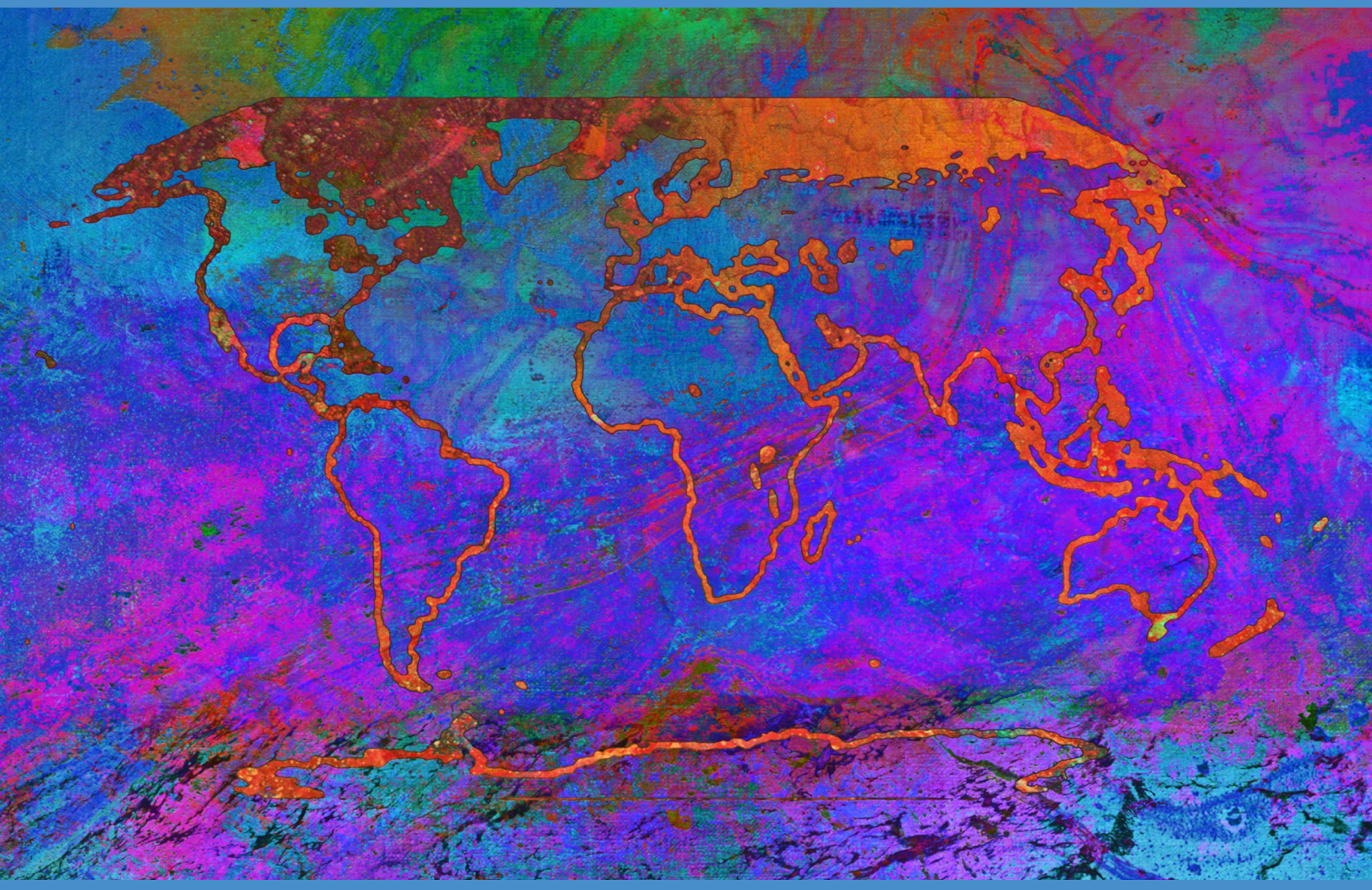
ipcc

INTERGOVERNMENTAL PANEL ON climate change

Climate Change 2021

The Physical Science Basis



WGI

Working Group I contribution to the
Sixth Assessment Report of the
Intergovernmental Panel on Climate Change

WMO UNEP

Summary for Policymakers

Drafting Authors:
Richard P. Allan (United Kingdom), Paola A. Arias (Colombia), Sophie Berger (France/Belgium), Josep G. Canadell (Australia), Christophe Cassou (France), Deliang Chen (Sweden), Annalisa Cherchi (Italy), Sarah L. Connors (France/United Kingdom), Erika Coppola (Italy), Faye Abigail Cruz (Philippines), Aïda Diongue-Niang (Senegal), Francisco J. Doblas-Reyes (Spain), Hervé Douville (France), Fatima Driouech (Morocco), Tamsin L. Edwards (United Kingdom), François Engelbrecht (South Africa), Veronika Eyring (Germany), Erich Fischer (Switzerland), Gregory M. Flato (Canada), Piers Forster (United Kingdom), Baylor Fox-Kemper (United States of America), Jan S. Fuglestvedt (Norway), John C. Fyfe (Canada), Nathan P. Gillett (Canada), Melissa I. Gomis (France/Switzerland), Sergey K. Gulev (Russian Federation), José Manuel Gutiérrez (Spain), Rafiq Hamdi (Belgium), Jordan Harold (United Kingdom), Mathias Hauser (Switzerland), Ed Hawkins (United Kingdom), Helene T. Hewitt (United Kingdom), Tom Gabriel Johansen (Norway), Christopher Jones (United Kingdom), Richard G. Jones (United Kingdom), Darrell S. Kaufman (United States of America), Zbigniew Klimont (Austria/Poland), Robert E. Kopp (United States of America), Charles Koven (United States of America), Gerhard Krinner (France/Germany, France), June-Yi Lee (Republic of Korea), Irene Lorenzoni (United Kingdom/Italy), Jochem Marotzke (Germany), Valérie Masson-Delmotte (France), Thomas K. Maycock (United States of America), Malte Meinshausen (Australia/Germany), Pedro M.S. Monteiro (South Africa), Angela Morelli (Norway/Italy), Vaishali Naik (United States of America), Dirk Notz (Germany), Friederike Otto (United Kingdom/Germany), Matthew D. Palmer (United Kingdom), Izidine Pinto (South Africa/Mozambique), Anna Pirani (Italy), Gian-Kasper Plattner (Switzerland), Krishnan Raghavan (India), Roshanka Ranasinghe (The Netherlands/Sri Lanka, Australia), Joeri Rogelj (United Kingdom/Belgium), Maisa Rojas (Chile), Alex C. Ruane (United States of America), Jean-Baptiste Sallée (France), Bjørn H. Samset (Norway), Sonia I. Seneviratne (Switzerland), Jana Sillmann (Norway/Germany), Anna A. Sörensson (Argentina), Tannecia S. Stephenson (Jamaica), Trude Storelvmo (Norway), Sophie Szopa (France), Peter W. Thorne (Ireland/United Kingdom), Blair Trewin (Australia), Robert Vautard (France), Carolina Vera (Argentina), Noureddine Yassaa (Algeria), Sönke Zaehle (Germany), Panmao Zhai (China), Xuebin Zhang (Canada), Kirsten Zickfeld (Canada/Germany)

Contributing Authors:
Krishna M. AchutaRao (India), Bhupesh Adhikary (Nepal), Edvin Aldrian (Indonesia), Kyle Armour (United States of America), Govindasamy Bala (India/United States of America), Rondrotiana Barimalala (South Africa/Madagascar), Nicolas Bellouin (United Kingdom/France), William Collins (United Kingdom), William D. Collins (United States of America), Susanna Corti (Italy), Peter M. Cox (United Kingdom), Frank J. Dentener (EU/The Netherlands), Claudine Dereczynski (Brazil), Alejandro Di Luca (Australia, Canada/Argentina), Alessandro Dosio (Italy), Leah Goldfarb (France/United States of America), Irina V. Gorodetskaya (Portugal/Belgium, Russian Federation), Pandora Hope (Australia), Mark Howden (Australia), Akm Saiful Islam (Bangladesh), Yu Kosaka (Japan), James Kossin (United States of America), Svitlana Krakovska (Ukraine), Chao Li (China), Jian Li (China), Thorsten Mauritsen (Germany/Denmark), Sebastian Milinski (Germany), Seung-Ki Min (Republic of Korea), Thanh Ngo Duc (Vietnam), Andy Reisinger (New Zealand), Lucas Ruiz (Argentina), Shubha Sathyendranath (United Kingdom/Canada, Overseas Citizen of India), Aimée B. A. Slangen (The Netherlands), Chris Smith (United Kingdom), Izuru Takayabu (Japan), Muhammad Irfan Tariq (Pakistan), Anne-Marie Treguier (France), Bart van den Hurk (The Netherlands), Karina von Schuckmann (France/Germany), Cunde Xiao (China)

Date of Document: 7 August 2021 17:00 CEST

This Summary for Policymakers should be cited as:
IPCC, 2021: Summary for Policymakers. In: *Climate Change 2021: The Physical Science Basis. Contribution of Working Group I to the Sixth Assessment Report of the Intergovernmental Panel on Climate Change* [Masson-Delmotte, V., P. Zhai, A. Pirani, S. L. Connors, C. Péan, S. Berger, N. Caud, Y. Chen, L. Goldfarb, M. I. Gomis, M. Huang, K. Leitzell, E. Lonnoy, J.B.R. Matthews, T. K. Maycock, T. Waterfield, O. Yelekçi, R. Yu and B. Zhou (eds.)]. Cambridge University Press. In Press.

This document is subject to final copy-editing.

Table of Contents

Introduction 4
A. The Current State of the Climate 5
B. Possible Climate Futures 15
C. Climate Information for Risk Assessment and Regional Adaptation 31
D. Limiting Future Climate Change 36

Introduction

This Summary for Policymakers (SPM) presents key findings of the Working Group I (WGI) contribution to the IPCC's Sixth Assessment Report (AR6)[1] on the physical science basis of climate change. The report builds upon the 2013 Working Group I contribution to the IPCC's Fifth Assessment Report (AR5) and the 2018–2019 IPCC Special Reports[2] of the AR6 cycle and incorporates subsequent new evidence from climate science[3].

This SPM provides a high-level summary of the understanding of the current state of the climate, including how it is changing and the role of human influence, the state of knowledge about possible climate futures, climate information relevant to regions and sectors, and limiting human-induced climate change.

Based on scientific understanding, key findings can be formulated as statements of fact or associated with an assessed level of confidence indicated using the IPCC calibrated language[4].

The scientific basis for each key finding is found in chapter sections of the main Report, and in the integrated synthesis presented in the Technical Summary (hereafter TS), and is indicated in curly brackets. The AR6 WGI Interactive Atlas facilitates exploration of these key synthesis findings, and supporting climate change information, across the WGI reference regions[5].

[1] Decision IPCC/XLVI-2.

[2] The three Special reports are: Global warming of 1.5°C: an IPCC Special Report on the impacts of global warming of 1.5°C above pre-industrial levels and related global greenhouse gas emission pathways, in the context of strengthening the global response to the threat of climate change, sustainable development, and efforts to eradicate poverty (SR1.5); Climate Change and Land: an IPCC Special Report on climate change, desertification, land degradation, sustainable land management, food security, and greenhouse gas fluxes in terrestrial ecosystems (SRCCL); IPCC Special Report on the Ocean and Cryosphere in a Changing Climate (SROCC).

[3] The assessment covers scientific literature accepted for publication by 31 January 2021.

[4] Each finding is grounded in an evaluation of underlying evidence and agreement. A level of confidence is expressed using five qualifiers: very low, low, medium, high and very high, and typeset in italics, for example, *medium confidence*. The following terms have been used to indicate the assessed likelihood of an outcome or a result: *virtually certain* 99–100% probability, *very likely* 90–100%, *likely* 66–100%, *about as likely as not* 33–66%, *unlikely* 0–33%, *very unlikely* 0–10%, *exceptionally unlikely* 0–1%. Additional terms (*extremely likely* 95–100%, *more likely than not* >50–100%, and *extremely unlikely* 0–5%) may also be used when appropriate. Assessed likelihood is typeset in italics, for example, *very likely*. This is consistent with AR5. In this Report, unless stated otherwise, square brackets [x to y] are used to provide the assessed *very likely* range, or 90% interval.

[5] The Interactive Atlas is available at https://interactive-atlas.ipcc.ch

A. The Current State of the Climate

Since AR5, improvements in observationally based estimates and information from paleoclimate archives provide a comprehensive view of each component of the climate system and its changes to date. New climate model simulations, new analyses, and methods combining multiple lines of evidence lead to improved understanding of human influence on a wider range of climate variables, including weather and climate extremes. The time periods considered throughout this Section depend upon the availability of observational products, paleoclimate archives and peer-reviewed studies.

A.1 It is unequivocal that human influence has warmed the atmosphere, ocean and land. Widespread and rapid changes in the atmosphere, ocean, cryosphere and biosphere have occurred.

{2.2, 2.3, Cross-Chapter Box 2.3, 3.3, 3.4, 3.5, 3.6, 3.8, 5.2, 5.3, 6.4, 7.3, 8.3, 9.2, 9.3, 9.5, 9.6, Cross-Chapter Box 9.1} **(Figure SPM.1, Figure SPM.2)**

A.1.1 Observed increases in well-mixed greenhouse gas (GHG) concentrations since around 1750 are unequivocally caused by human activities. Since 2011 (measurements reported in AR5), concentrations have continued to increase in the atmosphere, reaching annual averages of 410 ppm for carbon dioxide (CO_2), 1866 ppb for methane (CH_4), and 332 ppb for nitrous oxide (N_2O) in 2019[6]. Land and ocean have taken up a near-constant proportion (globally about 56% per year) of CO_2 emissions from human activities over the past six decades, with regional differences (*high confidence*)[7]. {2.2, 5.2, 7.3, TS.2.2, Box TS.5}

A.1.2 Each of the last four decades has been successively warmer than any decade that preceded it since 1850. Global surface temperature[8] in the first two decades of the 21st century (2001-2020) was 0.99 [0.84-1.10] °C higher than 1850-1900[9]. Global surface temperature was 1.09 [0.95 to 1.20] °C higher in 2011–2020 than 1850–1900, with larger increases over land (1.59 [1.34 to 1.83] °C) than over the ocean (0.88 [0.68 to 1.01] °C). The estimated increase in global surface temperature since AR5 is principally due to further warming since 2003–2012 (+0.19 [0.16 to 0.22] °C). Additionally, methodological advances and new datasets contributed approximately 0.1ºC to the updated estimate of warming in AR6[10].

[6] Other GHG concentrations in 2019 were: PFCs (109 ppt CF_4 equivalent); SF_6 (10 ppt); NF_3 (2 ppt); HFCs (237 ppt HFC-134a equivalent); other Montreal Protocol gases (mainly CFCs, HCFCs, 1032 ppt CFC-12 equivalent). Increases from 2011 are 19 ppm for CO_2, 63 ppb for CH_4 and 8 ppb for N_2O.

[7] Land and ocean are not substantial sinks for other GHGs.

[8] The term 'global surface temperature' is used in reference to both global mean surface temperature and global surface air temperature throughout this SPM. Changes in these quantities are assessed with *high confidence* to differ by at most 10% from one another, but conflicting lines of evidence lead to *low confidence* in the sign of any difference in long-term trend. {Cross-Section Box TS.1}

[9] The period 1850–1900 represents the earliest period of sufficiently globally complete observations to estimate global surface temperature and, consistent with AR5 and SR1.5, is used as an approximation for pre-industrial conditions.

[10] Since AR5, methodological advances and new datasets have provided a more complete spatial representation of changes in surface temperature, including in the Arctic. These and other improvements have additionally increased the estimate of global surface temperature change by approximately 0.1 ºC, but this increase does not represent additional physical warming since the AR5.

A.1.3 The *likely* range of total human-caused global surface temperature increase from 1850–1900 to 2010–2019[11] is 0.8°C to 1.3°C, with a best estimate of 1.07°C. It is *likely* that well-mixed GHGs contributed a warming of 1.0°C to 2.0°C, other human drivers (principally aerosols) contributed a cooling of 0.0°C to 0.8°C, natural drivers changed global surface temperature by –0.1°C to 0.1°C, and internal variability changed it by –0.2°C to 0.2°C. It is *very likely* that well-mixed GHGs were the main driver[12] of tropospheric warming since 1979, and *extremely likely* that human-caused stratospheric ozone depletion was the main driver of cooling of the lower stratosphere between 1979 and the mid-1990s.
{3.3, 6.4, 7.3, Cross-Section Box TS.1, TS.2.3} **(Figure SPM.2)**

A.1.4 Globally averaged precipitation over land has *likely* increased since 1950, with a faster rate of increase since the 1980s (*medium confidence*). It is *likely* that human influence contributed to the pattern of observed precipitation changes since the mid-20th century, and *extremely likely* that human influence contributed to the pattern of observed changes in near-surface ocean salinity. Mid-latitude storm tracks have *likely* shifted poleward in both hemispheres since the 1980s, with marked seasonality in trends (*medium confidence*). For the Southern Hemisphere, human influence *very likely* contributed to the poleward shift of the closely related extratropical jet in austral summer.
{2.3, 3.3, 8.3, 9.2, TS.2.3, TS.2.4, Box TS.6}

A.1.5 Human influence is *very likely* the main driver of the global retreat of glaciers since the 1990s and the decrease in Arctic sea ice area between 1979–1988 and 2010–2019 (about 40% in September and about 10% in March). There has been no significant trend in Antarctic sea ice area from 1979 to 2020 due to regionally opposing trends and large internal variability. Human influence *very likely* contributed to the decrease in Northern Hemisphere spring snow cover since 1950. It is *very likely* that human influence has contributed to the observed surface melting of the Greenland Ice Sheet over the past two decades, but there is only *limited evidence*, with *medium agreement*, of human influence on the Antarctic Ice Sheet mass loss.
{2.3, 3.4, 8.3, 9.3, 9.5, TS.2.5}

A.1.6 It is *virtually certain* that the global upper ocean (0–700 m) has warmed since the 1970s and *extremely likely* that human influence is the main driver. It is *virtually certain* that human-caused CO_2 emissions are the main driver of current global acidification of the surface open ocean. There is *high confidence* that oxygen levels have dropped in many upper ocean regions since the mid-20th century, and *medium confidence* that human influence contributed to this drop.
{2.3, 3.5, 3.6, 5.3, 9.2, TS.2.4}

A.1.7 Global mean sea level increased by 0.20 [0.15 to 0.25] m between 1901 and 2018. The average rate of sea level rise was 1.3 [0.6 to 2.1] mm yr^{-1} between 1901 and 1971, increasing to 1.9 [0.8 to 2.9] mm yr^{-1} between 1971 and 2006, and further increasing to 3.7 [3.2 to 4.2] mm yr^{-1} between 2006 and 2018 (*high confidence*). Human influence was *very likely* the main driver of these increases since at least 1971.
{2.3, 3.5, 9.6, Cross-Chapter Box 9.1, Box TS.4}

A.1.8 Changes in the land biosphere since 1970 are consistent with global warming: climate zones have shifted poleward in both hemispheres, and the growing season has on average lengthened by up to two days per decade since the 1950s in the Northern Hemisphere extratropics (*high confidence*).
{2.3, TS.2.6}

[11] The period distinction with A.1.2 arises because the attribution studies consider this slightly earlier period. The observed warming to 2010–2019 is 1.06 [0.88 to 1.21] °C.

[12] Throughout this SPM, 'main driver' means responsible for more than 50% of the change.

Human influence has warmed the climate at a rate that is unprecedented in at least the last 2000 years

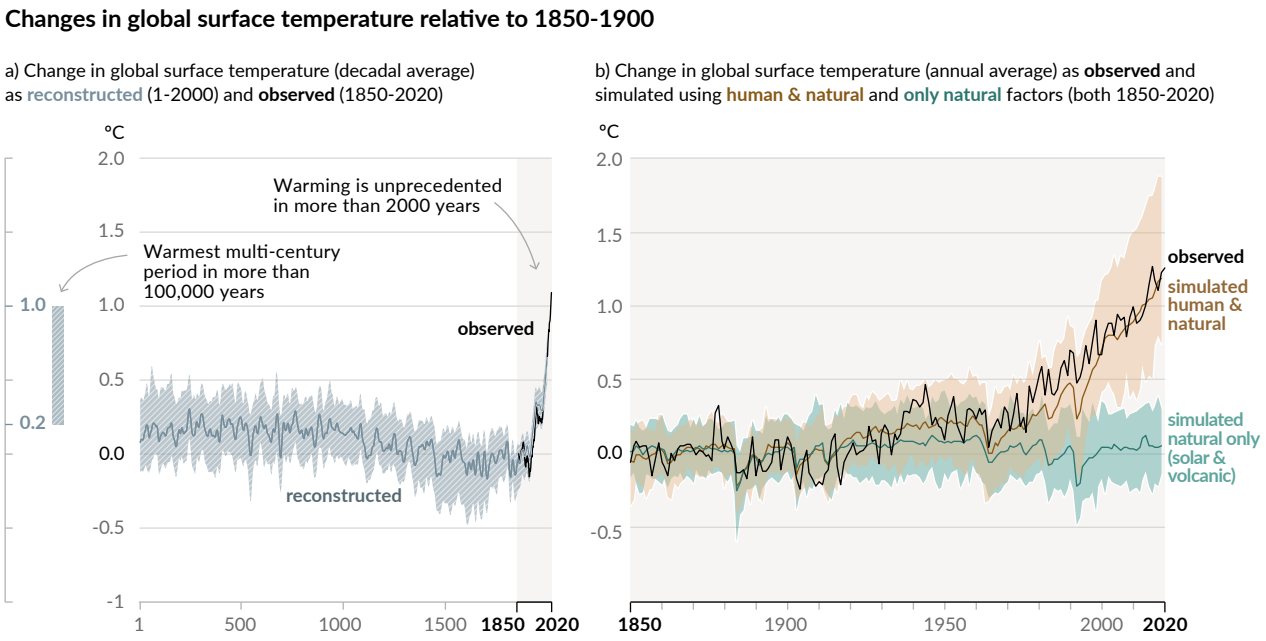


Figure SPM.1: History of global temperature change and causes of recent warming.

Panel a): Changes in global surface temperature reconstructed from paleoclimate archives (solid grey line, 1–2000) **and from direct observations** (solid black line, 1850–2020), both relative to 1850–1900 and decadally averaged. The vertical bar on the left shows the estimated temperature (*very likely* range) during the warmest multi-century period in at least the last 100,000 years, which occurred around 6500 years ago during the current interglacial period (Holocene). The Last Interglacial, around 125,000 years ago, is the next most recent candidate for a period of higher temperature. These past warm periods were caused by slow (multi-millennial) orbital variations. The grey shading with white diagonal lines shows the *very likely* ranges for the temperature reconstructions.

Panel b): Changes in global surface temperature over the past 170 years (black line) relative to 1850–1900 and annually averaged, compared to CMIP6 climate model simulations (see Box SPM.1) of the temperature response to both human and natural drivers (brown), and to only natural drivers (solar and volcanic activity, green). Solid coloured lines show the multi-model average, and coloured shades show the *very likely* range of simulations. (see Figure SPM.2 for the assessed contributions to warming).

{2.3.1, 3.3, Cross-Chapter Box 2.3, Cross-Section Box TS.1, Figure 1a, TS.2.2}

Observed warming is driven by emissions from human activities, with greenhouse gas warming partly masked by aerosol cooling

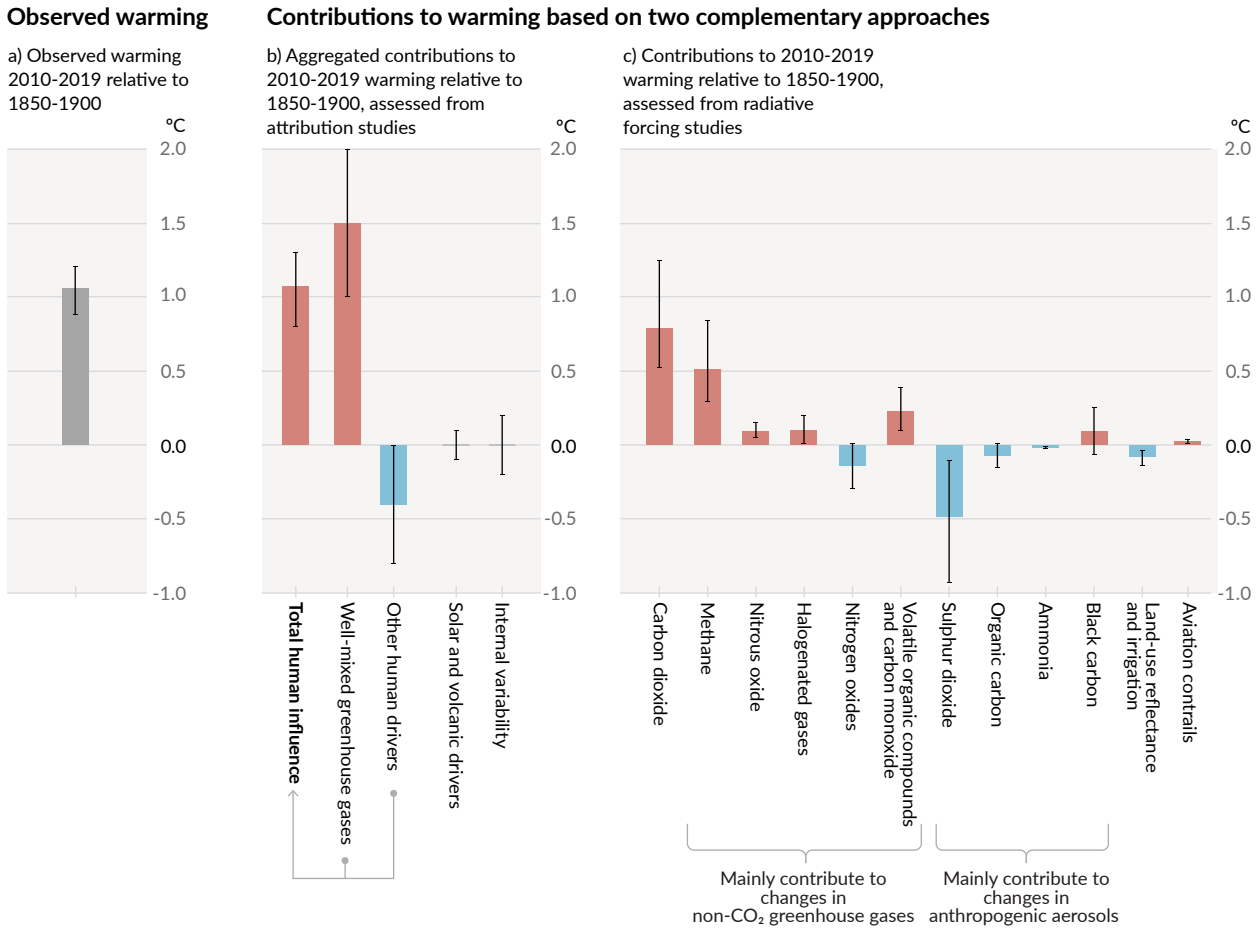


Figure SPM.2: Assessed contributions to observed warming in 2010–2019 relative to 1850–1900.

Panel a): Observed global warming (increase in global surface temperature) and its *very likely* range {3.3.1, Cross-Chapter Box 2.3}.

Panel b): Evidence from attribution studies, which synthesize information from climate models and observations. The panel shows temperature change attributed to total human influence, changes in well-mixed greenhouse gas concentrations, other human drivers due to aerosols, ozone and land-use change (land-use reflectance), solar and volcanic drivers, and internal climate variability. Whiskers show *likely* ranges {3.3.1}.

Panel c): Evidence from the assessment of radiative forcing and climate sensitivity. The panel shows temperature changes from individual components of human influence, including emissions of greenhouse gases, aerosols and their precursors; land-use changes (land-use reflectance and irrigation); and aviation contrails. Whiskers show *very likely* ranges. Estimates account for both direct emissions into the atmosphere and their effect, if any, on other climate drivers. For aerosols, both direct (through radiation) and indirect (through interactions with clouds) effects are considered.{6.4.2, 7.3}

A.2 The scale of recent changes across the climate system as a whole and the present state of many aspects of the climate system are unprecedented over many centuries to many thousands of years.

{Cross-Chapter Box 2.1, 2.2, 2.3, 5.1} **(Figure SPM.1)**

A.2.1 In 2019, atmospheric CO_2 concentrations were higher than at any time in at least 2 million years (*high confidence)*, and concentrations of CH_4 and N_2O were higher than at any time in at least 800,000 years (*very high confidence*). Since 1750, increases in CO_2 (47%) and CH_4 (156%) concentrations far exceed, and increases in N_2O (23%) are similar to, the natural multi-millennial changes between glacial and interglacial periods over at least the past 800,000 years (*very high confidence*).
{2.2, 5.1, TS.2.2}

A.2.2 Global surface temperature has increased faster since 1970 than in any other 50-year period over at least the last 2000 years (*high confidence*). Temperatures during the most recent decade (2011–2020) exceed those of the most recent multi-century warm period, around 6500 years ago[13] [0.2°C to 1°C relative to 1850–1900] (*medium confidence*). Prior to that, the next most recent warm period was about 125,000 years ago when the multi-century temperature [0.5°C to 1.5°C relative to 1850–1900] overlaps the observations of the most recent decade (*medium confidence*).
{Cross-Chapter Box 2.1, 2.3, Cross-Section Box TS.1} **(Figure SPM.1)**

A.2.3 In 2011–2020, annual average Arctic sea ice area reached its lowest level since at least 1850 (*high confidence*). Late summer Arctic sea ice area was smaller than at any time in at least the past 1000 years (*medium confidence*). The global nature of glacier retreat, with almost all of the world's glaciers retreating synchronously, since the 1950s is unprecedented in at least the last 2000 years (*medium confidence*).
{2.3, TS.2.5}

A.2.4 Global mean sea level has risen faster since 1900 than over any preceding century in at least the last 3000 years (*high confidence*). The global ocean has warmed faster over the past century than since the end of the last deglacial transition (around 11,000 years ago) (*medium confidence*). A long-term increase in surface open ocean pH occurred over the past 50 million years (*high confidence*), and surface open ocean pH as low as recent decades is unusual in the last 2 million years (*medium confidence*).
{2.3, TS.2.4, Box TS.4}

[13] As stated in section B.1, even under the very low emissions scenario SSP1-1.9, temperatures are assessed to remain elevated above those of the most recent decade until at least 2100 and therefore warmer than the century-scale period 6500 years ago.

A.3 Human-induced climate change is already affecting many weather and climate extremes in every region across the globe. Evidence of observed changes in extremes such as heatwaves, heavy precipitation, droughts, and tropical cyclones, and, in particular, their attribution to human influence, has strengthened since AR5.

{2.3, 3.3, 8.2, 8.3, 8.4, 8.5, 8.6, Box 8.1, Box 8.2, Box 9.2, 10.6, 11.2, 11.3, 11.4, 11.6, 11.7, 11.8, 11.9, 12.3} **(Figure SPM.3)**

A.3.1 It is *virtually certain* that hot extremes (including heatwaves) have become more frequent and more intense across most land regions since the 1950s, while cold extremes (including cold waves) have become less frequent and less severe, with *high confidence* that human-induced climate change is the main driver[14] of these changes. Some recent hot extremes observed over the past decade would have been *extremely unlikely* to occur without human influence on the climate system. Marine heatwaves have approximately doubled in frequency since the 1980s (*high confidence*), and human influence has *very likely* contributed to most of them since at least 2006.
{Box 9.2, 11.2, 11.3, 11.9, TS.2.4, TS.2.6, Box TS.10} **(Figure SPM.3)**

A.3.2 The frequency and intensity of heavy precipitation events have increased since the 1950s over most land area for which observational data are sufficient for trend analysis (*high confidence*), and human-induced climate change is *likely* the main driver. Human-induced climate change has contributed to increases in agricultural and ecological droughts[15] in some regions due to increased land evapotranspiration[16] (*medium confidence*).
{8.2, 8.3, 11.4, 11.6, 11.9, TS.2.6, Box TS.10} **(Figure SPM.3)**

A.3.3 Decreases in global land monsoon precipitation[17] from the 1950s to the 1980s are partly attributed to human-caused Northern Hemisphere aerosol emissions, but increases since then have resulted from rising GHG concentrations and decadal to multi-decadal internal variability (*medium confidence*). Over South Asia, East Asia and West Africa increases in monsoon precipitation due to warming from GHG emissions were counteracted by decreases in monsoon precipitation due to cooling from human-caused aerosol emissions over the 20th century (*high confidence*). Increases in West African monsoon precipitation since the 1980s are partly due to the growing influence of GHGs and reductions in the cooling effect of human-caused aerosol emissions over Europe and North America (*medium confidence*).
{2.3, 3.3, 8.2, 8.3, 8.4, 8.5, 8.6, Box 8.1, Box 8.2, 10.6, Box TS.13}

[14] Throughout this SPM, 'main driver' means responsible for more than 50% of the change.

[15] Agricultural and ecological drought (depending on the affected biome): a period with abnormal soil moisture deficit, which results from combined shortage of precipitation and excess evapotranspiration, and during the growing season impinges on crop production or ecosystem function in general. Observed changes in meteorological droughts (precipitation deficits) and hydrological droughts (streamflow deficits) are distinct from those in agricultural and ecological droughts and addressed in the underlying AR6 material (Chapter 11).

[16] The combined processes through which water is transferred to the atmosphere from open water and ice surfaces, bare soil, and vegetation that make up the Earth's surface.

[17] The global monsoon is defined as the area in which the annual range (local summer minus local winter) of precipitation is greater than 2.5 mm day^{-1}. Global land monsoon precipitation refers to the mean precipitation over land areas within the global monsoon.

A.3.4 It is *likely* that the global proportion of major (Category 3–5) tropical cyclone occurrence has increased over the last four decades, and the latitude where tropical cyclones in the western North Pacific reach their peak intensity has shifted northward; these changes cannot be explained by internal variability alone (*medium confidence*). There is *low confidence* in long-term (multi-decadal to centennial) trends in the frequency of all-category tropical cyclones. Event attribution studies and physical understanding indicate that human-induced climate change increases heavy precipitation associated with tropical cyclones (*high confidence*) but data limitations inhibit clear detection of past trends on the global scale. {8.2, 11.7, Box TS.10}

A.3.5 Human influence has *likely* increased the chance of compound extreme events[18] since the 1950s. This includes increases in the frequency of concurrent heatwaves and droughts on the global scale (*high confidence*); fire weather in some regions of all inhabited continents (*medium confidence*); and compound flooding in some locations (*medium confidence*). {11.6, 11.7, 11.8, 12.3, 12.4, TS.2.6, Table TS.5, Box TS.10}

[18] Compound extreme events are the combination of multiple drivers and/or hazards that contribute to societal or environmental risk. Examples are concurrent heatwaves and droughts, compound flooding (e.g., a storm surge in combination with extreme rainfall and/or river flow), compound fire weather conditions (i.e., a combination of hot, dry, and windy conditions), or concurrent extremes at different locations.

Climate change is already affecting every inhabited region across the globe with human influence contributing to many observed changes in weather and climate extremes

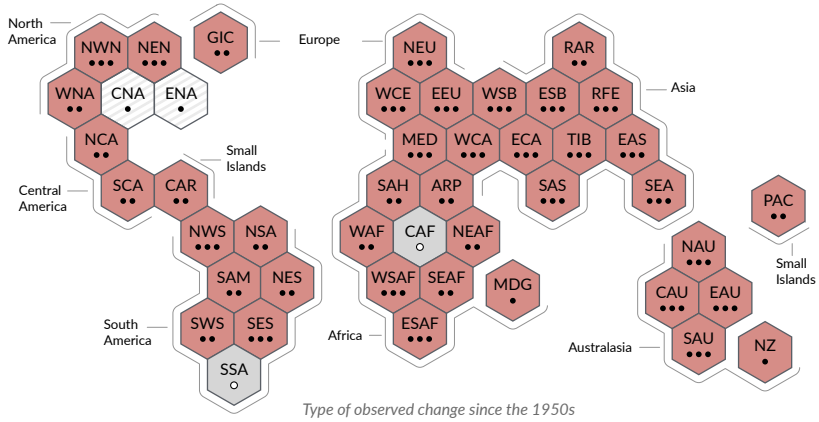
a) Synthesis of assessment of observed change in **hot extremes** and confidence in human contribution to the observed changes in the world's regions

Type of observed change in hot extremes

- Increase (41)
- Decrease (0)
- Low agreement in the type of change (2)
- Limited data and/or literature (2)

Confidence in human contribution to the observed change

- ●●● High
- ●● Medium
- ● Low due to limited agreement
- ○ Low due to limited evidence



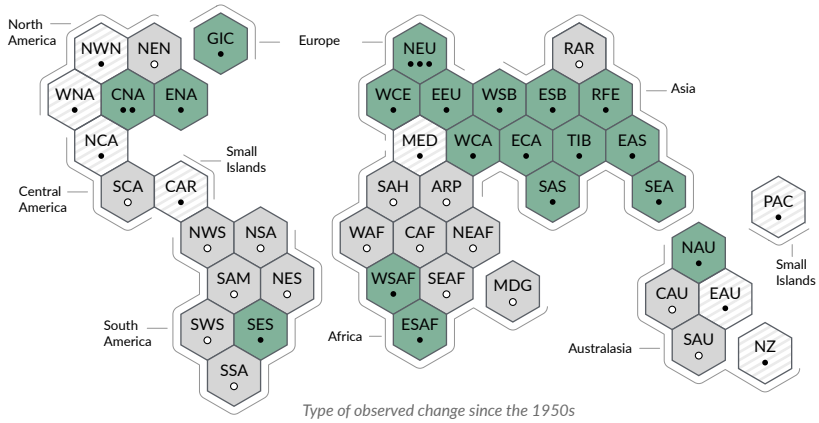
b) Synthesis of assessment of observed change in **heavy precipitation** and confidence in human contribution to the observed changes in the world's regions

Type of observed change in heavy precipitation

- Increase (19)
- Decrease (0)
- Low agreement in the type of change (8)
- Limited data and/or literature (18)

Confidence in human contribution to the observed change

- ●●● High
- ●● Medium
- ● Low due to limited agreement
- ○ Low due to limited evidence



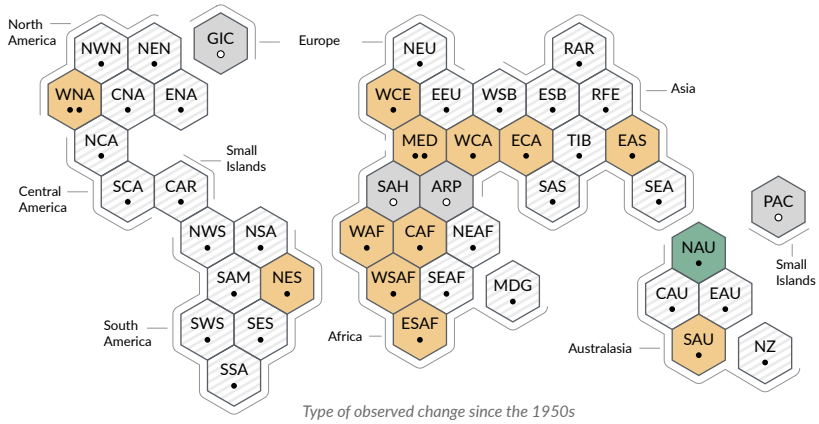
c) Synthesis of assessment of observed change in **agricultural and ecological drought** and confidence in human contribution to the observed changes in the world's regions

Type of observed change in agricultural and ecological drought

- Increase (12)
- Decrease (1)
- Low agreement in the type of change (28)
- Limited data and/or literature (4)

Confidence in human contribution to the observed change

- ●●● High
- ●● Medium
- ● Low due to limited agreement
- ○ Low due to limited evidence



Each hexagon corresponds to one of the IPCC AR6 WGI reference regions

NWN *North-Western North America*

IPCC AR6 WGI reference regions: **North America:** ***NWN*** *(North-Western North America),* ***NEN*** *(North-Eastern North America),* ***WNA*** *(Western North America),* ***CNA*** *(Central North America),* ***ENA*** *(Eastern North America),* **Central America:** ***NCA*** *(Northern Central America),* ***SCA*** *(Southern Central America),* ***CAR*** *(Caribbean),* **South America:** ***NWS*** *(North-Western South America),* ***NSA*** *(Northern South America),* ***NES*** *(North-Eastern South America),* ***SAM*** *(South American Monsoon),* ***SWS*** *(South-Western South America),* ***SES*** *(South-Eastern South America),* ***SSA*** *(Southern South America),* **Europe:** ***GIC*** *(Greenland/Iceland),* ***NEU*** *(Northern Europe),* ***WCE*** *(Western and Central Europe),* ***EEU*** *(Eastern Europe),* ***MED*** *(Mediterranean),* **Africa:** ***MED*** *(Mediterranean),* ***SAH*** *(Sahara),* ***WAF*** *(Western Africa),* ***CAF*** *(Central Africa),* ***NEAF*** *(North Eastern Africa),* ***SEAF*** *(South Eastern Africa),* ***WSAF*** *(West Southern Africa),* ***ESAF*** *(East Southern Africa),* ***MDG*** *(Madagascar),* **Asia:** ***RAR*** *(Russian Arctic),* ***WSB*** *(West Siberia),* ***ESB*** *(East Siberia),* ***RFE*** *(Russian Far East),* ***WCA*** *(West Central Asia),* ***ECA*** *(East Central Asia),* ***TIB*** *(Tibetan Plateau),* ***EAS*** *(East Asia),* ***ARP*** *(Arabian Peninsula),* ***SAS*** *(South Asia),* ***SEA*** *(South East Asia),* **Australasia:** ***NAU*** *(Northern Australia),* ***CAU*** *(Central Australia),* ***EAU*** *(Eastern Australia),* ***SAU*** *(Southern Australia),* ***NZ*** *(New Zealand),* **Small Islands:** ***CAR*** *(Caribbean),* ***PAC*** *(Pacific Small Islands)*

Figure SPM.3: Synthesis of assessed observed and attributable regional changes.

The IPCC AR6 WGI inhabited regions are displayed as **hexagons** with identical size in their approximate geographical location (see legend for regional acronyms). All assessments are made for each region as a whole and for the 1950s to the present. Assessments made on different time scales or more local spatial scales might differ from what is shown in the figure. The **colours** in each panel represent the four outcomes of the assessment on observed changes. White and light grey striped hexagons are used where there is *low agreement* in the type of change for the region as a whole, and grey hexagons are used when there is limited data and/or literature that prevents an assessment of the region as a whole. Other colours indicate at least *medium confidence* in the observed change. The **confidence level** for the human influence on these observed changes is based on assessing trend detection and attribution and event attribution literature, and it is indicated by the number of dots: three dots for *high confidence*, two dots for *medium confidence* and one dot for *low confidence* (filled: limited agreement; empty: limited evidence).

Panel a) For hot extremes, the evidence is mostly drawn from changes in metrics based on daily maximum temperatures; regional studies using other indices (heatwave duration, frequency and intensity) are used in addition. Red hexagons indicate regions where there is at least *medium confidence* in an observed increase in hot extremes.

Panel b) For heavy precipitation, the evidence is mostly drawn from changes in indices based on one-day or five-day precipitation amounts using global and regional studies. Green hexagons indicate regions where there is at least *medium confidence* in an observed increase in heavy precipitation.

Panel c) Agricultural and ecological droughts are assessed based on observed and simulated changes in total column soil moisture, complemented by evidence on changes in surface soil moisture, water balance (precipitation minus evapotranspiration) and indices driven by precipitation and atmospheric evaporative demand. Yellow hexagons indicate regions where there is at least *medium confidence* in an observed increase in this type of drought and green hexagons indicate regions where there is at least *medium confidence* in an observed decrease in agricultural and ecological drought.

For all regions, table TS.5 shows a broader range of observed changes besides the ones shown in this figure. Note that SSA is the only region that does not display observed changes in the metrics shown in this figure, but is affected by observed increases in mean temperature, decreases in frost, and increases in marine heatwaves.

{11.9, Table TS.5, Box TS.10, Figure 1, Atlas 1.3.3, Figure Atlas.2}

A.4 Improved knowledge of climate processes, paleoclimate evidence and the response of the climate system to increasing radiative forcing gives a best estimate of equilibrium climate sensitivity of 3°C with a narrower range compared to AR5. {2.2, 7.3, 7.4, 7.5, Box 7.2, Cross-Chapter Box 9.1, 9.4, 9.5, 9.6}

A.4.1 Human-caused radiative forcing of 2.72 [1.96 to 3.48] W m^{-2} in 2019 relative to 1750 has warmed the climate system. This warming is mainly due to increased GHG concentrations, partly reduced by cooling due to increased aerosol concentrations. The radiative forcing has increased by 0.43 W m^{-2} (19%) relative to AR5, of which 0.34 W m^{-2} is due to the increase in GHG concentrations since 2011. The remainder is due to improved scientific understanding and changes in the assessment of aerosol forcing, which include decreases in concentration and improvement in its calculation (*high confidence*).
{2.2, 7.3, TS.2.2, TS.3.1}

A.4.2 Human-caused net positive radiative forcing causes an accumulation of additional energy (heating) in the climate system, partly reduced by increased energy loss to space in response to surface warming. The observed average rate of heating of the climate system increased from 0.50 [0.32 to 0.69] W m^{-2} for the period 1971–2006[19], to 0.79 [0.52 to 1.06] W m^{-2} for the period 2006–2018[20] (*high confidence*). Ocean warming accounted for 91% of the heating in the climate system, with land warming, ice loss and atmospheric warming accounting for about 5%, 3% and 1%, respectively (*high confidence*).
{7.2, Box 7.2, TS.3.1}

A.4.3 Heating of the climate system has caused global mean sea level rise through ice loss on land and thermal expansion from ocean warming. Thermal expansion explained 50% of sea level rise during 1971–2018, while ice loss from glaciers contributed 22%, ice sheets 20% and changes in land water storage 8%. The rate of ice sheet loss increased by a factor of four between 1992–1999 and 2010–2019. Together, ice sheet and glacier mass loss were the dominant contributors to global mean sea level rise during 2006-2018. (*high confidence*)
{Cross-Chapter Box 9.1, 9.4, 9.5, 9.6}

A.4.4 The equilibrium climate sensitivity is an important quantity used to estimate how the climate responds to radiative forcing. Based on multiple lines of evidence[21], the *very likely* range of equilibrium climate sensitivity is between 2°C (*high confidence*) and 5°C (*medium confidence*). The AR6 assessed best estimate is 3°C with a *likely* range of 2.5°C to 4°C (*high confidence*), compared to 1.5°C to 4.5°C in AR5, which did not provide a best estimate.
{7.4, 7.5, TS.3.2}

[19] cumulative energy increase of 282 [177 to 387] ZJ over 1971–2006 (1 ZJ = 10^{21} J).

[20] cumulative energy increase of 152 [100 to 205] ZJ over 2006–2018.

[21] Understanding of climate processes, the instrumental record, paleoclimates and model-based emergent constraints (see glossary).

B. Possible Climate Futures

A set of five new illustrative emissions scenarios is considered consistently across this report to explore the climate response to a broader range of greenhouse gas (GHG), land use and air pollutant futures than assessed in AR5. This set of scenarios drives climate model projections of changes in the climate system. These projections account for solar activity and background forcing from volcanoes. Results over the 21st century are provided for the near-term (2021–2040), mid-term (2041–2060) and long-term (2081–2100) relative to 1850–1900, unless otherwise stated.

Box SPM.1: Scenarios, Climate Models and Projections

Box SPM.1.1: This report assesses the climate response to five illustrative scenarios that cover the range of possible future development of anthropogenic drivers of climate change found in the literature. They start in 2015, and include scenarios[22] with high and very high GHG emissions (SSP3-7.0 and SSP5-8.5) and CO_2 emissions that roughly double from current levels by 2100 and 2050, respectively, scenarios with intermediate GHG emissions (SSP2-4.5) and CO_2 emissions remaining around current levels until the middle of the century, and scenarios with very low and low GHG emissions and CO_2 emissions declining to net zero around or after 2050, followed by varying levels of net negative CO_2 emissions[23] (SSP1-1.9 and SSP1-2.6) as illustrated in Figure SPM.4. Emissions vary between scenarios depending on socio-economic assumptions, levels of climate change mitigation and, for aerosols and non-methane ozone precursors, air pollution controls. Alternative assumptions may result in similar emissions and climate responses, but the socio-economic assumptions and the feasibility or likelihood of individual scenarios is not part of the assessment.
{TS.1.3, 1.6, Cross-Chapter Box 1.4} **(Figure SPM.4)**

Box SPM.1.2: This report assesses results from climate models participating in the Coupled Model Intercomparison Project Phase 6 (CMIP6) of the World Climate Research Programme. These models include new and better representation of physical, chemical and biological processes, as well as higher resolution, compared to climate models considered in previous IPCC assessment reports. This has improved the simulation of the recent mean state of most large-scale indicators of climate change and many other aspects across the climate system. Some differences from observations remain, for example in regional precipitation patterns. The CMIP6 historical simulations assessed in this report have an ensemble mean global surface temperature change within 0.2°C of the observations over most of the historical period, and observed warming is within the *very likely* range of the CMIP6 ensemble. However, some CMIP6 models simulate a warming that is either above or below the assessed *very likely* range of observed warming.
{1.5, Cross-Chapter Box 2.2, 3.3, 3.8, TS.1.2, Cross-Section Box TS.1} (Figure SPM.1 b, Figure SPM.2)

Box SPM.1.3: The CMIP6 models considered in this Report have a wider range of climate sensitivity than in CMIP5 models and the AR6 assessed *very likely* range, which is based on multiple lines of evidence. These CMIP6 models also show a higher average climate sensitivity than CMIP5 and the AR6 assessed best estimate. The higher CMIP6 climate sensitivity values compared to CMIP5 can be traced to an amplifying cloud feedback that is larger in CMIP6 by about 20%.
{Box 7.1, 7.3, 7.4, 7.5, TS.3.2}

Box SPM.1.4: For the first time in an IPCC report, assessed future changes in global surface temperature, ocean warming and sea level are constructed by combining multi-model projections with observational constraints based on past simulated warming, as well as the AR6 assessment of climate sensitivity. For other quantities, such robust methods do not yet exist to constrain the projections. Nevertheless, robust projected

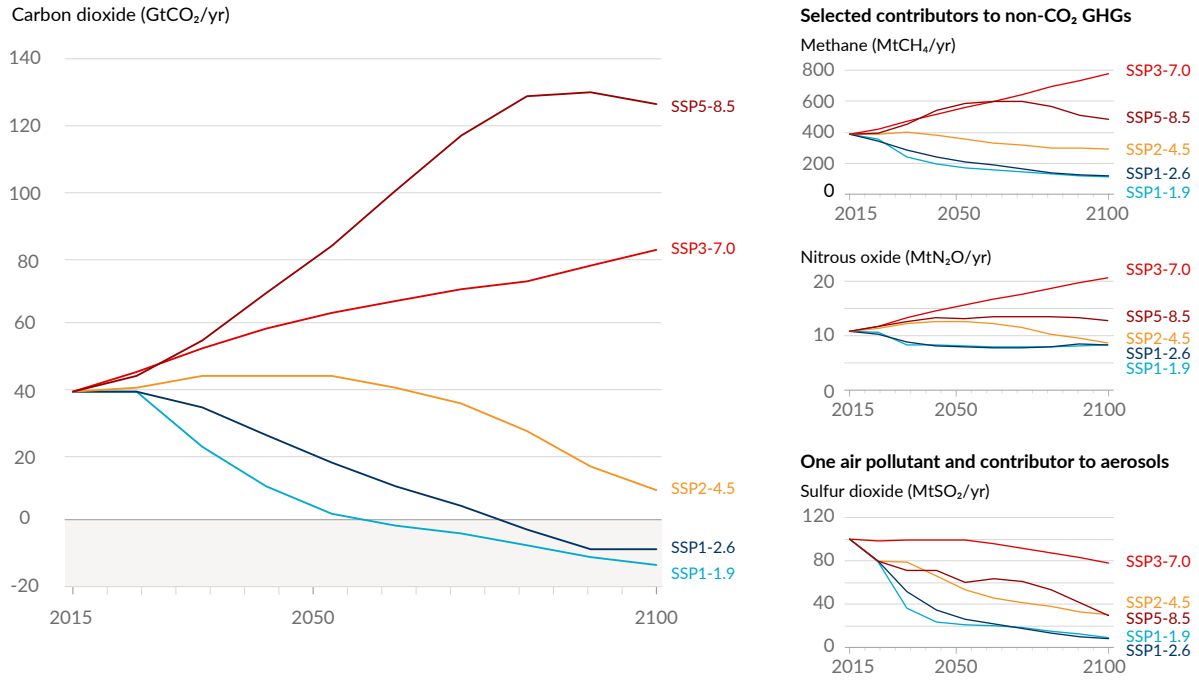
[22] Throughout this report, the five illustrative scenarios are referred to as SSPx-y, where 'SSPx' refers to the Shared Socio-economic Pathway or 'SSP' describing the socio-economic trends underlying the scenario, and 'y' refers to the approximate level of radiative forcing (in W m^{-2}) resulting from the scenario in the year 2100. A detailed comparison to scenarios used in earlier IPCC reports is provided in Section TS1.3 and 1.6 and 4.6. The SSPs that underlie the specific forcing scenarios used to drive climate models are not assessed by WGI. Rather, the SSPx-y labelling ensures traceability to the underlying literature in which specific forcing pathways are used as input to the climate models. IPCC is neutral with regard to the assumptions underlying the SSPs, which do not cover all possible scenarios. Alternative scenarios may be considered or developed.

[23] Net negative CO_2 emissions are reached when anthropogenic removals of CO_2 exceed anthropogenic emissions. {Glossary}

geographical patterns of many variables can be identified at a given level of global warming, common to all scenarios considered and independent of timing when the global warming level is reached.
{1.6, Box 4.1, 4.3, 4.6, 7.5, 9.2, 9.6, Cross-Chapter Box 11.1, Cross-Section Box TS.1}

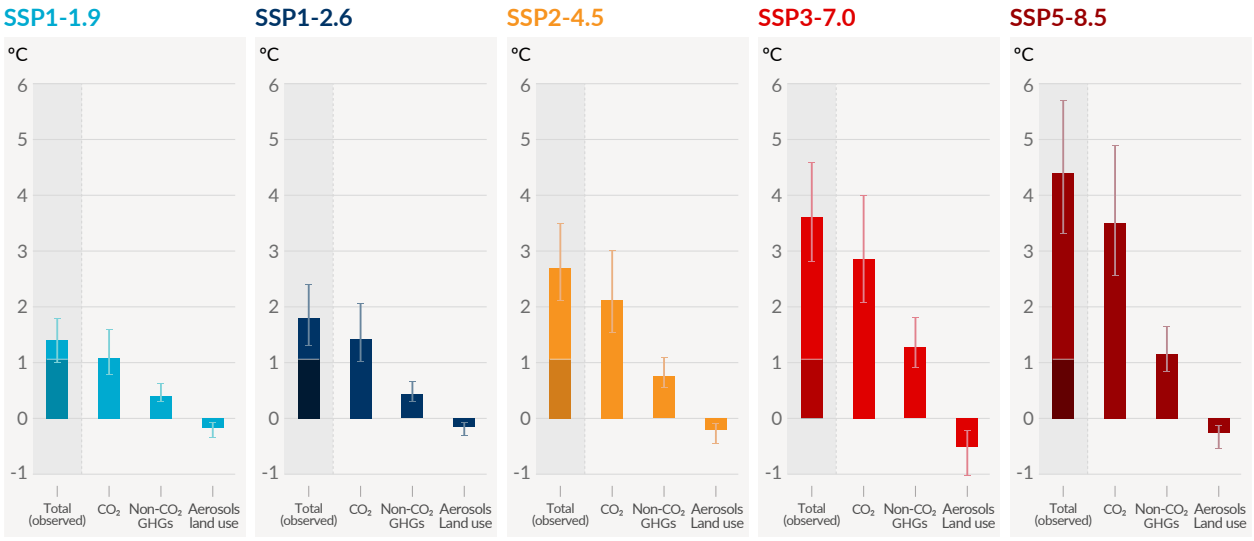
Future emissions cause future additional warming, with total warming dominated by past and future CO_2 emissions

a) Future annual emissions of CO_2 (left) and of a subset of key non-CO_2 drivers (right), across five illustrative scenarios



b) Contribution to global surface temperature increase from different emissions, with a dominant role of CO_2 emissions

Change in global surface temperature in 2081-2100 relative to 1850-1900 (°C)



Total warming (observed warming to date in darker shade), warming from CO_2, warming from non-CO_2 GHGs and cooling from changes in aerosols and land use

Figure SPM.4: Future anthropogenic emissions of key drivers of climate change and warming contributions by groups of drivers for the five illustrative scenarios used in this report.

The five scenarios are SSP1-1.9, SSP1-2.6, SSP2-4.5, SSP3-7.0 and SSP5-8.5.

Panel a) Annual anthropogenic (human-caused) emissions over the 2015–2100 period. Shown are emissions trajectories for carbon dioxide (CO_2) from all sectors ($GtCO_2$/yr) (left graph) and for a subset of three key non-CO_2 drivers considered in the scenarios: methane (CH_4, $MtCH_4$/yr, top-right graph), nitrous oxide (N_2O, MtN_2O/yr, middle-right graph) and sulfur dioxide (SO_2, $MtSO_2$/yr, bottom-right graph, contributing to anthropogenic aerosols in panel b).

Panel b) Warming contributions by groups of anthropogenic drivers and by scenario are shown as change in global surface temperature (°C) in 2081–2100 relative to 1850–1900, with indication of the observed warming to date. Bars and whiskers represent median values and the *very likely* range, respectively. Within each scenario bar plot, the bars represent total global warming (°C; total bar) (see Table SPM.1) and warming contributions (°C) from changes in CO_2 (CO_2 bar), from non-CO_2 greenhouse gases (non-CO_2 GHGs bar; comprising well-mixed greenhouse gases and ozone) and net cooling from other anthropogenic drivers (aerosols and land-use bar; anthropogenic aerosols, changes in reflectance due to land-use and irrigation changes, and contrails from aviation; see Figure SPM.2, panel c, for the warming contributions to date for individual drivers). The best estimate for observed warming in 2010–2019 relative to 1850–1900 (see Figure SPM.2, panel a) is indicated in the darker column in the total bar. Warming contributions in panel b are calculated as explained in Table SPM.1 for the total bar. For the other bars the contribution by groups of drivers are calculated with a physical climate emulator of global surface temperature which relies on climate sensitivity and radiative forcing assessments.

{Cross-Chapter Box 1.4, 4.6, Figure 4.35, 6.7, Figure 6.18, 6.22 and 6.24, Cross-Chapter Box 7.1, 7.3, Figure 7.7, Box TS.7, Figures TS.4 and TS.15}

B.1 Global surface temperature will continue to increase until at least the mid-century under all emissions scenarios considered. Global warming of 1.5°C and 2°C will be exceeded during the 21st century unless deep reductions in CO_2 and other greenhouse gas emissions occur in the coming decades.

{2.3, Cross-Chapter Box 2.3, Cross-Chapter Box 2.4, 4.3, 4.4, 4.5} **(Figure SPM.1, Figure SPM.4, Figure SPM.8, Table SPM.1, Box SPM.1)**

B.1.1 Compared to 1850–1900, global surface temperature averaged over 2081–2100 is *very likely* to be higher by 1.0°C to 1.8°C under the very low GHG emissions scenario considered (SSP1-1.9), by 2.1°C to 3.5°C in the intermediate scenario (SSP2-4.5) and by 3.3°C to 5.7°C under the very high GHG emissions scenario (SSP5-8.5)[24]. The last time global surface temperature was sustained at or above 2.5°C higher than 1850–1900 was over 3 million years ago (*medium confidence*).
{2.3, Cross-Chapter Box 2.4, 4.3, 4.5, Box TS.2, Box TS.4, Cross-Section Box TS.1} **(Table SPM.1)**

Table SPM.1: Changes in global surface temperature, which are assessed based on multiple lines of evidence, for selected 20-year time periods and the five illustrative emissions scenarios considered. Temperature differences relative to the average global surface temperature of the period 1850–1900 are reported in °C. This includes the revised assessment of observed historical warming for the AR5 reference period 1986–2005, which in AR6 is higher by 0.08 [–0.01 to 0.12] °C than in the AR5 (see footnote 10). Changes relative to the recent reference period 1995–2014 may be calculated approximately by subtracting 0.85°C, the best estimate of the observed warming from 1850–1900 to 1995–2014.
{Cross-Chapter Box 2.3, 4.3, 4.4, Cross-Section Box TS.1}

[24] Changes in global surface temperature are reported as running 20-year averages, unless stated otherwise.

	Near term, 2021–2040		Mid-term, 2041–2060		Long term, 2081–2100	
Scenario	Best estimate (°C)	*Very likely* range (°C)	Best estimate (°C)	*Very likely* range (°C)	Best estimate (°C)	*Very likely* range (°C)
SSP1-1.9	1.5	1.2 to 1.7	1.6	1.2 to 2.0	1.4	1.0 to 1.8
SSP1-2.6	1.5	1.2 to 1.8	1.7	1.3 to 2.2	1.8	1.3 to 2.4
SSP2-4.5	1.5	1.2 to 1.8	2.0	1.6 to 2.5	2.7	2.1 to 3.5
SSP3-7.0	1.5	1.2 to 1.8	2.1	1.7 to 2.6	3.6	2.8 to 4.6
SSP5-8.5	1.6	1.3 to 1.9	2.4	1.9 to 3.0	4.4	3.3 to 5.7

B.1.2 Based on the assessment of multiple lines of evidence, global warming of 2°C, relative to 1850–1900, would be exceeded during the 21st century under the high and very high GHG emissions scenarios considered in this report (SSP3-7.0 and SSP5-8.5, respectively). Global warming of 2°C would *extremely likely* be exceeded in the intermediate scenario (SSP2-4.5). Under the very low and low GHG emissions scenarios, global warming of 2°C is *extremely unlikely* to be exceeded (SSP1-1.9), or *unlikely* to be exceeded (SSP1-2.6)[25]. Crossing the 2°C global warming level in the mid-term period (2041–2060) is *very likely* to occur under the very high GHG emissions scenario (SSP5-8.5), *likely* to occur under the high GHG emissions scenario (SSP3-7.0), and *more likely than not* to occur in the intermediate GHG emissions scenario (SSP2-4.5)[26].
{4.3, Cross-Section Box TS.1} **(Table SPM.1, Figure SPM.4, Box SPM.1)**

B.1.3 Global warming of 1.5°C relative to 1850-1900 would be exceeded during the 21st century under the intermediate, high and very high scenarios considered in this report (SSP2-4.5, SSP3-7.0 and SSP5-8.5, respectively). Under the five illustrative scenarios, in the near term (2021-2040), the 1.5°C global warming level is *very likely* to be exceeded under the very high GHG emissions scenario (SSP5-8.5), *likely* to be exceeded under the intermediate and high GHG emissions scenarios (SSP2-4.5 and SSP3-7.0), *more likely than not* to be exceeded under the low GHG emissions scenario (SSP1-2.6) and *more likely than not* to be reached under the very low GHG emissions scenario (SSP1-1.9)[27]. Furthermore, for the very low GHG emissions scenario (SSP1-1.9), it is *more likely than not* that global surface temperature would decline back to below 1.5°C toward the end of the 21st century, with a temporary overshoot of no more than 0.1°C above 1.5°C global warming.
{4.3, Cross-Section Box TS.1} **(Table SPM.1, Figure SPM.4)**

[25] SSP1-1.9 and SSP1-2.6 are scenarios that start in 2015 and have very low and low GHG emissions and CO_2 emissions declining to net zero around or after 2050, followed by varying levels of net negative CO_2 emissions.

[26] Crossing is defined here as having the assessed global surface temperature change, averaged over a 20-year period, exceed a particular global warming level.

[27] The AR6 assessment of when a given global warming level is first exceeded benefits from the consideration of the illustrative scenarios, the multiple lines of evidence entering the assessment of future global surface temperature response to radiative forcing, and the improved estimate of historical warming. The AR6 assessment is thus not directly comparable to the SR1.5 SPM, which reported likely reaching 1.5°C global warming between 2030 and 2052, from a simple linear extrapolation of warming rates of the recent past. When considering scenarios similar to SSP1-1.9 instead of linear extrapolation, the SR1.5 estimate of when 1.5°C global

B.1.4 Global surface temperature in any single year can vary above or below the long-term human-induced trend, due to substantial natural variability[28]. The occurrence of individual years with global surface temperature change above a certain level, for example 1.5°C or 2ºC, relative to 1850–1900 does not imply that this global warming level has been reached[29].
{Cross-Chapter Box 2.3, 4.3, 4.4, Box 4.1, Cross-Section Box TS.1} **(Table SPM.1, Figure SPM.1, Figure SPM.8)**

B.2 Many changes in the climate system become larger in direct relation to increasing global warming. They include increases in the frequency and intensity of hot extremes, marine heatwaves, and heavy precipitation, agricultural and ecological droughts in some regions, and proportion of intense tropical cyclones, as well as reductions in Arctic sea ice, snow cover and permafrost. {4.3, 4.5, 4.6, 7.4, 8.2, 8.4, Box 8.2, 9.3, 9.5, Box 9.2, 11.1, 11.2, 11.3, 11.4, 11.6, 11.7, 11.9, Cross-Chapter Box 11.1, 12.4, 12.5, Cross-Chapter Box 12.1, Atlas.4, Atlas.5, Atlas.6, Atlas.7, Atlas.8, Atlas.9, Atlas.10, Atlas.11} **(Figure SPM.5, Figure SPM.6, Figure SPM.8)**

B.2.1 It is *virtually certain* that the land surface will continue to warm more than the ocean surface (*likely* 1.4 to 1.7 times more). It is *virtually certain* that the Arctic will continue to warm more than global surface temperature, with *high confidence* above two times the rate of global warming.
{2.3, 4.3, 4.5, 4.6, 7.4, 11.1, 11.3, 11.9, 12.4, 12.5, Cross-Chapter Box 12.1, Atlas.4, Atlas.5, Atlas.6, Atlas.7, Atlas.8, Atlas.9, Atlas.10, Atlas.11, Cross-Section Box TS.1, TS.2.6} **(Figure SPM.5)**

B.2.2 With every additional increment of global warming, changes in extremes continue to become larger. For example, every additional 0.5°C of global warming causes clearly discernible increases in the intensity and frequency of hot extremes, including heatwaves (*very likely*), and heavy precipitation (*high confidence*), as well as agricultural and ecological droughts[30] in some regions (*high confidence*). Discernible changes in intensity and frequency of meteorological droughts, with more regions showing increases than decreases, are seen in some regions for every additional 0.5°C of global warming (*medium confidence*). Increases in frequency and intensity of hydrological droughts become larger with increasing global warming in some regions (*medium confidence*). There will be an increasing occurrence of some extreme events unprecedented in the observational record with additional global warming, even at 1.5°C of global warming. Projected percentage changes in frequency are higher for rarer events (*high confidence*).
{8.2, 11.2, 11.3, 11.4, 11.6, 11.9, Cross-Chapter Box 11.1, Cross-Chapter Box 12.1, TS.2.6} **(Figure SPM.5, Figure SPM.6)**

warming is first exceeded is close to the best estimate reported here.

[28] Natural variability refers to climatic fluctuations that occur without any human influence, that is, internal variability combined with the response to external natural factors such as volcanic eruptions, changes in solar activity and, on longer time scales, orbital effects and plate tectonics.

[29] The internal variability in any single year is estimated to be ± 0.25°C (5–95% range, *high confidence*).

[30] Projected changes in agricultural and ecological droughts are primarily assessed based on total column soil moisture. See footnote 15 for definition and relation to precipitation and evapotranspiration.

B.2.3 Some mid-latitude and semi-arid regions, and the South American Monsoon region, are projected to see the highest increase in the temperature of the hottest days, at about 1.5 to 2 times the rate of global warming (*high confidence*). The Arctic is projected to experience the highest increase in the temperature of the coldest days, at about 3 times the rate of global warming (*high confidence*). With additional global warming, the frequency of marine heatwaves will continue to increase (*high confidence*), particularly in the tropical ocean and the Arctic *(medium confidence).*
{Box 9.2, 11.1, 11.3, 11.9, Cross-Chapter Box 11.1, Cross-Chapter Box 12.1, 12.4, TS.2.4, TS.2.6} **(Figure SPM.6)**

B.2.4 It is *very likely* that heavy precipitation events will intensify and become more frequent in most regions with additional global warming. At the global scale, extreme daily precipitation events are projected to intensify by about 7% for each 1°C of global warming (*high confidence*). The proportion of intense tropical cyclones (categories 4-5) and peak wind speeds of the most intense tropical cyclones are projected to increase at the global scale with increasing global warming (*high confidence*).
{8.2, 11.4, 11.7, 11.9, Cross-Chapter Box 11.1, Box TS.6, TS.4.3.1} **(Figure SPM.5, Figure SPM.6)**

B.2.5 Additional warming is projected to further amplify permafrost thawing, and loss of seasonal snow cover, of land ice and of Arctic sea ice (*high confidence*). The Arctic is *likely* to be practically sea ice free in September[31] at least once before 2050 under the five illustrative scenarios considered in this report, with more frequent occurrences for higher warming levels. There is *low confidence* in the projected decrease of Antarctic sea ice.
{4.3, 4.5, 7.4, 8.2, 8.4, Box 8.2, 9.3, 9.5, 12.4, Cross-Chapter Box 12.1, Atlas.5, Atlas.6, Atlas.8, Atlas.9, Atlas.11, TS.2.5} **(Figure SPM.8)**

[31] monthly average sea ice area of less than 1 million km^2 which is about 15% of the average September sea ice area observed in 1979-1988

With every increment of global warming, changes get larger in regional mean temperature, precipitation and soil moisture

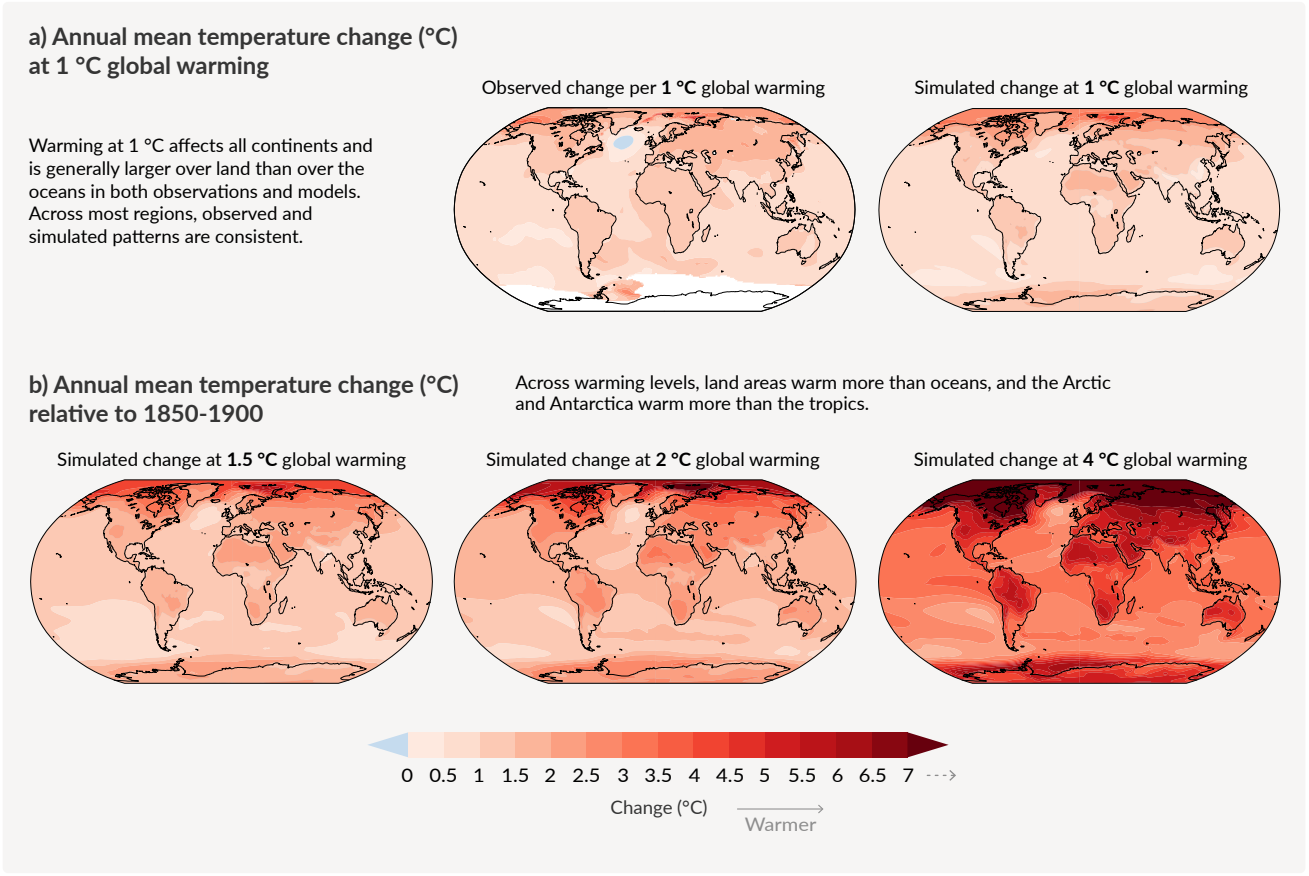
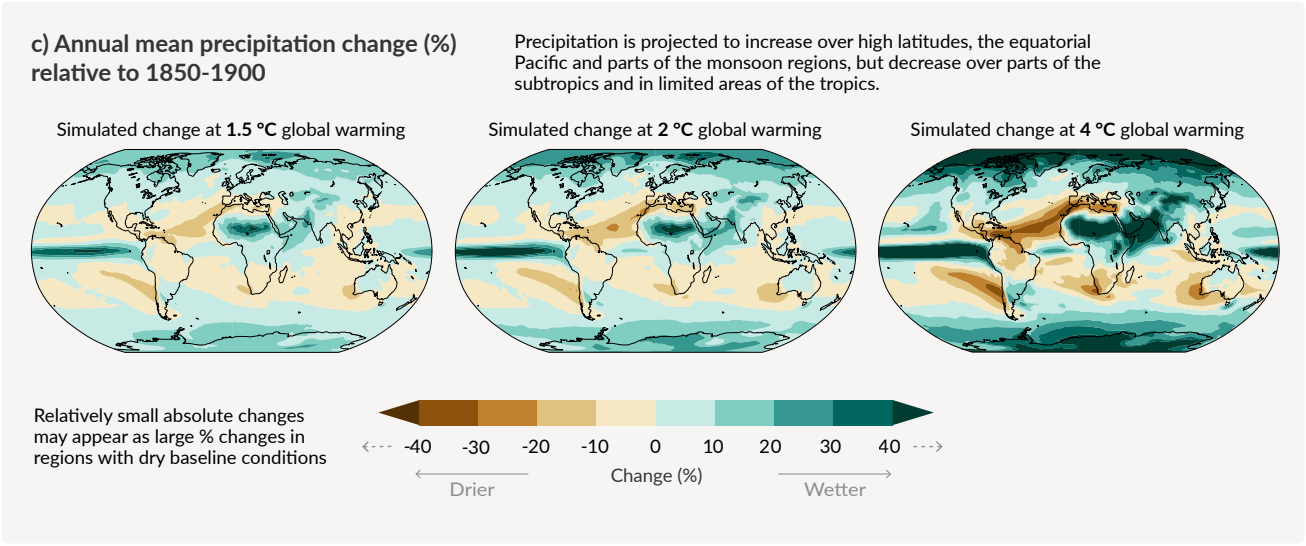
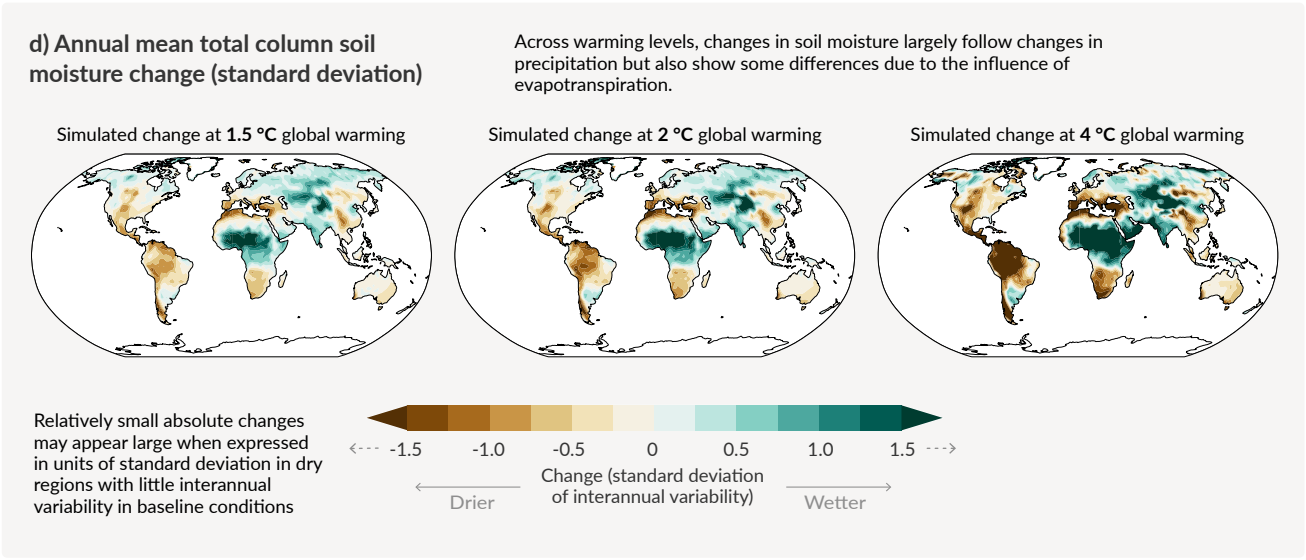


Figure SPM.5: Changes in annual mean surface temperature, precipitation, and soil moisture.

Panel a) Comparison of observed and simulated annual mean surface temperature change. The **left map** shows the observed changes in annual mean surface temperature in the period of 1850–2020 per °C of global warming (°C). The local (i.e., grid point) observed annual mean surface temperature changes are linearly regressed against the global surface temperature in the period 1850–2020. Observed temperature data are from Berkeley Earth, the dataset with the largest coverage and highest horizontal resolution. Linear regression is applied to all years for which data at the corresponding grid point is available. The regression method was used to take into account the complete observational time series and thereby reduce the role of internal variability at the grid point level. White indicates areas where time coverage was 100 years or less and thereby too short to calculate a reliable linear regression. The **right map** is based on model simulations and shows change in annual multi-model mean simulated temperatures at a global warming level of 1°C (20-year mean global surface temperature change relative to 1850–1900). The triangles at each end of the color bar indicate out-of-bound values, that is, values above or below the given limits.

Panel b) Simulated annual mean temperature change (°C), panel c) precipitation change (%), and panel d) total column soil moisture change (standard deviation of interannual variability) at global warming levels of 1.5°C, 2°C and 4°C (20-yr mean global surface temperature change relative to 1850–1900). Simulated changes correspond to CMIP6 multi-model mean change (median change for soil moisture) at the corresponding global warming level, i.e. the same method as for the right map in panel a).





In **panel c),** high positive percentage changes in dry regions may correspond to small absolute changes. In **panel d),** the unit is the standard deviation of interannual variability in soil moisture during 1850–1900. Standard deviation is a widely used metric in characterizing drought severity. A projected reduction in mean soil moisture by one standard deviation corresponds to soil moisture conditions typical of droughts that occurred about once every six years during 1850–1900. In panel d), large changes in dry regions with little interannual variability in the baseline conditions can correspond to small absolute change. The triangles at each end of the color bars indicate out-of-bound values, that is, values above or below the given limits. Results from all models reaching the corresponding warming level in any of the five illustrative scenarios (SSP1-1.9, SSP1-2.6, SSP2-4.5, SSP3-7.0 and SSP5-8.5) are averaged. Maps of annual mean temperature and precipitation changes at a global warming level of 3°C are available in Figure 4.31 and Figure 4.32 in Section 4.6.

Corresponding maps of panels b), c) and d) including hatching to indicate the level of model agreement at grid-cell level are found in Figures 4.31, 4.32 and 11.19, respectively; as highlighted in CC-box Atlas.1, grid-cell level hatching is not informative for larger spatial scales (e.g., over AR6 reference regions) where the aggregated signals are less affected by small-scale variability leading to an increase in robustness.

{TS.1.3.2, Figure TS.3, Figure TS.5, Figure 1.14, 4.6.1, Cross-Chapter Box 11.1, Cross-Chapter Box Atlas.1}

Projected changes in extremes are larger in frequency and intensity with every additional increment of global warming

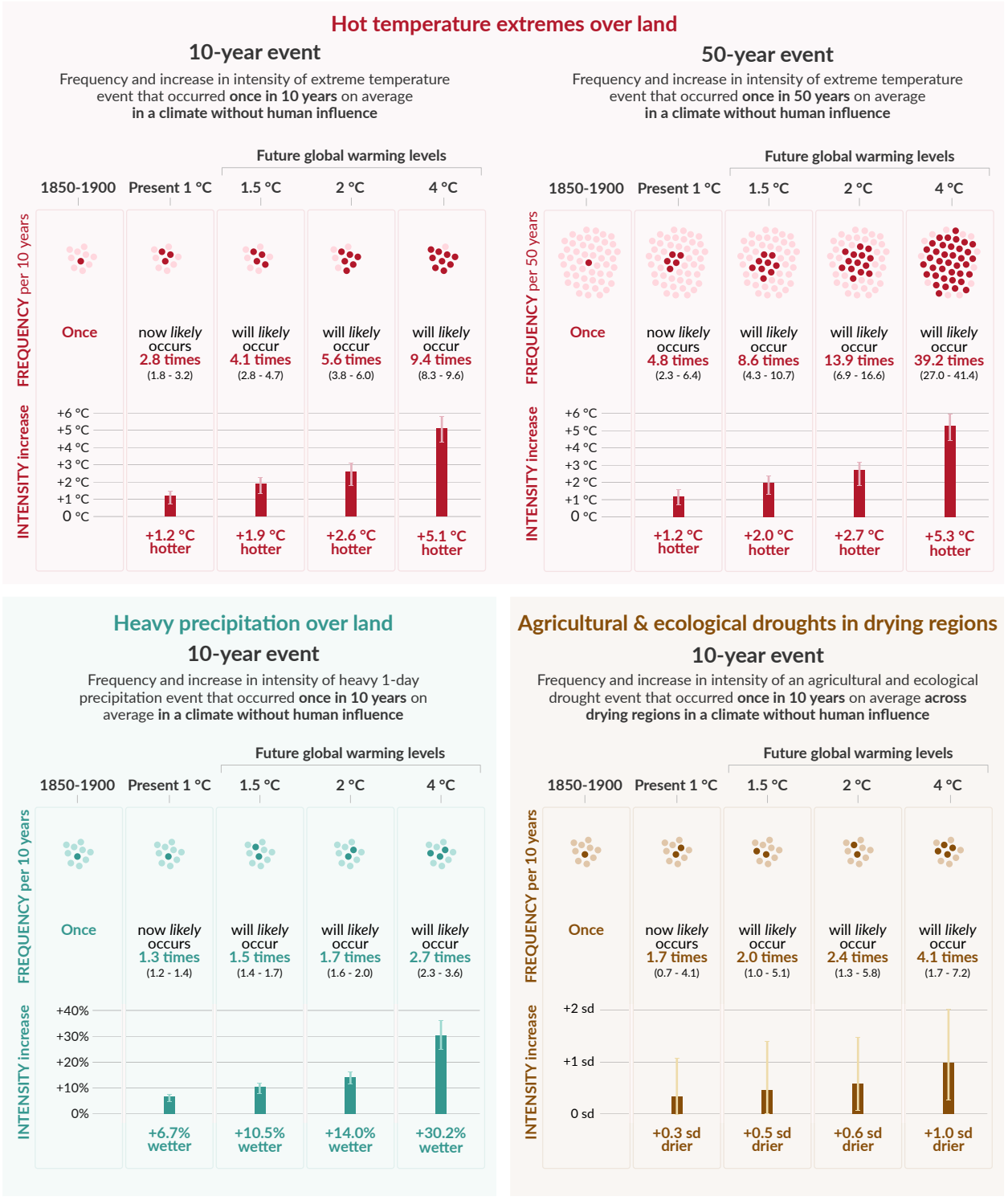


Figure SPM.6: Projected changes in the intensity and frequency of hot temperature extremes over land, extreme precipitation over land, and agricultural and ecological droughts in drying regions.

Projected changes are shown at global warming levels of 1°C, 1.5°C, 2°C, and 4°C and are relative to 1850-1900[9] representing a climate without human influence. The figure depicts frequencies and increases in intensity of 10- or 50-year extreme events from the base period (1850-1900) under different global warming levels.

Hot temperature extremes are defined as the daily maximum temperatures over land that were exceeded on average once in a decade (10-year event) or once in 50 years (50-year event) during the 1850–1900 reference period. **Extreme precipitation events** are defined as the daily precipitation amount over land that was exceeded on average once in a decade during the 1850–1900 reference period. **Agricultural and ecological drought events** are defined as the annual average of total column soil moisture below the 10th percentile of the 1850–1900 base period. These extremes are defined on model grid box scale. For hot temperature extremes and extreme precipitation, results are shown for the global land. For agricultural and ecological drought, results are shown for drying regions only, which correspond to the AR6 regions in which there is at least *medium confidence* in a projected increase in agricultural/ecological drought at the 2°C warming level compared to the 1850–1900 base period in CMIP6. These regions include W. North-America, C. North-America, N. Central-America, S. Central-America, Caribbean, N. South-America, N.E. South-America, South-American-Monsoon, S.W. South-America, S. South-America, West & Central-Europe, Mediterranean, W. Southern-Africa, E. Southern-Africa, Madagascar, E. Australia, S. Australia (Caribbean is not included in the calculation of the figure because of the too small number of full land grid cells). The non-drying regions do not show an overall increase or decrease in drought severity. Projections of changes in agricultural and ecological droughts in the CMIP5 multi-model ensemble differ from those in CMIP6 in some regions, including in part of Africa and Asia. Assessments on projected changes in meteorological and hydrological droughts are provided in Chapter 11. {11.6, 11.9}

In the **'frequency' section,** each year is represented by a dot. The dark dots indicate years in which the extreme threshold is exceeded, while light dots are years when the threshold is not exceeded. Values correspond to the medians (in bold) and their respective 5–95% range based on the multi-model ensemble from simulations of CMIP6 under different SSP scenarios. For consistency, the number of dark dots is based on the rounded-up median. In the **'intensity' section,** medians and their 5–95% range, also based on the multi-model ensemble from simulations of CMIP6, are displayed as dark and light bars, respectively. Changes in the intensity of hot temperature extremes and extreme precipitations are expressed as degree Celsius and percentage. As for agricultural and ecological drought, intensity changes are expressed as fractions of standard deviation of annual soil moisture.

{11.1, 11.3, 11.4, 11.6, Figure 11.12, Figure 11.15, Figure 11.6, Figure 11.7, Figure 11.18}

B.3 Continued global warming is projected to further intensify the global water cycle, including its variability, global monsoon precipitation and the severity of wet and dry events.

{4.3, 4.4, 4.5, 4.6, 8.2, 8.3, 8.4, 8.5, Box 8.2, 11.4, 11.6, 11.9, 12.4, Atlas.3} **(Figure SPM.5, Figure SPM.6)**

B.3.1 There is strengthened evidence since AR5 that the global water cycle will continue to intensify as global temperatures rise (*high confidence*), with precipitation and surface water flows projected to become more variable over most land regions within seasons (*high confidence*) and from year to year (*medium confidence*). The average annual global land precipitation is projected to increase by 0–5% under the very low GHG emissions scenario (SSP1-1.9), 1.5-8% for the intermediate GHG emissions scenario (SSP2-4.5) and 1–13% under the very high GHG emissions scenario (SSP5-8.5) by 2081–2100 relative to 1995-2014 (*likely* ranges). Precipitation is projected to increase over high latitudes, the equatorial Pacific and parts of the monsoon regions, but decrease over parts of the subtropics and limited areas in the tropics in SSP2-4.5, SSP3-7.0 and SSP5-8.5 (*very likely*). The portion of the global land experiencing detectable increases or decreases in seasonal mean precipitation is projected to increase (*medium confidence*). There is *high confidence* in an earlier onset of spring snowmelt, with higher peak flows at the expense of summer flows in snow-dominated regions globally.
{4.3, 4.5, 4.6, 8.2, 8.4, Atlas.3, TS.2.6, Box TS.6, TS.4.3} **(Figure SPM.5)**

B.3.2 A warmer climate will intensify very wet and very dry weather and climate events and seasons, with implications for flooding or drought (*high confidence*), but the location and frequency of these events depend on projected changes in regional atmospheric circulation, including monsoons and mid-latitude storm tracks. It is *very likely* that rainfall variability related to the El Niño–Southern Oscillation is projected to be amplified by the second half of the 21st century in the SSP2-4.5, SSP3-7.0 and SSP5-8.5 scenarios.
{4.3, 4.5, 4.6, 8.2, 8.4, 8.5, 11.4, 11.6, 11.9, 12.4, TS.2.6, TS.4.2, Box TS.6} **(Figure SPM.5, Figure SPM.6)**

B.3.3 Monsoon precipitation is projected to increase in the mid- to long term at global scale, particularly over South and Southeast Asia, East Asia and West Africa apart from the far west Sahel (*high confidence*). The monsoon season is projected to have a delayed onset over North and South America and West Africa (*high confidence*) and a delayed retreat over West Africa (*medium confidence*).
{4.4, 4.5, 8.2, 8.3, 8.4, Box 8.2, Box TS.13}

B.3.4 A projected southward shift and intensification of Southern Hemisphere summer mid-latitude storm tracks and associated precipitation is *likely* in the long term under high GHG emissions scenarios (SSP3-7.0, SSP5-8.5), but in the near term the effect of stratospheric ozone recovery counteracts these changes (*high confidence*). There is *medium confidence* in a continued poleward shift of storms and their precipitation in the North Pacific, while there is *low confidence* in projected changes in the North Atlantic storm tracks.
{TS.4.2, 4.4, 4.5, 8.4, TS.2.3}

B.4 Under scenarios with increasing CO_2 emissions, the ocean and land carbon sinks are projected to be less effective at slowing the accumulation of CO_2 in the atmosphere.

{4.3, 5.2, 5.4, 5.5, 5.6} **(Figure SPM.7)**

B.4.1 While natural land and ocean carbon sinks are projected to take up, in absolute terms, a progressively larger amount of CO_2 under higher compared to lower CO_2 emissions scenarios, they become less effective, that is, the proportion of emissions taken up by land and ocean decrease with increasing cumulative CO_2 emissions. This is projected to result in a higher proportion of emitted CO_2 remaining in the atmosphere (*high confidence*).
{5.2, 5.4, Box TS.5} **(Figure SPM.7)**

B.4.2 Based on model projections, under the intermediate scenario that stabilizes atmospheric CO_2 concentrations this century (SSP2-4.5), the rates of CO_2 taken up by the land and oceans are projected to decrease in the second half of the 21st century (*high confidence*). Under the very low and low GHG emissions scenarios (SSP1-1.9, SSP1-2.6), where CO_2 concentrations peak and decline during the 21st century, land and oceans begin to take up less carbon in response to declining atmospheric CO_2 concentrations (*high confidence*) and turn into a weak net source by 2100 under SSP1-1.9 (*medium confidence*). It is *very unlikely* that the combined global land and ocean sink will turn into a source by 2100 under scenarios without net negative emissions[32] (SSP2-4.5, SSP3-7.0, SSP5-8.5).
{4.3, 5.4, 5.5, 5.6, Box TS.5, TS.3.3}

B.4.3 The magnitude of feedbacks between climate change and the carbon cycle becomes larger but also more uncertain in high CO_2 emissions scenarios (*very high confidence*). However, climate model projections show that the uncertainties in atmospheric CO_2 concentrations by 2100 are dominated by the differences between emissions scenarios (*high confidence*). Additional ecosystem responses to warming not yet fully included in climate models, such as CO_2 and CH_4 fluxes from wetlands, permafrost thaw and wildfires, would further increase concentrations of these gases in the atmosphere (*high confidence*).
{5.4, Box TS.5, TS.3.2}

[32] These projected adjustments of carbon sinks to stabilization or decline of atmospheric CO_2 are accounted for in calculations of remaining carbon budgets.

The proportion of CO_2 emissions taken up by land and ocean carbon sinks is smaller in scenarios with higher cumulative CO_2 emissions

Total cumulative CO_2 emissions **taken up by land and oceans** (colours) and remaining in the atmosphere (grey) under the five illustrative scenarios from 1850 to 2100

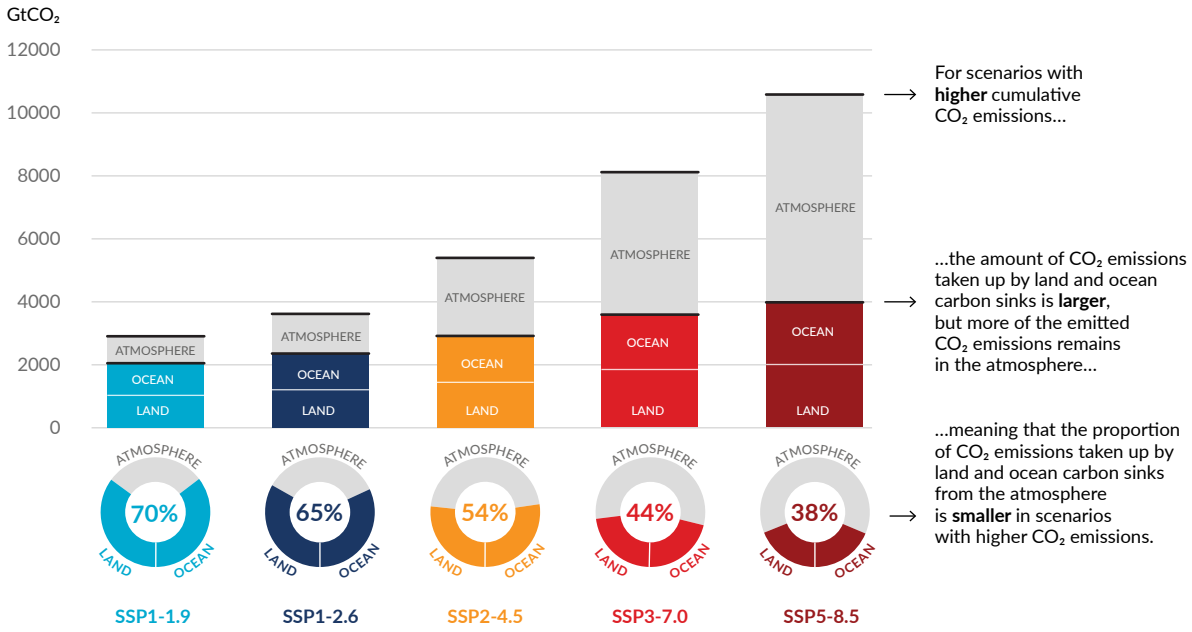


Figure SPM.7: Cumulative anthropogenic CO_2 emissions taken up by land and ocean sinks by 2100 under the five illustrative scenarios.

The cumulative anthropogenic (human-caused) carbon dioxide (CO_2) emissions taken up by the land and ocean sinks under the five illustrative scenarios (SSP1-1.9, SSP1-2.6, SSP2-4.5, SSP3-7.0 and SSP5-8.5) are simulated from 1850 to 2100 by CMIP6 climate models in the concentration-driven simulations. Land and ocean carbon sinks respond to past, current and future emissions, therefore cumulative sinks from 1850 to 2100 are presented here. During the historical period (1850-2019) the observed land and ocean sink took up 1430 $GtCO_2$ (59% of the emissions).

The **bar chart** illustrates the projected amount of cumulative anthropogenic CO_2 emissions ($GtCO_2$) between 1850 and 2100 remaining in the atmosphere (grey part) and taken up by the land and ocean (coloured part) in the year 2100. The **doughnut chart** illustrates the proportion of the cumulative anthropogenic CO_2 emissions taken up by the land and ocean sinks and remaining in the atmosphere in the year 2100. Values in % indicate the proportion of the cumulative anthropogenic CO_2 emissions taken up by the combined land and ocean sinks in the year 2100. The overall anthropogenic carbon emissions are calculated by adding the net global land use emissions from CMIP6 scenario database to the other sectoral emissions calculated from climate model runs with prescribed CO_2 concentrations[33]. Land and ocean CO_2 uptake since 1850 is calculated from the net biome productivity on land, corrected for CO_2 losses due to land-use change by adding the land-use change emissions, and net ocean CO_2 flux.

{Box TS.5, Box TS.5, Figure 1, 5.2.1, Table 5.1, 5.4.5, Figure 5.25}

[33] The other sectoral emissions are calculated as the residual of the net land and ocean CO_2 uptake and the prescribed atmospheric CO_2 concentration changes in the CMIP6 simulations. These calculated emissions are net emissions and do not separate gross anthropogenic emissions from removals, which are included implicitly.

B.5 Many changes due to past and future greenhouse gas emissions are irreversible for centuries to millennia, especially changes in the ocean, ice sheets and global sea level. {Cross-Chapter Box 2.4, 2.3, 4.3, 4.5, 4.7, 5.3, 9.2, 9.4, 9.5, 9.6, Box 9.4} **(Figure SPM.8)**

B.5.1 Past GHG emissions since 1750 have committed the global ocean to future warming (*high confidence*). Over the rest of the 21st century, *likely* ocean warming ranges from 2–4 (SSP1-2.6) to 4–8 times (SSP5-8.5) the 1971–2018 change. Based on multiple lines of evidence, upper ocean stratification (*virtually certain*), ocean acidification (*virtually certain*) and ocean deoxygenation (*high confidence*) will continue to increase in the 21st century, at rates dependent on future emissions. Changes are irreversible on centennial to millennial time scales in global ocean temperature (*very high confidence*), deep ocean acidification (*very high confidence*) and deoxygenation (*medium confidence*).
{4.3, 4.5, 4.7, 5.3, 9.2, TS.2.4} **(Figure SPM.8)**

B.5.2 Mountain and polar glaciers are committed to continue melting for decades or centuries (*very high confidence*). Loss of permafrost carbon following permafrost thaw is irreversible at centennial timescales (*high confidence*). Continued ice loss over the 21st century is *virtually certain* for the Greenland Ice Sheet and *likely* for the Antarctic Ice Sheet. There is *high confidence* that total ice loss from the Greenland Ice Sheet will increase with cumulative emissions. There is *limited evidence* for low-likelihood, high-impact outcomes (resulting from ice sheet instability processes characterized by deep uncertainty and in some cases involving tipping points) that would strongly increase ice loss from the Antarctic Ice Sheet for centuries under high GHG emissions scenarios[34]. {4.3, 4.7, 5.4, 9.4, 9.5, Box 9.4, Box TS.1, TS.2.5}

B.5.3 It is *virtually certain* that global mean sea level will continue to rise over the 21st century. Relative to 1995-2014, the *likely* global mean sea level rise by 2100 is 0.28-0.55 m under the very low GHG emissions scenario (SSP1-1.9), 0.32-0.62 m under the low GHG emissions scenario (SSP1-2.6), 0.44-0.76 m under the intermediate GHG emissions scenario (SSP2-4.5), and 0.63-1.01 m under the very high GHG emissions scenario (SSP5-8.5), and by 2150 is 0.37-0.86 m under the very low scenario (SSP1-1.9), 0.46-0.99 m under the low scenario (SSP1-2.6), 0.66-1.33 m under the intermediate scenario (SSP2-4.5), and 0.98-1.88 m under the very high scenario (SSP5-8.5) (*medium confidence*)[35]. Global mean sea level rise above the *likely* range – approaching 2 m by 2100 and 5 m by 2150 under a very high GHG emissions scenario (SSP5-8.5) (*low confidence*) – cannot be ruled out due to deep uncertainty in ice sheet processes.
{4.3, 9.6, Box 9.4, Box TS.4} **(Figure SPM.8)**

B.5.4 In the longer term, sea level is committed to rise for centuries to millennia due to continuing deep ocean warming and ice sheet melt, and will remain elevated for thousands of years (*high confidence*). Over the next 2000 years, global mean sea level will rise by about 2 to 3 m if warming is limited to 1.5°C, 2 to 6 m if limited to 2°C and 19 to 22 m with 5°C of warming, and it will continue to rise over subsequent millennia (*low confidence*). Projections of multi-millennial global mean sea level rise are consistent with reconstructed levels during past warm climate periods: *likely* 5–10 m higher than today around 125,000 years ago, when global temperatures were *very likely* 0.5°C–1.5°C higher than 1850–1900; and *very likely* 5–25 m higher roughly 3 million years ago, when global temperatures were 2.5°C–4°C higher (*medium confidence*).
{2.3, Cross-Chapter Box 2.4, 9.6, Box TS.2, Box TS.4, Box TS.9}

[34] Low-likelihood, high-impact outcomes are those whose probability of occurrence is low or not well known (as in the context of deep uncertainty) but whose potential impacts on society and ecosystems could be high. A tipping point is a critical threshold beyond which a system reorganizes, often abruptly and/or irreversibly. {Cross-Chapter Box 1.3, 1.4, 4.7}

[35] To compare to the 1986–2005 baseline period used in AR5 and SROCC, add 0.03 m to the global mean sea level rise estimates. To compare to the 1900 baseline period used in Figure SPM.8, add 0.16 m.

Human activities affect all the major climate system components, with some responding over decades and others over centuries

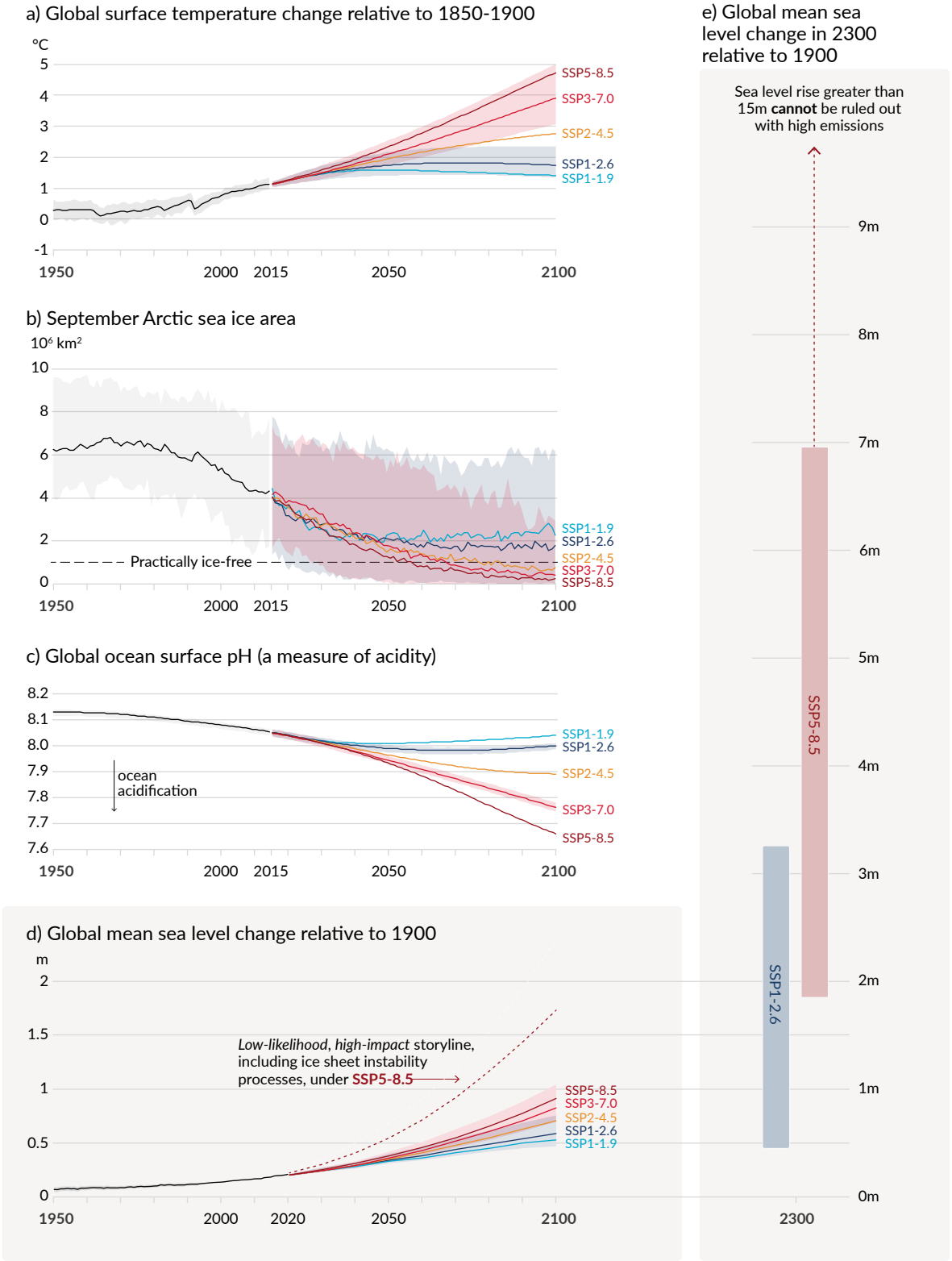


Figure SPM.8: Selected indicators of global climate change under the five illustrative scenarios used in this report.

The projections for each of the five scenarios are shown in colour. Shades represent uncertainty ranges – more detail is provided for each panel below. The black curves represent the historical simulations (panels a, b, c) or the observations (panel d). Historical values are included in all graphs to provide context for the projected future changes.

Panel a) Global surface temperature changes in °C relative to 1850–1900. These changes were obtained by combining CMIP6 model simulations with observational constraints based on past simulated warming, as well as an updated assessment of equilibrium climate sensitivity (see Box SPM.1). Changes relative to 1850–1900 based on 20-year averaging periods are calculated by adding 0.85°C (the observed global surface temperature increase from 1850–1900 to 1995–2014) to simulated changes relative to 1995–2014. *Very likely* ranges are shown for SSP1-2.6 and SSP3-7.0.

Panel b) September Arctic sea ice area in 10^6 km^2 based on CMIP6 model simulations. *Very likely* ranges are shown for SSP1-2.6 and SSP3-7.0. The Arctic is projected to be practically ice-free near mid-century under mid- and high GHG emissions scenarios.

Panel c) Global ocean surface pH (a measure of acidity) based on CMIP6 model simulations. *Very likely* ranges are shown for SSP1-2.6 and SSP3-7.0.

Panel d) Global mean sea level change in meters relative to 1900. The historical changes are observed (from tide gauges before 1992 and altimeters afterwards), and the future changes are assessed consistently with observational constraints based on emulation of CMIP, ice sheet, and glacier models. *Likely* ranges are shown for SSP1-2.6 and SSP3-7.0. Only *likely* ranges are assessed for sea level changes due to difficulties in estimating the distribution of deeply uncertain processes. The dashed curve indicates the potential impact of these deeply uncertain processes. It shows the 83rd percentile of SSP5-8.5 projections that include low-likelihood, high-impact ice sheet processes that cannot be ruled out; because of *low confidence* in projections of these processes, this curve does not constitute part of a *likely* range. Changes relative to 1900 are calculated by adding 0.158 m (observed global mean sea level rise from 1900 to 1995–2014) to simulated and observed changes relative to 1995–2014.

Panel e): Global mean sea level change at 2300 in meters relative to 1900. Only SSP1-2.6 and SSP5-8.5 are projected at 2300, as simulations that extend beyond 2100 for the other scenarios are too few for robust results. The 17th–83rd percentile ranges are shaded. The dashed arrow illustrates the 83rd percentile of SSP5-8.5 projections that include low-likelihood, high-impact ice sheet processes that cannot be ruled out.

Panels b) and c) are based on single simulations from each model, and so include a component of internal variability. Panels a), d) and e) are based on long-term averages, and hence the contributions from internal variability are small.

{Figure TS.8, Figure TS.11, Box TS.4 Figure 1, Box TS.4 Figure 1, 4.3, 9.6, Figure 4.2, Figure 4.8, Figure 4.11, Figure 9.27}

C. Climate Information for Risk Assessment and Regional Adaptation

Physical climate information addresses how the climate system responds to the interplay between human influence, natural drivers and internal variability. Knowledge of the climate response and the range of possible outcomes, including low-likelihood, high impact outcomes, informs climate services – the assessment of climate-related risks and adaptation planning. Physical climate information at global, regional and local scales is developed from multiple lines of evidence, including observational products, climate model outputs and tailored diagnostics.

C.1 Natural drivers and internal variability will modulate human-caused changes, especially at regional scales and in the near term, with little effect on centennial global warming. These modulations are important to consider in planning for the full range of possible changes.

{1.4, 2.2, 3.3, Cross-Chapter Box 3.1, 4.4, 4.6, Cross-Chapter Box 4.1, 4.4, Box 7.2, 8.3, 8.5, 9.2, 10.3, 10.4, 10.6, 11.3, 12.5, Atlas.4, Atlas.5, Atlas.8, Atlas.9, Atlas.10, Cross-Chapter Box Atlas.2, Atlas.11}

C.1.1 The historical global surface temperature record highlights that decadal variability has enhanced and masked underlying human-caused long-term changes, and this variability will continue into the future (*very high confidence*). For example, internal decadal variability and variations in solar and volcanic drivers partially masked human-caused surface global warming during 1998–2012, with pronounced regional and seasonal signatures (*high confidence*). Nonetheless, the heating of the climate system continued during this period, as reflected in both the continued warming of the global ocean (*very high confidence*) and in the continued rise of hot extremes over land (*medium confidence*).
{1.4, 3.3, Cross-Chapter Box 3.1, 4.4, Box 7.2, 9.2, 11.3, Cross-Section Box TS.1} **(Figure SPM.1)**

C.1.2 Projected human caused changes in mean climate and climatic impact-drivers (CIDs)[36], including extremes, will be either amplified or attenuated by internal variability[37] (*high confidence*). Near-term cooling at any particular location with respect to present climate could occur and would be consistent with the global surface temperature increase due to human influence (*high confidence*).
{1.4, 4.4, 4.6, 10.4, 11.3, 12.5, Atlas.5, Atlas.10, Atlas.11, TS.4.2}

C.1.3 Internal variability has largely been responsible for the amplification and attenuation of the observed human-caused decadal-to-multi-decadal mean precipitation changes in many land regions *(high confidence)*. At global and regional scales, near-term changes in monsoons will be dominated by the effects of internal variability (*medium confidence*). In addition to internal variability influence, near-term projected changes in precipitation at global and regional scales are uncertain because of model uncertainty and uncertainty in forcings from natural and anthropogenic aerosols (*medium confidence*).
{1.4, 4.4, 8.3, 8.5, 10.3, 10.4, 10.5, 10.6, Atlas.4, Atlas.8, Atlas.9, Atlas.10, Cross-Chapter Box Atlas.2, Atlas.11, TS.4.2, Box TS.6, Box TS.13}

[36] Climatic impact-drivers (CIDs) are physical climate system conditions (e.g., means, events, extremes) that affect an element of society or ecosystems. Depending on system tolerance, CIDs and their changes can be detrimental, beneficial, neutral, or a mixture of each across interacting system elements and regions. CID types include heat and cold, wet and dry, wind, snow and ice, coastal and open ocean.

[37] The main internal variability phenomena include El Niño–Southern Oscillation, Pacific Decadal variability and Atlantic Multi-decadal variability through their regional influence.

C.1.4 Based on paleoclimate and historical evidence, it is *likely* that at least one large explosive volcanic eruption would occur during the 21st century[38]. Such an eruption would reduce global surface temperature and precipitation, especially over land, for one to three years, alter the global monsoon circulation, modify extreme precipitation and change many CIDs (*medium confidence*). If such an eruption occurs, this would therefore temporarily and partially mask human-caused climate change.
{4.4, Cross-Chapter Box 4.1, 2.2, 8.5, TS.2.1}

C.2 With further global warming, every region is projected to increasingly experience concurrent and multiple changes in climatic impact-drivers. Changes in several climatic impact-drivers would be more widespread at 2°C compared to 1.5°C global warming and even more widespread and/or pronounced for higher warming levels.

{8.2, 9.3, 9.5, 9.6, Box 10.3, Box 11.3, Box 11.4, 11.3, 11.4, 11.5, 11.6, 11.7, 11.9, 12.2, 12.3, 12.4, 12.5, Atlas.4, Atlas.5, Atlas.6, Atlas.7, Atlas.8, Atlas.9, Atlas.10, Atlas.11, Cross-Chapter Box 11.1, Cross-Chapter Box 12.1} **(Table SPM.1, Figure SPM.9)**

C.2.1 All regions[39] are projected to experience further increases in hot climatic impact-drivers (CIDs) and decreases in cold CIDs (*high confidence*). Further decreases are projected in permafrost, snow, glaciers and ice sheets, lake and Arctic sea ice (*medium* to *high confidence*)[40]. These changes would be larger at 2°C global warming or above than at 1.5°C (*high confidence*). For example, extreme heat thresholds relevant to agriculture and health are projected to be exceeded more frequently at higher global warming levels (*high confidence*).
{9.3, 9.5, 11.3, 11.9, 12.3, 12.4, 12.5, Atlas.4, Atlas.5, Atlas.6, Atlas.7, Atlas.8, Atlas.9, Atlas.10, Atlas.11, TS.4.3, Cross-Chapter Box 11.1, Cross-Chapter Box 12.1} **(Table SPM.1, Figure SPM.9)**

C.2.2 At 1.5°C global warming, heavy precipitation and associated flooding are projected to intensify and be more frequent in most regions in Africa and Asia (*high confidence*), North America (*medium* to *high confidence*)[40] and Europe (*medium confidence*). Also**,** more frequent and/or severe agricultural and ecological droughts are projected in a few regions in all continents except Asia compared to 1850–1900 (*medium confidence*); increases in meteorological droughts are also projected in a few regions (*medium confidence*). A small number of regions are projected to experience increases or decreases in mean precipitation (*medium confidence*).
{11.4, 11.5, 11.6, 11.9, Atlas.4, Atlas.5, Atlas.7, Atlas.8, Atlas.9, Atlas.10, Atlas.11, TS.4.3} **(Table SPM.1)**

[38] Based on 2,500 year reconstructions, eruptions more negative than –1 W m^{-2} occur on average twice per century.

[39] Regions here refer to the AR6 WGI reference regions used in this Report to summarize information in sub-continental and oceanic regions. Changes are compared to averages over the last 20–40 years unless otherwise specified. {1.4, 12.4, Atlas.1, Interactive Atlas}.

[40] The specific level of confidence or likelihood depends on the region considered. Details can be found in the Technical Summary and the underlying Report.

C.2.3 At 2°C global warming and above, the level of confidence in and the magnitude of the change in droughts and heavy and mean precipitation increase compared to those at 1.5°C. Heavy precipitation and associated flooding events are projected to become more intense and frequent in the Pacific Islands and across many regions of North America and Europe (*medium* to *high confidence*)[40]. These changes are also seen in some regions in Australasia and Central and South America (*medium confidence*). Several regions in Africa, South America and Europe are projected to experience an increase in frequency and/or severity of agricultural and ecological droughts with *medium* to *high confidence*[40]; increases are also projected in Australasia, Central and North America, and the Caribbean with *medium confidence*. A small number of regions in Africa, Australasia, Europe and North America are also projected to be affected by increases in hydrological droughts, and several regions are projected to be affected by increases or decreases in meteorological droughts with more regions displaying an increase (*medium confidence*). Mean precipitation is projected to increase in all polar, northern European and northern North American regions, most Asian regions and two regions of South America (*high confidence*).
{11.4, 11.6, 11.9, 12.4, 12.5, Atlas.5, Atlas.7, Atlas.8, Atlas.9, Atlas.11, TS.4.3, Cross-Chapter Box 11.1, Cross-Chapter Box 12.1} **(Table SPM.1, Figure SPM.5, Figure SPM.6, Figure SPM.9)**

C.2.4 More CIDs across more regions are projected to change at 2°C and above compared to 1.5°C global warming (*high confidence*). Region-specific changes include intensification of tropical cyclones and/or extratropical storms (*medium confidence*), increases in river floods (*medium* to *high confidence*)[40], reductions in mean precipitation and increases in aridity (*medium* to *high confidence*)[40], and increases in fire weather (*medium* to *high confidence*)[40]. There is *low confidence* in most regions in potential future changes in other CIDs, such as hail, ice storms, severe storms, dust storms, heavy snowfall, and landslides.
{11.7, 11.9, 12.4, 12.5, Atlas.4, Atlas.6, Atlas.7, Atlas.8, Atlas.10, TS.4.3.1, TS.4.3.2, TS.5, Cross-Chapter Box, 11.1, Cross-Chapter Box 12.1} **(Table SPM.1, Figure SPM.9)**

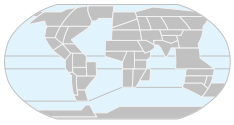
C.2.5 It is *very likely* to *virtually certain*[40] that regional mean relative sea level rise will continue throughout the 21st century, except in a few regions with substantial geologic land uplift rates. Approximately two-thirds of the global coastline has a projected regional relative sea level rise within ±20% of the global mean increase (*medium confidence*). Due to relative sea level rise, extreme sea level events that occurred once per century in the recent past are projected to occur at least annually at more than half of all tide gauge locations by 2100 (*high confidence*). Relative sea level rise contributes to increases in the frequency and severity of coastal flooding in low-lying areas and to coastal erosion along most sandy coasts (*high confidence*).
{9.6, 12.4, 12.5, Box TS.4, TS.4.3, Cross-Chapter Box 12.1} **(Figure SPM.9)**

C.2.6 Cities intensify human-induced warming locally, and further urbanization together with more frequent hot extremes will increase the severity of heatwaves (*very high confidence*). Urbanization also increases mean and heavy precipitation over and/or downwind of cities (*medium confidence*) and resulting runoff intensity (*high confidence*). In coastal cities, the combination of more frequent extreme sea level events (due to sea level rise and storm surge) and extreme rainfall/riverflow events will make flooding more probable (*high confidence*).
{8.2, Box 10.3, 11.3, 12.4, Box TS.14}

C.2.7 Many regions are projected to experience an increase in the probability of compound events with higher global warming (*high confidence*). In particular, concurrent heatwaves and droughts are *likely* to become more frequent. Concurrent extremes at multiple locations become more frequent, including in crop-producing areas, at 2°C and above compared to 1.5°C global warming (*high confidence*).
{11.8, Box 11.3, Box 11.4, 12.3, 12.4, TS.4.3, Cross-Chapter Box 12.1} **(Table SPM.1)**

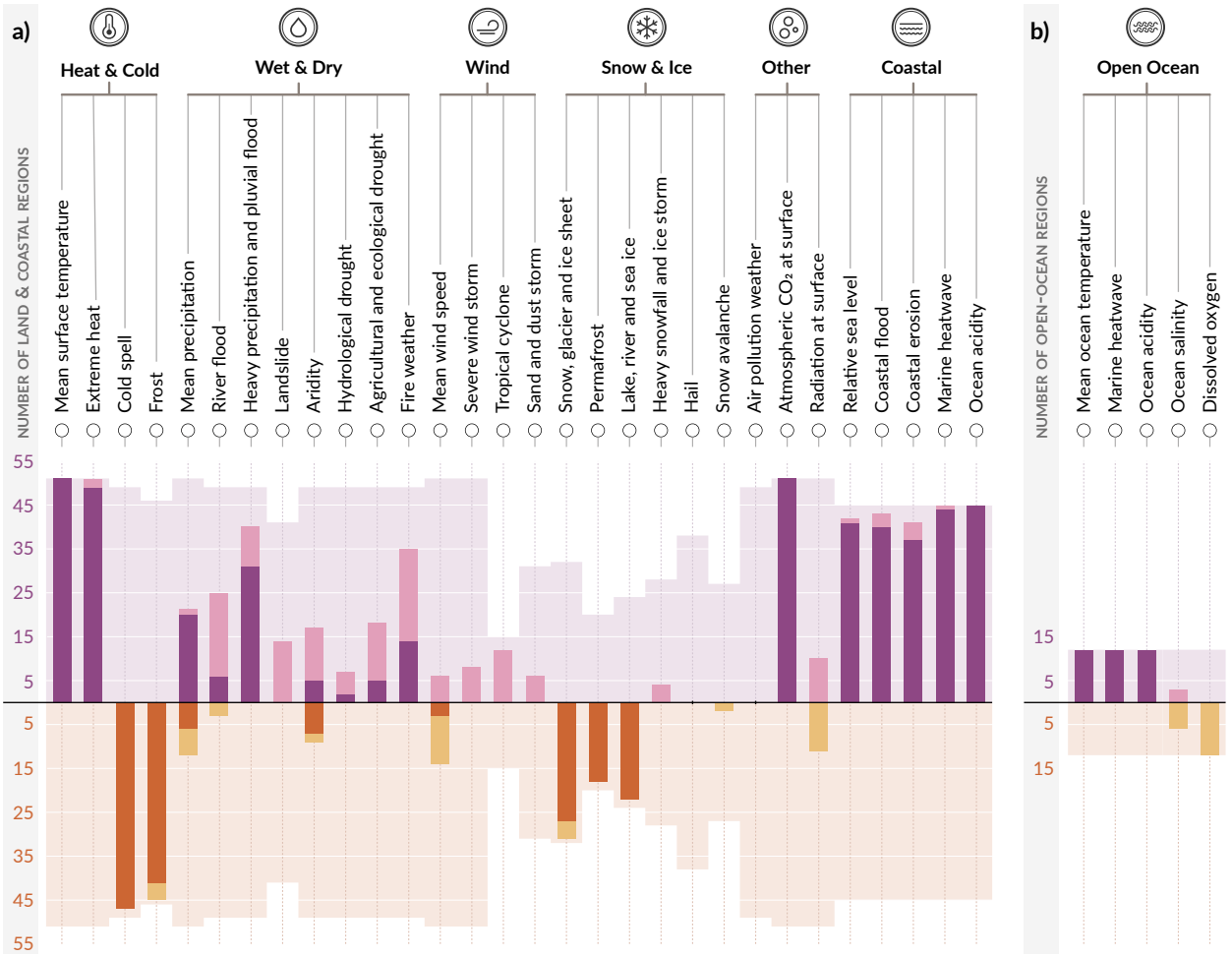
Multiple climatic impact-drivers are projected to change in all regions of the world

Climatic impact-drivers (CIDs) are physical climate system conditions (e.g., means, events, extremes) that affect an element of society or ecosystems. Depending on system tolerance, CIDs and their changes can be detrimental, beneficial, neutral, or a mixture of each across interacting system elements and regions. The CIDs are grouped into seven types, which are summarized under the icons in the figure. All regions are projected to experience changes in at least 5 CIDs. Almost all (96%) are projected to experience changes in at least 10 CIDs and half in at least 15 CIDs. For many CIDs there is wide geographical variation in where they change and so each region are projected to experience a specific set of CID changes. Each bar in the chart represents a specific geographical set of changes that can be explored in the WGI Interactive Atlas.



interactive-atlas.ipcc.ch

Number of land & coastal regions (a) and **open-ocean regions** (b) where each **climatic impact-driver** (CID) is projected to **increase** or **decrease** with ***high*** *confidence* (dark shade) or ***medium*** *confidence* (light shade)



BAR CHART LEGEND

- Regions with ***high*** *confidence* **increase**
- Regions with ***medium*** *confidence* **increase**
- Regions with ***high*** *confidence* **decrease**
- Regions with ***medium*** *confidence* **decrease**

LIGHTER-SHADED 'ENVELOPE' LEGEND

The height of the lighter shaded 'envelope' behind each bar represents the maximum number of regions for which each CID is relevant. The envelope is symmetrical about the x-axis showing the maximum possible number of relevant regions for CID increase (upper part) or decrease (lower part).

ASSESSED FUTURE CHANGES

Changes refer to a 20–30 year period centred around 2050 and/or consistent with 2°C global warming compared to a similar period within 1960-2014 or 1850-1900.

Figure SPM.9: Synthesis of the number of AR6 WGI reference regions where climatic impact-drivers are projected to change.

A total of 35 climatic impact-drivers (CIDs) grouped into seven types are shown: heat and cold, wet and dry, wind, snow and ice, coastal, open ocean and other. For each CID, the bar in the graph below displays the number of AR6 WGI reference regions where it is projected to change. The **colours** represent the direction of change and the level of confidence in the change: purple indicates an increase while brown indicates a decrease; darker and lighter shades refer to *high* and *medium confidence*, respectively. Lighter background colours represent the maximum number of regions for which each CID is broadly relevant.

Panel a) shows the 30 CIDs relevant to the **land and coastal regions** while **panel b)** shows the 5 CIDs relevant to the **open ocean regions.** Marine heatwaves and ocean acidity are assessed for coastal ocean regions in panel a) and for open ocean regions in panel b). Changes refer to a 20–30 year period centred around 2050 and/or consistent with 2°C global warming compared to a similar period within 1960-2014, except for hydrological drought and agricultural and ecological drought which is compared to 1850-1900. Definitions of the regions are provided in Atlas.1 and the Interactive Atlas (see *interactive-atlas.ipcc.ch*).

{Table TS.5, Figure TS.22, Figure TS.25, 11.9, 12.2, 12.4, Atlas.1} **(Table SPM.1)**

C.3 Low-likelihood outcomes, such as ice sheet collapse, abrupt ocean circulation changes, some compound extreme events and warming substantially larger than the assessed *very likely* range of future warming cannot be ruled out and are part of risk assessment.

{1.4, Cross-Chapter Box 1.3, Cross-Chapter Box 4.1, 4.3, 4.4, 4.8, 8.6, 9.2, Box 9.4, Box 11.2, 11.8, Cross-Chapter Box 12.1} **(Table SPM.1)**

C.3.1 If global warming exceeds the assessed *very likely* range for a given GHG emissions scenario, including low GHG emissions scenarios, global and regional changes in many aspects of the climate system, such as regional precipitation and other CIDs, would also exceed their assessed *very likely* ranges (*high confidence*). Such low-likelihood high-warming outcomes are associated with potentially very large impacts, such as through more intense and more frequent heatwaves and heavy precipitation, and high risks for human and ecological systems particularly for high GHG emissions scenarios.
{Cross-Chapter Box 1.3, 4.3, 4.4, 4.8, Box 9.4, Box 11.2, Cross-Chapter Box 12.1, TS.1.4, Box TS.3, Box TS.4} **(Table SPM.1)**

C.3.2 Low-likelihood, high-impact outcomes[34] could occur at global and regional scales even for global warming within the *very likely* range for a given GHG emissions scenario. The probability of low-likelihood, high impact outcomes increases with higher global warming levels (*high confidence*). Abrupt responses and tipping points of the climate system, such as strongly increased Antarctic ice sheet melt and forest dieback, cannot be ruled out (*high confidence*).
{1.4, 4.3, 4.4, 4.8, 5.4, 8.6, Box 9.4, Cross-Chapter Box 12.1, TS.1.4, TS.2.5, Box TS.3, Box TS.4, Box TS.9**} (Table SPM.1)**

C.3.3 If global warming increases, some compound extreme events[18] with low likelihood in past and current climate will become more frequent, and there will be a higher likelihood that events with increased intensities, durations and/or spatial extents unprecedented in the observational record will occur (*high confidence*).
{11.8, Box 11.2, Cross-Chapter Box 12.1, Box TS.3, Box TS.9}

C.3.4 The Atlantic Meridional Overturning Circulation is *very likely* to weaken over the 21st century for all emission scenarios. While there is *high confidence* in the 21st century decline, there is only *low confidence* in the magnitude of the trend. There is *medium confidence* that there will not be an abrupt collapse before 2100. If such a collapse were to occur, it would *very likely* cause abrupt shifts in regional weather patterns and water cycle, such as a southward shift in the tropical rain belt, weakening of the African and Asian monsoons and strengthening of Southern Hemisphere monsoons, and drying in Europe. {4.3, 8.6, 9.2, TS2.4, Box TS.3}

C.3.5 Unpredictable and rare natural events not related to human influence on climate may lead to low-likelihood, high impact outcomes. For example, a sequence of large explosive volcanic eruptions within decades has occurred in the past, causing substantial global and regional climate perturbations over several decades. Such events cannot be ruled out in the future, but due to their inherent unpredictability they are not included in the illustrative set of scenarios referred to in this Report. {2.2, Cross-Chapter Box 4.1, Box TS.3} **(Box SPM.1)**

D. Limiting Future Climate Change

Since AR5, estimates of remaining carbon budgets have been improved by a new methodology first presented in SR1.5, updated evidence, and the integration of results from multiple lines of evidence. A comprehensive range of possible future air pollution controls in scenarios is used to consistently assess the effects of various assumptions on projections of climate and air pollution. A novel development is the ability to ascertain when climate responses to emissions reductions would become discernible above natural climate variability, including internal variability and responses to natural drivers.

D.1 From a physical science perspective, limiting human-induced global warming to a specific level requires limiting cumulative CO_2 emissions, reaching at least net zero CO_2 emissions, along with strong reductions in other greenhouse gas emissions. Strong, rapid and sustained reductions in CH_4 emissions would also limit the warming effect resulting from declining aerosol pollution and would improve air quality.

{3.3, 4.6, 5.1, 5.2, 5.4, 5.5, 5.6, Box 5.2, Cross-Chapter Box 5.1, 6.7, 7.6, 9.6} **(Figure SPM.10, Table SPM.2)**

D.1.1 This Report reaffirms with *high confidence* the AR5 finding that there is a near-linear relationship between cumulative anthropogenic CO_2 emissions and the global warming they cause. Each 1000 $GtCO_2$ of cumulative CO_2 emissions is assessed to *likely* cause a 0.27°C to 0.63°C increase in global surface temperature with a best estimate of 0.45°C[41]. This is a narrower range compared to AR5 and SR1.5. This quantity is referred to as the transient climate response to cumulative CO_2 emissions (TCRE). This relationship implies that reaching net zero[42] anthropogenic CO_2 emissions is a requirement to stabilize human-induced global temperature increase at any level, but that limiting global temperature increase to a specific level would imply limiting cumulative CO_2 emissions to within a carbon budget[43]. {5.4, 5.5, TS.1.3, TS.3.3, Box TS.5} **(Figure SPM.10)**

[41] In the literature, units of °C per 1000 PgC are used, and the AR6 reports the TCRE *likely* range as 1.0°C to 2.3°C per 1000 PgC in the underlying report, with a best estimate of 1.65°C.

[42] condition in which anthropogenic carbon dioxide (CO_2) emissions are balanced by anthropogenic CO_2 removals over a specified period.

[43] The term carbon budget refers to the maximum amount of cumulative net global anthropogenic CO_2 emissions that would result in limiting global warming to a given level with a given probability, taking into account the effect of other anthropogenic climate forcers. This is referred to as the total carbon budget when expressed starting from the pre-industrial period, and as the remaining carbon budget when expressed from a recent specified date (see Glossary). Historical cumulative CO_2 emissions determine to a large degree warming to date, while future emissions cause future additional warming. The remaining carbon budget indicates how much CO_2 could still be emitted while keeping warming below a specific temperature level.

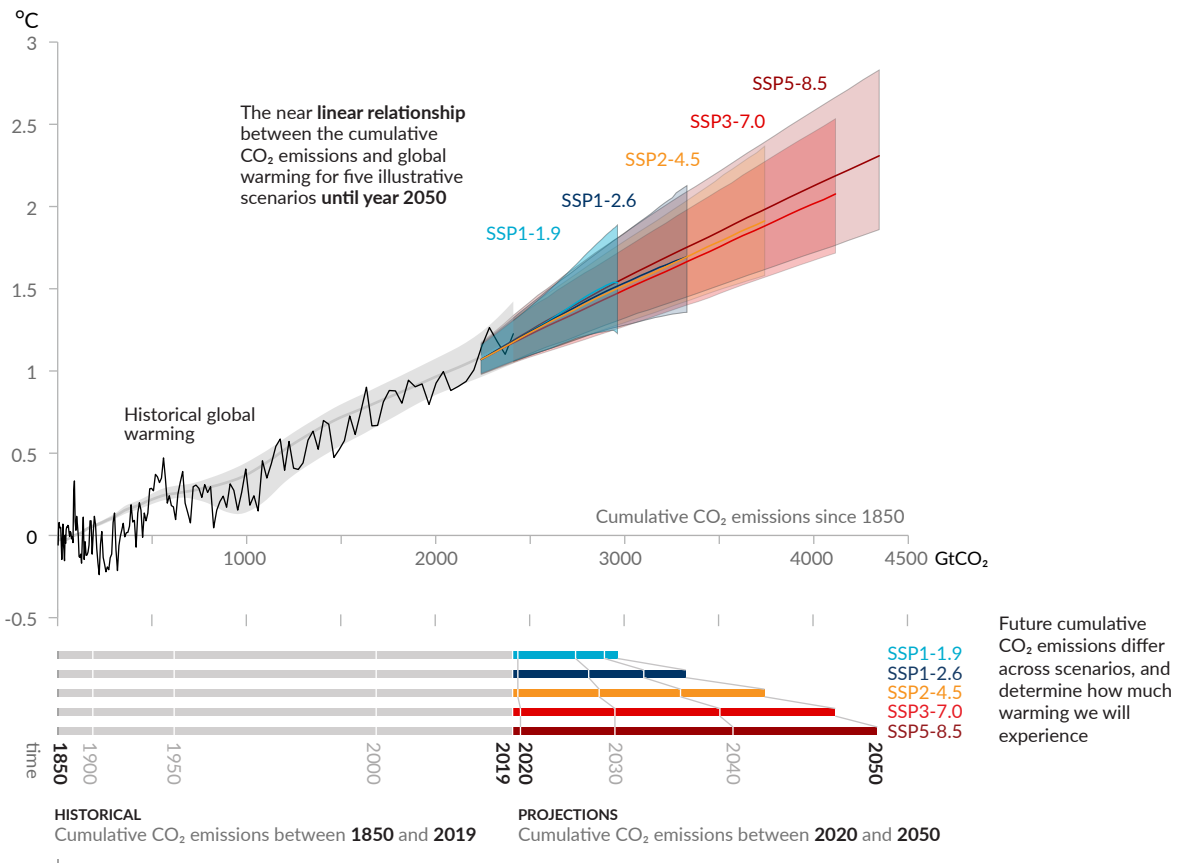


Figure SPM.10: Near-linear relationship between cumulative CO2 emissions and the increase in global surface temperature.

Top panel: Historical data (thin black line) shows observed global surface temperature increase in °C since 1850–1900 as a function of historical cumulative carbon dioxide (CO_2) emissions in $GtCO_2$ from 1850 to 2019. The grey range with its central line shows a corresponding estimate of the historical human-caused surface warming (see Figure SPM.2). Coloured areas show the assessed *very likely* range of global surface temperature projections, and thick coloured central lines show the median estimate as a function of cumulative CO_2 emissions from 2020 until year 2050 for the set of illustrative scenarios (SSP1-1.9, SSP1-2.6, SSP2-4.5, SSP3-7.0, and SSP5-8.5, see Figure SPM.4). Projections use the cumulative CO_2 emissions of each respective scenario, and the projected global warming includes the contribution from all anthropogenic forcers. The relationship is illustrated over the domain of cumulative CO_2 emissions for which there is *high confidence* that the transient climate response to cumulative CO_2 emissions (TCRE) remains constant, and for the time period from 1850 to 2050 over which global CO_2 emissions remain net positive under all illustrative scenarios as there is *limited evidence* supporting the quantitative application of TCRE to estimate temperature evolution under net negative CO_2 emissions.

Bottom panel: Historical and projected cumulative CO_2 emissions in $GtCO_2$ for the respective scenarios.

{Figure TS.18, Figure 5.31, Section 5.5}

D.1.2 Over the period 1850–2019, a total of 2390 ± 240 (*likely* range) $GtCO_2$ of anthropogenic CO_2 was emitted. Remaining carbon budgets have been estimated for several global temperature limits and various levels of probability, based on the estimated value of TCRE and its uncertainty, estimates of historical warming, variations in projected warming from non-CO_2 emissions, climate system feedbacks such as emissions from thawing permafrost, and the global surface temperature change after global anthropogenic CO_2 emissions reach net zero.
{5.1, 5.5, Box 5.2, TS.3.3} **(Table SPM.2)**

Table SPM.2: Estimates of historical CO_2 emissions and remaining carbon budgets. Estimated remaining carbon budgets are calculated from the beginning of 2020 and extend until global net zero CO_2 emissions are reached. They refer to CO_2 emissions, while accounting for the global warming effect of non-CO_2 emissions. Global warming in this table refers to human-induced global surface temperature increase, which excludes the impact of natural variability on global temperatures in individual years. {Table TS.3, Table 3.1, Table 5.1, Table 5.7, Table 5.8, 5.5.1, 5.5.2, Box 5.2}

Global warming between 1850–1900 and 2010–2019 *(°C)*	Historical cumulative CO_2 emissions from 1850 to 2019 *($GtCO_2$)*
1.07 (0.8–1.3; *likely* range)	2390 (± 240; *likely* range)

Approximate global warming relative to 1850–1900 until temperature limit *(°C)**(1)	Additional global warming relative to 2010–2019 until temperature limit *(°C)*	Estimated remaining carbon budgets from the beginning of 2020 *($GtCO_2$)* — *Likelihood of limiting global warming to temperature limit*(2)*					Variations in reductions in non-CO_2 emissions*(3)
		17%	*33%*	*50%*	*67%*	*83%*	
1.5	0.43	900	650	500	400	300	Higher or lower reductions in accompanying non-CO_2 emissions can increase or decrease the values on the left by 220 $GtCO_2$ or more
1.7	0.63	1450	1050	850	700	550	
2.0	0.93	2300	1700	1350	1150	900	

*(1) Values at each 0.1°C increment of warming are available in Tables TS.3 and 5.8.
*(2) This likelihood is based on the uncertainty in transient climate response to cumulative CO_2 emissions (TCRE) and additional Earth system feedbacks, and provides the probability that global warming will not exceed the temperature levels provided in the two left columns. Uncertainties related to historical warming (±550 $GtCO_2$) and non-CO_2 forcing and response (±220 $GtCO_2$) are partially addressed by the assessed uncertainty in TCRE, but uncertainties in recent emissions since 2015 (±20 $GtCO_2$) and the climate response after net zero CO_2 emissions are reached (±420 $GtCO_2$) are separate.
*(3) Remaining carbon budget estimates consider the warming from non-CO_2 drivers as implied by the scenarios assessed in SR1.5. The Working Group III Contribution to AR6 will assess mitigation of non-CO_2 emissions.

D.1.3 Several factors that determine estimates of the remaining carbon budget have been re-assessed, and updates to these factors since SR1.5 are small. When adjusted for emissions since previous reports, estimates of remaining carbon budgets are therefore of similar magnitude compared to SR1.5 but larger compared to AR5 due to methodological improvements[44].
{5.5, Box 5.2, TS.3.3} **(Table SPM.2)**

D.1.4 Anthropogenic CO_2 removal (CDR) has the potential to remove CO_2 from the atmosphere and durably store it in reservoirs (*high confidence*). CDR aims to compensate for residual emissions to reach net zero CO_2 or net zero GHG emissions or, if implemented at a scale where anthropogenic removals exceed anthropogenic emissions, to lower surface temperature. CDR methods can have potentially wide-ranging effects on biogeochemical cycles and climate, which can either weaken or strengthen the potential of these methods to remove CO_2 and reduce warming, and can also influence water availability and quality, food production and biodiversity[45] (*high confidence*).
{5.6, Cross-Chapter Box 5.1, TS.3.3}

D.1.5 Anthropogenic CO_2 removal (CDR) leading to global net negative emissions would lower the atmospheric CO_2 concentration and reverse surface ocean acidification (*high confidence*). Anthropogenic CO_2 removals and emissions are partially compensated by CO_2 release and uptake respectively, from or to land and ocean carbon pools (*very high confidence*). CDR would lower atmospheric CO_2 by an amount approximately equal to the increase from an anthropogenic emission of the same magnitude (*high confidence*). The atmospheric CO_2 decrease from anthropogenic CO_2 removals could be up to 10% less than the atmospheric CO_2 increase from an equal amount of CO_2 emissions, depending on the total amount of CDR (*medium confidence*). {5.3, 5.6, TS.3.3}

D.1.6 If global net negative CO_2 emissions were to be achieved and be sustained, the global CO_2-induced surface temperature increase would be gradually reversed but other climate changes would continue in their current direction for decades to millennia (*high confidence*). For instance, it would take several centuries to millennia for global mean sea level to reverse course even under large net negative CO_2 emissions (*high confidence*).
{4.6, 9.6, TS.3.3}

D.1.7 In the five illustrative scenarios, simultaneous changes in CH_4, aerosol and ozone precursor emissions, that also contribute to air pollution, lead to a net global surface warming in the near and long-term (*high confidence*). In the long term, this net warming is lower in scenarios assuming air pollution controls combined with strong and sustained CH_4 emission reductions (*high confidence*). In the low and very low GHG emissions scenarios, assumed reductions in anthropogenic aerosol emissions lead to a net warming, while reductions in CH_4 and other ozone precursor emissions lead to a net cooling. Because of the short lifetime of both CH_4 and aerosols, these climate effects partially counterbalance each other and reductions in CH_4 emissions also contribute to improved air quality by reducing global surface ozone (*high confidence*).
{6.7, Box TS.7} **(Figure SPM.2, Box SPM.1)**

[44] Compared to AR5, and when taking into account emissions since AR5, estimates in AR6 are about 300–350 $GtCO_2$ larger for the remaining carbon budget consistent with limiting warming to 1.5°C; for 2°C, the difference is about 400–500 $GtCO_2$.

[45] Potential negative and positive effects of CDR for biodiversity, water and food production are methods-specific, and are often highly dependent on local context, management, prior land use, and scale. IPCC Working Groups II and III assess the CDR potential, and ecological and socio-economic effects of CDR methods in their AR6 contributions.

D.1.8 Achieving global net zero CO_2 emissions is a requirement for stabilizing CO_2-induced global surface temperature increase, with anthropogenic CO_2 emissions balanced by anthropogenic removals of CO_2. This is different from achieving net zero GHG emissions, where metric-weighted anthropogenic GHG emissions equal metric-weighted anthropogenic GHG removals. For a given GHG emission pathway, the pathways of individual greenhouse gases determine the resulting climate response[46], whereas the choice of emissions metric[47] used to calculate aggregated emissions and removals of different GHGs affects what point in time the aggregated greenhouse gases are calculated to be net zero. Emissions pathways that reach and sustain net zero GHG emissions defined by the 100-year global warming potential are projected to result in a decline in surface temperature after an earlier peak (*high confidence*).
{4.6, 7.6, Box 7.3, TS.3.3}

D.2 Scenarios with very low or low GHG emissions (SSP1-1.9 and SSP1-2.6) lead within years to discernible effects on greenhouse gas and aerosol concentrations, and air quality, relative to high and very high GHG emissions scenarios (SSP3-7.0 or SSP5-8.5). Under these contrasting scenarios, discernible differences in trends of global surface temperature would begin to emerge from natural variability within around 20 years, and over longer time periods for many other climatic impact-drivers (*high confidence*).

{4.6, Cross-Chapter Box 6.1, 6.6, 6.7, 9.6, Cross-Chapter Box 11.1, 11.2, 11.4, 11.5, 11.6, 12.4, 12.5} **(Figure SPM.8, Figure SPM.10)**

D.2.1 Emissions reductions in 2020 associated with measures to reduce the spread of COVID-19 led to temporary but detectible effects on air pollution (*high confidence*), and an associated small, temporary increase in total radiative forcing, primarily due to reductions in cooling caused by aerosols arising from human activities (*medium confidence*). Global and regional climate responses to this temporary forcing are, however, undetectable above natural variability (*high confidence*). Atmospheric CO_2 concentrations continued to rise in 2020, with no detectable decrease in the observed CO_2 growth rate (*medium confidence*)[48].
{Cross-Chapter Box 6.1, TS.3.3}

D.2.2 Reductions in GHG emissions also lead to air quality improvements. However, in the near term[49], even in scenarios with strong reduction of GHGs, as in the low and very low GHG emission scenarios (SSP1-2.6 and SSP1-1.9), these improvements are not sufficient in many polluted regions to achieve air quality guidelines specified by the World Health Organization (*high confidence*). Scenarios with targeted reductions of air pollutant emissions lead to more rapid improvements in air quality within years compared to reductions in GHG emissions only, but from 2040, further improvements are projected in scenarios that combine efforts to reduce air pollutants as well as GHG emissions with the magnitude of the benefit varying between regions (*high confidence*). {6.6, 6.7, Box TS.7}.

[46] A general term for how the climate system responds to a radiative forcing (see Glossary).

[47] The choice of emissions metric depends on the purposes for which gases or forcing agents are being compared. This report contains updated emission metric values and assesses new approaches to aggregating gases.

[48] For other GHGs, there was insufficient literature available at the time of the assessment to assess detectable changes in their atmospheric growth rate during 2020.

[49] Near term: (2021–2040)

D.2.3 Scenarios with very low or low GHG emissions (SSP1-1.9 and SSP1-2.6) would have rapid and sustained effects to limit human-caused climate change, compared with scenarios with high or very high GHG emissions (SSP3-7.0 or SSP5-8.5), but early responses of the climate system can be masked by natural variability. For global surface temperature, differences in 20-year trends would *likely* emerge during the near term under a very low GHG emission scenario (SSP1-1.9), relative to a high or very high GHG emission scenario (SSP3-7.0 or SSP5-8.5). The response of many other climate variables would emerge from natural variability at different times later in the 21st century (*high confidence*).
{4.6, Cross-Section Box TS.1} **(Figure SPM.8, Figure SPM.10)**

D.2.4 Scenarios with very low and low GHG emissions (SSP1-1.9 and SSP1-2.6) would lead to substantially smaller changes in a range of CIDs[36] beyond 2040 than under high and very high GHG emissions scenarios (SSP3-7.0 and SSP5-8.5). By the end of the century, scenarios with very low and low GHG emissions would strongly limit the change of several CIDs, such as the increase in the frequency of extreme sea level events, heavy precipitation and pluvial flooding, and exceedance of dangerous heat thresholds, while limiting the number of regions where such exceedances occur, relative to higher GHG emissions scenarios (*high confidence*). Changes would also be smaller in very low compared to low emissions scenarios, as well as for intermediate (SSP2-4.5) compared to high or very high emissions scenarios (*high confidence*). {9.6, Cross-Chapter Box 11.1, 11.2, 11.3, 11.4, 11.5, 11.6, 11.9, 12.4, 12.5, TS.4.3}

Technical Summary

Coordinating Authors:
Paola A. Arias (Colombia), Nicolas Bellouin (United Kingdom/France), Erika Coppola (Italy), Richard G. Jones (United Kingdom), Gerhard Krinner (France/Germany, France), Jochem Marotzke (Germany), Vaishali Naik (United States of America), Matthew D. Palmer (United Kingdom), Gian-Kasper Plattner (Switzerland), Joeri Rogelj (United Kingdom /Belgium), Maisa Rojas (Chile), Jana Sillmann (Norway/Germany), Trude Storelvmo (Norway), Peter W. Thorne (Ireland/ United Kingdom), Blair Trewin (Australia)

Authors:
Krishna Achuta Rao (India), Bhupesh Adhikary (Nepal), Richard P. Allan (United Kingdom), Kyle Armour (United States of America), Govindasamy Bala (India/ United States of America), Rondrotiana Barimalala (South Africa/Madagascar), Sophie Berger (France/Belgium), Josep G. Canadell (Australia), Christophe Cassou (France), Annalisa Cherchi (Italy), William Collins (United Kingdom), William D. Collins (United States of America), Sarah L. Connors (France/ United Kingdom), Susanna Corti (Italy), Faye Cruz (Philippines), Frank J. Dentener (EU/The Netherlands), Claudine Dereczynski (Brazil), Alejandro Di Luca (Australia, Canada/Argentina), Aida Diongue Niang (Senegal), Francisco J. Doblas-Reyes (Spain), Alessandro Dosio (Italy), Hervé Douville (France), François Engelbrecht (South Africa), Veronika Eyring (Germany), Erich Fischer (Switzerland), Piers Forster (United Kingdom), Baylor Fox-Kemper (United States of America), Jan S. Fuglestvedt (Norway), John C. Fyfe (Canada), Nathan P. Gillett (Canada), Leah Goldfarb (France/ United States of America), Irina Gorodetskaya (Portugal/Russian Federation, Belgium), Jose Manuel Gutierrez (Spain), Rafiq Hamdi (Belgium), Ed Hawkins (United Kingdom), Helene T. Hewitt (United Kingdom), Pandora Hope (Australia), Akm Saiful Islam (Bangladesh), Christopher Jones (United Kingdom), Darrell S. Kaufman (United States of America), Robert E. Kopp (United States of America), Yu Kosaka (Japan), James Kossin (United States of America), Svitlana Krakovska (Ukraine), June-Yi Lee (Republic of Korea), Jian Li (China), Thorsten Mauritsen (Sweden, Denmark), Thomas K. Maycock (United States of America), Malte Meinshausen (Australia/Germany), Seung-Ki Min (Republic of Korea), Pedro M. S. Monteiro (South Africa), Thanh Ngo-Duc (Vietnam), Friederike Otto (United Kingdom /Germany), Izidine Pinto (South Africa/Mozambique), Anna Pirani (Italy/ United Kingdom, Italy), Krishnan Raghavan (India), Roshanka Ranasinghe (The Netherlands/Sri Lanka,Australia), Alex C. Ruane (United States of America), Lucas Ruiz (Argentina), Jean-Baptiste Sallée (France), Bjørn H. Samset (Norway), Shubha Sathyendranath (UK/Canada, United Kingdom, Overseas Citizen of India), Sonia I. Seneviratne (Switzerland), Anna A. Sörensson (Argentina), Sophie Szopa (France), Izuru Takayabu (Japan), Anne-Marie Treguier (France), Bart van den Hurk (The Netherlands), Robert Vautard (France), Karina von Schuckmann (France/Germany), Sönke Zaehle (Germany), Xuebin Zhang (Canada), Kirsten Zickfeld (Canada/Germany)

Contributing Authors:
Guðfinna Aðalgeirsdóttir (Iceland), Lincoln M. Alves (Brazil), Terje Berntsen (Norway), Sara M. Blichner (Norway), Lisa Bock (Germany), Gregory G. Garner (United States of America), Joelle Gergis (Australia), Sergey K. Gulev (Russian Federation), Mathias Hauser (Switzerland), Flavio Lehner (United States of America/Switzerland), Chao Li (China), Marianne T. Lund (Norway), Daniel J. Lunt (United Kingdom), Sebastian Milinski (Germany), Gemma Teresa Narisma (Philippines), Zebedee R. J. Nicholls (Australia), Dirk Notz (Germany), Sophie Nowicki (USA/France, USA), Bette Otto-Bliesner (USA), Brodie Pearson (United States of America / United Kingdom), Adam S. Phillips (United States of America), Lucas Ruiz (Argentina), Stéphane Sénési (France), Lucas Silva (Portugal/Switzerland), Aimee B. A. Slangen (The Netherlands), Thomas F. Stocker (Switzerland), Claudia Tebaldi (United States of America), Sabin Thazhe Purayil (India), Andrew Turner (United Kingdom), Steven Turnock (United Kingdom), Carolina Vera (Argentina), Cunde Xiao (China), Panmao Zhai (China)

Review Editors
Valérie Masson-Delmotte (France), Gregory M. Flato (Canada), Noureddine Yassa (Algeria)

ACCEPTED VERSION
SUBJECT TO FINAL EDITING

This Technical Summary should be cited as:
Arias, P. A., N. Bellouin, E. Coppola, R. G. Jones, G. Krinner, J. Marotzke, V. Naik, M. D. Palmer, G-K. Plattner, J. Rogelj, M. Rojas, J. Sillmann, T. Storelvmo, P. W. Thorne, B. Trewin, K. Achuta Rao, B. Adhikary, R. P. Allan, K. Armour, G. Bala, R. Barimalala, S. Berger, J. G. Canadell, C. Cassou, A. Cherchi, W. Collins, W. D. Collins, S. L. Connors, S. Corti, F. Cruz, F. J. Dentener, C. Dereczynski, A. Di Luca, A. Diongue Niang, F. J. Doblas-Reyes, A. Dosio, H. Douville, F. Engelbrecht, V. Eyring, E. Fischer, P. Forster, B. Fox-Kemper, J. S. Fuglestvedt, J. C. Fyfe, N. P. Gillett, L. Goldfarb, I. Gorodetskaya, J. M. Gutierrez, R. Hamdi, E. Hawkins, H. T. Hewitt, P. Hope, A. S. Islam, C. Jones, D. S. Kaufman, R. E. Kopp, Y. Kosaka, J. Kossin, S. Krakovska, J-Y. Lee, J. Li, T. Mauritsen, T. K. Maycock, M. Meinshausen, S-K. Min, P. M. S. Monteiro, T. Ngo-Duc, F. Otto, I. Pinto, A. Pirani, K. Raghavan, R. Ranasinghe, A. C. Ruane, L. Ruiz, J-B. Sallée, B. H. Samset, S. Sathyendranath, S. I. Seneviratne, A. A. Sörensson, S. Szopa, I. Takayabu, A-M. Treguier, B. van den Hurk, R. Vautard, K. von Schuckmann, S. Zaehle, X. Zhang, K. Zickfeld, 2021, Technical Summary. In: *Climate Change 2021: The Physical Science Basis. Contribution of Working Group I to the Sixth Assessment Report of the Intergovernmental Panel on Climate Change* [Masson-Delmotte, V., P. Zhai, A. Pirani, S. L. Connors, C. Péan, S. Berger, N. Caud, Y. Chen, L. Goldfarb, M. I. Gomis, M. Huang, K. Leitzell, E. Lonnoy, J.B.R. Matthews, T. K. Maycock, T. Waterfield, O. Yelekçi, R. Yu and B. Zhou (eds.)]. Cambridge University Press. In Press.

Date: August 2021

This document is subject to copy-editing, corrigenda and trickle backs.

ACCEPTED VERSION
SUBJECT TO FINAL EDITING

Table of Content

Introduction **4**
Box TS.1: Core Concepts Central to This Report **5**
TS.1 A Changing Climate **11**
TS.1.1 Context of a Changing Climate 11
Box TS.2: Paleoclimate **12**
TS.1.2 Progress in Climate Science 15
TS.1.2.1 Observation-based products and their assessments 15
TS.1.2.2 Climate Model Performance 16
TS.1.2.3 Understanding Climate Variability and Emerging Changes 18
TS.1.2.4 Understanding of Human Influence 20
TS.1.3 Assessing Future Climate Change 20
TS.1.3.1 Climate Change Scenarios 21
TS.1.3.2 Global Warming Levels and Cumulative CO_2 Emissions 23
TS.1.4 From Global to Regional Climate Information for Impact and Risk Assessment 25
Cross-Section Box TS.1: Global Surface Temperature Change **27**
TS.2 Large-scale Climate Change: Mean Climate, Variability and Extremes **31**
TS.2.1 Changes Across the Global Climate System 31
TS.2.2 Changes in the Drivers of the Climate System 35
TS.2.3 Upper Air Temperatures and Atmospheric Circulation 37
Box TS.3: Low-Likelihood, High-Warming Storylines **38**
TS.2.4 The Ocean 40
TS.2.5 The Cryosphere 42
Box TS.4: Sea Level **44**
Box TS.5: The Carbon Cycle **46**
TS.2.6 Land Climate, Including Biosphere and Extremes 48
Box TS.6: Water Cycle **50**
Infographic TS.1: Climate Futures **52**
TS.3 Understanding the Climate System Response and Implications for Limiting Global Warming **55**
TS.3.1 Radiative Forcing and Energy Budget 55
TS.3.2 Climate Sensitivity and Earth-System Feedbacks 57
TS.3.2.1 Equilibrium Climate Sensitivity, Transient Climate Response, and Transient Climate Response to Cumulative Carbon-dioxide Emissions 57
TS.3.2.2 Earth System Feedbacks 59
TS.3.3 Temperature Stabilization, Net Zero Emissions and Mitigation 61
TS.3.3.1 Remaining Carbon Budgets and Temperature Stabilization 61
TS.3.3.2 Carbon Dioxide Removal 64
TS.3.3.3 Relating Different Forcing Agents 66
Box TS.7: Climate and Air Quality Responses to Short-lived Climate Forcers in Shared

ACCEPTED VERSION SUBJECT TO FINAL EDITING

Socioeconomic Pathways **68**
Box TS.8: Earth System Response to Solar Radiation Modification **69**
Box TS.9: Irreversibility, Tipping Points and Abrupt Changes **71**
TS.4 Regional Climate Change **72**
TS.4.1 Generation and Communication of Regional Climate Change Information 72
TS.4.1.1 Sources and Methodologies for Generating Regional Climate Information 73
Box TS.10: Event Attribution **73**
TS.4.1.2 Regional Climate Information Distillation and Climate Services 75
Box TS.11: Climate Services **76**
Box TS.12: Multiple Lines of Evidence for Assessing Regional Climate Change and the Interactive Atlas **76**
TS.4.2 Drivers of Regional Climate Variability and Change 77
TS.4.2.1 Regional Fingerprints of Anthropogenic and Natural Forcing 78
TS.4.2.2 Modes of Variability and Regional Teleconnections 78
TS.4.2.3 Interplay Between Drivers of Climate Variability and Change at Regional Scales 81
Box TS.13: Monsoons **83**
TS.4.3 Regional Climate Change and Implications for Climate Extremes and Climatic Impact-Drivers 85
TS.4.3.1 Common Regional Changes in Climatic Impact-Drivers 87
TS.4.3.2 Region-by-Region Changes in Climatic Impact-Drivers 89
TS.4.3.2.1 Africa 90
TS.4.3.2.2 Asia 91
TS.4.3.2.3 Australasia 93
TS.4.3.2.4 Central and South America 94
TS.4.3.2.5 Europe 95
TS.4.3.2.6 North America 95
TS.4.3.2.7 Small Islands 96
TS.4.3.2.8 Polar 97
TS.4.3.2.9 Ocean 98
TS.4.3.2.10 Other Typological Domains 99
Box TS.14: Urban Areas **99**
Figures **101**

ACCEPTED VERSION
SUBJECT TO FINAL EDITING

Introduction

The Working Group I (WGI) contribution to the Intergovernmental Panel on Climate Change Sixth Assessment Report (AR6) assess the physical science basis of climate change. As part of that contribution, this Technical Summary (TS) is designed to bridge between the comprehensive assessment of the WGI Chapters and its Summary for Policymakers (SPM). It is primarily built from the Executive Summaries of the individual chapters and atlas and provides a synthesis of key findings based on multiple lines of evidence (e.g., analyses of observations, models, paleoclimate information and understanding of physical, chemical and biological processes and components of the climate system). All the findings and figures here are supported by and traceable to the underlying chapters, with relevant chapter sections indicated in curly brackets.

Throughout this Technical Summary, key assessment findings are reported using the IPCC calibrated uncertainty language (Chapter 1, Box 1.1). Two calibrated approaches are used to communicate the degree of certainty in key findings, which are based on author teams' evaluations of underlying scientific understanding:

(1) Confidence[1] is a qualitative measure of the validity of a finding, based on the type, amount, quality and consistency of evidence (e.g., data, mechanistic understanding, theory, models, expert judgment) and the degree of agreement; and
(2) Likelihood[2] provides a quantified measure of confidence in a finding expressed probabilistically (e.g., based on statistical analysis of observations or model results, or both, and expert judgement by the author team or from a formal quantitative survey of expert views, or both).

Where there is sufficient scientific confidence, findings can also be formulated as statements of fact without uncertainty qualifiers. Throughout IPCC reports, the calibrated language is clearly identified by being typeset in italics.

The context and progress in climate science (TS.1) is followed by a Cross-Section Box TS.1 on global surface temperature change. TS.2 provides information about past and future large-scale changes in all components of the climate system. TS.3 summarises knowledge and understanding of climate forcings, feedbacks and responses. Infographic TS.1 uses a storyline approach to integrate findings on possible climate futures. Finally, TS.4 provides a synthesis of climate information at regional scales.[3] The list of acronyms used in the WGI Report is in Annex VIII.

The AR6 WGI report promotes best practices in traceability and reproducibility, including through adoption of the Findable, Accessible, Interoperable, and Reusable (FAIR) principles for scientific data. Each chapter has a data table (in its Supplementary Material) documenting the input data and code used to generate its figures and tables. In addition, a collection of data and code from the report has been made freely-available online via long-term archives. ([URL to access WGI data to be added by 30 June])

ACCEPTED VERSION SUBJECT TO FINAL EDITING

[1] In this Technical Summary, the following summary terms are used to describe the available evidence: limited, medium, or robust; and for the degree of agreement: low, medium, or high. A level of confidence is expressed using five qualifiers: very low, low, medium, high, and very high, and typeset in italics, e.g., *medium confidence*. For a given evidence and agreement statement, different confidence levels can be assigned, but increasing levels of evidence and degrees of agreement are correlated with increasing confidence (see Chapter 1, Box 1.1 for more details).

[2] In this Technical Summary, the following terms have been used to indicate the assessed likelihood of an outcome or a result: *virtually certain* 99–100% probability, *very likely* 90–100%, likely 66–100%, *about as likely as not* 33–66%, *unlikely* 0–33%, *very unlikely* 0–10%, *exceptionally unlikely* 0–1%. Additional terms (extremely *likely*: 95–100%, *more likely than not* >50–100%, and *extremely unlikely* 0–5%) may also be used when appropriate. Assessed likelihood is typeset in italics, e.g., *very likely* (see Chapter 1, Box 1.1 for more details). Throughout the WGI report and unless stated otherwise, uncertainty is quantified using 90% uncertainty intervals. The 90% uncertainty interval, reported in square brackets [x to y], is estimated to have a 90% likelihood of covering the value that is being estimated. The range encompasses the median value, and there is an estimated 10% combined likelihood of the value being below the lower end of the range (x) and above its upper end (y). Often the distribution will be considered symmetric about the corresponding best estimate, but this is not always the case. In this report, an assessed 90% uncertainty interval is referred to as a '*very likely* range'. Similarly, an assessed 66% uncertainty interval is referred to as a '*likely* range'.

[3] The regional trackback matrices that provide the location of the assessment findings synthesized in TS.4 are in the Supplementary Material (SM) for Chapter 10.

These FAIR principles are central to the WGI Interactive Atlas, an online tool that complements the WGI Report by providing flexible spatial and temporal analyses of past, observed and projected climate change information. ([URL to access WGI data to be added by 30 June]).

Regarding the representation of robustness and uncertainty in maps, the method chosen for the AR6[4] differs from the method used in the Sixth Assessment Report (AR5). This choice is based on new research in the visualization of uncertainty and on user surveys.

[START BOX TS.1 HERE]

Box TS.1: Core Concepts Central to This Report

This box provides short descriptions of key concepts which are relevant to the AR6 WGI assessment, with a focus on their use in the Technical Summary and the Summary for Policymakers. The Glossary (Annex VII) includes more information on these concepts along with definitions of many other important terms and concepts used in this Report.

Characteristics of Climate Change Assessment

***Global warming*:** Global warming refers to the change of global surface temperature relative to a baseline depending upon the application. Specific global warming levels, such as 1.5°C, 2°C, 3°C or 4°C, are defined as changes in global surface temperature relative to the years 1850–1900 as the baseline (the earliest period of reliable observations with sufficient geographic coverage). They are used to assess and communicate information about global and regional changes, linking to scenarios and used as a common basis for WGII and WGIII assessments. (TS.1.3, Cross-Section Box TS.1) {1.4.1, 1.6.2, 4.6.1, Cross-Chapter Boxes 1.5, 2.3, 11.1, and 12.1, Atlas.3-Atlas.11, Glossary}

***Emergence*:** Emergence refers to the experience or appearance of novel conditions of a particular climate variable in a given region. This concept is often expressed as the ratio of the change in a climate variable relative to the amplitude of natural variations of that variable (often termed a 'signal-to-noise' ratio, with emergence occurring at a defined threshold of this ratio). Emergence can be expressed in terms of a time or a global warming level at which the novel conditions appear and can be estimated using observations or model simulations. (TS.1.2.3, TS.4.2) {1.4.2, FAQ 1.2, 7.5.5, 10.3, 10.4, 12.5.2, Cross-Chapter Box Atlas.1, Glossary}

***Cumulative carbon dioxide (CO_2) emissions*:** The total net amount of CO_2 emitted into the atmosphere as a result of human activities. Given the nearly linear relationship between cumulative CO_2 emissions and increases in global surface temperature, cumulative CO_2 emissions are relevant for understanding how past and future CO_2 emissions affect global surface temperature. A related term – remaining carbon budget – is used to describe the total net amount of CO_2 that could be released in the future by human activities while keeping global warming to a specific global warming level, such as 1.5°C, taking into account the warming contribution from non-CO_2 forcers as well. The remaining carbon budget is expressed from a recent specified date, while the total carbon budget is expressed starting from the pre-industrial period. (TS.1.3, TS.3.4) {1.6.3, 5.5, Glossary}

***Net zero CO_2 emissions*:** A condition that occurs when the amount of CO_2 emitted into the atmosphere by human activities equals the amount of CO_2 removed from the atmosphere by human activities over a specified period of time. Net negative CO_2 emissions occur when anthropogenic removals exceed anthropogenic emissions. (TS.3.3) {Box 1.4, Glossary}

[4] The AR6 figures follow either one of the following approaches. For observations, the absence of 'x' symbols shows areas with statistical significance (while the presence of 'x' indicates non-significance). For model projections, the method offers two approaches with varying complexity. In the simple approach, high agreement (≥80%) is indicated with no overlay, and diagonal lines (///) shows low agreement (<80%); In the advanced approach, areas with no overlay display robust signal (≥66% of models show change greater than the variability threshold and ≥80% of all models agree on the sign of change), reverse diagonal lines (\\\) shows no robust signal, and crossed lines show conflicting signals (i.e., significant change but low agreement). Cross-Chapter Box Atlas.1 provides more information on the AR6 method for visualizing robustness and uncertainty on maps.

ACCEPTED VERSION SUBJECT TO FINAL EDITING

Human Influence on the Climate System

***Earth's energy imbalance*:** In a stable climate, the amount of energy that the Earth receives from the Sun is approximately in balance with the amount of energy that is lost to space in the form of reflected sunlight and thermal radiation. 'Climate drivers', such as an increase in greenhouse gases or aerosols, interfere with this balance, causing the system to either gain or lose energy. The strength of a climate driver is quantified by its effective radiative forcing (ERF), measured in W m^{-2}. Positive ERF leads to warming and negative ERF leads to cooling. That warming or cooling in turn can change the energy imbalance through many positive (amplifying) or negative (dampening) climate feedbacks. (TS.2.2, TS.3.1, TS.3.2) {2.2.8, 7.2, 7.3, 7.4, Box 7.1, Box 7.2, Glossary}

***Attribution*:** Attribution is the process of evaluating the relative contributions of multiple causal factors to an observed change in climate variables (e.g., global surface temperature, global mean sea level change), or to the occurrence of extreme weather or climate-related events. Attributed causal factors include human activities (such as increases in greenhouse gas concentration and aerosols, or land-use change) or natural external drivers (solar and volcanic influences), and in some cases internal variability. (TS.1.2.4, TS.2, Box TS.10) {Cross-Working Group Box: Attribution, 3.5, 3.8, 10.4, 11.2.4, Glossary}

***Committed change, long-term commitment*:** Changes in the climate system, resulting from past, present and future human activities, which will continue long into the future (centuries to millennia) even with strong reductions in greenhouse gas emissions. Some aspects of the climate system, including the terrestrial biosphere, deep ocean and the cryosphere, respond much more slowly than surface temperatures to changes in greenhouse gas concentrations. As a result, there are already substantial committed changes associated with past greenhouse gas emissions. For example, global mean sea level will continue to rise for thousands of years, even if future CO_2 emissions are reduced to net zero and global warming halted, as excess energy due to past emissions continues to propagate into the deep ocean and as glaciers and ice sheets continue to melt. (TS.2.1, Box TS.4, Box TS.9) {1.2.1, 1.3, Box 1.2, Cross-Chapter Box 5.3}

Climate Information for Regional Climate Change and Risk Assessment

***Distillation*:** The process of synthesizing information about climate change from multiple lines of evidence obtained from a variety of sources, taking into account user context and values. It leads to an increase in the usability, usefulness, and relevance of climate information, enhances stakeholder trust, and expands the foundation of evidence used in climate services. It is particularly relevant in the context of co-producing regional-scale climate information to support decision-making. (TS.4.1, Box TS.11) {10.1, 10.5, 12.6}

***(Climate change) risk*:** The concept of risk is a key aspect of how the IPCC assesses and communicates to decision-makers about the potential for adverse consequences for human or ecological systems, recognising the diversity of values and objectives associated with such systems. In the context of climate change, risks can arise from potential impacts of climate change as well as human responses to climate change. WGI contributes to the common IPCC risk framing through the assessment of relevant climate information, including climatic impact-drivers and low-likelihood, high impact outcomes. (TS.1.4, TS.4.1, Box TS.4) {Cross-Chapter Boxes 1.3 and 12.1, Glossary}

***Climatic impact-drivers*:** Physical climate system conditions (e.g., means, events, extremes) that can be directly connected with having impacts on human or ecological systems are described as 'climatic impact-drivers' (CIDs) without anticipating whether their impacts are detrimental (i.e., as for hazards in the context of climate change risks) or provide potential opportunities. A range of indices may capture the sector- or application-relevant characteristics of a climatic impact-driver and can reflect exceedances of identified tolerance thresholds. (TS.1.4, TS.4.3) {12.1-12.3, FAQ12.1, Glossary}

***Storylines*:** The term storyline is used both in connection to scenarios (related to a future trajectory of emissions or socio-economic developments) or to describe plausible trajectories of weather and climate conditions or events, especially those related to high levels of risk. Physical climate storylines are introduced in AR6 to explore uncertainties in climate change and natural climate variability, to develop and communicate integrated

ACCEPTED VERSION SUBJECT TO FINAL EDITING

and context-relevant regional climate information, and to address issues with deep uncertainty[5], *including low-likelihood, high-impact outcomes.* (TS.1.4, Box TS.3, Infographic TS.1) {1.4.4, Box 10.2, Glossary}

***Low-likelihood, high impact outcomes*:** Events whose probability of occurrence is low or not well known (as in the context of deep uncertainty) but whose potential impacts on society and ecosystems could be high. To better inform risk assessment and decision-making, such low-likelihood outcomes are considered if they are associated with very large consequences and may therefore constitute material risks, even though those consequences do not necessarily represent the most likely outcome. (TS.1.4, Box TS.3, Figure TS.6) {1.4.4, 4.8, Cross Chapter Box 1.3, Glossary}

[END BOX TS.1 HERE]

As part of the AR6 cycle, the IPCC produced three Special Reports in 2018 and 2019: the Special Report on Global Warming of 1.5°C (SR1.5), the Special Report on Oceans and Cryosphere in a Changing Climate (SROCC), and the Special Report on Climate Change and Land (SRCCL).

The AR6 WGI Report provides a full and comprehensive assessment of the physical science basis of climate change that builds on the previous assessments and these Special Reports and consider new information and knowledge from the recent scientific literature[6], including longer observational datasets, new scenarios and model results.

The structure of the AR6 WGI report is designed to enhance the visibility of knowledge developments and to facilitate the integration of multiple lines of evidence, thereby improving confidence in findings. The Report has been peer-reviewed by the scientific community and governments (Annex X provides the Expert Reviewer list). The substantive introduction provided by Chapter 1 is followed by a first set of chapters dedicated to large-scale climate knowledge (Chapters 2–4), which encompasses observations and paleoclimate evidence, causes of observed changes, and projections, and are complemented by Chapter 11 for large-scale changes in extremes. The second set of chapters (Chapters 5–9) is orientated around the understanding of key climate system components and processes, including the global cycles of carbon, energy and water; short-lived climate forcers and their link to air quality; the ocean, cryosphere and sea level change. The last set of chapters (Chapters 10–12 and the Atlas) is dedicated to the assessment and distillation of regional climate information from multiple lines of evidence at sub-continental to local scales (including urban climate), with a focus on recent and projected regional changes in mean climate, extremes, and climatic impact-drivers. The new online Interactive Atlas allows users to interact in a flexible manner through maps, time series and summary statistics with climate information for a set of updated WGI reference regions. The Report also includes 34 Frequently Asked Questions and answers for the general public. [URL to access FAQs to be added by 30 June]

Together, this Technical Summary and the underlying chapters aim at providing a comprehensive picture of knowledge progress since the WGI AR5. Multiple lines of scientific evidence confirm that the climate is changing due to human influence. Important advances in the ability to understand past, present, and possible future changes should result in better-informed decision-making.

Some of the new results and main updates to key findings in AR6 WGI compared to AR5, SR1.5, SRCCL, and SROCC are summarized below. Relevant Technical Summary sections with further details are shown in

[5] Although not a core concept of the WGI Report, deep uncertainty is used in the Technical Summary in the following sense: 'A situation of deep uncertainty exists when experts or stakeholders do not know or cannot agree on: (1) appropriate conceptual models that describe relationships among key driving forces in a system; (2) the probability distributions used to represent uncertainty about key variables and parameters; and/or (3) how to weigh and value desirable alternative outcomes' (Lempert et al., 2003). Lempert, R. J., Popper, S. W., and Bankes, S. C. (2003). *Shaping the next one hundred years: New methods for quantitative long-term strategy analysis (MR-1626-RPC)*. Santa Monica, CA: The RAND Pardee Center.

[6] The assessment covers scientific literature accepted for publication by 31 January 2021.

ACCEPTED VERSION SUBJECT TO FINAL EDITING

parenthesis after each bullet point.

Selected Updates and/or New Results since AR5

- **Human influence[7] on the climate system is now an established fact:** The Fourth Assessment Report (AR4) stated in 2007 that 'warming of the climate system is unequivocal', and the AR5 stated in 2013 that 'human influence on the climate system is clear'. Combined evidence from across the climate system strengthens this finding. It is unequivocal that the increase of CO_2, methane (CH_4) and nitrous oxide (N_2O) in the atmosphere over the industrial era is the result of human activities and that human influence is the principal driver of many changes observed across the atmosphere, ocean, cryosphere and biosphere. (TS.1.2, TS.2.1)
- **Observed global warming to date:** A combination of improved observational records and a series of very warm years since AR5 have resulted in a substantial increase in the estimated level of global warming to date. The contribution of changes in observational understanding alone between AR5 and AR6 leads to an increase of about 0.1°C in the estimated warming since 1850–1900. For the decade 2011–2020, the increase in global surface temperature since 1850–1900 is assessed to be 1.09 [0.95 to 1.20] °C.[8] Estimates of crossing times of global warming levels and estimates of remaining carbon budgets are updated accordingly. (TS.1.2, Cross-Section Box TS.1)
- **Paleoclimate evidence:** The AR5 assessed that many of the changes observed since the 1950s are unprecedented over decades to millennia. Updated paleoclimate evidence strengthens this assessment; over the past several decades, key indicators of the climate system are increasingly at levels unseen in centuries to millennia and are changing at rates unprecedented in at least the last 2000 years. (Box TS.2, TS.2)
- **Updated assessment of recent warming:** The AR5 reported a smaller rate of increase in global mean surface temperature over the period 1998–2012 than the rate calculated since 1951**.** Based on updated observational datasets showing a larger trend over 1998–2012 than earlier estimates, there is now *high confidence* that the observed 1998–2012 global surface temperature trend is consistent with ensembles of climate model simulations, and there is now *very high confidence* that the slower rate of global surface temperature increase observed over this period was a temporary event induced by internal and naturally forced variability that partly offset the anthropogenic surface warming trend over this period, while heat uptake continued to increase in the ocean. Since 2012, strong warming has been observed, with the past five years (2016–2020) being the hottest five-year period in the instrumental record since at least 1850 (*high confidence*). (TS.1.2, Cross-Section Box TS.1)
- **Magnitude of climate system response:** In this Report, it has been possible to reduce the long-standing uncertainty ranges for metrics that quantify the response of the climate system to radiative forcing, such as the equilibrium climate sensitivity (ECS) and the transient climate response (TCR), due to substantial advances (e.g., a 50% reduction in the uncertainty range of cloud feedbacks) and improved integration of multiple lines of evidence, including paleoclimate information. Improved quantification of effective radiative forcing, the climate system radiative response, and the observed energy increase in the Earth system over the past five decades demonstrate improved consistency between independent estimates of climate drivers, the combined climate feedbacks, and the observed energy increase relative to AR5. (TS.3.2)
- **Improved constraints on projections of future climate change:** For the first time in an IPCC report, the assessed future change in global surface temperature is consistently constructed by combining scenario-based projections (which the AR5 focused on) with observational constraints based on past simulations of warming as well as the updated assessment of ECS and TCR. In addition, initialized forecasts have been used for the period 2019–2018. The inclusion of these lines of evidence reduces the assessed uncertainty for each scenario. (TS.1.3, Cross-Section Box TS.1)

[7] Human influence on the climate system refers to human-driven activities that lead to changes in the climate system due to perturbations of the Earth's energy budget (also called anthropogenic forcing). Human influence results from emissions of greenhouse gases, aerosols and tropospheric ozone precursors, ozone-depleting substances, and land-use change.

[8] Throughout the WGI report and unless stated otherwise, uncertainty is quantified using 90% uncertainty intervals. The 90% uncertainty interval, reported in square brackets [x to y], is estimated to have a 90% likelihood of covering the value that is being estimated. The range encompasses the median value and there is an estimated 10% combined likelihood of the value being below the lower end of the range (x) and above its upper end (y). Often the distribution will be considered symmetric about the corresponding best estimate, but this is not always the case. In this report, an assessed 90% uncertainty interval is referred to as a '*very likely* range'. Similarly, an assessed 66% uncertainty interval is referred to as a '*likely* range'

ACCEPTED VERSION SUBJECT TO FINAL EDITING

- **Air quality:** The AR5 assessed that projections of air quality are driven primarily by precursor emissions, including methane. New scenarios explore a diversity of future options in air pollution management. The AR6 WGI reports rapid recent shifts in the geographical distribution of some of these precursor emissions, confirms the AR5 finding, and shows higher warming effects of short-lived climate forcers in scenarios with the highest air pollution. (TS.1.3, TS.2.2, Box TS.7)
- **Effects of short-lived climate forcers on global warming:** The AR5 assessed the radiative forcing for emitted compounds. The AR6 has extended this by assessing the emission-based effective radiative forcings (ERFs) also accounting for aerosol–cloud interactions. The best estimates of ERF attributed to sulphur dioxide (SO_2) and CH_4 emissions are substantially greater than in AR5, while that of black carbon is substantially reduced. The magnitude of uncertainty in the ERF due to black carbon emissions has also been reduced relative to AR5.
- **Global water cycle:** The AR5 assessed that anthropogenic influences have *likely* affected the global water cycle since 1960. The dedicated chapter in the AR6 WGI (Chapter 8) concludes with *high confidence* that human-caused climate change has driven detectable changes in the global water cycle since the mid-20th century, with a better understanding of the response to aerosol and greenhouse gas changes. The AR6 WGI further projects with *high confidence* an increase in the variability of the water cycle in most regions of the world and under all emissions scenarios (Box TS.6)
- **Extreme events**: The AR5 assessed that human influence had been detected in changes in some climate extremes. A dedicated chapter in the AR6 (Chapter 11) concludes that it is now an established fact that human-induced greenhouse gas emissions have led to an increased frequency and/or intensity of some weather and climate extremes since 1850, in particular for temperature extremes. Evidence of observed changes and attribution to human influence has strengthened for several types of extremes since AR5, in particular for extreme precipitation, droughts, tropical cyclones and compound extremes (including fire weather). (TS.1.2, TS.2.1)

Selected Updates and/or New Results Since AR5 and SR1.5

- **Timing of crossing 1.5°C global warming:** Slightly different approaches are used in SR1.5 and in this Report. SR1.5 assessed a *likely* range of 2030 to 2052 for reaching a global warming level of 1.5°C (for a 30-year period), assuming a continued, constant rate of warming. In AR6, combining the larger estimate of global warming to date and the assessed climate response to all considered scenarios, the central estimate of crossing 1.5°C of global warming (for a 20-year period) occurs in the early 2030s, ten years earlier than the midpoint of the *likely* range assessed in the SR1.5, assuming no major volcanic eruption. (TS.1.3, Cross-Section Box TS.1)
- **Remaining carbon budgets:** The AR5 had assessed the transient climate response to cumulative emissions of CO_2 to be *likely* in the range of 0.8°C to 2.5°C per 1000 GtC (1 GtC = 1 PgC = 3.667 $GtCO_2$), and this was also used in SR1.5. The assessment in AR6, based on multiple lines of evidence, leads to a narrower *likely* range of 1.0°C–2.3°C per 1000 GtC. This has been incorporated in updated estimates of remaining carbon budgets (see TS.3.3.1), together with methodological improvements and recent observations. (TS.1.3, TS.3.3)
- **Effect of short-lived climate forcers on global warming in coming decades:** The SR1.5 stated that reductions in emissions of cooling aerosols partially offset greenhouse gas mitigation effects for two to three decades in pathways limiting global warming to 1.5°C. The AR6 assessment updates the AR5 assessment of the net cooling effect of aerosols and confirms that changes in short-lived climate forcers will *very likely* cause further warming in the next two decades across all scenarios (TS.1.3, Box TS.7)
- **COVID-19**: Temporary emission reductions in 2020 associated with COVID-19 containment led to small and positive net radiative effect (warming influence). However, global and regional climate responses to this forcing are undetectable above internal climate variability due to the temporary nature of emission reductions. (TS.3.3)

Selected Updates and/or New Results Since AR5, SRCCL and SROCC

- **Atmospheric concentration of methane:** SRCCL reported a resumption of atmospheric methane

ACCEPTED VERSION SUBJECT TO FINAL EDITING

concentration growth since 2007. WGI AR6 reports a faster growth over 2014–2019 and assesses growth since 2007 to be largely driven by emissions from the fossil fuels and agriculture (dominated by livestock) sectors. (TS.2.2)

- **Land and ocean carbon sinks:** SRCCL assessed that the persistence of the land carbon sink is uncertain due to climate change. WGI AR6 finds that land and ocean carbon sinks are projected to continue to grow until 2100 with increasing atmospheric concentrations of CO_2, but the fraction of emissions taken up by land and ocean is expected to decline as the CO_2 concentration increases, with a much larger uncertainty range for the land sink. AR5, SR1.5 and SRCCL assessed carbon dioxide removal options and scenarios. WGI AR6 finds that the carbon cycle response is asymmetric for pulse emissions or removals, which means that CO_2 emissions would be more effective at raising atmospheric CO_2 than CO_2 removals are at lowering atmospheric CO_2. (TS.3.3, Box TS.5)
- **Ocean stratification increase[9]:** Refined analyses of available observations in the AR6 lead to a reassessment of the rate of increase of the global stratification in the upper 200 m to be double that estimated in SROCC from 1970 to 2018. (TS.2.4)
- **Projected ocean oxygen loss:** Future subsurface oxygen decline in new projections assessed in WGI AR6 is substantially greater in 2080–2099 than assessed in SROCC. (TS.2.4)
- **Ice loss from glaciers and ice sheets:** since SROCC, globally resolved glacier changes have improved estimates of glacier mass loss over the past 20 years, and estimates of the Greenland and Antarctic Ice Sheet loss have been extended to 2020. (TS.2.5)
- **Observed global mean sea level change:** new observation-based estimates published since SROCC lead to an assessed sea level rise estimate from 1901 to 2018 that is now consistent with the sum of individual components and consistent with closure of the global energy budget. (Box TS.4)
- **Projected global mean sea level change:** AR6 projections of global mean sea level are based on projections from ocean thermal expansion and land ice contribution estimates, which are consistent with the assessed equilibrium climate sensitivity and assessed changes in global surface temperature. They are underpinned by new land ice model intercomparisons and consideration of processes associated with l*ow confidence* to characterise the deep uncertainty in future ice loss from Antarctica. AR6 projections based on new models and methods are broadly consistent with SROCC findings. (Box TS.4)

ACCEPTED VERSION
SUBJECT TO FINAL EDITING

[9] Increased stratification reduces the vertical exchange of heat, salinity, oxygen, carbon, and nutrients. Stratification is an important indicator for ocean circulation.

TS.1 A Changing Climate

This section introduces the assessment of the physical science basis of climate change in the AR6 and presents the climate context in which this assessment takes place, recent progress in climate science and the relevance of global and regional climate information for impact and risk assessments. The future emissions scenarios and global warming levels, used to integrate assessments across WGI AR6, are introduced and their applications for future climate projections are briefly addressed. Paleoclimate science provides a long-term context for observed climate change of the past 150 years and the projected changes in the 21st century and beyond (Box TS.2). The assessment of past, current and future global surface temperature changes relative to the standard baselines and reference periods[10] used throughout this Report is summarized in Cross-Section Box TS.1.

TS.1.1 Context of a Changing Climate

AR6 WGI assesses new scientific evidence relevant for a world whose climate system is rapidly changing, overwhelmingly due to human influence. The five IPCC assessment cycles since 1990 have comprehensively and consistently laid out the rapidly accumulating evidence of a changing climate system, with the Fourth Assessment Report (AR4) in 2007 being the first to conclude that warming of the climate system is unequivocal. Sustained changes have been documented in all major elements of the climate system: the atmosphere, land, cryosphere, biosphere and ocean (TS.2). Multiple lines of evidence indicate the recent large-scale climatic changes are unprecedented in a multi-millennial context, and that they represent a millennial-scale commitment for the slow-responding elements of the climate system, resulting in continued worldwide loss of ice, increase in ocean heat content, sea level rise and deep ocean acidification (Box TS.2; Section TS.2). {1.2.1, 1.3, Box 1.2, 2.2, 2.3, Figure 2.34, 5.1, 5.3, 9.2, 9.4-9.6, Appendix 1.A}

Earth's climate system has evolved over many millions of years, and evidence from natural archives provides a long-term perspective on observed and projected changes over the coming centuries. These reconstructions of past climate also show that atmospheric CO_2 concentrations and global surface temperature are strongly coupled (Figure TS.1), based on evidence from a variety of proxy records over multiple time scales (Box TS.2; TS.2). Levels of global warming (see Core Concepts Box) that have not been seen in millions of years could be reached by 2300, depending on the emissions pathway that is followed (TS.1.3). For example, there is *medium confidence* that, by 2300, an intermediate scenario[11] used in the report leads to global surface temperatures of 2.3°C–4.6°C higher than 1850–1900, similar to the mid-Pliocene Warm Period (2.5°C–4°C), about 3.2 million years ago, whereas the high CO_2 emissions scenario SSP5-8.5 leads to temperatures of 6.6°C–14.1°C by 2300, which overlaps with the Early Eocene Climate Optimum (10°C–18°C), about 50 million years ago. {Cross-Chapter Box 2.1 and 2.4, 2.3.1, 4.3.1.1, 4.7.1.2, 7.4.4.1}

[START FIGURE TS.1 HERE]

Figure TS.1: Changes in atmospheric CO_2 and global surface temperature (relative to 1850-1900) from the deep past to the next 300 years. *The intent is to show that CO_2 and temperature covary, both in the past and into the future, and that projected CO_2 and temperatures are similar to those only from many millions of years ago.* CO_2 concentrations from millions of years ago are reconstructed from multiple proxy records (grey dots are data from 2.2.3.1, Figure 2.3 shown with cubic-spline fit). CO_2 levels for the last 800,000 years through the mid-20th century are from air trapped in polar ice; recent values are

[10] Several baselines or reference periods are used consistently throughout AR6 WGI. Baseline refers to a period against which anomalies (i.e., differences from the average value for the baseline period) are calculated. Examples include the 1750 baseline (used for anthropogenic radiative forcings), the 1850–1900 baseline (an approximation for pre-industrial global surface temperature from which global warming levels are calculated) and the 1995–2014 baseline (used for many climate model projections). A reference period indicates a time period over which various statistics are calculated (e.g., the near-term reference period, 2021–2040). Paleo reference periods are listed in Box TS.2. {1.4.1, Cross-Chapter Box 1.2 and 2.1}

[11] Please refer to Section TS.1.3.1 for an overview of the climate change scenarios used in this report.

ACCEPTED VERSION SUBJECT TO FINAL EDITING

from direct air measurements (Figure TS.9). {1.2.1.2, 2.2.3, Figures 1.5, 2.4, 2.5} Global surface temperature prior to 1850 is estimated from marine oxygen isotopes, one of multiple sources of evidence used to assess paleo temperatures in this report. {2.3.1.1.1, Cross-Chapter Box 2.1, Figure 1} Temperature of the past 170 years is the AR6 assessed mean (Cross-Section Box TS.1). {2.3.1.1} CO_2 levels and global surface temperature change for the future are shown for three SSP scenarios (TS.1.3) through 2300 CE, using Earth System Model emulators calibrated to the assessed global surface temperatures. {4.7.1, Cross-Chapter Box 7.1} Their smooth trajectories do not account for inter-annual to inter-decadal variability, including transient response to potential volcanic eruptions. {Cross-Chapter Box 4.1} Global maps for two paleo reference periods are based on CMIP6 and pre-CMIP6 multi-model means, with site-level proxy data for comparison (squares and circles are marine and terrestrial, respectively) (Box TS.2). {Cross-Chapter Box 2.1, Figure 7.13} The map for 2020 is an estimate of the total observed warming since 1850-1900. {Figure 1.14} Global maps at right show two SSP scenarios at 2100 (2081-2100) {4.5.1} and at 2300 (2281-2300; map from CMIP6 models; temperature assessed in 4.7.1). A brief account of the major climate forcings associated with past global temperature changes is in Cross-Chapter Box 2.1.

[END FIGURE TS.1 HERE]

Understanding of the climate system's fundamental elements is robust and well established. Scientists in the 19th century identified the major natural factors influencing the climate system. They also hypothesized the potential for anthropogenic climate change due to carbon dioxide (CO_2) emitted by combustion of fossil fuels (petroleum, coal, natural gas). The principal natural drivers of climate change, including changes in incoming solar radiation, volcanic activity, orbital cycles, and changes in global biogeochemical cycles, have been studied systematically since the early 20th century. Other major anthropogenic drivers, such as atmospheric aerosols (fine solid particles or liquid droplets), land-use change and non-CO_2 greenhouse gases, were identified by the 1970s. Since systematic scientific assessments began in the 1970s, the influence of human activity on the warming of the climate system has evolved from theory to established fact (see also TS.2). The evidence for human influence on recent climate change strengthened from the IPCC First Assessment Report in 1990 to the IPCC Fifth Assessment Report in 2013/14, and is now even stronger in this assessment (TS.1.2.4, TS.2). Changes across a greater number of climate system components, including changes in regional climate and extremes can now be attributed to human influence (see TS.2 and TS.4). {1.3.1 - 1.3.5, 3.1, 11.2, 11.9}

[START BOX TS.2 HERE]

Box TS.2: Paleoclimate

Paleoclimate evidence is integrated within multiple lines of evidence across the WGI report to more fully understand the climate system. Paleo evidence extends instrument-based observations of climate variables and climate drivers back in time, providing the long-term context needed to gauge the extent to which recent and potential future changes are unusual (TS.2, Figure TS.1). Pre-industrial climate states complement evidence from climate model projections by providing real-world examples of climate characteristics for past global warming levels, with empirical evidence for how the slow-responding components of the climate system operate over centuries to millennia – the time scale for committed climate change (Core Concepts Box, Box TS.4, Box TS.9). Information about the state of the climate system during well-described paleoclimate reference periods helps narrow the uncertainty range in the overall assessment of Earth's sensitivity to climate forcing (TS.3.2.1). {Cross-Chapter Box 2.1, FAQ 1.3, FAQ 2.1}

Paleoclimate reference periods. Over the long evolution of the Earth's climate, several periods have received extensive research attention as examples of distinct climate states and rapid climate transitions (Box TS.2, Figure 1). These paleoclimate reference periods represent the present geological era (Cenozoic; past 65 million years) and are used across chapters to help structure the assessment of climate changes prior to industrialization. Cross-Chapter Box 2.1 describes the reference periods, along with a brief account of their climate forcings, and lists where each is discussed in other chapters. Cross-Chapter Box 2.4 summarizes

ACCEPTED VERSION SUBJECT TO FINAL EDITING

information on one of the reference periods, the mid-Pliocene Warm Period. The Interactive Atlas includes model output from the World Climate Research Programme Coupled Model Intercomparison Project Phase 6 (CMIP6) for four of the paleoclimate reference periods.

[START BOX TS.2, FIGURE 1 HERE]

Box TS.2, Figure 1: Paleoclimate and recent reference periods, with selected key indicators. *The intent of this figure is to list the paleoclimate reference periods used in the WGI report, to summarize three key global climate indicators, and compare CO_2 with global temperature over multiple periods*. (a) Three large-scale climate indicators (atmospheric CO_2, global surface temperature relative to 1850-1900, and global mean sea level relative to 1900), based on assessments in Chapter 2, with confidence levels ranging from *low* to *very high*. (b) Comparison between global surface temperature (relative to 1850-1900) and atmospheric CO_2 concentration for multiple reference periods (mid-points with 5–95% ranges). {2.2.3, 2.3.1.1, 2.3.3.3, Figure 2.34}

[END BOX TS.2, FIGURE 1 HERE]

Paleoclimate models and reconstructions. Climate models that target paleoclimate reference periods have been featured by the IPCC since the First Assessment Report. Under the framework of CMIP6-PMIP4 (Paleoclimate Modelling Intercomparison Project), new protocols for model intercomparisons have been developed for multiple paleoclimate reference periods. These modelling efforts have led to improved understanding of the climate response to different external forcings, including changes in Earth's orbital and plate movements, solar irradiance, volcanism, ice-sheet size, and atmospheric greenhouse gases. Likewise, quantitative reconstructions of climate variables from proxy records that are compared with paleoclimate simulations have improved as the number of study sites and variety of proxy types have expanded, and as records have been compiled into new regional and global datasets. {1.3.2, 1.5.1, Cross-Chapter Boxes 2.1 and 2.4}

Global surface temperature. Since AR5, updated climate forcings, improved models, new understanding of the strengths and weaknesses of a growing array of proxy records, better chronologies, and more robust proxy data products have led to better agreement between models and reconstructions. For global surface temperature, the mid-point of the AR6-assessed range and the median of the model-simulated temperatures differ by an average of 0.5°C across five reference periods; they overlap within their 90% ranges in four of five cases, which together span from about 6°C [5–7]°C colder during the Last Glacial Maximum to about 14 [10 to 18] °C warmer during the Early Eocene, relative to 1850–1900 (Box TS.2, Figure 2a). Changes in temperature by latitude in response to multiple forcings show that polar amplification (stronger warming at high latitudes than the global average) is a prominent feature of the climate system across multiple climate states, and the ability of models to simulate this polar amplification in past warm climates has improved since AR5 (*high confidence*). Over the past millennium, and especially since about 1300 CE, simulated global surface temperature anomalies are well within the uncertainty of reconstructions (*medium confidence*), except for some short periods immediately following large volcanic eruptions, for which different forcing datasets disagree (Box TS.2, Figure 2b). {2.3.1.1, 3.3.3.1, 3.8.2.1, 7.4.4.1.2}

[START BOX TS.2, FIGURE 2 HERE]

Box TS.2, Figure 2: Global surface temperature as estimated from proxy records (reconstructed) and climate models (simulated). *The intent of this figure is to show the agreement between observations and models of global temperatures during paleo reference periods*. (a) For individual paleoclimate reference periods. (b) For the last millennium, with instrumental temperature (AR6 assessed mean,10-year smoothed). Model uncertainties in (a) and (b) are 5-95% ranges of multi-model ensemble means; reconstructed uncertainties are 5-95% ranges (*medium confidence*) of (a) midpoints and (b) multi-method ensemble median. {2.3.1.1, Figure 2.34, Figure 3.2c, Figure 3.44}

ACCEPTED VERSION SUBJECT TO FINAL EDITING

[END BOX TS.2, FIGURE 2 HERE]

Equilibrium climate sensitivity. Paleoclimate data provide evidence to estimate equilibrium climate sensitivity (ECS[12]) (TS.3.2.1). In AR6, refinements in paleo data for paleoclimate reference periods indicate that ECS is *very likely* greater than 1.5°C and *likely* less than 4.5°C, which is largely consistent with other lines of evidence and helps narrow the uncertainty range of the overall assessment of ECS. Some of the CMIP6 climate models that have either high (> 5°C) or low (< 2°C) ECS also simulate past global surface temperature changes outside the range of proxy-based reconstructions for the coldest and warmest reference periods. Since AR5, independent lines of evidence, including proxy records from past warm periods and glacial-interglacial cycles, indicate that sensitivity to forcing increases as temperature increases (TS.3.2.2). {7.4.3.2, 7.5.3, 7.5.6, Table 7.11}

Water cycle. New hydroclimate reconstructions and model-data comparisons have improved the understanding of the causes and effects of long-term changes in atmospheric and ocean circulation, including monsoon variability and modes of variability (Box TS.13, TS.4.2). Climate models are able to reproduce decadal drought variability on large regional scales, including the severity, persistence and spatial extent of past megadroughts known from proxy records (*medium confidence*). Some long-standing discrepancies remain, however, such as the magnitude of African monsoon precipitation during the early Holocene, suggesting continuing knowledge gaps. Paleoclimate evidence shows that, in relatively high CO_2 climates such as the Pliocene, Walker circulation over the equatorial Pacific Ocean weakens, supporting the *high confidence* model projections of weakened Walker cells by the end of the 21st century. {3.3.2, 8.3.1.6, 8.4.1.6, 8.5.2.1, 9.2}

Sea level and ice sheets. Although past and future global warming differ in their forcings, evidence from paleoclimate records and modelling show that ice sheet mass and global mean sea level (GMSL) responded dynamically over multiple millennia (*high confidence*). This evidence helps to constrain estimates of the committed GMSL response to global warming (Box TS.4). For example, under a past global warming levels of around 2.5°C–4°C relative to 1850–1900, like during the mid-Pliocene Warm Period, sea level was 5–25 m higher than 1900 (*medium confidence*); under past global warming levels of 10°C–18°C, like during the Early Eocene, the planet was essentially ice free (*high confidence*). Constraints from these past warm periods, combined with physical understanding, glaciology and modelling, indicate a committed long-term GMSL rise over 10,000 years, reaching about 8–13 m for sustained peak global warming of 2°C and to 28–37 m for 5°C, which exceeds the AR5 estimate. {2.3.3.3, 9.4.1.4, 9.4.2.6, 9.6.2, 9.6.3.5}

Ocean. Since AR5, better integration of paleo-oceanographic data with modelling along with higher-resolution analyses of transient changes have improved understanding of long-term ocean processes. Low-latitude sea-surface temperatures at the Last Glacial Maximum cooled more than previously inferred, resolving some inconsistencies noted in AR5. This paleo context supports the assessment that ongoing increase in ocean heat content (OHC) represents a long-term commitment (see Core Concepts Box), essentially irreversible on human time scales (*high confidence*). Estimates of past global OHC variations generally track those of sea surface temperatures around Antarctica, underscoring the importance of Southern Ocean processes in regulating deep-ocean temperatures. Paleoclimate data, along with other evidence of glacial-interglacial changes, show that Antarctic Circumpolar flow strengthened and that ventilation of Antarctic Bottom Water accelerated during warming intervals, facilitating release of CO_2 stored in the deep ocean to the atmosphere. Paleo evidence suggests significant reduction of deep-ocean ventilation associated with meltwater input during times of peak warmth. {2.3.1.1, 2.3.3.1, 9.2.2, 9.2.3.2}

Carbon cycle. Past climate states were associated with substantial differences in the inventories of the various carbon reservoirs, including the atmosphere (TS.2.2). Since AR5, the quantification of carbon stocks has improved due to the development of novel sedimentary proxies and stable-isotope analyses of air trapped in polar ice. Terrestrial carbon storage decreased markedly during the Last Glacial Maximum by 300–600

[12] In this report, equilibrium climate sensitivity is defined as the equilibrium (steady state) change in the surface temperature following a doubling of the atmospheric carbon dioxide (CO_2) concentration from pre-industrial conditions.

ACCEPTED VERSION SUBJECT TO FINAL EDITING

PgC, possibly by 850 PgC when accounting for interactions with the lithosphere and ocean sediments, a larger reduction than previously estimated, owing to colder and drier climate. At the same time, the storage of remineralised carbon in the ocean interior increased by as much as 750–950 PgC, sufficient to balance the removal of carbon from the atmosphere (200 PgC) and terrestrial biosphere reservoirs combined (*high confidence*). {5.1.2.2}

[END BOX TS.2 HERE]

TS.1.2 Progress in Climate Science

TS.1.2.1 Observation-based products and their assessments

Observational capabilities have continued to improve and expand overall since AR5, enabling improved consistency between independent estimates of climate drivers, the combined climate feedbacks, and the observed energy and sea level increase. Satellite climate records and improved reanalyses are used as an additional line of evidence for assessing changes at the global and regional scales. However, there have also been reductions in some observational data coverage or continuity and limited access to data resulting from data policy issues. Natural archives of past climate, such as tropical glaciers, have also been subject to losses (in part due to anthropogenic climate change). {1.5.1, 1.5.2, 10.2.2}

Earth system observations are an essential driver of progress in our understanding of climate change. Overall, capabilities to observe the physical climate system have continued to improve and expand. Improvements are particularly evident in ocean observing networks and remote sensing systems. Records from several recently instigated satellite measurement techniques are now long enough to be relevant for climate assessments. For example, globally distributed, high-vertical-resolution profiles of temperature and humidity in the upper troposphere and stratosphere can be obtained from the early 2000s using global navigation satellite systems, leading to updated estimates of recent atmospheric warming. Improved measurements of ocean heat content, warming of the land surface, ice sheet mass loss, and sea level changes allow a better closure of the global energy and sea level budgets relative to AR5. For surface and balloon-based networks, apparent regional data reductions result from a combination of data policy issues, data curation/provision challenges, and real cessation of observations, and are to an extent counter-balanced by improvements elsewhere. Limited observational records of extreme events and spatial data gaps currently limit the assessment of some observed regional climate change. {1.5.1, 2.3.2, 7.2.2, Box 7.2, Cross-Chapter Box 9.1, 9.6.1, 10.2.2, 10.6, 11.2, 12.4}

New paleoclimate reconstructions from natural archives have enabled more robust reconstructions of the spatial and temporal patterns of past climate changes over multiple time scales (Box TS.2). However, paleoclimate archives, such as tropical glaciers and modern natural archives used for calibration (e.g., corals and trees), are rapidly disappearing owing to a host of pressures, including increasing temperatures (*high confidence*). Substantial quantities of past instrumental observations of weather and other climate variables, over both land and ocean, which could fill gaps in existing datasets, remain un-digitized or inaccessible. These include measurements of temperature (air and sea surface), rainfall, surface pressure, wind strength and direction, sunshine amount and many other variables dating back into the 19th century. {1.5.1}

Reanalyses combine observations and models (e.g., a numerical weather prediction model) using data assimilation techniques to provide a spatially complete, dynamically consistent estimate of multiple variables describing the evolving climate state. Since AR5, new reanalyses have been developed for the atmosphere and the ocean with various combinations of increased resolution, extended records, more consistent data assimilation and larger availability of uncertainty estimates. Limitations remain, for example, in how reanalyses represent global-scale changes to the water cycle. Regional reanalyses use high-resolution, limited-area models constrained by regional observations and with boundary conditions from global reanalyses. There is *high confidence* that regional reanalyses better represent the frequencies of extremes and variability in precipitation, surface air temperature and surface wind than global reanalyses and provide

ACCEPTED VERSION SUBJECT TO FINAL EDITING

estimates that are more consistent with independent observations than dynamical downscaling approaches. {1.5.2, 10.2.1.2, Annex I}

TS.1.2.2 Climate Model Performance

Developments in the latest generation CMIP6 climate and Earth system models, including new and better representation of physical, chemical and biological processes, as well as higher resolution, have improved the simulation of the recent mean climate of most large-scale indicators of climate change (*high confidence*, Figure TS.2) and many other aspects across the Earth system. Projections of the increase in global surface temperature, the pattern of warming, and global mean sea level rise from previous IPCC Assessment Reports and other studies are broadly consistent with subsequent observations, especially when accounting for the difference in radiative forcing scenarios used for making projections and the radiative forcings that actually occurred. While past warming is well simulated by the new generation of models, some individual models simulate past surface warming that is either below or above that observed. The information about how well models simulate past warming, as well as other insights from observations and theory, are used to assess projections of global warming. (see Cross-Section Box TS.1). Increasing horizontal resolution in global climate models improves the representation of small-scale features and the statistics of daily precipitation (*high confidence*). Earth system models, which include additional biogeochemical feedbacks, often perform as well as their lower-complexity global climate model counterparts, which do not account for these additional feedbacks (*medium confidence*). {1.3.6, 1.5.3, 3.1, 3.5.1, 3.8.2, 4.3.1, 4.3.4, 7.5, 8.5.1, 9.6.3.1}

Climate model simulations coordinated and collected as part of the World Climate Research Programme's Coupled Model Intercomparison Project Phase 6 (CMIP6), complemented by a range of results from the previous phase (CMIP5), constitute a key line of evidence supporting this Report. The latest generation of CMIP6 models have an improved representation of physical processes relative to previous generations, and a wider range of Earth system models now represent biogeochemical cycles. Higher-resolution models that better capture smaller-scale processes are also increasingly becoming available for climate change research (Figure TS.2, Panels a and b). Results from coordinated regional climate modelling initiatives, such as the Coordinated Regional Climate Downscaling Experiment (CORDEX) complement and add value to the CMIP global models, particularly in complex topography zones, coastal areas and small islands, as well as for extremes. {1.5.3, 1.5.4, 6.2.1.2, 6.3.6, 8.5.1, 10.3.3, Atlas.1.4}

Projections of the increase in global surface temperature and the pattern of warming from previous IPCC Assessment Reports and other studies are broadly consistent with subsequent observations (*limited evidence, high agreement*), especially when accounting for the difference in radiative forcing scenarios used for making projections and the radiative forcings that actually occurred. The AR5 and the SROCC projections of GMSL for the 2007–2018 period have been shown to be consistent with observed trends in GMSL and regional weighted mean tide gauges. {1.3.6, 9.6.3.1, Figure TS.3}

For most large-scale indicators of climate change, the simulated recent mean climate from CMIP6 models underpinning this assessment have improved compared to the CMIP5 models used in AR5 (*high confidence*). This is evident from the performance of 18 simulated atmospheric and land large-scale indicators of climate change between the three generations of models (CMIP3, CMIP5, and CMIP6) when benchmarked against reanalysis and observational data (Figure TS.2, Panel c). Earth system models, characterized by additional biogeochemical feedbacks, often perform at least as well as related, more constrained, lower-complexity models lacking these feedbacks (*medium confidence*). {3.8.2, 10.3.3.3}

The CMIP6 multi-model mean global surface temperature change from 1850–1900 to 2010–2019 is close to the best estimate of the observed warming. However, some CMIP6 models simulate a warming that is below or above the assessed *very likely* range. The CMIP6 models also reproduce surface temperature variations over the past millennium, including the cooling that follows periods of intense volcanism (*medium confidence*). For upper air temperature, an overestimation of the upper tropical troposphere warming by

ACCEPTED VERSION SUBJECT TO FINAL EDITING

about 0.1°C per decade between 1979 and 2014 persists in most CMIP5 and CMIP6 models (*medium confidence*), whereas the differences between simulated and improved satellite-derived estimates of change in global mean temperature through the depth of the stratosphere have decreased. {3.3.1}

Some CMIP6 models demonstrate an improvement in how clouds are represented. CMIP5 models commonly displayed a negative shortwave cloud radiative effect that was too weak in the present climate. These errors have been reduced, especially over the Southern Ocean, due to a more realistic simulation of supercooled liquid droplets with sufficient numbers and an associated increase in the cloud optical depth. Because a negative cloud optical depth feedback in response to surface warming results from 'brightening' of clouds via active phase change from ice to liquid cloud particles (increasing their shortwave cloud radiative effect), the extratropical cloud shortwave feedback in CMIP6 models tends to be less negative, leading to a better agreement with observational estimates (*medium confidence*). CMIP6 models generally represent more processes that drive aerosol–cloud interactions than the previous generation of climate models, but there is only *medium confidence* that those enhancements improve their fitness-for-purpose of simulating radiative forcing of aerosol–cloud interactions. {7.4.2, FAQ 7.2, 6.4}

CMIP6 models still have deficiencies in simulating precipitation patterns, particularly in the tropical ocean. Increasing horizontal resolution in global climate models improves the representation of small-scale features and the statistics of daily precipitation (*high confidence*). There is *high confidence* that high-resolution global, regional and hydrological models provide a better representation of land surfaces, including topography, vegetation and land-use change, which can improve the accuracy of simulations of regional changes in the terrestrial water cycle. {3.3.2, 8.5.1, 10.3.3, 11.2.3}

There is *high confidence* that climate models can reproduce the recent observed mean state and overall warming of temperature extremes globally and in most regions, although the magnitude of the trends may differ. There is *high confidence* in the ability of models to capture the large-scale spatial distribution of precipitation extremes over land. The overall performance of CMIP6 models in simulating the intensity and frequency of extreme precipitation is similar to that of CMIP5 models (*high confidence*). {Cross-Chapter Box 3.2, 11.3.3, 11.4.3}

The structure and magnitude of multi-model mean ocean temperature biases have not changed substantially between CMIP5 and CMIP6 (*medium confidence*). Since AR5, there is improved consistency between recent observed estimates and model simulations of changes in upper (<700 m) ocean heat content. The mean zonal and overturning circulations of the Southern Ocean and the mean overturning circulation of the North Atlantic (AMOC) are broadly reproduced by CMIP5 and CMIP6 models. {3.5.1, 3.5.4, 9.2.3, 9.3.2, 9.4.2}

CMIP6 models better simulate the sensitivity of Arctic sea ice area to anthropogenic CO_2 emissions, and thus better capture the time evolution of the satellite-observed Arctic sea ice loss (*high confidence*). The ability to model ice-sheet processes has improved substantially since AR5. As a consequence, we have *medium confidence* in the representation of key processes related to surface-mass balance and retreat of the grounding-line (the junction between a grounded ice sheet and an ice shelf, where the ice starts to float) in the absence of instabilities. However, there remains *low confidence* in simulations of ice-sheet instabilities, ice-shelf disintegration and basal melting owing to their high sensitivity to both uncertain oceanic forcing and uncertain boundary conditions and parameters. {1.5.3, 2.3.2, 3.4.1, 3.4.2, 3.8.2, 9.3.1, 9.3.2, 9.4.1, 9.4.2}

CMIP6 models are able to reproduce most aspects of the spatial structure and variance of the El Niño-Southern Oscillation (ENSO) and Indian Ocean Basin and Dipole modes of variability (*medium confidence*). However, despite a slight improvement in CMIP6, some underlying processes are still poorly represented. Models reproduce observed spatial features and variance of the Southern Annular Mode (SAM) and Northern Annular Modes (NAM) very well (*high confidence*). The summertime SAM trend is well captured, with CMIP6 models outperforming CMIP5 models (*medium confidence*). By contrast, the cause of the Northern Annular Mode (NAM) trend towards its positive phase is not well understood. In the Tropical Atlantic basin, which contains the Atlantic Zonal and Meridional modes, major biases in modelled mean state and variability remain. Model performance is limited in reproducing sea surface temperature anomalies for decadal modes of variability, despite improvements from CMIP5 to CMIP6 (*medium confidence*) (see

ACCEPTED VERSION SUBJECT TO FINAL EDITING

also TS.1.4.2.2, Table TS.4). {3.7.3-3.7.7}

Earth system models simulate globally averaged land carbon sinks within the range of observation-based estimates (*high confidence)*, but global-scale agreement masks large regional disagreements. There is also *high confidence* that the ESMs simulate the weakening of the global net flux of CO_2 into the ocean during the 1990s, as well as the strengthening of the flux from 2000. {3.6.1, 3.6.2}

Two important quantities used to estimate how the climate system responds to changes in GHG concentrations are the equilibrium climate sensitivity (ECS) and transient climate response (TCR[13]). The CMIP6 ensemble has broader ranges of ECS and TCR values than CMIP5 (see TS.3.2 for the assessed range). These higher sensitivity values can, in some models, be traced to changes in extratropical cloud feedbacks (*medium confidence*). To combine evidence from CMIP6 models and independent assessments of ECS and TCR, various emulators are used throughout the report. Emulators are a broad class of simple climate models or statistical methods that reproduce the behaviour of complex ESMs to represent key characteristics of the climate system, such as global surface temperature and sea level projections. The main application of emulators in AR6 is to extrapolate insights from ESMs and observational constraints to produce projections from a larger set of emissions scenarios, which is achieved due to their computational efficiency. These emulated projections are also used for scenario classification in WGIII. {Box 4.1, 4.3.4., 7.4.2, 7.5.6, CCB7.1, FAQ7.2}

[START FIGURE TS.2 HERE]

Figure TS.2: **Progress in climate models.** *The intent is to show present improvements in climate models in resolution, complexity and representation of key variables.* **(**a) Evolution of model horizontal resolution and vertical levels (based on Figure 1.19); (b) Evolution of inclusion of processes and resolution from CMIP Phase 3 (CMIP3) to CMIP6 (Annex II). (c) Centred pattern correlations between models and observations for the annual mean climatology over the period 1980–1999. Results are shown for individual CMIP3 (cyan), CMIP5 (blue) and CMIP6 (red) models (one ensemble member is used) as short lines, along with the corresponding ensemble averages (long lines). The correlations are shown between the models and the primary reference observational data set (from left to right: ERA5, GPCP-SG, CERES-EBAF, CERES-EBAF, CERES-EBAF, CERES-EBAF, JR-55, ERA5, ERA5, ERA5, ERA5, ERA5, ERA5, AIRS, ERA5, ESACCI-Soilmoisture, LAI3g, MTE). In addition, the correlation between the primary reference and additional observational data sets (from left to right: NCEP, GHCN, -, -, -, -, ERA5, HadISST, NCEP, NCEP, NCEP, NCEP, NCEP, NCEP, ERA5, NCEP, -, -, FLUXCOM) are shown (solid grey circles) if available. To ensure a fair comparison across a range of model resolutions, the pattern correlations are computed after regridding all datasets to a resolution of 4º in longitude and 5º in latitude. (Expanded from Figure 3.43; produced with ESMValTool version 2).

[END FIGURE TS.2 HERE]

TS.1.2.3 Understanding Climate Variability and Emerging Changes

Observed changes in climate are unequivocal at the global scale and are increasingly apparent on regional and local spatial scales. Both the rate of long-term change and the amplitude of year-to-year variations differ between regions and across climate variables, thus influencing when changes emerge or become apparent compared to natural variations (see Core Concepts Box). The signal of temperature change has emerged more clearly in tropical regions, where year-to-year variations tend to be small over land, than in regions with greater warming but larger year-to-year variations (*high confidence)* (Figure TS.3). Long-term changes in other variables have emerged in many regions, such as for some weather and climate extremes and Arctic sea ice area. {1.4.2, Cross-Chapter Box 3.1, 9.3.1, 11.3.2, 12.5.2}

[13] In this report, transient climate response is defined as the surface temperature response for the hypothetical scenario in which atmospheric carbon dioxide (CO_2) increases at 1% yr^{-1} from pre-industrial to the time of a doubling of atmospheric CO_2 concentration.

ACCEPTED VERSION SUBJECT TO FINAL EDITING

Observational datasets have been extended and improved since AR5, providing stronger evidence that the climate is changing and allowing better estimates of natural climate variability on decadal time scales. There is *very high confidence* that the slower rate of global surface temperature change observed over 1998–2012 compared to 1951–2012 was temporary, and was, with *high confidence*, induced by internal variability (particularly Pacific Decadal Variability) and variations in solar irradiance and volcanic forcing that partly offset the anthropogenic warming over this period. Global ocean heat content continued to increase throughout this period, indicating continuous warming of the entire climate system (*very high confidence*). Hot extremes also continued to increase during this period over land (*high confidence*). Even in a continually warming climate, periods of reduced and increased trends in global surface temperature at decadal time scales will continue to occur in the 21st century (*very high confidence*). {Cross-Chapter Box 3.1, 3.3.1, 3.5.1, 4.6.2, 11.3.2}

Since AR5, the increased use of 'large ensembles', or multiple simulations with the same climate model but using different initial conditions, supports improved understanding of the relative roles of internal variability and forced change in the climate system. Simulations and understanding of modes of climate variability, including teleconnections, have improved since AR5 (*medium confidence*), and larger ensembles allow a better quantification of uncertainty in projections due to internal climate variability. {1.4.2, 1.5.3, 1.5.4, 4.2, Box 4.1, 4.4.1, 8.5.2, 10.3.4, 10.4}

Changes in regional climate can be detected even though natural climate variations can temporarily increase or obscure anthropogenic climate change on decadal time scales. While anthropogenic forcing has contributed to multi-decadal mean precipitation changes in several regions, internal variability can delay emergence of the anthropogenic signal in long-term precipitation changes in many land regions (*high confidence*). {10.4.1, 10.4.2, 10.4.3}

Mean temperatures and heat extremes have emerged above natural variability in almost all land regions with *high confidence*. Changes in temperature-related variables, such as regional temperatures, growing season length, extreme heat and frost, have already occurred, and there is *medium confidence* that many of these changes are attributable to human activities. Several impact-relevant changes have not yet emerged from the natural variability but will emerge sooner or later in this century depending on the emissions scenario (*high confidence*). Ocean acidification and deoxygenation have already emerged over most of the global open ocean, as has a reduction in Arctic sea ice (*high confidence*). {9.3.1, 9.6.4, 11.2, 11.3, 12.4, 12.5, Atlas.3-Atlas.11}

[START FIGURE TS.3 HERE]

Figure TS.3: **Emergence of changes in temperature over the historical period.** *The intent of this figure is to show how observed changes in temperature have emerged and that the emergence pattern agrees with model simulations.* The observed change in temperature at a global warming level of 1°C (top map), and the signal-to-noise ratio (the change in temperature at a global warming level of 1°C, divided by the size of year-to-year variations, bottom map) using data from Berkeley Earth. The right panels show the zonal means of the maps and include data from different observational datasets (red) and the CMIP6 simulations (black, including the 5-95% range) processed in the same way as the observations. {1.4.2, 10.4.3}

[END FIGURE TS.3 HERE]

ACCEPTED VERSION SUBJECT TO FINAL EDITING

TS.1.2.4 Understanding of Human Influence

The evidence for human influence on recent climate change has strengthened progressively from the IPCC Second Assessment Report to the AR5 and is even stronger in this assessment, including for regional scales and for extremes. Human influence in the IPCC context refers to the human activities that lead to or contribute to a climate response, such as the human-induced emissions of greenhouse gases that subsequently alter the atmosphere's radiative properties, resulting in warming of the climate system. Other human activities influencing climate include the emission of aerosols and other short-lived climate forcers, and land-use change such as urbanisation. Progress in our understanding of human influence is gained from longer observational datasets, improved paleoclimate information, a stronger warming signal since AR5, and improvements in climate models, physical understanding and attribution techniques (see Core Concepts Box). Since AR5, the attribution to human influence has become possible across a wider range of climate variables and climatic impact-drivers (CIDs, see Core Concepts Box). New techniques and analyses drawing on several lines of evidence have provided greater confidence in attributing changes in regional weather and climate extremes to human influence (*high confidence*). {1.3, 1.5.1, Appendix 1A, 3.1-3.8, 5.2, 6.4.2, 7.3.5, 7.4.4, 8.3.1, 10.4, Cross-Chapter Box 10.3, 11.2-11.9, 12.4, TS.3}

Combining the evidence from across the climate system increases the level of confidence in the attribution of observed climate change to human influence and reduces the uncertainties associated with assessments based on single variables.

Since AR5, the accumulation of energy in the Earth system has become established as a robust measure of the rate of global climate change on interannual-to-decadal time scales. The rate of accumulation of energy is equivalent to the Earth's energy imbalance and can be quantified by changes in the global energy inventory for all components of the climate system, including global ocean heat uptake, warming of the atmosphere, warming of the land, and melting of ice. Compared to changes in global surface temperature, the Earth's energy imbalance (see Core Concepts Box) exhibits less variability, enabling more accurate identification and estimation of trends.

Identifying the human-induced components contributing to the energy budget provides an implicit estimate of the human influence on global climate change. {Cross-Working Group Box: Attribution, 3.8, 7.2.2, Box 7.2 and Cross Chapter Box 9.1, TS.2, TS.3.1}

Regional climate changes can be moderated or amplified by regional forcing from land use and land-cover changes or from aerosol concentrations and other short-lived climate forcers (SLCFs). For example, the difference in observed warming trends between cities and their surroundings can partly be attributed to urbanization (*very high confidence*). While established attribution techniques provide confidence in our assessment of human influence on large-scale climate changes (as described in TS.2), new techniques developed since AR5, including attribution of individual events, have provided greater confidence in attributing changes in climate extremes to climate change. Multiple attribution approaches support the contribution of human influence to several regional multi-decadal mean precipitation changes (*high confidence*). Understanding about past and future changes in weather and climate extremes has increased due to better observation-based datasets, physical understanding of processes, an increasing proportion of scientific literature combining different lines of evidence, and improved accessibility to different types of climate models (*high confidence*) (see TS.2, TS.4). {Cross-Working Group Box: Attribution, 1.5, 3.2, 3.5, 5.2, 6.4.3, 8.3, 9.6, 10.1, 10.2, 10.3.3, 10.4.1, 10.4.2, 10.4.3, 10.5, 10.6, Cross-Chapter Box 10.3, Box 10.3, 11.1.6, 11.2-11.9, 12.4}.

TS.1.3 Assessing Future Climate Change

Various frameworks can be used to assess future climatic changes and to synthesize knowledge across climate change assessment in WGI, WGII and WGIII. These frameworks include: (i) scenarios, (ii) global warming levels and (iii) cumulative CO_2 emissions (see Core Concepts Box). The latter two offer scenario-

ACCEPTED VERSION SUBJECT TO FINAL EDITING

and path-independent approaches to assess future projections. Additional choices, for instance with regard to common reference periods and time windows for which changes are assessed, can further help to facilitate integration across the WGI report and across the whole AR6 (see TS.1.1). {1.4.1, 1.6, Cross-Chapter Box 1.4, 4.2.2, 4.2.4, Cross-Chapter Box 11.1}

TS.1.3.1 Climate Change Scenarios

A core set of five scenarios based on the Shared Socioeconomic Pathways (SSPs) are used consistently across this report: SSP1-1.9, SSP1-2.6, SSP2-4.5, SSP3-7.0, and SSP5-8.5. These scenarios cover a broader range of greenhouse gas and air pollutant futures than assessed in earlier WGI reports, and they include high-CO_2 emissions pathways without climate change mitigation as well as new low-CO_2 emissions pathways (Figure TS.4). In these scenarios, differences in air pollution control and variations in climate change mitigation stringency strongly affect anthropogenic emission trajectories of SLCFs. Modelling studies relying on the Representative Concentration Pathways (RCPs) used in the AR5 complement the assessment based on SSP scenarios, for example at the regional scale. A comparison of simulations from CMIP5 using the RCPs with SSP-based simulations from CMIP6 shows that about half of the increase in simulated warming in CMIP6 versus CMIP5 arises because higher climate sensitivity is more prevalent in CMIP6 model versions; the other half arises from higher radiative forcing in nominally corresponding scenarios (e.g., RCP8.5 and SSP5-8.5; *medium confidence*). The feasibility or likelihood of individual scenarios is not part of this assessment, which focuses on the climate response to a large range of emissions scenarios. {1.5.4, 1.6, Cross-Chapter Box 1.4, 4.2, 4.3, 4.6, 6.6, 6.7, Cross-Chapter Box 7.1, Atlas.2.1}

Climate change projections with climate models require information about future emissions or concentrations of greenhouse gases, aerosols, ozone depleting substances, and land use over time (Figure TS.4). This information can be provided by scenarios, which are internally consistent projections of these quantities based on assumptions of how socio-economic systems could evolve over the 21st century. Emissions from natural sources, such as the ocean and the land biosphere, are usually assumed to be constant, or to evolve in response to changes in anthropogenic forcings or to projected climate change. Natural forcings, such as past changes in solar irradiance and historical volcanic eruptions, are represented in model simulations covering the historical era. Future simulations assessed in this report account for projected changes in solar irradiance and for the long-term mean background forcing from volcanoes, but not for individual volcanic eruptions. Scenarios have a long history in IPCC as a method for systematically examining possible futures and allow to follow the cause-effect chain: from anthropogenic emissions, to changes in atmospheric concentrations, to changes in the Earth' energy balance ('forcing'), to changes in global climate and ultimately regional climate and climatic impact-drivers (Figure TS.4; see TS.2; Infographic TS.1). {1.5.4, 1.6.1, 4.2.2, 4.4.4, Cross-Chapter Box 4.1, 11.1}

[START FIGURE TS.4 HERE]

Figure TS.4: **The climate change cause-effect chain:** from anthropogenic emissions, to changes in atmospheric concentration, to changes in the Earth's energy balance ('forcing'), to changes to changes in global climate and ultimately regional climate and climatic impact-drivers. Shown is the core set of five SSP scenarios as well as emission and concentration ranges for the previous RCP scenarios in year 2100; CO_2 emissions ($GtCO_2\ yr^{-1}$), panel top left; CH_4 emissions (middle) and SO_2, NO_x emissions (all in $Mt\ yr^{-1}$), top right; concentrations of atmospheric CO_2 (ppm) and CH4 (ppb), second row left and right; effective radiative forcing for both anthropogenic and natural forcings ($W\ m^{-2}$), third row; changes in global surface air temperature (°C) relative to 1850–1900, fourth row; maps of projected temperature change (°C) (left) and changes in annual-mean precipitation (%) (right) at GWL 2°C relative to 1850–1900 (see also Figure TS.5), bottom row. Carbon cycle and non-CO_2 biogeochemical feedbacks will also influence the ultimate response to anthropogenic emissions (arrows on the left). {1.6.1, Cross-Chapter Box 1.4, 4.2.2, 4.3.1, 4.6.1, 4.6.2}

[END FIGURE TS.4 HERE]

ACCEPTED VERSION SUBJECT TO FINAL EDITING

The uncertainty in climate change projections that results from assessing alternative socio-economic futures, the so-called scenario uncertainty, is explored through the use of scenario sets. Designed to span a wide range of possible future conditions, these scenarios do not intend to match how events actually unfold in the future, and they do not account for impacts of climate change on the socio-economic pathways. Besides scenario uncertainty, climate change projections are also subject to climate response uncertainty (i.e., the uncertainty related to our understanding of the key physical processes and structural uncertainties in climate models) and irreducible and intrinsic uncertainties related to internal variability. Depending on the spatial and temporal scales of the projection, and on the variable of interest, the relative importance of these different uncertainties may vary substantially. {1.4.3, 1.6, 4.2.5, Box 4.1, 8.5.1}

In this report, a core set of five scenarios is used to explore climate change over the 21st century and beyond (Section TS.2). They are labelled SSP1-1.9, SSP1-2.6, SSP2-4.5, SSP3-7.0, and SSP5-8.5[14], and span a wide range of radiative forcing levels in 2100. Scenarios in AR6 cover a broader range of emissions futures than considered in AR5, including high CO_2 emissions scenarios without climate change mitigation as well as a low CO_2 emissions scenario reaching net zero CO_2 emissions (see Core Concepts Box) around mid-century. These SSP scenarios offer unprecedented detail of input data for ESM simulations and allow for a more comprehensive assessment of climate drivers and responses, in particular because some aspects, such as the temporal evolution of pollutants, emissions or changes in land use and land cover, span a broader range in the SSP scenarios than in the RCPs used in the AR5. Modelling studies utilizing the RCPs complement the assessment based on SSP scenarios, for example, at the regional scale (Section TS.4). Scenario extensions are based on assumptions about the post-2100 evolution of emissions or of radiative forcing that is independent from the modelling of socio-economic dynamics, which does not extend beyond 2100. To explore specific dimensions, such as air pollution or temporary overshoot of a given warming level, scenario variants are used in addition to the core set. {1.6.1, Cross-Chapter Box 1.4, 4.2.2, 4.2.6, 4.7.1, Cross-Chapter Box 7.1}

SSP1-1.9 represents the low end of future emissions pathways, leading to warming below 1.5°C in 2100 and limited temperature overshoot over the course of the 21st century (see Figure TS.6). At the opposite end of the range, SSP5-8.5 represents the very high warming end of future emissions pathways from the literature. SSP3-7.0 has overall lower GHG emissions than SSP5-8.5 but, for example, CO_2 emissions still almost double by 2100 compared to today's levels. SSP2-4.5 and SSP1-2.6 represent scenarios with stronger climate change mitigation and thus lower GHG emissions. SSP1-2.6 was designed to limit warming to below 2°C. Infographic TS.1 presents a narrative depiction of SSP-related climate futures. No likelihood is attached to the scenarios assessed in this report, and the feasibility of specific scenarios in relation to current trends is best informed by the WGIII contribution to AR6. In the scenario literature, the plausibility of some scenarios with high CO_2 emissions, such as RCP8.5 or SSP5-8.5, has been debated in light of recent developments in the energy sector. However, climate projections from these scenarios can still be valuable because the concentration-levels reached in RCP8.5 or SSP5-8.5 and corresponding simulated climate futures cannot be ruled out. That is because of uncertainty in carbon-cycle feedbacks which in nominally lower emissions trajectories can result in projected concentrations that are higher than the central concentration-levels typically used to drive model projections {1.6.1; Cross-Chapter Box 1.4; 4.2.2, 5.4; SROCC; Chapter 3 in WGIII}.

The socio-economic narratives underlying SSP-based scenarios differ in their assumed level of air pollution control. Together with variations in climate change mitigation stringency, this difference strongly affects anthropogenic emission trajectories of SLCFs, some of which are also air pollutants. SSP1 and SSP5 assume strong pollution control, projecting a decline of global emissions of ozone precursors (except methane) and of aerosols and most of their precursors in the mid- to long term. The reductions due to air pollution controls are further strengthened in scenarios that assume a marked decarbonization, such as SSP1-1.9 or SSP1-2.6. SSP2-4.5 is a medium pollution-control scenario with air pollutant emissions following current trends, and SSP3-7.0 is a weak pollution-control scenario with strong increases in emissions of air pollutants over the 21st century. Methane emissions in SSP-based scenarios vary with the overall climate change mitigation

[14] Throughout this report, scenarios are referred to as SSPx-y, where "SSPx" refers to the Shared Socioeconomic Pathway or "SSP" describing the socio-economic trends underlying the scenario and "y" refers to the approximate target level of radiative forcing (in W m^{-2}) resulting from the scenario in the year 2100.

ACCEPTED VERSION SUBJECT TO FINAL EDITING

stringency, declining rapidly in SSP1-1.9 and SSP1-2.6 but declining only after 2070 in SSP5-8.5. SSP trajectories span a wider range of air pollutant emissions than considered in the RCP scenarios (see Figure TS.4), reflecting the potential for large regional differences in their assumed pollution policies. Their effects on climate and air pollution are assessed in Box TS.7. {4.4.4, 6.6.1, Figure 6.4; 6.7.1, Figure 6.19}

Since the RCPs are also labelled by the level of radiative forcing they reach in 2100, they can in principle be related to the core set of AR6 scenarios (Figure TS.4). However, the RCPs and SSP-based scenarios are not directly comparable. First, the gas-to-gas compositions differ; for example, the SSP5-8.5 scenario has higher CO_2 but lower methane concentrations compared to RCP8.5. Second, the projected 21st-century trajectories may differ, even if they result in the same radiative forcing by 2100. Third, the overall effective radiative forcing (see Core Concepts Box) may differ, and tends to be higher for the SSPs compared to RCPs that share the same nominal stratospheric-temperature-adjusted radiative forcing label. Comparing the differences between CMIP5 and CMIP6 projections (Cross-Section Box TS.1) that were driven by RCPs and SSP-based scenarios, respectively, indicates that about half of the difference in simulated warming arises because of higher climate sensitivity being more prevalent in CMIP6 model versions; the remainder arises from higher ERF in nominally corresponding scenarios (e.g., RCP8.5 and SSP5-8.5; *medium confidence*) (see TS.1.2.2). In SSP1-2.6 and SSP2-4.5, changes in effective radiative forcing also explain about half of the changes in the range of warming (*medium confidence*). For SSP5-8.5, higher climate sensitivity is the primary reason behind the upper end of the CMIP6-projected warming being higher than for RCP8.5 in CMIP5 (*medium confidence*). Note that AR6 uses multiple lines of evidence beyond CMIP6 results to assess global surface temperature under various scenarios (see Cross-Section Box TS.1 for the detailed assessment). {1.6, 4.2.2, 4.6.2.2, Cross-Chapter Box 7.1}

Earth system models can be driven by anthropogenic CO_2 emission ('emissions-driven' runs), in which case atmospheric CO_2 concentration is a projected variable; or by prescribed time-varying atmospheric concentrations ('concentration-driven' runs). In emissions-driven runs, changes in climate feed back on the carbon cycle and interactively modify the projected CO_2 concentration in each ESM, thus adding the uncertainty in the carbon cycle response to climate change to the projections. Concentration-driven simulations are based on a central estimate of carbon cycle feedbacks, while emissions-driven simulations help quantify the role of feedback uncertainty. The differences in the few ESMs for which both emission and concentration-driven runs were available for the same scenario are small and do not affect the assessment of global surface temperature projections discussed in Cross-Section Box TS.1 and Section TS.2 (*high confidence*). By the end of the 21st century, emission-driven simulations are on average around 0.1°C cooler than concentration-driven runs reflecting the generally lower CO_2 concentrations simulated by the emission driven ESMs, and a spread about 0.1°C greater reflecting the range of simulated CO_2 concentrations. However, these carbon cycle–climate feedbacks do affect the transient climate response to cumulative CO_2 emissions (TCRE[15]), and their quantification is crucial for the assessment of remaining carbon budgets consistent with global warming levels simulated by ESMs (see TS.3). {1.6.1, Cross-Chapter Box 1.4, 4.2, 4.3.1, 5.4.5, Cross-Chapter Box 7.1}

TS.1.3.2 Global Warming Levels and Cumulative CO_2 Emissions

Quantifying geographical response patterns of climate change at various global warming levels (GWLs), such as 1.5 or 2°C above the 1850–1900 period, is useful for characterizing changes in mean climate, extremes and climatic impact-drivers. GWLs are used in this report as a dimension of integration independent of the timing when the warming level is reached and of the emissions scenario that led to the warming. For many climate variables the response pattern for a given GWL is consistent across different scenarios. However, this is not the case for slowly responding processes, such as ice sheet and glacier mass loss, deep ocean warming, and the related sea level rise. The response of these variables depends on the time it takes to reach the GWL, differs if the warming is reached in a transient warming state or after a temporary overshoot of the warming level, and will continue to evolve, over centuries to millennia, even after global warming has stabilized. Different GWLs correspond closely to specific cumulative CO_2 emissions due to

[15] The transient surface temperature change per unit of cumulative CO_2 emissions, usually 1000 GtC;

ACCEPTED VERSION SUBJECT TO FINAL EDITING

their near-linear relationship with global surface temperature. This report uses 1.0°C, 1.5°C, 2.0°C, 3.0°C, and 4.0°C above 1850–1900 conditions as a primary set of GWLs. {1.6.2, 4.2.4, 4.6.1, 5.5, Cross-Chapter Box 11.1, Cross-chapter Box 12.1}

For many indicators of climate change, such as seasonal and annual mean and extreme surface air temperatures and precipitation, the geographical patterns of changes are well estimated by the level of global surface warming, independently of the details of the emission pathways that caused the warming, or the time at which the level of warming is attained. GWLs, defined as a global surface temperature increase of, for example, 1.5°C or 2°C relative to the mean of 1850–1900, are therefore a useful way to integrate climate information independently of specific scenarios or time periods. {1.6.2, 4.2.4, 4.6.1, 11.2.4, Cross-Chapter Box 11.1}

The use of GWLs allows disentangling the contribution of changes in global warming from regional aspects of the climate response, as scenario differences in response patterns at a given GWL are often smaller than model uncertainty and internal variability. The relationship between the GWL and response patterns is often linear, but integration of information can also be done for non-linear changes, like the frequency of heat extremes. The requirement is that the relationship to the GWL is broadly independent of the scenario and relative contribution of radiative forcing agents. {1.6, 11.2.4, Cross-Chapter Box 11.1}

The GWL approach to integration of climate information also has some limitations. Variables that are quick to respond to warming, like temperature and precipitation, including extremes, sea ice area, permafrost and snow cover, show little scenario dependence for a given GWL, whereas slow-responding variables such as glacier and ice sheet mass, warming of the deep ocean and their contributions to sea level rise, have substantial dependency on the trajectory of warming taken to reach the GWL. A given GWL can also be reached for different balances between anthropogenic forcing agents, such as long-lived greenhouse gas and SLCF emissions, and the response patterns may depend on this balance. Finally, there is a difference in the response even for temperature-related variables if a GWL is reached in a rapidly warming transient state or in an equilibrium state when the land–sea warming contrast is less pronounced. In this Report the climate responses at different GWLs are calculated based on climate model projections for the 21st century (see Figure TS.5), which are mostly not in equilibrium. The SSP1-1.9 scenario allows assessing the response to a GWL of about 1.5°C after a (relatively) short-term stabilization by the end of the 21st century. {4.6.2, 9.3.1.1, 9.5.2.3, 9.5.3.3, 11.2.4, Cross-Chapter Box 11.1, Cross-chapter Box 12.1}

Global warming levels are highly relevant as a dimension of integration across scientific disciplines and socio-economic actors and are motivated by the long-term goal in the Paris Agreement of ‘holding the increase in the global average temperature to well below 2°C above pre-industrial levels and to pursue efforts to limit the temperature increase to 1.5°C above pre-industrial levels’. The evolution of aggregated impacts with temperature levels has also been widely used and embedded in the WGII assessment. This includes the ‘Reasons for Concern’ (RFC) and other ‘burning ember’ diagrams in IPCC WGII. The RFC framework has been further expanded in the SR1.5, the SROCC and SRCCL by explicitly looking at the differential impacts between half-degree GWLs and the evolution of risk for different socio-economic assumptions. {1.4.4, 1.6.2, 11.2.4, 12.5.2, Cross-chapter Box 11.1, Cross-Chapter Box 12.1}

SR1.5 concluded, ‘climate models project robust differences in regional climate characteristics between present-day and global warming of 1.5°C, and between 1.5°C and 2°C’. This report adopts a set of common GWLs across which climate projections, impacts, adaptation challenges and climate change mitigation challenges can be integrated, within and across the three WGs, relative to 1850–1900. The core set of GWLs in this Report are 1.0°C (close to present day conditions), 1.5°C, 2.0°C, 3.0°C, and 4.0°C. {1.4, 1.6.2, Cross-Chapter Box 1.2, Table 1.5, Cross-chapter Box 11.1}

Connecting Scenarios and Global Warming Levels

In this report, scenario-based climate projections are translated into GWLs by aggregating the ESM model response at specific GWL across scenarios (see Figure TS.5 and Figure TS.6). The climate response pattern for the 20-year period around when individual simulations reach a given GWL are averaged across all

ACCEPTED VERSION SUBJECT TO FINAL EDITING

models and scenarios that reach that GWL. The best estimate and *likely* range of the timing of when a certain GWL is reached under a particular scenario (or 'GWL-crossing time'), however, is based not only on CMIP6 output, but on a combined assessment taking into account the observed warming to date, CMIP6 output and additional lines of evidence (see Cross-Section Box TS.1). {4.3.4, Cross-Chapter Box 11.1, Atlas.2, Interactive Atlas}

[START FIGURE TS.5 HERE]

Figure TS.5: How scenarios are linked to global warming levels (GWLs), and examples of the evolution of patterns of change with global warming levels. Left: Illustrative example of GWLs defined as global surface temperature response to anthropogenic emissions in unconstrained CMIP6 simulations, for two illustrative scenarios (SSP1-2.6 and SSP3-7.0). The time when a given simulation reaches a GWL, e.g., +2°C, relative to 1850-1900 is taken as the time when the central year of a 20-year running mean first reaches that level of warming. See the dots for +2°C, and how not all simulations reach all levels of warming. The assessment of the timing when a GWL is reached takes into account additional lines of evidence and is discussed in Cross-Section Box TS.1. Right: Multi-model, multi-simulation average response patterns of change in near-surface air temperature, precipitation (expressed as percentage change) and soil moisture (expressed in standard deviations of interannual variability), for three GWLs. The number to the top right of the panels shows the number of model simulations averaged across including all models that reach the corresponding GWL in any of the 5 SSPs. See TS.2 for discussion. (See also Cross-Chapter Box 11.1)

[END FIGURE TS.5 HERE]

Global warming levels are closely related to cumulative CO_2 (and in some cases CO_2-equivalent) emissions. This report confirms the assessment of the WGI AR5 and SR1.5 that a near-linear relationship exists between cumulative CO_2 emissions and the resulting increase in global surface temperature (Section TS.3.2). This implies that continued CO_2 emissions will cause further warming and associated changes in all components of the climate system. For declining cumulative CO_2 emissions (i.e., if negative net emissions are achieved), the relationship is less strong for some components, such as the hydrological cycle. The WGI report uses cumulative CO_2 emissions to compare climate response across scenarios and provides a link to the emission pathways assessment in WGIII. The advantage of using cumulative CO_2 emissions is that it is an inherent emissions scenario characteristic rather than an outcome of the scenario-based projections, where uncertainties in the cause–effect chain from emissions to temperature change are important (Figure TS.4), for example, the uncertainty in effective radiative forcing (ERF) and transient climate response (TCR). Cumulative CO_2 emissions can also provide a link to the assessments of mitigation options. Cumulative CO_2 emissions do not carry information about non-CO_2 emissions, although these can be included with specific emission metrics to estimate CO_2-equivalent emissions. (TS.3.3) {1.3.2, 1.6, 4.6.2, 5.5, 7.6, 8.4.3}

TS.1.4 From Global to Regional Climate Information for Impact and Risk Assessment

The WGI AR6 has an expanded focus on regional information supported by the increased availability of coordinated regional climate model ensemble projections and improvements in the sophistication and resolution of global and regional climate models (*high confidence*). Multiple lines of evidence can be used to construct climate information on a global to regional scale and can be further distilled in a co-production process to meet user needs (*high confidence*). To better support risk assessment, a common risk framework across all three Working Groups has been implemented in AR6, and low-likelihood but high-impact outcomes are explicitly addressed in WGI by using physical climate storylines (see Core Concepts Box). Climatic impact-drivers are physical climate system conditions (e.g., means, events, extremes) that affect an element of society or ecosystems. They are the WGI contribution to the risk framing without anticipating whether their impact provides potential opportunities or is detrimental (i.e., as for hazards). Many global and regional climatic impact-drivers have a direct relation to global warming levels (*high confidence*). {1.4.4, 1.5.2-1.5.4, 4.8, 10.1, 10.5.1, **11.2.4, 11.9,** 12.1-12.3, 12.6, Atlas.1.3.3-1.3.4, Atlas.1.4, Atlas.1.4.4, Boxes

ACCEPTED VERSION SUBJECT TO FINAL EDITING

10.2 and 11.2, Cross-Chapter Boxes 1.3, 10.3, 11.1, 12.1 and 12.2}

Climate change is a global phenomenon, but manifests differently in different regions. The impacts of climate change are generally experienced at local, national and regional scales, and these are also the scales at which decisions are typically made. Robust climate change information is increasingly available at regional scales for impact and risk assessments. Depending on the climate information context, geographical regions in AR6 may refer to larger areas, such as sub-continents and oceanic regions, or to typological regions, such as monsoon regions, coastlines, mountain ranges or cities, as used in TS.4. A new set of standard AR6 WGI reference regions has also been included in this report (Fig. TS.6 bottom panels). {1.4.5, 10.1, 11.9, 12.1-12.4, Atlas.1.3.3-1.3.4}

Global and regional climate models are important sources of climate information at the regional scale. Since AR5, a more comprehensive assessment of past and future evolution of a range of climate variables on a regional scale has been enabled by the increased availability of coordinated ensemble regional climate model projections and improvements in the level of sophistication and resolution of global and regional climate models. This has been complemented by observational, attribution and sectoral-vulnerability studies informing, for instance, about impact-relevant tolerance thresholds. {10.3.3, 11.9, 12.1, 12.3, 12.6, Atlas.3-Atlas.11, Interactive Atlas}

Multiple lines of evidence derived from observations, model simulations and other approaches can be used to construct climate information on a regional scale as described in detail in TS.4.1.1 and TS.4.1.2. Depending on the phenomena and specific context, these sources and methodologies include theoretical understanding of the relevant processes, drivers and feedbacks of climate at regional scale, trends in observed data from multiple datasets, and the attribution of these trends to specific drivers. Furthermore, simulations from different model types (including global and regional climate models, emulators, statistical downscaling methods, etc.) and experiments (e.g., CMIP, CORDEX, and large ensembles of single-model simulations with different initial conditions), attribution methodologies as well as other relevant local knowledge (e.g., indigenous knowledge) are utilized. (see Box TS.11). {1.5.3,1.5.4, Cross-Chapter Box 7.1, 10.2,10.3-10.6, 11.2, Atlas.1.4, Cross-Chapter Box 10.3}

From the multiple lines of evidence, climate information can be distilled in a co-production process that involves users, related stakeholders and producers of climate information, considering the specific context of the question at stake, the underlying values, and the challenge of communicating across different communities. The co-production process is an essential part of climate services, which are discussed in TS.4.1.2. {10.5, 12.6, Cross-Chapter Box 12.2}

[START FIGURE TS.6 HERE]

Figure TS.6: **A graphical abstract for key aspects of the Technical Summary related to observed and projected changes in global surface temperature and associated regional changes in climatic impact-drivers relevant for impact and risk assessment.** Top left: a schematic representation of the likelihood for equilibrium climate sensitivity (ECS), consistent with the AR6 assessment (see Chapter 7; TS.3). ECS values above 5°C and below 2°C are termed low-likelihood high warming (LLHW) and low-likelihood low warming, respectively. Top right: Observed (see Cross-Section Box TS.1) and projected global surface temperature changes, shown as global warming levels (GWL) relative to 1850-1900, using the assessed 95% (top), 50% (middle) and 5% (bottom) likelihood time series (see Chapter 4; TS.2). Bottom panels show maps of CMIP6 median projections of two climatic impact-drivers (CIDs) at three different GWLs (columns for 1.5, 2 and 4°C) for the AR6 land regions (see Chapters 1, 10, Atlas; TS.4). The heat warning index is the number of days per year averaged across each region at which a heat warning for human health at level 'danger' would be issued according to the U.S. National Oceanic and Atmospheric Administration (NOAA) (NOAA HI41, see Chapter 12 and Technical Annex VI). The maps of extreme rainfall changes show the percentage change in the amount of rain falling on the wettest day of a year (Rx1day, relative to 1995-2014, see Chapter 11) averaged across each region when the respective GWL is reached. Additional CIDs are discussed in TS.4.

ACCEPTED VERSION SUBJECT TO FINAL EDITING

[END FIGURE TS.6 HERE]

With the aim of informing decision-making at local or regional scales, a common risk framework has been implemented in AR6. Methodologies have been developed to construct more impact- and risk-relevant climate change information tailored to regions and stakeholders. Physical storyline approaches are used in order to build climate information based on multiple lines of evidence, and which can explicitly address physically plausible, but low-likelihood, high-impact outcomes and uncertainties related to climate variability for consideration in risk assessments (see Figure TS.6). {4.8, 12.1-12.3, 12.6, Box 9.4, 10.5, Box 10.2, Box 11.2, Cross-Chapter Box 1.3, Glossary}

The climatic impact-driver framework developed in AR6 supports an assessment of changing climate conditions that are relevant for sectoral impacts and risk assessment. Climatic impact-drivers (CIDs) are physical climate system conditions (e.g., means, extremes, events) that affect an element of society or ecosystems and are thus a potential priority for providing climate information. For instance, the heat index used by the U.S. National Oceanic and Atmospheric Administration (NOAA HI) for issuing heat warnings is a CID index that can be associated with adverse human health impacts due to heat stress (see Figure TS.6). Depending on system tolerance, CIDs and their changes can be detrimental (i.e., hazards in the risk framing), beneficial, neutral, or a mixture of each across interacting system elements, regions and sectors (aligning with WGII Sectoral Chapters 2–8). Each sector is affected by multiple CIDs, and each CID affects multiple sectors. Climate change has already altered CID profiles and resulted in shifting magnitude, frequency, duration, seasonality and spatial extent of associated indices (*high confidence*) (see regional details in TS.4.3). {12.1-12.4, Table 12.1, Table 12.2, Technical Annex VI}

Many global- and regional-scale CIDs, including extremes, have a direct relation to global warming levels (GWLs) and can thus inform the hazard component of 'Representative Key Risks' and 'Reasons for Concern' assessed by AR6 WGII. These include heat, cold, wet and dry hazards, both mean and extremes; cryospheric hazards (snow cover, ice extent, permafrost) and oceanic hazards (marine heatwaves) (*high confidence*) (Figure TS.6). Establishing links between specific GWLs with tipping points and irreversible behaviour is challenging due to model uncertainties and lack of observations, but their occurrence cannot be excluded, and their likelihood of occurrence generally increases at greater warming levels (Box TS.1, TS.9). {11.2.4, Box 11.2, Cross-Chapter Boxes 11.1 and 12.1}

[START CROSS-SECTION BOX TS.1 HERE]

Cross-Section Box TS.1: Global Surface Temperature Change

This box synthesizes the outcomes of the assessment of past, current and future global surface temperature. Global mean surface temperature (GMST) and global surface air temperature (GSAT) are the two primary metrics of global surface temperature used to estimate global warming in IPCC reports. GMST merges sea surface temperatures (SSTs) over the ocean and 2 m air temperature over land and sea ice areas and is used in most paleo, historical and present-day observational estimates. The GSAT metric is 2 m air temperature over all surfaces and is the diagnostic generally used from climate models. Changes in GMST and GSAT over time differ by at most 10% in either direction (*high confidence*), but conflicting lines of evidence from models and direct observations, combined with limitations in theoretical understanding, lead to *low confidence* in the sign of any difference in long-term trend. Therefore, long-term changes in GMST/GSAT are presently assessed to be identical, with expanded uncertainty in GSAT estimates. Hence the term global surface temperature is used in reference to both quantities in the text of the TS and SPM. {Cross-Chapter Box 2.3}

Global surface temperature has increased by 1.09 [0.95 to 1.20] °C from 1850–1900 to 2011–2020, and the last decade was *more likely than not* warmer than any multi-centennial period after the Last Interglacial, roughly 125,000 years ago. The *likely* range of human-induced warming in global surface temperature in 2010–2019 relative to 1850–1900 is 1.07 [0.8 to 1.3] °C, encompassing the observed warming, while the

ACCEPTED VERSION SUBJECT TO FINAL EDITING

change attributable to natural forcing is only –0.1°C to +0.1°C. Compared to 1850–1900, average global surface temperature over the period 2081–2100 is *very likely* to be higher by 1.0°C–1.8°C in the low CO_2 emissions scenario SSP1-1.9 and by 3.3°C–5.7°C in the high CO_2 emissions scenario SSP5-8.5. In all scenarios assessed here except SSP5-8.5, the central estimate of 20-year averaged global surface warming crossing the 1.5°C level lies in the early 2030s, which is about ten years earlier than the midpoint of the *likely* range (2030–2052) assessed in the SR1.5. It is *more likely than not* that under SSP1-1.9, global surface temperature relative to 1850–1900 will remain below 1.6°C throughout the 21st century, implying a potential temporary overshoot of 1.5°C global warming of no more than 0.1°C. Global surface temperature in any individual year, could exceed 1.5°C relative to 1850–1900 by 2030 with a likelihood between 40% and 60% across the scenarios considered here (*medium confidence*). A 2°C increase in global surface temperature relative to 1850–1900 will be crossed under SSP5-8.5 but is *extremely unlikely* to be crossed under SSP1-1.9. Periods of reduced and increased GSAT trends at decadal time scales will continue to occur in the 21st century (*very high confidence*). The effect of strong mitigation on 20-year global surface temperature trends would be *likely* to emerge during the near term (2021–2040), assuming no major volcanic eruptions occur. (Figure TS.8; Cross-Section Box TS.1, Figure 1), {2.3, 3.3, 4.3, 4.4, 4.6, 7.3}.

Surface Temperature History

Dataset innovations, particularly more comprehensive representation of polar regions, and the availability of new datasets have led to an assessment of increased global surface temperature change relative to the directly equivalent estimates reported in AR5. The contribution of changes in observational understanding alone between AR5 and AR6 in assessing temperature changes from 1850–1900 to 1986–2005 is estimated at 0.08 [–0.01 to 0.12] °C. From 1850–1900 to 1995–2014, global surface temperature increased by 0.85 [0.69 to 0.95] °C, and to the most recent decade (2011–2020) by 1.09 [0.95 to 1.20] °C. Each of the last four decades has in turn been warmer than any decade that preceded it since 1850. Temperatures have increased faster over land than over the ocean since 1850–1900, with warming to 2011–2020 of 1.59 [1.34 to 1.83] °C over land and 0.88 [0.68 to 1.01] °C over the ocean. {2.3.1, Cross-Chapter Box 2.3}

Global surface temperature during the period 1850–1900 is used as an approximation for pre-industrial conditions for consistency with AR5 and AR6 Special Reports, whilst recognizing that radiative forcings have a baseline of 1750 for the start of anthropogenic influences. It is *likely* that there was a net anthropogenic forcing of 0.0–0.3 Wm^{-2} in 1850–1900 relative to 1750 (*medium confidence*), and from the period around 1750 to 1850–1900 there was a change in global surface temperature of around 0.1°C (*likely* range –0.1 to +0.3°C, *medium confidence*), with an anthropogenic component of 0.0°C–0.2°C (*likely* range, *medium confidence*). {Cross-Chapter Box 1.2, 7.3.5}.

Global surface temperature has evolved over geological time (Figure TS.1, Box TS.2). Beginning approximately 6500 years ago, global surface temperature generally decreased, culminating in the coldest multi-century interval of the post-glacial period (since roughly 7000 years ago), which occurred between around 1450 and 1850 (*high confidence*). Over the last 50 years, global surface temperature has increased at an observed rate unprecedented in at least the last two thousand years (*medium confidence*), and it is *more likely than not* that no multi-centennial period after the Last Interglacial (roughly 125,000 years ago) was warmer globally than the most recent decade (Cross-Section Box TS.1, Figure 1). During the mid-Pliocene Warm Period, around 3.3–3.0 million years ago, global surface temperature was 2.5°C–4°C warmer, and during the Last Interglacial, it was 0.5°C–1.5°C warmer than 1850–1900 (*medium confidence*). {2.3.1, Cross-Chapter Box 2.1 and 2.4}

[START CROSS-SECTION BOX TS.1, FIGURE 1 HERE]

Cross-Section Box TS.1, Figure 1: Earth's surface temperature history and future with key findings annotated within each panel. *The intent of this figure is to show global surface temperature observed changes from the Holocene to now, and projected changes.* (a) Global surface temperature over the Holocene divided into three time scales. (i) 12,000 to 1000 years ago (10,000 BCE to 1000 CE) in 100-year time steps, (ii) 1000 to 1900

ACCEPTED VERSION SUBJECT TO FINAL EDITING

CE, 10-year smooth, and (iii) 1900 to 2020 CE (mean of four datasets in panel (c)). Median of the multi-method reconstruction (bold lines), with 5% and 95% percentiles of the ensemble members (thin lines). Vertical bars are 5th to 95th percentile ranges of estimated global surface temperature for the Last Interglacial and mid Holocene (*medium confidence*) (Section 2.3.1.1). All temperatures relative to 1850–1900. (b) Spatially resolved trends (°C per decade) for (upper map) HadCRUTv5 over 1981–2020, and (lower map, total change) multi-model mean projected changes from 1995–2014 to 2081–2010 in the SST3-7.0 scenario. Observed trends have been calculated where data are present in both the first and last decade and for at least 70% of all years within the period using OLS. Significance is assessed with AR(1) correction and denoted by stippling. Hatched areas in the lower map show areas of conflicting model evidence on significance of changes. (c) Temperature from instrumental data for 1850–2020, including annually resolved averages for the four global surface temperature datasets assessed in Section 2.3.1.1.3 (see text for references). The grey shading shows the uncertainty associated with the HadCRUTv5 estimate. All temperatures relative to the 1850–1900 reference period. (d) Recent past and 2015–2050 evolution of annual mean global surface temperature change relative to 1850–1900, from HadCRUTv5 (black), CMIP6 historical simulations (up to 2014, in grey, ensemble mean solid, 5% and 95% percentiles dashed, individual models thin), and CMIP6 projections under scenario SSP2-4.5, from four models that have an equilibrium climate sensitivity near the assessed central value (thick yellow). Solid thin coloured lines show the assessed central estimate of 20-year change in global surface temperature for 2015–2050 under three scenarios, and dashed thin coloured lines the corresponding 5% and 95% quantiles. (e) Assessed projected change in 20-year running mean global surface temperature for five scenarios (central estimate solid, *very likely* range shaded for SSP1-2.6 and SSP3-7.0), relative to 1995–2014 (left y-axis) and 1850–1900 (right y-axis). The y-axis on the right-hand side is shifted upward by 0.85°C, the central estimate of the observed warming for 1995–2014, relative to 1850–1900. The right y-axis in (e) is the same as the y-axis in (d).

[END CROSS-SECTION BOX TS.1, FIGURE 1 HERE]

Current Warming

There is *very high confidence* that the CMIP6 model ensemble reproduces observed global surface temperature trends and variability since 1850 with errors small enough for detection and attribution of human-induced warming. The CMIP6 multi-model mean global surface warming between 1850–1900 and 2010–2019 is close to the best estimate of observed warming, though some CMIP6 models simulate a warming that is outside the assessed *very likely* observed range. {3.3.1}

The *likely* range of human-induced change in global surface temperature in 2010–2019[16] relative to 1850–1900 is 1.07 [0.8 to 1.3] °C (Figure Cross-Section Box TS.1, Figure 1), encompassing the observed warming for that period of 1.06 [0.88 to 1.21] °C, while change attributable to natural forcing is only –0.1 to +0.1°C. This assessment is consistent with an estimate of the human-induced global surface temperature rise based on assessed ranges of perturbations to the top of the atmosphere (effective radiative forcing), and metrics of feedbacks of the climate response (equilibrium climate sensitivity and the transient climate response). Over the same period, well-mixed greenhouse gas forcing *likely* warmed global surface temperature by 1.0°C to 2.0°C, while aerosols and other anthropogenic forcings *likely* cooled global surface temperature by 0.0°C to 0.8°C. {2.3.1, 3.3.1, 7.3.5, Cross-Chapter Box 7.1}

The observed slower global surface temperature increase (relative to preceding and following periods) in the 1998–2012 period, sometimes referred to as 'the hiatus', was temporary (*very high confidence*). The increase

[16] Assessment of human-induced warming took place before 2020 data were available and hence concludes in 2019.

ACCEPTED VERSION SUBJECT TO FINAL EDITING

in global surface temperature during the 1998–2012 period is also greater in the data sets used in the AR6 assessment than in those available at the time of AR5. Using these updated observational data sets and a like-for-like consistent comparison of simulated and observed global surface temperature, all observed estimates of the 1998–2012 trend lie within the *very likely* range of CMIP6 trends. Since 2012, global surface temperature has warmed strongly, with the past five years (2016–2020) being the hottest five-year period between 1850 and 2020 (*high confidence*). {2.3.1, 3.3.1, 3.5.1, Cross-Chapter Box 3.1}

Future Changes in Global Surface Temperature

The AR6 assessment of future change in global surface temperature is, for the first time in an IPCC report, explicitly constructed by combining new projections for the SSP scenarios with observational constraints based on past simulated warming as well as the AR6-updated assessment of equilibrium climate sensitivity and transient climate response. Climate forecasts initialized from the observed climate state have in addition been used for the period 2019–2028. The inclusion of additional lines of evidence has reduced the assessed uncertainty ranges for each scenario (Cross-Section Box TS.1, Figure 1). {4.3.1, 4.3.4, Box 4.1, 7.5}

During the near term (2021–2040), a 1.5°C increase in global surface temperature, relative to 1850–1900, is *very likely* to occur in scenario SSP5-8.5, *likely* to occur in scenarios SSP2-4.5 and SSP3-7.0, and *more likely than not* to occur in scenarios SSP1-1.9 and SSP1-2.6. The time of crossing a warming level here is defined here as the midpoint of the first 20-year period during which the average global surface temperature exceeds the level. In all scenarios assessed here except SSP5-8.5, the central estimate of crossing the 1.5°C level lies in the early 2030s. This is about ten years earlier than the midpoint of the *likely* range (2030–2052) assessed in the SR1.5, which assumed continuation of the then-current warming rate; this rate has been confirmed in the AR6. Roughly half of the ten-year difference arises from a larger historical warming diagnosed in AR6. The other half arises because for central estimates of climate sensitivity, most scenarios show stronger warming over the near term than was estimated as 'current' in SR1.5 (*medium confidence*). (Cross-Section Box TS.1, Table 1) {2.3.1, Cross-Chapter Box 2.3, 3.3.1, 4.3.4, BOX 4.1}

It is *more likely than not* that under SSP1-1.9, global surface temperature relative to 1850–1900 will remain below 1.6°C throughout the 21st century, implying a potential temporary overshoot of 1.5°C global warming of no more than 0.1°C. If climate sensitivity lies near the lower end of the assessed *very likely* range, crossing the 1.5°C warming level is avoided in scenarios SSP1-1.9 and SSP1-2.6 (*medium confidence*). Global surface temperature in any individual year, in contrast to the 20-year average, could by 2030 exceed 1.5°C relative to 1850–1900 with a likelihood between 40% and 60%, across the scenarios considered here (*medium confidence*). (Cross-Section Box TS.1, Table 1) {4.3.4, 4.4.1, BOX 4.1, 7.5}

During the 21st century, a 2°C increase in global surface temperature relative to 1850–1900 will be crossed under SSP5-8.5 and SSP3-7.0, will *extremely likely* be crossed under SSP2-4.5, but is *unlikely* to be crossed under SSP1-2.6 and *extremely unlikely* to be crossed under SSP1-1.9. For the mid-term period 2041–2060, this 2°C global warming level is *very likely* to be crossed under SSP5-8.5, *likely* to be crossed under SSP3-7.0, and *more likely than not* to be crossed under SSP2-4.5. (Cross-Section Box TS.1, Table 1) {4.3.4}

Events of reduced and increased global surface temperature trends at decadal timescales will continue to occur in the 21st century, but will not affect the centennial warming (*very high confidence*). If strong mitigation is applied from 2020 onward as reflected in SSP1-1.9, its effect on 20-year trends in global surface temperature would *likely* emerge during the near term (2021–2040), measured against an assumed non-mitigation scenario such as SSP3-7.0 and SSP5-8.5. All statements about crossing the 1.5°C level assume that no major volcanic eruption occurs during the near term (Cross-Section Box TS.1, Table 1). {2.3.1, Cross-chapter Box 2.3, 4.3.4, 4.4.1, 4.6.3, Box 4.1}

Compared to 1850–1900, average global surface temperature over the period 2081–2100 is *very likely* to be higher by 1.0°C–1.8°C in the low CO_2 emissions scenario SSP1-1.9 and by 3.3°C–5.7°C in the high CO_2 emissions scenario SSP5-8.5. For the scenarios SSP1-2.6, SSP2-4.5, and SSP3-7.0, the corresponding *very likely* ranges are 1.3°C–2.4°C, 2.1°C–3.5°C, and 2.8°C–4.6°C, respectively. The uncertainty ranges for the period 2081–2100 continue to be dominated by the uncertainty in equilibrium climate sensitivity and

ACCEPTED VERSION SUBJECT TO FINAL EDITING

transient climate response (*very high confidence*) (Cross-Section Box TS.1, Table 1). {4.3.1, 4.3.4, 4.4.1, 7.5}

The CMIP6 models project a wider range of global surface temperature change than the assessed range (*high confidence*); furthermore, the CMIP6 global surface temperature increase tends to be larger than in CMIP5 (*very high confidence*). {4.3.1, 4.3.4, 4.6.2, 7.5.6}

[START CROSS-SECTION BOX TS.1, TABLE 1 HERE]

Cross-Section Box TS.1, Table 1: Assessment results for 20-year averaged change in global surface temperature based on multiple lines of evidence. The change is displayed in °C relative to the 1850–1900 reference period for selected time periods, and as the first 20-year period during which the average global surface temperature change exceeds the specified level relative to the period 1850–1900. The entries give both the central estimate and, in parentheses, the *very likely* (5–95%) range. An entry n.c. means that the global warming level is not crossed during the period 2021–2100.

	SSP1-1.9	SSP1-2.6	SSP2-4.5	SSP3-7.0	SSP5-8.5
Near term, 2021–2040	1.5 (1.2, 1.7)	1.5 (1.2, 1.8)	1.5 (1.2, 1.8)	1.5 (1.2, 1.8)	1.6 (1.3, 1.9)
Mid-term, 2041–2060	1.6 (1.2, 2.0)	1.7 (1.3, 2.2)	2.0 (1.6, 2.5)	2.1 (1.7, 2.6)	2.4 (1.9, 3.0)
Long term, 2081–2100	1.4 (1.0, 1.8)	1.8 (1.3, 2.4)	2.7 (2.1, 3.5)	3.6 (2.8, 4.6)	4.4 (3.3, 5.7)
1.5°C	2025–2044 (2013–2032, n.c.)	2023–2042 (2012–2031, n.c.)	2021–2040 (2012–2031, 2037–2056)	2021–2040 (2013–2032, 2033–2052)	2018–2037 (2011–2030, 2029–2048)
2°C	n.c. (n.c., n.c.)	n.c. (2031–2050, n.c.)	2043–2062 (2028–2047, 2075–2094)	2037–2056 (2026–2045, 2053–2072)	2032–2051 (2023–2042, 2044–2063)
3°C	n.c. (n.c., n.c.)	n.c. (n.c., n.c.)	n.c. (2061–2080, n.c.)	2066–2085 (2050–2069, n.c.)	2055–2074 (2042–2061, 2074–2093)
4°C	n.c. (n.c., n.c.)	n.c. (n.c., n.c.)	n.c. (n.c., n.c.)	n.c. (2070–2089, n.c.)	2075–2094 (2058–2077, n.c.)

[END CROSS-SECTION BOX TS.1, TABLE 1 HERE]

[END CROSS-SECTION BOX TS.1 HERE]

TS.2 Large-scale Climate Change: Mean Climate, Variability and Extremes

This section summarizes knowledge about observed and projected large-scale climate change (including variability and extremes), drivers and attribution of observed changes to human activities. It describes observed and projected large-scale changes associated with major components of the climate system: atmosphere, ocean (including sea level change), land, biosphere and cryosphere, and the carbon, energy and water cycles. In each subsection, reconstructed past, observed and attributed recent, and projected near- and long-term changes to mean climate, variability and extremes are presented, where possible, in an integrated way. See TS.1.3.1 for information on the scenarios used for projections.

TS.2.1 Changes Across the Global Climate System

In addition to global surface temperature (Cross-Section Box TS.1), a wide range of indicators across all components of the climate system is changing rapidly (Figure TS.7), with many at levels unseen in

ACCEPTED VERSION SUBJECT TO FINAL EDITING

millennia. The observed changes provide a coherent picture of a warming world, many aspects of which have now been formally attributed to human influences, and human influence on the climate system as a whole is assessed as unequivocal for the first time in IPCC assessment reports (Table TS.1, Figure TS.7). It is *virtually certain* that global surface temperature rise and associated changes can be limited through rapid and substantial reductions in global GHG emissions. Continued GHG emissions greatly increase the likelihood of potentially irreversible changes in the global climate system (Box TS.3), in particular with respect to the contribution of ice sheets to global sea level change (*high confidence*). {2.3, 3.8, 4.3, 4.6, 4.7, 7.2-7.4, 9.2-9.6, CCB 7.1}

Earth system model (ESM) simulations of the historical period since 1850 are only able to reproduce the observed changes in key climate indicators when anthropogenic forcings are included (Figure TS.7). Taken together with numerous formal attribution studies across an even broader range of indicators and theoretical understanding, this underpins the unequivocal attribution of observed warming of the climate system to human influence (Table TS.1). {2.3, 3.8}

[START FIGURE TS.7 HERE]

Figure TS.7: **Simulated and observed changes compared to the 1995–2014 average in key large-scale indicators of climate change across the climate system, for continents, ocean basins and globally up to 2014.** Black lines show observations, orange lines and shading show the multi-model mean and 5–95th percentile ranges for CMIP6 historical simulations including anthropogenic and natural forcing, and green lines and shading show corresponding ensemble means and 5-95th percentile ranges for CMIP6 natural-only simulations. Observations after 2014 (including, for example, a strong subsequent decrease of Antarctic sea-ice area that leads to no significant overall trend since 1979) are not shown because the CMIP6 historical simulations end in 2014. A 3-year running mean smoothing has been applied to all observational time series. {3.8, Figure 3.41}

[END FIGURE TS.7 HERE]

[START TABLE TS.1 HERE]

Table TS.1: Assessment of observed changes in large-scale indicators of mean climate across climate system components, and their attribution to human influence. The colour coding indicates the assessed confidence in / likelihood of the human contribution as a driver or main driver (specified in that case) where available (see colour key). Otherwise, explanatory text is provided in cells with white background. The relevant chapter section for more detailed information is listed in each table cell.

Change in indicator	Observed change assessment	Human contribution assessment
Atmosphere and water cycle		
Warming of global mean surface air temperature since 1850-1900	{2.3.1, CCB2.3}	*Likely* range of human contribution (0.8°C–1.3°C) encompasses observed warming (0.9°C–1.2°C) {3.3.1}
Warming of the troposphere since 1979	{2.3.1}	Main driver {3.3.1}
Cooling of the lower stratosphere	Since mid-20th century {2.3.1}	Main driver 1979 - mid-1990s {3.3.1}
Large-scale precipitation and upper troposphere humidity changes since 1979	{2.3.1}	{3.3.2, 3.3.3}
Expansion of the zonal mean Hadley Circulation since the 1980s	{2.3.1}	Southern Hemisphere {3.3.3}
Ocean		
Ocean heat content increase since the 1970s	{2.3.3, 2.3.4, 9.2.1, CCB 9.1}	Main driver {3.5.1}
Salinity changes since the mid-20th century	{2.3.3, 2.3.4, 9.2.2}	{3.5.2}
Global mean sea level rise since 1970	{2.3.3, 9.6.1}	Main driver {3.5.3}

ACCEPTED VERSION SUBJECT TO FINAL EDITING

Cryosphere		
Arctic sea ice loss since 1979	{2.3.2, 9.3.1}	Main driver {3.4.1}
Reduction in Northern Hemisphere spring snow cover since 1950	{2.3.2, 9.5.3}	{3.4.2}
Greenland Ice Sheet mass loss since 1990s	{2.3.2, 9.4.1}	{3.4.3}
Antarctic Ice Sheet mass loss since 1990s	{2.3.2, 9.4.2}	*Limited evidence & medium agreement* {3.4.3}
Retreat of glaciers	{2.3.2, 9.5.1}	Main driver {3.4.3}
Carbon cycle		
Increased amplitude of the seasonal cycle of atmospheric CO_2 since the early 1960s	{2.3.4}	Main driver {3.6.1}
Acidification of the global surface ocean	{SROCC, 5.3.2, CCB 5.3}	Main driver {3.6.2}
Land climate (extremes, see Table TS.12)		
Mean 2-m land warming since 1850–1900 (about 40% larger than global mean warming)	{2.3.1}	Main driver {3.3.1}
Synthesis		
Warming of the global climate system since preindustrial times	{2.3.5}	{3.8.1}

see text description	*medium confidence*	*likely / high confidence*	*very likely*	*extremely likely*	*virtually certain*	fact

[END TABLE TS.1 HERE]

Future climate change across a range of atmospheric, cryospheric, oceanic and biospheric indicators depends upon future emissions pathways. Outcomes for a broad range of indicators increasingly diverge through the 21st century across the different SSPs (TS.1.3.1; Figure TS.8). Due to the slow response of the deep ocean and ice sheets, this divergence continues long after 2100, and 21st century emissions choices will have implications for GMSL rise for centuries to millennia. Furthermore, it is *likely* that at least one large volcanic eruption will occur during the 21st century. Such an eruption would reduce global surface temperature for several years, decrease land precipitation, alter monsoon circulation and modify extreme precipitation, at both global and regional scales. {4.3, 4.7, 9.4, 9.6, Cross-Chapter Box 4.1}

[START FIGURE TS.8 HERE]

Figure TS.8: Observed, simulated and projected changes compared to the 1995–2014 average in 4 key indicators of the climate system through to 2100 differentiated by SSP scenario pathway. Past simulations are based on the CMIP6 multi-model ensemble. Future projections are based on the assessed ranges based upon multiple lines of evidence for (a) global surface temperature (Cross-Section Box TS.1) and (b) global ocean heat content and the associated thermosteric sea level contribution to Global Mean Sea Level (GMSL) change (right-hand axis) using a climate model emulator (Cross-Chapter Box 7.1), and CMIP6 simulations for (c) Arctic September sea ice and (d) Global land precipitation. SSP1-1.9 and SSP1-2.6 projections show that reduced GHG emissions lead to a stabilization of global surface temperature, Arctic sea ice area and global land precipitation over the 21st century. SSP1-2.6 shows that emissions reductions have the potential to substantially reduce the increase in ocean heat content and thermosteric sea level rise over the 21st century but that some increase is unavoidable. {4.3, 9.3, 9.6, Figure 4.2, Figure 9.6}

[END FIGURE TS.8 HERE]

Observational records show changes in a wide range of climate extremes that have been linked to human influence on the climate system (Table TS.2). In many cases, the frequency and intensity of future changes in extremes can be directly linked to the magnitude of future projected warming. Changes in extremes are widespread over land since the 1950s, including a *virtually certain* global increase in extreme air

ACCEPTED VERSION SUBJECT TO FINAL EDITING

temperatures and a *likely* intensification in global-scale extreme precipitation. It is *extremely likely* that human influence is the main contributor to the observed increase (decrease) in the likelihood and severity of hot (cold) extremes (Table TS.2). The frequency of extreme temperature and precipitation events in the current climate will change with warming, with warm extremes becoming more frequent (*virtually certain*), cold extremes becoming less frequent (*extremely likely*) and precipitation extremes becoming more frequent in most locations (*very likely*). {9.6.4, 11.2, 11,3, 11.4, 11.6, 11.7, 11.8, 11.9, Box 9.2}

[START TABLE TS.2 HERE]

Table TS.2: Summary table on observed changes in extremes, their attribution since 1950 (except where stated otherwise), and projected changes at +1.5°C, +2°C and +4°C of global warming, on global and continental scale. Warm/hot extremes refer to warmer and/or more frequent hot days and nights and warm spells/heat waves, over most land areas. Cold extremes refer to warmer and/or fewer cold days and nights, and cold spells/cold waves, over most land areas. Drought events are relative to a predominant fraction of land area. For tropical cyclones, observed changes and attribution refer to categories 3-5, while projected changes refer to categories 4-5. Tables 11.1 and 11.2 are more detailed versions of this table, containing in particular information on regional scales. In general, higher warming levels imply stronger projected changes also for indicators where the confidence level does not depend on the warming level and the table does not explicitly quantify the global sensitivity. {9.6, Box 9.2, 11.3, 11.7}

Change in indicator	Observed (since 1950)	Attributed (since 1950)	Projected at GWL (°C) +1.5	+2	+4
Warm/hot extremes: Frequency or intensity	↑	✔ Main driver	↑	↑	↑
Cold extremes: Frequency or intensity	↓	✔ Main driver	↓	↓	↓
Heavy precipitation events: Frequency, intensity and/or amount	↑ Over majority of land regions with good observational coverage	✔ Main driver of the observed intensification of heavy precipitation in land regions	↑ in most land regions	↑	↑ in most land regions
Agricultural and ecological droughts: Intensity and/or duration	↑ for predominant fraction of land area	✔ for predominant fraction of land area	↑ for predominant fraction of land area	↑ for predominant fraction of land area	↑ for predominant fraction of land area
Precipitation associated with tropical cyclones	↑	✔	↑ Rate +11%	↑ Rate +14%	↑ Rate +28%
Tropical cyclones: Proportion of intense cyclones	↑	✔	↑ +10%	↑ +13%	↑ +20%
Compound events: co-occurrent heat waves and droughts	↑ (Frequency)	✔ (Frequency)	↑ (Frequency and intensity increases with warming)		
Marine heatwaves: Intensity & frequency	↑ (since 1900)	✔ (since 2006)	↑ Strongest in tropical and Arctic Ocean		
Extreme sea levels: Frequency	↑ (since 1960)	✔	↑ (Scenario-based assessment for 21st century)		

medium confidence	*likely / high confidence*	*very likely*	*extremely likely*	*virtually certain*

[END TABLE TS.2 HERE]

ACCEPTED VERSION SUBJECT TO FINAL EDITING

TS.2.2 Changes in the Drivers of the Climate System

Since 1750, changes in the drivers of the climate system are dominated by the warming influence of increases in atmospheric GHG concentrations and a cooling influence from aerosols, both resulting from human activities. In comparison there has been negligible long-term influence from solar activity and volcanoes. Concentrations of CO_2, CH_4, and N_2O have increased to levels unprecedented in at least 800,000 years, and there is *high confidence* that current CO_2 concentrations have not been experienced for at least 2 million years. Global mean concentrations of anthropogenic aerosols peaked in the late 20th century and have slowly declined since in northern mid-latitudes, although they continue to increase in South Asia and East Africa (*high confidence*). The total anthropogenic effective radiative forcing (ERF) in 2019, relative to 1750, was 2.72 [1.96 to 3.48] W m^{-2} (*medium confidence*) and has *likely* been growing at an increasing rate since the 1970s. {2.2, 6.4, 7.2, 7.3}

Solar activity since 1900 was high but not exceptional compared to the past 9000 years (*high confidence*). The average magnitude and variability of volcanic aerosols since 1900 has not been unusual compared to at least the past 2500 years (*medium confidence*). However, sporadic strong volcanic eruptions can lead to temporary drops in global surface temperature lasting 2–5 years. {2.2.1, 2.2.2, 2.2.8, CCB4.1}

Atmospheric CO_2 concentrations have changed substantially over millions of years (Figure TS.1). Current levels of atmospheric CO_2 have not been experienced for at least 2 million years (*high confidence*, Figure TS.9a). Over 1750–2019, CO_2 increased by 131.6 ± 2.9 ppm (47.3%). The centennial rate of change of CO_2 since 1850 has no precedent in at least the past 800,000 years (Figure TS.9), and the fastest rates of change over the last 56 million years were at least a factor of 4 lower (*low confidence*) than over 1900–2019. Several networks of high-accuracy surface observations show that concentrations of CO_2 have exceeded 400 ppm, reaching 409.9 (± 0.3) ppm in 2019 (Figure TS.9c). The ERF from CO_2 in 2019 (relative to 1750) was 2.16 Wm^{-2}. {2.2.3, 5.1.2, 5.2.1, 7.3, Box TS.5}

By 2019, concentrations of CH_4 reached 1866.3 (± 3.3) ppb (Figure TS.9c). The increase since 1750 of 1137 ± 10 ppb (157.8%) far exceeds the range over multiple glacial-interglacial transitions of the past 800,000 years (*high confidence*). In the 1990s, CH_4 concentrations plateaued, but started to increase again around 2007 at an average rate of 7.6 ± 2.7 ppb yr^{-1} (2010–2019; *high confidence*). There is *high confidence* that this recent growth is largely driven by emissions from fossil fuel exploitation, livestock, and waste, with ENSO driving multi-annual variability of wetland and biomass burning emissions. In 2019, ERF from CH_4 was 0.54 Wm^{-2}. {2.2.3, 5.2.2, 7.3}

Since 1750, N_2O increased by 62.0 ± 6.0 ppb, reaching a level of 332.1 (± 0.4) ppb in 2019. The increase since 1750 is of comparable magnitude to glacial-interglacial fluctuations of the past 800,000 years (Figure TS.9c). N_2O concentration trends since 1980 are largely driven by a 30% increase in emissions from the expansion and intensification of global agriculture (*high confidence*). By 2019 its ERF was 0.21 Wm^{-2}. {2.2.3, 5.2.3}

[START FIGURE TS.9 HERE]

Figure TS.9: **Changes in well-mixed greenhouse gas (WMGHG) concentrations and Effective Radiative Forcing**. a) Changes in CO_2 from proxy records over the past 3.5 million years; b) Changes in all three WMGHGs from ice core records over the Common Era; c) directly observed WMGHG changes since the mid-20th century; d) Evolution of ERF and components since 1750. Further details on data sources and processing are available in the associated FAIR data table. {2.2, Figures 2.3, 2.4 and 2.10}

[END FIGURE TS.9 HERE]

ACCEPTED VERSION SUBJECT TO FINAL EDITING

Halogenated gases consist of chlorofluorocarbons (CFCs), hydrochlorofluorocarbons (HCFCs), hydrofluorocarbons (HFCs) and other gases, many of which can deplete stratospheric ozone and warm the atmosphere. In response to controls on production and consumption mandated by the Montreal Protocol on Substances that Deplete the Ozone Layer and its amendments, the atmospheric abundances of most CFCs have continued to decline since AR5. Abundances of of HFCs, which are replacements for CFCs and HCFCs, are increasing (*high confidence*), though increases of the major HCFCs have slowed in recent years. The ERF from halogenated components in 2019 was 0.41 Wm^{-2}. {2.2.4, 6.3.4, 7.3.2}

Tropospheric aerosols mainly act to cool the climate system, directly by reflecting solar radiation, and indirectly through enhancing cloud reflectance. Ice cores show increases in aerosols across the Northern Hemisphere mid-latitudes since 1700, and reductions since the late 20th century (*high confidence*). Aerosol optical depth (AOD), derived from satellite- and ground-based radiometers, has decreased since 2000 over the mid-latitude continents of both hemispheres, but increased over South Asia and East Africa (*high confidence*). Trends in AOD are more pronounced from sub-micrometre aerosols for which the anthropogenic contribution is particularly large. Global carbonaceous aerosol budgets and trends remain poorly characterised due to limited observations, but black carbon (BC), a warming aerosol component, is declining in several regions of the Northern Hemisphere (*low confidence*). Total aerosol ERF in 2019, relative to 1750, is −1.1 [−1.7 to −0.4] W m^{-2} (*medium confidence*), and *more likely than not* became less negative since the late 20th century, with *low confidence* in the magnitude of post-2014 changes due to conflicting evidence (TS.3.1). {2.2.6, 6.2.1, 6.3.5, 6.4.1, 7.3.3}

There is *high confidence* that tropospheric ozone has been increasing from 1750 in response to anthropogenic changes in ozone precursor emissions (nitrogen oxides, carbon monoxide, non-methane volatile organic compounds, and methane), but with *medium confidenc*e in the magnitude of this change, due to limited observational evidence and knowledge gaps. Since the mid-20th century, tropospheric ozone surface concentrations have increased by 30–70% across the Northern Hemisphere (*medium confidence*); since the mid-1990s free tropospheric ozone has increased by 2–7% per decade in most northern mid-latitude regions, and 2–12% per decade in sampled tropical regions. Future changes in surface ozone concentrations will be primarily driven by changes in precursor emissions rather than climate change (*high confidence*). Stratospheric ozone has declined between 60˚S–60˚N by 2.2% from 1964–1980 to 2014–2017 (*high confidence*), with the largest declines during 1980–1995. The strongest loss of stratospheric ozone continues to occur in austral spring over Antarctica (ozone hole), with emergent signs of recovery after 2000. The 1750–2019 ERF for total (stratospheric and tropospheric) ozone is 0.47 [0.24 to 0.71] W m^{-2}, which is dominated by tropospheric ozone changes. {2.2.5; 6.3.2., 7.3.2, 7.3.5}

The global mean abundance of hydroxyl (OH) radical, or 'oxidising capacity', chemically regulates the lifetimes of many short-lived climate forcers (SLCFs), and therefore the radiative forcing of methane, ozone, secondary aerosols and many halogenated species. Model estimates suggest no significant change in oxidising capacity from 1850 to 1980 (*low confidence*). Increases of about 9% over 1980–2014 computed by ESMs and carbon cycle models are not confirmed by observationally constrained inverse models, rendering an overall *medium confidence* in stable OH or positive trends since the 1980s, and implying that OH is not the primary driver of recent observed growth in CH_4. {6.3.6, CCB5.2}

Land use and land-cover change exert biophysical and biogeochemical effects. There is *medium confidence* that the biophysical effects of land-use change since 1750, most notably the increase in global albedo, have had an overall cooling on climate, whereas biogeochemical effects (i.e., changes in GHG and volatile organic compound emissions or sinks) led to net warming. Overall land use and land cover ERF is estimated at -0.2 [-0.3 to -0.1] W m^{-2}. {2.2.7, 7.3.4, SRCCL 2.5}

The total anthropogenic ERF (Figure TS.9) in 2019 relative to 1750 was 2.72 [1.96 to 3.48] W m^{-2} (Figure TS.9), dominated by GHGs (positive ERF) and partially offset by aerosols (negative ERF). The rate of change of ERF *likely* has increased since the 1970s, mainly due to growing CO_2 concentrations and less negative aerosol ERF. {2.2.8, 7.3}

ACCEPTED VERSION SUBJECT TO FINAL EDITING

TS.2.3 Upper Air Temperatures and Atmospheric Circulation

The effects of human-induced climate change have been clearly identified in observations of atmospheric temperature and some aspects of circulation, and these effects are *likely* to intensify in the future. Tropospheric warming and stratospheric cooling are *virtually certain* to continue with continued net emissions of greenhouse gases. Several aspects of the atmospheric circulation have *likely* changed since the mid-20th century, and human influence has *likely* contributed to the observed poleward expansion of the Southern Hemisphere Hadley Cell and *very likely* contributed to the observed poleward shift of the Southern Hemisphere extratropical jet in summer. It is *likely* that the mid-latitude jet will shift poleward and strengthen, accompanied by a strengthening of the storm track in the Southern Hemisphere by 2100 under the high CO_2 emissions scenarios. It is *likely* that the proportion of intense tropical cyclones has increased over the last four decades and that this cannot be explained entirely by natural variability. There is *low confidence* in observed recent changes in the total number of extratropical cyclones over both hemispheres. The proportion of tropical cyclones which are intense is expected to increase (*high confidence*) but the total global number of tropical cyclones is expected to decrease or remain unchanged (*medium confidence*). {2.3, 3.3, 4.3, 4.4, 4.5, 8.3, 8.4, 11.7}

The troposphere has warmed since at least the 1950s, and it is *virtually certain* that the stratosphere has cooled. It is *very likely* that human-induced increases in GHGs were the main driver of tropospheric warming since 1979. It is *extremely likely* that anthropogenic forcing, both from increases in GHG concentration and depletion of stratospheric ozone due to ozone-depleting substances, was the main driver of upper stratospheric cooling since 1979. It is *very likely* that global mean stratospheric cooling will be larger for scenarios with higher atmospheric CO_2 concentrations. In the tropics, since at least 2001 (when new techniques permit more robust quantification), the upper troposphere has warmed faster than the near-surface (*medium confidence*) (Figure TS.10). There is *medium confidence* that most CMIP5 and CMIP6 models overestimate the observed warming in the upper tropical troposphere over the period 1979–2014, in part because they overestimate tropical SST warming. It is *likely* that future tropical upper tropospheric warming will be larger than at the tropical surface. {2.3.1, 3.3.1, 4.5.1}

[START FIGURE TS.10 HERE]

Figure TS.10: Observed and projected upper air temperature and circulation changes. Upper panels: Left: Zonal cross-section of temperature trends for 2002-2019 in the upper troposphere region for the ROM SAF radio-occultation dataset. Middle: Change in the annual and zonal mean atmospheric temperature (°C) in 2081-2100 in SSP1-2.6 relative to 1995-2014 for 36 CMIP6 models. Right: the same in SSP3-7.0 for 32 models. Lower panels: Left: Long-term mean (thin black colour) and linear trend (colour) of zonal mean DJF zonal winds for ERA5. Middle: multi-model mean change in annual and zonal mean wind (m s^{-1}) in 2081-2100 in SSP1-2.6 relative to 1995-2014 based on 34 CMIP6 models. The 1995-2014 climatology is shown in contours with spacing 10 m s^{-1}. Right: the same for SSP3-7.0 for 31 models. {2.3.1, 4.5.1, Figures 2.12, 2.18, and 4.26}

[END FIGURE TS.10 HERE]

The Hadley Circulation has *likely* widened since at least the 1980s, predominantly in the Northern Hemisphere, although there is only *medium confidence* in the extent of the changes. This has been accompanied by a strengthening of the Hadley Circulation in the Northern Hemisphere (*medium confidence*). It is *likely* that human influence has contributed to the poleward expansion of the zonal mean Hadley cell in the Southern Hemisphere since the 1980s, which is projected to further expand with global warming (*high confidence*). There is *medium confidence* that the observed poleward expansion in the Northern Hemisphere is within the range of internal variability. {2.3.1, 3.3.3, 8.4.3}

Since the 1970s near-surface average winds have *likely* weakened over land. Over the ocean, near-surface average winds *likely* strengthened over 1980–2000, but divergent estimates lead to *low confidence* thereafter.

ACCEPTED VERSION SUBJECT TO FINAL EDITING

Extratropical storm tracks have *likely* shifted poleward since the 1980s. There is *low confidence* in projected poleward shifts of the Northern Hemisphere mid-latitude jet and storm tracks due to large internal variability and structural uncertainty in model simulations. There is *medium confidence* in a projected decrease of frequency of atmospheric blocking over Greenland and the North Pacific in boreal winter in 2081–2100 under the SSP3-7.0 and SSP5-8.5 scenarios. There is *high confidence* that Southern Hemisphere storm tracks and associated precipitation have migrated polewards over recent decades, especially in the austral summer and autumn, associated with a trend towards more positive phases of the Southern Annular Mode (SAM) (TS.4.2.2) and the strengthening and southward shift of the Southern Hemisphere extratropical jet in austral summer. In the long term (2081–2100), the Southern Hemisphere mid-latitude jet is *likely* to shift poleward and strengthen under SSP5-8.5 scenario relative to 1995–2014, accompanied by an increase in the SAM (TS.4.2.2). It is *likely* that wind speeds associated with extratropical cyclones will strengthen in the Southern Hemisphere storm track for SSP5-8.5. There is *low confidence* in the potential role of Arctic warming and sea ice loss on historical or projected mid-latitude atmospheric variability. {2.3.1, 3.3.3, 3.7.2, 4.3.3, 4.4.3, 4.5.1, 4.5.3, 8.2.2, 8.3.2, Cross-Chapter Box 10.1}

It is *likely* that the proportion of major (Category 3–5) tropical cyclones (TCs) and the frequency of rapid TC intensification events have increased over the past four decades. The average location of peak TC wind-intensity has *very likely* migrated poleward in the western North Pacific Ocean since the 1940s, and TC forward translation speed has *likely* slowed over the contiguous USA since 1900. It is *likely* that the poleward migration of TCs in the western North Pacific and the global increase in TC intensity rates cannot be explained entirely by natural variability**.** There is *high confidence* that average peak TC wind speeds and the proportion of Category 4–5 TCs will increase with warming and that peak winds of the most intense TCs will increase. There is *medium confidence* that the average location where TCs reach their maximum wind-intensity will migrate poleward in the western North Pacific Ocean, while the total global frequency of TC formation will decrease or remain unchanged with increasing global warming (*medium confidence*). {11.7}

There is *low confidence* in observed recent changes in the total number of extratropical cyclones over both hemispheres. There is also *low confidence* in past-century trends in the number and intensity of the strongest extratropical cyclones over the Northern Hemisphere due to the large interannual-to-decadal variability and temporal and spatial heterogeneities in the volume and type of assimilated data in atmospheric reanalyses, particularly before the satellite era. Over the Southern Hemisphere, it is *likely* that the number of extratropical cyclones with low central pressures (<980 hPa) has increased since 1979. The frequency of intense extratropical cyclones is projected to decrease (*medium confidence*). Projected changes in the intensity depend on the resolution of climate models (*medium confidence*). There is *medium confidence* that wind speeds associated with extratropical cyclones will change following changes in the storm tracks. {2.3.1, 3.3.3, 4.5.1, 4.5.3, 8.3.2, 8.4.2, 11.7.2, 11.7.2}

[START BOX TS.3 HERE]

Box TS.3: Low-Likelihood, High-Warming Storylines

Future global warming exceeding the assessed *very likely* range cannot be ruled out and is potentially associated with the highest risks for society and ecosystems. Such low-likelihood, high-warming storylines tend to exhibit substantially greater changes in the intensity of regional drying and wetting than the multi-model mean. Even at levels of warming within the *very likely* range, global and regional low-likelihood outcomes might occur, such as large precipitation changes, additional sea level rise associated with collapsing ice sheets, or abrupt ocean circulation changes. While there is *medium confidence* that the Atlantic Meridional Overturning circulation (AMOC) will not experience an abrupt collapse before 2100, if it were to occur, it would *very likely* cause abrupt shifts in regional weather patterns and water cycle. The probability of these low-likelihood outcomes increases with higher global warming levels. If the real-world climate sensitivity lies at the high end of the assessed range, then global and regional changes substantially outside the *very likely* range projections occur for a given emissions scenario. With increasing global warming, some very rare extremes and some compound events (multivariate or concurrent extremes) with low likelihood in past and current climate will become more frequent, and there is a higher chance that events unprecedented

ACCEPTED VERSION SUBJECT TO FINAL EDITING

in the observational record occur (*high confidence*). Finally, low likelihood, high-impact outcomes may also arise from a series of very large volcanic eruptions that could substantially alter the 21st century climate trajectory compared to SSP-based Earth system model projections. {Cross-Chapter Box 4.1, 4.3, 4.4, 4.8, 7.3, 7.4, 7.5, 8.6, 9.2, 9.6, Box TS.4, Box 9.4, Box 11.2, CCB 12.1}

Previous IPCC reports largely focused their assessment on the projected *very likely* range of future surface warming and associated climate change. However, a comprehensive risk assessment also requires considering the potentially larger changes in the physical climate system that are *unlikely* or *very unlikely* but possible and potentially associated with the highest risks for society and ecosystems (Figure TS.6). Since AR5, the development of physical climate storylines of high warming has emerged as a useful approach for exploring the future risk space that lies outside of the IPCC *very likely* range projections. {4.8}

Uncertainty in the true values of equilibrium climate sensitivity (ECS) and transient climate response (TCR) dominate uncertainty in projections of future warming under moderate to strong emissions scenarios (TS.3.2). A real-world ECS higher than the assessed *very likely* range (2°C–5°C) would require a strong historical aerosol cooling and/or a trend towards stronger warming from positive feedbacks linked to changes in SST patterns (pattern effects), combined with a strong positive cloud feedback and substantial biases in paleoclimate reconstructions – each of which is assessed as either *unlikely* or *very unlikely*, but not ruled out. Since CMIP6 contains several ESMs that exceed the upper bound of the assessed *very likely* range in future surface warming, these models can be used to develop low-likelihood, high warming storylines to explore risks and vulnerabilities, even in the absence of a quantitative assessment of likelihood. {4.3.4, 4.8, 7.3.2, 7.4.4, 7.5.2, 7.5.5, 7.5.7}

CMIP6 models with surface warming outside, or close to, the upper bound of the *very likely* range exhibit patterns of large widespread temperature and precipitation changes that differ substantially from the multi-model mean in all scenarios. For SSP5-8.5, the high-warming models exhibit widespread warming of more than 6°C over most extratropical land regions and parts of the Amazon. In the Arctic, annual mean temperatures increase by more than 10°C relative to present-day, corresponding to about 30% more than the best estimate of warming. Even for SSP1-2.6, high-warming models show on average 2°C–3°C warming relative to present-day conditions over much of Eurasia and North America (about 40% more than the best estimate of warming) and more than 4°C warming relative to the present over the Arctic (Box TS.3, Figure 1) in 2081–2100. Such a high global warming storyline would imply that the remaining carbon budget consistent with a 2°C warming is smaller than the assessed *very likely* range. Put another way, even if a carbon budget that *likely* limits warming to 2°C is met, a low-likelihood, high-warming storyline would result in warming of 2.5°C or more. {4.8}

CMIP6 models with global warming close to the upper bound of the assessed *very likely* warming range tend to exhibit greater changes in the intensity of regional drying and wetting than the multi-model mean. Furthermore, these model projections show a larger area of drying and tend to show a larger fraction of strong precipitation increases than the multi-model mean. However, regional precipitation changes arise from both thermodynamic and dynamic processes so that the most pronounced global warming levels are not necessarily associated with the strongest precipitation response. Abrupt human-caused changes to the water cycle cannot be ruled out. Positive land surface feedbacks, involving vegetation and dust, can contribute to abrupt changes in aridity, but there is only *low confidence* that such changes will occur during the 21st century. Continued Amazon deforestation, combined with a warming climate, raises the probability that this ecosystem will cross a tipping point into a dry state during the 21st century (*low confidence*). {4.8, 8.6.2, Box TS.9}

While there is *medium confidence* that the projected decline in the Atlantic Meridional Overturning Circulation (AMOC) (TS.2.4) will not involve an abrupt collapse before 2100, such a collapse might be triggered by an unexpected meltwater influx from the Greenland Ice Sheet. If an AMOC collapse were to occur, it would *very likely* cause abrupt shifts in the weather patterns and water cycle, such as a southward shift in the tropical rain belt, and could result in weakening of the African and Asian monsoons and strengthening of Southern Hemisphere monsoons. {4.7.2, 8.6.1, 9.2.3, Box TS.9, Box TS.13}

ACCEPTED VERSION SUBJECT TO FINAL EDITING

Very rare extremes and compound or concurrent events, such as the 2018 concurrent heatwaves across the Northern Hemisphere, are often associated with large impacts. The changing climate state is already altering the likelihood of extreme events, such as decadal droughts and extreme sea levels, and will continue to do so under future warming. Compound events and concurrent extremes contribute to increasing probability of low-likelihood, high-impact outcomes, and will become more frequent with increasing global warming (*high confidence*). Higher warming levels increase the likelihood of events unprecedented in the observational record. {Box 11.2, 9.6.4}

Finally, low likelihood storylines need not necessarily relate solely to the human-induced changes in climate. A low-likelihood, high-impact outcome, consistent with historical precedent in the past 2,500 years, would be to see several large volcanic eruptions that could greatly alter the 21st century climate trajectory compared to SSP-based Earth system model projections. {Cross-Chapter Box 4.1}

[START BOX TS.3, FIGURE 1 HERE]

Box TS.3, Figure 1: High-warming storylines. (a) CMIP6 multi-model mean linearly scaled to the assessed best global surface temperature estimate for SSP1-2.6 in 2081–2100 relative to 1995–2014, (b) mean across five high-warming models with global surface temperature changes warming nearest to the upper bound of the assessed very likely range, (c) mean across five very high-warming models with global surface temperature changes warming higher than the assessed very likely. (d-f) Same as (a-c) but for SSP5-8.5. Note the different colour bars in (a-c) and (d-f). {4.7, Figure 4.41}

[END BOX TS.3, FIGURE 1 HERE]

[END BOX TS.3 HERE]

TS.2.4 The Ocean

Observations, models and paleo-evidence indicate that recently observed changes in the ocean are unprecedented for centuries to millennia (*high confidence*). Over the past four to six decades, it is *virtually certain* that the global ocean has warmed, with human influence *extremely likely* the main driver since the 1970s, making climate change irreversible over centuries to millennia (*medium confidence*). It is *virtually certain* that upper ocean salinity contrasts have increased since the 1950s and *extremely likely* that human influence has contributed. It is *virtually certain* that upper ocean stratification has increased since 1970 and that sea water pH has declined globally over the last 40 years, with human influence the main driver of the observed ocean acidification (*virtually certain*). There is *high confidence* that marine heatwaves have become more frequent in the 20th century, and most of them have been attributed to anthropogenic warming since 2006 (*very likely*). There is *high confidence* that oxygen levels have dropped in many regions since the mid 20th century and that the geographic range of many marine organisms has changed over the last two decades. The amount of ocean warming observed since 1971 will *likely* at least double by 2100 under a low warming scenario (SSP1-2.6) and will increase by 4-8 times under a high warming scenario (SSP5-8.5). Stratification (*virtually certain*), acidification (*virtually certain*), deoxygenation (*high confidence*) and marine heatwave frequency (*high confidence*) will continue to increase in the 21st century. While there is *low confidence* in 20th century AMOC change, it is *very likely* that AMOC will decline over the 21st century (Figure TS.11). {2.3, 3.5, 3.6, 4.3, 5.3, 7.2, 9.2, 9.4, 9.6, Box 9.2, 12.4}

It is *virtually certain* that the global ocean has warmed since at least 1971, representing about 90% of the increase in the global energy inventory (TS.3.1). The ocean is currently warming faster than at any other time since at least the last deglacial transition (*medium confidence*), with warming extending to depths well below 2000 m (*very high confidence*). It is *extremely likely* that human influence was the main driver of ocean warming. Ocean warming will continue over the 21st century (*virtually certain*), and will *likely* continue until at least to 2300 even for low CO_2 emissions scenarios. Ocean warming is irreversible over centuries to millennia (*medium confidence*), but the magnitude of warming is scenario-dependent from about

ACCEPTED VERSION SUBJECT TO FINAL EDITING

the mid-21st century (*medium confidence*). The warming will not be globally uniform, with heat primarily stored in Southern Ocean water-masses and weaker warming in the subpolar North Atlantic (*high confidence*). Limitations in the understanding of feedback mechanisms limit our confidence in future ocean warming close to Antarctica and how this will affect sea ice and ice shelves. {2.3.3, 3.5.1, 4.7.2, 7.2.2, 9.2.2, 9.2.3, 9.2.4, 9.3.2, 9.6.1; Cross-Chapter Box 9.1}

Global mean SST has increased since the beginning of the 20th century by 0.88 [0.68 to 1.01] °C, and it is *virtually certain* it will continue to increase throughout the 21st century with increasing hazards to marine ecosystems (*medium confidence*). Marine heatwaves have become more frequent over the 20th century (*high confidence*), approximately doubling in frequency (*high confidence*) and becoming more intense and longer since the 1980s (*medium confidence*). Most of the marine heatwaves over 2006–2015 have been attributed to anthropogenic warming (*very likely*). Marine heatwaves will continue to increase in frequency, with a *likely* global increase of 2–9 times in 2081–2100 compared to 1995–2014 under SSP1-2.6, and 3–15 times under SSP5-8.5 (Figure TS.11a), with the largest changes in the tropical and Arctic ocean. {2.3.1, 9.2.1; Box 9.2; 12.4.8; Cross-Chapter Box 2.3}

Observed upper ocean stratification (0–200 m) has increased globally since at least 1970 *(virtually certain)*. Based on recent refined analyses of the available observations, there is *high confidence* that it increased by 4.9 ±1.5% from 1970–2018, which is about twice as much as assessed in the SROCC, and will continue to increase throughout the 21st century at a rate depending on the emissions scenario (*virtually certain*). {2.3.3, 9.2.1}

It is *virtually certain* that since 1950 near-surface high-salinity regions have become more saline, while low-salinity regions have become fresher, with *medium confidence* that this is linked to an intensification of the hydrological cycle (Box TS.6). It is *extremely likely* that human influence has contributed to this salinity change and that the large-scale pattern will grow in amplitude over the 21st century (*medium confidence*). {2.3.3, 3.5.2, 9.2.2, 12.4.8}

The AMOC was relatively stable during the past 8,000 years (*medium confidence*). There is *low confidence* in the quantification of AMOC changes in the 20th century because of *low agreement* in quantitative reconstructed and simulated trends, missing key processes in both models and measurements used for formulating proxies, and new model evaluations. Direct observational records since the mid-2000s are too short to determine the relative contributions of internal variability, natural forcing and anthropogenic forcing to AMOC change (*high confidence*). An AMOC decline over the 21st century is *very likely* for all SSP scenarios; a possible abrupt decline is assessed further in Box TS.3 (Figure TS.11b). {2.3.3, 3.5.4, 4.3.2, 8.6.1, 9.2.3, Cross-Chapter Box 12.3}

There is *high confidence* that many ocean currents will change in the 21st century in response to changes of wind stress. There is *low confidence* in 21st century change of Southern Ocean circulation, despite *high confidence* that it is sensitive to changes in wind patterns and increased ice-shelf melt. Western boundary currents and subtropical gyres have shifted poleward since 1993 (*medium confidence*). Subtropical gyres, the East Australian Current Extension, the Agulhas Current, and the Brazil Current are projected to intensify in the 21st century in response to changes in wind stress, while the Gulf Stream and the Indonesian Throughflow are projected to weaken (*medium confidence*). All of the four main eastern boundary upwelling systems are projected to weaken at low latitudes and intensify at high latitudes in the 21st century (*high confidence*). {2.3.3, 9.2.3}

It is *virtually certain* that surface pH has declined globally over the last 40 years and that the main driver is uptake of anthropogenic CO_2. Ocean acidification and associated reductions in the saturation state of calcium carbonate – a constituent of skeletons or shells of a variety of marine organisms – is expected to increase in the 21st century under all emissions scenarios (*high confidence*). There is *very high confidence* that present-day surface pH values are unprecedented for at least 26,000 years and current rates of pH change are unprecedented since at least that time. Over the past 2–3 decades, a pH decline in the ocean interior has been observed in all ocean basins (*high confidence*) (Figure TS.11d). {2.3.3, 2.3.4, 3.6.2, 4.3.2, 5.3.2, 5.3.3, 5.6.3, 12.4.8}

ACCEPTED VERSION SUBJECT TO FINAL EDITING

Open-ocean deoxygenation and expansion of oxygen minimum zones has been observed in many areas of the global ocean since the mid 20th century (*high confidence*), in part due to human influence (*medium confidence*). Deoxygenation is projected to continue to increase with ocean warming (*high confidence*) (Figure TS.11c). Higher climate sensitivity and reduced ocean ventilation in CMIP6 compared to CMIP5 results in substantially greater projections of subsurface (100–600 m) oxygen decline than reported in SROCC for the period 2080–2099. {2.3.3, 2.3.4, Cross-Chapter Box 2.4, 3.6.2, 5.3.3, 12.4.8}

Over at least the last two decades, the geographic range of many marine organisms has shifted towards the poles and towards greater depths (*high confidence*), indicative of shifts towards cooler waters. The range of a smaller subset of organisms has shifted equatorward and to shallower depths (*high confidence*). Phenological metrics associated with the life cycles of many organisms have also changed over the last two decades or longer (*high confidence*). Since the changes in the geographical range of organisms and their phenological metrics have been observed to differ with species and location, there is the possibility of disruption to major marine ecosystems. {2.3.4}

[START FIGURE TS.11 HERE]

Figure TS.11: **Past and future ocean and ice sheet changes.** Observed and simulated historical changes and projected future changes under varying greenhouse gas emissions scenarios. Simulated and projected ocean changes are shown as CMIP6 ensemble mean, and 5-95% range (shading) is provided for scenario SSP1-2.6 and SSP3-7.0 (except in panel a where range provided for scenario SSP1-2.6 and SSP5-8.5). Mean and 5-95% range in 2100 are shown as vertical bars on the right-hand side of each panel. (a) Change in multiplication factor in surface ocean marine heatwave days relative to 1995-2014 (defined as days exceeding the 99th percentile in SST from 1995-2014 distribution). Assessed observational change span 1982-2019 from AVHRR satellite SST. (b) AMOC transport relative to 1995-2014 (defined as maximum transport at 26°N). Assessed observational change spans 2004-2018 from the RAPID array smoothed with a 12-month running mean (shading around the mean shows the 12-month running standard deviation around the mean). (c) Global mean percent change in ocean oxygen (100–600 m depth), relative to 1995-2014. Assessed observational trends and *very likely* range are from the SROCC assessment, and spans 1970–2010 centered on 2005. (d) Global mean surface pH. Assessed observational change span 1985-2019, from the CMEMS SOCAT-based reconstruction (shading around the global mean shows the 90% confidence interval). (e), (f): Ice sheet mass changes. Projected ice sheet changes are shown as median, 5-95% range (light shading), and 17-83% range (dark shading) of cumulative mass loss and sea level equivalent from ISMIP6 emulation under SSP1-26 and SSP5-85 (shading and bold line), with individual emulated projections as thin lines. Median (dot), 17-83% range (thick vertical bar), and 5-95% range (thin vertical bar) in 2100 are shown as vertical bars on the right-hand side of each panel, from ISMIP6, ISMIP6 emulation, and LARMIP-2. Observation-based estimates: For Greenland (e), for 1972-2018 (Mouginot), for 1992-2016 (Bamber), for 1992-2020 (IMBIE) and total estimated mass loss range for 1840-1972 (Box). For Antarctica (f), estimates based on satellite data combined with simulated surface mass balance and glacial isostatic adjustment for 1992-2020 (IMBIE), 1992-2016 (Bamber), and 1979-2017 (Rignot). Left inset maps: mean Greenland elevation changes 2010-2017 derived from CryoSat-2 radar altimetry (e) and mean Antarctica elevation changes 1978-2017 derived from restored analog radar records (f). Right inset maps: ISMIP6 model mean (2093- 2100) projected changes under the MIROC5 climate model for the RCP8.5 scenario. {Box 9.2, 2.3.3, 2.3.4, 3.5.4, 4.3.2, 5.3.2, 5.3.3, 5.6.3, 9.2.3, 9.4.1, 9.4.2, Box 9.2 Figure 1, Figure 9.10, Figure 9.17, Figure 9.18}

[END FIGURE TS.11 HERE]

TS.2.5 The Cryosphere

Over recent decades, widespread loss of snow and ice has been observed, and several elements of the cryosphere are now in states unseen in centuries (*high confidence*). Human influence was *very likely* the main driver of observed reductions in Arctic sea ice since the late 1970s (with late-summer sea ice loss *likely* unprecedented for at least 1000 years) and the widespread retreat of glaciers (unprecedented in at least the last 2,000 years, *medium confidence*). Furthermore, human influence *very likely* contributed to the observed

ACCEPTED VERSION SUBJECT TO FINAL EDITING

Northern Hemisphere spring snow cover decrease since 1950. By contrast, Antarctic sea ice area experienced no significant net change since 1979, and there is only *low confidence* in its projected changes. The Arctic Ocean is projected to become practically sea ice-free in late summer under high CO_2 emissions scenarios by the end of the 21st century (*high confidence*). It is *virtually certain* that further warming will lead to further reductions of Northern Hemisphere snow cover, and there is *high confidence* that this is also the case for near-surface permafrost volume. Glaciers will continue to lose mass at least for several decades even if global temperature is stabilized (*very high confidence*), and mass loss over the 21st century is *virtually certain* for the Greenland Ice Sheet and *likely* for the Antarctic Ice Sheet. Deep uncertainty persists with respect to the possible evolution of the Antarctic Ice Sheet within the 21st century and beyond, in particular due to the potential instability of the West Antarctic Ice Sheet. {2.3, 3.4, 4.3, 8.3, 9.3-9.6, Box 9.4, 12.4}

Current Arctic sea ice coverage levels (both annual and late summer) are at their lowest since at least 1850 (*high confidence*), and for late summer for the past 1,000 years (*medium confidence*). Since the late 1970s, Arctic sea ice area and thickness have decreased in both summer and winter, with sea ice becoming younger, thinner and more dynamic (*very high confidence*). It is *very likely* that anthropogenic forcing, mainly due to greenhouse gas increases, was the main driver of this loss, although new evidence suggests that anthropogenic aerosol forcing has offset part of the greenhouse gas–induced losses since the 1950s (*medium confidence*). The annual Arctic sea ice area minimum will *likely* fall below 1 million km^2 at least once before 2050 under all assessed SSP scenarios. This practically sea ice-free state will become the norm for late summer by the end of the 21st century in high CO_2 emissions scenarios (*high confidence*). Arctic summer sea ice varies approximately linearly with global surface temperature, implying that there is no tipping point and observed/projected losses are potentially reversible (*high confidence*). {2.3.2, 3.4.1, 4.3.2, 9.3.1, 12.4.9}

For Antarctic sea ice, there is no significant trend in satellite-observed sea ice area from 1979 to 2020 in both winter and summer, due to regionally opposing trends and large internal variability. Due to mismatches between model simulations and observations, combined with a lack of understanding of reasons for substantial inter-model spread, there is *low confidence* in model projections of future Antarctic sea ice changes, particularly at the regional level. {2.3.2, 3.4.1, 9.3.2}

In permafrost regions, increases in ground temperatures in the upper 30 m over the past three to four decades have been widespread (*high confidence*). For each additional 1°C of warming (up to 4°C above the 1850–1900 level), the global volume of perennially frozen ground to 3 m below the surface is projected to decrease by about 25% relative to the present volume (*medium confidence*). However, these decreases may be underestimated due to an incomplete representation of relevant physical processes in ESMs (*low confidence*). Seasonal snow cover is treated in TS.2.6. {2.3.2, 9.5.2, 12.4.9}

There is *very high confidence* that, with few exceptions, glaciers have retreated since the second half of the 19th century; this behaviour is unprecedented in at least the last 2,000 years (*medium confidence*). Mountain glaciers *very likely* contributed 67.2 [41.8 to 92.6] mm to the observed GMSL change between 1901 and 2018. This retreat has occurred at increased rates since the 1990s, with human influences *very likely* being the main driver. Under RCP2.6 and RCP8.5, respectively, glaciers are projected to lose 18% ± 13% and 36% ± 20% of their current mass over the 21st century (*medium confidence*). {2.3.2, 3.4.3, 9.5.1, 9.6.1}

The Greenland Ice Sheet was smaller than at present during the Last Interglacial period (roughly 125,000 years ago) and the mid-Holocene (roughly 6,000 years ago) (*high confidence*). After reaching a recent maximum ice mass at some point between 1450 and 1850, the ice sheet retreated overall, with some decades *likely* close to equilibrium (i.e., mass loss approximately equalling mass gained). It is *virtually certain* that the Greenland Ice Sheet has lost mass since the 1990s, with human influence a contributing factor (*medium confidence*). There is *high confidence* that annual mass changes have been consistently negative since the early 2000s. Over the period 1992–2020, Greenland *likely* lost 4890 ± 460 Gt of ice, contributing 13.5 ± 1.3 mm to global mean sea level rise. There is *high confidence* that Greenland ice mass losses are increasingly dominated by surface melting and runoff, with large interannual variability arising from changes in surface mass balance. Projections of future Greenland ice-mass loss (Box TS.4, Table 1; Figure TS.11e) are dominated by increased surface melt under all emissions scenarios (*high confidence*). Potential irreversible long-term loss of the Greenland Ice Sheet, and of parts of the Antarctic Ice Sheet, is assessed in Box TS.9.

ACCEPTED VERSION SUBJECT TO FINAL EDITING

{2.3.2, 3.4.3, 9.4.1, 9.4.2, 9.6.3, Atlas.11.2}

It is *likely* that the Antarctic Ice Sheet has lost 2670 ± 530 Gt, contributing 7.4 ± 1.5 mm to global mean sea level rise over 1992–2020. The total Antarctic ice mass losses were dominated by the West Antarctic Ice Sheet, with combined West Antarctic and Peninsula annual loss rates increasing since about 2000 (*very high confidence*). Furthermore, it is *very likely* that parts of the East Antarctic Ice Sheet have lost mass since 1979. Since the 1970s, snowfall has *likely* increased over the western Antarctic Peninsula and eastern West Antarctica, with large spatial and interannual variability over the rest of Antarctica. Mass losses from West Antarctic outlet glaciers, mainly induced by ice shelf basal melt (*high confidence*), outpace mass gain from increased snow accumulation on the continent (*very high confidence*). However, there is only *limited evidence*, with *medium agreement*, of anthropogenic forcing of the observed Antarctic mass loss since 1992 (with *low confidence* in process attribution). Increasing mass loss from ice shelves and inland discharge will *likely* continue to outpace increasing snowfall over the 21st century (Figure TS.11f). Deep uncertainty persists with respect to the possible evolution of the Antarctic Ice Sheet along high-end mass-loss storylines within the 21st century and beyond, primarily related to the abrupt and widespread onset of Marine Ice Sheet Instability and Marine Ice Cliff Instability. {2.3.2, 3.4.3, 9.4.2, 9.6.3, Box 9.4, Atlas.11.1, Box TS.3, Box TS.4}

[START BOX TS.4 HERE]

Box TS.4: Sea Level

Global mean sea level (GMSL) increased by 0.20 [0.15 to 0.25] m over the period 1901 to 2018 with a rate of rise that has accelerated since the 1960s to 3.7 [3.2 to 4.2] mm yr^{-1} for the period 2006–2018 (*high confidence*). Human activity was *very likely* the main driver of observed GMSL rise since 1970, and new observational evidence leads to an assessed sea level rise over the period 1901 to 2018 that is consistent with the sum of individual components contributing to sea level rise, including expansion due to ocean warming and melting of glaciers and ice sheets (*high confidence*). It is *virtually certain* that GMSL will continue to rise over the 21st century in response to continued warming of the climate system (Box TS.4, Figure 1). Sea level responds to GHG emissions more slowly than global surface temperature, leading to weaker scenario dependence over the 21st century than for global surface temperature (*high confidence*). This slow response also leads to long-term committed sea level rise, associated with ongoing ocean heat uptake and the slow adjustment of the ice sheets, that will continue over the centuries and millennia following cessation of emissions (*high confidence*). By 2100, GMSL is projected to rise by 0.28–0.55 m (*likely* range) under SSP1-1.9 and 0.63–1.02 m (*likely* range) under SSP5-8.5 relative to the 1995–2014 average (*medium confidence*). Under the higher CO_2 emissions scenarios, there is deep uncertainty in sea level projections for 2100 and beyond associated with the ice-sheet responses to warming. In a low-likelihood, high-impact storyline and a high CO_2 emissions scenario, ice-sheet processes characterized by deep uncertainty could drive GMSL rise up to about 5 m by 2150. Given the long-term commitment, uncertainty in the timing of reaching different GMSL rise levels is an important consideration for adaptation planning. {2.3, 3.4, 3.5, 9.6, Box 9.4, Box TS.9 Cross-Chapter Box 9.1, Table 9.5}

GMSL change is driven by warming or cooling of the ocean (and the associated expansion/contraction) and changes in the amount of ice and water stored on land. Paleo-evidence shows that GMSL has been about 70 m higher and 130 m lower than present within the past 55 million years and was *likely* 5 to 10 m higher during the Last Interglacial (Box TS.2, Figure 1). Sea level observations show that GMSL rose by 0.20 [0.15 to 0.25] m over the period 1901–2018 at an average rate of 1.7 [1.3 to 2.2] mm yr^{-1}. New analyses and paleo-evidence since the AR5 show this rate is *very likely* faster than during any century over at least the last three millennia (*high confidence*). Since the AR5, there is strengthened evidence for an increase in the rate of GMSL rise since the mid-20th century, with an average rate of 2.3 [1.6–3.1] mm yr^{-1} over the period 1971–2018 increasing to 3.7 [3.2–4.2] mm yr^{-1} for the period 2006–2018 (*high confidence*). {2.3.3.3, 9.6.1, 9.6.2}

GMSL will continue to rise throughout the 21st century (Box TS.4, Figure 1a). Considering only those processes in whose projections we have at least *medium confidence*, relative to the period 1995–2014,

ACCEPTED VERSION SUBJECT TO FINAL EDITING

GMSL is projected to rise between 0.18 m (0.15–0.23 m, *likely range*) (SSP1-1.9) and 0.23 m (0.20–0.30 m, *likely range*) (SSP5-8.5) by 2050. By 2100, the projected rise is between 0.38 m (0.28–0.55 m, *likely range*) (SSP1-1.9) and 0.77 m (0.63–1.02 m, *likely range*) (SSP5-8.5) (Table 9.9). The methods, models and scenarios used for sea level projections in the AR6 are updated from those employed by the SROCC, with contributions informed by the latest model projections described in the ocean and cryosphere sections (TS.2.4 and TS.2.5). Despite these differences, the sea level projections are broadly consistent with those of the SROCC. {4.3.2, 9.6.3}

Importantly, *likely* range projections do not include those ice-sheet-related processes whose quantification is highly uncertain or that are characterized by deep uncertainty. Higher amounts of GMSL rise before 2100 could be caused by earlier-than-projected disintegration of marine ice shelves, the abrupt, widespread onset of Marine Ice Sheet Instability (MISI) and Marine Ice Cliff Instability (MICI) around Antarctica, and faster-than-projected changes in the surface mass balance and dynamical ice loss from Greenland (Box TS.4, Figure 1). In a low-likelihood, high-impact storyline and a high CO_2 emissions scenario, such processes could in combination contribute more than one additional meter of sea level rise by 2100. {Box TS.3, 4.3.2, 9.6.3, Box 9.4}

Beyond 2100, GMSL will continue to rise for centuries to millennia due to continuing deep ocean heat uptake and mass loss from ice sheets, and will remain elevated for thousands of years (*high confidence*). By 2150, considering only those processes in whose projections we have at least *medium confidence* and assuming no acceleration in ice-mass flux after 2100, GMSL is projected to rise between 0.6 m (0.4–0.9 m, *likely* range) (SSP1-1.9) and 1.4 m (1.0–1.9 m, *likely* range) (SSP5-8.5), relative to the period 1995–2014 based on the SSP scenario extensions. Under high CO_2 emissions, processes in which there is *low confidence*, such as Marine Ice Cliff Instability (MICI), could drive GMSL rise up to about 5 m by 2150 (Box TS.4, Figure 1a). By 2300, GMSL will rise 0.3–3.1 m under low CO_2 emissions (SSP1-2.6) (*low confidence*). Under high CO_2 emissions (SSP5-8.5), projected GMSL rise is between 1.7 and 6.8 m by 2300 in the absence of MICI and by up to 16 m considering MICI (*low confidence*). Over 2000 years, there is *medium agreemen*t and *limited evidence* that committed GMSL rise is projected to be about 2–3 m with 1.5°C peak warming, 2–6 m with 2°C of peak warming, 4–10 m with 3°C of peak warming, 12–16 m with 4°C of peak warming, and 19–22 m with 5°C of peak warming. {TS.1.3.1, 9.6.3}

Looking at uncertainty in time provides an alternative perspective on uncertainty in future sea-level rise (Box TS.4, Figure 1c). For example, considering only *medium confidence* processes, GMSL rise is likely to exceed 0.5 m between about 2080 and 2170 under SSP1-2.6 and between about 2070 and 2090 under SSP5-8.5. Given the long-term commitment, uncertainty in the timing of reaching different levels of GMSL rise is an important consideration for adaptation planning. {9.6.3}

At regional scales, additional processes come into play that modify the local sea level change relative to GMSL, including vertical land motion; ocean circulation and density changes and gravitational, rotational, and deformational effects arising from the redistribution of water and ice mass between land and the ocean. These processes give rise to a spatial pattern that tends to increase sea level rise at the low latitudes and reduce sea-level rise at high latitudes. However, over the 21st century, the majority of coastal locations have a median projected regional sea level rise within ± 20% of the projected GMSL change (*medium confidence*). Further details on regional sea level change and extremes are provided in TS.4. {9.6.3}

[START BOX TS.4, FIGURE 1 HERE]

Box TS.4, Figure 1: Global mean sea level change on different time scales and under different scenarios. (a) GMSL change from 1900 to 2150, observed (1900–2018) and projected under the SSP scenarios (2000–2150), relative to a 1995–2014 baseline. Solid lines show median projections. Shaded regions show *likely* ranges for SSP1-2.6 and SSP3-7.0. Dotted and dashed lines show respectively the 83rd and 95th percentile low-confidence projections for SSP5-8.5. Bars at right show *likely* ranges for SSP1-1.9, SSP1-2.6, SSP2-4.5, SSP3-7.0, and SSP5-8.5 in 2150. Lightly shaded thick/thin bars show 17th–83rd/5th–95th percentile *low-confidence* ranges in 2150 for SSP1-2.6 and SSP5-8.5, based upon projection methods incorporating structured expert judgement

ACCEPTED VERSION SUBJECT TO FINAL EDITING

and Marine Ice Cliff Instability. *Low-confidence* range for SSP5-8.5 in 2150 extends to 4.8/5.4 m at the 83rd/95th percentile. (b) GMSL change on 100- (blue), 2,000- (green) and 10,000-year (magenta) time scales as a function of global surface temperature, relative to 1850–1900. For 100-year projections, GMSL is projected for the year 2100, relative to a 1995-2014 baseline, and temperature anomalies are average values over 2081–2100. For longer-term commitments, warming is indexed by peak warming above 1850–1900 reached after cessation of emissions. Shaded regions show paleo-constraints on global surface temperature and GMSL for the Last Interglacial and mid-Pliocene Warm Period. Lightly shaded thick/thin blue bars show 17th–83rd/5th–95th percentile *low-confidence* ranges for SSP1-2.6 and SSP5-8.5 in 2100, plotted at 2°C and 5°C. (c) Timing of exceedance of GMSL thresholds of 0.5, 1.0, 1.5 and 2.0 m, under different SSPs. Lightly shaded thick/thin bars show 1th7–83rd/5th–95th percentile *low-confidence* ranges for SSP1-2.6 and SSP5-8.5.

[END BOX TS.4, FIGURE 1 HERE]

[END BOX TS.4 HERE]

[START BOX TS.5 HERE]

Box TS.5: The Carbon Cycle

The continued growth of atmospheric CO_2 concentrations over the industrial era is unequivocally due to emissions from human activities. Ocean and land carbon sinks slow the rise of CO_2 in the atmosphere. Projections show that while land and ocean sinks absorb more CO_2 under high emissions scenarios than low emissions scenarios, the fraction of emissions removed from the atmosphere by natural sinks decreases with higher concentrations (*high confidence*). Projected ocean and land sinks show similar responses for a given scenario, but the land sink has a much higher inter-annual variability and wider model spread. The slowed growth rates of the carbon sinks projected for the second half of this century are linked to strengthening carbon–climate feedbacks and stabilization of atmospheric CO_2 under medium-to-no-mitigation and high-mitigation scenarios respectively. {5.2, 5.4}

Carbon sinks for anthropogenic CO_2 are associated with mainly physical ocean and biospheric land processes that drive the exchange of carbon between multiple land, ocean and atmospheric reservoirs. These exchanges are driven by increasing atmospheric CO_2, but modulated by changes in climate (Box TS.5, Figure 1 c,d). The Northern and Southern Hemispheres dominate the land and ocean sinks, respectively (Box TS.5, Figure 1). Ocean circulation and thermodynamic processes also play a critical role in coupling the global carbon and energy (heat) cycles. There is *high confidence* that this ocean carbon–heat nexus is an important basis for one of the most important carbon–climate metrics, the transient climate response to cumulative CO_2 emissions (TCRE) (TS.3.2.1) used to determine the remaining carbon budget. {5.1, 5.2, 5.5, 9.2, Cross-Chapter Box 5.3}

Based on multiple lines of evidence using interhemispheric gradients of CO_2 concentrations, isotopes, and inventory data, it is unequivocal that the growth in CO_2 in the atmosphere since 1750 (see TS.2.2) is due to the direct emissions from human activities. The combustion of fossil fuels and land-use change for the period 1750–2019 resulted in the release of 700 ± 75 PgC (*likely* range, 1 PgC = 10^{15} g of carbon) to the atmosphere, of which about 41% ± 11% remains in the atmosphere today (*high confidence*). Of the total anthropogenic CO_2 emissions, the combustion of fossil fuels was responsible for about 64% ± 15%, growing to an 86% ± 14% contribution over the past 10 years. The remainder resulted from land-use change. During the last decade (2010–2019), average annual anthropogenic CO_2 emissions reached the highest levels in human history at 10.9 ± 0.9 PgC yr^{-1} (*high confidence*). Of these emissions, 46% accumulated in the atmosphere (5.1 ± 0.02 PgC yr^{-1}), 23% (2.5 ± 0.6 PgC yr^{-1}) was taken up by the ocean and 31% (3.4 ± 0.9 PgC yr^{-1}) was removed by terrestrial ecosystems (*high confidence*). {5.2.1, 5.2.2, 5.2.3}

The ocean (*high confidence*) and land (*medium confidence*) sinks of CO_2 have increased with anthropogenic emissions over the past six decades (Box TS.5, Figure 1). This coherence between emissions and the growth

ACCEPTED VERSION SUBJECT TO FINAL EDITING

in ocean and land sinks has resulted in the airborne fraction of anthropogenic CO_2 remaining at 44%±10% over the past 60 years (*high confidence*). Interannual and decadal variability of the ocean and land sinks indicate that they are sensitive to changes in the growth rate of emissions as well as climate variability, and therefore also sensitive to climate change (*high confidence*). {5.2.1}

The land CO_2 sink is driven by carbon uptake by vegetation, with large interannual variability, for example, linked to ENSO. Since the 1980s, carbon fertilization from rising atmospheric CO_2 has increased the strength of the net land CO_2 sink (*medium confidence*). During the historical period, the growth of the ocean sink has been primarily determined by the growth rate of atmospheric CO_2. However, there is *medium confidence* that changes to physical and chemical processes in the ocean and in the land biosphere, which govern carbon feedbacks, are already modifying the characteristics of variability, particularly the seasonal cycle of CO_2 in both the ocean and land. However, changes to the multi-decadal trends in the sinks have not yet been observed. {2.3.4, 3.6.1, 5.2.1, TS.2.3, TS.2.6}

In AR6, ESM projections are assessed with CO_2 concentrations by 2100 from about 400 ppm (SSP1-1.9) to above 1100 ppm (SSP5-8.5). Most simulations are performed with prescribed atmospheric CO_2 concentrations, which already account for a central estimate of climate–carbon feedback effects. CO_2 emissions-driven simulations account for uncertainty in these feedbacks, but do not significantly change the projected global surface temperature changes (*high confidence*). Although land and ocean sinks absorb more CO_2 under high emissions than low emissions scenarios, the fraction of emissions removed from the atmosphere decreases (*high confidence*). This means that the more CO_2 that is emitted, the less efficient the ocean and land sinks become (*high confidence*), an effect which compensates for the logarithmic relationship between CO_2 and its radiative forcing, which means that for each unit increase in additional atmospheric CO_2 the effect on global temperature decreases. (Box TS.5, Figure 1f,g). {4.3.1, 5.4.5, 5.5.1.2}

Ocean and land sinks show similar responses for a given scenario, but the land sink has a much higher inter-annual variability and wider model spread. Under SSP3-7.0 and SSP5-8.5, the initial growth of both sinks in response to increasing atmospheric concentrations of CO_2 is subsequently limited by emerging carbon–climate feedbacks (*high confidence*) (Box TS.5, Figure 1f). Projections show that the ocean and land sinks will stop growing from the second part of the 21st century under all emissions scenarios, but with different drivers for different emissions scenarios. Under SSP3-7.0 and SSP5-8.5, the weakening growth rate of the ocean CO_2 sink in the second half of the century is primarily linked to the strengthening positive feedback from reduced carbonate buffering capacity, ocean warming and altered ocean circulation (e.g., AMOC changes). In contrast, for SSP1-1.9, SSP1-2.6 and SSP2-4.5, the weakening growth rate of the ocean carbon sink is a response to the stabilizing or declining atmospheric CO_2 concentrations. Under high CO_2 emissions scenarios, it is *very likely* that the land carbon sink will grow more slowly due to warming and drying from the mid 21st century, but it is *very unlikely* that it will switch from being a sink to a source before 2100. Climate change alone is expected to increase land carbon accumulation in the high latitudes (not including permafrost, which is assessed in TS2.5 and TS.3.2.2), but also to lead to a counteracting loss of land carbon in the tropics (*medium confidence*). ESM projections show that the overall uncertainty of atmospheric CO_2 by 2100 is still dominated by the emission pathway, but carbon–climate feedbacks (see TS.3.3.2) are important, with increasing uncertainties in high emissions pathways (Box TS.5, Figure 1e). {4.3.2, 5.4.1, 5.4.2, 5.4.4, 5.4.5, 11.6, 11.9, Cross-Chapter Box 5.1, Cross-Chapter Box 5.3, TS.3.3.2}

Under three SSP scenarios with long-term extensions until 2300 (SSP5-8.5, SSP5-3.4-OS, SSP1-2.6), ESMs project a change of the land from a sink to a source (*medium confidence*). The scenarios make simplified assumptions about emissions reductions, with SSP1-2.6 and SSP5-3.4-OS reaching about 400 ppm by 2300, while SSP5-8.5 exceeds 2000 ppm. Under high emissions the transition is warming-driven, whereas it is linked to the decline in atmospheric CO_2 under net negative CO_2 emissions. The ocean remains a sink throughout the period to 2300 except under very large net negative emissions. The response of the natural aspects of the carbon cycle to carbon dioxide removal is further developed in TS.3.3.2. {5.4.9, TS.3.3.2; Figure Box TS.5f}

ACCEPTED VERSION SUBJECT TO FINAL EDITING

[START BOX TS.5, FIGURE 1 HERE]

Box TS.5, Figure 1: Carbon cycle processes and projections. Carbon cycle response to forcings. The figure shows changes in carbon storage in response to elevated CO_2 (a, b) and the response to climate warming (c, d). Maps show spatial patterns of changes in carbon uptake during simulations with 1% per year increase in CO_2 {section 5.4.5.5}, and zonal mean plots show distribution of carbon changes is dominated by the land (green lines) in the tropics and northern hemisphere and ocean (blue lines) in the southern hemisphere. Hatching indicates regions where fewer than 80% of models agree on the sign of response. (e) Future CO_2 projections: projected CO_2 concentrations in the SSP scenarios in response to anthropogenic emissions, results from coupled ESMs for SSP5-8.5 and from the MAGICC7 emulator for other scenarios {section 4.3.1}. (f) Future carbon fluxes: projected combined land and ocean fluxes (positive downward) up to 2100 for the SSP scenarios, and extended to 2300 for available scenarios, 5-95% uncertainty plumes shown for SSP1-2.6 and SSP3-7.0 {section 5.4.5.4, 5.4.10}. The numbers near the top show the number of model simulations used. (g) Sink fraction: the fraction of cumulative emissions of CO_2 removed by land and ocean sinks. The sink fraction is smaller under conditions of higher emissions. {5.4.5, 5.5.1; Figure 5.27; Figure 4.31; Figure 5.25; Figure 5.30; Figure 5.31}

[END BOX TS.5, FIGURE 1 HERE]

[END BOX TS.5 HERE]

TS.2.6 Land Climate, Including Biosphere and Extremes

Land surface air temperatures have risen faster than the global surface temperature since the 1850s, and it is *virtually certain* that this differential warming will persist into the future. It is *virtually certain* that the frequency and intensity of hot extremes and the intensity and duration of heat waves have increased since 1950 and will further increase in the future even if global warming is stabilized at 1.5°C. The frequency and intensity of heavy precipitation events have increased over a majority of those land regions with good observational coverage (*high confidence*) and will *extremely likely* increase over most continents with additional global warming. Over the past half century, key aspects of the biosphere have changed in ways that are consistent with large-scale warming: climate zones have shifted poleward, and the growing season length in the Northern Hemisphere extratropics has increased (*high confidence*). The amplitude of the seasonal cycle of atmospheric CO_2 poleward of 45°N has increased since the 1960s (*very high confidence*), with increasing productivity of the land biosphere due to the increasing atmospheric CO_2 concentration as the main driver (*medium confidence*). Global-scale vegetation greenness has increased since the 1980s (*high confidence*). {2.3, 3.6, 4.3, 4.5, 5.2, 11.3, 11.4, 11.9, 12.4}

Observed temperatures over land have increased by 1.61 [1.34–1.83] °C between the period 1850–1900 and 2011–2020. Warming of the land is about 45% larger than for global surface temperature, and about 80% larger than warming of the ocean surface. Warming of the land surface during the period 1971–2018 contributed about 5% of the increase in the global energy inventory (TS.3.1), nearly twice the estimate in AR5 (*high confidence*). It is *virtually certain* that the average surface warming over land will continue to be higher than over the ocean throughout the 21st century. The warming pattern will *likely* vary seasonally, with northern high latitudes warming more during winter than summer (*medium confidence*). {2.3.1, 4.3.1, 4.5.1, Box 7.2, 7.2.2, Cross-Chapter Box 9.1, 11.3, Atlas 11.2}

The frequency and intensity of hot extremes (warm days and nights) and the intensity and duration of heatwaves have increased globally and in most regions since 1950, while the frequency and intensity of cold extremes have decreased (*virtually certain*). There is *high confidence* that the increases in frequency and severity of hot extremes are due to human-induced climate change. Some recent extreme events would have been *extremely unlikely* to occur without human influence on the climate system. It is *virtually certain* that the further changes in hot and cold extremes will occur throughout the 21st century in nearly all inhabited

ACCEPTED VERSION SUBJECT TO FINAL EDITING

regions, even if global warming is stabilized at 1.5°C (Table TS.2, Figure TS.12a). {1.3, Cross-Chapter Box 3.2, 11.1.4, 11.3.2, 11.3.4, 11.3.5, 11.9, 12.4}

Greater warming over land alters key water cycle characteristics (Box TS.6). The rate of change in mean precipitation and runoff, and their variability, increases with global warming (Figure TS.12e,f). The majority of the land area has experienced decreases in available water during dry seasons due to the overall increase in evapotranspiration (*medium confidence*). The land area affected by increasing drought frequency and severity will expand with increasing global warming (*high confidence*; Figure TS.12c). There is *low confidence* that the increase of plant water-use efficiency due to higher atmospheric CO_2 concentration alleviates extreme agricultural and ecological droughts in conditions characterized by limited soil moisture and increased atmospheric evaporative demand. {2.3.1, CCB 5.1, 8.2.3, 8.4.1, Box 11.1, 11.2.4, 11.4, 11.6}

Northern Hemisphere spring snow cover has decreased since at least 1978 (*very high confidence*), and there is *high confidence* that trends in snow cover loss extend back to 1950. It is *very likely* that human influence contributed to these reductions. Earlier onset of snowmelt has contributed to seasonally dependent changes in streamflow (*high confidence*). A further decrease of Northern Hemisphere seasonal snow cover extent is *virtually certain* under further global warming (Figure TS.12d). {2.3.2, 3.4.2, 8.3.2. 9.5.3, 12.4, Atlas 8.2, 9.2, 11.2}

The frequency and intensity of heavy precipitation events have increased over a majority of land regions with good observational coverage since 1950 (*high confidence*, Box TS.6, Table TS.2). Human influence is *likely* the main driver of this change (Table TS.2). It is *extremely likely* that on most continents heavy precipitation will become more frequent and more intense with additional global warming (Table TS.2, Figure TS.12 b). The projected increase in heavy precipitation extremes translates to an increase in the frequency and magnitude of pluvial floods (*high confidence*) (Table TS.2). {Cross-Chapter Box 3.2, 8.4.1, 11.4.2, 11.4.4, 11.5.5, 12.4}

The probability of compound extreme events has *likely* increased due to human-induced climate change. Concurrent heat waves and droughts have become more frequent over the last century, and this trend will continue with higher global warming (*high confidence*). The probability of compound flooding (storm surge, extreme rainfall and/or river flow) has increased in some locations, and will continue to increase due to both sea level rise and increases in heavy precipitation, including changes in precipitation intensity associated with tropical cyclones (*high confidence*). {11.8.1, 11.8.2, 11.8.3}

Changes in key aspects of the terrestrial biosphere, such as an increase of the growing season length in much of the Northern Hemisphere extratropics since the mid-20th century (*high confidence*), are consistent with large-scale warming. At the same time an increase in the amplitude of the seasonal cycle of atmospheric CO_2 beyond 45°N since the early 1960s (*high confidence*) and a global-scale increase in vegetation greenness of the terrestrial surface since the early 1980s (*high confidence*) have been observed. Increasing atmospheric CO_2, warming at high latitudes and land management interventions have contributed to the observed greening trend, but there is *low confidence* in their relative roles. There is *medium confidence* that increased plant growth associated with CO_2 fertilization is the main driver of the observed increase in amplitude of the seasonal cycle of atmospheric CO_2 in the Northern hemisphere. Reactive nitrogen, ozone and aerosols affect terrestrial vegetation and carbon cycle through deposition and effects on large-scale radiation (*high confidence*), but the magnitude of these effects on the land carbon sink, ecosystem productivity and indirect CO_2 forcing remains uncertain. {2.3.4, 3.6.1, 5.2.1, 6.4.5, 12.3.7, 12.4}

Over the last century, there has been a poleward and upslope shift in the distribution of many land species (*very high confidence*) as well as increases in species turnover within many ecosystems (*high confidence*). There is *high confidence* that the geographical distribution of climate zones has shifted in many parts of the world in the last half century. SRCCL concluded that continued warming will exacerbate desertification processes (*medium confidence*) and ecosystems will become increasingly exposed to climates beyond those that they are currently adapted to (*high confidence*). There is *medium confidence* that climate change will increase disturbance by, for example, fire and tree mortality across several ecosystems. Increases are projected in drought, aridity, and fire weather in some regions (TS.4.3; *high confidence*). There is *low*

ACCEPTED VERSION SUBJECT TO FINAL EDITING

confidence in the magnitude of these changes, but the probability of crossing uncertain regional thresholds (e.g., fires, forest dieback) increases with further warming (*high confidence*). The response of biogeochemical cycles to the anthropogenic perturbation can be abrupt at regional scales, and irreversible on decadal to century time scales (*high confidence*). {2.3.4, 5.4.3, 5.4.9, 11.6, 11.8, 12.5, SRCCL 2.2, SRCCL 2.5, SR1.5 3.4}

[START FIGURE TS.12 HERE]

Figure TS.12: Land-related changes relative to the 1850-1900 as a function of global warming levels. a) Changes in the frequency (left scale) and intensity (in °C, right scale) of daily hot extremes occurring every 10- and 50-years; b) as a), but for daily heavy precipitation extremes, with intensity change in %; c) Changes in 10-year droughts aggregated over drought-prone regions (CNA, NCA, SCA, NSA, SAM, SWS, SSA, MED, WSAF, ESAF, MDG, SAU, and EAU; for definitions of these regions, see Atlas.2), with drought intensity (right scale) represented by the change of annual mean soil moisture, normalized with respect to interannual variability; d) Changes in Northern Hemisphere spring (March-April-May) snow cover extent relative to 1850-1900; e,f) Relative change (%) in annual mean of total precipitable water (grey line), precipitation (red solid lines), runoff (blue solid lines) and in standard deviation (i.e. variability) of precipitation (red dashed lines) and runoff (blue dashed lines) averaged over (e) tropical and (f) extratropical land as function of global warming levels. CMIP6 models that reached a 5°C warming level in the 21st century in SSP5-8.5 above the 1850-1900 average have been used. Precipitation and runoff variability are estimated by respective standard deviation after removing linear trends. Error bars show the 17-83% confidence interval for the warmest +5°C global warming level. {Figures 11.6, 11.7, 11.12, 11.15, 11.18, 9.24, 8.16, Atlas.2}

[END FIGURE TS.12 HERE]

[START BOX TS.6 HERE]

Box TS.6: Water Cycle

Human-caused climate change has driven detectable changes in the global water cycle since the mid-20th century (*high confidence*), and it is projected to cause substantial further changes at both global and regional scales (*high confidence*). Global land precipitation has *likely* increased since 1950, with a faster increase since the 1980s (*medium confidence*). Atmospheric water vapour has increased throughout the troposphere since at least the 1980s (*likely*). Annual global land precipitation will increase over the 21st century as global surface temperature increases (*high confidence*). Human influence has been detected in amplified surface salinity and precipitation minus evaporation (P-E) patterns over the ocean (*high confidence*). The severity of very wet and very dry events increase in a warming climate (*high confidence*), but changes in atmospheric circulation patterns affect where and how often these extremes occur. Water cycle variability and related extremes are projected to increase faster than mean changes in most regions of the world and under all emission scenarios (*high confidence*). Over the 21st century, the total land area subject to drought will increase and droughts will become more frequent and severe (*high confidence*). Near-term projected changes in precipitation are uncertain mainly because of internal variability, model uncertainty and uncertainty in forcings from natural and anthropogenic aerosols (*medium confidence*). Over the 21st century and beyond, abrupt human-caused changes to the water cycle cannot be excluded (*medium confidence*). {2.3, 3.3, 4.3, 4.4, 4.5, 4.6, 8.2, 8.3, 8.4, 8.5, 8.6, 11.4, 11.6, 11.9}

There is *high confidence* that the global water cycle has intensified since at least 1980 expressed by, for example, increased atmospheric moisture fluxes and amplified precipitation minus evaporation patterns. Global land precipitation has *likely* increased since 1950, with a faster increase since the 1980s (*medium confidence*), and a *likely* human contribution to patterns of change, particularly for increases in high-latitude precipitation over the Northern Hemisphere. Increases in global mean precipitation are determined by a robust response to global surface temperature (*very likely* 2–3% per °C) that is partly offset by fast atmospheric adjustments to atmospheric heating by GHGs and aerosols (TS.3.2.2). The overall effect of

ACCEPTED VERSION SUBJECT TO FINAL EDITING

anthropogenic aerosols is to reduce global precipitation through surface radiative cooling effects (*high confidence*). Over much of the 20th century, opposing effects of GHGs and aerosols on precipitation have been observed for some regional monsoons (*high confidence*) (Box TS.13). Global annual precipitation over land is projected to increase on average by 2.4% (–0.2% to 4.7% *likely* range) under SSP1-1.9, 4.6% (1.5% to 8.3% *likely* range) under SSP2-4.5, and 8.3% (0.9% to 12.9% *likely* range) under SSP5-8.5 by 2081–2100 relative to 1995–2014 (Box TS.6, Figure 1). Inter-model differences and internal variability contribute to a substantial range in projections of large-scale and regional water cycle changes (*high confidence*). The occurrence of volcanic eruptions can alter the water cycle for several years (*high confidence*). Projected patterns of precipitation change exhibit substantial regional differences and seasonal contrast as global surface temperature increases over the 21st century (Box TS.6, Figure 1). {2.3.1, 3.3.2, 3.3.3, 3.5.2, 4.3.1, 4.4.1, 4.5.1, 4.6.1, Cross-Chapter Box 4.1, 8.2.1, 8.2.2, 8.2.3, Box 8.1, 8.3.2.4, 8.4.1, 8.5.2, 10.4.2}

Global total column water vapour content has *very likely* increased since the 1980s, and it is *likely* that human influence has contributed to tropical upper tropospheric moistening. Near-surface specific humidity has increased over the ocean (*likely*) and land (*very likely*) since at least the 1970s, with a detectable human influence (*medium confidence*). Human influence has been detected in amplified surface salinity and precipitation minus evaporation (P-E) patterns over the ocean (*high confidence*). It is *virtually certain* that evaporation will increase over the ocean, and *very likely* that evapotranspiration will increase over land, with regional variations under future surface warming (Box TS.6, Figure 1). There is *high confidence* that projected increases in precipitation amount and intensity will be associated with increased runoff in northern high latitudes (Box TS.6, Figure 1). In response to cryosphere changes (TS.2.5), there have been changes in streamflow seasonality, including an earlier occurrence of peak streamflow in high-latitude and mountain catchments (*high confidence*). Projected runoff (Box TS.6, Figure 1c) is typically decreased by contributions from small glaciers because of glacier mass loss, while runoff from larger glaciers will generally increase with increasing global warming levels until their mass becomes depleted (*high confidence*). {2.3.1, 3.3.2, 3.3.3, 3.5.2, 8.2.3, 8.4.1, 11.5}

Warming over land drives an increase in atmospheric evaporative demand and in the severity of drought events (*high confidence*). Greater warming over land than over the ocean alters atmospheric circulation patterns and reduces continental near-surface relative humidity, which contributes to regional drying (*high confidence*). A *very likely* decrease in relative humidity has occurred over much of the global land area since 2000. Projected increases in evapotranspiration due to growing atmospheric water demand will decrease soil moisture (Box TS.6, Figure 1) over the Mediterranean region, southwestern North America, South Africa, southwestern South America and southwestern Australia (*high confidence*). Some tropical regions are also projected to experience enhanced aridity, including the Amazon basin and Central America (*high confidence*). The total land area subject to increasing drought frequency and severity will expand (*high confidence*), and in the Mediterranean, southwestern South America, and western North America, future aridification will far exceed the magnitude of change seen in the last millennium (*high confidence*). {4.5.1, 8.2.2, 8.2.3, 8.4.1, Box 8.2, 11.6, 11.9}

Land-use change and water extraction for irrigation have influenced local and regional responses in the water cycle (*high confidence*). Large-scale deforestation *likely* decreases evapotranspiration and precipitation and increases runoff over the deforested regions relative to the regional effects of climate change (*medium confidence*). Urbanization increases local precipitation (*medium confidence*) and runoff intensity (*high confidence*) (Box TS.14:). Increased precipitation intensities have enhanced groundwater recharge, most notably in tropical regions (*medium confidence*). There is *high confidence* that groundwater depletion has occurred since at least the start of the 21st century, as a consequence of groundwater withdrawals for irrigation in agricultural areas in drylands. {8.2.3, 8.3.1, 11.1.6, 11.4, 11.6, FAQ 8.1}

[START BOX TS.6, FIGURE 1 HERE]

Box TS.6, Figure 1: Projected water cycle changes. Long-term (2081–2100) projected annual mean changes (%) relative to present-day (1995–2014) in the SSP2-4.5 emissions scenario for (a) precipitation, (b) surface evapotranspiration, (c) total runoff and (d) surface soil moisture. Top-right panel numbers

ACCEPTED VERSION SUBJECT TO FINAL EDITING

indicate the number of CMIP6 models used for estimating the ensemble mean. For other scenarios, please refer to relevant figures in Chapter 8. Uncertainty is represented using the simple approach: No overlay indicates regions with high model agreement, where ≥80% of models agree on sign of change; diagonal lines indicate regions with low model agreement, where <80% of models agree on sign of change. For more information on the simple approach, please refer to the Cross-Chapter Box Atlas.1. {8.4.1, Figures 8.14, 8.17, 8.18, 8.19}

[END BOX TS.6, FIGURE 1 HERE]

Water cycle variability and related extremes are projected to increase faster than mean changes in most regions of the world and under all emissions scenarios (*high confidence*). A warmer climate increases moisture transport into weather systems, which intensifies wet seasons and events (*high confidence*). The magnitudes of projected precipitation increases and related extreme events depend on model resolution and the representation of convective processes (*high confidence*). Increases in near-surface atmospheric moisture capacity of about 7% per 1ºC of warming lead to a similar response in the intensification of heavy precipitation from sub-daily up to seasonal time scales, increasing the severity of flood hazards (*high confidence*). The average and maximum rain-rates associated with tropical and extratropical cyclones, atmospheric rivers and severe convective storms will therefore also increase with future warming (*high confidence*). For some regions, there is *medium confidence* that peak tropical cyclone rain-rates will increase by more than 7% per 1°C of warming due to increased low-level moisture convergence caused by increases in wind intensity. In the tropics year-round and in the summer season elsewhere, interannual variability of precipitation and runoff over land is projected to increase at a faster rate than changes in seasonal mean precipitation (Figure TS.12e,f) (*medium confidence*). Sub-seasonal precipitation variability is also projected to increase with fewer rainy days but increased daily mean precipitation intensity over many land regions (*high confidence*). {4.5.3, 8.2.3, 8.4.1, 8.4.2, 8.5.1, 8.5.2, 11.4,11.5, 11.7, 11.9}

[END BOX TS.6 HERE]

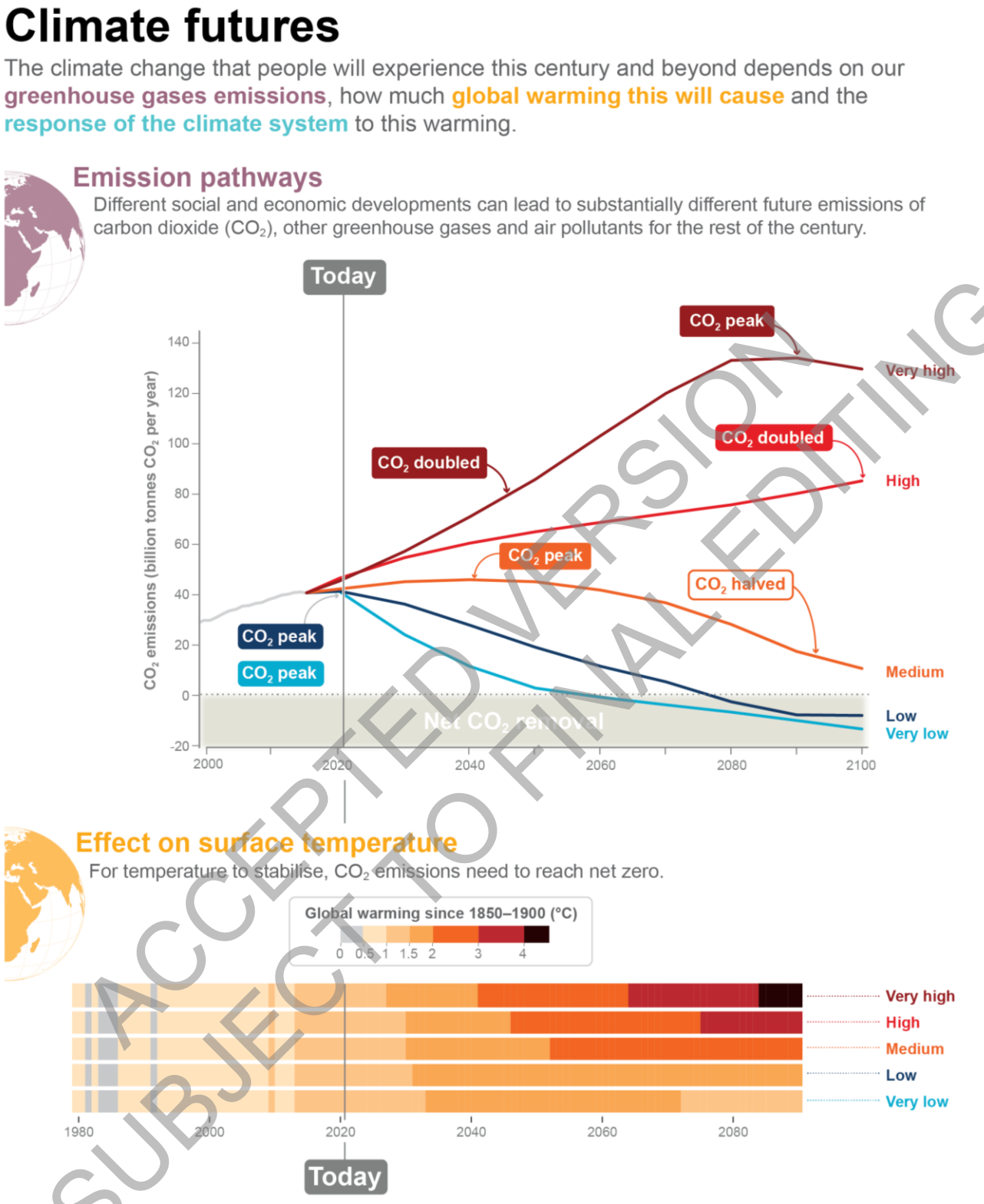
[START INFOGRAPHIC TS.1 HERE]

Infographic TS.1: Climate Futures.

(top left) Annual emissions of CO_2 for the five core Shared Socio-economic Pathway (SSP) scenarios (very low: SSP1-1.9, low: SSP1-2.6, medium: SSP2-4.5, high: SSP3-7.0, very high SSP5-8.5). (bottom left) Projected warming for each of these emissions scenarios. (top right) Response of some selected climate variables to 4 levels of global warming (°C). (bottom right) The long-term effect of each global warming level on sea level. See TS.1.3.1 for more detail on the SSP climate change scenarios.

ACCEPTED VERSION SUBJECT TO FINAL EDITING

1 a)

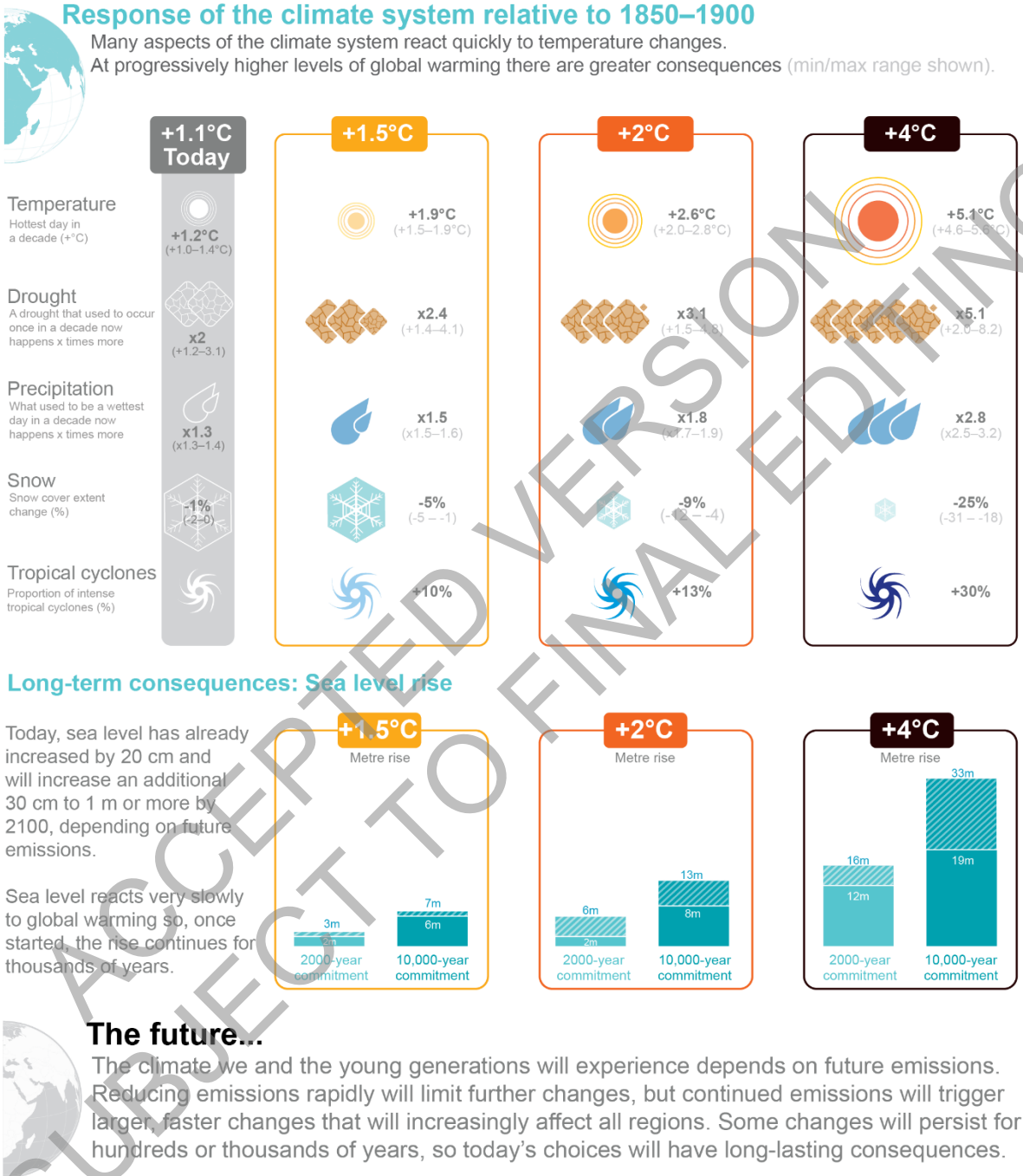


2
3
4

ACCEPTED VERSION SUBJECT TO FINAL EDITING

b)

Climate futures



ACCEPTED VERSION SUBJECT TO FINAL EDITING

[END INFOGRAPHIC TS.1 HERE]

TS.3 Understanding the Climate System Response and Implications for Limiting Global Warming

This section summarizes advances in our knowledge of the Earth's energy budget, including the time evolution of forcings and climate feedbacks that lead to the climate system responses summarized in TS.2. It assesses advances since AR5 and SR1.5 in the estimation of remaining carbon budgets, the Earth system response to carbon dioxide removal and quantification of metrics that allow comparison of the relative effects of different forcing agents. The section also highlights future climate and air pollution responses due to projected changes in short-lived climate forcers (SLCFs), the state of understanding of the climate response to potential interventions related to solar radiation modification (SRM), and irreversibility, tipping points and abrupt changes in the climate system.

TS.3.1 Radiative Forcing and Energy Budget

Since AR5, the accumulation of energy in the Earth system, quantified by observations of warming of the ocean, atmosphere, land and melting of ice, has become established as a robust measure of the rate of global climate change on interannual-to-decadal time scales. Compared to changes in global surface temperature, the increase in the global energy inventory exhibits less variability, and thus better indicates underlying climate trends. The global energy inventory increased by 435 [325 to 545] Zettajoules (ZJ, equal to 10^{21} Joules) for the period 1971–2018 and 153 [100 to 206] ZJ for the period 2006–2018 (Figure TS.13), with more than 90% accounted for by ocean warming. To put these numbers in context, the 2006–2018 average Earth system heating is equivalent to approximately 20 times the rate of global energy consumption in 2018. The accumulation of energy is driven by a positive total anthropogenic effective radiative forcing (ERF) relative to 1750. The best estimate ERF of 2.72 W m^{-2} has increased by 0.43 Wm^{-2} relative to that given in AR5 (for 1750–2014) due to an increase in the greenhouse gas ERF that is partly compensated by a more negative aerosol ERF compared to AR5. The greenhouse gas ERF has been revised due to changes in atmospheric concentrations and updates to forcing efficiencies, while the revision to aerosol ERF is due to increased understanding of aerosol–cloud interactions and is supported by improved agreement between different lines of evidence. Improved quantification of ERF, the climate system radiative response and the observed energy increase in the Earth system for the period 1971–2018 demonstrate improved closure of the global energy budget (i.e., the extent to which the sum of the integrated forcing and the integrated radiative response equals the energy gain of the Earth system) compared to AR5. (*high confidence*) {7.2.2, Box 7.2, Table 7.1, 7.3.5, 7.5.2, FAQ7.1}

[START FIGURE TS.13 HERE]

Figure TS.13: Estimates of the net cumulative energy change (ZJ = 10^{21} Joules) for the period 1971–2018 associated with: (a) observations of changes in the Global Energy Inventory (b) Integrated Radiative Forcing; (c) Integrated Radiative Response. *The intent is to show assessed changes in energy budget and ERFs.* Black dotted lines indicate the central estimate with *likely* and *very likely* ranges as indicated in the legend. The grey dotted lines indicate the energy change associated with an estimated 1850-1900 Earth energy imbalance of 0.2 W m^{-2} (panel a) and an illustration of an assumed pattern effect of –0.5 W m^{-2}°C^{-1} (panel c). Background grey lines indicate equivalent heating rates in W m^{-2} per unit area of Earth's surface. Panels (d) and (e) show the breakdown of components, as indicated in the legend, for the Global Energy Inventory and Integrated Radiative Forcing, respectively. Panel (f) shows the Global Energy Budget assessed for the period 1971–2018, i.e. the consistency between the change in the Global Energy Inventory relative to 1850-1900 and the implied energy change from Integrated Radiative Forcing plus Integrated Radiative Response under a number of different assumptions, as indicated in the figure legend, including assumptions of correlated and uncorrelated uncertainties in Forcing plus Response. Shading represents the *very likely* range for observed energy change relative to 1850-1900 and *likely* range for all other quantities. Forcing and Response timeseries are expressed relative to a baseline period of 1850–1900. {Box 7.2 Figure 1}

[END FIGURE TS.13 HERE]

ACCEPTED VERSION SUBJECT TO FINAL EDITING

The global energy inventory change for the period 1971–2018 corresponds to an Earth energy imbalance (Box TS.1) of 0.57 [0.43 to 0.72] W m^{-2}, increasing to 0.79 [0.52 to 1.06] W m^{-2} for the period 2006–2018. Ocean heat uptake is by far the largest contribution and accounts for 91% of the total energy change. Land warming, melting of ice and warming of the atmosphere account for about 5%, 3% and 1% of the total change, respectively. More comprehensive analysis of inventory components, cross-validation of satellite and in situ-based estimates of the global energy imbalance and closure of the global sea level budget have led to a strengthened assessment relative to AR5. (*high confidence*) {Box 7.2, 7.2.2, Table 7.1, 7.5.2.3, Cross-Chapter Box 9.1, 9.6.1, Table 9.5}

As in AR5, the perturbations to the Earth's top-of-atmosphere energy budget are quantified using ERFs (also see TS.2.2). These include any consequent adjustments to the climate system (e.g., from changes in atmospheric temperatures, clouds, and water vapour as shown in Figure TS.14), but exclude any surface temperature response. Since the AR5, ERFs have been estimated for a larger number of forcing agents and shown to be more closely related to the temperature response than the stratospheric-temperature adjusted radiative forcing. (*high confidence*) {7.3.1}

[START FIGURE TS.14 HERE]

Figure TS.14: Schematic representation of changes in the top-of atmosphere (TOA) radiation budget following a perturbation. *The intent of the figure is to illustrate the concept of adjustments in the climate system following a perturbation in the radiation budget*. The baseline TOA energy budget (a) responds instantaneously to perturbations (b), leading to adjustments in the atmospheric meteorology and composition, and land surface that are independent of changes in surface temperature (c). Surface temperature changes (here using an increase as an example) lead to physical, biogeophysical and biogeochemical feedback processes (d). Long term feedback processes, such as those involving ice sheets, are not shown here. {adapted from Chapter 7 Figure 7.2, FAQ 7.2 Figure 1, and Figure 8.3}

[END FIGURE TS.14 HERE]

Improved quantification of ERF, the climate system radiative response, and the observed energy increase in the Earth system for the period 1971–2018, demonstrate improved closure of the global energy budget relative to AR5 (Figure TS.13). Combining the *likely* range of ERF over this period with the central estimate of radiative response gives an expected energy gain of 340 [47 to 662] ZJ. Both estimates are consistent with an independent observation-based assessment of the global energy increase of 284 [96 to 471] ZJ, (*very likely range*) expressed relative to the estimated 1850–1900 Earth energy imbalance. (*high confidence*) {7.2.2, Box 7.2, 7.3.5}

The assessed greenhouse gas ERF over the 1750–2019 period (TS.2.2) has increased by 0.59 W m^{-2} over AR5 estimates for 1750–2011. This increase includes +0.34 W m^{-2} from increases in atmospheric concentrations of well-mixed greenhouse gases (including halogenated species) since 2011, +0.15 W m^{-2} from upwards revisions of their radiative efficiencies and +0.10 W m^{-2} from re-evaluation of the ozone and stratospheric water vapour ERF. {7.3.2, 7.3.4, 7.3.5}

For CO_2, CH_4, N_2O, and chlorofluorocarbons, there is now evidence to quantify the effect on ERF of tropospheric adjustments. The assessed ERF for a doubling of CO_2 compared to 1750 levels (3.9 ± 0.5 Wm^{-2}) is larger than in AR5. For CO_2, the adjustments include the physiological effects on vegetation. The reactive well-mixed greenhouse gases (methane, nitrous oxide, and halocarbons) cause additional chemical adjustments to the atmosphere through changes in ozone and aerosols (Figure TS.15a). The ERF due to methane emissions is 1.21 [0.90 to 1.51] W m^{-2}, of which 0.33 [0.25 to 0.41] W m^{-2} is attributed to chemical adjustments mainly via ozone. These chemical adjustments also affect the emission metrics (Section TS.3.3.3). SO_2 emission changes make the dominant contribution to the ERF from aerosol–cloud interactions (*high confidence*). Over the 1750–2019 period, the contributions from the emitted compounds to global surface temperature changes broadly match their contributions to the ERF (*high confidence*) (Figure TS.15b). Since a peak in emissions-induced SO_2 ERF has already occurred recently (TS.2.2) and since there

ACCEPTED VERSION SUBJECT TO FINAL EDITING

is a delay in the full global surface temperature response owing to the thermal inertia in the climate system, changes in SO_2 emissions have a slightly larger contribution to global surface temperature change compared with changes in CO_2 emissions, relative to their respective contributions to ERF. {6.4.2, 7.3.2}

Aerosols contributed an ERF of –1.3 [–2.0 to –0.6] W m^{-2} over the period 1750 to 2014 (*medium confidence*). The ERF due to aerosol–cloud interactions (ERFaci) contributes most to the magnitude of the total aerosol ERF (*high confidence*), and is assessed to be –1.0 [–1.7 to –0.3] W m^{-2} (*medium confidence*), with the remainder due to aerosol–radiation interactions (ERFari), assessed to be –0.3 [–0.6 to 0.0] W m^{-2} (*medium confidence*). There has been an increase in the estimated magnitude – but a reduction in the uncertainty – of the total aerosol ERF relative to AR5, supported by a combination of increased process-understanding and progress in modelling and observational analyses (Figure TS.15c). Effective radiative forcing estimates from these separate lines of evidence are now consistent with each other, in contrast to AR5, and support the assessment that it is *virtually certain* that the total aerosol ERF is negative. Compared to AR5, the assessed magnitude of ERFaci has increased, while that of ERFari has decreased. {7.3.3, 7.3.5}

[START FIGURE TS.15 HERE]

Figure TS.15: Contribution to ERF and b) global surface temperature change from component emissions between 1750 to 2019 based on CMIP6 models and c) net aerosol effective radiative forcing (ERF) from different lines of evidence. *The intent of the figure is to show advances since AR5 in the understanding of a) aerosol ERF from different lines of evidence as assessed in Chapter 7, b) emissions-based ERF and c) global surface temperature response for SLCFs as estimated in Chapter 6.* In panel a), ERFs for well-mixed greenhouse gases (WMGHGs) are from the analytical formulae. ERFs for other components are multi-model means based on ESM simulations that quantify the effect of individual components. The derived emission-based ERFs are rescaled to match the concentration-based ERFs in Figure 7.6. Error bars are 5-95% and for the ERF account for uncertainty in radiative efficiencies and multi-model error in the means. In panel b), the global mean temperature response is calculated from the ERF time series using an impulse response function. In panel c), the AR6 assessment is based on energy balance constraints, observational evidence from satellite retrievals, and climate model-based evidence. For each line of evidence, the assessed best-estimate contributions from ERF due to ERFari and ERFaci are shown with darker and paler shading, respectively. Estimates from individual CMIP5 and CMIP6 models are depicted by blue and red crosses, respectively. The observational assessment for ERFari is taken from the instantaneous forcing due to aerosol-radiation interactions (IRFari). Uncertainty ranges are given in black bars for the total aerosol ERF and depict *very likely* ranges. {Sections 7.3.3, 6.4.2, Cross-Chapter Box 7.1, Figures 6.12, 7.5 ; Table 7.8}

[END FIGURE TS.15 HERE]

TS.3.2 Climate Sensitivity and Earth-System Feedbacks

TS.3.2.1 Equilibrium Climate Sensitivity, Transient Climate Response, and Transient Climate Response to Cumulative Carbon-dioxide Emissions

Since AR5, substantial quantitative progress has been made in combining new evidence of Earth's climate sensitivity, with improvements in the understanding and quantification of Earth's energy imbalance, the instrumental record of global surface temperature change, paleoclimate change from proxy records, climate feedbacks and their dependence on time scale and climate state. A key advance is the broad agreement across these multiple lines of evidence, supporting a best estimate of equilibrium climate sensitivity (ECS) of 3°C, with a *very likely* range of 2°C to 5°C. The *likely* range of 2.5°C to 4°C is narrower than the AR5 *likely* range of 1.5°C to 4.5°C. {7.4, 7.5}

Constraints on ECS and TCR (see Glossary) are based on four main lines of evidence: feedback process understanding, climate change and variability seen within the instrumental record, paleoclimate evidence, and so-called 'emergent constraints', whereby a relationship between an observable quantity and either ECS

ACCEPTED VERSION SUBJECT TO FINAL EDITING

or TCR established within an ensemble of models is combined with observations to derive a constraint on ECS or TCR. In reports up to and including the IPCC third assessment report, ECS and TCR derived directly from ESMs were the primary line of evidence. However, since AR4, historical warming and paleoclimates provided useful additional evidence (Figure TS.16a). AR6 differs from previous reports in not directly using climate model estimates of ECS and TCR in the assessed ranges of climate sensitivity. {1.5, 7.5}

It is now clear that when estimating ECS and TCR, the dependence of feedbacks on time scales and the climate state must be accounted for. Feedback processes are expected to become more positive overall (more amplifying of global surface temperature changes) on multi-decadal time scales as the spatial pattern of surface warming evolves and global surface temperature increases, leading to an ECS that is higher than was inferred in AR5 based on warming over the instrumental record (*high confidence*). Historical surface temperature change since 1870 has shown relatively little warming in several key regions of positive feedbacks, including the eastern equatorial Pacific Ocean and the Southern Ocean, while showing greater warming in key regions of negative feedbacks, including the western Pacific warm pool. Based on process understanding, climate modelling, and paleoclimate reconstructions of past warm periods, it is expected that future warming will become enhanced over the eastern Pacific Ocean (*medium confidence*) and Southern Ocean (*high confidence*) on centennial time scales. This new understanding, along with updated estimates of historical temperature change, ERF, and energy imbalance, reconciles previously disparate ECS estimates. {7.4.4, 7.5.2, 7.5.3,}

The AR6 best estimate of ECS is 3°C, the *likely* range is 2.5 to 4°C and the *very likely* range is 2 to 5°C. There is a high level of agreement among the four main lines of evidence listed above (Figure TS.16b), and altogether it is *virtually certain* that ECS is larger than 1.5°C, but currently it is not possible to rule out ECS values above 5°C. Therefore, the 5°C upper end of the *very likely* range is assessed with *medium confidence* and the other bounds with *high confidence*. {7.5.5}

Based on process understanding, warming over the instrumental record, and emergent constraints, the best estimate of TCR is 1.8°C, the *likely* range is 1.4° to 2.2°C and the *very likely* range is 1.2° to 2.4°C. There is a high level of agreement among the different lines of evidence (Figure TS.16c) (*high confidence*). {7.5.5}

On average, CMIP6 models have higher mean ECS and TCR values than the CMIP5 generation of models and also have higher mean values and wider spreads than the assessed best estimates and *very likely* ranges within this Report. These higher mean ECS and TCR values can, in some models, be traced to changes in extratropical cloud feedbacks (*medium confidence*). The broader ECS and TCR ranges from CMIP6 also lead the models to project a range of future warming that is wider than the assessed future warming range, which is based on multiple lines of evidence (Cross-Section Box TS.1). However, some of the high-sensitivity CMIP6 models (TS.1.2.2) are less consistent with observed recent changes in global warming and with paleoclimate proxy records than models with ECS within the *very likely* range. Similarly, some of the low-sensitivity models are less consistent with the paleoclimate data. The CMIP6 models with the highest ECS and TCRs values provide insights into low-likelihood, high-impact futures, which cannot be excluded based on currently available evidence (Cross-Section Box TS.1). {4.3.1, 4.3.4, 7.4.2, 7.5.6}

Uncertainties regarding the true value of ECS and TCR are the dominant source of uncertainty in global temperature projections over the 21st century under moderate to high GHG concentrations scenarios. For scenarios that reach net zero CO_2 emissions (TS.3.3), the uncertainty in the ERF values of aerosol and other SLCFs contribute substantial uncertainty in projected temperature. Global ocean heat uptake is a smaller source of uncertainty in centennial warming. {7.5.7}

[START FIGURE TS.16 HERE]

Figure TS.16: **a) Evolution of equilibrium climate sensitivity (ECS) assessments from the Charney Report through a succession of IPCC Assessment Reports to AR6, and lines of evidence and combined assessment for (b) ECS and (c) transient climate response (TCR) in AR6.** In panel (a), the lines of evidence considered are listed below each assessment. Best estimates are marked by horizontal bars,

ACCEPTED VERSION SUBJECT TO FINAL EDITING

likely ranges by vertical bars, and very likely ranges by dotted vertical bars. In panel (b) and (c), assessed ranges are taken from Tables 7.13 and 7.14 for ECS and TCR respectively. Note that for the ECS assessment based on both the instrumental record and paleoclimates, limits (i.e., one-sided distributions) are given, which have twice the probability of being outside the maximum/minimum value at a given end, compared to ranges (i.e., two tailed distributions) which are given for the other lines of evidence. For example, the *extremely likely* limit of greater than 95% probability corresponds to one side of the *very likely* (5% to 95%) range. Best estimates are given as either a single number or by a range represented by grey box. CMIP6 ESM values are not directly used as a line of evidence but are presented on the Figure for comparison. {Sections 1.5, 7.5; Tables 7.13, 7.14; Figures 7.18}

[END FIGURE TS.16 HERE]

The transient climate response to cumulative CO_2 emissions (TCRE) is the ratio between globally averaged surface temperature increase and cumulative CO_2 emissions (see Glossary). This report reaffirms with *high confidence* the finding of AR5 that there is a near-linear relationship between cumulative CO_2 emissions and the increase in global average temperature caused by CO_2 over the course of this century for global warming levels up to at least 2°C relative to 1850–1900. The TCRE falls *likely* in the 1.0°C–2.3°C per 1000 PgC range, with a best estimate of 1.65°C per 1000 PgC. This range is about 15% narrower than the 0.8°–2.5°C per 1000 PgC assessment of the AR5 because of a better integration of evidence across chapters, in particular the assessment of TCR. Beyond this century, there is *low confidence* that the TCRE alone remains an accurate predictor of temperature changes in scenarios of very low or net negative CO_2 emissions because of uncertain Earth system feedbacks that can result in further changes in temperature or a path dependency of warming as a function of cumulative CO_2 emissions. {5.4, 5.5.1, 4.6.2}

TS.3.2.2 Earth System Feedbacks

The combined effect of all climate feedback processes is to amplify the climate response to forcing (*virtually certain*). While major advances in the understanding of cloud processes have increased the level of confidence and decreased the uncertainty range for the cloud feedback by about 50% compared to AR5, clouds remain the largest contribution to overall uncertainty in climate feedbacks (*high confidence*). Uncertainties in the ECS and other climate sensitivity metrics, such as the transient climate response (TCR) and the transient climate response to cumulative CO_2 emissions (TCRE), are the dominant source of uncertainty in global temperature projections over the 21st century under moderate to high GHG emissions scenarios. CMIP6 models have higher mean values and wider spreads in ECS and TCR than the assessed best estimates and *very likely* ranges within this Report, leading the models to project a range of future warming that is wider than the assessed future warming range (TS.2.2). {7.1, 7.4.2, 7.5}

Earth system feedbacks can be categorised into three broad groups: physical feedbacks, biogeophysical and biogeochemical feedbacks, and feedbacks associated with ice sheets. In previous assessments, the ECS has been associated with a distinct set of physical feedbacks (Planck response, water vapour, lapse rate, surface albedo, and cloud feedbacks). In this assessment, a more general definition of ECS is adopted whereby all biogeophysical and biogeochemical feedbacks that do not affect the atmospheric concentration of CO_2 are included. These include changes in natural methane emissions, natural aerosol emissions, nitrous oxide, ozone, and vegetation, which all act on time scales of years to decades and are therefore relevant for temperature change over the 21st century. Because the total biogeophysical and non-CO_2 biogeochemical feedback is assessed to have a central value that is near zero (*low confidence*), including it does not affect the assessed ECS but does contribute to the net feedback uncertainty. The biogeochemical feedbacks that affect the atmospheric concentration of CO_2 are not included because ECS is defined as the response to a sustained doubling of CO_2. Moreover, the long-term feedbacks associated with ice sheets are not included in the ECS owing to their long time scales of adjustment. {5.4, 6.4, 7.4, 7.5, Box 7.1}

The net effect of changes in clouds in response to global warming is to amplify human-induced warming, that is, the net cloud feedback is positive (*high confidence*). Compared to AR5, major advances in the understanding of cloud processes have increased the level of confidence and decreased the uncertainty range

ACCEPTED VERSION SUBJECT TO FINAL EDITING

in the cloud feedback by about 50% (Figure TS.17a). An assessment of the low-altitude cloud feedback over the subtropical ocean, which was previously the major source of uncertainty in the net cloud feedback, is improved owing to a combined use of climate model simulations, satellite observations, and explicit simulations of clouds, altogether leading to strong evidence that this type of cloud amplifies global warming. The net cloud feedback is assessed to be +0.42 [–0.10 to 0.94] W m^{-2} °C^{-1}. A net negative cloud feedback is *very unlikely*. The CMIP5 and CMIP6 ranges of cloud feedback are similar to this assessed range, with CMIP6 having a slightly more positive median cloud feedback (*high confidence*). The surface albedo feedback and combined water vapour-lapse rate feedback are positive (Figure TS.17a), with *high confidence* in the estimated value of each based on multiple lines of evidence, including observations, models, and theory. {7.4.2, Figure 7.14, Table 7.10, Box TS.6}

Natural sources and sinks of non-CO_2 greenhouse gases such as methane (CH_4) and nitrous oxide (N_2O) respond both directly and indirectly to atmospheric CO_2 concentration and climate change, and thereby give rise to additional biogeochemical feedbacks in the climate system. Many of these feedbacks are only partially understood and are not yet fully included in ESMs. There is *medium confidence* that the net response of natural ocean and land CH_4 and N_2O sources to future warming will be increased emissions, but the magnitude and timing of the responses of each individual process is known with *low confidence*. {5.4.7}

Non-CO_2 biogeochemical feedbacks induced from changes in emissions, abundances or lifetimes of SLCFs mediated by natural processes or atmospheric chemistry are assessed to decrease ECS (Figure TS.17b). These non-CO_2 biogeochemical feedbacks are estimated from ESMs, which since AR5 have advanced to include a consistent representation of biogeochemical cycles and atmospheric chemistry. However, process-level understanding of many biogeochemical feedbacks involving SLCFs, particularly natural emissions, is still emerging, resulting in *low confidence* in the magnitude and sign of the feedbacks. The central estimate of the total biogeophysical and non-CO_2 biogeochemical feedback is assessed to be −0.01 [–0.27 to +0.25] W m^{-2} °C^{-1} (Figure TS.17a). {5.4.7, 5.4.8, 6.2.2, 6.4.5, 7.4, Table 7.10}

The combined effect of all known radiative feedbacks (physical, biogeophysical, and non-CO_2 biogeochemical) is to amplify the base climate response (in the absence of feedbacks), also known as the Planck temperature response[17] (*virtually certain*). Combining these feedbacks with the Planck response, the net climate feedback parameter is assessed to be –1.16 [–1.81 to –0.51] W m^{-2} °C^{-1}, which is slightly less negative than that inferred from the overall ECS assessment. The combined water vapour and lapse rate feedback makes the largest single contribution to global warming, whereas the cloud feedback remains the largest contribution to overall uncertainty. Due to the state-dependence of feedbacks, as evidenced from paleoclimate observations and from models, the net feedback parameter will increase (become less negative) as global temperature increases. Furthermore, on long time scales the ice sheet feedback parameter is *very likely* positive, promoting additional warming on millennial timescales as ice sheets come into equilibrium with the forcing. (*high confidence*) {7.4.2, 7.4.3, Figure 7.14, Table 7.10}

The carbon cycle provides for additional feedbacks on climate owing to the sensitivity of land–atmosphere and ocean–atmosphere carbon fluxes and storage to changes in climate and in atmospheric CO_2 (Figure TS.17c). Because of the time scales associated with land and ocean carbon uptake, these feedbacks are known to be scenario dependent. Feedback estimates deviate from linearity in scenarios of stabilizing or reducing concentrations. With *high confidence*, increased atmospheric CO_2 will lead to increased land and ocean carbon uptake, acting as a negative feedback on climate change. It is *likely* that a warmer climate will lead to reduced land and ocean carbon uptake, acting as a positive feedback. {4.3.2, 5.4.1-5, Box TS.4}

Thawing terrestrial permafrost will lead to carbon release (*high confidence*), but there is *low confidence* in the timing, magnitude and the relative roles of CO_2 versus CH_4 as feedback processes. An ensemble of models projects CO_2 release from permafrost to be 3–41 PgC per 1ºC of global warming by 2100, leading to warming strong enough that it must be included in estimates of the remaining carbon budget but weaker than the warming from fossil fuel burning. However, the incomplete representation of important processes, such

[17] For reference, the Planck temperature response for a doubling of atmospheric CO_2 is approximately 1.2°C at equilibrium.

ACCEPTED VERSION SUBJECT TO FINAL EDITING

as abrupt thaw, combined with weak observational constraints, only allow *low confidence* in both the magnitude of these estimates and in how linearly proportional this feedback is to the amount of global warming. There is emerging evidence that permafrost thaw and thermokarst give rise to increased CH_4 and N_2O emissions, which leads to the combined radiative forcing from permafrost thaw being larger than from CO_2 emissions only. However, the quantitative understanding of these additional feedbacks is low, particularly for N_2O. These feedbacks, as well as potential additional carbon losses due to climate-induced fire feedback are not routinely included in Earth System models. {Box 5.1, 5.4.3, 5.4.7, 5.4.8, Box TS.9}

[START FIGURE TS.17 HERE]

Figure TS.17: An overview of physical and biogeochemical feedbacks in the climate system. *The intent is to summarize assessed estimates of physical, biogeophysical and biogeochemical feedbacks on global temperature based on Chapters 5, 6 and 7.* (a) Synthesis of physical, biogeophysical and non-CO_2 biogeochemical feedbacks that are included in the definition of ECS assessed in this Technical Summary. These feedbacks have been assessed using multiple lines of evidence including observations, models and theory. The net feedback is the sum of the Planck response, water vapour and lapse rate, surface albedo, cloud, and biogeophysical and non-CO_2 biogeochemical feedbacks. Bars denote the mean feedback values and uncertainties represent very likely ranges; (b) Estimated values of individual biogeophysical and non-CO_2 biogeochemical feedbacks. The atmospheric methane lifetime and other non-CO_2 biogeochemical feedbacks have been calculated using global Earth System Model simulations from AerChemMIP, while the CH_4 and N_2O source responses to climate have been assessed for the year 2100 using a range of modelling approaches using simplified radiative forcing equations. The estimates represent the mean and 5-95% range. The level of confidence in these estimates is *low* owing to the large model spread. (c) carbon-cycle feedbacks as simulated by models participating in the C4MIP of CMIP6. An independent estimate of the additional positive carbon-cycle climate feedbacks from permafrost thaw, which is not considered in most C4MIP models, is added. The estimates represent the mean and 5-95% range. Note that these feedbacks act through modifying the atmospheric concentration of CO_2 and thus are not included in the definition of ECS, which assumes a doubling of CO_2 but are included in the definition and assessed range of TCRE. {Sections Box 5.1, 5.4.7, 5.4.8, 6.4.5, 7.4.2, Figure 5.29, Tables 6.9, 7.10}

[END FIGURE TS.17 HERE]

TS.3.3 Temperature Stabilization, Net Zero Emissions and Mitigation

TS.3.3.1 Remaining Carbon Budgets and Temperature Stabilization

The near-linear relationship between cumulative CO_2 emissions and maximum global surface temperature increase caused by CO_2 implies that stabilizing human-induced global temperature increase at any level requires net anthropogenic CO_2 emissions to become zero. This near-linear relationship further implies that mitigation requirements for limiting warming to specific levels can be quantified in terms of a carbon budget (*high confidence*). Remaining carbon budget estimates have been updated since the AR5 with methodological improvements, resulting in larger estimates that are consistent with SR1.5. Several factors, including estimates of historical warming, future emissions from thawing permafrost, variations in projected non-CO_2 warming, and the global surface temperature change after cessation of CO_2 emissions, affect the exact value of carbon budgets (*high confidence*). {1.3.5, Box 1.2, 4.7.1, 5.5}

Limiting further climate change would require substantial and sustained reductions of GHG emissions. Without net zero CO_2 emissions, and a decrease in the net non-CO_2 forcing (or sufficient net negative CO_2 emissions to offset any further warming from net non-CO_2 forcing), the climate system will continue to warm. There is *high confidence* that mitigation requirements for limiting warming to specific levels over this century can be estimated using a carbon budget that relates cumulative CO_2 emissions to global mean temperature increase (Figure TS.18, Table TS.3). For the period 1850–2019, a total of 2390 ± 240 $GtCO_2$ of anthropogenic CO_2 has been emitted. Remaining carbon budgets (starting from 1 January 2020) for limiting

ACCEPTED VERSION SUBJECT TO FINAL EDITING

warming to 1.5°C, 1.7°C, and 2.0°C are estimated at 500 $GtCO_2$, 850 $GtCO_2$ and 1350 $GtCO_2$, respectively, based on the 50th percentile of TCRE. For the 67th percentile, the respective values are 400 $GtCO_2$, 700 $GtCO_2$ and 1150 $GtCO_2$. The remaining carbon budget estimates for different temperature limits assume that non-CO_2 emissions are mitigated consistent with the median reductions found in scenarios in the literature as assessed in SR1.5, but they may vary by an estimated ±220 $GtCO_2$ depending on how deeply future non-CO_2 emissions are assumed to be reduced (Table TS.3). {5.5.2, 5.6, Box 5.2, 7.6}

[START FIGURE TS.18 HERE]

Figure TS.18: Illustration of (a) relationship between cumulative emissions of CO_2 and global mean surface air temperature increase and (b) the assessment of the remaining carbon budget from its constituting components based on multiple lines of evidence. Carbon budgets consistent with various levels of additional warming are provided in Table 5.8 and should not be read from the illustrations in either panel. In panel (a) thin black line shows historical CO_2 emissions together with the assessed global surface temperature increase from 1850-1900 as assessed in Chapter 2 (Box 2.3). The orange-brown range with its central line shows the estimated human-induced share of historical warming. The vertical orange-brown line shows the assessed range of historical human-induced warming for the 2010–2019 period relative to 1850-1900 (Chapter 3). The grey cone shows the assessed *likely* range for the transient climate response to cumulative emissions of carbon dioxide (TCRE) (Section 5.5.1.4), starting from 2015. Thin coloured lines show CMIP6 simulations for the five scenarios of the WGI core set (SSP1-1.9, green; SSP1-2.6, blue; SSP2-4.5, yellow; SSP3-7.0, red; SSP5-8.5, maroon), starting from 2015 and until 2100. Diagnosed carbon emissions are complemented with estimated land-use change emissions for each respective scenario. Coloured areas show the Chapter 4 assessed *very likely* range of global surface temperature projections and thick coloured central lines the median estimate, for each respective scenario, relative to the original scenario emissions. For panel (b), the remaining allowable warming is estimated by combining the global warming limit of interest with the assessed historical human induced warming (Section 5.5.2.2.2), the assessed future potential non-CO_2 warming contribution (Section 5.5.2.2.3) and the ZEC (Section 5.5.2.2.4). The remaining allowable warming (vertical blue bar) is subsequently combined with the assessed TCRE (Section 5.5.1.4 and 5.5.2.2.1) and contribution of unrepresented Earth system feedbacks (Section 5.5.2.2.5) to provide an assessed estimate of the remaining carbon budget (horizontal blue bar, Table 5.8). Note that contributions in panel (b) are illustrative and are not to scale. For example, the central ZEC estimate was assessed to be zero. {Box 2.3; Sections 5.2.1, 5.2.2; Figure 5.31}

[END FIGURE TS.18 HERE]

[START TABLE TS.3 HERE]

Table TS.3: Estimates of remaining carbon budgets and their uncertainties. Assessed estimates are provided for additional human-induced warming, expressed as global surface temperature, since the recent past (2010–2019), which *likely* amounted to 0.8° to 1.3°C with a best estimate of 1.07°C relative to 1850–1900. Historical CO_2 emissions between 1850 and 2014 have been estimated at about 2180 ± 240 $GtCO_2$ (1-sigma range), while since 1 January 2015, an additional 210 $GtCO_2$ has been emitted until the end of 2019. $GtCO_2$ values to the nearest 50. {Table 5.8, Table 3.1, Table 5.1, Table 5.7, 5.5.1, 5.5.2, Box 5.2}

ACCEPTED VERSION SUBJECT TO FINAL EDITING

Global surface temperature change since 2010–2019	**Global surface temperature change since 1850–1900 *(1)**	**Estimated remaining carbon budgets starting from 1 January 2020 and subject to variations and uncertainties quantified in the columns on the right**					**Scenario variation**	**Geophysical uncertainties*(4)**			
°C	*°C*	Percentiles of TCRE*(2) *$GtCO_2$*					Non-CO_2 scenario variation *(3)	Non-CO_2 forcing and response uncertainty	Historical temperature uncertainty*(1)	ZEC uncertainty	Recent emissions uncertainty *(5)
		17th	*33rd*	*50th*	*67th*	*83rd*	*$GtCO_2$*	*$GtCO_2$*	*$GtCO_2$*	*$GtCO_2$*	*$GtCO_2$*
0.43	***1.5***	*900*	*650*	*500*	*400*	*300*	Values can vary by at least ±220 due to choices related to non-CO_2 emissions mitigation	Values can vary by at least ±220 due to uncertainty in the warming response to future non-CO_2 emissions	±550	±420	±20
0.53	***1.6***	*1200*	*850*	*650*	*550*	*400*					
0.63	***1.7***	*1450*	*1050*	*850*	*700*	*550*					
0.73	***1.8***	*1750*	*1250*	*1000*	*850*	*650*					
0.83	***1.9***	*2000*	*1450*	*1200*	*1000*	*800*					
0.93	***2***	*2300*	*1700*	*1350*	*1150*	*900*					

*(1) Human-induced global surface temperature increase between 1850–1900 and 2010–2019 is assessed at 0.8–1.3°C (*likely* range; Cross-Section Box TS.1) with a best estimate of 1.07°C. Combined with a central estimate of TCRE (1.65 °C EgC^{-1}) this uncertainty in isolation results in a potential variation of remaining carbon budgets of ±550 $GtCO_2$, which, however, is not independent of the assessed uncertainty of TCRE and thus not fully additional.

*(2) TCRE: transient climate response to cumulative emissions of carbon dioxide, assessed to fall *likely* between 1.0–2.3°C EgC^{-1} with a normal distribution, from which the percentiles are taken. Additional Earth system feedbacks are included in the remaining carbon budget estimates as discussed in Section 5.5.2.2.5.

*(3) Estimates assume that non-CO_2 emissions are mitigated consistent with the median reductions found in scenarios in the literature as assessed in SR1.5. Non-CO_2 scenario variations indicate how much remaining carbon budget estimates vary due to different scenario assumptions related to the future evolution of non-CO_2 emissions in mitigation scenarios from SR1.5 that reach net zero CO_2 emissions. This variation is additional to the uncertainty in TCRE. The WGIII Contribution to AR6 will reassess the potential for non-CO_2 mitigation based on literature since the SR1.5.

*(4) Geophysical uncertainties reported in these columns and TCRE uncertainty are not statistically independent, as uncertainty in TCRE depends on uncertainty in the assessment of historical temperature, non-CO_2 versus CO_2 forcing and uncertainty in emissions estimates. These estimates cannot be formally combined and these uncertainty variations are not directly additional to the spread of remaining carbon budgets due to TCRE uncertainty reported in columns 3 to 7.

*(5) Recent emissions uncertainty reflects the ±10% uncertainty in the historical CO_2 emissions estimate since 1 January 2015.

[END TABLE TS.3 HERE]

There is *high confidence* that several factors, including estimates of historical warming, future emissions from thawing permafrost, and variations in projected non-CO_2 warming, affect the value of carbon budgets but do not change the conclusion that global CO_2 emissions would need to decline to net zero to halt global warming. Estimates may vary by ±220 $GtCO_2$ depending on the level of non-CO_2 emissions at the time global anthropogenic CO_2 emissions reach net zero levels. This variation is referred to as non-CO_2 scenario uncertainty and will be further assessed in the AR6 Working Group III Contribution. Geophysical uncertainties surrounding the climate response to these non-CO_2 emissions result in an additional uncertainty of at least ±220 $GtCO_2$, and uncertainties in the level of historical warming result in a ±550 $GtCO_2$ uncertainty. {5.4, 5.5.2}

Methodological improvements and new evidence result in updated remaining carbon budget estimates. The assessment in AR6 applies the same methodological improvements as in SR1.5, which uses a recent observed baseline for historic temperature change and cumulative emissions. Changes compared to SR1.5 are therefore small: the assessment of new evidence results in updated median remaining carbon budget estimates for limiting warming to 1.5°C and 2°C being the same and about 60 $GtCO_2$ smaller, respectively, after accounting for emissions since SR1.5. Meanwhile, remaining carbon budgets for limiting warming to 1.5°C would be about 300–350 $GtCO_2$ larger if evidence and methods available at the time of the AR5 would be used. If a specific remaining carbon budget is exceeded, this results in a lower probability of keeping warming below a specified temperature level and higher irreversible global warming over decades to centuries, or alternatively a need for net negative CO_2 emissions or further reductions in non-CO_2 greenhouse gases after net zero CO_2 is achieved to return warming to lower levels in the long term. {5.5.2, 5.6, Box 5.2}

Based on idealized model simulations that explore the climate response once CO_2 emissions have been brought to zero, the magnitude of the zero CO_2 emissions commitment (ZEC, see Glossary) is assessed to be

ACCEPTED VERSION SUBJECT TO FINAL EDITING

likely smaller than 0.3°C for time scales of about half a century and cumulative CO_2 emissions broadly consistent with global warming of 2°C. However, there is *low confidence* about its sign on time scales of about half a century. For lower cumulative CO_2 emissions, the range would be smaller yet with equal uncertainty about the sign. If the ZEC is positive on decadal time scales, additional warming leads to a reduction in the estimates of remaining carbon budgets, and vice versa if it is negative. {4.7.1, 5.5.2}

Permafrost thaw is included in estimates together with other feedbacks that are often not captured by models. Limitations in modelling studies combined with weak observational constraints only allow *low confidence* in the magnitude of these estimates (TS.3.2.2). Despite the large uncertainties surrounding the quantification of the effect of additional Earth system feedback processes, such as emissions from wetlands and permafrost thaw, these feedbacks represent identified additional risk factors that scale with additional warming and mostly increase the challenge of limiting warming to specific temperature levels. These uncertainties do not change the basic conclusion that global CO_2 emissions would need to decline to net zero to halt global warming. {Box 5.1, 5.4.8, 5.5.2}

TS.3.3.2 Carbon Dioxide Removal

Deliberate carbon dioxide removal (CDR) from the atmosphere has the potential to compensate for residual CO_2 emissions to reach net zero CO_2 emissions or to generate net negative CO_2 emissions. In the same way that part of current anthropogenic net CO_2 emissions are taken up by land and ocean carbon stores, net CO_2 removal will be partially counteracted by CO_2 release from these stores (*very high confidence*). Asymmetry in the carbon cycle response to simultaneous CO_2 emissions and removals implies that a larger amount of CO_2 would need to be removed to compensate for an emission of a given magnitude to attain the same change in atmospheric CO_2 (*medium confidence*). CDR methods have wide-ranging side-effects that can either weaken or strengthen the carbon sequestration and cooling potential of these methods and affect the achievement of sustainable development goals (*high confidence*). {4.6.3, 5.6}

Carbon dioxide removal (CDR) refers to anthropogenic activities that deliberately remove CO_2 from the atmosphere and durably store it in geological, terrestrial or ocean reservoirs, or in products. Carbon dioxide is removed from the atmosphere by enhancing biological or geochemical carbon sinks or by direct capture of CO_2 from air. Emission pathways that limit global warming to 1.5°C or 2°C typically assume the use of CDR approaches in combination with GHG emissions reductions. CDR approaches could be used to compensate for residual emissions from sectors that are difficult or costly to decarbonize. CDR could also be implemented at a large scale to generate global net negative CO_2 emissions (i.e., anthropogenic CO_2 removals exceeding anthropogenic emissions), which could compensate for earlier emissions as a way to meet long-term climate stabilization goals after a temperature overshoot. This Report assesses the effects of CDR on the carbon cycle and climate. Co-benefits and trade-offs for biodiversity, water and food production are briefly discussed for completeness, but a comprehensive assessment of the ecological and socio-economic dimensions of CDR options is left to the WGII and WGIII reports. {4.6.3, 5.6}

CDR methods have the potential to sequester CO_2 from the atmosphere (*high confidence*). In the same way part of current anthropogenic net CO_2 emissions are taken up by land and ocean carbon stores, net CO_2 removal will be partially counteracted by CO_2 release from these stores, such that the amount of CO_2 sequestered by CDR will not result in an equivalent drop in atmospheric CO_2 (*very high confidence*). The fraction of CO_2 removed from the atmosphere that is not replaced by CO_2 released from carbon stores, a measure of CDR effectiveness, decreases slightly with increasing amounts of removal (*medium confidence*) and decreases strongly if CDR is applied at lower atmospheric CO_2 concentrations (*medium confidence*). The reduction in global surface temperature is approximately linearly related to cumulative CO_2 removal (*high confidence*). Because of this near-linear relationship, the amount of cooling per unit CO_2 removed is approximately independent of the rate and amount of removal (*medium confidence*). {4.6.3, 5.6.2.1, Figure 5.32, Figure 5.34}

Due to non-linearities in the climate system, the century-scale climate–carbon cycle response to a CO_2 removal from the atmosphere is not always equal and opposite to its response to a simultaneous CO_2 emission (*medium* confidence). For CO_2 emissions of 100 PgC released from a pre-industrial from a state in

ACCEPTED VERSION SUBJECT TO FINAL EDITING

equilibrium with pre-industrial atmospheric CO_2 levels, CMIP6 models simulate that 27± 6% (mean ± 1 standard deviation) of emissions remain in the atmosphere 80–100 years after the emissions, whereas for removals of 100 PgC only 23 ± 6% of removals remain out of the atmosphere. This asymmetry implies that an extra amount of CDR is required to compensate for a positive emission of a given magnitude to attain the same change in atmospheric CO_2. Due to *limited agreement* between models, there is *low confidence* in the sign of the asymmetry of the temperature response to CO_2 emissions and removals. {4.6.3, 5.6.2.1, Figure 5.35}

Simulations with ESMs indicate that under scenarios where CO_2 emissions gradually decline, reach net zero and become net negative during the 21st century (e.g., SSP1–2.6), land and ocean carbon sinks begin to weaken in response to declining atmospheric CO_2 concentrations, and the land sink eventually turns into a source (Figure TS.19). This sink-to-source transition occurs decades to a few centuries after CO_2 emissions become net negative. The ocean remains a sink of CO_2 for centuries after emissions become net negative. Under scenarios with large net negative CO_2 emissions (e.g., SSP5–3.4–OS) and rapidly declining CO_2 concentrations, the land source is larger than for SSP1–2.6 and the ocean also switches to a source. While the general response is robust across models, there is *low confidence* in the timing of the sink-to-source transition and the magnitude of the CO_2 source in scenarios with net negative CO_2 emissions. Carbon dioxide removal could reverse some aspects climate change if CO_2 emissions become net negative, but some changes would continue in their current direction for decades to millennia. For instance, sea level rise due to ocean thermal expansion would not reverse for several centuries to millennia (*high confidence*) (Box TS.4). {4.6.3, 5.4.10, 5.6.2.1, Figure 5.30, Figure 5.33}

[START FIGURE TS.19 HERE]

Figure TS.19: Carbon sink response in a scenario with net CO_2 removal from the atmosphere. *The intent of this figure is to show how atmospheric CO_2 evolves under negative emissions and its dependence on the negative emissions technologies. It also shows the evolution of the ocean and land sinks.* Shown are CO_2 flux components from concentration-driven Earth system model simulations during different emission stages of SSP1–2.6 and its long-term extension. (a) Large net positive CO_2 emissions, (b) small net positive CO_2 emissions, (c) – (d) net negative CO_2 emissions, (e) net zero CO_2 emissions. Positive flux components act to raise the atmospheric CO_2 concentration, whereas negative components act to lower the CO_2 concentration. Net CO_2 emissions, land and ocean CO_2 fluxes represent the multi-model mean and standard deviation (error bar) of four ESMs (CanESM5, UKESM1, CESM2-WACCM, IPSL-CM6a-LR) and one EMIC (UVic ESCM). Net CO_2 emissions are calculated from concentration-driven Earth system model simulations as the residual from the rate of increase in atmospheric CO_2 and land and ocean CO_2 fluxes. Fluxes are accumulated over each 50-year period and converted to concentration units (ppm). {5.6.2.1, Figure 5.33}

[END FIGURE TS.19 HERE]

CDR methods have a range of side effects that can either weaken or strengthen the carbon sequestration and cooling potential of these methods and affect the achievement of sustainable development goals (*high confidence*). Biophysical and biogeochemical side-effects of CDR methods are associated with changes in surface albedo, the water cycle, emissions of CH_4 and N_2O, ocean acidification and marine ecosystem productivity (*high confidence*). These side-effects and associated Earth system feedbacks can decrease carbon uptake and/or change local and regional climate and in turn limit the CO_2 sequestration and cooling potential of specific CDR methods (*medium confidence*). Deployment of CDR, particularly on land, can also affect water quality and quantity, food production and biodiversity (*high confidence*). These effects are often highly dependent on local context, management regime, prior land use, and scale (*high confidence*). The largest co-benefits are obtained with methods that seek to restore natural ecosystems or improve soil carbon sequestration (*medium confidence*). The climate and biogeochemical effects of terminating CDR are expected to be small for most CDR methods (*medium confidence*). {4.6.3, 5.6.2.2, 8.4.3, 8.6.3, Figure 5.36}

ACCEPTED VERSION SUBJECT TO FINAL EDITING

TS.3.3.3 Relating Different Forcing Agents

When including other GHGs, the choice of emission metric affects the quantification of net zero GHG emissions and their resulting temperature outcome (*high confidence*). Reaching and sustaining net zero GHG emissions typically leads to a peak and decline in temperatures when quantified with the global warming potential over a 100-year period (GWP-100). Carbon-cycle responses are more robustly accounted for in emission metrics compared to AR5 (*high confidence*). New emission metric approaches can be used to generate equivalent cumulative emissions of CO_2 for short-lived greenhouse gases based on their rate of emissions. {7.6.2}

Over 10- to 20-year time scales, the temperature response to a single year's worth of current emissions of SLCFs is at least as large as that of CO_2, but because the effect of SLCFs decays rapidly over the first few decades after emission, the net long-term temperature response to a single year's worth of emissions is predominantly determined by cumulative CO_2 emissions. Emission reductions in 2020 associated with COVID-19 containment led to small and positive global ERF; however, global and regional climate responses to the forcing are undetectable above internal variability due to the temporary nature of emission reductions. {6.6, Cross-Chapter Box 6.1}

The relative climate effects of different forcing agents are typically quantified using emission metrics that compare the effects of an idealised pulse of 1 kg of some climate forcing agent against a reference climate forcing agent, almost always CO_2. The two most prominent pulse emissions metrics are the global warming potential (GWP) and global temperature change potential (GTP) (see Glossary). The climate responses to CO_2 emissions by convention include the effects of warming on the carbon cycle, so for consistency these need to be determined also for non-CO_2 emissions. The methodology for doing this has been placed on a more robust scientific footing compared to AR5 (*high confidence*). Methane from fossil fuel sources has slightly higher emission metric values than those from biogenic sources since it leads to additional fossil CO_2 in the atmosphere (*high confidence*). Updates to the chemical adjustments for methane and nitrous oxide emissions (Section TS.3.1) and revisions in their lifetimes result in emission metrics for GWP and GTP that are slightly lower than in AR5 (*medium confidence*). Emission metrics for the entire suite of GHGs assessed in the AR6 have been calculated for various time horizons. {7.6.1, Table 7.15, Table 7.SM.7}

New emission metric approaches, such as GWP* and Combined-GTP (CGTP), relate changes in the emission rate of short-lived greenhouse gases to equivalent cumulative emissions of CO_2 (cumulative CO_2-e emissions). Global surface temperature response from aggregated emissions of short-lived greenhouse gases over time is determined by multiplying these cumulative CO_2-e by TCRE (see TS.3.2.1). When GHGs are aggregated using standard metrics such as GWP or GTP, cumulative CO_2-e emissions are not necessarily proportional to future global surface temperature outcomes (*high confidence*) {Box 7.3, 7.6.1}

Emission metrics are needed to aggregate baskets of gases to determine net zero GHG emissions. Generally, achieving net zero CO_2 emissions and declining non-CO_2 radiative forcing would halt human-induced warming. Reaching net zero GHG emissions quantified by GWP-100 typically leads to declining temperatures after net zero GHGs emissions are achieved if the basket includes short-lived gases, such as methane. Net zero GHG emissions defined by CGTP or GWP* imply net zero CO_2 and other long-lived GHG emissions and constant (CGTP) or gradually declining (GWP*) emissions of short-lived gases. The warming evolution resulting from net zero GHG emissions defined in this way corresponds approximately to reaching net zero CO_2 emissions, and would thus not lead to declining temperatures after net zero GHG emissions are achieved but to an approximate temperature stabilization (*high confidence*). The choice of emission metric hence affects the quantification of net zero GHG emissions, and therefore the resulting temperature outcome of reaching and sustaining net zero GHG emissions levels (*high confidence*). {7.6.1.4, 7.6.2, 7.6.3}

As pointed out in AR5, ultimately, it is a matter for policymakers to decide which emission metric is most applicable to their needs. This Report does not recommend the use of any specific emission metric as the most appropriate metric depends on the policy goal and context (see Chapter 7, Section 7.6). A detailed

ACCEPTED VERSION SUBJECT TO FINAL EDITING

assessment of GHG metrics to support climate change mitigation and associated policy contexts is provided in the WGIII contribution to the AR6.

The global surface temperature response following a climate change mitigation measure that affects emissions of both short- and long-lived climate forcers depends on their lifetimes, their ERFs, how fast and for how long the emissions are reduced, and the thermal inertia in the climate system. Mitigation, relying on emission reductions and implemented through new legislation or technology standards, implies that emissions reductions occur year after year. Global temperature response to a year's worth of current emissions from different sectors informs about the mitigation potential (Figure TS.20). Over 10- to 20-year time scales, the influence of SLCFs is at least as large as that of CO_2, with sectors producing the largest warming being fossil fuel production and distribution, agriculture, and waste management. Because the effect of the SLCFs decays rapidly over the first few decades after emission, the net long-term temperature effect from a single year's worth of current emissions is predominantly determined by CO_2. Fossil fuel combustion for energy, industry and land transportation are the largest contributing sectors on a 100-year time scale (*high confidence*). Current emissions of CO_2, N_2O and SLCFs from East Asia and North America are the largest regional contributors to additional net future warming on both short (*medium confidence*) and long time scales (10 and 100 year) (*high confidence*). {6.6.1, 6.6.2, Figure 6.16}

COVID-19 restrictions led to detectable reductions in global anthropogenic NO_x (about 35% in April 2020) and fossil CO_2 (7%, with estimates ranging from 5.8% to 13.0%) emissions, driven largely by reduced emissions from the transportation sector (*medium confidence*). There is *high confidence* that, with the exception of surface ozone, reductions in pollutant precursors contributed to temporarily improved air quality in most regions of the world. However, these reductions were lower than that would be expected from sustained implementation of policies addressing air quality and climate change (*medium confidence*). Overall, the net global ERF from COVID-19 containment was likely small and positive for 2020 (with a temporary peak value less than 0.2 W m^{-2}), thus temporarily adding to the total anthropogenic climate influence, with positive forcing (warming influence) from aerosol changes dominating over negative forcings (cooling influence) from CO_2, NO_x and contrail cirrus changes. Consistent with this small net radiative forcing, and against a large component of internal variability, Earth system models show no detectable effect on global or regional surface temperature or precipitation (*high confidence*). {Cross Chapter Box 6.1}

[START FIGURE TS.20 HERE]

Figure TS.20: Global surface temperature change 10 and 100 years after a one-year pulse of present-day emissions. *This figure shows the sectoral contribution to present-day climate change by specific climate forcers including CO_2 as well as SLCFs.* The temperature response is broken down by individual species and shown for total anthropogenic emissions (top), and sectoral emissions on 10-year (left) and 100-year time scales (right). Sectors are sorted by (high-to-low) net temperature effect on the 10-year time scale. Error bars in the top panel show the 5-95% range in net temperature effect due to uncertainty in radiative forcing only (calculated using a Monte Carlo approach and best estimate uncertainties from the literature). Emissions for 2014 are from the CMIP6 emissions dataset, except for HFCs and aviation H_2O which rely on other datasets (see Section 6.6.2 for more details). CO_2 emissions are excluded from open biomass burning and residential biofuel use. {6.6.2, Figure 6.16}

[END FIGURE TS.20 HERE]

ACCEPTED VERSION SUBJECT TO FINAL EDITING

[START BOX TS.7 HERE]

Box TS.7: Climate and Air Quality Responses to Short-lived Climate Forcers in Shared Socioeconomic Pathways

Future changes in emissions of short-lived climate forcers (SLCFs) are expected to cause an additional global mean warming with a large diversity in the end-of-century response across the WGI core set of SSPs, depending upon the level of climate change and air pollution mitigation. This additional warming is either due to reductions in cooling aerosols for air pollution regulation or due to increases in methane, ozone and HFCs. This additional warming is stable after 2040 in SSPs associated with lower global air pollution as long as methane emissions are also mitigated, but the overall warming induced by SLCF changes is higher in scenarios in which air quality continues to deteriorate (induced by growing fossil fuel use and limited air pollution control) (*high confidence*). Sustained methane mitigation reduces global surface ozone, contributing to air quality improvements and also reduces surface temperature in the longer term, but only sustained CO_2 emission reductions allow long-term climate stabilization (*high confidence*). Future changes in air quality (near-surface ozone and particulate matter, or PM) at global and local scales are predominantly driven by changes in ozone and aerosol precursor emissions rather than climate (*high confidence*). Air quality improvements driven by rapid decarbonization strategies, as in SSP1-1.9 and SSP1-2.6, are not sufficient in the near term to achieve air quality guidelines set by the World Health Organization in some highly polluted regions (*high confidence*). Additional policies (e.g., access to clean energy, waste management) envisaged to attain United Nations Sustainable Development Goals bring complementary SLCF reduction. {4,4,4, 6.6.3, 6.7.3, BOX TS.7 Figure 1, Box 6.2}

The net effect of SLCF emissions changes on temperature will depend on how emissions of warming and cooling SLCFs will evolve in the future. The magnitude of the cooling effect of aerosols remains the largest uncertainty in the effect of SLCFs in future climate projections. Since the SLCFs have undergone large changes over the past two decades, the temperature and air pollution responses are estimated relative to year 2019 instead of 1995–2014.

Temperature Response

In the next two decades, it is *very likely* that SLCF emission changes will cause a warming relative to 2019, across the WGI core set of SSPs (see TS.1.3.1), in addition to the warming from long-lived GHGs. The net effect of SLFC and HFC changes in global surface temperature across the SSPs is a *likely* warming of 0.06°C–0.35°C in 2040 relative to 2019. This near-term global mean warming linked to SLCFs is quite similar in magnitude across the SSPs due to competing effects of warming (methane, ozone) and cooling (aerosols) forcers (Box TS.7, Figure 1). There is greater diversity in the end-of-century response among the scenarios. SLCF changes in scenarios with no climate change mitigation (SSP3-7.0 and SSP5-8.5) will cause a warming in the *likely* range of 0.4°C–0.9°C in 2100 relative to 2019 due to increases in methane, tropospheric ozone and HFC levels. For the stringent climate change and pollution mitigation scenarios (SSP1-1.9 and SSP1-2.6), the cooling from reductions in methane, ozone and HFCs partially balances the warming from reduced aerosols, primarily sulphate, and the overall SLCF effect is a *likely* increase in global surface temperature of 0.0°C–0.3°C in 2100, relative to 2019. With intermediate climate change and air pollution mitigations, SLCFs in SSP2-4.5 add a *likely* warming of 0.2°C–0.5°C to global surface temperature change in 2100, with the largest warming resulting from reductions in aerosols. {4.4.4, 6.7.3}

Assuming implementation and efficient enforcement of both the Kigali Amendment to the Montreal Protocol on Ozone Depleting Substances and current national plans limit emissions (as in SSP1-2.6), the effects of HFCs on global surface temperature, relative to 2019, would remain below +0. 02°C from 2050 onwards versus about +0.04°C–0.08°C in 2050 and +0.1°C–0.3°C in 2100 considering only national HFC regulations decided prior to the Kigali Amendment (as in SSP5-8.5) (*medium confidence*). {6.6.3, 6.7.3}

Air Quality Responses

Air pollution projections range from strong reductions in global surface ozone and PM (e.g., SSP1-2.6, with stringent mitigation of both air pollution and climate change) to no improvement and even degradation (e.g.,

ACCEPTED VERSION SUBJECT TO FINAL EDITING

SSP3-7.0 without climate change mitigation and with only weak air pollution control) (*high confidence*). Under the SSP3-7.0 scenario, PM levels are projected to increase until 2050 over large parts of Asia, and surface ozone pollution is projected to worsen over all continental areas through 2100 (*high confidence*). In SSP5-8.5, a scenario without climate change mitigation but with stringent air pollution control, PM levels decline through 2100, but high methane levels hamper the decline in global surface ozone at least until 2080 (*high confidence*). {6.7.1}

[START BOX TS.7, FIGURE 1 HERE]

Box TS.7, Figure 1: Effects of short-lived climate forcers (SLCFs) on global surface temperature and air pollution across the WGI core set of Shared Socio-Economic Pathways (SSPs). *The intent of this figure is to show the climate and air quality (surface ozone and $PM_{2.5}$) response to SLCFs in the SSP scenarios for near and long-term.* Effects of net aerosols, tropospheric ozone, hydrofluorocarbons (HFCs) (with lifetimes less than 50 years), and methane are compared with those of total anthropogenic forcing for 2040 and 2100 relative to year 2019. The global surface temperature changes are based on historical and future evolution of Effective Radiative Forcing (ERF) as assessed in chapter 7 of this report. The temperature responses to the ERFs are calculated with a common impulse response function (R_T) for the climate response, consistent with the metric calculations in Chapter 7 (Box 7.1). The R_T has an equilibrium climate sensitivity of 3.0°C for a doubling of atmospheric CO_2 concentration (feedback parameter of -1.31 W m^{-2} $°C^{-1}$). The scenario total (grey bar) includes all anthropogenic forcings (long- and short-lived climate forcers, and land use changes). Uncertainties are 5-95% ranges. The global changes in air pollutant concentrations (ozone and $PM_{2.5}$) are based on multimodel CMIP6 simulations and represent changes in 5-year mean surface continental concentrations for 2040 and 2098 relative to 2019. Uncertainty bars represent inter-model ±1 standard deviation. {6.7.2, 6.7.3, Figure 6.24}

[END BOX TS.7, FIGURE 1 HERE]

[END BOX TS.7 HERE]

[START BOX TS.8 HERE]

Box TS.8: Earth System Response to Solar Radiation Modification

Since AR5, further modelling work has been conducted on aerosol-based solar radiation modification (SRM) options such as stratospheric aerosol injection, marine cloud brightening, and cirrus cloud thinning[18] and their climate and biogeochemical effects. These investigations have consistently shown that SRM could offset some of the effects of increasing GHGs on global and regional climate, including the carbon and water cycles (*high confidence*). However, there would be substantial residual or overcompensating climate change at the regional scales and seasonal time scales (*high confidence*), and large uncertainties associated with aerosol–cloud–radiation interactions persist. The cooling caused by SRM would increase the global land and ocean CO_2 sinks (*medium confidence*), but this would not stop CO_2 from increasing in the atmosphere or affect the resulting ocean acidification under continued anthropogenic emissions (*high confidence*). It is *likely* that abrupt water cycle changes will occur if SRM techniques are implemented rapidly. A sudden and sustained termination of SRM in a high CO_2 emissions scenario would cause rapid climate change (*high confidence*). However, a gradual phase-out of SRM combined with emission reduction and CDR would avoid these termination effects *(medium confidence*). {4.6.3, 5.6.3. 6.4.6, 8.6.3}.

Solar radiation modification (SRM) refers to deliberate large-scale climate intervention options that are studied as potential supplements to deep mitigation, for example, in scenarios that overshoot climate stabilization goals. SRM options aim to offset some of the warming effects of GHG emissions by

[18] Although cirrus cloud thinning aims to cool the planet by increasing longwave emissions to space, it is included in the portfolio of SRM options for consistency with AR5 and SR1.5. {4.6.3.3}

ACCEPTED VERSION SUBJECT TO FINAL EDITING

modification of the Earth's shortwave radiation budget. Following SR1.5, the SRM assessed in this report also includes some options, such as cirrus cloud thinning, that alter the longwave radiation budget. SRM contrasts with climate change mitigation activities, such as emission reductions and CDR, as it introduces a 'mask' to the climate change problem by altering the Earth's radiation budget, rather than attempting to address the root cause of the problem, which is the increase in GHGs in the atmosphere. By masking only the climate effects of GHG emissions, SRM does not address other issues related to atmospheric CO_2 increase, such as ocean acidification. The WGI report assesses physical understanding of the Earth system response to proposed SRM and is based primarily on idealized climate model simulations. There are important other considerations, such as risk to human and natural systems, perceptions, ethics, cost, governance, and trans-boundary issues and their relationship to the United Nations Sustainable Development Goals—issues that the WGII (Chapter 16) and WGIII (Chapter 14) reports address. {4.6.3}

SRM options include those that increase surface albedo, brighten marine clouds by increasing the amount of cloud condensation nuclei, or reduce the optical depth of cirrus clouds by seeding them with ice nucleating particles. However, the most commonly studied approaches attempt to mimic the cooling effects of major volcanic eruptions by injecting reflective aerosols (e.g., sulphates) or their precursors (e.g., sulphur dioxide) into the stratosphere. {4.6.3, 5.6.3, 6.4.6}

SRM could offset some effects of greenhouse gas-induced warming on global and regional climate, but there would be substantial residual and overcompensating climate change at the regional scale and seasonal time scales (*high confidence*). Since the AR5, more modelling work has been conducted with more sophisticated treatment of aerosol-based SRM approaches, but the uncertainties in cloud–aerosol–radiation interactions are still large (*high confidence*). Modelling studies suggest that it is possible to stabilize multiple large-scale temperature indicators simultaneously by tailoring the deployment strategy of SRM options (*medium confidence*) but with large residual or overcompensating regional and seasonal climate changes. {4.6.3}

SRM approaches targeting shortwave radiation are *likely* to reduce global mean precipitation, relative to future CO_2 emissions scenarios, if all global mean warming is offset. In contrast, cirrus cloud thinning, targeting longwave radiation, is expected to cause an increase in global mean precipitation (*medium confidence*). If shortwave approaches are used to offset global mean warming, the magnitude of reduction in regional precipitation minus evapotranspiration (P-E) (Box TS.5), which is more relevant to freshwater availability, is smaller than precipitation decrease because of simultaneous reductions in both precipitation and evapotranspiration (*medium confidence*). {4.6.3, 8.2.1, 8.6.3}.

If SRM is used to cool the planet, it would cause a reduction in plant and soil respiration and slow the reduction of ocean carbon uptake due to warming (*medium confidence*). The result would be an enhancement of the global land and ocean CO_2 sinks (*medium confidence*) and a slight reduction in atmospheric CO_2 concentration relative to unmitigated climate change. However, SRM would not stop CO_2 from increasing in the atmosphere or affect the resulting ocean acidification under continued anthropogenic emissions (*high confidence*). {5.6.3}

The effect of stratospheric aerosol injection on global temperature and precipitation is projected by models to be detectable after one to two decades, which is similar to the time scale for the emergence of the benefits of emissions reductions. A sudden and sustained termination of SRM in a high GHG emissions scenario would cause rapid climate change and a reversal of the SRM effects on the carbon sinks (*high confidence*). It is also *likely* that a termination of strong SRM would drive abrupt changes in the water cycle globally and regionally, especially in the tropical regions by shifting the ITCZ and Hadley cells. At the regional scale, non-linear responses cannot be excluded, due to changes in evapotranspiration. However, a gradual phase-out of SRM combined with emissions reductions and CDR would avoid larger rates of changes (*medium confidence*). {4.6.3, 5.6.3, 8.6.3}.

[END BOX TS.8 HERE]

ACCEPTED VERSION SUBJECT TO FINAL EDITING

[START BOX TS.9 HERE]

Box TS.9: Irreversibility, Tipping Points and Abrupt Changes

The present rate of response of many aspects of the climate system are proportionate to the rate of recent temperature change, but some aspects may respond disproportionately. Some climate system components are slow to respond, such as the deep ocean overturning circulation and the ice sheets. It is *virtually certain* that irreversible, committed change is already underway for the slow-to-respond processes as they come into adjustment for past and present emissions. The paleoclimate record indicates that tipping elements exist in the climate system where processes undergo sudden shifts toward a different sensitivity to forcing, such as during a major deglaciation, where one degree of temperature change might correspond to a large or small ice sheet mass loss during different stages. For global climate indicators, evidence for abrupt change is limited, but deep ocean warming, acidification and sea level rise are committed to ongoing change for millennia after global surface temperatures initially stabilize and are irreversible on human time scales (*very high confidence*). At the regional scale, abrupt responses, tipping points and even reversals in the direction of change cannot be excluded (*high confidence*). Some regional abrupt changes and tipping points could have severe local impacts, such as unprecedented weather, extreme temperatures and increased frequency of droughts and forest fires. Models that exhibit such tipping points are characterised by abrupt changes once the threshold is crossed, and even a return to pre-threshold surface temperatures or to atmospheric carbon dioxide concentrations, does not guarantee that the tipping elements return to their pre-threshold state. Monitoring and early warning systems are being put into place to observe tipping elements in the climate system. {Box TS.2, Box TS.4, TS 3.3.2, 1.3, 1.4.4, 1.5, 4.3.2, Table 4.10, 5.3.4, 5.4.9, 7.5.3, 9.2.2, 9.2.4, 9.4.1, 9.4.2, 9.6.3, Cross-chapter Box 12.1}

Understanding of multi-decadal reversibility (i.e., the system returns to the previous climate state within multiple decades after the radiative forcing is removed) has improved since AR5 for many atmospheric, land surface and sea ice climate metrics following sea surface temperature recovery. Some processes suspected of having tipping points, such as the Atlantic Meridional Overturning Circulation (AMOC), have been found to often undergo recovery after temperature stabilization with a time delay (*low confidence*). However, substantial irreversibility is further substantiated for some cryosphere changes, ocean warming, sea level rise, and ocean acidification. {4.7.2, 5.3.3, 5.4.9, 9.2.2, 9.2.4, 9.4.1, 9.4.2, 9.6.3}

Some climate system components are slow to respond, such as the deep ocean overturning circulation and the ice sheets. It is *likely* that under stabilization of global warming at 1.5°C, 2.0°C, or 3.0°C relative to 1850–1900, the AMOC will continue to weaken for several decades by about 15%, 20% and 30% of its strength and then recover to pre-decline values over several centuries (*medium confidence*). At sustained warming levels between 2°C and 3°C, there is limited evidence that the Greenland and West Antarctic Ice Sheets will be lost almost completely and irreversibly over multiple millennia; both the probability of their complete loss and the rate of mass loss increases with higher surface temperatures (*high confidence*). At sustained warming levels between 3°C and 5°C, near-complete loss of the Greenland Ice Sheet and complete loss of the West Antarctic Ice Sheet is projected to occur irreversibly over multiple millennia (*medium confidence*); with substantial parts or all of Wilkes Subglacial Basin in East Antarctica lost over multiple millennia (*low confidence*). Early-warning signals of accelerated sea-level-rise from Antarctica, could possibly be observed within the next few decades. For other hazards (e.g., ice sheet behaviour, glacier mass loss and global mean sea level change, coastal floods, coastal erosion, air pollution, and ocean acidification) the time and/or scenario dimensions remain critical, and a simple and robust relationship with global warming level cannot be established (*high confidence*). {4.3.2, 4.7.2, 5.4.3, 5.4.5, 5.4.8, 8.6, 9.2, 9.4, Box 9.3, Cross-Chapter Box 12.1}

For global climate indicators, evidence for abrupt change is limited. For global warming up to 2°C above 1850-1900 levels, paleoclimate records do not indicate abrupt changes in the carbon cycle (*low confidence*). Despite the wide range of model responses, uncertainty in atmospheric CO_2 by 2100 is dominated by future anthropogenic emissions rather than uncertainties related to carbon-climate feedbacks (*high confidence*). There is no evidence of abrupt change in climate projections of global temperature for the next century: there is a near-linear relationship between cumulative CO_2 emissions and maximum global mean surface air

ACCEPTED VERSION SUBJECT TO FINAL EDITING

temperature increase caused by CO_2 over the course of this century for global warming levels up to at least 2°C relative to 1850-1900. The increase in global ocean heat content (TS2.4) will likely continue until at least 2300 even for low-emission scenarios, and global mean sea level rise will continue to rise for centuries to millennia following cessation of emissions (Box TS.4) due to continuing deep ocean heat uptake and mass loss of the Greenland and Antarctic Ice Sheets (*high confidence*). {2.2.3; Cross-Chapter Box 2.1; 5.1.1; 5.4; Cross-Chapter Box 5.1; Figures 5.3, 5.4, 5.25, 5.26; 9.2.2; 9.2.4}

The response of biogeochemical cycles to anthropogenic perturbations can be abrupt at regional scales and irreversible on decadal to century time scales (*high confidence*). The probability of crossing uncertain regional thresholds increases with climate change (*high confidence*). It is *very unlikely* that gas clathrates (mostly methane) in deeper terrestrial permafrost and subsea clathrates will lead to a detectable departure from the emissions trajectory during this century. Possible abrupt changes and tipping points in biogeochemical cycles lead to additional uncertainty in 21st century atmospheric GHG concentrations, but future anthropogenic emissions remain the dominant uncertainty (*high confidence*). There is potential for abrupt water cycle changes in some high-emission scenarios, but there is no overall consistency regarding the magnitude and timing of such changes. Positive land surface feedbacks, including vegetation, dust, and snow, can contribute to abrupt changes in aridity, but there is only *low confidence* that such changes will occur during the 21st century. Continued Amazon deforestation, combined with a warming climate, raises the probability that this ecosystem will cross a tipping point into a dry state during the 21st century (*low confidence*). {TS3.2.2, 5.4.3, 5.4.5, 5.4.8, 5.4.9, 8.6.2, 8.6.3, Cross-chapter Box 12.1}

[END BOX TS.9 HERE]

TS.4 Regional Climate Change

This section focuses on how to generate regional climate change information and its relevance for climate services; the drivers of regional climate variability and change, and how they are being affected by anthropogenic factors; and observed, attributed and projected changes in climate, including extreme events and climatic impact-drivers (CID), across all regions of the world. There is a small set of CID changes common to all land or ocean regions and a specific set of changes from a broader range of CIDs seen in each region. This regional diversity results from regional climate being determined by a complex interplay between the seasonal-to-multidecadal variation of large-scale modes of climate variability, external natural and anthropogenic forcings, local climate processes and related feedbacks.

TS.4.1 Generation and Communication of Regional Climate Change Information

Climate change information at regional scale is generated using a range of data sources and methodologies. Multi-model ensembles and models with a range of resolutions are important data sources, and discarding models that fundamentally misrepresent relevant processes improves the credibility of ensemble information related to these processes. A key methodology is distillation, combining lines of evidence and accounting for stakeholder context and values, which helps ensure the information is relevant, useful and trusted for decision making (see Core Concepts Box) (*high confidence*). Since the AR5, physical climate storylines have emerged as a complementary approach to ensemble projections to generate more accessible climate information and promote a more comprehensive treatment of risk. They have been used as part of the distillation process within climate services to generate the required context-relevant, credible and trusted climate information. Since AR5, climate change information produced for climate services has increased significantly due to scientific and technological advancements and growing user awareness, requirements, and demand (*very high confidence*). The decision-making context, level of user engagement and co-production between scientists, practitioners and users are important determinants of the type of climate service developed and its utility in supporting adaptation, mitigation and risk management decisions. {Box TS.1, 10.3, Cross-Chapter Box 10.3, 10.6, 12.6, Cross-chapter Box 12.2, Box TS.3}

ACCEPTED VERSION SUBJECT TO FINAL EDITING

TS.4.1.1 Sources and Methodologies for Generating Regional Climate Information

Climate change information at regional scale is generated using a range of data sources and methodologies (TS.1.4). Understanding observed regional climate change and variability is based on the availability and analysis of multiple observational datasets that are suitable for evaluating the phenomena of interest (e.g., extreme events), including accounting for observational uncertainty. These datasets are combined with climate model simulations of observed changes and events to attribute causes of those changes and events to large- and regional-scale anthropogenic and natural drivers and to assess the performance of the models. Future simulations with many climate models (multi-model ensembles) are then used to generate and quantify ranges of projected regional climate responses. Discarding models that fundamentally misrepresent relevant processes improves the credibility of regional climate information generated from these ensembles (*high confidence*). However, multi-model mean and ensemble spread are not a full measure of the range of projection uncertainty and are not sufficient to characterize low-likelihood, high-impact changes (Box TS.3) or situations where different models simulate substantially different or even opposite changes (*high confidence*). Large single-model ensembles are now available and provide a more comprehensive spectrum of possible changes associated with internal variability (*high confidence*). {1.5.1, 1.5.4, 10.2, 10.3.3, 10.3.4, 10.4.1, 10.6.2, 11.2, Box 11.2, Cross-chapter Box 11.1, 12.4, Atlas.1.4.1, TS.1.2.1, TS.1.2.3, TS.4.2}

Depending on the region of interest, representing regionally important forcings (e.g., aerosols, land-use change and ozone concentrations) and feedbacks (e.g., between snow and albedo, soil-moisture and temperature, soil-moisture and precipitation) in climate models is a prerequisite for them to reproduce past regional trends to underpin the reliability of future projections (*medium confidence*). In some cases, even the sign of a projected change in regional climate cannot be trusted if relevant regional processes are not represented, for example, for variables such as precipitation and wind speed (*medium confidence*). In some regions, either geographical (e.g., Central Africa, Antarctica) or typological (e.g., mountainous areas, Small Islands and cities), and for certain phenomena, fewer observational records are available or accessible, which limits the assessment of regional climate change in these cases. {1.5.1, 1.5.3, 1.5.4, 8.5.1, 10.2, 10.3.3, 10.4.1, 11.1.6, 11.2, 12.4, Atlas.8.3, Atlas.11.1.5, Cross-Chapter Box Atlas.2, TS.1.2.2}

Methodologies such as statistical downscaling, bias adjustment and weather generators are beneficial as an interface between climate model projections and impact modelling and for deriving user-relevant indicators (*high confidence*). However, the performance of these techniques depends on that of the driving climate model: in particular, bias adjustment cannot overcome all consequences of unresolved or strongly misrepresented physical processes such as large-scale circulation biases or local feedbacks (*medium confidence*). {10.3.3, Cross-Chapter Box 10.2, 12.2, Atlas.2.2}

[START BOX TS.10 HERE]

Box TS.10: Event Attribution

The attribution of observed changes in extremes to human influence (including greenhouse gas and aerosol emissions and land-use changes) has substantially advanced since AR5, in particular for extreme precipitation, droughts, tropical cyclones, and compound extremes (*high confidence*). There is limited evidence for windstorms and convective storms. Some recent hot extreme events would have been *extremely unlikely* to occur without human influence on the climate system. (TS.1) {Cross-Working Group Box: Attribution, 11.2, 11.3, 11.4, 11.6, 11.7, 11.8}

Since AR5, the attribution of extreme weather events has emerged as a growing field of climate research with an increasing body of literature. It provides evidence that greenhouse gases and other external forcings have affected individual extreme weather events by disentangling anthropogenic drivers from natural variability. Event attribution is now an important line of evidence for assessing changes in extremes on regional scales. {Cross-Working Group Box: Attribution, TS.1, 11.1.4}

ACCEPTED VERSION SUBJECT TO FINAL EDITING

The regional extremes and events that have been studied are geographically uneven. A few events, for example, extreme rainfall events in the UK, heat waves in Australia, or Hurricane Harvey that hit Texas in 2017, have been heavily studied. Many highly impactful extreme weather events have not been studied in the event attribution framework, particularly in the developing world where studies are generally lacking. This is due to various reasons, including lack of observational data, lack of reliable climate models, and lack of scientific capacity. While the events that have been studied are not representative of all extreme events that have occurred, and results from these studies may also be subject to selection bias, the large number of event attribution studies provide evidence that changes in the properties of these local and individual events are in line with expected consequences of human influence on the climate and can be attributed to external drivers. {Cross-Working Group Box: Attribution, TS.4.1, 11.1.4, 11.2.2}

It is *very likely* that human influence is the main contributor to the observed increase in the intensity and frequency of hot extremes and the observed decrease in the intensity and frequency of cold extremes on continental scales. Some specific recent hot extreme events would have been *extremely unlikely* to occur without human influence on the climate system. Changes in aerosol concentrations have *likely* slowed the increase in hot extremes in some regions in particular from 1950–1980. No-till farming, irrigation, and crop expansion have similarly attenuated increases in summer hot extremes in some regions, such as central North America (*medium confidence*). {11.3.4}

Human influence has contributed to the intensification of heavy precipitation in three continents where observational data are most abundant, including North America, Europe and Asia (*high confidence*). On regional scales, evidence of human influence on extreme precipitation is limited, but new evidence from attributing individual heavy precipitation events found that human influence was a significant driver of the events. {11.4.4}

There is *low confidence* that human influence has affected trends in meteorological droughts in most regions, but *medium confidence* that they have contributed to the severity of some specific events. There is *medium confidence* that human-induced climate change has contributed to increasing trends in the probability or intensity of recent agricultural and ecological droughts, leading to an increase of the affected land area. {11.6.4}

Event attribution studies of specific strong tropical cyclones provide limited evidence for anthropogenic effects on tropical cyclone intensifications so far, but *high confidence* for increases in precipitation. There is *high confidence* that anthropogenic climate change contributed to extreme rainfall amounts during Hurricane Harvey (2017) and other intense tropical cyclones. {11.7.3}

The number of evident attribution studies on compound events is limited. There is *medium confidence* that weather conditions that promote wildfires have become more probable in southern Europe, northern Eurasia, the USA, and Australia over the last century. In Australia a number of event attribution studies show that there is *medium confidence* of increase in fire weather conditions due to human influence. {11.8.3, 12.4.3.2}

[START BOX TS.10, FIGURE 1 HERE]

Box TS.10, Figure 1: Synthesis of assessed observed changes and human influence of hot extremes (panel a), heavy precipitation (panel b) and agricultural and ecological drought (panel c) for the IPCC AR6 regions (displayed as hexagons). The colours in each panel represent the four outcomes of the assessment on the observed changes: In Panel a): red – at least *medium confidence* in an observed increase in hot extremes; blue – at least *medium confidence* in an observed decrease in hot extremes; white – no significant change in hot extremes is observed for the region as a whole; grey – the evidence in this region is insufficient (because of a lack of data and/or literature) to make an assessment for the region as a whole. In panel b): green – at least *medium confidence* in an observed increase in heavy rainfall; yellow - at least *medium confidence* in an observed decrease in heavy rainfall; white – no significant change in heavy rainfall is observed for the region as a whole; grey – the evidence in this region is insufficient

ACCEPTED VERSION SUBJECT TO FINAL EDITING

(because of a lack of data and/or literature) to make an assessment for the region as a whole. In panel c): yellow – at least *medium confidence* in an observed increase in agricultural and ecological drought; green - at least *medium confidence* in an observed decrease in agricultural and ecological drought; white – no significant change in agricultural and ecological drought is observed for the region as a whole; grey – the evidence in this region is insufficient (because of a lack of data and/or literature) to make an assessment for the region as a whole. Each panel represents in addition the synthesis of assessment of the human influence on the observed changes based on available trend detection and attribution and event attribution scientific publications. The level of confidence is indicated by a number of dots: *high confidence* (three dots), *medium confidence* (two dots), *low confidence* (one dot), and when no assessment is possible, due to insufficient evidence for the specific region (horizontal bar). For hot extremes, the evidence is mostly drawn from changes in metrics based on daily maximum temperatures, regional studies using other metrics (heatwave duration, frequency and intensity) are used in addition {11.9.2}. For heavy precipitation, the evidence is mostly drawn from changes in metrics based on one-day or five-day precipitation amounts using global and regional studies {11.9.3}. Agricultural and ecological droughts are assessed based on observed and projected changes in total column soil moisture, complemented by evidence on changes in surface soil moisture, water-balance (precipitation minus evapotranspiration) and metrics driven by precipitation and atmospheric evaporative demand. {11.9.3} All assessments are made for each AR6 region as a whole and for the timeframe from 1950 to present thus, more local or assessment made on shorter time scales might differ from what is shown in the figure. {11.9, Table TS.5}.

[END BOX TS.10, FIGURE 1 HERE]

[END BOX TS.10 HERE]

TS.4.1.2 Regional Climate Information Distillation and Climate Services

The construction of regional climate information involves people with a variety of backgrounds, from various disciplines, who have different sets of experiences, capabilities and values. The process of synthesizing climate information from different lines of evidence from a number of sources, taking into account the context of a user vulnerable to climate variability and change and the values of all relevant actors, is called distillation. Distillation is conditioned by the sources available, the actors involved and the context, which all depend heavily on the regions considered, and framed by the question being addressed. Distilling regional climate information from multiple lines of evidence and taking the user context into account increases fitness, usefulness, relevance and trust in that information for use in climate services (Box TS.11) and decision-making (*high confidence*). {1.2.3, 10.1.4, 10.5, Cross-Chapter Box 10.3, 12.6}

The distillation process can vary substantially, as it needs to consider multiple lines of evidence on all physically plausible outcomes (especially when they are contrasting) relevant to a specific decision required in response to a changing climate. Confidence in the distilled regional climate information is enhanced when there is agreement across multiple lines of evidence, so the outcome can be limited if these are inconsistent or contradictory. For example, in the Mediterranean region the agreement between different lines of evidence such as observations, projections by regional and global models, and understanding of the underlying mechanisms provides *high confidence* in summer warming that exceeds the global average (see Box TS.12). In a less clear-cut case for Cape Town, despite consistency among global model future projections, there is *medium confidence* in a projected future drier climate due to the lack of consistency in links between increasing greenhouse gases, changes in a key mode of variability (the Southern Annular Mode) and drought in Cape Town among different observation periods and in model simulations. {10.5.3, 10.6, 10.6.2, 10.6.4, Cross-Chapter Box 10.3, 12.4}

Since the AR5, physical climate storyline approaches have emerged as a complementary instrument to provide a different perspective on or additional climate information, to facilitate communication of the information or provide a more flexible consideration of risk. Storylines that condition climatic events and processes on a set of plausible but distinct large-scale climatic changes enable the exploration of uncertainties in regional climate projections. For example, they can explicitly address low-likelihood, high-impact outcomes, which would be

ACCEPTED VERSION SUBJECT TO FINAL EDITING

less emphasized in a probabilistic approach, and can be embedded in a user's risk landscape, taking account of socio-economic factors as well as physical climate changes. Storylines can also be used to communicate climate information by narrative elements describing and contextualising the main climatological features and the relevant consequences in the user context and, as such, can be used as part of a climate information distillation process. {1.4.4., Box 10.2, Box 11.2, 11.2, Cross-chapter Box 12.2}

[START BOX TS.11 HERE]

Box TS.11: Climate Services

Climate services involve providing climate information to assist decision-making, for example, about how extreme rainfall will change to inform improvements in urban drainage. Since AR5, there has been a significant increase in the range and diversity of climate service activities (*very high confidence*). The level of user-engagement, co-design and co-production are factors determining the utility of climate services, while resource limitations for these activities constrain their full potential. {12.6, Cross-Chapter Box 12.2}

Climate services include engagement from users and providers and an effective access mechanism; they are responsive to user needs and based on integrating scientifically credible information and relevant expertise. Climate services are being developed across regions, sectors, time scales and users-groups and include a range of knowledge brokerage and integration activities. These involve identifying knowledge needs; compiling, translating and disseminating knowledge; coordinating networks and building capacity through informed decision-making; analysis, evaluation and development of policy; and personal consultation.

Since AR5, climate change information produced in climate service contexts has increased significantly due to scientific and technological advancements and growing user awareness, requirements, and demand (*very high confidence*). Climate services are growing rapidly and are highly diverse in their practices and products. The decision-making context, level of user engagement and co-production between scientists, practitioners and intended users are important determinants of the type of climate service developed and their utility for supporting adaptation, mitigation and risk management decisions. They require different types of user–producer engagement depending on what the service aims to deliver (*high confidence*), and these fall into three broad categories: website-based services, interactive group activities and focused relationships.

Realization of the full potential of climate services is often hindered by limited resources for the co-design and co-production process, including sustained engagement between scientists, service providers and users (*high confidence*). Further challenges relate to the development and provision of climate services, generation of climate service products, communication with users, and evaluation of their quality and socio-economic benefit. {TS.4.1, 1.2.3, 10.5.4, 12.6, Cross-Chapter Box 12.2, Glossary}

[END BOX TS.11 HERE]

[START BOX TS.12 HERE]

Box TS.12: Multiple Lines of Evidence for Assessing Regional Climate Change and the Interactive Atlas

A key novel element in the AR6 is the WGI Atlas, which includes the Interactive Atlas. The Interactive Atlas provides the ability to explore much of the observational and climate model data used as lines of evidence in this assessment to generate regional climate information. {10.6.4, Atlas.2, Interactive Atlas}

A significant innovation in the AR6 WGI report is the Atlas. Part of its remit is to provide region-by-region assessment on changes in mean climate and to link with other WGI chapters to generate climate change information for the regions. An important component is the new online interactive tool, the Interactive Atlas,

ACCEPTED VERSION SUBJECT TO FINAL EDITING

with flexible spatial and temporal analyses of much of the observed, simulated past and projected future climate change data underpinning the WGI assessment. This includes the ability to generate global maps and a number of regionally aggregated products (time series, scatter plots, tables, etc.) for a range of observations and ensemble climate change projections of variables (such as changes in the CIDs summarized in Table TS.5) from CMIP5, CORDEX and CMIP6. The data can be displayed and summarized under a range of SSP-RCP scenarios and future time slices and also for different global warming levels, relative to several different baseline periods. The maps and various statistics can be generated for annual mean trends and changes or for any user-specified season. A new set of WGI reference regions is used for the regional summary statistics and applied widely throughout the report (with the regions available, along with aggregated datasets and the code to generate these at the ATLAS GitHub: https://github.com/IPCC-WG1/Atlas).

Box TS.12, Figure 1 shows how the Interactive Atlas products, together with other lines of evidence, can be used to generate climate information for an illustrative example of the Mediterranean summer warming. The lines of evidence include the understanding of relevant mechanisms, dynamic and thermodynamic processes and the effect of aerosols in this case (Box TS.12, Figure 1a), trends in observational datasets (which can have different spatial and temporal coverage – Box TS.12, Figure 1b, c), attribution of these trends and temperature projections from global and regional climate models at different resolutions, including single-model initial-condition large ensembles (SMILEs; Box TS.12, Figure 1d, e). Taken together, this evidence shows there is *high confidence* that the projected Mediterranean summer temperature increase will be larger than in the global mean with consistent results from CMIP5 and CMIP6 (Box TS.12, Figure 1e). However, CMIP6 results project both more pronounced warming than CMIP5 for a given emissions scenario and time period and a greater range of changes (Box TS.12, Figure 1d). {10.6.4, Atlas.2, Interactive Atlas}

[START BOX TS.12, FIGURE 1 HERE]

Box TS.12, Figure 1: **Example of generating regional climate information from multiple lines of evidence for the case of Mediterranean summer warming, with indication of the information available from the Interactive Atlas.** (a) Mechanisms and feedbacks involved in enhanced Mediterranean summer warming. (b) Locations of observing stations from different datasets. (c) Distribution of 1960–2014 summer temperature trends (°C per decade) for observations (black crosses), CMIP5 (blue circles), CMIP6 (red circles), HighResMIP (orange circles), CORDEX EUR-44 (light blue circles), CORDEX EUR-11 (green circles), and selected single Model Initial-condition Large Ensembles - SMILEs (grey boxplots, MIROC6, CSIRO-Mk3-6-0, MPI-ESM and d4PDF). (d) Time series of area averaged (25°N–50°N, 10°W–40°E) land point summer temperature anomalies (°C, baseline period is 1995–2014): the boxplot shows long term (2081–2100) temperature changes of different CMIP6 scenarios in respect to the baseline period. (e) Projected Mediterranean summer warming in comparison to global annual mean warming of CMIP5 (RCP2.6, RCP4.5, RCP6.0 and RCP8.5) and CMIP6 (SSP1-2.6, SSP2-4.5, SSP3-7.0 and SSP5-8.5) ensemble means (lines) and spread (shading). {Figure 10.20, Figure 10.21, Figure Atlas.8}

[END BOX TS.12, FIGURE 1 HERE]

[END BOX TS.12 HERE]

TS.4.2 Drivers of Regional Climate Variability and Change

Anthropogenic forcing, including GHGs and aerosols but also regional land use and irrigation have all affected observed regional climate changes (*high confidence*) and will continue to do so in the future (*high confidence*), with various degrees of influence and response times, depending on warming levels, the nature of the forcing and the relative importance of internal variability. Since the late 19th century, major modes of variability (MoVs) exhibited fluctuations in frequency and magnitude at multi-decadal time scales, but no sustained trends outside the range of internal variability (Table TS.4). An exception is the Southern Annular Mode (SAM), which has become systematically more positive (*high confidence*) and is projected to be more positive in all seasons, except for December-January-February (DJF), in high CO_2 emissions scenarios (*high confidence*).

ACCEPTED VERSION SUBJECT TO FINAL EDITING

The influence of stratospheric ozone forcing on the SAM trend has been reduced since the early 2000s compared to earlier decades, contributing to the weakening of its positive trend as observed over 2000–2019 (*medium confidence*). In the near-term, projected changes in most of the MoVs and related teleconnections will *likely* be dominated by internal variability. In the long-term, it is *very likely* that the precipitation variance related to El Niño–Southern Oscillation will increase. Physical climate storylines, including the complex interplay between climate drivers, MoVs, and local and remote forcing, increase confidence in the understanding and use of observed and projected regional changes. {2.4, 3.7, 4.3, 4.4, 4.5, 6.4, 8.3, 8.4, 10.3, 10.4, 11.3}

TS.4.2.1 Regional Fingerprints of Anthropogenic and Natural Forcing

While anthropogenic forcing has contributed to multi-decadal mean precipitation changes in several regions, internal variability can delay emergence of the anthropogenic signal in long-term precipitation changes in many land regions (*high confidence*). At the regional scale, the effect of human-induced GHG forcing on extreme temperature is moderated or amplified by soil moisture feedback, snow/ice-albedo feedback, regional forcing from land-use/land-cover changes, forcing from aerosol concentrations, or decadal/multi-decadal natural variability. Changes in local and remote aerosol forcings lead to south-north gradients of the effective radiative forcing (ERF) (hemispherical asymmetry). Along latitudes, it is more uniform with strong amplification of the temperature response towards the Arctic (*medium confidence*). The decrease of SO_2 emissions since the 1980s reduces the damping effect of aerosols, leading to a faster increase in surface air temperature that is most pronounced at mid- and high latitudes of the Northern Hemisphere, where the largest emission reductions have taken place (*medium confidence*). {1.3, 3.4.1, 6.3.4, 6.4.1, 6.4.3, 8.3.1, 8.3.2, Box 8.1, 10.4.2, 10.6, 11.1.6, 11.3}

Multidecadal dimming and brightening trends in incoming solar radiation at the Earth's surface occurred at widespread locations (*high confidence*). Multi-decadal variation in anthropogenic aerosol emissions are thought to be a major contributor (*medium confidence*), but multi-decadal variability in cloudiness may also have played a role. Volcanic eruptions affect regional climate through their spatially heterogeneous effect on the radiative budget as well as through triggering dynamical responses by favouring a given phase from some MoVs, for instance. {1.4.1, Cross-Chapter Box 1.2, 2.2.1, 2.2.2, 3.7.1, 3.7.3, 4.3.1, 4.4.1, 4.4.4, Cross-Chapter Box 4.1, 7.2.2, 8.5.2, 10.1.4, 11.1.6, 11.3.1}

Historical urbanization affects the observed warming trends in cities and their surroundings (*very high confidence*). Future urbanization will amplify the projected air temperature under different background climates, with a strong effect on minimum temperatures that could be as large as the global warming signal (*very high confidence*). Irrigation and crop expansion have attenuated increases in summer hot extremes in some regions, such as central North America (*medium confidence*). {Box 10.3, 11.1.6, 11.3, Box TS.6, Box TS.14}

TS.4.2.2 Modes of Variability and Regional Teleconnections

Modes of Variability (MoVs) (Annex IV, Table TS.4) have existed for millennia or longer (*high confidence*), but there is *low confidence* in detailed reconstructions of most of them prior to direct instrumental records. MoVs are treated as a main source of uncertainties associated with internal dynamics, as they can either accentuate or dampen, even mask, the anthropogenically-forced responses. {2.4, 8.5.2, 10.4, 10.6, 11.1.5, Atlas.3.1}

Since the late 19th century, major MoVs (Table TS.4) show no sustained trends, exhibiting fluctuations in frequency and magnitude at multi-decadal time scales, except for the Southern Annular Mode (SAM), which has become systematically more positive (*high confidence*) (Table TS.4). It is *very likely* that human influence has contributed to this trend from the 1970s to the 1990s, and to the associated strengthening and southward shift of the Southern Hemispheric extratropical jet in austral summer. The influence of stratospheric ozone forcing on the SAM trend has been reduced since the early 2000s compared to earlier decades, contributing to

ACCEPTED VERSION SUBJECT TO FINAL EDITING

the weakening of its positive trend observed over 2000–2019 (*medium confidence*). By contrast, the cause of the Northern Annular Mode (NAM) trend toward its positive phase since the 1960s and associated northward shifts of Northern Hemispheric extratropical jet and storm track in boreal winter is not well understood. The evaluation of model performance on simulating MoVs is assessed in TS.1.2.2. {2.3.3, 2.4, 3.3.3, 3.7.1, 3.7.2}

In the near term, the forced change in SAM in austral summer is *likely* to be weaker than observed during the late 20th century under all five SSPs assessed. This is because of the opposing influence in the near- to mid-term from stratospheric ozone recovery and increases in other greenhouse gases on the Southern Hemisphere summertime mid-latitude circulation (*high confidence*). In the near term, forced changes in the SAM in austral summer are therefore *likely* to be smaller than changes due to natural internal variability. In the long-term (2081–2100) under the SSP5-8.5 scenario, the SAM index is *likely* to increase in all seasons relative to 1995–2014. The CMIP6 multi-model ensemble projects a long-term (2081–2100) increase in the boreal wintertime NAM index under SSP3-7.0 and SSP5-8.5, but regional associated changes may deviate from a simple shift in the mid-latitude circulation due to a modified teleconnection resulting from interaction with a modified mean background state. {4.3.3, 4.4.3, 4.5.1, 4.5.3, 8.4.2}

Human influence has not affected the principal tropical modes of interannual climate variability (Table TS.4) and their associated regional teleconnections beyond the range of internal variability (*high confidence*). It is *virtually certain* that the ENSO will remain the dominant mode of interannual variability in a warmer world. There is no consensus from models for a systematic change in amplitude of ENSO SST variability over the 21st century in any of the SSP scenarios assessed (*medium confidence*). However, it is *very likely* that rainfall variability related to ENSO will be enhanced significantly by the latter half of the 21st century in the SSP2-4.5, SSP3-7.0, and SSP5-8.5 scenarios, regardless of the amplitude changes in SST variability related to the mode It is *very likely* that rainfall variability related to changes in the strength and spatial extent of ENSO teleconnections will lead to significant changes at regional scale. {3.7.3, 3.7.4, 3.7.5, 4.3.3, 4.5.3, 8.4.2, 10.3.3}

Modes of decadal and multidecadal variability over the Pacific and Atlantic Ocean exhibit no significant changes in variance over the period of observational records (*high confidence*). There is *medium confidence* that anthropogenic and volcanic aerosols contributed to observed temporal evolution in the Atlantic Multidecadal Variability (AMV) and associated regional teleconnections, especially since the 1960s, but there is *low confidence* in the magnitude of this influence and the relative contributions of natural and anthropogenic forcings. Internal variability is the main driver of Pacific Decadal Variability (PDV) observed since the start of the instrumental records (*high confidence*), despite some modelling evidence for potential external influence. There is *medium confidence* that the AMV will undergo a shift towards a negative phase in the near-term. {2.4, 3.7.6, 3.7.7, 8.5.2, 4.4.3}

[START TABLE TS.4 HERE]

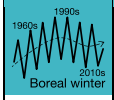
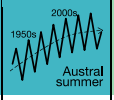
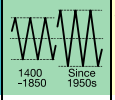
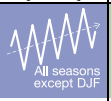
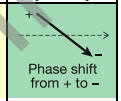
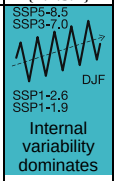
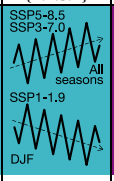
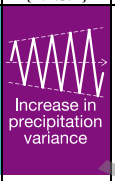
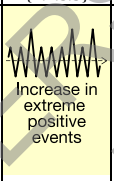
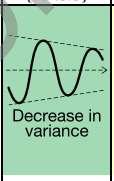
Table TS.4: Summary of the assessments on modes of variability (MoVs) and associated teleconnections. (a) Assessments on observed changes since the start of instrumental records, CMIP5 and CMIP6 model performance, human influence on the observed changes, and near-term (2021–2040) and mid- to long-term (2041–2100) changes. Curves schematically illustrate the assessed overall changes, with the horizontal axis indicating time, and are not intended to precisely represent the time evolution. (b) Fraction of surface air temperature (SAT) and precipitation (pr) variance explained at interannual timescale by each MoV for each AR6 region (numbers in each cell; in percent). Values correspond to the average of significant explained variance fractions based on HadCRUT, GISTEMP, BerkeleyEarth and CRU-TS (for SAT) and GPCC and CRU-TS (for precipitation). Significance is tested based on F-statistics at the 95% level confidence, and a slash indicates that the value is not significant in more than half of the available data sets. The colour scale corresponds to the sign and values of the explained variance as shown at the bottom. The corresponding anomaly maps are shown in Annex IV. DJF: December-January-February. MAM: March-April-May. JJA: June-July-August. SON: September-October-November. In (b), Northern Annular Mode (NAM) and El Niño–Southern Oscillation (ENSO) teleconnections are evaluated for 1959–2019, Southern Annular Mode (SAM) for 1979–2019, Indian Ocean Basin (IOB), Indian Ocean Dipole (IOD), Atlantic Zonal Mode (AZM) and Atlantic Meridional

ACCEPTED VERSION SUBJECT TO FINAL EDITING

Mode (AMM) for 1958–2019, and Pacific Decadal Variability (PDV) and Atlantic Multidecadal Variability (AMV) for 1900–2019. All data are linearly detrended prior to computation. {2.4, 3.7, 4.3.3, 4.4.3, 4.5.3, Table Atlas.1, Annex IV, TS.1.2.2}

(a) Assessments on MoV

(a) Assessments on MoV

	NAM	SAM	ENSO	IOB	IOD	AZM	AMM	PDV	AMV
Past changes since the start of observations				Within proxy-inferred variability range	Within proxy-inferred variability range	Limited evidence	Limited evidence	Dominated by multidecadal fluctuations	Dominated by multidecadal fluctuations
	{2.4.1.1}	{2.4.1.2}	{2.4.2}	{2.4.3}	{2.4.3}	{2.4.4}	{2.4.4}	{2.4.5}	{2.4.6}
CMIP5 and CMIP6 model performance	High performance	High performance	Medium performance	Medium performance	Medium performance	Low performance	Low performance	Medium performance	Medium performance
	{3.7.1}	{3.7.2}	{3.7.3}	{3.7.4}	{3.7.4}	{3.7.5}	{3.7.5}	{3.7.6}	{3.7.7}
Human influence on the observed changes	No robust evidence	Contributed through GHG (all seasons) &ozone (DJF)	Low agreement	No robust evidence	Not detected	No robust evidence	No robust evidence	Not detected	Contributed through aerosols
	{3.7.1}	{3.7.2}	{3.7.3}	{3.7.4}	{3.7.4}	{3.7.5}	{3.7.5}	{3.7.6}	{3.7.7}
Near-term future changes (2021–2040)	Internal variability dominates		Internal variability dominates	No robust evidence	No robust evidence	No robust evidence	No robust evidence	Limited evidence	
	{4.4.3.1}	{4.4.3.1}	{4.4.3.2}	{4.4.3.3}	{4.4.3.3}	{4.4.3.4}	{4.4.3.4}	{4.4.3.5}	{4.4.3.6}
Mid-to-long-term future changes (2041–2100)				No robust evidence		No robust evidence	No robust evidence		No changes
	{4.3.3.1; 4.5.3.1}	{4.3.3.1; 4.5.3.1}	{4.3.3.2; 4.5.3.2}	{4.5.3.3}	{4.5.3.3}	{4.5.3.4}	{4.5.3.4}	{4.5.3.5}	{4.5.3.6}

low confidence | *medium confidence* | *high confidence* | *more likely than not* | *likely* | *very likely*

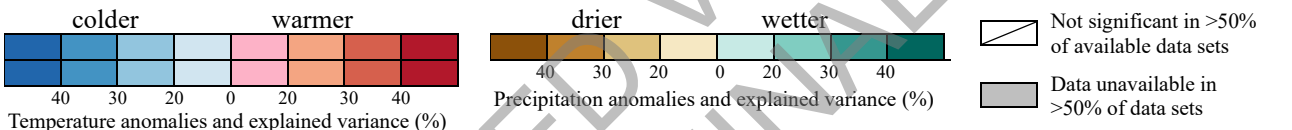
(b) Regional climate anomalies associated with MoV

(b) Regional climate anomalies associated with MoV

	Mode	NAM		SAM		ENSO		IOB		IOD		AZM		AMM		PDV		AMV	
	Season	DJF		DJF		DJF		MAM		SON		JJA		JJA		annual		annual	
	Variable	SAT	pr	SAT	pr	SAT	pr	SAT	pr	SAT	pr	SAT	pr	SAT	pr	SAT	pr	SAT	pr
Africa	Sahara	58						14				10	19		12		9	12	25
	Western Africa	25					15	45				21		10			6	6	23
	Central Africa	19	8		10	14		50				13					10	14	11
	North Eastern Africa	19	7				14	36			32					7		7	
	South Eastern Africa					14	22	36			57			10			4	9	
	West Southern Africa					49	26	27	16	8						4	12	5	
	East Southern Africa			13		75	34	35	7							4	6		
	Madagascar					24		24	7	11	10			9				5	
Asia	West Siberia	45					7						9						11
	East Siberia	52														3			11
	Russian Far East	8	10			11		6										5	5
	West Central Asia								15		21						4		
	East Central Asia								38										
	Tibetan Plateau		15							15	7		11			6	5	9	
	East Asia					7	20		23				9				9	13	
	South Asia	9						12			8			8				5	
	Southeast Asia					39	31	73	6		48					5	12		7
	Arabian Peninsula	32						10	24		20						5	13	7
Austr	Northern Australia					21	13	38			19				7	7	7		
	Central Australia			14		21	12	18		22	20		7		7	6	5		
	East Australia			22		20	11	18		9	8		7			7	8		

ACCEPTED VERSION SUBJECT TO FINAL EDITING

	Southern Australia						11			23	40		8				3		
	New Zealand			16															
Central & South America	Southern Central America					21	16	33		10	11			17		6		6	7
	Northwestern South America		7	14	16	82	17	54		18				13	16	7	8		
	Northern South America	7				56	58	61					22	17	24	9	12	7	
	Northeastern South America					25		58	19	9	12				8				
	South American Monsoon					54		31		22	7				6	7			
	Southwestern South America				10	16	14	17		10	16					8			
	Southeastern South America						21		13	21	10		12				5		6
	Southern South America				23					13	7								9
Europe	Mediterranean	28	58			7												19	
	Western & Central Europe	28	18							13	10						4		8
	Eastern Europe	35										7							
	Northern Europe	53	32															6	
North America	North Central America			10	26	13	27	18				7	12	15	12		6	19	
	Western North America															4		6	5
	Central North America	17			12		17					8					3	9	6
	Eastern North America	12										11	9			4		9	4
	Northeastern North America	18	26									8					10	9	4
	Northwestern North America		14			10	8	17								8	4		
Small Islands	Caribbean				10	15	18	26	8		10			17	12	7			5
	Pacific																		
Polar Terrestrial Regions	Greenland/Iceland	42	8												7			44	
	Russian Arctic	25	10														6	11	8
	West Antarctica											8		21					
	East Antarctica			38															



TS.4.2.3 Interplay Between Drivers of Climate Variability and Change at Regional Scales

Anthropogenic forcing has been a major driver of regional mean temperature change since 1950 in many subcontinental regions of the world (*virtually certain*). At regional scales, internal variability is stronger, and uncertainties in observations, models and external forcing are all larger than at the global scale, hindering a robust assessment of the relative contributions of greenhouse gases, stratospheric ozone, and different aerosol species in most of the cases. Multiple lines of evidence, combining multi-model ensemble global projections with those coming from single-model initial-condition large ensembles, show that internal variability is largely contributing to the delayed or absent emergence of the anthropogenic signal in long-term regional mean precipitation changes (*high confidence*). Internal variability in ocean dynamics dominates regional patterns on annual to decadal time scales (*high confidence*). The anthropogenic signal in regional sea level change will emerge in most regions by 2100 (*medium confidence*). {9.2.4, 9.6.1, 10.4.1, 10.4.2, 10.4.3}

Regional climate change is subject to the complex interplay between multiple external forcings and internal variability. Time evolution of mechanisms operating at different time scales can modify the amplitude of the regional-scale response of temperature, and both the amplitude and sign of the response of precipitation, to anthropogenic forcing (*high confidence*). These mechanisms include non-linear temperature, precipitation and soil moisture feedbacks, slow and fast responses of SST patterns and atmospheric circulation changes to increasing GHGs. Land use and aerosol forcings and land–atmosphere feedback play important roles in modulating regional changes, for instance in weather and climate extremes (*high confidence*). These can also lead to a higher warming of extreme temperatures compared to mean temperature (*high confidence*), and possibly cooling in some regions (*medium confidence*). The soil moisture–temperature feedback was shown to be relevant for past and present-day heat waves based on observations and model simulations. {10.4.3, 11.1.6, 11.3.1}

ACCEPTED VERSION SUBJECT TO FINAL EDITING

Southeastern South America (SES) is one of the AR6 WGI reference regions (outlined with black thick contour in Figure TS.21a) and it is used here as an illustrative example of the interplay between drivers of climate variability and change at regional scale. Austral summer (DJF) precipitation positive trends have been observed over the region during 1950–2014. Drivers of this change include MoVs, such as AMV, ENSO, and PDV, as well as external forcing, like GHG increases and ozone depletion together with aerosols (as illustrated in Figure TS.21a). MoVs and external forcing collectively affect climate phenomena, such as the Hadley cell width and strength, Rossby waves activity emerging from the large-scale tropical SST anomalies, and the Southern Hemisphere polar vortex, which are relevant for the region. In fact, local changes over SES in terms of moisture convergence, ascending motion and storm-track locations depend on these climate phenomena, and they are overall responsible for the observed precipitation trends. Projections suggest continuing positive trends in rainfall over SES in the near-term in response to GHG emissions scenarios. Multi-model mean and ensemble spread are not sufficient to characterise situations where different models simulate substantially different or even opposite changes (*high confidence*). In such cases, physical climate storylines addressing possible outcomes for climate phenomena shown to play a role in the variability of the region of interest can aid the interpretation of projection uncertainties. In addition, single-model initial-condition large ensembles of many realisations of internal variability are required to separate internal variability from forced changes (*high confidence*) and to partition the different sources of uncertainties as a function of future assessed periods. {10.3.4, 10.4.2, Figure 10.12a}

[START FIGURE TS.21 HERE]

Figure TS.21: Example of the interplay between drivers of climate variability and change at regional scale to understand past and projected changes. *The figure intent is to show an illustrative pathway for understanding past, and anticipating future, climate change at regional scale in the presence of uncertainties.* (a) Identification of the climate drivers and their influences on climate phenomena contributing through teleconnection to Southeastern South America summer (DJF) precipitation variability and trends observed over 1950–2014. Drivers (red squares) include MoVs as well as external forcing. Observed precipitation linear trend from GPCC is shown on continents (green-brown colour bar in mm month^{-1} per decade) and the SES AR6 WGI reference region is outlined with the thick black contour. Climate phenomena leading to local effect on SES are schematically presented (blue ovals). (b) Time series of decadal precipitation anomalies for DJF SES simulated from seven large ensembles of historical + RCP8.5 simulations over 1950–2100. Shading corresponds to the 5th–95th range of climate outcomes given from each large ensemble for precipitation (in mm/month) and thick coloured lines stand for their respective ensemble mean. The thick timeseries in white corresponds to the multi-model multi-member ensemble mean with model contribution being weighted according to their ensemble size. GPCC observation is shown in the light black line with squares over 1950–2014 and the 1995–2014 baseline period has been retained for calculation of anomalies in all datasets. (c) Quantification of the respective weight (in percent) between the individual sources of uncertainties (internal in grey, model in magenta and scenario in green) at near-term, mid-term and long-term temporal windows defined in AR6 and highlighted in (b) for SES DJF precipitation. All computations are done with respect to 1995–2014, taken as the reference period and the scenario uncertainty is estimated from CMIP5 using the same set of models as for the large ensembles that have run different RCP scenarios. {Figure 10.12a}

[END FIGURE TS.21 HERE]

ACCEPTED VERSION SUBJECT TO FINAL EDITING

[START BOX TS.13 HERE]

Box TS.13: Monsoons

Global land monsoon precipitation decreased from the 1950s to the 1980s, partly due to anthropogenic aerosols, but has increased since then in response to GHG forcing and large-scale multi-decadal variability (*medium confidence*). Northern Hemispheric anthropogenic aerosols weakened the regional monsoon circulations in South Asia, East Asia and West Africa during the second half of the 20th century, thereby offsetting the expected strengthening of monsoon precipitation in response to GHG-induced warming (*high confidence*). During the 21st century, global land monsoon precipitation is projected to increase in response to GHG warming in all time horizons and scenarios (*high confidence*). Over South and Southeast Asia, East Asia and the central Sahel, monsoon precipitation is projected to increase, whereas over North America and the far western Sahel it is projected to decrease (*medium confidence*). There is *low confidence* in projected precipitation changes in the South American and Australian-Maritime Continent monsoons. At global and regional scales, near-term monsoons changes will be dominated by the effects of internal variability (*medium confidence*). {2.3, Cross-Chapter Box 2.4, 3.3, 4.4, 4.5, 8.2, 8.3, 8.4, 8.5, Box 8.1, Box 8.2, 10.6}

Global Monsoon

Paleoclimate records indicate that during warm climates, like the mid-Pliocene Warm Period, monsoon systems were stronger (*medium confidence*). In the instrumental records, global summer monsoon precipitation intensity has *likely* increased since the 1980s, dominated by Northern Hemisphere summer trends and large multi-decadal variability. Contrary to the expected increase of precipitation under global warming, the Northern Hemisphere monsoon regions experienced declining precipitation from the 1950s to 1980s, which is partly attributable to the influence of anthropogenic aerosols (*medium confidence*) (Box TS.13, Figure 1). {2.3.1, Cross-Chapter Box 2.4, 3.3.2, 3.3.3}

With continued global warming, it is *likely* that global land monsoon precipitation will increase during this century (Box TS.13, Figure 1), particularly in the Northern Hemisphere, although the monsoon circulation is projected to weaken. A slowdown of the tropical circulation with global warming can partly offset the warming-induced strengthening of precipitation in monsoon regions (*high confidence*). In the near term, global monsoon changes are *likely* to be dominated by the effects of internal variability and model uncertainties (*medium confidence*). In the long term, global monsoon rainfall change will feature a robust north-south asymmetry characterized by a greater increase in the Northern Hemisphere than in the Southern Hemisphere and an east-west asymmetry characterized by enhanced Asian-African monsoons and a weakened North American monsoon (*medium confidence*). {4.4.1, 4.5.1, 8.4.1}

Regional Monsoons

Paleoclimate reconstructions indicate stronger monsoons in the Northern Hemisphere but weaker ones in the Southern Hemisphere during warm periods, particularly for the South and Southeast Asian, East Asian, North and South American monsoons, with the opposite occurring during cold periods (*medium confidence*). It is *very likely* that Northern Hemispheric anthropogenic aerosols weakened the regional monsoon circulations in South Asia, East Asia and West Africa during the second half of the 20th century, thereby offsetting the expected strengthening of monsoon precipitation in response to GHG-induced warming (Box TS.13, Figure 1). Multiple lines of evidence explain this contrast over South Asia, with the observed trends dominated by the effects of aerosols, while future projections are mostly driven by GHG increases. The recent partial recovery and enhanced intensity of monsoon precipitation over West Africa is related to the growing influence of GHGs with an additional contribution due to the reduced cooling effect of anthropogenic aerosols, emitted largely from North America and Europe (*medium confidence*). For other regional monsoons, that is, North and South America and Australia, there is *low confidence* in the attribution of recent changes in precipitation (Box TS.13, Figure 1) and winds. {2.3.1, 8.3.1, 8.3.2, Box 8.1, 10.6.3}

Projections of regional monsoons during the 21st century indicate contrasting (region-dependent) and

ACCEPTED VERSION SUBJECT TO FINAL EDITING

uncertain precipitation and circulation changes. The annual contrast between the wettest and driest month of the year is *likely* to increase by 3–5% per degree Celsius in most monsoon regions in terms of precipitation, precipitation minus evaporation, and runoff (*medium confidence*). For the North American monsoon, projections indicate a decrease in precipitation, whereas increased monsoon rainfall is projected over South and Southeast Asia and over East Asia (*medium confidence*) (Box TS.13, Figure 1). West African monsoon precipitation is projected to increase over the central Sahel and decrease over the far western Sahel (*medium confidence*). There is *low confidence* in projected precipitation changes in the South American and Australian-Maritime Continent regional monsoons (for both magnitude or sign) (Box TS.13, Figure 1). There is *medium confidence* that the monsoon season will be delayed in the Sahel and *high confidence* that it will be delayed in North and South America. {8.2.2, 8.4.2.4, Box 8.2}

Building the Assessment from Multiple Lines of Evidence

Large natural variability of monsoon precipitation across different time scales, found in both paleoclimate reconstructions and instrumental measurements, poses an inherent challenge for robust quantification of future changes in precipitation at regional and smaller spatial scales. At both global and regional scales, there is *medium confidence* that internal variability contributes the largest uncertainty related to projected changes, at least in the near term (2021–2040). A collapse of the Atlantic Multidecadal Overturning Circulation (AMOC) could weaken the African and Asian monsoons but strengthen the Southern Hemisphere monsoons (*high confidence*). {4.4.4, Cross-Chapter Box 4.1, 4.5.1, 8.5.2, 8.6.1, 9.2.3, 10.6.3}

Overall, long-term (2081–2100) future changes in regional monsoons like the South and Southeast Asian monsoon are generally consistent across global (including high-resolution) and regional climate models and supported by theoretical arguments. Uncertainties in simulating the observed characteristics of regional monsoon precipitation are related to varying complexities of regional monsoon processes and their responses to external forcing, internal variability, and deficiencies in representing monsoon warm rain processes, organized tropical convection, heavy orographic rainfall and cloud–aerosol interactions. {8.3.2, 8.5.1, 10.3.3, 10.6.3}

[START BOX TS.13, FIGURE 1 HERE]

Box TS.13, Figure 1: Global and regional monsoons: past trends and projected changes. *The intent of this figure is to show changes in precipitation over regional monsoon domains in terms of observed past trends, how greenhouse gases and aerosols relate to these changes, and in terms of future projections in one intermediate emission scenario in the near, medium and long terms.* (a) Global (black contour) and regional monsoons (colour shaded) domains. The global monsoon (*GM*) is defined as the area with local summer-minus-winter precipitation rate exceeding 2.5 mm day^{-1} (see Annex V). The regional monsoon domains are defined based on published literature and expert judgement (see Annex V), and also accounting for the fact that the climatological summer monsoon rainy season varies across the individual regions. Assessed regional monsoons are South and Southeast Asia (*SAsiaM, Jun-Jul-Aug-Sep*), East Asia (*EAsiaM, Jun-Jul-Aug*), West Africa (*WAfriM, Jun-Jul-Aug-Sep*), North America (*NAmerM, Jul-Aug-Sep*), South America (*SAmerM, Dec-Jan-Feb*), Australia and Maritime Continent Monsoon (*AusMCM, Dec-Jan-Feb*). Equatorial South America (*EqSAmer*) and South Africa (*SAfri*) regions are also shown, as they receive unimodal summer seasonal rainfall although their qualification as monsoons is subject to discussion. (b) Global and regional monsoons precipitation trends based on DAMIP CMIP6 simulations with both natural and anthropogenic (ALL), GHG only (GHG), aerosols only (AER) and natural only (NAT) radiative forcing. Weighted ensemble means are based on nine CMIP6 models contributing to the MIP (with at least 3 members). Observed trends computed from CRU GPCP, and APHRO (only for *SAsiaM* and *EAsiaM*) datasets are shown as well. (c) Percentage change in projected seasonal mean precipitation over global and regional monsoons domain in the near-term (2021–2040), mid-term (2041–2060), and long-term (2081–2100) under SSP2-4.5 based on 24 CMIP6 models. {Figure 8.11, Figure 8.22}

[END BOX TS.13, FIGURE 1 HERE]

ACCEPTED VERSION SUBJECT TO FINAL EDITING

[END BOX TS.13 HERE]

TS.4.3 Regional Climate Change and Implications for Climate Extremes and Climatic Impact-Drivers

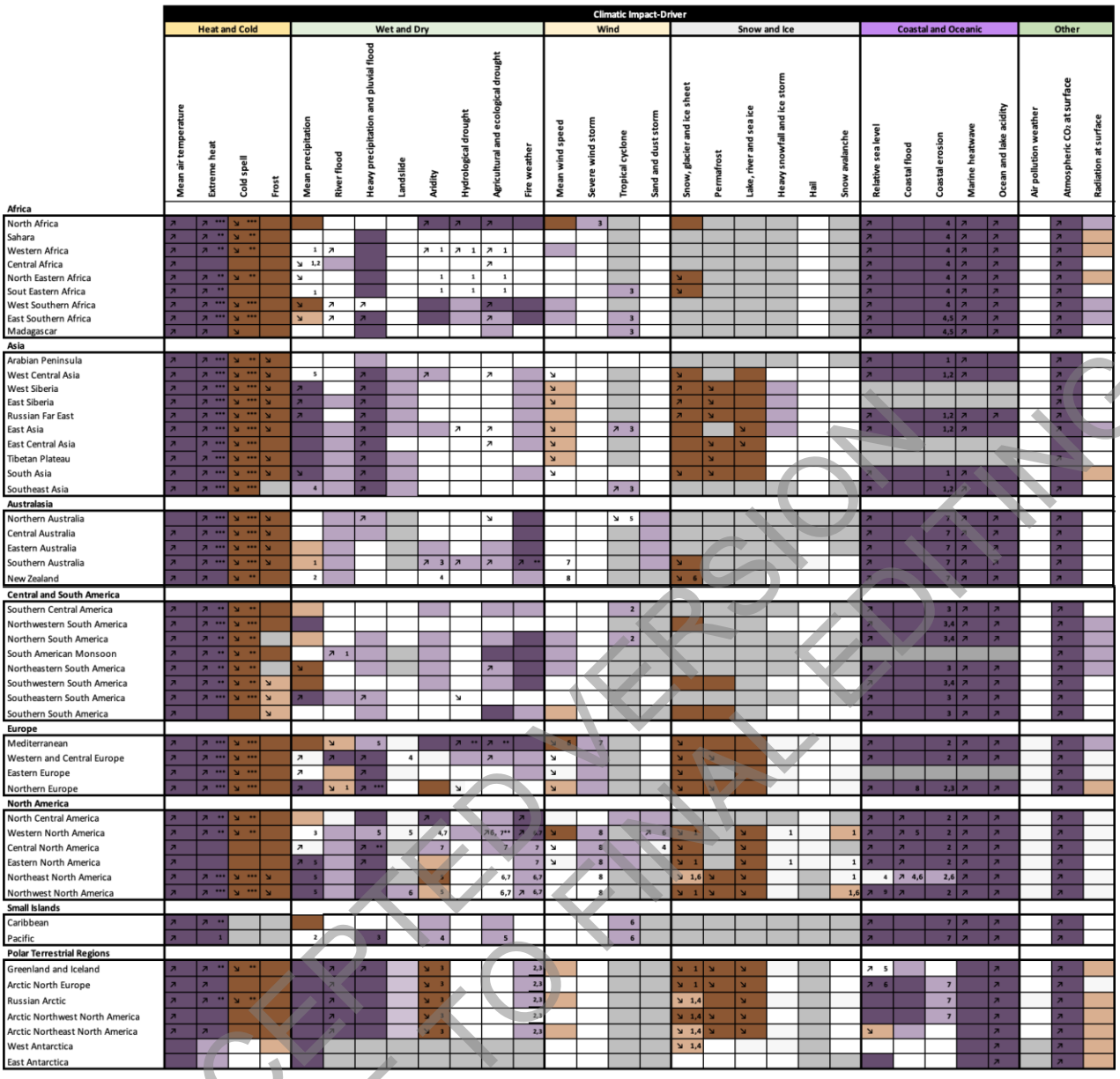
Current climate in all regions is already distinct from the climate of the early or mid-20th century with respect to several climatic impact-drivers (CIDs), resulting in shifting magnitude, frequency, duration, seasonality, and spatial extent of associated climate indices (*high confidence*). It is *very likely* that mean temperatures have increased in all land regions and will continue to increase at rates greater than the global average (*high confidence*). The frequency of heat and cold extremes have increased and decreased, respectively. These changes are attributed to human influence in almost all regions (*medium to high confidence*) and will continue through the 21st century (*high confidence*). In particular, extreme heat would exceed critical thresholds for health, agriculture and other sectors more frequently by the mid 21st century with 2°C of global warming (*high confidence*). Relative sea level rise is *very likely* to *virtually certain* (depending on the region) to continue during the 21st century, contributing to increased coastal flooding in low-lying areas (*high confidence*) and coastal erosion along most sandy coasts (*high confidence*). Sea level will continue to rise beyond 2100 (*high confidence*). Every region of the world will experience concurrent changes in multiple CIDs by mid-century (*high confidence*). Even for the current climate, climate change-induced shifts in CID distributions and event probabilities, some of which have occurred over recent decades, are relevant for risk assessments.{Box TS.4, 11.9, 12.1, 12.2, 12.4, 12.5, Atlas.3–Atlas.11}

An overview of changes in regional CIDs (introduced in TS.1) is given in Table TS.5, which summarizes multiple lines of evidence on regional climate change derived from observed trends, attribution of these trends and future projections. The level of confidence and the amplitude in the projected direction of change in CIDs at a given time-horizon depends on climate change mitigation efforts over the 21st century. It is evident from Table TS.5 that many heat, cold, snow and ice, coastal and oceanic CID changes are projected with *high confidence* in most regions starting from a global warming level (GWL) of 2°C, indicating worldwide challenges. Changes in many other regional CIDs have higher confidence later in the 21st century or at higher GWLs (*high confidence*), and another small subset are projected with *high confidence* for the 1.5°C GWL. This section focuses on the 2°C GWL and mid-century time period because the signal emerges from natural variability for a wider range of CIDs at this higher warming level. Figure TS.22 shows the geographical location of regions belonging to one of five groups characterized by a specific combination of changing climatic impact-drivers (CIDs). {Cross-Chapter Box 10.3, Box 11.1, 10.5, 11.1, 11.9, 12.1, 12.2, 12.4, 12.5}

[START TABLE TS.5 HERE]

Table TS.5: Summary of confidence for climatic impact-driver changes in each AR6 WG I reference region (illustrated in Figure TS.25) across multiple lines of evidence: observed, attributed and projected directional changes. The colours represent their projected aggregate characteristic changes for the mid-21st century, considering scenarios RCP4.5, SSP2-4.5, SRES A1B, or above (RCP6.0, RCP8.5, SSP3-7.0, SSP5-8.5, SRES A2), which approximately encompasses global warming levels of 2.0°C to 2.4°C. Arrows indicate *medium to high confidence* trends derived from observations, and asterisks indicate *medium* and *high confidence* in attribution of observed changes. (North Africa is not an AR6 WGI reference region, but assessment here is based upon the African portion of the Mediterranean reference region). {Tables 12.3–12.11 and Tables 11.4–11.21}

ACCEPTED VERSION SUBJECT TO FINAL EDITING



Key for observational trend evidence

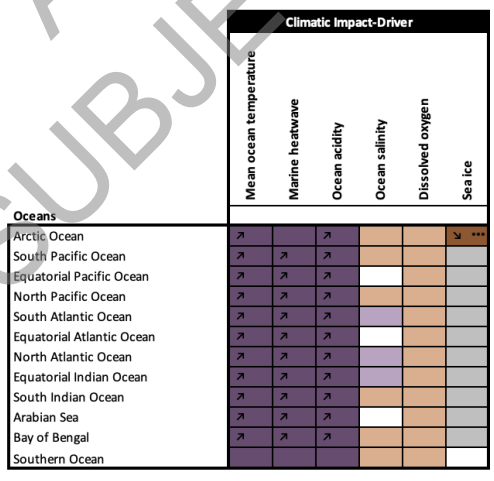
↗	Past upward trend *(medium or higher confidence)*
↘	Past downward trend *(medium or higher confidence)*

Key for level of confidence in future changes

High confidence of increase (or more)
Medium confidence of increase
Low confidence in direction of change
Medium confidence of decrease
High confidence of decrease (or more)
Not broadly relevant

Key for attribution evidence

***	High confidence (or more)
**	Medium confidence



Key for level of confidence in future changes

↗ Past upward trend *(medium or higher confidence)*
↘ Past downward trend *(medium or higher confidence)*

Key for level of confidence in future changes

High confidence of increase (or more)
Medium confidence of increase
Low confidence in direction of change
Medium confidence of decrease
High confidence of decrease (or more)
Not broadly relevant

Key for attribution evidence

***	High confidence (or more)
**	Medium confidence

ACCEPTED VERSION SUBJECT TO FINAL EDITING

[END TABLE TS.5 HERE]

[START FIGURE TS.22 HERE]

Figure TS.22: (Panel a): shows the geographical location of regions belonging to one of five groups characterized by a specific combination of changing climatic impact-drivers (CIDs). The five groups are represented by the five different colours, and the CID combinations associated with each group are represented in the corresponding 'fingerprint' and text below the map. Each fingerprint comprises a set of CIDs projected to change with *high confidence* in every region in the group, and a second set of CIDs, one or more of which are projected to change in each region with *high* or *medium confidence*. The CID combinations follow a progression from those becoming hotter and drier (group 1) to those becoming hotter and wetter (group 5). In between (groups 2–-4), the CIDs that change include some becoming drier and some wetter and always include a set of CIDs which are getting hotter. Tropical cyclones and severe wind CID changes are represented on the map with black dots in the regions affected. Regions affected by coastal CID changes are described by text on the map. The five groups are chosen to provide a reasonable level of detail for each region-specific detail whilst not overwhelming the map with a full summary all aspects of the assessment, which is available in Table TS.5. [Placeholder: This summary is also represented visually in the Interactive Atlas.] The CID changes summarized in the figure represent *high* and *medium confidence* changes projected if a level of 2°C of global warming is attained around 2050. The bar chart in panel b) shows the numbers of regions where each CID is increasing or decreasing with *medium* or *high confidence* for all land regions reported in the map of panel a) and for the ocean regions. The regions coloured in the map comprise the WG I AR6 reference regions, which include inhabited land areas and an additional non-continuous Pacific Islands region labelled PAC. Definitions of the acronyms of the other regions are provided in Atlas.1 and the Interactive Atlas. {Table TS.5, Figure TS.24}

[END FIGURE TS.22 HERE]

TS.4.3.1 Common Regional Changes in Climatic Impact-Drivers

Heat and cold: Changes in temperature-related CIDs such as mean temperatures, growing season length, and extreme heat and frost have already occurred (*high confidence*), and many of these changes have been attributed to human activities (*medium confidence*). Over all land regions with sufficient data (i.e., all except Antarctica), observed changes in temperature have already clearly emerged outside the range of internal variability, relative to 1850–1900 (Figure TS.24). In tropical regions, recent past temperature distributions have already shifted to a range different to that of the early 20th century (*high confidence*) (TS.1.2.4). Most land areas have *very likely* warmed by at least 0.1°C per decade since 1960, and faster in recent decades. On regional-to-continental scales, trends of increased frequency of hot extremes and decrease of cold extremes are generally consistent with the global-scale trends in mean temperature (*high confidence*). In a few regions, trends are difficult to assess due to limited data availability. {2.3.1.1, 11.3, 11.9, 12.4, Atlas.3.1, Interactive Atlas}

[START FIGURE TS.23 HERE]

Figure TS.23: **Time period during which the signals of temperature change in observed data aggregated over the reference regions emerged from the noise of annual variability in the respective aggregated data, using a signal-to-noise ratio of 2 as the threshold for emergence.** Emergence time is calculated for two global observational datasets, (a) Berkeley Earth and (b) CRUTEM5. Regions in the CRUTEM5 map are shaded grey when data are available over less than 50% of the area of the region. {Figure Atlas.11, TS.1.2.4}

[END FIGURE TS.23 HERE]

ACCEPTED VERSION SUBJECT TO FINAL EDITING

Warming trends observed in recent decades are projected to continue over the 21st century and over most land regions at a rate higher than the global average (*high confidence*). For given global warming levels, model projections from CMIP6 show future regional warming changes that are similar to those projected by CMIP5. However, projected regional warming in CMIP6 for given time periods and emissions scenarios has a wider range with a higher upper limit compared to CMIP5 because of the higher climate sensitivity in some CMIP6 models and differences in the forcings. {Atlas}

Under RCP8.5/SSP5-8.5, it is *likely* that most land areas will experience further warming of at least 4°C compared to a 1995–2014 baseline by the end of the 21st century, and in some areas significantly more. At increasing warming levels, extreme heat will exceed critical thresholds for health, agriculture and other sectors more frequently (*high confidence*), and it is *likely* that cold spells will become less frequent towards the end of the century. For example, by the end of the 21st century, dangerous humid heat thresholds, such as the NOAA Heat Index (HI) of 41°C, will be exceeded much more frequently under the SSP5-8.5 scenario than under SSP1-2.6 and will affect many regions (*high confidence*). In many tropical regions, the number of days per year where a HI of 41°C is exceeded would increase by more than 100 days relative to the recent past under SSP5-8.5, while this increase will be limited to less than 50 days under SSP1-2.6 (*high confidence*) (Figure TS.6). The number of days per year where temperature exceeds 35°C would increase by more than 150 days in many tropical areas by end of century for SSP5-8.5 scenario, such as the Amazon basin and South East Asia under SSP5-8.5, while it is expected to increase by less than 60 days in these areas under SSP1-2.6 (except for the Amazon Basin) (*high confidence*) (Figure TS.24). {4.6.1, 11.3, 11.9, 12.4, 12.5.2, Atlas}

[START FIGURE TS.24 HERE]

Figure TS.24: Projected change in the mean number of days per year with maximum temperature exceeding 35°C for CMIP5 (first column), CMIP6 (second column) and CORDEX (thirth column). The map shows the median change in the number of days per year between the mid-century (2041–2060) or end-century (2081–2100) and historical (1995–2014) periods for the CMIP5 and CORDEX RCP8.5 and RCP2.6 and CMIP6 SSP5-8.5 and SSP1-2.6 scenarios ensembles. Stippling indicates areas where less than 80% of the models agree on the sign of change. {Interactive Atlas}

[END FIGURE TS.24 HERE]

Wet and dry: Compared to the global scale, precipitation internal variability is stronger at the regional scale while uncertainties in observations, models and external forcing are all larger. However, GHG forcing has driven increased contrasts in precipitation amounts between wet and dry seasons and weather regimes over tropical land areas (*medium confidence*), with a detectable precipitation increase in the northern high latitudes (*high confidence*) (Box TS.6). The frequency and intensity of heavy precipitation events have increased over a majority of land regions with good observational coverage (*high confidence*). A majority of land areas have experienced decreases in available water in dry seasons due to human-induced climate change associated with changes in evapotranspiration (*medium confidence*). Global hydrological models project a larger fraction of land areas to be affected by an increase rather than by a decrease in river floods (*medium confidence*). Extreme precipitation and pluvial flooding will increase in many regions around the world on almost all continents (*high confidence*), but regional changes in river floods are more uncertain than changes in pluvial floods because complex hydrological processes, including land cover and human water management are involved. {Box 8.2, 8.2.2.1, 8.3.1, 10.4.1, 11.5, 11.6, 11.9, 12.4, 12.5.1, Atlas.3.1, Interactive Atlas}

Wind: Observed mean wind speed is decreasing over most land areas where observational coverage is high (*medium confidence*). It is *likely* that the global proportion of major tropical cyclone (TC) intensities (Categories 3–5) over the past four decades has increased. The proportion of intense TCs, average peak TC wind speeds, and peak wind speeds of the most intense TCs will increase on the global scale with increasing global warming (*high confidence*). {11.7.1}

Snow and ice: Many aspects of the cryosphere either have seen significant changes in the recent past or will see them during the 21st century (*high confidence*). Glaciers will continue to shrink and permafrost to thaw in

ACCEPTED VERSION SUBJECT TO FINAL EDITING

all regions where they are present (*high confidence*). Also, it is *virtually certain* that snow cover will experience a decline over most land regions during the 21st century, in terms of water equivalent, extent and annual duration. There is *high confidence* that the global warming-induced earlier onset of spring snowmelt and increased melting of glaciers have already contributed to seasonal changes in streamflow in high-latitude and low-elevation mountain catchments. Nevertheless, it is *very likely* that some high-latitude regions will experience an increase in winter snow water equivalent due to the effect of increased snowfall prevailing over warming-induced increased snowmelt. {TS.2.5, Box 8.2, 8.2.2.1, 8.3.1, 9.4, 9.5.1, 9.5.2, 12.4, Atlas}

Coastal and oceanic: There is *high confidence* that SST will increase in all oceanic regions, excepting the North Atlantic. Regional sea-level change has been the main driver of changes in extreme sea levels across the quasi-global tide gauge network over the 20th century (*high confidence*). With the exception of a few regions with substantial land uplift, relative sea-level rise is *very likely to virtually certain* (depending on the region) to continue along the 21st century, contributing to increased coastal flooding in low-lying areas (*high confidence*) and coastal erosion along most sandy coasts (*high confidence*) over the 21st century. In the open ocean, acidification, changes in sea ice and deoxygenation have already emerged in many areas (*high confidence*). Marine heatwaves (MWHs) are also expected to increase around the globe over the 21st century (*high confidence*). {TS.2.4, Box 9.2, 9.2.1.1, 9.6, 9.6.4, 9.6.4.2, 12.4}

Other variables and concurrent CID changes: It is *virtually certain* that atmospheric CO_2 and oceanic pH will increase in all climate scenarios, until net zero CO_2 emissions are achieved (TS.2.2). In nearly all regions, there is *low confidence* in changes in hail, ice storms, severe storms, dust storms, heavy snowfall, and avalanches, although this does not indicate that these CIDs will not be affected by climate change. For such CIDs, observations are often short-term or lack homogeneity, and models often do not have sufficient resolution or accurate parametrizations to adequately simulate them over climate change time scales. The probability of compound events has increased in the past due to human-induced climate change and will *likely* continue to increase with further global warming, including for concurrent heat waves and droughts, compound flooding and the possibility of connected sectors experiencing multiple regional extreme events at the same time (for example, in multiple breadbaskets) (*high confidence*). {5.3.4.2, 11.8, Box 11.3, Box 11.4, 12.4}

TS.4.3.2 Region-by-Region Changes in Climatic Impact-Drivers

This section provides a continental synthesis of changes in CIDs, some examples of which are presented in Figure TS.25.

With 2°C global warming, and as early as the mid-21st century, a wide range of CIDs, particularly related to the water cycle and storms, are expected to show simultaneous region-specific changes relative to recent past with *high* or *medium confidence*. In a number of regions (Southern Africa, the Mediterranean, North Central America, Western North America, the Amazon regions, South Western South America, and Australia), increases in one or more of drought, aridity and fire weather (*high confidence*) will affect a wide range of sectors, including agriculture, forestry, health and ecosystems. In another group of regions (Northwestern, Central and Eastern North America, Arctic regions, Northwestern South America, Northern and Central Western Europe, Siberia, Central, South and East Asia, Southern Australia and New Zealand), decreases in snow and ice or increases in pluvial/river flooding (*high confidence*) will affect sectors such as winter tourism, energy production, river transportation, and infrastructure. {11.9, 12.3, 12.4, 12.5, Table 12.2}

[START FIGURE TS.25 HERE]

Figure TS.25: Distribution of projected changes in selected climatic impact-driver indices for selected regions for CMIP6, CMIP5 and CORDEX model ensembles. Different indices are shown for different region: for east Europe and north Asia the mean number of days per year with maximum temperature exceeding 35°C, for Central America and the Caribbean, and the Arabian peninsula, western, southern and easten Asia the mean number of days per year with the NOAA Heat Index exceeding 41°C, for Australasia, East Asia and Russia far East the average shoreline position change, for South America,

ACCEPTED VERSION SUBJECT TO FINAL EDITING

Europe and Africa the mean change in 1-in-100-years river discharge per unit catchment area (m3 s–1 km–2), and for North America the median change in the number of days with snow water equivalent (SWE) over 100 mm. For each box plot the changes or the climatological values are reported respect to, or compared to, the recent past (1995–2014) period for 1.5 ºC, 2ºC and 4ºC global warming levels and for mid-century (2041–2060) or end-century (2081–2100) periods for the CMIP5 and CORDEX RCP8.5 and RCP2.6 and CMIP6 SSP5-8.5 and SSP1-2.6 scenarios ensembles {Figure 12.5, Figure 12.6, Figure 12.9, Figure 12.SM.1, Figure 12.SM.2, Figure 12.SM.6}.

[END FIGURE TS.25 HERE]

TS.4.3.2.1 Africa

Additional regional changes in Africa, besides those described in TS.4.3.1, include a projected decrease in total precipitation in the northernmost and southernmost regions (*high confidence*), with West and East Africa each having a west-to-east pattern of decreasing-to-increasing precipitation (*medium confidence*). Increases in heavy precipitation that can lead to pluvial floods (*high confidence*) are projected for most African regions, even as increasing dry CIDs (aridity, hydrological, agricultural and ecological droughts, fire weather) are projected in the western part of West Africa, North Africa, South Africa and the Mediterranean regions (*medium to high confidence*). {8.4, 11.3, 11.6, 11.9, 12.4, Atlas.4}

In addition to the main changes summarized above and in TS.4.3.1, additional details per CID are given below.

Heat and cold: Observed and projected increases in mean temperature and a shift toward heat extreme characteristics are broadly similar to the generic pattern described in TS.4.3.1. {2.3.1.1.2, 11.3, 11.9, 12.4.1.1, Atlas.4.2, Atlas.4.4}

Wet and dry: Mean precipitation changes have been observed over Africa, but the historical trends are not spatially coherent (*high confidence*). Northern East Africa, Eastern Southern Africa and Central Africa have experienced a decline in rainfall since about 1980 and parts of West Africa an increase (*high confidence*). Increases in the frequency and/or the intensity of heavy rainfall have been observed in Eastern and Western Southern Africa, and the eastern Mediterranean region (*medium confidence*). Increasing trends in river flood occurrences can be identified beyond 1980 in Eastern and Western Southern Africa (*medium confidence*) and West Africa (*high confidence*). However, Northern Africa and Western Southern Africa are *likely* to have a reduction in precipitation. Over West Africa, rainfall is projected to decrease in the Western Sahel subregion and increase along the Guinea Coast subregion (*medium confidence*). Rainfall is *likely* to reduce over the western part of East Africa but increase in the eastern part of the region (*medium confidence*). {8.3.1.6, 11.4, 11.9, 12.4.1.2, Atlas.4.2, Atlas.4.5, Interactive Atlas}

Precipitation declines and aridity trends in West Africa, Central Africa, Southern Africa and the Mediterranean co-occur with trends towards increased agricultural and ecological droughts in the same regions (*medium confidence*). Trends towards increased hydrological droughts have been observed in the Mediterranean (*high confidence*) and West Africa (*medium confidence*). These trends correspond with projected regional increases in aridity and fire weather conditions (*high confidence*). {8.3.1.6, 8.4.1.6, 11.6, 11.9, 12.4.1.2}

Wind: Mean wind, extreme winds and the wind energy potential in North Africa and the Mediterranean are projected to decrease across all scenarios (*high confidence*). Over West Africa and South Africa, a future significant increase in wind speed and wind energy potential is projected (*medium confidence*). There is a projected decrease in the frequency of tropical cyclones making landfall over Madagascar, Eastern Southern Africa and East Africa (*medium confidence*). {12.4.1.3}

Snow and ice: There is *high confidence* that African glaciers and snow have very significantly decreased in the last decades and that this trend will continue in the 21st century. {12.4.1.4}

Coastal and oceanic: Relative sea level has increased at a higher rate than GMSL around Africa over the last 3 decades. The present day 1-in-100-years Extreme Total Water Level (ETWL) is between 0.1 m and 1.2 m

ACCEPTED VERSION SUBJECT TO FINAL EDITING

around Africa, with values around 1 m or above along the South West, South East and Central East coasts. Satellite-derived shoreline retreat rates up to 1 m yr^{-1} have been observed around the continent from 1984 to 2015, except in Southeastern Africa, which has experienced a shoreline progradation (growth) rate of 0.1 m yr^{-1} over the same period. {12.4.1.5}

TS.4.3.2.2 Asia

Due to the high climatological and geographical heterogeneity of Asia, the assessment findings below are summarised over five sub-continental areas comprising one or more of the AR6 WG I reference regions (Box TS.12): East Asia (EAS+ECA), North Asia (WSB+ESB+RFE), South Asia (SAS+TIB), Southeast Asia (SEA) and Southwest Asia (ARP+WCA).

Additional regional changes in Asia, besides those features described in TS.4.3.1, include historical trends of annual precipitation that show considerable regional differences (*high confidence*). East Asian Monsoon precipitation has changed, with drying in the north and wetting in the south since the 1950s, and annual mean precipitation totals *very likely* have increased over most territories of North Asia since the mid-1970s (*high confidence*). South Asian summer monsoon precipitation decreased over several areas since the mid-20th century (*high confidence*) but is *likely* to increase during the 21st century, with enhanced interannual variability.

Increases in precipitation and rivers floods are projected over much of Asia: in the annual mean precipitation in East, North, South and Southeast Asia (*high confidence*); for extremes in East, South, West Central, North and Southeast Asia (*high confidence*) and Arabian Peninsula (*medium confidence*); and for river floods in East, South and Southeast Asia and East Siberia (*medium confidence*). Aridity in East and West Central Asia is projected to increase, especially beyond the middle of the 21st century and global warming levels beyond 2°C, (*medium confidence*). Fire weather seasons are projected to lengthen and intensify everywhere except Southeast Asia, Tibetan Plateau and Arabian Peninsula (*medium confidence*).

There is a large uncertainty in the future continuation of observed decreasing trends in surface wind speeds in Asia (*high confidence*), with *medium confidence* that mean wind speeds will decrease in North Asia, East Asia and Tibetan Plateau and that tropical cyclones will have decreasing frequency and increasing intensity overall in Southeast and East Asia.

Over North Asia, increases in permafrost temperature and its thawing have been observed over recent decades (*high confidence*). Future projections indicate continuing decline in seasonal snow duration, glacial mass, and permafrost area by mid-century (*high confidence*). Snow-covered areas and snow volumes will decrease in most regions of the Hindu Kush Himalaya during the 21st century and snowline elevations will rise (*high confidence)* and glacier volumes are *likely* to decline with greater mass loss in higher CO_2 emissions scenarios. Heavy snowfall is increasing in East Asia and North Asia (*medium confidence*) but with limited evidence on future changes in hail and snow avalanches.

{2.3, 8.3, 8.4, 9.5, 9.6, 10.6, Box 10.4, 11.4, 11.5, 11.7, 11.9, 12.4.2, Atlas.3.1, Atlas.5, Atlas.5.2, Atlas.5.3, Atlas.5.4, Atlas.5.5, Box TS.13}

In addition to the main changes summarized above and in TS.4.3.1, further details are given below.

Heat and cold: Over all regions of Asia, observed and projected increases in mean temperature and a shift toward heat extreme characteristics are broadly similar to the generic pattern described in TS.4.3.1. Over Southeast Asia annual mean surface temperature will *likely* increase by a slightly smaller amount than the global average. {Atlas.5.4.4}

Wet and dry: Over East Asia, historical trends of annual precipitation show considerable regional differences but with increases over northwest China and South Korea (*high confidence*). Daily precipitation extremes have increased over part of the region (*high confidence*). Extreme hydrological drought frequency has increased in a region extending from southwest to northeast China, with projected increases of agricultural and ecological drought for 4°C GWL and fire weather for 2°C and above (*medium confidence*). {8.3.2, 8.4.2, 11.4.4, 11.4.5,

ACCEPTED VERSION SUBJECT TO FINAL EDITING

11.9, 12.4.2.2, Atlas.5.1.2}

Over North Asia, annual mean precipitation totals have *very likely* increased, causing more intense flooding events, and there is *medium confidence* that the number of dry days has decreased. Concurrently total soil moisture is projected to decline extensively (*medium confidence*). {8.3.1.3, 8.4.1.6, 11.4.5, 11.5.2, 11.5.5, 12.4.2.2, Atlas.5.2.2}

Over South Asia, the summer monsoon precipitation decreased over several areas since the mid-20th century (*high confidence*), while it increased in parts of the western HKH and decreased over eastern-central HKH (*medium confidence*) (Box TS.12). The frequency of heavy precipitation and flood events has increased over several areas during the last few decades (*medium confidence*). {8.3.1.3, 8.3.2.4.1, 8.4.1.5, 8.4.2.4.1, 10.6.3.3, 10.6.3.5, 10.6.3.6, 10.6.3.8, Cross-Chapter Box 10.4, 11.4.1, 11.4.2, 11.4.5, 11.5.5, 12.4.2.2, Box 10.4, Atlas 5.3.2}

Over Southeast Asia, mean precipitation trends are not spatially coherent or consistent across datasets and seasons (*high confidence*). Most of the region has experienced an increase in rainfall intensity but with a reduced number of wet days (*medium confidence*). Rainfall is projected to increase in the northern parts of Southeast Asia and decrease in areas in the Maritime Continent (*medium confidence*). {8.4.1, 11.4.2, 11.5.5, 11.9, 12.4.2.2, Atlas.3.1, Atlas.5.4.2, Atlas.5.4.4}

Over Southwest Asia, an observed annual precipitation decline over the Arabian Peninsula since the 1980s of 6.3 mm per decade is contrasted with observed increases between 1.3 mm and 4.8 mm per decade during 1960–2013 over the elevated part of eastern West Central Asia *(very high confidence)*, along with an increase of the frequency and intensity of extreme precipitation. {Figure 8.19, Figure 8.20, 8.3.1.6, 8.4.1.6, Table 11.2A, 11.9, 12.4.2.2, Atlas.5.5}

Wind: Over East Asia, the terrestrial near-surface wind speed has decreased and is projected to decrease further in the future (*medium confidence*). Since the mid 1980's, there has been an increase in the number and intensification rate of intense TCs (*medium confidence*), with a significant northwestward shift in tracks and a northward shift in their average latitude, increasing exposure over East China, the Korean Peninsula and the Japanese Archipelago (*medium confidence*). {11.7.1, 12.4.2.3}

Over North Asia there is *medium confidence* for a decreasing trend in wind speed during 1979–2018 and for projected continuing decreases of terrestrial near-surface wind speed (*medium confidence*). {2.3.1.4.4, 12.4.2.3}

Over Southeast Asia, although there is no significant long-term trend in the number of TC, fewer but more extreme TCs have affected the Philippines during 1951–2013. {11.7.4, 12.4.2.4}

Snow and ice: Over East Asia, decreases have been observed in the frequency and increases in the mean intensity of snowfall in north-western, north-eastern and south-eastern China and the eastern Tibetan Plateau since the 1960s. Heavy snowfall is projected to occur more frequently in some parts of Japan (*medium confidence*). {12.4.2.4, Atlas.5.1.2}

Over North Asia, seasonal snow duration and extent have decreased in recent decades (*high confidence*), and maximum snow depth *likely* has increased since the mid-1970s, particularly over south of the Russian-Far-East. {2.3.2.5, 8.3.1.7.2, 9.5, 12.4.2.4, Atlas.5.2, Atlas.5.4}

Over South Asia, snow-cover has reduced over most of the HKH since the early 21st century, and glaciers have thinned, retreated, and lost mass since the 1970s (*high confidence*) although the Karakoram glaciers have either slightly gained mass or are in an approximately balanced state (*medium confidence*). {8.3.1.7.1, Cross-Chapter Box 10.4}

Over Southwest Asia, mountain permafrost degradation at high altitudes has increased the instability of mountain slopes in the past decade (*medium confidence*). More than 60% of glacier mass in the Caucasus is

ACCEPTED VERSION
SUBJECT TO FINAL EDITING

projected to disappear under RCP8.5 emissions by the end of the 21st century (*medium confidence*). {9.5.1, 9.5.3, 12.4.2.4}

Coastal and oceanic: Over the last three decades, relative sea level has increased at a rate higher than GMSL around Asia (*high confidence*). Gross coastal area loss and shoreline retreat has been observed over 1984–2015, but with localized shoreline progradation in the Russian Far East, East and Southeast Asia. {12.4.2.5}

Projections show that regional-mean sea level continues to rise (*high confidence*), ranging from 0.4–0.5 m under SSP1-2.6 to 0.8–1.0 m under SSP5-8.5 for 2081–2100 relative to 1995–2014 (median values). This will contribute to more frequent coastal flooding and higher Extreme Total Water Level (ETWL) in low-lying areas and coastal erosion along sandy beaches (*high confidence*). There is *high confidence* that compound effects of climate change, land subsidence, and human factors will lead to higher flood levels and prolonged inundation in the Mekong Delta and other Asian coasts. {9.6.1, 9.6.3, 12.4.2.5}

TS.4.3.2.3 Australasia

Additional regional changes in Australasia, besides those features described in TS.4.3.1, include a significant decrease in April to October rainfall in southwest Western Australia, observed from 1910 to 2019 and attributable to human influence (*high confidence*), which is *very likely* to continue in future. Agricultural and ecological and hydrological droughts have increased over southern Australia (*medium confidence*), and meteorological droughts have decreased over northern and central Australia (*medium confidence*). Relative sea level has increased over the period 1993–2018 at a rate higher than GMSL around Australasia (*high confidence*). Sandy shorelines have retreated around the region, except in southern Australia, where a shoreline progradation rate of 0.1 m yr^{-1} has been observed. In the future, heavy precipitation and pluvial flooding are *very likely* to increase over northern Australia and central Australia, and they are *likely* to increase elsewhere in Australasia for global warming levels (GWLs) exceeding 2°C and with *medium confidence* for a 2°C GWL. Agricultural and ecological droughts are projected to increase in southern and eastern Australia (*medium confidence*) for a 2°C GWL. Fire weather is projected to increase throughout Australia (*high confidence*) and New Zealand (*medium confidence*). Snowfall is expected to decrease throughout the region at high altitudes in both Australia (*high confidence*) and New Zealand (*medium confidence*), with glaciers receding in New Zealand (*high confidence*). {11.4, Table 11.6, 12.3, 12.4.3, Atlas.6.4, Atlas.6.5}

In addition to the main changes summarized above and in TS.4.3.1, further details are given below.

Heat and cold: Observed and projected increases in mean temperature and a shift toward heat extreme characteristics are broadly similar to the generic pattern described in TS.4.3.1. {11.9, 12.4.3.1, Atlas.6}

Wet and dry: There is *medium confidence* that heavy precipitation has increased in northern Australia since 1950. Annual mean precipitation is projected to increase in the south and west of New Zealand (*medium confidence*) and is projected to decrease in southwest western Australia (*high confidence*), eastern Australia (*medium confidence*), and in the north and east of New Zealand (*medium confidence*) for a GWL of 2°C. There is *medium confidence* that river flooding will increase in New Zealand and Australia, with higher increases in northern Australia. Aridity is projected to increase with *medium confidence* in southern Australia (*high confidence* in southwest Western Australia), eastern Australia (*medium confidence*) and in the north and east of New Zealand (*medium confidence*) for GWLs around 2°C. {11.4, Table 11.6, 11.9, 12.4.3.2, Atlas.6.2}

Wind: Mean wind speeds are projected to increase in parts of northeastern Australia (*medium confidence*) by the end of the 21st century, under high CO_2 emissions scenarios. TCs in north eastern and north Australia are projected to decrease in number (*high confidence*) but increase in intensity except for 'east coast lows' (*low confidence*). {12.4.3.3}

Snow and ice: Observations in Australia show that the snow season length has decreased by 5% in the last five decades. Furthermore, the date of peak snowfall in Australia has advanced by 11 days over the last 5

ACCEPTED VERSION SUBJECT TO FINAL EDITING

decades. Glacier ice volume in New Zealand has decreased by 33% from 1977 to 2018. {12.4.3.4, Atlas.6.2}

Coastal and oceanic: Observed changes in marine heat waves (MHWs) over the 20th century in the region show an increase in their occurrence frequency, except along the south east coast of New Zealand, an increase in duration per event, and the total number of MHW days per decade, with the change being stronger in the Tasman Sea than elsewhere. The present day 1-in-100-year ETWL is between 0.5–2.5 m around most of Australia, except the northwestern coast where 1-in-100-year ETWL can be as high as 6 m–7 m. {Box 9.1, 12.3.1.5, 12.4.3.5}

TS.4.3.2.4 Central and South America

Additional regional changes in Central and South America, besides those features described in TS.4.3.1, include increases in mean and extreme precipitation in Southeastern South America since the 1960s (*high confidence*) (TS.4.2.3). Decreasing trends in mean precipitation and increasing trends in agricultural and ecological drought are observed over Northeastern South America (*medium confidence*). The intensity and frequency of extreme precipitation and pluvial floods is projected to increase over Southeastern South America, Southern South America, Northern South America, South American Monsoon and Northeastern South America (*medium confidence*) for a 2°C GWL and above. Increases of agricultural and ecological drought are projected in South America Monsoon and Southern South America, and fire weather is projected to increase over several regions (Northern South America, the South American Monsoon, Northeastern South America and Southwestern South America) (*high confidence*). {8.3, 8.4, 11.3, 11.4, 11.9, Table 11.13, Table 11.14, Table 11.15, 12.4.4.2, Atlas.7.1, Atlas.7.2}

In addition to the main changes summarized above and in TS.4.3.1, further details are given below.

Heat and cold: Observed and projected increases in mean temperature and a shift toward heat extreme characteristics are broadly similar to the generic pattern described in TS.4.3.1. {11.3.2, 11.3.5, Table 11.13, 12.4.4.1, Atlas.7.1.2, Atlas.7.2.2, Atlas.7.2.4}

Wet and dry: Mean precipitation is projected to change in a dipole pattern with increases in Northwestern and Southeastern South America and decreases in Northeastern and Southwestern South America (*high confidence*) with further decreases in Northern South America and South Central America (*medium confidence*). In Northern South America and South Central America, aridity and agricultural and ecological droughts are increasing with *medium confidence*. Fire weather is projected to increase over Southern Central America and Southern South America with *medium confidence*. {8.3.1.3, 8.4.2.4.5, 11.4.2, 11.9, Table 11.14, Table 11.15, 12.4.4.2, Atlas.7.2.2, Atlas.7.2.4}

Wind: Climate projections indicate an increase in mean wind speed and in wind power potential over the Amazonian region (Northern South America, South American Monsoon, Northeastern South America) (*medium confidence*). {12.4.4.3}

Snow and ice: Glacier volume loss and permafrost thawing will *likely* continue in the Andes Cordillera under all climate scenarios, causing important reductions in river flow and potentially high-magnitude glacial lake outburst floods. {9.5.1.1, 12.4.4.4}

Coastal and oceanic: Around Central and South America, relative sea level has increased at a higher rate than GMSL in the South Atlantic and the subtropical North Atlantic, and at a rate lower than GMSL in the East Pacific over the last 3 decades. The present day 1-in-100-years ETWL is highest in Southern and Southwestern South America subregions, where it can be as large as 5 to 6 m. Satellite observations for 1984–2015 show shoreline retreat rates along the sandy coasts of Southern Central America, Southeastern South America and Southern South America, while shoreline progradation rates have been observed in Northwestern South America and Northern South America. Over the period 1982–2016, the coastlines experienced at least one MHW per year, and more along the Pacific coast of North Central America and the Atlantic coast of

ACCEPTED VERSION SUBJECT TO FINAL EDITING

Southeastern South America. {12.4.4.5}

TS.4.3.2.5 Europe

Additional regional changes in Europe, besides those features described in TS.4.3.1, include observed increases in pluvial flooding in northern Europe and hydrological and agricultural/ecological droughts in the Mediterranean (*high confidence*), which have been attributed to human contribution with *high* and *medium confidence*, respectively. Increased mean precipitation amounts at high latitudes in boreal winter and reduced summer precipitation in southern Europe are projected starting from a 2°C GWL (*high confidence*). Aridity, agricultural and hydrological droughts and fire weather conditions will increase in the Mediterranean region starting from 2°C GWL (*high confidence*). Pluvial flooding will increase everywhere with *high confidence* except for *medium confidence* in the Mediterranean; in Western and Central Europe this also applies to river flooding starting from a 2°C GWL (*high confidence*). Most periglacial processes in Northern Europe are projected to disappear by the end of the 21st century, even for a low warming scenario (*medium confidence*). {8.3, 11.3, 11.9, 12.4.5, 12.5.2, Atlas.8.2, Atlas.8.4}

In addition to the main changes summarized above and in TS.4.3.1, further details are given below.

Heat and cold: Observed and projected increases in mean temperature and a shift toward heat extreme characteristics are broadly similar to the generic pattern described in TS.4.3.1. {11.3, 11.9, 12.4.5.1, 12.5.2, Atlas.8.2, Atlas.8.4}

Wet and dry: There is *medium confidence* that annual mean precipitation in Northern Europe, West and Central Europe and Eastern Europe has increased since the early 20th century and *high confidence* for extreme precipitation. In the European Mediterranean, the magnitude and sign of observed land precipitation trends depend on time period and exact study region (*medium confidence*). There is *medium confidence* that river floods will decrease in Northern, Eastern and Southern Europe for high warming levels. {8.3.1.3, 11.3, 11.9, 12.4.5.2, Atlas.8.2, Atlas.8.4}

Wind: Mean wind speed over land has decreased (*medium confidence*), but the role of human-induced climate change has not been established. There is *high confidence* that mean wind speeds will decrease in Mediterranean areas and *medium confidence* of such decreases in Northern Europe for GWLs exceeding 2°C. The frequency of Medicanes (tropical-like cyclones in the Mediterranean) is projected to decrease (*medium confidence*). {11.9, 12.4.5.3}

Snow and ice: In the Alps, snow cover will decrease below elevations of 1500–2000 m throughout the 21st century (*high confidence*). A reduction of glacier ice volume is projected in the European Alps and Scandinavia with *high confidence* and with *medium confidence* for the timing and mass change rates. {12.4.5.4, 9.5.2}

Coastal and oceanic: Over the last three decades, relative sea level has increased at a lower rate than GMSL in the sub-polar North Atlantic coasts of Europe. The present day 1-in-100-years ETWL is between 0.5–1.5 m in the Mediterranean basin and 2.5–5.0 m in the western Atlantic European coasts, around the United Kingdom and along the North Sea coast, and lower at 1.5–2.5 m along the Baltic Sea coast. Satellite-derived shoreline change estimates over 1984–2015 indicate shoreline retreat rates of around 0.5 m yr^{-1} along the sandy coasts of Central Europe and the Mediterranean and more or less stable shorelines in Northern Europe. Over the period 1982–2016, the coastlines of Europe experienced on average more than 2.0 MHW per year, with the eastern Mediterranean and Scandinavia experiencing 2.5–3 MHWs per year. {12.4.5.5}

TS.4.3.2.6 North America

Additional regional changes in North America, besides those features described in TS.4.3.1, include changes in North American wet and dry CIDs, which are largely organized by the northeast (more wet) to southwest

ACCEPTED VERSION SUBJECT TO FINAL EDITING

(more dry) pattern of mean precipitation change, although heavy precipitation increases are widespread (*high confidence*). Increasing evaporative demand will expand agricultural and ecological drought and fire weather (particularly in summertime) in Central North America, Western North America and North Central America (from *medium* to *high confidence*). Severe wind storms, tropical cyclones, and dust storms in North America are shifting toward more extreme characteristics (*medium confidence*), and both observations and projections point to strong changes in the seasonal and geographic range of snow and ice conditions in the coming decades (*very high confidence*). General findings for relative sea level, coastal flooding and erosion will not apply for areas with substantial land uplift around the Hudson Bay and Southern Alaska. {8.4, 11.4, 11.5, 11.7, 11.9, 12.4, Atlas.9.4}

In addition to the main changes summarized above and in TS.4.3.1, further details are given below.

Heat and cold: Observed and projected increases in mean temperature and a shift toward heat extreme characteristics are broadly similar to the generic pattern described in TS.4.3.1. {11.3, 11.9, 12.4.6.1, Atlas.9.2, Atlas.9.4}

Wet and dry: Annual precipitation increased over parts of Eastern and Central North America during 1960–2015 (*high confidence*) and has decreased in parts of southwestern United States and northwestern Mexico (*medium confidence*). River floods are projected to increase for all North American regions other than north Central America (med*ium confidence*). {8.4.2.4, 11.4, 11.5, 11.9, 12.4.6.2, Atlas.9.2, Atlas.9.4}

Agricultural and ecological drought increases have been observed in Western North America (*medium confidence*), and aridity is projected to increase in the southwestern United States and Northern Central America, with lower summer soil moisture across much of the continental interior (*medium confidence*). {8.4.1, 11.6.2, 12.4.6.2}

Wind: Projections indicate a greater number of the most intense TCs, with slower translation speeds and higher rainfall potential for Mexico's Pacific Coast, the Gulf Coast and the United States East Coast (*medium confidence*). Mean wind speed and wind power potential are projected to decrease in Western North America (*high confidence*), with differences between global and regional models lending *low confidence* elsewhere. {11.4, 11.7, 12.4.6.3}

Snow and ice: It is *very likely* that some high-latitude regions will experience an increase in winter snow water equivalent, due to the snowfall increase prevailing over the warming trend. At sustained GWLs between 3°C and 5°C, nearly all glacial mass in Western Canada and Western North America will disappear (*medium confidence*). {9.5.1, 9.5.3, 12.4.6.4, Atlas.9.4}

Coastal and oceanic: Around North America, relative sea level has increased over the last 3 decades at a rate lower than GMSL in the subpolar North Atlantic and in the East Pacific, while it has increased at a rate higher than GMSL in the subtropical North Atlantic. Observations indicate that episodic coastal flooding is increasing along many coastlines in North America. Shoreline retreat rates of around 1 m yr^{-1} have been observed during 1984–2015 along the sandy coasts of Northwestern North America and Northern Central America, while portions of the United States Gulf Coast have seen a retreat rate approaching 2.5 m yr^{-1}. Sandy shorelines along Eastern North America and Western North America have remained more or less stable during 1984–2014, but a shoreline progradation rate of around 0.5 m yr^{-1} has been observed in Northeastern North America. {12.4.6.5}

TS.4.3.2.7 Small Islands

Additional regional changes in Small Islands, besides those features described in TS.4.3.1, include a *likely* decrease in rainfall during boreal summer in the Caribbean and in some parts of the Pacific islands poleward of 20° latitude in both the Northern and Southern Hemispheres. These drying trends will *likely* continue in coming decades. Fewer but more intense tropical cyclones are projected starting from a 2°C GWL (*medium*

ACCEPTED VERSION SUBJECT TO FINAL EDITING

confidence). {9.6, 11.3, 11.4, 11.7, 11.9, 12.4.7, Atlas.10.2, Atlas.10.4, Cross-Chapter Box Atlas.2}

In addition to the main changes summarized above and in TS.4.3.1, further details are given below.

Heat and cold: It is *very likely* that most Small Islands have warmed over the period of instrumental records, and continued temperature increases in the 21st century will further increase heat stress in these regions. {11.3.2, 11.9, 12.4.7.1, Atlas.10.2, Atlas.10.4, Cross-Chapter Box Atlas.2}

Wet and dry: Observed and projected rainfall trends vary spatially across the Small Islands. Higher evapotranspiration under a warming climate can partially offset future increases or amplify future reductions in rainfall resulting in increased aridity as well as more severe agricultural and ecological drought in the Small Islands (*medium confidence*). {11.4.2, 11.9, 12.4.7.2, Atlas.10.2, Atlas.10.4, Cross-Chapter Box Atlas.1}

Wind: Global changes indicate that Small Islands will face fewer but more intense TCs, with spatial inconsistency in projections given poleward shifts in TC tracks (*medium confidence*). {11.7.1.2, 11.7.1.5, 12.4.7.3}

Coastal and oceanic: Continued relative sea level rise is *very likely* in the ocean around Small Islands and, along with storm surges and waves, will exacerbate coastal inundation with the potential to increase saltwater intrusion into aquifers in small islands. Shoreline retreat is projected along sandy coasts of most small islands (*high confidence*). {9.6.3.3, 12.4.7.4, Cross-Chapter Box Atlas.1}

TS.4.3.2.8 Polar

It is *virtually certain* that surface warming in the Arctic will continue to be more pronounced than the global average warming over the 21st century. An intensification of the polar water cycle will increase mean precipitation, with precipitation intensity becoming stronger and more *likely* to be rainfall rather than snowfall (*high confidence*). Permafrost warming, loss of seasonal snow cover, and glacier melt will be widespread (*high confidence*). There is *high confidence* that both the Greenland and Antarctic Ice Sheets have lost mass since 1992 and will continue to lose mass throughout this century under all emissions scenarios. Relative sea level and coastal flooding are projected to increase in areas other than regions with substantial land uplift (*medium confidence*). {2.3, 3.4, 4.3, 4.5, 7.4, 8.2, 8.4, Box 8.2, 9.5, 12.4.9, Atlas.11.1, Atlas.11.2}

In addition to the main changes summarized above and in TS.4.3.1, further details are given below.

Heat and cold: Changes in Antarctica showed larger spatial variability, with *very likely* warming in the Antarctic Peninsula since the 1950s and no overall trend in East Antarctica. Less warming and weaker polar amplification are projected as *very likely* over the Antarctic than in the Arctic, with a weak polar amplification projected as *very likely* by the end of the 21st century. {4.3.1, 4.5.1, 7.4.4, 12.4.9.1, Atlas.11.1, Atlas.11.2}

Wet and dry: Recent decades have seen a general decrease in Arctic aridity (*high confidence*), with increased moisture transport leading to higher precipitation, humidity and streamflow and a corresponding decrease in dry days. Antarctic precipitation showed a positive trend during the 20th century. The water cycle is projected to intensify in both polar regions, leading to higher precipitation totals (and a shift to more heavy precipitation) and higher fraction of precipitation falling as rain. In the Arctic, this will result in higher river flood potential and earlier meltwater flooding, altering seasonal characteristics of flooding (*high confidence*). A lengthening of the fire season (*medium confidence*) and encroachment of fire regimes into tundra regions (*high confidence*) are projected. {8.2.3, 8.4.1, Box 8.2, 9.4.1, 9.4.2, 12.4.9.2, Atlas.11.1, Atlas.11.2}

Wind: There is *medium confidence* in mean wind decrease over the Russian Arctic and Arctic Northeast North America, but *low confidence* of changes in other Arctic regions and Antarctica. {12.4.9.3}

Snow and ice: Reductions in spring snow cover extent have occurred across the Northern Hemisphere since at least 1978 (*very high confidence*). Permafrost warming and thawing have been widespread in the Arctic

ACCEPTED VERSION SUBJECT TO FINAL EDITING

since the 1980s (*high confidence*), causing strong heterogeneity in surface conditions. There is *high confidence* in future glacier and ice sheet loss, permafrost warming, decreasing permafrost extent and decreasing seasonal duration and extent of snow cover in the Arctic. Decline in seasonal sea ice coverage along the majority of the Arctic coastline in recent decades is projected to continue, contributing to an increase in coastal hazards (including open water storm surge, coastal erosion and flooding). {2.3.2, 3.4.2, 3.4.3, 9.4.1, 9.4.2, 9.5, 12.4.6, 12.4.9, Atlas.11.2}

Coastal and oceanic: Higher sea levels contribute to *high confidence* for projected increases of Arctic coastal flooding and higher coastal erosion (aided by sea ice loss) (*medium confidence*), with lower confidence for those regions with substantial land uplift (Arctic Northeast North America and Greenland). {12.4.9.5}

TS.4.3.2.9 Ocean

The Indian Ocean, western equatorial Pacific Ocean and western boundary currents have warmed faster than the global average (*very high confidence*), with the largest changes in the frequency of marine heatwaves (MHWs) projected in the western tropical Pacific and the Arctic Ocean (*medium confidence*). The Pacific and Southern Ocean are projected to freshen and the Atlantic to become more saline (*medium confidence*). Anthropogenic warming is *very likely* to further decrease ocean oxygen concentrations, and this deoxygenation is expected to persist for thousands of years (*medium confidence*). Arctic sea ice losses are projected to continue, leading to a practically ice-free Arctic in September by the end of the 21st century under high CO_2 emissions scenarios (*high confidence*). {2.3, 5.3, 9.2, 9.3, Box 9.2, 12.4.8}

In addition to the main changes summarized above and in TS.4.3.1, further details are given below.

Ocean surface temperature: The Southern Ocean, the eastern equatorial Pacific, and the North Atlantic Ocean have warmed more slowly than the global average or slightly cooled. Global warming of 2°C above 1850–1900 levels would result in the exceedance of numerous hazard thresholds for pathogens, seagrasses, mangroves, kelp forests, rocky shores, coral reefs and other marine ecosystems (*medium confidence*). {9.2.13, 12.4.8}

Marine heatwaves: Moderate increases in MHW frequency are projected for mid-latitudes, and only small increases are projected for the Southern Ocean (*medium confidence*). Under the SSP5-8.5 scenario, permanent MHWs (more than 360 days per year) are projected to occur in the 21st century in parts of the tropical ocean, the Arctic Ocean and around 45°S; however, the occurrence of such permanent MHWs can be largely avoided under SSP1-2.6 scenario. {Box 9.2, 12.4.8}

Ocean acidity: With the rising CO_2 concentration, the ocean surface pH has declined globally over the past four decades (*virtually certain*). {2.3.3.5, 5.3.3.2, 12.4.8}

Ocean salinity: At the basin scale, it is *very likely* that the Pacific and the Southern Ocean have freshened while the Atlantic has become more saline. {2.3.3.2, 9.2.2.2, 12.4.8}

Dissolved oxygen: In recent decades, low oxygen zones in ocean ecosystems have expanded. {2.3.4.2, 5.3.3.2, 12.4.8}

Sea ice: Arctic perennial sea ice is being replaced by thin, seasonal ice, with earlier spring melt and delayed fall freeze up. There is no clear trend in the Antarctic sea ice area over the past few decades and l*ow confidence* in its future change. {2.3.2.1.1, 9.3.1.1, 12.4.8, 12.4.9}

ACCEPTED VERSION SUBJECT TO FINAL EDITING

TS.4.3.2.10 Other Typological Domains

Some types of regions found in different continents face common climate challenges regardless of their location. These include biodiversity hot spots that will *very likely* see even more extreme heat and droughts, mountain areas where a projected raising in the freezing level height will alter snow and ice conditions (*high confidence*), and tropical forests that are increasingly prone to fire weather (*medium confidence*). {Box 8.2, 8.4, 9.5, 12.3, 12.4}

Biodiversity hotspots located around the world will each face unique challenges in CID changes. Heat, drought and length of dry season, wildfire weather, sea surface temperature and deoxygenation are relevant drivers to terrestrial and freshwater ecosystems and have marked increasing trends. {12.3, 12.4.10.1}

Desert and semi-arid areas are strongly affected by CIDs such as extreme heat, drought and dust storms, with large-scale aridity trends contributing to expanding drylands in some regions (*high confidence*). {12.3, 12.4.10.3}

Average warming in mountain areas varies with elevation, but the pattern is not globally uniform (*medium confidence*). Extreme precipitation is projected to increase in major mountainous regions (*medium* to *high confidence* depending on location), with potential cascading consequences of floods, landslides and lake outbursts in all scenarios (*medium confidence*). {Box 8.2, 8.4.1.5, 9.5.1.3, 9.5.3.3, 9.5.2.3, Cross-Chapter Box 10.4, 11.5.5, 12.3, 12.4.1–12.4.6, 12.4.10.4}

Most tropical forests are challenged by a mix of emerging warming trends that are particularly large in comparison to historical variability (*medium confidence*). Water cycle changes bring prolonged drought, longer dry seasons, and increased fire weather to many tropical forests (*medium confidence*). {10.5, 12.3, 12.4}

[START BOX TS.14 HERE]

Box TS.14: Urban Areas

With global warming, urban areas and cities will be affected by more frequent occurrence of extreme climate events, such as heatwaves, with more hot days and warm nights as well as sea level rise and increases in tropical cyclone storm surge and rainfall intensity that will increase the probability of coastal city flooding (*high confidence*). {Box 10.3, 11.3, 11.5, 12.3, 12.4}

Urban areas have special interactions with the climate system, for instance in terms of heat islands and altering the water cycle, and thereby will be more affected by extreme climate events such as extreme heat (*high confidence*). With global warming, increasing relative sea level compounded by increasing tropical cyclone storm surge and rainfall intensity will increase the probability of coastal city flooding (*high confidence*). Arctic coastal settlements are particularly exposed to climate change due to sea ice retreat (*high confidence*). Improvements in urban climate modelling and climate monitoring networks have contributed to understanding the mutual interaction between regional and urban climate (*high confidence*). {Box 10.3, 11.3, 11.5, 12.3, 12.4}

Despite having a negligible effect on global surface temperature (*high confidence*), urbanization has exacerbated the effects of global warming through its contribution to the observed warming trend in and near cities, particularly in annual mean minimum temperature (*very high confidence*) and increases in mean and extreme precipitation over and downwind of the city, especially in the afternoon and early evening (*medium confidence*). {2.3, Box 10.3, 11.3, 11.4, 12.3, 12.4}

Combining climate change projections with urban growth scenarios, future urbanization will amplify (*very high confidence*) the projected local air temperature increase, particularly by strong influence on minimum temperatures, which is approximately comparable in magnitude to global warming (*high confidence*).

ACCEPTED VERSION SUBJECT TO FINAL EDITING

Compared to present day, large implications are expected from the combination of future urban development and more frequent occurrence of extreme climate events, such as heatwaves, with more hot days and warm nights adding to heat stress in cities (*very high confidence*). {Box 10.2, 11.3, 12.4}

Both sea levels and air temperatures are projected to rise in most coastal settlements (*high confidence*). There is *high confidence* in an increase in pluvial flood potential in urban areas where extreme precipitation is projected to increase, especially at high global warming levels. {11.4, 11.5, 12.4}

[END BOX TS.14 HERE]

ACCEPTED VERSION
SUBJECT TO FINAL EDITING

Figures

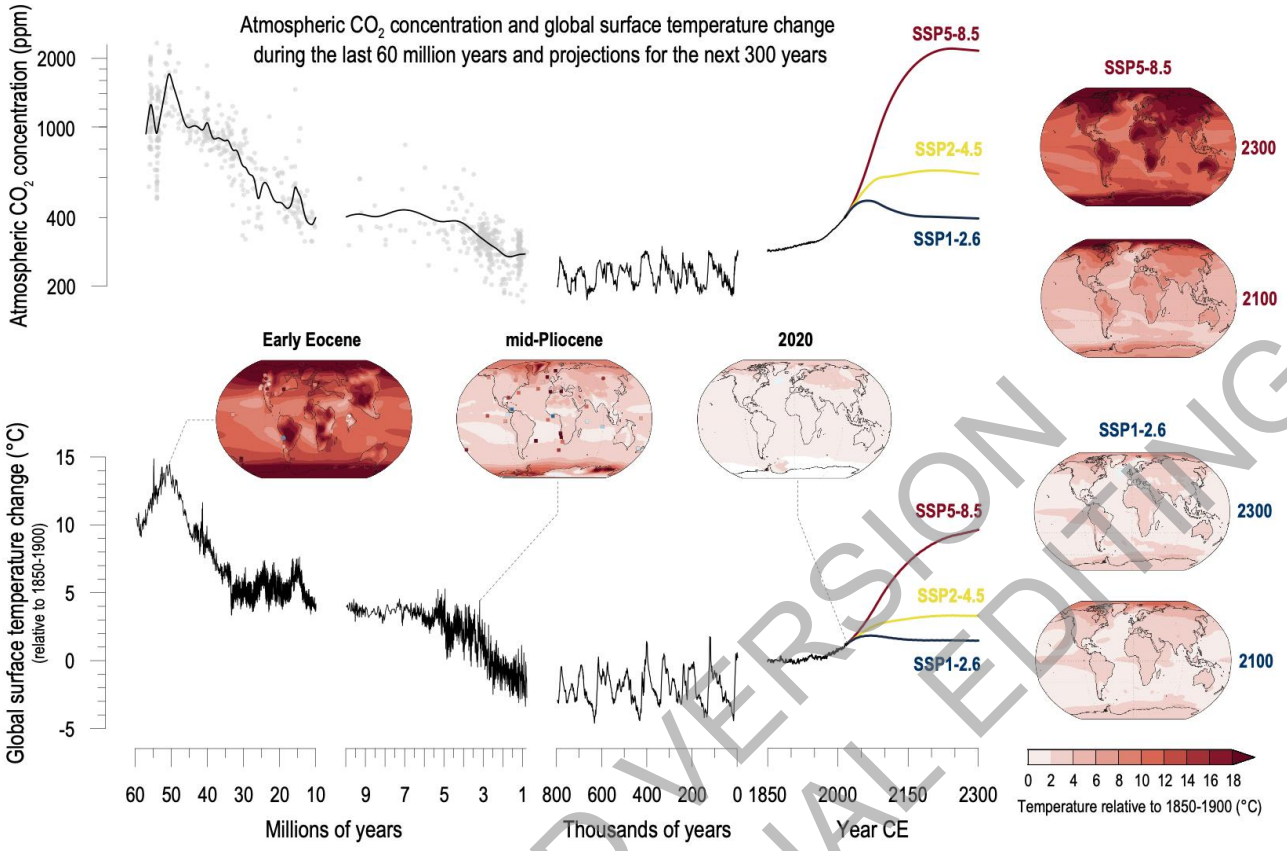
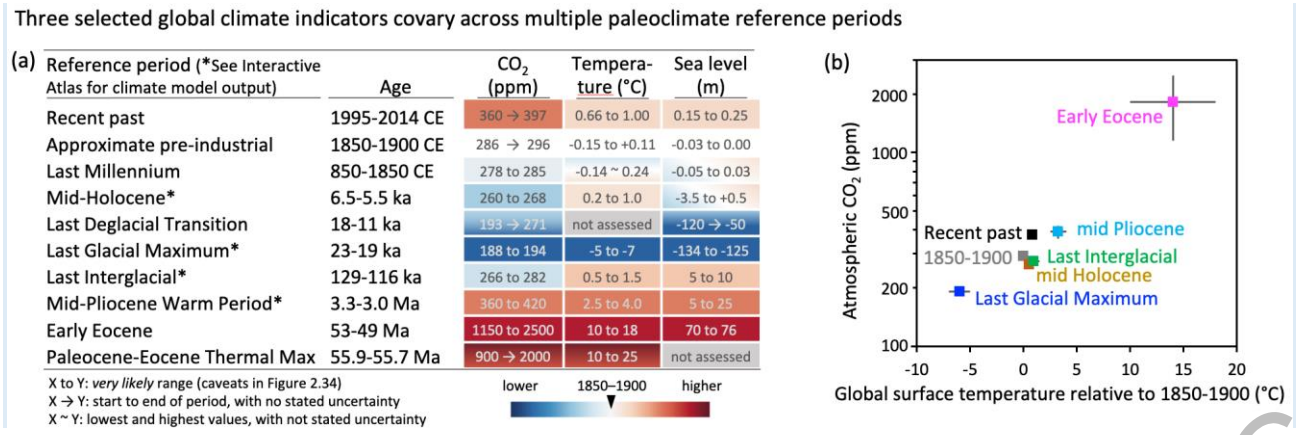


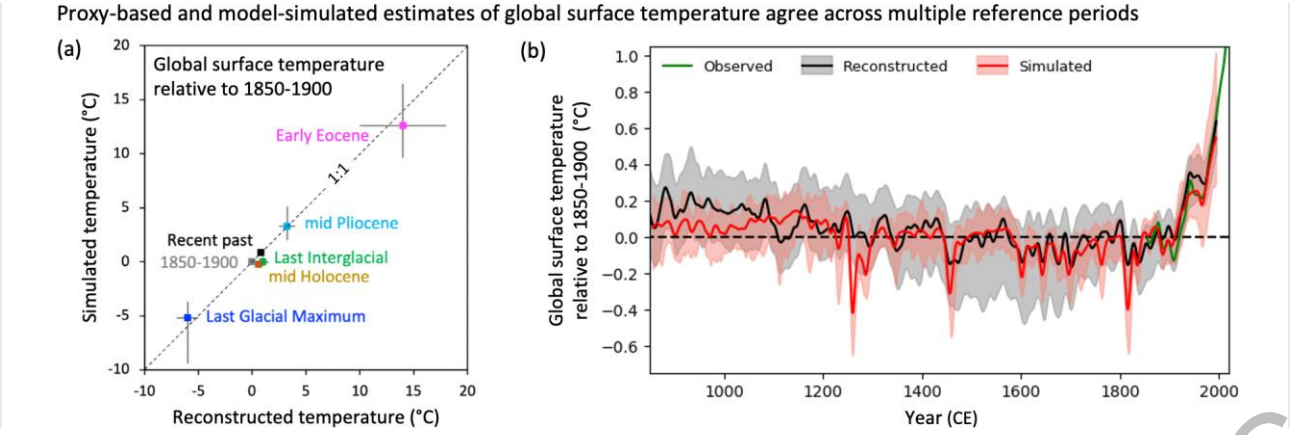
Figure TS.1: Changes in atmospheric CO_2 and global surface temperature (relative to 1850-1900) from the deep past to the next 300 years. *The intent is to show that CO_2 and temperature covary, both in the past and into the future, and that projected CO_2 and temperatures are similar to those only from many millions of years ago.* CO_2 concentrations from millions of years ago are reconstructed from multiple proxy records (grey dots are data from 2.2.3.1, Figure 2.3 shown with cubic-spline fit). CO_2 levels for the last 800,000 years through the mid-20th century are from air trapped in polar ice; recent values are from direct air measurements (Figure TS.9). {1.2.1.2, 2.2.3, Figures 1.5, 2.4, 2.5} Global surface temperature prior to 1850 is estimated from marine oxygen isotopes, one of multiple sources of evidence used to assess paleo temperatures in this report. {2.3.1.1.1, Cross-Chapter Box 2.1, Figure 1} Temperature of the past 170 years is the AR6 assessed mean (Cross-Section Box TS.1). {2.3.1.1} CO_2 levels and global surface temperature change for the future are shown for three SSP scenarios (TS.1.3) through 2300 CE, using Earth System Model emulators calibrated to the assessed global surface temperatures. {4.7.1, Cross-Chapter Box 7.1} Their smooth trajectories do not account for inter-annual to inter-decadal variability, including transient response to potential volcanic eruptions. {Cross-Chapter Box 4.1} Global maps for two paleo reference periods are based on CMIP6 and pre-CMIP6 multi-model means, with site-level proxy data for comparison (squares and circles are marine and terrestrial, respectively) (Box TS.2). {Cross-Chapter Box 2.1, Figure 7.13} The map for 2020 is an estimate of the total observed warming since 1850-1900. {Figure 1.14} Global maps at right show two SSP scenarios at 2100 (2081-2100) {4.5.1} and at 2300 (2281-2300; map from CMIP6 models; temperature assessed in 4.7.1). A brief account of the major climate forcings associated with past global temperature changes is in Cross-Chapter Box 2.1.

ACCEPTED VERSION SUBJECT TO FINAL EDITING



Box TS.2, Figure 1: Paleoclimate and recent reference periods, with selected key indicators. *The intent of this figure is to list the paleoclimate reference periods used in the WGI report, to summarize three key global climate indicators, and compare CO_2 with global temperature over multiple periods.* (a) Three large-scale climate indicators (atmospheric CO_2, global surface temperature relative to 1850-1900, and global mean sea level relative to 1900), based on assessments in Chapter 2, with confidence levels ranging from *low* to *very high*. (b) Comparison between global surface temperature (relative to 1850-1900) and atmospheric CO_2 concentration for multiple reference periods (mid-points with 5–95% ranges). {2.2.3, 2.3.1.1, 2.3.3.3, Figure 2.34}

ACCEPTED VERSION SUBJECT TO FINAL EDITING



Box TS.2, Figure 2: Global surface temperature as estimated from proxy records (reconstructed) and climate models (simulated). *The intent of this figure is to show the agreement between observations and models of global temperatures during paleo reference periods*. (a) For individual paleoclimate reference periods. (a) For individual paleoclimate reference periods. (b) For the last millennium, with instrumental temperature (AR6 assessed mean,10-year smoothed). Model uncertainties in (a) and (b) are 5-95% ranges of multi-model ensemble means; reconstructed uncertainties are 5-95% ranges (*medium confidence*) of (a) midpoints and (b) multi-method ensemble median. {2.3.1.1, Figure 2.34, Figure 3.2c, Figure 3.44}

ACCEPTED VERSION SUBJECT TO FINAL EDITING

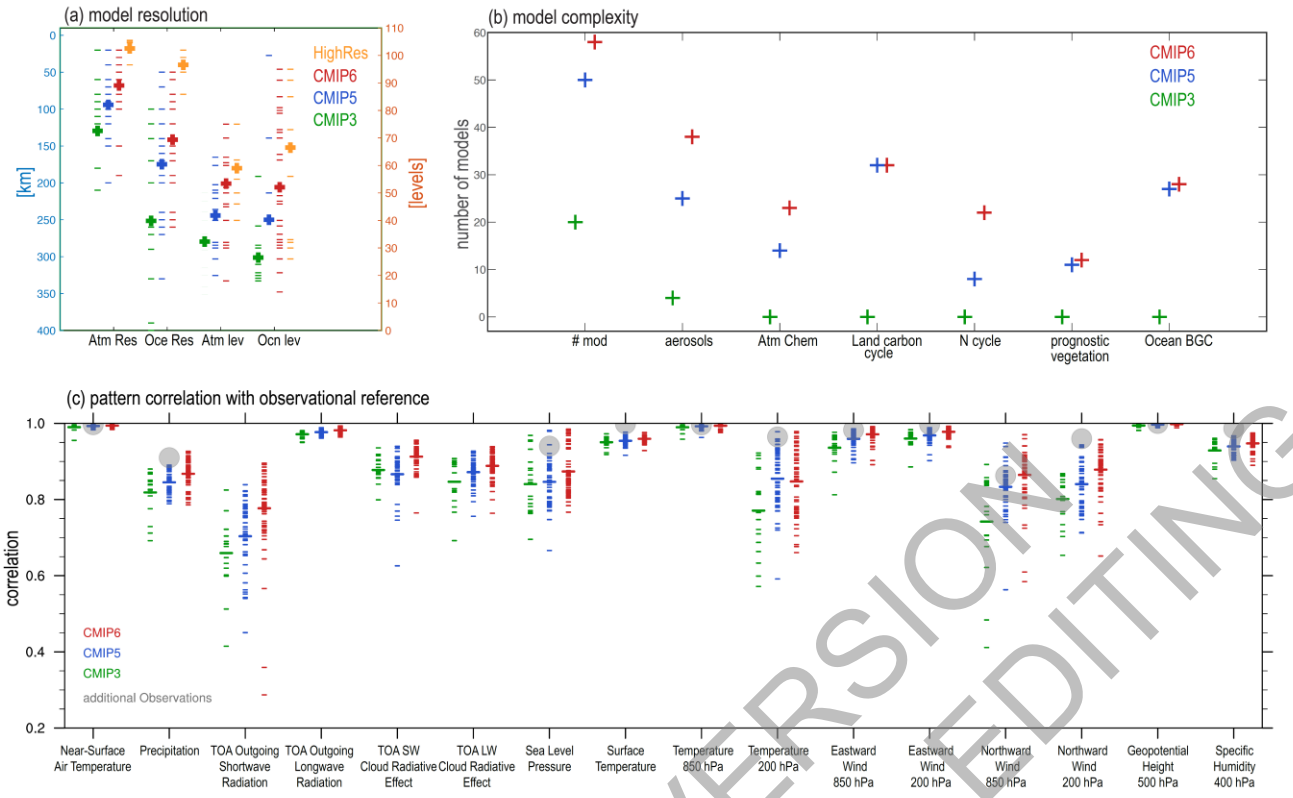


Figure TS.2: **Progress in climate models.** *The intent is to show present improvements in climate models in resolution, complexity and representation of key variables.* (a) Evolution of model horizontal resolution and vertical levels (based on Figure 1.19); (b) Evolution of inclusion of processes and resolution from CMIP Phase 3 (CMIP3) to CMIP6 (Annex II). (c) Centred pattern correlations between models and observations for the annual mean climatology over the period 1980–1999. Results are shown for individual CMIP3 (cyan), CMIP5 (blue) and CMIP6 (red) models (one ensemble member is used) as short lines, along with the corresponding ensemble averages (long lines). The correlations are shown between the models and the primary reference observational data set (from left to right: ERA5, GPCP-SG, CERES-EBAF, CERES-EBAF, CERES-EBAF, CERES-EBAF, JR-55, ERA5, ERA5, ERA5, ERA5, ERA5, ERA5, AIRS, ERA5, ESACCI-Soilmoisture, LAI3g, MTE). In addition, the correlation between the primary reference and additional observational data sets (from left to right: NCEP, GHCN, -, -, -, -, ERA5, HadISST, NCEP, NCEP, NCEP, NCEP, NCEP, NCEP, ERA5, NCEP, -, -, FLUXCOM) are shown (solid grey circles) if available. To ensure a fair comparison across a range of model resolutions, the pattern correlations are computed after regridding all datasets to a resolution of 4º in longitude and 5º in latitude. (Expanded from Figure 3.43; produced with ESMValTool version 2).

ACCEPTED VERSION. SUBJECT TO FINAL EDITING

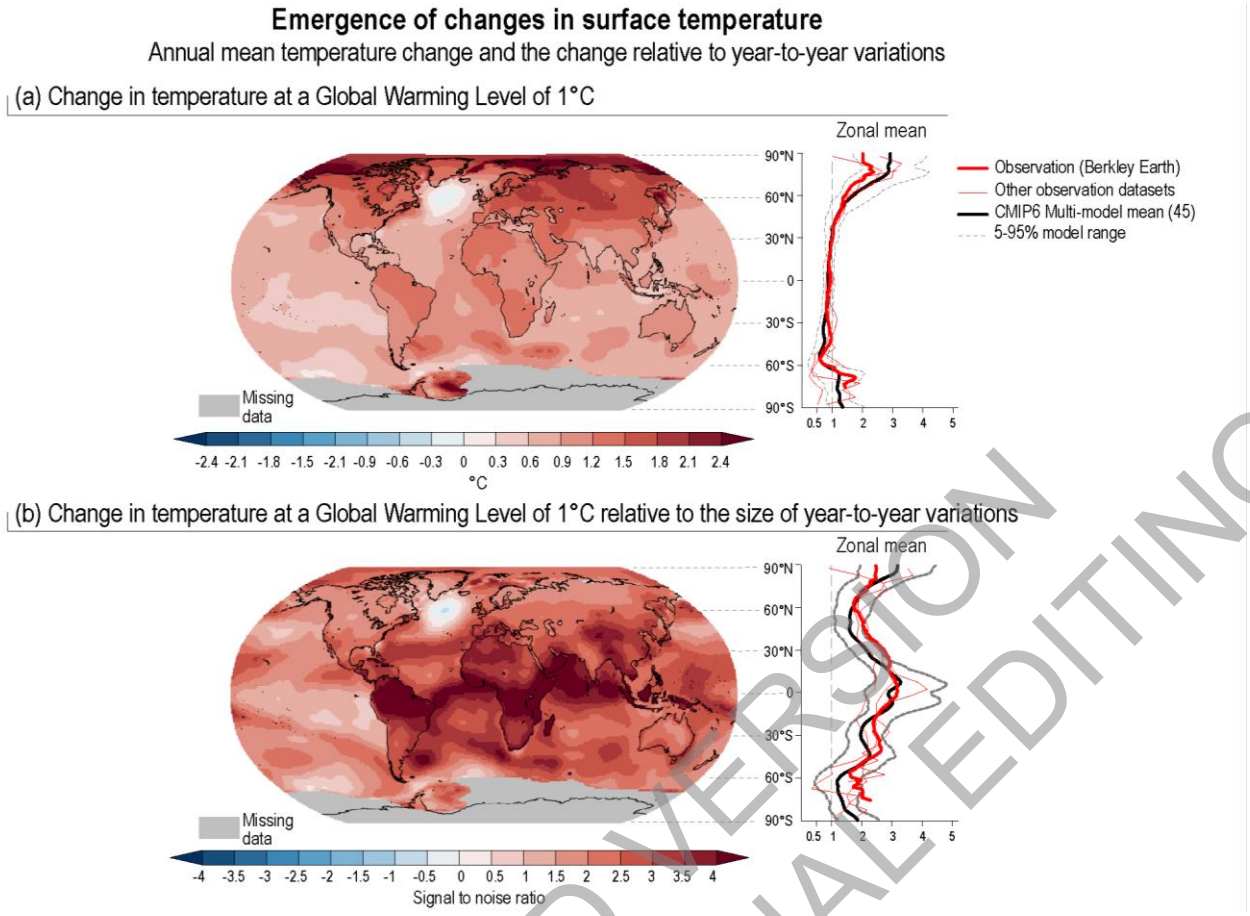
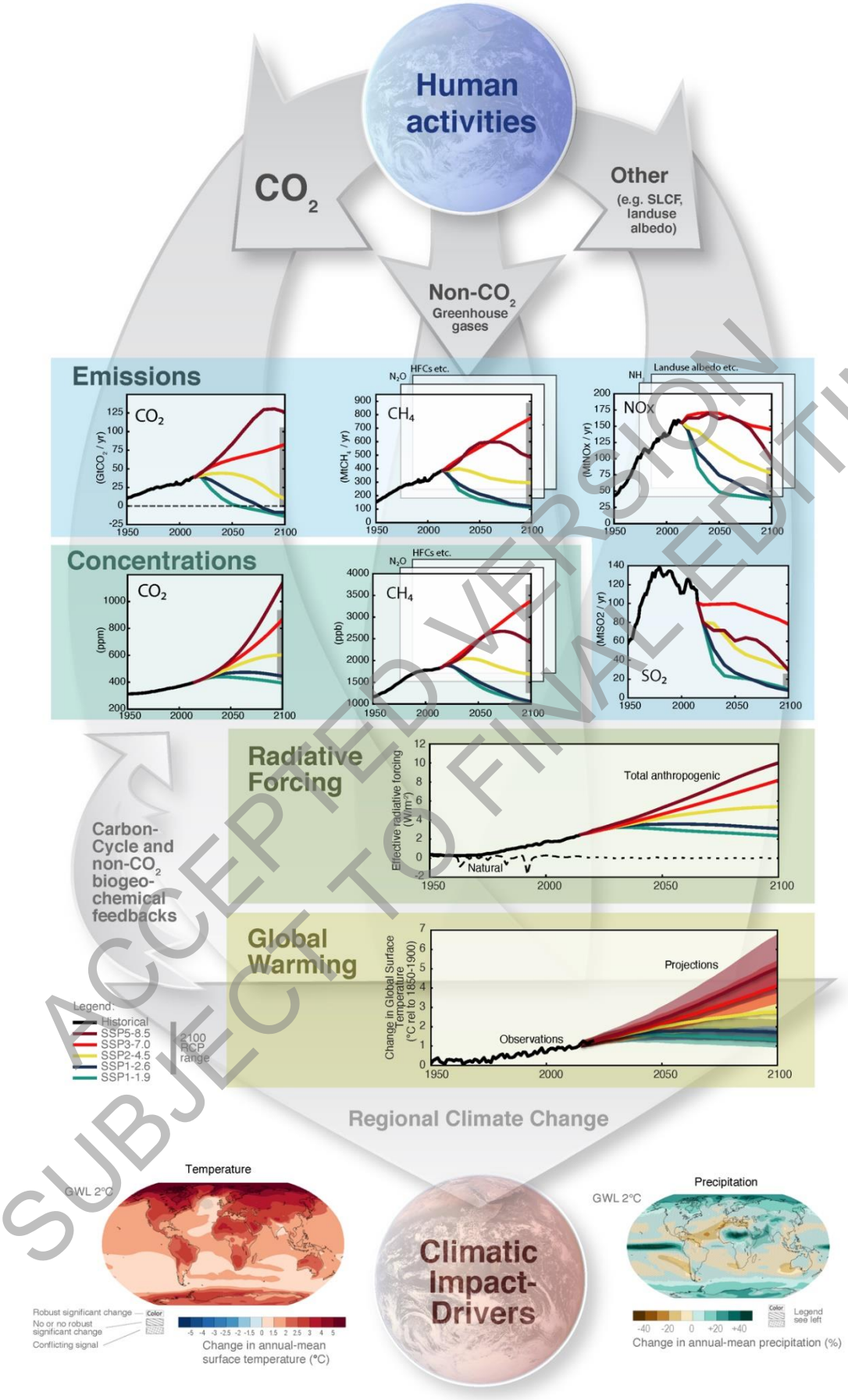


Figure TS.3: **Emergence of changes in temperature over the historical period.** *The intent of this figure is to show how observed changes in temperature have emerged and that the emergence pattern agrees with model simulations.* The observed change in temperature at a global warming level of 1°C (top map), and the signal-to-noise ratio (the change in temperature at a global warming level of 1°C, divided by the size of year-to-year variations, bottom map) using data from Berkeley Earth. The right panels show the zonal means of the maps and include data from different observational datasets (red) and the CMIP6 simulations (black, including the 5-95% range) processed in the same way as the observations. {1.4.2, 10.4.3}

ACCEPTED VERSION SUBJECT TO FINAL EDITING



ACCEPTED VERSION SUBJECT TO FINAL EDITING

Figure TS.4: **The climate change cause-effect chain:** from anthropogenic emissions, to changes in atmospheric concentration, to changes in the Earth's energy balance ('forcing'), to changes to changes in global climate and ultimately regional climate and climatic impact-drivers. Shown is the core set of five SSP scenarios as well as emission and concentration ranges for the previous RCP scenarios in year 2100; CO_2 emissions ($GtCO_2\ yr^{-1}$), panel top left; CH_4 emissions (middle) and SO_2, NO_x emissions (all in $Mt\ yr^{-1}$), top right; concentrations of atmospheric CO_2 (ppm) and CH4 (ppb), second row left and right; effective radiative forcing for both anthropogenic and natural forcings ($W\ m^{-2}$), third row; changes in global surface air temperature (°C) relative to 1850–1900, fourth row; maps of projected temperature change (°C) (left) and changes in annual-mean precipitation (%) (right) at GWL 2°C relative to 1850–1900 (see also Figure TS.5), bottom row. Carbon cycle and non-CO_2 biogeochemical feedbacks will also influence the ultimate response to anthropogenic emissions (arrows on the left). {1.6.1, Cross-Chapter Box 1.4, 4.2.2, 4.3.1, 4.6.1, 4.6.2}

ACCEPTED VERSION
SUBJECT TO FINAL EDITING

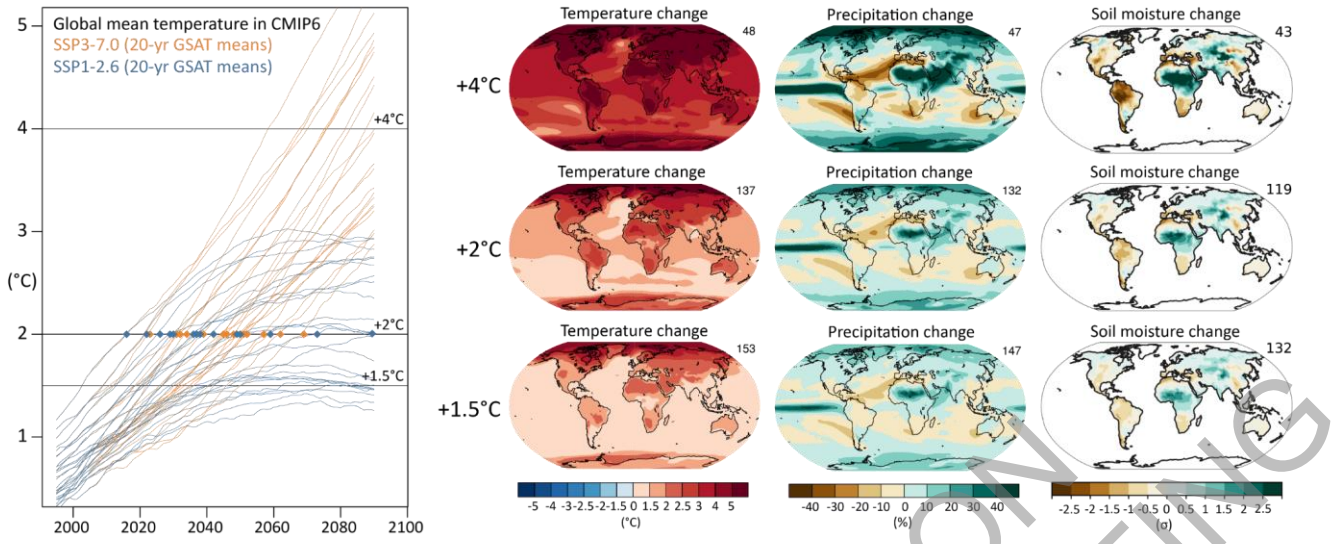


Figure TS.5: **How scenarios are linked to global warming levels (GWLs), and examples of the evolution of patterns of change with global warming levels.** Left: Illustrative example of GWLs defined as global surface temperature response to anthropogenic emissions in unconstrained CMIP6 simulations, for two illustrative scenarios (SSP1-2.6 and SSP3-7.0). The time when a given simulation reaches a GWL, e.g., +2°C, relative to 1850-1900 is taken as the time when the central year of a 20-year running mean first reaches that level of warming. See the dots for +2°C, and how not all simulations reach all levels of warming. The assessment of the timing when a GWL is reached takes into account additional lines of evidence and is discussed in Cross-Section Box TS.1. Right: Multi-model, multi-simulation average response patterns of change in near-surface air temperature, precipitation (expressed as percentage change) and soil moisture (expressed in standard deviations of interannual variability), for three GWLs. The number to the top right of the panels shows the number of model simulations averaged across including all models that reach the corresponding GWL in any of the 5 SSPs. See TS.2 for discussion. (See also Cross-Chapter Box 11.1)

ACCEPTED VERSION SUBJECT TO FINAL EDITING

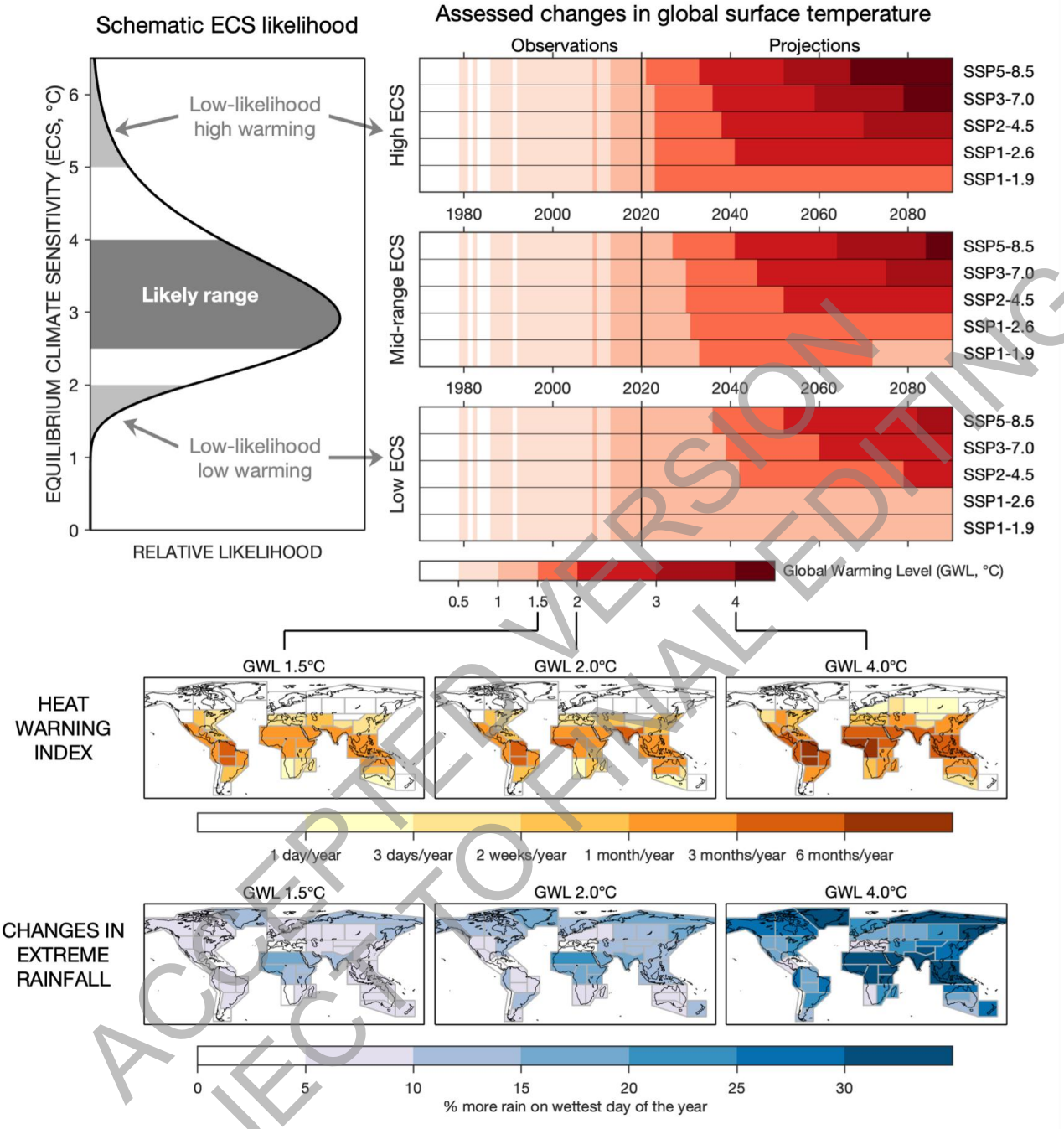
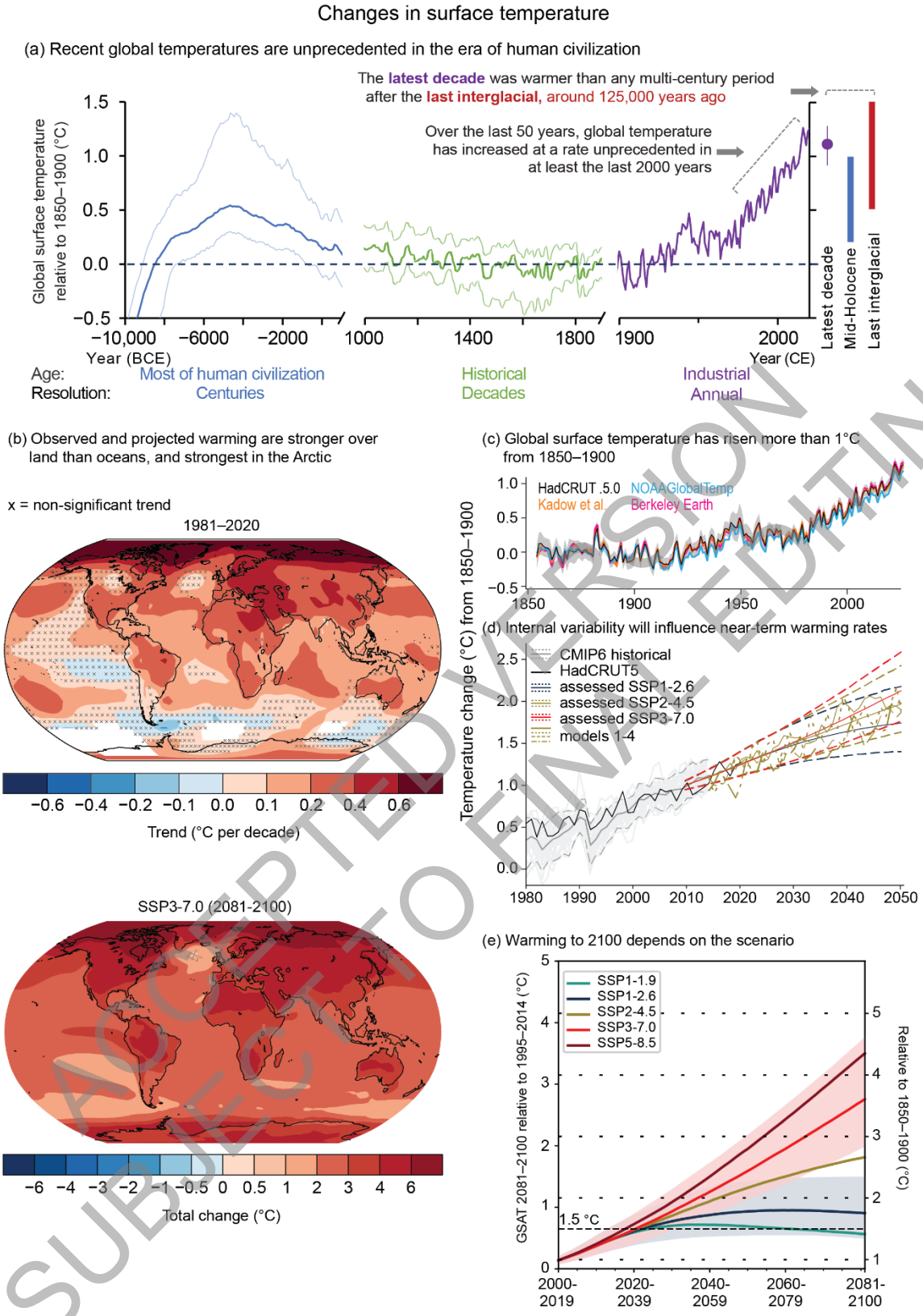


Figure TS.6: **A graphical abstract for key aspects of the Technical Summary related to observed and projected changes in global surface temperature and associated regional changes in climatic impact-drivers relevant for impact and risk assessment.** Top left: a schematic representation of the likelihood for equilibrium climate sensitivity (ECS), consistent with the AR6 assessment (see Chapter 7; TS.3). ECS values above 5°C and below 2°C are termed low-likelihood high warming (LLHW) and low-likelihood low warming, respectively. Top right: Observed (see Cross-Section Box TS.1) and projected global surface temperature changes, shown as global warming levels (GWL) relative to 1850-1900, using the assessed 95% (top), 50% (middle) and 5% (bottom) likelihood time series (see Chapter 4; TS.2). Bottom panels show maps of CMIP6 median projections of two climatic impact-drivers (CIDs) at three different GWLs (columns for 1.5, 2 and 4°C) for the AR6 land regions (see Chapters 1, 10, Atlas; TS.4). The heat warning index is the number of days per year averaged across each region at which a heat warning for human health at level 'danger' would be issued according to the U.S. National Oceanic and Atmospheric Administration (NOAA) (NOAA HI41, see Chapter 12

ACCEPTED VERSION SUBJECT TO FINAL EDITING

and Technical Annex VI). The maps of extreme rainfall changes show the percentage change in the amount of rain falling on the wettest day of a year (Rx1day, relative to 1995-2014, see Chapter 11) averaged across each region when the respective GWL is reached. Additional CIDs are discussed in TS.4.

ACCEPTED VERSION
SUBJECT TO FINAL EDITING

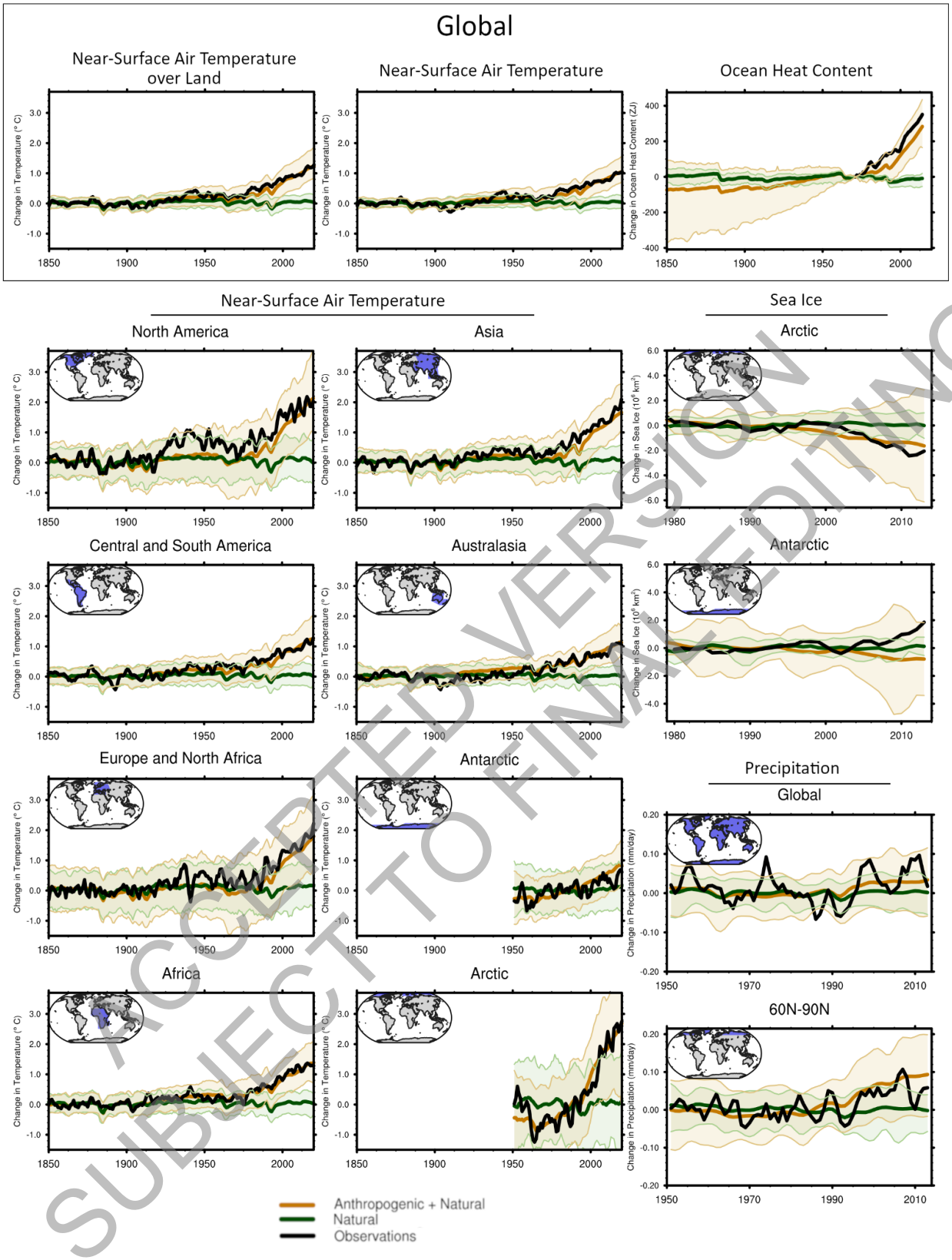


ACCEPTED VERSION SUBJECT TO FINAL EDITING

Cross-Section Box TS.1, Figure 1: Earth's surface temperature history and future with key findings annotated within each panel. *The intent of this figure is to show global surface temperature observed changes from the Holocene to now, and projected changes.* (a) Global

surface temperature over the Holocene divided into three time scales. (i) 12,000 to 1000 years ago (10,000 BCE to 1000 CE) in 100-year time steps, (ii) 1000 to 1900 CE, 10-year smooth, and (iii) 1900 to 2020 CE (mean of four datasets in panel (c)). Median of the multi-method reconstruction (bold lines), with 5% and 95% percentiles of the ensemble members (thin lines). Vertical bars are 5th to 95th percentile ranges of estimated global surface temperature for the Last Interglacial and mid Holocene (*medium confidence*) (Section 2.3.1.1). All temperatures relative to 1850–1900. (b) Spatially resolved trends (°C per decade) for (upper map) HadCRUTv5 over 1981–2020, and (lower map, total change) multi-model mean projected changes from 1995–2014 to 2081–2010 in the SST3-7.0 scenario. Observed trends have been calculated where data are present in both the first and last decade and for at least 70% of all years within the period using OLS. Significance is assessed with AR(1) correction and denoted by stippling. Hatched areas in the lower map show areas of conflicting model evidence on significance of changes. (c) Temperature from instrumental data for 1850–2020, including annually resolved averages for the four global surface temperature datasets assessed in Section 2.3.1.1.3 (see text for references). The grey shading shows the uncertainty associated with the HadCRUTv5 estimate. All temperatures relative to the 1850–1900 reference period. (d) Recent past and 2015–2050 evolution of annual mean global surface temperature change relative to 1850–1900, from HadCRUTv5 (black), CMIP6 historical simulations (up to 2014, in grey, ensemble mean solid, 5% and 95% percentiles dashed, individual models thin), and CMIP6 projections under scenario SSP2-4.5, from four models that have an equilibrium climate sensitivity near the assessed central value (thick yellow). Solid thin coloured lines show the assessed central estimate of 20-year change in global surface temperature for 2015–2050 under three scenarios, and dashed thin coloured lines the corresponding 5% and 95% quantiles. (e) Assessed projected change in 20-year running mean global surface temperature for five scenarios (central estimate solid, *very likely* range shaded for SSP1-2.6 and SSP3-7.0), relative to 1995–2014 (left y-axis) and 1850–1900 (right y-axis). The y-axis on the right-hand side is shifted upward by 0.85°C, the central estimate of the observed warming for 1995–2014, relative to 1850–1900. The right y-axis in (e) is the same as the y-axis in (d).

ACCEPTED VERSION
SUBJECT TO FINAL EDITING



ACCEPTED VERSION SUBJECT TO FINAL EDITING

Figure TS.7: **Simulated and observed changes compared to the 1995–2014 average in key large-scale indicators of climate change across the climate system, for continents, ocean basins and globally up to 2014.** Black lines show observations, orange lines and shading show the multi-model mean and 5–95th percentile ranges for CMIP6 historical simulations including anthropogenic and natural forcing, and green lines and shading show corresponding ensemble means and 5-95th percentile ranges for CMIP6 natural-only simulations. Observations after 2014 (including, for example, a strong

subsequent decrease of Antarctic sea-ice area that leads to no significant overall trend since 1979) are not shown because the CMIP6 historical simulations end in 2014. A 3-year running mean smoothing has been applied to all observational time series. {3.8, Figure 3.41}

ACCEPTED VERSION
SUBJECT TO FINAL EDITING

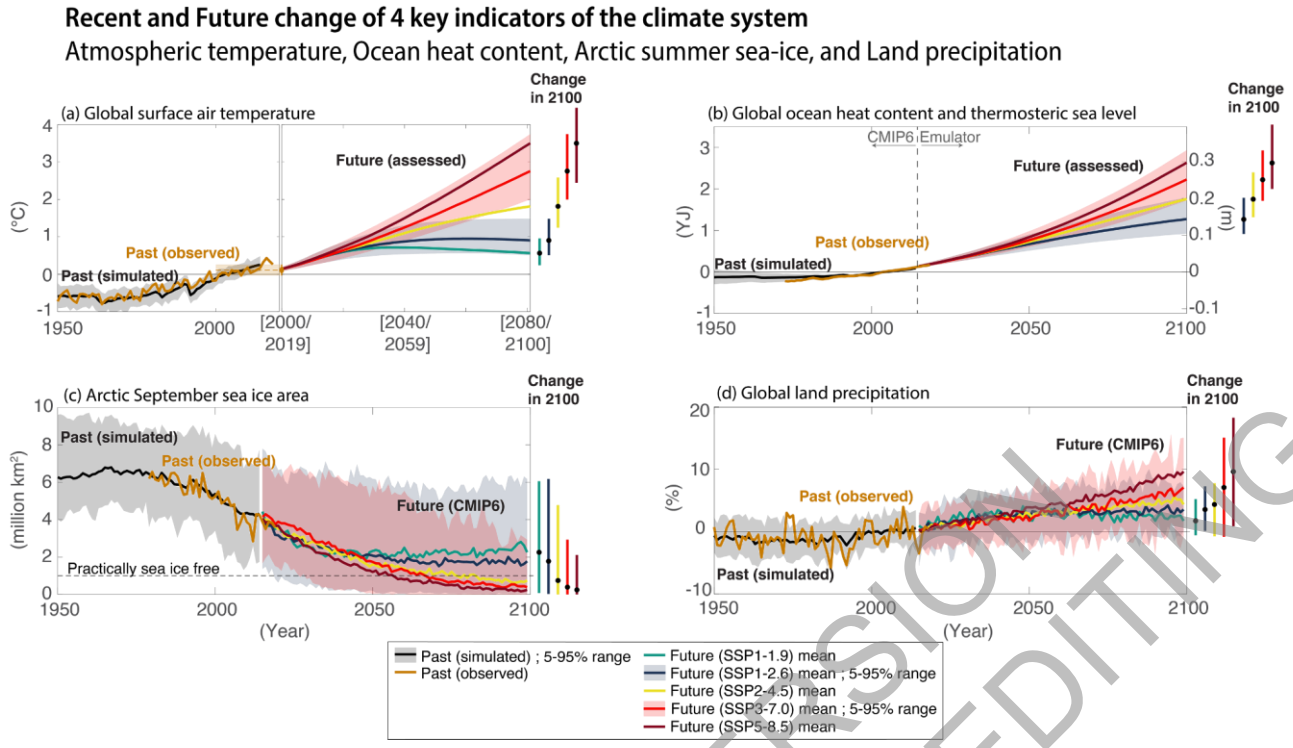
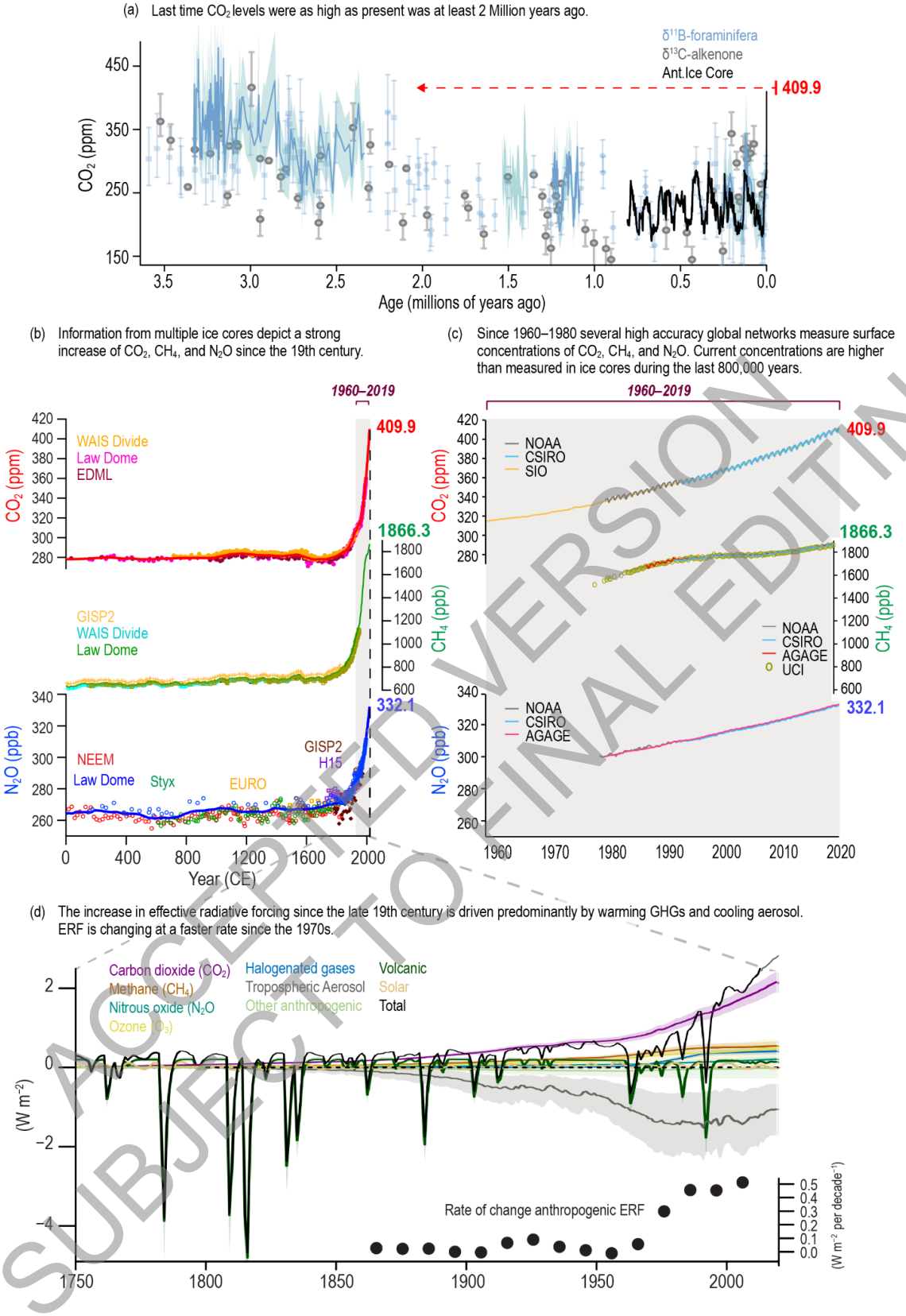


Figure TS.8: **Observed, simulated and projected changes compared to the 1995–2014 average in 4 key indicators of the climate system through to 2100 differentiated by SSP scenario pathway.** Past simulations are based on the CMIP6 multi-model ensemble. Future projections are based on the assessed ranges based upon multiple lines of evidence for (a) global surface temperature (Cross-Section Box TS.1) and (b) global ocean heat content and the associated thermosteric sea level contribution to Global Mean Sea Level (GMSL) change (right-hand axis) using a climate model emulator (Cross-Chapter Box 7.1), and CMIP6 simulations for (c) Arctic September sea ice and (d) Global land precipitation. SSP1-1.9 and SSP1-2.6 projections show that reduced GHG emissions lead to a stabilization of global surface temperature, Arctic sea ice area and global land precipitation over the 21st century. SSP1-2.6 shows that emissions reductions have the potential to substantially reduce the increase in ocean heat content and thermosteric sea level rise over the 21st century but that some increase is unavoidable. {4.3, 9.3, 9.6, Figure 4.2, Figure 9.6}

ACCEPTED VERSION SUBJECT TO FINAL EDITING



ACCEPTED VERSION SUBJECT TO FINAL EDITING

Figure TS.9: **Changes in well-mixed greenhouse gas (WMGHG) concentrations and Effective Radiative Forcing**. a) Changes in CO_2 from proxy records over the past 3.5 million years; b) Changes in all three WMGHGs from ice core records over the Common Era; c) directly observed WMGHG changes since the mid-20th century; d) Evolution of ERF and components since 1750. Further details on data sources and processing are available in the associated FAIR data table. {2.2, Figures 2.3, 2.4 and 2.10}

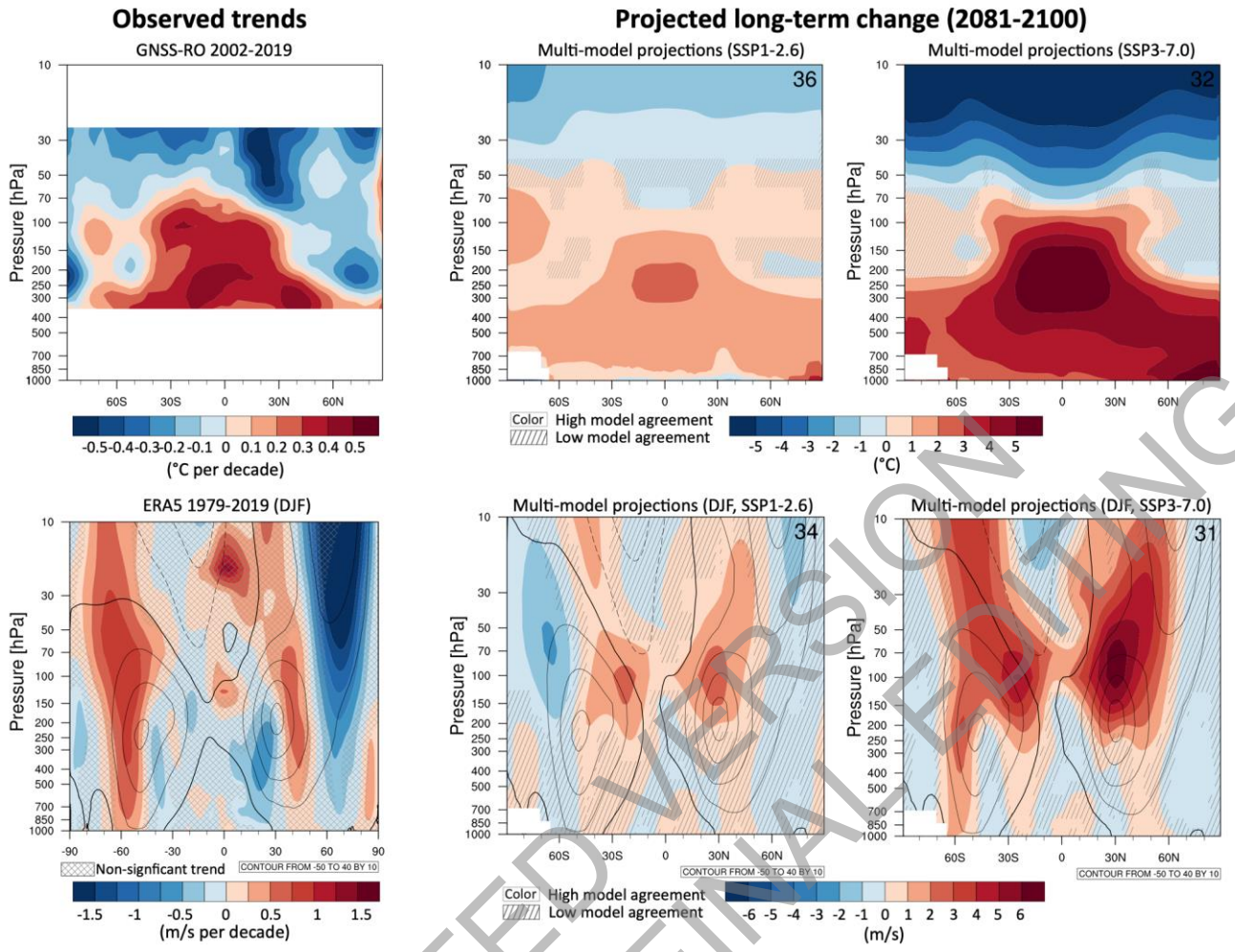
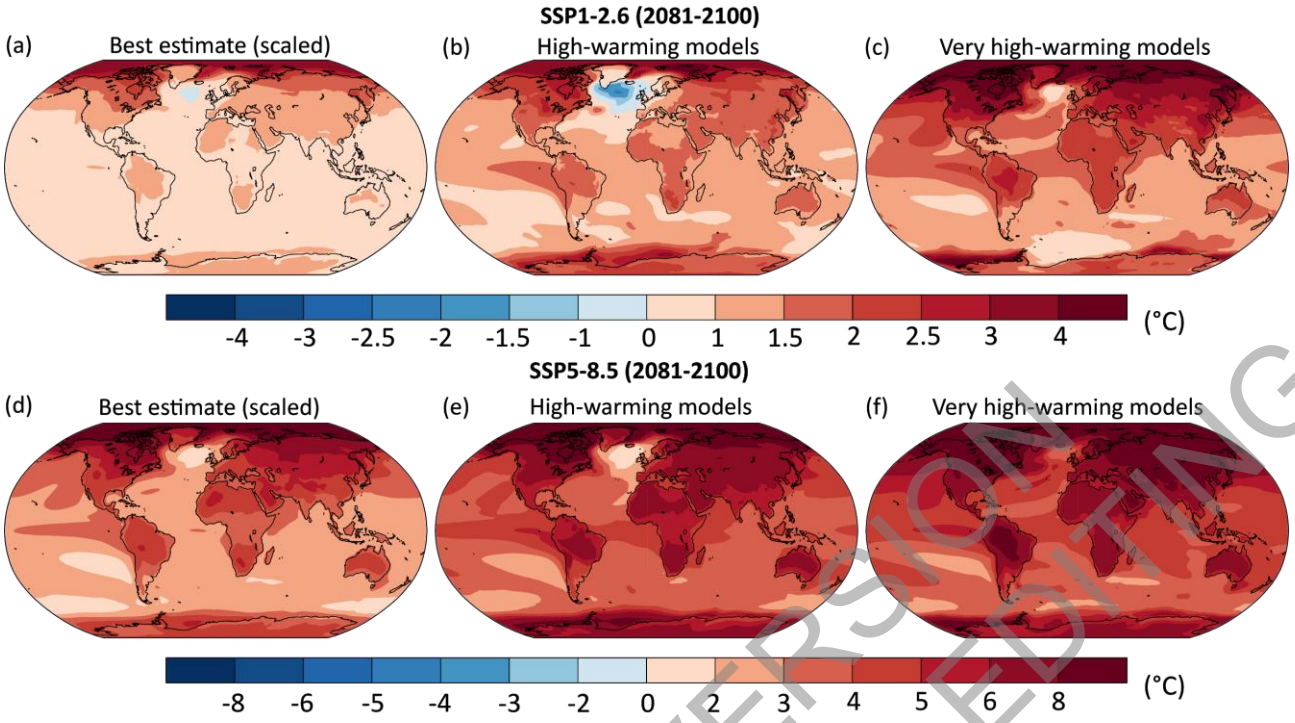


Figure TS.10: **Observed and projected upper air temperature and circulation changes.** Upper panels: Left: Zonal cross-section of temperature trends for 2002-2019 in the upper troposphere region for the ROM SAF radio-occultation dataset. Middle: Change in the annual and zonal mean atmospheric temperature (°C) in 2081-2100 in SSP1-2.6 relative to 1995-2014 for 36 CMIP6 models. Right: the same in SSP3-7.0 for 32 models. Lower panels: Left: Long-term mean (thin black colour) and linear trend (colour) of zonal mean DJF zonal winds for ERA5. Middle: multi-model mean change in annual and zonal mean wind (m s^{-1}) in 2081-2100 in SSP1-2.6 relative to 1995-2014 based on 34 CMIP6 models. The 1995-2014 climatology is shown in contours with spacing 10 m s^{-1}. Right: the same for SSP3-7.0 for 31 models. {2.3.1, 4.5.1, Figures 2.12, 2.18, and 4.26}

ACCEPTED VERSION SUBJECT TO FINAL EDITING



Box TS.3, Figure 1: High-warming storylines. (a) CMIP6 multi-model mean linearly scaled to the assessed best global surface temperature estimate for SSP1-2.6 in 2081–2100 relative to 1995–2014, (b) mean across five high-warming models with global surface temperature changes warming nearest to the upper bound of the assessed very likely range, (c) mean across five very high-warming models with global surface temperature changes warming higher than the assessed very likely. (d-f) Same as (a-c) but for SSP5-8.5. Note the different colour bars in (a-c) and (d-f). {4.7, Figure 4.41}

ACCEPTED VERSION SUBJECT TO FINAL EDITING

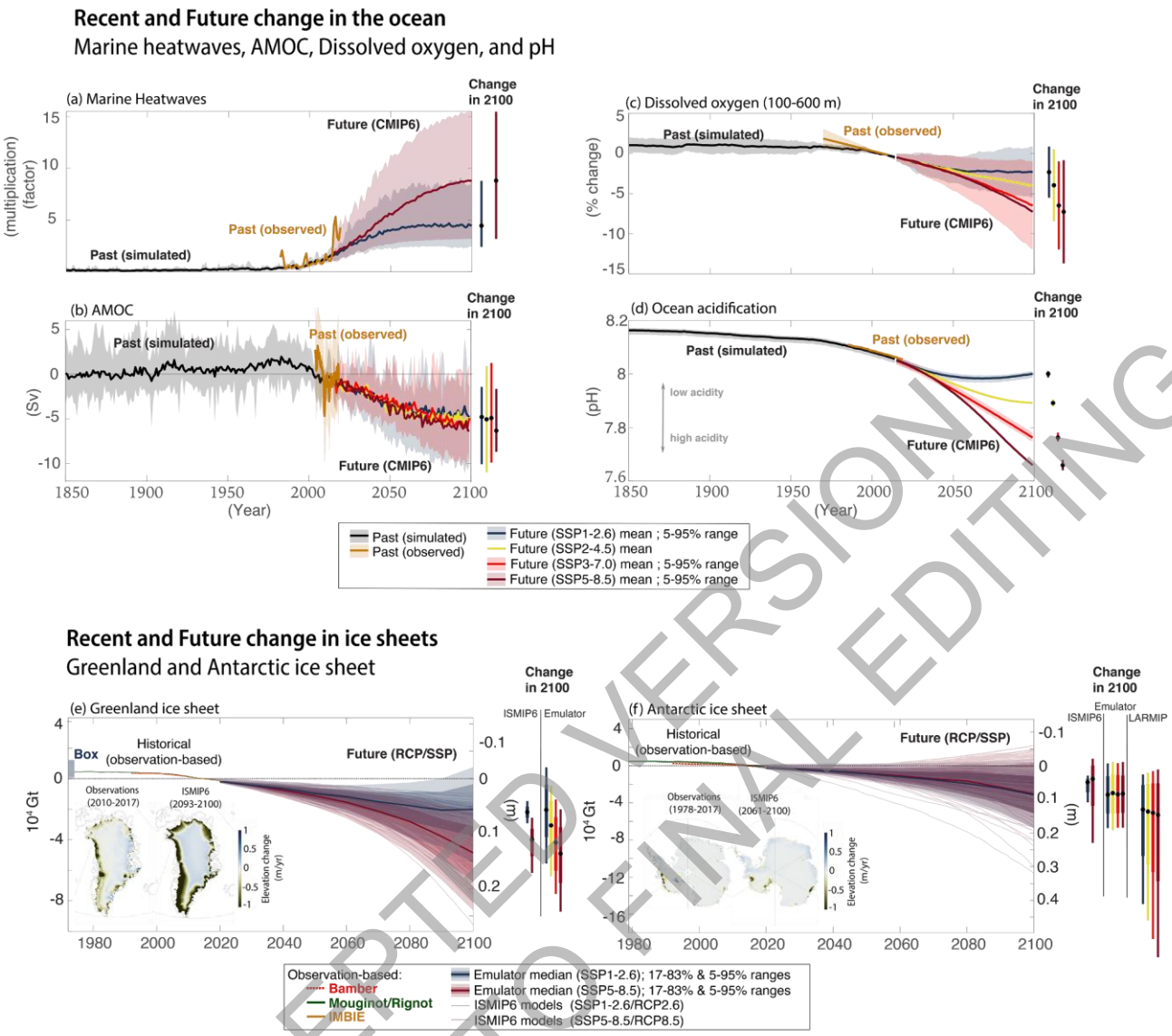
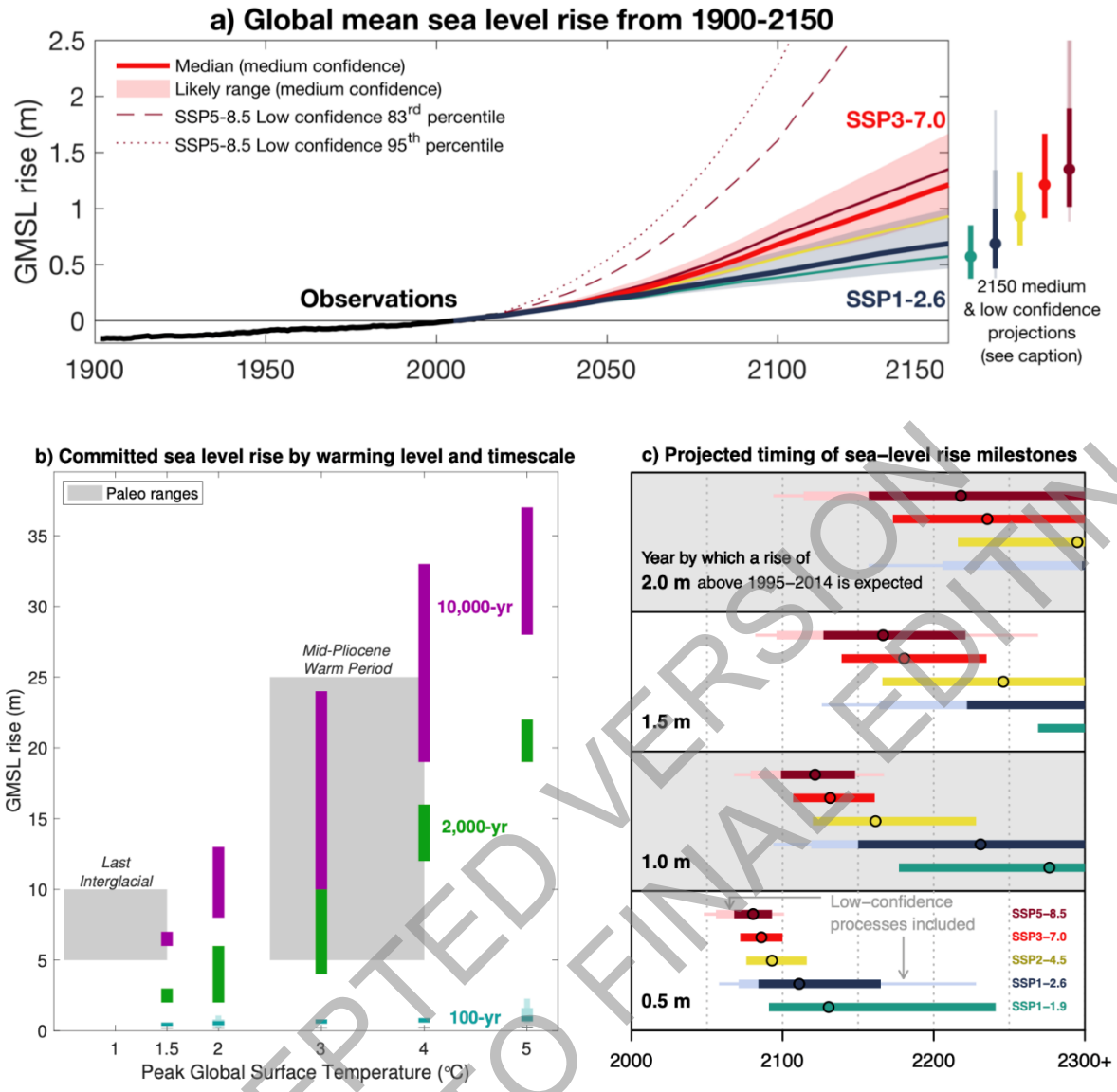


Figure TS.11: **Past and future ocean and ice sheet changes.** Observed and simulated historical changes and projected future changes under varying greenhouse gas emissions scenarios. Simulated and projected ocean changes are shown as CMIP6 ensemble mean, and 5-95% range (shading) is provided for scenario SSP1-2.6 and SSP3-7.0 (except in panel a where range provided for scenario SSP1-2.6 and SSP5-8.5). Mean and 5-95% range in 2100 are shown as vertical bars on the right-hand side of each panel. (a) Change in multiplication factor in surface ocean marine heatwave days relative to 1995-2014 (defined as days exceeding the 99th percentile in SST from 1995-2014 distribution). Assessed observational change span 1982-2019 from AVHRR satellite SST. (b) AMOC transport relative to 1995-2014 (defined as maximum transport at 26°N). Assessed observational change spans 2004-2018 from the RAPID array smoothed with a 12-month running mean (shading around the mean shows the 12-month running standard deviation around the mean). (c) Global mean percent change in ocean oxygen (100–600 m depth), relative to 1995-2014. Assessed observational trends and *very likely* range are from the SROCC assessment, and spans 1970–2010 centered on 2005. (d) Global mean surface pH. Assessed observational change span 1985-2019, from the CMEMS SOCAT-based reconstruction (shading around the global mean shows the 90% confidence interval). (e), (f): Ice sheet mass changes. Projected ice sheet changes are shown as median, 5-95% range (light shading), and 17-83% range (dark shading) of cumulative mass loss and sea level equivalent from ISMIP6 emulation under SSP1-26 and SSP5-85 (shading and bold line), with individual emulated projections as thin lines. Median (dot), 17-83% range (thick vertical bar), and 5-95% range (thin vertical bar) in 2100 are shown as vertical bars on the right-hand side of each panel, from ISMIP6, ISMIP6 emulation, and LARMIP-2. Observation-based estimates: For Greenland (e), for 1972-2018 (Mouginot), for 1992-2016 (Bamber), for 1992-2020 (IMBIE) and total estimated mass loss range for 1840-1972 (Box). For Antarctica (f),

ACCEPTED VERSION SUBJECT TO FINAL EDITING

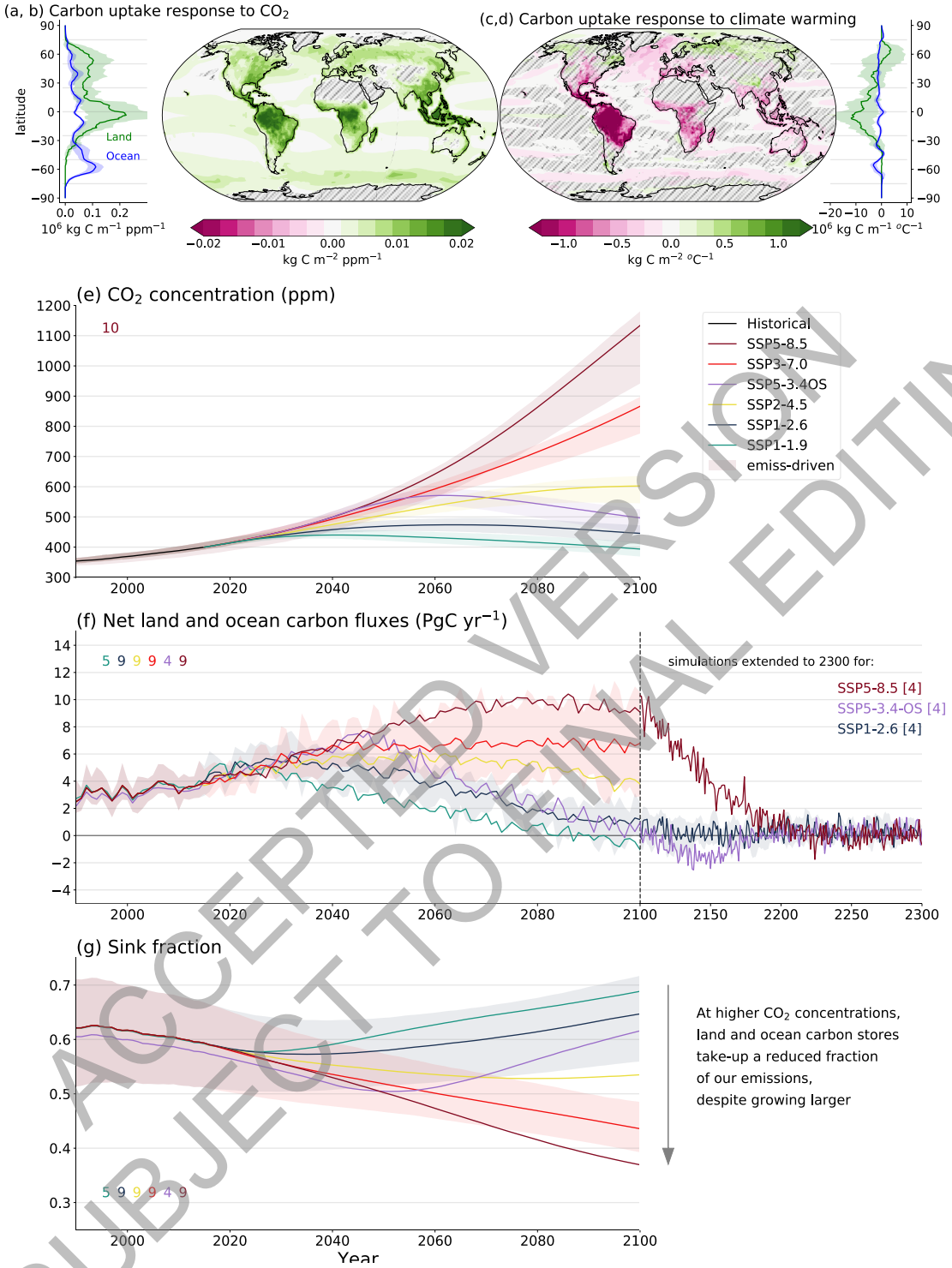
estimates based on satellite data combined with simulated surface mass balance and glacial isostatic adjustment for 1992-2020 (IMBIE), 1992-2016 (Bamber), and 1979-2017 (Rignot). Left inset maps: mean Greenland elevation changes 2010-2017 derived from CryoSat-2 radar altimetry (e) and mean Antarctica elevation changes 1978-2017 derived from restored analog radar records (f). Right inset maps: ISMIP6 model mean (2093- 2100) projected changes under the MIROC5 climate model for the RCP8.5 scenario. {Box 9.2, 2.3.3, 2.3.4, 3.5.4, 4.3.2, 5.3.2, 5.3.3, 5.6.3, 9.2.3, 9.4.1, 9.4.2, Box 9.2 Figure 1, Figure 9.10, Figure 9.17, Figure 9.18}

ACCEPTED VERSION
SUBJECT TO FINAL EDITING



Box TS.4, Figure 1: Global mean sea level change on different time scales and under different scenarios. (a) GMSL change from 1900 to 2150, observed (1900–2018) and projected under the SSP scenarios (2000–2150), relative to a 1995–2014 baseline. Solid lines show median projections. Shaded regions show *likely* ranges for SSP1-2.6 and SSP3-7.0. Dotted and dashed lines show respectively the 83rd and 95th percentile low-confidence projections for SSP5-8.5. Bars at right show *likely* ranges for SSP1-1.9, SSP1-2.6, SSP2-4.5, SSP3-7.0, and SSP5-8.5 in 2150. Lightly shaded thick/thin bars show 17th–83rd/5th–95th percentile *low-confidence* ranges in 2150 for SSP1-2.6 and SSP5-8.5, based upon projection methods incorporating structured expert judgement and Marine Ice Cliff Instability. *Low-confidence* range for SSP5-8.5 in 2150 extends to 4.8/5.4 m at the 83rd/95th percentile. (b) GMSL change on 100- (blue), 2,000- (green) and 10,000-year (magenta) time scales as a function of global surface temperature, relative to 1850–1900. For 100-year projections, GMSL is projected for the year 2100, relative to a 1995-2014 baseline, and temperature anomalies are average values over 2081–2100. For longer-term commitments, warming is indexed by peak warming above 1850–1900 reached after cessation of emissions. Shaded regions show paleo-constraints on global surface temperature and GMSL for the Last Interglacial and mid-Pliocene Warm Period. Lightly shaded thick/thin blue bars show 17th–83rd/5th–95th percentile *low-confidence* ranges for SSP1-2.6 and SSP5-8.5 in 2100, plotted at 2°C and 5°C. (c) Timing of exceedance of GMSL thresholds of 0.5, 1.0, 1.5 and 2.0 m, under different SSPs. Lightly shaded thick/thin bars show 1th7–83rd/5th–95th percentile *low-confidence* ranges for SSP1-2.6 and SSP5-8.5.

ACCEPTED VERSION SUBJECT TO FINAL EDITING

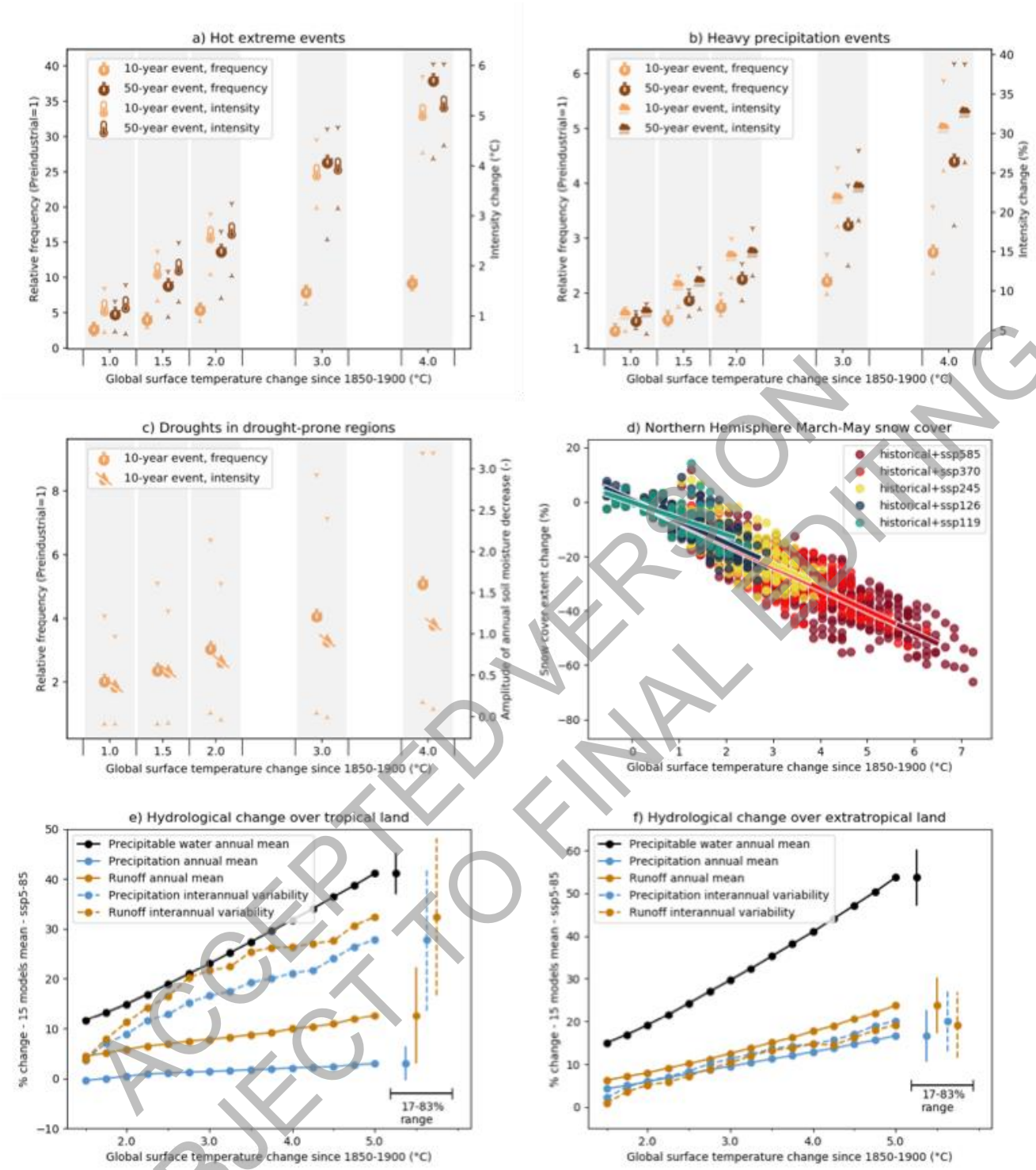


Box TS.5, Figure 1: Carbon cycle processes and projections. Carbon cycle response to forcings. The figure shows changes in carbon storage in response to elevated CO_2 (a, b) and the response to climate warming (c, d). Maps show spatial patterns of changes in carbon uptake during simulations with 1% per year increase in CO_2 {section 5.4.5.5}, and zonal mean plots show distribution of carbon changes is dominated by the land (green lines) in the tropics and northern hemisphere and ocean (blue lines) in the southern hemisphere. Hatching indicates regions where fewer than 80% of models agree on the sign of response. (e) Future CO_2 projections: projected CO_2 concentrations in the SSP scenarios in response to anthropogenic emissions, results from coupled ESMs for SSP5-8.5 and from the MAGICC7 emulator for other scenarios {section 4.3.1}. (f) Future carbon fluxes:

ACCEPTED VERSION SUBJECT TO FINAL EDITING

projected combined land and ocean fluxes (positive downward) up to 2100 for the SSP scenarios, and extended to 2300 for available scenarios, 5-95% uncertainty plumes shown for SSP1-2.6 and SSP3-7.0 {section 5.4.5.4, 5.4.10}. The numbers near the top show the number of model simulations used. (g) Sink fraction: the fraction of cumulative emissions of CO_2 removed by land and ocean sinks. The sink fraction is smaller under conditions of higher emissions. {5.4.5, 5.5.1; Figure 5.27; Figure 4.31; Figure 5.25; Figure 5.30; Figure 5.31}

ACCEPTED VERSION
SUBJECT TO FINAL EDITING

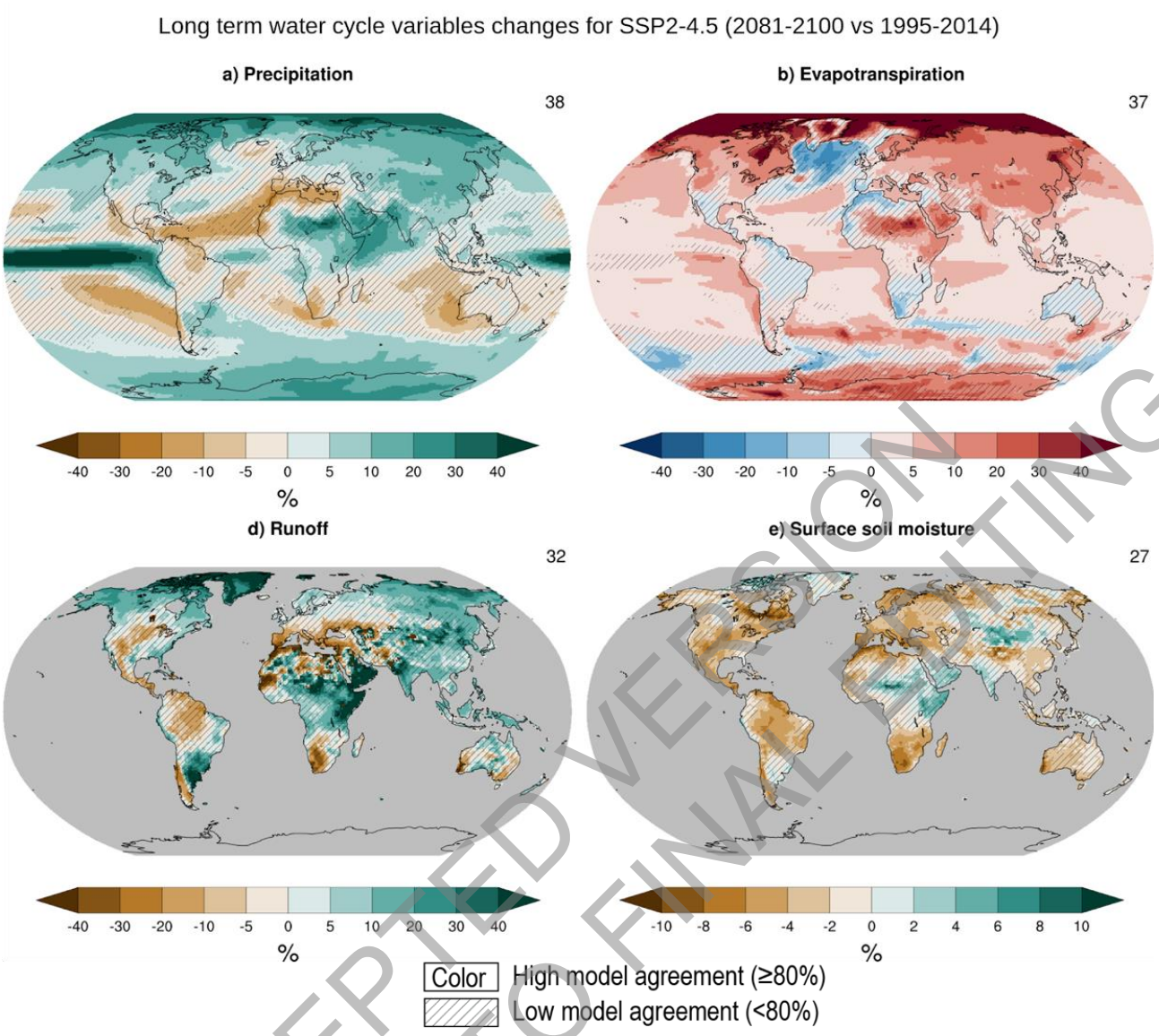


ACCEPTED VERSION SUBJECT TO FINAL EDITING

Figure TS.12: Land-related changes relative to the 1850-1900 as a function of global warming levels. a) Changes in the frequency (left scale) and intensity (in °C, right scale) of daily hot extremes occurring every 10- and 50-years; b) as a), but for daily heavy precipitation extremes, with intensity change in %; c) Changes in 10-year droughts aggregated over drought-prone regions (CNA, NCA, SCA, NSA, SAM, SWS, SSA, MED, WSAF, ESAF, MDG, SAU, and EAU; for definitions of these regions, see Atlas.2), with drought intensity (right scale) represented by the change of annual mean soil moisture, normalized with respect to interannual variability; d) Changes in Northern Hemisphere spring (March-April-May) snow cover extent relative to 1850-1900; e,f) Relative change (%) in annual mean of total precipitable water (grey line), precipitation (red solid lines), runoff (blue solid lines) and in standard deviation (i.e. variability) of precipitation (red dashed lines) and runoff (blue dashed lines) averaged over (e) tropical and (f) extratropical land as function of global warming levels. CMIP6 models that

reached a 5°C warming level in the 21st century in SSP5-8.5 above the 1850-1900 average have been used. Precipitation and runoff variability are estimated by respective standard deviation after removing linear trends. Error bars show the 17-83% confidence interval for the warmest +5°C global warming level. {Figures 11.6, 11.7, 11.12, 11.15, 11.18, 9.24, 8.16, Atlas.2}

ACCEPTED VERSION
SUBJECT TO FINAL EDITING



Box TS.6, Figure 1: Projected water cycle changes. Long-term (2081-2100) projected annual mean changes (%) relative to present-day (1995-2014) in the SSP2-4.5 emission scenario for (a) precipitation, (b) surface evapotranspiration, (c) total runoff and (d) surface soil moisture. Top-right panel numbers indicate the number of CMIP6 models used for estimating the ensemble mean. For other scenarios, please refer to relevant figures in Chapter 8. Uncertainty is represented using the simple approach: No overlay indicates regions with high model agreement, where ≥80% of models agree on sign of change; diagonal lines indicate regions with low model agreement, where <80% of models agree on sign of change. For more information on the simple approach, please refer to the Cross-Chapter Box Atlas.1. {8.4.1, Figures 8.14, 8.17, 8.18, 8.19}

ACCEPTED VERSION SUBJECT TO FINAL EDITING

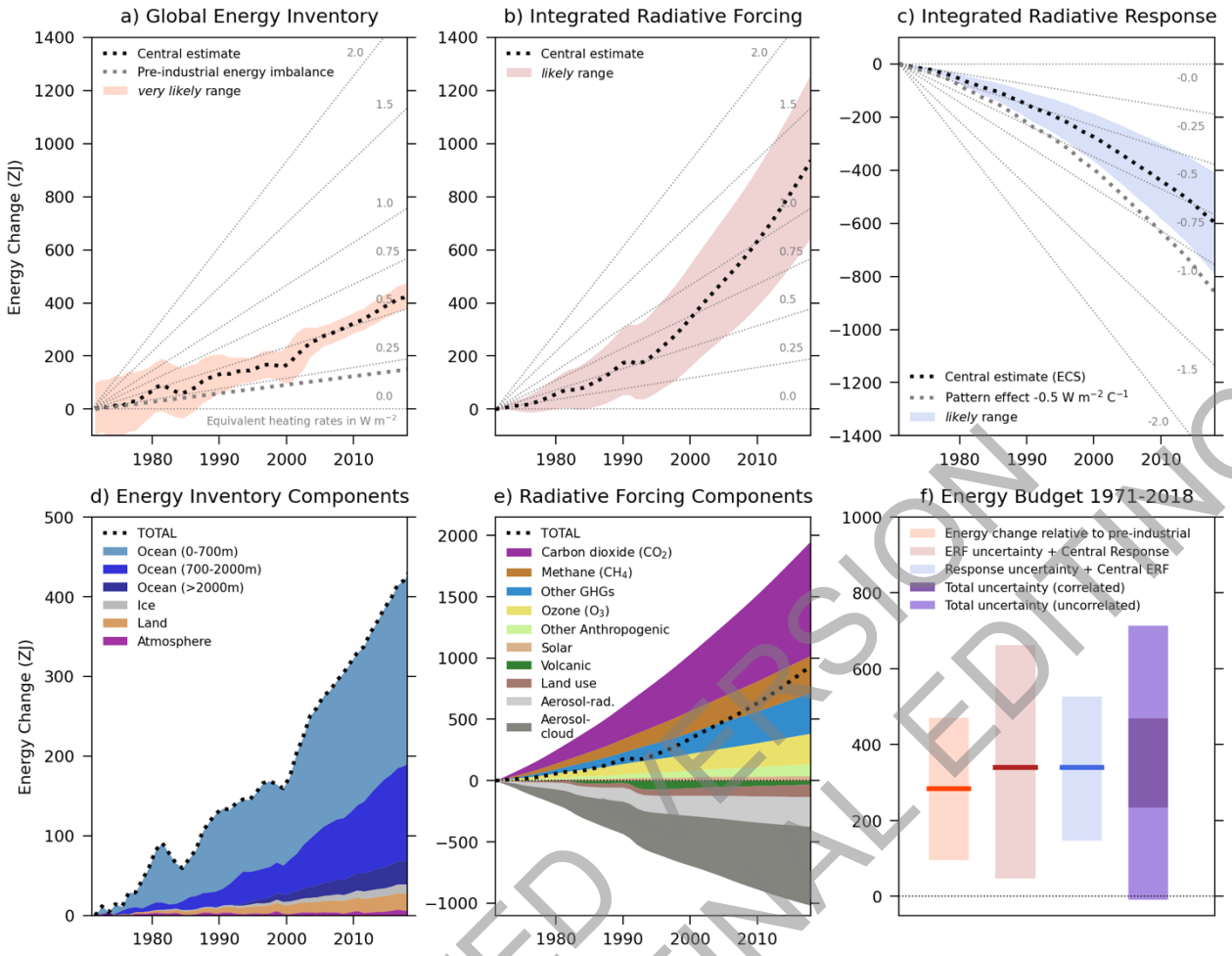


Figure TS.13: **Estimates of the net cumulative energy change (ZJ = 10^{21} Joules) for the period 1971–2018 associated with: (a) observations of changes in the Global Energy Inventory (b) Integrated Radiative Forcing; (c) Integrated Radiative Response.** *The intent is to show assessed changes in energy budget and ERFs.* Black dotted lines indicate the central estimate with *likely* and *very likely* ranges as indicated in the legend. The grey dotted lines indicate the energy change associated with an estimated pre-industrial Earth energy imbalance of 0.2 W m^{-2} (panel a) and an illustration of an assumed pattern effect of –0.5 W m^{-2} °C^{-1} (panel c). Background grey lines indicate equivalent heating rates in W m^{-2} per unit area of Earth's surface. Panels (d) and (e) show the breakdown of components, as indicated in the legend, for the Global Energy Inventory and Integrated Radiative Forcing, respectively. Panel (f) shows the Global Energy Budget assessed for the period 1971–2018, that is, the consistency between the change in the Global Energy Inventory relative to pre-industrial and the implied energy change from Integrated Radiative Forcing plus Integrated Radiative Response under a number of different assumptions, as indicated in the figure legend, including assumptions of correlated and uncorrelated uncertainties in Forcing plus Response. Shading represents the *very likely* range for observed energy change relative to pre-industrial and *likely* range for all other quantities. Forcing and Response timeseries are expressed relative to a baseline period of 1850–1900.

ACCEPTED VERSION SUBJECT TO FINAL EDITING

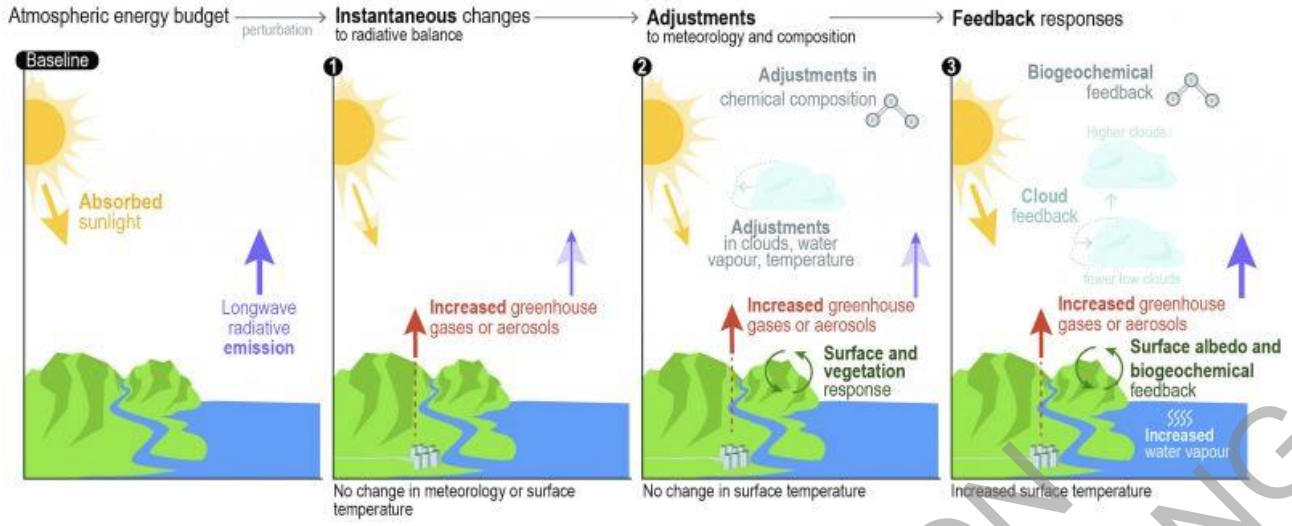


Figure TS.14: Schematic representation of changes in the top-of atmosphere (TOA) radiation budget following a perturbation. *The intent of the figure is to illustrate the concept of adjustments in the climate system following a perturbation in the radiation budget.* The baseline TOA energy budget (a) responds instantaneously to perturbations (b), leading to adjustments in the atmospheric meteorology and composition, and land surface that are independent of changes in surface temperature (c). Surface temperature changes (here using an increase as an example) lead to physical, biogeophysical and biogeochemical feedback processes (d). Long term feedback processes, such as those involving ice sheets, are not shown here. {adapted from Chapter 7 Figure 7.2, FAQ 7.2 Figure 1, and Figure 8.3}

ACCEPTED VERSION SUBJECT TO FINAL EDITING

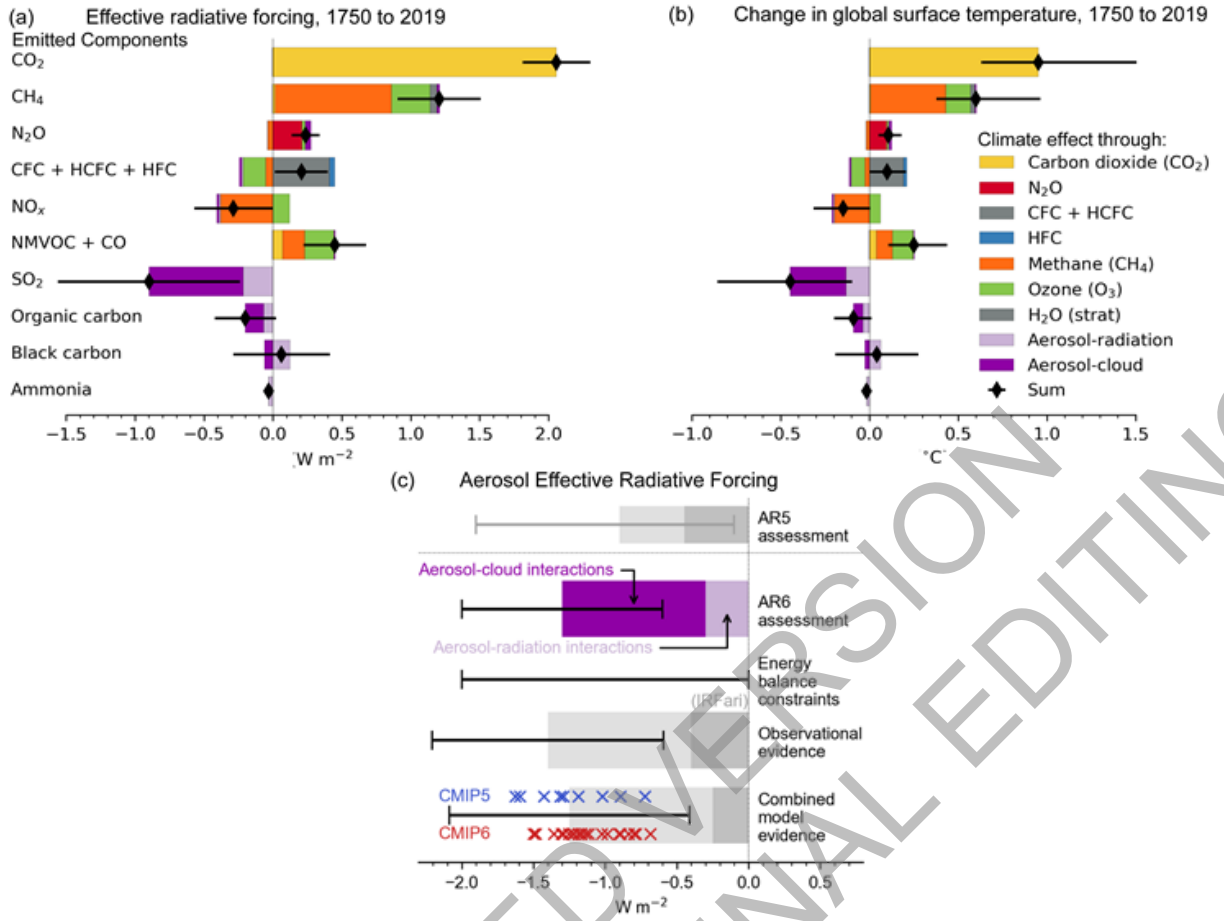
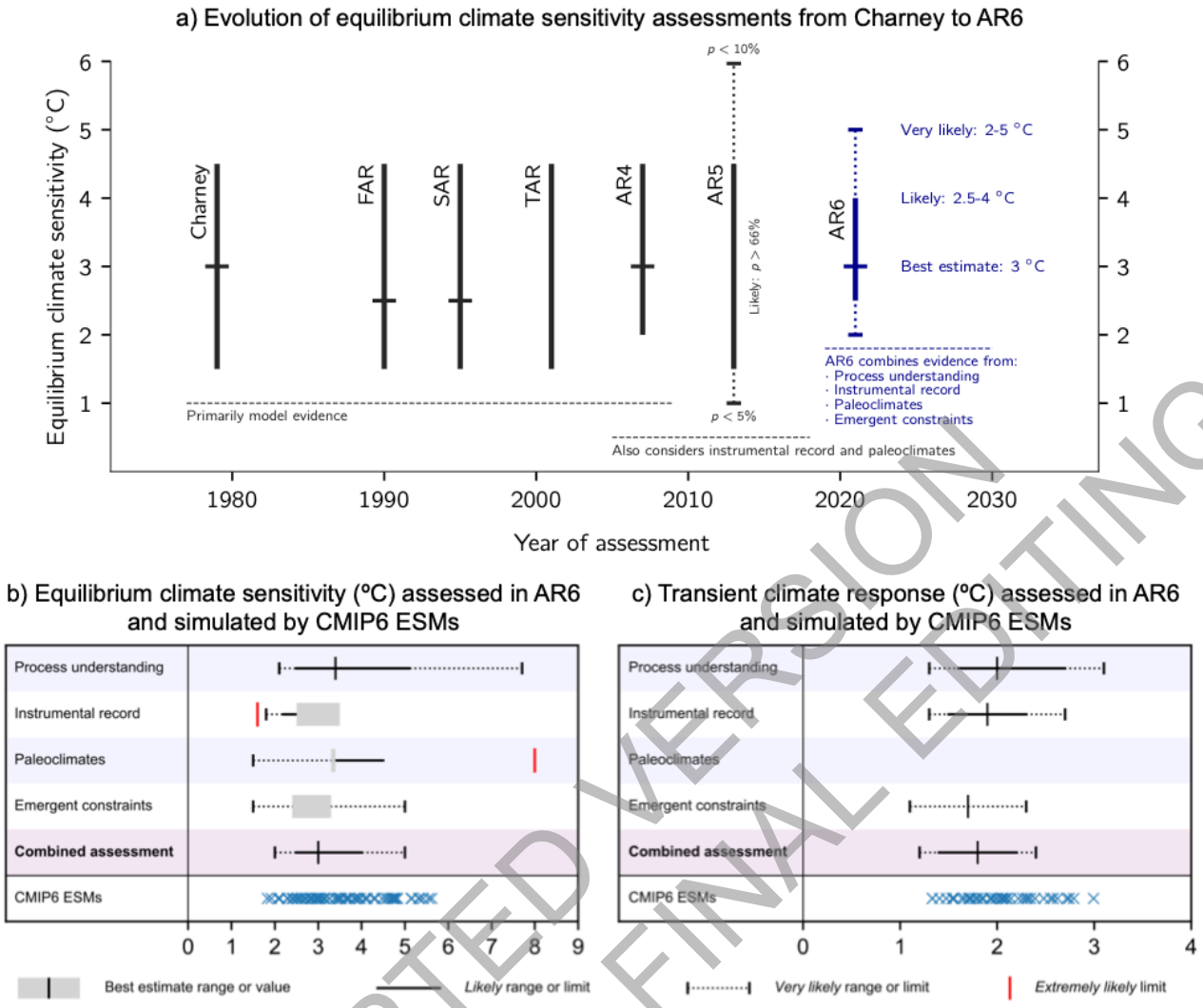


Figure TS.15: **Contribution to ERF and b) global surface temperature change from component emissions between 1750 to 2019 based on CMIP6 models and c) net aerosol effective radiative forcing (ERF) from different lines of evidence.** *The intent of the figure is to show advances since AR5 in the understanding of a) aerosol ERF from different lines of evidence as assessed in Chapter 7, b) emissions-based ERF and c) global surface temperature response for SLCFs as estimated in Chapter 6.* In panel a), ERFs for well-mixed greenhouse gases (WMGHGs) are from the analytical formulae. ERFs for other components are multi-model means based on ESM simulations that quantify the effect of individual components. The derived emission-based ERFs are rescaled to match the concentration-based ERFs in Figure 7.6. Error bars are 5-95% and for the ERF account for uncertainty in radiative efficiencies and multi-model error in the means. In panel b), the global mean temperature response is calculated from the ERF time series using an impulse response function. In panel c), the AR6 assessment is based on energy balance constraints, observational evidence from satellite retrievals, and climate model-based evidence. For each line of evidence the assessed best-estimate contributions from ERF due to ERFari and ERFaci are shown with darker and paler shading, respectively. Estimates from individual CMIP5 and CMIP6 models are depicted by blue and red crosses, respectively. The observational assessment for ERFari is taken from the instantaneous forcing due to aerosol-radiation interactions (IRFari). Uncertainty ranges are given in black bars for the total aerosol ERF and depict *very likely* ranges. {Sections 7.3.3, 6.4.2, Cross-Chapter Box 7.1, Figures 6.12, 7.5 ; Table 7.8}

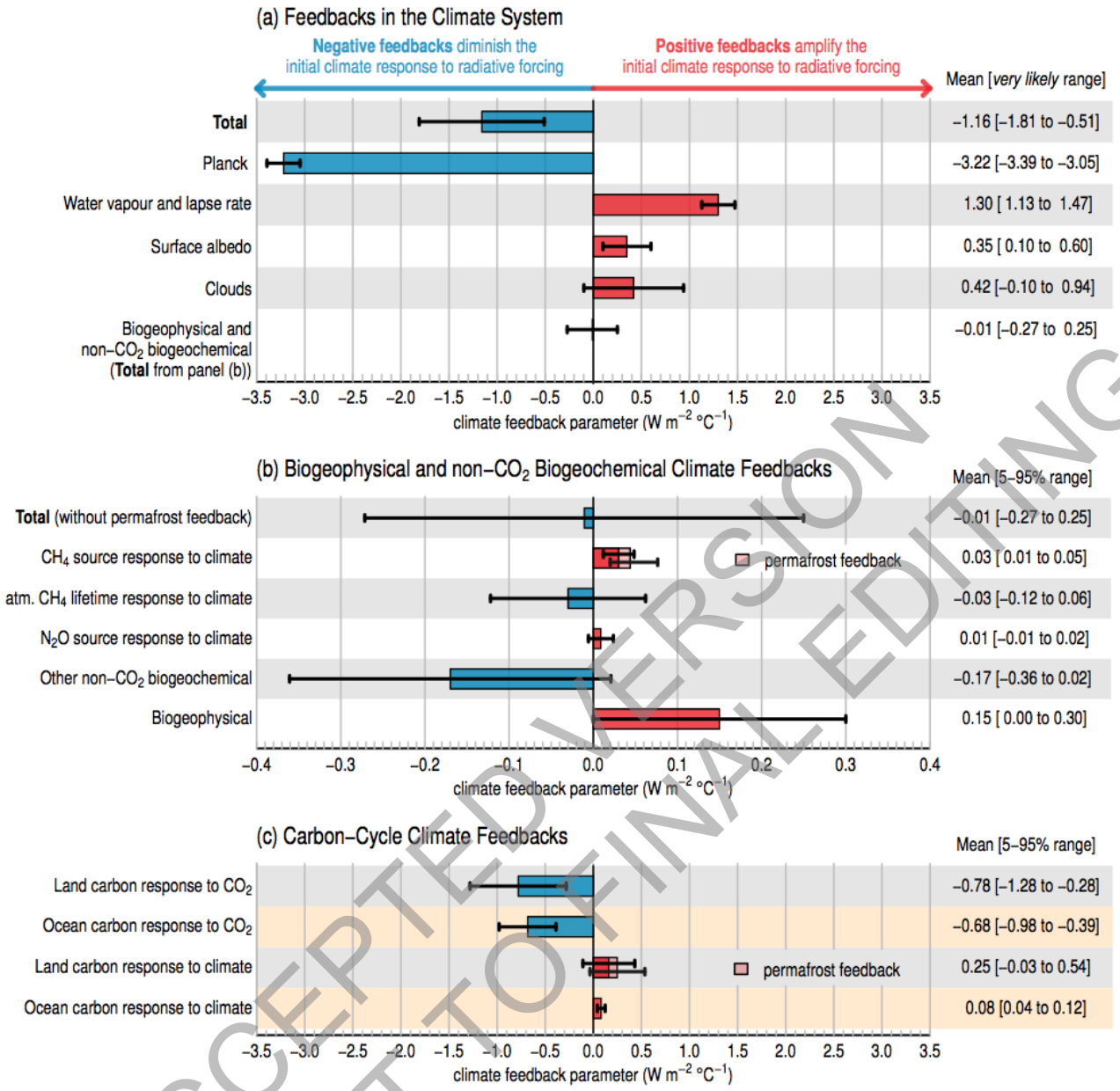
ACCEPTED VERSION SUBJECT TO FINAL EDITING



The intent is to show a) the progression in ECS including uncertainty and the lines of evidence used for assessment, b) and c) show the lines of assessment used to assess ECS and TCR in AR6.

Figure TS.16: **a) Evolution of equilibrium climate sensitivity (ECS) assessments from the Charney Report through a succession of IPCC Assessment Reports to AR6, and lines of evidence and combined assessment for (b) ECS and (c) transient climate response (TCR) in AR6.** In panel (a), the lines of evidence considered are listed below each assessment. Best estimates are marked by horizontal bars, likely ranges by vertical bars, and very likely ranges by dotted vertical bars. In panel (b) and (c), assessed ranges are taken from Tables 7.13 and 7.14 for ECS and TCR respectively. Note that for the ECS assessment based on both the instrumental record and paleoclimates, limits (i.e., one-sided distributions) are given, which have twice the probability of being outside the maximum/minimum value at a given end, compared to ranges (i.e., two tailed distributions) which are given for the other lines of evidence. For example, the *extremely likely* limit of greater than 95% probability corresponds to one side of the *very likely* (5% to 95%) range. Best estimates are given as either a single number or by a range represented by grey box. CMIP6 ESM values are not directly used as a line of evidence but are presented on the Figure for comparison. {Sections 1.5, 7.5; Tables 7.13, 7.14; Figures 7.18}

ACCEPTED VERSION SUBJECT TO FINAL EDITING

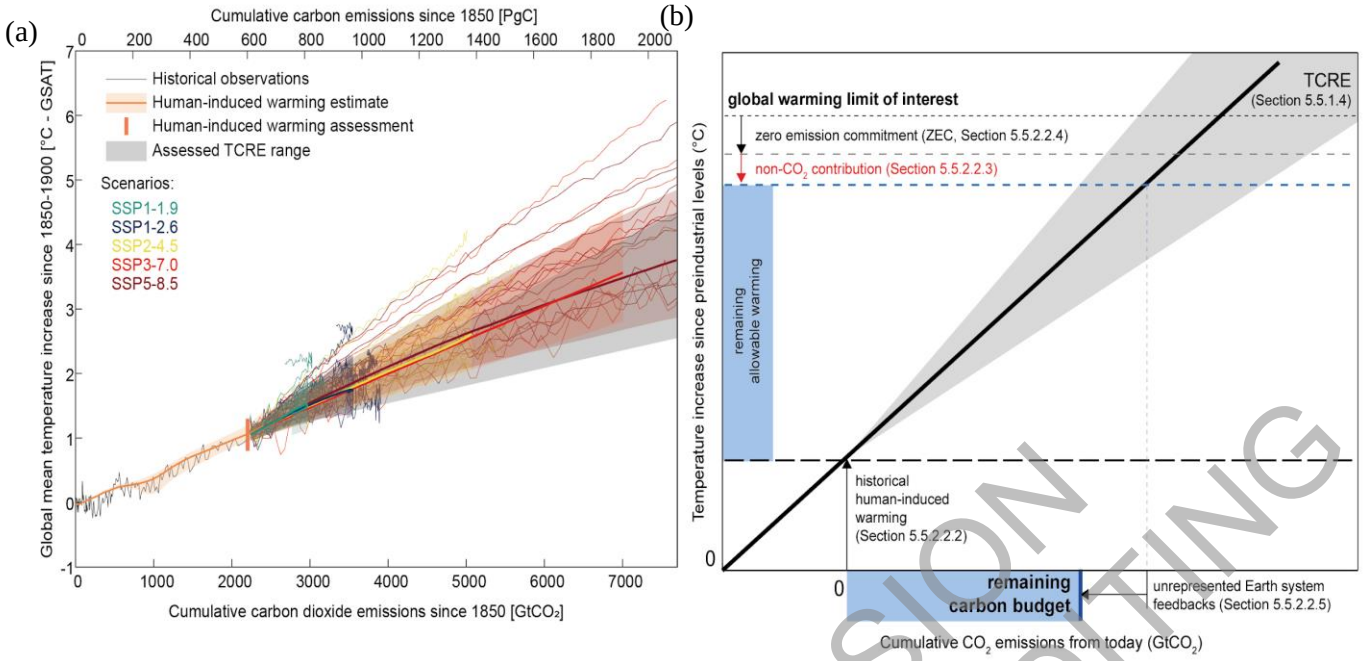


ACCEPTED VERSION SUBJECT TO FINAL EDITING

Figure TS.17: An overview of physical and biogeochemical feedbacks in the climate system. *The intent is to summarize assessed estimates of physical, biogeophysical and biogeochemical feedbacks on global temperature based on Chapters 5, 6 and 7.* (a) Synthesis of physical, biogeophysical and non-CO_2 biogeochemical feedbacks that are included in the definition of ECS assessed in this Technical Summary. These feedbacks have been assessed using multiple lines of evidence including observations, models and theory. The net feedback is the sum of the Planck response, water vapour and lapse rate, surface albedo, cloud, and biogeophysical and non-CO_2 biogeochemical feedbacks. Bars denote the mean feedback values and uncertainties represent *very likely* ranges; (b) Estimated values of individual biogeophysical and non-CO_2 biogeochemical feedbacks. The atmospheric methane lifetime and other non-CO_2 biogeochemical feedbacks have been calculated using global Earth System Model simulations from AerChemMIP, while the CH_4 and N_2O source responses to climate have been assessed for the year 2100 using a range of modelling approaches using simplified radiative forcing equations. The estimates represent the mean and 5-95% range. The level of confidence in these estimates is *low* owing to the large model spread. (c) carbon-cycle feedbacks as simulated by models participating in the C4MIP of CMIP6. An independent estimate of the additional positive carbon-cycle climate feedbacks from permafrost thaw, which is not considered in most C4MIP models, is added. The estimates represent the mean and 5-95% range. Note that these

feedbacks act through modifying the atmospheric concentration of CO_2 and thus are not included in the definition of ECS, which assumes a doubling of CO_2, but are included in the definition and assessed range of TCRE. {Sections Box 5.1, 5.4.7, 5.4.8, 6.4.5, 7.4.2, Figure 5.29, Tables 6.9, 7.10}

ACCEPTED VERSION
SUBJECT TO FINAL EDITING



The intent is to show the proportionality between cumulative CO_2 emissions and global surface air temperature in observations and models (left) as well as the assessed range of TCRE and the right-hand panel shows how information is combined to derive remaining carbon budgets consistent with limiting warming to a specific level.

Figure TS.18: Illustration of (a) relationship between cumulative emissions of CO_2 and global mean surface air temperature increase and (b) the assessment of the remaining carbon budget from its constituting components based on multiple lines of evidence. Carbon budgets consistent with various levels of additional warming are provided in Table 5.8 and should not be read from the illustrations in either panel. In panel (a) thin black line shows historical CO_2 emissions together with the assessed global surface temperature increase from 1850-1900 as assessed in Chapter 2 (Box 2.3). The orange-brown range with its central line shows the estimated human-induced share of historical warming. The vertical orange-brown line shows the assessed range of historical human-induced warming for the 2010–2019 period relative to 1850-1900 (Chapter 3). The grey cone shows the assessed *likely* range for the transient climate response to cumulative emissions of carbon dioxide (TCRE) (Section 5.5.1.4), starting from 2015. Thin coloured lines show CMIP6 simulations for the five scenarios of the WG1 core set (SSP1-1.9, green; SSP1-2.6, blue; SSP2-4.5, yellow; SSP3-7.0, red; SSP5-8.5, maroon), starting from 2015 and until 2100. Diagnosed carbon emissions are complemented with estimated land-use change emissions for each respective scenario. Coloured areas show the Chapter 4 assessed *very likely* range of global surface temperature projections and thick coloured central lines the median estimate, for each respective scenario, relative to the original scenario emissions. For panel (b), the remaining allowable warming is estimated by combining the global warming limit of interest with the assessed historical human induced warming (Section 5.5.2.2.2), the assessed future potential non-CO2 warming contribution (Section 5.5.2.2.3) and the ZEC (Section 5.5.2.2.4). The remaining allowable warming (vertical blue bar) is subsequently combined with the assessed TCRE (Section 5.5.1.4 and 5.5.2.2.1) and contribution of unrepresented Earth system feedbacks (Section 5.5.2.2.5) to provide an assessed estimate of the remaining carbon budget (horizontal blue bar, Table 5.8). Note that contributions in panel (b) are illustrative and are not to scale. For example, the central ZEC estimate was assessed to be zero. {Box 2.3; Sections 5.2.1, 5.2.2; Figure 5.31}

ACCEPTED VERSION SUBJECT TO FINAL EDITING

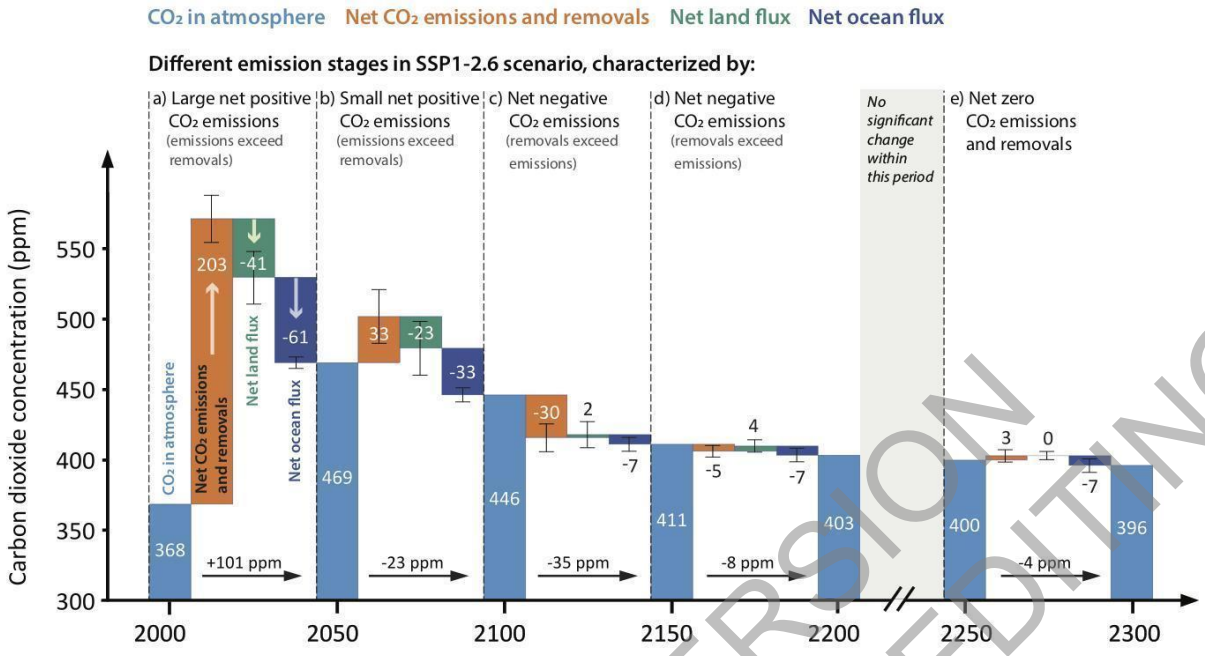


Figure TS.19: **Carbon sink response in a scenario with net CO_2 removal from the atmosphere. .** *The intent of this figure is to show how atmospheric CO_2 evolves under negative emissions and its dependence on the negative emissions technologies. It also shows the evolution of the ocean and land sinks.* Shown are CO_2 flux components from concentration-driven Earth system model simulations during different emission stages of SSP1–2.6 and its long-term extension. (a) Large net positive CO_2 emissions, (b) small net positive CO_2 emissions, (c) – (d) net negative CO_2 emissions, (e) net zero CO_2 emissions. Positive flux components act to raise the atmospheric CO_2 concentration, whereas negative components act to lower the CO_2 concentration. Net CO_2 emissions, land and ocean CO_2 fluxes represent the multi-model mean and standard deviation (error bar) of four ESMs (CanESM5, UKESM1, CESM2-WACCM, IPSL-CM6a-LR) and one EMIC (UVic ESCM). Net CO_2 emissions are calculated from concentration-driven Earth system model simulations as the residual from the rate of increase in atmospheric CO_2 and land and ocean CO_2 fluxes. Fluxes are accumulated over each 50-year period and converted to concentration units (ppm). {5.6.2.1, Figure 5.33}

ACCEPTED VERSION SUBJECT TO FINAL EDITING

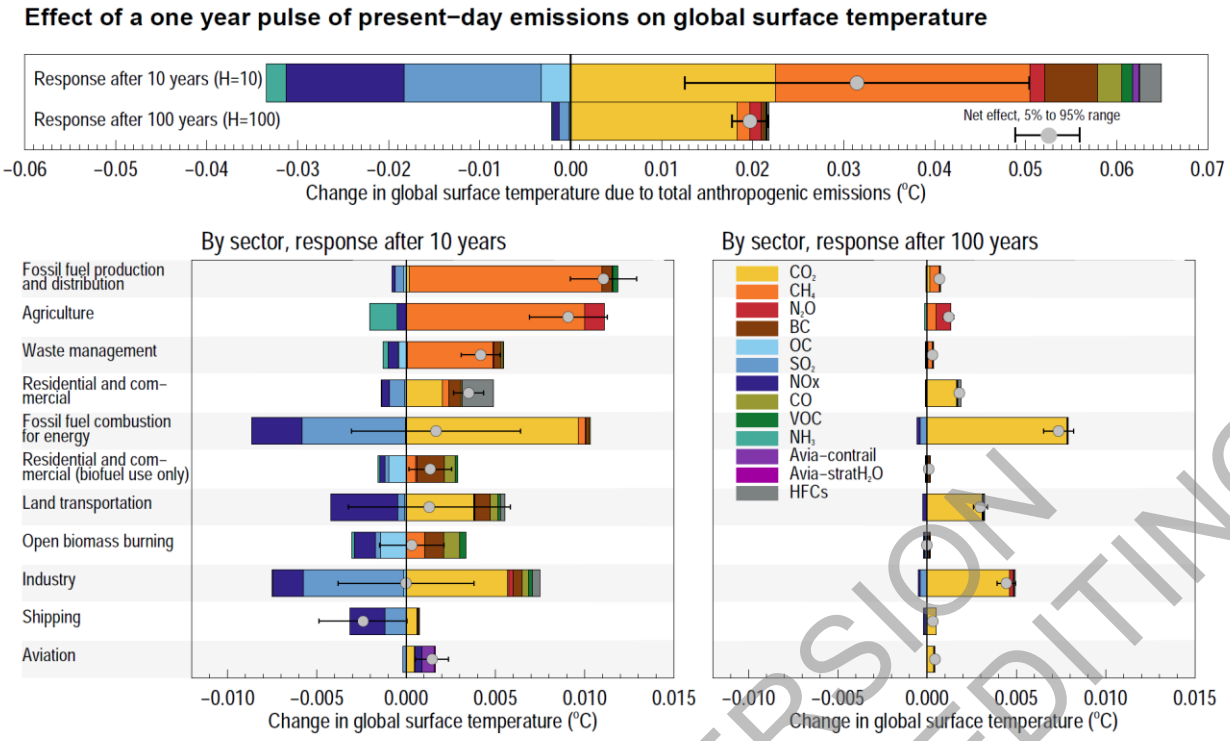
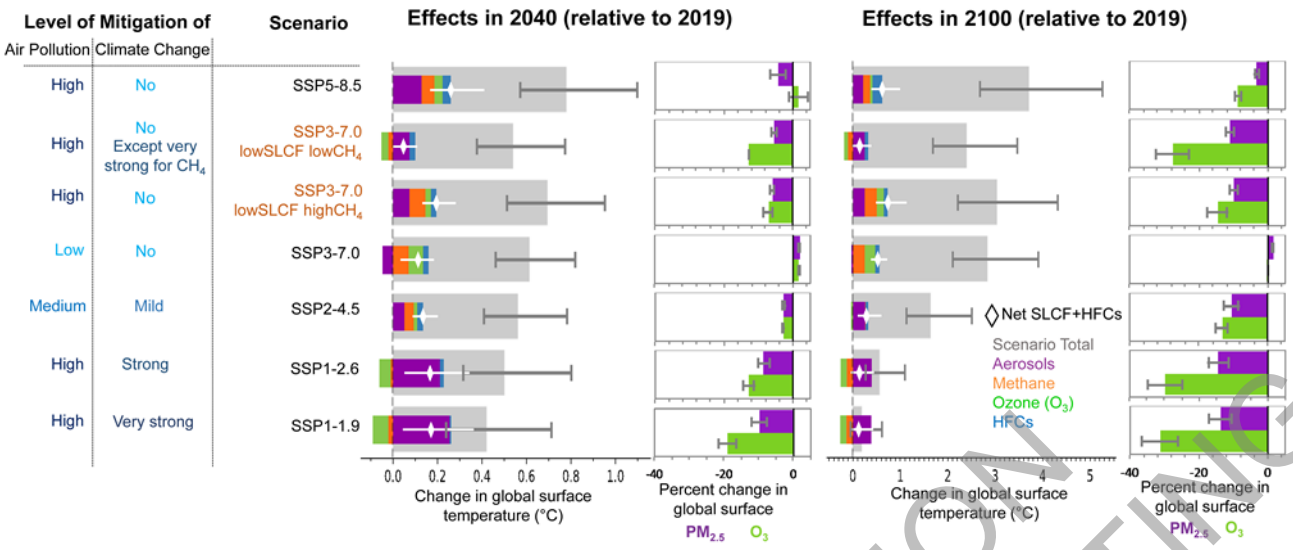


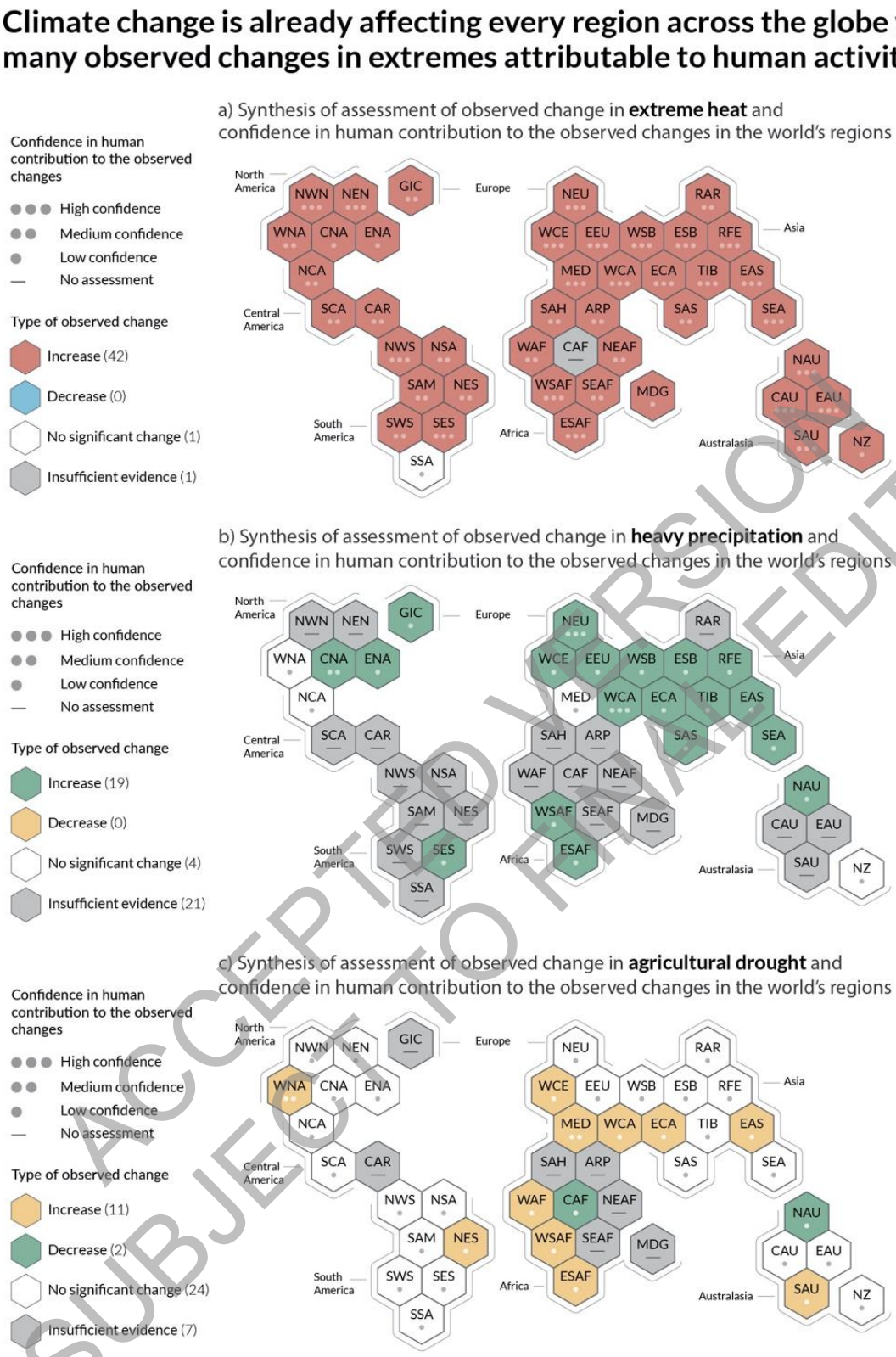
Figure TS.20: **Global surface temperature change 10 and 100 years after a one year pulse of present-day emissions**. *This figure shows the sectoral contribution to present-day climate change by specific climate forcers including CO_2 as well as SLCFs.* The temperature response is broken down by individual species and shown for total anthropogenic emissions (top), and sectoral emissions on 10-year (left) and 100-year time scales (right). Sectors are sorted by (high-to-low) net temperature effect on the 10-year time scale. Error bars in the top panel show the 5-95% range in net temperature effect due to uncertainty in radiative forcing only (calculated using a Monte Carlo approach and best estimate uncertainties from the literature). Emissions for 2014 are from the CMIP6 emissions dataset, except for HFCs and aviation H_2O which rely on other datasets (see Section 6.6.2 for more details). CO_2 emissions are excluded from open biomass burning and residential biofuel use. {6.6.2, Figure 6.16}

ACCEPTED VERSION SUBJECT TO FINAL EDITING



Box TS.7, Figure 1: Effects of short-lived climate forcers (SLCFs) on global surface temperature and air pollution across the WG1 core set of Shared Socio-Economic Pathways (SSPs). *The intent of this figure is to show the climate and air quality (surface ozone and $PM_{2.5}$) response to SLCFs in the SSP scenarios for near and long-term.* Effects of net aerosols, tropospheric ozone, hydrofluorocarbons (HFCs) (with lifetimes less than 50 years), and methane are compared with those of total anthropogenic forcing for 2040 and 2100 relative to year 2019. The global surface temperature changes are based on historical and future evolution of Effective Radiative Forcing (ERF) as assessed in chapter 7 of this report. The temperature responses to the ERFs are calculated with a common impulse response function (R_T) for the climate response, consistent with the metric calculations in Chapter 7 (Box 7.1). The R_T has an equilibrium climate sensitivity of 3.0°C for a doubling of atmospheric CO_2 concentration (feedback parameter of -1.31 W m^{-2} $°C^{-1}$). The scenario total (grey bar) includes all anthropogenic forcings (long- and short-lived climate forcers, and land use changes). Uncertainties are 5-95% ranges. The global changes in air pollutant concentrations (ozone and $PM_{2.5}$) are based on multimodel CMIP6 simulations and represent changes in 5-year mean surface continental concentrations for 2040 and 2098 relative to 2019. Uncertainty bars represent inter-model ±1 standard deviation. {6.7.2, 6.7.3, Figure 6.24}

ACCEPTED VERSION SUBJECT TO FINAL EDITING

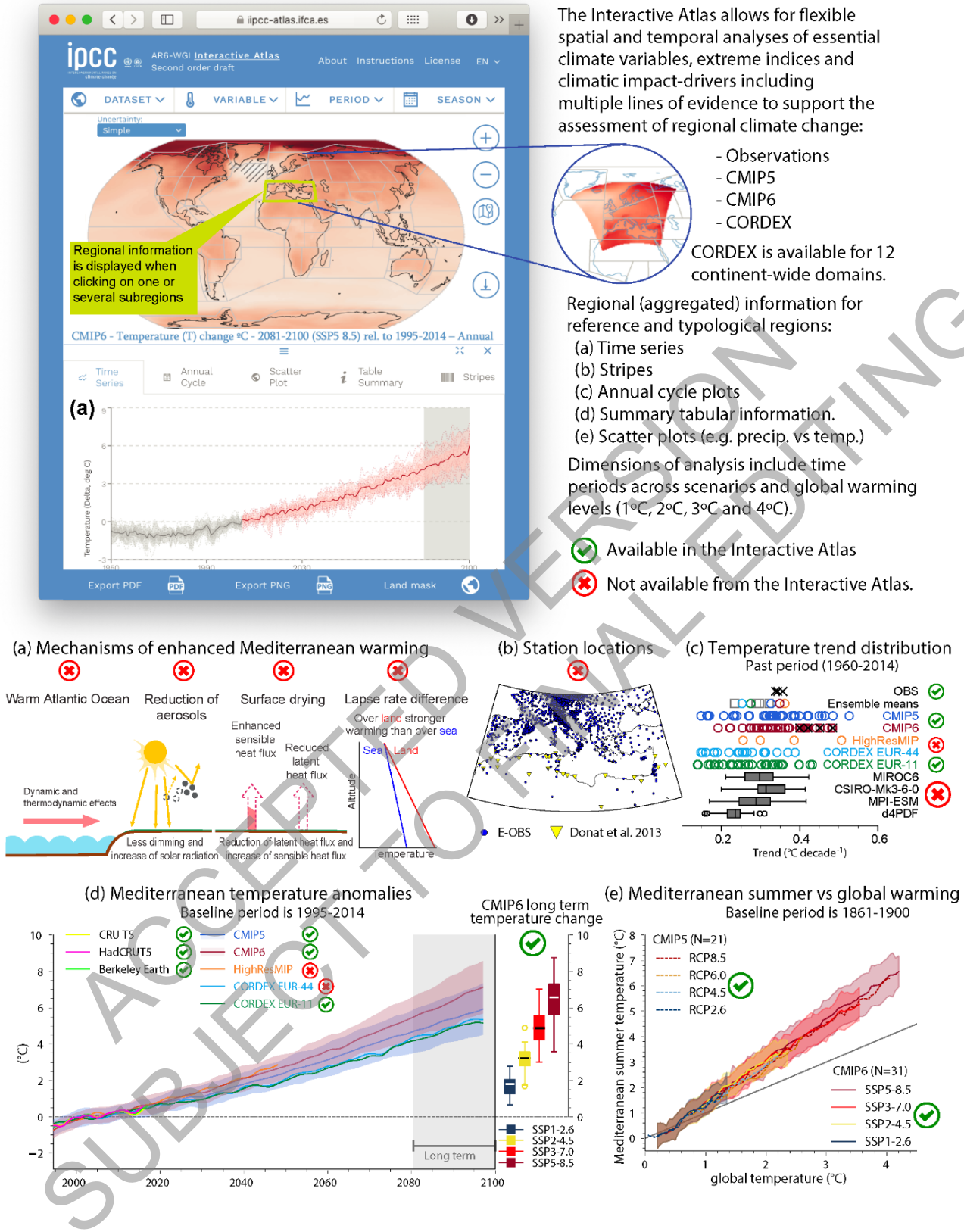


ACCEPTED VERSION SUBJECT TO FINAL EDITING

Box TS.10, Figure 1: Synthesis of assessed observed changes and human influence of hot extremes (panel a), heavy precipitation (panel b) and agricultural and ecological drought (panel c) for the IPCC AR6 regions (displayed as hexagons). The colours in each panel represent the four outcomes of the assessment on the observed changes: In Panel a): red – at least *medium confidence* in an observed increase in hot extremes; blue – at least *medium confidence* in an observed decrease in hot extremes; white – no significant change in hot extremes is observed for

the region as a whole; grey – the evidence in this region is insufficient (because of a lack of data and/or literature) to make an assessment for the region as a whole. In panel b): green – at least *medium confidence* in an observed increase in heavy rainfall; yellow - at least *medium confidence* in an observed decrease in heavy rainfall; white – no significant change in heavy rainfall is observed for the region as a whole; grey – the evidence in this region is insufficient (because of a lack of data and/or literature) to make an assessment for the region as a whole. In panel c): yellow – at least *medium confidence* in an observed increase in agricultural and ecological drought; green - at least *medium confidence* in an observed decrease in agricultural and ecological drought; white – no significant change in agricultural and ecological drought is observed for the region as a whole; grey – the evidence in this region is insufficient (because of a lack of data and/or literature) to make an assessment for the region as a whole. Each panel represents in addition the synthesis of assessment of the human influence on the observed changes based on available trend detection and attribution and event attribution scientific publications. The level of confidence is indicated by a number of dots: *high confidence* (three dots), *medium confidence* (two dots), *low confidence* (one dot), and when no assessment is possible, due to insufficient evidence for the specific region (horizontal bar). For hot extremes, the evidence is mostly drawn from changes in metrics based on daily maximum temperatures, regional studies using other metrics (heatwave duration, frequency and intensity) are used in addition {11.9.2}. For heavy precipitation, the evidence is mostly drawn from changes in metrics based on one-day or five-day precipitation amounts using global and regional studies {11.9.3}. Agricultural and ecological droughts are assessed based on observed and projected changes in total column soil moisture, complemented by evidence on changes in surface soil moisture, water-balance (precipitation minus evapotranspiration) and metrics driven by precipitation and atmospheric evaporative demand. {11.9.3} All assessments are made for each AR6 region as a whole and for the timeframe from 1950 to present thus, more local or assessment made on shorter time scales might differ from what is shown in the figure. {11.9, Table TS.5}.

ACCEPTED VERSION SUBJECT TO FINAL EDITING



ACCEPTED VERSION SUBJECT TO FINAL EDITING

Box TS.12, Figure 1: Example of generating regional climate information from multiple lines of evidence for the case of Mediterranean summer warming, with indication of the information available from the Interactive Atlas. (a) Mechanisms and feedbacks involved in enhanced Mediterranean summer warming. (b) Locations of observing stations from different datasets. (c) Distribution of 1960–2014 summer temperature trends (°C per decade) for observations (black crosses), CMIP5 (blue circles), CMIP6 (red circles), HighResMIP (orange circles), CORDEX EUR-44 (light blue

circles), CORDEX EUR-11 (green circles), and selected single Model Initial-condition Large Ensembles - SMILEs (grey boxplots, MIROC6, CSIRO-Mk3-6-0, MPI-ESM and d4PDF). (d) Time series of area averaged (25°N–50°N, 10°W–40°E) land point summer temperature anomalies (°C, baseline period is 1995–2014): the boxplot shows long term (2081–2100) temperature changes of different CMIP6 scenarios in respect to the baseline period. (e) Projected Mediterranean summer warming in comparison to global annual mean warming of CMIP5 (RCP2.6, RCP4.5, RCP6.0 and RCP8.5) and CMIP6 (SSP1-2.6, SSP2-4.5, SSP3-7.0 and SSP5-8.5) ensemble means (lines) and spread (shading). {Figure 10.20, Figure 10.21, Figure Atlas.8}

ACCEPTED VERSION
SUBJECT TO FINAL EDITING

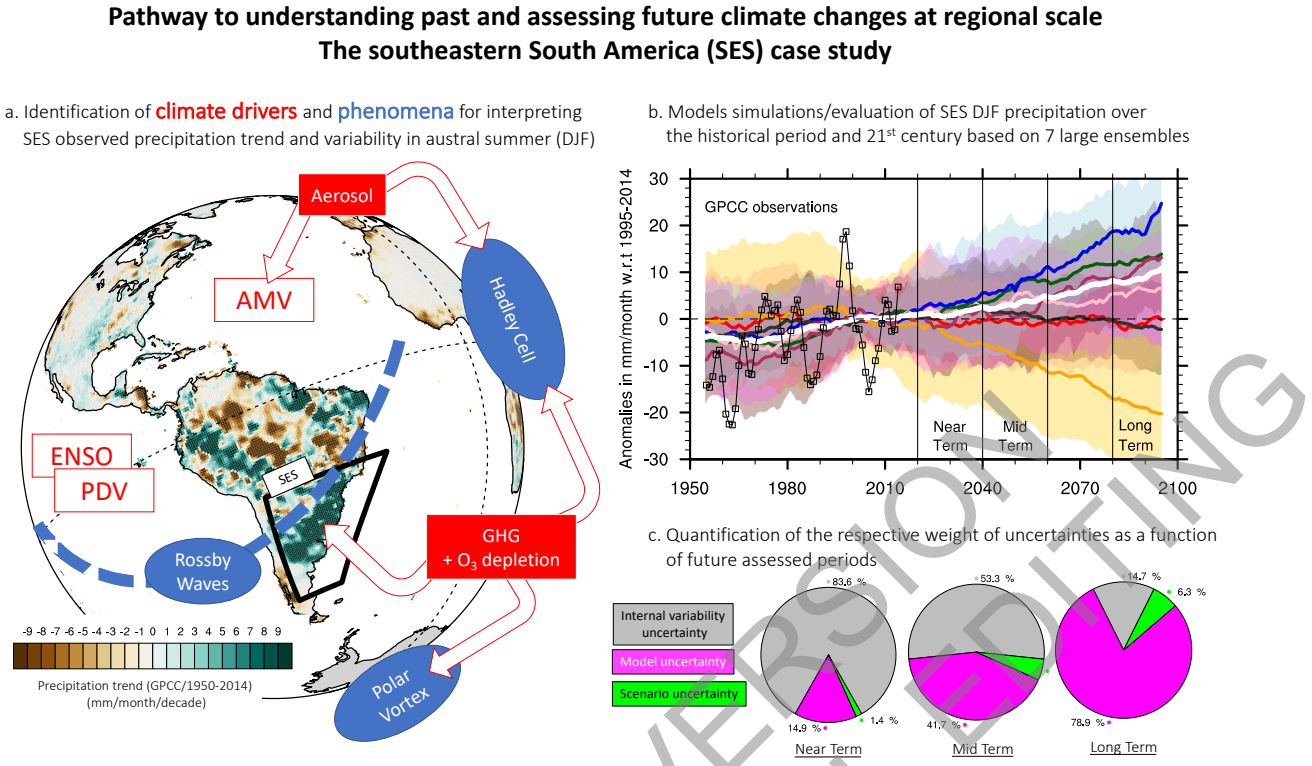
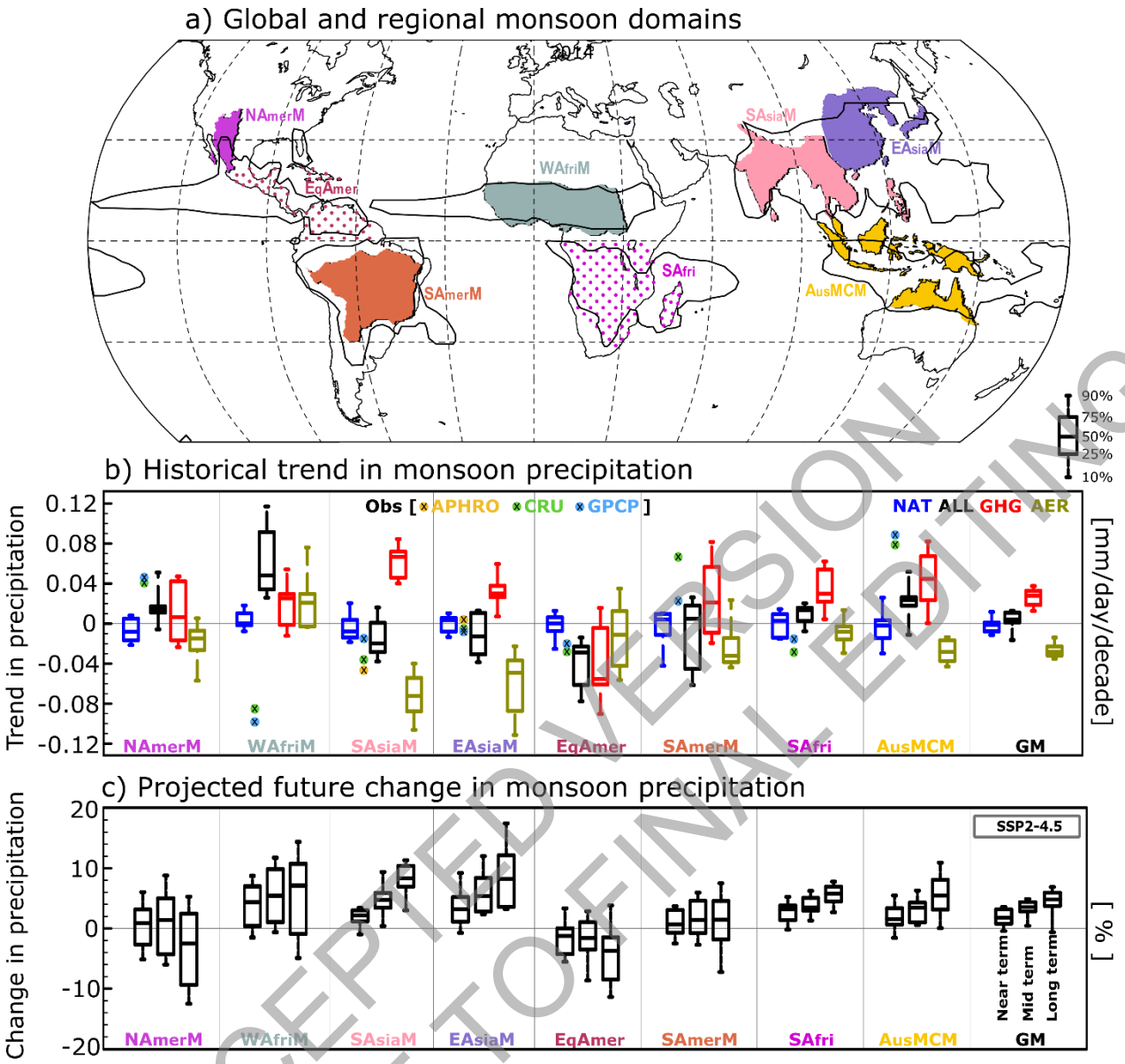


Figure TS.21: **Example of the interplay between drivers of climate variability and change at regional scale to understand past and projected changes.** *The figure intent is to show an illustrative pathway for understanding past, and anticipating future, climate change at regional scale in the presence of uncertainties.* (a) Identification of the climate drivers and their influences on climate phenomena contributing through teleconnection to Southeastern South America summer (DJF) precipitation variability and trends observed over 1950–2014. Drivers (red squares) include MoVs as well as external forcing. Observed precipitation linear trend from GPCC is shown on continents (green-brown colour bar in mm month^{-1} per decade) and the SES AR6 WGI reference region is outlined with the thick black contour. Climate phenomena leading to local impact on SES are schematically presented (blue ovals). (b) Time series of decadal precipitation anomalies for DJF SES simulated from seven large ensembles of historical + RCP8.5 simulations over 1950–2100. Shading corresponds to the 5th–95th range of climate outcomes given from each large ensemble for precipitation (in mm/month) and thick coloured lines stand for their respective ensemble mean. The thick timeseries in white corresponds to the multi-model multi-member ensemble mean with model contribution being weighted according to their ensemble size. GPCC observation is shown in the light black line with squares over 1950–2014 and the 1995–2014 baseline period has been retained for calculation of anomalies in all datasets. (c) Quantification of the respective weight (in percent) between the individual sources of uncertainties (internal in gray, model in magenta and scenario in green) at near-term, mid-term and long-term temporal windows defined in AR6 and highlighted in (b) for SES DJF precipitation. All computations are done with respect to 1995–2014, taken as the reference period and the scenario uncertainty is estimated from CMIP5 using the same set of models as for the large ensembles that have run different RCP scenarios. {Figure 10.12a}

ACCEPTED VERSION SUBJECT TO FINAL EDITING



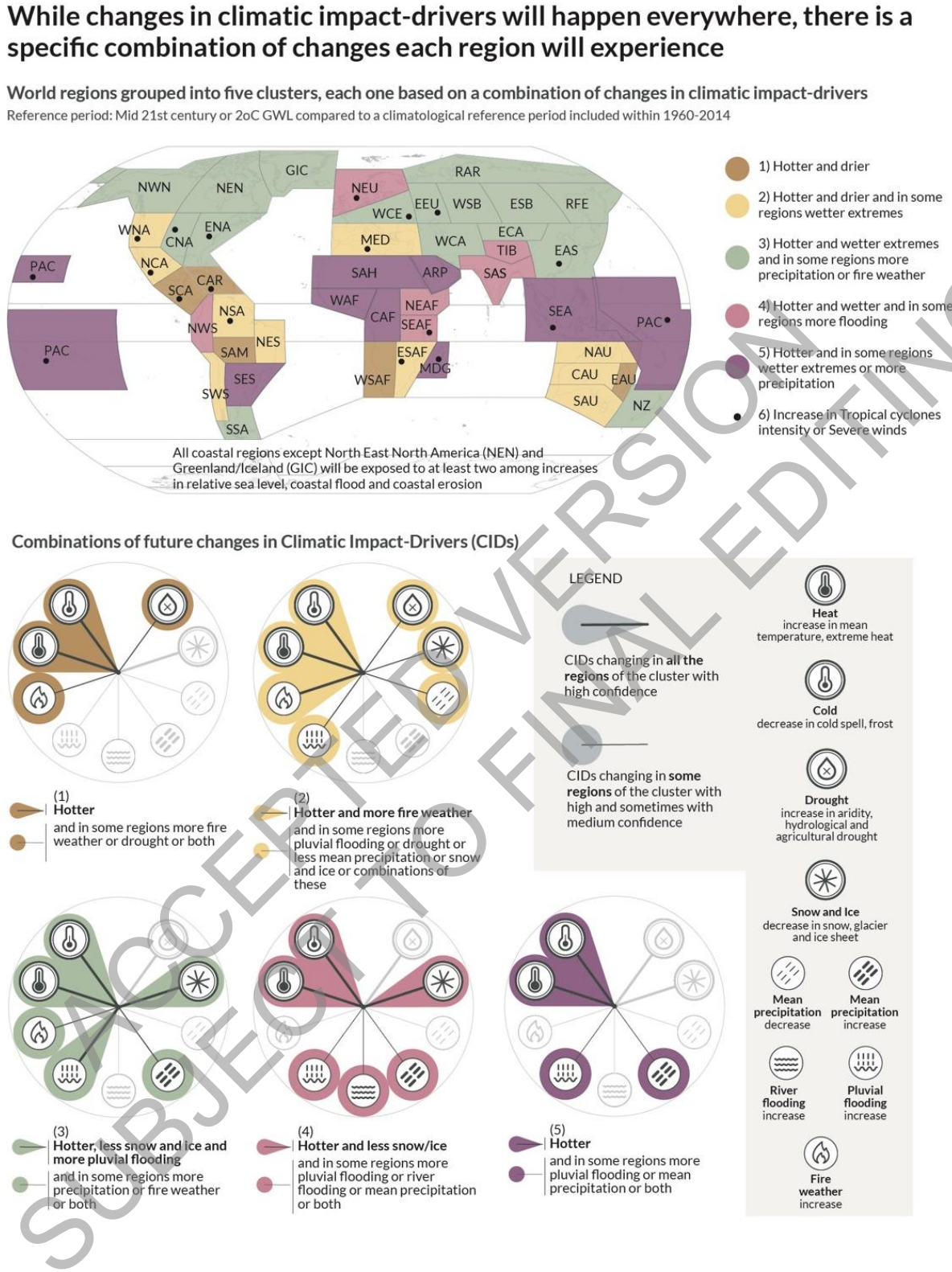
Box TS.13, Figure 1: Global and regional monsoons: past trends and projected changes: *The intent of this figure is to show changes in precipitation over regional monsoon domains in terms of observed past trends and related attribution, and in terms of future projections in one intermediate emission scenario in the near, medium and long terms.* (a) Global (black contour) and regional monsoons (color shaded) domains. The global monsoon (*GM*) is defined as the area with local summer-minus-winter precipitation rate exceeding 2.5 mm day^{-1} (see Annex V). The regional monsoon domains are defined based on published literature and expert judgement (see Annex V), and also accounting for the fact that the climatological summer monsoon rainy season varies across the individual regions. Assessed regional monsoons are South and Southeast Asia (*SAsiaM, Jun-Jul-Aug-Sep*), East Asia (*EAsiaM, Jun-Jul-Aug*), West Africa (*WAfriM, Jun-Jul-Aug-Sep*), North America (*NAmerM, Jul-Aug-Sep*), South America (*SAmerM, Dec-Jan-Feb*), Australia and Maritime Continent Monsoon (*AusMCM, Dec-Jan-Feb*). Equatorial South America (*EqSAmer*) and South Africa (*SAfri*) regions are also shown, as they receive unimodal summer seasonal rainfall although their qualification as monsoons is subject to discussion. (b) Global and regional monsoons precipitation trends based on DAMIP CMIP6 simulations with both natural and anthropogenic (ALL), GHG only (GHG), aerosols only (AER) and natural only (NAT) radiative forcing. Weighted ensemble means are based on nine CMIP6 models contributing to the MIP (with at least 3 members). Observed trends computed from CRU GPCP, and APHRO (only for *SAsiaM* and *EAsiaM*) datasets are shown as well. (c) Percentage change in projected seasonal mean precipitation over global and regional monsoons domain in the near-term (2021–2040),

ACCEPTED VERSION SUBJECT TO FINAL EDITING

mid-term (2041–2060), and long-term (2081–2100) under SSP2-4.5 based on 24 CMIP6 models. {Figure 8.11, Figure 8.22}

ACCEPTED VERSION
SUBJECT TO FINAL EDITING

a)



ACCEPTED VERSION SUBJECT TO FINAL EDITING

b)

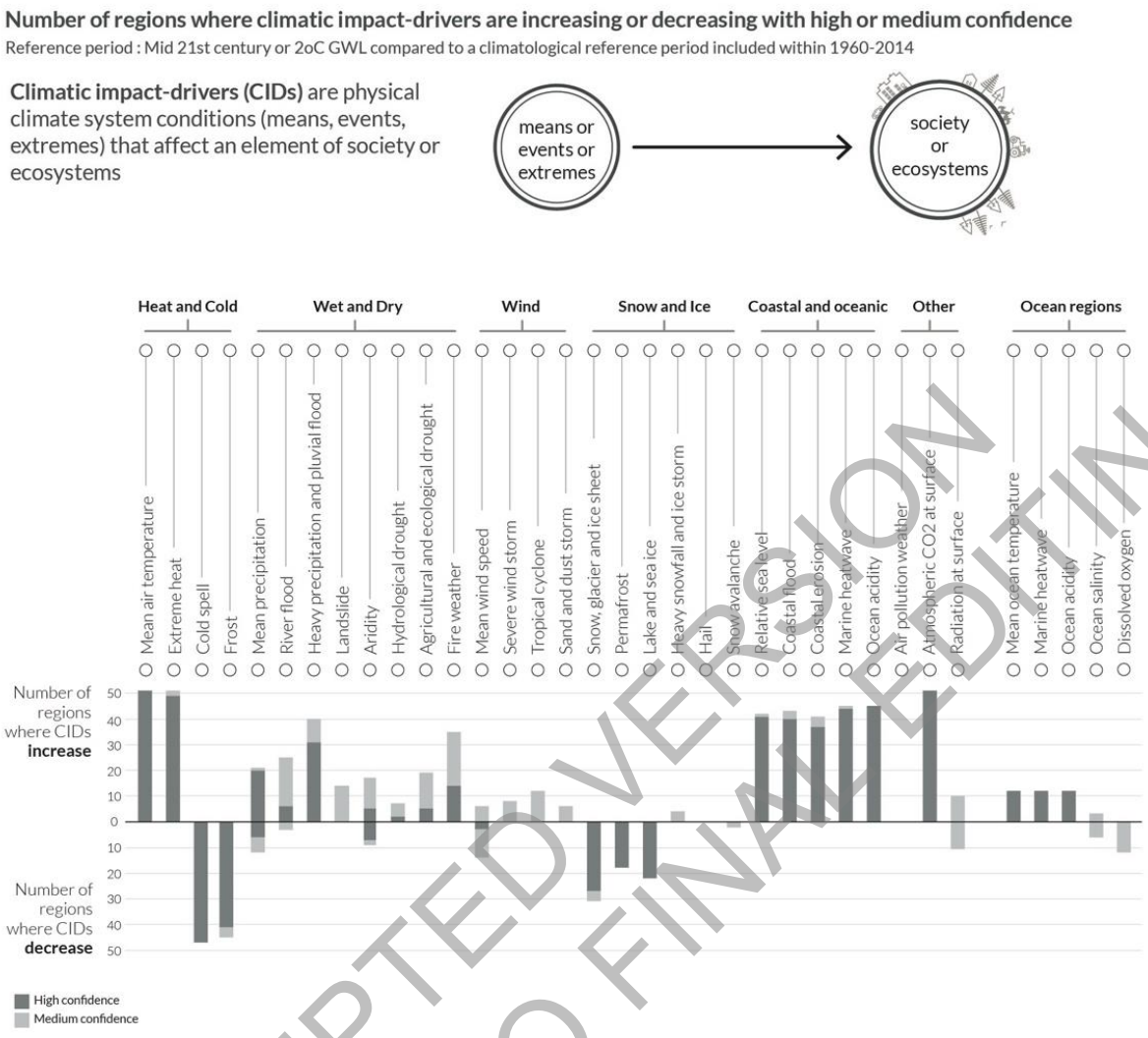
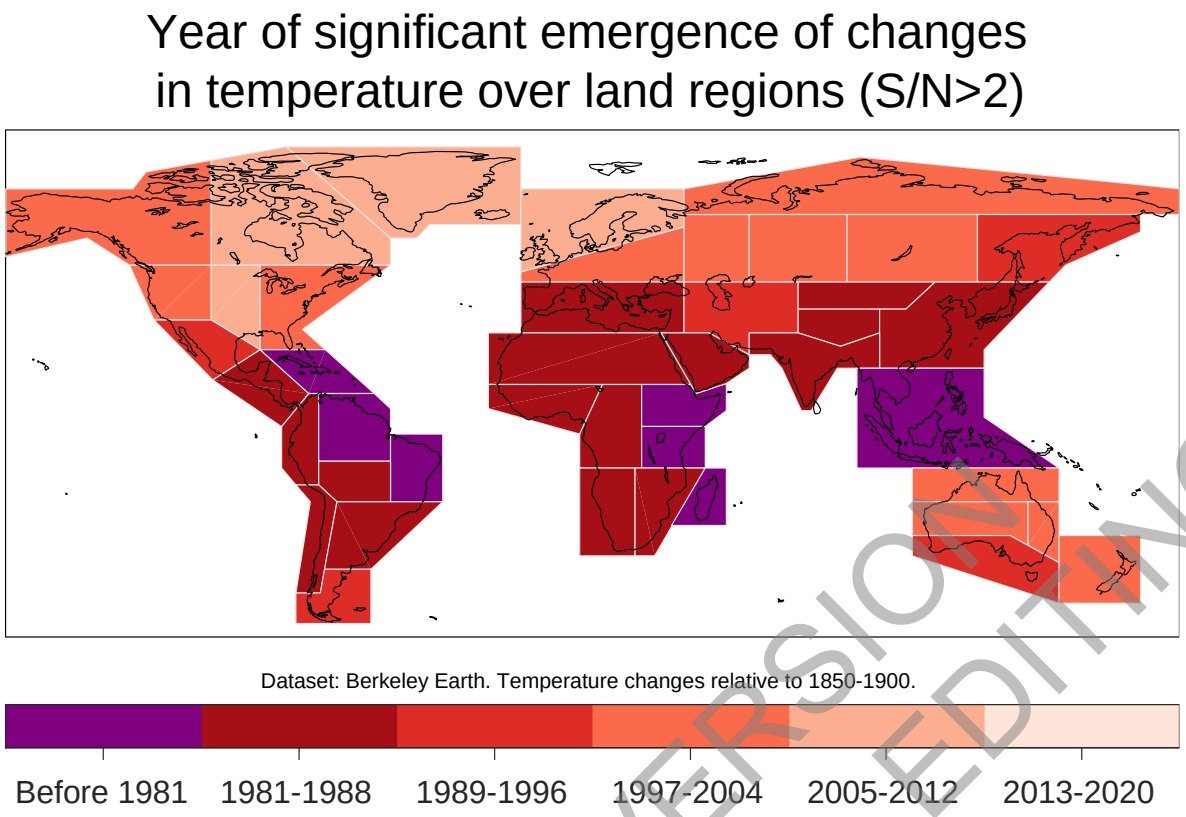
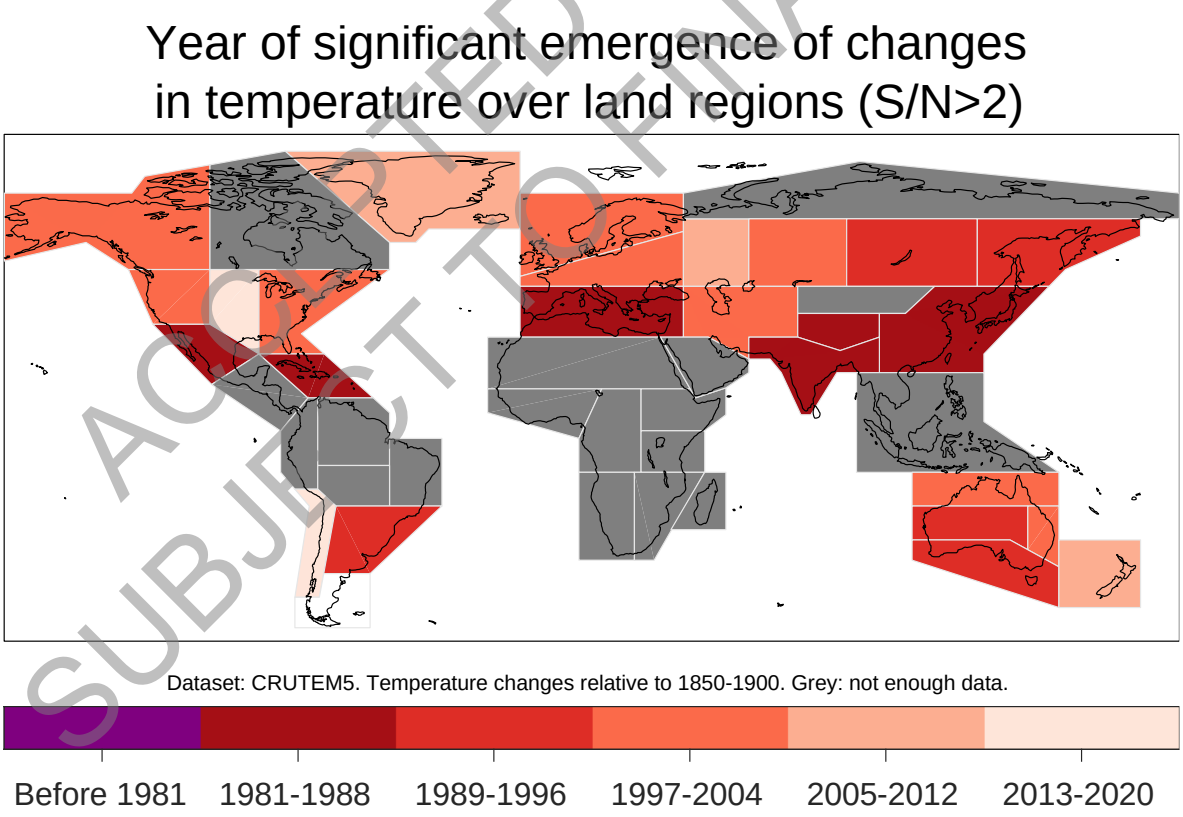


Figure TS.22: (Panel a): shows the geographical location of regions belonging to one of five groups characterized by a specific combination of changing climatic impact-drivers (CIDs). The five groups are represented by the five different colours, and the CID combinations associated with each group are represented in the corresponding 'fingerprint' and text below the map. Each fingerprint comprises a set of CIDs projected to change with high confidence in every region in the group, and a second set of CIDs, one or more of which are projected to change in each region with high or medium confidence. The CID combinations follow a progression from those becoming hotter and drier (group 1) to those becoming hotter and wetter (group 5). In between (groups 2–-4), the CIDs that change include some becoming drier and some wetter and always include a set of CIDs which are getting hotter. Tropical cyclones and severe wind CID changes are represented on the map with black dots in the regions affected. Regions affected by coastal CID changes are described by text on the map. The five groups are chosen to provide a reasonable level of detail for each region-specific detail whilst not overwhelming the map with a full summary all aspects of the assessment, which is available in Table TS.5. [Placeholder: This summary is also represented visually in the Interactive Atlas.] The CID changes summarized in the figure represent high and medium confidence changes projected if a level of 2°C of global warming is attained around 2050. The bar chart in panel b) shows the numbers of regions where each CID is increasing or decreasing with medium or high confidence for all land regions reported in the map of panel a) and for the ocean regions. The regions coloured in the map comprise the WG I AR6 reference regions, which include inhabited land areas and an additional non-continuous Pacific Islands region labelled PAC. Definitions of the acronyms of the other regions are provided in Atlas.1 and the Interactive Atlas. {Table TS.5, Figure TS.24}

ACCEPTED VERSION SUBJECT TO FINAL EDITING





ACCEPTED VERSION
SUBJECT TO FINAL EDITING

Figure TS.23: Time period during which the signals of temperature change in observed data aggregated over the reference regions emerged from the noise of annual variability in the respective aggregated data, using a signal-to-noise ratio of 2 as the threshold for emergence. Emergence time is

calculated for two global datasets (a) Berkeley Earth observations and (b) HadCRUT5 observations. Regions in the HadCRUT5 map are shaded grey when data are available over less than 50% of the area of the region. {Figure Atlas.11, TS.1.2.4}

ACCEPTED VERSION
SUBJECT TO FINAL EDITING

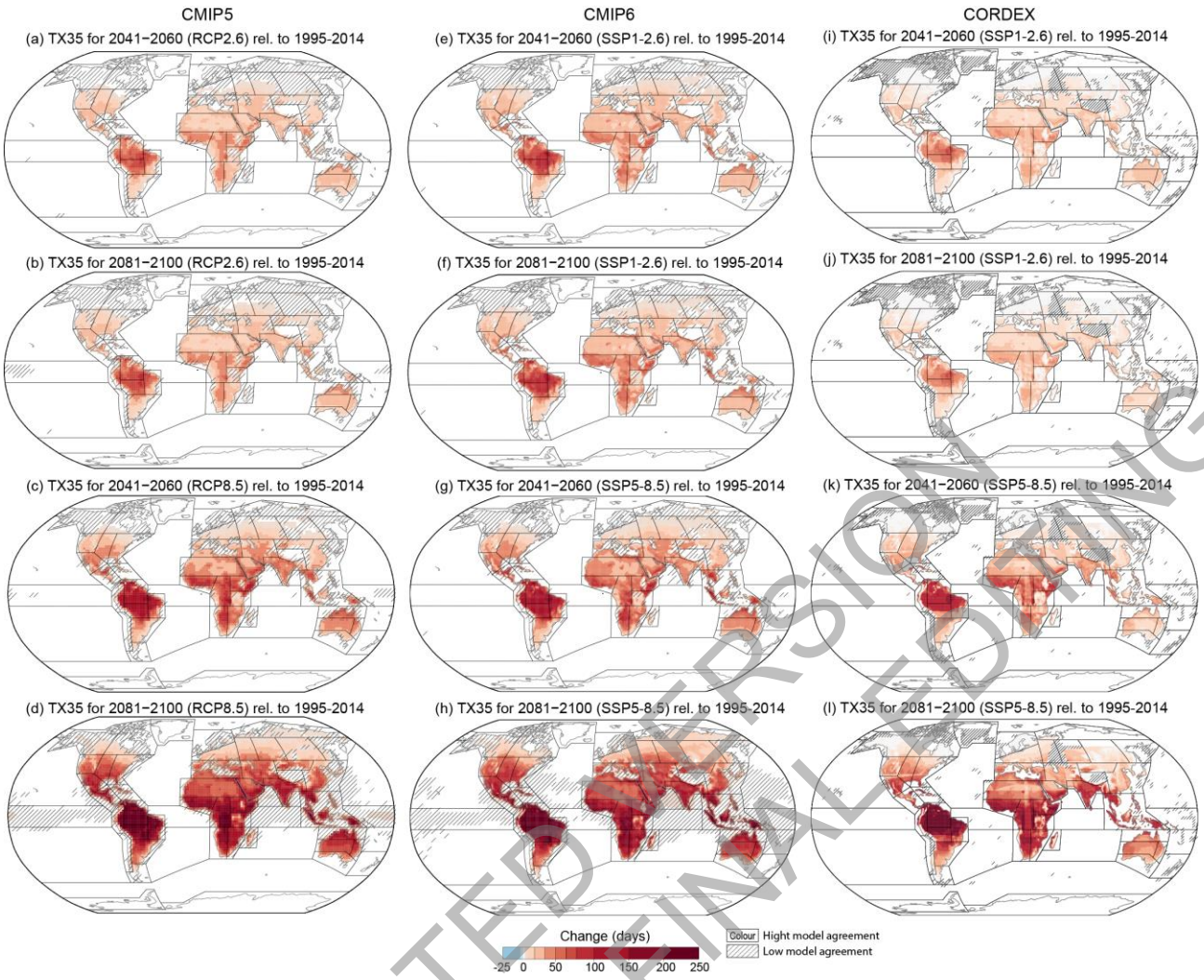
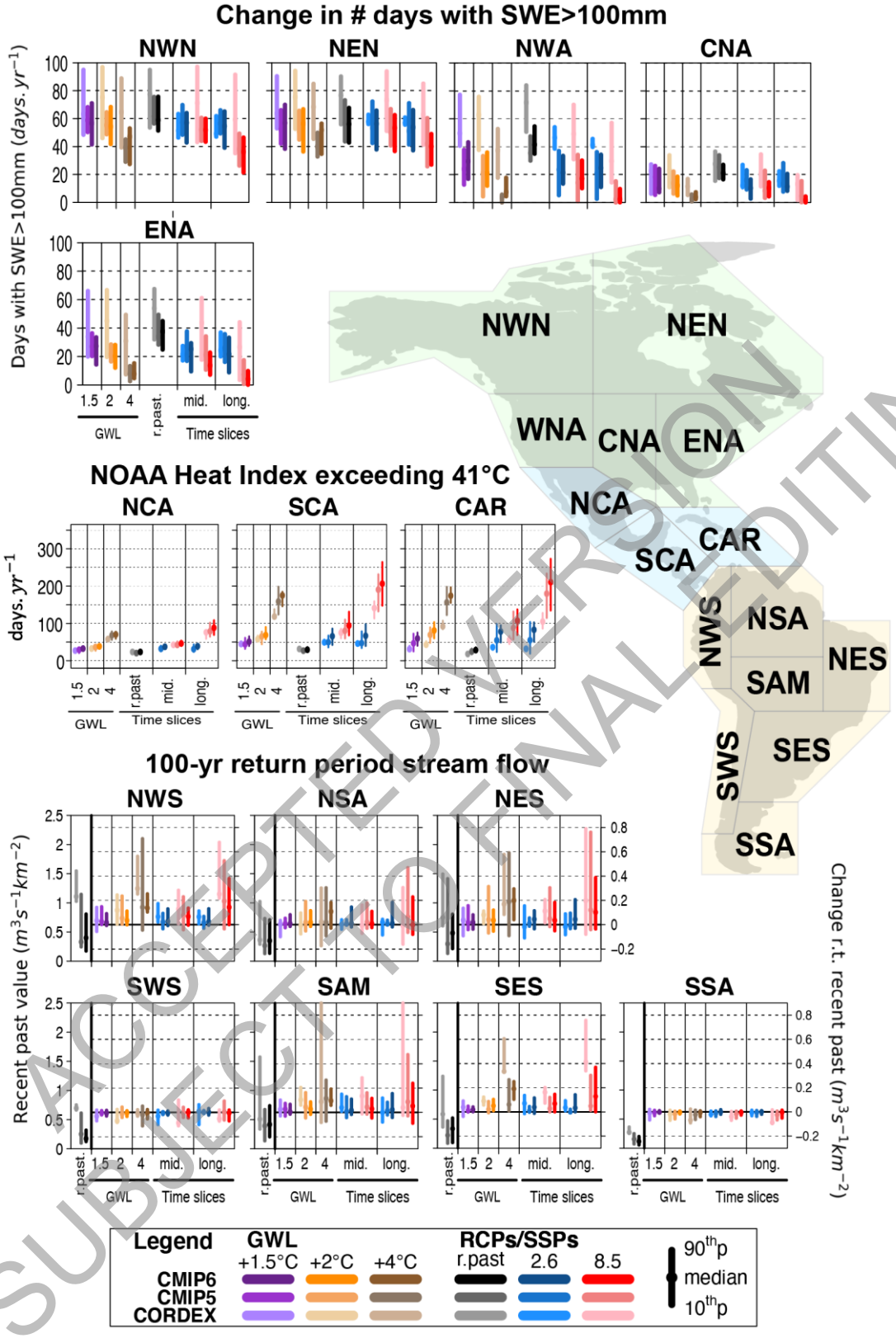


Figure TS.24: Projected change in the mean number of days per year with maximum temperature exceeding 35°C for CMIP5 (first column), CMIP6 (second column) and CORDEX (thirth column). The map shows the median change in the number of days per year between the mid-century (2041–2060) or end-century (2081–2100) and historical (1995–2014) periods for the CMIP5 and CORDEX RCP8.5 and RCP2.6 and CMIP6 SSP5-8.5 and SSP1-2.6 scenarios ensembles. Stippling indicates areas where less than 80% of the models agree on the sign of change. {Interactive Atlas}

ACCEPTED VERSION SUBJECT TO FINAL EDITING

a)



ACCEPTED VERSION SUBJECT TO FINAL EDITING

b)

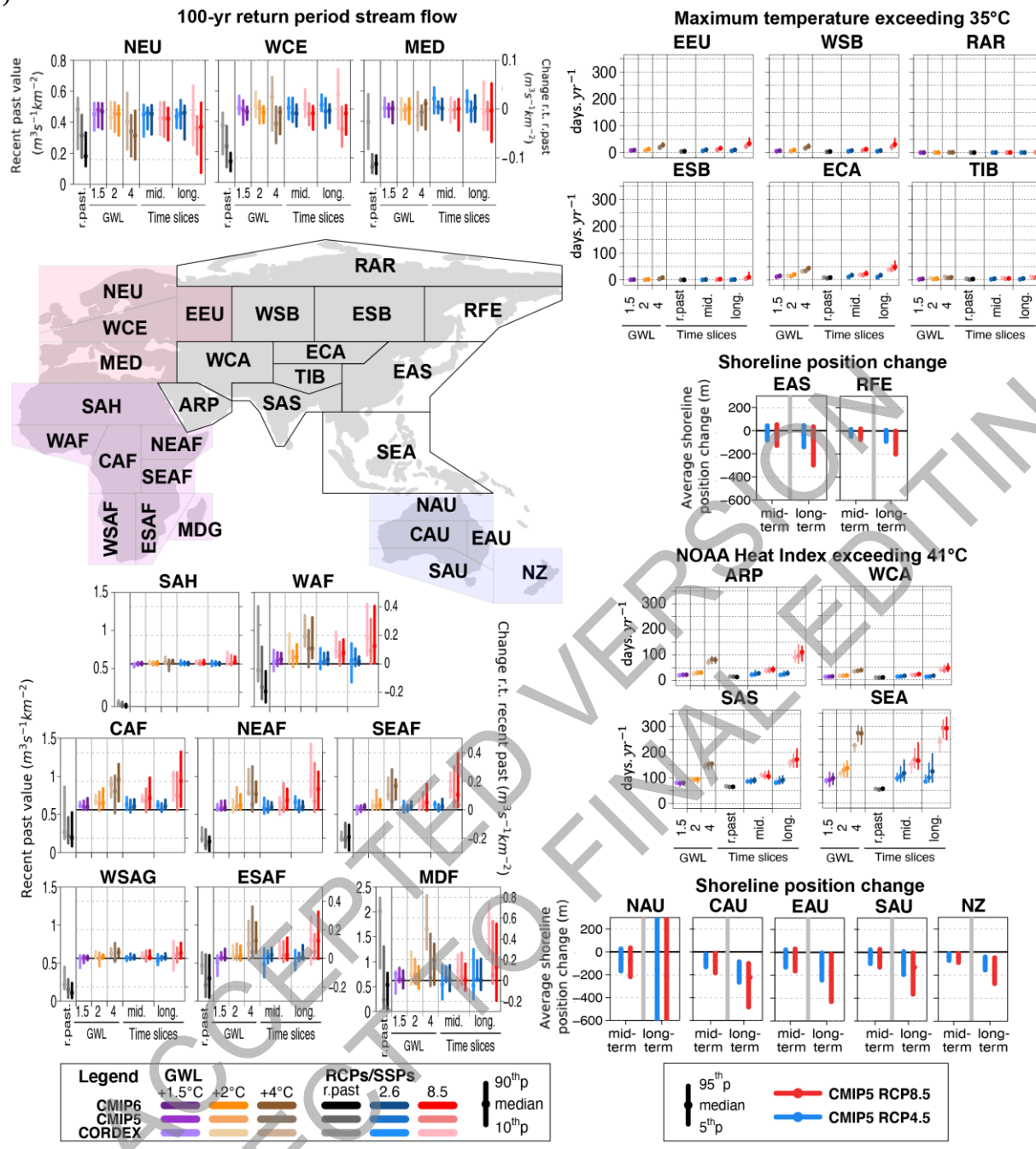


Figure TS.25: **Distribution of projected changes in selected climatic impact-driver indices for selected regions for CMIP6, CMIP5 and CORDEX model ensembles.** Different indices are shown for different region: for east Europe and north Asia the mean number of days per year with maximum temperature exceeding 35°C, for Central America and the Caribbean, and the Arabian peninsula, western, southern and easten Asia the mean number of days per year with the NOAA Heat Index exceeding 41°C, for Australasia, East Asia and Russia far East the average shoreline position change, for South America, Europe and Africa the mean change in 1-in-100-years river discharge per unit catchment area (m3 s–1 km–2), and for North America the median change in the number of days with snow water equivalent (SWE) over 100 mm. For each box plot the changes or the climatological values are reported respect to, or compared to, the recent past (1995–2014) period for 1.5 ºC, 2ºC and 4ºC global warming levels and for mid-century (2041–2060) or end-century (2081–2100) periods for the CMIP5 and CORDEX RCP8.5 and RCP2.6 and CMIP6 SSP5-8.5 and SSP1-2.6 scenarios ensembles {Figure 12.5, Figure 12.6, Figure 12.9, Figure 12.SM.1, Figure 12.SM.2, Figure 12.SM.6}.

ACCEPTED VERSION SUBJECT TO FINAL EDITING

Chapter 1: Framing, context, and methods

Coordinating Lead Authors:
Deliang Chen (Sweden), Maisa Rojas (Chile), Bjørn H. Samset (Norway)

Lead Authors:
Kim Cobb (United States of America), Aida Diongue-Niang (Senegal), Paul Edwards (United States of America), Seita Emori (Japan), Sergio Henrique Faria (Spain/Brazil), Ed Hawkins (United Kingdom), Pandora Hope (Australia), Philippe Huybrechts (Belgium), Malte Meinshausen (Australia/Germany), Sawsan Khair Elsied Abdel Rahim Mustafa (Sudan), Gian-Kasper Plattner (Switzerland), Anne Marie Treguier (France)

Contributing Authors:
Hui-Wen Lai (Sweden), Tania Villaseñor (Chile), Rondrotiana Barimalala (South Africa/Madagascar), Rosario Carmona (Chile), Peter M. Cox (United KingdomK), Wolfgang Cramer (France/Germany), Francisco J. Doblas-Reyes (Spain), Hans Dolman (The Netherlands), Alessandro Dosio (Italy), Veronika Eyring (Germany), Gregory M. Flato (Canada), Piers Forster (United Kingdom), David Frame (New Zealand), Katja Frieler (Germany), Jan S. Fuglestvedt (Norway), John C. Fyfe (Canada), Mathias Garschagen (Germany), Joelle Gergis (Australia), Nathan P. Gillett (Canada), Michael Grose (Australia), Eric Guilyardi (France), Celine Guivarch (France), Susan Hassol (United States of America), Zeke Hausfather (United States of America), Hans Hersbach (United Kingdom/The Netherlands), Helene T. Hewitt (United Kingdom), Mark Howden (Australia), Christian Huggel (Switzerland), Margot Hurlbert (Canada), Christopher Jones (United Kingdom), Richard G. Jones (United Kingdom), Darrell S. Kaufman (United States of America), Robert E. Kopp (United States of America), Anthony Leiserowitz (United States of America), Robert J. Lempert (United States of America), Jared Lewis (Australia/New Zealand), Hong Liao (China), Nikki Lovenduski (United States of America), Marianne T. Lund (Norway), Katharine Mach (United States of America), Douglas Maraun (Austria/Germany), Jochem Marotzke (Germany), Jan Minx (Germany), Zebedee R.J. Nicholls (Australia), Brian C. O'Neill (United States of America), M. Giselle Ogaz (Chile), Friederike Otto (United Kingdom /Germany), Wendy Parker (United Kingdom), Camille Parmesan (France, United Kingdom/United States of America), Warren Pearce (United Kingdom), Roque Pedace (Argentina), Andy Reisinger (New Zealand), James Renwick (New Zealand), Keywan Riahi (Austria), Paul Ritchie (United Kingdom), Joeri Rogelj (United Kingdom/Belgium), Rodolfo Sapiains (Chile), Yusuke Satoh (Japan), Sonia I. Seneviratne (Switzerland), Theodore G. Shepherd (United Kingdom/Canada), Jana Sillmann (Norway/Germany), Lucas Silva (Portugal/Switzerland), Aimée B.A. Slangen (The Netherlands), Anna A. Sörensson (Argentina), Peter Steinle (Australia), Thomas F. Stocker (Switzerland), Martina Stockhause (Germany), Daithi Stone (New Zealand), Abigail Swann (United States of America), Sophie Szopa (France), Izuru Takayabu (Japan), Claudia Tebaldi (United States of America), Laurent Terray (France), Peter W. Thorne (Ireland/ United Kingdom), Blair Trewin (Australia), Isabel Trigo (Portugal), Maarten K. van Aalst (The Netherlands), Bart van den Hurk (The Netherlands), Detlef van Vuuren (The Netherlands), Robert Vautard (France), Carolina Vera (Argentina), David Viner (United Kingdom), Axel von Engeln (Germany), Karina von Schuckmann (France/Germany), Xuebin Zhang (Canada)

Review Editors:
Nares Chuersuwan (Thailand), Gabriele Hegerl (United Kingdom/Germany), Tetsuzo Yasunari (Japan)

ACCEPTED VERSION
SUBJECT TO FINAL EDITS

Chapter Scientist:
Hui-Wen Lai (Sweden), Tania Villaseñor (Chile)

This chapter should be cited as:
Chen, D., M. Rojas, B. H. Samset, K. Cobb, A. Diongue Niang, P. Edwards, S. Emori, S. H. Faria, E. Hawkins, P. Hope, P. Huybrechts, M. Meinshausen, S. K. Mustafa, G. K. Plattner, A. M. Tréguier, 2021, Framing, Context, and Methods. In: *Climate Change 2021: The Physical Science Basis. Contribution of Working Group I to the Sixth Assessment Report of the Intergovernmental Panel on Climate Change* [Masson-Delmotte, V., P. Zhai, A. Pirani, S. L. Connors, C. Péan, S. Berger, N. Caud, Y. Chen, L. Goldfarb, M. I. Gomis, M. Huang, K. Leitzell, E. Lonnoy, J.B.R. Matthews, T. K. Maycock, T. Waterfield, O. Yelekçi, R. Yu and B. Zhou (eds.)]. In Press.

Date: August 2021

This document is subject to copy-editing, corrigenda and trickle backs

ACCEPTED VERSION
SUBJECT TO FINAL EDITS

Table of contents

Executive Summary **5**

1.1 Report and chapter overview **8**
1.1.1 The AR6 WGI Report 8
1.1.2 Rationale for the new AR6 WGI structure and its relation to the previous AR5 WGI Report 9
1.1.3 Integration of AR6 WGI assessments with other Working Groups 12
1.1.4 Chapter preview 13

1.2 Where we are now **13**
1.2.1 The changing state of the physical climate system 13
1.2.1.1 Recent changes in multiple climate indicators 14
1.2.1.2 Long-term perspectives on anthropogenic climate change 15
1.2.2 The policy and governance context 18

Cross-Chapter Box 1.1: The WGI contribution to the AR6 and its potential relevance for the global stocktake **19**

1.2.3 Linking science and society: communication, values, and the IPCC assessment process 29
1.2.3.1 Climate change understanding, communication, and uncertainties 29

Box 1.1: Treatment of uncertainty and calibrated uncertainty language in AR6 30

1.2.3.2 Values, science, and climate change communication 32
1.2.3.3 Climate information, co-production, and climate services 34
1.2.3.4 Media coverage of climate change 35

1.3 How we got here: the scientific context **36**
1.3.1 Lines of evidence: instrumental observations 36
1.3.2 Lines of evidence: paleoclimate 39
1.3.3 Lines of evidence: identifying natural and human drivers 40
1.3.4 Lines of evidence: understanding and attributing climate change 43
1.3.5 Projections of future climate change 45
1.3.6 How do previous climate projections compare with subsequent observations? 48

Box 1.2: Special Reports in the sixth IPCC assessment cycle: key findings 50

1.4 AR6 foundations and concepts **53**
1.4.1 Baselines, reference periods and anomalies 53

Cross-Chapter Box 1.2: Changes in global temperature between 1750 and 1850 ..... **55**

1.4.2 Variability and emergence of the climate change signal 56

ACCEPTED VERSION SUBJECT TO FINAL EDITS

1.4.2.1 Climate variability can influence trends over short periods 57
1.4.2.2 The emergence of the climate change signal 57
1.4.3 Sources of uncertainty in climate simulations 59
1.4.3.1 Sources of uncertainty 59
1.4.3.2 Uncertainty quantification 60
1.4.4 Considering an uncertain future 61
1.4.4.1 Low-likelihood outcomes 62
1.4.4.2 Storylines 62

Cross-Chapter Box 1.3: Risk framing in IPCC AR6 63

1.4.4.3 Abrupt change, tipping points and surprises 65

Cross-Working Group Box: Attribution 67

1.4.5 Climate regions used in AR6 70
1.4.5.1 Defining climate regions 70
1.4.5.2 Types of regions used in AR6 71

1.5 Major developments and their implications 72
1.5.1 Observational data and observing systems 72
1.5.1.1 Major expansions of observational capacity 73
1.5.1.2 Threats to observational capacity or continuity 77
1.5.2 New developments in reanalyses 78
1.5.3 Climate Models 82
1.5.3.1 Earth System Models 82
1.5.3.2 Model tuning and adjustment 84
1.5.3.3 From global to regional models 85
1.5.3.4 Models of lower complexity 86

Box 1.3: Emission metrics in AR6 WGI 88

1.5.4 Modelling techniques, comparisons and performance assessments 89
1.5.4.1 Model 'fitness for purpose' 89
1.5.4.2 Ensemble modelling techniques 89
1.5.4.3 The sixth phase of the Coupled Model Intercomparison Project (CMIP6) 91
1.5.4.4 Coordinated Regional Downscaling Experiment (CORDEX) 93
1.5.4.5 Model Evaluation Tools 94
1.5.4.6 Evaluation of process-based models against observations 94
1.5.4.7 Emergent constraints on climate feedbacks, sensitivities and projections 95
1.5.4.8 Weighting techniques for model comparisons 96

ACCEPTED VERSION SUBJECT TO FINAL EDITS

1.6 Dimensions of Integration: Scenarios, global warming levels and cumulative carbon emissions 97

1.6.1 Scenarios 98

1.6.1.1 Shared Socio-economic Pathways 100

Cross-Chapter Box 1.4: The SSP scenarios as used in Working Group I 102

1.6.1.2 Scenario generation process for CMIP6 107

1.6.1.3 History of scenarios within the IPCC 108

1.6.1.4 The likelihood of reference scenarios, scenario uncertainty and storylines 109

1.6.2 Global warming levels 111

1.6.3 Cumulative CO_2 emissions 112

Box 1.4: The relationships between 'net zero' emissions, temperature outcomes and carbon dioxide removal 113

1.7 Final remarks 114

Frequently Asked Questions 116

FAQ 1.1: Do we understand climate change better now compared to when the IPCC started? 116

FAQ 1.2: Where is climate change most apparent? 117

FAQ 1.3: What can past climate teach us about the future? 118

Acknowledgements 120

References 121

Appendix 1.A 165

Figures 175

ACCEPTED VERSION
SUBJECT TO FINAL EDITS

Executive Summary

Working Group I (WGI) of the Intergovernmental Panel on Climate Change (IPCC) assesses the current evidence on the physical science of climate change, evaluating knowledge gained from observations, reanalyses, paleoclimate archives and climate model simulations, as well as physical, chemical and biological climate processes. This chapter sets the scene for the WGI assessment, placing it in the context of ongoing global and regional changes, international policy responses, the history of climate science and the evolution from previous IPCC assessments, including the Special Reports prepared as part of this Assessment Cycle. Key concepts and methods, relevant recent developments, and the modelling and scenario framework used in this assessment are presented.

Framing and Context of the WGI Report

The WGI contribution to the IPCC Sixth Assessment Report (AR6) assesses new scientific evidence relevant for a world whose climate system is rapidly changing, overwhelmingly due to human influence. The five IPCC assessment cycles since 1990 have comprehensively and consistently laid out the rapidly accumulating evidence of a changing climate system, with the Fourth Assessment Report (AR4, 2007) being the first to conclude that warming of the climate system is unequivocal. Sustained changes have been documented in all major elements of the climate system, including the atmosphere, land, cryosphere, biosphere and ocean. Multiple lines of evidence indicate the unprecedented nature of recent large-scale climatic changes in context of all human history, and that they represent a millennial-scale commitment for the slow-responding elements of the climate system, resulting in continued worldwide loss of ice, increase in ocean heat content, sea level rise and deep ocean acidification. {1.2.1, 1.3, Box 1.2, Appendix 1.A}

Since the IPCC Fifth Assessment Report (AR5), the international policy context of IPCC reports has changed. The UN Framework Convention on Climate Change (UNFCCC, 1992) has the overarching objective of preventing 'dangerous anthropogenic interference with the climate system'. Responding to that objective, the Paris Agreement (2015) established the long-term goals of 'holding the increase in global average temperature to well below 2°C above pre-industrial levels and pursuing efforts to limit the temperature increase to 1.5°C above pre-industrial levels' and of achieving 'a balance between anthropogenic emissions by sources and removals by sinks of greenhouse gases in the second half of this century'. Parties to the Agreement have submitted Nationally Determined Contributions (NDCs) indicating their planned mitigation and adaptation strategies. However, the NDCs submitted as of 2020 are insufficient to reduce greenhouse gas emission enough to be consistent with trajectories limiting global warming to well below 2°C above pre-industrial levels (*high confidence*). {1.1, 1.2}

This report provides information of potential relevance to the 2023 global stocktake. The 5-yearly stocktakes called for in the Paris Agreement will evaluate alignment among the Agreement's long-term goals, its means of implementation and support, and evolving global efforts in climate change mitigation (efforts to limit climate change) and adaptation (efforts to adapt to changes that cannot be avoided). In this context, WGI assesses, among other topics, remaining cumulative carbon emission budgets for a range of global warming levels, effects of long-lived and short-lived climate forcers, projected changes in sea level and extreme events, and attribution to anthropogenic climate change. {Cross-Chapter Box 1.1}

Understanding of the fundamental features of the climate system is robust and well established. Scientists in the 19th-century identified the major natural factors influencing the climate system. They also hypothesized the potential for anthropogenic climate change due to carbon dioxide (CO_2) emitted by fossil fuel combustion. The principal natural drivers of climate change, including changes in incoming solar radiation, volcanic activity, orbital cycles, and changes in global biogeochemical cycles, have been studied systematically since the early 20th century. Other major anthropogenic drivers, such as atmospheric aerosols (fine solid particles or liquid droplets), land-use change and non-CO_2 greenhouse gases, were identified by the 1970s. Since systematic scientific assessments began in the 1970s, the influence of human activity on the warming of the climate system has evolved from theory to established fact. Past projections of global surface temperature and the pattern of warming are broadly consistent with subsequent observations (*limited evidence, high agreement*), especially when accounting for the difference in radiative forcing scenarios used

ACCEPTED VERSION SUBJECT TO FINAL EDITS

for making projections and the radiative forcings that actually occurred. {1.3.1 - 1.3.6}

Global surface temperatures increased by about 0.1°C (*likely* range –0.1°C to +0.3°C, *medium confidence*) between the period around 1750 and the 1850–1900 period, with anthropogenic factors responsible for a warming of 0.0°C–0.2°C (*likely* range, *medium confidence*). This assessed change in temperature before 1850–1900 is not included in the AR6 assessment of global warming to date, to ensure consistency with previous IPCC assessment reports, and because of the lower confidence in the estimate. There was *likely* a net anthropogenic forcing of 0.0–0.3 Wm^{-2} in 1850–1900 relative to 1750 (*medium confidence*), with radiative forcing from increases in atmospheric greenhouse gas concentrations being partially offset by anthropogenic aerosol emissions and land-use change. Net radiative forcing from solar and volcanic activity is estimated to be smaller than ±0.1 Wm^{-2} for the same period. {Cross Chapter Box 1.2, 1.4.1, Cross Chapter Box 2.3}

Natural climate variability can temporarily obscure or intensify anthropogenic climate change on decadal time scales, especially in regions with large internal interannual-to-decadal variability. At the current level of global warming, an observed signal of temperature change relative to the 1850–1900 baseline has emerged above the levels of background variability over virtually all land regions (*high confidence*). Both the rate of long-term change and the amplitude of interannual (year-to-year) variability differ from global to regional to local scales, between regions and across climate variables, thus influencing when changes become apparent. Tropical regions have experienced less warming than most others, but also exhibit smaller interannual variations in temperature. Accordingly, the signal of change is more apparent in tropical regions than in regions with greater warming but larger interannual variations (*high confidence*). {1.4.2, FAQ1.2}

The AR6 has adopted a unified framework of climate risk, supported by an increased focus in WGI on low-likelihood, high-impact events. Systematic risk framing is intended to aid the formulation of effective responses to the challenges posed by current and future climatic changes and to better inform risk assessment and decision-making. AR6 also makes use of the 'storylines' approach, which contributes to building a robust and comprehensive picture of climate information, allows a more flexible consideration and communication of risk, and can explicitly address low-likelihood, high-impact events. {1.1.2, 1.4.4, Cross-Chapter Box 1.3}

The construction of climate change information and communication of scientific understanding are influenced by the values of the producers, the users and their broader audiences. Scientific knowledge interacts with pre-existing conceptions of weather and climate, including values and beliefs stemming from ethnic or national identity, traditions, religion or lived relationships to land and sea (*high confidence*). Science has values of its own, including objectivity, openness and evidence-based thinking. Social values may guide certain choices made during the construction, assessment and communication of information (*high confidence*). {1.2.3, Box 1.1}

Data, Tools and Methods Used across the WGI Report

Capabilities for observing the physical climate system have continued to improve and expand overall, but some reductions in observational capacity are also evident (*high confidence*). Improvements are particularly evident in ocean observing networks and remote-sensing systems, and in paleoclimate reconstructions from proxy archives. However, some climate-relevant observations have been interrupted by the discontinuation of surface stations and radiosonde launches, and delays in the digitisation of records. Further reductions are expected to result from the COVID-19 pandemic. In addition, paleoclimate archives such as mid-latitude and tropical glaciers as well as modern natural archives used for calibration (e.g., corals and trees) are rapidly disappearing owing to a host of pressures, including increasing temperatures (*high confidence*). {1.5.1}

Reanalyses have improved since AR5 and are increasingly used as a line of evidence in assessments of the state and evolution of the climate system (*high confidence*). Reanalyses, where atmosphere or ocean forecast models are constrained by historical observational data to create a climate record of the past, provide

ACCEPTED VERSION SUBJECT TO FINAL EDITS

consistency across multiple physical quantities and information about variables and locations that are not directly observed. Since AR5, new reanalyses have been developed with various combinations of increased resolution, extended records, more consistent data assimilation, estimation of uncertainty arising from the range of initial conditions, and an improved representation of the ocean. While noting their remaining limitations, the WGI report uses the most recent generation of reanalysis products alongside more standard observation-based datasets. {1.5.2, Annex 1}

Since AR5, new techniques have provided greater confidence in attributing changes in climate extremes to climate change. Attribution is the process of evaluating the relative contributions of multiple causal factors to an observed change or event. This includes the attribution of the causal factors of changes in physical or biogeochemical weather or climate variables (e.g., temperature or atmospheric CO_2) as done in WGI, or of the impacts of these changes on natural and human systems (e.g., infrastructure damage or agricultural productivity), as done in WGII. Attributed causes include human activities (such as emissions of greenhouse gases and aerosols, or land-use change), and changes in other aspects of the climate, or natural or human systems. {Cross-WG Box 1.1}

The latest generation of complex climate models has an improved representation of physical processes, and a wider range of Earth system models now represent biogeochemical cycles. Since the AR5, higher-resolution models that better capture smaller-scale processes and extreme events have become available. Key model intercomparisons supporting this assessment include the Coupled Model Intercomparison Project Phase 6 (CMIP6) and the Coordinated Regional Climate Downscaling Experiment (CORDEX), for global and regional models respectively. Results using CMIP Phase 5 (CMIP5) simulations are also assessed. Since the AR5, large ensemble simulations, where individual models perform multiple simulations with the same climate forcings, are increasingly used to inform understanding of the relative roles of internal variability and forced change in the climate system, especially on regional scales. The broader availability of ensemble model simulations has contributed to better estimations of uncertainty in projections of future change (*high confidence*). A broad set of simplified climate models is assessed and used as emulators to transfer climate information across research communities, such as for evaluating impacts or mitigation pathways consistent with certain levels of future warming. {1.4.2, 1.5.3, 1.5.4, Cross-chapter Box 7.1}

Assessments of future climate change are integrated within and across the three IPCC Working Groups through the use of three core components: scenarios, global warming levels, and the relationship between cumulative carbon emissions and global warming. Scenarios have a long history in the IPCC as a method for systematically examining possible futures. A new set of scenarios, derived from the Shared Socio-economic Pathways (SSPs), is used to synthesize knowledge across the physical sciences, impact, and adaptation and mitigation research. The core set of SSP scenarios used in the WGI report, SSP1-1.9, SSP1-2.6, SSP2-4.5, SSP3-7.0 and SSP5-8.5, cover a broad range of emission pathways, including new low-emissions pathways. The feasibility or likelihood of individual scenarios is not part of this assessment, which focuses on the climate response to possible, prescribed emission futures. Levels of global surface temperature change (global warming levels), which are closely related to a range of hazards and regional climate impacts, also serve as reference points within and across IPCC Working Groups. Cumulative carbon emissions, which have a nearly linear relationship to increases in global surface temperature, are also used. {1.6.1-1.6.4, Cross-Chapter Box 1.5, Cross-Chapter Box 11.1}

ACCEPTED VERSION SUBJECT TO FINAL EDITS

1.1 Report and chapter overview

The role of the Intergovernmental Panel on Climate Change (IPCC) is to critically assess the scientific, technical, and socio-economic information relevant to understanding the physical science and impacts of human-induced climate change and natural variations, including the risks, opportunities and options for adaptation and mitigation. This task is performed through a comprehensive assessment of the scientific literature. The robustness of IPCC assessments stems from the systematic consideration and combination of multiple lines of independent evidence. In addition, IPCC reports undergo one of the most comprehensive, open, and transparent review and revision processes ever employed for science assessments.

Starting with the First Assessment Report (FAR; IPCC, 1990) the IPCC assessments have been structured into three working groups. Working Group I (WGI) assesses the physical science basis of climate change, Working Group II (WGII) assesses associated impacts, vulnerability and adaptation options, and Working Group III (WGIII) assesses mitigation response options. Each report builds on the earlier comprehensive assessments by incorporating new research and updating previous findings. The volume of knowledge assessed and the cross-linkages between the three working groups have substantially increased over time.

As part of its sixth assessment cycle, from 2015 to 2022, the IPCC is producing three Working Group Reports, three targeted Special Reports, a Refinement to the 2006 IPCC Guidelines for National Greenhouse Gas Inventories, and a Synthesis Report. The AR6 Special Reports covered the topics of 'Global Warming of 1.5°C' (SR1.5; IPCC, 2018), 'Climate Change and Land' (SRCCL; IPCC, 2019a) and 'The Ocean and Cryosphere in a Changing Climate' (SROCC; IPCC, 2019b). The SR1.5 and SRCCL are the first IPCC reports jointly produced by all three Working Groups. This evolution towards a more integrated assessment reflects a broader understanding of the interconnectedness of the multiple dimensions of climate change.

1.1.1 The AR6 WGI Report

The Sixth Assessment Report (AR6) of the IPCC marks more than 30 years of global collaboration to describe and understand, through expert assessments, one of the defining challenges of the 21st century: human-induced climate change. Since the inception of the IPCC in 1988, our understanding of the physical science basis of climate change has advanced markedly. The amount and quality of instrumental observations and information from paleoclimate archives have substantially increased. Understanding of individual physical, chemical and biological processes has improved. Climate model capabilities have been enhanced, through the more realistic treatment of interactions among the components of the climate system, and improved representation of the physical processes, in line with the increased computational capacities of the world's supercomputers.

This report assesses both observed changes, and the components of these changes that are attributable to anthropogenic influence (or human-induced), distinguishing between anthropogenic and naturally forced changes (see Section 1.2.1.1, Section 1.4.1, Cross Working Group Box: Attribution, and Chapter 3). The core assessment conclusions from previous IPCC reports are confirmed or strengthened in this report, indicating the robustness of our understanding of the primary causes and consequences of anthropogenic climate change.

The WGI contribution to AR6 is focused on physical and biogeochemical climate science information, with particular emphasis on regional climate changes. These are relevant for mitigation, adaptation and risk assessment in the context of complex and evolving policy settings, including the Paris Agreement, the Global Stocktake, the Sendai Framework and the Sustainable Development Goals (SDGs) Framework.

The core of this report consists of twelve chapters plus the Atlas (Figure 1.1), which can together be grouped into three categories (excluding this framing chapter):

Large-Scale Information (Chapters 2, 3 and 4). These chapters assess climate information from global to continental or ocean-basin scales. Chapter 2 presents an assessment of the changing state of the climate

ACCEPTED VERSION SUBJECT TO FINAL EDITS

system, including the atmosphere, biosphere, ocean and cryosphere. Chapter 3 continues with an assessment of the human influence on this changing climate, covering the attribution of observed changes, and introducing the fitness-for-purpose approach for the evaluation of climate models used to conduct the attribution studies. Finally, Chapter 4 assesses climate change projections, from the near to the long term, including climate change beyond 2100, as well as the potential for abrupt and 'low-likelihood, high-impact' changes.

Process Understanding (Chapters 5, 6, 7, 8 and 9). These five chapters provide end-to-end assessments of fundamental Earth system processes and components: the carbon budget and biogeochemical cycles (Chapter 5), short-lived climate forcers and their links to air quality (Chapter 6), the Earth's energy budget and climate sensitivity (Chapter 7), the water cycle (Chapter 8), and the ocean, cryosphere and sea-level changes (Chapter 9). All these chapters provide assessments of observed changes, including relevant paleoclimatic information and understanding of processes and mechanisms as well as projections and model evaluation.

Regional Information (Chapters 10, 11, 12 and Atlas). New knowledge on climate change at regional scales is reflected in this report with four chapters covering regional information. Chapter 10 provides a framework for assessment of regional climate information, including methods, physical processes, an assessment of observed changes at regional scales, and the performance of regional models. Chapter 11 addresses extreme weather and climate events, including temperature, precipitation, flooding, droughts and compound events. Chapter 12 provides a comprehensive, region-specific assessment of changing climatic conditions that may be hazardous or favourable (hence influencing climate risk) for various sectors to be assessed in WGII. Lastly, the Atlas assesses and synthesizes regional climate information from the whole report, focussing on the assessments of mean changes in different regions and on model assessments for the regions. It also introduces the online Interactive Atlas, a novel compendium of global and regional climate change observations and projections. It includes a visualization tool combining various warming levels and scenarios on multiple scales of space and time.

Embedded in the chapters are **Cross-Chapter Boxes** that highlight cross-cutting issues. Each chapter also includes an **Executive Summary (ES),** and several **Frequently Asked Questions (FAQs)**. To enhance traceability and reproducibility of report figures and tables, detailed information on the input data used to create them, as well as links to archived code, are provided in the **Input Data Tables** in chapter Supplementary Material. Additional metadata on the model input datasets is provided via the report website.

The AR6 WGI report includes a **Summary for Policy Makers (SPM)** and a **Technical Summary (TS)**. The integration among the three IPCC Working Groups is strengthened by the implementation of the **Cross-Working-Group Glossary**.

[START FIGURE 1.1 HERE]

Figure 1.1: The structure of the AR6 WGI Report. Shown are the three pillars of the AR6 WGI, its relation to the WGII and WGIII contributions, and the cross-working-group AR6 Synthesis Report (SYR).

[END FIGURE 1.1 HERE]

1.1.2 Rationale for the new AR6 WGI structure and its relation to the previous AR5 WGI Report

The AR6 WGI report, as a result of its scoping process, is structured around topics such as large-scale information, process understanding and regional information (Figure 1.1). This represents a rearrangement relative to the structure of the WGI contribution to the IPCC Fifth Assessment Report (AR5; IPCC, 2013a), as summarized in Figure 1.2. The AR6 approach aims at a greater visibility of key knowledge developments potentially relevant for policymakers, including climate change mitigation, regional adaptation planning based on a risk management framework, and the Global Stocktake.

ACCEPTED VERSION SUBJECT TO FINAL EDITS

[**START FIGURE 1.2 HERE**]

Figure 1.2: Main relations between AR5 WGI and AR6 WGI chapters. The left column shows the AR5 WGI chapter categories. The central column lists the AR5 WGI chapters, with the colour code indicating their relation to the AR6 WGI structure shown in Figure 1.1: Large-Scale Information (red), Process Understanding (gold), Regional Information (light blue), and Whole-Report Information (dark blue). AR5 WGI chapters depicted in white have their topics distributed over multiple AR6 WGI chapters and categories. The right column explains where to find related information in the AR6 WGI report.

[END FIGURE 1.2 HERE]

Two key subjects presented separately in AR5, paleoclimate and model evaluation, are now distributed among multiple AR6 WGI chapters. Various other cross-cutting themes are also distributed throughout this report. A summary of these themes and their integration across chapters is described in Table 1.1.

[START TABLE 1.1 HERE]

Table 1.1: Cross-cutting themes in AR6 WGI, and the main chapters that deal with them. Bold numbers in the table indicate the chapters that have extensive coverage.

Thematic focus	**Main chapters;** additional chapters
Aerosols	**2, 6, 7, 8, 9, 10, 11;** 3, 4, Atlas
Atmospheric circulation	**3, 4, 8;** 2, 5, 10, 11
Biosphere	**2, 3, 5, 11, Cross-Chapter Box 5.1;** 1, 4, 6, 8
Carbon dioxide removal (CDR)	**4, 5;** 8
Cities and urban aspects	**10, 11, 12;** 2, 8, 9, Atlas
Climate services	**12, Atlas, Cross-Chapter Box 12.2;** 1, 10
Climatic impact-drivers	**12, Annex VI;** 1, 9, 10, 11, Atlas
CO_2 concentration levels	**1, 2, 5, Cross-Chapter Box 1.1;** 12, Atlas
Coronavirus pandemic (COVID-19)	**Cross-Chapter Box 6.1;** 1
Cryosphere	**2, 3, 9;** 1, 4, 8, 12, Atlas
Deep uncertainty	**9;** 4, 7, 8, Cross-Chapter Box 11.2, Cross-Chapter Box 12.1

ACCEPTED VERSION SUBJECT TO FINAL EDITS

Detection and attribution	**3, 10, 11, Cross-Working Group Box: Attribution;** 5, 6, 8, 9, 12, Atlas
Emergence	**1, 10, 12;** 8, 11
Extremes and abrupt change	**11, 12;** 1, 5, 7, 8, 9, 10, Atlas, Cross-Chapter Box 12.1
Global warming hiatus	**Cross-Chapter Box 3.1;** 10, 11
Land use	**5;** 2, 7, 8, 10, 11
Limits of habitability	**9, 12;** 11
Low-likelihood, high-impact/warming	**1, 4, 11;** 7, 8, 9, 10, Cross-Chapter Box 1.1, Cross-Chapter Box 1.3, Cross-Chapter Box 4
Model evaluation	**1, 3, 9, 10, 11, Atlas;** 5, 6, 8
Modes of variability	**1, 2, 3, 4, 8, 9, Annex IV;** 7, 10, 11, 12, Atlas
Monsoons	**8;** 3, 4, 9, 10, 11, 12, Atlas
Natural variability	**1, 2, 3, 4, 9, 11;** 5, 8, 10
Ocean	**3, 5, 9;** 1, 2, 4, 7, 12, Atlas
Paleoclimate	**1, 2;** 3, 5, 7, 8, 9, Atlas, Box 11.3
Polar regions	**9, 12, Atlas;** 2, 3, 7, 8
Radiative Forcing	**7;** 1, 2, 6, 11
Regional case studies	**10, 11, Atlas;** 12, Box 8.1, Box 11.4, Cross-Chapter Box 12.2
Risk	**1, 11, 12, Cross-Chapter Box 1.3;** 4, 5, 9, Cross-Chapter Box 12.1
Sea level	**9, 12;** 1, 2, 3, 4, 7, 8, 10, 11, Atlas
Short-lived climate forcers (SLCF)	**6, 7;** 1, 2, 4, Atlas

ACCEPTED VERSION SUBJECT TO FINAL EDITS

Solar radiation modification (SRM)	**4, 5;** 6, 8
Tipping points	**5, 8, 9;** 4, 11, 12, Cross-Chapter Box 12.1
Values and beliefs	**1, 10;** 12
Volcanic forcing	**2, 4, 7, 8;** 1, 3, 5, 9, 10, Annex III
Water cycle	**8, 11;** 2, 3, 10, Box 11.1

[END TABLE 1.1 HERE]

1.1.3 Integration of AR6 WGI assessments with other Working Groups

Integration of assessments across the chapters of the WGI Report, and with WGII and WGIII, occurs in a number of ways, including work on a common Glossary, risk framework (see Cross-Chapter Box 1.3), scenarios and projections of future large-scale changes, and the presentation of results at various global warming levels (see Section 1.6).

Chapters 8 through 12, and the Atlas, cover topics also assessed by WGII in several areas, including regional climate information and climate-related risks. This approach produces a more integrated assessment of impacts of climate change across Working Groups. In particular, Chapter 10 discusses the generation of regional climate information for users, the co-design of research with users, and the translation of information into the user context (in particular directed towards WGII). Chapter 12 provides a direct bridge between physical climate information (climatic impact-drivers) and sectoral impacts and risk, following the chapter organization of the WGII assessment. Notably, Cross-Chapter Box 12.1 draws a connection to representative key risks and Reasons for Concern (RFC).

The science assessed in Chapters 2 to 7, such as the carbon budget, short-lived climate forcers and emission metrics, are topics in common with WGIII, and relevant for the mitigation of climate change. This includes a consistent presentation of the concepts of carbon budget and net zero emission targets within chapters, in order to support integration in the Synthesis Report. Emission-driven emulators (simple climate models), summarised in Cross-Chapter Box 7.1 in Chapter 7 are used to approximate large-scale climate responses of complex Earth System Models (ESMs) and have been used as tools to explore the expected GSAT response to multiple scenarios consistent with those assessed in WGI for the classification of scenarios in WGIII. Chapter 6 provides information about the impact of climate change on global air pollution, relevant for WGII, including Cross-Chapter Box 6.1 on the implications of the recent coronavirus pandemic (COVID-19) for climate and air quality. Cross-Chapter Box 2.3 in Chapter 2 presents an integrated cross-WG discussion of global temperature definitions, with implications for many aspects of climate change science.

In addition, Chapter 1 sets out a shared terminology on cross-cutting topics, including climate risk, attribution and storylines, as well as an introduction to emission scenarios, global warming levels and cumulative carbon emissions as an overarching topic for integration across all three Working Groups.

All these integration efforts are aimed at enhancing the bridges and ‘handshakes’ among Working Groups, enabling the final cross-working group exercise of producing the integrated Synthesis Report.

ACCEPTED VERSION SUBJECT TO FINAL EDITS

1.1.4 Chapter preview

The main purposes of this chapter are: (1) to set the scene for the WGI assessment and to place it in the context of ongoing global changes, international policy processes, the history of climate science and the evolution from previous IPCC assessments, including the Special Reports prepared as part of the sixth assessment cycle; (2) to describe key concepts and methods, relevant developments since AR5, and the modelling framework used in this assessment; and (3) together with the other chapters of this report, to provide context and support for the WGII and WGIII contributions to AR6, particularly on climate information to support mitigation, adaptation and risk management.

The chapter comprises seven sections (Figure 1.3). Section 1.2 describes the present state of Earth's climate, in the context of reconstructed and observed long-term changes and variations caused by natural and anthropogenic factors. It also provides context for the present assessment by describing recent changes in international climate change governance and fundamental scientific values. The evolution of knowledge about climate change and the development of earlier IPCC assessments are presented in Section 1.3. Approaches, methods, and key concepts of this assessment are introduced in Section 1.4. New developments in observing networks, reanalyses, modelling capabilities and techniques since the AR5 are discussed in Section 1.5. The three main 'dimensions of integration' across Working Groups in the AR6, i.e. emission scenarios, global warming levels and cumulative carbon emissions, are described in Section 1.6. The Chapter closes with a discussion of opportunities and gaps in knowledge integration in Section 1.7.

[START FIGURE 1.3 HERE]

Figure 1.3: A roadmap to the contents of Chapter 1.

[END FIGURE 1.3 HERE]

1.2 Where we are now

The IPCC sixth assessment cycle occurs in the context of increasingly apparent climatic changes observed across the physical climate system. Many of these changes can be attributed to anthropogenic influences, with impacts on natural and human systems. AR6 also occurs in the context of efforts in international climate governance such as the Paris Agreement, which sets a long-term goal to hold the increase in global average temperature to 'well below 2°C above pre-industrial levels, and to pursue efforts to limit the temperature increase to 1.5°C above pre-industrial levels, recognizing that this would significantly reduce the risks and impacts of climate change'. This section summarises key elements of the broader context surrounding the assessments made in the present report.

1.2.1 The changing state of the physical climate system

The WGI contribution to the AR5 (AR5 WGI; IPCC, 2013a) assessed that 'warming of the climate system is unequivocal', and that since the 1950s, many of the observed changes are unprecedented over decades to millennia. Changes are evident in all components of the climate system: the atmosphere and the ocean have warmed, amounts of snow and ice have diminished, sea level has risen, the ocean has acidified and its oxygen content has declined, and atmospheric concentrations of greenhouse gases have increased (IPCC, 2013b). This Report documents that, since the AR5, changes to the state of the physical and biogeochemical climate system have continued, and these are assessed in full in later chapters. Here, we summarize changes to a set of key large-scale climate indicators over the modern era (1850 to present). We also discuss the changes in relation to the longer-term evolution of the climate. These ongoing changes throughout the climate system form a key part of the context of the present report.

ACCEPTED VERSION SUBJECT TO FINAL EDITS

1.2.1.1 Recent changes in multiple climate indicators

The physical climate system comprises all processes that combine to form weather and climate. The early chapters of this report broadly organize their assessments according to overarching realms: the atmosphere, the biosphere, the cryosphere (surface areas covered by frozen water, such as glaciers and ice sheets), and the ocean. Elsewhere in the report, and in previous IPCC assessments, the land is also used as an integrating realm that includes parts of the biosphere and the cryosphere. These overarching realms have been studied and measured in increasing detail by scientists, institutions, and the general public since the 18th century, over the era of instrumental observation (see Section 1.3). Today, observations include those taken by numerous land surface stations, ocean surface measurements from ships and buoys, underwater instrumentation, satellite and surface-based remote sensing, and in situ atmospheric measurements from airplanes and balloons. These instrumental observations are combined with paleoclimate reconstructions and historical documentations to produce a highly detailed picture of the past and present state of the whole climate system, and to allow assessments about rates of change across the different realms (see Chapter 2 and Section 1.5).

Figure 1.4 documents that the climate system is undergoing a comprehensive set of changes. It shows a selection of key indicators of change through the instrumental era that are assessed and presented in the subsequent chapters of this report. Annual mean values are shown as stripes, with colours indicating their value. The transitions from one colour to another over time illustrate how conditions are shifting in all components of the climate system. For these particular indicators, the observed changes go beyond the yearly and decadal variability of the climate system. In this Report, this is termed an 'emergence' of the climate signal (see Section 1.4.2 and FAQ 1.2).

Warming of the climate system is most commonly presented through the observed increase in global mean surface temperature (GMST). Taking a baseline of 1850–1900, GMST change until present (2011–2020) is 1.09 °C (0.95–1.20 °C) (see Chapter 2, Section 2.3, Cross-Chapter Box 2.3). This evolving change has been documented in previous Assessment Reports, with each reporting a higher total global temperature change (see Section 1.3, Cross-Chapter Box 1.2). The total change in Global Surface Air Temperature (GSAT; see Section 1.4.1 and Cross-Chapter Box 2.3 in Chapter 2) attributable to anthropogenic activities is assessed to be consistent with the observed change in GSAT (see Chapter 3, Section 3.3)[1].

Similarly, atmospheric concentrations of a range of greenhouse gases are increasing. Carbon dioxide (CO_2, shown in Figure 1.4 and Figure 1.5a), found in AR5 and earlier reports to be the current strongest driver of anthropogenic climate change, has increased from 285.5 ± 2.1 ppm in 1850 to 409.9 ± 0.4 ppm in 2019; concentrations of methane (CH_4), and nitrous oxide (N_2O) have increased as well (see Chapter 2, Sections 2.2, Chapter 5, section 5.2, and Annex V). These observed changes are assessed to be in line with known anthropogenic and natural emissions, when accounting for observed and inferred uptake by land, ocean, and biosphere respectively (see Chapter 5, Section 5.2), and are a key source of anthropogenic changes to the global energy balance (or radiative forcing; see Chapter 2, Section 2.2 and Chapter 7, Section 7.3).

The hydrological (or water) cycle is also changing and is assessed to be intensifying, through a higher exchange of water between the surface and the atmosphere (see Chapter 3, Section 2.3 and Chapter 8, Section 8.3). The resulting regional patterns of changes to precipitation are, however, different from surface temperature change, and interannual variability is larger, as illustrated in Figure 1.4. Annual land area mean precipitation in the Northern Hemisphere temperate regions has increased, while the sub-tropical dry regions have experienced a decrease in precipitation in recent decades (see Chapter 2, Section 2.3).

The cryosphere is undergoing rapid changes, with increased melting and loss of frozen water mass in most

[1] Note that GMST and GSAT are physically distinct but closely related quantities, see Section 1.4.1 and Cross-Chapter Box 2.3 in Chapter 2.

ACCEPTED VERSION SUBJECT TO FINAL EDITS

regions. This includes all frozen parts of the globe, such as terrestrial snow, permafrost, sea ice, glaciers, freshwater ice, solid precipitation, and the ice sheets covering Greenland and Antarctica (see Chapter 9; SROCC, IPCC, 2019b). Figure 1.4 illustrates how, globally, glaciers have been increasingly losing mass for the last fifty years. The total glacier mass in the most recent decade (2010-2019) was the lowest since the beginning of the 20th century. (See Chapter 2, Section 2.3 and Chapter 9, Section 9.5).

The global ocean has warmed unabatedly since at least 1970 (Sections 1.3, 2.3, 9.2; SROCC, IPCC, 2019b) . Figure 1.4 shows how the averaged ocean heat content is steadily increasing, with a total increase of [0.28–0.55] yottajoule (10^{24} joule) between 1971 and 2018. (see Chapter 9, Section 9.2). In response to this ocean warming, as well as to the loss of mass from glaciers and ice sheets, the global mean sea level (GMSL) has risen by 0.20 [0.15 to 0.25] metres between 1900 and 2018. GMSL rise has accelerated since the late 1960s. (See Chapter 9, Section 9.6).

Overall, the changes in these selected climatic indicators have progressed beyond the range of natural year-to-year variability (see Chapters 2, 3, 8, and 9, and further discussion in Sections 1.2.1.2 and 1.4.2). The indicators presented in Figure 1.4 document a broad set of concurrent and emerging changes across the physical climate system. All indicators shown here, along with many others, are further presented in the coming chapters, together with a rigorous assessment of the supporting scientific literature. Later chapters (Chapter 10, 11, 12, and the Atlas) present similar assessments at the regional level, where observed changes do not always align with the global mean picture shown here.

[START FIGURE 1.4 HERE]

Figure 1.4: Changes are occurring throughout the climate system. Left: Main realms of the climate system: atmosphere, biosphere, cryosphere, and ocean. Right: Six key indicators of ongoing changes since 1850, or the start of the observational or assessed record, through 2018. Each stripe indicates the global (except for precipitation which shows two latitude band means), annual mean anomaly for a single year, relative to a multi-year baseline (except for CO_2 concentration and glacier mass loss, which are absolute values). Grey indicates that data are not available. Datasets and baselines used are: (1) CO_2: Antarctic ice cores (Lüthi et al., 2008; Bereiter et al., 2015) and direct air measurements (Tans and Keeling, 2020) (see Figure 1.5 for details); (2) precipitation: Global Precipitation Climatology Centre (GPCC) V8 (updated from Becker et al. 2013), baseline 1961-1990 using land areas only with latitude bands 33°N–66°N and 15°S–30°S; (3) glacier mass loss: Zemp et al., 2019; (4) global surface air temperature (GMST): HadCRUT5 (Morice et al., 2021), baseline 1961–1990; (5) sea level change: (Dangendorf et al., 2019), baseline 1900–1929; (6) ocean heat content (model-observation hybrid): Zanna et al., (2019), baseline 1961–1990. Further details on data sources and processing are available in the chapter data table (Table 1.SM.1).

[END FIGURE 1.4 HERE]

1.2.1.2 Long-term perspectives on anthropogenic climate change

Paleoclimate archives (e.g. ice cores, corals, marine and lake sediments, speleothems, tree rings, borehole temperatures, soils) permit the reconstruction of climatic conditions before the instrumental era. This establishes an essential long-term context for the climate change of the past 150 years and the projected changes in the 21st century and beyond (IPCC, 2013a; Masson-Delmotte et al., 2013) Chapter 3). Figure 1.5 shows reconstructions of three key indicators of climate change over the past 800,000 years[2] – atmospheric CO_2 concentrations, global mean surface temperature (GMST) and global mean sea level (GMSL) –

[2] as old as the longest continuous climate records based on the ice core from EPICA Dome Concordia (Antarctica). Polar ice cores are the only paleoclimatic archive providing direct information on past greenhouse gas concentrations.

ACCEPTED VERSION SUBJECT TO FINAL EDITS

comprising at least eight complete glacial-interglacial cycles (EPICA Community Members, 2004; Jouzel et al., 2007) that are largely driven by oscillations in the Earth's orbit and consequent feedbacks on multi-millennial time scales (Berger, 1978; Laskar et al., 1993). The dominant cycles – recurring approximately every 100,000 years – can be found imprinted in the natural variations of these three key indicators. Before industrialisation, atmospheric CO_2 concentrations varied between 174 ppm and 300 ppm, as measured directly in air trapped in ice at Dome Concordia, Antarctica (Bereiter et al., 2015; Nehrbass-Ahles et al., 2020). Relative to 1850–1900, the reconstructed GMST changed in the range of -6 to +1°C across these glacial-interglacial cycles (see Chapter 2, Section 2.3.1 for an assessment of different paleo reference periods). GMSL varied between about -130 m during the coldest glacial maxima and +5 to +25 m during the warmest interglacial periods (Spratt and Lisiecki, 2016; Chapter 2). They represent the amplitudes of natural, global-scale climate variations over the last 800,000 years prior to the influence of human activity. Further climate information from a variety of paleoclimatic archives are assessed in Chapters 2, 5, 7, 9.

Paleoclimatic information also provides a long-term perspective on rates of change of these three key indicators. The rate of increase in atmospheric CO_2 observed over 1919-2019 CE is one order of magnitude higher than the fastest CO_2 fluctuations documented during the last glacial maximum and the last deglacial transition in high-resolution reconstructions from polar ice cores (Marcott et al., 2014, see Chapter 2, Section 2.2.3.2.1). Current multi-decadal GMST exhibit a higher rate of increase than over the past two thousand years (PAGES 2k Consortium, 2019; Chapter 2, Section 2.3.1.1.2), and in the 20th century GMSL rise was faster than during any other century over the past three thousand years (Chapter 2, Section 2.3.3.3).

[START FIGURE 1.5 HERE]

Figure 1.5: Long-term context of anthropogenic climate change based on selected paleoclimatic reconstructions over the past 800,000 years for three key indicators: atmospheric CO_2 concentrations, Global Mean Surface Temperature (GMST), and Global Mean Sea Level (GMSL). a) Measurements of CO_2 in air enclosed in Antarctic ice cores (Lüthi et al., 2008; Bereiter et al., 2015 [a compilation]; uncertainty ±1.3ppm; see Chapter 2, Section 2.2.3 and Chapter 5, Section 5.1.2 for an assessment) and direct air measurements (Tans and Keeling, 2020; uncertainty ±0.12 ppm). Projected CO_2 concentrations for five Shared Socioeconomic Pathways (SSP) scenarios are indicated by dots on the right-hand side panels of the figure (grey background) (Meinshausen et al., 2020; SSPs are described in Section 1.6). b) Reconstruction of GMST from marine paleoclimate proxies (light grey: Snyder (2016); dark grey: Hansen et al. (2013); see Chapter 2, Section 2.3.1 for an assessment). Observed and reconstructed temperature changes since 1850 are the AR6 assessed mean (referenced to 1850–1900; Box TS.3; 2.3.1.1); dots/whiskers on the right-hand side panels of the figure (grey background) indicate the projected mean and ranges of warming derived from Coupled Model Intercomparison Project Phase 6 (CMIP6) SSP-based (2081–2100) and Model for the Assessment of Greenhouse Gas Induced Climate Change (MAGICC7) (2300) simulations (Chapter 4, Tables 4.5 and 4.9). c) Sea level changes reconstructed from a stack of oxygen isotope measurements on seven ocean sediment cores (Spratt and Lisiecki, 2016; see Chapter 2, Section 2.3.3.3 and Chapter 9, Section 9.6.2 for an assessment). The sea level record from 1850 to 1900 is from Kopp et al. (2016), while the 20th century record is an updated ensemble estimate of GMSL change (Palmer et al., 2021; see also Chapter 2, Section 2.3.3.3 and Chapter 9, Section 9.6.1.1). Dots/whiskers on the right-hand side panels of the figure (grey background) indicate the projected median and ranges derived from SSP-based simulations (2081–2100: Chapter 9, Table 9.9; 2300: Chapter 9, Section 9.6.3.5). Best estimates (dots) and uncertainties (whiskers) as assessed by Chapter 2 are included in the left and middle panels for each of the three indicators and selected paleo-reference periods used in this report (CO_2: Chapter 2, Table 2.1; GMST: Chapter 2, Section 2.3.1.1 and Cross-Chapter Box 2.3, Table 1 in Chapter 2; GMSL: Chapter 2, Section 2.3.3.3 and Chapter 9, Section 9.6.2. See also Cross-Chapter Box 2.1 in Chapter 2). Selected paleo-reference periods: LIG – Last Interglacial; LGM – Last Glacial Maximum; MH – mid-Holocene (Cross-Chapter Box 2.1, Table 1 in Chapter 2). The non-labelled best estimate in panel c) corresponds to the sea level high-stand during Marine Isotope Stage 11, about 410,000 years ago (see Chapter 9, Section 9.6.2). Further details on data sources and processing are available in the chapter data table (Table 1.SM.1).

[END FIGURE 1.5 HERE]

ACCEPTED VERSION SUBJECT TO FINAL EDITS

Paleoclimate reconstructions also shed light on the causes of these variations, revealing processes that need to be considered when projecting climate change. The paleorecords show that sustained changes in global mean temperature of a few degrees Celsius are associated with increases in sea level of several tens of metres (Figure 1.5). During two extended warm periods (interglacials) of the last 800,000 years, sea level is estimated to have been at least six metres higher than today (Chapter 2; Dutton et al., 2015). During the last interglacial, sustained warmer temperatures in Greenland preceded the peak of sea level rise (Figure 5.15 in Masson-Delmotte et al., 2013). The paleoclimate record therefore provides substantial evidence directly linking warmer GMST to substantially higher GMSL.

GMST will remain above present-day levels for many centuries even if net CO_2 emissions are reduced to zero, as shown in simulations with coupled climate models (Plattner et al., 2008; Section 12.5.3 in Collins et al., 2013; Zickfeld et al., 2013; MacDougall et al., 2020; Chapter 4, Section 4.7.1). Such persistent warm conditions in the atmosphere represent a multi-century commitment to long-term sea level rise, summer sea ice reduction in the Arctic, substantial ice sheet melting, potential ice sheet collapse, and many other consequences in all components of the climate system (Clark et al., 2016; Pfister and Stocker, 2016; Fischer et al., 2018; see also Chapter 9, Section 9.4) (Figure 1.5).

Paleoclimate records also show centennial- to millennial-scale variations, particularly during the ice ages, which indicate rapid or abrupt changes of the Atlantic Meridional Overturning Circulation (AMOC; see Chapter 9, Section 9.2.3.1) and the occurrence of a 'bipolar seesaw' (opposite-phase surface temperature changes in both hemispheres; Stocker and Johnsen, 2003; EPICA Community Members, 2006; Members WAIS Divide Project et al., 2015; Lynch-Stieglitz, 2017; Pedro et al., 2018; Weijer et al., 2019, see Chapter 2, Section 2.3.3.4.1). This process suggests that instabilities and irreversible changes could be triggered if critical thresholds are passed (Section 1.4.4.3). Several other processes involving instabilities are identified in climate models (Drijfhout et al., 2015), some of which may now be close to critical thresholds (Joughin et al., 2014; Section 1.4.4.3; see also Chapters 5, 8 and 9 regarding tipping points).

Based on Figure 1.5, the reconstructed, observed and projected ranges of changes in the three key indicators can be compared. By the first decade of the 20th century, atmospheric CO_2 concentrations had already moved outside the reconstructed range of natural variation over the past 800,000 years. On the other hand, global mean surface temperature and sea level were higher than today during several interglacials of that period (Chapter 2, Section 2.3.1, Figure 2.34 and Section 2.3.3). Projections for the end of the 21st century, however, show that GMST will have moved outside of its natural range within the next few decades, except for the strong mitigation scenarios (Section 1.6). There is a risk that GMSL may potentially leave the reconstructed range of natural variations over the next few millennia (Clark et al., 2016; Chapter 9, Section 9.6.3.5; SROCC (IPCC, 2019b). In addition, abrupt changes can not be excluded (Section 1.4.4.3).

An important time period in the assessment of anthropogenic climate change is the last 2000 years. Since AR5, new global datasets have emerged, aggregating local and regional paleorecords (PAGES 2k Consortium, 2013, 2017, 2019; McGregor et al., 2015; Tierney et al., 2015; Abram et al., 2016; Hakim et al., 2016; Steiger et al., 2018; Brönnimann et al., 2019b). Before the global warming that began around the mid-19th century (Abram et al., 2016), a slow cooling in the Northern Hemisphere from roughly 1450 to 1850 is consistently recorded in paleoclimate archives (PAGES 2k Consortium, 2013; McGregor et al., 2015). While this cooling, primarily driven by an increased number of volcanic eruptions (PAGES 2k Consortium, 2013; Owens et al., 2017; Brönnimann et al., 2019b; Chapter 3, Section 3.3.1), shows regional differences, the subsequent warming over the past 150 years exhibits a global coherence that is unprecedented in the last 2000 years (Neukom et al., 2019).

The rate, scale, and magnitude of anthropogenic changes in the climate system since the mid-20th century suggested the definition of a new geological epoch, the Anthropocene (Crutzen and Stoermer, 2000; Steffen et al., 2007), referring to an era in which human activity is altering major components of the Earth system and leaving measurable imprints that will remain in the permanent geological record (IPCC, 2018) (Figure 1.5). These alterations include not only climate change itself, but also chemical and biological changes in the Earth system such as rapid ocean acidification due to uptake of anthropogenic carbon dioxide, massive destruction of tropical forests, a worldwide loss of biodiversity and the sixth mass extinction of species

ACCEPTED VERSION SUBJECT TO FINAL EDITS

(Hoegh-Guldberg and Bruno, 2010; Ceballos et al., 2017; IPBES, 2019). According to the key messages of the last global assessment of the Intergovernmental Science-Policy Platform on Biodiversity and Ecosystem Services (IPBES, 2019), climate change is a 'direct driver that is increasingly exacerbating the impact of other drivers on nature and human well-being', and 'the adverse impacts of climate change on biodiversity are projected to increase with increasing warming'.

1.2.2 The policy and governance context

The contexts of both policymaking and societal understanding about climate change have evolved since the AR5 was published (2013–2014). Increasing recognition of the urgency of the climate change threat, along with still-rising emissions and unresolved issues of mitigation and adaptation, including aspects of sustainable development, poverty eradication and equity, have led to new policy efforts. This section summarizes these contextual developments and how they have shaped, and been used during the preparation of this Report.

IPCC reports and the UN Framework Convention on Climate Change (UNFCCC). The IPCC First Assessment Report (FAR, IPCC, 1990a) provided the scientific background for the establishment of the United Nations Framework Convention on Climate Change (UNFCCC, 1992), which committed parties to negotiate ways to 'prevent dangerous anthropogenic interference with the climate system' (the ultimate objective of the UNFCCC). The Second Assessment Report (SAR, IPCC, 1995a) informed governments in negotiating the Kyoto Protocol (1997), the first major agreement focusing on mitigation under the UNFCCC. The Third Assessment report (TAR, IPCC, 2001a) highlighted the impacts of climate change and need for adaptation and introduced the treatment of new topics such as policy and governance in IPCC reports. The Fourth and Fifth Assessment Reports (AR4, IPCC, 2007a; AR5, IPCC, 2013a) provided the scientific background for the second major agreement under the UNFCCC: the Paris Agreement (2015), which entered into force in 2016.

The Paris Agreement (PA). Parties to the PA commit to the goal of limiting global average temperature increase to 'well below 2°C above pre-industrial levels, and to pursue efforts to limit the temperature increase to 1.5°C in order to 'significantly reduce the risks and impacts of climate change'. In AR6, as in many previous IPCC reports, observations and projections of changes in global temperature are expressed relative to 1850-1900 as an approximation for pre-industrial levels (Cross-Chapter Box 1.2).

The PA further addresses mitigation (Article 4) and adaptation to climate change (Article 7), as well as loss and damage (Article 8), through the mechanisms of finance (Article 9), technology development and transfer (Article 10), capacity-building (Article 11) and education (Article 12). To reach its long-term temperature goal, the PA recommends 'achieving a balance between anthropogenic emissions by sources and removals by sinks of greenhouse gases in the second half of this century', a state commonly described as 'net zero' emissions (Article 4) (Section 6, Box 1.4). Each Party to the PA is required to submit a Nationally Determined Contribution (NDC) and pursue, on a voluntary basis, domestic mitigation measures with the aim of achieving the objectives of its NDC (Article 4).

Numerous studies of the NDCs submitted since adoption of the PA in 2015 (Fawcett et al., 2015; UNFCCC, 2015, 2016; Lomborg, 2016; Rogelj et al., 2016, 2017; Benveniste et al., 2018; Gütschow et al., 2018; United Nations Environment Programme (UNEP), 2019) conclude that they are insufficient to meet the Paris temperature goal. In the present IPCC Sixth Assessment cycle, a Special Report on Global Warming of 1.5°C (SR1.5, IPCC, 2018) assessed *high agreement* that current NDCs 'are not in line with pathways that limit warming to 1.5°C by the end of the century'. The PA includes a ratcheting mechanism designed to increase the ambition of voluntary national pledges over time. Under this mechanism, NDCs will be communicated or updated every five years. Each successive NDC will represent a 'progression beyond' the 'then current' NDC and reflect the 'highest possible ambition' (Article 4). These updates will be informed by a five-yearly periodic review including the 'Structured Expert Dialogue' (SED), as well as a 'global stocktake', to assess collective progress toward achieving the PA long-term goals. These processes will rely upon the assessments prepared during the IPCC sixth assessment cycle (e.g., Schleussner et al., 2016b;

ACCEPTED VERSION SUBJECT TO FINAL EDITS

Cross-Chapter Box 1.1).

The Structured Expert Dialogue (SED). Since AR5, the formal dialogue between the scientific and policy communities has been strengthened through a new science-policy interface, the Structured Expert Dialogue (SED). The SED was established by UNFCCC to support the work of its two subsidiary bodies, the Subsidiary Body for Scientific and Technological Advice (SBSTA) and the Subsidiary Body for Implementation (SBI). The first SED aimed to 'ensure the scientific integrity of the first periodic review' of the UNFCCC, the 2013-2015 review. The Mandate of the periodic review is to 'assess the adequacy of the long-term (temperature) goal in light of the ultimate objective of the convention' and the 'overall progress made towards achieving the long-term global goal, including a consideration of the implementation of the commitments under the Convention'.

The SED of the first periodic review (2013-2015) provided an important opportunity for face-to-face dialogue between decision makers and experts on review themes, based on 'the best available scientific knowledge, including the assessment reports of the IPCC'. That SED was instrumental in informing the long-term global goal of the PA and in providing the scientific argument of the consideration of limiting warming to 1.5°C warming (Fischlin et al., 2015; Fischlin, 2017). The SED of the second periodic review, initiated in the second half of 2020, focuses on, inter alia, 'enhancing Parties' understanding of the long-term global goal and the scenarios towards achieving it in the light of the ultimate objective of the Convention'. The second SED provides a formal venue for the scientific and the policy communities to discuss the requirements and benchmarks to achieve the 'long-term temperature goal' (LTTG) of 1.5°C and well below 2°C global warming. The discussions also concern the associated timing of net zero emissions targets and the different interpretations of the PA LTTG, including the possibility of overshooting the 1.5° C warming level before returning to it by means of negative emissions (e.g., Schleussner and Fyson, 2020; Section 1.6). The second periodic review is planned to continue until November 2022 and its focus includes the review of the progress made since the first review, with minimising 'possible overlaps' and profiting from 'synergies with the Global Stocktake'.

[START CROSS-CHAPTER BOX 1.1 HERE]

Cross-Chapter Box 1.1: The WGI contribution to the AR6 and its potential relevance for the global stocktake

Contributing Authors: Malte Meinshausen (Australia/Germany), Gian-Kasper Plattner (Switzerland), Aïda Diongue-Niang (Senegal), Francisco Doblas-Reyes (Spain), David Frame (New Zealand), Nathan Gillett (Canada/UK), Helene Hewitt (UK), Richard Jones (UK), Hong Liao (China), Jochem Marotzke (Germany), James Renwick (New Zealand), Joeri Rogelj (Belgium), Maisa Rojas (Chile), Sonia I. Seneviratne (Switzerland), Claudia Tebaldi (USA), Blair Trewin (Australia)

The global stocktake under the Paris Agreement (PA) evaluates the collective progress of countries' actions towards attaining the Agreement's purpose and long-term goals every five years. The first global stocktake is due in 2023, and then every five years thereafter, unless otherwise decided by the Conference of the Parties. The purpose and long-term goals of the PA are captured in Article 2: to 'strengthen the global response to the threat of climate change, in the context of sustainable development and efforts to eradicate poverty, including by': *mitigation*[3], specifically, 'holding the increase in the global average temperature to well below 2°C above pre-industrial levels and to pursue efforts to limit the temperature increase to 1.5°C above pre-industrial levels, recognizing that this would significantly reduce

[3] the labels of mitigation, adaptation and means of implementation and support are here provided for reader's guidance only, with no presumption about the actual legal content of the paragraphs and to which extent they encompass mitigation, adaptation and means of implementation in its entirety.

ACCEPTED VERSION SUBJECT TO FINAL EDITS

the risks and impacts of climate change'; *adaptation*, that is, 'Increasing the ability to adapt to the adverse impacts of climate change and foster climate resilience and low greenhouse gas emissions development, in a manner that does not threaten food production'; and *means of implementation and support*, that is, 'Making finance flows consistent with a pathway towards low greenhouse gas emissions and climate-resilient development'.

The PA further specifies that the stocktake shall be undertaken in a 'comprehensive and facilitative manner, considering mitigation, adaptation and the means of implementation and support, and in the light of equity and the best available science' (Article 14).

The sources of input envisaged for the global stocktake include the 'latest reports of the Intergovernmental Panel on Climate Change' as a central source of information[4]. The global stocktake is one of the key formal avenues for scientific inputs into the UNFCCC and PA negotiation process alongside, for example, the Structured Expert Dialogues under the UNFCCC[5] (Section 1.2.2).

The WGI assessment provides a wide range of information potentially relevant for the global stocktake, complementing the IPCC AR6 Special Reports, the contributions from WGII and WGIII and the Synthesis Report. This includes the state of greenhouse gas emissions and concentrations, the current state of the climate, projected long-term warming levels under different scenarios, near-term projections, the attribution of extreme events, and remaining carbon budgets. Cross-Chapter Box 1.1, Table 1 provide pointers to the in-depth material that WGI has assessed and may be relevant for the global stocktake.

The following tabularised overview of potentially relevant information from the WGI contribution for the global stocktake is structured into three sections: the current state of the climate, the long-term future, and the near-term. These sections and their order align with the three questions of the Talanoa dialogue, launched during COP23 based on the Pacific concept of talanoa[6]: '*Where are we', 'Where do we want to go'* and '*How do we get there?'*.

[START CROSS-CHAPTER BOX 1.1, TABLE 1 HERE]

Cross-Chapter Box 1.1, Table 1: WGI assessment findings and their potential relevance for the global stocktake. The table combines information assessed in this report that could potentially be relevant for the global stocktake process. Section 1 focuses on the current state of the climate and its recent past. Section 2 focuses on long-term projections in the context of the PA's 1.5°C and 2.0°C goals and on progress towards net zero greenhouse gas emissions. Section 3 considers challenges and key insights for mitigation and adaptation in the near term from a WGI perspective. Further Information on potential relevance of the aspects listed here in terms of, for example, impacts and socio-economic aspects can be found in the WGII and WGIII reports

Section 1: State of the Climate – '*Where are we?'* *WGI assessment to inform about past changes in the climate system, current climate and committed changes.*		
Question	**Chapter**	**Potential Relevance and Explanatory Remarks**

ACCEPTED VERSION SUBJECT TO FINAL EDITS

[4] paragraph 37b in 19/CMA.1 in FCCC/PA/CMA/2018/3/Add.2, pursuant decision 1/CP.21, paragraph 99 of the adoption of the PA in FCCC/CP/2015/10/Add.1, available at: https://unfccc.int/documents/193408

[5] Decision 5/CP.25, available at: https://unfccc.int/sites/default/files/resource/cp2019_13a01E.pdf

[6] Decision 1/CP.23, in FCCC/CP/2017/L.13, available at https://unfccc.int/resource/docs/2017/cop23/eng/l13.pdf

How much warming have we observed in global mean surface air temperatures?	Cross-Chapter Box 1.2; Cross-Chapter Box 2.3; 2.3.1.1, especially 2.3.1.1.3	Knowledge about the current warming relative to pre-industrial levels allows us to quantify the remaining distance to the PA goal of keeping global mean temperatures well below 2°C above pre-industrial level or pursue best efforts to limit warming to 1.5°C above pre-industrial level. Many of the report's findings are provided against a proxy for pre-industrial temperature levels with Cross-Chapter Box 1.2 examining the difference between pre-industrial levels and the 1850–1900 period.
How much has the ocean warmed?	2.3.3.1, 9.2.1.1; Box 9.1; 7.2; Box 7.2	A warming ocean can affect marine life (e.g., coral bleaching) and also are among the main contributors to long-term sea level rise (thermal expansion). Marine heatwaves can accentuate the impacts of ocean warming on marine ecosystems. Also, knowing the heat uptake of the ocean helps to better understand the response of the climate system and hence helps to project future warming.
How much have the land areas warmed and how has precipitation changed?	2.3.4; 5.4.3; 5.4.8; 8.2.1; 8.2.3; 8.5.1;	A stronger than global-average warming over land, combined with changing precipitation patterns, and/or increased aridity in some regions (like the Mediterranean) can severely affect land ecosystems and species distributions, the terrestrial carbon cycle and food production systems. Amplified warming in the Arctic can enhance permafrost thawing, which in turn can result in overall stronger anthropogenic warming (a positive feedback loop). Intensification of heavy precipitation events can cause more severe impacts related to flooding.
How did the sea ice area change in recent decades in both the Arctic and Antarctic?	2.3.2.1.1; 2.3.2.1.2; 9.3; Cross-Chapter Box 10.1; 12.4.9	Sea ice area influences mass and energy (ice-albedo, heat and momentum) exchange between the atmosphere and the ocean, and its changes in turn impact polar life, adjacent land and ice masses and complex dynamical flows in the atmosphere. The loss of a year-round sea-ice cover in the Arctic can severely impact Arctic ecosystems, affect the livelihood of First Nations in the Arctic, and amplify Arctic warming with potential consequences for the warming of the surrounding permafrost regions and ice sheets.
How much have atmospheric CO_2 and other GHG concentrations increased?	2.2.3; 2.2.4; 5.1.1; 5.2.2; 5.2.3; 5.2.4	The main human influence on the climate is via combustion of fossil fuels and land use-change-related CO_2 emissions, the principal causes of increased CO_2 concentrations since the pre-industrial period. Historical observations indicate that current atmospheric concentrations are unprecedented within at least the last 800,000 years. An understanding of historical fossil fuel emissions and the carbon cycle interactions, as well as CH_4 and N_2O sinks and sources are crucial for better estimates of future GHG emissions compatible with the PA's long-term goals.

ACCEPTED VERSION SUBJECT TO FINAL EDITS

How much did sea level rise in past centuries and how large is the long-term commitment?	2.3.3.3; 9.6.1; 9.6.2; FAQ 9.1; Box 9.1; 9.6.3; 9.6.4	Sea level rise is a comparatively slow consequence of a warming world. Historical warming committed the world already to long-term sea level rise that is not reversed in even the lowest emissions scenarios (such as 1.5°C), which come with a multimeter sea level commitment. Regional sea level change near the coastlines differs from global-mean sea level change due to vertical land movement, ice mass changes, and ocean dynamical changes.
How much has the ocean acidified and how much oxygen have they lost?	2.3.4.3; 2.3.4.2; 5.3	Ocean acidification is affecting marine life, especially organisms that build calciferous shells and structures (e.g., coral reefs). Together with less oxygen in upper ocean waters and increasingly widespread oxygen minimum zones and in addition to ocean warming, this poses adaptation challenges for coastal and marine ecosystems and their services, including seafood supply.
How much of the observed warming was due to anthropogenic influences?	3.3.1	To monitor progress toward the PA's long-term goals it is important to know how much of the observed warming is due to human activities. Chapter 3 assesses human-induced warming in global mean near-surface air temperature for the decade 2010–2019, relative to 1850–1900 with associated uncertainties, based on detection and attribution studies. This estimate can be compared with observed estimates of warming for the same decade reported in Chapter 2, and is typically used to calculate carbon budgets consistent with remaining below a particular temperature threshold.
How much has anthropogenic influence changed other aspects of the climate system?	3.3.2; 3.3.3; 3.4; 3.5; 3.6; 3.7; 8; 12; 10.4	Climate change impacts are driven by changes in many aspects of the climate system, including changes in the water cycle, atmospheric circulation, ocean, cryosphere, biosphere and modes of variability, and to better plan climate change adaptation it is relevant to know which observed changes have been driven by human influence.
How much are anthropogenic emissions contributing to changes in the severity and frequency of extreme events?	9.6.4; 11.3-11.8; 12.3; Cross-Chapter Box 3.2; 1.5; Cross-Chapter Box 1.3	Adaptation challenges are often accentuated in the face of extreme events, including floods, droughts, bushfires, and tropical cyclones. For agricultural management, infrastructure planning, and designing for climate resilience it is relevant to know whether extreme events will become more frequent in the near future. In that respect it is important to understand whether observed extreme events are part of a natural background variability or caused by past anthropogenic emissions. This attribution of extreme events is therefore key to understanding current events, as well as to better project the future evolution of these events, such as temperature extremes; heavy precipitation; floods; droughts; extreme storms and compound events; extreme sea level. Also, loss and damage events are often related to extreme events, which means that future disasters can be fractionally attributed to

ACCEPTED VERSION SUBJECT TO FINAL EDITS

		past human emissions

Section 2: Long-term climate futures. – *'Where do we want to go?'*
WGI assessment to inform how long-term climate change could unfold depending on chosen emission futures.

Question	Chapter	Potential Relevance and Explanatory Remarks
How are climate model projections used to project the range of future global and regional climate changes?	Box 4.1; 3.8.2; Cross-Chapter Box 3.1; 10.3; 10.4; 12.4	The scientific literature provides new insights in a developing field of scientific research regarding evaluating model performance and weighting. This can lead to more constrained projection ranges for a given scenario and some variables, which take into account the performance of climate models and interdependencies among them. These techniques have a strong relevance to quantifying future uncertainties, for example regarding the likelihood of the various scenarios exceeding the PA's long-term temperature goals of 1.5°C or 2°C.
If emission scenarios are pursued that achieve mitigation goals by 2050, what are the differences in climate over the 21st century compared to emission scenarios where no additional climate policies are implemented?	1.2.2; 4.6, FAQ 4.2, 12.4, 9, 11; Atlas; Interactive Atlas;	Understanding of the response to a change of anthropogenic emissions is important to estimate the scale and timing of mitigation compatible with the PA's long-term goals. The new generation of scenarios spans the response space from very low emission scenarios (SSP1-1.9) under the assumption of accelerated and effective climate policy implementation, to very high emission scenarios in the absence of additional climate policies (SSP3-7.0 or SSP5-8.5). It can be informative to place current NDCs and their emission mitigation pledges within this low and high-end scenario range, that is, in the context of medium-high emission scenarios (RCP4.5, RCP6.0 or SSP4-6.0). Climate response differences between those future medium or high emission scenarios and those compatible with the PA's long-term temperature goals can help inform policymakers about the corresponding adaptation challenges.

ACCEPTED VERSION SUBJECT TO FINAL EDITS

What is the climatic effect of net zero GHG emissions and a balance between anthropogenic sources and anthropogenic sinks?	Box 1.4; 4.7.2; 5.2.2; 5.2.3 and 5.2.4; 7.6	Understanding the long-term climate effect of global emission levels, including the effect of net zero emission targets adopted by countries as part of their long-term climate strategies, can be important when assessing whether the collective level of mitigation action is consistent with long-term goals of the PA. Understanding the dynamics of natural sources of CO_2, CH_4 and N_2O is a fundamental prerequisite to derive climate projections. Net zero GHG emissions, that is, the balance between anthropogenic sources and anthropogenic sinks of CO_2 and other greenhouse gases, will halt human-induced global warming and/or lead to slight reversal below peak warming levels. Net zero CO_2 emissions will approximately lead to a stabilisation of CO_2-induced global warming.
What is the remaining carbon budget that is consistent with the PA's long-term temperature goals?	5.5	The remaining carbon budget provides an estimate of how much CO_2 can still be emitted into the atmosphere by human activities while keeping global mean surface temperature to a specific warming level. It thus provides key geophysical information about emissions limits consistent with limiting global warming to well below 2°C above pre-industrial levels and to pursue efforts to limit the temperature increase to 1.5°C. Remaining carbon budgets can be seen in the context of historical CO_2 emissions to date. The concept of the transient climate response to cumulative emissions of CO_2 (TCRE) indicates that one tonne of CO_2 has the same effect on global warming irrespective of whether it is emitted in the past, today, or in the future. In contrast, the global warming from short-lived climate forcers is dependent on their rate of emission rather than their cumulative emission.
What is our current knowledge on the 'Reasons for Concern' related to the PA's long-term temperature goals and higher warming levels?	Cross-Chapter Box 12.1; with individual domains discussed in 2.3.3, 3.5.4, 4.3.2; 5.3; 8.4.1; 9.4.2, 9.5; 11; 12	Synthesis information on projected changes in indices of climatic impact-drivers feeds into different 'Reasons for Concern'. Where possible, an explicit transfer function between different warming levels and indices quantifying characteristics of these hazards is provided, or the difficulties in doing so documented. Those indices include Arctic sea ice area in September; global average change in ocean acidification; volume of glaciers or snow cover; ice volume change for the West Antarctic Ice Sheet (WAIS) and Greenland Ice Sheet (GIS); Atlantic Meridional Overturning Circulation (AMOC) strength ; amplitude and variance of El Niño Southern Oscillation (ENSO) mode (Nino3.4 index); and weather and climate extremes.
What are the climate effects and air pollution co-benefits of rapid decarbonisation due to the reduction of co-emitted short-lived climate forcers (SLCF)?	6.6.3 ; 6.7.3 ; Box 6.2	Understanding to what degree rapid decarbonisation strategies bring about reduced air pollution due to reductions in co-emitted short-lived climate forcers can be useful to consider integrated and/or complementary policies, with synergies for pursuing the PA goals, the World Health Organization (WHO) air quality guidelines and the Sustainable Development Goals (SDGs).

ACCEPTED VERSION SUBJECT TO FINAL EDITS

What are the Equilibrium Climate Sensitivity, the Transient Climate Response, and Transient Climate Response to Emissions and what do these indicators tell us about expected warming over the 21st century under various scenarios?	Box 4.1; 5.4, 5.5.1, 7.5	Equilibrium Climate Sensitivity (ECS) measures the long-term global-mean warming in response to doubling CO_2 concentrations from pre-industrial levels, while Transient Climate Response (TCR) also takes into account the inertia of the climate system and is an indicator for the near- and medium-term warming. TCRE is similar to TCR, but asks the question of what is the implied warming is in response to cumulative CO_2 emissions (rather than CO_2 concentration changes). The higher the ECS, TCR or TCRE, the lower are the greenhouse gas emissions that are consistent with the PA's long-term temperature goals.
What is the Earth's energy imbalance and why does it matter?	7.2.2	The current global energy imbalance implies that one can expect additional warming before the Earth's climate system attains equilibrium with the current level of concentrations and radiative forcing. Note though, that future warming commitments can be different depending on how future concentrations and radiative forcing change.
What are the regional and long-term changes in precipitation, evaporation and runoff?	8.4.1, 8.5; 8.6; 10.4; 10.6; 12.4; 11.4; 11.9; 11.6; 11.7; Atlas; Interactive Atlas	Changes in regional precipitation – in terms of both extremes and long-term averages – are important for estimating adaptation challenges. Projected changes of precipitation minus evaporation (P-E) are closely related to surface water availability and drought probability. Understanding water cycle changes over land, including seasonality, variability and extremes, and their uncertainties, is important to estimate a broad range of climate impacts and adaptation, including food production, water supply and ecosystem functioning.
Are we committed to irreversible sea level rise and what is the expected sea level rise by the end of the century if we pursue strong mitigation or high emission scenarios?	4.7.2; 9.6.3; 9.6.4; 12.4; Interactive Atlas	Unlike many regional climate responses, global-mean sea level keeps rising even in the lowest scenarios and is not halted when warming is halted. This is due to the long timescales on which ocean heat uptake, glacier melt, ice sheets react to temperature changes. Tipping points and thresholds in polar ice sheets need to be considered. Thus, sea level rise commitments and centennial-scale irreversibility of ocean warming and sea level rise are important for future impacts under even the lowest of the emission scenarios.
Can we project future climate extremes under various global warming levels in the long term?	11, 12.4; Interactive Atlas	Projections of future weather and climate extreme events and their regional occurrence, including at different global warming levels, are important for adaptation and disaster risk reduction. The attribution of these extreme events to natural variability and human-induced changes can be of relevance for both assessing adaptation challenges and issues of loss and damage.

ACCEPTED VERSION SUBJECT TO FINAL EDITS

What is the current knowledge of potential surprises, abrupt changes, tipping points and low-likelihood, high impact events related to different levels of future emissions or warming?	1.4.4; 4.7.2; 4.8; 5.4.8; Box 5.1; 8.5.3.2; 8.6.2; Box 9.4; 11.2.4; Cross-Chapter Box 4.1; Cross-Chapter Box 12.1	From a risk perspective, it is useful to have information of lower probability events and system changes, if they could potentially result in high impacts, given the dynamic interactions between climate-related hazards and socio-economic drivers (exposure, vulnerability of the affected human or ecological systems). Examples include permafrost thaw, CH_4 clathrate feedbacks, ice sheet mass loss, ocean turnover circulation changes, either accelerating warming globally or yielding particular regional responses and impacts.

Section 3: The near term. – '*How do we get there?'*
WGI assessment to inform near-term adaptation and mitigation options

Questions	**Chapter**	**Potential Relevance and Explanatory Remarks**
What are projected key climate indices under low, medium and high emission scenarios in the near term, that is, the next 20 years?	4.3; 4.4; FAQ 4.1, 10.6; 12.3; Atlas; Interactive Atlas	Much of the near-term information and comparison to historical observations allows us to quantify the climate adaptation challenges for the next decades as well as the opportunities to reduce climate change by pursuing lower emissions. For this timescale both the forced changes and the internal variability are important.
How can the climate benefit of mitigating emissions of different greenhouse gases be compared?	7.6	For mitigation challenges, it is important to compare efforts to reduce emissions of CO_2 versus emissions of other climate forcers, such as, short-lived CH_4 or long-lived N_2O. Global Warming Potentials (GWPs), which are used in the UNFCCC and in emission inventories, are updated and various other metrics are also investigated. While the NDCs of Parties to the PA, emission inventories under the UNFCCC, and various emission trading schemes work on the basis of GWP-weighted emissions, some recent discussion in the scientific literature also considers projecting temperatures induced by short-lived climate forcers on the basis of emission changes, not emissions per se.
Do mountain glaciers shrink currently and in the near-future in regions that are currently dependent on this seasonal freshwater supply?	2.3.2.3; 9.5; Cross-chapter Box 10.4; 12.4: 8.4.1; Atlas.5.2.2; Atlas.5.3.2; Atlas.6.2; Atlas.9.2	Mountain glaciers and seasonal snow cover often feed downstream river systems during the melting period, and can be an important source of freshwater. Changing river discharge can pose adaptation challenges. Melting mountain glaciers are among the main contributors to observed global mean sea level rise.

ACCEPTED VERSION SUBJECT TO FINAL EDITS

What are the capacities and limitations in the provision of regional climate information for adaptation and risk management?	10.5;10.6; Box 10.2; Cross-Chapter Box 10.4; 11.9; Cross-Chapter Box 1.3; 12.6; Cross-Chapter Box 12.1	Challenges for adaptation and risk management are predominantly local, even if globally interlinked. There are a number of approaches used in the production of regional climate information for adaptation purposes focusing on regional scales. All of them consider a range of sources of data and knowledge that are distilled into, at times contextual, climate information. A wealth of examples can be found in this Report, including assessments of extremes and climatic impact-drivers, and attribution at regional scales. Specific regions and case studies for regional projections are considered, like the Sahel and West African monsoon drought and recovery, the Southern Australian rainfall decline, the Caribbean small island summer drought, and regional projections are discussed for Cape Town, the Mediterranean region and Hindu Kush Himalaya.
How important are reductions in short-lived climate forcers compared to the reduction of CO_2 and other long-lived greenhouse gases?	6.1; 6.6; 6.7; 7.6	While most of the radiative forcing which causes climate change comes from CO_2 emissions, short-lived climate forcers also play an important role in the anthropogenic effect on climate change. Many aerosol species, especially SO_4, tend to cool the climate and their reduction leads to a masking of greenhouse gas induced warming. On the other hand, many short-lived species themselves exert a warming effect, including black carbon and CH_4, the second most important anthropogenic greenhouse gas (in terms of current radiative forcing). Notably, the climate response to aerosol emissions has a strong regional pattern and is different from that of greenhouse gas driven warming.
What are potential co-benefits and side-effects of climate change mitigation?	5.6.2; 6.1; 6.7.5	The reduction of fossil-fuel-related emissions often goes hand-in-hand with a reduction of air pollutants, such as aerosols and ozone. Reductions will improve air quality and result in broader environmental benefits (reduced acidification, eutrophication, and often tropospheric ozone recovery). More broadly, various co-benefits are discussed in WGII and WGIII, as well as co-benefits and side-effects related to certain mitigation actions, like increased biomass use and associated challenges to food security and biodiversity conservation.
What large near-term surprises could result in particular adaptation challenges?	1.4; 4.4.4; Cross-Chapter Box 4.1; 8.5.2; 11.2.4; Cross-	Surprises can come from a range of sources: from incomplete understanding of the climate system, from surprises in emissions of natural (e.g., volcanic) sources, or from disruptions to the carbon cycle associated with a warming climate (e.g., methane release from permafrost thawing, tropical forest dieback). There could be large natural variability in the near-term; or also accelerated climate

ACCEPTED VERSION SUBJECT TO FINAL EDITS

	Chapter Box 12.1	change due to a markedly more sensitive climate than previously thought. When the next large explosive volcanic eruption will happen is unknown. The largest volcanic eruptions over the last few hundred years led to substantial but temporary cooling, including precipitation changes.

[END CROSS-CHAPTER BOX 1.1, TABLE 1 HERE]

[END CROSS-CHAPTER BOX 1.1 HERE]

Sustainable Development Goals (SDGs). Many interactions among environmental problems and development are addressed in the United Nations 2030 Agenda for Sustainable Development and its Sustainable Development Goals. The 2030 Agenda, supported by the finance-oriented Addis Ababa Action Agenda (UN DESA, 2015), calls on nations to 'take the bold and transformative steps which are urgently needed to shift the world onto a sustainable and resilient path.' The 2030 Agenda recognizes that 'climate change is one of the greatest challenges of our time and its adverse impacts undermine the ability of all countries to achieve sustainable development.' SDG 13 deals explicitly with climate change, establishing several targets for adaptation, awareness-raising and finance. Climate and climate change are also highly relevant to most other SDGs, while acknowledging UNFCCC as the main forum to negotiate the global response to climate change. For example, both long-lived greenhouse gases (LLGHGs), through mitigation decisions, and SLCFs, through air quality, are relevant to SDG 11 (sustainable cities and communities). Chapter 6 assesses SLCF effects on climate and the implications of changing climate for air quality, including opportunities for mitigation relevant to the SDGs (Chapter 6, Box 6.2). Also, the UN Conference on Housing and Sustainable Development established a New Urban Agenda (United Nations, 2017) envisaging cities as part of the solutions for sustainable development, climate change adaptation and mitigation.

The Sendai Framework for Disaster Risk Reduction (SFDRR). The Sendai Framework for Disaster Risk Reduction is a non-binding agreement to reduce risks associated with disasters of all scales, frequencies and onset rates caused by natural or human-made hazards, including climate change. The SFDRR outlines targets and priorities for action including 'Understanding disaster risk', along the dimensions of vulnerability, exposure of persons and assets and hazard characteristics. Chapter 12 assesses climate information relevant to regional impact and risk assessment with a focus on climate hazards and other aspects of climate that influence society and ecosystem and makes the link with Working Group II. AR6 adopts a consistent risk and solution-oriented framing (Cross-Chapter Box 1.3) that calls for a multidisciplinary approach and cross-working group coordination in order to ensure integrative discussions of major scientific issues associated with integrative risk management and sustainable solutions (IPCC, 2017).

The Intergovernmental Science-Policy Platform on Biodiversity and Ecosystem Services (IPBES). Efforts to address climate change take place alongside and in the context of other major environmental problems, such as biodiversity loss. The Intergovernmental Science-Policy Platform on Biodiversity and Ecosystem Services (IPBES), established in 2012, builds on the IPCC model of a science-policy interface and assessment. The Platform's objective is to 'strengthen the science-policy interface for biodiversity and ecosystem services for the conservation and sustainable use of biodiversity, long-term human well-being and sustainable development' (UNEP, 2012). SROCC (IPCC, 2019b) and SRCCL (IPCC, 2019a) assessed the relations between changes in biodiversity and in the climate system. The rolling work programme of IPBES up to 2030 will address interlinkages among biodiversity, water, food and health. This assessment will use a nexus approach to examine interlinkages between biodiversity and the above-mentioned issues, including climate change mitigation and adaptation. Furthermore, IPBES and IPCC will directly collaborate on biodiversity and climate change under the rolling work programme.

Addressing climate change alongside other environmental problems, while simultaneously supporting

ACCEPTED VERSION SUBJECT TO FINAL EDITS

sustainable socioeconomic development, requires a holistic approach. Since AR5, there is increasing attention on the need for coordination among previously independent international agendas, recognizing that climate change, disaster risk, economic development, biodiversity conservation and human well-being are tightly interconnected. The current COVID-19 pandemic provides an example of the need for such interconnection, with its widespread impacts on economy, society and environment (e.g., Shan et al., 2020). Cross Chapter Box 6.1 in Chapter 6 assesses the consequences of the COVID-19 lockdowns on emissions of GHGs and SLCFs and related implications for the climate. Another example is the close link between SLCF emissions, climate evolution and air quality concerns (see Chapter 6). Emissions of halocarbons have previously been successfully regulated under the Montreal Protocol and its Kigali Amendment. This has been achieved in an effort to reduce ozone depletion that has also modulated anthropogenic climate influence (Estrada et al., 2013; Wu et al., 2013). In the process, emissions of some SLCFs are jointly regulated to reduce environmental and health impacts from air pollution (e.g., Gothenburg Protocol; Reis et al., 2012). Considering the recognized importance of SLCFs for climate, the IPCC decided in May 2019 to approve that the IPCC Task Force on National Greenhouse Gas Inventories produces an IPCC Methodology Report on SLCFs to develop guidance for national SLCFs inventories.

The evolving governance context since AR5 challenges the IPCC to provide policymakers and other actors with information relevant for both adaptation to and mitigation of climate change and for the loss and damage induced.

1.2.3 Linking science and society: communication, values, and the IPCC assessment process

This section assesses how the process of communicating climate information has evolved since AR5. It summarizes key issues regarding scientific uncertainty addressed in previous IPCC assessments and introduces the IPCC calibrated uncertainty language. Next it discusses the role of values in problem-driven, multidisciplinary science assessments such as this one. The section introduces climate services and how climate information can be tailored for greatest utility in specific contexts, such as the global stocktake. Finally, we briefly evaluate changes in media coverage of climate information since AR5, including the increasing role of internet sources and social media.

1.2.3.1 Climate change understanding, communication, and uncertainties

The response to climate change is facilitated when leaders, policymakers, resource managers, and their constituencies share basic understanding of the causes, effects, and possible future course of climate change (SR1.5, IPCC, 2018; SRCCL, IPCC, 2019a). Achieving shared understanding is complicated, since scientific knowledge interacts with pre-existing conceptions of weather and climate built up in diverse world cultures over centuries and often embedded in strongly held values and beliefs stemming from ethnic or national identities, traditions, religion, and lived relationships to weather, land and sea (Van Asselt and Rotmans, 1996; Rayner and Malone, 1998; Hulme, 2009, 2018; Green et al., 2010; Jasanoff, 2010; Orlove et al., 2010; Nakashima et al., 2012; Shepherd and Sobel, 2020). These diverse, more local understandings can both contrast with and enrich the planetary-scale analyses of global climate science (*high confidence*).

Political cultures also give rise to variation in how climate science knowledge is interpreted, used, and challenged (Leiserowitz, 2006; Oreskes and Conway, 2010; Brulle et al., 2012; Dunlap and Jacques, 2013; Mahony, 2014, 2015; Brulle, 2019). A meta-analysis of 87 studies carried out between 1998 and 2016 (62 USA national, 16 non-USA national, 9 cross-national) found that political orientation and political party identification were the second-most important predictors of views on climate change after environmental values (the strongest predictor) (McCright et al. 2016). Ruiz et al. (2020) systematically reviewed 34 studies of non-US nations or clusters of nations and 30 studies of the USA alone. They found that in the non-US studies, ‘changed weather’ and ‘socio-altruistic values’ were the most important drivers of public attitudes. For the USA case, by contrast, political affiliation and the influence of corporations were most important. Widely varying media treatment of climate issues also affects public responses (see Section 1.2.3.4). In summary, environmental and socio-altruistic values are the most significant influences on public opinion

ACCEPTED VERSION SUBJECT TO FINAL EDITS

about climate change globally, while political views, political party affiliation, and corporate influence also had strong effects, especially in the USA (*high confidence*).

Furthermore, climate change itself is not uniform. Some regions face steady, readily observable change, while others experience high variability that masks underlying trends (Section 1.4.1); most regions are subject to hazards, but some may also experience benefits, at least temporarily (see Chapters 11, 12, and Atlas). This non-uniformity may lead to wide variation in public climate change awareness and risk perceptions at multiple scales (Howe et al., 2015; Lee et al., 2015). For example, short-term temperature trends, such as cold spells or warm days, have been shown to influence public concern (Hamilton and Stampone, 2013; Zaval et al., 2014; Bohr, 2017).

Given these manifold influences and the highly varied contexts of climate change communication, special care is required when expressing findings and uncertainties, including IPCC assessments that inform decision making. Throughout the IPCC's history, all three Working Groups (WGs) have sought to explicitly assess and communicate scientific uncertainty (Le Treut et al., 2007; Cubasch et al., 2013). Over time, the IPCC has developed and revised a framework to treat uncertainties consistently across assessment cycles, reports, and Working Groups through the use of calibrated language (Moss and Schneider, 2000; IPCC, 2005). Since its First Assessment Report (IPCC, 1990a), the IPCC specified terms and methods for communicating authors' expert judgments (Mastrandrea and Mach, 2011). During the AR5 cycle, this calibrated uncertainty language was updated and unified across all WGs (Mastrandrea et al., 2010, 2011). Box 1.1 summarizes this framework as used in AR6.

[START BOX 1.1 HERE]

Box 1.1: Treatment of uncertainty and calibrated uncertainty language in AR6

The AR6 follows the approach developed for AR5 (Box 1.1, Figure 1), as described in the 'Guidance Notes for Lead Authors of the IPCC Fifth Assessment Report on Consistent Treatment of Uncertainties' (Mastrandrea et al., 2010). The uncertainty Guidance Note used in AR6 clarifies the relationship between the qualitative description of confidence and the quantitative representation of uncertainty expressed by the likelihood scale. The calibrated uncertainty language emphasizes traceability of the assessment throughout the process. Key chapter findings presented in the chapter Executive Summary are supported in the chapter text by a summary of the underlying literature that is assessed in terms of evidence and agreement, confidence, and also likelihood if applicable.

In all three WGs, author teams evaluate underlying scientific understanding and use two metrics to communicate the degree of certainty in key findings. These metrics are:

1. *Confidence:* a qualitative measure of the validity of a finding, based on the type, amount, quality and consistency of evidence (e.g., data, mechanistic understanding, theory, models, expert judgment) and the degree of agreement.
2. *Likelihood:* a quantitative measure of uncertainty in a finding, expressed probabilistically (e.g., based on statistical analysis of observations or model results, or both, and expert judgement by the author team or from a formal quantitative survey of expert views, or both).

Throughout IPCC reports, the calibrated language indicating a formal confidence assessment is clearly identified by *italics* (e.g., *medium confidence*). Where appropriate, findings can also be formulated as statements of fact without uncertainty qualifiers.

[START BOX 1.1, FIGURE 1 HERE]

Box 1.1, Figure 1: The IPCC AR6 approach for characterizing understanding and uncertainty in assessment findings. This diagram illustrates the step-by-step process authors use to evaluate and communicate the state

ACCEPTED VERSION SUBJECT TO FINAL EDITS

of knowledge in their assessment (Mastrandrea et al., 2010). Authors present evidence/agreement, confidence, or likelihood terms with assessment conclusions, communicating their expert judgments accordingly. Example conclusions drawn from this report are presented in the box at the bottom of the figure. [adapted from Mach et al. (2017)].

[END BOX 1.1, FIGURE 1 HERE]

Box.1.1, Figure 1 (adapted from Mach et al., 2017) shows the idealized step-by-step process by which IPCC authors assess scientific understanding and uncertainties. It starts with the evaluation of the available evidence and agreement (Steps 1–2). The following summary terms are used to describe the available evidence: *limited, medium,* or *robust*; and the degree of agreement: *low, medium,* or *high*. Generally, evidence is most robust when there are multiple, consistent, independent lines of high-quality evidence.

If the author team concludes that there is sufficient evidence and agreement, the level of confidence can be evaluated. In this step, assessments of evidence and agreement are combined into a single metric (Steps 3–5). The assessed level of confidence is expressed using five qualifiers: *very low, low, medium, high,* and *very high*. Step 4 depicts how summary statements for evidence and agreement relate to confidence levels. For a given evidence and agreement statement, different confidence levels can be assigned depending on the context, but increasing levels of evidence and degrees of agreement correlate with increasing confidence. When confidence in a finding is assessed to be *low*, this does not necessarily mean that confidence in its opposite is *high,* and vice versa. Similarly, *low confidence* does not imply distrust in the finding; instead, it means that the statement is the best conclusion based on currently available knowledge. Further research and methodological progress may change the level of confidence in any finding in future assessments.

If the expert judgement of the author team concludes that there is sufficient confidence and quantitative/probabilistic evidence, assessment conclusions can be expressed with likelihood statements (Box.1.1, Figure 1, Steps 5–6). Unless otherwise indicated, likelihood statements are related to findings for which the authors' assessment of confidence is '*high*' or '*very high*'. Terms used to indicate the assessed likelihood of an outcome include: *virtually certain*: 99–100% probability, *very likely*: 90–100%, *likely*: 66–100%, *about as likely as not*: 33–66%, *unlikely*: 0–33%, *very unlikely*: 0–10%, *exceptionally unlikely*: 0–1%. Additional terms (*extremely likely*: 95–100%, *more likely than not* >50–100%, and *extremely unlikely* 0–5%) may also be used when appropriate.

Likelihood can indicate probabilities for single events or broader outcomes. The probabilistic information may build from statistical or modelling analyses, other quantitative analyses, or expert elicitation. The framework encourages authors, where appropriate, to present probability more precisely than can be done with the likelihood scale, for example with complete probability distributions or percentile ranges, including quantification of tails of distributions important for risk management (Mach et al., 2017; see also Sections 1.2.2 and 1.4.4). In some instances, multiple combinations of confidence and likelihood are possible to characterize key findings. For example, a *very likely* statement might be made with *high confidence*, whereas a *likely* statement might be made with *very high confidence*. In these instances, the author teams consider which statement will convey the most balanced information to the reader.

Throughout this WGI report and unless stated otherwise, uncertainty is quantified using 90% uncertainty intervals. The 90% uncertainty interval, reported in square brackets [x to y], is estimated to have a 90% likelihood of covering the value that is being estimated. The range encompasses the median value and there is an estimated 10% combined likelihood of the value being below the lower end of the range (x) and above its upper end (y). Often the distribution will be considered symmetric about the corresponding best estimate (as in the illustrative example in the figure), but this is not always the case. In this report, an assessed 90% uncertainty interval is referred to as a '*very likely* range'. Similarly, an assessed 66% uncertainty interval is referred to as a '*likely* range'.

[END BOX 1.1 HERE]

ACCEPTED VERSION SUBJECT TO FINAL EDITS

Considerable critical attention has focused on whether applying the IPCC framework effectively achieves consistent treatment of uncertainties and clear communication of findings to users (Shapiro et al., 2010; Adler and Hirsch Hadorn, 2014). Specific concerns include, for example, the transparency and traceability of expert judgements underlying the assessment conclusions (Oppenheimer et al., 2016) and the context-dependent representations and interpretations of probability terms (Budescu et al., 2009, 2012; Janzwood, 2020). Budescu et al. (2014) surveyed 25 samples in 24 countries (a total of 10,792 individual responses), finding that even when shown IPCC uncertainty guidance, lay readers systematically misunderstood IPCC likelihood statements. When presented with a 'high likelihood' statement, they understood it as indicating a lower likelihood than intended by the IPCC authors. Conversely, they interpreted 'low likelihood' statements as indicating a higher likelihood than intended. In another study, British lay readers interpreted uncertainty language somewhat differently from IPCC guidance, but Chinese lay people reading the same uncertainty language translated into Chinese differed much more in their interpretations (Harris et al., 2013). Further, even though it is objectively more probable that wide uncertainty intervals will encompass true values, wide intervals were interpreted by lay people as implying subjective uncertainty or lack of knowledge on the part of scientists (Løhre et al., 2019). Mach et al. (2017) investigated the advances and challenges in approaches to expert judgment in the AR5. Their analysis showed that the shared framework increased the overall comparability of assessment conclusions across all WGs and topics related to climate change, from the physical science basis to resulting impacts, risks, and options for response. Nevertheless, many challenges in developing and communicating assessment conclusions persist, especially for findings drawn from multiple disciplines and Working Groups, for subjective aspects of judgments, and for findings with substantial uncertainties (Adler and Hirsch Hadorn, 2014). In summary, the calibrated language cannot entirely prevent misunderstandings, including a tendency to systematically underestimate the probability of the IPCC's higher-likelihood conclusions and overestimate the probability of the lower-likelihood ones (*high confidence*), however a consistent and systematic approach across Working Groups to communicate the assessment outcomes is an important characteristic of the IPCC.

Some suggested alternatives are impractical, such as always including numerical values along with calibrated language (Budescu et al., 2014). Others, such as using positive instead of negative expressions of low to medium probabilities, show promise but were not proposed in time for adoption in AR6 (Juanchich et al., 2020). This report therefore retains the same calibrated language used in AR5 (Box 1.1). Like previous reports, AR6 also includes FAQs that express its chief conclusions in plain language designed for lay readers.

The framework for communicating uncertainties does not address when "deep uncertainty" is identified in the assessment (Adler and Hirsch Hadorn, 2014). The definition of deep uncertainty in IPCC assessments has been described in the context of the SROCC (IPCC, 2019b; Box 5 in Abram et al. (2019)). A situation of deep uncertainty exists when experts or stakeholders do not know or cannot agree on: (1) appropriate conceptual models that describe relationships among key driving forces in a system; (2) the probability distributions used to represent uncertainty about key variables and parameters; and/or (3) how to weigh and value desirable alternative outcomes (Abram et al., 2019). (See also Cross-Chapter Box 1.2, Annex VII Glossary) Since AR5, the 'storylines' or 'narratives' approach has been used to address issues related to deep uncertainty, for example low-likelihood events that would have high impact if they occurred, to better inform risk assessment and decision making (see Section 1.4.4). Chapter 9 (Section 9.2.3) notes deep uncertainty in long term projections for sea level rise, and in processes related to Marine Ice Sheet Instability and Marine Ice Cliff Instability.

1.2.3.2 Values, science, and climate change communication

As noted above, values — fundamental attitudes about what is important, good, and right — play critical roles in all human endeavours, including climate science. In AR5, Chapters 3 and 4 of the WGIII assessment addressed the role of cultural, social, and ethical values in climate change mitigation and sustainable development (Fleurbaey et al., 2014; Kolstad et al., 2014). These values include widely accepted concepts of human rights, enshrined in international law, that are relevant to climate impacts and policy objectives (Hall

ACCEPTED VERSION SUBJECT TO FINAL EDITS

and Weiss, 2012; Peel and Osofsky, 2018; Setzer and Vanhala, 2019). Specific values – human life, subsistence, stability, and equitable distribution of the costs and benefits of climate impacts and policies – are explicit in the texts of the UNFCCC and the PA (Breakey et al., 2016; Dooley and Parihar, 2016). Here we address the role of values in how scientific knowledge is created, verified, and communicated. Chapters 10, 12, and Cross-Chapter Box 12.2 address how the specific values and contexts of users can be addressed in the co-production of climate information.

The epistemic (knowledge-related) values of science include explanatory power, predictive accuracy, falsifiability, replicability, and justification of claims by explicit reasoning (Popper, 1959; Kuhn, 1977). These are supported by key institutional values, including openness, 'organized scepticism,' and objectivity or 'disinterestedness' (Merton, 1973), operationalized as well-defined methods, documented evidence, publication, peer review, and systems for institutional review of research ethics (COSEPUP, 2009). In recent decades, open data, open code, and scientific cyberinfrastructure (notably the Earth System Grid Federation, a partnership of climate modeling centers dedicated to supporting climate research by providing secure, web-based, distributed access to climate model data) have facilitated scrutiny from a larger range of participants, and FAIR data stewardship principles – making data Findable, Accessible, Interoperable and Reusable (FAIR) – are being mainstreamed in many fields (Wilkinson et al., 2016). Climate science norms and practices embodying these scientific values and principles include the publication of data and model code, multiple groups independently analysing the same problems and data, model intercomparison projects (MIPs), explicit evaluations of uncertainty, and comprehensive assessments by national academies of science and the IPCC.

The formal Principles Governing IPCC Work (1998, amended 2003, 2006, 2012, 2013) specify that assessments should be 'comprehensive, objective, open and transparent.' The IPCC assessment process seeks to achieve these goals in several ways: by evaluating evidence and agreement across all relevant peer-reviewed literature, especially that published or accepted since the previous assessment; by maintaining a traceable, transparent process that documents the reasoning, data, and tools used in the assessment; and by maximizing the diversity of participants, authors, experts, reviewers, institutions, and communities represented, across scientific discipline, geographical location, gender, ethnicity, nationality, and other characteristics. The multi-stage review process is critical to ensure an objective, comprehensive and robust assessment, with hundreds of scientists, other experts, and governments providing comments to a series of drafts before the report is finalised.

Social values are implicit in many choices made during the construction, assessment, and communication of climate science information (Heymann et al., 2017; Skelton et al., 2017). Some climate science questions are prioritised for investigation, or given a specific framing or context, because of their relevance to climate policy and governance. One example is the question of how the effects of a 1.5°C global warming would differ from those of a 2°C warming, an assessment specifically requested by Parties to the PA. SR1.5 (2018) explicitly addressed this issue 'within the context of sustainable development; considerations of ethics, equity and human rights; and the problem of poverty' (Chapters 1 and 5; see also Hoegh-Guldberg et al., 2019) following the outcome of the approval of the outline of the Special Report by the IPCC during its 44th Session (Bangkok, Thailand, 17-20 October 2016). Likewise, particular metrics are sometimes prioritized in climate model improvement efforts because of their practical relevance for specific economic sectors or stakeholders. Examples include reliable simulation of precipitation in a specific region, or attribution of particular extreme weather events to inform rebuilding and future policy (see Chapters 8 and 11; Intemann, 2015; Otto et al., 2018; James et al., 2019). Sectors or groups whose interests do not influence research and modelling priorities may thus receive less information in support of their climate-related decisions (Parker and Winsberg, 2018).

Recent work also recognizes that choices made throughout the research process can affect the relative likelihood of false alarms (overestimating the probability and/or magnitude of hazards) or missed warnings (underestimating the probability and/or magnitude of hazards), known respectively as Type I and Type II errors. Researchers may choose different methods depending on which type of error they view as most important to avoid, a choice that may reflect social values (Douglas, 2009; Knutti, 2018; Lloyd and Oreskes, 2018). This reflects a fundamental trade-off between the values of reliability and informativeness. When

ACCEPTED VERSION SUBJECT TO FINAL EDITS

uncertainty is large, researchers may choose to report a wide range as '*very likely*', even though it is less informative about potential consequences. By contrast, high-likelihood statements about a narrower range may be more informative, yet also prove less reliable if new evidence later emerges that widens the range. Furthermore, the difference between narrower and wider uncertainty intervals has been shown to be confusing to lay readers, who often interpret wider intervals as less certain (Løhre et al., 2019).

1.2.3.3 Climate information, co-production, and climate services

In AR6, 'climate information' refers to specific information about the past, current, or future state of the climate system that is relevant for mitigation, adaptation and risk management. Cross-Chapter Box 1.1 is an example of climate information at the global scale. It provides climate change information potentially relevant to the global stocktake, and indicates where in AR6 this information may be found.

Responding to national and regional policymakers' needs for tailored information relevant to risk assessment and adaptation, AR6 emphasizes assessment of regional information more than earlier reports. Here the phrase 'regional climate information' refers to predefined reference sets of land and ocean regions; various typological domains (such as mountains or monsoons); temporal frames including baseline periods as well as near-term (2021–2040), medium-term (2041–2060), and long-term (2081–2100); and global warming levels (Sections 1.4.1 and 1.4.5; Chapters 10, 12, and Atlas). Regional climate change information is constructed from multiple lines of evidence including observations, paleoclimate proxies, reanalyses, attribution of changes and climate model projections from both global and regional climate models (Section 1.5.3, Chapter 10, Section 10.2 to 10.4). The constructed regional information needs to take account of user context and values for risk assessment, adaptation and policy decisions (Section 1.2.3, Chapter 10, Section 10.5).

As detailed in Chapter 10, scientific climate information often requires 'tailoring' to meet the requirements of specific decision-making contexts. In a study of the UK Climate Projections 2009 project, researchers concluded that climate scientists struggled to grasp and respond to users' information needs because they lacked experience interacting with users, institutions, and scientific idioms outside the climate science domain (Porter and Dessai, 2017). Economic theory predicts the value of 'polycentric' approaches to climate change informed by specific global, regional, and local knowledge and experience (Ostrom, 1996, 2012). This is confirmed by numerous case studies of extended, iterative dialogue among scientists, policymakers, resource managers, and other stakeholders to produce mutually understandable, usable, task-related information and knowledge, policymaking and resource management around the world (Lemos and Morehouse, 2005; Lemos et al., 2012, 2014, 2018; see Vaughan and Dessai, 2014 for a critical view). SR1.5 (2018) assessed that 'education, information, and community approaches, including those that are informed by indigenous knowledge and local knowledge, can accelerate the wide-scale behaviour changes consistent with adapting to and limiting global warming to 1.5°C. These approaches are more effective when combined with other policies and tailored to the motivations, capabilities and resources of specific actors and contexts (*high confidence*).' These extended dialogic 'co-production' and education processes have thus been demonstrated to improve the quality of both scientific information and governance (*high confidence*) (Chapter 10, Section 10.5; Cross Chapter Box 12.2 in Chapter 12).

Since AR5, 'climate services' have increased at multiple levels (local, national, regional, and global) to aid decision-making of individuals and organizations and to enable preparedness and early climate change action. These services include appropriate engagement from users and providers, are based on scientifically credible information and producer and user expertise, have an effective access mechanism, and respond to the users' needs (Hewitt et al., 2012; Annex VII Glossary). A Global Framework for Climate Services (GFCS) was established in 2009 by the World Meteorological Organization (WMO) in support of these efforts (Hewitt et al., 2012; Lúcio and Grasso, 2016). Climate services are provided across sectors and timescales, from sub-seasonal to multi-decadal and support co-design and co-production processes that involve climate information providers, resource managers, planners, practitioners and decision makers (Brasseur and Gallardo, 2016; Trenberth et al., 2016; Hewitt et al., 2017). For example, they may provide high-quality data on temperature, rainfall, wind, soil moisture and ocean conditions, as well as maps, risk and vulnerability analyses, assessments, and future projections and scenarios. These data and information

ACCEPTED VERSION SUBJECT TO FINAL EDITS

products may be combined with non-meteorological data, such as agricultural production, health trends, population distributions in high-risk areas, road and infrastructure maps for the delivery of goods, and other socio-economic variables, depending on users' needs (WMO, 2020a). Cross-chapter Box 12.2 in Chapter 12 illustrates the diversity of climate services with three examples from very different contexts.

The current landscape of climate services is assessed in detail in Chapter 12 (Section 12.6), with a focus on multi-decadal timescales relevant for climate change risk assessment. Other information relevant to improving climate services for decision making includes the assessment of methods to construct regional information (Chapter 10), as well as projections at the regional level (Atlas) relevant for impact and risk assessment in different sectors (Chapter 12).

1.2.3.4 Media coverage of climate change

Climate services focus on users with specific needs for climate information, but most people learn about climate science findings from media coverage. Since AR5, research has expanded on how mass media report climate change and how their audiences respond (Dewulf, 2013; Jaspal and Nerlich, 2014; Jaspal et al., 2014). For example, in five European Union (EU) countries, television coverage of the AR5 used 'disaster' and 'opportunity' as its principal themes, but virtually ignored the 'risk' framing introduced by AR5 WGII (Painter, 2015) and now extended by the AR6 (see Cross-Chapter Box 1.3). Other studies show that people react differently to climate change news when it is framed as a catastrophe (Hine et al., 2015), as associated with local identities (Sapiains et al., 2016), or as a social justice issue (Howell, 2013). Similarly, audience segmentation studies show that responses to climate change vary between groups of people with different, although not necessarily opposed, views on this phenomenon (e.g., Maibach et al., 2011; Sherley et al., 2014; Detenber et al., 2016). In Brazil, two studies have shown the influence of mass media on the high level of public climate change concern in that country (Rodas and DiGiulio, 2017; Dayrell, 2019). In the USA, analyses of television network news show that climate change receives minimal attention, is most often framed in a political context, and largely fails to link extreme weather events to climate change using appropriate probability framing (Hassol et al., 2016). However, recent evidence suggests that Climate Matters (an Internet resource for US TV weathercasters to link weather to climate change trends) may have had a positive effect on public understanding of climate change (Myers et al., 2020). Also, some media outlets have recently adopted and promoted terms and phrases stronger than the more neutral 'climate change' and 'global warming', including 'climate crisis', 'global heating', and 'climate emergency' (Zeldin-O'Neill, 2019). Google searches on those terms, and on 'climate action,' increased 20-fold in 2019, when large social movements such as the School Strikes for Climate gained worldwide attention (Thackeray et al., 2020). We thus assess that specific characteristics of media coverage play a major role in climate understanding and perception (*high confidence*), including how IPCC assessments are received by the general public.

Since AR5, social media platforms have dramatically altered the mass-media landscape, bringing about a shift from uni-directional transfer of information and ideas to more fluid, multi-directional flows (Pearce et al., 2019). A survey covering 18 Latin American countries (StatKnows-CR2, 2019) found that the main sources of information about climate change mentioned were the Internet (52% of mentions), followed by social media (18%). There are well-known challenges with social media, such as misleading or false presentations of scientific findings, incivility that diminishes the quality of discussion around climate change topics, and 'filter bubbles' that restrict interactions to those with broadly similar views (Anderson and Huntington, 2017). However, at certain moments (such as at the release of the AR5 WGI report), Twitter studies have found that more mixed, highly-connected groups existed, within which members were less polarized (Pearce et al., 2014; Williams et al., 2015). Thus, social media platforms may in some circumstances support dialogic or co-production approaches to climate communication. Because the contents of IPCC reports speak not only to policymakers, but also to the broader public, the character and effects of media coverage are important considerations across Working Groups.

ACCEPTED VERSION SUBJECT TO FINAL EDITS

1.3 How we got here: the scientific context

Scientific understanding of the climate system's fundamental features is robust and well established. This section briefly presents the major lines of evidence in climate science (Figure 1.6). It illustrates their long history and summarises key findings from the WGI contribution to AR5, where relevant referencing previous IPCC assessments for comparison. Box 1.2 summarises major findings from three Special Reports already released during the sixth IPCC assessment cycle. This chapter's Appendix 1A summarises the principal findings of all six IPCC WGI Assessment Reports, including the present one, in a single table for ready reference.

[START FIGURE 1.6 HERE]

Figure 1.6: Climate science milestones, between 1817-2021. Milestones in observations (top); Curves of global surface air temperature (GMST) using HadCRUT5 (Morice et al., 2021) and atmospheric CO_2 concentrations from Antarctic ice cores (Lüthi et al., 2008; Bereiter et al., 2015) and direct air measurements from 1957 onwards (Tans and Keeling, 2020) (see Figure 1.4 for details) (middle). Milestone in scientific understanding of the CO2 enhanced greenhouse effect (bottom). Further details on each milestone are available in Chapter 1, Section 1.3, and Chapter 1 of AR4.

[END FIGURE 1.6 HERE]

1.3.1 Lines of evidence: instrumental observations

Instrumental observations of the atmosphere, ocean, land, biosphere, and cryosphere underpin all understanding of the climate system. This section describes the evolution of instrumental data for major climate variables at Earth's land and ocean surfaces, at altitude in the atmosphere, and at depth in the ocean. Many data records exist, of varying length, continuity, and spatial distribution; Figure 1.7 gives a schematic overview of temporal coverage.

Instrumental weather observation at the Earth's surface dates to the invention of thermometers and barometers in the 1600s. National and colonial weather services built networks of surface stations in the 1800s. By the mid-19th century, semi-standardized naval weather logs recorded winds, currents, precipitation, air pressure, and temperature at sea, initiating the longest continuous quasi-global instrumental record (Maury, 1849, 1855, 1860). Because the ocean covers over 70% of global surface area and constantly exchange energy with the atmosphere, both air and sea surface temperatures (SST) recorded in these naval logs are crucial variables in climate studies. Dove (1853) mapped seasonal isotherms over most of the globe. By 1900, a patchy weather data-sharing system reached all continents except Antarctica. Regular compilation of climatological data for the world began in 1905 with the Réseau Mondial (Meteorological Office and Shaw, 1920), and the similar compilations World Weather Records (Clayton, 1927) and Monthly Climatic Data for the World (est. 1948) have been published continuously since their founding.

Land and ocean surface temperature data have been repeatedly evaluated, refined, and extended (Section 1.5.1). As computer power increased and older data were recovered from handwritten records, the number of surface station records used in published global land temperature time series grew. A pioneering study for 1880–1935 used fewer than 150 stations (Callendar, 1938). A benchmark study of 1880–2005 incorporated 4300 stations (Brohan et al., 2006). A study of the 1753–2011 period included previously unused station data, for a total of 36,000 stations (Rohde et al., 2013); recent versions of this dataset comprise over 40,000 land stations (Rohde and Hausfather, 2020). Several centres, including NOAA, Hadley, and Japan Meteorological Agency (JMA), each produce SST datasets independently calculated from instrumental records. In the 2000s, adjustments for bias due to different measurement methods (buckets, engine intake thermometers, moored and drifting buoys) resulted in major improvements of SST data (Thompson et al., 2008), and these improvements continue (Huang et al., 2017; Kennedy et al., 2019). SST and land-based data are incorporated into global surface temperature datasets calculated independently by multiple research

ACCEPTED VERSION SUBJECT TO FINAL EDITS

groups, including NOAA, NASA, Berkeley Earth, Hadley-CRU, JMA, and China Meteorological Administration (CMA). Each group aggregates the raw measurement data, applies various adjustments for non-climatic biases such as urban heat-island effects, and addresses unevenness in geospatial and temporal sampling with various techniques (see Chapter 2, Section 2.3.1.1.3 and Table 2.4 for references). Other research groups provide alternative interpolations of these datasets using different methods (e.g., Cowtan and Way, 2014; Kadow et al., 2020). Using the then available global surface temperature datasets, WGI AR5 assessed that the global mean surface temperature (GMST) increased by 0.85°C from 1880 to 2012 and found that each of the three decades following 1980 was successively warmer at the Earth's surface than any preceding decade since 1850 (IPCC, 2013b). Marine air temperatures, especially those measured during night-time, are increasingly also used to examine variability and long-term trends (e.g., Rayner et al., 2006; Kent et al., 2013; Cornes et al., 2020; Junod and Christy, 2020). Cross-Chapter Box 2.3 in Chapter 2 discusses updates to the global temperature datasets, provides revised estimates for the observed changes and considers whether marine air temperatures are changing at the same rate as SSTs.

Data at altitude came initially from scattered mountain summits, balloons, and kites, but the upper troposphere and stratosphere were not systematically observed until radiosonde (weather balloon) networks emerged in the 1940s and 1950s. These provide the longest continuous quasi-global record of the atmosphere's vertical dimension (Stickler et al., 2010). New methods for spatial and temporal homogenisation (intercalibration and quality control) of radiosonde records were introduced in the 2000s (Sherwood et al., 2008, 2015; Haimberger et al., 2012). Since 1978, Microwave Sounding Units (MSU) mounted on Earth-orbiting satellites have provided a second high-altitude data source, measuring temperature, humidity, ozone, and liquid water throughout the atmosphere. Over time, these satellite data have required numerous adjustments to account for such factors as orbital precession and decay (Edwards, 2010). Despite repeated adjustments, however, marked differences remain in the temperature trends from surface, radiosonde, and satellite observations; between the results from three research groups that analyse satellite data (UAH, RSS, and NOAA); and between modelled and satellite-derived tropospheric warming trends (Thorne et al., 2011; Santer et al., 2017). These differences are the subject of ongoing research (Maycock et al., 2018). In the 2000s, Atmospheric Infrared Sounder (AIRS) and radio occultation (GNSS-RO) measurements provided new ways to measure temperature at altitude, complementing data from the MSU. GNSS-RO is a new independent, absolutely calibrated source, using the refraction of radio-frequency signals from the Global Navigation Satellite System (GNSS) to measure temperature, pressure, and water vapour (Chapter 2, Section 2.3.1.2.1; Foelsche et al., 2008; Anthes, 2011).

Heat-retaining properties of the atmosphere's constituent gases were closely investigated in the 19th century. Foote, (1856) measured solar heating of CO_2 experimentally and argued that higher concentrations in the atmosphere would increase Earth's temperature. Water vapour, ozone, carbon dioxide, and certain hydrocarbons were found to absorb longwave (infrared) radiation, the principal mechanism of the greenhouse effect (Tyndall, 1861). 19th-century investigators also established the existence of a natural biogeochemical carbon cycle. CO_2 emitted by volcanoes is removed from the atmosphere through a combination of silicate rock weathering, deep-sea sedimentation, oceanic absorption, and biological storage in plants, shellfish, and other organisms. On multi-million-year timescales, the compression of fossil organic matter stores carbon as coal, oil, and natural gas (Chamberlin, 1897, 1898; Ekholm, 1901).

Arrhenius (1896) calculated that a doubling of atmospheric carbon dioxide would produce a 5–6°C warming, but in 1900 new measurements seemed to rule out CO_2 as a greenhouse gas due to overlap with the absorption bands of water vapour (Ångström, 1900; Very and Abbe, 1901). Further investigation and more sensitive instruments later overturned Ångström's conclusion (Fowle, 1917; Callendar, 1938). Nonetheless, the major role of CO_2 in the energy balance of the atmosphere was not widely accepted until the 1950s (Callendar, 1949; Plass, 1956, 1961; Manabe and Möller, 1961; Weart, 2008; Edwards, 2010). Revelle and Keeling established carbon dioxide monitoring stations in Antarctica and Hawaii during the 1957–1958 International Geophysical Year (Revelle and Suess, 1957; Keeling, 1960). These stations have tracked rising atmospheric CO_2 concentrations from 315 ppm in 1958 to 414 ppm in 2020. Ground-based monitoring of other greenhouse gases followed. The Greenhouse Gases Observing Satellite (GOSat) was launched in 2009, and two Orbiting Carbon Observatory satellite instruments have been in orbit since 2014.

ACCEPTED VERSION SUBJECT TO FINAL EDITS

WGI AR5 highlighted 'the other CO_2 problem' (Doney et al., 2009), that is, ocean acidification caused by the absorption of some 20–30% of anthropogenic carbon dioxide from the atmosphere and its conversion to carbonic acid in seawater. WGI AR5 assessed that the pH of ocean surface water has decreased by 0.1 since the beginning of the industrial era (*high confidence*), indicating approximately a 30% increase in acidity (IPCC, 2013b).

With a heat capacity about 1000 times greater than that of the atmosphere, Earth's ocean stores the vast majority of energy retained by the planet. Ocean currents transport the stored heat around the globe and, over decades to centuries, from the surface to its greatest depths. The ocean's thermal inertia moderates faster changes in radiative forcing on land and in the atmosphere, reaching full equilibrium with the atmosphere only after hundreds to thousands of years (Yang and Zhu, 2011). The earliest subsurface measurements in the open ocean date to the 1770s (Abraham et al., 2013). From 1872–76, the research ship *HMS Challenger* measured global ocean temperature profiles at depths up to 1700 m along its cruise track. By 1900, research ships were deploying instruments such as Nansen bottles and Mechanical BathyThermographs (MBTs) to develop profiles of the upper 150 m in areas of interest to navies and commercial shipping (Abraham et al., 2013). Starting in 1967, eXpendable BathyThermographs (XBTs) were deployed by scientific and commercial ships along repeated transects to measure temperature to 700 m (Goni et al., 2019). Ocean data collection expanded in the 1980s with the Tropical Ocean Global Experiment (TOGA; Gould, 2003). Marine surface observations for the globe, assembled in the mid-1980s in the International Comprehensive Ocean-Atmosphere Data Set (ICOADS; Woodruff et al., 1987, 2005), were extended to 1662–2014 using newly recovered marine records and metadata (Woodruff et al., 1998; Freeman et al., 2017). The Argo submersible float network developed in the early 2000s provided the first systematic global measurements of the 700–2000 m layer. Comparing the *HMS Challenger* data to data from Argo submersible floats revealed global subsurface ocean warming on the centennial scale (Roemmich et al., 2012). WGI AR5 assessed with *high confidence* that ocean warming accounted for more than 90% of the additional energy accumulated by the climate system between 1971 and 2010 (IPCC, 2013b). In comparison, warming of the atmosphere corresponds to only about 1% of the additional energy accumulated over that period (IPCC, 2013a). Chapter 2 summarises the ocean heat content datasets used in AR6 (Chapter 2, Section 2.3.3.1; Table 2.7).

Water expands as it warms. This thermal expansion, along with glacier mass loss, were the dominant contributors to global mean sea level rise during the 20th century (*high confidence*) according to AR5 (IPCC, 2013b). Sea level can be measured by averaging across tide gauges, some of which date to the 18th century. However, translating tide gauge readings into global mean sea levevl (GMSL) is challenging, since their spatial distribution is limited to continental coasts and islands, and their readings are relative to local coastal conditions that may shift vertically over time. Satellite radar altimetry, introduced operationally in the 1990s, complements the tide gauge record with geocentric measurements of GMSL at much greater spatial coverage (Katsaros and Brown, 1991; Fu et al., 1994). WGI AR5 assessed that global mean sea level rose by 0.19 [0.17 to 0.21] m over the period 1901–2010, and that the rate of sea level rise increased from 2.0 [1.7 to 2.3] mm yr^{-1} in 1971–2010 to 3.2 [2.8 to 3.6] mm yr^{-1} from 1993–2010. Warming of the ocean *very likely* contributed 0.8 [0.5 to 1.1] mm yr^{-1} of sea level change during 1971–2010, with the majority of that contribution coming from the upper 700 m (IPCC, 2013b). Chapter 2, Section 2.3.3.3 assesses current understanding of the extent and rate of sea level rise, past and present.

Satellite remote sensing also revolutionised studies of the cryosphere (Chapter 2, Section 2.3.2 and Chapter 9, Sections 9.3 to 9.5), particularly near the poles where conditions make surface observations very difficult. Satellite mapping and measurement of snow cover began in 1966, with land and sea ice observations following in the mid-1970s. Yet prior to the Third Assessment Repor, researchers lacked sufficient data to tell whether the Greenland and Antarctic Ice Sheets were shrinking or growing. Through a combination of satellite and airborne altimetry and gravity measurements, and improved knowledge of surface mass balance and perimeter fluxes, a consistent signal of ice loss for both ice sheets was established by the time of AR5 (Shepherd et al., 2012). After 2000, satellite radar interferometry revealed rapid changes in surface velocity at ice-sheet margins, often linked to reduction or loss of ice shelves (Scambos et al., 2004; Rignot and Kanagaratnam, 2006). Whereas sea ice area and concentration were continuously monitored since 1979 from microwave imagery, datasets for ice thickness emerged later from upward sonar profiling by submarines (Rothrock et al., 1999) and radar altimetry of sea-ice freeboards (Laxon et al., 2003). A recent reconstruction

ACCEPTED VERSION SUBJECT TO FINAL EDITS

of Arctic sea ice extent back to 1850 found no historical precedent for the Arctic sea ice minima of the 21st century (Walsh et al., 2017). Glacier length has been monitored for decades to centuries; internationally coordinated activities now compile worldwide glacier length and mass balance observations (World Glacier Monitoring Service, Zemp et al., 2015), global glacier outlines (Randolph Glacier Inventory, Pfeffer et al., 2014), and ice thickness of about 1100 glaciers (GlaThiDa, Gärtner-Roer et al., 2014). In summary, these data allowed WGI AR5 to assess that over the last two decades, the Greenland and Antarctic Ice Sheets have been losing mass, glaciers have continued to shrink almost worldwide, and Arctic sea ice and Northern Hemisphere spring snow cover have continued to decrease in extent (*high confidence*) (IPCC, 2013b).

[START FIGURE 1.7 HERE]

Figure 1.7: Schematic of temporal coverage of selected instrumental climate observations (top) and selected paleoclimate archives (bottom). The satellite era began in 1979 CE (Common Era). The width of the taper gives an indication of the amount of available records.

[END FIGURE 1.7 HERE]

1.3.2 Lines of evidence: paleoclimate

With the gradual acceptance of geological 'deep time' in the 19th century came investigation of fossils, geological strata, and other evidence pointing to large shifts in the Earth's climate, from ice ages to much warmer periods, across thousands to billions of years. This awareness set off a search for the causes of climatic changes. The long-term perspective provided by paleoclimate studies is essential to understanding the causes and consequences of natural variations in climate, as well as crucial context for recent anthropogenic climatic change. The reconstruction of climate variability and change over recent millennia began in the 1800s (Brückner et al., 2000; Brückner, 2018 [1890]; Coen, 2018, 2020). In brief, paleoclimatology reveals the key role of carbon dioxide and other greenhouse gases in past climatic variability and change, the magnitude of recent climate change in comparison to past glacial-interglacial cycles, and the unusualness recent climate change (Section 1.2.1.2; Cross Chapter Box 2.1 in Chapter 2; Tierney et al., 2020). FAQ 1.3 provides a plain-language summary of its importance.

Paleoclimate studies reconstruct the evolution of Earth's climate over hundreds to billions of years using pre-instrumental historical archives, indigenous knowledge and natural archives left behind by geological, chemical, and biological processes (Figure 1.7). Paleoclimatology covers a wide range of temporal scales, ranging from the human historical past (decades to millennia) to geological deep time (millions to billions of years). Paleoclimate reference periods are presented in Cross Chapter Box 2.1 in Chapter 2.

Historical climatology aids near-term paleoclimate reconstructions using media such as diaries, almanacs, and merchant accounts that describe climate-related events such as frosts, thaws, flowering dates, harvests, crop prices, and droughts (Lamb, 1965, 1995; Le Roy Ladurie, 1967; Brázdil et al., 2005). Meticulous records by Chinese scholars and government workers, for example, have permitted detailed reconstructions of China's climate back to 1000 CE, and even beyond (Louie and Liu, 2003; Ge et al., 2008). Climatic phenomena such as large-scale, regionally and temporally distributed warmer and cooler periods of the past 2000 years were originally reconstructed from European historical records (Lamb, 1965, 1995; Le Roy Ladurie, 1967; Neukom et al., 2019).

Indigenous and local knowledge have played an increasing role in historical climatology, especially in areas where instrumental observations are sparse. Peruvian fishermen named the periodic El Niño warm current in the Pacific, linked by later researchers to the Southern Oscillation (Cushman, 2004). Inuit communities have contributed to climatic history and community based monitoring across the Arctic (Riedlinger and Berkes, 2001; Gearheard et al., 2010). Indigenous Australian knowledge of climatic patterns has been offered as a complement to sparse observational records (Green et al., 2010; Head et al., 2014), such as those of sea-level

ACCEPTED VERSION SUBJECT TO FINAL EDITS

rise (Nunn and Reid, 2016). Ongoing research seeks to conduct further dialogue, utilise Indigenous and local knowledge as an independent line of evidence complementing scientific understanding, and analyse their utility for multiple purposes, especially adaptation (Laidler, 2006; Alexander et al., 2011; IPCC, 2019c). Indigenous and local knowledge are used most extensively by IPCC Working Group II.

Certain geological and biological materials preserve evidence of past climate changes. These 'natural archives' include corals, trees, glacier ice, speleothems (stalactites and stalagmites), loess deposits (dust sediments), fossil pollen, peat, lake sediment, and marine sediment (Stuiver, 1965; Eddy, 1976; Haug et al., 2001; Wang et al., 2001; Jones et al., 2009; Bradley, 2015). By the early 20th century, laboratory research had begun using tree rings to reconstruct precipitation and the possible influence of sunspots on climatic change (Douglass, 1914, 1919, 1922). Radiocarbon dating, developed in the 1940s (Arnold and Libby, 1949), allows accurate determination of the age of carbon-containing materials from the past 50,000 years; this dating technique ushered in an era of rapid progress in paleoclimate studies.

On longer timescales, tiny air bubbles trapped in polar ice sheets provide direct evidence of past atmospheric composition, including CO_2 levels (Petit et al., 1999), and the ^{18}O isotope in frozen precipitation serves as a proxy marker for temperature (Dansgaard, 1954). Sulphate deposits in glacier ice and as ash layers within sediment record major volcanic eruptions, providing another mechanism for dating. The first paleoclimate reconstructions used an almost 100,000-year ice core taken at Camp Century, Greenland (Dansgaard et al., 1969; Langway Jr, 2008). Subsequent cores from Antarctica extended this climatic record to 800,000 years (EPICA Community Members, 2004; Jouzel, 2013). Comparisons of air contained in these ice samples against measurements from the recent past enabled WGI AR5 to assess that atmospheric concentrations of CO_2, methane (CH_4), and nitrous oxide (N_2O) had all increased to levels unprecedented in at least the last 800,000 years (IPCC, 2013b) (see Section 1.2.1.2, Figure 1.5).

Global reconstructions of sea surface temperature were developed from material contained in deep-sea sediment cores (CLIMAP Project Members et al., 1976), providing the first quantitative constraints for model simulations of ice age climates (e.g., Rind and Peteet, 1985). Paleoclimate data and modelling showed that the Atlantic Ocean circulation has not been stable over glacial-interglacial time periods, and that many changes in ocean circulation are associated with abrupt transitions in climate in the North Atlantic region (Ruddiman and McIntyre, 1981; Broecker et al., 1985; Boyle and Keigwin, 1987; Manabe and Stouffer, 1988).

By the early 20th century, cyclical changes in insolation due to the interacting periodicities of orbital eccentricity, axial tilt, and axial precession had been hypothesised as a chief pacemaker of ice age-interglacial cycles on multi-millennial timescales (Milankovich, 1920). Paleoclimate information derived from marine sediment provides quantitative estimates of past temperature, ice volume, and sea level over millions of years (Section 1.2.1.2, Figure 1.5) (Emiliani, 1955; Shackleton and Opdyke, 1973; Siddall et al., 2003; Lisiecki and Raymo, 2005; Past Interglacials Working Group of PAGES, 2016). These estimates have bolstered the orbital cycles hypothesis (Hays et al., 1976; Berger, 1977, 1978). However, paleoclimatology of multi-million to billion-year periods reveals that methane, carbon dioxide, continental drift, silicate rock weathering, and other factors played a greater role than orbital cycles in climate changes during ice-free 'hothouse' periods of Earth's distant past (Frakes et al., 1992; Bowen et al., 2015; Zeebe et al., 2016).

The WGI AR5 (IPCC, 2013b) used paleoclimatic evidence to put recent warming and sea level rise in a multi-century perspective and assessed that 1983–2012 was *likely* the warmest 30-year period of the last 1400 years in the Northern Hemisphere (*medium confidence*). AR5 also assessed that the rate of sea level rise since the mid-19th century has been larger than the mean rate during the previous two millennia (*high confidence)*.

1.3.3 Lines of evidence: identifying natural and human drivers

The climate is a globally interconnected system driven by solar energy. Scientists in the 19th-century established the main physical principles governing Earth's temperature. By 1822, the principle of radiative

ACCEPTED VERSION SUBJECT TO FINAL EDITS

equilibrium (the balance between absorbed solar radiation and the energy Earth re-radiates into space) had been articulated, and the atmosphere's role in retaining heat had been likened to a greenhouse (Fourier, 1822). The primary explanations for natural climate change — greenhouse gases, orbital factors, solar irradiance, continental position, volcanic outgassing, silicate rock weathering, and the formation of coal and carbonate rock — were all identified by the late 1800s (Fleming, 1998; Weart, 2008).

The natural and anthropogenic factors responsible for climate change are known today as radiative 'drivers' or 'forcers'. The net change in the energy budget at the top of the atmosphere, resulting from a change in one or more such drivers, is termed radiative forcing (RF; see Annex VII: Glossary) and measured in Watts per square metre (W m^{-2}). The total radiative forcing over a given time interval (often since 1750) represents the sum of positive drivers (inducing warming) and negative ones (inducing cooling). Past IPCC reports have assessed scientific knowledge of these drivers, quantified their range for the period since 1750, and presented the current understanding of how they interact in the climate system. Like all previous IPCC reports, AR5 assessed that total radiative forcing has been positive at least since 1850–1900, leading to an uptake of energy by the climate system, and that the largest single contribution to total radiative forcing is the rising atmospheric concentration of CO_2 since 1750 (IPCC, 2013a; see Cross-Chapter Box 1.2 and Chapter 7).

Natural drivers include changes in solar irradiance, ocean currents, naturally occurring aerosols, and natural sources and sinks of radiatively active gases such as water vapour, carbon dioxide, methane, and sulphur dioxide. Detailed global measurements of surface-level solar irradiance were first conducted during the 1957–1958 International Geophysical Year (Landsberg, 1961), while top-of-atmosphere irradiance has been measured by satellites since 1959 (House et al., 1986). Measured changes in solar irradiance have been small and slightly negative since about 1980 (Matthes et al., 2017). Water vapour is the most abundant radiatively active gas, accounting for about 75% of the terrestrial greenhouse effect, but because its residence time in the atmosphere averages just 8–10 days, its atmospheric concentration is largely governed by temperature (van der Ent and Tuinenburg, 2017; Nieto and Gimeno, 2019). As a result, non-condensing greenhouse gases with much longer residence times serve as 'control knobs', regulating planetary temperature, with water vapour concentrations as a feedback effect (Lacis et al., 2010, 2013). The most important of these non-condensing gases is carbon dioxide (a positive driver), released naturally by volcanism at about 637 $MtCO_2$ yr^{-1} in recent decades, or roughly 1.6% of the 37 $GtCO_2$ emitted by human activities in 2018 (Burton et al., 2013; Le Quéré et al., 2018). Absorption by the ocean and uptake by plants and soils are the primary natural CO_2 sinks on decadal to centennial time scales (see Chapter 5, Section 5.1.2 and Figure 5.3).

Aerosols (tiny airborne particles) interact with climate in numerous ways, some direct (e.g. reflecting solar radiation back into space) and others indirect (e.g., cloud droplet nucleation); specific effects may cause either positive or negative radiative forcing. Major volcanic eruptions inject sulphur dioxide (SO_2, a negative driver) into the stratosphere, creating aerosols that can cool the planet for years at a time by reflecting some incoming solar radiation. The history and climatic effects of volcanic activity have been traced through historical records, geological traces, and observations of major eruptions by aircraft, satellites, and other instruments (Dörries, 2006). The negative RF of major volcanic eruptions was considered in the First Assessment Report (FAR; IPCC, 1990a). In subsequent assessments, the negative RF of smaller eruptions has also been considered (e.g., Chapter 2, section 2.4.3 in IPCC, 1995; Cross-Chapter Box 4.1 in Chapter 4 of this report). Dust and other natural aerosols have been studied since the 1880s (e.g., Aitken, 1889; Ångström, 1929, 1964; Twomey, 1959), particularly in relation to their role in cloud nucleation, an aerosol indirect effect whose RF may be either positive or negative depending on such factors as cloud altitude, depth, and albedo (Stevens and Feingold, 2009; Boucher et al., 2013).

Anthropogenic (human) drivers of climatic change were hypothesised as early as the 17th century, with a primary focus on forest clearing and agriculture (Grove, 1995; Fleming, 1998). In the 1890s, Arrhenius was first to calculate the effects of increased or decreased CO_2 concentrations on planetary temperature, and Högbom estimated that worldwide coal combustion of about 500 Mt yr^{-1} had already completely offset the natural absorption of CO_2 by silicate rock weathering (Högbom, 1894; Arrhenius, 1896; Berner, 1995; Crawford, 1997). As coal consumption reached 900 Mt yr^{-1} only a decade later, Arrhenius wrote that anthropogenic carbon dioxide from fossil fuel combustion might eventually warm the planet (Arrhenius, 1908). In 1938, analysing records from 147 stations around the globe, Callendar calculated atmospheric

ACCEPTED VERSION SUBJECT TO FINAL EDITS

warming over land at 0.3-0.4°C from 1880-1935 and attributed about half of this warming to anthropogenic CO_2 (Callendar, 1938; Fleming, 2007; Hawkins and Jones, 2013; Figure 1.8).

[START FIGURE 1.8 HERE]

Figure 1.8: G.S. Callendar's estimates of global land temperature variations and their possible causes. (a) The original figure from Callendar (1938), using measurements from 147 surface stations for 1880–1935, showing: (top) ten-year moving departures from the mean of 1901-1930 (°C), with the dashed line representing his estimate of the 'CO_2 effect' on temperature rise, and (bottom) annual departures from the 1901–1930 mean (°C). (b) Comparing the estimates of global land (60°S–60°N) temperatures tabulated in Callendar (1938, 1961) with a modern reconstruction (Osborn et al., 2021) for the same period, after (Hawkins and Jones (2013). Further details on data sources and processing are available in the chapter data table (Table 1.SM.1).

[END FIGURE 1.8 HERE]

Studies of radiocarbon (^{14}C) in the 1950s established that increasing atmospheric CO_2 concentrations were due to fossil fuel combustion. Since all the ^{14}C once contained in fossil fuels long ago decayed into non-radioactive ^{12}C, the CO_2 produced by their combustion reduces the overall concentration of atmospheric ^{14}C (Suess, 1955). Related work demonstrated that while the ocean was absorbing around 30% of anthropogenic CO_2, these emissions were also accumulating in the atmosphere and biosphere (see Section 1.3.1 and Chapter 5, Section 5.2.1.5). Further work later established that atmospheric oxygen levels were decreasing in inverse relation to the anthropogenic CO_2 increase, because combustion of carbon consumes oxygen to produce CO_2 (Keeling and Shertz, 1992; IPCC, 2013a, Chapters 2 and 6). Revelle and Suess (1957) famously described fossil fuel emissions as a 'large scale geophysical experiment', in which 'within a few centuries we are returning to the atmosphere and ocean the concentrated organic carbon stored in sedimentary rocks over hundreds of millions of years'. The 1960s saw increasing attention to other radiatively active gases, especially ozone (Manabe and Möller, 1961; Plass, 1961). Methane and nitrous oxide were not considered systematically until the 1970s, when anthropogenic increases in those gases were first noted (Wang et al., 1976). In the 1970s and 1980s, scientists established that synthetic halocarbons (see Annex VII: Glossary), including widely used refrigerants and propellants, were extremely potent greenhouse gases (Ramanathan, 1975; Chapter 2, Section 2.2.4.3; Chapter 6, section 6.2.2.9). When these chemicals were also found to be depleting the stratospheric ozone layer, they were stringently and successfully regulated on a global basis by the 1987 Montreal Protocol on the Ozone Layer and successor agreements (Parson, 2003).

Radioactive fallout from atmospheric nuclear weapons testing (1940s–1950s) and urban smog (1950s–1960s) first provoked widespread attention to anthropogenic aerosols and ozone in the troposphere (Edwards, 2012). Theory, measurement, and modelling of these substances developed steadily from the 1950s (Hidy, 2019). However, the radiative effects of anthropogenic aerosols did not receive sustained study until around 1970 (Bryson and Wendland, 1970; Rasool and Schneider, 1971), when their potential as cooling agents was recognised (Peterson et al., 2008). The US Climatic Impact Assessment Program (CIAP) found that proposed fleets of supersonic aircraft, flying in the stratosphere, might cause substantial aerosol cooling and depletion of the ozone layer, stimulating efforts to understand and model stratospheric circulation, atmospheric chemistry, and aerosol radiative effects (Mormino et al., 1975; Toon and Pollack, 1976). Since the 1980s, aerosols have increasingly been integrated into comprehensive modelling studies of transient climate evolution and anthropogenic influences, through treatment of volcanic forcing, links to global dimming and cloud brightening, and their influence on cloud nucleation and other properties (e.g., thickness, lifetime, and extent) and precipitation (e.g., Hansen et al., 1981; Charlson et al., 1987, 1992; Albrecht, 1989; Twomey, 1991).

The FAR (1990) focused attention on human emissions of carbon dioxide, methane, tropospheric ozone, chlorofluorocarbons (CFCs), and nitrous oxide. Of these, at that time only the emissions of CO_2 and CFCs were well measured, with methane sources known only 'semi-quantitatively' (IPCC, 1990a). The FAR

ACCEPTED VERSION SUBJECT TO FINAL EDITS

assessed that some other trace gases, especially CFCs, have global warming potentials hundreds to thousands of times greater than CO_2 and methane, but are emitted in much smaller amounts. As a result, CO_2 remains by far the most important positive anthropogenic driver, with methane next most significant (Section 1.6.3); anthropogenic methane stems from such sources as fossil fuel extraction, natural gas pipeline leakage, agriculture, and landfills. In 2001, increased greenhouse forcing attributable to CO_2, methane, ozone, CFC-11, and CFC-12 was detected by comparing satellite measurements of outgoing longwave radiation measurements taken in 1970 and in 1997 (Harries et al., 2001). AR5 assessed that the 40% increase in atmospheric CO_2 contributed most to positive RF since 1750. Together, changes in atmospheric concentrations of CO_2, methane, nitrous oxide, and halocarbons from 1750–2011 were assessed to contribute a positive RF of 2.83 [2.26 to 3.40] W m^{-2} (IPCC, 2013b).

All IPCC reports have assessed the total RF as positive when considering all sources. However, due to the considerable variability of both natural and anthropogenic aerosol loads, the FAR characterised total aerosol RF as 'highly uncertain' and was unable even to determine its sign (positive or negative). Major advances in quantification of aerosol loads and their effects have taken place since then, and IPCC reports since 1992 have consistently assessed total forcing by anthropogenic aerosols as negative (IPCC, 1992, 1995a, 1996). However, due to their complexity and the difficulty of obtaining precise measurements, aerosol effects have been consistently assessed as the largest single source of uncertainty in estimating total RF (Stevens and Feingold, 2009; IPCC, 2013a). Overall, AR5 assessed that total aerosol effects, including cloud adjustments, resulted in a negative RF of –0.9 [–1.9 to −0.1] W m^{-2} (*medium confidence*), offsetting a substantial portion of the positive RF resulting from the increase in greenhouse gases (*high confidence*) (IPCC, 2013b). Chapter 7 provides an updated assessment of the total and per-component RF for the WGI contribution to AR6.

1.3.4 Lines of evidence: understanding and attributing climate change

Understanding the global climate system requires both theoretical understanding and empirical measurement of the major forces and factors that govern the transport of energy and mass (air, water and water vapour) around the globe; the chemical and physical properties of the atmosphere, ocean, cryosphere, and land surfaces; and the biological and physical dynamics of natural ecosystems, as well as the numerous feedbacks (both positive and negative) among these processes. Attributing climatic changes or extreme weather events to human activity (see Cross Working Group Box: Attribution) requires, additionally, understanding of the many ways that human activities may affect the climate, along with statistical and other techniques for separating the 'signal' of anthropogenic climate change from the 'noise' of natural climate variability (see Section 1.4.2). This inter- and trans-disciplinary effort requires contributions from many sciences.

Due to the complexity of many interacting processes ranging in scale from the molecular to the global, and occurring on timescales from seconds to millennia, attribution makes extensive use of conceptual, mathematical, and computer simulation models. Modelling allows scientists to combine a vast range of theoretical and empirical understanding from physics, chemistry, and other natural sciences, producing estimates of their joint consequences as simulations of past, present, or future states and trends (Nebeker, 1995; Edwards, 2010, 2011).

In addition to radiative transfer (discussed above in Section 1.3.3), forces and factors such as thermodynamics (energy conversions), gravity, surface friction, and the Earth's rotation govern the planetary-scale movements or 'circulation' of air and water in the climate system. The scientific theory of climate began with Halley (1686), who hypothesized vertical atmospheric circulatory cells driven by solar heating, and Hadley (1735), who showed how the Earth's rotation affects that circulation. Ferrel (1856) added the Coriolis force to existing theory, explaining the major structures of the global atmospheric circulation. In aggregate, prevailing winds and ocean currents move energy poleward from the equatorial regions where the majority of incoming solar radiation is received.

Climate models provide the ability to simulate these complex circulatory processes, and to improve the physical theory of climate by testing different mathematical formulations of those processes. Since controlled experiments at planetary scale are impossible, climate simulations provide one important way to

ACCEPTED VERSION SUBJECT TO FINAL EDITS

explore the differential effects and interactions of variables such as solar irradiance, aerosols, and greenhouse gases. To assess their quality, models or compontents of models may be compared with observations. For this reason, they can be used to attribute observed climatic effects to different natural and human drivers (Hegerl et al., 2011). As early as Arrhenius (1896), simple mathematical models were used to calculate the effects of doubling atmospheric carbon dioxide over pre-industrial concentrations (~550 ppm vs ~275 ppm). In the early 1900s Bjerknes formulated the Navier-Stokes equations of fluid dynamics for motion of the atmosphere (Bjerknes, 1906; Bjerknes et al., 1910), and Richardson (1922) developed a system for numerical weather prediction based on these equations. When electronic computers became available in the late 1940s, the methods of Bjerknes and Richardson were successfully applied to weather forecasting (Charney et al., 1950; Nebeker, 1995; Harper, 2008).

In the 1960s similar approaches to modelling the weather were used to model the climate, but with much longer runs than daily forecasting (Smagorinsky et al., 1965; Manabe and Wetherald, 1967). Simpler statistical and one- and two-dimensional modelling approaches continued in tandem with the more complex General Circulation Models (GCMs) (Manabe and Wetherald, 1967; Budyko, 1969; Sellers, 1969). The first coupled atmosphere-ocean model (AOGCM) with realistic topography appeared in 1975 (Bryan et al., 1975; Manabe et al., 1975). Rapid increases in computer power enabled higher resolutions, longer model simulations, and the inclusion of additional physical processes in GCMs, such as aerosols, atmospheric chemistry, sea ice, and snow.

In the 1990s, AOGCMs were state of the art. By the 2010s, Earth system models (ESMs, also known as coupled carbon-cycle climate models) incorporated land surface, vegetation, the carbon cycle, and other elements of the climate system. Since the 1990s, some major modelling centres have deployed 'unified' models for both weather prediction and climate modelling, with the goal of a seamless modelling approach that uses the same dynamics, physics, and parameterisations at multiple scales of time and space (Cullen, 1993; Brown et al., 2012; NRC Committee on a National Strategy for Advancing Climate Modeling, 2012; Brunet et al., 2015; Chapter 10, Section 10.1.2). Because weather forecast models make short-term predictions that can be frequently verified, and improved models are introduced and tested iteratively on cycles as short as 18 months, this approach allows major portions of the climate model to be evaluated as a weather model and more frequently improved. However, all climate models exhibit biases of different degrees and types, and the practice of 'tuning' parameter values in models to make their outputs match variables such as historical warming trajectories has generated concern throughout their history (Randall and Wielicki, 1997; Edwards, 2010; Hourdin et al., 2017; see also 1.5.3.2). Overall, the WGI AR5 assessed that climate models had improved since previous reports (IPCC, 2013b) .

Since climate models vary along many dimensions, such as grid type, resolution, and parameterizations, comparing their results requires special techniques. To address this problem, the climate modelling community developed increasingly sophisticated Model Intercomparison Projects (MIPs) (Gates et al., 1999; Covey et al., 2003). MIPs prescribe standardised experiment designs, time periods, output variables, or observational reference data, to facilitate direct comparison of model results. This aids in diagnosing the reasons for biases and other differences among models, and furthers process understanding (Section 1.5). Both the CMIP3 and CMIP5 model intercomparison projects included experiments testing the ability of models to reproduce 20th century global surface temperature trends both with and without anthropogenic forcings. Although some individual model runs failed to achieve this (Hourdin et al., 2017), the mean trends of multi-model ensembles did so successfully (Meehl et al., 2007a; Taylor et al., 2012). When only natural forcings were included (creating the equivalent of a 'control Earth' without human influences), similar multi-model ensembles could not reproduce the observed post-1970 warming at either global or regional scales (Edwards, 2010; Jones et al., 2013). The GCMs and ESMs compared in CMIP6 (used in this report) offer more explicit documentation and evaluation of tuning procedures (Schmidt et al., 2017; Burrows et al., 2018; Mauritsen and Roeckner, 2020); see Section 1.5).

The FAR (IPCC, 1990a) concluded that while both theory and models suggested that anthropogenic warming was already well underway, its signal could not yet be detected in observational data against the 'noise' of natural variability (also see Barnett and Schlesinger (1987) and Section 1.4.2). Since then, increased warming and progressively more conclusive attribution studies have identified human activities as

ACCEPTED VERSION SUBJECT TO FINAL EDITS

the 'dominant cause of the observed warming since the mid-20th century' (IPCC, 2013b). 'Fingerprint' studies seek to detect specific observed changes – expected from theoretical understanding and model results – that could not be explained by natural drivers alone, and to attribute statistically the proportion of such changes that is due to human influence. These include global-scale surface warming, nights warming faster than days, tropospheric warming and stratospheric cooling, a rising tropopause, increasing ocean heat content, changed global patterns of precipitation and sea-level air pressure, increasing downward longwave radiation, and decreasing upward longwave radiation (Hasselmann, 1979; Schneider, 1994; Karoly et al., 1994; Santer et al., 1995, 2013, Hegerl et al., 1996, 1997; Gillett et al., 2003; Santer, 2003; Zhang et al., 2007; Stott et al., 2010; Davy et al., 2017; Mann et al., 2017). Cross Working Group Box 1.1 outlines attribution methods and uses from across the AR6, now including event attribution (specifying the influence of climate change on individual extreme events such as floods, or on the frequency of classes of events such as tropical cyclones). Overall, the evidence for human influence has grown substantially over time and from each IPCC report to the subsequent one.

A key indicator of climate understanding is whether theoretical climate system budgets or 'inventories', such as the balance of incoming and outgoing energy at the surface and at the top of the atmosphere, can be quantified and closed observationally. The global energy budget, for example, includes energy retained in the atmosphere, upper ocean, deep ocean, ice, and land surface. Church et al. (2013) assessed in AR5 with *high confidence* that independent estimates of effective radiative forcing (ERF), observed heat storage, and surface warming combined to give an energy budget for the Earth that is consistent with the WGI AR5 assessed *likely* range of equilibrium climate sensitivity (ECS) [1.5°C to 4.5°C] to within estimated uncertainties (IPCC, 2013a; on ECS, see Section 1.3.5 below). Similarly, over the period 1993 to 2010, when observations of all sea level components were available, WGI AR5 assessed the observed global mean sea level rise to be consistent with the sum of the observed contributions from ocean thermal expansion (due to warming) combined with changes in glaciers, the Antarctic and Greenland Ice Sheets, and land water storage (*high confidence*). Verification that the terms of these budgets balance over recent decades provides strong evidence for our understanding of anthropogenic climate change (Cross-Chapter Box 9.1 in Chapter 9).

The Appendix to Chapter 1 (Appendix 1A) lists the key detection and attribution statements in the Summaries for Policymakers of WGI reports since 1990. The evolution of these statements over time reflects the improvement of scientific understanding and the corresponding decrease in uncertainties regarding human influences. The SAR stated that 'the balance of evidence suggests a discernible human influence on global climate' (IPCC, 1995b). Five years later, the TAR concluded that 'there is new and stronger evidence that most of the warming observed over the last 50 years is attributable to human activities' (IPCC, 2001b). AR4 further strengthened previous statements, concluding that 'most of the observed increase in global average temperatures since the mid-20th century is *very likely* due to the observed increase in anthropogenic greenhouse gas concentrations' (IPCC, 2007b). AR5 assessed that a human contribution had been detected to changes in warming of the atmosphere and ocean; changes in the global water cycle; reductions in snow and ice; global mean sea level rise; and changes in some climate extremes. AR5 concluded that 'it is *extremely likely* that human influence has been the dominant cause of the observed warming since the mid-20th century' (IPCC, 2013b).

1.3.5 Projections of future climate change

It was recognised in IPCC AR5 that information about the near term was increasingly relevant for adaptation decisions. In response, WGI AR5 made a specific assessment for how global surface temperature was projected to evolve over the next two decades, concluding that the change for the period 2016–2035 relative to 1986–2005 will *likely* be in the range of 0.3°C to 0.7°C (*medium confidence*), assuming no major volcanic eruptions or secular changes in total solar irradiance (IPCC, 2013b). AR5 was also the first IPCC assessment report to assess 'decadal predictions' of the climate, where the observed state of the climate system was used to start forecasts for a few years ahead. AR6 examines updates to these decadal predictions (Chapter 4, Section 4.4.1).

The assessments and predictions for the near-term evolution of global climate features are largely

ACCEPTED VERSION SUBJECT TO FINAL EDITS

independent of future carbon emissions pathways. However, WGI AR5 assessed that limiting climate change in the long-term future will require substantial and sustained reductions of greenhouse gas emissions (IPCC, 2013b). This assessment results from decades of research on understanding the climate system and its perturbations, and projecting climate change into the future. Each IPCC report has considered a range of emission scenarios, typically including a scenario in which societies choose to continue on their present course as well as several others reflecting socioeconomic and policy responses that may limit emissions and/or increase the rate of carbon dioxide removal from the atmosphere. Climate models are used to project the outcomes of each scenario. However, future human climate influence cannot be precisely predicted because greenhouse gas and aerosol emissions, land use, energy use, and other human activities may change in numerous ways. Common emission scenarios used in the WGI contribution to AR6 are detailed in Section 1.6.

Based on model results and steadily increasing CO_2 concentrations (Bolin and Bischof, 1970; SMIC, 1971; Meadows et al., 1972), concerns about future 'risk of effects on climate' were addressed in Recommendation 70 of the Stockholm Action Plan, resulting from the 1972 United Nations Conference on the Human Environment. Numerous other scientific studies soon amplified these concerns (summarised in Schneider (1975), and Williams (1978); see also Nordhaus (1975, 1977). In 1979, a US National Research Council (NRC) group led by Jule Charney reported on the 'best present understanding of the carbon dioxide/climate issue for the benefit of policymakers', initiating an era of regular and repeated large-scale assessments of climate science findings.

The 1979 Charney NRC report estimated equilibrium climate sensitivity (ECS) at 3°C, stating the range as 2°C–4.5°C, based on 'consistent and mutually supporting' model results and expert judgment (NRC, 1979). ECS is defined in IPCC assessments as the global surface air temperature (GSAT) response to CO_2 doubling (from pre-industrial levels) after the climate has reached equilibrium (stable energy balance between the atmosphere and ocean). Another quantity, transient climate response (TCR), was later introduced as the global surface air temperature change, averaged over a 20-year period, at the time of CO_2 doubling in a scenario of concentration increasing at 1% per year). Calculating ECS from historical or paleoclimate temperature records in combination with energy budget models has produced estimates both lower and higher than those calculated using GCMs and ESMs; in AR6, these are assessed in Chapter 7, Section 7.5.2.

ECS is typically characterised as most relevant on centennial timescales, while TCR was long seen as a more appropriate measure of the 50-100 year response to gradually increasing CO_2; however, recent studies have raised new questions about how accurately both quantities are estimated by GCMs and ESMs (Grose et al., 2018; Meehl et al., 2020; Sherwood et al., 2020). Further, as climate models evolved to include a full-depth ocean, the time scale for reaching full equilibrium became longer and new methods to estimate ECS had to be developed (Gregory et al., 2004; Meehl et al., 2020; Meinshausen et al., 2020). Because of these considerations as well as new estimates from observation-based, paleoclimate, and emergent-constraints studies (Sherwood et al., 2020), the AR6 definition of ECS has changed from previous reports; it now includes all feedbacks except those associated with ice sheets. Accordingly, unlike previous reports, the AR6 assessments of ECS and TCR are not based primarily on GCM and ESM model results (see Chapter 7, Box. 7.1 and Section 7.5.5 for a full discussion).

Today, other sensitivity terms are sometimes used, such as transient climate response to emissions (TCRE, defined as the ratio of warming to cumulative CO_2 emissions in a CO_2-only simulation) and Earth system sensitivity (ESS), which includes multi-century Earth system feedbacks such as changes in ice sheets. Table 1.2 shows estimates of ECS and TCR for major climate science assessments since 1979. The table shows that despite some variation in the range of GCM and (for the later assessments) ESM results, expert assessment of ECS changed little between 1979 and the present report. Based on multiple lines of evidence, AR6 has narrowed the *likely* range of ECS to 2.5-4.0 °C (Chapter 7, Section 7.5.5).

[START TABLE 1.2 HERE]

ACCEPTED VERSION SUBJECT TO FINAL EDITS

Table 1.2: Estimates of equilibrium climate sensitivity (ECS) and transient climate response (TCR) from successive major scientific assessments since 1979. No likelihood statements are available for reports prior to 2001 because those reports did not use the IPCC calibrated uncertainty language. The assessed range of ECS differs from the range derived from General Circulation Model (GCM) and Earth System Model (ESM) results because assessments take into account other evidence, other types of models, and expert judgment. The AR6 definition of ECS differs from previous reports, now including all long-term feedbacks except those associated with ice sheets. AR6 estimates of ECS are derived primarily from process understanding, historical observations, and emergent constraints, informed by (but not based on) GCM and ESM model results. CMIP6 is the 6th phase of the Coupled Model Intercomparison Project. See Chapter 7, Box 7.1 and Section 7.5.5.

Assessment	ECS range derived from GCM and ESM results (°C)	Assessed range of ECS (°C)	Assessed central estimate of ECS (°C)	Assessed range of TCR (°C)
NAS 1979 (NRC, 1979)	2.0–3.5	1.5–4.5	3.0	
NAS 1983 (National Research Council and Carbon Dioxide Assessment Committee, 1983)	2.0–3.5	1.5–4.5	3.0	
Villach 1985 (WMO/UNEP/ICSU, 1986)	1.5–5.5	1.5–4.5	3.0	
IPCC FAR 1990 (IPCC, 1990a)	1.9–5.2	1.5–4.5	2.5	
IPCC 1992 Supplementary Report (IPCC, 1992)	1.7–5.4	1.5–4.5	2.5	discussed but not assessed
IPCC 1994 Radiative Forcing report (IPCC, 1995a)	not given	1.5–4.5	2.5	
IPCC SAR (IPCC, 1996)	1.9–5.2	1.5–4.5	2.5	discussed but not assessed
IPCC TAR (IPCC, 2001a)	2.0–5.1	1.5–4.5 *(likely)*	2.5	1.1–3.1
IPCC AR4 (IPCC, 2007a)	2.1–4.4	2.0–4.5 *(likely)*	3.0	1.0–3.0
IPCC AR5 (IPCC, 2013a)	2.1–4.7	1.5–4.5 *(likely)*	not given	1.0–2.5
World Climate Research Programme (Sherwood et al., 2020)	Models not used in estimate	2.6–3.9 (66% uncertainty interval, *likely*) 2.3–4.7 (90% uncertainty interval, *very likely*)	not given	not given
IPCC AR6 2021	1.8–5.6 (CMIP6). Not used directly in assessing ECS range (Ch 7).	2.5–4.0 *(likely)* 2.0-5.0 (*very likely*)	3.0	1.4–2.2 *(likely)*

[END TABLE 1.2 HERE]

WGI AR5 assessed that there is a close relationship of cumulative total emissions of CO_2 and global mean

ACCEPTED VERSION SUBJECT TO FINAL EDITS

surface temperature response that is approximately linear (IPCC, 2013b). This finding implies that continued emissions of carbon dioxide will cause further warming and changes in all components of the climate system, independent of any specific scenario or pathway. Scenario-based climate projections using the Representative Concentration Pathways (RCPs) assessed in WGI AR5 result in continued warming over the 21st century in all scenarios except a strong climate change mitigation scenario (RCP2.6). Similarly, under all RCP scenarios, AR5 assessed that the rate of sea level rise over the 21st century will *very likely* exceed that observed during 1971–2010 due to increased ocean warming and increased loss of mass from glaciers and ice sheets. Further increases in atmospheric CO_2 will also lead to further uptake of carbon by the ocean, which will increase ocean acidification. By the mid-21st century the magnitudes of the projected changes are substantially affected by the choice of scenario. The set of scenarios used in climate change projections assessed as part of the AR6 are discussed in Section 1.6.

From the close link between cumulative emissions and warming it follows that any given level of global warming is associated with a total budget of GHG emissions, especially CO_2 as it is the largest long-lasting contributor to radiative forcing (Allen et al., 2009; Collins et al., 2013; Rogelj et al., 2019). Higher emissions in earlier decades imply lower emissions later on to stay within the Earth's carbon budget. Stabilising the anthropogenic influence on global surface temperature thus requires that CO_2 emissions and removals reach net zero once the remaining carbon budget is exhausted (see Cross-Chapter Box 1.4).

Past, present and future emissions of CO_2 therefore commit the world to substantial multi-century climate change, and many aspects of climate change would persist for centuries even if emissions of CO_2 were stopped immediately (IPCC, 2013b). According to AR5, a large fraction of this change is essentially irreversible on a multi-century to millennial time scale, barring large net removal ('negative emissions') of CO_2 from the atmosphere over a sustained period through as yet unavailable technological means (IPCC, 2013a, 2018; see Chapters 4 and 5). However, significant reductions of warming due to SLCFs could reduce the level at which temperature stabilises once CO_2 emissions reach net zero, and also reduce the long-term global warming commitment by reducing radiative forcing from SLCFs (Chapter 5).

In summary, major lines of evidence – observations, paleoclimate, theoretical understanding, and natural and human drivers — have been studied and developed for over 150 years. Methods for projecting climate futures have matured since the 1950s and attribution studies since the 1980s. We conclude that understanding of the principal features of the climate system is robust and well established.

1.3.6 How do previous climate projections compare with subsequent observations?

Many different sets of climate projections have been produced over the past several decades, so it is valuable to assess how well those projections have compared against subsequent observations. Consisent findings build confidence in the process of making projections for the future. For example, Stouffer and Manabe (2017) compared projections made in the early 1990s with subsequent observations. They found that the projected surface pattern of warming, and the vertical structure of temperature change in both the atmosphere and ocean, were realistic. Rahmstorf et al. (2007, 2012) examined projections of global surface temperatureand global mean sea level assessed by the TAR and AR4 and found that the global surface temperature projections were in good agreement with the subsequent observations, but that sea level projections were underestimates compared to subsequent observations. WGI AR5 also examined earlier IPCC Assessment Reports to evaluate their projections of how global surface temperature and global mean sea level would change (Cubasch et al., 2013) with similar conclusions.

Although these studies generally showed good agreement between the past projections and subsequent observations, this type of analysis is complicated because the scenarios of future radiative forcing used in earlier projections do not precisely match the actual radiative forcings that subsequently occurred. Mismatches between the projections and subsequent observations could be due to incorrectly projected radiative forcings (e.g., aerosol emissions, greenhouse gas concentrations or volcanic eruptions that were not included), an incorrect modelled response to those forcings, or both. Alternatively, agreement between projections and observations may be fortuitous due to a compensating balance of errors, for example, too low

ACCEPTED VERSION SUBJECT TO FINAL EDITS

climate sensitivity but too strong radiative forcings.

One approach to partially correct for mismatches between the forcings used in the projections and the forcings that actually occurred is described by Hausfather et al. (2020). Model projections of global surface temperatureand estimated radiative forcings were taken from several historical studies, along with the baseline no-policy scenarios from the first four IPCC assessment reports. These model projections of temperature and radiative forcing are then compared to (a) the observed change in temperature through time over the projection period, and (b) the observed change in temperature relative to the observationally-estimated radiative forcing over the projection period (Figure 1.9; data from Hausfather et al. (2020)).

Although this approach has limitations when the modelled forcings differ greatly from the forcings subsequently experienced, they were generally able to project actual future global warming when the mismatches between forecast and observed radiative forcings are accounted for. For example, the Scenario B presented in Hansen et al. (1988) projected around 50% more warming than has been observed during the 1988–2017 period, but this is largely because it overestimated subsequent radiative forcings. Similarly, while the FAR (IPCC, 1990a) projected a higher rate of global surface temperature warming than has been observed, this is largely because it overestimated future greenhouse gas concentrations: the FAR's projected increase in total anthropogenic forcing between 1990 and 2017 was 1.6 W m^{-2}, while the observational estimate of actual forcing during that period is 1.1 W m^{-2} (Dessler and Forster, 2018). Under these actual forcings, the change in temperature in the FAR aligns with observations (Hausfather et al., 2020).

[START FIGURE 1.9 HERE]

Figure 1.9: Assessing past projections of global temperature change. Projected temperature change post-publication on a temperature vs time (1970–2020, top panel) and temperature vs radiative forcing (1970–2017, bottom panel) basis for a selection of prominent climate model projections (taken from Hausfather et al., 2020). Model projections (using global surface air temperature, GSAT) are compared to temperature observations (using global mean surface temperature, GMST) from HadCRUT5 (black) and anthropogenic forcings (through 2017) from Dessler and Forster (2018), and have a baseline generated from the first five years of the projection period. Projections shown are: Manabe (1970), Rasool and Schneider (1971), Broecker (1975), Nordhaus (1977), Hansen et al. (1981, H81), Hansen et al. (1988, H88), Manabe and Stouffer (1993), along with the Energy Balance Model (EBM) projections from the FAR, SAR and TAR, and the multi-model mean projection using CMIP3 simulations of the Special Reports on Emission Scenarios (SRES) A1B scenario from AR4. H81 and H88 show most excpected scenarios 1 and B, respectively. See Hausfather et al. (2020) for more details of the projections. Further details on data sources and processing are available in the chapter data table (Table 1.SM.1).

[END FIGURE 1.9 HERE]

In addition to global surface temperature, past regional projections can be evaluated. For example, the FAR presented a series of temperature projections for 1990 to 2030 for several regions around the world. Regional projections were given for a best global warming estimate of 1.8°C since 1850-1900 by 2030, and were assigned *low confidence*. The FAR also suggested that regional temperature changes should be scaled by -30% to +50% to account for the uncertainty in projected global warming.

The regional projections presented in the FAR are compared to the observed temperature change in the period since 1990 (Figure 1.10), following Grose et al. (2017). Subsequent observed temperature change has tracked within the FAR projected range for the best estimate of regional warming in the Sahel, South Asia and Southern Europe. Temperature change has tracked at or below this range for the Central North America and Australia, yet remains within the range reduced by 30% to generate the FAR's lower global warming estimate, consistent with the smaller observed estimate of radiative forcing compared to the FAR central estimate. Note that the projections assessed in Chapter 4 of AR6 WGI suggest that global temperatures will be around 1.2°C–1.8°C above 1850–1900 by 2030, also lower than the FAR central estimate.

ACCEPTED VERSION SUBJECT TO FINAL EDITS

Overall, there is *medium confidence* that past projections of global temperature are consistent with subsequent observations, especially when accounting for the difference in radiative forcings used and those which actually occurred (*limited evidence, high agreement*). FAR regional projections are broadly consistent with subsequent observations, allowing for regional-scale climate variability and differences in projected and actual forcings. There is *medium confidence* that the spatial warming pattern has been reliably projected in past IPCC reports (*limited evidence, high agreement*).

[START FIGURE 1.10 HERE]

Figure 1.10: Range of projected temperature change for 1990–2030 for various regions defined in IPCC First Assessment Report (FAR). The left panel shows the FAR projections (IPCC, 1990a) for Southern Europe, with darker red bands representing the range of projected change given for the best estimate of 1.8°C global warming since pre-industrial to 2030, and the fainter red bands show the range scaled by –30% to +50% for lower and higher estimates of global warming. Blue lines show the regionally averaged observations from several global temperature gridded datasets, and blue dashed lines show the linear trends in those datasets for 1990–2020 extrapolated to 2030. Observed datasets are: HadCRUT5, Cowtan and Way, GISTEMP, Berkeley Earth and NOAA GlobalTemp. The inset map shows the definition of the FAR regions used. The right panel shows projected temperature changes by 2030 for the various FAR regions, compared to the extrapolated observational trends, following Grose et al. (2017). Further details on data sources and processing are available in the chapter data table (Table 1.SM.1).

[END FIGURE 1.10 HERE]

[START BOX 1.2 HERE]

Box 1.2: Special Reports in the sixth IPCC assessment cycle: key findings

The Sixth Assessment Cycle started with three Special Reports. The Special Report on Global Warming of 1.5°C (SR1.5, (IPCC, 2018), invited by the Parties to the UNFCCC in the context of the Paris Agreement, assessed current knowledge on the impacts of global warming of 1.5°C above pre-industrial levels and related global greenhouse gas (GHG) emission pathways. The Special Report on Climate Change and Land (SRCCL, IPCC, 2019a) addressed GHG fluxes in land-based ecosystems, land use and sustainable land management in relation to climate change adaptation and mitigation, desertification, land degradation and food security. The Special Report on the Ocean and Cryosphere in a Changing Climate (SROCC, IPCC, 2019b) assessed new literature on observed and projected changes of the ocean and the cryosphere, and their associated impacts, risks, and responses.

The SR1.5 and SRCCL were produced through a collaboration between the three IPCC Working Groups, the SROCC by only WGs I and II. Here we focus on key findings relevant to the physical science basis covered by WGI.

1) Observations of climate change

The SR1.5 estimated with *high confidence* that human activities caused a global warming of approximately 1°C between the 1850-1900 and 2017. For the period 2006–2015, observed global mean surface temperature (GMST[7]) was 0.87±0.12°C higher than the average over the 1850–1900 period (*very high confidence*). Anthropogenic global warming was estimated to be increasing at 0.2±0.1°C per decade *(high confidence)* and *likely* matches the level of observed warming to within ±20%. The SRCCL found with *high confidence* that over land, mean surface air temperature increased by 1.53±0.15°C from 1850–1900 to 2006–2015, or nearly twice as much as the global average. This observed warming has already led to increases in the

[7] Box 1.2 reproduces the temperature metrics as they appeared in the respective SPMs of the SRs. In AR6 long-term changes of GMST (Global Mean Surface Temperature) and GSAT (Global Surface Air Temperature) are considered to be equivalent, differing in uncertainty estimates only (see Cross-Chapter Box 2.3 in Chapter 2).

ACCEPTED VERSION SUBJECT TO FINAL EDITS

frequency and intensity of climate and weather extremes in many regions and seasons, including heat waves in most land regions (*high confidence*), increased droughts in some regions (*medium confidence*), and increases in the intensity of heavy precipitation events at the global scale (*medium confidence*). These climate changes have contributed to desertification and land degradation in many regions (*high confidence*). Increased urbanisation can enhance warming in cities and their surroundings (heat island effect), especially during heat waves (*high confidence),* and intensify extreme rainfall (*medium confidence*).

With respect to the ocean, the SROCC assessed that it is *virtually certain* that the ocean has warmed unabated since 1970 and has taken up more than 90% of the excess heat contributed by global warming. The rate of ocean warming has *likely* more than doubled since 1993. Over the period 1982–2016, marine heatwaves have *very likely* doubled in frequency and are increasing in intensity (*very high confidence*). In addition, the surface ocean acidified further (*virtually certain*) and loss of oxygen occurred from the surface to a depth of 1000 m (*medium confidence*). The report expressed *medium confidence* that the Atlantic Meridional Overturning Circulation (AMOC) weakened in 2004–2017 relative to 1850–1900.

Concerning the cryosphere, the SROCC reported widespread continued shrinking of nearly all components. Mass loss from the Antarctic Ice Sheet tripled over the period 2007–2016 relative to 1997–2006, while mass loss doubled for the Greenland Ice Sheet (*likely, medium confidence*). The report concludes with *very high confidence* that due to the combined increased loss from the ice sheets, global mean sea level (GMSL) rise has accelerated (*extremely likely*). The rate of recent GMSL rise (3.6±0.5 mm yr^{-1} for 2006–2015) is about 2.5 times larger than for 1901–1990. The report also found that Arctic sea ice extent has *very likely* decreased for all months of the year since 1979 and that September sea ice reductions of 12.8±2.3% per decade are *likely* unprecedented for at least 1000 years. Feedbacks from the loss of summer sea ice and spring snow cover on land have contributed to amplified warming in the Arctic (*high confidence*), where surface air temperature *likely* increased by more than double the global average over the last two decades. By contrast, Antarctic sea ice extent overall saw no statistically significant trend for the period 1979 to 2018 (*high confidence*).

The SROCC assessed that anthropogenic climate change has increased observed precipitation (*medium confidence*), winds (*low confidence*), and extreme sea level events (*high confidence*) associated with some tropical cyclones. It also found evidence for an increase in annual global proportion of Category 4 or 5 tropical cyclones in recent decades (*low confidence*).

2) Drivers of climate change

The SRCCL stated that the land is simultaneously a source and sink of CO_2 due to both anthropogenic and natural drivers. It estimates with *medium confidence* that Agriculture, Forestry and Other Land Use (AFOLU) activities accounted for around 13% of CO_2, 44% of methane, and 82% of nitrous oxide emissions from human activities during 2007–2016, representing 23% (12.0±3.0 $GtCO_2$ equivalent yr^{-1}) of the total net anthropogenic emissions of GHGs. The natural response of land to human-induced environmental change such as increasing atmospheric CO_2 concentration, nitrogen deposition, and climate change, caused a net CO_2 sink equivalent of around 29% of total CO_2 emissions (*medium confidence*); however, the persistence of the sink is uncertain due to climate change (*high confidence*).

The SRCCL also assessed how changes in land conditions affect global and regional climate. It found that changes in land cover have led to both a net release of CO_2, contributing to global warming, and an increase in global land albedo, causing surface cooling. However, the report estimated that the resulting net effect on globally averaged surface temperature was small over the historical period (*medium confidence*).

The SROCC found that the carbon content of Arctic and boreal permafrost is almost twice that of the atmosphere (*medium confidence)*, and assessed *medium evidence* with *low agreement* that thawing northern permafrost regions are currently releasing additional net methane and CO_2.

3) Projections of climate change

ACCEPTED VERSION SUBJECT TO FINAL EDITS

The SR1.5 concluded that global warming is *likely* to reach 1.5°C between 2030 and 2052 if it continues to increase at the current rate (*high confidence*). However, even though warming from anthropogenic emissions will persist for centuries to millennia and will cause ongoing long-term changes, past emissions alone are *unlikely* to raise global surface temperatur to 1.5°C above 1850-1900 levels.

The SR1.5 also found that reaching and sustaining net zero anthropogenic CO_2 emissions and reducing net non-CO_2 radiative forcing would halt anthropogenic global warming on multi-decadal time scales (*high confidence*). The maximum temperature reached is then determined by cumulative net global anthropogenic CO_2 emissions up to the time of net zero CO_2 emissions (*high confidence*) and the level of non-CO_2 radiative forcing in the decades prior to the time that maximum temperatures are reached (*medium confidence*).

Furthermore, climate models project robust differences in regional climate characteristics between the present day and a global warming of 1.5°C, and between 1.5°C and 2°C, including mean temperature in most land and ocean regions and hot extremes in most inhabited regions (*high confidence*). There is *medium confidence* in robust differences in heavy precipitation events in several regions and the probability of droughts in some regions.

The SROCC projected that global-scale glacier mass loss, permafrost thaw, and decline in snow cover and Arctic sea ice extent will continue in the near term (2031–2050) due to surface air temperature increases (*high confidence*). The Greenland and Antarctic Ice Sheets are projected to lose mass at an increasing rate throughout the 21st century and beyond (*high confidence*). Sea level rise will also continue at an increasing rate. For the period 2081–2100 with respect to 1986–2005, the *likely* ranges of global mean sea level (GMSL) rise are projected at 0.26–0.53 m for RCP2.6 and 0.51–0.92 m for RCP8.5. For the RCP8.5 scenario, projections of GMSL rise by 2100 are higher by 0.1 m than in AR5 due to a larger contribution from the Antarctic Ice Sheet (*medium confidence*). Extreme sea level events that occurred once per hundred years in the recent past are projected to occur at least once per year at many locations by 2050, especially in tropical regions, under all RCP scenarios *(high confidence*). According to SR1.5, by 2100, GMSL rise would be around 0.1 m lower with 1.5°C global warming compared to 2°C (*medium confidence*). If warming is held to 1.5°, GMSLwill still continue to rise well beyond 2100, but at a slower rate and a lower magnitude. However, instability and/or irreversible loss of the Greenland and Antarctic Ice Sheets, resulting in multi-metre rise in sea level over hundreds to thousands of years, could be triggered at 1.5°C to 2°C of global warming (*medium confidence*). According to the SROCC, sea level rise in an extended RCP2.6 scenario would be limited to around 1 m in 2300 (*low confidence*) while multi-metre sea-level rise is projected under RCP8.5 by then (*medium confidence*).

The SROCC projected that over the 21st century, the ocean will transition to unprecedented conditions with increased temperatures (*virtually certain*), further acidification (*virtually certain*), and oxygen decline (*medium confidence*). Marine heatwaves are projected to become more frequent (*very high confidence*) as are extreme El Niño and La Niña events (*medium confidence*). The AMOC is projected to weaken during the 21st century (*very likely*), but a collapse is deemed *very unlikely* (albeit with *medium confidence* due to known biases in the climate models used for the assessment).

4) Emission pathways to limit global warming

The SR1.5 focused on emission pathways and system transitions consistent with 1.5°C global warming over the 21st century. Building upon the understanding from WGI AR5 of the quasi-linear relationship between cumulative net anthropogenic CO_2 emissions since 1850–1900 and maximum global mean temperature, the report assessed the remaining carbon budgets compatible with the 1.5°C or 2°C warming goals of the Paris Agreement. Starting from year 2018, the remaining carbon budget for a one-in-two chance of limiting global warming to 1.5°C is about 580 $GtCO_2$, and about 420 $GtCO_2$ for a two-in-three chance (*medium confidence*). At constant 2017 emissions, these budgets would be depleted by about the years 2032 and 2028, respectively. Using GMST instead of GSAT gives estimates of 770 and 570 $GtCO_2$, respectively (*medium confidence*). Each budget is further reduced by approximately 100 $GtCO_2$ over the course of this century when permafrost and other less well represented Earth-system feedbacks are taken into account.

ACCEPTED VERSION SUBJECT TO FINAL EDITS

It is concluded that all emission pathways with no or limited overshoot of 1.5°C imply that global net anthropogenic CO_2 emissions would need to decline by about 45% from 2010 levels by 2030, reaching net zero around 2050, together with deep reductions in other anthropogenic emissions, such as methane and black carbon. To limit global warming to below 2°C, CO_2 emissions would have to decline by about 25% by 2030 and reach net zero around 2070.

[END BOX 1.2 HERE]

1.4 AR6 foundations and concepts

AR6 WGI builds on previous assessments using well established foundations and concepts. This section highlights some of the cross-cutting methods applied in the climate change literature and topics discussed repeatedly throughout this report. The choices related to baseline, or reference periods, are first highlighted (Section 1.4.1), including a specific discussion on the pre-industrial baseline used in AR6 WGI (Cross-Chapter Box 1.2). The relationships between long-term trends, climate variability and the concept of emergence of changes (Section 1.4.2) and the sources of uncertainty in climate simulations (Section 1.4.3) are discussed next. The topic of low-likelihood outcomes, storylines, abrupt changes and surprises follows (Section 1.4.4), including a description of the AR6 WGI risk framing (Cross-Chapter Box 1.3). The Cross-Working Group Box: Attribution describes attribution methods, including those for extreme events. Various sets of geographical regions used in later Chapters are also defined and introduced (Section 1.4.5).

1.4.1 Baselines, reference periods and anomalies

Several 'baselines' or 'reference periods' are used consistently throughout AR6 WGI. Baseline refers to a period against which differences are calculated whereas reference period is used more generally to indicate a time period of interest, or a period over which some relevant statistics are calculated (see Annex VII: Glossary). Variations in observed and simulated climate variables over time are often presented as 'anomalies', i.e., the differences relative to a baseline, rather than using the absolute values. This is done for several reasons.

First, anomalies are often used when combining data from multiple locations, because the absolute values can vary over small spatial scales which are not densely observed or simulated, whereas anomalies are representative for much larger scales (e.g., for temperature, Hansen and Lebedeff 1987). Since their baseline value is zero by definition, anomalies are also less susceptible to biases arising from changes in the observational network. Second, the seasonality in different climate indicators can be removed using anomalies to more clearly distinguish variability from long-term trends.

Third, different datasets can have different absolute values for the same climate variable that should be removed for effective comparisons of variations with time. This is often required when comparing climate simulations with each other, or when comparing simulations with observations, as simulated climate variables are also affected by model bias that can be removed when they are presented as anomalies. It can also be required when comparing observational datasets or reanalyses (see Section 1.5.2) with each other, due to systematic differences in the underlying measurement system (see Figure 1.11). Understanding the reasons for any absolute difference is important, but whether the simulated absolute value matters when projecting future change will depend on the variable of interest. For example, there is not a strong relationship between climate sensitivity of a model (which is an indicator of the degree of future warming) and the simulated absolute global surface temperature (Mauritsen et al. 2012; Hawkins and Sutton 2016).

For some variables, such as precipitation, anomalies are often expressed as percentages in order to more easily compare changes in regions with very different climatological means. However, for situations where there are important thresholds (e.g., phase transitions around 0°C) or for variables which can only take a particular sign or be in a fixed range (e.g., sea ice extent or relative humidity), absolute values are normally used.

ACCEPTED VERSION SUBJECT TO FINAL EDITS

The choice of a baseline period has important consequences for evaluating both observations and simulations of the climate, for comparing observations with simulations, and for presenting climate projections. There is usually no perfect choice of baseline as many factors have to be considered and compromises may be required (Hawkins and Sutton 2016). It is important to evaluate the sensitivity of an analysis or assessment to the choice of the baseline.

For example, the collocation of observations and reanalyses within the model ensemble spread depends on the choice of the baseline, and uncertainty in future projections of climate is reduced if using a more recent baseline, especially for the near-term (Figure 1.11). The length of an appropriate baseline or reference period depends on the variable being considered, the rates of change of the variable and the purpose of the period, but is usually 20 to 50 years long. The World Meteorological Organization (WMO) uses 30-year periods to define 'climate normals', which indicate conditions expected to be experienced in a given location.

[START FIGURE 1.11 HERE]

Figure 1.11: Choice of baseline matters when comparing observations and model simulations. Global surface air temperature (GSAT, grey) from a range of CMIP6 historical simulations (1850–2014, 25 models) and SSP1-2.6 (2015–2100) using absolute values (top) and anomalies relative to two different baselines: 1850–1900 (middle) and 1995–2014 (bottom). An estimate of GSAT from a reanalysis (ERA-5, orange, 1979–2020) and an observation-based estimate of global mean surface air temperature (GMST) (Berkeley Earth, black, 1850–2020) are shown, along with the mean GSAT for 1961–1990 estimated by Jones et al. (1999), light blue shading, 14.0±0.5°C). Using the more recent baseline (bottom) allows the inclusion of datasets which do not include the periods of older baselines. The middle and bottom panels have scales which are the same size but offset. Further details on data sources and processing are available in the chapter data table (Table 1.SM.1).

[END FIGURE 1.11 HERE]

For AR6 WGI, the period 1995–2014 is used as a baseline to calculate the changes in future climate using model projections and also as a 'modern' or 'recent past' reference period when estimating past observed warming. The equivalent period in AR5 was 1986–2005, and in SR1.5, SROCC and SRCCL it was 2006–2015. The primary reason for the different choice in AR6 is that 2014 is the final year of the historical CMIP6 simulations. These simulations subsequently assume different emission scenarios and so choosing any later baseline end date would require selecting a particular emissions scenario. For certain assessments, the most recent decade possible (e.g. 2010–2019 or 2011–2020, depending on the availability of observations) is also used as a reference period (see Cross Chapter Box 2.3 in Chapter 2).

Figure 1.12 shows changes in observed global mean surface temperature (GMST) relative to 1850–1900 and illustrates observed global warming levels for a range of reference periods that are either used in AR6 or were used in previous IPCC Reports. This allows changes to be calculated between different periods and compared to previous assessments. For example, AR5 assessed the change in GMST from the 1850–1900 baseline to 1986–2005 reference period as 0.61 (0.55–0.67) °C, whereas it is now assessed to be 0.69 (0.52–0.82) °C using improved GMST datasets (also see Cross-Chapter Box 2.3 in Chapter 2).

The commonly used metric for global surface warming tends to be global mean surface temperature (GMST) but, as shown in Figure 1.11, climate model simulations tend to use global surface air temperature (GSAT). Although GMST and GSAT are closely related, the two measures are physically distinct. GMST is a combination of land surface air temperatures (LSAT) and sea surface temperatures (SSTs), whereas GSAT is surface air temperatures over land, ocean and ice. A key development in AR6 is the assessment that long-term changes in GMST and GSAT differ by at most 10% in either direction, with *low confidence* in the sign of any differences (see Cross Chapter Box 2.3 for details).

Three future reference periods are used in AR6 WGI for presenting projections: *near-term* (2021–2040),

ACCEPTED VERSION SUBJECT TO FINAL EDITS

mid-term (2041–2060) and *long-term* (2081–2100) (see Figure 1.11). In AR6, 20-year reference periods are considered long enough to show future changes in many variables when averaging over ensemble members of multiple models, and short enough to enable the time dependence of changes to be shown throughout the 21st century. Projections with alternative recent baselines (such as 1986–2005 or the current WMO climate normal period of 1981–2010) and a wider range of future reference periods are presented in the Interactive Atlas. Note that 'long-term' is also sometimes used to refer to durations of centuries to millennia when examining past climate, as well as future climate change beyond the year 2100. Cross-Chapter Box 2.1 in Chapter 2 discusses the paleo reference periods used in AR6.

[START FIGURE 1.12 HERE]

Figure 1.12: Global warming over the instrumental period. Observed global mean surface temperature (GMST) from four datasets, relative to the average temperature of 1850–1900 in each dataset (see Cross-Chapter Box 2.3 and Section 2.3.1.1 for more details). The shaded grey band indicates the assessed *likely* range for the period around 1750 (see Cross-Chapter Box 1.2). Different reference periods are indicated by the coloured horizontal lines, and an estimate of total GMST change up to that period is given, enabling a translation of the level of warming between different reference periods. The reference periods are all chosen because they have been used in the AR6 or previous IPCC assessment reports. The value for the 1981–2010 reference period, used as a 'climate normal' period by the World Meteorological Organization, is the same as the 1986–2005 reference period shown. Further details on data sources and processing are available in the chapter data table (Table 1.SM.1).

[END FIGURE 1.12 HERE]

[START CROSS-CHAPTER BOX 1.2 HERE]

Cross-Chapter Box 1.2: Changes in global temperature between 1750 and 1850

Contributing Authors: Ed Hawkins (UK), Paul Edwards (USA), Piers Forster (UK), Darrell Kaufman (USA), Jochem Marotzke (Germany), Malte Meinshausen (Australia/Germany), Maisa Rojas (Chile), Bjørn H. Samset (Norway), Peter Thorne (Ireland/UK).

The Paris Agreement aims to limit global temperatures to specific thresholds '*above pre-industrial levels*'. In AR6 WGI, as in previous IPCC reports, observations and projections of changes in global temperature are generally expressed relative to 1850–1900 as an approximate pre-industrial state (SR1.5, IPCC, 2018). This is a pragmatic choice based upon data availability considerations, though both anthropogenic and natural changes to the climate occurred before 1850. The remaining carbon budgets, the chance of crossing global temperature thresholds, and projections of extremes and sea level rise at a particular level of global warming can all be sensitive to the chosen definition of the approximate pre-industrial baseline (Millar et al., 2017a; Schurer et al., 2017; Pfleiderer et al., 2018; Rogelj et al., 2019; Tokarska et al., 2019). This Cross-Chapter Box assesses the evidence on change in radiative forcing and global temperature from the period around 1750 to 1850–1900; variations in the climate before 1750 are discussed in Chapter 2.

Although there is some evidence for human influence on climate before 1750 (e.g., Ruddiman and Thomson, 2001; Koch et al., 2019), the magnitude of the effect is still disputed (e.g., Joos et al., 2004; Beck et al., 2018b; see Chapter 5, Section 5.1.2.3), and most studies analyse the human influence on climate over the industrial period. Historically, the widespread use of coal-powered machinery started the Industrial Revolution in Britain in the late 18th century (Ashton, 1997), but the global effects were small for several decades. In line with this, previous IPCC assessment reports considered changes in radiative forcing relative to 1750, and temperature changes were often reported relative to the 'late 19th century'. AR5 and SR1.5 made the specific pragmatic choice to approximate pre-industrial global temperatures by the average of the 1850–1900 period, when permanent surface observing networks emerged that provide sufficiently accurate

ACCEPTED VERSION SUBJECT TO FINAL EDITS

and continuous measurements on a near-global scale (see Sections 1.3.1 and Chapter 2, Section 2.3.1.1), and because the model simulations of the historical period used 1850 as their start date. For the same reasons, to ensure continuity with previous assessments, and because of larger uncertainties and lower confidence in climatic changes before 1850 than after, AR6 makes the same choice to approximate pre-industrial global temperatures by the average of the 1850-1900 period.

Here we assess improvements in our understanding of climatic changes in the period 1750-1850. Anthropogenic influences on climate between 1750 and 1900 were primarily increased anthropogenic GHG and aerosol emissions, and changes in land use. Between 1750 and 1850 atmospheric CO_2 levels increased by from about 278 ppm to about 285 ppm (Chapter 2, Section 2.2.3, equivalent to around 3 years of current rates of increase), corresponding to about 55 $GtCO_2$ in the atmosphere. Estimates of emissions from fossil fuel burning (about 4 $GtCO_2$, Boden et al., 2017) cannot explain the pre-1850 increase, so CO_2 emissions from land use changes are implicated as the dominant source. The atmospheric concentration of other GHGs also increased over the same period, and there was a cooling influence from other anthropogenic radiative forcings (such as aerosols and land use changes), but with a larger uncertainty than for GHGs (e.g., Carslaw et al., 2017; Owens et al., 2017; Hamilton et al., 2018; Chapter 2, Section 2.2.6; Chapter 7, Section 7.3.5.2; Cross-Chapter Box 1.2, Figure 1). It is *likely* that there was a net anthropogenic forcing of 0.0–0.3 Wm^{-2} in 1850–1900 relative to 1750 (*medium confidence*). The net radiative forcing from changes in solar activity and volcanic activity in 1850–1900, compared to the period around 1750, is estimated to be smaller than ± 0.1 W m^{-2}, but note there were several large volcanic eruptions between 1750 and 1850 (Cross-Chapter Box 1.2, Figure 1).

Several studies since AR5 have estimated changes in global temperatures following industrialisation and before 1850. Hawkins et al. (2017) used observations, radiative forcing estimates and model simulations to estimate the warming from 1720–1800 until 1986–2005 and assessed a *likely* range of 0.55°C–0.80°C, slightly broader than the equivalent range starting from 1850–1900 (0.6°C–0.7°C). From proxy evidence, PAGES 2k Consortium (2019) found that GMST for 1850–1900 was 0.02°C [-0.22 to 0.16°C] warmer than the 30-year period centred on 1750. Schurer et al. (2017) used climate model simulations of the last millennium to estimate that the increase in GHG concentrations before 1850 caused an additional *likely* range of 0.0–0.2°C global warming when considering multiple reference periods. Haustein et al. (2017) implies an additional warming of around 0.05°C attributable to human activity from 1750 to 1850–1900, and the AR6 emulator (Chapter 7, Section 7.3.5.3) estimates the *likely* range of this warming to be 0.04°C–0.14°C.

Combining these different sources of evidence, we assess that from the period around 1750 to 1850–1900 there was a change in global temperature of around 0.1°C [-0.1 to +0.3°C](*medium confidence*), with an anthropogenic component of a *likely* range of 0.0°C–0.2°C (*medium confidence*).

[START CROSS-CHAPTER BOX1.2, FIGURE 1 HERE]

Cross-Chapter Box 1.2, Figure 1: **Changes in radiative forcing from 1750 to 2019**. The radiative forcing estimates from the AR6 emulator (see Cross-Chapter Box 7.1 in Chapter 7) are split into GHG, other anthropogenic (mainly aerosols and land use) and natural forcings, with the average over the 1850–1900 baseline shown for each. Further details on data sources and processing are available in the chapter data table (Table 1.SM.1).

[END FIGURE CROSS-CHAPTER 1.2, FIGURE 1 HERE]

[END CROSS-CHAPTER BOX 1.2 HERE]

1.4.2 Variability and emergence of the climate change signal

Climatic changes since the pre-industrial era are a combination of long-term anthropogenic changes and

ACCEPTED VERSION SUBJECT TO FINAL EDITS

natural variations on time scales from days to decades. The relative importance of these two factors depends on the climate variable or region of interest. Natural variations consist of both natural radiatively forced trends (e.g. due to volcanic eruptions or solar variations) and 'internal' fluctuations of the climate system which occur even in the absence of any radiative forcings. The internal 'modes of variability', such as ENSO and the NAO, are discussed further in Annex IV.

1.4.2.1 Climate variability can influence trends over short periods

Natural variations in both weather and longer timescale phenomena can temporarily obscure or intensify any anthropogenic trends (e.g., Deser et al., 2012; Kay et al., 2015). These effects are more important on small spatial and temporal scales but can also occur on the global scale as well (see Cross-Chapter Box 3.1in Chapter 3).

Since AR5, many studies have examined the role of internal variability through the use of 'large ensembles'. Each such ensemble consists of many different simulations by a single climate model for the same time period and using the same radiative forcings. These simulations differ only in their phasing of the internal climate variations (also see Section 1.5.4.2). A set of illustrative examples using one such large ensemble (Maher et al., 2019) demonstrates how variability can influence trends on decadal timescales (Figure 1.13). The long-term anthropogenic trends in this set of climate indicators are clearly apparent when considering the ensemble as a whole (grey shading), and all the individual ensemble members have very similar trends for ocean heat content (OHC), which is a robust estimate of the total energy stored in the climate system (e.g., Palmer and McNeall, 2014). However, the individual ensemble members can exhibit very different decadal trends in global surface air temperature (GSAT), UK summer temperatures, and Arctic sea-ice variations. More specifically, for a representative 11-year period, both positive and negative trends can be found in all these surface indicators, even though the long-term trend is for increasing temperatures and decreasing sea ice. Periods in which the long-term trend is substantially obscured or intensified for more than 20 years are also visible in these regional examples, highlighting that observations are expected to exhibit short-term trends which are larger or smaller than the long-term trend or differ from the average projected trend from climate models, especially on continental spatial scales or smaller (see Cross Chapter Box 3.1 in Chapter 3). The actual observed trajectory can be considered as one realisation of many possible alternative worlds which experienced different weather, as also demonstrated by the construction of 'observation-based large ensembles' that are alternate possible realisations of historical observations, which retain the statistical properties of observed regional weather (e.g., McKinnon and Deser, 2018).

[START FIGURE 1.13 HERE]

Figure 1.13: Simulated changes in various climate indicators under historical and RCP4.5 scenarios using the MPI ESM Grand Ensemble. The grey shading shows the 5–95% range from the 100-member ensemble. The coloured lines represent individual example ensemble members, with linear trends for the 2011–2021 period indicated by the thin dashed lines. Changes in Ocean Heat Content (OHC) over the top 2000m represents the integrated signal of global warming (left). The top row shows surface air temperature-related indicators (annual GSAT change and UK summer temperatures) and the bottom row shows Arctic sea-ice related indicators (annual ice volume and September sea ice extent). For smaller regions and for shorter time period averages the variability increases and simulated short-term trends can temporarily obscure or intensify anthropogenic changes in climate. Data from Maher et al., (2019). Further details on data sources and processing are available in the chapter data table (Table 1.SM.1).

[END FIGURE 1.13 HERE]

1.4.2.2 The emergence of the climate change signal

In the 1930s it was noted that temperatures were increasing at both local and global scales (Kincer, 1933; Callendar, 1938; Figure 1.8). At the time it was unclear whether the observed changes were part of a longer-

ACCEPTED VERSION SUBJECT TO FINAL EDITS

term trend or a natural fluctuation; the 'signal' had not yet clearly emerged from the 'noise' of natural variability. Numerous studies have since focused on the emergence of changes in temperature using instrumental observations (e.g., Madden and Ramanathan, 1980; Wigley and Jones, 1981; Mahlstein et al., 2011, 2012; Lehner and Stocker, 2015; Lehner et al., 2017) and paleo-temperature data (e.g., Abram et al., 2016).

Since the IPCC Third's Assessment report in 2001, the observed signal of climate change has been unequivocally detected at the global scale (see Section 1.3), and this signal is increasingly emerging from the noise of natural variability on smaller spatial scales and in a range of climate variables (see also FAQ1.2). In this Report emergence of a climate change signal or trend refers to when a change in climate (the 'signal') becomes larger than the amplitude of natural or internal variations (defining the 'noise'). This concept is often expressed as a 'signal to-noise' ratio (S/N) and emergence occurs at a defined threshold of this ratio (e.g. S/N > 1 or 2). Emergence can be estimated using observations and/or model simulations and can refer to changes relative to a historical or modern baseline (see Chapter 12, Section 12.5.2, Annex VII: Glossary). The concept can also be expressed in terms of time (the 'time of emergence'; Annex VII: Glossary) or in terms of a global warming level (Kirchmeier- Young et al., 2019; see Chapter 11, Section 11.2.5) and is also used to refer to a time when we can expect to see a response of mitigation activities that reduce emissions of greenhouse gases or enhance their sinks (emergence with respect to mitigation, see Chapter 4, Section 4.6.3.1). Whenever possible, emergence should be discussed in the context of a clearly defined level of S/N or other quantification, such as 'the signal has emerged at the level of S/N > 2', rather than as a simple binary statement. For an extended discussion, see Chapter 10 (Section 10.4.3).

Related to the concept of emergence is the detection of change (see Chapter 3). Detection of change is defined as the process of demonstrating that some aspect of the climate or a system affected by climate has changed in some defined statistical sense, often using spatially aggregating methods that try to maximise S/N, such as 'fingerprints' (e.g., Hegerl et al., 1996), without providing a reason for that change. An identified change is detected in observations if its likelihood of occurrence by chance due to internal variability alone is determined to be small, for example, <10% (Annex VII: Glossary).

An example of observed emergence in surface air temperatures is shown in Figure 1.14. Both the largest changes in temperature and the largest amplitude of year-to-year variations are observed in the Arctic, with lower latitudes showing less warming and smaller year-to-year variations. For the six example regions shown (Figure 1.14), the emergence of changes in temperature is more apparent in northern South America, East Asia and central Africa, than for northern North America or northern Europe. This pattern was predicted by Hansen et al. (1988) and noted in subsequent observations by Mahlstein et al. (2011) (see Chapter 10, Section 10.3.4.3, Chapter 12, Section 12.5.2). Overall, tropical regions show earlier emergence of temperature changes than at higher latitudes (*high confidence*).

Since AR5, the emergence of projected future changes has also been extensively examined, in variables including surface air temperature (Hawkins and Sutton, 2012; Kirtman et al., 2013; Tebaldi and Friedlingstein, 2013), ocean temperatures and salinity (Banks and Wood, 2002), mean precipitation (Giorgi and Bi, 2009; Maraun, 2013), drought (Orlowsky and Seneviratne, 2013), extremes (Diffenbaugh and Scherer, 2011; Fischer et al., 2014; King et al., 2015; Schleussner and Fyson, 2020), and regional sea level change (Lyu et al., 2014). The concept has also been applied to climate change impacts such as effects on crop growing regions (Rojas et al., 2019). In AR6, the emergence of oceanic signals such as regional sea level change and changes in water mass properties is assessed in Chapter 9 (Section 9.6.1.4), emergence of future regional changes is assed in Chapter 10 (Section 10.4.3), the emergence of extremes as a function of global warming levels is assessed in Chapter 11 (Section 11.2.5) and the emergence of climatic impact-drivers for AR6 regions and many climate variables is assessed in Chapter 12 (Section 12.5.2).

Although the magnitude of any change is important, regions which have a larger signal of change relative to the background variations will potentially face greater risks than other regions, as they will see unusual or novel climate conditions more quickly (Frame et al., 2017). As in Figure 1.14, the signal of temperature change is often smaller in tropical countries, but their lower amplitude of variability means they may experience the effects of climate change earlier than the mid-latitudes. In addition, these tropical countries

ACCEPTED VERSION SUBJECT TO FINAL EDITS

are often amongst the most exposed, due to large populations (Lehner and Stocker, 2015), and often more vulnerable (Harrington et al., 2016; Harrington and Otto, 2018; Russo et al., 2019); both of these factors increase the risk from climate-related impacts (Cross Chapter Box 1.3). The rate of change is also important for many hazards (e.g., Loarie et al., 2009). Providing more information about changes and variations on regional scales, and the associated attribution to particular causes (see Cross-Working Group Box: Attribution), is therefore important for adaptation planning.

[START FIGURE 1.14 HERE]

Figure 1.14: The observed emergence of changes in temperature. Top left: the total change in temperature estimated for 2020 relative to 1850–1900 (following Hawkins et al. 2020), showing the largest warming in the Arctic. Top right: the amplitude of estimated year-to-year variations in temperature. Middle left: the ratio of the observed total change in temperature and the amplitude of temperature variability (the 'signal-to-noise (S/N) ratio'), showing that the warming is most apparent in the tropical regions (also see FAQ1.2). Middle right: the global warming level at which the change in local temperature becomes larger than the local year-to-year variability. The bottom panels show time series of observed annual mean surface air temperatures over land in various example regions, as indicated as boxes in the top left panel. The 1 and 2 standard deviations of estimated year-to-year variations for that region are shown by the pink shaded bands. Observed temperature data from Berkeley Earth (Rohde and Hausfather, 2020). Further details on data sources and processing are available in the chapter data table (Table 1.SM.1).

[END FIGURE 1.14 HERE]

1.4.3 Sources of uncertainty in climate simulations

When evaluating and analysing simulations of the physical climate system, several different sources of uncertainty need to be considered (e.g., Hawkins and Sutton, 2009; Lehner et al., 2020). Broadly, these sources are: uncertainties in radiative forcings (both those observed in the past and those projected for the future); uncertainty in the climate response to particular radiative forcings; internal and natural variations of the climate system (which may be somewhat predictable) and interactions among these sources of uncertainty.

Ensembles of climate simulations (see Section 1.5.4.2), such as those produced as part of the sixth phase of the Coupled Model Intercomparison Project (CMIP6), can be used to explore these different sources of uncertainty and estimate their magnitude. Relevant experiments with climate models include both historical simulations constrained by past radiative forcings and projections of future climate which are constrained by specified drivers, such as GHG concentrations, emissions, or radiative forcings. (The term 'prediction' is usually reserved for estimates of the future climate state which are also constrained by the observed initial conditions of the climate system, analogous to a weather forecast.)

1.4.3.1 Sources of uncertainty

Radiative forcing uncertainty

Future radiative forcing is uncertain due to as-yet-unknown societal choices that will determine future anthropogenic emissions; this is considered '*scenario uncertainty*'. The RCP and SSP scenarios, which form the basis for climate projections assessed in this report, are designed to span a plausible range of future pathways (see Section 1.6) and can be used to estimate the magnitude of scenario uncertainty, but the real world may also differ from any one of these example pathways.

Uncertainties also exist regarding past emissions and radiative forcings. These are especially important for simulations of paleoclimate time periods, such as the Pliocene, Last Glacial Maximum or the last millennium, but are also relevant for the CMIP historical simulations of the instrumental period since 1850. In particular, historical radiative forcings due to anthropogenic and natural aerosols are less well constrained

ACCEPTED VERSION SUBJECT TO FINAL EDITS

by observations than the greenhouse gas radiative forcings. There is also uncertainty in the size of large volcanic eruptions (and in the location for some that occurred before around 1850), and the amplitude of changes in solar activity, before satellite observations. The role of historical radiative forcing uncertainty was considered previously (Knutti et al., 2002; Forster et al., 2013) but, since AR5, specific simulations have been performed to examine this issue, particularly for the effects of uncertainty in anthropogenic aerosol radiative forcing (e.g., Jiménez-de-la-Cuesta and Mauritsen, 2019; Dittus et al., 2020).

Climate response uncertainty

Under any particular scenario (see Section 1.6.1), there is uncertainty in how the climate will respond to the specified emissions or radiative forcing combinations. A range of climate models is often used to estimate the range of uncertainty in our understanding of the key physical processes and to define the '*model response uncertainty*' (see Section 1.5.4 and Chapter 4, Section 4.2.5). However, this range does not necessarily represent the full '*climate response uncertainty'* in how the climate may respond to a particular radiative forcing or emissions scenario. This is because, for example, the climate models used in CMIP experiments have structural uncertainties not explored in a typical multi-model exercise (e.g., Murphy et al., 2004) and are not entirely independent of each other (Masson and Knutti, 2011; Abramowitz et al., 2019; see Section 1.5.4.8); there are small spatial-scale features which cannot be resolved; and long time-scale processes or tipping points are not fully represented. Section 1.4.4 discusses how some of these issues can still be considered in a risk assessment context. For some metrics, such as Equilibrium Climate Sensitivity (ECS), the CMIP6 model range is found to be broader than the *very likely* range assessed by combining multiple lines of evidence (see Chapter 4, Section 4.3.4 and Chapter 7, Section 7.5.6).

Natural and internal climate variations

Even without any anthropogenic radiative forcing, there would still be uncertainty in projecting future climate because of unpredictable natural factors such as variations in solar activity and volcanic eruptions. For projections of future climate, such as those presented in Chapter 4, the uncertainty in these factors is not normally considered. However, the potential effects on the climate of large volcanic eruptions (Cross-Chapter Box 4.1in Chapter 4, Zanchettin et al., 2016; Bethke et al., 2017) and large solar variations (Feulner and Rahmstorf, 2010; Maycock et al., 2015) are studied. On longer timescales, orbital effects and plate tectonics also play a role.

Further, even in the absence of any anthropogenic or natural changes in radiative forcing, Earth's climate fluctuates on timescales from days to decades or longer. These 'internal' variations, such as those associated with modes of variability (e.g., ENSO, Pacific Decadal Variability (PDV), or Atlantic Multi-decadal Variability (AMV) – see Annex IV) are unpredictable on timescales longer than a few years ahead and are a source of uncertainty for understanding how the climate might become in a particular decade, especially regionally. The increased use of 'large ensembles' of complex climate model simulations to sample this component of uncertainty is discussed above in Section 1.4.2.1 and further in Chapter 4.

Interactions between variability and radiative forcings

It is plausible that there are interactions between radiative forcings and climate variations, such as influences on the phasing or amplitude of internal or natural climate variability (Zanchettin, 2017). For example, the timing of volcanic eruptions may influence Atlantic multi-decadal variability (e.g., Otterå et al., 2010; Birkel et al., 2018) or ENSO (e.g., Maher et al., 2015; Khodri et al., 2017; Zuo et al., 2018), and anthropogenic aerosols may influence decadal modes of variability in the Pacific (e.g., Smith et al., 2016). In addition, melting of glaciers and ice caps due to anthropogenic influences has been speculated to increase volcanic activity (e.g., a specific example for Iceland is discussed in Swindles et al., 2018).

1.4.3.2 Uncertainty quantification

Not all of these listed sources of uncertainty are of the same type. For example, internal climate variations are an intrinsic uncertainty that can be estimated probabilistically, and could be more precisely quantified, but cannot usually be reduced. However, advances in decadal prediction offer the prospect of narrowing uncertainties in the trajectory of the climate for a few years ahead (e.g., Meehl et al., 2014; Yeager and

ACCEPTED VERSION SUBJECT TO FINAL EDITS

Robson, 2017; Chapter 4, Section 4.2.3).

Other sources of uncertainty, such as model response uncertainty, can in principle be reduced, but are not amenable to a frequency-based interpretation of probability, and Bayesian methods to quantify the uncertainty have been considered instead (e.g., Tebaldi, 2004; Rougier, 2007; Sexton et al., 2012). The scenario uncertainty component is distinct from other uncertainties, given that future anthropogenic emissions can be considered as the outcome of a set of societal choices (see Section 1.6.1).

For climate model projections it is possible to approximately quantify the relative amplitude of various sources of uncertainty (e.g., Hawkins and Sutton, 2009; Lehner et al., 2020). A range of different climate models are used to estimate the model response uncertainty to a particular emissions pathway, and multiple pathways are used to estimate the scenario uncertainty. The unforced component of internal variability can be estimated from individual ensemble members of the same climate model (e.g., Deser et al., 2012; Maher et al., 2019; Section 1.5.4.8).

Figure 1.15 illustrates the relative size of these different uncertainty components using a 'cascade of uncertainty' (Wilby and Dessai, 2010), with examples shown for global mean temperature, northern South American annual temperatures and East Asian summer precipitation changes. For global mean temperature, the role of internal variability is small, and the total uncertainty is dominated by emissions scenario and model response uncertainties. Note that there is considerable overlap between individual simulations for different emissions scenarios even for the mid-term (2041–2060). For example, the slowest-warming simulation for SSP5-8.5 produces less mid-term warming than the fastest-warming simulation for SSP1-1.9. For the long-term, emissions scenario uncertainty becomes dominant.

The relative uncertainty due to internal variability and model uncertainty increases for smaller spatial scales. In the regional example shown for changes in temperature, the same scenario and model combination has produced two simulations which differ by 1°C in their projected 2081–2100 averages due solely to internal climate variability. For regional precipitation changes, emissions scenario uncertainty is often small relative to model response uncertainty. In the example shown, the SSPs overlap considerably, but SSP1-1.9 shows the largest precipitation change in the near-term even though global mean temperature warms the least; this is due to differences between regional aerosol emissions projected in this and other scenarios (Wilcox et al., 2020). These cascades of uncertainty would branch out further if applying the projections to derive estimates of changes in hazard (e.g., Wilby and Dessai, 2010; Halsnæs and Kaspersen, 2018; Hattermann et al., 2018).

[START FIGURE 1.15 HERE]

Figure 1.15: The 'cascade of uncertainties' in CMIP6 projections. Changes in GSAT (left), northern South America (region NSA) temperature change (middle), and East Asia (region EAS) summer (JJA) precipitation change (right) are shown for two time periods (2041–2060, top, and 2081–2100, bottom). The SSP-radiative forcing combination is indicated at the top of each cascade at the value of the multi-model mean for each scenario. This branches downwards to show the ensemble mean for each model, and further branches into the individual ensemble members, although often only a single member is available. These diagrams highlight the relative importance of different sources of uncertainty in climate projections, which varies for different time periods, regions and climate variables. See Section 1.4.5 for the definition of the regions used. Further details on data sources and processing are available in the chapter data table (Table 1.SM.1).

[END FIGURE 1.15 HERE]

1.4.4 Considering an uncertain future

Since AR5 there have been developments in how to consider and describe future climate outcomes which are considered possible but *very unlikely,* highly uncertain, or potentially surprising. To examine such futures there is a need to move beyond the usual *'likely'* or *'very likely'* assessed ranges and consider low-likelihood

ACCEPTED VERSION SUBJECT TO FINAL EDITS

outcomes, especially those that would result in significant impacts if they occurred (e.g., Sutton, 2018; Sillmann et al., 2021). This section briefly outlines some of the different approaches used in the AR6 WGI.

1.4.4.1 Low-likelihood outcomes

In the AR6, certain low-likelihood outcomes are described and assessed because they may be associated with high levels of risk and the greatest risks may not be associated with the most expected outcome. The aim of assessing these possible futures is to better inform risk assessment and decision making. Two types are considered: (1) low-likelihood high warming (LLHW) scenarios, which describe the climate in a world with very high climate sensitivity, and (2) low-likelihood high impact (LLHI) events that have a low likelihood of occurring, but would cause large potential impacts on society or ecosystems.

An illustrative example of how low-likelihood outcomes can produce significant additional risks is shown in Figure 1.16. The Reasons for Concern (RFCs) produced by the IPCC AR5 WGII define the additional risks due to climate change at different global warming levels. These have been combined with Chapter 4 assessments of projected global temperature for different emissions scenarios (SSPs; see Section 1.6), and Chapter 7 assessments about ECS. For example, even following a medium emissions scenario could result in high levels of additional risk if ECS is at the upper end of the *very likely* range. However, not all possible low-likelihood outcomes relate to ECS, and AR6 considers these issues in more detail than previous IPCC assessment reports (see Table 1.1 and below for some examples).

[START FIGURE 1.16 HERE]

Figure 1.16: Illustrating concepts of low-likelihood scenarios. Left: schematic likelihood distribution consistent with the IPCC AR6 assessments that equilibrium climate sensitivity (ECS) is *likely* in the range 2.5 to 4.0°C, and *very likely* between 2.0 and 5.0°C (Chapter 7). ECS values outside the assessed *very likely* range are designated low-likelihood scenarios in this example (light grey). Middle and right columns: additional risks due to climate change for 2020–2090 using the Reasons For Concern (RFCs, see IPCC, 2014), specifically RFC1 describing the risks to unique and threatened systems and RFC3 describing risks from the distribution of impacts (O'Neill et al., 2017b; Zommers et al., 2020). The projected changes of GSAT used are the 95%, median and 5% assessed ranges from Chapter 4 for each SSP (top, middle and bottom); these are designated High ECS, Mid-range ECS and Low ECS respectively. The burning-ember risk spectrum is usually associated with levels of committed GSAT change; instead, this illustration associates the risk spectrum with the GSAT reached in each year from 2020 to 2090. Note that this illustration does not include the vulnerability aspect of each SSP scenario. Further details on data sources and processing are available in the chapter data table (Table 1.SM.1).

[END FIGURE 1.16 HERE]

1.4.4.2 Storylines

As societies are increasingly experiencing the impacts of climate change related events, the climate science community is developing climate information tailored for particular regions and sectors. There is a growing focus on explaining and exploring complex physical chains of events or on predicting climate under various future socio-economic developments. Since AR5, 'storylines' or 'narratives' approaches have been used to better inform risk assessment and decision making, to assist understanding of regional processes, and represent and communicate climate projection uncertainties more clearly. The aim is to help build a cohesive overall picture of potential climate change pathways that moves beyond the presentation of data and figures (Annex VII: Glossary; Fløttum and Gjerstad, 2017; Moezzi et al., 2017; Dessai et al., 2018; Shepherd et al., 2018b).

In the broader IPCC context, the term 'scenario storyline' refers to a narrative description of one or more scenarios, highlighting their main characteristics, relationships between key driving forces and the dynamics

ACCEPTED VERSION SUBJECT TO FINAL EDITS

of their evolution (for example, short-lived climate forcers emissions assessed in Chapter 6 are driven by 'scenario storylines', see Section 1.6). WGI is mainly concerned with 'physical climate storylines'. These are self-consistent and possible unfolding of a physical trajectory of the climate system, or a weather or climate event, on timescales from hours to multiple decades (Shepherd et al., 2018b). This approach can be used to constrain projected changes or specific events on specified explanatory elements such as projected changes of large-scale indicators (Chapter 10, Box 10.2). For example, Hazeleger et al. (2015) suggested using 'tales of future weather', blending numerical weather prediction with a climate projection to illustrate the potential behaviour of future high-impact events (also see Hegdahl et al. 2020). Several studies describe how possible large changes in atmospheric circulation would affect regional precipitation and other climate variables, and discuss the various climate drivers which could cause such a circulation response (James et al., 2015; Zappa and Shepherd, 2017; Mindlin et al., 2020). Physical climate storylines can also help frame the causal factors of extreme weather events (Shepherd, 2016) and then be linked to event attribution (Chapter 11, Section 11.2.2; Cross Working Group Box: Attribution).

Storyline approaches can be used to communicate and contextualise climate change information in the context of risk for policymakers and practitioners (e.g., de Bruijn et al., 2016; Dessai et al., 2018; Scott et al., 2018; Jack et al., 2020; Chapter 10, Box 10.2). They can also help in assessing risks associated with LLHI events (Weitzman, 2011; Sutton, 2018), because they consider the 'physically self-consistent unfolding of past events, or of plausible future events or pathways' (Shepherd et al., 2018b), which would be masked in a probabilistic approach. These aspects are important as the greatest risk need not be associated with the highest-likelihood outcome, and in fact will often be associated with low-likelihood outcomes. The storyline approach can also acknowledge that climate-relevant decisions in a risk-oriented framing will rarely be taken on the basis of physical climate change alone; instead, such decisions will normally take into account socio-economic factors as well (Shepherd, 2019).

In the AR6 WGI Assessment Report, these different storyline approaches are used in several places (see Table 1.1). Chapter 4 uses a storyline approach to assess the upper tail of the distribution of global warming levels (the storylines of high global warming levels) and their manifestation in global patterns of temperature and precipitation changes. Chapter 9 uses a storyline approach to examine the potential for, and early warning signals of, a high-end sea-level scenario, in the context of deep uncertainty related to our current understanding the physical processes that contribute to long-term sea-level rise. Chapter 10 assesses the use of physical climate storylines and narratives as a way to explore uncertainties in regional climate projections, and to link to the specific risk and decision context relevant to a user, for developing integrated and context-relevant regional climate change information. Chapter 11 uses the term storyline in the framework of extreme event attribution. Chapter 12 assesses the use of a storylines approach with narrative elements for communicating climate (change) information in the context of climate services (Cross-Chapter Box 12.2 in Chapter 12).

[START CROSS-CHAPTER BOX 1.3 HERE]

Cross-Chapter Box 1.3: Risk framing in IPCC AR6

Contributing Authors: Andy Reisinger (New Zealand), Maisa Rojas (Chile), Maarten van Aalst (Netherlands), Aïda Diongue-Niang (Senegal), Mathias Garschagen (Germany), Mark Howden (Australia), Margot Hurlbert (Canada), Katie Mach (USA), Sawsan Mustafa (Sudan), Brian O'Neill (USA), Roque Pedace (Argentina), Jana Sillmann (Norway), Carolina Vera (Argentina), David Viner (UK).

The IPCC SREX presented a framework for assessing risks from climate change, linking hazards (due to changes in climate) with exposure and vulnerability (Cardona et al., 2012). This framework was further developed by AR5 WGII (IPCC, 2014b), while AR5 WGI focussed only on the hazard component of risk. As part of AR6, a cross-Working Group process expanded and refined the concept of risk to allow for a consistent risk framing to be used across the three IPCC working groups (IPCC, 2019b; Box 2 in Abram et al., 2019; Reisinger et al., 2020).

ACCEPTED VERSION SUBJECT TO FINAL EDITS

In this revised definition, risk is the 'potential for adverse consequences for human or ecological systems, recognising the diversity of values and objectives associated with such systems. In the context of climate change, risks can arise not only from **impacts of climate change**, but also from potential human **responses to climate change**. Relevant adverse consequences include those on lives, livelihoods, health and wellbeing, economic, social and cultural assets and investments, infrastructure, services (including ecosystem services), ecosystems and species.

In the context of climate change impacts, risks result from dynamic interactions between climate-related hazards with the exposure and vulnerability of the affected human or ecological system to hazards. Hazards, exposure and vulnerability may each be subject to uncertainty in terms of magnitude and likelihood of occurrence, and each may change over time and space due to socio-economic changes and human decision-making.

In the context of climate change responses, risks result from the potential for such responses not achieving the intended objective(s), or from potential trade-offs with, or negative side-effects on, other societal objectives, such as the Sustainable Development Goals. Risks can arise for example from uncertainty in implementation, effectiveness or outcomes of climate policy, climate-related investments, technology development or adoption, and system transitions'.

The following concepts are also relevant for the definition of risk (see Annex VII: Glossary):

Exposure: The presence of people, livelihoods, species or ecosystems, environmental functions, services, and resources, infrastructure, or economic, social, or cultural assets in places and settings that could be adversely affected.

Vulnerability: The propensity or predisposition to be adversely affected. Vulnerability encompasses a variety of concepts and elements including sensitivity or susceptibility to harm and lack of capacity to cope and adapt.

Hazard: The potential occurrence of a natural or human-induced physical event or trend that may cause loss of life, injury, or other health impacts, as well as damage and loss to property, infrastructure, livelihoods, service provision, ecosystems and environmental resources.

Impacts: The consequences of realised risks on natural and human systems, where risks result from the interactions of climate-related hazards (including extreme weather and climate events), exposure, and vulnerability. Impacts generally refer to effects on lives, livelihoods, health and wellbeing, ecosystems and species, economic, social and cultural assets, services (including ecosystem services), and infrastructure. Impacts may be referred to as consequences or outcomes, and can be adverse or beneficial.

Risk in AR6 WGI

The revised risk framing clarifies the role and contribution of WGI to risk assessment. Risk in IPCC terminology applies only to human or ecological systems, not to physical systems on their own.

Climatic impact-drivers: CIDs are physical climate system conditions (e.g., means, extremes, events) that affect an element of society or ecosystems. Depending on system tolerance, CIDs and their changes can be detrimental, beneficial, neutral, or a mixture of each across interacting system elements and regions.

In AR6, WGI uses the term 'climatic impact-drivers' (CIDs) to describe changes in physical systems rather than 'hazards', because the term hazard already assumes an adverse consequence. The terminology of 'climatic impact-driver' therefore allows WGI to provide a more value-neutral characterisation of climatic changes that may be relevant for understanding potential impacts, without pre-judging whether specific climatic changes necessarily lead to adverse consequences, as some could also result in beneficial outcomes depending on the specific system and associated values. Chapter 12 and the Atlas assess and provide information on climatic impact-drivers for different regions and sectors to support and link to WGII

ACCEPTED VERSION SUBJECT TO FINAL EDITS

assessment of the impacts and risks (or opportunities) related to the changes in the climatic impact-drivers. Although CIDs can lead to adverse or beneficial outcomes, focus is given to CIDs connected to hazards, and hence inform risk.

'Extremes' are a category of CID, corresponding to unusual events with respect to the range of observed values of the variable. Chapter 11 assesses changes in weather and climate extremes, their attribution and future projections.

As examples of the use of this terminology, the term 'flood risk' should not be used if it only describes changes in the frequency and intensity of flood events (a hazard); the risk from flooding to human and ecological systems is caused by the flood hazard, the exposure of the system affected (e.g., topography, human settlements or infrastructure in the area potentially affected by flooding) and the vulnerability of the system (e.g., design and maintenance of infrastructure, existence of early warning systems). As another example, climate-related risk to food security can arise from both potential climate change impacts and responses to climate change and can be exacerbated by other stressors. Drivers for risks related to climate change impacts include climate hazards (e.g., drought, temperature extremes, humidity), mediated by other climatic impact-drivers (e.g., increased CO_2 fertilisation of certain types of crops may help increase yields), the potential for indirect climate-related impacts (e.g., pest outbreaks triggered by ecosystem responses to weather patterns), exposure of people (e.g., how many people depend on a particular crop) and vulnerability or adaptability (how able are affected people to substitute other sources of food, which may be related to financial access and markets).

Information provided by WGI may or may not be relevant to understand risks related to climate change responses. For example, the risk to a company arising from emissions pricing, or the societal risk from reliance on an unproven mitigation technology, are not directly dependent on actual or projected changes in climate but arise largely from human choices. However, WGI climate information may be relevant to understand the potential for maladaptation, such as the potential for specific adaptation responses not achieving the desired outcome or having negative side-effects. For example, WGI information about the range of sea level rise can help inform understanding of whether coastal protection, accommodation, or retreat would be the most effective risk management strategy in a particular context.

From a WGI perspective also relevant for risk assessment are low-likelihood high impact events and the concept of deep uncertainty.

Low-likelihood, high-impact events: (LLHI) 'These are events whose probability of occurrence is low but whose potential impacts on society and ecosystems are high. To better inform risk assessment and decision making, such low likelihood outcomes are described as they may be associated with very high levels of risk and because the greatest risks might not be associated with the most expected outcome.

The AR6 WGI report provides more detailed information about these types of events compared to the AR5 (see Table 1.1, Section 1.4.4).

Recognising the need for assessing and managing risk in situations of high uncertainty, the SROCC advanced the treatment of situations with deep uncertainty (IPCC, 2019b; Box 5 in Abram et al., 2019); Section 1.2.3). A situation of deep uncertainty exists when experts or stakeholders do not know or cannot agree on: (1) appropriate conceptual models that describe relationships among key driving forces in a system; (2) the probability distributions used to represent uncertainty about key variables and parameters; and/or (3) how to weigh and value desirable alternative outcomes (Abram et al., 2019). The concept of deep uncertainty can complement the IPCC calibrated language and thereby broaden the communication of risk.

[END CROSS-CHAPTER BOX 1.3 HERE]

1.4.4.3 Abrupt change, tipping points and surprises

ACCEPTED VERSION SUBJECT TO FINAL EDITS

An *abrupt change* is defined in this report as a change that takes place substantially faster than the rate of change in the recent history of the affected component of a system (see Annex VII: Glossary). In some cases, abrupt change occurs because the system state actually becomes unstable, such that the subsequent rate of change is independent of the forcing. We refer to this class of abrupt change as a *tipping point,* defined as a critical threshold beyond which a system reorganizes, often abruptly and/or irreversibly (Lenton et al., 2008); Annex VII: Glossary). Some of the abrupt climate changes and climate tipping points discussed in this report could have severe local climate responses, such as extreme temperature, droughts, forest fires, ice sheet loss and collapse of the thermohaline circulation (see Chapter 4, Section 4.7.2, Chapter 5, Section 5.4.9, Chapter 8, Section 8.6 and Chapter 9, Section 9.2.3).

There is evidence of abrupt change in Earth's history, and some of these events have been interpreted as tipping points (Dakos et al., 2008) . Some of these are associated with significant changes in the global climate, such as deglaciations in the Quaternary (past 2.5 million years) and rapid warming at the Palaeocene-Eocene Thermal Maximum (around 55.5 million years ago) (Bowen et al., 2015; Hollis et al., 2019). Such events changed the planetary climate for tens to hundreds of thousands of years, but at a rate that is actually much slower than projected anthropogenic climate change over this century, even in the absence of tipping points.

Such paleoclimate evidence has even fuelled concerns that anthropogenic GHGs could tip the global climate into a permanent hot state (Steffen et al., 2018). However, there is no evidence of such non-linear responses at the global scale in climate projections for the next century, which indicate a near-linear dependence of global temperature on cumulative GHG emissions (Section 1.3.5, Chapter 5, Section 5.5 and Chapter 7, Section 7.4.3.1). At the regional scale, abrupt changes and tipping points, such as Amazon forest dieback and permafrost collapse, have occurred in projections with Earth System Models (Drijfhout et al., 2015; Bathiany et al., 2020; Chapter 4, Section 4.7.3). In such simulations, tipping points occur in narrow regions of parameter space (e.g., CO_2 concentration or temperature increase), and for specific climate background states. This makes them difficult to predict using ESMs relying on parmeterizations of known processes. In some cases, it is possible to detect forthcoming tipping points through time-series analysis that identifies increased sensitivity to perturbations as the tipping point is approached (e.g., 'critical slowing-down', Scheffer et al., 2012).

Some suggested climate tipping points prompt transitions from one steady state to another (see Figure 1.17). Transitions can be prompted by perturbations such as climate extremes which force the system outside of its current well of attraction in the stability landscape; this is called noise-induced tipping (Ashwin et al., 2012; Figure 1.17, panels a/b). For example, the tropical forest dieback seen in some ESM projections is accelerated by longer and more frequent droughts over tropical land (Good et al., 2013).

Alternatively, transitions from one state to another can occur if a critical threshold is exceeded; this is called bifurcation tipping (Ashwin et al., 2012; Figure 1.17, panels c/d). The new state is defined as *irreversible* on a given timescale if the recovery from this state takes substantially longer than the timescale of interest, which is decades to centuries for the projections presented in this report. A well-known example is the modelled irreversibility of the ocean's thermohaline circulation in response to North Atlantic changes such as freshwater input from rainfall and ice-sheet melt (Rahmstorf et al., 2005; Alkhayuon et al., 2019), which is assessed in detail in Chapter 9, Section 9.2.3.

The tipping point concept is most commonly framed for systems in which the forcing changes relatively slowly. However, this is not the case for most scenarios of anthropogenic forcing projected for the 21st century. Systems with inertia lag behind rapidly-increasing forcing, which can lead to the failure of early warning signals or even the possibility of temporarily overshooting a bifurcation point without provoking tipping (Ritchie et al., 2019).

[START FIGURE 1.17 HERE]

Figure 1.17: Illustration of two types of tipping points: noise-induced (panels a, b) and bifurcation (panels c, d).

ACCEPTED VERSION SUBJECT TO FINAL EDITS

(a), (c) example time-series (coloured lines) through the tipping point with black solid lines indicating stable climate states (e.g., low or high rainfall) and dashed lines represent the boundary between stable states. (b), (d) stability landscapes provide an intuitive understanding for the different types of tipping point. The valleys represent different climate states the system can occupy, with hill tops separating the stable states. The resilience of a climate state is implied by the depth of the valley. The current state of the system is represented by a ball. Both scenarios assume that the ball starts in the left-hand valley (black dashed lines) and then through different mechanisms dependent on the type of tipping transitions to the right valley (coloured lines). Noise-induced tipping events, for instance drought events causing sudden dieback of the Amazonian rainforest, develop from fluctuations within the system. The stability landscape in this scenario remains fixed and stationary. A series of perturbations in the same direction or one large perturbation are required to force the system over the hill top and into the alternative stable state. Bifurcation tipping events, such as a collapse of the thermohaline circulation in the Atlantic Ocean under climate change, occur when a critical level in the forcing is reached. Here the stability landscape is subjected to a change in shape. Under gradual anthropogenic forcing the left valley begins to shallow and eventually vanishes at the tipping point, forcing the system to transition to the right-hand valley.

[END FIGURE 1.17 HERE]

Surprises are a class of risk that can be defined as low-likelihood but well-understood events, and events that cannot be predicted with current understanding. The risk from such surprises can be accounted for in risk assessments (Parker and Risbey, 2015). Examples relevant to climate science include: a series of major volcanic eruptions or a nuclear war, either of which would cause substantial planetary cooling (Robock et al., 2007; Mills et al., 2014); significant 21st century sea level rise due to marine ice sheet instability (MISI, Chapter 9, Box 9.4); the potential for collapse of the stratocumulus cloud decks (Schneider et al., 2019) or other substantial changes in climate feedbacks (see Chapter 7, Section 7.4); and unexpected biological epidemics among humans or other species, such as the COVID-19 pandemic (Forster et al., 2020; Le Quéré et al., 2020; see Cross-Chapter Box 6.1 in Chapter 6). The discovery of the ozone hole was also a surprise even though some of the relevant atmospheric chemistry was known at the time. The term 'unknown unknowns' (Parker and Risbey, 2015) is also sometimes used in this context to refer to events that cannot be anticipated with present knowledge or were of an unanticipated nature before they occurred.

[START CROSS-WORKING GROUP BOX: ATTRIBUTION HERE]

Cross-Working Group Box: Attribution

Contributing Authors: Wolfgang Cramer (France/Germany), Pandora Hope (Australia), Maarten van Aalst (Netherlands), Greg Flato (Canada), Katja Frieler (Germany), Nathan Gillett (Canada/UK), Christian Huggel (Switzerland), Jan Minx (Germany), Friederike Otto (UK/Germany), Camille Parmesan (France/UK/USA), Joeri Rogelj (UK/Belgium), Maisa Rojas (Chile), Sonia I. Seneviratne (Switzerland), Aimee Slangen (Netherlands), Daithi Stone (New Zealand), Laurent Terray (France), Robert Vautard (France), Xuebin Zhang (Canada)

Introduction

Changes in the climate system are becoming increasingly apparent, as are the climate-related impacts on natural and human systems. Attribution is the process of evaluating the contribution of one or more causal factors to such observed changes or events. Typical questions addressed by the IPCC are for example: 'To what degree is an observed change in global temperature induced by anthropogenic greenhouse gas and aerosol concentration changes or influenced by natural variability?' or 'What is the contribution of climate change to observed changes in crop yields that are also influenced by changes in agricultural management?' Changes in the occurrence and intensity of extreme events can also be attributed, addressing questions such as: 'Have human greenhouse gas emissions increased the likelihood or intensity of an observed heat wave?'

This Cross-Working Group Box briefly describes why attribution studies are important. It also describes

ACCEPTED VERSION SUBJECT TO FINAL EDITS

some new developments in the methods used and provides recommendations for interpretation.

Attribution studies serve to evaluate and communicate linkages associated with climate change, for example: between the human-induced increase in greenhouse gas concentrations and the observed increase in air temperature or extreme weather events (WGI Chapter 3, 10, 11); or between observed changes in climate and changing species distributions and food production (WGII Chapters 2 and others, summarised in Chapter 16) (e.g., Verschuur et al., 2021); or between climate change mitigation policies and atmospheric greenhouse gas concentrations (WGI Chapter 5; WGIII Chapter 14). As such, they support numerous statements made by the IPCC (IPCC, 2013b, 2014b; WGI Chapter 1, Section 1.3, Appendix 1A).

Attribution assessments can also serve to monitor mitigation and assess the efficacy of applied climate protection policies (e.g., Nauels et al., 2019; Banerjee et al., 2020; WGI Chapter 4, Section 4.6.3), inform and constrain projections (Gillett et al., 2021; Ribes et al., 2021; WGI Chapter 4, Section 4.2.3) or inform the loss and damages estimates and potential climate litigation cases by estimating the costs of climate change (Huggel et al., 2015; Marjanac et al., 2017; Frame et al., 2020). These findings can thus inform mitigation decisions as well as risk management and adaptation planning (e.g., CDKN, 2017).

Steps towards an attribution assessment

The unambiguous framing of what is being attributed to what is a crucial first step for an assessment (Easterling et al., 2016; Hansen et al., 2016; Stone et al., 2021), followed by the identification of the possible and plausible drivers of change and the development of a hypothesis or theory for the linkage (see Cross-Working Group Box: Attribution, Figure 1). The next step is to clearly define the indicators of the observed change or event and note the quality of the observations. There has been significant progress in the compilation of fragmented and distributed observational data, broadening and deepening the data basis for attribution research (e.g., Poloczanska et al., 2013; Ray et al., 2015; Cohen et al., 2018; WGI Chapter 1, Section 1.5). The quality of the observational record of drivers should also be considered (e.g., volcanic eruptions: WGI Chapter 2, section 2.2.2). Impacted systems also change in the absence of climate change; this baseline and its associated modifiers such as agricultural developments or population growth need to be considered, alongside the exposure and vulnerability of people depending on these systems.

There are many attribution approaches, and several methods are detailed below. In physical and biological systems, attribution often builds on the understanding of the mechanisms behind the observed changes and numerical models are used, while in human systems other methods of evidence-building are employed. Confidence in the attribution can be increased if more than one approach is used and the model is evaluated as fit-for-purpose (Hegerl et al., 2010; Vautard et al., 2019; Otto et al., 2020; Philip et al., 2020) (WGI Chapter 1, Section 1.5). Finally, appropriate communication of the attribution assessment and the accompanying confidence in the result (e.g., Lewis et al., 2019).

Attribution methods

Attribution of changes in atmospheric greenhouse gas concentrations to anthropogenic activity

AR6 WGI Chapter 5 presents multiple lines of evidence that unequivocally establish the dominant role of human activities in the growth of atmospheric CO_2, including through analysing changes in atmospheric carbon isotope ratios and the atmospheric O_2-N_2 ratio (WGI Chapter 5, Section 5.2.1.1). Decomposition approaches can be used to attribute emissions underlying those changes to various drivers such as population, energy efficiency, consumption or carbon intensity (Hoekstra and van den Bergh, 2003; Raupach et al., 2007; Rosa and Dietz, 2012). Combined with attribution of their climate outcomes, the attribution of the sources of greenhouse gas emissions can inform the attribution of anthropogenic climate change to specific countries or actors (Matthews, 2016; Otto et al., 2017; Skeie et al., 2017; Nauels et al., 2019), and in turn inform discussions on fairness and burden sharing (WGIII Chapter 14).

Attribution of observed climate change to anthropogenic forcing

ACCEPTED VERSION SUBJECT TO FINAL EDITS

Changes in large-scale climate variables (e.g., global mean temperature) have been reliably attributed to anthropogenic and natural forcings (e.g., Hegerl et al., 2010; Bindoff et al., 2013; WGI Chapter 1, Section 1.3.4). The most established method is to identify the 'fingerprint' of the expected space-time response to a particular climate forcing agent such as the concentration of anthropogenically induced greenhouse gases or aerosols, or natural variation of solar radiation. This technique disentangles the contribution of individual forcing agents to an observed change (e.g., Gillett et al., 2021). New statistical approaches have been applied to better account for internal climate variability and the uncertainties in models and observations (e.g., Naveau et al., 2018; Santer et al., 2019) (WGI, Chapter 3 Section 3.2). There are many other approaches, for example, global mean sea-level change has been attributed to anthropogenic climate forcing by attributing the individual contributions from, for example, glacier melt or thermal expansion, while also examining which aspects of the observed change are inconsistent with internal variability (WGI Chapter 3, Section 3.5.2 and WGI Chapter 9, Section 9.6.1.4).

Specific regional conditions and responses may simplify or complicate attribution on those scales. For example, some human forcings, such as regional land use change or aerosols, may enhance or reduce regional signals of change (Lejeune et al., 2018; Undorf et al., 2018; Boé et al., 2020; Thiery et al., 2020; see also WGI Chapter 10, Section 10.4.2; WGI Chapter 11, Sections 11.1.6 and 11.2.2. In general, regional climate variations are larger than the global mean climate, adding additional uncertainty to attribution (e.g., in regional sea-level change, WGI Chapter 9, Section 9.6.1). These statistical limitations may be reduced by 'process-based attribution', focusing on the physical processes known to influence the response to external forcing and internal variability (WGI Chapter 10, Section 10.4.2).

Attribution of weather and climate events to anthropogenic forcing

New methods have emerged since AR5 to attribute the change in likelihood or characteristics of weather or climate events or classes of events to underlying drivers (National Academies of Sciences Engineering and Medicine, 2016; Stott et al., 2016; Jézéquel et al., 2018; Wehner et al., 2018; Wang et al., 2020; WGI Chapter 10, Section 10.4.1; WG1 Chapter 11, Section 11.2.2). Typically, historical changes, simulated under observed forcings, are compared to a counterfactual climate simulated in the absence of anthropogenic forcing. Another approach examines facets of the weather and thermodynamic status of an event through process-based attribution (Hauser et al., 2016; Shepherd et al., 2018b; Grose et al., 2019; WGI Chapter 10 Section 10.4.1 and Chapter 11). Events where attributable human influences have been found include hot and cold temperature extremes (including some with wide-spread impacts), heavy precipitation, and certain types of droughts and tropical cyclones (e.g., Vogel et al., 2019; Herring et al., 2021; AR6 WGI Chapter 11, Section 11.9). Event attribution techniques have sometimes been extended to 'end-to-end' assessments from climate forcing to the impacts of events on natural or human systems (Otto, 2017, examples in WGII Table 16.1, SI of WGII Chapter 16, Section 16.2).

Attribution of observed changes in natural or human systems to climate-related drivers

The attribution of observed changes to climate-related drivers across a diverse set of sectors, regions and systems is part of each chapter in the WGII contribution to the AR6 and is synthesised in WGII Chapter 16 (Section 16.2). The number of attribution studies on climate change impacts has grown substantially since AR5, generally leading to higher confidence levels in attributing the causes of specific impacts. New studies include the attribution of changes in socio-economic indicators such as economic damages due to river floods (e.g., Schaller et al., 2016; Sauer et al., 2021), the occurrence of heat related human mortality (e.g., Sera et al., 2020, Vicedo-Cabrera et al., 2018;) or economic inequality (e.g., Diffenbaugh and Burke, 2019).

Impact attribution covers a diverse set of qualitative and quantitative approaches, building on experimental approaches, observations from remote sensing, long-term in situ observations, and monitoring efforts, teamed with local knowledge, process understanding and empirical or dynamical modelling (WGII Chapter 16, Section 16.2; Stone et al., 2013; Cramer et al., 2014). The attribution of a change in a natural or human system (e.g., wild species, natural ecosystems, crop yields, economic development, infrastructure or human health) to changes in climate-related systems (i.e., climate, and ocean acidification, permafrost thawing or

ACCEPTED VERSION SUBJECT TO FINAL EDITS

sea-level rise) requires accounting for other potential drivers of change, such as technological and economic changes in agriculture affecting crop production (Hochman et al., 2017; Butler et al., 2018), changes in human population patterns and vulnerability affecting flood or wildfire induced damages (Huggel et al., 2015; Sauer et al., 2021), or habitat loss driving declines in wild species (IPBES, 2019). These drivers are accounted for by estimating a baseline condition that would exist in the absence of climate change. The baseline might be stationary and be approximated by observations from the past, or it may change over time and be simulated by statistical or process-based impact models (Cramer et al. 2014, WGII Chapter 16, Section 16.2). Assessment of multiple independent lines of evidence, taken together, can provide rigorous attribution when more quantitative approaches are not available (Parmesan et al., 2013). These include paleodata, physiological and ecological experiments, natural 'experiments' from very long-term datasets indicating consistent responses to the same climate trend/event, and 'fingerprints' in species' responses that are uniquely expected from climate change (e.g. poleward range boundaries expanding and equatorial range boundaries contracting in a coherent pattern world-wide, Parmesan and Yohe, 2003). Meta-analyses of species/ecosystem responses, when conducted with wide geographic coverage, also provide a globally coherent signal of climate change at an appropriate scale for attribution to anthropogenic climate change (Parmesan and Yohe, 2003; Parmesan et al., 2013).

Impact attribution does not always involve attribution to anthropogenic climate forcing. However, a growing number of studies include this aspect (e.g., Frame et al., 2020 for the attribution of damages induced by hurricane Harvey; or Diffenbaugh and Burke, 2019 for the attribution of economic inequality between countries; or Schaller et al., 2016 for flood damages).

[START CROSS-WORKING GROUP BOX: ATTRIBUTION, FIGURE 1 HERE]

Cross-Working Group Box: Attribution, Figure 1: Schematic of the steps to develop an attribution assessment, and the purposes of such assessments. Methods and systems used to test the attribution hypothesis or theory include model-based fingerprinting, other model-based methods, evidence-based fingerprinting, process-based approaches, empirical or decomposition methods and the use of multiple lines of evidence. Many of the methods are based on the comparison of the observed state of a system to a hypothetical counterfactual world that does not include the driver of interest to help estimate the causes of the observed response.

[END CROSS-WORKING GROUP BOX: ATTRIBUTION, FIGURE 1 HERE]

[END CROSS-WORKING GROUP BOX: ATTRIBUTION HERE]

1.4.5 Climate regions used in AR6

1.4.5.1 Defining climate regions

AR5 assessed regional scale detection and attribution and assessed key regional climate phenomena and their relevance for future regional climate projections. This report shows that past and future climate changes and extreme weather events can be substantial on local and regional scales (Chapters 8–12, Atlas), where they may differ considerably from global trends, not only in intensity but even in sign (e.g., Fischer et al., 2013).

Although the evolution of global climate trends emerges as the net result of regional phenomena, average or aggregate estimates often do not reflect the intensity, variability, and complexity of regional climate changes (Stammer et al., 2018; Shepherd, 2019). A fundamental aspect of the study of regional climate changes is the definition of characteristic climate zones, clusters or regions, across which the emergent climate change signal can be properly analysed and projected (see Atlas). Suitable sizes and shapes of such zones strongly

ACCEPTED VERSION SUBJECT TO FINAL EDITS

depend not only on the climate variable and process of interest, but also on relevant multiscale feedbacks.

There are several approaches to the classification of climate regions. When climate observation data was sparse and limited, the aggregation of climate variables was implicitly achieved through the consideration of biomes, giving rise to the traditional vegetation-based classification of Köppen (1936). In the last decades, the substantial increases in climate observations, climate modelling, and data processing capabilities have allowed new approaches to climate classification, e.g., through interpolation of aggregated global data from thousands of stations (Peel et al., 2007; Belda et al., 2014; Beck et al., 2018a) or through data-driven approaches applied to delineate ecoregions that behave in a coherent manner in response to climate variability (Papagiannopoulou et al., 2018). Experience shows that each method has strengths and weaknesses through trade-offs between detail and convenience. For instance, a very detailed classification, with numerous complexly shaped regions derived from a large set of variables, may be most useful for the evaluation of climate models (Rubel and Kottek, 2010; Belda et al., 2015; Beck et al., 2018a) and climate projections (Feng et al., 2014; Belda et al., 2016). In contrast, geometrically simple regions are often best suited for regional climate modelling and downscaling (e.g., the Coordinated Regional Climate Downscaling Experiment (CORDEX) domains; see Giorgi and Gutowski, 2015, and Section 1.5.3).

1.4.5.2 Types of regions used in AR6

IPCC's recognition of the importance of regional climates can be traced back to its First Assessment Report (IPCC, 1990a), where climate projections for 2030 were presented for five subcontinental regions (see Section 1.3.6 for an assessment of those projections). In subsequent reports, there has been a growing emphasis on the analysis of regional climate, including two special reports: one on regional impacts (IPCC, 1998) and another on extreme events (SREX, IPCC, 2012). A general feature of previous IPCC reports is that the number and coverage of climate regions vary according to the subject and across WGs. Such varied definitions have the advantage of optimizing the results for a particular application (e.g., national boundaries are crucial for decision making, but they rarely delimit distinctive climate regions), whereas variable region definitions may have the disadvantage of hindering multidisciplinary assessments and comparisons between studies or WGs.

In this Report, regional climate change is primarily addressed through the introduction of four classes of regions (unless otherwise explicitly mentioned and justified). The first two are the unified WGI Reference Sets of (1) Land and (2) Ocean Regions, which are used in the entire Report. These are supplemented by additional sets of (3) Typological Regions — used in Chapters 5, 8–12 and Atlas — and (4) Continental Regions, which are mainly used for linking Chapters 11, 12 and Atlas with WGII (Figure 1.18). All four classes of regions are defined and described in detail in the Atlas. Here we summarize their basic features.

[START FIGURE 1.18 HERE]

Figure 1.18: Main types of regions used in this report. (a) AR6 WGI Reference Set of Land and Ocean Regions (Iturbide et al., 2020), consisting of 46 land regions and 15 ocean regions, including 3 hybrid regions (CAR, MED, SEA) that are both land and ocean regions. Acronyms are explained on the right of the map. Notice that RAR, SPO, NPO and EPO extend beyond the 180º meridian, therefore appearing at both sides of the map (indicated by dashed lines). A comparison with the previous reference regions of AR5 WGI (IPCC, 2013a) is presented in the Atlas. (b) Example of typological regions: monsoon domains adopted in Chapter 8. Acronyms are explained on the right of the map. The black contour lines represent the global monsoon zones, while the coloured regions denote the regional monsoon domains. The two stippled regions (EqAmer and SAfri) do receive seasonal rainfall, but their classification as monsoon regions is still under discussion. (c) Continental Regions used mainly in Chapter 12 and the Atlas. Stippled zones define areas that are assessed in both regions (e.g., the Caribbean is assessed as Small Islands and also as part of Central America). Small Islands are ocean regions containing small islands with consistent climate signals and/or climatological coherence.

[END FIGURE 1.18 HERE]

ACCEPTED VERSION SUBJECT TO FINAL EDITS

Reference Land and Ocean Regions are polygonal, sub-continental domains defined through a combination of environmental, climatic and non-climatic (e.g., pragmatic, technical, historical) factors, in accordance with the literature and climatological reasoning based on observed and projected future climate. Merging the diverse functions and purposes of the regions assessed in the literature into a common reference set implies a certain degree of compromise between simplicity, practicality, and climate consistency. For instance, Spain is fully included in the Mediterranean (MED) Reference Region, but is one of the most climatically diverse countries in the world. Likewise, a careful comparison of panels (a) and (b) of Figure 1.18) reveals that the simplified southern boundary of the Sahara (SAH) Reference Region slightly overlaps the northern boundary of the West African Monsoon Typological Region. As such, the resulting Reference Regions are not intended to precisely represent climates, but rather to provide simple domains suitable for regional synthesis of observed and modelled climate and climate change information (Iturbide et al., 2020). In particular, CMIP6 model results averaged over Reference Regions are presented in the Atlas.

The starting point for defining the AR6 Reference Sets of Land Regions was the collection of 26 regions introduced in SREX (IPCC, 2012). The SREX collection was then revised, reshaped, complemented and optimized to reflect the recent scientific literature and observed climate-change trends, giving rise to the novel AR6 reference set of 46 land regions. Additionally, AR6 introduces a new reference set of 15 ocean regions (including 3 hybrid regions that are treated as both, land and ocean), which complete the coverage of the whole Earth (Iturbide et al., 2020).

Particular aspects of regional climate change are described by specialized domains called Typological Regions (Figure 1.18b). These regions cover a wide range of spatial scales and are defined by specific features, called typologies. Examples of typologies include: tropical forests, deserts, mountains, monsoon regions, and megacities, among others. Typological Regions are powerful tools to summarize complex aspects of climate defined by a combination of multiple variables. For this reason, they are used in many chapters of AR6 WGI and WGII (e.g., Chapters 8–12 and the Atlas).

Finally, consistency with WGII is also pursued in Chapter 11, 12 and Atlas through the use of a set of Continental Regions (Figure 1.18c), based on the nine continental domains defined in AR5 WGII Part B (Hewitson et al., 2014). These are classical geopolitical divisions of Africa, Asia, Australasia, Europe, North America, Central and South America, plus Small Islands, Polar Regions, and the Ocean. In AR6 WGI, five hybrid zones (Caribbean–Small islands, East Europe–Asia, European Arctic, North American Arctic, and North Central America) are also identified, which are assessed in more than one continental region. Additional consistency with WGIII is pursued by Chapter 6 through the use of sub-continental domains which essentially form a subset of the Continental Set of Regions (Figure 1.18c and Chapter 6, Section 6.1).

1.5 Major developments and their implications

This section presents a selection of key developments since the AR5 of the capabilities underlying the lines of evidence used in the present report: observational data and observing systems (Section 1.5.1), new developments in reanalyses (Section 1.5.2), climate models (Section 1.5.3), and modelling techniques, comparisons and performance assessments (Section 1.5.4). For brevity, we focus on the developments that are of particular importance to the conclusions drawn in later chapters, though we also provide an assessment of potential losses of climate observational capacity.

1.5.1 Observational data and observing systems

Progress in climate science relies on the quality and quantity of observations from a range of platforms: surface-based instrumental measurements, aircraft, radiosondes and other upper-atmospheric observations, satellite-based retrievals, ocean observations, and paleoclimatic records. An historical perspective to these types of observations is presented in Section 1.3.1.

ACCEPTED VERSION SUBJECT TO FINAL EDITS

Observed large-scale climatic changes assessed in Chapter 2, attribution of these changes in Chapter 3, and regional observations of specific physical or biogeochemical processes presented in other Chapters, are supported by improvements in observational capacity since the AR5. Attribution assessments can be made at a higher likelihood level than AR5, due in part to the availability of longer observational datasets (Chapter 3). Updated assessments are made based on new and improved datasets, for example of global temperature change (Cross-Chapter Box 2.3 in Chapter 2) or regional climate information (Chapter 10, Section 10.2). Of particular relevance to the AR6 assessment are the 'Essential Climate Variables' (ECVs, Hollmann et al., 2013; Bojinski et al., 2014), and 'Essential Ocean Variables' (EOVs; Lindstrom et al., 2012), compiled by the Global Climate Observing System (GCOS; WMO, 2016), and the Global Ocean Observing System (GOOS), respectively. These variables include physical, chemical, and biological variables or groups of linked variables and underpin 'headline indicators' for climate monitoring (Trewin et al., 2021).

We highlight below the key advances in observational capacity since the AR5, including major expansions of existing observational platforms as well as new and/or emerging observational platforms that play a key role in AR6. We then discuss potential near-term losses in key observational networks due to climate change or other adverse human-caused influence.

1.5.1.1 Major expansions of observational capacity

Atmosphere, land and hydrological cycle

Satellites provide observations of a large number of key atmospheric and land surface variables, ensuring sustained observations over wide areas. Since AR5, such observations have expanded to include satellite retrievals of atmospheric CO_2 via the NASA Orbiting Carbon Observatory satellites (OCO-2 and OCO-3, Eldering et al., 2017), following on from similar efforts employing the Greenhouse Gases Observing Satellite (GOSAT, Yokota et al., 2009; Inoue et al., 2016). Improved knowledge of fluxes between the atmosphere and land surface results from combining remote sensing and in situ measurements (Rebmann et al., 2018). FLUXNET (https://fluxnet.org/) has been providing eddy covariance measurements of carbon, water, and energy fluxes between the land and the atmosphere, with some of the stations operating for over 20 years (Pastorello et al., 2017), while the Baseline Surface Radiation Network (BSRN) has been maintaining high-quality radiation observations since the 1990s (Ohmura et al., 1998; Driemel et al., 2018).

Observations of the composition of the atmosphere have been further improved through expansions of existing surface observation networks (Bodeker et al., 2016; De Mazière et al., 2018) and through in situ measurements such as aircraft campaigns (Chapter 2, Section 2.2; Chapter 5, Section 5.2; Chapter 6, Section 6.2). Examples of expanded networks include Aerosols, Clouds, and Trace Gases Research InfraStructure (ACTRIS) (Pandolfi et al., 2018), which focuses on short-lived climate forcers, and the Integrated Carbon Observation System (ICOS), which allows scientists to study and monitor the global carbon cycle and greenhouse gas emissions (Colomb et al., 2018). Examples of recent aircraft observations include the Atmospheric Tomography Mission (ATom), which has flown repeatedly along the north-south axis of both the Pacific and Atlantic oceans, and the continuation of the In-service Aircraft for a Global Observing System (IAGOS) effort, which measures atmospheric composition from commercial aircraft (Petzold et al., 2015).

Two distinctly different but important remote sensing systems can provide information about temperature and humidity since the early 2000s. Global Navigation Satellite Systems (e.g., GPS) radio occultation and limb soundings provide information, although only data for the upper troposphere and lower stratosphere are suitable to support climate change assessments (Angerer et al., 2017; Scherllin-Pirscher et al., 2017; Steiner et al., 2019; Gleisner et al., 2020). These measurements complement those from the Atmospheric Infrared Sounder (AIRS; Chahine et al., 2006). AIRS has limitations in cloudy conditions, although these limitations have been partly solved using new methods of analysis (Blackwell and Milstein, 2014; Susskind et al., 2014). These new data sources now have a sufficient length of the record to strengthen the analysis of atmospheric warming in Chapter 2, Section 2.3.1.2.

ACCEPTED VERSION SUBJECT TO FINAL EDITS

Assessments of the hydrological cycle in Chapters 2 and 8 are supported by longer time series and new developments. Examples are new satellites (McCabe et al., 2017) and measurements of water vapor using commercial laser absorption spectrometers and water vapor isotopic composition (Steen-Larsen et al., 2015; Zannoni et al., 2019). Data products of higher quality have been developed since AR5, such as the multi-source weighted ensemble precipitation (Beck et al., 2017), and multi-satellite terrestrial evaporation (Fisher et al., 2017). Longer series are available for satellite-derived global inundation (Prigent et al., 2020). Observations of soil moisture are now available via the Soil Moisture and Ocean Salinity (SMOS) and the Soil Moisture Active Passive (SMAP) satellite retrievals, filling critical gaps in the observation of hydrological trends and variability over land (Dorigo et al., 2017). Similarly, the Gravity Recovery and Climate Experiment GRACE and GRACE-FO satellites (Tapley et al., 2019) have provided key constraints on groundwater variability and trends around the world (Frappart and Ramillien, 2018). The combination of new observations with other sources of information has led to updated estimates of heat storage in inland waters (Vanderkelen et al., 2020), contributing to revised estimates of heat storage on the continents (von Schuckmann et al., 2020; Chapter 7, Section 7.2.2.3).

The ongoing collection of information about the atmosphere as it evolves is supplemented by the reconstruction and digitization of data about past conditions. Programs aimed at recovering information from sources such as handwritten weather journals and ship logs continue to make progress, and are steadily improving spatial coverage and extending our knowledge backward in time. For example, Brönnimann et al. (2019) has recently identified several thousand sources of climate data for land areas in the pre-1890 period, with many from the 18th century. The vast majority of these data are not yet contained in international digital data archives, and substantial quantities of undigitized ship's weather log data exist for the same period (Kaspar et al., 2015). Since the AR5 there has been a growth of 'citizen science' activities to rapidly transcribe substantial quantities of weather observations involving volunteers. Examples of projects include: oldWeather.org, and SouthernWeatherDiscovery.org that both used ship-based logbook sources, and the DRAW (Data Rescue: Archival and Weather) project, WeatherRescue.org, JungleWeather.org and the Climate History Australia project, which recovered land-based station data from Canada, Europe, the Congo and Australia respectively (e.g., Park et al., 2018; Hawkins et al., 2019). Undergraduate students have also been recruited to successfully digitise rainfall data in Ireland (Ryan et al., 2018). Such observations are an invaluable source of weather and climate information for the early historical period that continues to expand the digital archives (e.g., Freeman et al., 2017) which underpin observational datasets used across several Chapters.

Ocean

Observations of the ocean have expanded significantly since the AR5, with expanded global coverage of in situ ocean temperature and salinity observations, in situ ocean biogeochemistry observations, and satellite retrievals of a variety of EOVs. Many recent advances are extensively documented in a compilation by Lee et al. (2019). Below we discuss those most relevant for the current assessment.

Argo is a global network of nearly 4000 autonomous profiling floats (Roemmich et al., 2019), delivering detailed constraints on the horizontal and vertical structure of temperature and salinity across the global ocean. Argo has greatly expanded since AR5, including biogeochemistry and measurements deeper than 2000 m (Jayne et al., 2017), and the longer timeseries enable more rigorous climate assessments of direct relevance to estimates of ocean heat content (Chapter 2, Section 2.3.3.1 ; Chapter 7, section 7.2.2.2). Argo profiles are complemented by animal-borne sensors in several key areas, such as the seasonally ice-covered sectors of the Southern Ocean (Harcourt et al., 2019).

Most basin-scale arrays of moored ocean instruments have expanded since AR5, providing decades-long records of the ocean and atmosphere properties relevant for climate, such as the El Niño-Southern Oscillation (Chen et al., 2018), deep convection (de Jong et al., 2018) or transports through straits (Woodgate, 2018). Key basin-scale arrays include transport-measuring arrays in the Atlantic Ocean, continuing (McCarthy et al., 2020) or newly added since AR5 (Lozier et al., 2019), supporting the assessment of regional ocean circulation (Chapter 9, section 9.2.3). Tropical ocean moorings in the Pacific,

ACCEPTED VERSION SUBJECT TO FINAL EDITS

Indian and Atlantic oceans include new sites, improved capability for real time transmission, and new oxygen and CO_2 sensors (Bourlès et al., 2019; Hermes et al., 2019; Smith et al., 2019b).

A decade of observations of sea-surface salinity is now available via the SMOS and SMAP satellite retrievals, providing continuous and global monitoring of surface salinity in the open ocean and coastal areas for the first time (Vinogradova et al., 2019; Reul et al., 2020) (Chapter 9, Section 9.2.2.2).

The global network of tide gauges, complemented by a growing number of satellite-based altimetry datasets, allows for more robust estimates of global and regional sea level rise (Chapter 2, Section 2.3.3.3; Chapter 9, Section 9.6.1.3). Incorporating vertical land motion derived from the Global Positioning System (GPS), the comparison with tide gauges has allowed the correction of a drift in satellite altimetry series over the period 1993–1999 (Watson et al., 2015; Chen et al., 2017), thus improving our knowledge of the recent acceleration of sea level rise (Chapter 2, Section 2.3.3.3). These datasets, combined with Argo and observations of the cryosphere, allow a consistent closure of the global mean sea level budget (Cross-Chapter Box 9.1 in Chapter 9; WCRP Global Sea Level Budget, 2018).

Cryosphere

For the cryosphere, there has been much recent progress in synthesizing global datasets covering larger areas and longer time periods from multi-platform observations. For glaciers, the Global Terrestrial Network for Glaciers, which combines data on glacier fluctuations, mass balance and elevation change with glacier outlines and ice thickness, has expanded and provided input for assessing global glacier evolution and its role in sea level rise (Chapter 2, Section 2.3.2.3; Chapter 9, Section 9.5.1; Zemp et al., 2019). New data sources include archived and declassified aerial photographs and satellite missions, and high-resolution (10 m or less) digital elevation models (Porter et al., 2018; Braun et al., 2019).

Improvements have also been made in the monitoring of permafrost. The Global Terrestrial Network for Permafrost (Biskaborn et al., 2015) provides long-term records of permafrost temperature and active layer thickness at key sites to assess their changes over time. Substantial improvements to our assessments of large-scale snow changes come from intercomparison and blending of several datasets, for snow water equivalent (Mortimer et al., 2020) and snow cover extent (Mudryk et al., 2020), and from bias corrections of combined datasets using in situ data (Pulliainen et al., 2020; Chapter 2, Section 2.3.2.5; Chapter 9, Section 9.5.2).

The value of gravity-based estimates of changes in ice sheet mass has increased as the time series from the GRACE and GRACE-FO satellites, homogenised and absolutely calibrated, is close to 20 years in length. The ESA's Cryosat-2 radar altimetry satellite mission has continued to provide measurements of the changes in the thickness of sea ice and the elevation of the Greenland and Antarctic Ice Sheets (Tilling et al., 2018). Other missions include NASA's Operation IceBridge, collecting airborne remote sensing measurements to bridge the gap between ICESat (Ice, Cloud and land Elevation Satellite) and the upcoming ICESat-2 laser altimetry missions. Longer time series from multiple missions have led to considerable advances in understanding the origin of inconsistencies between the mass balances of different glaciers and reducing uncertainties in estimates of changes in the Greenland and Antarctic Ice Sheets (Bamber et al., 2018; Shepherd et al., 2018a, 2020). Last, the first observed climatology of snowfall over Antarctica was obtained using the cloud/precipitation radar onboard NASA's CloudSat (Palerme et al., 2014).

Biosphere

Satellite observations have recently expanded to include data on the fluorescence of land plants as a measure of photosynthetic activity via the Global Ozone Monitoring Experiment (Guanter et al., 2014; Yang et al., 2015) and OCO-2 satellites (Sun et al., 2017). Climate data records of Leaf Area Index (LAI), characterizing the area of green leaves per unit of ground area, and the fraction of absorbed photosynthetically active radiation (FAPAR) – an important indicator of photosynthetic activity and plant health (Gobron et al., 2009) – are now available for over 30-years (Claverie et al., 2016). In addition, key indicators such as fire disturbances/burned areas are now retrieved via satellite (Chuvieco et al., 2019). In the US, the National

ACCEPTED VERSION SUBJECT TO FINAL EDITS

Ecological Observational Network (NEON) provides continental-scale observations relevant to the assessment of changes in aquatic and terrestrial ecosystems via a wide variety of ground-based, airborne, and satellite platforms (Keller et al., 2008). All these long-term records reveal range shifts in ecosystems (Chapter 2, Section 2.3.4).

The ability to estimate changes in global land biomass has improved due to the use of different microwave satellite data (Liu et al., 2015) and in situ forest census data and co-located lidar, combined with the MODerate resolution Imaging Spectroradiometer (MODIS; Baccini et al., 2017). This has allowed for improved quantification of land temperature (Duan et al., 2019), carbon stocks and human-induced changes due to deforestation (Chapter 2, Section 2.2.7). Time series of Normalized Difference Vegetation Index (NDVI) from MODIS and other remote sensing platforms is widely applied to assess the effects of climate change on vegetation in drought-sensitive regions (Atampugre et al., 2019). New satellite imaging capabilities for meteorological observations, such as the advanced multi-spectral imager aboard Himawari-8 (Bessho et al., 2016), also allow for improved monitoring of challenging quantities such as seasonal changes of vegetation in cloudy regions (Miura et al., 2019; Chapter 2, section 2.3.4.3).

In the ocean, efforts are underway to coordinate observations of biologically-relevant EOVs around the globe (Muller-Karger et al., 2018; Canonico et al., 2019) and to integrate observations across disciplines (e.g., the Global Ocean Acidification Observing Network; Tilbrook et al., 2019). A large number of coordinated field campaigns during the 2015/2016 El Niño event enabled the collection of short-lived biological phenomena such as coral bleaching and mortality caused by a months-long ocean heatwave (Hughes et al., 2018); beyond this event, coordinated observations of coral reef systems are increasing in number and quality (Obura et al., 2019). Overall, globally coordinated efforts focused on individual components of the biosphere (e.g., the Global Alliance of Continuous Plankton Recorder Surveys; Batten et al., 2019) contribute to improved knowledge of the changing marine ecosystems (Chapter 2, Section 2.3.4.2).

Given widespread evidence for decreases in global biodiversity in recent decades related to climate change and other forms of human disturbance (IPBES, 2019), a new international effort to identify a set of Essential Biodiversity Variables is underway (Pereira et al., 2013; Navarro et al., 2017).

In summary, the observational coverage of ongoing changes to the climate system is improved at the time of AR6, relative to what was available for AR5 (*high confidence*).

Paleoclimate

Major paleo reconstruction efforts completed since AR5 include a variety of large-scale, multi-proxy temperature datasets and associated reconstructions spanning the last 2000 years (PAGES 2k Consortium, 2017, 2019; Neukom et al., 2019), the Holocene (Kaufman et al., 2020), the Last Glacial Maximum (Cleator et al., 2020; Tierney et al., 2020b), the Mid-Pliocene Warm Period (McClymont et al., 2020), and the Early Eocene Climate Optimum (Hollis et al., 2019). Newly compiled borehole data (Cuesta-Valero et al., 2019), as well as advances in statistical applications to tree ring data, result in more robust reconstructions of key indices such as Northern Hemisphere temperature over the last millennium (e.g., Wilson et al., 2016; Anchukaitis et al., 2017). Such reconstructions provide a new context for recent warming trends (Chapter 2) and serve to constrain the response of the climate system to natural and anthropogenic forcing (Chapters 3 and 7).

Ongoing efforts have expanded the number of large-scale, tree-ring-based drought reconstructions that span the last centuries to millennium at annual resolution (Chapter 8; Cook et al., 2015; Stahle et al., 2016; Aguilera-Betti et al., 2017; Morales et al., 2020). Likewise, stalagmite records of oxygen isotopes have increased in number, resolution, and geographic distribution since AR5, providing insights into regional to global-scale hydrological change over the last centuries to millions of years (Chapter 8; Cheng et al., 2016; Denniston et al., 2016; Comas-Bru and Harrison, 2019). A new global compilation of water isotope-based paleoclimate records spanning the last 2,000 years (PAGES Iso2K) lays the groundwork for quantitative multi-proxy reconstructions of regional to global scale hydrological and temperature trends and extremes (Konecky et al., 2020).

ACCEPTED VERSION SUBJECT TO FINAL EDITS

Recent advances in the reconstruction of climate extremes beyond temperature and drought include expanded datasets of past El Niño-Southern Oscillation extremes (Chapter 2, Section 2.4.2; e.g., Barrett et al., 2018; Freund et al., 2019; Grothe et al., 2019) and other modes of variability (Hernández et al., 2020), hurricane activity (e.g., Burn and Palmer, 2015; Donnelly et al., 2015), jet stream variability (Trouet et al., 2018), and wildfires (e.g., Taylor et al., 2016).

New datasets as well as recent data compilations and syntheses of sea level over the last millennia (Kopp et al., 2016; Kemp et al., 2018), the last 20,000 years (Khan et al., 2019), the last interglacial period (Dutton et al., 2015; Chapter 2, Section 2.3.3.3), and the Pliocene (Dumitru et al., 2019; Grant et al., 2019; Cross-Chapter Box 2.4 in Chapter 2) help constrain sea level variability and its relationship to global and regional temperature variability, and to contributions from different sources on centennial to millennial timescales (Chapter 9, Section 9.6.2).

Reconstructions of paleoocean pH (Chapter 2, Section 2.3.3.5) have increased in number and accuracy, providing new constraints on ocean pH across the last centuries (e.g., Wu et al., 2018), the last glacial cycles (e.g., Moy et al., 2019), and the last several million years (e.g., Anagnostou et al., 2020). Such reconstructions inform processes and act as benchmarks for Earth system models of the global carbon cycle over the recent geologic past (Chapter 5, Section 5.3.1), including previous high-CO_2 warm intervals such as the Pliocene (Cross-Chapter Box 2.4 in Chapter 2). Particularly relevant to such investigations are reconstructions of atmospheric CO_2 (Hönisch et al., 2012; Foster et al., 2017) that span the past millions to tens of millions of years.

Constraints on the timing and rates of past climate changes have improved since AR5. Analytical methods have increased the precision and reduced sample-size requirements for key radiometric dating techniques including radiocarbon (Gottschalk et al., 2018; Lougheed et al., 2018) and Uranium-Thorium dating (Cheng et al., 2013). More accurate ages of many paleoclimate records are also facilitated by recent improvements in the radiocarbon calibration datasets (IntCal20, Reimer et al., 2020). A recent compilation of global cosmogenic nuclide-based exposure dates (Balco, 2020b) allows for a more rigorous assessment of the evolution of glacial landforms since the Last Glacial Maximum (Balco, 2020a).

Advances in paleoclimate data assimilation (Chapter 10, Section 10.2.3.2) leverage the expanded set of paleoclimate observations to create physically consistent gridded fields of climate variables for data-rich intervals of interest (e.g., over the last millennium, Hakim et al. 2016) or last glacial period (Cleator et al., 2020; Tierney et al., 2020b). Such efforts mirror advances in our understanding of the relationship between proxy records and climate variables of interest, as formalized in so-called proxy system models (e.g., Tolwinski-Ward et al., 2011; Dee et al., 2015; Dolman and Laepple, 2018).

Overall, the number, temporal resolution, and chronological accuracy of paleoclimate reconstructions have increased since AR5, leading to improved understanding of climate system processes (or Earth system processes) (*high confidence*).

1.5.1.2 Threats to observational capacity or continuity

The lock-downs and societal outcomes arising due to the COVID-19 pandemic pose a new threat to observing systems. For example, WMO and UNESCO-IOC published a summary of the changes to Earth system observations during COVID-19 (WMO, 2020b). Fewer aircraft flights (down 75–90% in May 2020, depending on region) and ship transits (down 20% in May 2020) mean that onboard observations from those networks have reduced in number and frequency (James et al., 2020; Ingleby et al., 2021). Europe has deployed more radiosonde soundings to account for the reduction in data from air traffic. Fewer ocean observing buoys were deployed during 2020, and reductions have been particularly prevalent in the tropics and Southern Hemisphere. The full consequences of the pandemic and responses will come to light over time. Estimates of the effect of the reduction in aircraft data assimilation on weather forecasting skill are small (James et al., 2020; Ingleby et al., 2021), potentially alleviating concerns about veracity of future

ACCEPTED VERSION SUBJECT TO FINAL EDITS

atmospheric reanalyses of the COVID-19 pandemic period.

Surface-based networks have reduced in their coverage or range of variables measured due to COVID-19 and other factors. Over land, several factors, including the ongoing transition from manual to automatic observations of weather, have reduced the spatial coverage of certain measurement types including rainfall intensity, radiosonde launches and pan evaporation, posing unique risks to datasets used for climate assessment (WMO, 2017; Lin and Huybers, 2019). Ship-based measurements, which are important for ocean climate and reanalyses through time (Smith et al., 2019c), have been in decline due to the number of ships contributing observations. There has also been a decline in the number of variables recorded by ships, but an increase in the quality and time-resolution of others (e.g., sea level pressure, Kent et al. 2019).

Certain satellite frequencies are used to detect meteorological features that are vital to climate change monitoring. These can be disturbed by certain radio communications (Anterrieu et al., 2016), although scientists work to remove noise from the signal (Oliva et al., 2016). For example, water vapour in the atmosphere naturally produces a weak signal at 23.8 gigahertz, which is within the range of frequencies of the 5G communications network (Liu et al., 2021). Concern has been raised about potential leakage from 5G network transmissions into the operating frequencies of passive sensors on existing weather satellites, which could adversely influence their ability to remotely observe water vapour in the atmosphere (Yousefvand et al., 2020).

Threats to observational capacity also include the loss of natural climate archives that are disappearing as a direct consequence of warming temperatures. Ice core records from vulnerable alpine glaciers in the tropics (Permana et al., 2019) and the mid-latitudes (Gabrielli et al., 2016; Winski et al., 2018; Moreno et al., 2021) document more frequent melt layers in recent decades, with glacial retreat occurring at a rate and geographic scale that is unusual in the Holocene (Solomina et al., 2015). The scope and severity of coral bleaching and mortality events have increased in recent decades (Hughes et al., 2018), with profound implications for the recovery of coral climate archives from new and existing sites. An observed increase in the mortality of larger, long-lived trees over the last century is attributed to a combination of warming, land use change, and disturbance (e.g., McDowell et al., 2020). The ongoing loss of these natural, high-resolution climate archives endanger an end in their coverage over recent decades, given that many of the longest monthly- to annually-resolved paleoclimate records were collected in the 1960s to 1990s (e.g., the PAGES2K database as represented in PAGES 2k Consortium, 2017). This gap presents a barrier to the calibration of existing decades-to-centuries-long records needed to constrain past temperature and hydrology trends and extremes.

Historical archives of weather and climate observations contained in ship's logs, weather diaries, observatory logbooks and other sources of documentary data are also at jeopardy of loss from natural disasters or accidental destruction. These include measurements of temperature (air and sea surface), rainfall, surface pressure, wind strength and direction, sunshine amount, and many other variables back into the 19th century. While internationally coordinated data rescue efforts are focused on recovering documentary sources of past weather and climate data (e.g., Allan et al., 2011), no such coordinated efforts exist for vulnerable paleoclimate archives. Furthermore, oral traditions about local and regional weather and climate from indigenous peoples represent valuable sources of information, especially when used in combination with instrumental climate data (Makondo and Thomas, 2018), but are in danger of being lost as indigenous knowledge-holders pass away.

In summary, while the quantity, quality, and diversity of climate system observations have grown since AR5, the loss or potential loss of several critical components of the observational network is also evident (*high confidence*).

1.5.2 New developments in reanalyses

Reanalyses are usually the output of a model (e.g., a numerical weather prediction model) constrained by observations using data assimilation techniques, but the term has also been used to describe observation-based datasets produced using simpler statistical methods and models (see Annex I). This section focuses on

ACCEPTED VERSION SUBJECT TO FINAL EDITS

the model-based methods and their recent developments.

Reanalyses complement datasets of observations in describing changes through the historical record and are sometimes considered as 'maps without gaps' because they provide gridded output in space and time, often global, with physical consistency across variables on sub-daily timescales, and information about sparsely-observed variables (such as evaporation) (Hersbach et al., 2020). They can be globally complete, or regionally focussed and constrained by boundary conditions from a global reanalysis (Chapter 10, Section 10.2.1.2). They can also provide feedback about the quality of the observations assimilated, including estimates of biases and critical gaps for some observing systems.

Many early reanalyses are described in Box 2.3 of Hartmann et al. (2013). These were often limited by the underlying model, the data assimilation schemes and observational issues (Thorne and Vose, 2010; Zhou et al., 2018). Observational issues include the lack of underlying observations in some regions, changes in the observational systems over time (e.g., spatial coverage, introduction of satellite data), and time-dependent errors in the underlying observations or in the boundary conditions, which may lead to stepwise biases in time. The assimilation of sparse or inconsistent observations can introduce mass or energy imbalances (Valdivieso et al., 2017; Trenberth et al., 2019). Further limitations and some efforts to reduce the implications of these observational issues will be detailed below.

The methods used in the development of reanalyses have progressed since AR5 and, in some cases, this has important implications for the information they provide on how the climate is changing. Annex I includes a list of reanalysis datasets used in the AR6. Recent major developments in reanalyses include the assimilation of a wider range of observations, higher spatial and temporal resolution, extensions further back in time, and greater efforts to minimise the influence of a temporally varying observational network.

Atmospheric reanalyses

Extensive improvements have been made in global atmospheric reanalyses since AR5. The growing demand for high-resolution data has led to the development of higher-resolution atmospheric reanalyses, such as the Modern-Era Retrospective Analysis for Research and Applications, version 2 (MERRA2; Gelaro et al., 2017) and ERA5 (Hersbach et al., 2020). There is a focus on ERA5 here because it has been assessed as of high enough quality to present temperature trends alongside more traditional observational datasets (Chapter 2, Section 2.3.1.1) and is also used in the Interactive Atlas.

Atmospheric reanalyses that were assessed in AR5 are still being used in the literature, and results from ERA-Interim (Dee et al., 2011, ~80 km resolution, production stopped in August 2019), the Japanese 55-year Reanalysis (JRA-55) (Ebita et al., 2011; Kobayashi et al., 2015; Harada et al., 2016) and Climate Forecast System Reanalysis (CFSR) (Saha et al., 2010) are assessed in AR6. Some studies still also use the NCEP/NCAR reanalysis, particularly because it extends back to 1948 and is updated in near real-time (Kistler et al., 2001). Older reanalyses have a number of limitations, which have to be accounted for when assessing the results of any study that uses them.

ERA5 provides hourly atmospheric fields at about 31 km resolution on 137 levels in the vertical, as well as land surface variables and ocean waves, and is available from 1979 onwards and is updated in near real-time, with plans to extend back to 1950. A 10-member ensemble is also available at coarser resolution, allowing uncertainty estimates to be provided (e.g., Chapter 2, Section 2.3). MERRA-2 includes many updates from the earlier version, including the assimilation of aerosol observations, several improvements to the representation of the stratosphere, including ozone, and improved representations of cryospheric processes. All of these improvements increase the usefulness of these reanalyses (Hoffmann et al., 2019; Chapter 7, Section 7.3).

Models of atmospheric composition and emission sources and sinks allow the forecast and reanalysis of constituents such as O_3, CO, NO_x and aerosols. The Copernicus Atmosphere Monitoring Service (CAMS) reanalysis shows improvement against earlier atmospheric composition reanalyses, giving greater confidence for its use to study trends and evaluate models (e.g., Inness et al., 2019; Chapter 7, Section 7.3).

ACCEPTED VERSION SUBJECT TO FINAL EDITS

The inter-comparison of reanalyses with each other, or with earlier versions, is often done for particular variables or aspects of the simulation. ERA5 is assessed as the most reliable reanalysis for climate trend assessment (Chapter 2, Section 2.3). Compared to ERA-Interim, the ERA5 forecast model and assimilation system, as well as the availability of improved reprocessing of observations, resulted in relatively smaller errors when compared to observations, including a better representation of global energy budgets, radiative forcing from volcanic eruptions (e.g., Mt. Pinatubo: Allan et al., 2020), the partitioning of surface energy (Martens et al., 2020) and wind (Kaiser-Weiss et al., 2015, 2019; Borsche et al., 2016; Scherrer, 2020). In ERA5, higher resolution means a better representation of Lagrangian motion convective updrafts, gravity waves, tropical cyclones, and other meso- to synoptic-scale features of the atmosphere (Hoffmann et al., 2019; Martens et al., 2020). Low-frequency variability is found to be generally well represented and, from 10 hPa downwards, patterns of anomalies in temperature match those from the ERA-Interim, MERRA-2 and JRA-55 reanalyses. Inhomogeneities in the water cycle have also been reduced (Hersbach et al., 2020).

Precipitation is not usually assimilated in reanalyses and, depending on the region, reanalysis precipitation can differ from observations by more than the observational error (Zhou and Wang, 2017; Sun et al., 2018; Alexander et al., 2020; Bador et al., 2020), although these studies did not include ERA5. Assimilation of radiance observations from microwave imagers which, over ice-free ocean surfaces, improve the analysis of lower-tropospheric humidity, cloud liquid water and ocean surface wind speed have resulted in improved precipitation outputs in ERA5 (Hersbach et al., 2020). Global averages of other fields, particularly temperature, from ERA-Interim and JRA-55 reanalyses continue to be consistent over the last 20 years with surface observational data sets that include the polar regions (Simmons and Poli, 2015), although biases in precipitation and radiation can influence temperatures regionally (Zhou et al., 2018). The global average surface temperature from MERRA-2 is far cooler in recent years than temperatures derived from ERA-Interim and JRA-55, which may be due to the assimilation of aerosols and their interactions (see Chapter 2, Section 2.3).

A number of regional atmospheric reanalyses (see Chapter 10, Section 10.2.1.2) have been developed, such as COSMO-REA (Wahl et al., 2017), and the Australian Bureau of Meteorology Atmospheric high-resolution Regional Reanalysis for Australia (BARRA) (Su et al., 2019). Regional reanalyses can add value to global reanalyses due to the lower computational requirements, and can allow multiple numerical weather prediction models to be tested (e.g., Kaiser-Weiss et al., 2019). There is some evidence that these higher resolution reanalyses better capture precipitation variability than global lower resolution reanalyses (Jermey and Renshaw, 2016; Cui et al., 2017) and are further assessed in Chapter 10, Section 10.2.1.2 and used in the Interactive Atlas.

In summary, the improvements in atmospheric reanalyses, and the greater number of years since the routine ingestion of satellite data began relative to AR5, mean that there is increased confidence in using atmospheric reanalyses products alongside more standard observation-based datasets in AR6 (*high confidence*).

Sparse input reanalyses of the instrumental era

Although reanalyses such as ERA5 take advantage of new observational datasets and present a great improvement in atmospheric reanalyses, the issues introduced by the evolving observational network remain. Sparse input reanalyses, where only a limited set of reliable and long observed records are assimilated, address these issues, with the limitation of fewer observational constraints. These efforts are sometimes called centennial-scale reanalyses. One example is the atmospheric 20th Century Reanalysis (Compo et al., 2011; Slivinski et al., 2021) which assimilates only surface and sea-level pressure observations, and is constrained by time-varying observed changes in atmospheric constituents, prescribed sea surface temperatures and sea ice concentration, creating a reconstruction of the weather over the whole globe every 3 hours for the period 1806–2015. The ERA-20C atmospheric reanalysis (covering 1900–2010; Poli et al., 2016) also assimilates marine wind observations, and CERA-20C is a centennial-scale reanalysis that assimilates both atmospheric and oceanic observations for the 1901–2010 period (Laloyaux et al., 2018). These centennial-scale reanalyses are often run as ensembles that provide an estimate of the uncertainty in the simulated variables over space and time. Slivinski et al. (2021) conclude that the uncertainties in surface

ACCEPTED VERSION SUBJECT TO FINAL EDITS

circulation fields in version 3 of the 20th Century Reanalysis are reliable and that there is also skill in its tropospheric reconstruction over the 20th century. Long-term changes in other variables, such as precipitation, also agree well with direct observation-based datasets (Chapter 2, Section 2.3.1.3; Chapter 8, Section 8.3.2.8).

Ocean reanalyses

Since AR5, ocean reanalyses have improved due to: increased model resolution (Zuo et al., 2017; Lellouche et al., 2018; Heimbach et al., 2019); improved physics (Storto et al., 2019); improvements in the atmospheric forcing from atmospheric reanalyses (see preceding subsection); and improvements in the data quantity and quality available for assimilation (e.g., Lellouche et al., 2018; Heimbach et al., 2019), particularly due to Argo observations (Zuo et al., 2019) (see Annex I).

The first Ocean Reanalyses Intercomparison project (Balmaseda et al., 2015) focussed on the uncertainty in key climate indicators, such as ocean heat content (Palmer et al., 2017), thermosteric sea level (Storto et al., 2017, 2019), salinity (Shi et al., 2017), sea ice extent (Chevallier et al., 2017), and the AMOC (Karspeck et al., 2017). Reanalysis uncertainties occur in areas of inhomogeneous or sparse observational data sampling, such as for the deep ocean, the Southern Ocean and western boundary currents (Lellouche et al., 2018; Storto et al., 2019). Intercomparisons have also been dedicated to specific variables such as mixed-layer depths (Toyoda et al., 2017), eddy kinetic energy (Masina et al., 2017) of the polar regions (Uotila et al., 2019). Karspeck et al. (2017) found disagreement in the Atlantic meridional overturning circulation (AMOC)` variability and strength in reanalyses over observation-sparse periods, whereas Jackson et al. (2019) reported a lower spread in AMOC strength across an ensemble of ocean reanalyses of the recent period (1993-2010) linked to improved observation availability for assimilation. Reanalyses also have a larger spread of ocean heat uptake than data-only products and can produce spurious overestimates of heat uptake (Palmer et al., 2017), which is important in the context of estimating climate sensitivity (Storto et al., 2019). The ensemble approach for ocean reanalyses provides another avenue for estimating uncertainties across ocean reanalyses (Storto et al., 2019).

While there are still limitations in their representation of oceanic features, ocean reanalyses add value to observation-only based products and are used to inform assessments in AR6 (Chapters 2, 3, 7 and 9). Reanalyses of the atmosphere or ocean alone may not account for important atmosphere-ocean coupling, motivating the development of coupled reanalyses (Laloyaux et al., 2018; Schepers et al., 2018; Penny et al., 2019), but these are not assessed in AR6.

Reanalyses of the pre-instrumental era

Longer reanalyses that extend further back in time than the beginning of the instrumental record are being developed. They include the complete integration of paleoclimate archives and newly available early instrumental data into extended reanalysis datasets. Such integration leverages ongoing development of climate models that can simulate paleoclimate records in their units of analysis (i.e., oxygen isotope composition, tree ring width, etc.), in many cases using physical climate variables as input for so-called 'proxy system models' (Evans et al., 2013; Dee et al., 2015). Ensemble Kalman filter data assimilation approaches allow to combine paleoclimate data and climate model data to generate annually resolved fields (Last Millenium Reanalysis, Hakim et al., 2016; Tardif et al., 2018) or even monthly fields (Franke et al., 2017). This allows for a greater understanding of decadal variability (Parsons and Hakim, 2019) and greater certainty around the full range of the frequency and severity of climate extremes, allowing for better-defined detection of change. It also helps to identify the links between biogeochemical cycles, ecosystem structure and ecosystem functioning, and to provide initial conditions for further model experiments or downscaling (see Chapter 2).

Applications of reanalyses

The developments in reanalyses described above mean that they are now used across a range of applications. In AR6, reanalyses provide information for fields and in regions where observations are limited. There is

ACCEPTED VERSION SUBJECT TO FINAL EDITS

growing confidence that modern reanalyses can provide another line of evidence in describing recent temperature trends (see Chapter 2, Tables 2.4 and 2.5) As their spatial resolution increases, the exploration of fine-scale extremes in both space and time becomes possible (e.g., wind; Kaiser-Weiss et al., 2015). Longer reanalyses can be used to describe the change in the climate over the last 100 to 1000 years. Reanalyses have been used to help post-process climate model output, and drive impact models, however, they are often bias adjusted first (e.g., Weedon et al., 2014). See Cross-Chapter Box 10.2 in Chapter 10. Copernicus Climate Change Service (C3S) provides a bias adjusted dataset for global land areas based on ERA5 called WFDE5 (Cucchi et al., 2020) which, combined with ERA5 information over the ocean (W5E5; Lange, 2019), is used as the AR6 Interactive Atlas reference for the bias adjustment of model output.

The growing interest in longer-term climate forecasts (from seasonal to multi-year and decadal) means that reanalyses are now more routinely being used to develop the initial state for these forecasts, such as for the Decadal Climate Prediction Project (DCPP; Boer et al., 2016). Ocean reanalyses are now being used routinely in the context of climate monitoring, (e.g., the Copernicus Marine Environment Monitoring Service Ocean State Report; von Schuckmann et al., 2019).

In summary, reanalyses have improved since AR5 and can increasingly be used as a line of evidence in assessments of the state and evolution of the climate system (*high confidence*). Reanalyses provide consistency across multiple physical quantities, and information about variables and locations that are not directly observed. Since AR5, new reanalyses have been developed with various combinations of increased resolution, extended records, more consistent data assimilation, estimation of uncertainty arising from the range of initial conditions, and an improved representation of the atmosphere or ocean system. While noting their remaining limitations, the WGI Report uses the most recent generation of reanalysis products alongside more standard observation-based datasets.

1.5.3 Climate Models

A wide range of numerical models are widely used in climate science to study the climate system and its behaviour across multiple temporal and spatial scales. These models are the main tools available to look ahead into possible climate futures under a range of scenarios (see Section 1.6). Global Earth System Models (ESMs) are the most complex models which contribute to AR6. At the core of each ESM is a GCM (General Circulation Model) representing the dynamics of the atmosphere and ocean. ESMs are complemented by regional models (see Chapter 10, Section 10.3.1) and by a hierarchy of models of lower complexity. This section summarizes major developments in these different types of models since AR5. Past IPCC reports have made use of multi-model ensembles generated through various phases of the World Climate Research Programme (WCRP) Coupled Model Intercomparison Project (CMIP). Analysis of the latest CMIP Phase 6 (CMIP6, Eyring et al., 2016) simulations constitute a key line of evidence supporting this assessment report (see Section 1.5.4). The key characteristics of models participating in CMIP6 are listed in Annex II.

1.5.3.1 Earth System Models

Earth system models are mathematical formulations of the natural laws that govern the evolution of climate-relevant systems: atmosphere, ocean, cryosphere, land, and biosphere, and the carbon cycle (Flato, 2011). They build on the fundamental laws of physics (e.g., Navier-Stokes or Clausius-Clapeyron equations) or empirical relationships established from observations and, when possible, constrained by fundamental conservation laws (e.g., mass and energy). The evolution of climate-relevant variables is computed numerically using high performance computers (André et al., 2014; Balaji et al., 2017), on three-dimensional discrete grids (Staniforth and Thuburn, 2012). The spatial (and temporal) resolution of these grids in both the horizontal and vertical directions determines which processes need to be parameterised or whether they can be explicitly resolved. Developments since AR5 in model resolution, parameterizations and modelling of the land and ocean biosphere and of biogeochemical cycles are discussed below.

Model grids and resolution

ACCEPTED VERSION SUBJECT TO FINAL EDITS

The horizontal resolution and the number of vertical levels in ESMs is generally higher in CMIP6 than in CMIP5 (Figure 1.19). Global models with finer horizontal grids represent better many aspects of the circulation of the atmosphere (Gao et al., 2020; Schiemann et al., 2020) and ocean (Bishop et al., 2016; Storkey et al., 2018), bringing improvements in the simulation of the global hydrological cycle (Roberts et al., 2018). CMIP6 includes a dedicated effort (HighResMIP, Haarsma et al., 2016) to explore the effect of higher horizontal resolution, such as ~50 km, ~25 km and even ~10 km (see 1.5.4.2 and Annex II, Table AII.6). Improvements are documented in the highest resolution coupled models used for HighResMip (Hewitt et al., 2017b; Roberts et al., 2019). Flexible grids allowing spatially variable resolution are more widely used than at the time of the AR5 in the atmosphere (McGregor, 2015; Giorgetta et al., 2018) and in the ocean (Wang et al., 2014; Petersen et al., 2019).

The number of vertical levels in the atmosphere of global models has increased (Figure 1.19) partly to enable simulations to include higher levels in the atmosphere and better represent stratospheric processes (Charlton-Perez et al., 2013; Kawatani et al., 2019). Half the modelling groups now use 'high top' models with a top level above the stratopause (a pressure of about 1 hPa). The number of vertical levels in the ocean models has also increased in order to achieve finer resolution over the water column and especially in the upper mixed layer, and better resolve the diurnal cycle (Bernie et al., 2008) (see Chapter 3, Section 3.5 and Annex II).

Despite the documented progress of higher resolution, the model evaluation carried out in subsequent chapters shows that improvements between CMIP5 and CMIP6 remain modest at the global scale (Bock et al., 2020; Chapter 3, Section 3.8.2). Lower resolution alone does not explain all model biases, for example, a low blocking frequency (Davini and D'Andrea, 2020) or a wrong shape of the Intertropical Convergence Zone (Tian and Dong, 2020). Model performance depends on model formulation and parameterizations as much as on resolution (Chapter 3, Chapter 8, Chapter 10).

[START FIGURE 1.19 HERE]

Figure 1.19: Resolution of the atmospheric and oceanic components of global climate models participating in CMIP5, CMIP6, and HighResMIP: (a) (b) horizontal resolution (km), and (c) (d) number of vertical levels. Darker colour circles indicate high-top models (whose top of the atmosphere is above 50 km). The crosses are the median values. These models are documented in Annex II. Note that duplicated models in a modelling group are counted as one entry when their horizontal and vertical resolutions are same. For HighResMIP, one atmosphere-ocean coupled model with the highest resolution from each modelling group is used. The horizontal resolution (rounded to 10km) is the square root of the number of grid points divided by the surface area of the Earth, or the number of surface ocean grid points divided by the area of the ocean surface, for the atmosphere and ocean respectively.

[END FIGURE 1.19 HERE]

Representation of physical and chemical processes in ESMs

Atmospheric models include representations of physical processes such as clouds, turbulence, convection and gravity waves that are not fully represented by grid-scale dynamics. The CMIP6 models have undergone updates in some of their parameterization schemes compared to their CMIP5 counterparts, with the aim of better representing the physics and bringing the climatology of the models closer to newly available observational datasets. Most notable developments are to schemes involving radiative transfer, cloud microphysics, and aerosols, in particular a more explicit representation of the aerosol indirect effects through aerosol-induced modification of cloud properties. Broadly, aerosol-cloud microphysics has been a key topic for the aerosol and chemistry modelling communities since AR5, leading to improved understanding of the climate influence of short-lived climate forcers, but they remain the single largest source of spread in ESM calculations of climate sensitivity (Meehl et al., 2020), with numerous parameterization schemes in use (Gettelman and Sherwood, 2016; Zhao et al., 2018; Gettelman et al., 2019). See also Chapter 6, section 6.4. The treatment of droplet size and mixed-phase clouds (liquid and ice) was found to lead to changes in

ACCEPTED VERSION SUBJECT TO FINAL EDITS

climate sensitivity (Annex VII: Glossary) of some models between AR5 and AR6 (Bodas-Salcedo et al., 2019; Gettelman et al., 2019; Zelinka et al., 2020, Chapter 7, Section 7.4).

The representation of ocean and cryosphere processes has also evolved significantly since CMIP5. The explicit representation of ocean eddies, due to increased grid resolution (typically, from 1° to ¼°), is a major advance in a number of CMIP6 ocean model components (Hewitt et al., 2017b). Advances in sea ice models have been made, for example, through correcting known shortcomings in CMIP5 simulations, in particular the persistent underestimation of the rapid decline in summer Arctic sea ice extent (Rosenblum and Eisenman, 2016, 2017; Turner and Comiso, 2017; Notz and Stroeve, 2018). The development of glacier and ice-sheet models has been motivated and guided by an improved understanding of key physical processes, including grounding line dynamics, stratigraphy and microstructure evolution, sub-shelf melting, and glacier and ice-shelf calving, among others (Faria et al., 2014, 2018; Hanna et al., 2020). The resolution of ice sheet models has continuously increased, including the use of nested grids, sub-grid interpolation schemes, and adaptive mesh approaches (Cornford et al., 2016), mainly for a more accurate representation of grounding-line migration and data assimilation (Pattyn, 2018). Ice-sheet models are increasingly interactively coupled with global and regional climate models, accounting for the height mass-balance feedback (Vizcaino et al., 2015; Le clec'h et al., 2019), and enabling a better representation of ice-ocean processes, in particular for the Antarctic Ice Sheet (Asay-Davis et al., 2017).

Sea level rise is caused by multiple processes acting on multiple time scales: ocean warming, glaciers and ice sheet melting, change in water storage on land, glacial isostatic adjustment (Chapter 9, Box 9.1) but no single model can represent all these processes (Chapter 9, Section 9.6). In this report, the contributions are computed separately (Chapter 9, Figure 9.28) and merged into a common probabilistic framework and updated from AR5 (Church et al., 2013; Kopp et al., 2014; Chapter 9, Section 9.6).

Another notable development since AR5 is the inclusion of stochastic parameterizations of sub-grid processes in some comprehensive climate models (Sanchez et al., 2016). Here, the deterministic differential equations that govern the dynamical evolution of the model are complemented by knowledge of the stochastic variability in unresolved processes. While not yet widely implemented, the approach has been shown to improve the forecasting skill of weather models, to reduce systematic biases in global models (Berner et al., 2017; Palmer, 2019) and to influence simulated climate sensitivity (Strommen et al., 2019).

Representation of biogeochemistry, including the carbon cycle

Since AR5, more sophisticated land use and land cover change representations in ESMs have been developed to simulate the effects of land management on surface fluxes of carbon, water and energy (Lawrence et al., 2016), although the integration of many processes (e.g., wetland drainage, fire as a management tool) remains a challenge (Pongratz et al., 2018). The importance of nitrogen availability to limit the terrestrial carbon sequestration has been recognised (Zaehle et al., 2014; Chapter 5, Section 5.4) and so an increasing number of models now include a prognostic representation of the terrestrial nitrogen cycle and its coupling to the land carbon cycle (Jones et al., 2016a; Arora et al., 2020), leading to a reduction in uncertainty for carbon budgets (Jones and Friedlingstein, 2020; Chapter 5, Section 5.1). As was the case in CMIP5 (Ciais et al., 2013), the land surface processes represented vary across CMIP6 models, with at least some key processes (fire, permafrost carbon, microbes, nutrients, vegetation dynamics, plant demography) absent from any particular ESM land model (Chapter 5, Table 5.4). Ocean biogeochemical models have evolved to enhance the consistency of the exchanges between ocean, atmosphere and land, through riverine input and dust deposition (Stock et al., 2014; Aumont et al., 2015). Other developments include flexible plankton stoichiometric ratios (Galbraith and Martiny, 2015), improvements in the representation of nitrogen fixation (Paulsen et al., 2017), and the limitation of plankton growth by iron (Aumont et al., 2015). Due to the long time scale of biogeochemical processes, spin-up strategies have been shown to affect the performance of models used in AR5 (Séférian et al., 2016).

1.5.3.2 Model tuning and adjustment

When developing climate models, choices have to be made in a number of areas. Besides model formulation

ACCEPTED VERSION SUBJECT TO FINAL EDITS

and resolution, parameterizations of unresolved processes also involve many choices as, for each of these, several parameters can be set. The acceptable range for these parameters is set by mathematical consistency (e.g., convergence of a numerical scheme), physical considerations (e.g., energy conservation), observations, or a combination of factors. Model developers choose a set of parameters that both falls within this range and mimics observations of individual processes or their statistics.

An initial set of such choices is usually made by (often extensive) groups of modellers working on individual components of the Earth system (e.g., ocean, atmosphere, land or sea ice). As components are assembled to build an ESM, the choices are refined so that the simulated climate best represents a number of pre-defined climate variables, or 'tuning targets'. When these are met the model is released for use in intercomparisons such as CMIP. Tuning targets can be one of three types: mean climate, regional phenomena and features, and historical trends (Hourdin et al., 2017). One example of such a goal is that the climate system should reach a mean equilibrium temperature close to observations when energy received from the sun is close to its observed value. Whether tuning should be performed to accurate simulating long-term trends such as changes in global mean temperature over the historical era, or rather be performed for each process independently such that all collective behaviour is emergent, is an open question (Schmidt et al., 2017; Burrows et al., 2018).

Each modelling group has its own strategy and, after AR5, a survey was conducted to understand the tuning approach used in 23 CMIP5 modelling centres. The results are discussed in Hourdin et al. (2017), which stresses that the behaviour of ESMs depends on the tuning strategy. An important recommendation is that the calibration steps that lead to particular model tuning should be carefully documented. In CMIP6 each modelling group now describes the three levels of tuning, both for the complete ESM and for the individual components (available at https://explore.es-doc.org/ and in the published model descriptions, Annex II). The most important global tuning target for CMIP6 models is the net top-of-the-atmosphere (TOA) heat flux and its radiative components. Other global targets include: the decomposition of each of these TOA fluxes into a clear sky component and a component due to the radiative effect of clouds, global mean air and ocean temperature, sea ice extent, sea ice volume, glacial mass balance, global root mean square error of precipitation. The TOA heat flux balance is achieved using a diversity of approaches, usually unique to each modelling group. Adjustments are made for parameters associated with uncertain or poorly constrained processes (Schmidt et al., 2017), for example the aerosol indirect effects, adjustments to ocean albedo, marine dimethyl sulfide (DMS) parameterization, or cloud properties (Mauritsen and Roeckner, 2020).

Regional tuning targets include the meridional overturning circulation in the Atlantic Ocean, the Southern Ocean circulation and temperature profiles in ocean basins (Golaz et al., 2019; Sellar et al., 2019); regional land properties and precipitations (Mauritsen et al., 2019; Yukimoto et al., 2019), latitudinal distribution of radiation (Boucher et al., 2020), spatial contrasts in TOA radiative fluxes or surface fluxes, and stationary waves in the Northern Hemisphere (Schmidt et al., 2017; Yukimoto et al., 2019).

Even with some core commonalities of approaches to model tuning, practices can differ, such as the use of initial drift from initialized forecasts, the explicit use of the transient observed record for the historical period, or the use of the present-day radiative imbalance at the TOA as a tuning target rather than an equilibrated pre-industrial balance. The majority of CMIP6 modelling groups report that they do not tune their model for the observed trends during the historical period (23 out of 29), nor for equilibrium climate sensitivity (25 out of 29). ECS and TCR are thus emergent properties for a large majority of models. The effect of tuning on model skill and ensemble spread in CMIP6 is further discussed in Chapter 3, Section 3.3.

1.5.3.3 From global to regional models

The need for accurate climate information at the regional scale is increasing (Chapter 10, Section 10.1). High-resolution global climate models, such as those taking part in HighResMIP, provide more detailed information at the regional scale (Roberts et al., 2018). However, due to the large computational resources required by these models, only a limited number of simulations per model are available. In addition to CMIP global models, regional information can be derived using Regional Climate Models (RCMs) and

ACCEPTED VERSION SUBJECT TO FINAL EDITS

downscaling techniques, presented in Chapter 10 and the Atlas. RCMs are dynamical models similar to GCMs that simulate a limited region and are forced with boudary conditions from a global simulation, often correcting for biases (Chapter 10, Section 10.3 and Cross-Chapter Box 10.2, Annex II). This approach allows the use of a higher resolution within the chosen domain, and thus better represent important drivers of regional climate such as mountain ranges, land management and urban effects. RCMs resolving atmospheric convection explicitly are now included in intercomparisons (Coppola et al., 2020) and used in Chapters 10, 11 and 12. Other approaches are also used to generate regional climate projections, such as statistical downscaling (Maraun and Widmann, 2018; Chapter 10, Section 10.3).

The number of climate centres or consortia that carry out global climate simulations and projections has grown from 11 in the first CMIP to 19 in CMIP5 and 28 for CMIP6 (see Section 1.5.4.2 and Annex II). Regional climate models participating in the Coordinated Regional Downscaling Experiment (CORDEX) are more diverse than the global ESMs (see Section 1.5.4.3 and Annex II) and engage an even wider international community (Figure 1.20).

[START FIGURE 1.20 HERE]

Figure 1.20: A world map showing the increased diversity of modelling centres contributing to CMIP and CORDEX. Climate models are often developed by international consortia. EC-Earth is shown as an example (involving SMHI, Sweden; KNMI, The Netherlands; DMI, Denmark; AEMET, Spain; Met Éireann, Ireland; CNR-ISAC, Italy; Instituto de Meteorologia, Portugal; FMI, Finland), but there are too many such collaborations to display all of them on this map. More complete information about institutions contributing to CORDEX and CMIP6 is found in Annex II.

[END FIGURE 1.20 HERE]

1.5.3.4 Models of lower complexity

Earth System Models of Intermediate Complexity (EMICs) complement the model hierarchy and fill the gap between conceptual, simple climate models and complex GCMs or ESMs (Claussen et al., 2002). EMICs are simplified; they include processes in a more parameterized, rather than explicitly calculated, form and generally have lower spatial resolution compared to the complex ESMs. As a result, EMICs require much less computational resource and can be integrated for many thousands of years without supercomputers (Hajima et al., 2014). The range of EMICs used in climate change research is highly heterogeneous, ranging from zonally averaged or mixed-layer ocean models coupled to statistical-dynamical models of the atmosphere to low-resolution 3-dimensional ocean models coupled to simplified dynamical models of the atmosphere. An increasing number of EMICs include interactive representations of the global carbon cycle, with varying levels of complexity and numbers of processes considered (Plattner et al., 2008; Zickfeld et al., 2013; MacDougall et al., 2020). Given the heterogeneity of the EMIC community, modelers tend to focus on specific research questions and develop individual models accordingly. As for any type of models assessed in this report, the set of EMICs undergoes thorough evaluation and fit-for-purpose testing before being applied to address specific climate aspects.

EMICs have been used extensively in past IPCC reports, providing long-term integrations on paleoclimate and future timescales, including stabilization pathways and a range of commitment scenarios, with perturbed physics ensembles and sensitivity studies, or with simulations targeting the uncertainty in global climate-carbon cycle systems (e.g., Meehl et al., 2007; Collins et al., 2013). More recently, a number of studies have pointed to the possibility of systematically different climate responses to external forcings in EMICs and complex ESMs (Frölicher and Paynter, 2015; Pfister and Stocker, 2017, 2018) that need to be considered in the context of this report. For example, Frölicher and Paynter (2015) showed that EMICs have a higher simulated realized warming fraction (i.e., the TCR/ECS ratio) than CMIP5 ESMs and speculated that this may bias the temperature response to zero carbon emissions. But, in a recent comprehensive multi-model analysis of the zero CO_2 emissions commitment, MacDougall et al. (2020) did not find any significant

ACCEPTED VERSION SUBJECT TO FINAL EDITS

differences in committed temperatures 90 years after halting emissions between EMICs and ESMs. While some EMICs contribute to parts of the CMIP6-endorsed MIPs, a coordinated EMICs modeling effort similar to the ones for the AR4 (Plattner et al., 2008) and AR5 (Eby et al., 2013; Zickfeld et al., 2013) is not in place for IPCC AR6; however, EMICs are assessed in a number of chapters. For example, Chapters 4 and 5 use EMICs in the assessment of long-term climate change beyond 2100 (Chapter 5, Section 5.5), zero-emission commitments, overshoot and recovery (Chapter 4, Section 4.7), consequences of carbon dioxide removal (CDR) on the climate system and the carbon cycle (Chapter 4, Sections 4.6 and Chapter 5, Section 5.6) and long-term carbon cycle–climate feedbacks (Chapter 5, Section 5.4).

Physical emulators and simple climate models make up a broad class of heavily parametrized models designed to reproduce the responses of the more complex, process-based models, and provide rapid translations of emissions, via concentrations and radiative forcing, into probabilistic estimates of changes to the physical climate system. The main application of emulators is to extrapolate insights from ESMs and observational constraints to a larger set of emission scenarios (see Cross-Chapter Box 7.1 in Chapter 7). The computational efficiency of various emulating approaches opens new analytical possibilities given that ESMs take a lot of computational resources for each simulation. The applicability and usefulness of emulating approaches are however constrained by their skill in capturing the global mean climate responses simulated by the ESMs (mainly limited to global-mean or hemispheric land/ocean temperatures) and by their ability to extrapolate skilfully outside the calibrated range.

The terms emulator and simple climate model (SCM) are different, although they are sometimes used interchangeably. SCM refers to a broad class of lower-dimensional models of the energy balance, radiative transfer, carbon cycle, or a combination of such physical components. SCMs can also be tuned to reproduce the calculations of climate-mean variables of a given ESM, assuming that their structural flexibility can capture both the parametric and structural uncertainties across process-oriented ESM responses. When run in this setup, they are termed emulators. Simple climate models do not have to be run in 'emulation' mode, though, as they can also be used to test consistency across multiple lines of evidence with regard to ranges in ECS, TCR, TCRE and carbon cycle feedbacks (see Chapters 5 and 7). Physical emulation can also be performed with very simple parameterisations ('one-or-few-line climate models'), statistical methods like neural networks, genetic algorithms, or other artificial intelligence approaches, where the emulator behaviour is explicitly tuned to reproduce the response of a given ESM or model ensemble (Chapters 4, 5, and 7).

Current emulators and SCMs include the generic impulse response model outlined in Chapter 8 of the AR5 (AR5-IR (Supplementary Material 8.SM.11 of Myhre et al. (2013)), two-layer models (Held et al., 2010; Rohrschneider et al., 2019; Nicholls et al., 2020), and higher complexity approaches that include upwelling, diffusion and entrainment in the ocean component (e.g., MAGICC Version 5.3 (Raper et al., 2001; Wigley et al., 2009), Version 6/7 (Meinshausen et al., 2011a)**;** OSCAR (Gasser et al., 2017); CICERO SCM (Skeie et al., 2017); FaIR (Millar et al., 2017b; Smith et al., 2018); and a range of statistical approaches (Schwarber et al., 2019; Beusch et al., 2020b)). An example of recent use of an emulator approach is an early estimate of the climate implications of the COVID-19 lockdowns (Forster et al. 2020; see Cross-Chapter Box 6.1 in Chapter 6).

Since AR5, simplified climate models have been developed further, and their use is increasing. Different purposes motivating development include: being as simple as possible for teaching purposes (e.g., a two-layer energy balance model), as comprehensive as possible to allow for propagation of uncertainties across multiple Earth System domains (MAGICC and others), or focus on higher complexity representation of specific domains (e.g., OSCAR). The common theme in many models is to improve parameterisations that reflect the latest findings in complex ESM interactions, such as the nitrogen cycle addition to the carbon cycle, or tropospheric and stratospheric ozone exchange, with the aim of emulating their global mean temperature response. Also, within the simple models that have a rudimentary representation of spatial heterogeneity (e.g., four-box simple climate models), the ambition is to represent heterogeneous forcers such as black carbon more adequately (Stjern et al., 2017), provide an appropriate representation of the forcing-feedback framework (see e.g., Sherwood et al., 2015), investigate new parameterisations of ocean heat uptake, and implement better representations of volcanic aerosol induced cooling (Gregory et al., 2016a).

ACCEPTED VERSION SUBJECT TO FINAL EDITS

MAGICC (Wigley et al., 2009; Meinshausen et al., 2011a) and FaIR (Smith et al., 2018) were used in the SR1.5 (IPCC, 2018) to categorize mitigation pathways into classes of scenarios that peak near 1.5°C, overshoot 1.5°C, or stay below 2°C. The SR1.5 (Rogelj et al., 2018) concluded that there was a *high agreement* in the relative temperature response of pathways, but *medium agreement* on the precise absolute magnitude of warming, introducing a level of imprecision in the attribution of a single pathway to a given category.

In this Report, there are two notable uses of simple climate models. One is the connection between the assessed range of ECS in Chapter 7, and the projections of future global surface air temperature (GSAT) change in Chapter 4, which is done via a two-layer model based on Held et al. (2010). It is also used as input to sea level projections in Chapter 9. The other usage is the transfer of Earth system assessment knowledge to Working Group III, via a set of models (MAGICC, FaIR, CICERO-SCM) specifically tuned to represent the Working Group I assessment. For an overview of the uses, and an assessment of the related Reduced Complexity Model Intercomparison Project (RCMIP), see Nicholls et al. (2020) and Cross-Chapter Box 7.1 in Chapter 7.

[START BOX 1.3 HERE]

Box 1.3: Emission metrics in AR6 WGI

Emission metrics compare the radiative forcing, temperature change, or other climate effects arising from emissions of CO_2 versus those from emissions of non-CO_2 radiative forcing agents (such as CH_4 or N_2O). They have been discussed in the IPCC since the First Assessment Report and are used as a means of aggregating emissions and removals of different gases and placing them on a common ('CO_2 equivalent', or 'CO_2-eq') scale.

AR5 included a thorough assessment of common pulse emission metrics, and how these address various indicators of future climate change (Myhre et al., 2013). Most prominently used are the Global Warming Potentials (GWPs), which integrate the calculated radiative forcing contribution following an idealized pulse (or one-time) emission, over a chosen time horizon (IPCC, 1990a), or the Global Temperature-change Potential (GTP), which considers the contribution of emission to the global-mean temperature at a specific time after emission. Yet another metric is the Global Precipitation change Potential (GPP), used to quantify the precipitation change per unit mass of emission of a given forcing agent (Shine et al., 2015).

As an example of usage, the Paris Rulebook [Decision 18/CMA.1, annex, paragraph 37] states that 'Each Party shall use the 100-year time-horizon global warming potential (GWP) values from the IPCC Fifth Assessment Report, or 100-year time-horizon GWP values from a subsequent IPCC assessment report as agreed upon by the 'Conference of the Parties serving as the meeting of the Parties to the Paris Agreement' (CMA), to report aggregate emissions and removals of GHGs, expressed in CO_2-eq. Each Party may in addition also use other metrics (e.g., global temperature potential) to report supplemental information on aggregate emissions and removals of GHGs, expressed in CO_2-eq'.

Since AR5, improved knowledge of the radiative properties, lifetimes, and other characteristics of emitted species, and the response of the climate system, have led to updates to the numerical values of a range of metrics; see Chapter 7, Table 7.15. Another key development is a set of metrics that compare a pulse emission of CO_2 (as considered by GWP and GTP) to step-changes of emission rates for short-lived components (i.e., also considering emission trends). Termed GWP* (which also includes a pulse component) and Combined Global Temperature change Potential (CGTP), these metrics allow the construction of a near-linear relationship between global surface temperature change and cumulative CO_2 and CO_2-equivalent emissions of both short and long lived forcing agents (Allen et al., 2016; Cain et al., 2019; Collins et al., 2019). For example, the temperature response to a sustained methane reduction has a similar behaviour to the temperature response to a pulse CO_2 removal (or avoided emission).

In this Report, recent scientific developments underlying emission metrics, as relevant for Working Group I,

ACCEPTED VERSION SUBJECT TO FINAL EDITS

are assessed in full in Chapter 7, Section 7.6. In particular, see Box 7.3, which discusses the choice of metric for different usages, and Section 7.6.1, which treats the challenge of comparing the climate implication of emissions of short-lived and long-lived compounds. Also, the choice of metric is of key importance when defining and quantifying net zeronet-zero greenhouse gas emissions; see Box 1.4 and Chapter 7, Section 7.6.2. Chapter 6 applies metrics to attribute GSAT change to short-lived climate forcer (SLCF) and long-lived greenhouse gas (LLGHG) emissions from different sectors and regions (Section 6.6.2).

The metrics assessed in this Report are also used, and separately assessed, by Working Group III. See Cross-Chapter Box 2: GHG emissions metrics and Annex B in Chapter 2 of the WGIII contribution to the AR6.

[END BOX 1.3 HERE]

1.5.4 Modelling techniques, comparisons and performance assessments

Numerical models, however complex, cannot be a perfect representation of the real world. Results from climate modelling simulations constitute a key line of evidence for the present report, which requires considering the limitations of each model simulation. This section presents recent developments in techniques and approaches to robustly extract, quantify and compare results from multiple, independent climate models, and how their performance can be assessed and validated.

1.5.4.1 Model 'fitness for purpose'

A key issue addressed in this report is whether climate models are adequate or 'fit' for purposes of interest, that is, whether they can be used to successfully answer particular research questions, especially about the causes of recent climate change and the future evolution of climate (e.g., Parker, 2009; Notz, 2015; Knutti, 2018; Winsberg, 2018). Assessment of a model's fitness-for-purpose can be informed both by how the model represents relevant physical processes and by relevant performance metrics (Baumberger et al., 2017; Parker, 2020). The processes and metrics that are most relevant can vary with the question of interest, for example, a question about changes in deep ocean circulation versus a question about changes in regional precipitation (Notz, 2015; Gramelsberger et al., 2020). New model evaluation tools (Section 1.5.4.5) and emergent constraint methodologies (Section 1.5.4.7) can also aid the assessment of fitness-for-purpose, especially in conjunction with process understanding (Klein and Hall, 2015; Knutti, 2018). The broader availability of large model ensemble may allow for novel tests of fitness that better account for natural climate variability (see Section 1.5.4.2). Fitness-for-purpose of models used in this report is discussed in Chapter 3 (Section 3.8.4) for the global scale, in Chapter 10 (Section 10.3) for regional climate, and in the other chapters at the process level.

Typical strategies for enhancing the fitness-for-purpose of a model include increasing resolution in order to explicitly simulate key processes, improving relevant parameterizations, and careful tuning. Changes to a model that enhance its fitness for one purpose can sometimes decrease its fitness for others, by upsetting a pre-existing balance of approximations. When it is unclear whether a model is fit for a purpose of interest, there is often a closely-related purpose for which the evidence of fitness is clearer; for example, it might be unclear whether a model is fit for providing highly accurate projections of precipitation changes in a region, but reasonable to think that the model is fit for providing projections of precipitation changes that cannot yet be ruled out (Parker, 2009). Such information about plausible or credible changes can be useful to inform adaptation. Note that challenges associated with assessing model fitness-for-purpose need not prevent reaching conclusions with high confidence if there are multiple other lines of evidence supporting those same conclusions.

1.5.4.2 Ensemble modelling techniques

A key approach in climate science is the comparison of results from multiple model simulations with each

ACCEPTED VERSION SUBJECT TO FINAL EDITS

other and against observations. These simulations have typically been performed by separate models with consistent boundary conditions and prescribed emissions or radiative forcings, as in the Coupled Model Intercomparison Project phases (CMIP, Meehl et al., 2000, 2007a; Taylor et al., 2012; Eyring et al., 2016). Such multi-model ensembles (MMEs) have proven highly useful in sampling and quantifying model uncertainty, within and between generations of climate models. They also reduce the influence on projections of the particular sets of parametrizations and physical components simulated by individual models. The primary usage of MMEs is to provide a well quantified model range, but when used carefully they can also increase confidence in projections (Knutti et al., 2010). Presently, however, many models also share provenance (Masson and Knutti, 2011) and may have common biases that should be acknowledged when presenting and building on MME-derived conclusions (Boé, 2018; Abramowitz et al., 2019) (see Section 1.5.4.6).

Since AR5, an increase in computing power has made it possible to investigate simulated internal variability and to provide robust estimates of forced model responses, using Large Initial Condition Ensembles (ICEs), also referred to as Single Model Initial condition Large Ensembles (SMILEs). Examples using GCMs or ESMs that support assessments in AR6 include the CESM Large Ensemble (Kay et al., 2015), the MPI Grand Ensemble (Maher et al., 2019), and the CanESM2 large ensembles (Kirchmeier-Young et al., 2017). Such ensembles employ a single GCM or ESM in a fixed configuration, but starting from a variety of different initial states. In some experiments, these initial states only differ slightly. As the climate system is chaotic, such tiny changes in initial conditions lead to different evolutions for the individual realizations of the system as a whole. Other experiments start from a set of well-separated ocean initial conditions to sample the uncertainty in the circulation state of the ocean and its role in longer-timescale variations. These two types of ICEs have been referred to as 'micro' and 'macro' perturbation ensembles respectively (Hawkins et al., 2016). In support of this report, most models contributing to CMIP6 have produced ensembles of multiple realizations of their historical and scenario simulations (see Chapters 3 and 4).

Recently, the ICE technique has been extended to atmosphere-only simulations (Mizuta et al., 2017), single-forcer influences such as volcanic eruptions (Bethke et al., 2017) to regional modelling (Mote et al., 2015; Fyfe et al., 2017; Schaller et al., 2018; Leduc et al., 2019) and to attribution of extreme weather events using crowd-sourced computing (climateprediction.net; Massey et al., 2015).

ICEs can also be used to evaluate climate model parameterizations, if models are initialized appropriately (Phillips et al., 2004; Williams et al., 2013), mostly within the framework of seamless weather and climate predictions (e.g., Palmer et al., 2008; Hurrell et al., 2009; Brown et al., 2012). Initializing an atmospheric model in hindcast mode and observing the biases as they develop permits testing of the parameterized processes, by starting from a known state rather than one dominated by quasi-random short term variability (Williams et al., 2013; Ma et al., 2014; Vannière et al., 2014). However, single-model initial-conditions ensembles cannot cover the same degrees of freedom as a multi-model ensemble, because model characteristics substantially affect model behaviour (Flato et al., 2013).

A third common modelling technique is the perturbed parameter ensemble (PPE; note that the abbreviation also sometimes refers to the sub-category 'perturbed physics ensemble'). These methods are used to assess uncertainty based on a single model, with individual parameters perturbed to reflect the full range of their uncertainty (Murphy et al., 2004; Knutti et al., 2010; Lee et al., 2011; Shiogama et al., 2014). Statistical methods can then be used to detect which parameters are the main causes of uncertainty across the ensemble. PPEs have been used frequently in simpler models, such as EMICs, and are being applied to more complex models. A caveat of PPEs is that the estimated uncertainty will depend on the specific parameterizations of the underlying model and may well be an underestimation of the 'true' uncertainty. It is also challenging to disentangle forced responses from internal variability using a PPE alone.

Together, the three ensemble methods (MMEs, ICEs, PPEs) allow investigation of climate model uncertainty arising from internal variability, initial and internal boundary conditions, model formulations and parameterizations (Parker, 2013). Figure 1.21 illustrates the different ensemble types. Recent studies have also started combining multiple ensemble types or using ensembles in combination with statistical analytical techniques. For example, Murphy et al. (2018) combine MMEs and PPEs to give a fuller assessment of

ACCEPTED VERSION SUBJECT TO FINAL EDITS

modelling uncertainty. Wagman and Jackson (2018) use PPEs to evaluate the robustness of MME-based emergent constraints. Sexton et al. (2019) study the robustness of ICE approaches by identifying parameters and processes responsible for model errors at the two different timescales.

Overall, we assess that increases in computing power and the broader availability of larger and more varied ensembles of model simulations have contributed to better estimations of uncertainty in projections of future change (*high confidence*). Note, however, that despite their widespread use in climate science today, the cost of the ensemble approach in human and computational resources, and the challenges associated with the interpretation of multi-model ensembles, has been questioned (Palmer and Stevens, 2019; Touzé-Peiffer et al., 2020).

[START FIGURE 1.21 HERE]

Figure 1.21: Illustration of common types of model ensemble, simulating the time evolution of a quantity Q (such as global mean surface temperature). (a) Multi-model ensemble, where each model has its own realization of the processes affecting Q, and its own internal variability around the baseline value (dashed line). The multi-model mean (black) is commonly taken as the ensemble average. (b) Initial condition ensemble, where several realizations from a single model are compared. These differ only by minute ('micro') perturbations to the initial conditions of the simulation, such that over time, internal variability will progress differently in each ensemble member. (c) Perturbed physics ensemble, which also compares realizations from a single model, but where one or more internal parameters that may affect the simulations of Q are systematically changed to allow for a quantification of the effects of those quantities on the model results. Additionally, each parameter set may be taken as the starting point for an initial condition ensemble. In this figure, each set has three ensemble members.

[END FIGURE 1.21 HERE]

1.5.4.3 The sixth phase of the Coupled Model Intercomparison Project (CMIP6)

The Coupled Model Intercomparison Project (CMIP) provides a framework to compare the results of different GCMs or ESMs performing similar experiments. Since its creation in the mid-1990s, it has evolved in different phases, involving all major climate modelling centres in the world (Figure 1.20). The results of these phases have played a key role in previous IPCC reports, and the present Report assesses a range of results from CMIP5 that were not published until after the AR5, as well as the first results of the 6th phase of CMIP (CMIP6) (Eyring et al., 2016). The CMIP6 experiment design is somewhat different from previous phases. It now consists of a limited set of DECK (Diagnostic, Evaluation and Characterization of Klima) simulations and an historical simulation that must be performed by all participating models, as well as a wide range of CMIP6-endorsed Model Intercomparison Projects (MIPs) covering specialized topics (Eyring et al., 2016) (see Figure 1.22). Each MIP activity consists of a series of model experiments, documented in the literature (see Table 1.3) and in an online database (https://es-doc.org, see Pascoe et al. (2019) and Annex II).

The CMIP DECK simulations form the basis for a range of assessments and projections in the following chapters. As in CMIP5, they consist of a 'pre-industrial' control simulation (piControl, where 'pre-industrial' is taken as fixed 1850 conditions in these experiments), an idealized, abrupt quadrupling of CO_2 concentrations relative to piControl (to estimate equilibrium climate sensitivity), a 1% per year increase in CO_2 concentrations relative to piControl (to estimate the transient climate response), and a transient simulation with prescribed sea-surface temperatures for the period 1979–2014 (termed 'AMIP' for historical reasons). In addition, all participating models perform a historical simulation for the period 1850–2014. For the latter, common CMIP6 forcings are prescribed (Cross-Chapter Box 1.4, Table 2). Depending on the model setup, these include emissions and concentrations of short-lived species (Hoesly et al., 2018; Gidden et al., 2019), long-lived greenhouse gases (Meinshausen et al., 2017), biomass burning emissions (van Marle et al., 2017), global gridded land use forcing data (Ma et al., 2020a), solar forcing (Matthes et al., 2017), and stratospheric aerosol data from volcanoes (Zanchettin et al., 2016). The methods for generating gridded datasets are described in (Feng et al., 2019). For AMIP simulations, common sea surface temperatures

ACCEPTED VERSION SUBJECT TO FINAL EDITS

(SSTs) and sea ice concentrations (SICs) are prescribed. For simulations with prescribed aerosol abundances (i.e., not calculated from emissions), optical properties and fractional changes in cloud droplet effective radius are generally prescribed in order to provide a more consistent representation of aerosol forcing relative to earlier CMIP phases (Fiedler et al., 2017; Stevens et al., 2017). For models without ozone chemistry, time-varying gridded ozone concentrations and nitrogen deposition are also provided (Checa-Garcia et al., 2018).

Beyond the DECK and the historical simulations, the CMIP6-endorsed MIPs aim to investigate how models respond to specific forcings, their potential systematic biases, their variability, and their responses to detailed future scenarios such as the Shared Socioeconomic Pathways (SSPs, Section 1.6). Table 1.3 lists the 23 CMIP6-endorsed MIPs and key references. Results from a range of these MIPs, and many others outside of the most recent CMIP6 cycle, will be assessed in the following chapters (also shown in Table 1.3). References to all the CMIP6 datasets used in the report are found in Annex II, Table AII.10.

[START FIGURE 1.22 HERE]

Figure 1.22: Structure of CMIP6, the 6th phase of the Coupled Model Intercomparison Project. The centre shows the common DECK (Diagnostic, Evaluation and Characterization of Klima) and historical experiments that all participating models must perform. The outer circles show the topics covered by the endorsed (blue) and other MIPs (red). See Table 1.3 for explanation of the MIP acronyms. (Expanded from Eyring et al., 2016).

[END FIGURE 1.22 HERE]

[START TABLE 1.3 HERE]

Table 1.3: CMIP6-Endorsed MIPs, their key references, and where they are used or referenced throughout this report.

CMIP6-Endorsed MIP name	Long name	Key references	Used in chapters
AerChemMIP	Aerosols and Chemistry Model Intercomparison Project	(Collins et al., 2017)	4, 6, Atlas
C4MIP	Coupled Climate Carbon Cycle Model Intercomparison Project	(Jones et al., 2016a)	4, 5, Atlas
CDRMIP	The Carbon Dioxide Removal Model Intercomparison Project	(Keller et al., 2018)	4, 5, Atlas
CFMIP	Cloud Feedback Model Intercomparison Project	(Webb et al., 2017)	4, 7, Atlas
CORDEX	Coordinated Regional Climate Downscaling Experiment	(Gutowski Jr. et al., 2016)	4, 8, 9, 10, 11, 12, Atlas
DAMIP	Detection and Attribution Model Intercomparison Project	(Gillett et al., 2016)	3, 10, Atlas
DCPP	Decadal Climate Prediction Project	(Boer et al., 2016)	4, 8, Atlas
DynVarMIP	Dynamics and Variability Model Intercomparison Project	(Gerber and Manzini, 2016)	Atlas

ACCEPTED VERSION SUBJECT TO FINAL EDITS

FAFMIP	Flux-Anomaly-Forced Model Intercomparison Project	(Gregory et al., 2016b)	9, Atlas
GeoMIP	Geoengineering Model Intercomparison Project	(Kravitz et al., 2015)	4, 5, 8, 12, Atlas
GMMIP	Global Monsoons Model Intercomparison Project	(Zhou et al., 2016)	2,3,4, 10, Atlas
HighResMIP	High Resolution Model Intercomparison Project	(Haarsma et al., 2016)	3, 8, 9, 10, 11, Atlas
ISMIP6	Ice Sheet Model Intercomparison Project for CMIP6	(Nowicki et al., 2016)	3, 7, 9, Atlas
LS3MIP	Land Surface, Snow and Soil Moisture	(van den Hurk et al., 2016)	3, 9, 11, Atlas
LUMIP	Land Use Model Intercomparison Project	(Lawrence et al., 2016)	4, 6, Atlas
OMIP	Ocean Model Intercomparison Project	(Griffies et al., 2016; Orr et al., 2017)	3, 9, Atlas
PAMIP	Polar Amplification Model Intercomparison Project	(Smith et al., 2019a)	10, Atlas
PMIP	Paleoclimate Modelling Intercomparison Project	(Haywood et al., 2016; Jungclaus et al., 2017; Otto-Bliesner et al., 2017; Kageyama et al., 2018)	2, 3, 7, 8, 9, 10, Atlas
RFMIP	Radiative Forcing Model Intercomparison Project	(Pincus et al., 2016)	6, 7, Atlas
ScenarioMIP	Scenario Model Intercomparison Project	(O'Neill et al., 2016)	4, 5, 6, 9, 10, 12, Atlas
SIMIP	Sea Ice Model Intercomparison Project	(Notz et al., 2016)	4, 9, 12, Atlas
VIACS AB	Vulnerability, Impacts, Adaptation and Climate Services Advisory Board	(Ruane et al., 2016)	12, Atlas
VolMIP	Volcanic Forcings Model Intercomparison Project	(Zanchettin et al., 2016)	4, 8, Atlas

[END TABLE 1.3 HERE]

1.5.4.4 Coordinated Regional Downscaling Experiment (CORDEX)

The Coordinated Regional Downscaling Experiment (CORDEX, Gutowski Jr. et al., 2016) is an intercomparison project for regional models and statistical downscaling techniques, coordinating simulations on common domains and under common experimental conditions in a similar way to the CMIP effort. Dynamical and statistical downscaling techniques can provide higher-resolution climate information than is available directly from global climate models (Chapter 10, Section 10.3). These techniques require evaluation and quantification of their performance before they can be considered appropriate as usable regional climate information or be used in support of climate services. CORDEX simulations have been provided by a range of regional downscaling models, for 14 regions together covering much of the globe

ACCEPTED VERSION SUBJECT TO FINAL EDITS

(Atlas, Figure Atlas.7), and they are used extensively in the AR6 WGI Atlas (Atlas.1.4; see also Annex II).

In support of AR6, CORDEX has undertaken a new experiment (CORDEX-CORE) where regional climate models downscale a common set of global model simulations, performed at a coarser resolution, to a spatial resolution spanning from 12 to 25 km over most of the CORDEX domains (Atlas, Box Atlas.1). CORDEX-CORE represents an improved level of coordinated intercomparison of downscaling models (Remedio et al., 2019).

1.5.4.5 Model Evaluation Tools

For the first time in CMIP, a range of comprehensive evaluation tools are now available that can run alongside the commonly used distributed data platform Earth System Grid Federation (ESGF, see Annex II), to produce comprehensive results as soon as the model output is published to the CMIP archive.

For instance, the Earth System Model Evaluation Tool (ESMValTool; Eyring et al., 2020; Lauer et al., 2020; Righi et al., 2020) is used by a number of chapters. It is an open-source community software tool that includes a large variety of diagnostics and performance metrics relevant for coupled Earth System processes, such as for the mean, variability and trends, and it can also examine emergent constraints (see Section 1.5.4.7). ESMValTool also includes routines provided by the WMO Expert Team on Climate Change Detection and Indices for the evaluation of extreme events (Min et al., 2011; Sillmann et al., 2013) and diagnostics for key processes and variability. Another example of evaluation tool is the CLIVAR 2020 ENSO metrics package (Planton et al., 2021).

These tools are used in several chapters of this report for the creation of the figures that show CMIP results. Together with the Interactive Atlas, they allow for traceability of key results, and an additional level of quality control on whether published figures can be reproduced. It also provides the capability to update published figures with, as much as possible, the same set of models in all figures, and to assess model improvements across different phases of CMIP (Chapter 3, Section 3.8.2).

These new developments are facilitated by the definition of common formats for CMIP model output (Balaji et al., 2018) and the availability of reanalyses and observations in the same format as CMIP output (obs4MIPs, Ferraro et al., 2015). The tools are also used to support routine evaluation at individual model centres and simplify the assessment of improvements of individual models or generations of model ensembles (Eyring et al., 2019). Note, however, that while tools such as ESMValTool can produce an estimate of overall model performance, dedicated model evaluation still needs to be performed when analysing projections for a particular purpose, such as assessing changing hazards in a given particular region. Such evaluation is discussed in the next section, and in greater detail in later chapters of this Report.

1.5.4.6 Evaluation of process-based models against observations

Techniques used for evaluating process-based climate models against observations were assessed in AR5 (Flato et al., 2013), and have progressed rapidly since (Eyring et al., 2019). The most widely used technique is to compare climatologies (long-term averages of specific climate variables) or time series of simulated (process-based) model output with observations, considering the observational uncertainty. A further approach is to compare the results of process-based models with those from statistical models. In addition to a comparison of climatological means, trends and variability, AR5 already made use of a large set of performance metrics for a quantitative evaluation of the models.

Since AR5, a range of studies has investigated model agreement with observations well beyond large scale mean climate properties (e.g., Bellenger et al., 2014; Covey et al., 2016; Pendergrass and Deser, 2017; Goelzer et al., 2018; Beusch et al., 2020a), providing information on the performance of recent model simulations across multiple variables and components of the Earth system (e.g., Anav et al., 2013; Guan and Waliser, 2017). Based on such studies, this Report assesses model improvements across different CMIP

ACCEPTED VERSION SUBJECT TO FINAL EDITS

DECK, CMIP6 historical and CMIP6-Endorsed MIP simulations, and of differences in model performance between different classes of models, such as high- versus low-resolution models (see e.g., Chapter 3, Section 3.8.2).

In addition, process- or regime-oriented evaluation of models has been expanded since AR5. By focusing on processes, causes of systematic errors in the models can be identified and insights can be gained as to whether a mean state or trend is correctly simulated for the right reasons. This approach is commonly used for the evaluation of clouds (e.g., Williams and Webb, 2009; Konsta et al., 2012; Bony et al., 2015; Dal Gesso et al., 2015; Jin et al., 2017), dust emissions (e.g., Parajuli et al., 2016; Wu et al., 2016) as well as aerosol-cloud (e.g., Gryspeerdt and Stier, 2012) and chemistry-climate (SPARC, 2010) interactions. Process-oriented diagnostics have also been used to evaluate specific phenomena such as the El Niño Southern Oscillation (ENSO, Guilyardi et al., 2016), the Madden–Julian Oscillation (MJO; Ahn et al., 2017; Jiang et al., 2018), Southern Ocean clouds (Hyder et al., 2018), monsoons (Boo et al., 2011; James et al., 2015), and tropical cyclones (Kim et al., 2018).

Instrument simulators provide estimates of what a satellite would see if looking down on the model simulated planet, and improve the direct comparison of modelled variables such as clouds, precipitation and upper tropospheric humidity with observations from satellites (e.g., Kay et al., 2011; Klein et al., 2013; Cesana and Waliser, 2016; Konsta et al., 2016; Jin et al., 2017; Chepfer et al., 2018; Swales et al., 2018; Zhang et al., 2018). Within the framework of the Cloud Feedback Model Intercomparison Project (CFMIP) contribution to CMIP6 (Webb et al., 2017), a new version of the Cloud Feedback Model Intercomparison Project Observational Simulator (COSP, Swales et al., 2018) has been released which makes use of a collection of observation proxies or satellite simulators. Related approaches in this rapidly evolving field include simulators for Arctic Ocean observations (Burgard et al., 2020) and measurements of aerosol observations along aircraft trajectories (Watson-Parris et al., 2019).

In this Report, model evaluation is performed in the individual chapters, rather than in a separate chapter as was the case for AR5. This applies to the model types discussed above, and also to dedicated models of subsystems that are not (or not yet) part of usual climate models, for example, glacier or ice sheet models (Annex II). Further discussions are found in Chapter 3 (attribution), Chapter 5 (carbon cycle), Chapter 6 (short-lived climate forcers), Chapter 8 (water cycle), Chapter 9 (ocean, cryosphere and sea level), Chapter 10 (regional scale information) and the Atlas (regional models).

1.5.4.7 Emergent constraints on climate feedbacks, sensitivities and projections

An emergent constraint is the relationship between an uncertain aspect of future climate change and an observable feature of the Earth System, evident across an ensemble of models (Allen and Ingram, 2002; Mystakidis et al., 2016; Wenzel et al., 2016; Hall et al., 2019; Winkler et al., 2019). Complex Earth System Models (ESMs) simulate variations on timescales from hours to centuries, telling us how aspects of the current climate relate to its sensitivity to anthropogenic forcing. Where an ensemble of different ESMs displays a relationship between a short-term observable variation and a longer-term sensitivity, an observation of the short-term variation in the real world can be converted, via the model-based relationship, into an 'emergent constraint' on the sensitivity. This is shown schematically in Figure 1.23 (Eyring et al., 2019), see also Annex VII: Glossary.

Emergent constraints use the spread in model projections to estimate the sensitivities of the climate system to anthropogenic forcing, providing another type of ensemble-wide information that is not readily available from simulations with one ESM alone. As emergent constraints depend on identifying those observable aspects of the climate system that are most related to climate projections, they also help to focus model evaluation on the most relevant observations (Hall et al., 2019). However, there is a chance that indiscriminate data-mining of the multi-dimensional outputs from ESMs could lead to spurious correlations (Caldwell et al., 2014; Wagman and Jackson, 2018) and less than robust emergent constraints on future changes (Bracegirdle and Stephenson, 2013). To avoid this, emergent constraints need to be tested 'out of sample' on parts of the dataset that were not included in its construction (Caldwell et al., 2018) and should

ACCEPTED VERSION SUBJECT TO FINAL EDITS

also always be based on sound physical understanding and mathematical theory (Hall et al., 2019). Their conclusions should also be reassessed when a new generation of MMEs becomes available, such as CMIP6. As an example, Chapter 7 (Section 7.5.4) discusses and assesses recent studies where equilibrium climate sensitivities (ECS) diagnosed in a multi-model ensemble are compared with the same models' estimates of an observable quantity, such as post-1970s global warming or tropical sea-surface temperatures of past climates like the last glacial maximum or the Pliocene. Assessments of other emergent constraints appear throughout later chapters, such as Chapter 4 (Section 4.2.5), Chapter 5 (Section 5.4.6) and Chapter 7 (Section 7.5.4).

[START FIGURE 1.23 HERE]

Figure 1.23: The principle of emergent constraints. An ensemble of models (blue dots) defines a relationship between an observable, mean, trend or variation in the climate (x-axis) and an uncertain projection, climate sensitivity or feedback (y-axis). An observation of the x-axis variable can then be combined with the model-derived relationship to provide a tighter estimate of the climate projection, sensitivity or feedback on the y-axis (adapted from Eyring et al. 2019).

[END FIGURE 1.23 HERE]

1.5.4.8 Weighting techniques for model comparisons

Assessments of climate model ensembles have commonly assumed that each individual model is of equal value ('model democracy') and when combining simulations to estimate the mean and variance of quantities of interest, they are typically unweighted (Haughton et al., 2015). This practice has been noted to diminish the influence of models exhibiting a good match with observations (Tapiador et al., 2020). However, exceptions to this approach exist, notably AR5 projections of sea ice, which only selected a few models which passed a model performance assessment (Collins et al., 2013), and more studies on this topic have appeared since the AR5 (e.g., Eyring et al., 2019). Ensembles are typically sub-selected by removing either poorly performing model simulations (McSweeney et al., 2015) or model simulations that are perceived to add little additional information, typically where multiple simulations have come from the same model. They may also be weighted based on model performance.

Several recent studies have attempted to quantify the effect of various strategies for selection or weighting of ensemble members based on some set of criteria (Haughton et al., 2015; Olonscheck and Notz, 2017; Sanderson et al., 2017). Model weighting strategies have been further employed since AR5 to reduce the spread in climate projections for a given scenario by using weights based on one or more model performance metrics (Wenzel et al., 2016; Knutti et al., 2017; Sanderson et al., 2017; Lorenz et al., 2018; Liang et al., 2020). However, models may share representations of processes, parameterization schemes, or even parts of code, leading to common biases. The models may therefore not be fully independent, calling into question inferences derived from multi-model ensembles (Abramowitz et al., 2019). Emergent constraints (see Section 1.5.4.5) also represent an implicit weighting technique that explicitly links present performance to future projections (Bracegirdle and Stephenson, 2013).

Concern has been raised about the large extent to which code is shared within the CMIP5 multi-model ensemble (Sanderson et al., 2015a). Boé (2018) showed that a clear relationship exists between the number of components shared by climate models and how similar the simulations are. The resulting similarities in behaviour need to be accounted for in the generation of best-estimate multi-model climate projections. This has led to calls to move beyond equally-weighted multi-model means towards weighted means that take into account both model performance and model independence (Sanderson et al., 2015b, 2017; Knutti et al., 2017). Model independence has been defined in terms of performance differences within an ensemble (Masson and Knutti, 2011; Knutti et al., 2013, 2017, Sanderson et al., 2015b, 2015a, 2017; Lorenz et al., 2018). However, this definition is sensitive to the choice of variable, observational data set, metric, time period, and region, and a performance ranked ensemble has been shown to sometimes perform worse than a

ACCEPTED VERSION SUBJECT TO FINAL EDITS

random selection (Herger et al., 2018a). The adequacy of the constraint provided by the data and experimental methods can be tested using a calibration-validation style partitioning of observations into two sets (Bishop and Abramowitz, 2013), or a 'perfect model approach' where one of the ensemble members is treated as the reference dataset and all model weights are calibrated against it (Bishop and Abramowitz, 2013; Wenzel et al., 2016; Knutti et al., 2017; Sanderson et al., 2017; Herger et al., 2018a, 2018b). Sunyer et al. (2014) use a Bayesian framework to account for model dependencies and changes in model biases. Annan and Hargreaves (2017) provides a statistical, quantifiable definition of independence that is independent of performance-based measures.

The AR5 quantified uncertainty in CMIP5 climate projections by selecting one realization per model per scenario, and calculating the 5–95% range of the resulting ensemble (see Chapter 4, Box 4.1) and the same strategy is generally still used in AR6. Broadly, the following chapters take the CMIP6 5–95% ensemble range as the *likely* uncertainty range for projections[8], with no further weighting or consideration of model ancestry and as long as no universal, robust method for weighting a multi-model projection ensemble is available (Box 4.1, Chapter 4). A notable exception to this approach is the assessment of future changes in global surface air temperature (GSAT), which also draws on the updated best estimate and range of equilibrium climate sensitivity assessed in Chapter 7. For a thorough description of the model weighting choices made in this Report, and the assessment of GSAT, see Chapter 4 (Box 4.1). Model selection and weighting in downscaling approaches for regional assessment is discussed in Chapter 10 (Section 10.3.4).

1.6 Dimensions of Integration: Scenarios, global warming levels and cumulative carbon emissions

This section introduces three ways to synthesize climate change knowledge across topics and chapters. These 'dimensions of integration' include (1) emission and concentration scenarios underlying the climate change projections assessed in this report, (2) levels of global mean surface warming relative to the 1850-1900 baseline ('global warming levels'), and (3) cumulative carbon emissions (Figure 1.24). All three dimensions can, in principle, be used to synthesize physical science knowledge across WGI, and also across climate change impacts, adaptation, and mitigation research. Scenarios, in particular, have a long history of serving as a common reference point within and across IPCC Working Groups and research communities. Similarly, cumulative carbon emissions and global warming levels provide key links between WGI assessments and those of the other WGs; these two dimensions frame the cause-effect chain investigated by WGI. The closest links to WGIII are the emissions scenarios, as WGIII considers drivers of emissions and climate change mitigation options. The links to WGII are the geophysical climate projections from the Earth System Models which the climate impacts and adaptation literature often uses as their starting point.

[START FIGURE 1.24 HERE]

Figure 1.24: The Dimensions of Integration across Chapters and Working Groups in the IPCC AR6 assessment. This report adopts three explicit dimensions of integration to integrate knowledge across chapters and Working Groups. The first dimension is scenarios, the second dimension is global-mean warming levels relative to 1850-1900, and the third dimension is cumulative CO_2 emissions. For the scenarios, illustrative 2100 end-points are also indicated (white circles). Further details on data sources and processing are available in the chapter data table (Table 1.SM.1).

[END FIGURE 1.24 HERE]

The section is structured as follows: first, the scenarios used in AR6 are introduced and discussed in relation to scenarios used in earlier IPCC assessments (Section 1.6.1). Cross-Chapter Box 1.4 provides an overview of the new scenarios and how they are used in this report. Next, the two additional dimensions of integration are introduced: global warming levels (Section 1.6.2) and cumulative emissions (Section 1.6.3). Net zero

[8] Note that the 5–95% is a *very likely* range (See Box 1.1 on the use of calibrated uncertainty language in AR6), though if this is purely a multi-model likelihood range, it is generally treated as *likely*, in absence of other lines of evidence

ACCEPTED VERSION SUBJECT TO FINAL EDITS

emissions are discussed in Box 1.4. The relation between global warming levels and scenarios is further assessed in Cross-Chapter Box 11.1 in Chapter 11.

1.6.1 Scenarios

A scenario is a description of how the future may develop based on a coherent and internally consistent set of assumptions about key drivers including demography, economic processes, technological innovation, governance, lifestyles and relationships among these driving forces (IPCC, 2000; Rounsevell and Metzger, 2010; O'Neill et al., 2014; see Section 1.6.1.1). Scenarios can also be defined by geophysical driving forces only, such as emissions or abundances of greenhouse gases, aerosols, and aerosol precursors or land use patterns. Scenarios are not predictions; instead, they provide a 'what-if' investigation of the implications of various developments and actions (Moss et al., 2010). WGI investigates potential future climate change principally by assessing climate model simulations using emission scenarios originating from the WGIII community (Section 1.6.1.2). The scenarios used in this WGI report cover various hypothetical 'baseline scenarios' or 'reference futures' that could unfold in the absence of any or any additional climate policies (see Annex VII: Glossary). These 'reference scenarios' originate from a comprehensive analysis of a wide array of socio-economic drivers, such as population growth, technological development, and economic development, and their broad spectrum of associated energy, land use and emission implications (Riahi et al., 2017). With direct policy relevance to the Paris Agreement's 1.5°C and 'well below' 2°C goals, this report also assesses climate futures where the effects of additional climate change mitigation action are explored, i.e., so-called mitigation scenarios (for a broader discussion on scenarios and futures analysis, see Cross-Chapter Box 1, Table 1 in SRCCL, IPCC, 2019b).

For this Report, the main emissions, concentration and land use scenarios considered are a subset of scenarios recently developed using the Shared Socioeconomic Pathways framework (SSPs) (Riahi et al., 2017; see Section 1.6.1.1 and Cross-Chapter Box 1.4). Initially, the term 'SSP' described five broad narratives of future socio-economic development only (O'Neill et al., 2014). However, at least in the WGI community, the term 'SSP scenario' is now more widely used to refer directly to future emission and concentration scenarios that result from combining these socio-economic development pathways with climate change mitigation assumptions. These are assessed in detail in WGIII (WGIII, Chapter 3; Cross-Chapter Box 1.4, Table 1).

The WGI report uses a core set of five SSP scenarios to assist cross-Chapter integration and cross-WG applications: SSP1-1.9, SSP1-2.6, SSP2-4.5, SSP3-7.0 and SSP5-8.5 (Cross-Chapter Box 1.4, Table 1). These scenarios span a wide range of plausible societal and climatic futures from potentially below 1.5°C best-estimate warming to over 4°C warming by 2100 (Figure 1.25). The set of five SSP scenarios includes those in 'Tier 1' simulations of the CMIP6 ScenarioMIP intercomparison project (O'Neill et al., 2016; see Section 1.5.4) that participating climate modelling groups were asked to prioritize (SSP1-2.6, SSP2-4.5, SSP3-7.0 and SSP5-8.5), plus the low emission scenario SSP1-1.9. SSP1-1.9 is used in combination with SSP1-2.6 to explore differential outcomes of approximately 1.5 and 2.0 °C warming relative to pre-industrial levels, relevant to the Paris Agreement goals. Further SSP scenarios are used in this report to assess specific aspects, e.g., air pollution policies in Chapter 6 (Cross-Chapter Box 1.4). In addition, the previous generation of Representative Concentration Pathways (RCPs) is also used in this report when assessing future climate change (Section 1.6.1.3; Cross-Chapter Box 1.4, Table 1).

Climatic changes over the 21st century (and beyond) are projected and assessed in subsequent chapters, using a broad range of climate models, conditional on the various SSP scenarios. The projected future changes can then be put into the context of longer-term paleoclimate data and historical observations, showing how the higher emission and higher concentration scenarios diverge further from the range of climate conditions that ecosystems and human societies experienced in the past 2000 years in terms of global mean temperature and other key climate variables (Figure 1.26; see also Figure 1.5).

[START FIGURE 1.25 HERE]

ACCEPTED VERSION SUBJECT TO FINAL EDITS

Figure 1.25: Global mean surface air temperature (GSAT) illustrated as warming stripes from blue (cold) to red (warm) over three different time periods. From 1750 to 1850 based on PAGES 2K reconstructions (2017, 2019); from 1850 to 2018 showing the composite GSAT time series assessed in Chapter 2; and from 2020 onwards using the assessed GSAT projections for each Shared Socio-economic Pathway (SSP) (from Chapter 4). For the projections, the upper end of each arrow aligns with colour corresponding to the 95th percentile of the projected temperatures and the lower end aligns with the colour corresponding to the 5th percentile of the projected temperature range. Projected temperatures are shown for five scenarios from 'very low' SSP1-1.9 to 'very high' SSP5-8.5 (see Cross-Chapter Box 1.4 for more details on the scenarios). For illustrative purposes, natural variability has been added from a single CMIP6 Earth system model (MRI ESM2). The points in time when total CO_2 emissions peak, reach halved levels of the peak and reach net-zero emissions are indicated with arrows, '½' and '0' marks, respectively. Further details on data sources and processing are available in the chapter data table (Table 1.SM.1).

[END FIGURE 1.25 HERE]

While scenarios are a key tool for integration across IPCC Working Groups, they also allow the integration of knowledge among scientific communities and across timescales. For example, agricultural yield, infrastructure and human health impacts of increased drought frequency, extreme rainfall events and hurricanes are often examined in isolation. New insights on climate impacts in WGII can be gained if compound effects of multiple cross-sectoral impacts are considered across multiple research communities under consistent scenario frameworks (Leonard et al., 2014; Warszawski et al., 2014; see also Chapter 11, Section 11.8). Similarly, a synthesis of WGI knowledge on sea level rise contributions is enabled by a consistent application of future scenarios across all specialised research communities, such as ice-sheet mass balance analyses, glacier loss projections and thermosteric change from ocean heat uptake (e.g. Kopp et al., 2014; see Chapter 9).

[START FIGURE 1.26 HERE]

Figure 1.26: Historical and projected future concentrations of CO_2, CH_4 and N_2O and global mean surface temperatures (GMST). GMST temperature reconstructions over the last 2000 years were compiled by the PAGES 2k Consortium (2017, 2019) (grey line, with 95% uncertainty range), joined by historical GMST timeseries assessed in Chapter 2 (black line) – both referenced against the 1850-1900 period. Future GSAT temperature projections are from CMIP6 ESM models across all concentration-driven SSP scenario projections (Chapter 4). The discontinuity around year 2100 for CMIP6 temperature projections results from the fact that not all ESM models ran each scenario past 2100. The grey vertical band indicates the future 2015-2300 period. The concentrations used to drive CMIP6 Earth System Models are derived from ice core, firn and instrumental datasets (Meinshausen et al., 2017) and projected using an emulator (Cross-Chapter Box 7.1 in Chapter 7; Meinshausen et al., 2020). The colours of the lines indicate the SSP scenarios used in this report (see Cross-Chapter Box 1.4, Figure 1). Further details on data sources and processing are available in the chapter data table (Table 1.SM.1).

[END FIGURE 1.26 HERE]

In addition to the comprehensive SSP scenario set and the RCPs, multiple idealized scenarios and time-slice experiments using climate models are assessed in this report. Idealized scenarios refer to experiments where, for example, CO_2 concentrations are increased by 1% per year, or instantly quadrupled. Such idealized experiments have been extensively used in previous model intercomparison projects and constitute the core 'DECK' set of model experiments of CMIP6 (see Section 1.5.4). They are, for example, used to diagnose the patterns of climate feedbacks across the suite of models assessed in this report (Chapter 7).

In the following, we further introduce the SSP scenarios and how they relate to the Shared Socioeconomic Pathways framework (Section 1.6.1.1), describe the scenario generation process (Section 1.6.1.2), and

ACCEPTED VERSION SUBJECT TO FINAL EDITS

provide a historical review of scenarios used in IPCC assessment reports (Section 1.6.1.3), before briefly discussing questions of scenario likelihood, scenario uncertainty and the use of scenario storylines (Section 1.6.1.4).

1.6.1.1 Shared Socio-economic Pathways

The Shared Socioeconomic Pathways SSP1 to SSP5 describe a range of plausible trends in the evolution of society over the 21st century. They were developed in order to connect a wide range of research communities (Nakicenovic et al., 2014) and consist of two main elements: a set of qualitative, narrative storylines describing societal futures (O'Neill et al., 2017a) and a set of quantified measures of development at aggregated and/or spatially resolved scales. Each pathway is an internally consistent, plausible and integrated description of a socio-economic future, but these socio-economic futures do not account for the effects of climate change, and no new climate policies are assumed. The SSPs' quantitative projections of socio-economic drivers include population, gross domestic product (GDP) and urbanization (Dellink et al., 2017; Jiang and O'Neill, 2017; Samir and Lutz, 2017). By design, the SSPs differ in terms of the socio-economic challenges they present for climate change mitigation and adaptation (Rothman et al., 2014; Schweizer and O'Neill, 2014) and the evolution of these drivers within each SSP reflects this design. Broadly, the five SSPs represent 'sustainability' (SSP1), a 'middle of the road' path (SSP2), 'regional rivalry' (SSP3), 'inequality' (SSP4), and 'fossil fuel intensive' development (SSP5) (Cross-Chapter Box 1.4, Figure 1) (O'Neill et al., 2017a). More specific information on the SSP framework and the assumptions underlying the SSPs will be provided in the IPCC WGIII report (WGIII, Chapter 3; see also Box SPM.1 in SRCCL (IPCC, 2019d)).

The SSP narratives and drivers were used to develop scenarios of energy use, air pollution control, land use and greenhouse gas (GHG) emissions developments using integrated assessment models (IAMs) (Riahi et al., 2017; Rogelj et al., 2018a). An IAM can derive multiple emission futures for each socio-economic development pathway, assuming no new mitigation policies or various levels of additional mitigation action (in the case of reference scenarios and mitigation scenarios, respectively (Riahi et al., 2017). By design, the evolution of drivers and emissions within the SSP scenarios do not take into account the effects of climate change.

The SSPX-Y scenarios and the RCP scenarios are categorized similarly, by reference to the approximate radiative forcing levels each one entails at the end of the 21st century. For example, the '1.9' in the SSP1-1.9 scenario stands for an approximate radiative forcing level of 1.9 W m^{-2} in 2100. The first number (X) in the 'SSPX-Y' acronym refers to one of the five shared socio-economic development pathways (Cross-Chapter Box 1.4, Figure 1; Table 1.4).

[START TABLE 1.4 HERE]

Table 1.4: Overview of different RCP and SSP acronyms as used in this report.

Scenario Acronym	Description
'**SSPX**' with X standing for the shared socioeconomic pathway family (1, 2, …, 5)	The shared socioeconomic pathway family, i.e., the socioeconomic developments with storylines regarding (among other things) GDP, population, urbanisation, economic collaboration, human and technological development projections that describe different future worlds in the absence of climate change and additional climate policy (O'Neill et al., 2014). The quantification of energy, land use and emission implications in those storylines is not part of the SSPX narratives, but follows in a second step in which their climate outcomes are defined. This second step is dependent upon the IAM that is used for this quantification (Riahi et al., 2017) (see SSPX-Y)
'**RCPY**' with Y	Representative Concentration Pathways (Moss et al., 2010; van Vuuren et al., 2011).

ACCEPTED VERSION SUBJECT TO FINAL EDITS

standing for approximate radiative forcing level in 2100, at levels 2.6, 4.5, 6.0 or 8.5.	These are GHG concentrations (Meinshausen et al., 2011b) , aerosol emissions (Lamarque et al., 2011) and land use pattern time series (Hurtt et al., 2011) derived from several IAMs. The pathways were originally generated from specific sets of socio-economic drivers, but these are no longer considered. Instead, these RCP emission and concentration time series are used in combination with a range of socio-economic futures (see SSPX-RCPY). For example, the CMIP5 intercomparison (assessed in IPCC AR5) developed climate futures based on these emission and concentration pathways from the RCPs.
The SSP and RCP combination '**SSPX-RCPY**' with X and Y as above.	Combination of the SSP socioeconomic pathway X with climate futures stemming from GCMs, AOGCMs or Earth system model runs that used the RCPY. This combination is widely used in the impact literature assessed by WGII (see for example the Special Issue on SSPs by van Vuuren et al. (2014) and the large literature collection in the International Committee On New Integrated Climate change assessment Scenarios database (ICONICS, 2021). These SSPX-RCPY scenarios differ from the SSPX-Y group (below) in that the respective socio-economic futures (SSPXs) and emission and concentration futures (RCPYs) were developed separately before being used in combination.
'**SSPX-Y**' with X and Y as above.	SSPX-Y is the abbreviation for a scenario, where X is the numbering of the SSP socioeconomic family (1 to 5) that was used to develop the emission pathway, and the Y indicates the approximate radiative forcing value reached by the end of the century. The SSPX-Y scenarios span the nominal range from 1.9 to 8.5 W m^2. A range of different IAMs were used to quantify the SSPX-Y scenarios, but each IAM quantified both the scenario-economic futures (energy use, land use, population etc) and various emission futures within the same IAM modelling framework, thus enhancing the consistency between the socio-economic backgrounds and their resulting emission futures. In contrast, the SSPX-RCPY framework combines the SSP socio-economic futures and RCP emission and concentration futures at random (see above). For more details, see Section 1.6.1.1.

[END TABLE 1.4 HERE]

This SSP scenario categorisation, focused on end-of-century radiative forcing levels, reflects how scenarios were conceptualized until recently, namely, to reach a particular climate target in 2100 at the lowest cost and irrespective of whether the target was exceeded over the century. More recently, and in particular since the IPCC SR1.5 report focused attention on peak warming scenarios (Rogelj et al., 2018b), scenario development started to explicitly consider peak warming, cumulative emissions and the amount of net negative emissions (Rogelj et al., 2018b; Fujimori et al., 2019).

The SSP scenarios can be used for either emission- or concentration-driven model experiments (Cross-Chapter Box 1.4). ESMs can be run with emissions and concentrations data for GHGs and aerosols and land use or landcover maps and calculate levels of radiative forcing internally. The radiative forcing labels of the RCP and SSP scenarios, such as '2.6' in RCP2.6 or SSP1-2.6, are thus approximate labels for the year 2100 only. The actual global mean effective radiative forcing varies across ESMs due to different radiative transfer schemes, uncertainties in aerosol-cloud interactions and different feedback mechanisms, among other reasons. Nonetheless, using approximate radiative forcing labels is advantageous because it establishes a clear categorization of scenarios, with multiple climate forcings and different combinations in those scenarios summarized in a single number. The classifications according to cumulative carbon emissions (see Section 1.6.3) and global warming level (see Section 1.6.2 and Cross-Chapter Box 7.1 on emulators in Chapter 7) complement those forcing labels.

A key advance of the SSP scenarios relative to the RCPs is a wider span of assumptions on future air quality

ACCEPTED VERSION SUBJECT TO FINAL EDITS

mitigation measures, and hence emissions of short-lived climate forcers (SLCFs) (Rao et al., 2017; Lund et al., 2020). This allows for a more detailed investigation into the relative roles of GHG and SLCF emissions in future global and regional climate change, and hence the implications of policy choices. For instance, SSP1-2.6 builds on an assumption of stringent air quality mitigation policy, leading to rapid reductions in particle emissions, while SSP3-7.0 assumes slow improvements, with pollutant emissions over the 21st century comparable to current levels (Cross-Chapter Box 1.4, Figure 2, Chapter 6, Figure 6.19).

One limitation of the SSP scenarios used for CMIP6 and in this Report is that they reduce emissions from all the major ozone-depleting substances controlled under the Montreal Protocol (CFCs, halons, and hydrochlorofluorocarbons (HCFCs)) uniformly, rather than representing a fuller range of possible high and low emission futures (UNEP, 2016). Hydrofluorocarbon (HFC) emissions, on the other hand, span a wider range within the SSPs than in the RCPs (Cross-Chapter Box 1.4, Figure 2).

The SSP scenarios and previous RCP scenarios are not directly comparable. First, the gas-to-gas compositions differ; for example, the SSP5-8.5 scenario has higher CO_2 concentrations but lower methane concentrations compared to RCP8.5. Second, the projected 21st-century trajectories may differ, even if they result in the same radiative forcing by 2100. Third, the overall effective radiative forcing (see Chapter 7) may differ, and tends to be higher for the SSPs compared to RCPs that share the same nominal stratospheric-temperature adjusted radiative forcing label. The stratospheric-temperature adjusted radiative forcings of the SSPs and RCPs, however, remain relatively close, at least by 2100 (Tebaldi et al., 2021). In summary, differences in, for example, CMIP5 RCP8.5 and CMIP6 SSP5-8.5 ESM outputs, are partially due to different scenario characteristics rather than different ESM characteristics only (Chapter 4, Section 4.6.2).

When investigating various mitigation futures, WGIII goes beyond the core set of SSP scenarios assessed in WGI (SSP1-1.9, SSP1-2.6, etc.) to consider the characteristics of more than 1000 scenarios (see Cross-Chapter Box 7.1 in Chapter 7). In addition, while staying within the framework of socio-economic development pathways (SSP1 to SSP5), WGIII also considers various mitigation possibilities through so-called illustrative pathways (IPs). These illustrative pathways help to highlight key narratives in the literature concerning various technological, social and behavioral options for mitigation, various timings for implementation, or varying emphasis on different GHG and land use options. Just as with the SSPX-Y scenarios considered in this report, these illustrative pathways can be placed in relation to the matrix of SSP families and approximate radiative forcing levels in 2100 (see Cross-Chapter Box 1.4, Figure 1 and Working Group III, Chapter 3).

No likelihood is attached to the scenarios assessed in this report, and the feasibility of specific scenarios in relation to current trends is best informed by the WGIII contribution to AR6. In the scenario literature, the plausibility of the high emissions levels underlying scenarios such as RCP8.5 or SSP5-8.5 has been debated in light of recent developments in the energy sector. (see Section 1.6.1.4).

[START CROSS CHAPTER BOX 1.4 HERE]

Cross-Chapter Box 1.4: The SSP scenarios as used in Working Group I

Contributing Authors: Jan Fuglestvedt (Norway), Celine Guivarch (France), Chris Jones (UK), Malte Meinshausen (Australia/Germany), Zebedee Nicholls (Australia), Gian-Kasper Plattner (Switzerland), Keywan Riahi (Austria), Joeri Rogelj (UK/Belgium), Sophie Szopa (France), Claudia Tebaldi (USA/Italy), Anne-Marie Treguier (France), and Detlef van Vuuren (Netherlands)

The new nine SSP emission and concentration scenarios (SSP1-1.9 to SSP5-8.5; Cross-Chapter Box 1.4, Table 1) offer unprecedented detail of input data for climate model simulations. They allow for a more comprehensive assessment of climate drivers and responses than has previously been available, in particular because some of the scenarios' time series, e.g., pollutants, emissions or changes in land use and land cover, are more diverse in the SSP scenarios than in the RCPs used in AR5 (e.g., Chuwah et al., 2013) (Cross-Chapter Box 1.4, Figure 2).

ACCEPTED VERSION SUBJECT TO FINAL EDITS

The core set of five SSP scenarios SSP1-1.9, SSP1-2.6, SSP2-4.5, SSP3-7.0 and SSP5-8.5 was selected in this Report to align with the objective that the new generation of SSP scenarios should fill certain gaps identified in the RCPs. For example, a scenario assuming reduced air pollution control and thus higher aerosol emissions was missing from the RCPs. Likewise, nominally the only 'no-additional-climate-policy' scenario in the set of RCPs was RCP8.5. The new SSP3-7.0 'no-additional-climate-policy' scenario fills both these gaps. A very strong mitigation scenario in line with the 1.5°C goal of the Paris Agreement was also missing from the RCPs, and the SSP1-1.9 scenario now fills this gap, complementing the other strong mitigation scenario SSP1-2.6. The five core SSPs were also chosen to ensure some overlap with the RCP levels for radiative forcing at the year 2100 (specifically 2.6, 4.5, and 8.5) (O'Neill et al., 2016; Tebaldi et al., 2021), although effective radiative forcings are generally higher in the SSP scenarios compared to the equivalently-named RCP pathways (Cross-Chapter Box 1.4, Figure 1; Chapter 4, Section 4.6.2). In theory, running scenarios with similar radiative forcings would permit analysis of the CMIP5 and CMIP6 outcomes for pairs of scenarios (e.g., RCP8.5 and SSP5-8.5) in terms of varying model characteristics rather than differences in the underlying scenarios. In practice, however, there are limitations to this approach (Section 1.6.1.1 and Chapter 4, Section 4.6.2).

[START Cross-Chapter Box 1.4, FIGURE 1 HERE]

Cross-Chapter Box 1.4, Figure 1: The SSP scenarios used in this report, their indicative temperature evolution and radiative forcing categorization, and the five socio-economic storylines upon which they are built. The core set of scenarios used in this report, i.e., SSP1-1.9, SSP1-2.6, SSP2-4.5, SSP3-7.0 and SSP5-8.5, is shown together with an additional four SSPs that are part of ScenarioMIP, as well as previous RCP scenarios. In the left panel, the indicative temperature evolution is shown (adapted from Meinshausen et al., 2020). The black stripes on the respective scenario family panels on the left side indicate a larger set of IAM-based SSP scenarios that span the scenario range more fully, but are not used in this report. The SSP-radiative forcing matrix is shown on the right, with the SSP socioeconomic narratives shown as columns and the indicative radiative forcing categorisation by 2100 shown as rows. Note that the descriptive labels for the five SSP narratives refer mainly to the reference scenario futures without additional climate policies. For example, SSP5 can accommodate strong mitigation scenarios leading to net zero emissions; these do not match a 'fossil-fueled development' label. Further details on data sources and processing are available in the chapter data table (Table 1.SM.1).

[END Cross-Chapter Box 1.4, FIGURE 1 HERE]

[START Cross-Chapter Box 1.4, TABLE 1 HERE]

Cross-Chapter Box 1.4, Table 1: Overview of SSP scenarios used in this report. The middle column briefly describes the SSP scenarios and the right column indicates the previous RCP scenarios that most closely match that SSP's assessed global-mean temperatures (GSAT) trajectory. RCP scenarios are generally found to result in larger modelled warming for the same nominal radiative forcing label (Chapter 4, Section 4.6.2.2). The five core SSP scenarios used most commonly in this report are highlighted in bold. Further SSP scenarios are used where they allow assessment of specific aspects, e.g., air pollution policies in Chapter 6 (SSP3-7.0-lowNTCF). RCPs are used in this report wherever the relevant scientific literature makes substantial use of regional or domain-specific model output that is based on these previous RCP pathways, such as sea level rise projections in Chapter 9 (Section 9.6.3.1) or regional climate aspects in Chapters 10 and 12. See Chapter 4 (Section 4.3.4) for the GSAT assessment for the SSP scenarios and Section 4.6.2.2 for a comparison between SSPs and RCPs in terms of both radiative forcing and global surface temperature.

SSPX-Y scenario	Description from an emission / concentration and temperature perspective (Chapter 4, Table 4.2)	Closest RCP scenarios
SSP1-1.9	Holds warming to approximately 1.5°C above 1850-1900 in 2100 after slight overshoot (median) and implied net zero	Not available. No equivalently low RCP scenario exists.

ACCEPTED VERSION SUBJECT TO FINAL EDITS

	CO_2 emissions around the middle of the century.	
SSP1-2.6	Stays below 2.0°C warming relative to 1850-1900 (median) with implied net zero emissions in the second half of the century.	RCP2.6, although RCP2.6 might be cooler for the same model settings.
SSP4-3.4	A scenario in between SSP1-2.6 and SSP2-4.5 in terms of end-of-century radiative forcing. It does not stay below 2.0°C in most CMIP6 runs (Chapter 4) relative to 1850-1900.	No 3.4 level of end-of-century radiative forcing was available in the RCPs. Nominally SSP4-3.4 sits between RCP 2.6 and RCP 4.5, although SSP4-3.4 might be more similar to RCP4.5. Also, in the early decades of the 21st century, SSP4-3.4 is close to RCP6.0, which featured lower radiative forcing than RCP4.5 in the first decades of the 21st century.
SSP2-4.5	Scenario approximately in line with the upper end of aggregate NDC emission levels by 2030 (see Section 1.2.2 and Chapter 4, Section 4.3; SR1.5, (IPCC, 2018) , Box 1). SR1.5 assessed temperature projections for NDCs to be between 2.7 and 3.4°C by 2100 (Section 1.2.2; SR1.5 (IPCC, 2018); Cross-Chapter Box 11 in Chapter 11), corresponding to the upper half of projected warming under SSP2-4.5 (Chapter 4). New or updated NDCs by the end of 2020 did not significantly change the emissions projections up to 2030, although more countries adopted 2050 net zero targets in line with SSP1-1.9 or SSP1-2.6. The SSP2-4.5 scenario deviates mildly from a 'no-additional-climate-policy' reference scenario, resulting in a best-estimate warming around 2.7°C by the end of the 21st century relative to 1850-1900 (Chapter 4).	RCP4.5 and, until 2050, also RCP6.0. Forcing in the latter was even lower than RCP4.5 in the early decades of the 21st century.
SSP4-6.0	The end-of-century nominal radiative forcing level of 6.0 W/m^2 can be considered a 'no-additional-climate-policy' reference scenario, under SSP1 and SSP4 socioeconomic development narratives.	RCP6.0 is nominally closest in the second half of the century, although global mean temperatures are estimated to be generally lower in RCPs compared to SSPs. Furthermore, RCP6.0 features lower warming than SSP4-6.0, as it has very similar temperature projections compared to the nominally lower RCP4.5 scenario in the first half of the century.
SSP3-7.0	A medium to high reference scenario resulting from no additional climate policy under the SSP3 socioeconomic development narrative. SSP3-7.0 has particularly high non-CO_2 emissions, including high aerosols emissions.	In between RCP6.0 and RCP8.5, although SSP3-7.0 non-CO_2 emissions and aerosols are higher than in any of the RCPs.
SSP3-7.0-lowNTCF	A variation of the medium to high reference scenario SSP3-7.0 but with	SSP3-7.0-lowNTCF is between RCP6.0 and RCP8.5, as RCP scenarios generally

ACCEPTED VERSION SUBJECT TO FINAL EDITS

	mitigation of CH_4 and/or short-lived species such as black carbon and other short-lived climate forcers (SLCF). Note that variants of SSP3-7.0-lowNTCF differ in terms of whether methane emissions are reduced[9] (Chapter 4, Section 4.4 and Chapter 6, Section 6.6).	incorporated a narrow and comparatively low level of SLCF emissions across the range of RCPs.
SSP5-3.4 OS (Overshoot)	A mitigation-focused variant of SSP5-8.5 that initially follows unconstrained emission growth in a fossil-intensive setting until 2040 and then implements the largest net negative CO_2 emissions of all SSP scenarios in the second half of 21st century to reach SSP1-2.6 forcing levels in the 22nd century. Used to consider reversibility and strong overshoot scenarios in, e.g., Chapters 4 and 5.	Not available. Initially, until 2040, similar to RCP8.5.
SSP5-8.5	A high reference scenario with no additional climate policy. Emission levels as high as SSP5-8.5 are not obtained by Integrated Assessment Models (IAMs) under any of the SSPs other than the fossil fueled SSP5 socioeconomic development pathway.	RCP8.5, although CO_2 emissions under SSP5-8.5 are higher towards the end of the century (Cross-Chapter Box 1.4, Figure 2). Methane emissions under SSP5-8.5 are lower than under RCP 8.5. When used with the same model settings, SSP5-8.5 may result in slightly higher temperatures than RCP8.5 (Chapter 4, Section 4.6.2).

[END Cross-Chapter Box 1.4, TABLE 1 HERE]

In contrast to stylized assumptions about the future evolution of emissions (e.g., a linear phase-out from year A to year B), these SSP scenarios are the result of a detailed scenario generation process (see Sections 1.6.1.1 and 1.6.1.2). While IAMs produce internally-consistent future emission time series for CO_2, CH_4, N_2O, and aerosols for the SSP scenarios (Riahi et al., 2017; Rogelj et al., 2018a), these emission scenarios are subject to several processing steps for harmonisation (Gidden et al., 2018) and in-filling (Lamboll et al., 2020), before also being complemented by several datasets so that ESMs can run these SSPs (Durack et al., 2018; Tebaldi et al., 2021). Although five scenarios are the primary focus of WGI, a total of nine SSP scenarios have been prepared with all the necessary detail to drive the ESMs as part of the CMIP6 (Cross-Chapter Box 1.4, Figure 1 and Table 2).

[START Cross-Chapter Box 1.4, TABLE 2 HERE]

Cross-Chapter Box 1.4, Table 2: Overview of key climate forcer datasets used as input by ESMs for historical and future SSP scenario experiments. The data is available from the Earth System Grid Federation (ESGF, 2021) described in Eyring et al. (2016).

[9] The AerChemMIP variant of SSP3-7.0-lowNTCF (Collins et al., 2017) only reduced aerosol and ozone precursors compared to SSP3-7.0, not methane. The SSP3-7.0-lowNTCF variant by the Integrated Assessment Models also reduced methane emissions (Gidden et al., 2019), which creates differences between SSP3-7.0-lowNTCF and SSP3-7.0 also in terms of methane concentrations and some fluorinated gas concentrations that have OH related sinks (Meinshausen et al., 2020).

ACCEPTED VERSION SUBJECT TO FINAL EDITS

Climate Forcer	Description
CO_2 emissions (emission-driven runs only)	Harmonized historical and future gridded emissions of anthropogenic CO_2 emissions (Hoesly et al., 2018; Gidden et al., 2019) are used instead of the prescribed CO_2 concentrations. See Chapter 4 (Section 4.3.1).
Historical and future greenhouse gas concentrations	Greenhouse gas surface air mole fractions of 43 species, including CO_2, CH_4, N_2O, HFCs, PFCs, halons, HCFCs, CFCs, SF_6, NF_3, including latitudinal gradients and seasonality from year 1 to 2500 (Meinshausen et al., 2017, 2020)
Land use change and management patterns	Globally gridded land use and land cover change datasets (Hurtt et al., 2020; Ma et al., 2020b)
Biomass burning emissions	Historical fire-related gridded emissions, including SO_2, NO_x, CO, BC, OC, NH_3, NMVOCs, relevant to concentration-driven historical and future SSP scenario runs (van Marle et al., 2017).
Stratospheric and tropospheric ozone	Historical and future ozone dataset, also with total column ozone (CCMI, 2021).
Reactive gas emissions	Gridded global anthropogenic emissions of reactive gases and aerosol precursors, including CO, SO_x, CH_4, NO_x, NMVOCs, or NH_3 (Hoesly et al., 2018; Feng et al., 2020)
Solar forcing	Radiative and particle input of solar variability from 1850 through to 2300 (Matthes et al., 2017). Future variations in solar forcing also reflect long-term multi-decadal trends.
Volcanic forcing	Historical stratospheric aerosol climatology (Thomason et al., 2018), with the mean stratospheric volcanic aerosol prescribed in future projections.

[END Cross-Chapter Box 1.4, TABLE 2 HERE]

ESMs are driven by either emission or concentration scenarios. Inferring concentration changes from emission time series requires using carbon cycle and other gas cycle models. To aid comparability across ESMs, and in order to allow participation of ESMs that do not have coupled carbon and other gas cycles models in CMIP6, most of the CMIP6 ESM experiments are so-called 'concentration-driven' runs, with concentrations of CO_2, CH_4, N_2O and other well-mixed GHGs prescribed in conjunction with aerosol emissions, ozone changes and effects from human-induced land cover changes that may be radiatively active via albedo changes (Cross-Chapter Box 1.4, Figure 2). In these concentration-driven climate projections, the uncertainty in projected future climate change resulting from our limited understanding of how the carbon cycle and other gas cycles will evolve in the future is not captured. For example, when deriving the default concentrations for these scenarios, permafrost and other carbon cycle feedbacks are considered using default settings, with a single time series prescribed for all ESMs (Meinshausen et al., 2020). Thus, associated uncertainties (Joos et al., 2013; Schuur et al., 2015) are not considered.

The so-called 'emission-driven' experiments (Jones et al., 2016b) use the same input datasets as concentration-driven ESM experiments, except that they use CO_2 emissions rather than concentrations (Chapter 4, Section 4.3.1; Chapter 5). In these experiments, atmospheric CO_2 concentrations are calculated internally using the ESM interactive carbon cycle module and thus differ from the prescribed default CO_2 concentrations used in the concentration-driven runs. In the particular case of SSP5-8.5, the emission-driven runs are assessed to add no significant additional uncertainty to future global surface air temperature (GSAT) projections (Chapter 4, Section 4.3.1). However, generally, when assessing uncertainties in future climate

ACCEPTED VERSION SUBJECT TO FINAL EDITS

projections, it is important to consider which elements of the cause-effect chain from emissions to the resulting climate change are interactively included as part of the model projections, and which are externally prescribed using default settings.

[START Cross-Chapter Box 1.4, FIGURE 2 HERE]

Cross-Chapter Box 1.4, Figure 2: Comparison between the Shared Socio-economic Pathways (SSP) scenarios and the Representative Concentration Pathway (RCP) scenarios in terms of their CO_2, CH_4 and N_2O atmospheric concentrations (panels a-c), and their global emissions (panels d-o). Also shown are gridded emission differences for sulfur (panel p) and black carbon (panel q) for the year 2000 between the input emission datasets that underpinned the CMIP5 and CMIP6 model intercomparisons. Historical emission estimates are provided in black in panels d to o. The range of concentrations and emissions investigated under the RCP pathways is grey shaded. Panels p and q adapted from Figure 7 in Hoesly et al. (2018). Further details on data sources and processing are available in the chapter data table (Table 1.SM.1).

[END Cross-Chapter Box 1.4, FIGURE 2 HERE]

[END CROSS CHAPTER BOX 1.4 HERE]

1.6.1.2 Scenario generation process for CMIP6

The scenario generation process involves research communities linked to all three IPCC Working Groups (Figure 1.27). It generally starts in the scientific communities associated with WGII and WGIII with the definition of new socio-economic scenario storylines (IPCC, 2000; O'Neill et al., 2014) that are quantified in terms of their drivers, i.e., GDP, population, technology, energy and land use and their resulting emissions (Riahi et al., 2017). Then, numerous complementation and harmonisation steps are necessary for datasets within the WGI and WGIII science communities, including gridding emissions of anthropogenic short-lived forcers, providing open biomass burning emission estimates, preparing land use patterns, aerosol fields, stratospheric and tropospheric ozone, nitrogen deposition datasets, solar irradiance and aerosol optical property estimates, and observed and projected greenhouse gas concentration time series (documented for CMIP6 through input4mips; Durack et al., 2018; Cross-Chapter Box 1.4, Table 2).

Once these datasets are completed, ESMs are run in coordinated model intercomparison projects in the WGI science community, using standardized simulation protocols and scenario data. The most recent example of such a coordinated effort is the CMIP6 exercise (Eyring et al., 2016; see also Section 1.5.4) with, in particular, ScenarioMIP (O'Neill et al., 2016). The WGI science community feeds back climate information to WGIII via climate emulators (Cross-Chapter Box 7.1 in Chapter 7) that are updated and calibrated with the ESMs' temperature responses and other lines of evidence. Next, this climate information is used to compute several high-level global climate indicators (e.g., atmospheric concentrations, global temperatures) for a much wider set of hundreds of scenarios that are assessed as part of IPCC WGIII assessment (WGIII Annex C). The outcomes from climate models run under the different scenarios are then used to calculate the evolution of climatic impact-drivers (Chapter 12), and utilized by impact researchers together with exposure and vulnerability information, in order to characterize risk from future climate change to human and natural systems. The climate impacts associated with these scenarios or different warming levels are then assessed as part of WGII reports (Figure 1.27).

[START FIGURE 1.27 HERE]

Figure 1.27: A simplified illustration of the scenario generation process that involves the scientific communities represented in the three IPCC Working Groups. The circular set of arrows at the top indicate the main set of models and workflows used in that scenario generation process, with the lower level indicating the datasets.

ACCEPTED VERSION SUBJECT TO FINAL EDITS

[END FIGURE 1.27 HERE]

1.6.1.3 History of scenarios within the IPCC

Scenario modelling experiments have been a core element of physical climate science since the first transient simulations with a General Circulation Model in 1988 (Hansen et al., 1988; see Section 1.3). Scenarios and modelling experiments assessed in IPCC reports have evolved over time, which provides a 'history of how the future was seen'. The starting time for the scenarios moves as actual emissions supersede earlier emission assumptions, while new scientific insights into the range of plausible population trends, behavioural changes and technology options and other key socioeconomic drivers of emissions also emerge (see WGIII; Legget, 1992; IPCC, 2000; Moss et al., 2010; Riahi et al., 2017). Many different sets of climate projections have been produced over the past several decades, using different sets of scenarios. Here, we compare those earlier scenarios against the most recent ones.

Climate science research involving scenarios necessarily follows a series of consecutive steps (see Figure 1.27). As each step waits for input from the preceding one, delays often occur that result in the impact literature basing its analyses on earlier scenarios than those most current in the climate change mitigation and climate system literature. It is hence important to provide an approximate comparison across the various scenario generations (Figure 1.28; Cross-Chapter Box 1.4, Table 1; Chapter 4).

[START FIGURE 1.28 HERE]

Figure 1.28: Comparison of the range of fossil and industrial CO_2 emissions from scenarios used in previous assessments up to AR6. Previous assessments are the IS92 scenarios from 1992 (top panel), the Special Report on Emissions Scenarios (SRES) scenarios from the year 2000 (second panel), the Representative Concentration Pathway (RCP) scenarios designed around 2010 (third panel) and the Shared Socio-economic Pathways (SSP) scenarios (second bottom panel). In addition, historical emissions are shown (black line) (Chapter 5, Figure 5.5); a more complete set of scenarios is assessed in SR1.5 (bottom panel) (Huppmann et al., 2018). Further details on data sources and processing are available in the chapter data table (Table 1.SM.1).

[END FIGURE 1.28 HERE]

The first widely used set of IPCC emission scenarios was the IS92 scenarios in 1992 (Leggett et al., 1992). Apart from reference scenarios, IS92 also included a set of stabilisation scenarios, the so-called 'S' scenarios. Those 'S' pathways were designed to lead to CO_2 stabilisation levels such as 350 ppm or 450 ppm. By 1996, those latter stabilisation levels were complemented in the scientific literature by alternative trajectories that assumed a delayed onset of climate change mitigation action (Figure 1.28; Wigley et al., 1996).

By 2000, the IPCC Special Report on Emission Scenarios (SRES) produced the SRES scenarios (IPCC, 2000), albeit without assuming any climate-policy-induced mitigation. The four broad groups of SRES scenarios (scenario 'families') A1, A2, B1 and B2 were the first scenarios to emphasize socio-economic scenario storylines, and also first to emphasize other greenhouse gases, land use change and aerosols. Represented by three scenarios for the high-growth A1 scenario family, those 6 SRES scenarios (A1FI, A1B, A1T, A2, B1, and B2) can still sometimes be found in today's climate impact literature. The void of missing climate change mitigation scenarios was filled by a range of community exercises, including the so-called post-SRES scenarios (Swart et al., 2002).

The RCP scenarios (van Vuuren et al., 2011) then broke new ground by providing low emission pathways that implied strong climate change mitigation including an example with negative CO_2 emissions on a large scale, namely RCP2.6. As shown in Figure 1.28, the upper end of the scenario range has not substantially

ACCEPTED VERSION SUBJECT TO FINAL EDITS

shifted. Building on the SRES multi-gas scenarios, the RCPs include time series of emissions and concentrations of the full suite of greenhouse gases and aerosols and chemically active gases, as well as land use and land cover (Moss et al., 2010). The word 'representative' signifies that each RCP is only one of many possible scenarios that would lead to the specific radiative forcing characteristics. The term pathway emphasizes that not only the long-term concentration levels are of interest, but also the trajectory taken over time to reach that outcome (Moss et al., 2010). RCPs usually refer to the concentration pathway extending to 2100, for which IAMs produced corresponding emission scenarios. Four RCPs produced from IAMs were selected from the published literature and are used in AR5 as well as in this report, spanning approximately the range from below 2°C warming to high (>4°C) warming best-estimates by the end of the 21st century: RCP2.6, RCP4.5 and RCP6.0 and RCP8.5 (Cross-Chapter Box 1.4, Table 1). Extended Concentration Pathways (ECPs) describe extensions of the RCPs from 2100 to 2300 that were calculated using simple rules generated by stakeholder consultations; these do not represent fully consistent scenarios (Meinshausen et al., 2011b).

By design, the RCP emission and concentration pathways were originally developed using particular socio-economic development pathways, but those are no longer considered (Moss et al., 2010). The different levels of emissions and climate change represented in the RCPs can hence be explored against the backdrop of different socio-economic development pathways (SSP1 to SSP5) (Section 1.6.1.1; Cross-Chapter Box 1.4). This integrative SSP-RCP framework ('SSPX-RCPY' in Table 1.4) is now widely used in the climate impact and policy analysis literature (e.g., ICONICS, 2021; Green et al., 2020; O'Neill et al., 2020), where climate projections obtained under the RCP scenarios are analysed against the backdrop of various SSPs. Considering various levels of future emissions and climate change for each socio-economic development pathway was an evolution from the previous SRES framework (IPCC, 2000), in which socio-economic and emission futures were closely aligned.

The new set of scenarios (SSP1-1.9 to SSP5-8.5) now features a higher top level of CO_2 emissions (SSP5-8.5 compared to RCP8.5), although the most significant change is again the addition of a very low climate change mitigation scenario (SSP1-1.9, compared to the previous low scenario, RCP2.6). Also, historically, none of the previous scenario sets featured a scenario that involves a very pronounced peak-and-decline emissions trajectory, but SSP1-1.9 does so now. The full set of nine SSP scenarios now includes a high aerosol emission scenario (SSP3-7.0). The RCPs featured more uniformly low aerosol trajectories across all scenarios (Cross-Chapter Box 1.4, Figure 2). More generally, the SSP scenarios feature a later peak of global emission for the lower scenarios, simply as a consequence of historical emissions not having followed the trajectory projected by previous low scenarios (Figure 1.28).

Over the last decades, discussions around scenarios have often focussed on whether recent trends make certain future scenarios more or less probable or whether all scenarios are too high or too low. When the SRES scenarios first appeared, the debate was often whether the scenarios were overestimating actual world emissions developments (e.g., Castles and Henderson, 2003). With the strong emissions increase throughout the 2000s, that debate then shifted towards the question of whether the lower future climate change mitigation scenarios were rendered unfeasible (Pielke et al., 2008; van Vuuren and Riahi, 2008). Historical emissions over 2000 to 2010 approximately track the upper half of SRES and RCP projections (Figure 1.28). More generally, the global fossil and industrial CO_2 emissions of recent decades tracked approximately the middle of the projected scenario ranges (see Fig 1.28), although with regional differences (Pedersen et al., 2020).

1.6.1.4 The likelihood of reference scenarios, scenario uncertainty and storylines

In general, no likelihood is attached to the scenarios assessed in this Report. The use of different scenarios for climate change projections allows to explore 'scenario uncertainty' (Collins et al., 2013; SR1.5; see also Section 1.4.4). Scenario uncertainty is fundamentally different from geophysical uncertainties, which result from limitations in the understanding and predictability of the climate system (Smith and Stern, 2011). In scenarios, by contrast, future emissions depend to a large extent on the collective outcome of choices and processes related to population dynamics and economic activity, or on choices that affect a given activity's

ACCEPTED VERSION SUBJECT TO FINAL EDITS

energy and emissions intensity (Jones, 2000; Knutti et al., 2008; Kriegler et al., 2012; van Vuuren et al., 2014). Even if identical socio-economic futures are assumed, the associated future emissions still face uncertainties, since different experts and model frameworks diverge in their estimates of future emission ranges (Ho et al., 2019).

When exploring various climate futures, scenarios with no, or no additional, climate policies are often referred to as 'baseline' or 'reference scenarios' (Section 1.6.1.1; Annex VII: Glossary). Among the five core scenarios used most in this report, SSP3-7.0 and SSP5-8.5 are explicit 'no-climate-policy' scenarios (Gidden et al., 2019; Cross-Chapter Box 1.4, Table 1), assuming a carbon price of zero. These future 'baseline' scenarios are hence counterfactuals that include less climate policies compared to 'business-as-usual' scenarios – given that 'business-as-usual' scenarios could be understood to imply a continuation of existing climate policies. Generally, future scenarios are meant to cover a broad range of plausible futures, due for example to unforeseen discontinuities in development pathways (Raskin and Swart, 2020), or to large uncertainties in underlying long-term projections of economic drivers (Christensen et al., 2018). However, the likelihood of high emission scenarios such as RCP8.5 or SSP5-8.5 is considered low in light of recent developments in the energy sector (Hausfather and Peters, 2020a, 2020b). Studies that consider possible future emission trends in the absence of additional climate policies, such as the recent IEA 2020 World Energy Outlook 'stated policy' scenario (International Energy Agency, 2020), project approximately constant fossil and industrial CO_2 emissions out to 2070, approximately in line with the medium RCP4.5, RCP6.0 and SSP2-4.5 scenarios (Hausfather and Peters, 2020b) and the 2030 global emission levels that are pledged as part of the Nationally Determined Contributions (NDCs) under the Paris Agreement (Section 1.2.2; (Fawcett et al., 2015; Rogelj et al., 2016; UNFCCC, 2016; IPCC, 2018). On the other hand, the default concentrations aligned with RCP8.5 or SSP5-8.5 and resulting climate futures derived by ESMs could be reached by lower emission trajectories than RCP8.5 or SSP5-8.5. That is because the uncertainty range on carbon-cycle feedbacks includes stronger feedbacks than assumed in the default derivation of RCP8.5 and SSP5-8.5 concentrations (Ciais et al., 2013; Friedlingstein et al., 2014; Booth et al., 2017; see also Chapter 5, Section 5.4).

To address long-term scenario uncertainties, scenario storylines (or 'narratives') are often used (Rounsevell and Metzger, 2010; O'Neill et al., 2014) (see Section 1.4.4 for a more general discussion on 'storylines' also covering 'physical climate storylines'). Scenario storylines are descriptions of a future world, and the related large-scale socio-economic development path towards that world that are deemed plausible within the current state of knowledge and historical experience (WGIII; Section 1.2.3). Scenario storylines attempt to 'stimulate, provoke, and communicate visions of what the future could hold for us' (Rounsevell and Metzger, 2010) in settings where either limited knowledge or inherent unpredictability in social systems prevent a forecast or numerical prediction. Scenario storylines have been used in previous climate research, and they are the explicit or implicit starting point of any scenario exercise, including for the SRES scenarios (IPCC, 2000) and the SSPs (e.g., O'Neill et al., 2017a).

Recent technological or socio-economic trends might be informative for bounding near-term future trends, for example, if technological progress renders a mitigation technology cheaper than previously assumed. However, short-term emission trends alone do not generally rule out an opposite trend in the future (van Vuuren et al., 2010). The ranking of individual RCP emission scenarios from the IAMs with regard to emission levels is different for different time horizons, e.g., 2020 versus longer-term emission levels; For example, the strongest climate change mitigation scenario RCP2.6 was in fact the second highest CO_2 emission scenario (jointly with RCP4.5) before 2020 in the set of RCPs and the strong global emission decline in RCP2.6 only followed after 2020. Implicitly, this scenario feature was cautioning against the assumption that short-term trends predicate particular long-term trajectories. This is also the case in relation to the COVID-19 related drop in 2020 emissions. Potential changes in underlying drivers of emissions, such as those potentially incentivised by COVID-19 recovery stimulus packages, are more significant for longer-term emissions than the short-term deviation from recent emission trends (Cross-Chapter Box 6.1 on COVID-19 in Chapter 6).

ACCEPTED VERSION SUBJECT TO FINAL EDITS

1.6.2 Global warming levels

The global mean surface temperature change, or 'global warming level' (GWL), is a 'dimension of integration' that is highly relevant across scientific disciplines and socioeconomic actors. First, global warming levels relative to pre-industrial conditions are the quantity in which the 1.5°C and 'well below 2°C' Paris Agreement goals were formulated. Second, global mean temperature change has been found to be nearly-linearly related to a number of regional climate effects (Mitchell et al., 2000; Mitchell, 2003; Tebaldi and Arblaster, 2014; Seneviratne et al., 2016; Li et al., 2020; Seneviratne and Hauser, 2020). Even where non-linearities are found, some regional climate effects can be considered to be almost scenario-independent for a given level of warming (Cross-Chapter Box 11.1 in Chapter 11; Chapter 4, Sections 4.2.4 and 4.6.1; Chapter 8, Section 8.5.3; Chapter 10, Section 10.4.3.1). Finally, the evolution of aggregated impacts with warming levels has been widely used and embedded in the assessment of the 'Reasons for Concern' (RFC) in IPCC WGII (Smith et al., 2009; IPCC, 2014a). The RFC framework was further expanded in SR1.5 (2018), SROCC (2019) and SRCCL (2019) by explicitly describing the differential impacts of half-degree warming steps (cf. King et al., 2017) (Section 1.4.4; Cross-Chapter Box 12.1 in Chapter 12).

In this Report, the term 'global warming level' refers to the categorisation of global and regional climate change, associated impacts, emission and concentration scenarios by global mean surface temperature relative to 1850-1900, which is the period used as a proxy for pre-industrial levels (see Cross-Chapter Box 11.1 in Chapter 11). By default, GWLs are expressed as global surface air temperature (GSAT; see Section 1.4.1; Cross-Chapter Box 2.3 in Chapter 2).

As the SR1.5 concluded, even half-degree global mean temperature steps carry robust differences in climate impacts (see SR1.5,IPCC, 2018; Schleussner et al., 2016a; Wartenburger et al., 2017; see also Chapter 11). This Report adopts half-degree warming levels which allows integration within and across the three WGs for climate projections, impacts, adaptation challenges and mitigation challenges. The core set of - GWLs 1.5, 2.0, 3.0 and 4.0°C - are highlighted (Chapters 4, 8, 11, 12 and the Atlas). Given that much impact analysis is based on previous scenarios, i.e., RCPs or SRES, and climate change mitigation analysis is based on new emission scenarios in addition to the main SSP scenarios, these global warming levels assist in the comparison of climate states across scenarios and in the synthesis across the broader literature.

The transient and equilibrium states of certain global warming levels can differ in their climate impacts (IPCC, 2018; King et al., 2020). Climate impacts in a 'transient' world relate to a scenario in which the world is continuing to warm. On the other hand, climate impacts at the same warming levels can also be estimated from equilibrium states after a (relatively) short-term stabilisation by the end of the 21st century or at a (near-) equilibrium state after a long-term (multi-decadal to multi-millennial) stabilisation. Different methods to estimate these climate states come with challenges and limitations (Chapter 4, Section 4.6.1; Cross-Chapter Box 11.1 in Chapter 11). First, information can be drawn from GCM or ESM simulations that 'pass through' the respective warming levels (as used and demonstrated in the Interactive Atlas to this report), also called 'epoch' or 'time-shift' approaches (Chapter 4, Sections 4.2.4 and 4.6.1) (Herger et al., 2015; James et al., 2017; Tebaldi and Knutti, 2018). Information from transient simulations can also be used through an empirical scaling relationship (Seneviratne et al., 2016, 2018; Wartenburger et al., 2017) or using 'time sampling' approaches, as described in James et al. (2017). Second, information can be drawn from large ESM ensembles with prescribed SST at particular global warming levels (Mitchell et al., 2017), although an underrepresentation of variability can arise when using prescribed SST temperatures (Fischer et al., 2018a).

In order to fully derive climate impacts, warming levels will need to be complemented by additional information, such as their associated CO_2 concentrations (e.g., fertilization or ocean acidification), composition of the total radiative forcing (aerosols vs greenhouse gases, with varying regional distributions) or socioeconomic conditions (e.g., to estimate societal impacts). More fundamentally, while a global warming level is a good proxy for the state of the climate (Cross-Chapter Box 11.1 in Chapter 11), it does not uniquely define a change in global or regional climate state. For example, regional precipitation responses depend on the details of the individual forcing mechanisms that caused the change (Samset et al., 2016), on whether the temperature level is stabilized or transient (King et al., 2020; Zappa et al., 2020), on

ACCEPTED VERSION SUBJECT TO FINAL EDITS

the vertical structure of the troposphere (Andrews et al., 2010), and, in particular, on the global distribution of atmospheric aerosols (Frieler et al., 2012). Another aspect is how Earth system components with century to millennial response timescales, such as long-term sea level rise or permafrost thaw, are affected by global mean warming. For example, sea level rise 50 years after a 1°C warming will be lower than sea level rise 150 years after that same 1°C warming (Chapter 9).

Also, forcing or response patterns that vary in time can create differences in regional climates for the same global mean warming level, or can create non-linearities when scaling patterns from one warming level to another (King et al., 2018), depending on whether near-term transient climate, end of the century, equilibrium climate or climate states after an initial overshoot are considered.

In spite of these challenges, and thanks to recent methodological advances in quantifying or overcoming them, global warming levels provide a robust and useful integration mechanism. They allow knowledge from various domains within WGI and across the three WGs to be integrated and communicated (Cross Chapter Box 11.1). In this report, Chapters 4, 8, 11, 12 and the Atlas provide information specific to certain warming levels, highlighting the regional differences, but also the approximate scalability of regional climate change, that can arise from even a 0.5°C shift in global-mean temperatures. Furthermore, building on WGI insights into physical climate system responses (Cross-Chapter Box 7.1 in Chapter 7), WGIII will use peak and end-of-century global warming levels to classify a broad set of scenarios.

1.6.3 Cumulative CO_2 emissions

The WGI AR5 (IPCC, 2013a) and the SR1.5 (IPCC, 2018) highlighted the near-linear relationship between cumulative carbon emissions and global mean warming (Section 1.3; Section 5.5). This implies that continued CO_2 emissions will cause further warming and changes in all components of the climate system, independent of any specific scenario or pathway. This is captured in the TCRE concept, which relates CO_2-induced global mean warming to cumulative carbon emissions (Chapter 5). This Report thus uses cumulative CO_2 emissions to compare the climate response across scenarios, and to categorise emission scenarios (Figure 1.29). The advantage of using cumulative CO_2 emissions is that it is an inherent emission scenario characteristic rather than an outcome of the scenario-based projections, where uncertainties in the cause-effect chain from emissions to atmospheric concentrations to temperature change are important.

There is also a close relationship between cumulative total greenhouse gas emissions and cumulative CO_2 emissions for scenarios in the SR1.5 scenario database (IPCC, 2018; Figure 1.29). The dominance of CO_2 compared to other well-mixed greenhouse gases (Figure 1.29; Chapter 5, Section 5.2.4) allows policymakers to make use of the carbon budget concept (Chapter 5, Section 5.5) in a policy context, in which GWP-weighted combinations of multiple greenhouse gases are used to define emission targets. A caveat is that cumulative GWP-weighted CO_2 equivalent emissions over the next decades do not yield exactly the same temperature outcomes as the same amount of cumulative CO_2 emissions, because atmospheric perturbation lifetimes of the various greenhouse gases differ. While carbon budgets are not derived using GWP-weighted emission baskets but rather by explicit modelling of non-CO_2 induced warming (Chapter 5, Section 5.5; Cross-Chapter Box 7.1 in Chapter 7), the policy frameworks based on GWP-weighted emission baskets can still make use of the insights from remaining cumulative carbon emissions for different warming levels.

The same cumulative CO_2 emissions could lead to a slightly different level of warming over time (Box 1.4). Rapid emissions followed by steep cuts and potentially net-negative emissions would be characterised by a higher maximum warming and faster warming rate, compared with the same cumulative CO_2 emissions spread over a longer period. As further explored in the WGIII assessment, one potential limitation when presenting emission pathway characteristics in cumulative emission budget categories is that path dependencies and lock-in effects (e.g. today's decisions regarding fossil fuel related infrastructure) play an important role in long-term mitigation strategies (Davis et al., 2010; Luderer et al., 2018). Similarly, high emissions early on might imply strongly net negative emissions (Minx et al., 2018) later on to reach the same cumulative emission and temperature target envelope by the end of the century (Box 1.4). This report explores options to address some of those potential issues from a WGI perspective (see Chapter 5, Sections

ACCEPTED VERSION SUBJECT TO FINAL EDITS

5.5.2 and 5.6.2).

[START FIGURE 1.29 HERE]

Figure 1.29: The role of CO_2 in driving future climate change in comparison to other greenhouse gases (GHGs). The GHGs included here are CH_4, N_2O, and 40 other long-lived, well-mixed GHGs. The blue shaded area indicates the approximate forcing exerted by CO_2 in Shared Socio-economic Pathways (SSP) scenarios, ranging from very low SSP1-1.9 to very high SSP5-8.5 (Chapter 7). The CO_2 concentrations under the SSP1-1.9 scenarios reach approximately 350 ppm after 2150, while those of SSP5-8.5 exceed 2000 ppm CO_2 in the longer term (through year 2300). Similarly to the dominant radiative forcing share at each point in time (lower area plots), cumulative GWP-100-weighted GHG emissions happen to be closely correlated with cumulative CO_2 emissions, allowing policymakers to make use of the carbon budget concept in a policy context with multi-gas GHG baskets as it exhibits relatively low variation across scenarios with similar cumulative emissions until 2050 (inset panel). Further details on data sources and processing are available in the chapter data table (Table 1.SM.1).

[END FIGURE 1.29 HERE]

[START BOX 1.4 HERE]

Box 1.4: The relationships between 'net zero' emissions, temperature outcomes and carbon dioxide removal

Article 4 of the Paris Agreement sets an objective to 'achieve a balance between anthropogenic emissions by sources and removals by sinks of greenhouse gases' (Section 1.2). This box addresses the relationship between such a balance and the corresponding evolution of global surface temperature, with or without the deployment of large-scale Carbon Dioxide Removal (CDR), using the definitions of 'net zero CO_2 emissions' and 'net zero greenhouse gas (GHG) emissions' of the AR6 Glossary (Annex VII: Glossary).

'Net zero CO_2 emissions' is defined in AR6 as the condition in which anthropogenic CO_2 emissions are balanced by anthropogenic CO_2 removals over a specified period. Similarly, 'net zero GHG emissions' is the condition in which metric-weighted anthropogenic GHG emissions are balanced by metric-weighted anthropogenic GHG removals over a specified period. The quantification of net zero GHG emissions thus depends on the GHG emission metric chosen to compare emissions of different gases, as well as the time horizon chosen for that metric. (For a broader discussion of metrics, see Box 1.3 and Chapter 7, Section 7.6, and WGIII Cross-Chapter Box 2.)

Technical notes expanding on these definitions can be found as part of their respective entries in the Annex VII: Glossary. The notes clarify the relation between 'net zero' CO_2 and GHG emissions and the concept of carbon and GHG neutrality, and the metric usage set out in the Paris Rulebook (Decision 18/CMA.1, annex, paragraph 37).

A global net zero level of CO_2, or GHG, emissions will be achieved when the sum of anthropogenic emissions and removals across all countries, sectors, sources and sinks reaches zero. Achieving net zero CO_2 or GHG emissions globally, at a given time, does not imply that individual entities (i.e., countries, sectors) have to reach net zero emissions at that same point in time, or even at all (see WGIII, TS Box 4 and Chapter 3).

Net zero CO_2 and net zero GHG emissions differ in their implications for the subsequent evolution of global surface temperature. Net zero CO_2 emissions result in approximately stable CO_2-induced warming, but overall warming will depend on any further warming contribution of non-CO_2 GHGs. The effect of net zero GHG emissions on global surface temperature depends on the GHG emission metric chosen to aggregate emissions and removals of different gases. For GWP100 (the metric in which Parties to the Paris Agreement have decided to report their aggregated emissions and removals), net zero GHG emissions would generally imply a peak in global surface temperature, followed by a gradual decline (Chapter 7, Section 7.6.2; see also

ACCEPTED VERSION SUBJECT TO FINAL EDITS

Chapter 4, Section 4.7.1 regarding the Zero Emission Commitment). However, other anthropogenic factors, such as aerosol emissions or land use-induced changes in albedo, may still affect the climate.

The definitions of net zero CO_2 and GHG should also be seen in relation to the various CDR methods discussed in the context of climate change mitigation (see Chapter 5, Section 5.6, which also includes an assessment of the response of natural sinks to CDR), and how it is employed in scenarios used throughout the WG I and III reports, as described in Section 1.6.1. (See also WGIII, Chapters 3, 7 and 12.)

For virtually all scenarios assessed by the IPCC, CDR is necessary to reach both global net zero CO_2 and net zero GHG emissions, to compensate for residual anthropogenic emissions. This is in part because for some sources of CO_2 and non-CO_2 emissions, abatement options to eliminate them have not yet been identified. For a given scenario, the choice of GHG metric determines how much net CDR is necessary to compensate for residual non-CO_2 emissions, in order to reach net zero GHG emissions (Chapter 7, Section 7.6.2).

If CDR is further used to go beyond net zero, to a situation with net-negative CO_2 emissions (i.e., where anthropogenic removals exceed anthropogenic emissions), anthropogenic CO_2-induced warming will decline. A further increase of CDR, until a situation with net zero or even net-negative GHG emissions is reached, would increase the pace at which historical human-induced warming is reversed after its peak (SR1.5, IPCC, 2018). Net-negative anthropogenic GHG emissions may become necessary to stabilize the global surface temperature in the long term, should climate feedbacks further affect natural GHG sinks and sources (see Chapter 5).

CDR can be achieved through a number of measures (Chapter 5, Section 5.6, and SRCCL). These include additional afforestation, reforestation, soil carbon management, biochar, direct air capture and carbon capture and storage (DACCS), and bioenergy with carbon capture and storage (BECCS) (de Coninck et al., 2018, SR1.5 Ch4; Minx et al., 2018; see also WGIII Chapters 7 and 12). Differences between Land Use, Land Use Change and Forestry (LULUCF) accounting rules, and scientific book-keeping approaches for CO_2 emissions and removals from the terrestrial biosphere, can result in significant differences between the amount of CDR that is reported in different studies (Grassi et al., 2017). Different measures to achieve CDR come with different risks, negative side effects and potential co-benefits – also in conjunction with sustainable development goals – that can inform choices around their implementation (Fuss et al., 2018; Roe et al., 2019, Chapter 5, Section 5.6). Technologies to achieve direct large-scale anthropogenic removals of non-CO_2 GHGs are speculative at present (Yoon et al., 2009; Ming et al., 2016; Kroeger et al., 2017; Jackson et al., 2019).

[END BOX 1.4 HERE]

1.7 Final remarks

The assessment in this Report is based on a rapidly growing body of new evidence from the peer-reviewed literature. Recently, scientific climate change research has doubled in output every 5–6 years; the majority of publications deal with issues related to the physical climate system (Burkett et al., 2014; Haunschild et al., 2016). The sheer volume of published, peer-reviewed literature on climate change presents a challenge to comprehensive, robust and transparent assessment.

The enhanced focus on regional climate in WGI AR6 further expands the volume of literature relative to AR5, including non-English language publications sometimes presented as reports (‘grey’ literature), particularly on topics such as regional observing networks and climate services. These factors enhance the challenge of discovering, accessing and assessing the relevant literature. The international, multi-lingual author teams of the IPCC AR6, combined with the open expert review process, help to minimise these concerns, but they remain a challenge.

Despite the key role of CMIP6 in this Report (Section 1.5), the number of studies evaluating its results and modelling systems remains relatively limited. At the time of publication, additional model results are still

ACCEPTED VERSION SUBJECT TO FINAL EDITS

becoming available. This reflects the need for close temporal alignment of the CMIP cycle with the IPCC assessment process, and the growing complexity of coordinated international modelling efforts.

Indigenous and local knowledge includes information about past and present climate states. However, assessing this knowledge, and integrating it with the scientific literature, remains a challenge to be met. This lack of assessment capability and integration leads to most WGI chapters still not including Indigenous and local knowledge in their assessment findings.

Spatial and temporal gaps in both historical and current observing networks, and the limited extent of paleoclimatic archives, have always posed a challenge for IPCC assessments. A relative paucity of long-term observations is particularly evident in Antarctica and in the depths of the ocean. Knowledge of previous cryospheric and oceanic processes is therefore incomplete. Sparse instrumental temperature observations prior to the industrial revolution makes it difficult to uniquely characterize a 'pre-industrial' baseline, although this report extends the assessment of anthropogenic temperature change further back in time than previous assessment cycles (Cross-Chapter Box 1.2, Chapter 7).

Common, integrating scenarios can never encompass all possible events that might induce radiative forcing in the future (Section 1.4). These may include large volcanic eruptions (see Cross-Chapter Box 4.1 in Chapter 4), the consequences of a major meteorite, smoke plumes following a conflict involving nuclear weapons, extensive geo-engineering, or a major pandemic (Cross-Chapter Box 1.6). Scenario-related research also often focuses on the 21st century. Post-2100 climate changes are not covered as comprehensively, and their assessment is limited. Those long-term climate changes, potentially induced by forcing over the 21st century (as in the case of sea level rise), are nevertheless relevant for decision making.

At the time of publication, the consequences of the COVID-19 pandemic on emissions, atmospheric abundances, radiative forcing and the climate (see Cross-Chapter Box 6.1 in Chapter 6), and on observations (Section 1.5.1), are not yet fully evident. Their assessment in this report is thus limited.

ACCEPTED VERSION
SUBJECT TO FINAL EDITS

Frequently Asked Questions

FAQ 1.1: Do we understand climate change better now compared to when the IPCC started?

Yes, much better. The first IPCC report, released in 1990, concluded that human-caused climate change would soon become evident, but could not yet confirm that it was already happening. Today, evidence is overwhelming that the climate has indeed changed since the pre-industrial era and that human activities are the principal cause of that change. With much more data and better models, we also understand more about how the atmosphere interacts with the ocean, ice, snow, ecosystems and land surfaces of the Earth. Computer climate simulations have also improved dramatically, incorporating many more natural processes and providing projections at much higher resolutions.

Since the first IPCC report in 1990, large numbers of new instruments have been deployed to collect data in the air, on land, at sea and from outer space. These instruments measure temperature, clouds, winds, ice, snow, ocean currents, sea level, soot and dust in the air, and many other aspects of the climate system. New satellite instruments have also provided a wealth of increasingly fine-grained data. Additional data from older observing systems and even hand-written historical records are still being incorporated into observational datasets, and these datasets are now better integrated and adjusted for historical changes in instruments and measurement techniques. Ice cores, sediments, fossils, and other new evidence from the distant past have taught us much about how Earth's climate has changed throughout its history.

Understanding of climate system processes has also improved. For example, in 1990 very little was known about how the deep ocean responds to climate change. Today, reconstructions of deep ocean temperatures extend as far back as 1871. We now know that the oceans absorb most of the excess energy trapped by greenhouse gases and that even the deep ocean is warming up. As another example, in 1990, relatively little was known about exactly how or when the gigantic ice sheets of Greenland and Antarctica would respond to warming. Today, much more data and better models of ice sheet behaviour reveal unexpectedly high melt rates that will lead to major changes within this century, including substantial sea level rise (see FAQ 9.2).

The major natural factors contributing to climate change on time scales of decades to centuries are volcanic eruptions and variations in the sun's energy output. Today, data show that changes in incoming solar energy since 1900 have contributed only slightly to global warming, and they exhibit a slight downward trend since the 1970s. Data also show that major volcanic eruptions have sometimes cooled the entire planet for relatively short periods of time (typically several years) by erupting aerosols (tiny airborne particles) high into the atmosphere.

The main human causes of climate change are the heat-absorbing greenhouse gases released by fossil fuel combustion, deforestation, and agriculture, which warm the planet, and aerosols such as sulphate from burning coal, which have a short-term cooling effect that partially counteracts human-caused warming. Since 1990, we have more and better observations of these human factors as well as improved historical records, resulting in more precise estimates of human influences on the climate system (see FAQ 3.1).

While most climate models in 1990 focused on the atmosphere, using highly simplified representations of oceans and land surfaces, today's Earth system simulations include detailed models of oceans, ice, snow, vegetation and many other variables. An important test of models is their ability to simulate Earth's climate over the period of instrumental records (since about 1850). Several rounds of such testing have taken place since 1990, and the testing itself has become much more rigorous and extensive. As a group and at large scales, models have predicted the observed changes well in these tests (see FAQ 3.3). Since there is no way to do a controlled laboratory experiment on the actual Earth, climate model simulations can also provide a kind of 'alternate Earth' to test what would have happened without human influences. Such experiments show that the observed warming would not have occurred without human influence. .

Finally, physical theory predicts that human influences on the climate system should produce specific patterns of change, and we see those patterns in both observations and climate simulations. For example, nights are warming faster than days, less heat is escaping to space, and the lower atmosphere (troposphere) is warming but the upper atmosphere (stratosphere) has cooled. These confirmed predictions are all evidence of

ACCEPTED VERSION SUBJECT TO FINAL EDITS

changes driven primarily by increases in greenhouse gas concentrations rather than natural causes.

[START FAQ 1.1, FIGURE 1 HERE]

FAQ 1.1, Figure 1: Sample elements of climate understanding, observations and models as assessed in the IPCC First Assessment Report (1990) and Sixth Assessment Report (2021). Many other advances since 1990, such as key aspects of theoretical understanding, geological records and attribution of change to human influence, are not included in this figure because they are not readily represented in this simple format. Fuller explications of the history of climate knowledge are available in the introductory chapters of the IPCC Fourth and Sixth Assessment Reports.

[END FAQ 1.1, FIGURE 1 HERE]

FAQ 1.2: Where is climate change most apparent?

The signs of climate change are unequivocal at the global scale and are increasingly apparent on smaller spatial scales. The high northern latitudes show the largest temperature increase with clear effects on sea ice and glaciers. The warming in the tropical regions is also apparent because the natural year-to-year variations in temperature there are small. Long-term changes in other variables such as rainfall and some weather and climate extremes have also now become apparent in many regions.

It was first noticed that the planet's land areas were warming in the 1930s. Although increasing atmospheric carbon dioxide concentrations were suggested as part of the explanation, it was not certain at the time whether the observed warming was part of a long-term trend or a natural fluctuation – global warming had not yet become apparent. But the planet continued to warm, and by the 1980s the changes in temperature had become obvious or, in other words, the signal had *emerged*.

Imagine you had been monitoring temperatures at the same location for the past 150 years. What would you have experienced? When would the warming have become noticeable in your data? The answers to these questions depend on where on the planet you are.

Observations and climate model simulations both demonstrate that the largest long-term warming trends are in the high northern latitudes and the smallest warming trends over land are in tropical regions. However, the year-to-year variations in temperature are smallest in the tropics, meaning that the changes there are also apparent, relative to the range of past experiences (see FAQ 1.2, Figure 1).

Changes in temperature also tend to be more apparent over land areas than over the open ocean and are often most apparent in regions which are more vulnerable to climate change. It is expected that future changes will continue to show the largest signals at high northern latitudes, but with the most apparent warming in the tropics. The tropics also stand to benefit the most from climate change mitigation in this context, as limiting global warming will also limit how far the climate shifts relative to past experience.

Changes in other climate variables have also become apparent at smaller spatial scales. For example, changes in average rainfall are becoming clear in some regions, but not in others, mainly because natural year-to-year variations in precipitation tend to be large relative to the magnitude of the long-term trends. However, extreme rainfall is becoming more intense in many regions, potentially increasing the impacts from inland flooding (see FAQ 8.2). Sea levels are also clearly rising on many coastlines, increasing the impacts of inundation from coastal storm surges, even without any increase in the number of storms reaching land. A decline in the amount of Arctic sea ice is apparent, both in the area covered and in its thickness, with implications for polar ecosystems.

When considering climate-related impacts, it is not necessarily the size of the change which is most important. Instead, it can be the rate of change or it can also be the size of the change relative to the natural variations of the climate to which ecosystems and society are adapted. As the climate is pushed further away

ACCEPTED VERSION SUBJECT TO FINAL EDITS

from past experiences and enters an unprecedented state, the impacts can become larger, along with the challenge of adapting to them.

How and when a long-term trend becomes distinguishable from shorter-term natural variations depends on the aspect of climate being considered (e.g., temperature, rainfall, sea ice or sea level), the region being considered, the rate of change, and the magnitude and timing of natural variations. When assessing the local impacts from climate change, both the size of the change and the amplitude of natural variations matter.

[START FAQ 1.2, FIGURE 1 HERE]

FAQ 1.2, Figure 1: **Observed variations in regional temperatures since 1850** (data from Berkeley Earth). Regions in high latitudes, such as mid-North America (40ºN–64ºN, 140ºW–60ºW, left), have warmed by a larger amount than regions at lower latitudes, such as Tropical South America (10ºS–10ºN, 84ºW–16ºW, right), but the natural variations are also much larger at high latitudes (darker and lighter shading represents 1 and 2 standard deviations, respectively, of natural year-to-year variations). The signal of observed temperature change emerged earlier in Tropical South America than mid-North America even though the changes were of a smaller magnitude. (Note that those regions were chosen because of the longer length of their observational record, see Figure 1.14 for more regions).

[END FAQ 1.2, FIGURE 1 HERE]

FAQ 1.3: What can past climate teach us about the future?

In the past, the Earth has experienced prolonged periods of elevated greenhouse gas concentrations that caused global temperatures and sea levels to rise. Studying these past warm periods informs us about the potential long-term consequences of increasing greenhouse gases in the atmosphere.

Rising greenhouse gas concentrations are driving profound changes to the Earth system, including global warming, sea level rise, increases in climate and weather extremes, ocean acidification, and ecological shifts (see FAQ 2.2, FAQ 7.1). The vast majority of instrumental observations of climate began during the 20th century, when greenhouse gas emissions from human activities became the dominant driver of changes in Earth's climate (see FAQ 3.1).

As scientists seek to refine our understanding of Earth's climate system and how it may evolve in coming decades to centuries, past climate states provide a wealth of insights. Data about these past states help to establish the relationship between natural climate drivers and the history of changes in global temperature, global sea levels, the carbon cycle, ocean circulation, and regional climate patterns, including climate extremes. Guided by such data, scientists use Earth system models to identify the chain of events underlying the transitions between past climatic states (see FAQ 3.3). This is important because during present-day climate change, just as in past climate changes, some aspects of the Earth system (e.g., surface temperature) respond to changes in greenhouse gases on a time scale of decades to centuries, while others (e.g., sea level and the carbon cycle) respond over centuries to millennia (see FAQ 5.3). In this way, past climate states serve as critical benchmarks for climate model simulations, improving our understanding of the sequences, rates, and magnitude of future climate change over the next decades to millennia.

Analyzing previous warm periods caused by natural factors can help us understand how key aspects of the climate system evolve in response to warming. For example, one previous warm-climate state occurred roughly 125,000 years ago, during the Last Interglacial period, when slight variations in the Earth's orbit triggered a sequence of changes that caused about 1°C–2°C of global warming and about 2–8 m of sea level rise relative to the 1850-1900, even though atmospheric carbon dioxide concentrations were similar to 1850-1900 values (FAQ 1.3, Figure 1). Modelling studies highlight that increased summer heating in the higher latitudes of the Northern Hemisphere during this time caused widespread melting of snow and ice, reducing the reflectivity of the planet and increasing the absorption of solar energy by the Earth's surface. This gave rise to global-scale warming, which led in turn to further ice loss and sea level rise. These self-reinforcing positive *feedback cycles* are a pervasive feature of Earth's climate system, with clear implications for future

ACCEPTED VERSION SUBJECT TO FINAL EDITS

climate change under continued greenhouse gas emissions. In the case of sea level rise, these cycles evolved over several centuries to millennia, reminding us that the rates and magnitude of sea level rise in the 21st century are just a fraction of the sea level rise that will ultimately occur after the Earth system fully adjusts to current levels of global warming.

Roughly 3 million years ago, during the Pliocene Epoch, the Earth witnessed a prolonged period of elevated temperatures (2.5°C–4°C higher than 1850-1900) and higher sea levels (5–25 m higher than 1850-1900), in combination with atmospheric carbon dioxide concentrations similar to present-day. The fact that Pliocene atmospheric carbon dioxide concentrations were similar to present, while global temperatures and sea levels were significantly higher, reflects the difference between an Earth system that has fully-adjusted to changes in natural drivers (the Pliocene) and one where greenhouse gases concentrations, temperature, and sea level rise are still increasing (present-day). Much about the transition into the Pliocene climate state – in terms of key causes, the role of cycles that hastened or slowed the transition, and the rate of change in climate indicators such as sea level – remain topics of intense study by climate researchers using a combination of paleoclimate observations and Earth system models. Insights from such studies may help to reduce the large uncertainties around estimates of global sea level rise by 2300, which range from 0.3 m to 3 m above 1850-1900 (in a low-emissions scenario) to as much as 16 m higher than 1850-1900 (in a very high-emissions scenario that includes accelerating structural disintegration of the polar ice sheets).

While present-day warming is unusual in the context of the recent geologic past in several different ways (see FAQ 2.1), past warm climate states present a stark reminder that the long-term adjustment to present-day atmospheric carbon dioxide concentrations has only just begun. That adjustment will continue over the coming centuries to millennia.

[START FAQ 1.3, FIGURE 1 HERE]

FAQ 1.3, Figure 1: Comparison of past, present and future. Schematic of atmospheric carbon dioxide concentrations, global temperature, and global sea level during previous warm periods as compared to 1850-1900, present-day (2011-2020), and future (2100) climate change scenarios corresponding to low-emissions scenarios (SSP1-2.6; lighter colour bars) and very high emissions scenarios (SSP5-8.5; darker colour bars).

[END FAQ 1.3, FIGURE 1 HERE]

ACCEPTED VERSION SUBJECT TO FINAL EDITS

Acknowledgements

We thank Alejandro Cearreta (UPV/EHU, Spain) for his invaluable contribution to the Glossary.

ACCEPTED VERSION
SUBJECT TO FINAL EDITS

References

Abraham, J.P. et al., 2013: A review of global ocean temperature observations: Implications for ocean heat content estimates and climate change. *Reviews of Geophysics*, **51(3)**, 450–483, doi:10.1002/rog.20022.

Abram, N. et al., 2019: Framing and Context of the Report. In: *IPCC Special Report on the Ocean and Cryosphere in a Changing Climate* []. In Press, pp. 73–129.

Abram, N.J. et al., 2016: Early onset of industrial-era warming across the oceans and continents. *Nature*, **536(7617)**, 411–418, doi:10.1038/nature19082.

Abramowitz, G. et al., 2019: ESD Reviews: Model dependence in multi-model climate ensembles: weighting, sub-selection and out-of-sample testing. *Earth System Dynamics*, **10(1)**, 91–105, doi:10.5194/esd-10-91-2019.

Adler, C.E. and G. Hirsch Hadorn, 2014: The IPCC and treatment of uncertainties: topics and sources of dissensus. *Wiley Interdisciplinary Reviews: Climate Change*, **5(5)**, 663–676, doi:10.1002/wcc.297.

Aguilera-Betti, I. et al., 2017: The First Millennium-Age Araucaria Araucana in Patagonia. *Tree-Ring Research*, **73(1)**, 53–56, doi:10.3959/1536-1098-73.1.53.

Ahn, M.-S. et al., 2017: MJO simulation in CMIP5 climate models: MJO skill metrics and process-oriented diagnosis. *Climate Dynamics*, **49(11–12)**, 4023–4045, doi:10.1007/s00382-017-3558-4.

Aitken, J., 1889: I. – On the Number of Dust Particles in the Atmosphere. *Transactions of the Royal Society of Edinburgh*, **35(1)**, 1–19, doi:10.1017/s0080456800017592.

Albrecht, B.A., 1989: Aerosols, Cloud Microphysics, and Fractional Cloudiness. *Science*, **245(4923)**, 1227–1230, doi:10.1126/science.245.4923.1227.

Alexander, C. et al., 2011: Linking Indigenous and Scientific Knowledge of Climate Change. *BioScience*, **61(6)**, 477–484, doi:10.1525/bio.2011.61.6.10.

Alexander, L. et al., 2020: Intercomparison of annual precipitation indices and extremes over global land areas from in situ , space-based and reanalysis products. *Environmental Research Letters*, **15(5)**, 055002, doi:10.1088/1748-9326/ab79e2.

Alkhayuon, H., P. Ashwin, L.C. Jackson, C. Quinn, and R.A. Wood, 2019: Basin bifurcations, oscillatory instability and rate-induced thresholds for Atlantic meridional overturning circulation in a global oceanic box model. *Proceedings of the Royal Society A: Mathematical, Physical and Engineering Sciences*, **475(2225)**, 20190051, doi:10.1098/rspa.2019.0051.

Allan, R. et al., 2011: The International Atmospheric Circulation Reconstructions over the Earth (ACRE) Initiative. *Bulletin of the American Meteorological Society*, **92(11)**, 1421–1425, doi:10.1175/2011bams3218.1.

Allan, R.P. et al., 2020: Advances in understanding large-scale responses of the water cycle to climate change. *Annals of the New York Academy of Sciences*, **1472(1)**, 49–75, doi:10.1111/nyas.14337.

Allen, M.R. and W.J. Ingram, 2002: Constraints on future changes in climate and the hydrologic cycle. *Nature*, **419(6903)**, 228–232, doi:10.1038/nature01092.

Allen, M.R. et al., 2009: Warming caused by cumulative carbon emissions towards the trillionth tonne. *Nature*, **458(7242)**, 1163–1166, doi:10.1038/nature08019.

Allen, M.R. et al., 2016: New use of global warming potentials to compare cumulative and short-lived climate pollutants. *Nature Climate Change*, **6(8)**, 773–776, doi:10.1038/nclimate2998.

Anagnostou, E. et al., 2020: Proxy evidence for state-dependence of climate sensitivity in the Eocene greenhouse. *Nature Communications*, **11(1)**, 4436, doi:10.1038/s41467-020-17887-x.

Anav, A. et al., 2013: Evaluating the Land and Ocean Components of the Global Carbon Cycle in the CMIP5 Earth System Models. *Journal of Climate*, **26(18)**, 6801–6843, doi:10.1175/jcli-d-12-00417.1.

Anchukaitis, K.J. et al., 2017: Last millennium Northern Hemisphere summer temperatures from tree rings: Part II, spatially resolved reconstructions. *Quaternary Science Reviews*, **163**, 1–22, doi:10.1016/j.quascirev.2017.02.020.

Anderson, A.A. and H.E. Huntington, 2017: Social Media, Science, and Attack Discourse: How Twitter Discussions of Climate Change Use Sarcasm and Incivility. *Science Communication*, **39(5)**, 598–620, doi:10.1177/1075547017735113.

André, J.-C. et al., 2014: High-Performance Computing for Climate Modeling. *Bulletin of the American Meteorological Society*, **95(5)**, ES97–ES100, doi:10.1175/bams-d-13-00098.1.

Andrews, T., P.M. Forster, O. Boucher, N. Bellouin, and A. Jones, 2010: Precipitation, radiative forcing and global temperature change. *Geophysical Research Letters*, **37(14)**, n/a–n/a, doi:10.1029/2010gl043991.

Angerer, B. et al., 2017: Quality aspects of the Wegener Center multi-satellite GPS radio occultation record OPSv5.6. *Atmospheric Measurement Techniques*, **10(12)**, 4845–4863, doi:10.5194/amt-10-4845-2017.

Ångström, A., 1929: On the Atmospheric Transmission of Sun Radiation and on Dust in the Air. *Geografiska Annaler*, **11(2)**, 156–166, doi:10.1080/20014422.1929.11880498.

Ångström, A., 1964: The parameters of atmospheric turbidity. *Tellus*, **16(1)**, 64–75, doi:10.3402/tellusa.v16i1.8885.

Ångström, K., 1900: Über die Bedeutung des Wasserdampfes und der Kohlensäure bei der Absorption der Erdatmosphäre. *Annalen der Physik*, **3**, 720–732.

ACCEPTED VERSION SUBJECT TO FINAL EDITS

Annan, J.D. and J.C. Hargreaves, 2017: On the meaning of independence in climate science. *Earth System Dynamics*, **8(1)**, 211–224, doi:10.5194/esd-8-211-2017.

Anterrieu, E., A. Khazaal, F. Cabot, and Y. Kerr, 2016: Geolocation of RFI sources with sub-kilometric accuracy from SMOS interferometric data. *Remote Sensing of Environment*, **180**, 76–84, doi:10.1016/j.rse.2016.02.007.

Anthes, R.A., 2011: Exploring Earth's atmosphere with radio occultation: contributions to weather, climate and space weather. *Atmospheric Measurement Techniques*, **4(6)**, 1077–1103, doi:10.5194/amt-4-1077-2011.

Arnold, J.R. and W.F. Libby, 1949: Age determinations by radiocarbon content: Checks with samples of known age. *Science*, **110**, 678–680, doi:10.1126/science.110.2869.678.

Arora, V.K. et al., 2020: Carbon--concentration and carbon--climate feedbacks in CMIP6 models and their comparison to CMIP5 models. *Biogeosciences*, **17(16)**, 4173–4222, doi:10.5194/bg-17-4173-2020.

Arrhenius, S., 1896: On the influence of carbonic acid in the air upon the temperature of the ground. *The London, Edinburgh, and Dublin Philosophical Magazine and Journal of Science*, **41(251)**, 237–276, doi:10.1080/14786449608620846.

Arrhenius, S., 1908: *Worlds in the Making: The Evolution of the Universe*. Harper & Brothers Publishers, New York, NY, USA and London, UK, 230 pp.

Asay-Davis, X.S., N.C. Jourdain, and Y. Nakayama, 2017: Developments in Simulating and Parameterizing Interactions Between the Southern Ocean and the Antarctic Ice Sheet. *Current Climate Change Reports*, **3(4)**, 316–329, doi:10.1007/s40641-017-0071-0.

Ashton, T.S., 1997: *The Industrial Revolution 1760-1830*. Oxford University Press, Oxford, UK, 162 pp.

Ashwin, P., S. Wieczorek, R. Vitolo, and P. Cox, 2012: Tipping points in open systems: bifurcation, noise-induced and rate-dependent examples in the climate system. *Philosophical Transactions of the Royal Society A: Mathematical, Physical and Engineering Sciences*, **370(1962)**, 1166–1184, doi:10.1098/rsta.2011.0306.

Atampugre, G., M. Nursey-Bray, and R. Adade, 2019: Using geospatial techniques to assess climate risks in savannah agroecological systems. *Remote Sensing Applications: Society and Environment*, **14**, 100–107, doi:10.1016/j.rsase.2019.01.006.

Aumont, O., C. Ethé, A. Tagliabue, L. Bopp, and M. Gehlen, 2015: PISCES-v2: an ocean biogeochemical model for carbon and ecosystem studies. *Geoscientific Model Development*, **8(8)**, 2465–2513, doi:10.5194/gmd-8-2465-2015.

Baccini, A. et al., 2017: Tropical forests are a net carbon source based on aboveground measurements of gain and loss. *Science*, **358(6360)**, 230–234, doi:10.1126/science.aam5962.

Bador, M. et al., 2020: Impact of Higher Spatial Atmospheric Resolution on Precipitation Extremes Over Land in Global Climate Models. *Journal of Geophysical Research: Atmospheres*, **125(13)**, e2019JD032184, doi:10.1029/2019jd032184.

Balaji, V. et al., 2017: CPMIP: measurements of real computational performance of Earth system models in CMIP6. *Geoscientific Model Development*, **10(1)**, 19–34, doi:10.5194/gmd-10-19-2017.

Balaji, V. et al., 2018: Requirements for a global data infrastructure in support of CMIP6. *Geoscientific Model Development*, **11(9)**, 3659–3680, doi:10.5194/gmd-11-3659-2018.

Balco, G., 2020a: Glacier Change and Paleoclimate Applications of Cosmogenic-Nuclide Exposure Dating. *Annual Review of Earth and Planetary Sciences*, **48(1)**, 21–48, doi:10.1146/annurev-earth-081619-052609.

Balco, G., 2020b: Technical note: A prototype transparent-middle-layer data management and analysis infrastructure for cosmogenic-nuclide exposure dating. *Geochronology*, **2(2)**, 169–175, doi:10.5194/gchron-2-169-2020.

Balmaseda, M.A. et al., 2015: The Ocean Reanalyses Intercomparison Project (ORA-IP). *Journal of Operational Oceanography*, **8(sup1)**, s80–s97, doi:10.1080/1755876x.2015.1022329.

Bamber, J.L., R.M. Westaway, B. Marzeion, and B. Wouters, 2018: The land ice contribution to sea level during the satellite era. *Environmental Research Letters*, **13(6)**, 063008, doi:10.1088/1748-9326/aac2f0.

Banerjee, A., J.C. Fyfe, L.M. Polvani, D. Waugh, and K.L. Chang, 2020: A pause in Southern Hemisphere circulation trends due to the Montreal Protocol. *Nature*, **579(7800)**, 544–548, doi:10.1038/s41586-020-2120-4.

Banks, H. and R. Wood, 2002: Where to look for anthropogenic climate change in the ocean. *Journal of Climate*, doi:10.1175/1520-0442(2002)015<0879:wtlfac>2.0.co;2.

Barnett, T.P. and M.E. Schlesinger, 1987: Detecting changes in global climate induced by greenhouse gases. *Journal of Geophysical Research*, **92(D12)**, 14772, doi:10.1029/jd092id12p14772.

Barrett, H.G., J.M. Jones, and G.R. Bigg, 2018: Reconstructing El Niño Southern Oscillation using data from ships' logbooks, 1815–1854. Part II: Comparisons with existing ENSO reconstructions and implications for reconstructing ENSO diversity. *Climate Dynamics*, **50(9–10)**, 3131–3152, doi:10.1007/s00382-017-3797-4.

Bathiany, S., J. Hidding, and M. Scheffer, 2020: Edge Detection Reveals Abrupt and Extreme Climate Events. *Journal of Climate*, **33(15)**, 6399–6421, doi:10.1175/jcli-d-19-0449.1.

Batten, S.D. et al., 2019: A Global Plankton Diversity Monitoring Program . *Frontiers in Marine Science* , **6** , 321.

Baumberger, C., R. Knutti, and G. Hirsch Hadorn, 2017: Building confidence in climate model projections: an analysis of inferences from fit. *WIREs Climate Change*, **8(3)**, e454, doi:10.1002/wcc.454.

Beck, H.E. et al., 2017: MSWEP: 3-hourly 0.25° global gridded precipitation (1979–2015) by merging gauge, satellite, and reanalysis data. *Hydrology and Earth System Sciences*, **21(1)**, 589–615, doi:10.5194/hess-21-589-2017.

ACCEPTED VERSION SUBJECT TO FINAL EDITS

Beck, H.E. et al., 2018: Present and future Köppen-Geiger climate classification maps at 1-km resolution. *Scientific Data*, **5**, 180214.
Beck, J. et al., 2018: Bipolar carbon and hydrogen isotope constraints on the Holocene methane budget. *Biogeosciences*, **15(23)**, 7155–7175, doi:10.5194/bg-15-7155-2018.
Becker, A. et al., 2013: A description of the global land-surface precipitation data products of the Global Precipitation Climatology Centre with sample applications including centennial (trend) analysis from 1901–present. *Earth System Science Data*, **5(1)**, 71–99, doi:10.5194/essd-5-71-2013.
Belda, M., E. Holtanová, T. Halenka, and J. Kalvová, 2014: Climate classification revisited: from Köppen to Trewartha. *Climate Research*, **59(1)**, 1–13, doi:10.3354/cr01204.
Belda, M., E. Holtanová, J. Kalvová, and T. Halenka, 2016: Global warming-induced changes in climate zones based on CMIP5 projections. *Climate Research*, **71(1)**, 17–31, doi:10.3354/cr01418.
Belda, M., E. Holtanová, T. Halenka, J. Kalvová, and Z. Hlávka, 2015: Evaluation of CMIP5 present climate simulations using the Köppen-Trewartha climate classification. *Climate Research*, **64(3)**, 201–212, doi:10.3354/cr01316.
Bellenger, H., E. Guilyardi, J. Leloup, M. Lengaigne, and J. Vialard, 2014: ENSO representation in climate models: from CMIP3 to CMIP5. *Climate Dynamics*, **42(7–8)**, 1999–2018, doi:10.1007/s00382-013-1783-z.
Benveniste, H., O. Boucher, C. Guivarch, H. Treut, and P. Criqui, 2018: Impacts of nationally determined contributions on 2030 global greenhouse gas emissions: uncertainty analysis and distribution of emissions. *Environmental Research Letters*, **13(1)**, 014022, doi:10.1088/1748-9326/aaa0b9.
Bereiter, B. et al., 2015: Revision of the EPICA Dome C CO2 record from 800 to 600 kyr before present. *Geophysical Research Letters*, **42(2)**, 542–549, doi:10.1002/2014gl061957.
Berger, A.L., 1977: Support for the astronomical theory of climatic change. *Nature*, **269(5623)**, 44–45, doi:10.1038/269044a0.
Berger, A.L., 1978: Long-Term Variations of Daily Insolation and Quaternary Climatic Changes. *Journal of the Atmospheric Sciences*, **35(12)**, 2362–2367, doi:10.1175/1520-0469(1978)035<2362:ltvodi>2.0.co;2.
Berner, J. et al., 2017: Stochastic Parameterization: Toward a New View of Weather and Climate Models. *Bulletin of the American Meteorological Society*, **98(3)**, 565–588, doi:10.1175/bams-d-15-00268.1.
Berner, R.A., 1995: A. G. Högbom and the development of the concept of the geochemical carbon cycle. *American Journal of Science*, **295(5)**, 491–495, doi:10.2475/ajs.295.5.491.
Bernie, D.J. et al., 2008: Impact of resolving the diurnal cycle in an ocean–atmosphere GCM. Part 2: A diurnally coupled CGCM. *Climate Dynamics*, **31(7)**, 909–925, doi:10.1007/s00382-008-0429-z.
Bessho, K. et al., 2016: An Introduction to Himawari-8/9— Japan’s New-Generation Geostationary Meteorological Satellites. *Journal of the Meteorological Society of Japan. Ser. II*, **94(2)**, 151–183, doi:10.2151/jmsj.2016-009.
Bethke, I. et al., 2017: Potential volcanic impacts on future climate variability. *Nature Climate Change*, **7(11)**, 799–805, doi:10.1038/nclimate3394.
Beusch, L., L. Gudmundsson, and S.I. Seneviratne, 2020a: Crossbreeding CMIP6 Earth System Models With an Emulator for Regionally Optimized Land Temperature Projections. *Geophysical Research Letters*, **47(15)**, e2019GL086812, doi:10.1029/2019gl086812.
Beusch, L., L. Gudmundsson, and S.I. Seneviratne, 2020b: Emulating Earth system model temperatures with MESMER: from global mean temperature trajectories to grid-point-level realizations on land. *Earth System Dynamics*, **11(1)**, 139–159, doi:10.5194/esd-11-139-2020.
Bindoff, N.L. et al., 2013: Detection and Attribution of Climate Change: from Global to Regional. In: *Climate Change 2013: The Physical Science Basis. Contribution of Working Group I to the Fifth Assessment Report of the Intergovernmental Panel on Climate Change* [Stocker, T.F., D. Qin, G.-K. Plattner, M. Tignor, S.K. Allen, J. Boschung, A. Nauels, Y. Xia, V. Bex, and P.M. Midgley (eds.)]. Cambridge University Press, Cambridge, United Kingdom and New York, NY, USA, pp. 867–952, doi:10.1017/cbo9781107415324.022.
Birkel, S.D., P.A. Mayewski, K.A. Maasch, A. Kurbatov, and B. Lyon, 2018: Evidence for a volcanic underpinning of the Atlantic multidecadal oscillation. *npj Climate and Atmospheric Science*, **1(1)**, 24, doi:10.1038/s41612-018-0036-6.
Bishop, C.H. and G. Abramowitz, 2013: Climate model dependence and the replicate Earth paradigm. *Climate Dynamics*, **41(3–4)**, 885–900, doi:10.1007/s00382-012-1610-y.
Bishop, S.P. et al., 2016: Southern Ocean Overturning Compensation in an Eddy-Resolving Climate Simulation. *Journal of Physical Oceanography*, **46(5)**, 1575–1592, doi:10.1175/jpo-d-15-0177.1.
Biskaborn, B.K. et al., 2015: The new database of the Global Terrestrial Network for Permafrost (GTN-P). *Earth System Science Data*, **7(2)**, 245–259, doi:10.5194/essd-7-245-2015.
Bjerknes, V.F.K., 1906: *Fields of force; supplementary lectures, applications to meteorology; a course of lectures in mathematical physics delivered December 1 to 23, 1905*. Columbia University Press, New York, NY, USA, 160 pp.
Bjerknes, V.F.K., J.W. Sandström, T. Hesselberg, and O.M. Devik, 1910: *Dynamic Meteorology and Hydrography*. Carnegie Institution of Washington, Washington, DC, USA, 2 v. pp.

ACCEPTED VERSION SUBJECT TO FINAL EDITS

Blackwell, W.J. and A.B. Milstein, 2014: A Neural Network Retrieval Technique for High-Resolution Profiling of Cloudy Atmospheres. *IEEE Journal of Selected Topics in Applied Earth Observations and Remote Sensing*, **7(4)**, 1260–1270, doi:10.1109/jstars.2014.2304701.

Bock, L. et al., 2020: Quantifying Progress Across Different CMIP Phases With the ESMValTool. *Journal of Geophysical Research: Atmospheres*, **125(21)**, e2019JD032321, doi:10.1029/2019jd032321.

Bodas-Salcedo, A. et al., 2019: Strong Dependence of Atmospheric Feedbacks on Mixed-Phase Microphysics and Aerosol-Cloud Interactions in HadGEM3. *Journal of Advances in Modeling Earth Systems*, **11(6)**, 1735–1758, doi:10.1029/2019ms001688.

Bodeker, G.E. et al., 2016: Reference Upper-Air Observations for Climate: From Concept to Reality. *Bulletin of the American Meteorological Society*, **97(1)**, 123–135, doi:10.1175/bams-d-14-00072.1.

Boden, T., G. Marland, and R.J. Andres, 2017: Global, Regional, and National Fossil-Fuel CO2 Emissions (1751 - 2014) (V. 2017). Carbon Dioxide Information Analysis Center (CDIAC), Oak Ridge National Laboratory (ORNL), Oak Ridge, TN, USA.

Boé, J., 2018: Interdependency in Multimodel Climate Projections: Component Replication and Result Similarity. *Geophysical Research Letters*, **45(6)**, 2771–2779, doi:10.1002/2017gl076829.

Boé, J. et al., 2020: Past long-term summer warming over western Europe in new generation climate models: Role of large-scale atmospheric circulation. *Environmental Research Letters*, **15(8)**, doi:10.1088/1748-9326/ab8a89.

Boer, G.J. et al., 2016: The Decadal Climate Prediction Project (DCPP) contribution to CMIP6. *Geoscientific Model Development*, **9(10)**, 3751–3777, doi:10.5194/gmd-9-3751-2016.

Bohr, J., 2017: Is it hot in here or is it just me? Temperature anomalies and political polarization over global warming in the American public. *Climatic Change*, **142(1–2)**, 271–285, doi:10.1007/s10584-017-1934-z.

Bojinski, S. et al., 2014: The Concept of Essential Climate Variables in Support of Climate Research, Applications, and Policy. *Bulletin of the American Meteorological Society*, **95(9)**, 1431–1443, doi:10.1175/bams-d-13-00047.1.

Bolin, B.E.R.T. and W.A.L.T.E.R. Bischof, 1970: Variations of the carbon dioxide content of the atmosphere in the northern hemisphere. *Tellus*, **22(4)**, 431–442, doi:10.1111/j.2153-3490.1970.tb00508.x.

Bony, S. et al., 2015: Clouds, circulation and climate sensitivity. *Nature Geoscience*, **8(4)**, 261–268, doi:10.1038/ngeo2398.

Boo, K.-O., G. Martin, A. Sellar, C. Senior, and Y.-H. Byun, 2011: Evaluating the East Asian monsoon simulation in climate models. *Journal of Geophysical Research*, **116(D1)**, D01109, doi:10.1029/2010jd014737.

Booth, B.B.B. et al., 2017: Narrowing the Range of Future Climate Projections Using Historical Observations of Atmospheric CO 2 . *Journal of Climate*, **30(8)**, 3039–3053, doi:10.1175/jcli-d-16-0178.1.

Borsche, M., A.K. Kaiser-Weiss, and F. Kaspar, 2016: Wind speed variability between 10 and 116\\,m height from the regional reanalysis COSMO-REA6 compared to wind mast measurements over Northern Germany and~the~Netherlands. *Advances in Science and Research*, **13**, 151–161, doi:10.5194/asr-13-151-2016.

Boucher, O. et al., 2013: Clouds and Aerosols. In: *Climate Change 2013: The Physical Science Basis. Contribution of Working Group I to the Fifth Assessment Report of the Intergovernmental Panel on Climate Change* [Stocker, T.F., D. Qin, G.-K. Plattner, M. Tignor, S.K. Allen, J. Boschung, A. Nauels, Y. Xia, V. Bex, and P.M. Midgley (eds.)]. Cambridge University Press, Cambridge, United Kingdom and New York, NY, USA, pp. 571–658, doi:10.1017/cbo9781107415324.016.

Boucher, O. et al., 2020: Presentation and Evaluation of the IPSL-CM6A-LR Climate Model. *Journal of Advances in Modeling Earth Systems*, **12(7)**, doi:10.1029/2019ms002010.

Bourlès, B. et al., 2019: PIRATA: A Sustained Observing System for Tropical Atlantic Climate Research and Forecasting. *Earth and Space Science*, **6(4)**, 577–616, doi:10.1029/2018ea000428.

Bowen, G.J. et al., 2015: Two massive, rapid releases of carbon during the onset of the Palaeocene–Eocene thermal maximum. *Nature Geoscience*, **8(1)**, 44–47, doi:10.1038/ngeo2316.

Boyle, E.A. and L. Keigwin, 1987: North Atlantic thermohaline circulation during the past 20,000 years linked to high-latitude surface temperature. *Nature*, **330(6143)**, 35–40, doi:10.1038/330035a0.

Bracegirdle, T.J. and D.B. Stephenson, 2013: On the Robustness of Emergent Constraints Used in Multimodel Climate Change Projections of Arctic Warming. *Journal of Climate*, **26(2)**, 669–678, doi:10.1175/jcli-d-12-00537.1.

Bradley, R.S., 2015: *Paleoclimatology*. Elsevier, 675 pp., doi:10.1016/c2009-0-18310-1.

Brasseur, G.P. and L. Gallardo, 2016: Climate services: Lessons learned and future prospects. *Earth's Future*, **4(3)**, 79–89, doi:10.1002/2015ef000338.

Braun, M.H. et al., 2019: Constraining glacier elevation and mass changes in South America. *Nature Climate Change*, **9(2)**, 130–136, doi:10.1038/s41558-018-0375-7.

Brázdil, R., C. Pfister, H. Wanner, H. Storch, and J. Luterbacher, 2005: Historical Climatology In Europe – The State Of The Art. *Climatic Change*, **70(3)**, 363–430, doi:10.1007/s10584-005-5924-1.

Breakey, H., T. Cadman, and C. Sampford, 2016: Governance values and institutional integrity. In: *Governing the Climate Change Regime* [Cadman, T., R. Maguire, and C. Sampford (eds.)]. Routledge, London, UK, pp. 34–62, doi:10.4324/9781315442365.

Broecker, W.S., 1975: Climatic Change: Are We on the Brink of a Pronounced Global Warming? *Science*, **189(4201)**, 460–463, doi:10.1126/science.189.4201.460.

ACCEPTED VERSION SUBJECT TO FINAL EDITS

Broecker, W.S., D.M. Peteet, and D. Rind, 1985: Does the ocean–atmosphere system have more than one stable mode of operation? *Nature*, **315(6014)**, 21–26, doi:10.1038/315021a0.
Brohan, P., J.J. Kennedy, I. Harris, S.F.B. Tett, and P.D. Jones, 2006: Uncertainty estimates in regional and global observed temperature changes: A new data set from 1850. *Journal of Geophysical Research: Atmospheres*, **111(D12)**, doi:10.1029/2005jd006548.
Brönnimann, S. et al., 2019a: Unlocking pre-1850 instrumental meteorological records: A global inventory. *Bulletin of the American Meteorological Society*, doi:10.1175/bams-d-19-0040.1.
Brönnimann, S. et al., 2019b: Last phase of the Little Ice Age forced by volcanic eruptions. *Nature Geoscience*, **12(8)**, 650–656, doi:10.1038/s41561-019-0402-y.
Brown, A. et al., 2012: Unified Modeling and Prediction of Weather and Climate: A 25-Year Journey. *Bulletin of the American Meteorological Society*, **93(12)**, 1865–1877, doi:10.1175/bams-d-12-00018.1.
Brückner, E., 1890: *Klima-Schwankungen Seit 1700, Nebst Bemerkungen über Die Klimaschwankungen Der Diluvialzeit*. Eduard Hölzel, Vienna and Olmütz, 324 pp.
Brulle, R.J., 2019: Networks of Opposition: A Structural Analysis of U.S. Climate Change Countermovement Coalitions 1989–2015. *Sociological Inquiry*, soin.12333, doi:10.1111/soin.12333.
Brulle, R.J., J. Carmichael, and J.C. Jenkins, 2012: Shifting public opinion on climate change: an empirical assessment of factors influencing concern over climate change in the U.S., 2002–2010. *Climatic Change*, **114(2)**, 169–188, doi:10.1007/s10584-012-0403-y.
Bryan, K., S. Manabe, and R.C. Pacanowski, 1975: A Global Ocean-Atmosphere Climate Model. Part II. The Oceanic Circulation. *Journal of Physical Oceanography*, **5(1)**, 30–46, doi:10.1175/1520-0485(1975)005<0030:agoacm>2.0.co;2.
Bryson, R.A. and W.M. Wendland, 1970: Climatic effects of atmospheric pollution. In: *Global Effects of Environmental Pollution: A Symposium Organized by the American Association for the Advancement of Science Held in Dallas, Texas, December 1968* [Singer, S.F. (ed.)]. Springer, Dordrecht, The Netherlands, pp. 139–147, doi:10.1007/978-94-010-3290-2_14.
Budescu, D., S. Broomell, and H.-H. Por, 2009: Improving Communication of Uncertainty in the Reports of the Intergovernmental Panel on Climate Change. *Psychological Science*, **20(3)**, 299–308, doi:10.1111/j.1467-9280.2009.02284.x.
Budescu, D., H.-H. Por, and S.B. Broomell, 2012: Effective communication of uncertainty in the IPCC reports. *Climatic Change*, **113(2)**, 181–200, doi:10.1007/s10584-011-0330-3.
Budescu, D., H.-H. Por, S.B. Broomell, and M. Smithson, 2014: The interpretation of IPCC probabilistic statements around the world. *Nature Climate Change*, **4(6)**, 508–512, doi:10.1038/nclimate2194.
Budyko, M.I., 1969: The effect of solar radiation variations on the climate of the Earth. *Tellus*, doi:10.3402/tellusa.v21i5.10109.
Burgard, C., D. Notz, L.T. Pedersen, and R.T. Tonboe, 2020: The Arctic Ocean Observation Operator for 6.9 GHz (ARC3O) – Part 2: Development and evaluation. *The Cryosphere*, **14(7)**, 2387–2407, doi:10.5194/tc-14-2387-2020.
Burkett, V.R. et al., 2014: Point of departure. In: *Climate Change 2014: Impacts, Adaptation, and Vulnerability. Part A: Global and Sectoral Aspects. Contribution of Working Group II to the Fifth Assessment Report of the Intergovernmental Panel on Climate Change* [Field, C.B., V.R. Barros, D.J. Dokken, K.J. Mach, M.D. Mastrandrea, T.E. Bilir, M. Chatterjee, K.L. Ebi, Y.O. Estrada, R.C. Genova, B. Girma, E.S. Kissel, A.N. Levy, S. MacCracken, P.R. Mastrandrea, and L.L. White (eds.)]. Cambridge University Press, Cambridge, United Kingdom and New York, NY, USA, pp. 169–194, doi:10.1017/cbo9781107415379.006.
Burn, M.J. and S.E. Palmer, 2015: Atlantic hurricane activity during the last millennium. *Scientific Reports*, **5(1)**, 12838, doi:10.1038/srep12838.
Burrows, S.M. et al., 2018: Characterizing the Relative Importance Assigned to Physical Variables by Climate Scientists when Assessing Atmospheric Climate Model Fidelity. *Advances in Atmospheric Sciences*, **35(9)**, 1101–1113, doi:10.1007/s00376-018-7300-x.
Burton, M.R., G.M. Sawyer, and D. Granieri, 2013: Deep Carbon Emissions from Volcanoes. *Reviews in Mineralogy and Geochemistry*, **75(1)**, 323–354, doi:10.2138/rmg.2013.75.11.
Butler, E.E., N.D. Mueller, and P. Huybers, 2018: Peculiarly pleasant weather for US maize. *Proceedings of the National Academy of Sciences of the United States of America*, **115(47)**, 11935–11940, doi:10.1073/pnas.1808035115.
Cain, M. et al., 2019: Improved calculation of warming-equivalent emissions for short-lived climate pollutants. *npj Climate and Atmospheric Science*, **2(1)**, doi:10.1038/s41612-019-0086-4.
Caldwell, P.M., M.D. Zelinka, and S.A. Klein, 2018: Evaluating Emergent Constraints on Equilibrium Climate Sensitivity. *Journal of Climate*, **31(10)**, 3921–3942, doi:10.1175/jcli-d-17-0631.1.
Caldwell, P.M. et al., 2014: Statistical significance of climate sensitivity predictors obtained by data mining. *Geophysical Research Letters*, **41(5)**, 1803–1808, doi:10.1002/2014gl059205.
Callendar, G.S., 1938: The artificial production of carbon dioxide and its influence on temperature. *Quarterly Journal of the Royal Meteorological Society*, **64(275)**, 223–240, doi:10.1002/qj.49706427503.

ACCEPTED VERSION SUBJECT TO FINAL EDITS

Callendar, G.S., 1949: Can Carbon Dioxide Influence Climate? *Weather*, **4(10)**, 310–314, doi:10.1002/j.1477-8696.1949.tb00952.x.
Callendar, G.S., 1961: Temperature Fluctuations and Trends over the Earth. *Quarterly Journal of the Royal Meteorological Society*, **87(371)**, 1–12, doi:10.1002/qj.49708737102.
Canonico, G. et al., 2019: Global Observational Needs and Resources for Marine Biodiversity. *Frontiers in Marine Science*, **6**, 367, doi:10.3389/fmars.2019.00367.
Cardona, O.-D. et al., 2012: Determinants of Risk: Exposure and Vulnerability. In: *Managing the Risks of Extreme Events and Disasters to Advance Climate Change Adaptation* [Field, C.B., V. Barros, T.F. Stocker, and Q. Dahe (eds.)]. Cambridge University Press, Cambridge, United Kingdom and New York, NY, USA, pp. 65–108, doi:10.1017/cbo9781139177245.005.
Carslaw, K.S. et al., 2017: Aerosols in the Pre-industrial Atmosphere. *Current Climate Change Reports*, **3(1)**, 1–15, doi:10.1007/s40641-017-0061-2.
CCMI, 2021: IGAC/SPARC CCMI Ozone Database and Mitrogen-Deposition Fields in Support of CMIP6. International Global Atmospheric Chemistry (IGAC) / Stratosphere-troposphere Processes And their Role in Climate (SPARC) Chemistry Climate Model Initiative (CCMI). Retrieved from: https://blogs.reading.ac.uk/ccmi/forcing-databases-in-support-of-cmip6.
CDKN, 2017: Building capacity for risk management in a changing climate: A synthesis report from the Raising Risk Awareness project. , 30.
Ceballos, G., P.R. Ehrlich, and R. Dirzo, 2017: Biological annihilation via the ongoing sixth mass extinction signaled by vertebrate population losses and declines. *Proceedings of the National Academy of Sciences*, **114(30)**, E6089–E6096, doi:10.1073/pnas.1704949114.
Cesana, G. and D.E. Waliser, 2016: Characterizing and understanding systematic biases in the vertical structure of clouds in CMIP5/CFMIP2 models. *Geophysical Research Letters*, **43(19)**, 10,538–10,546, doi:10.1002/2016gl070515.
Chahine, M.O.U.S.T.A.F.A.T. et al., 2006: AIRS: Improving Weather Forecasting and Providing New Data on Greenhouse Gases. *Bulletin of the American Meteorological Society*, **87(7)**, 911–926, doi:10.1175/bams-87-7-911.
Chamberlin, T.C., 1897: A Group of Hypotheses Bearing on Climatic Changes. *Journal of Geology*, **5**, 653–683, doi:10.1086/607921.
Chamberlin, T.C., 1898: The Influence of Great Epochs of Limestone Formation upon the Constitution of the Atmosphere. *Journal of Geology*, **6**, 609–621, doi:10.1086/608185.
Charlson, R.J., J.E. Lovelock, M.O. Andreae, and S.G. Warren, 1987: Oceanic phytoplankton, atmospheric sulphur, cloud albedo and climate. *Nature*, **326(6114)**, 655–661, doi:10.1038/326655a0.
Charlson, R.J. et al., 1992: Climate Forcing by Anthropogenic Aerosols. *Science*, **255(5043)**, 423–430, doi:10.1126/science.255.5043.423.
Charlton-Perez, A.J. et al., 2013: On the lack of stratospheric dynamical variability in low-top versions of the CMIP5 models. *Journal of Geophysical Research: Atmospheres*, **118(6)**, 2494–2505, doi:10.1002/jgrd.50125.
Charney, J.G., R. Fjörtoft, and J. Neumann, 1950: Numerical Integration of the Barotropic Vorticity Equation. *Tellus*, **2(4)**, 237–254, doi:10.1111/j.2153-3490.1950.tb00336.x.
Checa-Garcia, R., M.I. Hegglin, D. Kinnison, D.A. Plummer, and K.P. Shine, 2018: Historical Tropospheric and Stratospheric Ozone Radiative Forcing Using the CMIP6 Database. *Geophysical Research Letters*, **45(7)**, 3264–3273, doi:10.1002/2017gl076770.
Chen, D., N. Smith, and W. Kessler, 2018: The evolving ENSO observing system. *National Science Review*, **5(6)**, 805–807, doi:10.1093/nsr/nwy137.
Chen, X. et al., 2017: The increasing rate of global mean sea-level rise during 1993–2014. *Nature Climate Change*, **7(7)**, 492–495, doi:10.1038/nclimate3325.
Cheng, H. et al., 2013: Improvements in 230Th dating, 230Th and 234U half-life values, and U–Th isotopic measurements by multi-collector inductively coupled plasma mass spectrometry. *Earth and Planetary Science Letters*, **371–372**, 82–91, doi:10.1016/j.epsl.2013.04.006.
Cheng, H. et al., 2016: Climate variations of Central Asia on orbital to millennial timescales. *Scientific Reports*, **6(1)**, 36975, doi:10.1038/srep36975.
Chepfer, H. et al., 2018: The Potential of a Multidecade Spaceborne Lidar Record to Constrain Cloud Feedback. *Journal of Geophysical Research: Atmospheres*, **123(10)**, 5433–5454, doi:10.1002/2017jd027742.
Chevallier, M. et al., 2017: Intercomparison of the Arctic sea ice cover in global ocean–sea ice reanalyses from the ORA-IP project. *Climate Dynamics*, **49(3)**, 1107–1136, doi:10.1007/s00382-016-2985-y.
Christensen, P., K. Gillingham, and W. Nordhaus, 2018: Uncertainty in forecasts of long-run economic growth. *Proceedings of the National Academy of Sciences*, **115(21)**, 5409–5414, doi:10.1073/pnas.1713628115.
Church, J.A. et al., 2013: Sea Level Change. In: *Climate Change 2013: The Physical Science Basis. Contribution of Working Group I to the Fifth Assessment Report of the Intergovernmental Panel on Climate Change* [Stocker, T.F., D. Qin, G.-K. Plattner, M. Tignor, S.K. Allen, J. Boschung, A. Nauels, Y. Xia, V. Bex, and P.M. Midgley (eds.)]. Cambridge University Press, Cambridge, United Kingdom and New York, NY, USA, pp. 1137–1216,

ACCEPTED VERSION SUBJECT TO FINAL EDITS

doi:10.1017/cbo9781107415324.026.
Chuvieco, E. et al., 2019: Historical background and current developments for mapping burned area from satellite Earth observation. *Remote Sensing of Environment*, **225**, 45–64, doi:10.1016/j.rse.2019.02.013.
Chuwah, C. et al., 2013: Implications of alternative assumptions regarding future air pollution control in scenarios similar to the Representative Concentration Pathways. *Atmospheric Environment*, **79**, 787–801, doi:10.1016/j.atmosenv.2013.07.008.
Ciais, P. et al., 2013: Carbon and Other Biogeochemical Cycles. In: *Climate Change 2013: The Physical Science Basis. Contribution of Working Group I to the Fifth Assessment Report of the Intergovernmental Panel on Climate Change* [Stocker, T.F., D. Qin, G.-K. Plattner, M. Tignor, S.K. Allen, J. Boschung, A. Nauels, Y. Xia, V. Bex, and P.M. Midgley (eds.)]. Cambridge University Press, Cambridge, United Kingdom and New York, NY, USA, pp. 465–570, doi:10.1017/cbo9781107415324.015.
Clark, P.U. et al., 2016: Consequences of twenty-first-century policy for multi-millennial climate and sea-level change. *Nature Climate Change*, **6(4)**, 360–369, doi:10.1038/nclimate2923.
Claussen, M. et al., 2002: Earth system models of intermediate complexity: closing the gap in the spectrum of climate system models. *Climate Dynamics*, **18(7)**, 579–586, doi:10.1007/s00382-001-0200-1.
Claverie, M., J.L. Matthews, E.F. Vermote, and C.O. Justice, 2016: A 30+ Year AVHRR LAI and FAPAR Climate Data Record: Algorithm Description and Validation. *Remote Sensing*, **8(3)**, doi:10.3390/rs8030263.
Clayton, H.H., 1927: *World Weather Records*. Smithsonian Institution, Washington, DC, USA, 1199 pp.
Cleator, S.F., S.P. Harrison, N.K. Nichols, I.C. Prentice, and I. Roulstone, 2020: A new multivariable benchmark for Last Glacial Maximum climate simulations. *Climate of the Past*, **16(2)**, 699–712, doi:10.5194/cp-16-699-2020.
CLIMAP Project Members et al., 1976: The Surface of the Ice-Age Earth. *Science*, **191(4232)**, 1131–1137, doi:10.1126/science.191.4232.1131.
Coen, D.R., 2018: *Climate in Motion: Science, Empire, and the Problem of Scale*. University of Chicago Press, Chicago, IL, USA, 423 pp., doi:10.7208/chicago/9780226555027.001.0001.
Coen, D.R., 2020: The Advent of Climate Science. In: *Oxford Research Encyclopedia of Climate Science*. Oxford University Press, Oxford, UK, doi:10.1093/acrefore/9780190228620.013.716.
Cohen, J.M., M.J. Lajeunesse, and J.R. Rohr, 2018: A global synthesis of animal phenological responses to climate change. *Nature Climate Change*, **8(3)**, 224–228, doi:10.1038/s41558-018-0067-3.
Collins, M. et al., 2013: Long-term Climate Change: Projections, Commitments and Irreversibility. In: *Climate Change 2013: The Physical Science Basis. Contribution of Working Group I to the Fifth Assessment Report of the Intergovernmental Panel on Climate Change* [Stocker, T.F., D. Qin, G.-K. Plattner, M. Tignor, S.K. Allen, J. Boschung, A. Nauels, Y. Xia, V. Bex, and P.M. Midgley (eds.)]. Cambridge University Press, Cambridge, United Kingdom and New York, NY, USA, pp. 1029–1136, doi:10.1017/cbo9781107415324.024.
Collins, W.J., D.J. Frame, J. Fuglestvedt, and K.P. Shine, 2019: Stable climate metrics for emissions of short and long-lived species – combining steps and pulses. *Environmental Research Letters*, doi:10.1088/1748-9326/ab6039.
Collins, W.J. et al., 2017: AerChemMIP: quantifying the effects of chemistry and aerosols in CMIP6. *Geoscientific Model Development*, **10(2)**, 585–607, doi:10.5194/gmd-10-585-2017.
Colomb, A. et al., 2018: ICOS Atmospheric Greenhouse Gas Mole Fractions of CO2, CH4, CO, 14CO2 and Meteorological Observations 2016-2018, final quality controlled Level 2 data. Integrated Carbon Observation System (ICOS) – European Research Infrastructure Consortium (ERIC).
Comas-Bru, L. and S.P. Harrison, 2019: SISAL: Bringing Added Value to Speleothem Research. *Quaternary*, **2(1)**, doi:10.3390/quat2010007.
Compo, G.P. et al., 2011: The Twentieth Century Reanalysis Project. *Quarterly Journal of the Royal Meteorological Society*, **137(654)**, 1–28, doi:10.1002/qj.776.
Cook, E.R. et al., 2015: Old World megadroughts and pluvials during the Common Era. *Science Advances*, **1(10)**, doi:10.1126/sciadv.1500561.
Coppola, E. et al., 2020: A first-of-its-kind multi-model convection permitting ensemble for investigating convective phenomena over Europe and the Mediterranean. *Climate Dynamics*, **55(1)**, 3–34, doi:10.1007/s00382-018-4521-8.
Cornes, R.C., E.C. Kent, D.I. Berry, and J.J. Kennedy, 2020: CLASSnmat: A global night marine air temperature data set, 1880–2019. *Geoscience Data Journal*, **7(2)**, 170–184, doi:10.1002/gdj3.100.
Cornford, S.L., D.F. Martin, V. Lee, A.J. Payne, and E.G. Ng, 2016: Adaptive mesh refinement versus subgrid friction interpolation in simulations of Antarctic ice dynamics. *Annals of Glaciology*, **57(73)**, 1–9, doi:10.1017/aog.2016.13.
COSEPUP, 2009: *On Being a Scientist: A Guide to Responsible Conduct in Research (3rd Edition)*. Committee on Science, Engineering, and Public Policy (COSEPUP), National Academy of Science, National Academy of Engineering, and Institute of Medicine of the National Academies. The National Academies Press, Washington, DC, USA, 63 pp.
Covey, C. et al., 2003: An overview of results from the Coupled Model Intercomparison Project. *Global and Planetary Change*, **37(1–2)**, 103–133, doi:10.1016/s0921-8181(02)00193-5.
Covey, C. et al., 2016: Metrics for the Diurnal Cycle of Precipitation: Toward Routine Benchmarks for Climate

ACCEPTED VERSION SUBJECT TO FINAL EDITS

Models. *Journal of Climate*, **29(12)**, 4461–4471, doi:10.1175/jcli-d-15-0664.1.
Cowtan, K. and R.G. Way, 2014: Coverage bias in the HadCRUT4 temperature series and its impact on recent temperature trends. *Quarterly Journal of the Royal Meteorological Society*, doi:10.1002/qj.2297.
Cramer, W. et al., 2014: Detection and attribution of observed impacts. In: *Climate Change 2014: Impacts, Adaptation, and Vulnerability. Part A: Global and Sectoral Aspects. Contribution of Working Group II to the Fifth Assessment Report of the Intergovernmental Panel on Climate* [Field, C.B., V.R. Barros, D.J. Dokken, K.J. Mach, M.D. Mastrandrea, T.E. Bilir, M. Chatterjee, K.L. Ebi, Y.O. Estrada, R.C. Genova, B. Girma, E.S. Kissel, A.N. Levy, S. MacCracken, P.R. Mastrandrea, and L.L. White (eds.)]. Cambridge University Press, Cambridge, United Kingdom and New York, NY, USA, pp. 979–1037, doi:10.1017/cbo9781107415379.023.
Crawford, E., 1997: Arrhenius' 1896 Model of the Greenhouse Effect in Context. *Ambio*, **26(1)**, 6–11.
Crutzen, P.J. and E.F. Stoermer, 2000: The "Anthropocene". *IGBP Newsletter*, 17–18.
Cubasch, U. et al., 2013: Introduction. In: *Climate Change 2013: The Physical Science Basis. Contribution of Working Group I to the Fifth Assessment Report of the Intergovernmental Panel on Climate Change* [Stocker, T.F., D. Qin, G.-K. Plattner, M. Tignor, S.K. Allen, J. Boschung, A. Nauels, Y. Xia, V. Bex, and P.M. Midgley (eds.)]. Cambridge University Press, Cambridge, United Kingdom and New York, NY, USA, pp. 119–158, doi:10.1017/cbo9781107415324.007.
Cucchi, M. et al., 2020: WFDE5: bias-adjusted ERA5 reanalysis data for impact studies. *Earth System Science Data*, **12(3)**, 2097–2120, doi:10.5194/essd-12-2097-2020.
Cuesta-Valero, F.J., A. Garcia-Garcia, H. Beltrami, E. Zorita, and F. Jaume-Santero, 2019: Long-term Surface Temperature (LoST) database as a complement for GCM preindustrial simulations. *Climate of the Past*, **15(3)**, 1099–1111, doi:10.5194/cp-15-1099-2019.
Cui, W., X. Dong, B. Xi, and A. Kennedy, 2017: Evaluation of Reanalyzed Precipitation Variability and Trends Using the Gridded Gauge-Based Analysis over the CONUS. *Journal of Hydrometeorology*, **18(8)**, 2227–2248, doi:10.1175/jhm-d-17-0029.1.
Cullen, M.J.P., 1993: The unified forecast/climate model. *Meteorological Magazine*, **122(1449)**, 81–94.
Cushman, G.T., 2004: Enclave Vision: Foreign Networks in Peru and the Internationalization of El Niño Research during the 1920s. In: *Proceedings of the International Commission on History of Meteorology 1.1*. International Commission on the History of Meteorology, pp. 65–74.
Dakos, V. et al., 2008: Slowing down as an early warning signal for abrupt climate change. *Proceedings of the National Academy of Sciences*, **105(38)**, 14308–14312, doi:10.1073/pnas.0802430105.
Dal Gesso, S., A.P. Siebesma, and S.R. de Roode, 2015: Evaluation of low-cloud climate feedback through single-column model equilibrium states. *Quarterly Journal of the Royal Meteorological Society*, **141(688)**, 819–832, doi:10.1002/qj.2398.
Dangendorf, S. et al., 2019: Persistent acceleration in global sea-level rise since the 1960s. *Nature Climate Change*, **9(9)**, 705–710, doi:10.1038/s41558-019-0531-8.
Dansgaard, W., 1954: The O18-abundance in fresh water. *Geochimica et Cosmochimica Acta*, **6**, 241–260.
Dansgaard, W., S.J. Johnsen, J. Möller, and C.C. Langway, 1969: One thousand centuries of climatic record from Camp Century on the Greenland ice sheet. *Science*, **166(3903)**, 377–380, doi:10.1126/science.166.3903.377.
Davini, P. and F. D'Andrea, 2020: From CMIP3 to CMIP6: Northern Hemisphere Atmospheric Blocking Simulation in Present and Future Climate. *Journal of Climate*, **33(23)**, 10021–10038, doi:10.1175/jcli-d-19-0862.1.
Davis, S.J., K. Caldeira, and H.D. Matthews, 2010: Future CO2 Emissions and Climate Change from Existing Energy Infrastructure. *Science*, **329(5997)**, 1330–1333, doi:10.1126/science.1188566.
Davy, R., I. Esau, A. Chernokulsky, S. Outten, and S. Zilitinkevich, 2017: Diurnal asymmetry to the observed global warming. *International Journal of Climatology*, **37(1)**, 79–93, doi:10.1002/joc.4688.
Dayrell, C., 2019: Discourses around climate change in Brazilian newspapers: 2003–2013. *Discourse and Communication*, **13(2)**, 149–171, doi:10.1177/1750481318817620.
de Bruijn, K.M., N. Lips, B. Gersonius, and H. Middelkoop, 2016: The storyline approach: a new way to analyse and improve flood event management. *Natural Hazards*, **81(1)**, 99–121, doi:10.1007/s11069-015-2074-2.
de Coninck, H. et al., 2018: Strengthening and Implementing the Global Response. In: *Global Warming of 1.5°C. An IPCC Special Report on the impacts of global warming of 1.5°C above pre-industrial levels and related global greenhouse gas emission pathways, in the context of strengthening the global response to the threat of climate change*. [Masson-Delmotte, V., P. Zhai, H.-O. Pörtner, D. Roberts, J. Skea, P.R. Shukla, A. Pirani, W. Moufouma-Okia, C. Péan, R. Pidcock, S. Connors, J.B.R. Matthews, Y. Chen, X. Zhou, M.I. Gomis, E. Lonnoy, T. Maycock, M. Tignor, and T. Waterfield (eds.)]. In Press, pp. 313–443.
de Jong, M.F., M. Oltmanns, J. Karstensen, and L. de Steur, 2018: Deep Convection in the Irminger Sea Observed with a Dense Mooring Array. *Oceanography*, **31(1)**, 50–59, doi:10.5670/oceanog.2018.109.
De Mazière, M. et al., 2018: The Network for the Detection of Atmospheric Composition Change (NDACC): history, status and perspectives. *Atmospheric Chemistry and Physics*, **18(7)**, 4935–4964, doi:10.5194/acp-18-4935-2018.
Dee, D.P. et al., 2011: The ERA-Interim reanalysis: Configuration and performance of the data assimilation system. *Quarterly Journal of the Royal Meteorological Society*, **137(656)**, 553–597, doi:10.1002/qj.828.

ACCEPTED VERSION SUBJECT TO FINAL EDITS

Dee, S. et al., 2015: PRYSM: An open-source framework for PRoxY System Modeling, with applications to oxygen-isotope systems. *Journal of Advances in Modeling Earth Systems*, **7(3)**, 1220–1247, doi:10.1002/2015ms000447.
Dellink, R., J. Chateau, E. Lanzi, and B. Magné, 2017: Long-term economic growth projections in the Shared Socioeconomic Pathways. *Global Environmental Change*, **42**, 200–214, doi:10.1016/j.gloenvcha.2015.06.004.
Denniston, R.F. et al., 2016: Expansion and Contraction of the Indo-Pacific Tropical Rain Belt over the Last Three Millennia. *Scientific Reports*, **6(1)**, 34485, doi:10.1038/srep34485.
Deser, C., R. Knutti, S. Solomon, and A.S. Phillips, 2012: Communication of the role of natural variability in future North American climate. *Nature Climate Change*, **2(11)**, 775–779, doi:10.1038/nclimate1562.
Dessai, S. et al., 2018: Building narratives to characterise uncertainty in regional climate change through expert elicitation. *Environmental Research Letters*, **13(7)**, 074005, doi:10.1088/1748-9326/aabcdd.
Dessler, A.E. and P.M. Forster, 2018: An Estimate of Equilibrium Climate Sensitivity From Interannual Variability. *Journal of Geophysical Research: Atmospheres*, **123(16)**, 8634–8645, doi:10.1029/2018jd028481.
Detenber, B., S. Rosenthal, Y. Liao, and S. Ho, 2016: Audience Segmentation for Campaign Design: Addressing Climate Change in Singapore.. *International Journal of Communication*, **10**, 4736–4758.
Dewulf, A., 2013: Contrasting frames in policy debates on climate change adaptation. *Wiley Interdisciplinary Reviews: Climate Change*, **4(4)**, 321–330, doi:10.1002/wcc.227.
Diffenbaugh, N.S. and M. Scherer, 2011: Observational and model evidence of global emergence of permanent, unprecedented heat in the 20th and 21st centuries. *Climatic Change*, **107(3–4)**, 615–624, doi:10.1007/s10584-011-0112-y.
Diffenbaugh, N.S. and M. Burke, 2019: Global warming has increased global economic inequality. *Proceedings of the National Academy of Sciences*, **116(20)**, 9808–9813, doi:10.1073/pnas.1816020116.
Ditlevsen, P.D. and S.J. Johnsen, 2010: Tipping points: Early warning and wishful thinking. *Geophysical Research Letters*, **37(19)**, n/a–n/a, doi:10.1029/2010gl044486.
Dittus, A.J. et al., 2020: Sensitivity of Historical Climate Simulations to Uncertain Aerosol Forcing. *Geophysical Research Letters*, **47(13)**, doi:10.1029/2019gl085806.
Dolman, A.M. and T. Laepple, 2018: Sedproxy: a forward model for sediment-archived climate proxies. *Climate of the Past*, **14(12)**, 1851–1868, doi:10.5194/cp-14-1851-2018.
Doney, S.C., V.J. Fabry, R.A. Feely, and J.A. Kleypas, 2009: Ocean Acidification: The Other CO2 Problem. *Annual Review of Marine Science*, **1(1)**, 169–192, doi:10.1146/annurev.marine.010908.163834.
Donnelly, J.P. et al., 2015: Climate forcing of unprecedented intense-hurricane activity in the last 2000 years. *Earth's Future*, **3(2)**, 49–65, doi:10.1002/2014ef000274.
Dooley, K. and G. Parihar, 2016: Human rights and equity: Governing values for the international climate regime. In: *Governing the Climate Change Regime: Institutional Integrity and Integrity Systems* [Cadman, T., R. Maguire, and C. Sampford (eds.)]. Routledge, London, UK, pp. 136–154, doi:10.4324/9781315442365.
Dorigo, W. et al., 2017: ESA CCI Soil Moisture for improved Earth system understanding: State-of-the art and future directions. *Remote Sensing of Environment*, **203**, 185–215, doi:10.1016/j.rse.2017.07.001.
Dörries, M., 2006: In the public eye: Volcanology and climate change studies in the 20th century. *Historical Studies in the Physical and Biological Sciences*, **37(1)**, 87–125, doi:10.1525/hsps.2006.37.1.87.
Douglas, H.E., 2009: *Science, Policy, and the Value-Free Ideal*. University of Pittsburgh Press, Pittsburgh, PA, USA, 256 pp.
Douglass, A.E., 1914: A method of estimating rainfall by the growth of trees. *Bulletin of the American Geographical Society*, **46(5)**, 321–335, doi:10.2307/201814.
Douglass, A.E., 1919: *Climatic cycles and tree-growth. A study of the annual rings of trees in relation to climate and solar activity*. Carnegie Institution of Washington, Washington, DC, USA, 126 pp.
Douglass, A.E., 1922: Some aspects of the use of the annual rings of trees in climatic study. *The Scientific Monthly*, **15(1)**, 5–21.
Dove, H.W., 1853: *The Distribution of Heat over the Surface of the Globe: Illustrated by Isothermal, Thermic Isabnormal, and Other Curves of Temperature*. Taylor and Francis, London, UK, 27 pp.
Driemel, A. et al., 2018: Baseline Surface Radiation Network (BSRN): structure and data description (1992–2017). *Earth System Science Data*, **10(3)**, 1491–1501, doi:10.5194/essd-10-1491-2018.
Drijfhout, S. et al., 2015: Catalogue of abrupt shifts in Intergovernmental Panel on Climate Change climate models. *Proceedings of the National Academy of Sciences*, **112(43)**, E5777–E5786, doi:10.1073/pnas.1511451112.
Duan, S.-B. et al., 2019: Validation of Collection 6 MODIS land surface temperature product using in situ measurements. *Remote Sensing of Environment*, **225**, 16–29, doi:10.1016/j.rse.2019.02.020.
Dumitru, O.A. et al., 2019: Constraints on global mean sea level during Pliocene warmth. *Nature*, **574(7777)**, 233–236, doi:10.1038/s41586-019-1543-2.
Dunlap, R.E. and P.J. Jacques, 2013: Climate Change Denial Books and Conservative Think Tanks. *American Behavioral Scientist*, **57(6)**, 699–731, doi:10.1177/0002764213477096.
Durack, P. et al., 2018: Toward Standardized Data Sets for Climate Model Experimentation. *Eos*, **99**, doi:10.1029/2018eo101751.

ACCEPTED VERSION SUBJECT TO FINAL EDITS

Dutton, A. et al., 2015: Sea-level rise due to polar ice-sheet mass loss during past warm periods. *Science*, **349(6244)**, aaa4019–aaa4019, doi:10.1126/science.aaa4019.
Easterling, D.R., K.E. Kunkel, M.F. Wehner, and L. Sun, 2016: Detection and attribution of climate extremes in the observed record. *Weather and Climate Extremes*, **11**, 17–27, doi:10.1016/j.wace.2016.01.001.
Ebita, A. et al., 2011: The Japanese 55-year Reanalysis “JRA-55”: An Interim Report. *SOLA*, **7**, 149–152, doi:10.2151/sola.2011-038.
Eby, M. et al., 2013: Historical and idealized climate model experiments: an intercomparison of Earth system models of intermediate complexity. *Climate of the Past*, **9(3)**, 1111–1140, doi:10.5194/cp-9-1111-2013.
Eddy, J.A., 1976: The Maunder Minimum. *Science*, **192(4245)**, 1189–1202, doi:10.1126/science.192.4245.1189.
Edwards, P.N., 2010: *A Vast Machine: Computer Models, Climate Data, and the Politics of Global Warming*. MIT Press, Cambridge. MA, USA, 552 pp.
Edwards, P.N., 2011: History of climate modeling. *Wiley Interdisciplinary Reviews: Climate Change*, **2(1)**, 128–139, doi:10.1002/wcc.95.
Edwards, P.N., 2012: Entangled histories: Climate science and nuclear weapons research. *Bulletin of the Atomic Scientists*, **68(4)**, 28–40, doi:10.1177/0096340212451574.
Ekholm, N., 1901: On the variations of the climate of the geological and historical past and their causes. *Quarterly Journal of the Royal Meteorological Society*, **27(117)**, 1–62, doi:10.1002/qj.49702711702.
Eldering, A. et al., 2017: The Orbiting Carbon Observatory-2: first 18~months of science data products. *Atmospheric Measurement Techniques*, **10(2)**, 549–563, doi:10.5194/amt-10-549-2017.
Elliott, K.C., 2017: *A Tapestry of Values: An Introduction to Values in Science*. Oxford University Press, Oxford, UK, 224 pp.
Emiliani, C., 1955: Pleistocene Temperatures. *The Journal of Geology*, **63(6)**, 538–578, doi:10.1086/626295.
EPICA Community Members, 2004: Eight glacial cycles from an Antarctic ice core. *Nature*, **429(6992)**, 623–628, doi:10.1038/nature02599.
EPICA Community Members, 2006: One-to-one coupling of glacial climate variability in Greenland and Antarctica. *Nature*, **444(7116)**, 195–198, doi:10.1038/nature05301.
ESGF, 2021: input4MIPs Data Search on Earth System Grid Federation. Earth System Grid Federation (ESGF). Retrieved from: https://esgf-node.llnl.gov/search/input4mips.
Estrada, F., P. Perron, and B. Martínez-López, 2013: Statistically derived contributions of diverse human influences to twentieth-century temperature changes. *Nature Geoscience*, **6(12)**, 1050–1055, doi:10.1038/ngeo1999.
Evans, M.N., S.E. Tolwinski-Ward, D.M. Thompson, and K.J. Anchukaitis, 2013: Applications of proxy system modeling in high resolution paleoclimatology. *Quaternary Science Reviews*, **76**, 16–28, doi:10.1016/j.quascirev.2013.05.024.
Eyring, V. et al., 2016: Overview of the Coupled Model Intercomparison Project Phase 6 (CMIP6) experimental design and organization. *Geoscientific Model Development*, **9(5)**, 1937–1958, doi:10.5194/gmd-9-1937-2016.
Eyring, V. et al., 2019: Taking climate model evaluation to the next level. *Nature Climate Change*, **9(2)**, 102–110, doi:10.1038/s41558-018-0355-y.
Eyring, V. et al., 2020: Earth System Model Evaluation Tool (ESMValTool) v2.0 – an extended set of large-scale diagnostics for quasi-operational and comprehensive evaluation of Earth system models in CMIP. *Geoscientific Model Development*, **13(7)**, 3383–3438, doi:10.5194/gmd-13-3383-2020.
Faria, S.H., I. Weikusat, and N. Azuma, 2014: The microstructure of polar ice. Part II: State of the art. *Journal of Structural Geology*, **61**, 21–49, doi:10.1016/j.jsg.2013.11.003.
Faria, S.H., S. Kipfstuhl, and A. Lambrecht, 2018: *The EPICA-DML Deep Ice Core: A Visual Record*. Springer-Verlag, Berlin and Heidelberg, Germany, 305 pp., doi:10.1007/978-3-662-55308-4.
Fawcett, A.A. et al., 2015: Can Paris pledges avert severe climate change? *Science*, **350(6265)**, 1168–1169, doi:10.1126/science.aad5761.
Feng, L. et al., 2019: Gridded Emissions for CMIP6. *Geoscientific Model Development Discussions*, 1–25, doi:10.5194/gmd-2019-195.
Feng, L. et al., 2020: The generation of gridded emissions data for CMIP6. *Geoscientific Model Development*, **13(2)**, 461–482, doi:10.5194/gmd-13-461-2020.
Feng, S. et al., 2014: Projected climate regime shift under future global warming from multi-model, multi-scenario CMIP5 simulations. *Global and Planetary Change*, **112**, 41–52, doi:10.1016/j.gloplacha.2013.11.002.
Ferraro, R., D.E. Waliser, P. Gleckler, K.E. Taylor, and V. Eyring, 2015: Evolving Obs4MIPs to Support Phase 6 of the Coupled Model Intercomparison Project (CMIP6). *Bulletin of the American Meteorological Society*, **96(8)**, ES131–ES133, doi:10.1175/bams-d-14-00216.1.
Ferrel, W., 1856: An Essay on the Winds and Currents of the Ocean. *Nashville Journal of Medicine and Surgery*, **11(4–5)**, 287–301,375–389.
Feulner, G. and S. Rahmstorf, 2010: On the effect of a new grand minimum of solar activity on the future climate on Earth. *Geophysical Research Letters*, doi:10.1029/2010gl042710.
Fiedler, S., B. Stevens, and T. Mauritsen, 2017: On the sensitivity of anthropogenic aerosol forcing to model-internal variability and parameterizing a Twomey effect. *Journal of Advances in Modeling Earth Systems*, **9(2)**, 1325–

ACCEPTED VERSION SUBJECT TO FINAL EDITS

1341, doi:10.1002/2017ms000932.
Fischer, E.M., U. Beyerle, and R. Knutti, 2013: Robust spatially aggregated projections of climate extremes. *Nature Climate Change*, **3**, 1033, doi:10.1038/nclimate2051.
Fischer, E.M., J. Sedláček, E. Hawkins, and R. Knutti, 2014: Models agree on forced response pattern of precipitation and temperature extremes. *Geophysical Research Letters*, **41(23)**, 8554–8562, doi:10.1002/2014gl062018.
Fischer, E.M., U. Beyerle, C.F. Schleussner, A.D. King, and R. Knutti, 2018: Biased Estimates of Changes in Climate Extremes From Prescribed SST Simulations. *Geophysical Research Letters*, **45(16)**, 8500–8509, doi:10.1029/2018gl079176.
Fischer, H. et al., 2018: Palaeoclimate constraints on the impact of 2°C anthropogenic warming and beyond. *Nature Geoscience*, **11(7)**, 474–485, doi:10.1038/s41561-018-0146-0.
Fischlin, A., 2017: Background and role of science. In: *The Paris Agreement on Climate Change* [Klein, D., M.P. Carazo, M. Doelle, J. Bulmer, and A. Higham (eds.)]. Oxford University Press, Oxford, UK, pp. 3–16.
Fischlin, A., Z. Ji, F. Vladu, and A. Bisiaux, 2015: *Report on the Structured Expert Dialogue on the 2013-2015 Review of the United Nations Framework Convention on Climate Change (UNFCCC)*. FCCC/SB/2015/INF.1, Subsidiary Body for Implementation (SBI) and Subsidiary Body for Scientific and Technological Advice (SBSTA). UNFCCC Secretariat, Bonn, Germany, 182 pp.
Fisher, J.B. et al., 2017: The future of evapotranspiration: Global requirements for ecosystem functioning, carbon and climate feedbacks, agricultural management, and water resources. *Water Resources Research*, **53(4)**, 2618–2626, doi:10.1002/2016wr020175.
Flato, G. et al., 2013: Evaluation of Climate Models. In: *Climate Change 2013: The Physical Science Basis. Contribution of Working Group I to the Fifth Assessment Report of the Intergovernmental Panel on Climate Change* [Stocker, T.F., D. Qin, G.-K. Plattner, M. Tignor, S.K. Allen, J. Boschung, A. Nauels, Y. Xia, V. Bex, and P.M. Midgley (eds.)]. Cambridge University Press, Cambridge, United Kingdom and New York, NY, USA, pp. 741–866, doi:10.1017/cbo9781107415324.020.
Flato, G.M., 2011: Earth system models: an overview. *WIREs Climate Change*, **2(6)**, 783–800, doi:10.1002/wcc.148.
Fleming, J.R., 1998: *Historical Perspectives on Climate Change*. Oxford University Press, New York, NY, USA and Oxford, UK, 194 pp.
Fleming, J.R., 2007: *The Callendar Effect: The Life and Work of Guy Stewart Callendar (1898–1964), the Scientist Who Established the Carbon Dioxide Theory of Climate Change*. American Meteorological Society (AMS), Boston, MA, USA, 155 pp.
Fleurbaey, M. et al., 2014: Sustainable Development and Equity. In: *Climate Change 2014: Mitigation of Climate Change. Contribution of Working Group III to the Fifth Assessment Report of the Intergovernmental Panel on Climate Change* [Edenhofer, O., R. Pichs-Madruga, Y. Sokona, E. Farahani, S. Kadner, K. Seyboth, A. Adler, I. Baum, S. Brunner, P. Eickemeier, B. Kriemann, J. Savolainen, S. Schlömer, C. von Stechow, T. Zwickel, and J.C. Minx (eds.)]. Cambridge University Press, Cambridge, United Kingdom and New York, NY, USA, pp. 283–350, doi:10.1017/cbo9781107415416.010.
Fløttum, K. and Gjerstad, 2017: Narratives in climate change discourse. *Wiley Interdisciplinary Reviews: Climate Change*, **8(1)**, e429, doi:10.1002/wcc.429.
Foelsche, U. et al., 2008: An observing system simulation experiment for climate monitoring with GNSS radio occultation data: Setup and test bed study. *Journal of Geophysical Research*, **113(D11)**, D11108, doi:10.1029/2007jd009231.
Foote, E., 1856: Circumstances affecting the Heat of the Sun's Rays. *The American Journal of Science and Arts*, **22(65)**, 382–383.
Forster, P.M. et al., 2013: Evaluating adjusted forcing and model spread for historical and future scenarios in the CMIP5 generation of climate models. *Journal of Geophysical Research: Atmospheres*, **118(3)**, 1139–1150, doi:10.1002/jgrd.50174.
Forster, P.M. et al., 2020: Current and future global climate impacts resulting from COVID-19. *Nature Climate Change*, **10(10)**, 913–919, doi:10.1038/s41558-020-0883-0.
Foster, G.L., D.L. Royer, and D.J. Lunt, 2017: Future climate forcing potentially without precedent in the last 420 million years. *Nature Communications*, **8**, 14845, doi:10.1038/ncomms14845.
Fourier, J.B.J., 1822: *Théorie Analytique de la Chaleur*. Firmin Didot, Paris, France, 639 pp.
Fowle, F.E., 1917: Water-Vapor Transparency to Low-Temperature Radiation. *Smithsonian Miscellaneous Collections*, **68(8)**, 1–68.
Frakes, L.A., J.E. Francis, and J.I. Syktus, 1992: *Climate modes of the Phanerozoic*. Cambridge University Press, Cambridge, UK, 274 pp., doi:10.1017/cbo9780511628948.
Frame, D., M.F. Wehner, I. Noy, and S.M. Rosier, 2020: The economic costs of Hurricane Harvey attributable to climate change. *Climatic Change*, **160(2)**, 271–281, doi:10.1007/s10584-020-02692-8.
Frame, D., M. Joshi, E. Hawkins, L.J. Harrington, and M. de Roiste, 2017: Population-based emergence of unfamiliar climates. *Nature Climate Change*, **7(6)**, 407, doi:10.1038/nclimate3297.
Franke, J., S. Brönnimann, J. Bhend, and Y. Brugnara, 2017: A monthly global paleo-reanalysis of the atmosphere from 1600 to 2005 for studying past climatic variations. *Scientific Data*, **4(1)**, 170076, doi:10.1038/sdata.2017.76.

ACCEPTED VERSION SUBJECT TO FINAL EDITS

Frappart, F. and G. Ramillien, 2018: Monitoring Groundwater Storage Changes Using the Gravity Recovery and Climate Experiment (GRACE) Satellite Mission: A Review. *Remote Sensing*, **10(6)**, 829, doi:10.3390/rs10060829.

Freeman, E. et al., 2017: ICOADS Release 3.0: a major update to the historical marine climate record. *International Journal of Climatology*, **37(5)**, 2211–2232, doi:10.1002/joc.4775.

Freund, M.B. et al., 2019: Higher frequency of Central Pacific El Niño events in recent decades relative to past centuries. *Nature Geoscience*, **12(6)**, 450–455, doi:10.1038/s41561-019-0353-3.

Friedlingstein, P. et al., 2014: Uncertainties in CMIP5 Climate Projections due to Carbon Cycle Feedbacks. *Journal of Climate*, **27(2)**, 511–526, doi:10.1175/jcli-d-12-00579.1.

Frieler, K. et al., 2012: A Scaling Approach to Probabilistic Assessment of Regional Climate Change. *Journal of Climate*, **25(9)**, 3117–3144, doi:10.1175/jcli-d-11-00199.1.

Frölicher, T.L. and D.J. Paynter, 2015: Extending the relationship between global warming and cumulative carbon emissions to multi-millennial timescales. *Environmental Research Letters*, **10(7)**, 075002, doi:10.1088/1748-9326/10/7/075002.

Fu, L.-L. et al., 1994: TOPEX/POSEIDON mission overview. *Journal of Geophysical Research*, **99(C12)**, 24369, doi:10.1029/94jc01761.

Fujimori, S., K. Oshiro, H. Shiraki, and T. Hasegawa, 2019: Energy transformation cost for the Japanese mid-century strategy. *Nature Communications*, **10(1)**, 4737, doi:10.1038/s41467-019-12730-4.

Fuss, S. et al., 2018: Negative emissions-Part 2: Costs, potentials and side effects. *Environmental Research Letters*, **13(6)**, 063002, doi:10.1088/1748-9326/aabf9f.

Fyfe, J.C. et al., 2017: Large near-term projected snowpack loss over the western United States. *Nature Communications*, **8(1)**, 14996, doi:10.1038/ncomms14996.

Gabrielli, P. et al., 2016: Age of the Mt.~Ortles ice cores, the Tyrolean Iceman and glaciation of the highest summit of South Tyrol since the Northern Hemisphere Climatic Optimum. *The Cryosphere*, **10(6)**, 2779–2797, doi:10.5194/tc-10-2779-2016.

Galbraith, E.D. and A.C. Martiny, 2015: A simple nutrient-dependence mechanism for predicting the stoichiometry of marine ecosystems. *Proceedings of the National Academy of Sciences*, **112(27)**, 8199–8204, doi:10.1073/pnas.1423917112.

Gao, J. et al., 2020: Influence of model resolution on bomb cyclones revealed by HighResMIP-PRIMAVERA simulations. *Environmental Research Letters*, **15(8)**, 84001, doi:10.1088/1748-9326/ab88fa.

Gärtner-Roer, I. et al., 2014: A database of worldwide glacier thickness observations. *Global and Planetary Change*, **122**, 330–344, doi:10.1016/j.gloplacha.2014.09.003.

Gasser, T. et al., 2017: The compact Earth system model OSCAR v2.2: description and first results. *Geosci. Model Dev*, **10**, 271–319, doi:10.5194/gmd-10-271-2017.

Gates, W.L. et al., 1999: An Overview of the Results of the Atmospheric Model Intercomparison Project (AMIP I). *Bulletin of the American Meteorological Society*, **80(1)**, 29–55, doi:10.1175/1520-0477(1999)080<0029:aootro>2.0.co;2.

Ge, Q. et al., 2008: Coherence of climatic reconstruction from historical documents in China by different studies. *International Journal of Climatology*, **28(8)**, 1007–1024, doi:10.1002/joc.1552.

Gearheard, S., M. Pocernich, R. Stewart, J. Sanguya, and H.P. Huntington, 2010: Linking Inuit knowledge and meteorological station observations to understand changing wind patterns at Clyde River, Nunavut. *Climatic Change*, **100(2)**, 267–294, doi:10.1007/s10584-009-9587-1.

Gelaro, R. et al., 2017: The modern-era retrospective analysis for research and applications, version 2 (MERRA-2). *Journal of Climate*, **30(14)**, 5419–5454, doi:10.1175/jcli-d-16-0758.1.

Gerber, E.P. and E. Manzini, 2016: The Dynamics and Variability Model Intercomparison Project (DynVarMIP) for CMIP6: assessing the stratosphere–troposphere system. *Geoscientific Model Development*, **9(9)**, 3413–3425, doi:10.5194/gmd-9-3413-2016.

Gettelman, A. and S.C. Sherwood, 2016: Processes Responsible for Cloud Feedback. *Current Climate Change Reports*, **2(4)**, 179–189, doi:10.1007/s40641-016-0052-8.

Gettelman, A. et al., 2019: High Climate Sensitivity in the Community Earth System Model Version 2 (CESM2). *Geophysical Research Letters*, **46(14)**, 8329–8337, doi:10.1029/2019gl083978.

Gidden, M.J. et al., 2018: A methodology and implementation of automated emissions harmonization for use in Integrated Assessment Models. *Environmental Modelling & Software*, **105**, 187–200, doi:10.1016/j.envsoft.2018.04.002.

Gidden, M.J. et al., 2019: Global emissions pathways under different socioeconomic scenarios for use in CMIP6: a dataset of harmonized emissions trajectories through the end of the century. *Geoscientific Model Development*, **12(4)**, 1443–1475, doi:10.5194/gmd-12-1443-2019.

Gillett, N.P., F.W. Zwiers, A.J. Weaver, and P.A. Stott, 2003: Detection of human influence on sea-level pressure. *Nature*, **422(6929)**, 292–294, doi:10.1038/nature01487.

Gillett, N.P. et al., 2016: The Detection and Attribution Model Intercomparison Project (DAMIP v1.0) contribution to CMIP6. *Geoscientific Model Development*, **9(10)**, 3685–3697, doi:10.5194/gmd-9-3685-2016.

ACCEPTED VERSION SUBJECT TO FINAL EDITS

Gillett, N.P. et al., 2021: Constraining human contributions to observed warming since the pre-industrial period. *Nature Climate Change*, **11**, doi:10.1038/s41558-020-00965-9.
Giorgetta, M.A. et al., 2018: ICON-A, the Atmosphere Component of the ICON Earth System Model: I. Model Description. *Journal of Advances in Modeling Earth Systems*, **10(7)**, 1613–1637, doi:10.1029/2017ms001242.
Giorgi, F. and X. Bi, 2009: Time of emergence (TOE) of GHG-forced precipitation change hot-spots. *Geophysical Research Letters*, **36(6)**, 653–656, doi:10.1029/2009gl037593.
Giorgi, F. and W.J. Gutowski, 2015: Regional Dynamical Downscaling and the CORDEX Initiative. *Annual Review of Environment and Resources*, **40(1)**, 467–490, doi:10.1146/annurev-environ-102014-021217.
Gleisner, H., K.B. Lauritsen, J.K. Nielsen, and S. Syndergaard, 2020: Evaluation of the 15-year ROM SAF monthly mean GPS radio occultation climate data record. *Atmospheric Measurement Techniques*, **13(6)**, 3081–3098, doi:10.5194/amt-13-3081-2020.
Gobron, N., M.M. Verstraete, B. Pinty, M. Taberner, and O. Aussedat, 2009: Potential of long time series of FAPAR products for assessing and monitoring land surface changes: Examples in Europe and the Sahel. In: *Recent Advances in Remote Sensing and Geoinformation Processing for Land Degradation Assessment* [Roeder, A. and H. Joachim (eds.)]. CRC Press, London, UK, pp. 89–102.
Goelzer, H. et al., 2018: Design and results of the ice sheet model initialisation experiments initMIP-Greenland: an ISMIP6 intercomparison. *The Cryosphere*, **12(4)**, 1433–1460, doi:10.5194/tc-12-1433-2018.
Golaz, J.-C. et al., 2019: The DOE E3SM Coupled Model Version 1: Overview and Evaluation at Standard Resolution. *Journal of Advances in Modeling Earth Systems*, **11(7)**, 2089–2129, doi:10.1029/2018ms001603.
Goni, G.J. et al., 2019: More Than 50 Years of Successful Continuous Temperature Section Measurements by the Global Expendable Bathythermograph Network, Its Integrability, Societal Benefits, and Future. *Frontiers in Marine Science*, **6**, doi:10.3389/fmars.2019.00452.
Good, P., C. Jones, J. Lowe, R. Betts, and N. Gedney, 2013: Comparing Tropical Forest Projections from Two Generations of Hadley Centre Earth System Models, HadGEM2-ES and HadCM3LC. *Journal of Climate*, **26(2)**, 495–511, doi:10.1175/jcli-d-11-00366.1.
Gottschalk, J. et al., 2018: Radiocarbon Measurements of Small-Size Foraminiferal Samples with the Mini Carbon Dating System (MICADAS) at the University of Bern: Implications for Paleoclimate Reconstructions. *Radiocarbon*, **60(2)**, 469–491, doi:10.1017/rdc.2018.3.
Gould, J., 2003: WOCE and TOGA-The Foundations of the Global Ocean Observing System. *Oceanography*, **16(4)**, 24–30, doi:10.5670/oceanog.2003.05.
Gramelsberger, G., J. Lenhard, and W.S. Parker, 2020: Philosophical Perspectives on Earth System Modeling: Truth, Adequacy, and Understanding. *Journal of Advances in Modeling Earth Systems*, **12(1)**, e2019MS001720, doi:10.1029/2019ms001720.
Grant, G.R. et al., 2019: The amplitude and origin of sea-level variability during the Pliocene epoch. *Nature*, **574(7777)**, 237–241, doi:10.1038/s41586-019-1619-z.
Grassi, G. et al., 2017: The key role of forests in meeting climate targets requires science for credible mitigation. *Nature Climate Change*, **7(3)**, 220–226, doi:10.1038/nclimate3227.
Green, C. et al., 2020: Shared Socioeconomic Pathways (SSPs) Literature Database, Version 1, 2014-2019. National Aeronautics and Space Administration (NASA) Socioeconomic Data and Applications Center (SEDAC), Palisades, NY, USA.
Green, D., J. Billy, and A. Tapim, 2010: Indigenous Australians' knowledge of weather and climate. *Climatic Change*, **100(2)**, 337–354, doi:10.1007/s10584-010-9803-z.
Gregory, J.M., T. Andrews, P. Good, T. Mauritsen, and P.M. Forster, 2016a: Small global-mean cooling due to volcanic radiative forcing. *Climate Dynamics*, **47(12)**, 3979–3991, doi:10.1007/s00382-016-3055-1.
Gregory, J.M. et al., 2004: A new method for diagnosing radiative forcing and climate sensitivity. *Geophysical Research Letters*, **31(3)**, L03205, doi:10.1029/2003gl018747.
Gregory, J.M. et al., 2016b: The Flux-Anomaly-Forced Model Intercomparison Project (FAFMIP) contribution to CMIP6: investigation of sea-level and ocean climate change in response to CO2 forcing. *Geoscientific Model Development*, **9(11)**, 3993–4017, doi:10.5194/gmd-9-3993-2016.
Griffies, S.M. et al., 2016: OMIP contribution to CMIP6: experimental and diagnostic protocol for the physical component of the Ocean Model Intercomparison Project. *Geoscientific Model Development*, **9(9)**, 3231–3296, doi:10.5194/gmd-9-3231-2016.
Grose, M.R., J.S. Risbey, and P.H. Whetton, 2017: Tracking regional temperature projections from the early 1990s in light of variations in regional warming, including 'warming holes'. *Climatic Change*, **140(2)**, 307–322, doi:10.1007/s10584-016-1840-9.
Grose, M.R., J. Gregory, R. Colman, and T. Andrews, 2018: What Climate Sensitivity Index Is Most Useful for Projections? *Geophysical Research Letters*, **45(3)**, 1559–1566, doi:10.1002/2017gl075742.
Grose, M.R. et al., 2019: The warm and extremely dry spring in 2015 in Tasmania contained the fingerprint of human influence on the climate. *Journal of Southern Hemisphere Earth Systems Science*, **69(1)**, 183, doi:10.1071/es19011.
Grothe, P.R. et al., 2019: Enhanced El Niño-Southern Oscillation variability in recent decades. *Geophysical Research*

ACCEPTED VERSION SUBJECT TO FINAL EDITS

Letters, **46(n/a)**, doi:10.1029/2019gl083906.
Grove, R.H., 1995: *Green Imperialism: Colonial Expansion, Tropical Island Edens and the Origins of Environmentalism, 1600-1860*. Cambridge University Press, Cambridge, UK, 540 pp.
Gryspeerdt, E. and P. Stier, 2012: Regime-based analysis of aerosol-cloud interactions. *Geophysical Research Letters*, **39(21)**, n/a–n/a, doi:10.1029/2012gl053221.
Guan, B. and D.E. Waliser, 2017: Atmospheric rivers in 20 year weather and climate simulations: A multimodel, global evaluation. *Journal of Geophysical Research: Atmospheres*, **122(11)**, 5556–5581, doi:10.1002/2016jd026174.
Guanter, L. et al., 2014: Global and time-resolved monitoring of crop photosynthesis with chlorophyll fluorescence. *Proceedings of the National Academy of Sciences*, **111(14)**, E1327 LP – E1333, doi:10.1073/pnas.1320008111.
Guilyardi, E. et al., 2016: Fourth CLIVAR Workshop on the Evaluation of ENSO Processes in Climate Models: ENSO in a Changing Climate. *Bulletin of the American Meteorological Society*, **97(5)**, 817–820, doi:10.1175/bams-d-15-00287.1.
Gutowski Jr., W.J. et al., 2016: WCRP COordinated Regional Downscaling EXperiment (CORDEX): a diagnostic MIP for CMIP6. *Geoscientific Model Development*, **9(11)**, 4087–4095, doi:10.5194/gmd-9-4087-2016.
Gütschow, J., M.L. Jeffery, M. Schaeffer, and B. Hare, 2018: Extending Near-Term Emissions Scenarios to Assess Warming Implications of Paris Agreement NDCs. *Earth's Future*, **6(9)**, 1242–1259, doi:10.1002/2017ef000781.
Haarsma, R.J. et al., 2016: High Resolution Model Intercomparison Project (HighResMIP v1.0) for CMIP6. *Geoscientific Model Development*, **9(11)**, 4185–4208, doi:10.5194/gmd-9-4185-2016.
Hadley, G., 1735: Concerning the Cause of the General Trade-Winds. *Philosophical Transactions of the Royal Society of London*, **39**, 58–62, doi:10.1098/rstl.1735.0014.
Haimberger, L., C. Tavolato, and S. Sperka, 2012: Homogenization of the global radiosonde temperature dataset through combined comparison with reanalysis background series and neighboring stations. *Journal of Climate*, **25(23)**, 8108–8131, doi:10.1175/jcli-d-11-00668.1.
Hajima, T. et al., 2014: Modeling in Earth system science up to and beyond IPCC AR5. *Progress in Earth and Planetary Science*, **1(1)**, 29, doi:10.1186/s40645-014-0029-y.
Hakim, G.J. et al., 2016: The last millennium climate reanalysis project: Framework and first results. *Journal of Geophysical Research: Atmospheres*, **121(12)**, 6745–6764, doi:10.1002/2016jd024751.
Hall, A., P. Cox, C. Huntingford, and S. Klein, 2019: Progressing emergent constraints on future climate change. *Nature Climate Change*, **9(4)**, 269–278, doi:10.1038/s41558-019-0436-6.
Hall, M.J. and D.C. Weiss, 2012: Avoiding Adaptation Apartheid: Climate Change Adaptation and Human Rights Law. *Yale Journal of International Law*, **37(2)**, 310–366.
Halley, E., 1686: An Historical Account of the Trade Winds, and Monsoons, Observable in the Seas between and Near the Tropicks, with an Attempt to Assign the Phisical Cause of the Said Winds. *Philosophical Transactions of the Royal Society of London*, **1(183)**, 153–168, doi:10.1098/rstl.1686.0026.
Halsnæs, K. and P.S. Kaspersen, 2018: Decomposing the cascade of uncertainty in risk assessments for urban flooding reflecting critical decision-making issues. *Climatic Change*, **151(3–4)**, 491–506, doi:10.1007/s10584-018-2323-y.
Hamilton, D.S. et al., 2018: Reassessment of pre-industrial fire emissions strongly affects anthropogenic aerosol forcing. *Nature Communications*, **9(1)**, 3182, doi:10.1038/s41467-018-05592-9.
Hamilton, L.C. and M.D. Stampone, 2013: Blowin' in the Wind: Short-Term Weather and Belief in Anthropogenic Climate Change. *Weather, Climate, and Society*, **5(2)**, 112–119, doi:10.1175/wcas-d-12-00048.1.
Hanna, E. et al., 2020: Mass balance of the ice sheets and glaciers – Progress since AR5 and challenges. *Earth-Science Reviews*, **201**, 102976, doi:10.1016/j.earscirev.2019.102976.
Hansen, G., D. Stone, M. Auffhammer, C. Huggel, and W. Cramer, 2016: Linking local impacts to changes in climate: a guide to attribution. *Regional Environmental Change*, **16(2)**, 527–541, doi:10.1007/s10113-015-0760-y.
Hansen, J. and S. Lebedeff, 1987: Global Trends of Measured Surface Air Temperature. *Journal of Geophysical Research*, doi:10.1029/jd092id11p13345.
Hansen, J., M. Sato, G. Russell, and P. Kharecha, 2013: Climate sensitivity, sea level and atmospheric carbon dioxide. *Philosophical Transactions of the Royal Society A: Mathematical, Physical and Engineering Sciences*, **371(2001)**, 20120294, doi:10.1098/rsta.2012.0294.
Hansen, J. et al., 1981: Climate Impact of Increasing Atmospheric Carbon Dioxide. *Science*, **213(4511)**, 957–966, doi:10.1126/science.213.4511.957.
Hansen, J. et al., 1988: Global climate changes as forecast by Goddard Institute for Space Studies three-dimensional model. *Journal of Geophysical Research*, **93(D8)**, 9341, doi:10.1029/jd093id08p09341.
Harada, Y. et al., 2016: The JRA-55 Reanalysis: Representation of Atmospheric Circulation and Climate Variability. *Journal of the Meteorological Society of Japan. Ser. II*, **94(3)**, 269–302, doi:10.2151/jmsj.2016-015.
Harcourt, R. et al., 2019: Animal-Borne Telemetry: An Integral Component of the Ocean Observing Toolkit. *Frontiers in Marine Science*, **6**, 326, doi:10.3389/fmars.2019.00326.
Harper, K.C., 2008: *Weather by the Numbers: The Genesis of Modern Meteorology*. MIT Press, Cambridge, MA, USA,

ACCEPTED VERSION SUBJECT TO FINAL EDITS

320 pp.
Harries, J.E., H.E. Brindley, P.J. Sagoo, and R.J. Bantges, 2001: Increases in greenhouse forcing inferred from the outgoing longwave radiation spectra of the Earth in 1970 and 1997. *Nature*, **410(6826)**, 355–357, doi:10.1038/35066553.
Harrington, L.J. and F.E.L. Otto, 2018: Changing population dynamics and uneven temperature emergence combine to exacerbate regional exposure to heat extremes under 1.5 ◦C and 2 ◦C of warming. *Environmental Research Letters*, doi:10.1088/1748-9326/aaaa99.
Harrington, L.J. et al., 2016: Poorest countries experience earlier anthropogenic emergence of daily temperature extremes. *Environmental Research Letters*, **11(5)**, 055007, doi:10.1088/1748-9326/11/5/055007.
Harris, A.J.L., A. Corner, J. Xu, and X. Du, 2013: Lost in translation? Interpretations of the probability phrases used by the Intergovernmental Panel on Climate Change in China and the UK. *Climatic Change*, **121(2)**, 415–425, doi:10.1007/s10584-013-0975-1.
Hartmann, D.L. et al., 2013: Observations: Atmosphere and Surface. In: *Climate Change 2013: The Physical Science Basis. Contribution of Working Group I to the Fifth Assessment Report of the Intergovernmental Panel on Climate Change* [Stocker, T.F., D. Qin, G.-K. Plattner, M. Tignor, S.K. Allen, J. Boschung, A. Nauels, Y. Xia, V. Bex, and P.M. Midgley (eds.)]. Cambridge University Press, Cambridge, United Kingdom and New York, NY, USA, pp. 159–254, doi:10.1017/cbo9781107415324.008.
Hasselmann, K., 1979: On the signal-to-noise problem in atmospheric response studies. In: *Meteorology Over the Tropical Oceans* [Shaw, D.B. (ed.)]. Royal Meteorological Society, Bracknell, UK, pp. 251–259.
Hassol, S.J., S. Torok, and S.L. Lewis Patrick, 2016: (Un)Natural Disasters: Communicating Linkages Between Extreme Events and Climate Change. *WMO Bulletin*, **65(2)**.
Hattermann, F.F. et al., 2018: Sources of uncertainty in hydrological climate impact assessment: a cross-scale study. *Environmental Research Letters*, **13(1)**, 015006, doi:10.1088/1748-9326/aa9938.
Haug, G.H., K.A. Hughen, D.M. Sigman, L.C. Peterson, and U. Röhl, 2001: Southward Migration of the Intertropical Convergence Zone Through the Holocene. *Science*, **293(5533)**, 1304–1308, doi:10.1126/science.1059725.
Haughton, N., G. Abramowitz, A. Pitman, and S.J. Phipps, 2015: Weighting climate model ensembles for mean and variance estimates. *Climate Dynamics*, **45(11–12)**, 3169–3181, doi:10.1007/s00382-015-2531-3.
Haunschild, R., L. Bornmann, and W. Marx, 2016: Climate Change Research in View of Bibliometrics. *PLOS ONE*, **11(7)**, e0160393, doi:10.1371/journal.pone.0160393.
Hauser, M., R. Orth, and S.I. Seneviratne, 2016: Role of soil moisture versus recent climate change for the 2010 heat wave in western Russia. *Geophysical Research Letters*, **43(6)**, 2819–2826, doi:10.1002/2016gl068036.
Hausfather, Z. and G.P. Peters, 2020a: Emissions – the 'business as usual' story is misleading. *Nature*, **577(7792)**, 618–620, doi:10.1038/d41586-020-00177-3.
Hausfather, Z. and G.P. Peters, 2020b: RCP8.5 is a problematic scenario for near-term emissions. *Proceedings of the National Academy of Sciences*, **117(45)**, 27791–27792, doi:10.1073/pnas.2017124117.
Hausfather, Z., H.F. Drake, T. Abbott, and G.A. Schmidt, 2020: Evaluating the performance of past climate model projections. *Geophysical Research Letters*, **47**, e2019GL085378, doi:10.1029/2019gl085378.
Haustein, K. et al., 2017: A real-time Global Warming Index. *Scientific Reports*, **7(1)**, 15417, doi:10.1038/s41598-017-14828-5.
Hawkins, E. and R. Sutton, 2009: The Potential to Narrow Uncertainty in Regional Climate Predictions. *Bulletin of the American Meteorological Society*, **90(8)**, 1095–1108, doi:10.1175/2009bams2607.1.
Hawkins, E. and R. Sutton, 2012: Time of emergence of climate signals. *Geophysical Research Letters*, **39(1)**, doi:10.1029/2011gl050087.
Hawkins, E. and P.D. Jones, 2013: On increasing global temperatures: 75 years after Callendar. *Quarterly Journal of the Royal Meteorological Society*, **139(677)**, doi:10.1002/qj.2178.
Hawkins, E. and R. Sutton, 2016: Connecting climate model projections of global temperature change with the real world. *Bulletin of the American Meteorological Society*, **97(6)**, doi:10.1175/bams-d-14-00154.1.
Hawkins, E., R.S. Smith, J.M. Gregory, and D.A. Stainforth, 2016: Irreducible uncertainty in near-term climate projections. *Climate Dynamics*, **46(11)**, 3807–3819, doi:10.1007/s00382-015-2806-8.
Hawkins, E. et al., 2017: Estimating changes in global temperature since the preindustrial period. *Bulletin of the American Meteorological Society*, **98(9)**, doi:10.1175/bams-d-16-0007.1.
Hawkins, E. et al., 2019: Hourly weather observations from the Scottish Highlands (1883–1904) rescued by volunteer citizen scientists. *Geoscience Data Journal*, **n/a(n/a)**, doi:10.1002/gdj3.79.
Hawkins, E. et al., 2020: Observed emergence of the climate change signal: from the familiar to the unknown. *Geophysical Reasearch Letters*, **47(6)**, e2019GL086259.
Hays, J.D., J. Imbrie, and N.J. Shackleton, 1976: Variations in the Earth's Orbit: Pacemaker of the Ice Ages. *Science*, **194(4270)**, 1121–1132, doi:10.1126/science.194.4270.1121.
Haywood, A.M. et al., 2016: The Pliocene Model Intercomparison Project (PlioMIP) Phase 2: scientific objectives and experimental design. *Climate of the Past*, **12(3)**, 663–675, doi:10.5194/cp-12-663-2016.
Hazeleger, W. et al., 2015: Tales of future weather. *Nature Climate Change*, **5(2)**, 107–113, doi:10.1038/nclimate2450.
Head, L., M. Adams, H. Mcgregor, and S. Toole, 2014: Climate change and Australia. *WIREs Clim Change*, **5**, 175–

ACCEPTED VERSION SUBJECT TO FINAL EDITS

197, doi:10.1002/wcc.255.
Hegdahl, T.J., K. Engeland, M. Müller, and J. Sillmann, 2020: An Event-Based Approach to Explore Selected Present and Future Atmospheric River–Induced Floods in Western Norway. *Journal of Hydrometeorology*, **21(9)**, 2003–2021, doi:10.1175/jhm-d-19-0071.1.
Hegerl, G. et al., 2011: Influence of human and natural forcing on European seasonal temperatures. *Nature Geoscience*, **4(2)**, 99–103, doi:10.1038/ngeo1057.
Hegerl, G.C. et al., 1996: Detecting Greenhouse-Gas-Induced Climate Change with an Optimal Fingerprint Method. *Journal of Climate*, **9(10)**, 2281–2306, doi:10.1175/1520-0442(1996)009<2281:dggicc>2.0.co;2.
Hegerl, G.C. et al., 1997: Multi-fingerprint detection and attribution analysis of greenhouse gas, greenhouse gas-plus-aerosol and solar forced climate change. *Climate Dynamics*, **13(9)**, 613–634, doi:10.1007/s003820050186.
Hegerl, G.C. et al., 2010: Good Practice Guidance Paper on Detection and Attribution Related to Anthropogenic Climate Change. In: *Meeting Report of the Intergovernmental Panel on Climate Change Expert Meeting on Detection and Attribution of Anthropogenic Climate Change* []. IPCC Working Group I Technical Support Unit, Bern, Switzerland, pp. 1–8.
Heimbach, P. et al., 2019: Putting It All Together: Adding Value to the Global Ocean and Climate Observing Systems With Complete Self-Consistent Ocean State and Parameter Estimates. *Frontiers in Marine Science*, **6**, 55, doi:10.3389/fmars.2019.00055.
Held, I.M. et al., 2010: Probing the Fast and Slow Components of Global Warming by Returning Abruptly to Preindustrial Forcing. *Journal of Climate*, **23(9)**, 2418–2427, doi:10.1175/2009jcli3466.1.
Herger, N., B.M. Sanderson, and R. Knutti, 2015: Improved pattern scaling approaches for the use in climate impact studies. *Geophysical Research Letters*, **42(9)**, 3486–3494, doi:10.1002/2015gl063569.
Herger, N. et al., 2018a: Selecting a climate model subset to optimise key ensemble properties. *Earth System Dynamics*, **9(1)**, 135–151, doi:10.5194/esd-9-135-2018.
Herger, N. et al., 2018b: Calibrating Climate Model Ensembles for Assessing Extremes in a Changing Climate. *Journal of Geophysical Research: Atmospheres*, **123(11)**, 5988–6004, doi:10.1029/2018jd028549.
Hermes, J.C. et al., 2019: A Sustained Ocean Observing System in the Indian Ocean for Climate Related Scientific Knowledge and Societal Needs. *Frontiers in Marine Science*, **6**, 355, doi:10.3389/fmars.2019.00355.
Hernández, A. et al., 2020: Modes of climate variability: Synthesis and review of proxy-based reconstructions through the Holocene. *Earth-Science Reviews*, **209**, 103286, doi:10.1016/j.earscirev.2020.103286.
Herring, S.C., N. Christidis, A. Hoell, M.P. Hoerling, and P.A. Stott, 2021: Explaining Extreme Events of 2019 from a Climate Perspective. *Bulletin of the American Meteorological Society*, **102(1)**, S1–S116, doi:10.1175/bams-explainingextremeevents2019.1.
Hersbach, H. et al., 2020: The ERA5 global reanalysis. *Quarterly Journal of the Royal Meteorological Society*, doi:10.1002/qj.3803.
Hewitson, B. et al., 2014: Regional context. In: *Climate Change 2014: Impacts, Adaptation, and Vulnerability. Part B: Regional Aspects. Contribution of Working Group II to the Fifth Assessment Report of the Intergovernmental Panel on Climate Change* [Barros, V.R., C.B. Field, D.J. Dokken, M.D. Mastrandrea, K.J. Mach, T.E. Bilir, M. Chatterjee, K.L. Ebi, Y.O. Estrada, R.C. Genova, B. Girma, E.S. Kissel, A.N. Levy, S. MacCracken, P.R. Mastrandrea, and L.L. White (eds.)]. Cambridge University Press, Cambridge, United Kingdom and New York, NY, USA, pp. 1133–1197, doi:10.1017/cbo9781107415386.001.
Hewitt, C., S. Mason, and D. Walland, 2012: The Global Framework for Climate Services. *Nature Climate Change*, **2(12)**, 831–832, doi:10.1038/nclimate1745.
Hewitt, C.D., R.C. Stone, and A.B. Tait, 2017: Improving the use of climate information in decision-making. *Nature Climate Change*, **7(9)**, doi:10.1038/nclimate3378.
Hewitt, H.T. et al., 2017: Will high-resolution global ocean models benefit coupled predictions on short-range to climate timescales? *Ocean Modelling*, **120**, 120–136, doi:10.1016/j.ocemod.2017.11.002.
Heymann, M., G. Gramelsberger, and M. Mahony (eds.), 2017: *Cultures of Prediction in Atmospheric and Climate Science: Epistemic and Cultural Shifts in Computer-based Modelling and Simulation*. Taylor & Francis, Abingdon, Oxon, UK and New York, NY, USA, 272 pp.
Hidy, G.M., 2019: Atmospheric Aerosols: Some Highlights and Highlighters, 1950 to 2018. *Aerosol Science and Engineering*, **3(1)**, 1–20, doi:10.1007/s41810-019-00039-0.
Hine, D.W. et al., 2015: Preaching to different choirs: How to motivate dismissive, uncommitted, and alarmed audiences to adapt to climate change? *Global Environmental Change*, **36**, 1–11.
Ho, E., D. Budescu, V. Bosetti, D.P. van Vuuren, and K. Keller, 2019: Not all carbon dioxide emission scenarios are equally likely: a subjective expert assessment. *Climatic Change*, **155(4)**, 545–561, doi:10.1007/s10584-019-02500-y.
Hochman, Z., D.L. Gobbett, and H. Horan, 2017: Climate trends account for stalled wheat yields in Australia since 1990. *Global Change Biology*, **23(5)**, 2071–2081, doi:10.1111/gcb.13604.
Hoegh-Guldberg, O. and J.F. Bruno, 2010: The Impact of Climate Change on the World's Marine Ecosystems. *Science*, **328(5985)**, 1523–1528, doi:10.1126/science.1189930.
Hoegh-Guldberg, O. et al., 2019: The human imperative of stabilizing global climate change at 1.5°C. *Science*,

ACCEPTED VERSION SUBJECT TO FINAL EDITS

365(6459), eaaw6974, doi:10.1126/science.aaw6974.
Hoekstra, R. and J.C.J.M. van den Bergh, 2003: Comparing structural decomposition analysis and index. *Energy Economics*, **25(1)**, 39–64, doi:10.1016/s0140-9883(02)00059-2.
Hoesly, R.M. et al., 2018: Historical (1750–2014) anthropogenic emissions of reactive gases and aerosols from the Community Emissions Data System (CEDS). *Geoscientific Model Development*, **11(1)**, 369–408, doi:10.5194/gmd-11-369-2018.
Hoffmann, L. et al., 2019: From ERA-Interim to ERA5: The considerable impact of ECMWF's next-generation reanalysis on Lagrangian transport simulations. *Atmospheric Chemistry and Physics*, **19(5)**, 3097–3214, doi:10.5194/acp-19-3097-2019.
Högbom, A., 1894: Om sannolikheten för sekulära förändringar i atmosfärens kolsyrehalt. *Svensk Kemisk Tidskrift*, **4**, 169–177.
Hollis, C.J. et al., 2019: The DeepMIP contribution to PMIP4: methodologies for selection, compilation and analysis of latest Paleocene and early Eocene climate proxy data, incorporating version 0.1 of the DeepMIP database. *Geoscientific Model Development*, **12(7)**, 3149–3206, doi:10.5194/gmd-12-3149-2019.
Hollmann, R. et al., 2013: The ESA Climate Change Initiative: Satellite Data Records for Essential Climate Variables. *Bulletin of the American Meteorological Society*, **94(10)**, 1541–1552, doi:10.1175/bams-d-11-00254.1.
Hönisch, B. et al., 2012: The Geological Record of Ocean Acidification. *Science*, **335(6072)**, 1058 LP – 1063, doi:10.1126/science.1208277.
Hourdin, F. et al., 2017: The Art and Science of Climate Model Tuning. *Bulletin of the American Meteorological Society*, **98(3)**, 589–602, doi:10.1175/bams-d-15-00135.1.
House, F.B., A. Gruber, G.E. Hunt, and A.T. Mecherikunnel, 1986: History of satellite missions and measurements of the Earth Radiation Budget (1957–1984). *Reviews of Geophysics*, **24(2)**, 357–377, doi:10.1029/rg024i002p00357.
Howe, P.D., M. Mildenberger, J.R. Marlon, and A. Leiserowitz, 2015: Geographic variation in opinions on climate change at state and local scales in the USA. *Nature Climate Change*, **5(6)**, 596–603, doi:10.1038/nclimate2583.
Howell, R.A., 2013: It's not (just) "the environment, stupid!" Values, motivations, and routes to engagement of people adopting lower-carbon lifestyles. *Global Environmental Change*, **23(1)**, 281–290, doi:10.1016/j.gloenvcha.2012.10.015.
Huang, B. et al., 2017: Extended Reconstructed Sea Surface Temperature, Version 5 (ERSSTv5): Upgrades, Validations, and Intercomparisons. *Journal of Climate*, **30(20)**, 8179–8205, doi:10.1175/jcli-d-16-0836.1.
Huggel, C., D. Stone, H. Eicken, and G. Hansen, 2015: Potential and limitations of the attribution of climate change impacts for informing loss and damage discussions and policies. *Climatic Change*, **133(3)**, 453–467, doi:10.1007/s10584-015-1441-z.
Hughes, T.P. et al., 2018: Spatial and temporal patterns of mass bleaching of corals in the Anthropocene. *Science*, **359(6371)**, 80–83, doi:10.1126/science.aan8048.
Hulme, M., 2009: *Why We Disagree about Climate Change: Understanding Controversy, Inaction and Opportunity*. Cambridge University Press, Cambridge, UK, 432 pp.
Hulme, M., 2018: "Gaps" in Climate Change Knowledge. *Environmental Humanities*, **10(1)**, 330–337, doi:10.1215/22011919-4385599.
Huppmann, D., J. Rogelj, E. Kriegler, V. Krey, and K. Riahi, 2018: A new scenario resource for integrated 1.5°C research. *Nature Climate Change*, **8(12)**, 1027–1030, doi:10.1038/s41558-018-0317-4.
Hurrell, J. et al., 2009: A Unified Modeling Approach to Climate System Prediction. *Bulletin of the American Meteorological Society*, **90(12)**, 1819–1832, doi:10.1175/2009bams2752.1.
Hurtt, G.C. et al., 2011: Harmonization of land-use scenarios for the period 1500–2100: 600 years of global gridded annual land-use transitions, wood harvest, and resulting secondary lands. *Climatic Change*, **109(1–2)**, 117–161, doi:10.1007/s10584-011-0153-2.
Hurtt, G.C. et al., 2020: Harmonization of global land use change and management for the period 850–2100 (LUH2) for CMIP6. *Geoscientific Model Development*, **13(11)**, 5425–5464, doi:10.5194/gmd-13-5425-2020.
Hyder, P. et al., 2018: Critical Southern Ocean climate model biases traced to atmospheric model cloud errors. *Nature Communications*, **9(1)**, 3625, doi:10.1038/s41467-018-05634-2.
ICONICS, 2021: International Committee On New Integrated Climate change assessment Scenarios. Retrieved from: http://iconics-ssp.org.
Ingleby, B. et al., 2021: The Impact of COVID-19 on Weather Forecasts: A Balanced View. *Geophysical Research Letters*, **48(4)**, e2020GL090699, doi:10.1029/2020gl090699.
Inness, A. et al., 2019: The CAMS reanalysis of atmospheric composition. *Atmospheric Chemistry and Physics*, **19(6)**, 3515–3556, doi:10.5194/acp-19-3515-2019.
Inoue, M. et al., 2016: Bias corrections of GOSAT SWIR XCO2 and XCH4 with TCCON data and their evaluation using aircraft measurement data. *Atmospheric Measurement Techniques*, **9(8)**, 3491–3512, doi:10.5194/amt-9-3491-2016.
Intemann, K., 2015: Distinguishing Between Legitimate and Illegitimate Values in Climate Modeling. *European*

ACCEPTED VERSION SUBJECT TO FINAL EDITS

Journal for Philosophy of Science, **5**, doi:10.1007/s13194-014-0105-6.
IPBES, 2019: Summary for policymakers of the global assessment report on biodiversity and ecosystem services of the Intergovernmental Science-Policy Platform on Biodiversity and Ecosystem Services. In: *Global assessment report on biodiversity and ecosystem services of the Intergovernmental Science-Policy Platform on Biodiversity and Ecosystem Services* [Díaz, S., J. Settele, E.S. Brondízio, H.T. Ngo, M. Guèze, J. Agard, A. Arneth, P. Balvanera, K.A. Brauman, S.H.M. Butchart, K.M.A. Chan, L.A. Garibaldi, K. Ichii, J. Liu, S.M. Subramanian, G.F. Midgley, P. Miloslavich, Z. Molnár, D. Obura, A. Pfaff, S. Polasky, A. Purvis, J. Razzaque, B. Reyers, R.R. Chowdhury, Y.J. Shin, I.J. Visseren-Hamakers, K.J. Willis, and C.N. Zayas (eds.)]. Intergovernmental Science-Policy Platform on Biodiversity and Ecosystem Services (IPBES) Secretariat, Bonn, Germany, pp. 56, doi:10.5281/zenodo.3553579.
IPCC, 1990a: Climate Change: The IPCC Scientific Assessment. [Houghton, J.T., G.J. Jenkins, and J.J. Ephraums (eds.)]. Cambridge University Press, Cambridge, United Kingdom and New York, NY, USA, 365 pp.
IPCC, 1990b: Policymaker summary of Working Group I. *IPCC First Assessment Report*, 24.
IPCC, 1992: Climate Change 1992: The Supplementary Report to the IPCC Scientific Assessment. [Houghton, J.T., B.A. Callander, and S.K. Varney (eds.)]. Cambridge University Press, Cambridge, United Kingdom and New York, NY, USA, 200 pp.
IPCC, 1995a: Climate Change 1994: Radiative Forcing of Climate change and An Evaluation of the IPCC IS92 Emission Scenarios. [Houghton, J.T., L.G.M. Filho, J. Bruce, H. Lee, B.A. Callander, E. Haites, N. Harris, and K. Maskell. (eds.)]. Cambridge University Press, Cambridge, United Kingdom and New York, NY, USA, 339 pp.
IPCC, 1995b: Summary for Policymakers. *Climate Change 1995: The Science of Climate Change. Contribution of Working Group I to the Second Assessment Report of the Intergovernmental Panel on Climate Change*, 6.
IPCC, 1996: Climate Change 1995: The Science of Climate Change. Contribution of Working Group I to the Second Assessment Report of the Intergovernmental Panel on Climate Change. [Houghton, J.T., L.G.M. Filho, B.A. Callander, N. Harris, A. Kattenberg, and K. Maskell (eds.)]. Cambridge University Press, Cambridge, United Kingdom and New York, NY, USA, 584 pp.
IPCC, 1998: The Regional Impacts of Climate Change: An Assessment of Vulnerability. A Special Report of IPCC Working Group II. [Watson, R.T., M.C. Zinyowera, and R.H. Moss (eds.)]. Cambridge University Press, Cambridge, United Kingdom and New York, NY, USA, 517 pp.
IPCC, 2000: Special Report on Emissions Scenarios. A Special Report of Working Group III of the Intergovernmental Panel on Climate Change. [Nakićenović, N. and R. Swart (eds.)]. Cambridge University Press, Cambridge, United Kingdom and New York, NY, USA, 570 pp.
IPCC, 2001a: Climate Change 2001: The Scientific Basis. Contribution of Working Group I to the Third Assessment Report of the Intergovernmental Panel on Climate Change. [Houghton, J.T., Y. Ding, D.J. Griggs, M. Noguer, P.J. van der Linden, X. Dai, K. Maskell, and C.A. Johnson (eds.)]. Cambridge University Press, Cambridge, United Kingdom and New York, NY, USA, 881 pp.
IPCC, 2001b: Summary for Policymakers. *Climate Change 2001: The Scientific Basis. Contribution of Worling Group I to the Thirs Assessment Report of the Intergovernmental Panel on Climate Change*, 20.
IPCC, 2005: *Guidance notes for lead authors of the IPCC Fourth Assessment Report on addressing uncertainties*. Intergovernmental Panel on Climate Change (IPCC) Secretariat, Geneva, Switzerland, 4 pp.
IPCC, 2007a: Climate Change 2007: The Physical Science Basis. Contribution of Working Group I to the Fourth Assessment Report of the Intergovernmental Panel on Climate Change. [Solomon, S., D. Qin, M. Manning, Z. Chen, M. Marquis, K.B. Averyt, M. Tignor, and H.L. Miller (eds.)]. Cambridge University Press, Cambridge, United Kingdom and New York, NY, USA, 996 pp.
IPCC, 2007b: Summary for Policymakers. *Climate Change 2007: The Physical Science Basis. Contribution of Working Group I to the Fourth Assessment Report of the Intergovernmental Panel on Climate Changelimate Change 2007: The Physical Science Basis. Contribution of Working Group I to the Fourth*.
IPCC, 2012: Managing the Risks of Extreme Events and Disasters to Advance Climate Change Adaptation. A Special Report of Working Groups I and II of the Intergovernmental Panel on Climate Change. [Field, C.B., V. Barros, T.F. Stocker, D. Qin, D.J. Dokken, K.L. Ebi, M.D. Mastrandrea, K.J. Mach, G.-K. Plattner, S.K. Allen, M. Tignor, and P.M. Midgley (eds.)]. Cambridge University Press, Cambridge, United Kingdom, and New York, NY, USA, 582 pp., doi:10.1017/cbo9781139177245.
IPCC, 2013a: Climate Change 2013: The Physical Science Basis. Contribution of Working Group I to the Fifth Assessment Report of the Intergovernmental Panel on Climate Change. , 1535, doi:10.1017/cbo9781107415324.004.
IPCC, 2013b: Summary for Policymakers. In: *Climate Change 2013: The Physical Science Basis. Contribution of Working Group I to the Fifth Assessment Report of the Intergovernmental Panel on Climate Change* [Stocker, T.F., D. Qin, G.-K. Plattner, M. Tignor, S.K. Allen, J. Boschung, A. Nauels, Y. Xia, V. Bex, and P.M. Midgley (eds.)]. Cambridge University Press, Cambridge, United Kingdom and New York, NY, USA, pp. 1–30, doi:10.1017/cbo9781107415324.004.
IPCC, 2014a: Climate Change 2014: Impacts, Adaptation, and Vulnerability. Part A: Global and Sectoral Aspects.

ACCEPTED VERSION SUBJECT TO FINAL EDITS

Contribution of Working Group II to the Fifth Assessment Report of the Intergovernmental Panel on Climate Change. [Field, C.B., V.R. Barros, D.J. Dokken, K.J. Mach, M.D. Mastrandrea, T.E. Bilir, M. Chatterjee, K.L. Ebi, Y.O. Estrada, R.C. Genova, B. Girma, E.S. Kissel, A.N. Levy, S. MacCracken, P.R. Mastrandrea, and L.L. White (eds.)]. Cambridge University Press, Cambridge, United Kingdom and New York, NY, USA, 1132 pp., doi:10.1017/cbo9781107415379.

IPCC, 2014b: Summary for Policymakers. In: *Climate Change 2014: Impacts,Adaptation, and Vulnerability. Part A: Global and Sectoral Aspects. Contribution of Working Group II to the Fifth Assessment Report of the Intergovernmental Panel on Climate Change* [Field, C.B., V.R. Barros, D.J. Dokken, K.J. Mach, M.D. Mastrandrea, T.E. Bilir, M. Chatterjee, K.L. Ebi, Y.O. Estrada, R.C. Genova, B. Girma, E.S. Kissel, A.N. Levy, S. MacCracken, P.R. Mastrandrea, and L.L. White (eds.)]. Cambridge University Press, Cambridge, United Kingdom and New York, NY, USA, pp. 1–32, doi:10.1017/cbo9781107415379.003.

IPCC, 2017: *AR6 Scoping Meeting – Chair's Vision Paper*. Intergovernmental Panel on Climate Change (IPCC) Secretariat, Geneva, Switzerland, 44 pp.

IPCC, 2018: Global Warming of 1.5°C. An IPCC Special Report on the impacts of global warming of 1.5°C above pre-industrial levels and related global greenhouse gas emission pathways, in the context of strengthening the global response to the threat of climate change,. [Masson-Delmotte, V., P. Zhai, H.-O. Pörtner, D. Roberts, J. Skea, P.R. Shukla, A. Pirani, W. Moufouma-Okia, C. Péan, R. Pidcock, S. Connors, J.B.R. Matthews, Y. Chen, X. Zhou, M.I. Gomis, E. Lonnoy, T. Maycock, M. Tignor, and T. Waterfield (eds.)]. In Press, 616 pp.

IPCC, 2019a: Climate Change and Land, An IPCC special report on climate change, desertification, land degradation, sustainable land management, food security, and greenhouse gas fluxes in terrestrial ecosystems. [Shukla, P.R., J. Skea, E.C. Buendia, V. Masson-Delmotte, H.-O. Pörtner, D.C. Roberts, P. Zhai, R. Slade, S. Connors, R. Diemen, M. Ferrat, E. Haughey, S. Luz, S. Neogi, M. Pathak, J. Petzold, J.P. Pereira, P. Vyas, E. Huntley, K. Kissick, M. Belkacemi, and J. Malley (eds.)]. In Press, 896 pp.

IPCC, 2019b: IPCC Special Report on the Ocean and Cryosphere in a Changing Climate. [Pörtner, H.-O., D.C. Roberts, V. Masson-Delmotte, P. Zhai, M. Tignor, E. Poloczanska, K. Mintenbeck, A. Alegría, M. Nicolai, and A. Okem (eds.)]. In Press, 755 pp.

IPCC, 2019c: Summary for Policymakers. [Pörtner, H.-O., D.C. Roberts, V. Masson-Delmotte, P. Zhai, M. Tignor, E. Poloczanska, K. Mintenbeck, A. Alegría, M. Nicolai, A. Okem, J. Petzold, B. Rama, and N.M. Weyer (eds.)]. In Press, 755 pp.

IPCC, 2019d: Summary for Policymakers. *Climate Change and Land: an IPCC special report on climate change, desertification, land degradation, sustainable land management, food security, and greenhouse gas fluxes in terrestrial ecosystems*, doi:10.4337/9781784710644.

Iturbide, M. et al., 2020: An update of IPCC climate reference regions for subcontinental analysis of climate model data: definition and aggregated datasets. *Earth System Science Data*, **12(4)**, 2959–2970, doi:10.5194/essd-12-2959-2020.

Jack, C.D., R. Jones, L. Burgin, and J. Daron, 2020: Climate risk narratives: An iterative reflective process for co-producing and integrating climate knowledge. *Climate Risk Management*, **29**, 100239, doi:10.1016/j.crm.2020.100239.

Jackson, L.C. et al., 2019: The Mean State and Variability of the North Atlantic Circulation: A Perspective From Ocean Reanalyses. *Journal of Geophysical Research: Oceans*, **124(12)**, 9141–9170, doi:10.1029/2019jc015210.

James, E.P., S.G. Benjamin, and B.D. Jamison, 2020: Commercial-Aircraft-Based Observations for NWP: Global Coverage, Data Impacts, and COVID-19. *Journal of Applied Meteorology and Climatology*, **59(11)**, 1809–1825, doi:10.1175/jamc-d-20-0010.1.

James, R., R. Washington, and R. Jones, 2015: Process-based assessment of an ensemble of climate projections for West Africa. *Journal of Geophysical Research: Atmospheres*, **120(4)**, 1221–1238, doi:10.1002/2014jd022513.

James, R., R. Washington, C.-F. Schleussner, J. Rogelj, and D. Conway, 2017: Characterizing half-a-degree difference: a review of methods for identifying regional climate responses to global warming targets. *Wiley Interdisciplinary Reviews: Climate Change*, **8(2)**, e457, doi:10.1002/wcc.457.

James, R.A. et al., 2019: Attribution: How Is It Relevant for Loss and Damage Policy and Practice? In: *Loss and Damage from Climate Change: Concepts, Methods and Policy Options* [Mechler, R., L.M. Bouwer, T. Schinko, S. Surminski, and J.A. Linnerooth-Bayer (eds.)]. Springer, Cham, Switzerland, pp. 113–154, doi:10.1007/978-3-319-72026-5_5.

Janzwood, S., 2020: Confident, likely, or both? The implementation of the uncertainty language framework in IPCC special reports. *Climatic Change*, doi:10.1007/s10584-020-02746-x.

Jasanoff, S., 2010: A New Climate for Society. *Theory, Culture & Society*, **27(2–3)**, 233–253, doi:10.1177/0263276409361497.

Jaspal, R. and B. Nerlich, 2014: When climate science became climate politics: British media representations of climate change in 1988. *Public Understanding of Science*, **23(2)**, 122–141, doi:10.1177/0963662512440219.

Jaspal, R., B. Nerlich, and M. Cinnirella, 2014: Human Responses to Climate Change: Social Representation, Identity and Socio-psychological Action. *Environmental Communication*, **8(1)**, 110–130, doi:10.1080/17524032.2013.846270.

ACCEPTED VERSION SUBJECT TO FINAL EDITS

Jayne, S.R. et al., 2017: The Argo Program: Present and Future. *Oceanography*, **30(2)**, 18–28.
Jermey, P.M. and R.J. Renshaw, 2016: Precipitation representation over a two-year period in regional reanalysis. *Quarterly Journal of the Royal Meteorological Society*, **142(696)**, 1300–1310, doi:10.1002/qj.2733.
Jézéquel, A. et al., 2018: Behind the veil of extreme event attribution. *Climatic Change*, **149(3–4)**, 367–383, doi:10.1007/s10584-018-2252-9.
Jiang, L. and B.C. O'Neill, 2017: Global urbanization projections for the Shared Socioeconomic Pathways. *Global Environmental Change*, **42**, 193–199, doi:10.1016/j.gloenvcha.2015.03.008.
Jiang, X., F. Adames, M. Zhao, D. Waliser, and E. Maloney, 2018: A Unified Moisture Mode Framework for Seasonality of the Madden–Julian Oscillation. *Journal of Climate*, **31(11)**, 4215–4224, doi:10.1175/jcli-d-17-0671.1.
Jiménez-de-la-Cuesta, D. and T. Mauritsen, 2019: Emergent constraints on Earth's transient and equilibrium response to doubled CO2 from post-1970s global warming. *Nature Geoscience*, **12(11)**, 902–905, doi:10.1038/s41561-019-0463-y.
Jin, D., L. Oreopoulos, and D. Lee, 2017: Regime-based evaluation of cloudiness in CMIP5 models. *Climate Dynamics*, **48(1–2)**, 89–112, doi:10.1007/s00382-016-3064-0.
Jones, C.D. and P. Friedlingstein, 2020: Quantifying process-level uncertainty contributions to {TCRE} and carbon budgets for meeting Paris Agreement climate targets. *Environmental Research Letters*, **15(7)**, 74019, doi:10.1088/1748-9326/ab858a.
Jones, C.D. et al., 2016a: The C4MIP experimental protocol for CMIP6. *Geoscientific Model Development Discussions*, 1–52, doi:10.5194/gmd-2016-36.
Jones, C.D. et al., 2016b: C4MIP - The Coupled Climate–Carbon Cycle Model Intercomparison Project: experimental protocol for CMIP6. *Geoscientific Model Development*, **9(8)**, 2853–2880, doi:10.5194/gmd-9-2853-2016.
Jones, G.S., P.A. Stott, and N. Christidis, 2013: Attribution of observed historical near-surface temperature variations to anthropogenic and natural causes using CMIP5 simulations. *Journal of Geophysical Research: Atmospheres*, **118(10)**, 4001–4024, doi:10.1002/jgrd.50239.
Jones, P.D., M. New, D.E. Parker, S. Martin, and I.G. Rigor, 1999: Surface air temperature and its changes over the past 150 years. *Reviews of Geophysics*, **37(2)**, 173–199, doi:10.1029/1999rg900002.
Jones, P.D. et al., 2009: High-resolution palaeoclimatology of the last millennium: a review of current status and future prospects. *The Holocene*, **19(1)**, 3–49, doi:10.1177/0959683608098952.
Jones, R.N., 2000: Managing Uncertainty in Climate Change Projections – Issues for Impact Assessment. *Climatic Change*, **45**, 403–419, doi:10.1023/a:1005551626280.
Joos, F., S. Gerber, I.C. Prentice, B.L. Otto-Bliesner, and P.J. Valdes, 2004: Transient simulations of Holocene atmospheric carbon dioxide and terrestrial carbon since the Last Glacial Maximum. *Global Biogeochemical Cycles*, **18(2)**, n/a–n/a, doi:10.1029/2003gb002156.
Joos, F. et al., 2013: Carbon dioxide and climate impulse response functions for the computation of greenhouse gas metrics: a multi-model analysis. *Atmos. Chem. Phys*, **13**, 2793–2825, doi:10.5194/acp-13-2793-2013.
Joughin, I., B.E. Smith, and B. Medley, 2014: Marine Ice Sheet Collapse Potentially Under Way for the Thwaites Glacier Basin, West Antarctica. *Science*, **344(6185)**, 735–738, doi:10.1126/science.1249055.
Jouzel, J., 2013: A brief history of ice core science over the last 50 yr. *Climate of the Past*, **9(6)**, 2525–2547, doi:10.5194/cp-9-2525-2013.
Jouzel, J. et al., 2007: Orbital and Millennial Antarctic Climate Variability over the Past 800,000 Years. *Science*, **317(5839)**, 793–796, doi:10.1126/science.1141038.
Juanchich, M., T.G. Shepherd, and M. Sirota, 2020: Negations in uncertainty lexicon affect attention, decision-making and trust. *Climatic Change*, doi:10.1007/s10584-020-02737-y.
Jungclaus, J.H. et al., 2017: The PMIP4 contribution to CMIP6 -- Part 3: The last millennium, scientific objective, and experimental design for \\hack{\\newline} the PMIP4 \\textit{past1000} simulations. *Geoscientific Model Development*, **10(11)**, 4005–4033, doi:10.5194/gmd-10-4005-2017.
Junod, R.A. and J.R. Christy, 2020: A new compilation of globally gridded night-time marine air temperatures: The UAHNMATv1 dataset. *International Journal of Climatology*, **40(5)**, 2609–2623, doi:10.1002/joc.6354.
Kadow, C., D.M. Hall, and U. Ulbrich, 2020: Artificial intelligence reconstructs missing climate information. *Nature Geoscience*, **13(6)**, 408–413, doi:10.1038/s41561-020-0582-5.
Kageyama, M. et al., 2018: The PMIP4 contribution to CMIP6 – Part 1: Overview and over-arching analysis plan. *Geoscientific Model Development*, **11(3)**, 1033–1057, doi:10.5194/gmd-11-1033-2018.
Kaiser-Weiss, A.K. et al., 2015: Comparison of regional and global reanalysis near-surface winds with station observations over Germany. *Advances in Science and Research*, **12(1)**, 187–198, doi:10.5194/asr-12-187-2015.
Kaiser-Weiss, A.K. et al., 2019: Added value of regional reanalyses for climatological applications. *Environmental Research Communications*, **1(7)**, 071004, doi:10.1088/2515-7620/ab2ec3.
Karoly, D.J. et al., 1994: An example of fingerprint detection of greenhouse climate change. *Climate Dynamics*, **10(1–2)**, 97–105, doi:10.1007/bf00210339.
Karspeck, A.R. et al., 2017: Comparison of the Atlantic meridional overturning circulation between 1960 and 2007 in

ACCEPTED VERSION SUBJECT TO FINAL EDITS

six ocean reanalysis products. *Climate Dynamics*, **49(3)**, 957–982, doi:10.1007/s00382-015-2787-7.
Kaspar, F., B. Tinz, H. Mächel, and L. Gates, 2015: Data rescue of national and international meteorological observations at Deutscher Wetterdienst. *Advances in Science and Research*, **12(1)**, 57–61, doi:10.5194/asr-12-57-2015.
Katsaros, K.B. and R.A. Brown, 1991: Legacy of the Seasat Mission for Studies of the Atmosphere and Air-Sea-Ice Interactions. *Bulletin of the American Meteorological Society*, **72(7)**, 967–981, doi:10.1175/1520-0477(1991)072<0967:lotsmf>2.0.co;2.
Kaufman, D. et al., 2020: A global database of Holocene paleotemperature records. *Scientific Data*, **7(1)**, 115, doi:10.1038/s41597-020-0445-3.
Kawatani, Y. et al., 2019: The effects of a well-resolved stratosphere on the simulated boreal winter circulation in a climate model. *Journal of the Atmospheric Sciences*, JAS–D–18–0206.1, doi:10.1175/jas-d-18-0206.1.
Kay, J.E., M.M. Holland, and A. Jahn, 2011: Inter-annual to multi-decadal Arctic sea ice extent trends in a warming world. *Geophysical Research Letters*, **38(15)**, doi:10.1029/2011gl048008.
Kay, J.E. et al., 2015: The Community Earth System Model (CESM) Large Ensemble Project: A Community Resource for Studying Climate Change in the Presence of Internal Climate Variability. *Bulletin of the American Meteorological Society*, **96(8)**, 1333–1349, doi:10.1175/bams-d-13-00255.1.
Keeling, C.D., 1960: The Concentration and Isotopic Abundances of Carbon Dioxide in the Atmosphere. *Tellus*, **12(2)**, 200–203, doi:10.3402/tellusa.v12i2.9366.
Keeling, R.F. and S.R. Shertz, 1992: Seasonal and interannual variations in atmospheric oxygen and implications for the global carbon cycle. *Nature*, **358(6389)**, 723–727, doi:10.1038/358723a0.
Keller, D.P. et al., 2018: The Carbon Dioxide Removal Model Intercomparison Project (CDRMIP): rationale and experimental protocol for CMIP6. *Geoscientific Model Development*, **11(3)**, 1133–1160, doi:10.5194/gmd-11-1133-2018.
Keller, M., D.S. Schimel, W.W. Hargrove, and F.M. Hoffman, 2008: A continental strategy for the National Ecological Observatory Network. *Frontiers in Ecology and the Environment*, **6(5)**, 282–284, doi:10.1890/1540-9295(2008)6[282:acsftn]2.0.co;2.
Kemp, A.C. et al., 2018: Relative sea-level change in Newfoundland, Canada during the past ~3000 years. *Quaternary Science Reviews*, **201**, 89–110, doi:10.1016/j.quascirev.2018.10.012.
Kennedy, J.J., N.A. Rayner, C.P. Atkinson, and R.E. Killick, 2019: An Ensemble Data Set of Sea Surface Temperature Change From 1850: The Met Office Hadley Centre HadSST.4.0.0.0 Data Set. *Journal of Geophysical Research: Atmospheres*, **124(14)**, 7719–7763, doi:10.1029/2018jd029867.
Kent, E.C. et al., 2013: Global analysis of night marine air temperature and its uncertainty since 1880: The HadNMAT2 data set. *Journal of Geophysical Research: Atmospheres*, **118(3)**, 1281–1298, doi:10.1002/jgrd.50152.
Kent, E.C. et al., 2019: Observing Requirements for Long-Term Climate Records at the Ocean Surface. *Frontiers in Marine Science*, **6**, 441, doi:10.3389/fmars.2019.00441.
Khan, N.S. et al., 2019: Inception of a global atlas of sea levels since the Last Glacial Maximum. *Quaternary Science Reviews*, **220**, 359–371, doi:10.1016/j.quascirev.2019.07.016.
Khodri, M. et al., 2017: Tropical explosive volcanic eruptions can trigger El Niño by cooling tropical Africa. *Nature Communications*, **8(1)**, 778, doi:10.1038/s41467-017-00755-6.
Kim, W.M., S. Yeager, P. Chang, and G. Danabasoglu, 2018: Low-Frequency North Atlantic Climate Variability in the Community Earth System Model Large Ensemble. *Journal of Climate*, **31(2)**, 787–813, doi:10.1175/jcli-d-17-0193.1.
Kincer, J., 1933: Is our climate changing? A study of long-time temperature trends. *Monthly Weather Review*, doi:10.1175/1520-0493(1933)61<251:ioccas>2.0.co;2.
King, A.D., D.J. Karoly, and B.J. Henley, 2017: Australian climate extremes at 1.5°C and 2°C of global warming. *Nature Climate Change*, **7(6)**, 412–416, doi:10.1038/nclimate3296.
King, A.D., T.P. Lane, B.J. Henley, and J.R. Brown, 2020: Global and regional impacts differ between transient and equilibrium warmer worlds. *Nature Climate Change*, **10(1)**, 42–47, doi:10.1038/s41558-019-0658-7.
King, A.D. et al., 2015: The timing of anthropogenic emergence in simulated climate extremes. *Environmental Research Letters*, **10(9)**, 094015, doi:10.1088/1748-9326/10/9/094015.
King, A.D. et al., 2018: On the Linearity of Local and Regional Temperature Changes from 1.5°C to 2°C of Global Warming. *Journal of Climate*, **31(18)**, 7495–7514, doi:10.1175/jcli-d-17-0649.1.
Kirchmeier-Young, M.C., F.W. Zwiers, and N.P. Gillett, 2017: Attribution of Extreme Events in Arctic Sea Ice Extent. *Journal of Climate*, **30(2)**, 553–571, doi:10.1175/jcli-d-16-0412.1.
Kirchmeier-Young, M.C., H. Wan, X. Zhang, and S.I. Seneviratne, 2019: Importance of Framing for Extreme Event Attribution: The Role of Spatial and Temporal Scales. *Earth's Future*, **7(10)**, 1192–1204, doi:10.1029/2019ef001253.
Kirtman, B. et al., 2013: Near-term Climate Change: Projections and Predictability. In: *Climate Change 2013: The Physical Science Basis. Contribution of Working Group I to the Fifth Assessment Report of the Intergovernmental Panel on Climate Change* [Stocker, T.F., D. Qin, G.-K. Plattner, M. Tignor, S.K. Allen, J. Boschung, A. Nauels, Y. Xia, V. Bex, and P.M. Midgley (eds.)]. Cambridge University Press, Cambridge,

ACCEPTED VERSION SUBJECT TO FINAL EDITS

United Kingdom and New York, NY, USA, pp. 953–1028, doi:10.1017/cbo9781107415324.023.
Kistler, R. et al., 2001: The NCEP-NCAR 50-year reanalysis: Monthly means CD-ROM and documentation. *Bulletin of the American Meteorological Society*, **74**, 247–268, doi:10.1175/1520-0477(2001)082<0247:tnnyrm>2.3.co;2.
Klein, S.A. and A. Hall, 2015: Emergent Constraints for Cloud Feedbacks. *Current Climate Change Reports*, **1(4)**, 276–287, doi:10.1007/s40641-015-0027-1.
Klein, S.A. et al., 2013: Are climate model simulations of clouds improving? An evaluation using the ISCCP simulator. *Journal of Geophysical Research: Atmospheres*, **118(3)**, 1329–1342, doi:10.1002/jgrd.50141.
Knutti, R., 2018: Climate Model Confirmation: From Philosophy to Predicting Climate in the Real World. In: *Climate Modelling: Philosophical and Conceptual Issues* [A. Lloyd, E. and E. Winsberg (eds.)]. Palgrave Macmillan, Cham, Switzerland, pp. 325–359, doi:10.1007/978-3-319-65058-6_11.
Knutti, R., D. Masson, and A. Gettelman, 2013: Climate model genealogy: Generation CMIP5 and how we got there. *Geophysical Research Letters*, **40(6)**, 1194–1199, doi:10.1002/grl.50256.
Knutti, R., T.F. Stocker, F. Joos, and G.-K. Plattner, 2002: Constraints on radiative forcing and future climate change from observations and climate model ensembles. *Nature*, **416(6882)**, 719–723, doi:10.1038/416719a.
Knutti, R., R. Furrer, C. Tebaldi, J. Cermak, and G.A. Meehl, 2010: Challenges in Combining Projections from Multiple Climate Models. *Journal of Climate*, **23(10)**, 2739–2758, doi:10.1175/2009jcli3361.1.
Knutti, R. et al., 2008: A Review of Uncertainties in Global Temperature Projections over the Twenty-First Century. *Journal of Climate*, **21(11)**, 2651–2663, doi:10.1175/2007jcli2119.1.
Knutti, R. et al., 2017: A climate model projection weighting scheme accounting for performance and interdependence. *Geophysical Research Letters*, doi:10.1002/2016gl072012.
Kobayashi, S. et al., 2015: The JRA-55 reanalysis: General specifications and basic characteristics. *Journal of the Meteorological Society of Japan*, **93(1)**, 5–48, doi:10.2151/jmsj.2015-001.
Koch, A., C. Brierley, M.M. Maslin, and S.L. Lewis, 2019: Earth system impacts of the European arrival and Great Dying in the Americas after 1492. *Quaternary Science Reviews*, **207**, 13–36, doi:10.1016/j.quascirev.2018.12.004.
Kolstad, C. et al., 2014: Social, Economic and Ethical Concepts and Methods. In: *Climate Change 2014: Mitigation of Climate Change. Contribution of Working Group III to the Fifth Assessment Report of the Intergovernmental Panel on Climate Change* [Edenhofer, O., R. Pichs-Madruga, Y. Sokona, E. Farahani, S. Kadner, K. Seyboth, A. Adler, I. Baum, S. Brunner, P. Eickemeier, B. Kriemann, J. Savolainen, S. Schlömer, C. von Stechow, T. Zwickel, and J.C. Minx (eds.)]. Cambridge University Press, Cambridge, United Kingdom and New York, NY, USA, pp. 207–282, doi:10.1017/cbo9781107415416.009.
Konecky, B.L. et al., 2020: The Iso2k database: a global compilation of paleo-δ18O and δ2H records to aid understanding of Common Era climate. *Earth System Science Data*, **12(3)**, 2261–2288, doi:10.5194/essd-12-2261-2020.
Konsta, D., H. Chepfer, and J.-L. Dufresne, 2012: A process oriented characterization of tropical oceanic clouds for climate model evaluation, based on a statistical analysis of daytime A-train observations. *Climate Dynamics*, **39(9–10)**, 2091–2108, doi:10.1007/s00382-012-1533-7.
Konsta, D., J.-L. Dufresne, H. Chepfer, A. Idelkadi, and G. Cesana, 2016: Use of A-train satellite observations (CALIPSO-PARASOL) to evaluate tropical cloud properties in the LMDZ5 GCM. *Climate Dynamics*, **47(3–4)**, 1263–1284, doi:10.1007/s00382-015-2900-y.
Kopp, R.E. et al., 2014: Probabilistic 21st and 22nd century sea-level projections at a global network of tide-gauge sites. *Earth's Future*, **2(8)**, 383–406, doi:10.1002/2014ef000239.
Kopp, R.E. et al., 2016: Temperature-driven global sea-level variability in the Common Era. *Proceedings of the National Academy of Sciences*, **113(11)**, E1434–E1441, doi:10.1073/pnas.1517056113.
Köppen, W., 1936: Das geographische System der Klimate. In: *Handbuch der Klimatologie (Band I)*. Gebrueder Borntraeger, Berlin, Germany, pp. 43.
Kravitz, B. et al., 2015: The Geoengineering Model Intercomparison Project Phase 6 (GeoMIP6): simulation design and preliminary results. *Geoscientific Model Development*, **8(10)**, 3379–3392, doi:10.5194/gmd-8-3379-2015.
Kriegler, E. et al., 2012: The need for and use of socio-economic scenarios for climate change analysis: A new approach based on shared socio-economic pathways. *Global Environmental Change*, **22(4)**, 807–822, doi:10.1016/j.gloenvcha.2012.05.005.
Kroeger, K.D., S. Crooks, S. Moseman-Valtierra, and J. Tang, 2017: Restoring tides to reduce methane emissions in impounded wetlands: A new and potent Blue Carbon climate change intervention. *Scientific Reports*, **7(1)**, 11914, doi:10.1038/s41598-017-12138-4.
Kuhn, T.S., 1977: *The Essential Tension: Selected Studies in Scientific Tradition and Change*. University of Chicago Press, Chicago, IL, USA, 390 pp.
Lacis, A.A., G.A. Schmidt, D. Rind, and R.A. Ruedy, 2010: Atmospheric CO2: Principal Control Knob Governing Earth's Temperature. *Science*, **330(6002)**, 356–359, doi:10.1126/science.1190653.
Lacis, A.A., J.E. Hansen, G.L. Russell, V. Oinas, and J. Jonas, 2013: The role of long-lived greenhouse gases as principal LW control knob that governs the global surface temperature for past and future climate change. *Tellus B: Chemical and Physical Meteorology*, **65(1)**, 19734, doi:10.3402/tellusb.v65i0.19734.

ACCEPTED VERSION SUBJECT TO FINAL EDITS

Laidler, G.J., 2006: Inuit and Scientific Perspectives on the Relationship Between Sea Ice and Climate Change: The Ideal Complement? *Climatic Change*, **78(2–4)**, 407–444, doi:10.1007/s10584-006-9064-z.
Laloyaux, P. et al., 2018: CERA-20C: A Coupled Reanalysis of the Twentieth Century. *Journal of Advances in Modeling Earth Systems*, **10(5)**, 1172–1195, doi:10.1029/2018ms001273.
Lamarque, J.-F. et al., 2011: Global and regional evolution of short-lived radiatively-active gases and aerosols in the Representative Concentration Pathways. *Climatic Change*, **109(1–2)**, 191–212, doi:10.1007/s10584-011-0155-0.
Lamb, H.H., 1965: The early medieval warm epoch and its sequel. *Palaeogeography, Palaeoclimatology, Palaeoecology*, **1**, 13–37, doi:10.1016/0031-0182(65)90004-0.
Lamb, H.H., 1995: *Climate, History, and the Modern World*. Routledge, London, UK, 464 pp.
Lamboll, R.D., Z.R.J. Nicholls, J.S. Kikstra, M. Meinshausen, and J. Rogelj, 2020: Silicone v1.0.0: an open-source Python package for inferringmissing emissions data for climate change research. *Geosci. Model Dev.*, **13**, 5259–5275.
Landsberg, H.E., 1961: Solar radiation at the earth's surface. *Solar Energy*, **5(3)**, 95–98, doi:10.1016/0038-092x(61)90051-2.
Lange, S., 2019: WFDE5 over land merged with ERA5 over the ocean (W5E5). V. 1.0.. *GFZ Data Services*, doi:10.5880/pik.2019.023.
Langway Jr, C.C., 2008: *The history of early polar ice cores*. ERDC/CRREL TR-08-1, U.S. Army Engineer Research and Development Center (ERDC), Cold Regions Research and Engineering Laboratory (CRREL), Hanover, NH, USA, 47 pp.
Laskar, J.; Joutel, F.; Boudin, F., 1993: Orbital, precessional, and insolation quantities for the earth from -20 Myr to +10 Myr. *Astronomy and Astrophysics*, **270**, 522–533.
Lauer, A. et al., 2020: Earth System Model Evaluation Tool (ESMValTool) v2.0 -- diagnostics for emergent constraints and future projections from Earth system models in CMIP. *Geoscientific Model Development*, **13(9)**, 4205–4228, doi:10.5194/gmd-13-4205-2020.
Lawrence, D.M. et al., 2016: The Land Use Model Intercomparison Project (LUMIP) contribution to CMIP6: rationale and experimental design. *Geoscientific Model Development*, **9(9)**, 2973–2998, doi:10.5194/gmd-9-2973-2016.
Laxon, S., N. Peacock, and D. Smith, 2003: High interannual variability of sea ice thickness in the Arctic region. *Nature*, **425(6961)**, 947–950, doi:10.1038/nature02050.
Le clec'h, S. et al., 2019: A rapidly converging initialisation method to simulate the present-day Greenland ice sheet using the GRISLI ice sheet model (version 1.3). *Geoscientific Model Development*, **12(6)**, 2481–2499, doi:10.5194/gmd-12-2481-2019.
Le Quéré, C. et al., 2018: Global Carbon Budget 2018. *Earth System Science Data*, **10(4)**, 2141–2194, doi:10.5194/essd-10-2141-2018.
Le Quéré, C. et al., 2020: Temporary reduction in daily global CO2 emissions during the COVID-19 forced confinement. *Nature Climate Change*, **10(7)**, 647–653, doi:10.1038/s41558-020-0797-x.
Le Roy Ladurie, E., 1967: *Histoire du climat depuis l'an mil*. Flammarion, Paris, France, 376 pp.
Le Treut, H. et al., 2007: Historical Overview of Climate Change. In: *Climate Change 2007: The Physical Science Basis. Contribution of Working Group I to the Fourth Assessment Report of the Intergovernmental Panel on Climate Change* [Solomon, S., D. Qin, M. Manning, Z. Chen, M. Marquis, K.B. Averyt, M. Tignor, and H.L. Miller (eds.)]. Cambridge University Press, Cambridge, United Kingdom and New York, NY, USA, pp. 93–127.
Leduc, M. et al., 2019: The ClimEx Project: A 50-Member Ensemble of Climate Change Projections at 12-km Resolution over Europe and Northeastern North America with the Canadian Regional Climate Model (CRCM5). *Journal of Applied Meteorology and Climatology*, **58(4)**, 663–693, doi:10.1175/jamc-d-18-0021.1.
Lee, L.A., K.S. Carslaw, K.J. Pringle, G.W. Mann, and D. Spracklen, 2011: Emulation of a complex global aerosol model to quantify sensitivity to uncertain parameters. *Atmospheric Chemistry and Physics*, **11(23)**, 12253–12273, doi:10.5194/acp-11-12253-2011.
, 2019: OceanObs'19: An Ocean of Opportunity. Volume 1. Frontiers Media, 783 pp.
Lee, T.M., E.M. Markowitz, P.D. Howe, C.-Y. Ko, and A.A. Leiserowitz, 2015: Predictors of public climate change awareness and risk perception around the world. *Nature Climate Change*, **5(11)**, 1014–1020, doi:10.1038/nclimate2728.
Leggett, J., W.J. Pepper, and R.J. Swart, 1992: Emissions scenarios for the IPCC: an Update. In: *Climate change 1992: The Supplementary Report to the IPCC Scientific Assessment* [Houghton, J.T., B.A. Callander, and S.K. Varney (eds.)]. Cambridge University Press, Cambridge, United Kingdom and New York, NY, USA, pp. 69–95.
Lehner, F. and T.F. Stocker, 2015: From local perception to global perspective. *Nature Climate Change*, **5(8)**, 731–734, doi:10.1038/nclimate2660.
Lehner, F., C. Deser, and L. Terray, 2017: Toward a New Estimate of "Time of Emergence" of Anthropogenic Warming: Insights from Dynamical Adjustment and a Large Initial-Condition Model Ensemble. *Journal of Climate*, **30(19)**, 7739–7756, doi:10.1175/jcli-d-16-0792.1.

ACCEPTED VERSION SUBJECT TO FINAL EDITS

Lehner, F. et al., 2020: Partitioning climate projection uncertainty with multiple large ensembles and CMIP5/6. *Earth System Dynamics*, **11(2)**, 491–508, doi:10.5194/esd-11-491-2020.
Leiserowitz, A., 2006: Climate Change Risk Perception and Policy Preferences: The Role of Affect, Imagery, and Values. *Climatic Change*, **77(1–2)**, 45–72, doi:10.1007/s10584-006-9059-9.
Lejeune, Q., E.L. Davin, L. Gudmundsson, J. Winckler, and S.I. Seneviratne, 2018: Historical deforestation locally increased the intensity of hot days in northern mid-latitudes. *Nature Climate Change*, **8(5)**, 386–390, doi:10.1038/s41558-018-0131-z.
Lellouche, J.-M. et al., 2018: Recent updates to the Copernicus Marine Service global ocean monitoring and forecasting real-time 1⁄12° high-resolution system. *Ocean Science*, **14(5)**, 1093–1126, doi:10.5194/os-14-1093-2018.
Lemos, M.C. and B.J. Morehouse, 2005: The co-production of science and policy in integrated climate assessments. *Global Environmental Change*, doi:10.1016/j.gloenvcha.2004.09.004.
Lemos, M.C., C.J. Kirchhoff, and V. Ramprasad, 2012: Narrowing the climate information usability gap. *Nature Climate Change*, **2(11)**, 789–794, doi:10.1038/nclimate1614.
Lemos, M.C., C.J. Kirchhoff, S.E. Kalafatis, D. Scavia, and R.B. Rood, 2014: Moving Climate Information off the Shelf: Boundary Chains and the Role of RISAs as Adaptive Organizations. *Weather, Climate, and Society*, **6(2)**, 273–285, doi:10.1175/wcas-d-13-00044.1.
Lemos, M.C. et al., 2018: To co-produce or not to co-produce. *Nature Sustainability*, **1(12)**, 722–724, doi:10.1038/s41893-018-0191-0.
Lenton, T.M. et al., 2008: Tipping elements in the Earth's climate system. *Proceedings of the National Academy of Sciences*, **105(6)**, 1786–1793, doi:10.1073/pnas.0705414105.
Leonard, M. et al., 2014: A compound event framework for understanding extreme impacts. *Wiley Interdisciplinary Reviews: Climate Change*, **5(1)**, 113–128, doi:10.1002/wcc.252.
Lewis, S.C., A.D. King, S.E. Perkins-Kirkpatrick, and M.F. Wehner, 2019: Toward Calibrated Language for Effectively Communicating the Results of Extreme Event Attribution Studies. *Earth's Future*, **7(9)**, 1020–1026, doi:10.1029/2019ef001273.
Li, D., J. Yuan, and R.E. Kopp, 2020: Escalating global exposure to compound heat-humidity extremes with warming. *Environmental Research Letters*, **15(6)**, 064003, doi:10.1088/1748-9326/ab7d04.
Liang, Y., N.P. Gillett, and A.H. Monahan, 2020: Climate Model Projections of 21st Century Global Warming Constrained Using the Observed Warming Trend. *Geophysical Research Letters*, **47(12)**, e2019GL086757, doi:10.1029/2019gl086757.
Lin, M. and P. Huybers, 2019: If Rain Falls in India and No One Reports It, Are Historical Trends in Monsoon Extremes Biased? *Geophysical Research Letters*, **46(3)**, 1681–1689, doi:10.1029/2018gl079709.
Lindstrom, E., J. Gunn, A. Fischer, A. McCurdy, and L.K. Glover, 2012: A Framework for ocean observing. , 28, doi:10.5270/oceanobs09-foo.
Lisiecki, L.E. and M.E. Raymo, 2005: A Pliocene-Pleistocene stack of 57 globally distributed benthic δ 18 O records. *Paleoceanography*, **20(1)**, n/a–n/a, doi:10.1029/2004pa001071.
Liu, Q.M., C. Cao, C. Grassotti, and Y.K. Lee, 2021: How can microwave observations at 23.8 GHz help in acquiring water vapor in the atmosphere over land? *Remote Sensing*, **13(3)**, 1–10, doi:10.3390/rs13030489.
Liu, Y.Y. et al., 2015: Recent reversal in loss of global terrestrial biomass. *Nature Climate Change*, **5**, 470, doi:10.1038/nclimate2581.
Lloyd, E.A. and N. Oreskes, 2018: Climate Change Attribution: When Is It Appropriate to Accept New Methods? *Earth's Future*, **6(3)**, 311–325, doi:10.1002/2017ef000665.
Loarie, S.R. et al., 2009: The velocity of climate change. *Nature*, **462(7276)**, 1052–1055, doi:10.1038/nature08649.
Løhre, E., M. Juanchich, M. Sirota, K.H. Teigen, and T.G. Shepherd, 2019: Climate Scientists' Wide Prediction Intervals May Be More Likely but Are Perceived to Be Less Certain. *Weather, Climate, and Society*, **11(3)**, 565–575, doi:10.1175/wcas-d-18-0136.1.
Lomborg, B., 2016: Impact of Current Climate Proposals. *Global Policy*, **7(1)**, 109–118, doi:10.1111/1758-5899.12295.
Lorenz, R. et al., 2018: Prospects and Caveats of Weighting Climate Models for Summer Maximum Temperature Projections Over North America. *Journal of Geophysical Research: Atmospheres*, **123(9)**, 4509–4526, doi:10.1029/2017jd027992.
Lougheed, B.C., B. Metcalfe, U.S. Ninnemann, and L. Wacker, 2018: Moving beyond the age–depth model paradigm in deep-sea palaeoclimate archives: dual radiocarbon and stable isotope analysis on single foraminifera. *Climate of the Past*, **14(4)**, 515–526, doi:10.5194/cp-14-515-2018.
Louie, K.- and K.- Liu, 2003: Earliest historical records of typhoons in China. *Journal of Historical Geography*, **29(3)**, 299–316, doi:10.1006/jhge.2001.0453.
Lozier, M.S. et al., 2019: A sea change in our view of overturning in the subpolar North Atlantic. *Science*, **363(6426)**, 516–521, doi:10.1126/science.aau6592.
Lúcio, F.D.F. and V. Grasso, 2016: The Global Framework for Climate Services (GFCS). *Climate Services*, **2–3**, 52–53, doi:10.1016/j.cliser.2016.09.001.
Luderer, G. et al., 2018: Residual fossil CO2 emissions in 1.5–2°C pathways. *Nature Climate Change*, **8(7)**, 626–633, doi:10.1038/s41558-018-0198-6.

ACCEPTED VERSION SUBJECT TO FINAL EDITS

Lund, M.T. et al., 2020: A continued role of short-lived climate forcers under the Shared Socioeconomic Pathways. *Earth System Dynamics*, **11(4)**, 977–993, doi:10.5194/esd-11-977-2020.
Lüthi, D. et al., 2008: High-resolution carbon dioxide concentration record 650,000–800,000 years before present. *Nature*, **453(7193)**, 379–382, doi:10.1038/nature06949.
Lynch-Stieglitz, J., 2017: The Atlantic Meridional Overturning Circulation and Abrupt Climate Change. *Annual Review of Marine Science*, **9(1)**, 83–104, doi:10.1146/annurev-marine-010816-060415.
Lyu, K., X. Zhang, J.A. Church, A.B.A. Slangen, and J. Hu, 2014: Time of emergence for regional sea-level change. *NATURE CLIMATE CHANGE*, **4(11)**, 1006–1010, doi:10.1038/nclimate2397.
Ma, H.-Y. et al., 2014: On the Correspondence between Mean Forecast Errors and Climate Errors in CMIP5 Models. *Journal of Climate*, **27(4)**, 1781–1798, doi:10.1175/jcli-d-13-00474.1.
Ma, L. et al., 2020a: Global rules for translating land-use change (LUH2) to land-cover change for CMIP6 using GLM2. *Geoscientific Model Development*, **13(7)**, 3203–3220, doi:10.5194/gmd-13-3203-2020.
Ma, L. et al., 2020b: Global rules for translating land-use change (LUH2) to land-cover change for CMIP6 using GLM2. *Geoscientific Model Development*, **13(7)**, 3203–3220, doi:10.5194/gmd-13-3203-2020.
MacDougall, A.H. et al., 2020: Is there warming in the pipeline? A multi-model analysis of the Zero Emissions Commitment from CO2. *Biogeosciences*, **17(11)**, 2987–3016, doi:10.5194/bg-17-2987-2020.
Mach, K.J., M.D. Mastrandrea, P.T. Freeman, and C.B. Field, 2017: Unleashing expert judgment in assessment. *Global Environmental Change*, **44**, 1–14, doi:10.1016/j.gloenvcha.2017.02.005.
Madden, R.A. and V. Ramanathan, 1980: Detecting climate change due to increasing carbon dioxide. *Science*, doi:10.1126/science.209.4458.763.
Maher, N., S. McGregor, M.H. England, and A. Gupta, 2015: Effects of volcanism on tropical variability. *Geophysical Research Letters*, doi:10.1002/2015gl064751.
Maher, N. et al., 2019: The Max Planck Institute Grand Ensemble: Enabling the Exploration of Climate System Variability. *Journal of Advances in Modeling Earth Systems*, **11(7)**, 2050–2069, doi:10.1029/2019ms001639.
Mahlstein, I., G. Hegerl, and S. Solomon, 2012: Emerging local warming signals in observational data. *Geophysical Research Letters*, **39(21)**, n/a–n/a, doi:10.1029/2012gl053952.
Mahlstein, I., R. Knutti, S. Solomon, and R.W. Portmann, 2011: Early onset of significant local warming in low latitude countries. *Environmental Research Letters*, **6(3)**, 034009, doi:10.1088/1748-9326/6/3/034009.
Mahony, M., 2014: The predictive state: Science, territory and the future of the Indian climate. *Social Studies of Science*, **44(1)**, 109–133, doi:10.1177/0306312713501407.
Mahony, M., 2015: Climate change and the geographies of objectivity: the case of the IPCC's burning embers diagram. *Transactions of the Institute of British Geographers*, **40(2)**, 153–167, doi:10.1111/tran.12064.
Maibach, E.W., A. Leiserowitz, C. Roser-Renouf, and C.K. Mertz, 2011: Identifying Like-Minded Audiences for Global Warming Public Engagement Campaigns: An Audience Segmentation Analysis and Tool Development. *PLoS ONE*, **6(3)**, e17571, doi:10.1371/journal.pone.0017571.
Makondo, C.C. and D.S.G. Thomas, 2018: Climate change adaptation: Linking indigenous knowledge with western science for effective adaptation. *Environmental Science & Policy*, **88**, 83–91, doi:10.1016/j.envsci.2018.06.014.
Manabe, S., 1970: The Dependence of Atmospheric Temperature on the Concentration of Carbon Dioxide. In: *Global Effects of Environmental Pollution* [Singer, S.F. (ed.)]. Springer, Dordrecht, The Netherlands, pp. 25–29, doi:10.1007/978-94-010-3290-2_4.
Manabe, S. and F. Möller, 1961: On the Radiative Equilibrium and Heat Balance of the AtmosphereE. *Monthly Weather Review*, **89(12)**, 503–532, doi:10.1175/1520-0493(1961)089<0503:otreah>2.0.co;2.
Manabe, S. and R.T. Wetherald, 1967: Thermal Equilibrium of the Atmosphere with a Given Distribution of Relative Humidity. *Journal of the Atmospheric Sciences*, **24(3)**, 241–259, doi:10.1175/1520-0469(1967)024<0241:teotaw>2.0.co;2.
Manabe, S. and R.J. Stouffer, 1988: Two Stable Equilibria of a Coupled Ocean-Atmosphere Model. *Journal of Climate*, **1(9)**, 841–866, doi:10.1175/1520-0442(1988)001<0841:tseoac>2.0.co;2.
Manabe, S. and R.J. Stouffer, 1993: Century-scale effects of increased atmospheric C02 on the ocean-atmosphere system. *Nature*, doi:10.1038/364215a0.
Manabe, S., K. Bryan, and M.J. Spelman, 1975: A Global Ocean-Atmosphere Climate Model. Part I. The Atmospheric Circulation. *Journal of Physical Oceanography*, **5(1)**, 3–29, doi:10.1175/1520-0485(1975)005<0003:agoacm>2.0.co;2.
Mann, M.E., S.K. Miller, S. Rahmstorf, B.A. Steinman, and M. Tingley, 2017: Record temperature streak bears anthropogenic fingerprint. *Geophysical Research Letters*, **44(15)**, 7936–7944, doi:10.1002/2017gl074056.
Maraun, D., 2013: When will trends in European mean and heavy daily precipitation emerge? *Environmental Research Letters*, **8(1)**, 014004, doi:10.1088/1748-9326/8/1/014004.
Maraun, D. and M. Widmann, 2018: *Statistical Downscaling and Bias Correction for Climate Research*. Cambridge University Press, Cambridge, UK, 347 pp., doi:10.1017/9781107588783.
Marcott, S.A. et al., 2014: Centennial-scale changes in the global carbon cycle during the last deglaciation. *Nature*, **514(7524)**, 616–619, doi:10.1038/nature13799.

ACCEPTED VERSION SUBJECT TO FINAL EDITS

Marjanac, S., L. Patton, and J. Thornton, 2017: Acts of god, human infuence and litigation. *Nature Geoscience*, **10(9)**, 616–619, doi:10.1038/ngeo3019.
Martens, B. et al., 2020: Evaluating the land-surface energy partitioning in ERA5. *Geoscientific Model Development*, **13(9)**, 4159–4181, doi:10.5194/gmd-13-4159-2020.
Masina, S. et al., 2017: An ensemble of eddy-permitting global ocean reanalyses from the MyOcean project. *Climate Dynamics*, **49(3)**, 813–841, doi:10.1007/s00382-015-2728-5.
Massey, N. et al., 2015: weather@home-development and validation of a very large ensemble modelling system for probabilistic event attribution. *Quarterly Journal of the Royal Meteorological Society*, **141(690)**, 1528–1545, doi:10.1002/qj.2455.
Masson, D. and R. Knutti, 2011: Climate model genealogy. *Geophysical Research Letters*, **38(8)**, n/a–n/a, doi:10.1029/2011gl046864.
Masson-Delmotte, V. et al., 2013: Information from Paleoclimate Archives. In: *Climate Change 2013: The Physical Science Basis. Contribution of Working Group I to the Fifth Assessment Report of the Intergovernmental Panel on Climate Change* [Stocker, T.F., D. Qin, G.-K. Plattner, M. Tignor, S.K. Allen, J. Boschung, A. Nauels, Y. Xia, V. Bex, and P.M. Midgley (eds.)]. Cambridge University Press, Cambridge, United Kingdom and New York, NY, USA, pp. 383–464, doi:10.1017/cbo9781107415324.013.
Mastrandrea, M.D. and K.J. Mach, 2011: Treatment of uncertainties in IPCC Assessment Reports: past approaches and considerations for the Fifth Assessment Report. *Climatic Change*, **108(4)**, 659–673, doi:10.1007/s10584-011-0177-7.
Mastrandrea, M.D. et al., 2010: *Guidance Note for Lead Authors of the IPCC Fifth Assessment Report on Consistent Treatment of Uncertainties*. Intergovernmental Panel on Climate Change (IPCC), 7 pp.
Mastrandrea, M.D. et al., 2011: The IPCC AR5 guidance note on consistent treatment of uncertainties: A common approach across the working groups. *Climatic Change*, **108(4)**, 675–691, doi:10.1007/s10584-011-0178-6.
Matthes, K. et al., 2017: Solar forcing for CMIP6 (v3.2). *Geoscientific Model Development*, **10(6)**, 2247–2302, doi:10.5194/gmd-10-2247-2017.
Matthews, H.D., 2016: Quantifying historical carbon and climate debts among nations. *Nature Climate Change*, **6(1)**, 60–64, doi:10.1038/nclimate2774.
Mauritsen, T. and E. Roeckner, 2020: Tuning the MPI-ESM1.2 Global Climate Model to Improve the Match With Instrumental Record Warming by Lowering Its Climate Sensitivity. *Journal of Advances in Modeling Earth Systems*, **12(5)**, e2019MS002037, doi:10.1029/2019ms002037.
Mauritsen, T. et al., 2012: Tuning the climate of a global model. *Journal of Advances in Modeling Earth Systems*, doi:10.1029/2012ms000154.
Mauritsen, T. et al., 2019: Developments in the MPI-M Earth System Model version 1.2 (MPI-ESM 1.2) and its response to increasing CO2. *Journal of Advances in Modeling Earth Systems*, doi:10.1029/2018ms001400.
Maury, M.F., 1849: *Wind and Current Charts of the North and South Atlantic*. National Observatory, Washington, DC, USA, 31 maps pp.
Maury, M.F., 1855: *The Physical Geography of the Sea*. Harper & Brothers Publishers, New York, NY, USA, 274 pp.
Maury, M.F., 1860: *The Physical Geography of the Sea, and its Meteorology*. Harper & Brothers Publishers, New York, NY, USA, 474 pp.
Maycock, A.C. et al., 2015: Possible impacts of a future grand solar minimum on climate: Stratospheric and global circulation changes. *Journal of Geophysical Research: Atmospheres*, **120(18)**, 9043–9058, doi:10.1002/2014jd022022.
Maycock, A.C. et al., 2018: Revisiting the Mystery of Recent Stratospheric Temperature Trends. *Geophysical Research Letters*, **45(18)**, 9919–9933, doi:10.1029/2018gl078035.
McCabe, M.F. et al., 2017: The future of Earth observation in hydrology. *Hydrology and Earth System Sciences*, **21(7)**, 3879–3914, doi:10.5194/hess-21-3879-2017.
McCarthy, G.D. et al., 2020: Sustainable Observations of the AMOC: Methodology and Technology. *Reviews of Geophysics*, **58(1)**, e2019RG000654, doi:10.1029/2019rg000654.
McClymont, E.L. et al., 2020: Lessons from a high-CO2 world: an ocean view from ~3million years ago. *Climate of the Past*, **16(4)**, 1599–1615, doi:10.5194/cp-16-1599-2020.
McCright, A.M., S.T. Marquart-Pyatt, R.L. Shwom, S.R. Brechin, and S. Allen, 2016: Ideology, capitalism, and climate: Explaining public views about climate change in the United States. *Energy Research & Social Science*, **21**, 180–189, doi:10.1016/j.erss.2016.08.003.
McDowell, N.G. et al., 2020: Pervasive shifts in forest dynamics in a changing world. *Science*, **368(6494)**, eaaz9463, doi:10.1126/science.aaz9463.
McGregor, H. et al., 2015: Robust global ocean cooling trend for the pre-industrial Common Era. *Nature Geoscience*, **8(9)**, 671–677, doi:10.1038/ngeo2510.
McGregor, J.L., 2015: Recent developments in variable-resolution global climate modelling. *Climatic Change*, **129(3)**, 369–380, doi:10.1007/s10584-013-0866-5.
McKinnon, K.A. and C. Deser, 2018: Internal Variability and Regional Climate Trends in an Observational Large Ensemble. *Journal of Climate*, **31(17)**, 6783–6802, doi:10.1175/jcli-d-17-0901.1.

ACCEPTED VERSION
SUBJECT TO FINAL EDITS

McSweeney, C.F., R.G. Jones, R.W. Lee, and D.P. Rowell, 2015: Selecting CMIP5 GCMs for downscaling over multiple regions. *Climate Dynamics*, **44(11–12)**, 3237–3260, doi:10.1007/s00382-014-2418-8.
Meadows, D.H., D.L. Meadows, J. Randers, and W.W. Behrens III, 1972: *The Limits to Growth: A Report for the Club of Rome's Project on the Predicament of Mankind*. Universe Books, New York, NY, USA, 205 pp.
Meehl, G.A., G.J. Boer, C. Covey, M. Latif, and R.J. Stouffer, 2000: The Coupled Model Intercomparison Project (CMIP). *Bulletin of the American Meteorological Society*, **81(2)**, 313–318, doi:10.1175/1520-0477(2000)081<0313:tcmipc>2.3.co;2.
Meehl, G.A. et al., 2007a: The WCRP CMIP3 Multimodel Dataset: A New Era in Climate Change Research. *Bulletin of the American Meteorological Society*, **88(9)**, 1383–1394, doi:10.1175/bams-88-9-1383.
Meehl, G.A. et al., 2007b: Global Climate Projections. In: *Climate Change 2007: The Physical Science Basis. Contribution of Working Group I to the Fourth Assessment Report of the Intergovernmental Panel on Climate Change* [Solomon, S., D. Qin, M. Manning, Z. Chen, M. Marquis, K.B. Averyt, M. Tignor, and H.L. Miller (eds.)]. Cambridge University Press, Cambridge, United Kingdom and New York, NY, USA, pp. 747–846.
Meehl, G.A. et al., 2014: Decadal climate prediction an update from the trenches. *Bulletin of the American Meteorological Society*, doi:10.1175/bams-d-12-00241.1.
Meehl, G.A. et al., 2020: Context for interpreting equilibrium climate sensitivity and transient climate response from the CMIP6 Earth system models. *Science Advances*, **6(26)**, doi:10.1126/sciadv.aba1981.
Meinshausen, M., S.C.B. Raper, and T.M.L. Wigley, 2011a: Emulating coupled atmosphere-ocean and carbon cycle models with a simpler model, MAGICC6 – Part 1: Model description and calibration. *Atmospheric Chemistry and Physics*, **11(4)**, 1417–1456, doi:10.5194/acp-11-1417-2011.
Meinshausen, M. et al., 2011b: The RCP greenhouse gas concentrations and their extensions from 1765 to 2300. *Climatic Change*, **109(1–2)**, 213–241, doi:10.1007/s10584-011-0156-z.
Meinshausen, M. et al., 2017: Historical greenhouse gas concentrations for climate modelling (CMIP6). *Geoscientific Model Development*, **10(5)**, 2057–2116, doi:10.5194/gmd-10-2057-2017.
Meinshausen, M. et al., 2020: The shared socio-economic pathway (SSP) greenhouse gas concentrations and their extensions to 2500. *Geoscientific Model Development*, **13(8)**, 3571–3605, doi:10.5194/gmd-13-3571-2020.
Members WAIS Divide Project et al., 2015: Precise interpolar phasing of abrupt climate change during the last ice age. *Nature*, **520(7549)**, 661–665, doi:10.1038/nature14401.
Merton, R.K., 1973: *The Sociology of Science: Theoretical and Empirical Investigations*. University of Chicago Press, Chicago, IL, USA, 636 pp.
Meteorological Office and N. Shaw, 1920: *Réseau Mondial, 1910: Monthly and Annual Summaries of Pressure, Temperature, and Precipitation at Land Stations*. H. M. Stationery Office, London, UK.
Milankovich, M., 1920: *Théorie Mathématique des Phénomènes Thermiques Produits par la Radiation Solaire*. Gauthier-Villars et Cie, Paris, France, 338 pp.
Millar, R.J., Z.R. Nicholls, P. Friedlingstein, and M.R. Allen, 2017a: A modified impulse-response representation of the global near-surface air temperature and atmospheric concentration response to carbon dioxide emissions. *Atmospheric Chemistry and Physics*, **17(11)**, 7213–7228, doi:10.5194/acp-17-7213-2017.
Millar, R.J. et al., 2017b: Emission budgets and pathways consistent with limiting warming to 1.5°C. *Nature Geoscience*, **10(10)**, 741–747, doi:10.1038/ngeo3031.
Mills, M.J., O.B. Toon, J. Lee-Taylor, and A. Robock, 2014: Multidecadal global cooling and unprecedented ozone loss following a regional nuclear conflict. *Earth's Future*, **2(4)**, 161–176, doi:10.1002/2013ef000205.
Min, S.-K., X. Zhang, F.W. Zwiers, and G.C. Hegerl, 2011: Human contribution to more-intense precipitation extremes. *Nature*, **470(7334)**, 378–381, doi:10.1038/nature09763.
Mindlin, J. et al., 2020: Storyline description of Southern Hemisphere midlatitude circulation and precipitation response to greenhouse gas forcing. *Climate Dynamics*, **54(9–10)**, 4399–4421, doi:10.1007/s00382-020-05234-1.
Ming, T., R. de_Richter, S. Shen, and S. Caillol, 2016: Fighting global warming by greenhouse gas removal: destroying atmospheric nitrous oxide thanks to synergies between two breakthrough technologies. *Environmental Science and Pollution Research*, **23(7)**, 6119–6138, doi:10.1007/s11356-016-6103-9.
Minx, J.C. et al., 2018: Negative emissions-Part 1: Research landscape and synthesis. *Environmental Research Letters*, **13(6)**, 063001, doi:10.1088/1748-9326/aabf9b.
Mitchell, D. et al., 2017: Half a degree additional warming, prognosis and projected impacts (HAPPI): background and experimental design. *Geoscientific Model Development*, **10(2)**, 571–583, doi:10.5194/gmd-10-571-2017.
Mitchell, J.F.B., T.C. Johns, W.J. Ingram, and J.A. Lowe, 2000: The effect of stabilising atmospheric carbon dioxide concentrations on global and regional climate change. *Geophysical Research Letters*, **27(18)**, 2977–2980, doi:10.1029/1999gl011213.
Mitchell, T.D., 2003: Pattern Scaling: An Examination of the Accuracy of the Technique for Describing Future Climates. *Climatic Change*, **60(3)**, 217–242, doi:10.1023/a:1026035305597.
Miura, T., S. Nagai, M. Takeuchi, K. Ichii, and H. Yoshioka, 2019: Improved Characterisation of Vegetation and Land Surface Seasonal Dynamics in Central Japan with Himawari-8 Hypertemporal Data. *Scientific Reports*, **9(1)**, doi:10.1038/s41598-019-52076-x.
Mizuta, R. et al., 2017: Over 5,000 Years of Ensemble Future Climate Simulations by 60-km Global and 20-km

ACCEPTED DIVISION SUBJECT TO FINAL EDITS

Regional Atmospheric Models. *Bulletin of the American Meteorological Society*, **98(7)**, 1383–1398, doi:10.1175/bams-d-16-0099.1.
Moezzi, M., K.B. Janda, and S. Rotmann, 2017: Using stories, narratives, and storytelling in energy and climate change research. *Energy Research & Social Science*, **31**, 1–10, doi:10.1016/j.erss.2017.06.034.
Morales, M.S. et al., 2020: Six hundred years of South American tree rings reveal an increase in severe hydroclimatic events since mid-20th century. *Proceedings of the National Academy of Sciences*, **117(29)**, 16816 LP – 16823, doi:10.1073/pnas.2002411117.
Moreno, A. et al., 2021: The case of a southern European glacier which survived Roman and medieval warm periods but is disappearing under recent warming. *The Cryosphere*, **15(2)**, 1157–1172, doi:10.5194/tc-15-1157-2021.
Morice, C.P. et al., 2021: An Updated Assessment of Near-Surface Temperature Change From 1850: The HadCRUT5 Data Set. *Journal of Geophysical Research: Atmospheres*, **126(3)**, doi:10.1029/2019jd032361.
Mormino, J., D. Sola, and C. Patten, 1975: *Climatic Impact Assessment Program: Development and Accomplishments, 1971-1975*. DOT-TST-76-41, U. S. Dept. of Transportation, Climatic Impact Assessment Program Office, 206 pp.
Mortimer, C. et al., 2020: Evaluation of long-term Northern Hemisphere snow water equivalent products. *The Cryosphere*, **14(5)**, 1579–1594, doi:10.5194/tc-14-1579-2020.
Moss, R.H. and S.H. Schneider, 2000: Uncertainties in the IPCC TAR: Recommendations to lead authors for more consistent assessment and reporting. In: *Guidance Papers on the Cross Cutting Issues of the Third Assessment Report of the IPCC* [Pachauri, R., T. Taniguchi, and K. Tanaka (eds.)]. World Meteorological Organization (WMO), Geneva, Switzerland, pp. 33–51.
Moss, R.H. et al., 2010: The next generation of scenarios for climate change research and assessment. *Nature*, **463**, 747, doi:10.1038/nature08823.
Mote, P.W. et al., 2015: Superensemble Regional Climate Modeling for the Western United States. *Bulletin of the American Meteorological Society*, **97(2)**, 203–215, doi:10.1175/bams-d-14-00090.1.
Moy, A.D. et al., 2019: Varied contribution of the Southern Ocean to deglacial atmospheric CO2 rise. *Nature Geoscience*, **12(12)**, 1006–1011, doi:10.1038/s41561-019-0473-9.
Mudryk, L. et al., 2020: Historical Northern Hemisphere snow cover trends and projected changes in the CMIP6 multi-model ensemble. *The Cryosphere*, **14(7)**, 2495–2514, doi:10.5194/tc-14-2495-2020.
Muller-Karger, F.E. et al., 2018: Advancing Marine Biological Observations and Data Requirements of the Complementary Essential Ocean Variables (EOVs) and Essential Biodiversity Variables (EBVs) Frameworks. *Frontiers in Marine Science*, **5**, doi:10.3389/fmars.2018.00211.
Murphy, J.M. et al., 2004: Quantification of modelling uncertainties in a large ensemble of climate change simulations. *Nature*, **430(7001)**, 768–772, doi:10.1038/nature02771.
Murphy, J.M. et al., 2018: *UKCP18 Land Projections: Science Report*. 00830/d, Met Office, Exeter, UK, 191 pp.
Myers, T.A. et al., 2020: Impact of the Climate Matters Program on Public Understanding of Climate Change. *Weather, Climate, and Society*, **12(4)**, 863–876, doi:10.1175/wcas-d-20-0026.1.
Myhre, G. et al., 2013: Anthropogenic and Natural Radiative Forcing Supplementary Material. In: *Climate Change 2013: The Physical Science Basis. Contribution of Working Group I to the Fifth Assessment Report of the Intergovernmental Panel on Climate Change* [Stocker, T.F., D. Qin, G.-K. Plattner, M. Tignor, S.K. Allen, J. Boschung, A. Nauels, Y. Xia, V. Bex, and P.M. Midgley (eds.)]. Cambridge University Press, Cambridge, United Kingdom and New York, NY, USA, pp. 44.
Mystakidis, S., E.L. Davin, N. Gruber, and S.I. Seneviratne, 2016: Constraining future terrestrial carbon cycle projections using observation-based water and carbon flux estimates. *Global Change Biology*, **22(6)**, 2198–2215, doi:10.1111/gcb.13217.
NA SEM, 2016: *Attribution of Extreme Weather Events in the Context of Climate Change*. National Academies of Sciences Engineering and Medicine (NA SEM). The National Academies Press, Washington, DC, USA, 200 pp., doi:10.17226/21852.
Nakashima, D.J., K. Galloway McLean, H.D. Thulstrup, A. Ramos Castillo, and J.T. Rubis, 2012: *Weathering Uncertainty: Traditional knowledge for climate change assessment and adaptation*. United Nations Educational, Scientific and Cultural Organization (UNESCO) and United Nations University Traditional Knowledge Initiative, Paris, France and Darwin, Australia, 120 pp.
Nakicenovic, N., R.J. Lempert, and A.C. Janetos, 2014: A Framework for the Development of New Socio-economic Scenarios for Climate Change Research: Introductory Essay. *Climatic Change*, **122(3)**, 351–361, doi:10.1007/s10584-013-0982-2.
National Research Council and Carbon Dioxide Assessment Committee, 1983: *Changing Climate*. National Academies Press, Washington, D.C, doi:10.17226/18714.
Nauels, A. et al., 2019: Attributing long-term sea-level rise to Paris Agreement emission pledges. *Proceedings of the National Academy of Sciences of the United States of America*, **116(47)**, 23487–23492, doi:10.1073/pnas.1907461116.
Navarro, L.M. et al., 2017: Monitoring biodiversity change through effective global coordination. *Current Opinion in Environmental Sustainability*, **29**, 158–169, doi:10.1016/j.cosust.2018.02.005.

SUBJECT TO FINAL EDITS ACCEPTED VERSION

Naveau, P. et al., 2018: Revising return periods for record events in a climate event attribution context. *Journal of Climate*, **31(9)**, 3411–3422, doi:10.1175/jcli-d-16-0752.1.
Nebeker, F., 1995: *Calculating the Weather: Meteorology in the 20th Century*. Academic Press, San Diego, CA, USA, 265 pp.
Nehrbass-Ahles, C. et al., 2020: Abrupt CO 2 release to the atmosphere under glacial and early interglacial climate conditions. *Science*, **369(6506)**, 1000–1005, doi:10.1126/science.aay8178.
Neukom, R., N. Steiger, J.J. Gómez-Navarro, J. Wang, and J.P. Werner, 2019: No evidence for globally coherent warm and cold periods over the preindustrial Common Era. *Nature*, **571(7766)**, 550–554, doi:10.1038/s41586-019-1401-2.
Nicholls, R.J.Z. et al., 2020: Reduced complexity model intercomparison project phase 1: Protocol, results and initial observations. *Geoscientific Model Development Discussions*, **13(11)**, 5175–5190, doi:10.5194/gmd-13-5175-2020.
Nieto, R. and L. Gimeno, 2019: A database of optimal integration times for Lagrangian studies of atmospheric moisture sources and sinks. *Scientific Data*, **6(1)**, 59, doi:10.1038/s41597-019-0068-8.
Nordhaus, W.D., 1975: *Can We Control Carbon Dioxide?* IIASA Working Paper WP-75-63, International Institute for Applied Systems Analysis (IIASA), Laxenberg, Austria, 47 pp.
Nordhaus, W.D., 1977: *Strategies for the Control of Carbon Dioxide*. Cowles Foundation Discussion Paper No. 443, Cowles Foundation for Research in Economics. Yale University, New Haven, CN, USA, 79 pp.
Notz, D., 2015: How well must climate models agree with observations? *Philosophical Transactions of the Royal Society A: Mathematical, Physical and Engineering Sciences*, **373(2052)**, 20140164, doi:10.1098/rsta.2014.0164.
Notz, D. and J. Stroeve, 2018: The Trajectory Towards a Seasonally Ice-Free Arctic Ocean. *Current Climate Change Reports*, **4(4)**, 407–416, doi:10.1007/s40641-018-0113-2.
Notz, D. et al., 2016: The CMIP6 Sea-Ice Model Intercomparison Project (SIMIP): understanding sea ice through climate-model simulations. *Geoscientific Model Development*, **9(9)**, 3427–3446, doi:10.5194/gmd-9-3427-2016.
Nowicki, S.M.J. et al., 2016: Ice Sheet Model Intercomparison Project (ISMIP6) contribution to CMIP6. *Geoscientific Model Development*, **9(12)**, 4521–4545, doi:10.5194/gmd-9-4521-2016.
NRC, 1979: *Carbon Dioxide and Climate: A Scientific Assessment*. National Research Council (NRC) Ad Hoc Study Group on Carbon Dioxide and Climate. The National Academies Press, Washington, DC, USA, 34 pp., doi:10.17226/12181.
NRC, 2012: Synergies Between Weather and Climate Modeling. In: *A National Strategy for Advancing Climate Modeling*. National Research Council (NRC) Committee on a National Strategy for Advancing Climate Modeling. The National Academies Press, Washington, DC, USA, pp. 197–208, doi:10.17226/13430.
Nunn, P.D. and N.J. Reid, 2016: Aboriginal Memories of Inundation of the Australian Coast Dating from More than 7000 Years Ago. *Australian Geographer*, **47(1)**, 11–47, doi:10.1080/00049182.2015.1077539.
O'Neill, B.C. et al., 2014: A new scenario framework for climate change research: The concept of shared socioeconomic pathways. *Climatic Change*, **122(3)**, 387–400, doi:10.1007/s10584-013-0905-2.
O'Neill, B.C. et al., 2016: The Scenario Model Intercomparison Project (ScenarioMIP) for CMIP6. *Geoscientific Model Development*, **9(9)**, 3461–3482, doi:10.5194/gmd-9-3461-2016.
O'Neill, B.C. et al., 2017a: The roads ahead: Narratives for shared socioeconomic pathways describing world futures in the 21st century. *Global Environmental Change*, **42**, 169–180, doi:10.1016/j.gloenvcha.2015.01.004.
O'Neill, B.C. et al., 2017b: IPCC reasons for concern regarding climate change risks. *Nature Climate Change*, **7(1)**, 28–37, doi:10.1038/nclimate3179.
O'Neill, B.C. et al., 2020: Achievements and needs for the climate change scenario framework. *Nature Climate Change*, **10(12)**, 1074–1084, doi:10.1038/s41558-020-00952-0.
Obura, D.O. et al., 2019: Coral Reef Monitoring, Reef Assessment Technologies, and Ecosystem-Based Management. *Frontiers in Marine Science*, **6**, 580, doi:10.3389/fmars.2019.00580.
Ohmura, A. et al., 1998: Baseline Surface Radiation Network (BSRN/WCRP): New Precision Radiometry for Climate Research. *Bulletin of the American Meteorological Society*, **79(10)**, 2115–2136, doi:10.1175/1520-0477(1998)079<2115:bsrnbw>2.0.co;2.
Oliva, R. et al., 2016: Status of Radio Frequency Interference (RFI) in the 1400–1427MHz passive band based on six years of SMOS mission. *Remote Sensing of Environment*, **180**, 64–75, doi:10.1016/j.rse.2016.01.013.
Olonscheck, D. and D. Notz, 2017: Consistently estimating internal climate variability from climate model simulations. *Journal of Climate*, **30(23)**, 9555–9573, doi:10.1175/jcli-d-16-0428.1.
Oppenheimer, M., C.M. Little, and R.M. Cooke, 2016: Expert judgement and uncertainty quantification for climate change. *Nature Climate Change*, **6(5)**, 445–451, doi:10.1038/nclimate2959.
Oreskes, N. and E.M. Conway, 2010: *Merchants of Doubt: How a Handful of Scientists Obscured the Truth on Issues from Tobacco Smoke to Global Warming*. Bloomsbury Press, New York, NY, USA, 368 pp.
Orlove, B., C. Roncoli, M. Kabugo, and A. Majugu, 2010: Indigenous climate knowledge in southern Uganda: the multiple components of a dynamic regional system. *Climatic Change*, **100(2)**, 243–265, doi:10.1007/s10584-

ACCEPTED VERSION SUBJECT TO FINAL EDITS

009-9586-2.
Orlowsky, B. and S.I. Seneviratne, 2013: Elusive drought: uncertainty in observed trends and short- and long-term CMIP5 projections. *Hydrology and Earth System Sciences*, **17(5)**, 1765–1781, doi:10.5194/hess-17-1765-2013.
Orr, J.C. et al., 2017: Biogeochemical protocols and diagnostics for the CMIP6 Ocean Model Intercomparison Project (OMIP). *Geoscientific Model Development*, **10(6)**, 2169–2199, doi:10.5194/gmd-10-2169-2017.
Osborn, T.J. et al., 2021: Land Surface Air Temperature Variations Across the Globe Updated to 2019: The CRUTEM5 Data Set. *Journal of Geophysical Research: Atmospheres*, **126(2)**, e2019JD032352, doi:10.1029/2019jd032352.
Ostrom, E., 1996: Crossing the great divide: Coproduction, synergy, and development. *World Development*, **24(6)**, 1073–1087, doi:10.1016/0305-750x(96)00023-x.
Ostrom, E., 2012: Nested externalities and polycentric institutions: must we wait for global solutions to climate change before taking actions at other scales? *Economic Theory*, **49(2)**, 353–369, doi:10.1007/s00199-010-0558-6.
Otterå, O.H., M. Bentsen, H. Drange, and L. Suo, 2010: External forcing as a metronome for Atlantic multidecadal variability. *Nature Geoscience*, doi:10.1038/ngeo955.
Otto, F.E.L., 2017: Attribution of Weather and Climate Events. *Annual Review of Environment and Resources*, **42(1)**, 627–646, doi:10.1146/annurev-environ-102016-060847.
Otto, F.E.L., R.B. Skeie, J.S. Fuglestvedt, T. Berntsen, and M.R. Allen, 2017: Assigning historic responsibility for extreme weather events. *Nature Publishing Group*, **7**, 757–759, doi:10.1038/nclimate3419.
Otto, F.E.L. et al., 2018: Attributing high-impact extreme events across timescales-a case study of four different types of events. *Climatic Change*, **149(3–4)**, 399–412, doi:10.1007/s10584-018-2258-3.
Otto, F.E.L. et al., 2020: Toward an Inventory of the Impacts of Human-Induced Climate Change. *Bulletin of the American Meteorological Society*, **101(11)**, E1972–E1979, doi:10.1175/bams-d-20-0027.1.
Otto-Bliesner, B.L. et al., 2017: The PMIP4 contribution to CMIP6 -- Part 2: Two interglacials, scientific objective and experimental design for Holocene and \\hack{\\newline} Last Interglacial simulations. *Geoscientific Model Development*, **10(11)**, 3979–4003, doi:10.5194/gmd-10-3979-2017.
Owens, M.J. et al., 2017: The Maunder minimum and the Little Ice Age: an update from recent reconstructions and climate simulations. *Journal of Space Weather and Space Climate*, **7**, A33, doi:10.1051/swsc/2017034.
PAGES 2k Consortium, 2013: Continental-scale temperature variability during the past two millennia. *Nature Geoscience*, **6(5)**, 339–346, doi:10.1038/ngeo1797.
PAGES 2k Consortium, 2017: A global multiproxy database for temperature reconstructions of the Common Era. *Scientific Data*, **4**, 170088, doi:10.1038/sdata.2017.88.
PAGES 2k Consortium, 2019: Consistent multidecadal variability in global temperature reconstructions and simulations over the Common Era. *Nature Geoscience*, **12(8)**, 643–649, doi:10.1038/s41561-019-0400-0.
Painter, J., 2015: Disaster, uncertainty, opportunity or risk? Key messages from the television coverage of the IPCC's 2013/2014 reports. *MÈTODE Science Studies Journal*, 81–87, doi:10.7203/metode.85.4179.
Palerme, C. et al., 2014: How much snow falls on the Antarctic ice sheet? *The Cryosphere*, **8(4)**, 1577–1587, doi:10.5194/tc-8-1577-2014.
Palmer, M.D. and D.J. McNeall, 2014: Internal variability of Earth's energy budget simulated by CMIP5 climate models. *Environmental Research Letters*, doi:10.1088/1748-9326/9/3/034016.
Palmer, M.D., C.M. Domingues, A.B.A. Slangen, and F. Boeira Dias, 2021: An ensemble approach to quantify global mean sea-level rise over the 20th century from tide gauge reconstructions. *Environmental Research Letters*, doi:10.1088/1748-9326/abdaec.
Palmer, M.D. et al., 2017: Ocean heat content variability and change in an ensemble of ocean reanalyses. *Climate Dynamics*, **49(3)**, 909–930, doi:10.1007/s00382-015-2801-0.
Palmer, T. and B. Stevens, 2019: The scientific challenge of understanding and estimating climate change. *Proceedings of the National Academy of Sciences*, **116(49)**, 24390 LP – 24395, doi:10.1073/pnas.1906691116.
Palmer, T.N., 2019: Stochastic weather and climate models. *Nature Reviews Physics*, **1(7)**, 463–471, doi:10.1038/s42254-019-0062-2.
Palmer, T.N., F.J. Doblas-Reyes, A. Weisheimer, and M.J. Rodwell, 2008: Toward Seamless Prediction: Calibration of Climate Change Projections Using Seasonal Forecasts. *Bulletin of the American Meteorological Society*, **89(4)**, 459–470, doi:10.1175/bams-89-4-459.
Pandolfi, M. et al., 2018: A European aerosol phenomenology – 6: scattering properties of atmospheric aerosol particles from 28 ACTRIS sites. *Atmospheric Chemistry and Physics*, **18(11)**, 7877–7911, doi:10.5194/acp-18-7877-2018.
Papagiannopoulou, C., D.G. Miralles, M. Demuzere, N.E.C. Verhoest, and W. Waegeman, 2018: Global hydro-climatic biomes identified via multitask learning. *Geosci. Model Dev.*, **11(10)**, 4139–4153, doi:10.5194/gmd-11-4139-2018.
Parajuli, S.P., Z.-L. Yang, and D.M. Lawrence, 2016: Diagnostic evaluation of the Community Earth System Model in simulating mineral dust emission with insight into large-scale dust storm mobilization in the Middle East and North Africa (MENA). *Aeolian Research*, **21**, 21–35, doi:10.1016/j.aeolia.2016.02.002.

ACCEPTED VERSION SUBJECT TO FINAL EDITS

Park, E.G., G. Burr, V. Slonosky, R. Sieber, and L. Podolsky, 2018: Data rescue archive weather (DRAW). *Journal of Documentation*, **74(4)**, 763–780.
Parker, W.S., 2009: Confirmation and adequacy-for-purpose in climate modelling. *Aristotelian Society Supplementary Volume*, **83(1)**, 233–249, doi:10.1111/j.1467-8349.2009.00180.x.
Parker, W.S., 2013: Ensemble modeling, uncertainty and robust predictions. *WIREs Climate Change*, **4(3)**, 213–223, doi:10.1002/wcc.220.
Parker, W.S., 2020: Model Evaluation: An Adequacy-for-Purpose View. *Philosophy of Science*, **87(3)**, 457–477, doi:10.1086/708691.
Parker, W.S. and J.S. Risbey, 2015: False precision, surprise and improved uncertainty assessment. *Philosophical Transactions of the Royal Society A: Mathematical, Physical and Engineering Sciences*, **373(2055)**, 20140453, doi:10.1098/rsta.2014.0453.
Parker, W.S. and E. Winsberg, 2018: Values and evidence: how models make a difference. *European Journal for Philosophy of Science*, **8(1)**, 125–142, doi:10.1007/s13194-017-0180-6.
Parmesan, C. and G. Yohe, 2003: A globally coherent fingerprint of climate change. *Nature*, **421**, 37–42, doi:10.1038/nature01286.
Parmesan, C. et al., 2013: Beyond climate change attribution in conservation and ecological research. *Ecology Letters*, **16**, 58–71, doi:10.1111/ele.12098.
Parson, E.A., 2003: *Protecting the Ozone Layer: Science and Strategy*. Oxford University Press, Oxford, UK, 400 pp., doi:10.1093/0195155491.001.0001.
Parsons, L.A. and G.J. Hakim, 2019: Local Regions Associated With Interdecadal Global Temperature Variability in the Last Millennium Reanalysis and CMIP5 Models. *Journal of Geophysical Research: Atmospheres*, doi:10.1029/2019jd030426.
Pascoe, C., B.N. Lawrence, E. Guilyardi, M. Juckes, and K.E. Taylor, 2019: Designing and Documenting Experiments in CMIP6. *Geoscientific Model Development Discussions*, **2019**, 1–27, doi:10.5194/gmd-2019-98.
Past Interglacials Working Group of PAGES, 2016: Interglacials of the last 800,000 years. *Reviews of Geophysics*, **54(1)**, 162–219, doi:10.1002/2015rg000482.
Pastorello, G.Z. et al., 2017: A new data set to keep a sharper eye on land-air exchanges. *Eos, Transactions American Geophysical Union*, doi:10.1029/2017eo071597.
Pattyn, F., 2018: The paradigm shift in Antarctic ice sheet modelling. *Nature Communications*, **9(1)**, 2728, doi:10.1038/s41467-018-05003-z.
Paulsen, H., T. Ilyina, K.D. Six, and I. Stemmler, 2017: Incorporating a prognostic representation of marine nitrogen fixers into the global ocean biogeochemical model HAMOCC. *Journal of Advances in Modeling Earth Systems*, **9(1)**, 438–464, doi:10.1002/2016ms000737.
Pearce, W., K. Holmberg, I. Hellsten, and B. Nerlich, 2014: Climate Change on Twitter: Topics, Communities and Conversations about the 2013 IPCC Working Group 1 Report. *PLoS ONE*, **9(4)**, e94785, doi:10.1371/journal.pone.0094785.
Pearce, W., S. Niederer, S.M. Özkula, and N. Sánchez Querubín, 2019: The social media life of climate change: Platforms, publics, and future imaginaries. *Wiley Interdisciplinary Reviews: Climate Change*, **10(2)**, e569, doi:10.1002/wcc.569.
Pedersen, J.S.T. et al., 2020: Variability in historical emissions trends suggests a need for a wide range of global scenarios and regional analyses. *Communications Earth & Environment*, **1(1)**, 41, doi:10.1038/s43247-020-00045-y.
Pedro, J.B. et al., 2018: Beyond the bipolar seesaw: Toward a process understanding of interhemispheric coupling. *Quaternary Science Reviews*, **192**, 27–46, doi:10.1016/j.quascirev.2018.05.005.
Peel, J. and H.M. Osofsky, 2018: A Rights Turn in Climate Change Litigation? *Transnational Environmental Law*, **7(1)**, 37–67, doi:10.1017/s2047102517000292.
Peel, M.C., B.L. Finlayson, and T.A. McMahon, 2007: Updated world map of the Köppen-Geiger climate classification. *Hydrology and Earth System Sciences*, **11(5)**, 1633–1644, doi:10.5194/hess-11-1633-2007.
Pendergrass, A.G. and C. Deser, 2017: Climatological Characteristics of Typical Daily Precipitation. *Journal of Climate*, **30(15)**, 5985–6003, doi:10.1175/jcli-d-16-0684.1.
Penny, S.G. et al., 2019: Observational Needs for Improving Ocean and Coupled Reanalysis, S2S Prediction, and Decadal Prediction. *Frontiers in Marine Science*, **6**, 391, doi:10.3389/fmars.2019.00391.
Pereira, H.M. et al., 2013: Essential Biodiversity Variables. *Science*, **339(6117)**, 277–278, doi:10.1126/science.1229931.
Permana, D.S. et al., 2019: Disappearance of the last tropical glaciers in the Western Pacific Warm Pool (Papua, Indonesia) appears imminent. *Proceedings of the National Academy of Sciences*, **116(52)**, 26382 LP – 26388, doi:10.1073/pnas.1822037116.
Petersen, M.R. et al., 2019: An Evaluation of the Ocean and Sea Ice Climate of E3SM Using MPAS and Interannual CORE-II Forcing. *Journal of Advances in Modeling Earth Systems*, **11(5)**, 1438–1458, doi:10.1029/2018ms001373.
Peterson, T.C., W.M. Connolley, and J. Fleck, 2008: The Myth of the 1970s Global Cooling Consensus. *Bulletin of the*

ACCEPTED VERSION SUBJECT TO FINAL EDITS

American Meteorological Society, **89(9)**, 1325–1338, doi:10.1175/2008bams2370.1.
Petit, J.R. et al., 1999: Climate and atmospheric history of the past 420,000 years from the Vostok ice core, Antarctica. *Nature*, **399(6735)**, 429–436, doi:10.1038/20859.
Petzold, A. et al., 2015: Global-scale atmosphere monitoring by in-service aircraft – current achievements and future prospects of the European Research Infrastructure IAGOS. *Tellus B: Chemical and Physical Meteorology*, **67(1)**, 28452, doi:10.3402/tellusb.v67.28452.
Pfeffer, W.T. et al., 2014: The Randolph Glacier Inventory: a globally complete inventory of glaciers. *Journal of Glaciology*, **60(221)**, 537–552, doi:10.3189/2014jog13j176.
Pfister, P.L. and T.F. Stocker, 2016: Earth system commitments due to delayed mitigation. *Environmental Research Letters*, **11(1)**, 014010, doi:10.1088/1748-9326/11/1/014010.
Pfister, P.L. and T.F. Stocker, 2017: State-Dependence of the Climate Sensitivity in Earth System Models of Intermediate Complexity. *Geophysical Research Letters*, **44(20)**, 10,643–10,653, doi:10.1002/2017gl075457.
Pfister, P.L. and T.F. Stocker, 2018: The realized warming fraction: a multi-model sensitivity study. *Environmental Research Letters*, **13(12)**, 124024, doi:10.1088/1748-9326/aaebae.
Pfleiderer, P., C.-F. Schleussner, M. Mengel, and J. Rogelj, 2018: Global mean temperature indicators linked to warming levels avoiding climate risks. *Environmental Research Letters*, doi:10.1088/1748-9326/aac319.
Philip, S. et al., 2020: A protocol for probabilistic extreme event attribution analyses. *Advances in Statistical Climatology, Meteorology and Oceanography*, **6(2)**, 177–203, doi:10.5194/ascmo-6-177-2020.
Phillips, T.J. et al., 2004: Evaluating Parameterizations in General Circulation Models: Climate Simulation Meets Weather Prediction. *Bulletin of the American Meteorological Society*, **85(12)**, 1903–1916, doi:10.1175/bams-85-12-1903.
Pielke, R., T. Wigley, and C. Green, 2008: Dangerous assumptions. *Nature*, **452(7187)**, 531–532, doi:10.1038/452531a.
Pincus, R., P.M. Forster, and B. Stevens, 2016: The Radiative Forcing Model Intercomparison Project (RFMIP): experimental protocol for CMIP6. *Geoscientific Model Development*, **9(9)**, 3447–3460, doi:10.5194/gmd-9-3447-2016.
Planton, Y.Y. et al., 2021: Evaluating Climate Models with the CLIVAR 2020 ENSO Metrics Package. *Bulletin of the American Meteorological Society*, **102(2)**, E193–E217, doi:10.1175/bams-d-19-0337.1.
Plass, G.N., 1956: Effect of Carbon Dioxide Variations on Climate. *American Journal of Physics*, **24(5)**, 376–387, doi:10.1119/1.1934233.
Plass, G.N., 1961: The Influence of Infrared Absorptive Molecules on the Climate. *Annals of the New York Academy of Sciences*, **95(1)**, 61–71, doi:10.1111/j.1749-6632.1961.tb50025.x.
Plattner, G.-K. et al., 2008: Long-Term Climate Commitments Projected with Climate–Carbon Cycle Models. *Journal of Climate*, **21(12)**, 2721–2751, doi:10.1175/2007jcli1905.1.
Poli, P. et al., 2016: ERA-20C: An atmospheric reanalysis of the twentieth century. *Journal of Climate*, **29(11)**, 4083–4097, doi:10.1175/jcli-d-15-0556.1.
Poloczanska, E.S. et al., 2013: Global imprint of climate change on marine life. *Nature Climate Change*, **3(10)**, 919–925, doi:10.1038/nclimate1958.
Pongratz, J. et al., 2018: Models meet data: Challenges and opportunities in implementing land management in Earth system models. *Global Change Biology*, **24(4)**, 1470–1487, doi:10.1111/gcb.13988.
Popper, S.K.R., 1959: *The Logic of Scientific Discovery*. Hutchinson & Co., London, UK, 480 pp.
Porter, C. et al., 2018: ArcticDEM V1. Harvard Dataverse.
Porter, J.J. and S. Dessai, 2017: Mini-me: Why do climate scientists' misunderstand users and their needs? *Environmental Science & Policy*, **77**, 9–14, doi:10.1016/j.envsci.2017.07.004.
Prigent, C., C. Jimenez, and P. Bousquet, 2020: Satellite-Derived Global Surface Water Extent and Dynamics Over the Last 25 Years (GIEMS-2). *Journal of Geophysical Research: Atmospheres*, **125(3)**, e2019JD030711, doi:10.1029/2019jd030711.
Pulliainen, J. et al., 2020: Patterns and trends of Northern Hemisphere snow mass from 1980 to 2018. *Nature*, **581(7808)**, 294–298, doi:10.1038/s41586-020-2258-0.
Rahmstorf, S., G. Foster, and A. Cazenave, 2012: Comparing climate projections to observations up to 2011. *Environmental Research Letters*, **7(4)**, 044035, doi:10.1088/1748-9326/7/4/044035.
Rahmstorf, S. et al., 2005: Thermohaline circulation hysteresis: A model intercomparison. *Geophysical Research Letters*, **32(23)**, L23605, doi:10.1029/2005gl023655.
Rahmstorf, S. et al., 2007: Recent Climate Observations Compared to Projections. *Science*, **316(5825)**, 709–709, doi:10.1126/science.1136843.
Ramanathan, V., 1975: Greenhouse Effect Due to Chlorofluorocarbons: Climatic Implications. *Science*, **190(4209)**, 50–52, doi:10.1126/science.190.4209.50.
Randall, D.A. and B.A. Wielicki, 1997: Measurements, Models, and Hypotheses in the Atmospheric Sciences. *Bulletin of the American Meteorological Society*, **78(3)**, 399–406, doi:10.1175/1520-0477(1997)078<0399:mmohit>2.0.co;2.
Rao, S. et al., 2017: Future air pollution in the Shared Socio-economic Pathways. *Global Environmental Change*, **42**, 346–358, doi:10.1016/j.gloenvcha.2016.05.012.

ACCEPTED VERSION SUBJECT TO FINAL EDITS

Raper, S.C.B., J.M. Gregory, and T.J. Osborn, 2001: Use of an upwelling-diffusion energy balance climate model to simulate and diagnose A/OGCM results. *Climate Dynamics*, **17(8)**, 601–613, doi:10.1007/pl00007931.
Raskin, P. and R. Swart, 2020: Excluded futures: the continuity bias in scenario assessments. *Sustainable Earth*, **3(1)**, 8, doi:10.1186/s42055-020-00030-5.
Rasool, S.I. and S.H. Schneider, 1971: Atmospheric Carbon Dioxide and Aerosols: Effects of Large Increases on Global Climate. *Science*, **173(3992)**, 138–141, doi:10.1126/science.173.3992.138.
Raupach, M.R. et al., 2007: Global and regional drivers of accelerating CO2 emissions. *Proceedings of the National Academy of Sciences*, **104(24)**, 10288–10293, doi:10.1073/pnas.0700609104.
Ray, D.K., J.S. Gerber, G.K. Macdonald, and P.C. West, 2015: Climate variation explains a third of global crop yield variability. *Nature Communications*, **6**, doi:10.1038/ncomms6989.
Rayner, N.A. et al., 2006: Improved Analyses of Changes and Uncertainties in Sea Surface Temperature Measured In Situ since the Mid-Nineteenth Century: The HadSST2 Dataset. *Journal of Climate*, **19(3)**, 446–469, doi:10.1175/jcli3637.1.
Rayner, S. and E.L. Malone, 1998: *Human Choice and Climate Change: The Societal Framework*. Battelle Press, Columbus, OH, USA, 536 pp.
Rebmann, C. et al., 2018: ICOS eddy covariance flux-station site setup: a review. *International Agrophysics*, **32(4)**, 471–494.
Reimer, P.J. et al., 2020: The IntCal20 Northern Hemisphere Radiocarbon Age Calibration Curve (0–55 cal kBP). *Radiocarbon*, **62(4)**, 725–757, doi:10.1017/rdc.2020.41.
Reis, S. et al., 2012: From acid rain to climate change. *Science*, **338(6111)**, 1153–1154, doi:10.1126/science.1226514.
Reisinger, A. et al., 2020: *The concept of risk in the IPCC Sixth Assessment Report: a summary of crossWorking Group discussions*. Intergovernmental Panel on Climate Change (IPCC), Geneva, Switzerland, 15 pp.
Remedio, A.R. et al., 2019: Evaluation of New CORDEX Simulations Using an Updated Köppen-Trewartha Climate Classification. *Atmosphere*, **10(11)**, doi:10.3390/atmos10110726.
Reul, N. et al., 2020: Sea surface salinity estimates from spaceborne L-band radiometers: An overview of the first decade of observation (2010–2019). *Remote Sensing of Environment*, **242**, 111769, doi:10.1016/j.rse.2020.111769.
Revelle, R. and H.E. Suess, 1957: Carbon Dioxide Exchange Between the Atmosphere and Ocean and the Question of an Increase of Atmospheric CO2 during the Past Decades. *Tellus*, **9(1)**, 18–27, doi:10.1111/j.2153-3490.1957.tb01849.x.
Riahi, K. et al., 2017: The Shared Socioeconomic Pathways and their energy, land use, and greenhouse gas emissions implications: An overview. *Global Environmental Change*, **42**, 153–168, doi:10.1016/j.gloenvcha.2016.05.009.
Ribes, A., S. Qasmi, and N.P. Gillett, 2021: Making climate projections conditional on historical observations. *Science Advances*, **7(4)**, 1–10, doi:10.1126/sciadv.abc0671.
Richardson, L.F., 1922: *Weather Prediction by Numerical Process*. Cambridge University Press, Cambridge, UK, 236 pp.
Riedlinger, D. and F. Berkes, 2001: Contributions of traditional knowledge to understanding climate change in the Canadian Arctic. *Polar Record*, **37(203)**, 315–328.
Righi, M. et al., 2020: Earth System Model Evaluation Tool (ESMValTool) v2.0 – technical overview. *Geoscientific Model Development*, **13(3)**, 1179–1199, doi:10.5194/gmd-13-1179-2020.
Rignot, E. and P. Kanagaratnam, 2006: Changes in the Velocity Structure of the Greenland Ice Sheet. *Science*, **311(5763)**, 986–990, doi:10.1126/science.1121381.
Rind, D. and D. Peteet, 1985: Terrestrial Conditions at the Last Glacial Maximum and CLIMAP Sea-Surface Temperature Estimates: Are They Consistent? *Quaternary Research*, **24(01)**, 1–22, doi:10.1016/0033-5894(85)90080-8.
Ritchie, P., Karabacak, and J. Sieber, 2019: Inverse-square law between time and amplitude for crossing tipping thresholds. *Proceedings of the Royal Society A: Mathematical, Physical and Engineering Sciences*, **475(2222)**, 20180504, doi:10.1098/rspa.2018.0504.
Roberts, M.J. et al., 2018: The benefits of global high-resolution for climate simulation: process-understanding and the enabling of stakeholder decisions at the regional scale.. *Bulletin of the American Meteorological Society*, null, doi:10.1175/bams-d-15-00320.1.
Roberts, M.J. et al., 2019: Description of the resolution hierarchy of the global coupled HadGEM3-GC3.1 model as used in CMIP6 HighResMIP experiments. *Geoscientific Model Development*, **12(12)**, 4999–5028, doi:10.5194/gmd-12-4999-2019.
Robock, A., L. Oman, and G.L. Stenchikov, 2007: Nuclear winter revisited with a modern climate model and current nuclear arsenals: Still catastrophic consequences. *Journal of Geophysical Research: Atmospheres*, **112(D13)**, n/a–n/a, doi:10.1029/2006jd008235.
Rodas, C.D.A. and G.M. Di Giulio, 2017: Mídia brasileira e mudanças climáticas: uma análise sobre tendências da cobertura jornalística, abordagens e critérios de noticiabilidade. *Desenvolvimento e Meio Ambiente*, **40**, 101–124, doi:10.5380/dma.v40i0.49002.

ACCEPTED VERSION SUBJECT TO FINAL EDITS

Roe, S. et al., 2019: Contribution of the land sector to a 1.5°C world. *Nature Climate Change*, **9(11)**, 817–828, doi:10.1038/s41558-019-0591-9.
Roemmich, D., W. John Gould, and J. Gilson, 2012: 135 years of global ocean warming between the Challenger expedition and the Argo Programme. *Nature Climate Change*, **2(6)**, 425–428, doi:10.1038/nclimate1461.
Roemmich, D. et al., 2019: On the Future of Argo: A Global, Full-Depth, Multi-Disciplinary Array. *Frontiers in Marine Science*, **6**, 439, doi:10.3389/fmars.2019.00439.
Rogelj, J., P.M. Forster, E. Kriegler, C.J. Smith, and R. Séférian, 2019: Estimating and tracking the remaining carbon budget for stringent climate targets. *Nature*, **571(7765)**, 335–342, doi:10.1038/s41586-019-1368-z.
Rogelj, J. et al., 2016: Paris Agreement climate proposals need a boost to keep warming well below 2°C. *Nature*, **534(7609)**, 631–639, doi:10.1038/nature18307.
Rogelj, J. et al., 2017: Understanding the origin of Paris Agreement emission uncertainties. *Nature Communications*, **8(1)**, doi:10.1038/ncomms15748.
Rogelj, J. et al., 2018a: Scenarios towards limiting global mean temperature increase below 1.5°C. *Nature Climate Change*, **8(4)**, 325–332, doi:10.1038/s41558-018-0091-3.
Rogelj, J. et al., 2018b: Mitigation Pathways Compatible with 1.5°C in the Context of Sustainable Development. In: *Global Warming of 1.5°C. An IPCC Special Report on the impacts of global warming of 1.5°C above pre-industrial levels and related global greenhouse gas emission pathways, in the context of strengthening the global response to the threat of climate change,* [Masson-Delmotte, V., P. Zhai, H.-O. Pörtner, D. Roberts, J. Skea, P.R. Shukla, A. Pirani, W. Moufouma-Okia, C. Péan, R. Pidcock, S. Connors, J.B.R. Matthews, Y. Chen, X. Zhou, M.I. Gomis, E. Lonnoy, T. Maycock, M. Tignor, and T. Waterfield (eds.)]. In Press, pp. 93–174.
Rohde, R., R.A. Muller, R. Jacobsen, E. Muller, and C. Wickham, 2013: A New Estimate of the Average Earth Surface Land Temperature Spanning 1753 to 2011. *Geoinformatics & Geostatistics: An Overview*, **01(01)**, doi:10.4172/2327-4581.1000101.
Rohde, R.A. and Z. Hausfather, 2020: The Berkeley Earth Land/Ocean Temperature Record. *Earth System Science Data*, **12(4)**, 3469–3479, doi:10.5194/essd-12-3469-2020.
Rohrschneider, T., B. Stevens, and T. Mauritsen, 2019: On simple representations of the climate response to external radiative forcing. *Climate Dynamics*, **53(5)**, 3131–3145, doi:10.1007/s00382-019-04686-4.
Rojas, M., F. Lambert, J. Ramirez-Villegas, and A.J. Challinor, 2019: Emergence of robust precipitation changes across crop production areas in the 21st century. *Proceedings of the National Academy of Sciences*, **116(14)**, 6673–6678, doi:10.1073/pnas.1811463116.
Rosa, E.A. and T. Dietz, 2012: Human drivers of national greenhouse-gas emissions. *Nature Climate Change*, **2**, 581–586.
Rosenblum, E. and I. Eisenman, 2016: Faster Arctic Sea Ice Retreat in CMIP5 than in CMIP3 due to Volcanoes. *Journal of Climate*, **29(24)**, 9179–9188, doi:10.1175/jcli-d-16-0391.1.
Rosenblum, E. and I. Eisenman, 2017: Sea Ice Trends in Climate Models Only Accurate in Runs with Biased Global Warming. *Journal of Climate*, **30(16)**, 6265–6278, doi:10.1175/jcli-d-16-0455.1.
Rothman, D.S., P. Romero-Lankao, V.J. Schweizer, and B.A. Bee, 2014: Challenges to adaptation: a fundamental concept for the shared socio-economic pathways and beyond. *Climatic Change*, **122(3)**, 495–507, doi:10.1007/s10584-013-0907-0.
Rothrock, D.A., Y. Yu, and G.A. Maykut, 1999: Thinning of the Arctic sea-ice cover. *Geophysical Research Letters*, **26(23)**, 3469–3472, doi:10.1029/1999gl010863.
Rougier, J., 2007: Probabilistic Inference for Future Climate Using an Ensemble of Climate Model Evaluations. *Climatic Change*, **81(3–4)**, 247–264, doi:10.1007/s10584-006-9156-9.
Rounsevell, M.D.A. and M.J. Metzger, 2010: Developing qualitative scenario storylines for environmental change assessment. *Wiley Interdisciplinary Reviews: Climate Change*, **1(4)**, 606–619, doi:10.1002/wcc.63.
Ruane, A.C. et al., 2016: The Vulnerability, Impacts, Adaptation and Climate Services Advisory Board (VIACS AB v1.0) contribution to CMIP6. *Geoscientific Model Development*, **9(9)**, 3493–3515, doi:10.5194/gmd-9-3493-2016.
Rubel, F. and M. Kottek, 2010: Observed and projected climate shifts 1901-2100 depicted by world maps of the Köppen-Geiger climate classification. *Meteorologische Zeitschrift*, **19(2)**, 135–141, doi:10.1127/0941-2948/2010/0430.
Ruddiman, W.F. and A. McIntyre, 1981: The North Atlantic Ocean during the last deglaciation. *Palaeogeography, Palaeoclimatology, Palaeoecology*, **35**, 145–214, doi:10.1016/0031-0182(81)90097-3.
Ruddiman, W.F. and J.S. Thomson, 2001: The case for human causes of increased atmospheric CH4 over the last 5000 years. *Quaternary Science Reviews*, **20(18)**, 1769–1777, doi:10.1016/s0277-3791(01)00067-1.
Ruiz, I., S.H. Faria, and M.B. Neumann, 2020: Climate change perception: Driving forces and their interactions. *Environmental Science & Policy*, **108**, 112–120, doi:10.1016/j.envsci.2020.03.020.
Russo, S. et al., 2019: Half a degree and rapid socioeconomic development matter for heatwave risk. *Nature Communications*, **10(1)**, 136, doi:10.1038/s41467-018-08070-4.
Ryan, C. et al., 2018: Integrating Data Rescue into the Classroom. *Bulletin of the American Meteorological Society*,

ACCEPTED VERSION SUBJECT TO FINAL EDITS

99(9), 1757–1764, doi:10.1175/bams-d-17-0147.1.
Saha, S. et al., 2010: The NCEP climate forecast system reanalysis. *Bulletin of the American Meteorological Society*, **91(8)**, 1015–1057, doi:10.1175/2010bams3001.1.
Samir, K.C. and W. Lutz, 2017: The human core of the shared socioeconomic pathways: Population scenarios by age, sex and level of education for all countries to 2100. *Global Environmental Change*, **42**, 181–192, doi:10.1016/j.gloenvcha.2014.06.004.
Samset, B.H. et al., 2016: Fast and slow precipitation responses to individual climate forcers: A PDRMIP multimodel study. *Geophysical Research Letters*, **43(6)**, 2782–2791, doi:10.1002/2016gl068064.
Sanchez, C., K.D. Williams, and M. Collins, 2016: Improved stochastic physics schemes for global weather and climate models. *Quarterly Journal of the Royal Meteorological Society*, **142(694)**, 147–159, doi:10.1002/qj.2640.
Sanderson, B.M., R. Knutti, and P. Caldwell, 2015a: A Representative Democracy to Reduce Interdependency in a Multimodel Ensemble. *Journal of Climate*, **28(13)**, 5171–5194, doi:10.1175/jcli-d-14-00362.1.
Sanderson, B.M., R. Knutti, and P. Caldwell, 2015b: Addressing Interdependency in a Multimodel Ensemble by Interpolation of Model Properties. *Journal of Climate*, **28(13)**, 5150–5170, doi:10.1175/jcli-d-14-00361.1.
Sanderson, B.M., M. Wehner, and R. Knutti, 2017: Skill and independence weighting for multi-model assessments. *Geosci. Model Dev*, **10**, 2379–2395, doi:10.5194/gmd-10-2379-2017.
Santer, B.D., 2003: Contributions of Anthropogenic and Natural Forcing to Recent Tropopause Height Changes. *Science*, **301(5632)**, 479–483, doi:10.1126/science.1084123.
Santer, B.D. et al., 1995: Towards the detection and attribution of an anthropogenic effect on climate. *Climate Dynamics*, **12(2)**, 77–100, doi:10.1007/bf00223722.
Santer, B.D. et al., 2013: Human and natural influences on the changing thermal structure of the atmosphere. *Proceedings of the National Academy of Sciences*, **110(43)**, 17235–17240, doi:10.1073/pnas.1305332110.
Santer, B.D. et al., 2017: Causes of differences in model and satellite tropospheric warming rates. *Nature Geoscience*, **10(7)**, 478–485, doi:10.1038/ngeo2973.
Santer, B.D. et al., 2019: Quantifying stochastic uncertainty in detection time of human-caused climate signals. *Proceedings of the National Academy of Sciences*, **116(40)**, 19821–19827, doi:10.1073/pnas.1904586116.
Sapiains, R., R.J.S. Beeton, and I.A. Walker, 2016: Individual responses to climate change: Framing effects on pro-environmental behaviors. *Journal of Applied Social Psychology*, **46(8)**, 483–493, doi:10.1111/jasp.12378.
Sauer, I. et al., 2021: Climate Signals in River Flood Damages Emerge under Sound Regional Disaggregation. *Nature Communications*, 1–24, doi:10.21203/rs.3.rs-37259/v1.
Scambos, T.A., J.A. Bohlander, C.A. Shuman, and P. Skvarca, 2004: Glacier acceleration and thinning after ice shelf collapse in the Larsen B embayment, Antarctica. *Geophysical Research Letters*, **31(18)**, L18402, doi:10.1029/2004gl020670.
Schaller, N. et al., 2016: Human influence on climate in the 2014 southern England winter floods and their impacts. *Nature Climate Change*, **6(6)**, 627–634, doi:10.1038/nclimate2927.
Schaller, N. et al., 2018: Influence of blocking on Northern European and Western Russian heatwaves in large climate model ensembles. *Environmental Research Letters*, **13(5)**, 054015, doi:10.1088/1748-9326/aaba55.
Scheffer, M. et al., 2012: Anticipating Critical Transitions. *Science*, **338(6105)**, 344–348, doi:10.1126/science.1225244.
Schepers, D., E. de Boisseson, R. Eresmaa, C. Lupu, and P. Rosnay, 2018: CERA-SAT: A coupled satellite-era reanalysis. *ECMWF Newsletter*, **155**, 32–37, doi:10.21957/sp619ds74g.
Scherllin-Pirscher, B., A.K. Steiner, G. Kirchengast, M. Schwärz, and S.S. Leroy, 2017: The power of vertical geolocation of atmospheric profiles from GNSS radio occultation. *Journal of Geophysical Research: Atmospheres*, **122(3)**, 1595–1616, doi:10.1002/2016jd025902.
Scherrer, S.C., 2020: Temperature monitoring in mountain regions using reanalyses: lessons from the Alps. *Environmental Research Letters*, **15(4)**, 044005, doi:10.1088/1748-9326/ab702d.
Schiemann, R. et al., 2020: Northern Hemisphere blocking simulation in current climate models: evaluating progress from the Climate Model Intercomparison Project Phase~5 to 6 and sensitivity to resolution. *Weather and Climate Dynamics*, **1(1)**, 277–292, doi:10.5194/wcd-1-277-2020.
Schleussner, C.-F. and C.L. Fyson, 2020: Scenarios science needed in UNFCCC periodic review. *Nature Climate Change*, **10(4)**, 272–272, doi:10.1038/s41558-020-0729-9.
Schleussner, C.-F. et al., 2016a: Differential climate impacts for policy-relevant limits to global warming: the case of 1.5°C and 2°C. *Earth System Dynamics*, **7(2)**, 327–351, doi:10.5194/esd-7-327-2016.
Schleussner, C.-F. et al., 2016b: Science and policy characteristics of the Paris Agreement temperature goal. *Nature Climate Change*, **6(9)**, 827–835, doi:10.1038/nclimate3096.
Schmidt, G.A. et al., 2017: Practice and philosophy of climate model tuning across six US modeling centers. *Geoscientific Model Development*, **10(9)**, 3207–3223, doi:10.5194/gmd-10-3207-2017.
Schneider, S.H., 1975: On the Carbon Dioxide–Climate Confusion. *Journal of the Atmospheric Sciences*, **32(11)**, 2060–2066, doi:10.1175/1520-0469(1975)032<2060:otcdc>2.0.co;2.
Schneider, S.H., 1994: Detecting Climatic Change Signals: Are There Any "Fingerprints"? *Science*, **263(5145)**, 341–347, doi:10.1126/science.263.5145.341.
Schneider, T., C.M. Kaul, and K.G. Pressel, 2019: Possible climate transitions from breakup of stratocumulus decks

ACCEPTED VERSION SUBJECT TO FINAL EDITS

under greenhouse warming. *Nature Geoscience*, **12(3)**, 163–167, doi:10.1038/s41561-019-0310-1.
Schurer, A.P., M.E. Mann, E. Hawkins, S.F.B. Tett, and G.C. Hegerl, 2017: Importance of the pre-industrial baseline for likelihood of exceeding Paris goals. *Nature Climate Change*, **7(8)**, doi:10.1038/nclimate3345.
Schuur, E.A.G. et al., 2015: Climate change and the permafrost carbon feedback. *Nature*, **520(7546)**, 171–179, doi:10.1038/nature14338.
Schwarber, A.K., S.J. Smith, C.A. Hartin, B.A. Vega-Westhoff, and R. Sriver, 2019: Evaluating climate emulation: fundamental impulse testing of simple climate models. *Earth System Dynamics*, **10(4)**, 729–739, doi:10.5194/esd-10-729-2019.
Schweizer, V.J. and B.C. O'Neill, 2014: Systematic construction of global socioeconomic pathways using internally consistent element combinations. *Climatic Change*, **122(3)**, 431–445, doi:10.1007/s10584-013-0908-z.
Scott, D. et al., 2018: The Story of Water in Windhoek: A Narrative Approach to Interpreting a Transdisciplinary Process. *Water*, **10(10)**, 1366, doi:10.3390/w10101366.
Séférian, R. et al., 2016: Inconsistent strategies to spin up models in CMIP5: implications for ocean biogeochemical model performance assessment. *Geoscientific Model Development*, **9(5)**, 1827–1851, doi:10.5194/gmd-9-1827-2016.
Sellar, A.A. et al., 2019: UKESM1: Description and Evaluation of the U.K. Earth System Model. *Journal of Advances in Modeling Earth Systems*, **n/a(n/a)**, doi:10.1029/2019ms001739.
Sellers, W.D., 1969: A Global Climatic Model Based on the Energy Balance of the Earth-Atmosphere System. *Journal of Applied Meteorology*, **8(3)**, 392–400, doi:10.1175/1520-0450(1969)008<0392:agcmbo>2.0.co;2.
Seneviratne, S.I. and M. Hauser, 2020: Regional Climate Sensitivity of Climate Extremes in CMIP6 Versus CMIP5 Multimodel Ensembles. *Earth's Future*, **8(9)**, doi:10.1029/2019ef001474.
Seneviratne, S.I., M.G. Donat, A.J. Pitman, R. Knutti, and R.L. Wilby, 2016: Allowable CO2 emissions based on regional and impact-related climate targets. *Nature*, **529(7587)**, 477–483, doi:10.1038/nature16542.
Seneviratne, S.I. et al., 2018: Climate extremes, land–climate feedbacks and land-use forcing at 1.5°C. *Philosophical Transactions of the Royal Society A: Mathematical,\n\t\t\t\tPhysical and Engineering Sciences*, **376(2119)**, 20160450, doi:10.1098/rsta.2016.0450.
Sera, F. et al., 2020: Air Conditioning and Heat-related Mortality. *Epidemiology*, **31(6)**, 779–787, doi:10.1097/ede.0000000000001241.
Setzer, J. and L.C. Vanhala, 2019: Climate change litigation: A review of research on courts and litigants in climate governance. *Wiley Interdisciplinary Reviews: Climate Change*, **10(3)**, e580, doi:10.1002/wcc.580.
Sexton, D.M.H., J.M. Murphy, M. Collins, and M.J. Webb, 2012: Multivariate probabilistic projections using imperfect climate models part I: outline of methodology. *Climate Dynamics*, **38(11–12)**, 2513–2542, doi:10.1007/s00382-011-1208-9.
Sexton, D.M.H. et al., 2019: Finding plausible and diverse variants of a climate model. Part 1: establishing the relationship between errors at weather and climate time scales. *Climate Dynamics*, **53(1)**, 989–1022, doi:10.1007/s00382-019-04625-3.
Shackleton, N.J. and N.D. Opdyke, 1973: Oxygen Isotope and Palaeomagnetic Stratigraphy of Equatorial Pacific Core V28-238: Oxygen Isotope Temperatures and Ice Volumes on a 105 Year and 106 Year Scale. *Quaternary Research*, **3(01)**, 39–55, doi:10.1016/0033-5894(73)90052-5.
Shan, Y. et al., 2020: Impacts of COVID-19 and fiscal stimuli on global emissions and the Paris Agreement. *Nature Climate Change*, doi:10.1038/s41558-020-00977-5.
Shapiro, H.T. et al., 2010: *Climate change assessments: Review of the processes and procedures of the IPCC*. InterAcademy Council, Amsterdam, The Netherlands.
Shepherd, A. et al., 2012: A Reconciled Estimate of Ice-Sheet Mass Balance. *Science*, **338(6111)**, 1183–1189, doi:10.1126/science.1228102.
Shepherd, A. et al., 2018: Mass balance of the Antarctic Ice Sheet from 1992 to 2017. *Nature*, **558(7709)**, 219–222, doi:10.1038/s41586-018-0179-y.
Shepherd, A. et al., 2020: Mass balance of the Greenland Ice Sheet from 1992 to 2018. *Nature*, **579(7798)**, 233–239, doi:10.1038/s41586-019-1855-2.
Shepherd, T.G., 2016: A Common Framework for Approaches to Extreme Event Attribution. *Current Climate Change Reports*, **2(1)**, 28–38, doi:10.1007/s40641-016-0033-y.
Shepherd, T.G., 2019: Storyline approach to the construction of regional climate change information. *Proceedings of the Royal Society A: Mathematical, Physical and Engineering Sciences*, **475(2225)**, 20190013, doi:10.1098/rspa.2019.0013.
Shepherd, T.G. and A.H. Sobel, 2020: Localness in Climate Change. *Comparative Studies of South Asia, Africa and the Middle East*, **40(1)**, 7–16, doi:10.1215/1089201x-8185983.
Shepherd, T.G. et al., 2018: Storylines: an alternative approach to representing uncertainty in physical aspects of climate change. *Climatic Change*, **151(3–4)**, 555–571, doi:10.1007/s10584-018-2317-9.
Sherley, C., M. Morrison, R. Duncan, and K. Parton, 2014: Using Segmentation and Prototyping in Engaging Politically-Salient Climate-Change Household Segments. *Journal of Nonprofit & Public Sector Marketing*, **26(3)**, 258–280, doi:10.1080/10495142.2014.918792.

ACCEPTED VERSION SUBJECT TO FINAL EDITS

Sherwood, S.C., C.L. Meyer, R.J. Allen, and H.A. Titchner, 2008: Robust Tropospheric Warming Revealed by Iteratively Homogenized Radiosonde Data. *Journal of Climate*, **21(20)**, 5336–5352, doi:10.1175/2008jcli2320.1.

Sherwood, S.C. et al., 2015: Adjustments in the Forcing-Feedback Framework for Understanding Climate Change. *Bulletin of the American Meteorological Society*, **96(2)**, 217–228, doi:10.1175/bams-d-13-00167.1.

Sherwood, S.C. et al., 2020: An Assessment of Earth's Climate Sensitivity Using Multiple Lines of Evidence. *Reviews of Geophysics*, **58(4)**, doi:10.1029/2019rg000678.

Shi, L. et al., 2017: An assessment of upper ocean salinity content from the Ocean Reanalyses Inter-comparison Project (ORA-IP). *Climate Dynamics*, **49(3)**, 1009–1029, doi:10.1007/s00382-015-2868-7.

Shine, K.P., R.P. Allan, W.J. Collins, and J.S. Fuglestvedt, 2015: Metrics for linking emissions of gases and aerosols to global precipitation changes. *Earth System Dynamics*, **6(2)**, 525–540, doi:10.5194/esd-6-525-2015.

Shiogama, H., M. Watanabe, T. Ogura, T. Yokohata, and M. Kimoto, 2014: Multi-parameter multi-physics ensemble (MPMPE): a new approach exploring the uncertainties of climate sensitivity. *Atmospheric Science Letters*, **15(2)**, 97–102, doi:10.1002/asl2.472.

Siddall, M. et al., 2003: Sea-level fluctuations during the last glacial cycle. *Nature*, **423(6942)**, 853–858, doi:10.1038/nature01690.

Sillmann, J., V. Kharin, X. Zhang, F.W. Zwiers, and D. Bronaugh, 2013: Climate extremes indices in the CMIP5 multimodel ensemble: Part 1. Model evaluation in the present climate. *Journal of Geophysical Research: Atmospheres*, **118(4)**, 1716–1733, doi:10.1002/jgrd.50203.

Sillmann, J. et al., 2021: Event-Based Storylines to Address Climate Risk. *Earth's Future*, **9(2)**, doi:10.1029/2020ef001783.

Simmons, A.J. and P. Poli, 2015: Arctic warming in ERA-Interim and other analyses. *Quarterly Journal of the Royal Meteorological Society*, **141(689)**, 1147–1162, doi:10.1002/qj.2422.

Skeie, R.B. et al., 2017: Perspective has a strong effect on the calculation of historical contributions to global warming. *Environmental Research Letters*, **12(2)**, 024022, doi:10.1088/1748-9326/aa5b0a.

Skelton, M., J.J. Porter, S. Dessai, D.N. Bresch, and R. Knutti, 2017: The social and scientific values that shape national climate scenarios: a comparison of the Netherlands, Switzerland and the UK. *Regional Environmental Change*, **17(8)**, 2325–2338, doi:10.1007/s10113-017-1155-z.

Slivinski, L.C. et al., 2021: An Evaluation of the Performance of the Twentieth Century Reanalysis Version 3. *Journal of Climate*, **34(4)**, 1417–1438, doi:10.1175/jcli-d-20-0505.1.

Smagorinsky, J., S. Manabe, and J.L. Holloway, 1965: Numerical results from a Nine-level General Circulation Model of the Atmosphere. *Monthly Weather Review*, **93(12)**, 727–768, doi:10.1175/1520-0493(1965)093<0727:nrfanl>2.3.co;2.

SMIC, 1971: *Inadvertent Climate Modification: Report of the Study of Man's Impact on Climate*. Study of Man's Impact on Climate (SMIC). MIT Press, Cambridge, MA, USA, 334 pp.

Smith, C.J. et al., 2018: FAIR v1.3: a simple emissions-based impulse response and carbon cycle model. *Geoscientific Model Development*, **11(6)**, 2273–2297, doi:10.5194/gmd-11-2273-2018.

Smith, D.M. et al., 2016: Role of volcanic and anthropogenic aerosols in the recent global surface warming slowdown. *Nature Climate Change*, **6(10)**, 936–940, doi:10.1038/nclimate3058.

Smith, D.M. et al., 2019: The Polar Amplification Model Intercomparison Project (PAMIP) contribution to CMIP6: investigating the causes and consequences of polar amplification. *Geoscientific Model Development*, **12(3)**, 1139–1164, doi:10.5194/gmd-12-1139-2019.

Smith, J.B. et al., 2009: Assessing dangerous climate change through an update of the Intergovernmental Panel on Climate Change (IPCC) "reasons for concern". *Proceedings of the National Academy of Sciences*, **106(11)**, 4133–4137, doi:10.1073/pnas.0812355106.

Smith, L.A. and N. Stern, 2011: Uncertainty in science and its role in climate policy. *Philosophical Transactions of the Royal Society A: Mathematical, Physical and Engineering Sciences*, **369(1956)**, 4818–4841, doi:10.1098/rsta.2011.0149.

Smith, N. et al., 2019: Tropical Pacific Observing System. *Frontiers in Marine Science*, **6**, 31, doi:10.3389/fmars.2019.00031.

Smith, S.R. et al., 2019: Ship-Based Contributions to Global Ocean, Weather, and Climate Observing Systems. *Frontiers in Marine Science*, **6**, 434, doi:10.3389/fmars.2019.00434.

Snyder, C.W., 2016: Evolution of global temperature over the past two million years. *Nature*, **538(7624)**, 226–228, doi:10.1038/nature19798.

Solomina, O.N. et al., 2015: Holocene glacier fluctuations. *Quaternary Science Reviews*, **111**, 9–34, doi:10.1016/j.quascirev.2014.11.018.

Eyring, V., T.G. Shepherd, and D.W. Waugh (eds.), 2010: *SPARC CCMVal Report on the Evaluation of Chemistry-Climate Models*. SPARC Report No. 5, WCRP-30/2010, WMO/TD – No. 40, Stratosphere-troposphere Processes And their Role in Climate (SPARC), 426 pp.

Spratt, R.M. and L.E. Lisiecki, 2016: A Late Pleistocene sea level stack. *Climate of the Past*, **12(4)**, 1079–1092, doi:10.5194/cp-12-1079-2016.

ACCEPTED VERSION SUBJECT TO FINAL EDITS

Stahle, D.W. et al., 2016: The Mexican Drought Atlas: Tree-ring reconstructions of the soil moisture balance during the late pre-Hispanic, colonial, and modern eras. *Quaternary Science Reviews*, **149**, 34–60, doi:10.1016/j.quascirev.2016.06.018.

Stammer, D. et al., 2018: Science Directions in a Post COP21 World of Transient Climate Change: Enabling Regional to Local Predictions in Support of Reliable Climate Information. *Earth's Future*, **6(11)**, 1498–1507, doi:10.1029/2018ef000979.

Staniforth, A. and J. Thuburn, 2012: Horizontal grids for global weather and climate prediction models: a review. *Quarterly Journal of the Royal Meteorological Society*, **138(662)**, 1–26, doi:10.1002/qj.958.

StatKnows-CR2, 2019: *International Survey on Climate Change*. StatKnows and the Center for Climate and Resilience Research (CR2), 30 pp.

Steen-Larsen, H.C. et al., 2015: Moisture sources and synoptic to seasonal variability of North Atlantic water vapor isotopic composition. *Journal of Geophysical Research: Atmospheres*, **120(12)**, 5757–5774, doi:10.1002/2015jd023234.

Steffen, W., P.J. Crutzen, and J.R. McNeill, 2007: The Anthropocene: Are Humans Now Overwhelming the Great Forces of Nature. *AMBIO: A Journal of the Human Environment*, **36(8)**, 614–621, doi:10.1579/0044-7447(2007)36[614:taahno]2.0.co;2.

Steffen, W. et al., 2018: Trajectories of the Earth System in the Anthropocene. *Proceedings of the National Academy of Sciences of the United States of America*, doi:10.1073/pnas.1810141115.

Stehr, N. and H. Storch (eds.), 2000: *Eduard Brückner: The Sources and Consequences of Climate Change and Climate Variability in Historical Times*. Springer, Dordrecth, The Netherlands, 338 pp., doi:10.1007/978-94-015-9612-1.

Steiger, N.J., J.E. Smerdon, E.R. Cook, and B.I. Cook, 2018: A reconstruction of global hydroclimate and dynamical variables over the Common Era. *Scientific Data*, **5(1)**, 180086, doi:10.1038/sdata.2018.86.

Steiner, A.K. et al., 2019: Consistency and structural uncertainty of multi-mission GPS radio occultation records. *Atmospheric Measurement Techniques Discussions*, **2019**, 1–43, doi:10.5194/amt-2019-358.

Stevens, B. and G. Feingold, 2009: Untangling aerosol effects on clouds and precipitation in a buffered system. *Nature*, **461(7264)**, 607–613, doi:10.1038/nature08281.

Stevens, B. et al., 2017: MACv2-SP: a parameterization of anthropogenic aerosol optical properties and an associated Twomey effect for use in CMIP6. *Geoscientific Model Development*, **10(1)**, 433–452, doi:10.5194/gmd-10-433-2017.

Stickler, A. et al., 2010: The Comprehensive Historical Upper-Air Network. *Bulletin of the American Meteorological Society*, **91(6)**, 741–752, doi:10.1175/2009bams2852.1.

Stjern, C.W. et al., 2017: Rapid Adjustments Cause Weak Surface Temperature Response to Increased Black Carbon Concentrations. *Journal of Geophysical Research: Atmospheres*, **122(21)**, 11,462–11,481, doi:10.1002/2017jd027326.

Stock, C.A., J.P. Dunne, and J.G. John, 2014: Global-scale carbon and energy flows through the marine planktonic food web: An analysis with a coupled physical–biological model. *Progress in Oceanography*, **120(Complete)**, 1–28, doi:10.1016/j.pocean.2013.07.001.

Stocker, T.F. and S.J. Johnsen, 2003: A minimum thermodynamic model for the bipolar seesaw. *Paleoceanography*, **18(4)**, n/a–n/a, doi:10.1029/2003pa000920.

Stone, D. et al., 2013: The challenge to detect and attribute effects of climate change on human and natural systems. *Climatic Change*, **121(2)**, 381–395, doi:10.1007/s10584-013-0873-6.

Stone, D.A., S.M. Rosier, and D.J. Frame, 2021: The question of life, the universe and event attribution. *Nature Climate Change*, **11(4)**, 276–278, doi:10.1038/s41558-021-01012-x.

Storkey, D. et al., 2018: UK Global Ocean GO6 and GO7: a traceable hierarchy of model resolutions. *Geoscientific Model Development*, **11(8)**, 3187–3213, doi:10.5194/gmd-11-3187-2018.

Storto, A. et al., 2017: Steric sea level variability (1993–2010) in an ensemble of ocean reanalyses and objective analyses. *Climate Dynamics*, **49(3)**, 709–729, doi:10.1007/s00382-015-2554-9.

Storto, A. et al., 2019: The added value of the multi-system spread information for ocean heat content and steric sea level investigations in the CMEMS GREP ensemble reanalysis product. *Climate Dynamics*, **53(1–2)**, 287–312, doi:10.1007/s00382-018-4585-5.

Stott, P.A. et al., 2010: Detection and attribution of climate change: a regional perspective. *Wiley Interdisciplinary Reviews: Climate Change*, **1(2)**, 192–211, doi:10.1002/wcc.34.

Stott, P.A. et al., 2016: Attribution of extreme weather and climate-related events. *Wiley Interdisciplinary Reviews: Climate Change*, **7(1)**, 23–41, doi:10.1002/wcc.380.

Stouffer, R.J. and S. Manabe, 2017: Assessing temperature pattern projections made in 1989. *Nature Climate Change*, doi:10.1038/nclimate3224.

Strommen, K., P.A.G. Watson, and T.N. Palmer, 2019: The Impact of a Stochastic Parameterization Scheme on Climate Sensitivity in EC-Earth. *Journal of Geophysical Research: Atmospheres*, **124(23)**, 12726–12740, doi:10.1029/2019jd030732.

Stuiver, M., 1965: Carbon-14 Content of 18th- and 19th-Century Wood: Variations Correlated with Sunspot Activity.

ACCEPTED VERSION SUBJECT TO FINAL EDITS

Science, **149(3683)**, 533–534, doi:10.1126/science.149.3683.533.
Su, C.-H. et al., 2019: BARRA v1.0: the Bureau of Meteorology Atmospheric high-resolution Regional Reanalysis for Australia. *Geoscientific Model Development*, **12(5)**, 2049–2068, doi:10.5194/gmd-12-2049-2019.
Suess, H.E., 1955: Radiocarbon Concentration in Modern Wood. *Science*, **122(3166)**, 415–417, doi:10.1126/science.122.3166.415-a.
Sun, Q. et al., 2018: A Review of Global Precipitation Data Sets: Data Sources, Estimation, and Intercomparisons. *Reviews of Geophysics*, **56(1)**, 79–107, doi:10.1002/2017rg000574.
Sun, Y. et al., 2017: OCO-2 advances photosynthesis observation from space via solar-induced chlorophyll fluorescence. *Science*, **358(6360)**, eaam5747, doi:10.1126/science.aam5747.
Sunyer, M.A., H. Madsen, D. Rosbjerg, and K. Arnbjerg-Nielsen, 2014: A Bayesian Approach for Uncertainty Quantification of Extreme Precipitation Projections Including Climate Model Interdependency and Nonstationary Bias. *Journal of Climate*, **27(18)**, 7113–7132, doi:10.1175/jcli-d-13-00589.1.
Susskind, J., J.M. Blaisdell, and L. Iredell, 2014: Improved methodology for surface and atmospheric soundings, error estimates, and quality control procedures: the atmospheric infrared sounder science team version-6 retrieval algorithm. *Journal of Applied Remote Sensing*, **8(1)**, 1–34, doi:10.1117/1.jrs.8.084994.
Sutton, R.T., 2018: ESD Ideas: a simple proposal to improve the contribution of IPCC WGI to the assessment and communication of climate change risks. *Earth System Dynamics*, **9(4)**, 1155–1158, doi:10.5194/esd-9-1155-2018.
Swales, D.J., R. Pincus, and A. Bodas-Salcedo, 2018: The Cloud Feedback Model Intercomparison Project Observational Simulator Package: Version 2. *Geoscientific Model Development*, **11(1)**, 77–81, doi:10.5194/gmd-11-77-2018.
Swart, R., J. Mitchell, T. Morita, and S. Raper, 2002: Stabilisation scenarios for climate impact assessment. *Global Environmental Change*, **12(3)**, 155–165, doi:10.1016/s0959-3780(02)00039-0.
Swindles, G.T. et al., 2018: Climatic control on Icelandic volcanic activity during the mid-Holocene. *Geology*, doi:10.1130/g39633.1.
Tanoue, M., Y. Hirabayashi, and H. Ikeuchi, 2016: Global-scale river flood vulnerability in the last 50 years. *Scientific Reports*, **6(1)**, 36021, doi:10.1038/srep36021.
Tans, P. and R.F. Keeling, 2020: Trends in Atmospheric Carbon Dioxide. Global Monitoring Laboratory, National Oceanic & Atmospheric Administration Earth System Research Laboratories (NOAA/ESRL). Retrieved from: www.esrl.noaa.gov/gmd/ccgg/trends.
Tapiador, F.J., A. Navarro, R. Moreno, J.L. Sánchez, and E. García-Ortega, 2020: Regional climate models: 30 years of dynamical downscaling. *Atmospheric Research*, **235**, 104785, doi:10.1016/j.atmosres.2019.104785.
Tapley, B.D. et al., 2019: Contributions of GRACE to understanding climate change. *Nature Climate Change*, **9(5)**, 358–369, doi:10.1038/s41558-019-0456-2.
Tardif, R. et al., 2019: Last Millennium Reanalysis with an expanded proxy database and seasonal proxy modeling. *Climate of the Past*, **15(4)**, 1251–1273, doi:10.5194/cp-15-1251-2019.
Taylor, A.H., V. Trouet, C.N. Skinner, and S. Stephens, 2016: Socioecological transitions trigger fire regime shifts and modulate fire–climate interactions in the Sierra Nevada, USA, 1600–2015 CE. *Proceedings of the National Academy of Sciences*, **113(48)**, 13684 LP – 13689, doi:10.1073/pnas.1609775113.
Taylor, K.E., R.J. Stouffer, and G.A. Meehl, 2012: An Overview of CMIP5 and the Experiment Design. *Bulletin of the American Meteorological Society*, **93(4)**, 485–498, doi:10.1175/bams-d-11-00094.1.
Tebaldi, C., 2004: Regional probabilities of precipitation change: A Bayesian analysis of multimodel simulations. *Geophysical Research Letters*, **31(24)**, L24213, doi:10.1029/2004gl021276.
Tebaldi, C. and P. Friedlingstein, 2013: Delayed detection of climate mitigation benefits due to climate inertia and variability. *Proceedings of the National Academy of Sciences of the United States of America*, doi:10.1073/pnas.1300005110.
Tebaldi, C. and J.M. Arblaster, 2014: Pattern scaling: Its strengths and limitations, and an update on the latest model simulations. *Climatic Change*, **122(3)**, 459–471, doi:10.1007/s10584-013-1032-9.
Tebaldi, C. and R. Knutti, 2018: Evaluating the accuracy of climate change pattern emulation for low warming targets. *Environmental Research Letters*, **13(5)**, 055006, doi:10.1088/1748-9326/aabef2.
Tebaldi, C. et al., 2021: Climate model projections from the Scenario Model Intercomparison Project (ScenarioMIP) of CMIP6. *Earth System Dynamics*, **12(1)**, 253–293, doi:10.5194/esd-12-253-2021.
Thackeray, S.J. et al., 2020: Civil disobedience movements such as School Strike for the Climate are raising public awareness of the climate change emergency. *Global Change Biology*, **26(3)**, 1042–1044, doi:10.1111/gcb.14978.
Thiery, W. et al., 2020: Warming of hot extremes alleviated by expanding irrigation. *Nature Communications*, **11(1)**, 290, doi:10.1038/s41467-019-14075-4.
Thomason, L.W. et al., 2018: A global space-based stratospheric aerosol climatology: 1979–2016. *Earth System Science Data*, **10(1)**, 469–492, doi:10.5194/essd-10-469-2018.
Thompson, D.W.J., J.J. Kennedy, J.M. Wallace, and P.D. Jones, 2008: A large discontinuity in the mid-twentieth century in observed global-mean surface temperature. *Nature*, **453(7195)**, 646–649, doi:10.1038/nature06982.

ACCEPTED VERSION SUBJECT TO FINAL EDITS

Thorne, P.W. and R.S. Vose, 2010: Reanalyses suitable for characterizing long-term trends. *Bulletin of the American Meteorological Society*, **91(3)**, 353–361, doi:10.1175/2009bams2858.1.
Thorne, P.W., J.R. Lanzante, T.C. Peterson, D.J. Seidel, and K.P. Shine, 2011: Tropospheric temperature trends: history of an ongoing controversy. *Wiley Interdisciplinary Reviews: Climate Change*, **2(1)**, 66–88, doi:10.1002/wcc.80.
Tian, B. and X. Dong, 2020: The Double-ITCZ Bias in CMIP3, CMIP5, and CMIP6 Models Based on Annual Mean Precipitation. *Geophysical Research Letters*, **47(8)**, e2020GL087232, doi:10.1029/2020gl087232.
Tierney, J.E. et al., 2015: Tropical sea surface temperatures for the past four centuries reconstructed from coral archives. *Paleoceanography*, **30(3)**, 226–252, doi:10.1002/2014pa002717.
Tierney, J.E. et al., 2020a: Past climates inform our future. *Science*, **370(6517)**, eaay3701, doi:10.1126/science.aay3701.
Tierney, J.E. et al., 2020b: Glacial cooling and climate sensitivity revisited. *Nature*, **584(7822)**, 569–573, doi:10.1038/s41586-020-2617-x.
Tilbrook, B. et al., 2019: An Enhanced Ocean Acidification Observing Network: From People to Technology to Data Synthesis and Information Exchange. *Frontiers in Marine Science*, **6**, 337, doi:10.3389/fmars.2019.00337.
Tilling, R.L., A. Ridout, and A. Shepherd, 2018: Estimating Arctic sea ice thickness and volume using CryoSat-2 radar altimeter data. *Advances in Space Research*, **62(6)**, 1203–1225, doi:10.1016/j.asr.2017.10.051.
Tokarska, K.B. et al., 2019: Recommended temperature metrics for carbon budget estimates, model evaluation and climate policy. *Nature Geoscience*, **12(12)**, 964–971, doi:10.1038/s41561-019-0493-5.
Tolwinski-Ward, S.E., M.N. Evans, M.K. Hughes, and K.J. Anchukaitis, 2011: An efficient forward model of the climate controls on interannual variation in tree-ring width. *Climate Dynamics*, **36(11)**, 2419–2439, doi:10.1007/s00382-010-0945-5.
Toon, O.B. and J.B. Pollack, 1976: A Global Average Model of Atmospheric Aerosols for Radiative Transfer Calculations. *Journal of Applied Meteorology*, **15(3)**, 225–246, doi:10.1175/1520-0450(1976)015<0225:agamoa>2.0.co;2.
Touzé-Peiffer, L., A. Barberousse, and H. Le Treut, 2020: The Coupled Model Intercomparison Project: History, uses, and structural effects on climate research. *WIREs Climate Change*, **11(4)**, e648, doi:10.1002/wcc.648.
Toyoda, T. et al., 2017: Interannual-decadal variability of wintertime mixed layer depths in the North Pacific detected by an ensemble of ocean syntheses. *Climate Dynamics*, **49(3)**, 891–907, doi:10.1007/s00382-015-2762-3.
Trenberth, K.E., M. Marquis, and S. Zebiak, 2016: The vital need for a climate information system. *Nature Climate Change*, doi:10.1038/nclimate3170.
Trenberth, K.E., Y. Zhang, J.T. Fasullo, and L. Cheng, 2019: Observation-based estimates of global and basin ocean meridional heat transport time series. *Journal of Climate*, **32(14)**, 4567–4583, doi:10.1175/jcli-d-18-0872.1.
Trewin, B. et al., 2021: Headline Indicators for Global Climate Monitoring. *Bulletin of the American Meteorological Society*, **102(1)**, E20–E37, doi:10.1175/bams-d-19-0196.1.
Trouet, V., F. Babst, and M. Meko, 2018: Recent enhanced high-summer North Atlantic Jet variability emerges from three-century context. *Nature Communications*, **9(1)**, 180, doi:10.1038/s41467-017-02699-3.
Turner, J. and J. Comiso, 2017: Solve Antarctica's sea-ice puzzle. *Nature*, **547**, 275–277, doi:10.1038/547275a.
Twomey, S., 1959: The nuclei of natural cloud formation part II: The supersaturation in natural clouds and the variation of cloud droplet concentration. *Geofisica Pura e Applicata*, **43(1)**, 243–249, doi:10.1007/bf01993560.
Twomey, S., 1991: Aerosols, clouds and radiation. *Atmospheric Environment. Part A. General Topics*, **25(11)**, 2435–2442, doi:10.1016/0960-1686(91)90159-5.
Tyndall, J., 1861: I. The Bakerian Lecture – On the absorption and radiation of heat by gases and vapours, and on the physical connexion of radiation, absorption, and conduction. *Philosophical Transactions of the Royal Society of London*, **151**, 1–36, doi:10.1098/rstl.1861.0001.
UN DESA, 2015: *Addis Ababa Action Agenda of the Third International Conference on Financing for Development (Addis Ababa Action Agenda)*. UN Department of Economic and Social Affairs (UN DESA), 61 pp.
Undorf, S. et al., 2018: Detectable Impact of Local and Remote Anthropogenic Aerosols on the 20th Century Changes of West African and South Asian Monsoon Precipitation. *Journal of Geophysical Research: Atmospheres*, **123(10)**, 4871–4889, doi:10.1029/2017jd027711.
UNEP, 2012: *Report of the second session of the plenary meeting to determine modalities and institutional arrangements for an intergovernmental science-policy platform on biodiversity and ecosystem services*. UNEP/IPBES.MI/2/9, United Nations Environment Programme (UNEP), Nairobi, Kenya, 26 pp.
UNEP, 2016: *The Montreal Protocol on Substances that Deplete the Ozone Layer – as adjusted and amended up to 15 October 2016 (Kigali Agreement)*. United Nations Environment Programme (UNEP), Nairobi, Kenya, 33 pp.
UNFCCC, 1992: *United Nations Framework Convention on Climate Change*. FCCC/INFORMAL/84, United Nations Framework Convention on Climate Change (UNFCCC), 24 pp.
UNFCCC, 2015: *Report on the Structured Expert Dialogue on the 2013–2015 Review*. FCCC/SB/2015/INF.1, 182 pp.
UNFCCC, 2016: *Aggregate effect of the Intended Nationally Determined Contributions: An Update – Synthesis Report by the Secretariat*. FCCC/CP/2016/2, United Nations Framework Convention on Climate Change (UNFCCC), 75 pp.

ACCEPTED VERSION SUBJECT TO FINAL EDITS

United Nations, 2017: *New Urban Agenda*. A/RES/71/256, Conference on Housing and Sustainable Urban Development (Habitat III) Secretariat, 66 pp.
United Nations Environment Programme (UNEP), 2019: *Emissions Gap Report 2018*. United Nations Environment Programme (UNEP), Nairobi, Kenya, 112 pp.
Uotila, P. et al., 2019: An assessment of ten ocean reanalyses in the polar regions. *Climate Dynamics*, **52(3–4)**, 1613–1650, doi:10.1007/s00382-018-4242-z.
Valdivieso, M. et al., 2017: An assessment of air–sea heat fluxes from ocean and coupled reanalyses. *Climate Dynamics*, **49(3)**, 983–1008, doi:10.1007/s00382-015-2843-3.
Van Asselt, M. and J. Rotmans, 1996: Uncertainty in perspective. *Global Environmental Change*, **6(2)**, 121–157, doi:10.1016/0959-3780(96)00015-5.
van den Hurk, B. et al., 2016: LS3MIP (v1.0) contribution to CMIP6: the Land Surface, Snow and Soil moisture Model Intercomparison Project – aims, setup and expected outcome. *Geoscientific Model Development*, **9(8)**, 2809–2832, doi:10.5194/gmd-9-2809-2016.
van der Ent, R.J. and O.A. Tuinenburg, 2017: The residence time of water in the atmosphere revisited. *Hydrology and Earth System Sciences*, **21(2)**, 779–790, doi:10.5194/hess-21-779-2017.
van Marle, M.J.E. et al., 2017: Historic global biomass burning emissions for CMIP6 (BB4CMIP) based on merging satellite observations with proxies and fire models (1750–2015). *Geoscientific Model Development*, **10(9)**, 3329–3357, doi:10.5194/gmd-10-3329-2017.
van Vuuren, D.P. and K. Riahi, 2008: Do recent emission trends imply higher emissions forever? *Climatic Change*, **91(3–4)**, 237–248, doi:10.1007/s10584-008-9485-y.
van Vuuren, D.P. et al., 2010: What do near-term observations tell us about long-term developments in greenhouse gas emissions? *Climatic Change*, **103(3–4)**, 635–642, doi:10.1007/s10584-010-9940-4.
van Vuuren, D.P. et al., 2011: The representative concentration pathways: an overview. *Climatic Change*, **109(1–2)**, 5–31, doi:10.1007/s10584-011-0148-z.
van Vuuren, D.P. et al., 2014: A new scenario framework for Climate Change Research: scenario matrix architecture. *Climatic Change*, **122(3)**, 373–386, doi:10.1007/s10584-013-0906-1.
Vanderkelen, I. et al., 2020: Global Heat Uptake by Inland Waters. *Geophysical Research Letters*, **47(12)**, e2020GL087867, doi:10.1029/2020gl087867.
Vannière, B., E. Guilyardi, T. Toniazzo, G. Madec, and S. Woolnough, 2014: A systematic approach to identify the sources of tropical SST errors in coupled models using the adjustment of initialised experiments. *Climate Dynamics*, **43(7–8)**, 2261–2282, doi:10.1007/s00382-014-2051-6.
Vaughan, C. and S. Dessai, 2014: Climate services for society: origins, institutional arrangements, and design elements for an evaluation framework. *Wiley Interdisciplinary Reviews: Climate Change*, **5(5)**, 587–603, doi:10.1002/wcc.290.
Vautard, R. et al., 2019: Evaluation of the HadGEM3-A simulations in view of detection and attribution of human influence on extreme events in Europe. *Climate Dynamics*, **52(1–2)**, 1187–1210, doi:10.1007/s00382-018-4183-6.
Verschuur, J., S. Li, P. Wolski, and F.E.L. Otto, 2021: Climate change as a driver of food insecurity in the 2007 Lesotho-South Africa drought. *Scientific Reports*, **11(1)**, 3852, doi:10.1038/s41598-021-83375-x.
Very, F.W. and C. Abbe, 1901: Knut Angstrom on Atmospheric Absorption. 268 pp., doi:10.1175/1520-0493(1901)29[268a:kaoaa]2.0.co;2.
Vicedo-Cabrera, A.M. et al., 2018: A multi-country analysis on potential adaptive mechanisms to cold and heat in a changing climate. *Environment International*, **111**, 239–246, doi:10.1016/j.envint.2017.11.006.
Vinogradova, N. et al., 2019: Satellite Salinity Observing System: Recent Discoveries and the Way Forward. *Frontiers in Marine Science*, **6**, 243, doi:10.3389/fmars.2019.00243.
Vizcaino, M. et al., 2015: Coupled simulations of Greenland Ice Sheet and climate change up to A.D. 2300. *Geophysical Research Letters*, **42(10)**, 3927–3935, doi:10.1002/2014gl061142.
Vogel, M.M., J. Zscheischler, R. Wartenburger, D. Dee, and S.I. Seneviratne, 2019: Concurrent 2018 Hot Extremes Across Northern Hemisphere Due to Human-Induced Climate Change. *Earth's Future*, **7(7)**, 692–703, doi:10.1029/2019ef001189.
von Schuckmann, K. et al., 2019: Copernicus Marine Service Ocean State Report, Issue 3. *Journal of Operational Oceanography*, **12(sup1)**, S1–S123, doi:10.1080/1755876x.2019.1633075.
von Schuckmann, K. et al., 2020: Heat stored in the Earth system: where does the energy go? *Earth System Science Data*, **12(3)**, 2013–2041, doi:10.5194/essd-12-2013-2020.
Wagman, B.M. and C.S. Jackson, 2018: A Test of Emergent Constraints on Cloud Feedback and Climate Sensitivity Using a Calibrated Single-Model Ensemble. *Journal of Climate*, **31(18)**, 7515–7532, doi:10.1175/jcli-d-17-0682.1.
Wahl, S. et al., 2017: A novel convective-scale regional reanalysis COSMO-REA2: Improving the representation of precipitation. *Meteorologische Zeitschrift*, **26(4)**, 345–361, doi:10.1127/metz/2017/0824.
Walsh, J.E., F. Fetterer, J. Scott Stewart, and W.L. Chapman, 2017: A database for depicting Arctic sea ice variations back to 1850. *Geographical Review*, **107(1)**, 89–107, doi:10.1111/j.1931-0846.2016.12195.x.

ACCEPTED VERSION SUBJECT TO FINAL EDITS

Wang, H. et al., 2020: Aerosols in the E3SM Version 1: New Developments and Their Impacts on Radiative Forcing. *Journal of Advances in Modeling Earth Systems*, **12(1)**, e2019MS001851, doi:10.1029/2019ms001851.
Wang, Q. et al., 2014: The Finite Element Sea Ice-Ocean Model (FESOM) v.1.4: formulation of an ocean general circulation model. *Geoscientific Model Development*, **7(2)**, 663–693, doi:10.5194/gmd-7-663-2014.
Wang, W.C., Y.L. Yung, A.A. Lacis, T. Mo, and J.E. Hansen, 1976: Greenhouse Effects due to Man-Made Perturbations of Trace Gases. *Science*, **194(4266)**, 685–690, doi:10.1126/science.194.4266.685.
Wang, Y.J. et al., 2001: A high-resolution absolute-dated late pleistocene monsoon record from Hulu Cave, China. *Science*, **294(5550)**, 2345–2348, doi:10.1126/science.1064618.
Warszawski, L. et al., 2014: The Inter-Sectoral Impact Model Intercomparison Project (ISI-MIP): project framework.. *Proceedings of the National Academy of Sciences of the United States of America*, **111(9)**, 3228–32, doi:10.1073/pnas.1312330110.
Wartenburger, R. et al., 2017: Changes in regional climate extremes as a function of global mean temperature: an interactive plotting framework. *Geoscientific Model Development*, **10(9)**, 3609–3634, doi:10.5194/gmd-10-3609-2017.
Watson, C.S. et al., 2015: Unabated global mean sea-level rise over the satellite altimeter era. *Nature Climate Change*, **5(6)**, 565–568, doi:10.1038/nclimate2635.
Watson-Parris, D. et al., 2019: In situ constraints on the vertical distribution of global aerosol. *Atmospheric Chemistry and Physics*, **19(18)**, 11765–11790, doi:10.5194/acp-19-11765-2019.
WCRP Global Sea Level Budget, 2018: Global sea-level budget 1993--present. *Earth System Science Data*, **10(3)**, 1551–1590, doi:10.5194/essd-10-1551-2018.
Weart, S.R., 2008: *The Discovery of Global Warming: Revised and Expanded Edition (2nd edition)*. Harvard University Press, Cambridge, MA, USA, 240 pp.
Webb, M.J. et al., 2017: The Cloud Feedback Model Intercomparison Project (CFMIP) contribution to CMIP6. *Geoscientific Model Development*, **10(1)**, 359–384, doi:10.5194/gmd-10-359-2017.
Weedon, G.P. et al., 2014: The WFDEI meteorological forcing data set: WATCH Forcing data methodology applied to ERA-Interim reanalysis data. *Water Resources Research*, **50(9)**, 7505–7514, doi:10.1002/2014wr015638.
Wehner, M.F., C. Zarzycki, and C. Patricola, 2018: Estimating the human influence on tropical cyclone intensity as the climate changes. In: *Hurricane Risk* [Collins, J.M. and K. Walsh (eds.)]. Springer, Cham, Switzerland, pp. 235–260, doi:10.1007/978-3-030-02402-4_12.
Weijer, W. et al., 2019: Stability of the Atlantic Meridional Overturning Circulation: A Review and Synthesis. *Journal of Geophysical Research: Oceans*, **124(8)**, 5336–5375, doi:10.1029/2019jc015083.
Weitzman, M.L., 2011: Fat-Tailed Uncertainty in the Economics of Catastrophic Climate Change. *Review of Environmental Economics and Policy*, **5(2)**, 275–292, doi:10.1093/reep/rer006.
Wenzel, S., V. Eyring, E.P. Gerber, and A.Y. Karpechko, 2016: Constraining Future Summer Austral Jet Stream Positions in the CMIP5 Ensemble by Process-Oriented Multiple Diagnostic Regression. *Journal of Climate*, **29(2)**, 673–687, doi:10.1175/jcli-d-15-0412.1.
Wigley, T.M.L. and P.D. Jones, 1981: Detecting CO2-induced climatic change. *Nature*, doi:10.1038/292205a0.
Wigley, T.M.L., R. Richels, and J.A. Edmonds, 1996: Economic and environmental choices in the stabilization of atmospheric CO2concentrations. *Nature*, **379(6562)**, 240–243, doi:10.1038/379240a0.
Wigley, T.M.L. et al., 2009: Uncertainties in climate stabilization. *Climatic Change*, **97(1–2)**, 85–121, doi:10.1007/s10584-009-9585-3.
Wilby, R.L. and S. Dessai, 2010: Robust adaptation to climate change. *Weather*, **65(7)**, 180–185, doi:10.1002/wea.543.
Wilcox, L.J. et al., 2020: Accelerated increases in global and Asian summer monsoon precipitation from future aerosol reductions. *Atmospheric Chemistry and Physics*, **20(20)**, 11955–11977, doi:10.5194/acp-20-11955-2020.
Wilkinson, M.D. et al., 2016: The FAIR Guiding Principles for scientific data management and stewardship. *Scientific Data*, **3(1)**, 160018, doi:10.1038/sdata.2016.18.
Williams, H.T.P., J.R. McMurray, T. Kurz, and F. Hugo Lambert, 2015: Network analysis reveals open forums and echo chambers in social media discussions of climate change. *Global Environmental Change*, **32**, 126–138, doi:10.1016/j.gloenvcha.2015.03.006.
Williams, J. (ed.), 1978: Carbon Dioxide, Climate and Society: Proceedings of a IIASA Workshop cosponsored by WMO, UNEP, and SCOPE, February 21-24, 1978. Pergamon Press, Oxford, UK, 332 pp.
Williams, K.D. and M.J. Webb, 2009: A quantitative performance assessment of cloud regimes in climate models. *Climate Dynamics*, **33(1)**, 141–157, doi:10.1007/s00382-008-0443-1.
Williams, K.D. et al., 2013: The Transpose-AMIP II Experiment and Its Application to the Understanding of Southern Ocean Cloud Biases in Climate Models. *Journal of Climate*, **26(10)**, 3258–3274, doi:10.1175/jcli-d-12-00429.1.
Wilson, R. et al., 2016: Last millennium northern hemisphere summer temperatures from tree rings: Part I: The long term context. *Quaternary Science Reviews*, **134**, 1–18, doi:10.1016/j.quascirev.2015.12.005.
Winkler, A.J., R.B. Myneni, and V. Brovkin, 2019: Investigating the applicability of emergent constraints. *Earth System Dynamics*, **10(3)**, 501–523, doi:10.5194/esd-10-501-2019.
Winsberg, E., 2018: *Philosophy and Climate Science*. Cambridge University Press, Cambridge, UK, 270 pp.,

ACCEPTED VERSION SUBJECT TO FINAL EDITS

doi:10.1017/9781108164290.
Winski, D. et al., 2018: A 400-Year Ice Core Melt Layer Record of Summertime Warming in the Alaska Range. *Journal of Geophysical Research: Atmospheres*, **123(7)**, 3594–3611, doi:10.1002/2017jd027539.
WMO, 2015: *Seamless Prediction of the Earth System: From Minutes to Months*. WMO-No. 1156, World Meteorological Organization (WMO), Geneva, Switzerland, 471 pp.
WMO, 2016: *The Global Observing System for Climate: Implementation Needs*. GCOS No. 200, Global Climate Observing System (GCOS) Secretariat, World Meteorological Organization (WMO), Geneva, Switzerland, 315 pp.
WMO, 2017: *Challenges in the Transition from Conventional to Automatic Meteorological Observing Networks for Long-term Climate Records*. WMO-No. 1202, World Meteorological Organization (WMO), Geneva, Switzerland, 20 pp.
WMO, 2020a: *State of Climate Services 2020: Risk Information and Early Warning Systems*. WMO-No. 1252, World Meteorological Organization (WMO), Geneva, Switzerland, 47 pp.
WMO, 2020b: *United In Science: A multi-organization high-level compilation of the latest climate science information*. World Meteorological Organization (WMO), Geneva, Switzerland, 25 pp.
WMO/UNEP/ICSU, 1986: *Report of the International Conference on the Assessment of the Role of Carbon Dioxide and of Other Greenhouse Gases in Climate Variations and Associated Impacts, Villach, Austria, 9-15 October 1985*. WMO - No.661, World Meteorological Organization (WMO), United Nations Environment Programme (UNEP), International Council of Scientific Unions (ICSU). WMO, Geneva, Switzerland, 78 pp.
Woodgate, R.A., 2018: Increases in the Pacific inflow to the Arctic from 1990 to 2015, and insights into seasonal trends and driving mechanisms from year-round Bering Strait mooring data. *Progress in Oceanography*, **160**, 124–154, doi:10.1016/j.pocean.2017.12.007.
Woodruff, S.D., R.J. Slutz, R.L. Jenne, and P.M. Steurer, 1987: A Comprehensive Ocean-Atmosphere Data Set. *Bulletin of the American Meteorological Society*, **68(10)**, 1239–1250, doi:10.1175/1520-0477(1987)068<1239:acoads>2.0.co;2.
Woodruff, S.D., H.F. Diaz, J.D. Elms, and S.J. Worley, 1998: COADS Release 2 data and metadata enhancements for improvements of marine surface flux fields. *Physics and Chemistry of the Earth*, **23(5–6)**, 517–526, doi:10.1016/s0079-1946(98)00064-0.
Woodruff, S.D., H.F. Diaz, S.J. Worley, R.W. Reynolds, and S.J. Lubker, 2005: Early Ship Observational Data and Icoads. *Climatic Change*, **73(1–2)**, 169–194, doi:10.1007/s10584-005-3456-3.
Wu, C. et al., 2016: A process-oriented evaluation of dust emission parameterizations in CESM: Simulation of a typical severe dust storm in East Asia. *Journal of Advances in Modeling Earth Systems*, **8(3)**, 1432–1452, doi:10.1002/2016ms000723.
Wu, H.C. et al., 2018: Surface ocean pH variations since 1689 CE and recent ocean acidification in the tropical South Pacific. *Nature Communications*, **9(1)**, 2543, doi:10.1038/s41467-018-04922-1.
Wu, Y., L.M. Polvani, and R. Seager, 2013: The importance of the montreal protocol in protecting Earth's hydroclimate. *Journal of Climate*, **26(12)**, 4049–4068, doi:10.1175/jcli-d-12-00675.1.
Yang, H. and J. Zhu, 2011: Equilibrium thermal response timescale of global oceans. *Geophysical Research Letters*, **38(14)**, n/a–n/a, doi:10.1029/2011gl048076.
Yang, X. et al., 2015: Solar-induced chlorophyll fluorescence that correlates with canopy photosynthesis on diurnal and seasonal scales in a temperate deciduous forest. *Geophysical Research Letters*, **42(8)**, 2977–2987, doi:10.1002/2015gl063201.
Yeager, S.G. and J.I. Robson, 2017: Recent Progress in Understanding and Predicting Atlantic Decadal Climate Variability. *Current Climate Change Reports*, doi:10.1007/s40641-017-0064-z.
Yokota, T. et al., 2009: Global Concentrations of CO₂ and CH₄ Retrieved from GOSAT: First Preliminary Results. *SOLA*, **5**, 160–163, doi:10.2151/sola.2009-041.
Yoon, S., J.N. Carey, and J.D. Semrau, 2009: Feasibility of atmospheric methane removal using methanotrophic biotrickling filters. *Applied Microbiology and Biotechnology*, **83(5)**, 949–956, doi:10.1007/s00253-009-1977-9.
Yousefvand, M., C.-T.M. Wu, R.-Q. Wang, J. Brodie, and N. Mandayam, 2020: Modeling the Impact of 5G Leakage on Weather Prediction. *2020 IEEE 3rd 5G World Forum (5GWF)*, 291–296, doi:10.1109/5gwf49715.2020.9221472.
Yukimoto, S. et al., 2019: The Meteorological Research Institute Earth System Model Version 2.0, MRI-ESM2.0: Description and Basic Evaluation of the Physical Component. *Journal of the Meteorological Society of Japan. Ser. II*, **97(5)**, 931–965, doi:10.2151/jmsj.2019-051.
Zaehle, S., C.D. Jones, B. Houlton, J.-F. Lamarque, and E. Robertson, 2014: Nitrogen Availability Reduces CMIP5 Projections of Twenty-First-Century Land Carbon Uptake. *Journal of Climate*, **28(6)**, 2494–2511, doi:10.1175/jcli-d-13-00776.1.
Zanchettin, D., 2017: Aerosol and Solar Irradiance Effects on Decadal Climate Variability and Predictability. *Current Climate Change Reports*, doi:10.1007/s40641-017-0065-y.
Zanchettin, D. et al., 2016: The Model Intercomparison Project on the climatic response to Volcanic forcing (VolMIP):

ACCEPTED VERSION SUBJECT TO FINAL EDITS

experimental design and forcing input data for CMIP6. *Geoscientific Model Development*, **9(8)**, 2701–2719, doi:10.5194/gmd-9-2701-2016.

Zanna, L., S. Khatiwala, J.M. Gregory, J. Ison, and P. Heimbach, 2019: Global reconstruction of historical ocean heat storage and transport. *Proceedings of the National Academy of Sciences of the United States of America*, **116(4)**, 1126–1131, doi:10.1073/pnas.1808838115.

Zannoni, D. et al., 2019: The atmospheric water cycle of a coastal lagoon: An isotope study of the interactions between water vapor, precipitation and surface waters. *Journal of Hydrology*, **572**, 630–644, doi:10.1016/j.jhydrol.2019.03.033.

Zappa, G. and T.G. Shepherd, 2017: Storylines of atmospheric circulation change for European regional climate impact assessment. *Journal of Climate*, **30(16)**, 6561–6577, doi:10.1175/jcli-d-16-0807.1.

Zappa, G., P. Ceppi, and T.G. Shepherd, 2020: Time-evolving sea-surface warming patterns modulate the climate change response of subtropical precipitation over land. *Proceedings of the National Academy of Sciences*, **117(9)**, 4539–4545, doi:10.1073/pnas.1911015117.

Zaval, L., E.A. Keenan, E.J. Johnson, and E.U. Weber, 2014: How warm days increase belief in global warming. *Nature Climate Change*, **4(2)**, 143–147, doi:10.1038/nclimate2093.

Zeebe, R.E., A. Ridgwell, and J.C. Zachos, 2016: Anthropogenic carbon release rate unprecedented during the past 66 million years. *Nature Geoscience*, **9(4)**, 325–329, doi:10.1038/ngeo2681.

Zeldin-O'Neill, S., 2019: 'It's a crisis, not a change': the six Guardian language changes on climate matters. *The Guardian*.

Zelinka, M.D. et al., 2020: Causes of Higher Climate Sensitivity in CMIP6 Models. *Geophysical Research Letters*, **47(1)**, e2019GL085782, doi:10.1029/2019gl085782.

Zemp, M. et al., 2015: Historically unprecedented global glacier decline in the early 21st century. *Journal of Glaciology*, **61(228)**, 745–762, doi:10.3189/2015jog15j017.

Zemp, M. et al., 2019: Global glacier mass changes and their contributions to sea-level rise from 1961 to 2016. *Nature*, **568(7752)**, 382–386, doi:10.1038/s41586-019-1071-0.

Zhang, X. et al., 2007: Detection of human influence on twentieth-century precipitation trends. *Nature*, **448(7152)**, 461–465, doi:10.1038/nature06025.

Zhang, Y. et al., 2018: The ARM Cloud Radar Simulator for Global Climate Models: Bridging Field Data and Climate Models. *Bulletin of the American Meteorological Society*, **99(1)**, 21–26, doi:10.1175/bams-d-16-0258.1.

Zhao, M. et al., 2018: The GFDL Global Atmosphere and Land Model AM4.0/LM4.0: 1. Simulation Characteristics With Prescribed SSTs. *Journal of Advances in Modeling Earth Systems*, **10(3)**, 691–734, doi:10.1002/2017ms001208.

Zhou, C. and K. Wang, 2017: Contrasting Daytime and Nighttime Precipitation Variability between Observations and Eight Reanalysis Products from 1979 to 2014 in China. *Journal of Climate*, **30(16)**, 6443–6464, doi:10.1175/jcli-d-16-0702.1.

Zhou, C., Y. He, and K. Wang, 2018: On the suitability of current atmospheric reanalyses for regional warming studies over China. *Atmospheric Chemistry and Physics*, **18(11)**, 8113–8136, doi:10.5194/acp-18-8113-2018.

Zhou, T. et al., 2016: GMMIP (v1.0) contribution to CMIP6: Global Monsoons Model Inter-comparison Project. *Geoscientific Model Development*, **9(10)**, 3589–3604, doi:10.5194/gmd-9-3589-2016.

Zickfeld, K. et al., 2013: Long-Term Climate Change Commitment and Reversibility: An EMIC Intercomparison. *Journal of Climate*, **26(16)**, 5782–5809, doi:10.1175/jcli-d-12-00584.1.

Zommers, Z. et al., 2020: Burning embers: towards more transparent and robust climate-change risk assessments. *Nature Reviews Earth & Environment*, **1(10)**, 516–529, doi:10.1038/s43017-020-0088-0.

Zuo, H., M.A. Balmaseda, and K. Mogensen, 2017: The new eddy-permitting ORAP5 ocean reanalysis: description, evaluation and uncertainties in climate signals. *Climate Dynamics*, **49(3)**, 791–811, doi:10.1007/s00382-015-2675-1.

Zuo, H., M.A. Balmaseda, S. Tietsche, K. Mogensen, and M. Mayer, 2019: The ECMWF operational ensemble reanalysis--analysis system for ocean and sea ice: a description of the system and assessment. *Ocean Science*, **15(3)**, 779–808, doi:10.5194/os-15-779-2019.

Zuo, M., W. Man, T. Zhou, and Z. Guo, 2018: Different Impacts of Northern, Tropical, and Southern Volcanic Eruptions on the Tropical Pacific SST in the Last Millennium. *Journal of Climate*, **31(17)**, 6729–6744, doi:10.1175/jcli-d-17-0571.1.

ACCEPTED VERSION SUBJECT TO FINAL EDITS

Appendix 1.A

[START TABLE 1.A.1 HERE]

Table 1.A.1: Historical overview of major conclusions of IPCC assessment reports. The table repeats Table 1.1 from the IPCC Fifth Assessment Report (AR5; Cubasch et al., 2013) and extends it with the AR5 and AR6 key findings. The table provides a non-comprehensive selection of key Summary for Policymakers (SPM) statements from previous assessment reports—IPCC First Assessment Report (FAR; IPCC, 1990b), IPCC Second Assessment Report (SAR; IPCC, 1995b), IPCC Third Assessment Report (TAR; IPCC, 2001b), IPCC Fourth Assessment Report (AR4; IPCC, 2007b) , IPCC Fifth Assessment Report (AR5; IPCC, 2013b), and the IPCC Sixth Assessment Report (AR6; IPCC, 2021) —with a focus on global mean surface air temperature and sea level change as two policy relevant quantities that have been covered in IPCC since the FAR.

[Placeholder: the column for AR6 will be filled out once the SPM is drafted, and this column will be finalized once the final version of the AR6 SPM is approved]

Topic	FAR SPM Statement (1990)	SAR SPM Statement (1995)	TAR SPM Statement (2001)	AR4 SPM Statement (2007)	AR5 SPM statement (2013)	AR6 SPM statement (2021)
Human and Natural Drivers of Climate Change	There is a natural greenhouse effect, which already keeps the Earth warmer than it would otherwise be. Emissions resulting from human activities are substantially increasing the atmospheric concentrations of the greenhouse gases carbon dioxide, methane, chlorofluorocarbons and nitrous oxide. These increases will enhance the greenhouse effect, resulting on average in an additional warming of the Earth's surface.	Greenhouse gas concentrations have continued to increase. These trends can be attributed largely to human activities, mostly fossil fuel use, land use change and agriculture.	Emissions of greenhouse gases and aerosols due to human activities continue to alter the atmosphere in ways that are expected to affect the climate. The atmospheric concentration of CO_2 has increased by 31% since 1750 and that of methane by 151%.	Global atmospheric concentrations of carbon dioxide, methane and nitrous oxide have increased markedly as a result of human activities since 1750 and now far exceed pre-industrial values determined from ice cores spanning many thousands of years. The global increases in carbon dioxide concentration are due primarily to fossil fuel use and land use change, while those of	Total radiative forcing is positive, and has led to an uptake of energy by the climate system. The largest contribution to total radiative forcing is caused by the increase in the atmospheric concentration of CO_2 since 1750.	

ACCEPTED VERSION SUBJECT TO FINAL EDITS

				methane and nitrous oxide are primarily due to agriculture.		
	Continued emissions of these gases at present rates would commit us to increased concentrations for centuries ahead.	Anthropogenic aerosols are short-lived and tend to produce negative radiative forcing.	Anthropogenic aerosols are short-lived and mostly produce negative radiative forcing by their direct effect. There is more evidence for their indirect effect, which is negative, although of very uncertain magnitude.	*Very high confidence* that the global average net effect of human activities since 1750 has been one of warming, with a radiative forcing of +1.6 [+0.6 to +2.4] W m^{-2}.	The total anthropogenic radiative forcing (RF) for 2011 relative to 1750 is 2.29 [1.13 to 3.33] W m^{-2}), and it has increased more rapidly since 1970 than during prior decades. The total anthropogenic RF best estimate for 2011 is 43% higher than that reported in AR4 for the year 2005.	
			Natural factors have made small contributions to radiative forcing over the past century.		The total natural RF from solar irradiance changes and stratospheric volcanic aerosols made only a small contribution to the net radiative forcing throughout the last century, except for brief periods after large volcanic eruptions.	
Observations of Recent Climate Change - Temperature	Global mean surface air temperature has increased by 0.3°C to 0.6°C over the last 100 years, with the five global-average	Climate has changed over the past century. Global mean surface temperature has increased by between	An increasing body of observations gives a collective picture of a warming world and other changes in the	Warming of the climate system is unequivocal, as is now evident from observations of	Warming of the climate system is unequivocal, and since the 1950s, many of the observed changes are	

ACCEPTED VERSION SUBJECT TO FINAL EDITS

	warmest years being in the 1980s.	about 0.3 and 0.6°C since the late 19th century. Recent years have been among the warmest since 1860, despite the cooling effect of the 1991 Mt. Pinatubo volcanic eruption.	climate system.	increases in global average air and ocean temperatures, widespread melting of snow and ice, and rising global average sea level.	unprecedented over decades to millennia. The atmosphere and ocean have warmed, the amounts of snow and ice have diminished, sea level has risen, and the concentrations of greenhouse gases have increased.	
			The global average temperature has increased since 1861. Over the 20th century the increase has been 0.6°C.	Eleven of the last twelve years (1995–2006) rank among the 12 warmest years in the instrumental record of global surface temperature (since 1850). The updated 100-year linear trend (1906 to 2005) of 0.74°C [0.56°C to 0.92°C] is therefore larger than the corresponding trend for 1901 to 2000 given in the TAR of 0.6°C [0.4°C to 0.8°C].	Each of the last three decades has been successively warmer at the Earth's surface than any preceding decade since 1850. The globally averaged combined land and ocean surface temperature data as calculated by a linear trend, show a warming of 0.85 [0.65 to 1.06] °C, over the period 1880 to 2012.	
			Some important aspects of climate appear not to have changed.	Some aspects of climate have not been observed to change.		
Observations of Recent Climate Change - Sea	Over the same period global sea level has increased by 10 to 20 cm. These increases have not	Global sea level has risen by between 10 and 25 cm over the past 100 years and	Tide gauge data show that global average sea level rose between 0.1 and 0.2 m during the	Global average sea level rose at an average rate of 1.8 [1.3 to 2.3] mm yr^{-1} over	The rate of sea level rise since the mid-19th century has been larger than the mean rate	

ACCEPTED VERSION SUBJECT TO FINAL EDITS

Level	been smooth with time nor uniform over the globe.	much of the rise may be related to the increase in global mean temperature.	20th century.	1961 to 2003. The rate was faster over 1993 to 2003: about 3.1 [2.4 to 3.8] mm yr^{-1}. The total 20th century rise is estimated to be 0.17 [0.12 to 0.22] m.	during the previous two millennia (*high confidence*). Over the period 1901 to 2010, global mean sea level rose by 0.19 [0.17 to 0.21] m.	
Observations of Recent Climate Change - Ocean Heat Content			Global ocean heat content has increased since the late1950s, the period for which adequate observations of sub-surface ocean temperatures have been available.	Observations since 1961 show that the average temperature of the global ocean has increased to depths of at least 3000 m and that the ocean has been absorbing more than 80% of the heat added to the climate system. Such warming causes seawater to expand, contributing to sea level rise.	Ocean warming dominates the increase in energy stored in the climate system, accounting for more than 90% of the energy accumulated between 1971 and 2010 (*high confidence*). It is *virtually certain* that the upper ocean (0−700 m) warmed from 1971 to 2010, and it *likely* warmed between the 1870s and 1971. On a global scale, the ocean warming is largest near the surface, and the upper 75 m warmed by 0.11 [0.09 to 0.13] °C per decade over the period 1971 to 2010. Instrumental biases in upper-ocean temperature records have been identified	

ACCEPTED VERSION SUBJECT TO FINAL EDITS

					and reduced, enhancing confidence in the assessment of change.	
Observations of Recent Climate Change - Carbon Cycle / Ocean Acidification				Increasing atmospheric carbon dioxide concentrations lead to increasing acidification of the ocean. Projections based on SRES scenarios give reductions in average global surface ocean pH of between 0.14 and 0.35 units over the 21st century, adding to the present decrease of 0.1 units since pre-industrial times.	The atmospheric concentrations of carbon dioxide, methane, and nitrous oxide have increased to levels unprecedented in at least the last 800,000 years. Carbon dioxide concentrations have increased by 40% since pre-industrial times, primarily from fossil fuel emissions and secondarily from net land use change emissions. The ocean has absorbed about 30% of the emitted anthropogenic carbon dioxide, causing ocean acidification.	
A Palaeoclimatic Perspective	Climate varies naturally on all timescales from hundreds of millions of years down to the year-to-year. Prominent in the Earth's history have been the 100,000-year glacial–interglacial cycles when climate was mostly cooler	The limited available evidence from proxy climate indicators suggests that the 20th century global mean temperature is at least as warm as any other century since at least 1400 AD. Data prior to	New analyses of proxy data for the Northern Hemisphere indicate that the increase in temperature in the 20th century is *likely* to have been the largest of any century during the past 1,000 years. It is also	Palaeoclimatic information supports the interpretation that the warmth of the last half-century is unusual in at least the previous 1,300 years.	In the Northern Hemisphere, 1983–2012 was *likely* the warmest 30-year period of the last 1400 years (*medium confidence*).	
				The last time the polar regions were	There is *very high confidence* that	

ACCEPTED VERSION SUBJECT TO FINAL EDITS

	than at present. Global surface temperatures have typically varied by 5°C to 7°C through these cycles, with large changes in ice volume and sea level, and temperature changes as great as 10°C to 15°C in some middle and high latitude regions of the Northern Hemisphere. Since the end of the last ice age, about 10,000 years ago, global surface temperatures have probably fluctuated by little more than 1°C. Some fluctuations have lasted several centuries, including the period 1400-1900 which ended in the 19th century and which appears to have been global in extent.	1400 are too sparse to allow the reliable estimation of global mean temperature.	*likely* that, in the Northern Hemisphere, the 1990s was the warmest decade and 1998 the warmest year. Because less data are available, less is known about annual averages prior to 1,000 years before present and for conditions prevailing in most of the Southern Hemisphere prior to 1861.	significantly warmer than present for an extended period (about 125,000 years ago), reductions in polar ice volume led to 4 to 6 m of sea level rise.	maximum global mean sea level during the last interglacial period (129,000 to 116,000 years ago) was, for several thousand years, at least 5 m higher than present, and *high confidence* that it did not exceed 10 m above present.	
Understanding and Attributing Climate Change	The size of this warming is broadly consistent with predictions of climate models, but it is also of the same magnitude as natural climate variability. Thus, the observed increase could be largely due to this natural variability; alternatively, this variability and other	The balance of evidence suggests a discernible human influence on global climate. Simulations with coupled atmosphere–ocean models have provided important information about decade to century timescale	There is new and stronger evidence that most of the warming observed over the last 50 years is attributable to human activities. There is a longer and more scrutinized temperature record and new model estimates of variability.	Most of the observed increase in global average temperatures since the mid-20th century is *very likely* due to the observed increase in anthropogenic greenhouse gas concentrations. Discernible human	Human influence on the climate system is clear. It is *extremely likely* that more than half of the observed increase in global average surface temperature from 1951 to 2010 was caused by the anthropogenic increase in greenhouse	

ACCEPTED VERSION SUBJECT TO FINAL EDITS

	human factors could have offset a still larger human-induced greenhouse warming. The unequivocal detection of the enhanced greenhouse effect from observations is *not likely* for a decade or more.	natural internal climate variability.	Reconstructions of climate data for the past 1,000 years indicate this warming was unusual and is *unlikely* to be entirely natural in origin.	influences now extend to other aspects of climate, including ocean warming, continental-average temperatures, temperature extremes and wind patterns.	gas concentrations and other anthropogenic forcings together. The best estimate of the human-induced contribution to warming is similar to the observed warming over this period.	
Projections of Future Changes in Climate - Temperature	Under the IPCC Business-as-Usual emissions of greenhouse gases, a rate of increase of global mean temperature during the next century of about 0.3°C per decade (with an uncertainty range of 0.2°C to 0.5°C per decade); this is greater than that seen over the past 10,000 years.	Climate is expected to continue to change in the future. For the mid-range IPCC emission scenario, IS92a, assuming the 'best estimate' value of climate sensitivity and including the effects of future increases in aerosols, models project an increase in global mean surface air temperature relative to 1990 of about 2°C by 2100.	Global average temperature and sea level are projected to rise under all IPCC SRES scenarios. The globally averaged surface temperature is projected to increase by 1.4°C to 5.8°C over the period 1990 to 2100.	For the next two decades, a warming of about 0.2°C per decade is projected for a range of SRES emission scenarios. Even if the concentrations of all greenhouse gases and aerosols had been kept constant at year 2000 levels, a further warming of about 0.1°C per decade would be expected.	Global surface temperature change for the end of the 21st century is *likely* to exceed 1.5°C relative to 1850 to 1900 for all RCP scenarios except RCP2.6. It is likely to exceed 2°C for RCP6.0 and RCP8.5, and *more likely than not* to exceed 2°C for RCP4.5. Warming will continue beyond 2100 under all RCP scenarios except RCP2.6. Warming will continue to exhibit interannual-to-decadal variability and will not be regionally uniform.	
			Confidence in the ability of models to project future climate has increased.	There is now higher confidence in projected patterns of warming and other regional-scale features,	Climate models have improved since the AR4. Models reproduce observed continental-scale	

ACCEPTED VERSION SUBJECT TO FINAL EDITS

				including changes in wind patterns, precipitation and some aspects of extremes and of ice.	surface temperature patterns and trends over many decades, including the more rapid warming since the mid-20th century and the cooling immediately following large volcanic eruptions.	
			Anthropogenic climate change will persist for many centuries.	Anthropogenic warming and sea level rise would continue for centuries, even if greenhouse gas concentrations were to be stabilised.	Cumulative emissions of CO_2 largely determine global mean surface warming by the late 21st century and beyond. Most aspects of climate change will persist for many centuries even if emissions of CO_2 are stopped. This represents a substantial multi-century climate change commitment created by past, present and future emissions of CO_2.	
Projections of Future Changes in Climate - Sea Level	An average rate of global mean sea level rise of about 6 cm per decade over the next century (with an uncertainty range of 3 to 10 cm per decade) is projected.	For the IS92a scenario, assuming the 'best estimate' values of climate sensitivity and of ice melt sensitivity to warming and including the effects of future	Global mean sea level is projected to rise by 0.09 to 0.88 m between 1990 and 2100.	Global sea level rise for the range of scenarios is projected as 0.18 to 0.59 m by the end of the 21st century.	Global mean sea level rise for 2081–2100 relative to 1986–2005 will *likely* be in the ranges of 0.26 to 0.55 m for RCP2.6, 0.32 to 0.63 m for RCP4.5, 0.33 to 0.63 m for	

ACCEPTED VERSION SUBJECT TO FINAL EDITS

		changes in aerosol concentrations, models project a sea level rise of about 50 cm from the present to 2100. The corresponding 'low' and 'high' projections are 15 and 95 cm.			RCP6.0, and 0.45 to 0.82 m for RCP8.5.	
Projections of Future Changes in Climate - AMOC		Most simulations show a reduction in the strength of the North Atlantic thermohaline circulation. Future unexpected, large and rapid climate system changes are difficult to predict. These arise from the non-linear nature of the climate system. Examples include rapid circulation changes in the North Atlantic.	Most models show weakening of the ocean thermohaline circulation, which leads to a reduction of the heat transport into high latitudes of the Northern Hemisphere. However, even in models where the thermohaline circulation weakens, there is still a warming over Europe due to increased greenhouse gases. The current projections using climate models do not exhibit a complete shut-down of the thermohaline circulation by 2100. Beyond 2100, the thermohaline circulation could completely, and possibly irreversibly, shut-down in either hemisphere if	Based on current model simulations, it is *very likely* that the meridional overturning circulation (MOC) of the Atlantic Ocean will slow down during the 21st century. It is *very unlikely* that the MOC will undergo a large abrupt transition during the 21st century. Longer-term changes in the MOC cannot be assessed with confidence.	It is *very likely* that the Atlantic Meridional Overturning Circulation (AMOC) will weaken over the 21st century. It is *very unlikely* that the AMOC will undergo an abrupt transition or collapse in the 21st century for the scenarios considered. There is *low confidence* in assessing the evolution of the AMOC beyond the 21st century because of the limited number of analyses and equivocal results. However, a collapse beyond the 21st century for large sustained warming cannot be excluded.	

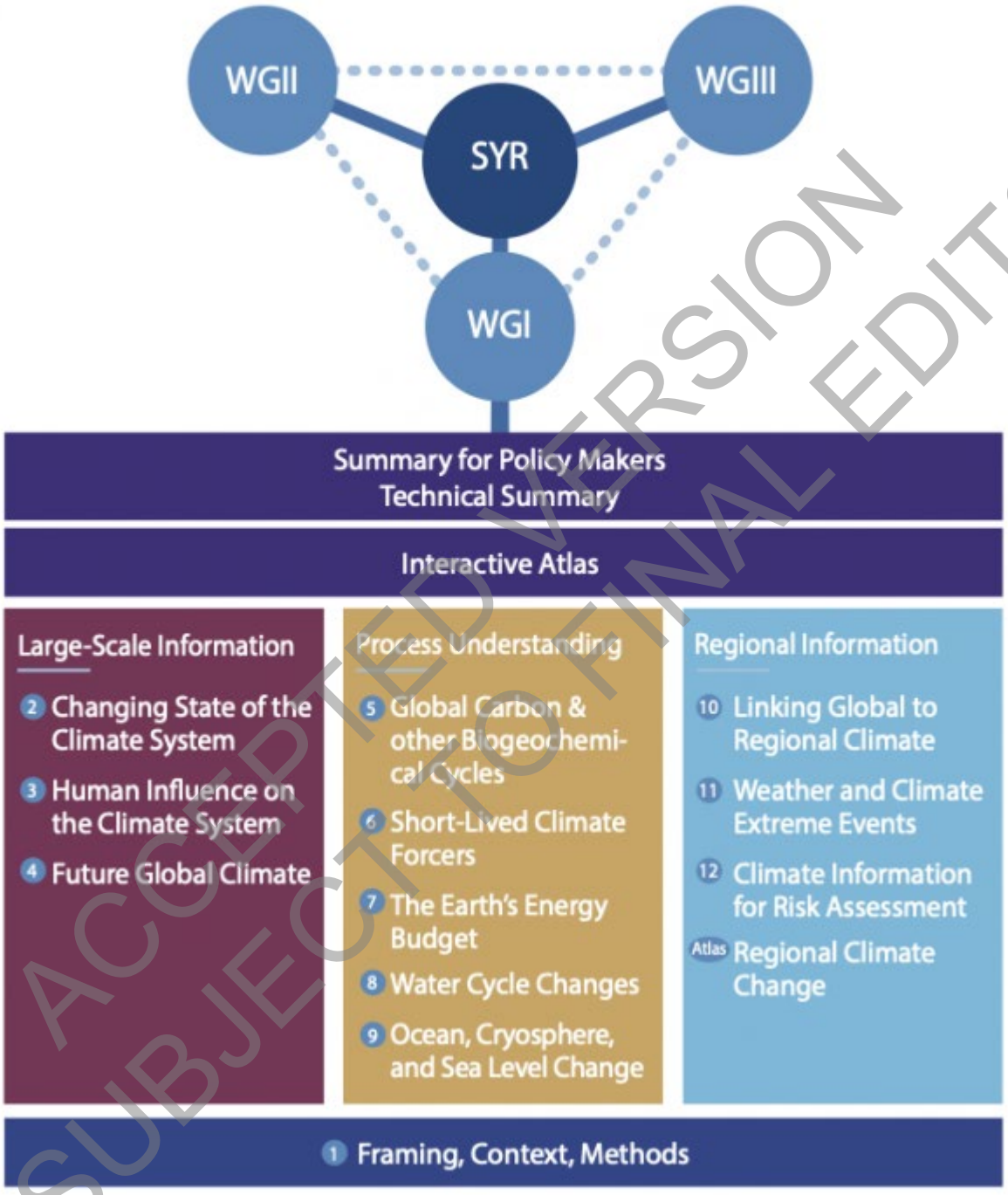
ACCEPTED VERSION SUBJECT TO FINAL EDITS

			the change in radiative forcing is large enough and applied long enough.			

[END TABLE 1.A.1 HERE]

ACCEPTED VERSION
SUBJECT TO FINAL EDITS

Figures



ACCEPTED VERSION SUBJECT TO FINAL EDITS

Figure 1.1: **The structure of the AR6 WGI Report**. Shown are the three pillars of AR6 WGI, its relation to the WGII and WGIII contributions, and the cross-working-group AR6 Synthesis Report (SYR).

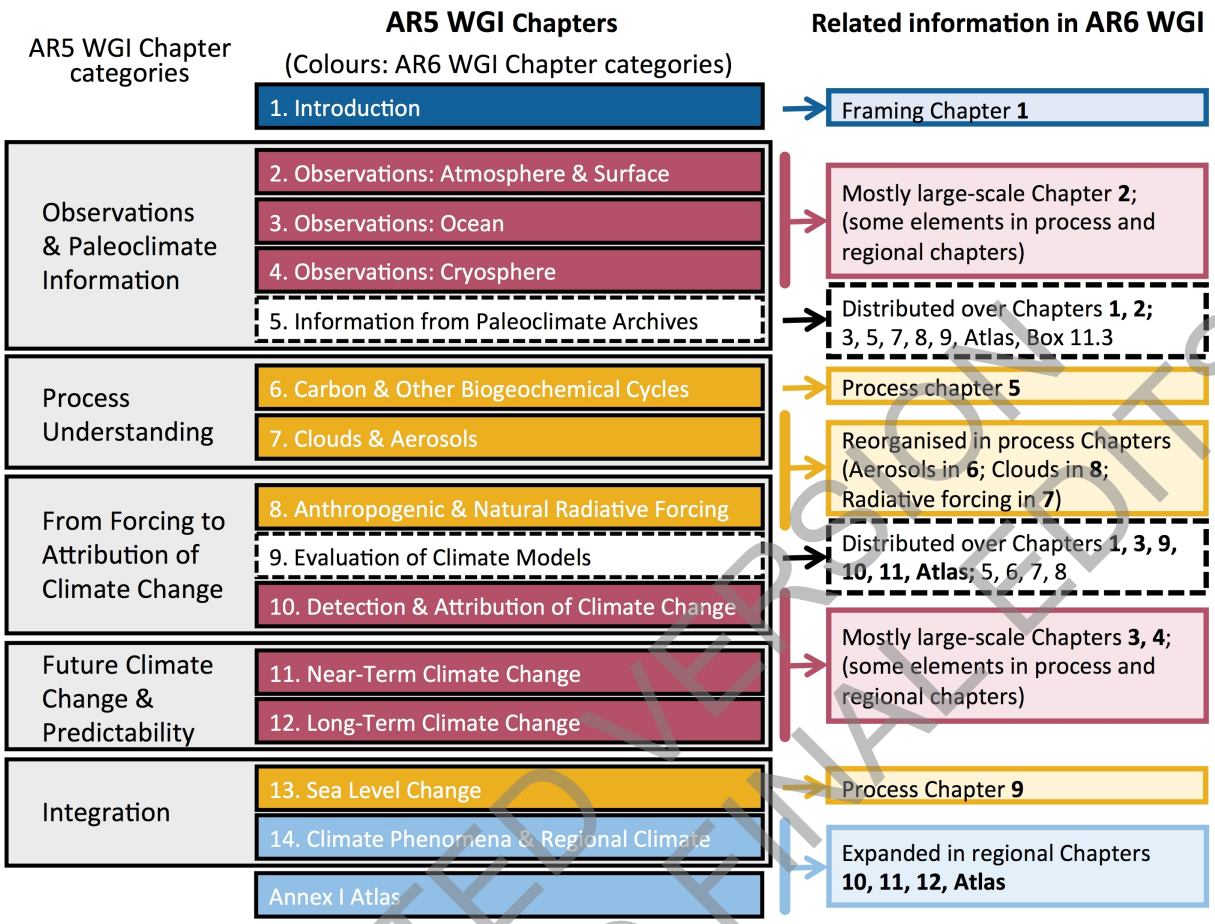


Figure 1.2: Main relations between AR5 WGI and AR6 WGI chapters. The left column shows the AR5 WGI chapter categories. The central column lists the AR5 WGI chapters, with the colour code indicating their relation to the AR6 WGI structure shown in Figure 1.1: Large-Scale Information (red), Process Understanding (gold), Regional Information (light blue), and Whole-Report Information (dark blue). AR5 WGI chapters depicted in white have their topics distributed over multiple AR6 WGI chapters and categories. The right column explains where to find related information in the AR6 WGI report.

ACCEPTED VERSION SUBJECT TO FINAL EDITS

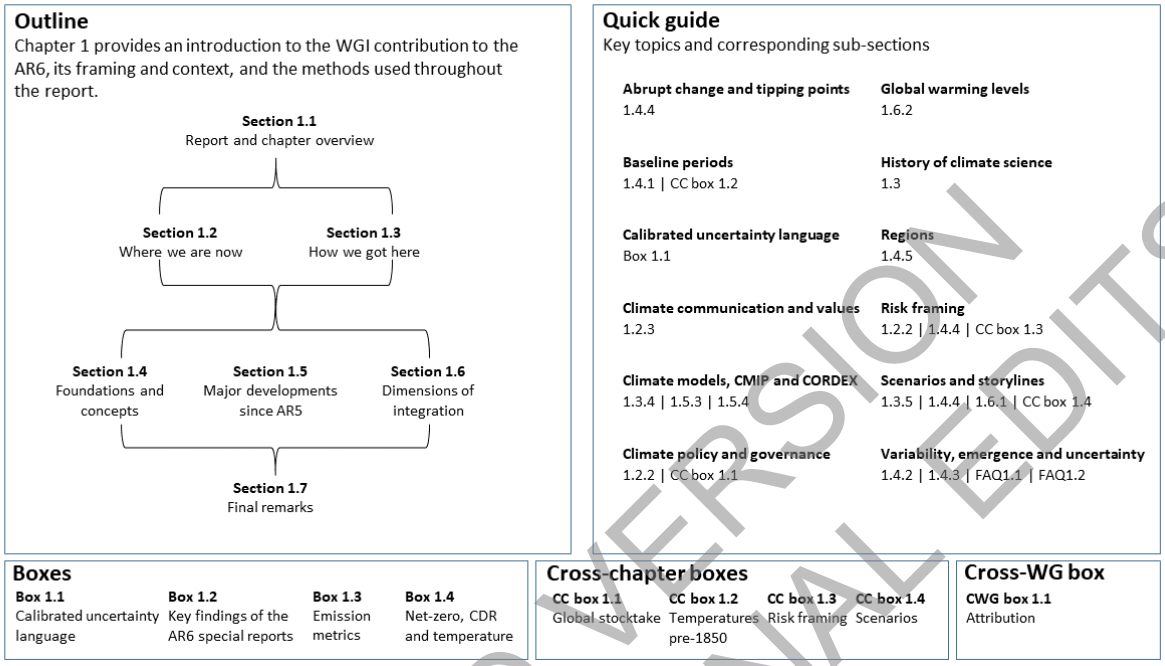


Figure 1.3: A roadmap to the contents of Chapter 1.

ACCEPTED VERSION
SUBJECT TO FINAL EDITS

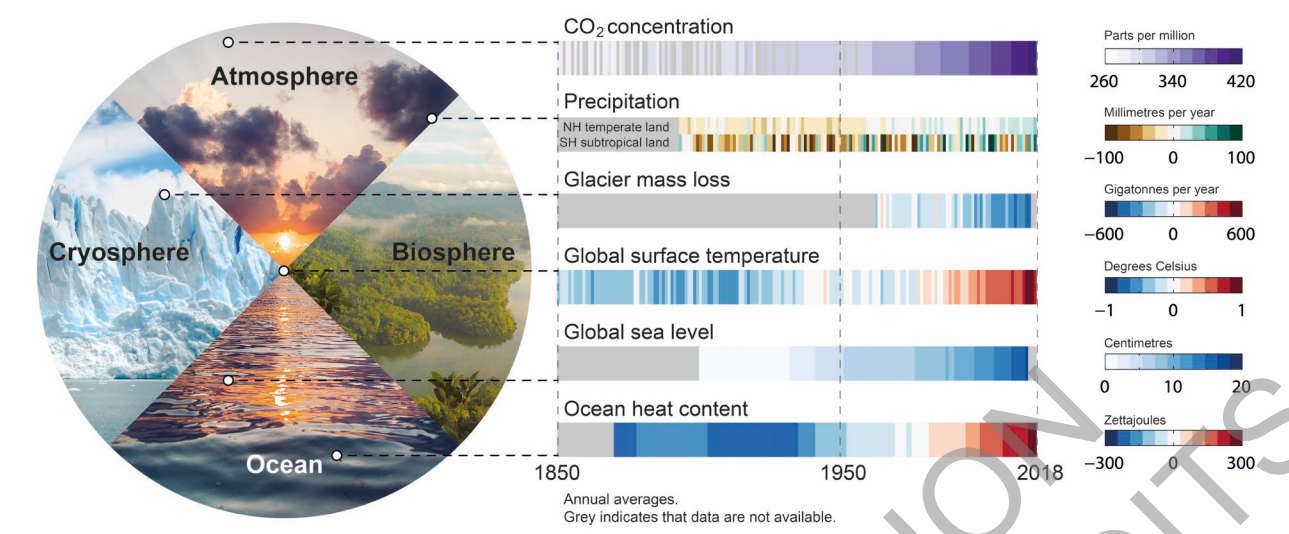
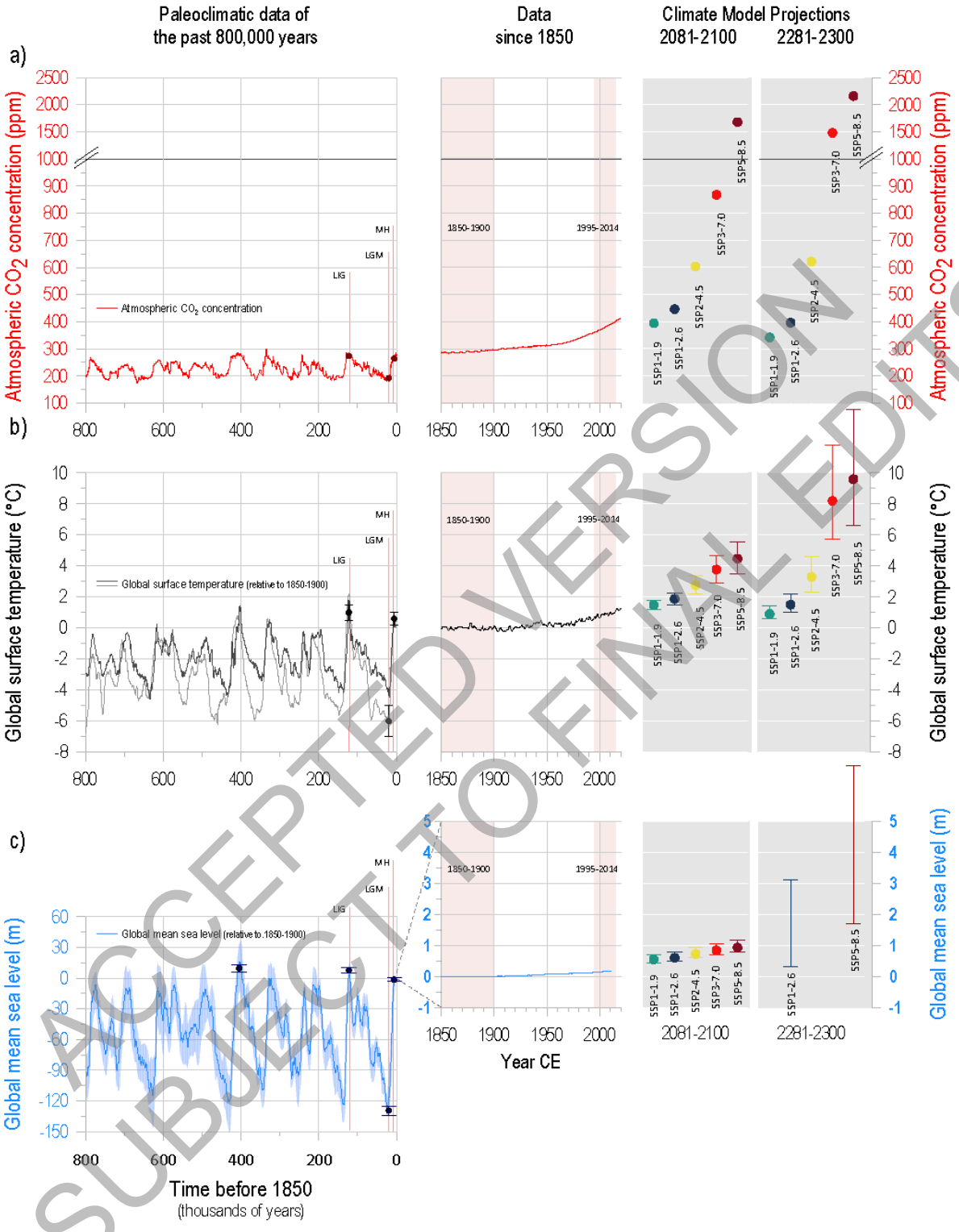


Figure 1.4: **Changes are occurring throughout the climate system.** Left: Main realms of the climate system: atmosphere, biosphere, cryosphere, and ocean. Right: Six key indicators of ongoing changes since 1850, or the start of the observational or assessed record, through 2018. Each stripe indicates the global (except for precipitation which shows two latitude band means), annual mean anomaly for a single year, relative to a multi-year baseline (except for CO_2 concentration and glacier mass loss, which are absolute values). Grey indicates that data are not available. Datasets and baselines used are: (1) CO_2: Antarctic ice cores (Lüthi et al., 2008; Bereiter et al., 2015) and direct air measurements (Tans and Keeling, 2020) (see Figure 1.5 for details); (2) precipitation: Global Precipitation Climatology Centre (GPCC) V8 (updated from Becker et al. 2013), baseline 1961-1990 using land areas only with latitude bands 33°N–66°N and 15°S–30°S; (3) glacier mass loss: Zemp et al., 2019; (4) global surface air temperature (GMST): HadCRUT5 (Morice et al., 2021), baseline 1961–1990; (5) sea level change: (Dangendorf et al., 2019), baseline 1900–1929; (6) ocean heat content (model-observation hybrid): Zanna et al., (2019), baseline 1961–1990. Further details on data sources and processing are available in the chapter data table (Table 1.SM.1).

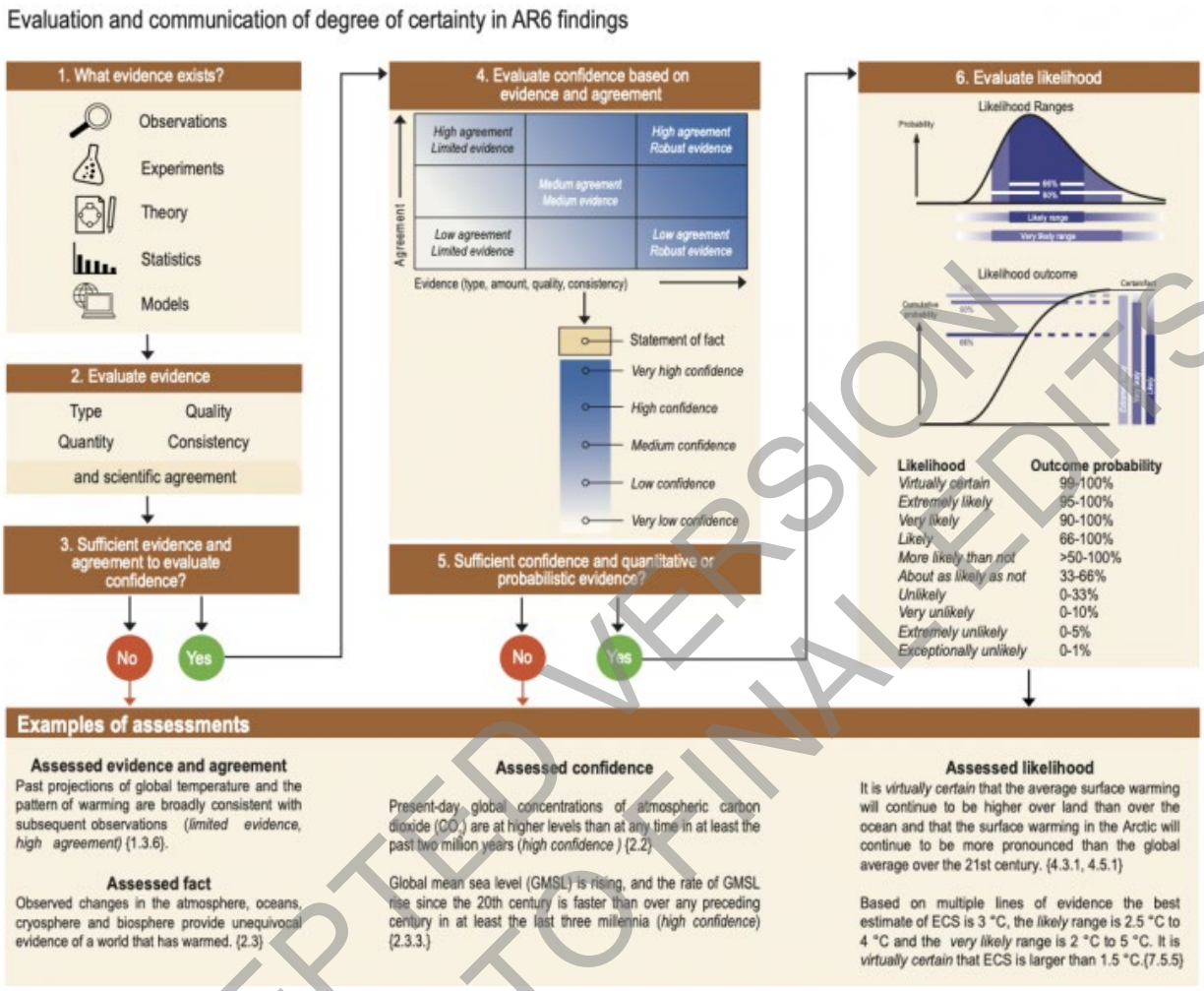
ACCEPTED VERSION SUBJECT TO FINAL EDITS



ACCEPTED VERSION SUBJECT TO FINAL EDITS

Figure 1.5: Long-term context of anthropogenic climate change based on selected paleoclimatic reconstructions over the past 800,000 years for three key indicators: atmospheric CO_2 concentrations, Global Mean Surface Temperature (GMST), and Global Mean Sea Level (GMSL). a) Measurements of CO_2 in air enclosed in Antarctic ice cores (Lüthi et al., 2008; Bereiter et al., 2015 [a compilation]; uncertainty ±1.3ppm; see Chapter 2, Section 2.2.3 and Chapter 5, Section 5.1.2 for an assessment) and direct air measurements (Tans and Keeling, 2020; uncertainty ±0.12 ppm). Projected CO_2 concentrations for five Shared Socioeconomic Pathways (SSP) scenarios are indicated by dots on the right-hand side panels of the figure (grey background) (Meinshausen et al., 2020; SSPs are described in Section 1.6). b) Reconstruction of GMST from marine paleoclimate proxies (light grey: Snyder (2016); dark grey: Hansen et al. (2013); see Chapter 2, Section 2.3.1 for an assessment). Observed and reconstructed temperature changes since 1850 are the AR6 assessed mean (referenced to 1850–1900; Box TS.3; 2.3.1.1); dots/whiskers on the right-hand side panels of the figure (grey background) indicate the projected mean and ranges of warming derived from Coupled Model Intercomparison Project Phase 6 (CMIP6) SSP-based (2081–2100) and Model for the Assessment of Greenhouse Gas Induced Climate Change (MAGICC7) (2300) simulations (Chapter 4, Tables 4.5 and 4.9). c) Sea level changes reconstructed from a stack of oxygen isotope measurements on seven ocean sediment cores (Spratt and Lisiecki, 2016; see Chapter 2, Section 2.3.3.3 and Chapter 9, Section 9.6.2 for an assessment). The sea level record from 1850 to 1900 is from Kopp et al. (2016), while the 20th century record is an updated ensemble estimate of GMSL change (Palmer et al., 2021; see also Chapter 2, Section 2.3.3.3 and Chapter 9, Section 9.6.1.1). Dots/whiskers on the right-hand side panels of the figure (grey background) indicate the projected median and ranges derived from SSP-based simulations (2081–2100: Chapter 9, Table 9.9; 2300: Chapter 9, Section 9.6.3.5). Best estimates (dots) and uncertainties (whiskers) as assessed by Chapter 2 are included in the left and middle panels for each of the three indicators and selected paleo-reference periods used in this report (CO_2: Chapter 2, Table 2.1; GMST: Chapter 2, Section 2.3.1.1 and Cross-Chapter Box 2.3, Table 1 in Chapter 2; GMSL: Chapter 2, Section 2.3.3.3 and Chapter 9, Section 9.6.2. See also Cross-Chapter Box 2.1 in Chapter 2). Selected paleo-reference periods: LIG – Last Interglacial; LGM – Last Glacial Maximum; MH – mid-Holocene (Cross-Chapter Box 2.1, Table 1 in Chapter 2). The non-labelled best estimate in panel c) corresponds to the sea level high-stand during Marine Isotope Stage 11, about 410,000 years ago (see Chapter 9, Section 9.6.2). Further details on data sources and processing are available in the chapter data table (Table 1.SM.1).

ACCEPTED VERSION SUBJECT TO FINAL EDITS



Box 1.1, Figure 1: The IPCC AR6 approach for characterizing understanding and uncertainty in assessment findings. This diagram illustrates the step-by-step process authors use to evaluate and communicate the state of knowledge in their assessment (Mastrandrea et al., 2010). Authors present evidence/agreement, confidence, or likelihood terms with assessment conclusions, communicating their expert judgments accordingly. Example conclusions drawn from this report are presented in the box at the bottom of the figure. [adapted from Mach et al. (2017)].

ACCEPTED VERSION SUBJECT TO FINAL EDITS

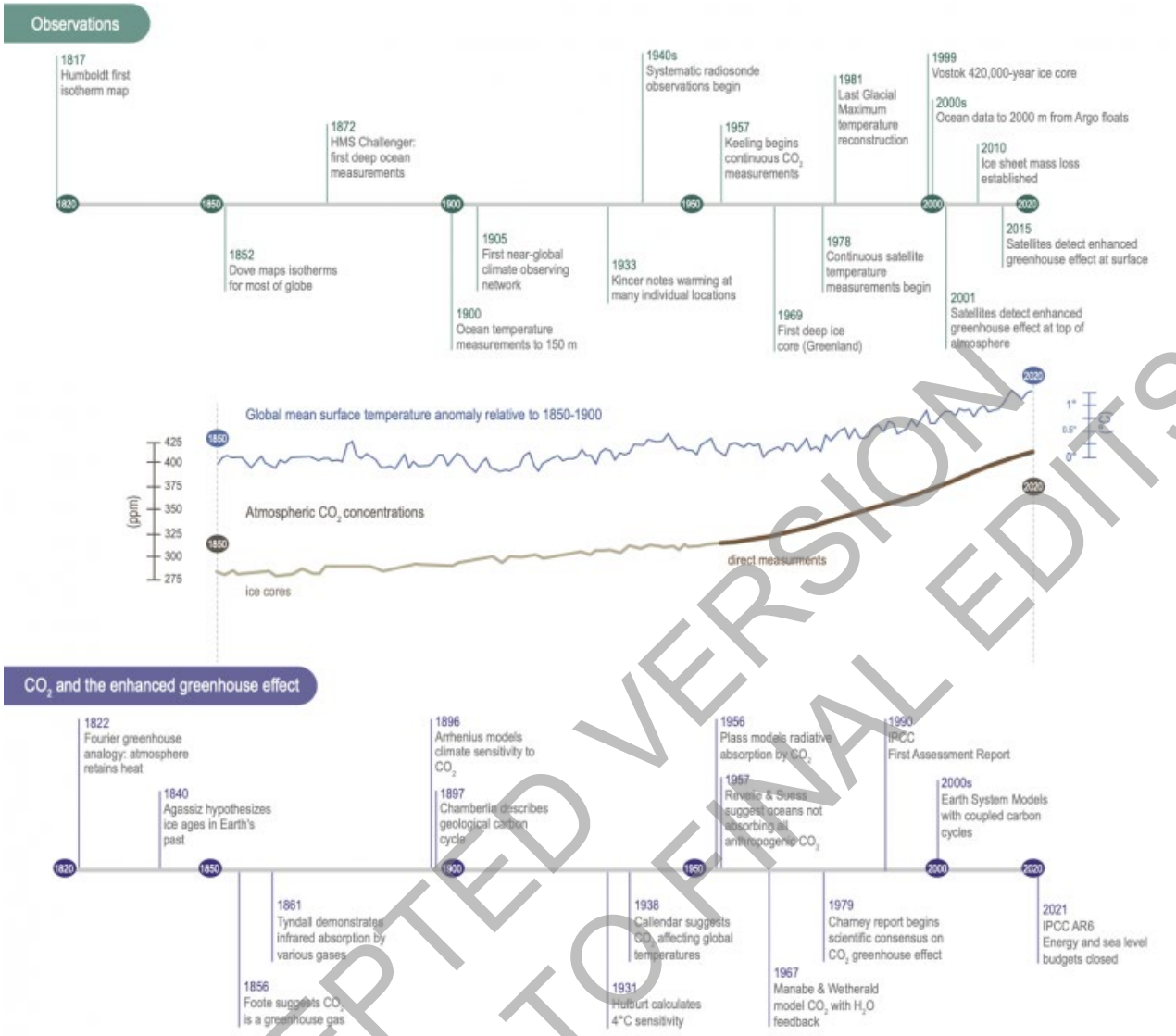


Figure 1.6: **Climate science milestones, between 1817-2021**. Milestones in observations (top); Curves of global surface air temperature (GMST) using HadCRUT5 (Morice et al., 2021) and atmospheric CO_2 concentrations from Antarctic ice cores (Lüthi et al., 2008; Bereiter et al., 2015) and direct air measurements from 1957 onwards (Tans and Keeling, 2020) (see Figure 1.4 for details) (middle). Milestone in scientific understanding of the CO2 enhanced greenhouse effect (bottom). Further details on each milestone are available in Chapter 1, Section 1.3, and Chapter 1 of AR4.

ACCEPTED VERSION SUBJECT TO FINAL EDITS

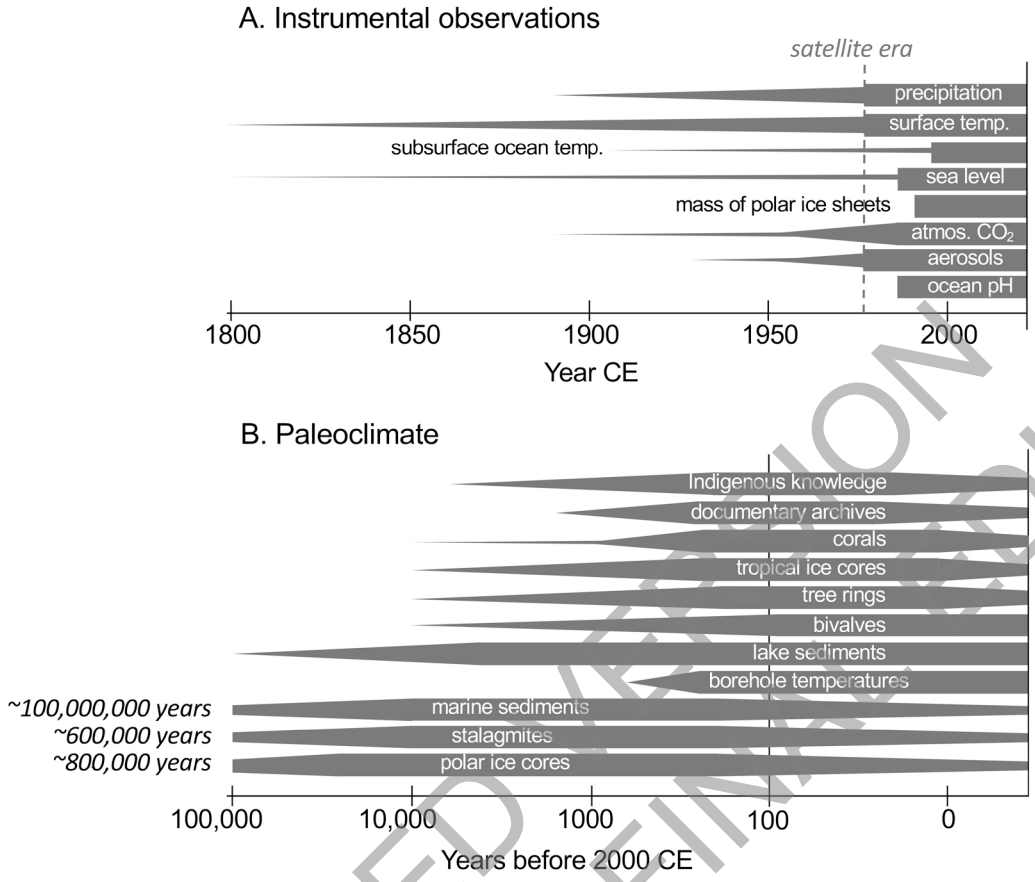
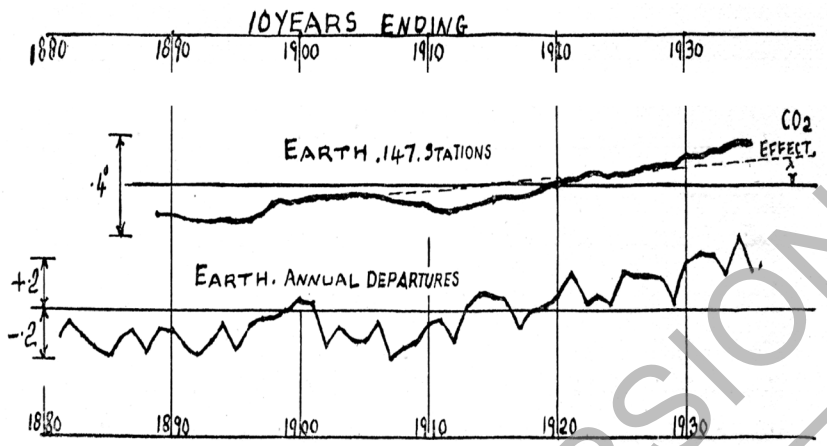


Figure 1.7: Schematic of temporal coverage of selected instrumental climate observations (top) and selected paleoclimate archives (bottom). The satellite era began in 1979 CE (Common Era). The width of the taper gives an indication of the amount of available records.

ACCEPTED VERSION SUBJECT TO FINAL EDITS

Changes in global land temperature (60°S-60°N) relative to a 1901-1930 baseline (°C)

(a) Callendar (1938)



(b) Comparing Callendar (1938, 1961) with CRUTEM5 (Osborn et al. 2020)

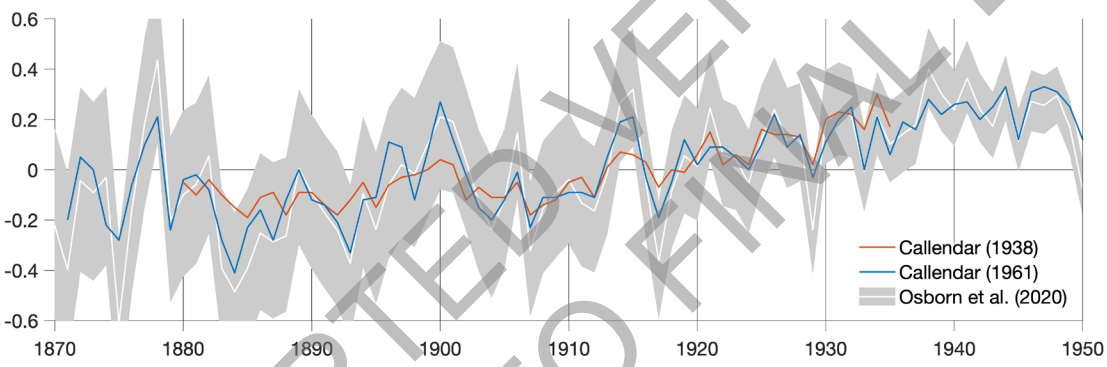
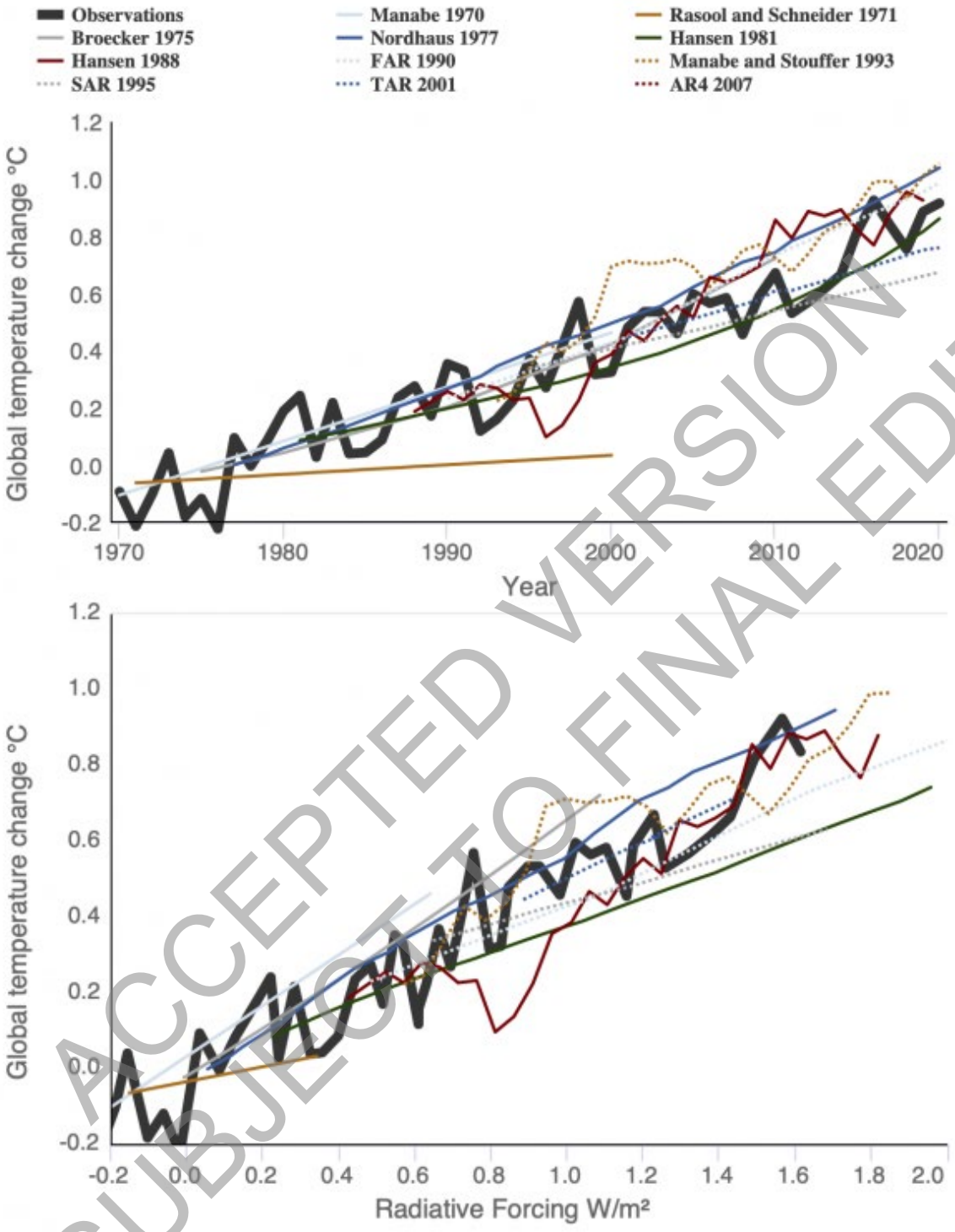


Figure 1.8: **G.S. Callendar's estimates of global land temperature variations and their possible causes.** (a) The original figure from Callendar (1938), using measurements from 147 surface stations for 1880–1935, showing: (top) ten-year moving departures from the mean of 1901-1930 (°C), with the dashed line representing his estimate of the 'CO_2 effect' on temperature rise, and (bottom) annual departures from the 1901–1930 mean (°C). (b) Comparing the estimates of global land (60°S–60°N) temperatures tabulated in Callendar (1938, 1961) with a modern reconstruction (Osborn et al., 2021) for the same period, after (Hawkins and Jones (2013). Further details on data sources and processing are available in the chapter data table (Table 1.SM.1).

ACCEPTED VERSION SUBJECT TO FINAL EDITS



ACCEPTED VERSION SUBJECT TO FINAL EDITS

Figure 1.9: Assessing past projections of global temperature change. Projected temperature change post-publication on a temperature vs time (1970–2020, top panel) and temperature vs radiative forcing (1970–2017, bottom panel) basis for a selection of prominent climate model projections (taken from Hausfather et al., 2020). Model projections (using global surface air temperature, GSAT) are compared to temperature observations (using global mean surface temperature, GMST) from HadCRUT5 (black) and anthropogenic forcings (through 2017) from Dessler and Forster (2018), and have a baseline generated from the first five years of the projection period. Projections shown are: Manabe (1970), Rasool and

Schneider (1971), Broecker (1975), Nordhaus (1977), Hansen et al. (1981, H81), Hansen et al. (1988, H88), Manabe and Stouffer (1993), along with the Energy Balance Model (EBM) projections from the FAR, SAR and TAR, and the multi-model mean projection using CMIP3 simulations of the Special Reports on Emission Scenarios (SRES) A1B scenario from AR4. H81 and H88 show most expected scenarios 1 and B, respectively. See Hausfather et al. (2020) for more details of the projections. Further details on data sources and processing are available in the chapter data table (Table 1.SM.1).

ACCEPTED VERSION
SUBJECT TO FINAL EDITS

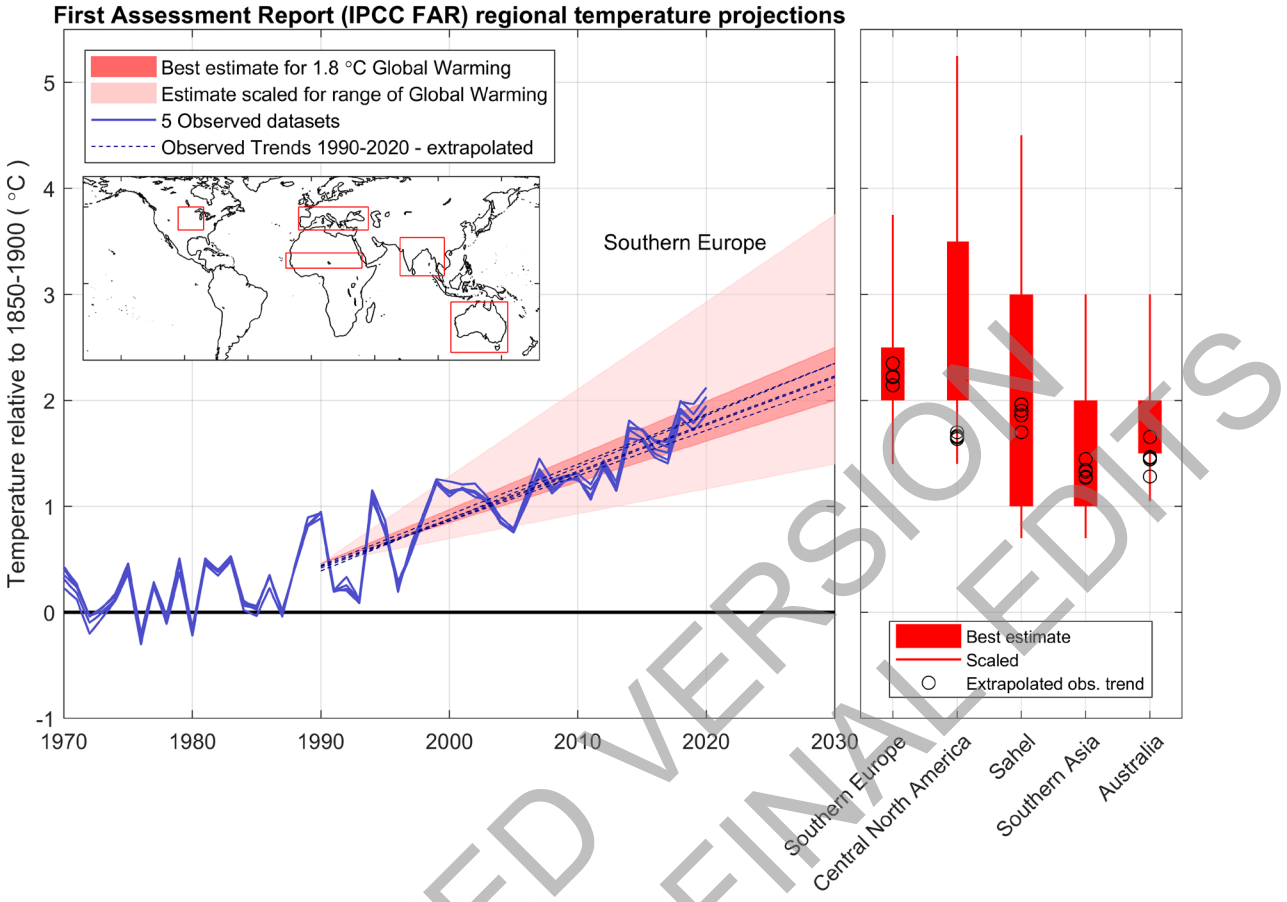


Figure 1.10: Range of projected temperature change for 1990–2030 for various regions defined in IPCC First Assessment Report (FAR). The left panel shows the FAR projections (IPCC, 1990) for Southern Europe, with darker red bands representing the range of projected change given for the best estimate of 1.8°C global warming since pre-industrial to 2030, and the fainter red bands show the range scaled by –30% to +50% for lower and higher estimates of global warming. Blue lines show the regionally averaged observations from several global temperature gridded datasets, and blue dashed lines show the linear trends in those datasets for 1990–2020 extrapolated to 2030. Observed datasets are: HadCRUT5, Cowtan and Way, GISTEMP, Berkeley Earth and NOAA GlobalTemp. The inset map shows the definition of the FAR regions used. The right panel shows projected temperature changes by 2030 for the various FAR regions, compared to the extrapolated observational trends, following Grose et al. (2017). Further details on data sources and processing are available in the chapter data table (Table 1.SM.1).

ACCEPTED VERSION SUBJECT TO FINAL EDITS

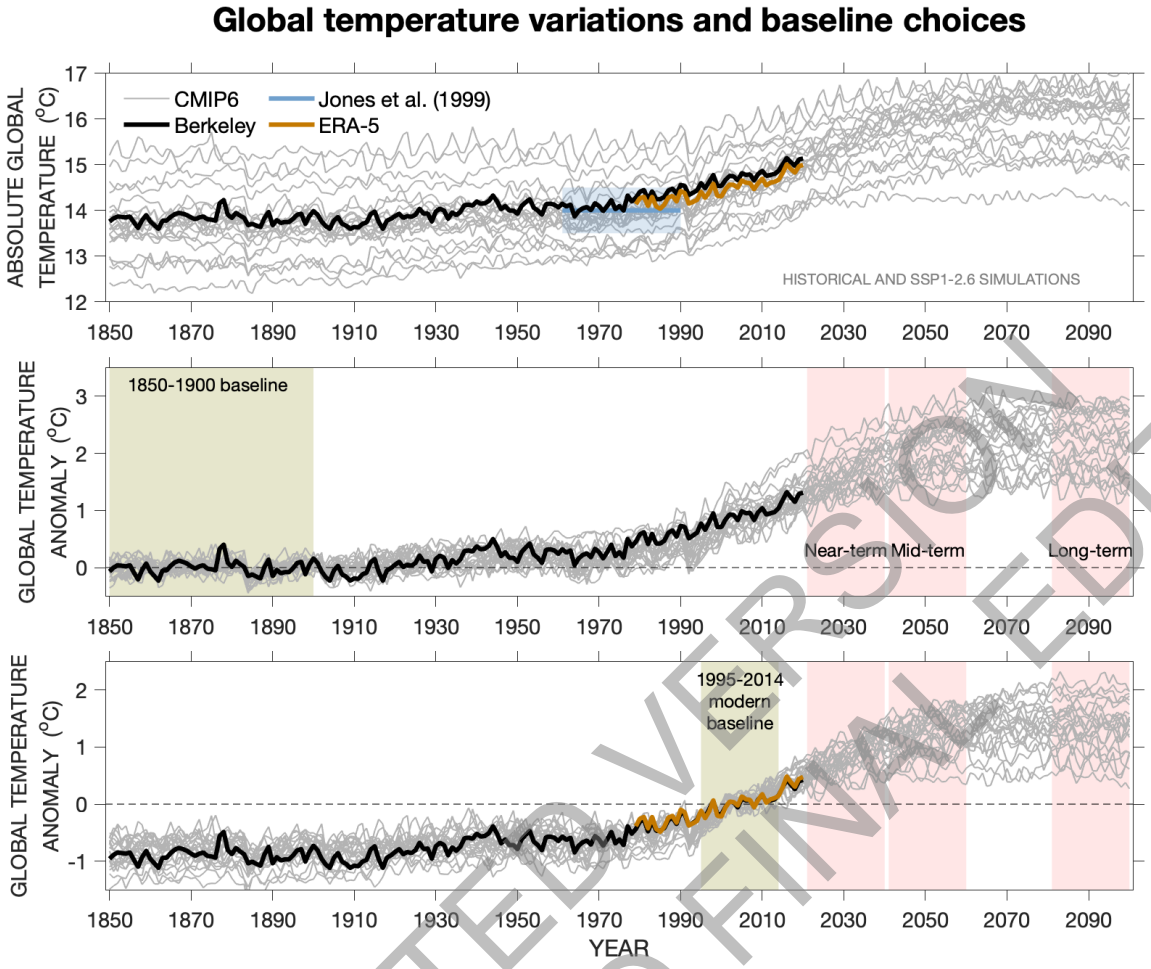


Figure 1.11: Choice of baseline matters when comparing observations and model simulations. Global mean surface air temperature (GSAT, grey) from a range of CMIP6 historical simulations (1850–2014, 25 models) and SSP1-2.6 (2015–2100) using absolute values (top) and anomalies relative to two different baselines: 1850–1900 (middle) and 1995–2014 (bottom). An estimate of GSAT from a reanalysis (ERA-5, orange, 1979–2020) and an observation-based estimate of global mean surface air temperature (GMST) (Berkeley Earth, black, 1850–2020) are shown, along with the mean GSAT for 1961–1990 estimated by Jones et al. (1999), light blue shading, 14.0±0.5°C). Using the more recent baseline (bottom) allows the inclusion of datasets which do not include the periods of older baselines. The middle and bottom panels have scales which are the same size but offset. Further details on data sources and processing are available in the chapter data table (Table 1.SM.1).

ACCEPTED VERSION SUBJECT TO FINAL EDITS

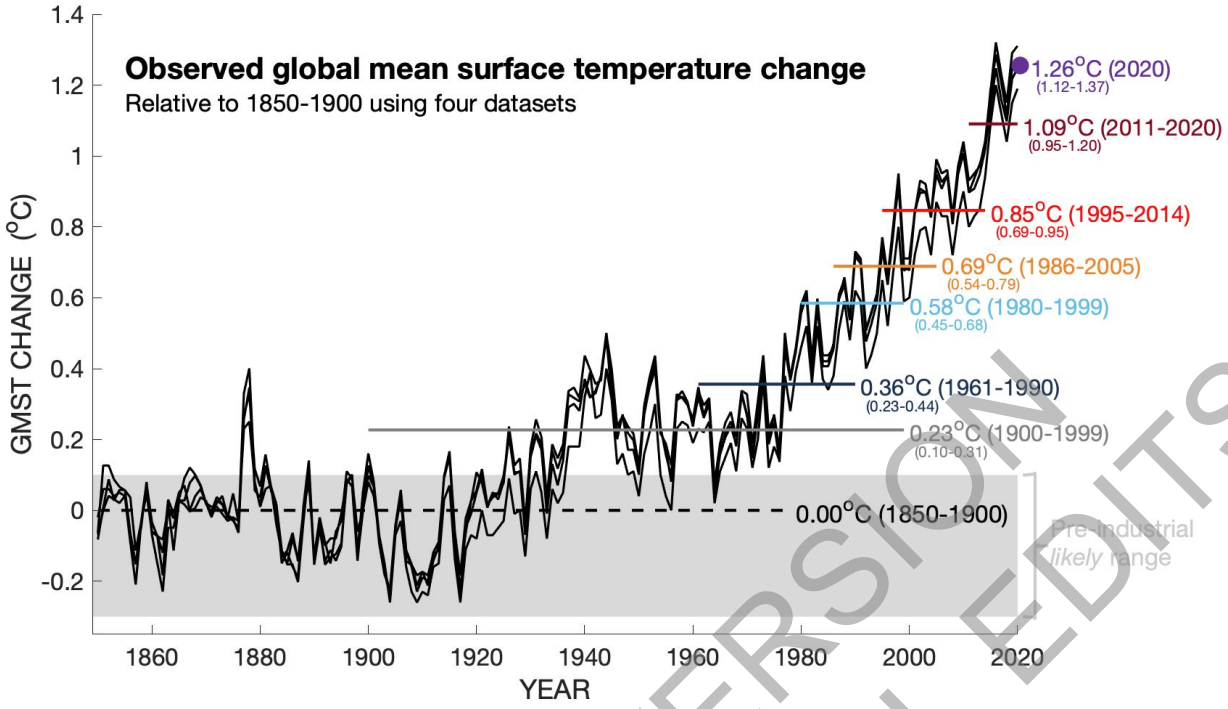
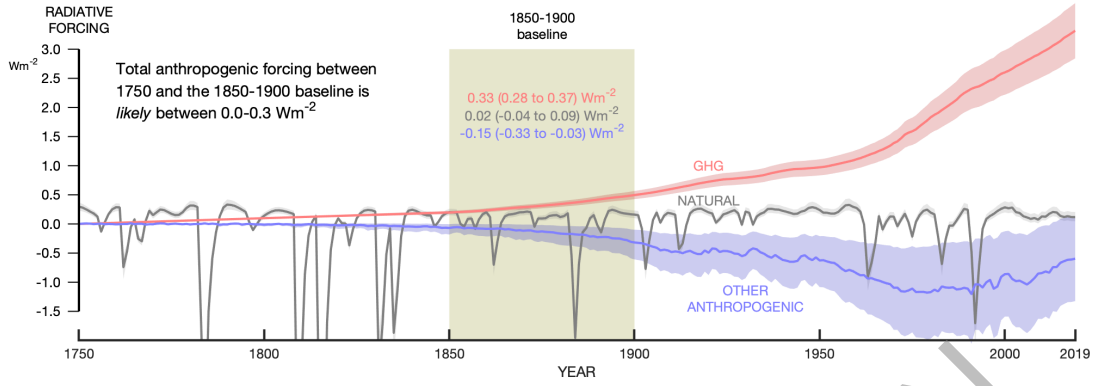


Figure 1.12: Global warming over the instrumental period. Observed global mean surface temperature (GMST) from four datasets, relative to the average temperature of 1850–1900 in each dataset (see Cross-Chapter Box 2.3 and Section 2.3.1.1 for more details). The shaded grey band indicates the assessed *likely* range for the period around 1750 (see Cross-Chapter Box 1.2). Different reference periods are indicated by the coloured horizontal lines, and an estimate of total GMST change up to that period is given, enabling a translation of the level of warming between different reference periods. The reference periods are all chosen because they have been used in the AR6 or previous IPCC assessment reports. The value for the 1981–2010 reference period, used as a 'climate normal' period by the World Meteorological Organization, is the same as the 1986–2005 reference period shown. Further details on data sources and processing are available in the chapter data table (Table 1.SM.1).

ACCEPTED VERSION SUBJECT TO FINAL EDITS



Cross-Chapter Box 1.2, Figure 1: Changes in radiative forcing from 1750 to 2019. The radiative forcing estimates from the AR6 emulator (see Cross-Chapter Box 7.1 in Chapter 7) are split into GHG, other anthropogenic (mainly aerosols and land use) and natural forcings, with the average over the 1850–1900 baseline shown for each. Further details on data sources and processing are available in the chapter data table (Table 1.SM.1).

ACCEPTED VERSION SUBJECT TO FINAL EDITS

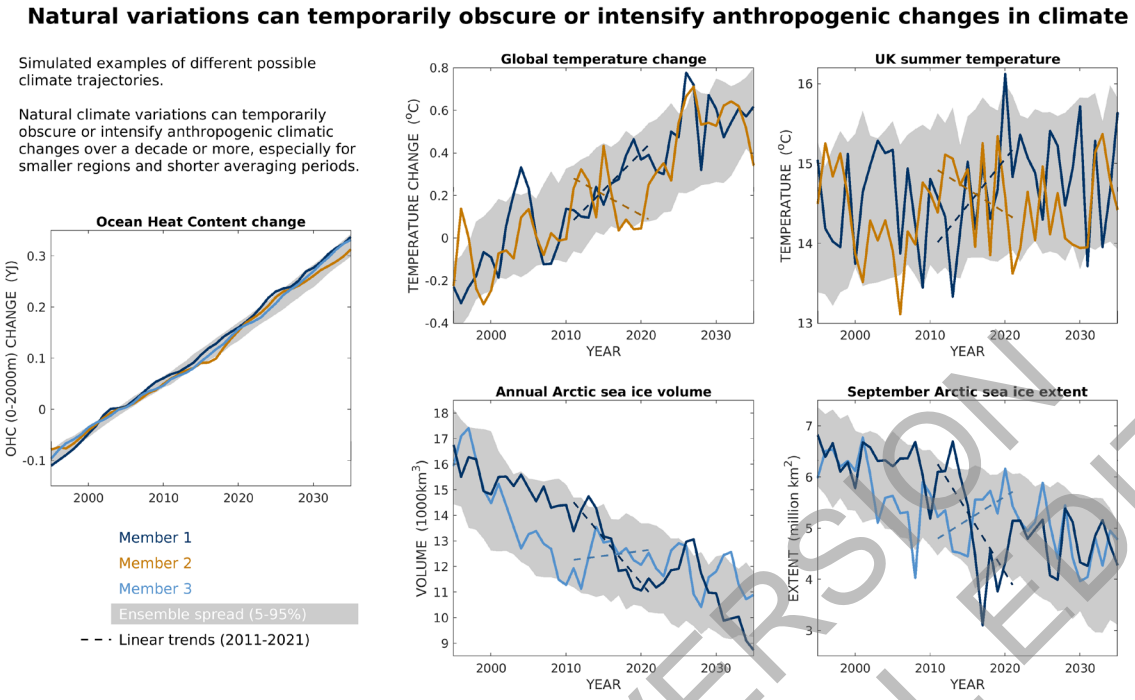
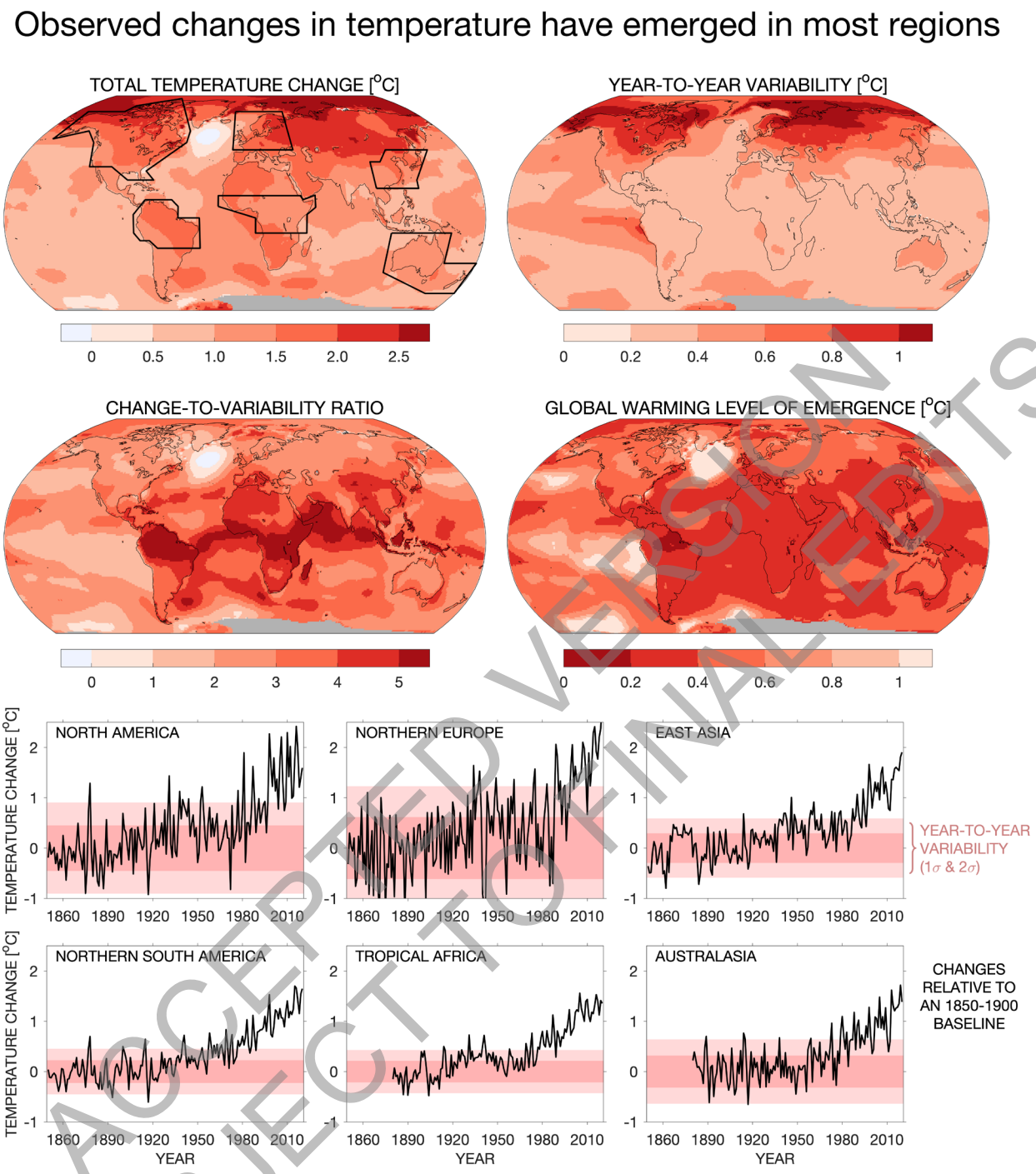


Figure 1.13: Simulated changes in various climate indicators under historical and RCP4.5 scenarios using the MPI ESM Grand Ensemble. The grey shading shows the 5–95% range from the 100-member ensemble. The coloured lines represent individual example ensemble members, with linear trends for the 2011–2021 period indicated by the thin dashed lines. Changes in Ocean Heat Content (OHC) over the top 2000m represents the integrated signal of global warming (left). The top row shows surface air temperature-related indicators (annual GSAT change and UK summer temperatures) and the bottom row shows Arctic sea-ice related indicators (annual ice volume and September sea ice extent). For smaller regions and for shorter time period averages the variability increases and simulated short-term trends can temporarily obscure or intensify anthropogenic changes in climate. Data from Maher et al., (2019). Further details on data sources and processing are available in the chapter data table (Table 1.SM.1).

ACCEPTED VERSION SUBJECT TO FINAL EDITS



ACCEPTED VERSION SUBJECT TO FINAL EDITS

Figure 1.14: The observed emergence of changes in temperature. Top left: the total change in temperature estimated for 2020 relative to 1850–1900 (following Hawkins et al. 2020), showing the largest warming in the Arctic. Top right: the amplitude of estimated year-to-year variations in temperature. Middle left: the ratio of the observed total change in temperature and the amplitude of temperature variability (the 'signal-to-noise (S/N) ratio'), showing that the warming is most apparent in the tropical regions (also see FAQ1.2). Middle right: the global warming level at which the change in local temperature becomes larger than the local year-to-year variability. The bottom panels show time series of observed annual mean surface air temperatures over land in various example regions, as indicated as boxes in the top left panel. The 1 and 2 standard deviations of estimated year-to-year variations for that region are shown by the pink shaded bands. Observed temperature data from Berkeley Earth (Rohde and Hausfather, 2020). Further details on data sources and processing are available in the chapter data table (Table 1.SM.1).

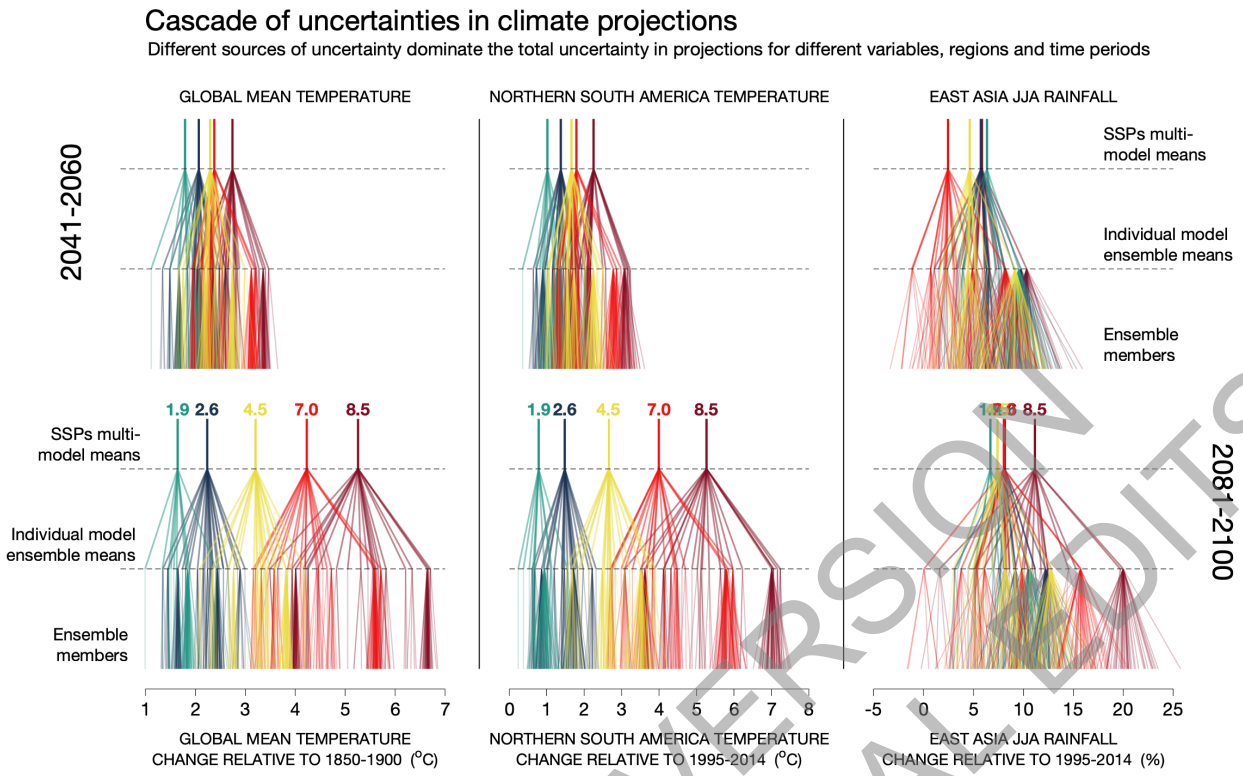


Figure 1.15: The 'cascade of uncertainties' in CMIP6 projections. Changes in GSAT (left), northern South America (region NSA) temperature change (middle), and East Asia (region EAS) summer (JJA) precipitation change (right) are shown for two time periods (2041–2060, top, and 2081–2100, bottom). The SSP-radiative forcing combination is indicated at the top of each cascade at the value of the multi-model mean for each scenario. This branches downwards to show the ensemble mean for each model, and further branches into the individual ensemble members, although often only a single member is available. These diagrams highlight the relative importance of different sources of uncertainty in climate projections, which varies for different time periods, regions and climate variables. See Section 1.4.5 for the definition of the regions used. Further details on data sources and processing are available in the chapter data table (Table 1.SM.1).

ACCEPTED VERSION SUBJECT TO FINAL EDITS

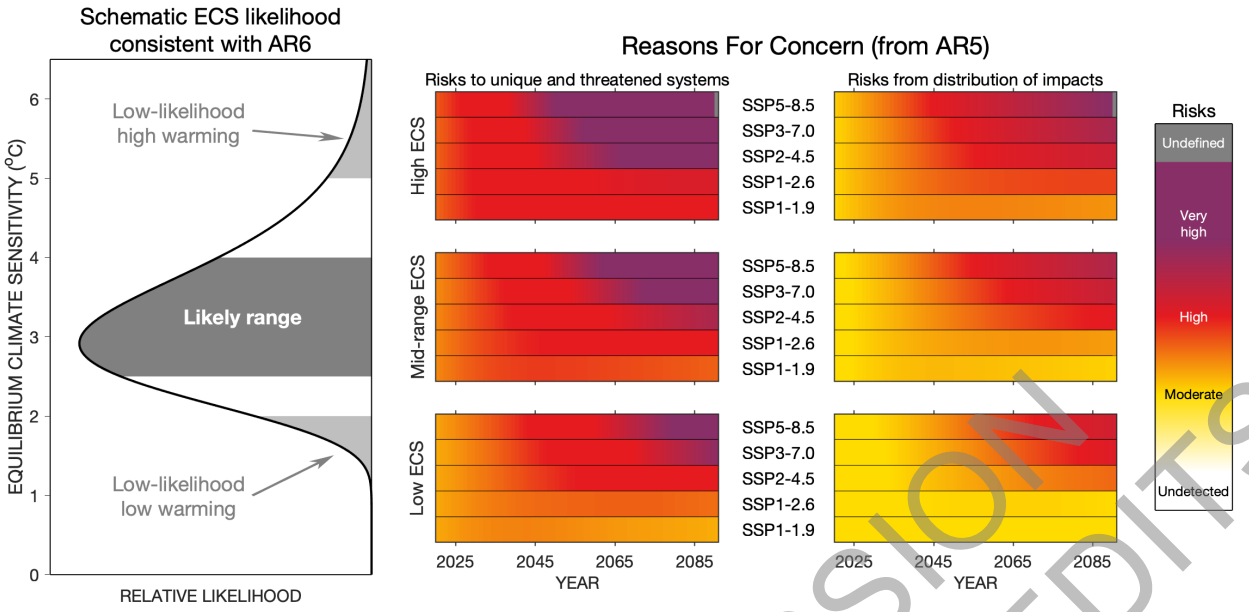


Figure 1.16: Illustrating concepts of low-likelihood scenarios. Left: schematic likelihood distribution consistent with the IPCC AR6 assessments that equilibrium climate sensitivity (ECS) is *likely* in the range 2.5 to 4.0°C, and *very likely* between 2.0 and 5.0°C (Chapter 7). ECS values outside the assessed *very likely* range are designated low-likelihood scenarios in this example (light grey). Middle and right columns: additional risks due to climate change for 2020–2090 using the Reasons For Concern (RFCs, see IPCC, 2014), specifically RFC1 describing the risks to unique and threatened systems and RFC3 describing risks from the distribution of impacts (O'Neill et al., 2017; Zommers et al., 2020). The projected changes of GSAT used are the 95%, median and 5% assessed ranges from Chapter 4 for each SSP (top, middle and bottom); these are designated High ECS, Mid-range ECS and Low ECS respectively. The burning-ember risk spectrum is usually associated with levels of committed GSAT change; instead, this illustration associates the risk spectrum with the GSAT temperature reached in each year from 2020 to 2090. Note that this illustration does not include the vulnerability aspect of each SSP scenario. Further details on data sources and processing are available in the chapter data table (Table 1.SM.1).

ACCEPTED VERSION SUBJECT TO FINAL EDITS

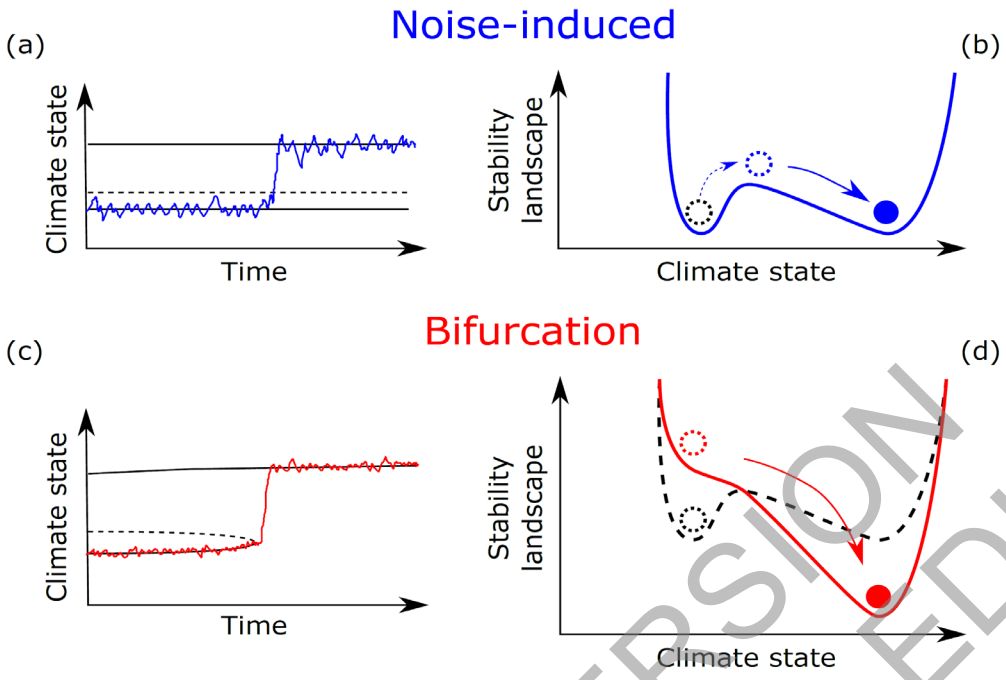
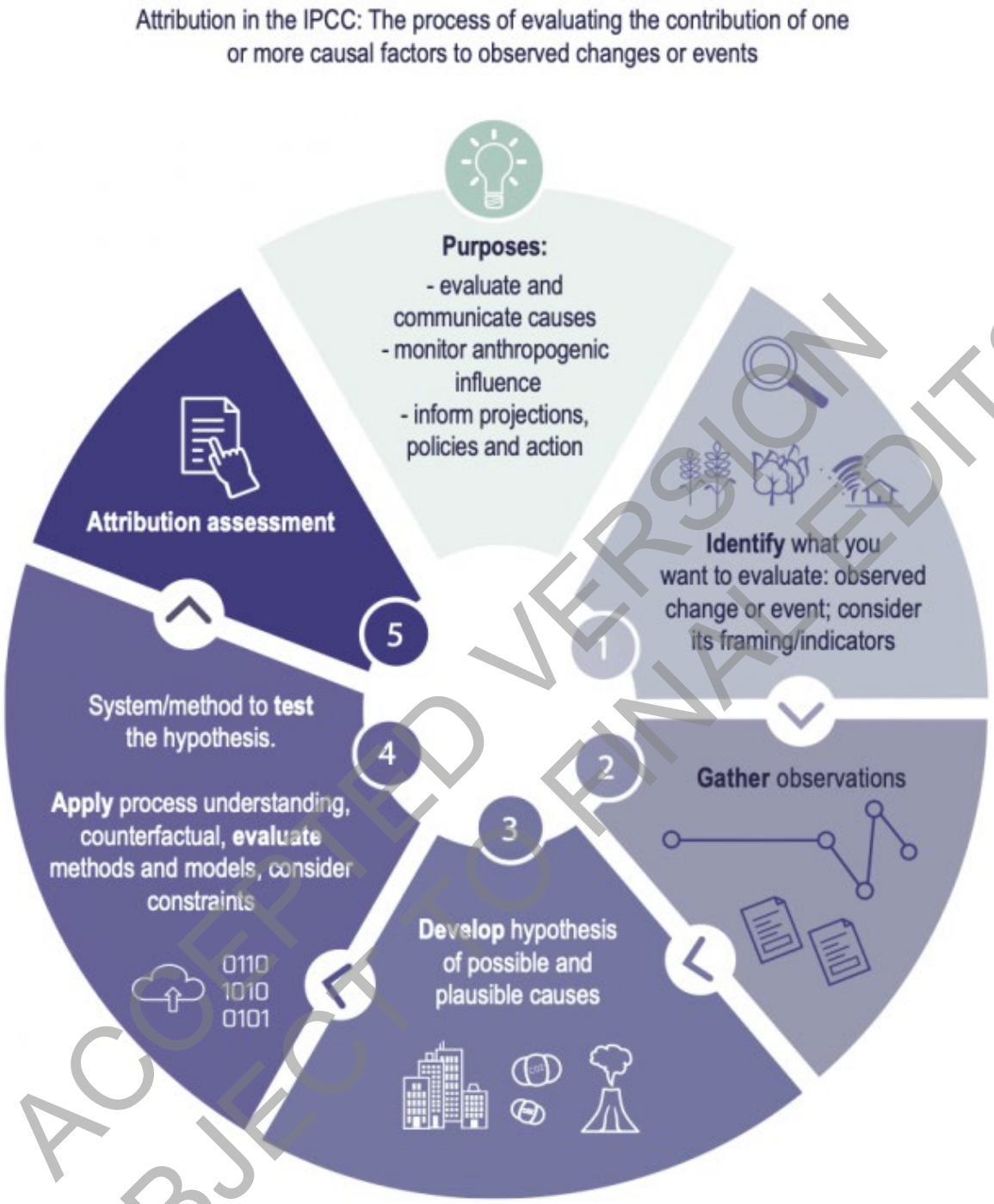


Figure 1.17: Illustration of two types of tipping points: noise-induced (panels a, b) and bifurcation (panels c, d). (a), (c) example time-series (coloured lines) through the tipping point with black solid lines indicating stable climate states (e.g., low or high rainfall) and dashed lines represent the boundary between stable states. (b), (d) stability landscapes provide an intuitive understanding for the different types of tipping point. The valleys represent different climate states the system can occupy, with hill tops separating the stable states. The resilience of a climate state is implied by the depth of the valley. The current state of the system is represented by a ball. Both scenarios assume that the ball starts in the left-hand valley (black dashed lines) and then through different mechanisms dependent on the type of tipping transitions to the right valley (coloured lines). Noise-induced tipping events, for instance drought events causing sudden dieback of the Amazonian rainforest, develop from fluctuations within the system. The stability landscape in this scenario remains fixed and stationary. A series of perturbations in the same direction or one large perturbation are required to force the system over the hill top and into the alternative stable state. Bifurcation tipping events, such as a collapse of the thermohaline circulation in the Atlantic Ocean under climate change, occur when a critical level in the forcing is reached. Here the stability landscape is subjected to a change in shape. Under gradual anthropogenic forcing the left valley begins to shallow and eventually vanishes at the tipping point, forcing the system to transition to the right-hand valley.

ACCEPTED VERSION SUBJECT TO FINAL EDITS



ACCEPTED VERSION SUBJECT TO FINAL EDITS

Cross-Working Group Box: Attribution, Figure 1: **Schematic of the steps to develop an attribution assessment, and the purposes of such assessments.** Methods and systems used to test the attribution hypothesis or theory include model-based fingerprinting, other model-based methods, evidence-based fingerprinting, process-based approaches, empirical or decomposition methods and the use of multiple lines of evidence. Many of the methods are based on the comparison of the observed state of a system to a hypothetical counterfactual world that does not include the driver of interest to help estimate the causes of the observed response.

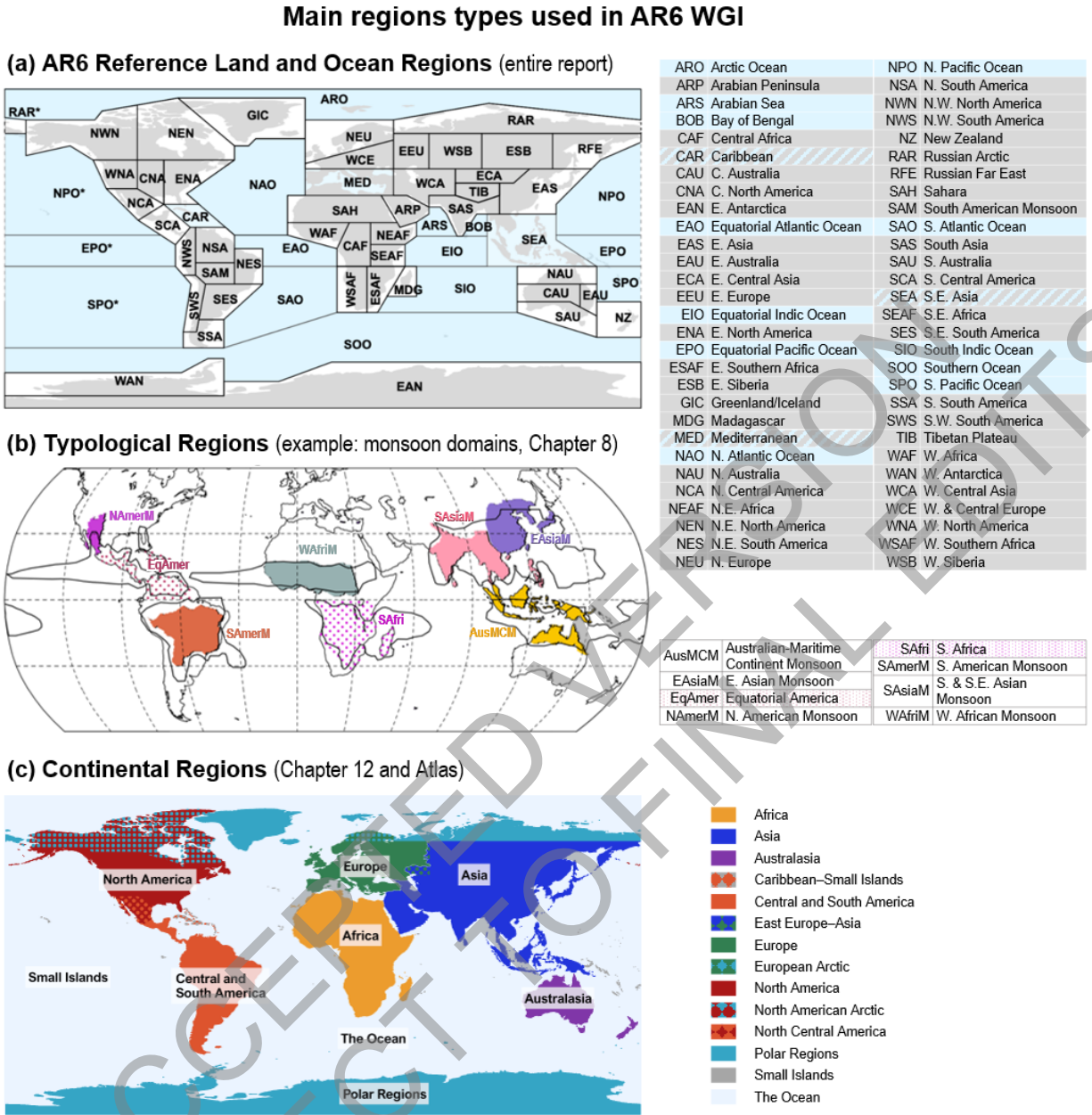


Figure 1.18: Main types of regions used in this report. (a) AR6 WGI Reference Set of Land and Ocean Regions (Iturbide et al., 2020), consisting of 46 land regions and 15 ocean regions, including 3 hybrid regions (CAR, MED, SEA) that are both land and ocean regions. Acronyms are explained on the right of the map. Notice that RAR, SPO, NPO and EPO extend beyond the 180º meridian, therefore appearing at both sides of the map (indicated by dashed lines). A comparison with the previous reference regions of AR5 WGI (IPCC, 7777) is presented in the Atlas. (b) Example of typological regions: monsoon domains adopted in Chapter 8. Acronyms are explained on the right of the map. The black contour lines represent the global monsoon zones, while the coloured regions denote the regional monsoon domains. The two stippled regions (EqAmer and SAfri) do receive seasonal rainfall, but their classification as monsoon regions is still under discussion. (c) Continental Regions used mainly in Chapter 12 and the Atlas. Stippled zones define areas that are assessed in both regions (e.g., the Caribbean is assessed as Small Islands and also as part of Central America). Small Islands are ocean regions containing small islands with consistent climate signals and/or climatological coherence.

ACCEPTED VERSION SUBJECT TO FINAL EDITS

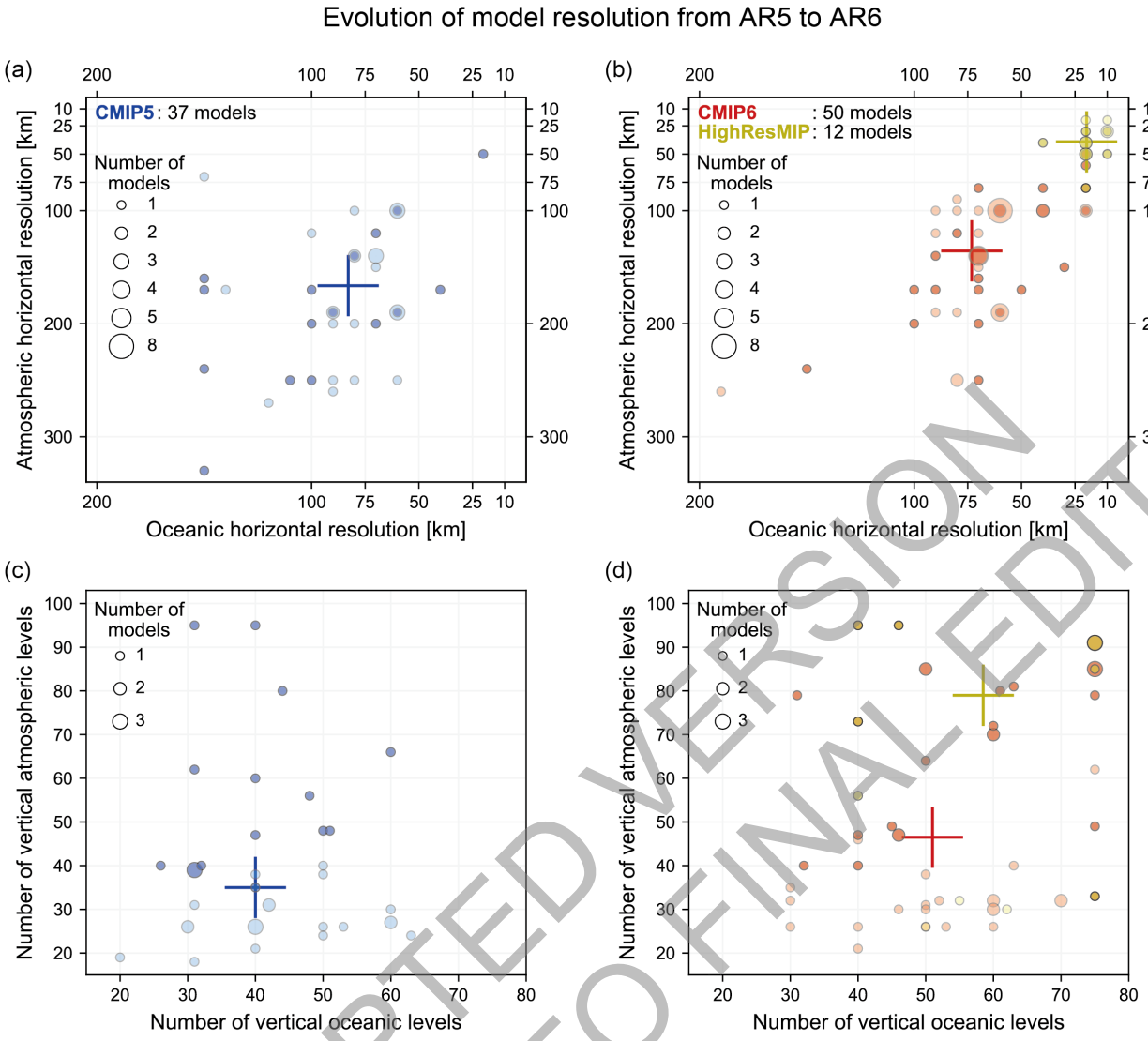


Figure 1.19: Resolution of the atmospheric and oceanic components of global climate models participating in CMIP5, CMIP6, and HighResMIP: (a) (b) horizontal resolution (km), and (c) (d) number of vertical levels. Darker colour circles indicate high-top models (whose top of the atmosphere is above 50 km). The crosses are the median values. These models are documented in Annex II. Note that duplicated models in a modelling group are counted as one entry when their horizontal and vertical resolutions are same. For HighResMIP, one atmosphere-ocean coupled model with the highest resolution from each modelling group is used. The horizontal resolution (rounded to 10km) is the square root of the number of grid points divided by the surface area of the Earth, or the number of surface ocean grid points divided by the area of the ocean surface, for the atmosphere and ocean respectively.

ACCEPTED VERSION SUBJECT TO FINAL EDITS

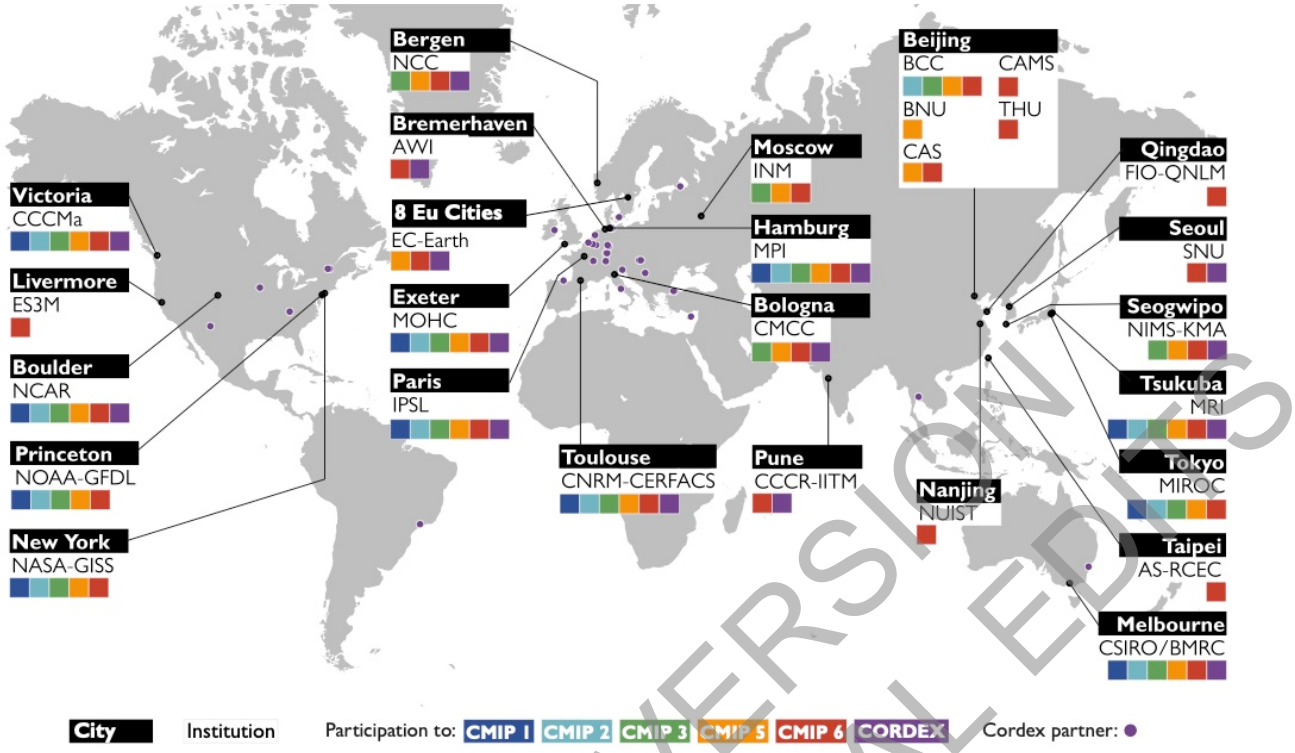


Figure 1.20: A world map showing the increased diversity of modelling centres contributing to CMIP and CORDEX. Climate models are often developed by international consortia. EC-Earth is shown as an example (involving SMHI, Sweden; KNMI, The Netherlands; DMI, Denmark; AEMET, Spain; Met Éireann, Ireland; CNR-ISAC, Italy; Instituto de Meteorologia, Portugal; FMI, Finland), but there are too many such collaborations to display all of them on this map. More complete information about institutions contributing to CORDEX and CMIP6 is found in Annex II.

ACCEPTED VERSION SUBJECT TO FINAL EDITS

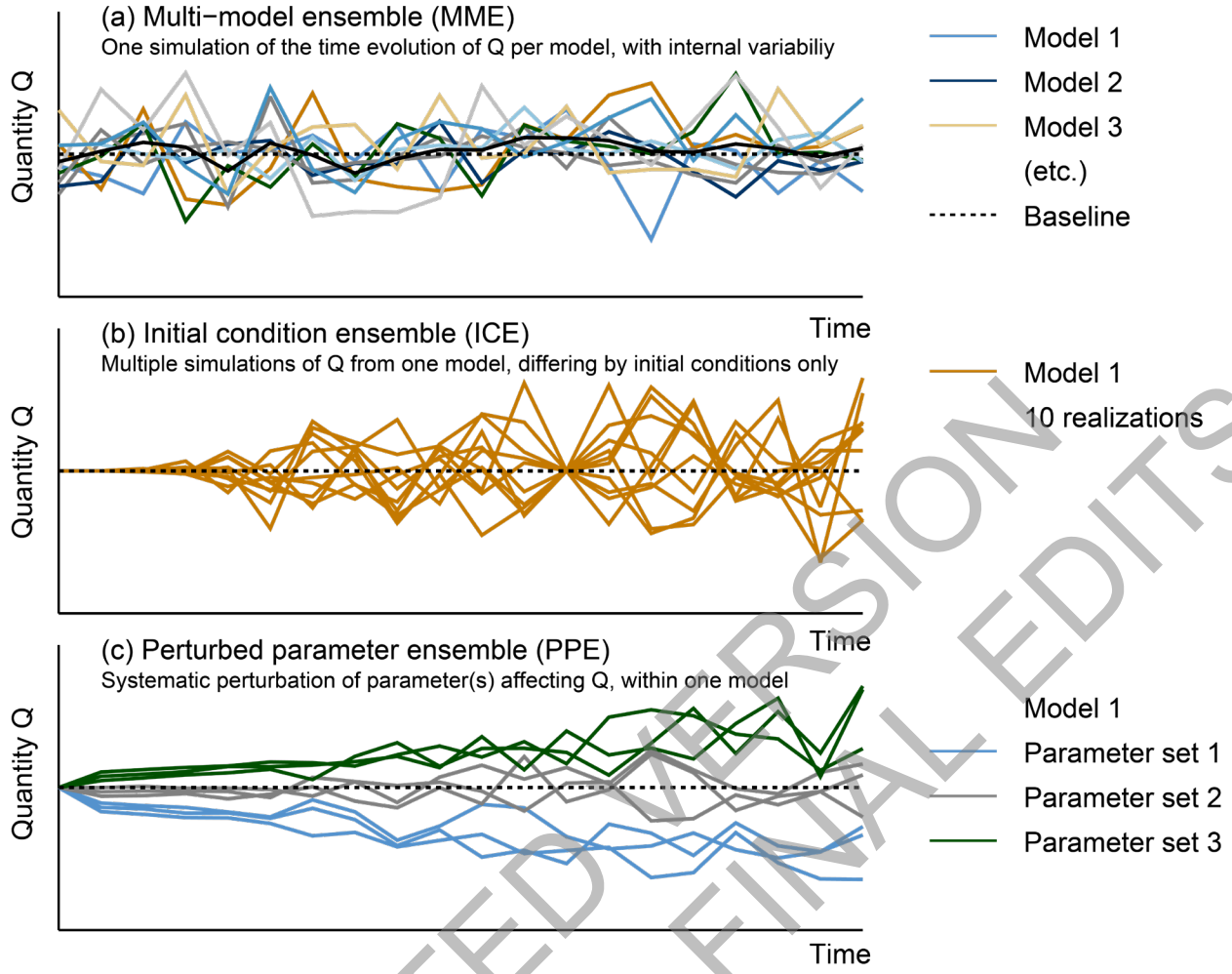


Figure 1.21: Illustration of common types of model ensemble, simulating the time evolution of a quantity Q (such as global mean surface temperature). (a) Multi-model ensemble, where each model has its own realization of the processes affecting Q, and its own internal variability around the baseline value (dashed line). The multi-model mean (black) is commonly taken as the ensemble average. (b) Initial condition ensemble, where several realizations from a single model are compared. These differ only by minute ('micro') perturbations to the initial conditions of the simulation, such that over time, internal variability will progress differently in each ensemble member. (c) Perturbed physics ensemble, which also compares realizations from a single model, but where one or more internal parameters that may affect the simulations of Q are systematically changed to allow for a quantification of the impact of those quantities on the model results. Additionally, each parameter set may be taken as the starting point for an initial condition ensemble. In this figure, each set has three ensemble members.

ACCEPTED VERSION SUBJECT TO FINAL EDITS

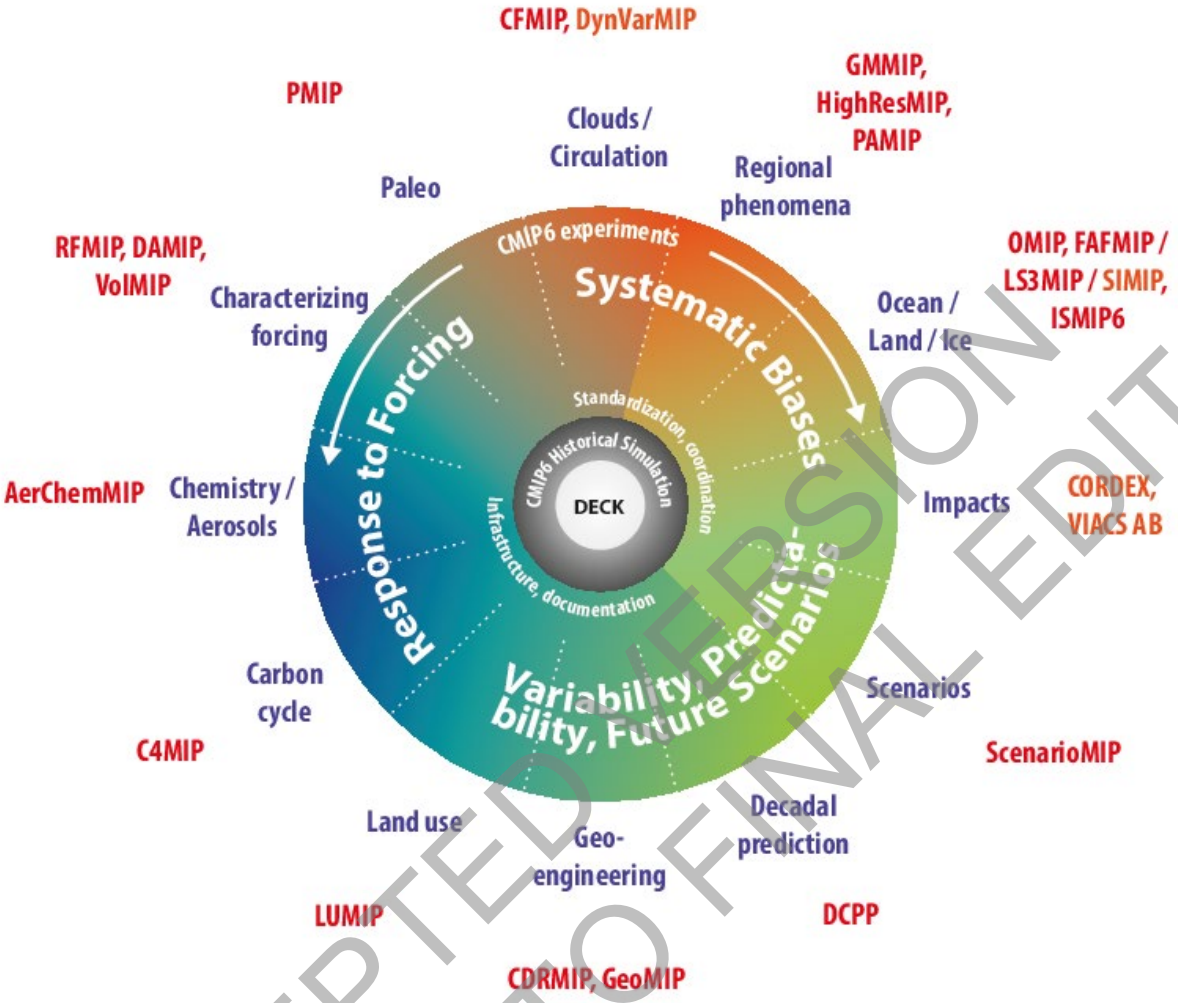


Figure 1.22: Structure of CMIP6, the 6th phase of the Coupled Model Intercomparison Project. The centre shows the common DECK (Diagnostic, Evaluation and Characterization of Klima) and historical experiments that all participating models must perform. The outer circles show the topics covered by the endorsed (blue) and other MIPs (red). See Table 1.3 for explanation of the MIP acronyms. (expanded from Eyring et al., 2016).

ACCEPTED VERSION SUBJECT TO FINAL EDITS

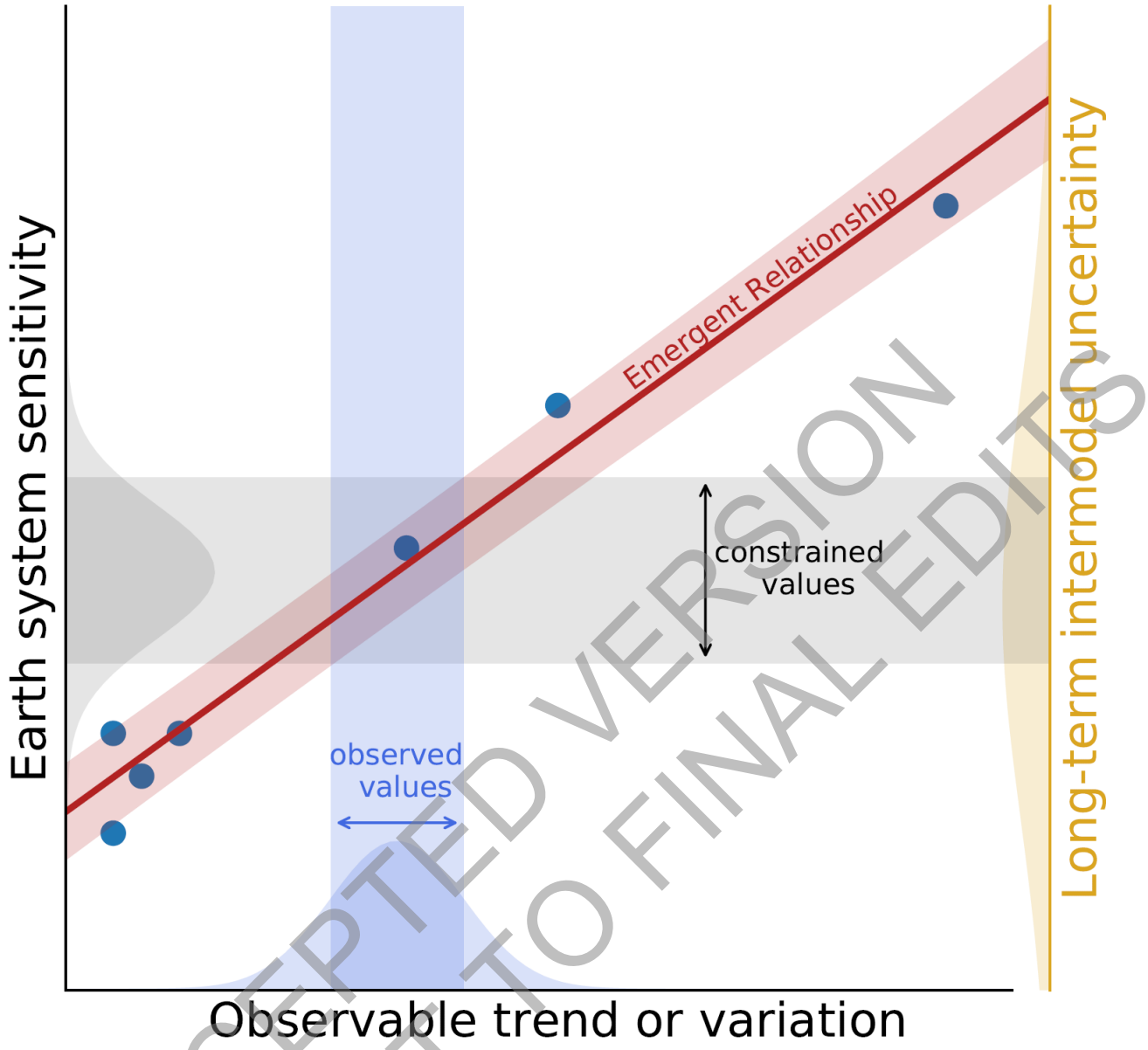


Figure 1.23: The principle of emergent constraints. An ensemble of models (blue dots) defines a relationship between an observable, mean, trend or variation in the climate (x-axis) and an uncertain projection, climate sensitivity or feedback (y-axis). An observation of the x-axis variable can then be combined with the model-derived relationship to provide a tighter estimate of the climate projection, sensitivity or feedback on the y-axis (adapted from Eyring et al. 2019).

ACCEPTED VERSION SUBJECT TO FINAL EDITS

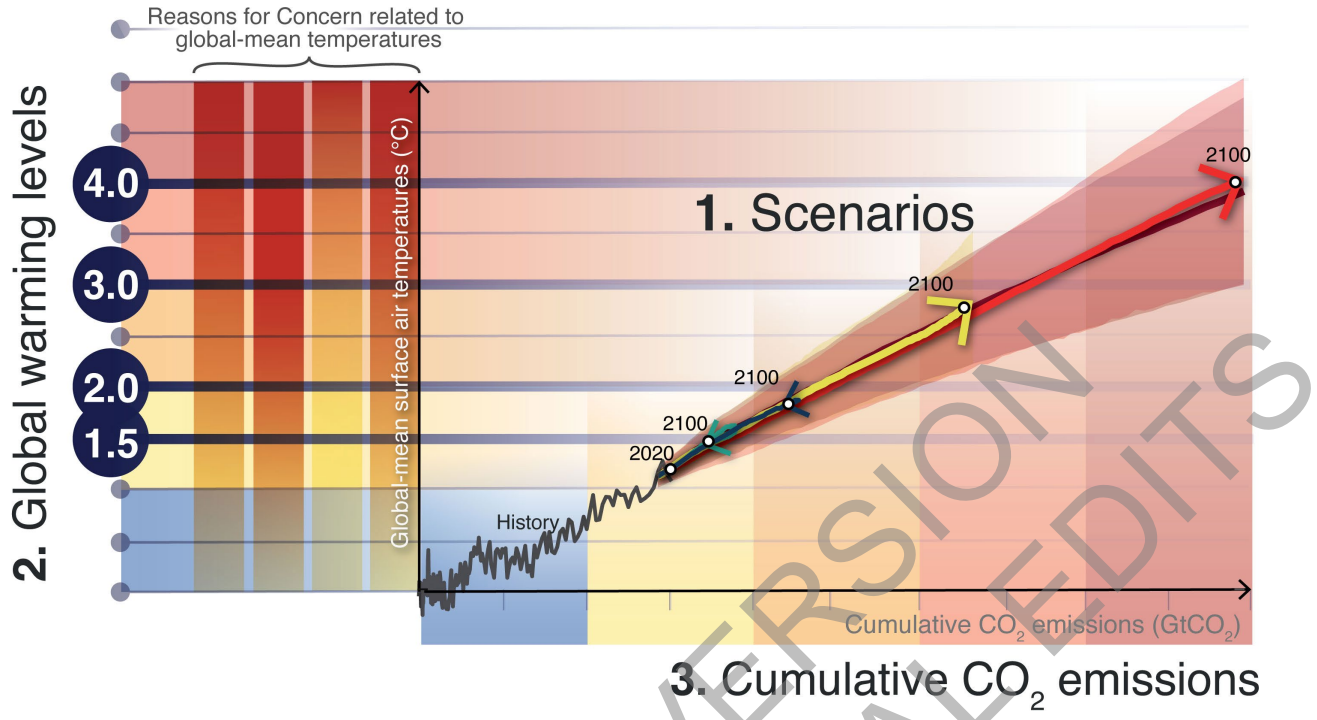


Figure 1.24: The Dimensions of Integration across Chapters and Working Groups in the IPCC AR6 assessment. This report adopts three explicit dimensions of integration to integrate knowledge across chapters and Working Groups. The first dimension is scenarios, the second dimension is global-mean warming levels relative to pre-industrial levels and the third dimension is cumulative CO_2 emissions. For the scenarios, illustrative 2100 end-points are also indicated (white circles). Further details on data sources and processing are available in the chapter data table (Table 1.SM.1).

ACCEPTED VERSION SUBJECT TO FINAL EDITS

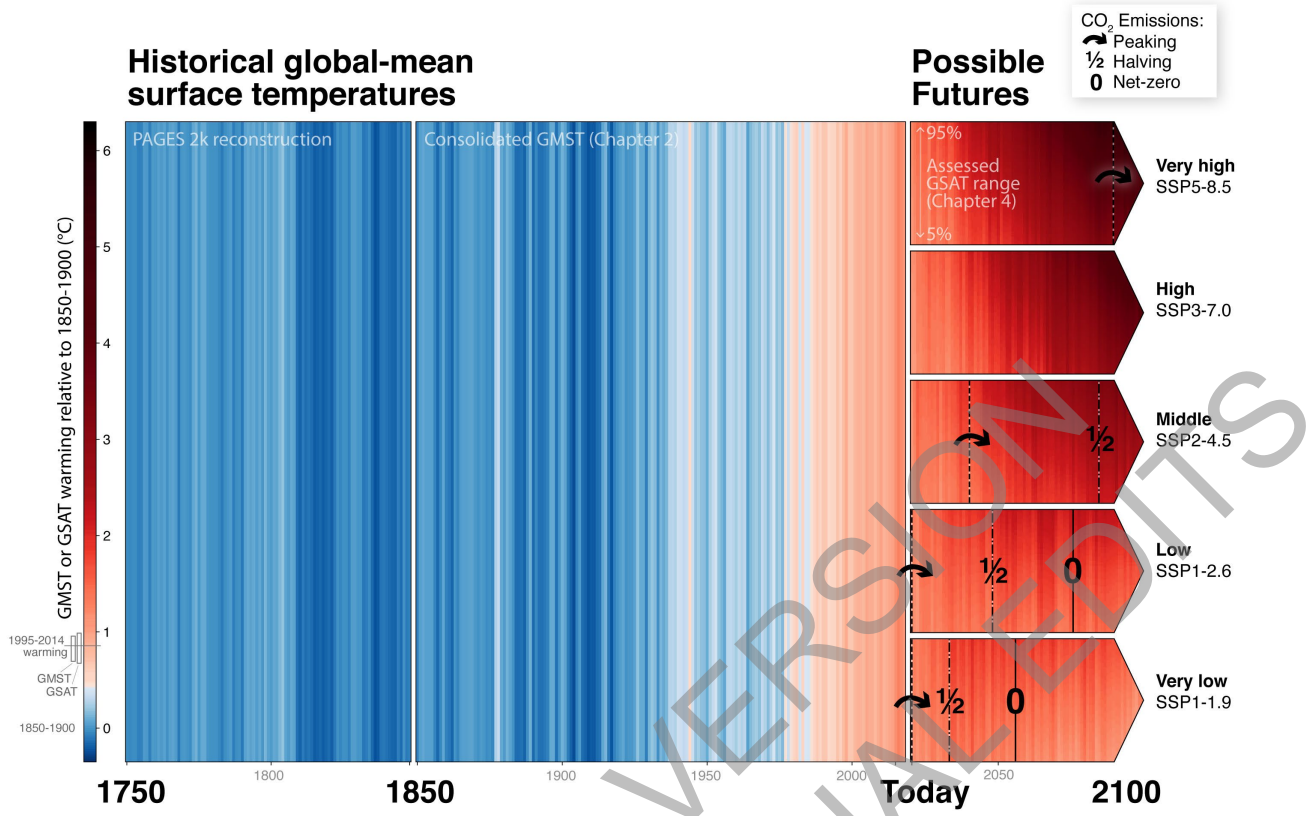


Figure 1.25: Global mean surface air temperature (GSAT) illustrated as warming stripes from blue (cold) to red (warm) over three different time periods. From 1750 to 1850 based on PAGES 2K reconstructions (2017, 2019); from 1850 to 2018 showing the composite GSAT time series assessed in Chapter 2; and from 2020 onwards using the assessed GSAT projections for each Shared Socio-economic Pathway (SSP) (from Chapter 4). For the projections, the upper end of each arrow aligns with colour corresponding to the 95th percentile of the projected temperatures and the lower end aligns with the colour corresponding to the 5th percentile of the projected temperature range. Projected temperatures are shown for five scenarios from 'very low' SSP1-1.9 to 'very high' SSP5-8.5 (see Cross-Chapter Box 1.4 for more details on the scenarios). For illustrative purposes, natural variability has been added from a single CMIP6 Earth system model (MRI ESM2). The points in time when total CO_2 emissions peak, reach halved levels of the peak and reach net-zero emissions are indicated with arrows, '½' and '0' marks, respectively. Further details on data sources and processing are available in the chapter data table (Table 1.SM.1).

ACCEPTED VERSION SUBJECT TO FINAL EDITS

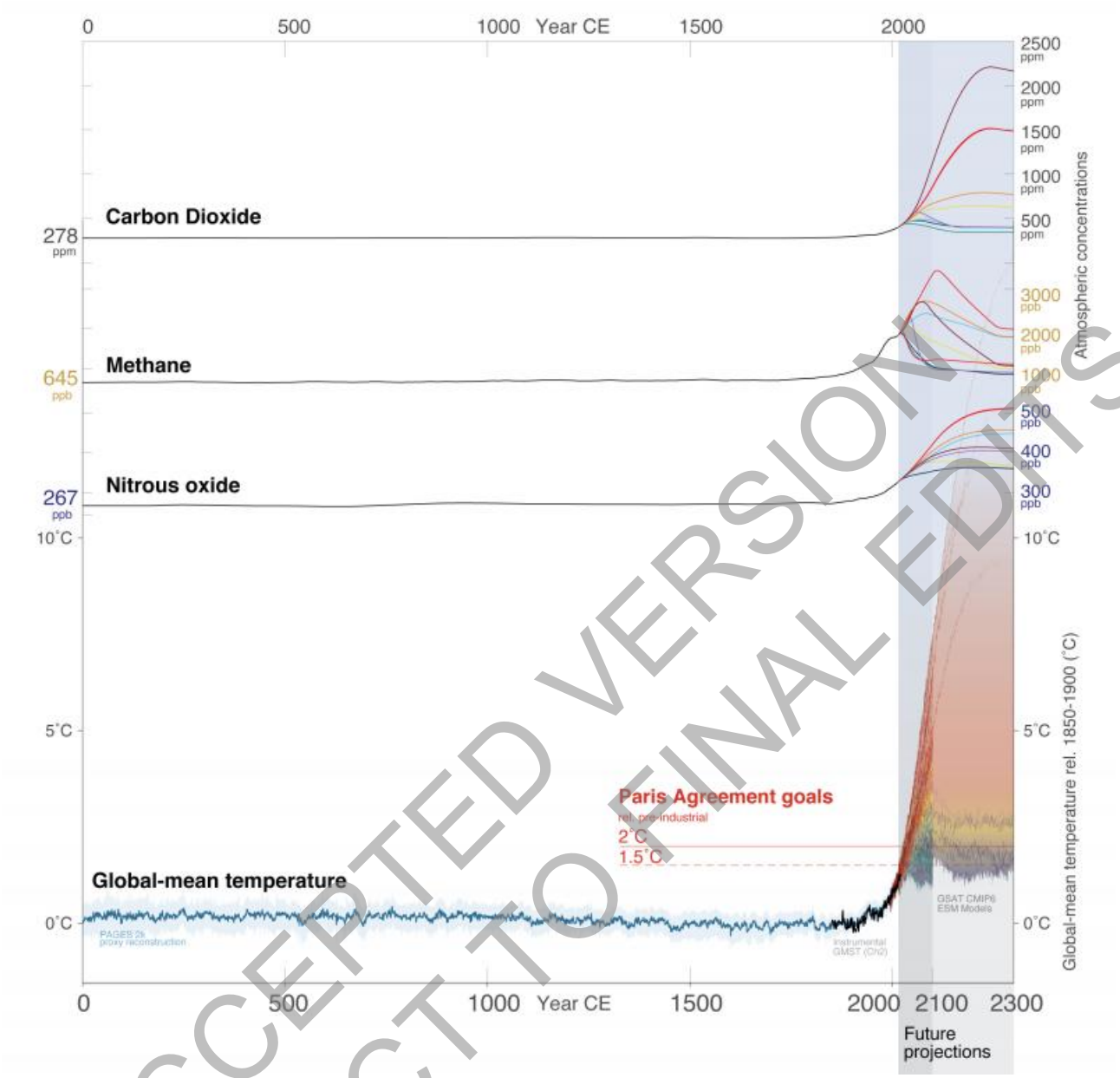
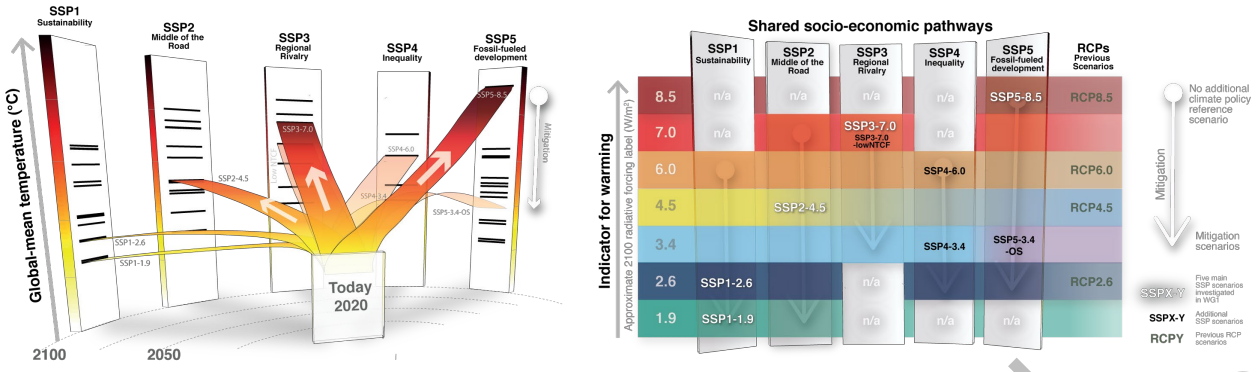


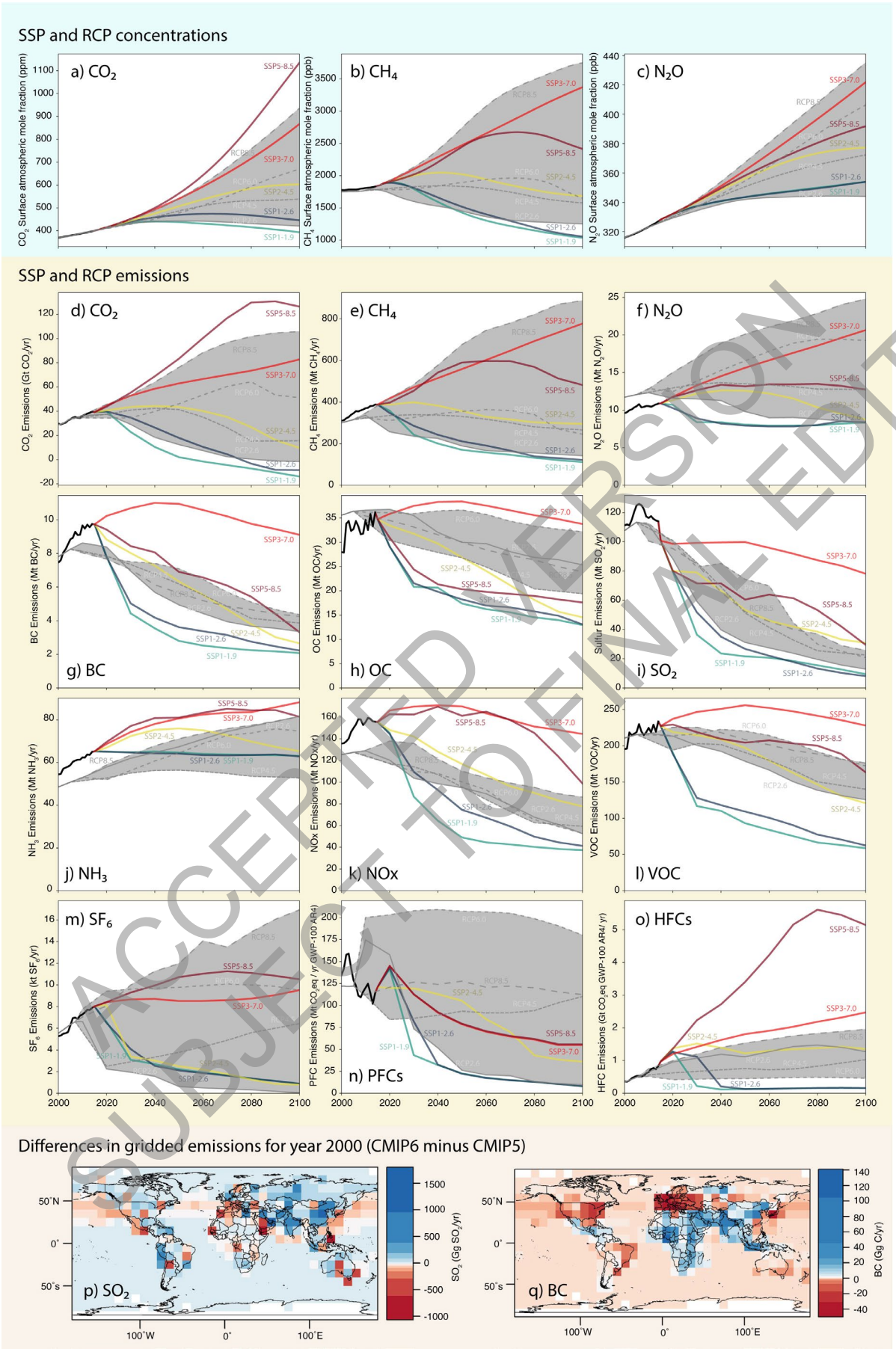
Figure 1.26: Historical and projected future concentrations of CO_2, CH_4 and N_2O and global mean temperatures (GMST). GMST temperature reconstructions over the last 2000 years were compiled by the PAGES 2k Consortium (2017, 2019) (grey line, with 95% uncertainty range), joined by historical GMST timeseries assessed in Chapter 2 (black line) – both referenced against the 1850-1900 period. Future GSAT temperature projections are from CMIP6 ESM models across all concentration-driven SSP scenario projections (Chapter 4). The discontinuity around year 2100 for CMIP6 temperature projections results from the fact that not all ESM models ran each scenario past 2100. The grey vertical band indicates the future 2015-2300 period. The concentrations used to drive CMIP6 Earth System Models are derived from ice core, firn and instrumental datasets (Meinshausen et al., 2017) and projected using an emulator (Cross-Chapter Box 7.1 in Chapter 7; Meinshausen et al., 2020). The colours of the lines indicate the SSP scenarios used in this report (see Cross-Chapter Box 1.4, Figure 1). Further details on data sources and processing are available in the chapter data table (Table 1.SM.1).

ACCEPTED VERSION SUBJECT TO FINAL EDITS



Cross-Chapter Box 1.4, Figure 1: The SSP scenarios used in this report, their indicative temperature evolution and radiative forcing categorization, and the five socio-economic storylines upon which they are built. The core set of scenarios used in this report, i.e., SSP1-1.9, SSP1-2.6, SSP2-4.5, SSP3-7.0 and SSP5-8.5, is shown together with an additional four SSPs that are part of ScenarioMIP, as well as previous RCP scenarios. In the left panel, the indicative temperature evolution is shown (adapted from Meinshausen et al., 2020). The black stripes on the respective scenario family panels on the left side indicate a larger set of IAM-based SSP scenarios that span the scenario range more fully, but are not used in this report. The SSP-radiative forcing matrix is shown on the right, with the SSP socioeconomic narratives shown as columns and the indicative radiative forcing categorisation by 2100 shown as rows. Note that the descriptive labels for the five SSP narratives refer mainly to the reference scenario futures without additional climate policies. For example, SSP5 can accommodate strong mitigation scenarios leading to net-zero emissions; these do not match a 'fossil-fueled development' label. Further details on data sources and processing are available in the chapter data table (Table 1.SM.1).

ACCEPTED VERSION SUBJECT TO FINAL EDITS



ACCEPTED VERSION SUBJECT TO FINAL EDITS

Cross-Chapter Box 1.4, Figure 2: Comparison between the Shared Socio-economic Pathways (SSP) scenarios and the Representative Concentration Pathway (RCP) scenarios in terms of their CO_2, CH_4 and N_2O atmospheric concentrations (panels a-c), and their global emissions (panels d-o). Also shown are gridded emission differences for sulfur (panel p) and black carbon (panel q) for the year 2000 between the input emission datasets that underpinned the CMIP5 and CMIP6 model intercomparisons. Historical emission estimates are provided in black in panels d to o. The range of concentrations and emissions investigated under the RCP pathways is grey shaded. Panels p and q adapted from Figure 7 in Hoesly et al. (2018). Further details on data sources and processing are available in the chapter data table (Table 1.SM.1).

ACCEPTED VERSION
SUBJECT TO FINAL EDITS

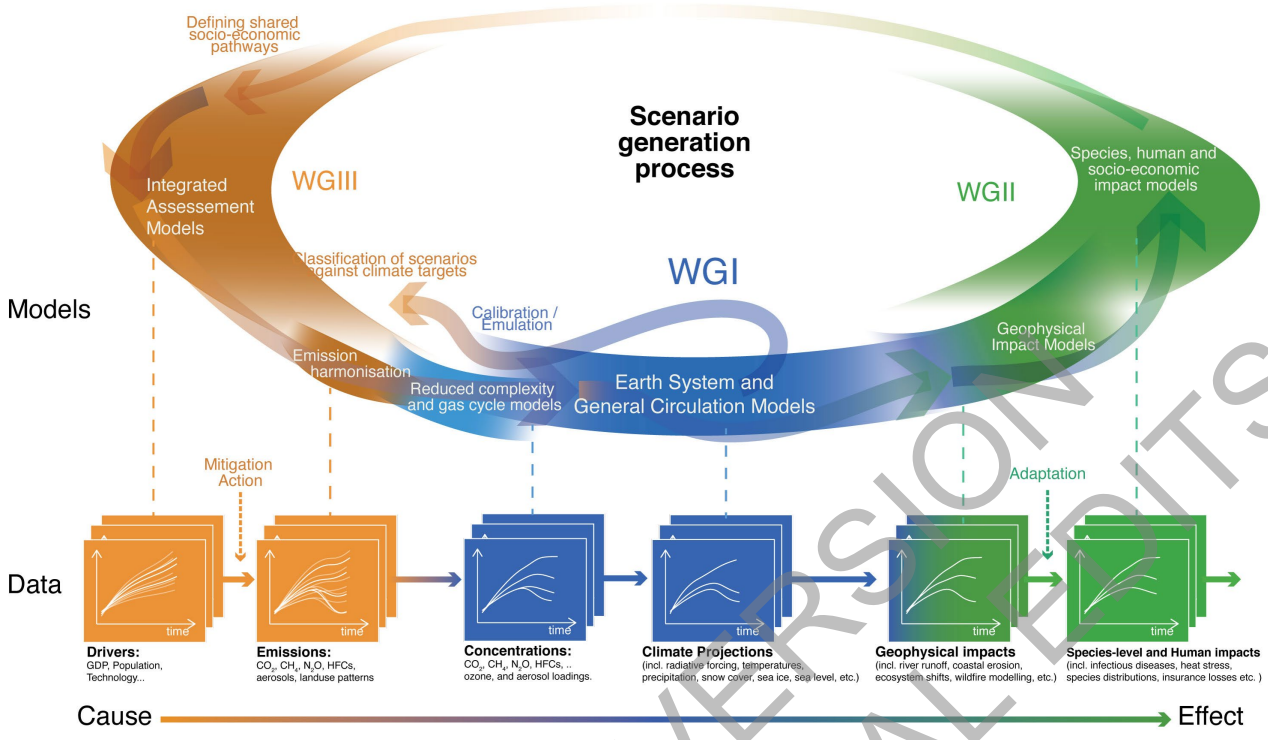
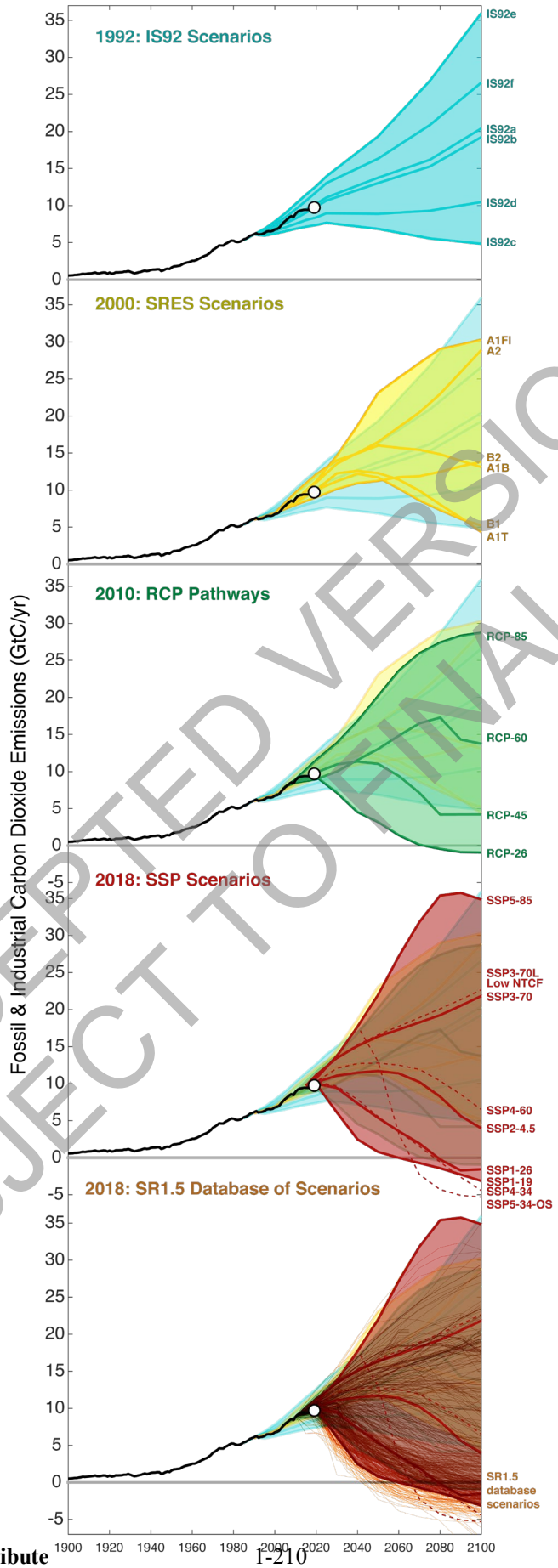


Figure 1.27: A simplified illustration of the scenario generation process that involves the scientific communities represented in the three IPCC Working Groups. The circular set of arrows at the top indicate the main set of models and workflows used in that scenario generation process, with the lower level indicating the datasets.

ACCEPTED VERSION SUBJECT TO FINAL EDITS



ACCEPTED VERSION
SUBJECT TO FINAL EDITS

Figure 1.28: Comparison of the range of fossil and industrial CO_2 emissions from scenarios used in previous assessments up to AR6. Previous assessments are the IS92 scenarios from 1992 (top panel), the Special Report on Emissions Scenarios (SRES) scenarios from the year 2000 (second panel), the Representative Concentration Pathway (RCP) scenarios designed around 2010 (third panel) and the Shared Socio-economic Pathways (SSP) scenarios (second bottom panel). In addition, historical emissions are shown (black line) (Chapter 5, Figure 5.5); a more complete set of scenarios is assessed in SR1.5 (bottom panel) (Huppmann et al., 2018). Further details on data sources and processing are available in the chapter data table (Table 1.SM.1).

ACCEPTED VERSION
SUBJECT TO FINAL EDITS

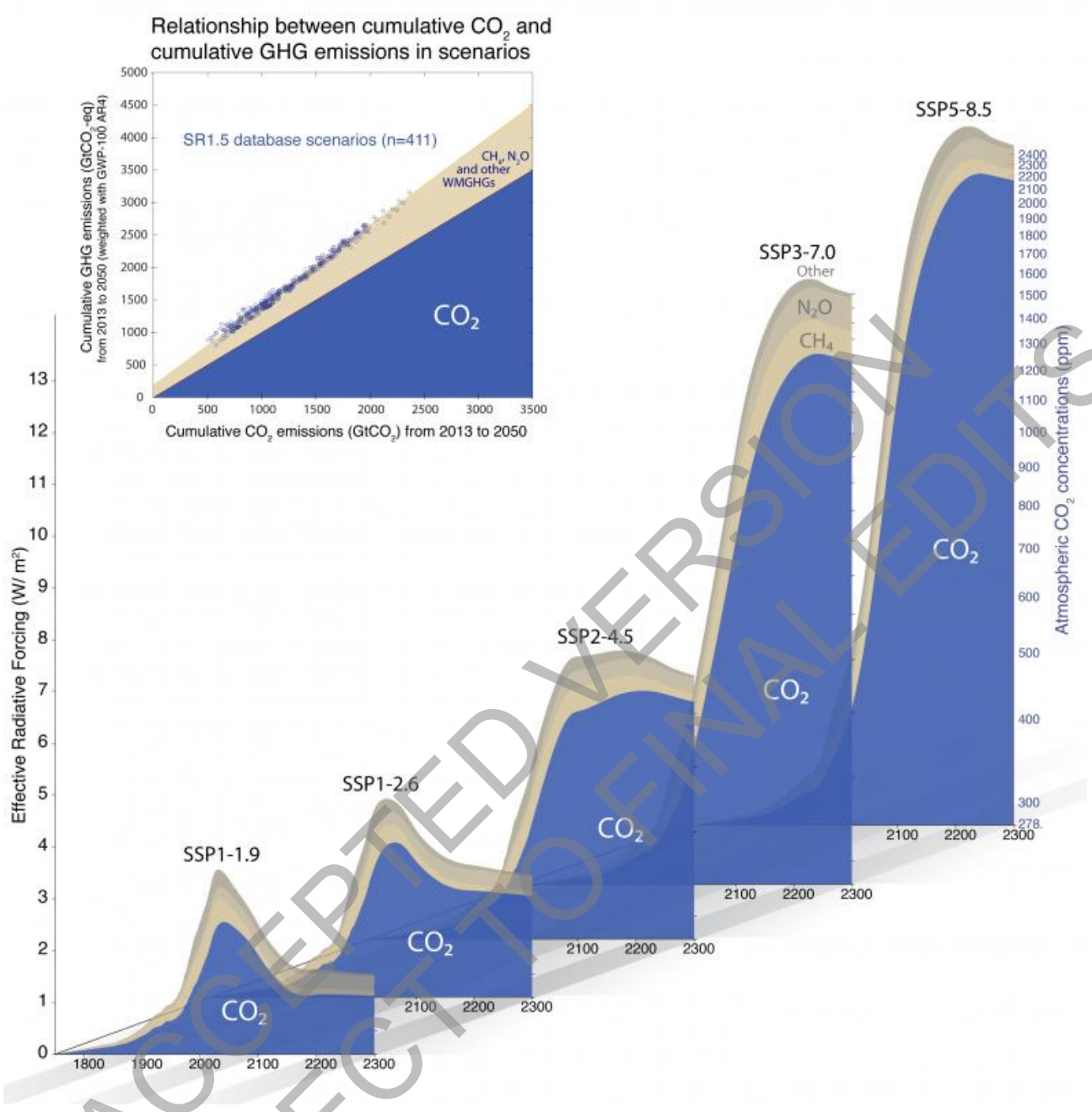
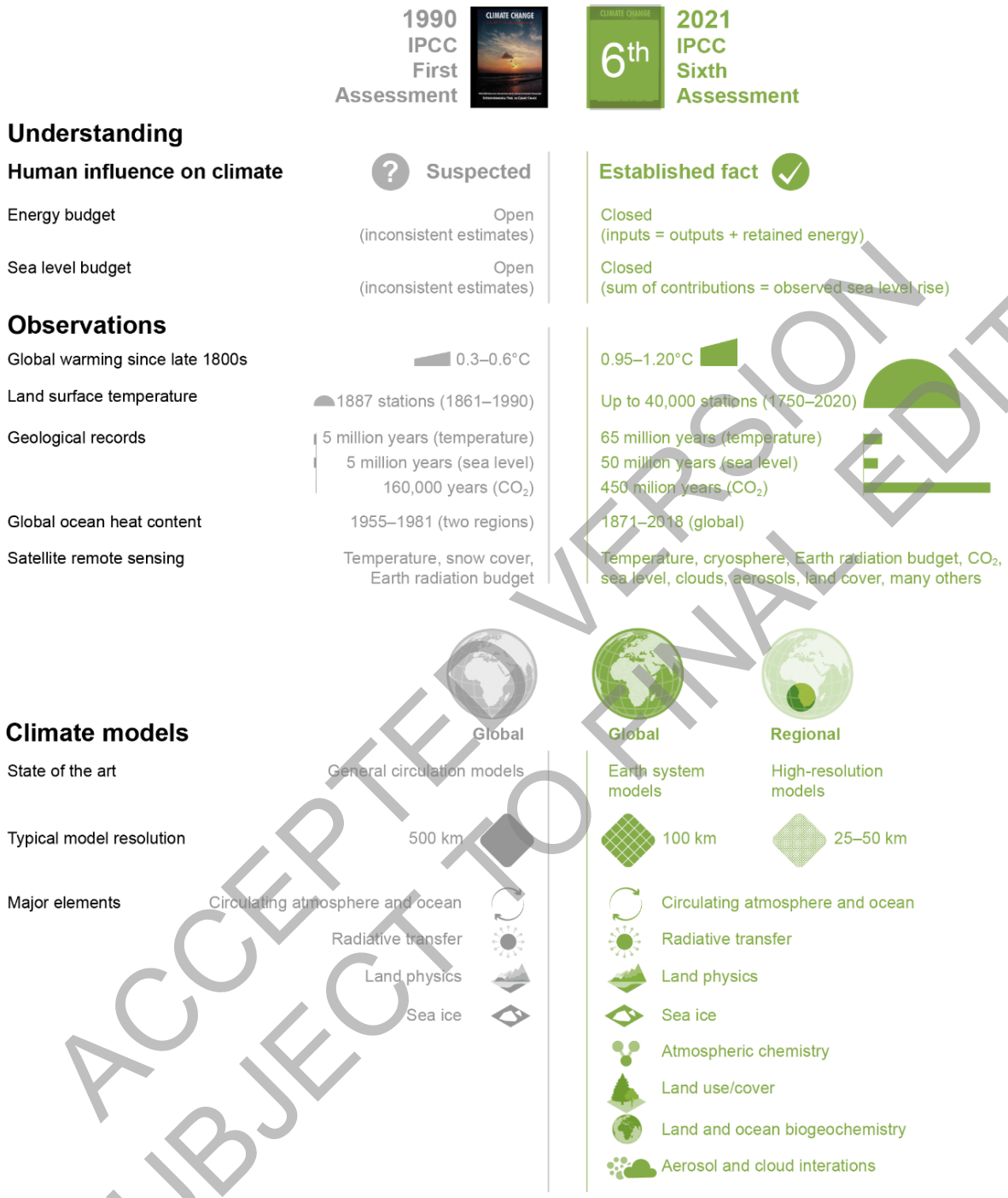


Figure 1.29: The role of CO_2 in driving future climate change in comparison to other greenhouse gases (GHGs). The GHGs included here are CH_4, N_2O, and 40 other long-lived, well-mixed GHGs. The blue shaded area indicates the approximate forcing exerted by CO_2 in Shared Socio-economic Pathways (SSP) scenarios, ranging from very low SSP1-1.9 to very high SSP5-8.5 (Chapter 7). The CO_2 concentrations under the SSP1-1.9 scenarios reach approximately 350 ppm after 2150, while those of SSP5-8.5 exceed 2000 ppm CO_2 in the longer term (through year 2300). Similarly to the dominant radiative forcing share at each point in time (lower area plots), cumulative GWP-100-weighted GHG emissions happen to be closely correlated with cumulative CO_2 emissions, allowing policymakers to make use of the carbon budget concept in a policy context with multi-gas GHG baskets as it exhibits relatively low variation across scenarios with similar cumulative emissions until 2050 (inset panel). Further details on data sources and processing are available in the chapter data table (Table 1.SM.1).

ACCEPTED VERSION SUBJECT TO FINAL EDITS

FAQ 1.1: **Do we understand climate change better than when the IPCC started?**

Yes. Between 1990 and 2021, observations, models and climate understanding improved, while the dominant role of human influence in global warming was confirmed.

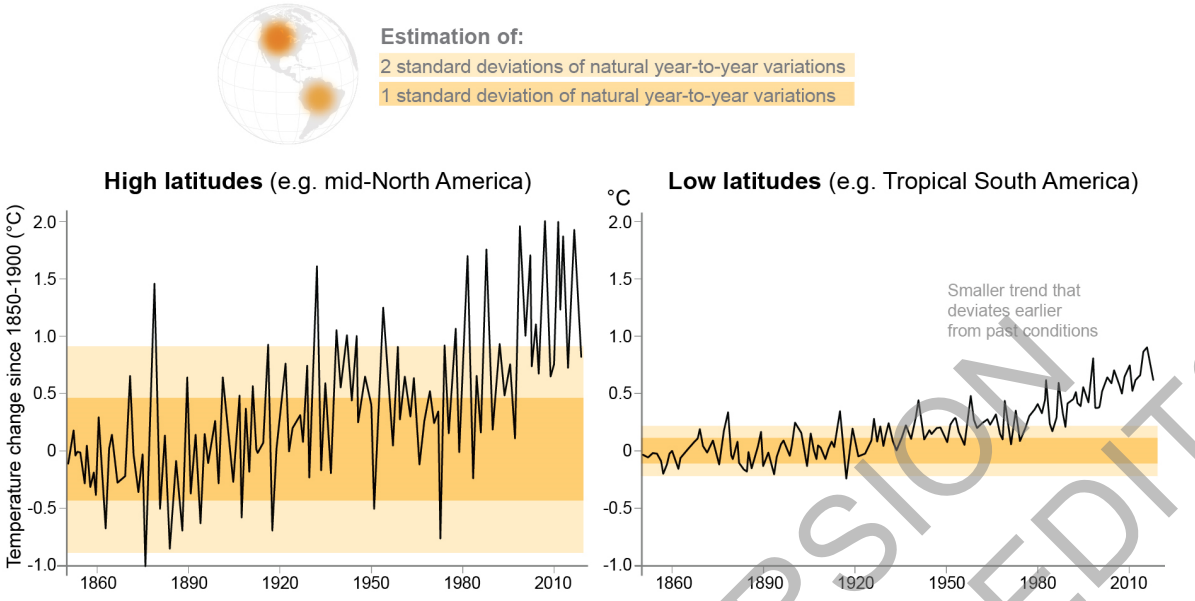


FAQ 1.1, Figure 1: Sample elements of climate understanding, observations and models as assessed in the IPCC First Assessment Report (1990) and Sixth Assessment Report (2021). Many other advances since 1990, such as key aspects of theoretical understanding, geological records and attribution of change to human influence, are not included in this figure because they are not readily represented in this simple format. Fuller explications of the history of climate knowledge are available in the introductory chapters of the IPCC fourth and sixth Assessment Reports.

ACCEPTED VERSION SUBJECT TO FINAL EDITS

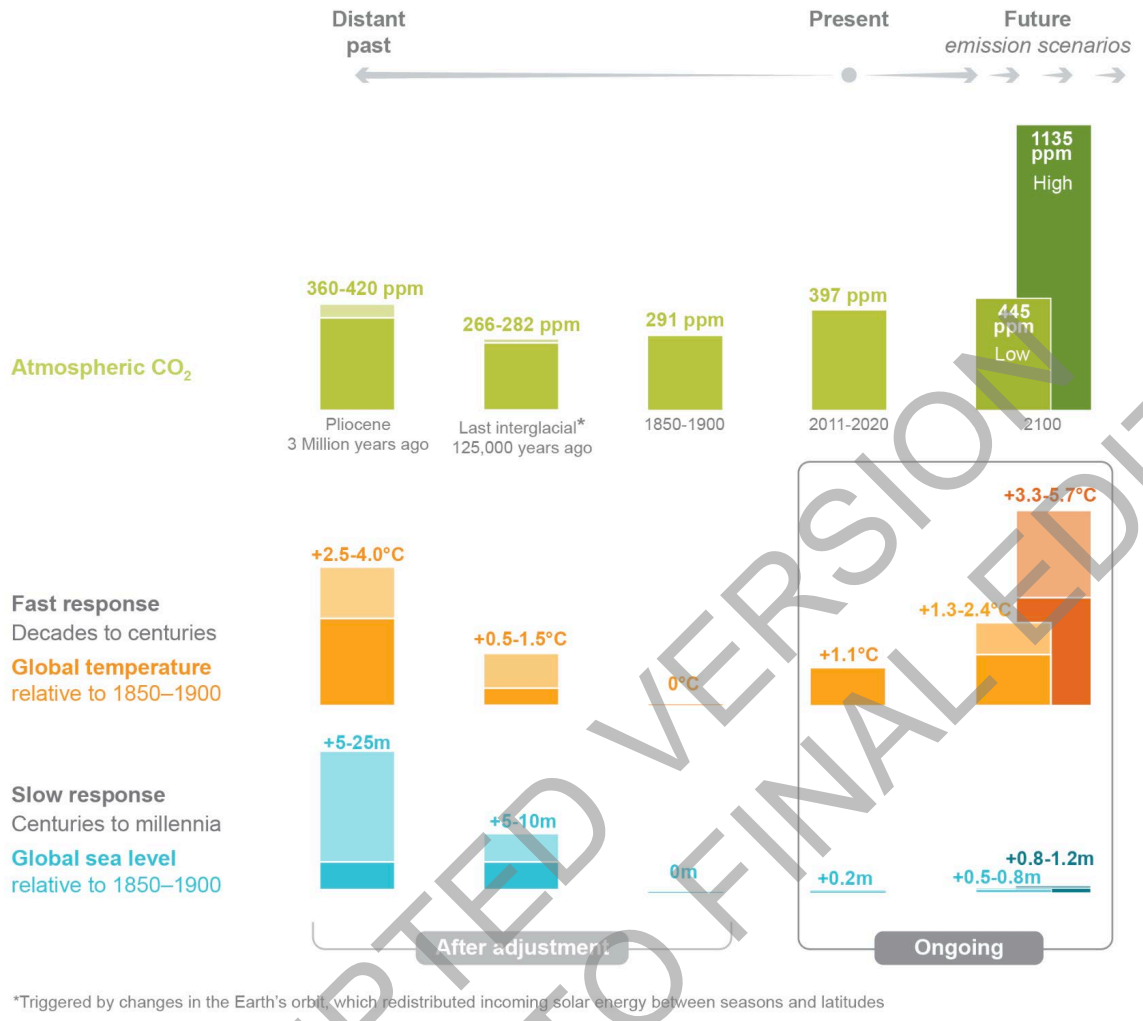
FAQ 1.2: **Where is climate change most apparent?**

Temperature changes are most apparent in regions with smaller natural variations.



FAQ 1.2, Figure 1: **Observed variations in regional temperatures since 1850** (data from Berkeley Earth). Regions in high latitudes, such as mid-North America (40ºN–64ºN, 140ºW–60ºW, left), have warmed by a larger amount than regions at lower latitudes, such as Tropical South America (10ºS–10ºN, 84ºW–16ºW, right), but the natural variations are also much larger at high latitudes (darker and lighter shading represents 1 and 2 standard deviations, respectively, of natural year-to-year variations). The signal of observed temperature change emerged earlier in Tropical South America than mid-North America even though the changes were of a smaller magnitude. (Note that those regions were chosen because of the longer length of their observational record, see Figure 1.14 for more regions).

ACCEPTED VERSION
SUBJECT TO FINAL EDITS



FAQ 1.3, Figure 1: **Comparison of past, present and future.** Schematic of atmospheric carbon dioxide concentrations, global temperature, and global sea level during previous warm periods as compared to 1850-1900, present-day (2011-2020), and future (2100) climate change scenarios corresponding to low-emissions scenarios (SSP1-2.6; lighter colour bars) and very high emissions scenarios (SSP5-8.5; darker colour bars).

ACCEPTED VERSION SUBJECT TO FINAL EDITS

Chapter 1: Framing, context, methods - Supplementary Material

Coordinating Lead Authors:
Deliang Chen (Sweden), Maisa Rojas (Chile), Bjørn H. Samset (Norway)

Lead Authors:
Kim Cobb (United States of America), Aida Diongue-Niang (Senegal), Paul Edwards (United States of America), Seita Emori (Japan), Sergio Henrique Faria (Spain/Brazil), Ed Hawkins (United Kingdom), Pandora Hope (Australia), Philippe Huybrechts (Belgium), Malte Meinshausen (Australia/Germany), Sawsan Khair Elsied Abdel Rahim Mustafa (Sudan), Gian-Kasper Plattner (Switzerland), Anne Marie Treguier (France)

Contributing Authors:
Hui-Wen Lai (Sweden), Tania Villaseñor (Chile), Rondrotiana Barimalala (South Africa/Madagascar), Rosario Carmona (Chile), Peter M. Cox (United KingdomK), Wolfgang Cramer (France/Germany), Francisco J. Doblas-Reyes (Spain), Hans Dolman (The Netherlands), Alessandro Dosio (Italy), Veronika Eyring (Germany), Gregory M. Flato (Canada), Piers Forster (United Kingdom), David Frame (New Zealand), Katja Frieler (Germany), Jan S. Fuglestvedt (Norway), John C. Fyfe (Canada), Mathias Garschagen (Germany), Joelle Gergis (Australia), Nathan P. Gillett (Canada), Michael Grose (Australia), Eric Guilyardi (France), Celine Guivarch (France), Susan Hassol (United States of America), Zeke Hausfather (United States of America), Hans Hersbach (United Kingdom/The Netherlands), Helene T. Hewitt (United Kingdom), Mark Howden (Australia), Christian Huggel (Switzerland), Margot Hurlbert (Canada), Christopher Jones (United Kingdom), Richard G. Jones (United Kingdom), Darrell S. Kaufman (United States of America), Robert E. Kopp (United States of America), Anthony Leiserowitz (United States of America), Robert J. Lempert (United States of America), Jared Lewis (Australia/New Zealand), Hong Liao (China), Nikki Lovenduski (United States of America), Marianne T. Lund (Norway), Katharine Mach (United States of America), Douglas Maraun (Austria/Germany), Jochem Marotzke (Germany), Jan Minx (Germany), Zebedee R.J. Nicholls (Australia), Brian C. O'Neill (United States of America), M. Giselle Ogaz (Chile), Friederike Otto (United Kingdom /Germany), Wendy Parker (United Kingdom), Camille Parmesan (France, United Kingdom/United States of America), Warren Pearce (United Kingdom), Roque Pedace (Argentina), Andy Reisinger (New Zealand), James Renwick (New Zealand), Keywan Riahi (Austria), Paul Ritchie (United Kingdom), Joeri Rogelj (United Kingdom/Belgium), Rodolfo Sapiains (Chile), Yusuke Satoh (Japan), Sonia I. Seneviratne (Switzerland), Theodore G. Shepherd (United Kingdom/Canada), Jana Sillmann (Norway/Germany), Lucas Silva (Portugal/Switzerland), Aimée B.A. Slangen (The Netherlands), Anna A. Sörensson (Argentina), Peter Steinle (Australia), Thomas F. Stocker (Switzerland), Martina Stockhause (Germany), Daithi Stone (New Zealand), Abigail Swann (United States of America), Sophie Szopa (France), Izuru Takayabu (Japan), Claudia Tebaldi (United States of America), Laurent Terray (France), Peter W. Thorne (Ireland/ United Kingdom), Blair Trewin (Australia), Isabel Trigo (Portugal), Maarten K. van Aalst (The Netherlands), Bart van den Hurk (The Netherlands), Detlef van Vuuren (The Netherlands), Robert Vautard (France), Carolina Vera (Argentina), David Viner (United Kingdom), Axel von Engeln (Germany), Karina von Schuckmann (France/Germany), Xuebin Zhang (Canada)

Review Editors:
Nares Chuersuwan (Thailand), Gabriele Hegerl (United Kingdom/Germany), Tetsuzo Yasunari (Japan)

ACCEPTED VERSION SUBJECT TO FINAL EDITING

Chapter Scientist:
Hui-Wen Lai (Sweden), Tania Villaseñor (Chile)

This Supplementary Material should be cited as:
Chen, D., M. Rojas, B. H. Samset, K. Cobb, A. Diongue Niang, P. Edwards, S. Emori, S. H. Faria, E. Hawkins, P. Hope, P. Huybrechts, M. Meinshausen, S. K. Mustafa, G. K. Plattner, A. M. Tréguier, 2021, Framing, Context, and Methods Supplementary Material. In: *Climate Change 2021: The Physical Science Basis. Contribution of Working Group I to the Sixth Assessment Report of the Intergovernmental Panel on Climate Change* [Masson-Delmotte, V., P. Zhai, A. Pirani, S. L. Connors, C. Péan, S. Berger, N. Caud, Y. Chen, L. Goldfarb, M. I. Gomis, M. Huang, K. Leitzell, E. Lonnoy, J. B. R. Matthews, T. K. Maycock, T. Waterfield, O. Yelekçi, R. Yu and B. Zhou (eds.)]. Available from https://ipcc.ch/static/ar6/wg1.

Date: August 2021

This document is subject to copy-editing, corrigenda and trickle backs.

ACCEPTED VERSION
SUBJECT TO FINAL EDITING

Table of Contents

1.SM.1 Data Table 3

References 18

ACCEPTED VERSION
SUBJECT TO FINAL EDITING

1.SM.1 Data Table

[START TABLE 1.SM.1 HERE]

Table 1.SM.1: Input Data Table. Input datasets and code used to create chapter figures.

Figure number / Table number / Chapter section (for calculations)	**Dataset / Code name**	**Type**	**Filename / Specificities**	**License type**	**Dataset / Code citation**	**Dataset / Code URL**	**Related publications / Software used**	**Notes** [Can add info on data processing, e.g., reference period conversion]
Figure 1.4	CO2: Antarctic ice core	Input dataset	grl52461-sup-0003-supplementary.xls			https://agupubs.onlinelibrary.wiley.com/action/downloadSupplement?doi=10.1002%2F2014GL061957&file=grl52461-sup-0003-supplementary.xls	Lüthi et al. (2008); Bereiter et al. (2015)	
	CO2: direct air measurements	Input dataset	co2_trend_gl.txt			https://www.esrl.noaa.gov/gmd/ccgg/trends/gl_data.html	Tans and Keeling (2019)	
	Precipitation: Global Precipitation Climatology Centre (GPCC) V8	Input dataset	baseline 1961-1990 using land areas only. Latitude bands are 33ºN-66ºN and 15ºS-30ºS.			https://psl.noaa.gov/data/gridded/data.gpcc.html	Becker et al. (2013)	
	Glacier mass loss	Input dataset	Zemp_etal_results_regions_glob	Creative Commons	10.5281/zenodo.1492141	https://doi.org/10.5281/zenodo.149	Zemp et al. (2019)	

ACCEPTED VERSION SUBJECT TO FINAL EDITING

			al.zip	Attribution 4.0 International		2141		
	Surface air temperature (GMST): Hadley Centre/Climatic Research Unit Temperature (HadCRUT) 5.0	Input dataset	baseline 1961-1990.	Open Government License v3.		https://www.metoffice.gov.uk/hadobs/hadcrut5/data/current/download.html	Morice et al. (2021)	
	Sea leve change	Input dataset	Baseline 1900-1929.			https://static-content.springer.com/esm/art%3A10.1038%2Fs41558-019-0531-8/MediaObjects/41558_2019_531_MOESM2_ESM.txt	Dangendorf et al. (2019)	
	Ocean heat content	Input dataset	baseline1961-1990.			https://www.ncei.noaa.gov/access/global-ocean-heat-content/heat_global.html	Zanna et al. (2019)	
Figure 1.5, panel a	Left. CO2, air enclosed in ice measurements	Input dataset	grl52461-sup-0003-supplementary.xls			https://agupubs.onlinelibrary.wiley.com/action/downloadSupplement?doi=10.1002%2F2014GL061957&file=grl52461-sup-	Bereiter et al. (2015) AR6 Chapter 2 Table 2.1	

ACCEPTED VERSION SUBJECT TO FINAL EDITING

						0003-supplementary.xls https://agupubs.onlinelibrary.wiley.com/doi/full/10.1002/2014GL061957		
	Middle. CO2, direct air measurements	Input dataset	uncertainty +/- 0.12 ppm			https://agupubs.onlinelibrary.wiley.com/doi/full/10.1002/2014GL061957 https://www.esrl.noaa.gov/gmd/ccgg/trends/gl_data.html	Bereiter et al. (2015); Tans and Keeling (2019) (consulted on 02.12.2020)	
	Right. CO2, Projected concentration for five SSPs	Input dataset	uncertainty +/- 2ppm.	Creative Commons Attribution-ShareAlike 4.0 International License (CC BY-SA 4.0)		https://gmd.copernicus.org/articles/13/3571/2020/gmd-13-3571-2020-discussion.html	Meinshausen et al. (2020)	
Figure 1.5, panel b	Left. Global Mean Surface Air Temperature	Input dataset	Only 50% column used (Snyder, 2016) Referenced to 1850-1900 by adding +0.36°C (Hansen et al., 2013)			https://www.nature.com/articles/nature19798 (Snyder, 2016) ; https://doi.org/10.1098/rsta.2012.0294 (Hansen et al., 2013); https://science.sciencemag.org/high	Hansen et al. (2013); Snyder (2016); Westerhold et al. (2020) AR6 Chapter 2 Section 2.3.1.1; Cross-chapter Box 2.3 Table 1	

ACCEPTED VERSION SUBJECT TO FINAL EDITING

						wire/filestream/749806/field_highwire_adjunct_files/0/aba6853_Tables_S8_S34.xlsx (Westerhold et al., 2020)		
	Middle. Observed and reconstructed temperature changes since 1850, Hadley Centre/Climatic Research Unit Temperature (HadCRUT) 5.0	Input dataset	referenced to 1850-1900 baseline AR6 assessed 4-dataset mean	Open Government License v3.		https://www.metoffice.gov.uk/hadobs/hadcrut5/data/current/download.html	Morice et al. (2021)	
	Right. Projected mean and ranges of warming; **CMIP6 MODEL & EXPERIMENTS (2081-2100)**	Input dataset	CMIP6 MODEL & EXPERIMENTS (2081-2100)				AR6 Chapter 4 Table 4.5	
	Right. Projected mean and ranges of warming; **Model for the Assessment of Greenhouse**	Input dataset	(2300) simulations				AR6 Chapter 4 Table 4.9	

ACCEPTED VERSION SUBJECT TO FINAL EDITING

	Gas Induced Climate Change (MAGICC7)							
Figure 1.5, panel c	Left. Sea level reconstruction	Input dataset	https://www1.ncdc.noaa.gov/pub/data/paleo/contributions_by_author/spratt2016/spratt2016.txt. Uncertainty +/- 5m Only long time series used			https://www.ncdc.noaa.gov/paleo-search/study/19982	Spratt and Lisiecki (2016) AR6 Chapter 2 Section 2.3.3.3 and Chapter 9 Section 9.6.2	
	Middle. Sea level record over the historial period	Input dataset	first referenced to its own 1850-1900 average Sea level record from 1850 to 1900			https://www.pnas.org/content/113/11/E1434	Kopp et al. (2016)	
	Middle. Sea level record over the historial period	Input dataset	20th century sea level record referenced to 1850-1900	CC BY 3.0 licence		https://iopscience.iop.org/article/10.1088/1748-9326/abdaec	Palmer et al. (2021)	
	Right. Sea level projections based on SSPs-based simulations (2081-2100). **CMIP6 MODELS & EXPERIMENTS**	Input dataset	Relative to 1850-1900, by adding +0.16m				AR6 Chapter 4 Table 9.9 Total (2100)	
	Right. Sea level	Input dataset					AR6 Chapter 4	

ACCEPTED VERSION SUBJECT TO FINAL EDITING

	projections based on SSPs-based simulations (2281-2300).						Section 9.6.3.5	
Figure 1.6	Surface air temperature (GMST): Hadley Centre/Climatic Research Unit Temperature (HadCRUT) 5.0	Input dataset	baseline 1961-1990.	Open Government License v3.		https://www.metoffice.gov.uk/hadobs/hadcrut5/data/current/download.html	Morice et al. (2021)	see Cross-Chapter Box 2.3 and section 2.3.1.1 for details
	CO2: Antarctic ice core	Input dataset	grl52461-sup-0003-supplementary.xls			https://agupubs.onlinelibrary.wiley.com/action/downloadSupplement?doi=10.1002%2F2014GL061957&file=grl52461-sup-0003-supplementary.xls		
	CO2: direct air measurements	Input dataset	co2_trend_gl.txt (??)			https://www.esrl.noaa.gov/gmd/ccgg/trends/gl_data.html	Tans and Keeling (2019)	
Figure 1.8, panel a	Annual mean surface temperatures, 60°N to 60°S, as calculated by G.S. Callendar.	Input dataset	https://rmets.onlinelibrary.wiley.com/action/downloadSupplement?doi=10.1002%2Fqj.2178&file=qj_2178_sm_s			https://rmets.onlinelibrary.wiley.com/action/downloadSupplement?doi=10.1002%2Fqj.2178&file=qj_2178_sm_suppinforS	Callendar (1938); Hawkins and Jones (2013)	

ACCEPTED VERSION SUBJECT TO FINAL EDITING

	Transcribed by Ed Hawkins		uppinforS1.dat			1.dat		
Figure 1.8, panel b	Surface temperature, Climatic Research Unit Temperature (CRUTEM) 5	Input dataset	Processed to produce 60S-60N average	Open Government License v3.		https://www.metoffice.gov.uk/hadobs/crutem5/	Osborn et al. (2021)	
Figure 1.9	Past model projections of global temperature change	Input dataset				https://github.com/hausfath/OldModels	Hausfather et al. (2020)	
	Hadley Centre/Climatic Research Unit Temperature (HadCRUT) 5.0	Input dataset		Open Government License v3.		https://www.metoffice.gov.uk/hadobs/hadcrut5/data/current/download.html	Morice et al. (2021)	
	Anthropogenic forcing	Input dataset				https://zenodo.org/record/1323162#.X2tTzNZ7mHo	Dessler and Forster (2018)	
Figure 1.10	Temperature projection 1990-2030	Input dataset					IPCC (1990)	
	Hadley Centre/Climatic Research Unit Temperature (HadCRUT) 5.0	Input dataset		Open Government License v3.		https://www.metoffice.gov.uk/hadobs/hadcrut5/data/current/download.html	Morice et al. (2021)	
	Cowtan and Way	Input dataset				https://www-users.york.ac.uk/~	Cowtan and Way (2014)	

ACCEPTED VERSION SUBJECT TO FINAL EDITING

						kdc3/papers/coverage2013/series.html		
	NASA GISTEMP	Input dataset				https://data.giss.nasa.gov/gistemp/	GISTEMP Team, 2020: GISS Surface Temperature Analysis (GISTEMP), version 4. NASA Goddard Institute for Space Studies. https://data.giss.nasa.gov/gistemp/.	
	Berkeley Earth	Input dataset				http://berkeleyearth.org/data-new/		
	NOAAGlobalTemp	Input dataset				https://www.ncdc.noaa.gov/data-access/marineocean-data/noaa-global-surface-temperature-noaaglobaltemp		
	Projected temperature change by 2030	Input dataset					Grose et al. (2017)	
Figure 1.11	GSAT ERA-5	Input dataset	1979-2020			https://www.ecmwf.int/en/forecasts/datasets/browse-reanalysis-datasets		
	GMST Berkeley Earth (1850-2020)	Input dataset				http://berkeleyearth.org/data/		
	GMST Jones (1961-1990)	Input dataset					Jones et al. (1999)	

ACCEPTED VERSION SUBJECT TO FINAL EDITING

	GSAT, CMIP6 historical simulation (1850-2014)	Input dataset				https://doi.org/10.5281/zenodo.3951890	Nicholls et al. (2021)	The data archive grows as new CMIP6 results are added. An up-to-date full collection can be found at https://cmip6.science.unimelb.edu.au
	GSAT, CMIP6 SSP1-2.6	Input dataset				https://doi.org/10.5281/zenodo.3951890	Nicholls et al. (2021)	
Figure 1.12	Hadley Centre/Climatic Research Unit Temperature (HadCRUT) 5.0	Input dataset			Data provided by Chapter 2		Morice et al. (2021); Data provided by Chapter 2	
	Berkeley Earth	Input dataset			Data provided by Chapter 2		Data provided by Chapter 2	
	NOAAGlobalTemp	Input dataset			Data provided by Chapter 2		Data provided by Chapter 2	
	Kadow et al (2020) (updated)	Input dataset			Data provided by Chapter 2		Kadow et al. (2020); Data provided by Chapter 2	
Cross-chapter Box 1.2 , Figure 1.	Radiative forcing estimates from	Input dataset			Data provided by Chapter 7		AR6 Chapter 7.	see Cross-Chapter Box 7.1 in

ACCEPTED VERSION SUBJECT TO FINAL EDITING

	AR6 emulator							Chapter 7
Figure 1.13	Ocean heat content; Surface air t°; Ice volume: **Historical and RCP4.5 experiments**	Input dataset	MPI Large Ensemble			https://esgf-data.dkrz.de/projects/mpi-ge/	Maher et al. (2019)	
Figure 1.14, top panel	Left. Total change in t° since 1850-1900	Input dataset					Hawkins et al. (2020)	
	Right. Year to year variability	Input dataset					Hawkins et al. (2020)	
Figure 1.14, middle panel	Left. Signal-to-noise ratio	Input dataset					Hawkins et al. (2020)	
	Right. Global warming level of emergence	Input datset					Hawkins et al. (2020)	
Figure 1.14, bottom panel	Annual mean surface air temperatures: N North America, Northern Europe, East Asia, N South America, Tropical Africa, Australasia	Input dataset	Berkeley Earth air temperature over land dataset	Creative Commons BY-4.0		https://doi.org/10.5281/zenodo.3634713	Rohde and Hausfather (2020).	
Figure 1.15, left	GSAT projections (CMIP6 Model	Input dataset				https://cmip6.science.unimelb.edu.au	Nicholls et al. (2021)	

ACCEPTED VERSION SUBJECT TO FINAL EDITING

	outputs)							
Figure 1.15, middle	Northern South America temperature change projections (CMIP6 Model outputs)	Input dataset				https://cmip6.science.unimelb.edu.au	Nicholls et al. (2021)	
Figure 1.15, right	East Asia JJA rainfall change projections (CMIP6 Model outputs)	Input dataset				https://cmip6.science.unimelb.edu.au	Nicholls et al. (2021)	
Figure 1.16	GSAT projections	Input dataset	Projected changes for 2020-2090 in Chapter 4				AR6 Chapter 4	
Figure 1.24	Historical GMST	Input dataset						
	GMST projections	Input dataset						
	Historical cumulative CO2	Input dataset						
	Cumulative CO2 projections	Input dataset						
Figure 1.25	Historical global-mean surface air temperatures	Input dataset	from 1750 to 1850				PAGES 2k Consortium (2017, 2019)	
	Historical global-mean surface air temperatures	Input dataset	from 1850 to 2018			Chapter 2		

ACCEPTED VERSION SUBJECT TO FINAL EDITING

	CMIP6 temperature projections under five SSPs	Input dataset	Projections from 2020			https://doi.org/10.22033/ESGF/input4MIPs.9864 https://doi.org/10.22033/ESGF/input4MIPs.9865 https://doi.org/10.22033/ESGF/input4MIPs.9866 https://doi.org/10.22033/ESGF/input4MIPs.9861 https://doi.org/10.22033/ESGF/input4MIPs.9868		
	CMIP6.ScenarioMIP.MIROC.MIROC6	Input dataset	CMIP6.ScenarioMIP.MIROC.MIROC6					
Figure 1.26	CO2, CH4, N2O historical concentration	Input dataset				greenhousegases.science.unimelb.edu.au	Meinshausen et al. (2017)	
	Temperature proxies (PAGES 2k consortium)	Input dataset					PAGES 2k Consortium (2017, 2019)	http://www.pastglobalchanges.org/science/wg/2k-network/data/phase-2-data
	GMST Hadley Centre/Climatic Research Unit Temperature (HadCRUT) 5.0	Input dataset					Chapter 2	
	Temperature	Input dataset				cmip6.science.uni		

ACCEPTED VERSION SUBJECT TO FINAL EDITING

	projections (CMIP6 ScenarioMIP experiment examined in Chapter 4)					melb.edu.au		
Cross-chapter box 1.4, Figure 1	(left panel) temperature evolution from ScenarioMIP	Input dataset				greenhousegases.science.unimelb.edu.au	Meinshausen et al. (2020)	
Cross-chapter box 1.4, Figure 2	International Institute for Applied Systems Analysis (IIASA) SSP database	Input dataset	annual			IIASA SSP database: https://secure.iiasa.ac.at/web-apps/ene/SspDb/dsd?Action=htmlpage&page=about	(Riahi et al., 2017; Gidden et al., 2019; Rogelj et al., 2019)	
	RCP database	Input dataset						
	panel (p) and (q) CMIP6-CMIP5	Input dataset					Hoesly et al. (2018)	Figure 7 in Hoesly et al. (2018)
	Cross-chapter box 1.4, Figure 2 code	Code				https://gitlab.com/magicc/ar6-wg1/-/blob/master/notebooks/SSPSCENDAT-rcp-ssp-comparisons/100-SSPSCENDAT-rcp-ssp-comparison-plot.ipynb	Figure code	
Figure 1.28	Range of CO2 emissions from IS92	Input dataset	since 1992			https://sedac.ciesin.columbia.edu/data/set/ipcc-is92-emissions-		

ACCEPTED VERSION SUBJECT TO FINAL EDITING

						scenarios-v1-1		
	Range of CO2 emissions from SRES	Input dataset	since 2000			https://sedac.ciesin.columbia.edu/ddc/sres/		
	Range of CO2 emissions from RCP	Input dataset	since 2010			http://www.iiasa.ac.at/web-apps/tnt/RcpDb		
	Range of CO2 emissions from SSP	Input dataset				https://doi.org/10.22033/ESGF/input4MIPs.9868 https://doi.org/10.22033/ESGF/input4MIPs.9824 https://doi.org/10.22033/ESGF/input4MIPs.9861 https://doi.org/10.22033/ESGF/input4MIPs.9863 https://doi.org/10.22033/ESGF/input4MIPs.9866 https://doi.org/10.22033/ESGF/input4MIPs.9865 https://doi.org/10.22033/ESGF/input4MIPs.9864 https://doi.org/10.22033/ESGF/input4MIPs.9862 https://doi.org/10.22033/ESGF/input4MIPs.9867		
	Scenarios IPCC	Input dataset				https://data.ene.iia	Huppmann et al.	

ACCEPTED VERSION SUBJECT TO FINAL EDITING

	SR1.5					sa.ac.at/iamc-1.5c-explorer/#/login?redirect=%2Fworkspaces	(2018)	
	CO2 historical emissions	Input dataset				https://www.pik-potsdam.de/paris-reality-check/primap-hist/	Gütschow et al. (2016)	
Figure 1.29	SR1.5 scenario database	Input dataset				https://data.ene.iiasa.ac.at/iamc-1.5c-explorer		
	SSP1-1.9	Input dataset				https://doi.org/10.22033/ESGF/input4MIPs.9864	Chapter 7	
	SSP1-2.6	Input dataset				https://doi.org/10.22033/ESGF/input4MIPs.9865	Chapter 7	
	SSP2-4.5	Input dataset				https://doi.org/10.22033/ESGF/input4MIPs.9866	Chapter 7	
	SSP3-7.0	Input dataset				https://doi.org/10.22033/ESGF/input4MIPs.9861	Chapter 7	
	SSP5-8.5	Input dataset				https://doi.org/10.22033/ESGF/input4MIPs.9868	Chapter 7	
	Figure 1.29 code	Code			Will be generated by TSU	https://gitlab.com/magicc/ar6-wg1/-/tree/master/notebooks/CO2DRIVER-ghg-erf-contributions		

ACCEPTED VERSION SUBJECT TO FINAL EDITING

[END TABLE 1.SM.1 HERE]

References

Becker, A., Finger, P., Meyer-Christoffer, A., Rudolf, B., Schamm, K., Schneider, U., et al. (2013). A description of the global land-surface precipitation data products of the Global Precipitation Climatology Centre with sample applications including centennial (trend) analysis from 1901–present. *Earth Syst. Sci. Data* 5, 71–99. doi:10.5194/essd-5-71-2013.

Bereiter, B., Eggleston, S., Schmitt, J., Nehrbass-Ahles, C., Stocker, T. F., Fischer, H., et al. (2015). Revision of the EPICA Dome C CO2 record from 800 to 600 kyr before present. *Geophys. Res. Lett.* 42, 542–549. doi:10.1002/2014GL061957.

Callendar, G. S. (1938). The artificial production of carbon dioxide and its influence on temperature. *Q. J. R. Meteorol. Soc.* 64, 223–240. doi:10.1002/qj.49706427503.

Cowtan, K., and Way, R. G. (2014). Coverage bias in the HadCRUT4 temperature series and its impact on recent temperature trends. *Q. J. R. Meteorol. Soc.* doi:10.1002/qj.2297.

Dangendorf, S., Hay, C., Calafat, F. M., Marcos, M., Piecuch, C. G., Berk, K., et al. (2019). Persistent acceleration in global sea-level rise since the 1960s. *Nat. Clim. Chang.* 9, 705–710. doi:10.1038/s41558-019-0531-8.

Dessler, A. E., and Forster, P. M. (2018). An Estimate of Equilibrium Climate Sensitivity From Interannual Variability. *J. Geophys. Res. Atmos.* 123, 8634–8645. doi:10.1029/2018JD028481.

Gidden, M. J., Riahi, K., Smith, S. J., Fujimori, S., Luderer, G., Kriegler, E., et al. (2019). Global emissions pathways under different socioeconomic scenarios for use in CMIP6: a dataset of harmonized emissions trajectories through the end of the century. *Geosci. Model Dev.* 12, 1443–1475. doi:10.5194/gmd-12-1443-2019.

Grose, M. R., Risbey, J. S., and Whetton, P. H. (2017). Tracking regional temperature projections from the early 1990s in light of variations in regional warming, including 'warming holes.' *Clim. Change* 140, 307–322. doi:10.1007/s10584-016-1840-9.

Gütschow, J., Jeffery, M. L., Gieseke, R., Gebel, R., Stevens, D., Krapp, M., et al. (2016). The PRIMAP-hist national historical emissions time series. *Earth Syst. Sci. Data* 8, 571–603. doi:10.5194/essd-8-571-2016.

Hansen, J., Sato, M., Russell, G., and Kharecha, P. (2013). Climate sensitivity, sea level and atmospheric carbon dioxide. *Philos. Trans. R. Soc. A Math. Phys. Eng. Sci.* 371, 20120294. doi:10.1098/rsta.2012.0294.

Hausfather, Z., Drake, H. F., Abbott, T., and Schmidt, G. A. (2020). Evaluating the performance of past climate model projections. *Geophys. Res. Lett.* 47, e2019GL085378. doi:10.1029/2019GL085378.

Hawkins, E., Frame, D., Harrington, L. J., Joshi, M., King, A., Rojas, M., et al. (2020). Observed emergence of the climate change signal: from the familiar to the unknown. *Geophys. Reasearch Lett.* 47, e2019GL086259. Available at: 10.1029/2019GL086259.

Hawkins, E., and Jones, P. D. (2013). On increasing global temperatures: 75 years after Callendar. *Q. J. R. Meteorol. Soc.* 139. doi:10.1002/qj.2178.

Hoesly, R. M., Smith, S. J., Feng, L., Klimont, Z., Janssens-Maenhout, G., Pitkanen, T., et al. (2018). Historical (1750–2014) anthropogenic emissions of reactive gases and aerosols from the Community Emissions Data System (CEDS). *Geosci. Model Dev.* 11, 369–408. doi:10.5194/gmd-11-369-2018.

Huppmann, D., Rogelj, J., Kriegler, E., Krey, V., and Riahi, K. (2018). A new scenario resource for integrated 1.5 °C research. *Nat. Clim. Chang.* 8, 1027–1030. doi:10.1038/s41558-018-0317-4.

IPCC (1990). Climate Change: The IPCC Scientific Assessment. , eds. J. T. Houghton, G. J. Jenkins, and J. J. Ephraums Cambridge, United Kingdom and New York, NY, USA: Cambridge University Press Available at: https://www.ipcc.ch/report/ar1/wg1.

Jones, P. D., New, M., Parker, D. E., Martin, S., and Rigor, I. G. (1999). Surface air temperature and its changes over the past 150 years. *Rev. Geophys.* 37, 173–199. doi:10.1029/1999RG900002.

Kadow, C., Hall, D. M., and Ulbrich, U. (2020). Artificial intelligence reconstructs missing climate information. *Nat. Geosci.* 13, 408–413. doi:10.1038/s41561-020-0582-5.

Kopp, R. E., Kemp, A. C., Bittermann, K., Horton, B. P., Donnelly, J. P., Gehrels, W. R., et al. (2016). Temperature-driven global sea-level variability in the Common Era. *Proc. Natl. Acad. Sci.* 113, E1434–E1441. doi:10.1073/pnas.1517056113.

Lüthi, D., Le Floch, M., Bereiter, B., Blunier, T., Barnola, J.-M., Siegenthaler, U., et al. (2008). High-resolution carbon dioxide concentration record 650,000–800,000 years before present. *Nature* 453, 379–382. doi:10.1038/nature06949.

Maher, N., Milinski, S., Suarez-Gutierrez, L., Botzet, M., Dobrynin, M., Kornblueh, L., et al. (2019). The Max Planck Institute Grand Ensemble: Enabling the Exploration of Climate System Variability. *J. Adv. Model. Earth Syst.* 11, 2050–2069. doi:10.1029/2019MS001639.

Meinshausen, M., Nicholls, Z. R. J., Lewis, J., Gidden, M. J., Vogel, E., Freund, M., et al. (2020). The shared socio-economic pathway (SSP) greenhouse gas concentrations and their extensions to 2500. *Geosci. Model Dev.* 13,

ACCEPTED VERSION SUBJECT TO FINAL EDITING

3571–3605. doi:10.5194/gmd-13-3571-2020.
Meinshausen, M., Vogel, E., Nauels, A., Lorbacher, K., Meinshausen, N., Etheridge, D. M., et al. (2017). Historical greenhouse gas concentrations for climate modelling (CMIP6). *Geosci. Model Dev.* 10, 2057–2116. doi:10.5194/gmd-10-2057-2017.
Morice, C. P., Kennedy, J. J., Rayner, N. A., Winn, J. P., Hogan, E., Killick, R. E., et al. (2021). An Updated Assessment of Near-Surface Temperature Change From 1850: The HadCRUT5 Data Set. *J. Geophys. Res. Atmos.* 126. doi:10.1029/2019JD032361.
Nicholls, Z., Lewis, J., Makin, M., Nattala, U., Zhang, G. Z., Mutch, S. J., et al. (2021). Regionally aggregated, stitched and de-drifted CMIP-climate data, processed with netCDF-SCM v2.0.0. *Geosci. Data J.* 00, 1–45. doi:https://doi.org/10.1002/gdj3.113.
Osborn, T. J., Jones, P. D., Lister, D. H., Morice, C. P., Simpson, I. R., Winn, J. P., et al. (2021). Land Surface Air Temperature Variations Across the Globe Updated to 2019: The CRUTEM5 Data Set. *J. Geophys. Res. Atmos.* 126, e2019JD032352. doi:10.1029/2019JD032352.
PAGES 2k Consortium (2017). A global multiproxy database for temperature reconstructions of the Common Era. *Sci. Data* 4, 170088. doi:10.1038/sdata.2017.88.
PAGES 2k Consortium (2019). Consistent multidecadal variability in global temperature reconstructions and simulations over the Common Era. *Nat. Geosci.* 12, 643–649. doi:10.1038/s41561-019-0400-0.
Palmer, M. D., Domingues, C. M., Slangen, A. B. A., and Boeira Dias, F. (2021). An ensemble approach to quantify global mean sea-level rise over the 20th century from tide gauge reconstructions. *Environ. Res. Lett.* doi:10.1088/1748-9326/abdaec.
Riahi, K., van Vuuren, D. P., Kriegler, E., Edmonds, J., O'Neill, B. C., Fujimori, S., et al. (2017). The Shared Socioeconomic Pathways and their energy, land use, and greenhouse gas emissions implications: An overview. *Glob. Environ. Chang.* 42, 153–168. doi:10.1016/j.gloenvcha.2016.05.009.
Rogelj, J., Huppmann, D., Krey, V., Riahi, K., Clarke, L., Gidden, M., et al. (2019). A new scenario logic for the Paris Agreement long-term temperature goal. *Nature* 573, 357–363. doi:10.1038/s41586-019-1541-4.
Rohde, R. A., and Hausfather, Z. (2020). The Berkeley Earth Land/Ocean Temperature Record. *Earth Syst. Sci. Data* 12, 3469–3479. doi:10.5194/essd-12-3469-2020.
Snyder, C. W. (2016). Evolution of global temperature over the past two million years. *Nature* 538, 226–228. doi:10.1038/nature19798.
Spratt, R. M., and Lisiecki, L. E. (2016). A Late Pleistocene sea level stack. *Clim. Past* 12, 1079–1092. doi:10.5194/cp-12-1079-2016.
Tans, P., and Keeling, R. F. (2020). Trends in Atmospheric Carbon Dioxide. Available at: www.esrl.noaa.gov/gmd/ccgg/trends/ [Accessed March 1, 2021].
Westerhold, T., Marwan, N., Drury, A. J., Liebrand, D., Agnini, C., Anagnostou, E., et al. (2020). An astronomically dated record of Earth's climate and its predictability over the last 66 million years. *Science (80-.).* 369, 1383–1387. doi:10.1126/science.aba6853.
Zanna, L., Khatiwala, S., Gregory, J. M., Ison, J., and Heimbach, P. (2019). Global reconstruction of historical ocean heat storage and transport. *Proc. Natl. Acad. Sci. U. S. A.* 116, 1126–1131. doi:10.1073/pnas.1808838115.
Zemp, M., Huss, M., Thibert, E., Eckert, N., McNabb, R., Huber, J., et al. (2019). Global glacier mass changes and their contributions to sea-level rise from 1961 to 2016. *Nature* 568, 382–386. doi:10.1038/s41586-019-1071-0.

ACCEPTED VERSION
SUBJECT TO FINAL EDITING

Chapter 2: Changing state of the climate system

Coordinating Lead Authors:
Sergey K. Gulev (Russian Federation), Peter W. Thorne (Ireland/United Kingdom)

Lead Authors:
Jinho Ahn (Republic of Korea), Frank J. Dentener (EU/The Netherlands), Catia M. Domingues (Australia, United Kingdom/Brazil), Sebastian Gerland (Norway/Germany), Daoyi Gong (China), Darrell S. Kaufman (United States of America), Hyacinth C. Nnamchi (Nigeria, Germany/Nigeria), Johannes Quaas (Germany), Juan A. Rivera (Argentina), Shubha Sathyendranath (United Kingdom/Canada, Overseas Citizen of India, United Kingdom), Sharon L. Smith (Canada), Blair Trewin (Australia), Karina von Schuckmann (France/Germany), Russell S. Vose (United States of America)

Contributing Authors:
Guðfinna Aðalgeirsdóttir (Iceland), Samuel Albani (Italy), Richard P. Allan (United Kingdom), Richard A. Betts (United Kingdom), Lea Beusch (Switzerland), Kinfe Beyene (Ethiopia), Jason E. Box (Denmark/United States of America), Denise Breitburg (United States of America), Kevin D. Burke (United States of America), Michael P. Byrne (United Kingdom/Ireland), John A. Church (Australia), Sloane Coats (United States of America), Naftali Cohen (United States of America), William Collins (United Kingdom), Owen R. Cooper (United States of America), Pedro Di Nezio (United States of America), Fabio Boeira Dias (Finland/Brazil), Ed J. Dlugokencky (United States of America), Timothy Dunkerton (United States of America), Paul J. Durack (United States of America/Australia), Tamsin L. Edwards (United Kingdom), Veronika Eyring (Germany), Chris Fairall (United States of America), Vitali Fioletov (Canada), Piers Forster (United Kingdom), Gavin L. Foster (United Kingdom), Baylor Fox-Kemper (United States of America), Qiang Fu (United States of America), Jan S. Fuglestvedt (Norway), John C. Fyfe (Canada), Marie-José Gaillard (Sweden/Switzerland, Sweden), Joelle Gergis (Australia), Nathan P. Gillett (Canada), Hans Gleisner (Denmark/Sweden), Nadine Gobron (EU/France), Nicholas R. Golledge (New Zealand/United Kingdom), Bradley Hall (United States of America), Ed Hawkins (United Kingdom), Alan M. Haywood (United Kingdom), Armand Hernández (Spain), Forrest M. Hoffman (United States of America), Yongyun Hu (China), Dale F. Hurst (United States of America), Masao Ishii (Japan), Samuel Jaccard (Switzerland), Dabang Jiang (China), Christopher Jones (United Kingdom), Bror Jönsson (United Kingdom/Sweden), Andreas Kääb (Norway/Germany), Ralph Keeling (United States of America), Noel S. Keenlyside (Norway/Australia, United Kingdom), John Kennedy (United Kingdom), Elizabeth Kent (United Kingdom), Nichol S. Khan (Hong Kong, China/United States of America), Wolfgang Kiessling (Germany), Stefan Kinne (Germany), Robert E. Kopp (United States of America), Svitlana Krakovska (Ukraine), Elmar Kriegler (Germany), Gerhard Krinner (France/Germany, France), Natalie Krivova (Germany), Paul B. Krummel (Australia), Werner L. Kutsch (EU/Germany), Ron Kwok (United States of America), Florian Ladstädter (Austria), Peter Landschützer (Germany/Austria), June-Yi Lee (Republic of Korea), Andrew Lenton (Australia), Lisa A. Levin (United States of America), Daniel J. Lunt (United Kingdom), Jochem Marotzke (Germany), Gareth J. Marshall (United Kingdom), Robert A. Massom (Australia), Katja Matthes (Germany), Damon H. Matthews (Canada), Thorsten Mauritsen (Sweden/Denmark), Gerard D. McCarthy (Ireland), Erin L. McClymont (United Kingdom), Shayne McGregor (Australia), Jerry F. McManus (United States of America), Walter N. Meier (United States of America), Alan Mix (United States of America), Olaf Morgenstern (New Zealand/Germany), Lawrence R. Mudryk (Canada), Jens Mühle (United States of America/Germany), Dirk Notz (Germany), Lisa C. Orme (Ireland/United Kingdom), Scott M. Osprey (United Kingdom), Matthew D. Palmer (United Kingdom), Anna Pirani (Italy/United Kingdom, Italy), Chris Polashenski (United States of America), Elvira Poloczsanka (Australia/United Kingdom), Anthony Richardson (Australia), Belén Rodríguez-Fonseca (Spain), Joeri Rogelj (United Kingdom/Belgium), Steven K. Rose (United States of America), Yair Rosenthal (United States of America/Israel, United States of

ACCEPTED VERSION SUBJECT TO FINAL EDITS

America), Alessio Rovere (Germany/Italy), Lucas Ruiz (Argentina), Ulrich Salzmann (United Kingdom/Germany, United Kingdom), Bjørn H. Samset (Norway), Abhishek Savita (Australia/India), Margit Schwikowski (Switzerland), Sonia I. Seneviratne (Switzerland), Isobel J. Simpson (Canada), Aimée B. A. Slangen (The Netherlands), Chris Smith (United Kingdom), Olga N. Solomina (Russian Federation), Joshua H. P. Studholme (United States of America/United Kingdom, New Zealand), Alessandro Tagliabue (United Kingdom), Claudia Tebaldi (United States of America), Jessica Tierney (United States of America), Matthew Toohey (Canada, Germany/Canada), Andrew Turner (United Kingdom), Osvaldo Ulloa (Chile), Caroline C. Ummenhofer (United States of America/Germany, United States of America), Axel von Engeln (Germany), Rachel Warren (United Kingdom), Kate Willett (United Kingdom), John W. Williams (United States of America)

Review Editors:
Timothy J. Osborn (United Kingdom), Azar Zarrin (Iran)

Chapter Scientists:
Katherine J. Dooley (Ireland), Therese A. Myslinski (Ireland), David N. Smyth (Ireland/United Kingdom)

This chapter should be cited as:
Gulev, S. K., P. W. Thorne, J. Ahn, F. J. Dentener, C. M. Domingues, S. Gerland, D. Gong, D. S. Kaufman, H. C. Nnamchi, J. Quaas, J. A. Rivera, S. Sathyendranath, S. L. Smith, B. Trewin, K. von Shuckmann, R. S. Vose, 2021, Changing State of the Climate System. In: *Climate Change 2021: The Physical Science Basis. Contribution of Working Group I to the Sixth Assessment Report of the Intergovernmental Panel on Climate Change* [Masson-Delmotte, V., P. Zhai, A. Pirani, S. L. Connors, C. Péan, S. Berger, N. Caud, Y. Chen, L. Goldfarb, M. I. Gomis, M. Huang, K. Leitzell, E. Lonnoy, J. B. R. Matthews, T. K. Maycock, T. Waterfield, O. Yelekçi, R. Yu and B. Zhou (eds.)]. Cambridge University Press. In Press.

Date: August 2021

This document is subject to copy-editing, corrigenda and trickle backs.

ACCEPTED VERSION SUBJECT TO FINAL EDITS

Table of Contents

Executive Summary **5**

2.1 Introduction **9**

Cross-Chapter Box 2.1: Paleoclimate Reference Periods in the Assessment Report *10*

2.2 Changes in Climate Drivers **12**

2.2.1 Solar and Orbital Forcing *12*

2.2.2 Volcanic Aerosol Forcing *14*

2.2.3 Well-mixed Greenhouse Gases (WMGHGs) *15*

2.2.3.1 CO_2 during 450 Ma to 800 ka 15

2.2.3.2 Glacial-interglacial WMGHG Fluctuations from 800 ka 17

2.2.3.2.1 CO_2 17

2.2.3.2.2 CH_4 18

2.2.3.2.3 N_2O 18

2.2.3.3 Modern measurements of WMGHGs 18

2.2.3.3.1 Carbon Dioxide (CO_2) 20

2.2.3.3.2 Methane (CH_4) 20

2.2.3.3.3 Nitrous Oxide (N_2O) 20

2.2.3.4 Summary of changes in WMGHGs 20

2.2.4 Halogenated Greenhouse Gases (CFCs, HCFCs, HFCs, PFCs, SF6 and others) *21*

2.2.4.1 CFCs 21

2.2.4.2 HCFCs 21

2.2.4.3 HFCs, PFCs, SF6 and other radiatively important halogenated gases 22

2.2.4.4 Summary of changes in halogenated gases 22

2.2.5 Other short-lived gases *23*

2.2.5.1 Stratospheric water vapour 23

2.2.5.2 Stratospheric ozone 23

2.2.5.3 Tropospheric ozone 24

2.2.6 Aerosols *26*

2.2.7 Land use and land cover *27*

2.2.8 Effective radiative forcing (ERF) exerted by the assessed climate drivers *28*

2.3 Changes in large-scale climate **30**

Cross-Chapter Box 2.2: Large-scale indicators of climate change *30*

2.3.1 Atmosphere and Earth's surface *32*

2.3.1.1 Surface temperatures 32

2.3.1.1.1 Temperatures of the deep past (65 Ma to 8 ka) 32

2.3.1.1.2 Temperatures of the post-glacial period (past 7000 years) 34

Cross-Chapter Box 2.3: New estimates of global warming to date and key implications *35*

2.3.1.1.3 Temperatures during the instrumental period – surface 42

2.3.1.2 Temperatures during the instrumental period – free atmosphere 47

2.3.1.2.1 Dataset developments 47

2.3.1.2.2 Assessment of trends 48

2.3.1.3 Global hydrological cycle 50

2.3.1.3.1 Paleo perspective of the global hydrological cycle 50

2.3.1.3.2 Surface humidity 51

2.3.1.3.3 Total column water vapour 52

2.3.1.3.4 Global precipitation 53

2.3.1.3.5 Precipitation minus Evaporation 54

2.3.1.3.6 Streamflow 55

2.3.1.4 Atmospheric circulation 56

2.3.1.4.1 The Hadley and Walker circulations 56

2.3.1.4.2 Global monsoon changes 58

ACCEPTED VERSION SUBJECT TO FINAL EDITS

2.3.1.4.3 Extratropical jets, storm tracks, and blocking 59
2.3.1.4.4 Surface wind and sea level pressure 61
2.3.1.4.5 Stratospheric polar vortex and sudden warming events 62
2.3.2 Cryosphere *63*
2.3.2.1 Sea ice coverage and thickness 63
2.3.2.1.1 Arctic Sea Ice 63
2.3.2.1.2 Antarctic Sea Ice 65
2.3.2.2 Terrestrial snow cover 67
2.3.2.3 Glacier mass 67
2.3.2.4 Ice sheet mass and extent 69
2.3.2.4.1 Greenland Ice Sheet 69
2.3.2.4.2 Antarctic Ice Sheet 70
2.3.2.5 Terrestrial permafrost 71
2.3.3 Ocean *73*
2.3.3.1 Ocean temperature, heat content and thermal expansion 73
2.3.3.2 Ocean salinity 75
2.3.3.3 Sea level 76
2.3.3.4 Ocean circulation 79
2.3.3.4.1 Atlantic Meridional Overturning circulation (AMOC) 79
2.3.3.4.2 Western boundary currents and inter-basin exchanges 81
2.3.3.5 Ocean pH 82
2.3.3.6 Ocean deoxygenation 83
2.3.4 Biosphere *84*
2.3.4.1 Seasonal Cycle of CO_2 85
2.3.4.2 Marine biosphere 85
2.3.4.2.1 Large-scale distribution of marine biota 85
2.3.4.2.2 Marine Primary production 87
2.3.4.2.3 Marine phenology 87
2.3.4.3 Terrestrial biosphere 88
2.3.4.3.1 Growing season and phenology changes 88
2.3.4.3.2 Terrestrial ecosystems 89
2.3.4.3.3 Global greening and browning 91
2.3.5 Synthesis of evidence for past changes *92*
Cross-Chapter Box 2.4: The climate of the Pliocene (around 3 million years ago), when CO_2 concentrations were last similar to those of present day *93*
2.4 Changes in modes of variability 95
2.4.1 Annular modes *95*
2.4.1.1 Northern Annular Mode (NAM) / North Atlantic Oscillation (NAO) 95
2.4.1.2 Southern Annular Mode (SAM) 96
2.4.2 El Niño-Southern Oscillation (ENSO) *97*
2.4.3 Indian Ocean Basin and dipole modes *99*
2.4.4 Atlantic Meridional and Zonal Modes *100*
2.4.5 Pacific Decadal Variability *101*
2.4.6 Atlantic Multidecadal Variability *102*
2.5 Final remarks 103
Frequently asked questions 104
Acknowledgements 107
References 108
Figures 170

ACCEPTED VERSION SUBJECT TO FINAL EDITS

Executive Summary

Chapter 2 assesses observed large-scale changes in climate system drivers, key climate indicators and principal modes of variability. Chapter 3 considers model performance and detection/attribution, and Chapter 4 covers projections for a subset of these same indicators and modes of variability. Collectively, these chapters provide the basis for later chapters, which focus upon processes and regional changes. Within Chapter 2, changes are assessed from in situ and remotely sensed data and products and from indirect evidence of longer-term changes based upon a diverse range of climate proxies. The time-evolving availability of observations and proxy information dictate the periods that can be assessed. Wherever possible, recent changes are assessed for their significance in a longer-term context, including target proxy periods, both in terms of mean state and rates of change.

Changes in Climate System Drivers

Climate system drivers lead to climate change by altering the Earth's energy balance. The influence of a climate driver is described in terms of its effective radiative forcing (ERF), measured in W m^{-2}. Positive ERF values exert a warming influence and negative ERF values exert a cooling influence (Chapter 7).

Present-day global concentrations of atmospheric carbon dioxide (CO_2) are at higher levels than at any time in at least the past two million years (*high confidence*). Changes in ERF since the late 19th century are dominated by increases in concentrations of greenhouse gases and trends in aerosols; the net ERF is positive and changing at an increasing rate since the 1970s (*medium confidence*). {2.2, 7.2, 7.3}

Change in ERF from natural factors since 1750 is negligible in comparison to anthropogenic drivers (*very high confidence*). Solar activity since 1900 was high but not exceptional compared to the past 9000 years (*high confidence*). The average magnitude and variability of volcanic aerosol forcing since 1900 have not been unusual compared to the past 2500 years (*medium confidence*). {2.2.1, 2.2.2}

In 2019, concentrations of CO_2, methane (CH_4) and nitrous oxide (N_2O) reached levels of 409.9 (±0.4) ppm, 1866.3 (±3.3) ppb and 332.1 (±0.4) ppb, respectively. Since 1850, these well-mixed greenhouse gases (GHGs) have increased at rates that have no precedent on centennial time scales in at least the past 800,000 years. Concentrations of CO_2, CH_4, and N_2O increased from 1750 to 2019 by 131.6 ± 2.9 ppm (47.3%), 1137 ± 10 ppb (156%), and 62 ± 6 ppb (23.0%) respectively. These changes are larger than those between glacial and interglacial periods over the last 800,000 years for CO_2 and CH_4 and of comparable magnitude for N_2O (*very high confidence*). The best estimate of the total ERF from CO_2, CH_4 and N_2O in 2019 relative to 1750 is 2.9 W m^{-2}, an increase of 12.5 % from 2011. ERF from halogenated components in 2019 was 0.4 W m^{-2}, an increase of 3.5% since 2011. {2.2.3, 2.2.4, 7.3.2}

Tropospheric aerosol concentrations across the Northern Hemisphere mid-latitudes increased from 1700 to the last quarter of the 20th century, but have subsequently declined (*high confidence*). Aerosol optical depth (AOD) has decreased since 2000 over Northern Hemisphere mid-latitudes and Southern Hemisphere mid-latitude continents, but increased over South Asia and East Africa (*high confidence*). These trends are even more pronounced in AOD from sub-micrometre aerosols for which the anthropogenic contribution is particularly large. The best-estimate of aerosol ERF in 2019 relative to 1750 is –1.1 W m^{-2}. {2.2.6, 7.3.3}

Changes in other short-lived gases are associated with an overall positive ERF (*medium confidence*). Stratospheric ozone has declined between 60˚S and 60˚N by 2.2% from the 1980s to 2014–2017 (*high confidence*). Since the mid-20th century, tropospheric ozone has increased by 30–70% across the Northern Hemisphere (*medium confidence*). Since the mid-1990s, free tropospheric ozone increases were 2–7% per decade in the northern mid-latitudes (*high confidence*), 2–12% per decade in the tropics (*high confidence*) and <5% per decade in southern mid-latitudes (*medium confidence*). The best estimate of ozone column ERF (0.5 W m^{-2} relative to 1750) is dominated by changes in tropospheric ozone. Due to discrepancies in satellite and in situ records, there is *low confidence* in estimates of stratospheric water vapour change. {2.2.5, 7.3.2}

ACCEPTED VERSION SUBJECT TO FINAL EDITS

Biophysical effects from historical changes in land use have an overall negative ERF (*medium confidence*). The best-estimate ERF from the increase in global albedo is –0.15 W m^{-2} since 1700 and –0.12 W m^{-2} since 1850 (*medium confidence*). {2.2.7, 7.3.4}

Changes in Key Indicators of Global Climate Change

Observed changes in the atmosphere, oceans, cryosphere and biosphere provide unequivocal evidence of a world that has warmed. Over the past several decades, key indicators of the climate system are increasingly at levels unseen in centuries to millennia, and are changing at rates unprecedented in at least the last 2000 years (*high confidence*). In the last decade, global mean surface temperature (GMST) was *more likely than not* higher than for any multi-century average during the Holocene (past 11,700 years) and was comparable to temperatures of the Last Interglacial period (roughly 125,000 years ago). {2.3}

GMST increased by 0.85 [0.69 to 0.95] °C between 1850–1900 and 1995–2014 and by 1.09 [0.95 to 1.20] °C between 1850–1900 and 2011–2020. From 1850–1900 to 2011–2020, the temperature increase over land (1.59 [1.34 to 1.83] °C) has been faster than over the oceans (0.88 [0.68 to 1.01] °C). Over the last 50 years, observed GMST has increased at a rate unprecedented in at least the last 2000 years (*medium confidence*). The increase in GMST since the mid-19th century was preceded by a slow decrease that began in the mid-Holocene (around 6500 years ago) (*medium confidence*). {2.3.1.1, Cross-Chapter Box 2.1}

Changes in GMST and global surface air temperature (GSAT) over time differ by at most 10% in either direction *(high confidence)*, and the long-term changes in GMST and GSAT are presently assessed to be identical. There is expanded uncertainty in GSAT estimates, with the assessed change from 1850–1900 to 1995–2014 being 0.85 [0.67 to 0.98] °C. {Cross-Chapter box 2.3}

The troposphere has warmed since at least the 1950s, and it is *virtually certain* that the stratosphere has cooled. In the Tropics, the upper troposphere has warmed faster than the near-surface since at least 2001, the period over which new observation techniques permit more robust quantification (*medium confidence*). It is *virtually certain* that the tropopause height has risen globally over 1980–2018, but there is *low confidence* in the magnitude. {2.3.1.2}

Changes in several components of the global hydrological cycle provide evidence for overall strengthening since at least 1980 (*high confidence*). However, there is *low confidence* in comparing recent changes with past variations due to limitations in paleoclimate records at continental and global scales. Global land precipitation has *likely* increased since 1950, with a faster increase since the 1980s (*medium confidence*). Near-surface specific humidity has increased over both land (*very likely*) and the oceans (*likely*) since at least the 1970s. Relative humidity has *very likely* decreased over land areas since 2000. Global total column water vapour content has *very likely* increased during the satellite era. Observational uncertainty leads to *low confidence* in global trends in precipitation minus evaporation and river runoff. {2.3.1.3}

Several aspects of the large-scale atmospheric circulation have *likely* changed since the mid-20th century, but limited proxy evidence yields *low confidence* in how these changes compare to longer-term climate. The Hadley circulation has *very likely* widened since at least the 1980s, and extratropical storm tracks have *likely* shifted poleward in both hemispheres. Global monsoon precipitation has *likely* increased since the 1980s, mainly in the Northern Hemisphere (*medium confidence*). Since the 1970s, near-surface winds have *likely* weakened over land. Over the oceans, near-surface winds *likely* strengthened over 1980–2000, but divergent estimates lead to *low confidence* in the sign of change thereafter. It is *likely* that the northern stratospheric polar vortex has weakened since the 1980s and experienced more frequent excursions toward Eurasia. {2.3.1.4}

Current Arctic sea ice coverage levels are the lowest since at least 1850 for both annual mean and late-summer values (*high confidence*) and for the past 1000 years for late-summer values (*medium confidence*). Between 1979 and 2019, Arctic sea ice area has decreased in both summer and winter, with sea ice becoming younger, thinner and more dynamic (*very high confidence*). Decadal means for Arctic sea ice area decreased from 6.23 million km^2 in 1979–1988 to 3.76 million km^2 in 2010–2019 for September and

ACCEPTED VERSION SUBJECT TO FINAL EDITS

from 14.52 to 13.42 million km^2 for March. Antarctic sea ice area has experienced little net change since 1979 (*high confidence*), with only minor differences between sea ice area decadal means for 1979–1988 (2.04 million km^2 for February, 15.39 million km^2 for September) and 2010–2019 (2.17 million km^2 for February, 15.75 million km^2 for September). {2.3.2.1}

Changes across the terrestrial cryosphere are widespread, with several indicators now in states unprecedented in centuries to millennia (*high confidence*). Reductions in spring snow cover extent have occurred across the Northern Hemisphere since at least 1978 (*very high confidence*). With few exceptions, glaciers have retreated since the second half of the 19th century and continued to retreat with increased rates since the 1990s (*very high confidence*); this behaviour is unprecedented in at least the last 2000 years (*medium confidence*). Greenland Ice Sheet mass loss has increased substantially since 2000 (*high confidence*). The Greenland Ice Sheet was smaller than at present during the Last Interglacial period (*high confidence*) and the mid-Holocene (*high confidence*). The Antarctic Ice Sheet (AIS) lost mass between 1992 and 2020 (*very high confidence*), with an increasing rate of mass loss over this period (*medium confidence*). Although permafrost persists in areas of the Northern Hemisphere where it was absent prior to 3000 years ago, increases in temperatures in the upper 30 m over the past three to four decades have been widespread (*high confidence*). {2.3.2}

Global mean sea level (GMSL) is rising, and the rate of GMSL rise since the 20th century is faster than over any preceding century in at least the last three millennia (*high confidence*). Since 1901, GMSL has risen by 0.20 [0.15–0.25] m, and the rate of rise is accelerating. Further back in time, there is *medium confidence* that GMSL was within –3.5 to 0.5 m (*very likely*) of present during the mid-Holocene (6000 years ago), 5 to 10 m (*likely*) higher during the Last Interglacial (125,000 years ago), and 5 to 25 m (*very likely*) higher during the mid-Pliocene Warm Period (MPWP) (3.3 million years ago). {2.3.3.3}

Recent ocean changes are widespread, and key ocean indicators are in states unprecedented for centuries to millennia (*high confidence*). Since 1971, it is *virtually certain* that global ocean heat content has increased for the upper (0–700 m) layer, *very likely* for the intermediate (700–2000 m) layer and *likely* below 2000 m, and is currently increasing faster than at any point since at least the last deglacial transition (18-11 thousand years ago) (*medium confidence*). It is *virtually certain* that large-scale near-surface salinity contrasts have intensified since at least 1950. The Atlantic Meridional Overturning Circulation (AMOC) was relatively stable during the past 8000 years (*medium confidence*) but declined during the 20th century (*low confidence*). Ocean pH has declined globally at the surface over the past four decades (*virtually certain*) and in all ocean basins in the ocean interior (*high confidence*) over the past 2–3 decades. Deoxygenation has occurred in most open ocean regions during the mid 20th to early 21st centuries (*high confidence*), with decadal variability (*medium confidence*). Oxygen minimum zones are expanding at many locations (*high confidence*). {2.3.3}

Changes in the marine biosphere are consistent with large-scale warming and changes in ocean geochemistry (*high confidence*). The ranges of many marine organisms are shifting towards the poles and towards greater depths (*high confidence*), but a minority of organisms are shifting in the opposite directions. This mismatch in responses across species means that the species composition of ecosystems is changing (*medium confidence*). At multiple locations, various phenological metrics for marine organisms have changed in the last 50 years, with the nature of the changes varying with location and with species (*high confidence*). In the last two decades, the concentration of phytoplankton at the base of the marine food web, as indexed by chlorophyll concentration, has shown weak and variable trends in low and mid-latitudes and an increase in high latitudes (*medium confidence*). Global marine primary production decreased slightly from 1998–2018, with increasing production in the Arctic (*medium confidence*). {2.3.4.2}

Changes in key global aspects of the terrestrial biosphere are consistent with large-scale warming (*high confidence*). Over the last century, there have been poleward and upslope shifts in the distributions of many land species (*very high confidence*) as well as increases in species turnover within many ecosystems (*high confidence*). Over the past half century, climate zones have shifted poleward, accompanied by an increase in the length of the growing season in the Northern Hemisphere extratropics and an increase in the amplitude of the seasonal cycle of atmospheric CO_2 above 45°N (*high confidence*). Since the early 1980s, there has been a global-scale increase in the greenness of the terrestrial surface (*high confidence*). {2.3.4.1,

ACCEPTED VERSION SUBJECT TO FINAL EDITS

2.3.4.3}

During the Mid-Pliocene warm period (MPWP, 3.3–3.0 million years ago) slowly changing large-scale indicators reflect a world that was warmer than present, with CO_2 similar to current levels. CO_2 levels during the MPWP were similar to present for a sustained period, within a range of 360–420 ppm (*medium confidence*). Relative to the present, GMST, GMSL and precipitation rate were all higher, the Northern Hemisphere latitudinal temperature gradient was lower, and major terrestrial biomes were shifted northward (*very high confidence*). There is *high confidence* that cryospheric indicators were diminished and *medium confidence* that the Pacific longitudinal temperature gradient weakened and monsoon systems strengthened. {2.3, Cross-Chapter Box 2.4, 9.6.2}

Inferences from past climate states based on proxy records can be compared with climate projections over coming centuries to place the range of possible futures into a longer-term context. There is *medium confidence* in the following mappings between selected paleo periods and future projections: During the Last Interglacial, GMST is estimated to have been 0.5°C–1.5°C warmer than the 1850–1900 reference for a sustained period, which overlaps the low end of the range of warming projected under SSP1-2.6, including its negative-emissions extension to the end of the 23rd century [1.0–2.2] °C. During the mid-Pliocene Warm Period, the GMST estimate [2.5-4.0] °C is similar to the range projected under SSP2-4.5 for the end of the 23rd century [2.3-4.6] °C. GMST estimates for the Miocene Climatic Optimum [5–10] °C and Early Eocene Climatic Optimum [10–18] °C, about 15 and 50 million years ago, respectively, overlap with the range projected for the end of the 23rd century under SSP5-8.5 [6.6–14.1] °C. {Cross-Chapter Box 2.1, 2.3.1, 4.3.1.1, 4.7.1.1}

Changes in Modes of Variability

Since the late 19th century, major modes of climate variability show no sustained trends but do exhibit fluctuations in frequency and magnitude at inter-decadal time scales, with the notable exception of the Southern Annular Mode, which has become systematically more positive (*high confidence*). There is *high confidence* that these modes of variability have existed for millennia or longer, but *low confidence* in detailed reconstructions of most modes prior to direct instrumental records. Both polar annular modes have exhibited strong positive trends toward increased zonality of midlatitude circulation over multi-decadal periods, but these trends have not been sustained for the Northern Annular Mode since the early 1990s (*high confidence*). For tropical ocean modes, a sustained shift beyond multi-centennial variability has not been observed for El Niño–Southern Oscillation (*medium confidence*), but there is *low evidence* and *low agreement* about the long-term behaviour of other tropical ocean modes. Modes of decadal and multi-decadal variability over the Pacific and Atlantic oceans exhibit no significant trends over the period of observational records (*high confidence*). {2.4}

ACCEPTED VERSION SUBJECT TO FINAL EDITS

2.1 Introduction

This chapter assesses the evidence-basis for large-scale past changes in selected components of the climate system. As such, it combines much of the assessment performed in Chapters 2 through 5 of the Fifth Assessment Report (AR5) WGI contribution (IPCC, 2013) that, taken together, supported a finding of unequivocal recent warming of the climate system. The Sixth Assessment Report (AR6) WGI Report structure differs substantially from that in AR5 (Section 1.1.2). The current chapter focuses upon observed changes in climate system drivers and changes in key selected large-scale indicators of climate change and in important modes of variability (Cross-Chapter Box 2.2), which allow for an assessment of changes in the global climate system in an integrated manner. This chapter is complemented by Chapters 3 and 4, which respectively consider model assessment / detection and attribution, and future climate projections for subsets of these same indicators and modes. It does not consider changes in observed extremes, which are assessed in Chapter 11. The chapter structure is outlined in the visual abstract (Figure 2.1).

[START FIGURE 2.1 HERE]

Figure 2.1: Chapter 2 visual abstract of contents.

[END FIGURE 2.1 HERE]

Use is made of paleoclimate, in situ, ground- and satellite-based remote sensing, and reanalysis data products where applicable (Section 1.5). All observational products used in the chapter are detailed in Annex I, and information on data sources and processing for each figure and table can be found in the associated chapter table 2.SM.1 available as an electronic supplement to the chapter. Use of common periods ranging from 56 million years ago through to the recent past is applied to the extent permitted by available data (Section 1.4.1 and Cross-Chapter Box 2.1). In all cases, the narrative proceeds from as far in the past as the data permit through to the present. Each sub-section starts by highlighting the key findings from AR5 and any relevant AR6-cycle special reports (SROCC, SR1.5, SRCCL), and then outlines the new evidence-basis arising from a combination of: i) new findings reported in the literature, including new datasets and new versions of existing datasets; and ii) recently observed changes, before closing with a new summary assessment.

Trends, when calculated as part of this assessment, have wherever possible been calculated using a common approach following that adopted in Box 2.2 of Chapter 2 of AR5 (Hartmann et al., 2013). In addition to trends, consideration is also made of changes between various time slices / periods in performing the assessment (Section 1.4.1 and Cross-Chapter Box 2.1). Statistical significance of trends and changes are assessed at the two-tailed 90% confidence (*very likely*) level unless otherwise stated. Limited use is also made of published analyses that have employed a range of methodological choices. In each such case the method / metric is stated.

There exist a variety of inevitable and, in some cases, irreducible uncertainties in performing an assessment of the observational evidence for climate change. In some instances, a combination of sources of uncertainty is important. For example, the assessment of global surface temperature over the instrumental record in Section 2.3.1.1.3 considers a combination of observational-dataset and trend-estimate uncertainties. Furthermore, estimates of parametric uncertainty are often not comprehensive in their consideration of all possible factors and, when such estimates are constructed in distinct manners, there are often significant limitations to their direct comparability (Hartmann et al., 2013; their Box 2.1).

ACCEPTED VERSION SUBJECT TO FINAL EDITS

[START CROSS-CHAPTER BOX 2.1 HERE]

Cross-Chapter Box 2.1: Paleoclimate Reference Periods in the Assessment Report

Contributing Authors: Darrell Kaufman (USA), Kevin Burke (USA), Samuel Jaccard (Switzerland), Chris Jones (UK), Wolfgang Kiessling (Germany), Daniel Lunt (UK), Olaf Morgenstern (New Zealand), John W. Williams (USA)

Over the long evolution of the Earth's climate system, several periods have been extensively studied as examples of distinct climate states. This Cross-Chapter Box places multiple paleoclimate reference periods into the unifying context of Earth's long-term climate history, and points to sections in the report with additional information about each period. Other reference periods, including those of the industrialized era, are described in Section 1.4.1.

The reference periods represent times that were both colder and warmer than present, and periods of rapid climate change, many with informative parallels to projected climate (Cross-Chapter Box 2.1, Table 1). They are used to address a wide variety of questions related to natural climate variations in the past (FAQ 1.3). Most of them are used as targets to evaluate the performance of climate models under different climate forcings (Section 3.8.2), while also providing insight into the ocean-atmospheric circulation changes associated with various radiative forcings and geographical changes.

Global Mean Surface Temperature (GMST) is a key indicator of the changing state of the climate system. Earth's mean temperature history during the current geological era (Cenozoic, beginning 66 Ma) can be broadly characterized as follows (Cross-Chapter Box 2.1, Figure 1): (1) transient warming during the first 15 million years of the Cenozoic, punctuated by the Paleocene-Eocene Thermal Maximum; (2) a long-term cooling over tens of millions of years beginning around 50 Ma, driven by (among other factors) the slow drift of tectonic plates, which drove mountain building, erosion and volcanism, and reconfigured ocean passages, all of which ultimately moved carbon from the atmosphere to other reservoirs and led to the development of the Antarctic Ice Sheet (AIS) about 35–30 Ma; (2) the intensification of cooling by climate feedbacks involving interactions among tectonics, ice albedo, ocean circulation, land cover and greenhouse gases, causing ice sheets to develop in the Northern Hemisphere (NH) by about 3 Ma; (3) glacial-interglacial fluctuations paced by slow changes in Earth's astronomical configuration (orbital forcing) and modulated by changes in the global carbon cycle and ice sheets on time scales of tens to hundreds of thousands of years, with particular prominence during the last 1 Myr; (4) a transition with both gradual and abrupt shifts from the Last Glacial Maximum to the present interglacial epoch (Holocene), with sporadic ice-sheet breakup disrupting ocean circulation; (5) continued warming followed by minor cooling following the mid-Holocene, with superposed centennial- to decadal-scale fluctuations caused by volcanic activity, among other factors; (6) recent warming related to the build-up of anthropogenic greenhouse gases (Sections 2.2.3, 3.3.1).

GMST estimated for each of the reference periods based on proxy evidence (Section 2.3.1.1) can be compared with climate projections over coming centuries to place the range of possible futures into a longer-term context (Cross-Chapter Box 2.1, Figure 1). Here, the *very likely* range of GMST for the warmer world reference periods are compared with the *very likely* range of GSAT projected for the end the 21st century (2080–2100; Table 4.5 and the *likely* range for the end of the 23rd century (2300; Table 4.9) under multiple Shared Socioeconomic Pathway (SSP) scenarios. From this comparison, there is *medium confidence* in the following: GMST estimated for the warmest long-term period of the Last Interglacial about 125 ka (0.5–1.5°C relative to 1850–1900) overlaps with the low end of the range of temperatures projected under SSP1-2.6 including its negative emissions extension to the end of the 23rd century [1.0 to 2.2°C]. GMST estimated for a period of prolonged warmth during the mid-Pliocene Warm Period about 3 Ma [2.5 to 4.0°C] is similar to temperatures projected under SSP2-4.5 for the end of the 23rd century [2.3 to 4.6°C]. GMST estimated for the Miocene Climatic Optimum [5°C to 10°C] and Early Eocene Climatic Optimum [10 to 18°C], about 15 and 50 million years ago, respectively, overlap with the range projected for the end of the 23rd century under SSP5-8.5 [6.6 to 14.1°C].

ACCEPTED VERSION SUBJECT TO FINAL EDITS

[START CROSS-CHAPTER BOX 2.1, TABLE 1 HERE]

Cross-Chapter Box 2.1, Table 1: Paleo reference periods, listed from oldest to youngest. See 'AR6 sections' for literature citations related to each 'Sketch of the climate state.' See Working Group II (Chapters 1, 2, 3) for citations related to paleontological changes. See Interactive Atlas for simulated climate variables for MPWP, LIG, LGM and MH.

Period	**Age/ year***	**Sketch of the climate state (relative to 1850–1900), and *model experiment protocols*.** Values for large-scale climate indicators including global temperature, sea level and atmospheric CO_2 are shown in Figure 2.34.	**AR6 sections** partial list
Paleocene-Eocene thermal maximum (PETM)	55.9–55.7 Ma	A geologically rapid, large-magnitude warming event at the start of the Eocene when a large pulse of carbon was released to the ocean-atmosphere system, decreasing ocean pH and oxygen content. Terrestrial plant and animal communities changed composition, and species distributions shifted poleward. Many deep-sea species went extinct and tropical coral reefs diminished. *DeepMIP* (Lunt et al., 2017)	2.2.3.1 2.3.1.1.1 5.1.2.1 5.3.1.1 7.5.3.4
Early Eocene climatic optimum** (EECO)	53–49 Ma	Prolonged "hothouse" period with atmospheric CO_2 concentration >1000 ppm, similar to SSP5-8.5 end-of-century values. Continental positions were somewhat different to present due to tectonic plate movements; polar ice was absent and there was more warming at high latitudes than in the equatorial regions. Near-tropical forests grew at 70°S, despite seasonal polar darkness. *DeepMIP*, about 50 Ma (Lunt et al., 2017, 2021)	2.2.3.1 2.3.1.1.1 7.4.4.1.2 7.5.3.4 7.5.6
Miocene climatic optimum** (MCO)	16.9–14.7 Ma	Prolonged warm period with atmospheric CO_2 concentrations 400–600 ppm, similar to SSP2-4.5 end-of-century values. Continental geography was broadly similar to modern. At times, Arctic sea ice may have been absent, and the AIS was much smaller or perhaps absent. Peak in Cenozoic reef development. *MioMIP1*, Early and Middle Miocene (Steinthorsdottir et al., 2020)	2.2.3.1 2.3.1.1.1
Mid-Pliocene warm period (MPWP)	3.3–3.0 Ma	Warm period when atmospheric CO_2 concentration was similar to present (Cross-Chapter Box 2.4). The Arctic was much warmer, but tropical temperatures were only slightly warmer. Sea level was high. Treeline extended to the northern coastline of the NH continents. Also called, "Piacenzian warm period." *PMIP4 midPliocene-eoi400*, 3.2 Ma (Haywood et al., 2016; 2020)	CCB2.4 7.4.4.1.2 7.5.3.3 8.2.2.2 9.6.2
Last Interglacial (LIG)	129–116 ka	Most recent interglacial period, similar to mid-Holocene, but with more pronounced seasonal insolation cycle. Northern high latitudes were warmer, with reduced sea ice. Greenland and West Antarctic Ice Sheets were smaller and sea level was higher. Monsoon was enhanced. Boreal forests extended into Greenland and subtropical animals such as *Hippopotamus* occupied Britain. Coral reefs expanded latitudinally and contracted equatorially. *PMIP4 lig127k*, 127 ka (Otto-Bliesner, et al.,2017; 2021)	2.2.3.2 2.3.1.1.1 2.3.3.3 9.2.2.1 9.6.2
Last Glacial Maximum (LGM)	23–19 ka	Most recent glaciation when global temperatures were lower, with greater cooling toward the poles. Ice sheets covered much of North America and northwest Eurasia, and sea level was commensurately lower. Atmospheric CO_2 was lower; more carbon was sequestered in the ocean interior. Precipitation was generally lower over most regions; the atmosphere was dustier, and ranges of many plant species contracted into glacial refugia; forest extent and coral reef distribution was reduced worldwide. *PMIP4lgm*, 21 ka (Kageyama et al., 2017; 2021)	2.2.3.2 2.3.1.1.1 3.3.1.1 3.8.2.1 5.1.2.2 7.4.4.1.2 7.5.3.1 8.3.2.4 9.6.2
Last deglacial transition (LDT)	18–11 ka	Warming that followed the Last Glacial Maximum, with decreases in the extent of the cryosphere in both polar regions. Sea level, ocean meridional overturning circulation, and atmospheric CO_2 increased during two main steps. Temperate and boreal species ranges expanded northwards. Community turnover was large. Megafauna populations declined or went extinct.	2.2.3.2 5.1.2.2 5.3.1.2 8.6.1 9.6.2
Mid-Holocene (MH)	6.5–5.5 ka	Middle of the present interglacial when the CO_2 concentration was similar to the onset of the industrial era, but the orbital configuration led to warming and shifts in the hydrological cycle, especially NH monsoons. Approximate time during the current interglacial and before the onset of major industrial activities when GMST was highest. Biome-scale loss of North African grasslands caused by weakened monsoons and collapses of temperate tree populations linked to hydroclimate variability. *PMIP4 mid-Holocene*, 6 ka (Brierley et al., 2020; Otto-Bliesner et al., 2017)	2.3.1.1.2 2.3.2.4 2.3.3.3 3.3.1.1 3.8.2.1 8.3.2.4 8.6.2.2 9.6.2
Last millennium***	850-1850 CE	Climate variability during this period is better documented on annual to centennial scales than during previous reference periods. Climate changes were driven by solar, volcanic, land cover, and anthropogenic forcings, including strong increases in	2.3.1.1.2 2.3.2.3 8.3.1.6

ACCEPTED VERSION SUBJECT TO FINAL EDITS

		greenhouse gasses since 1750. *PMIP4 past1000,* 850–1849 CE (Jungclaus et al., 2017)	8.5.2.1 Box 11.3

* CE: Common Era; ka: thousands of years ago; Ma: millions of years ago.
** The word "optimum" is traditionally used in geosciences to refer to the warmest interval of a geologic period.
*** The terms "Little Ice Age" and "Medieval Warm Period" (or "Medieval Climate Anomaly") are not used extensively in this report because the timing of these episodes is not well defined and varies regionally. Since AR5, new proxy records have improved climate reconstructions at decadal scale across the last millennium. Therefore, the dates of events within these two roughly defined periods are stated explicitly when possible.

[END CROSS-CHAPTER BOX 2.1, TABLE 1 HERE]

[START CROSS-CHAPTER BOX 2.1, FIGURE 1 HERE]

Cross-Chapter Box 2.1, Figure 1: Global mean surface temperature (GMST) over the past 60 million years relative to 1850–1900 shown on three time scales. Information about each of the nine paleo reference periods (blue font) and sections in AR6 that discuss these periods are listed in Cross-Chapter Box 2.1 Table 1. Grey horizontal bars at the top mark important events. Characteristic uncertainties are based on expert judgement and are representative of the approximate midpoint of their respective time scales; uncertainties decrease forward in time. GMST estimates for most paleo reference periods (Figure 2.34) overlap with this reconstruction, but take into account multiple lines of evidence. Future projections span the range of global surface air temperature best estimates for SSP1–2.6 and SSP5–8.5 scenarios described in Section 1.6. Range shown for 2100 is based on CMIP6 multi-model mean for 2081–2100 from Table 4.5; range for 2300 is based upon an emulator and taken from Table 4.9. Further details on data sources and processing are available in the chapter data table (Table 2.SM.1).

[END CROSS-CHAPTER BOX 2.1, FIGURE 1 HERE]

[END CROSS-CHAPTER BOX 2.1 HERE]

2.2 Changes in Climate Drivers

This section assesses the magnitude and rates of changes in both natural and anthropogenically mediated climate drivers over a range of time scales. First, changes in insolation (orbital and solar; 2.2.1), and volcanic stratospheric aerosol (2.2.2) are assessed. Next, well-mixed greenhouse gases (GHGs) (CO_2, N_2O and CH_4) are covered in 2.2.3, with climate feedbacks and other processes involved in the carbon cycle assessed in Chapter 5. The section continues with the assessment of changes in halogenated GHGs (2.2.4), stratospheric water vapour, stratospheric and tropospheric ozone (2.2.5), and tropospheric aerosols (2.2.6). Short-lived Climate Forcers (SLCFs), their precursor emissions and key processes are assessed in more detail in Chapter 6. Section 2.2.7 assesses the effect of historical land cover change on climate, including biophysical and biogeochemical processes. Section 2.2.8 summarizes the changes in the Earth's energy balance since 1750 using the comprehensive assessment of Effective Radiative Forcing (ERF) performed in Section 7.3. For some SLCFs with insufficient spatial or temporal observational coverage, ERFs are based on model estimates, but also reported here for completeness and context. Tabulated global mixing ratios of all well-mixed GHGs and ERFs from 1750–2019 are provided in Annex III.

2.2.1 Solar and Orbital Forcing

AR5 assessed solar variability over multiple time scales, concluding that total solar irradiance (TSI) multi-millennial fluctuations over the past 9 kyr were <1 W m^{-2}, but with no assessment of confidence provided. For multi-decadal to centennial variability over the last millennium, AR5 emphasized reconstructions of TSI that show little change (<0.1%) since the Maunder Minimum (1645–1715) when solar activity was particularly low, again without providing a confidence level. AR5 further concluded that the best estimate of radiative forcing due to TSI changes for the period 1750–2011 was 0.05–0.10 W m^{-2} (*medium confidence*),

ACCEPTED VERSION SUBJECT TO FINAL EDITS

and that TSI *very likely* changed by –0.04 [–0.08–0.00 W m^{-2}] between 1986 and 2008. Potential solar influences on climate due to feedbacks arising from interactions with Galactic Cosmic Rays are assessed in Section 7.3.4.5.

Slow periodic changes in the Earth's orbit around the Sun mainly cause variations in seasonal and latitudinal receipt of incoming solar radiation. Precise calculations of orbital variations are available for tens of millions of years (Berger and Loutre, 1991; Laskar et al., 2011). The range of insolation averaged over boreal summer at 65°N was about 83 W m^{-2} during the past million years, and 3.2 W m^{-2} during the past millennium, but there was no substantial effect upon global average radiative forcing (0.02 W m^{-2} during the past millennium).

A new reconstruction of solar irradiance extends back 9 kyr based upon updated cosmogenic isotope datasets and improved models for production and deposition of cosmogenic nuclides (Poluianov et al., 2016), and shows that solar activity during the second half of the 20th century was in the upper decile of the range. TSI features millennial-scale changes with typical magnitudes of 1.5 [1.4 to 2.1] W m^{-2} (Wu et al., 2018). Although stronger variations in the deeper past cannot be ruled out completely (Egorova, T. et al., 2018; Reinhold et al., 2019), there is no indication of such changes having happened over the last 9 kyr.

Recent estimates of TSI and spectral solar irradiance (SSI) for the past millennium are based upon updated irradiance models (e.g., Egorova et al., 2018; Wu et al., 2018) and employ updated and revised direct sunspot observations over the last three centuries (Clette et al., 2014; Chatzistergos et al., 2017) as well as records of sunspot numbers reconstructed from cosmogenic isotope data prior to this (Usoskin et al., 2016). These reconstructed TSI timeseries (Figure 2.2a) feature little variation in TSI averaged over the past millennium. The TSI between the Maunder Minimum (1645–1715) and second half of the 20th century increased by 0.7–2.7 W m^{-2} (Jungclaus et al., 2017; Egorova et al., 2018; Lean, 2018; Wu, C.-J. et al., 2018; Yeo et al., 2020; Lockwood & Ball, 2020). This TSI increase implies a change in ERF of 0.09–0.35 W m^{-2} (Section 7.3.4.4).

Estimation of TSI changes since 1900 (Figure 2.2b) has further strengthened, and confirms a small (less than about 0.1 W m^{-2}) contribution to global climate forcing (Section 7.3.4.4). New reconstructions of TSI over the 20th century (Lean, 2018; Wu C-J. et al., 2018) support previous results that the TSI averaged over the solar cycle *very likely* increased during the first seven decades of the 20th century and decreased thereafter (Figure 2.2b). TSI did not change significantly between 1986 and 2019. Improved insights (Coddington et al., 2016; Yeo et al., 2015, 2017a; Krivova et al., 2006) show that variability in the 200–400 nm UV range was greater than previously assumed. Building on these results, the forcing proposed by Matthes et al. (2017) has a 16% stronger contribution to TSI variability in this wavelength range compared to the forcing used in the 5th Phase of the Coupled Model Intercomparison Project (CMIP5).

To conclude, solar activity since the late 19th century was relatively high but not exceptional in the context of the past 9 kyr (*high confidence*). The associated global-mean ERF is in the range of –0.06 to 0.08 W m^{-2} (Section 7.3.4.4).

[START FIGURE 2.2 HERE]

Figure 2.2: Time series of solar and volcanic forcing for the past 2.5 kyr (panels a, c) and since 1850 (panels b, d). (a) Total solar irradiance (TSI) reconstruction (10-year running averages) recommended for CMIP6 / PMIP4 millennial experiments based on the radiocarbon dataset before 1850 (blue) scaled to the CMIP6 historical forcing after 1850 (purple). (b) TSI time series (6-month running averages) from CMIP6 historical forcing as inferred from sunspot numbers (blue), compared to CMIP5 forcing based on (red) and an update to CMIP6 by a TSI composite (orange). (c) Volcanic forcing represented as reconstructed Stratospheric aerosol optical depth (SAOD; as presented in Section 7.3.4.6) at 550 nm. Estimates covering 500 BCE to 1900 CE (green) and 1850–2015 (blue). (d) SAOD reconstruction from CMIP6 (v 4) (blue), compared to CMIP5 forcing (red). Note the change in y-axis range between panels c and d. Further details on data sources and processing are available in the chapter data table (Table 2.SM.1).

[END FIGURE 2.2 HERE]

ACCEPTED VERSION SUBJECT TO FINAL EDITS

2.2.2 Volcanic Aerosol Forcing

AR5 concluded that, on inter-annual time scales, the radiative effects of volcanic aerosols are a dominant natural driver of climate variability, with the greatest effects occurring within the first 2–5 years following a strong eruption. Reconstructions of radiative forcing by volcanic aerosols used in the Paleoclimate Modelling Intercomparison Project Phase III (PMIP3) simulations and in AR5 featured short-lived perturbations of a range of magnitudes, with events of greater magnitude than –1 W m^{-2} (annual mean) occurring on average every 35–40 years, although no associated assessment of confidence was given. This section focuses on advances in reconstructions of stratospheric aerosol optical depth (SAOD), whereas Chapter 7 focuses on the effective radiative forcing of volcanic aerosols, and Chapter 5 assesses volcanic emissions of CO_2 and CH_4; tropospheric aerosols are discussed in Section 2.2.6. Cross-Chapter Box 4.1 undertakes an integrative assessment of volcanic effects including potential for 21st century effects.

Advances in analysis of sulphate records from the Greenland Ice Sheet (GrIS) and AIS have resulted in improved dating and completeness of SAOD reconstructions over the past 2.5 kyr (Sigl et al., 2015), a more uncertain extension back to 10 ka (Kobashi et al., 2017; Toohey and Sigl, 2017), and a better differentiation of sulphates that reach high latitudes via stratospheric (strong eruptions) versus tropospheric pathways (Burke et al., 2019; Gautier et al., 2019). The PMIP4 volcanic reconstruction extends the period analysed in AR5 by 1 kyr (Jungclaus et al., 2017; Figure 2.2c) and features multiple strong events that were previously misdated, underestimated or not detected, particularly before about 1500 CE. The period between successive large volcanic eruptions (Negative ERF greater than –1 W m^{-2}), ranges from 3–130 years, with an average of 43 ± 7.5 years between such eruptions over the past 2.5 kyr (data from Toohey & Sigl, 2017). The most recent such eruption was that of Mt Pinatubo in 1991. Century-long periods that lack such large eruptions occurred once every 400 years on average. Systematic uncertainties related to the scaling of sulphate abundance in glacier ice to radiative forcing have been estimated to be about 60% (Hegerl et al., 2006). Uncertainty in the timing of eruptions in the proxy record is ± 2 years (95% confidence interval) back to 1.5 ka and ± 4 years before (Toohey and Sigl, 2017).

SAOD averaged over the period 950–1250 CE (0.012) was lower than for the period 1450–1850 CE (0.017) and similar to the period 1850–1900 (0.011). Uncertainties associated with these inter-period differences are not well quantified but have little effect because the uncertainties are mainly systematic throughout the record. Over the past 100 years, SAOD averaged 14% lower than the mean of the previous 24 centuries (back to 2.5 ka), and well within the range of centennial-scale variability (Toohey and Sigl, 2017).

Direct observations of volcanic gas-phase sulphur emissions (mostly SO_2), sulphate aerosols, and their radiative effects are available from a variety of sources (Kremser et al., 2016). New estimates of SO_2 emissions from explosive eruptions have been derived from satellite (beginning in 1979) and in situ measurements (Höpfner et al., 2015; Carn et al., 2016; Neely and Schmidt, 2016; Brühl, 2018). Satellite observations of aerosol extinction after recent eruptions have uncertainties of about 15–25% (Vernier et al., 2011; Bourassa et al., 2012). Additional uncertainties occur when gaps in the satellite records are filled by complementary observations or using statistical methods (Thomason et al., 2018). Merged datasets (Thomason et al., 2018) and sparse ground-based measurements (Stothers, 1997) allow for volcanic forcing estimates back to 1850. In contrast to the CMIP5 historical volcanic forcing datasets (Ammann et al., 2003), updated time series (Luo et al., 2018; Figure 2.2d) feature a more comprehensive set of optical properties including latitude-, height- and wavelength-dependent aerosol extinction, single scattering albedo and asymmetry parameters. A series of small-to-moderate eruptions since 2000 resulted in perturbations in SAOD of 0.004–0.006 (Andersson et al., 2015; Schmidt et al., 2018).

To conclude, strong individual volcanic eruptions cause multi-annual variations in radiative forcing. However, the average magnitude and variability of SAOD and its associated volcanic aerosol forcing since 1900 are not unusual in the context of at least the past 2.5 kyr (*medium confidence*).

ACCEPTED VERSION SUBJECT TO FINAL EDITS

2.2.3 Well-mixed Greenhouse Gases (WMGHGs)

Well-mixed greenhouse gases generally have lifetimes of more than several years. AR5 assigned *medium confidence* to the values of atmospheric CO_2 concentrations (mixing ratios) during the warm geological periods of the early Eocene and Pliocene. It concluded with *very high confidence* that, by 2011, the mixing ratios of CO_2, CH_4, and N_2O in the atmosphere exceeded the range derived from ice cores for the previous 800 kyr, and that the observed rates of increase of the greenhouse gases were unprecedented on centennial timescales over at least the past 22 kyr. It reported that over 2005–2011 atmospheric burdens of CO_2, CH_4, and N_2O increased, with 2011 levels of 390.5 ppm, 1803.2 ppb and 324.2 ppb, respectively. Increases of CO_2 and N_2O over 2005–2011 were comparable to those over 1996–2005, while CH_4 resumed increasing in 2007, after remaining nearly constant over 1999–2006. A comprehensive process-based assessment of changes in CO_2, CH_4, and N_2O is undertaken in Chapter 5.

2.2.3.1 CO_2 during 450 Ma to 800 ka

Isotopes from continental and marine sediments using improved analytical techniques and sampling resolution have reinforced the understanding of long-term changes in atmospheric CO_2 during the past 450 Myr (Table 2.1, Figure 2.3). In particular, for the last 60 Myr, sampling resolution and accuracy of the boron isotope proxy in ocean sediments has improved (Anagnostou et al., 2016; 2020; Babila et al., 2018; Chalk et al., 2017; de la Vega et al., 2020; Dyez et al., 2018; Gutjahr et al., 2017; Harper et al., 2020; Henehan et al., 2019; 2020; Penman et al., 2014; Raitzsch et al., 2018; Sosdian et al., 2018), the understanding of the alkenone CO_2 proxy has increased (e.g., Badger et al., 2019; Rae et al., 2021; Stoll et al., 2019; Zhang et al., 2019; 2020) and new phytoplankton proxies have been developed and applied (e.g. Witkowski et al., 2018). Understanding of the boron isotope CO_2 proxy has improved since AR5 with studies showing very good agreement between boron-CO_2 estimates and co-existing ice core CO_2 (Chalk et al., 2017; Foster, 2008; Henehan et al., 2013; Hönisch & Hemming, 2005; Raitzsch et al., 2018; Figure 2.3c). Such independent validation has proven difficult to achieve with the other available CO_2 proxies (e.g. Badger et al., 2019; Da et al., 2019; Stoll et al., 2019; Zhang et al., 2019). Remaining uncertainties in these ocean sediment based proxies (Hollis et al., 2019) partly limit the applicability of the alkenone $\delta^{13}C$ and boron $\delta^{11}B$ proxies beyond the Cenozoic, although new records are emerging, e.g. Jurikova et al., (2020). CO_2 estimates from the terrestrial CO_2 proxies, such as stomatal density in fossil plants and $\delta^{13}C$ of palaeosol carbonates, are available for much of the last 420 Myr. Given the low sampling density, relatively large CO_2 uncertainty, and high age uncertainty (relative to marine sediments) of the terrestrial proxies, preference here is given to the marine based proxies (and boron in particular) where possible.

Levels were close to 1750 values during at least one prolonged interval during the Carboniferous and Permian (350–252 Ma). During the Triassic (251.9–201.3 Ma), atmospheric CO_2 mixing ratios reached a maximum between 2000–5000 ppm (200–220 Ma). During the PETM (56 Ma) CO_2 rapidly rose from about 900 ppm to about 2000 ppm (Anagnostou et al., 2020; Gutjahr et al., 2017; Schubert & Jahren, 2013; Table 2.1) in 3–20 kyr (Gutjahr et al., 2017; Turner, 2018; Zeebe et al., 2016). Estimated multi-millennial rates of CO_2 accumulation during this event range from 0.3–1.5 PgC yr^{-1} (Gingerich, 2019); were at least 4-5 times lower than current centennial rates (Section 5.3.1.1). Based on boron and carbon isotope data, supported by other proxies (Hollis et al., 2019), atmospheric CO_2 during the EECO (50 Ma) was between 1150 and 2500 ppm (*medium confidence*), and then gradually declined over the last 50 Myr at a long-term rate of about 16 ppm Myr^{-1} (Figure 2.3). The last time the CO_2 mixing ratio was as high as 1000 ppm (the level reached by some high emission scenarios by 2100; Annex III) was prior to the Eocene-Oligocene transition (33.5 Ma; Figure 2.3) that was associated with the first major advance of the AIS (Anagnostou et al., 2016; Hollis et al., 2019; Pagani et al., 2011; Pearson et al., 2009; Witkowski et al., 2018). The compilation of Foster et al., (2017) constrained CO_2 concentration to between 290 and 450 ppm during the MPWP, based primarily on the boron-isotope data reported by Martínez-Botí et al. (2015b), consistent with the AR5 range of 300–450 ppm. A more recent high-resolution boron isotope-based study revealed that CO_2 cycled during the MPWP from about 330 to about 390 ppm on orbital timescales, with a mean of about 370 ppm (de la Vega et al., 2020). Although data from other proxy types (e.g., stomatal density or $\delta^{13}C$ of alkenones) have too low resolution to resolve the orbital variability of CO_2 during this interval (e.g. Kürschner et al., 1996; Stoll et al.,

ACCEPTED VERSION SUBJECT TO FINAL EDITS

2019) there is general agreement among the different proxy types with the boron-derived mean (e.g. Stoll et al., 2019). High-resolution sampling (about 1 sample per 3 kyr) with the boron-isotope proxy indicates mean CO_2 mixing ratios for the Marine Isotope Stage KM5c interglacial were 360–420 ppm (*medium confidence*) (de la Vega et al., 2020).

Following the MPWP, the atmospheric CO_2 mixing ratio generally decreased at a rate of about 30 ppm Myr^{-1}. It is *very likely* that CO_2 levels as high as the present were not experienced in the last 2 Myr (Bartoli et al., 2011; Chalk et al., 2017; Da et al., 2019; Dyez et al., 2018; Hönisch et al., 2009; Martínez-Botí et al., 2015a; Stoll et al., 2019). Related to the shift of glacial-interglacial cycle frequency from 40 to 100 kyr at 0.8–1.2 Ma, there was a decrease of glacial-period CO_2 (Chalk et al., 2017; Dyez et al., 2018). These boron isotope-based CO_2 results agree with available records based on ancient ice exposed near the surface of the AIS (Yan et al., 2019), however, direct comparison is limited due to a lack of ancient ice cores with sufficiently continuous stratigraphy (Higgins et al., 2015; Brook and Buizert, 2018).

To conclude, there is *high confidence* that average EECO and MPWP (KM5c) CO_2 concentration was higher than those preceding industrialisation at 1150-2500 ppm and 360-420 ppm, respectively. Although there is some uncertainty due to the non-continuous nature of marine sediment records, the last time atmospheric CO_2 mixing ratio was as high as present was *very likely* more than 2 million years ago.

[START TABLE 2.1 HERE]

Table 2.1: Concentration (mixing ratios) and, where applicable, century time-scale rate of change of atmospheric CO_2 based on multiple datasets for target paleoclimate reference (Cross-Chapter Box 2.1, and Figure 2.34) and selected other periods. Modern data are from 2.2.3.3 and Annex III. 'AR6' denotes best estimates assessed in this report and propagated to Figure 2.34. Units for the rate of change are given only for centennial periods characterized by rapid changes. *Confidence* levels are *very high* for instrumentally derived concentrations, *high* for values derived from air in glacier ice (back to LIG), *medium* for values supported by multiple proxy types (MPWP, EECO), and *low* for values from a single sedimentary proxy type (PETM). '→' indicates transition from the beginning to the end of the time interval. Uncertainties for Modern are based on 2019 estimates. Last Millennium rate of range shows lowest and highest values attained during this period; LDT shows highest rate of change. See chapter data table for bibliographic citation and auxiliary information for each dataset (Table SM.1).

Reference period	**CO_2 concentration (ppm) and dataset details**	**Rate of change (ppm per century)**
Modern (1995-2014)	359.6 to 360.4 → 396.7 to 397.5 (AR6)	192.3 to 198.3* (AR6)
Last 100 years (1919-2019)	302.8 to 306.0 → 409.5 to 410.3 (AR6)	103.9 to 107.1 (AR6)
Approximate pre-industrial baseline (1850-1900) (See CCB1.2)	283.4 to 287.6 → 294.8 to 298.0 (AR6); 284.3† → 295.7† (CMIP6)	16.5 to 27.1* (AR6) 22.8†,* (CMIP6)
Last millennium (1000- 1750)	278.0 to 285.0 (AR6; average of WAIS Divide, Law Dome and EDML core data)	-6.9 ~ 4.7† (Law Dome); -1.9 ~ 3.2† (EDML); -5.2 ~ 4.2† (WAIS Divide)
MH	260.1 to 268.1 (Dome C; CMIP6)	
LDT	193.2† → 271.2† (AR6); 195.2† → 265.3† (Dome C); 191.2† → 277.0† (WAIS Divide)	9.6† (WAIS Divide); 7.1† (Dome C)

ACCEPTED VERSION SUBJECT TO FINAL EDITS

LGM	188.4 to 194.2 (AR6); 190.5 to 200.1 (WAIS Divide); 186.8 to 202.0 (Byrd); 184.9 to 193.1 (Dome C); 180.5 to 192.7 (Siple Dome); 190† (PMIP6); 174.2 to 205.8 (δ^{11}B proxy)	
LIG	265.9 to 281.5 (AR6); 259.4 to 283.8 (Vostok); 266.2 to 285.4 (Dome C); 275† (PMIP4) 282.2 to 305.8 (δ^{11}B proxy)	
MPWP (KM5c)	360 to 420 (AR6)	
EECO	1150 to 2500 (AR6)	
PETM	800 to 1000 → 1400 to 3150 (AR6)	4 to 42 (AR6)

*centennial rate of change estimated by extrapolation of data from a shorter time period. The values (x to y) represent *very likely* ranges (90% CIs)
† data uncertainty is not estimated.

[END TABLE 2.1 HERE]

[START FIGURE 2.3 HERE]

Figure 2.3: The evolution of atmospheric CO_2 through the last 450 million years. The periods covered are 0–450 Ma (a), 0–58 Ma (b), and 0–3500 ka (c), reconstructed from continental rock, marine sediment and ice core records. Note different timescales and axes ranges in panels (a), (b) and (c). Dark and light green bands in (a) are uncertainty envelopes at 68% and 95% uncertainty, respectively. 100 ppm in each panel is shown by the marker in the lower right hand corner to aid comparison between panels. In panel (b) and (c) the major paleoclimate reference periods (CCB2.1) have been labelled, and in addition: MPT (Mid Pleistocene Transition), MCO (Miocene Climatic Optimum). Further details on data sources and processing are available in the chapter data table (Table 2.SM.1).

[END FIGURE 2.3 HERE]

2.2.3.2 Glacial-interglacial WMGHG Fluctuations from 800 ka

Since AR5, the number of ice cores for the last 800 kyr has increased and their temporal resolution has improved (Figure 2.4), especially for the last 60 kyr and when combined with analyses of firn air, leading to improved quantification of greenhouse gas concentrations prior to the mid-20th century.

2.2.3.2.1 CO_2

Records of CO_2 from the AIS formed during the last glacial period and the LDT show century-scale fluctuations of up to 9.6 ppm (Ahn et al., 2012; Ahn & Brook, 2014; Bauska et al., 2015; Marcott et al., 2014; Rubino et al., 2019). Although these rates are an order of magnitude lower than those directly observed over 1919–2019 CE (Section 2.2.3.3.1), they provide information on non-linear responses of climate-biogeochemical feedbacks (Section 5.1.2). Multiple records for 0–1850 CE show CO_2 mixing ratios of 274–285 ppm. Offsets among ice core records are about 1%, but the long-term trends agree well and show coherent multi-centennial variations of about 10 ppm (Ahn et al., 2012; Bauska et al., 2015; Rubino et al., 2019). Multiple records show CO_2 concentrations of 278.3 ± 2.9 ppm in 1750 and 285.5 ± 2.1 ppm in 1850 (Ahn et al., 2012, 2019; Bauska et al., 2015; MacFarling Meure et al., 2006; Siegenthaler et al., 2005). CO_2 concentration increased by 5.0 ± 0.8 ppm during 970–1130 CE, followed by a decrease of 4.6 ± 1.7 ppm during 1580–1700 CE. The greatest rate of change over the CE prior to 1750 is observed at about 1600 CE, and ranges from –6.9 to 4.7 ppm per century in multiple high-resolution ice core records (Ahn et al., 2012; Bauska et al., 2015; MacFarling Meure et al., 2006; Rubino et al., 2019; Siegenthaler et al., 2005). Although ice core records present low-pass filtered time series due to gas diffusion and gradual bubble close-off in the snow layer over the ice sheet (Fourteau et al., 2020), the rate of increase since 1850 CE (about 125 ppm

ACCEPTED VERSION SUBJECT TO FINAL EDITS

increase over about 170 years) is far greater than implied for any 170-year period by ice core records that cover the last 800 ka (*very high confidence*).

2.2.3.2.2 CH_4

CH_4 concentrations over the past 110 kyr are higher in the Northern Hemisphere (NH) than in the Southern Hemisphere (SH), but closely correlated on centennial and millennial timescales (WAIS Divide Project Members, 2015). On glacial to interglacial cycles, approximately 450 ppb oscillations in CH_4 concentrations have occurred (Loulergue et al., 2008). On millennial timescales, most rapid climate changes observed in Greenland and other regions are coincident with rapid CH_4 changes (Rhodes et al., 2015, 2017; WAIS Divide Project Members, 2015). The variability of CH_4 on centennial timescales during the early Holocene does not significantly differ from that of the late Holocene prior to about 1850 (Rhodes et al., 2013; Yang et al., 2017). The LGM concentration was 390.5 ± 6.0 ppb (Kageyama et al., 2017). The global mean concentrations during 0–1850 CE varied between 625 and 807 ppb. High-resolution ice core records from Antarctica and Greenland exhibit the same trends with an inter-polar difference of 36–47 ppb (Mitchell et al., 2013b; Sapart et al., 2012). There is a long-term positive trend of about 0.5 ppb per decade during the Common Era (CE) until 1750 CE. The most rapid CH_4 changes prior to industrialisation were as large as 30–50 ppb on multi-decadal timescales. Global mean CH_4 concentrations estimated from Antarctic and Greenland ice cores are 729.2 ± 9.4 ppb in 1750 and 807.6 ± 13.8 ppb in 1850 (Mitchell et al., 2013b).

2.2.3.2.3 N_2O

New records show that N_2O concentration changes are associated with glacial-interglacial transitions (Schilt et al., 2014). The most rapid change during the last glacial termination is a 30 ppb increase in a 200-year period, which is an order of magnitude smaller than the modern rate (Section 2.2.3.3). During the LGM, N_2O was 208.5 ± 7.7 ppb (Kageyama et al., 2017). Over the Holocene the lowest value was 257 ± 6.6 ppb during 6–8 ka, but millennial variation is not clearly detectable due to analytical uncertainty and insufficient ice core quality (Flückiger et al., 2002; Schilt et al., 2010). Recently acquired high-resolution records from Greenland and Antarctica for the last 2 kyr consistently show multi-centennial variations of about 5–10 ppb (Figure 2.4), although the magnitudes vary over time (Ryu et al., 2020). Three high temporal resolution records exhibit a short-term minimum at about 600 CE of 261 ± 4 ppb (MacFarling Meure et al., 2006; Ryu et al., 2020). It is *very likely* that industrial N_2O increase started before 1900 CE (Machida et al., 1995; Sowers, 2001; MacFarling Meure et al., 2006; Ryu et al., 2020). Multiple ice cores show N_2O concentrations of 270.1 ± 6.0 ppb in 1750 and 272.1 ± 5.7 ppb in 1850 (Flückiger et al., 1999; Machida et al., 1995; Rubino et al., 2019; Ryu et al., 2020; Sowers, 2001).

[START FIGURE 2.4 HERE]

Figure 2.4: Atmospheric WMGHG concentrations from ice cores. (a) Records during the last 800 kyr with the LGM to Holocene transition as inset. (b) Multiple high-resolution records over the CE. The horizontal black bars in the panel a inset indicate Last Glacial Maximum (LGM) and Last Deglacial Termination (LDT) respectively. The red and blue lines in (b) are 100-year running averages for CO_2 and N_2O concentrations, respectively. The numbers with vertical arrows in (b) are instrumentally measured concentrations in 2019. Further details on data sources and processing are available in the chapter data table (Table 2.SM.1).

[END FIGURE 2.4 HERE]

2.2.3.3 Modern measurements of WMGHGs

In this section and for calculation of ERF, surface global averages are determined from measurements representative of the well-mixed lower troposphere. Global averages that include sites subject to significant anthropogenic activities or influenced by strong regional biospheric emissions are typically larger than those

ACCEPTED VERSION SUBJECT TO FINAL EDITS

from remote sites, and require weighting accordingly (Table 2.2). This section focusses on global mean mixing ratios estimated from networks with global spatial coverage, and updated from the CMIP6 historical dataset (Meinshausen et al., 2017) for periods prior to the existence of global networks.

[START TABLE 2.2 HERE]

Table 2.2: Atmospheric global annual mean mixing ratios (dry-air mole fraction) observed in 2011 and 2019, and relative changes since 2011, for selected well-mixed, radiatively important gases (ERF > 0.001 W m^{-2}), estimated from various measurement networks or compilations. Units are parts-per-million (ppm) for CO_2, parts-per-billion (ppb) for CH_4 and N_2O, parts-per-trillion (ppt) for all other gases. Time series since 1750, data for additional gases, references, and network information can be found in Annex III and the corresponding electronic supplement. Further details on data sources and processing are available in the chapter data table (Table 2.SM.1).

Species	Lifetime, AR6, ERF	2011	2019	Chg.	Network
CO_2	#	390.5	409.9 (0.17)	5.0%	NOAA*
	409.9 (0.4)	389.7	409.5 (0.37)	5.1%	SIO
	2.156	390.2	409.6 (0.31)	5.0%	CSIRO
		390.9	410.5 (0.30)	5.0%	WMO
		390.9			CMIP6
CH_4	9.1-11.8	1803.1	1866.6 (1.0)	3.5%	NOAA*
	1866.3 (3.3)	1803.6	1866.1 (2.0)	3.5%	AGAGE*
	0.544	1791.8	1860.8 (3.5)	3.9%	UCI
		1802.3	1862.5 (2.4)	3.3%	CSIRO
		1813	1877 (3)	3.5%	WMO
		1813.1			CMIP6
N_2O	116-109	324.2	331.9 (0.2)	2.4%	NOAA*
	332.1 (0.4)	324.7	332.3 (0.1)	2.4%	AGAGE*
	0.208	324.0	331.6 (0.3)	2.3%	CSIRO
		324.3	332.0 (0.2)	2.4%	WMO
		324.2			CMIP6
CFC-12	102	526.9	501.5 (0.3)	–4.8%	NOAA*
	503.1 (3.2)	529.6	504.6 (0.2)	–4.7%	AGAGE*
	0.180	525.3	508.4 (2.5)	–3.2%	UCI
CFC-11	52	237.2	226.5 (0.2)	–4.5%	NOAA*
	226.2 (1.1)	237.4	225.9 (0.1)	–4.8%	AGAGE*
	0.066	237.9	224.9 (1.3)	–5.5%	UCI
CFC-113	93	74.5	69.7 (0.1)	–6.4%	NOAA*
	69.8 (0.3)	74.6	69.9 (0.1)	–6.3%	AGAGE*
	0.021	74.9	70.0 (0.5)	–6.5%	UCI
CFC-114	189	16.36	16.28 (0.03)	–0.5%	AGAGE*
	16.0 (0.05)				
	0.005				
CFC-115	540	8.39	8.67 (0.02)	3.3%	AGAGE*
	8.67 (0.02)				
	0.002				
CCl_4	32	86.9	78.4 (0.1)	–9.8%	NOAA*
	77.9 (0.7)	85.3	77.3 (0.1)	–9.4%	AGAGE*
	0.013	87.8	77.7 (0.7)	–11.5%	UCI

Species	Lifetime, AR6, ERF	2011	2019	Chg.	Network
HCFC-22	11.9	212.6	246.8 (0.5)	16.1%	NOAA*
	246.8 (0.6)	213.7	246.7 (0.4)	15.5%	AGAGE*
	0.053	209.0	244.1 (3.0)	22.0%	UCI
HCFC-141b	9.4	21.3	24.4 (0.1)	14.4%	NOAA*
	24.4 (0.3)	21.4	24.3 (0.1)	13.7%	AGAGE*
	0.004	20.8	26.0 (0.3)	25.0%	UCI
HCFC-142b	18	20.9	22.0 (0.1)	5.3%	NOAA*
	22.3 (0.4)	21.5	22.5 (0.1)	5.0%	AGAGE*
	0.004	21.0	22.8 (0.2)	8.6%	UCI
HFC-134a	14	62.7	107.8 (0.4)	72%	NOAA*
	107.6 (1.0)	62.8	107.4 (0.2)	71%	AGAGE*
	0.018	63.4	107.6 (1.7)	70%	UCI
HFC-125	30	10.1	29.1 (0.3)	187%	NOAA*
	29.4 (0.6)	10.4	29.7 (0.1)	186%	AGAGE*
	0.007				
HFC-23	228	24.1	32.4 (0.1)	35%	AGAGE*
	32.4 (0.1)				
	0.006				
HFC-143a	51	11.9	23.8 (0.1)	100%	NOAA*
	24.0 (0.4)	12.1	24.2 (0.1)	100%	AGAGE*
	0.004				
HFC-32	5.4	4.27	19.2 (0.3)	350%	NOAA*
	20.0 (1.4)	5.15	20.8 (0.2)	304%	AGAGE*
	0.002				
CF_4	50,000	79.0	85.5 (0.1)	8.2%	AGAGE*
	85.5 (0.2)				
	0.005				
C_2F_6	10,000	4.17	4.85 (0.01)	16.3%	AGAGE*
	4.85 (0.1)				
	0.001				
SF_6	About 1000	7.32	9.96 (0.02)	36.1%	NOAA*
	9.95 (0.01)	7.28	9.94 (0.02)	36.5%	AGAGE*
	0.006				

AGAGE = Advanced Global Atmospheric Gases Experiment; SIO = Scripps Institution of Oceanography; NOAA = National Oceanic and Atmospheric Administration, Global Monitoring Laboratory; UCI = University of California, Irvine; CSIRO = Commonwealth Scientific and Industrial Research Organization, Aspendale, Australia; WMO = World Meteorological Organization, Global Atmosphere Watch, CMIP6 (Climate Model Intercomparison Project – Phase 6). Mixing ratios denoted by AR6 are representative of the remote, unpolluted troposphere, derived from one or more measurement networks (denoted by *). Minor differences between 2011 values reported here and in the previous Assessment Report (AR5) are due to updates in calibration and data processing. ERF in 2019 is taken from Table 7.5, and the difference with the AR5 assessment reflects updates in the estimates of AR6 global mixing ratios and updated radiative calculations. Uncertainties, in parenthesis, are estimated at 90% confidence interval. Networks use different methods to estimate uncertainties. Some uncertainties have been rounded up to be consistent with the number of decimal places shown. Lifetime is reported in years: # indicates multiple lifetimes for CO_2. For CH_4 and N_2O the two values represent total atmospheric lifetime and perturbation lifetime.

[END TABLE 2.2 HERE]

ACCEPTED VERSION SUBJECT TO FINAL EDITS

2.2.3.3.1 Carbon Dioxide (CO_2)

There has been a positive trend in globally averaged surface CO_2 mixing ratios since 1958 (Figure 2.5a), that reflects the imbalance of sources and sinks (Section 5.2). The growth rate has increased overall since the 1960s (Figure 2.5a inset), while annual growth rates have varied substantially, e.g. reaching a peak during the strong El Niño events of 1997–1998 and 2015–2016 (Bastos et al., 2013; Betts et al., 2016). The average annual CO_2 increase from 2000 through 2011 was 2.0 ppm yr^{-1} (standard deviation 0.3 ppm yr^{-1}), similar to what was reported in AR5. From 2011 through 2019 it was 2.4 ppm yr^{-1} (standard deviation 0.5 ppm yr^{-1}), which is higher than that of any comparable time period since global measurements began. Global networks consistently show that the globally averaged annual mean CO_2 has increased by 5.0% since 2011, reaching 409.9 ± 0.4 ppm in 2019 (NOAA measurements). Further assessment of changing seasonality is undertaken in Section 2.3.4.1.

[START FIGURE 2.5 HERE]

Figure 2.5: Globally averaged dry-air mole fractions of well-mixed greenhouse gases. (a) CO_2 from SIO, CSIRO, and NOAA/GML (b) CH_4 from NOAA, AGAGE, CSIRO, and UCI; and (c) N_2O from NOAA, AGAGE, and CSIRO (see Table 2.2). Growth rates, calculated as the time derivative of the global means after removing seasonal cycle are shown as inset figures. Note that the CO_2 series is 1958–2019 whereas CH_4, and N_2O are 1979–2019. Further details on data are in Annex III, and on data sources and processing are available in the chapter data table (Table 2.SM.1).

[END FIGURE 2.5 HERE]

2.2.3.3.2 Methane (CH_4)

The globally averaged surface mixing ratio of CH_4 in 2019 was 1866.3 ± 3.3 ppb, which is 3.5% higher than 2011, while observed increases from various networks range from 3.3–3.9% (Table 2.2; Figure 2.5b). There are marked growth rate changes over the period of direct observations, with a decreasing rate from the late-1970s through the late-1990s, very little change in concentrations from 1999–2006, and resumed increases since 2006. Atmospheric CH_4 fluctuations result from complex variations of sources and sinks. A detailed discussion of recent methane trends and our understanding of their causes is presented in Cross-Chapter Box 5.2.

2.2.3.3.3 Nitrous Oxide (N_2O)

AR5 reported 324.2 ± 0.1 ppb for global surface annual mean N_2O in 2011; since then, it has increased by 2.4% to 332.1 ± 0.4 ppb in 2019. Independent measurement networks agree well for both the global mean mixing ratio and relative change since 2011 (Table 2.2). Over 1995–2011, N_2O increased at an average rate of 0.79 ± 0.05 ppb yr^{-1}. The growth rate has been higher in recent years, amounting to 0.96 ± 0.05 ppb yr^{-1} from 2012 to 2019 (Figure 2.5c) (Section 5.2.3.5).

2.2.3.4 Summary of changes in WMGHGs

In summary, CO_2 has fluctuated by at least 2000 ppm over the last 450 Myr (*medium confidence*). The last time CO_2 concentrations were similar to the present-day was over 2 Ma (*high confidence*). Further, it is certain that WMGHG mixing ratios prior to industrialisation were lower than present-day levels and the growth rates of the WMGHGs from 1850 are unprecedented on centennial timescales in at least the last 800 kyr. During the glacial-interglacial climate cycles over the last 800 kyr, the concentration variations of the WMGHG were 50–100 ppm for CO_2, 210–430 ppb for CH_4 and 60–90 ppb for N_2O. Between 1750–2019 mixing ratios increased by 131.6 ± 2.9 ppm (47%), 1137 ± 10 ppb (156%), and 62 ± 6 ppb (23%), for CO_2, CH_4, and N_2O, respectively (*very high confidence*). Since 2011 (AR5) mixing ratios of CO_2, CH_4, and N_2O have further increased by 19 ppm, 63 ppb, and 7.7 ppb, reaching in 2019 levels of 409.9 (± 0.4) ppm, 1866.3 (± 3.3) ppb, and 332.1 (± 0.4) ppb, respectively. By 2019, the combined ERF (relative to 1750) of CO_2, CH_4 and N_2O was 2.9 ± 0.5 W m^{-2} (Table 2.2; Section 7.3.2).

ACCEPTED VERSION SUBJECT TO FINAL EDITS

2.2.4 Halogenated Greenhouse Gases (CFCs, HCFCs, HFCs, PFCs, SF6 and others)

This category includes ozone depleting substances (ODS), their replacements, and gases used industrially or produced as by-products. Some have natural sources (Section 6.2.2.4). AR5 reported that atmospheric abundances of chlorofluorocarbons (CFCs) were decreasing in response to controls on production and consumption mandated by the Montreal Protocol on Substances that Deplete the Ozone Layer and its amendments. In contrast, abundances of both hydrochlorofluorocarbons (HCFCs, replacements for CFCs) and hydrofluorocarbons (HFCs, replacements for HCFCs) were increasing. Atmospheric abundances of perfluorocarbons (PFCs), SF_6, and NF_3 were also increasing.

Further details on ODS and other minor greenhouse gases can be found in the Scientific Assessment of Ozone Depletion: 2018 (Engel & Rigby, 2018; Montzka & Velders, 2018). Updated mixing ratios of the most radiatively important gases (ERF > 0.001 W m^{-2}) are reported in Table 2.2, and additional gases (ERF <0.001 W m^{-2}) are shown in Annex III.

2.2.4.1 CFCs

Atmospheric abundances of most CFCs have continued to decline since 2011 (AR5). The globally-averaged abundance of CFC-12 decreased by 25 ppt (4.8%) from 2011 to 2019, while CFC-11 decreased by about 11 ppt (4.7%) over the same period (Table 2.2, Figure 2.6). Atmospheric abundances of some minor CFCs (CFC-13, CFC-115, CFC-113a) have increased since 2011 (Annex III), possibly related to use of HFCs (Laube et al., 2014). Overall, as of 2019 the ERF from CFCs has declined by 9 ± 0.5% from its maximum in 2000, and 4.7 ± 0.6% since 2011 (Table 7.5).

While global reporting indicated that CFC-11 production had essentially ceased by 2010, and the atmospheric abundance of CFC-11 is still decreasing, emissions inferred from atmospheric observations began increasing in 2013–2014 and remained elevated for 5–6 years, suggesting renewed and unreported production (Montzka et al., 2018; 2021; Park et al., 2021; Rigby et al., 2019). The global lifetimes of several ozone-depleting substances have been updated (SPARC, 2013), in particular for CFC-11 from 45 to 52 years.

[START FIGURE 2.6 HERE]

Figure 2.6: Global mean atmospheric mixing ratios of select ozone-depleting substances and other greenhouse gases. Data shown are based on the CMIP6 historical dataset and data from NOAA and AGAGE global networks. PFCs include CF_4, C_2F_6, and C_3F_8, and *c*-C_4F_8; Halons include halon-1211, halon-1301, and halon-2402; other HFCs include HFC-23, HFC-32, HFC-125, HFC-143a, HFC-152a, HFC-227ea, HFC-236fa, HFC-245fa, and HFC-365mfc, and HFC-43-10mee. Note that the y-axis range is different for a, b and c and a 25 ppt yardstick is given next to each panel to aid interpretation. Further data are in Annex III, and details on data sources and processing are available in the chapter data table (Table 2.SM.1).

[END FIGURE 2.6 HERE]

2.2.4.2 HCFCs

The atmospheric abundances of the major HCFCs (HCFC-22, HCFC-141b, HCFC-142b), primarily used in refrigeration and foam blowing, are increasing, but rates of increase have slowed in recent years (Figure 2.6). Global mean mixing ratios (Table 2.2) showed good concordance at the time of AR5 for the period 2005–2011. For the period 2011–2019, the UCI network detected larger increases in HCFC-22, HCFC-141b, and HCFC-142b compared to the NOAA and AGAGE networks. Reasons for the discrepancy are presently unverified, but could be related to differences in sampling locations in the networks (Simpson et al., 2012). Emissions of HCFC-22, derived from atmospheric data, have remained relatively stable since 2012, while those of HCFC-141b and HCFC-142b have declined (Engel et al., 2018). Minor HCFCs, HCFC-133a and

ACCEPTED VERSION SUBJECT TO FINAL EDITS

HCFC-31, have been detected in the atmosphere (currently less than 1 ppt) and may be unintentional by-products of HFC production (Engel et al., 2018).

2.2.4.3 HFCs, PFCs, SF6 and other radiatively important halogenated gases

Hydrofluorocarbons (HFCs) are replacements for CFCs and HCFCs. The atmospheric abundances of many HFCs increased between 2011 and 2019. HFC-134a (mobile air conditioning, foam blowing, and domestic refrigerators) increased by 71 % from 63 ppt in 2011 to 107.6 ppt in 2019 (Table 2.2). The UCI network detected a slightly smaller relative increase (53%). HFC-23, which is emitted as a by-product of HCFC-22 production, increased by 8.4 ppt (35%) over 2011–2019. HFC-32 used as a substitute for HCFC-22, increased at least by 300%, and HFC-143a and HFC-125 showed increases of 100% and 187%, respectively. While the ERF of HFC-245fa is currently < 0.001 W m^{-2}, its atmospheric abundance doubled since 2011 to 3.1 ppt in 2019 (Annex III). In contrast, HFC-152a is showing signs of stable (steady-state) abundance.

Other radiatively important gases with predominantly anthropogenic sources also continue to increase in abundance. SF_6, used in electrical distribution systems, magnesium production, and semi-conductor manufacturing, increased from 7.3 ppt in 2011 to 10.0 ppt in 2019 (+36%). Alternatives to SF_6 or SF_6-free equipment for electrical systems have become available in recent years, but SF_6 is still widely in use in electrical switch gear (Simmonds et al., 2020). The global lifetime of SF_6 has been revised from 3200 years to about 1000 years (Kovács et al., 2017; Ray et al., 2017) with implications for climate emission metrics (Section 7.6.2). NF_3, which is used in the semi-conductor industry, increased 147% over the same period to 2.05 ppt in 2019. Its contribution to ERF remains small, however, at 0.0004 W m^{-2}. The atmospheric abundance of SO_2F_2, which is used as a fumigant in place of ozone-depleting methyl bromide, reached 2.5 ppt in 2019, a 46% increase from 2011. Its ERF also remains small at 0.0005 W m^{-2}.

The global abundance of CCl_4 continues to decline, down about 9.6% since 2011. Following a revision of the global lifetime from 26 to 32 years, and discovery of previously unknown sources (e.g. biproduct industrial emissions), knowledge of the CCl_4 budget has improved. There is now better agreement between top-down emissions estimates (based on atmospheric measurements) and industry-based estimates (Engel et al., 2018). Halon-1211, mainly used for fire suppression, is also declining, and its ERF dropped below 0.001 W m^{-2} in 2019. While CH_2Cl_2 has a short atmospheric lifetime (6 months), and is not well-mixed, its abundance is increasing and its ERF is approaching 0.001 W m^{-2}.

Perfluorocarbons CF_4 and C_2F_6, which have exceedingly long global lifetimes, showed modest increases from 2011 to 2019. CF_4, which has both natural and anthropogenic sources, increased 8.2% to 85.5 ppt, and C_2F_6 increased 16.3% to 4.85 ppt. *c*-C_4F_8, which is used in the electronics industry and may also be generated during the production of polytetrafluoroethylene (PTFE, "Teflon") and other fluoropolymers (Mühle et al., 2019), has increased 34% since 2011 to 1.75 ppt, although its ERF remains below 0.001 W m^{-2}. Other PFCs, present at mixing ratios < 1 ppt, have also been quantified (Droste et al., 2020; Annex III).

2.2.4.4 Summary of changes in halogenated gases

In summary, by 2019 the ERF of halogenated GHGs has increased 3.5% since 2011, reflecting predominantly a decrease in the atmospheric mixing ratios of CFCs and an increase in their replacements. However, average annual ERF growth rates associated with halogenated gases since 2011 are a factor of seven lower than in the 1970s and 1980s. Direct radiative forcings from CFCs, HCFCs, HFCs, and other halogenated greenhouse gases were 0.28, 0.06, 0.04, and 0.03 W m^{-2} respectively, totalling 0.41 ± 0.07 W m^{-2} in 2019 (see Table 7.5).

ACCEPTED VERSION SUBJECT TO FINAL EDITS

2.2.5 Other short-lived gases

2.2.5.1 Stratospheric water vapour

AR5 assessed *low confidence* in stratospheric water vapour (SWV) trends based on substantial seasonal and interannual variability in satellite data from 1992 to 2011. The 1980–2010 record of balloon-borne frost point hygrometer measurements over Boulder, Colorado (40°N), showed an average net increase of 1.0 ± 0.2 ppm (27 ± 6%) in the 16–26 km layer.

Since AR5, bias-adjusted spatially comprehensive SWV measurements by different satellite sensors were merged to form continuous records (Hegglin et al., 2014; Froidevaux et al., 2015; Davis et al., 2016). These indicate no net global increase of SWV in the lower stratosphere since the late 1980s. Hegglin et al. (2014) reported a latitudinal dependence of SWV trends and suggested that the upward trend over Boulder should not be considered representative of the global stratosphere, while Lossow et al. (2018) showed insignificant differences between SWV trends at Boulder and those for the 35–45°N zonal mean from 1980 to 2010 using model simulations and satellite observations.

Recent studies of dynamical influences on SWV (Eguchi et al., 2015; Evan et al., 2015; Tao et al., 2015; Konopka et al., 2016; Diallo et al., 2018; Garfinkel et al., 2018) have demonstrated that the quasi-biennial oscillation (QBO), El Niño-Southern Oscillation (ENSO), Sudden Stratospheric Warming (SSW) events and possibly also Pacific Decadal Variability (PDV) (Wang W. et al., 2016), can significantly influence SWV abundance and the tropical cold point tropopause temperatures that largely control water vapour entering the stratosphere. It has also been shown that the convective lofting of ice can moisten the lower stratosphere over large regions (Dessler et al., 2016; Anderson et al., 2017; Avery et al., 2017). Near-global observations of SWV have revealed unusually strong and abrupt interannual changes, especially in the tropical lower stratosphere. Between December 2015 and November 2016, the tropical mean SWV anomaly at 82 hPa dropped from 0.9 ± 0.1 ppm to –1.0 ± 0.1 ppm, accompanied by highly anomalous QBO-related dynamics in the tropical stratosphere (Newman P. et al., 2016; Tweedy et al., 2017) and the transition of ENSO from strong El Niño to La Niña conditions (Davis et al., 2017). The tropical mean SWV anomaly then rose sharply to 0.7 ± 0.1 ppm in June 2017 as warm westerlies returned to the tropical lower stratosphere and ENSO neutral conditions prevailed (Davis et al., 2017).

In summary, in situ measurements at a single mid-latitude location indicate about a 25% net increase in stratospheric water vapour since 1980, while merged satellite data records since the late 1980s suggest little net change. Recent studies of dynamical influences on SWV have highlighted their substantial roles in driving large interannual variability that complicates trend detection. There thus continues to be *low confidence* in trends of SWV over the instrumental period. Disregarding dynamic influences on SWV, an ERF of 0.05 ± 0.05 W m^{-2} is estimated for SWV produced by CH_4 oxidation (Section 7.3.2.6), unchanged from AR5.

2.2.5.2 Stratospheric ozone

AR5 assessed that it was certain that global stratospheric ozone from the mid-1990s to 2011 was nearly constant and about 3.5% lower than in the reference period 1964–1980. Most of the declines occurred prior to the mid-1990s.

Global annual mean total ozone (Figure 2.7) significantly declined by about 3.5% during the 1980s and the early 1990s and by 2.5% over 60°S–60°N (near-global). Then, during 2000–2017, both global and near-global concentrations increased slightly, but not significantly, all in line with production and consumption limits of ODS regulated under the Montreal Protocol and its amendments. Near-global 2014–2017 mean total ozone is about 2.2% below the pre-ozone depletion 1964–1980 average (Braesicke et al., 2018). At southern and northern mid-latitudes, declines are 5.5% and 3.0% compared to the 1964–1980 average respectively. Total ozone remained practically unchanged in the tropics (Braesicke et al., 2018). Emission of ODS started before 1980 and some estimates suggest that as much as 40% of the long-term ozone loss

ACCEPTED VERSION SUBJECT TO FINAL EDITS

occurred between 1960 and 1980 (Shepherd et al., 2014), lowering the 1964–1980 baseline values by about 1% (outside the polar regions), a value close to observational uncertainties. The world's longest record of total ozone measurements from Arosa, Switzerland, initiated in 1926, does not show any substantial long-term changes before about 1980 (Staehelin et al., 2018).

[START FIGURE 2.7 HERE]

Figure 2.7: Time series of annual mean total column ozone from 1964-2019. Values are in Dobson Units (DU), a good proxy for vertically integrated stratospheric ozone. Time series are shown for (a) near-global domain, (b-d) three zonal bands and (e) polar (60°–90°) total ozone in March (NH) and October (SH) ; the months when polar ozone losses usually are largest. Further details on data sources and processing are available in the chapter data table (Table 2.SM.1).

[END FIGURE 2.7 HERE]

ERF depends strongly on the altitude of ozone changes. Two stratospheric regions are mainly responsible for long-term changes outside the polar regions. In the upper stratosphere (35–45 km), there was a strong decline (about 10%) from the start of observations in 1979 up to the mid-1990s and a subsequent increase by about 4% to present (SPARC/IO3C/GAW, 2019). In the lower stratosphere (20–25 km), there also was a statistically significant decline (7–8%) up to the mid-1990s, followed by stabilization or a small further decline (Ball et al., 2018; 2019), although the natural variability is too strong to make a conclusive statement (Chipperfield et al., 2018).

The strongest ozone loss in the stratosphere continues to occur in austral spring over Antarctica (ozone hole) with emergent signs of recovery after 2000 (Langematz et al., 2018). Interannual variability in polar stratospheric ozone is driven by large scale winds and temperatures, and, to a lesser extent, by the stratospheric aerosol loading and the solar cycle. This variability is particularly large in the Arctic, where the largest depletion events, comparable to a typical event in the Antarctic, occurred in 2011 (Manney et al., 2011; Langematz et al., 2018) and again in 2020 (Grooß and Müller, 2020; Manney et al., 2020). Further details on trends and ERF can be found in sections 6.3.2 and 7.3.2.5.

In summary, compared to the 1964–1980 average, stratospheric ozone columns outside polar regions (60°S–60°N) declined by about 2.5% over 1980–1995, and stabilized after 2000, with 2.2% lower values in 2014–2017. Large ozone depletions continue to appear in spring in the Antarctic and, in particularly cold years, also in the Arctic. Model based estimates disagree on the sign of the ERF due to stratospheric ozone changes, but agree that it is much smaller in magnitude than that due to tropospheric ozone changes (Section 7.3.2.5).

2.2.5.3 Tropospheric ozone

AR5 assessed *medium confidence* in large-scale increases of tropospheric ozone at rural surface sites across the NH (1970–2010), and in a doubling of European surface ozone during the 20th century, with the increases of surface ozone in the SH being of *low confidence*. Surface ozone *likely* increased in East Asia, but levelled off or decreased in the eastern USA and Western Europe. Free tropospheric trends (1971–2010) from ozonesondes and aircraft showed positive trends in most, but not all, assessed regions, and for most seasons and altitudes. This section focuses on large scale ozone changes; chemical and physical processes and regional changes in tropospheric ozone are assessed in Section 6.3.2.1 and Section 7.3.2.5 assesses radiative forcing.

Prior to 1850 ozone observations do not exist, but a recent analysis using clumped-isotope composition of molecular oxygen ($^{18}O^{18}O$ in O_2) trapped in polar firn and ice, combined with atmospheric chemistry model simulations, constrains the global tropospheric ozone increase to less than 40% between 1850 and 2005, with most of this increase occurring between 1950 and 1980 (Yeung et al., 2019). Recently, the Tropospheric Ozone Assessment Report identified and evaluated 60 records of surface ozone observations collected at

ACCEPTED VERSION SUBJECT TO FINAL EDITS

rural locations worldwide between 1896 and 1975, which were based on a range of measurement techniques with potentially large uncertainties (Tarasick et al., 2019). They found that from the mid-20th century (1930s to the early 1970s) to 1990–2014, rural surface ozone increased by 30–70% across the northern extra-tropics. This is smaller than the 100% 20th century increase reported in AR5, which relied on far fewer measurement sites, all in Europe. In the northern tropics limited low-elevation historical data (1954–1975) provide no clear indication of surface ozone increases (Tarasick et al., 2019). However, similar to the northern mid-latitude increases, lower-free tropospheric ozone at Mauna Loa, Hawaii increased by approximately 50% from the late 1950s to present (Cooper et al., 2020). Historical observations are too limited to draw conclusions on surface ozone trends in the SH tropics and mid-latitudes since the mid-20th century, with tropospheric ozone exhibiting little change across Antarctica (Tarasick et al., 2019; Cooper et al., 2020). Based on reliable UV absorption measurements at remote locations (surface and lower troposphere), ozone trends since the mid-1990s varied spatially at northern mid-latitudes, but increased in the northern tropics (2-17%; 1-6 ppbv per decade) (Cooper et al., 2020; Gaudel et al., 2020). Across the SH these more recent observations are too limited to determine zonal trends (e.g. tropics, mid-latitudes, high latitudes).

The earliest observations of free tropospheric ozone (1934–1955) are available from northern mid-latitudes where limited data indicate a tropospheric column ozone increase of 48 ± 30% up to 1990–2012 (Tarasick et al., 2019). Starting in the 1960s, records from ozonesondes show no significant changes in the free troposphere over the Arctic and mid-latitude regions of Canada, but trends are mainly positive elsewhere in the northern mid-latitudes (Cooper et al., 2020; Oltmans et al., 2013). Tropospheric column and free tropospheric trends since the mid-1990s based on commercial aircraft, ozonesonde observations and satellite retrievals (Figure 2.8b,c), are overwhelmingly positive across the northern mid-latitudes (2–7%; 1–4 ppbv per decade) and tropics (2–14%; 1–5 ppbv per decade), with the largest increases (8–14%; 3–6 ppbv per decade) in the northern tropics in the vicinity of southern Asia and Indonesia. Observations in the SH are limited, but indicate average tropospheric column ozone increases of 2–12% (1–5 ppbv) per decade in the tropics (Figure 2.8c), and weak tropospheric column ozone increases (< 5%, < 1 ppbv per decade) at mid-latitudes (Cooper et al., 2020). Above Antarctica, mid-tropospheric ozone has increased since the late 20th century (Oltmans et al., 2013). The total ozone ERF from 1750 to 2019 best estimate is assessed as 0.47 W m^{-2} (7.3.2.5) and this is dominated by increases in the troposphere. The underlying modelled global tropospheric ozone column increase (Skeie et al., 2020) from 1850 to 2010 of 40–60%, is somewhat higher than the isotope based upper-limit of Yeung et al., (2019). At mid-latitudes (30°–60° N) model increases of 30–40% since the mid-20th century are broadly consistent with observations.

In summary, *limited* available isotopic *evidence* constrains the global tropospheric ozone increase to less than 40% between 1850 and 2005 (*low confidence*). Based on sparse historical surface/low altitude data tropospheric ozone has increased since the mid-20th century by 30–70% across the NH (*medium confidence*). Surface / low altitude ozone trends since the mid-1990s are variable at northern mid-latitudes, but positive in the tropics [2 to 17% per decade] (*high confidence*). Since the mid-1990s, free tropospheric ozone has increased by 2–7% per decade in most regions of the northern mid-latitudes, and 2–12% per decade in the sampled regions of the northern and southern tropics (*high confidence*). Limited coverage by surface observations precludes identification of zonal trends in the SH, while observations of tropospheric column ozone indicate increases of less than 5% per decade at southern mid-latitudes (*medium confidence*).

[START FIGURE 2.8 HERE]

Figure 2.8: Surface and tropospheric ozone trends. (a) Decadal ozone trends by latitude at 28 remote surface sites and in the lower free troposphere (650 hPa, about 3.5 km) as measured by IAGOS aircraft above 11 regions. All trends are estimated for the time series up to the most recently available year, but begin in 1995 or 1994. Colours indicate significance (p-value) as denoted in the in-line key. See Figure 6.5 for a depiction of these trends globally. (b) Trends of ozone since 1994 as measured by IAGOS aircraft in 11 regions in the mid-troposphere (700–300 hPa; about 3–9 km) and upper troposphere (about 10-12 km), as measured by IAGOS aircraft and ozonesondes. (c) Trends of average tropospheric column ozone mixing ratios from the TOST composite ozonesonde product and three composite satellite products based on TOMS, OMI/MLS (Sat1), GOME, SCIAMACHY, OMI, GOME-2A, GOME-2B (Sat2), and GOME, SCIAMACHY, GOME-II (Sat3). Vertical bars indicate the latitude range of each product, while horizontal lines indicate the *very likely* uncertainty range.. Further details on data sources and processing

ACCEPTED VERSION SUBJECT TO FINAL EDITS

are available in the chapter data table (Table 2.SM.1).

[END FIGURE 2.8 HERE]

2.2.6 Aerosols

AR5 assessed large-scale Aerosol Optical Depth (AOD) trends over 2000–2009, concluding that there was *low confidence* in a global trend, but that AOD *very likely* decreased from 1990 onwards over Europe and the eastern USA, and increased since 2000 over eastern and southern Asia. The ERF associated with aerosol-radiation interactions for 2011 (relative to 1750) was estimated to be -0.45 ± 0.5 W m^{-2} and of aerosol-cloud interaction estimated as -0.45 [-1.2–0.0] W m^{-2}. Aerosol ERF uncertainty was assessed as the largest contributor to the overall ERF uncertainty since 1750.

This section assesses the observed large-scale temporal evolution of tropospheric aerosols. Aerosol-related processes, chemical and physical properties, and links to air quality, are assessed in Chapter 6. An in-depth assessment of aerosol interactions with radiation and clouds is provided in Section 7.3.3.

Aerosol proxy records of improved temporal resolution and quality are now available (Dornelas et al., 2018; Jacobel et al., 2017; Kylander et al., 2016; Middleton et al., 2018; Stevens et al., 2016; 2018), which further advance synthesis of new global compilations of aerosol loadings (Lambert et al., 2015; Albani et al., 2016). Estimates of the glacial / interglacial ratio in global dust deposition are within the range of 2–4 (Albani et al., 2015; Lambert et al., 2015). New reconstructions indicate a ratio of 3–5 for the glacial / interglacial loadings for mid- and high-latitude ocean of both hemispheres (Lamy et al., 2014; Martinez-Garcia et al., 2014; Serno et al., 2015). Improved quantification of changes in dust deposition from North Africa and North Atlantic sediment records confirms dust deposition rates lower by a factor 2–5 during the African Humid Period (10–5 ka) compared to the late Holocene (McGee et al., 2013; Albani et al., 2015; Middleton et al., 2018; Palchan & Torfstein, 2019). During the Holocene, biogenic emissions and volcanic activity drove significant variability (up to one order of magnitude) in sulphate concentrations (Schüpbach et al., 2018).

Ice cores allow for estimation of multi-centennial trends in mid- and high-latitude aerosol deposition, including those for sulphate and black carbon (Figure 2.9 a, b). Sulphate in ice cores increased by a factor of 8 from the end of the 19th century to the 1970s in continental Europe, by a factor of 4 from the 1940s to the 1970s in Russia, and by a factor of 3 from the end of the 19th century to 1950 in the Arctic (Svalbard). In all regions studied, concentrations have declined by about a factor of 2 following their peak (around 1970 in Europe and Russia, and 1950 in the Arctic). Strong increases of black carbon (BC) were observed in the 20th century over Europe, Russia, Greenland (primarily originating from emissions from North America), and in the Arctic (Svalbard). South America exhibits a small positive trend (Figure 2.9). BC concentrations in various Antarctic ice cores were below 1 ng g^{-1} without a clear trend.

Spatially resolved trends of AOD derived from Aqua/Terra MISR and MODIS instruments over 2000–2019 range between -2% and 2% per year (Figure 2.9c). Ground-based solar attenuation networks help to constrain and improve the satellite-derived retrievals of AOD, and trends derived from the AERONET network (Figure 2.9c, d) corroborate satellite results (Bauer et al., 2020; Georgoulias et al., 2016; Wei et al., 2019; Yu et al., 2020) in particular for declines over Europe (Stjern et al., 2011; Cherian et al., 2014; Li et al., 2014) and the USA (Jongeward et al., 2016; Li et al., 2014). The tendency in AOD over East Asia reversed from positive (2000–2010) to negative (since 2010) (Filonchyk et al., 2019; Ma et al., 2019; Samset et al., 2019; Sogacheva et al., 2018). Over southern Asia, however, AOD from satellite (MODIS / MISR) and AERONET retrievals show continuing increases (Li et al., 2014; Zhao et al., 2017), with similar trends from UV-based aerosol retrievals from the Ozone Monitoring Instrument (OMI) on the Aura satellite (Dahutia et al., 2018; Hammer et al., 2018). A comparison of MODIS and MISR radiometric observations with the broadband CERES satellite instrument (Corbett and Loeb, 2015) showed that drifts in calibration are *unlikely* to affect the satellite derived trends. CERES shows patterns for clear-sky broadband radiation consistent with the aerosol spatio-temporal changes (Loeb et al., 2018; Paulot et al., 2018).

Satellite-derived trends are further supported by in situ regional surface concentration measurements,

ACCEPTED VERSION SUBJECT TO FINAL EDITS

operational since the 1980s (sulphate) and 1990s (PM2.5) from a global compilation (Coen et al., 2020) of networks over Europe (Stjern et al., 2011), North America (Jongeward et al., 2016), and China (Zheng et al., 2018). Collaud Coen et al. (2020) report from surface observations across the NH mid-latitudes that aerosol absorption coefficients decreased since the first decade of the 21st century.

Anthropogenic aerosol is predominantly found in the fraction of particles with radii <1 μm that comprise the fine-mode AOD (AODf) (Kinne, 2019) (Figure 2.9d). A significant decline in AODf of more than 1.5% per year from 2000 to 2019 has occurred over Europe and North America, while there have been positive trends of up to 1.5% per year over Southern Asia and East Africa. The global-scale trend in AODf of –0.03% per year (Figure 2.9) is significant. The results are consistent with trend estimates from an aerosol reanalysis (Bellouin et al., 2020), and the trends in satellite-derived cloud droplet number concentrations are consistent with the aerosol trends (Cherian and Quaas, 2020). Cloudiness and cloud radiative properties trends are, however, less conclusive possibly due to their large variability (Norris et al., 2016; Cherian and Quaas, 2020). Further details on aerosol-cloud interactions are assessed in Section 7.3.3.2.

[START FIGURE 2.9 HERE]

Figure 2.9: Aerosol evolution from ice-core measurements. Changes are shown as 10-yr averaged time series (a, b) and trends in remote-sensing aerosol optical depth (AOD) and AODf (c, d). (a) Concentrations of non-sea salt (nss) sulphate (ng g^{-1}). (b) Black carbon (BC) in glacier ice from the Arctic (Lomonosovfonna), Russia (Belukha), Europe (Colle Gnifetti), South America (Illimani), Antarctica (stacked sulphate record, and BC from the B40 core), and BC from Greenland (stacked rBC record from Greenland and Eastern Europe (Elbrus)). (c) Linear trend in annual mean AOD retrieved from satellite data for the 2000–2019 period (% yr^{-1}). The average trend from MODerate Resolution Imaging Spectroradiometer (MODIS) and Multi-Angle Imaging Spectroradiometer (MISR) is shown. Trends are calculated using OLS regression with significance assessed following AR(1) adjustment after Santer et al., (2008a). Superimposed are the trends in annual-mean AOD from the AERONET surface sunphotometer network for 2000–2019. (d) Linear trend in 2000–2019 as in (c), but for fine-mode AOD, AODf, and using only MISR over land. Significance is assessed following AR(1) adjustment after Santer et al., (2008a), 'x' marks denote non-significant trends. Further details on data sources and processing are available in the chapter data table (Table 2.SM.1).

[END FIGURE 2.9 HERE]

To conclude, atmospheric aerosols sampled by ice cores, influenced by northern mid-latitude emissions, show positive trends from 1700 until the last quarter of the 20th century and decreases thereafter (*high confidence)*, but there is *low confidence* in observations of systematic changes in other parts of the world in these periods. Satellite data and ground-based records indicate that AOD exhibits predominantly negative trends since 2000 over NH mid-latitudes and SH continents, but increased over South Asia and East Africa (*high confidence*). A globally deceasing aerosol abundance is thus assessed with *medium confidence*. This implies increasing net positive ERF, since the overall negative aerosol ERF has become smaller.

2.2.7 Land use and land cover

AR5 assessed that land use change *very likely* increased the Earth's albedo with a radiative forcing of -0.15 (± 0.10) W m^{-2}. AR5 also assessed that a net cooling of the surface, accounting for processes that are not limited to the albedo, was *about as likely as not*. SRCCL concluded with *medium confidence* that the biophysical effects of land cover change (mainly increased albedo) had a cooling effect on surface temperatures. SRCCL also concluded with *very high confidence* that the biogeochemical effects of land cover change (i.e., GHG emissions) resulted in a mean annual surface warming.

Much of the global land surface has been modified or managed to some extent by human activities during the Holocene. Reconstructions based on pollen data indicate that natural vegetation probably covered most of

ACCEPTED VERSION SUBJECT TO FINAL EDITS

the Earth's ice-free terrestrial surface until roughly the mid-Holocene (Harrison et al., 2020; Li et al., 2020; Marquer et al., 2017). Reconstructions based on pollen, archaeological, and historical data indicate deforestation at the regional scale since at least 6 ka (Harrison et al., 2020; Li et al., 2020; Marquer et al., 2017; Stephens et al., 2019). From a global perspective, land-use forcing datasets (Lawrence et al., 2016) estimate that changes in land use (and related deforestation) were small on the global scale until the mid-19th century and accelerated markedly thereafter, with larger uncertainties prior to industrialization (Kaplan et al., 2017). Since the early 1980s, about 60% of all land cover changes have been associated with direct human activities, with spatial patterns emphasizing the regional character of land use and land management, including tropical deforestation, temperate afforestation, cropland intensification, and increased urbanization (Song et al., 2018, Zeng et al., 2018). At present, nearly three-quarters of the ice-free terrestrial surface is under some form of human use (Venter et al., 2016; Erb et al., 2017), particularly in agriculture and forest management.

The impact of historical land-cover change on global climate is assessed with model simulations that consider multiple climate and biophysical processes (e.g., changes in albedo, evapotranspiration, and roughness) and / or biogeochemical processes (e.g., changes in atmospheric composition such as carbon release from deforestation). The dominant biophysical response to land cover changes is albedo, which is estimated (using a MODIS albedo product and a historical land-use harmonization product) to have increased gradually prior to the mid-19th century and then strongly through the mid-20th century, with a slightly slower rise thereafter (Ghimire et al., 2014). Recent radiative forcing estimates arising from biophysical processes generally fall at the lower end of the AR5 assessed range. For instance, based on historical simulations from 13 CMIP6 models, Smith et al., (2020) estimated that the ERF from surface albedo changes (including snow cover and leaf area) was -0.08 [-0.22 to 0.06] W m^{-2} since 1850. Similarly, based on simulations from 13 CMIP5 models, Lejeune et al., (2020) estimated the radiative forcing from transitions between trees, crops, and grasslands was -0.11 [-0.16 to 0.04] W m^{-2} since 1860. Andrews et al., (2017) identified an ERF of -0.40 W m^{-2} since 1860, ascribing much of the effect to increases in albedo (including the unmasking of underlying snow cover); notably, however, the analysis was based on a single model with a known tendency to overestimate the ERF (Collins et al., 2011). Ward et al. (2014) examined the combined effects of biophysical and biogeochemical processes, obtaining an RF of 0.9 ± 0.5 W m^{-2} since 1850 that was driven primarily by increases in land-use related GHG emissions from deforestation and agriculture (Ward and Mahowald, 2015). According to a large suite of historical simulations, the biophysical effects of changes in land cover (i.e. increased surface albedo and decreased turbulent heat fluxes) led to a net global cooling of 0.10 ± 0.14 °C at the surface (SRCCL). Available model simulations suggest that biophysical and biogeochemical effects jointly may have contributed to a small global warming of 0.078 ± 0.093 ℃ at the surface over about the past two centuries (SRCCL), with a potentially even larger warming contribution over the Holocene as a whole (He et al., 2014).

In summary, biophysical effects from historical changes in land use have an overall negative ERF (*medium confidence*). The best-estimate ERF from the increase in global albedo is -0.15 W m^{-2} since 1700 and -0.12 W m^{-2} since 1850 (*medium confidence*; Section 7.3.4.1). Biophysical effects of land-use change *likely* resulted in a net global cooling of about 0.1°C since 1750 (*medium confidence*; Section 7.3.5.3).

2.2.8 Effective radiative forcing (ERF) exerted by the assessed climate drivers

AR5 concluded that changes in climate drivers over the industrial period corresponded to a positive ERF which increased more rapidly after 1970 than before. There was *very high confidence* in the positive ERF due to WMGHG, with CO_2 the single largest contributor. AR5 concluded that there was *high confidence* that aerosols have offset a substantial portion of the WMGHG forcing.

This section reports the evolution in ERF with respect to 1750 as assessed in Section 7.3 and relies on the observed changes in climate drivers as assessed in Section 2.2 wherever possible, and models otherwise. The ERF is assessed using the methods and details described in Section 7.3.1 and includes, in addition to the radiative forcing, the rapid adjustments, especially implied by clouds. The time series are shown in Figure 2.10.

ACCEPTED VERSION SUBJECT TO FINAL EDITS

Increasing TSI (Section 2.2.1) implies a small ERF of less than 0.1 W m^{-2} between 1900 and 1980. TSI varies over the 11-year solar cycle with ERF of order ± 0.1 W m^{-2} in the assessed period. Strong volcanic eruptions (Section 2.2.2) with periods of strong negative ERF lasting 2–5 years in duration occurred in the late 19th and early 20th centuries. There followed a relatively quiescent period between about 1920 and 1960, and then three strong eruptions in 1963, 1982 and 1991, and only small-to-moderate eruptions thereafter (Schmidt et al., 2018).

The atmospheric concentrations of WMGHGs (Section 2.2.3) have continuously increased since the early 19th century, with CO_2 contributing the largest share of the positive ERF. Compared to the last two decades of the 20th century, the growth rate of CO_2 in the atmosphere increased in the 21st century, showed strong fluctuations for CH_4, and was about constant for N_2O. Mixing ratios of the most abundant CFCs declined (Section 2.2.4). Mixing ratios of HCFCs increased, but growth rates are starting to decelerate. Mixing ratios of HFCs and some other human-made components are increasing (Section 2.2.4). The ERF for CO_2 alone is stronger than for all the other anthropogenic WMGHGs taken together throughout the industrial period, and its relative importance has increased in recent years (Figures 2.10, 7.6).

[START FIGURE 2.10 HERE]

Figure 2.10: Temporal evolution of effective radiative forcing (ERF) related to the drivers assessed in Section 2.2. ERFs are based upon the calculations described in Chapter 7, of which the global annual mean, central assessment values are shown as lines and the 5 to 95% uncertainty range as shading (Section 7.3, see Figures 7.6 to 7.8 for more detail on uncertainties). The inset plot shows the rate of change (linear trend) in total anthropogenic ERF (total without TSI and volcanic ERF) for 30-year periods centred at each dot. Further details on data sources and processing are available in the chapter data table (Table 2.SM.1).

[END FIGURE 2.10 HERE]

Among the gaseous short-lived climate forcers (Section 2.2.5, Chapter 6, Section 7.3; excluding CH_4 here), ozone (O_3) is the component with the largest (positive) ERF. Concentrations from direct observations have increased since the mid-20th century and, mostly based on models, this extends to since 1750. Other gaseous short-lived climate forcers have small contributions to total ERF.

The net effect of aerosols (Sections 2.2.6, 6.4) on the radiation budget, including their effect on clouds, and cloud adjustments, as well as the deposition of black carbon on snow (Section 7.3.4.3), was negative throughout the industrial period (*high confidence*). The net effect strengthened (becoming more negative) over most of the 20th century, but *more likely than not* weakened (becoming less negative) since the late 20th century. These trends are reflected in measurements of surface solar radiation (Section 7.2.2.3) and the Earth's energy imbalance (Section 7.2.2.1). The relative importance of aerosol forcing compared to other forcing agents has decreased globally in the most recent 30 years (*medium confidence*) and the reduction of the negative forcing in the 21st century enhances the overall positive ERF.

Land use and land cover changes (Section 2.2.7) over the industrial period introduce a negative radiative forcing by increasing the surface albedo. This effect increased since 1750, reaching current values of about –0.20 W m^{-2} (*medium confidence*). This ERF value is taken from Section 7.3.4.1 and is different from the assessment in Section 2.2.7 in that it also includes the effect of irrigation. It also includes uncertain rapid adjustments and thus there is *low confidence* in its magnitude. Biogeochemical feedbacks can be substantial (Section 5.4) and are not included in ERF.

In conclusion, the net ERF due to all observed changes in climate drivers is positive, except for short periods (up to a few years in duration) following moderate to large volcanic eruptions, and has grown in magnitude since the late 19th century. The rate of change *likely* has increased in the last 30 years, since CO_2 concentrations increased at an increasing rate due to growing CO_2 emissions (*very likely*), and since the aerosol forcing became less negative (*more likely than not*).

ACCEPTED VERSION SUBJECT TO FINAL EDITS

2.3 Changes in large-scale climate

[START CROSS-CHAPTER BOX 2.2 HERE]

Cross-Chapter Box 2.2: Large-scale indicators of climate change

Contributing Authors: Veronika Eyring (Germany), Nathan Gillett (Canada), Sergey Gulev (Russian Federation), Jochem Marotzke (Germany), June-Yi Lee (Republic of Korea), Peter Thorne (Ireland/UK)

Chapters 2, 3 and 4 assess the current evidence basis for climatic changes, their causes, and their potential future under different possible emissions pathways using a combination of observations and state-of-the-art Earth System Models (ESMs). The assessment in these chapters focuses on selected large-scale indicators and modes as defined in this Box. These indicators and modes of variability taken together characterise overall changes to the climate system as a whole.

Defining large-scale

Understanding of large-scale climate variability and change requires knowledge of both the response to forcings and the role of internal variability. Many forcings have substantial hemispheric or continental scale variations. Modes of climate variability are generally driven by ocean basin scale processes. The climate system involves process interactions from the micro- to the global-scale and as such, any threshold for defining "large-scale" is arbitrary, but, within these chapters on the basis of these considerations large-scale is defined to include ocean basin and continental scales as well as hemispheric and global scales.

Defining a key set of climate indicators

Key climate indicators should constitute a finite set of distinct variables and / or metrics that may collectively point to important overall changes in the climate system that provide a synthesis of climate system evolution and are of broad societal relevance. Key indicators have been selected across the atmospheric, oceanic, cryospheric and biospheric domains, with land as a cross-cutting component. These indicators, and their use across chapters 2 to 4, as well as the broader report, are summarized in Cross-Chapter Box 2.2 Table 1. All selected indicators are Essential Climate Variables as defined by the Global Climate Observing System (Bojinski et al., 2014).

[START CROSS-CHAPTER BOX 2.2, TABLE 1 HERE]

Cross-Chapter Box 2.2, Table 1: Summary of the large-scale indicators used across chapters 2 through 4 and their principal applications in remaining chapters. Indicators are sub-divided by Earth-system domain and their inclusion in individual chapters is indicated by an orange solid fill. The list of additional chapters is limited to those where the variable is a principal consideration.

Selected large-scale indicator of climate change	Used in Chapters			Additional regional or process-based assessments undertaken in Chapters
	2	3	4	
Atmosphere and surface				
Surface and upper air temperatures	■	■	■	7, 10, 11, 12, Atlas
Hydrological cycle components (surface humidity, precipitable water vapour, precipitation, runoff, Precipitation-Evaporation)	■	■	■	8, 10, 11, 12, Atlas
Atmospheric circulation (sea level pressure and winds, Hadley / Walker circulation, global monsoons, blocking, storm tracks and jets, sudden stratospheric warmings)	■	■	■	8, 10, 11, 12
Cryosphere				
Sea ice extent / area, seasonality and thickness	■	■	■	9, 12, Atlas
Terrestrial snow cover	■	■		8, 9, 12, Atlas
Glacier mass and extent	■	■		8, 9, 12
Ice sheet mass and extent	■	■		9, 12, Atlas
Terrestrial permafrost temperature and active layer	■			5, 9, 12

ACCEPTED VERSION SUBJECT TO FINAL EDITS

thickness				
Ocean				
Temperature / ocean heat content				5, 7, 9, 12, Atlas
Salinity				8, 9, 12
Sea-level				9, 12
Circulation				5, 9
pH and deoxygenation				5, 12, Atlas
Biosphere				
Seasonal cycle of CO_2				5, 12
Marine biosphere (distribution of marine biota, primary production, phenology)				
Terrestrial biosphere (distribution of terrestrial biota, global greening / browning, growing season)				5, 12

[END CROSS-CHAPTER BOX 2.2, TABLE 1 HERE]

Atmospheric indicators

Monitoring surface temperatures is integral to the negotiations of UNFCCC and the global mean temperature goals of the Paris Agreement. Upper-air temperatures are a key indicator of different causal mechanisms underlying climate change and underpinned the very first conclusion in the Second Assessment Report of a 'discernible human influence' (Santer et al., 1996). To ascertain large-scale changes of and human influence on the global hydrological cycle (which includes terrestrial and oceanic components), a small subset of indicators across this cycle are chosen: ocean and land precipitaion-evaproation (P-E), global precipitation, total column water vapour, surface humidity (specific and relative), and global river runoff. Chapter 8 performs a substantive and holistic assessment of a much broader range of components. Finally, a warming world may be accompanied by a change in large-scale circulation patterns linked through energy / mass / momentum constraints such as the extent and strength of the Hadley circulation (HC), monsoon systems, and / or the position and strength of the sub-tropical and polar jets.

Cryospheric indicators

Changes in ice sheets are indicators of the longest-term impacts of climate change and associated with changes in global and regional sea level. Seasonal snow cover has many implications for mid- to high-latitude regions (albedo, hydrological cycle, etc.) with impacts on biospheric components of the system. Changes in sea ice extent, seasonality and thickness have potential impacts for hemispheric-scale circulation (Cross-Chapter Box 10.1). Changes in glacier mass balance contribute to changes in sea level but also have substantial implications for water supply for a substantial proportion of the global population. Finally, changes in permafrost and the seasonally thawed active layer have substantial implications in mid- to high-latitudes and have been hypothesised to be important in potential feedbacks through degassing of WMGHGs as the permafrost thaws.

Oceanic indicators

Most of the energy imbalance (Box 7.2) in the climate system is taken up by the ocean, resulting in changes in ocean temperature and heat content. Salinity changes indicate broad-scale hydrological cycle and circulation changes. Global-mean sea-level change is a key indicator of the impacts of both global warming and changes in global ice volume. Furthermore, it is integral to assessing the global energy budget (Cross-Chapter Box 9.1). The oceanic overturning circulation redistributes heat, carbon, oxygen and salinity within the ocean. Declines in ocean pH result from air-sea exchange of carbon dioxide and loss of ocean oxygen results from ocean warming; both lead to changes in marine ecosystems.

Biospheric indicators

The seasonal cycle of CO_2 is an integrated measure of the biogeochemical activity across the global biosphere. Changes in marine and terrestrial ecosystems can also be observed directly at large scales. For small, free-floating organisms such as phytoplankton, the dynamics can be rapid in nature, whereas on land slower changes in plant assemblages may occur, with commensurate changes in altitude and latitude of the tree-line. Lengthening of the growing season and the associated changes in phenology, distribution and abundance of species would be expected in most of the extratropics. Biospheric indicators and their impacts

ACCEPTED VERSION SUBJECT TO FINAL EDITS

are assessed in much greater detail in WGII Chapters 2 and 3.

Defining a selection of modes of variability

Many modes of climate variability affect global, hemispheric or regional climate across a range of timescales. Conversely, their behaviour may be influenced by global climate change. Modes were selected for inclusion that: i) have effects at large spatial scales; and ii) have substantial potential to modify interannual to multidecadal climate. The selected modes are considered in multiple chapters (Cross-Chapter Box 2.2 Table 2) and are defined in Annex IV.

[START CROSS-CHAPTER BOX 2.2, TABLE 2 HERE]

Cross-Chapter Box 2.2, Table 2: Summary of the modes of variability used across Chapters 2 through 4 and their principal applications in remaining chapters. Inclusion in each of Chapters 2 through 4 is indicated by a solid fill of the relevant table cell. The list of remaining chapters is limited to those where the mode of variability is a principal consideration of that chapter and is not intended to be exhaustive.

Selected mode of variability	Used in Chapters			Additional regional or process-based assessments undertaken in chapters
	2	3	4	
El Niño Southern Oscillation				8
Indian Ocean Basin and dipole modes				8, 10
Atlantic Multidecadal Variability				8, 10
Pacific Decadal Variability				8, 10
Annular modes (NAO / NAM, SAM)				8, 10
Atlantic Meridional and Zonal Modes				8

[END CROSS-CHAPTER BOX 2.2, TABLE 2 HERE]

[END CROSS-CHAPTER BOX 2.2 HERE]

2.3.1 Atmosphere and Earth's surface

2.3.1.1 Surface temperatures

2.3.1.1.1 Temperatures of the deep past (65 Ma to 8 ka)

This assessment of the paleo reference periods (Cross-Chapter Box 2.1) draws from studies based mostly or entirely on indirect observational evidence from geological archives (i.e. proxy records) rather than reconstructions that rely more heavily on modelled parameters and those based on deep-ocean temperatures (e.g. Köhler et al., 2015; Friedrich et al., 2016). In contrast to AR5, temperature estimates from climate models are not included in the assessed values for paleo reference periods in this chapter. AR5 concluded that the reconstructed GMST during the PETM was 4°C–7°C warmer than pre-PETM mean climate (*low confidence*), and that the EECO and the MPWP were 9°C–14°C and 1.9°C–3.6°C warmer than pre-industrial, respectively (*medium confidence*). The GMST during the LIG was assessed at 1°C–2°C warmer than pre-industrial (*medium confidence*), whereas SROCC narrowed the range to 0.5°C–1.0°C warmer, but did not state a confidence level. AR5 further concluded that it was *very likely* that the LGM was 3°C–8°C colder than pre-industrial, and *likely* that the maximum rate of global warming during the subsequent deglacial period was 1°C–1.5°C kyr^{-1}.

For the PETM, new reconstructions agree with those assessed by AR5. A major new compilation of proxy temperature data (Hollis et al., 2019) analysed using multiple statistical approaches (Inglis et al., 2020) indicates that GMST was 10°C–25°C (90% range) warmer than 1850–1900, or about 5°C warmer relative to the pre-PETM state. A related synthesis study also estimates that PETM warmed by 5°C (no uncertainty assigned; Zhu et al., 2019). A recent benthic isotope compilation (Westerhold et al., 2020) transformed to GMST based on the formulation by Hansen et al. (2013c) (Cross-Chapter Box 2.1, Figure 1), and adjusted to 1850-1900 by adding 0.36°C, shows an increase of GMST by about 10°C during the PETM. This reflects the

ACCEPTED VERSION SUBJECT TO FINAL EDITS

expected higher variability at single sites that were used to splice together the composite time series, compared to the globally averaged composite time series of Zachos et al. (2008). The latter was originally used by Hansen et al. (2013c) to reconstruct GMST, and is the preferred representation of the global average bottom water conditions, despite its less well-refined chronology.

For the EECO, new GMST reconstructions fall at the high end of the range assessed by AR5. These include estimates of 7°C–18°C (90% range; Inglis et al., 2020) and 12°C–18°C (95% range; Zhu et al., 2019) warmer than 1850–1900, and 10°C–16°C warmer than 1995-2014 "recent past" conditions (2 standard error range; Caballero & Huber, 2013). Together, they indicate that GMST was 10°C–18°C warmer during the EECO compared with 1850–1900 (*medium confidence*).

AR5 did not assess the GMST for the MCO. Reconstructions based on data from multiple study sites include estimates of about 4°C (uncertainty range not specified; You et al., 2009) and 5°C–10°C (2 standard error range; Goldner et al., 2014) warmer than 1850–1900. Together, these studies indicate that GMST was 4°C–10°C warmer during the MCO (*medium confidence*).

For the MPWP, new proxy-based estimates of global sea surface temperatures (SST) are about 2.0°C–3.5°C warmer than 1850–1900, depending on which proxy types are included in the analysis (Foley and Dowsett, 2019; McClymont et al., 2020). On the basis of model-derived relationships between land versus sea surface temperatures under different climate states (Section 3.3.1.1, Figure 3.2b), the increase in GMST is estimated to have been roughly 15% greater than the increase in global SST. Therefore, GMST during the MPWP is estimated to have been 2.5°C–4.0°C warmer than 1850–1900 (*medium confidence*).

For the LIG (Cross-Chapter Box 2.1, Figure 1; Figure 2.11), a major new compilation of marine proxy data (Turney et al., 2020) from 203 sites indicates that the average SST from 129–125 ka was 1.0°C ± 0.2°C (2SD) warmer than 1850–1900 (reported relative to 1981–2010 and adjusted here by 0.8°C). These temperatures represent the time of peak warmth, which may not have been synchronous among these sites. This compares with two other SST estimates for 125 ka of 0.5°C ± 0.3°C (± 2 SD) warmer at 125 ka relative to 1870–1889 (Hoffman et al., 2017), and about 1.4°C (no uncertainty stated) warmer at 125 ka relative to 1850–1900 (Friedrich and Timmermann, 2020; reported relative to 10–5 ka and adjusted here by 0.4°C; (Kaufman et al., 2020a)). The average of these post-AR5 global SST anomalies is 1°C. Commensurately (Figure 3.2b), GMST is estimated to have been roughly 1.1°C above 1850-1900 values, although this value could be too high if peak warmth was not globally synchronous (Capron et al., 2017). A further estimate of peak GMST anomalies of 1.0°C–3.5°C (90% range; adjusted here to 1850–1900 by adding 0.2°C) based on 59 marine sediment cores (Snyder, 2016) is considerably warmer than remaining estimates and are therefore given less weight in the final assessment. The warmest millennium of the LIG GMST reconstruction in the Hansen et al. (2013c) is 1.5°C above 1850-1900. In summary, GMST during the warmest millennia of the LIG (within the interval of around 129–125 ka) is estimated to have reached 0.5°C–1.5°C higher values than the 1850–1990 reference period (*medium confidence*).

New GMST reconstructions for the LGM fall near the middle of AR5's *very likely* range, which was based on a combination of proxy reconstructions and model simulations. Two of these new reconstructions use marine proxies to reconstruct global SST that were scaled to GMST based on different assumptions. One indicates that GMST was 6.2 [4.5 to 8.1°C; 95% range] cooler than the late Holocene average (Snyder, 2016), and the other, 5.7°C ± 0.8°C (2 SD) cooler than the average of the first part of the Holocene (10–5 ka) (Friedrich and Timmermann, 2020). A third new estimate (Tierney et al., 2020) uses a much larger compilation of marine proxies along with a data-assimilation procedure, rather than scaling, to reconstruct a GMST of 6.1°C ± 0.4°C (2 SD) cooler than the late Holocene. Assuming that the 1850–1900 reference period was 0.2°C and 0.4°C cooler than the late and first part of the Holocene, respectively (Kaufman et al., 2020a), the midpoints of these three new GMST reconstructions average -5.8°C relative to 1850–1900. The coldest multi-century period of the LGM in the Hansen et al. (2013c) reconstruction is 4.3°C colder than 1850–1900. This compares to land- and SST-only estimates of about -6.1°C ± 2°C and -2.2°C ± 1°C, respectively (2 SD), which are based on AR5-generation studies that imply a warmer GMST than more recent reconstructions (Fig. 1c in Harrison et al., 2015; Fig. 7 in Harrison et al., 2016). A major new pollen-based data-assimilation reconstruction averages 6.9°C cooler over northern extratropical land (Cleator et al., 2020). LGM temperature variability on centennial scales was about four times higher globally than during

ACCEPTED VERSION SUBJECT TO FINAL EDITS

the Holocene, and even greater at high latitudes (Rehfeld et al., 2018). In summary, GMST is estimated to have been 5°C–7°C lower during the LGM (around 23–19 ka) compared with 1850–1900 (*medium confidence*).

For the LDT (Cross-Chapter Box 2.1, Figure 1), no new large-scale studies have been published since AR5 (Shakun et al., 2012) to further assess the rate of GMST change during this period of rapid global warming (estimated at 1°C–1.5°C per kyr). The reconstruction of Shakun et al. (2012) was based primarily on SST records and therefore underrepresents the change in GMST during the LDT. Temperature over Greenland increased by about ten times that rate during the centuries of most rapid warming (Jansen et al., 2020).

2.3.1.1.2 Temperatures of the post-glacial period (past 7000 years)

AR5 did not include an assessment of large-scale temperature estimates for the MH, although it assigned *high confidence* to the long-term cooling trend over mid- to high-latitudes of the NH during the 5 kyr that preceded recent warming. For average annual NH temperatures, the period 1983–2012 was assessed as *very likely* the warmest 30-year period of the past 800 years (*high confidence*) and *likely* the warmest 30-year period of the past 1.4 kyr (*medium confidence*); the warm multi-decadal periods prior to the 20th century were unsynchronized across regions, in contrast to the warming since the mid-20th century (*high confidence*), although only sparse information was available from the SH.

This section concerns the Holocene period prior to industrialization when GMST was overall highest. Whereas SR1.5 focussed upon the 'Holocene thermal maximum' when regional temperatures were up to 1°C higher than 1850-1900, though peak warming occurred regionally at different times between around 10 and 5 ka greatly complicating interpretation. A multi-method reconstruction (Kaufman et al., 2020a) based on a quality-controlled, multi-proxy synthesis of paleo-temperature records from 470 terrestrial and 209 marine sites globally (Kaufman et al., 2020b) indicates that the median GMST of the warmest two-century-long interval was 0.7 [0.3 to 1.8] °C warmer than 1800–1900 (which averaged 0.03°C colder than 1850–1900; PAGES 2k Consortium, 2019), and was centred around 6.5 ka. This is similar to Marcott et al. (2013), which is based on a smaller dataset (73 sites) and different procedures to estimate a maximum warmth of 0.8°C ± 0.3°C (2 SD) at around 7.0 ka, adjusted here by adding 0.3°C to account for differences in reference periods. These may be underestimates because averaging inherently smoothed proxy records with uncertain chronologies reduces the variability in the temperature reconstruction (e.g., Dolman & Laepple (2018) for sedimentary archives). However, the general coincidence between peak warmth and astronomically driven boreal summer insolation might reflect a bias toward summer conditions (Bova et al., 2021; Hou et al., 2019; Liu et al., 2014), suggesting that the estimate is too high. This possibility is supported by AR5-generation proxy data focusing on 6 ka (Harrison et al., 2014), the long-standing MH modelling target (Cross-Chapter Box 2.1), that indicate surface temperatures for land and ocean were indistinguishable from 'pre-industrial' climate (Fig. 1c in Harrison et al., 2015; Fig. 7 in Harrison et al., 2016). In contrast, the GMST estimate from the multi-method global reconstruction (Kaufman et al., 2020a) for the millennium centred on 6 ka is only about 0.1°C colder than the warmest millennium.

Taking all lines of evidence into account, the GMST averaged over the warmest centuries of the current interglacial period (sometime between around 6 and 7 ka) is estimated to have been 0.2°C–1.0°C higher than 1850–1900 (*medium confidence*). It is therefore *more likely than not* that no multi-centennial interval during the post-glacial period was warmer globally than the most recent decade (which was 1.1°C warmer than 1850–1900; Section 2.3.1.1.3); the LIG (129–116 ka) is the next most recent candidate for a period of higher global temperature. Zonally averaged mean annual temperature reconstructions (Routson et al., 2019) indicate that MH warmth was most pronounced north of 30°N latitude, and that GMST subsequently decreased in general, albeit with multi-century variability, with greater cooling in the NH than in the SH (Kaufman et al., 2020a).

The temperature history of the last millennium and the methods used to reconstruct it have been studied extensively, both prior to and following AR5, as summarized recently by Smerdon and Pollack (2016) and Christiansen and Ljungqvist (2017). New regional (e.g., Shi et al., 2015; Stenni et al., 2017; Werner et al., 2018), global ocean (McGregor et al., 2015), quasi-hemispheric (Neukom et al., 2014; Schneider et al., 2015;

ACCEPTED VERSION SUBJECT TO FINAL EDITS

Anchukaitis et al., 2017), and global (Tardif et al., 2019) temperature reconstructions, and new regional proxy data syntheses (Lüning et al., 2019a,b) have been published, extending back 1-2 kyr. In addition, a major new global compilation of multiproxy, annually resolved paleo-temperature records for the CE (PAGES 2k Consortium, 2017) has been analysed using a variety of statistical methods for reconstructing temperature (PAGES 2k Consortium, 2019). The median of the multi-method GMST reconstruction from this synthesis (Figure 2.11a) generally agrees with the AR5 assessment, while affording more robust estimates of the following major features of GMST during the CE: (1) an overall millennial-scale cooling trend of –0.18 [–0.28 to 0.00] °C kyr^{-1} prior to 1850; (2) a multi-centennial period of relatively low temperature beginning around the 15th century, with GMST averaging –0.03 [–0.30 to 0.06] °C between 1450 and 1850 relative to 1850–1900; (3) the warmest multi-decadal period occurring most recently; and (4) the rate of warming during the second half of the 20th century (from instrumental data) exceeding the 99th percentile of all 51-year trends over the past 2 kyr. Moreover, the new proxy data compilation shows that the warming of the 20th century was more spatially uniform than any other century-scale temperature change of the CE (*medium confidence*) (Neukom et al., 2019). A new independent temperature reconstruction extending back to 1580 is based on an expanded database of subsurface borehole temperature profiles, along with refined methods for inverse modelling (Cuesta-Valero et al., 2021). The borehole data, converted to GMST based on the modelled relation between changes in land versus sea surface temperature outlined previously, indicate that average GMST for 1600–1650 was 0.12°C colder than 1850–1900, which is similar to the PAGES 2k reconstruction (0.09°C colder), although both estimates are associated with relatively large uncertainties (0.8°C (95% range) and 0.5°C (90% range), respectively).

To conclude, following approximately 6 ka, GMST generally decreased, culminating in the coldest multi-century interval of the post-glacial period (since 8 ka), which occurred between around 1450 and 1850 (*high confidence*). This multi-millennial cooling trend was reversed in the mid-19th century. Since around 1950, GMST has increased at an observed rate unprecedented for any 50-year period in at least the last 2000 years (*medium confidence*).

[START FIGURE 2.11 HERE]

Figure 2.11: Earth's surface temperature history with key findings annotated within each panel. (a) GMST over the Holocene divided into three time scales. (i) 12 kyr–1 kyr in 100-year time steps, (ii) 1000–1900 CE, 10-year smooth, and (iii) 1900–2020 CE (from panel c). Median of the multi-method reconstruction (bold lines), with 5th and 95th percentiles of the ensemble members (thin lines). Vertical bars are the assessed *medium confidence* ranges of GMST for the Last Interglacial and mid-Holocene (Section 2.3.1.1). The last decade value and *very likely* range arises from 2.3.1.1.3. (b) Spatially resolved trends (°C per decade) for HadCRUTv5 over (upper map) 1900–1980, and (lower map) 1981–2020. Significance is assessed following AR(1) adjustment after Santer et al., (2008a), 'x' marks denote non-significant trends. (c) Temperature from instrumental data for 1850–2020, including (upper panel) multi-product mean annual timeseries assessed in Section 2.3.1.1.3 for temperature over the ocean (blue line) and temperature over the land (red line) and indicating the warming to the most recent 10 years; and annually (middle panel) and decadally (bottom panel) resolved averages for the GMST datasets assessed in Section 2.3.1.1.3. The grey shading in each panel shows the uncertainty associated with the HadCRUT5 estimate (Morice et al., 2021). All temperatures relative to the 1850–1900 reference period. Further details on data sources and processing are available in the chapter data table (Table 2.SM.1).

[END FIGURE 2.11 HERE]

[START CROSS-CHAPTER BOX 2.3 HERE]

Cross-Chapter Box 2.3: New estimates of global warming to date and key implications

Contributing Authors: Blair Trewin (Australia), Peter Thorne (Ireland / UK), Richard Allan (UK), Richard Betts (UK), Lea Beusch (Switzerland), Chris Fairall (USA), Piers Forster (UK), Baylor Fox-Kemper (USA), Jan Sigurd Fuglestvedt (Norway), John Fyfe (Canada), Nathan Gillett (Canada), Ed Hawkins (UK), Chris

ACCEPTED VERSION SUBJECT TO FINAL EDITS

Jones (UK), Elizabeth Kent (UK), Svitlana Krakovska (Ukraine), Elmar Kriegler (Germany), Jochem Marotzke (Germany), H. Damon Matthews (Canada), Thorsten Mauritsen (Germany / Denmark / Sweden), Anna Pirani (Italy), Joeri Rogelj (Austria / UK / Belgium), Steven Rose (USA), Bjørn H. Samset (Norway), Sonia I. Seneviratne (Switzerland), Claudia Tebaldi (USA), Andrew Turner (UK), Russell Vose (USA), Rachel Warren (UK)

This Cross-Chapter Box presents the AR6 WGI assessment of observed global warming and describes improvements and updates since AR5 and subsequent Special Reports. The revised estimates result from: the availability of new and revised observational datasets; the occurrence of recent record warm years; and the evaluation of the two primary metrics used to estimate global warming in past IPCC reports: "Global mean surface temperature" (GMST) and "Global surface air temperature" (GSAT). Implications for threshold crossing times, remaining carbon budgets and impacts assessments across AR6 WGs are discussed.

Dataset innovations

Since AR5, all major datasets used for assessing observed temperature change based upon GMST have been updated and improved (Section 2.3.1.1.3). A number of new products have also become available, including new datasets (e.g. Berkeley Earth, Rohde & Hausfather, 2020) and new interpolations based on existing datasets (e.g. Cowtan and Way (2014) and Kadow et al. (2020a)). These various estimates are not fully independent.

Improvements in global temperature datasets since AR5 have addressed two major systematic issues. First, new SST datasets (Huang et al., 2017; Kennedy et al., 2019) address deficiencies previously identified in AR5 relating to the shift from predominantly ship-based to buoy-based measurements; these improvements result in larger warming trends, particularly in recent decades. Second, all datasets now employ interpolation to improve spatial coverage. This is particularly important in the Arctic, which has warmed faster than the rest of the globe in recent decades (Atlas 5.9.2.2); under-sampling of the Arctic leads to a cool bias in recent decades (Simmons et al., 2017; Benestad et al., 2019). Some datasets are now spatially complete (Cowtan and Way, 2014; Kadow et al., 2020a) while others have expanded spatial coverage (Lenssen et al., 2019; Morice et al., 2021; Rohde & Hausfather, 2020; Vose et al., 2021). Several interpolation methods have been benchmarked against test cases (e.g. Lenssen et al., 2019), and comparisons with reanalyses further confirm the value of such interpolation (Simmons et al., 2017). It is *extremely likely* that interpolation produces an improved estimate of the changes in GMST compared to ignoring data-void regions.

Overall, dataset innovations and the availability of new datasets have led to an assessment of increased GMST change relative to the directly equivalent estimates reported in AR5 (Cross-Chapter Box 2.3, Table 1 and Figure 1).

Effects of warming since AR5 and choice of metrics of global mean temperature change

Each of the six years from 2015 to 2020 has *likely* been warmer than any prior year in the instrumental record. GMST for the decade 2011–2020 has been 0.19 [0.16 to 0.22] °C warmer than 2003–2012, the most recent decade used in AR5 (Cross-Chapter Box 2.3, Figure 1). A linear trend has become a poorer representation of observed change over time since most of the sustained warming has occurred after the 1970s (Cross-Chapter Box 2.3 Figure 1) and all values since 2012 are at least 0.2°C above a linear trendline for 1850–2020. For this reason, the primary method used to assess observed warming in this report is the change in temperature from 1850–1900 to the most recent decade (2011–2020) or the recent past (1995–2014), replacing the trend-based methods used in AR5 and earlier assessments. The effect of this change from trend-based to change-based metrics is currently relatively minor at -0.03°C (<5%) for the most recent decade, but this may not remain the case in future (*high confidence*).

Observed changes in global mean temperature since the pre-industrial era

AR5 used 1850–1900 as an approximate pre-industrial baseline for global temperature change, whilst using an earlier pre-industrial baseline of 1750 for radiative forcings. Cross-Chapter Box 1.2 assesses that there

ACCEPTED VERSION SUBJECT TO FINAL EDITS

was an observed GMST change from the period around 1750 to 1850–1900 of around 0.1°C (*likely* range -0.1 to +0.3°C, *medium confidence*). This additional global temperature change before 1850–1900 is not included when making AR6 assessments on global warming to date, global temperature threshold crossing times, or remaining carbon budgets to ensure consistency with previous ARs.

Addressing the non-equivalence of GMST and GSAT

GMST is a combination of land surface air temperatures (LSAT) and SSTs, whereas GSAT is a combination of LSAT and marine air temperatures (MATs). Although GMST and GSAT are closely related, the two measures are physically distinct. The implications have become more apparent since AR5 (Cowtan et al., 2015; IPCC, 2018 (SR1.5); Merchant et al., 2013; Richardson et al., 2018; Simmons et al., 2017), and it has been shown (Rubino et al., 2020) that MAT and SST can show distinct multidecadal-scale trends and patterns of interannual variability. Although the SR1.5 used GMST for observational-based and GSAT for model-based headline warming statements, they noted the importance of the difference for their assessment (SR1.5 Section 1.2.1.1). SR1.5 used information from CMIP5 models to estimate a GSAT equivalent from observation-based GMST for certain applications such as remaining carbon budgets. The following subsections assess available lines of evidence related to the equivalence between GMST and GSAT.

Physical understanding

A well-understood physical constraint on the vertical gradient between the air and sea surface temperature is that it is approximately proportional to the turbulent sensible heat flux in the atmospheric surface layer (Chor et al., 2020). Similarly, the latent heat flux scales with the vertical humidity gradient and, in the global mean and in most oceanic regions, the latent heat flux is substantially larger than the sensible heat flux (Sections 7.2.1, 9.2.1.3). If GSAT were to warm faster than GMST, the sensible surface heat flux would respond so as to reduce this difference. However, it is the sum of the sensible, latent, and radiative heat fluxes that controls GMST, so the sensible heat flux effect cannot be considered in isolation. Attempts to further constrain the combination of fluxes (e.g., Lorenz et al., 2010; Siler et al., 2019) rely on parameterisations or output from Earth system models (ESMs) or reanalyses and so are not considered independent. Apart from the above global considerations, regional and seasonal effects such as changes to the frequency and intensity of storms, sea state, cloudiness, sea ice cover, vegetation and land use may all affect the GSAT to GMST difference, either directly or by altering the relationships between gradients and energy fluxes. These changing energy flux relationships are monitored through observing the stratification of the upper ocean (Section 9.2.1.3) and the response of upper ocean processes (Cross-Chapter Box 5.3) in ESMs and reanalyses, but such monitoring tasks rival the observational challenge of directly observing SSTs and 2 m air temperature under a wide range of conditions. In summary, because of the lack of physical constraints and the complexity of processes driving changes in the GSAT to GMST temperature differences, there is no simple explanation based on physical grounds alone for how this difference responds to climate change.

Direct observational evidence

There is currently no regularly updated, entirely observation-based dataset for GSAT. The best available observations of near-surface air temperature over ocean are datasets of night-time marine air temperature (NMAT) (e.g. Cornes et al., 2020; Junod & Christy, 2020), though spatial coverage is less extensive than for SST. Night-time measurements are used to avoid potential biases from daytime heating of ship superstructures. Kennedy et al. (2019) show little difference between HadNMAT2 and HadSST4 between 1920 and 1990, but a warming of SST relative to NMAT manifesting as a step change of 0.05°C–0.10°C in the early 1990s, which may reflect an actual change, the impact of increasingly divergent spatial coverage between SST and MAT measurements, or unresolved structural uncertainties in one or both datasets. This leads to NMAT warming around 10% more slowly than SST over the last century. In contrast, Junod and Christy (2020a) find NMAT trends which are 8–17% larger than those for SST in the ERSSTv4 and HadISST datasets for the period 1900 to 2010, but 11–15% smaller than the SST trends for the same datasets from 1979 to 2010. However, ERSSTv4 uses NMAT data as a basis for homogeneity adjustment so is not fully independent. Kent and Kennedy (2021) note sensitivity to methodological choices in comparisons but find that NMAT is warming more slowly than SST products over most periods considered. Rubino et al.

ACCEPTED VERSION SUBJECT TO FINAL EDITS

(2020) exploit tropical Pacific moored buoy arrays, available since the early 1980s, and find differences in NMAT and SST anomalies, which are sensitive to the choice of period and show spatio-temporal ENSO-related (Annex IV) signals in the differences.

Overall, with *medium evidence* and *low agreement*, available observational products suggest that NMAT is warming less than SST by up to 15%. Given that these ocean observations cover roughly two thirds of the globe, this implies that GMST is warming up to at most 10% faster than GSAT. Substantial uncertainty remains and the effect is highly sensitive to the choice of both time period and choice of NMAT and SST observational products to compare. Observed NMAT warming faster than observed SST cannot be precluded.

CMIP model-based evidence

CMIP historical simulations and projections agree that GSAT increases faster than GMST, the reverse of what is indicated by many marine observations. Several studies approximate the approach used to derive GMST from observations by blending SST over open ocean and SAT over land and sea ice from model output (Cowtan et al., 2015; Richardson et al., 2018; Beusch et al., 2020; Gillett et al., 2021). Cowtan et al. (2015) found that trends in GSAT are of the order of 9% larger than for GMST in CMIP5, based on data from 1850–2100 (historical + RCP8.5), if anomalies are blended and sea ice is allowed to vary over time. Broadly consistent numbers are found for both CMIP5 and CMIP6, across a range of SSP and RCP scenarios and time periods (Richardson et al., 2018; Beusch et al., 2020; Gillett et al., 2021). Blending monthly anomalies and allowing sea ice to vary, the change in GSAT for 2010–2019 relative to 1850–1900 is 2–8% larger than spatially-complete GMST in CMIP6 historical and SSP2-4.5 simulations (Gillett et al., 2021), and 6–12% larger in CMIP5 historical and RCP2.6 and 8.5 simulations for 2007–2016 relative to 1861–1880 (Richardson et al., 2018). However, a true like-for-like comparison to observational products is challenging because methodological choices have a large impact on the relationship between modelled GMST and GSAT and none of these studies fully reproduces the methods used to derive estimates of GMST in recent observational datasets, which use various ways to infill areas lacking in situ observations (Jones, 2020).

Marine boundary layer behaviour and parameterisations in all CMIP models are based upon Monin-Obukhov similarity theory (e.g. Businger et al., 1971), which informs assumptions around gradients in the near-surface boundary layer dependent upon temperature, wind speed and humidity. This leaves open the possibility of a common model bias, while Druzhinin et al. (2019) also point to departures of temperature profiles from theoretical predictions under certain conditions. There remain inadequacies in understanding and modelling of key processes (Edwards et al., 2020), and biases in the representation of the absolute SST-MAT difference have been identified in climate models and reanalyses (Găinuşă-Bogdan et al., 2015; Zhou et al., 2020).

Reanalysis-based evidence

Simmons et al. (2017) found that in JRA-55 and ERA-Interim (following an adjustment to account for an apparent discontinuity), GSAT increased 2–4% faster than GMST over the period 1979–2016.
In atmospheric reanalyses, SST is given as a lower boundary condition from an observed globally interpolated product (such as HadISST; Rayner et al., 2003) whereas the air temperature is reliant upon model parameterisations and assimilated observations that do not include MAT observations (Simmons et al., 2017), thereby limiting their capability to constrain differences in GMST and GSAT trends. Furthermore, it is unclear what the lack of dynamic coupling at the ocean-atmosphere interface might imply for the representativeness of reanalysis-based estimates.

Representation of surface temperatures in sea ice regions

There is a significant issue in areas where sea-ice melts or grows, where the quantity used in observational-based GMST estimates switches between air temperature and sea surface temperature. This primarily affects analyses combining SAT anomalies over land and ice with SST anomalies over ocean. In areas where sea ice has recently melted, the climatological value changes from an air-temperature based estimate to an SST estimate based upon the freezing point of seawater (–1.8°C). This switch in climatology to, in general, a warmer climatology, leads to a bias towards reduced warming in anomalies compared with analyses based

ACCEPTED VERSION SUBJECT TO FINAL EDITS

on absolute temperatures. Richardson et al. (2018) found this underestimation to amount to approximately 3% of observed warming in historical model simulations. Given the projected future sea-ice losses, the effect will grow in future (*low confidence*), with potential effects of the order of 0.1°C in the second half of the 21st century under high warming scenarios, although with some uncertainty arising from the large spread of sea-ice loss in model projections (Tokarska et al., 2019).

Summary of lines of evidence

GMST and GSAT are physically distinct. There is *high confidence* that long-term changes in GMST and GSAT differ by at most 10% in either direction. However, conflicting lines of evidence from models and direct observations combined with limitations in theoretical understanding lead to *low confidence* in the sign of any difference in long-term trends. The *very likely* range of estimated historical GMST warming is combined with the assessed ± 10% uncertainty in the relationship between GMST and GSAT changes to infer a GSAT equivalent, accounting for any possible real-world physical difference. Improvements in understanding may yield a robust basis to apply a scaling-factor to account for the difference in future assessments.

[START CROSS-CHAPTER BOX 2.3, TABLE 1 HERE]

Cross Chapter Box 2.3, Table 1: Summary of key observationally-based global warming estimates (in °C) to various periods in the present report and selected prior reports and their principal applications. Further details on data sources and processing are available in the chapter data table (Table 2.SM.1).

Period	**AR6 GMST (°C)**	**AR6 GSAT* (°C)**	**AR5 and / or *SR1.5* (only where reported) (°C)**	**Principal use of this period in reports**
1850–1900 to 2011–2020	1.09 (0.95–1.20)	1.09 (0.91–1.23)		Warming to present in AR6 WGI
1850–1900 to 2010–2019	1.06 (0.92–1.17)	1.06 (0.88–1.21)		Attributable warming in AR6 WGI
1850–1900 to 2006–2019	1.03 (0.89–1.14)	1.03 (0.86–1.18)		Energy budget constraints in AR6 on ECS and TCR
1850–1900 to 2006–2015	0.94 (0.79–1.04)	0.94 (0.76–1.08)	*0.87 (0.75–0.99) - GMST* *0.97 (0.85–1.09) – GSAT*[#]	Warming to date in SR1.5. GSAT value used for remaining carbon budgets (RCBs) in SR1.5.
1850–1900 to 2003–2012	0.90 (0.74–1.00)	0.90 (0.72–1.03)	0.78 (0.72–0.85)	Warming to date in AR5 WGI.
1850–1900 to 1995–2014	0.85 (0.69–0.95)	0.85 (0.67–0.98)		Warming to recent past in AR6 WGI.

ACCEPTED VERSION SUBJECT TO FINAL EDITS

1850–1900 to 1986–2005	0.69 (0.54–0.79)	0.69 (0.52–0.82)	0.61 (0.55–0.67)^	Warming to recent past in AR5 WGI.
1850–1900 to 1961–1990	0.36 (0.23–0.44)	0.36 (0.22–0.45)		Warming to reference period recommended by WMO for national-level data sets used for climate change assessment (included in the WGI Atlas)
1880–2012 OLS trend	0.92 (0.68–1.17)		0.85 (0.65–1.06)	Warming to date in AR5 WGI

* As the uncertainty in the relationship between GMST and GSAT changes is independent of the uncertainty in the assessed change in GMST, these uncertainties are combined in quadrature.
SR1.5 derived a GSAT estimate by taking the CMIP5 ensemble mean GSAT change of 0.99°C, sub-sampling to HadCRUTv4.6, noting the offset in trends (0.84°C HadCRUT4 observed GMST vs. 0.86°C modelled GMST) and adjusting by this to arrive at an estimate of 0.97 °C change in GSAT. The *likely* uncertainty range of ±0.12°C was not further adjusted.
^ Note that the AR5 approach for the change from 1850–1900 to both 1986–2005 and 2003–2012 was based upon one dataset (HadCRUT4) and its parametric uncertainty estimates are known to underestimate the true uncertainty.

[END CROSS-CHAPTER BOX 2.3, TABLE 1 HERE]

Mapping between AR5 and AR6 assessments

The AR5 assessed estimate for historical warming between 1850–1900 and 1986–2005 is 0.61 [0.55 to 0.67] °C. The equivalent in AR6 is 0.69 [0.54 to 0.79] °C, and the 0.08 [-0.01 to 0.12] °C difference is an estimate of the contribution of changes in observational understanding alone (Cross-Chapter Box 2.3, Table 1). The exact value of this contribution depends upon the metric being compared (GMST/GSAT, trend or change, exact period). The AR6-assessed GMST warming between 1850–1900 and 2011–2020 is 1.09 [0.95 to 1.20] °C. An AR5-equivalent assessment using this estimated difference in observational understanding is thus 1.01 [0.94 to 1.08] °C. These updates and improvements in observational datasets affect other quantities that derive from the assessment of GSAT warming, including estimates of remaining carbon budgets and estimates of crossing times of 1.5°C and 2°C of global warming (See Cross Chapter Box 2.3 Table 1**).**

Updates to estimated Global Warming Level (GWL) crossing times

The updated estimate of historical warming is one contribution to the revised time of projected crossing of the threshold of 1.5°C global warming in comparison with SR1.5, but is not the only reason for this update. The AR6 assessment of future change in GSAT (Section 4.3.4, Table 4.5) results in the following threshold-crossing times, based on 20-year moving averages. The threshold-crossing time is defined as the midpoint of the first 20-year period during which the average GSAT exceeds the threshold. During the near term (2021–2040), a 1.5°C GSAT increase relative to the average over the period 1850–1900 is *very likely* to occur in scenario SSP5-8.5, *likely* to occur in scenarios SSP2-4.5 and SSP3-7.0, and *more likely than not* to occur in scenarios SSP1-1.9 and SSP1-2.6. In all scenarios assessed here except SSP5-8.5, the central estimate of crossing the 1.5°C global warming level lies in the early 2030s. This is about ten years earlier than the midpoint of the *likely* range (2030–2052) assessed in the SR1.5, which assumed continuation of the then-reported warming rate; this estimated rate has been confirmed in AR6 (Section 3.3.1). Roughly half of the ten-year difference arises from the higher diagnosed historical warming in AR6. The other half arises because, for central estimates of climate sensitivity, most scenarios show stronger warming over the near term than was assessed as 'current' in SR1.5 (*medium confidence*).

Implications for assessment of emission scenarios and remaining carbon budgets

To estimate the global warming implications of emissions scenarios, AR5 and SR1.5 combined estimates of observed GMST changes from 1850–1900 to 1986–2005 (Cross-Chapter Box 2.3, Table 1) with GSAT projections of subsequent warming. AR6 undertakes three changes to this approach. First, the AR6

ACCEPTED VERSION SUBJECT TO FINAL EDITS

assessment of improved observational records is used. Second, the recent past baseline period is updated from 1986–2005 to 1995–2014, and, third, historical estimates are expressed in GSAT instead of GMST for consistency of historical estimates with future projections. The updated estimates of warming to date in AR6 lead to higher estimates of future warming, all else being equal. The temperature classification of emissions scenarios in the WGIII report adopts the definition of temperature classes as introduced in SR1.5, and assigns emission scenarios to these classes based on their AR6 assessed GSAT outcomes (Cross-Chapter Box 7.1, WGIII Annex C.II.2.4).

Both in AR5 and SR1.5, remaining carbon budgets were expressed as a function of GSAT warming, while also highlighting the implications of using historical warming estimates expressed in GMST. AR5 reported total carbon budgets for GSAT warming relative to 1861–1880. AR5 SYR also includes remaining carbon budget estimates based on AR5 WGIII scenario projections that use the method for AR5 scenario projections described above. SR1.5 integrated several methodological advancements to estimate remaining carbon budgets and reported budgets for additional GSAT warming since the 2006–2015 period, estimating, following the application of an adjustment (Richardson et al., 2016, Table 1.1. SR1.5) to GMST, that 0.97°C (± 0.12°C) of GSAT warming occurred historically between 1850–1900 and 2006–2015. The AR6 assessment, above, leads to an estimate of 0.94°C of warming between 1850–1900 and 2006–2015. All other factors considered equal, the AR6 estimate thus implies that 0.03°C more warming is considered for remaining carbon budgets compared to SR1.5. Combining this 0.03°C value with the SR1.5 transient climate response to cumulative emissions of CO_2 (TCRE) translates into remaining carbon budgets about 70 $GtCO_2$ [40 to 140 $GtCO_2$] larger compared to SR1.5 on a like-for-like basis. Meanwhile, on the same like-for-like basis, updates to historical observational products would reduce remaining carbon budgets reported in AR5 SYR based on WGIII scenario projections by about 180 $GtCO_2$ [120 to 370 $GtCO_2$]. Box 5.2 provides a further overview of updates to estimates of the remaining carbon budget since AR5.

Implications for assessment of impacts and adaptation

The assessment of global warming to date now being larger than previously assessed has no consequence on the assessment of past climate impacts, nor does it generally imply that projected climate impacts are now expected to occur earlier. The implications are mainly that the level of warming associated with a particular impact has been revised. This has very limited practical implications for the assessment of the benefits of limiting global warming to specific levels, as well as for the urgency of adaptation action. For example, impacts that occurred in the period 1986–2005 were previously associated with a GMST increase of 0.61°C relative to 1850–1900, relative to AR5 estimates. These impacts are now instead associated with a GMST increase of 0.69°C, relative to the assessment in this Report. The impacts themselves have not changed. Similarly, the impacts previously associated with a GMST or GSAT increase of 1.5°C will now generally be associated with a slightly different global warming level. This is because projections of future warming and its impacts relative to 1850–1900 are normally made by adding projected warming from a recent past baseline to an estimate of the observed warming from 1850–1900, as in AR5 and SR1.5.

Most of the previously projected impacts and risks associated with global warming of 1.5°C have therefore not changed and are still associated with the same level of future warming (0.89°C) relative to 1986–2005. With this warming now estimated as 0.08°C larger than in AR5, the future impacts previously associated with 1.5°C warming are now associated with 1.58°C warming. Similarly, the impacts now associated with 1.5°C warming would have previously been associated with 1.42°C warming. There are exceptions where impacts studies have used a baseline earlier than 1986–2005 (e.g. King et al., 2017), for which the new estimate of the historical warming would mean an earlier occurrence of the projected impacts. However, even in these cases, the ostensible difference in impacts associated with a 0.08°C difference in global mean temperature will be small in comparison with the uncertainties. There are also substantial uncertainties in regional climate changes and the magnitude of climate impact-drivers projected to occur with global warming of 1.5°C (Betts et al., 2018; Seneviratne et al., 2018). Furthermore, the time of reaching global warming of 1.5°C is subject to uncertainties of approximately ± 10 years associated with uncertainties in climate sensitivity, and ± 3 to 4 years associated with the different SSP forcing scenarios (Section 4.3.4, Table 4.5 see prior discussion). There is therefore *high confidence* that assessment of the magnitude and timing of impacts-related climate quantities at 1.5°C is not substantially affected by the revised estimate of

ACCEPTED VERSION SUBJECT TO FINAL EDITS

historical global warming.

The assessment of the implications of limiting global warming to 1.5°C compared to 2°C will also remain broadly unchanged by the updated estimate of historical warming, as this depends on the relative impacts rather than the absolute impacts at any specific definition of global temperature anomaly *(high confidence)*.

[START CROSS-CHAPTER BOX 2.3, FIGURE 1 HERE]

Cross-chapter Box 2.3, Figure 1: Changes in assessed historical surface temperature changes since AR5. (a) Summary of the impact of various steps from AR5 headline warming-to-date number for 1880–2012 using a linear trend fit to the AR6 assessment based upon the difference between 1850–1900 and 2011–2020. Whiskers provide 90% (*very likely*) ranges. AR6 assessment in addition denotes additional warming since the period around 1750 (Cross-Chapter Box 1.2). (b) Time series of the average of assessed AR5 series (orange, faint prior to 1880 when only HadCRUT4 was available) and AR6 assessed series (blue) and their differences (offset) including an illustration of the two trend fitting metrics used in AR5 and AR6. Further details on data sources and processing are available in the chapter data table (Table 2.SM.1).

[END CROSS-CHAPTER BOX 2.3, FIGURE 1 HERE]

[END CROSS-CHAPTER BOX 2.3 HERE]

2.3.1.1.3 Temperatures during the instrumental period – surface

AR5 concluded that it was certain that GMST had increased since the late 19th century. Total warming in GMST was assessed as 0.85 [0.65 to 1.06] °C over 1880–2012, whilst the change from 1850–1900 to 2003–2012 was assessed at 0.78 [0.72 to 0.85] °C, and from 1850–1900 to 1986–2005 at 0.61 [0.55 to 0.67] °C. SR1.5 reported warming of GMST from 1850–1900 to 2006–2015 of 0.87°C, with an 1880–2012 trend of 0.86°C and an 1880–2015 trend of 0.92°C. SRCCL concluded that since the pre-industrial period, surface air temperature over land areas has risen nearly twice as much as the global mean surface temperature (*high confidence*).

Since AR5, there have been substantial improvements in the availability of instrumental archive data both over the ocean and on land. A new version of the International Comprehensive Ocean-Atmosphere Dataset (ICOADS Release 3.0, Freeman et al., 2017) comprises over 450 million in situ marine reports and incorporates newly digitised data, increasing coverage in data sparse regions and times (e.g. polar oceans and World War I). The International Surface Temperature Initiative released a much improved collection of fundamental land surface air temperature records (Rennie et al., 2014) comprising more than 35,000 station records. These advances, both of which have substantially improved spatial coverage, have reduced uncertainties in assessments of both land and marine data.

Marine domain

For SST analyses, three products – HadSST4 (1850–present, Kennedy et al., 2019), ERSSTv5 (1850–present, Huang et al., 2017) and COBE SST2 (1880–present, (Hirahara et al., 2014) – now have bias adjustments applied throughout the record. The new SST datasets account for two major issues previously identified in AR5: that globally averaged buoy SSTs are about 0.12°C cooler than ship-based SSTs (Huang et al., 2015; Kennedy et al., 2011), and that SSTs from ship engine room intakes may have biases for individual ships depending upon the sensor set-up (Kent & Kaplan, 2006) but have an overall warm bias when globally aggregated (Kennedy et al., 2019). The first issue primarily affects data since 1990, when buoys began to increasingly contribute to the observation network (Woodruff et al., 2011), and the second issue has its largest effect from the 1940s to the 1970s. From the standpoint of uncertainty, ERSSTv4 (Liu W. et al., 2015a; Huang et al., 2016) and subsequent versions (Huang et al., 2017), and HadSST4 have

ACCEPTED VERSION SUBJECT TO FINAL EDITS

estimates presented as ensembles that sample parametric uncertainty. Comparisons between these independently-derived analyses and the assessed uncertainties (Kennedy, 2014; Kent et al., 2017) show unambiguously that global mean SST increased since the start of the 20th century, a conclusion that is insensitive to the method used to treat gaps in data coverage (Kennedy, 2014).

A number of recent studies also corroborate important components of the SST record (Cowtan et al., 2018; Hausfather et al., 2017; Kennedy et al., 2019; Kent et al., 2017). In particular, ATSR SST satellite retrievals (Merchant et al., 2012; Berry et al., 2018), the near-surface records from hydrographical profiles (Gouretski et al., 2012; Huang et al., 2018), and coastal observations (Cowtan et al., 2018) have all been shown to be broadly consistent with the homogenized SST analyses. Hausfather et al. (2017) also confirmed the new estimate of the rate of warming seen in ERSSTv4 since the late 1990s through comparison with independent SST data sources such as Argo floats and satellite retrievals. Nevertheless, dataset differences remain in the mid-20th century when there were major, poorly-documented, changes in instrumentation and observational practices (Kent et al., 2017), particularly during World War II, when ship observations were limited and disproportionately originated from US naval sources (Thompson et al., 2008). Kennedy et al. (2019) also identify differences between the new HadSST4 dataset and other SST datasets in the 1980s and 1990s, indicating that some level of structural uncertainty remains during this period, whilst Chan et al. (2019) and Davis et al. (2019) document residual uncertainties in the early and later 20th century records respectively.

Historically, SST has been used as a basis for global temperature assessment on the premise that the less variable SST data provides a better estimate of marine temperature changes than marine air temperature (MAT) (Kent & Kennedy, 2021). However, MAT products are used to adjust SST biases in the NOAA SST product because they are assessed to be more homogeneous (Huang et al., 2017). Observational datasets exist for night-marine air temperature (NMAT) (e.g. (Cornes et al., 2020; Junod & Christy, 2019; Rayner et al., 2020) and there are methods to adjust daytime MATs (Berry et al., 2004), but there is to date no regularly updated dataset which combines MAT with temperatures over land. MAT datasets are more sparse in recent decades than SST datasets as marine datasets have become increasingly dependent on drifting buoys (Centurioni et al., 2019) which generally measure SST but not MAT, and there are almost no recent winter MAT data south of 40°S (Swart et al., 2019). However, the situation reverses in the 19th Century with a greater prevalence of MAT than SST measurements available in the ICOADS data repository (Freeman et al., 2017, 2019; Kent & Kennedy, 2021).

Land domain

The GHCNMv4 dataset (Menne et al., 2018) includes many more land stations than GHCNMv3, arising from the databank efforts of Rennie et al. (2014), and calculates a 100-member parametric uncertainty ensemble drawing upon the benchmarking analysis of Williams et al. (2012), as well as accounting for sampling effects. A new version of the CRUTEM dataset (CRUTEMv5, Osborn et al., 2021) has increased data completeness and additional quality control measures. A new global land dataset, the China Land Surface Air Temperature (CLSAT) dataset (Xu et al., 2018) has higher network density in some regions (particularly Asia) than previously existing datasets. Global trends derived from CLSAT are generally consistent with those derived from other land datasets through 2014 (Xu et al., 2018).

AR5 identified diurnal temperature range (DTR) as a substantial knowledge gap. The most recent analysis of Thorne et al. (2016a,b) compared a broad range of gridded estimates of change in DTR, including a new estimate derived from the ISTI databank release using the pairwise homogenization algorithm used to create GHCNMv4, and estimates derived from the Vose et al. (2005), HadEX2 (Donat et al., 2013a), HadGHCND (Donat et al., 2013a), GHCNDEX (Donat et al., 2013b), Berkeley Earth (Rohde et al., 2013), and CRU TS (Harris et al., 2014). The analysis highlighted substantial ambiguity in pre-1950 estimates arising from sparse data availability. After 1950 estimates agreed that DTR had decreased globally with most of that decrease occurring over the period 1960–1980. A subsequent DTR analysis using CLSAT further confirmed this behaviour (Sun et al., 2018).

No recent literature has emerged to alter the AR5 finding that it is *unlikely* that any uncorrected effects from urbanization (Box 10.3), or from changes in land use or land cover (Section 2.2.7), have raised global Land Surface Air Temperature (LSAT) trends by more than 10%, although larger signals have been identified in

ACCEPTED VERSION SUBJECT TO FINAL EDITS

some specific regions, especially rapidly urbanizing areas such as eastern China (Li Y. et al., 2013; Liao et al., 2017; Shi et al., 2019). There is also no clear indication that site-specific data homogeneity issues have had any significant impact on global trends since the early 20th century; there is more uncertainty in the 19th century, mainly arising from a lack of standardization of instrument shelters, which has been largely accounted for in data from central Europe (Jones et al., 2012), but less so elsewhere.

Combined data products

At the time of AR5 a limitation of conventional datasets was the lack of coverage, especially in high latitudes, which although recognised as an issue (Simmons et al., 2010a) had not been addressed in most products. Interpolation involves the statistical imputation of values across regions with limited data and can add both systematic and random uncertainties (Lenssen et al., 2019). Cowtan and Way (2014) applied a kriging-based method to extend existing datasets to polar regions, while Kadow et al. (2020a) used an artificial intelligence-based method, and Vaccaro et al. (2021) used gaussian random Markov fields, for the same purpose, although only Kadow et al. (2020) uses the most recent generation of datasets as its base. The Berkeley Earth merged product (Rohde & Hausfather, 2020), HadCRUT5 (Morice et al., 2021) and NOAA GlobalTemp - Interim (Vose et al., 2021) all include interpolation over reasonable distances across data sparse regions which results in quasi-global estimates from the late 1950s when continuous Antarctic observations commenced. Interpolated datasets with substantial coverage of high latitudes show generally stronger warming of GMST than those with limited data in polar regions (Vose et al., 2021), and their strong warming at high northern latitudes is consistent with independent estimates from reanalyses (Simmons et al., 2017; Lenssen et al., 2019) and satellites (Cowtan and Way, 2014). Given the spatial scales of surface temperature variations and the verification of the methods, it is *extremely likely* that interpolation results in a less-biased estimate of the actual global temperature change than ignoring regions with limited or no data.

In total there are five conventional datasets which meet spatial coverage requirements and draw from the most recent generation of SST analyses, four of which have sufficient data in the 1850–1900 period to allow an assessment of changes from that baseline (Table 2.3). A fifth dataset is added to the assessment for changes over land areas. Datasets share SST and LSAT data products and in several cases differ solely in the post-processing interpolation applied meaning that there are far fewer methodological degrees of freedom than implied by a straight count of the number of available estimates.

[START TABLE 2.3 HERE]

Table 2.3: Principal characteristics of GMST in-situ data products considered in AR6 WGI highlighting interdependencies in underlying land and SST products and whether inclusion criteria are met.

Dataset	Period of record	Land component	SST component	Ensemble uncertainties?	Meets all inclusion criteria?	Principal reference
HadCRUT5	1850-2020	CRUTEM5	HadSST4	Yes	Yes	Morice et al. (2021)
NOAA GlobalTemp - Interim	1850-2020	GHCNv4	ERSSTv5	Yes, on earlier version	Yes	Vose et al. (2021)
Berkeley Earth	1850-2020	Berkeley	HadSST4	No	Yes	Rohde and Hausfather (2020)
Kadow et al	1850-2020	CRUTEM5	HadSST4	No	Yes	Kadow et al (2020a)
China - MST	1856-2020	CLSAT	ERSSTv5	No	Land only	Sun et al. (2021)
GISTEMP	1880-2020	GHCNv4	ERSSTv5	Yes	Post-1880 only	Lenssen et al (2019)

ACCEPTED VERSION SUBJECT TO FINAL EDITS

Cowtan and Way	1850-2020	CRUTEM4	HadSST3	Yes	No	Cowtan and Way (2014)
Vaccaro et al	1850-2020	CRUTEM4	HadSST3	No	No	Vaccaro et al (2021)

[END TABLE 2.3 HERE]

Estimates of GMST have also benefitted from improved estimation of parametric uncertainties. New versions of three long-standing products from NASA GISTEMP v4 (Lenssen et al., 2019), NOAA GlobalTempv5 (Huang et al., 2019) and HadCRUT5 (Morice et al., 2021) are all now available as ensemble estimates. These ensembles each account for a variety of systematic and random uncertainty effects in slightly different ways, giving broadly similar results, which are incorporated into the present assessment, with the total uncertainty generally declining up until the mid-20th century as data coverage improves.

Another significant development has been the incorporation of reanalysis products (Section 1.5.2) into operational monitoring of GSAT. It was reported in AR5 that various reanalyses were broadly consistent with conventional surface datasets in the representation of trends since the mid-20th century. Since that time, Simmons et al. (2017) found that the ERA-Interim (Dee et al., 2011) and JRA-55 (Kobayashi et al., 2015) reanalyses continued to be consistent, over the last 20 years, with those surface datasets which fully represented the polar regions. GSAT trends from ERA5 reanalysis (Hersbach et al., 2020) are also broadly consistent with GMST trends from conventional surface datasets. However, the MERRA-2 reanalysis (Gelaro et al., 2017) GSAT spuriously cooled sharply relative to ERA-Interim and JRA-55 in about 2007 (Funk et al., 2019). Since the early 2000s, analyses of surface temperature, from which near-surface temperature may be derived, have also been available from various satellites (Famiglietti et al., 2018; Prakash et al., 2018; Susskind et al., 2019), which have the potential to improve assessments of temperature changes over data-sparse regions.

Most land areas in the extratropical NH have warmed faster than the GMST average over both the 1900–2020 and 1980–2020 periods (Figure 2.11b), although at more regional scales, particularly in data sparse regions, considerable uncertainty is introduced by sometimes large differences in trends between different LSAT datasets (Rao et al., 2018). Temperatures averaged over land areas globally have warmed by 1.59 [1.34 to 1.83] °C from 1850–1900 to 2011–2020, substantially higher than the SST warming of 0.88 [0.68 to 1.01] °C. The four conventional surface temperature products which meet all criteria to be included in the final assessment (Table 2.4) agree that each of the last four decades has consecutively been the warmest globally since the beginning of their respective records (Figure 2.11c, Table 2.4). Each of the six years 2015 to 2020 has *very likely* been at least 0.9°C warmer than the 1850–1900 average.

[START TABLE 2.4 HERE]

Table 2.4: Observed increase (°C) in GMST and underlying LSAT and SST estimates in various datasets. Numbers in square brackets indicate 5–95% confidence ranges. Trend values are calculated with ordinary least squares following Santer et al. (2008a) and expressed as a total change over the stated period. Datasets considered in this table are those with data for at least 90% of global gridpoints in each year from 1960 onwards. GMST and SST are shown only for data sets which use air temperature (as opposed to climatological SST values) over sea ice. Changes from an 1850–1900 baseline are calculated only for those datasets which have data in at least 80% of years over 1850–1900. GMST values for each year are calculated as the mean of hemispheric means for the NH and SH, while LSAT and SST values are calculated from hemispheric means weighted according to the proportion of land (ocean) in the two hemispheres. This may vary from the methods used by individual data set providers in their own reporting. Products which meet all criteria to be included in the final assessment and contribute to the average are shown in italics. Further details on data sources and processing are available in the chapter data table (Table 2.SM.1).

ACCEPTED VERSION SUBJECT TO FINAL EDITS

Diagnostic/ Dataset		**1850–1900 to 1995–2014** (°C)	**1850–1900 to 2011–2020** (°C)	**Trend 1880–2020** (°C)	**Trend 1960–2020** (°C)	**Trend 1980–2020** (°C)
HadCRUT5	GMST	*0.87 [0.81–0.94]*	*1.12 [1.06–1.18]*	*1.10 [0.89–1.32]*	*1.04 [0.93–1.14]*	*0.76 [0.65–0.87]*
	LSAT	*1.23 [1.06–1.38]*	*1.55 [1.39–1.70]*	*1.43 [1.16–1.70]*	*1.50 [1.33–1.67]*	*1.20 [1.04–1.36]*
	SST	*0.73 [0.69–0.78]*	*0.94 [0.90–0.99]*	*1.03 [0.80–1.25]*	*0.90 [0.80–0.99]*	*0.62 [0.51–0.72]*
NOAAGlobalTemp - Interim	GMST	*0.76*	*1.02*	*1.06 [0.80–1.32]*	*1.01 [0.90–1.11]*	*0.75 [0.63–0.87]*
	LSAT	*1.34*	*1.69*	*1.58 [1.32–1.84]*	*1.54 [1.40–1.68]*	*1.19 [1.04–1.35]*
	SST	*0.53*	*0.75*	*0.85 [0.59–1.12]*	*0.79 [0.69–0.89]*	*0.57 [0.44–0.70]*
GISTEMP v4	GMST			*1.07 [0.80–1.34]*	*1.05 [0.94–1.16]*	*0.79 [0.67–0.90]*
	LSAT			*1.48 [1.19–1.78]*	*1.56 [1.40–1.72]*	*1.23 [1.07–1.39]*
	SST			*0.91 [0.65–1.17]*	*0.84 [0.74–0.95]*	*0.61 [0.49–0.72]*
Berkeley Earth	GMST	*0.89*	*1.14*	*1.17 [0.94–1.40]*	*1.09 [1.00–1.19]*	*0.79 [0.68–0.90]*
	LSAT	*1.28*	*1.60*	*1.50 [1.25–1.76]*	*1.51 [1.36–1.66]*	*1.16 [1.00–1.32]*
	SST	*0.73*	*0.96*	*1.04 [0.81–1.26]*	*0.93 [0.84–1.01]*	*0.64 [0.54–0.74]*
China-MST	LSAT	*1.18*	*1.49*	*1.48 [1.21–1.75]*	*1.48 [1.31–1.65]*	*1.16 [1.00–1.32]*
Kadow et al.	GMST	*0.86*	*1.09*	*1.15 [0.95–1.35]*	*1.01 [0.92–1.10]*	*0.73 [0.63–0.82]*
	LSAT	*1.29*	*1.61*	*1.60 [1.37–1.82]*	*1.46 [1.30–1.61]*	*1.14 [0.99–1.30]*
	SST	*0.69*	*0.88*	*0.97 [0.78–1.16]*	*0.83 [0.76–0.90]*	*0.56 [0.48–0.65]*
Cowtan-Way	GMST	0.82 [0.75–0.89]	1.04 [0.97–1.11]	1.03 [0.84–1.22]	0.94 [0.82–1.07]	0.77 [0.67–0.87]
	LSAT	1.23	1.54	1.42 [1.15–1.68]	1.48 [1.31–1.65]	1.20 [1.04–1.36]
	SST	0.66	0.84	0.88 [0.71–1.05]	0.73 [0.61–0.84]	0.61 [0.52–0.69]
Vaccaro et al	GMST	0.76	0.97	0.99 [0.81−1.17]	0.89 [0.77−1.00]	0.72 [0.63−0.81]
	LSAT	1.15	1.47	1.40 [1.13−1.67]	1.47 [1.29−1.64]	1.21 [1.06−1.36]
	SST	0.60	0.77	0.82 [0.67−0.97]	0.66 [0.55−0.76]	0.53 [0.44−0.61]
ERA5	GSAT					0.78 [0.64–0.92]
	LSAT					1.21 [1.02–1.40]
Average – GMST		0.85	1.09	1.11	1.04	0.76
Average – LSAT		1.27	1.59	1.50	1.51	1.18
Average – SST		0.67	0.88	0.96	0.86	0.60

[END TABLE 2.4 HERE]

ACCEPTED VERSION SUBJECT TO FINAL EDITS

To conclude, from 1850–1900 to 1995–2014, GMST increased by 0.85 [0.69 to 0.95] °C, and to the most recent decade (2011–2020) by 1.09 [0.95 to 1.20] °C. Each of the last four decades has in turn been warmer than any decade that preceded it since 1850. Temperatures have increased faster over land than over the oceans since 1850–1900, with warming to 2011–2020 of 1.59 [1.34 to 1.83] °C versus 0.88 [0.68 to 1.01] °C, respectively.

2.3.1.2 Temperatures during the instrumental period – free atmosphere

AR5 reported that it was *virtually certain* that tropospheric temperatures have risen, and stratospheric temperatures fallen, since the mid-20th century, but that assessments of the rate of change and its vertical structure had only *medium confidence* in the NH extratropics and *low confidence* elsewhere. In particular there was *low confidence* in the vertical structure of temperature trends in the upper tropical troposphere.

2.3.1.2.1 Dataset developments

There have been updated radiosonde estimates from the University of Vienna (RAOBCORE and RICH; Haimberger et al., 2012) and a new dataset from the State University of New York (SUNY, (Zhou et al., 2020). There are new versions of AMSU products from the University of Alabama in Huntsville (UAHv6.0; Spencer et al., 2017) and Remote Sensing Systems (RSSv4.0; Mears and Wentz, 2017). These updates have led to convergence in the lower stratosphere layer (Maycock et al., 2018); in particular, the move to UAHv6.0 has addressed homogeneity issues identified by Seidel et al. (2016), although residual differences remain (Christy et al., 2018). Reanalyses products had identified limitations near the 300 hPa level where the contribution of aircraft observations has increased rapidly in recent years (Dee et al., 2011; Gelaro et al., 2017), leading to identified biases (Dee and Uppala, 2009), that have been addressed in ERA5 (Hersbach et al., 2020). Modern reanalyses are generally well aligned with radiosonde and satellite observations in the middle and lower troposphere and lower stratosphere. A new operational mid- and upper-stratospheric dataset (STAR) has been developed by Zou & Qian (2016), merging the previous 1979–2006 SSU dataset (Zou et al., 2014) with a dataset from 1998 onwards drawn from relevant AMSU channels (Wang & Zou, 2014). Further stratospheric satellite-based datasets from various combinations of satellites have been developed by McLandress et al. (2015) and Randel et al. (2016).

New assessments of free-atmosphere temperature are available through radio occultation (RO) and Atmospheric Infrared Sounder (AIRS) products which begin in the early 2000s (Section 1.5.1.1). Global Navigation Satellite System (GNSS)-RO datasets have been compared against AMSU data records, finding almost identical trends (Khaykin et al., 2017). Comparison of RO with collocated radiosondes, Vaisala RS90/92 and GCOS Reference Upper Air Network data (RS92-GDP; Dirksen et al., 2014), show very good correspondence with global annual mean differences of less than 0.2°C in the upper troposphere and lower stratosphere. Radiosonde daytime radiation biases were identified at higher altitudes (Ho et al., 2017; Ladstädter et al., 2015). The stability of RO makes this data a useful comparator for AMSU (Chen & Zou, 2014) and radiosondes (Ho et al., 2017; Tradowsky et al., 2017), as well as anchoring post-2006 reanalyses datasets and improving their consistency in the lower and middle stratosphere (Ho et al., 2020; Long et al., 2017). The effective vertical resolution of RO measurements in the upper troposphere and lower stratosphere was found to be up to 100 m at the tropical tropopause (Zeng et al., 2019a), which is favourable for resolving atmospheric variability (Scherllin-Pirscher et al., 2012; Stocker et al., 2019; Wilhelmsen et al., 2018). Temperature trends in RO products are most consistent with each other and with other observations between 8 km and 25 km (Ho et al., 2012; Steiner et al., 2013, 2020a). The uncertainty increases above 25 km for the early RO period, for which data are based on the single-satellite CHAMP mission, but data at higher altitudes become more reliable for later missions based on advanced receivers (Steiner et al., 2020a), along with the application of corrections for ionospheric effects (Danzer et al., 2020). The uncertainty due to the changing number of observations is reduced by correcting for the sampling uncertainty in RO climatological fields (e.g., Scherllin-Pirscher et al., 2011). For AIRS, thus far, stability of the instrument has been constrained to less than 0.03 °C per decade for selected window channels in a comparison to SSTs measured by ocean buoys (Aumann et al., 2019). Trends were inter-compared with trends in RO data and reanalysis data to assess systematic uncertainties (Leroy et al., 2018).

ACCEPTED VERSION SUBJECT TO FINAL EDITS

2.3.1.2.2 Assessment of trends

Warming has continued in the lower troposphere according to all radiosonde, reanalyses and satellite datasets, with a rate over 1980–2019 similar to surface warming rates (Table 2.5; c.f. Table 2.4). Radiosonde-based products generally show greater warming rates for 1980–2019 than satellite-based products and reanalyses. They also extend further back to the 1950s and trends since quasi-global coverage around 1960 also show warming (Table 2.5). Trends in RO and AIRS data, supported by radiosonde datasets, exhibit a warming trend in most of the mid- to upper- troposphere at all non-polar latitudes over 2002–2019. These also exhibit faster warming rates in the tropics in the upper troposphere than those observed at or near the surface (Figure 2.12); with the lowermost stratosphere also warming while above it is cooling. There is some spread between different data types in the tropics near the 15 km level, although these differences are reduced to near zero if a subset of radiosonde data, using only high-quality instruments, is used (Steiner et al., 2020b). AMSU tropical middle troposphere data also show that warming rates are near or above those in the lower troposphere, but they are measuring much broader layers which greatly complicates interpretation (Steiner et al., 2020b).

Temperatures averaged through the full lower stratosphere (roughly 10–25 km) have decreased over 1980–2019 in all data products, with the bulk of the decrease prior to 2000. The decrease holds even if the influence of the El Chichon (1982) and Pinatubo (1991) volcanic eruptions on the trend, found by Steiner et al. (2020b) to have increased the 1979–2018 cooling trend by 0.06°C per decade, is removed. Most datasets show no significant or only marginally significant trends over 2000–2019, and the results of Philipona et al. (2018) show weak increases over 2000–2015 in the very lowermost stratosphere sampled by radiosondes.

The STAR dataset shows cooling in the middle and upper stratosphere with a trend of –0.56°C ± 0.16°C per decade for the mid-stratosphere and –0.62°C ± 0.29°C per decade for the upper stratosphere over 1980–2019, although both cooling rates have slowed substantially since the mid-1990s. The overall post-1980 trend is reduced in magnitude by about 0.10°C per decade at both levels if the influences of the El Chichon and Pinatubo eruptions, and the solar cycle, are removed (Zou and Qian, 2016). The results obtained by McLandress et al. (2015) for 1980–2012, Randel et al. (2016) for 1979–2015, and Maycock et al. (2018) for 1979-2016 are broadly consistent with this.

A rise in the tropopause height of 40 to 120 m per decade between 1981 and 2015 was determined from both radiosonde and reanalysis datasets (Xian and Homeyer, 2018). Local studies (e.g. Tang et al., 2017; Chen X. et al., 2019) found stronger trends in some regions near the subtropical jet linked to tropical expansion (Section 2.3.1.4.1). Whilst Seidel and Randel (2006) found that the tropopause height was more closely coupled with temperatures in the stratosphere than those in the troposphere, it is not yet clear whether the rate of increase in tropopause height has experienced a similar recent slowdown to that of the cooling of the lower stratosphere, as short-period trends are typically inconclusive due to significant natural variability (Scherllin-Pirscher et al., 2020). RO data (Gao P. et al., 2015) indicate little change in tropopause height over the short period from 2006 to 2014, but a warming below the tropopause is observed over 2002 to 2019 (Figure 2.12).

In summary, the troposphere has warmed since the mid-20th century. There is *medium confidence* that temperatures in the tropical upper troposphere have warmed faster than those at the surface since 2001, but *low confidence* in changes prior to 2001. It is *virtually certain* that the lower stratosphere has cooled since the mid-20th century. However, most datasets show that lower stratospheric temperatures have stabilized since the mid-1990s with no significant change over the last 20 years. It is *likely* that middle and upper stratospheric temperatures have decreased since 1980, but there is *low confidence* in the magnitude. It is *virtually certain* that the tropopause height has risen over 1980–2019 but there is *low confidence* in the magnitude of this rise, or whether the rate of change has reduced commensurate with stabilized lower stratospheric temperatures.

ACCEPTED VERSION SUBJECT TO FINAL EDITS

[START TABLE 2.5 HERE]

Table 2.5: Observed change (°C) in free atmospheric temperatures in various datasets, for the lower tropospheric and lower stratospheric layers. Numbers in square brackets indicate 5–95% confidence ranges. Trend values are calculated with ordinary least squares following (Santer et al., 2008b) and are expressed as a total change over the stated period. Further details on data sources and processing are available in the chapter data table (Table 2.SM.1).

Diagnostic/ Dataset	Trend 1960–2019	Trend 1980–2019	Trend 2000–2019
Lower troposphere			
RAOBCORE	1.08 [0.94–1.23]	0.74 [0.57–0.91]	0.52 [0.26–0.78]
RICH	1.20 [1.06–1.34]	0.79 [0.63–0.96]	0.53 [0.28–0.77]
SUNY	0.97 [0.80−1.13]	0.91 [0.76−1.05]	0.53 [0.35−0.72]
UAH		0.51 [0.37–0.65]	0.29 [0.07–0.50]
RSS		0.79 [0.66–0.92]	0.41 [0.24–0.58]
ERA5		0.68 [0.53–0.84]	0.54 [0.32–0.75]
Average	1.14	0.70	0.46
Lower stratosphere			
RAOBCORE	–1.37 [–1.80– –0.93]	–1.00 [–1.56– –0.45]	–0.05 [–0.20–0.09]
RICH	–1.45 [–1.99– –0.92]	–1.19 [–1.95– –0.42]	0.02 [–0.20–0.23]
SUNY	−1.25 [−1.51− −0.98]	−0.79 [−1.16− −0.43]	−0.11 [−0.25−0.03]
UAH		–1.14 [–1.61– –0.67]	–0.24 [–0.37– –0.12]
RSS		–0.90 [–1.37– –0.43]	–0.14 [–0.26– –0.03]
STAR		–0.97 [–1.45– –0.49]	–0.17 [–0.29– –0.04]
ERA5		–1.23 [–2.14– –0.32]	0.33 [0.07–0.60]
Average	–1.41	–1.07	–0.04

[END TABLE 2.5 HERE]

[START FIGURE 2.12 HERE]

Figure 2.12: Temperature trends in the upper air. (a) Zonal cross-section of temperature anomaly trends (2007–2016 baseline) for 2002–2019 in the upper troposphere and lower stratosphere region. The climatological tropopause altitude is marked as a grey line. Significance is not indicated due to the short period over which trends are shown, and because the assessment findings associated to this figure relate to difference

ACCEPTED VERSION SUBJECT TO FINAL EDITS

between trends at different heights, not the absolute trends. (b) Trends in temperature at various atmospheric heights for 1980–2019 and 2002–2019 for the near-global (70°N–70°S) domain. (d) (e) as for (b) (c) but for the tropical (20°N–20°S) region. Further details on data sources and processing are available in the chapter data table (Table 2.SM.1).

[END FIGURE 2.12 HERE]

2.3.1.3 Global hydrological cycle

This section focuses on large-scale changes in a subset of components of the hydrological cycle (Cross-Chapter Box 2.2). Chapter 8 undertakes a holistic assessment of changes in the hydrological cycle integrating observations, modelling and theoretical understanding, while Chapter 11 assesses hydrological cycle extremes such as droughts and floods.

2.3.1.3.1 Paleo perspective of the global hydrological cycle

AR5 assessed large-scale indicators of terrestrial paleo hydroclimate, including as part of its assessment of paleo floods and droughts, but did not assess proxy evidence for paleo hydroclimate indicators over continental and larger scales. The paleoclimate evidence assessed in AR5 was broadly consistent with global hydroclimate scaling with temperature: warmer periods were wetter (e.g., the Pliocene; increased precipitation) with colder periods being drier (e.g., the LGM; decreased precipitation).

Substantial limitations exist in reconstructing the global hydrological cycle prior to the Quaternary, particularly during the Eocene, due to the lack of high-resolution proxy records and their sparsity. Spatial heterogeneity complicates identification of wetting and drying signals during the PETM and the EECO, with paleo data and model simulations suggesting an intensified global hydrological cycle (Carmichael et al., 2016, 2017; Hyland et al., 2017; West et al., 2020), in particular an increased specific humidity (Winnick et al., 2015; van Dijk et al., 2020). Conditions wetter than present were inferred for the MPWP (Cross Chapter Box 2.4), with intensified Asian monsoons (An et al., 2015) and with nevertheless drier conditions over tropical and subtropical SH locations (Pontes et al., 2020). A new global reconstruction of hydroclimate proxies for the LIG points to stronger boreal precipitation compared to 1850–1900 over high latitudes and especially over monsoon areas, with a more heterogeneous signal for the SH (Scussolini et al., 2019). This heterogeneity is also present in the tropics, characterized by large zonal differences in precipitation change due to the variations in the intensity of Walker circulation (section 2.3.1.4.1). Available records indicate reduced global vegetation cover and abundant atmospheric dust deposition during the LGM (increased aridity), particularly over the tropics and high latitudes (Lamy et al., 2014; Újvári et al., 2017). This agrees with models and moisture-sensitive proxies, suggesting an overall decrease in global precipitation during the LGM relative to recent decades, albeit with regional-scale heterogeneity (Cao et al., 2019). Despite lower global precipitation amounts, research since AR5 has identified a wetting of mid-latitudes during the LGM (Putnam and Broecker, 2017; Lowry and Morrill, 2018; Morrill et al., 2018), thereby complicating the characterization of the LGM as a relatively "dry" period. Low evaporation rates and increased top-soil moisture during the LGM may have contributed to elevated levels of large closed-basin lakes located in the 30°–45° latitudinal belts (Putnam and Broecker, 2017; Scheff et al., 2017), such as the southwest US (e.g. Ibarra et al., 2018), southern Australia (Fitzsimmons et al., 2015; Petherick et al., 2013; Sniderman et al., 2019) and Patagonia (e.g. Quade & Kaplan, 2017).

New analyses suggest that during the Holocene, the NH mid-latitudes became increasingly wet, in phase with the strength of the latitudinal temperature and insolation gradients (Shuman and Marsicek, 2016; Routson et al., 2019). Nevertheless, there was also considerable spatial heterogeneity and variability on centennial to millennial timescales (Liefert & Shuman, 2020; Newby et al., 2014; Shuman & Marsicek, 2016; Zhang H. et al., 2018). The NH tropics and many regions of the SH deep tropics experienced wetting up until the early to mid-Holocene but drying thereafter (Muñoz et al., 2017; Nash et al., 2016; Quade et al., 2018; Shanahan et al., 2015). *Evidence* for the SH is *limited*, with a wetting trend during the Holocene in low latitudes of South America (Kanner et al., 2013; Mollier-Vogel et al., 2013) and parts of the African tropics (Schefuß et al., 2011; Chevalier and Chase, 2015) but a drying tendency over southern Australia and New

ACCEPTED VERSION SUBJECT TO FINAL EDITS

Zealand (Barr et al., 2019; van den Bos et al., 2018) and South America (Moreno et al., 2018; Quade & Kaplan, 2017).

For the CE, new proxy records have led to the creation of continental drought atlases (Cook et al., 2015; Morales et al., 2020; Palmer et al., 2015; Stahle et al., 2016) and millennial reanalyses (Steiger et al., 2018; Tardif et al., 2019). These reconstructions highlighted the occurrence of multi-decadal regional mega-droughts in the NH before 1600 CE, particularly during 800–1200 CE, with a predominance of wet periods after 1700 CE (Cook et al., 2015; Rodysill et al., 2018; Shuman et al., 2018). In the SH, much of South America and the African tropics experienced a reduction of precipitation during 900–1200 CE and a wetting peak during 1500–1800 CE (Campos et al., 2019; Fletcher et al., 2018; Lüning et al., 2018; Nash et al., 2016; Tierney et al., 2015), with an opposite pattern in southern subtropical Africa (Lüning et al., 2018; Woodborne et al., 2015). Large multidecadal variability was documented over Australia and New Zealand during the 800–1300 CE period, followed by a well-defined wet period during 1500–1800 CE (Barr et al., 2014; Evans et al, 2019).

To summarise, since AR5 there has been considerable progress in detecting the variations of the global hydrological cycle prior to the instrumental period. There are indications from multiple sources of a wetting trend during the Holocene, particularly for the NH and parts of the SH tropics (*medium confidence*). Hydroclimate during the CE is dominated by regional variability, generally precluding definitive statements on changes at continental and larger scales, with a general reduction of mega-drought occurrences over the last about 500 years (*medium confidence*). Availability of proxy data for assessing Holocene hydroclimate variability is biased towards the NH, with *medium evidence* but *low agreement* for the assessment of SH changes.

2.3.1.3.2 Surface humidity

AR5 reported *very likely* widespread increases in near-surface air specific humidity since the 1970s, abating from around 2000 to 2012 (*medium confidence*). This abatement resulted in a recent decline in relative humidity over the land.

Near surface humidity has been monitored using in situ data (e.g. NOCSv2.0; Berry and Kent, 2011), satellite-derived estimations (e.g. HOAPS3, Liman et al., 2018; J-OFURO3, Tomita et al., 2019), global gridded products such as HadISDH (Willett et al., 2014; 2020), and reanalyses (e.g. ERA5, JRA-55 and 20CRv3). In situ based humidity products suffer from uncertainties over poorly sampled regions particularly in the SH (Berry & Kent, 2011; Kent et al., 2014; Willett et al., 2014). There is general consensus in the inter-annual variability and sign of trends implying *high confidence* in increasing specific humidity since the 1970s and decreasing relative humidity since 2000, particularly over land (Simmons et al., 2010; Willett et al., 2014; 2020). Since 2012, specific humidity over land and ocean has remained well above the 1973–2019 average and reached record or near-record values (Figure 2.13b), with the strong 2015–2016 El Niño event boosting surface moisture levels (Byrne and O'Gorman, 2018). The abatement from around 2000 to 2012 reported in AR5 has not persisted. This is consistent with increases in total column water vapour (Section 2.3.1.3.3) and a resumption of rapid warming in surface temperatures (Section 2.3.1.1.3). The global averaged relative humidity however has remained depressed since 2000 (Figure 2.13d) (Dunn et al., 2017; Simmons et al., 2010; Vicente-Serrano et al., 2018; Willett et al., 2014; 2020).

Since 1973, increases in specific humidity have been widespread and significant across the majority of the land and ocean regions where observations are available (Figure 2.13a). In contrast, trends in relative humidity show distinct spatial patterns with generally increasing trends over the higher latitudes and the tropics and generally decreasing trends over the sub-tropics and mid-latitudes, particularly over land areas (Figure 2.13c). Near-surface specific humidity over the oceans has increased since the 1970s according to several in situ, satellite and reanalysis data records (Kent et al., 2014; Robertson et al., 2020; Willett et al., 2020). According to the HadISDH product, increases in specific humidity and decreases in relative humidity are significant particularly over the NH mid-latitudes (Figure 2.13a,c). Poor data coverage over the SH south of 20°S does not allow for the robust assessment of trends. Sources of uncertainty include the initial measurement accuracy, homogenisation over land, observational height at ships and instrument bias

ACCEPTED VERSION SUBJECT TO FINAL EDITS

adjustment over ocean, and sparse spatio-temporal sampling (Prytherch et al., 2015; Roberts et al., 2019; Willett et al., 2020).

In summary, observations since the 1970s show a *very likely* increase in near surface specific humidity over both land and oceans. A *very likely* decrease in relative humidity has occurred over much of the global land area since 2000, particularly over mid-latitude regions of the NH, with increases at northern high latitudes.

[START FIGURE 2.13 HERE]

Figure 2.13: Changes in surface humidity. (a) Trends in surface specific humidity over 1973–2019. Trends are calculated using OLS regression with significance assessed following AR(1) adjustment after Santer et al (2008a) ('x' marks denote non-significant trends). (b) Global average surface specific humidity annual anomalies (1981–2010 base period). (c) as (a) but for the relative humidity. (d) as (b) but for the global average surface relative humidity annual anomalies. Further details on data sources and processing are available in the chapter data table (Table 2.SM.1).

[END FIGURE 2.13 HERE]

2.3.1.3.3 Total column water vapour

AR5 concluded that total column water vapour (TCWV) *very likely* increased since the 1970s, at a rate that was overall consistent with the Clausius-Clapeyron relationship (about 7% per °C) given the observed increase in atmospheric temperature.

Records prior to the instigation of quasi-global coverage by radiosondes require the use of statistical relationships to infer TCWV from historical SST observations or the evaluation of centennial-scale reanalysis products (Smith and Arkin, 2015). These approaches reveal two periods of positive trends, one during 1910–1940 and the other from 1975 onwards (Zhang et al., 2013; Mieruch et al., 2014; Shi et al., 2018), concurrent with periods of positive SST trends (Figure 2.11). Potential sources of errors in the SST-based estimation of TCWV include both uncertainties in historical SST and uncertainties in the parameters that define the relationship between the variables (Smith & Arkin, 2015). Trends based on 20CRv2c, ERA-20C and ERA-20CM indicate an increase in TCWV over much of the global ocean since the beginning of the 20th century, particularly over the tropics (Bordi et al., 2015; Poli et al., 2016; Smith & Arkin, 2015). TCWV trends estimated since the middle of the 20th century from radiosonde observations show significant increases over North America and large portions of Eurasia, while decreases are restricted to Australia, Eastern Asia and the Mediterranean region (Zhang Y. et al., 2018). Overall, there is a significant increase in TCWV over global land areas since 1979 (Chen & Liu, 2016).

Since the late 1970s a range of satellite missions permit a quasi-global assessment of TCWV. Several satellite products provide water vapour retrievals based upon distinct spectral domains, in addition to products from radiosondes, reanalyses and GNSS radio occultation. The GEWEX Water Vapour Assessment (G-VAP) provided an intercomparison of several TCWV data records, with global coverage but limited timespan (Schröder et al., 2018). The various global products generally exhibit a positive trend since 1979 (Figure 2.14) (Allan et al., 2014; Mieruch et al., 2014; Schröder et al., 2016; Wang X.L. et al., 2016a), most evident over the tropics (Chen & Liu, 2016; Gu & Adler, 2013; Mears et al., 2018; Salamalikis et al., 2021; Wang R. & Liu, 2020). The existence of apparent breakpoints in several products, which are generally coincident with changes in the observing system, lead to trend estimates that are not in line with theoretical expectations imposed by the Clausius-Clapeyron relationship (Schröder et al., 2019a), although other factors such as regional moisture divergence/convergence could account for the observed TCWV-temperature scaling. Substantial potential inhomogeneities affect trend estimates based on satellite, reanalysis and merged products in particular over Central Africa, the Sahara and central South America (Schröder et al., 2016, 2019; Wang et al., X.L. 2016). Moreover, data gaps in observations from ground-based GNSS receivers and radiosondes lead to *low confidence* in TCWV estimation in these regions.

ACCEPTED VERSION SUBJECT TO FINAL EDITS

[START FIGURE 2.14 HERE]

Figure 2.14: Timeseries of global mean total column water vapour annual anomalies (mm) relative to a 1988–2008 base period. Further details on data sources and processing are available in the chapter data table (Table 2.SM.1).

[END FIGURE 2.14 HERE]

In summary, positive trends in global total column water vapour are *very likely* since 1979 when globally representative direct observations began, although uncertainties associated with changes in the observing system imply *medium confidence* in estimation of the trend magnitudes. *Low confidence* in longer-term trends arises from uncertainties in the SST-TCWV relationship and current centennial scale reanalyses, particularly during the first half of the 20th century.

2.3.1.3.4 Global precipitation

AR5 concluded that there was *low confidence* in precipitation change averaged over global land areas prior to 1950, and *medium confidence* thereafter with no significant global trends. There was a *likely* overall increase in precipitation in the well-sampled NH mid-latitudes, with *high confidence* after 1951.

In situ precipitation records over land extend back for centuries in a few locations, and to the early to mid-20th century quasi-globally. Datasets differ in their input data, completeness of records, period covered, and the gridding procedures which, given spatial clustering and the small spatial scales of precipitation, results in differences in global and regional estimates of precipitation changes (Nogueira, 2020; Sun Q. et al., 2018). The spatial variability of observed long-term trends (1901–2019) based on GPCC V2020 and CRU TS 4.04 (Figure 2.15a,b) indicates significant increases in precipitation mainly over eastern North America, northern Eurasia, southern South America and northwestern Australia. Decreases are strongest across tropical western and equatorial Africa and southern Asia. The temporal evolution of global annual land precipitation anomalies exhibits little consistency between GPCC V2020, CRU TS 4.04 and GHCNv4 datasets, especially prior to 1950, that is associated with limitations in data coverage (Figure 2.15c, (Gu & Adler, 2015; Shen et al., 2014; Wu et al., 2013). These disagreements between datasets prior to the 1950s result in differences in trend estimates over global land (Table 2.6). A qualitative consistency in decadal and interdecadal variations between the products is only observed since the 1950s, with primarily positive land precipitation anomalies during the 1950s, 1970s and after the 2000s (Figure 2.15c).

Several satellite-based precipitation datasets improve the representation of the spatio-temporal changes since the late 20th century. Some of these are based exclusively on satellite data (e.g. CMORPH, Joyce et al., 2004; GSMaP, Okamoto et al., 2005), with others being combinations of in situ observations, reanalyses and satellite retrievals (e.g. CMAP, Xie and Arkin, 1997; TRMM 3B43 V7, Huffman et al., 2007; PERSIANN-CDR, Ashouri et al., 2015; CHIRPS, Funk et al., 2015; GPCP V2.3, Adler et al., 2018). These can be affected by systematic and random uncertainties due to inhomogeneities in the satellite-derived precipitation and station data and the uncertainties of blending algorithms (Hegerl et al., 2015; Sun et al., 2018a). The spatial coverage of these products is near-global, with available estimations formally covering 60°S–60°N with decreasing quality from low to high latitudes, depending on the sensors and algorithms used (Hu Q. et al., 2019). A detailed description of the most relevant satellite products is provided in section 10.2.1.1.

Recent trends (1980–2019) for GPCC V2020, CRU TS 4.04 and GPCP V2.3 show significant increases in land precipitation over tropical Africa, the eastern portions of Europe and North America, central Asia and the Maritime Continent (Figure 2.14, d, e and f). Significant decreases are observed over central South America, western North America, northern Africa and the Middle East. A detailed assessment of the recent regional precipitation trends using the same datasets can be found in the Atlas. Global trends for 1980–2019 show a general increase in annual precipitation over land, which is particularly marked for CRU TS 4.04 and GHCNv4 (Table 2.6). These changes have been accompanied by a strengthening of precipitation seasonality over tropical land areas, although with broad spread between different satellite-based (GPCP, MSWEP_V1.2, PERSIANN-CDR) and in situ gridded datasets (GPCC, CRU TS) (Chou et al., 2013; Li X.

ACCEPTED VERSION SUBJECT TO FINAL EDITS

et al., 2016; Tan et al., 2020). Increasing trends since 1980, in contrast to longer-term declining trends since 1901, are particularly evident over much of Africa, while more widespread negative trends were observed over much of southern South America in the more recent period (Knutson and Zeng, 2018) (Atlas 7.2). A faster recent increase in precipitation over global land is inferred comparing the precipitation trends over 1960–2019 with 1980–2019 (Table 2.6). Over the global ocean, the comparison between precipitation datasets is compromised by the different measurement periods, as well as the spatial coverage of the available products (Adler et al., 2017; Jaber & Abu-Allaban, 2020; Nguyen et al., 2018; Nogueira, 2020), limiting the ability to assess the sign and magnitude of precipitation trends. The GPCPv2.3 database (Adler et al., 2017, 2018) exhibits an increase of 2.94 mm yr^{-1} per decade over 1980–2019, principally due to the trends over the Indian ocean and in the tropical western Pacific (Figure 2.15f). The regional patterns of recent trends are consistent with the documented increase in precipitation over tropical wet regions and the decrease over dry areas, estimated through GPCP v2.2 data (Kao et al., 2017; Liu & Allan, 2013; Polson & Hegerl, 2017; Trammell et al., 2015).

[START FIGURE 2.15 HERE]

Figure 2.15: Changes in observed precipitation. (a, b) Spatial variability of observed precipitation trends over land for 1901–2019 for two global in-situ products. Trends are calculated using OLS regression with significance assessed following AR(1) adjustment after Santer et al (2008a) ('x' marks denote non-significant trends). (c) Annual time series and decadal means from 1891 to date relative to a 1981–2010 climatology (note that different products commence at distinct times). (d, e) as (a, b), but for the periods starting in 1980. (f) is for the same period for the globally complete merged GPCP v2.3 product. Further details on data sources and processing are available in the chapter data table (Table 2.SM.1).

[END FIGURE 2.15 HERE]

[START TABLE 2.6 HERE]

Table 2.6: Globally averaged trend estimates over land and 90% confidence intervals for annual precipitation for each time series in Figure 2.15(c) over three periods all ending in 2019. Trends are calculated using OLS regression with significance assessed after Santer et al (2008a). Further details on data sources and processing are available in the chapter data table (Table 2.SM.1).

Dataset	Trends in annual precipitation (mm yr^{-1} per decade)		
	1901-2019	**1960-2019**	**1980-2019**
GPCCv2020	1.01* ± 0.99	1.67 ± 3.23	5.60 ± 6.38
CRU TS 4.04	0.57 ± 2.08	0.17 ± 3.12	5.75* ± 5.09
GHCNv4	3.19*± 1.48	5.03* ± 4.87	11.06* ± 9.17
GPCPv2.3			5.41* ± 5.20

* Trend values significant at the 10% level.

[END TABLE 2.6 HERE]

In summary, globally averaged land precipitation has *likely* increased since the middle of the 20th century (*medium confidence*), with *low confidence* in trends prior to 1950. A faster increase in global land precipitation was observed since the 1980s (*medium confidence*), with large interannual variability and regional heterogeneity. Over the global ocean there is *low confidence* in the estimates of precipitation trends, linked to uncertainties in satellite retrievals, merging procedures and limited in situ observations.

2.3.1.3.5 Precipitation minus Evaporation

AR5 concluded that the pattern of precipitation minus evaporation (P-E) over the ocean had been enhanced since the 1950s (*medium confidence*). Saline surface waters had become saltier, while the relatively fresh

ACCEPTED VERSION SUBJECT TO FINAL EDITS

surface waters had become fresher. The inferred changes in P-E were consistent with the observed increased TCWV, although uncertainties in the available products prevented identifying robust trends.

Estimating global-scale trends in P-E using direct observations alone is challenging due to limited evaporation measurements and inhomogeneities in satellite-derived precipitation and evaporation datasets (Hegerl et al., 2015; López et al., 2017). Hence, the assessment of global P-E trends is generally performed using reanalyses, although changes in the observing system imply considerable uncertainty (Skliris et al., 2014a). Since the second half of the 20th century, several reanalyses and observational datasets have shown increases in P-E over global land, although 75% of land areas exhibit no significant changes and both internal variability and observational uncertainty are substantial (Greve et al., 2014; Robertson et al., 2016). The recently released ERA5 (Hersbach et al., 2020) showed improvements in the representation of tropical precipitation, although it overestimates global precipitation trends in comparison to ERA-Interim and GPCP (Nogueira, 2020), and suffers from temporal changes in the annual balance between precipitation and evaporation (Hersbach et al., 2020). The spatial pattern of P-E trends over 1980–2019 (Figure 2.16a) are largely consistent with the trends in the GPCP v2.3 precipitation dataset (Figure 2.15f, Section 2.3.1.3.4) and agrees in sign with the trends from other reanalyses such as JRA-55 and MERRA-2 (Yu L. et al., 2020).

A variety of reanalysis products exhibit diverse temporal evolutions of P-E (Figure 2.16b-d). Globally MERRA-2, ERA20C and ERA20CM exhibit little change whereas JRA-55, ERA5 and 20CRv3 all imply long-term changes (Figure 2.16d). A potential limitation in estimating P-E from some reanalysis products is readily apparent when considering the temporal evolution of global P-E from CFSR and MERRA (Figure 2.16d) which both exhibit strong discontinuities over the global ocean in the late 1990s. Over global land as a whole, precipitation exceeds evaporation (P-E > 0) for all the reanalysis products (Figure 2.16c), with decreasing trends in P-E for ERA5 and JRA-55 and increasing trends for MERRA-2 and CFSR. The P-E over the global ocean is negative (evaporation exceeding precipitation) for most reanalyses (Figure 2.16d), with declining trends in ERA5 and MERRA-2 dominated by trends in evaporation (Bosilovich et al., 2017; Hersbach et al., 2020) (Figure 2.16d). The recent increase in ocean evaporation was also documented for several reanalyses (Craig et al., 2017) and in satellite data (Andersson et al., 2011; Robertson et al., 2014), although with considerable differences between available estimates (Chandanpurkar et al., 2017, Yu L. et al., 2020). An alternative indirect approach to estimate P-E changes is based on near-surface ocean salinity (Section 2.3.3.2), which is partially driven by the freshwater flux at the ocean surface. The near-surface salinity trends are more spatially coherent compared to those revealed by P-E estimates from reanalyses, with an intensification of the water cycle over oceans, especially in subtropical regions (Yu L. et al., 2020, Durack et al., 2012; Skliris et al., 2014). However, the precise rate of water cycle intensification implied by salinity trends is sensitive to methodological choices (e.g., Skliris et al., 2016; Zika et al., 2018).

[START FIGURE 2.16 HERE]

Figure 2.16: Changes in precipitation minus evaporation. (a) Trends in precipitation minus evaporation (P-E) between 1980 and 2019. Trends are calculated using OLS regression with significance assessed following AR(1) adjustment after (Santer et al., 2008; 'x' marks denote non-significant trends). Time series of (b) global, (c) land-only and (d) ocean-only average annual P-E (mm/day). Further details on data sources and processing are available in the chapter data table (Table 2.SM.1).

[END FIGURE 2.16 HERE]

In conclusion, observational uncertainty yields *low confidence* in globally averaged trends in P-E over the 20th century, with a spatial pattern dominated by precipitation changes over land and by evaporation increases over the ocean. Different reanalyses disagree on the sign of long-term changes in the global mean P-E.

2.3.1.3.6 Streamflow

AR5 concluded that there was *low confidence* in a positive trend in global river discharge during the 20th

ACCEPTED VERSION SUBJECT TO FINAL EDITS

century. It noted that many of the largest rivers with long term streamflow records have been impacted by non-climatic human influences such as dam construction or land-use change.

River discharge is monitored widely, although gaps remain at a subcontinental scale over central Asia and Africa (Wei et al., 2020). Substantial recent efforts have been made to generate new global streamflow datasets, consolidating observations from many stream gauges to create streamflow indices (Do et al., 2018; Gudmundsson et al., 2018) and gridded products using neural networks (Barbarossa et al., 2018) or combinations between observations and reanalyses (Suzuki et al., 2018; Ghiggi et al., 2019).

Human intervention on river discharge linked to increases in evapotranspiration and some reduction of intra-annual streamflow variability (Jaramillo and Destouni, 2015, Chai et al., 2020) might affect the detection of trends in extreme daily streamflow events (Do et al., 2017; Gudmundsson et al., 2019). However, these activities have a minor impact on annual streamflow compared to climate variations (Dai et al., 2009; Alkama et al., 2013). Available global studies post-1950 generally concur that there have been more rivers experiencing decreases than increases in runoff (Do et al., 2017; Gudmundsson et al., 2019; X. Shi et al., 2019; Su et al., 2018). Most of the rivers have not experienced statistically significant changes in streamflow, and when globally aggregated there is no significant change (Dai and Zhao, 2017). Global streamflow variability is strongly modulated by ENSO and PDV, with below-normal global streamflow as a response to El Niño events and vice-versa during La Niña episodes (Dai, 2016; Kim, 2019; Liang et al., 2016). The response of streamflow to changes in precipitation associated with ENSO and PDV has heterogeneous regional patterns at subcontinental scales (Section 8.3.2.9.1). No significant trends are found for reanalysis-based discharge estimates over 1993 to 2015 (Chandanpurkar et al., 2017). Uncertainties in global streamflow trends arise predominantly from changes in instrumentation, gauge restoration, recalibration of rating curves, flow regulation or channel engineering (Alkama et al., 2011; Gudmundsson et al., 2018; Ghiggi et al., 2019).

In summary, the sign of global streamflow trends remains uncertain, with slightly more globally gauged rivers experiencing significantly decreasing flows than significantly increasing flows since the 1950s (*low confidence*).

2.3.1.4 Atmospheric circulation

This section focuses on large-scale changes in a subset of components of the atmospheric circulation (Cross-Chapter Box 2.2). Chapter 8 assesses large-scale as well as regional aspects of circulation components and their impact on the hydrological cycle, while Chapter 11 assesses the association of circulation changes and variability with extreme events.

2.3.1.4.1 The Hadley and Walker circulations

AR5 reported *low confidence* in trends in the strength of the Hadley circulation (HC) and the Walker circulation (WC) due to uncertainties in available reanalysis datasets and the large interannual-to-decadal variability of associated circulation patterns. However, AR5 indicated a *likely* widening of the tropical belt since the 1970s, albeit with large uncertainty in the magnitude of this change. There was *high confidence* that the post-1990s strengthening trends of the Pacific WC reversed its weakening observed from the mid-19th century to the 1990s.

Paleo reconstructions of rainfall and trade winds extending over the last 100 kyr show an intensification of the NH HC concurrently with a weakening of the SH HC and a southward shift of the inter tropical convergence zone (ITCZ) during Heinrich stadials (Deplazes et al., 2013; McGee et al., 2018; Stríkis et al., 2018; Wendt et al., 2019). An intensification of the HC associated with conditions similar to La Niña (northward migrations of both the ITCZ and the SH westerlies) was found in reconstructions for the MH (McGee et al., 2014; Mollier-Vogel et al., 2019). Changes in insolation from the mid to late Holocene favoured a southward migration in the position of the ITCZ and the descending branch of the HC in the NH, approaching its current width and position (Wirth et al., 2013a; Thatcher et al., 2020). Tree ring chronologies

ACCEPTED VERSION SUBJECT TO FINAL EDITS

from the NH mid-latitudes over the last 800 years show that the northern edge of the HC tended to migrate southward during positive phases of ENSO and PDV, with northward shifts during negative phases (Alfaro-Sánchez et al., 2018). Between 1400 and 1850 CE the HC over both hemispheres and the ITCZ were displaced southward, consistent with occurrence of drought conditions in several NH regions (Alfaro-Sánchez et al., 2018; Burn and Palmer, 2014; Flores-Aqueveque et al., 2020; Lechleitner et al., 2017; Wirth et al., 2013). Moreover, several proxy records showed not only inter-hemispheric shifts in the ITCZ but a contraction of the tropical belt during 1400–1850 CE, which followed an expansion during 950–1250 CE (Denniston et al., 2016; Griffiths et al., 2016).

From centennial-scale reanalyses, Liu et al. (2012) and D'Agostino and Lionello (2017) found divergent results on HC extent over the last 150 years, although with unanimity upon an intensification of the SH HC. A substantial discrepancy between HC characteristics in centennial-scale reanalyses and in ERA-Interim (D'Agostino and Lionello, 2017) since 1979 yields significant questions regarding their ability to capture changes in HC behaviour. Taken together with the existence of apparent non-climatic artefacts in the dataset (Nguyen et al., 2015), this implies *low confidence* in changes in the extent and intensity of HC derived from centennial-scale reanalyses. However, using multiple observational datasets and centennial-scale reanalyses, Bronnimann et al. (2015) identified a southward shift in the NH HC edge from 1945 to 1980 of about 0.25° latitude per decade, consistent with observed changes in global land monsoon precipitation (Section 2.3.1.4.2).

Since AR5 several studies based upon a range of metrics and different reanalyses products have suggested that the annual mean HC extent has shifted poleward at an approximate rate of 0.1°–0.5° latitude per decade over the last about 40 years (Allen & Kovilakam, 2017; Davis & Birner, 2017; Grise et al., 2018; Staten et al., 2020; Staten et al., 2018; Studholme & Gulev, 2018; Grise & Davis, 2020). The observed widening of the annual mean HC, revealed by a variety of metrics, is primarily due to poleward shift of the NH HC. There have been stronger upward trends in the NH extent of HC after 1992 (Figure 2.17a). The estimated magnitude of the recent changes based on modern-era reanalyses is not as large as that in AR5, due to apparent biases in older-generation reanalyses (Grise et al., 2019). Moreover, large interannual variability leads to uncertainties in estimates of long-term changes (Nguyen et al., 2013, Garfinkel et al., 2015b; Seviour et al., 2018; Staten et al., 2018), particularly for the NH given its zonal asymmetries (Staten et al., 2020; Wang et al., 2020). These large-scale features of the HC based on reanalyses agree with estimates revealed from the Integrated Global Radiosonde Archive (IGRA) during 1979–2012 (Lucas & Nguyen, 2015; Mathew et al., 2016). Recent trends based on reanalyses indicate a larger seasonal widening in the HC for summer and autumn in each hemisphere, although the magnitude of changes in HC extent is strongly dependent on dataset and metrics used (Grise et al., 2018; Hu Y. et al., 2018; Staten et al., 2018). The shifts in the HC position were accompanied by a narrowing ITCZ over the Atlantic and Pacific basins, with no significant change in its location and increases in the precipitation intensity (Byrne et al., 2018).

Trends in the HC intensity since 1979 differ between reanalyses, although there is a tendency toward HC intensification (Figure 2.17b) (Nguyen et al., 2013; Chen et al., 2014; D'Agostino and Lionello, 2017; Huang et al., 2019), which is more marked in the NH than the SH (Studholme and Gulev, 2018). However, the ability of reanalyses to represent the HC strength has been questioned due to inaccurate representation of latent heating distribution, which is directly related to tropical convection and influences the HC dynamics (Chemke and Polvani, 2019; Mathew and Kumar, 2019).

[START FIGURE 2.17 HERE]

Figure 2.17: Timeseries of the annual mean Northern Hemisphere (NH, top curves) and Southern Hemisphere (SH, bottom curves) Hadley Cell extent (a) and Hadley Cell intensity (b) since 1979. Further details on data sources and processing are available in the chapter data table (Table 2.SM.1).

[END FIGURE 2.17 HERE]

Paleo evidence during the LGM indicates a weaker WC over the Indian Ocean (Windler et al., 2019,

ACCEPTED VERSION SUBJECT TO FINAL EDITS

DiNezio et al., 2018), with a stronger Pacific WC (DiNezio and Tierney, 2013). During the Holocene, a transition from a strong WC located more westward during the Early-to-Mid Holocene towards a weak and eastward shifted WC during the late Holocene was inferred from proxy records from the Pacific Warm Pool and South-eastern Asia (Barr et al., 2019; Dang et al., 2020; Griffiths et al., 2020), in concurrence with changes in ENSO activity (section 2.4.2). Reconstructions for the CE showed weakened WC during 1000–1250 and since 1850, with an intensified circulation during 1500–1850 CE (Deng et al., 2017; Xu et al., 2016).

Considering instrumental records, there is considerable interdecadal variability in the strength of the WC, resulting in time-period dependent magnitude and even sign of trends (Bordbar et al., 2017; Carilli et al., 2015; Hou et al., 2018), with some studies reporting weakening over the 20th century (e.g. Liu et al., 2019; Power and Kociuba, 2011), while others reported strengthening (Li Z. et al., 2020), particularly over the last 30-40 years (e.g. Hu et al., 2013; L'Heureux et al., 2013, Yim et al., 2017). Based on estimation of changes in mid-tropospheric velocity from changes in observed cloud cover, Bellomo and Clement (2015) suggest a weakening and eastward shift of the WC over 1920–2010, however the robustness of this signal is questionable due to high uncertainty in the ship reported cloud data records used before 1954. Using centennial-scale 20CR reanalysis Tseng et al. (2019) showed that the vertical westerly wind shear over the western Pacific does not indicate any long-term change during 1900–1980, but shows a marked increase since the 1980s that is not present in ERA-Interim and JRA-55, again calling into question the ability of centennial-scale reanalyses to capture tropical circulation changes. Recent strengthening together with a westward shift of the WC (Bayr et al., 2014; Ma & Zhou, 2016) was identified across several reanalysis products and observational datasets, and using different metrics for quantifying WC. Nevertheless, satellite observations of precipitation and analyses of upper tropospheric humidity suggest substantially weaker strengthening of the WC than implied by reanalyses (Chung et al., 2019). This recent strengthening in the WC is associated with enhanced precipitation in the tropical western Pacific, anomalous westerlies in the upper troposphere, strengthened downwelling in the central and eastern tropical Pacific, and anomalous surface easterlies in the western and central tropical Pacific (Dong and Lu, 2013; Choi et al., 2016, McGregor et al., 2014). Positive trends in sea level pressure over the eastern Pacific and concurrent negative trends over the Indonesian region result in a pattern implying a shift towards a La Niña-like WC regime, with strengthening of the Pacific Trade Winds mainly over 1979–2012 (England et al., 2014; L'Heureux et al., 2013; Sohn et al., 2016; Zhao & Allen, 2019). Seasonal assessment of the WC showed significant changes in the vertical westerly wind shear over the Pacific during the austral summer and autumn implying a strengthening (Clem et al., 2017).

In summary, there has been a *likely* widening of the Hadley circulation since the 1980s, mostly due to its extension in the NH, although there is only *medium confidence* in the extent of the changes. This has been accompanied by a strengthening of the Hadley circulation, particularly in the NH (*medium confidence*). There is *low confidence* in the estimation of long-term trends in the strength of the Walker circulation, which are time period dependent and subject to dataset uncertainties. Trends since 1980 are better characterised and consistent with a *very likely* strengthening that resembles a La Niña-like Walker circulation and a westward shift of the Walker circulation, although with *medium confidence* in the magnitude of the changes, arising from the differences between satellite observations and reanalysis products.

2.3.1.4.2 Global monsoon changes

AR5 reported a weakening of the global monsoon (GM) circulation as well as a decrease of global land monsoon rainfall over the second half of the 20th century. Nevertheless, there was *low confidence* in the observed circulation trends due to uncertainties in reanalysis products and in the definition of the monsoon area. From a paleo perspective, AR5 only assessed regional monsoon changes.

New research based on high-resolution proxies reinforces previous findings on the influence of orbital cycles on GM variability on millennial time scales. The intensity of the monsoon systems is generally out of phase between hemispheres, being associated with the precession cycle (~21–23 kyr) (An et al., 2015; Seth et al., 2019; Wang P.X. et al., 2017), with intensified NH monsoon systems during precession minima (Toucanne et al., 2015; Wagner et al., 2019). The eccentricity forcing (about 100 kyr cycle) shows stronger GM during

ACCEPTED VERSION SUBJECT TO FINAL EDITS

interglacial periods (An et al., 2015; Mohtadi et al., 2016; Wang P. X. et al., 2014; 2017). Changes in obliquity (about 41 kyr cycle) modify the strength of monsoon systems, with increased summer monsoon rainfall when obliquity is maximal (Liu Yi et al., 2015; Mohtadi et al., 2016). Millennial scale variability in GM during the LDT was also linked to the occurrences of Heinrich stadials, resulting in weakened NH monsoons and intensified SH monsoons (An et al., 2015; Margari et al., 2020; Wang P.X. et al., 2017).

An intensification of the NH monsoons in the early to mid-Holocene with increased precipitation and regional expansions of rainfall areas identified through a variety of proxy records is shown by Biasutti et al., (2018) and Wang P.X. et al. (2017). The response for the SH monsoons during this period indicates a weakening in both summer and winter precipitation (Sachs et al., 2018; Wang P.X. et al., 2014; 2017). A decline in GM precipitation and a retraction of the northern fringes of monsoon areas was inferred from the mid-Holocene onwards, with some regions experiencing wetter conditions during the mid to late Holocene compared with present and a strengthening of the SH monsoons (Sachs et al., 2018; Wang P.X. et al., 2014; 2017). For the CE, GM reconstructions exhibit inter-hemispheric contrast during the period 950–1250 CE, with intensified NH monsoons and weakened SH monsoons, and the opposite pattern during 1400–1850 CE (An et al., 2015; Wang P. X. et al., 2014).

Direct observations highlight that the GM land precipitation, particularly over the NH, experienced a slight increase from 1900 through the early 1950s, followed by an overall decrease from the 1950s to the 1980s, and then an increase to present (Huang X. et al., 2019; Kitoh et al., 2013; Wang B. et al., 2018; 2020). This highlights the existence of multidecadal variations in the NH monsoon circulation patterns and precipitation intensity (Monerie et al., 2019; Wang B. et al., 2013; Wang P.X. et al., 2014; 2017). An overall increase in monsoon precipitation during extended boreal summer (JJAS) over the NH since 1979 is revealed by GPCP (Deng et al., 2018; Han et al., 2019) and CMAP for 1980–2010 (Jiang et al. 2016). SH summer monsoon behaviour is dominated by strong interannual variability and large regional differences (Deng et al., 2018; Han et al., 2019; Jiang et al., 2016; Kamae et al., 2017; Kitoh et al., 2013; Lin et al., 2014), with no significant trends reported by GPCP and CMAP (Deng et al., 2018). Uncertainty predominantly arises from the observed increase in tropical precipitation seasonality (Feng et al., 2013) and the estimation of GM precipitation over the ocean areas, leading to a large apparent spread across datasets (Kitoh et al., 2013b; Kamae et al., 2017).

In summary, observed trends during the last century indicate that the GM precipitation decline reported in AR5 has reversed since the 1980s, with a *likely* increase mainly due to a significant positive trend in the NH summer monsoon precipitation (*medium confidence*). However, GM precipitation has exhibited large multi-decadal variability over the last century, creating *low confidence* in the existence of centennial-length trends in the instrumental record. Proxy reconstructions show a *likely* NH monsoons weakening since the mid-Holocene, with opposite behaviour for the SH monsoons.

2.3.1.4.3 Extratropical jets, storm tracks, and blocking

AR5 reported a *likely* poleward shift of storm tracks and jet streams since the 1970s from different datasets, variables and approaches. These trends were consistent with the HC widening and the poleward shifting of the circulation features since the 1970s. There was *low confidence* in any large-scale change in blocking.

Proxy records consistent with modelling results imply a southward shift of the storm tracks over the North Atlantic during the LGM (Raible et al., 2021). A variety of proxies are available for the changes in the position of the extratropical jets / westerlies during the Holocene. Recent syntheses of moisture-sensitive proxy records indicate drier-than-present conditions over mid-latitudes of western North America (Hermann et al., 2018; Liefert and Shuman, 2020) during the MH, which together with a weakened Aleutian Low (Bailey et al., 2018) implies that the winter North Pacific jetstream was shifted northward. A synthesis of lines of evidence from the SH indicates that the westerly winds were stronger over 14–5 ka, followed by regional asymmetry after 5 ka (Fletcher & Moreno, 2012). There is no consensus on the shifts of the SH westerlies with some studies implying poleward migrations (Lamy et al., 2010; Voigt et al., 2015; Turney et al., 2017; Anderson et al., 2018) and others suggesting an equatorward shift (Kaplan et al., 2016) in the MH.

ACCEPTED VERSION SUBJECT TO FINAL EDITS

During 950–1400 CE, hydroclimate indicators suggest a northward shift of Pacific storm tracks over North America (McCabe-Glynn et al., 2013; Steinman et al., 2014) which was comparable in magnitude to that over 1979–2015 (Wang et al., 2017). Storm tracks over the North Atlantic-European sector shifted northward as indicated by multi-proxy indicators over the North Atlantic (Wirth et al., 2013; Orme et al., 2017) and Mediterranean (Roberts et al., 2012). Reconstructed westerly winds in the SH suggest a poleward shift (Goodwin et al., 2014; Koffman et al., 2014; Lamy et al., 2010; Moreno et al., 2018; Schimpf et al., 2011), with latitudinal change comparable to that during recent decades (Swart and Fyfe, 2012; Manney and Hegglin, 2018).

Multiple reanalyses show that since 1979 the subtropical jet wind speeds have generally increased in winter and decreased in summer in both hemispheres, but the trends are regionally dependent (Pena-Ortiz et al., 2013; Manney and Hegglin, 2018; Lee et al., 2019). Over NH mid-latitudes, the summer zonal wind speeds have weakened in the mid-troposphere (Francis and Vavrus, 2012; Coumou et al., 2014, 2015; Haimberger and Mayer, 2017). Meanwhile there are indications of enhanced jetstream meandering in boreal autumn at the hemispheric scale (Francis and Vavrus, 2015; Di Capua and Coumou, 2016), whereas the regional arrangement of meandering depends on the background atmospheric state (Cohen et al., 2020). These meandering trends, however, are sensitive to the metrics used (Cattiaux et al., 2016; Hassanzadeh et al., 2014; Screen & Simmonds, 2013; Vavrus, 2018). Hypothesised links to Arctic warming are assessed in Cross-Chapter Box 10.1.

Multiple reanalyses and radiosonde observations show an increasing number of extratropical cyclones over the NH since the 1950s (Chang & Yau, 2016; Wang X. L. et al., 2016). The positive trends are generally consistent among reanalyses since 1979, though with considerable spread (Tilinina et al., 2013; Wang X. L. et al., 2016). In recent decades the number of deep extratropical cyclones has increased over the SH (Reboita et al., 2015; Wang X. L. et al., 2016) (Section 8.3.2.8.1, Figure 8.12), while the number of deep cyclones has decreased in the NH in both winter and summer (Neu et al., 2013; Wang et al., 2017, Chang et al., 2016; Coumou et al., 2015; Gertler & O'Gorman, 2019). The regional changes for different intensity extratropical cyclones are assessed in Section 8.3.2.8.1. The assessment of trends is complicated by strong interannual-decadal variability, sensitivity to dataset choice and resolution (Tilinina et al., 2013; Lucas et al., 2014; Wang et al., 2016; Pepler et al., 2018; Rohrer et al., 2018) and cyclone identification / tracking methods (Neu et al., 2013; Grieger et al., 2018). Thus there is overall *low confidence* for recent changes in global extratropical storm tracks.

A consistent poleward shift of the tropospheric extratropical jets since 1979 is reported by multiple reanalyses (Davis and Rosenlof, 2012; Davis and Birner, 2013; Pena-Ortiz et al., 2013; Manney and Hegglin, 2018) (Figure 2.18), and radiosonde winds (Allen et al., 2012). This is generally consistent with the earlier reported shifts retrieved from satellite temperature observations (Fu and Lin, 2011; Davis and Rosenlof, 2012). After the 1960s the magnitude of meridional shifts in extratropical jets over both the North Atlantic and North Pacific in August is enhanced compared to multi-century variability (Trouet et al., 2018). Despite some regional differences (Ma & Zhang, 2018; Melamed-Turkish et al., 2018; Norris et al., 2016; Wang J. et al., 2017a; Woollings et al., 2014; Xue & Zhang, 2018), overall poleward deflection of storm tracks in boreal winter over both the North Atlantic and the North Pacific was identified during 1979–2010 (Tilinina et al., 2013). Over the SH extra-tropics there is a similarly robust poleward shift in the polar jet since 1979 (Pena-Ortiz et al., 2013; Manney and Hegglin, 2018; WMO, 2018), although after 2000 the December-January-February (DJF) tendency to poleward shift of the SH jet stream position ceased (Banerjee et al., 2020). The general poleward movement in midlatitude jet streams (Lucas et al., 2014) is consistent with the expansion of the tropical circulation (Section 2.3.1.4.1). The changes of extratropical jets and westerlies are also related to the annular modes of variability (Section 2.4, Annex IV).

Robust trends in blocking have only been found in certain regions and specific seasons during recent decades. Increases in blocking frequency have occurred over low-latitude regions in the North Atlantic in boreal winter (Davini et al., 2012), the South Atlantic in austral summer (Dennison et al., 2016) and the southern Indian Ocean in austral spring (Schemm, 2018). Over the subpolar North Atlantic sustained periods of positive Greenland blocking were identified during 1870–1900 and from the late 1990s to 2015 (Hanna et al., 2015). Further analysis of association of Greenland blocking with the NAM is provided in Section 2.4.1.1. Meanwhile, a reduced blocking frequency has been found over winter in Siberia (Davini et al., 2012)

ACCEPTED VERSION SUBJECT TO FINAL EDITS

and the southwestern Pacific in austral spring (Schemm, 2018). Over Eastern European Russia and Western Siberia (40–100E) a tendency towards longer blocking events was reported by Luo et al. (2016) for 2000–2013 and by Tyrlis et al. (2020) for 1979–2017. Inter-annual variance in the number of blocking events over the SH (Oliveira et al., 2014) and North Atlantic (Kim & Ha, 2015) has enhanced. Blocking events and their trends are sensitive to choice of datasets, calculation periods and methods (Barnes et al., 2014; Cheung et al., 2013; Kononova & Lupo, 2020; Pepler et al., 2018; Rohrer et al., 2018; Woollings et al., 2018b). As a result, hemispheric and global trends in blocking frequency have overall *low confidence.*

In summary, the total number of extratropical cyclones has *likely* increased since the 1980s in the NH (*low confidence*), but with fewer deep cyclones particularly in summer. The number of strong extratropical cyclones has *likely* increased in the SH (*medium confidence*). The extratropical jets and cyclone tracks have *likely* been shifting poleward in both hemispheres since the 1980s with marked seasonality in trends (*medium confidence*). There is *low confidence* in shifting of extratropical jets in the NH during the mid-Holocene and over 950–1400 CE to latitudes that *likely* were similar to those since 1979. There is *low confidence* in observed global-scale changes in the occurrence of blocking events.

[START FIGURE 2.18 HERE]

Figure 2.18: Trends in ERA5 zonal-mean zonal wind speed. Shown are (a) DJF (December-January-February), (b) MAM (March-April-May), (c) JJA (June-July-August) and (d) SON (September-October-November). Climatological zonal winds during the data period are shown in solid contour lines for westerly winds and in dashed lines for easterly. Trends are calculated using OLS regression after Santer et al (2008a) ('x' marks denote non-significant trends). Further details on data sources and processing are available in the chapter data table (Table 2.SM.1).

[END FIGURE 2.18 HERE]

2.3.1.4.4 Surface wind and sea level pressure

AR5 concluded that surface winds over land had generally weakened. The *confidence* for both land and ocean surface wind trends was *low* owing to uncertainties in datasets and measures used. Sea level pressure (SLP) was assessed to have *likely* decreased from 1979–2012 over the tropical Atlantic and increased over large regions of the Pacific and South Atlantic, but trends were sensitive to the period analysed.

Terrestrial in situ wind datasets have been updated and the quality-control procedures have been improved, with particular attention to homogeneity and to better retaining true extreme values (Dunn et al., 2012; 2014; 2016). Global mean land wind speed (excluding Australia) from HadISD for 1979–2018 shows a reduction (stilling) of 0.063 m s^{-1} per decade (Azorin-Molina et al., 2019). Trends are broadly insensitive to the subsets of stations used. Although the meteorological stations are unevenly distributed worldwide and scarce in South America and Africa, the majority exhibit stilling particularly in the NH (Figure 2.19). Regionally, strong decreasing trends are reported in central Asia and North America (–0.106 and –0.084 m s^{-1} per decade respectively) during 1979–2018 (McVicar et al., 2012; Vautard et al., 2012; Wu et al., 2018; Azorin-Molina et al., 2019). This stilling tendency has reversed after 2010 and the global mean surface winds have strengthened (Azorin-Molina et al., 2020; Zeng et al., 2019), although the robustness of this reversal is unclear given the short period and interannual variability (Kousari et al., 2013; Kim and Paik, 2015; Azorin-Molina et al., 2019).

[START FIGURE 2.19 HERE]

Figure 2.19: Trends in surface wind speed. (a) Station observed winds from the integrated surface database (HadISD v2.0.2.2017f); (b) Cross-Calibrated Multi-Platform wind product; (c) ERA5; and (d) wind speed from the Objectively Analyzed Air-Sea Heat Fluxes dataset, release 3. White areas indicate incomplete or missing data. Trends are calculated using OLS regression with significance assessed following AR(1) adjustment after Santer et al (2008c) ('x' marks denote non-significant trends). Further details on data sources and processing are available in the chapter data table (Table 2.SM.1).

ACCEPTED VERSION SUBJECT TO FINAL EDITS

[END FIGURE 2.19 HERE]

Over the ocean, datasets demonstrate considerable disagreement in surface wind speed trends and spatial features (Kent et al., 2013). Global ocean surface winds from NOCv2.0 demonstrate upward trends of about 0.11 m s^{-1} per decade (1979–2015) with somewhat smaller trends from WASwind for 1979–2011 (Azorin-Molina et al., 2017, 2019). The datasets are consistent until 1998, but diverge thereafter. Both ERA5 and JRA-55 reanalyses show consistently increasing global marine wind speeds over 1979–2015, though flattening since 2000, whereas MERRA-2 agrees until 1998, but then exhibits increased variability and an overall decrease in the last two decades (Azorin-Molina et al., 2019). This agrees with estimates by Sharmar et al. (2021) showing upward ocean wind trends from 1979 to 2000 which are consistent in ERA-Interim, ERA5 and MERRA-2, but disagree with CFSR trends for the same period. Over 2000–2019 all reanalyses show diverging tendencies. An updated multiplatform satellite database (comprising data from altimeters, radiometers, and scatterometers) from 1985–2018 shows small increases in mean wind speed over the global ocean, with the largest increase observed in the Southern Ocean (Young & Ribal, 2019), consistent with signals in ERA-Interim, ERA5 and MERRA-2 (Sharmar et al., 2021). Overall, most products suggest positive trends over the Southern Ocean, western North Atlantic and the tropical eastern Pacific since the early 1980s.

The modern era reanalyses exhibit SLP increases over the SH subtropics with stronger increases in austral winter over 1979–2018. Over the NH, SLP increased over the mid-latitude Pacific in boreal winter and decreased over the eastern subtropical and mid-latitude North Atlantic in boreal summer. Discrepancies in the low-frequency variations during the first half of the 20th century exist in the centennial-scale reanalysis products (Befort et al., 2016). Overall, modern reanalysis datasets support the AR5 conclusion that there is no clear signal for trends in the strength and position of the permanent and quasi-permanent pressure centres of action since the 1950s. Instead, they highlight multi-decadal variations. Large-scale SLP is strongly associated with the changes in modes of variability (Section 2.4, Annex IV).

In summary, since the 1970s a worldwide weakening of surface wind has *likely* occurred over land, particularly marked in the NH, with *low confidence* in a recent partial recovery since around 2010. Differences between available wind speed estimates lead to *low confidence* in trends over the global ocean as a whole but with most estimates showing strengthening globally over 1980–2000 and over the last four decades in the Southern Ocean, western North Atlantic and the tropical eastern Pacific.

2.3.1.4.5 Stratospheric polar vortex and sudden warming events

AR5 assessed changes in the polar vortices and reported a *likely* decrease in the lower-stratospheric geopotential heights over Antarctica in spring and summer at least since 1979.

Multiple definitions for the polar vortex strength and sudden stratospheric warming (SSW) events have been proposed and compared (Butler et al., 2015; Palmeiro et al., 2015; Waugh et al., 2017; Butler and Gerber, 2018), and new techniques identifying daily vortex patterns and SSWs have been developed (Kretschmer et al., 2018; Mitchell et al., 2013a). Errors in reanalysis stratospheric winds were assessed and discrepancies in stratospheric atmospheric circulation and temperatures between reanalyses, satellites and radiosondes have been reported (Mitchell et al., 2013a; Duruisseau et al., 2017).

The northern stratospheric polar vortex has varied seasonally and with altitude during recent decades. Multiple reanalysis and radiosonde datasets show that the midwinter lower stratospheric geopotential height (150 hPa) over the polar region north of 60°N has increased significantly since the early 1980s (Bohlinger et al., 2014; Garfinkel et al., 2017). This signal extends to the middle and upper stratosphere. In January-February zonal winds north of 60°N at 10 hPa have been weakening (Kim et al., 2014; Kretschmer et al., 2018). Daily atmospheric circulation patterns over the northern polar stratosphere exhibit a decreasing frequency of strong vortex events and commensurate increase in more-persistent weak events, which largely explains the observed significant weakening of the vortex during 1979–2015 (Kretschmer et al., 2018). The northern polar vortex has weakened in early winter but strengthened during late winter (Bohlinger et al.,

ACCEPTED VERSION SUBJECT TO FINAL EDITS

2014; Garfinkel et al., 2015a; 2017; Ivy et al., 2016; Kretschmer et al., 2018; Seviour, 2017). In the middle and upper stratosphere, a strengthening trend of the northern polar vortex during DJF has occurred since 1998, contrasting the weakening trend beforehand (Hu et al., 2018). The position of the polar vortex also has long-term variations, exhibiting a persistent shift toward Northern Siberia and away from North America in February over the period 1979–2015 (Zhang J. et al., 2016, 2018). Multiple measures show similar location changes (Seviour, 2017).

The SSW, a phenomenon of rapid stratospheric air temperature increases (sometimes by more than 50°C in 1–2 days), is tightly associated with the reversal of upper stratospheric zonal winds, and a resulting collapse or substantial weakening of the stratospheric polar vortex (Butler et al., 2015; Butler and Gerber, 2018) and on average occurs approximately 6 times per decade in the NH winter (Charlton et al., 2007; Butler et al., 2015). The SSW record from all modern reanalyses is very consistent. There is a higher occurrence of major midwinter SSWs in the 1980s and 2000s with no SSW events during 1990–1997 (Reichler et al., 2012, Butler et al., 2015). An assessment of multidecadal variability and change in SSW events is sensitive to both chosen metric and methods (Palmeiro et al., 2015). Due to the lack of assimilation of upper air data, the centennial-scale reanalyses do not capture SSW events, even for the most recent decades (Butler et al., 2015, 2017) and hence cannot inform on earlier behaviour. There has been considerably less study of trends in the southern hemispheric stratosphere vortex strength despite the interest in the ozone hole and the *likely* impact of the southern hemispheric stratosphere vortex strength on it. The occurrence of SSW events in the SH is not as frequent as in the NH, with only 3 documented events in the last 40 years (Shen et al., 2020).

In summary, it is *likely* that the northern lower stratospheric vortex has weakened since the 1980s in midwinter, and its location has shifted more frequently toward the Eurasian continent. The short record and substantial decadal variability yields *low confidence* in any trends in the occurrence of SSW events in the NH winter and such events in the SH are rare.

2.3.2 Cryosphere

This section focuses on large-scale changes in a subset of components of the cryosphere (Cross-Chapter Box 2.2). Chapter 9 undertakes a holistic assessment of past and possible future changes at the process level in the cryosphere, including those at regional scales, integrating observations, modelling and theoretical understanding, while, here in chapter 2, the focus is on past large-scale, observation-based cryospheric changes.

2.3.2.1 Sea ice coverage and thickness

2.3.2.1.1 Arctic Sea Ice

AR5 reported that the annual mean Arctic sea ice extent (SIE) *very likely* decreased by 3.5–4.1% per decade between 1979 and 2012 with the summer sea ice minimum (perennial sea ice) *very likely* decreasing by 9.4–13.6% per decade. This was confirmed by SROCC reporting the strongest reductions in September (12.8 ± 2.3% per decade; 1979–2018) and stating that these changes were *likely* unprecedented in at least 1 kyr (*medium confidence*). The spatial extent had decreased in all seasons, with the largest decrease for September (*high confidence*). AR5 reported also that the average winter sea ice thickness within the Arctic Basin had *likely* decreased by between 1.3 m and 2.3 m from 1980 to 2008 (*high confidence*), consistent with the decline in multi-year and perennial ice extent. SROCC stated further that it was *virtually certain* that Arctic sea ice had thinned, concurrent with a shift to younger ice. Lower sea ice volume in 2010–2012 compared to 2003–2008 was documented in AR5 (*medium confidence*). There was *high confidence* that, where the sea ice thickness had decreased, the sea ice drift speed had increased.

Proxy records are used in combination with modelling to assess Arctic paleo sea-ice conditions to the extent possible. For the Pliocene, *limited* proxy *evidence* of a reduced sea-ice cover compared to ‘modern’ winter conditions (Knies et al., 2014; Clotten et al., 2018) and model simulations of a largely ice-free Arctic Ocean during summer (Feng et al., 2019; Howell et al., 2016; Li F. et al., 2020) imply *medium confidence* that the

ACCEPTED VERSION SUBJECT TO FINAL EDITS

Arctic Ocean was seasonally ice covered. Over the LIG, sparse proxy reconstructions (Stein et al., 2017; Kremer et al., 2018) and proxy evidence from marine sediment (Kageyama et al., 2021) provide *medium confidence* of perennial sea-ice cover.

Over the past 13 kyr proxy records suggest extensive sea ice coverage during the Younger Dryas (at the end of the LDT), followed by a decrease in sea ice coverage during the Early Holocene, and increasing sea ice coverage from the MH to the mid-1400s (De Vernal et al., 2013; Belt et al., 2015; Cabedo-Sanz et al., 2016; Armand et al., 2017; Belt, 2018). There is *limited evidence* that the Canadian Arctic had less multiyear sea ice during the Early Holocene than today (Spolaor et al., 2016). For more regional details on paleo arctic sea ice see Section 9.3.1.1.

Current pan-Arctic SIE conditions (annual means and late summer) are unprecedented since at least 1850 (Brennan et al., 2020; Walsh et al., 2017; 2019, Figure 2.20a), while, as reported in SROCC, there remains *medium confidence* that the current September (late summer) Arctic sea ice loss is unprecedented during the past 1 kyr. Sea ice charts since 1850 (Walsh et al., 2017; 2019) suggest that there was no significant trend before the 1990s, but the uncertainty of these estimates is large and could mask a trend, a possibility illustrated by Brennan et al. (2020), who found a loss of Arctic sea ice between 1910 and 1940 in an estimate based on a data assimilation approach.

There has been a continuing decline in SIE and Arctic sea ice area (SIA) in recent years (Figure 2.20a). To reduce grid-geometry associated biases and uncertainties (Notz, 2014; Ivanova et al., 2016; Meier and Stewart, 2019) SIA is used in addition to, or instead of SIE herein (see also section 9.3.1). A record-low Arctic SIA since the start of the satellite era (1979) occurred in September 2012 (Figure 2.20a). Decadal SIA means based on the average of three different satellite products decreased from 6.23–3.76 million km^2 for September and 14.52–13.42 million km^2 for March SIA (Figure 2.20a). Initial SIA data for 2020 (OSISAF) are within the range of these recent decadal means or slightly below (Figure 2.20a). SIA has declined since 1979 across the seasonal cycle (Figure 9.13). Most of this decline in SIA has occurred after 2000, and is superimposed by substantial interannual variability. The sharp decline in Arctic summer SIA coincides with earlier surface melt onset (Mortin et al., 2016; Bliss et al., 2017), later freeze-up, and thus a longer ice retreat and open water period (Stammerjohn et al., 2012; Parkinson, 2014; Peng et al., 2018).

[START FIGURE 2.20 HERE]

Figure 2.20: Changes in Arctic and Antarctic sea ice area. (a) Three time series of Arctic sea ice area (SIA) for March and September from 1979 to 2020 (passive microwave satellite era). In addition, the range of SIA from 1850–1978 is indicated by the vertical bar to the left. Decadal means for the three series for the first and most recent decades of observations are shown by horizontal lines in grey (1979–1988) and black (2010–2019). (b): Three time series of Antarctic sea ice area for September and February (1979–2020). Sea ice area values have been calculated from sea ice concentration fields. Available data for 2020 (OSISAF) is shown in both (a) and (b). Further details on data sources and processing are available in the chapter data table (Table 2.SM.1).

[END FIGURE 2.20 HERE]

Over the past two decades, first-year sea ice has become more dominant and the oldest multiyear ice (older than 4 years) which in March 1985 made up 33% of the Arctic sea ice cover, has nearly disappeared, making up 1.2% in March 2019 (Perovich et al., 2020). The loss of older ice is indicative of a thinning overall of ice cover (Tschudi et al., 2016), but also the remaining older ice has become thinner (Hansen E. et al., 2013). Since in situ ice thickness measurements are sparse, information about ice thickness is mainly based on airborne and satellite surveys. Records from a combination of different platforms show for the central and western Arctic Ocean (Arctic Ocean north of Canada and Alaska) negative trends since the mid-1970s (Kwok, 2018; Lindsay & Schweiger, 2015), with a particularly rapid decline during the 2000s, which coincided with a large loss of multiyear sea ice. Direct observations from 2004 and 2017 indicate a decrease

ACCEPTED VERSION SUBJECT TO FINAL EDITS

of modal ice thickness in the Arctic Ocean north of Greenland by 0.75 m, but with little thinning between 2014 and 2017 (Haas et al., 2017). This agrees with data based on satellite altimetry and airborne observations, showing no discernible thickness trend since 2010 (Kwok & Cunningham, 2015; Kwok, 2018; Kwok and Kacimi, 2018) (Figure 2.21). However, sea ice thickness derived from airborne and spaceborne data is still subject to uncertainties imposed by snow loading. For radar altimeters, insufficient penetration of radar signal into the snowpack results in overestimation of ice thickness (e.g., Ricker et al., 2015; King et al., 2018a; Nandan et al., 2020). Negative trends in ice thickness since the 1990s are also reported from the Fram Strait in the Greenland Sea, and north of Svalbard (Hansen E. et al., 2013; King et al., 2018; Renner et al., 2014; Rösel et al., 2018; Spreen et al., 2020). Thickness data collected in the Fram Strait originate from ice exported from the interior of the Arctic Basin and are representative of a larger geographical area upstream in the transpolar drift. A reduction of survival rates of sea ice exported from the Siberian shelves by 15% per decade has interrupted the transpolar drift and affected the long-range transport of sea ice (Krumpen et al., 2019). The thinner and on average younger ice has less resistance to dynamic forcing, resulting in a more dynamic ice cover (Hakkinen et al., 2008; Spreen et al., 2011; Vihma et al., 2012; Kwok et al., 2013).

[START FIGURE 2.21 HERE]

Figure 2.21: Arctic sea ice thickness changes (means) for autumn (red/dotted red) and winter (blue/dotted blue). Shadings (blue and red) show 1 S.E. ranges from the regression analysis of submarine ice thickness and expected uncertainties in satellite ice thickness estimates. Data release area of submarine data ice thickness data is shown in inset. Satellite ice thickness estimates are for the Arctic south of 88°N. Thickness estimates from more localized airborne/ground electromagnetic surveys near the North Pole (diamonds) and from Operation IceBridge (circles) are shown within the context of the larger scale changes in the submarine and satellite records. Further details on data sources and processing are available in the chapter data table (Table 2.SM.1).

[END FIGURE 2.21 HERE]

SROCC noted the lack of continuous records of snow on sea ice. Nevertheless in recent decades, more snow on sea ice has been observed in the Atlantic sector in the Arctic than in the Western Arctic Ocean (Webster et al., 2018). Previously, Warren et al. (1999) showed that over 1954–1991 there were weak trends towards declining snow depth on sea ice in the Pacific sector. Recent observations indicate a substantial thinning of the spring snowpack in the western Arctic (Cavalieri et al., 2012; Brucker and Markus, 2013; Kurtz et al., 2013; Laxon et al., 2013; Webster et al., 2018). In contrast, thick snow over Arctic sea ice in the Atlantic sector north of Svalbard (snow thickness around 0.4 m or more) has been observed in the 1970s and since the 1990s (Rösel et al., 2018), but data are too sparse to detect trends.

In summary, over 1979–2019 Arctic SIA has decreased for all months, with the strongest decrease in summer (*very high confidence*). Decadal means for SIA decreased from the first to the last decade in that period from 6.23 to 3.76 million km^2 for September, and from 14.52 to 13.42 million km^2 for March. Arctic sea ice has become younger, thinner and faster moving (*very high confidence*). Snow thickness on sea ice has decreased in the western Arctic Ocean (*medium confidence*). Since the Younger Dryas at the end of the LDT, proxy indicators show that Arctic sea ice has fluctuated on multiple time scales with a decrease in sea ice coverage during the Early Holocene and an increase from the MH to the mid-1400s. Current pan-Arctic sea ice coverage levels (annual mean and late summer) are unprecedentedly low since 1850 (*high confidence),* and with *medium confidence* for late summer for at least the past 1 kyr.

2.3.2.1.2 Antarctic Sea Ice

AR5 reported a small but significant increase in the total annual mean Antarctic SIE that was *very likely* in the range of 1.2–1.8% per decade between 1979 and 2012 (0.13–0.20 million km^2 per decade) (*very high confidence*), while SROCC reported that total Antarctic sea ice coverage exhibited no significant trend over the period of satellite observations (1979–2018) (*high confidence*). SROCC noted that a significant positive

ACCEPTED VERSION SUBJECT TO FINAL EDITS

trend in mean annual ice cover between 1979 and 2015 had not persisted, due to three consecutive years of below-average ice cover (2016–2018). SROCC stated also that historical Antarctic sea ice data from different sources indicated a decrease in overall Antarctic sea ice cover since the early 1960s, but was too small to be separated from natural variability (*high confidence*).

There is only *limited evidence* from predominantly regional paleo proxies for the evolution of Southern Ocean sea ice before the instrumental record and estimates are not available for all proxy target periods (Section 9.3.2). Proxies from marine sediments for intervals preceding and following the MPWP indicate open water conditions with less sea-ice than modern conditions (Taylor-Silva and Riesselman, 2018; Ishino and Suto, 2020). During the LGM, proxies indicate that summer sea ice coverage reached the polar ocean front (e.g., Nair et al., 2019). More recently, sea ice coverage appears to have fluctuated substantially throughout the Holocene (e.g., for the western Amundsen Sea, Lamping et al., 2020). At the beginning of the CE, regional summer sea ice coverage in the north-western Ross Sea was lower than today (Tesi et al., 2020). Crosta et al. (2021) suggest, based on different proxies, four different phases with 7–10 months periods of sea ice occurrence per year in the Antarctic region off Adelie Land during the CE, where each phase was several hundred years long.

More recent sea ice reconstructions are based on diverse sources including whaling records (De La Mare, 1997, 2009; Cotté and Guinet, 2007), old ship logbooks (Ackley et al., 2003; Edinburgh and Day, 2016), and ice core records (Curran et al., 2003; Abram et al., 2010; Sinclair et al., 2014), amongst other methods (e.g. Murphy et al., 2014). These reconstructions, in combination with recent satellite-based observations indicate: i) a decrease in summer SIE across all Antarctic sectors since the early- to mid-20th century; ii) a decrease in winter SIE in the East Antarctic, and Amundsen-Bellingshausen Seas sectors starting in the 1960s; and iii) small fluctuations in winter SIE in the Weddell Sea over the 20th century (Hobbs et al., 2016a,b). There are also ice-core indications that the pronounced Ross Sea increase dates back to the mid-1960s (Sinclair et al., 2014; Thomas & Abram, 2016). While there is reasonable broad-scale concurrence across these estimates, the uncertainties are large, there is considerable interannual variability, and reconstructions require further validation (Hobbs et al., 2016a,b). New reconstructions (Thomas et al., 2019) from Antarctic land ice cores show that SIE in the Ross Sea had increased between 1900 and 1990, while the Bellingshausen Sea had experienced a decline in SIE; this dipole pattern is consistent with satellite-based observations from 1979 to 2019 (Parkinson, 2019), but the recent rate of change then has been larger. Records of Antarctic SIE for the late 19th and early 20th centuries (Edinburgh and Day, 2016), show SIE comparable with the satellite era, although with marked spatial heterogeneity (e.g., Thomas et al., 2019).

Early Nimbus satellite visible and infrared imagery from the 1960s (Meier et al., 2013; Gallaher et al., 2014) indicate higher overall SIE compared to 1979–2013 (Hobbs et al., 2016a,b), but with large uncertainties and poorly quantified biases (NA SEM, 2017). The continuous satellite passive-microwave record shows that there was a modest increase in overall Antarctic SIA of 2.5% ± 0.2% per decade (1 standard error over 1979–2015 (Comiso et al., 2017). For overall ice coverage and for this period, positive long-term trends were most pronounced during austral autumn advance (Maksym, 2019), being moderate in summer and winter, and lowest in spring (Comiso et al., 2017; Hobbs et al., 2016a,b; Holland, 2014; Turner et al., 2015). Since 2014, overall Antarctic SIE (and SIA) has exhibited major fluctuations from record-high to record-low satellite era extents (Comiso et al., 2017; Massonnet et al., 2015; Parkinson, 2019; Reid, and Massom, 2015; Reid et al., 2015). After setting record-high extents each September from 2012 through 2014, Antarctic SIE (and SIA) dipped rapidly in mid-2016 and remained predominantly below average through 2019 (Reid et al., 2020). For the most recent decade of observations (2010–2019), the decadal means of three SIA products (Figure 2.20b) were 2.17 million km^2 for February and 15.75 million km^2 for September, respectively. The corresponding levels for the means for the first decade of recordings (1979–1988) were 2.04 million km^2 for February and 15.39 million km^2 for September indicating little overall change. Initial SIA data for 2020 (OSISAF) show SIA for September above, and for February slightly below the recent decadal means (Fig. 2.20b). The 2020 September level (OSISAF) remains below the levels observed over 2012–2014.

In summary, Antarctic sea ice has experienced both increases and decreases in SIA over 1979–2019, and substantively lower levels since 2016, with only minor differences between decadal means of SIA for the first (for February 2.04 million km^2, for September 15.39 million km^2) and last decades (for February 2.17 million km^2, for September 15.75 million km^2) of satellite observations (*high confidence*). There remains *low*

ACCEPTED VERSION SUBJECT TO FINAL EDITS

confidence in all aspects of Antarctic sea ice prior to the satellite era owing to a paucity of records that are highly regional in nature and often seemingly contradictory.

2.3.2.2 Terrestrial snow cover

AR5 concluded that snow cover extent (SCE) had decreased in the NH, especially in spring *(very high confidence)*. For 1967–2012, the largest change was in June and March-April SCE *very likely* declined. No trends were identified for the SH due to limited records and large variability. SROCC concluded with *high confidence* that Arctic June SCE declined between 1967 and 2018 and in nearly all mountain regions, snow cover declined in recent decades.

Analysis of the combined in situ observations (Brown, 2002) and the multi-observation product (Mudryk et al. 2020) indicates that since 1922, April SCE in the NH has declined by 0.29 million km^2 per decade, with significant interannual variability (Figure 2.22) and regional differences (Section 9.5.3.1). The limited pre-satellite era data does not allow for a similar assessment for the entire spring-summer period. Assessment of SCE trends in the NH since 1978 indicates that for the October to February period there is substantial uncertainty in trends with the sign dependent on the observational product. Analysis using the NOAA Climate Data Record shows an increase in October to February SCE (Hernández-Henríquez et al., 2015; Kunkel et al., 2016) while analyses based on satellite borne optical sensors (Hori et al., 2017) or multi-observation products (Mudryk et al., 2020) show a negative trend for all seasons (section 9.5.3.1, Figure 9.23). The greatest declines in SCE have occurred during boreal spring and summer, although the estimated magnitude is dataset dependent (Rupp et al., 2013; Estilow et al., 2015; Bokhorst et al., 2016; Thackeray et al., 2016; Connolly et al., 2019).

[START FIGURE 2.22 HERE]

Figure 2.22: April snow cover extent (SCE) for the Northern Hemisphere (1922–2018). Shading shows *very likely* range. The trend over the entire 1922–2018 period (black line) is –0.29 (± 0.07) million km^2 per decade. Further details on data sources and processing are available in the chapter data table (Table 2.SM.1).

[END FIGURE 2.22 HERE]

There has been a commensurate decrease in the snow-cover duration and persistence, particularly in higher latitudes due to earlier spring melt and, in some cases, later autumn onset of snow cover (Chen Xiaona et al., 2015; Derksen et al., 2015; Hammond et al., 2018; Hori et al., 2017). Arctic snow-cover duration has decreased by 2–4 days per decade since the 1970s (Brown et al., 2017). Significant decreases in snow-cover duration have been documented over western Eurasia since 1978 (Hori et al., 2017).

For the NH, maximum snow depth has generally decreased since the 1960s, with more robust trends for North America and greater uncertainty for Eurasia (Kunkel et al., 2016). Several satellite-based passive microwave and other products indicate general declines in pre-melt snow water equivalent since 1981 although there is regional and inter-dataset variability (Brown et al., 2017; Jeong et al., 2017; Marty et al., 2017; Mortimer et al., 2020; Mudryk et al., 2020; Pulliainen et al., 2020, Section 9.5.3).

In summary, substantial reductions in spring snow cover extent have occurred in the NH since 1978 (*very high confidence*) with *limited evidence* that this decline extends back to the early 20th century. Since 1981 there has been a general decline in NH spring snow water equivalent (*high confidence*).

2.3.2.3 Glacier mass

AR5 concluded with *high confidence* that, during the Holocene, glaciers were at times smaller than at the

ACCEPTED VERSION SUBJECT TO FINAL EDITS

end of the 20th century. AR5 stated further with *very high confidence* that most glaciers had been shrinking since the mid-1800s, and the mass loss from all glaciers worldwide *very likely* increased from 1970 to 2009. SROCC reported a globally coherent picture of continued glacier recession in recent decades (*very high confidence*) based on in situ and satellite observations of changes in glacier area, length and mass, although there were considerable inter-annual and regional variations. Between 2006 and 2015 the global glacier mass change assessed by SROCC was –278 ± 113 Gt yr^{-1}.

Two recent global reviews on glaciers over the Holocene (Solomina et al., 2015) and the past 2 kyr (Solomina et al., 2016) summarize the chronologies of respectively 189 and 275 glaciers. The former shows that glaciers retreated during the LDT and retracted to their minimum extent between 8 ka and 6 ka. Except for some glaciers in the SH and tropics, glaciers expanded thereafter, reaching their maximum extent beyond their present-day margins during the mid-1400s to late-1800s CE. With few exceptions, glacier margins worldwide have retreated since the 19th century, with the rate of retreat and its global character since the late 20th century being unusual in the context of the Holocene (Solomina et al., 2016, Figure 2.23a). However, the areal extents of modern glaciers in most places in the NH are still larger than those of the early and/or middle Holocene (Solomina et al., 2015). When considering Holocene and present glaciers extents, it is important to account for the relatively long adjustment time of glaciers (often referred to as response time; Section 9.5.1.3); the majority of modern glaciers are currently out of equilibrium with current climate, even without further global warming (Christian et al., 2018; Marzeion et al., 2018; Mernild et al., 2013; Zekollari et al., 2020). The size of glaciers during other periods warmer than the Early to Mid-Holocene, such as the MPWP and LIG, is largely unknown because the deposits marking previous extents were in almost all cases over-ridden by later glaciations. For Arctic glaciers, different regional studies consistently indicate that in many places glaciers are now smaller than they have been in millennia (Harning et al., 2016, 2018; Lowell et al., 2013; Miller et al., 2013, 2017; Pendleton et al., 2019; Schweinsberg et al., 2017, 2018)

New glacier outline (RGI Consortium, 2017) and glacier mass compilations (Ciracì et al., 2020; Hugonnet et al., 2021; Zemp et al., 2019; 2020) improve, refine and update the quantification of glacier areal and mass changes based on observations from in situ and remote sensing data. Observations between the 1960s and 2019 indicate that mass loss has increased over recent decades (Figure 2.23b). The overall global glacier mass loss rate has increased from 240 ± 9 Gt yr^{-1} over 2000–2009 to 290 ± 10 Gt yr^{-1} over 2010–2019 (Hugonnet et al., 2021), confirming that the last decade exhibits the most negative glacier mass balance since the beginning of the observational record. Observations are in general consistent with trends revealed by global glacier mass change modelling for almost the entire 20th century (1901–1990) implying an estimated mass loss (without uncharted glaciers (Parkes and Marzeion, 2018) and excluding peripheral glaciers of Greenland and Antarctica) of *very likely* 210 ± 90 Gt yr^{-1} and *very likely* 170 ± 80 Gt yr^{-1} for the period 1971–2019 (Marzeion et al., 2015; Section 9.5.1 and Table 9.5).

[START FIGURE 2.23 HERE]

Figure 2.23: Glacier advance and annual mass change. (a) Number of a finite selection of surveyed glaciers that advanced during the past 2000 years. (b) Annual and decadal global glacier mass change (Gt yr^{-1}) from 1961 until 2018. In addition, mass change mean estimates are shown. Ranges show the 90% confidence interval. Further details on data sources and processing are available in the chapter data table (Table 2.SM.1).

[END FIGURE 2.23 HERE]

In summary, there is *very high confidence* that, with few exceptions, glaciers worldwide have retreated since the second half of the 19th century, and continue to retreat. The current global character of glacier mass loss is highly unusual (almost all glaciers simultaneously receding) in the context of at least the last 2 kyr (*medium confidence*). Glacier mass loss rates have increased since the 1970s (*high confidence*). Although many surveyed glaciers are currently more extensive than during the MH (*high confidence*), they generally are in disequilibrium with respect to current climate conditions and hence are committed to further ice loss.

ACCEPTED VERSION SUBJECT TO FINAL EDITS

2.3.2.4 Ice sheet mass and extent

During glacial periods, ice sheets were more extensive and the state of knowledge on their paleo-reconstruction can be found in recent publications (e.g. Batchelor et al., 2019; Stokes et al., 2015). This section focuses only on the large-scale aspects of those ice sheets, Greenland and Antarctic, that still exist today.

2.3.2.4.1 Greenland Ice Sheet

AR5 concluded the volume of the Greenland Ice Sheet (GrIS) was reduced compared to present during periods of the past few million years that were globally warmer than present (*high confidence*). It reported that the GrIS had lost ice during the prior two decades (*very high confidence*), that the ice loss had occurred in several sectors, and that high rates of mass loss had both expanded to higher elevations (*high confidence)* and *very likely* accelerated since 1992. SROCC concluded that it was *extremely likely* that ice loss increased through the early 21st century. SROCC also found that summer melting rate had increased since the 1990s to a rate unprecedented over the last 350 years *(very high confidence*), being two to five times greater than the pre-industrial rates (*medium confidence*).

Details of the history of GrIS fluctuations during warm interglacials continue to be elucidated. Oscillations over the past 7.5 Myr, including the Pliocene and through the glacial - interglacial cycles of the Pleistocene are not well-constrained, but most studies indicate that Greenland was at least partially glaciated over this time with extended periods when it was predominantly deglaciated (Schaefer et al., 2016, Bierman et al., 2016). Geological evidence and modelling studies suggest periods of glacial intensification during the Pliocene at 4.9 Myr, 4.0 Myr, 3.6 Myr and 3.3 Myr (De Schepper et al., 2014; Bierman et al., 2016; Bachem et al., 2017). Retreat of the GrIS occurred during the MPWP and GrIS extent was reduced compared to today with some studies suggesting that the ice sheet was limited to the highest elevations (Blake-Mizen et al., 2019; De Schepper et al., 2014; Haywood et al., 2016; Koenig et al., 2015). There is apparent glacial intensification following the MPWP, 2.75–2.72 Myr (Nielsen and Kuijpers, 2013; De Schepper et al., 2014; Blake-Mizen et al., 2019; Knutz et al., 2019). Several studies agree that during the LIG the total GrIS extent was *likely* less than present day (Section 9.4.1, Figure 9.17) with the total mass loss ranging from 0.3–6.2 m sea level equivalent (SLE), although timing and magnitude of this mass loss are not well constrained (Clark et al., 2020; Goelzer et al., 2016; Helsen et al., 2013; Sinclair et al., 2016; Stone et al., 2013; Vasskog et al., 2015; Yau et al., 2016). During the LGM, the GrIS reached a peak ice volume greater than present (2–5 m SLE), as revealed by limited number of available geological records (Lecavalier et al., 2014; Simpson et al., 2009; Batchelor et al. 2019).

Recent studies of marine and lake sediments, glacier ice, and geomorphic features show that the GrIS retreated rapidly during the early Holocene but halted periodically, with a complex ice-margin chronology (Briner et al., 2016; Carlson et al., 2014; Larsen et al., 2014, 2015; Young et al., 2020; Young & Briner, 2015). It is probable that its total volume during 8–3 ka was smaller than today (Briner et al., 2016; Larsen et al., 2015; Young & Briner, 2015), but uncertainties exist regarding precisely when the minimum MH extent and volume was reached, due to uncertainties in reconstructions. The GrIS then re-advanced reaching its maximum extent in most places during 1450–1850 CE, although the timing and extent of this maximum differed by sector (Briner et al., 2016; Larsen et al., 2015).

Greenland-wide estimates of mass change based on direct observations were limited prior to 1992 at the time of AR5 (Kjeldsen et al., 2015). Combined records based on airborne observations, model-based estimates and geodetic approaches indicate an average mass loss of 75 ± 29.4 Gt yr^{-1} for 1900–1983 (Kjeldsen et al., 2015). Integration of proxies and modelling indicates that the last time the rate of mass loss of GrIS was plausibly similar to 20th century rates was during the early Holocene (Briner et al., 2020; Buizert et al., 2018).

Since AR5, a combination of remote sensing, in situ observations and modelling has provided new insights regarding surface processes and their contribution to recent GrIS mass changes (AMAP, 2017; Bamber et al., 2018; IMBIE Consortium, 2020; Khan et al., 2020; Mouginot et al., 2019; van den Broeke et al., 2017).

ACCEPTED VERSION SUBJECT TO FINAL EDITS

Estimates of total ice loss during the post-1850 period (Kjeldsen et al., 2015) and recent observations show that the rate of loss has increased since the beginning of the 21st century (IMBIE Consortium, 2020; Sasgen et al., 2020; Velicogna et al., 2020) (Figure 2.24, Section 9.4.1.1 Figure 9.17).

The GrIS lost 4890 [4140–5640] Gt (SLE 13.5 [11.4–15.6] mm) of ice between 1992 and 2020 (IMBIE Consortium, 2020) (Figure 2.24, Section 9.4.1). The ice sheet was close to mass balance in the 1990s, but increases in mass loss have occurred since (Bamber et al., 2018; WCRP Global Sea Level Budget Group, 2018; Mouginot et al., 2019; IMBIE Consortium, 2020). The rate of ice sheet (including peripheral glaciers) mass loss rose from 120 [70 to 170] Gt yr^{-1} (SLE 0.33 [0.18 to 0.47] mm yr^{-1}) in 1901–1990 to 330 [290 to 370] Gt yr^{-1} (SLE 0.91 [0.79 to 1.02] mm yr^{-1}) for 2006–2018 (Section 9.4.1, Table 9.5).

[START FIGURE 2.24 HERE]

Figure 2.24: Cumulative Antarctic Ice Sheet (AIS) and Greenland Ice Sheet (GrIS) mass changes. Values shown are in gigatons and come from satellite-based measurements (IMBIE Consortium, 2018, 2020) for the period 1992–2018 for GrIS and 1992–2017 for AIS. The estimated uncertainties, *very likely* range, for the respective cumulative changes are shaded. Further details on data sources and processing are available in the chapter data table (Table 2.SM.1).

[END FIGURE 2.24 HERE]

In summary, the GrIS was smaller than present during the MPWP (*medium confidence*), LIG (*high confidence*) and the MH (*high confidence*). GrIS mass loss began following a peak volume attained during the 1450–1850 period and the rate of loss has increased substantially since the turn of the 21st century (*high confidence*).

2.3.2.4.2 Antarctic Ice Sheet

AR5 reported that there was *high confidence* that the AIS was losing mass. The average ice mass loss from Antarctica was 97 [58 to 135] Gt yr^{-1} (GMSL equivalent of 0.27 [0.16 to 0.37] mm yr^{-1}) over 1993–2010, and 147 [74 to 221] Gt yr^{-1} (0.41 [0.20 to 0.61] mm yr^{-1}) over 2005–2010. These assessments included the Antarctic peripheral glaciers. AR5 reported with *high confidence* that the volume of the West Antarctic Ice Sheet (WAIS) was reduced during warm periods of the past few million years. SROCC concluded that over 2006–2015, the AIS lost mass at an average rate of 155 ± 19 Gt yr^{-1} (*very high confidence*). SROCC stated also that it is *virtually certain* that the Antarctic Peninsula and WAIS combined have cumulatively lost mass since widespread measurements began in 1992, and that the rate of loss has increased since around 2006.

Process understanding and, to some extent, paleoclimate records show that changes in parts of the AIS can occur over multi-century time scales (<2kyr) (e.g. Dowdeswell et al., 2020; Sections 9.4.2.3 and 9.6.2). Based on physical understanding, paleo evidence and numerical simulations, it is *very likely* that the AIS has been smaller than today during at least some past warm climates (such as MCO and LIG), in particular the WAIS (de Boer et al., 2015; Deconto & Pollard, 2016; Golledge et al., 2014; Levy et al., 2016) (Figure 9.18). Results from sediment studies suggest a smaller AIS during the MPWP compared with current levels, with main differences in the WAIS (SROCC, Bertram et al., 2018; Shakun et al., 2018, Section 9.6.2). Marine sediments indicate that during the Pleistocene repeated ungrounding and loss of large marine-based parts of the AIS occurred during interglacial periods, with at least seven transitions between floating and grounded ice in the Ross Sea during the last 780 kyr (McKay et al., 2012) and at least three reductions in ice volume in the Wilkes Basin during the last 500 kyr (Wilson et al., 2018). Proxies, modelling and process understanding (Rohling et al., 2019; Clark et al., 2020) indicate that the AIS was smaller during the LIG than present.

Geological evidence has been used to reconstruct Holocene glacial fluctuations of the ice sheet margin and lowerings of its surface, which occurred at different times in different places, as recently reviewed by Noble et al. (2020). In West Antarctica, marine sediments below the ice sheet (Kingslake et al., 2018) corroborate a

ACCEPTED VERSION SUBJECT TO FINAL EDITS

previous glacial isostatic adjustment modelling study (Bradley et al., 2015), which suggests that ice had retreated behind the present grounding line prior to about 10 ka, and then readvanced. Geophysical imaging indicates a readvance in this area around 6 ± 2 ka (Wearing and Kingslake, 2019). Other studies from the region conclude that ice sheet retreat and thinning was fastest from 9 to 8 ka (Johnson et al., 2014; McKay et al., 2016; Spector et al., 2017), or millennia later, during the MH (Hein et al., 2016; Johnson et al., 2019), with indications of a subsequent readvance (Venturelli et al., 2020). In East Antarctica, rapid ice sheet thinning occurred between around 9 and 5 ka (Jones et al., 2015), consistent with previous work indicating that the ice sheet in many regions was at or close to its current position by 5 ka (Bentley et al., 2014). Overall, during the MH, the AIS was retreating, but remained more extensive than present, while some parts of the ice sheet might have been smaller than now (*low confidence*).

Improved estimates of surface mass balance (SMB) in Antarctica from 67 ice core records do not show any substantial changes in accumulation rates over most of Antarctica since 1200 CE (Frezzotti et al., 2013). The SMB growth rate in Antarctica is estimated to be 7.0 ± 0.1 Gt per decade between 1800 and 2010 and 14.0 ± 1.8 Gt per decade since 1900 (Thomas et al., 2017). For the period 1979–2000, an insignificant Antarctic-wide negative SMB trend has been estimated (Medley and Thomas, 2019). The Antarctic Ice Sheet lost 2670 [1800 to 3540] Gt (SLE 7.4 [5.0 to 9.8] mm) of ice between 1992 and 2020. The rate of ice sheet (including peripheral glaciers) mass loss rose from 0 [–36 to 40] Gt yr^{-1} (SLE 0.0 [–0.10 to 0.11] mm yr^{-1}) in 1901–1990 to 192 [145 to 239] Gt yr^{-1} (SLE 0.54 [0.47 to 0.61] mm yr^{-1}) for 2006–2018 (Figure 2.24, Section 9.4.2, Table 9.5). Within quantified uncertainties, this estimate agrees with other recent estimates (Rignot et al., 2019; Smith et al., 2020; Velicogna et al., 2020). There is therefore *very high confidence* that the AIS has been losing mass over 1992–2020 (Figure 2.24, Section 9.4.2.1). Major contributions to recent AIS changes arise from West Antarctica and Wilkes Land in East Antarctica (Rignot et al., 2019). For the East Antarctic most studies suggest that the mass balance is not significantly different from zero (Bamber et al., 2018; IMBIE Consortium, 2018; Mohajerani et al., 2018; Rignot et al., 2019).

In summary, the AIS has lost mass between 1992 and 2020 (*very high confidence*), and there is *medium confidence* that this mass loss has increased. During the MPWP and LIG, the ice sheet was smaller than present (*medium confidence*). There is *low confidence* as to whether the total mass of the ice sheet was larger or smaller around 6 ka compared to now.

2.3.2.5 Terrestrial permafrost

AR5 concluded that in most regions and at most monitoring sites permafrost temperatures since the 1980s had increased (*high confidence*). Negligible change was observed at a few sites, mainly where permafrost temperatures were close to 0°C, with slight cooling at a limited number of sites. AR5 also noted positive trends in active layer thickness (ALT; the seasonally thawed layer above the permafrost) since the 1990s for many high latitude sites (*medium confidence*). SROCC concluded permafrost temperatures have increased to record high levels since the 1980s (*very high confidence*) with a recent increase by 0.29°C ± 0.12°C from 2007 to 2016 averaged across polar and high mountain regions globally.

Permafrost occurrence during the Pliocene has been inferred from pollen in lake sediments in NE Arctic Russia and permafrost-vegetation relationships which indicate that permafrost was absent during the MPWP in this region (Brigham-Grette et al., 2013; Herzschuh et al., 2016). Analysis of speleothem records in Siberian caves, indicates that permafrost was absent in the current continuous permafrost zone at 60°N at the start of the 1.5 Ma record, with aggradation occurring around 0.4 Ma (Vaks et al., 2020). There are indications of extensive permafrost thaw during subsequent interglacials especially further south in the current permafrost zone (Vaks et al., 2013). Reconstruction of permafrost distribution during the LGM indicates that permafrost was more extensive in exposed areas (Vandenberghe et al., 2014). In non-glaciated areas of the North American Arctic there is permafrost that survived the LIG (French and Millar, 2014). Trends and timing of permafrost aggradation and thaw over the last 6 kyr in peatlands of the NH were recently summarized (Hiemstra, 2018; Treat and Jones, 2018a). Three multi-century periods (ending 1000 Before the Common Era (BCE), 500 CE and 1850 CE) of permafrost aggradation, associated with neoglaciation periods are inferred resulting in more extensive permafrost in peatlands of the present-day discontinuous permafrost zone, which reached a peak approximately 250 years ago, with thawing occurring

ACCEPTED VERSION SUBJECT TO FINAL EDITS

concurrently with post 1850 warming (Treat and Jones, 2018b). Although permafrost persists in peatlands at the southern extent of the permafrost zone where it was absent prior to 3 ka, there has been thawing since the 1960s (Holloway & Lewkowicz, 2020; James et al., 2013; Jones et al., 2016).

Records of permafrost temperature measured in several boreholes located throughout the northern polar regions indicate general warming of permafrost over the last 3–4 decades (Figure 2.25), with marked regional variations (Romanovsky et al., 2017a,b; 2020; Biskaborn et al., 2019). Recent (2018–2019) permafrost temperatures in the upper 20–30 m layer (at depths where seasonal variation is minimal) were the highest ever directly observed at most sites (Romanovsky et al., 2020), with temperatures in colder permafrost of northern North America being more than 1°C higher than they were in 1978. Increases in temperature of colder Arctic permafrost are larger (average 0.4°C–0.6°C per decade) than for warmer (temperature >–2°C) permafrost (average 0.17°C per decade) of sub-Arctic regions (Figures 2.25, 9.22).

[START FIGURE 2.25 HERE]

Figure 2.25: Changes in permafrost temperature. Average departures of permafrost temperature (measured in the upper 20–30 m) from a baseline established during International Polar Year (2007–2009) for Arctic regions. Further details on data sources and processing are available in the chapter data table (Table 2.SM.1).

[END FIGURE 2.25 HERE]

Increases in permafrost temperature over the last 10–30 years of up to 0.3°C per decade have been documented at depths of about 20 m in high elevation regions in the NH (European Alps, the Tibetan Plateau and some other high elevation areas in Asia; Biskaborn et al., 2019; Cao et al., 2018; Liu G. et al., 2017; Noetzli et al., 2020; Zhao et al., 2020). In Antarctica, where records are limited and short (most < 10 years) trends are less evident (Noetzli et al. 2019).

Assessment of trends in ALT is complicated by considerable ALT interannual variability. For example, in north-western North America during the extreme warm year of 1998, ALT was greater than in prior years. Although ALT decreased over the following few years, it has generally increased again since the late 2000s (Duchesne, et al. 2015; Romanovsky et al., 2017b; 2020). However, at some sites there has been little change in ALT due to ground subsidence that accompanies thaw of ice-rich permafrost (Streletskiy et al., 2017; O'Neill et al., 2019). In the European and Russian Arctic there has been a broad-scale increase in ALT during the 21st century (Streletskiy et al., 2015; Romanovsky et al., 2020). In high elevation areas in Europe and Asia, increases in ALT have occurred since the mid-1990s (Cao et al., 2018; Liu, Y. et al., 2017; Noetzli et al., 2019; 2020; Zhao et al., 2020). Limited and shorter records for Antarctica show marked interannual variability and no apparent trend with ALT being relatively stable or decreasing at some sites since 2006 (Hrbáček et al., 2018).

Observations of ground subsidence and other landscape change (e.g. thermokarst, slope instability) since the middle of the 20th century in the Arctic associated with ground ice melting have been documented in several studies and provide additional indications of thawing permafrost (Borge et al., 2017; Derksen et al., 2019; Farquharson et al., 2019; Kokelj et al., 2017; Lewkowicz & Way, 2019; Liljedahl et al., 2016; Nitze et al., 2017; O'Neill et al., 2019; Séjourné et al., 2015; Streletskiy et al., 2017; Section 9.5.2.1). In mountain areas, destabilization and acceleration of rock glacier complexes that may be associated with warming permafrost have also been observed (Eriksen et al., 2018; Marcer et al., 2019).

In summary, increases in permafrost temperatures in the upper 30 m have been observed since the start of observational programs over the past three to four decades throughout the permafrost regions (*high confidence*). *Limited evidence* suggests that permafrost was less extensive during the MPWP (*low confidence*). Permafrost that formed after 3ka still persists in areas of the NH, but there are indications of thaw after the mid-1800s (*medium confidence*).

ACCEPTED VERSION SUBJECT TO FINAL EDITS

2.3.3 Ocean

This section focuses on large-scale changes in a subset of physical components of the ocean (Cross-Chapter Box 2.2). Chapter 7 assesses the role of the ocean in Earth system heating and evaluates the Earth's energy budget. Chapter 9 undertakes a holistic assessment of changes in the ocean integrating observations, modelling and theoretical understanding. Chapter 11 assesses extremes such as marine heat waves and storm surges. SSTs are assessed in Section 2.3.1.1 as they constitute a critical component of GMST estimation.

2.3.3.1 Ocean temperature, heat content and thermal expansion

AR5 assessed that since 1971, global ocean warming was *virtually certain* for the upper 700 m and *likely* for the 700–2000 m layer. SROCC reported linear warming trends for the 0–700 m and 700–2000 m layers of the ocean of 4.35 ± 0.8 and 2.25 ± 0.64 ZJ yr^{-1} over 1970-2017; 6.28 ± 0.48 and 3.86 ± 2.09 ZJ yr^{-1} over 1993–2017; and 5.31 ± 0.48 and 4.02 ± 0.97 ZJ yr^{-1} over 2005–2017. Both AR5 and SROCC assessed that the ocean below 2000 m had *likely* warmed since 1992. SROCC reported global mean thermosteric sea level (ThSL) rise, associated with thermal expansion of the ocean, with a trend of 0.89 ± 0.05 mm yr^{-1} for 1970–2015; 1.36 ± 0.40 mm yr^{-1} for 1993–2015; and 1.40 ± 0.40 mm yr^{-1} for 2006–2015, and also reported that the rate of ocean warming over 1993-2017 had *likely* more than doubled since 1969–1992.

New ocean heat content (OHC) reconstructions derived from paleo proxies (Baggenstos et al., 2019; Bereiter et al., 2018; Gebbie, 2021; Shackleton et al., 2019) indicate that the global ocean warmed by 2.57°C ± 0.24°C, at an average rate of ~0.3°C ka^{-1} (equivalent to an OHC change rate of 1.3 ZJ yr^{-1}) from the LGM (~20 ka) to the early Holocene (~10 ka) (Figure 9.9, Section 9.2.2.1). Over the LDT, ocean warming occurred in two stages, offset by some heat loss during the Antarctic Cold Reversal (14.58–12.75 ka). Only during a short period of rapid warming at the end of the Younger Dryas (12.75–11.55 ka) were rates comparable to those observed since the 1970s (Bereiter et al., 2018; Shackleton et al., 2019). Ice cores imply a small decrease in the global mean ocean temperature during the early Holocene (<0.4°C) (Baggenstos et al., 2019; Bereiter et al., 2018). Sediment cores from the equatorial Pacific and Atlantic Ocean (0–1000 m) indicate a stronger regional cooling (compared to mean ocean temperature) of 1.0°C ± 0.7°C to 1.8°C ± 0.4°C from the early/mid-Holocene to ca.1750 CE (Kalansky et al., 2015; Morley et al., 2014; Rosenthal et al., 2017; 2013). Sediment cores from the western equatorial Pacific suggest 0.8°C ± 0.1°C higher temperatures in the upper 700 m of the ocean during 950–1100 CE compared to 1400–1750 CE. These changes are consistent with a global estimate derived from combined surface and subsurface ocean temperature proxy records (McGregor et al., 2015; PAGES 2k Consortium, 2013). A combined study of model and observational data further confirmed these results, treating temperature as a passive tracer (Gebbie & Huybers, 2019) and addressing the role of circulation dynamics (Scheen and Stocker, 2020). Collectively, the proxy records indicate a global OHC decrease of ~400 ± 70 ZJ (~170 ± 100 ZJ in the Pacific) in the upper 700 m between 950–1100 CE and 1400–1750 CE, and also suggest that the deep Pacific is still adjusting to this cooling (Rosenthal et al., 2013), partially offsetting the global increase since 1750 CE (Gebbie & Huybers, 2019; Gebbie, 2021).

For the instrumental era, since AR5 and SROCC, new and updated OHC (and ThSL) observation-based analyses (Johnson et al., 2020; von Schuckmann et al., 2020) enhance an existing large ensemble of direct and indirect OHC estimates (Figure 2.26), although some rely to varying degrees upon information from ocean-climate models. Direct estimates benefit from improved: bias adjustments (e.g. Bagnell & DeVries, 2020; Cheng et al., 2018; Gouretski & Cheng, 2020; Leahy et al., 2018; Palmer et al., 2018; Ribeiro et al., 2018; Wang et al., 2018); interpolation methods (Kuusela & Stein, 2018; Su et al., 2020); and characterization of sources of uncertainty (e.g.(Allison et al., 2019; Garry et al., 2019; Good, 2017; Meyssignac et al., 2019; Palmer et al., 2021; Wunsch, 2018), including those originating from forced and intrinsic ocean variability (Penduff et al. 2018). After 2006 direct OHC estimates for the upper 2000 m layer benefit from the near-global ARGO array with its superior coverage over 60°S–60°N (Roemmich et al., 2019). Indirect estimates include OHC and ThSL series inferred from satellite altimetry and gravimetry since 2003 (Meyssignac et al., 2019), the passive uptake of OHC (ThSL) at centennial timescales inferred from observed SST anomalies, and time-invariant circulation processes from an ocean state estimation (e.g. Zanna

ACCEPTED VERSION SUBJECT TO FINAL EDITS

et al., 2019). Resplandy et al. (2019) estimate the rate of global OHC uptake over 1991–2016 from changes in atmospheric composition and physical relationships based on CMIP5 model simulations. The uncertainties are broader than from direct estimates but the estimate is qualitatively consistent.

Collectively, the new and updated analyses strengthen AR5 and SROCC findings of a sustained increase in global OHC (Figure 2.26, Table 2.7) and associated ThSL rise. Larger warming rates are observed in the upper 700 m compared to deeper layers, with more areas exhibiting significant warming than significant cooling (Johnson & Lyman, 2020). There is an improved consistency among available estimates of OHC rates in the upper 2000 m since 2006. Cheng et al. (2020), von Schuckmann et al. (2020) and Johnson et al. (2020) have further confirmed that the central estimates of rates of OHC change in the upper 2000 m depths have increased after 1993 and particularly since 2010 (Section 3.5.1.3, Figures 2.26, 3.26), although uncertainties are large (Table 2.7). Ocean reanalyses support findings of continued upper ocean warming (Balmaseda et al., 2013; Meyssignac et al., 2019; von Schuckmann et al., 2018), albeit with higher spread than solely observational estimates, particularly in the poorly sampled deep ocean below 2000 m (Palmer et al., 2018; Storto et al., 2017).

In summary, current multidecadal to centennial rates of OHC gain are greater than at any point since the last deglaciation (*medium confidence*). At multi-centennial timescales, changes in OHC based upon proxy indicators demonstrate a tight link with surface temperature changes during the last deglaciation (*high confidence*), as well as during the Holocene and CE (*low confidence*). It is *likely* the global ocean has warmed since 1871, consistent with the observed increase in sea surface temperature. It is *virtually certain* that OHC increased between 1971 and 2018 in the upper 700 m and *very likely* in the 700–2000 m layer, with *high confidence* since 2006. It is *likely* the OHC below 2000 m has increased since 1992. Confidence in the assessment of multidecadal OHC increase is further strengthened by consistent closure of both global sea level and energy budgets (Section 7.2.2.2, Box 7.2, Cross-Chapter Box 9.1).

[START FIGURE 2.26 HERE]

Figure 2.26: Changes in Ocean heat content (OHC). Changes are shown over (a) full depth of the ocean from 1871 to 2019 from a selection of indirect and direct measurement methods. The series from Table 2.7 is shown in solid black in both (a) and (b) (see Table 2.7 caption for details). (b) as (a) but for 0–2000 m depths only and reflecting the broad range of available estimates over this period all of which are broadly similar. For further details see chapter data table (Table 2.SM.1).

[END FIGURE 2.26 HERE]

[START TABLE 2.7 HERE]

Table 2.7: Rates of global ocean heat content (OHC) and global mean thermosteric sea level ThSL change for four depth integrations over different periods. For the period up to 1971, the assessment for all depth layers is based on Zanna et al (2019). From 1971 onwards, consistent with AR5, Domingues et al. (2008, updated) is the central estimate for 0–700 m along with uncertainty from a 5-member ensemble (Cheng et al., 2017; Domingues et al., 2008; updated; Good et al., 2013; Ishii et al., 2017; Levitus et al., 2012), following the approach of Palmer et al (2021). Similarly, Ishii et al. (2017) is the central estimate for 700–2000 m with uncertainty based on a 3-member ensemble (Cheng et al., 2017; Ishii et al., 2017; Levitus et al., 2012). For depths below 2000 m, both central estimate and uncertainty are from Purkey and Johnson (2010, updated). In cases when OHC estimates do not have a ThSL counterpart (e.g. Cheng et al., 2017; Good et al., 2013), OHC was converted into ThSL using the average linear regression coefficients for 0–700 m and 700–2000 m from all available ensemble members. For consistency with the energy and sea-level budgets presented in Chapters 7 and 9, reported rates are based on the difference between the first and last annual mean value in each period (Palmer et al., 2021, Box 7.2, Cross-Chapter Box 9.1). Further details on data sources and processing are available in the chapter data table (Table 2.SM.1).

ACCEPTED VERSION SUBJECT TO FINAL EDITS

Depth	*Period*	*OHC rate (ZJ yr^{-1})*	*ThSL rate (mm yr^{-1})*	*Relative full ocean depth contribution*	
				OHC	*ThSL*
0 to 700 m	1901-1990	2.50 [1.16–3.85]	0.31 [0.16–0.45]	81%	86%
	1901-2018	3.11 [2.18–4.04]	0.40 [0.30–0.50]	66%	74%
	1971-2018	5.14 [3.46–6.82]	0.71 [0.51–0.90]	61%	70%
	1993-2018	6.06 [4.56–7.55]	0.89 [0.69–1.10]	58%	68%
	2006-2018	6.28 [4.06–8.50]	0.91 [0.51–1.31]	54%	65%
700 to 2000 m	1901-1990	0.50 [-0.59–1.60]	0.04 [-0.07–0.16]	16%	11%
	1901-2018	1.26 [0.43–2.09]	0.11 [0.02–0.19]	27%	20%
	1971-2018	2.62 [2.04–3.20]	0.23 [0.16–0.31]	31%	23%
	1993-2018	3.31 [2.40–4.22]	0.30 [0.19–0.41]	32%	23%
	2006-2018	4.14 [2.41–5.86]	0.36 [0.15–0.58]	36%	26%
>2000 m	1901-1990	0.07 [0.02–0.12]	0.01 [0.00–0.01]	2%	3%
	1901-2018	0.32 [0.18–0.46]	0.03 [0.02–0.05]	7%	6%
	1971-2018	0.66 [0.33–0.99]	0.07 [0.03–0.10]	8%	7%
	1993-2018	1.15 [0.58–1.72]	0.12 [0.06–0.18]	11%	9%
	2006-2018	1.15 [0.58–1.72]	0.12 [0.06–0.18]	10%	9%
Full-depth	1901-1990	3.08 [1.36–4.79]	0.36 [0.17–0.54]		
	1901-2018	4.68 [3.45–5.92]	0.54 [0.40–0.68]		
	1971-2018	8.42 [6.08–10.77]	1.01 [0.73–1.29]		
	1993-2018	10.52 [7.76–13.28]	1.31 [0.95–1.66]		
	2006-2018	11.57 [7.20–15.94]	1.39 [0.74–2.05]		

[END TABLE 2.7 HERE]

2.3.3.2 Ocean salinity

AR5 concluded that subtropical regions of high salinity (where evaporation dominates over precipitation) had become more saline, while regions of low salinity (mostly in the tropics and high latitudes) had *very likely* become fresher since the 1950s, both at the near-surface, and in the ocean interior along ventilation pathways. From 1950 to 2008, the mean surface contrast between high- and low-salinity regions increased by 0.13 [0.08 to 0.17] (PSS-78, Unesco, 1981). Across basins, the Atlantic Ocean had become saltier and the Pacific and Southern Oceans had freshened (*very likely*).

Prior to the instrumental record, reconstructions of near-surface salinity change are accomplished by combining isotopic and elemental proxy data from microfossil plankton shells and skeletons preserved in deep-sea sediments. These data highlight changes in the salinity contrast between the Pacific and Atlantic oceans during past ice ages (Broecker, 1989; Keigwin and Cook, 2007; Costa et al., 2018) and for repeated

ACCEPTED VERSION SUBJECT TO FINAL EDITS

episodes of increased subtropical salinity (Schmidt et al., 2004, 2006) and subpolar freshening (Cortijo et al., 1997; Thornalley et al., 2011) in the North Atlantic ocean. These episodes were associated with disruptions to the large-scale deep ocean circulation (Buizert et al., 2015; Henry et al., 2016; Lynch-Stieglitz, 2017). Further quantification of paleo salinity changes is complicated by incomplete understanding on how proxy-salinity relationships and the relative influence of atmospheric and ocean processes vary across regions and paleo periods (Conroy et al., 2017; Holloway et al., 2016; LeGrande & Schmidt, 2011; Rohling, 2007).

Since AR5, new and extended multidecadal analyses have strengthened the observational support for increased contrast between high and low near-surface salinity regions and inter-basin contrast since the mid-20th century (Section 9.2.2.2; Aretxabaleta et al., 2017; Cheng et al., 2020; Durack & Wijffels, 2010; Good et al., 2013; Skliris et al., 2014). These analyses employ different statistical algorithms for interpolation, and only Cheng et al., (2020) use CMIP5 model simulations to constrain observation-based signals in data-sparse regions.

The 1950–2019 trends reveal near-surface freshening of the northern and western Warm (and fresh) Pool of the Pacific and increased salinity maxima in the subtropical Atlantic, strengthening the inter-basin contrast (Figure 2.27a). There are indications that the subpolar freshening and subtropical salinification of the Atlantic ocean may extend back to at least 1896 (Friedman et al., 2017). Over recent decades, new observations from Argo floats and ocean reanalyses provide general support that changes in the global patterns of near-surface salinity contrast are broadly associated with an intensification of the hydrological cycle (Sections 2.3.1.3.5; 8.3.1.1). However, this assessment is complicated by changing observational techniques (Section 1.5.1), temporally and spatially inhomogeneous sampling and uncertainties in interpolation algorithms and the substantial influence of modes of natural variabiltity and ocean circulation processes over interannual timescales (Aretxabaleta et al., 2017; Durack, 2015; Grist et al., 2016; Liu et al., 2020; Skliris et al., 2014; Vinogradova & Ponte, 2017). Following AR5, based on the updated analysis from Durack and Wijffels (2010) which infills in situ gaps to recover large-scale patterns the mean salinity contrast between high- and low- near-surface salinity regions increased by 0.14 [0.07 to 0.20] from 1950 to 2019.

Changes in the global patterns of near-surface salinity contrast are transferred to the ocean interior via ventilation pathways (Figure 2.27b). Large scale similarities in subsurface salinity changes across observational estimates point to decreasing (increasing) salinity in regions where salinity is lower (higher) than the global average, with freshening in subpolar regions and salinification in the subtropical gyres (Aretxabaleta et al., 2017; Cheng et al., 2020; Durack, 2015; Durack & Wijffels, 2010; Good et al., 2013; Skliris et al., 2014). Regional changes in salinity are assessed in Section 9.2.2.2.

In summary, it is *virtually certain* that since 1950 near-surface high salinity regions have become more saline, while low salinity regions have become fresher, and it is *very likely* that this extends to the ocean interior along ventilation pathways. Across basins, it is *very likely* that the Atlantic has become saltier and the Pacific and Southern oceans have freshened. The differences between high-salinity and low-salinity regions are linked to an intensification of the hydrological cycle (*medium confidence*).

[START FIGURE 2.27 HERE]

Figure 2.27: Changes in ocean salinity. Estimates of salinity trends using a total least absolute differences fitting method for (a) global near-surface salinity (SSS) changes and (b) global zonal mean subsurface salinity changes. Black contours show the associated climatological mean salinity (either near-surface (a) or subsurface (b)) for the analysis period (1950–2019). Both panels represent changes of Practical Salinity Scale 1978 [PSS-78], per decade. In both panels green denotes freshening regions and orange/brown denotes regions with enhanced salinities. 'x' marks denote non-significant changes. Further details on data sources and processing are available in the chapter data table (Table 2.SM.1).

[END FIGURE 2.27 HERE]

2.3.3.3 Sea level

ACCEPTED VERSION SUBJECT TO FINAL EDITS

AR5 concluded based on proxy and instrumental data that the rate of global mean sea level (GMSL) rise since the mid-19th century was larger than the mean rate during the previous two millennia (*high confidence*). SROCC reported with *high confidence* that GMSL increases were 1.5 [1.1 to 1.9] mm yr^{-1} for 1902–2010 (with an acceleration rate between -0.002–0.019 mm yr^{-2}), 2.1 [1.8 to 2.3] mm yr^{-1} for 1970–2015, 3.2 [2.8 to 3.5] mm yr^{-1} for 1993–2015 and 3.6 [3.1 to 4.1] mm yr^{-1} for 2006–2015. AR5 reported that GMSL during the LIG was, over several thousand years, between 5 and 10 m higher than 1985–2004 (*medium confidence*) whereas SROCC concluded it was *virtually certain* that GMSL exceeded current levels (*high confidence*), and reached a peak that was *likely* 6–9 m higher than today, but did not exceed 10 m (*medium confidence*). AR5 concluded with *high confidence* that there were two intra-LIG GMSL peaks and that the millennial-scale rate during these periods exceeded 2mm yr^{-1}. AR5 had *high confidence* that GMSL during the MPWP did not exceed 20 m above present. Based on new understanding, SROCC placed the upper bound at 25 m but with *low confidence*.

The Earth was largely ice free during the EECO (Cramer et al., 2011; Miller et al., 2020, Section 9.6.2), and complete loss of current land ice reservoirs would raise GMSL by 65.6 ± 1.8 m (Farinotti et al., 2019; Morlighem et al., 2017; 2020). Given that GMSL change must be due to some combination of transient land ice growth and changes in terrestrial water storage, additional global mean thermosteric sea-level increase of 7 ± 2 m (Fischer et al., 2018) implies a peak EECO GMSL of 70–76 m (*low confidence*). Changes in ocean basin size driven by plate tectonics contributed a comparable amount to global mean geocentric sea level in the Eocene, but are definitionally excluded from GMSL assessment (Wright et al., 2020).

For the MPWP, several studies of coastal features have provided additional quantitative sea-level estimates of: 5.6–19.2 m from Spain (Dumitru et al., 2019), approximately 14 m from South Africa (Hearty et al., 2020), 15 m from the United States (Moucha and Ruetenik, 2017), and 25 m from New Zealand (Grant et al., 2019). Thus, consistent with SROCC, GMSL during the MPWP was higher than present by 5–25 m (*medium confidence*).

Reconstructions of GMSL from marine oxygen isotopes in foraminifera shells show variations of more than 100 m over intervals of 10–100 kyr during glacial-interglacial cycles of the Quaternary (McManus et al., 1999; Miller et al., 2020; Shackleton, 1987; Waelbroeck et al., 2002). Correction for past temperatures and a calibration for ice-volume changes implies uncertainty estimates of ± 10–13 m (1 SD) (Grant et al., 2014; Shakun et al., 2015; Spratt & Lisiecki, 2016). A recent marine oxygen-isotope-based GMSL reconstruction (Spratt and Lisiecki, 2016) agrees with previous reconstructions, while focusing on the past 800 kyr (Figure 2.28). It shows that GMSL during the Holocene was among the highest over this entire interval, and was surpassed only during the LIG (Marine Isotope Stage (MIS 5e)) and MIS 11 (*medium confidence*); however, relatively brief (about 2 kyr) highstands during other interglacial periods might be obscured by dating limitations.

Few sites globally have well-preserved MIS 11 sea-level indicators (Dutton et al., 2015). As reported in AR5, Raymo and Mitrovica (2012) used glacial isostatic adjustment models to correct the elevation of MIS 11 sea-level proxies from Bermuda and Bahamas to estimate a peak MIS 11 GMSL between 6 and 13 m above present-day. This agrees with the elevation of 13 ± 2 m for the MIS 11 subtidal–intertidal transition in South Africa (Roberts et al., 2012). A revised glacial isostatic adjustment at this location resulted in a peak GMSL estimate of 8–11.5 m (Chen et al., 2014). In light of these data, and the review by Dutton et al. (2015), the AR5 estimate of 6–13 m for MIS 11 remains the best available (*medium confidence*).

Recent studies have highlighted uncertainties in estimates of GMSL during the LIG, including the extent of GMSL variability (Capron et al., 2019). Vertical land motions (Austermann et al., 2017) are starting to be considered quantitatively (e.g., Stephenson et al., 2019), but are still bounded by large uncertainties. The distribution and thickness of pre-LIG ice sheets (Dendy et al., 2017; Rohling et al., 2017) and isostasy driven by sediment loading since the LIG (Pico, 2020) add further uncertainty. In light of these recent studies and previous assessments, there is *medium confidence* that peak GMSL during the LIG was *likely* between 5 and 10 m higher than modern. Relative sea-level estimates from some sites (e.g., Bahamas and Seychelles) report ephemeral, metre-scale fluctuations (Vyverberg et al., 2018). Different generations of LIG reef growth at other sites (e.g., Yucatan Peninsula, Western Australia) suggest the occurrence of sudden accelerations in

ACCEPTED VERSION SUBJECT TO FINAL EDITS

GMSL change (Blanchon et al., 2009; O'Leary et al., 2013). However, other sites (e.g., South Australia, Mediterranean), indicate that LIG sea level was substantially stable (Pan, Y-T. et al., 2018; Polyak et al., 2018). In addition, there are uncertainties in the interpretation of local relative sea level from some GMSL reconstructions (Barlow et al., 2018). Therefore, *low confidence* is assigned to any GMSL rate of change estimated within the LIG.

New geological proxies and glacial isostatic adjustment (GIA) modelling studies confirm that, at the LGM, GMSL was 125–134 m below present (Lambeck et al., 2014; Yokoyama et al., 2018). During the LDT, GMSL rose from approximately -120 m to -50 m, implying an average rate of about 10 mm yr^{-1} (Lambeck et al., 2014). The fastest rise occurred during Meltwater Pulse 1A, at about 14.6–14.3 ka (Deschamps et al., 2012; Sanborn et al., 2017), when GMSL rose by between 8 m and 15 m (*medium confidence*) (Liu J. et al., 2016) at an average rate of 24–44 mm yr^{-1}.

Recent GIA modelling studies tuned to both near- and far-field relative sea level (RSL) data yield MH GMSL estimates of -3.8 to -1.0 m (Lambeck et al., 2014; Peltier et al., 2015; Bradley et al., 2016; Roy and Peltier, 2017). Estimates from relatively stable locations where the effects of GIA are small and relatively insensitive to parameters defining Earth rheology, and where RSL is expected to approximate GMSL to within about 1 m (e.g., Milne & Mitrovica, 2008), suggest that RSL was between about -6 to 1.5 m at around 6 ka at multiple locations (Braithwaite et al., 2000; Camoin et al., 1997; Frank et al., 2006; Hibbert et al., 2018; Khan et al., 2017; Montaggioni & Faure, 2008; Vacchi et al., 2016). The assessment of GMSL change at 6 kyr is challenging considering the proportionately large GIA effect (Kopp et al., 2016a), insufficient resolution of marine geochemical proxies ($\delta^{18}O$, Mg/Ca) and uncertainties in the contribution of the Antarctic Ice Sheet during the MH (Section 2.3.2.4). The possibility that GMSL was at least somewhat higher than present cannot be excluded.

For the last 3 kyr, GMSL has been estimated from global databases of sea-level proxies, including numerous densely-sampled high-resolution salt-marsh records with decimetre scale vertical resolution and sub-centennial temporal resolution (Kopp et al., 2016b; Kemp et al., 2018a). Over the last about 1.5 kyr, the most prominent century-scale GMSL trends include average maximum rates of lowering and rising of -0.7 ± 0.5 mm yr^{-1} (2 SD) over 1020–1120 CE, and 0.3 ± 0.5 (2 SD) over 1460–1560, respectively. Between 1000 and 1750 CE, GMSL is estimated to have been within the range of about -0.11–0.09 m relative to 1900 (Kemp et al., 2018b). This was followed by a sustained increase of GMSL that began between 1820 and 1860 and has continued to the present day. New analyses demonstrate that it is *very likely* that GMSL rise over the 20th century was faster than over any preceding century in at least 3 kyr (Kopp et al., 2016a; Kemp et al., 2018a) (Figure 2.28).

[START FIGURE 2.28 HERE]

Figure 2.28: Changes in global mean sea level. (a) Reconstruction of sea-level from ice core oxygen isotope analysis for the last 800 kyr. For target paleo periods (CCB2.1) and MIS11 the estimates based upon a broader range of sources are given as box whiskers. Note the much broader axis range (200 m) than for later panels (tenths of metres). (b) Reconstructions for the last 2500 years based upon a range of proxy sources with direct instrumental records superposed since the late 19th century. (c) Tide-gauge and, more latterly, altimeter based estimates since 1850. The consensus estimate used in various calculations in Chapters 7 and 9 is shown in black. (d) The most recent period of record from tide-gauge and altimeter based records. Further details on data sources and processing are available in the chapter data table (Table 2.SM.1).

[END FIGURE 2.28 HERE]

Since SROCC, two new tide gauge reconstructions of 20th century GMSL change have been published, although both rely upon CMIP models to varying degrees (Figure 2.28). Frederikse et al (2020) used a "virtual station" method and a probabilistic framework to estimate GMSL change and its uncertainties since 1900. Dangendorf et al (2019) combined a Kalman Smoother (Hay et al., 2015) with Reduced Space

ACCEPTED VERSION SUBJECT TO FINAL EDITS

Optimal Interpolation (Church & White, 2011; Ray & Douglas, 2011) in an effort to better represent both the long-term GMSL change while preserving information on sea-level variability. In addition, new ensemble-based methods for quantifying GMSL change have been presented that account for both structural and parametric uncertainty (Palmer et al., 2021). Altimeter timeseries of GMSL change (Figure 2.28) have been extended to 2019/2020 but bias adjustments (Ablain et al., 2019; Beckley et al., 2017; Dieng et al., 2017; Legeais et al., 2020; Watson et al., 2015) did not change since SROCC.

Based on the ensemble approach of Palmer et al (2021) and an updated WCRP (2018) assessment (Figure 2.28) GMSL rose at a rate of 1.35 [0.78 to 1.92] mm yr^{-1} for the period 1901–1990 and 3.25 [2.88 to 3.61] mm yr^{-1} for 1993–2018 (*high confidence*). The average rate for 1901–2018 was 1.73 [1.28 to 2.17] mm yr^{-1} with a total rise of 0.20 [0.15 to 0.25] m (Table 9.5). The acceleration rate *very likely* is 0.094 [0.082 to 0.115] mm yr^{-2} for 1993–2018 (WCRP, 2018, updated), consistent with other estimates (Ablain et al., 2019; Chen X. et al., 2017; Legeais et al. 2020; Nerem et al., 2018; Watson et al., 2015; WCRP, 2018). For the period 1902–2010 the updated tide gauge reconstructions published since the SROCC also show a robust acceleration over the 20th century and the ensemble estimate of Palmer et al (2021) gives a value of 0.0053 [0.0042 to 0.0073] mm yr^{-2}, based on an unweighted quadratic fit.

In summary, GMSL is rising, and the rate of GMSL rise since the 20th century is faster than over any preceding century in at least the last three millennia (*high confidence*). Since 1901, GMSL has risen by 0.20 [0.15 to 0.25] m at an accelerating rate. Further back in time, there is *medium confidence* that GMSL was within –3.5–0.5 m (*very likely* range) of present during the MH, 5–10 m higher (*likely range*) during the LIG, and 5–25 m higher (*very likely* range) during the MPWP.

2.3.3.4 Ocean circulation

2.3.3.4.1 Atlantic Meridional Overturning circulation (AMOC)

AR5 concluded that there was no evidence of a trend in the AMOC during the period of instrumental observations. However, AR5 also stressed insufficient evidence to support a finding of change in the heat transport of the AMOC. SROCC assessed that there was emerging evidence in sustained observations, both in situ (2004–2017) and revealed from SST-based reconstructions, that the AMOC had weakened during the instrumental era relative to 1850–1900 (*medium confidence*), although there were insufficient data to quantify the magnitude of the weakening. SROCC also concluded with *low confidence* an increase of the Southern Ocean upper cell overturning circulation. SROCC also reported with *medium confidence* that the production of Antarctic Bottom Water had decreased since the 1950s consistent with a decreased lower cell overturning circulation, and potentially modulating the strength of the AMOC.

On multi-millennial timescales, proxy evidence indicates that the AMOC varied repeatedly in strength and vertical structure. During the last glacial period, particularly around the LGM, AMOC was estimated to be shallower than present, although there is continued debate about the magnitude of the shoaling (Gebbie, 2014; Lynch-Stieglitz et al., 2007), and whether this change was associated with a weaker overturning (Ritz et al., 2013; Menviel et al., 2017; Muglia et al., 2018). There are indications that substantial variations in AMOC were associated with abrupt climate changes during the glacial intervals, including Dansgaard-Oeschger and Heinrich events (14–70 ka) (Böhm et al., 2015; Henry et al., 2016; Lynch-Stieglitz, 2017; McManus et al., 2004). During these millennial-scale oscillations, weakened AMOC was associated with dramatic cooling in the northern hemisphere and warming in the southern hemisphere (Buizert et al., 2015; Henry et al., 2016), while hemispheric changes of opposite sign accompanied strengthened AMOC. After the final demise of the Laurentide ice sheet about 8 ka, the mean overall strength of AMOC has been relatively stable throughout the rest of the Holocene compared to the preceding 100 kyr (Hoffmann et al., 2018; Lippold et al., 2019). There are however indications of episodic variations in AMOC during the Holocene (Bianchi and McCave, 1999; Oppo et al., 2003; Thornalley et al., 2013; Ayache et al., 2018), and past interglacial intervals (Galaasen et al., 2014, 2020; Hayes et al., 2014; Huang et al., 2020; Mokeddem et al., 2014). Over the last 3 kyr, there are indications that AMOC variability was potentially linked to decreasing production of Labrador Sea Water (LSW), one of the water masses contributing to AMOC (Alonso-Garcia et al., 2017; McClymont et al., 2020; Moffa-Sánchez et al., 2019; Moffa-Sánchez & Hall, 2017).

ACCEPTED VERSION SUBJECT TO FINAL EDITS

Numerous proxy records collectively imply that AMOC is currently at its weakest point in the past 1.6 ka (Caesar et al., 2018, 2021; Rahmstorf et al., 2015; Thibodeau et al., 2018; Thornalley et al., 2018). Caesar et al. (2021) analyse a compilation of various available indirect AMOC proxies from marine sediments, in situ-based reconstructions and terrestrial proxies, which show a decline beginning in the late 19th century and over the 20th century superimposed by large decadal variability in the second half of the 20th century. Indirect reconstructions of AMOC components based on coastal sea level records in the western North Atlantic (Ezer, 2013; McCarthy et al., 2015; Piecuch, 2020) show an AMOC decline since the late 1950s, with only a short period of recovery during the 1990s.

However, other studies highlight that proxy records do not show such clear signals (Moffa-Sánchez et al., 2019), and the use of SST- and coastal sea level-based proxies of AMOC places uncertainties on these results (Jackson & Wood, 2020; Little et al., 2019; Menary et al., 2020). For instance, SSTs are additionally influenced by atmospheric and non-AMOC related ocean variability (Josey et al., 2018; Keil et al., 2020; Menary et al., 2020), while sea level responds to a variety of factors (e.g. atmospheric pressure and local winds) independent of the AMOC (Woodworth et al., 2014; Piecuch and Ponte, 2015; Piecuch et al., 2016). Finally, large decadal variability is present in many reconstructions and obscures estimation of the long-term trend over the 20th century (Caesar et al., 2021; Ezer, 2013; McCarthy et al., 2015; Thornalley et al., 2018; Yashayaev & Loder, 2016). It is also noted that the proxy reported AMOC decline, beginning in the late 19th century, is not supported by model-based evidence (Sections 3.5.4.1. and 9.2.3.l).

Since the 1980s, multiple lines of observational evidence for AMOC change exist. Ship-based hydrographic estimates of AMOC as far back as the 1980s show no overall decline in AMOC strength (Fu et al., 2020; Worthington et al., 2020). Direct indications from in-situ observations report a –2.5 ± 1.4 Sv change between 1993 and 2010 across the OVIDE section, superimposed on large interannual to decadal variability (Mercier et al., 2015). At 41°N and 26°N, a decline of –3.1 ± 3.2 Sv per decade and –2.5 ± 2.1 Sv per decade respectively has been reported over 2004–2016 (Baringer et al., 2018; Smeed et al., 2018). However, Moat et al. (2020) report an increase in AMOC strength at 26°N over 2009–2018. Recent time series of moored observations at 11ºS (Hummels et al., 2015), 34ºS (Meinen et al., 2018; Kersalé et al., 2020), and between 57 and 60ºN (Lozier et al., 2019a) are currently too short to permit robust conclusions about changes. The directly observed AMOC weakening since 2004, while significant, is over too short a period to assess whether it is part of a longer term trend or dominated by decadal-scale internal variability (Smeed et al., 2014; Collins et al., 2019; Moat et al., 2020). Notably an increase and subsequent decline in the 1990s is present in estimates of AMOC and associated heat transport constructed from reanalyses or auxiliary data (Frajka-Williams, 2015; Jackson & Wood, 2020; Jackson et al., 2016; Trenberth & Fasullo, 2017) (Section 9.2.3.1).

Repeated full depth in situ measurements report that deep convection - a major driver for AMOC - has recently returned to the Labrador Sea (particularly in 2015; Rhein et al., 2017; Yashayaev & Loder, 2016), and Irminger Sea (de Jong et al., 2018; de Jong & de Steur, 2016; Gladyshev et al., 2016) following an extended period with weak convection since 2000. An associated strengthening of the outflow from the Labrador Sea has not been observed (Zantopp et al., 2017; Lozier et al., 2019b), while strengthening of the AMOC is tentative (Desbruyères et al., 2019; Moat et al., 2020). A long-term increase of the upper overturning cell in the Southern Ocean since the 1990s can be assessed with *low confidence*, and there is *medium confidence* of a decrease in Antarctic bottom water (AABW) volume and circulation, which has potential implications for the strength of the AMOC (Section 9.2.3.2).

In summary, proxy-based reconstructions suggested that the AMOC was relatively stable during the past 8 kyr (*medium confidence*), with a weakening beginning since the late 19th century (*medium confidence*), but due to a lack of direct observations, *confidence* in an overall decline of AMOC during the 20th century *is low*. From mid-2000s to mid-2010s, the directly observed weakening in AMOC *(high confidence)* cannot be distinguished between decadal-scale variability or a long-term trend (*high confidence*).

ACCEPTED VERSION SUBJECT TO FINAL EDITS

2.3.3.4.2 Western boundary currents and inter-basin exchanges

Both AR5 and SROCC reported that western boundary currents (WBCs) have undergone an intensification, warming and poleward expansion, except for the Gulf Stream and the Kuroshio, but did not provide confidence statements. AR5 reported with *medium* to *high confidence* intensification of the North Pacific subpolar gyre, the South Pacific subtropical gyre, and the subtropical cells, along with an expansion of the North Pacific subtropical gyre since the 1990s. It was pointed out that these changes are *likely* predominantly due to interannual-to-decadal variability, and in the case of the subtropical cells represent a reversal of earlier multi-decadal change. SROCC concluded that it was *unlikely* that there has been a statistically significant net southward movement of the mean Antarctic Circumpolar Current (ACC) position over the past 20 years, in contrast to AR5, where this change had been assessed with *medium confidenc*e.

The intensity of the Kuroshio current system in the northwest Pacific varied in conjunction with the glaciation cycles over the last 1 Myr, with some limited glacial-interglacial variability in position (Jian et al., 2000; Gallagher et al., 2015). The Agulhas current has strengthened substantially during the warming associated with deglaciations of the past 1 Myr (Peeters et al., 2004; Bard and Rickaby, 2009; Martínez-Méndez et al., 2010; Marino et al., 2013; Ballalai et al., 2019). According to sediment core analyses, the Agulhas leakage varied by about 10 Sv during major climatic transitions over the past 640 kyr (Caley et al., 2014). Available data suggests that there was relatively little change in the net flow of the ACC in the LGM, with no consensus on the sign of changes (Lamy et al., 2015; Lynch-Stieglitz et al., 2016; McCave et al., 2013), except at one location at the northern edge of the Drake Passage where a 40% decrease of transport had been reported (Lamy et al., 2015). Longer time series from the northern entrance to Drake Passage suggest a consistent transport variability of 6–16% through glacial climate cycles, with higher current speeds during interglacial times and reduced current speeds during glacial intervals (Toyos et al., 2020). Inferred variability in the size and strength of the North Atlantic subpolar gyre was substantial, and included rapid changes on millennial time scales during both interglacial and glacial intervals over the last 150 kyr (Born and Levermann, 2010; Mokeddem et al., 2014b; Irvalı et al., 2016; Mokeddem and McManus, 2016). North Atlantic – Arctic exchange has also varied in the past, with indications of an increasing inflow of Atlantic waters into the Arctic during the late Holocene (Ślubowska et al., 2005) with an acceleration to the recent inflow that is now the largest of the past 2 kyr (Spielhagen et al., 2011).

A latitudinal shift of subtropical/subpolar gyres on the order of 0.1 ± 0.04° per decade is derived by an indirect method using remote sensing data during 1993–2018 (Yang H. et al., 2020). Direct observations show a systematic poleward migration of WBCs (Bisagni et al., 2017; Wu L. et al., 2012; Yang H. et al., 2016, 2020). However, they do not support an intensification of WBCs, with a weakening, broadening, or little change reported for the Kuroshio (Collins et al., 2019; Wang & Wu, 2018; Wang et al., 2016), Gulf Stream (Andres et al., 2020; Collins et al., 2019; Dong et al., 2019; McCarthy et al., 2018), Agulhas (Beal and Elipot, 2016; Elipot and Beal, 2018) and East Australian (Sloyan and O'Kane, 2015) currents. The Gulf Stream has recently reversed a long-term poleward migration (Bisagni et al., 2017). Multidecadal variability of the strength and position of WBCs (Bisagni et al., 2017; Hsin, 2015; McCarthy et al., 2018) and short records from direct observations obscure the detection of any long-term trends (Yang H. et al., 2020).

The Pacific to Arctic exchange at the Bering Strait plays a minor role in the total Arctic exchange with the global ocean, which has increased from 0.8 Sv to 1.0 Sv over 1990–2015 (Woodgate, 2018). For Atlantic-Arctic exchange, major branches of Atlantic Water inflow from the North Atlantic into the Arctic across the Greenland-Scotland Ridge have remained stable since the mid-1990s (Berx et al., 2013; Hansen et al., 2015; Jochumsen et al., 2017; Østerhus et al., 2019), with only the smaller pathway of Atlantic Water north of Iceland showing a strengthening trend during 1993–2018 (Casanova-Masjoan et al., 2020), but with associated heat transport strengthening through the 1990s (Rossby et al., 2020; Tsubouchi et al., 2021). The Arctic outflow remained broadly stable from the mid-1990s to the mid 2010 (Osterhus et al., 2019). The heat and mass transport of the Indonesian throughflow (ITF) shows substantial variability at seasonal to decadal time scales (Feng M. et al., 2017, 2018; Li M. et al., 2018; Liu Q.-Y. et al., 2015; Sprintall et al., 2019; Susanto & Song, 2015; Xie T. et al., 2019; Zhuang et al., 2013). Liu et al. (2015) reported an increasing trend in the ITF geostrophic transport of 1 Sv per decade over 1984–2013, consistent with direct estimates (Sprintall et al., 2014), and results from reanalyses (Li et al., 2018), and this appears to be linked to multi-decadal scale variability rather than a long-term trend (England et al., 2014; Kosaka & Xie, 2013; Lee S.-K.

ACCEPTED VERSION SUBJECT TO FINAL EDITS

et al., 2015). Southern Ocean circulation changes are assessed in SROCC (Meredith et al., 2019), and are confirmed and synthesized in Section 9.2.3.2 which shows that there is no indication of ACC transport change, and that it is *unlikely* that the mean meridional position of the ACC has moved southward in recent decades.

In summary, over the past 3–4 decades, the WBC strength is highly variable (*high confidence*), and WBCs and subtropical gyres have shifted poleward since 1993 (*medium confidence*). Net Arctic Ocean volume exchanges with the other ocean basins remained stable over the mid-1990s to the mid-2010s (*high confidence*). There is *high confidence* that the ITF shows strong multi-decadal scale variability since the 1980s.

2.3.3.5 Ocean pH

AR5 assessed with *high confidence* that the pH of the ocean surface has decreased since preindustrial times, primarily as a result of ocean uptake of CO_2. SROCC concluded that the global ocean absorbed 20–30% of total CO_2 emissions since the 1980s, with *virtually certain* ocean surface pH decline. The SROCC assessed a rate of surface pH decline of 0.017–0.027 pH units per decade across a range of time series of pH observations longer than 15 years. The decline in surface open ocean pH was assessed by SROCC as having *very likely* already emerged from background natural variability for more than 95% of the global surface open ocean.

Understanding of changes in surface pH at paleo time-scales has increased since AR5 (Anagnostou et al., 2020; Clarkson et al., 2015; Foster & Rae, 2016; Gutjahr et al., 2017; Harper et al., 2020; Henehan et al., 2019; Müller et al., 2020; Sosdian et al., 2018; Zeebe et al., 2016). Over the last 65 million years there have been several intervals when the pH of surface waters varied concurrently with climate change such as during the PETM, EECO, and MCO (Figure 2.29a) (Section 5.3.1.1). However, only during the PETM is the change sufficiently well-constrained to allow for a direct comparison with recent and current trends (Turner, 2018). This event was associated with profound perturbations of the global carbon cycle, ocean warming, deoxygenation and a surface ocean pH decrease *likely* ranging from 0.15 to 0.30 units (Penman et al., 2014; Gutjahr et al., 2017; Babila et al., 2018) - a rate that was *likely* at least an order of magnitude slower than today (Cui et al., 2011; Bowen et al., 2015; Frieling et al., 2016; Zeebe et al., 2016; Gutjahr et al., 2017; Kirtland Turner, 2018; Gingerich, 2019).

[START FIGURE 2.29 HERE]

Figure 2.29: Low latitude surface ocean pH over the last 65 million years. (a) Low-latitude (30°N–30°S) surface ocean pH over the last 65 million years, reconstructed using boron isotopes in foraminifera. (b) as (a) but for the last 3.5 million years. Double headed arrow shows the approximate magnitude of glacial-interglacial pH changes. (c) Multisite composite of surface pH. In a)-c), uncertainty is shown at 95% confidence as a shaded band. Relevant paleoclimate reference periods (CCB2.1) have been labelled. Period windows for succeeding panels are shown as horizontal black lines in a) and b). (d) Estimated low-latitude surface pH from direct observations (BATS, HOT) and global mean pH (65°S–65°N) from two indirect estimates (CMEMS, OCEAN-SODA). Further details on data sources and processing are available in the chapter data table (Table 2.SM.1).

[END FIGURE 2.29 HERE]

Paleo evidence suggests that surface ocean pH has gradually increased over the last 50 Myr (Anagnostou et al., 2016; 2020; Sosdian et al., 2018) (Figure 2.29a). Global mean surface pH values as low as observed during recent decades are uncommon in the last 2 Myr (Figure 2.29b) (Chalk et al., 2017; Dyez et al., 2018; Martínez-Botí et al., 2015a; Sosdian et al., 2018), and have not been experienced in at least the last 25 kyr (Figure 2.29c) (Ezat et al., 2017; Foster, 2008; Gray et al., 2018; Henehan et al., 2013; Kirschke et al., 2013; Martínez-Botí et al., 2015a; Naik et al., 2015; Palmer et al., 2010; Palmer & Pearson, 2003; Shao et al.,

ACCEPTED VERSION SUBJECT TO FINAL EDITS

2019). The magnitude of pH change during the Pleistocene glacial-interglacial cycles was 0.1–0.15 pH units - similar to recent changes in the modern era (Figure 2.29c) (Hönisch et al., 2009; Chalk et al., 2017; Shao et al., 2019) (Section 5.3.1.2). Maximum rates of pH change during the LDT, inferred from changes in atmospheric CO_2 recorded in ice cores (Marcott et al., 2014b) and the established relationships between pH and CO_2 changes and the boron isotope proxy (Hain et al. 2018), reached -0.02 pH units per century at about 11.7 ka, about 14.8 ka and about 16.3 ka, as previously sequestered CO_2 was transferred from the ocean interior to the subsurface ocean (Jaccard et al., 2016; Martínez-Botí et al., 2015a; Rae et al., 2018).

Since the 1980s, the global ocean has experienced a decline in surface pH of 0.016 ± 0.006 pH units per decade based on indirect pH products (Figure 2.29d) (Gehlen et al., 2020; Hurd et al., 2018; IPCC, 2019; Lauvset et al., 2015) that agrees with the decline of 0.017–0.025 pH units per decade assessed in SROCC from direct time-series measurements of pH. Section 5.3.2.2 assesses a decline that ranges from 0.01 to 0.026 pH units per decade for the tropical and subtropical open ocean areas, and 0.003–0.026 pH units per decade for the polar and subpolar open ocean regions by using time series and ship-based datasets from the surface ocean CO_2 measurement network (Bakker et al., 2016; Gehlen et al. 2020; Gregor & Gruber, 2021). There is general consensus that global surface ocean pH trends over the past two decades have exceeded the natural background variability (Bindoff et al., 2019; Gehlen et al., 2020; Lauvset et al., 2015). However, for some areas sparse data coverage, and large year-to-year variations hinders the detection of long-term surface ocean pH trends; for example in the Southern Ocean (Bindoff et al., 2019; Lauvset et al., 2015) and in the Arctic Ocean (Bindoff et al., 2019; Lauvset et al., 2015; Meredith et al., 2019).

For subsurface pH changes, estimates arise from direct ship measurements from repeated hydrography programs (Carter et al., 2019), indirect estimates of pH through calcite and aragonite saturation horizons (Osborne et al., 2020; Ross et al., 2020), and the very recent biogeochemical Argo floats equipped with pH sensors (Claustre et al., 2020). Global subsurface pH has decreased over the past 20–30 years, with signals observed to at least 1000 m depths (Lauvset et al., 2020). Global findings are supplemented by regional findings from the Pacific Ocean (Carter et al., 2019; Ross et al., 2020); the South Atlantic (Salt et al., 2015) and Southern Ocean (Jones et al., 2017); the North Atlantic Ocean and along the AMOC (Woosley et al., 2016; Perez et al., 2018), the Arctic Ocean (Qi et al., 2017) and marginal seas (Chen C.-T. A. et al., 2017). Further details are given in Section 5.3.3.1.

To conclude, it is *virtually certain* that surface open ocean pH has declined globally over the last 40 years by 0.003–0.026 pH per decade, and a decline in the ocean interior has been observed in all ocean basins over the past 2–3 decades (*high confidence*). A long-term increase in surface open ocean pH occurred over the past 50 Myr (*high confidence*), and surface open ocean pH as low as recent times is uncommon in the last 2 Myr (*medium confidence*). There is *very high confidence* that open ocean surface pH is now the lowest it has been for at least 26 kyr and current rates of pH change are unprecedented since at least that time.

2.3.3.6 Ocean deoxygenation

SROCC concluded that there has *very likely* been a net loss of oxygen over all ocean depths since the 1960s linked to global ocean deoxygenation at a range of 0.3–2.0%, and that the oxygen levels in the global upper 1000 m of the ocean had decreased by 0.5–3.3% during 1970–2010 (*medium confidence*), alongside an expansion of oxygen minimum zones (OMZ) by 3–8%. For the surface ocean (0–100 m) and the thermocline at 100–600 m, the *very likely* range of oxygen decline was assessed to be 0.2–2.1% and 0.7–3.5%, respectively. Multidecadal rates of deoxygenation showed variability throughout the water column and across ocean basins (*high confidence*).

Since AR5 evidence for changes in oxygen content based on new proxy reconstructions has increased (Anderson et al., 2019; Gottschalk et al., 2016, 2020; Hoogakker et al., 2015, 2018). Paleo records point to past periods of reduced oceanic oxygen levels during the late Permian (about 250 Ma), the Jurassic and Cretaceous (180–100 Ma), alongside associated global scale disturbances of the global carbon cycle. Emerging studies for the Cenozoic Era suggest more stable ocean oxygenation conditions throughout the interval on million-year time scales (Wang X. et al., 2016). Sedimentary proxy data indicate, however, that the seemingly stable Cenozoic was punctuated by transient, widespread deoxygenation during the PETM

ACCEPTED VERSION SUBJECT TO FINAL EDITS

(Dickson et al., 2012; Winguth et al., 2012; Remmelzwaal et al., 2019), with parts of the ocean reaching anoxic levels (Yao et al., 2018) (Section 5.3.1.1). Since the LGM, there was an overall emergence and expansion of low-oxygen waters into the ocean intermediate depths as a result of rapid warming and a reorganization of the global overturning circulation (Galbraith and Jaccard, 2015). The maximum expansion of oxygen-depleted waters during the LDT occurred coincidently with rapid warming in the NH at 14.7–12.9 ka (Hoogakker et al., 2018; Jaccard & Galbraith, 2012; Moffitt et al., 2015). Deep (> 1500m) ocean oxygen levels increased by 100–150 μmol kg^{-1} since the LGM, reaching modern oxygen levels at about 10 ka (Anderson et al., 2019; Gottschalk et al., 2016; Hoogakker et al., 2015) (Section 5.3.1.2).

New findings for ocean oxygen content since SROCC are limited to regional scale assessments. The magnitude of change is difficult to compare across regions to arrive at a global assessment due to differences in depth range, time period, baseline climatology, methodology, and particularly the use of different units. To facilitate comparisons, data are presented as change per decade, and conversions of the SROCC global mean percentage of oxygen decline estimates are provided as a loss of 3.2 μmol kg^{-1} in the upper 1000 m of the global ocean (1.93%), and 2.0 μmol kg^{-1} (0.8 μmol kg^{-1} per decade) in the upper 1000 m of the global ocean (1.93%), and 2.0 μmol kg^{-1} (0.5 μmol kg^{-1} per decade) in the entire water column (1.15%) between 1970 and 2010 (Bindoff et al., 2019). Oxygen change also shows decadal variability (Ito et al., 2016; Stramma et al., 2020) that can influence estimates of trends.

Subsurface (100–400 m) oxygen in the California Current system is estimated to have declined by 24 ± 2 μmol kg^{-1} (1.0 μmol kg^{-1} per decade) between 1993 and 2018, a rate similar to the global upper 1000 m average (Bindoff et al. 2019). In some locations, however, the magnitude of oxygen loss substantially exceeds global averages (Queste et al., 2018; Bronselaer et al., 2020; Cummins and Ross, 2020; Stramma et al., 2020). For example, a decline in oxygen content of 11.7 ± 3.5% in the upper 4000 m, including a decline of 20.4 ± 7.2% in the upper 1550 m, is reported in the North Pacific over the period 1958–2018 (Cummins and Ross, 2020) (equivalent to 2.3 μmol kg^{-1} per decade in the upper 1550 m and 2.0 μmol kg^{-1} $decade^{-1}$ throughout the 4000 m water column). In some regions of the Southern Ocean south of 65°S oxygen in the upper 2000 m has declined by 60 μmol kg^{-1} (~52 μmol kg^{-1} per decade) based on comparisons of 2014–2019 and 1985–2005 observations (Bronselaer et al., 2020). Within some OMZs regions of the Indian ocean, oxygen has declined from 6–12 to < 2 μmol kg^{-1} between the 1960s and 2015–2016 (Bristow et al., 2017; Naqvi et al., 2018; Queste et al., 2018).

Findings since SROCC provide further support that the volume of severely oxygen-depleted water has expanded in some locations of the global ocean (Section 5.3.3.2). For example, vertical expansion of low oxygen zones is reported in the North Pacific at a rate of 3.1 ± 0.5 m yr^{-1} (Ross et al., 2020), and suboxic waters have increased by 20% at a rate of about 19 m per decade from 1982–2010 in the Arabian Sea (Naqvi et al., 2018; Lachkar et al., 2019), and expanded off the coast of Mexico (Sánchez-Velasco et al., 2019).

In summary, episodes of widespread and long-lasting (100 ka scales) open-ocean deoxygenation were related to warm climate intervals of the Permian-Cretaceous, with conditions becoming generally better oxygenated as the climate cooled over the course of the Cenozoic (*high confidence*). The largest expansions of oxygen depleted waters over the past 25 ka were strongly linked to rapid warming rates (*medium confidence*). Open-ocean deoxygenation has occurred in most regions of the open ocean during the mid- 20th to early 21st centuries (*high confidence*), and shows decadal variability (*medium confidence*). Evidence further confirms SROCC that OMZs are expanding at many locations (*high confidence*).

2.3.4 Biosphere

This section is limited to a few biological indicators to demonstrate the close links between the biosphere and physical forcing. In selecting the indicators, we focussed on those (i) that are observable at large (global) spatial scales and over long (two decades or more) temporal scales, using standardised and consistent procedures; and (ii) those that are illustrative of the influence of the physical system on the biological realm. Chapters 2 and 3 of WGII AR6 undertake a more holistic assessment of biospheric impacts.

ACCEPTED VERSION SUBJECT TO FINAL EDITS

2.3.4.1 Seasonal Cycle of CO_2

AR5 noted that because CO_2 uptake by photosynthesis occurs only during the growing season, the greater land mass in the NH imparts a characteristic 'sawtooth' seasonal cycle in atmospheric CO_2. SRCCL similarly stated that due to strong seasonal patterns of growth, NH terrestrial ecosystems are largely responsible for the seasonal variations in global atmospheric CO_2 concentrations. Neither AR5 nor SRCCL made a confidence statement about observed changes in the amplitude of the seasonal cycle of CO_2.

In situ observations of CO_2 generally depict a rising amplitude of the seasonal cycle over the past half century, especially north of about 45°N (Figure 2.30). For example, an amplitude increase of 6 ± 2.6% per decade has been observed at the Barrow surface observatory in Alaska over 1961–2011 (Graven et al., 2013), with slightly slower increases thereafter. Aircraft data north of 45°N exhibit an amplitude increase of 57 ± 7% at 500 mb versus an increase of 26 ± 18% for 35°N–45°N between field campaigns in 1958–1961 and 2009–2011 (Graven et al., 2013b). Increases in amplitude for the period 1980–2012 are apparent at eight surface observatories north of 50°N (Piao et al., 2018), related primarily to a larger drawdown in June and July. Trends in seasonal cycle amplitude at lower latitudes are smaller (if present at all); for instance, the increase at the Mauna Loa observatory in Hawaii since the early 1960s is only about half as large as at Barrow (Graven et al., 2013a), and only one other low-latitude observatory has a significant increase from 1980–2012 (Piao et al., 2018). There is a weak signal of an increase in amplitude at the Sinhagad observatory in western India in recent years (Chakraborty et al., 2020). Generally speaking, larger increases in the Arctic and boreal regions are indicative of changes in vegetation and carbon cycle dynamics in northern ecosystems (Forkel et al., 2016), though increased carbon uptake can also result from other factors such as warmer- and wetter-than-normal conditions.

Recent satellite-based, global-scale estimates of seasonal variations in atmospheric CO_2 for the period 2003–2018 show that the seasonal variations in the SH are out of phase with those in the NH (Reuter et al., 2020), which is consistent with the phenological shifts in primary productivity between hemispheres. The net effect of the phase shift between the two hemispheres is to dampen the amplitude of the global average seasonal cycle. These integrated results also show that the amplitude of the oscillations has been increasing in the SH, from about 2009, but comparison with data from Baring head suggests that periods of high seasonal oscillation had occurred at that location in the SH prior to 1995.

[START FIGURE 2.30 HERE]

Figure 2.30: Changes in the amplitude of the seasonal cycle of CO_2. (a) Observed peak-to-trough seasonal amplitude given by the day of year of downward zero crossing, of CO_2 concentration at Barrow (71°N, blue) and Mauna Loa (20°N, black). Seasonal CO_2 cycles observed at (b) Barrow and (c) Mauna Loa for the 1961–1963 or 1958–1963 and 2017–2019 time periods. The first six months of the year are repeated. Reprinted with permission from AAAS. Further details on data sources and processing are available in the chapter data table (Table 2.SM.1).

[END FIGURE 2.30 HERE]

In summary, there is *very high confidence* that the amplitude of the seasonal cycle of atmospheric CO_2 has increased at mid-to-high NH latitudes since the early 1960s. The observed increase is generally consistent with greater greening during the growing season and an increase in the length of the growing season over the high northern high latitudes. Similarly, globally-integrated results from the SH also show an increase in seasonal amplitude of atmospheric CO_2 signal, from around 2009 to 2018 (*low confidence*).

2.3.4.2 Marine biosphere

2.3.4.2.1 Large-scale distribution of marine biota

SROCC pointed out that long-term global observations of many key ocean variables, including

ACCEPTED VERSION SUBJECT TO FINAL EDITS

phytoplankton, have not reached the density and accuracy necessary for detecting change. But SROCC noted the good comparability between short time-scale single-sensor ocean-colour products and a longer time-scale, climate-quality time series of multi-sensor, inter-sensor-bias-corrected, and error characterised, global data on chlorophyll-a concentration in the surface layers of the ocean. With respect to oligotrophic gyres, AR5 WGII concluded that the oligotrophic subtropical gyres of the Atlantic and Pacific Oceans are expanding and that they indicate declining phytoplankton stocks in these waters (*limited evidence, low agreement*). With respect to distributions of marine organisms, AR5 WGII reported range shifts of benthic, pelagic, and demersal species and communities (*high confidence*), though the shifts were not uniform.

Phytoplankton are responsible for marine primary production through photosynthesis; they are a major player in the ocean carbon cycle. They have a high metabolic rate, and respond fast to changes in environmental conditions (light, temperature, nutrients, mixing), and as such, serve as a sentinel for change in marine ecosystems. Concentration of chlorophyll-a, the major photosynthetic pigment in all phytoplankton, is often used as a measure of phytoplankton biomass. As primary producers, they are also food for organisms at higher trophic levels. The multi-sensor time series of chlorophyll-a concentration has now been updated (Sathyendranath et al., 2019) to cover 1998–2018. Figure 2.31 shows that global trends in chlorophyll-a for the last two decades are insignificant over large areas of the global ocean (von Schuckmann et al., 2019), but some regions exhibit significant trends, with positive trends in parts of the Arctic and the Antarctic waters (>3% yr^{-1}), and both negative and positive trends (within ± 3% yr^{-1}) in parts of the tropics, subtropics and temperate waters. The interannual variability in chlorophyll-a data in many regions is strongly tied to indices of climate variability (Section 2.4, Annex IV) and changes in total concentration are typically associated with changes in phytoplankton community structure (e.g., Brewin et al., 2012; Racault et al., 2017a). Variability in community structure related to El Niño has, in turn, been linked to variability in fisheries, for example in the catch of anchovy (*Engraulis ringens*) in the Humboldt current ecosystem (Jackson et al., 2011).

[START FIGURE 2.31 HERE]

Figure 2.31: Phytoplankton dynamics in the ocean. (a) Climatology of chlorophyll-a concentration derived from ocean-colour data (1998–2018); (b) Linear trends in chlorophyll concentration. Trends are calculated using OLS regression with significance assessed following AR(1) adjustment after Santer et al (2008c) ('x' marks denote non-significant changes). (c) Histogram of linear trends in chlorophyll concentration, after area weighting and with per-pixel uncertainty estimates based on comparison with in situ data. Further details on data sources and processing are available in the chapter data table (Table 2.SM.1).

[END FIGURE 2.31 HERE]

Since AR5 WGII, analysis of a longer time series of ocean-colour data (1998–2012) has shown (Aiken et al., 2017) that the expansion of the low nutrient part of the North Atlantic oligotrophic gyre was significant, at 0.27 x 10^6 km^2 per decade, but that the rate was much lower than that reported earlier by Polovina et al. (2008). Furthermore, Aiken et al. (2017) reported no significant trend in the oligotrophic area of the South Atlantic Gyre. With the time series extended to 2016, von Schuckmann et al. (2018) reported that since 2007, there was a general decreasing trend in the areas of the North and South Pacific oligotrophic Gyres, while the North and South Atlantic oligotrophic Gyres remained stable, with little change in area, consistent with Aiken et al. (2017). The changing sign of trends in the areal extent of the oligotrophic gyres with increase in the length of the time series raises the possibility that these changes arise from interannual to multi-decadal variability. The time series of ocean-colour data is too short to discern any trend that might be superimposed on such variability.

Similarly, there is limited consistent and long-term information on large-scale distributions of marine organisms at higher trophic levels. But there are increased indications since AR5 and SROCC that the distributions of various higher trophic-level organisms are shifting both polewards and to deeper levels (Atkinson et al., 2019; Edwards et al., 2016; Haug et al., 2017; Lenoir et al., 2020; Pinsky et al., 2020), mostly consistent with changes in temperature. However observations also show a smaller set of counter-

ACCEPTED VERSION SUBJECT TO FINAL EDITS

intuitive migrations towards warmer and shallower waters, which could be related to changes in phenology and in larval transport by currents (Fuchs et al., 2020). There are also strengthening indications of greater representation by species with warm-water affinity in marine communities, consistent with expectations under observed warming (Burrows et al., 2019). There are indications that pre-1850 CE plankton communities are different from their modern counterparts globally (Jonkers et al., 2019). Indicators of geographical distributions of species (mostly from coastal waters) suggest that the rates at which some species are leaving or arriving at an ecosystem are variable, leading to changes in community composition (Blowes et al. 2019), with *likely* greater representation of warm-water species in some locations (Burrows et al., 2019).

In summary, there is *high confidence* that the latitudinal and depth limits of the distribution of various organisms in the marine biome are changing. There is *medium confidence* that there are differences in the responses of individual species relative to each other, such that the species compositions of ecosystems are changing. There is *medium confidence* that chlorophyll concentration in the surface shows weak negative and positive trends in parts of low and mid latitudes, and weak positive trends in some high-latitude areas. There is *medium confidence* that the large-scale distribution of the oligotrophic gyre provinces is subject to significant inter-annual variations, but *low confidence* in the long-term trends in the areal extent of these provinces because of insufficient length of direct observations.

2.3.4.2.2 Marine Primary production

SROCC expressed *low confidence* in satellite-based estimates of trends in marine primary production, citing insufficient length of the time series and lack of corroborating in situ measurements and independent validation time series. The report also cites significant mismatches in absolute values and decadal trends in primary production when different satellite-based products are compared.

Recent model-based results with assimilation of satellite data (Gregg and Rousseaux, 2019), show global annual mean marine primary production of around 38 (±1.13) PgC yr^{-1} over 1998–2015. This new result lies towards the low end of values reported in earlier, satellite-based, studies (range 36.5–67 PgC yr^{-1}, reported in Sathyendranath et al., 2020). Reconciling the results of Gregg & Rousseaux (2019) with earlier satellite-based studies leads to a mean of 47 (±7.8) PgC yr^{-1}. There is a strong correlation between interannual regional variability in marine primary production and climate variability (Gregg & Rousseaux, 2019; Racault et al., 2017b). The increase in primary production in the Arctic has been associated with retreating sea ice and with increases in nutrient supply and chlorophyll concentration (Lewis et al., 2020). Gregg and Rousseaux (2019) reported a decreasing trend in marine primary production, of -0.8 PgC (-2.1%) per decade globally. There is *low confidence* in this trend because of the small number of studies and the short length of the time series (<20 years).

In conclusion, there is *low confidence* because of the small number of recent studies and the insufficient length of the time series analysed that marine primary production is 47 (± 7.8) PgC yr^{-1}. A small decrease in productivity is evident globally for the period 1998–2015, but regional changes are larger and of opposing signs (*low confidence*).

2.3.4.2.3 Marine phenology

Phenology is the study of the timing of important events in the annual life cycle of organisms (plants or animals) (see also Annex VII: Glossary). AR5 WGII noted that the timing of various seasonal biological events in the ocean had advanced by more than four days per decade over the previous 50-year period and concluded that there was *high confidence* in observed changes in the phenological metrics of marine organisms. AR5 WGII further reported that, of those observations that showed a response, 81% of changes in phenology, distribution and abundance were consistent with anticipated responses to climate warming according to theoretical expectations, corroborated by updates in SROCC. The consequent current and future impacts on interactions between species, including competition and predator-prey dynamics, were noted with *high confidence*.

ACCEPTED VERSION SUBJECT TO FINAL EDITS

There are additional indications that phenological metrics related to different species are changing, but not always in a similar manner. For example, many seabirds are breeding earlier, while others are breeding later (Sydeman et al., 2015). Planktonic organisms in the North Atlantic are also responding differently to each other when subjected to the same environmental changes (Edwards & Richardson, 2004). Furthermore, different factors could be responsible for triggering phenological responses in different stages in the life cycle of a single organism (Koeller et al., 2009). The shift in the distribution of many benthic invertebrates on the North-West Atlantic shelf, including some commercially-important shellfish, could be explained by phenology and larval transport and the shift and contraction of species range have been associated with higher mortality (Fuchs et al., 2020). Changes in phytoplankton phenological indicators globally (Racault et al., 2012; Sapiano et al., 2012) have been linked to indicators of climate variability, such as the multivariate ENSO Index (Racault et al., 2017a) with responses varying across ecological provinces of the ocean (Longhurst, 2007).

Phenological links between multiple components of an ecosystem have to be maintained intact, to retain system integrity. Since all higher pelagic organisms depend on phytoplankton for their food, either directly or indirectly, a match favours survival, and a mismatch is antagonistic to survival. Match represents synchonicity in the phenological events of both prey and predator. There are indications from ocean-colour data used in conjunction with fisheries data that the survival rate of various larger marine organisms depends on phenological metrics related to the seasonality of phytoplankton growth. Such links have been demonstrated, for example, for haddock (*Melanogrammus aeglefinus*) in the North-West Atlantic (Platt et al., 2003); northern shrimp in the North Atlantic (Koeller et al., 2009; Ouellet et al., 2011); sardine (*Sardinella aurita*) off the Ivory coast (Kassi et al., 2018); cod (*Gadus morhua*) and haddock (*Melanogrammus aeglefinus*) larvae in the North-West Atlantic (Trzcinski et al., 2013); and oil sardine (*Sardinella longiceps*) off the south-west coast of India. Borstad et al. (2011) showed that fledgling production rate of rhinoceros auklets (*Cerorhinca monocerata*) on a remote island in coastal north-eastern Pacific was related to seasonal values of chlorophyll-a biomass in the vicinity of the island.

In summary, new in situ data as well as satellite observations strengthen AR5 and SROCC findings that various phenological metrics for many species of marine organisms have changed in the last half century (*high confidence*), though many regions and many species of marine organisms remain under-sampled or even unsampled. The changes vary with location and with species (*high confidence*). There is a strong dependence of survival in higher trophic-level organisms (fish, exploited invertebrates, birds) on the availability of food at various stages in their life cycle, which in turn depends on phenologies of both (*high confidence*). There is a gap in our understanding of how the varied responses of marine organisms to climate change, from a phenological perspective, might threaten the stability and integrity of entire ecosystems.

2.3.4.3 Terrestrial biosphere

2.3.4.3.1 Growing season and phenology changes

AR5 WGII briefly discussed large-scale changes in the length of the growing season but made no confidence statement about observed trends. However, AR5 did conclude with *high confidence* that warming contributed to an overall spring advancement in the NH.

Recent in situ analyses document increases in the length of the thermal growing season (i.e., the period of the year when temperatures are warm enough to support growth) over much of the extratropical land surface since at least the mid-20th century. Over the NH as a whole, an increase of about 2.0 days per decade is evident for 1951–2018 (Dunn et al., 2020), with slightly larger increases north of 45°N (Barichivich et al., 2013). Over North America, a rise of about 1.3 days per decade is apparent in the United States for 1900–2014 (Kukal and Irmak, 2018), with larger increases after 1980 (McCabe et al., 2015); likewise, all ecozones in Canada experienced increases from 1950–2010 (Pedlar et al., 2015). Growing season length in China increased by at least 1.0 days per decade since 1960 (Xia et al., 2018) and by several days per decade in South Korea since 1970 (Jung et al., 2015). In general, changes in phenological indicators are consistent with the increase in growing season length documented by instrumental data (Parmesan and Hanley, 2015). Several long-term, site-specific records illustrate the unusualness of recent phenological changes relative to

ACCEPTED VERSION SUBJECT TO FINAL EDITS

interannual variability; for example, peak bloom dates for cherry blossoms in Kyoto, Japan have occurred progressively earlier in the growing season in recent decades, as have grape harvest dates in Beaune, France (Figure 2.32).

[START FIGURE 2.32 HERE]

Figure 2.32: Phenological indicators of changes in growing season. (a) cherry blossom peak bloom in Kyoto, Japan; (b) grape harvest in Beaune, France; (c) spring phenology index in eastern China; (d) full flower of Piedmont species in Philadelphia, USA; (e) Grape harvest in Central Victoria, Australia; (f) start of growing season in Tibetan Plateau, China. Red lines depict the 25-year moving average (top row) or the 9-year moving average (middle and bottom rows) with the minimum roughness boundary constraint of Mann (2004). Further details on data sources and processing are available in the chapter data table (Table 2.SM.1).

[END FIGURE 2.32 HERE]

Changes in the length of the photosynthetically active growing season (derived from the Normalised Difference Vegetation Index (NDVI)) are also evident over many land areas since the early 1980s. Increases of about 2.0 days per decade are apparent north of 45°N since the early 1980s (centred over mid-latitude Eurasia and north-eastern North America), with indications of a reversal to a decline in season length starting in the early 2000s (Barichivich et al., 2013; Garonna et al., 2016; Liu Q. et al., 2016; Park et al., 2016; Zhao J. et al., 2015). Satellite-based records suggest that most NH regions have experienced both an earlier start and a later end to the growing season, a finding supported by ground-based data (Piao et al., 2020). A number of studies also capture increases in growing season length over the Canadian Arctic (Chen, 2016), Fennoscandia (Hogda et al., 2013), most of Europe (Garonna et al., 2014), and parts of sub-Saharan Africa (Vrieling et al., 2013).

The general consistency between in situ and satellite estimates over the NH is noteworthy given that many factors independently contribute to uncertainty in observed changes. For example, there is no universally accepted definition of growing season length across in situ analyses; some define the growing season as the period based on a temperature threshold (e.g., 5°C) whereas others use the frost-free period. Spatial and temporal coverage can also affect conclusions based upon in situ studies (Donat et al., 2013). For satellite analyses, uncertainties can be related to the satellite datasets themselves (e.g., satellite drift, sensor differences, calibration uncertainties, atmospheric effects); and to the methods for determining phenological metrics (e.g., start, end, and length of season) (Wang S. et al., 2016).

In summary, based on multiple independent analyses of in situ, satellite, and phenological data, there is *high confidence* that the length of the growing season has increased over much of the extratropical NH since at least the mid-20th century.

2.3.4.3.2 Terrestrial ecosystems

AR5 WGII concluded that many terrestrial species have shifted their geographic ranges in recent decades (*high confidence*). Similarly, SRCCL assessed that many land species have experienced range size and location changes as well as altered abundances over recent decades (*high confidence*). SROCC noted that species composition and abundance have markedly changed in high mountain ecosystems in recent decades (*very high confidence*).

Paleoclimate reconstructions document large-scale biome shifts from the deep past through the Holocene (e.g., Hoogakker et al., 2016). The northernmost location of the treeline is a representative indicator in this regard (Figure 2.34). During the MPWP, boreal forest extended to the Arctic coast, with the northernmost treeline being about 4° to 10° latitude further north than at present; temperate forests and grasslands were also shifted poleward (with reduced tundra extent), while savannahs and woodlands were more expansive in Africa and Australia at the expense of deserts (Salzmann et al., 2008, 2013; Sniderman et al, 2016; Andrae et

ACCEPTED VERSION SUBJECT TO FINAL EDITS

al., 2018) (Cross-Chapter Box 2.4 Figure 1b). During the LGM, tundra and steppe expanded whereas forests were globally reduced in extent (Binney et al., 2017; Prentice et al., 2000), the northern treeline being about 17° to 23° latitude south of its present day location in most areas. During the LDT, pervasive ecosystem transformations occurred in response to warming and other climatic changes (Nolan et al., 2018; Fordham et al., 2020). By the MH, North Africa had experienced a widespread conversion from grasslands to desert (Hoelzmann et al., 1998; Prentice et al., 2000; Sha, 2019), and the northernmost treeline had shifted poleward again to about 1° to 3° latitude north of its current location (Binney et al., 2009; MacDonald et al., 2000; Williams et al., 2011). Over the past half century, there has been an increase in the spatial synchrony of annual tree growth across all continents that is unprecedented during the past millennium (Manzanedo et al., 2020). Elevated rates of vegetation change in the Holocene are consistent with climate variability (Shuman et al., 2019), intensified human land use (Fyfe et al., 2015; Marquer et al., 2017c), and resulting increased ecosystem novelty (Finsinger et al., 2017; Burke et al., 2019).

Long-term ecological records capture extensive range shifts during the 20th and early 21st centuries (Lenoir & Svenning, 2015; Pecl et al., 2017). Research has been most extensive for North America and western Eurasia, with fewer studies for central Africa, eastern Asia, South America, Greenland, and Antarctica (Lenoir & Svenning, 2015). Most documented changes are toward cooler conditions - i.e., poleward and upslope (Lenoir et al., 2008; Harsch et al., 2009; Elmendorf et al., 2015; Parmesan and Hanley, 2015; Evans and Brown, 2017). Notably, a large, quasi-global analysis (Chen et al., 2011) estimated that many insect, bird, and plant species had shifted by 17 (± 3) km per decade toward higher latitudes and 11 (± 2) m per decade toward higher elevations since the mid-20th century, with changes in both the leading and trailing edges of species ranges (Rumpf et al., 2018). Over the past century, long-term ecological surveys also show that species turnover (i.e., the total number of gains and losses of species within an area) has significantly increased across a broad array of ecosystems (Dornelas et al., 2014; 2019), including undisturbed montane areas worldwide (Gibson-Reinemer et al., 2015). Despite global losses to biodiversity, however, most local assemblages have experienced a change in biodiversity rather than a systematic loss (Pimm et al., 2014). With increased species turnover, the novelty of contemporary communities relative to historical baselines has risen (Hobbs et al., 2009; Radeloff et al., 2015) due to greater spatial homogenization, mixtures of exotic and native species, altered disturbance regimes, and legacies of current or historic land use (Olden and Rooney, 2006; Schulte et al., 2007; Thompson et al., 2013; Goring et al., 2016). In general, terrestrial species have had lower rates of turnover than marine species (Dornelas et al., 2018; Blowes et al., 2019).

There are exceptions to the general pattern of poleward / upslope migration. For some species, various biotic and abiotic factors (such as precipitation and land use) supersede the physiological effects of temperature (Vanderwal et al., 2013; Gibson-Reinemer and Rahel, 2015; Ordonez et al., 2016; Scheffers et al., 2016; Lenoir et al., 2020). For other species, poleward migration is slower than expectations from the observed temperature increases. Trees are one such example because of their long lifespan and gradual maturity (Renwick and Rocca, 2015); in fact, poleward advance is only evident at about half of the sites in a large global dataset of treeline dynamics for 1900-present (Harsch et al., 2009b). Furthermore, the northernmost extent of treeline at present (roughly 73°N) is actually somewhat south of its location in the MH (MacDonald et al., 2008) despite an expanding growing season in the extratropical NH since the mid-20th century (Section 2.3.4.3.1).

Consistent with species range shifts, SRCCL noted that there have been changes in the geographical distribution of climate zones. Poleward shifts in temperate and continental climates are evident across the globe over 1950–2010, with decreases in the area (and increases in the average elevation) of polar climates (Chan and Wu, 2015). Zonal changes towards higher latitudes in winter plant hardiness regions are apparent since the 1970s over the central and eastern United States, with elevational changes also being important in the western united states (Daly et al., 2012). A clear northward shift in winter plant hardiness zones is detectable across western Canada since 1930, with somewhat lesser changes in the south eastern part of the country (McKenney et al., 2014). A northward migration of agro-climate zones is also evident over Europe since the mid-1970s (Ceglar et al., 2019). In addition, a shift toward more arid climate zones is apparent in some areas, such as the Asian monsoon region (Son and Bae, 2015) as well as parts of South America and Africa (Spinoni et al., 2015).

ACCEPTED VERSION SUBJECT TO FINAL EDITS

In summary, there is *very high confidence* that many terrestrial species have shifted their geographic ranges poleward and/or upslope over the past century, with increased rates of species turnover. There is *high confidence* that the geographical distribution of climate zones has shifted in many parts of the world.

2.3.4.3.3 Global greening and browning

AR5 WGII briefly discussed changes in global vegetation greenness derived from satellite proxies for photosynthetic activity. Observed trends varied in their strength and consistency, and AR5 thus made no confidence statement on observed changes. SRCCL subsequently concluded that greening had increased globally over the past 2–3 decades (*high confidence*).

Vegetation index data derived from AVHRR and MODIS depicts increases in aspects of vegetation greenness (i.e., green leaf area and/or mass) over the past four decades (Piao et al., 2020). NDVI increased globally from the early 1980s through the early 2010s (Liu et al., 2015c). Pan et al. (2018a) found NDVI increases over about 70% of the Earth's vegetated surface through 2013, and Osborne et al. (2018) noted strong upward changes in NDVI in the circumpolar Arctic through 2016. Globally integrated Leaf Area Index (LAI) also rose from the early 1980s through at least the early 2010s (Zhu et al., 2016; Forzieri et al., 2017; Jiang et al., 2017; Xiao et al., 2017) and probably through near-present; for example, Chen et al. (2019) documented an LAI increase over one-third of the global vegetated area from 2000–2017. Although less frequently analysed for temporal trends, Fraction of Absorbed Photosynthetically Active Radiation (FAPAR) likewise increased over many global land areas (particularly China, India, and Eastern Europe) in the past two decades (Figure 2.33) (Forkel et al., 2014; Gobron, 2018; Keenan & Riley, 2018). There are also documented changes in specific vegetation types, such as a 7% rise in global tree cover for 1982–2016 (Song et al., 2018) and an expansion of shrub extent in the Arctic tundra over 1982–2017 (Myers-Smith et al., 2020). The increased greening is largely consistent with CO_2 fertilization at the global scale, with other changes being noteworthy at the regional level (Piao et al., 2020); examples include agricultural intensification in China and India (Chen et al., 2019; Gao et al., 2019) and temperature increases in the northern high latitudes (Kong et al., 2017; Keenan and Riley, 2018) and in other areas such as the Loess Plateau in central China (Wang et al., 2018). Notably, some areas (such as parts of Amazonia, central Asia, and the Congo basin) have experienced browning (i.e., decreases in green leaf area and/or mass) (Anderson et al., 2019; Gottschalk et al., 2016; Hoogakker et al., 2015). Because rates of browning have exceeded rates of greening in some regions since the late 1990s, the increase in global greening has been somewhat slower in the last two decades (Pan et al., 2018a).

[START FIGURE 2.33 HERE]

Figure 2.33: Satellite-based trends in Fraction of Absorbed Photosynthetically Active Radiation (per decade) for 1998–2019. Trends are calculated using OLS regression with significance assessed following AR(1) adjustment after Santer et al (2008c) ('x' marks denote non-significant trend). Unvegetated areas such as barren deserts (grey) and ice sheets (white) have no trend in FAPAR. Further details on data sources and processing are available in the chapter data table (Table 2.SM.1).

[END FIGURE 2.33 HERE]

Global-scale linear trends differ substantially across products for the same periods and trend metrics used (Jiang et al., 2017). Several factors contribute to this large span in estimated changes. Remotely sensed vegetation products vary in their spatial and temporal completeness as well as resolution and are sensitive to contamination from atmospheric composition, clouds, snow cover, and anisotropy, as well as orbital changes and sensor degradations (de Jong et al., 2012; Zhu et al., 2016; Jiang et al., 2017; Xiao et al., 2017; Pan et al., 2018a). Ground-based measurements suitable for calibration and validation are scarce before 2000 (Xiao et al., 2017), and the recalibration of satellite records (e.g., as in from MODIS Collection 5 to 6) can affect trends (Piao et al., 2020). It is possible that the increase in greenness over 2000–2015 is larger than the increase in gross primary production (based on flux tower measurements and MODIS Collection 6 data) (Zhang L. et al., 2018). Land use changes and altered disturbance regimes (e.g. floods, fires, diseases) may

ACCEPTED VERSION SUBJECT TO FINAL EDITS

mask large-scale signals (Franklin et al., 2016). In addition, there is a plethora of models for the identification of phenological metrics from satellite data as well as a variety of statistical techniques for analysing historical changes (Wang et al., 2016).

In summary, there is *high confidence* that vegetation greenness (i.e., green leaf area and/or mass) has increased globally since the early 1980s. However, there is *low confidence* in the magnitude of this increase owing to the large range in available estimates.

2.3.5 Synthesis of evidence for past changes

Section 2.3 has assessed the observational evidence for changes in key indicators across the atmosphere, cryosphere, ocean and biosphere starting, where applicable, from paleoclimate proxy records and coming up to the present day. This synthesis serves as an assessment of the evidence for change across the climate system as represented by the instrumental record and its unusualness in the longer-term context. Building upon previous sections assessing the observational evidence for each key indicator individually, this section integrates the evidence across multiple indicators to arrive at a holistic and robust final assessment.

Climate has varied across a broad range of timescales (Figure 2.34). During the Cenozoic Era temperatures generally decreased over tens of millions of years, leading to the development of ice sheets. During the last two million years, climate has fluctuated between glacials and interglacials. Within the current Holocene interglacial and, with increasing detail in the CE, it is possible to reconstruct a history both of more indicators of the climate system and, with increasing fidelity, the rates of change. Solely for the last 150 years or so are instrumental observations of globally distributed climate indicators available. However, only since the late 20th century have observational systems attained essentially global monitoring capabilities. The direct observations point unequivocally to rapid change across many indicators of the climate system since the mid-19th century. These are all consistent in indicating a world that has warmed rapidly.

Assessing the long-term context of recent changes is key to understanding their potential importance and implications. The climate system consists of many observable aspects that vary over a very broad range of timescales. Some biogeochemical indicators of change such as atmospheric CO_2 concentrations and ocean pH have shifted rapidly and CO_2 concentrations are currently at levels unseen in at least 800 kyr (the period of continuous polar ice-core records) and *very likely* for millions of years. The GMST in the past decade is *likely* warmer than it has been on a centennially-averaged basis in the CE and *more likely than not* since the peak of the LIG. Many more integrative components of the climate system (e.g., glaciers, GMSL) are experiencing conditions unseen in millennia, whereas the most slowly responding components (e.g. ice-sheet extent, permafrost, tree line) are at levels unseen in centuries (*high confidence*). The rate at which several assessed climate indicators (e.g., GMSL, OHC, GSAT) have changed over recent decades is highly unusual in the context of preceding slower changes during the current post-glacial period (*high confidence*).

In summary, directly observed changes in the atmosphere, ocean, cryosphere and biosphere are unequivocal evidence of a warming world. Key climate indicators are now at levels not experienced for centuries to millennia. Since the late 19th century many indicators of the global climate system have changed at a rate unprecedented over at least the last two thousand years.

[START FIGURE 2.34 HERE]

Figure 2.34: Selected large-scale climate indicators during paleoclimate and recent reference periods of the Cenozoic Era. Values are based upon assessments carried out in this chapter, with *confidence* levels ranging from *low* to *very high*. Refer to Cross-Chapter Box 2.1 for description of paleoclimate reference periods and Section 1.4.1 for recent reference periods. Values are reported as either the *very likely* range (x to y), or best estimates from beginning to end of the reference period with no stated uncertainty (x → y), or lowest and highest values with no stated uncertainty (x ~ y). Temperature is global mean surface temperature. Glacier extent is relative and colour scale is inverted so that more extensive glacier extent is intuitively blue.

ACCEPTED VERSION SUBJECT TO FINAL EDITS

[END FIGURE 2.34 HERE]

[START CROSS-CHAPTER BOX 2.4 HERE]

Cross-Chapter Box 2.4: The climate of the Pliocene (around 3 million years ago), when CO_2 concentrations were last similar to those of present day

Contributing Authors: Alan Haywood (UK), Darrell Kaufman (USA), Nicholas Golledge (New Zealand), Dabang Jiang (China), Daniel Lunt (UK), Erin McClymont (UK), Ulrich Salzmann (UK), Jessica Tierney (USA)

Throughout this Report, information about past climate states is presented in the context of specific climate variables, processes or regions. This Cross-Chapter Box focuses on a single paleoclimate reference period as an example of how proxy data, models and process understanding come together to form a more complete representation of a warm climate state that occurred during the relatively recent geologic past.

Introduction. The Pliocene Epoch is one of the best-documented examples of a warmer world during which the slow responding components of the climate system were approximately in balance with concentrations of atmospheric CO_2, similar to present (e.g., Haywood et al., 2016). It provides a means to constrain Earth's equilibrium climate sensitivity (Section 7.5.3) and to assess climate model simulations (Section 7.4.4.1.2). During the Pliocene, continental configurations were similar to present (Cross-Chapter Box 2.4 Figure 1a), and many plant and animal species living then also exist today. These similarities increase reliability of paleo-environmental reconstructions compared with those for older geological periods. Within the well-studied mid-Pliocene Warm Period (MPWP, also called the mid-Piacenzian Warm Period, 3.3–3.0 Ma), the interglacial period KM5c (3.212–3.187 Ma) has become a focus of research because its orbital configuration, and therefore insolation forcing, was similar to present (global mean insolation = –0.022 W m^{-2} relative to modern; Haywood et al., 2013), allowing for the climatic state associated with relatively high atmospheric CO_2 to be assessed with fewer confounding variables.

Major global climate indicators. During the KM5c interglacial, atmospheric CO_2 concentration was typically between 360 and 420 ppm (Section 2.2.3.1). New climate simulations of this interval from the Pliocene Model Intercomparison Project Phase 2 (PlioMIP2) show a multi-model mean global surface air temperature of 3.2°C [2.1–4.8] °C warmer than control simulations (Haywood et al., 2020; Cross-Chapter Box 2.4 Figure 1a). This is consistent with proxy evidence for the broader MPWP, which indicates that global mean surface temperature was 2.5°C–4.0°C higher than 1850–1900 (Section 2.3.1.1.1). Global mean sea level was between 5 and 25 m higher than present (Section 2.3.3.3). Geological evidence (Section 2.3.2.4) and ice-sheet modelling (Section 9.6.2) indicate that both the Antarctic and Greenland Ice Sheets were substantially smaller than present (Cross-Chapter Box 2.4 Figure 1c). Attribution of sea level highstands to particular ice sheet sources (Section 9.6.2) is challenging (DeConto & Pollard, 2016; Golledge, 2020), but improving (Berends et al., 2019; Grant et al., 2019).

Northern high latitudes. The latitudinal temperature gradient during the MPWP was reduced relative to present-day and the consistency between proxy and modelled temperatures has improved since AR5 (Section 7.4.4.1.2). Northern high latitude (> 60°N) SSTs were up to 7°C higher than 1850–1900 (Bachem et al., 2016; McClymont et al., 2020; Sánchez-Montes et al., 2020), and terrestrial biomes were displaced poleward (e.g., Dowsett et al., 2019) (Cross-Chapter Box 2.4, Figure 1b). Arctic tundra regions currently underlain by permafrost were warm enough to support boreal forests, which shifted northward by approximately 250 km in Siberia, and up to 2000 km in the Canadian Arctic Archipelago (Fletcher et al., 2017; Salzmann et al., 2013). The shift caused high-latitude surface albedo changes, which further amplified the Pliocene global warming (Zhang & Jiang, 2014). Vegetation changes in northeast Siberia indicate that MPWP summer temperatures were up to 6°C higher than present day (Brigham-Grette et al., 2013). Farther south, modern boreal forest regions in Russia and eastern North America were covered with temperate forests and grasslands, whereas highly diverse, warm-temperate forests with subtropical taxa were widespread in central

ACCEPTED VERSION SUBJECT TO FINAL EDITS

and eastern Europe (Cross-Chapter Box 2.4, Figure 1). While seasonal sea ice was present in the North Atlantic and Arctic oceans, its winter extent was reduced relative to present (Knies et al., 2014; Clotten et al., 2018), and some models suggest that the Arctic was sea ice free during the summer (Feng et al., 2020; Howell et al., 2016).

Tropical Pacific. The average longitudinal temperature gradient in the tropical Pacific was weaker during the Pliocene than during 1850–1900 (Section 7.4.4.2.2). Changes in Pacific SSTs and SST gradients had far-reaching impacts on regional climates through atmospheric teleconnections, affecting rainfall patterns in western North America (Burls & Fedorov, 2017; Ibarra et al., 2018). The reduced zonal SST gradient has led some to propose that the Pliocene Pacific experienced a "permanent El Niño" state (Molnar and Cane, 2002; Fedorov, 2006). However, there is no direct geological evidence, nor support from climate models, that ENSO variability collapsed during the Pliocene. Although not located in the centre-of-action region for ENSO, Pliocene corals show temperature variability over 3–7 year timescales (Watanabe et al., 2011). In addition, a multi-model intercomparison indicates that ENSO existed, albeit with reduced variability (Brierley, 2015). Thus, there is *high confidence* that ENSO variability existed during the Pliocene.

Hydrological cycle. Vegetation reconstructions for the late Pliocene indicate regionally wetter conditions resulting in an expansion of tropical savannas and woodlands in Africa and Australia at the expense of deserts (Cross-Chapter Box 2.4, Figure 1b). PlioMIP2 climate models generally simulate higher rates of mean annual precipitation in the tropics and high latitudes, and a decrease in the subtropics, with a multi-model mean global increase of 0.19 mm day^{-1} [0.13–0.32 mm day^{-1}] relative to control simulations (Haywood et al., 2020) (Cross-Chapter Box 2.4, Figure 1a). Both simulations and *limited* proxy *evidence* indicate stronger monsoons in northern Africa, Asia, and northern Australia relative to present, but trends are uncertain in other monsoon regions (Huang X. et al., 2019; Li X. et al., 2018; Yang et al., 2018; Zhang et al., 2019). There is thus *medium confidence* that monsoon systems were stronger during the Pliocene. Simulations of MPWP climate show that global tropical cyclone intensity and duration increased during the MPWP (Yan et al., 2016); however, there is *low confidence* in this result because inter-model variability is high.

Summary. During the MPWP (3.3–3.0 Ma) the atmospheric CO_2 concentration was similar to present, and the slow-response, large-scale indicators reflect a world that was warmer than present. With *very high confidence*, relative to present, global surface temperature, sea level, and precipitation rate were higher, NH latitudinal temperature gradient was lower, and major terrestrial biomes expanded poleward. With *medium confidence* from proxy-based evidence alone (Section 2.3.2), combined with numerical modelling, analysis of the sea-level budget, and process understanding (Section 9.6.2), there is *high confidence* that cryospheric indicators were diminished. There is *medium confidence* that the Pacific longitudinal temperature gradient was weaker and monsoon systems were stronger.

[START CROSS-CHAPTER BOX 2.4, FIGURE 1 HERE]

Cross-Chapter Box 2.4, Figure 1: Climate indicators of the mid-Pliocene Warm Period (3.3–3.0 Ma) from models and proxy data. (a) Simulated surface air temperature (left) and precipitation rate anomaly (right) anomaly (relative to 1850–1900) from the Pliocene Model Intercomparison Project Phase 2 multi-model mean, including CMIP6 (n = 4) and non-CMIP6 (n = 12) models. Symbols represent site-level proxy-based estimates of sea-surface temperature for KM5c (n = 32), and terrestrial temperature (n = 8) and precipitation rate for the MPWP (n = 8). (b) Distribution of terrestrial biomes was considerably different during the Piacenzian Stage (3.6–2.6 Ma) (upper) compared with present-day (lower). Biome distributions simulated with a model (BIOME4) in which Pliocene biome classifications are based on 208 locations, with model-predicted biomes filling spatial gaps, and the present day, with the model adjusted for CO_2 concentration of 324 ppm. (c) Ice-sheet extent predicted using modelled climate forcing and showing where multiple models consistently predict the former presence or absence of ice on Greenland (n = 8 total) and Antarctica (n = 10 total). Further details on data sources and processing are available in the chapter data table (Table 2.SM.1).

ACCEPTED VERSION SUBJECT TO FINAL EDITS

[END CROSS-CHAPTER BOX 2.4, FIGURE 1 HERE]

[END CROSS-CHAPTER BOX 2.4 HERE]

2.4 Changes in modes of variability

Modes of climate variability that are important for large-scale climate on interannual and longer timescales (Cross-Chapter Box 2.2) are assessed herein and defined and summarised in Annex IV. Though the modes of variability discussed here are assessed and classified on the basis of physical variables, it is important to recognise that the distribution and function of various components of the terrestrial and marine biospheres are modified in response to them.

2.4.1 Annular modes

2.4.1.1 Northern Annular Mode (NAM) / North Atlantic Oscillation (NAO)

AR5 reported that the shift towards a positive NAO, a mode of variability in the North Atlantic that is closely related to the hemispheric-scale NAM, from the 1950s to the 1990s was largely reversed by more recent changes (*high confidence*). Moreover, periods of persistent negative or positive NAO states observed during the latter part of the 20th century were not unusual, based on NAO reconstructions spanning the last half millennium (*high confidence*).

New multi-millennial-timescale NAO reconstructions are derived from marine and lake sediments, speleothems, tree rings and ice cores (Ortega et al., 2015; Faust et al., 2016; Sjolte et al., 2018). NAO variability over the past 8 kyr suggests the presence of a significant 1.5 kyr periodicity (Darby et al., 2012). Positive NAO conditions dominated during the MH, while the prevailing NAO sign during the early and late Holocene was negative according to most reconstructions (Brahim et al., 2019; Hernández et al., 2020; Olsen et al., 2012; Røthe et al., 2019). For the CE, reconstructions developed since AR5 indicate no dominant NAO phase during 1000–1300 CE (Baker et al., 2015; Hernández et al., 2020; Jones et al., 2014; Lasher & Axford, 2019; Ortega et al., 2015), with either negative (Baker et al., 2015; Faust et al., 2016; Mellado-Cano et al., 2019) or a more variable phase of the NAO (Jones et al., 2014; Ortega et al., 2015; Sjolte et al., 2018; Cook et al., 2019) between 1400 and 1850 CE. Several instrument-based NAO reconstructions extending back to the 17th and 18th centuries highlight the presence of multidecadal variations in the NAO phases (Cornes et al., 2013; Cropper et al., 2015), although these studies have limitations considering the seasonality of the centres of action and the locations of the stations used. Recent reconstructions of the large scale sea level pressure field yield more robust NAO analysis, showing a persistently negative NAO phase from the 1820s to the 1870s, with positive values dominating during the beginning of the 20th century followed by a declining trend over 1920–1970, with a recovery thereafter to a period of consistently high values between 1970 and the early 1990s (Delaygue et al., 2019; Mellado-Cano et al., 2019). Based on the evaluation of several NAO reconstructions for recent centuries, Hernández et al. (2020) highlighted that the strong positive NAO phases of the 1990s and early 21st century were not unusual.

The predominantly positive phase during the 1990s was followed by partial reversal and a tendency towards stronger variability in boreal winter NAM and NAO since the late 1990s (Hanna et al., 2018; Pinto & Raible, 2012). This is particularly evident in December NAO (Hanna et al., 2015) and NAM (Overland and Wang, 2015) indices, and is not unusual on multidecadal time scales (Woollings et al., 2018a). Since the 1990s, a statistically significant summer NAO decline was reported, which is, to a lesser extent, also evident in the winter NAO, linked to an enhanced blocking activity over Greenland (Hanna et al., 2015; 2016; Wachowicz et al., 2021). However, this was moderated by a persistent positive NAO values since 2015 (Annex IV 2.1). Based on observations and reanalysis datasets, multidecadal fluctuations were found for the NAM patterns: the Atlantic centre remained unchanged throughout 1920–2010, whereas the Pacific centre was stronger during 1920–1959 and 1986–2010 and weaker during 1960–1985 (Gong et al., 2018). Multidecadal changes were also observed in the position of the centres of action of the NAO (Moore et al., 2013; Zuo et al., 2016).

ACCEPTED VERSION SUBJECT TO FINAL EDITS

In summary, positive trends for the NAM / NAO winter indices were observed between the 1960s and the early 1990s, but these indices have become less positive or even negative thereafter (*high confidence*). The NAO variability in the instrumental record was *very likely* not unusual in the millennial and multi-centennial context.

2.4.1.2 Southern Annular Mode (SAM)

AR5 concluded that it was *likely* that the SAM had become more positive since the 1950s and that this increase was unusual in the context of the prior 400 years (*medium confidence*). Both AR5 and SROCC reported statistically significant trends in the SAM during the instrumental period for the austral summer and autumn.

Several studies have attempted to reconstruct the evolution of the SAM during the Holocene using proxies of the position and strength of the zonal winds, although with no clear consensus regarding the timing and phase of the SAM (Hernández et al., 2020). The early Holocene was dominated by SAM positive phases (Moreno et al., 2018; Reynhout et al., 2019), consistent with increasing westerly wind strength (Lamy et al., 2010), with some reconstructions showing significant centennial and millennial variability but no consistent trend after 5 ka (Hernández et al., 2020). For the CE, enhanced westerly winds occurred over 0–1000 CE, as reflected in increased burning activity in Patagonia (Turney et al., 2016a) and tree ring records from southern New Zealand (Turney et al., 2016b), imply a predominantly positive SAM phase. Pollen records and lake sediments from Tasmania, southern mainland Australia, New Zealand and southern South America, inferred the period of 1000 to 1400 CE to be characterized by anomalously dry conditions south of 40°S, implying a positive SAM (Evans et al., 2019; Fletcher et al., 2018; Matley et al., 2020; Moreno et al., 2014). Nevertheless, proxy reconstructions of the SAM based on temperature-sensitive records from tree rings, ice cores, lake sediments and corals spanning the mid-to-polar latitudes show altering positive and negative phases (Figure 2.35).

Prolonged periods of negative SAM values were identified during the period 1400–1700 CE in several reconstructions (Figure 2.35, Abram et al., 2014; Dätwyler et al., 2018; Villalba et al., 2012), with a minimum identified during the 15th century (Hernández et al., 2020), although some disagreements exist between proxy records before 1800 CE (Hessl et al., 2017). Abram et al. (2014) concluded that the mean SAM index during recent decades is at its highest levels for at least the last 1 kyr. Similarly, the summer SAM reconstruction by Dätwyler et al. (2018) indicates a strengthening over the last 60 years that is outside the *very likely* range of the last millennium natural variability. The largest 30- and 50-year trends in the annual SAM index occurred at the end of the 20th century (after 1969 and 1950 respectively), indicating that the recent increase in the SAM is unprecedented in the context of at least the past three centuries (Yang & Xiao, 2018).

Before the mid-1950s, SAM indices derived from station-based datasets, and centennial reanalyses show pronounced interannual and decadal variability but no significant trends, with low correlation between SAM indices due to the diversity across different datasets and sensitivity to the definition used for the index calculation (Barrucand et al., 2018; Lee J. et al., 2019a; Schneider & Fogt, 2018). Various SAM indices exhibit significant positive trends since the 1950s, particularly during austral summer and autumn (Barrucand et al., 2018; Lee J. et al., 2019a; Schneider & Fogt, 2018), unprecedented for austral summer over the last 150 years (Fogt & Marshall, 2020; Jones et al., 2016b). This indicates a strengthening of the surface westerly winds around Antarctica, related to both the position and intensity of the subpolar jet in the SH (IPCC, 2019b; Ivy et al., 2017) (Section 2.3.1.4.3). The SAM trends have slightly weakened after about 2000 (Fogt and Marshall, 2020).

[START FIGURE 2.35 HERE]

Figure 2.35: Southern Annular Mode (SAM) reconstruction over the last millennium. (a) SAM reconstructions as 7-year moving averages (thin lines) and 70-year LOESS filter (thick lines). (b) observed SAM index

ACCEPTED VERSION SUBJECT TO FINAL EDITS

during 1900–2019. Further details on data sources and processing are available in the chapter data table (Table 2.SM.1).

[END FIGURE 2.35 HERE]

In summary, historical station-based reconstructions of the SAM show that there has been a robust positive trend in the SAM index, particularly since 1950 and for the austral summer (*high confidence*). The recent positive trend in the SAM is *likely* unprecedented in at least the past millennium, although *medium confidence* arises due to the differences between proxy records before 1800 CE.

2.4.2 El Niño-Southern Oscillation (ENSO)

AR5 reported with *medium confidence* that ENSO-like variability existed, at least sporadically, during the warm background state of the Pliocene. It was also found (*high confidence*) that ENSO has remained highly variable during the last 7 kyr with no discernible orbital modulation. AR5 concluded that large variability on interannual to decadal timescales, and differences between datasets, precluded robust conclusions on any changes in ENSO during the instrumental period. SROCC reported epochs of strong ENSO variability throughout the Holocene, with no indications of a systematic trend in ENSO amplitude, but with some indication that the ENSO amplitude over 1979–2009 was greater than at any point in the period from 1590–1880 CE. It was also reported that the frequency and intensity of El Niño events in the period from 1951–2000 was high relative to 1901–1950.

Manucharyan and Fedorov (2014) found that ENSO-like variability has been present, at least sporadically, during epochs of millions of years (including the MPWP; Cross-Chapter Box 2.4), with proxy records indicating that this was the case even when cross-Pacific SST gradients were much weaker than present. There is substantial disagreement between proxy records for ENSO activity during the early Holocene (White et al., 2018; Zhang et al., 2014), and for ENSO activity and mean state at the LGM (Ford et al., 2015,2018; Koutavas & Joanides, 2012; Leduc et al., 2009; Sadekov et al., 2013; Tierney et al., 2020; Zhu et al., 2017). A number of studies (Carré et al., 2014; Cobb et al., 2013; Emile-Geay et al., 2016; Grothe et al., 2019; McGregor H. et al., 2013; Thompson et al., 2017; Tian et al., 2017; White et al., 2018) have found that ENSO was substantially weaker than at present at various times in the mid-Holocene within the period from 6 to 3 ka, with stronger decreases in variability revealed by remote proxies than by those close to the core region of ENSO activity. However, Karamperidou et al. (2015) find that weakening in ENSO-related variability in eastern Pacific proxies does not necessarily correspond to weakening in central Pacific proxies. Barrett et al. (2018) concluded that multi-proxy reconstructions are more efficient at identifying eastern Pacific than central Pacific events. This suggests that a weakening of proxy-based signals may indicate an along-equatorial shift in ENSO activity rather than a weakening of ENSO during some periods. Following the period of weak ENSO variability in the mid-Holocene, a number of studies find an increase in ENSO activity which, depending upon the study, commences between 4.4 and 3 ka (Chen et al., 2016; Cobb et al., 2013; Du et al., 2021; Emile-Geay et al., 2016; Koutavas & Joanides, 2012; Thompson et al., 2017; Zhang et al., 2014).

Numerous studies (Hope et al., 2017; Li J. et al., 2013; Liu Y. et al., 2017; McGregor S. et al., 2013; Rustic et al., 2015) find substantial variability in ENSO activity on multi-decadal to centennial timescales over the last 500 to 1 kyr (Figure 2.36). Different proxies show a wide spread in the specific timing and magnitude of events in the pre-instrumental period (e.g. Dätwyler et al., 2019). Most investigators find that ENSO activity in recent decades was higher than the most recent centuries prior to the instrumental period. Grothe et al. (2019) also found that ENSO variance of the last 50 years was 25% higher than the average of the last millennium, and was substantially higher than the average of the mid- to late Holocene. McGregor S. et al., (2010, 2013) looked for common variance changes in pre-existing ENSO proxies, finding stronger ENSO variance for the 30-year period 1979–2009 compared to any 30-year period within the timespan 1590–1880 CE. This finding also holds when adding more recently developed ENSO proxies (Figure 2.36). Koutavas & Joanides (2012), Ledru et al. (2013) and Thompson et al., (2017) identify various periods within the range 1000 BCE to 1300 CE when ENSO activity was greater than in the following centuries, and more

ACCEPTED VERSION SUBJECT TO FINAL EDITS

closely comparable to the mid-20th century onwards behaviour.

[START FIGURE 2.36 HERE]

Figure 2.36: Reconstructed and historical variance ratio of El Niño–Southern Oscillation (ENSO). (a) 30-year running variance of the reconstructed annual mean Niño 3.4 or related indicators from various published reconstructions. (b) variance of June-November Southern Oscillation Index (SOI) and April-March mean Niño 3.4 (1981–2010 base period) along with the mean reconstruction from (a). Further details on data sources and processing are available in the chapter data table (Table 2.SM.1).

[END FIGURE 2.36 HERE]

Since AR5, updates to datasets used widely in prior ENSO assessments resulted in substantial and important revisions to observed tropical Pacific SST data (Section 2.3.1.1). In particular, ERSSTv4, and then ERSSTv5, addressed known SST biases in ERSSTv3 in the equatorial Pacific which affected the derived mean state and amplitude of indices based on that dataset (Huang et al., 2015). During the instrumental period, there is no robust indication of any significant century-scale trend in the east-west SST gradient across the equatorial Pacific Ocean, with periods when gradients have been stronger and weaker than the long-term average on decadal timescales, associated with a predominance of La Niña or El Niño events respectively. The frequency of El Niño and La Niña events is also subject to considerable decadal variability (e.g. Hu et al., 2013) but with no indication of a long-term signal in the frequency of events. The ENSO amplitude since 1950 has increased relative to the 1910–1950 period, as confirmed by independent proxy records (e.g., Gergis & Fowler, 2009), the Southern Oscillation Index (SOI) (Braganza et al., 2009) and SSTs (e.g., Ohba, 2013; Yu & Kim, 2013), although there is a spread between different proxy and instrumental sources as to the magnitude of that increase (Figure 2.36). The El Niño events of 1982–1983, 1997–1998 and 2015–2016 had the strongest anomalies in the Niño 3.4 SST index since 1950. Their predominance was less evident from indices based on de-trended data such as the Oceanic Niño Index (ONI) (which still ranked them as the three strongest events since 1950, but only by a small margin), and in the SOI. Huang B. et al. (2019d) also note that analyses based upon buoy and Argo data, which are only available since the 1990s, are more capable of resolving strong events than analyses which do not include such data.

Prior to the 1950s, SST observations in the tropical Pacific were much sparser and hence uncertainties in Niño indices are much larger (Huang B. et al., 2020). SOI data and some newer SST-based studies show high ENSO amplitude, comparable to the post-1950 period, in the period from the mid-late 19th century to about 1910, but proxy indicators generally indicate that the late 19th and early 20th century were less active than the late 20th century (Figure 2.36). Yu & Kim's (2013) implementation of the ONI found a number of events with the ONI above 1.5°C between 1888 and 1905, then no such events until 1972, whilst the SOI indicates comparable or stronger events to the three strongest post-1950 events in 1896 and 1905. Giese & Ray (2011) also found a number of such events between 1890 and 1920 in the SODA ocean reanalysis, corroborated further by Huang B. et al. (2020a) and Vaccaro et al. (2021), who found that the strength of the 1877–1878 event was comparable with that of the 1982–1983, 1997–1998 and 2015–2016 events. There have also been a number of strong La Niña events (e.g. 1973–1974, 1975–1976 and 2010–2011), with few clear analogues in the 1920–1970 period; the proxy-based analysis of McGregor et al. (2010) indicates that the mid-1970s La Niña period was also extreme in a multi-centennial context. There is no indication that the frequency of high-amplitude events since the 1970s reflects a long-term trend which can be separated from multi-decadal variability, given apparent presence of several high-amplitude events in the late 19th and early 20th centuries, and the relatively large uncertainty in pre-1950 SST data in the tropical Pacific region.

There is a distinction (Annex IV 2.3.1) between El Niño events centred in the eastern Pacific ('Eastern Pacific' (EP) or 'classical' events) and those centred in the Central Pacific ('Central Pacific' (CP) or 'Modoki' events), which have different typical teleconnections (e.g. Ashok et al., 2007; Capotondi et al., 2015; Ratnam et al., 2014; Timmermann et al., 2018). A number of studies, using a range of indicators, have found an increase in recent decades of the fraction of CP El Niño events, particularly after 2000 (Yu and

ACCEPTED VERSION SUBJECT TO FINAL EDITS

Kim, 2013; Lübbecke and McPhaden, 2014; Pascolini-Campbell et al., 2015; Jiang and Zhu, 2018). Johnson (2013) found that the frequency of CP El Niño events had increased (although not significantly) over the 1950–2011 period, being accompanied by a significant increase in the frequency of La Niña events with a warm (as opposed to cool) western Pacific warm pool. A coral-based reconstruction starting in 1600 CE (Freund et al., 2019) found that the ratio of CP to EP events in the last 30 years was substantially higher than at any other time over the last 400 years. Variations in the proportion of CP and EP events have also been found in earlier periods, with Carré et al. (Carré et al., 2014) finding a period of high CP activity around 7 ka.

There is no robust indication of any changes in ENSO teleconnections over multi-centennial timescales (Hernández et al., 2020) despite multi-decadal variability. Shi and Wang (2018) found that teleconnections with the broader Asian summer monsoon, including the Indian and the East Asian monsoon, were generally stable since the 17th century during the developing phase of the monsoon, and showed substantial decadal variability, but no clear trend, during the decaying phase. They also found that the weakening of teleconnections between the Indian summer monsoon and ENSO in recent decades had numerous precedents over the last few centuries. Räsänen et al. (2016) also found substantial decadal variability, but little trend, in the strength of the relationship between ENSO and monsoon precipitation in South-East Asia between 1650 and 2000. Dätwyler et al., (2019) identified a number of multi-decadal periods with apparently changed teleconnections at times over the last 400 years.

In the instrumental period, teleconnections associated with ENSO are well known to vary on decadal to multi-decadal timescales (e.g. Ashcroft et al., 2016; He et al., 2013; Jin et al., 2016; Lee & Ha, 2015; Wang Q. et al., 2019). Yun and Timmermann (2018) found that decadal variations in teleconnections between ENSO and the Indian monsoon did not extend beyond what would be expected from a stochastic process. Many observed decadal changes in teleconnections in the instrumental period are consistent with a shift to more central Pacific El Niño events (Evtushevsky et al., 2018; Yeh et al., 2018; Yu & Sun, 2018; Zhao & Wang, 2019). Effects of the PDV (Kwon et al. 2013; Wang S. et al., 2014; Dong et al., 2018) and the AMV (Kayano et al., 2019) can also modulate ENSO teleconnections, and affect the frequency of CP versus EP events (Ashok et al., 2007). Chiodi and Harrison (2015) found that teleconnections over the most recent decades are broadly consistent with those over the last 100 years. Variability in teleconnections can also occur on timescales longer than characteristic PDV timescales (e.g. Gallant et al., 2013).

In summary, there is *medium confidence* that both ENSO amplitude and the frequency of high-magnitude events since 1950 are higher than over the period from 1850 as far back as 1400, but *low confidence* that they are outside the range of variability over periods prior to 1400, or higher than the average of the Holocene as a whole. Overall, there is no indication of a recent sustained shift in ENSO or associated features such as the Walker Circulation, or in teleconnections associated with these, being beyond the range of variability on decadal to millennial timescales. A high proportion of El Niño events in the last 20–30 years has been based in the central, rather than eastern Pacific, but there is *low confidence* that this represents a long-term change.

2.4.3 Indian Ocean Basin and dipole modes

AR5 did not provide an assessment of the Indian Ocean Dipole (IOD) records based on paleo reconstructions. For the instrumental era, AR5 reported that there were no trends in the IOD behaviour. However, the strength of the Indian Ocean Basin-wide (IOB) mode, quantified by the basin-scale averaged SST index, increased in all assessed periods except 1979–2012, but the AR5 neither quantified trends nor provided a confidence statement.

For the LGM, enhanced equatorial Indian Ocean productivity in marine sediment records was associated with strengthened westerly jets, in line with a shallower central-western Indian Ocean thermocline and stronger negative IOD events (Punyu et al., 2014). The LGM Indian Ocean basin was substantially modified by the exposure of the tropical shelves (DiNezio et al., 2018) and this has been associated with an Indian Ocean "El Niño" (Thirumalai et al., 2019). Wurtzel et al. (2018) contend that during the LDT, including the

ACCEPTED VERSION SUBJECT TO FINAL EDITS

Younger Dryas event, Indian Ocean precipitation did not mirror the zonal asymmetry observed in Indian Ocean SSTs in the Holocene based upon a speleothem record from Sumatra, but instead reflected shifts in moisture transport pathways and sources. Using Seychelles corals, representing the western pole of the IOD, spanning from the MH to present, Zinke et al. (2014) identified changes in seasonality, with the lowest seasonal SST range in the MH and then again around 2 ka, while the largest seasonal range occurred around 4.6 ka and then again during the near-present (1990–2003). Reconstructions from fossil corals for the eastern Indian Ocean point to stronger negative IOD SST anomalies due to the enhanced upwelling and cooling driven by a stronger monsoon with enhanced anomalous easterly winds in the eastern Indian Ocean during the MH (Abram et al., 2020a). Niedermeyer et al. (2014) from the analysis of stable isotopes in terrestrial plant waxes, suggest that the period 6.5 ka to 4.5 ka was characterized by an anomalously positive IOD mean state. During various parts of the Holocene, periods of a mean positive IOD-like state were associated with increased IOD variability, including events that exceed the magnitude of the strongest events during the instrumental period (Abram et al., 2020b).

From the coral $\delta^{18}O$ record from the Seychelles over 1854–1994, Du et al. (2014) showed a 3–7 year dominant period associated with the IOB in response to ENSO forcing. They identified multi-decadal variability in the IOB, with more active IOB phases during 1870–1890, 1930–1955, and 1975–1992, while decadal variability in the IOB dominated during 1940–1975 (Du Y. et al., 2014). *Evidence* for changes in IOB characteristics during earlier periods (e.g., MH, LGM) is *limited*.

The role of decadal to multi-decadal variability has recently emerged as an important aspect of the IOD with many indications of the effects of Pacific Ocean processes on IOD variability through atmospheric and oceanic mechanisms (Dong et al., 2016; Jin et al., 2018; Krishnamurthy & Krishnamurthy, 2016; Zhou et al., 2017). Positive events in the 1960s and 1990s were linked to a relatively shallow eastern Indian Ocean thermocline, and a primarily negative IOD state in the 1970s and 1980s was related to a deeper thermocline (Ummenhofer et al., 2016). Positive IOD events may have increased in frequency during the second half of the 20th century (Abram et al., 2020a,b). Earlier observations of apparent changes in the frequency and / or magnitude of the IOD events are considered unreliable, particularly prior to the 1960s (Hernández et al., 2020). Although the seasonal evolution and the type of ENSO (Section 2.4.2) may influence the character of the IOD (Guo et al., 2015; Zhang et al., 2015; Fan et al., 2016), the occurrence of some IOD events may be independent of ENSO (Sun et al., 2015).

To summarize, there is *low confidence* in any multi-decadal IOD variability trend in the instrumental period due to data uncertainty especially before the 1960s. In addition to data uncertainty, understanding of the IOB variability during the instrumental period is also limited by large-scale warming of the Indian Ocean. Neither the IOD nor the IOB have exhibited behaviour outside the range implied by proxy records (*low confidence*).

[START FIGURE 2.37 HERE]

Figure 2.37: Indices of interannual climate variability from 1950–2019 based upon several sea surface temperature based data products. Shown are the following indices from top to bottom: IOB mode, IOD, Niño4, AMM and AZM. All indices are based on area-averaged annual data (see Technical Annex IV). Further details on data sources and processing are available in the chapter data table (Table 2.SM.1).

[END FIGURE 2.37 HERE]

2.4.4 Atlantic Meridional and Zonal Modes

AR5 reported no changes in the Atlantic Meridional Mode (AMM) during the 20th century or shorter periods thereof. For the Atlantic Zonal Mode (AZM), also referred as the Atlantic Niño, the AR5 reported increases during the 1950–2012 period but neither assessed trends nor provided a confidence statement. The AR5 did not assess paleo evidence for the AZM and AMM.

Paleo-reconstructions of these two modes remain rather limited. Nonetheless, the interhemispheric cross-

ACCEPTED VERSION SUBJECT TO FINAL EDITS

equatorial SST gradients linked to changes in ITCZ locations characteristic of the AMM has been found during the LGM, Heinrich Stadial 1 and the MH, with the largest shift occurring during HS1 (McGee et al., 2014). Similarly, the dipole-like SST pattern in the South Atlantic subtropics, which is related to the AZM (Foltz et al., 2019; Lübbecke et al., 2018; Morioka et al., 2011; Nnamchi et al., 2016, 2017; Rouault et al., 2018; Venegas et al., 1996), has been reconstructed using SST proxies from marine sediment cores during the past 12 kyr (Wainer et al., 2014). The reconstructed index captures two significant cold events that occurred during the 12.9–11.6 ka and 8.6–8.0 ka periods in the South Atlantic (Wainer et al., 2014).

During the observational period the AZM and AMM (Figure 2.37) are related to the AMV largely controlling the interhemispheric gradient of the SST at decadal to multi-decadal timescales (Li et al., 2015; Lübbecke et al., 2018; Polo et al., 2013; Svendsen et al., 2014; Tokinaga & Xie, 2011). The AZM interannual variability is enhanced (Foltz et al., 2019; Lübbecke et al., 2018), and is more strongly related to ENSO during the negative phase of the AMV (Martín-Rey et al., 2014, 2018; Polo et al., 2015; Nnamchi et al., 2020). The AZM displayed a persistent weakened variability over the 1960–2009 period associated with declined cold tongue upwelling (Tokinaga and Xie, 2011), which became pronounced since 2000 (Prigent et al., 2020a,b). Despite these multi-decadal fluctuations, there is *limited evidence* for any sustained change in the AMM (Chang et al., 2011; Martín-Rey et al., 2018) and AZM (Martín-Rey et al., 2018; Nnamchi et al., 2020) during the instrumental period. The AZM and AMM interact on interannual timescales (Foltz & McPhaden, 2010; Pottapinjara et al., 2019; Servain et al., 1999) leading in 2009 to extremes of both modes in which the negative phase of the AMM (Burmeister et al., 2016) (Foltz et al., 2012) preceded an equatorial cold tongue cold event that was unprecedented in the prior 30 years (Burmeister et al., 2016; Foltz & McPhaden, 2010).

In summary, *confidence* is *low* in any sustained changes to the AZM and AMM variability in instrumental observations. There is *very low confidence* in changes of the paleo AZM and AMM due to extremely limited availability of paleo reconstructions.

2.4.5 Pacific Decadal Variability

Pacific Decadal Variability (PDV) refers to the ocean-atmosphere climate variability over the Pacific Ocean at decadal-to-interdecadal time scales and is usually described by the Pacific Decadal Oscillation (PDO) or the Interdecadal Pacific Oscillation (IPO) indices. AR5 and SROCC reported a large shift of the PDO in the late 1970s, with a predominantly positive phase until the end of the 1990s, being mainly negative afterwards. There was no significant change assessed in the PDO during the instrumental period as a whole, and no confidence level was assigned. Changes in the pre-instrumental era PDO were not assessed in AR5.

The existence of the PDV in the centuries prior to the instrumental period is evidenced by a variety of proxy records based on tree rings (Biondi et al., 2001; D'Arrigo and Ummenhofer, 2015), corals (Deng et al., 2013; Felis et al., 2010; Linsley et al., 2015) and sediments (Lapointe et al., 2017; O'Mara et al., 2019). There is little coherence between the various paleo-proxy indices prior to the instrumental record, and neither these nor the instrumental records provide indications of a clearly defined spectral peak (Buckley et al., 2019; Chen & Wallace, 2015; Henley, 2017; Newman M. et al., 2016; Zhang L. et al., 2018). For instance, spectral analysis from millennia length PDV reconstructions shows spectral peaks at multi-decadal, centennial and bi-centennial time scales (Beaufort and Grelaud, 2017), while only multi-decadal oscillations can be detected in the shorter (less than 400 years into the past) paleoclimate reconstructions. A variety of proxies suggest a shift in the PDV from the early-mid Holocene, which was characterized by a persistently negative phase of the PDO (i.e. weak Aleutian Low), to the late Holocene, and a more variable and more positive PDO (i.e. strong Aleutian Low) conditions. This shift at around 4.5 ka is also evident in the PDO periodicities, changing from bidecadal and pentadecadal variability in the early Holocene to only pentadecadal periodicities in the late Holocene (Hernández et al., 2020). Several proxy records indicate that the strengthening in the Aleutian Low inferred since the late 17th century is unprecedented over the last millennium (Liu Z. et al., 2017; Osterberg et al., 2017; Winski et al., 2017), in line with an increase in PDV low-frequency variability (Hernández et al., 2020; Williams et al., 2017).

ACCEPTED VERSION SUBJECT TO FINAL EDITS

The PDO and IPO indices are significantly correlated during the instrumental period, showing regime shifts in the 1920s, 1940s, 1970s and around 1999. Positive PDV phases were observed from the 1920s to the mid-1940s and from the late 1970s to the late 1990s, while negative phases occurred from mid-1940s until the late 1970s, and since 1999 (Figure 2.38; Han et al., 2013; Chen and Wallace, 2015; Newman M. et al., 2016). The associated spatial patterns are quite similar, but the PDO pattern exhibits stronger SST anomalies in the extra-tropical North Pacific than the IPO (Chen & Wallace, 2015). The strength and structure of the SST patterns also differ among the periods (Newman M. et al., 2016).

[START FIGURE 2.38 HERE]

Figure 2.38: Indices of multi-decadal climate variability from 1854–2019 based upon several sea surface temperature based data products. Shown are the indices of the AMV and PDV based on area averages for the regions indicated in Technical Annex IV. Further details on data sources and processing are available in the chapter data table (Table 2.SM.1).

[END FIGURE 2.38 HERE]

Instrumental observations are sparse prior to 1950, and thus the fidelity of any PDV index derived for the second part of the 19th century and early decades of the 1900s is relatively low (Deng et al., 2013; Wen et al., 2014) (Figure 2.38). This results in *low agreement* in the classification of the PDO / IPO phase among several indices, even during recent years with the availability of high-quality data. Nevertheless, the teleconnection patterns are robust regardless of the index used to characterize the PDO (McAfee, 2017). Analysis of time series of PDO and IPO highlights the (multi-) decadal nature of this mode of variability with no significant trends, but highlights a recent switch from a positive to a negative phase since 1999 / 2000 across all indicators (England et al., 2014; Henley, 2017).

In summary, the PDV in the instrumental record is dominated by (multi-) decadal-scale shifts between positive and negative phases over the last 150 years with no overall trend (*high confidence*). There is *low confidence* in paleo-PDV reconstructions due to discrepancies among the various available time series in terms of phasing and timing. However, there is *high confidence* in the occurrence of a shift from predominantly negative to positive PDO conditions from the middle to the late Holocene.

2.4.6 Atlantic Multidecadal Variability

AR5 reported no robust changes in Atlantic Multidecadal Variability (AMV) reconstructions based on paleo records due to low consistency between different AMV reconstructions prior to 1900. AR5 concluded that there have been no significant trends in the AMV index during the instrumental period and there was difficulty in interpreting the AMV signal because of the long-term underlying SST warming trend.

The AR5 conclusions about large uncertainties in AMV paleo reconstructions (Hernández et al., 2020) have been reinforced by recent studies of tree rings (Wang et al., 2017b), Greenland ice (Chylek et al., 2012), and corals (Kilbourne et al., 2014; Svendsen et al., 2014a; Wang et al., 2017b). The AMV exhibited a generally positive state over the first millennium of the CE (Mann et al., 2009; Singh et al., 2018). Paleo reconstructions over the last millennium consistently show a negative AMV phase during 1400–1850 CE and a positive phase during 900–1200 CE (Mann et al., 2009; Singh et al., 2018; Wang J. et al., 2017), consistent with warmer surface temperatures from tropical Atlantic records (Kilbourne et al., 2014).

Instrumental observations show that AMV is characterized by basin-wide warm and cool periods with an average variation in SST of about 0.4°C, but with larger variations in the North Atlantic subpolar gyre. Despite small differences in indices used to define the AMV (Annex IV), they all show warm periods occurring approximately between 1880–1900, 1940–1960, and from the mid-1990s to present, with cool periods in between (Figure 2.38) but no overall sustained change during the instrumental period (Bellomo et

ACCEPTED VERSION SUBJECT TO FINAL EDITS

al., 2018; Booth et al., 2012; Gulev et al., 2013; Sun et al., 2017).

The oceanic changes are seen in salinity and temperature variations over the upper 3000 m of the North Atlantic (Polyakov et al., 2005; Keenlyside et al., 2015), and in sea level variations in the Western North Atlantic along the Gulf Stream passage (McCarthy et al., 2015). The pattern and strength of the AMV differs among the periods (e.g., Svendsen et al., 2014a; Reynolds et al., 2018) and there are indications that there may have been a shift since 2005 toward a negative phase of the AMV (Robson et al., 2016).

In summary, no sustained change in AMV indices has been observed over the instrumental period (*high confidence*). However, instrumental records may not be long enough to distinguish any oscillatory behaviour from trends in the AMV. There is *low confidence* in the paleo AMV reconstructions due to a paucity of high-resolution records.

2.5 Final remarks

The assessment in this chapter is based upon an ever-expanding volume of available proxy and observational records and a growing body of literature. Since AR5, improvements have been made in all aspects of data collection, data curation, data provision and data analysis permitting improved scientific insights. The chapter has also benefitted from the availability of new products from a range of emerging, mainly space-based, observing capabilities and new generations of reanalysis products. However, a number of key challenges still remain which, if addressed, would serve to strengthen future reports.

- Development of new techniques and exploitation of existing and new proxy sources may help address challenges around the low temporal resolution of most paleoclimate proxy records, particularly prior to the Common Era, and ambiguities around converting paleoclimate proxy data into estimates of climate-relevant variables. Conversions rely upon important proxy-specific assumptions and biases can be large due to limited accounting of seasonality, non-climatic effects, or the influence of multiple climate variables. These challenges currently limit the ability to ascertain the historical unusualness of recent directly observed climate changes for many indicators. {2.2, 2.3}

- Improved sharing of historical instrumental and proxy records (including metadata) along with significant efforts at data rescue of presently undigitised records would serve to significantly strengthen many aspects of the present assessment. Longer observational time series help to better understand variability, and any underlying periodicity in climate indicators and climate forcers, especially for components of the climate system where the dominant response is on multi-decadal and longer time scales. Targeted rescue of early marine data records, especially from waters of the tropical oceans and the Southern Ocean could help constrain modes of variability and important teleconnection changes in, for example, the hydrological cycle and patterns of global temperature change. {2.2, 2.3, 2.4}

- Contemporary observing systems have limitations in parts of the Earth system with limited accessibility or coverage, for example coastal and shallow ocean, polar regions, marine biosphere, and the deep sea, leading to seasonal-dependency and regional variability in data coverage and uncertainty which serve to limit confidence in the present assessment of changes. {2.3}

- Contradictory lines of evidence exist between observations and models on the relationship between the rates of warming in GMST and GSAT, compounded by limitations in theoretical understanding. Improvements in air temperature datasets over the ocean and an improved understanding of the representation of the lowermost atmosphere over the ocean in models would reduce uncertainty in assessed changes in GSAT. {Cross-Chapter Box 2.3}

ACCEPTED VERSION SUBJECT TO FINAL EDITS

Frequently asked questions

FAQ 2.1: The Earth's temperature has varied before. How is the current warming any different?

Earth's climate has always changed naturally, but both the global extent and rate of recent warming are unusual. The recent warming has reversed a slow, long-term cooling trend, and research indicates that global surface temperature is higher now than it has been for millennia.

While climate can be characterised by many variables, temperature is a key indicator of the overall climate state, and global surface temperature is fundamental to characterising and understanding global climate change, including Earth's energy budget. A rich variety of geological evidence shows that temperature has changed throughout Earth's history. A variety of natural archives from around the planet, such as ocean and lake sediments, glacier ice and tree rings, shows that there were times in the past when the planet was cooler, and times when it was warmer. While our confidence in quantifying large-scale temperature changes generally decreases the farther back in time we look, scientists can still identify at least four major differences between the recent warming and those of the past.

It's warming almost everywhere. During decades and centuries of the past 2000 years, some regions warmed more than the global average while, at the same time, other regions cooled. For example, between the 10th and 13th centuries, the North Atlantic region warmed more than many other regions. In contrast, the pattern of recent surface warming is globally more uniform than for other decadal to centennial climate fluctuations over at least the past two millennia.

It's warming rapidly. Over the past 2 million years, Earth's climate has fluctuated between relatively warm interglacial periods and cooler glacial periods, when ice sheets grew over vast areas of the northern continents. Intervals of rapid warming coincided with the collapse of major ice sheets, heralding interglacial periods such as the present Holocene Epoch, which began about 12,000 years ago. During the shift from the last glacial period to the current interglacial, the total temperature increase was about 5°C. That change took about 5000 years, with a maximum warming rate of about 1.5°C per thousand years, although the transition was not smooth. In contrast, Earth's surface has warmed approximately 1.1°C since 1850–1900. However, even the best reconstruction of global surface temperature during the last deglacial period is too coarsely resolved for direct comparison with a period as short as the past 150 years. But for the past 2000 years, we have higher-resolution records that show that the rate of global warming during the last 50 years has exceeded the rate of any other 50-year period.

Recent warming reversed a long-term global cooling trend. Following the last major glacial period, global surface temperature peaked by around 6500 years ago, then slowly cooled. The long-term cooling trend was punctuated by warmer decades and centuries. These fluctuations were minor compared with the persistent and prominent warming that began in the mid-19th century when the millennial-scale cooling trend was reversed.

It's been a long time since it's been this warm. Averaged over the globe, surface temperatures of the past decade were probably warmer than when the long cooling trend began around 6500 years ago. If so, we need to look back to at least the previous interglacial period, around 125,000 years ago, to find evidence for multi-centennial global surface temperatures that were warmer than now.

Previous temperature fluctuations were caused by large-scale natural processes, while the current warming is largely due to human causes (see, for example, FAQ 1.3, FAQ 3.1). But understanding how and why temperatures have changed in the past is critical for understanding the current warming and how human and natural influences will interact to determine what happens in the future. Studying past climate changes also makes it clear that, unlike previous climate changes, the effects of recent warming are occurring on top of stresses that make humans and nature vulnerable to changes in ways that they have never before experienced (for example, see FAQ 11.2, FAQ12.3).

ACCEPTED VERSION SUBJECT TO FINAL EDITS

[START FAQ 2.1, FIGURE 1 HERE]

FAQ 2.1, Figure 1: Evidence for the unusualness of recent warming.

[END FAQ 2.1, FIGURE 1 HERE]

FAQ 2.2: What is the evidence for climate change?

The evidence for climate change rests on more than just increasing surface temperatures. A broad range of indicators collectively leads to the inescapable conclusion that we are witnessing rapid changes to many aspects of our global climate. We are seeing changes in the atmosphere, ocean, cryosphere, and biosphere. Our scientific understanding depicts a coherent picture of a warming world.

We have long observed our changing climate. From the earliest scientists taking meteorological observations in the 16th and 17th centuries to the present, we have seen a revolution in our ability to observe and diagnose our changing climate. Today we can observe diverse aspects of our climate system from space, from aircraft and weather balloons, using a range of ground-based observing technologies, and using instruments that can measure to great depths in the ocean.

Observed changes in key indicators point to warming over land areas. Global surface temperature over land has increased since the late 19th century, and changes are apparent in a variety of societally relevant temperature extremes. Since the mid-1950s the troposphere (i.e., the lowest 6–10 km of the atmosphere) has warmed, and precipitation over land has increased. Near-surface specific humidity (i.e., water vapour) over land has increased since at least the 1970s. Aspects of atmospheric circulation have also evolved since the mid-20th century, including a poleward shift of mid-latitude storm tracks.

Changes in the global ocean point to warming as well. Global average sea surface temperature has increased since the late 19th century. The heat content of the global ocean has increased since the 19th century, with more than 90% of the excess energy accumulated in the climate system being stored in the ocean. This ocean warming has caused ocean waters to expand, which has contributed to the increase in global sea level in the past century. The relative acidity of the ocean has also increased since the early 20th century, caused by the uptake of carbon dioxide from the atmosphere, and oxygen loss is evident in the upper ocean since the 1970s.

Significant changes are also evident over the cryosphere – the portion of the Earth where water is seasonally or continuously frozen as snow or ice. There have been decreases in Arctic sea ice area and thickness and changes in Antarctic sea ice extent since the mid-1970s. Spring snow cover in the Northern Hemisphere has decreased since the late-1970s, along with an observed warming and thawing of permafrost (perennially frozen ground). The Greenland and Antarctic ice sheets are shrinking, as are the vast majority of glaciers worldwide, contributing strongly to the observed sea level rise.

Many aspects of the biosphere are also changing. Over the last century, long-term ecological surveys show that many land species have generally moved poleward and to higher elevations. There have been increases in green leaf area and/or mass (i.e., global greenness) since the early 1980s, and the length of the growing season has increased over much of the extratropical Northern Hemisphere since at least the mid-20th century. There is also strong evidence that various phenological metrics (such as the timing of fish migrations) for many marine species have changed in the last half century.

Change is apparent across many components of the climate system. It has been observed using a very broad range of techniques and analysed independently by numerous groups around the world. The changes are consistent in pointing to a climate system that has undergone rapid warming since the industrial revolution.

[START FAQ 2.2, FIGURE 1 HERE]

ACCEPTED VERSION SUBJECT TO FINAL EDITS

FAQ 2.2, Figure 1: Synthesis of significant changes observed in the climate system over the past several decades. Upwards, downwards and circling arrows indicate increases, decreases and changes, respectively. Independent analyses of many components of the climate system that would be expected to change in a warming world exhibit trends consistent with warming. Note that this list is not comprehensive.

[END FAQ 2.2, FIGURE 1 HERE]

ACCEPTED VERSION
SUBJECT TO FINAL EDITS

Acknowledgements

The authors of Chapter 2 would like to extend their gratitude to Sara Veasey, Deborah Riddle, Deborah Misch (all NOAA NCEI, USA) and Robert Fawcett (BoM, Australia) for providing substantial support in the production and finalisation of all figures. We wish to acknowledge Raphael Neukom (U. Bern, Switzerland) and Michael Bosilovich (NASA/GFSC, USA) for their assistance in the provision of data. In addition, we wish to acknowledge the work of David Schoeman (USC, USA), Camille Parmesan (U. Plymouth, UK) and Marie-Fanny Racault (PML, UK) (all WGII) in providing input on the coordination of biospheric aspects.

ACCEPTED VERSION
SUBJECT TO FINAL EDITS

References

Ablain, M. et al., 2019: Uncertainty in satellite estimates of global mean sea-level changes, trend and acceleration. *Earth System Science Data*, **11(3)**, 1189–1202, doi:10.5194/essd-11-1189-2019.

Abram, N.J. et al., 2010: Ice core evidence for a 20th century decline of sea ice in the Bellingshausen Sea, Antarctica. *Journal of Geophysical Research Atmospheres*, **115**, D23101, doi:10.1029/2010jd014644.

Abram, N.J. et al., 2014: Evolution of the Southern Annular Mode during the past millennium. *Nature Climate Change*, **4(7)**, 564–569, doi:10.1038/nclimate2235.

Abram, N.J. et al., 2020a: Palaeoclimate perspectives on the Indian Ocean Dipole (2020b). *Quaternary Science Reviews*, **237**, 106302, doi:10.1016/j.quascirev.2020.106302.

Abram, N.J. et al., 2020b: Coupling of Indo-Pacific climate variability over the last millennium (2020a). *Nature*, **579(7799)**, 385–392, doi:10.1038/s41586-020-2084-4.

Ackley, S., P. Wadhams, J.C. Comiso, and A.P. Worby, 2003: Decadal decrease of Antarctic sea ice extent inferred from whaling records revisited on the basis of historical and modern sea ice records. *Polar Research*, **22**, 19–25, doi:10.1111/j.1751-8369.2003.tb00091.x.

Adler, R.F., G. Gu, M. Sapiano, J.J. Wang, and G.J. Huffman, 2017: Global Precipitation: Means, Variations and Trends During the Satellite Era (1979–2014). *Surveys in Geophysics*, **38(4)**, 679–699, doi:10.1007/s10712-017-9416-4.

Adler, R.F. et al., 2018: The Global Precipitation Climatology Project (GPCP) monthly analysis (New Version 2.3) and a review of 2017 global precipitation. *Atmosphere*, **9(4)**, doi:10.3390/atmos9040138.

Ahn, J. and E.J. Brook, 2014: Siple Dome ice reveals two modes of millennial CO2 change during the last ice age. *Nature Communications*, **5(3723)**, doi:10.1038/ncomms4723.

Ahn, J., S. Marcott, and E. Brook, 2019: Atmospheric CO2 during the late Holocene. *in prep.*

Ahn, J., E.J. Brook, A. Schmittner, and K. Kreutz, 2012: Abrupt change in atmospheric CO2 during the last ice age. *Geophysical Research Letters*, **39**, L18711, doi:10.1029/2012gl053018.

Aiken, J. et al., 2017: A synthesis of the environmental response of the North and South Atlantic Sub-Tropical Gyres during two decades of AMT. *Progress in Oceanography*, **158**, 236–254, doi:10.1016/j.pocean.2016.08.004.

Ait Brahim, Y. et al., 2019: North Atlantic Ice-Rafting, Ocean and Atmospheric Circulation During the Holocene: Insights From Western Mediterranean Speleothems. *Geophysical Research Letters*, **46(13)**, 7614–7623, doi:10.1029/2019gl082405.

Albani, S. et al., 2015: Twelve thousand years of dust: the Holocene global dust cycle constrained by natural archives. *Climate of the Past*, **11(6)**, 869–903, doi:10.5194/cp-11-869-2015.

Albani, S. et al., 2016: Paleodust variability since the Last Glacial Maximum and implications for iron inputs to the ocean. *Geophysical Research Letters*, **43(8)**, 3944–3954, doi:10.1002/2016gl067911.

Alfaro-Sánchez, R. et al., 2018: Climatic and volcanic forcing of tropical belt northern boundary over the past 800 years. *Nature Geoscience*, doi:10.1038/s41561-018-0242-1.

Alkama, R., B. Decharme, H. Douville, and A. Ribes, 2011: Trends in Global and Basin-Scale Runoff over the Late Twentieth Century: Methodological Issues and Sources of Uncertainty. *Journal of Climate*, **24(12)**, 3000–3014, doi:10.1175/2010jcli3921.1.

Alkama, R., L. Marchand, A. Ribes, and B. Decharme, 2013: Detection of global runoff changes: results from observations and CMIP5 experiments. *Hydrology and Earth System Sciences*, **17**, 2967–2979, doi:10.5194/hess-17-2967-2013.

Allan, R.P. et al., 2014: Physically Consistent Responses of the Global Atmospheric Hydrological Cycle in Models and Observations. *Surveys in Geophysics*, **35**, 533–552, doi:10.1007/s10712-012-9213-z.

Allen, R.J. and M. Kovilakam, 2017: The Role of Natural Climate Variability in Recent Tropical Expansion. *Journal of Climate*, **30**, 6329–6350, doi:10.1175/jcli-d-16-0735.1.

Allen, R.J., S.C. Sherwood, J.R. Norris, and C.S. Zender, 2012: Recent Northern Hemisphere tropical expansion primarily driven by black carbon and tropospheric ozone. *Nature*, **485**, 350–354.

Allison, L.C. et al., 2019: Towards quantifying uncertainty in ocean heat content changes using synthetic profiles. *Environmental Research Letters*, **14(8)**, 84037, doi:10.1088/1748-9326/ab2b0b.

Alonso-Garcia, M. et al., 2017: Freshening of the Labrador Sea as a trigger for Little Ice Age development. *Clim. Past*, **13(4)**, 317–331, doi:10.5194/cp-13-317-2017.

AMAP, 2017: *Snow, Water, Ice and Permafrost in the Arctic (SWIPA)*. Arctic Monitoring and Assessment Programme (AMAP), Oslo, Norway, 269 pp.

Ammann, C.M., G.A. Meehl, W.M. Washington, and C.S. Zender, 2003: A monthly and latitudinally varying volcanic forcing dataset in simulations of 20th century climate. *Geophysical Research Letters*, **30(12)**, doi:10.1029/2003gl016875.

An, Z. et al., 2015: Global Monsoon Dynamics and Climate Change. *Annual Review of Earth and Planetary Sciences*, **43(1)**, 29–77, doi:10.1146/annurev-earth-060313-054623.

Anagnostou, E. et al., 2016: Changing atmospheric CO2 concentration was the primary driver of early Cenozoic climate. *Nature*, **533**, 380–384, doi:10.1038/nature17423.

ACCEPTED VERSION SUBJECT TO FINAL EDITS

Anagnostou, E. et al., 2020a: Proxy evidence for state-dependence of climate sensitivity in the Eocene greenhouse. *Nature Communications*, **11(1)**, 4436, doi:10.1038/s41467-020-17887-x.
Anagnostou, E. et al., 2020b: Proxy evidence for state-dependence of climate sensitivity in the Eocene greenhouse. *Nature Communications*, **11(1)**, 4436, doi:10.1038/s41467-020-17887-x.
Anchukaitis, K.J. et al., 2017: Last millennium Northern Hemisphere summer temperatures from tree rings: Part II, spatially resolved reconstructions. *Quaternary Science Reviews*, **163**, 1–22, doi:10.1016/j.quascirev.2017.02.020.
Anderson, H.J. et al., 2018: Southern Hemisphere westerly wind influence on southern New Zealand hydrology during the Lateglacial and Holocene. *Journal of Quaternary Science*, **33(6)**, 689–701, doi:10.1002/jqs.3045.
Anderson, J.G. et al., 2017: Stratospheric ozone over the United States in summer linked to observations of convection and temperature via chlorine and bromine catalysis. *Proceedings of the National Academy of Sciences*, doi:10.1073/pnas.1619318114.
Anderson, R.F. et al., 2019: Deep-Sea Oxygen Depletion and Ocean Carbon Sequestration During the Last Ice Age. *Global Biogeochemical Cycles*, **33(3)**, 301–317, doi:10.1029/2018gb006049.
Andersson, A. et al., 2011: Evaluation of HOAPS-3 Ocean Surface Freshwater Flux Components. *Journal of Applied Meteorology and Climatology*, **50**, 379–398, doi:10.1175/2010jamc2341.1.
Andersson, S.M. et al., 2015: Significant radiative impact of volcanic aerosol in the lowermost stratosphere. *Nature Communications*, **6**, 7692, doi:10.1038/ncomms8692.
Andres, M., K.A. Donohue, and J.M. Toole, 2020: The Gulf Stream's path and time-averaged velocity structure and transport at 68.5°W and 70.3°W. *Deep Sea Research Part I: Oceanographic Research Papers*, **156**, 103179, doi:10.1016/j.dsr.2019.103179.
Andrews, T., R.A. Betts, B.B.B. Booth, C.D. Jones, and G.S. Jones, 2017: Effective radiative forcing from historical land use change. *Climate Dynamics*, doi:10.1007/s00382-016-3280-7.
Aretxabaleta, A.L., K.W. Smith, and T.S. Kalra, 2017: Regime Changes in Global Sea Surface Salinity Trend. *Journal of Marine Science and Engineering*, **5(4)**, doi:10.3390/jmse5040057.
Armand, L., A. Ferry, and A. Leventer, 2017: Advances in palaeo sea ice estimation. In: *Sea Ice (Third Edition)* [Thomas, D.N. (ed.)]. John Wiley & Sons, Ltd, Chichester, UK and Hoboken, NJ, USA, pp. 600–629, doi:10.1002/9781118778371.ch26.
Ashcroft, L., J. Gergis, and D.J. Karoly, 2016: Long-term stationarity of El Niño--Southern Oscillation teleconnections in southeastern Australia. *Climate Dynamics*, **46(9)**, 2991–3006, doi:10.1007/s00382-015-2746-3.
Ashok, K., S.K. Behera, S.A. Rao, H. Weng, and T. Yamagata, 2007: El Niño Modoki and its possible teleconnection. *Journal of Geophysical Research: Oceans*, **112(C11)**, doi:10.1029/2006jc003798.
Ashouri, H. et al., 2015: PERSIANN-CDR: Daily Precipitation Climate Data Record from Multisatellite Observations for Hydrological and Climate Studies. *Bull. Amer. Meteor. Soc*, 69–84, doi:10.1175/bams-d-13-00068.1.
Atkinson, A. et al., 2019: Krill (Euphausia superba) distribution contracts southward during rapid regional warming. *Nature Climate Change*, **9(2)**, 142–147, doi:10.1038/s41558-018-0370-z.
Aumann, H.H., S. Broberg, E. Manning, and T. Pagano, 2019: Radiometric Stability Validation of 17 Years of AIRS Data Using Sea Surface Temperatures. *Geophysical Research Letters*, **46(21)**, 12504–12510, doi:10.1029/2019gl085098.
Austermann, J., J.X. Mitrovica, P. Huybers, and A. Rovere, 2017: Detection of a dynamic topography signal in last interglacial sea-level records. *Science Advances*, **3(7)**, doi:10.1126/sciadv.1700457.
Avery, M.A., S.M. Davis, K.H. Rosenlof, H. Ye, and A.E. Dessler, 2017: Large anomalies in lower stratospheric water vapour and ice during the 2015-2016 El Ninõ. *Nature Geoscience*, **10(6)**, 405–409, doi:10.1038/ngeo2961.
Ayache, M., D. Swingedouw, Y. Mary, F. Eynaud, and C. Colin, 2018: Multi-centennial variability of the AMOC over the Holocene: A new reconstruction based on multiple proxy-derived SST records. *Global and Planetary Change*, **170**, 172–189, doi:10.1016/j.gloplacha.2018.08.016.
Azorin-Molina, C., J.H. Dunn, C.A. Mears, P. Berrisford, and T.R. McVicar, 2017: Surface winds: Land surface wind speed [in "State of the Climate in 2016"]. *Bulletin of the American Meteorological Soceity*, **98(8)**, S37–S39, doi:10.1175/2017bamsstateoftheclimate.1.
Azorin-Molina, C. et al., 2019: Surface winds [in "State of the Climate in 2018"]. *Bulletin of the American Meteorological Society*, **100(9)**, S43–S45, doi:10.1175/2019bamsstateoftheclimate.1.
Azorin-Molina, C. et al., 2020: Land and ocean surface winds. *State of the Climate in 2019. Bulletin of the American Meteorological Society*, **101(8)**, S63–S65, doi:10.1175/2020bamsstateoftheclimate.1.
Babila, T.L. et al., 2018: Capturing the global signature of surface ocean acidification during the Palaeocene-Eocene Thermal Maximum. *Philosophical Transactions of the Royal Society A: Mathematical, Physical and Engineering Sciences*, **376(2130)**, doi:10.1098/rsta.2017.0072.
Bachem, P.E., B. Risebrobakken, and E.L. McClymont, 2016: Sea surface temperature variability in the Norwegian Sea during the late Pliocene linked to subpolar gyre strength and radiative forcing. *Earth and Planetary Science Letters*, **446**, 113–122, doi:10.1016/j.epsl.2016.04.024.
Bachem, P.E., B. Risebrobakken, S. De Schepper, and E.L. McClymont, 2017: Highly variable Pliocene sea surface conditions in the Norwegian Sea. *Climate of the Past*, **13(9)**, doi:10.5194/cp-13-1153-2017.

ACCEPTED VERSION SUBJECT TO FINAL EDITS

Badger, M.P.S. et al., 2019: Insensitivity of alkenone carbon isotopes to atmospheric CO2 at low to moderate CO2 levels. *Climate of the Past*, **15(2)**, 539–554, doi:10.5194/cp-15-539-2019.

Baggenstos, D. et al., 2019: Earth{\\textquoteright}s radiative imbalance from the Last Glacial Maximum to the present. *Proceedings of the National Academy of Sciences*, **116(30)**, 14881–14886, doi:10.1073/pnas.1905447116.

Bagnell, A. and T. DeVries, 2020: Correcting Biases in Historical Bathythermograph Data Using Artificial Neural Networks. *Journal of Atmospheric and Oceanic Technology*, **37(10)**, 1781–1800, doi:10.1175/jtech-d-19-0103.1.

Bailey, H.L. et al., 2018: Holocene atmospheric circulation in the central North Pacific : A new terrestrial diatom and d 18 O dataset from the Aleutian Islands. *Quaternary Science Reviews*, **194**, 27–38, doi:10.1016/j.quascirev.2018.06.027.

Baker, A., J. C. Hellstrom, B.F.J. Kelly, G. Mariethoz, and V. Trouet, 2015: A composite annual-resolution stalagmite record of North Atlantic climate over the last three millennia. *Scientific Reports*, **5(1)**, 10307, doi:10.1038/srep10307.

Bakker, D.C.E. et al., 2016: A multi-decade record of high-quality fCO2 data in version 3 of the Surface Ocean CO2 Atlas (SOCAT). *Earth Syst. Sci. Data*, **8(2)**, 383–413, doi:10.5194/essd-8-383-2016.

Ball, W.T. et al., 2018: Evidence for a continuous decline in lower stratospheric ozone offsetting ozone layer recovery. *Atmos. Chem. Phys.*, **18(2)**, 1379–1394, doi:10.5194/acp-18-1379-2018.

Ball, W.T. et al., 2019: Stratospheric ozone trends for 1985--2018: sensitivity to recent large variability. *Atmospheric Chemistry and Physics*, **19(19)**, 12731–12748, doi:10.5194/acp-19-12731-2019.

Ballalai, J.M. et al., 2019: Tracking Spread of the Agulhas Leakage Into the Western South Atlantic and Its Northward Transmission During the Last Interglacial. *Paleoceanography and Paleoclimatology*, **34(11)**, 1744–1760, doi:10.1029/2019pa003653.

Balmaseda, M.A., K.E. Trenberth, and E. Källén, 2013: Distinctive climate signals in reanalysis of global ocean heat content. *Geophysical Research Letters*, **40(9)**, 1754–1759, doi:10.1002/grl.50382.

Bamber, J.L., R.M. Westaway, B. Marzeion, and B. Wouters, 2018: The land ice contribution to sea level during the satellite era. *Environmental Research Letters*, **13(6)**, 63008, doi:10.1088/1748-9326/aac2f0.

Banerjee, A., F. J C, L.M. Polvani, D. Waugh, and K.-L. Chang, 2020: A pause in southern hemisphere circulation trends due to the Montreal Protocol. *Nature*, **579**, 544–548, doi:10.1038/s41586-020-2120-4.

Barbarossa, V. et al., 2018: Data Descriptor: FLO1K, global maps of mean, maximum and minimum annual streamflow at 1 km resolution from 1960 through 2015. *Scientific Data*, **5**, 1–11, doi:10.1038/sdata.2018.52.

Bard, E. and R.E.M. Rickaby, 2009: Migration of the subtropical front as a modulator of glacial climate. *Nature*, **460(7253)**, 380–383, doi:10.1038/nature08189.

Barichivich, J. et al., 2013: Large-scale variations in the vegetation growing season and annual cycle of atmospheric CO2 at high northern latitudes from 1950 to 2011. *Global Change Biology*, doi:10.1111/gcb.12283.

Baringer, M.O. et al., 2018: Meridional overturning and oceanic heat transport circulation observations in the North Atlantic Ocean [in “State of the Climate in 2017”]. *Bulletin of the American Meteorological Society*, **99(8)**, S91–S94, doi:10.1175/2018bamsstateoftheclimate.1.

Barlow, N.L.M. et al., 2018: Lack of evidence for a substantial sea-level fluctuation within the Last Interglacial. *Nature Geoscience*, **11(9)**, 627–634, doi:10.1038/s41561-018-0195-4.

Barnes, E.A., E. Dunn-Sigouin, G. Masato, and T. Woollings, 2014: Exploring recent trends in Northern Hemisphere blocking. *Geophysical Research Letters*, **41(2)**, 638–644, doi:10.1002/2013gl058745.

Barr, C. et al., 2014: Climate variability in south-eastern Australia over the last 1500 years inferred from the high-resolution diatom records of two crater lakes. *Quaternary Science Reviews*, **95**, 115–131, doi:10.1016/j.quascirev.2014.05.001.

Barr, C. et al., 2019: Holocene El Niño–Southern Oscillation variability reflected in subtropical Australian precipitation. *Scientific Reports*, **9(1)**, 1627, doi:10.1038/s41598-019-38626-3.

Barrett, H.G., J.M. Jones, and G.R. Bigg, 2018: Reconstructing El Niño Southern Oscillation using data from ships’ logbooks, 1815--1854. Part II: Comparisons with existing ENSO reconstructions and implications for reconstructing ENSO diversity. *Climate Dynamics*, **50(9)**, 3131–3152, doi:10.1007/s00382-017-3797-4.

Barrucand, M.G., M.E Zitto, R. Piotrkowski, P. Canziani, and A. O’Neill, 2018: Historical SAM index time series: linear and nonlinear analysis. *International Journal of Climatology*, **38**, e1091–e1106, doi:10.1002/joc.5435.

Bartoli, G., B. Hönisch, and R.E. Zeebe, 2011: Atmospheric CO2 decline during the Pliocene intensification of Northern Hemisphere glaciations. *Paleoceanography*, **26(4)**, doi:10.1029/2010pa002055.

Bastos, A., S.W. Running, C. Gouveia, and R.M. Trigo, 2013: The global NPP dependence on ENSO: La Niña and the extraordinary year of 2011. *Journal of Geophysical Research: Biogeosciences*, **118**, 1247– 1255, doi:10.1002/jgrg.20100.

Batchelor, C.L. et al., 2019: The configuration of Northern Hemisphere ice sheets through the Quaternary. *Nature Communications*, **10(1)**, 3713, doi:10.1038/s41467-019-11601-2.

Bauer, S.E. et al., 2020: Historical (1850–2014) Aerosol Evolution and Role on Climate Forcing Using the GISS ModelE2.1 Contribution to CMIP6. *Journal of Advances in Modeling Earth Systems*, **12(8)**, e2019MS001978,

ACCEPTED VERSION SUBJECT TO FINAL EDITS

doi:10.1029/2019ms001978.
Bauska, T.K. et al., 2015: Links between atmospheric carbon dioxide, the land carbon reservoir and climate over the past millennium. *Nature Geoscience*, **8**, 383–387, doi:10.1038/ngeo2422.
Bayr, T., D. Dommenget, T. Martin, and S.B. Power, 2014: The eastward shift of the Walker Circulation in response to global warming and its relationship to ENSO variability. *Climate Dynamics*, **43(9–10)**, 2747–2763, doi:10.1007/s00382-014-2091-y.
Beal, L.M. and S. Elipot, 2016: Broadening not strengthening of the Agulhas Current since the early 1990s. *Nature*, **540**, 570–573, doi:10.1038/nature19853.
Beaufort, L. and M. Grelaud, 2017: A 2700-year record of ENSO and PDO variability from the Californian margin based on coccolithophore assemblages and calcification. *Progress in Earth and Planetary Science*, **4(1)**, 5, doi:10.1186/s40645-017-0123-z.
Beckley, B.D., P.S. Callahan, D.W. Hancock III, G.T. Mitchum, and R.D. Ray, 2017: On the "Cal-Mode" Correction to TOPEX Satellite Altimetry and Its Effect on the Global Mean Sea Level Time Series. *Journal of Geophysical Research: Oceans*, **122(11)**, 8371–8384, doi:10.1002/2017jc013090.
Befort, D.J., S. Wild, T. Kruschke, U. Ulbrich, and G.C. Leckebusch, 2016: Different long-term trends of extra-tropical cyclones and windstorms in ERA-20C and NOAA-20CR reanalyses. *Atmospheric Science Letters*, **17**, 586–595, doi:10.1002/asl.694.
Bellomo, K. and A.C. Clement, 2015: Evidence for weakening of the Walker circulation from cloud observations. *Geophysical Research Letters*, **42(18)**, 7758–7766, doi:10.1002/2015gl065463.
Bellomo, K., L.N. Murphy, M.A. Cane, A.C. Clement, and L.M. Polvani, 2018: Historical forcings as main drivers of the Atlantic multidecadal variability in the CESM large ensemble. *Climate Dynamics*, **50(9)**, 3687–3698, doi:10.1007/s00382-017-3834-3.
Bellouin, N. et al., 2020: Radiative forcing of climate change from the Copernicus reanalysis of atmospheric composition. *Earth System Science Data*, **12(3)**, 1649–1677, doi:10.5194/essd-12-1649-2020.
Belt, S.T., 2018: Source-specific biomarkers as proxies for Arctic and Antarctic sea ice. *Organic Geochemistry*, doi:10.1016/j.orggeochem.2018.10.002.
Belt, S.T. et al., 2015: Identification of paleo Arctic winter sea ice limits and the marginal ice zone: Optimised biomarker-based reconstructions of late Quaternary Arctic sea ice. *Earth and Planetary Science Letters*, **431**, 127–139, doi:10.1016/j.epsl.2015.09.020.
Benestad, R.E., H.B. Erlandsen, A. Mezghani, and K.M. Parding, 2019: Geographical Distribution of Thermometers Gives the Appearance of Lower Historical Global Warming. *Geophysical Research Letters*, **46(13)**, 7654–7662, doi:10.1029/2019gl083474.
Bentley, M.J. et al., 2014: A community-based geological reconstruction of Antarctic Ice Sheet deglaciation since the Last Glacial Maximum. *Quaternary Science Reviews*, **100**, 1–9, doi:10.1016/j.quascirev.2014.06.025.
Bereiter, B. et al., 2018: Mean global ocean temperatures during the last glacial transition. *Nature*, **553(39)**, 39, doi:10.1038/nature25152.
Berends, C.J., B. de Boer, A.M. Dolan, D.J. Hill, and R.S.W. van de Wal, 2019: Modelling ice sheet evolution and atmospheric CO2 during the Late Pliocene. *Climate of the Past*, **15(4)**, 1603–1619, doi:10.5194/cp-15-1603-2019.
Berger, A. and M.F. Loutre, 1991: Insolation values for the climate of the last 10 million years. *Quaternary Science Reviews*, **10(4)**, 297–317, doi:10.1016/0277-3791(91)90033-q.
Berry, D.I. and E.C. Kent, 2011a: Air-Sea fluxes from ICOADS : the construction of a new gridded dataset with uncertainty estimates. *International Journal of Climatology*, **31**, 987–1001, doi:10.1002/joc.2059.
Berry, D.I. and E.C. Kent, 2011b: Air-Sea fluxes from ICOADS : the construction of a new gridded dataset with uncertainty estimates. *International Journal of Climatology*, **31**, 987–1001, doi:10.1002/joc.2059.
Berry, D.I., E.C. Kent, and P.K. Taylor, 2004: An Analytical Model of Heating Errors in Marine Air Temperatures from Ships. *Journal of Atmospheric and Oceanic Technology*, **21(8)**, 1198–1215, doi:10.1175/1520-0426(2004)021<1198:aamohe>2.0.co;2.
Berry, D.I., G.K. Corlett, O. Embury, and C.J. Merchant, 2018: Stability Assessment of the (A)ATSR Sea Surface Temperature Climate Dataset from the European Space Agency Climate Change Initiative. *Remote Sensing*, **10(1)**, doi:10.3390/rs10010126.
Bertram, R.A. et al., 2018: Pliocene deglacial event timelines and the biogeochemical response offshore Wilkes Subglacial Basin, East Antarctica. *Earth and Planetary Science Letters*, **494**, 109–116, doi:10.1016/j.epsl.2018.04.054.
Berx, B. et al., 2013: Combining in situ measurements and altimetry to estimate volume, heat and salt transport variability through the Faroe–Shetland Channel. *Ocean Sci.*, **9(4)**, 639–654, doi:10.5194/os-9-639-2013.
Betts, R.A., C.D. Jones, J.R. Knight, R.F. Keeling, and J.J. Kennedy, 2016: El Niño and a record CO2 rise. *Nature Climate Change*, **6**, 806–810, doi:10.1038/nclimate3063.
Betts, R.A. et al., 2018: Changes in climate extremes, fresh water availability and vulnerability to food insecurity projected at 1.5°C and 2°C global warming with a higher-resolution global climate model. *Philosophical Transactions of the Royal Society A: Mathematical, Physical and Engineering Sciences*, **376(2119)**, 20160452,

ACCEPTED VERSION SUBJECT TO FINAL EDITS

doi:10.1098/rsta.2016.0452.
Beusch, L., L. Gudmundsson, and S.I. Seneviratne, 2020: Crossbreeding CMIP6 Earth System Models With an Emulator for Regionally Optimized Land Temperature Projections. *Geophysical Research Letters*, **47(15)**, e2019GL086812, doi:10.1029/2019gl086812.
Bianchi, G.G. and I.N. McCave, 1999: Holocene periodicity in North Atlantic climate and deep-ocean flow south of Iceland. *Nature*, **397(6719)**, 515–517, doi:10.1038/17362.
Biasutti, M. et al., 2018: Global energetics and local physics as drivers of past, present and future monsoons. *Nature Geoscience*, **11(6)**, 392–400, doi:10.1038/s41561-018-0137-1.
Bierman, P.R., J.D. Shakun, L.B. Corbett, S.R. Zimmerman, and D.H. Rood, 2016: A persistent and dynamic East Greenland Ice Sheet over the past 7.5 million years. *Nature*, **540(7632)**, 256–260, doi:10.1038/nature20147.
Bindoff, N.L. et al., 2019: Changing Ocean, Marine Ecosystems, and Dependent Communities. In: *IPCC Special Report on the Ocean and Cryosphere in a Changing Climate* [Pörtner, H.-O., D.C. Roberts, V. Masson-Delmotte, P. Zhai, M. Tignor, E. Poloczanska, K. Mintenbeck, A. Alegría, M. Nicolai, and A. Okem (eds.)]. In Press, pp. 447–587.
Binney, H. et al., 2017: Vegetation of Eurasia from the last glacial maximum to present: Key biogeographic patterns. *Quaternary Science Reviews*, **157**, 80–97, doi:10.1016/j.quascirev.2016.11.022.
Binney, H.A. et al., 2009: The distribution of late-Quaternary woody taxa in northern Eurasia: evidence from a new macrofossil database. *Quaternary Science Reviews*, doi:10.1016/j.quascirev.2009.04.016.
Biondi, F., A. Gershunov, and D.R. Cayan, 2001: North Pacific Decadal Climate Variability since 1661. *Journal of Climate*, **14(1)**, 5–10, doi:10.1175/1520-0442(2001)014<0005:npdcvs>2.0.co;2.
Bisagni, J.J., A. Gangopadhyay, and A. Sanchez-Franks, 2017: Secular change and inter-annual variability of the Gulf Stream position, 1993–2013, 70°-55°W. *Deep-Sea Research Part I: Oceanographic Research Papers*, **25**, 1–10, doi:10.1016/j.dsr.2017.04.001.
Biskaborn, B.K. et al., 2019a: Permafrost is warming at a global scale. *Nature Communications*, **10(1)**, 264, doi:10.1038/s41467-018-08240-4.
Biskaborn, B.K. et al., 2019b: Permafrost is warming at a global scale. *Nature Communications*, **10(1)**, 264, doi:10.1038/s41467-018-08240-4.
Blake-Mizen, K. et al., 2019: Southern Greenland glaciation and Western Boundary Undercurrent evolution recorded on Eirik Drift during the late Pliocene intensification of Northern Hemisphere glaciation. *Quaternary Science Reviews*, **209**, 40–51, doi:10.1016/j.quascirev.2019.01.015.
Blanchon, P., A. Eisenhauer, J. Fietzke, and V. Liebetrau, 2009: Rapid sea-level rise and reef back-stepping at the close of the last interglacial highstand. *Nature*, **458(7240)**, 881–884, doi:10.1038/nature07933.
Bliss, A.C., J.A. Miller, and W.N. Meier, 2017: Comparison of passive microwave-derived early melt onset records on Arctic sea ice. *Remote Sensing*, doi:10.3390/rs9030199.
Blowes, S.A. and Blowes, S., Supp, S., Antao, L., Bates, A., Bruelheide, Chase, J., Moyes, F., Magurran, A., McGill, B., Myers-Smith, I., Winter, M., Bjorkman, A., Bowler, D., Byrnes, J., Bonzalez, A., hines, J., Isbell, F., Jones, H., Navarro, L., Thompson, P., 2019: The geography of biodiversity change in marine and terrestrial assemblages. *Science*, **366(6463)**, 339–345, doi:10.1126/science.aaw1620.
Blunden, J. and D.S. Arndt, 2019: State of the Climate in 2018. *Bulletin of the American Meteorological Society*, **100(9)**, Si–S306, doi:10.1175/2019bamsstateoftheclimate.1.
Bohlinger, P., B.M. Sinnhuber, R. Ruhnke, and O. Kirner, 2014: Radiative and dynamical contributions to past and future Arctic stratospheric temperature trends. *Atmospheric Chemistry and Physics*, **14(3)**, 1679–1688, doi:10.5194/acp-14-1679-2014.
Böhm, E. et al., 2015: Strong and deep Atlantic meridional overturning circulation during the last glacial cycle. *Nature*, **517(7532)**, 73–76, doi:10.1038/nature14059.
Bojinski, S. et al., 2014: The Concept of Essential Climate Variables in Support of Climate Research, Applications, and Policy. *Bulletin of the American Meteorological Society*, **95(9)**, 1431–1443, doi:10.1175/bams-d-13-00047.1.
Bokhorst, S. et al., 2016: Changing Arctic snow cover: A review of recent developments and assessment of future needs for observations, modelling, and impacts. *Ambio*, **45**, 516–537, doi:10.1007/s13280-016-0770-0.
Booth, B.B.B., N.J. Dunstone, P.R. Halloran, T. Andrews, and N. Bellouin, 2012: Aerosols implicated as a prime driver of twentieth-century North Atlantic climate variability. *Nature*, **484(7393)**, 228–232, doi:10.1038/nature10946.
Bordbar, M.H., T. Martin, M. Latif, and W. Park, 2017: Role of internal variability in recent decadal to multidecadal tropical Pacific climate changes. *Geophysical Research Letters*, **44(9)**, 4246–4255, doi:10.1002/2016gl072355.
Bordi, I., R. Bonis, K. Fraedrich, and A. Sutera, 2015: Interannual variability patterns of the world' s total column water content: Amazon River basin. *Theoretical and Applied Climatology*, **122**, 441–455, doi:10.1007/s00704-014-1304-y.
Borge, A.F., S. Westermann, I. Solheim, and B. Etzelmüller, 2017: Strong degradation of palsas and peat plateaus in northern Norway during the last 60 years. *Cryosphere*, **11(1)**, 1–16, doi:10.5194/tc-11-1-2017.
Born, A. and A. Levermann, 2010: The 8.2 ka event: Abrupt transition of the subpolar gyre toward a modern North Atlantic circulation. *Geochemistry, Geophysics, Geosystems*, **11(6)**, doi:10.1029/2009gc003024.
Borstad, G., W. Crawford, J.M. Hipfner, R. Thomson, and K. Hyatt, 2011: Environmental control of the breeding

ACCEPTED VERSION SUBJECT TO FINAL EDITS

success of rhinoceros auklets at Triangle Island, British Columbia. *Marine Ecology Progress Series*, **424**, 285–302, doi:10.3354/meps08950.
Bosilovich, M.G., F.R. Robertson, L. Takacs, A. Molod, and D. Mocko, 2017: Atmospheric Water Balance and Variability in the MERRA-2 Reanalysis. *Journal of Climate*, **30**, 1177–1196, doi:10.1175/jcli-d-16-0338.1.
Bourassa, A.E., C.A. McLinden, A.F. Bathgate, B.J. Elash, and D.A. Degenstein, 2012: Precision estimate for Odin-OSIRIS limb scatter retrievals. *Journal of Geophysical Research*, **117(D4)**, D04303, doi:10.1029/2011jd016976.
Bova, S., Y. Rosenthal, Z. Liu, S.P. Godad, and M. Yan, 2021: Seasonal origin of the thermal maxima at the Holocene and the last interglacial. *Nature*, **589(7843)**, 548–553, doi:10.1038/s41586-020-03155-x.
Bowen, G.J. et al., 2015: Two massive, rapid releases of carbon during the onset of the Palaeocene–Eocene thermal maximum. *Nature Geoscience*, **8(1)**, 44–47, doi:10.1038/ngeo2316.
Bradley, S.L., G.A. Milne, B.P. Horton, and Y. Zong, 2016: Modelling sea level data from China and Malay-Thailand to estimate Holocene ice-volume equivalent sea level change. *Quaternary Science Reviews*, **137**, 54–68, doi:10.1016/j.quascirev.2016.02.002.
Bradley, S.L., R.C.A. Hindmarsh, P.L. Whitehouse, M.J. Bentley, and M.A. King, 2015: Low post-glacial rebound rates in the Weddell Sea due to Late Holocene ice-sheet readvance. *Earth and Planetary Science Letters*, **413**, 79–89, doi:10.1016/j.epsl.2014.12.039.
Braesicke, A.P. et al., 2018: Update on Global Ozone: Past, Present and Future. In: *Scientific Assessment of Ozone Depletion: 2018*. Global Ozone Research and Monitoring Project – Report No. 58, World Meteorological Organization (WMO), Geneva, Switzerland, pp. 3.1–3.74.
Braganza, K., J.L. Gergis, S.B. Power, J.S. Risbey, and A.M. Fowler, 2009: A multiproxy index of the El Niño–Southern Oscillation, A.D. 1525–1982. *Journal of Geophysical Research: Atmospheres*, **114(D5)**, doi:10.1029/2008jd010896.
Braithwaite, C.J.R. et al., 2000: Origins and development of Holocene coral reefs: a revisited model based on reef boreholes in the Seychelles, Indian Ocean. *International Journal of Earth Sciences*, **89(2)**, 431–445, doi:10.1007/s005310000078.
Brennan, M.K., G.J. Hakim, and E. Blanchard-Wrigglesworth, 2020: Arctic Sea-Ice Variability During the Instrumental Era. *Geophysical Research Letters*, **47(7)**, e2019GL086843, doi:10.1029/2019gl086843.
Brewin, R.J.W. et al., 2012: The influence of the Indian Ocean Dipole on interannual variations in phytoplankton size structure as revealed by Earth Observation. *Deep Sea Research Part II: Topical Studies in Oceanography*, **77–80**, 117–127, doi:10.1016/j.dsr2.2012.04.009.
Brierley, C.M., 2015: Interannual climate variability seen in the Pliocene Model Intercomparison Project. *Climate of the Past*, **11(3)**, 605–618, doi:10.5194/cp-11-605-2015.
Brierley, C.M. et al., 2020: Large-scale features and evaluation of the PMIP4-CMIP6 midHolocene simulations. *Climate of the Past*, **16(5)**, 1847–1872, doi:10.5194/cp-16-1847-2020.
Brigham-Grette, J. et al., 2013: Pliocene Warmth, Polar Amplification, and Stepped Pleistocene Cooling Recorded in NE Arctic Russia. *Science*, **340(6139)**, doi:10.1126/science.1233137.
Briner, J.P. et al., 2016: Holocene climate change in Arctic Canada and Greenland. *Quaternary Science Reviews*, **147**, 340–364, doi:10.1016/j.quascirev.2016.02.010.
Briner, J.P. et al., 2020: Rate of mass loss from the Greenland Ice Sheet will exceed Holocene values this century. *Nature*, **586(7827)**, 70–74, doi:10.1038/s41586-020-2742-6.
Bristow, L.A. et al., 2017: N2 production rates limited by nitrite availability in the Bay of Bengal oxygen minimum zone. *Nature Geoscience*, **10(1)**, 24–29, doi:10.1038/ngeo2847.
Broecker, W.S., 1989: The salinity contrast between the Atlantic and Pacific oceans during glacial time. *Paleoceanography*, **4(2)**, 207–212, doi:10.1029/pa004i002p00207.
Bronnimann, S. et al., 2015: Southward shift of the northern tropical belt from 1945 to 1980. *Nature Geoscience*, **8(12)**, 969–974, doi:10.1038/ngeo2568.
Bronselaer, B. et al., 2020: Importance of wind and meltwater for observed chemical and physical changes in the Southern Ocean. *Nature Geoscience*, **13(1)**, 35–42, doi:10.1038/s41561-019-0502-8.
Brook, E.J. and C. Buizert, 2018: Antarctic and global climate history viewed from ice cores. *Nature*, **558**, 200–208, doi:10.1038/s41586-018-0172-5.
Brown, R.D., 2002: Reconstructed North American, Eurasian, and Northern Hemisphere Snow Cover Extent, 1915-1997, Version 1. National Snow and Ice Center, Boulder, Colorado, USA. , doi:10.7265/n5v985z6.
Brown, R., Shuler, D. V., Bulygina, O., Derksen, C., Luojus, K., Mudryk, L., 2017: Arctic terrestrial snow cover. In: *Snow, Water, Ice and Permafrost in the Arctic (SWIPA) 2017*. Arctic Monitoring and Assessment Programme (AMAP), Oslo, Norway, pp. 25–64.
Brühl, C., 2018: Volcanic SO2 data derived from limb viewing satellites for the lower stratosphere from 1998 to 2012, and from nadir viewing satellites for the troposphere. World Data Center for Climate (WDCC) at DKRZ.
Buckley, B.M. et al., 2019: Interdecadal Pacific Oscillation reconstructed from trans-Pacific tree rings : 1350 – 2004 CE. *Climate Dynamics*, **53**, 3181–3196, doi:10.1007/s00382-019-04694-4.
Buizert, C. et al., 2015: Precise interpolar phasing of abrupt climate change during the last ice age. *Nature*, **520**, 661,

ACCEPTED VERSION SUBJECT TO FINAL EDITS

doi:10.1038/nature14401.
Buizert, C. et al., 2018: Greenland-Wide Seasonal Temperatures During the Last Deglaciation. *Geophysical Research Letters*, **45(4)**, 1905–1914, doi:10.1002/2017gl075601.
Burke, K.D. et al., 2019: Differing climatic mechanisms control transient and accumulated vegetation novelty in Europe and eastern North America. *Philosophical transactions of the Royal Society of London. Series B, Biological sciences*, **374**, 20190218, doi:10.1098/rstb.2019.0218.
Burls, N.J. and A. Fedorov, 2017: Wetter subtropics in a warmer world : Contrasting past and future hydrological cycles. *Proceedings of the National Academy of Sciences of the United States of America*, **114(49)**, 12888–12893, doi:10.1073/pnas.1703421114.
Burmeister, K., P. Brandt, and J.F. Lübbecke, 2016: Revisiting the cause of the eastern equatorial Atlantic cold event in 2009. *Journal of Geophysical Research: Oceans*, **121(7)**, 4777–4789, doi:10.1002/2016jc011719.
Burn, M.J. and S.E. Palmer, 2014: Solar forcing of Caribbean drought events during the last millennium. *Journal of Quaternary Science*, **29(8)**, 827–836, doi:10.1002/jqs.2660.
Burrows, M.T. et al., 2019: Ocean community warming responses explained by thermal affinities and temperature gradients. *Nature Climate Change*, **9(12)**, 959–963, doi:10.1038/s41558-019-0631-5.
Businger, J.A., J.C. Wyngaard, Y. Izumi, and E.F. Bradley, 1971: Flux-Profile Relationships in the Atmospheric Surface Layer. *Journal of the Atmospheric Sciences*, **28(2)**, 181–189, doi:10.1175/1520-0469(1971)028<0181:fprita>2.0.co;2.
Butler, A.H. and E.P. Gerber, 2018: Optimizing the definition of a sudden stratospheric warming. *Journal of Climate*, **31(6)**, 2337–2344, doi:10.1175/jcli-d-17-0648.1.
Butler, A.H., J.P. Sjoberg, D.J. Seidel, and K.H. Rosenlof, 2017: A sudden stratospheric warming compendium. , 63–76, doi:10.7289/v5ns0rwp.
Butler, A.H. et al., 2015: Defining sudden stratospheric warmings. *Bulletin of the American Meteorological Society*, **96(11)**, 1913–1928, doi:10.1175/bams-d-13-00173.1.
Byrne, M.P. and P.A. O'Gorman, 2018: Trends in continental temperature and humidity directly linked to ocean warming. *Proceedings of the National Academy of Sciences*, **115(19)**, 4863–4868, doi:10.1073/pnas.1722312115.
Byrne, M.P., A.G. Pendergrass, A.D. Rapp, and K.R. Wodzicki, 2018: Response of the Intertropical Convergence Zone to Climate Change : Location, Width, and Strength. *Current Climate Change Reports*, **4(4)**, 355–370, doi:10.1007/s40641-018-0110-5.
Caballero, R. and M. Huber, 2013: State-dependent climate sensitivity in past warm climates and its implications for future climate projections.. *Proceedings of the National Academy of Sciences of the United States of America*, **110(35)**, 14162–7, doi:10.1073/pnas.1303365110.
Caesar, L., S. Rahmstorf, A. Robinson, G. Feulner, and V. Saba, 2018: Observed fingerprint of a weakening Atlantic Ocean overturning circulation. *Nature*, **556(7700)**, 191, doi:10.1038/s41586-018-0006-5.
Caesar, L., G.D. McCarthy, D.J.R. Thornalley, N. Cahill, and S. Rahmstorf, 2021: Current Atlantic Meridional Overturning Circulation weakest in last millennium. *Nature Geoscience*, doi:10.1038/s41561-021-00699-z.
Caley, T. et al., 2014: Quantitative estimate of the paleo-Agulhas leakage. *Geophysical Research Letters*, **41(4)**, 1238–1246, doi:10.1002/2014gl059278.
Camoin, G.F. et al., 1997: Holocene sea level changes and reef development in the southwestern Indian Ocean. *Coral Reefs*, **16(4)**, 247–259, doi:10.1007/s003380050080.
Campos, J.L.P.S. et al., 2019: Coherent South American Monsoon Variability During the Last Millennium Revealed Through High-Resolution Proxy Records. *Geophysical Research Letters*, **46(14)**, 8261–8270, doi:10.1029/2019gl082513.
Cao, B. et al., 2018: Thermal Characteristics and Recent Changes of Permafrost in the Upper Reaches of the Heihe River Basin, Western China. *Journal of Geophysical Research: Atmospheres*, **123**, 7935– 7949, doi:10.1029/2018jd028442.
Cao, J., B. Wang, and J. Liu, 2019: Attribution of the Last Glacial Maximum climate formation. *Climate Dynamics*, **53(3)**, 1661–1679, doi:10.1007/s00382-019-04711-6.
Capotondi, A. et al., 2015: Understanding ENSO Diversity. *Bulletin of the American Meteorological Society*, **96(6)**, 921–938, doi:10.1175/bams-d-13-00117.1.
Capron, E., A. Govin, R. Feng, B.L. Otto-Bliesner, and E.W. Wolff, 2017: Critical evaluation of climate syntheses to benchmark CMIP6/PMIP4 127 ka Last Interglacial simulations in the high-latitude regions. *Quaternary Science Reviews*, **168**, 137–150, doi:10.1016/j.quascirev.2017.04.019.
Capron, E. et al., 2019: Challenges and research priorities to understand interactions between climate, ice sheets and global mean sea level during past interglacials. *Quaternary Science Reviews*, **219**, 308–311, doi:10.1016/j.quascirev.2019.06.030.
Carilli, J.E. et al., 2015: Reply to comment by Karnauskas et al. on "Equatorial Pacific coral geochemical records show recent weakening of the Walker circulation". *Paleoceanography*, **30**, 575–582, doi:10.1002/2014pa002683.received.
Carlson, A.E. et al., 2014: Earliest Holocene south Greenland ice sheet retreat within its late Holocene extent.

ACCEPTED VERSION SUBJECT TO FINAL EDITS

Geophysical Research Letters, **41(15)**, 5514–5521, doi:10.1002/2014gl060800.
Carmichael, M.J. et al., 2016: A model–model and data–model comparison for the early Eocene hydrological cycle. *Climate of the Past*, **12(2)**, 455–481, doi:10.5194/cp-12-455-2016.
Carmichael, M.J. et al., 2017: Hydrological and associated biogeochemical consequences of rapid global warming during the Paleocene-Eocene Thermal Maximum. *Global and Planetary Change*, **157**, 114–138, doi:10.1016/j.gloplacha.2017.07.014.
Carn, S.A., L. Clarisse, and A.J. Prata, 2016: Multi-decadal satellite measurements of global volcanic degassing. *Journal of Volcanology and Geothermal Research*, **311**, 99–134, doi:10.1016/j.jvolgeores.2016.01.002.
Carré, M. et al., 2014: Holocene history of ENSO variance and asymmetry in the eastern tropical Pacific. *Science*, **345(6200)**, 1045–1048, doi:10.1126/science.1252220.
Carter, B.R. et al., 2019: Pacific Anthropogenic Carbon Between 1991 and 2017. *Global Biogeochemical Cycles*, **33(5)**, 597–617, doi:10.1029/2018gb006154.
Casanova-Masjoan, M. et al., 2020: Along-Stream, Seasonal, and Interannual Variability of the North Icelandic Irminger Current and East Icelandic Current Around Iceland. *Journal of Geophysical Research: Oceans*, **125(9)**, e2020JC016283, doi:10.1029/2020jc016283.
Cattiaux, J., Y. Peings, D. Saint-Martin, N. Trou-Kechout, and S.J. Vavrus, 2016: Sinuosity of midlatitude atmospheric flow in a warming world. *Geophyiscal Research Letters*, **43(15)**, doi.org/10.1002/2016GL070309.
Ceglar, A., M. Zampieri, A. Toreti, and F. Dentener, 2019: Observed Northward Migration of Agro-Climate Zones in Europe Will Further Accelerate Under Climate Change. *Earth's Future*, doi:10.1029/2019ef001178.
Centurioni, L.R. et al., 2019: Global in situ Observations of Essential Climate and Ocean Variables at the Air-Sea Interface. *Frontiers in Marine Science*, **6**, 419, doi:10.3389/fmars.2019.00419.
Chai, Y. et al., 2020: Homogenization and polarization of the seasonal water discharge of global rivers in response to climatic and anthropogenic effects. *Science of the Total Environment*, **709**, 136062, doi:10.1016/j.scitotenv.2019.136062.
Chakraborty, S., Y.K. Tiwari, P.K.D. Burman, S.B. Roy, and V. Valsala, 2020: Observations and Modeling of GHG Concentrations and Fluxes Over India. In: *Assessment of Climate Change over the Indian Region: A Report of the Ministry of Earth Sciences (MoES), Government of India* [Krishnan, R., J. Sanjay, C. Gnanaseelan, M. Mujumdar, A. Kulkarni, and S. Chakraborty (eds.)]. Springer, Singapore, pp. 73–92, doi:10.1007/978-981-15-4327-2_4.
Chalk, T.B. et al., 2017: Causes of ice age intensification across the Mid-Pleistocene Transition. *Proceedings of the National Academy of Sciences*, doi:10.1073/pnas.1702143114.
Chan, D. and Q. Wu, 2015: Significant anthropogenic-induced changes of climate classes since 1950. *Scientific Reports*, **5(13487)**, doi:10.1038/srep13487.
Chan, D., E.C. Kent, D.I. Berry, and P. Huybers, 2019: Correcting datasets leads to more homogeneous early-twentieth-century sea surface warming. *Nature*, **571(7765)**, 393–397, doi:10.1038/s41586-019-1349-2.
Chandanpurkar, H.A., J.T. Reager, J.S. Famiglietti, and T.H. Syed, 2017: Satellite- and reanalysis-based mass balance estimates of global continental discharge (1993-2015). *Journal of Climate*, **30(21)**, 8481–8495, doi:10.1175/jcli-d-16-0708.1.
Chang, C.-Y., J.C.H. Chiang, M.F. Wehner, A.R. Friedman, and R. Ruedy, 2011: Sulfate Aerosol Control of Tropical Atlantic Climate over the Twentieth Century. *Journal of Climate*, **24(10)**, 2540–2555, doi:10.1175/2010jcli4065.1.
Chang, E.K.M. and A.M.W. Yau, 2016: Northern Hemisphere winter storm track trends since 1959 derived from multiple reanalysis datasets. *Climate Dynamics*, **47(5–6)**, 1435–1454, doi:10.1007/s00382-015-2911-8.
Charlton, A.J. et al., 2007: A New Look at Stratospheric Sudden Warmings. Part II: Evaluation of Numerical Model Simulations. *J. Climate*, **20**, 470–488, doi:10.1175/jcli3994.1.
Chatzistergos, Theodosios, Usoskin, Ilya G., Kovaltsov, Gennady A., Krivova, Natalie A., and Solanki, Sami K., 2017: New reconstruction of the sunspot group numbers since 1739 using direct calibration and "backbone" methods. *A&A*, **602**, A69, doi:10.1051/0004-6361/201630045.
Chemke, R. and L.M. Polvani, 2019: Opposite tropical circulation trends in climate models and in reanalyses. *Nature Geoscience*, **12(7)**, 528–532, doi:10.1038/s41561-019-0383-x.
Chen, 2016: Decoupling between Plant Productivity and Growing Season Length under a Warming Climate in Canada's Arctic. *American Journal of Climate Change*, **5**, 344–359, doi:10.4236/ajcc.2016.53026.
Chen, B. and Z. Liu, 2016: Global water vapor variability and trend from the latest 36 year (1979 to 2014) data of ECMWF and NCEP reanalyses, radiosonde, GPS, and microwave satellite. *Journal of Geophysical Research: Atmospheres*, **121**, 11442–11462, doi:10.1002/2016jd024917.
Chen, C. et al., 2019: China and India lead in greening of the world through land-use management. *Nature Sustainability*, **2**, 122–129, doi:10.1038/s41893-019-0220-7.
Chen, C.-T.A. et al., 2017: Deep oceans may acidify faster than anticipated due to global warming. *Nature Climate Change*, **7(12)**, 890–894, doi:10.1038/s41558-017-0003-y.
Chen, I.C., J.K. Hill, R. Ohlemüller, D.B. Roy, and C.D. Thomas, 2011: Rapid range shifts of species associated with high levels of climate warming. *Science*, **333(6045)**, 1024–1026, doi:10.1126/science.1206432.

ACCEPTED VERSION SUBJECT TO FINAL EDITS

Chen, S., K. Wei, W. Chen, and L. Song, 2014: Regional changes in the annual mean Hadley circulation in recent decades. *Journal of Geophysical Research: Atmospheres*, **119(13)**, 7815–7832, doi:10.1002/2014jd021540.
Chen, S. et al., 2016: A high-resolution speleothem record of western equatorial Pacific rainfall: Implications for Holocene ENSO evolution. *Earth and Planetary Science Letters*, **442**, 61–71, doi:10.1016/j.epsl.2016.02.050.
Chen, X. and X. Zou, 2014: Postlaunch calibration and bias characterization of AMSU-A upper air sounding channels using GPS RO Data. *Journal of Geophysical Research: Atmospheres*, **119(7)**, 3924–3941, doi:10.1002/2013jd021037.
Chen, X. and J.M. Wallace, 2015: ENSO-Like Variability: 1900–2013. *Journal of Climate*, **28(24)**, 9623–9641, doi:10.1175/jcli-d-15-0322.1.
Chen, X., S. Liang, Y. Cao, T. He, and D. Wang, 2015: Observed contrast changes in snow cover phenology in northern middle and high latitudes from 2001-2014. *Scientific Reports*, **5(1)**, 16820, doi:10.1038/srep16820.
Chen, X. et al., 2017: The increasing rate of global mean sea-level rise during 1993–2014. *Nature Climate Change*, **7(7)**, 492–495, doi:10.1038/nclimate3325.
Chen, X. et al., 2019a: Tropopause trend across China from 1979 to 2016: A revisit with updated radiosonde measurements. *International Journal of Climatology*, **39(2)**, 1117–1127, doi:10.1002/joc.5866.
Chen, X. et al., 2019b: Tropopause trend across China from 1979 to 2016: A revisit with updated radiosonde measurements. *International Journal of Climatology*, **39(2)**, 1117–1127, doi:10.1002/joc.5866.
Cheng, L. et al., 2017a: Improved estimates of ocean heat content from 1960 to 2015. *Science Advances*, **3(3)**, doi:10.1126/sciadv.1601545.
Cheng, L. et al., 2017b: Improved estimates of ocean heat content from 1960 to 2015. *Science Advances*, **3(3)**, doi:10.1126/sciadv.1601545.
Cheng, L. et al., 2018: How Well Can We Correct Systematic Errors in Historical XBT Data? *Journal of Atmospheric and Oceanic Technology*, **35(5)**, 1103–1125, doi:10.1175/jtech-d-17-0122.1.
Cheng, L. et al., 2020: Improved estimates of changes in upper ocean salinity and the hydrological cycle. *Journal of Climate*, **33(23)**, 10357–10381, doi:10.1175/jcli-d-20-0366.1.
Cherian, R. and J. Quaas, 2020: Trends in AOD, Clouds, and Cloud Radiative Effects in Satellite Data and CMIP5 and CMIP6 Model Simulations Over Aerosol Source Regions. *Geophysical Research Letters*, **47(9)**, e2020GL087132, doi:10.1029/2020gl087132.
Cherian, R., J. Quaas, M. Salzmann, and M. Wild, 2014: Pollution trends over Europe constrain global aerosol forcing as simulated by climate models. *Geophysical Research Letters*, **41(6)**, 2176–2181, doi:10.1002/2013gl058715.
Cheung, H.N., W. Zhou, H.Y. Mok, M.C. Wu, and Y. Shao, 2013: Revisiting the Climatology of Atmospheric Blocking in the Northern Hemisphere. *Advances in Atmospheric Sciences*, **30**, 397–410.
Chevalier, M. and B.M. Chase, 2015: Southeast African records reveal a coherent shift from high- to low-latitude forcing mechanisms along the east African margin across last glacial-interglacial transition. *Quaternary Science Reviews*, **125**, 117–130, doi:10.1016/j.quascirev.2015.07.009.
Chiodi, A.M. and D.E. Harrison, 2015: Global Seasonal Precipitation Anomalies Robustly Associated with El Niño and La Niña Events – An OLR Perspective. *Journal of Climate*, **28(15)**, 6133–6159, doi:10.1175/jcli-d-14-00387.1.
Chipperfield, M.P. et al., 2018: On the Cause of Recent Variations in Lower Stratospheric Ozone. *Geophysical Research Letters*, **45(11)**, 5718–5726, doi:10.1029/2018gl078071.
Choi, J.-W., I.-G. Kim, J.-Y. Kim, and C.-H. Park, 2016: The Recent Strengthening of Walker Circulation. *Sola*, **12(0)**, 96–99, doi:10.2151/sola.2016-022.
Chor, T., J.C. McWilliams, and M. Chamecki, 2020: Diffusive-Nondiffusive Flux Decompositions in Atmospheric Boundary Layers. *Journal of the Atmospheric Sciences*, **77(10)**, 3479–3494, doi:10.1175/jas-d-20-0093.1.
Chou, C. et al., 2013: Increase in the range between wet and dry season precipitation. *Nature Geoscience*, **6(4)**, 263–267, doi:10.1038/ngeo1744.
Christian, J.E., M. Koutnik, and G. Roe, 2018: Committed retreat: controls on glacier disequilibrium in a warming climate. *Journal of Glaciology*, **64(246)**, 675–688, doi:10.1017/jog.2018.57.
Christiansen, B. and F.C. Ljungqvist, 2017: Challenges and perspectives for large-scale temperature reconstructions of the past two millennia. *Reviews of Geophysics*, **55(1)**, 40–96, doi:10.1002/2016rg000521.
Christy, J.R., R.W. Spencer, W.D. Braswell, and R. Junod, 2018: Examination of space-based bulk atmospheric temperatures used in climate research. *International Journal of Remote Sensing*, **39(11)**, 3580–3607, doi:10.1080/01431161.2018.1444293.
Chung, E.S. et al., 2019: Reconciling opposing Walker circulation trends in observations and model projections. *Nature Climate Change*, **9(5)**, 405–412, doi:10.1038/s41558-019-0446-4.
Church, J.A. and N.J. White, 2011: Sea-level rise from the late 19th to the early 21st Century. *Surveys in Geophysics*, **32**, 585, doi:10.1007/s10712-011-9119-1.
Chylek, P. et al., 2012: Greenland ice core evidence for spatial and temporal variability of the Atlantic Multidecadal Oscillation. *Geophysical Research Letters*, **39(9)**, doi:10.1029/2012gl051241.
Ciracì, E., I. Velicogna, and S. Swenson, 2020: Continuity of the Mass Loss of the World's Glaciers and Ice Caps From the GRACE and GRACE Follow-On Missions. *Geophysical Research Letters*, **47(9)**, e2019GL086926,

ACCEPTED VERSION SUBJECT TO FINAL EDITS

doi:10.1029/2019gl086926.
Clark, P.U. et al., 2020: Oceanic forcing of penultimate deglacial and last interglacial sea-level rise. *Nature*, **577(7792)**, 660–664, doi:10.1038/s41586-020-1931-7.
Clarkson, M.O. et al., 2015: Ocean acidification and the Permo-Triassic mass extinction. *Science*, **348(6231)**, 229, doi:10.1126/science.aaa0193.
Claustre, H., K.S. Johnson, and Y. Takeshita, 2020: Observing the Global Ocean with Biogeochemical-Argo. *Annual Review of Marine Science*, **12(1)**, 23–48, doi:10.1146/annurev-marine-010419-010956.
Cleator, S.F., S.P. Harrison, N.K. Nichols, I.C. Prentice, and I. Roulstone, 2020: A new multivariable benchmark for Last Glacial Maximum climate simulations. *Climate of the Past*, **16(2)**, 699–712, doi:10.5194/cp-16-699-2020.
Clem, K.R., J.A. Renwick, and J. McGregor, 2017: Relationship between eastern tropical Pacific cooling and recent trends in the Southern Hemisphere zonal-mean circulation. *Climate Dynamics*, **49(1–2)**, 113–129, doi:10.1007/s00382-016-3329-7.
Clette, F., L. Svalgaard, J.M. Vaquero, and E.W. Cliver, 2014: Revisiting the Sunspot Number. *Space Science Reviews*, **186(1–4)**, 35–103, doi:10.1007/s11214-014-0074-2.
Clotten, C., R. Stein, K. Fahl, and S. De Schepper, 2018: Seasonal sea ice cover during the warm Pliocene: Evidence from the Iceland Sea (ODP Site 907). *Earth and Planetary Science Letters*, **481**, 61–72, doi:10.1016/j.epsl.2017.10.011.
Cobb, K.M. et al., 2013: Highly Variable El Niño-Southern Oscillation Throughout the Holocene. *Science*, **339(6115)**, 67–70, doi:10.1126/science.1228246.
Coddington, O., J.L. Lean, P. Pilewskie, M. Snow, and D. Lindholm, 2016: A Solar Irradiance Climate Data Record. *Bulletin of the American Meteorological Society*, **97(7)**, 1265–1282, doi:10.1175/bams-d-14-00265.1.
Coen, M.C. et al., 2020: Multidecadal trend analysis of aerosol radiative properties at a global scale. *Atmospheric Chemistry and Physics*, **20(14)**, 8867–8908, doi:10.5194/acp-20-8867-2020.
Cohen, J. et al., 2020: Divergent consensuses on Arctic amplification influence on midlatitude severe winter weather. *Nature Climate Change*, **10**, 20–29, doi:10.1038/s41558-019-0662-y.
Collins, M., M. Sutherland, L. Bower, and S.-M. Cheong, 2019: Extremes, Abrupt Changes and Managing Risks. In: *IPCC Special Report on the Ocean and Cryosphere in a Changing Climate* [Pörtner, H.-O., D.C. Roberts, V. Masson-Delmotte, P. Zhai, M. Tignor, E. Poloczanska, K. Mintenbeck, A. Alegría, M. Nicolai, and A. Okem (eds.)]. In Press, pp. 589–655.
Collins, W.J. et al., 2011: Development and evaluation of an Earth-System model – HadGEM2. *Geoscientific Model Development*, **4(4)**, doi:10.5194/gmd-4-1051-2011.
Comiso, J.C. et al., 2017: Positive Trend in the Antarctic Sea Ice Cover and Associated Changes in Surface Temperature.. *Journal of Climate*, **30(6)**, 2251–2267, doi:10.1175/jcli-d-16-0408.1.
Connolly, R. et al., 2019: Northern Hemisphere Snow-Cover Trends (1967–2018): A Comparison between Climate Models and Observations. *Geosciences*, **9(3)**, doi:10.3390/geosciences9030135.
Conroy, J.L. et al., 2017: Spatiotemporal variability in the δ18O-salinity relationship of seawater across the tropical Pacific Ocean. *Paleoceanography*, **32(5)**, 484–497, doi:10.1002/2016pa003073.
Cook, B.I., J.E. Smerdon, R. Seager, and E.R. Cook, 2014: Pan-Continental Droughts in North America over the Last Millennium. *Journal of Climate*, **27(1)**, 383–397, doi:10.1175/jcli-d-13-00100.1.
Cook, E.R. et al., 2015: Old World megadroughts and pluvials during the Common Era. *Science Advances*, **1(10)**, e1500561, doi:10.1126/sciadv.1500561.
Cook, E.R. et al., 2019: A Euro-Mediterranean tree-ring reconstruction of the winter NAO index since 910 C . E .. *Climate Dynamics*, **53(3–4)**, 1567–1580, doi:10.1007/s00382-019-04696-2.
Cooper, O.R. et al., 2020: Multi-decadal surface ozone trends at globally distributed remote locations. *Elementa Sci. Anthropocene*, **8(1)**, 23, doi:10.1525/elementa.420.
Corbett, J.G. and N.G. Loeb, 2015: On the relative stability of CERES reflected shortwave and MISR and MODIS visible radiance measurements during the Terra satellite mission. *Journal of Geophysical Research: Atmospheres*, **120(22)**, 11,608–11,616, doi:10.1002/2015jd023484.
Cornes, R.C., P.D. Jones, K.R. Briffa, and T.J. Osborn, 2013: Estimates of the North Atlantic Oscillation back to 1692 using a Paris-London westerly index. *International Journal of Climatology*, **33(1)**, 228–248, doi:10.1002/joc.3416.
Cornes, R.C., E.C. Kent, D.I. Berry, and J.J. Kennedy, 2020: CLASSnmat: A global night marine air temperature data set, 1880–2019. *Geoscience Data Journal*, **7(n/a)**, 170–184, doi:10.1002/gdj3.100.
Cortijo, E. et al., 1997: Changes in sea surface hydrology associated with Heinrich event 4 in the North Atlantic Ocean between 40° and 60°N. *Earth and Planetary Science Letters*, **146(1–2)**, 29–45, doi:10.1016/s0012-821x(96)00217-8.
Costa, K.M., J.F. McManus, and R.F. Anderson, 2018: Paleoproductivity and Stratification Across the Subarctic Pacific Over Glacial-Interglacial Cycles. *Paleoceanography and Paleoclimatology*, **33(9)**, 914–933, doi:10.1029/2018pa003363.
Cotté, C. and C. Guinet, 2007: Historical whaling records reveal major regional retreat of Antarctic sea ice. *Deep-Sea Research Part I: Oceanographic Research Papers*, **57**, 243–252, doi:10.1016/j.dsr.2006.11.001.

ACCEPTED VERSION SUBJECT TO FINAL EDITS

Coumou, D., J. Lehmann, and J. Beckmann, 2015: The weakening summer circulation in the Northern Hemisphere mid-latitudes. *Science*, **348(6232)**, 324–327, doi:10.1126/science.1261768.
Coumou, D., V. Petoukhov, S. Rahmstorf, S. Petri, and H.J. Schellnhuber, 2014: Quasi-resonant circulation regimes and hemispheric synchronization of extreme weather in boreal summer. *Proceedings of the National Academy of Sciences*, **111(34)**, 12331–12336, doi:10.1073/pnas.1412797111.
Coumou, D., G. Di Capua, S. Vavrus, L. Wang, and S. Wang, 2018: The influence of Arctic amplification on mid-latitude summer circulation. *Nature Communications*, **9(1)**, 2959, doi:10.1038/s41467-018-05256-8.
Cowtan, K. and R.G. Way, 2014: Coverage bias in the HadCRUT4 temperature series and its impact on recent temperature trends. *Quarterly Journal of the Royal Meteorological Society*, **140(683)**, 1935–1944, doi:10.1002/qj.2297.
Cowtan, K., R. Rohde, and Z. Hausfather, 2018: Evaluating biases in sea surface temperature records using coastal weather stations. *Quarterly Journal of the Royal Meteorological Society*, **144(712)**, 670–681, doi:10.1002/qj.3235.
Cowtan, K. et al., 2015: Robust comparison of climate models with observations using blended land air and ocean sea surface temperatures. *Geophysical Research Letters*, **42(15)**, 6526–6534, doi:10.1002/2015gl064888.
Craig, P.M., D. Ferreira, and J. Methven, 2017: The contrast between Atlantic and Pacific surface water fluxes. *Tellus A: Dynamic Meteorology and Oceanography*, **69(1)**, 1–15, doi:10.1080/16000870.2017.1330454.
Cramer, B.S., K.G. Miller, P.J. Barrett, and J.D. Wright, 2011: Late Cretaceous-Neogene trends in deep ocean temperature and continental ice volume: Reconciling records of benthic foraminiferal geochemistry (δ18O and Mg/Ca) with sea level history. *Journal of Geophysical Research: Oceans*, **116(C12)**, doi:10.1029/2011jc007255.
Cropper, T., E. Hanna, M.A. Valente, and T. Jónsson, 2015: A daily Azores-Iceland North Atlantic Oscillation index back to 1850. *Geoscience Data Journal*, **2(1)**, 12–24, doi:10.1002/gdj3.23.
Crosta, X. et al., 2021: Multi-decadal trends in Antarctic sea-ice extent driven by ENSO-SAM over the last 2,000 years. *Nature Geoscience*, **14**, 156–160, doi:10.1038/s41561-021-00697-1.
Cuesta-Valero, F.J., A. Garcia-Garcia, H. Beltrami, J.F. González-Rouco, and E. Garcia-Bustamante, 2021: Long-Term Global Ground Heat Flux and Continental Heat Storage from Geothermal Data. *Climate of the Past*, **17(1)**, 451–468, doi:10.5194/cp-17-451-2021.
Cui, Y. et al., 2011: Slow release of fossil carbon during the palaeocene-eocene thermal maximum. *Nature Geoscience*, **4(7)**, 481–485, doi:10.1038/ngeo1179.
Cummins, P.F. and T. Ross, 2020: Secular trends in water properties at Station P in the northeast Pacific: An updated analysis. *Progress in Oceanography*, **186**, 102329, doi:10.1016/j.pocean.2020.102329.
Curran, M.A.J., T.D. Van Ommen, V.I. Morgan, K.L. Phillips, and A.S. Palmer, 2003: Ice Core Evidence for Antarctic Sea Ice Decline since the 1950s. *Science*, **302(5648)**, 1203–1206, doi:10.1126/science.1087888.
D'Agostino, R. and P. Lionello, 2017: Evidence of global warming impact on the evolution of the Hadley Circulation in ECMWF centennial reanalyses. *Climate Dynamics*, **48(9–10)**, 3047–3060, doi:10.1007/s00382-016-3250-0.
D'Arrigo, R. and C.C. Ummenhofer, 2015: The climate of Myanmar: evidence for effects of the Pacific Decadal Oscillation. *International Journal of Climatology*, **35(4)**, 634–640, doi:10.1002/joc.3995.
Da, J., Y.G. Zhang, G. Li, X. Meng, and J. Ji, 2019: Low CO2 levels of the entire Pleistocene epoch. *Nature Communications*, **10(1)**, 4342, doi:10.1038/s41467-019-12357-5.
Dahutia, P., B. Pathak, and P.K. Bhuyan, 2018: Aerosols characteristics, trends and their climatic implications over Northeast India and adjoining South Asia. *International Journal of Climatology*, **38(3)**, 1234–1256, doi:10.1002/joc.5240.
Dai, A., 2016: Historical and Future Changes in Streamflow and Continental Runoff: A Review. *Terrestrial Water Cycle and Climate Change: Natural and Human-Induced Impacts*, 17–37, doi:10.1002/9781118971772.ch2.
Dai, A. and T. Zhao, 2017: Uncertainties in historical changes and future projections of drought . Part I : estimates of historical drought changes. *Climatic Change*, **144**, 519–533, doi:10.1007/s10584-016-1705-2.
Dai, A., T. Qian, K.E. Trenberth, and J.D. Milliman, 2009: Changes in continental freshwater discharge from 1948 to 2004. *Journal of Climate*, **22(10)**, 2773–2792, doi:10.1175/2008jcli2592.1.
Daly, C., M.P. Widrlechner, M.D. Halbleib, J.I. Smith, and W.P. Gibson, 2012: Development of a new USDA plant hardiness zone map for the United States. *Journal of Applied Meteorology and Climatology*, **51(2)**, 242–264, doi:10.1175/2010jamc2536.1.
Dang, H. et al., 2020: Pacific warm pool subsurface heat sequestration modulated Walker circulation and ENSO activity during the Holocene. *Science Advances*, **6(42)**, eabc0402, doi:10.1126/sciadv.abc0402.
Dangendorf, S. et al., 2019: Persistent acceleration in global sea-level rise since the 1960s. *Nature Climate Change*, **9(9)**, 705–710, doi:10.1038/s41558-019-0531-8.
Danzer, J., M. Schwaerz, G. Kirchengast, and S.B. Healy, 2020: Sensitivity Analysis and Impact of the Kappa-Correction of Residual Ionospheric Biases on Radio Occultation Climatologies. *Earth and Space Science*, **7(7)**, e2019EA000942, doi:10.1029/2019ea000942.
Darby, D.A., J.D. Ortiz, C.E. Grosch, and S.P. Lund, 2012: 1,500-year cycle in the Arctic Oscillation identified in Holocene Arctic sea-ice drift. *Nature Geoscience*, **5(12)**, 897–900, doi:10.1038/ngeo1629.

ACCEPTED VERSION SUBJECT TO FINAL EDITS

Dätwyler, C., N.J. Abram, M. Grosjean, E.R. Wahl, and R. Neukom, 2019: El Niño-Southern Oscillation variability, teleconnection changes and responses to large volcanic eruptions since AD 1000. *International Journal of Climatology*, **39(5)**, 2711–2724, doi:10.1002/joc.5983.

Dätwyler, C. et al., 2018: Teleconnection stationarity, variability and trends of the Southern Annular Mode (SAM) during the last millennium. *Climate Dynamics*, **51(5–6)**, 2321–2339, doi:10.1007/s00382-017-4015-0.

Davini, P., C. Cagnazzo, S. Gualdi, and A. Navarra, 2012: Bidimensional diagnostics, variability, and trends of Northern Hemisphere blocking. *Journal of Climate*, **25(19)**, 6496–6509, doi:10.1175/jcli-d-12-00032.1.

Davis, L.L.B., D.W.J. Thompson, J.J. Kennedy, and E.C. Kent, 2019: The Importance of Unresolved Biases in Twentieth-Century Sea Surface Temperature Observations. *Bulletin of the American Meteorological Society*, **100(4)**, 621–629, doi:10.1175/bams-d-18-0104.1.

Davis, N. and T. Birner, 2017: On the Discrepancies in Tropical Belt Expansion between Reanalyses and Climate Models and among Tropical Belt Width Metrics. *Journal of Climate*, **30**, 1211–1231, doi:10.1175/jcli-d-16-0371.1.

Davis, N.A. and T. Birner, 2013: Seasonal to multi-decadal variability of the width of the tropical belt. *Journal of Geophysical Research*, **118(14)**, 7773–7787, doi:10.1002/jgrd.50610.

Davis, S.M. and K.H. Rosenlof, 2012: A multi-diagnostic intercomparison of tropical width time series using reanalyses and satellite observations. *Journal of Climate*, **25(4)**, 1061–1078, doi:10.1175/jcli-d-11-00127.1.

Davis, S.M., K.H. Rosenlof, D.F. Hurst, H.B. Selkirk, and H. Vömel, 2017: Global Climate: Atmospheric Composition] Stratospheric Water Vapor. *State of the Climate in 2016. Bulletin of the American Meteorological Soceity*, **98, S51–S5**, doi:10.1175/2017bamsstateoftheclimate.1.

Davis, S.M. et al., 2016: The Stratospheric Water and Ozone Satellite Homogenized (SWOOSH) database: a long-term database for climate studies. *Earth System Science Data*, **8(2)**, 461–490, doi:10.5194/essd-8-461-2016.

de Boer, B. et al., 2015: Simulating the Antarctic ice sheet in the late-Pliocene warm period: PLISMIP-ANT, an ice-sheet model intercomparison project. *The Cryosphere*, **9(3)**, 881–903, doi:10.5194/tc-9-881-2015.

de Jong, M.F. and L. de Steur, 2016: Strong winter cooling over the Irminger Sea in winter 2014–2015, exceptional deep convection, and the emergence of anomalously low SST. *Geophysical Research Letters*, **43(13)**, 7106–7113, doi:10.1002/2016gl069596.

de Jong, M.F., M. Oltmanns, J. Karstensen, and L. de Steur, 2018: Deep convection in the Irminger Sea observed with a dense mooring array. *Oceanography*, **31(1)**, 50–59, doi:10.5670/oceanog.2018.109.

de Jong, R., J. Verbesselt, M.E. Schaepman, and S. de Bruin, 2012: Trend changes in global greening and browning: Contribution of short-term trends to longer-term change. *Global Change Biology*, **18(2)**, 642–655, doi:10.1111/j.1365-2486.2011.02578.x.

De La Mare, W.K., 1997: Abrupt mid-twentieth-century decline in Antarctic sea-ice extent from whaling records. *Nature*, **389**, 57–60, doi:10.1038/37956.

De La Mare, W.K., 2009: Changes in Antarctic sea-ice extent from direct historical observations and whaling records. *Climatic Change*, **92**, 461–493, doi:10.1007/s10584-008-9473-2.

de la Vega, E., T.B. Chalk, P.A. Wilson, R.P. Bysani, and G.L. Foster, 2020: Atmospheric CO2 during the Mid-Piacenzian Warm Period and the M2 glaciation. *Scientific Reports*, **10(1)**, 11002, doi:10.1038/s41598-020-67154-8.

De Schepper, S., P.L. Gibbard, U. Salzmann, and J. Ehlers, 2014: A global synthesis of the marine and terrestrial evidence for glaciation during the Pliocene Epoch. *Earth-Science Reviews*, **135**, doi:10.1016/j.earscirev.2014.04.003.

De Vernal, A. et al., 2013: Dinocyst-based reconstructions of sea ice cover concentration during the Holocene in the Arctic Ocean, the northern North Atlantic Ocean and its adjacent seas. *Quaternary Science Reviews*, **79**, 111–121, doi:10.1016/j.quascirev.2013.07.006.

DeConto, R.M. and D. Pollard, 2016: Contribution of Antarctica to past and future sea-level rise. *Nature*, **531(7596)**, 591–597, doi:10.1038/nature17145.

Dee, D.P. and S. Uppala, 2009: Variational bias correction of satellite radiance data in the ERA-Interim reanalysis. *Quarterly Journal of the Royal Meteorological Society*, **135(644)**, 1830–1841, doi:10.1002/qj.493.

Dee, D.P. et al., 2011: The ERA-Interim reanalysis: configuration and performance of the data assimilation system. *Quarterly Journal of the Royal Meteorological Society*, **137(656)**, 553–597, doi:10.1002/qj.828.

Delaygue, G., S. Brönnimann, P.D. Jones, J. Blanchet, and M. Schwander, 2019: Reconstruction of Lamb weather type series back to the eighteenth century. *Climate Dynamics*, **52**, 6131–6148, doi:10.1007/s00382-018-4506-7.

Dendy, S., J. Austermann, J.R. Creveling, and J.X. Mitrovica, 2017: Sensitivity of Last Interglacial sea-level high stands to ice sheet configuration during Marine Isotope Stage 6. *Quaternary Science Reviews*, **171**, 234–244, doi:10.1016/j.quascirev.2017.06.013.

Deng, K., S. Yang, M. Ting, Y. Tan, and S. He, 2018: Global Monsoon Precipitation: Trends, Leading Modes, and Associated Drought and Heat Wave in the Northern Hemisphere. *Journal of Climate*, **31(17)**, 6947–6966, doi:10.1175/jcli-d-17-0569.1.

Deng, W. et al., 2013: Variations in the Pacific Decadal Oscillation since 1853 in a coral record from the northern South China Sea. *Journal of Geophysical Research: Oceans*, **118(5)**, 2358–2366, doi:10.1002/jgrc.20180.

ACCEPTED VERSION SUBJECT TO FINAL EDITS

Deng, W. et al., 2017: A comparison of the climates of the Medieval Climate Anomaly, Little Ice Age, and Current Warm Period reconstructed using coral records from the northern South China Sea. *Journal of Geophysical Research: Oceans*, **122(1)**, 264–275, doi:10.1002/2016jc012458.

Dennison, F.W., A.J. McDonald, and O. Morgenstern, 2016: The Influence of Ozone Forcing on Blocking in the Southern Hemisphere. *Journal of Geophysical Research: Atmospheres*, **121(24)**, 14358–14371, doi:10.1002/2016jd025033.

Denniston, R.F. et al., 2016: Expansion and contraction of the indo-pacific tropical rain belt over the last three millennia. *Scientific Reports*, **6**, 1–9, doi:10.1038/srep34485.

Deplazes, G. et al., 2013: Links between tropical rainfall and North Atlantic climate during the last glacial period. *Nature Geoscience*, **6(3)**, 213–217, doi:10.1038/ngeo1712.

Derksen, C. et al., 2019: Changes in Snow, Ice and Permafrost Across Canada. In: *Canada's Changing Climate Report* [Bush, E. and D.S. Lemmen (eds.)]. Government of Canada, Ottawa, ON, Canada, pp. 194–260.

Derksen, C., Brown, R., Mudryk, L., Luojus, K., Helfrich, S., 2018: Terrestrial snow cover in the Arctic [in "State of the Climate in 2017"]. *Bulletin of the American Meteorological Society*, **99**, S169–S171, doi:10.1175/2018bamsstateoftheclimate.1.

Derksen, C., R. Brown, L. Mudryk, K.L., 2015: Snow. In: *Arctic Report Card 2015*.

Desbruyères, D.G., H. Mercier, G. Maze, and N. Daniault, 2019: Surface predictor of overturning circulation and heat content change in the subpolar North Atlantic. *Ocean Sci.*, **15(3)**, 809–817, doi:10.5194/os-15-809-2019.

Deschamps, P. et al., 2012: Ice-sheet collapse and sea-level rise at the Bølling warming 14,600 years ago. *Nature*, **483(7391)**, 559–564, doi:10.1038/nature10902.

Dessler, A.E. et al., 2016: Transport of ice into the stratosphere and the humidification of the stratosphere over the 21st century. *Geophysical research letters*, **43(5)**, 2323–2329, doi:10.1002/2016gl067991.

Di Capua, G. and D. Coumou, 2016: Changes in meandering of the Northern Hemisphere circulation. *Environmental Research Letters*, **11**, 094028,doi:10.1088/1748–9326/11/9/094028.

Diallo, M. et al., 2018: Response of stratospheric water vapor and ozone to the unusual timing of El Niño and the QBO disruption in 2015–2016. *Atmospheric Chemistry and Physics*, **18(17)**, 13055–13073, doi:10.5194/acp-18-13055-2018.

Dickson, A.J., A.S. Cohen, and A.L. Coe, 2012: Seawater oxygenation during the Paleocene-Eocene Thermal Maximum. *Geology*, **40(7)**, 639–642, doi:10.1130/g32977.1.

Dieng, H.B., A. Cazenave, B. Meyssignac, and M. Ablain, 2017: New estimate of the current rate of sea level rise from a sea level budget approach. *Geophysical Research Letters*, **44(8)**, 3744–3751, doi:10.1002/2017gl073308.

DiNezio, P.N. and J.E. Tierney, 2013: The effect of sea level on glacial Indo-Pacific climate. *Nature Geoscience*, **6(6)**, 485–491, doi:10.1038/ngeo1823.

DiNezio, P.N. et al., 2018: Glacial changes in tropical climate amplified by the Indian Ocean. *Science Advances*, **4(12)**, 1–12, doi:10.1126/sciadv.aat9658.

Dirksen, R.J. et al., 2014: Reference quality upper-air measurements: GRUAN data processing for the Vaisala RS92 radiosonde. *Atmospheric Measurement Techniques*, **7(12)**, 4463–4490, doi:10.5194/amt-7-4463-2014.

Do, H.X., S. Westra, and M. Leonard, 2017: A global-scale investigation of trends in annual maximum streamflow. *Journal of Hydrology*, **552**, 28–43, doi:10.1016/j.jhydrol.2017.06.015.

Do, H.X., L. Gudmundsson, M. Leonard, and S. Westra, 2018: The Global Streamflow Indices and Metadata Archive (GSIM)-Part 1: The production of a daily streamflow archive and metadata. *Earth System Science Data*, **10(2)**, 765–785, doi:10.5194/essd-10-765-2018.

Dolman, A.M. and T. Laepple, 2018: Sedproxy: a forward model for sediment-archived climate proxies. *Climate of the Past*, **14(12)**, 1851–1868, doi:10.5194/cp-14-1851-2018.

Domingues, C.M. et al., 2008: Improved estimates of upper-ocean warming and multi-decadal sea-level rise. *Nature*, **453(7198)**, 1090–1093, doi:10.1038/nature07080.

Donat, M.G. et al., 2013a: Global land-based datasets for monitoring climatic extremes. *Bulletin of the American Meteorological Society*, **94(7)**, 997–1006, doi:10.1175/bams-d-12-00109.1.

Donat, M.G. et al., 2013b: Updated analyses of temperature and precipitation extreme indices since the beginning of the twentieth century: The HadEX2 dataset. *Journal of Geophysical Research Atmospheres*, **118(5)**, 2098–2118, doi:10.1002/jgrd.50150.

Dong, B. and R. Lu, 2013: Interdecadal enhancement of the walker circulation over the Tropical Pacific in the late 1990s. *Advances in Atmospheric Sciences*, **30(2)**, 247–262, doi:10.1007/s00376-012-2069-9.

Dong, B., A. Dai, M. Vuille, and O.E. Timm, 2018: Asymmetric Modulation of ENSO Teleconnections by the Interdecadal Pacific Oscillation. *Journal of Climate*, **31(18)**, 7337–7361, doi:10.1175/jcli-d-17-0663.1.

Dong, L. et al., 2016: The Footprint of the Inter-decadal Pacific Oscillation in Indian Ocean Sea Surface Temperatures. *Scientific Reports*, **6**, 21251, doi:10.1038/srep21251.

Dong, S., M.O. Baringer, and G.J. Goni, 2019: Slow Down of the Gulf Stream during 1993–2016. *Scientific Reports*, **9(1)**, 6672, doi:10.1038/s41598-019-42820-8.

Dornelas, M. et al., 2014: Assemblage Time Series Reveal Biodiversity Change but Not Systematic Loss. *Science*, **344(6181)**, 296–299, doi:10.1126/science.1248484.

ACCEPTED VERSION SUBJECT TO FINAL EDITS

Dornelas, M. et al., 2018: BioTIME: A database of biodiversity time series for the Anthropocene. *Global Ecology and Biogeography*, **27(7)**, 760–786, doi:10.1111/geb.12729.
Dowdeswell, J.A. et al., 2020: Delicate seafloor landforms reveal past Antarctic grounding-line retreat of kilometers per year. *Science*, **368(6494)**, 1020–1024, doi:10.1126/science.aaz3059.
Dowsett, H.J. et al., 2019: The mid-Piacenzian of the North Atlantic Ocean. *Stratigraphy*, **16(3)**, 119–144, doi:10.29041/strat.16.3.119-144.
Droste, E.S. et al., 2020: Trends and emissions of six perfluorocarbons in the Northern Hemisphere and Southern Hemisphere. *Atmospheric Chemistry and Physics*, **20(8)**, 4787–4807, doi:10.5194/acp-20-4787-2020.
Druzhinin, O., Y. Troitskaya, and S. Zilitinkevich, 2019: The study of the unstably-stratified marine atmospheric boundary layer by direct numerical simulation. *Journal of Physics: Conference Series*, **1163**, 12018, doi:10.1088/1742-6596/1163/1/012018.
Du, X. et al., 2021: High-resolution interannual precipitation reconstruction of Southern California: Implications for Holocene ENSO evolution. *Earth and Planetary Science Letters*, **554**, 116670, doi:10.1016/j.epsl.2020.116670.
Du, Y., J.J. Xiao, and K.F. Yu, 2014: Tropical Indian Ocean Basin Mode recorded in coral oxygen isotope data from the Seychelles over the past 148 years. *Science China Earth Sciences*, **57(11)**, 2597–2605, doi:10.1007/s11430-014-4956-7.
Duchesne, C., Smith, S. L., Ednie, M., Bonnaventure, P.P., 2015: Active layer variability and Change in the Mackenzie Valley, Northwest Territories. In: *68th Canadian Geotechnical Conference and 7th Canadian Permafrost Conference*.
Dumitru, O.A. et al., 2019: Constraints on global mean sea level during Pliocene warmth. *Nature*, **574(7777)**, 233–236, doi:10.1038/s41586-019-1543-2.
Dunn, R.J.H., K.M. Willett, C.P. Morice, and D.E. Parker, 2014: Pairwise homogeneity assessment of HadISD. *Climate of the Past*, **10(4)**, 1501–1522, doi:10.5194/cp-10-1501-2014.
Dunn, R.J.H., K.M. Willett, D.E. Parker, and L. Mitchell, 2016: Expanding HadISD: quality-controlled, sub-daily station data from 1931. *Geoscientific Instrumentation, Methods and Data Systems*, **5(2)**, 473–491, doi:10.5194/cpd-11-4569-2015.
Dunn, R.J.H., K.M. Willett, A. Ciavarella, and P.A. Stott, 2017: Comparison of land surface humidity between observations and CMIP5 models. *Earth System Dynamics*, **8(3)**, 719–747, doi:10.5194/esd-8-719-2017.
Dunn, R.J.H. et al., 2012: HadISD: A Quality Controlled global synoptic report database for selected variables at long-term stations from 1973-2011. *Climate of the Past*, **8(5)**, 1649–1679, doi:10.5194/cp-8-1649-2012.
Dunn, R., 2020: Development of an updated global in situ-based dataset of temperature and precipitation extremes: HadEX3. *Journal of Geophysical Research - Atmospheres*, **125(16)**, doi:10.1029/2019jd032263.
Durack, P.J., 2015: Ocean salinity and the global water cycle. *Oceanography*, **28**, 20–31, doi:10.5670/oceanog.2015.03.
Durack, P.J. and S.E. Wijffels, 2010: Fifty-Year Trends in Global Ocean Salinities and Their Relationship to Broad-Scale Warming. *Journal of Climate*, **23(16)**, 4342–4362, doi:10.1175/2010jcli3377.1.
Durack, P.J., S.E. Wijffels, and R.J. Matear, 2012: Ocean salinities reveal strong global water cycle intensification during 1950 to 2000. *Science*, **336(6080)**, 455–458, doi:10.1126/science.1212222.
Duruisseau, F., N. Huret, A. Andral, and C. Camy-Peyret, 2017: Assessment of the ERA-Interim Winds Using High-Altitude Stratospheric Balloons. *Journal of the Atmospheric Sciences*, **74(6)**, 2065–2080, doi:10.1175/jas-d-16-0137.1.
Dutton, A. et al., 2015: Sea-level rise due to polar ice-sheet mass loss during past warm periods. *Science*, **349(6244)**, doi:10.1126/science.aaa4019.
Dyez, K.A., B. Hönisch, and G.A. Schmidt, 2018: Early Pleistocene Obliquity-Scale pCO2 Variability at ~1.5 Million Years Ago. *Paleoceanography and Paleoclimatology*, **33(11)**, 1270–1291, doi:10.1029/2018pa003349.
Ebita, A. et al., 2011: The Japanese 55-year Reanalysis "JRA-55": An Interim Report. *SOLA*, **7**, 149–152, doi:10.2151/sola.2011-038.
Edinburgh, T. and J.J. Day, 2016: Estimating the extent of Antarctic summer sea ice during the Heroic Age of Antarctic exploration. *Cryosphere*, **10(6)**, 2721–2730, doi:10.5194/tc-10-2721-2016.
Edwards, J.M., A.C.M. Beljaars, A.A.M. Holtslag, and A.P. Lock, 2020: Representation of Boundary-Layer Processes in Numerical Weather Prediction and Climate Models. *Boundary-Layer Meteorology*, **177**, 511–539, doi:10.1007/s10546-020-00530-z.
Edwards, M. and A.J. Richardson, 2004: Impact of climate change on marine pelagic phenology and trophic mismatch. *Nature*, **430(7002)**, 881–884, doi:10.1038/nature02808.
Edwards, M., Helaouet P., Alhaija, R.A., Batten S., Beaugrand G., C.S., 2016: *Global Marine Ecological Status Report: results from the global CPR survey 2014/2015*. Global Marine Ecological Status Report No. 11. Sir Alister Hardy Foundation for Continuous Plankton Recorder Survey, Plymouth, UK, 32 pp.
Egorova, T. et al., 2018: Revised historical solar irradiance forcing. *A&A*, **615**, A85, doi:10.1051/0004-6361/201731199.
Eguchi, N., K. Kodera, and T. Nasuno, 2015: A global non-hydrostatic model study of a downward coupling through the tropical tropopause layer during a stratospheric sudden warming. *Atmospheric Chemistry and Physics*,

ACCEPTED VERSION SUBJECT TO FINAL EDITS

15(1), 297–304, doi:10.5194/acp-15-297-2015.
Elipot, S. and L.M. Beal, 2018: Observed Agulhas Current sensitivity to interannual and long-term trend atmospheric forcings. *Journal of Climate*, **31(8)**, 3077–3098, doi:10.1175/jcli-d-17-0597.1.
Elmendorf, S.C. et al., 2015: Experiment, monitoring, and gradient methods used to infer climate change effects on plant communities yield consistent patterns. *Proceedings of the National Academy of Sciences*, **112(2)**, 448–452, doi:10.1073/pnas.1410088112.
Emile-Geay, J. et al., 2016: Links between tropical Pacific seasonal, interannual and orbital variability during the Holocene. *Nature Geoscience*, **9**, 168, doi:10.1038/ngeo2608.
Engel, A. et al., 2018: Update on Ozone-Depleting Substances (ODSs) and Other Gases of Interest to the Montreal Protocol. In: *Scientific Assessment of Ozone Depletion: 2018*. Global Ozone Research and Monitoring Project – Report No. 58, World Meteorological Organization (WMO), Geneva, Switzerland, pp. 1.1–1.87.
England, M.H. et al., 2014: Recent intensification of wind-driven circulation in the Pacific and the ongoing warming hiatus. *Nature Climate Change*, **4(3)**, 222–227, doi:10.1038/nclimate2106.
Erb, K.H. et al., 2017: Land management: data availability and process understanding for global change studies. *Global Change Biology*, **23(2)**, doi:10.1111/gcb.13443.
Eriksen, H. et al., 2018: Recent Acceleration of a Rock Glacier Complex, Ádjet, Norway, Documented by 62 Years of Remote Sensing Observations. *Geophysical Research Letters*, **45(16)**, 8314–8323, doi:10.1029/2018gl077605.
Estilow, T.W., A.H. Young, and D.A. Robinson, 2015: A long-term Northern Hemisphere snow cover extent data record for climate studies and monitoring. *Earth System Science Data*, **7(1)**, 137–142, doi:10.5194/essd-7-137-2015.
Evan, S., K.H. Rosenlof, T. Thornberry, A. Rollins, and S. Khaykin, 2015: TTL cooling and drying during the January 2013 stratospheric sudden warming. *Quarterly Journal of the Royal Meteorological Society*, **141(693)**, 3030–3039, doi:10.1002/qj.2587.
Evans, G., P. Augustinus, P. Gadd, A. Zawadzki, and A. Ditchfield, 2019: A multi-proxy µ-XRF inferred lake sediment record of environmental change spanning the last ca. 2230 years from Lake Kanono, Northland, New Zealand. *Quaternary Science Reviews*, **225**, doi:10.1016/j.quascirev.2019.106000.
Evans, P. and C.D. Brown, 2017: The boreal–temperate forest ecotone response to climate change. *Environmental Reviews*, **25(4)**, doi:10.1139/er-2017-0009.
Evtushevsky, O.M., A. Grytsai, and G.P. Milinevsky, 2018: Decadal changes in the central tropical Pacific teleconnection to the Southern Hemisphere extratropics. *Climate Dynamics*, **52**, 4027–4055, doi:10.1007/s00382-018-4354-5.
Ezat, M.M., T.L. Rasmussen, B. Hönisch, J. Groeneveld, and P. deMenocal, 2017: Episodic release of CO2 from the high-latitude North Atlantic Ocean during the last 135 kyr. *Nature Communications*, **8(1)**, 14498, doi:10.1038/ncomms14498.
Ezer, T., 2013: Sea level rise, spatially uneven and temporally unsteady: why the US east coast, the global tide gauge record and the global altimeter data show different trends. *Geophysical Research Letters*, **40(20)**, 5439–5444, doi:10.1002/2013gl057952.
Famiglietti, C.A., J.B. Fisher, G. Halverson, and E.E. Borbas, 2018: Global Validation of MODIS Near-Surface Air and Dew Point Temperatures. *Geophysical Research Letters*, **45(15)**, 7772–7780, doi:10.1029/2018gl077813.
Fan, L., Q. Liu, C. Wang, and F. Guo, 2016: Indian Ocean Dipole Modes Associated with Different Types of ENSO Development. *Journal of Climate*, **30(6)**, 2233–2249, doi:10.1175/jcli-d-16-0426.1.
Farinotti, D. et al., 2019: A consensus estimate for the ice thickness distribution of all glaciers on Earth. *Nature Geoscience*, **12**, 168–173, doi:10.1038/s41561-019-0300-3.
Farquharson, L.M. et al., 2019: Climate Change Drives Widespread and Rapid Thermokarst Development in Very Cold Permafrost in the Canadian High Arctic. *Geophysical Research Letters*, **46(12)**, 6681–6689, doi:10.1029/2019gl082187.
Faust, J.C., K. Fabian, G. Milzer, J. Giraudeau, and J. Knies, 2016: Norwegian fjord sediments reveal NAO related winter temperature and precipitation changes of the past 2800 years. *Earth and Planetary Science Letters*, **435**, 84–93, doi:10.1016/j.epsl.2015.12.003.
Fedorov, A., 2006: The Pliocene Paradox (Mechanisms for a Permanent El Nino). *Science*, **312(5779)**, 1485–1489, doi:10.1126/science.1122666.
Felis, T., A. Suzuki, H. Kuhnert, N. Rimbu, and H. Kawahata, 2010: Pacific Decadal Oscillation documented in a coral record of North Pacific winter temperature since 1873. *Geophysical Research Letters*, **37(14)**, doi:10.1029/2010gl043572.
Feng, M., X. Zhang, B. Sloyan, and M. Chamberlain, 2017: Contribution of the deep ocean to the centennial changes of the Indonesian Throughflow. *Geophysical Research Letters*, **44(6)**, 2859–2867, doi:10.1002/2017gl072577.
Feng, M., N. Zhang, Q. Liu, and S. Wijffels, 2018: The Indonesian throughflow, its variability and centennial change. *Geoscience Letters*, **5(1)**, 3, doi:10.1186/s40562-018-0102-2.
Feng, R., B.L. Otto-Bliesner, E.C. Brady, and N. Rosenbloom, 2020: Increased Climate Response and Earth System Sensitivity From CCSM4 to CESM2 in Mid-Pliocene Simulations. *Journal of Advances in Modeling Earth Systems*, **12(8)**, e2019MS002033, doi:10.1029/2019ms002033.

ACCEPTED VERSION SUBJECT TO FINAL EDITS

Feng, R. et al., 2019: Contributions of aerosol-cloud interactions to mid-Piacenzian seasonally sea ice-free Arctic Ocean. *Geophysical Research Letters*, **46(16)**, 9920–9929, doi:10.1029/2019gl083960.
Feng, X., A. Porporato, and I. Rodriguez-iturbe, 2013: Changes in rainfall seasonality in the tropics. *Nature Climate Change*, **3(6)**, 1–5, doi:10.1038/nclimate1907.
Filonchyk, M. et al., 2019: Combined use of satellite and surface observations to study aerosol optical depth in different regions of China. *Scientific Reports*, **9(1)**, 6174, doi:10.1038/s41598-019-42466-6.
Finsinger, W., T. Giesecke, S. Brewer, and M. Leydet, 2017: Emergence patterns of novelty in European vegetation assemblages over the past 15 000 years. *Ecology Letters*, **20**, 336–346, doi:10.1111/ele.12731.
Fischer, H. et al., 2018: Palaeoclimate constraints on the impact of 2°C anthropogenic warming and beyond. *Nature Geoscience*, **11(7)**, 474–485, doi:10.1038/s41561-018-0146-0.
Fitzsimmons, K.E., N. Stern, C. Murray-Wallace, W. Truscott, and C. Pop, 2015: The Mungo mega-lake event, semi-arid Australia: Non-linear descent into the last ice age, implications for human behaviour. *PLoS ONE*, **10(6)**, 1–19, doi:10.1371/journal.pone.0127008.
Fletcher, M.- et al., 2018: Centennial-scale trends in the Southern Annular Mode revealed by hemisphere-wide fire and hydroclimatic trends over the past 2400 years. *Geology*, **46(4)**, 363–366, doi:10.1130/g39661.1.
Fletcher, M.S. and P.I. Moreno, 2012: Have the Southern Westerlies changed in a zonally symmetric manner over the last 14,000 years? A hemisphere-wide take on a controversial problem. *Quaternary International*, **253**, 32–46, doi:10.1016/j.quaint.2011.04.042.
Fletcher, T., R. Feng, A.M. Telka, J. Matthews, and A. Ballantyne, 2017: Floral Dissimilarity and the Influence of Climate in the Pliocene High Arctic: Biotic and Abiotic Influences on Five Sites on the Canadian Arctic Archipelago. *Frontiers in Ecology and Evolution*, **5**, 19, doi:10.3389/fevo.2017.00019.
Flores-Aqueveque, V., M. Rojas, C. Aguirre, P.A. Arias, and C. González, 2020: South Pacific Subtropical High from the late Holocene to the end of the 21st century: insights from climate proxies and general circulation models. *Climate of the Past*, **16(1)**, 79–99, doi:10.5194/cp-16-79-2020.
Flückiger, J. et al., 1999: Variations in atmospheric N2O concentration during abrupt climatic changes. *Science*, **285(5425)**, 227–230, doi:10.1126/science.285.5425.227.
Flückiger, J. et al., 2002: High-resolution Holocene N2O ice core record and its relationship with CH4 and CO2. *Global Biogeochemical Cycles*, **16(1)**, 10–18, doi:10.1029/2001gb001417.
Fogt, R.L. and G.J. Marshall, 2020: The Southern Annular Mode: Variability, trends, and climate impacts across the Southern Hemisphere. *Wiley Interdisciplinary Reviews: Climate Change*, **11(4)**, 1–24, doi:10.1002/wcc.652.
Foley, K.M. and H.J. Dowsett, 2019: Community sourced mid-Piacenzian sea surface temperature (SST) data. , doi:10.5066/p9yp3dtv.
Foltz, G.R. and M.J. McPhaden, 2010: Abrupt equatorial wave-induced cooling of the Atlantic cold tongue in 2009. *Geophysical Research Letters*, **37(24)**, doi:10.1029/2010gl045522.
Foltz, G.R., M.J. McPhaden, and R. Lumpkin, 2012: A Strong Atlantic Meridional Mode Event in 2009: The Role of Mixed Layer Dynamics. *Journal of Climate*, **25(1)**, 363–380, doi:10.1175/jcli-d-11-00150.1.
Foltz, G.R. et al., 2019: The Tropical Atlantic Observing System. *Frontiers in Marine Science*, **6**, 206, doi:10.3389/fmars.2019.00206.
Ford, H.L., A.C. Ravelo, and P.J. Polissar, 2015: Reduced El Niño-Southern Oscillation during the last glacial maximum. *Science*, **347(6219)**, 255–258, doi:10.1126/science.1258437.
Ford, H.L., C.L. McChesney, J.E. Hertzberg, and J.F. McManus, 2018: A Deep Eastern Equatorial Pacific Thermocline During the Last Glacial Maximum. *Geophysical Research Letters*, **45(21)**, 11,806–811,816, doi:10.1029/2018gl079710.
Forkel, M. et al., 2014: Identifying environmental controls on vegetation greenness phenology through model-data integration. *Biogeosciences*, **11(23)**, 7025–7050, doi:10.5194/bg-11-7025-2014.
Forkel, M. et al., 2016: Enhanced seasonal CO2 exchange caused by amplified plant productivity in northern ecosystems. *Science*, **351(6274)**, doi:10.1126/science.aac4971.
Forzieri, G., R. Alkama, D.G. Miralles, and A. Cescatti, 2017: Satellites reveal contrasting responses of regional climate to the widespread greening of Earth. *Science*, **356(6343)**, 1180–1184, doi:10.1126/science.aal1727.
Foster, G.L., 2008: Seawater pH, pCO2 and [CO2-3] variations in the Caribbean Sea over the last 130 kyr: A boron isotope and B/Ca study of planktic foraminifera. *Earth and Planetary Science Letters*, **271(1)**, 254–266, doi:10.1016/j.epsl.2008.04.015.
Foster, G.L. and J.W.B. Rae, 2016: Reconstructing Ocean pH with Boron Isotopes in Foraminifera. *Annual Review of Earth and Planetary Sciences*, **44(1)**, 207–237, doi:10.1146/annurev-earth-060115-012226.
Foster, G.L., D.L. Royer, and D.J. Lunt, 2017: Future climate forcing potentially without precedent in the last 420 million years. *Nature Communications*, **8(14845)**, doi:10.1038/ncomms14845.
Fourteau, K. et al., 2020: Estimation of gas record alteration in very low-accumulation ice cores. *Climate of the Past*, **16(2)**, 503–522, doi:10.5194/cp-16-503-2020.
Frajka-Williams, E., 2015: Estimating the Atlantic overturning at 26°N using satellite altimetry and cable measurements. *Geophysical Research Letters*, **42(9)**, 3458–3464, doi:10.1002/2015gl063220.
Francis, J.A. and S.J. Vavrus, 2012: Evidence linking Arctic amplification to extreme weather in mid-latitudes.

ACCEPTED VERSION SUBJECT TO FINAL EDITS

Geophysical Research Letters, **39(L06801)**, doi:10.1029/2012GL051000.
Francis, J.A. and S.J. Vavrus, 2015: Evidence for a wavier jet stream in response to rapid Arctic warming. *Environmental Research Letters*, **10(1)**, doi:10.1088/1748-9326/10/1/014005.
Frank, N. et al., 2006: Open system U-series ages of corals from a subsiding reef in New Caledonia: Implications for sea level changes, and subsidence rate. *Earth and Planetary Science Letters*, **249(3)**, 274–289, doi:10.1016/j.epsl.2006.07.029.
Franklin, J., J.M. Serra-Diaz, A.D. Syphard, and H.M. Regan, 2016: Global change and terrestrial plant community dynamics. *Proceedings of the National Academy of Sciences*, **113(14)**, 3725–3734, doi:10.1073/pnas.1519911113.
Frederikse, T. et al., 2020: The causes of sea-level rise since 1900. *Nature*, **584(7821)**, 393–397, doi:10.1038/s41586-020-2591-3.
Freeman, E. et al., 2017: ICOADS Release 3.0: a major update to the historical marine climate record. *International Journal of Climatology*, **37(5)**, 2211–2232, doi:10.1002/joc.4775.
Freeman, E. et al., 2019: The International Comprehensive Ocean-Atmosphere Data Set – Meeting Users Needs and Future Priorities. *Frontiers in Marine Science*, **6**, 435, doi:10.3389/fmars.2019.00435.
French, H.M. and S.W.S. Millar, 2014: Permafrost at the time of the Last Glacial Maximum (LGM) in North America. *Boreas*, **43(3)**, doi:10.1111/bor.12036.
Freund, M.B. et al., 2019: Higher frequency of Central Pacific El Nino events in recent decades relative to past centuries. *Nature Geoscience*, **12(6)**, 450–455, doi:10.1038/s41561-019-0353-3.
Frezzotti, M., C. Scarchilli, S. Becagli, M. Proposito, and S. Urbini, 2013: A synthesis of the Antarctic surface mass balance during the last 800 yr. *Cryosphere*, **7(1)**, 303–319, doi:10.5194/tc-7-303-2013.
Friedman, A.R., G. Reverdin, M. Khodri, and G. Gastineau, 2017: A new record of Atlantic sea surface salinity from 1896 to 2013 reveals the signatures of climate variability and long-term trends. *Geophysical Research Letters*, **44(4)**, 1866–1876, doi:10.1002/2017gl072582.
Friedrich, T. and A. Timmermann, 2020: Using Late Pleistocene sea surface temperature reconstructions to constrain future greenhouse warming. *Earth and Planetary Science Letters*, **530**, 115911, doi:10.1016/j.epsl.2019.115911.
Friedrich, T., A. Timmermann, M. Tigchelaar, O. Elison Timm, and A. Ganopolski, 2016: Nonlinear climate sensitivity and its implications for future greenhouse warming. *Science Advances*, **2(11)**, doi:10.1126/sciadv.1501923.
Frieling, J. et al., 2016: Thermogenic methane release as a cause for the long duration of the PETM. *Proceedings of the National Academy of Sciences*, 201603348, doi:10.1073/pnas.1603348113.
Froidevaux, L. et al., 2015: Global OZone Chemistry And Related trace gas Data records for the Stratosphere (GOZCARDS): methodology and sample results with a focus on HCl, H2O, and O3. *Atmospheric Chemistry and Physics*, **15(18)**, 10471–10507, doi:10.5194/acp-15-10471-2015.
Fu, Q. and P. Lin, 2011: Poleward shift of subtropical jets inferred from satellite-observed lower-stratospheric temperatures. *Journal of Climate*, **24(21)**, 5597–5603, doi:10.1175/jcli-d-11-00027.1.
Fu, Y., F. Li, J. Karstensen, and C. Wang, 2020: A stable Atlantic Meridional Overturning Circulation in a changing North Atlantic Ocean since the 1990s. *Science Advances*, **6(48)**, doi:10.1126/sciadv.abc7836.
Fuchs, H.L. et al., 2020: Wrong-way migrations of benthic species driven by ocean warming and larval transport. *Nature Climate Change*, **10(11)**, 1052–1056, doi:10.1038/s41558-020-0894-x.
Funk, C. et al., 2015: The climate hazards infrared precipitation with stations - a new environmental record for monitoring extremes. *Scientific Data*, 1–21, doi:10.1038/sdata.2015.66.
Funk, C. et al., 2019: A High-Resolution 1983–2016 Tmax Climate Data Record Based on Infrared Temperatures and Stations by the Climate Hazard Center. *Journal of Climate*, **32(17)**, 5639–5658, doi:10.1175/jcli-d-18-0698.1.
Fyfe, R.M., J. Woodbridge, and N. Roberts, 2015: From forest to farmland: Pollen-inferred land cover change across Europe using the pseudobiomization approach. *Global Change Biology*, **21(3)**, 1197–1212, doi:10.1111/gcb.12776.
Găinuşă-Bogdan, A., P. Braconnot, and J. Servonnat, 2015: Using an ensemble data set of turbulent air-sea fluxes to evaluate the IPSL climate model in tropical regions. *Journal of Geophysical Research: Atmospheres*, **120(10)**, 4483–4505, doi:10.1002/2014jd022985.
Galaasen, E.V. et al., 2014: Rapid Reductions in North Atlantic Deep Water During the Peak of the Last Interglacial Period. *Science*, **343(6175)**, 1129, doi:10.1126/science.1248667.
Galaasen, E.V. et al., 2020: Interglacial instability of North Atlantic Deep Water ventilation. *Science*, **367(6485)**, 1485, doi:10.1126/science.aay6381.
Galbraith, E.D. and S.L. Jaccard, 2015: Deglacial weakening of the oceanic soft tissue pump: Global constraints from sedimentary nitrogen isotopes and oxygenation proxies. *Quaternary Science Reviews*, **109**, 38–48, doi:10.1016/j.quascirev.2014.11.012.
Gallagher, S.J. et al., 2015: The Pliocene to recent history of the Kuroshio and Tsushima Currents: a multi-proxy approach. *Progress in Earth and Planetary Science*, **2(1)**, 17, doi:10.1186/s40645-015-0045-6.
Gallaher, D.W., G.G. Campbell, and W.N. Meier, 2014: Anomalous variability in Antarctic sea ice extents during the 1960s with the use of Nimbus data. *IEEE Journal of Selected Topics in Applied Earth Observations and*

ACCEPTED VERSION SUBJECT TO FINAL EDITS

Remote Sensing, **7(3)**, doi:10.1109/jstars.2013.2264391.
Gallant, A.J.E., S.J. Phipps, D.J. Karoly, A.B. Mullan, and A.M. Lorrey, 2013: Nonstationary Australasian Teleconnections and Implications for Paleoclimate Reconstructions. *Journal of Climate*, **26(22)**, 8827–8849, doi:10.1175/jcli-d-12-00338.1.
Gao, P., X. Xu, and X. Zhang, 2015: Characteristics of the Trends in the Global Tropopause Estimated From COSMIC Radio Occultation Data. *IEEE Transactions on Geoscience and Remote Sensing*, **53(12)**, 6813–6822, doi:10.1109/tgrs.2015.2449338.
Gao, X., S. Liang, and B. He, 2019: Detected global agricultural greening from satellite data. *Agricultural and Forest Meteorology*, **276–277**, doi:10.1016/j.agrformet.2019.107652.
Garfinkel, C.I., M.M. Hurwitz, and L.D. Oman, 2015a: Effect of recent sea surface temperature trends on the Arctic stratospheric vortex (2015a). *Journal of Geophysical Research*, **120(11)**, 5404–5416, doi:10.1002/2015jd023284.
Garfinkel, C.I., D.W. Waugh, and L.M. Polvani, 2015b: Recent Hadley cell expansion : The role of internal atmospheric variability in reconciling modeled and observed trends (2015b). *Geophysical Research Letters*, **42**, 10824–10831, doi:10.1002/2015gl066942.1.
Garfinkel, C.I., S.W. Son, K. Song, V. Aquila, and L.D. Oman, 2017: Stratospheric variability contributed to and sustained the recent hiatus in Eurasian winter warming. *Geophysical Research Letters*, **44(1)**, 374–382, doi:10.1002/2016gl072035.
Garfinkel, C.I. et al., 2018: Nonlinear response of tropical lower-stratospheric temperature and water vapor to ENSO. *Atmospheric Chemistry and Physics*, **18(7)**, 4597–4615, doi:10.5194/acp-18-4597-2018.
Garonna, I., R. de Jong, and M.E. Schaepman, 2016: Variability and evolution of global land surface phenology over the past three decades (1982-2012). *Global Change Biology*, **22(4)**, 1456–1468, doi:10.1111/gcb.13168.
Garonna, I. et al., 2014: Strong contribution of autumn phenology to changes in satellite-derived growing season length estimates across Europe (1982-2011). *Global Change Biology*, **20(11)**, 3457–3470, doi:10.1111/gcb.12625.
Garry, F.K. et al., 2019: Model-Derived Uncertainties in Deep Ocean Temperature Trends Between 1990 and 2010. *Journal of Geophysical Research: Oceans*, **124(2)**, 1155–1169, doi:10.1029/2018jc014225.
Gautier, E. et al., 2019: 2600-years of stratospheric volcanism through sulfate isotopes. *Nature Communications*, **10(1)**, 466, doi:10.1038/s41467-019-08357-0.
Gebbie, G., 2014: How much did Glacial North Atlantic Water shoal? *Paleoceanography*, **29(3)**, 190–209, doi:10.1002/2013pa002557.
Gebbie, G., 2021: Combining Modern and Paleoceanographic Perspectives on Ocean Heat Uptake. *Annual Review of Marine Science*, **13(1)**, 255–281, doi:10.1146/annurev-marine-010419-010844.
Gebbie, G. and P. Huybers, 2019: The Little Ice Age and 20th-century deep Pacific cooling. *Science*, **363(6422)**, 70–74, doi:10.1126/science.aar8413.
Gehlen, M., T.t..T. Chau, A. Conchon, A. Denvil-Sommer, F. Chevallier, M. Vrac, C.M., 2020: Ocean acidification. In The Copernicus Marine Service Ocean State Report, issue 4. *Journal of Operational Oceanography*, **13(supp1)**, s64–s67, doi: 10.1080/1755876x.2020.1785097.
Gelaro, R. et al., 2017: The Modern-Era Retrospective Analysis for Research and Applications, Version 2 (MERRA-2). *Journal of Climate*, **30(14)**, 5419–5454, doi:10.1175/jcli-d-16-0758.1.
Georgoulias, A.K. et al., 2016: Spatiotemporal variability and contribution of different aerosol types to the aerosol optical depth over the Eastern Mediterranean. *Atmospheric Chemistry and Physics*, **16(21)**, 13853–13884, doi:10.5194/acp-16-13853-2016.
Gergis, J.L. and A.M. Fowler, 2009: A history of ENSO events since A.D. 1525: implications for future climate change. *Climatic Change*, **92(3)**, 343–387, doi:10.1007/s10584-008-9476-z.
Ghiggi, G., V. Humphrey, S.I. Seneviratne, and L. Gudmundsson, 2019: GRUN: An observations-based global gridded runoff dataset from 1902 to 2014. *Earth System Science Data*, **11**, 1655–1674, doi:10.5194/essd-2019-32.
Ghimire, B. et al., 2014: Global albedo change and radiative cooling from anthropogenic land cover change, 1700 to 2005 based on MODIS, land use harmonization, radiative kernels, and reanalysis. *Geophysical Research Letters*, **41(24)**, 9087–9096, doi:10.1002/2014gl061671.
Gibson-Reinemer, D.K. and F.J. Rahel, 2015: Inconsistent range shifts within species highlight idiosyncratic responses to climate warming. *PLoS ONE*, **10(7)**, e0132103, doi:10.1371/journal.pone.0132103.
Gibson-Reinemer, D.K., K.S. Sheldon, and F.J. Rahel, 2015: Climate change creates rapid species turnover in montane communities. *Ecology and Evolution*, **5(12)**, 2340–2347, doi:10.1002/ece3.1518.
Giese, B.S. and S. Ray, 2011: El Niño variability in simple ocean data assimilation (SODA), 1871–2008. *Journal of Geophysical Research: Oceans*, **116(C2)**, doi:10.1029/2010jc006695.
Gillett, N.P. et al., 2021: Constraining human contributions to observed warming since the pre-industrial period. *Nature Climate Change*, doi:10.1038/s41558-020-00965-9.
Gingerich, P.D., 2019: Temporal Scaling of Carbon Emission and Accumulation Rates: Modern Anthropogenic Emissions Compared to Estimates of PETM-Onset Accumulation. *Paleoceanography and Paleoclimatology*, **34(3)**, 329–335, doi:10.1029/2018pa003379.
Giraudeau, J. et al., 2010: Millennial-scale variability in Atlantic water advection to the Nordic Seas derived from

ACCEPTED VERSION SUBJECT TO FINAL EDITS

Holocene coccolith concentration records. *Quaternary Science Reviews*, **29(9–10)**, 1276–1287, doi:10.1016/j.quascirev.2010.02.014.
Gladyshev, S., V.S. Gladyshev, S.K. Gulev, and A. Sokov, 2016: Anomalously deep convection in the Irminger Sea during the winter of 2014–2015. *Doklady Earth Sciences*, **469(1)**, 766–770, doi:10.1134/s1028334x16070229.
Gobron, N., 2018: Terrestrial Vegetation Activity [in "State of the Climate in 2017"]. *Bulletin of the American Meteorological Society*, **99**, S62–S63, doi:10.1175/2018bamsstateoftheclimate.1.
Goelzer, H., P. Huybrechts, M.-F.M.-F.M.-F. Loutre, and T. Fichefet, 2016: Last Interglacial climate and sea-level evolution from a coupled ice sheet-climate model. *Clim. Past*, **12(12)**, 2195–2213, doi:10.5194/cp-12-2195-2016.
Goldner, A., N. Herold, and M. Huber, 2014: The challenge of simulating the warmth of the mid-Miocene climatic optimum in CESM1. *Climate of the Past*, **10(2)**, 523–536, doi:10.5194/cp-10-523-2014.
Golledge, N.R., 2020: Long-term projections of sea-level rise from ice sheets. *WIREs Climate Change*, **11(2)**, e634, doi:10.1002/wcc.634.
Golledge, N.R. et al., 2014: Antarctic contribution to meltwater pulse 1A from reduced Southern Ocean overturning. *Nature Communications*, **5**, doi:10.1038/ncomms6107.
Gong, H., L. Wang, W. Chen, and D. Nath, 2018: Multidecadal fluctuation of the wintertime Arctic Oscillation pattern and its implication. *Journal of Climate*, **31(14)**, 5595–5608, doi:10.1175/jcli-d-17-0530.1.
Good, S.A., 2017: The impact of observational sampling on time series of global 0–700 m ocean average temperature: a case study. *International Journal of Climatology*, **37(5)**, 2260–2268, doi:10.1002/joc.4654.
Good, S.A., M.J. Martin, and N.A. Rayner, 2013a: EN4: Quality controlled ocean temperature and salinity profiles and monthly objective analyses with uncertainty estimates. *Journal of Geophysical Research: Oceans*, **118(12)**, 6704–6716, doi:10.1002/2013jc009067.
Good, S.A., M.J. Martin, and N.A. Rayner, 2013b: EN4: Quality controlled ocean temperature and salinity profiles and monthly objective analyses with uncertainty estimates. *Journal of Geophysical Research: Oceans*, **118(12)**, 6704–6716, doi:10.1002/2013jc009067.
Goodwin, I.D. et al., 2014: A reconstruction of extratropical Indo-Pacific sea-level pressure patterns during the Medieval Climate Anomaly. *Climate Dynamics*, **43(5–6)**, 1197–1219, doi:10.1007/s00382-013-1899-1.
Goring, S.J. et al., 2016: Novel and lost forests in the upper Midwestern United States, from new estimates of settlement-era composition, stem density, and biomass. *PLoS ONE*, **11(12)**, e0151935, doi:10.1371/journal.pone.0151935.
Gottschalk, J. et al., 2016: Biological and physical controls in the Southern Ocean on past millennial-scale atmospheric CO2 changes. *Nature Communications*, **7**, doi:10.1038/ncomms11539.
Gottschalk, J. et al., 2020: Southern Ocean link between changes in atmospheric CO2 levels and northern-hemisphere climate anomalies during the last two glacial periods. *Quaternary Science Reviews*, **230**, 106067, doi:10.1016/j.quascirev.2019.106067.
Gouretski, V. and L. Cheng, 2020: Correction for Systematic Errors in the Global Dataset of Temperature Profiles from Mechanical Bathythermographs. *Journal of Atmospheric and Oceanic Technology*, **37(5)**, 841–855, doi:10.1175/jtech-d-19-0205.1.
Gouretski, V., J. Kennedy, T. Boyer, and A. Köhl, 2012: Consistent near-surface ocean warming since 1900 in two largely independent observing networks. *Geophysical Research Letters*, **39(19)**, doi:10.1029/2012gl052975.
Graham, N.E., C.M. Ammann, D. Fleitmann, K.M. Cobb, and J. Luterbacher, 2011: Support for global climate reorganization during the 'Medieval Climate Anomaly'. *Climate Dynamics*, **37(5)**, 1217–1245, doi:10.1007/s00382-010-0914-z.
Grant, G.R. et al., 2019: The amplitude and origin of sea-level variability during the Pliocene epoch. *Nature*, **574(7777)**, 237–241, doi:10.1038/s41586-019-1619-z.
Grant, K.M. et al., 2014: Sea-level variability over five glacial cycles. *Nature Communications*, **5(1)**, 5076, doi:10.1038/ncomms6076.
Graven, H.D. et al., 2013a: Enhanced seasonal exchange of CO2by Northern ecosystems since 1960. *Science*, doi:10.1126/science.1239207.
Graven, H.D. et al., 2013b: Enhanced seasonal exchange of CO2by Northern ecosystems since 1960. *Science*, doi:10.1126/science.1239207.
Gray, A.R. et al., 2018: Autonomous Biogeochemical Floats Detect Significant Carbon Dioxide Outgassing in the High-Latitude Southern Ocean. *Geophysical Research Letters*, **45(17)**, 9049–9057, doi:10.1029/2018gl078013.
Gregg, W.W. and C.S. Rousseaux, 2019: Global ocean primary production trends in the modern ocean color satellite record (1998–2015). *Environmental Research Letters*, **14(12)**, 124011, doi:10.1088/1748-9326/ab4667.
Gregor, L. and N. Gruber, 2021: OceanSODA-ETHZ: a global gridded data set of the surface ocean carbonate system for seasonal to decadal studies of ocean acidification. *Earth System Science Data*, **13(2)**, 777–808, doi:10.5194/essd-13-777-2021.
Greve, P. et al., 2014: Global assessment of trends in wetting and drying over land. *Nature Geoscience*, **7(10)**, 716–721, doi:10.1038/ngeo2247.

ACCEPTED VERSION SUBJECT TO FINAL EDITS

Grieger, J., G.C. Leckebusch, C.C. Raible, I. Rudeva, and I. Simmonds, 2018: Subantarctic cyclones identified by 14 tracking methods, and their role for moisture transports into the continent. *Tellus A: Dynamic Meteorology and Oceanography*, **70(1)**, 1454808, doi:10.1080/16000870.2018.1454808.
Griffiths, M.L. et al., 2016: Western Pacific hydroclimate linked to global climate variability over the past two millennia. *Nature Communications*, **7**, 1–9, doi:10.1038/ncomms11719.
Griffiths, M.L. et al., 2020: End of Green Sahara amplified mid- to late Holocene megadroughts in mainland Southeast Asia. *Nature Communications*, **11(1)**, 4204, doi:10.1038/s41467-020-17927-6.
Grise, K., S. Davis, P. Staten, and O. Adam, 2018: Regional and Seasonal Characteristics of the Recent Expansion of the Tropics. *Journal of Climate*, **31(17)**, 6839–6856, doi:10.1175/jcli-d-18-0060.1.
Grise, K.M. and S.M. Davis, 2020: Hadley cell expansion in CMIP6 models. *Atmospheric Chemistry and Physics*, **20(9)**, 5249–5268, doi:10.5194/acp-20-5249-2020.
Grise, K.M. et al., 2019: Recent tropical expansion: Natural variability or forced response? *Journal of Climate*, **32(5)**, 1551–1571, doi:10.1175/jcli-d-18-0444.1.
Grist, J.P., S.A. Josey, J.D. Zika, D.G. Evans, and N. Skliris, 2016: Assessing recent air-sea freshwater flux changes using a surface temperature-salinity space framework. *Journal of Geophysical Research: Oceans*, **121(12)**, 8787–8806, doi:10.1002/2016jc012091.
Grooß, J.-U. and R. Müller, 2020: Simulation of the record Arctic stratospheric ozone depletion in 2020. *JGR*. 17, doi:10.1002/essoar.10503569.1.
Grothe, P.R. et al., 2019: Enhanced El Niño-Southern Oscillation variability in recent decades. *Geophysical Research Letters*, **46(7)**, e2019GL083906, doi:10.1029/2019gl083906.
Gu, G. and R.F. Adler, 2013: Interdecadal variability/long-term changes in global precipitation patterns during the past three decades: Global warming and/or pacific decadal variability? *Climate Dynamics*, **40(11–12)**, 3009–3022, doi:10.1007/s00382-012-1443-8.
Gu, G. and R.F. Adler, 2015: Spatial patterns of global precipitation change and variability during 1901-2010. *Journal of Climate*, **28(11)**, 4431–4453, doi:10.1175/jcli-d-14-00201.1.
Gudmundsson, L., H.X. Do, M. Leonard, and S. Westra, 2018: The Global Streamflow Indices and Metadata Archive (GSIM)-Part 2: Quality control, time-series indices and homogeneity assessment. *Earth System Science Data*, **10(2)**, 787–804, doi:10.5194/essd-10-787-2018.
Gudmundsson, L., M. Leonard, H.X. Do, S. Westra, and S.I. Seneviratne, 2019a: Observed Trends in Global Indicators of Mean and Extreme Streamflow. *Geophys. Res. Lett.*, **46(2)**, 756–766, doi:10.1029/2018gl079725.
Gudmundsson, L., M. Leonard, H.X. Do, S. Westra, and S.I. Seneviratne, 2019b: Observed Trends in Global Indicators of Mean and Extreme Streamflow. *Geophys. Res. Lett.*, **46(2)**, 756–766, doi:10.1029/2018gl079725.
Gulev, S.K., M. Latif, N. Keenlyside, W. Park, and K.P. Koltermann, 2013: North Atlantic Ocean control on surface heat flux on multidecadal timescales. *Nature*, **499**, 464, doi:10.1038/nature12268.
Guo, F., Q. Liu, S. Sun, and J. Yang, 2015: Three Types of Indian Ocean Dipoles. *Journal of Climate*, **28(8)**, 3073–3092, doi:10.1175/jcli-d-14-00507.1.
Gutjahr, M. et al., 2017: Very large release of mostly volcanic carbon during the Palaeocene-Eocene Thermal Maximum. *Nature*, **548(7669)**, 573–577, doi:10.1038/nature23646.
Haas, C. et al., 2017: Ice and Snow Thickness Variability and Change in the High Arctic Ocean Observed by In Situ Measurements. *Geophysical Research Letters*, **44(20)**, 10,410–462,469, doi:10.1002/2017gl075434.
Haimberger, L. and M. Mayer, 2018: Upper air winds [in "State of the Climate in 2017"]. *Bulletin of the American Meteorological Soceity*, **98(8)**, S39–S41, doi:10.1175/2017bamsstateoftheclimate.1.
Haimberger, L., C. Tavolato, and S. Sperka, 2012: Homogenization of the Global Radiosonde Temperature Dataset through Combined Comparison with Reanalysis Background Series and Neighboring Stations. *Journal of Climate*, **25(23)**, 8108–8131, doi:10.1175/jcli-d-11-00668.1.
Hain, M.P., G.L. Foster, and T. Chalk, 2018: Robust Constraints on Past CO2 Climate Forcing From the Boron Isotope Proxy. *Paleoceanography and Paleoclimatology*, **33(10)**, 1099–1115, doi:10.1029/2018pa003362.
Hakkinen, S., A. Proshutinsky, and I. Ashik, 2008: Sea ice drift in the Arctic since the 1950s. *Geophysical Research Letters*, **35(19)**, doi:10.1029/2008gl034791.
Hammer, M.S. et al., 2018: Insight into global trends in aerosol composition from 2005 to 2015 inferred from the OMI Ultraviolet Aerosol Index. *Atmospheric Chemistry and Physics*, **18(11)**, 8097–8112, doi:10.5194/acp-18-8097-2018.
Hammond, J.C., F.A. Saavedra, and S.K. Kampf, 2018: Global snow zone maps and trends in snow persistence 2001-2016. *International Journal of Climatology*, **38(12)**, 4369–4383, doi:10.1002/joc.5674.
Han, W. et al., 2014: Intensification of decadal and multi-decadal sea level variability in the western tropical Pacific during recent decades. *Climate Dynamics*, **43(5–6)**, 1357–1379, doi:10.1007/s00382-013-1951-1.
Han, Z. et al., 2019: Changes in global monsoon precipitation and the related dynamic and thermodynamic mechanisms in recent decades. *International Journal of Climatology*, **39(3)**, 1490–1503, doi:10.1002/joc.5896.
Hanna, E., T.E. Cropper, R.J. Hall, and J. Cappelen, 2016: Greenland Blocking Index 1851–2015: a regional climate change signal. *International Journal of Climatology*, **36(15)**, 4847–4861, doi:10.1002/joc.4673.
Hanna, E., T.E. Cropper, P.D. Jones, A.A. Scaife, and R. Allan, 2015: Recent seasonal asymmetric changes in the NAO

ACCEPTED VERSION SUBJECT TO FINAL EDITS

(a marked summer decline and increased winter variability) and associated changes in the AO and Greenland Blocking Index. *International Journal of Climatology*, **35(9)**, 2540–2554, doi:10.1002/joc.4157.
Hanna, E. et al., 2018: Greenland blocking index daily series 1851–2015: Analysis of changes in extremes and links with North Atlantic and UK climate variability and change. *International Journal of Climatology*, **38(9)**, 3546–3564, doi:10.1002/joc.5516.
Hansen, B. et al., 2015: Transport of volume, heat, and salt towards the Arctic in the Faroe Current 1993–2013. *Ocean Sci.*, **11(5)**, 743–757, doi:10.5194/os-11-743-2015.
Hansen, E. et al., 2013a: Thinning of Arctic sea ice observed in Fram Strait: 1990-2011. *Journal of Geophysical Research: Oceans*, doi:10.1002/jgrc.20393.
Hansen, E. et al., 2013b: Thinning of Arctic sea ice observed in Fram Strait: 1990-2011. *Journal of Geophysical Research: Oceans*, doi:10.1002/jgrc.20393.
Hansen, J., M. Sato, G. Russell, and P. Kharecha, 2013: Climate sensitivity, sea level and atmospheric carbon dioxide. *Philosophical transactions. Series A, Mathematical, physical, and engineering sciences*, **371(2001)**, 20120294, doi:10.1098/rsta.2012.0294.
Harada, Y. et al., 2016: The JRA-55 Reanalysis: Representation of atmospheric circulation and climate variability. *Journal of the Meteorological Society of Japan*, **94(3)**, 269–302, doi:10.2151/jmsj.2016-015.
Harning, D.J., Geirsdóttir, and G.H. Miller, 2018: Punctuated Holocene climate of Vestfirdir, Iceland, linked to internal/external variables and oceanographic conditions. *Quaternary Science Reviews*, **189**, 31–42, doi:10.1016/j.quascirev.2018.04.009.
Harning, D.J., Geirsdóttir, G.H. Miller, and L. Anderson, 2016: Episodic expansion of Drangajökull, Vestfirdir, Iceland, over the last 3 ka culminating in its maximum dimension during the Little Ice Age. *Quaternary Science Reviews*, **152**, 118–131, doi:10.1016/j.quascirev.2016.10.001.
Harper, D.T. et al., 2020: The Magnitude of Surface Ocean Acidification and Carbon Release During Eocene Thermal Maximum 2 (ETM-2) and the Paleocene-Eocene Thermal Maximum (PETM). *Paleoceanography and Paleoclimatology*, **35(2)**, e2019PA003699, doi:10.1029/2019pa003699.
Harris, I., P.D. Jones, T.J. Osborn, and D.H. Lister, 2014: Updated high-resolution grids of monthly climatic observations - the CRU TS3.10 Dataset. *International Journal of Climatology*, **34(3)**, 623–642, doi:10.1002/joc.3711.
Harrison, S.P., P.J. Bartlein, and I.C. Prentice, 2016: What have we learnt from palaeoclimate simulations? *Journal of Quaternary Science*, **31(4)**, 363–385, doi:10.1002/jqs.2842.
Harrison, S.P. et al., 2014: Climate model benchmarking with glacial and mid-Holocene climates. *Climate Dynamics*, **43(3)**, 671–688, doi:10.1007/s00382-013-1922-6.
Harrison, S.P. et al., 2015: Evaluation of CMIP5 palaeo-simulations to improve climate projections. *Nature Climate Change*, **5**, 735, doi:10.1038/nclimate2649.
Harrison, S.P. et al., 2020: Development and testing scenarios for implementing land use and land cover changes during the Holocene in Earth system model experiments. *Geoscientific Model Development*, **13(2)**, 805–824, doi:10.5194/gmd-13-805-2020.
Harsch, M.A., P.E. Hulme, M.S. McGlone, and R.P. Duncan, 2009a: Are treelines advancing? A global meta-analysis of treeline response to climate warming. *Ecology Letters*, doi:10.1111/j.1461-0248.2009.01355.x.
Harsch, M.A., P.E. Hulme, M.S. McGlone, and R.P. Duncan, 2009b: Are treelines advancing? A global meta-analysis of treeline response to climate warming. *Ecology Letters*, doi:10.1111/j.1461-0248.2009.01355.x.
Hartmann, D.L. et al., 2013: Observations: Atmosphere and surface. *Climate Change 2013 the Physical Science Basis: Working Group I Contribution to the Fifth Assessment Report of the Intergovernmental Panel on Climate Change*, **9781107057**, 159-254, doi:10.1017/cbo9781107415324.008.
Hassanzadeh, P., Z. Kuang, and B.F. Farrell, 2014: Responses of midlatitude blocks and wave amplitude to changes in the meridional temperature gradient in an idealized dry GCM. *Geophyiscal Research Letters*, **41(14)**, 5223–5232, doi:10.1002/2014gl060764.
Haug, T. et al., 2017: Future harvest of living resources in the Arctic Ocean north of the Nordic and Barents Seas: A review of possibilities and constraints. *Fisheries Research*, **188**, 38–57, doi:10.1016/j.fishres.2016.12.002.
Hausfather, Z. et al., 2017: Assessing recent warming using instrumentally homogeneous sea surface temperature records. *Science Advances*, **3(1)**, doi:10.1126/sciadv.1601207.
Haustein, K. et al., 2019: A Limited Role for Unforced Internal Variability in Twentieth-Century Warming. *Journal of Climate*, **32(16)**, 4893–4917, doi:10.1175/jcli-d-18-0555.1.
Hay, C.C., E. Morrow, R.E. Kopp, and J.X. Mitrovica, 2015: Probabilistic reanalysis of twentieth-century sea-level rise. *Nature*, **517(7535)**, 481–484, doi:10.1038/nature14093.
Hayes, C.T. et al., 2014: A stagnation event in the deep South Atlantic during the last interglacial period. *Science*, **346(6216)**, 1514, doi:10.1126/science.1256620.
Haywood, A.M., H.J. Dowsett, and A.M. Dolan, 2016: Integrating geological archives and climate models for the mid-Pliocene warm period. *Nature Communications*, **7**, 10646, doi:10.1038/ncomms10646.
Haywood, A.M. et al., 2013: On the identification of a pliocene time slice for data-model comparison. *Philosophical Transactions of the Royal Society A: Mathematical, Physical and Engineering Sciences*, **371(2001)**, 20120515,

ACCEPTED VERSION SUBJECT TO FINAL EDITS

doi:10.1098/rsta.2012.0515.
Haywood, A.M. et al., 2020: The Pliocene Model Intercomparison Project Phase 2: large-scale climate features and climate sensitivity. *Climate of the Past*, **16(6)**, 2095–2123, doi:10.5194/cp-16-2095-2020.
He, F. et al., 2014: Simulating global and local surface temperature changes due to Holocene anthropogenic land cover change. *Geophysical Research Letters*, **41(2)**, 623–631, doi:10.1002/2013gl058085.
He, S., H. Wang, and J. Liu, 2013: Changes in the Relationship between ENSO and Asia–Pacific Midlatitude Winter Atmospheric Circulation. *Journal of Climate*, **26(10)**, 3377–3393, doi:10.1175/jcli-d-12-00355.1.
Hearty, P.J. et al., 2020: Pliocene-Pleistocene Stratigraphy and Sea-Level Estimates, Republic of South Africa With Implications for a 400 ppmv CO2 World. *Paleoceanography and Paleoclimatology*, **35(7)**, e2019PA003835, doi:10.1029/2019pa003835.
Hegerl, G.C., T.J. Crowley, W.T. Hyde, and D.J. Frame, 2006: Climate sensitivity constrained by temperature reconstructions over the past seven centuries. *Nature*, **440(7087)**, 1029–1032, doi:10.1038/nature04679.
Hegerl, G.C. et al., 2015: Challenges in quantifying changes in the global water cycle. *Bull. Amer. Meteor. Soc*, **96(7)**, 1097–1116, doi:10.1175/bams-d-13-00212.1.
Hegglin, M.I. et al., 2014: Vertical structure of stratospheric water vapour trends derived from merged satellite data. *Nature Geoscience*, **7**, 768, doi:10.1038/ngeo2236.
Hein, A.S. et al., 2016: Mid-Holocene pulse of thinning in the Weddell Sea sector of the West Antarctic ice sheet. *Nature Communications*, **7(12511)**, doi:10.1038/ncomms12511.
Helsen, M.M., W.J. van de Berg, R.S.W. van de Wal, M.R. van den Broeke, and J. Oerlemans, 2013: Coupled regional climate-ice-sheet simulation shows limited Greenland ice loss during the Eemian. *Clim. Past*, **9(4)**, 1773–1788, doi:10.5194/cp-9-1773-2013.
Henehan, M. et al., 2020: Revisiting the Middle Eocene Climatic Optimum "Carbon Cycle Conundrum" With New Estimates of Atmospheric pCO 2 From Boron Isotopes. *Paleoceanography and Paleoclimatology*, **35**, e2019PA003713, doi:10.1029/2019pa003713.
Henehan, M.J. et al., 2013a: Calibration of the boron isotope proxy in the planktonic foraminifera Globigerinoides ruber for use in palaeo-CO2 reconstruction. *Earth and Planetary Science Letters*, **364**, 111–122, doi:10.1016/j.epsl.2012.12.029.
Henehan, M.J. et al., 2013b: Calibration of the boron isotope proxy in the planktonic foraminifera Globigerinoides ruber for use in palaeo-CO2 reconstruction. *Earth and Planetary Science Letters*, **364**, 111–122, doi:10.1016/j.epsl.2012.12.029.
Henehan, M.J. et al., 2019: Rapid ocean acidification and protracted Earth system recovery followed the end-Cretaceous Chicxulub impact. *Proceedings of the National Academy of Sciences*, **116(45)**, 22500, doi:10.1073/pnas.1905989116.
Henley, B.J., 2017: Pacific decadal climate variability: Indices, patterns and tropical- extratropical interactions. *Global and Planetary Change*, **155**, 42–55, doi:10.1016/j.gloplacha.2017.06.004.
Henry, L.G. et al., 2016a: North Atlantic ocean circulation and abrupt climate change during the last glaciation. *Science*, **353(6298)**, 470–474, doi:10.1126/science.aaf5529.
Henry, L.G. et al., 2016b: North Atlantic ocean circulation and abrupt climate change during the last glaciation. *Science*, **353(6298)**, 470–474, doi:10.1126/science.aaf5529.
Hermann, N.W., J.L. Oster, and D.E. Ibarra, 2018: Spatial patterns and driving mechanisms of mid-Holocene hydroclimate in western North America. *Journal of Quaternary Science*, **33(4)**, 421–434, doi:10.1002/jqs.3023.
Hernández, A. et al., 2020: Modes of climate variability: Synthesis and review of proxy-based reconstructions through the Holocene. *Earth-Science Reviews*, **209(103286)**, 103286, doi:10.1016/j.earscirev.2020.103286.
Hernández-Henríquez, M.A., S.J. Déry, and C. Derksen, 2015: Polar amplification and elevation-dependence in trends of Northern Hemisphere snow cover extent, 1971-2014. *Environmental Research Letters*, **10(044010)**, doi:10.1088/1748-9326/10/4/044010.
Hersbach, H. et al., 2020: The ERA5 global reanalysis. *Quarterly Journal of the Royal Meteorological Society*, **146**, 1999–2049, doi:10.1002/qj.3803.
Herzschuh, U. et al., 2016: Glacial legacies on interglacial vegetation at the Pliocene-Pleistocene transition in NE Asia. *Nature Communications*, **7(1)**, doi:10.1038/ncomms11967.
Hessl, A., K.J. Allen, T. Vance, N.J. Abram, and K.M. Saunders, 2017: Reconstructions of the southern annular mode (SAM) during the last millennium. *Progress in Physical Geography*, **41(6)**, 834–849, doi:10.1177/0309133317743165.
Hibbert, F.D., F.H. Williams, S.J. Fallon, and E.J. Rohling, 2018: A database of biological and geomorphological sea-level markers from the Last Glacial Maximum to present. *Scientific Data*, **5(1)**, 180088, doi:10.1038/sdata.2018.88.
Hiemstra, J.F., 2018: Permafrost and environmental dynamics: A virtual issue of The Holocene. *Holocene*, **28(8)**, 1201–1204, doi:10.1177/0959683618785835.
Higgins, J.A. et al., 2015: Atmospheric composition 1 million years ago from blue ice in the Allan Hills, Antarctica. *Proceedings of the National Academy of Sciences*, **112(22)**, 6887–6891, doi:10.1073/pnas.1420232112.

ACCEPTED VERSION SUBJECT TO FINAL EDITS

Hirahara, S., M. Ishii, and Y. Fukuda, 2014: Centennial-Scale Sea Surface Temperature Analysis and Its Uncertainty. *Journal of Climate*, **27(1)**, 57–75, doi:10.1175/jcli-d-12-00837.1.

Ho, S.- et al., 2012: Reproducibility of GPS radio occultation data for climate monitoring: Profile-to-profile inter-comparison of CHAMP climate records 2002 to 2008 from six data centers. *Journal of Geophysical Research: Atmospheres*, **117(D18)**, doi:10.1029/2012jd017665.

Ho, S.-P., L. Peng, and H. Vömel, 2017: Characterization of the long-term radiosonde temperature biases in the upper troposphere and lower stratosphere using COSMIC and Metop-A/GRAS data from 2006 to 2014. *Atmospheric Chemistry and Physics*, **17(7)**, 4493–4511, doi:10.5194/acp-17-4493-2017.

Ho, S.-P. et al., 2020: The COSMIC/FORMOSAT-3 Radio Occultation Mission after 12 years: Accomplishments, Remaining Challenges, and Potential Impacts of COSMIC-2. *Bulletin of the American Meteorological Society*, **101**, E1107–E1136, doi:10.1175/bams-d-18-0290.1.

Hobbs, R.J., E. Higgs, and J.A. Harris, 2009: Novel ecosystems: implications for conservation and restoration. *Trends in Ecology and Evolution*, **24(11)**, 599–605, doi:10.1016/j.tree.2009.05.012.

Hobbs, W., M. Curran, N. Abram, and E.R. Thomas, 2016: Century-scale perspectives on observed and simulated Southern Ocean sea ice trends from proxy reconstructions. *Journal of Geophysical Research: Oceans*, **121(10)**, 7804–7818, doi:10.1002/2016jc012111.

Hobbs, W.R. et al., 2016: A review of recent changes in Southern Ocean sea ice, their drivers and forcings. *Global and Planetary Change*, **143**, 228–250, doi:10.1016/j.gloplacha.2016.06.008.

Hodges, K.I., R.W. Lee, and L. Bengtsson, 2011: A comparison of extratropical cyclones in recent reanalyses ERA-Interim, NASA MERRA, NCEP CFSR, and JRA-25. *Journal of Climate*, **24**, 4888–4906, doi:10.1175/2011jcli4097.1.

Hoelzmann, P. et al., 1998: Mid-Holocene land-surface conditions in northern Africa and the Arabian peninsula: A data set for the analysis of biogeophysical feedbacks in the climate system. *Global Biogeochemical Cycles*, **12(1)**, 35–51, doi:10.1029/97gb02733.

Hoffman, J.S., P.U. Clark, A.C. Parnell, and F. He, 2017: Regional and global sea-surface temperatures during the last interglaciation. *Science*, **355(6322)**, 276–279, doi:10.1126/science.aai8464.

Hoffmann, S.S., J.F. McManus, and E. Swank, 2018: Evidence for Stable Holocene Basin-Scale Overturning Circulation Despite Variable Currents Along the Deep Western Boundary of the North Atlantic Ocean. *Geophysical Research Letters*, **45(24)**, 13, 413–427, 436, doi:10.1029/2018gl080187.

Hogda, K., H. Tømmervik, and S. Karlsen, 2013: Trends in the Start of the Growing Season in Fennoscandia 1982-2011. *Remote Sensing, vol. 5, issue 9, pp. 4304-4318*, **5(9)**, 4304–4318, doi:10.3390/rs5094304.

Holland, P.R., 2014: The seasonality of Antarctic sea ice trends. *Geophysical Research Letters*, **41(12)**, 4230–4237, doi:10.1002/2014gl060172.

Hollis, C.J. et al., 2019: The DeepMIP contribution to PMIP4: methodologies for selection, compilation and analysis of latest Paleocene and early Eocene climate proxy data, incorporating version 0.1 of the DeepMIP database. *Geoscientific Model Development Discussions*, **2019**, 1–98, doi:10.5194/gmd-2018-309.

Holloway, J.E. and A.G. Lewkowicz, 2020: Half a century of discontinuous permafrost persistence and degradation in western Canada. *Permafrost and Periglacial Processes*, **31(1)**, 85–96, doi:10.1002/ppp.2017.

Holloway, M.D. et al., 2016: Antarctic last interglacial isotope peak in response to sea ice retreat not ice-sheet collapse. *Nature Communications*, **7**, 1–9, doi:10.1038/ncomms12293.

Hönisch, B. and N.G. Hemming, 2005: Surface ocean pH response to variations in pCO2 through two full glacial cycles. *Earth and Planetary Science Letters*, **236(1)**, 305–314, doi:10.1016/j.epsl.2005.04.027.

Hönisch, B., N.G. Hemming, D. Archer, M. Siddall, and J.F. McManus, 2009: Atmospheric carbon dioxide concentration across the mid-pleistocene transition. *Science*, doi:10.1126/science.1171477.

Hoogakker, B.A.A., H. Elderfield, G. Schmiedl, I.N. McCave, and R.E.M. Rickaby, 2015: Glacial-interglacial changes in bottom-water oxygen content on the Portuguese margin. *Nature Geoscience*, **8(1)**, 40–43, doi:10.1038/ngeo2317.

Hoogakker, B.A.A. et al., 2016: Terrestrial biosphere changes over the last 120 kyr. *Climate of the Past*, **12(1)**, doi:10.5194/cp-12-51-2016.

Hoogakker, B.A.A. et al., 2018: Glacial expansion of oxygen-depleted seawater in the eastern tropical Pacific. *Nature*, **562(7727)**, 410–413, doi:10.1038/s41586-018-0589-x.

Hope, P., B.J. Henley, J. Gergis, J. Brown, and H. Ye, 2017: Time-varying spectral characteristics of ENSO over the Last Millennium. *Climate Dynamics*, **49(5–6)**, 1705–1727, doi:10.1007/s00382-016-3393-z.

Höpfner, M. et al., 2015: Sulfur dioxide (SO$_{2}$) from MIPAS in the upper troposphere and lower stratosphere 2002–2012. *Atmospheric Chemistry and Physics*, **15(12)**, 7017–7037, doi:10.5194/acp-15-7017-2015.

Hori, M. et al., 2017: A 38-year (1978–2015) Northern Hemisphere daily snow cover extent product derived using consistent objective criteria from satellite-borne optical sensors. *Remote Sensing of Environment*, **191**, 402–418, doi:10.1016/j.rse.2017.01.023.

Hou, J., C.-G. Li, and S. Lee, 2019: The temperature record of the Holocene: progress and controversies. *Science Bulletin*, **64(9)**, 565–566, doi:10.1016/j.scib.2019.02.012.

Hou, X., J. Cheng, S. Hu, and G. Feng, 2018: Interdecadal variations in the walker circulation and its connection to

ACCEPTED VERSION SUBJECT TO FINAL EDITS

inhomogeneous air temperature changes from 1961-2012. *Atmosphere*, **9(12)**, doi:10.3390/atmos9120469.
Howell, F.W. et al., 2016: Arctic sea ice simulation in the PlioMIP ensemble. *Climate of the Past*, **12(3)**, 749–767, doi:10.5194/cp-12-749-2016.
Howell, S.E.L., C.R. Duguay, and T. Markus, 2009: Sea ice conditions and melt season duration variability within the Canadian Arctic Archipelago: 1979-2008. *Geophysical Research Letters*, **36(10)**, doi:10.1029/2009gl037681.
Hrbáček, F. et al., 2018: Active layer monitoring in Antarctica: an overview of results from 2006 to 2015. *Polar Geography*, doi:10.1080/1088937x.2017.1420105.
Hsin, Y.C., 2015: Multidecadal variations of the surface Kuroshio between 1950s and 2000s and its impacts on surrounding waters. *Journal of Geophysical Research: Oceans*, **120(3)**, 1792–1808, doi:10.1002/2014jc010582.
Hu, D., Z. Guan, W. Tian, and R. Ren, 2018: Recent strengthening of the stratospheric Arctic vortex response to warming in the central North Pacific. *Nature Communications*, **9(1)**, doi:10.1038/s41467-018-04138-3.
Hu, Q. et al., 2019: Rainfall spatial estimations: A review from spatial interpolation to multi-source data merging. *Water (Switzerland)*, **11(3)**, 1–30, doi:10.3390/w11030579.
Hu, Y., H. Huang, and C. Zhou, 2018: Widening and weakening of the Hadley circulation under global warming. *Science Bulletin*, **63(10)**, 640–644, doi:10.1016/j.scib.2018.04.020.
Hu, Z.-Z. et al., 2013: Weakened Interannual Variability in the Tropical Pacific Ocean since 2000. *Journal of Climate*, **26(8)**, 2601–2613, doi:10.1175/jcli-d-12-00265.1.
Huang, B., M. L'Heureux, Z.-Z. Hu, X. Yin, and H.-M. Zhang, 2020: How Significant Was the 1877/78 El Niño? *Journal of Climate*, **33(11)**, 4853–4869, doi:10.1175/jcli-d-19-0650.1.
Huang, B. et al., 2015: Extended Reconstructed Sea Surface Temperature Version 4 (ERSST.v4). Part I: Upgrades and Intercomparisons. *Journal of Climate*, **28(3)**, 911–930, doi:10.1175/jcli-d-14-00006.1.
Huang, B. et al., 2016: Further Exploring and Quantifying Uncertainties for Extended Reconstructed Sea Surface Temperature (ERSST) Version 4 (v4). *Journal of Climate*, **29(9)**, 3119–3142, doi:10.1175/jcli-d-15-0430.1.
Huang, B. et al., 2017: Extended Reconstructed Sea Surface Temperature, Version 5 (ERSSTv5): Upgrades, Validations, and Intercomparisons. *Journal of Climate*, **30(20)**, 8179–8205, doi:10.1175/jcli-d-16-0836.1.
Huang, B. et al., 2018: Evaluating SST Analyses with Independent Ocean Profile Observations. *Journal of Climate*, **31(13)**, 5015–5030, doi:10.1175/jcli-d-17-0824.1.
Huang, B. et al., 2019: Uncertainty estimates for sea surface temperature and land surface air temperature in NOAAGlobalTemp version 5. *Journal of Climate*, **33(4)**, 1351–1379, doi:10.1175/jcli-d-19-0395.1.
Huang, H., M. Gutjahr, A. Eisenhauer, and G. Kuhn, 2020: No detectable Weddell Sea Antarctic Bottom Water export during the Last and Penultimate Glacial Maximum. *Nature Communications*, **11(1)**, 424, doi:10.1038/s41467-020-14302-3.
Huang, R., S. Chen, W. Chen, P. Hu, and B. Yu, 2019: Recent Strengthening of the Regional Hadley Circulation over the Western Pacific during Boreal Spring. *Advances in Atmospheric Sciences*, **36**, 1251–1264.
Huang, X. et al., 2019a: Northwestward Migration of the Northern Edge of the East Asian Summer Monsoon During the Mid-Pliocene Warm Period: Simulations and Reconstructions. *Journal of Geophysical Research: Atmospheres*, **124(3)**, 1392–1404, doi:10.1029/2018jd028995.
Huang, X. et al., 2019b: Northern Hemisphere land monsoon precipitation changes in the twentieth century revealed by multiple reanalysis datasets. *Climate Dynamics*, **53(11)**, 7131–7149, doi:10.1007/s00382-019-04982-z.
Huffman, G.J. et al., 2007: The TRMM Multisatellite Precipitation Analysis (TMPA): Quasi-Global , Multiyear , Combined-Sensor Precipitation Estimates at Fine Scales. *Journal of Hydrometeorology*, **8**, 38–55, doi:10.1175/jhm560.1.
Hugonnet, R. et al., 2021: Accelerated global glacier mass loss in the early twenty-first century. *Nature* (in press).
Hummels, R. et al., 2015: Interannual to decadal changes in the western boundary circulation in the Atlantic at 11°S. *Geophysical Research Letters*, **42(18)**, 7615–7622, doi:10.1002/2015gl065254.
Hurd, C.L., A. Lenton, B. Tilbrook, and P.W. Boyd, 2018: Current understanding and challenges for oceans in a higher-CO2 world. *Nature Climate Change*, **8(8)**, 686–694, doi:10.1038/s41558-018-0211-0.
Hyland, E.G., N.D. Sheldon, and J.M. Cotton, 2017: Constraining the early Eocene climatic optimum: A terrestrial interhemispheric comparison. *Geological Society of America Bulletin*, **129(1–2)**, 244–252, doi:10.1130/b31493.1.
Ibarra, D.E. et al., 2018: Warm and cold wet states in the western United States during the Pliocene-Pleistocene. *Geology*, **46(4)**, 355–358, doi:10.1130/g39962.1.
IMBIE Consortium, 2018: Mass balance of the Antarctic Ice Sheet from 1992 to 2017. *Nature*, doi:10.1038/s41586-018-0179-y.
IMBIE Consortium, 2020: BB Mass balance of the Greenland Ice Sheet from 1992 to 2018. *Nature*, **579(7798)**, 233–239, doi:10.1038/s41586-019-1855-2.
Inglis, G.N. et al., 2020: Global mean surface temperature and climate sensitivity of the EECO, PETM and latest Paleocene. *Climate of the Past*, **16(5)**, 1953–1968, doi:10.5194/cp-16-1953-2020.
IPCC, 2013: Summary for Policymakers. In: *Climate Change 2013: The Physical Science Basis. Contribution of Working Group I to the Fifth Assessment Report of the Intergovernmental Panel on Climate Change* [Stocker,

ACCEPTED VERSION SUBJECT TO FINAL EDITS

T.F., D. Qin, G.K. Plattner, M. Tignor, S.K. Allen, J. Boschung, A. Nauels, Y. Xia, V. Bex, and P.M. Midgley (eds.)]. Cambridge University Press, Cambridge, United Kingdom and New York, NY, USA, United Kingdom and New York, NY, USA, pp. 3–29, doi:10.1017/cbo9781107415324.004.

IPCC, 2018: Global Warming of 1.5°C. An IPCC Special Report on the impacts of global warming of 1.5°C above pre-industrial levels and related global greenhouse gas emission pathways, in the context of strengthening the global response to the threat of climate change,. [Masson-Delmotte, V., P. Zhai, H.-O. Pörtner, D. Roberts, J. Skea, P.R. Shukla, A. Pirani, W. Moufouma-Okia, C. Péan, R. Pidcock, S. Connors, J.B.R. Matthews, Y. Chen, X. Zhou, M.I. Gomis, E. Lonnoy, T. Maycock, M. Tignor, and T. Waterfield (eds.)]. In Press, 616 pp.

IPCC, 2019: IPCC Special Report on the Ocean and Cryosphere in a Changing Climate. [Pörtner, H.-O., D.C. Roberts, V. Masson-Delmotte, P. Zhai, M. Tignor, E. Poloczanska, K. Mintenbeck, A. Alegría, M. Nicolai, and A. Okem (eds.)]. In Press, 755 pp.

Irvalı, N. et al., 2016: Evidence for regional cooling, frontal advances, and East Greenland Ice Sheet changes during the demise of the last interglacial. *Quaternary Science Reviews*, **150**, 184–199, doi:10.1016/j.quascirev.2016.08.029.

Ishii, M., Fakuda, Y., Hirahara, S., Yasui, S., Suzuki, T., and Sato, K., 2017: Accuracy of global upper ocean heat content estimation expected from present observational data sets. *SOLA*, **13**, 163–167, doi:10.2151/sola.2017-030.

Ishino, S. and I. Suto, 2020: Late Pliocene sea-ice expansion and its influence on diatom species turnover in the Southern Ocean. *Marine Micropaleontology*, **160**, 101895, doi:10.1016/j.marmicro.2020.101895.

Ito, T., A. Nenes, M.S. Johnson, N. Meskhidze, and C. Deutsch, 2016: Acceleration of oxygen decline in the tropical Pacific over the past decades by aerosol pollutants. *Nature Geoscience*, **9(6)**, 443–447, doi:10.1038/ngeo2717.

Ivanova, D.P., P.J. Gleckler, K.E. Taylor, P.J. Durack, and K.D. Marvel, 2016: Moving beyond the total sea ice extent in gauging model biases. *Journal of Climate*, **29(24)**, 8965–8987, doi:10.1175/jcli-d-16-0026.1.

Ivy, D.J., S. Solomon, and H.E. Rieder, 2016: Radiative and dynamical influences on polar stratospheric temperature trends. *Journal of Climate*, **29(13)**, 4927–4938, doi:10.1175/jcli-d-15-0503.1.

Ivy, D.J. et al., 2017: Observed changes in the Southern Hemispheric circulation in May. *Journal of Climate*, **30(2)**, 527–536, doi:10.1175/jcli-d-16-0394.1.

Jaber, S.M. and M.M. Abu-Allaban, 2020: TRMM 3B43 Product-Based Spatial and Temporal Anatomy of Precipitation Trends: Global Perspective. *Environmental Monitoring and Assessment*, **192(7)**, doi:10.1007/s10661-020-08405-z.

Jaccard, S.L. and E.D. Galbraith, 2012: Large climate-driven changes of oceanic oxygen concentrations during the last deglaciation. *Nature Geoscience*, **5(2)**, 151–156, doi:10.1038/ngeo1352.

Jaccard, S.L., E.D. Galbraith, A. Martínez-Garciá, and R.F. Anderson, 2016: Covariation of deep Southern Ocean oxygenation and atmospheric CO2 through the last ice age. *Nature*, **530(7589)**, 207–210, doi:10.1038/nature16514.

Jackson, L.C. and R.A. Wood, 2020: Fingerprints for Early Detection of Changes in the AMOC. *Journal of Climate*, **33(16)**, 7027–7044, doi:10.1175/jcli-d-20-0034.1.

Jackson, L.C., K.A. Peterson, C.D. Roberts, and R.A. Wood, 2016: Recent slowing of Atlantic overturning circulation as a recovery from earlier strengthening. *Nature Geoscience*, **9(7)**, 518–522, doi:10.1038/ngeo2715.

Jackson, T., H.A. Bouman, S. Sathyendranath, and E. Devred, 2011: Regional-scale changes in diatom distribution in the Humboldt upwelling system as revealed by remote sensing: implications for fisheries. *ICES Journal of Marine Science*, **68(4)**, 729–736, doi:10.1093/icesjms/fsq181.

Jacobel, A.W., J.F. McManus, R.F. Anderson, and G. Winckler, 2017: Climate-related response of dust flux to the central equatorial Pacific over the past 150 kyr. *Earth and Planetary Science Letters*, **457**, 160–172, doi:10.1016/j.epsl.2016.09.042.

James, M., A.G. Lewkowicz, S.L. Smith, and C.M. Miceli, 2013: Multi-decadal degradation and persistence of permafrost in the Alaska Highway corridor, northwest Canada. *Environmental Research Letters*, **8(4)**, 045013, doi:10.1088/1748-9326/8/4/045013.

Jansen, E. et al., 2020: Past perspectives on the present era of abrupt Arctic climate change. *Nature Climate Change*, **10(8)**, 714–721, doi:10.1038/s41558-020-0860-7.

Jaramillo, F. and G. Destouni, 2015: Local flow regulation and irrigation raise global human water consumption and footprint. *Science*, **350(6265)**, 1248–1251, doi:10.1126/science.aad1010.

Jeong, D., L. Sushama, and M. Naveed Khaliq, 2017: Attribution of spring snow water equivalent (SWE) changes over the northern hemisphere to anthropogenic effects. *Climate Dynamics*, **48**, 3645–3658, doi:10.1007/s00382-016-3291-4.

Jian, Z. et al., 2000: Holocene variability of the Kuroshio Current in the Okinawa Trough, northwestern Pacific Ocean. *Earth and Planetary Science Letters*, **184(1)**, 305–319, doi:10.1016/s0012-821x(00)00321-6.

Jiang, C. et al., 2017: Inconsistencies of interannual variability and trends in long-term satellite leaf area index products. *Global Change Biology*, **23(10)**, 4133–4146, doi:10.1111/gcb.13787.

Jiang, N. and C. Zhu, 2018: Asymmetric Changes of ENSO Diversity Modulated by the Cold Tongue Mode Under Recent Global Warming. *Geophysical Research Letters*, **45(22)**, 12,506–512,513, doi:10.1029/2018gl079494.

ACCEPTED VERSION SUBJECT TO FINAL EDITS

Jiang, N., W. Qian, and J.C.H. Leung, 2016: The global monsoon division combining the k-means clustering method and low-level cross-equatorial flow. *Climate Dynamics*, **47(7–8)**, 2345–2359, doi:10.1007/s00382-015-2967-5.
Jin, D., S.N. Hameed, and L. Huo, 2016: Recent Changes in ENSO Teleconnection over the Western Pacific Impacts the Eastern China Precipitation Dipole. *Journal of Climate*, **29(21)**, 7587–7598, doi:10.1175/jcli-d-16-0235.1.
Jin, X. et al., 2018: Influences of Pacific Climate Variability on Decadal Subsurface Ocean Heat Content Variations in the Indian Ocean. *Journal of Climate*, **31(10)**, 4157–4174, doi:10.1175/jcli-d-17-0654.1.
Johnson, G.C. and J.M. Lyman, 2020: Warming trends increasingly dominate global ocean. *Nature Climate Change*, **10(8)**, 757–761, doi:10.1038/s41558-020-0822-0.
Johnson, G.C. et al., 2020: Ocean heat content. In State of the Climate in 2019, Global Oceans. *Bull. Am. Meteorol. Soc.*, **101(8)**, S140–S144, doi:10.1175/bams-d-20-0105.1.
Johnson, J.S., K.A. Nichols, B.M. Goehring, G. Balco, and J.M. Schaefer, 2019: Abrupt mid-Holocene ice loss in the western Weddell Sea Embayment of Antarctica. *Earth and Planetary Science Letters*, **518**, 127–135, doi:10.1016/j.epsl.2019.05.002.
Johnson, J.S. et al., 2014: Rapid thinning of pine island glacier in the early holocene. *Science*, **343(6174)**, 999–1001, doi:10.1126/science.1247385.
Johnson, N.C., 2013: How Many ENSO Flavors Can We Distinguish? *Journal of Climate*, **26(13)**, 4816–4827, doi:10.1175/jcli-d-12-00649.1.
Jones, B.M. et al., 2016: Presence of rapidly degrading permafrost plateaus in south-central Alaska. *The Cryosphere*, **10(6)**, 2673–2692, doi:10.5194/tc-10-2673-2016.
Jones, E.M. et al., 2017: Ocean acidification and calcium carbonate saturation states in the coastal zone of the West Antarctic Peninsula. *Deep Sea Research Part II: Topical Studies in Oceanography*, **139**, 181–194, doi:10.1016/j.dsr2.2017.01.007.
Jones, G.S., 2020: 'Apples and Oranges': On comparing simulated historic near-surface temperature changes with observations. *Quarterly Journal of the Royal Meteorological Society*, **146**, 3747–3771, doi:10.1002/qj.3871.
Jones, J.M. et al., 2016: Assessing recent trends in high-latitude Southern Hemisphere surface climate. *Nature Climate Change*, **6**, 917, doi:10.1038/nclimate3103.
Jones, P.D., C. Harpham, and B.M. Vinther, 2014: Winter-responding proxy temperature reconstructions and the North Atlantic Oscillation. *Journal of Geophysical Research: Atmospheres*, **119**, 6497–6505, doi:10.1002/2014jd021561.
Jones, P.D. et al., 2012: Hemispheric and large-scale land-surface air temperature variations: An extensive revision and an update to 2010. *Journal of Geophysical Research: Atmospheres*, **117(D5)**, doi:10.1029/2011jd017139.
Jones, R.S. et al., 2015: Rapid Holocene thinning of an East Antarctic outlet glacier driven by marine ice sheet instability. *Nature Communications*, **8910**, doi:10.1038/ncomms9910.
Jongeward, A.R., Z. Li, H. He, and X. Xiong, 2016: Natural and Anthropogenic Aerosol Trends from Satellite and Surface Observations and Model Simulations over the North Atlantic Ocean from 2002 to 2012. *Journal of the Atmospheric Sciences*, **73(11)**, 4469–4485, doi:10.1175/jas-d-15-0308.1.
Jonkers, L., H. Hillebrand, and M. Kucera, 2019: Global change drives modern plankton communities away from the pre-industrial state. *Nature*, **570(7761)**, 372–375, doi:10.1038/s41586-019-1230-3.
Josey, S.A. et al., 2018: The Recent Atlantic Cold Anomaly: Causes, Consequences, and Related Phenomena. *Annual Review of Marine Science*, **10**, 475–501, doi:10.1146/annurev-marine-121916-063102.
Joyce, R.J., J.E. Janowiak, P.A. Arkin, and P. Xie, 2004: CMORPH : A Method that Produces Global Precipitation Estimates from Passive Microwave and Infrared Data at High Spatial and Temporal Resolution. *Journal of Hydrometeorology*, **5(3)**, 487–503, doi:10.1175/1525-7541(2004)005<0487:camtpg>2.0.co;2.
Jung, M.-P., K.-M. Shim, Y. Kim, and I.-T. Choi, 2015: Change of Climatic Growing Season in Korea. *Korean Journal of Environmental Agriculture*, **34**, 192–195, doi:10.5338/kjea.2015.34.3.27.
Jungclaus, J.H. et al., 2017: The PMIP4 contribution to CMIP6 - Part 3: The last millennium, scientific objective, and experimental design for the PMIP4 past1000 simulations. *Geoscientific Model Development*, **10(11)**, 4005–4033, doi:10.5194/gmd-10-4005-2017.
Junod, R.A. and J.R. Christy, 2020a: A new compilation of globally gridded night-time marine air temperatures: The UAHNMATv1 dataset. *International Journal of Climatology*, **40(5)**, 2609–2623, doi:10.1002/joc.6354.
Junod, R.A. and J.R. Christy, 2020b: A new compilation of globally gridded night-time marine air temperatures: The UAHNMATv1 dataset. *International Journal of Climatology*, **40(5)**, 2609–2623, doi:10.1002/joc.6354.
Jurikova, H. et al., 2020: Permian–Triassic mass extinction pulses driven by major marine carbon cycle perturbations. *Nature Geoscience*, **13(11)**, 745–750, doi:10.1038/s41561-020-00646-4.
Kadow, C., D.M. Hall, and U. Ulbrich, 2020a: Artificial intelligence reconstructs missing climate information. *Nature Geoscience*, **13(6)**, 408–413, doi:10.1038/s41561-020-0582-5.
Kadow, C., D.M. Hall, and U. Ulbrich, 2020b: Artificial intelligence reconstructs missing climate information. *Nature Geoscience*, **13(6)**, 408–413, doi:10.1038/s41561-020-0582-5.
Kageyama, M. et al., 2017: The PMIP4 contribution to CMIP6 – Part 4: Scientific objectives and experimental design of the PMIP4-CMIP6 Last Glacial Maximum experiments and PMIP4 sensitivity experiments. *Geoscientific Model Development*, **10(11)**, 4035–4055, doi:10.5194/gmd-10-4035-2017.

ACCEPTED VERSION SUBJECT TO FINAL EDITS

Kageyama, M. et al., 2020: The PMIP4-CMIP6 Last Glacial Maximum experiments: preliminary results and comparison with the PMIP3-CMIP5 simulations. *Climate of the Past Discussions*, **2020**, 1–37, doi:10.5194/cp-2019-169.
Kageyama, M. et al., 2021: A multi-model CMIP6-PMIP4 study of Arctic sea ice at 127ka: sea ice data compilation and model differences. *Climate of the Past*, **17(1)**, 37–62, doi:10.5194/cp-17-37-2021.
Kalansky, J., Rosenthal, Y., Herbert, T., Bova, S., Altabet, M., 2015: Southern Ocean contributions to the Eastern Equatorial Pacific heat content during the Holocene. *Earth and Planetary Science Letters*, **424**, 158–167, doi:10.1016/j.epsl.2015.05.013.
Kamae, Y., X. Li, S.P. Xie, and H. Ueda, 2017: Atlantic effects on recent decadal trends in global monsoon. *Climate Dynamics*, **49(9–10)**, 3443–3455, doi:10.1007/s00382-017-3522-3.
Kanner, L.C., S.J. Burns, H. Cheng, R.L. Edwards, and M. Vuille, 2013: High-resolution variability of the South American summer monsoon over the last seven millennia: Insights from a speleothem record from the central Peruvian Andes. *Quaternary Science Reviews*, **75**, 1–10, doi:10.1016/j.quascirev.2013.05.008.
Kao, A., X. Jiang, L. Li, H. Su, and Y. Yung, 2017: Precipitation, circulation, and cloud variability over the past two decades. *Earth and Space Science*, **4**, 597–606, doi:10.1002/2017ea000319.
Kaplan, J. et al., 2017: Constraining the Deforestation History of Europe: Evaluation of Historical Land Use Scenarios with Pollen-Based Land Cover Reconstructions. *Land*, **6(4)**, 91, doi:10.3390/land6040091.
Kaplan, M.R. et al., 2016: Patagonian and southern South Atlantic view of Holocene climate. *Quaternary Science Reviews*, doi:10.1016/j.quascirev.2016.03.014.
Karamperidou, C., P.N. Di Nezio, A. Timmermann, F.-F. Jin, and K.M. Cobb, 2015: The response of ENSO flavors to mid-Holocene climate: Implications for proxy interpretation. *Paleoceanography*, **30(5)**, 527–547, doi:10.1002/2014pa002742.
Kassi, J.-B. et al., 2018: Remotely Sensing the Biophysical Drivers of Sardinella aurita Variability in Ivorian Waters. *Remote Sensing*, **10(5)**, 785, doi:10.3390/rs10050785.
Kaufman, D. et al., 2020a: Holocene global mean surface temperature, a multi-method reconstruction approach (2020a). *Scientific Data*, **7(1)**, 201, doi:10.1038/s41597-020-0530-7.
Kaufman, D. et al., 2020b: A global database of Holocene paleotemperature records (2020b). *Scientific Data*, **7(1)**, 115, doi:10.1038/s41597-020-0445-3.
Kayano, M.T., R.V. Andreoli, and R.A.F. Souza, 2019: El Niño–Southern Oscillation related teleconnections over South America under distinct Atlantic Multidecadal Oscillation and Pacific Interdecadal Oscillation backgrounds: La Niña. *International Journal of Climatology*, **39(3)**, 1359–1372, doi:10.1002/joc.5886.
Keeling, C.D., J.F.S. Chin, and T.P. Whorf, 1996: Increased activity of northern vegetation inferred from atmospheric CO2 measurements. *Nature*, **382**, 146–149, doi:10.1038/382146a0.
Keenan, T.F. and W.J. Riley, 2018: Greening of the land surface in the world's cold regions consistent with recent warming. *Nature Climate Change*, **8**, 825–828, doi:10.1038/s41558-018-0258-y.
Keenlyside, N. et al., 2015: North Atlantic Multi-Decadal Variability – Mechanisms and Predictability. In: *Climate Change: Multidecadal and Beyond* [Chang, C.-P., M. Ghil, M. Latif, and J.M. Wallace (eds.)]. World Scientific, pp. 141–157, doi:10.1142/9789814579933_0007.
Keigwin, L.D. and M.S. Cook, 2007: A role for North Pacific salinity in stabilizing North Atlantic climate. *Paleoceanography*, **22(3)**, doi:10.1029/2007pa001420.
Keil, P. et al., 2020: Multiple drivers of the North Atlantic warming hole. *Nature Climate Change*, **10(7)**, 667–671, doi:10.1038/s41558-020-0819-8.
Kemp, A.C. et al., 2018a: Relative sea-level change in Newfoundland, Canada, during the past ~3000 years. *Quaternary Science Reviews*, **201**, 89–110, doi:10.1016/j.quascirev.2018.10.012.
Kemp, A.C. et al., 2018b: Relative sea-level change in Newfoundland, Canada, during the past ~3000 years. *Quaternary Science Reviews*, **201**, 89–110, doi:10.1016/j.quascirev.2018.10.012.
Kennedy, J.J., 2014: A review of uncertainty in in situ measurements and data sets of sea surface temperature. *Reviews of Geophysics*, **52(1)**, 1–32, doi:10.1002/2013rg000434.
Kennedy, J.J., N.A. Rayner, C.P. Atkinson, and R.E. Killick, 2019: An ensemble data set of sea-surface temperature change from 1850: the Met Office 1 Hadley Centre HadSST.4.0.0.0 data set. *Journal of Geophysical Research Atmospheres*, **124(14)**, 7719–7763, doi:10.1029/2018jd029867.
Kennedy, J.J., N.A. Rayner, R.O. Smith, D.E. Parker, and M. Saunby, 2011: Reassessing biases and other uncertainties in sea surface temperature observations measured in situ since 1850: 1. Measurement and sampling uncertainties. *Journal of Geophysical Research: Atmospheres*, **116(D14)**, doi:10.1029/2010jd015218.
Kent, E.C. and A. Kaplan, 2006: Toward Estimating Climatic Trends in SST. Part III: Systematic Biases. *Journal of Atmospheric and Oceanic Technology*, **23(3)**, 487–500, doi:10.1175/jtech1845.1.
Kent, E.C. and J.J. Kennedy, 2021: Historical Estimates of Surface Marine Temperatures. *Annual Review of Marine Science*, **13(1)**, 283–311, doi:10.1146/annurev-marine-042120-111807.
Kent, E.C., S. Fangohr, and D.I. Berry, 2013: A comparative assessment of monthly mean wind speed products over the global ocean. *International Journal of Climatology*, **33**, 2520–2541, doi:10.1002/joc.3606.
Kent, E.C., D.I. Berry, and J.B. Roberts, 2014a: A comparison of global marine surface-specific humidity datasets from

ACCEPTED VERSION SUBJECT TO FINAL EDITS

in situ observations and atmospheric reanalysis. *International Journal of Climatology*, **376**, 355–376, doi:10.1002/joc.3691.
Kent, E.C., D.I. Berry, and J.B. Roberts, 2014b: A comparison of global marine surface-specific humidity datasets from in situ observations and atmospheric reanalysis. *International Journal of Climatology*, **376**, 355–376, doi:10.1002/joc.3691.
Kent, E.C. et al., 2017: A Call for New Approaches to Quantifying Biases in Observations of Sea Surface Temperature. *Bulletin of the American Meteorological Society*, **98(8)**, 1601–1616, doi:10.1175/bams-d-15-00251.1.
Kersalé, M. et al., 2020: Highly variable upper and abyssal overturning cells in the South Atlantic. *Science Advances*, **6(32)**, eaba7573, doi:10.1126/sciadv.aba7573.
Khan, N.S. et al., 2017: Drivers of Holocene sea-level change in the Caribbean. *Quaternary Science Reviews*, **155**, 13–36, doi:10.1016/j.quascirev.2016.08.032.
Khan, S.A. et al., 2020: Centennial response of Greenland's three largest outlet glaciers. *Nature Communications*, **11(1)**, doi:10.1038/s41467-020-19580-5.
Khaykin, S.M. et al., 2017: Postmillennium changes in stratospheric temperature consistently resolved by GPS radio occultation and AMSU observations. *Geophysical Research Letters*, **44(14)**, 7510–7518, doi:10.1002/2017gl074353.
Kilbourne, K.H., M.A. Alexander, and J.A. Nye, 2014: A low latitude paleoclimate perspective on Atlantic multidecadal variability. *Journal of Marine Systems*, **133**, 4–13, doi:10.1016/j.jmarsys.2013.09.004.
Kim, B.-M. et al., 2014: Weakening of the stratospheric polar vortex by Arctic sea-ice loss. *Nature Communications*, **5(1)**, 4646, doi:10.1038/ncomms5646.
Kim, H., 2019: Hydrological cycle: river discharge and runoff [in "State of the Climate in 2018"]. *Bull. Am. Meteorol. Soc.*, **100(9)**, S35–S37, doi:10.1175/2019bamsstateoftheclimate.1.
Kim, J.C. and K. Pai, 2015: Recent recovery of surface wind speed after decadal decrease: a focus on South Korea. *Climate Dynamics*, **45**, 1699–1712, doi:10.1007/s00382-015-2546-9.
Kim, S.-H. and K.-J. Ha, 2015: Two leading modes of Northern Hemisphere blocking variability in the boreal wintertime and their relationship with teleconnection patterns. *Climate Dynamics*, **44**, 2479–2491, doi:10.1007/s00382-014-2304-4.
King, A.D., D.J. Karoly, and B.J. Henley, 2017: Australian climate extremes at 1.5 °C and 2 °C of global warming. *Nature Climate Change*, **7(6)**, 412–416, doi:10.1038/nclimate3296.
King, J. et al., 2018: Comparison of Freeboard Retrieval and Ice Thickness Calculation From ALS, ASIRAS, and CryoSat-2 in the Norwegian Arctic to Field Measurements Made During the N-ICE2015 Expedition. *Journal of Geophysical Research: Oceans*, **123(2)**, 1123–1141, doi:10.1002/2017jc013233.
King, J.C. and S.A. Harangozo, 1998: Climate change in the western Antarctic Peninsula since 1945: Observations and possible causes. *Annals of Glaciology*, 571–575, doi:10.3189/1998aog27-1-571-575.
Kingslake, J. et al., 2018: Extensive retreat and re-advance of the West Antarctic Ice Sheet during the Holocene. *Nature*, **558(7710)**, 430–434, doi:10.1038/s41586-018-0208-x.
Kinne, S., 2019: Aerosol radiative effects with MACv2. *Atmospheric Chemistry and Physics*, **19(16)**, 10919–10959, doi:10.5194/acp-19-10919-2019.
Kirschke, S. et al., 2013: Three decades of global methane sources and sinks. *Nature Geoscience*, **6**, 813–823, doi:10.1038/ngeo1955.
Kirtland Turner, S., 2018: Constraints on the onset duration of the Paleocene–Eocene Thermal Maximum. *Philosophical Transactions of the Royal Society A: Mathematical, Physical and Engineering Sciences*, doi:10.1098/rsta.2017.0082.
Kitoh, A. et al., 2013a: Monsoons in a changing world : A regional perspective in a global context. *Journal of Geophysical Research Atmospheres*, **118**, 3053–3065, doi:10.1002/jgrd.50258.
Kitoh, A. et al., 2013b: Monsoons in a changing world : A regional perspective in a global context. *Journal of Geophysical Research Atmospheres*, **118**, 3053–3065, doi:10.1002/jgrd.50258.
Kjeldsen, K.K. et al., 2015: Spatial and temporal distribution of mass loss from the Greenland Ice Sheet since AD 1900. *Nature*, **528**, 396–400, doi:10.1038/nature16183.
Knies, J. et al., 2014: The emergence of modern sea ice cover in the Arctic Ocean. *Nature Communications*, **5(1)**, 5608, doi:10.1038/ncomms6608.
Knutson, T.R. and F. Zeng, 2018: Model assessment of observed precipitation trends over land regions: Detectable human influences and possible low bias in model trends. *Journal of Climate*, **31(12)**, 4617–4637, doi:10.1175/jcli-d-17-0672.1.
Knutz, P.C. et al., 2019: Eleven phases of Greenland Ice Sheet shelf-edge advance over the past 2.7 million years. *Nature Geoscience*, **12(5)**, doi:10.1038/s41561-019-0340-8.
Kobashi, T. et al., 2017: Volcanic influence on centennial to millennial Holocene Greenland temperature change. *Scientific Reports*, **7(1)**, 1441, doi:10.1038/s41598-017-01451-7.
Kobayashi, S. et al., 2015: The JRA-55 reanalysis: General specifications and basic characteristics. *Journal of the Meteorological Society of Japan. Ser. II*, **93(1)**, 5–48, doi:10.2151/jmsj.2015-001.
Koeller, P. et al., 2009: Basin-Scale Coherence in Phenology of Shrimps and Phytoplankton in the North Atlantic

ACCEPTED VERSION SUBJECT TO FINAL EDITS

Ocean. *Science*, **324(5928)**, 791, doi:10.1126/science.1170987.
Koenig, S.J. et al., 2015: Ice sheet model dependency of the simulated Greenland Ice Sheet in the mid-Pliocene. *Climate of the Past*, **11(3)**, doi:10.5194/cp-11-369-2015.
Koffman, B.G. et al., 2014: Centennial-scale variability of the Southern Hemisphere westerly wind belt in the eastern Pacific over the past two millennia. *Climate of the Past*, **10(3)**, 112–125, doi:10.5194/cp-10-1125-2014.
Köhler, P., B. de Boer, A.S. von der Heydt, L.B. Stap, and R.S.W. van de Wal, 2015: On the state dependency of the equilibrium climate sensitivity during the last 5 million years. *Climate of the Past*, **11(12)**, 1801–1823, doi:10.5194/cp-11-1801-2015.
Kokelj, S., T.C. Lantz, J. Tunnicliffe, R. Segal, and D. Lacelle, 2017: Climate-driven thaw of permafrost preserved glacial landscapes, northwestern Canada. *Geology*, **45(4)**, 371–374, doi:10.1130/g38626.1.
Kong, D., Q. Zhang, V.P. Singh, and P. Shi, 2017: Seasonal vegetation response to climate change in the Northern Hemisphere (1982–2013). *Global and Planetary Change*, doi:10.1016/j.gloplacha.2016.10.020.
Kononova, N.K. and A.R. Lupo, 2020: Changes in the dynamics of the Northern Hemisphere atmospheric circulation and the relationship to surface temperature in the 20th and 21st centuries. *Atmosphere*, **11(255)**, doi:10.3390/atmos11030255.
Konopka, P., F. Ploeger, M. Tao, and M. Riese, 2016: Zonally resolved impact of ENSO on the stratospheric circulation and water vapor entry values. *Journal of Geophysical Research: Atmospheres*, **121(19)**, 11,411–486,501, doi:10.1002/2015jd024698.
Kopp, R.E. et al., 2016a: Temperature-driven global sea-level variability in the Common Era. *Proceedings of the National Academy of Sciences*, **113(11)**, E1434–E1441, doi:10.1073/pnas.1517056113.
Kopp, R.E. et al., 2016b: Temperature-driven global sea-level variability in the Common Era. *Proceedings of the National Academy of Sciences*, **113(11)**, E1434–E1441, doi:10.1073/pnas.1517056113.
Kosaka, Y. and S.-P. Xie, 2013: Recent global-warming hiatus tied to equatorial Pacific surface cooling. *Nature*, **501(7467)**, 403–407, doi:10.1038/nature12534.
Kousari, M.R., H. Ahani, and H. Hakimelahi, 2013: An investigation of near-surface wind speed trends in arid and semiarid regions of Iran. *Theoretical and Applied Climatology*, **114**, 153–168, doi:10.1007/s00704-012-0811-y.
Koutavas, A. and S. Joanides, 2012: El Niño–Southern Oscillation extrema in the Holocene and Last Glacial Maximum. *Paleoceanography*, **27(4)**, PA4208, doi:10.1029/2012pa002378.
Kovács, T. et al., 2017: Determination of the atmospheric lifetime and global warming potential of sulfur hexafluoride using a three-dimensional model. *Atmospheric Chemistry and Physics*, **17(2)**, 883–898, doi:10.5194/acp-17-883-2017.
Kremer, A. et al., 2018: Changes in sea ice cover and ice sheet extent at the Yermak Plateau during the last 160 ka – Reconstructions from biomarker records. *Quaternary Science Reviews*, **182**, 93–108, doi:10.1016/j.quascirev.2017.12.016.
Kremser, S. et al., 2016: Stratospheric aerosol - Observations, processes, and impact on climate. *Reviews of Geophysics*, **54**, doi:10.1002/2015rg000511.
Kretschmer, M. et al., 2018: More-persistent weak stratospheric polar vortex States linked to cold extremes. *Bulletin of the American Meteorological Society*, **99(1)**, 49–60, doi:10.1175/bams-d-16-0259.1.
Krishnamurthy, L. and V. Krishnamurthy, 2016: Decadal and interannual variability of the Indian Ocean SST. *Climate Dynamics*, **46(1)**, 57–70, doi:10.1007/s00382-015-2568-3.
Krivova, N. A., Solanki, S. K., and Floyd, L., 2006: Reconstruction of solar UV irradiance in cycle~23. *A&A*, **452(2)**, 631–639, doi:10.1051/0004-6361:20064809.
Krumpen, T. et al., 2019: Arctic warming interrupts the Transpolar Drift and affects long-range transport of sea ice and ice-rafted matter. *Scientific Reports*, **9(1)**, 5459, doi:10.1038/s41598-019-41456-y.
Kukal, M.S. and S. Irmak, 2018: U.S. Agro-Climate in 20thCentury: Growing Degree Days, First and Last Frost, Growing Season Length, and Impacts on Crop Yields. *Scientific Reports*, **8(6977)**, doi:10.1038/s41598-018-25212-2.
Kunkel, K.E. et al., 2016: Trends and Extremes in Northern Hemisphere Snow Characteristics. *Current Climate Change Reports*, **2**, 65–73, doi:10.1007/s40641-016-0036-8.
Kürschner, W.M., J. van der Burgh, H. Visscher, and D.L. Dilcher, 1996: Oak leaves as biosensors of late neogene and early pleistocene paleoatmospheric CO2 concentrations. *Marine Micropaleontology*, **27(1–4)**, 299–312, doi:10.1016/0377-8398(95)00067-4.
Kuusela, M. and M.L. Stein, 2018: Locally stationary spatio-temporal interpolation of Argo profiling float data. *Proceedings of the Royal Society A: Mathematical, Physical and Engineering Sciences*, **474(2220)**, 20180400, doi:10.1098/rspa.2018.0400.
Kwok, R., 2018a: Arctic sea ice thickness, volume, and multiyear ice coverage: Losses and coupled variability (1958-2018). *Environmental Research Letters*, **13(10)**, 105005, doi:10.1088/1748-9326/aae3ec.
Kwok, R., 2018b: Arctic sea ice thickness, volume, and multiyear ice coverage: Losses and coupled variability (1958-2018). *Environmental Research Letters*, **13(10)**, 105005, doi:10.1088/1748-9326/aae3ec.
Kwok, R. and G.F. Cunningham, 2015: Variability of arctic sea ice thickness and volume from CryoSat-2.

ACCEPTED VERSION SUBJECT TO FINAL EDITS

Philosophical Transactions of the Royal Society A: Mathematical, Physical and Engineering Sciences, **373**, 2045, doi:10.1098/rsta.2014.0157.
Kwon, M.H., S.-W. Yeh, Y.-G. Park, and Y.-K. Lee, 2013: Changes in the linear relationship of ENSO–PDO under the global warming. *International Journal of Climatology*, **33(5)**, 1121–1128, doi:10.1002/joc.3497.
Kylander, M.E. et al., 2016: Potentials and problems of building detailed dust records using peat archives: An example from Store Mosse (the "Great Bog"), Sweden. *Geochim. Cosmochim*, **190**, 156–174, doi:10.1016/j.gca.2016.06.028.
L'Heureux, M.L., S. Lee, and B. Lyon, 2013: Recent multidecadal strengthening of the Walker circulation across the tropical Pacific. *Nature Climate Change*, **3(6)**, 571–576, doi:10.1038/nclimate1840.
Lachkar, Z., M. Lévy, and K.S. Smith, 2019: Strong Intensification of the Arabian Sea Oxygen Minimum Zone in Response to Arabian Gulf Warming. *Geophysical Research Letters*, **46(10)**, 5420–5429, doi:10.1029/2018gl081631.
Ladstädter, F., A.K. Steiner, M. Schwärz, and G. Kirchengast, 2015: Climate intercomparison of GPS radio occultation, RS90/92 radiosondes and GRUAN from 2002 to 2013. *Atmospheric Measurement Techniques*, **8(4)**, 1819–1834, doi:10.5194/amt-8-1819-2015.
Lambeck, K., H. Rouby, A. Purcell, Y. Sun, and M. Sambridge, 2014: Sea level and global ice volumes from the Last Glacial Maximum to the Holocene. *Proceedings of the National Academy of Sciences*, **111(43)**, 15296–15303, doi:10.1073/pnas.1411762111.
Lambert, F. et al., 2015: Dust fluxes and iron fertilization in Holocene and Last Glacial Maximum climates. *Geophysical Research Letters*, **42(14)**, 6014–6023, doi:10.1002/2015gl064250.
Lamping, N. et al., 2020: Highly branched isoprenoids reveal onset of deglaciation followed by dynamic sea-ice conditions in the western Amundsen Sea, Antarctica. *Quaternary Science Reviews*, **228**, 106103, doi:10.1016/j.quascirev.2019.106103.
Lamy, F. et al., 2010: Holocene changes in the position and intensity of the southern westerly wind belt. *Nature Geoscience*, **3(10)**, 695–699, doi:10.1038/ngeo959.
Lamy, F. et al., 2014: Increased Dust Deposition in the Pacific Southern Ocean During Glacial Periods. *Science*, **343(6169)**, 403–407, doi:10.1126/science.1245424.
Lamy, F. et al., 2015: Glacial reduction and millennial-scale variations in Drake Passage throughflow. *Proceedings of the National Academy of Sciences*, **112(44)**, 13496, doi:10.1073/pnas.1509203112.
Langematz, U. et al., 2018: Polar Stratospheric Ozone: Past, Present and Future. In: *Scientific Assessment of Ozone Depletion: 2018*. Global Ozone Research and Monitoring Project – Report No. 58, pp. 4.1–4.63.
Lapointe, F. et al., 2017: Influence of North Pacific decadal variability on the western Canadian Arctic over the past 700 years. *Climate of the Past*, **13(4)**, 411–420, doi:10.5194/cp-13-411-2017.
Larsen, N.K. et al., 2014: Rapid early Holocene ice retreat in West Greenland. *Quaternary Science Reviews*, **92**, 310–323, doi:10.1016/j.quascirev.2013.05.027.
Larsen, N.K. et al., 2015: The response of the southern Greenland ice sheet to the Holocene thermal maximum. *Geology*, **43(4)**, 291–294, doi:10.1130/g36476.1.
Lasher, G.E. and Y. Axford, 2019: Medieval warmth confirmed at the Norse Eastern Settlement in Greenland. *Geology*, **47(3)**, 267–270, doi:10.1130/g45833.1.
Laskar, J., A. Fienga, M. Gastineau, and H. Manche, 2011: La2010: a new orbital solution for the long-term motion of the Earth. *Astronomy & Astrophysics*, **532**, A89, doi:10.1051/0004-6361/201116836.
Laube, J.C. et al., 2014: Newly detected ozone-depleting substances in the atmosphere. *Nature Geoscience*, **7**, 266–269, doi:10.1038/ngeo2109.
Lauvset, S.K., N. Gruber, P. Landschützer, A. Olsen, and J. Tjiputra, 2015: Trends and drivers in global surface ocean pH over the past 3 decades. *Biogeosciences*, **12(5)**, 1285–1298, doi:10.5194/bg-12-1285-2015.
Lauvset, S.K. et al., 2020: Processes Driving Global Interior Ocean pH Distribution. *Global Biogeochemical Cycles*, **34(1)**, e2019GB006229, doi:10.1029/2019gb006229.
Lawrence, D.M. et al., 2016: The Land Use Model Intercomparison Project (LUMIP) contribution to CMIP6: Rationale and experimental design. *Geoscientific Model Development*, **9(9)**, 2973–2998, doi:10.5194/gmd-9-2973-2016.
Leahy, T. P., F. P. Llopis, M. D. Palmer, N.H.R., 2018: Using neural networks to correct historical climate observations. *Journal of Atmospheric and Oceanic Technology*, **35**, 2053–2059.
Lean, J.L., 2018a: Estimating Solar Irradiance Since 850 CE. *Earth and Space Science*, **5(4)**, 133–149, doi:10.1002/2017ea000357.
Lean, J.L., 2018b: Estimating Solar Irradiance Since 850 CE. *Earth and Space Science*, **5(4)**, 133–149, doi:10.1002/2017ea000357.
Lecavalier, B.S. et al., 2014: A model of Greenland ice sheet deglaciation constrained by observations of relative sea level and ice extent. *Quaternary Science Reviews*, **102**, 54–84, doi:10.1016/j.quascirev.2014.07.018.
Lechleitner, F.A. et al., 2017: Tropical rainfall over the last two millennia: Evidence for a low-latitude hydrologic seesaw. *Scientific Reports*, **7**, 1–9, doi:10.1038/srep45809.
Ledru, M.-P. et al., 2013: The Medieval Climate Anomaly and the Little Ice Age in the eastern Ecuadorian Andes. *Climate of the Past*, **9(1)**, 307–321, doi:10.5194/cp-9-307-2013.

ACCEPTED VERSION SUBJECT TO FINAL EDITS

Leduc, G., L. Vidal, O. Cartapanis, and E. Bard, 2009: Modes of eastern equatorial Pacific thermocline variability: Implications for ENSO dynamics over the last glacial period. *Paleoceanography*, **24(3)**, doi:10.1029/2008pa001701.

Lee, J., K.R. Sperber, P.J. Gleckler, C.J.W. Bonfils, and K.E. Taylor, 2019: Quantifying the agreement between observed and simulated extratropical modes of interannual variability. *Climate Dynamics*, **52**, 4057–4089, doi:10.1007/s00382-018-4355-4.

Lee, J.-Y. and K.-J. Ha, 2015: Understanding of Interdecadal Changes in Variability and Predictability of the Northern Hemisphere Summer Tropical–Extratropical Teleconnection. *Journal of Climate*, **28(21)**, 8634–8647, doi:10.1175/jcli-d-15-0154.1.

Lee, S.H., P.D. William, and T.A. Frame, 2019: Increased shear in the North Atlantic upper-level jet strean over the past four decades. *Nature*, **572**, 639–643, doi:10.1038/s41586-019-1465-z.

Lee, S.-K. et al., 2015: Pacific origin of the abrupt increase in Indian Ocean heat content during the warming hiatus. *Nature Geoscience*, **8(6)**, 445–449, doi:10.1038/ngeo2438.

Legeais, J.-F., W. Llovel, A.M.B.M., 2020: Evidence of the TOPEX-A Altimeter Instrumental Anomaly and Acceleration of the Global Mean Sea Level. *In Copernicus Marine Service Ocean State Report Journal of Operational Oceanography*, S1–S172, doi:10.1080/1755876x.2020.1785097.

LeGrande, A.N. and G.A. Schmidt, 2011: Water isotopologues as a quantitative paleosalinity proxy. *Paleoceanography*, **26(3)**, doi:10.1029/2010pa002043.

Lejeune, Q. et al., 2020: Biases in the albedo sensitivity to deforestation in CMIP5 models and their impacts on the associated historical Radiative Forcing. *Earth System Dynamics*, **11(4)**, 1209–1232, doi:10.5194/esd-2019-94.

Lenoir, J. and J.C. Svenning, 2015: Climate-related range shifts – a global multidimensional synthesis and new research directions. *Ecography*, **38(1)**, 15–28, doi:10.1111/ecog.00967.

Lenoir, J., J.C. Gégout, P.A. Marquet, P. De Ruffray, and H. Brisse, 2008: A significant upward shift in plant species optimum elevation during the 20th century. *Science*, doi:10.1126/science.1156831.

Lenoir, J. et al., 2020: Species better track climate warming in the oceans than on land. *Nature Ecology and Evolution*, **4(8)**, doi:10.1038/s41559-020-1198-2.

Lenssen, N.J.L. et al., 2019: Improvements in the GISTEMP Uncertainty Model. *Journal of Geophysical Research: Atmospheres*, **124(12)**, 6307–6326, doi:10.1029/2018jd029522.

Leroy, S.S., C.O. Ao, and O.P. Verkhoglyadova, 2018: Temperature Trends and Anomalies in Modern Satellite Data: Infrared Sounding and GPS Radio Occultation. *Journal of Geophysical Research: Atmospheres*, **123(20)**, 11,411–431,444, doi:10.1029/2018jd028990.

Levitus, S. et al., 2012: World ocean heat content and thermosteric sea level change (0–2000 m), 1955–2010. *Geophysical Research Letters*, **39(10)**, doi:10.1029/2012gl051106.

Levy, R. et al., 2016: Antarctic ice sheet sensitivity to atmospheric CO2 variations in the early to mid-Miocene.. *Proceedings of the National Academy of Sciences of the United States of America*, **113(13)**, 3453–8, doi:10.1073/pnas.1516030113.

Lewis, K., G. Dijken, and K. Arrigo, 2020: Changes in phytoplankton concentration now drive increased Arctic Ocean primary production. *Science*, **369**, 198–202, doi:10.1126/science.aay8380.

Lewkowicz, A.G. and R.G. Way, 2019: Extremes of summer climate trigger thousands of thermokarst landslides in a High Arctic environment. *Nature Communications*, **10(1)**, 1329, doi:10.1038/s41467-019-09314-7.

Li, F. et al., 2020: Towards quantification of Holocene anthropogenic land-cover change in temperate China: A review in the light of pollen-based REVEALS reconstructions of regional plant cover. *Earth-Science Reviews*, **203**, doi:10.1016/j.earscirev.2020.103119.

Li, J., B.E. Carlson, O. Dubovik, and A.A. Lacis, 2014: Recent trends in aerosol optical properties derived from AERONET measurements. *Atmospheric Chemistry and Physics*, **14(22)**, 12271–12289, doi:10.5194/acp-14-12271-2014.

Li, J. et al., 2013: El Niño modulations over the past seven centuries. *Nature Climate Change*, **3**, 822, doi:10.1038/nclimate1936.

Li, M., A.L. Gordon, J. Wei, L.K. Gruenburg, and G. Jiang, 2018: Multi-decadal timeseries of the Indonesian throughflow. *Dynamics of Atmospheres and Oceans*, **81**, 84–95, doi:10.1016/j.dynatmoce.2018.02.001.

Li, X., D. Jiang, Z. Tian, and Y. Yang, 2018: Mid-Pliocene global land monsoon from PlioMIP1 simulations. *Palaeogeography, Palaeoclimatology, Palaeoecology*, **512**, 56–70, doi:10.1016/j.palaeo.2018.06.027.

Li, X. et al., 2015: Mid-Pliocene westerlies from PlioMIP simulations. *Advances in Atmospheric Sciences*, **32(7)**, 909–923, doi:10.1007/s00376-014-4171-7.

Li, X. et al., 2016: Trend and seasonality of land precipitation in observations and CMIP5 model simulations. *International Journal of Climatology*, **36(11)**, 3781–3793, doi:10.1002/joc.4592.

Li, Y., L. Zhu, X. Zhao, S. Li, and Y. Yan, 2013: Urbanization Impact on Temperature Change in China with Emphasis on Land Cover Change and Human Activity. *Journal of Climate*, **26(22)**, 8765–8780, doi:10.1175/jcli-d-12-00698.1.

Li, Z., S. Yang, C.-Y. Tam, and C. Hu, 2020: Strengthening western equatorial Pacific and Maritime Continent atmospheric convection and its modulation on the trade wind during spring of 1901–2010. *International*

ACCEPTED VERSION SUBJECT TO FINAL EDITS

Journal of Climatology, **41(2)**, 1455–1464, doi:10.1002/joc.6856.
Liang, Y.C., C.C. Chou, J.Y. Yu, and M.H. Lo, 2016: Mapping the locations of asymmetric and symmetric discharge responses in global rivers to the two types of El Niño. *Environmental Research Letters*, **11(4)**, doi:10.1088/1748-9326/11/4/044012.
Liao, W., D. Wang, X. Liu, G. Wang, and J. Zhang, 2017: Estimated influence of urbanization on surface warming in Eastern China using time-varying land use data. *International Journal of Climatology*, **37(7)**, 3197–3208, doi:10.1002/joc.4908.
Liefert, D.T. and B.N. Shuman, 2020: Pervasive Desiccation of North American Lakes During the Late Quaternary. *Geophyiscal Research Letters*, **47**, e2019GL086412, doi:10.1029/2019gl086412.
Liljedahl, A.K. et al., 2016: Pan-Arctic ice-wedge degradation in warming permafrost and its influence on tundra hydrology. *Nature Geoscience*, **9**, 312–318, doi:10.1038/ngeo2674.
Liman, J., M. Schröder, K. Fennig, A. Andersson, and R. Hollmann, 2018: Uncertainty characterization of HOAPS 3.3 latent heat-flux-related parameters. *Atmospheric Measurement Techniques*, **11(3)**, 1793–1815, doi:10.5194/amt-11-1793-2018.
Lin, R., T. Zhou, and Y. Qian, 2014: Evaluation of global monsoon precipitation changes based on five reanalysis datasets. *Journal of Climate*, **27(3)**, 1271–1289, doi:10.1175/jcli-d-13-00215.1.
Lindsay, R. and A. Schweiger, 2015: Arctic sea ice thickness loss determined using subsurface, aircraft, and satellite observations. *Cryosphere*, **9(1)**, 269–283, doi:10.5194/tc-9-269-2015.
Linsley, B.K., H.C. Wu, E.P. Dassié, and D.P. Schrag, 2015: Decadal changes in South Pacific sea surface temperatures and the relationship to the Pacific decadal oscillation and upper ocean heat content. *Geophysical Research Letters*, **42(7)**, 2358–2366, doi:10.1002/2015gl063045.
Lippold, J. et al., 2019: Constraining the Variability of the Atlantic Meridional Overturning Circulation During the Holocene. *Geophysical Research Letters*, **46(20)**, 11338–11346, doi:10.1029/2019gl084988.
Little, C.M. et al., 2019: The Relationship Between U.S. East Coast Sea Level and the Atlantic Meridional Overturning Circulation: A Review. *Journal of Geophysical Research: Oceans*, **124(9)**, 6435–6458, doi:10.1029/2019jc015152.
Liu, C. and R.P. Allan, 2013: Observed and simulated precipitation responses in wet and dry regions 1850 – 2100. *Environ. Res. Lett.*, **8(034002)**, 1–11, doi:10.1088/1748-9326/8/3/034002.
Liu, C., X. Liang, D.P. Chambers, and R.M. Ponte, 2020: Global Patterns of Spatial and Temporal Variability in Salinity from Multiple Gridded Argo Products. *Journal of Climate*, **33(20)**, 8751–8766, doi:10.1175/jcli-d-20-0053.1.
Liu, G. et al., 2017: Permafrost Warming in the Context of Step-wise Climate Change in the Tien Shan Mountains, China. *Permafrost and Periglacial Processes*, **28(1)**, 130–139, doi:10.1002/ppp.1885.
Liu, J., M. Song, Y. Hu, and X. Ren, 2012: Changes in the strength and width of the Hadley Circulation since 1871. *Climate of the Past*, **8(4)**, 1169–1175, doi:10.5194/cp-8-1169-2012.
Liu, J., G.A. Milne, R.E. Kopp, P.U. Clark, and I. Shennan, 2016: Sea-level constraints on the amplitude and source distribution of Meltwater Pulse 1A. *Nature Geoscience*, **9(2)**, 130–134, doi:10.1038/ngeo2616.
Liu, Q. et al., 2016: Delayed autumn phenology in the Northern Hemisphere is related to change in both climate and spring phenology. *Global Change Biology*, **22(11)**, 3702–3711, doi:10.1111/gcb.13311.
Liu, Q.-Y., M. Feng, D. Wang, and S. Wijffels, 2015: Interannual variability of the Indonesian Throughflow transport: A revisit based on 30 year expendable bathythermograph data. *Journal of Geophysical Research: Oceans*, **120(12)**, 8270–8282, doi:10.1002/2015jc011351.
Liu, W. et al., 2015: Extended Reconstructed Sea Surface Temperature Version 4 (ERSST.v4): Part II. Parametric and Structural Uncertainty Estimations. *Journal of Climate*, **28(3)**, 931–951, doi:10.1175/jcli-d-14-00007.1.
Liu, Y., Y. Li, S. Li, and S. Motesharrei, 2015a: Spatial and temporal patterns of global NDVI trends: Correlations with climate and human factors. *Remote Sensing*, doi:10.3390/rs71013233.
Liu, Y. et al., 2015b: Obliquity pacing of the western Pacific Intertropical Convergence Zone over the past 282,000 years. *Nature Communications*, **6(10018)**, 1–7, doi:10.1038/ncomms10018.
Liu, Y. et al., 2017a: Recent enhancement of central Pacific El Niño variability relative to last eight centuries. *Nature Communications*, **8**, 15386, doi:10.1038/ncomms15386.
Liu, Y. et al., 2017b: Recent enhancement of central Pacific El Niño variability relative to last eight centuries. *Nature Communications*, **8**, 15386, doi:10.1038/ncomms15386.
Liu, Z., Z. Jian, C.J. Poulsen, and L. Zhao, 2019: Isotopic evidence for twentieth-century weakening of the Pacific Walker circulation. *Earth and Planetary Science Letters*, **507**, 85–93, doi:10.1016/j.epsl.2018.12.002.
Liu, Z. et al., 2014: The Holocene temperature conundrum. *Proceedings of the National Academy of Sciences*, **111(34)**, E3501–E3505, doi:10.1073/pnas.1407229111.
Liu, Z. et al., 2017: Pacific North American circulation pattern links external forcing and North American hydroclimatic change over the past millennium. *Proceedings of the National Academy of Sciences of the United States of America*, **114(13)**, 3340–3345, doi:10.1073/pnas.1618201114.
Lockwood, M. and W.T. Ball, 2020: Placing limits on long-term variations in quiet-Sun irradiance and their contribution to total solar irradiance and solar radiative forcing of climate. *Proceedings of the Royal Society A:*

ACCEPTED VERSION SUBJECT TO FINAL EDITS

Mathematical, Physical and Engineering Sciences, **476(2238)**, 20200077, doi:10.1098/rspa.2020.0077.
Loeb, N.G., T.J. Thorsen, J.R. Norris, H. Wang, and W. Su, 2018: Changes in Earth's energy budget during and after the "Pause" in global warming: An observational perspective. *Climate*, **6(3)**, doi:10.3390/cli6030062.
Long, C.S., M. Fujiwara, S. Davis, D.M. Mitchell, and C.J. Wright, 2017: Climatology and interannual variability of dynamic variables in multiple reanalyses evaluated by the SPARC Reanalysis Intercomparison Project (S-RIP). *Atmospheric Chemistry and Physics*, **17(23)**, 14593–14629, doi:10.5194/acp-17-14593-2017.
Longhurst, A.R., 2007: *Ecological Geography of the Sea*. Academic Press, 560 pp., doi:10.1016/b978-0-12-455521-1.x5000-1.
López, O., R. Houborg, and M.F. McCabe, 2017: Evaluating the hydrological consistency of evaporation products using satellite-based gravity and rainfall data. *Hydrology and Earth System Sciences*, **21**, 323–343, doi:10.5194/hess-21-323-2017.
Lorenz, D.J., E.T. DeWeaver, and D.J. Vimont, 2010: Evaporation Change and Global Warming: The Role of Net Radiation and Relative Humidity. *Journal of Geophysical Research: Atmospheres*, **115(D20)**, doi:10.1029/2010jd013949.
Lossow, S. et al., 2018: Trend differences in lower stratospheric water vapour between Boulder and the zonal mean and their role in understanding fundamental observational discrepancies. *Atmospheric Chemistry and Physics*, **18(11)**, 8331–8351, doi:10.5194/acp-18-8331-2018.
Loulergue, L. et al., 2008: Orbital and millennial-scale features of atmospheric CH4 over the past 800,000 years. *Nature*, **453**, 383, doi:10.1038/nature06950.
Lowell, T. et al., 2013: Late Holocene expansion of Istorvet ice cap, Liverpool Land, east Greenland. *Quaternary Science Reviews*, **63**, 128–140, doi:10.1016/j.quascirev.2012.11.012.
Lowry, D.P. and C. Morrill, 2018: Is the Last Glacial Maximum a reverse analog for future hydroclimate changes in the Americas ? *Climate Dynamics*, **52(8)**, 4407–4427, doi:10.1007/s00382-018-4385-y.
Lozier, M.S. et al., 2019a: A sea change in our view of overturning in the subpolar North Atlantic. *Science*, **363(6426)**, 516–521, doi:10.1126/science.aau6592.
Lozier, M.S. et al., 2019b: A sea change in our view of overturning in the subpolar North Atlantic. *Science*, **363(6426)**, 516–521, doi:10.1126/science.aau6592.
Lübbecke, J.F. and M.J. McPhaden, 2014: Assessing the Twenty-First-Century Shift in ENSO Variability in Terms of the Bjerknes Stability Index. *Journal of Climate*, **27(7)**, 2577–2587, doi:10.1175/jcli-d-13-00438.1.
Lübbecke, J.F. et al., 2018: Equatorial Atlantic variability – Modes, mechanisms, and global teleconnections. *Wiley Interdisciplinary Reviews: Climate Change*, **9(4)**, e527, doi:10.1002/wcc.527.
Lucas, C. and H. Nguyen, 2015: Regional characteristics of tropical expansion and the role of climate variability. *Journal of Geophysical Research*, **120**, 6809–6824, doi:10.1002/2015jd023130.
Lucas, C., B. Timbal, and H. Nguyen, 2014: The expanding tropics: A critical assessment of the observational and modeling studies. *Wiley Interdisciplinary Reviews: Climate Change*, **5(1)**, 89–112, doi:10.1002/wcc.251.
Lüning, S., M. Ga, I.B. Danladi, T.A. Adagunodo, and F. Vahrenholt, 2018a: Hydroclimate in Africa during the Medieval Climate Anomaly. *Palaeogeography, Palaeoclimatology, Palaeoecology*, **495**, 309–322, doi:10.1016/j.palaeo.2018.01.025.
Lüning, S., M. Ga, I.B. Danladi, T.A. Adagunodo, and F. Vahrenholt, 2018b: Hydroclimate in Africa during the Medieval Climate Anomaly. *Palaeogeography, Palaeoclimatology, Palaeoecology*, **495**, 309–322, doi:10.1016/j.palaeo.2018.01.025.
Lüning, S., M. Gałka, F.P. Bamonte, F.G. Rodríguez, and F. Vahrenholt, 2019a: The Medieval Climate Anomaly in South America. *Quaternary International*, **508**, 70–87, doi:10.1016/j.quaint.2018.10.041.
Lüning, S., L. Schulte, S. Garcés-Pastor, I.B. Danladi, and M. Gałka, 2019b: The Medieval Climate Anomaly in the Mediterranean Region. *Paleoceanography and Paleoclimatology*, **34(10)**, 1625–1649, doi:10.1029/2019pa003734.
Lunt, D.J. et al., 2017: The DeepMIP contribution to PMIP4: experimental design for model simulations of the EECO, PETM, and pre-PETM (version 1.0). *Geosci. Model Dev.*, **10(2)**, 889–901, doi:10.5194/gmd-10-889-2017.
Lunt, D.J. et al., 2021: DeepMIP: Model intercomparison of early Eocene climatic optimum (EECO) large-scale climate features and comparison with proxy data. *Climate of the Past*, **17(1)**, 203–227, doi:10.5194/cp-17-203-2021.
Luo, B., 2018: Aerosol Radiative Forcing and SAD version v4.0.0 1850–2016. Retrieved from: ftp://iacftp.ethz.ch/pub_read/luo/cmip6_sad_radforcing_v4.0.0.
Luo, D. et al., 2016: Impact of Ural blocking on winter warm Arctic–cold Eurasian anomalies. Part I: Blocking-induced amplification. *Journal of Climate*, **29**, 3925–3947, doi:10.1175/jcli-d-15-0611.1.
Lynch-Stieglitz, J., 2017: The Atlantic Meridional Overturning Circulation and Abrupt Climate Change. *Annual Review of Marine Science*, **9**, 83–104, doi:10.1146/annurev-marine-010816-060415.
Lynch-Stieglitz, J., T. Ito, and E. Michel, 2016: Antarctic density stratification and the strength of the circumpolar current during the Last Glacial Maximum. *Paleoceanography*, **31(5)**, 539–552, doi:10.1002/2015pa002915.
Lynch-Stieglitz, J. et al., 2007: Atlantic Meridional Overturning Circulation During the Last Glacial Maximum. *Science*, **316(5821)**, 66, doi:10.1126/science.1137127.
Ma, S. and T. Zhou, 2016: Robust Strengthening and westward shift of the tropical Pacific Walker circulation during

ACCEPTED VERSION SUBJECT TO FINAL EDITS

1979-2012: A comparison of 7 sets of reanalysis data and 26 CMIP5 models. *Journal of Climate*, **29(9)**, 3097–3118, doi:10.1175/jcli-d-15-0398.1.

Ma, X. and Y. Zhang, 2018: Interannual variability of the North Pacific winter storm track and its relationship with extratropical atmospheric circulation. *Climate Dynamics*, **51**, 3685–3698, doi:10.1007/s00382-018-4104-8.

Ma, Z., R. Liu, Y. Liu, and J. Bi, 2019: Effects of air pollution control policies on PM2.5 pollution improvement in China from 2005 to 2017: a satellite-based perspective. *Atmospheric Chemistry and Physics*, **19(10)**, 6861–6877, doi:10.5194/acp-19-6861-2019.

MacDonald, G.M., K. Kremenetski, and D.W. Beilman, 2008: Climate change and the northern Russian treeline zone. *Philosophical Transactions of the Royal Society B: Biological Sciences*, **363(1501)**, doi:10.1098/rstb.2007.2200.

MacDonald, G.M. et al., 2000: Holocene treeline history and climate change across northern Eurasia. *Quaternary Research*, **53(3)**, 302 – 311, doi:10.1006/qres.1999.2123.

MacFarling Meure, C. et al., 2006: Law Dome CO2, CH4 and N2O ice core records extended to 2000 years BP. *Geophysical Research Letters*, **33(14)**, L14810, doi:10.1029/2006gl026152.

Machida, T., T. Nakazawa, Y. Fujii, S. Aoki, and O. Watanabe, 1995: Increase in the atmospheric nitrous oxide concentration during the last 250 years. *Geophysical Research Letters*, **22(21)**, 2921–2924, doi:10.1029/95gl02822.

Maksym, T., 2019: Arctic and Antarctic Sea Ice Change: Contrasts, Commonalities, and Causes. *Annual Review of Marine Science*, **11(1)**, 187–213, doi:10.1146/annurev-marine-010816-060610.

Mann, M.E. et al., 2009: Global Signatures and Dynamical Origins of the Little Ice Age and Medieval Climate Anomaly. *Science*, **326(5957)**, 1256, doi:10.1126/science.1177303.

Manney, G.L. and M.I. Hegglin, 2018: Seasonal and regional variations of long-term changes in upper-tropospheric jets from reanalyses. *Journal of Climate*, **31(1)**, 423–448, doi:10.1175/jcli-d-17-0303.1.

Manney, G.L. et al., 2011: Unprecedented Arctic ozone loss in 2011. *Nature*, **478(7370)**, 469–475, doi:10.1038/nature10556.

Manney, G.L. et al., 2020: Record-low Arctic stratospheric ozone in 2020: MLS observations of chemical processes and comparisons with previous extreme winters. *Geophysical Research Letters*, **47(16)**, e2020GL089063, doi:10.1029/2020gl089063.

Manucharyan, G.E. and A. Fedorov, 2014: Robust ENSO across a Wide Range of Climates. *Journal of Climate*, **27(15)**, 5836–5850, doi:10.1175/jcli-d-13-00759.1.

Manzanedo, R.D., J. HilleRisLambers, T.T. Rademacher, and N. Pederson, 2020: Evidence of unprecedented rise in growth synchrony from global tree ring records. *Nature Ecology and Evolution*, **4**, 1622–1629, doi:10.1038/s41559-020-01306-x.

Marcer, M. et al., 2019: Evaluating the destabilization susceptibility of active rock glaciers in the French Alps. *The Cryosphere*, **13(1)**, 141–155, doi:10.5194/tc-13-141-2019.

Marcott, S.A., J.D. Shakun, P.U. Clark, and A.C. Mix, 2013: A Reconstruction of Regional and Global Temperature for the Past 11,300 Years. *Science*, **339(6124)**, 1198 LP – 1201, doi:10.1126/science.1228026.

Marcott, S.A. et al., 2014a: Centennial-scale changes in the global carbon cycle during the last deglaciation. *Nature*, **514(7524)**, 616–619, doi:10.1038/nature13799.

Marcott, S.A. et al., 2014b: Centennial-scale changes in the global carbon cycle during the last deglaciation. *Nature*, **514(7524)**, 616–619, doi:10.1038/nature13799.

Margari, V. et al., 2020: Fast and slow components of interstadial warming in the North Atlantic during the last glacial. *Communications Earth & Environment*, **1(1)**, 1–9, doi:10.1038/s43247-020-0006-x.

Marino, G. et al., 2013: Agulhas salt-leakage oscillations during abrupt climate changes of the Late Pleistocene. *Paleoceanography*, **28(3)**, 599–606, doi:10.1002/palo.20038.

Marquer, L. et al., 2017a: Quantifying the effects of land use and climate on Holocene vegetation in Europe. *Quaternary Science Reviews*, doi:10.1016/j.quascirev.2017.07.001.

Marquer, L. et al., 2017b: Quantifying the effects of land use and climate on Holocene vegetation in Europe. *Quaternary Science Reviews*, **171**, 20–37, doi:10.1016/j.quascirev.2017.07.001.

Marquer, L. et al., 2017c: Quantifying the effects of land use and climate on Holocene vegetation in Europe. *Quaternary Science Reviews*, **171**, 20–37, doi:10.1016/j.quascirev.2017.07.001.

Martínez-Botí, M.A. et al., 2015a: Plio-Pleistocene climate sensitivity evaluated using high-resolution CO2 records. *Nature*, **518(7537)**, 49–54, doi:10.1038/nature14145.

Martínez-Botí, M.A. et al., 2015b: Boron isotope evidence for oceanic carbon dioxide leakage during the last deglaciation. *Nature*, **518(7538)**, 219–222, doi:10.1038/nature14155.

Martinez-Garcia, A. et al., 2014: Iron Fertilization of the Subantarctic Ocean During the Last Ice Age. *Science*, **343(6177)**, 1347–1350, doi:10.1126/science.1246848.

Martínez-Méndez, G. et al., 2010: Contrasting multiproxy reconstructions of surface ocean hydrography in the Agulhas Corridor and implications for the Agulhas Leakage during the last 345,000 years. *Paleoceanography*, **25(4)**, doi:10.1029/2009pa001879.

Martín-Rey, M., B. Rodríguez-Fonseca, I. Polo, and F. Kucharski, 2014: On the Atlantic–Pacific Niños connection: a

ACCEPTED VERSION SUBJECT TO FINAL EDITS

multidecadal modulated mode. *Climate Dynamics*, **43(11)**, 3163–3178, doi:10.1007/s00382-014-2305-3.
Martín-Rey, M., I. Polo, B. Rodríguez-Fonseca, T. Losada, and A. Lazar, 2018: Is There Evidence of Changes in Tropical Atlantic Variability Modes under AMO Phases in the Observational Record? *Journal of Climate*, **31(2)**, 515–536, doi:10.1175/jcli-d-16-0459.1.
Marty, C., A.-M. Tilg, and T. Jonas, 2017: Recent Evidence of Large-Scale Receding Snow Water Equivalents in the European Alps. *Journal of Hydrometeorology*, **18(4)**, 1021–1031, doi:10.1175/jhm-d-16-0188.1.
Marzeion, B., P.W. Leclercq, J.G. Cogley, and A.H. Jarosch, 2015: Brief Communication: Global reconstructions of glacier mass change during the 20th century are consistent. *The Cryosphere*, **9(6)**, 2399–2404, doi:10.5194/tc-9-2399-2015.
Marzeion, B., G. Kaser, F. Maussion, and N. Champollion, 2018: Limited influence of climate change mitigation on short-term glacier mass loss. *Nature Climate Change*, **8(4)**, 305–308, doi:10.1038/s41558-018-0093-1.
Massonnet, F., V. Guemas, N.S. Fuèkar, and F.J. Doblas-Reyes, 2015: The 2014 high record of antarctic sea ice extent. *Bulletin of the American Meteorological Society*, **96(12)**, S163–S167, doi:10.1175/bams-d-15-00093.1.
Mathew, S.S. and K.K. Kumar, 2019: On the role of precipitation latent heating in modulating the strength and width of the Hadley circulation. *Theoretical and Applied Climatology*, **136**, 661–673, doi:10.1007/s00704-018-2515-4.
Mathew, S.S., K.K. Kumar, and K.V. Subrahmanyam, 2016: Hadley cell dynamics in Japanese Reanalysis-55 dataset: evaluation using other reanalysis datasets and global radiosonde network observations. *Climate Dynamics*, **47(12)**, 3917–3930, doi:10.1007/s00382-016-3051-5.
Matley, K.A., J.M.K. Sniderman, A.N. Drinnan, and J.C. Hellstrom, 2020: Late-Holocene environmental change on the Nullarbor Plain, southwest Australia, based on speleothem pollen records. *Holocene*, **30(5)**, 672–681, doi:10.1177/0959683619895589.
Matthes, K. et al., 2017: Solar forcing for CMIP6 (v3.2). *Geoscientific Model Development*, **10(6)**, 2247–2302, doi:10.5194/gmd-10-2247-2017.
Maycock, A.C. et al., 2018: Revisiting the mystery of recent stratospheric temperature trends. *Geophysical Research Letters*, **45(18)**, 9919–9933, doi:10.1029/2018gl078035.
McAfee, S.A., 2017: Uncertainty in Pacific decadal oscillation indices does not contribute to teleconnection instability. *International Journal of Climatology*, **37(8)**, 3509–3516, doi:10.1002/joc.4918.
McCabe, G.J., J.L. Betancourt, and S. Feng, 2015: Variability in the start, end, and length of frost-free periods across the conterminous United States during the past century. *International Journal of Climatology*, doi:10.1002/joc.4315.
McCabe-Glynn, S. et al., 2013: Variable North Pacific influence on drought in southwestern North America since AD 854. *Nature Geoscience*, **6(8)**, 617–621.
McCarthy, G.D., T.M. Joyce, and S.A. Josey, 2018: Gulf Stream variability in the context of quasi-decadal and multi-decadal Atlantic climate variability. *Geophysical Research Letters*, **45(20)**, 11,257–11,264, doi:10.1029/2018gl079336.
McCarthy, G.D., I.D. Haigh, J.J.M. Hirschi, J.P. Grist, and D.A. Smeed, 2015: Ocean impact on decadal Atlantic climate variability revealed by sea-level observations. *Nature*, **521(7553)**, 508–510, doi:10.1038/nature14491.
McCave, I.N., S.J. Crowhurst, G. Kuhn, C.-D. Hillenbrand, and M.P. Meredith, 2013: Minimal change in Antarctic Circumpolar Current flow speed between the last glacial and Holocene. *Nature Geoscience*, **7**, 113, doi:10.1038/ngeo2037.
McClymont, E.L. et al., 2020: Lessons from a high CO2 world: an ocean view from ~ 3 million years ago. *Climate of the Past*, **16(4)**, 1599–1615, doi:10.5194/cp-2019-161.
McGee, D., A. Donohoe, J. Marshall, and D. Ferreira, 2014a: Changes in ITCZ location and cross-equatorial heat transport at the Last Glacial Maximum, Heinrich Stadial 1, and the mid-Holocene. *Earth and Planetary Science Letters*, **390**, 69–79, doi:10.1016/j.epsl.2013.12.043.
McGee, D., A. Donohoe, J. Marshall, and D. Ferreira, 2014b: Changes in ITCZ location and cross-equatorial heat transport at the Last Glacial Maximum, Heinrich Stadial 1, and the mid-Holocene. *Earth and Planetary Science Letters*, **390**, 69–79, doi:10.1016/j.epsl.2013.12.043.
McGee, D., P.B. DeMenocal, G. Winckler, J.B.W. Stuut, and L.I. Bradtmiller, 2013: The magnitude, timing and abruptness of changes in North African dust deposition over the last 20,000yr. *Earth and Planetary Science Letters*, **371–372**, 163–176, doi:10.1016/j.epsl.2013.03.054.
McGee, D. et al., 2018: Hemispherically asymmetric trade wind changes as signatures of past ITCZ shifts. *Quaternary Science Reviews*, **180**, 214–228, doi:10.1016/j.quascirev.2017.11.020.
McGregor, H. et al., 2013: A weak El Niño/Southern Oscillation with delayed seasonal growth around 4,300 years ago. *Nature Geoscience*, **6**, 949, doi:10.1038/ngeo1936.
McGregor, H. et al., 2015: Robust global ocean cooling trend for the pre-industrial Common Era. *Nature Geoscience*, **8(9)**, 671–677, doi:10.1038/ngeo2510.
McGregor, S., A. Timmermann, and O. Timm, 2010: A unified proxy for ENSO and PDO variability since 1650. *Climate of the Past*, **6(1)**, 1–17, doi:10.5194/cp-6-1-2010.
McGregor, S., A. Timmermann, M.H. England, O. Elison Timm, and A.T. Wittenberg, 2013a: Inferred changes in El Niño–Southern Oscillation variance over the past six centuries. *Climate of the Past*, **9(5)**, 2269–2284,

ACCEPTED VERSION SUBJECT TO FINAL EDITS

doi:10.5194/cp-9-2269-2013.
McGregor, S., A. Timmermann, M.H. England, O. Elison Timm, and A.T. Wittenberg, 2013b: Inferred changes in El Niño–Southern Oscillation variance over the past six centuries. *Climate of the Past*, **9(5)**, 2269–2284, doi:10.5194/cp-9-2269-2013.
McGregor, S. et al., 2014: Recent Walker circulation strengthening and Pacific cooling amplified by Atlantic warming. *Nature Climate Change*, **4(10)**, 888–892, doi:10.1038/nclimate2330.
McKay, R. et al., 2012: Pleistocene variability of Antarctic Ice Sheet extent in the Ross Embayment. *Quaternary Science Reviews*, **34**, 93–112, doi:10.1016/j.quascirev.2011.12.012.
McKay, R. et al., 2016: Antarctic marine ice-sheet retreat in the Ross Sea during the early Holocene. *Geology*, **44(1)**, 7–10, doi:10.1130/g37315.1.
McKenney, D.W. et al., 2014: Change and evolution in the plant hardiness zones of Canada. *BioScience*, doi:10.1093/biosci/biu016.
McLandress, C., T.G. Shepherd, A.I. Jonsson, T. von Clarmann, and B. Funke, 2015: A method for merging nadir-sounding climate records, with an application to the global-mean stratospheric temperature data sets from SSU and AMSU. *Atmospheric Chemistry and Physics*, **15(16)**, 9271–9284, doi:10.5194/acp-15-9271-2015.
McManus, J.F., D.W. Oppo, and J.L. Cullen, 1999: A 0.5-Million-Year Record of Millennial-Scale Climate Variability in the North Atlantic. *Science*, **283(5404)**, 971–975, doi:10.1126/science.283.5404.971.
McManus, J.F., R. Francois, J.-M. Gherardi, L.D. Keigwin, and S. Brown-Leger, 2004: Collapse and rapid resumption of Atlantic meridional circulation linked to deglacial climate changes. *Nature*, **428(6985)**, 834–837, doi:10.1038/nature02494.
McVicar, T.R. et al., 2012: Global review and synthesis of trends in observed terrestrial near-surface wind speeds: Implications for evaporation. *Journal of Hydrology*, **416–417**, 182–205, doi:10.1016/j.jhydrol.2011.10.024.
Mears, C.A. and F.J. Wentz, 2017: A Satellite-Derived Lower-Tropospheric Atmospheric Temperature Dataset Using an Optimized Adjustment for Diurnal Effects. *Journal of Climate*, **30(19)**, 7695–7718, doi:10.1175/jcli-d-16-0768.1.
Mears, C.A., S.P. Ho, O. Bock, X. Zhou, and J. Nicolas, 2019: Hydrological cycle: Total column water vapor [in "State of the Climate in 2018"]. *Bull. Am. Meteorol. Soc.*, **100(9)**, S27–S28, doi:10.1175/2019bamsstateoftheclimate.1.
Mears, C.A. et al., 2018: Construction and Uncertainty Estimation of a Satellite-Derived Total Precipitable Water Data Record Over the World's Oceans. *Earth and Space Science*, **5(5)**, 197–210, doi:10.1002/2018ea000363.
Medley, B. and E.R. Thomas, 2019: Increased snowfall over the Antarctic Ice Sheet mitigated twentieth-century sea-level rise. *Nature Climate Change*, **9(1)**, 34–39, doi:10.1038/s41558-018-0356-x.
Meier, W.N. and J.S. Stewart, 2019: Assessing uncertainties in sea ice extent climate indicators. *Environmental Research Letters*, **14(3)**, 35005, doi:10.1088/1748-9326/aaf52c.
Meier, W.N., D. Gallaher, and G.G. Campbell, 2013: New estimates of Arctic and Antarctic sea ice extent during September 1964 from recovered Nimbus I satellite imagery. *The Cryosphere*, **7(2)**, 699–705, doi:10.5194/tc-7-699-2013.
Meinen, C.S. et al., 2018: Meridional Overturning Circulation Transport Variability at 34.5°S During 2009–2017: Baroclinic and Barotropic Flows and the Dueling Influence of the Boundaries. *Geophysical Research Letters*, **45(9)**, 4180–4188, doi:10.1029/2018gl077408.
Meinshausen, M. et al., 2017: Historical greenhouse gas concentrations for climate modelling (CMIP6). *Geosci. Model Dev.*, **10(5)**, 2057–2116, doi:10.5194/gmd-10-2057-2017.
Melamed-Turkish, K., P.A. Taylor, and J. Liu, 2018: Upper-level winds over eastern North America: A regional jet stream climatology. *International Journal of Climatology*, 1–18, doi:10.1002/joc.5693.
Mellado-Cano, J., D. Barriopedro, R. García-Herrera, R.M. Trigo, and A. Hernández, 2019: Examining the North Atlantic Oscillation, East Atlantic pattern and jet variability since 1685. *Journal of Climate*, **32**, 6285–6298, doi:10.1175/jcli-d-18-0135.1.
Menary, M.B. et al., 2020: Aerosol-Forced AMOC Changes in CMIP6 Historical Simulations. *Geophysical Research Letters*, **47(14)**, e2020GL088166, doi:10.1029/2020gl088166.
Menne, M.J., C.N. Williams, B.E. Gleason, J.J. Rennie, and J.H. Lawrimore, 2018: The Global Historical Climatology Network Monthly Temperature Dataset, Version 4. *Journal of Climate*, **31(24)**, 9835–9854, doi:10.1175/jcli-d-18-0094.1.
Menviel, L. et al., 2017: Poorly ventilated deep ocean at the Last Glacial Maximum inferred from carbon isotopes: A data-model comparison study. *Paleoceanography*, **32(1)**, 2–17, doi:10.1002/2016pa003024.
Merchant, C.J. et al., 2012: A 20 year independent record of sea surface temperature for climate from Along-Track Scanning Radiometers. *Journal of Geophysical Research: Oceans*, **117(C12)**, doi:10.1029/2012jc008400.
Merchant, C.J. et al., 2013: The surface temperatures of Earth: steps towards integrated understanding of variability and change. *Geoscientific Instrumentation, Methods and Data Systems*, **2(2)**, 305–321, doi:10.5194/gi-2-305-2013.
Mercier, H. et al., 2015: Variability of the meridional overturning circulation at the Greenland–Portugal OVIDE section from 1993 to 2010. *Progress in Oceanography*, **132**, 250–261, doi:10.1016/j.pocean.2013.11.001.
Meredith, M. et al., 2019: Polar Regions. In: *IPCC Special Report on the Ocean and Cryosphere in a Changing Climate*

ACCEPTED VERSION SUBJECT TO FINAL EDITS

[Pörtner, H.-O., D.C. Roberts, V. Masson-Delmotte, P. Zhai, M. Tignor, E. Poloczanska, K. Mintenbeck, A. Alegría, M. Nicolai, A. Okem, J. Petzold, B. Rama, and N.M. Weyer (eds.)]. In Press, pp. 203–320.

Mernild, S.H., W.H. Lipscomb, D.B. Bahr, V. Radić, and M. Zemp, 2013: Global glacier changes: a revised assessment of committed mass losses and sampling uncertainties. *The Cryosphere*, **7(5)**, 1565–1577, doi:10.5194/tc-7-1565-2013.

Meyssignac, B. et al., 2019: Measuring Global Ocean Heat Content to Estimate the Earth Energy Imbalance. *Frontiers in Marine Science*, **6**, 432, doi:10.3389/fmars.2019.00432.

Middleton, J.L., S. Mukhopadhyay, C.H. Langmuir, J.F. McManus, and P.J. Huybers, 2018: Millennial-scale variations in dustiness recorded in Mid-Atlantic sediments from 0 to 70 ka. *Earth and Planetary Science Letters*, **482**, 12–22, doi:10.1016/j.epsl.2017.10.034.

Mieruch, S., M. Schröder, S. Noël, and J. Schulz, 2014: Comparison of decadal global water vapor changes derived from independent satellite time series. *Journal of Geophysical Research Atmospheres*, **119(22)**, 12489–12499, doi:10.1002/2014jd021588.

Miller, G.H., J.Y. Landvik, S.J. Lehman, and J.R. Southon, 2017: Episodic Neoglacial snowline descent and glacier expansion on Svalbard reconstructed from the14C ages of ice-entombed plants. *Quaternary Science Reviews*, **155**, 67–78, doi:10.1016/j.quascirev.2016.10.023.

Miller, G.H., S.J. Lehman, K.A. Refsnider, J.R. Southon, and Y. Zhong, 2013: Unprecedented recent summer warmth in Arctic Canada. *Geophysical Research Letters*, **40(21)**, 5745–5751, doi:10.1002/2013gl057188.

Miller, K.G. et al., 2020: Cenozoic sea-level and cryospheric evolution from deep-sea geochemical and continental margin records. *Science Advances*, **6(20)**, doi:10.1126/sciadv.aaz1346.

Milne, G.A. and J.X. Mitrovica, 2008: Searching for eustasy in deglacial sea-level histories. *Quaternary Science Reviews*, **27(25)**, 2292–2302, doi:10.1016/j.quascirev.2008.08.018.

Mitchell, D.M., L.J. Gray, J. Anstey, M.P. Baldwin, and A.J. Charlton-Perez, 2013: The influence of stratospheric vortex displacements and splits on surface climate. *Journal of Climate*, **26(8)**, 2668–2682, doi:10.1175/jcli-d-12-00030.1.

Mitchell, L., E. Brook, J.E. Lee, C. Buizert, and T. Sowers, 2013a: Constraints on the late Holocene anthropogenic contribution to the atmospheric methane budget (2013b). *Science*, **342(6161)**, 964–966, doi:10.1126/science.1238920.

Mitchell, L., E. Brook, J.E. Lee, C. Buizert, and T. Sowers, 2013b: Constraints on the late Holocene anthropogenic contribution to the atmospheric methane budget (2013b). *Science*, **342(6161)**, 964–966, doi:10.1126/science.1238920.

MK, T., E. Devred, T. Platt, and S. Sathyendranath, 2013: Variation in ocean colour may help predict cod and haddock recruitment. *Marine Ecology Progress Series*, **491**, 187–197, doi:10.3354/meps10451.

Moat, B.I. et al., 2020: Pending recovery in the strength of the meridional overturning circulation at 26° N. *Ocean Science*, **16(4)**, 863–874, doi:10.5194/os-16-863-2020.

Moffa-Sánchez, P. and I.R. Hall, 2017: North Atlantic variability and its links to European climate over the last 3000 years. *Nature Communications*, **8(1)**, 1726, doi:10.1038/s41467-017-01884-8.

Moffa-Sánchez, P. et al., 2019: Variability in the Northern North Atlantic and Arctic Oceans Across the Last Two Millennia: A Review. *Paleoceanography and Paleoclimatology*, **34(8)**, 1399–1436, doi:10.1029/2018pa003508.

Moffitt, S.E. et al., 2015: Paleoceanographic Insights on Recent Oxygen Minimum Zone Expansion: Lessons for Modern Oceanography. *PLOS ONE*, **10(1)**, e0115246, doi:10.1371/journal.pone.0115246.

Mohajerani, Y., I. Velicogna, and E. Rignot, 2018: Mass Loss of Totten and Moscow University Glaciers, East Antarctica, Using Regionally Optimized GRACE Mascons. *Geophysical Research Letters*, **45(14)**, 7010–7018, doi:10.1029/2018gl078173.

Mohtadi, M., M. Prange, and S. Steinke, 2016: Review Palaeoclimatic insights into forcing and response of monsoon rainfall. *Nature*, **533(7602)**, 191–199, doi:10.1038/nature17450.

Mokeddem, Z. and J.F. McManus, 2016: Persistent climatic and oceanographic oscillations in the subpolar North Atlantic during the MIS 6 glaciation and MIS 5 interglacial. *Paleoceanography*, **31(6)**, 758–778, doi:10.1002/2015pa002813.

Mokeddem, Z., J.F. McManus, and D.W. Oppo, 2014a: Oceanographic dynamics and the end of the last interglacial in the subpolar North Atlantic. *Proceedings of the National Academy of Sciences*, **111(31)**, 11263, doi:10.1073/pnas.1322103111.

Mokeddem, Z., J.F. McManus, and D.W. Oppo, 2014b: Oceanographic dynamics and the end of the last interglacial in the subpolar North Atlantic. *Proceedings of the National Academy of Sciences*, **111(31)**, 11263, doi:10.1073/pnas.1322103111.

Mollier-Vogel, E., G. Leduc, T. Böschen, P. Martinez, and R.R. Schneider, 2013: Rainfall response to orbital and millennial forcing in northern Peru over the last 18ka. *Quaternary Science Reviews*, **76**, 29–38, doi:10.1016/j.quascirev.2013.06.021.

Mollier-Vogel, E. et al., 2019: Mid-Holocene deepening of the Southeast Pacific oxycline. *Global and Planetary Change*, **172**, 365–373, doi:10.1016/j.gloplacha.2018.10.020.

ACCEPTED VERSION SUBJECT TO FINAL EDITS

Molnar, P. and M.A. Cane, 2002: El Niño's tropical climate and teleconnections as a blueprint for pre-Ice Age climates. *Paleoceanography*, **17(2)**, 11, doi:10.1029/2001pa000663.
Monerie, P.A., J. Robson, B. Dong, D.L.R. Hodson, and N.P. Klingaman, 2019: Effect of the Atlantic Multidecadal Variability on the Global Monsoon. *Geophysical Research Letters*, **46(3)**, 1765–1775, doi:10.1029/2018gl080903.
Montaggioni, L.F. and G. Faure, 2008: Response of reef coral communities to sea-level rise: a Holocene model from Mauritius (Western Indian Ocean). *Sedimentology*, **44(6)**, 1053–1070, doi:10.1111/j.1365-3091.1997.tb02178.x.
Montzka, S.A. et al., 2018a: An unexpected and persistent increase in global emissions of ozone-depleting CFC-11. *Nature*, **557(7705)**, 413–417, doi:10.1038/s41586-018-0106-2.
Montzka, S.A. et al., 2018b: Hydrofluorocarbons (HFCs). In: *Scientific Assessment of Ozone Depletion: 2018*. Global Ozone Research and Monitoring Project – Report No. 58, World Meteorological Organization (WMO), Geneva, Switzerland, pp. 2.1–2.56.
Montzka, S.A. et al., 2021: A decline in global CFC-11 emissions during 2018-2019. *Nature*, **590(7846)**, 428–432, doi:10.1038/s41586-021-03260-5.
Moore, G.W.K., I.A. Renfrew, and R.S. Pickart, 2013: Multidecadal mobility of the north atlantic oscillation. *Journal of Climate*, **26(8)**, 2453–2466, doi:10.1175/jcli-d-12-00023.1.
Morales, M.S. et al., 2020: Six hundred years of South American tree rings reveal an increase in severe hydroclimatic events since mid-20th century. *Proceedings of the National Academy of Sciences*, **117(29)**, 16816–16823, doi:10.1073/pnas.2002411117.
Moreno, P.I. et al., 2014: Southern Annular Mode-like changes in southwestern Patagonia at centennial timescales over the last three millennia. *Nature Communications*, **5(1)**, 4375, doi:10.1038/ncomms5375.
Moreno, P.I. et al., 2018: Onset and evolution of southern annular mode-like changes at centennial timescale. *Scientific Reports*, **8(1)**, 3458, doi:10.1038/s41598-018-21836-6.
Morice, C.P. et al., 2021: An updated assessment of near-surface temperature change from 1850: the HadCRUT5 dataset. *Journal of Geophysical Research: Atmospheres*, **126(3)**, doi:10.1029/2019jd032361.
Morioka, Y., T. Tozuka, and T. Yamagata, 2011: On the Growth and Decay of the Subtropical Dipole Mode in the South Atlantic. *Journal of Climate*, **24(21)**, 5538–5554, doi:10.1175/2011jcli4010.1.
Morley, A., Y. Rosenthal, P. DeMenocal, and P. Morley, A., Rosenthal, Y., deMenocal, 2014: Ocean-atmosphere climate shift during the mid-to-late Holocene transition. *Earth and Planetary Science Letters*, **388**, 18–26, doi:10.1016/j.epsl.2013.11.039.
Morlighem, M. et al., 2017: BedMachine v3: Complete Bed Topography and Ocean Bathymetry Mapping of Greenland From Multibeam Echo Sounding Combined With Mass Conservation. *Geophysical Research Letters*, **44(21)**, 11,11–51,61, doi:10.1002/2017gl074954.
Morlighem, M. et al., 2020: Deep glacial troughs and stabilizing ridges unveiled beneath the margins of the Antarctic ice sheet. *Nature Geoscience*, **13(2)**, 132–137, doi:10.1038/s41561-019-0510-8.
Morrill, C., D.P. Lowry, and A. Hoell, 2018: Thermodynamic and Dynamic Causes of Pluvial Conditions During the Last Glacial Maximum in Western North America. *Geophyiscal Research Letters*, **45**, 335–345, doi:10.1002/2017gl075807.
Mortimer, C. et al., 2020: Evaluation of long-term Northern Hemisphere snow water equivalent products. *The Cryosphere*, **14(5)**, 1579–1594, doi:10.5194/tc-14-1579-2020.
Mortin, J. et al., 2016: Melt onset over Arctic sea ice controlled by atmospheric moisture transport. *Geophysical Research Letters*, **43(12)**, 6636–6642, doi:10.1002/2016gl069330.
Moucha, R. and G.A. Ruetenik, 2017: Interplay between dynamic topography and flexure along the U.S. Atlantic passive margin: Insights from landscape evolution modeling. *Global and Planetary Change*, **149**, 72–78, doi:10.1016/j.gloplacha.2017.01.004.
Mouginot, J. et al., 2019: Forty-six years of Greenland Ice Sheet mass balance from 1972 to 2018. *Proceedings of the National Academy of Sciences*, **116(19)**, 9239–9244, doi:10.1073/pnas.1904242116.
Mudryk, L. et al., 2020: Historical Northern Hemisphere snow cover trends and projected changes in the CMIP6 multi-model ensemble. *The Cryosphere*, **14(7)**, 2495–2514, doi:10.5194/tc-14-2495-2020.
Mudryk, L.R. et al., 2018: Canadian snow and sea ice: Historical trends and projections. *Cryosphere*, **12**, 1157–1176, doi:10.5194/tc-12-1157-2018.
Muglia, J., L.C. Skinner, and A. Schmittner, 2018: Weak overturning circulation and high Southern Ocean nutrient utilization maximized glacial ocean carbon. *Earth and Planetary Science Letters*, **496**, 47–56, doi:10.1016/j.epsl.2018.05.038.
Mühle, J. et al., 2019: Perfluorocyclobutane (PFC-318, C4F8) in the global atmosphere. *Atmospheric Chemistry and Physics*, **19(15)**, 10335–10359, doi:10.5194/acp-19-10335-2019.
Müller, T. et al., 2020: Ocean acidification during the early Toarcian extinction event: Evidence from boron isotopes in brachiopods. *Geology*, **48(12)**, 1184–1188, doi:10.1130/g47781.1.
Muñoz, P. et al., 2017: Holocene climatic variations in the Western Cordillera of Colombia: A multiproxy high-resolution record unravels the dual influence of ENSO and ITCZ. *Quaternary Science Reviews*, **155**, 159–178,

ACCEPTED VERSION SUBJECT TO FINAL EDITS

doi:10.1016/j.quascirev.2016.11.021.
Murphy, E.J., A. Clarke, C. Symon, and J. Priddle, 1995: Temporal Variation in Antarctic Sea-Ice - Analysis of a Long-Term Fast-Ice Record from the South-Orkney Islands. *Deep-Sea Research Part I-Oceanographic Research Papers*, doi:10.1016/0967-0637(95)00057-d.
Murphy, E.J., A. Clarke, N.J. Abram, and J. Turner, 2014: Variability of sea-ice in the northern Weddell Sea during the 20th century. *Journal of Geophysical Research: Oceans*, **119(7)**, 4549–4572, doi:10.1002/2013jc009511.
Myers-Smith, I.H. et al., 2020: Complexity revealed in the greening of the Arctic. *Nature Climate Change*, **10(2)**, doi:10.1038/s41558-019-0688-1.
NA SEM, 2017: *Antarctic Sea Ice Variability in the Southern Ocean-Climate System: Proceedings of a Workshop*. National Academies of Sciences, Engineering, and Medicine. The National Academies Press, Washington, DC, USA, 82 pp., doi:10.17226/24696.
Naik, S.S., P. Divakar Naidu, G.L. Foster, and M.A. Martínez-Botí, 2015: Tracing the strength of the southwest monsoon using boron isotopes in the eastern Arabian Sea. *Geophysical Research Letters*, **42(5)**, 1450–1458, doi:10.1002/2015gl063089.
Nair, A. et al., 2019: Southern Ocean sea ice and frontal changes during the Late Quaternary and their linkages to Asian summer monsoon. *Quaternary Science Reviews*, **213**, 93–104, doi:10.1016/j.quascirev.2019.04.007.
Naqvi, A.-S.T.S.W.A., F. Al-Yamani, A. Goncharov, and L. Fernandes, 2018: High total organic carbon in surface waters of the northern Arabian Gulf: Implications for the oxygen minimum zone of the Arabian Sea. *Marine Pollution Bulletin*, **129(1)**, 35–42, doi:10.1016/j.marpolbul.2018.02.013.
Nash, D.J. et al., 2016: African hydroclimatic variability during the last 2000 years. *Quaternary Science Reviews*, **154**, 1–22, doi:10.1016/j.quascirev.2016.10.012.
Neely III, R.R. and A. Schmidt, 2016: VolcanEESM: Global volcanic sulphur dioxide (SO2) emissions database from 1850 to present - Version 1.0. Centre for Environmental Data Analysis, 04 February 2016.
Nerem, R.S. et al., 2018: Climate-change–driven accelerated sea-level rise detected in the altimeter era. *Proceedings of the National Academy of Sciences*, **115**, 201717312, doi:10.1073/pnas.1717312115.
Neu, U. et al., 2013: IMILAST: A Community Effort to Intercompare Extratropical Cyclone Detection and Tracking Algorithms. *Bulletin of the American Meteorological Society*, **94**, 529–547, doi:10.1175/bams-d-11-00154.1.
Neukom, R., N. Steiger, J.J. Gómez-Navarro, J. Wang, and J.P. Werner, 2019: No evidence for globally coherent warm and cold periods over the preindustrial Common Era. *Nature*, **571(7766)**, 550–554, doi:10.1038/s41586-019-1401-2.
Neukom, R. et al., 2014: Inter-hemispheric temperature variability over the past millennium. *Nature Climate Change*, **4**, 362, doi:10.1038/nclimate2174.
Newby, P.E., B.N. Shuman, J.P. Donnelly, K.B. Karnauskas, and J. Marsicek, 2014: Centennial-to-millennial hydrologic trends and variability along the North Atlantic Coast, USA, during the Holocene. *Geophys. Res. Lett.*, **41**, 4300–4307, doi:10.1002/2014gl060183.
Newman, M. et al., 2016: The Pacific Decadal Oscillation, Revisited. *Journal of Climate*, **29(12)**, 4399–4427, doi:10.1175/jcli-d-15-0508.1.
Newman, P.A., L. Coy, S. Pawson, and L.R. Lait, 2016: The anomalous change in the QBO in 2015–2016. *Geophysical Research Letters*, **43(16)**, 8791–8797, doi:10.1002/2016gl070373.
Nguyen, H., A. Evans, C. Lucas, I. Smith, and B. Timbal, 2013: The Hadley Circulation in Reanalyses : Climatology, Variability, and Change. *Journal of Climate*, **26**, 3357–3376, doi:10.1175/jcli-d-12-00224.1.
Nguyen, H., C. Lucas, A. Evans, B. Timbal, and L. Hanson, 2015: Expansion of the Southern Hemisphere Hadley Cell in Response to Greenhouse Gas Forcing. *Journal of Climate*, **28**, 8067–8077, doi:10.1175/jcli-d-15-0139.1.
Nguyen, P. et al., 2018: Global precipitation trends across spatial scales using satellite observations. *Bulletin of the American Meteorological Society*, **99(4)**, 689–697, doi:10.1175/bams-d-17-0065.1.
Niedermeyer, E.M., A.L. Sessions, S.J. Feakins, and M. Mohtadi, 2014: Hydroclimate of the western Indo-Pacific Warm Pool during the past 24,000 years. *Proceedings of the National Academy of Sciences*, **111(26)**, 9402, doi:10.1073/pnas.1323585111.
Nielsen, T. and A. Kuijpers, 2013: Only 5 southern Greenland shelf edge glaciations since the early Pliocene. *Scientific Reports*, **3(1)**, doi:10.1038/srep01875.
Nitze, I. et al., 2017: Landsat-based trend analysis of lake dynamics across Northern Permafrost Regions. *Remote Sensing*, **9(7)**, 640, doi:10.3390/rs9070640.
Nnamchi, H.C., F. Kucharski, N.S. Keenlyside, and R. Farneti, 2017: Analogous seasonal evolution of the South Atlantic SST dipole indices. *Atmospheric Science Letters*, **18(10)**, 396–402, doi:10.1002/asl.781.
Nnamchi, H.C. et al., 2016: An Equatorial–Extratropical Dipole Structure of the Atlantic Niño. *Journal of Climate*, **29(20)**, 7295–7311, doi:10.1175/jcli-d-15-0894.1.
Noble, T.L. et al., 2020: The Sensitivity of the Antarctic Ice Sheet to a Changing Climate: Past, Present, and Future. *Reviews of Geophysics*, **58(4)**, e2019RG000663, doi:10.1029/2019rg000663.
Noetzli J, Biskaborn B, Christiansen HH, Isaksen K, Schroeneich P, Smith S, Vieira G, Zhao L, S., 2019: Permafrost Thermal State [in "State of the Climate in 2018"]. *Bulletin of the American Meteorological Society*, **100(9)**, S21–S22, doi:10.1175/2019bamsstateoftheclimate.1.

ACCEPTED VERSION SUBJECT TO FINAL EDITS

Noetzli J, Christiansen HH, Isaksen K, Smith S, Zhao L, S., 2020: Permafrost Thermal State [in "State of the Climate in 2019"]. *Bulletin of the American Meteorological Society*, **101(8)**, S34–S36, doi:10.1175/bams-d-20-0104.1.

Nogueira, M., 2020: Inter-comparison of ERA-5, ERA-interim and GPCP rainfall over the last 40 years: Process-based analysis of systematic and random differences. *Journal of Hydrology*, **583**, 124632, doi:10.1016/j.jhydrol.2020.124632.

Nolan, C. et al., 2018: Past and future global transformation of terrestrial ecosystems under climate change. *Science*, **361(6405)**, 920–923, doi:10.1126/science.aan5360.

Norris, J.R. et al., 2016: Evidence for climate change in the satellite cloud record. *Nature*, **536(7614)**, 72–75, doi:10.1038/nature18273.

Notz, D., 2014: Sea-ice extent and its trend provide limited metrics of model performance. *Cryosphere*, **8(1)**, 229–243, doi:10.5194/tc-8-229-2014.

O'Leary, M.J. et al., 2013: Ice sheet collapse following a prolonged period of stable sea level during the last interglacial. *Nature Geoscience*, **6(9)**, 796–800, doi:10.1038/ngeo1890.

O'Mara, N.A. et al., 2019: Subtropical Pacific Ocean Temperature Fluctuations in the Common Era: Multidecadal Variability and Its Relationship With Southwestern North American Megadroughts. *Geophysical Research Letters*, **46(24)**, 14662–14673, doi:10.1029/2019gl084828.

O'Neill, H.B., S.L. Smith, and C. Duchesne, 2019: Long-Term Permafrost Degradation and Thermokarst Subsidence in the Mackenzie Delta Area Indicated by Thaw Tube Measurements. *Cold Regions Engineering 2019*, 643–651, doi:10.1061/9780784482599.074.

Ohba, M., 2013: Important factors for long-term change in ENSO transitivity. *International Journal of Climatology*, **33(6)**, 1495–1509, doi:10.1002/joc.3529.

Okamoto, K., T. Ushio, T. Iguchi, N. Takahashi, and K. Iwanami, 2005: The Global Satellite Mapping of Precipitation (GSMaP) Project. *Proceedings. 2005 IEEE International Geoscience and Remote Sensing Symposium, 2005. IGARSS '05.*, **5(3)**, 3414–3416, doi:10.1109/igarss.2005.1526575.

Olden, J.D. and T.P. Rooney, 2006: On defining and quantifying biotic homogenization. *Global Ecology and Biogeography*, **15(2)**, 113–120, doi:10.1111/j.1466-822x.2006.00214.x.

Oliveira, F.N.M., L.M. Carvalho, and T. Ambrizzi, 2014: A new climatology for Southern Hemisphere blockings in the winter and the combined effect of ENSO and SAM phases. *International Journal of Climatology*, **34**, 1676–1692.

Olsen, J., N.J. Anderson, and M.F. Knudsen, 2012: Variability of the North Atlantic Oscillation over the past 5 , 200 years. *Nature Geoscience*, **5(11)**, 808–812, doi:10.1038/ngeo1589.

Oltmans, S.J. et al., 2013: Recent tropospheric ozone changes - A pattern dominated by slow or no growth. *Atmospheric Environment*, **67**, 331–351, doi:10.1016/j.atmosenv.2012.10.057.

Oppo, D.W., J.F. McManus, and J.L. Cullen, 2003: Deepwater variability in the Holocene epoch. *Nature*, **422(6929)**, 277, doi:10.1038/422277b.

Ordonez, A., J.W. Williams, and J.C. Svenning, 2016: Mapping climatic mechanisms likely to favour the emergence of novel communities. *Nature Climate Change*, **6**, 1104–1109, doi:10.1038/nclimate3127.

Orme, L.C. et al., 2017: Past changes in the North Atlantic storm track driven by insolation and sea-ice forcing. *Geology*, **45(4)**, 335–338, doi:10.1130/g38521.1.

Ortega, P. et al., 2015a: A model-tested North Atlantic Oscillation reconstruction for the past millennium. *Nature*, **523(7558)**, 71–74, doi:10.1038/nature14518.

Ortega, P. et al., 2015b: A model-tested North Atlantic Oscillation reconstruction for the past millennium. *Nature*, **523(7558)**, 71–74, doi:10.1038/nature14518.

Ortega, P. et al., 2015c: A model-tested North Atlantic Oscillation reconstruction for the past millennium. *Nature*, **523(7558)**, 71–74, doi:10.1038/nature14518.

Osborn, T.J. et al., 2021: Land Surface Air Temperature Variations Across the Globe Updated to 2019: The CRUTEM5 Data Set. *Journal of Geophysical Research: Atmospheres*, **126(2)**, e2019JD032352, doi:10.1029/2019jd032352.

Osborne, E., J. Richter-Menge, and M. Jeffries (eds.), 2018: *Arctic Report Card 2018*.

Osborne, E.B., R.C. Thunell, N. Gruber, R.A. Feely, and C.R. Benitez-Nelson, 2020: Decadal variability in twentieth-century ocean acidification in the California Current Ecosystem. *Nature Geoscience*, **13(1)**, 43–49, doi:10.1038/s41561-019-0499-z.

Osterberg, E.C. et al., 2017: The 1200 year composite ice core record of Aleutian Low intensification. *Geophysical Research Letters*, **44(14)**, 7447–7454, doi:10.1002/2017gl073697.

Osterhus, S. et al., 2019: Arctic Mediterranean exchanges: a consistent volume budget and trends in transports from two decades of observations. *Ocean Sci.*, **15(2)**, 379–399, doi:10.5194/os-15-379-2019.

Otto-Bliesner, B.L. et al., 2017: Amplified North Atlantic warming in the late Pliocene by changes in Arctic gateways: Arctic Gateways and Pliocene Climate. *Geophysical Research Letters*, **44(2)**, 957–964, doi:10.1002/2016gl071805.

Otto-Bliesner, B.L. et al., 2021a: Large-scale features of Last Interglacial climate: Results from evaluating the lig127k simulations for CMIP6-PMIP4. *Climate of the Past*, **17(1)**, 63–94, doi:10.5194/cp-17-63-2021.

ACCEPTED VERSION SUBJECT TO FINAL EDITS

Otto-Bliesner, B.L. et al., 2021b: Large-scale features of Last Interglacial climate: results from evaluating the lig127k simulations for the Coupled Model Intercomparison Project (CMIP6)--Paleoclimate Modeling Intercomparison Project (PMIP4). *Climate of the Past*, **17(1)**, 63–94, doi:10.5194/cp-17-63-2021.
Ouellet, P. et al., 2011: Ocean surface characteristics influence recruitment variability of populations of northern shrimp (Pandalus borealis) in the Northwest Atlantic. *ICES Journal of Marine Science*, **68(4)**, 737–744, doi:10.1093/icesjms/fsq174.
Overland, J.E. and M. Wang, 2015: Increased variability in the early winter subarctic North American atmospheric circulation. *Journal of Climate*, **28(18)**, 7297–7305, doi:10.1175/jcli-d-15-0395.1.
Pagani, M. et al., 2011: The role of carbon dioxide during the onset of antarctic glaciation. *Science*, **334(6060)**, 1261–1264, doi:10.1126/science.1203909.
PAGES 2k Consortium, 2013: Continental-scale temperature variability during the past two millennia. *Nature Geoscience*, **6(5)**, 339–346, doi:10.1038/ngeo1797.
PAGES 2k Consortium, 2019: Consistent multidecadal variability in global temperature reconstructions and simulations over the Common Era. *Nature Geoscience*, **12(8)**, 643–649, doi:10.1038/s41561-019-0400-0.
PAGES 2k Consortium et al., 2017: A global multiproxy database for temperature reconstructions of the Common Era. *Scientific Data*, **4**, 170088, doi:10.1038/sdata.2017.88.
Palchan, D. and A. Torfstein, 2019: A drop in Sahara dust fluxes records the northern limits of the African Humid Period. *Nature Communications*, **10(1)**, 3803, doi:10.1038/s41467-019-11701-z.
Palmeiro, F.M., D. Barriopedro, R. Garcia-Herrera, and N. Calvo, 2015: Comparing sudden stratospheric warming definitions in reanalysis data. *Journal of Climate*, **28(17)**, 6823–6840, doi:10.1175/jcli-d-15-0004.1.
Palmer, J.G. et al., 2015: Drought variability in the eastern Australia and New Zealand summer drought atlas (ANZDA, CE 1500–2012) modulated by the Interdecadal Pacific Oscillation. *Environmental Research Letters*, **10(12)**, 124002, doi:10.1088/1748-9326/10/12/124002.
Palmer, M.D., C.M. Domingues, A.B.A. Slangen, and F. Boeira Dias, 2021: An ensemble approach to quantify global mean sea-level rise over the 20th century from tide gauge reconstructions. *Environmental Research Letters*, **16(4)**, 044043, doi:10.1088/1748-9326/abdaec.
Palmer, M.D. et al., 2018: An Algorithm for Classifying Unknown Expendable Bathythermograph (XBT) Instruments Based on Existing Metadata. *Journal of Atmospheric and Oceanic Technology*, **35(3)**, 429–440, doi:10.1175/jtech-d-17-0129.1.
Palmer, M.R. and P.N. Pearson, 2003: A 23,000-year record of surface water pH and PCO2 in the western equatorial Pacific Ocean.. *Science (New York, N.Y.)*, **300(5618)**, 480–482, doi:10.1126/science.1080796.
Palmer, M.R. et al., 2010: Multi-proxy reconstruction of surface water pCO2 in the northern Arabian Sea since 29ka. *Earth and Planetary Science Letters*, **295(1)**, 49–57, doi:10.1016/j.epsl.2010.03.023.
Pan, N. et al., 2018: Increasing global vegetation browning hidden in overall vegetation greening: Insights from time-varying trends (2018a). *Remote Sensing of Environment*, **214**, 59–72, doi:10.1016/j.rse.2018.05.018.
Pan, T.-Y., C. Murray-Wallace, A. Dosseto, and R.P. Bourman, 2018: The last interglacial (MIS 5e) sea level highstand from a tectonically stable far-field setting, Yorke Peninsula, southern Australia (2018b). *Marine Geology*, **398**, 126–136, doi:10.1016/j.margeo.2018.01.012.
Park, S. et al., 2021: A decline in emissions of CFC-11 and related chemicals from eastern China. *Nature*, **590(7846)**, 433–437, doi:10.1038/s41586-021-03277-w.
Park, T. et al., 2016: Changes in growing season duration and productivity of northern vegetation inferred from long-term remote sensing data. *Environmental Research Letters*, **11(084001)**, doi:10.1088/1748-9326/11/8/084001.
Parkes, D. and B. Marzeion, 2018: Twentieth-century contribution to sea-level rise from uncharted glaciers. *Nature*, **563(7732)**, 551–554, doi:10.1038/s41586-018-0687-9.
Parkinson, C.L., 2014: Spatially mapped reductions in the length of the Arctic sea ice season. *Geophysical Research Letters*, **41(12)**, 4316–4322, doi:10.1002/2014gl060434.
Parkinson, C.L., 2019: A 40-y record reveals gradual Antarctic sea ice increases followed by decreases at rates far exceeding the rates seen in the Arctic. *Proceedings of the National Academy of Sciences*, **116(29)**, 14414–14423, doi:10.1073/pnas.1906556116.
Parmesan, C. and M. Hanley, 2015: Plants and climate change: complexities and surprises. *Annals of botany*, **116**, 849–864, doi:10.1093/aob/mcv169.
Pascolini-Campbell, M. et al., 2015: Toward a record of Central Pacific El Niño events since 1880. *Theoretical and Applied Climatology*, **119(1)**, 379–389, doi:10.1007/s00704-014-1114-2.
Paulot, F., D. Paynter, P. Ginoux, V. Naik, and L.W. Horowitz, 2018: Changes in the aerosol direct radiative forcing from 2001 to 2015: observational constraints and regional mechanisms. *Atmospheric Chemistry and Physics*, **18(17)**, 13265–13281, doi:10.5194/acp-18-13265-2018.
Pearson, P.N., G.L. Foster, and B.S. Wade, 2009: Atmospheric carbon dioxide through the Eocene–Oligocene climate transition. *Nature*, **461**, 1110, doi:10.1038/nature08447.
Pecl, G.T. et al., 2017: Biodiversity redistribution under climate change: Impacts on ecosystems and human well-being. *Science*, **355(6332)**, eaai9214, doi:10.1126/science.aai9214.
Pedlar, J.H. et al., 2015: A comparison of two approaches for generating spatial models of growing-season variables for

ACCEPTED VERSION SUBJECT TO FINAL EDITS

Canada. *Journal of Applied Meteorology and Climatology*, **54(2)**, 506–518, doi:10.1175/jamc-d-14-0045.1.
Peeters, F.J.C. et al., 2004: Vigorous exchange between the Indian and Atlantic oceans at the end of the past five glacial periods. *Nature*, **430(7000)**, 661–665, doi:10.1038/nature02785.
Peltier, W.R., D.F. Argus, and R. Drummond, 2015: Space geodesy constrains ice age terminal deglaciation: The global ICE-6G_C (VM5a) model. *Journal of Geophysical Research: Solid Earth*, **120(1)**, 450–487, doi:10.1002/2014jb011176.
Pena-Ortiz, C., D. Gallego, P. Ribera, P. Ordonez, and M.D.C. Alvarez-Castro, 2013: Observed trends in the global jet stream characteristics during the second half of the 20th century. *Journal of Geophysical Research Atmospheres*, **118**, 2702–2713, doi:10.1002/jgrd.50305.
Pendleton, S.L. et al., 2019: Rapidly receding Arctic Canada glaciers revealing landscapes continuously ice-covered for more than 40,000 years. *Nature communications*, **10(1)**, 445, doi:10.1038/s41467-019-08307-w.
Penduff, T., G. Sérazin, S. Leroux, S. Close, J.-M. Molines, B. Barnier, L. Bessières, L. Terray, G.M., 2018: Chaotic variability of ocean heat content: Climate-relevant features and observational implications. *Oceanography*, **31(2)**, 63–71, doi:10.5670/oceanog.2018.210.
Peng, G., M. Steele, A.C. Bliss, W.N. Meier, and S. Dickinson, 2018: Temporal means and variability of Arctic sea ice melt and freeze season climate indicators using a satellite climate data record. *Remote Sensing*, **10(9)**, 1328, doi:10.3390/rs10091328.
Penman, D.E., B. Hönisch, R.E. Zeebe, E. Thomas, and J.C. Zachos, 2014: Rapid and sustained surface ocean acidification during the Paleocene-Eocene Thermal Maximum. *Paleoceanography*, **29(5)**, 357–369, doi:10.1002/2014pa002621.
Pepler, A.S., A. Di Luca, and J.P. Evans, 2018: Independently assessing the representation of midlatitude cyclones in high-resolution reanalyses using satellite observed winds. *International Journal of Climatology*, **38(3)**, 1314–1327, doi:10.1002/joc.5245.
Perez, F.F. et al., 2018: Meridional overturning circulation conveys fast acidification to the deep Atlantic Ocean. *Nature*, **554(7693)**, 515–518, doi:10.1038/nature25493.
Petherick, L. et al., 2013: Climatic records over the past 30 ka from temperate Australia e a synthesis from the Oz-INTIMATE workgroup. *Quaternary Science Reviews*, **74**, 58–77, doi:10.1016/j.quascirev.2012.12.012.
Philipona, R. et al., 2018: Radiosondes Show That After Decades of Cooling, the Lower Stratosphere Is Now Warming. *Journal of Geophysical Research: Atmospheres*, **123(22)**, 12,509–512,522, doi:10.1029/2018jd028901.
Piao, S. et al., 2018: On the causes of trends in the seasonal amplitude of atmospheric CO2. *Global Change Biology*, **24(2)**, 608–616, doi:10.1111/gcb.13909.
Piao, S. et al., 2020: Characteristics, drivers and feedbacks of global greening. *Nature Reviews Earth & Environment*, **1(1)**, 14–27, doi:10.1038/s43017-019-0001-x.
Pico, T., 2020: Towards assessing the influence of sediment loading on Last Interglacial sea level. *Geophysical Journal International*, **220(1)**, 384–392, doi:10.1093/gji/ggz447.
Piecuch, C.G., 2020: Likely weakening of the Florida Current during the past century revealed by sea-level observations. *Nature Communications*, **11(1)**, 3973, doi:10.1038/s41467-020-17761-w.
Piecuch, C.G. and R.M. Ponte, 2015: Inverted barometer contributions to recent sea level changes along the northeast coast of North America. *Geophysical Research Letters*, **42(14)**, 5918–5925, doi:10.1002/2015gl064580.
Piecuch, C.G., S. Dangendorf, R.M. Ponte, and M. Marcos, 2016: Annual sea level changes on the North American Northeast Coast: influence of local winds and barotropic motions. *Journal of Climate*, **29(13)**, 4801–4816, doi:10.1175/jcli-d-16-0048.1.
Pimm, S.L. et al., 2014: The biodiversity of species and their rates of extinction, distribution, and protection. *Science*, **344(6187)**, 1246752, doi:10.1126/science.1246752.
Pinsky, M.L., R.L. Selden, and Z.J. Kitchel, 2020: Climate-Driven Shifts in Marine Species Ranges: Scaling from Organisms to Communities. *Annual Review of Marine Science*, **12(1)**, 153–179, doi:10.1146/annurev-marine-010419-010916.
Pinto, J.G. and C.C. Raible, 2012: Past and recent changes in the North Atlantic oscillation. *WIREs Climate Change*, **3(1)**, 79–90, doi:10.1002/wcc.150.
Platt, T., C. Fuentes-Yaco, and K.T. Frank, 2003: Spring algal bloom and larval fish survival. *Nature*, **423(6938)**, 398–399, doi:10.1038/423398b.
Poli, P. et al., 2016: ERA-20C: An Atmospheric Reanalysis of the Twentieth Century. *Journal of Climate*, **29(11)**, 4083–4097, doi:10.1175/jcli-d-15-0556.1.
Polo, I., B.W. Dong, and R.T. Sutton, 2013: Changes in tropical Atlantic interannual variability from a substantial weakening of the meridional overturning circulation. *Climate Dynamics*, **41(9)**, 2765–2784, doi:10.1007/s00382-013-1716-x.
Polo, I., M. Martin-Rey, B. Rodriguez-Fonseca, F. Kucharski, and C.R. Mechoso, 2015: Processes in the Pacific La Niña onset triggered by the Atlantic Niño. *Climate Dynamics*, **44(1)**, 115–131, doi:10.1007/s00382-014-2354-7.
Polovina, J.J., E.A. Howell, and M. Abecassis, 2008: Ocean's least productive waters are expanding. *Geophysical Research Letters*, **35(3)**, doi:10.1029/2007gl031745.

ACCEPTED VERSION SUBJECT TO FINAL EDITS

Polson, D. and G.C. Hegerl, 2017: Strengthening contrast between precipitation in tropical wet and dry regions. *Geophysical Research Letters*, **44(1)**, 365–373, doi:10.1002/2016gl071194.
Poluianov, S., G.A. Kovaltsov, A.L. Mishev, and I.G. Usoskin, 2016: Production of cosmogenic isotopes 7Be, 10Be, 14C, 22Na, and 36Cl in the atmosphere: Altitudinal profiles of yield functions. *Journal of Geophysical Research: Atmospheres*, **121(13)**, 8125–8136, doi:10.1002/2016jd025034.
Polyak, V.J. et al., 2018: A highly resolved record of relative sea level in the western Mediterranean Sea during the last interglacial period. *Nature Geoscience*, **11(11)**, 860–864, doi:10.1038/s41561-018-0222-5.
Polyakov, I. et al., 2005: Multidecadal Variability of North Atlantic Temperature and Salinity during the Twentieth Century. *Journal of Climate*, **18(21)**, 4562–4581, doi:10.1175/jcli3548.1.
Pontes, G.M. et al., 2020: Drier tropical and subtropical Southern Hemisphere in the mid-Pliocene Warm Period. *Scientific Reports*, **10(1)**, 13458, doi:10.1038/s41598-020-68884-5.
Pottapinjara, V., M.S. Girishkumar, R. Murtugudde, K. Ashok, and M. Ravichandran, 2019: On the Relation between the Boreal Spring Position of the Atlantic Intertropical Convergence Zone and Atlantic Zonal Mode. *Journal of Climate*, **32(15)**, 4767–4781, doi:10.1175/jcli-d-18-0614.1.
Power, S.B. and G. Kociuba, 2011: What Caused the Observed Twentieth-Century Weakening of the Walker Circulation? *Journal of Climate*, **24(24)**, 6501–6514, doi:10.1175/2011jcli4101.1.
Prakash, S., F. Shati, H. Norouzi, and R. Blake, 2018: Observed differences between near-surface air and skin temperatures using satellite and ground-based data. *Theoretical and Applied Climatology*, **137(1–2)**, 587–600, doi:10.1007/s00704-018-2623-1.
Prentice, I.C. et al., 2000: Mid-Holocene and glacial-maximum vegetation geography of the northern continents and Africa. *Journal of Biogeography*, **27(3)**, 507–519, doi:10.1046/j.1365-2699.2000.00425.x.
Prigent, A., R.A. Imbol Koungue, J.F. Lübbecke, P. Brandt, and M. Latif, 2020a: Origin of Weakened Interannual Sea Surface Temperature Variability in the Southeastern Tropical Atlantic Ocean. *Geophysical Research Letters*, **47(20)**, e2020GL089348, doi:10.1029/2020gl089348.
Prigent, A., J.F. Lübbecke, T. Bayr, M. Latif, and C. Wengel, 2020b: Weakened SST variability in the tropical Atlantic Ocean since 2000. *Climate Dynamics*, **54(5)**, 2731–2744, doi:10.1007/s00382-020-05138-0.
Prytherch, J., E.C. Kent, and D.I. Berry, 2015: A comparison of SSM / I-derived global marine surface-specific humidity datasets. *International Journal of Climatology*, **35**, 2359–2381, doi:10.1002/joc.4150.
Pulliainen, J. et al., 2020: Patterns and trends of Northern Hemisphere snow mass from 1980 to 2018. *Nature*, **581(7808)**, 294–298, doi:10.1038/s41586-020-2258-0.
Punyu, V.R., V.K. Banakar, and A. Garg, 2014: Equatorial Indian Ocean productivity during the last 33kyr and possible linkage to Westerly Jet variability. *Marine Geology*, **348**, 44–51, doi:10.1016/j.margeo.2013.11.010.
Purkey, S.G. and G.C. Johnson, 2010: Warming of Global Abyssal and Deep Southern Ocean Waters between the 1990s and 2000s: Contributions to Global Heat and Sea Level Rise Budgets. *Journal of Climate*, **23(23)**, 6336–6351, doi:10.1175/2010jcli3682.1.
Putnam, A.E. and W.S. Broecker, 2017: Human-induced changes in the distribution of rainfall. *Science Advances*, **3(5)**, e1600871, doi:10.1126/sciadv.1600871.
Qi, D. et al., 2017: Increase in acidifying water in the western Arctic Ocean. *Nature Climate Change*, 195–199, doi:10.1038/nclimate3228.
Quade, J. and M.R. Kaplan, 2017: Lake-level stratigraphy and geochronology revisited at Lago (Lake) Cardiel, Argentina, and changes in the Southern Hemispheric Westerlies over the last 25 ka. *Quaternary Science Reviews*, **177**, 173–188, doi:10.1016/j.quascirev.2017.10.006.
Quade, J. et al., 2018: Megalakes in the Sahara ? A Review. *Quaternary Research*, **90**, 253–275, doi:10.1017/qua.2018.46.
Queste, B.Y., C. Vic, K.J. Heywood, and S.A. Piontkovski, 2018: Physical Controls on Oxygen Distribution and Denitrification Potential in the North West Arabian Sea. *Geophysical Research Letters*, **45(9)**, 4143–4152, doi:10.1029/2017gl076666.
Racault, M.-F., S. Sathyendranath, N. Menon, and T. Platt, 2017a: Phenological Responses to ENSO in the Global Oceans (2017a). *Surveys in Geophysics*, **38(1)**, 277–293, doi:10.1007/s10712-016-9391-1.
Racault, M.-F., C. Le Quéré, E. Buitenhuis, S. Sathyendranath, and T. Platt, 2012: Phytoplankton phenology in the global ocean. *Ecological Indicators*, **14(1)**, 152–163, doi:10.1016/j.ecolind.2011.07.010.
Racault, M.-F. et al., 2017b: Impact of El Niño Variability on Oceanic Phytoplankton. *Frontiers in Marine Science*, **4**, 133, doi:10.3389/fmars.2017.00133.
Radeloff, V.C. et al., 2015: The rise of novelty in ecosystems. *Ecological Applications*, **25(8)**, 2051–2068, doi:10.1890/14-1781.1.
Rae, J.W.B., Y.-G. Zhang, X. Liu, G.L. Foster, and H.M. Stoll, 2021: Atmospheric CO2 over the last 66 million years from marine archives. *Annual Review of Earth and Planetary Sciences*, doi:10.1146/annurev-earth-082420-063026.
Rae, J.W.B. et al., 2018: CO2 storage and release in the deep Southern Ocean on millennial to centennial timescales. *Nature*, **562(7728)**, 569–573, doi:10.1038/s41586-018-0614-0.
Rahmstorf, S. et al., 2015: Exceptional twentieth-century slowdown in Atlantic Ocean overturning circulation. *Nature*

ACCEPTED VERSION SUBJECT TO FINAL EDITS

Climate Change, **5**, 475–480, doi:10.1038/nclimate2554.
Raible, C.C., J.G. Pinto, P. Ludwig, and M. Messmer, 2021: A review of past changes in extratropical cyclones in the northern hemisphere and what can be learned for the future. *WIREs Climate Change*, **12(1)**, e680, doi:10.1002/wcc.680.
Raitzsch, M. et al., 2018: Boron isotope-based seasonal paleo-pH reconstruction for the Southeast Atlantic – A multispecies approach using habitat preference of planktonic foraminifera. *Earth and Planetary Science Letters*, **487**, 138–150, doi:10.1016/j.epsl.2018.02.002.
Randel, W.J., A.K. Smith, F. Wu, C.-Z. Zou, and H. Qian, 2016: Stratospheric Temperature Trends over 1979–2015 Derived from Combined SSU, MLS, and SABER Satellite Observations. *Journal of Climate*, **29(13)**, 4843–4859, doi:10.1175/jcli-d-15-0629.1.
Rao, Y., S. Liang, and Y. Yu, 2018: Land Surface Air Temperature Data Are Considerably Different Among BEST-LAND, CRU-TEM4v, NASA-GISS, and NOAA-NCEI. *Journal of Geophysical Research: Atmospheres*, **123(11)**, 5881–5900, doi:10.1029/2018jd028355.
Räsänen, T.A., V. Lindgren, J.H.A. Guillaume, B.M. Buckley, and M. Kummu, 2016: On the spatial and temporal variability of ENSO precipitation and drought teleconnection in mainland Southeast Asia. *Climate of the Past*, **12(9)**, 1889–1905, doi:10.5194/cp-12-1889-2016.
Ratnam, J., S.K. Behera, Y. Masumoto, and T. Yamagata, 2014: Remote Effects of El Niño and Modoki Events on the Austral Summer Precipitation of Southern Africa. *Journal of Climate*, **27(10)**, 3802–3815, doi:10.1175/jcli-d-13-00431.1.
Ray, E.A. et al., 2017: Quantification of the SF6 lifetime based on mesospheric loss measured in the stratospheric polar vortex. *Journal of Geophysical Research*, **122(8)**, 4626–4638, doi:10.1002/2016jd026198.
Ray, R.D. and B.C. Douglas, 2011: Experiments in reconstructing twentieth-century sea levels. *Progress in Oceanography*, **91(4)**, 496–515, doi:10.1016/j.pocean.2011.07.021.
Raymo, M.E. and J.X. Mitrovica, 2012: Collapse of polar ice sheets during the stage 11 interglacial. *Nature*, **483(7390)**, 453–456, doi:10.1038/nature10891.
Rayner, N.A. et al., 2003: Global analyses of sea surface temperature, sea ice, and night marine air temperature since the late nineteenth century. *Journal of Geophysical Research: Atmospheres*, **108(D14)**, doi:10.1029/2002jd002670.
Rayner, N.A. et al., 2020: The EUSTACE project: delivering global, daily information on surface air temperature. *Bulletin of the American Meteorological Society*, 1–79, doi:10.1175/bams-d-19-0095.1.
Reboita, M.S., R.P. da Rocha, T. Ambrizzi, and C.D. Gouveia, 2015: Trend and teleconnection patterns in the climatology of extratropical cyclones over the Southern Hemisphere. *Climate Dynamics*, **45**, 1929–1944, doi:10.1007/s00382-014-2447-3.
Rehfeld, K., T. Münch, S.L. Ho, and T. Laepple, 2018: Global patterns of declining temperature variability from the Last Glacial Maximum to the Holocene. *Nature*, **554**, 356, doi:10.1038/nature25454.
Reid, P. and R.A. Massom, 2015: Successive Antarctic sea ice extent records during 2012, 2013 and 2014 [in "State of the Climate in 2014"]. *Bulletin of the American Meteorological Society*, **96(7)**, S163–S164, 2015bamsstateoftheclimate.1.
Reid, P., S. Stammerjohn, R. Massom, T. Scambos, and J. Lieser, 2015: The record 2013 Southern Hemisphere sea-ice extent maximum. *Annals of Glaciology*, **56(69)**, doi:10.3189/2015aog69a892.
Reid, P. et al., 2020: Sea ice extent, concentration, and seasonality [in "State of the Climate in 2019"]. *Bull. Amer. Meteor. Soc.*, **101(8)**, S304–S306, doi:10.1175/bams-d-20-0090.1.
Reinhold, T. et al., 2019: The Sun is less active than other solar-type stars. *Science*, **368(6490)**, 518–521, doi:10.1126/science.aay3821.
Remmelzwaal, S.R.C. et al., 2019: Investigating Ocean Deoxygenation During the PETM Through the Cr Isotopic Signature of Foraminifera. *Paleoceanography and Paleoclimatology*, **34(6)**, 917–929, doi:10.1029/2018pa003372.
Renner, A.H.H. et al., 2014: Evidence of Arctic sea ice thinning from direct observations. *Geophysical Research Letters*, **41(14)**, 5029–5036, doi:10.1002/2014gl060369.
Rennie, J.J. et al., 2014: The international surface temperature initiative global land surface databank: monthly temperature data release description and methods. *Geoscience Data Journal*, **1(2)**, 75–102, doi:10.1002/gdj3.8.
Renwick, K.M. and M.E. Rocca, 2015: Temporal context affects the observed rate of climate-driven range shifts in tree species. *Global Ecology and Biogeography*, **24(1)**, 44–51, doi:10.1111/geb.12240.
Resplandy, L. et al., 2019: Quantification of ocean heat uptake from changes in atmospheric O2 and CO2 composition. *Scientific Reports*, **9(1)**, 20244, doi:10.1038/s41598-019-56490-z.
Reuter, M. et al., 2020: Ensemble-based satellite-derived carbon dioxide and methane column-averaged dry-air mole fraction data sets (2003--2018) for carbon and climate applications. *Atmospheric Measurement Techniques*, **13(2)**, 789–819, doi:10.5194/amt-13-789-2020.
Reynhout, S.A. et al., 2019: Holocene glacier fluctuations in Patagonia are modulated by summer insolation intensity and paced by Southern Annular Mode-like variability. *Quaternary Science Reviews*, **220**, 178–187, doi:10.1016/j.quascirev.2019.05.029.

ACCEPTED VERSION SUBJECT TO FINAL EDITS

Reynolds, D.J. et al., 2018: Isolating and Reconstructing Key Components of North Atlantic Ocean Variability From a Sclerochronological Spatial Network. *Paleoceanography and Paleoclimatology*, **33(10)**, 1086–1098, doi:10.1029/2018pa003366.
RGI Consortium, 2017: Randolph Glacier Inventory – A Dataset of Global Glacier Outlines: Version 6.0. Technical Report, Global Land Ice Measurements from Space, CO, USA.
Rhein, M., R. Steinfeldt, D. Kieke, I. Stendardo, and I. Yashayaev, 2017: Ventilation variability of Labrador Sea Water and its impact on oxygen and anthropogenic carbon: a review. *Philosophical Transactions of the Royal Society A: Mathematical, Physical and Engineering Sciences*, **375(2102)**, 20160321, doi:10.1098/rsta.2016.0321.
Rhodes, R.H. et al., 2013: Continuous methane measurements from a late Holocene Greenland ice core: Atmospheric and in-situ signals. *Earth and Planetary Science Letters*, **368**, 9–19, doi:10.1016/j.epsl.2013.02.034.
Rhodes, R.H. et al., 2015: Enhanced tropical methane production in response to iceberg discharge in the North Atlantic. *Science*, **348(6238)**, 1016–1019, doi:10.1126/science.1262005.
Rhodes, R.H. et al., 2017: Atmospheric methane variability: Centennial-scale signals in the Last Glacial Period. *Global Biogeochemical Cycles*, **31(3)**, 575–590, doi:10.1002/2016gb005570.
Ribeiro, N., M.M. Mata, J.L.L. De Azevedo, and M. Cirano, 2018: An assessment of the XBT fall-rate equation in the Southern Ocean. *Journal of Atmospheric and Oceanic Technology*, **35(4)**, 911–926, doi:10.1175/jtech-d-17-0086.1.
Richardson, M., K. Cowtan, and R.J. Millar, 2018: Global temperature definition affects achievement of long-term climate goals. *Environmental Research Letters*, **13(5)**, 54004, doi:10.1088/1748-9326/aab305.
Richardson, M., K. Cowtan, E. Hawkins, and M.B. Stolpe, 2016: Reconciled climate response estimates from climate models and the energy budget of Earth. *Nature Climate Change*, **6(10)**, 931–935, doi:10.1038/nclimate3066.
Ricker, R., S. Hendricks, D.K. Perovich, V. Helm, and R. Gerdes, 2015: Impact of snow accumulation on CryoSat-2 range retrievals over Arctic sea ice: An observational approach with buoy data. *Geophysical Research Letters*, **42(11)**, 4447–4455, doi:10.1002/2015gl064081.
Rigby, M. et al., 2019: Increase in CFC-11 emissions from eastern China based on atmospheric observations. *Nature*, **569(7757)**, 546–550, doi:10.1038/s41586-019-1193-4.
Rignot, E. et al., 2019: Four decades of Antarctic Ice Sheet mass balance from 1979–2017. *Proceedings of the National Academy of Sciences*, **116(4)**, 1095–1103, doi:10.1073/pnas.1812883116.
Ritz, S.P., T.F. Stocker, J.O. Grimalt, L. Menviel, and A. Timmermann, 2013: Estimated strength of the Atlantic overturning circulation during the last deglaciation. *Nature Geoscience*, **6(3)**, 208–212, doi:10.1038/ngeo1723.
Roberts, J.B., C.A. Clayson, and F.R. Robertson, 2019: Improving Near - Surface Retrievals of Surface Humidity Over the Global Open Oceans From Passive Microwave Observations. *Earth and Space Science*, **6**, 1220–1233, doi:10.1029/2018ea000436.
Roberts, N. et al., 2012a: Palaeolimnological evidence for an east–west climate see-saw in the Mediterranean since AD 900. *Global and Planetary Change*, **84–85(s1)**, 23–34, doi:10.1016/j.gloplacha.2011.11.002.
Roberts, N. et al., 2012b: Palaeolimnological evidence for an east–west climate see-saw in the Mediterranean since AD 900. *Global and Planetary Change*, **84–85(s1)**, 23–34, doi:10.1016/j.gloplacha.2011.11.002.
Robertson, F.R., M.G. Bosilovich, and J.B. Roberts, 2016: Reconciling Land – Ocean Moisture Transport Variability in Reanalyses with P - ET in Observationally Driven Land Surface Models. *Journal of Climate*, **29**, 8625–8646, doi:10.1175/jcli-d-16-0379.1.
Robertson, F.R. et al., 2014: Consistency of Estimated Global Water Cycle Variations over the Satellite Era. *Journal of Climate*, **27**, 6135–6154, doi:10.1175/jcli-d-13-00384.1.
Robertson, F.R. et al., 2020: Uncertainties in Ocean Latent Heat Flux Variations Over Recent Decades in Satellite-Based Estimates and Reduced Observation Reanalyses. *Journal of Climate*, **33**, 8415–8437, doi:10.1175/jcli-d-19-0954.1.
Robson, J., P. Ortega, and R. Sutton, 2016: A reversal of climatic trends in the North Atlantic since 2005. *Nature Geoscience*, **9**, 513.
Rodysill, J.R. et al., 2018: A North American Hydroclimate Synthesis (NAHS) of the Common Era. *Global and Planetary Change*, **162**, 175–198, doi:10.1016/j.gloplacha.2017.12.025.
Roemmich, D. et al., 2019: On the Future of Argo: A Global, Full-Depth, Multi-Disciplinary Array. *Frontiers in Marine Science*, **6**, 439, doi:10.3389/fmars.2019.00439.
Rohde, R. et al., 2013: Berkeley Earth Temperature Averaging Process. *Geoinformatics & Geostatistics: An Overview*, **1(2)**, doi:10.4172/gigs.1000103.
Rohde, R.A. and Z. Hausfather, 2020: The Berkeley Earth Land/Ocean Temperature Record. *Earth System Science Data*, **12(4)**, 3469–3479, doi:10.5194/essd-12-3469-2020.
Rohling, E.J., 2007: Progress in paleosalinity: Overview and presentation of a new approach. *Paleoceanography*, **22(3)**, doi:10.1029/2007pa001437.
Rohling, E.J. et al., 2017: Differences between the last two glacial maxima and implications for ice-sheet, δ18O, and sea-level reconstructions. *Quaternary Science Reviews*, **176**, 1–28, doi:10.1016/j.quascirev.2017.09.009.
Rohling, E.J. et al., 2019: Asynchronous Antarctic and Greenland ice-volume contributions to the last interglacial sea-level highstand. *Nature Communications*, **10(1)**, 5040, doi:10.1038/s41467-019-12874-3.

ACCEPTED VERSION SUBJECT TO FINAL EDITS

Rohrer, M. et al., 2018: Representation of extratropical cyclones, blocking anticyclones, and alpine circulation types in multiple reanalyses and model simulations. *Journal of Climate*, **31(8)**, 3009–3031, doi:10.1175/jcli-d-17-0350.1.

Romanovsky, V. et al., 2017: Changing permafrost and its impacts. In: *Snow, Water, Ice and Permafrost in the Arctic (SWIPA) 2017*. Arctic Monitoring and Assessment Program (AMAP), Oslo, Norway, pp. 65–102.

Romanovsky, V.E. et al., 2020: Terrestrial Permafrost [in "State of the Climate in 2019"]. *Bulletin of the American Meteorological Society*, **101(8)**, 265–269, doi:10.1175/bams-d-20-0086.1.

Romanovsky, V. E., Smith, S. L., Isaksen, K., Shiklomanov, N. I., Streletskiy, D. A., Kholodov, A. L., Christiansen, H. H., Drozdov, D. S., Malkova, G. V., Marchenko, S.S., 2017: Terrestrial Permafrost. In: Arctic Report Card 2017.. , doi:10.1175 /2018bamsstateoftheclimate.1.

Romanovsky, V. E., Smith, S. L., Isaksen, K., Shiklomanov, N. I., Streletskiy, D. A., Kholodov, A. L., Christiansen, H. H., Drozdov, D. S., Malkova, G. V., Marchenko, S.S., 2018: [Arctic] Terrestrial Permafrost [in "State of the Climate in 2017"]. *Bulletin of the American Meteorological Society (supplement)*, **99(9)**, S161–S165, doi:10.1175 /2018bamsstateoftheclimate.1.

Rösel, A. et al., 2018: Thin Sea Ice, Thick Snow, and Widespread Negative Freeboard Observed During N-ICE2015 North of Svalbard. *Journal of Geophysical Research: Oceans*, **123(2)**, 1156–1176, doi:10.1002/2017jc012865.

Rosenthal, Y., B.K. Linsley, and D.W. Oppo, 2013: Pacific Ocean Heat Content During the Past 10,000 Years. *Science*, **342(6158)**, 617–621, doi:10.1126/science.1240837.

Rosenthal, Y., Kalansky, J., Morley, A., Linsley, B., 2017: A paleo-perspective on ocean heat content: Lessons from the Holocene and Common Era. *Quaternary Science Reviews*, **155**, 1–12, doi:10.1016/j.quascirev.2016.10.017.

Ross, T., C. Du Preez, and D. Ianson, 2020: Rapid deep ocean deoxygenation and acidification threaten life on Northeast Pacific seamounts. *Global Change Biology*, **n/a(n/a)**, doi:10.1111/gcb.15307.

Rossby, T., L. Chafik, and L. Houpert, 2020: What can Hydrography Tell Us About the Strength of the Nordic Seas MOC Over the Last 70 to 100 Years? *Geophysical Research Letters*, **47(12)**, e2020GL087456, doi:10.1029/2020gl087456.

Røthe, T.O., J. Bakke, E.W.N. Støren, and S.O. Dahl, 2019: Wintertime extreme events recorded by lake sediments in Arctic Norway. *The Holocene*, **29(8)**, 1305–1321, doi:10.1177/0959683619846983.

Rouault, M., S. Illig, J. Lübbecke, and R.A.I. Koungue, 2018: Origin, development and demise of the 2010–2011 Benguela Niño. *Journal of Marine Systems*, **188**, 39–48, doi:10.1016/j.jmarsys.2017.07.007.

Routson, C.C. et al., 2019: Mid-latitude net precipitation decreased with Arctic warming during the Holocene. *Nature*, **568**, 83–87, doi:10.1038/s41586-019-1060-3.

Roy, K. and W.R. Peltier, 2017: Space-geodetic and water level gauge constraints on continental uplift and tilting over North America: regional convergence of the ICE-6G_C (VM5a/VM6) models. *Geophysical Journal International*, **210(2)**, 1115–1142, doi:10.1093/gji/ggx156.

Rubino, A., D. Zanchettin, F. De Rovere, and M.J. McPhaden, 2020: On the interchangeability of sea-surface and near-surface air temperature anomalies in climatologies. *Scientific Reports*, **10(1)**, 7433, doi:10.1038/s41598-020-64167-1.

Rubino, M. et al., 2019: Revised records of atmospheric trace gases CO2, CH4, N2O, and delta13C-CO2 over the last 2000 years from Law Dome, Antarctica. *Earth System Science Data*, **11(2)**, 473–492, doi:10.5194/essd-11-473-2019.

Rumpf, S.B., K. Hülber, N.E. Zimmermann, and S. Dullinger, 2018: Elevational rear edges shifted at least as much as leading edges over the last century. *Global Ecology and Biogeography*, **28(4)**, 533–543, doi:10.1111/geb.12865.

Rupp, D.E., P.W. Mote, N.L. Bindoff, P.A. Stott, and D.A. Robinson, 2013: Detection and attribution of observed changes in northern hemisphere spring snow cover. *Journal of Climate*, **26(18)**, 6904–6914, doi:10.1175/jcli-d-12-00563.1.

Rustic, G.T., A. Koutavas, T.M. Marchitto, and B.K. Linsley, 2015: Dynamical excitation of the tropical Pacific Ocean and ENSO variability by Little Ice Age cooling. *Science*, **350(6267)**, 1537–1541, doi:10.1126/science.aac9937.

Ryu, Y. et al., 2020: Ice core nitrous oxide over the past 2000 years. PANGAEA. Retrieved from: https://doi.org/10.1594/pangaea.923434.

Sachs, J.P. et al., 2018: Southward Shift of the Pacific ITCZ During the Holocene. *Paleoceanography and Paleoclimatology*, **33**, 1383–1395, doi:10.1029/2018pa003469.

Sadekov, A.Y. et al., 2013: Palaeoclimate reconstructions reveal a strong link between El Niño-Southern Oscillation and Tropical Pacific mean state. *Nature Communications*, **4(1)**, 2692, doi:10.1038/ncomms3692.

Salamalikis, V., I. Vamvakas, C.A. Gueymard, and A. Kazantzidis, 2021: Atmospheric water vapor radiative effects on shortwave radiation under clear skies: A global spatiotemporal analysis. *Atmospheric Research*, **251**, 105418, doi:10.1016/j.atmosres.2020.105418.

Salt, L.A., S.M.A.C. van Heuven, M.E. Claus, E.M. Jones, and H.J.W. de Baar, 2015: Rapid acidification of mode and intermediate waters in the southwestern Atlantic Ocean. *Biogeosciences*, **12(5)**, 1387–1401, doi:10.5194/bg-12-1387-2015.

Salzmann, U., A.M. Haywood, D.J. Lunt, P.J. Valdes, and D.J. Hill, 2008: A new global biome reconstruction and data-

ACCEPTED VERSION SUBJECT TO FINAL EDITS

model comparison for the Middle Pliocene. *Global Ecology and Biogeography*, **17(3)**, 432–447, doi:10.1111/j.1466-8238.2008.00381.x.
Salzmann, U. et al., 2013a: Challenges in quantifying Pliocene terrestrial warming revealed by data-model discord. *Nature Climate Change*, **3**, 969–974, doi:10.1038/nclimate2008.
Salzmann, U. et al., 2013b: Challenges in quantifying Pliocene terrestrial warming revealed by data-model discord. *Nature Climate Change*, **3**, 969–974, doi:10.1038/nclimate2008.
Samset, B.H., M.T. Lund, M. Bollasina, G. Myhre, and L. Wilcox, 2019: Emerging Asian aerosol patterns. *Nature Geoscience*, **12(8)**, 582–584, doi:10.1038/s41561-019-0424-5.
Sanborn, K.L. et al., 2017: New evidence of Hawaiian coral reef drowning in response to meltwater pulse-1A. *Quaternary Science Reviews*, **175**, 60–72, doi:10.1016/j.quascirev.2017.08.022.
Sánchez-Montes, M.L. et al., 2020: Late Pliocene Cordilleran Ice Sheet development with warm Northeast Pacific sea surface temperatures. *Climate of the Past*, **16(1)**, 299–313, doi:10.5194/cp-2019-29.
Sánchez-Velasco, L. et al., 2019: Larval Fish Habitats and Deoxygenation in the Northern Limit of the Oxygen Minimum Zone off Mexico. *Journal of Geophysical Research: Oceans*, **124(12)**, 9690–9705, doi:10.1029/2019jc015414.
Santer, B.D. et al., 2008a: Consistency of modelled and observed temperature trends in the tropical troposphere. *International Journal of Climatology*, **28(13)**, 1703–1722, doi:10.1002/joc.1756.
Santer, B.D. et al., 2008b: Consistency of modelled and observed temperature trends in the tropical troposphere. *International Journal of Climatology*, **28(13)**, 1703–1722, doi:10.1002/joc.1756.
Santer, B.D. et al., 2008c: Consistency of modelled and observed temperature trends in the tropical troposphere. *International Journal of Climatology*, **28(13)**, 1703–1722, doi:10.1002/joc.1756.
Santer, B.D., T.M.L. Wigley, T.P. Barnett, E.A., 1996: Detection of climate change and attribution of causes. In: *Climate Change 1995: The Science of Climate Change. Contribution of Working Group I to the Second Assessment Report of the Intergovernmental Panel on Climate Change* [Houghton, J.T., L.G.M. Filho, B.A. Callander, N. Harris, A. Kattenberg, and K. Maskell (eds.)]. Cambridge University Press, Cambridge, United Kingdom and New York, NY, USA, pp. 407–444.
Sapart, C.J. et al., 2012: Natural and anthropogenic variations in methane sources during the past two millennia. *Nature*, **490**, 85–88, doi:10.1038/nature11461.
Sapiano, M.R.P., C.W. Brown, S. Schollaert Uz, and M. Vargas, 2012: Establishing a global climatology of marine phytoplankton phenological characteristics. *Journal of Geophysical Research: Oceans*, **117(C8)**, doi:10.1029/2012jc007958.
Sasgen, I. et al., 2020: Return to rapid ice loss in Greenland and record loss in 2019 detected by the GRACE-FO satellites. *Communications Earth & Environment*, **1(1)**, 8, doi:10.1038/s43247-020-0010-1.
Sathyendranath, S. et al., 2019: An Ocean-Colour Time Series for Use in Climate Studies: The Experience of the Ocean-Colour Climate Change Initiative (OC-CCI). *Sensors*, **19(19)**, doi:10.3390/s19194285.
Sathyendranath, S. et al., 2020: Reconciling models of primary production and photoacclimation. *Appl. Opt.*, **59(10)**, C100—C114, doi:10.1364/ao.386252.
Sato, M., J.E. Hansen, M.P. McCormick, and J.B. Pollack, 1993: Stratospheric Aerosol Optical Depths, 1850–1990. *Journal of Geophysical Research*, **98(D12)**, 22987–22994, doi:10.1029/93jd02553.
Schaefer, J.M. et al., 2016: Greenland was nearly ice-free for extended periods during the Pleistocene. *Nature*, **540(7632)**, 252–255, doi:10.1038/nature20146.
Scheen, J. and T.F. Stocker, 2020: Effect of changing ocean circulation on deep ocean temperature in the last millennium. *Earth System Dynamics*, **11(4)**, 925–951, doi:10.5194/esd-11-925-2020.
Scheff, J., R. Seager, and H. Liu, 2017: Are Glacials Dry? Consequences for Paleoclimatology and for Greenhouse Warming. *Journal of Climate*, **30**, 6593–6609, doi:10.1175/jcli-d-16-0854.1.
Scheffers, B.R. et al., 2016: The broad footprint of climate change from genes to biomes to people. *Science*, **354(6313)**, doi:10.1126/science.aaf7671.
Schefuß, E., H. Kuhlmann, G. Mollenhauer, M. Prange, and J. Pätzold, 2011: Forcing of wet phases in southeast Africa over the past 17,000 years. *Nature*, **480(7378)**, 509–512, doi:10.1038/nature10685.
Schemm, S., 2018: Regional trends in weather systems help explain Antarctic sea ice trends. *Geophyiscal Research Letters*, **45**, 7165–7175, doi:10.1029/2018gl079109.
Scherllin-Pirscher, B., G. Kirchengast, A.K. Steiner, Y.-H. Kuo, and U. Foelsche, 2011: Quantifying uncertainty in climatological fields from GPS radio occultation: an empirical-analytical error model. *Atmospheric Measurement Techniques*, **4(9)**, 2019–2034, doi:10.5194/amt-4-2019-2011.
Scherllin-Pirscher, B. et al., 2012: The vertical and spatial structure of ENSO in the upper troposphere and lower stratosphere from GPS radio occultation measurements. *Geophysical Research Letters*, **39(20)**, doi:10.1029/2012gl053071.
Scherllin-Pirscher B., A. K. Steiner, R. A. Anthes, S. Alexander, R. Biondi, T. Birner, J. Kim, W. J. Randel, S-W. Son, T. Tsuda, Z.Z., 2020: Tropical temperature variability in the UTLS: New insights from GPS radio occultation observations. *J. Climate*, **In Press**, 1–92, doi:10.1175/jcli-d-20-0385.1.
Schilt, A. et al., 2010: Glacial–interglacial and millennial-scale variations in the atmospheric nitrous oxide

ACCEPTED VERSION SUBJECT TO FINAL EDITS

concentration during the last 800,000 years. *Quaternary Science Reviews*, **29(1)**, 182–192, doi:10.1016/j.quascirev.2009.03.011.
Schilt, A. et al., 2014: Isotopic constraints on marine and terrestrial N2O emissions during the last deglaciation. *Nature*, **516**, 234, doi:10.1038/nature13971.
Schimpf, D. et al., 2011: The significance of chemical, isotopic, and detrital components in three coeval stalagmites from the superhumid southernmost Andes (53 S) as high-resolution palaeo-climate proxies. *Quaternary Science Reviews*, **30(3–4)**, 443–459, doi:10.1016/j.quascirev.2010.12.006.
Schmidt, A. et al., 2018a: Volcanic Radiative Forcing From 1979 to 2015. *Journal of Geophysical Research: Atmospheres*, **123(22)**, 12,412–491,508, doi:10.1029/2018jd028776.
Schmidt, A. et al., 2018b: Volcanic Radiative Forcing From 1979 to 2015. *Journal of Geophysical Research: Atmospheres*, **123(22)**, 12,412–491,508, doi:10.1029/2018jd028776.
Schmidt, M.W., H.J. Spero, and D.W. Lea, 2004: Links between salinity variation in the Caribbean and North Atlantic thermohaline circulation. *Nature*, **428(6979)**, 160–163, doi:10.1038/nature02346.
Schmidt, M.W., M.J. Vautravers, and H.J. Spero, 2006: Rapid subtropical North Atlantic salinity oscillations across Dansgaard-Oeschger cycles. *Nature*, **443(7111)**, 561–564, doi:10.1038/nature05121.
Schneider, D.P. and R.L. Fogt, 2018: Artifacts in Century-Length Atmospheric and Coupled Reanalyses Over Antarctica Due To Historical Data Availability. *Geophysical Research Letters*, **45(2)**, 964–973, doi:10.1002/2017gl076226.
Schneider, L. et al., 2015: Revising midlatitude summer temperatures back to A.D. 600 based on a wood density network. *Geophysical Research Letters*, **42(11)**, 4556–4562, doi:10.1002/2015gl063956.
Schröder, M. et al., 2016: The GEWEX water vapor assessment: Results from intercomparison, trend, and homogeneity analysis of total column water vapor. *Journal of Applied Meteorology and Climatology*, **55(7)**, 1633–1649, doi:10.1175/jamc-d-15-0304.1.
Schröder, M. et al., 2018: The GEWEX Water Vapor Assessment archive of water vapour products from satellite observations and reanalyses. *Earth System Science Data*, **10(2)**, 1093–1117, doi:10.5194/essd-10-1093-2018.
Schröder, M. et al., 2019a: The GEWEX Water Vapor Assessment: Overview and Introduction to Results and Recommendations. *Remote Sensing*, **11**, 1–28, doi:10.3390/rs11030251.
Schröder, M. et al., 2019b: The GEWEX Water Vapor Assessment: Overview and Introduction to Results and Recommendations. *Remote Sensing*, **11**, 1–28, doi:10.3390/rs11030251.
Schubert, B.A. and A. Hope Jahren, 2013: Reconciliation of marine and terrestrial carbon isotope excursions based on changing atmospheric CO2 levels. *Nature Communications*, **4(1)**, 1653, doi:10.1038/ncomms2659.
Schulte, L.A., D.J. Mladenoff, T.R. Crow, L.C. Merrick, and D.T. Cleland, 2007: Homogenization of northern U.S. Great Lakes forests due to land use. *Landscape Ecology*, **22**, 1089–1103, doi:10.1007/s10980-007-9095-5.
Schüpbach, S. et al., 2018: Greenland records of aerosol source and atmospheric lifetime changes from the Eemian to the Holocene. *Nature Communications*, **9(1)**, 1476, doi:10.1038/s41467-018-03924-3.
Schweinsberg, A.D., J.P. Briner, G.H. Miller, O. Bennike, and E.K. Thomas, 2017: Local glaciation in West Greenland linked to North Atlantic Ocean circulation during the Holocene. *Geology*, **45(3)**, 195–198, doi:10.1130/g38114.1.
Schweinsberg, A.D. et al., 2018: Holocene mountain glacier history in the Sukkertoppen Iskappe area, southwest Greenland. *Quaternary Science Reviews*, **197**, 142–161, doi:10.1016/j.quascirev.2018.06.014.
Screen, J.A. and I. Simmonds, 2013: Exploring links between Arctic amplification and mid-latitude weather. *Geophysical Research Letters*, **40(5)**, 959–964, doi:10.1002/grl.50174.
Scussolini, P. et al., 2019: Agreement between reconstructed and modeled boreal precipitation of the last interglacial. *Science Advances*, **5(11)**, 1–12, doi:10.1126/sciadv.aax7047.
Seidel, D.J. and W.J. Randel, 2006: Variability and trends in the global tropopause estimated from radiosonde data. *Journal of Geophysical Research: Atmospheres*, **111(D21)**, doi:10.1029/2006jd007363.
Seidel, D.J. et al., 2016: Stratospheric temperature changes during the satellite era. *Journal of Geophysical Research: Atmospheres*, **121(2)**, 664–681, doi:10.1002/2015jd024039.
Séjourné, A. et al., 2015: Evolution of the banks of thermokarst lakes in Central Yakutia (Central Siberia) due to retrogressive thaw slump activity controlled by insolation. *Geomorphology*, doi:10.1016/j.geomorph.2015.03.033.
Seneviratne, S.I. et al., 2018: The many possible climates from the Paris Agreement's aim of 1.5°C warming. *Nature*, **558(7708)**, 41–49, doi:10.1038/s41586-018-0181-4.
Serno, S. et al., 2015: Comparing dust flux records from the Subarctic North Pacific and Greenland: Implications for atmospheric transport to Greenland and for the application of dust as a chronostratigraphic tool. *Paleoceanography*, **30(6)**, 583–600, doi:10.1002/2014pa002748.
Servain, J., I. Wainer, J.P. McCreary Jr., and A. Dessier, 1999: Relationship between the equatorial and meridional modes of climatic variability in the tropical Atlantic. *Geophysical Research Letters*, **26(4)**, 485–488, doi:10.1029/1999gl900014.
Seth, A. et al., 2019: Monsoon Responses to Climate Changes - Connecting Past , Present and Future. *Current Climate Change Reports*, **5(2)**, 63–79, doi:10.1007/s40641-019-00125-y.

ACCEPTED VERSION SUBJECT TO FINAL EDITS

Seviour, W.J.M., 2017: Weakening and shift of the Arctic stratospheric polar vortex: Internal variability or forced response? *Geophysical Research Letters*, **44(7)**, 3365–3373, doi:10.1002/2017gl073071.
Seviour, W.J.M., S.M. Davis, K.M. Grise, and D.W. Waugh, 2018: Large Uncertainty in the Relative Rates of Dynamical and Hydrological Tropical Expansion. *Geophysical Research Letters*, **45(2)**, 1106–1113, doi:10.1002/2017gl076335.
Sha, L., 2019: How Far North Did the African Monsoon Fringe Expand During the African Humid Period? Insights From Southwest Moroccan Speleothems. *Geophysical Research Letters*, **46(23)**, 14093–14102, doi:10.1029/2019gl084879.
Shackleton, N.J., 1987: Oxygen isotopes, ice volume and sea level. *Quaternary Science Reviews*, **6(3)**, 183–190, doi:10.1016/0277-3791(87)90003-5.
Shackleton, S. et al., 2019: Is the Noble Gas-Based Rate of Ocean Warming During the Younger Dryas Overestimated? *Geophysical Research Letters*, **46(11)**, 5928–5936, doi:10.1029/2019gl082971.
Shakun, J.D., D.W. Lea, L.E. Lisiecki, and M.E. Raymo, 2015: An 800-kyr record of global surface ocean δ18O and implications for ice volume-temperature coupling. *Earth and Planetary Science Letters*, **426**, 58–68, doi:10.1016/j.epsl.2015.05.042.
Shakun, J.D. et al., 2012: Global warming preceded by increasing carbon dioxide concentrations during the last deglaciation. *Nature*, **484**, 49, doi:10.1038/nature10915.
Shakun, J.D. et al., 2018: Minimal East Antarctic Ice Sheet retreat onto land during the past eight million years. *Nature*, **558(7709)**, 284–287, doi:10.1038/s41586-018-0155-6.
Shanahan, T.M. et al., 2015: The time-transgressive termination of the African Humid Period. *Nature Geoscience*, **8(2)**, 140–144, doi:10.1038/ngeo2329.
Shao, J. et al., 2019: Atmosphere-Ocean CO2 Exchange Across the Last Deglaciation From the Boron Isotope Proxy. *Paleoceanography and Paleoclimatology*, **34(10)**, 1650–1670, doi:10.1029/2018pa003498.
Sharmar, V.D., M.Y. Markina, and S.K. Gulev, 2021: Global Ocean Wind-Wave Model Hindcasts Forced by Different Reanalyzes: A Comparative Assessment. *Journal of Geophysical Research: Oceans*, **126(1)**, e2020JC016710, doi:10.1029/2020jc016710.
Shen, S.S.P., N. Tafolla, T.M. Smith, and P.A. Arkin, 2014: Multivariate Regression Reconstruction and Its Sampling Error for the Quasi-Global Annual Precipitation from 1900 to 2011. *Journal of the atmospheric sciences*, **71**, 3250–3268, doi:10.1175/jas-d-13-0301.1.
Shen, X., L. Wang, and S. Osprey, 2020: The Southern Hemisphere sudden stratospheric warming of September 2019. *Science Bulletin*, **65(21)**, 1800–1802, doi:10.1016/j.scib.2020.06.028.
Shepherd, T.G. et al., 2014: Reconciliation of halogen-induced ozone loss with the total-column ozone record. *Nature Geoscience*, **7**, 443–449, doi:10.1038/ngeo2155.
Shi, F. et al., 2015: A multi-proxy reconstruction of spatial and temporal variations in Asian summer temperatures over the last millennium. *Climatic Change*, **131(4)**, 663–676, doi:10.1007/s10584-015-1413-3.
Shi, H. and B. Wang, 2018: How does the Asian summer precipitation-ENSO relationship change over the past 544 years? *Climate Dynamics*, **52**, 4583–4598, doi:10.1007/s00382-018-4392-z.
Shi, L., C.J. Schreck, and M. Schröder, 2018: Assessing the Pattern Differences between Satellite-Observed Upper Tropospheric Humidity and Total Column Water Vapor during Major El Niño Events. *Remote Sensing*, **10(1188)**, 1–15, doi:10.3390/rs10081188.
Shi, X., T. Qin, H. Nie, B. Weng, and S. He, 2019: Changes in major global river discharges directed into the ocean. *International Journal of Environmental Research and Public Health*, **16(8)**, doi:10.3390/ijerph16081469.
Shi, Z., G. Jia, Y. Hu, and Y. Zhou, 2019: The contribution of intensified urbanization effects on surface warming trends in China. *Theoretical and Applied Climatology*, **138(1)**, 1125–1137, doi:10.1007/s00704-019-02892-y.
Shuman, B.N. and J. Marsicek, 2016: The structure of Holocene climate change in mid-latitude North America. *Quaternary Science Reviews*, **141**, 38–51, doi:10.1016/j.quascirev.2016.03.009.
Shuman, B.N., J. Marsicek, W.W. Oswald, and D.R. Foster, 2019: Predictable hydrological and ecological responses to Holocene North Atlantic variability. *Proceedings of the National Academy of Sciences of the United States of America*, **116(13)**, 5985–5990, doi:10.1073/pnas.1814307116.
Shuman, B.N. et al., 2018: Placing the Common Era in a Holocene context: millennial to centennial patterns and trends in the hydroclimate of North America over the past 2000 years. *Climate of the Past*, **14(5)**, 665–686, doi:10.5194/cp-14-665-2018.
Siegenthaler, U. et al., 2005: Supporting evidence from the EPICA Dronning Maud Land ice core for atmospheric CO2 changes during the past millennium. *Tellus B*, **57(1)**, 51–57, doi:10.1111/j.1600-0889.2005.00131.x.
Sigl, M. et al., 2015: Timing and climate forcing of volcanic eruptions for the past 2,500 years. *Nature*, **523**, 543–549, doi:10.1038/nature14565.
Siler, N., G.H. Roe, K.C. Armour, and N. Feldl, 2019: Revisiting the surface-energy-flux perspective on the sensitivity of global precipitation to climate change. *Climate Dynamics*, **52(7)**, 3983–3995, doi:10.1007/s00382-018-4359-0.
Simmonds, P.G. et al., 2020: The increasing atmospheric burden of the greenhouse gas sulfur hexafluoride (SF6). *Atmospheric Chemistry and Physics*, **20(12)**, 7271–7290, doi:10.5194/acp-20-7271-2020.

ACCEPTED VERSION SUBJECT TO FINAL EDITS

Simmons, A.J., K.M. Willett, P.D. Jones, P.W. Thorne, and D.P. Dee, 2010a: Low-frequency variations in surface atmospheric humidity, temperature, and precipitation: Inferences from reanalyses and monthly gridded observational data sets. *Journal of Geophysical Research*, **115**, 1–21, doi:10.1029/2009jd012442.

Simmons, A.J., K.M. Willett, P.D. Jones, P.W. Thorne, and D.P. Dee, 2010b: Low-frequency variations in surface atmospheric humidity, temperature, and precipitation: Inferences from reanalyses and monthly gridded observational data sets. *Journal of Geophysical Research*, **115**, 1–21, doi:10.1029/2009jd012442.

Simmons, A.J. et al., 2017: A reassessment of temperature variations and trends from global reanalyses and monthly surface climatological datasets. *Quarterly Journal of the Royal Meteorological Society*, **143(702)**, 101–119, doi:10.1002/qj.2949.

Simpson, I.J. et al., 2012: Long-term decline of global atmospheric ethane concentrations and implications for methane. *Nature*, **488**, 490–494, doi:10.1038/nature11342.

Simpson, M.J.R., G.A. Milne, P. Huybrechts, and A.J. Long, 2009: Calibrating a glaciological model of the Greenland ice sheet from the Last Glacial Maximum to present-day using field observations of relative sea level and ice extent. *Quaternary Science Reviews*, **28(17)**, 1631–1657, doi:10.1016/j.quascirev.2009.03.004.

Sinclair, G. et al., 2016: Diachronous retreat of the Greenland ice sheet during the last deglaciation. *Quaternary Science Reviews*, **145**, 243–258, doi:10.1016/j.quascirev.2016.05.040.

Sinclair, K.E., N.A.N. Bertler, M.M. Bowen, and K.R. Arrigo, 2014: Twentieth century sea-ice trends in the Ross Sea from a high-resolution, coastal ice-core record. *Geophysical Research Letters*, **41(10)**, 3510–3516, doi:10.1002/2014gl059821.

Singh, H.K.A., G.J. Hakim, R. Tardif, J. Emile-Geay, and D.C. Noone, 2018: Insights into Atlantic multidecadal variability using the Last Millennium Reanalysis framework. *Clim. Past*, **14(2)**, 157–174, doi:10.5194/cp-14-157-2018.

Sjolte, J. et al., 2018: Solar and volcanic forcing of North Atlantic climate inferred from a process-based reconstruction. *Climate of the Past*, **14(8)**, 1179–1194, doi:10.5194/cp-14-1179-2018.

Skeie, R.B. et al., 2020: Historical total ozone radiative forcing derived from CMIP6 simulations. *npj Climate and Atmospheric Science*, **3(1)**, 32, doi:10.1038/s41612-020-00131-0.

Skliris, N., J.D. Zika, G. Nurser, S.A. Josey, and R. Marsh, 2016: Global water cycle amplifying at less than the Clausius-Clapeyron rate. *Nature Publishing Group*, 1–9, doi:10.1038/srep38752.

Skliris, N. et al., 2014a: Salinity changes in the World Ocean since 1950 in relation to changing surface freshwater fluxes. *Climate Dynamics*, **43(3–4)**, 709–736, doi:10.1007/s00382-014-2131-7.

Skliris, N. et al., 2014b: Salinity changes in the World Ocean since 1950 in relation to changing surface freshwater fluxes. *Climate Dynamics*, **43(3–4)**, 709–736, doi:10.1007/s00382-014-2131-7.

Sloyan, B.M. and T.J. O'Kane, 2015: Drivers of decadal variability in the Tasman Sea. *Journal of Geophysical Research: Oceans*, **120(5)**, 3193–3210, doi:10.1002/2014jc010550.

Ślubowska, M.A., N. Koç, T.L. Rasmussen, and D. Klitgaard-Kristensen, 2005: Changes in the flow of Atlantic water into the Arctic Ocean since the last deglaciation: Evidence from the northern Svalbard continental margin, 80°N. *Paleoceanography*, **20(4)**, doi:10.1029/2005pa001141.

Smeed, D.A. et al., 2014: Observed decline of the Atlantic Meridional Overturning Circulation 2004 to 2012. *Ocean Science*, **10**, 38–39.

Smeed, D.A. et al., 2018: The North Atlantic Ocean is in a state of reduced overturning. *Geophysical Research Letters*, **45(3)**, 1527–1533, doi:10.1002/2017gl076350.

Smerdon, J.E. and H.N. Pollack, 2016: Reconstructing Earth's surface temperature over the past 2000 years: the science behind the headlines. *Wiley Interdisciplinary Reviews: Climate Change*, **7(5)**, 746–771, doi:10.1002/wcc.418.

Smith, B. et al., 2020: Pervasive ice sheet mass loss reflects competing ocean and atmosphere processes. *Science*, **368(6496)**, 1239–1242, doi:10.1126/science.aaz5845.

Smith, C.J. et al., 2020: Effective radiative forcing and adjustments in CMIP6 models. *Atmospheric Chemistry and Physics*, **20(16)**, doi:10.5194/acp-20-9591-2020.

Smith, T.M. and P.A. Arkin, 2015: Improved historical analysis of oceanic total precipitable water. *Journal of Climate*, **28(8)**, 3099–3121, doi:10.1175/jcli-d-14-00601.1.

Sniderman, J.M.K. et al., 2019: Vegetation and Climate Change in Southwestern Australia During the Last Glacial Maximum. *Geophyiscal Research Letters*, **46(3)**, 1709–1720, doi:10.1029/2018gl080832.

Snyder, C.W., 2016: Evolution of global temperature over the past two million years. *Nature*, **538**, 226, doi:10.1038/nature19798.

Sogacheva, L. et al., 2018: Spatial and seasonal variations of aerosols over China from two decades of multi-satellite observations – Part 1: ATSR (1995–2011) and MODIS C6.1 (2000–2017). *Atmospheric Chemistry and Physics*, **18(15)**, 11389–11407, doi:10.5194/acp-18-11389-2018.

Sohn, B.J., S. Lee, E.S. Chung, and H.J. Song, 2016: The role of the dry static stability for the recent change in the Pacific Walker circulation. *Journal of Climate*, **29(8)**, 2765–2779, doi:10.1175/jcli-d-15-0374.1.

Solomina, O.N. et al., 2015: Holocene glacier fluctuations. *Quaternary Science Reviews*, **111**, 9–34, doi:10.1016/j.quascirev.2014.11.018.

Solomina, O.N. et al., 2016: Glacier fluctuations during the past 2000 years. *Quaternary Science Reviews*, **149**, 61–90,

ACCEPTED VERSION SUBJECT TO FINAL EDITS

doi:10.1016/j.quascirev.2016.04.008.
Solomon, S. et al., 2011: The Persistently Variable "Background" Stratospheric Aerosol Layer and Global Climate Change.. *Science (New York, N.Y.)*, **333(6044)**, 866–70, doi:10.1126/science.1206027.
Son, K.H. and D.H. Bae, 2015: Drought analysis according to shifting of climate zones to arid climate zone over Asia monsoon region. *Journal of Hydrology*, **529**, doi:10.1016/j.jhydrol.2015.09.010.
Song, X.-P. et al., 2018: Global land change from 1982 to 2016. *Nature*, **560**, 639–643, doi:10.1038/s41586-018-0411-9.
Sosdian, S.M. et al., 2018: Constraining the evolution of Neogene ocean carbonate chemistry using the boron isotope pH proxy (2018a). *Earth and Planetary Science Letters*, **248**, 362–376, doi:10.1016/j.epsl.2018.06.017.
Sowers, T., 2001: N2O record spanning the penultimate deglaciation from the Vostok ice core. *Journal of Geophysical Research: Atmospheres*, **106(D23)**, 31903–31914, doi:10.1029/2000jd900707.
Ko, M.K.W., P.A. Newman, S. Reimann, and S.E. Strahan (eds.), 2013: *SPARC Report on the Lifetimes of Stratospheric Ozone-Depleting Substances, Their Replacements, and Related Species*. SPARC Report No. 6, WCRP-15/2013, 255 pp.
Petropavlovskikh, I., S. Godin-Beekmann, D. Hubert, R. Damadeo, B. Hassler, and V. Sofieva (eds.), 2019: *SPARC/IO3C/GAW Report on Long-term Ozone Trends and Uncertainties in the Stratosphere*. SPARC Report No. 9, GAW Report No. 241, WCRP-17/2018, 78 pp., doi:10.17874/f899e57a20b.
Spector, P. et al., 2017: Rapid early-Holocene deglaciation in the Ross Sea, Antarctica. *Geophysical Research Letters*, doi:10.1002/2017gl074216.
Spencer, R.W., J.R. Christy, and W.D. Braswell, 2017: UAH Version 6 Global Satellite Temperature Products: Methodology and Results. *Asia-Pacific Jouurnal of Atmospheric Science*, **53(1)**, 121–130, doi:10.1007/s13143-017-0010-y.
Spielhagen, R.F. et al., 2011: Enhanced Modern Heat Transfer to the Arctic by Warm Atlantic Water. *Science*, **331(6016)**, 450–453, doi:10.1126/science.1197397.
Spinoni, J., J. Vogt, G. Naumann, H. Carrao, and P. Barbosa, 2015: Towards identifying areas at climatological risk of desertification using the Köppen-Geiger classification and FAO aridity index. *International Journal of Climatology*, **35(9)**, doi:10.1002/joc.4124.
Spolaor, A. et al., 2016: Canadian Arctic sea ice reconstructed from bromine in the Greenland NEEM ice core. *Scientific Reports*, **6(1)**, 33925, doi:10.1038/srep33925.
Spratt, R.M. and L.E. Lisiecki, 2016: A Late Pleistocene sea level stack. *Climate of the Past*, **12(4)**, 1079–1092, doi:10.5194/cp-12-1079-2016.
Spreen, G., R. Kwok, and D. Menemenlis, 2011: Trends in Arctic sea ice drift and role of wind forcing: 1992–2009. *Geophysical Research Letters*, **38(19)**, doi:10.1029/2011gl048970.
Spreen, G. et al., 2020: Arctic Sea Ice Volume Export Through Fram Strait From 1992 to 2014. *Journal of Geophysical Research: Oceans*, **125(6)**, doi:10.1029/2019jc016039.
Sprintall, J. et al., 2014: The Indonesian seas and their role in the coupled ocean–climate system. *Nature Geoscience*, **7(7)**, 487–492, doi:10.1038/ngeo2188.
Sprintall, J. et al., 2019: Detecting Change in the Indonesian Seas. *Frontiers in Marine Science*, **6**, 257, doi:10.3389/fmars.2019.00257.
Staehelin, J., P. Viatte, R. Stübi, F. Tummon, and T. Peter, 2018: Stratospheric ozone measurements at Arosa (Switzerland): History and scientific relevance. *Atmospheric Chemistry and Physics*, **18(9)**, 6567–6584, doi:10.5194/acp-18-6567-2018.
Stahle, D.W. et al., 2016: The Mexican Drought Atlas: Tree-ring reconstructions of the soil moisture balance during the late pre-Hispanic, colonial, and modern eras. *Quaternary Science Reviews*, **149**, 34–60, doi:10.1016/j.quascirev.2016.06.018.
Staten, P.W., J. Lu, K.M. Grise, S.M. Davis, and T. Birner, 2018: Re-examining tropical expansion. *Nature Climate Change*, **8(9)**, 768–775, doi:10.1038/s41558-018-0246-2.
Staten, P.W. et al., 2020: Tropical Widening: From Global Variations to Regional Impacts. *Bulletin of the American Meteorological Society*, **101(6)**, E897–E904, doi:10.1175/bams-d-19-0047.1.
Steiger, N.J., J.E. Smerdon, E.R. Cook, and B.I. Cook, 2018: A reconstruction of global hydroclimate and dynamical variables over the Common Era. *Scientific Data*, **5**, 1–15, doi:10.1038/sdata.2018.86.
Stein, R., K. Fahl, P. Gierz, F. Niessen, and G. Lohmann, 2017: Arctic Ocean sea ice cover during the penultimate glacial and the last interglacial. *Nature Communications*, **8(1)**, 373, doi:10.1038/s41467-017-00552-1.
Steiner, A.K. and Co-Authors, 2020: Observed temperature changes in the troposphere and stratosphere from 1979 to 2018. *Journal of Climate*, **33**, 8165–8194, doi:10.1175/jcli-d-19-0998.1.
Steiner, A.K. et al., 2013: Quantification of structural uncertainty in climate data records from GPS radio occultation. *Atmospheric Chemistry and Physics*, **13(3)**, 1469–1484, doi:10.5194/acp-13-1469-2013.
Steiner, A.K. et al., 2020: Consistency and structural uncertainty of multi-mission GPS radio occultation records. *Atmospheric Measurement Techniques*, **13(5)**, 2547–2575, doi:10.5194/amt-13-2547-2020.
Steinman, B.A. et al., 2014: Ocean-atmosphere forcing of centennial hydroclimate variability in the Pacific Northwest. *Geophysical Research Letters*, **41(7)**, 2553–2560, doi:10.1002/2014gl059499.

ACCEPTED VERSION SUBJECT TO FINAL EDITS

Steinthorsdottir, M. et al., 2020: The Miocene: the Future of the Past. *Paleoceanography and Paleoclimatology*, **35(n/a)**, e2020PA004037, doi:10.1029/2020pa004037.
Stenni, B. et al., 2017: Antarctic climate variability on regional and continental scales over the last 2000 years. *Climate of the Past*, **13(11)**, 1609–1634, doi:10.5194/cp-13-1609-2017.
Stephens, L. et al., 2019: Archaeological assessment reveals Earth's early transformation through land use. *Science*, **365(6456)**, doi:10.1126/science.aax1192.
Stephenson, S.N., N.J. White, T. Li, and L.F. Robinson, 2019: Disentangling interglacial sea level and global dynamic topography: Analysis of Madagascar. *Earth and Planetary Science Letters*, **519**, 61–69, doi:10.1016/j.epsl.2019.04.029.
Stevens, T. et al., 2018: Ice-volume-forced erosion of the Chinese Loess Plateau global Quaternary stratotype site. *Nature Communications*, doi:10.1038/s41467-018-03329-2.
Stevens T, Buylaert J-P, Lu H, Thiel C, Murray A, Frechen M, 2016: Mass accumulation rate and monsoon records from Xifeng, Chinese Loess Plateau, based on a luminescence age model. *J Quat Sci*, **31(4)**, 391–405, doi:10.1002/jqs.2848.
Stjern, C.W., A. Stohl, and J.E. Kristjánsson, 2011: Have aerosols affected trends in visibility and precipitation in Europe? *Journal of Geophysical Research*, **116(D2)**, D02212, doi:10.1029/2010jd014603.
Stocker, M., F. Ladstädter, H. Wilhelmsen, and A.K. Steiner, 2019: Quantifying Stratospheric Temperature Signals and Climate Imprints From Post-2000 Volcanic Eruptions. *Geophysical Research Letters*, **46(21)**, 12486–12494, doi:10.1029/2019gl084396.
Stokes, C.R. et al., 2015: On the reconstruction of palaeo-ice sheets: Recent advances and future challenges. *Quaternary Science Reviews*, **125**, 15–49, doi:10.1016/j.quascirev.2015.07.016.
Stoll, H.M. et al., 2019: Upregulation of phytoplankton carbon concentrating mechanisms during low CO2 glacial periods and implications for the phytoplankton pCO2 proxy. *Quaternary Science Reviews*, **208**, 1–20, doi:10.1016/j.quascirev.2019.01.012.
Stone, E.J., D.J. Lunt, J.D. Annan, and J.C. Hargreaves, 2013: Quantification of the Greenland ice sheet contribution to Last Interglacial sea level rise. *Clim. Past*, **9(2)**, 621–639, doi:10.5194/cp-9-621-2013.
Storto, A. et al., 2017: Steric sea level variability (1993–2010) in an ensemble of ocean reanalyses and objective analyses. *Climate Dynamics*, **49(3)**, 709–729, doi:10.1007/s00382-015-2554-9.
Stothers, R.B., 1997: Stratospheric aerosol clouds due to very large volcanic eruptions of the early twentieth century: Effective particle sizes and conversion from pyrheliometric to visual optical depth. *Journal of Geophysical Research*, **102(D5)**, 6143, doi:10.1029/96jd03985.
Stramma, L. et al., 2020: Trends and decadal oscillations of oxygen and nutrients at 50 to 300m depth in the equatorial and North Pacific. *Biogeosciences*, **17(3)**, 813–831, doi:10.5194/bg-17-813-2020.
Streletskiy, D.A., A.B. Sherstiukov, O.W. Frauenfeld, and F.E. Nelson, 2015: Changes in the 1963-2013 shallow ground thermal regime in Russian permafrost regions. *Environmental Research Letters*, **10(12)**, 125005, doi:10.1088/1748-9326/10/12/125005.
Streletskiy, D.A. et al., 2017: Thaw Subsidence in Undisturbed Tundra Landscapes, Barrow, Alaska, 1962-2015. *Permafrost and Periglacial Processes*, **28(3)**, 566–572, doi:10.1002/ppp.1918.
Stríkis, N.M. et al., 2018: South American monsoon response to iceberg discharge in the North Atlantic. *Proceedings of the National Academy of Sciences of the United States of America*, **115(15)**, 3788–3793, doi:10.1073/pnas.1717784115.
Studholme, J. and S. Gulev, 2018: Concurrent changes to hadley circulation and the meridional distribution of tropical cyclones. *Journal of Climate*, **31(11)**, 4367–4389, doi:10.1175/jcli-d-17-0852.1.
Su, H. et al., 2020: OPEN: A New Estimation of Global Ocean Heat Content for Upper 2000 Meters from Remote Sensing Data. *Remote Sensing*, **12(14)**, 2294, doi:10.3390/rs12142294.
Su, L. et al., 2018: Long-term trends in global river flow and the causal relationships between river flow and ocean signals. *Journal of Hydrology*, **563**, 818–833, doi:10.1016/j.jhydrol.2018.06.058.
Sun, Q. et al., 2018: A Review of Global Precipitation Data Sets: Data Sources, Estimation, and Intercomparisons. *Reviews of Geophysics*, **56(1)**, 79–107, doi:10.1002/2017rg000574.
Sun, S., J. Lan, Y. Fang, Tana, and X. Gao, 2015: A Triggering Mechanism for the Indian Ocean Dipoles Independent of ENSO. *Journal of Climate*, **28(13)**, 5063–5076, doi:10.1175/jcli-d-14-00580.1.
Sun, W. et al., 2021: The Assessment of Global Surface Temperature Change from 1850s: The C-LSAT2.0 Ensemble and the CMST-Interim Datasets. *Advances in Atmospheric Sciences*, doi:10.1007/s00376-021-1012-3.
Sun, X. et al., 2018: Global diurnal temperature range (DTR) changes since 1901. *Climate Dynamics*, **52**, 3343–3356, doi:10.1007/s00382-018-4329-6.
Susanto, R.D. and Y.T. Song, 2015: Indonesian throughflow proxy from satellite altimeters and gravimeters. *Journal of Geophysical Research: Oceans*, **120(4)**, 2844–2855, doi:10.1002/2014jc010382.
Susskind, J., G.A. Schmidt, J.N. Lee, and L. Iredell, 2019: Recent global warming as confirmed by AIRS. *Environmental Research Letters*, **14(4)**, 044030, doi:10.1088/1748-9326/aafd4e.
Suzuki, T. et al., 2018: A dataset of continental river discharge based on JRA-55 for use in a global ocean circulation model. *Journal of Oceanography*, **74(4)**, 421–429, doi:10.1007/s10872-017-0458-5.

ACCEPTED VERSION SUBJECT TO FINAL EDITS

Svendsen, L., N.G. Kvamstø, and N. Keenlyside, 2014a: Weakening AMOC connects Equatorial Atlantic and Pacific interannual variability. *Climate Dynamics*, **43(11)**, 2931–2941, doi:10.1007/s00382-013-1904-8.
Svendsen, L., S. Hetzinger, N. Keenlyside, and Y. Gao, 2014b: Marine-based multiproxy reconstruction of Atlantic multidecadal variability. *Geophysical Research Letters*, **41(4)**, 1295–1300, doi:10.1002/2013gl059076.
Swart, N.C. and J.C. Fyfe, 2012: Observed and simulated changes in the Southern Hemisphere surface westerly wind-stress. *Geophysical Research Letters*, **39(16)**, 6–11, doi:10.1029/2012gl052810.
Swart, S. et al., 2019: Constraining Southern Ocean Air-Sea-Ice Fluxes Through Enhanced Observations. *Frontiers in Marine Science*, **6**, 421, doi:10.3389/fmars.2019.00421.
Sydeman, W.J., E. Poloczanska, T.E. Reed, and S.A. Thompson, 2015: Climate change and marine vertebrates. *Science*, **350(6262)**, 772–777, doi:10.1126/science.aac9874.
Tan, X., Y. Wu, B. Liu, and S. Chen, 2020: Inconsistent changes in global precipitation seasonality in seven precipitation datasets. *Climate Dynamics*, **54(5–6)**, 3091–3108, doi:10.1007/s00382-020-05158-w.
Tang, C. et al., 2017: Distribution and trends of the cold-point tropopause over China from 1979 to 2014 based on radiosonde dataset. *Atmospheric Research*, **193**, 1–9, doi:10.1016/j.atmosres.2017.04.008.
Tao, M. et al., 2015: Impact of the 2009 major sudden stratospheric warming on the composition of the stratosphere. *Atmospheric Chemistry and Physics*, **15(15)**, 8695–8715, doi:10.5194/acp-15-8695-2015.
Tarasick, D. et al., 2019: Tropospheric Ozone Assessment Report: Tropospheric ozone from 1877 to 2016, observed levels, trends and uncertainties.. *Elem Sci Anth*, **7(1)**, 39, doi:10.1525/elementa.376.
Tardif, R. et al., 2019: Last Millennium Reanalysis with an expanded proxy database and seasonal proxy modeling. *Climate of the Past*, **15(4)**, 1251–1273, doi:10.5194/cp-15-1251-2019.
Taylor-Silva, B.I. and C.R. Riesselman, 2018: Polar Frontal Migration in the Warm Late Pliocene: Diatom Evidence From the Wilkes Land Margin, East Antarctica. *Paleoceanography and Paleoclimatology*, **33(1)**, 76–92, doi:10.1002/2017pa003225.
Tesi, T. et al., 2020: Resolving sea ice dynamics in the north-western Ross Sea during the last 2.6 ka: From seasonal to millennial timescales. *Quaternary Science Reviews*, **237**, 106299, doi:10.1016/j.quascirev.2020.106299.
Thackeray, C.W., C.G. Fletcher, L.R. Mudryk, and C. Derksen, 2016: Quantifying the Uncertainty in Historical and Future Simulations of Northern Hemisphere Spring Snow Cover. *Journal of Climate*, **29(23)**, 8647–8663, doi:10.1175/jcli-d-16-0341.1.
Thatcher, D.L. et al., 2020: Hydroclimate variability from western Iberia (Portugal) during the Holocene: Insights from a composite stalagmite isotope record. *Holocene*, **30(7)**, 966–981, doi:10.1177/0959683620908648.
Thibodeau, B. et al., 2018: Last Century Warming Over the Canadian Atlantic Shelves Linked to Weak Atlantic Meridional Overturning Circulation. *Geophysical Research Letters*, **45(22)**, 12, 312–376, 385, doi:10.1029/2018gl080083.
Thirumalai, K., P.N. DiNezio, J.E. Tierney, M. Puy, and M. Mohtadi, 2019: An El Niño Mode in the Glacial Indian Ocean? *Paleoceanography and Paleoclimatology*, **34(8)**, 1316–1327, doi:10.1029/2019pa003669.
Thomas, E.R. and N.J. Abram, 2016: Ice core reconstruction of sea ice change in the Amundsen-Ross Seas since 1702 A.D.. *Geophysical Research Letters*, **43(10)**, 5309–5317, doi:10.1002/2016gl068130.
Thomas, E.R. et al., 2017: Regional Antarctic snow accumulation over the past 1000 years. *Climate of the Past*, **13(11)**, 1491–1513, doi:10.5194/cp-13-1491-2017.
Thomas, E.R. et al., 2019: Antarctic Sea Ice Proxies from Marine and Ice Core Archives Suitable for Reconstructing Sea Ice over the Past 2000 Years. *Geosciences*, **9(12)**, doi:10.3390/geosciences9120506.
Thomason, L.W. et al., 2018: A global space-based stratospheric aerosol climatology: 1979–2016. *Earth System Science Data*, **10(1)**, 469–492, doi:10.5194/essd-10-469-2018.
Thompson, D.M. et al., 2017: Tropical Pacific climate variability over the last 6000 years as recorded in Bainbridge Crater Lake, Galápagos. *Paleoceanography*, **32(8)**, 903–922, doi:10.1002/2017pa003089.
Thompson, D.W.J., J.J. Kennedy, J.M. Wallace, and P.D. Jones, 2008: A large discontinuity in the mid-twentieth century in observed global-mean surface temperature. *Nature*, **453**, 646, doi:10.1038/nature06982.
Thompson, J.R., D.N. Carpenter, C. Cogbill, and D.R. Foster, 2013: Four Centuries of Change in Northeastern United States Forests. *PLoS ONE*, doi:10.1371/journal.pone.0072540.
Thornalley, D.J.R., H. Elderfield, and I.N. McCave, 2011: Reconstructing North Atlantic deglacial surface hydrography and its link to the Atlantic overturning circulation. *Global and Planetary Change*, **79(3–4)**, 163–175, doi:10.1016/j.gloplacha.2010.06.003.
Thornalley, D.J.R., S. Barker, J. Becker, I.R. Hall, and G. Knorr, 2013: Abrupt changes in deep Atlantic circulation during the transition to full glacial conditions. *Paleoceanography*, **28(2)**, 253–262, doi:10.1002/palo.20025.
Thornalley, D.J.R. et al., 2018: Anomalously weak Labrador Sea convection and Atlantic overturning during the past 150 years. *Nature*, **556**, 227–230, doi:10.1038/s41586-018-0007-4.
Thorne, P.W. et al., 2016a: Reassessing changes in diurnal temperature range: Intercomparison and evaluation of existing global data set estimates (2016b). *Journal of Geophysical Research: Atmospheres*, **121(10)**, 5138–5158, doi:10.1002/2015jd024584.
Thorne, P.W. et al., 2016b: Reassessing changes in diurnal temperature range: A new data set and characterization of data biases (2016a). *Journal of Geophysical Research: Atmospheres*, **121(10)**, 5115–5137,

ACCEPTED VERSION SUBJECT TO FINAL EDITS

doi:10.1002/2015jd024583.
Tian, Z., T. Li, D. Jiang, and L. Chen, 2017: Causes of ENSO weakening during the mid-Holocene. *Journal of Climate*, **30(17)**, 7049–7070, doi:10.1175/jcli-d-16-0899.1.
Tierney, J.E., C.C. Ummenhofer, and P.B. DeMenocal, 2015: Past and future rainfall in the Horn of Africa. *Science Advances*, **1(9)**, e1500682, doi:10.1126/sciadv.1500682.
Tierney, J.E. et al., 2020: Glacial cooling and climate sensitivity revisited. *Nature*, **584**, 569–573, doi:10.1038/s41586-020-2617-x.
Tilinina, N., S.K. Gulev, I. Rudeva, and P. Koltermann, 2013: Comparing Cyclone Life Cycle Characteristics and Their Interannual Variability in Different Reanalyses. *Journal of Climate*, **26**, 6419–6438, doi:10.1175/jcli-d-12-00777.1.
Timmermann, A. et al., 2018: El Niño–Southern Oscillation complexity. *Nature*, **559(7715)**, 535–545, doi:10.1038/s41586-018-0252-6.
Tokarska, K.B. et al., 2019: Recommended temperature metrics for carbon budget estimates, model evaluation and climate policy. *Nature Geoscience*, **12(12)**, 964–971, doi:10.1038/s41561-019-0493-5.
Tokinaga, H. and S.-P. Xie, 2011: Weakening of the equatorial Atlantic cold tongue over the past six decades. *Nature Geoscience*, **4(4)**, 222–226, doi:10.1038/ngeo1078.
Tomita, H., T. Hihara, S. Kako, M. Kubota, and K. Kutsuwada, 2019: An introduction to J-OFURO3, a third-generation Japanese ocean flux data set using remote-sensing observations. *Journal of Oceanography*, **75(2)**, 171–194, doi:10.1007/s10872-018-0493-x.
Toohey, M. and M. Sigl, 2017: Volcanic stratospheric sulfur injections and aerosol optical depth from 500 BCE to 1900 CE. *Earth System Science Data*, **9(2)**, 809–831, doi:10.5194/essd-9-809-2017.
Toucanne, S. et al., 2015: Tracking rainfall in the northern Mediterranean borderlands during sapropel deposition. *Quaternary Science Reviews*, **129**, 178–195, doi:10.1016/j.quascirev.2015.10.016.
Toyos, M.H. et al., 2020: Antarctic Circumpolar Current Dynamics at the Pacific Entrance to the Drake Passage Over the Past 1.3 Million Years. *Paleoceanography and Paleoclimatology*, **35(7)**, e2019PA003773, doi:10.1029/2019pa003773.
Tradowsky, J.S., C.P. Burrows, S.B. Healy, and J.R. Eyre, 2017: A New Method to Correct Radiosonde Temperature Biases Using Radio Occultation Data. *Journal of Applied Meteorology and Climatology*, **56(6)**, 1643–1661, doi:10.1175/jamc-d-16-0136.1.
Trammell, J.H. et al., 2015: Investigation of Precipitation Variations over Wet and Dry Areas from Observation and Model. *Advances in Meteorology*, **2015(981092)**, 1–9, doi:10.1155/2015/981092.
Treat, C.C. and M.C. Jones, 2018a: Near-surface permafrost aggradation in Northern Hemisphere peatlands shows regional and global trends during the past 6000 years. *Holocene*, **28(6)**, doi:10.1177/0959683617752858.
Treat, C.C. and M.C. Jones, 2018b: Near-surface permafrost aggradation in Northern Hemisphere peatlands shows regional and global trends during the past 6000 years. *Holocene*, **28(6)**, doi:10.1177/0959683617752858.
Trenberth, K.E. and J.T. Fasullo, 2017: Atlantic meridional heat transports computed from balancing Earth's energy locally. *Geophysical Research Letters*, **44(4)**, 1919–1927, doi:10.1002/2016gl072475.
Trouet, V., F. Babst, and M. Meko, 2018: Recent enhanced high-summer North Atlantic jet variability emerges from three-century context. *Nature Communications*, **9:180**, doi:10.1038/s41467–017–02699–3.
Tschudi, M.A., J.C. Stroeve, and J.S. Stewart, 2016: Relating the age of Arctic sea ice to its thickness, as measured during nasa's ICESat and IceBridge campaigns. *Remote Sensing*, **8(6)**, 457, doi:10.3390/rs8060457.
Tseng, W.L., S.Y. Simon Wang, H.H. Hsu, and J.D.D. Meyer, 2019: Intensification of the decadal activity in Equatorial Rossby Waves and linkage to changing tropical circulation. *Terrestrial, Atmospheric and Oceanic Sciences*, **30(4)**, 563–574, doi:10.3319/tao.2019.01.18.02.
Tsubouchi, T. et al., 2021: Increased ocean heat transport into the Nordic Seas and Arctic Ocean over the period 1993–2016. *Nature Climate Change*, **11(1)**, 21–26, doi:10.1038/s41558-020-00941-3.
Turner, J., J.S. Hosking, T.J. Bracegirdle, G.J. Marshall, and T. Phillips, 2015: Recent changes in Antarctic Sea Ice. *Philosophical Transactions of the Royal Society A: Mathematical, Physical and Engineering Sciences*, **373(2045)**, doi:10.1098/rsta.2014.0163.
Turner, S.K., 2018: Constraints on the onset duration of the Paleocene-Eocene Thermal Maximum. *Philosophical Transactions of the Royal Society A: Mathematical, Physical and Engineering Sciences*, **376(2130)**, doi:10.1098/rsta.2017.0082.
Turney, C.S.M. et al., 2016a: A 250-year periodicity in Southern Hemisphere westerly winds over the last 2600 years (2016a). *Climate of the Past*, **12**, 189–200, doi:10.5194/cp-12-189-2016.
Turney, C.S.M. et al., 2016b: Intensification of Southern Hemisphere westerly winds 2000-1000 years ago: evidence from the subantarctic Campbell and Auckland Islands (52-50°S). *Journal of Quaternary Science*, **31(1)**, 12–19, doi:10.1002/jqs.2828.
Turney, C.S.M. et al., 2017: Reconstructing atmospheric circulation over southern New Zealand: Establishment of modern westerly airflow 5500 years ago and implications for Southern Hemisphere Holocene climate change. *Quaternary Science Reviews*, **159**, 77–87, doi:10.1016/j.quascirev.2016.12.017.
Turney, C.S.M. et al., 2020: A global mean sea-surface temperature dataset for the Last Interglacial (129-116 kyr) and

SUBJECT TO FINAL EDITS ACCEPTED VERSION

contributin of thermal expansin to sea-level change. *Earth System Science Data*, **12(4)**, 3341–3356, doi:10.5194/essd-12-3341-2020.
Tweedy, O. et al., 2017: Response of trace gases to the disrupted 2015--2016 quasi-biennial oscillation. *Atmospheric Chemistry and Physics*, **17(11)**, 6813–6823, doi:10.5194/acp-17-6813-2017.
Tyrlis, E. et al., 2020: On the role of Ural Blocking in driving the Warm Arctic–Cold Siberia pattern. *Quarterly Journal of the Royal Meteorological Society*, **145**, 2138–2153, doi:10.1002/qj.3784.
Újvári, G. et al., 2017: Coupled European and Greenland last glacial dust activity driven by North Atlantic climate. *Proceedings of the National Academy of Sciences of the United States of America*, **114(50)**, E10632–E10638, doi:10.1073/pnas.1712651114.
Ummenhofer, C.C., A. Biastoch, and C.W. Böning, 2016: Multidecadal Indian Ocean Variability Linked to the Pacific and Implications for Preconditioning Indian Ocean Dipole Events. *Journal of Climate*, **30(5)**, 1739–1751, doi:10.1175/jcli-d-16-0200.1.
UNESCO/ICES/SCOR/IAPSO, 1981: *Background papers and supporting data on the Practical Salinity Scale 1978*. UNESCO Technical Papers in Marine Science No. 37. United Nations Educational, Scientific and Cultural Organization (UNESCO), Paris, France, 144 pp.
Usoskin, I.G., Y. Gallet, F. Lopes, G.A. Kovaltsov, and G. Hulot, 2016: Solar activity during the Holocene: the Hallstatt cycle and its consequence for grand minima and maxima. *A&A*, **587**, A150, doi:10.1051/0004-6361/201527295.
Vaccaro, A. et al., 2021: Climate field completion via Markov random fields – Application to the HadCRUT4.6 temperature dataset. *Journal of Climate*, 1–66, doi:10.1175/jcli-d-19-0814.1.
Vacchi, M. et al., 2016: Multiproxy assessment of Holocene relative sea-level changes in the western Mediterranean: Sea-level variability and improvements in the definition of the isostatic signal. *Earth-Science Reviews*, **155**, 172–197, doi:10.1016/j.earscirev.2016.02.002.
Vaks, A. et al., 2013: Speleothems Reveal 500,000-Year History of Siberian Permafrost. *Science*, **340(6129)**, doi:10.1126/science.1228729.
Vaks, A. et al., 2020: Palaeoclimate evidence of vulnerable permafrost during times of low sea ice. *Nature*, **577(7789)**, doi:10.1038/s41586-019-1880-1.
van den Bos, V. et al., 2018: Holocene temperature , humidity and seasonality in northern New Zealand linked to Southern Hemisphere summer insolation. *Quaternary Science Reviews*, **201**, 77–88, doi:10.1016/j.quascirev.2018.10.008.
van den Broeke, M. et al., 2017: Greenland Ice Sheet Surface Mass Loss: Recent Developments in Observation and Modeling. *Current Climate Change Reports*, **3**, 345–356, doi:10.1007/s40641-017-0084-8.
van Dijk, J. et al., 2020: Spatial pattern of super-greenhouse warmth controlled by elevated specific humidity. *Nature Geoscience*, **13(11)**, 739–744, doi:10.1038/s41561-020-00648-2.
Vandenberghe, J. et al., 2014: The Last Permafrost Maximum (LPM) map of the Northern Hemisphere: permafrost extent and mean annual air temperatures, 25-17 ka BP. *Boreas*, **43(3)**, doi:10.1111/bor.12070.
Vanderwal, J. et al., 2013: Focus on poleward shifts in species' distribution underestimates the fingerprint of climate change. *Nature Climate Change*, **3**, 239–243, doi:10.1038/nclimate1688.
Vasskog, K., P.M. Langebroek, J.T. Andrews, J.E. Nilsen, and A. Nesje, 2015: The Greenland Ice Sheet during the last glacial cycle: Current ice loss and contribution to sea-level rise from a palaeoclimatic perspective. *Earth-Science Reviews*, **150**, 45–67, doi:10.1016/j.earscirev.2015.07.006.
Vautard, R., T.R. McVicar, J.N. Thepaut, and M.L. Roderic, 2012: Land surface winds and atmospheric evaporative demand [in "State of the Climate in 2011"]. *Bulletin of the American Meteorological Society*, **93(7)**, S36–S38, doi:10.1175/2012bamsstateoftheclimate.1.
Velicogna, I. et al., 2020: Continuity of Ice Sheet Mass Loss in Greenland and Antarctica From the GRACE and GRACE Follow-On Missions. *Geophysical Research Letters*, **47(8)**, doi:10.1029/2020gl087291.
Venegas, S.A., L.A. Mysak, and D.N. Straub, 1996: Evidence for interannual and interdecadal climate variability in the South Atlantic. *Geophysical Research Letters*, **23(19)**, 2673–2676, doi:10.1029/96gl02373.
Venter, O. et al., 2016: Sixteen years of change in the global terrestrial human footprint and implications for biodiversity conservation. *Nature Communications*, **7**, doi:10.1038/ncomms12558.
Venturelli, R.A. et al., 2020: Mid-Holocene Grounding Line Retreat and Readvance at Whillans Ice Stream, West Antarctica. *Geophysical Research Letters*, **47(15)**, e2020GL088476, doi:10.1029/2020gl088476.
Vernier, J.-P. et al., 2011: Major influence of tropical volcanic eruptions on the stratospheric aerosol layer during the last decade. *Geophysical Research Letters*, **38(12)**, doi:10.1029/2011gl047563.
Vicente-Serrano, S.M. et al., 2018: Recent changes of relative humidity: regional connections with land and ocean processes. *Earth System Dynamics*, **9(2)**, 915–937, doi:10.5194/esd-9-915-2018.
Vihma, T., P. Tisler, and P. Uotila, 2012: Atmospheric forcing on the drift of Arctic sea ice in 1989–2009. *Geophysical Research Letters*, **39(2)**, doi:10.1029/2011gl050118.
Villalba, R. et al., 2012: Unusual Southern Hemisphere tree growth patterns induced by changes in the Southern Annular Mode. *Nature Geoscience*, **5**, 793–798, doi:10.1038/ngeo1613.
Vinogradova, N.T. and R.M. Ponte, 2017: In Search of Fingerprints of the Recent Intensification of the Ocean Water

ACCEPTED VERSION SUBJECT TO FINAL EDITS

Cycle. *Journal of Climate*, **30(14)**, 5513–5528, doi:10.1175/jcli-d-16-0626.1.
Voigt, I. et al., 2015: Holocene shifts of the southern westerlies across the South Atlantic. *Paleoceanography*, **30(2)**, 39–51, doi:10.1002/2014pa002677.
von Schuckmann, K. et al., 2018: Copernicus Marine Service Ocean State Report. *Journal of Operational Oceanography*, **11(sup1)**, S1–S142, doi:10.1080/1755876x.2018.1489208.
von Schuckmann, K. et al., 2019: Copernicus Marine Service Ocean State Report, Issue 3. *Journal of Operational Oceanography*, **12(sup1)**, S1–S123, doi:10.1080/1755876x.2019.1633075.
von Schuckmann, K. et al., 2020: Heat stored in the Earth system: where does the energy go? *Earth System Science Data*, **12(3)**, 2013–2041, doi:10.5194/essd-12-2013-2020.
Vose, R.S., D.R. Easterling, and B. Gleason, 2005: Maximum and minimum temperature trends for the globe: An update through 2004. *Geophysical Research Letters*, **32(23)**, doi:10.1029/2005gl024379.
Vose, R.S. et al., 2021: Implementing Full Spatial Coverage in NOAA's Global Temperature Analysis. *Geophysical Research Letters*, **48(4)**, e2020GL090873, doi:10.1029/2020gl090873.
Vrieling, A., J. De Leeuw, and M.Y. Said, 2013: Length of growing period over africa: Variability and trends from 30 years of NDVI time series. *Remote Sensing*, **5(2)**, 982–1000, doi:10.3390/rs5020982.
Vyverberg, K. et al., 2018: Episodic reef growth in the granitic Seychelles during the Last Interglacial: Implications for polar ice sheet dynamics. *Marine Geology*, **399**, 170–187, doi:10.1016/j.margeo.2018.02.010.
Wachowicz, L.J., J.R. Preece, T.L. Mote, B.S. Barrett, and G.R. Henderson, 2021: Historical trends of seasonal Greenland blocking under different blocking metrics. *International Journal of Climatology*, **41(S1)**, joc.6923, doi:10.1002/joc.6923.
Waelbroeck, C. et al., 2002: Sea-level and deep water temperature changes derived from benthic foraminifera isotopic records. *Quaternary Science Reviews*, **21(1)**, 295–305, doi:10.1016/s0277-3791(01)00101-9.
Wagner, B. et al., 2019: Mediterranean winter rainfall in phase with African monsoons during the past 1.36 million years. *Nature*, **573**, 256–260, doi:10.1038/s41586-019-1529-0.
Wainer, I., L.F. Prado, M. Khodri, and B. Otto-Bliesner, 2014: Reconstruction of the South Atlantic Subtropical Dipole index for the past 12,000 years from surface temperature proxy. *Scientific Reports*, **4(1)**, 5291, doi:10.1038/srep05291.
WAIS Divide Project Members. et al., 2015: Precise interpolar phasing of abrupt climate change during the last ice age. *Nature*, **520(7549)**, 661, doi:10.1038/nature14401.
Walsh, J.E., F. Fetterer, J. Scott Stewart, and W.L. Chapman, 2017: A database for depicting Arctic sea ice variations back to 1850. *Geographical Review*, **107(1)**, 89–107, doi:10.1111/j.1931-0846.2016.12195.x.
Walsh, J.E., W.L. Chapman, F. Fetterer, and J.S. Stewart, 2019: Gridded Monthly Sea Ice Extent and Concentration, 1850 Onward, Version 2. National Snow and Ice Data Center (NSIDC), Boulder, CO, USA. Retrieved from: https://nsidc.org/data/g10010.
Wang, B. et al., 2013: Northern Hemisphere summer monsoon intensi fi ed by mega-El Niño / southern oscillation and Atlantic multidecadal oscillation. *Proceedings of the National Academy of Sciences of the United States of America*, **110(14)**, 5347–5352, doi:10.1073/pnas.1219405110.
Wang, B. et al., 2018: Toward predicting changes in the land monsoon rainfall a decade in advance. *Journal of Climate*, **31(7)**, 2699–2714, doi:10.1175/jcli-d-17-0521.1.
Wang, B. et al., 2021: Monsoons Climate Change Assessment. *Bulletin of the American Meteorological Society*, **102(1)**, E1–E19, doi:10.1175/bams-d-19-0335.1.
Wang, C., Y. Hu, X. Wen, C. Zhou, and J. Liu, 2020: Inter-model spread of the climatological annual mean Hadley circulation and its relationship with the double ITCZ bias in CMIP5. *Climate Dynamics*, **55(9)**, doi:10.1007/s00382-020-05414-z.
Wang, J., A. Dai, and C. Mears, 2016: Global water vapor trend from 1988 to 2011 and its diurnal asymmetry based on GPS, radiosonde, and microwave satellite measurements. *Journal of Climate*, **29(14)**, 5205–5222, doi:10.1175/jcli-d-15-0485.1.
Wang, J., H.-M. Kim, and E.K.M. Chang, 2017a: Changes in Northern Hemisphere Winter Storm Tracks under the Background of Arctic Amplification. *Journal of Climate*, **30(10)**, 3705–3724, doi:10.1175/jcli-d-16-0650.1.
Wang, J. et al., 2017b: Internal and external forcing of multidecadal Atlantic climate variability over the past 1,200 years. *Nature Geoscience*, **10(7)**, 512–517, doi:10.1038/ngeo2962.
Wang, P.X. et al., 2014: The global monsoon across timescales: Coherent variability of regional monsoons. *Climate of the Past*, **10(6)**, 2007–2052, doi:10.5194/cp-10-2007-2014.
Wang, P.X. et al., 2017: The global monsoon across time scales: Mechanisms and outstanding issues. *Earth-Science Reviews*, **174**, 84–121, doi:10.1016/j.earscirev.2017.07.006.
Wang, Q. et al., 2019: Response of Southern China Winter Rainfall to El Niño Diversity and Its Relevance to Projected Southern China Rainfall Change. *Journal of Climate*, **32(11)**, 3343–3356, doi:10.1175/jcli-d-18-0571.1.
Wang, R. and Y. Liu, 2020: Recent declines in global water vapor from MODIS products: Artifact or real trend? *Remote Sensing of Environment*, **247**, 111896, doi:10.1016/j.rse.2020.111896.
Wang, S., J. Huang, Y. He, and Y. Guan, 2014: Combined effects of the Pacific Decadal Oscillation and El Niño-Southern Oscillation on Global Land Dry–Wet Changes. *Scientific Reports*, **4**, 6651.

ACCEPTED VERSION SUBJECT TO FINAL EDITS

Wang, S. et al., 2016: Temporal trends and spatial variability of vegetation phenology over the Northern Hemisphere during 1982-2012. *PLoS ONE*, doi:10.1371/journal.pone.0157134.
Wang, W. and C.-Z. Zou, 2014: AMSU-A-Only Atmospheric Temperature Data Records from the Lower Troposphere to the Top of the Stratosphere. *Journal of Atmospheric and Oceanic Technology*, **31(4)**, 808–825, doi:10.1175/jtech-d-13-00134.1.
Wang, W., K. Matthes, N.E. Omrani, and M. Latif, 2016: Decadal variability of tropical tropopause temperature and its relationship to the Pacific Decadal Oscillation. *Scientific Reports*, **6(29537)**, doi:10.1038/srep29537.
Wang, X., N.J. Planavsky, C.T. Reinhard, J.R. Hein, and T.M. Johnson, 2016: A cenozoic seawater redox record derived from 238U/235U in ferromanganese crusts. *American Journal of Science*, **315(11)**, 64–83, doi:10.2475/01.2016.02.
Wang, X.L., Y. Feng, R. Chan, and V. Isaac, 2016: Inter-comparison of extra-tropical cyclone activity in nine reanalysis datasets. *Atmospheric Research*, **181**, 133–153, doi:10.1016/j.atmosres.2016.06.010.
Wang, Y.L., C.R. Wu, and S.Y. Chao, 2016: Warming and weakening trends of the Kuroshio during 1993–2013. *Geophysical Research Letters*, doi:10.1002/2016gl069432.
Wang, Y.-L. and C.-R. Wu, 2018: Discordant multi-decadal trend in the intensity of the Kuroshio along its path during 1993--2013. *Scientific Reports*, **8(1)**, 14633, doi:10.1038/s41598-018-32843-y.
Wang, Y., Brandt, M., Zhao, M., Tong, X., Xing, K., Xue, F., Kang, M., Wang, L., Jiang, Y., Fensholt, R. and Wang, Y., 2018: Major forest increase on the Loess Plateau, China (2001–2016). *Land Degradation and Development*, **29(11)**, 4080–4091, doi:10.1002/ldr.3174.
Ward, D.S. and N.M. Mahowald, 2015: Local sources of global climate forcing from different categories of land use activities. *Earth System Dynamics*, **6(1)**, 175–194, doi:10.5194/esd-6-175-2015.
Ward, D.S., N.M. Mahowald, and S. Kloster, 2014: Potential climate forcing of land use and land cover change. *Atmospheric Chemistry and Physics*, **14(23)**, 12701–12724, doi:10.5194/acp-14-12701-2014.
Warren, S.G. et al., 1999: Snow depth on Arctic sea ice. *Journal of Climate*, **12(6)**, 1814–1829, doi:10.1175/1520-0442(1999)012<1814:sdoasi>2.0.co;2.
Watanabe, T. et al., 2011: Permanent El Niño during the Pliocene warm period not supported by coral evidence. *Nature*, **471**, 209–211, doi:10.1038/nature09777.
Watson, C.S. et al., 2015: Unabated global mean sea-level rise over the satellite altimeter era. *Nature Climate Change*, **5(6)**, 565–568, doi:10.1038/nclimate2635.
Waugh, D.W., A.H. Sobel, and L.M. Polvani, 2017: What is the polar vortex and how does it influence weather? *Bulletin of the American Meteorological Society*, **98(1)**, 37–44, doi:10.1175/bams-d-15-00212.1.
WCRP Global Sea Level Budget Group, 2018: AA Global sea-level budget 1993–present. *Earth System Science Data*, **10(3)**, 1551–1590, doi:10.5194/essd-10-1551-2018.
Wearing, M.G. and J. Kingslake, 2019: Holocene Formation of Henry Ice Rise, West Antarctica, Inferred From Ice-Penetrating Radar. *Journal of Geophysical Research: Earth Surface*, **124(8)**, 2224–2240, doi:10.1029/2018jf004988.
Webster, M. et al., 2018a: Snow in the changing sea-ice systems. *Nature Climate Change*, **8**, 946–953, doi:10.1038/s41558-018-0286-7.
Webster, M. et al., 2018b: Snow in the changing sea-ice systems. *Nature Climate Change*, **8**, 946–953, doi:10.1038/s41558-018-0286-7.
Webster, M.A. et al., 2014: Interdecadal changes in snow depth on Arctic sea ice. *Journal of Geophysical Research: Oceans*, **119(8)**, 5395–5406, doi:10.1002/2014jc009985.
Wei, J., Y. Peng, R. Mahmood, L. Sun, and J. Guo, 2019: Intercomparison in spatial distributions and temporal trends derived from multi-source satellite aerosol products. *Atmospheric Chemistry and Physics*, **19(10)**, 7183–7207, doi:10.5194/acp-19-7183-2019.
Wei, Z. et al., 2020: Identification of uncertainty sources in quasi-global discharge and inundation simulations using satellite-based precipitation products. *Journal of Hydrology*, **589**, doi:10.1016/j.jhydrol.2020.125180.
Wen, C., A. Kumar, and Y. Xue, 2014: Factors contributing to uncertainty in Pacific Decadal Oscillation index. *Geophysical Research Letters*, **41(22)**, 7980–7986, doi:10.1002/2014gl061992.
Wendt, K.A. et al., 2019: Three-phased Heinrich Stadial 4 recorded in NE Brazil stalagmites. *Earth and Planetary Science Letters*, **510**, 94–102, doi:10.1016/j.epsl.2018.12.025.
Werner, J.P., D. Divine, F. Charpentier Ljungqvist, T. Nilsen, and P. Francus, 2018: Spatio-temporal variability of Arctic summer temperatures over the past 2 millennia. *Climate of the Past*, **14(4)**, 527–557, doi:10.5194/cp-14-527-2018.
West, C.K. et al., 2020: Paleobotanical proxies for early Eocene climates and ecosystems in northern North America from middle to high latitudes. *Climate of the Past*, **16(4)**, 1387–1410, doi:10.5194/cp-16-1387-2020.
Westerhold, T. et al., 2020: An astronomically dated record of Earth's climate and its predictability over the last 66 million years. *Science*, **369(6509)**, 1383–1387, doi:10.1126/science.aba6853.
White, S.M., A.C. Ravelo, and P.J. Polissar, 2018a: Dampened El Niño in the Early and Mid-Holocene Due To Insolation-Forced Warming/Deepening of the Thermocline. *Geophysical Research Letters*, **45(1)**, 316–326, doi:10.1002/2017gl075433.

ACCEPTED VERSION SUBJECT TO FINAL EDITS

White, S.M., A.C. Ravelo, and P.J. Polissar, 2018b: Dampened El Niño in the Early and Mid-Holocene Due To Insolation-Forced Warming/Deepening of the Thermocline. *Geophysical Research Letters*, **45(1)**, 316–326, doi:10.1002/2017gl075433.
Wilhelmsen, H., F. Ladstädter, B. Scherllin-Pirscher, and A.K. Steiner, 2018: Atmospheric QBO and ENSO indices with high vertical resolution from GNSS radio occultation temperature measurements. *Atmospheric Measurement Techniques*, **11(3)**, 1333–1346, doi:10.5194/amt-11-1333-2018.
Willett, K.M., R.J.H. Dunn, J.J. Kennedy, and D.I. Berry, 2020: Development of the HadISDH.marine humidity climate monitoring dataset. *Earth System Science Data*, **12(4)**, 2853–2880, doi:10.5194/essd-12-2853-2020.
Willett, K.M. et al., 2014: HadISDH land surface multi-variable humidity and temperature record for climate monitoring. *Climate of the Past*, **10**, 1983–2006, doi:10.5194/cp-10-1983-2014.
Williams, B. et al., 2017: North Pacific twentieth century decadal-scale variability is unique for the past 342 years. *Geophys. Res. Lett.*, **44**, 3761–3769, doi:10.1002/2017gl073138.
Williams, C.N., M.J. Menne, and P.W. Thorne, 2012: Benchmarking the performance of pairwise homogenization of surface temperatures in the United States. *Journal of Geophysical Research: Atmospheres*, **117(D5)**, doi:10.1029/2011jd016761.
Williams, J.W., P. Tarasov, S. Brewer, and M. Notaro, 2011: Late Quaternary variations in tree cover at the northern forest-tundra ecotone. *Journal of Geophysical Research: Biogeosciences*, **116(G1)**, doi:10.1029/2010jg001458.
Wilson, R. et al., 2018: Glacial lakes of the Central and Patagonian Andes. *Global and Planetary Change*, **162**, 275–291, doi:10.1016/j.gloplacha.2018.01.004.
Windler, G., J.E. Tierney, P.N. DiNezio, K. Gibson, and R. Thunell, 2019: Shelf exposure influence on Indo-Pacific Warm Pool climate for the last 450,000 years. *Earth and Planetary Science Letters*, **516**, 66–76, doi:10.1016/j.epsl.2019.03.038.
Winguth, A.M.E., E. Thomas, and C. Winguth, 2012: Global decline in ocean ventilation, oxygenation, and productivity during the Paleocene-Eocene Thermal Maximum: Implications for the benthic extinction. *Geology*, **40(3)**, 263–266, doi:10.1130/g32529.1.
Winnick, M.J., J.K. Caves, and C.P. Chamberlain, 2015: A mechanistic analysis of early Eocene latitudinal gradients of isotopes in precipitation. *Geophysical Research Letters*, **42(19)**, 8216–8224, doi:10.1002/2015gl064829.
Winski, D. et al., 2017: Industrial-age doubling of snow accumulation in the Alaska Range linked to tropical ocean warming. *Scientific Reports*, **7(1)**, 1–12, doi:10.1038/s41598-017-18022-5.
Wirth, S.B., L. Glur, A. Gilli, and F.S. Anselmetti, 2013a: Holocene flood frequency across the Central Alps – solar forcing and evidence for variations in North Atlantic atmospheric circulation. *Quaternary Science Reviews*, **80**, 112–128, doi:10.1016/j.quascirev.2013.09.002.
Wirth, S.B., L. Glur, A. Gilli, and F.S. Anselmetti, 2013b: Holocene flood frequency across the Central Alps – solar forcing and evidence for variations in North Atlantic atmospheric circulation. *Quaternary Science Reviews*, **80**, 112–128, doi:10.1016/j.quascirev.2013.09.002.
Witkowski, C.R., J.W.H. Weijers, B. Blais, S. Schouten, and J.S. Sinninghe Damsté, 2018a: Molecular fossils from phytoplankton reveal secular PCO2 trend over the phanerozoic. *Science Advances*, **4(11)**, eaat4556, doi:10.1126/sciadv.aat4556.
Witkowski, C.R., J.W.H. Weijers, B. Blais, S. Schouten, and J.S. Sinninghe Damsté, 2018b: Molecular fossils from phytoplankton reveal secular PCO2 trend over the phanerozoic. *Science Advances*, **4(11)**, eaat4556, doi:10.1126/sciadv.aat4556.
WMO, 2018: *Scientific Assessment of Ozone Depletion: 2018*. Global Ozone Research and Monitoring Project – Report No. 58, World Meteorological Organization (WMO), Geneva, Switzerland, 588 pp.
Woodborne, S. et al., 2015: A 1000-year carbon isotope rainfall proxy record from South African baobab trees (Adansonia digitata L.). *PLoS ONE*, **10(5)**, 1–18, doi:10.1371/journal.pone.0124202.
Woodgate, R.A., 2018: Increases in the Pacific inflow to the Arctic from 1990 to 2015, and insights into seasonal trends and driving mechanisms from year-round Bering Strait mooring data. *Progress in Oceanography*, **160**, 124–154, doi:10.1016/j.pocean.2017.12.007.
Woodruff, S.D. et al., 2011: ICOADS Release 2.5: extensions and enhancements to the surface marine meteorological archive. *International Journal of Climatology*, **31(7)**, 951–967, doi:10.1002/joc.2103.
Woodworth, P.L., M.M. Maqueda, V.M. Roussenov, R.G. Williams, and C.W. Hughes, 2014: Mean sea-level variability along the northeast American Atlantic coast and the roles of the wind and the overturning circulation. *Journal of Geophysical Research C: Oceans*, **119(12)**, 8916–8935, doi:10.1002/2014jc010520.
Woollings, T., C. Czuchnicki, and C. Franzke, 2014: Twentieth century North Atlantic jet variability. *Quarterly Journal of the Royal Meteorological Society*, **140(680)**, 783–791, doi:10.1002/qj.2197.
Woollings, T. et al., 2018a: Daily to Decadal Modulation of Jet Variability (2018a). *Journal of Climate*, **31**, 1297–1314, doi:10.1175/jcli-d-17-0286.1.
Woollings, T. et al., 2018b: Blocking and its Response to Climate Change (2018b). *Current Climate Change Reports*, **4(3)**, 287–300, doi:10.1007/s40641-018-.
Woosley, R.J., F.J. Millero, and R. Wanninkhof, 2016: Rapid anthropogenic changes in CO2 and pH in the Atlantic

ACCEPTED VERSION SUBJECT TO FINAL EDITS

Ocean: 2003–2014. *Global Biogeochemical Cycles*, **30(1)**, 70–90, doi:10.1002/2015gb005248.
Worthington, E.L. et al., 2020: A 30-year reconstruction of the Atlantic meridional overturning circulation shows no decline. *Ocean Sci. Discuss.*, **17(1)**, 285–299, doi:10.5194/os-2020-71.
Wright, N.M., M. Seton, S.E. Williams, J.M. Whittaker, and R.D. Müller, 2020: Sea-level fluctuations driven by changes in global ocean basin volume following supercontinent break-up. *Earth-Science Reviews*, **208**, 103293, doi:10.1016/j.earscirev.2020.103293.
Wu, J., J. Zha, D. Zhao, and Q. Yang, 2018: Changes in terrestrial near-surface wind speed and their possible causes: an overview. *Climate Dynamics*, **51**, 2039–2078, doi:10.1007/s00382-017-3997-y.
Wu, L. et al., 2012: Enhanced warming over the global subtropical western boundary currents. *Nature Climate Change*, **2(3)**, 161–166, doi:10.1038/nclimate1353.
Wu, P., N. Christidis, and P. Stott, 2013: Anthropogenic impact on Earth's hydrological cycle. *Nature Climate Change*, **3(9)**, 807–810, doi:10.1038/nclimate1932.
Wu, C.-J., Krivova, N. A., Solanki, S. K., and Usoskin, I. G., 2018: Solar total and spectral irradiance reconstruction over the last 9000 years. *A&A*, **620**, A120, doi:10.1051/0004-6361/201832956.
Wunsch, C., 2018: Towards determining uncertainties in global oceanic mean values of heat, salt, and surface elevation. *Tellus A: Dynamic Meteorology and Oceanography*, **70(1)**, 1–14, doi:10.1080/16000870.2018.1471911.
Wurtzel, J.B. et al., 2018: Tropical Indo-Pacific hydroclimate response to North Atlantic forcing during the last deglaciation as recorded by a speleothem from Sumatra, Indonesia. *Earth and Planetary Science Letters*, **492**, 264–278, doi:10.1016/j.epsl.2018.04.001.
Xia, J. et al., 2018: Shifts in timing of local growing season in China during 1961–2012. *Theoretical and Applied Climatology*, **137**, 1637–1642, doi:10.1007/s00704-018-2698-8.
Xian, T. and C.R. Homeyer, 2019: Global Tropopause Altitudes in Radiosondes and Reanalyses. *Atmospheric Chemistry and Physics*, **19(8)**, 5661–5678, doi:10.5194/acp-19-5661-2019.
Xiao, Z., S. Liang, and B. Jiang, 2017: Evaluation of four long time-series global leaf area index products. *Agricultural and Forest Meteorology*, **246**, 218–230, doi:10.1016/j.agrformet.2017.06.016.
Xie, P. and P.A. Arkin, 1997: Global Precipitation : A 17-Year Monthly Analysis Based on Gauge Observations , Satellite Estimates , and Numerical Model Outputs. *Bull. Amer. Meteor. Soc*, **78(11)**, 2539–2558, doi:10.1175/1520-0477(1997)078<2539:gpayma>2.0.co;2.
Xie, T., R. Newton, P. Schlosser, C. Du, and M. Dai, 2019: Long-Term Mean Mass, Heat and Nutrient Flux Through the Indonesian Seas, Based on the Tritium Inventory in the Pacific and Indian Oceans. *Journal of Geophysical Research: Oceans*, **124(6)**, 3859–3875, doi:10.1029/2018jc014863.
Xu, H. et al., 2016: Hydroclimatic contrasts over Asian monsoon areas and linkages to tropical Pacific SSTs. *Scientific Reports*, **6(1)**, 33177, doi:10.1038/srep33177.
Xu, W. et al., 2018a: A new integrated and homogenized global monthly land surface air temperature dataset for the period since 1900. *Climate Dynamics*, **50(7)**, 2513–2536, doi:10.1007/s00382-017-3755-1.
Xu, W. et al., 2018b: A new integrated and homogenized global monthly land surface air temperature dataset for the period since 1900. *Climate Dynamics*, **50(7)**, 2513–2536, doi:10.1007/s00382-017-3755-1.
Xue, D.K. and Y.C. Zhang, 2018: Concurrent variations in the location and intensity of the Asian winter jet streams and the possible mechanism. *Climate Dynamics*, 37–52, doi:10.1007/s00382-016-3325-y.
Yan, Q. et al., 2016: Enhanced intensity of global tropical cyclones during the mid-{Pliocene} warm period. *Proceedings of the National Academy of Sciences*, **113(46)**, 12963–12967, doi:10.1073/pnas.1608950113.
Yan, Y. et al., 2019: Two-million-year-old snapshots of atmospheric gases from Antarctic ice. *Nature*, **574(7780)**, 663–666, doi:10.1038/s41586-019-1692-3.
Yang, H. et al., 2016: Intensification and poleward shift of subtropical western boundary currents in a warming climate. *Journal of Geophysical Research: Oceans*, **121(7)**, 4928–4945, doi:10.1002/2015jc011513.
Yang, H. et al., 2020: Poleward Shift of the Major Ocean Gyres Detected in a Warming Climate. *Geophysical Research Letters*, **47(5)**, e2019GL085868, doi:10.1029/2019gl085868.
Yang, J. and C. Xiao, 2018: The evolution and volcanic forcing of the southern annular mode during the past 300 years. *International Journal of Climatology*, **38(4)**, 1706–1717, doi:10.1002/joc.5290.
Yang, J.-W., J. Ahn, E.J. Brook, and Y. Ryu, 2017: Atmospheric methane control mechanisms during the early Holocene. *Climate of the Past*, **13(9)**, 1227–1242, doi:10.5194/cp-13-1227-2017.
Yang, S. et al., 2018: A strengthened East Asian Summer Monsoon during Pliocene warmth: Evidence from 'red clay' sediments at Pianguan, northern China. *Journal of Asian Earth Sciences*, **155**, 124–133, doi:10.1016/j.jseaes.2017.10.020.
Yao, W., A. Paytan, and U.G. Wortmann, 2018: Large-scale ocean deoxygenation during the Paleocene-Eocene Thermal Maximum. *Science*, **361(6404)**, 804–806, doi:10.1126/science.aar8658.
Yashayaev, I. and J.W. Loder, 2016: Recurrent replenishment of Labrador Sea Water and associated decadal-scale variability. *Journal of Geophysical Research: Oceans*, **121(11)**, 8095–8114, doi:10.1002/2016jc012046.
Yau, A.M., M.L. Bender, A. Robinson, and E.J. Brook, 2016: Reconstructing the last interglacial at Summit, Greenland: Insights from GISP2. *Proceedings of the National Academy of Sciences*, **113(35)**, 9710–9715, doi:10.1073/pnas.1524766113.

ACCEPTED VERSION SUBJECT TO FINAL EDITS

Yeh, S.-W. et al., 2018: ENSO Atmospheric Teleconnections and Their Response to Greenhouse Gas Forcing. *Reviews of Geophysics*, **56(1)**, 185–206, doi:10.1002/2017rg000568.
Yeo, K.L., N.A. Krivova, and S.K. Solanki, 2017: EMPIRE: A robust empirical reconstruction of solar irradiance variability. *Journal of Geophysical Research: Space Physics*, **122(4)**, 3888–3914, doi:10.1002/2016ja023733.
Yeo, K.L. et al., 2015: UV solar irradiance in observations and the NRLSSI and SATIRE-S models. *Journal of Geophysical Research: Space Physics*, **120(8)**, 6055–6070, doi:10.1002/2015ja021277.
Yeo, K.L. et al., 2020: The Dimmest State of the Sun. *Geophysical Research Letters*, **47(19)**, doi:10.1029/2020gl090243.
Yeung, L.Y. et al., 2019: Isotopic constraint on the twentieth-century increase in tropospheric ozone. *Nature*, **570(7760)**, 224–227, doi:10.1038/s41586-019-1277-1.
Yim, B.Y., S.W. Yeh, H.J. Song, D. Dommenget, and B.J. Sohn, 2017: Land-sea thermal contrast determines the trend of Walker circulation simulated in atmospheric general circulation models. *Geophysical Research Letters*, **44(11)**, 5854–5862, doi:10.1002/2017gl073778.
Yokoyama, Y. et al., 2018: Rapid glaciation and a two-step sea level plunge into the Last Glacial Maximum. *Nature*, **559(7715)**, 603–607, doi:10.1038/s41586-018-0335-4.
You, Y., M. Huber, R.D. Müller, C.J. Poulsen, and J. Ribbe, 2009: Simulation of the Middle Miocene Climate Optimum. *Geophysical Research Letters*, **36(4)**, doi:10.1029/2008gl036571.
Young, I.R. and A. Ribal, 2019: Multiplatform evaluation of global trends in wind speed and wave height. *Science*, **364(6440)**, 548–552, doi:10.1126/science.aav9527.
Young, N.E. and J.P. Briner, 2015: Holocene evolution of the western Greenland Ice Sheet: Assessing geophysical ice-sheet models with geological reconstructions of ice-margin change. *Quaternary Science Reviews*, **114**, 1–17, doi:10.1016/j.quascirev.2015.01.018.
Young, N.E. et al., 2020: Deglaciation of the Greenland and Laurentide ice sheets interrupted by glacier advance during abrupt coolings. *Quaternary Science Reviews*, **229**, 106091, doi:10.1016/j.quascirev.2019.106091.
Yu, H. et al., 2020: Interannual variability and trends of combustion aerosol and dust in major continental outflows revealed by MODIS retrievals and CAM5 simulations during 2003–2017. *Atmospheric Chemistry and Physics*, **20(1)**, 139–161, doi:10.5194/acp-20-139-2020.
Yu, J.-Y. and S.T. Kim, 2013: Identifying the types of major El Niño events since 1870. *International Journal of Climatology*, **33(8)**, 2105–2112, doi:10.1002/joc.3575.
Yu, L., S.A. Josey, F.M. Bingham, and T. Lee, 2020: Intensification of the global water cycle and evidence from ocean salinity: a synthesis review. *Annals of the New York Academy of Sciences*, **1472(1)**, 76–94, doi:10.1111/nyas.14354.
Yu, S. and J. Sun, 2018: Revisiting the relationship between El Niño-Southern Oscillation and the East Asian winter monsoon. *International Journal of Climatology*, **38(13)**, 4846–4859, doi:10.1002/joc.5702.
Yun, K.-S. and A. Timmermann, 2018: Decadal Monsoon-ENSO Relationships Reexamined. *Geophysical Research Letters*, **45(4)**, 2014–2021, doi:10.1002/2017gl076912.
Zachos, J.C., G.R. Dickens, and R.E. Zeebe, 2008: An early Cenozoic perspective on greenhouse warming and carbon-cycle dynamics. *Nature*, **451(7176)**, 279–283, doi:10.1038/nature06588.
Zanna, L., S. Khatiwala, J.M. Gregory, J. Ison, and P. Heimbach, 2019: Global reconstruction of historical ocean heat storage and transport. *Proceedings of the National Academy of Sciences*, **116(4)**, 1126–1131, doi:10.1073/pnas.1808838115.
Zantopp, R., J. Fischer, M. Visbeck, and J. Karstensen, 2017: From interannual to decadal: 17 years of boundary current transports at the exit of the Labrador Sea. *Journal of Geophysical Research: Oceans*, **122(3)**, 1724–1748, doi:10.1002/2016jc012271.
Zeebe, R.E., A. Ridgwell, and J.C. Zachos, 2016: Anthropogenic carbon release rate unprecedented during the past 66 million years. *Nature Geoscience*, **9(4)**, 325–329, doi:10.1038/ngeo2681.
Zekollari, H., M. Huss, and D. Farinotti, 2020: On the Imbalance and Response Time of Glaciers in the European Alps. *Geophysical Research Letters*, **47(2)**, e2019GL085578, doi:10.1029/2019gl085578.
Zemp, M. et al., 2019: Global glacier mass changes and their contributions to sea-level rise from 1961 to 2016. *Nature*, **568(7752)**, 382–386, doi:10.1038/s41586-019-1071-0.
Zemp, M. et al., 2020: Brief communication: Ad hoc estimation of glacier contributions to sea-level rise from the latest glaciological observations. *Cryosphere*, **14(3)**, doi:10.5194/tc-14-1043-2020.
Zeng, Z., S. Sokolovskiy, W.S. Schreiner, and D. Hunt, 2019a: Representation of vertical atmospheric structures by radio occultation observations in the UTLS: comparison to high resolution radiosonde profiles. *Journal of Atmospheric and Oceanic Technology*, **58(2)**, 199–211, doi:10.1175/jtech-d-18-0105.1.
Zeng, Z. et al., 2019b: A reversal in global terrestrial stilling and its implications for wind energy production. *Nature Climate Change*, **9**, 979–985, doi:10.1038/s41558-019-0622-6.
Zhang, H. et al., 2018: East Asian hydroclimate modulated by the position of the westerlies during Termination I. *Science*, **362**, 580–583, doi:10.1126/science.aat9393.
Zhang, J., W. Tian, M.P. Chipperfield, F. Xie, and J. Huang, 2016: Persistent shift of the Arctic polar vortex towards the Eurasian continent in recent decades. *Nature Climate Change*, **6(12)**, 1094–1099,

ACCEPTED VERSION SUBJECT TO FINAL EDITS

doi:10.1038/nclimate3136.
Zhang, J. et al., 2018: Stratospheric ozone loss over the Eurasian continent induced by the polar vortex shift. *Nature Communications*, **9(1)**, 1–8, doi:10.1038/s41467-017-02565-2.
Zhang, L., L. Wu, and B. Gan, 2013: Modes and mechanisms of global water vapor variability over the twentieth century. *Journal of Climate*, **26(15)**, 5578–5593, doi:10.1175/jcli-d-12-00585.1.
Zhang, L., G. Kuczera, A.S. Kiem, and G. Willgoose, 2018: Using paleoclimate reconstructions to analyse hydrological epochs associated with Pacific decadal variability. *Hydrology and Earth System Sciences*, **22(12)**, 6399–6414, doi:10.5194/hess-22-6399-2018.
Zhang, R. and D. Jiang, 2014: Impact of vegetation feedback on the mid-Pliocene warm climate. *Advances in Atmospheric Sciences*, **31(6)**, 1407–1416, doi:10.1007/s00376-014-4015-5.
Zhang, R., D. Jiang, Z. Zhang, Q. Yan, and X. Li, 2019: Modeling the late Pliocene global monsoon response to individual boundary conditions. *Climate Dynamics*, **53(7)**, 4871–4886, doi:10.1007/s00382-019-04834-w.
Zhang, W., Y. Wang, F.-F. Jin, M.F. Stuecker, and A.G. Turner, 2015: Impact of different El Niño types on the El Niño/IOD relationship. *Geophysical Research Letters*, **42(20)**, 8570–8576, doi:10.1002/2015gl065703.
Zhang, Y., J. Xu, N. Yang, and P. Lan, 2018: Variability and Trends in Global Precipitable Water Vapor Retrieved from COSMIC Radio Occultation and Radiosonde Observations. *Atmosphere*, **9(5)**, 174, doi:10.3390/atmos9050174.
Zhang, Y., C. Song, L.E. Band, and G. Sun, 2019: No Proportional Increase of Terrestrial Gross Carbon Sequestration From the Greening Earth. *Journal of Geophysical Research: Biogeosciences*, **124(8)**, doi:10.1029/2018jg004917.
Zhang, Y.G., J. Henderiks, and X. Liu, 2020: Refining the alkenone-pCO2 method II: Towards resolving the physiological parameter 'b'. *Geochimica et Cosmochimica Acta*, **281**, 118–134, doi:10.1016/j.gca.2020.05.002.
Zhang, Z., G. Leduc, and J.P. Sachs, 2014: El Niño evolution during the Holocene revealed by a biomarker rain gauge in the Galápagos Islands. *Earth and Planetary Science Letters*, **404**, 420–434, doi:10.1016/j.epsl.2014.07.013.
Zhao, B. et al., 2017: Decadal-scale trends in regional aerosol particle properties and their linkage to emission changes. *Environmental Research Letters*, **12(5)**, 054021, doi:10.1088/1748-9326/aa6cb2.
Zhao, H. and C. Wang, 2019: On the relationship between ENSO and tropical cyclones in the western North Pacific during the boreal summer. *Climate Dynamics*, **52(1–2)**, 275–288, doi:10.1007/s00382-018-4136-0.
Zhao, J. et al., 2015: Spatial and temporal changes in vegetation phenology at middle and high latitudes of the northern hemisphere over the past three decades. *Remote Sensing*, **7(8)**, 10973–10995, doi:10.3390/rs70810973.
Zhao, L. et al., 2020: Changing climate and the permafrost environment on the Qinghai–Tibet (Xizang) plateau. *Permafrost and Periglacial Processes*, **31(3)**, 396–405, doi:10.1002/ppp.2056.
Zhao, S.-P., Z.-T. Nan, Y.-B. Huang, and L. Zhao, 2017: The Application and Evaluation of Simple Permafrost Distribution Models on the Qinghai-Tibet Plateau. *Permafrost and Periglacial Processes*, **28(2)**, 391–404, doi:10.1002/ppp.1939.
Zhao, X. and R.J. Allen, 2019: Strengthening of the Walker Circulation in recent decades and the role of natural sea surface temperature variability. *Environmental Research Communications*, **1(2)**, 021003, doi:10.1088/2515-7620/ab0dab.
Zheng, B. et al., 2018: Trends in China's anthropogenic emissions since 2010 as the consequence of clean air actions. *Atmospheric Chemistry and Physics*, **18(19)**, 14095–14111, doi:10.5194/acp-18-14095-2018.
Zhou, X., P. Ray, B.S. Barrett, and P.-C. Hsu, 2020a: Understanding the bias in surface latent and sensible heat fluxes in contemporary AGCMs over tropical oceans. *Climate Dynamics*, **55(11)**, 2957–2978, doi:10.1007/s00382-020-05431-y.
Zhou, X., P. Ray, B.S. Barrett, and P.-C. Hsu, 2020b: Understanding the bias in surface latent and sensible heat fluxes in contemporary AGCMs over tropical oceans. *Climate Dynamics*, **55(11)**, 2957–2978, doi:10.1007/s00382-020-05431-y.
Zhou, X., O. Alves, S.J. Marsland, D. Bi, and A.C. Hirst, 2017: Multi-decadal variations of the South Indian Ocean subsurface temperature influenced by Pacific Decadal Oscillation. *Tellus A: Dynamic Meteorology and Oceanography*, **69(1)**, 1308055, doi:10.1080/16000870.2017.1308055.
Zhu, J., C.J. Poulsen, and J.E. Tierney, 2019: Simulation of Eocene extreme warmth and high climate sensitivity through cloud feedbacks. *Science Advances*, **5(9)**, doi:10.1126/sciadv.aax1874.
Zhu, J. et al., 2017: Reduced ENSO variability at the LGM revealed by an isotope-enabled Earth system model. *Geophysical Research Letters*, **44(13)**, 6984–6992, doi:10.1002/2017gl073406.
Zhu, Z. et al., 2016: Greening of the Earth and its drivers. *Nature Climate Change*, **6**, 791–795, doi:10.1038/nclimate3004.
Zhuang, W., M. Feng, Y. Du, A. Schiller, and D. Wang, 2013: Low-frequency sea level variability in the southern Indian Ocean and its impacts on the oceanic meridional transports. *Journal of Geophysical Research: Oceans*, **118(3)**, 1302–1315, doi:10.1002/jgrc.20129.
Zika, J.D. et al., 2018: Improved estimates of water cycle change from ocean salinity: the key role of ocean warming. *Environmental Research Letters*, **13(7)**, 074036, doi:10.1088/1748-9326/aace42.

ACCEPTED VERSION SUBJECT TO FINAL EDITS

Zinke, J. et al., 2014: Corals record long-term Leeuwin current variability including Ningaloo Niño/Niña since 1795. *Nature Communications*, **5**, 3607, doi:10.1038/ncomms4607.

Zou, C.-Z. and H. Qian, 2016: Stratospheric Temperature Climate Data Record from Merged SSU and AMSU-A Observations. *Journal of Atmospheric and Oceanic Technology*, **33(9)**, 1967–1984, doi:10.1175/jtech-d-16-0018.1.

Zou, C.-Z., H. Qian, W. Wang, L. Wang, and C. Long, 2014: Recalibration and merging of SSU observations for stratospheric temperature trend studies. *Journal of Geophysical Research: Atmospheres*, **119(23)**, 13,113–180,205, doi:10.1002/2014jd021603.

Zuo, J., H.-L. Ren, W. Li, and L. Wang, 2016: Interdecadal Variations in the Relationship between the Winter North Atlantic Oscillation and Temperature in South-Central China. *Journal of Climate*, **29**, 7477–7493, doi:10.1175/jcli-d-15-0873.1.

ACCEPTED VERSION
SUBJECT TO FINAL EDITS

Figures

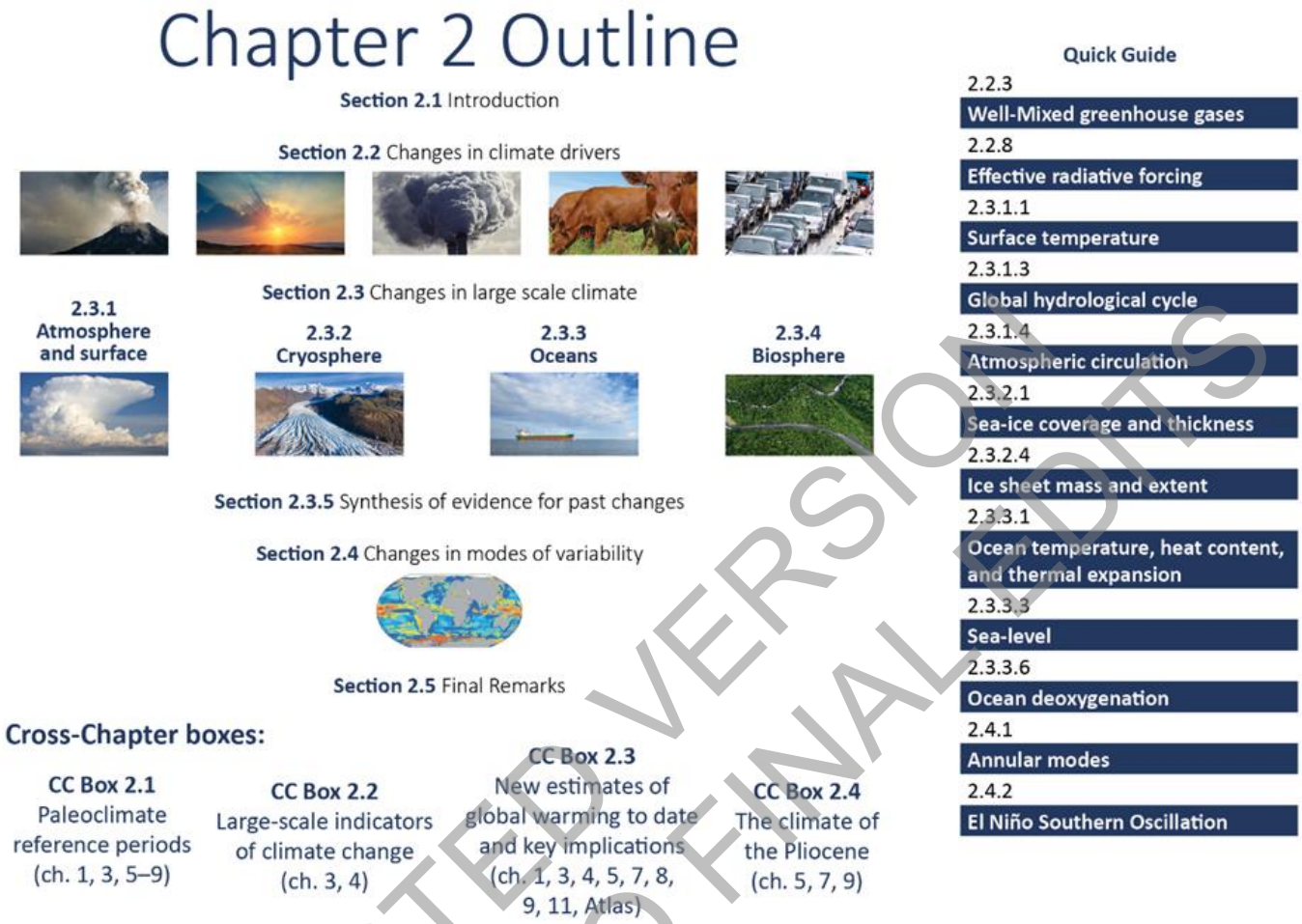
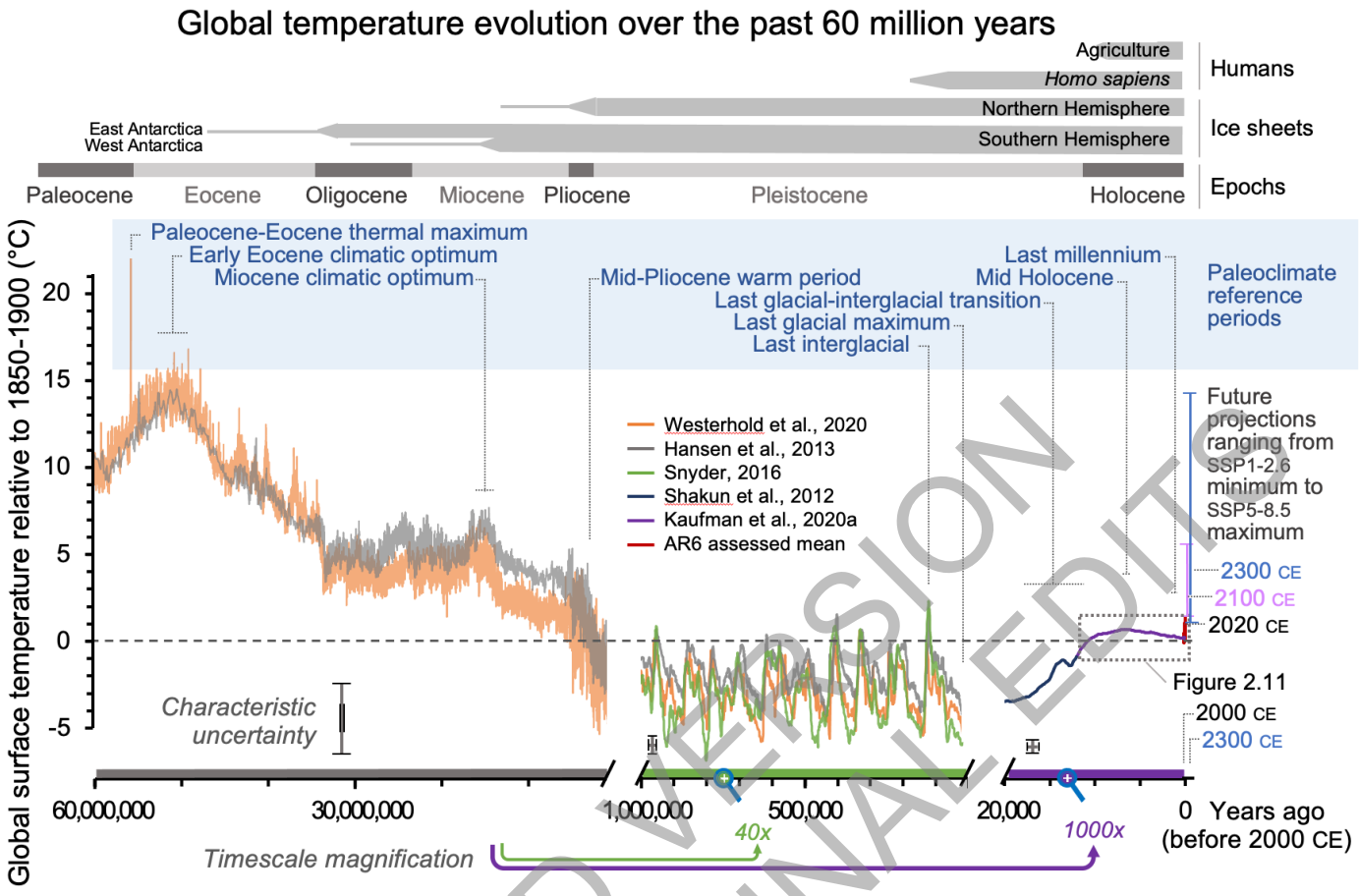


Figure 2.1: Chapter 2 visual abstract of contents.

ACCEPTED VERSION SUBJECT TO FINAL EDITS



Cross-Chapter Box 2.1, Figure 1: Global mean surface temperature (GMST) over the past 60 million years relative to 1850–1900 shown on three time scales. Information about each of the nine paleo reference periods (blue font) and sections in AR6 that discuss these periods are listed in Cross-Chapter Box 2.1 Table 1. Grey horizontal bars at the top mark important events. Characteristic uncertainties are based on expert judgement and are representative of the approximate midpoint of their respective time scales; uncertainties decrease forward in time. GMST estimates for most paleo reference periods (Figure 2.34) overlap with this reconstruction, but take into account multiple lines of evidence. Future projections span the range of global surface air temperature best estimates for SSP1–2.6 and SSP5–8.5 scenarios described in Section 1.6. Range shown for 2100 is based on CMIP6 multi-model mean for 2081–2100 from Table 4.5; range for 2300 is based upon an emulator and taken from Table 4.9. Further details on data sources and processing are available in the chapter data table (Table 2.SM.1).

ACCEPTED VERSION SUBJECT TO FINAL EDITS

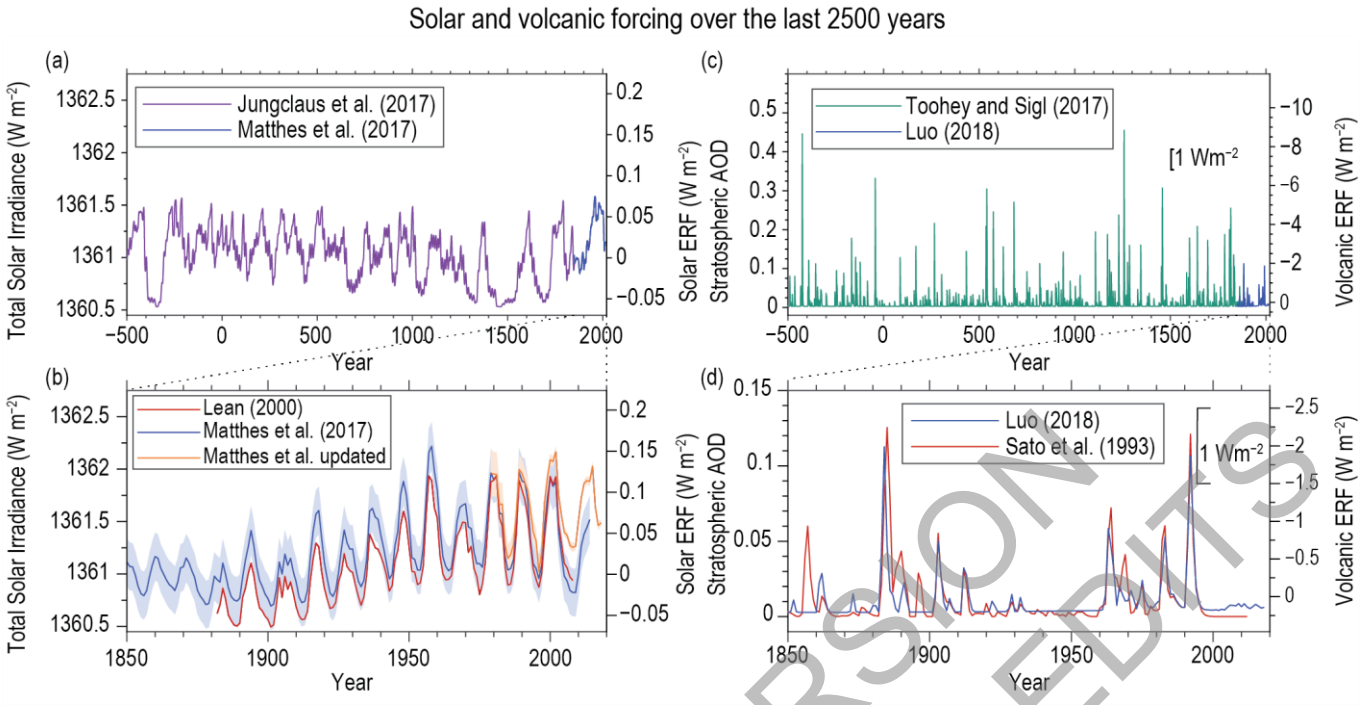


Figure 2.2: Time series of solar and volcanic forcing for the past 2.5 kyr (panels a, c) and since 1850 (panels b, d). (a) Total solar irradiance (TSI) reconstruction (10-year running averages) recommended for CMIP6 / PMIP4 millennial experiments based on the radiocarbon dataset before 1850 (blue) scaled to the CMIP6 historical forcing after 1850 (purple). (b) TSI time series (6-month running averages) from CMIP6 historical forcing as inferred from sunspot numbers (blue), compared to CMIP5 forcing based on (red) and an update to CMIP6 by a TSI composite (orange). (c) Volcanic forcing represented as reconstructed Stratospheric aerosol optical depth (SAOD; as presented in Section 7.3.4.6) at 550 nm. Estimates covering 500 BCE to 1900 CE (green) and 1850–2015 (blue). (d) SAOD reconstruction from CMIP6 (v 4) (blue), compared to CMIP5 forcing (red). Note the change in y-axis range between panels c and d. Further details on data sources and processing are available in the chapter data table (Table 2.SM.1).

ACCEPTED VERSION SUBJECT TO FINAL EDITS

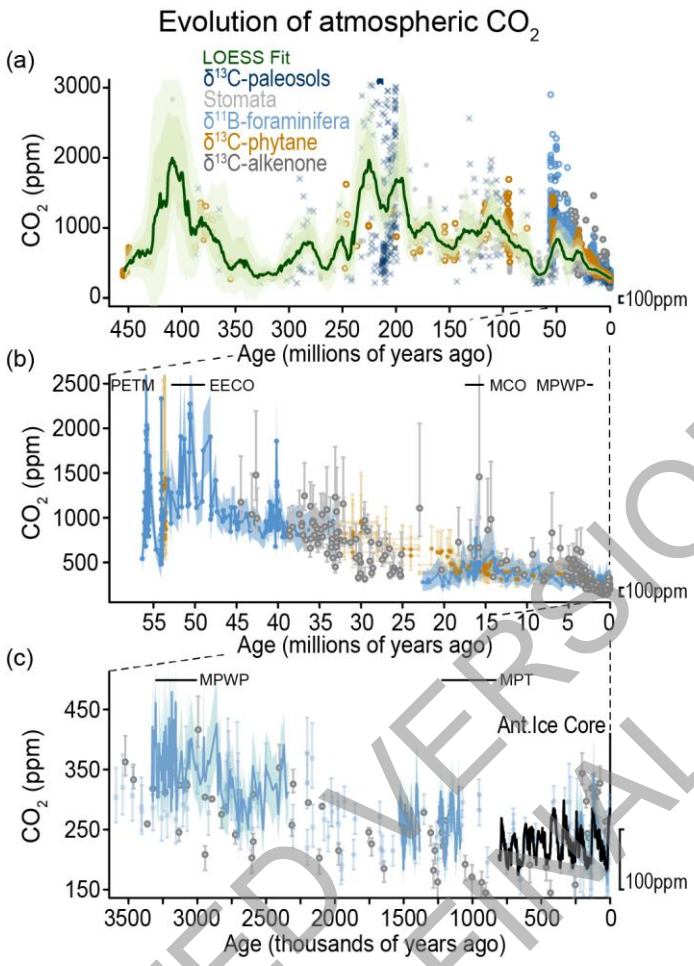
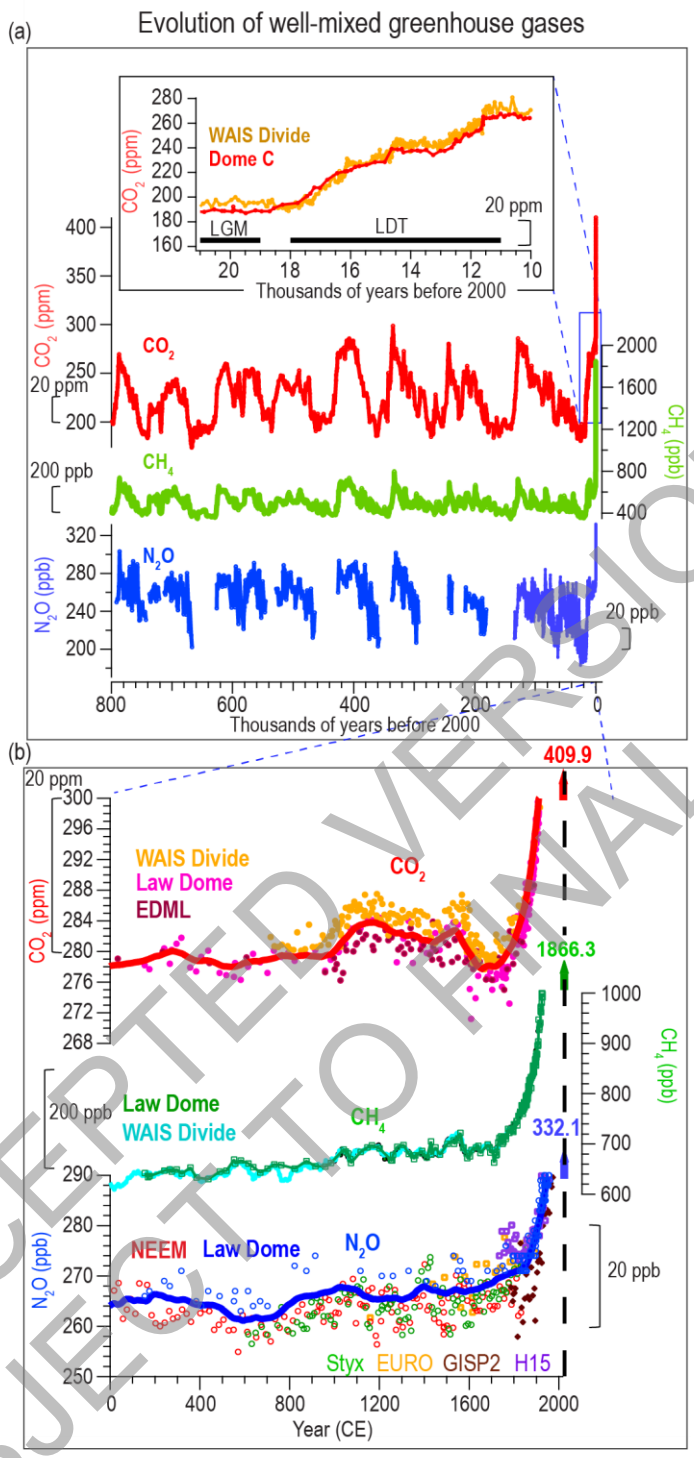


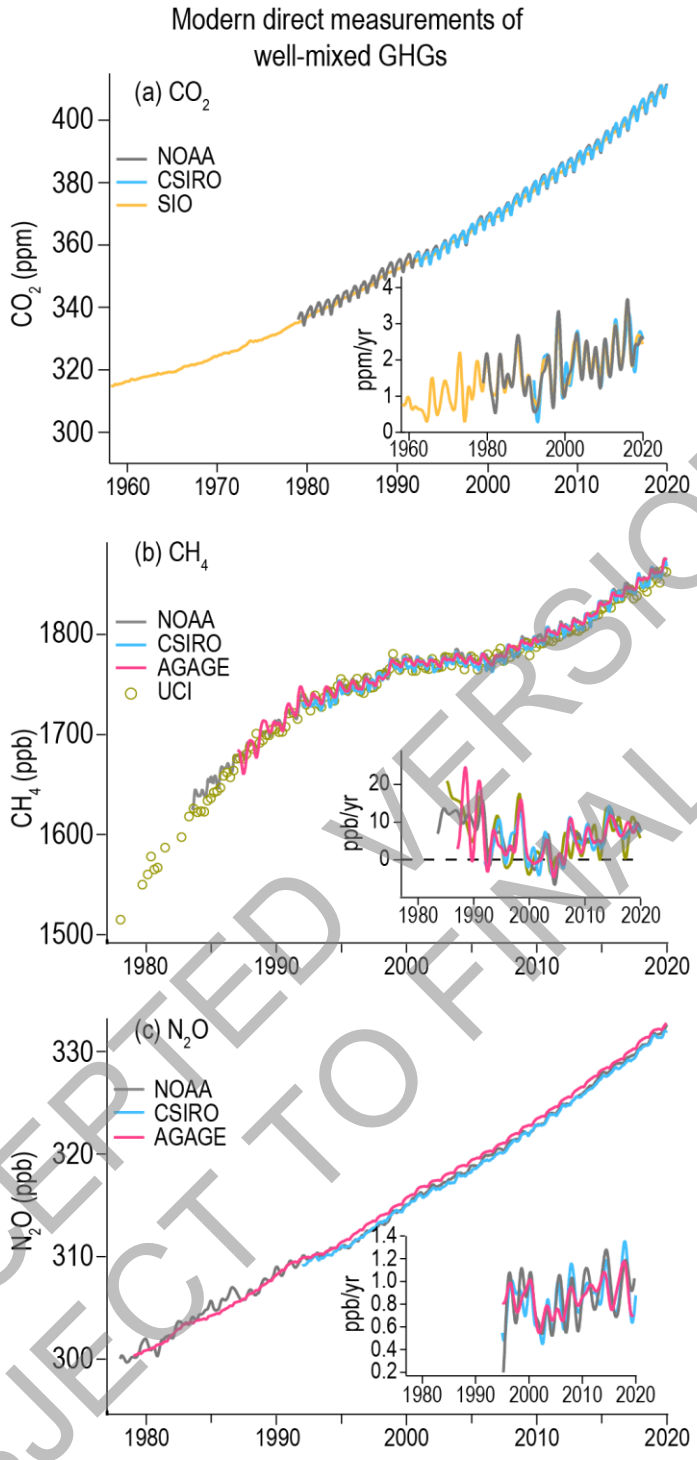
Figure 2.3: **The evolution of atmospheric CO_2 through the last 450 million years.** The periods covered are 0–450 Ma (a), 0–58 Ma (b), and 0–3500 ka (c), reconstructed from continental rock, marine sediment and ice core records. Note different timescales and axes ranges in panels (a), (b) and (c). Dark and light green bands in (a) are uncertainty envelopes at 68% and 95% uncertainty, respectively. 100 ppm in each panel is shown by the marker in the lower right hand corner to aid comparison between panels. In panel (b) and (c) the major paleoclimate reference periods (CCB2.1) have been labelled, and in addition: MPT (Mid Pleistocene Transition), MCO (Miocene Climatic Optimum). Further details on data sources and processing are available in the chapter data table (Table 2.SM.1).

ACCEPTED VERSION SUBJECT TO FINAL EDITS



ACCEPTED VERSION
SUBJECT TO FINAL EDITS

Figure 2.4: **Atmospheric WMGHG concentrations from ice cores.** (a) Records during the last 800 kyr with the LGM to Holocene transition as inset. (b) Multiple high-resolution records over the CE. The horizontal black bars in the panel a inset indicate Last Glacial Maximum (LGM) and Last Deglacial Termination (LDT) respectively. The red and blue lines in (b) are 100-year running averages for CO_2 and N_2O concentrations, respectively. The numbers with vertical arrows in (b) are instrumentally measured concentrations in 2019. Further details on data sources and processing are available in the chapter data table (Table 2.SM.1).



ACCEPTED VERSION SUBJECT TO FINAL EDITS

Figure 2.5: Globally averaged dry-air mole fractions of greenhouse gases. (a) CO_2 from SIO, CSIRO, and NOAA/GML (b) CH_4 from NOAA, AGAGE, CSIRO, and UCI; and (c) N_2O from NOAA, AGAGE, and CSIRO (see Table 2.2). Growth rates, calculated as the time derivative of the global means after removing seasonal cycle are shown as inset figures. Note that the CO_2 series is 1958–2019 whereas CH_4, and N_2O are 1979–2019. Further details on data are in Annex III, and on data sources and processing are available in the chapter data table (Table 2.SM.1).

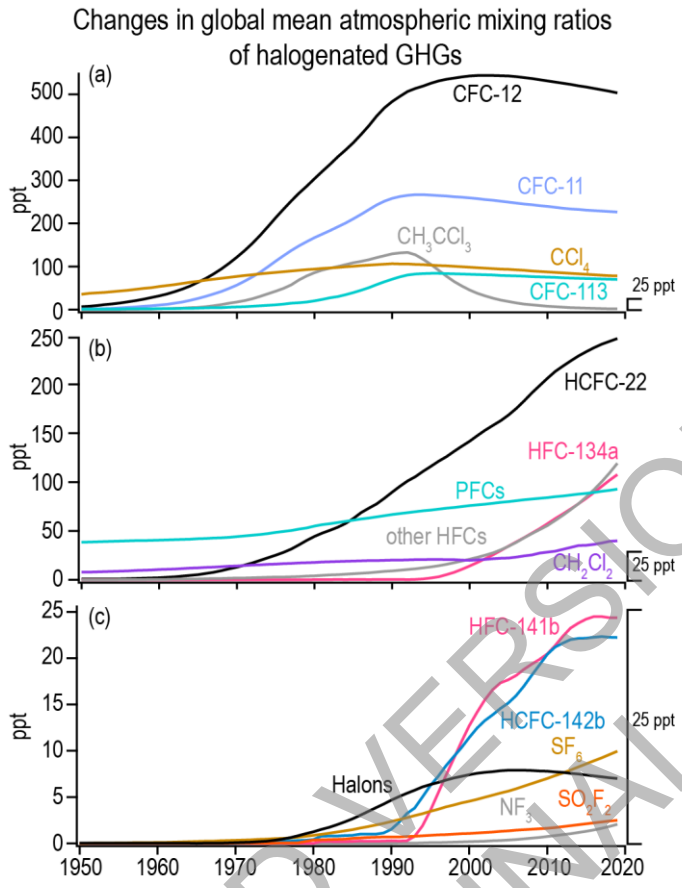


Figure 2.6: **Global mean atmospheric mixing ratios of select ozone-depleting substances and other greenhouse gases**. Data shown are based on the CMIP6 historical dataset and data from NOAA and AGAGE global networks. PFCs include CF_4, C_2F_6, and C_3F_8, and *c*-C_4F_8; Halons include halon-1211, halon-1301, and halon-2402; other HFCs include HFC-23, HFC-32, HFC-125, HFC-143a, HFC-152a, HFC-227ea, HFC-236fa, HFC-245fa, and HFC-365mfc, and HFC-43-10mee. Note that the y-axis range is different for a, b and c and a 25 ppt yardstick is given next to each panel to aid interpretation. Further data are in Annex III, and details on data sources and processing are available in the chapter data table (Table 2.SM.1).

ACCEPTED VERSION SUBJECT TO FINAL EDITS

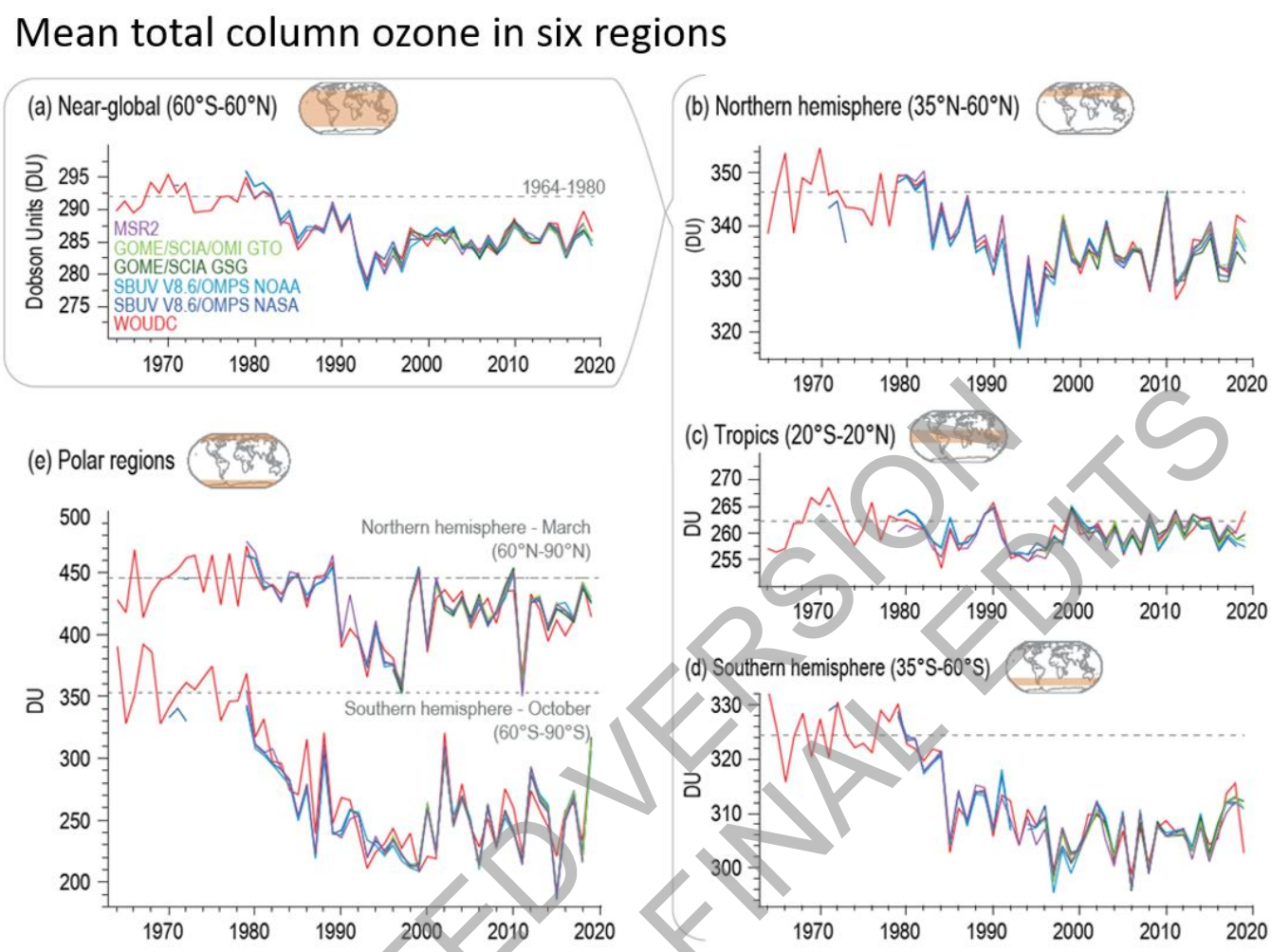


Figure 2.7: **Time series of annual mean total column ozone from 1964-2019.** Values are in Dobson Units (DU), a good proxy for vertically integrated stratospheric ozone. Time series are shown for (a) near-global domain, (b-d) three zonal bands and (e) polar (60°–90°) total ozone in March (NH) and October (SH) ; the months when polar ozone losses usually are largest. Further details on data sources and processing are available in the chapter data table (Table 2.SM.1).

ACCEPTED VERSION SUBJECT TO FINAL EDITS

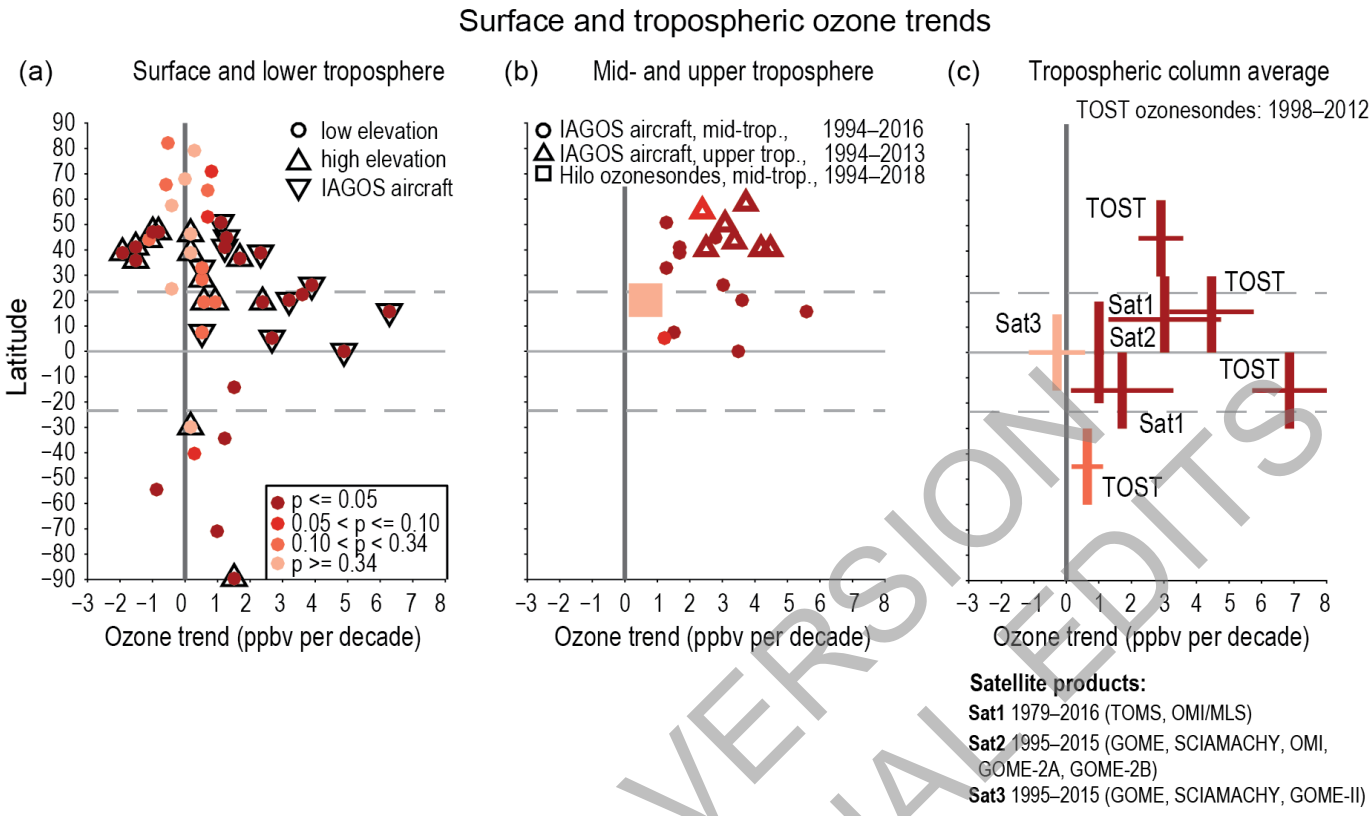


Figure 2.8: **Surface and tropospheric ozone trends.** (a) Decadal ozone trends by latitude at 28 remote surface sites and in the lower free troposphere (650 hPa, about 3.5 km) as measured by IAGOS aircraft above 11 regions. All trends are estimated for the time series up to the most recently available year, but begin in 1995 or 1994. Colours indicate significance (p-value) as denoted in the in-line key. See Figure 6.5 for a depiction of these trends globally. (b) Trends of ozone since 1994 as measured by IAGOS aircraft in 11 regions in the mid-troposphere (700–300 hPa; about 3–9 km) and upper troposphere (about 10-12 km), as measured by IAGOS aircraft and ozonesondes. (c) Trends of average tropospheric column ozone mixing ratios from the TOST composite ozonesonde product and three composite satellite products based on TOMS, OMI/MLS (Sat1), GOME, SCIAMACHY, OMI, GOME-2A, GOME-2B (Sat2), and GOME, SCIAMACHY, GOME-II (Sat3). Vertical bars indicate the latitude range of each product, while horizontal lines indicate the *very likely* uncertainty range.. Further details on data sources and processing are available in the chapter data table (Table 2.SM.1).

ACCEPTED VERSION SUBJECT TO FINAL EDITS

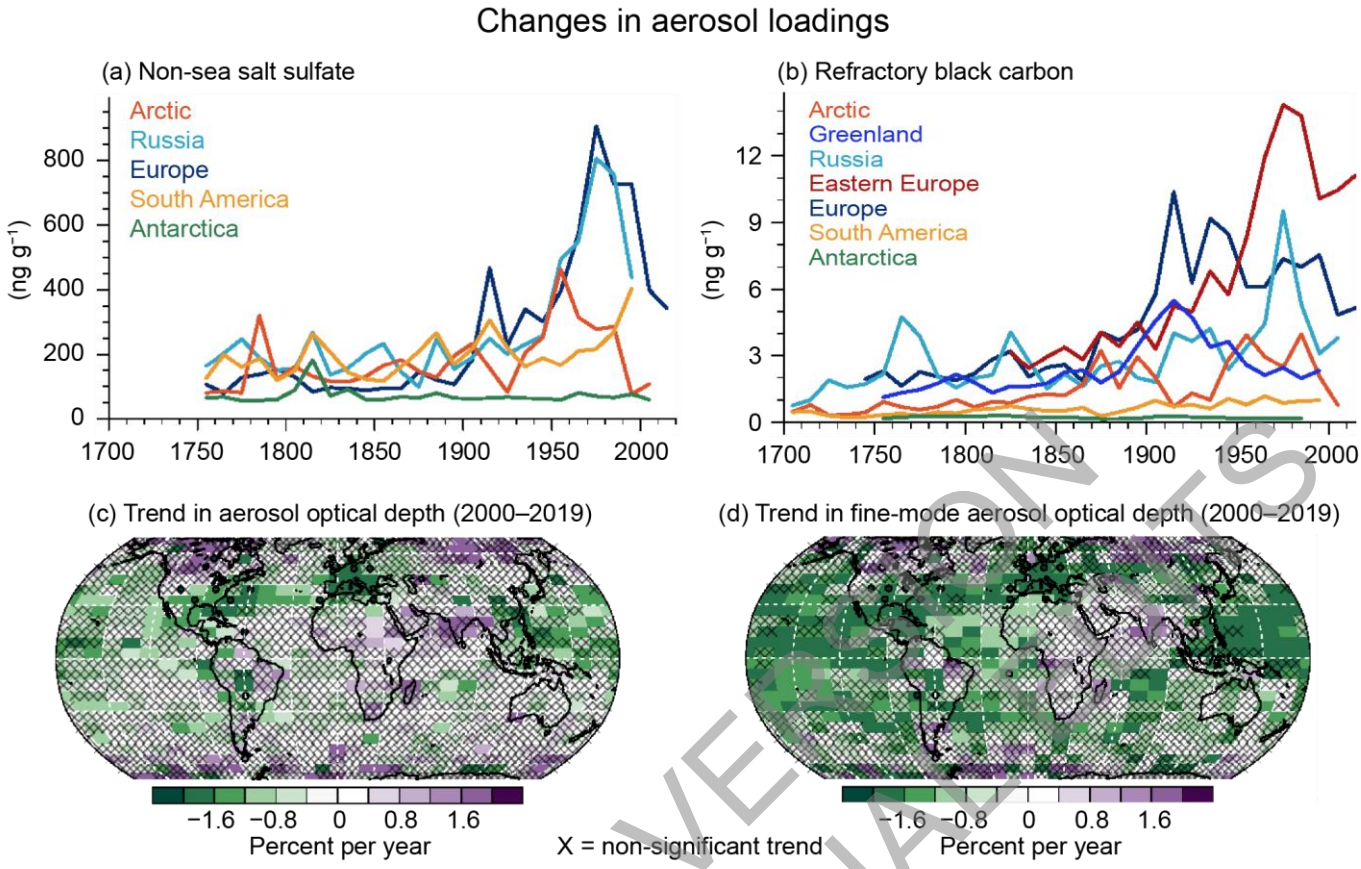


Figure 2.9: **Aerosol evolution from ice-core measurements**. Changes are shown as 10-yr averaged time series (a, b) and trends in remote-sensing aerosol optical depth (AOD) and AODf (c, d). (a) Concentrations of non-sea salt (nss) sulphate (ng g^{-1}). (b) Black carbon (BC) in glacier ice from the Arctic (Lomonosovfonna), Russia (Belukha), Europe (Colle Gnifetti), South America (Illimani), Antarctica (stacked sulphate record, and BC from the B40 core), and BC from Greenland (stacked rBC record from Greenland and Eastern Europe (Elbrus)). (c) Linear trend in annual mean AOD retrieved from satellite data for the 2000–2019 period (% yr^{-1}). The average trend from MODerate Resolution Imaging Spectroradiometer (MODIS) and Multi-Angle Imaging Spectroradiometer (MISR) is shown. Trends are calculated using OLS regression with significance assessed following AR(1) adjustment after Santer et al., (2008a). Superimposed are the trends in annual-mean AOD from the AERONET surface sunphotometer network for 2000–2019. (d) Linear trend in 2000–2019 as in (c), but for fine-mode AOD, AODf, and using only MISR over land. 'x' marks denote non-significant trends. Further details on data sources and processing are available in the chapter data table (Table 2.SM.1).

ACCEPTED VERSION SUBJECT TO FINAL EDITS

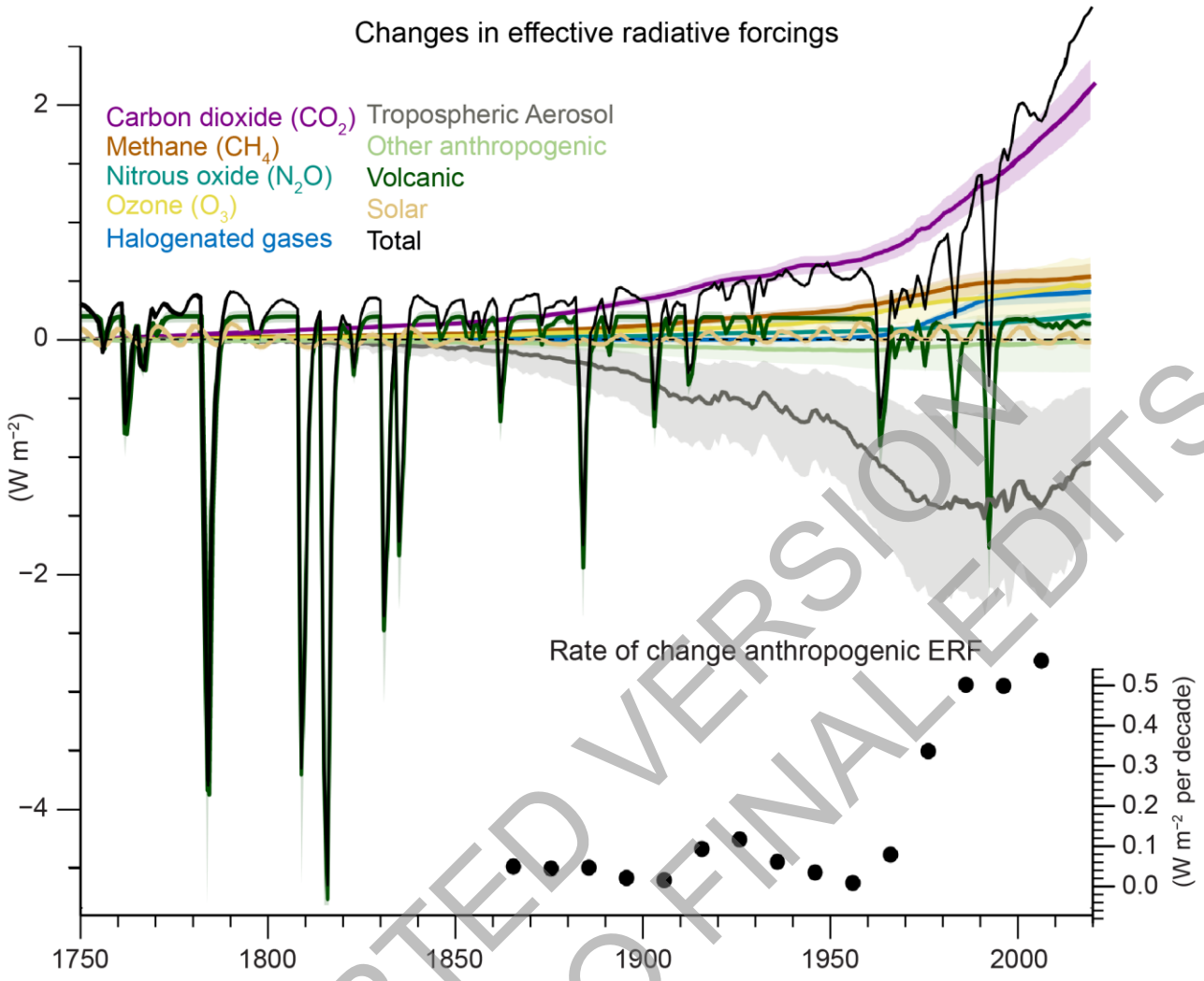
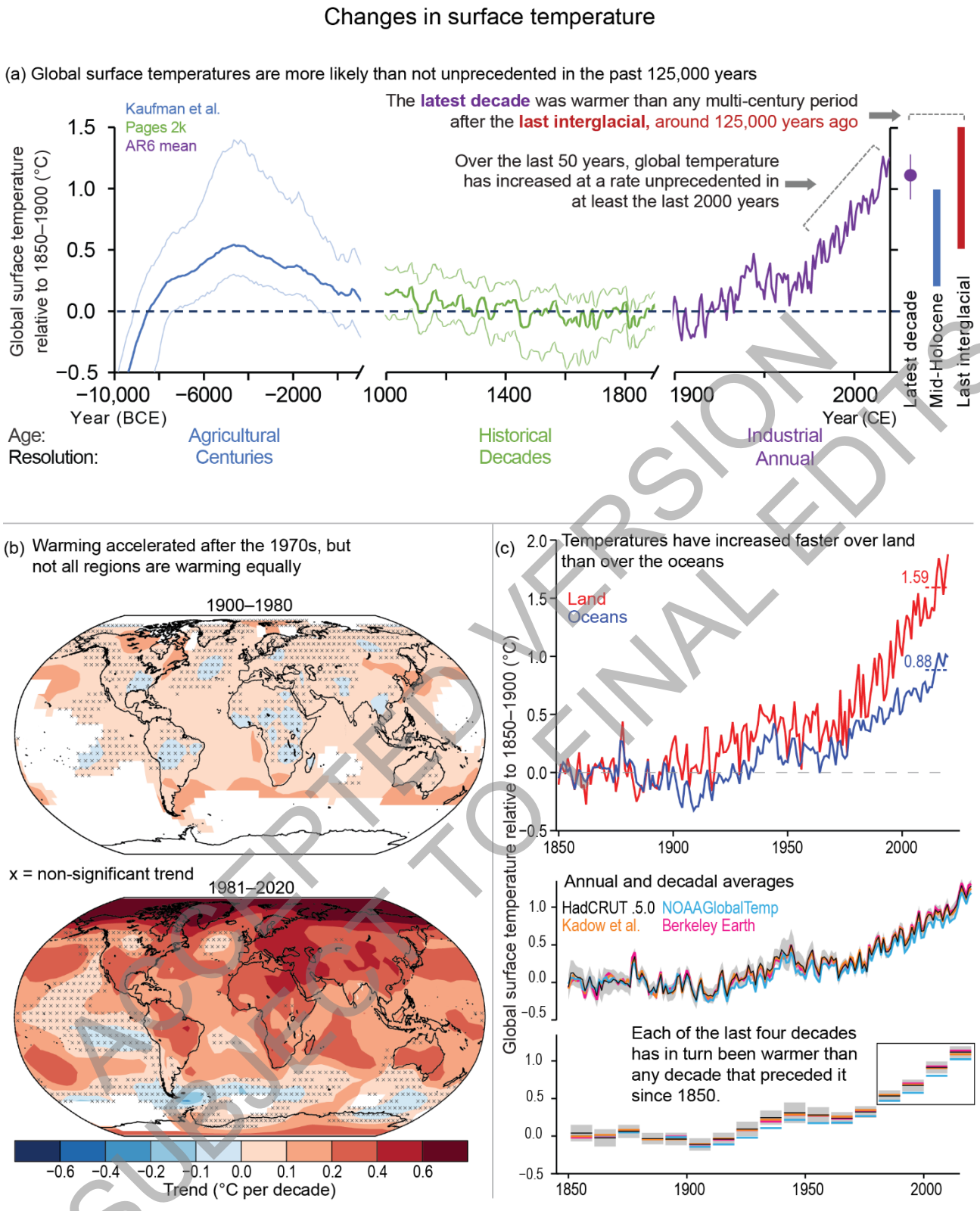


Figure 2.10: Temporal evolution of effective radiative forcing (ERF) related to the drivers assessed in Section 2.2. ERFs are based upon the calculations described in Chapter 7, of which the global annual mean, central assessment values are shown as lines and the 5 to 95% uncertainty range as shading (Section 7.3, see Figures 7.6 to 7.8 for more detail on uncertainties). The inset plot shows the rate of change (linear trend) in total anthropogenic ERF (total without TSI and volcanic ERF) for 30-year periods centred at each dot. Further details on data sources and processing are available in the chapter data table (Table 2.SM.1).

ACCEPTED VERSION SUBJECT TO FINAL EDITS

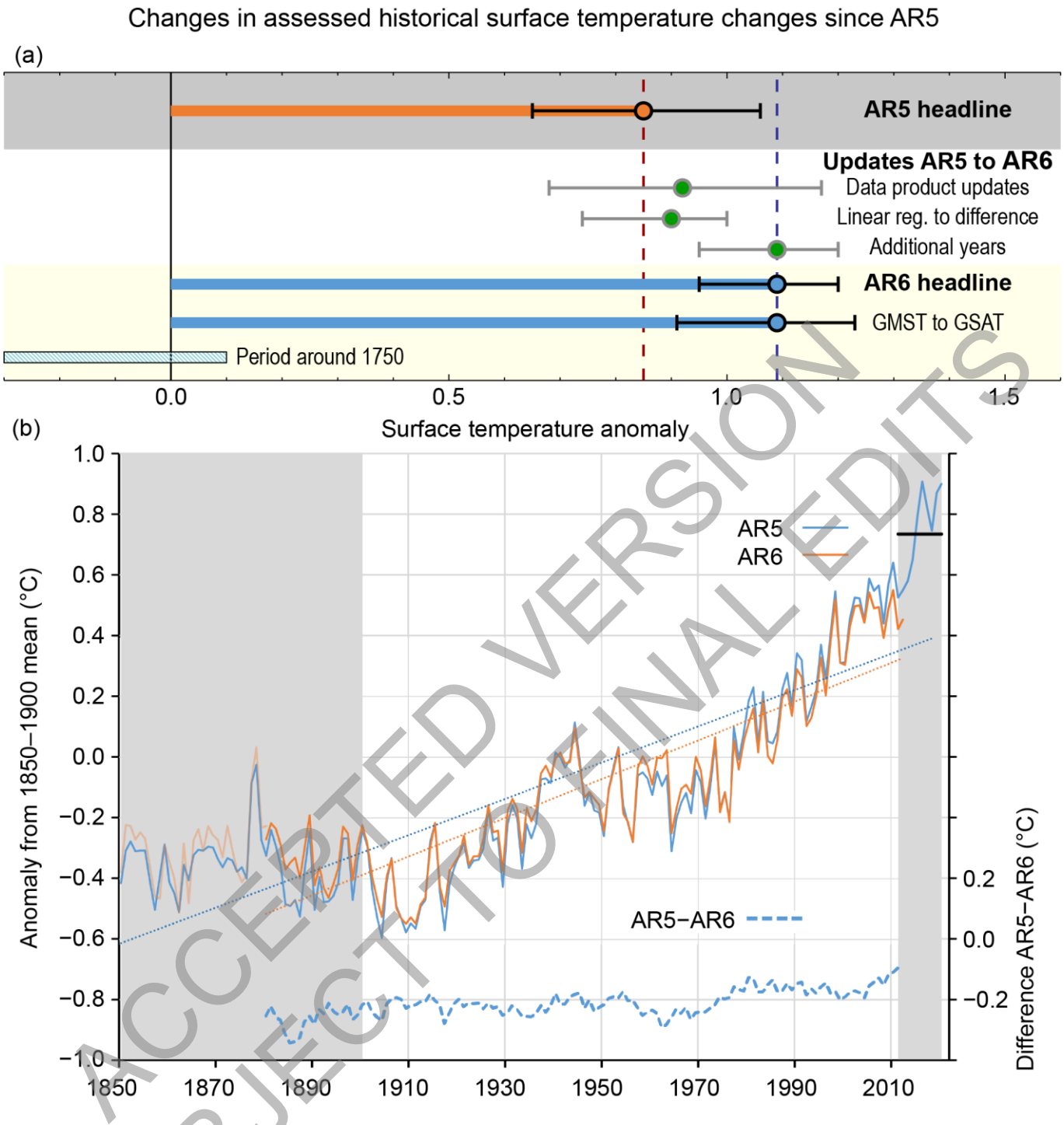


ACCEPTED VERSION SUBJECT TO FINAL EDITS

Figure 2.11: Earth's surface temperature history with key findings annotated within each panel. (a) GMST over the Holocene divided into three time scales. (i) 12 kyr–1 kyr in 100-year time steps, (ii) 1000–1900 CE, 10-year smooth, and (iii) 1900–2020 CE (from panel c). Median of the multi-method reconstruction (bold lines), with 5th and 95th percentiles of the ensemble members (thin lines). Vertical bars are the assessed *medium confidence* ranges of GMST for the Last Interglacial and mid-Holocene (Section 2.3.1.1). The last decade value and *very likely* range arises from 2.3.1.1.3. (b) Spatially resolved trends (°C per decade) for HadCRUTv5 over (upper map) 1900–1980, and (lower map) 1981–2020. 'x' marks denote non-significant trends. (c) Temperature from instrumental data for 1850–2020, including (upper panel) multi-

product mean annual timeseries assessed in Section 2.3.1.1.3 for temperature over the oceans (blue line) and temperature over the land (red line) and indicating the warming to the most recent 10 years; and annually (middle panel) and decadally (bottom panel) resolved averages for the GMST datasets assessed in Section 2.3.1.1.3. The grey shading in each panel shows the uncertainty associated with the HadCRUT5 estimate (Morice et al., 2021). All temperatures relative to the 1850–1900 reference period. Further details on data sources and processing are available in the chapter data table (Table 2.SM.1).

ACCEPTED VERSION
SUBJECT TO FINAL EDITS



ACCEPTED VERSION SUBJECT TO FINAL EDITS

Cross-Chapter Box 2.3, Figure 1: Changes in assessed historical surface temperature changes since AR5. (a) Summary of the impact of various steps from AR5 headline warming-to-date number for 1880–2012 using a linear trend fit to the AR6 assessment based upon the difference between 1850–1900 and 2011–2020. Whiskers provide 90% (*very likely*) ranges. AR6 assessment in addition denotes additional warming since the period around 1750 AR6 assessment in addition denotes additional warming since the period around 1750 (Cross-Chapter Box 1.2). (b) Time series of the average of assessed AR5 series (orange, faint prior to 1880 when only HadCRUT4 was available) and AR6 assessed series (blue) and their differences (offset) including an illustration of the two trend fitting metrics used in AR5 and AR6. Further details on data sources and processing are available in the chapter data table (Table 2.SM.1).

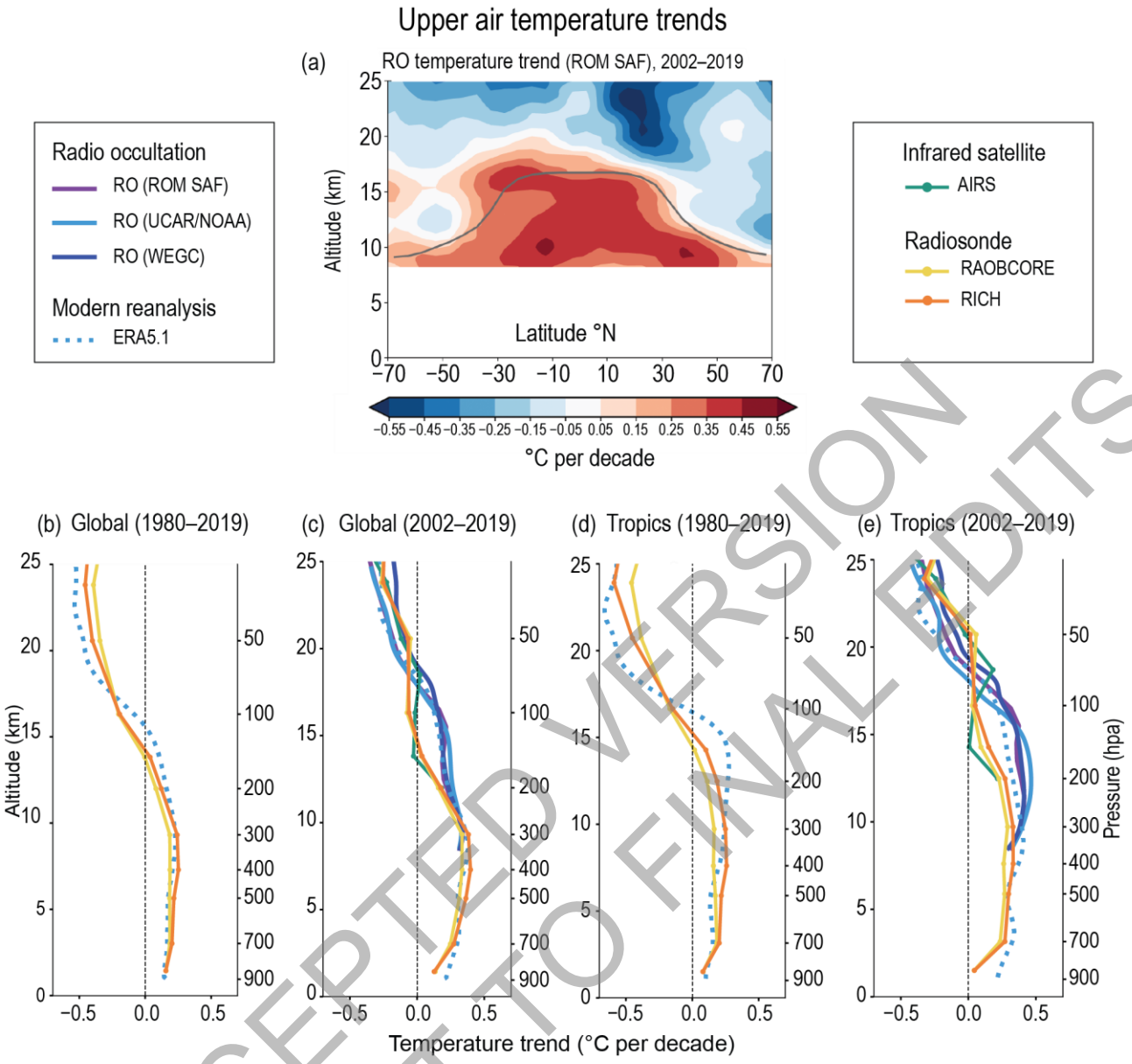


Figure 2.12: Temperature trends in the upper air. (a) Zonal cross-section of temperature anomaly trends (2007–2016 baseline) for 2002–2019 in the upper troposphere and lower stratosphere region. The climatological tropopause altitude is marked as a grey line. Significance is not indicated due to the short period over which trends are shown, and because the assessment findings associated to this figure relate to difference between trends at different heights, not the absolute trends. (b) Trends in temperature at various atmospheric heights for 1980–2019 and 2002–2019 for the near-global (70°N–70°S) domain. (d) (e) as for (b) (c) but for the tropical (20°N–20°S) region. Further details on data sources and processing are available in the chapter data table (Table 2.SM.1).

ACCEPTED VERSION SUBJECT TO FINAL EDITS

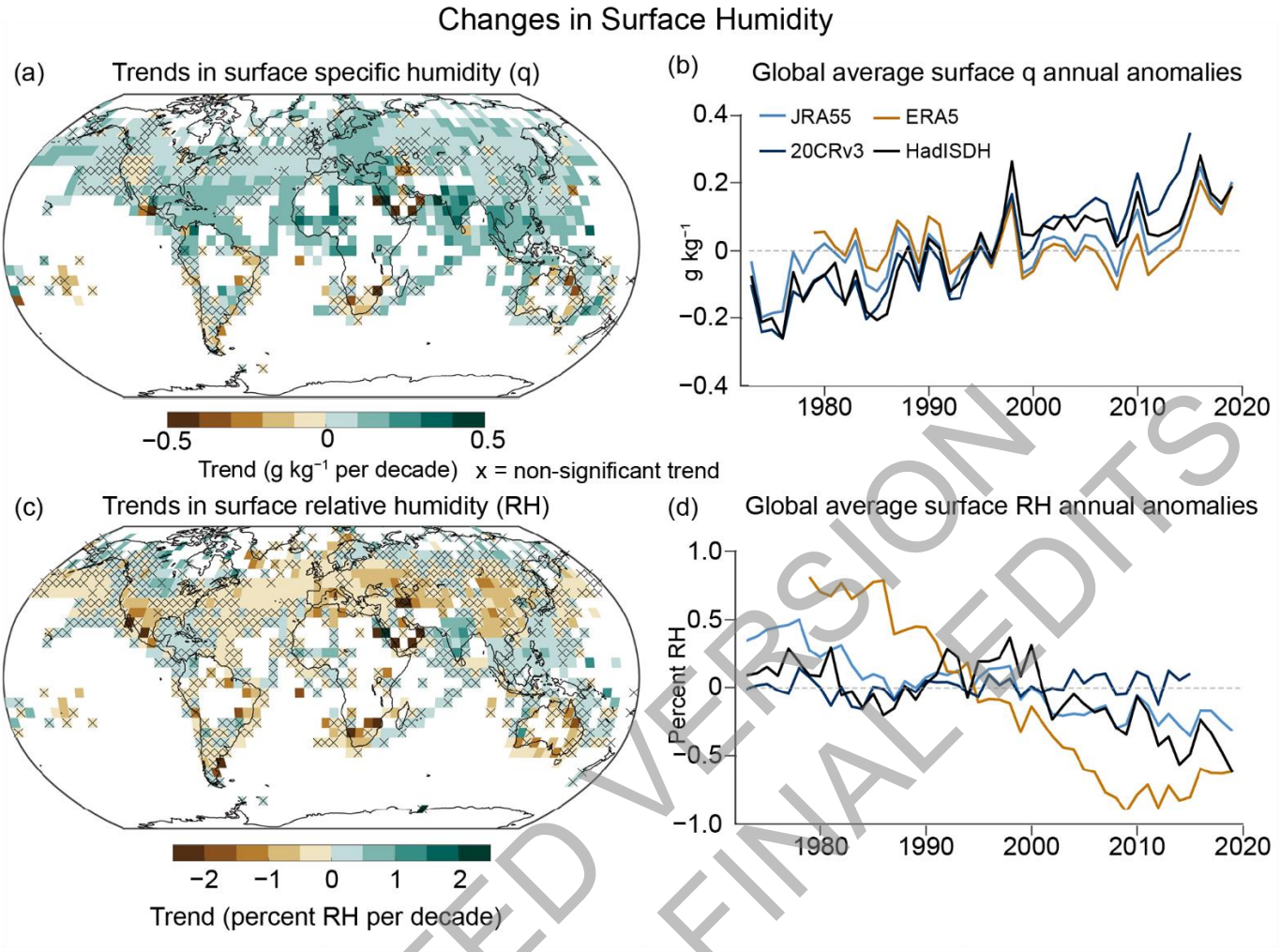


Figure 2.13: Changes in surface humidity. (a) Trends in surface specific humidity over 1973–2019. Trends are calculated using OLS regression with significance assessed following AR(1) adjustment after Santer et al (2008a) ('x' marks denote non-significant trends). (b) Global average surface specific humidity annual anomalies (1981–2010 base period). (c) as (a) but for the relative humidity. (d) as (b) but for the global average surface relative humidity annual anomalies. Further details on data sources and processing are available in the chapter data table (Table 2.SM.1).

ACCEPTED VERSION SUBJECT TO FINAL EDITS

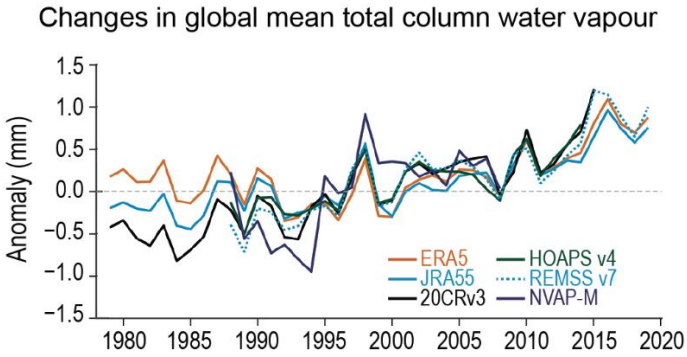


Figure 2.14: Timeseries of global mean total column water vapour annual anomalies (mm) relative to a 1988–2008 base period. Further details on data sources and processing are available in the chapter data table (Table 2.SM.1).

ACCEPTED VERSION
SUBJECT TO FINAL EDITS

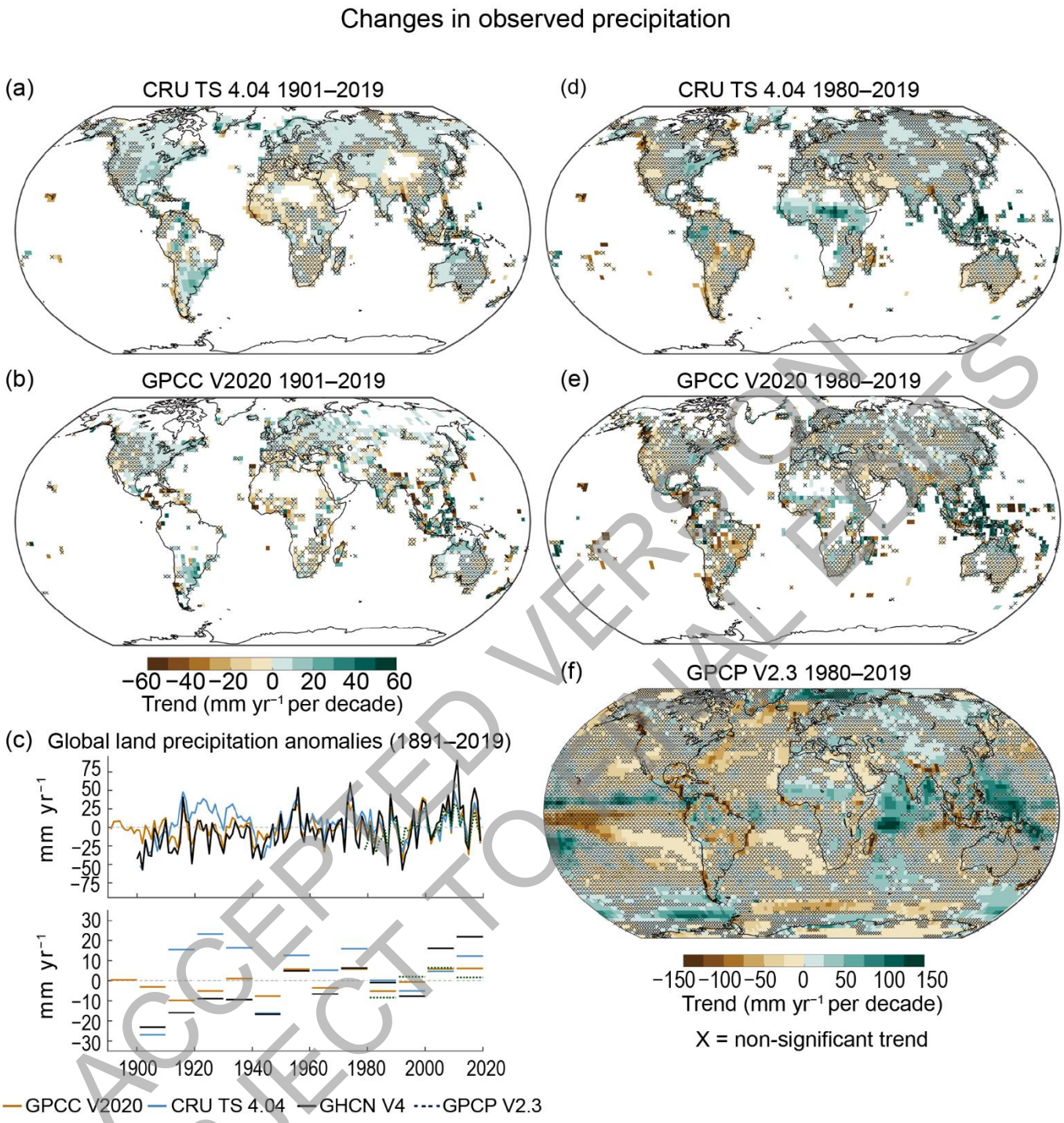


Figure 2.15: Changes in observed precipitation. (a, b) Spatial variability of observed precipitation trends over land for 1901–2019 for two global in-situ products. Trends are calculated using OLS regression with significance assessed following AR(1) adjustment after Santer et al (2008a) ('x' marks denote non-significant trends). (c) Annual time series and decadal means from 1891 to date relative to a 1981–2010 climatology (note that different products commence at distinct times). (d, e) as (a, b), but for the periods starting in 1980. (f) is for the same period for the globally complete merged GPCP v2.3 product. Further details on data sources and processing are available in the chapter data table (Table 2.SM.1).

ACCEPTED VERSION SUBJECT TO FINAL EDITS

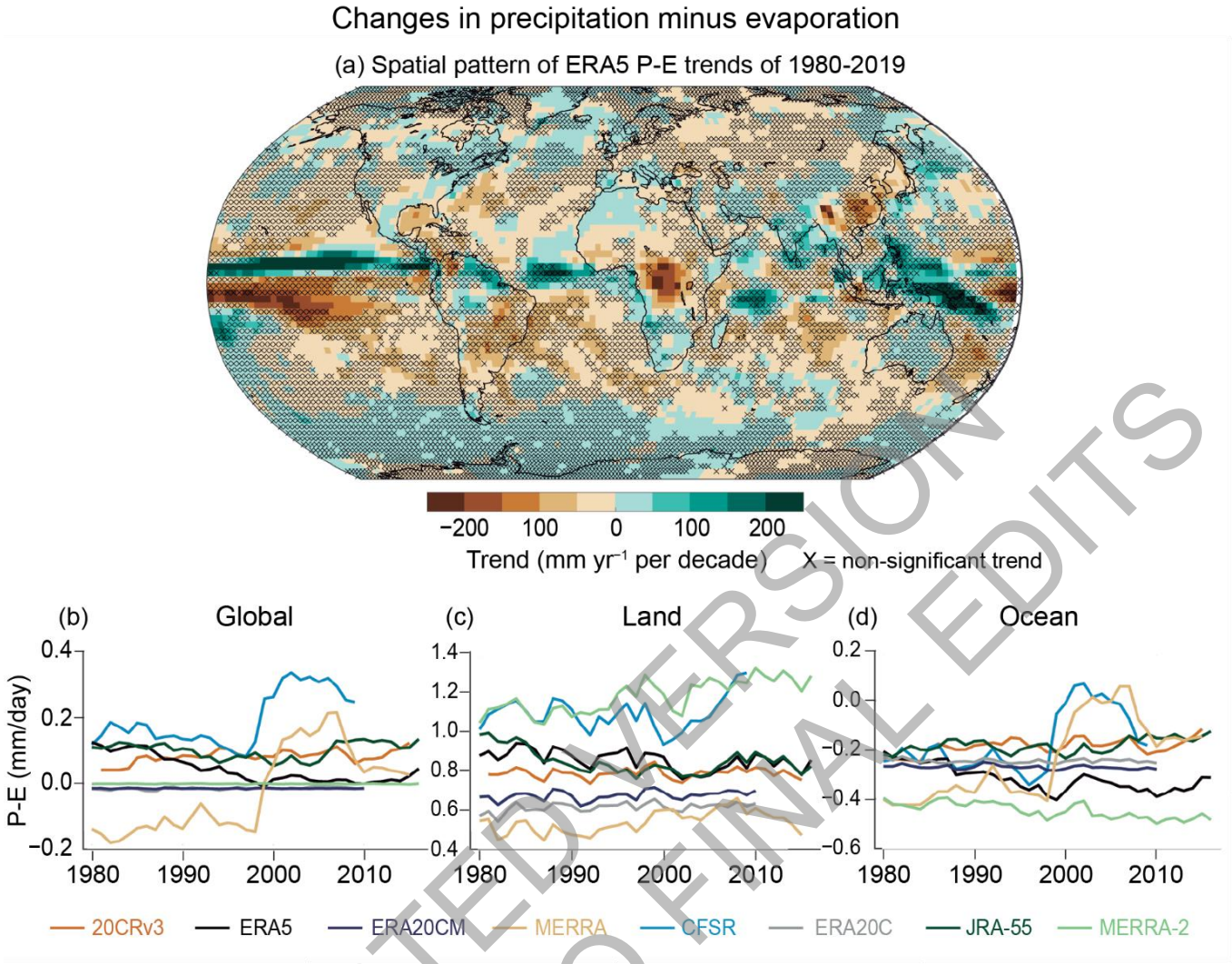


Figure 2.16: Changes in precipitation minus evaporation. (a) Trends in precipitation minus evaporation (P-E) between 1980 and 2019. Trends are calculated using OLS regression with significance assessed following AR(1) adjustment after (Santer et al., 2008; 'x' marks denote non-significant trends). Time series of (b) global, (c) land-only and (d) ocean-only average annual P-E (mm/day). Further details on data sources and processing are available in the chapter data table (Table 2.SM.1).

ACCEPTED VERSION SUBJECT TO FINAL EDITS

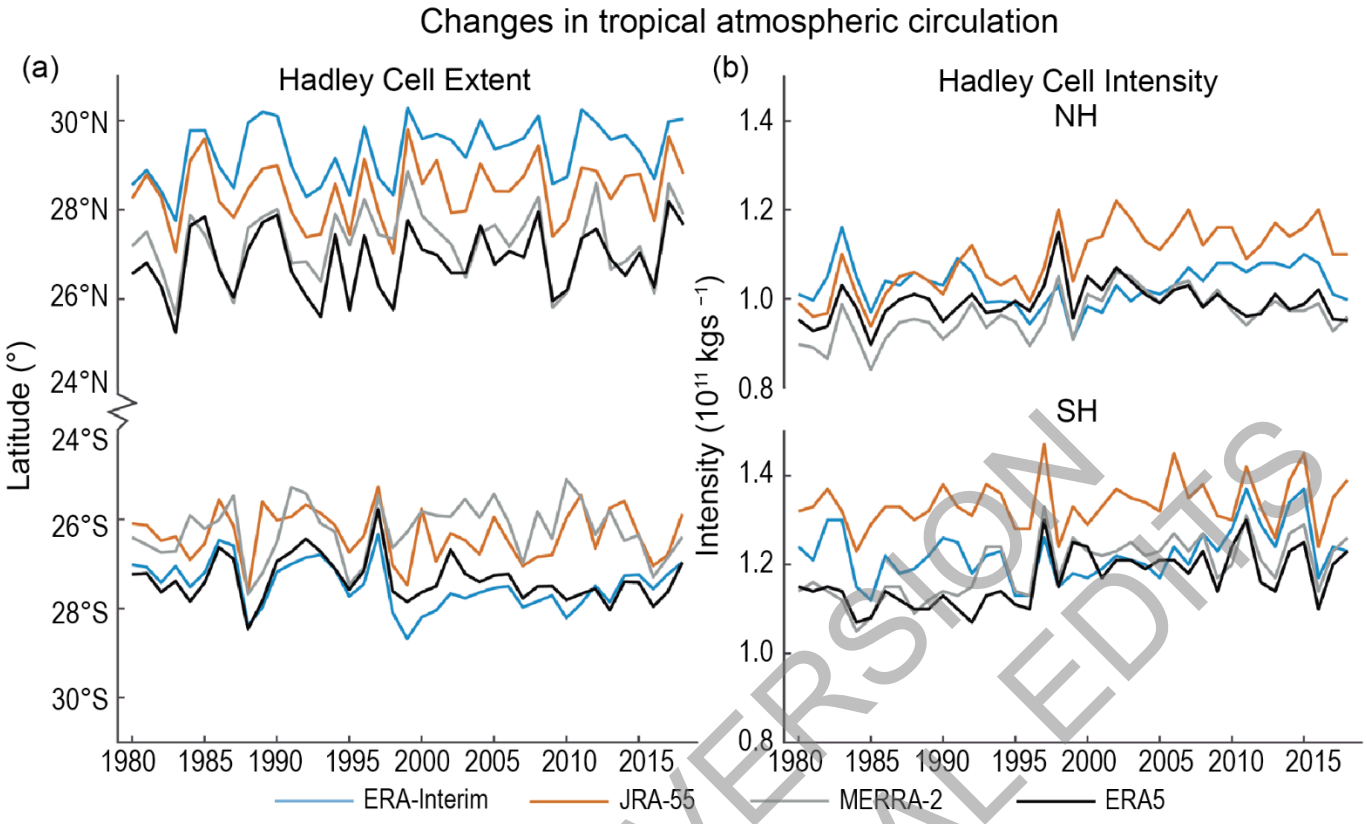


Figure 2.17: Timeseries of the annual mean Northern Hemisphere (NH, top curves) and Southern Hemisphere (SH, bottom curves) Hadley Cell extent (a) and Hadley Cell intensity (b) since 1979. Further details on data sources and processing are available in the chapter data table (Table 2.SM.1).

ACCEPTED VERSION SUBJECT TO FINAL EDITS

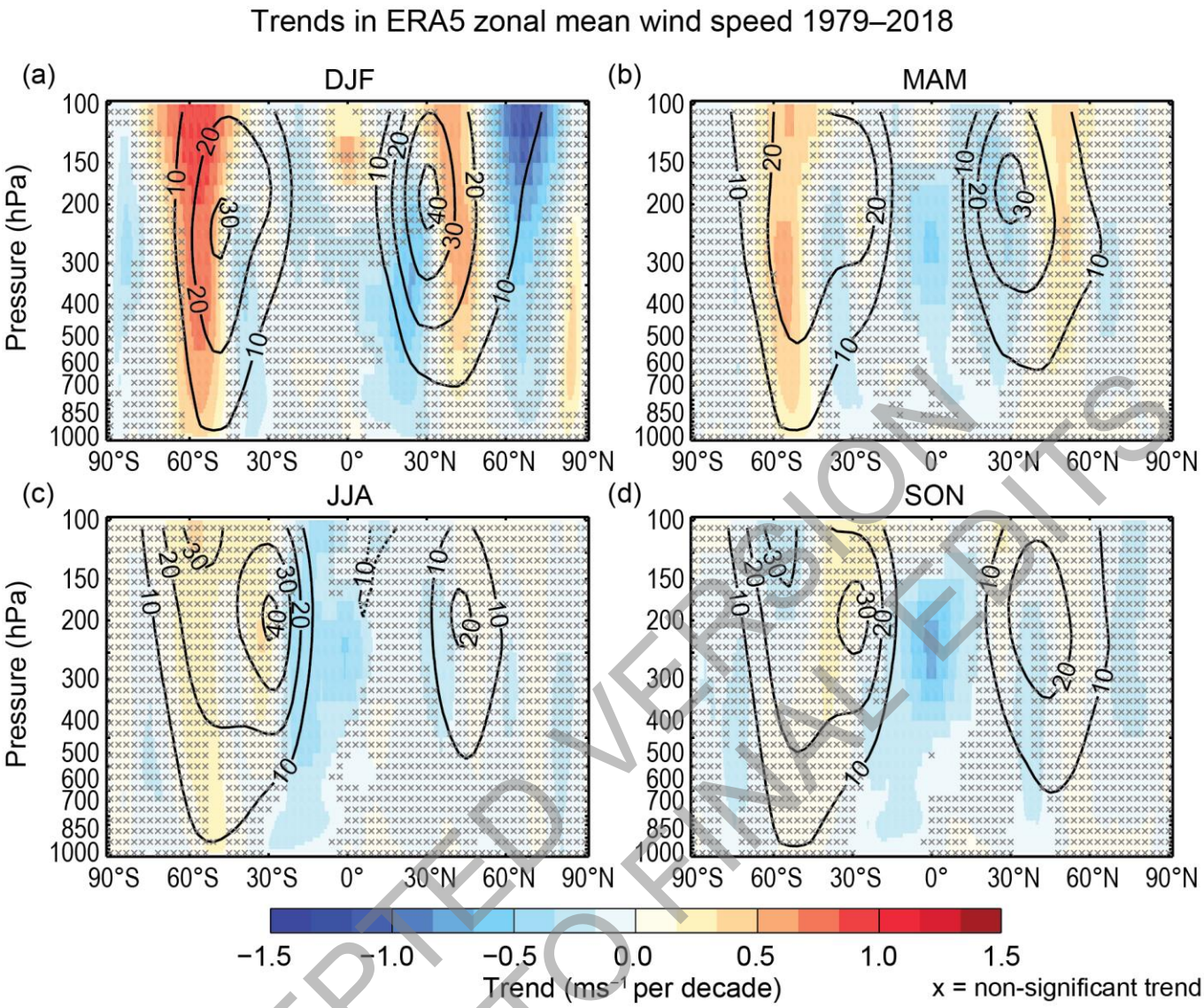


Figure 2.18: Trends in ERA5 zonal-mean zonal wind speed. Shown are (a) DJF (December-January-February), (b) MAM (March-April-May), (c) JJA (June-July-August) and (d) SON (September-October-November). Climatological zonal winds during the data period are shown in solid contour lines for westerly winds and in dashed lines for easterly. Trends are calculated using OLS regression with significance assessed following AR(1) adjustment after Santer et al (2008a) ('x' marks denote non-significant trends). Further details on data sources and processing are available in the chapter data table (Table 2.SM.1).

ACCEPTED VERSION SUBJECT TO FINAL EDITS

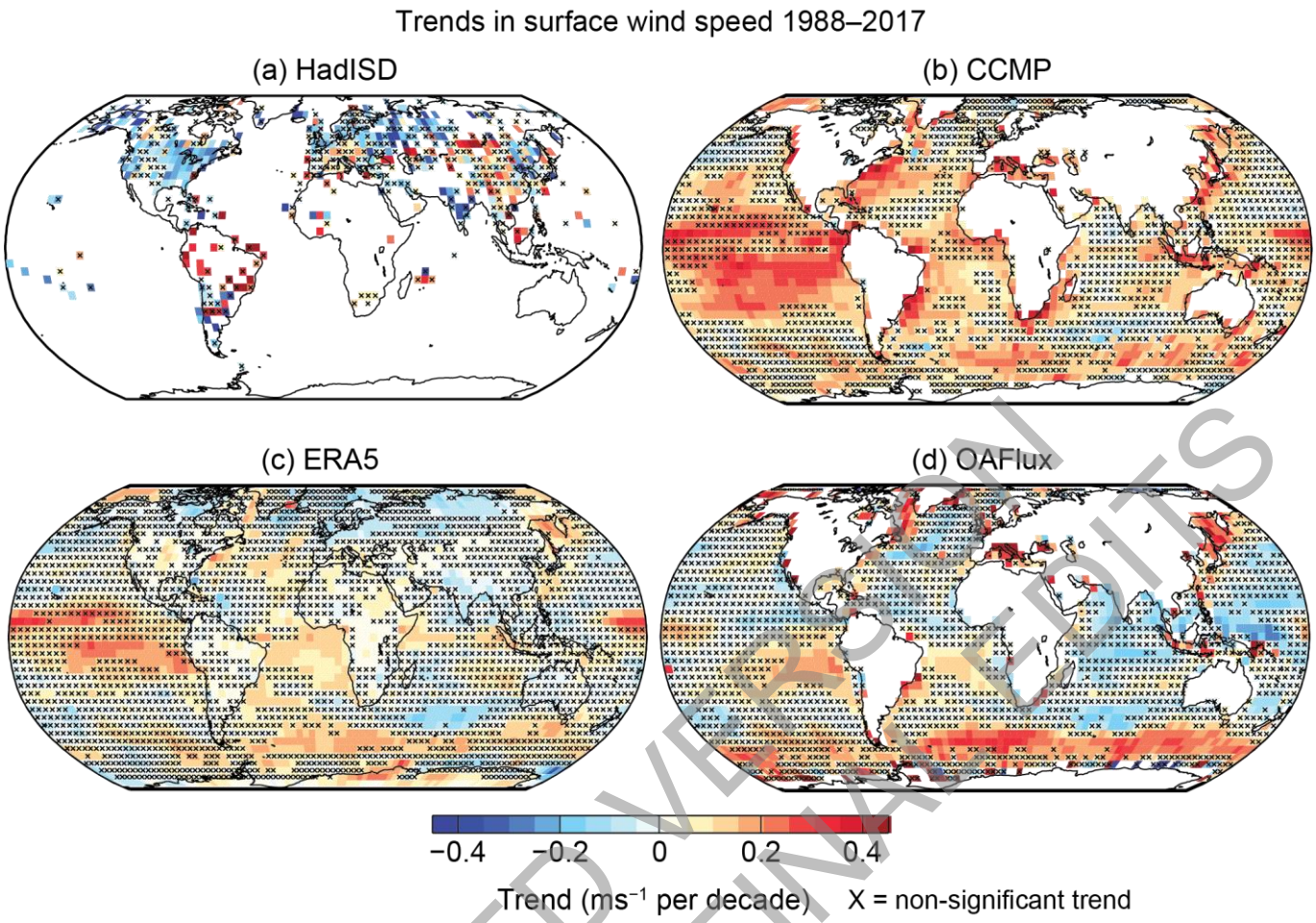


Figure 2.19: Trends in surface wind speed. (a) Station observed winds from the integrated surface database (HadISD v2.0.2.2017f); (b) Cross-Calibrated Multi-Platform wind product; (c) ERA5; and (d) wind speed from the Objectively Analyzed Air-Sea Heat Fluxes dataset, release 3. White areas indicate incomplete or missing data. Trends are calculated using OLS regression with significance assessed following AR(1) adjustment after Santer et al (2008b) ('x' marks denote non-significant trends). Further details on data sources and processing are available in the chapter data table (Table 2.SM.1).

ACCEPTED VERSION SUBJECT TO FINAL EDITS

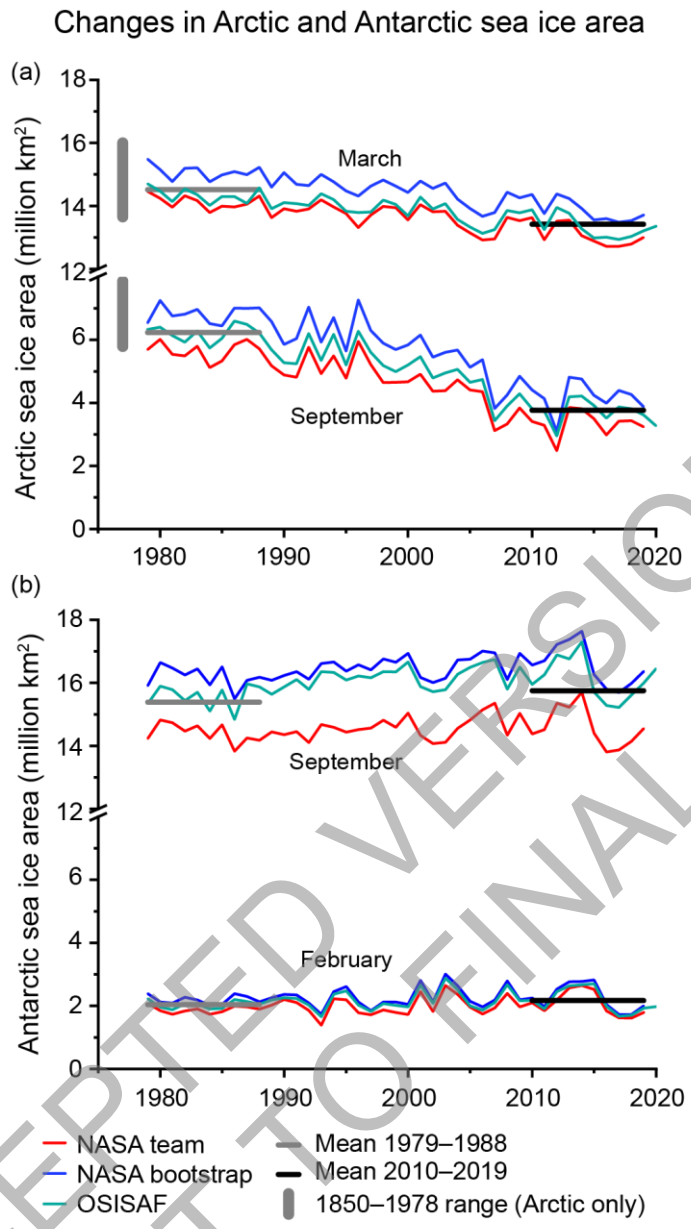


Figure 2.20: Changes in Arctic and Antarctic sea ice area. (a) Three time series of Arctic sea ice area (SIA) for March and September from 1979 to 2020 (passive microwave satellite era). In addition, the range of SIA from 1850–1978 is indicated by the vertical bar to the left. Decadal means for the three series for the first and most recent decades of observations are shown by horizontal lines in grey (1979–1988) and black (2010–2019). (b): Three time series of Antarctic sea ice area for September and February (1979–2020). Sea ice area values have been calculated from sea ice concentration fields. Available data for 2020 (OSISAF) is shown in both (a) and (b). Further details on data sources and processing are available in the chapter data table (Table 2.SM.1).

ACCEPTED VERSION SUBJECT TO FINAL EDITS

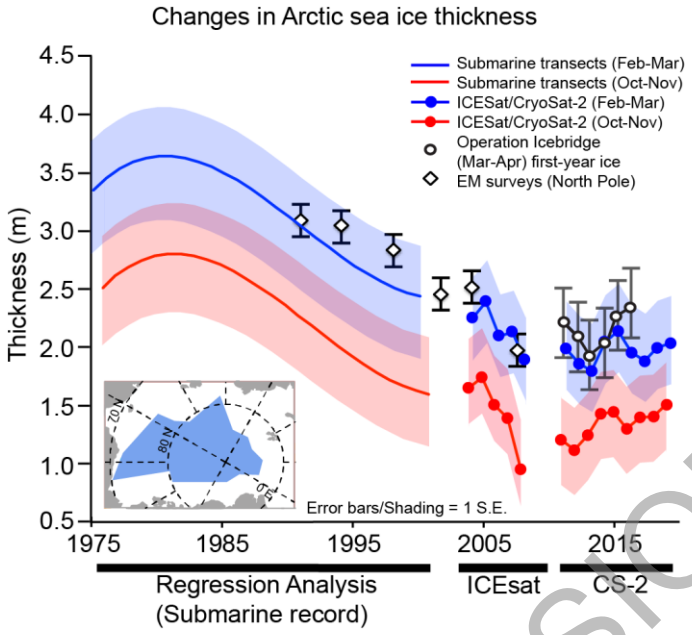


Figure 2.21: Arctic sea ice thickness changes (means) for autumn (red/dotted red) and winter (blue/dotted blue). Shadings (blue and red) show 1 S.E. ranges from the regression analysis of submarine ice thickness and expected uncertainties in satellite ice thickness estimates. Data release area of submarine data ice thickness data is shown in inset. Satellite ice thickness estimates are for the Arctic south of 88°N. Thickness estimates from more localized airborne/ground electromagnetic surveys near the North Pole (diamonds) and from Operation IceBridge (circles) are shown within the context of the larger scale changes in the submarine and satellite records. Further details on data sources and processing are available in the chapter data table (Table 2.SM.1).

ACCEPTED VERSION
SUBJECT TO FINAL EDITS

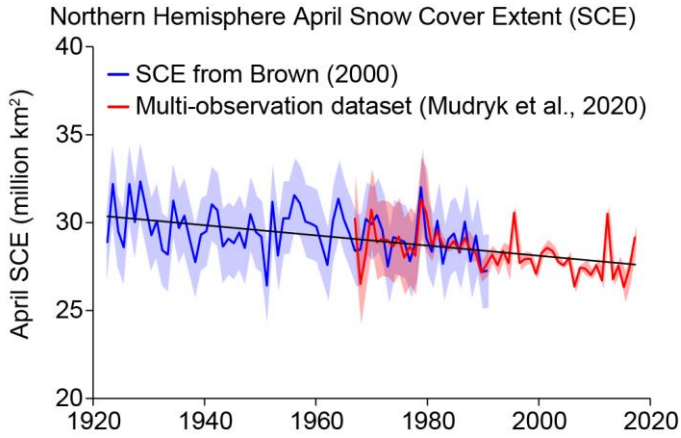


Figure 2.22: April snow cover extent (SCE) for the Northern Hemisphere (1922–2018). Shading shows *very likely* range. The trend over the entire 1922–2018 period (black line) is –0.29 (± 0.07) million km^2 per decade. Further details on data sources and processing are available in the chapter data table (Table 2.SM.1).

ACCEPTED VERSION
SUBJECT TO FINAL EDITS

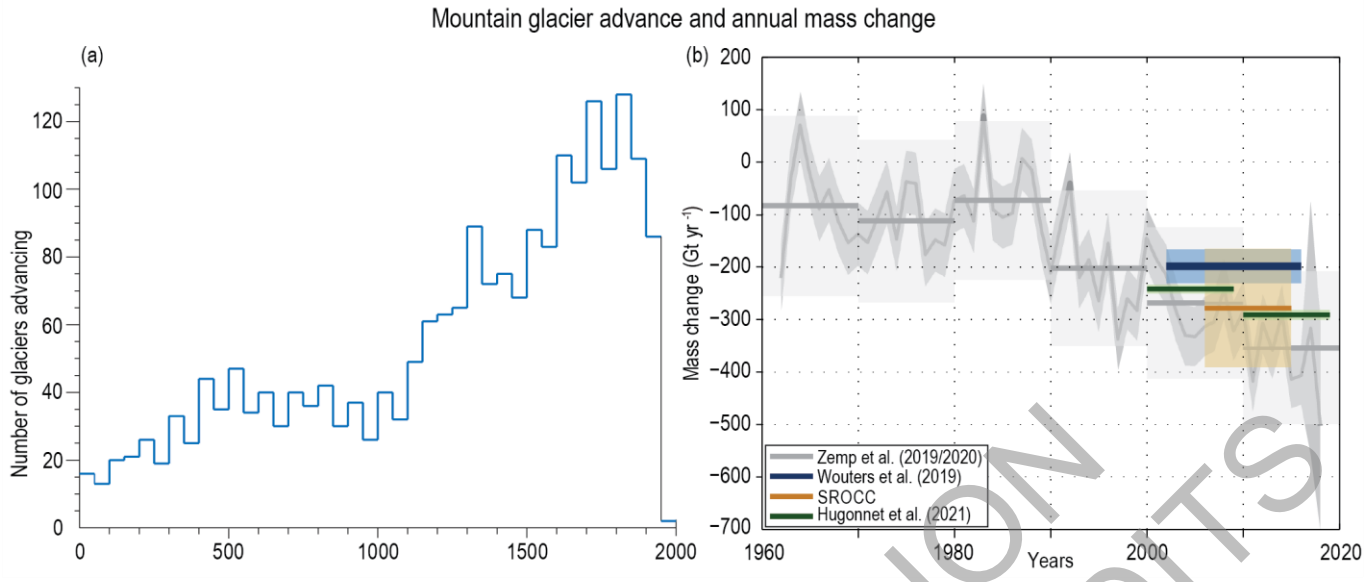


Figure 2.23: Glacier advance and annual mass change. (a) Number of a finite selection of surveyed glaciers that advanced during the past 2000 years. (b) Annual and decadal global glacier mass change (Gt yr^{-1}) from 1961 until 2018. In addition, mass change mean estimates are shown. Ranges show the 90% confidence interval. Further details on data sources and processing are available in the chapter data table (Table 2.SM.1).

ACCEPTED VERSION
SUBJECT TO FINAL EDITS

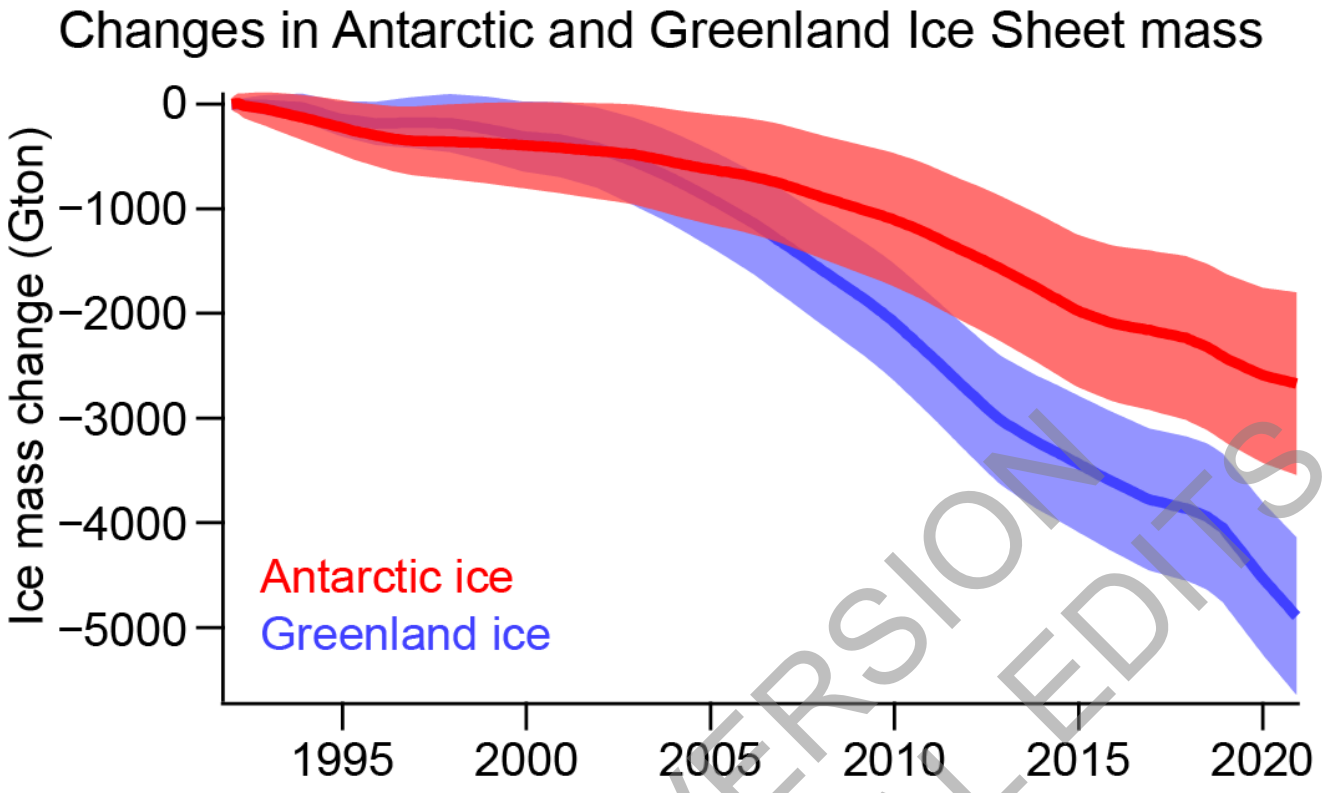


Figure 2.24: Cumulative Antarctic Ice Sheet (AIS) and Greenland Ice Sheet (GrIS) mass changes. Values shown are in gigatons and come from satellite-based measurements (IMBIE Consortium, 2018, 2020) for the period 1992–2018 for GrIS and 1992–2017 for AIS. The estimated uncertainties, *very likely* range, for the respective cumulative changes are shaded. Further details on data sources and processing are available in the chapter data table (Table 2.SM.1).

ACCEPTED VERSION SUBJECT TO FINAL EDITS

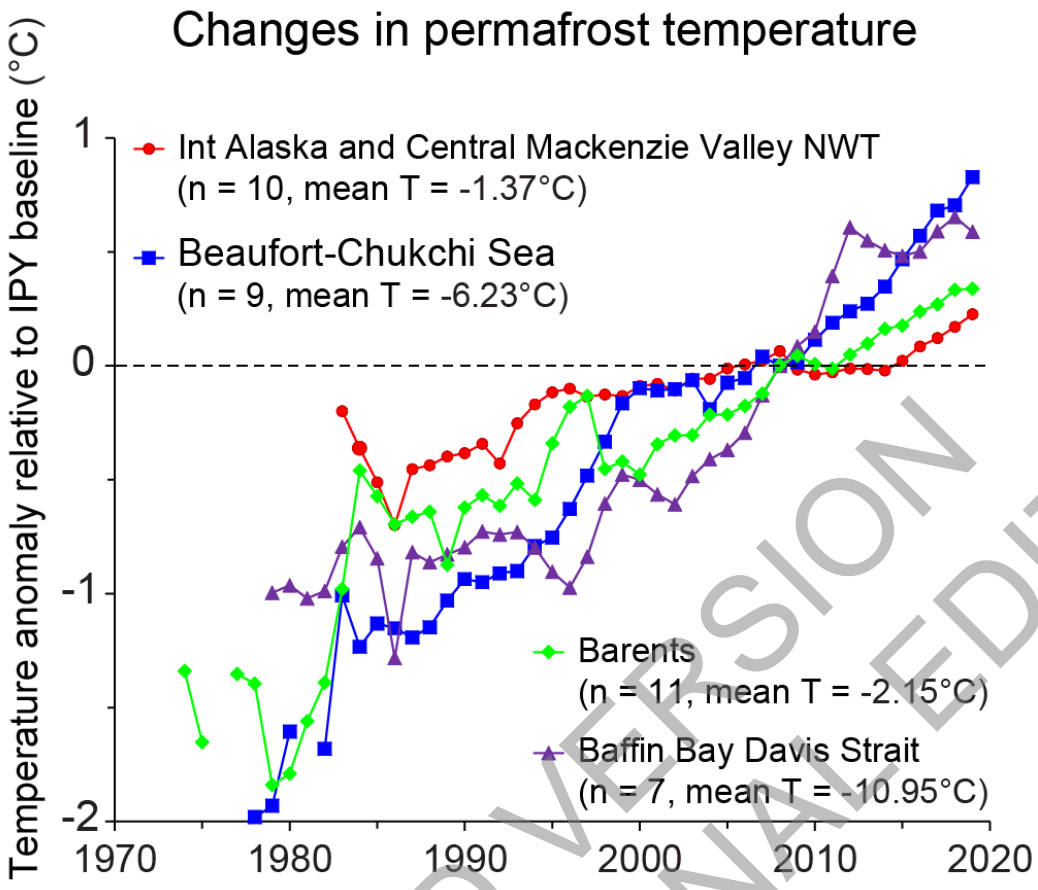


Figure 2.25: Changes in permafrost temperature. Average departures of permafrost temperature (measured in the upper 20–30m) from a baseline established during International Polar Year (2007–2009) for Arctic regions. Further details on data sources and processing are available in the chapter data table (Table 2.SM.1).

ACCEPTED VERSION SUBJECT TO FINAL EDITS

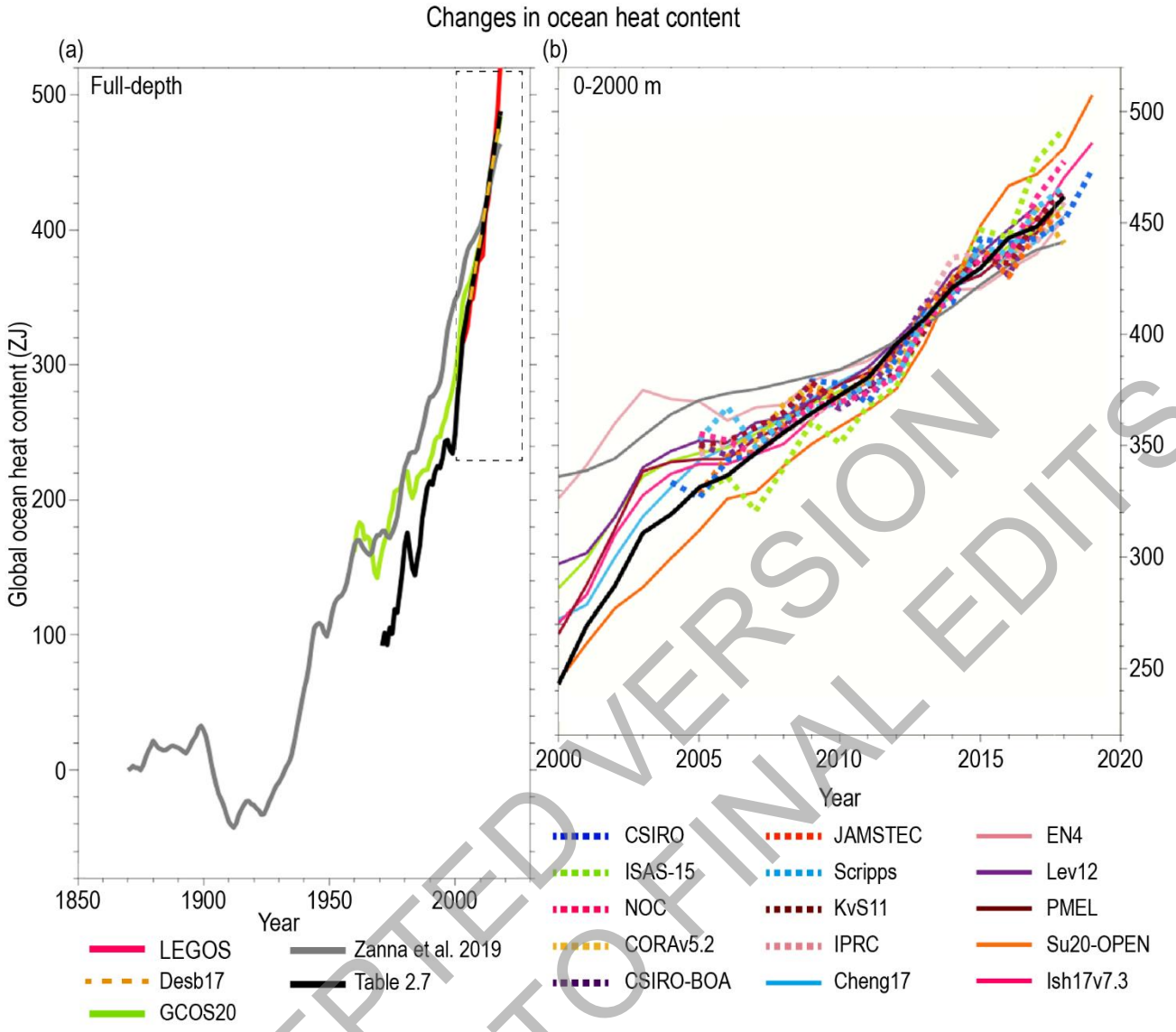


Figure 2.26: Changes in Ocean heat content (OHC). Changes are shown over (a) full depth of the ocean from 1871 to 2019 from a selection of indirect and direct measurement methods. The series from Table 2.7 is shown in solid black in both (a) and (b) (see Table 2.7 caption for details). (b) as (a) but for 0–2000 m depths only and reflecting the broad range of available estimates over this period all of which are broadly similar. Further details on data sources and processing are available in the chapter data table (Table 2.SM.1).

ACCEPTED VERSION SUBJECT TO FINAL EDITS

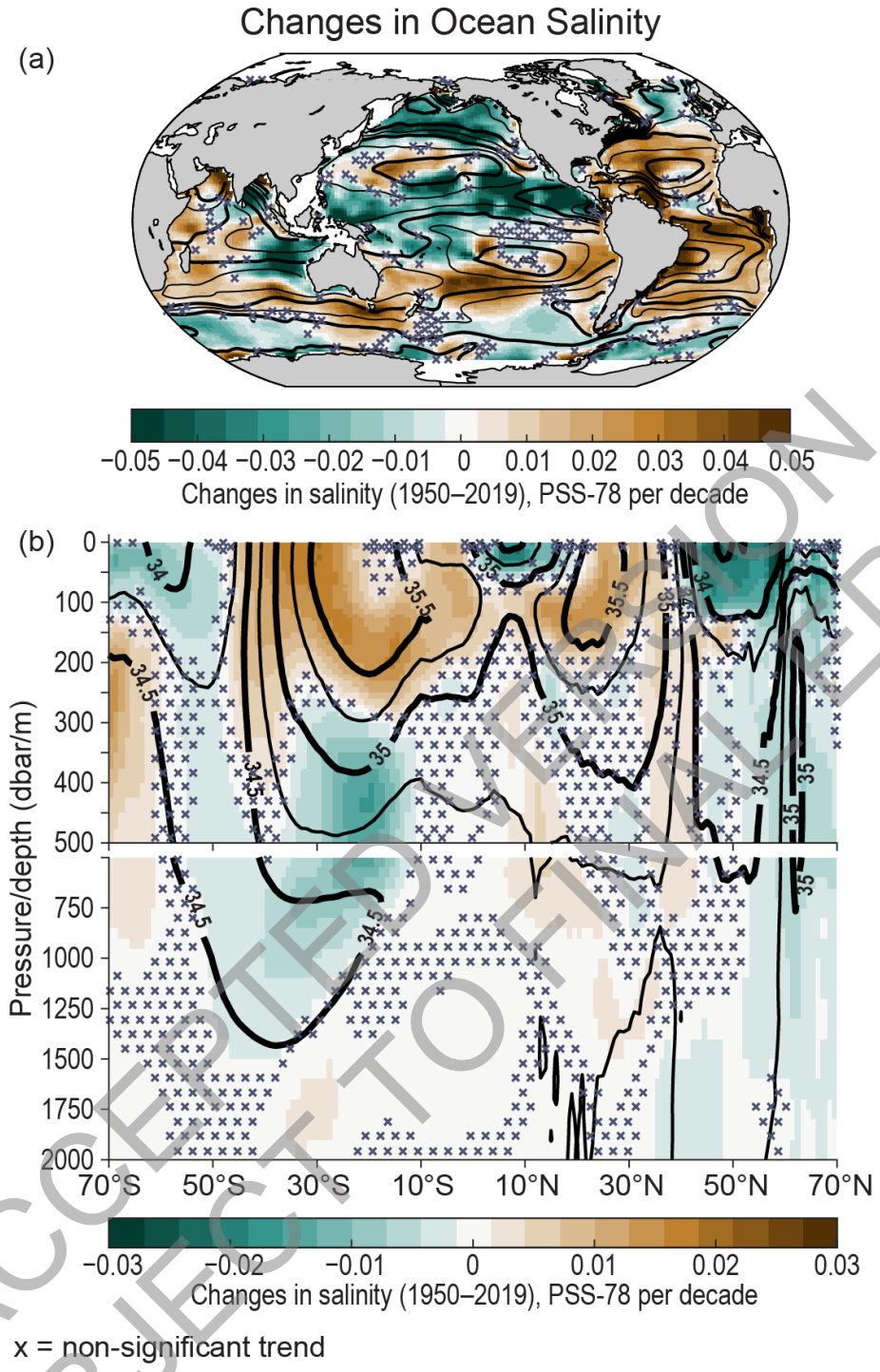
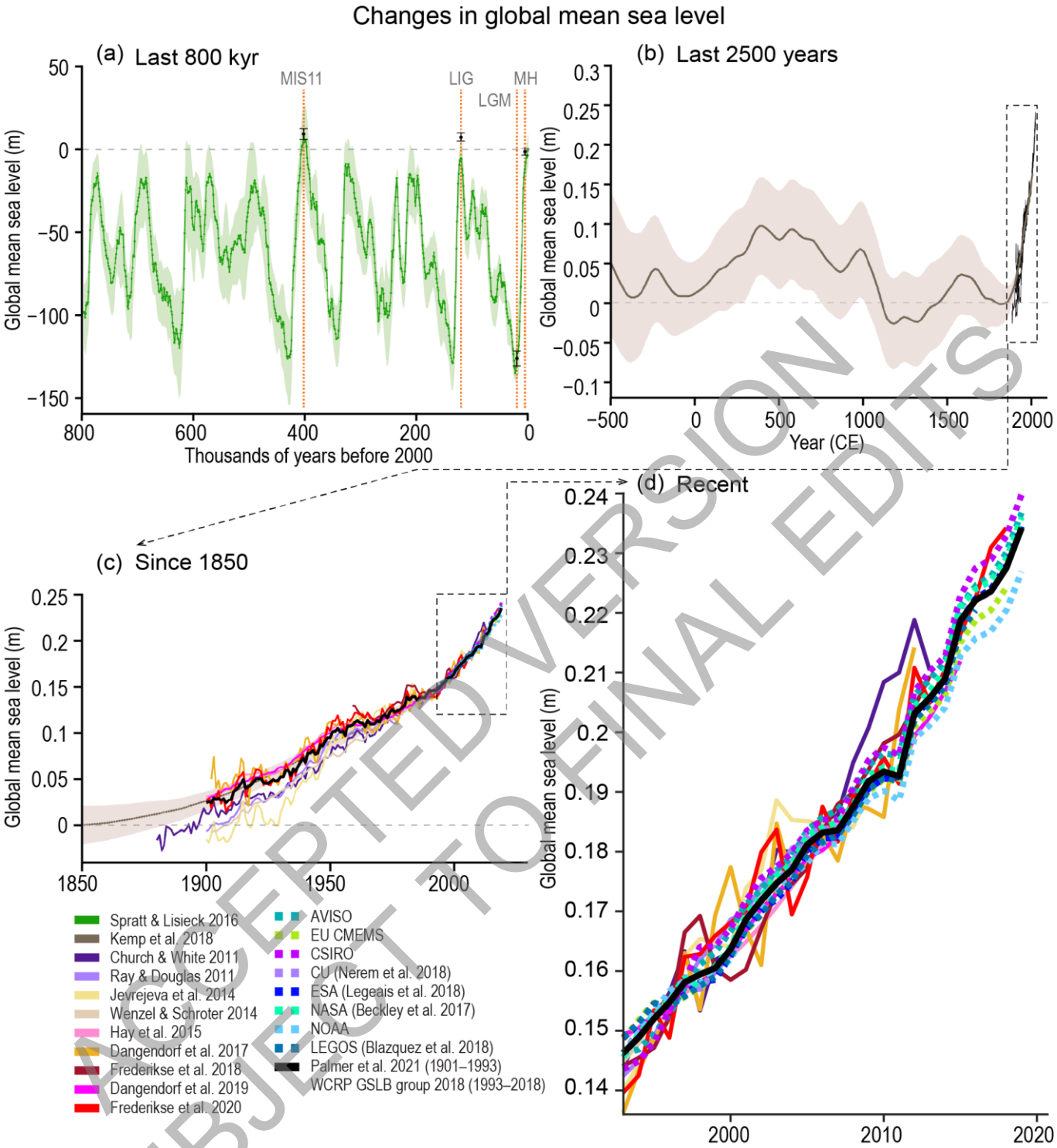


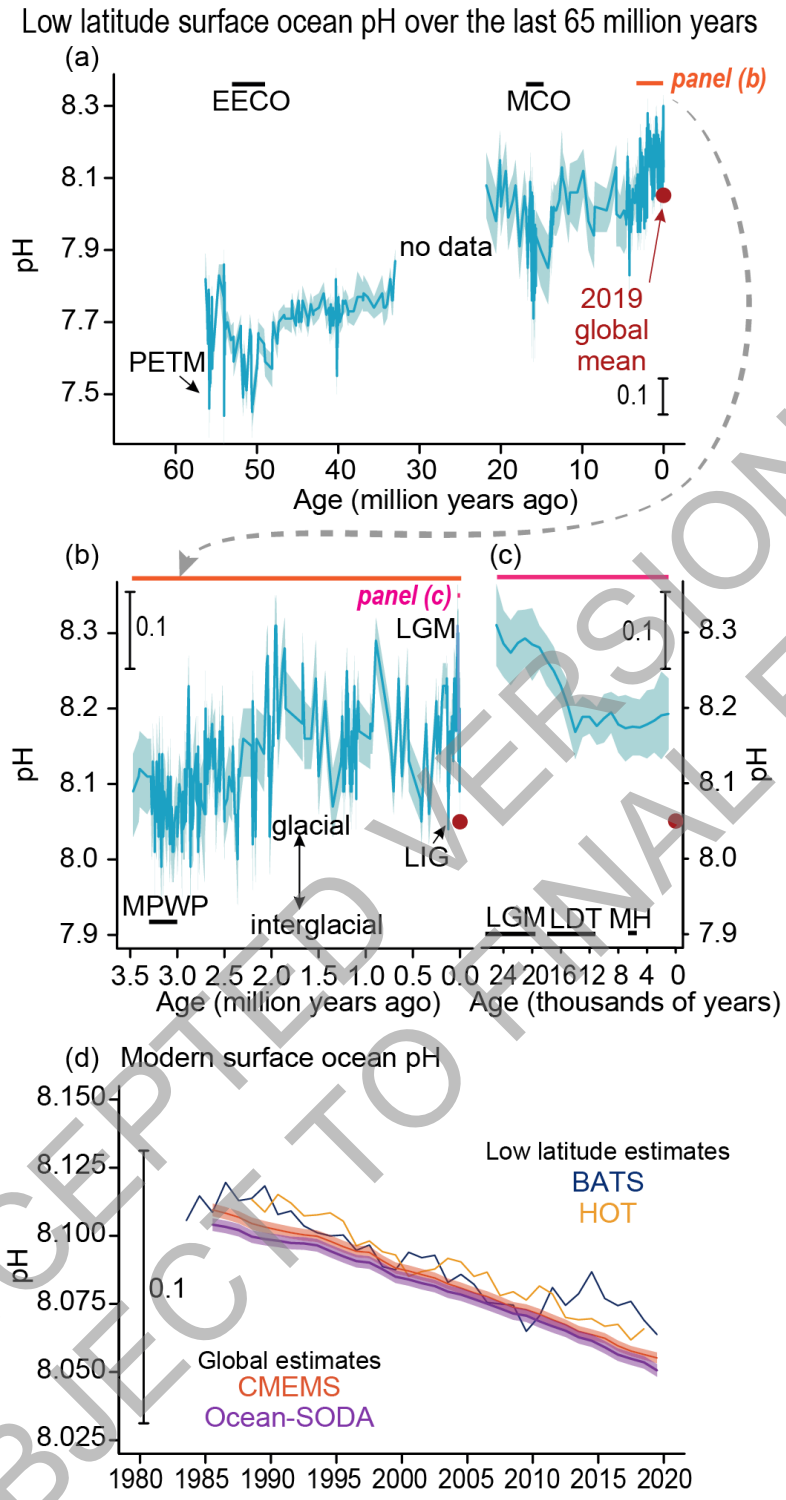
Figure 2.27: Changes in ocean salinity. Estimates of salinity trends using a total least absolute differences fitting method for (a) global near-surface salinity (SSS) changes and (b) global zonal mean subsurface salinity changes. Black contours show the associated climatological mean salinity (either near-surface (a) or subsurface (b)) for the analysis period (1950–2019). Both panels represent changes of Practical Salinity Scale 1978 [PSS-78], per decade. In both panels green denotes freshening regions and orange/brown denotes regions with enhanced salinities. 'x' marks denote non-significant changes. Further details on data sources and processing are available in the chapter data table (Table 2.SM.1).

ACCEPTED VERSION SUBJECT TO FINAL EDITS



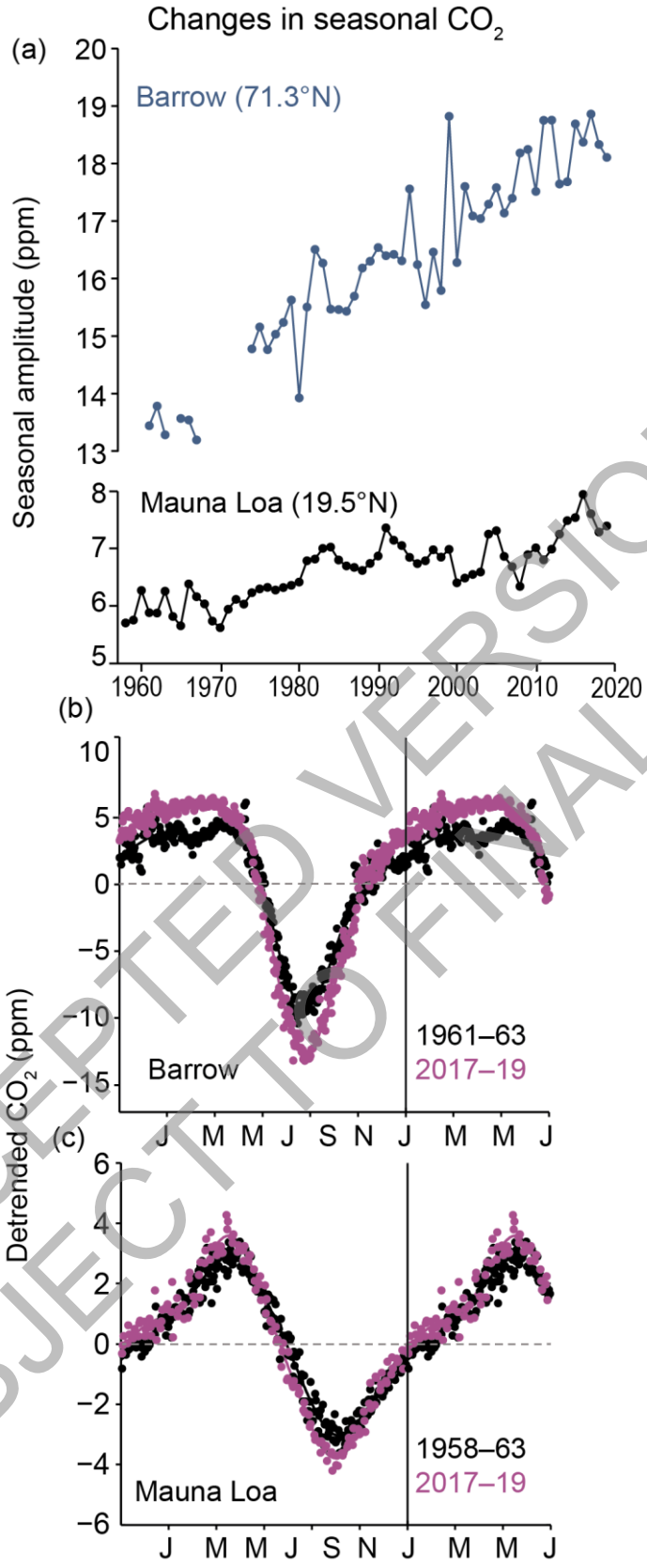
ACCEPTED VERSION SUBJECT TO FINAL EDITS

Figure 2.28: Changes in global mean sea level. (a) Reconstruction of sea-level from ice core oxygen isotope analysis for the last 800 kyr. For target paleo periods (CCB2.1) and MIS11 the estimates based upon a broader range of sources are given as box whiskers. Note the much broader axis range (200 m) than for later panels (tenths of metres). (b) Reconstructions for the last 2500 years based upon a range of proxy sources with direct instrumental records superposed since the late 19th century. (c) Tide-gauge and, more latterly, altimeter based estimates since 1850. The consensus estimate used in various calculations in Chapters 7 and 9 is shown in black. (d) The most recent period of record from tide-gauge and altimeter based records. Further details on data sources and processing are available in the chapter data table (Table 2.SM.1).



ACCEPTED VERSION SUBJECT TO FINAL EDITS

Figure 2.29: Low latitude surface ocean pH over the last 65 million years. (a) Low-latitude (30°N–30°S) surface ocean pH over the last 65 million years, reconstructed using boron isotopes in foraminifera. (b) as (a) but for the last 3.5 million years. Double headed arrow shows the approximate magnitude of glacial-interglacial pH changes. (c) Multisite composite of surface pH. In a)-c), uncertainty is shown at 95% confidence as a shaded band. Relevant paleoclimate reference periods (CCB2.1) have been labelled. Period windows for succeeding panels are shown as horizontal black lines in a) and b). (d) Estimated low-latitude surface pH from direct observations (BATS, HOT) and global mean pH (65°S–65°N) from two indirect estimates (CMEMS, OCEAN-SODA). Further details on data sources and processing are available in the chapter data table (Table 2.SM.1).



ACCEPTED VERSION SUBJECT TO FINAL EDITS

Figure 2.30: Changes in the amplitude of the seasonal cycle of CO_2. (a) Observed peak-to-trough seasonal amplitude given by the day of year of downward zero crossing, of CO_2 concentration at Barrow (71°N, blue) and Mauna Loa (20°N, black). Seasonal CO_2 cycles observed at (b) Barrow and (c) Mauna Loa for the 1961–1963 or 1958–1963 and 2017–2019 time periods. The first six months of the year are repeated. Reprinted with permission from AAAS. Further details on data sources and processing are available in the chapter data table (Table 2.SM.1).

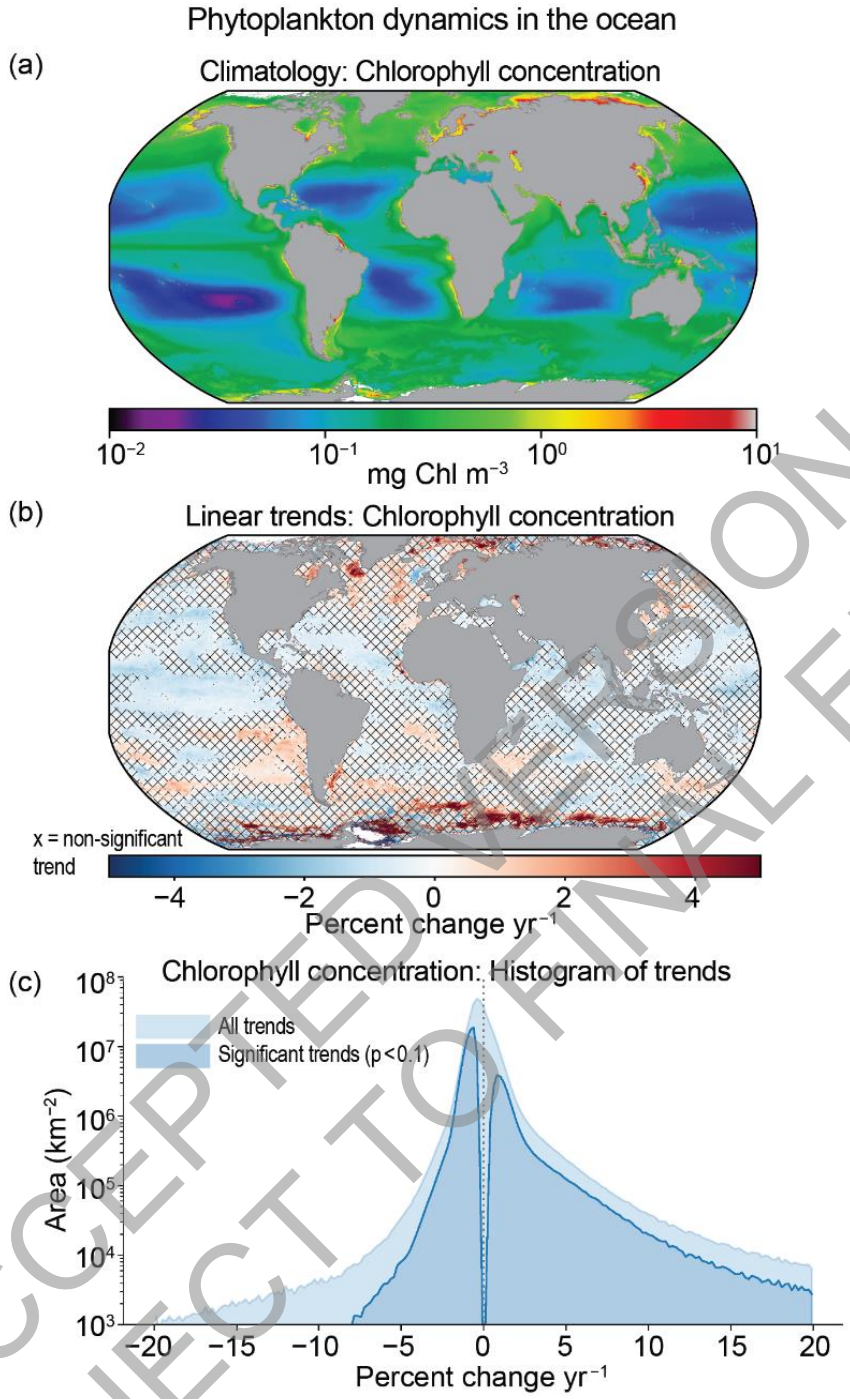
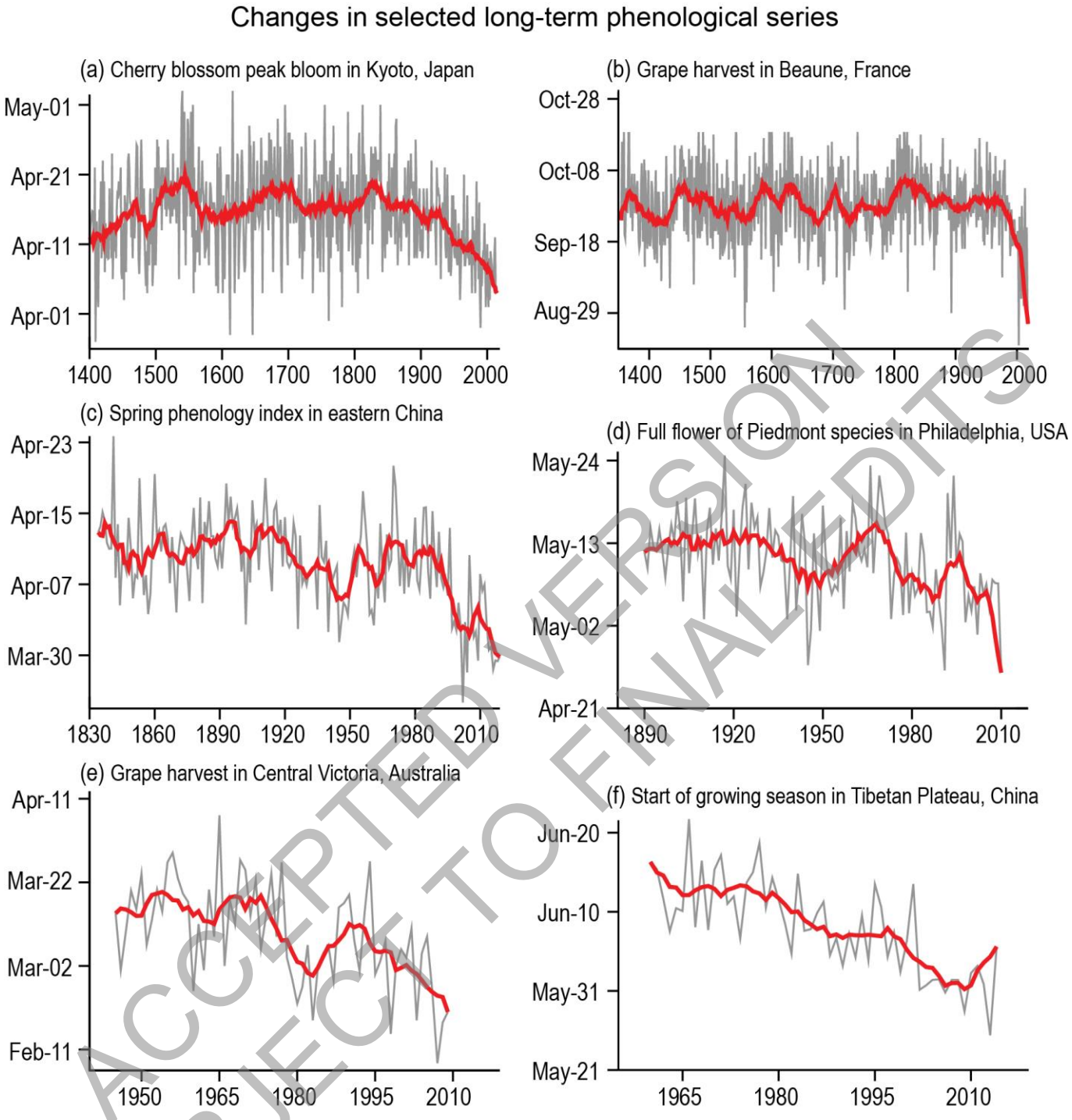


Figure 2.31: Phytoplankton dynamics in the ocean. (a) Climatology of chlorophyll-a concentration derived from ocean-colour data (1998–2018); (b) Linear trends in chlorophyll concentration. Trends are calculated using OLS regression with significance assessed following AR(1) adjustment after Santer et al (2008b) ('x' marks denote non-significant changes). (c) Histogram of linear trends in chlorophyll concentration, after area weighting and with per-pixel uncertainty estimates based on comparison with in situ data. Further details on data sources and processing are available in the chapter data table (Table 2.SM.1).

ACCEPTED VERSION SUBJECT TO FINAL EDITS



ACCEPTED VERSION SUBJECT TO FINAL EDITS

Figure 2.32: Phenological indicators of changes in growing season. (a) cherry blossom peak bloom in Kyoto, Japan; (b) grape harvest in Beaune, France; (c) spring phenology index in eastern China; (d) full flower of Piedmont species in Philadelphia, USA; (e) Grape harvest in Central Victoria, Australia; (f) start of growing season in Tibetan Plateau, China. Red lines depict the 25-year moving average (top row) or the 9-year moving average (middle and bottom rows) with the minimum roughness boundary constraint of Mann (2004). Further details on data sources and processing are available in the chapter data table (Table 2.SM.1).

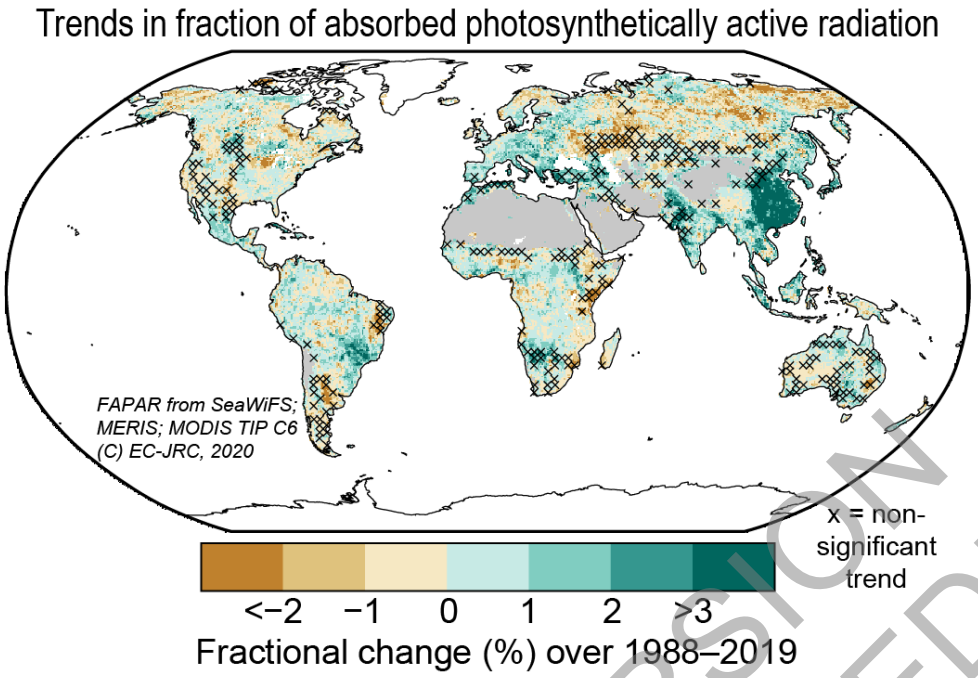


Figure 2.33: Satellite-based trends in Fraction of Absorbed Photosynthetically Active Radiation (per decade) for 1998–2019. Trends are calculated using OLS regression with significance assessed following AR(1) adjustment after Santer et al (2008b) ('x' marks denote non-significant trend). Unvegetated areas such as barren deserts (grey) and ice sheets (white) have no trend in FAPAR. Further details on data sources and processing are available in the chapter data table (Table 2.SM.1).

ACCEPTED VERSION SUBJECT TO FINAL EDITS

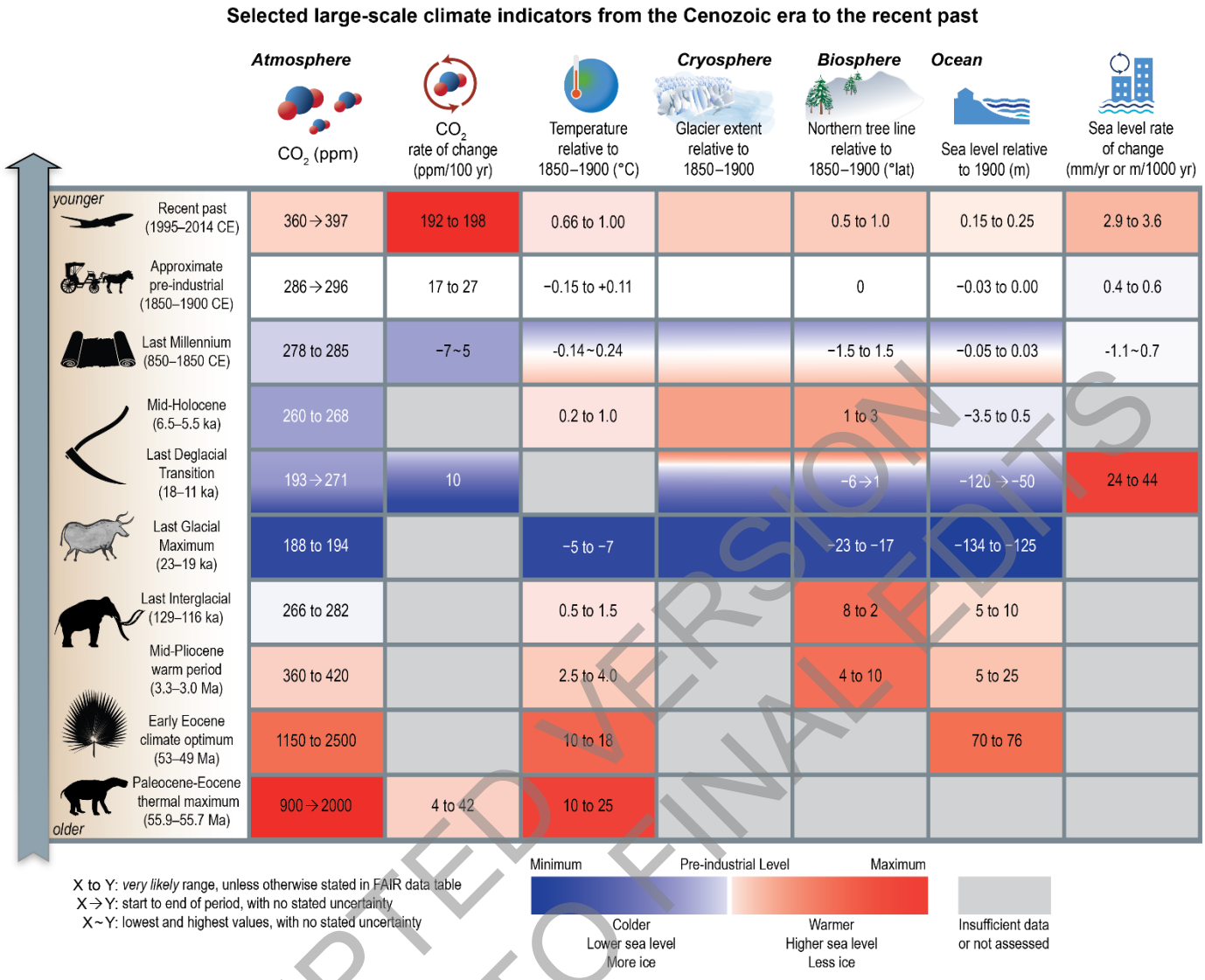
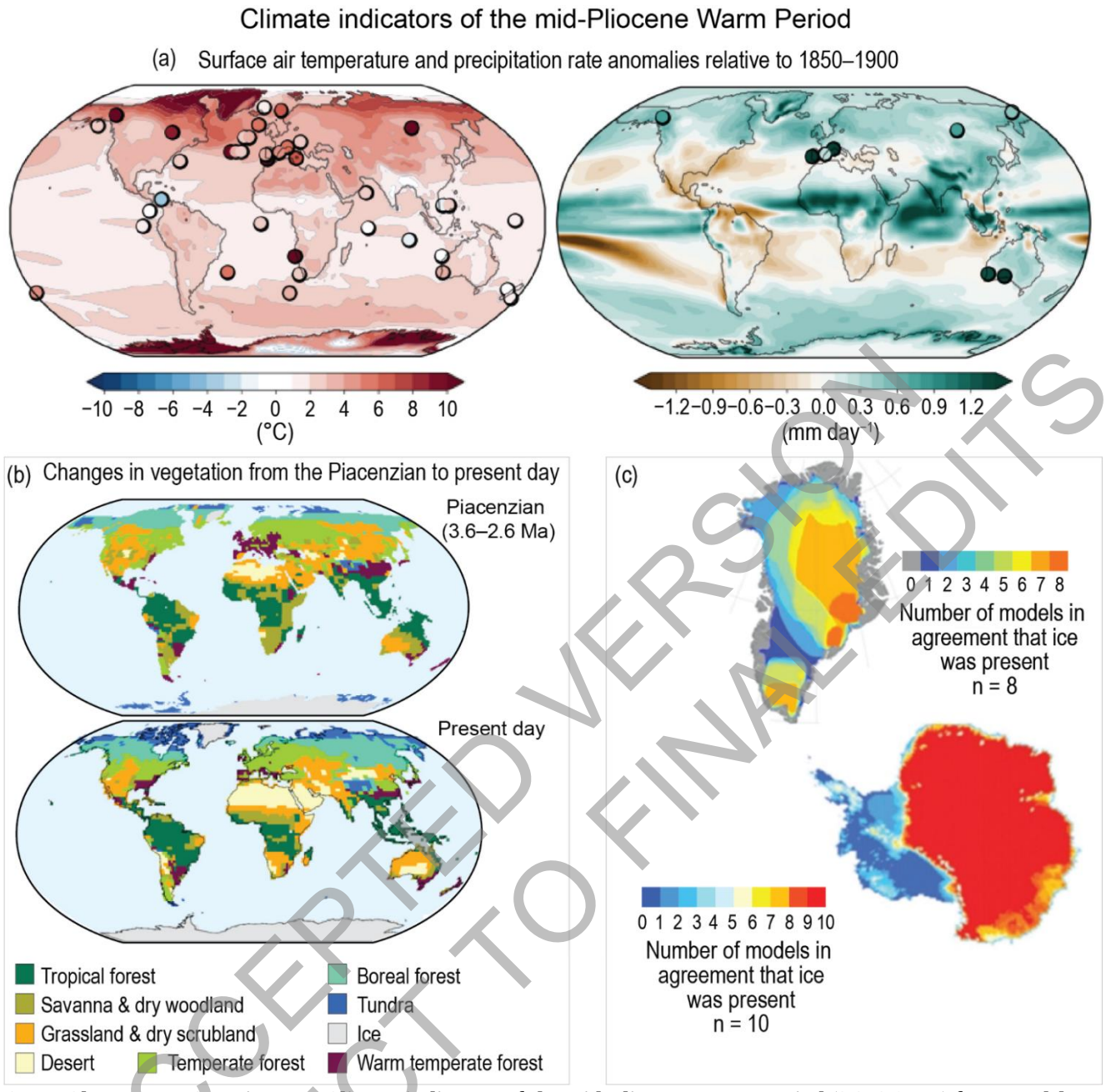


Figure 2.34: Selected large-scale climate indicators during paleoclimate and recent reference periods of the Cenozoic Era. Values are based upon assessments carried out in this chapter, with *confidence* levels ranging from *low* to *very high*. Refer to Cross-Chapter Box 2.1 for description of paleoclimate reference periods and Section 1.4.1 for recent reference periods. Values are reported as either the *very likely* range (x to y), or best estimates from beginning to end of the reference period with no stated uncertainty (x → y), or lowest and highest values with no stated uncertainty (x ~ y). Temperature is global mean surface temperature. Glacier extent is relative and colour scale is inverted so that more extensive glacier extent is intuitively blue.

ACCEPTED VERSION SUBJECT TO FINAL EDITS



Cross-Chapter Box 2.4, Figure 1: Climate indicators of the mid-Pliocene Warm Period (3.3–3.0 Ma) from models and proxy data. (a) Simulated surface air temperature (left) and precipitation rate anomaly (right) anomaly (relative to 1850–1900) from the Pliocene Model Intercomparison Project Phase 2 multi-model mean, including CMIP6 (n = 4) and non-CMIP6 (n = 12) models. Symbols represent site-level proxy-based estimates of sea-surface temperature for KM5c (n = 32), and terrestrial temperature (n = 8) and precipitation rate for the MPWP (n = 8). (b) Distribution of terrestrial biomes was considerably different during the Piacenzian Stage (3.6–2.6 Ma) (upper) compared with present-day (lower). Biome distributions simulated with a model (BIOME4) in which Pliocene biome classifications are based on 208 locations, with model-predicted biomes filling spatial gaps, and the present day, with the model adjusted for CO_2 concentration of 324 ppm. (c) Ice-sheet extent predicted using modelled climate forcing and showing where multiple models consistently predict the former presence or absence of ice on Greenland (n = 8 total) and Antarctica (n = 10 total). Further details on data sources and processing are available in the chapter data table (Table 2.SM.1).

ACCEPTED VERSION SUBJECT TO FINAL EDITS

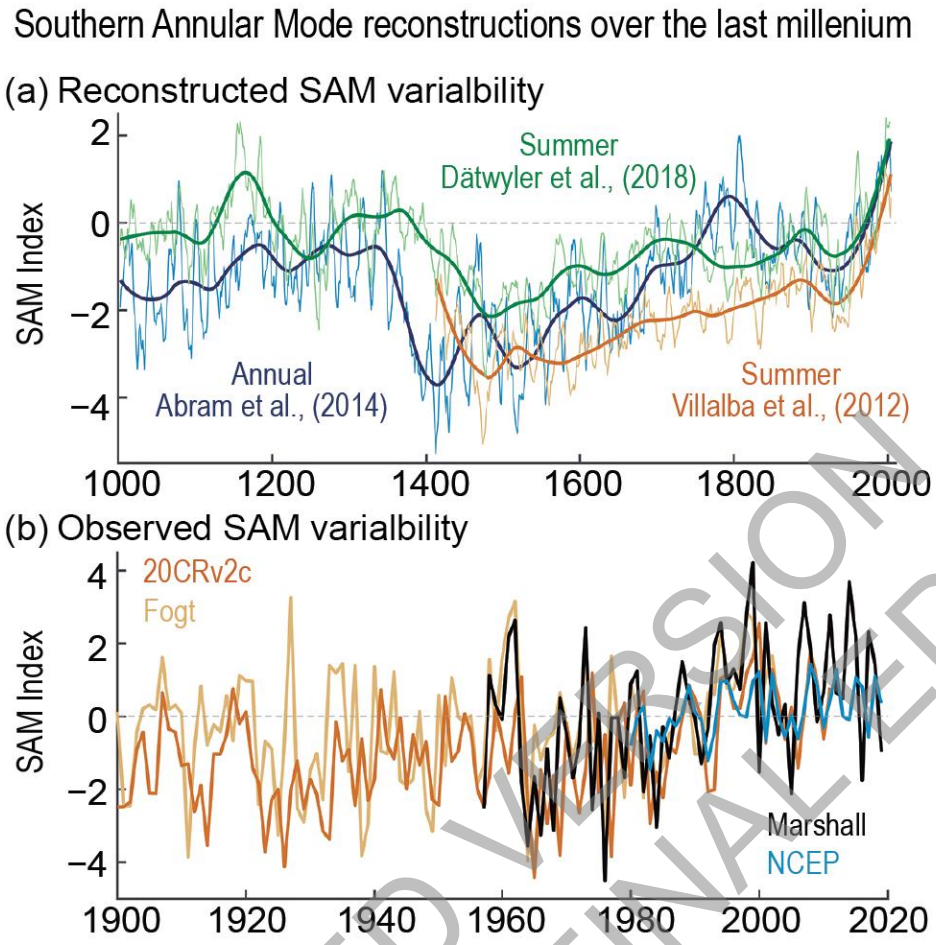


Figure 2.35: Southern Annular Mode (SAM) reconstruction over the last millennium. (a) SAM reconstructions as 7-year moving averages (thin lines) and 70-year LOESS filter (thick lines). (b) observed SAM index during 1900–2019. Further details on data sources and processing are available in the chapter data table (Table 2.SM.1).

ACCEPTED VERSION SUBJECT TO FINAL EDITS

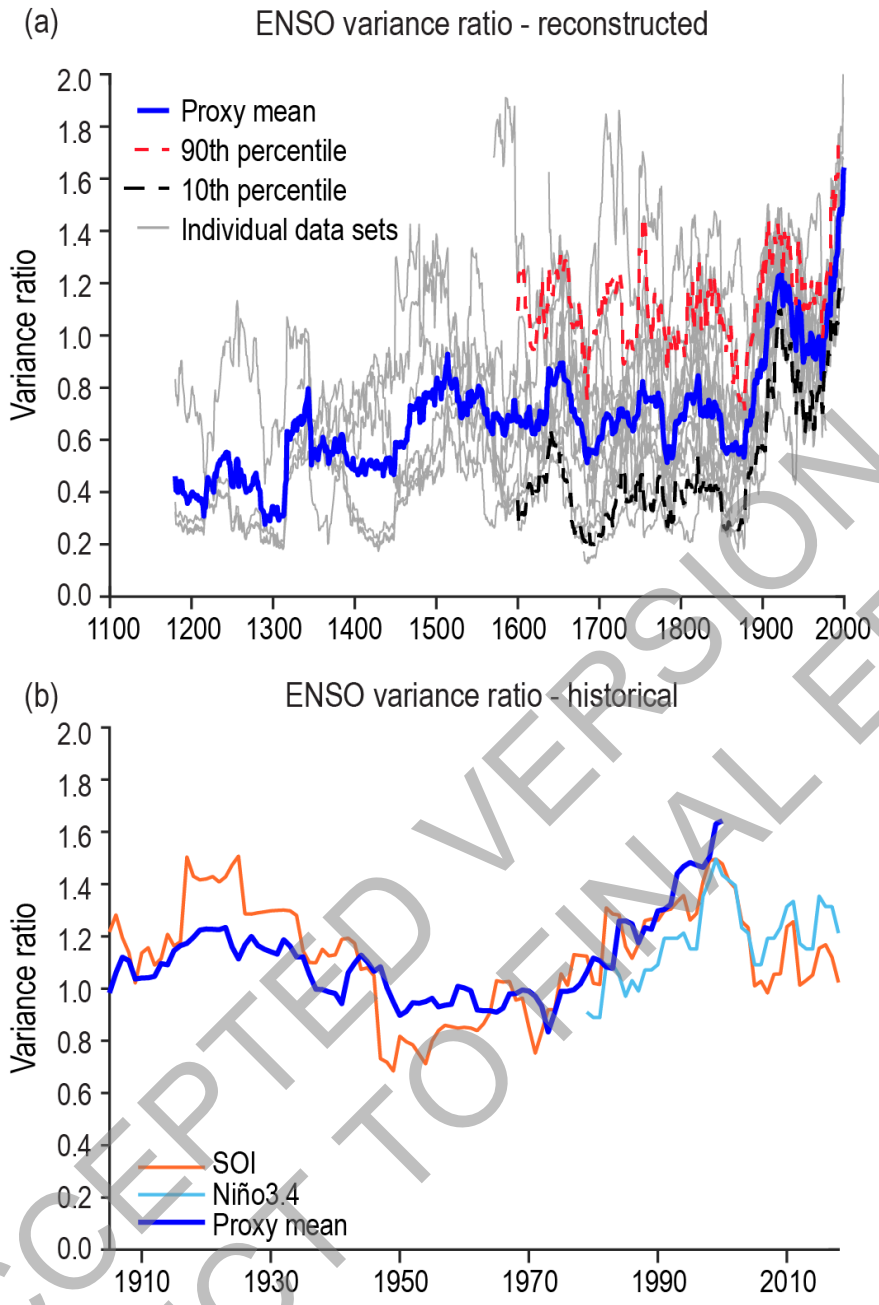
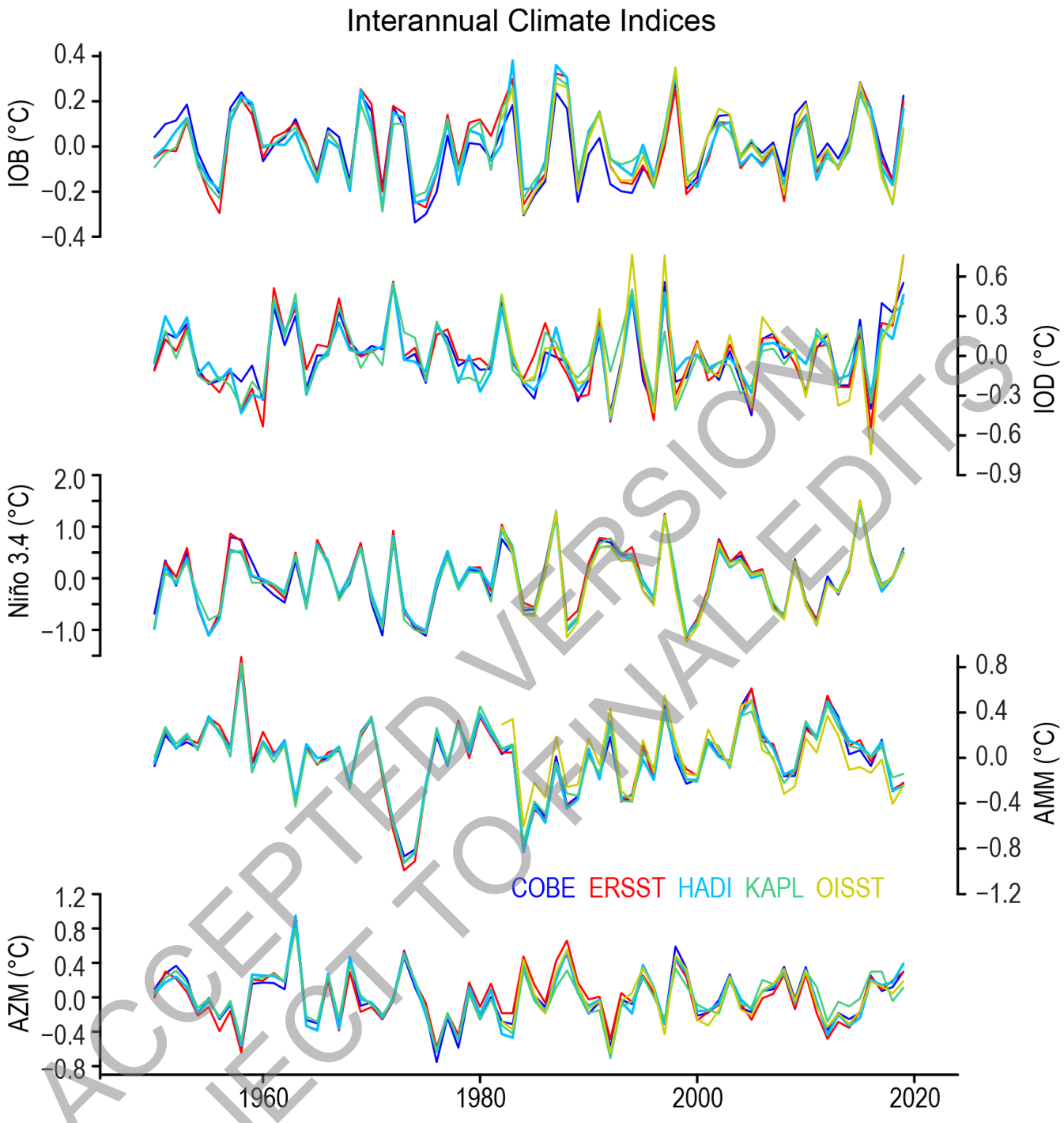


Figure 2.36: Reconstructed and historical variance ratio of El Niño–Southern Oscillation (ENSO). (a) 30-year running variance of the reconstructed annual mean Niño 3.4 or related indicators from various published reconstructions. (b) variance of June-November Southern Oscillation Index (SOI) and April-March mean Niño 3.4 (1981–2010 base period) along with the mean reconstruction from (a). Further details on data sources and processing are available in the chapter data table (Table 2.SM.1).

ACCEPTED VERSION SUBJECT TO FINAL EDITS



ACCEPTED VERSION SUBJECT TO FINAL EDITS

Figure 2.37: Indices of interannual climate variability from 1950–2019 based upon several sea surface temperature based data products. Shown are the following indices from top to bottom: IOB mode, IOD, Niño4, AMM and AZM. All indices are based on area-averaged annual data (see Technical Annex IV). Further details on data sources and processing are available in the chapter data table (Table 2.SM.1).

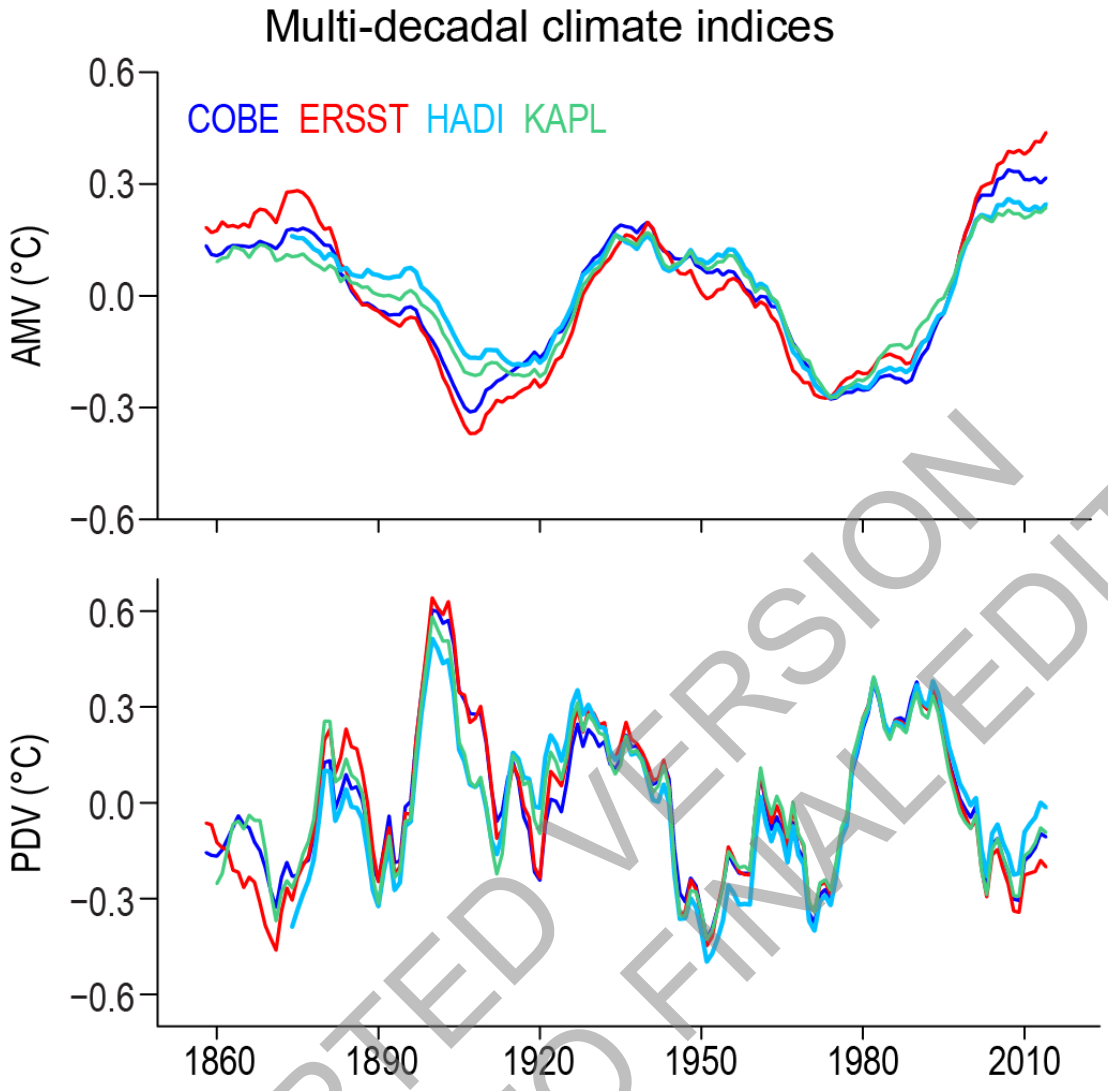


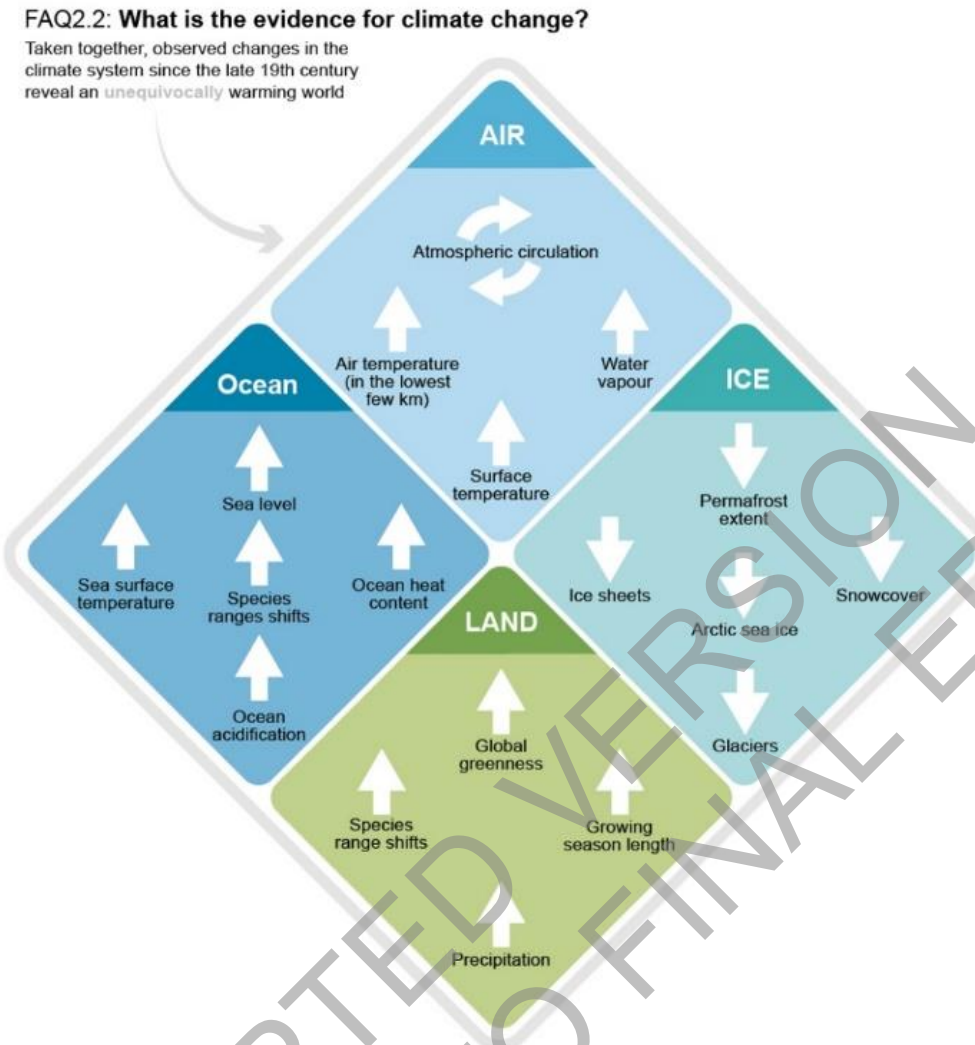
Figure 2.38: Indices of multi-decadal climate variability from 1854–2019 based upon several sea surface temperature based data products. Shown are the indices of the AMV and PDV based on area averages for the regions indicated in Technical Annex IV. Further details on data sources and processing are available in the chapter data table (Table 2.SM.1).

ACCEPTED VERSION SUBJECT TO FINAL EDITS



FAQ 2.1, Figure 1: Evidence for the unusualness of recent warming.

ACCEPTED VERSION SUBJECT TO FINAL EDITS



FAQ 2.2, Figure 1: Synthesis of significant changes observed in the climate system over the past several decades. Upwards, downwards and circling arrows indicate increases, decreases and changes, respectively. Independent analyses of many components of the climate system that would be expected to change in a warming world exhibit trends consistent with warming. Note that this list is not comprehensive.

ACCEPTED VERSION SUBJECT TO FINAL EDITS

Chapter 2: Changing state of the climate system - Supplementary Material

Coordinating Lead Authors:
Sergey K. Gulev (Russian Federation), Peter W. Thorne (Ireland/United Kingdom)

Lead Authors:
Jinho Ahn (Republic of Korea), Frank J. Dentener (EU/The Netherlands), Catia M. Domingues (Australia, United Kingdom/Brazil), Sebastian Gerland (Norway/Germany), Daoyi Gong (China), Darrell S. Kaufman (United States of America), Hyacinth C. Nnamchi (Nigeria, Germany/Nigeria), Johannes Quaas (Germany), Juan A. Rivera (Argentina), Shubha Sathyendranath (United Kingdom/Canada, Overseas Citizen of India, United Kingdom), Sharon L. Smith (Canada), Blair Trewin (Australia), Karina von Schuckmann (France/Germany), Russell S. Vose (United States of America)

Contributing Authors:
Guðfinna Aðalgeirsdóttir (Iceland), Samuel Albani (Italy), Richard P. Allan (United Kingdom), Richard A. Betts (United Kingdom), Lea Beusch (Switzerland), Kinfe Beyene (Ethiopia), Jason E. Box (Denmark/United States of America), Denise Breitburg (United States of America), Kevin D. Burke (United States of America), Michael P. Byrne (United Kingdom/Ireland), John A. Church (Australia), Sloane Coats (United States of America), Naftali Cohen (United States of America), William Collins (United Kingdom), Owen R. Cooper (United States of America), Pedro Di Nezio (United States of America), Fabio Boeira Dias (Finland/Brazil), Ed J. Dlugokencky (United States of America), Timothy Dunkerton (United States of America), Paul J. Durack (United States of America/Australia), Tamsin L. Edwards (United Kingdom), Veronika Eyring (Germany), Chris Fairall (United States of America), Vitali Fioletov (Canada), Piers Forster (United Kingdom), Gavin L. Foster (United Kingdom), Baylor Fox-Kemper (United States of America), Qiang Fu (United States of America), Jan S. Fuglestvedt (Norway), John C. Fyfe (Canada), Marie-José Gaillard (Sweden/Switzerland, Sweden), Joelle Gergis (Australia), Nathan P. Gillett (Canada), Hans Gleisner (Denmark/Sweden), Nadine Gobron (EU/France), Nicholas R. Golledge (New Zealand/United Kingdom), Bradley Hall (United States of America), Ed Hawkins (United Kingdom), Alan M. Haywood (United Kingdom), Armand Hernández (Spain), Forrest M. Hoffman (United States of America), Yongyun Hu (China), Dale F. Hurst (United States of America), Masao Ishii (Japan), Samuel Jaccard (Switzerland), Dabang Jiang (China), Christopher Jones (United Kingdom), Bror Jönsson (United Kingdom/Sweden), Andreas Kääb (Norway/Germany), Ralph Keeling (United States of America), Noel S. Keenlyside (Norway/Australia, United Kingdom), John Kennedy (United Kingdom), Elizabeth Kent (United Kingdom), Nichol S. Khan (Hong Kong, China/United States of America), Wolfgang Kiessling (Germany), Stefan Kinne (Germany), Robert E. Kopp (United States of America), Svitlana Krakovska (Ukraine), Elmar Kriegler (Germany), Gerhard Krinner (France/Germany, France), Natalie Krivova (Germany), Paul B. Krummel (Australia), Werner L. Kutsch (EU/Germany), Ron Kwok (United States of America), Florian Ladstädter (Austria), Peter Landschützer (Germany/Austria), June-Yi Lee (Republic of Korea), Andrew Lenton (Australia), Lisa A. Levin (United States of America), Daniel J. Lunt (United Kingdom), Jochem Marotzke (Germany), Gareth J. Marshall (United Kingdom), Robert A. Massom (Australia), Katja Matthes (Germany), Damon H. Matthews (Canada), Thorsten Mauritsen (Sweden/Denmark), Gerard D. McCarthy (Ireland), Erin L. McClymont (United Kingdom), Shayne McGregor (Australia), Jerry F. McManus (United States of America), Walter N. Meier (United States of America), Alan Mix (United States of America), Olaf Morgenstern (New Zealand/Germany), Lawrence R. Mudryk (Canada), Jens Mühle (United States of America/Germany), Dirk Notz (Germany), Lisa C. Orme (Ireland/United Kingdom), Scott M. Osprey (United Kingdom), Matthew D. Palmer (United Kingdom), Anna Pirani (Italy/United Kingdom, Italy), Chris Polashenski (United States of America), Elvira Poloczsanka (Australia/United Kingdom), Anthony Richardson (Australia), Belén Rodríguez-Fonseca (Spain), Joeri Rogelj (United Kingdom/Belgium), Steven K. Rose (United States of America), Yair Rosenthal (United States of America/Israel, United States of

ACCEPTED VERSION SUBJECT TO FINAL EDITS

America), Alessio Rovere (Germany/Italy), Lucas Ruiz (Argentina), Ulrich Salzmann (United Kingdom/Germany, United Kingdom), Bjørn H. Samset (Norway), Abhishek Savita (Australia/India), Margit Schwikowski (Switzerland), Sonia I. Seneviratne (Switzerland), Isobel J. Simpson (Canada), Aimée B. A. Slangen (The Netherlands), Chris Smith (United Kingdom), Olga N. Solomina (Russian Federation), Joshua H. P. Studholme (United States of America/United Kingdom, New Zealand), Alessandro Tagliabue (United Kingdom), Claudia Tebaldi (United States of America), Jessica Tierney (United States of America), Matthew Toohey (Canada, Germany/Canada), Andrew Turner (United Kingdom), Osvaldo Ulloa (Chile), Caroline C. Ummenhofer (United States of America/Germany, United States of America), Axel von Engeln (Germany), Rachel Warren (United Kingdom), Kate Willett (United Kingdom), John W. Williams (United States of America)

Review Editors:
Timothy J. Osborn (United Kingdom), Azar Zarrin (Iran)

Chapter Scientists:
Katherine J. Dooley (Ireland), Therese A. Myslinski (Ireland), David N. Smyth (Ireland/United Kingdom)

This Supplementary Material should be cited as:
Gulev, S. K., P. W. Thorne, J. Ahn, F. J. Dentener, C. M. Domingues, S. Gerland, D. Gong, D. S. Kaufman, H. C. Nnamchi, J. Quaas, J. A. Rivera, S. Sathyendranath, S. L. Smith, B. Trewin, K. von Shuckmann, R. S. Vose, 2021, Changing State of the Climate System Supplementary Material. In: *Climate Change 2021: The Physical Science Basis. Contribution of Working Group I to the Sixth Assessment Report of the Intergovernmental Panel on Climate Change* [Masson-Delmotte, V., P. Zhai, A. Pirani, S. L. Connors, C. Péan, S. Berger, N. Caud, Y. Chen, L. Goldfarb, M. I. Gomis, M. Huang, K. Leitzell, E. Lonnoy, J. B. R. Matthews, T. K. Maycock, T. Waterfield, O. Yelekçi, R. Yu and B. Zhou (eds.)]. Available from https://ipcc.ch/static/ar6/wg1.

Date: August 2021

This document is subject to copy-editing, corrigenda and trickle backs.

ACCEPTED VERSION SUBJECT TO FINAL EDITS

2.SM.1 Data Table

[START TABLE 2.SM.1 HERE]

Table 2.SM.1: Input Data Table. Input datasets and code used to create chapter figures.

Figure number / Table number / Chapter section (for calculations)	Dataset / Codename	Type	Filename / Specificities	License type	Dataset / Code citation	Dataset / Code URL	Related publication / Software used	Notes
CCB2.1 Figure 1	Hansen – Cenozoic (60 to 0.02 Ma GMST reconstruction from benthic marine isotope stack	Input dataset		CC0 for metadata CC-BY for data	Converted to GMST based on equations in Hansen et al. (2013)	http://www.columbia.edu/~mhs119/Sensitivity+SL+CO2/Table.txt (accessed 3/27/2021)	Hansen et al. (2013); isotope dataset from Zachos et al. (2008)	Added 0.36°C to adjust GMST estimated for 1961-1900 to 1850-1900.
	Westerhold – Cenozoic (60 to 0.02 Ma) GMST reconstruction from benthic marine isotope splice, binned & interpolated (CENOGRID)	Input dataset	https://doi.pangaea.de/10.1594/PANGAEA.917717?format=html#mcol6_ds13915407; 2000-year-binned dataset	CC0 for metadata CC-BY for data	Converted to GMST based on equations in Hansen et al. (2013)	https://doi.org/10.1594/PANGAEA.917717 (accessed 1/11/2020)	Westerhold et al. (2020)	Added 0.36°C to adjust GMST estimated for 1961-1900 to 1850-1900.
	Snyder – Pleistocene (1 to 0.02 Ma) GMST reconstruction from sea surface temperature stack	Input dataset	https://www.nature.com/articles/nature19798" https://www.nature.com/articles/nature19798 (Supplementary Data)			https://static-content.springer.com/esm/art%3A10.1038%2Fnature19798/MediaObjects/41586_2016_BFnature19798_MOESM258_ESM.xlsx	Snyder (2016)	

ACCEPTED VERSION SUBJECT TO FINAL EDITS

	Shakun – 20 to 12 ka global mean surface temperature reconstruction	Input dataset	https://www.nature.com/articles/nature10915#Sec14 (Supplementary Data, Temperature Stacks tab)				Shakun et al. (2012)	Added 0.24°C to splice temperature at 12 ka to Holocene temperature reconstruction.
	Kaufman – Holocene global mean surface temperature reconstruction (Temp12k multi-method)	Input dataset	https://www.ncei.noaa.gov/pub/data/paleo/reconstructions/kaufman2020/temp12k_allmethods_percentiles.csv			https://www.ncdc.noaa.gov/paleo/study/29712 (accessed 1/11/2020)	Kaufman et al., (2020a; 2020b)	Median ensemble reconstruction.
	1850 to 2020 global mean surface temperature (AR6 assessed mean)	Same as Figure 2.11c						
Figure 2.2a	Total Solar Irradiance (TSI) reconstruction PMIP4 SATRIRE-M solar forcing data	Input dataset	SSI_14C_cycle_yearly_cmip_v20160613_fc.nc			https://pmip4.lsce.ipsl.fr/doku.php/data:solar_satire (accessed 7 December 2020)	Jungclaus et al. (2017)	The right axis is the ERF derived on the basis of TSI as in Section 7.3.4.4.

ACCEPTED VERSION SUBJECT TO FINAL EDITS

Figure 2.2a, b	Total Solar Irradiance (TSI) reconstruction CMIP6 solar forcing data	Input dataset	solarforcing-ref-mon_input4MIPs_solar_CMIP_SOLARIS-HEPPA-3-2_gn_18500101-22991231.nc			https://solarisheppa.geomar.de/cmip6 (accessed 7 December 2020)	Matthes et al. (2017)	
Figure 2.2b	Total Solar Irradiance (TSI) time series CMIP5 solar forcing data	Input dataset	TSI_WLS_mon_1882_2008.txt			http://solarisheppa.geomar.de/cmip5 (accessed 7 December 2020)	Lean (2000); Wang et al. (2005)	TSI by definition includes the UV range, 200-400 nm, contributing particularly strongly to the TSI changes
	Total Solar Irradiance (TSI) time series	Input dataset	TSI_Composite.txt			https://spot.colorado.edu/~koppg/TSI/ (accessed 7 December 2020)	Dudok de Wit et al. (2017) .	
Figure 2.2c	Reconstructed volcanic stratospheric sulfur injections and aerosol optical depth, 500 BCE to 1900 CE, version 3. World Data Center for Climate (WDCC) at DKRZ	Input dataset	eVolv2k_v3_ds_1.nc	**CC BY-NC-SA 2.0 DE**	Toohey and Sigl (2019)	https://cera-www.dkrz.de/WDCC/ui/cerasearch/entry?acronym=eVolv2k_v3 (accessed 7 December 2020)	Toohey and Sigl (2017)	
Figure 2.2c, d	Stratospheric Aerosol Optical Depth (SAOD)	Input dataset	CMIP_1850_2014_extinction_550nm_strat_only_v3.nc			ftp://iacftp.ethz.ch/pub_read/luo/CMIP6/ (accessed 7 December 2020)	Luo (2018)	See unit bars for a visual guide as to scale mismatch. TSI values refer to changes in solar radiation and do not account for the spherical Earth.
Figure 2.2d	Stratospheric Aerosol Optical Depth (SAOD)	Input dataset	tau.map_2012.12.txt			https://data.giss.nasa.gov/modelforce/strataer/ (accessed 7 December 2020)	Sato et al. (1993); Luo (2018)	
Table 2.1	Atmospheric CO_2 during 1995-2014	Input dataset	Refer to file in zenodo			zenodo	NOAA, references in Annex 5	The uncertainty of CO_2 in 1995 and 2014 is assumed the same as that of 2019.

ACCEPTED VERSION SUBJECT TO FINAL EDITS

								To estimate centennial rate of change, the CO_2 data are extrapolated using the mean rate of change during 1995 to 2014.
	Atmospheric CO_2 during 1850-1900	Input dataset	Refer to file in zenodo			zenodo	Ahn et al., (2012); Bauska et al., (2015); MacFarling Meure et al., (2006); Siegenthaler et al., (2005); Annex 5; Meinshausen et al. (2017)	
	Atmospheric CO_2 during 1850-1900 (CMIP6)	Input dataset				zenodo	Meinshausen et al. (2017)	
	Atmospheric CO_2 during the last millennium (1000-1750)	Input dataset	Fig2.4_data_Feb_2021			https://www.ncdc.noaa.gov/paleo/study/18316 ; https://data.csiro.au/collections/collection/CIcsiro:37077v1; https://www.ncdc.noaa.gov/paleo-search/study/2488	Ahn et al. (2012); Rubino et al. (2019); Siegenthaler et al. (2005)	Rate of CO2 concentration change (ppm/century) was estimated from 100-year running mean average for each ice core record
	Atmospheric CO_2 during MH	Input dataset	Ice core CO2.xls			https://www.ncdc.noaa.gov/paleo/study/17975	Monnin et al. (2004)	CO_2 is averaged during the given time period
	Atmospheric CO_2 during LDT	Input dataset	Ice core CO2.xls			https://www.ncdc.noaa.gov/paleo-search/study/18636 ; https://www.ncdc.noaa.gov/paleo-search/study/17975	Bereiter et al. (2015); Marcott et al. (2014)	rate of CO2 concentration change (ppm/century) was estimated from 100-year running mean average for each ice core record

ACCEPTED VERSION SUBJECT TO FINAL EDITS

	Atmospheric CO_2 during LGM	Input dataset	Ice core CO2.xls		(Ahn & Brook, 2014) Schmitt et al. (2012a)	https://www.ncdc.noaa.gov/paleo-search/study/18636 ; https://www.ncdc.noaa.gov/paleo-search/study/17975 ; https://www.ncdc.noaa.gov/paleo/study/6178	Bereiter et al. (2015); Ahn & Brook (2008); Ahn et al. (2014); Marcott et al. (2014); Schmitt et al. (2012b)	CO_2 is averaged during the given time period
	Atmospheric CO_2 during LIG	Input dataset	Ice core CO2.xls		Schneider et al. (2013a) Köhler et al. (2017)	https://www.ncdc.noaa.gov/paleo-search/study/17975	Petit et al. (1999); Schneider et al. (2013b); Lourantou et al. (2010)	CO_2 is averaged during the given time period
	Atmospheric CO_2 during MPWP (KM5c)	Input dataset				http://www.pangaea.de/ https://paleo-co2.org/		
	Atmospheric CO_2 during EECO	Input dataset				http://www.pangaea.de/ https://paleo-co2.org/		
	Atmospheric CO_2 during PETM	Input dataset				http://www.pangaea.de/ https://paleo-co2.org/		To calculate the average rate of CO2 change across the PETM a Monte Carlo approach was used to fully propagate the uncertainty in age and CO2 estimates. A normal distribution for the uncertainty on the CO2 estimates across the PETM from Anagnostou et al. (2020) was assumed, whereas for the onset duration a uniform

ACCEPTED VERSION SUBJECT TO FINAL EDITS

								probability was assumed from 3-20 kyr.
Figure 2.3a	Atmospheric CO_2 0 to 22.6 myrs estimated from $\delta^{11}B$ Planktic Foraminifera (the Planktic-HO-SI-LE option of Sosdian et al. 2018)	Input dataset	Sosdian.txt	CC BY 4.0 (Sosdian et al., 2018); CC BY-NC-ND (Chalk et al., 2017); Free access (Bartoli et al., 2011)	(Bartoli et al., 2011; Martínez-Botí et al., 2015)		Sosdian et al. (2018) plus recalculations of: Hönisch et al. (2009) ; Chalk et al. (2017) ; Bartoli et al. (2011) ; Martinez-Boti et al. (2015)	See note below regarding the quality of the Plio-Pleistocene data in this dataset.
	Atmospheric CO_2 from 33 to 56.3 myr estimated from $\delta^{11}B$ Planktic Foraminifera	Input dataset	Anagnostou.txt	CC BY 4.0 (Anagnostou et al., 2020)	(Anagnostou et al., 2016; 2020; Gutjahr et al., 2017; Pearson et al., 2009)		Anagnostou et al. (2020) plus recalculations of : Pearson et al. (2009); Anagnostou et al. (2016); Gutjahr et al. (2017); Harper et al. (2020); Henehan et al. (2020) ; Penman et al. (2014)	
	Atmospheric CO_2 from 0 to 450 myr estimated from $\delta^{13}C$ of Phytane	Input dataset	wit.txt	CC BY-NC 4.0		https://advances.sciencemag.org/content/suppl/2018/11/26/4.11.eaat4556.DC1	Witkowski et al. (2018)	
	Atmospheric CO_2 estimated Alkenone $\delta^{13}C$	Input dataset	Akenonecompilation.txt				Stoll et al. (2019) ; Pagani et al. (2005, 2011); Zhang et al. (2013)	For <22.9 Ma the data CO_2 is calculated using the model of Stoll et al. (2019), for >22.9 Ma a diffusive model is used as outlined in Pagani et al. (2005). Following Rae et al. (2021), the $\delta^{13}C$ alkenone based CO_2 estimates of Stoll et al. (2019) are used for

ACCEPTED VERSION SUBJECT TO FINAL EDITS

								<23 Ma in preference to those of Super et al. (2018) and Pagani et al. (2010) due to the more accurate model applied by Stoll et al. (2019) to account for non-diffusive CO_2 uptake by alkenone producing coccolithophorids at low CO_2.
	Atmospheric CO_2 over the last 450 million years estimated using $\delta^{13}C$ in palaeosol CaCO3 and plant stomata	Input dataset	PhanCO2F.txt	CC BY 4.0	(Foster et al., 2017)		Foster et al. (2017)	
	Smoothed fit through all the above data	Input dataset	PhanCO2sm.exp.txt					Smoothed fit through all the above data using the methods described in Foster et al. (2017).
Figure 2.3b	Atmospheric CO_2 estimated Alkenone $\delta^{13}C$	Input dataset	Akenone compilation.txt				Stoll et al. (2019) ; Pagani et al. (2005, 2011); Zhang et al. (2013)	For <22.9 Ma the data CO_2 is calculated using the model of Stoll et al. (2019), for >22.9 Ma a diffusive model is used as outlined in Pagani et al. (2005). Following Rae et al. (2021), the $\delta^{13}C$ alkenone based CO_2 estimates of Stoll et al. (2019) are used for <23 Ma in preference to those of Super et al. (2018) and Pagani et al. (2010) due to the

ACCEPTED VERSION SUBJECT TO FINAL EDITS

								more accurate model applied by Stoll et al. (2019) to account for non-diffusive CO_2 uptake by alkenone producing coccolithophorids at low CO_2.
	Atmospheric CO_2 0 to 22.6 myrs estimated from $\delta^{11}B$ Planktic Foraminifera (the Planktic-HO-SI-LE option of Sosdian et al. 2018)	Input dataset	Sosdian.txt	CC BY 4.0 (Sosdian et al., 2018); CC BY-NC-ND (Chalk et al., 2017); Free access (Bartoli et al., 2011)	(Bartoli et al., 2011; Martínez-Botí et al., 2015)		Sosdian et al. (2018) plus recalculations of: Hönisch et al. (2009) ; Chalk et al. (2017) ; Bartoli et al. (2011) ; Martinez-Boti et al. (2015)	
	Atmospheric CO_2 from 33 to 56.3 myr estimated from $\delta^{11}B$ Planktic Foraminifera	Input dataset	Anagnostou.txt	CC BY 4.0 (Anagnostou et al., 2020) (Henehan et al., 2020)	(Anagnostou et al., 2016; 2020; Gutjahr et al., 2017; Henehan et al., 2020; Pearson et al., 2009)		Anagnostou et al. (2020) plus recalculations of : Pearson et al. (2009); Anagnostou et al. (2016); Gutjahr et al. (2017); Harper et al. (2020); Henehan et al. (2020)	
	Atmospheric CO_2 from 0 to 450 myr estimated from $\delta^{13}C$ of Phytane	Input dataset	wit.txt	CC BY-NC 4.0		https://advances.sciencemag.org/content/suppl/2018/11/26/4.11.eaat4556.DC1	Witkowski et al. (2018)	
Figure 2.3c	Atmospheric CO_2 estimated Alkenone $\delta^{13}C$	Input dataset	Akenone compilation.txt				Stoll et al. (2019) ; Pagani et al. (2005, 2011); Zhang et al. (2013)	For <22.9 Ma the data CO_2 is calculated using the model of Stoll et al. (2019), for >22.9 Ma a diffusive model is used as outlined in Pagani et al. (2005).

ACCEPTED VERSION SUBJECT TO FINAL EDITS

								Following Rae et al. (2021), the $\delta^{13}C$ alkenone based CO_2 estimates of Stoll et al. (2019) are used for <23 Ma in preference to those of Super et al. (2018) and Pagani et al. (2010) due to the more accurate model applied by Stoll et al. (2019) to account for non-diffusive CO_2 uptake by alkenone producing coccolithophorids at low CO_2.
	Antarctic Ice Core CO_2 from various sources	Input dataset	Ice_core.txt	CC BY 4.0(Siegenthaler et al., 2005)	(Bereiter et al., 2015)		Petit et al. (1999); Siegenthaler et al. (2005); Bereiter et al. (2015)	
	Atmospheric CO_2 from 0 to 3500 ka estimated from $\delta^{11}B$ Planktic Foraminifera	Input dataset	Plio_Pleisto_Final.txt	Open access (de la Vega et al. 2020)	(Bartoli et al., 2011; Dyez et al., 2018; Martínez-Botí et al., 2015)		De la Vega (2020) plus recalculation of Martinez-Boti et al. (2015) Bartoli et al. (2011) data recalculated by Sosdian et al. (2018) Other datasets as published: Chalk et al. (2017) Hönisch et al. (2009) Raitzsch et al. (2018) Dyez et al., (2018)	These data are preferred for this interval than the recalculations in Sosdian.txt because the Plio-Pleistocene data reported in Sosdian et al. (2018) are not representative due to the large uncertainties propagated in the long-term Neogene reconstruction (i.e. seawater composition; see Sosdian et al.,

ACCEPTED VERSION SUBJECT TO FINAL EDITS

								2018 for more details).
	Figure 2.3 code	Code	CO2_IPCC_colours_clear.R			https://github.com/gavinfoster d11B/IPCC-AR5-Figure-2.3		
Figure 2.4a Atmospheric CO2 concentration during the last 800,000 years	EPICA Dome C – 800KYr CO2 Data; Antarctic Ice Cores Revised 800KYr CO2 Data	Input dataset	Fig2.4_data_Nov_2020		Lüthi et al. (2008); Bereiter et al. (2015)	https://www.ncdc.noaa.gov/paleo-search/study/6091; https://www.ncdc.noaa.gov/paleo-search/study/17975	Petit et al. (1999)	
Figure 2.4a Atmospheric CO2 concentration during the glacial termination	WAIS Divide Ice Core 9-23KYrBP CO2 Data; Antarctic Ice Cores Revised 800KYr CO2 Data	Input dataset	Fig2.4_data_Nov_2020		Marcott et al. (2014); Bereiter et al. (2015)	https://www.ncdc.noaa.gov/paleo-search/study/18636; https://www.ncdc.noaa.gov/paleo-search/study/17975		
Figure 2.4a Atmospheric CH4 concentration during the last 800,000 years	EPICA Dome C – 800KYr Methane Data	Input dataset	Fig2.4_data_Nov_2020		Loulergue et al. (2008)	https://www.ncdc.noaa.gov/paleo-search/study/6093		
Figure 2.4a Atmospheric N2O concentration during the last 800,000 years	EPICA Dronning Maud Land, EPICA Dome C – 140KYr N2O Data, 800KYr N2O Data	Input dataset	Fig2.4_data_Nov_2020		Schilt et al. (2010); Köhler et al. (2017)	https://www.ncdc.noaa.gov/paleo-search/study/8615 https://doi.pangaea.de/10.1594/PANGAEA.871273		

ACCEPTED VERSION SUBJECT TO FINAL EDITS

Figure 2.4b Atmospheric CO2 concentration during the last 2,000 years	WAIS Divide Core 1,200 Year Atmospheric CO2 and CO2 Stable Isotope Data; Law Dome Ice Core 2000-Year CO2, CH4, N20 and d13C-CO2; EPICA Dronning Maud Land, EPICA South Pole – CO2 Data for the Last Millennium; West Antarctic Ice Sheet (WAIS) Ice Core WDC – 05a 1000 Year CO2 Data	Input dataset	Fig2.4_data_Nov_2020	https://confluence.csiro.au/display/daphelp/CSIRO+Data+Licence	Bauska et al. (2015); Rubino et al. (2019); Siegenthaler et al. (2005); Ahn et al. (2012)	https://www.ncdc.noaa.gov/paleo/study/18316; https://data.csiro.au/collections/collection/CIcsiro:37077v1; https://www.ncdc.noaa.gov/paleo-search/study/2488 https://www.ncdc.noaa.gov/paleo/study/12949	MacFarling Meure et al. (2006)	
Figure 2.4b Atmospheric CH4 concentration during the last 2,000 years	Law Dome Ice Core 2000-Year CO2, CH4, N2O and d13C-CO2	Input dataset	Fig2.4_data_Nov_2020	https://confluence.csiro.au/display/daphelp/CSIRO+Data+Licence	Rubino et al. (2019);	https://data.csiro.au/collections/collection/CIcsiro:37077v1	Mitchell et al. (2013)	
Figure 2.4b Atmospheric N2O concentration during the last 2,000 years	NEEM and Styx Polar Ice Cores 2,000 Year Nitrous Oxide Data; Law Dome Ice Core 2000-Year CO2, CH4, N2O and d13C-CO2; EPICA Dome C – Nitrous Oxide, CO2, and CH4 Data	Input dataset	Fig2.4_data_Nov_2020	https://confluence.csiro.au/display/daphelp/CSIRO+Data+Licence	(Flückiger et al., 1999; Rubino et al., 2019; Ryu et al., 2020)	https://www.ncdc.noaa.gov/paleo-search/study/30752; https://data.csiro.au/collections/collection/CIcsiro:37077v1 https://www.ncdc.noaa.gov/paleo/study/2457	Machida et al. (1995); Sowers (2001)	
Table 2.2	Global annual mean mixing ratios of WMGHGs: CO2/CH4 (NOAA)	Input Dataset	See Annex III			https://zenodo.org/xxxx	Updated from Conway et al. (1994); Dlugokencky et al. (1994); Masarie and Tans (2004)	Derived from measurements in the remote, unpolluted troposphere

ACCEPTED VERSION SUBJECT TO FINAL EDITS

	Global annual mean mixing ratios of WMGHGs: N2O/SF6 (NOAA)	Input Dataset	See Annex III			zenodo	Updated from Hall et al. (2011)	Derived from measurements in the remote, unpolluted troposphere
	Global annual mean mixing ratios of WMGHGs: other (NOAA)	Input Dataset	See Annex III			zenodo	Updated from Montzka et al. (2015)	Derived from measurements in the remote, unpolluted troposphere
	Global annual mean mixing ratios of WMGHGs: all (AGAGE)	Input Dataset	See Annex III			zenodo	Updated from Prinn et al. (2018); Rigby et al. (2014)	Derived from measurements in the remote, unpolluted troposphere
	Global annual mean mixing ratios of WMGHGs: CO2 (SIO)	Input Dataset	See Annex III			zenodo	Updated from Keeling et al. (2005)	Derived from measurements at Mauna Loa, Hawaii and South Pole
	Global annual mean mixing ratios of WMGHGs (UCI)	Input Dataset	See Annex III			zenodo	Updated from Simpson et al. (2012)	
	Global annual mean mixing ratios of WMGHGs (CSIRO)	Input Dataset	See Annex III			zenodo	Updated from Kirschke et al. (2013); Langenfelds et al. (2002)	
	Global annual mean mixing ratios of WMGHGs (WMO-GAW)	Input Dataset	See Annex III	Free and open access		https://gaw.kishou.go.jp/publications/global_mean_mole_fractions#content1 (accessed November 30 2020)	Updated from (WMO, 2019)	WMO global means include data from NOAA, AGAGE, CSIRO, and SIO, and may include observations subject to regional and local influence
	Global annual mean mixing ratios of WMGHGs (CMIP6)	Input Dataset	See Annex III				Updated from Meinshausen et al. (2017)	May include observations subject to regional and local influence

ACCEPTED VERSION SUBJECT TO FINAL EDITS

	CFC-114, CFC-113	Input Dataset	See Annex III			zenodo		CFC-114 is a combination of CFC-114 and an unquantified amount of the minor isomer CFC-114a. CFC-113 includes the minor isomer CFC-113a. For ERF, the 2019 CFC-114 value was adjusted by factor 0.98 to be consistent with values used in WMO (2018).
	Lifetime (except SF6, CH4, and N2O)	Input Dataset			(Witkowski et al., 2018)	https://advances.sciencemag.org/content/4/11/eaat4556/tab-figures-data	Appendix A in (WMO, 2018)	
	SF6 lifetime						(Kovács et al., 2017; E. A. Ray et al., 2017)	
	CH4 lifetime		See Chapter 6					Total atmospheric lifetime of 9.1 ±0.9 years (1 s.d.) and the perturbation residence time of 11.8±1.8 years, respectively (see 6.3.1).
	N2O liftime		See Chapter 5				(Prather et al., 2015)	N2O atmospheric lifetime is 116 ± 9 years (1 s.d.) and perturbation residence time 109 ± 10 years (see 5.2.3; Prather et al., 2015).

ACCEPTED VERSION SUBJECT TO FINAL EDITS

Figure 2.5a	CO_2 from Scripps Institution of Oceanography (SIO) based on measurements from Mauna Loa, Hawaii and South Pole	Input Dataset	See Annex III				Keeling et al. (2005)	At monthly time resolution based on measurements from Mauna Loa, Hawaii and South Pole (deseasonalised).
	CO_2 from Commonwealth Scientific and Industrial Research Organization, Aspendale, Australia (CSIRO)	Input dataset	See Annex III				Kirschke et al. (2013); Langenfelds et al. (2002)	At monthly time resolution.
	CO_2 from National Oceanic and Atmospheric Administration, Global Monitoring Laboratory (NOAA/GML)	Input dataset	See Annex III					At quasi-weekly time resolution.
Figure 2.5b	CH_4 from National Oceanic and Atmospheric Administration (NOAA)	Input dataset	See Annex III				Conway et al. (1994); Dlugokencky et al. (1994); Masarie and Tans (1995)	
	CH_4 from Advanced Global Atmospheric Gases Experiment (AGAGE)	Input dataset	See Annex III				Prinn et al. (2018); Rigby et al. (2014)	
	CH_4 from Commonwealth Scientific and Industrial Research Organization, Aspendale, Australia (CSIRO)	Input dataset	See Annex III				Kirschke et al. (2013); Langenfelds et al. (2002)	

ACCEPTED VERSION SUBJECT TO FINAL EDITS

	CH_4 from University of California, Irvine (UCI)	Input dataset	See Annex III				Simpson et al. (2012)	
Figure 2.5c	N_2O from National Oceanic and Atmospheric Administration (NOAA)	Input dataset	See Annex III				Conway et al. (1994); Dlugokencky et al. (1994); Masarie and Tans (1995)	Insufficient and noisy data prevent the calculation of accurate growth rates for N_2O prior to 1995.
	N_2O from Advanced Global Atmospheric Gases Experiment (AGAGE)	Input dataset	See Annex III				Prinn et al. (2018); Rigby et al. (2014)	
	N_2O from Commonwealth Scientific and Industrial Research Organization, Aspendale, Australia (CSIRO)	Input dataset	See Annex III				Kirschke et al. (2013); Langenfelds et al. (2002)	
Figure 2.6	Climate Model Intercomparison Project – Phase 6 (CMIP6)	Input Dataset	See Annex III				Meinshausen et al. (2017)	
	National Oceanic and Atmospheric Administration (NOAA)	Input Dataset	See Annex III				Montzka et al. (2009)	

ACCEPTED VERSION SUBJECT TO FINAL EDITS

	Advanced Global Atmospheric Gases Experiment (AGAGE)	Input Dataset	See Annex III				Prinn et al. (2018); Rigby et al. (2014)	
Figure 2.7	Multi Sensor Reanalysis (MSR-2) of total ozone	Input dataset				https://www.temis.nl/protocols/O3global.php (date accessed 24 February 2021)	Braesicke et al. (2018); Blunden (2020); Chipperfield et al. (2018); Weber et al. (2018, 2020)	The values are given in Dobson units (see glossary).
	GOME-type Total Ozone (GTO) data record GOME/SCIA/OMI	Input dataset		https://climate.esa.int/en/terms-and-conditions/		http://www.esa-ozone-cci.org/?q=node/163		
	GOME-SCIAMACHY-GOME-2A (GSG) total ozone time series	Input dataset		https://www.uni-bremen.de/en/data-privacy/disclaimer		http://www.iup.uni-bremen.de/gome/wfdoas	Weber et al. (2018, 2020),	
	Solar Backscatter Ultraviolet Radiometer (SBUV) NOAA Cohesive data record (COH) v8.6	Input dataset				ftp://ftp.cpc.ncep.noaa.gov/SBUV_CDR		
	Solar Backscatter Ultraviolet Radiometer (SBUV) NASA Merged Ozone Data Set (MOD) v8.6 (release 6)	Input dataset				http://acdb-ext.gsfc.nasa.gov/Data_services/merged		
	World Ozone and Ultraviolet Radiation Data Centre (WOUDC)	Input dataset				http://woudc.org/archive/Projects-Campaigns/ZonalMeans		

ACCEPTED VERSION SUBJECT TO FINAL EDITS

Figure 2.8a	Surface stations	Input dataset	Archive link will be made available	CC BY 4.0 (Cooper et al., 2020)	(Cooper et al., 2020)		Cooper et al. (2020); Wang et al. (2019)	High elevation surface sites are >1500 m a.s.l.
	IAGOS	Input dataset	Archive link will be made available			https://doi.org/10.25326/20	Gaudel et al. (2020); Cohen et al. (2018)	Above Europe, northeastern USA, southeastern USA, western North America, NE China, SE Asia, southern India, Persian Gulf, Malaysia / Indonesia, Gulf of Guinea and northern South America.
Figure 2.8b	IAGOS	Input dataset	Archive link will be made available			https://doi.org/10.25326/20	Gaudel et al. (2020); Cohen et al. (2018)	Mid-troposphere (700–300 hPa; about 3–9 km and 7 regions of the upper troposphere (about 10–12 km)
	Sondes	Input dataset	Archive link will be made available			ftp://aftp.cmdl.noaa.gov/data/ozwv/Ozonesonde	Chang et al. (2020)	Analysed using a similar method as the aircraft observations) above Hilo, Hawaii, which are representative of the central North Pacific region
Figure 2.8c	TOST composite ozonesonde product	Input dataset	Archive link will be made available			http://woudc.org/archive/products/ozone/vertical-ozone-profile/ozonesonde/1.0/tost/ ; https://woudc.org/archive/products/ozone/vertical-ozone-	Gaudel et al. (2018)	

ACCEPTED VERSION SUBJECT TO FINAL EDITS

						profile/ozonesonde/1.0/tost/tropospheric_column/TROPOSPHERIC_OZONE_DATA/ANNUAL/SEA_LEVEL/		
	SAT1 (TOMS, OMI/MLS)	Input dataset	Archive link will be made available			https://acd-ext.gsfc.nasa.gov/Data_services/cloud_slice/new_data.html (accessed 20 Nov 2019)	Ziemke et al. (2019)	
	SAT2 (GOME, SCIAMACHY, OMI, GOME-2A, GOME-2B)	Input dataset	Archive link will be made available				Heue et al. (2016)	
	SAT3 (GOME, SCIAMACHY, GOME-II)	Input dataset	Archive link will be made available				Leventidou et al. (2018)	
	OMI/MLS tropospheric column ozone	Input dataset	Archive link will be made available			https://acd-ext.gsfc.nasa.gov/Data_services/cloud_slice/new_data.html (accessed 20 Nov 2019)	Ziemke et al. (2019)	Conversion of DU to tropospheric weighted average ozone mixing ratios is based on data from URL link.
		Software	plot_tropospheric_ozone_trends_for_IPCC_AR6_Chapter_2.m					
Figure 2.9a,b	Non sea salt sulfate ice core data	Input dataset			Will be available through the code uploaded onto DMS		Wendl et al. (2015); Osmont et al. (2018)	Arctic (Svalbard,78.82°N / 17.43°E)
		Input dataset			Will be available through the code uploaded onto DMS		Olivier et al. (2006)	Russia (Belukha, 49.81°N / 86.58°E)

ACCEPTED VERSION SUBJECT TO FINAL EDITS

		Input dataset			Will be available through the code uploaded onto DMS		Engardt et al. (2017); Sigl et al. (2018)	Europe (Colle Gnifetti, 45.93°N / 7.88°E)
		Input dataset			Will be available through the code uploaded onto DMS		Kellerhals et al. (2010)	South America (Illimani, 16.62°S / 67.77°W) ex-sulphate, corrected for mineral dust input
		Input dataset			Will be available through the code uploaded onto DMS		Sigl et al. (2014)	Antarctica (stacked sulphate record from Antarctica including the four ice cores DIV2010, 77.95°S / 95.96°W; B40, 70.0°S / 0.06°E; Talos Dome, 72.48°S / 159.46°E, and DFS10, 77.40°S / 39.62°W)
	Refractory black carbon ice core data	Input dataset			Will be available through the code uploaded onto DMS		Arienzo et al. (2017)	BC from the B40 core
		Input dataset			Will be available through the code uploaded onto DMS		McConnell et al. (2007); Sigl et al. (2015; 2013, 2018); Keegan et al. (2014); Mernild et al. (2015)	BC in addition from Greenland (stacked rBC record from Greenland including the four ice cores NEEM-2011-S1, 77.45°N / 51.06°W; D4, 71.4°N / 44.0°W; TUNU2013, 78.0°N / 33.88°W; and Summit2010, 72.6°N / 38.5°W)

ACCEPTED VERSION SUBJECT TO FINAL EDITS

		Input dataset			Will be available through the code uploaded onto DMS		Lim et al. (2017) reproduced from Sigl et al. (2018) and Osmont et al. (2019)	Eastern Europe (Elbrus, 43.35°N / 42.43°E) The record for Eastern Europe goes back to 1820 only.
								Sulphate concentrations were not corrected for sea-salt input, which is negligible at the ice core locations. The exception is Antarctica, for which non-sea-salt sulphate is shown, calculated from total sulphur concentrations using sodium concentrations as a sea-salt tracer and assuming a sulphur to sodium ratio in bulk sea water of 0.084. Non-sea-salt sulphate was calculated from the non-sea-salt sulphur concentration using $[nssSO_4^{2-}] = [nssS]*3$ for conversion.
Figure 2.9c	First link: MODIS Aerosol Parameters Integrated Climate Data Center (ICDC) Second link: MODerate Resolution Imaging Spectroradiometer	Input dataset	MOD08_D3 (Terra), MYD08_D3 (Aqua)	Second link: https://modaps.modaps.eosdis.nasa.gov/services/faq/LAADS_Data-	Platnick et al. (2015)	https://icdc.cen.uni-hamburg.de/en/modis-aerosol-properties.html; https://ladsweb.modaps.eosdis.nasa.gov/search/order/	Levy et al. (2010); Santer et al. (2008) ;	MODIS and MISR data from the Terra satellite are analysed starting 2000, and are enhanced by MODIS on Aqua starting 2002. Areas without crosses show trend that is significant at the 0.9

ACCEPTED VERSION SUBJECT TO FINAL EDITS

	MODIS AOD			Use_Citation_Policies.pdf				level (two-sided t-test with correction. Superimposed are the trends in annual-mean AOD from the AERONET surface sunphotometer network for 2000–2019
	Multi-Angle Imaging Spectroradiometer MISR AOD	Input dataset	MIL3MAEN			https://opendap.larc.nasa.gov/opendap/MISR/MIL3YAEN.004	Garay et al. (2017)	
	AErosol RObotic NETwork AERONET AOD	Input dataset	Level 2.0, V3, monthly			https://aeronet.gsfc.nasa.gov/data_push/AOT_Level2_Monthly.tar.gz	Holben et al. (1998); Giles et al. (2019); Santer et al. (2008)	
	AERONET AODf	Input dataset	Level 2.0, V3, monthly			https://aeronet.gsfc.nasa.gov/data_push/AOT_Level2_Monthly.tar.gz	Holben et al. (1998); Giles et al. (2019)	
Figure 2.9d	MODerate Resolution Imaging Spectroradiometer MODIS AODf	Input dataset	MOD08_D3 (Terra), MYD08_D3 (Aqua)	Licence link for LAADS DAAC: https://modaps.modaps.eosdis.nasa.gov/services/faq/LAADS_Data-Use_Citation_Policies.pdf	Platnick et al. (2015)	https://icdc.cen.uni-hamburg.de/en/modis-aerosol-properties.html; https://ladsweb.modaps.eosdis.nasa.gov/search/order/	Levy et al. (2010)	

ACCEPTED VERSION SUBJECT TO FINAL EDITS

	Multi-Angle Imaging Spectroradiometer MISR AODf	Input dataset	MIL3MAEN			https://opendap.larc.nasa.gov/opendap/MISR/MIL3YAEN.004	Garay et al. (2017)	
Figure 2.10	Effective Radiative Forcings (ERF)	Input dataset	Forcing time series			See Annex III	Section 7.3	ERF of changes to the atmospheric composition are shown for the gases carbon dioxide (CO_2), methane (CH_4), nitrous oxide (N_2O), ozone (O_3), and halogenated gases. Aerosol changes include the sum of the ERF due to aerosol – radiation and aerosol – cloud interactions. Other anthropogenic forcings include stratospheric ozone, stratospheric water vapour, land use / land cover changes, black carbon deposition on snow, and contrails. Volcanic ERF is defined such that there is zero mean forcing in the past 2.5 kyr. The sum of the best estimates for all forcings is shown as the total forcing. Further uncertainty ranges are provided in Figures 7.10 and 7.11.

ACCEPTED VERSION SUBJECT TO FINAL EDITS

Figure 2.11a	Holocene global mean surface temperature reconstruction (Temp12k multi-method)	Input dataset	https://www.ncei.noaa.gov/pub/data/paleo/reconstructions/kaufman2020/temp12k_allmethods_percentiles.csv			https://www.ncdc.noaa.gov/paleo/study/29712 (accessed 1/11/2020)	Kaufman et al. (2020a; 2020b)	Multi-method reconstruction, 5-95 percentile
	Last millennium global mean surface temperature reconstruction (PAGES2k multi method) PAGES2k Common Era Surface Temperature Reconstructions	Input dataset	https://www.ncei.noaa.gov/pub/data/paleo/pages2k/neukom2019temp/recons/Full_ensemble_median_and_95pct_range.txt			https://www.ncdc.noaa.gov/paleo/study/26872 (accessed 1/11/2020)	PAGES 2k Consortium (2019; 2017)	Median ensemble reconstruction, adjusted to mean of 1850-1900 from the reconstruction (+ 0.38°C)
	1900-2020 global mean surface temperature (multi-dataset mean)	Same as in panel (c) of this figure						
Figure 2.11b, c	HadCRUT Version 5.0	Input dataset	Archive link will be made available	https://www.metoffice.gov.uk/about-us/legal/tandc#Use-of-Crown-Copyright		https://www.metoffice.gov.uk/hadobs/	Morice et al. (2021)	Trends have been calculated where data are present in both the first and last decade and for at least 70% of all years within the period using OLS. Significance is

ACCEPTED VERSION SUBJECT TO FINAL EDITS

	NOAAGlobalTemp Version 5 – Arctic variant (not yet officially named)	Input dataset	Archive link will be made available			ftp://ftp.ncdc.noaa.gov/pub/data/cmb/ersst/v5/2020.grl.dat/interim/ (expected to be superseded)	Vose et al. (2021)	assessed with AR(1) correction as described in (Santer et al., 2008) and denoted by stippling.
	Berkeley Earth	Input dataset	Archive link will be made available			http://berkeleyearth.org/archive/data/	Rohde and Hausfather (2020)	
	FREVA-CLINT/climateronstructionAl: Updated reconstruction Version 1.0.1	Input dataset	Archive link will be made available	Open access	Kadow et al. (2020)	http://doi.org/10.5281/zenodo.3873044		
	China-MST	Input dataset	Archive link will be made available				Sun et al. (2021)	
CCB2.3 Table 1	HadCRUT Version 5.0	Input dataset	Archive link will be made available	https://www.metoffice.gov.uk/about-us/legal/tandc#Use-of-Crown-Copyright		None as yet. Once public, will appear through: https://www.metoffice.gov.uk/hadobs/		
	NOAAGlobalTemp Version – Arctic variant (not yet officially named)	Input dataset	Archive link will be made available			ftp://ftp.ncdc.noaa.gov/pub/data/cmb/ersst/v5/2020.grl.dat/interim/ (expected to be superseded)		
	Berkeley Earth	Input dataset	Archive link will be made available			http://berkeleyearth.org/archive/data/		

ACCEPTED VERSION SUBJECT TO FINAL EDITS

	Global temperature reconstructions version 2	Input dataset	Archive link will be made available		Cowtan and Way (2014)	https://pure.york.ac.uk/portal/en/datasets/global-temperature-reconstructions-version-2-cowtan-and-way(20ee85c3-f53c-4ab6-8e50-270b0ddd3686).html		
	FREVA-CLINT/climateronstructionAl: Updated reconstruction Version 1.0.1	Input dataset	Archive link will be made available	Open access	Kadow et al. (2020)	http://doi.org/10.5281/zenodo.3873044		
CCB2.3 Figure 1	HadCRUT Version 5.0	Input dataset	Archive link will be made available	https://www.metoffice.gov.uk/about-us/legal/tandc#Use-of-Crown-Copyright		https://www.metoffice.gov.uk/hadobs/hadcrut5/		
	NOAAGlobalTemp Version – Arctic variant (not yet officially named)	Input dataset	Archive link will be made available			ftp://ftp.ncdc.noaa.gov/pub/data/cmb/ersst/v5/2020.grl.dat/interim/ (expected to be superseded)		
	Berkeley Earth	Input dataset	Archive link will be made available			http://berkeleyearth.org/archive/data/		
	Global temperature reconstructions version 2	Input dataset	Archive link will be made available		Cowtan and Way (2014)	https://pure.york.ac.uk/portal/en/datasets/global-temperature-reconstructions-version-2-cowtan-and-way(20ee85c3-f53c-4ab6-8e50-270b0ddd3686).html		

ACCEPTED VERSION SUBJECT TO FINAL EDITS

	FREVA-CLINT/climateronstructionAl: Updated reconstruction Version 1.0.1	Input dataset	Archive link will be made available	Open access	Kadow et al. (2020)	http://doi.org/10.5281/zenodo.3873044		
Table 2.3	HadCRUT Version 5.0	Input dataset	Archive link will be made available	https://www.metoffice.gov.uk/about-us/legal/tandc#Use-of-Crown-Copyright		https://www.metoffice.gov.uk/hadobs/	Morice et al. (2021)	
	NOAAGlobalTemp Version 5 – Arctic variant (not yet officially named)	Input dataset	Archive link will be made available			ftp://ftp.ncdc.noaa.gov/pub/data/cmb/ersst/v5/2020.grl.dat/interim/ (expected to be superseded)	Vose et al. (2021)	
	Berkeley Earth	Input dataset	Archive link will be made available			http://berkeleyearth.org/archive/data/	Rohde and Hausfather (2020)	
	FREVA-CLINT/climateronstructionAl: Updated reconstruction Version 1.0.1	Input dataset	Archive link will be made available	Open access	Kadow et al. (2020)	http://doi.org/10.5281/zenodo.3873044		
	China-MST	Input dataset	Archive link will be made available				Sun et al. (2021)	
	GISTEMP Version 4	Input dataset	Archive link will be made available			https://data.giss.nasa.gov/gistemp/	Lenssen et al. (2019)	
	Global temperature reconstructions version 2	Input dataset	Archive link will be made available	CC BY 4.0	Cowtan and Way (2014)	https://doi.org/10.15124/20ee85c3-f53c-4ab6-8e50-270b0ddd3686	Cowtan and Way (2014)	

ACCEPTED VERSION SUBJECT TO FINAL EDITS

	GraphEM-infilled temperature data	Input dataset	Archive link will be made available	https://creativecommons.org/licenses/by/4.0/legalcode	Vaccaro et al (2021)	https://zenodo.org/record/4469607		
Table 2.4	HadCRUT Version 5.0	Input dataset	Archive link will be made available	https://www.metoffice.gov.uk/about-us/legal/tandc#Use-of-Crown-Copyright		https://www.metoffice.gov.uk/hadobs/	Morice et al. (2021)	
	NOAAGlobalTemp Version 5 – Arctic variant (not yet officially named)	Input dataset	Archive link will be made available			ftp://ftp.ncdc.noaa.gov/pub/data/cmb/ersst/v5/2020.grl.dat/interim/ (expected to be superseded)	Vose et al. (2021)	
	GISTEMP Version 4	Input dataset	Archive link will be made available			https://data.giss.nasa.gov/gistemp/	Lenssen et al. (2019)	
	Berkeley Earth	Input dataset	Archive link will be made available			http://berkeleyearth.org/archive/data/	Rohde and Hausfather (2020)	
	China-MST	Input dataset	Archive link will be made available				Sun et al. (2021)	
	FREVA-CLINT/climateronstructionAl: Updated reconstruction Version 1.0.1	Input dataset	Archive link will be made available	Open access	Kadow et al. (2020)	http://doi.org/10.5281/zenodo.3873044		
	Global temperature reconstructions version 2	Input dataset	Archive link will be made available	CC BY 4.0	Cowtan and Way (2014)	https://doi.org/10.15124/20ee85c3-f53c-4ab6-8e50-270b0ddd3686	Cowtan and Way (2014)	
	GraphEM-infilled temperature data	Input dataset	Archive link will be made available	https://creativecommons.org/licenses/by/4.0/legalcode	Vaccaro et al (2021)	https://zenodo.org/record/4469607		

ACCEPTED VERSION SUBJECT TO FINAL EDITS

	ERA5 Version 5.1	Input dataset	Archive link will be made available	https://cds.climate.copernicus.eu/api/v2/terms/static/licence-to-use-copernicus-products.pdf		https://www.ecmwf.int/en/forecasts/datasets/reanalysis-datasets/era5	Hersbach et al. (2020)	
Table 2.5	RAOBCORE Version 1.7	Input dataset	Archive link will be made available			ftp://srvx1.img.univie.ac.at/pub/	Haimberger et al. (2012)	The running variance is plotted against the end of the 30-year period concerned. All values are expressed as a ratio with the 1900−1970 variance (for Niño 3.4, the 1900−1970 variance is estimated by scaling the observed 1950−2018 variance with the ratio of the SOI variances from 1900−1970 and 1950−2018).
	RICH Version 1.7	Input dataset	Archive link will be made available			ftp://srvx1.img.univie.ac.at/pub/	Haimberger et al. (2012)	
	SUNY	Input dataset	Archive link will be made available				Zhou et al (2021)	
	UAH Version 6.0	Input dataset	Archive link will be made available			https://www.nsstc.uah.edu/climate/	Spencer et al. (2017)	
	RSS Version 4.0	Input dataset	Archive link will be made available			http://www.remss.com/measurements/upper-air-temperature/	Mears and Wentz (2017)	
	ERA5 Version 5.1	Input dataset	Archive link will be made available	https://cds.climate.copernicus.eu/api/v2/terms/static/licence-to-use-copernicus-products.pdf		https://www.ecmwf.int/en/forecasts/datasets/reanalysis-datasets/era5	Hersbach et al. (2020)	

ACCEPTED VERSION SUBJECT TO FINAL EDITS

	STAR Version 3.0	Input dataset	Archive link will be made available			ftp://ftp.star.nesdis.noaa.gov/pub/smcd/emb/mscat/data/SSU/SSU_v3.0/	Zou and Qian (2016)	
Figure 2.12	ERA5 Version 5.1	Input dataset	Archive link will be made available	https://cds.climate.copernicus.eu/api/v2/terms/static/licence-to-use-copernicus-products.pdf		https://www.ecmwf.int/en/forecasts/datasets/reanalysis-datasets/era5	Hersbach et al. (2020)	
	RAOBCORE Version 1.7	Input dataset	Archive link will be made available			ftp://srvx1.img.univie.ac.at/pub/	Haimberger et al. (2012)	
	RICH Version 1.7	Input dataset	Archive link will be made available			ftp://srvx1.img.univie.ac.at/pub/	Haimberger et al. (2012)	
	Radio Occultation Meteorology Satellite Application Facility (ROM SAF) CDR (and ICDR) Version 1.0	Input dataset	Archive link will be made available			https://www.romsaf.org/product_archive.php	Gleisner et al. (2019)	
	University Corporation for Atmospheric Research / National Oceanic and Atmospheric Administration (UCAR/NOAA)	Input dataset	Archive link will be made available			https://cdaac-www.cosmic.ucar.edu/	Steiner et al. (2020)	

ACCEPTED VERSION SUBJECT TO FINAL EDITS

	Wegener Center (WEGC) Ops v5.6	Input dataset	Archive link will be made available	CC-BY 4.0		http://doi.org/10.25364/WEGC/OPS5.6:2020.1	Angerer et al. (2017)	
	Atmospheric InfraRed Sounder (AIRS) Version 6.0	Input dataset	Archive link will be made available			https://cmr.earthdata.nasa.gov/search/concepts/C1238517301-GES_DISC.html	Susskind et al. (2014)	
Figure 2.13a	Met Office Hadley Centre HadISDH.blend gridded global surface specific humidity version 1.0.0.2019f	Input dataset	https://www.metoffice.gov.uk/hadobs/hadisdh/data/HadISDH.blendq.1.0.0.2019f_FLATgridIDPHABClocalSHIPboth5by5_anoms8110_JAN2020_cf.nc	http://www.nationalarchives.gov.uk/doc/open-government-licence/version/3/		https://www.metoffice.gov.uk/hadobs/hadisdh/downloadblend1002020.html	Willett et al. (2013; 2014; 2020;); Santer et al. (2008)	Blend (land and marine) in situ monitoring product.
Figure 2.13b	Met Office Hadley Centre HadISDH.blend gridded global surface specific humidity version 1.0.0.2019f	Input dataset	HadISDH.blendq.1.0.0.2019f_FLATgridIDPHABClocalSHIPboth5by5_anoms8110_JAN2020_cf.nc	http://www.nationalarchives.gov.uk/doc/open-government-licence/version/3/		https://www.metoffice.gov.uk/hadobs/hadisdh/downloadblend1002020.html	Willett et al., (2013; 2014; 2020)	
	ERA5 Specific humidity	Input dataset	qERA5.nc	https://www.romsaf.org/product_archive.php		https://cds.climate.copernicus.eu/cdsapp#!/dataset/reanalysis-era5-pressure-levels-monthly-means?tab=form (accessed 29 January 2021)	Hersbach et al. (2019; 2020);	

ACCEPTED VERSION SUBJECT TO FINAL EDITS

	The Japanese 55-year Reanalysis (JRA55) Specific humidity	Input dataset	jraq19732019.nc	CC BY 4.0	Japan Meteorological Agency (2013)	https://rda.ucar.edu/datasets/ds628.1/ (accessed 29 January 2021)	Kobayashi et al. (2015)	
	20th Century Reanalysis V3 (20CRv3) Specific humidity	Input dataset	shum.2m.mon.mean.nc			ftp://ftp2.psl.noaa.gov/Datasets/20thC_ReanV3/Monthlies/2mSI-MO/shum.2m.mon.mean.nc; https://psl.noaa.gov/data/gridded/data.20thC_ReanV3.monolevel.html	Slivinski et al. (2019)	
Figure 2.13c	Met Office Hadley Centre HadISDH.blend gridded global surface relative humidity version 1.0.0.2019f	Input dataset	HadISDH.blendRH.1.0.0.2019f_FLATgridIDPHABClocalSHIPboth5by5_anoms8110_JAN2020_cf.nc	https://www.metoffice.gov.uk/about-us/legal/tandc#Use-of-Crown-Copyright		https://www.metoffice.gov.uk/hadobs/hadisdh/downloadblend1002020.html	Willett et al., (2013; 2014; 2020)	Blend (land and marine) in situ monitoring product.
Figure 2.13d	Met Office Hadley Centre HadISDH.blend gridded global surface relative humidity version 1.0.0.2019f	Input dataset	HadISDH.blendRH.1.0.0.2019f_FLATgridIDPHABClocalSHIPboth5by5_anoms8110_JAN2020_cf.nc	https://www.metoffice.gov.uk/about-us/legal/tandc#Use-of-Crown-Copyright		https://www.metoffice.gov.uk/hadobs/hadisdh/downloadblend1002020.html	(Willett et al., 2013, 2014; 2020)	

ACCEPTED VERSION SUBJECT TO FINAL EDITS

	ERA5 Relative humidity	Input dataset	RHERA5.nc	https://cds.climate.copernicus.eu/api/v2/terms/static/licence-to-use-copernicus-products.pdf		https://cds.climate.copernicus.eu/cdsapp#!/dataset/reanalysis-era5-pressure-levels-monthly-means?tab=form (accessed 30 January 2021)	Hersbach et al. (2019; 2020);	
	The Japanese 55-year Reanalysis (JRA55) Relative humidity	Input dataset	jrarh19732019.nc	CC BY 4.0	Japan Meteorological Agency (2013)	https://rda.ucar.edu/datasets/ds628.1/ (accessed 30 January 2021)	Kobayashi et al. (2015)	
	20th Century Reanalysis V3 (20CRv3) Relative humidity	Input dataset	rhum.2m.mon.mean.nc			ftp://ftp2.psl.noaa.gov/Datasets/20thC_ReanV3/Monthlies/2mSI-MO/rhum.2m.mon.mean.nc ; https://psl.noaa.gov/data/gridded/data.20thC_ReanV3.monolevel.html	Slivinski et al. (2019)	
Figure 2.14	ERA5	Input dataset	tcwvera5.nc	https://cds.climate.copernicus.eu/api/v2/terms/static/licence-to-use-copernicus-products.pdf		https://cds.climate.copernicus.eu/cdsapp#!/dataset/reanalysis-era5-single-levels-monthly-means?tab=overview (accessed 21 December 2020)	Hersbach et al. (2019; 2020);	Reanalyses covering the 1979-2019 period
	The Japanese 55-year Reanalysis (JRA55)	Input dataset	jrapwat19792019.nc	CC BY 4.0	Japan Meteorological Agency (2013)	https://rda.ucar.edu/datasets/ds628.1/ (accessed 21 December 2020)	Kobayashi et al. (2015)	

ACCEPTED VERSION SUBJECT TO FINAL EDITS

	20th Century Reanalysis V3 (20CRv3)	Input dataset	pr_wtr.eatm.mon.mean.nc			ftp://ftp2.psl.noaa.gov/Datasets/20thC_ReanV3/Monthlies/miscSI-MO/pr_wtr.eatm.mon.mean.nc ; https://psl.noaa.gov/data/gridded/data.20thC_ReanV3.monolevel.html	Slivinski et al. (2019)	
	The Hamburg Ocean Atmosphere Parameters and Fluxes from Satellite (HOAPS) v4	Input dataset	HOAPS4.nc		Andersson et al. (2017)	https://wui.cmsaf.eu/safira/action/viewDoiDetails?acronym=HOAPS_V002	Andersson et al. (2017) (Product User Manual SSM/I and SSMIS)	Observations covering the 1979-2019 period.
	Remote Sensing Systems (REMSS) v7	Input dataset	tpw_v07r01_198801_202012.nc4.nc			ftp://ftp.remss.com/vapor/monthly_1deg/ ; http://www.remss.com/measurements/atmospheric-water-vapor/tpw-1-deg-product/	Wentz and Meissner (2007)	
	NASA Water Vapor Project MEaSURsS (NVAP-M)	Input dataset	TCWV_MERGED_NVAPM_TOTAL_V01_long_commongrid_198801_200812_v1.0.nc			https://public.satproj.klima.dwd.de/data/GVAP_data_archive/v1.0/TCWV/long/ (accessed 6 November 2020)	Vonder Haar, Bytheway and Forsythe (2012)	
Figure 2.15 a, d	Climatic Research Unit (CRU) Time-series (TS) data version 4.04	Input dataset	https://crudata.uea.ac.uk/cru/data/hrg/cru_ts_4.04/cruts.2004151855.v4.04/pre/cru_ts4.04.1901.2019.pre.dat.nc.gz			https://crudata.uea.ac.uk/cru/data/hrg/cru_ts_4.04/cruts.2004151855.v4.04/pre/	Harris et al. (2020)	Data products have been masked to regions with an observational constraint.

ACCEPTED VERSION SUBJECT TO FINAL EDITS

Figure 2.15 b, e	Global Precipitation Climatology Centre (GPCC) version 2020	Input dataset	gpcc_v2020_f.nc	https://www.dwd.de/EN/service/imprint/imprint_node.html		https://opendata.dwd.de/climate_environment/GPCC/html/fulldata-monthly_v2020_doi_download.html	Becker et al. (2013)	
Figure 2.15c	Climatic Research Unit (CRU) Time-series (TS) data version 4.04	Input dataset	https://crudata.uea.ac.uk/cru/data/hrg/cru_ts_4.04/cruts.2004151855.v4.04/pre/cru_ts4.04.1901.2019.pre.dat.nc.gz			https://crudata.uea.ac.uk/cru/data/hrg/cru_ts_4.04/cruts.2004151855.v4.04/pre/	Harris et al. (2020)	
	Global Historical Climatology Network Monthly (GHCN) – Version 4	Input dataset	GHCNv4-pave_BASE1961-1990.dat			https://www.ncei.noaa.gov/data/global-historical-climatology-network-monthly/v4beta/	Updated from Vose et al. (1992)	
	Global Precipitation Climatology Project (GPCP) version 2.3 combined precipitation data set	Input dataset	ftp://ftp.cdc.noaa.gov/Datasets/gpcp/precip.mon.mean.nc			https://psl.noaa.gov/data/gridded/data.gpcp.html	Adler et al. (2018)	Land-only
	Global Precipitation Climatology Centre (GPCC) version 2020	Input dataset	gpcc_v2020_f.nc			https://opendata.dwd.de/climate_environment/GPCC/html/fulldata-monthly_v2020_doi_download.html	Becker et al. (2013)	
Figure 2.15f	Global Precipitation Climatology Project (GPCP) version 2.3	Input dataset	ftp://ftp.cdc.noaa.gov/Datasets/gpcp/precip.mon.mean.nc			https://psl.noaa.gov/data/gridded/data.gpcp.html	Adler et al. (2018)	

ACCEPTED VERSION SUBJECT TO FINAL EDITS

Table 2.6	Global Precipitation Climatology Centre (GPCC) version 2020	Input dataset	gpcc_v2020_f.nc			https://opendata.dwd.de/climate_environment/GPCC/html/fulldata-monthly_v2020_doi_download.html	Becker et al. (2013)	
	Climatic Research Unit (CRU) Time-series (TS) data version 4.04	Input dataset	https://crudata.uea.ac.uk/cru/data/hrg/cru_ts_4.04/cruts.2004151855.v4.04/pre/cru_ts4.04.1901.2019.pre.dat.nc.gz			https://crudata.uea.ac.uk/cru/data/hrg/cru_ts_4.04/cruts.2004151855.v4.04/pre/	Harris et al. (2020)	
	Global Historical Climatology Network (GHCN) Monthly - Version 4	Input dataset	GHCNv4-pave_BASE1961-1990.dat			https://www.ncei.noaa.gov/data/global-historical-climatology-network-monthly/v4beta/	Vose et al. (1992)	
	Global Precipitation Climatology Project (GPCP) version 2.3	Input dataset	ftp://ftp.cdc.noaa.gov/Datasets/gpcp/precip.mon.mean.nc			https://psl.noaa.gov/data/gridded/data.gpcp.html	Adler et al. (2018)	
Figure 2.16a	ERA5 total precipitation and evaporation	Input dataset	era5_tp_2.nc era5_evap_2.nc	https://cds.climate.copernicus.eu/api/v2/terms/static/licence-to-use-copernicus-products.pdf		https://cds.climate.copernicus.eu/cdsapp#!/dataset/reanalysis-era5-single-levels-monthly-means?tab=form (accessed 19 December 2020)	Hersbach et al. (2019; 2020); Santer et al. (2008)	Blue shading shows regions that have moistened at the surface [δ(P-E) > 0] and red shading shows regions that have dried [δ (P-E) < 0]. The X indicates regions where the trends are non-significant at the p = 0.1 level.

ACCEPTED VERSION SUBJECT TO FINAL EDITS

Figure 2.16b, c, d	ERA5 total precipitation and evaporation	Input dataset	era5_tp_2.nc era5_evap_2.nc	https://cds.climate.copernicus.eu/api/v2/terms/static/licence-to-use-copernicus-products.pdf		https://cds.climate.copernicus.eu/cdsapp#!/dataset/reanalysis-era5-single-levels-monthly-means?tab=form (accessed 19 December 2020)	Hersbach et al. (2020)	
	Japanese 55-year Reanalysis (JRA-55) precipitation minus evaporation	Input dataset	fcst_phy2m125		Japan Meteorological Agency (2013) https://doi.org/10.5065/D60G3H5B	http://search.diasjp.net/en/dataset/JRA55 (accessed 19 December 2020)	Kobayashi et al. (2015)	
	20th Century Reanalysis version 3 (20CRv3) precipitation minus evaporation	Input dataset	lhtfl.mon.mean.nc, prate.mon.mean.nc			ftp://ftp.cdc.noaa.gov/Datasets/20thC_ReanV3/Monthlies/sfcFlxSI/lhtfl.mon.mean.nc; ftp://ftp.cdc.noaa.gov/Datasets/20thC_ReanV3/Monthlies/sfcSI/prate.mon.mean.nc ; https://psl.noaa.gov/data/gridded/data.20thC_ReanV3.monolevel.html (accessed 19 December 2020)	Slivinski et al. (2019)	

ACCEPTED VERSION SUBJECT TO FINAL EDITS

	Climate Forecast System Reanalysis (CFSR) precipitation minus evaporation	Input dataset	flxf06.gdas.grb2			https://www.ncei.noaa.gov/data/climate-forecast-system/access/reanalysis/monthly-means/ (accessed 19 December 2020)	Saha et al. (2010)	
	ERA20C precipitation minus evaporation	Input dataset	ERA20C_MMfcst_1978-2010.nc			https://www.ecmwf.int/en/forecasts/datasets/reanalysis-datasets/era-20c (accessed 19 December 2020)	Poli et al. (2016)	
	ERA20CM precipitation minus evaporation	Input dataset	ERA20CM_FLX.nc			https://www.ecmwf.int/en/forecasts/datasets/reanalysis-datasets/era-20cm-model-integrations (accessed 19 December 2020)	Hersbach et al. (2015)	
	Modern-Era Retrospective analysis for Research and Applications (MERRA) precipitation minus evaporation Version 5.2.0	Input dataset	tavgM_2d_flx_Nx		Global Modeling and Assimilation Office (GMAO) (2008)	https://disc.sci.gsfc.nasa.gov/datasets?keywords=%22MERRA%22%20tavgM_2d_flx_Nx&page=1 (accessed 19 December 2020)	Rienecker et al. (2011)	
	Modern-Era Retrospective analysis for Research and Applications, version 2 (MERRA-2) precipitation minus evaporation Version 5.12.4	Input dataset	tavgM_2d_flx_Nx DOI : 10.5067/0JRLVL8YV2Y4		Global Modeling and Assimilation Office (GMAO) (2015)	https://disc.sci.gsfc.nasa.gov/datasets?keywords=%22MERRA%22%20tavgM_2d_flx_Nx&page=1 (accessed 19 December 2020)	Gelaro et al. (2017)	
Figure 2.17	ERA5	Input dataset	Monthly averaged reanalysis, V-component of	https://cds.climate.copernicus.eu/api/v2/ter		https://cds.climate.copernicus.eu/cdsapp#!/dataset/reanalysis-era5-pressure-	Hersbach et al. (2019; 2020)	The edge of the Hadley Cell is taken as the average latitude of the zero cross of

ACCEPTED VERSION SUBJECT TO FINAL EDITS

			Wind, all pressure levels	ms/static/licence-to-use-copernicus-products.pdf		levels-monthly-means?tab=form (accessed 19 December 2020)		mean meridional mass streamfunction averaged between 800 and 400 hPa (Studholme & Gulev, 2018). Hadley Cell intensity is taken as the vertically averaged maximum value of the meridional stream function between 900 and 200 hPa in each overturning cell
	ERA-Interim	Input dataset	Monthly means of daily means, V-component of Wind, all pressure levels			https://apps.ecmwf.int/datasets/data/interim-full-moda/levtype=pl/ (accessed 19 December 2020)	Dee et al. (2011)	
	Japanese 55-year Reanalysis (JRA-55)	Input dataset	JRA-55/Hist/Monthly//anl_p125/anl_p125_vgrd.{YEAR}{MONTH}.nc		Japan Meteorological Agency (2013)	http://search.diasjp.net/en/dataset/JRA55 (accessed 19 December 2020)	Kobayashi et al. (2015)	
	Modern-Era Retrospective analysis for Research and Applications, version 2 (MERRA-2)	Input dataset	M2IMNPASM.5.12.4:MERRA2_100.instM_3d_asm_Np.{YEAR}{MONTH}.nc4		Global Modeling and Assimilation Office (GMAO) (2015)	https://disc.gsfc.nasa.gov/datasets/M2IMNPASM_5.12.4/summary?keywords=merra2 (accessed 19 December 2020)	Gelaro et al. (2017)	
Figure 2.18	ERA5 zonal wind	Input dataset	https://cds.climate.copernicus.eu/cdsapp#!/dataset/reanalysis-era5-pressure-levels-monthly-means?tab=form	https://cds.climate.copernicus.eu/api/v2/terms/static/licence-to-use-copernicus-products.pdf		https://cds.climate.copernicus.eu/cdsapp#!/dataset/reanalysis-era5-pressure-levels-monthly-means?tab=form	Hersbach et al. (2019; 2020); Santer et al. (2008)	

ACCEPTED VERSION SUBJECT TO FINAL EDITS

Figure 2.19a	HadISD station wind speed v2.0.2.2017f	Input dataset	https://www.metoffice.gov.uk/hadobs/hadisd/v202_2017f/station_download.html More than 8000 stations	https://www.metoffice.gov.uk/about-us/legal/tandc#Use-of-Crown-Copyright		https://www.metoffice.gov.uk/hadobs/hadisd/	Dunn et al. (2016)	To improve readability of plots, all datasets (including land station data) are interpolated into a uniform 4×4 longitude-latitude grid. Trends for HadISD were computed only if at least 36 years had values and each year has at least 3 seasons of observations available.
Figure 2.19b	ERA5 surface wind	Input dataset	https://cds.climate.copernicus.eu/cdsapp#!/dataset/reanalysis-era5-pressure-levels-monthly-means?tab=form	https://cds.climate.copernicus.eu/api/v2/terms/static/licence-to-use-copernicus-products.pdf		https://cds.climate.copernicus.eu/cdsapp#!/dataset/reanalysis-era5-single-levels-monthly-means?tab=form	Hersbach et al. (2019; 2020);	
Figure 2.19c	Cross-Calibrated Multi-Platform (CCMP) gridded surface vector winds, version 2	Input dataset	http://data.remss.com/ccmp/v02.0		Wentz et al. (2015)	http://www.remss.com/measurements/ccmp/	Atlas et al. (2011)	
Figure 2.19d	Objectively Analyzed Air-Sea Heat Fluxes (OAFlux) data set surface wind, release 3	Input dataset	ftp://ftp.whoi.edu/pub/science/oaflux/wind_v1			http://oaflux.whoi.edu/data.html	Yu et al. (2008)	

ACCEPTED VERSION SUBJECT TO FINAL EDITS

Figure 2.20	Ocean and Sea Ice Satellite Application Facility (OSISAF); NOAA/NSIDC Climate Data Record of Passive Microwave Sea Ice Concentration version 3: NASA Team (NOAA CDR) v3.0); NASA Bootstrap (NOAA CDR) v3.0; Gridded Monthly Sea Ice Extent and Concentration, 1850 Onward, version 2 - Walsh NSIDC G10010 (Arctic only); UHH Sea Ice Area Product	Input dataset	SIA_nh_September_1850-2020.csv SIA_nh_March_1850-2020.csv SIA_sh_September_1979-2020.csv SIA_sh_February_1979-2020.csv	Doerr et al. (2021): https://creativecommons.org/licenses/by/4.0/legalcode	Walsh et al. (2019) https://doi.org/10.7265/jj4s-tq79 Doerr et al. (2021)	OSISAF: OSI-450 and OSI-430-b under http://osisaf.met.no/p/ice/#conc-reproc-v2 NASA Team and Bootstrap: https://nsidc.org/data/g02202	OSISAF: Lavergne et al. (2019) NASA Bootstrap: Comiso (2017) NASA Team: Cavalieri et al. (1996) Walsh: Walsh et al. (2019; 2017) Doerr et al. (2021)	Sea ice area values have been calculated from sea ice concentration fields provided by OSISAF/CCI, NASA Team, and NASA Bootstrap from NOAA CDR 3.0
Figure 2.21	Arctic sea ice thickness from submarine transects	Input dataset			Rothrock et al. (2008)			The orbit inclination of both satellite altimeters allows mapping of Arctic sea ice to 88 °N.
	Ice, Clouds, and Land Elevation Satellite (ICESat)	Input dataset			Kwok et al. (2009**)**			
	CryoSat-2 European Space Agency (ESA)	Input dataset				https://science-pds.cryosat.esa.int/	Kwok and Cunningham (2015)	
	Electromagnetic (EM)	Input dataset					Haas et al. (2008, 2010, 2011)	
	Operation IceBridge	Input dataset			Studinger (2013, 2014) ; Paden et al. (2014)	ATM L1B elevation and echo strength: https://doi.org/10.5067/19SIM5TXKPGT ;	Kwok and Kacimi (2018)	

ACCEPTED VERSION SUBJECT TO FINAL EDITS

						Narrow swath ATM L1B elevation and echo strength: https://doi.org/10.5067/CXEQS8KVIXEI ; Snow radar L1B geolocated radar echo strength profiles: https://doi.org/10.5067/FAZTWP500V70		
Figure 2.22	Northern Hemisphere Blended Snow Cover Extent and Snow Mass Time Series	Input dataset (for Snow cover extent only)	1922-1991 : SCE_NH_index_april.nc 1967-2018 : SCE_timeseries.nc	Open access	Mudryk et al. (2020)	http://data.ec.gc.ca/data/climate/scientificknowledge/climate-research-publication-based-data/northern-hemisphere-blended-snow-extent-and-snow-mass-time-series/ (accessed 16 December 2020)	Mudryk et al. (2020); Brown (2000; 2002)	Data are from multi-observation dataset, based on method of Mudryk et al. (2020) for the satellite era (1967–2018) with the earlier part of the record based on in situ data (Brown, 2000;2002), recalibrated to the multi-observational dataset as described in Mudryk et al. (2020).
Figure 2.23a	A global compilation of glacier advances and retreats for the past two millennia grouped by 17 regions (excluding Antarctica)	Input dataset	Data stored locally but link will be made available once archived		(Solomina et al., 2016)		Solomina et al. (2016)	Time series is based on 275 studied glaciers in both hemispheres from an extensive compilation. The increasing number of glaciers with recorded advances between the12th and 19th century represents both widespread glacier expansion and better preservation of

ACCEPTED VERSION SUBJECT TO FINAL EDITS

								evidence left during more recent advances, especially where those advances were large and therefore obliterated evidence of younger advances.
Figure 2.23b	Global and regional glacier mass changes from 1961 to 2016	Input dataset	Zemp_etal_results_global.xlsx	https://creativecommons.org/licenses/by/4.0/legalcode	Zemp et al. (2019; 2020)		Zemp et al. (2020) Table 1	From 450 glacial and 19,130 geodetic glacier datasets
	GRACE satellite mission	Input dataset	annual_MB_Gtyr.mat			https://gracefo.jpl.nasa.gov/data/grace-fo-data/	Wouters et al. (2019)	
	Special Report on the Ocean and Cryosphere in a Changing Climate (SROCC)	Input dataset	SROCC_table_A2.xlsx				SROCC	
	Hugonnet et al. (2021)	Input dataset	table_hugonnet_regions_10yr_ar6period.xlsx		Hugonnet et al. (2021)			
Figure 2.24	Ice Sheet Mass Balance Inter-comparison Exercise (IMBIE) 2019 Greenland Dataset	Input dataset	imbie_dataset_greenland_dynamics-2020_02_28.xlsx			http://imbie.org/data-downloads/ (accessed 16 December 2020)	Greenland: IMBIE Consortium (2020)	
	Ice Sheet Mass Balance Inter-comparison Exercise (IMBIE) 2018 Antarctic Dataset	Input dataset	imbie_dataset-2018_07_23.xlsx			http://imbie.org/data-downloads/ (accessed 16 December 2020)	Antarctic: IMBIE Consortium (2018)	

ACCEPTED VERSION SUBJECT TO FINAL EDITS

Figure 2.25	State of Climate in 2019 Arctic Permafrost Temperature Data	Input dataset	May be available through link			https://gtnp.arcticportal.org/	Romanovsky et al (2017; 2020); updated from SROCC Ch 3	Regions are those described in (Romanovsky et al., 2020; 2017). Nordic region and Russia / Siberia 1974–2019 (note: six sites started 1998 or later); high and eastern Canadian Arctic 1978–2019 (note: four sites initiated 2008); northern Alaska, Northwest Territories and eastern Siberia 1978–2019 (note: four sites initiated 2003 or later); Interior Alaska & Central Mackenzie Valley discontinuous permafrost 1983–2019 (note: one site initiated 2001)
Figure 2.26	CSIRO	Input dataset	gmts.2019-11-27.mat			https://www.dropbox.com/sh/1crel1zq3bcmjq9/AADiidW4nJwVI5_kdLzKIB7Ba?dl=0	Wijffels et al. (2016); Roemmich et al. (2015)	
	ISAS-15	Input dataset	GOHC_2005_2018.mat			https://www.dropbox.com/sh/rgc99ra61q8y2wg/AAD4I3wZ5uBTFVrrXjcy5Hmaa?dl=0	Kolodziejczyk et al. (2017); Gaillard et al. (2016)	
	LEGOS	Input dataset	/V1.2/OHC_LEGOS1.dat			https://www.dropbox.com/sh/vyz1091l104lrpz/AAC_zyqrXhaNORGtNVPdL8iIa?dl=0 ; https://marine.copernicus.eu/access-data		This OHC solution is based on the altimetry-based sea-level from CMEMS (www.marine.copernicus.eu), the gravimetry-based ocean mass

ACCEPTED VERSION SUBJECT TO FINAL EDITS

								from the GRACE LEGOS V1.2 updated from Blazquez et al. (2018), and the expansion efficiency of heat from Meyssignac et al (2019). Annual Sub annual frequencies have been removed Uncertainties are expressed at 90% confidence level (1.65 sigma)
	NOC	Input dataset				https://www.dropbox.com/sh/a3wtx5rr2rns4bh/AAA8HoXLBs4qig5tFXHrIUJ3a?dl=0		
	CORA v5.2 Area Averaged Ocean Heat Content Anomaly	Input dataset	INSITU_GLO_TS_REP_OBSERVATIONS_013_001_b.	http://marine.copernicus.eu/services-portfolio/service-commitments-and-licence/		https://www.dropbox.com/sh/gwgmia1xns6t1mt/AAAkx1244scq_TOmfaQsqKn8a?dl=0 http://marine.copernicus.eu		Period : 2005-2018. Used climatology : 2005-2017. Global between 60°N-60°S.'
	CSIRO-BOA Area Averaged Ocean Heat Content Anomaly (0-700m)	Input dataset				https://www.dropbox.com/sh/g4yysjvw9mqpkb5/AAAMYwMSHiGiZ9uKj0IAAS-Ja?dl=0	CSIO website (argo) : http://www.argo.ucsd.edu/Gridded_fields.html	Period : 2005-2018. Used climatology : 2005-2017. Global between 60°N-60°S.
	IPRC	Input dataset				https://www.dropbox.com/sh/yc9jclqrdyh14uc/AABy		Period : 2005-2018. Used climatology :

ACCEPTED VERSION SUBJECT TO FINAL EDITS

						o_4H0e-ITCig6Xgjebs1a?dl=0 IPRC website (argo) : http://apdrc.soest.hawaii.edu/projects/Argo/data/gridded/On_standard_levels/index-1.html		2005-2017. Global between 60°N-60°S.
	JAMSTEC	Input dataset				https://www.dropbox.com/sh/gm67r4qm1r3lxp2/AABBgtEvsibMXrPOSxsu7emma?dl=0	'JAMSTEC website (argo) : http://www.jamstec.go.jp/ARGO/argo_web/argo/?page_id=83&lang=en	Period : 2005-2018. Used climatology : 2005-2017. Global between 60°N-60°S.
	Scripps	Input dataset				https://www.dropbox.com/sh/9ojeql7caccjqcl/AAD1gg5Ake0sn9nCLxEF4_9na?dl=0		Period : 2005-2018. Used climatology : 2005-2017. Global between 60°N-60°S
	KvS11	Input dataset	CORA5.1 : INSITU_GLO_TS_REP_OBSERVATIONS_013_001_b.	http://marine.copernicus.eu/services-portfolio/service-commitments-and-licence/		https://www.dropbox.com/sh/lca41zwv9vv4i2m/AADsRmKtofG9prda_eTKiKO_a?dl=0	von Schuckmann & Le Traon (2011)	Period : 2005-2018. Used climatology : same years. Global between 60°N-60°S.'
	Cheng17	Input dataset	2019_10_25/IAP_OHC_estimate_update.txt			https://www.dropbox.com/sh/tskdbmvntpmnm0g/AADKpG7Am-wQLqD1oAHS1n-Na?dl=0 Accessed 19/03/2019	Cheng & Zhu (2016); Cheng et al. (2017)	Unit of OHC: *10^22 Joules Smoothed-OHC is 12-month running mean. Baseline: 2006-2015 Note: in this version (v3), we included the Arctic Ocean,

ACCEPTED VERSION SUBJECT TO FINAL EDITS

								improved land mask, and used updated CH14 XBT correction. Information of updated CH14 scheme for XBT data provided in http://159.226.119.60/cheng/ and https://www.nodc.noaa.gov/OC5/XBT_BIAS/xbt_bias.html Note: Reliable records are after 1955 Link to Ocean Gridded Temperature Analysis: ftp://ds1.iap.ac.cn/ftp/cheng/CZ16_v3_IAP_Temperature_gridded_1month_netcdf/ OR: http://ddl.escience.cn/f/FiL0
	GCOS20	Input dataset	GCOS_all_heat_content_1960-2018_ZJ_v22062020.nc			https://www.dropbox.com/sh/99xpvl4tlc9r5c2/AADDvOnKGYzVU__NcW-Eabwma?dl=0	Von Schuckmann et al. (2020)	Period : 1960-2018.
	EN4	Input dataset				https://www.dropbox.com/sh/te1ol2kazaet1gs/AAAyUSAXSG969PGbnstnbccga?dl=0	Good et al. (2013)	

ACCEPTED VERSION SUBJECT TO FINAL EDITS

						https://www.metoffice.gov.uk/hadobs/en4/download-en4-2-1.html		
	Lev12-NCEI	Input dataset				https://www.dropbox.com/sh/un7zkln9d0mfjgj/AADtaHXhF1oZJjMck8hOahcya?dl=0 https://www.ncei.noaa.gov/access/global-ocean-heat-content/	Levitus et al. (2012)	
	Ish17v7.3	Input dataset			Ishii et al. (2017)	https://www.dropbox.com/sh/pct4t51wg3e8ggh/AAAV0wGWXn8KARNvW49gn5WZa?dl=0 https://climate.mri-jma.go.jp/pub/ocean/ts/v7.3/ (Accessed 21/01/2021)		
	PMEL	Input dataset				https://www.dropbox.com/sh/8ken8wamye6rxk6/AADy_1InfSqpUFF0BNmmcT7ja?dl=0 (Accessed 27/03/2019)	Lyman & Johnson (2014) Johnson et al. (2018)	
	Su20-OPEN	Input dataset	OHC_recons_Su/2020_11_14_WF/OPEN_ToCatia.mat			https://www.dropbox.com/sh/o5l3gqararkxddv/AABBstLQnLks-LyHdc-ukGdBa?dl=0		
	Zanna	Input dataset				https://www.dropbox.com/sh/1wd75jd5umilvdf/AAABHlBwQZxCJa3GIMWgspq2a?dl=0	Zanna et al. (2019)	

ACCEPTED VERSION SUBJECT TO FINAL EDITS

						https://laurezanna.github.io/#about https://zenodo.org/record/4603700#.YG5vEC3L0lI		
	Desb17					https://www.dropbox.com/sh/82uxgu2ew4ankgi/AADuy_aDsdl1mw1Gj0cbmXi5a?dl=0	Desbruyeres et al. (2017) ; Purkey & Johnson (2010)	Desbruyeres published an estimate of the full-depth GOHC and ThSLR during the 2000's using a blended Argo-hydrography product : 1.45 ZJ/yr and 0.2 mm/yr, respectively.
Table 2.7	Cheng ocean heat content	Input dataset			Cheng et al. (2017)	http://159.226.119.60/cheng/		
	CSIRO ocean heat content / thermosteric sea level	Input dataset			Domingues et al. (2008)	https://www.cmar.csiro.au/sealevel/thermal_expansion_ocean_heat_timeseries.html		
	EN4 ocean subsurface profiles	Input dataset		Non-Commercial Government License (UK)	Good et al (2013)	https://www.metoffice.gov.uk/hadobs/en4/		
	Ishii et al ocean heat content / thermosteric sea level	Input dataset		https://www.jma.go.jp/jma/en/copyright.html	Ishii et al. (2017)	https://www.data.jma.go.jp/gmd/kaiyou/english/ohc/ohc_data_en.html		
	NCEI Ocean Heat Content / thermosteric sea level	Input dataset			Levitus et al. (2012)	https://www.ncei.noaa.gov/access/global-ocean-heat-content/		
	Purkey and Johnson ocean heat content / thermosteric sea level	Input dataset			Purkey and Johnson (2010)		Desbruyères et al (2016)	

ACCEPTED VERSION SUBJECT TO FINAL EDITS

	Zanna et al ocean heat content / thermosteric sea level	Input dataset			Zanna et al. (2019)	https://laurezanna.github.io/post/ohc_pnas_dataset/		
Figure 2.27	Durack and Wijffels (2010)	Input dataset	DurackandWijffels_GlobalOceanChanges_19500101-20191231__210122-205355_beta.nc		Durack and Wijffels (2010)	https://www.cmar.csiro.au/oceanchange/download.php		
			DurackandWijffels_GlobalOceanChanges_19700101-20191231__210122-205448_beta.nc					
Figure 2.28	KE2018 Kemp et al. (2018)	Input dataset				https://www.dropbox.com/s/6nna1xdsfvqziwn/sealevel.xlsx?dl=0 (Accessed 27/07/2020)	Kemp et al. (2018)	
	RD2011 Ray & Douglas (2011)	Input dataset				https://www.dropbox.com/s/6nna1xdsfvqziwn/sealevel.xlsx?dl=0 (Accessed 27/07/2020)	Ray & Douglas (2011)	
	JE2014 Jevrejeva et al. (2014)	Input dataset				https://www.dropbox.com/s/6nna1xdsfvqziwn/sealevel.xlsx?dl=0 (Accessed 27/07/2020) https://www.psmsl.org/products/reconstructions/gslGPChange2014.txt	Jevrejeva et al. (2014)	https://www.sciencedirect.com/science/article/abs/pii/S0921818113002750?via%3Dihub
	DA2017 Dangendorf et al. (2017)	Input dataset				https://www.dropbox.com/s/6nna1xdsfvqziwn/sealevel.xlsx?dl=0 (Accessed 27/07/2020)	Dangendorf et al. (2017)	

ACCEPTED VERSION SUBJECT TO FINAL EDITS

	DA2019 Dangendorf et al. (2019)	Input dataset				https://www.dropbox.com/s/6nna1xdsfvqziwn/sealevel.xlsx?dl=0 (Accessed 27/07/2020)	Dangendorf et al. (2019)	
	CW2011 Church & White (2011)	Input dataset				https://www.dropbox.com/sh/yqxi73t6l7mbapp/AABdh4zVUjTlmpon4nstYgXca?dl=0 https://www.cmar.csiro.au/sealevel/GMSL_SG_2011_up.html https://www.cmar.csiro.au/sealevel/sl_data_cmar.html	Church & White (2011) ; Church et al. (2011)	
	WS2014 Wenzel & Schroter (2014)	Input dataset				https://www.dropbox.com/sh/e9n2p4d89br233q/AABDMt4ZFPlgdS658LXkFk8Fa?dl=0 (Accessed 5/8/2020) http://store.pangaea.de/Publications/WenzelM_SchroeterJ_2014/WS2014_RSLA_EOF_decomposition.nc	Wenzel & Schroter (2014)	
	HA2015 Hay et al. (2015)	Input dataset				https://www.dropbox.com/sh/ubvlpanfjkj9oxt/AAB5GekySRF-80pVzCnWWfQ6a?dl=0 https://static-content.springer.com/esm/art%3A10.1038%2Fnature14093/MediaObjects/41586_2015_BFnature14093_MOESM60_ESM.xls (Accessed 24/09/2020)	Hay et al. (2014; 2015, 2017)	

ACCEPTED VERSION SUBJECT TO FINAL EDITS

	FR2018 Frederikse et al. (2018)	Input dataset				https://www.dropbox.com/sh/89sh77lvjpadwpl/AADiSEDBA-nzbzKa2-tfD9JFa?dl=0 (Accessed 01/09/2020)	Frederikse et al. (2018)	
	FR2020 Frederikse et al. (2020)	Input dataset				https://www.dropbox.com/sh/lvrysjuccqic5je/AACWcbC4gmbEvvdUzorED8kLa?dl=0 https://github.com/thomasfrederikse/sealevelbudget_20c. https://zenodo.org/record/3862995#.YG3rQxNKglI	Frederikse et al. (2020)	
	AVISO	Input dataset	netcdf file: MSL_Serie_MERGED_Global_AVISO_GIA_Adjust_Filter2m.nc			https://www.dropbox.com/sh/jzjbzqx0x2ehtlv/AAAvdT6bLYyNgpMjTkkLyo5oa?dl=0 https://www.aviso.altimetry.fr/index.php?id=1599		
	EU CMEMS	Input dataset				https://www.dropbox.com/sh/8zaziptcs40tk2o/AAB_s8m5C6Lm_BU2jvObU4DOa?dl=0 http://www.esa-sealevel-cci.org/products	Ablain et al. (2017, 2019) ; WCRP Global Sea Level Budget Group (2018)	
	CSIRO	Input dataset				https://www.dropbox.com/sh/y2eb3uqx99gjox4/AAA8AhrhpUiRakna9gKJ1y6Pa?dl=0		

ACCEPTED VERSION SUBJECT TO FINAL EDITS

						https://www.cmar.csiro.au/sealevel/sl_data_cmar.html		
	CU (Nerem et al. (2018))	Input dataset				https://www.dropbox.com/sh/4930xp6v110q65k/AABk5b2oSkPWXnuScFL7iD07a?dl=0 https://sealevel.colorado.edu/	Nerem et al. (2018)	
	ESA (Legeais et al. (2018))	Input dataset				https://www.dropbox.com/sh/prso9p9sa99nw9l/AAAmhADZJWyINLX5bd5EeItda?dl=0	Legeais et al. (2018) ; Quartly et al. (2017)	
	NASA (Beckley et al. (2017))	Input dataset	GMSL_TPJAOS_199209_201411.txt		Beckley et al. (2017)	https://www.dropbox.com/sh/giqkd23763fqbjs/AABOSOoMojE3cSuajM5LoA0Aa?dl=0 https://podaac.jpl.nasa.gov/MEaSUREs-SSH?sections=about%2Bdata		If this data is used please cite Beckley et al. (2016)
	NOAA	Input dataset	slr_sla_gbl_free_txj1j2_90.nc			https://www.dropbox.com/sh/5sccjwsijplbc9b/AADbU26hWwrbyd4_mvD5uCNUa?dl=0 https://www.star.nesdis.noaa.gov/socd/lsa/SeaLevelRise/LSA_SLR_timeseries.php		
	LEGOS (Blazquez et al. (2018))	Input dataset			Blazquez et al. (2018)	https://www.dropbox.com/sh/j6mgodlgtt0fnto/AAArZyPhbsV3dCgpnGb4vXMPa?dl=0 ftp://ftp.legos.obs-mip.fr/pub/soa/gravimetrie		

ACCEPTED VERSION SUBJECT TO FINAL EDITS

						/grace_legos/V1.2/ocean_mass_and_contributors.dat		
	Palmer et al. (2021) (1901-1993) + WCRP GSLB group (1993-2018)	Input dataset	gmsl_altimeter+TG_ensemble_12022021.mat		Palmer et al. (2021) ; WCRP Global Sea Level Budget Group (2018)	https://www.dropbox.com/s/a5wx1k15fd84czh/GOHC_GThSL_timeseries.mat?dl=0		
	Spratt and Lisiecki (2016)	Input dataset				https://www.dropbox.com/sh/ahprl53ibnqfp3f/AABjeYtZBcDjVjBnRmGiISqIa?dl=0 http://www.ncdc.noaa.gov/paleo/study/19982	Spratt and Lisiecki (2016)	Preferred reconstruction: Figure 2c - composite of the short (0–431 ka) and long (431–798 ka) time windows
Figure 2.29a	High-resolution boron isotope-based CO_2 record; Table mmc5 for the Pliocene (0 to 3.5 myr) and the older than 3.5 myr data from Table mmc4, using the G17 reconstruction of seawater d11B OA_IPCC_clean.R Panel a	Input dataset	Anag2020.txt Sos.GR.txt	CC BY 4.0	Anagnostou et al. (2020) Sosdian et al. (2018)		Anagnostou et al. (2016); Pearson et al. (2009); Harper et al. (2020); Gutjahr et al. (2017); Henehan et al. (2020); Badger et al. (2013); Bartoli et al. (2011); Chalk et al. (2017); Foster et al. (2012); Greenop et al. (2014); Hönisch et al. (2009); Martínez-Botí et al. (2015); Seki et al. (2010); Sosdian et al. (2018)	
Figure 2.29b	Data from mmc5 – Sosdian et al. (2018) OA_IPCC_clean.R Panel b	Input dataset	Plio.pH.txt	CC BY 4.0	Sosdian et al. (2018)		Anagnostou et al. (2016); Bartoli et al. (2011); Chalk et al. (2017); Gutjahr et al. (2017); Hönisch et al.	

ACCEPTED VERSION SUBJECT TO FINAL EDITS

							(2009); Martínez-Botí et al. (2015); Seki et al. (2010); Sosdian et al. (2018)	
Figure 2.29c	Boron isotope records OA_IPCC_clean.R Panel c	Input dataset	Shao.txt		Shao et al. (2019)		Shao et al. (2019); Martinez-Boti et al. (2015); Palmer et al. (2010); Pearson and Palmer (2003); Gray et al. (2018); Ezat et al. (2017); Foster (2008); Henehan et al. (2013); Foster and Sexton (2014); Naik et al. (2015)	
Figure 2.29d	BATS pH	Input dataset	Ocean_pH_BAT.txt		http://bats.bios.edu/bats-data/	http://bats.bios.edu/bats-data/	Bates and Johnson (2020)	
	HOT pH	Input dataset	Ocean_pH_HOT.txt		Karl and Lukas (1996)	https://hahana.soest.hawaii.edu/hot/crequest/main.html	Dore et al. (2009)	
	Copernicus Marine Environment Monitoring Service (CMEMS) pH	Input dataset	global_omi_health_carbon_ph_area_averaged_1985_P20200930.nc		Gehlen et al. (2020)	https://resources.marine.copernicus.eu/?option=com_csw&view=details&product_id=GLOBAL_OMI_HEALTH_carbon_ph_area_averaged	Gehlen et al. (2020)	
	OceanSODA-ETHZ	Input dataset	ipcc_oceanSODA_pH_65N-65S_1985-2019_annualAvg_areaWeighted.csv		Gregor and Gruber (2021)	https://www.ncei.noaa.gov/access/metadata/landing-page/bin/iso?id=gov.noaa.nodc:0220059	Gregor and Gruber (2021)	

ACCEPTED VERSION SUBJECT TO FINAL EDITS

Figure 2.30	Barrow CO_2	Input dataset		Open access		https://www.esrl.noaa.gov/gmd/dv/data/index.php?site=BRW&parameter_name=Carbon%2BDioxide	Graven et al. (2013)	
	Mauna Loa CO_2	Input dataset		Open access		https://www.esrl.noaa.gov/gmd/dv/data/index.php?site=MLO&parameter_name=Carbon%2BDioxide	Graven et al. (2013)	
Figure 2.31	Ocean Colour Climate Change Initiative (OC-CCI Version 4.2)	Input dataset	OC-CCI Version 4.2	Free and Open		https://catalogue.ceda.ac.uk/uuid/99348189bd33459cbd597a58c30d8d10 ; https://climate.esa.int/en/projects/ocean-colour/; www.oceancolour.org	Sathyendranath et al. (2019); Santer et al. (2008)	The climatology and trends are calculated from climate-quality ocean-colour products generated as part of the Climate Change Initiative of the European Space Agency. These are multi-sensor products, with inter-sensor bias correction applied to minimise artefacts in trends, with processing algorithms selected after round-robin comparisons
Figure 2.32a	Cherry blossom peak bloom in Kyoto, Japan	Input dataset		Open access		http://atmenv.envi.osakafu-u.ac.jp/aono/kyophenotemp4/	Aono & Saito (2010)	
Figure 2.32b	Grape harvest in Beaune, France	Input dataset				https://www.euroclimhist.unibe.ch/en/	Labbe et al. (2019)	
Figure 2.32c	Spring phenology index in eastern China	Input dataset	Archive link will be made available				Ge et al. (2014)	
Figure 2.32d	Full flower of Piedmont species in Philadelphia, USA	Input dataset	Archive link will be made available				Panchen et al. (2012)	

ACCEPTED VERSION SUBJECT TO FINAL EDITS

Figure 2.32e	Grape harvest in Central Victoria, Australia	Input dataset	Archive link will be made available				Webb et al. (2011)	
Figure 2.32f	Start of growing season in Tibetan Plateau, China	Input dataset		Open access		https://www.ncdc.noaa.gov/paleo-search/study/22641	Yang et al. (2017)	
Figure 2.33	MERIS	Input dataset		Open access		http://earth.esa.int/level3/meris-level3/	Gobron (2018)	
	MODIS-TIP	Input dataset		Open access		https://ladsweb.modaps.eosdis.nasa.gov/	Gobron (2018)	
	SeaWIFS v 2010.0	Input dataset		Open access		http://fapar.jrc.ec.europa.eu/	Gobron (2018)	
Figure 2.34 CO_2	Refer to Table 2.1 and Section 2.2.3							LM age range is from 1000 to 1750 CE; MPWP value is for interglacial KM5c, 95% range
Figure 2.34 CO_2 rate of change	Refer to Table 2.1 and Section 2.2.3							LM age range is from 1000 to 1750 CE based on data from Law Dome; last deglacial transition is maximum rate based on data from WAIS Divide
Figure 2.34 Temperature relative to 1850-1900	Refer to Section 2.3.1.1 and 4-dataset mean for modern and 1850-1900							Modern and 1850-1900 is based on 4-dataset mean; LM warmest and coldest 20-year periods are 873-892 CE and 1454-1473 CE, respectively, from PAGES 2k Consortium(2019)

ACCEPTED VERSION SUBJECT TO FINAL EDITS

Figure 2.34 Glacier extent relative to 1850-1900al	Refer to Section 2.3.2.3 and CCB2.4 for MPWP							1850-1900 and LM are based on Solomina et al., (2016); MH is based on Solomina et al., (2015)
Figure 2.34 Northern tree line relative to 1850-1900	Refer to Section 2.3.4.3.2							Modern based on Binney et al. (2009); LM and MH are based on MacDonald et al. (2008) and Binney et al. (2017); LGM is based on Williams et al. (2011) and Binney et al. (2017); LIG is based on CAPE Last Interglacial Project Members (2006); MPWP is based on Salzmann et al. (2008; 2013)
Figure 2.34 Sea level relative to 1900	Refer to Section 2.3.3.3							Modern is for 2018; 1850-1900 and LM are from Kemp et al. (2018); LIG and EECO are *likely* ranges
Figure 2.34 Sea level rate of change	Refer to Section 2.3.3.3							Modern is for 1993-2018; LM values are maximum centennial rates of lowering and rising: –1.1 to –0.2 (1020-1120 CE) and –0.1 to 0.7 (1460-1560 CE), respectively, from Kemp et al. (2018); LGT is for meltwater pulse 1A about 14.6-14.3 ka

ACCEPTED VERSION SUBJECT TO FINAL EDITS

CCB2.4 Figure 1a (left side)	Multi-model mean, annual near-surface air temperature (PlioMIP2) The Pliocene Model Intercomparison Project Phase 2	Input dataset	Replotted from Haywood et al. (2020) (Figure 1b); supplement file: data_for_1b_1d.nc			https://doi.org/10.5194/cp-16-2095-2020-supplement	Haywood et al. (2020)	
	Site-level proxy data, sea-surface temperature for KM5c	Input dataset	McClymont et al. (2020a) (UK37 using BAYSPLINE (column 14), and Mg/Ca using BAYMAG (column 16), both for KM5c). Same as Figure 7.17k	CC BY-4.0		https://doi.org/10.1594/PANGAEA.911847 (accessed 1/11/2020)	McClymont et al. (2020b)	
	Site-level proxy data, terrestrial temperature for MPWP	Input dataset	Same as Figure 7.17b				Salzmann et al. (2013); Vieira et al. (2018)	
CCB2.4 Figure 1a (right side)	Multi-model mean, annual precipitation rate (PlioMIP2) The Pliocene Model Intercomparison Project Phase 2	Input dataset	Replotted from Haywood et al. (2020) (Figure 5b) supplement file: data_for_5b_5c.nc			https://doi.org/10.5194/cp-16-2095-2020-supplement	Haywood et al. (2020)	
	Site-level proxy data, terrestrial precipitation rate for MPWP	Input dataset					Ager et al. (1994); Fauquette et al. (1999); Demske et al. (2002); Dodson and Macphail (2004); Brigham-Grette et al.	Site-level data from individual studies.

ACCEPTED VERSION SUBJECT TO FINAL EDITS

							(2013); Sniderman et al. (2016); Vieira et al. (2018)	
CCB2.4 Figure 1b (top)	Biome distributions MPWP (PRISM4)	Input dataset	Replotted from Dowsett et al. (2016) (Figure 3c)				Dowsett et al. (2016)	
CCB2.4 Figure 1b (bottom)	Biome distributions present-day (BOME4)	Input dataset	Replotted from Salzmann et al. (2008) (Figure 1b)				Salzmann et al. (2008)	
CCB2.4 Figure 1c (top)	Modelled ice sheet extent, Greenland, MPWP	Input dataset	Replotted from Haywood et al. (2019) (Figure 4a)				Haywood et al. (2019)	
CCB2.4 Figure 1c (bottom)	Modelled ice sheet extent, Antarctica, MPWP	Input dataset	Replotted from Dolan et al. (2018) (Figure 3e)				Dolan et al. (2018)	
Figure 2.35	Southern Annular Mode (SAM) Index 1,000 Year Annual Reconstruction – Dätwyler et al. (2018)	Input dataset	Reconstructions_Annual_LC.txt			https://www1.ncdc.noaa.gov/pub/data/paleo/reconstructions/datwyler2017/	Dätwyler et al. (2018)	
	Southern Annular Mode (SAM) Index 1,000 Year DJF Reconstruction – Dätwyler et al. (2018)	Input dataset	Reconstructions_DJF_LC.txt			https://www1.ncdc.noaa.gov/pub/data/paleo/reconstructions/datwyler2017/	Dätwyler et al. (2018)	
	Southern Annular Mode (SAM) Index 600 Year DJF Tree Ring Reconstruction – Villalba et al. (2012)	Input dataset	villalba2012sam.txt			ftp://ftp.ncdc.noaa.gov/pub/data/paleo/treering/reconstructions/villalba2012sam.txt ; https://www.ncdc.noaa.gov/paleo-search/	Villalba et al. (2012)	

ACCEPTED VERSION SUBJECT TO FINAL EDITS

	Southern Annular Mode (SAM) Index 1000 Year Reconstruction – Abram et al. (2014)	Input dataset	abram2014sam.txt			ftp://ftp.ncdc.noaa.gov/pub/data/paleo/contributions_by_author/abram2014/abram2014sam.txt ; https://www.ncdc.noaa.gov/paleo-search/	Abram et al. (2014)	
	Observation-based Southern Hemisphere Annular Mode Index (SAM Marshall)	Input dataset	newsam.1957.2007.txt			https://legacy.bas.ac.uk/met/gjma/sam.html	Marshall (2003)	
	Southern Annular Mode (SAM) 20th Century Reanalysis v2c (20CRv2c)	Input dataset	sam.20crv2c.long.data			https://psl.noaa.gov/data/20thC_Rean/timeseries/monthly/SAM/sam.20crv2c.long.data	Gong and Wang (1999)	
	Seasonal Southern Hemisphere Annular Mode (SAM) Reconstructions – SAM Fogt	Input dataset	recons_mean7100.txt			http://polarmet.osu.edu/ACD/sam/sam_recon.html	Fogt et al. (2009); Jones et al. (2009)	
	Antarctic Oscillation (AAO) (NCEP) – SAM NCEP	Input dataset	monthly.aao.index.b79.current.ascii			https://www.cpc.ncep.noaa.gov/products/precip/CWlink/daily_ao_index/aao/aao.shtml	Mo (2000)	
Figure 2.36	Stahle et al. (1998) Southern Oscillation Index Reconstruction	Input dataset	Archive link may be provided			http://www.ncdc.noaa.gov/paleo-search/study/6238	Stahle et al. (1998)	Individual studies represented with grey lines, while the overlying thick blue line is the mean reconstruction and the dashed black lines the *very likely* range for the period where there
	Nino 3 Index Reconstruction	Input dataset				http://www.ncdc.noaa.gov/paleo-search/study/6250	Cook (2000)	

ACCEPTED VERSION SUBJECT TO FINAL EDITS

	Mann et al. (2000) El Niño Reconstructions	Input dataset	Archive link may be provided			http://www.meteo.psu.edu/holocene/public_html/shared/research/old/mbh99b.html	Mann et al. (2000)	are sufficient data to estimate it
	Evans et al. (2001) Proxy-Based Pacific SST Reconstructions	Input dataset	Archive link may be provided			ftp://ftp.ncdc.noaa.gov/pub/data/paleo/coral/east_pacific/sst_evans2002/	Evans et al. (2001)	
	Evans et al. (2002) Proxy-Based Pacific SST Reconstructions	Input dataset	Archive link may be provided			http://www.ncdc.noaa.gov/paleo-search/study/6348	Evans et al. (2002)	
	Cook et al. (2008) 700 Year Tree-Ring ENSO Index Reconstructions	Input dataset	Archive link may be provided			http://www.ncdc.noaa.gov/paleo-search/study/8704	Cook et al. (2008)	
	Braganza et al. (2009) Multiproxy ENSO Reconstructions	Input dataset	Archive link may be provided			http://www.ncdc.noaa.gov/paleo-search/study/8409	Braganza et al. (2009)	
	McGregor et al. (2010) 350 Year Unified ENSO Proxy Reconstructions	Input dataset	Archive link may be provided			http://www.ncdc.noaa.gov/paleo-search/study/8732	McGregor et al. (2010)	

ACCEPTED VERSION SUBJECT TO FINAL EDITS

	Nino 3.4 SST 460 Year Reconstructions	Input dataset	Archive link may be provided			http://www.ncdc.noaa.gov/paleo-search/study/11749	Wilson et al. (2010)	
	1100 Year ENSO Index Reconstruction	Input dataset	Archive link may be provided			http://www.ncdc.noaa.gov/paleo-search/study/11194	Li et al. (2011)	
	700 Year ENSO Nino 3.4 Index Reconstruction	Input dataset	Archive link may be provided			http://www.ncdc.noaa.gov/paleo-search/study/14632	Li et al. (2013)	
	Central Equatorial Pacific Nino 3.4 850 Year SST Reconstruction	Input dataset	Archive link may be provided			http://www.ncdc.noaa.gov/paleo-search/study/13684	Emile-Geay et al. (2013)	
	PAGES Ocean 2K 400 Year Coral Data and Tropical SST Record	Input dataset	Archive link may be provided			http://www.ncdc.noaa.gov/paleo-search/study/17955	Tierney et al. (2015)	
	Southern Oscillation Index (SOI)	Input dataset	Archive link may be provided	**Creative Commons (CC) Attribution 3.0 licence**		http://www.bom.gov.au/climate/current/soi2.shtml	Troup (1965)	
	Nino 3.4 (from Extended Reconstructed Sea Surface Temperature (ERSST) v5)	Input dataset	Archive link may be provided			https://www.cpc.ncep.noaa.gov/data/indices/	Huang et al. (2017)	
Figure 2.37	Centennial-scale sea surface temperature	Input dataset	ftp://ftp.cdc.noaa.gov/Datasets/			https://psl.noaa.gov/data/gridded/data.cobe2.html	Hirahara et al. (2014)	

ACCEPTED VERSION SUBJECT TO FINAL EDITS

	analysis and its uncertainty, version 2 (COBE)		COBE2/sst.mon.mean.nc					
	NOAA Extended Reconstructed Sea Surface Temperature V5 (ERSST)	Input dataset	ftp://ftp.cdc.noaa.gov/Datasets/noaa.ersst.v5/sst.mnmean.nc			https://psl.noaa.gov/data/gridded/data.noaa.ersst.v5.html	Huang et al. (2017)	
	Hadley Centre Sea Ice and Sea Surface Temperature data set (HadISST)	Input dataset	https://www.metoffice.gov.uk/hadobs/hadisst/data/HadISST_sst.nc.gz	http://www.nationalarchives.gov.uk/doc/non-commercial-government-licence/version/2/		https://www.metoffice.gov.uk/hadobs/hadisst/	Rayner et al. (2003)	
	Kaplan Extended SST V2 (KAPLAN)	Input dataset	ftp://ftp.cdc.noaa.gov/Datasets/kaplan_sst/sst.mon.anom.nc			https://www.psl.noaa.gov/data/gridded/data.kaplan_sst.html	Kaplan et al. (1998)	
	NOAA Optimum Interpolation (OI) Sea Surface Temperature V2 (OISST)	Input dataset	ftp://ftp.cdc.noaa.gov/Datasets/noaa.oisst.v2/sst.mnmean.nc			https://www.psl.noaa.gov/data/gridded/data.noaa.oisst.v2.html	Reynolds et al. (2002)	
Figure 2.38	Centennial-scale sea surface temperature analysis and its uncertainty, version 2 (COBE)	Input dataset	ftp://ftp.cdc.noaa.gov/Datasets/COBE2/sst.mon.mean.nc			https://psl.noaa.gov/data/gridded/data.cobe2.html	Hirahara et al. (2014)	Both indices are based on annual data, with the long-term mean and linear trend removed using the least-squares method and then low-pass filtered using a 10-year running mean.
	NOAA Extended Reconstructed Sea Surface Temperature V5 (ERSST)	Input dataset	ftp://ftp.cdc.noaa.gov/Datasets/noaa.ersst.v5/sst.mnmean.nc			https://psl.noaa.gov/data/gridded/data.noaa.ersst.v5.html	Huang et al. (2017)	

ACCEPTED VERSION SUBJECT TO FINAL EDITS

	Hadley Centre Sea Ice and Sea Surface Temperature data set (HadISST)	Input dataset	https://www.metoffice.gov.uk/hadobs/hadisst/data/HadISST_sst.nc.gz			https://www.metoffice.gov.uk/hadobs/hadisst/	Rayner et al. (2003)	
	Kaplan Extended SST V2 (KAPLAN)	Input dataset	ftp://ftp.cdc.noaa.gov/Datasets/kaplan_sst/sst.mon.anom.nc			https://www.psl.noaa.gov/data/gridded/data.kaplan_sst.html	Kaplan et al. (1998)	

[END TABLE 2.SM.1 HERE]

ACCEPTED VERSION
SUBJECT TO FINAL EDITS

References

(GMAO), G. M. and A. O. (2008). *tavgM_2d_flx_Nx: MERRA 2D IAU Diagnostic, Surface Fluxes, Monthly Mean V5.2.0, Greenbelt, MD, USA,*. Goddard Earth Sciences Data and Information Services Center (GES DISC). https://doi.org/10.5067/JX8Q6J3NH5QD

(GMAO), G. M. and A. O. (2015). *MERRA-2 tavgM_2d_flx_Nx: 2d,Monthly mean,Time-Averaged,Single-Level,Assimilation,Surface Flux Diagnostics V5.12.4, Greenbelt, MD, USA*. Goddard Earth Sciences Data and Information Services Center (GES DISC). https://doi.org/10.5067/0JRLVL8YV2Y4

Ablain, M., Legeais, J. F., Prandi, P., Marcos, M., Fenoglio-Marc, L., Dieng, H. B., Benveniste, J., & Cazenave, A. (2017). *Satellite Altimetry-Based Sea Level at Global and Regional Scales* (pp. 9–33). https://doi.org/10.1007/978-3-319-56490-6_2

Ablain, M., Meyssignac, B., Zawadzki, L., Jugier, R., Ribes, A., Spada, G., Benveniste, J., Cazenave, A., & Picot, N. (2019). Uncertainty in satellite estimates of global mean sea-level changes, trend and acceleration. *Earth System Science Data*, *11*(3), 1189–1202. https://doi.org/10.5194/essd-11-1189-2019

Abram, N. J., Mulvaney, R., Vimeux, F., Phipps, S. J., Turner, J., & England, M. H. (2014). Evolution of the Southern Annular Mode during the past millennium (I2, Trans.). *Nature Climate Change*, *4*(7), 564–569. https://doi.org/10.1038/nclimate2235

Adler, R. F., Sapiano, M. R. P., Huffman, G. J., Wang, J. J., Gu, G., Bolvin, D., Chiu, L., Schneider, U., Becker, A., Nelkin, E., Xie, P., Ferraro, R., & Shin, D. Bin. (2018). The Global Precipitation Climatology Project (GPCP) monthly analysis (New Version 2.3) and a review of 2017 global precipitation (I7, Trans.). *Atmosphere*, *9*(4). https://doi.org/10.3390/atmos9040138

Ager, T. A., Matthews, J. V, & Yeend, W. (1994). Pliocene terrace gravels of the ancestral Yukon River near Circle, Alaska: Palynology, paleobotany, paleoenvironmental reconstruction and regional correlation. *Quaternary International*, *22–23*, 185–206. https://doi.org/10.1016/1040-6182(94)90012-4

Ahn, J.;, Brook, E. J. ., Mitchell, L. E. ., Rosen, J. ., McConnell, J. R. ., Taylor, K. C. ., Etheridge, D. M. ., & Rubino, D. L. (2012). Atmospheric CO2 over the last 1000 years: A high-resolution record from the West Antarctic Ice Sheet (WAIS) Divide ice core. *Global Biogeochemical Cycles*, *26*(2). https://doi.org/10.1029/2011GB004247

Ahn, J., & Brook, E. J. (2014). Siple Dome ice reveals two modes of millennial CO2 change during the last ice age. *Nature Communications*, *5*(3723). https://doi.org/10.1038/ncomms4723

Ahn, J, & Brook, E. J. (2008). Supporting Online Material for Atmospheric CO2 and Climate on Millennial Time Scales During the Last Glacial Period. *Science*, *322*(5898), 83–85. https://science.sciencemag.org/content/sci/suppl/2008/09/11/1160832.DC1/Ahn.SOM.pdf

Ahn, Jinho, Brook, E. J., Schmittner, A., & Kreutz, K. (2012). Abrupt change in atmospheric CO2 during the last ice age. *Geophysical Research Letters*, *39*, L18711. https://doi.org/10.1029/2012GL053018

Anagnostou, E, John, E. H., Babila, T. L., Sexton, P. F., Ridgwell, A., Lunt, D. J., Pearson, P. N., Chalk, T. B., Pancost, R. D., & Foster, G. L. (2020). Proxy evidence for state-dependence of climate sensitivity in the Eocene greenhouse. *Nature Communications*, *11*(1), 4436. https://doi.org/10.1038/s41467-020-17887-x

Anagnostou, Eleni, John, E. H., Edgar, K. M., Foster, G. L., Ridgwell, A., Inglis, G. N., Pancost, R. D., Lunt, D. J., & Pearson, P. N. (2016). Changing atmospheric CO2 concentration was the primary driver of early Cenozoic climate. *Nature*. https://doi.org/10.1038/nature17423

Andersson, A., Graw, K., Schröder, M., Fennig, K., Liman, J., Bakan, S., Hollmann, R., & Klepp, C. (2017). *Hamburg Ocean Atmosphere Parameters and Fluxes from Satellite Data - HOAPS 4.0*. Satellite Application Facility on Climate Monitoring. https://doi.org/10.5676/EUM_SAF_CM/HOAPS/V002

Angerer, B., Ladstädter, F., Scherllin-Pirscher, B., Schwärz, M., Steiner, A. K., Foelsche, U., & Kirchengast, G. (2017). Quality aspects of the Wegener Center multi-satellite GPS radio occultation record OPSv5.6. *Atmospheric Measurement Techniques*, *10*(12), 4845–4863. https://doi.org/10.5194/amt-10-4845-2017

Aono, Y., & Saito, S. (2010). Clarifying springtime temperature reconstructions of the medieval period by gap-filling the cherry blossom phenological data series at Kyoto, Japan. *International Journal of Biometeorology*, *54*(2), 211–219. https://doi.org/10.1007/s00484-009-0272-x

Arienzo, M. M., McConnell, J. R., Murphy, L. N., Chellman, N., Das, S., Kipfstuhl, S., & Mulvaney, R. (2017). Holocene black carbon in Antarctica paralleled Southern Hemisphere climate. *Journal of Geophysical Research: Atmospheres*, *122*(13), 6713–6728. https://doi.org/10.1002/2017JD026599

Atlas, R., Hoffman, R. N., Ardizzone, J., Leidner, S. M., Jusem, J. C., Smith, D. K., & Gombos, D. (2011). A cross-calibrated, multiplatform ocean surface wind velocity product for meteorological and oceanographic applications (I17, Trans.). *Bulletin of the American Meteorological Society*, *92*(2), 157–174. https://doi.org/10.1175/2010BAMS2946.1

Badger, M. P. S., Schmidt, D. N., Mackensen, A., & Pancost, R. D. (2013). High-resolution alkenone palaeobarometry indicates relatively stable pCO2 during the Pliocene (3.3–2.8 Ma). *Philosophical Transactions of the Royal Society A: Mathematical, Physical and Engineering Sciences*, *371*(2001), 20130094. https://doi.org/10.1098/rsta.2013.0094

ACCEPTED VERSION SUBJECT TO FINAL EDITS

Bartoli, G., Hönisch, B., & Zeebe, R. E. (2011). Atmospheric CO2 decline during the Pliocene intensification of Northern Hemisphere glaciations. *Paleoceanography*, *26*(4). https://doi.org/10.1029/2010PA002055

Bates, N. R., & Johnson, R. J. (2020). Acceleration of ocean warming, salinification, deoxygenation and acidification in the surface subtropical North Atlantic Ocean. *Communications Earth & Environment*, *1*(1), 33. https://doi.org/10.1038/s43247-020-00030-5

Bauska, T. K., Joos, F., Mix, A. C., Roth, R., Ahn, J., & Brook, E. J. (2015). Links between atmospheric carbon dioxide, the land carbon reservoir and climate over the past millennium. *Nature Geoscience*, *8*, 383–387. https://doi.org/10.1038/ngeo2422

Becker, A., Finger, P., Meyer-Christoffer, A., Rudolf, B., Schamm, K., Schneider, U., & Ziese, M. (2013). A description of the global land-surface precipitation data products of the Global Precipitation Climatology Centre with sample applications including centennial (trend) analysis from 1901-present (I34, Trans.). *Earth System Science Data*, *5*(1), 71–99. https://doi.org/10.5194/essd-5-71-2013

Beckley, B. ., Zelensky, N. P. ., Holmes, S. A. ., Lemoine, F. G. ., Ray, R. D. ., Mitchum, G. T. ., Desai, S. ., & Brown, S. T. (2016). *Global Mean Sea Level Trend from Integrated Multi-Mission Ocean Altimeters TOPEX/Poseidon Jason-1 and OSTM/Jason-2 Version 4.2*. NASA Physical Oceanography DAAC. https://doi.org/10.5067/GMSLM-TJ142

Beckley, B. D., Callahan, P. S., Hancock III, D. W., Mitchum, G. T., & Ray, R. D. (2017). On the "Cal-Mode" Correction to TOPEX Satellite Altimetry and Its Effect on the Global Mean Sea Level Time Series. *Journal of Geophysical Research: Oceans*, *122*(11), 8371–8384. https://doi.org/10.1002/2017JC013090

Bereiter, B., Eggleston, S., Schmitt, J., Nehrbass-Ahles, C., Stocker, T. F., Fischer, H., Kipfstuhl, S., & Chappellaz, J. (2015). Revision of the EPICA Dome C CO2 record from 800 to 600-kyr before present. *Geophysical Research Letters*, *42*(2), 542– 549. https://doi.org/10.1002/2014GL061957

Binney, H. A., Willis, K. J., Edwards, M. E., Bhagwat, S. A., Anderson, P. M., Andreev, A. A., Blaauw, M., Damblon, F., Haesaerts, P., Kienast, F., Kremenetski, K. V., Krivonogov, S. K., Lozhkin, A. V., MacDonald, G. M., Novenko, E. Y., Oksanen, P., Sapelko, T. V., Väliranta, M., & Vazhenina, L. (2009). The distribution of late-Quaternary woody taxa in northern Eurasia: evidence from a new macrofossil database. *Quaternary Science Reviews*. https://doi.org/10.1016/j.quascirev.2009.04.016

Binney, H., Edwards, M., Macias-Fauria, M., Lozhkin, A., Anderson, P., Kaplan, J. O., Andreev, A., Bezrukova, E., Blyakharchuk, T., Jankovska, V., Khazina, I., Krivonogov, S., Kremenetski, K., Nield, J., Novenko, E., Ryabogina, N., Solovieva, N., Willis, K., & Zernitskaya, V. (2017). Vegetation of Eurasia from the last glacial maximum to present: Key biogeographic patterns. *Quaternary Science Reviews*, *157*, 80–97. https://doi.org/10.1016/j.quascirev.2016.11.022

Blazquez, A., Meyssignac, B., Lemoine, J. M., Berthier, E., Ribes, A., & Cazenave, A. (2018). Exploring the uncertainty in GRACE estimates of the mass redistributions at the Earth surface: Implications for the global water and sea level budgets. *Geophysical Journal International*, *215*(1), 415–430. https://doi.org/10.1093/gji/ggy293

Blunden, J. (2020). Relevant Datasets and sources. *Bull. Am. Meteorol. Soc.*, *101*(8), S421. https://doi.org/10.1175/2020BAMSStateoftheClimate_Chapter8.1

Braesicke, A. P., Neu, J., Fioletov, V., Godin-Beekman, S., Hubert, D., Petropavlovskikh, I., Shiotani, M., & B.-M. Sinnhuber. (2018). *Chapter 3 "Update on Global Ozone: Past, Present and Future", in WMO/UNEP Scientific Assessment of Ozone Depletion: 2018, Global Ozone Research and Monitoring Project–Report No. 58, Geneva, Switzerland* (I. Rt14 (trans.)).

Braganza, K., Gergis, J. L., Power, S. B., Risbey, J. S., & Fowler, A. M. (2009). A multiproxy index of the El Niño–Southern Oscillation, A.D. 1525–1982 (I60, Trans.). *Journal of Geophysical Research: Atmospheres*, *114*(D5). https://doi.org/10.1029/2008JD010896

Brigham-Grette, J., Melles, M., Minyuk, P., Andreev, A., Tarasov, P., DeConto, R., Koenig, S., Nowaczyk, N., Wennrich, V., Rosen, P., Haltia, E., Cook, T., Gebhardt, C., Meyer-Jacob, C., Snyder, J., & Herzschuh, U. (2013). Pliocene Warmth, Polar Amplification, and Stepped Pleistocene Cooling Recorded in NE Arctic Russia. *Science*, *340*(6139). https://doi.org/10.1126/science.1233137

Brown, R. D. (2002). *Reconstructed North American, Eurasian, and Northern Hemisphere Snow Cover Extent, 1915-1997, Version 1. National Snow and Ice Center, Boulder, Colorado, USA*. https://doi.org/10.7265/N5V985Z6

Brown, Ross D. (2000). Northern Hemisphere Snow Cover Variability and Change, 1915–97. *Journal of Climate*, *13*(13). https://doi.org/10.1175/1520-0442(2000)013<2339:NHSCVA>2.0.CO;2

CAPE Last Interglacial Project Members. (2006). Last Interglacial Arctic warmth confirms polar amplification of climate change. *Quaternary Science Reviews*, *25*(13–14), 1383–1400. https://doi.org/10.1016/j.quascirev.2006.01.033

Cavalieri, D. J., C. L. Parkinson, P. Gloersen, and H. J. Z. (1996). *Sea Ice Concentrations from Nimbus-7 SMMR and DMSP SSM/I-SSMIS Passive Microwave Data, Version 1*. NASA National Snow and Ice Data Center Distributed Active Archive Center. https://doi.org/10.5067/8GQ8LZQVL0VL

Chalk, T. B., Hain, M. P., Foster, G. L., Rohling, E. J., Sexton, P. F., Badger, M. P. S., Cherry, S. G., Hasenfratz, A. P., Haug, G. H., Jaccard, S. L., Martínez-García, A., Pälike, H., Pancost, R. D., & Wilson, P. A. (2017). Causes of ice age intensification across the Mid-Pleistocene Transition. *Proceedings of the National Academy of Sciences*.

ACCEPTED VERSION SUBJECT TO FINAL EDITS

https://doi.org/10.1073/PNAS.1702143114
Chang, K.-L., Cooper, O. R., Gaudel, A., Petropavlovskikh, I., & Thouret, V. (2020). Statistical regularization for trend detection: An integrated approach for detecting long-term trends from sparse tropospheric ozone profiles. *Atmos. Chem. Phys.*, *20*(16), 9915–9938. https://doi.org/10.5194/acp-20-9915-2020
Cheng, L., Trenberth, K. E., Fasullo, J., Boyer, T., Abraham, J., & Zhu, J. (2017). Improved estimates of ocean heat content from 1960 to 2015. *Science Advances*, *3*(3). https://doi.org/10.1126/sciadv.1601545
Cheng, L., & Zhu, J. (2016). Benefits of CMIP5 Multimodel Ensemble in Reconstructing Historical Ocean Subsurface Temperature Variations. *Journal of Climate*, *29*(15), 5393–5416. https://doi.org/10.1175/JCLI-D-15-0730.1
Chipperfield, M. P., Dhomse, S., Hossaini, R., Feng, W., Santee, M. L., Weber, M., Burrows, J. P., Wild, J. D., Loyola, D., & Coldewey-Egbers, M. (2018). On the Cause of Recent Variations in Lower Stratospheric Ozone. *Geophysical Research Letters*, *45*(11), 5718–5726. https://doi.org/10.1029/2018GL078071
Church, J. A., & White, N. J. (2011). Sea-level rise from the late 19th to the early 21st Century. *Surveys in Geophysics*, *32*, 585. https://doi.org/10.1007/s10712-011-9119-1.
Church, J. A., White, N. J., Konikow, L. F., Domingues, C. M., Cogley, J. G., Rignot, E., Gregory, J. M., van den Broeke, M. R., Monaghan, A. J., & Velicogna, I. (2011). Revisiting the Earth's sea-level and energy budgets from 1961 to 2008. *Geophysical Research Letters*, *38*(18). https://doi.org/10.1029/2011GL048794
Cohen, Y., Petetin, H., Thouret, V., Marécal, V., Josse, B., Clark, H., Sauvage, B., Fontaine, A., Athier, G., Blot, R., Boulanger, D., Cousin, J.-M. J.-M., & Nédélec, P. (2018). Climatology and long-term evolution of ozone and carbon monoxide in the upper troposphere--lower stratosphere (UTLS) at northern midlatitudes, as seen by IAGOS from 1995 to 2013 (I106, Trans.). *Atmospheric Chemistry and Physics*, *18*(8), 5415–5453. https://doi.org/10.5194/acp-18-5415-2018
Comiso, J. C. (2017). *Bootstrap Sea Ice Concentrations from Nimbus-7 SMMR and DMSP SSM/I-SSMIS, Version 3.* NASA National Snow and Ice Data Center Distributed Active Archive Center. https://doi.org/10.5067/7Q8HCCWS4I0R
Conway, T. J., Tans, P. P., Waterman, L. S., Thoning, K. W., Kitzis, D. R., Masarie, K. A., & Zhang, N. (1994). Evidence for interannual variability of the carbon cycle from the National Oceanic and Atmospheric Administration/Climate Monitoring and Diagnostics Laboratory Global Air Sampling Network. *Journal of Geophysical Research*, *99*(D11), 22831– 22855. https://doi.org/10.1029/94JD01951
Cook, E. R. (2000). *Niño 3 index reconstruction in: International Tree-Ring Data Bank, IGBP PAGES/World Data Center A for Paleoclimatology Data Contribution Series*.
Cook, E. R., D'Arrigo, R. D., & Anchukaitis, K. J. (2008). ENSO reconstructions from long tree ring chronologies: unifying the differences? *Reconciling ENSO Chronologies for the Past 500 Years, Moorea, French Polynesia, April 2-3 2008*.
Cooper, O. R., Schultz, M. G., Schröder, S., Chang, K.-L., Gaudel, A., Carbajal Benítez, G., Cuevas, E., Fröhlich, M., Galbally, I. E., Kubistin, D., Lu, X., McClure-Begley, A., Molloy, S., Nédélec, P., O'Brien, J., Oltmans, S. J., Petropavlovskikh, I., Ries, L., Senik, I., … X. Xu. (2020). Multi-decadal surface ozone trends at globally distributed remote locations. *Elementa Sci. Anthropocene*, *8*(1), 23. https://doi.org/10.1525/elementa.420
Cowtan, K., & Way, R. G. (2014). Coverage bias in the HadCRUT4 temperature series and its impact on recent temperature trends. *Quarterly Journal of the Royal Meteorological Society*, *140*(683), 1935–1944. https://doi.org/10.1002/qj.2297
Dangendorf, S., Hay, C. C., Calafat, F. M., Marcos, M., Berk, K., Jensen, J., Piecuch, C. G., Berk, K., & Jensen, J. (2019). Persistent acceleration in global sea-level rise since the 1960s. *Nature Climate Change*, *9*(9), 705–710. https://doi.org/10.1038/s41558-019-0531-8
Dangendorf, S., Marcos, M., Wöppelmann, G., Conrad, C. P., Frederikse, T., & Riva, R. (2017). Reassessment of 20th century global mean sea level rise. *Proceedings of the National Academy of Sciences*, *114*(23), 5946–5951. https://doi.org/10.1073/pnas.1616007114
Dätwyler, C., Neukom, R., Abram, N. J., Gallant, A. J. E., Grosjean, M., Jacques-Coper, M., Karoly, D. J., & Villalba, R. (2018). Teleconnection stationarity, variability and trends of the Southern Annular Mode (SAM) during the last millennium (I128, Trans.). *Climate Dynamics*, *51*(5–6), 2321–2339. https://doi.org/10.1007/s00382-017-4015-0
de la Vega, E., Chalk, T. B., Wilson, P. A., Bysani, R. P., & Foster, G. L. (2020). Atmospheric CO2 during the Mid-Piacenzian Warm Period and the M2 glaciation. *Scientific Reports*, *10*(1), 11002. https://doi.org/10.1038/s41598-020-67154-8
Dee, D. P., Uppala, S. M., Simmons, A. J., Berrisford, P., Poli, P., Kobayashi, S., Andrae, U., Balmaseda, M. A., Balsamo, G., Bauer, P., Bechtold, P., Beljaars, A. C. M., van de Berg, L., Bidlot, J., Bormann, N., Delsol, C., Dragani, R., Fuentes, M., Geer, A. J., … Vitart, F. (2011). The ERA-interim reanalysis: configuration and performance of the data assimilation system (I136, Trans.). *Q. J. R. Meteorol. Soc.*, *137*(656), 553–597. https://doi.org/10.1002/qj.828
Demske, D., Mohr, B., & Oberhänsli, H. (2002). Late Pliocene vegetation and climate of the Lake Baikal region, southern East Siberia, reconstructed from palynological data. *Palaeogeography, Palaeoclimatology, Palaeoecology*, *184*(1), 107–129. https://doi.org/10.1016/S0031-0182(02)00251-1

ACCEPTED VERSION SUBJECT TO FINAL EDITS

Desbruyères, D. G., Purkey, S. G., McDonagh, E. L., Johnson, G. C., & King, B. A. (2016). Deep and abyssal ocean warming from 35 years of repeat hydrography. *Geophysical Research Letters*, *43*(19), 10,310-356,365. https://doi.org/10.1002/2016GL070413

Desbruyères, D., McDonagh, E. L., King, B. A., & Thierry, V. (2017). Global and Full-Depth Ocean Temperature Trends during the Early Twenty-First Century from Argo and Repeat Hydrography. *Journal of Climate*, *30*(6), 1985–1997. https://doi.org/10.1175/JCLI-D-16-0396.1

Dlugokencky, E. J., Masaire, K. A., Lang, P. M., Tans, P. P., Steele, L. P., & Nisbet, E. G. (1994). A dramatic decrease in the growth rate of atmospheric methane in the northern hemisphere during 1992. *Geophysical Research Letters*, *21*(1), 45–48. https://doi.org/10.1029/93GL03070

Dodson, J. R., & Macphail, M. K. (2004). Palynological evidence for aridity events and vegetation change during the Middle Pliocene, a warm period in Southwestern Australia. *Global and Planetary Change*, *41*(3), 285–307. https://doi.org/https://doi.org/10.1016/j.gloplacha.2004.01.013

Doerr, Jakob; Notz, Dirk; Kern, S. (2021). *UHH Sea Ice Area Product (Version 2019_fv0.01)*. http://doi.org/10.25592/uhhfdm.8559

Dolan, A. M., de Boer, B., Bernales, J., Hill, D. J., & Haywood, A. M. (2018). High climate model dependency of Pliocene Antarctic ice-sheet predictions. *Nature Communications*, *9*(1), 2799. https://doi.org/10.1038/s41467-018-05179-4

Domingues, C. M., Church, J. A., White, N. J., Gleckler, P. J., Wijffels, S. E., Barker, P. M., & Dunn, J. R. (2008). Improved estimates of upper-ocean warming and multi-decadal sea-level rise. *Nature*, *453*(7198), 1090–1093. https://doi.org/10.1038/nature07080

Dore, J. E., Lukas, R., Sadler, D. W., Church, M. J., & Karl, D. M. (2009). Physical and biogeochemical modulation of ocean acidification in the central North Pacific. *Proceedings of the National Academy of Sciences*, *106*(30), 12235. https://doi.org/10.1073/pnas.0906044106

Dowsett, H., Dolan, A., Rowley, D., Moucha, R., Forte, A. M., Mitrovica, J. X., Pound, M., Salzmann, U., Robinson, M., Chandler, M., Foley, K., & Haywood, A. (2016). The PRISM4 (mid-Piacenzian) paleoenvironmental reconstruction. *Climate of the Past*, *12*(7), 1519–1538. https://doi.org/10.5194/cp-12-1519-2016

Dudok de Wit, T., Kopp, G., Fröhlich, C., & Schöll, M. (2017). Methodology to create a new total solar irradiance record: Making a composite out of multiple data records (I154, Trans.). *Geophysical Research Letters*, *44*(3), 1196–1203. https://doi.org/10.1002/2016GL071866

Dunn, R. J. H., Azorin-Molina, C., Mears, C. A., Berrisford, P., & McVicar, T. R. (2016). Global climate; Atmospheric circulation; Surface winds. [in "State of the Climate in 2015"] (I155, Trans.). *Bulletin of the American Meteorological Society*, *97*(8), S38–S40.

Dyez, K. A., Hönisch, B., & Schmidt, G. A. (2018). Early Pleistocene Obliquity-Scale pCO2 Variability at ~1.5 Million Years Ago. *Paleoceanography and Paleoclimatology*, *33*(11), 1270–1291. https://doi.org/10.1029/2018PA003349

Emile-Geay, J., Cobb, K. M., Mann, M. E., & Wittenberg, A. T. (2013). Estimating central equatorial pacific SST variability over the past millennium. Part I: Methodology and validation. *Journal of Climate*, *26*(7), 2302–2328. https://doi.org/10.1175/JCLI-D-11-00510.1

Engardt, M., Simpson, D., Schwikowski, M., & Granat, L. (2017). Deposition of sulphur and nitrogen in Europe 1900–2050. Model calculations and comparison to historical observations. *Tellus B: Chemical and Physical Meteorology*, *69*(1), 1328945. https://doi.org/10.1080/16000889.2017.1328945

Evans, M. N., Cane, M. A., Schrag, D. P., Kaplan, A., Linsley, B. K., Villalba, R., & Wellington, G. M. (2001). Support for tropically-driven pacific decadal variability based on paleoproxy evidence. *Geophysical Research Letters*, *28*(19), 3689–3692. https://doi.org/10.1029/2001GL013223

Evans, M. N., Kaplan, A., & Cane, M. A. (2002). Pacific sea surface temperature field reconstruction from coral δ18O data using reduced space objective analysis. *Paleoceanography*, *17*(1), 7–13. https://doi.org/10.1029/2000PA000590

Ezat, M. M., Rasmussen, T. L., Hönisch, B., Groeneveld, J., & deMenocal, P. (2017). Episodic release of CO2 from the high-latitude North Atlantic Ocean during the last 135 kyr. *Nature Communications*, *8*(1), 14498. https://doi.org/10.1038/ncomms14498

Fauquette, S., Suc, J.-P., Guiot, J., Diniz, F., Feddi, N., Zheng, Z., Bessais, E., & Drivaliari, A. (1999). Climate and biomes in the West Mediterranean area during the Pliocene. *Palaeogeography, Palaeoclimatology, Palaeoecology*, *152*(1), 15–36. https://doi.org/10.1016/S0031-0182(99)00031-0

Flückiger, J., Dällenbach, A., Blunier, T., Stauffer, B., Stocker, T. F., Raynaud, D., & Barnola, J. M. (1999). Variations in atmospheric N2O concentration during abrupt climatic changes. *Science*, *285*(5425), 227–230. https://doi.org/10.1126/science.285.5425.227

Fogt, R. L., Perlwitz, J., Monaghan, A. J., Bromwich, D. H., Jones, J. M., & Marshall, G. J. (2009). Historical SAM variability. Part II: Twentieth-century variability and trends from reconstructions, Observations, and the IPCC AR4 models. *Journal of Climate*, *22*(20), 5346–5365. https://doi.org/10.1175/2009JCLI2786.1

Foster, G L. (2008). Seawater pH, pCO2 and [CO2−3] variations in the Caribbean Sea over the last 130 kyr: A boron isotope and B/Ca study of planktic foraminifera. *Earth and Planetary Science Letters*, *271*(1), 254–266.

ACCEPTED VERSION SUBJECT TO FINAL EDITS

https://doi.org/10.1016/j.epsl.2008.04.015
Foster, G L, & Sexton, P. F. (2014). Enhanced carbon dioxide outgassing from the eastern equatorial Atlantic during the last glacial. *Geology*, *42*(11), 1003–1006. https://doi.org/10.1130/G35806.1
Foster, Gavin L., Royer, D. L., & Lunt, D. J. (2017). Future climate forcing potentially without precedent in the last 420 million years. *Nature Communications*, *8*(14845). https://doi.org/10.1038/ncomms14845
Foster, Gavin L, Lear, C. H., & Rae, J. W. B. (2012). The evolution of pCO2, ice volume and climate during the middle Miocene. *Earth and Planetary Science Letters*, *341–344*, 243–254. https://doi.org/10.1016/j.epsl.2012.06.007
Frederikse, T., Jevrejeva, S., Riva, R. E. M., & Dangendorf, S. (2018). A consistent sea-level reconstruction and its budget on basin and global scales over 1958-2014. *Journal of Climate*, *31*(3), 1267–1280. https://doi.org/10.1175/JCLI-D-17-0502.1
Frederikse, T., Landerer, F., Caron, L., Adhikari, S., Parkes, D., Humphrey, V. W., Dangendorf, S., Hogarth, P., Zanna, L., Cheng, L., & Wu, Y. H. (2020). The causes of sea-level rise since 1900. *Nature*, *584*(7821), 393–397. https://doi.org/10.1038/s41586-020-2591-3
Gaillard, F., Reynaud, T., Thierry, V., Kolodziejczyk, N., & von Schuckmann, K. (2016). In Situ–Based Reanalysis of the Global Ocean Temperature and Salinity with ISAS: Variability of the Heat Content and Steric Height. *Journal of Climate*, *29*(4), 1305–1323. https://doi.org/10.1175/JCLI-D-15-0028.1
Garay, M. J., Kalashnikova, O. V., & Bull, M. A. (2017). Development and assessment of a higher-spatial-resolution (4.4 km) MISR aerosol optical depth product using AERONET-DRAGON data (I193, Trans.). *Atmospheric Chemistry and Physics*, *17*(8), 5095–5106. https://doi.org/10.5194/acp-17-5095-2017
Gaudel, A., Cooper, O. R., Ancellet, G., Barret, B., Boynard, A., Burrows, J. P., Clerbaux, C., Coheur, P.-F., Cuesta, J., Cuevas, E., Doniki, S., Dufour, G., Ebojie, F., Foret, G., Garcia, O., Muños, M. J. G., Hannigan, J. W., Hase, F., Huang, G., … Ziemke, J. (2018). Tropospheric Ozone Assessment Report: Present-day distribution and trends of tropospheric ozone relevant to climate and global atmospheric chemistry model evaluation. *Elem Sci Anth*, *6*(39). https://doi.org/10.1525/elementa.291
Gaudel, A., Cooper, O. R., Chang, K.-L., Bourgeois, I., Ziemke, J. R., Strode, S. A., Oman, L. D., Sellitto, P., Nedelec, P., Blot, R., Thouret, V., & Granier, C. (2020). Aircraft observations since the 1990s reveal increases of tropospheric ozone at multiple locations across the Northern Hemisphere. *Sci. Adv.*, *6*(34). https://doi.org/10.1126/sciadv.aba8272
Ge, Q., Wang, H., Zheng, J., This, R., & Dai, J. (2014). A 170year spring phenology index of plants in eastern China. *Journal of Geophysical Research: Biogeosciences*, *119*(3). https://doi.org/10.1002/2013JG002565
Gehlen, M., T.t..T. Chau, A. Conchon, A. Denvil-Sommer, F. Chevallier, M. Vrac, C. M. (2020). Ocean acidification. In The Copernicus Marine Service Ocean State Report, issue 4. *Journal of Operational Oceanography*, *13*(supp1), s64–s67. https://doi.org/DOI: 10.1080/1755876X.2020.1785097
Gelaro, R., McCarty, W., Suárez, M. J., Todling, R., Molod, A., Takacs, L., Randles, C. A., Darmenov, A., Bosilovich, M. G., Reichle, R., Wargan, K., Coy, L., Cullather, R., Draper, C., Akella, S., Buchard, V., Conaty, A., da Silva, A. M., Gu, W., … Zhao, B. (2017). The Modern-Era Retrospective Analysis for Research and Applications, Version 2 (MERRA-2) (I200, Trans.). *Journal of Climate*, *30*(14), 5419–5454. https://doi.org/10.1175/JCLI-D-16-0758.1
Giles, D. M., Sinyuk, A., Sorokin, M. G., Schafer, J. S., Smirnov, A., Slutsker, I., Eck, T. F., Holben, B. N., Lewis, J. R., Campbell, J. R., Welton, E. J., Korkin, S. V., & Lyapustin, A. I. (2019). Advancements in the Aerosol Robotic Network (AERONET) Version 3 database – automated near-real-time quality control algorithm with improved cloud screening for Sun photometer aerosol optical depth (AOD) measurements. *Atmospheric Measurement Techniques*, *12*(1), 169–209. https://doi.org/10.5194/amt-12-169-2019
Gleisner, H., Lauritsen, K. B., Nielsen, J. K., & Syndergaard, S. (2019). Evaluation of the 15-year ROM SAF monthly mean GPS radio occultation climate data record. *Atmospheric Measurement Techniques Discussions*, *2019*, 1–26. https://doi.org/10.5194/amt-2019-417
Gobron, N. (2018). Terrestrial Vegetation Activity [in "State of the Climate in 2017"]. *Bulletin of the American Meteorological Society*, *99*, S62–S63. https://doi.org/10.1175/2018BAMSStateoftheClimate.1
Gong, D., & Wang, S. (1999). Definition of Antarctic oscillation index. *Geophysical Research Letters*, *26*(4), 459–462. https://doi.org/10.1029/1999GL900003
Good, S. A., Martin, M. J., & Rayner, N. A. (2013). EN4: Quality controlled ocean temperature and salinity profiles and monthly objective analyses with uncertainty estimates. *Journal of Geophysical Research: Oceans*, *118*(12), 6704–6716. https://doi.org/10.1002/2013JC009067
Graven, H. D., Keeling, R. F., Piper, S. C., Patra, P. K., Stephens, B. B., Wofsy, S. C., Welp, L. R., Sweeney, C., Tans, P. P., Kelley, J. J., Daube, B. C., Kort, E. A., Santoni, G. W., & Bent, J. D. (2013). Enhanced seasonal exchange of CO2by Northern ecosystems since 1960. In *Science*. https://doi.org/10.1126/science.1239207
Gray, A. R., Johnson, K. S., Bushinsky, S. M., Riser, S. C., Russell, J. L., Talley, L. D., Wanninkhof, R., Williams, N. L., & Sarmiento, J. L. (2018). Autonomous Biogeochemical Floats Detect Significant Carbon Dioxide Outgassing in the High-Latitude Southern Ocean. *Geophysical Research Letters*, *45*(17), 9049–9057. https://doi.org/10.1029/2018GL078013
Greenop, R., Foster, G. L., Wilson, P. A., & Lear, C. H. (2014). Middle Miocene climate instability associated with

ACCEPTED VERSION SUBJECT TO FINAL EDITS

high-amplitude CO2 variability. *Paleoceanography*, *29*(9), 845–853. https://doi.org/10.1002/2014PA002653
Gregor, L., & Gruber, N. (2021). OCEAN-SODA: A global gridded data set of the surface ocean carbonate system for seasonal to decadal studies of ocean acidification. *Earth System Science Data*, *13*(2), 777–808. https://doi.org/10.5194/essd-13-777-2021
Gutjahr, M., Ridgwell, A., Sexton, P. F., Anagnostou, E., Pearson, P. N., Pälike, H., Norris, R. D., Thomas, E., & Foster, G. L. (2017). Very large release of mostly volcanic carbon during the Palaeocene-Eocene Thermal Maximum. *Nature*. https://doi.org/10.1038/nature23646
Haas, C., Goff, H. Le, Audrain, S., Perovich, D., & Haapala, J. (2011). Comparison of seasonal sea-ice thickness change in the Transpolar Drift observed by local ice mass-balance observations and floe-scale EM surveys. *Annals of Glaciology*, *52*(57), 97–102. https://doi.org/10.3189/172756411795931778
Haas, C., Hendricks, S., Eicken, H., & Herber, A. (2010). Synoptic airborne thickness surveys reveal state of Arctic sea ice cover. *Geophysical Research Letters*, *37*(9). https://doi.org/10.1029/2010GL042652
Haas, C., Pfaffling, A., Hendricks, S., Rabenstein, L., Etienne, J.-L., & Rigor, I. (2008). Reduced ice thickness in Arctic Transpolar Drift favors rapid ice retreat. *Geophysical Research Letters*, *35*(17). https://doi.org/10.1029/2008GL034457
Haimberger, L., Tavolato, C., & Sperka, S. (2012). Homogenization of the Global Radiosonde Temperature Dataset through Combined Comparison with Reanalysis Background Series and Neighboring Stations (I221, Trans.). *Journal of Climate*, *25*(23), 8108–8131. https://doi.org/10.1175/JCLI-D-11-00668.1
Hall, B. D., Dutton, G. S., Mondeel, D. J., Nance, J. D., Rigby, M., Butler, J. H., Moore, F. L., Hurst, D. F., & Elkins, J. W. (2011). Improving measurements of SF6 for the study of atmospheric transport and emissions. *Atmospheric Measurement Techniques*. https://doi.org/10.5194/amt-4-2441-2011
Hansen, J., Sato, M., Russell, G., & Kharecha, P. (2013). Climate sensitivity, sea level and atmospheric carbon dioxide. *Philosophical Transactions. Series A, Mathematical, Physical, and Engineering Sciences*, *371*(2001), 20120294. https://doi.org/10.1098/rsta.2012.0294
Harper, D. T., Hönisch, B., Zeebe, R. E., Shaffer, G., Haynes, L. L., Thomas, E., & Zachos, J. C. (2020). The Magnitude of Surface Ocean Acidification and Carbon Release During Eocene Thermal Maximum 2 (ETM-2) and the Paleocene-Eocene Thermal Maximum (PETM). *Paleoceanography and Paleoclimatology*, *35*(2), e2019PA003699. https://doi.org/10.1029/2019PA003699
Harris, I., Osborn, T. J., Jones, P., & Lister, D. (2020). Version 4 of the CRU TS monthly high-resolution gridded multivariate climate dataset. *Scientific Data*, *7*(1), 109. https://doi.org/10.1038/s41597-020-0453-3
Hay, C. C., Morrow, E. D., Kopp, R. E., & Mitrovica, J. X. (2017). On the robustness of bayesian fingerprinting estimates of global sea level change. *Journal of Climate*, *30*(8), 3025–3038. https://doi.org/10.1175/JCLI-D-16-0271.1
Hay, C. C., Morrow, E., Kopp, R. E., & Mitrovica, J. X. (2015). Probabilistic reanalysis of twentieth-century sea-level rise. *Nature*, *517*(7535), 481–484. https://doi.org/10.1038/nature14093
Hay, C., Mitrovica, J. X., Gomez, N., Creveling, J. R., Austermann, J., & Kopp, R. R. (2014). The sea-level fingerprints of ice-sheet collapse during interglacial periods. *Quaternary Science Reviews*, *87*, 60–69. https://doi.org/10.1016/j.quascirev.2013.12.022
Haywood, A. M., Tindall, J. C., Dowsett, H. J., Dolan, A. M., Foley, K. M., Hunter, S. J., Hill, D. J., Chan, W.-L., Abe-Ouchi, A., Stepanek, C., Lohmann, G., Chandan, D., Peltier, W. R., Tan, N., Contoux, C., Ramstein, G., Li, X., Zhang, Z., Guo, C., … Lunt, D. J. (2020). The Pliocene Model Intercomparison Project Phase 2: large-scale climate features and climate sensitivity. *Climate of the Past*, *16*(6), 2095–2123. https://doi.org/10.5194/cp-16-2095-2020
Haywood, A. M., Valdes, P. J., Aze, T., Barlow, N., Burke, A., Dolan, A. M., von der Heydt, A. S., Hill, D. J., Jamieson, S. S. R., Otto-Bliesner, B. L., Salzmann, U., Saupe, E., & Voss, J. (2019). What can Palaeoclimate Modelling do for you? *Earth Systems and Environment*, *3*(1), 1–18. https://doi.org/10.1007/s41748-019-00093-1
Henehan, M., Edgar, K., Foster, G., Penman, D., Hull, P., Greenop, R., Anagnostou, E., & Pearson, P. (2020). Revisiting the Middle Eocene Climatic Optimum "Carbon Cycle Conundrum" With New Estimates of Atmospheric pCO 2 From Boron Isotopes. *Paleoceanography and Paleoclimatology*, *35*, e2019PA003713. https://doi.org/10.1029/2019PA003713
Henehan, M. J., Rae, J. W. B., Foster, G. L., Erez, J., Prentice, K. C., Kucera, M., Bostock, H. C., Martínez-Botí, M. A., Milton, J. A., Wilson, P. A., Marshall, B. J., & Elliott, T. (2013). Calibration of the boron isotope proxy in the planktonic foraminifera Globigerinoides ruber for use in palaeo-CO2 reconstruction. *Earth and Planetary Science Letters*, *364*, 111–122. https://doi.org/10.1016/j.epsl.2012.12.029
Hersbach, H., Bell, B., Berrisford, P., Biavati, G., Horányi, A., Muñoz Sabater, J., Nicolas, J., Peubey, C., Radu, R., Rozum, I., Schepers, D., Simmons, A., Soci, C., Dee, D., & Thépaut, J.-N. (2019). *ERA5 monthly averaged data on pressure levels from 1979 to present.* Copernicus Climate Change Service (C3S) Climate Data Store (CDS). https://doi.org/10.24381/cds.6860a573
Hersbach, Hans, Bell, B., Berrisford, P., Hirahara, S., Horányi, A., Muñoz-Sabater, J., Nicolas, J., Peubey, C., Radu, R., Schepers, D., Simmons, A., Soci, C., Abdalla, S., Abellan, X., Balsamo, G., Bechtold, P., Biavati, G., Bidlot, J., Bonavita, M., … Thépaut, J. N. (2020). The ERA5 global reanalysis. *Quarterly Journal of the Royal*

ACCEPTED VERSION SUBJECT TO FINAL EDITS

Meteorological Society, *146*, 1999–2049. https://doi.org/10.1002/qj.3803
Hersbach, Hans, Peubey, C., Simmons, A., Berrisford, P., Poli, P., & Dee, D. (2015). ERA-20CM: a twentieth-century atmospheric model ensemble. *Quarterly Journal of the Royal Meteorological Society*, *141*(691), 2350–2375. https://doi.org/10.1002/qj.2528
Heue, K.-P., Coldewey-Egbers, M., Delcloo, A., Lerot, C., Loyola, D., Valks, P., & van Roozendael, M. (2016). Trends of tropical tropospheric ozone from 20 years of \hack{\break}European satellite measurements and perspectives for \hack{\break}the Sentinel-5 Precursor. *Atmospheric Measurement Techniques*, *9*(10), 5037–5051. https://doi.org/10.5194/amt-9-5037-2016
Hirahara, S., Ishii, M., & Fukuda, Y. (2014). Centennial-Scale Sea Surface Temperature Analysis and Its Uncertainty. *Journal of Climate*, *27*(1), 57–75. https://doi.org/10.1175/JCLI-D-12-00837.1
Holben, B. N., Eck, T. F., Slutsker, I., Tanré, D., Buis, J. P., Setzer, A., Vermote, E., Reagan, J. A., Kaufman, Y. J., Nakajima, T., Lavenu, F., Jankowiak, I., & Smirnov, A. (1998). AERONET—A Federated Instrument Network and Data Archive for Aerosol Characterization (I254, Trans.). *Remote Sensing of Environment*, *66*(1), 1–16. https://doi.org/10.1016/S0034-4257(98)00031-5
Hönisch, B., Hemming, N. G., Archer, D., Siddall, M., & McManus, J. F. (2009). Atmospheric Carbon Dioxide Concentration Across the Mid-Pleistocene Transition. *Science*, *324*(5934), 1551. https://doi.org/10.1126/science.1171477
Huang, B., Thorne, P. W., Banzon, V. F., Boyer, T., Chepurin, G., Lawrimore, J. H., Menne, M. J., Smith, T. M., Vose, R. S., & Zhang, H.-M. (2017). Extended Reconstructed Sea Surface Temperature, Version 5 (ERSSTv5): Upgrades, Validations, and Intercomparisons. *Journal of Climate*, *30*(20), 8179–8205. https://doi.org/10.1175/JCLI-D-16-0836.1
Hugonnet, R., McNabb, R., Berthier, E., Menounos, B., Nuth, C., Girod, L., Farinotti, D., Huss, M., Dussaillant, I., Brun, F., & Kääb, A. (2021). Accelerated global glacier mass loss in the early twenty-first century. *Nature (in Press)*.
IMBIE Consortium. (2018). Mass balance of the Antarctic Ice Sheet from 1992 to 2017. In *Nature*. https://doi.org/10.1038/s41586-018-0179-y
IMBIE Consortium. (2020). BB Mass balance of the Greenland Ice Sheet from 1992 to 2018. *Nature*, *579*(7798), 233–239. https://doi.org/10.1038/s41586-019-1855-2
Ishii, M., Fukuda, Y., Hirahara, S., Yasui, S., Suzuki, T., and Sato, K. (2017). Accuracy of global upper ocean heat content estimation expected from present observational data sets. *SOLA*, *13*, 163–167. https://doi.org/10.2151/sola.2017-030
Japan Meteorological Agency, Japan. (2013). *JRA-55: Japanese 55-year Reanalysis, Monthly Means and Variances*. Research Data Archive at the National Center for Atmospheric Research, Computational and Information Systems Laboratory. https://doi.org/10.5065/D60G3H5B
Jevrejeva, S., Moore, J. C., Grinsted, A., Matthews, A. P., & Spada, G. (2014). Trends and acceleration in global and regional sea levels since 1807. *Global and Planetary Change*, *113*, 11–22. https://doi.org/https://doi.org/10.1016/j.gloplacha.2013.12.004
Johnson, G. C., Lyman, J. M., Boyer, T., Cheng, L., Domingues, C. M., Gilson, J., et al. (2018). Global oceans: ocean heat content. *Bull. Am. Meteorol. Soc.*, *99*, s72–s77.
Jones, J. M., Fogt, R. L., Widmann, M., Marshall, G. J., Jones, P. D., & Visbeck, M. (2009). Historical SAM variability. Part I: Century-length seasonal reconstructions. *Journal of Climate*, *22*(20), 5319–5345. https://doi.org/10.1175/2009JCLI2785.1
Jungclaus, J. H., Bard, E., Baroni, M., Braconnot, P., Cao, J., Chini, L. P., Egorova, T., Evans, M., Fidel González-Rouco, J., Goosse, H., Hurtt, G. C., Joos, F., Kaplan, J. O., Khodri, M., Klein Goldewijk, K., Krivova, N., Legrande, A. N., Lorenz, S. J., Luterbacher, J., … Zorita, E. (2017). The PMIP4 contribution to CMIP6 - Part 3: The last millennium, scientific objective, and experimental design for the PMIP4 past1000 simulations (I287, Trans.). *Geoscientific Model Development*, *10*(11), 4005–4033. https://doi.org/10.5194/gmd-10-4005-2017
Kadow, C., Hall, D. M., & Ulbrich, U. (2020). Artificial intelligence reconstructs missing climate information. *Nature Geoscience*, *13*(6), 408–413. https://doi.org/10.1038/s41561-020-0582-5
Kaplan, A., Cane, M. A., Kushnir, Y., Clement, A. C., Blumenthal, M. B., & Rajagopalan, B. (1998). Analyses of global sea surface temperature 1856–1991. *Journal of Geophysical Research: Oceans*, *103*(C9), 18567–18589. https://doi.org/10.1029/97JC01736
Karl, D. M., & Lukas, R. (1996). The Hawaii Ocean Time-series (HOT) program: Background, rationale and field implementation. *Deep Sea Research Part II: Topical Studies in Oceanography*, *43*(2), 129–156. https://doi.org/10.1016/0967-0645(96)00005-7
Kaufman, D., McKay, N., Routson, C., Erb, M., Dätwyler, C., Sommer, P. S., Heiri, O., & Davis, B. (2020). Holocene global mean surface temperature, a multi-method reconstruction approach (2020a). *Scientific Data*, *7*(1), 201. https://doi.org/10.1038/s41597-020-0530-7
Kaufman, D., McKay, N., Routson, C., Erb, M., Davis, B., Heiri, O., Jaccard, S., Tierney, J., Dätwyler, C., Axford, Y., Brussel, T., Cartapanis, O., Chase, B., Dawson, A., de Vernal, A., Engels, S., Jonkers, L., Marsicek, J., Moffa-Sánchez, P., … Zhilich, S. (2020). A global database of Holocene paleotemperature records (2020b). *Scientific*

ACCEPTED VERSION SUBJECT TO FINAL EDITS

Data, *7*(1), 115. https://doi.org/10.1038/s41597-020-0445-3
Keegan, K. M., Albert, M. R., McConnell, J. R., & Baker, I. (2014). Climate change and forest fires synergistically drive widespread melt events of the Greenland Ice Sheet. *Proceedings of the National Academy of Sciences*, *111*(22), 7964–7967. https://doi.org/10.1073/pnas.1405397111
Keeling, C. D., Piper, S. C., Bacastow, R. B., Wahlen, M., Whorf, T. P., Heimann, M., & Meijer, H. A. (2005). Atmospheric CO2 and 13CO2 exchange with the terrestrial biosphere and oceans from 1978 to 2000: observations and carbon cycle implications, pages 83-113, in "A History of Atmospheric CO2 and its effects on Plants, Animals, and Ecosystems. In J. R. Ehleringer, T. E. Cerling, & M. D. Dearing (Eds.), *A History of Atmospheric CO2 and its effects on Plants, Animals, and Ecosystems, editors Ehleringer, J.R., T. E. Cerling, M. D. Dearing* (pp. 83–113). Springer Verlag.
Kellerhals, T., Brütsch, S., Sigl, M., Knüsel, S., Gäggeler, H. W., & Schwikowski, M. (2010). Ammonium concentration in ice cores: A new proxy for regional temperature reconstruction? *Journal of Geophysical Research*, *115*(D16), D16123. https://doi.org/10.1029/2009JD012603
Kemp, A. C., Wright, A. J., Edwards, R. J., Barnett, R. L., Brain, M. J., Kopp, R. E., Cahill, N., Horton, B. P., Charman, D. J., Hawkes, A. D., Hill, T. D., & van de Plassche, O. (2018). Relative sea-level change in Newfoundland, Canada, during the past ~3000 years. *Quaternary Science Reviews*, *201*, 89–110. https://doi.org/10.1016/j.quascirev.2018.10.012
Kirschke, S., Bousquet, P., Ciais, P., Saunois, M., Canadell, J. G., Dlugokencky, E. J., Bergamaschi, P., Bergmann, D., Blake, D. R., Bruhwiler, L., Cameron-Smith, P., Castaldi, S., Chevallier, F., Feng, L., Fraser, A., Heimann, M., Hodson, E. L., Houweling, S., Josse, B., … Zeng, G. (2013). Three decades of global methane sources and sinks. *Nature Geoscience*, *6*, 813–823. https://doi.org/10.1038/ngeo1955
Kobayashi, S., Ota, Y., Harada, Y., Ebita, A., Moriya, M., Onoda, H., Onogi, K., Kamahori, H., Kobayashi, C., Endo, H., & others. (2015). The JRA-55 reanalysis: General specifications and basic characteristics. *Journal of the Meteorological Society of Japan. Ser. II*, *93*(1), 5–48. https://doi.org/10.2151/jmsj.2015-001
Köhler, P., Nehrbass-Ahles, C., Schmitt, J., Stocker, T. F., & Fischer, H. (2017). A 156 kyr smoothed history of the atmospheric greenhouse gases CO2, CH4, and N2O and their radiative forcing. *Earth System Science Data*, *9*(1), 363–387. https://doi.org/10.5194/essd-9-363-2017
Kolodziejczyk, N., A. Prigent-Mazella, F. G. (2017). ISAS-15 temperature and salinity griddedfields. *SEANOE*. https://doi.org/10.17882/52367
Kovács, T., Feng, W., Totterdill, A., Plane, J. M. C., Dhomse, S., Gómez-Martín, J. C., Stiller, G. P., Haenel, F. J., Smith, C., Forster, P. M., Garcia, R. R., Marsh, D. R., & Chipperfield, M. P. (2017). Determination of the atmospheric lifetime and global warming potential of sulfur hexafluoride using a three-dimensional model. *Atmospheric Chemistry and Physics*, *17*(2), 883–898. https://doi.org/10.5194/acp-17-883-2017
Kwok, R., & Cunningham, G. F. (2015). Variability of arctic sea ice thickness and volume from CryoSat-2 (I322, Trans.). *Philosophical Transactions of the Royal Society A: Mathematical, Physical and Engineering Sciences*, *373*, 2045. https://doi.org/10.1098/rsta.2014.0157
Kwok, R., Cunningham, G. F., Wensnahan, M., Rigor, I., Zwally, H. J., & Yi, D. (2009). Thinning and volume loss of the Arctic Ocean sea ice cover: 2003-2008. *Journal of Geophysical Research: Oceans*, *114*(C7). https://doi.org/10.1029/2009JC005312
Kwok, Ron, & Kacimi, S. (2018). Three years of sea ice freeboard, snow depth, and ice thickness of the weddell sea from operation icebridge and cryosat-2. *Cryosphere*, *12*(8), 2789–2801. https://doi.org/10.5194/tc-12-2789-2018
Labbe, T., C. Pfister, S. Bronnimann, D. Rousseau, J. Franke, and B. B. (2019). The longest homogeneous series of grape harvest dates, Beaune 1354-2018, and its significance for the understanding of past and present climate. *Climates of the Past Forum*, *15*(4), 1485–1501. https://doi.org/10.5194/cp-2018-179
Langenfelds, R. L., Francey, R. J., Pak, B. C., Steele, L. P., Lloyd, J., Trudinger, C. M., & Allison, C. E. (2002). Interannual growth rate variations of atmospheric CO2 and its δ13C, H2, CH4, and CO between 1992 and 1999 linked to biomass burning. *Global Biogeochemical Cycles*, *16*(3), 21-1-21–22. https://doi.org/10.1029/2001GB001466
Lavergne, T., Macdonald Sørensen, A., Kern, S., Tonboe, R., Notz, D., Aaboe, S., Bell, L., Dybkjær, G., Eastwood, S., Gabarro, C., Heygster, G., Anne Killie, M., Brandt Kreiner, M., Lavelle, J., Saldo, R., Sandven, S., & Pedersen, L. T. (2019). Version 2 of the EUMETSAT OSI SAF and ESA CCI sea-ice concentration climate data records. *Cryosphere*, *13*(1), 49–78. https://doi.org/10.5194/tc-13-49-2019
Lean, J. (2000). Evolution of the Sun's Spectral Irradiance Since the Maunder Minimum. *Geophysical Research Letters*, *27*(16), 2425–2428. https://doi.org/10.1029/2000GL000043
Legeais, J.-F., Ablain, M., Zawadzki, L., Zuo, H., Johannessen, J. A., Scharffenberg, M. G., Fenoglio-Marc, L., Fernandes, M. J., Andersen, O., Rudenko, S., & others. (2018). An improved and homogeneous altimeter sea level record from the ESA Climate Change Initiative. *Earth System Science Data*, *10*, 281–301. https://doi.org/10.5194/essd-10-281-2018
Lenssen, N. J. L., Schmidt, G. A., Hansen, J. E., Menne, M. J., Persin, A., Ruedy, R., & Zyss, D. (2019). Improvements in the GISTEMP Uncertainty Model. *Journal of Geophysical Research: Atmospheres*, *124*(12), 6307–6326. https://doi.org/10.1029/2018JD029522

ACCEPTED VERSION SUBJECT TO FINAL EDITS

Leventidou, E., Weber, M., Eichmann, K.-U. K. U., Burrows, J. P., Heue, K.-P. K. P., Thompson, A. M., & Johnson, B. J. (2018). Harmonisation and trends of 20-year tropical tropospheric ozone data. *Atmospheric Chemistry and Physics*, *18*(13), 9189–9205. https://doi.org/10.5194/acp-18-9189-2018

Levitus, S., Antonov, J. I., Boyer, T. P., Baranova, O. K., Garcia, H. E., Locarnini, R. A., Mishonov, A. V, Reagan, J. R., Seidov, D., Yarosh, E. S., & Zweng, M. M. (2012). World ocean heat content and thermosteric sea level change (0–2000 m), 1955–2010. *Geophysical Research Letters*, *39*(10). https://doi.org/10.1029/2012GL051106

Levy, R. C., Remer, L. A., Kleidman, R. G., Mattoo, S., Ichoku, C., Kahn, R., & Eck, T. F. (2010). Global evaluation of the Collection 5 MODIS dark-target aerosol products over land (I333, Trans.). *Atmospheric Chemistry and Physics*, *10*(21), 10399–10420. https://doi.org/10.5194/acp-10-10399-2010

Li, J., Xie, S.-P., Cook, E. R., Huang, G., D'Arrigo, R., Liu, F., Ma, J., & Zheng, X.-T. (2011). Interdecadal modulation of El Niño amplitude during the past millennium (I336, Trans.). *Nature Climate Change*, *1*, 114. http://dx.doi.org/10.1038/nclimate1086

Li, J., Xie, S.-P., Cook, E. R., Morales, M. S., Christie, D. A., Johnson, N. C., Chen, F., D'Arrigo, R., Fowler, A. M., Gou, X., & Fang, K. (2013). El Niño modulations over the past seven centuries (I337, Trans.). *Nature Climate Change*, *3*, 822. http://dx.doi.org/10.1038/nclimate1936

Lim, S., Faïn, X., Ginot, P., Mikhalenko, V., Kutuzov, S., Paris, J.-D., Kozachek, A., & Laj, P. (2017). Black carbon variability since preindustrial times in the eastern part of Europe reconstructed from Mt. Elbrus, Caucasus, ice cores. *Atmospheric Chemistry and Physics*, *17*(5), 3489–3505. https://doi.org/10.5194/acp-17-3489-2017

Loulergue, L., Schilt, A., Spahni, R., Masson-Delmotte, V., Blunier, T., Lemieux, B., Barnola, J.-M., Raynaud, D., Stocker, T. F., & Chappellaz, J. (2008). Orbital and millennial-scale features of atmospheric CH4 over the past 800,000 years. *Nature*, *453*, 383. https://doi.org/10.1038/nature06950

Lourantou, A., Chappellaz, J., Barnola, J.-M., Masson-Delmotte, V., & Raynaud, D. (2010). Changes in atmospheric CO2 and its carbon isotopic ratio during the penultimate deglaciation. *Quaternary Science Reviews*, *29*(17), 1983–1992. https://doi.org/https://doi.org/10.1016/j.quascirev.2010.05.002

Luo, B. (2018). *Aerosol Radiative Forcing and SAD version v4.0.0 1850 – 2016* (Rt17 (trans.)). ftp://iacftp.ethz.ch/pub_read/luo/CMIP6_SAD_radForcing_v4.0.0/

Lüthi, D., Le Floch, M., Bereiter, B., Blunier, T., Barnola, J.-M., Siegenthaler, U., Raynaud, D., Jouzel, J., Fischer, H., Kawamura, K., & Stocker, T. F. (2008). High-resolution carbon dioxide concentration record 650,000–800,000 years before present. *Nature*, *453*, 379. https://doi.org/10.1038/nature06949

Lyman, J. M., & Johnson, G. C. (2014). Estimating Global Ocean Heat Content Changes in the Upper 1800 m since 1950 and the Influence of Climatology Choice. *Journal of Climate*, *27*(5), 1945–1957. https://doi.org/10.1175/JCLI-D-12-00752.1

MacDonald, G. M., Kremenetski, K. V., & Beilman, D. W. (2008). Climate change and the northern Russian treeline zone. *Philosophical Transactions of the Royal Society B: Biological Sciences*, *363*(1501). https://doi.org/10.1098/rstb.2007.2200

MacFarling Meure, C., Etheridge, D., Trudinger, C., Steele, P., Langenfelds, R., van Ommen, T., Smith, A., & Elkins, J. (2006). Law Dome CO_2, CH_4 and N_2O ice core records extended to 2000 years BP. *Geophysical Research Letters*, *33*(14), L14810. https://doi.org/10.1029/2006GL026152

Machida, T., Nakazawa, T., Fujii, Y., Aoki, S., & Watanabe, O. (1995). Increase in the atmospheric nitrous oxide concentration during the last 250 years. *Geophysical Research Letters*, *22*(21), 2921–2924. https://doi.org/10.1029/95GL02822

Mann, M. E., Bradley, R. S., & Hughes, M. K. (2000). Long-term variability in the El Niño Southern Oscillation and associated teleconnections. In *El Niño and the Southern Oscillation: Multiscale Variability and its Impacts on Natural Ecosystems and Society* (pp. 357–412). https://doi.org/10.1017/CBO9780511573125.011

Marcott, S. A., Bauska, T. K., Buizert, C., Steig, E. J., Rosen, J. L., Cuffey, K. M., Fudge, T. J., Severinghaus, J. P., Ahn, J., Kalk, M. L., McConnell, J. R., Sowers, T., Taylor, K. C., White, J. W. C., & Brook, E. J. (2014). Centennial-scale changes in the global carbon cycle during the last deglaciation. *Nature*, *514*(7524), 616–619. https://doi.org/10.1038/nature13799

Marshall, G. J. (2003). Trends in the Southern Annular Mode from observations and reanalyses. *Journal of Climate*, *16*, 4134–4143.

Martínez-Botí, M. A., Foster, G. L., Chalk, T. B., Rohling, E. J., Sexton, P. F., Lunt, D. J., Pancost, R. D., Badger, M. P. S., & Schmidt, D. N. (2015). AA Plio-Pleistocene climate sensitivity evaluated using high-resolution CO2 records (2015a). *Nature*, *518*(7537), 49. https://doi.org/10.1038/nature14145

Masarie, K. A., & Tans, P. P. (1995). Extension and integration of atmospheric carbon dioxide data into a globally consistent measurement record. *Journal of Geophysical Research: Atmospheres*, *100*(D6), 11593–11610. https://doi.org/10.1029/95JD00859

Masarie, K. A., & Tans, P. P. (2004). Extension and integration of atmospheric carbon dioxide data into a globally consistent measurement record. *Journal of Geophysical Research*. https://doi.org/10.1029/95jd00859

Matthes, K., Funke, B., Andersson, M. E., Barnard, L., Beer, J., Charbonneau, P., Clilverd, M. A., Dudok de Wit, T., Haberreiter, M., Hendry, A., Jackman, C. H., Kretzschmar, M., Kruschke, T., Kunze, M., Langematz, U., Marsh, D. R., Maycock, A. C., Misios, S., Rodger, C. J., … Versick, S. (2017). Solar forcing for CMIP6 (v3.2) (I378,

ACCEPTED VERSION SUBJECT TO FINAL EDITS

Trans.). *Geoscientific Model Development*, *10*(6), 2247–2302. https://doi.org/10.5194/gmd-10-2247-2017
McClymont, E L, Ford, H. L., Ho, S. L., Tindall, J. C., Haywood, A. M., Alonso-Garcia, M., Bailey, I., Berke, M. A., Littler, K., Patterson, M. O., Petrick, B., Peterse, F., Ravelo, A. C., Risebrobakken, B., De Schepper, S., Swann, G. E. A., Thirumalai, K., Tierney, J. E., van der Weijst, C., … Zhang, Z. (2020). Lessons from a high CO2 world: an ocean view from ~ 3 million years ago (2020b). *Climate of the Past*, *16*(4), 1599–1615. https://doi.org/10.5194/cp-16-1599-2020
McClymont, Erin L, Ford, H. L., Ho, S. L., Alonso-Garcia, M., Bailey, I., Berke, M. A., Littler, K., Patterson, M. O., Petrick, B. F., Peterse, F., Ravelo, A. C., Risebrobakken, B., De Schepper, S., Swann, G. E. A., Thirumalai, K., Tierney, J. E., van der Weijst, C., & White, S. (2020). *Sea surface temperature anomalies for Pliocene interglacial KM5c (PlioVAR) (2020a)*. PANGAEA. https://doi.org/10.1594/PANGAEA.911847
McConnell, J. R., Edwards, R., Kok, G. L., Flanner, M. G., Zender, C. S., Saltzman, E. S., Banta, J. R., Pasteris, D. R., Carter, M. M., & Kahl, J. D. W. (2007). 20th-Century Industrial Black Carbon Emissions Altered Arctic Climate Forcing. *Science*, *317*(5843), 1381–1384. https://doi.org/10.1126/science.1144856
McGregor, S., Timmermann, A., & Timm, O. (2010). A unified proxy for ENSO and PDO variability since 1650 (I382, Trans.). *Climate of the Past*, *6*(1), 1–17. https://doi.org/10.5194/cp-6-1-2010
Mears, C. A., & Wentz, F. J. (2017). A Satellite-Derived Lower-Tropospheric Atmospheric Temperature Dataset Using an Optimized Adjustment for Diurnal Effects (I385, Trans.). *Journal of Climate*, *30*(19), 7695–7718. https://doi.org/10.1175/JCLI-D-16-0768.1
Meinshausen, M., Vogel, E., Nauels, A., Lorbacher, K., Meinshausen, N., Etheridge, D. M., Fraser, P. J., Montzka, S. A., Rayner, P. J., Trudinger, C. M., Krummel, P. B., Beyerle, U., Canadell, J. G., Daniel, J. S., Enting, I. G., Law, R. M., Lunder, C. R., O'Doherty, S., Prinn, R. G., … Weiss, R. (2017). Historical greenhouse gas concentrations for climate modelling (CMIP6). *Geosci. Model Dev.*, *10*(5), 2057–2116. https://doi.org/10.5194/gmd-10-2057-2017
Mernild, S. H., Hanna, E., McConnell, J. R., Sigl, M., Beckerman, A. P., Yde, J. C., Cappelen, J., Malmros, J. K., & Steffen, K. (2015). Greenland precipitation trends in a long-term instrumental climate context (1890-2012): evaluation of coastal and ice core records. *International Journal of Climatology*, *35*(2), 303–320. https://doi.org/10.1002/joc.3986
Meyssignac, B., Boyer, T., Zhao, Z., Hakuba, M. Z., Landerer, F. W., Stammer, D., Köhl, A., Kato, S., L'Ecuyer, T., Ablain, M., Abraham, J. P., Blazquez, A., Cazenave, A., Church, J. A., Cowley, R., Cheng, L., Domingues, C. M., Giglio, D., Gouretski, V., … Zilberman, N. (2019). Measuring Global Ocean Heat Content to Estimate the Earth Energy Imbalance. *Frontiers in Marine Science*, *6*, 432. https://doi.org/10.3389/fmars.2019.00432
Mitchell, D. M., Gray, L. J., Anstey, J., Baldwin, M. P., & Charlton-Perez, A. J. (2013). The influence of stratospheric vortex displacements and splits on surface climate (I392, Trans.). *Journal of Climate*, *26*(8), 2668–2682. https://doi.org/10.1175/JCLI-D-12-00030.1
Mo, K. C. (2000). Relationships between low-frequency variability in the Southern Hemisphere and sea surface temperature anomalies. *Journal of Climate*, *13*(20), 3599–3610. https://doi.org/10.1175/1520-0442(2000)013<3599:RBLFVI>2.0.CO;2
Monnin, E., Steig, E. J., Siegenthaler, U., Kawamura, K., Schwander, J., Stauffer, B., Stocker, T. F., Morse, D. L., Barnola, J.-M., Bellier, B., Raynaud, D., & Fischer, H. (2004). Evidence for substantial accumulation rate variability in Antarctica during the Holocene, through synchronization of CO2 in the Taylor Dome, Dome C and DML ice cores. *Earth and Planetary Science Letters*, *224*(1), 45–54. https://doi.org/https://doi.org/10.1016/j.epsl.2004.05.007
Montzka, S. A., Hall, B. D., & Elkins, J. W. (2009). Accelerated increases observed for hydrochlorofluorocarbons since 2004 in the global atmosphere. *Geophysical Research Letters*, *36*(3). https://doi.org/10.1029/2008GL036475
Montzka, S. A., Mcfarland, M., Andersen, S. O., Miller, B. R., Fahey, D. W., Hall, B. D., Hu, L., Siso, C., & Elkins, J. W. (2015). Recent trends in global emissions of hydrochlorofluorocarbons and hydrofluorocarbons: Reflecting on the 2007 Adjustments to the Montreal protocol. *Journal of Physical Chemistry A*, *119*(19), 4439–4449. https://doi.org/10.1021/jp5097376
Morice, C. P., Kennedy, J. J., Rayner, N. A., Winn, J. P., Hogan, E., Killick, R. E., Dunn, R. J. H., Osborn, T. J., Jones, P. D., & Simpson, I. R. (2021). An updated assessment of near-surface temperature change from 1850: the HadCRUT5 dataset. *Journal of Geophysical Research: Atmospheres*, *126*(3). https://doi.org/10.1029/2019JD032361
Mudryk, L., Santolaria-Otín, M., Krinner, G., Ménégoz, M., Derksen, C., Brutel-Vuilmet, C., Brady, M., & Essery, R. (2020). Historical Northern Hemisphere snow cover trends and projected changes in the CMIP6 multi-model ensemble. *The Cryosphere*, *14*(7), 2495–2514. https://doi.org/10.5194/tc-14-2495-2020
Naik, S. S., Divakar Naidu, P., Foster, G. L., & Martínez-Botí, M. A. (2015). Tracing the strength of the southwest monsoon using boron isotopes in the eastern Arabian Sea. *Geophysical Research Letters*, *42*(5), 1450–1458. https://doi.org/10.1002/2015GL063089
Nerem, R. S., Beckley, B. D., Fasullo, J. T., Hamlington, B. D., Masters, D., & Mitchum, G. T. (2018). Climate-change–driven accelerated sea-level rise detected in the altimeter era. *Proceedings of the National Academy of Sciences*, *115*, 201717312. https://doi.org/10.1073/pnas.1717312115

ACCEPTED VERSION SUBJECT TO FINAL EDITS

Olivier, S., Blaser, C., Brütsch, S., Frolova, N., Gäggeler, H. W., Henderson, K. A., Palmer, A. S., Papina, T., & Schwikowski, M. (2006). Temporal variations of mineral dust, biogenic tracers, and anthropogenic species during the past two centuries from Belukha ice core, Siberian Altai. *Journal of Geophysical Research Atmospheres*, *111*(5). https://doi.org/10.1029/2005JD005830

Osmont, D., Sigl, M., Eichler, A., Jenk, T. M., Schwikowski, M., & Osmont, D., Sigl, M., Eichler, A., Jenk, T. M., and Schwikowski, M. (2019). A Holocene black carbon ice-core record of biomass burning in the Amazon Basin from Illimani, Bolivia. *Climate of the Past*, *15*, 579–592. https://doi.org/10.5194/cp-2018-136

Osmont, D., Wendl, I. A., Schmidely, L., Sigl, M., Vega, C. P., Isaksson, E., & Schwikowski, M. (2018). An 800-year high-resolution black carbon ice core record from Lomonosovfonna, Svalbard (I417, Trans.). *Atmospheric Chemistry and Physics*, *18*(17), 12777–12795. https://doi.org/10.5194/acp-18-12777-2018

Paden, J., Li, J., Leuschen, C., Rodriguez-Morales, F., & Hale, R. (2014). *IceBridge Snow Radar L1B Geolocated Radar Echo Strength Profiles, Version 2 (2014, updated 2019)*. NASA National Snow and Ice Data Center Distributed Active Archive Center. https://doi.org/10.5067/FAZTWP500V70

Pagani, M., Huber, M., Liu, Z., Bohaty, S. M., Henderiks, J., Sijp, W., Krishnan, S., & DeConto, R. M. (2011). The role of carbon dioxide during the onset of antarctic glaciation. *Science*, *334*(6060), 1261–1264. https://doi.org/10.1126/science.1203909

Pagani, M., Liu, Z., LaRiviere, J., & Ravelo, A. C. (2010). High Earth-system climate sensitivity determined from Pliocene carbon dioxide concentrations. *Nature Geoscience*, *3*(1), 27–30. https://doi.org/10.1038/ngeo724

Pagani, M., Zachos, J. C., Freeman, K. H., Tipple, B., & Bohaty, S. (2005). Marked decline in atmospheric carbon dioxide concentrations during the Paleogene. *Science*, *309*(5734), 600–603. https://doi.org/10.1126/science.1110063

PAGES 2k Consortium. (2019). Consistent multidecadal variability in global temperature reconstructions and simulations over the Common Era. *Nature Geoscience*, *12*(8), 643–649. https://doi.org/10.1038/s41561-019-0400-0

PAGES 2k Consortium, Emile-Geay, J., McKay, N. P., Kaufman, D. S., von Gunten, L., Wang, J., Anchukaitis, K. J., Abram, N. J., Addison, J. A., Curran, M. A. J., Evans, M. N., Henley, B. J., Hao, Z., Martrat, B., McGregor, H. V, Neukom, R., Pederson, G. T., Stenni, B., Thirumalai, K., … Zinke, J. (2017). A global multiproxy database for temperature reconstructions of the Common Era (I419, Trans.). *Scientific Data*, *4*, 170088. http://dx.doi.org/10.1038/sdata.2017.88

Palmer, M. D., Domingues, C. M., Slangen, A. B. A., & Dias, F. B. (2021). An ensemble approach to quantify global mean sea-level rise over the 20th century from tide gauge reconstructions. *Environmental Research Letters*. http://iopscience.iop.org/article/10.1088/1748-9326/abdaec

Palmer, M. R., Brummer, G. J., Cooper, M. J., Elderfield, H., Greaves, M. J., Reichart, G. J., Schouten, S., & Yu, J. M. (2010). Multi-proxy reconstruction of surface water pCO2 in the northern Arabian Sea since 29ka. *Earth and Planetary Science Letters*, *295*(1), 49–57. https://doi.org/10.1016/j.epsl.2010.03.023

Palmer, M. R., & Pearson, P. N. (2003). A 23,000-Year Record of Surface Water pH and PCO₂ in the Western Equatorial Pacific Ocean. *Science*, *300*(5618), 480 LP – 482. https://doi.org/10.1126/science.1080796

Panchen, Z. A., Primack, R. B., Anisko, T., & Lyons, R. E. (2012). Herbarium specimens, photographs, and field observations show philadelphia area plants are responding to climate change. *American Journal of Botany*, *99*(4). https://doi.org/10.3732/ajb.1100198

Pearson, P. N., Foster, G. L., & Wade, B. S. (2009). Atmospheric carbon dioxide through the Eocene–Oligocene climate transition. *Nature*, *461*, 1110. https://doi.org/10.1038/nature08447

Petit, J. R., Jouzel, J., Raynaud, D., Barkov, N. I., Barnola, J.-M., Basile, I., Bender, M., Chappellaz, J., Davis, M., Delaygue, G., Delmotte, M., Kotlyakov, V. M., Legrand, M., Lipenkov, V. Y., Lorius, C., PÉpin, L., Ritz, C., Saltzman, E., & Stievenard, M. (1999). Climate and atmospheric history of the past 420,000 years from the Vostok ice core, Antarctica. *Nature*, *399*(6735), 429–436. https://doi.org/10.1038/20859

Platnick, S., & et al. (2015). *MODIS Atmosphere L3 Daily Product.* NASA MODIS Adaptive Processing System, Goddard Space Flight Center, USA. https://doi.org/10.5067/MODIS/MOD08_D3.061

Poli, P., Hersbach, H., Dee, D. P., Berrisford, P., Simmons, A. J., Vitart, F., Laloyaux, P., Tan, D. G. H., Peubey, C., Thépaut, J.-N., Trémolet, Y., Hólm, E. V, Bonavita, M., Isaksen, L., & Fisher, M. (2016). ERA-20C: An Atmospheric Reanalysis of the Twentieth Century. *Journal of Climate*, *29*(11), 4083–4097. https://doi.org/10.1175/JCLI-D-15-0556.1

Prather, M. J., Hsu, J., DeLuca, N. M., Jackman, C. H., Oman, L. D., Douglass, A. R., Fleming, E. L., Strahan, S. E., Steenrod, S. D., Søvde, O. A., Isaksen, I. S. A., Froidevaux, L., & Funke, B. (2015). Measuring and modeling the lifetime of nitrous oxide including its variability. *Journal of Geophysical Research: Atmospheres*, *120*(11), 5693–5705. https://doi.org/10.1002/2015JD023267

Prinn, R. G., Weiss, R. F., Arduini, J., Arnold, T., Langley Dewitt, H., Fraser, P. J., Ganesan, A. L., Gasore, J., Harth, C. M., Hermansen, O., Kim, J., Krummel, P. B., Li, S., Loh, Z. M., Lunder, C. R., Maione, M., Manning, A. J., Miller, B. R., Mitrevski, B., … Zhou, L. (2018). History of chemically and radiatively important atmospheric gases from the Advanced Global Atmospheric Gases Experiment (AGAGE). *Earth System Science Data*, *10*(2),

ACCEPTED VERSION SUBJECT TO FINAL EDITS

985–1018. https://doi.org/10.5194/essd-10-985-2018
Purkey, S. G., & Johnson, G. C. (2010). Warming of Global Abyssal and Deep Southern Ocean Waters between the 1990s and 2000s: Contributions to Global Heat and Sea Level Rise Budgets. *Journal of Climate*, *23*(23), 6336–6351. https://doi.org/10.1175/2010JCLI3682.1
Quartly, G. D., Legeais, J. F., Ablain, M., Zawadzki, L., Joana Fernandes, M., Rudenko, S., Carrère, L., Nilo Garciá, P., Cipollini, P., Andersen, O. B., Poisson, J. C., Mbajon Njiche, S., Cazenave, A., & Benveniste, J. (2017). A new phase in the production of quality-controlled sea level data. *Earth System Science Data*, *9*(2), 557–572. https://doi.org/10.5194/essd-9-557-2017
Rae, J. W. B., Zhang, Y.-G., Liu, X., Foster, G. L., & Stoll, H. M. (2021). Atmospheric CO2 over the last 66 million years from marine archives. *Annual Review of Earth and Planetary Sciences*. https://doi.org/10.1146/annurev-earth-082420-063026
Raitzsch, M., Bijma, J., Benthien, A., Richter, K.-U., Steinhoefel, G., & Kučera, M. (2018). Boron isotope-based seasonal paleo-pH reconstruction for the Southeast Atlantic – A multispecies approach using habitat preference of planktonic foraminifera. *Earth and Planetary Science Letters*, *487*, 138–150. https://doi.org/10.1016/j.epsl.2018.02.002
Ray, E. A., Moore, F. L., Elkins, J. W., Rosenlof, K. H., Laube, J. C., Röckmann, T., Marsh, D. R., & Andrews, A. E. (2017). Quantification of the SF6 lifetime based on mesospheric loss measured in the stratospheric polar vortex. *Journal of Geophysical Research*, *122*(8), 4626–4638. https://doi.org/10.1002/2016JD026198
Ray, R. D., & Douglas, B. C. (2011). Experiments in reconstructing twentieth-century sea levels. *Progress in Oceanography*, *91*(4), 496–515. https://doi.org/10.1016/j.pocean.2011.07.021
Rayner, N. A., Parker, D. E., Horton, E. B., Folland, C. K., Alexander, L. V, Rowell, D. P., Kent, E. C., & Kaplan, A. (2003). Global analyses of sea surface temperature, sea ice, and night marine air temperature since the late nineteenth century. *Journal of Geophysical Research: Atmospheres*, *108*(D14). https://doi.org/10.1029/2002JD002670
Reynolds, R. W., Rayner, N. A., Smith, T. M., Stokes, D. C., & Wang, W. (2002). An Improved In Situ and Satellite SST Analysis for Climate. *Journal of Climate*, *15*(13), 1609–1625. https://doi.org/10.1175/1520-0442(2002)015<1609:AIISAS>2.0.CO;2
Rienecker, M. M., Suarez, M. J., Gelaro, R., Todling, R., Bacmeister, J., Liu, E., Bosilovich, M. G., Schubert, S. D., Takacs, L., Kim, G.-K., Bloom, S., Chen, J., Collins, D., Conaty, A., da Silva, A., Gu, W., Joiner, J., Koster, R. D., Lucchesi, R., … Woollen, J. (2011). MERRA: NASA's Modern-Era Retrospective Analysis for Research and Applications (I449, Trans.). *Journal of Climate*, *24*(14), 3624–3648. https://doi.org/10.1175/JCLI-D-11-00015.1
Rigby, M., Prinn, R. G., O'Doherty, S., Miller, B. R., Ivy, D., Mühle, J., Harth, C. M., Salameh, P. K., Arnold, T., Weiss, R. F., Krummel, P. B., Steele, L. P., Fraser, P. J., Young, D., & Simmonds, P. G. (2014). Recent and future trends in synthetic greenhouse gas radiative forcing. *Geophysical Research Letters*, *41*(7), 2623–2630. https://doi.org/10.1002/2013GL059099
Roemmich, D., Church, J., Gilson, J., Monselesan, D., Sutton, P., & Wijffels, S. (2015). Unabated planetary warming and its ocean structure since 2006. *Nature Climate Change*, *5*, 240. https://doi.org/10.1038/nclimate2513
Rohde, R. A., & Hausfather, Z. (2020). The Berkeley Earth Land/Ocean Temperature Record. *Earth System Science Data*, *12*(4), 3469–3479. https://doi.org/10.5194/essd-12-3469-2020
Romanovsky, V., Isaksen, K., Drozdov, D., Anisimov, O., Instanes, A., Leibman, M., McGuire, A. D., Shiklomanov, N., Smith, S. L., Walker, D. (2017). *Chapter 4, Changing permafrost and its impacts. In: Snow, Water, Ice and Permafrost in the Arctic (SWIPA) 2017*. https://www.researchgate.net/publication/321330914_Changing_permafrost_and_its_impacts_In_Snow_Water_Ice_and_Permafrost_in_the_Arctic_SWIPA_2017
Romanovsky, V., Smith, S., Isaksen, K., Nyland, K., Kholodov, A., Shiklomanov, N., Streletskiy, D., Farquharson, L., Drozdov, D., Malkova, G., & Christiansen, H. (2020). [Arctic] Terrestrial Permafrost [in "State of the Climate in 2019"]. *Bulletin of the American Meteorological Society (Supplement)*, *101*(8), 265–269. https://doi.org/10.1175/BAMS-D-20-0086.1
Rothrock, D. A., Percival, D. B., & Wensnahan, M. (2008). The decline in arctic sea-ice thickness: Separating the spatial, annual, and interannual variability in a quarter century of submarine data. *Journal of Geophysical Research: Oceans*, *113*(C5). https://doi.org/10.1029/2007JC004252
Rubino, M., Etheridge, D. M., Thornton, D. P., Howden, R., Allison, C. E., Francey, R. J., Langenfelds, R. L., Steele, L. P., Trudinger, C. M., Spencer, D. A., Curran, M. A. J., van Ommen, T. D., & Smith, A. M. (2019). Revised records of atmospheric trace gases CO2, CH4, N2O, and delta13C-CO2 over the last 2000 years from Law Dome, Antarctica. *Earth System Science Data*, *11*(2), 473–492. https://doi.org/10.5194/essd-11-473-2019
Ryu, Y., Ahn, J., Yang, J.-W., Jang, Y., Brook, E., Timmermann, A., Hong, S., Han, Y., Hur, S., & Kim, S. (2020). Atmospheric nitrous oxide variations on centennial time scales during the past two millennia. *Global Biogeochemical Cycles*, *34*(9), e2020GB006568. https://doi.org/10.1029/2020GB006568
Saha, S., Moorthi, S., Pan, H. L., Wu, X., Wang, J., Nadiga, S., Tripp, P., Kistler, R., Woollen, J., Behringer, D., Liu, H., Stokes, D., Grumbine, R., Gayno, G., Wang, J., Hou, Y. T., Chuang, H. Y., Juang, H. M. H., Sela, J., … Goldberg, M. (2010). The NCEP climate forecast system reanalysis. *Bulletin of the American Meteorological*

ACCEPTED VERSION SUBJECT TO FINAL EDITS

Society, *91*(8), 1015–1057. https://doi.org/10.1175/2010BAMS3001.1
Salzmann, U., Haywood, A. M., Lunt, D. J., Valdes, P. J., & Hill, D. J. (2008). A new global biome reconstruction and data-model comparison for the Middle Pliocene. *Global Ecology and Biogeography*, *17*(3), 432–447. https://doi.org/10.1111/j.1466-8238.2008.00381.x
Salzmann, Ulrich, Dolan, A. M., Haywood, A. M., Chan, W. Le, Voss, J., Hill, D. J., Abe-Ouchi, A., Otto-Bliesner, B., Bragg, F. J., Chandler, M. A., Contoux, C., Dowsett, H. J., Jost, A., Kamae, Y., Lohmann, G., Lunt, D. J., Pickering, S. J., Pound, M. J., Ramstein, G., … Zhang, Z. (2013). Challenges in quantifying Pliocene terrestrial warming revealed by data-model discord. *Nature Climate Change*, *3*, 969–974. https://doi.org/10.1038/nclimate2008
Santer, B. D., Thorne, P. W., Haimberger, L., Taylor, K. E., Wigley, T. M. L., Lanzante, J. R., Solomon, S., Free, M., Gleckler, P. J., Jones, P. D., Karl, T. R., Klein, S. A., Mears, C., Nychka, D., Schmidt, G. A., Sherwood, S. C., & Wentz, F. J. (2008). Consistency of modelled and observed temperature trends in the tropical troposphere. *International Journal of Climatology*, *28*(13), 1703–1722. https://doi.org/10.1002/joc.1756
Sathyendranath, S., Brewin, R. J. W., Brockmann, C., Brotas, V., Calton, B., Chuprin, A., Cipollini, P., Couto, A. B., Dingle, J., Doerffer, R., Donlon, C., Dowell, M., Farman, A., Grant, M., Groom, S., Horseman, A., Jackson, T., Krasemann, H., Lavender, S., … Platt, T. (2019). An Ocean-Colour Time Series for Use in Climate Studies: The Experience of the Ocean-Colour Climate Change Initiative (OC-CCI). *Sensors*, *19*(19). https://doi.org/10.3390/s19194285
Sato, M., Hansen, J. E., McCormick, M. P., & Pollack, J. B. (1993). Stratospheric Aerosol Optical Depths, 1850–1990 (I460, Trans.). *Journal of Geophysical Research*, *98*(D12), 22987–22994. https://doi.org/10.1029/93JD02553
Schilt, A., Baumgartner, M., Blunier, T., Schwander, J., Spahni, R., Fischer, H., & Stocker, T. F. (2010). Glacial–interglacial and millennial-scale variations in the atmospheric nitrous oxide concentration during the last 800,000 years. *Quaternary Science Reviews*, *29*(1), 182–192. https://doi.org/https://doi.org/10.1016/j.quascirev.2009.03.011
Schmitt, J., Schneider, R., Elsig, J., Leuenberger, D., Lourantou, A., Chappellaz, J. A., Köhler, P., Joos, F., Stocker, T. F., Leuenberger, M. C., & Fischer, H. (2012a). *Stable carbon isotope ratio of atmospheric CO2 of ice core EDC96, Grenoble ball mill*. PANGAEA. https://doi.org/10.1594/PANGAEA.772706
Schmitt, J., Schneider, R., Elsig, J., Leuenberger, D., Lourantou, A., Chappellaz, J., Köhler, P., Joos, F., Stocker, T. F., Leuenberger, M., & Fischer, H. (2012b). Carbon isotope constraints on the deglacial CO2rise from ice cores. *Science*. https://doi.org/10.1126/science.1217161
Schneider, R., Schmitt, J., Köhler, P., Joos, F., & Fischer, H. (2013a). A reconstruction of atmospheric carbon dioxide and its stable carbon isotopic composition from the penultimate glacial maximum to the glacial inception (Supplement to paper). *PANGAEA*. https://doi.org/10.1594/PANGAEA.817041
Schneider, R., Schmitt, J., Köhler, P., Joos, F., & Fischer, H. (2013b). A reconstruction of atmospheric carbon dioxide and its stable carbon isotopic composition from the penultimate glacial maximum to the last glacial inception. *Climate of the Past*, *9*(6), 2507–2523. https://doi.org/10.5194/cp-9-2507-2013
Seki, O., Foster, G. L., Schmidt, D. N., Mackensen, A., Kawamura, K., & Pancost, R. D. (2010). Alkenone and boron-based Pliocene pCO2 records. *Earth and Planetary Science Letters*, *292*(1–2), 201–211. https://doi.org/10.1016/j.epsl.2010.01.037
Shakun, J. D., Clark, P. U., He, F., Marcott, S. A., Mix, A. C., Liu, Z., Otto-Bliesner, B., Schmittner, A., & Bard, E. (2012). Global warming preceded by increasing carbon dioxide concentrations during the last deglaciation. *Nature*, *484*, 49. https://doi.org/10.1038/nature10915
Shao, J., Stott, L. D., Gray, W. R., Greenop, R., Pecher, I., Neil, H. L., Coffin, R. B., Davy, B., & Rae, J. W. B. (2019). Atmosphere-Ocean CO2 Exchange Across the Last Deglaciation From the Boron Isotope Proxy. *Paleoceanography and Paleoclimatology*, *34*(10), 1650–1670. https://doi.org/10.1029/2018PA003498
Siegenthaler, U. R. S., Monnin, E., Kawamura, K., Spahni, R., Schwander, J., Stauffer, B., Stocker, T. F., Barnola, J.-M., & Fischer, H. (2005). Supporting evidence from the EPICA Dronning Maud Land ice core for atmospheric CO2 changes during the past millennium. *Tellus B*, *57*(1), 51–57. https://doi.org/10.1111/j.1600-0889.2005.00131.x
Sigl, M., Winstrup, M., McConnell, J. R., Welten, K. C., Plunkett, G., Ludlow, F., Büntgen, U., Caffee, M., Chellman, N., Dahl-Jensen, D., Fischer, H., Kipfstuhl, S., Kostick, C., Maselli, O. J., Mekhaldi, F., Mulvaney, R., Muscheler, R., Pasteris, D. R., Pilcher, J. R., … Woodruff, T. E. (2015). Timing and climate forcing of volcanic eruptions for the past 2,500 years (I491, Trans.). *Nature*, *523*, 543–549. https://doi.org/10.1038/nature14565
Sigl, Michael, Abram, N. J., Gabrieli, J., Jenk, T. M., Osmont, D., & Schwikowski, M. (2018). 19th century glacier retreat in the Alps preceded the emergence of industrial black carbon deposition on high-alpine glaciers (I492, Trans.). *The Cryosphere*, *12*, 3311–3331. https://doi.org/10.5194/tc-12-3311-2018
Sigl, Michael, McConnell, J. R., Layman, L., Maselli, O., McGwire, K., Pasteris, D., Dahl-Jensen, D., Steffensen, J. P., Vinther, B., Edwards, R., Mulvaney, R., & Kipfstuhl, S. (2013). A new bipolar ice core record of volcanism from WAIS Divide and NEEM and implications for climate forcing of the last 2000 years. *Journal of Geophysical Research: Atmospheres*, *118*(3), 1151–1169. https://doi.org/10.1029/2012JD018603
Sigl, Michael, McConnell, J. R., Toohey, M., Curran, M., Das, S. B., Edwards, R., Isaksson, E., Kawamura, K.,

ACCEPTED VERSION SUBJECT TO FINAL EDITS

Kipfstuhl, S., Krüger, K., Layman, L., Maselli, O. J., Motizuki, Y., Motoyama, H., Pasteris, D. R., & Severi, M. (2014). Insights from Antarctica on volcanic forcing during the Common Era. *Nature Climate Change*, *4*(8), 693–697. https://doi.org/10.1038/nclimate2293

Simpson, I. J., Andersen, M. P. S., Meinardi, S., Bruhwiler, L., Blake, N. J., Helmig, D., Sherwood Rowland, F., & Blake, D. R. (2012). Long-term decline of global atmospheric ethane concentrations and implications for methane. *Nature*, *488*, 490–494. https://doi.org/10.1038/nature11342

Slivinski, L. C., Compo, G. P., Whitaker, J. S., Sardeshmukh, P. D., Giese, B. S., McColl, C., Allan, R., Yin, X., Vose, R., Titchner, H., Kennedy, J., Spencer, L. J., Ashcroft, L., Brönnimann, S., Brunet, M., Camuffo, D., Cornes, R., Cram, T. A., Crouthamel, R., … Wyszyński, P. (2019). Towards a more reliable historical reanalysis: Improvements for version 3 of the Twentieth Century Reanalysis system. *Quarterly Journal of the Royal Meteorological Society*, *145*(724), 2876–2908. https://doi.org/10.1002/qj.3598

Sniderman, J. M. K., Woodhead, J. D., Hellstrom, J., Jordan, G. J., Drysdale, R. N., Tyler, J. J., & Porch, N. (2016). Pliocene reversal of late Neogene aridification. *Proceedings of the National Academy of Sciences of the United States of America*, *113*(8). https://doi.org/10.1073/pnas.1520188113

Snyder, C. W. (2016). Evolution of global temperature over the past two million years (I501, Trans.). *Nature*, *538*, 226. http://dx.doi.org/10.1038/nature19798

Solomina, O. N., Bradley, R. S., Hodgson, D. A., Ivy-Ochs, S., Jomelli, V., Mackintosh, A. N., Nesje, A., Owen, L. A., Wanner, H., Wiles, G. C., & Young, N. E. (2015). Holocene glacier fluctuations (I503, Trans.). *Quaternary Science Reviews*, *111*, 9–34. https://doi.org/10.1016/j.quascirev.2014.11.018

Solomina, O. N., Bradley, R. S., Jomelli, V., Geirsdottir, A., Kaufman, D. S., Koch, J., McKay, N. P., Masiokas, M., Miller, G., Nesje, A., Nicolussi, K., Owen, L. A., Putnam, A. E., Wanner, H., Wiles, G., & Yang, B. (2016). Glacier fluctuations during the past 2000 years (I504, Trans.). *Quaternary Science Reviews*, *149*, 61–90. https://doi.org/10.1016/j.quascirev.2016.04.008

Sosdian, S. M., Greenop, R., Hain, M. P., Foster, G. L., Pearson, P. N., & Lear, C. H. (2018). Constraining the evolution of Neogene ocean carbonate chemistry using the boron isotope pH proxy (2018a). *Earth and Planetary Science Letters*, *248*, 362–376. https://doi.org/10.1016/j.epsl.2018.06.017

Sowers, T. (2001). N2O record spanning the penultimate deglaciation from the Vostok ice core. *Journal of Geophysical Research: Atmospheres*, *106*(D23), 31903–31914. https://doi.org/10.1029/2000JD900707

Spencer, R. W., Christy, J. R., & Braswell, W. D. (2017). UAH Version 6 Global Satellite Temperature Products: Methodology and Results (I507, Trans.). *Asia-Pacific Jouurnal of Atmospheric Science*, *53*(1), 121–130. https://doi.org/10.1007/s13143-017-0010-y

Spratt, R. M., & Lisiecki, L. E. (2016). A Late Pleistocene sea level stack. *Climate of the Past*, *12*(4), 1079–1092. https://doi.org/10.5194/cp-12-1079-2016

Stahle, D. W., D'Arrigo, R. D., Krusic, P. J., Cleaveland, M. K., Cook, E. R., Allan, R. J., Cole, J. E., Dunbar, R. B., Therrell, M. D., Gay, D. A., Moore, M. D., Stokes, M. A., Burns, B. T., Villanueva-Diaz, J., & Thompson, L. G. (1998). Experimental Dendroclimatic Reconstruction of the Southern Oscillation. *Bulletin of the American Meteorological Society*, *79*, 2137–2152. https://doi.org/10.1175/1520-0477(1998)079<2137:EDROTS>2.0.CO;2

Steiner, A. K., Ladstädter, F., Ao, C. O., Gleisner, H., Ho, S.-P., Hunt, D., Schmidt, T., Foelsche, U., Kirchengast, G., Kuo, Y.-H., Lauritsen, K. B., Mannucci, A. J., Nielsen, J. K., Schreiner, W., Schwärz, M., Sokolovskiy, S., Syndergaard, S., & Wickert, J. (2020). Consistency and structural uncertainty of multi-mission GPS radio occultation records. *Atmospheric Measurement Techniques*, *13*(5), 2547–2575. https://doi.org/https://doi.org/10.5194/amt-13-2547-2020

Stoll, H. M., Guitian, J., Hernandez-Almeida, I., Mejia, L. M., Phelps, S., Polissar, P., Rosenthal, Y., Zhang, H., & Ziveri, P. (2019). Upregulation of phytoplankton carbon concentrating mechanisms during low CO2 glacial periods and implications for the phytoplankton pCO2 proxy. *Quaternary Science Reviews*, *208*, 1–20. https://doi.org/10.1016/j.quascirev.2019.01.012

Studholme, J., & Gulev, S. (2018). Concurrent changes to hadley circulation and the meridional distribution of tropical cyclones (I516, Trans.). *Journal of Climate*, *31*(11), 4367–4389. https://doi.org/10.1175/JCLI-D-17-0852.1

Studinger, M. (2013). IceBridge ATM L1B Elevation and Return Strength, Version 2. (2013, updated 2020). In *NASA National Snow and Ice Data Center Distributed Active Archive Center*. https://doi.org/10.5067/19SIM5TXKPGT

Studinger, M. (2014). *IceBridge Narrow Swath ATM L1B Elevation and Return Strength, Version 2 (2014, updated 2020)*. NASA National Snow and Ice Data Center Distributed Active Archive Center. https://doi.org/10.5067/CXEQS8KVIXEI

Sun, W., Li, Q., Huang, B., Cheng, J., Song, Z., Li, H., Dong, W., Zhai, P., & Jones, P. (2021). The Assessment of Global Surface Temperature Change from 1850s: The C-LSAT2.0 Ensemble and the CMST-Interim Datasets. *Advances in Atmospheric Sciences*. https://doi.org/10.1007/s00376-021-1012-3

Super, J. R., Thomas, E., Pagani, M., Huber, M., O'Brien, C., & Hull, P. M. (2018). North Atlantic temperature and pCO2 coupling in the early-middle Miocene. *Geology*, *46*(6), 519–522. https://doi.org/10.1130/G40228.1

Susskind, J., Blaisdell, J. M., & Iredell, L. (2014). Improved methodology for surface and atmospheric soundings, error estimates, and quality control procedures: the atmospheric infrared sounder science team version-6 retrieval algorithm. *Journal of Applied Remote Sensing*, *8*(1), 1–34. https://doi.org/10.1117/1.JRS.8.084994

ACCEPTED VERSION SUBJECT TO FINAL EDITS

Tierney, J. E., Abram, N. J., Anchukaitis, K. J., Evans, M. N., Giry, C., Kilbourne, K. H., Saenger, C. P., Wu, H. C., & Zinke, J. (2015). Tropical sea surface temperatures for the past four centuries reconstructed from coral archives. *Paleoceanography*, *30*(3), 226–252. https://doi.org/10.1002/2014PA002717

Toohey, M., & Sigl, M. (2017). Volcanic stratospheric sulfur injections and aerosol optical depth from 500 BCE to 1900 CE (I539, Trans.) [Article]. *Earth System Science Data*, *9*(2), 809–831. https://doi.org/10.5194/essd-9-809-2017

Toohey, M., & Sigl, M. (2019). *Reconstructed volcanic stratospheric sulfur injections and aerosol optical depth, 500 BCE to 1900 CE, version 3*. World Data Center for Climate (WDCC) at DKRZ. https://doi.org/10.26050/WDCC/eVolv2k_v3

Troup, A. J. (1965). The 'southern oscillation.' *Quarterly Journal of the Royal Meteorological Society*, *91*(390), 490–506. https://doi.org/10.1002/qj.49709139009

Vaccaro, A., Emile-Geay, J., Guillot, D., Verna, R., Morice, C., Kennedy, J., & Rajaratnam, B. (2021). Climate field completion via Markov random fields – Application to the HadCRUT4.6 temperature dataset. *Journal of Climate*, 1–66. https://doi.org/10.1175/JCLI-D-19-0814.1

Vieira, M., Pound, M. J., & Pereira, D. I. (2018). The late Pliocene palaeoenvironments and palaeoclimates of the western Iberian Atlantic margin from the Rio Maior flora. *Palaeogeography, Palaeoclimatology, Palaeoecology*, *495*, 245–258. https://doi.org/10.1016/j.palaeo.2018.01.018

Villalba, R., Lara, A., Masiokas, M. H., Urrutia, R., Luckman, B. H., Marshall, G. J., Mundo, I. A., Christie, D. A., Cook, E. R., Neukom, R., Allen, K., Fenwick, P., Boninsegna, J. A., Srur, A. M., Morales, M. S., Araneo, D., Palmer, J. G., Cuq, E., Aravena, J. C., … Lequesne, C. (2012). Unusual Southern Hemisphere tree growth patterns induced by changes in the Southern Annular Mode. *Nature Geoscience*, *5*(October), 793–798. https://doi.org/10.1038/ngeo1613

von Schuckmann, K., Cheng, L., Palmer, M. D., Hansen, J., Tassone, C., Aich, V., Adusumilli, S., Beltrami, H., Boyer, T., Cuesta-Valero, F. J., Desbruyères, D., Domingues, C., Garcia-Garcia, A., Gentine, P., Gilson, J., Gorfer, M., Haimberger, L., Ishii, M., Johnson, G. C., … Wijffels, S. E. (2020). Heat stored in the Earth system: where does the energy go? *Earth System Science Data*, *12*(3), 2013–2041. https://doi.org/10.5194/essd-12-2013-2020

von Schuckmann, K., & Le Traon, P.-Y. (2011). How well can we derive Global Ocean Indicators from Argo data? *Ocean Sci.*, *7*(6), 783–791. https://doi.org/10.5194/os-7-783-2011

Vonder Haar, T. H., Bytheway, J. L., & Forsythe, J. M. (2012). Weather and climate analyses using improved global water vapor observations. *Geophysical Research Letters*, *39*(15), 1–6. https://doi.org/10.1029/2012GL052094

Vose, R. S., Huang, B., Yin, X., Arndt, D., Easterling, D. R., Lawrimore, J. H., Menne, M. J., Sanchez-Lugo, A., & Zhang, H. M. (2021). Implementing Full Spatial Coverage in NOAA's Global Temperature Analysis. *Geophysical Research Letters*, *48*(4), e2020GL090873. https://doi.org/10.1029/2020GL090873

Vose, R., Schmoyer, R., Steurer, P., Peterson, T., Heim, R., Karl, T., & Eischeid, J. (1992). *The Global Historical Climatology Network: Long-term monthly temperature, precipitation, sea level pressure, and station pressure data* (I. Rt0 (trans.)). https://doi.org/10.2172/10178730

Walsh, J. E., W. L. Chapman, F. Fetterer, and J. S. S. (2019). *Gridded Monthly Sea Ice Extent and Concentration, 1850 Onward, Version 2*. NSIDC: National Snow and Ice Data Center. https://doi.org/org/10.7265/jj4s-tq79

Walsh, J. E., Fetterer, F., Scott Stewart, J., & Chapman, W. L. (2017). A database for depicting Arctic sea ice variations back to 1850 (I557, Trans.). *Geographical Review*, *107*(1), 89–107. https://doi.org/10.1111/j.1931-0846.2016.12195.x

Wang, T., Dai, J., Lam, K. S., Nan Poon, C., & Brasseur, G. P. (2019). Twenty-Five Years of Lower Tropospheric Ozone Observations in Tropical East Asia: The Influence of Emissions and Weather Patterns. *Geophysical Research Letters*, *46*(20), 11463–11470. https://doi.org/10.1029/2019GL084459

Wang, Y.-M., Lean, J. L., & N. R. Sheeley, J. (2005). Modeling the Sun's Magnetic Field and Irradiance since 1713. *The Astrophysical Journal*, *625*(1), 522–538. https://doi.org/10.1086/429689

WCRP Global Sea Level Budget Group. (2018). Global sea-level budget 1993–present. *Earth Syst. Sci. Data*, *10*(3), 1551–1590. https://doi.org/10.5194/essd-10-1551-2018

Webb, L. B., Whetton, P. H., & Barlow, E. W. R. (2011). Observed trends in winegrape maturity in Australia. *Global Change Biology*, *17*(8). https://doi.org/10.1111/j.1365-2486.2011.02434.x

Weber, M., Steinbrecht, W., A, R. van der, Frith, S. M., Anderson, J., Coldewey-Egbers, M., Davis, S., Degenstein, D., Fioletov, V. E., Froidevaux, L., Hubert, D., Laat, J. de, Long, C. S., Loyola, D., Sofieva, V., Tourpali, K., Roth, C., Wang, R., & Wild, J. D. (2018). Stratospheric ozone in "State of the Climate in 2017 (I572, Trans.). *Bull. Amer. Meteor. Soc*, *99*, S51-s54. https://doi.org/10.1175/2018BAMSStateoftheClimate.1

Weber, M., Steinbrecht, W., Arosio, C., A, R. van der, Frith, S. M., Anderson, M., Coldewey-Egbers, S. Davis, D., Degenstein, V. E. Fioletov Froidevaux, L., Hubert, D., Long, C. S., Loyola, D., Rozanov, A., Roth, C., Sofieva, V., Tourpali, K., Wang, R., & Wild, J. D. (2020). Stratospheric ozone, in State of the Climate in 2019. *Bull. Amer. Meteor., 101 (8), S81–S83, 101*(8), S81–S83. https://doi.org/10.1175/ BAMS-D-20-0104.1.

Weber, Mark, Coldewey-Egbers, M., Fioletov, V. E., Frith, S. M., Wild, J. D., Burrows, J. P., Long, C. S., & Loyola, D. (2018). Total ozone trends from 1979 to 2016 derived from five merged observational datasets-the emergence into ozone recovery. In *Atmospheric Chemistry and Physics*. https://doi.org/10.5194/acp-18-2097-2018

ACCEPTED VERSION SUBJECT TO FINAL EDITS

Wendl, I. A., Eichler, A., Isaksson, E., Martma, T., & Schwikowski, M. (2015). 800-year ice-core record of nitrogen deposition in Svalbard linked to ocean productivity and biogenic emissions (I577, Trans.). *Atmospheric Chemistry and Physics*, *15*(13), 7287–7300. https://doi.org/10.5194/acp-15-7287-2015

Wentz, F. J., Scott, J., Hoffman, R., Leidner, M., Atlas, R., & Ardizzone, J. (2015). *Remote Sensing Systems Cross-Calibrated Multi-Platform (CCMP) 6-hourly ocean vector wind analysis product on 0.25 deg grid, Version 2.0.* Remote Sensing Systems, Santa Rosa, CA. www.remss.com/measurements/ccmp

Wentz, F. J., & T., M. (2007). *Supplement 1 Algorithm Theoretical Basis Document for AMSR-E Ocean Algorithms*. http://images.remss.com/papers/rsstech/2007_051707_Wentz_AMSR_Ocean_V2_Supplement_1.pdf

Wenzel, M., & Schröter, J. (2014). Global and regional sea level change during the 20th century. *Journal of Geophysical Research: Oceans*, *119*(11), 7493–7508. https://doi.org/10.1002/2014JC009900

Westerhold, T., Marwan, N., Drury, A. J., Liebrand, D., Agnini, C., Anagnostou, E., Barnet, J. S. K., Bohaty, S. M., De Vleeschouwer, D., Florindo, F., Frederichs, T., Hodell, D. A., Holbourn, A. E., Kroon, D., Lauretano, V., Littler, K., Lourens, L. J., Lyle, M., Pälike, H., … Zachos, J. C. (2020). An astronomically dated record of Earth's climate and its predictability over the last 66 million years. *Science*, *369*(6509), 1383–1387. https://doi.org/10.1126/science.aba6853

Wijffels, S., Roemmich, D., Monselesan, D., Church, J., & Gilson, J. (2016). Ocean temperatures chronicle the ongoing warming of Earth. *Nature Climate Change*, *6*(2), 116–118. https://doi.org/10.1038/nclimate2924

Willett, K., Dunn, R., Kennedy, J., & Berry, D. (2020). Development of the HadISDH.marine humidity climate monitoring dataset. *Earth Syst. Sci. Data*, *12*(4), 2853–2880. https://doi.org/10.5194/essd-2019-190

Willett, K. M., Dunn, R. J. H., Thorne, P. W., Bell, S., Podesta, M. De, Parker, D. E., Jones, P. D., & Jr, C. N. W. (2014). HadISDH land surface multi-variable humidity and temperature record for climate monitoring. *Climate of the Past*, *10*, 1983–2006. https://doi.org/10.5194/cp-10-1983-2014

Willett, K. M., Williams, C. N., Dunn, R. J. H., Thorne, P. W., Bell, S., de Podesta, M., Jones, P. D., & Parker, D. E. (2013). HadISDH: an updateable land surface specific humidity product for climate monitoring. *Climate of the Past*, *9*(2), 657–677. https://doi.org/10.5194/cp-9-657-2013

Williams, J. W., Tarasov, P., Brewer, S., & Notaro, M. (2011). Late Quaternary variations in tree cover at the northern forest-tundra ecotone. *Journal of Geophysical Research: Biogeosciences*, *116*(G1). https://doi.org/10.1029/2010JG001458

Wilson, R., Cook, E., D'Arrigo, R., Riedwyl, N., Evans, M. N., Tudhope, A., & Allan, R. (2010). Reconstructing ENSO: the influence of method, proxy data, climate forcing and teleconnections. *Journal of Quaternary Science*, *25*(1), 62–78. https://doi.org/10.1002/jqs.1297

Witkowski, C. R., Weijers, J. W. H., Blais, B., Schouten, S., & Sinninghe Damsté, J. S. (2018). Molecular fossils from phytoplankton reveal secular PCO2 trend over the phanerozoic. *Science Advances*, *4*(11), eaat4556. https://doi.org/10.1126/sciadv.aat4556

WMO. (2018). *19th WMO/IAEA Meeting on Carbon Dioxide, Other Greenhouse Gases and Related Measurement Techniques (GGMT-2017)*,.

WMO. (2019). WMO Greenhouse Gas Bulletin (GHG Bulletin) - No. 15: The State of Greenhouse Gases in the Atmosphere Based on Global Observations through 2018. *WMO Greenhouse Gas Bulletin (GHG Bulletin)*, *15*. https://library.wmo.int/index.php?lvl=notice_display&id=21620#.YCEa8uj7SUk

Wouters, B., Gardner, A. S., & Moholdt, G. (2019). Global Glacier Mass Loss During the GRACE Satellite Mission (2002-2016). *Frontiers in Earth Science*, *7*, 96. https://doi.org/10.3389/feart.2019.00096

Yang, J.-W., Ahn, J., Brook, E. J., & Ryu, Y. (2017). Atmospheric methane control mechanisms during the early Holocene. *Climate of the Past*, *13*(9), 1227–1242. https://doi.org/10.5194/cp-13-1227-2017

Yu, L., Jin, X., & Weller, R. A. (2008). *Multidecade Global Flux Datasets from the Objectively Analyzed Air-sea Fluxes (OAFlux) Project: Latent and sensible heat fluxes, ocean evaporation, and related surface meteorological variables* (I. Rt7 (trans.)). Woods Hole Oceanographic Institution, OAFlux Project Technical Report. OA-2008-01, Woods Hole, Massachusetts. https://www.researchgate.net/publication/237440650_Multidecade_Global_Flux_Datasets_from_the_Objectively_Analyzed_Air-sea_Fluxes_OAFlux_Project_Latent_and_Sensible_Heat_Fluxes_Ocean_Evaporation_and_Related_Surface_Meteorological_Variables

Zachos, J. C., Dickens, G. R., & Zeebe, R. E. (2008). An early Cenozoic perspective on greenhouse warming and carbon-cycle dynamics. *Nature*, *451*(7176), 279–283. https://doi.org/10.1038/nature06588

Zanna, L., Khatiwala, S., Gregory, J. M., Ison, J., & Heimbach, P. (2019). Global reconstruction of historical ocean heat storage and transport. *Proceedings of the National Academy of Sciences*, *116*(4), 1126–1131. https://doi.org/10.1073/pnas.1808838115

Zemp, M, Huss, M., Thibert, E., Eckert, N., McNabb, R., Huber, J., Barandun, M., Machguth, H., Nussbaumer, S. U., Gärtner-Roer, I., Thomson, L., Paul, F., Maussion, F., Kutuzov, S., & Cogley, J. G. (2019). Global glacier mass changes and their contributions to sea-level rise from 1961 to 2016. *Nature*, *568*(7752), 382–386. https://doi.org/10.1038/s41586-019-1071-0

Zemp, Michael, Huss, M., Eckert, N., Thibert, E., Paul, F., Nussbaumer, U. S., & Gärtner-Roer, I. (2020). Brief

ACCEPTED VERSION SUBJECT TO FINAL EDITS

communication: Ad hoc estimation of glacier contributions to sea-level rise from the latest glaciological observations. *Cryosphere*, *14*(3). https://doi.org/10.5194/tc-14-1043-2020

Zhang, Y. G., Pagani, M., Liu, Z., Bohaty, S. M., & DeConto, R. (2013). A 40-million-year history of atmospheric CO2. *Philosophical Transactions of the Royal Society A: Mathematical, Physical and Engineering Sciences*, *371*(2001), 20130096. https://doi.org/10.1098/rsta.2013.0096

Zhou, C., Wang, J., Dai, A., & Thorne, P. W. (2021). A New Approach to Homogenize Global Subdaily Radiosonde Temperature Data from 1958 to 2018. *Journal of Climate*, *34*(3), 1163–1183. https://doi.org/10.1175/JCLI-D-20-0352.1

Ziemke, J. R., Oman, L. D., Strode, S. A., Douglass, A. R., Olsen, M. A., McPeters, R. D., Bhartia, P. K., Froidevaux, L., Labow, G. J., Witte, J. C., Thompson, A. M., Haffner, D. P., Kramarova, N. A., Frith, S. M., Huang, L. K., Jaross, G. R., Seftor, C. J., Deland, M. T., & Taylor, S. L. (2019). Trends in global tropospheric ozone inferred from a composite record of TOMS/OMI/MLS/OMPS satellite measurements and the MERRA-2 GMI simulation. *Atmospheric Chemistry and Physics*, *19*(5), 3257–3269. https://doi.org/10.5194/acp-19-3257-2019

Zou, C.-Z., & Qian, H. (2016). Stratospheric Temperature Climate Data Record from Merged SSU and AMSU-A Observations (I616, Trans.). *Journal of Atmospheric and Oceanic Technology*, *33*(9), 1967–1984. https://doi.org/10.1175/JTECH-D-16-0018.1

ACCEPTED VERSION
SUBJECT TO FINAL EDITS

Chapter 3: Human influence on the climate system

Coordinating Lead Authors:
Veronika Eyring (Germany) and Nathan P. Gillett (Canada)

Lead Authors:
Krishna M. Achuta Rao (India), Rondrotiana Barimalala (South Africa/Madagascar), Marcelo Barreiro Parrillo (Uruguay), Nicolas Bellouin (United Kingdom/France), Christophe Cassou (France), Paul J. Durack (United States of America/Australia), Yu Kosaka (Japan), Shayne McGregor (Australia), Seung-Ki Min (Republic of Korea), Olaf Morgenstern (New Zealand/Germany), Ying Sun (China)

Contributing Authors:
Lisa Bock (Germany), Elizaveta Malinina (Canada/Russian Federation), Guðfinna Aðalgeirsdóttir (Iceland), Jonathan L. Bamber (United Kingdom), Chris Brierley (United Kingdom), Lee de Mora (United Kingdom), John P. Dunne (United States of America), John C. Fyfe (Canada), Peter J. Gleckler (United States of America), Peter Greve (Austria/Germany), Lukas Gudmundsson (Switzerland/Germany, Iceland), Karsten Haustein (United Kingdom, Germany /Germany), Ed Hawkins (United Kingdom), Benjamin J. Henley (Australia), Marika M. Holland (United States of America), Chris Huntingford (United Kingdom), Colin Jones (United Kingdom), Masa Kageyama (France), Rémi Kazeroni (Germany/France), Yeon-Hee Kim (Republic of Korea), Charles Koven (United States of America), Gerhard Krinner (France/Germany, France), Eunice Lo (United Kingdom/China), Daniel J. Lunt (United Kingdom), Sophie Nowicki (United States of America/France, United States of America), Adam S. Phillips (United States of America), Valeriu Predoi (United Kingdom), Krishnan Raghavan (India), Malcolm J. Roberts (United Kingdom), Jon Robson (United Kingdom), Lucas Ruiz (Argentina), Jean-Baptiste Sallée (France), Benjamin D. Santer (United States of America), Andrew P. Schurer (United Kingdom), Jessica Tierney (United States of America), Blair Trewin (Australia), Katja Weigel (Germany), Xuebin Zhang (Canada), Anni Zhao (United Kingdom/China), Tianjun Zhou (China)

Review Editors:
Tomas Halenka (Czech Republic), Jose A. Marengo Orsini (Brazil/Peru), Daniel Mitchell (United Kingdom)

Chapter Scientists:
Lisa Bock (Germany), Elizaveta Malinina (Canada/Russian Federation)

This Chapter should be cited as:
Eyring, V., N. P. Gillett, K. M. Achuta Rao, R. Barimalala, M. Barreiro Parrillo, N. Bellouin, C. Cassou, P. J. Durack, Y. Kosaka, S. McGregor, S. Min, O. Morgenstern, Y. Sun, 2021, Human Influence on the Climate System. In: *Climate Change 2021: The Physical Science Basis. Contribution of Working Group I to the Sixth Assessment Report of the Intergovernmental Panel on Climate Change* [Masson-Delmotte, V., P. Zhai, A. Pirani, S. L. Connors, C. Péan, S. Berger, N. Caud, Y. Chen, L. Goldfarb, M. I. Gomis, M. Huang, K. Leitzell, E. Lonnoy, J. B. R. Matthews, T. K. Maycock, T. Waterfield, O. Yelekçi, R. Yu and B. Zhou (eds.)]. Cambridge University Press. In Press.

Date: August 2021

This document is subject to copy-editing, corrigenda and trickle backs.

ACCEPTED VERSION SUBJECT TO FINAL EDITING

Table of Contents

Executive Summary **4**

3.1 Scope and Overview **9**

3.2 Methods **10**

3.2.1 Methods Based on Regression 11

3.2.2 Other Probabilistic Approaches 12

3.3 Human Influence on the Atmosphere and Surface **12**

3.3.1 Temperature 12

3.3.1.1 Surface Temperature 12

3.3.1.2 Upper-Air Temperature 23

Cross-Chapter Box 3.1: Global Surface Warming over the Early 21st Century **26**

3.3.2 Precipitation, Humidity and Streamflow 29

3.3.2.1 Atmospheric Water Vapour 31

3.3.2.2 Precipitation 32

3.3.2.3 Streamflow 36

Cross-Chapter Box 3.2:Human Influence on Large-scale Changes in Temperature and Precipitation Extremes **37**

3.3.3 Atmospheric Circulation 39

3.3.3.1 The Hadley and Walker Circulations 39

3.3.3.2 Global Monsoon 42

3.3.3.3 Extratropical Jets, Storm Tracks and Blocking 44

3.3.3.4 Sudden Stratospheric Warming Activity 47

3.4 Human Influence on the Cryosphere **47**

3.4.1 Sea Ice 47

3.4.1.1 Arctic Sea Ice 47

3.4.1.2 Antarctic Sea Ice 49

3.4.2 Snow Cover 51

3.4.3 Glaciers and Ice Sheets 52

3.4.3.1 Glaciers 52

3.4.3.2 Ice Sheets 53

3.5 Human Influence on the Ocean **55**

3.5.1 Ocean Temperature 55

3.5.1.1 Sea Surface and Zonal Mean Ocean Temperature Evaluation 55

3.5.1.2 Tropical Sea Surface Temperature Evaluation 57

3.5.1.3 Ocean Heat Content Change Attribution 58

ACCEPTED VERSION
SUBJECT TO FINAL EDITING

3.5.2 Ocean Salinity 60
3.5.2.1 Sea Surface and Depth-profile Salinity Evaluation 61
3.5.2.2 Salinity Change Attribution 62
3.5.3 Sea Level 63
3.5.3.1 Sea Level Evaluation 63
3.5.3.2 Sea Level Change Attribution 64
3.5.4 Ocean Circulation 65
3.5.4.1 Atlantic Meridional Overturning Circulation (AMOC) 65
3.5.4.2 Southern Ocean Circulation 67
3.6 Human Influence on the Biosphere 68
3.6.1 Terrestrial Carbon Cycle 68
3.6.2 Ocean Biogeochemical Variables 71
3.7 Human Influence on Modes of Climate Variability 73
3.7.1 North Atlantic Oscillation and Northern Annular Mode 73
3.7.2 Southern Annular Mode 77
3.7.3 El Niño-Southern Oscillation 79
3.7.4 Indian Ocean Basin and Dipole Modes 83
3.7.5 Atlantic Meridional and Zonal Modes 85
3.7.6 Pacific Decadal Variability 86
3.7.7 Atlantic Multidecadal Variability 88
3.8 Synthesis across Earth System Components 91
3.8.1 Multivariate Attribution of Climate Change 91
3.8.2 Multivariate Model Evaluation 92
3.8.2.1 Integrative Measures of Model Performance 92
3.8.2.2 Process Representation in Different Classes of Models 97
Frequently Asked Questions 100
FAQ 3.1: How do we Know Humans are Responsible for Climate Change? 100
FAQ 3.2: What is Natural Variability and How has it Influenced Recent Climate Changes? 102
FAQ 3.3: Are Climate Models Improving? 104
Acknowledgements 106
References 107
Figures 153

ACCEPTED VERSION
SUBJECT TO FINAL EDITING

Executive Summary

The evidence for human influence on recent climate change strengthened from the IPCC Second Assessment Report to the IPCC Fifth Assessment Report, and is now even stronger in this assessment. The IPCC Second Assessment Report (1995) concluded 'the balance of evidence suggests that there is a discernible human influence on global climate'. In subsequent assessments (TAR, 2001; AR4, 2007 and AR5, 2013), the evidence for human influence on the climate system was found to have progressively strengthened. AR5 concluded that human influence on the climate system is clear, evident from increasing greenhouse gas concentrations in the atmosphere, positive radiative forcing, observed warming, and physical understanding of the climate system. This chapter updates the assessment of human influence on the climate system for large-scale indicators of climate change, synthesizing information from paleo records, observations and climate models. It also provides the primary evaluation of large-scale indicators of climate change in this report, that is complemented by fitness-for-purpose evaluation in subsequent chapters.

Synthesis across the Climate System

It is unequivocal that human influence has warmed the global climate system since pre-industrial times. Combining the evidence from across the climate system increases the level of confidence in the attribution of observed climate change to human influence and reduces the uncertainties associated with assessments based on single variables. Large-scale indicators of climate change in the atmosphere, ocean, cryosphere and at the land surface show clear responses to human influence consistent with those expected based on model simulations and physical understanding. {3.8.1}

For most large-scale indicators of climate change, the simulated recent mean climate from the latest generation Coupled Model Intercomparison Project Phase 6 (CMIP6) climate models underpinning this assessment has improved compared to the CMIP5 models assessed in the AR5 (*high confidence*). High-resolution models exhibit reduced biases in some but not all aspects of surface and ocean climate (*medium confidence*), and most Earth system models, which include biogeochemical feedbacks, perform as well as their lower-complexity counterparts (*medium confidence*). The multi-model mean captures most aspects of observed climate change well (*high confidence*). The multi-model mean captures the proxy-reconstructed global-mean surface air temperature (GSAT) change during past high- and low-CO_2 climates (*high confidence*) and the correct sign of temperature and precipitation change in most assessed regions in the mid-Holocene (*medium confidence*). The simulation of paleoclimates on continental scales has improved compared to AR5 (*medium confidence*), but models often underestimate large temperature and precipitation differences relative to the present day (*high confidence*). {3.8.2}

Human Influence on the Atmosphere and Surface

The *likely* range of human-induced warming in global-mean surface air temperature (GSAT) in 2010–2019 relative to 1850–1900 is 0.8°C–1.3°C, encompassing the observed warming of 0.9°C–1.2°C, while the change attributable to natural forcings is only −0.1°C–0.1°C. The best estimate of human-induced warming is 1.07°C. Warming can now be attributed since 1850–1900, instead of since 1951 as done in the AR5, thanks to a better understanding of uncertainties and because observed warming is larger. The *likely* ranges for human-induced GSAT and global mean surface temperature (GMST) warming are equal (*medium confidence*). Attributing observed warming to specific anthropogenic forcings remains more uncertain. Over the same period, forcing from greenhouse gases[1] *likely* increased GSAT by 1.0°C–2.0°C, while other anthropogenic forcings including aerosols *likely* decreased GSAT by 0.0°C–0.8°C. It is *very likely* that human-induced greenhouse gas increases were the main driver[2] of tropospheric warming since comprehensive satellite observations started in 1979, and *extremely likely* that human-induced stratospheric ozone depletion was the main driver of cooling in the lower stratosphere between 1979 and the mid-1990s. {3.3.1}

[1] In this chapter, 'greenhouse gases' refers to well-mixed greenhouse gases.

[2] In this chapter, 'main driver' means responsible for more than 50% of the change.

ACCEPTED VERSION SUBJECT TO FINAL EDITING

The CMIP6 model ensemble reproduces the observed historical global surface temperature trend and variability with biases small enough to support detection and attribution of human-induced warming (*very high confidence*). The CMIP6 multi-model mean GSAT anomaly between 1850–1900 and 2010–2019 is close to the best estimate of observed warming, but some CMIP6 models simulate a warming that is outside the assessed 5–95% range of observed warming. CMIP6 models broadly reproduce surface temperature variations over the past millennium, including the cooling that follows periods of intense volcanism (*medium confidence*). For upper air temperature, there is *medium confidence* that most CMIP5 and CMIP6 models overestimate observed warming in the upper tropical troposphere by at least 0.1°C per decade over the period 1979 to 2014. The latest updates to satellite-derived estimates of stratospheric temperature have resulted in decreased differences between simulated and observed changes of global mean temperature through the depth of the stratosphere (*medium confidence*). {3.3.1}

The slower rate of GMST increase observed over 1998–2012 compared to 1951–2012 was a temporary event followed by a strong GMST increase (*very high confidence*). Improved observational data sets since AR5 show a larger GMST trend over 1998–2012 than earlier estimates. All the observed estimates of the 1998–2012 GMST trend lie within the 10th–90th percentile range of CMIP6 simulated trends (*high confidence*). Internal variability, particularly Pacific Decadal Variability, and variations in solar and volcanic forcings partly offset the anthropogenic surface warming trend over the 1998–2012 period (*high confidence*). Global ocean heat content continued to increase throughout this period, indicating continuous warming of the entire climate system (*very high confidence*). Since 2012, GMST has warmed strongly, with the past five years (2016–2020) being the warmest five-year period in the instrumental record since at least 1850 (*high confidence*). {Cross-Chapter Box 3.1, 3.3.1; 3.5.1}

It is *likely* that human influence has contributed to[3] moistening in the upper troposphere since 1979. Also, there *is medium confidence* that human influence contributed to a global increase in annual surface specific humidity, and *medium confidence* that it contributed to a decrease in surface relative humidity over mid-latitude Northern Hemisphere continents during summertime. {3.3.2}

It is *likely* that human influence has contributed to observed large-scale precipitation changes since the mid-20th century. New attribution studies strengthen previous findings of a detectable increase in Northern Hemisphere mid- to high-latitude land precipitation (*high confidence*). Human influence has contributed to strengthening the zonal mean precipitation contrast between the wet tropics and dry subtropics (*medium confidence*). Yet, anthropogenic aerosols contributed to decreasing global land summer monsoon precipitation from the 1950s to 1980s (*medium confidence*). There is also *medium confidence* that human influence has contributed to high-latitude increases and mid-latitude decreases in Southern Hemisphere summertime precipitation since 1979 associated with the trend of the Southern Annular Mode toward its positive phase. Despite improvements, models still have deficiencies in simulating precipitation patterns, particularly over the tropical ocean (*high confidence*). {3.3.2, 3.3.3, 3.5.2}

Human-induced greenhouse gas forcing is the main driver of the observed changes in hot and cold extremes on the global scale (*virtually certain*) and on most continents (*very likely*). It is *likely* that human influence, in particular due to greenhouse gas forcing, is the main driver of the observed intensification of heavy precipitation in global land regions during recent decades. There is *high confidence* in the ability of models to capture the large-scale spatial distribution of precipitation extremes over land. The magnitude and frequency of extreme precipitation simulated by CMIP6 models are similar to those simulated by CMIP5 models (*high confidence*). {Cross-Chapter Box 3.2}

It is *likely* that human influence has contributed to the poleward expansion of the zonal mean Hadley cell in the Southern Hemisphere since the 1980s. There is *medium confidence* that the observed poleward expansion of the zonal mean Hadley cell in the Northern Hemisphere is within the range of internal variability. The causes of the observed strengthening of the Pacific Walker circulation since the 1980s are not well understood, and the observed strengthening trend is outside the range of trends simulated in the

[3] In this chapter the phrase 'human influence has contributed to' an observed change means that the response to human influence is nonzero and consistent in sign with the observed change.

ACCEPTED VERSION SUBJECT TO FINAL EDITING

coupled models (*medium confidence*). While CMIP6 models capture the general characteristics of the tropospheric large-scale circulation (*high confidence*), systematic biases exist in the mean frequency of atmospheric blocking events, especially in the Euro-Atlantic sector, some of which reduce with increasing model resolution (*medium confidence*). {3.3.3}

Human Influence on the Cryosphere

It is *very likely* that anthropogenic forcing, mainly due to greenhouse gas increases, was the main driver of Arctic sea ice loss since the late 1970s. There is new evidence that increases in anthropogenic aerosols have offset part of the greenhouse gas-induced Arctic sea ice loss since the 1950s (*medium confidence*). In the Arctic, despite large differences in the mean sea ice state, loss of sea ice extent and thickness during recent decades is reproduced in all CMIP5 and CMIP6 models (*high confidence*). By contrast, global climate models do not generally capture the small observed increase in Antarctic sea ice extent during the satellite era, and there is *low confidence* in attributing the causes of this change. {3.4.1}

It is *very likely* that human influence contributed to the observed reductions in Northern Hemisphere spring snow cover since 1950. The seasonal cycle in Northern Hemisphere snow cover is better reproduced by CMIP6 than by CMIP5 models (*high confidence*). Human influence was *very likely* the main driver of the recent global, near-universal retreat of glaciers. It is *very likely* that human influence has contributed to the observed surface melting of the Greenland Ice Sheet over the past two decades, and there is *medium confidence* in an anthropogenic contribution to recent overall mass loss from the Greenland Ice Sheet. However, there is only *limited evidence*, with *medium agreement*, of human influence on Antarctic Ice Sheet mass balance through changes in ice discharge. {3.4.2, 3.4.3}

Human Influence on the Ocean

It is *extremely likely* that human influence was the main driver of the ocean heat content increase observed since the 1970s, which extends into the deeper ocean (*very high confidence*). Since AR5, there is improved consistency between recent observed estimates and model simulations of changes in upper (<700 m) ocean heat content, when accounting for both natural and anthropogenic forcings. Updated observations and model simulations show that warming extends throughout the entire water column (*high confidence*), with CMIP6 models simulating 58% of industrial-era heat uptake (1850 to 2014) in the upper layer (0–700 m), 21% in the intermediate layer (700–2000 m) and 22% in the deep layer (>2000 m). The structure and magnitude of multi-model mean ocean temperature biases have not changed substantially between CMIP5 and CMIP6 (*medium confidence*). {3.5.1}

It is *extremely likely* that human influence has contributed to observed near-surface and subsurface oceanic salinity changes since the mid-20th century. The associated pattern of change corresponds to fresh regions becoming fresher and salty regions becoming saltier (*high confidence*). Changes to the coincident atmospheric water cycle and ocean–atmosphere fluxes (evaporation and precipitation) are the primary drivers of the observed basin-scale salinity changes (*high confidence*). The observed depth-integrated basin-scale salinity changes have been attributed to human influence, with CMIP5 and CMIP6 models able to reproduce these patterns only in simulations that include greenhouse gas increases (*medium confidence*). The basin-scale changes are consistent across models and intensify through the historical period (*high confidence*). The structure of the biases in the multi-model mean has not changed substantially between CMIP5 and CMIP6 (*medium confidence*). {3.5.2}

Combining the attributable contributions from glaciers, ice sheet surface mass balance and thermal expansion, it is *very likely* that human influence was the main driver of the observed global mean sea level rise since at least 1970. Since the AR5, studies have shown that simulations that exclude anthropogenic greenhouse gases are unable to capture the sea level rise due to thermal expansion (thermosteric) during the historical period and that model simulations that include all forcings (anthropogenic and natural) most closely match observed estimates. It is *very likely* that human influence was the main driver of the observed global mean thermosteric sea level increase since 1970. {3.5.3, 3.5.1, 3.4.3}

ACCEPTED VERSION SUBJECT TO FINAL EDITING

While observations show that the Atlantic Meridional Overturning Circulation (AMOC) has weakened from the mid-2000s to the mid-2010s (*high confidence*) and the Southern Ocean upper overturning cell has strengthened since the 1990s (*low confidence*), observational records are too short to determine the relative contributions of internal variability, natural forcing, and anthropogenic forcing to these changes (*high confidence*). No changes in Antarctic Circumpolar Current transport or meridional position have been observed. The mean zonal and overturning circulations of the Southern Ocean and the mean overturning circulation of the North Atlantic (AMOC) are broadly reproduced by CMIP5 and CMIP6 models. However, biases are apparent in the modelled circulation strengths (*high confidence*) and their variability (*medium confidence*). {3.5.4}

Human Influence on the Biosphere

The main driver of the observed increase in the amplitude of the seasonal cycle of atmospheric CO_2 is enhanced fertilization of plant growth by the increasing concentration of atmospheric CO_2 (*medium confidence*). However, there is only *low confidence* that this CO_2 fertilization has also been the main driver of observed greening because land management is the dominating factor in some regions. Earth system models simulate globally averaged land carbon sinks within the range of observation-based estimates (*high confidence*), but global-scale agreement masks large regional disagreements. {3.6.1}

It is *virtually certain* that the uptake of anthropogenic CO_2 was the main driver of the observed acidification of the global ocean. The observed increase in CO_2 concentration in the subtropical and equatorial North Atlantic since 2000 is *likely* associated in part with an increase in ocean temperature, a response that is consistent with the expected weakening of the ocean carbon sink with warming. Consistent with AR5 there is *medium confidence* that deoxygenation in the upper ocean is due in part to human influence. There is *high confidence* that Earth system models simulate a realistic time evolution of the global mean ocean carbon sink. {3.6.2}

Human Influence on Modes of Climate Variability

It is *very likely* that human influence has contributed to the observed trend towards the positive phase of the Southern Annular Mode (SAM) since the 1970s and to the associated strengthening and southward shift of the Southern Hemispheric extratropical jet in austral summer. The influence of ozone forcing on the SAM trend has been small since the early 2000s compared to earlier decades, contributing to a weaker SAM trend observed over 2000–2019 (*medium confidence*). Climate models reproduce the summertime SAM trend well, with CMIP6 models outperforming CMIP5 models (*medium confidence*). By contrast, the cause of the Northern Annular Mode (NAM) trend towards its positive phase since the 1960s and associated northward shifts of Northern Hemispheric extratropical jet and storm track in boreal winter is not well understood. Models reproduce observed spatial features and variance of the SAM and NAM very well (*high confidence*). {3.3.3, 3.7.1, 3.7.2}

Human influence has not affected the principal tropical modes of interannual climate variability or their associated regional teleconnections beyond the range of internal variability (*high confidence*). Further assessment since the AR5 confirms that climate and Earth system models are able to reproduce most aspects of the spatial structure and variance of the El Niño–Southern Oscillation and Indian Ocean Basin and Dipole modes (*medium confidence*). However, despite a slight improvement in CMIP6, some underlying processes are still poorly represented. In the Tropical Atlantic basin, which contains the Atlantic Zonal and Meridional modes, major biases in modelled mean state and variability remain. {3.7.3 to 3.7.5}

There is *medium confidence* that anthropogenic and volcanic aerosols contributed to observed changes in the Atlantic Multi-decadal Variability (AMV) index and associated regional teleconnections since the 1960s, but there is *low confidence* in the magnitude of this influence There is *high confidence* that internal variability is the main driver of Pacific Decadal Variability (PDV) observed since pre-industrial times, despite some modelling evidence for potential human influence. Uncertainties remain in quantification of the human influence on AMV and PDV due to brevity of the observational records, limited model

ACCEPTED VERSION SUBJECT TO FINAL EDITING

performance in reproducing related sea surface temperature anomalies despite improvements from CMIP5 to CMIP6 (*medium confidence*), and limited process understanding of their key drivers. {3.7.6, 3.7.7}

ACCEPTED VERSION
SUBJECT TO FINAL EDITING

3.1 Scope and Overview

This chapter assesses the extent to which the climate system has been affected by human influence and to what extent climate models are able to simulate observed mean climate, changes and variability. This assessment is the basis for understanding what impacts of anthropogenic climate change may already be occurring and informs our confidence in climate projections. Moreover, an understanding of the amount of human-induced global warming to date is key to assessing our status with respect to the Paris Agreement goals of holding the increase in global average temperature to well below 2°C above pre-industrial levels and pursuing efforts to limit the temperature increase to 1.5°C (COP21, UNFCCC (2015)).

The evidence of human influence on the climate system has strengthened progressively over the course of the previous five IPCC assessments, from the Second Assessment Report that concluded 'the balance of evidence suggests a discernible human influence on climate' through to the Fifth Assessment Report (AR5) which concluded that 'it is *extremely likely* that human influence caused more than half of the observed increase in global mean surface temperature (GMST) from 1951 to 2010' (see also Sections 1.3.4 and 3.3.1.1). AR5 concluded that climate models had been developed and improved since the Fourth Assessment Report (AR4) and were able to reproduce many features of observed climate. Nonetheless, several systematic biases were identified (Flato et al., 2013). This chapter additionally builds on the assessment of attribution of global temperatures contained in the IPCC Special Report on Global Warming of 1.5°C (SR1.5; IPCC, 2018), assessments of attribution of changes in the ocean and cryosphere in the IPCC Special Report on the Ocean and Cryosphere in a Changing Climate (SROCC; IPCC, 2019), and assessments of attribution in changes in the terrestrial carbon cycle in the IPCC Special Report on Climate Change and Land (IPCC, 2019a).

This chapter assesses the evidence for human influence on observed large-scale indicators of climate change that are described in Cross-Chapter Box 2.2 and assessed in Chapter 2. It takes advantage of the longer period of record now available in many observational datasets. The assessment of the human-induced contribution to observed climate change requires an estimate of the expected response to human influence, as well as an estimate of the expected climate evolution due to natural forcings and an estimate of variability internal to the climate system (internal climate variability). For this we need high quality models, primarily climate and Earth system models. Since the AR5, a new set of coordinated model results from the World Climate Research Programme (WCRP) Coupled Model Intercomparison Project Phase 6 (CMIP6; Eyring et al.,2016a) has become available. Together with updated observations of large-scale indicators of climate change (Chapter 2), CMIP simulations are a key resource for assessing human influences on the climate system. Pre-industrial control and historical simulations are of most relevance for model evaluation and assessment of internal variability, and these simulations are evaluated to assess fitness-for-purpose for attribution, which is the focus of this chapter (see also Section 1.5.4). This chapter provides the primary evaluation of large-scale indicators of climate change in this report, and is complemented by other fitness-for-purpose evaluations in subsequent chapters. CMIP6 also includes an extensive set of idealized and single forcing experiments for attribution (Eyring et al., 2016a; Gillett et al., 2016a). In addition to the assessment of model performance and human influence on the climate system during the instrumental era up to the present-day, this chapter also includes evidence from paleo-observations and simulations over past millennia (Kageyama et al., 2018a).

Whereas in previous IPCC Assessment Reports the comparison of simulated and observed climate change was done separately in a model evaluation chapter and a chapter on detection and attribution, in AR6 these comparisons are integrated together. This has the advantage of allowing a single discussion of the full set of explanations for any inconsistency in simulated and observed climate change, including missing forcings, errors in the simulated response to forcings, and observational errors, as well as an assessment of the application of detection and attribution techniques to model evaluation. Where simulated and observed changes are consistent, this can be interpreted both as supporting attribution statements, and as giving confidence in simulated future change in the variable concerned (see also Box 4.1). However, if a model's simulation of historical climate change has been tuned to agree with observations, or if the models used in an attribution study have been selected or weighted on the basis of the realism of their simulated climate response, this information would need to be considered in the assessment and any attribution results

ACCEPTED VERSION SUBJECT TO FINAL EDITING

correspondingly tempered. An integrated discussion of evaluation and attribution supports such a robust and transparent assessment.

This chapter starts with a brief description of methods for detection and attribution of observed changes in Section 3.2, which builds on the more general introduction to attribution approaches in Cross-Working Group Box: Attribution (Chapter 1). In this chapter we assess the detection of anthropogenic influence on climate on large spatial scales and long temporal scales, a concept related to, but distinct from, that of emergence of anthropogenically-induced climate change from the range of internal variability on local scales and shorter timescales (Section 1.4.2.2). The following sections address the climate system component-by-component, in each case assessing human influence and evaluating climate models' simulations of the relevant aspects of climate and climate change. This chapter assesses the evaluation and attribution of continental and ocean basin-scale indicators of climate change in the atmosphere and at the Earth's surface (Section 3.3), cryosphere (Section 3.4), ocean (Section 3.5), and biosphere (Section 3.6), and the evaluation and attribution of modes of variability (Section 3.7), the period of slower warming in the early 21st century (Cross-Chapter Box 3.1) and large-scale changes in extremes (Cross-Chapter Box 3.2). Model evaluation and attribution on sub-continental scales are not covered here, since these are assessed in the Atlas and in Chapter 10, and extreme event attribution is not covered since it is assessed in Chapter 11. Section 3.8 assesses multivariate attribution and integrative measures of model performance based on multiple variables, as well as process representation in different classes of models. The chapter structure is summarised in Figure 3.1.

[START FIGURE 3.1 HERE]

Figure 3.1: Visual Abstract for Chapter 3: Human influence on the climate system.

[END FIGURE 3.1 HERE]

3.2 Methods

New methods for model evaluation that are used in this chapter are described in Section 1.5.4. These include new techniques for process-based evaluation of climate and Earth system models against observations that have rapidly advanced since the publication of AR5 (Eyring et al., 2019) as well as newly developed CMIP evaluation tools that allow a more rapid and comprehensive evaluation of the models with observations (Eyring et al., 2016b, 2016a).

In this chapter, we use the Earth System Model Evaluation Tool (ESMValTool, Eyring et al. (2020); Lauer et al. (2020); Righi et al. (2020)) and the NCAR Climate Variability Diagnostic Package (CVDP, Phillips et al., 2014) that is included in the ESMValTool to produce most of the figures. This ensures traceability of the results and provides an additional level of quality control. The ESMValTool code to produce the figures in this chapter is released as open source software at the time of the publication of AR6 (see details in the Chapter Data Table, Table SM.3.1). Figures in this chapter are produced either using one ensemble member from each model, or using all available ensemble members and weighting each simulation by $1/(NM_i)$, where N is the number of models and M_i is the ensemble size of the i^{th} model, prior to calculating means and percentiles. Both approaches ensure that each model used is given equal weight in the figures, and details on which approach is used are provided in the figure captions.

An introduction to recent developments in detection and attribution methods in the context of this report is provided in Cross-Working Group Box: Attribution (in Chapter 1). Here we discuss new methods and improvements applicable to the attribution of changes in large-scale indicators of climate change which are used in this chapter.

ACCEPTED VERSION SUBJECT TO FINAL EDITING

3.2.1 Methods Based on Regression

Regression-based methods, also known as fingerprinting methods, have been widely used for detection of climate change and attribution of the change to different external drivers. Initially, these methods were applied to detect changes in global surface temperature, and were then extended to other climate variables at different time and spatial scales (e.g., Hegerl et al., 1996; Hasselmann, 1997; Allen and Tett, 1999; Gillett et al., 2003b; Zhang et al., 2007; Min et al., 2008a, 2011). These approaches are based on multivariate linear regression and assume that the observed change consists of a linear combination of externally forced signals plus internal variability, which generally holds for large-scale variables (Hegerl and Zwiers, 2011). The regressors are the expected space-time response patterns to different climate forcings (fingerprints), and the residuals represent internal variability. Fingerprints are usually estimated from climate model simulations following spatial and temporal averaging. A regression coefficient which is significantly different from zero implies that a detectable change is identified in the observations. When the confidence interval of the regression coefficient includes unity and is inconsistent with zero, the magnitude of the model simulated fingerprints is assessed to be consistent with the observations, implying that the observed changes can be attributed in part to a particular forcing. Variants of linear regression have been used to address uncertainty in the fingerprints due to internal variability (Allen and Stott, 2003) as well as the structural model uncertainty (Huntingford et al., 2006).

In order to improve the signal-to-noise ratio, observations and model-simulated responses are usually normalized by an estimate of internal variability derived from climate model simulations. This procedure requires an estimate of the inverse covariance matrix of the internal variability, and some approaches have been proposed for more reliable estimation of this (Ribes et al., 2009). A signal can be spuriously detected due to too small noise, and hence simulated internal variability needs to be evaluated with care. Model-simulated variability is typically checked through comparing modelled variance from unforced simulations with the observed residual variance using a standard residual consistency test (Allen and Tett, 1999b), or an improved one (Ribes and Terray, 2013). Imbers et al. (2014) tested the sensitivity of detection and attribution results to the different representations of internal variability associated with short-memory and long-memory processes. Their results supported the robustness of previous detection and attribution statements for the global mean temperature change but they also recommended the use of a wider variety of robustness tests.

Some recent studies focused on the improved estimation of the scaling factor (regression coefficient) and its confidence interval. Hannart et al. (2014) describe an inference procedure for scaling factors which avoids making the assumption that model error and internal variability have the same covariance structure. An integrated approach to optimal fingerprinting was further suggested in which all uncertainty sources (i.e., observational error, model error, and internal variability) are treated in one statistical model without a preliminary dimension reduction step (Hannart, 2016). Katzfuss et al. (2017) introduced a similar integrated approach based on a Bayesian model averaging. On the other hand, DelSole et al. (2019) suggested a bootstrap method to better estimate the confidence intervals of scaling factors even in a weak-signal regime. It is notable that some studies do not optimise fingerprints, as uncertainty in the covariance introduces a further layer of complexity, but results in only a limited improvement in detection (Polson and Hegerl, 2017).

Another fingerprinting approach uses pattern similarity between observations and fingerprints, in which the leading empirical orthogonal function obtained from the time-evolving multi-model forced simulation is usually defined as a fingerprint (e.g., Santer et al., 2013; Marvel et al., 2019; Bonfils et al., 2020). Observations and model simulations are then projected onto the fingerprint to measure the degree of spatial pattern similarity with the expected physical response to a given forcing. This projection provides the signal time series, which is in turn tested against internal variability, as estimated from long control simulations. As a way to extend this pattern-based approach to a high-dimensional detection variable at daily timescales, Sippel et al. (2019, 2020) proposed using the relationship pattern with a global climate change metric as a fingerprint. To solve the high-dimensional regression problem which makes regression coefficients not well constrained, they incorporated a statistical learning technique based on a regularized linear regression, which optimizes a global warming signal by giving lower weight to regions with large internal variability.

ACCEPTED VERSION SUBJECT TO FINAL EDITING

3.2.2 Other Probabilistic Approaches

Considering the difficulty in accounting for climate modelling uncertainties in the regression-based approaches, Ribes et al. (2017) introduced a new statistical inference framework based on an additivity assumption and likelihood maximization, which estimates climate model uncertainty based on an ensemble of opportunity and tests whether observations are inconsistent with internal variability and consistent with the expected response from climate models. The method was further developed by Ribes et al. (2021), who applied it to narrow the uncertainty range in the estimated human-induced warming. Hannart and Naveau (2018), on the other hand, extended the application of standard causal theory (Pearl, 2009) to the context of detection and attribution by converting a time series into an event, and calculating the probability of causation, an approach which maximizes the causal evidence associated with the forcing. On the other hand, Schurer et al. (2018) employed a Bayesian framework to explicitly consider climate modelling uncertainty in the optimal regression method. Application of these approaches to attribution of large-scale temperature changes supports the dominant anthropogenic contribution to the observed global warming.

Climate change signals can vary with time and discriminant analysis has been used to obtain more accurate estimates of time-varying signals, and has been applied to different variables such as seasonal temperatures (Jia and DelSole, 2012) and the South Asian monsoon (Srivastava and DelSole, 2014). The same approach was applied to separate aerosol forcing responses from other forcings (Yan et al., 2016b) and results using climate model output indicated that detectability of the aerosol response is maximised by using a combination of temperature and precipitation data. Paeth et al. (2017) introduced a detection and attribution method applicable for multiple variables based on a discriminant analysis and a Bayesian classification method. Finally, a systematic approach has been proposed to translating quantitative analysis into a description of confidence in the detection and attribution of a climate response to anthropogenic drivers (Stone and Hansen, 2016).

Overall, these new fingerprinting and other probabilistic methods for detection and attribution as well as efforts to better incorporate the associated uncertainties have addressed a number of shortcomings in previously applied detection and attribution techniques. They further strengthen the confidence in attribution of observed large-scale changes to a combination of external forcings as assessed in the following sections.

3.3 Human Influence on the Atmosphere and Surface

3.3.1 Temperature

3.3.1.1 Surface Temperature

Surface temperature change is the aspect of climate in which the climate research community has had most confidence over past IPCC Assessment Reports. This confidence comes from the availability of longer observational records compared to other indicators, a large response to anthropogenic forcing compared to variability in the global mean, and a strong theoretical understanding of the key thermodynamics driving its changes (Collins et al., 2010; Shepherd, 2014). AR5 assessed that it was *extremely likely* that human activities had caused more than half of the observed increase in global mean surface temperature from 1951 to 2010, and *virtually certain* that internal variability alone could not account for the observed global warming since 1951 (Bindoff et al., 2013). The AR5 also assessed with *very high confidence* that climate models reproduce the general features of the global-scale annual mean surface temperature increase over 1850-2011 and with *high confidence* that models reproduce global and Northern Hemisphere (NH) temperature variability on a wide range of time scales (Flato et al., 2013). This section assesses the performance of the new generation CMIP6 models (see Table AII.5) in simulating the patterns, trends, and variability of surface temperature, and the evidence from detection and attribution studies of human influence on large-scale changes in surface temperature.

Model evaluation

ACCEPTED VERSION SUBJECT TO FINAL EDITING

To be fit for detecting and attributing human influence on globally-averaged surface temperatures, climate models need to represent, based on physical principles, both the response of surface temperature to external forcings and the internal variability in surface temperature over various time scales. This section assesses the performance of those aspects in the latest generation CMIP6 climate models. See Section 3.8 for evaluation at continental scales, Chapter 10 for model evaluation in the context of regional climate information, and the Atlas for region-by-region assessments of model performance.

Reconstructions of past temperature from paleoclimate proxies (Cross-Chapter Box 2.1, Section 2.3.1.1) have been used to evaluate modelled past climate temperature change patterns. The AR5 found that CMIP5 (Taylor et al., 2012) models were able to reproduce the large-scale patterns of temperature during the Last Glacial Maximum (LGM) (Flato et al., 2013) and simulated a polar amplification broadly consistent with reconstructions for warm (Pliocene and Eocene) and cold (LGM) periods (Masson-Delmotte et al., 2013a). Since AR5, a better understanding of temperature proxies and their uncertainties and in some cases the forcing applied to model simulations has led to better agreement between models and reconstructions over a wide range of past climates. For the Pliocene and Eocene warm periods, understanding of uncertainties in temperature proxies (Hollis et al., 2019; McClymont et al., 2020) and the boundary conditions used in climate simulations (Haywood et al., 2016; Lunt et al., 2017) has improved, and some models now agree better with temperature proxies for these time periods compared to models assessed in AR5 (Zhu et al., 2019; Haywood et al., 2020; Lunt et al., 2021) (Sections 7.4.4.1.2; 7.4.4.2.2; Cross-Chapter Box 2.4). For the Last Interglacial (LIG), improved temporal resolution of temperature proxies (Capron et al., 2017) and better appreciation of the importance of freshwater forcing (Stone et al., 2016) have clarified the reasons behind apparent model-data inconsistencies. Regional LIG temperature responses simulated by CMIP6 are within the uncertainty ranges of reconstructed temperature responses, except in regions where unresolved changes in regional ocean circulation, meltwater, or vegetation changes may cause model mismatches (Otto-Bliesner et al., 2021). For the LGM, the CMIP5 and CMIP6 ensembles compare similarly to new sea surface temperature (SST) and surface air temperature (SAT) proxy reconstructions (Cleator et al., 2020; Tierney et al., 2020b) (Figure 3.2a). The very cold CMIP6 LGM simulation by CESM2.1 is an exception related to the high Equilibrium Climate Sensitivity (ECS) of that model (Section 7.5.6) (Kageyama et al., 2021a; Zhu et al., 2021). Figure 3.2a illustrates the wide range of simulated global LGM temperature responses in both ensembles. CMIP6 models tend to underestimate the cooling over land, but agree better with oceanic reconstructions. For the mid-Holocene, the regional biases found in CMIP5 simulations are similar to those in pre-industrial and historical simulations (Harrison et al., 2015; Ackerley et al., 2017), suggesting common causes. CMIP5 models underestimate Arctic warming in the mid-Holocene (Yoshimori and Suzuki, 2019). CMIP6 models simulate a mid-latitude, subtropical, and tropical cooling compared to pre-industrial, whereas temperature proxies indicate a warming (Brierley et al., 2020; Kaufman et al., 2020; see also Section 2.3.1.1.2), although accounting for seasonal effects in the proxies may reduce the discrepancy (Bova et al., 2021). Over the past millennium, reconstructed and simulated temperature anomalies, internal variability, and forced response agree well over NH continents, but those statistics disagree strongly in the Southern Hemisphere (SH), where models seem to overestimate the response (PAGES 2k-PMIP3, 2015). That disagreement is partly explained by the lower quality of the reconstructions in the SH, but model and/or forcing errors may also contribute (Neukom et al., 2018). Figure 3.2b shows that land/sea warming contrast behaves coherently in model simulations across multiple periods, with a slight non-linearity in land warming due to a smaller contribution of snow cover to temperature response in warmer climates. A metric-based assessment of paleoclimate model simulations is carried out in Section 3.8.2.

[START FIGURE 3.2 HERE]

Figure 3.2: Changes in surface temperature for different paleoclimates. (a) Comparison of reconstructed and modelled surface temperature anomalies for the Last Glacial Maximum over land and ocean in the Tropics (30°N to 30°S). Land-based reconstructions are from Cleator et al., (2020). Ocean-based reconstructions are from Tierney et al. (2020). Model points are calculated as the difference between Last Glacial Maximum and pre-industrial control simulations of the PMIP3 and PMIP4 ensembles, sampled at the reconstruction data points. (b) Land-sea contrast in global mean surface temperature change for different paleoclimates. Crosses show individual model simulations from the CMIP5 and CMIP6 ensembles. Filled symbols show ensemble means and assessed values. Acronyms are LGM Last Glacial

ACCEPTED VERSION SUBJECT TO FINAL EDITING

Maximum, LIG Last Inter Glacial, MPWP mid-Pliocene Warm Period, EECO Early Eocene Climatic Optimum. (c) Upper panel shows time series of volcanic radiative forcing, in W m^{-2}, as used in the CMIP5 (Gao et al., 2008; Crowley and Unterman, 2013; see also Schmidt et al., 2011) and CMIP6 (850 BCE to 1900 CE from Toohey and Sigl (2017), 1850-2015 from Luo (2018)). The forcing has been calculated from the stratospheric aerosol optical depth at 550 nm shown in Figure 2.2. Lower panel shows time series of global mean surface temperature anomalies, in K, with respect to 1850-1900 for the CMIP5 and CMIP6 past1000 simulations and their historical continuation simulations. Simulations are coloured according to the volcanic radiative forcing dataset they used. The temperature median reconstruction by PAGES 2k Consortium (2019) is shown in black, the 5-95% confidence interval by grey lines and the grey envelopes show the 1, 5, 15, 25, 35, 45, 55, 65, 75, 85, 95, and 99 percentiles. All data in both panels are band-passed, where frequencies longer than 20 years have been retained. Further details on data sources and processing are available in the chapter data table (Table 3.SM.1).

[END FIGURE 3.2 HERE]

For the historical period, AR5 assessed with *very high confidence* that CMIP5 models reproduced observed large-scale mean surface temperature patterns, although errors of several degrees appear in elevated regions, like the Himalayas and Antarctica, near the edge of the sea ice in the North Atlantic, and in upwelling regions. This assessment is updated here for the CMIP6 simulations. Figure 3.3 shows the annual-mean surface air temperature at 2 m for the CMIP5 and CMIP6 multi-model means, both compared to the ERA5 reanalysis (see Section 1.5.2) for the period 1995-2014. The distribution of biases is similar in CMIP5 and CMIP6 models, as already noted by several studies (Crueger et al., 2018; Găinușă-Bogdan et al., 2018; Kuhlbrodt et al., 2018; Lauer et al., 2018). Arctic temperature biases seem more widespread in both ensembles than assessed at the time of the AR5. The fundamental causes of temperature biases remain elusive, with errors in clouds (Lauer et al., 2018), oceanic circulation (Kuhlbrodt et al., 2018), winds (Lauer et al., 2018), and surface energy budget (Hourdin et al., 2015; Séférian et al., 2016; Găinușă-Bogdan et al., 2018) being frequently cited candidates. Increasing horizontal resolution shows promise of decreasing long-standing biases in surface temperature over large regions (Bock et al., 2020). Panels e and f of Figure 3.3 show that biases in the mean High-Resolution Model Intercomparison Project (HighResMIP, Haarsma et al., 2016) models (see also Table AII.6) are smaller than those in the mean of the corresponding lower-resolution versions of the same models simulating the same period (see also Section 3.8.2.2). However, the bias reduction is modest (Palmer and Stevens, 2019). In addition, the biases of the limited number of models participating in HighResMIP are not entirely representative of overall CMIP6 biases, especially in the Southern Ocean, as indicated by comparing panels b and f of Figure 3.3.

[START FIGURE 3.3 HERE]

Figure 3.3: Annual-mean surface (2 m) air temperature (°C) for the period 1995–2014. (a) Multi-model (ensemble) mean constructed with one realization of the CMIP6 historical experiment from each model. (b) Multi-model mean bias, defined as the difference between the CMIP6 multi-model mean and the climatology of the Fifth generation of ECMWF atmospheric reanalyses of the global climate (ERA5). (c) Multi-model mean of the root mean square error calculated over all months separately and averaged with respect to the climatology from ERA5. (d) Multi-model-mean bias as the difference between the CMIP6 multi-model mean and the climatology from ERA5. Also shown is the multi-model mean bias as the difference between the multi-model mean of (e) high resolution and (f) low resolution simulations of four HighResMIP models and the climatology from ERA5. Uncertainty is represented using the advanced approach: No overlay indicates regions with robust signal, where ≥66% of models show change greater than variability threshold and ≥80% of all models agree on sign of change; diagonal lines indicate regions with no change or no robust signal, where <66% of models show a change greater than the variability threshold; crossed lines indicate regions with conflicting signal, where ≥66% of models show change greater than variability threshold and <80% of all models agree on sign of change. For more information on the advanced approach, please refer to the Cross-Chapter Box Atlas.1. Dots in panel e) mark areas where the bias in high resolution versions of the HighResMIP models is lower in at least 3 out of 4 models than in the corresponding low resolution versions. Further details on data sources and processing are available in the chapter data table (Table 3.SM.1).

ACCEPTED VERSION SUBJECT TO FINAL EDITING

[END FIGURE 3.3 HERE]

AR5 assessed with *very high confidence* that models reproduce the general history of the increase in global-scale annual mean surface temperature since the year 1850, although AR5 also reported that an observed reduction in the rate of warming over the period 1998-2012 was not reproduced by the models (Flato et al., 2013) (see Cross-Chapter Box 3.1). Figure 3.2c and Figure 3.4 show time series of anomalies in annually and globally averaged surface temperature simulated by CMIP5 and CMIP6 models for the past millennium and the period 1850 to 2020, respectively, with the baseline set to 1850-1900 (see Section 1.4.1). As also indicated by Figure 3.4, the spread in simulated absolute temperatures is large (Palmer and Stevens, 2019). But the discussion is based on temperature anomaly time series instead of absolute temperatures because our focus is on evaluation of the simulation of climate change in these models, and also because anomalies are more uniformly distributed and are more easily deseasonalised to isolate long-term trends (see Section 1.4.1). CMIP6 models broadly reproduce surface temperature variations over the past millennium, including the cooling that follows periods of intense volcanism (*medium confidence*) (Figure 3.2c). Simulated GMST anomalies are well within the uncertainty range of temperature reconstructions (*medium confidence*) since about the year 1300, except for some short periods immediately following large volcanic eruptions, for which simulations driven by different forcing datasets disagree (Figure 3.2c). Before the year 1300, larger disagreements between models and temperature reconstructions can be expected because forcing and temperature reconstructions are increasingly uncertain further back in time, but specific causes have not been identified conclusively (Ljungqvist et al., 2019; PAGES 2k Consortium, 2019) (*medium confidence*). For the historical period, results for CMIP6 shown in Figure 3.4 suggest that the qualitative history of surface temperature increase is well reproduced, including the increase in warming rates beginning in the 1960s and the temporary cooling that follows large volcanic eruptions.

Although virtually all CMIP6 modelling groups report improvements in their model's ability to simulate current climate compared to the CMIP5 version (Gettelman et al., 2019; Golaz et al., 2019; Mauritsen et al., 2019; Swart et al., 2019; Voldoire et al., 2019b; Wu et al., 2019c; Bock et al., 2020; Boucher et al., 2020a; Dunne et al., 2020), it does not necessarily follow that the simulation of temperature trends is also improved (Bock et al., 2020; Fasullo et al., 2020). The CMIP6 multi-model ensemble encompasses observed warming and the multi-model mean tracks those observations within 0.2°C over most of the historical period. Figure 3.4 confirms the findings of Papalexiou et al. (2020), who highlighted based on 29 CMIP6 models that most models replicate the period of slow warming between 1942 and 1975 and the late twentieth century warming (1975–2014). The CMIP6 multi-model mean is cooler over the period 1980-2000 than both observations and CMIP5 (Bock et al., 2020; Flynn and Mauritsen, 2020; Gillett et al., 2021; Figure 3.4). Biases of several tenths of a degree in some CMIP6 models over that period may be due to an overestimate in aerosol radiative forcing (Andrews et al., 2020; Dittus et al., 2020; Flynn and Mauritsen, 2020) (see also Section 6.3.5, Figure 6.8, and Section 7.3.3). Papalexiou et al. (2020), Stolpe et al. (2020) and Tokarska et al. (2020) all report that CMIP6 models on average overestimate warming from the 1970s or 1980s to the 2010s, although quantitative conclusions depend on which observational dataset is compared against (see also Table 2.4). However, Figure 3.4, which includes a larger number of models than available to those studies, indicates that the average CMIP6 model tracks observed warming better than CMIP5 models after the year 2000. The CMIP6 multi-model mean GSAT warming between 1850-1900 and 2010-2019 and associated 5-95% range is 1.09°C (0.66 to 1.64°C). Cross-Chapter Box 2.3 assessed GSAT warming over the same period at 1.06°C (0.88 to 1.21°C). So some CMIP6 models simulate a warming that is smaller than the assessed observed range, and other CMIP6 models simulate a warming that is larger. That overestimated warming may be an early symptom of overestimated equilibrium climate sensitivities (ECS) in some CMIP6 models (Meehl et al., 2020; Schlund et al., 2020) (see also Section 7.5.6), and has implications for projections of GSAT changes (see Chapter 4) (Liang et al., 2020; Nijsse et al., 2020; Tokarska et al., 2020; Ribes et al., 2021). In some models, a large ECS and a strong aerosol forcing lead to too large a mid-20th century cooling followed by overestimated warming rates in the late 20th century when aerosol emissions decrease (Golaz et al., 2019; Flynn and Mauritsen, 2020). Temperature biases are driven by both model physics and prescribed forcing, which is a challenge for model development.

Chylek et al. (2020) argue that CMIP5 models overestimate the temperature response to volcanic eruptions.

ACCEPTED VERSION SUBJECT TO FINAL EDITING

Lehner et al. (2016), Rypdal (2018) and Stolpe et al. (2020) point instead to missed compensating effects on surface temperature change associated with the El-Nino Southern Oscillation (ENSO) or the Atlantic Multidecadal Oscillation (AMO). An alternative view sees those ENSO and AMO responses as expressions of changes in climate feedbacks driven by the geographical pattern of SST changes (Andrews et al., 2018). At least one model is able to reproduce such pattern effects (Gregory and Andrews, 2016). Errors in the volcanic forcing prescribed in simulations, including for CMIP6 (Rieger et al., 2020), also introduce differences with the observed temperature response, independently of the quality of the model physics. In addition, comparisons of the modelled temperature response to large eruptions over the past millennium to temperature reconstructions based on tree rings show a much better agreement (Lücke et al., 2019; Zhu et al., 2020a) than comparisons to the annual, multi-temperature proxy reconstructions shown in Figure 3.2c. These considerations, and Figures 3.2c and 3.4, suggest that CMIP6 models do not systematically overestimate the cooling that follows large volcanic eruptions (see also Cross-Chapter Box 4.1).

When interpreting model simulations of historical temperature change, it is important to keep in mind that some models are tuned towards representing the observed trend in global mean surface temperature over the historical period (Hourdin et al., 2017). In Figure 3.4 the CMIP6 models that are documented to be tuned to reproduce observed warming, typically by tuning aerosol forcing or factors that influence the model's ECS, are marked with an asterisk. Such tuning of a model can strongly impact its temperature projections (Mauritsen and Roeckner, 2020). However, Bock et al. (2020) reported that there is no statistically significant difference in multi-model mean GSAT between the models that had been tuned based on observed warming compared to those which had not. Moreover, only two of thirteen models used for the DAMIP simulations on which CMIP6 attribution studies are based were tuned towards historical warming (Bock et al., 2020; Gillett et al., 2021). Further, tuning is done on globally averaged quantities, so does not substantially change the spatio-temporal pattern of response on which many regression-based attribution studies are based (Bock et al., 2020). Therefore, we assess with *high confidence* that the tuning of a small number of CMIP6 models to observed warming has not substantially influenced attribution results assessed in this chapter.

[START FIGURE 3.4 HERE]

Figure 3.4: Observed and simulated time series of the anomalies in annual and global mean near-surface air temperature (GSAT). All anomalies are differences from the 1850–1900 time-mean of each individual time series. The reference period 1850–1900 is indicated by grey shading. (a) Single simulations from CMIP6 models (thin lines) and the multi-model mean (thick red line). Observational data (thick black lines) are HadCRUT5, and are blended surface temperature (2 m air temperature over land and sea surface temperature over the ocean). All models have been subsampled using the HadCRUT5 observational data mask. Vertical lines indicate large historical volcanic eruptions. CMIP6 models which are marked with an asterisk are either tuned to reproduce observed warming directly, or indirectly by tuning equilibrium climate sensitivity. Inset: GSAT for each model over the reference period, not masked to any observations. (b). Multi-model means of CMIP5 (blue line) and CMIP6 (red line) ensembles and associated 5 to 95 percentile ranges (shaded regions). Observational data are HadCRUT5, Berkeley Earth, NOAAGlobalTemp-Interim and Kadow et al. (2020). Masking was done as in (a). CMIP6 historical simulations are extended with SSP2-4.5 simulations for the period 2015-2020 and CMIP5 simulations are extended with RCP4.5 simulations for the period 2006-2020. All available ensemble members were used (see Section 3.2). The multi-model means and percentiles were calculated solely from simulations available for the whole time span (1850-2020). Figure is updated from Bock et al. (2020), their Figures 1 and 2. / CC BY4.0 https://creativecommons.org/licenses/by/4.0/. Further details on data sources and processing are available in the chapter data table (Table 3.SM.1).

[END FIGURE 3.4 HERE]

The reliance of detection and attribution studies on climate models (see Section 3.2) requires that those models simulate realistic statistics of internal variability on multi-decadal timescales. An incorrect estimate of variability in models would affect confidence in the conclusions from detection and attribution. AR5 found that CMIP5 models simulate realistic variability in global-mean surface temperature on decadal time

ACCEPTED VERSION SUBJECT TO FINAL EDITING

scales, with variability on multi-decadal time scales being more difficult to evaluate because of the short observational record (Flato et al., 2013). Since AR5, new work has characterized the contributions of variability in different ocean areas to SST variability, with tropical modes of variability like ENSO dominant on time scales of 5 to 10 years, while longer time scales see the variance maxima move poleward to the North Atlantic, North Pacific, and Southern oceans (Monselesan et al., 2015). There may, however, be sizeable, two-way interdependencies between ENSO and sea surface temperature variability in different basins (Kumar et al., 2014; Cai et al., 2019), and ENSO's influence on global surface temperature variability may not be confined only to decadal timescales (Triacca et al., 2014). Studies based on large ensembles of 20th and 21st century climate change simulations confirm that internal variability has a substantial influence on global warming trends over periods shorter than 30-40 years (Kay et al., 2015; Dai and Bloecker, 2019). Although the equatorial Pacific seems to be the main source of internal variability on decadal timescales, Brown et al. (2016) linked diversity in modelled oceanic convection, sea ice, and energy budget in high-latitude regions to overall diversity in modelled internal variability.

Interest in internal variability since publication of the AR5 stems in part from its importance in understanding the slower global surface temperature warming over the early 21st century (see Cross-Chapter Box 3.1). Evidence coming mostly from paleo studies is mixed on whether CMIP5 models underestimate decadal and multi-decadal variability in global mean temperature. Schurer et al. (2013) found good agreement between internal variability derived from paleo reconstructions, estimated as the fraction of variance that is not explained by forced responses, and modelled variability, although the subset of CMIP5 models they used may have been associated with larger variability than the full CMIP5 ensemble. PAGES 2k Consortium (2019) found that the largest 51-year trends in both reconstructions of global mean temperature and fully forced climate simulations over the period 850 to 1850 were almost identical. Zhu et al. (2019a) showed agreement in the modelled and reconstructed temporal spectrum of global surface temperatures on annual to multi-millennial timescales. However, they suggest that decadal-to-centennial variability is partly forced by slow orbital changes that predate the last millennium. This is consistent with Gebbie and Huybers (2019), who showed that the deep ocean has been out of equilibrium over that period. Laepple and Huybers (2014) found good agreement between modelled and proxy-derived decadal ocean temperature variability, but underestimates of variance by models by at least a factor of ten at centennial timescales because models underestimate the difference between the warm and cold periods of the last millennium. Parsons et al. (2020) found that some CMIP6 models exhibit much higher multidecadal variability in GSAT than CMIP5 models, with indications that variability in these models is also higher than that from proxy reconstructions. CMIP6 models may not share the underestimation by CMIP5 models of variability in decadal to multidecadal modes of variability, such as Pacific decadal variability (Section 3.7.6) (England et al., 2014; Thompson et al., 2014; Schurer et al., 2015) and Atlantic Multidecadal Variability (AMV, which may be partly forced, see Section 3.7.7) but this assessment is limited by the small number of available studies. For the SH, Hegerl et al. (2018) found an instance of internal variability in the early 20th century larger than that modelled, but indicated that could be an observational issue. Friedman et al. (2020) found biases in interhemispheric SST contrast in some models that may be consistent with underestimated cooling after early-20th century eruptions or underestimated Pacific decadal variability, but could also be due to an imperfect separation between internal variability and forced signal in the observations. Figure 3.2c, updated from PAGES 2k Consortium (2019), compares modelled temperatures to reconstructions over the last millennium. It indicates that models reproduce the observed variability well, at least for the timescales between 20 and 50 years that paleo reconstructions typically resolve and that the figure represents. In summary, decadal GMST variability simulated in CMIP6 models spans the range of residual decadal variability in large-scale reconstructions (*medium evidence, low agreement*).

In addition, new literature suggests that anthropogenic forcing itself may locally increase or decrease variability in surface temperatures (Screen et al., 2014; Qian and Zhang, 2015; Brown et al., 2017; Park et al., 2018; Santer et al., 2018; Weller et al., 2020). Those studies imply limitations in the use of pre-industrial control simulations to quantify the role of unforced variability over the historical period. Some recent attribution studies (Gillett et al., 2021; Ribes et al., 2021) have estimated variability from ensembles of forced simulations instead, which would be expected to resolve any such changes in variability.

Figure 3.5 shows the standard deviation of zonal-mean surface temperature in CMIP6 pre-industrial control

ACCEPTED VERSION SUBJECT TO FINAL EDITING

simulations and observed temperature datasets. Results are consistent with those based on CMIP5 models, which showed the largest model spread where variability is also large, in the tropics and mid- to high-latitudes (Flato et al., 2013). Modelled variability is within a factor two of observed variability over most of the globe. The apparent overestimation of high latitude variability in models compared to observations may be due to interpolation and infilling over data sparse high latitude regions in the observational products shown here (Jones, 2016).

[START FIGURE 3.5 HERE]

Figure 3.5: The standard deviation of annually averaged zonal-mean near-surface air temperature. This is shown for four detrended observed temperature datasets (HadCRUT5, Berkeley Earth, NOAAGlobalTemp-Interim and Kadow et al. (2020), for the years 1995-2014) and 59 CMIP6 pre-industrial control simulations (one ensemble member per model, 65 years) (after Jones et al., 2013). For line colours see the legend of Figure 3.4. Additionally, the multi-model mean (red) and standard deviation (grey shading) are shown. Observational and model datasets were detrended by removing the least-squares quadratic trend. Further details on data sources and processing are available in the chapter data table (Table 3.SM.1).

[END FIGURE 3.5 HERE]

The previous paragraph took an ensemble-mean view of model performance, but individual models disagree on unforced variability. Figure 3.6 illustrates the large differences in GSAT variability in unforced CMIP6 pre-industrial control simulations, following the method of Parsons et al. (2020). Surface temperatures in pre-industrial conditions are especially variable in the ten models highlighted in Figure 3.6a, and some models substantially exceed the variability seen in CMIP5 models (Parsons et al., 2020). Figure 3.6b shows that the distribution of warming trends simulated by CMIP6 models in historical simulations is clearly distinct from that simulated in unforced piControl simulations. Still, the unforced variability of the five most variable models approaches half that observed over the historical period under anthropogenically forced conditions (Figure 3.6c) (Parsons et al., 2020; Ribes et al., 2021). For the Centre National de la Recherche Météorologique (CNRM) models, which are among the most variable, the large, low-frequency variability is attributed to strong simulated Atlantic Multidecadal Variability (Séférian et al., 2019; Voldoire et al., 2019b), which is difficult to disprove because of the short observational record (Cassou et al., 2018; Section 3.7.7). But, importantly, patterns of temperature variability simulated by even the most variable models differ from the pattern of forced temperature change (Parsons et al., 2020). Taken together, this discussion and Figures 3.2, 3.5 and 3.6 indicate that the statistics of internal variability in models compare well in most cases to observational estimates and temperature proxy reconstructions, though some CMIP6 models appear to have higher multidecadal variability than CMIP5 models or proxy reconstructions. When used in attribution studies, models with overestimated variability would increase estimated uncertainties and make results statistically conservative.

[START FIGURE 3.6 HERE]

Figure 3.6: Simulated internal variability of global surface air temperature (GSAT) versus observed changes. (a) Time series of 5-year running mean GSAT anomalies in 45 CMIP6 pre-industrial control (unforced) simulations. The 10 most variable models in terms of 5-year running mean GSAT are coloured according to the legend on Figure 3.4. (b) Histograms of GSAT changes in CMIP6 historical simulations (extended by SSP2-4.5 simulations) from 1850-1900 to 2010-2019 are shown by pink shading in (c), and GSAT changes from the first 51 years average to the last 20 years average of 170-year overlapping segments of the pre-industrial control simulations shown in (a) are shown by blue shading. GMST changes in observational datasets for the same period are indicated by black vertical lines. (c) Observed GMST anomaly time series relative to the 1850-1900 average. Black lines represent the 5-year running means while grey lines show unfiltered annual time series. Further details on data sources and processing are available in the chapter data table (Table 3.SM.1).

ACCEPTED VERSION SUBJECT TO FINAL EDITING

[END FIGURE 3.6 HERE]

In summary, there is *high confidence* that CMIP6 models reproduce observed large-scale mean surface temperature patterns and internal variability as well as their CMIP5 predecessors, but with little evidence for reduced biases. CMIP6 models also reproduce historical GSAT changes similarly to their CMIP5 counterparts (*medium confidence*). However, in spite of model imperfections, there is *very high confidence* that biases in surface temperature trends and variability simulated by the CMIP5 and CMIP6 ensembles are small enough to support detection and attribution of human-induced warming.

Detection and attribution

Looking at periods preceding the instrumental record, AR5 assessed with *high confidence* that the 20th century annual mean surface temperature warming reversed a 5000-year cooling trend in NH mid-to-high latitudes caused by orbital forcing, and attributed the reversal to anthropogenic forcing with *high confidence* (see also Section 2.3.1.1). Since AR5, the combined response to solar, volcanic and greenhouse gas forcing was detected in all NH continents (PAGES 2k-PMIP3, 2015) over the period 864 to 1840. In contrast, the effect of those forcings was not detectable in the SH (Neukom et al., 2018). Global and NH temperature changes from reconstructions over this period have been attributed mostly to volcanic forcing (Schurer et al., 2014a; McGregor et al., 2015; Otto-Bliesner et al., 2016; PAGES 2k Consortium, 2019; Büntgen et al., 2020), with a smaller role for changes in greenhouse forcing, and solar forcing playing a minor role (Schurer et al., 2014b; PAGES 2k Consortium, 2019).

Focusing now on warming over the historical period, AR5 assessed that it was *extremely likely* that human influence was the dominant cause of the observed warming since the mid-20th century, and that it was *virtually certain* that warming over the same period cannot be explained by internal variability alone. Since AR5 many new attribution studies of changes in global surface temperature have focused on methodological advances (see also Section 3.2). Those advances include better accounting for observational and model uncertainties, and internal variability (Ribes and Terray, 2013; Hannart, 2016; Ribes et al., 2017; Schurer et al., 2018); formulating the attribution problem in a counterfactual framework (Hannart and Naveau, 2018); and reducing the dependence of the attribution on uncertainties in climate sensitivity and forcing (Otto et al., 2015; Haustein et al., 2017, 2019). Studies now account for the uncertainties in the statistics of internal variability, either explicitly (Hannart, 2016; Hannart and Naveau, 2018; Ribes et al., 2021) or implicitly (Ribes and Terray, 2013; Schurer et al., 2018; Gillett et al., 2021), thus addressing concerns about over-confident attribution conclusions. Accounting for observational uncertainty increases the range of warming attributable to greenhouse gases by only 10 to 30% (Jones and Kennedy, 2017; Schurer et al., 2018). While some attribution studies estimate attributable changes in globally-complete GSAT (Schurer et al., 2018; Gillett et al., 2021; Ribes et al., 2021), others attribute changes in observational GMST, but this makes little difference to attribution conclusions (Schurer et al., 2018). Moreover, based on a synthesis of observational and modelling evidence, Cross-Chapter Box 2.3 assesses that the current best estimate of the scaling factor between GMST and GSAT is one, and therefore attribution studies of GMST and GSAT are here treated together in deriving assessed warming ranges. Studies also increasingly validate their multi-model approaches using imperfect model tests (Schurer et al., 2018; Gillett et al., 2021; Ribes et al., 2021). Alternative techniques, based purely on statistical or econometric approaches, without the need for climate modelling, have also been applied (Estrada et al., 2013; Stern and Kaufmann, 2014; Dergiades et al., 2016) and match the results of physically-based methods. The larger range of attribution techniques and improvements to those techniques increase confidence in the results compared to AR5.

In contrast, studies published since the AR5 indicate that closely constraining the separate contributions of greenhouse gas changes and aerosol changes to observed temperature changes remains challenging. Attribution of warming to greenhouse gas forcing is made as early as the end of the 19th century (Schurer et al., 2014b; Owens et al., 2017; PAGES 2k Consortium, 2019). Hegerl et al. (2019) found that volcanism cooled global temperatures by about 0.1°C between 1870 and 1910, then a lack of volcanic activity warmed temperatures by about 0.1°C between 1910 and 1950, with aerosols cooling temperatures throughout the 20th century, especially between 1950 and 1980 when the estimated range of aerosol cooling was about 0.1 to 0.5°C. Jones et al. (2016a) attributed a warming of 0.87 to 1.22°C per century over the period 1906 to 2005

ACCEPTED VERSION SUBJECT TO FINAL EDITING

to greenhouse gases, partially offset by a cooling of −0.54 to −0.22°C per century attributed to aerosols. But they also found that detection of the greenhouse gas or the aerosol signal often fails, because of uncertainties in modelled patterns of change and internal variability. That point is illustrated by Figure 3.7, which shows two- and three-way fingerprinting regression coefficients for 13 CMIP6 models and the corresponding attributable warming ranges, derived using HadCRUT4 (Gillett et al., 2021). Regression coefficients with an uncertainty range that includes zero mean that detection has failed. Models with regression coefficients significantly less than 1 significantly overpredict the temperature response to the corresponding forcing. Conversely, models with regression coefficients significantly greater than 1 underpredict the response to these forcings. While estimates of warming attributable to anthropogenic influence derived using individual models are generally consistent, estimates of warming attributable to greenhouse gases and aerosols separately based on individual models are not all consistent, and detection of the aerosol influence fails more often than that of greenhouse gases. Hence, results of recent studies emphasize the need to use multi-model means to better constrain estimates of GSAT changes attributable to greenhouse gas and aerosol forcing (Schurer et al., 2018; Gillett et al., 2021; Ribes et al., 2021).

[START FIGURE 3.7 HERE]

Figure 3.7: Regression coefficients and corresponding attributable warming estimates for individual CMIP6 models. Upper panels show regression coefficients based on a two-way regression (left) and three-way regression (right), of observed 5-yr mean global mean masked and blended surface temperature (HadCRUT4) onto individual model response patterns, and a multi-model mean, labelled 'Multi'. Anthropogenic, natural, greenhouse gas, and other anthropogenic (aerosols, ozone, land-use change) regression coefficients are shown. Regression coefficients are the scaling factors by which the model responses must be multiplied to best match observations. Regression coefficients consistent with one indicate a consistent magnitude response in observations and models, and regression coefficients inconsistent with zero indicate a detectable response to the forcing concerned. Lower panels show corresponding observationally-constrained estimates of attributable warming in globally-complete GSAT for the period 2010-2019, relative to 1850-1900, and the horizontal black line shows an estimate of observed warming in GSAT for this period. Figure is adapted from Gillett et al. (2021), their Extended Data Figure 3. Further details on data sources and processing are available in the chapter data table (Table 3.SM.1).

[END FIGURE 3.7 HERE]

Figure 3.8 compares attributable trends in globally-complete GSAT for the period 2010-2019 compared to 1850-1900 from three detection and attribution studies, two of which use CMIP6 multi-model means (Gillett et al., 2021; Ribes et al., 2021), and an estimate based on assessed effective radiative forcing and transient and equilibrium climate sensitivity (see Section 7.3.5.3). The reference period 1850-1900 is used to assess attributable temperature changes because this is when the earliest gridded surface temperature records start, this is when the CMIP6 historical simulations start, this is the earliest base period used in attribution literature, and this is a reference period used in IPCC SR1.5 and earlier reports. It should however be noted that Cross-Chapter Box 1.2 assesses with *medium confidence* that there was an anthropogenic warming with a *likely* range of 0.0°C-0.2°C between 1750 and 1850-1900. Figure 3.8 also shows the GSAT changes directly simulated in response to these forcings in thirteen CMIP6 models. In spite of their different methodologies and input datasets, the three attribution approaches yield very similar results, with the anthropogenic attributable warming range encompassing observed warming, and the natural attributable warming being close to zero. The warming driven by greenhouse gas increases is offset in part by cooling due to other anthropogenic forcing agents, mostly aerosols, although uncertainties in these contributions are larger than the uncertainty in the net anthropogenic warming, as discussed above. Estimates based on physical understanding of forcing and ECS made by Chapter 7 are close to estimates from attribution studies, despite being the products of a different approach. This agreement enhances confidence in the magnitude and causes of attributable surface temperature warming.

ACCEPTED VERSION SUBJECT TO FINAL EDITING

[START FIGURE 3.8 HERE]

Figure 3.8: Assessed contributions to observed warming, and supporting lines of evidence. Shaded bands show assessed *likely* ranges of temperature change in GSAT, 2010-2019 relative to 1850-1900, attributable to net human influence, well-mixed greenhouse gases, other human forcings (aerosols, ozone, and land-use change), natural forcings, and internal variability, and the 5-95% range of observed warming. Bars show 5-95% ranges based on (left to right) Haustein et al. (2017), Gillett et al. (2021) and Ribes et al. (2021), and crosses show the associated best estimates. No 5-95% ranges were provided for the Haustein et al. (2017) greenhouse gas or other human forcings contributions. The Ribes et al. (2021) results were updated using a revised natural forcing time series, and the Haustein et al. (2017) results were updated using HadCRUT5. The Chapter 7 best estimates and ranges are derived using assessed forcing time series and a two-layer energy balance model as described in Section 7.3.5.3. Coloured symbols show the simulated responses to the forcings concerned in each of the models indicated. Further details on data sources and processing are available in the chapter data table (Table 3.SM.1).

[END FIGURE 3.8 HERE]

The AR5 found *high confidence* for a major role for anthropogenic forcing in driving warming over each of the inhabited continents, except for Africa where they found only *medium confidence* because of limited data availability (Bindoff et al., 2013). At the hemispheric scale, Friedman et al. (2020) and Bonfils et al. (2020) detected an anthropogenically forced response of inter-hemispheric contrast in surface temperature change, which has a complex time evolution but showing the NH cooling more than the SH until around 1975 but then warming after that. Bonfils et al. (2020) attribute the NH reversal to a combination of reduced aerosol forcing and greenhouse gas induced warming of NH land masses. Friedman et al. (2020) found that CMIP5 models simulate the correct sign of the inter-hemispheric contrast when forced with all forcings but underestimate its magnitude. Figure 3.9 shows global surface temperature change in CMIP6 all-forcing and natural-only simulations globally, averaged over continents, and separately over land and ocean surfaces. All-forcing simulations encompass observed temperature changes for all regions, while natural-only simulations fail to do so in recent decades except in Antarctica, based on the annual means shown. As stated above, warming results from a partial offset of greenhouse warming by aerosol cooling. That offset is stronger over land than ocean. Regionally, models show a large range of possible temperature responses to greenhouse gas and aerosol forcing, which complicates single-forcing attribution. A more detailed discussion of regional attribution can be found in Section 10.4. Over global land surfaces, Chan and Wu (2015) used CMIP5 simulations to attribute a warming trend of 0.3 (2.5%–97.5% confidence interval: 0.2–0.36) °C per decade to anthropogenic forcing, with natural forcing only contributing 0.05 (0.02–0.06) °C per decade. Accounting for unsampled sources of uncertainty and the availability of only a single study, their result suggests that it is *very likely* that human influence is the main driver of warming over land.

[START FIGURE 3.9 HERE]

Figure 3.9: Global, land, ocean and continental annual mean near-surface air temperatures anomalies in CMIP6 models and observations. Time series are shown for CMIP6 historical anthropogenic and natural (brown), natural-only (green), greenhouse gas only (grey) and aerosol only (blue) simulations (multi-model means shown as thick lines, and shaded ranges between the 5th and 95th percentiles) and for HadCRUT5 (black). All models have been subsampled using the HadCRUT5 observational data mask. Temperatures anomalies are shown relative to 1950-2010 for Antarctica and relative to 1850–1900 for other continents. CMIP6 historical simulations are expand by the SSP2-4.5 scenario simulations. All available ensemble members were used (see Section 3.2). Regions are defined by Iturbide et al. (2020). Further details on data sources and processing are available in the chapter data table (Table 3.SM.1).

[END FIGURE 3.9 HERE]

In summary, since the publication of the AR5, new literature has emerged which better accounts for methodological and climate model uncertainties in attribution studies (Ribes et al., 2017; Hannart and

ACCEPTED VERSION SUBJECT TO FINAL EDITING

Naveau, 2018) and concluded that anthropogenic warming is approximately equal to observed warming over the 1951-2010 period. The IPCC SR1.5 reached the same conclusion for 2017 relative to 1850-1900 based on anthropogenic warming and associated uncertainties calculated using the method of Haustein et al. (2017). Moreover, the improved understanding of the causes of the apparent slowdown in warming over the beginning of the 21st century and the difference in simulated and observed warming trends over this period (Cross-Chapter Box 3.1) further improve our confidence in the assessment of the dominant anthropogenic contribution to observed warming. In deriving our assessments, these considerations are balanced against new literature that raises questions about the ability of some models to simulate variability in surface temperatures over a range of time scales (Laepple and Huybers, 2014; Parsons et al., 2017; Friedman et al., 2020), and the finding that some CMIP6 models exhibit substantially higher multidecadal internal variability than that seen in CMIP5, which remains to be fully understood (Parsons et al., 2020; Ribes et al., 2021). Further, uncertainties in simulated aerosol-cloud interactions are still large (Section 7.3.3.2.2), resulting in very diverse spatial responses of different climate models to aerosol forcing and differences in the historical global mean temperature evolution and in diagnosed cooling attributable to aerosol (Figure 3.8). Moreover, like previous generations of coupled model simulations, historical and single forcing CMIP6 simulations follow a common experimental design (Eyring et al., 2016a; Gillett et al., 2016b) and are thus all driven by the same common set of forcings, even though these forcings are uncertain. Hence, forcing uncertainty is not directly accounted for in most of the attribution and model evaluation studies assessed here, although this limitation can to some extent be addressed by comparing with previous generation multi-model ensembles or individual model studies using different sets of forcings.

The IPCC SR1.5 best estimate and *likely* range of anthropogenic attributable GMST warming was 1.0±0.2°C in 2017 with respect to the period 1850-1900. Here, the best estimate is expressed in terms of GSAT and is calculated as the average of the three estimates shown in Figure 3.9, yielding a value of 1.07°C. Ranges for attributable GSAT warming are derived by finding the smallest ranges with a precision of 0.1°C which span all of the 5-95% ranges from the attribution studies shown in Figure 3.9. These ranges are then assessed as *likely* rather than *very likely* because the studies may underestimate the importance of the structural limitations of climate models, which probably do not represent all possible sources of internal variability; use too simple climate models, which may underestimate the role of internal variability; or underestimate model uncertainty, especially when using model ensembles of limited size and inter-dependent models, for example through common errors in forcings across models, as discussed above. This leads to a *likely* range for anthropogenic attributable warming in 2010-2019 relative to 1850-1900 of 0.8 to 1.3°C in terms of GSAT. Consequently, that range encompasses the best estimate and *very likely* range of observed GSAT warming of 1.06 °C [0.88 to 1.21 °C] over the same period (Cross-Chapter Box 2.3). There is *medium confidence* that the best estimate and *likely* ranges of attributable warming expressed in terms of GMST are equal to those for GSAT (Cross-Chapter Box 2.3). Repeating the process for other time periods leads to the best estimates and *likely* ranges listed in Table 3.1. GSAT change attributable to natural forcings is −0.1 to 0.1°C. The *likely* range of GSAT warming attributable to greenhouse gases is assessed in the same way to be 1.0 to 2.0°C while the GSAT change attributable to aerosols, ozone and land-use change is −0.8 to 0.0°C. Progress in attribution techniques allows the important advance of attributing observed surface temperature warming since 1850-1900, instead of since 1951 as was done in the AR5.

[START TABLE 3.1 HERE]

Table 3.1: Estimates of warming in GSAT attributable to human influence for different periods in °C, all relative to the 1850-1900 base period. Uncertainty ranges are 5-95% ranges for individual studies and *likely* ranges for the assessment. The results shown in the table use the methods described in the three studies indicated, but applied to additional periods and the warming trend. Ribes et al. (2021) results were updated using a corrected natural forcing time series, and Haustein et al. (2017) results were updated to use HadCRUT5.

	1986-2005	1995-2014	2006-2015	2010-2019	Warming rate 2010-2019
Ribes et al. (2021)	0.65 (0.52 – 0.77)	0.82 (0.69 – 0.94)	0.94 (0.81 – 1.08)	1.03 (0.89 – 1.17)	0.23 (0.18 – 0.29)

ACCEPTED VERSION SUBJECT TO FINAL EDITING

Gillett et al. (2021)	0.63 (0.32 – 0.94)	0.84 (0.63 – 1.06)	0.98 (0.74 – 1.22)	1.11 (0.92 – 1.30)	0.36 (0.30 – 0.41)
Haustein et al. (2017)	0.73 (0.58 – 0.82)	0.88 (0.75 – 0.98)	0.98 (0.87 – 1.10)	1.06 (0.94 – 1.22)	0.23 (0.19 – 0.35)
Assessment	0.68 (0.3 – 1.0)	0.85 (0.6 – 1.1)	0.97 (0.7 – 1.3)	1.07 (0.8 – 1.3)	0.2 (0.1 – 0.3)

[END TABLE 3.1 HERE]

The IPCC AR5 assessed the *likely* range of the contribution of internal variability to GMST warming to be −0.1 to 0.1°C over the period 1951-2010. Since then, several studies have downplayed the contribution of internal modes of variability to global temperature variability, often by arguing for a forced component to those internal modes (Mann et al., 2014; Folland et al., 2018; Haustein et al., 2019; Liguori et al., 2020). Haustein et al. (2017) found a 5-95% confidence interval of −0.09 to +0.12 °C for the contribution of internal variability to warming between 1850–1879 and 2017. Ribes et al. (2021) imply a contribution of internal variability of −0.02 ± 0.16°C to warming between 2010-2019 and 1850-1900, assuming independence between errors in the observations and in the estimate of the forced response. Based on these studies, but allowing for unsampled sources of error, we assess the *likely* range of the contribution of internal variability to GSAT warming between 2010-2019 and 1850-1900 to be −0.2 to 0.2°C.

The IPCC SR1.5 gave a *likely* range for the human-induced warming rate of 0.1°C to 0.3°C per decade in 2017, with a best estimate of 0.2°C per decade (Allen et al., 2018). Table 3.1 lists the estimates of attributable anthropogenic warming rate over the period 2010-2019 by the three studies that underpin the assessment of GSAT warming (Haustein et al., 2017; Gillett et al., 2021; Ribes et al., 2021). Estimates from Haustein et al. (2017), based on observed warming, and Ribes et al. (2021), based on CMIP6 simulations constrained by observed warming, are in good agreement. Gillett et al. (2021), also based on CMIP6 models, corresponds to a larger anthropogenic attributable warming rate, because of a smaller warming rate attributed to natural forcing than in Ribes et al. (2021). This disagreement does not support a decrease in uncertainty compared to the SR1.5 assessment. So the range for anthropogenic attributable surface temperature warming rate of 0.1°C to 0.3°C per decade is again assessed to be *likely*, with a best estimate of 0.2°C per decade.

3.3.1.2 Upper-Air Temperature

Chapter 2 assessed that the troposphere has warmed since at least the 1950s, that it is *virtually certain* that the stratosphere has cooled, and that there is *medium confidence* that the upper troposphere in the tropics has warmed faster than the near-surface since at least 2001 (Section 2.3.1.2). The AR5 assessed that anthropogenic forcings, dominated by greenhouse gases, *likely* contributed to the warming of the troposphere since 1961 and that anthropogenic forcings, dominated by the depletion of the ozone layer due to ozone-depleting substances, *very likely* contributed to the cooling of the lower stratosphere since 1979. Since the AR5, understanding of observational uncertainties in the radiosonde and satellite data has improved with more available data and longer coverage, and differences between models and observations in the tropical atmosphere have been investigated further.

Tropospheric temperature

The AR5 assessed with *low confidence* that most, though not all, CMIP3 (Meehl et al., 2007) and CMIP5 (Taylor et al., 2012) models overestimated the observed warming trend in the tropical troposphere during the satellite period 1979-2012, and that a third to a half of this difference was due to an overestimate of the SST trend during this period (Flato et al., 2013). Since the AR5, additional studies based on CMIP5 and CMIP6 models show that this warming bias in tropospheric temperatures remains. Recent studies have investigated the role of observational uncertainty, the model response to external forcings, the influence of the time period considered, and the role of biases in SST trends in contributing to this bias.

Several studies since AR5 have continued to demonstrate an inconsistency between simulated and observed

ACCEPTED VERSION SUBJECT TO FINAL EDITING

temperature trends in the tropical troposphere, with models simulating more warming than observations (Mitchell et al., 2013, 2020, Santer et al., 2017a, 2017b; McKitrick and Christy, 2018; Po-Chedley et al., 2021). Santer et al. (2017b) used updated and improved satellite retrievals to investigate model performance in simulating the tropical mid- to upper-troposphere trends, and removed the influence of stratospheric cooling by regression. These factors were found to reduce the size of the discrepancy in mid- to upper-tropospheric temperature trends between models and observations over the satellite era, but a discrepancy remained. Santer et al. (2017a) found that during the late 20th century, the discrepancies between simulated and satellite-derived mid- to upper-tropospheric temperature trends were consistent with internal variability, while during most of the early 21st century, simulated tropospheric warming is significantly larger than observed, which they relate to systematic deficiencies in some of the external forcings used after year 2000 in the CMIP5 models. However, in CMIP6, differences between simulated and observed upper tropospheric temperature trends persist despite updated forcing estimates (Mitchell et al., 2020). Figure 3.10 shows that CMIP6 models forced by combined anthropogenic and natural forcings overestimate temperature trends compared to radiosonde data (Haimberger et al., 2012) throughout the tropical troposphere (Mitchell et al., 2020). Over the 1979-2014 period, models are more consistent with observations in the lower troposphere, and least consistent in the upper troposphere around 200 hPa, where biases exceed 0.1°C per decade. Several studies using CMIP6 models suggest that differences in climate sensitivity may be an important factor contributing to the discrepancy between the simulated and observed tropospheric temperature trends (McKitrick and Christy, 2020; Po-Chedley et al., 2021), though it is difficult to deconvolve the influence of climate sensitivity, changes in aerosol forcing and internal variability in contributing to tropospheric warming biases (Po-Chedley et al., 2021). Another study found that the absence of a hypothesized negative tropical cloud feedback could explain half of the upper troposphere warming bias in one model (Mauritsen and Stevens, 2015).

Mitchell et al. (2013) and Mitchell et al. (2020) found a smaller discrepancy in tropical tropospheric temperature trends in models forced with observed SSTs (see also Figure 3.10a), and CMIP5 models and observations were found to be consistent below 150 hPa when viewed in terms of the ratio of temperature trends aloft to those at the surface (Mitchell et al., 2013). Flannaghan et al. (2014) and Tuel (2019) showed that most of the tropospheric temperature difference between CMIP5 models and the satellite-based trend over the 1970-2018 period is due to respective differences in SST warming trends in regions of deep convection, and Po-Chedley et al. (2021) show that CMIP6 models with a more realistic SST simulation in the central and eastern Pacific show a better performance than other models. Though systematic biases still remain, this indicates that the bias in tropospheric temperature warming in models is in part linked to surface temperature warming biases, especially in the lower troposphere.

In summary, studies continue to find that CMIP5 and CMIP6 model simulations warm more than observations in the tropical mid- and upper-troposphere over the 1979-2014 period (Mitchell et al., 2013, 2020, Santer et al., 2017a, 2017b; Suárez-Gutiérrez et al., 2017; McKitrick and Christy, 2018), and that overestimated surface warming is partially responsible (Mitchell et al., 2013; Po-Chedley et al., 2021). Some studies point to forcing errors in the CMIP5 simulations in the early 21st century as a possible contributor (Mitchell et al., 2013; Sherwood and Nishant, 2015; Santer et al., 2017a), but CMIP6 simulations use updated forcing estimates yet generally still warm more than observations. Although accounting for internal variability and residual observational errors can reconcile models with observations to some extent (Suárez-Gutiérrez et al., 2017; Mitchell et al., 2020), some studies suggest that climate sensitivity also plays a role (Mauritsen and Stevens, 2015; McKitrick and Christy, 2020; Po-Chedley et al., 2021). Hence, we assess with *medium confidence* that CMIP5 and CMIP6 models continue to overestimate observed warming in the upper tropical troposphere over the 1979-2014 period by at least 0.1°C per decade, in part because of an overestimate of the tropical SST trend pattern over this period.

[START FIGURE 3.10 HERE]

Figure 3.10: Observed and simulated tropical mean temperature trends through the atmosphere. Vertical profiles of temperature trends in the tropics (20°S-20°N) for three periods: (a) 1979-2014 (b) 1979-1997 (ozone depletion era) (c) 1998-2014 (ozone stabilisation era). The black lines show trends in the RICH

ACCEPTED VERSION SUBJECT TO FINAL EDITING

1.7 (long dashed) and RAOBCORE 1.7 (dashed) radiosonde datasets (Haimberger et al., 2012), and in the ERA5/5.1 reanalysis (solid). Grey envelopes are centred on the RICH 1.7 trends, but show the uncertainty based on 32 RICH-obs members of version 1.5.1 of the dataset, which used version 1.7.3 of the RICH software but with the parameters of version 1.5.1. ERA5 was used as reference for calculating the adjustments between 2010 and 2019, and ERA-Interim was used for the years before that. Red lines show trends in CMIP6 historical simulations from one realization of 60 models. Blue lines show trends in 46 CMIP6 models that used prescribed, rather than simulated, sea surface temperatures (SSTs). Figure is adapted from Mitchell et al. (2020), their Figure 1. Further details on data sources and processing are available in the chapter data table (Table 3.SM.1).

[END FIGURE 3.10 HERE]

The AR5 assessed as *likely* that anthropogenic forcings, dominated by greenhouse gases, contributed to the warming of the troposphere since 1961 (Bindoff et al., 2013). Since then, there has been further progress in detecting and attributing tropospheric temperature changes. Mitchell et al. (2020) used CMIP6 models to find that the main driver of tropospheric temperature changes are greenhouse gases. Previous detection of the anthropogenic influence on tropospheric warming may have overestimated uncertainties: Pallotta and Santer (2020) found that CMIP5 climate models overestimate the observed natural variability in global mean tropospheric temperature on timescales of 5-20 years. Nevertheless, Santer et al. (2019) found that stochastic uncertainty is greater for tropospheric warming (8-15 years) than stratospheric cooling (1-3 years) because of larger noise and slower recovery time from the Pinatubo eruption in the troposphere. The detection time of the anthropogenic signal in the tropospheric warming can be affected by both the model climate sensitivity and the model response to aerosol forcing. Volcanic forcing is also important, as models that do not consider the influence of volcanic eruptions in the early 21st century overestimate the observed tropospheric warming since 1998 (Santer et al., 2014). Changes in the amplitude of the seasonal cycle of tropospheric temperatures have also been attributed to human influences. Santer et al. (2018) found that satellite data and climate models driven by anthropogenic forcing show consistent amplitude increases at mid-latitudes in both hemispheres, amplitude decreases at high latitudes in the SH, and small changes in the tropics.

In summary, these studies confirm the dominant role of human activities in tropospheric temperature trends. We therefore assess that it is *very likely* that anthropogenic forcing, dominated by greenhouse gases, was the main driver of the warming of the troposphere since 1979.

Stratospheric temperature

The AR5 concluded that the CMIP5 models simulated a generally realistic evolution of lower stratospheric temperatures (Bindoff et al., 2013; Flato et al., 2013), which was better than the CMIP3 models, in part because they generally include time-varying ozone concentrations, unlike many of the CMIP3 models. Nonetheless, it was noted that there was a tendency for the simulations to underestimate stratospheric cooling compared to observations. Bindoff et al. (2013) concluded that it was *very likely* that anthropogenic forcing, dominated by stratospheric ozone depletion by chemical reactions involving trace species known as ozone-depleting substances (ODS), had contributed to the cooling of the lower stratosphere since 1979. Increased greenhouse gases cause near-surface warming but cooling of stratospheric temperatures.

For the lower stratosphere, a debate has been ongoing since the AR5 between studies finding that models underestimate the cooling of stratospheric temperature (Santer et al., 2017b), in part because of underestimated stratospheric ozone depletion (Eyring et al., 2013; Young et al., 2013), and studies finding that lower stratospheric temperature trends are within the range of observed trends (Young et al., 2013; Maycock et al., 2018). Different observational data and different time periods explain the different conclusions. Aquila et al. (2016) used forced chemistry-climate models with prescribed SST to investigate the influence of different forcings on global stratospheric temperature changes. They found that in the lower stratosphere, the simulated cooling trend due to increasing greenhouse gases was roughly constant over the satellite era, while changes in ODS concentrations amplified that stratospheric cooling trend during the era of increasing ozone depletion up until the mid-1990s, with a flattening of the temperature trend over the subsequent period over which stratospheric ozone has stabilised (Section 2.2.5.2). Mitchell et al. (2020) showed that while models simulate realistic trends in tropical lower stratospheric temperature over the whole

ACCEPTED VERSION SUBJECT TO FINAL EDITING

1979-2014 period when compared with radiosonde data, they tend to overestimate the cooling trend over the ozone depletion era (1979-1997) and underestimate it over the ozone recovery era (1998-2014) (Figure 3.10b and 3.10c). They speculate that those disagreements are due to poor representations of stratospheric ozone forcing.

Upper stratospheric temperature changes were not assessed in the context of attribution or model evaluation in AR5, but this is an area where there has been considerable progress over recent years (see Section 2.3.1.2.1). Simulated temperature changes in chemistry-climate models show good consistency with the reprocessed dataset from NOAA STAR but are less consistent with the revised UK Met Office record (Karpechko et al., 2018b). The latter still shows stronger cooling than simulated in chemistry-climate models (Maycock et al., 2018). Reanalyses, which assimilate AMSU and SSU datasets, indicate an upper-stratospheric cooling from 1979 to 2009 of about 3°C at 5 hPa and 4°C at 1 hPa that agrees well with the cooling in simulations with prescribed SST and using CMIP5 forcings (Simmons et al., 2014). Mitchell (2016) used regularized optimal fingerprinting techniques to carry out an attribution analysis of annual mid to upper stratospheric temperature in response to external forcings. They found that anthropogenic forcing has caused a cooling of approximately 2-3°C in the upper stratosphere over the period of 1979-2015, with greenhouse gases contributing two thirds of this change and ozone depletion contributing one third. They find a large upper stratospheric temperature change in response to volcanic forcing (0.4-0.6 °C for Mount Pinatubo) but that change is still smaller than the lower-stratospheric signal. Aquila et al. (2016) found that the cooling of the middle and upper stratosphere after 1979 is mainly due to changes in greenhouse gas concentrations. Volcanic eruptions and the solar cycle were not found to affect long-term stratospheric temperature trends but to have short-term influences.

In summary, based on the latest updates to satellite observations of stratospheric temperature, we assess that simulated and observed trends in global mean temperature through the depth of the stratosphere are more consistent than based on previous datasets, but some differences remain (*medium confidence*). Studies published since the AR5 increase our confidence in the simulated stratospheric temperature response to greenhouse gas and ozone changes, and support an assessment that it is *extremely likely* that stratospheric ozone depletion due to ozone-depleting substances was the main driver of the cooling of the lower stratosphere between 1979 and the mid-1990s, as expected from physical understanding. Similarly, revised observations and new studies support an assessment that it is *extremely likely* that anthropogenic forcing, both from increases in greenhouse gas concentration and depletion of stratospheric ozone due to ozone-depleting substances, was the main driver of upper stratospheric cooling since 1979.

[START CROSS-CHAPTER BOX 3.1 HERE]

Cross-Chapter Box 3.1: Global Surface Warming over the Early 21st Century

Contributors: Christophe Cassou (France), Yu Kosaka (Japan), John Fyfe (Canada), Nathan Gillett (Canada), Edward Hawkins (UK), Blair Trewin (Australia)

AR5 found that the rate of global mean surface temperature (GMST) increase inferred from observations over the 1998-2012 period was lower than the rate of increase over the 1951-2012 period, and lower than the ensemble mean increase in historical simulations from CMIP5 climate models extended by RCP scenario simulations beyond 2005 (Flato et al., 2013). This apparent slowdown of surface global warming compared to the 62-year rate was assessed with *medium confidence* to have been caused in roughly equal measure by a cooling contribution from internal variability and a reduced trend in external forcing (particularly associated with solar and volcanic forcing) in the AR5 based on expert judgement (Flato et al., 2013). In AR5 it was assessed that almost all CMIP5 simulations did not reproduce the observed slower warming, and that there was *medium confidence* that the trend difference from the CMIP5 ensemble mean was to a substantial degree caused by internal variability with possible contributions from forcing error and model response uncertainty. This Cross-Chapter Box assesses new findings from observational products and statistical and physical models on trends over the 1998-2012 period considered in AR5.

ACCEPTED VERSION SUBJECT TO FINAL EDITING

Updated observational and reanalyses data sets and comparison with model simulations

Since the AR5, there have been version updates and new releases of most observational GMST data sets (Cross-Chapter Box 2.3). All the updated products now available consistently find stronger positive trends for 1998-2012 than those assessed in AR5 (Cowtan and Way, 2014; Karl et al., 2015; Hausfather et al., 2017; Medhaug et al., 2017; Simmons et al., 2017; Risbey et al., 2018). Simmons et al. (2017) reported that the 1998-2012 GMST trends in the updated observational and reanalysis data sets available at that time range from 0.06 °C to 0.14°C per decade, compared with the 0.05 °C per decade on average as reported in AR5, whilst the latest data products reported in Chapter 2 Table 2.4 show GMST or global mean near-surface air temperature (GSAT) trends over that period ranging from 0.12°C to 0.14°C per decade. The lowest trend in Simmons et al. (2017) is from HadCRUT4, now superseded by HadCRUT5, which shows a trend of 0.12 ºC per decade. The upward revision is mainly due to improved sea surface temperature (SST) data sets and infilling of surface temperature in locations with missing records in observational products, mainly in the Arctic (see Cross-Chapter Box 2.3 for details).

With these updates, all the observed trends assessed here lie within the 10^{th}-90^{th} percentile range of the simulated trends in the CMIP5 and CMIP6 simulations (Cross-Chapter Box 3.1, Figure 1a). This result is insensitive to whether model GSAT (based on surface air temperature) or GMST (based on a blend of surface air temperature over land and sea ice and SST over open ocean) is used, and to whether or not masking with the observational data coverage is applied. Therefore, the observed 1998-2012 trend is consistent with both the CMIP5 or CMIP6 multi-model ensemble of trends over the same period (*high confidence*).

Internal variability

All the observation-based GMST and GSAT trends are lower than the multi-model mean GMST and GSAT trends of both CMIP5 and CMIP6 for 1998-2012 (Cross-Chapter Box 3.1, Figure 1a). This suggests a possible cooling contribution from internal variability during this period. This is supported by initialized decadal hindcasts, which account for the phase of the multidecadal modes of variability (Sections 3.7.6 and 3.7.7), and which better reproduce observed global mean SST and GSAT trends than uninitialized historical simulations (Guemas et al., 2013; Meehl et al., 2014).

Studies since AR5 identify Pacific Decadal Variability (PDV) as the leading mode of variability associated with unforced decadal GSAT fluctuations, with additional influence from Atlantic Multidecadal Variability (Brown et al., 2015; Dai et al., 2015; Steinman et al., 2015; Pasini et al., 2017; Annex IV.2.6, IV.2.7). PDV transitioned from positive (El Niño-like) to negative (La Niña-like) phases during the slow warming period (Figure 3.39f, Cross-Chapter Box 3.1, Figure 1c). Model ensemble members that capture the observed slower decadal warming under transient forcing, and time segments of model simulations that show decadal GSAT decreases under fixed radiative forcing, also feature negative PDV trends (Maher et al., 2014; Meehl et al., 2011, 2013, 2014; Middlemas and Clement, 2016; Cross-Chapter Box 3.1, Figure 1d), suggesting the influence of PDV. This is confirmed by statistical models with the PDV-GSAT relationship estimated from observations and model simulations (Schmidt et al., 2014; Meehl et al., 2016b; Hu and Fedorov, 2017), selected ensemble members and time segments from model simulations where PDV by chance evolves in phase with observations over the slow warming period (Huber and Knutti, 2014; Risbey et al., 2014), and coupled model experiments in which PDV evolution is constrained to follow the observations (Kosaka and Xie, 2013, 2016; England et al., 2014; Watanabe et al., 2014; Delworth et al., 2015). Part of the PDV trend may be driven by anthropogenic aerosols (Smith et al., 2016); however, this result is model-dependent, and internally-driven PDV dominates the forced PDV signal in the CMIP6 multi-model ensemble (Section 3.7.6). It is also notable that there is large uncertainty in the magnitude of the PDV influence on GSAT across models (Deser et al., 2017a; Wang et al., 2017a) and among the studies cited above. In addition to PDV, contributions to the reduced warming trend from wintertime Northern Hemisphere atmospheric internal variability, particularly associated with a trend towards the negative phase of the Northern Annular Mode/North Atlantic Oscillation (Annex IV.2.1; Guan et al., 2015; Saffioti et al., 2015; Iles and Hegerl, 2017) or the Cold Ocean-Warm Land pattern (Molteni et al., 2017; Yang et al., 2020) have been suggested, leading to regional continental cooling over a large part of Eurasia and North America (Li et al., 2015; Deser et al., 2017; Gan et al., 2019; Cross-Chapter Box 3.1, Figure 1c).

ACCEPTED VERSION SUBJECT TO FINAL EDITING

Such internally-driven variation of decadal GSAT trends is not unique to the 1998-2012 period (Section 1.4.2.1; Lovejoy, 2014; Roberts et al., 2015; Dai and Bloecker, 2019). Due to the nature of internal variability, surface temperature changes over the 1998-2012 period are regionally- and seasonally-varying (Trenberth et al., 2014; Zang et al., 2019; Cross-Chapter Box 3.1, Figure 1c). Further, there was no slowdown in the increasing occurrence of hot extremes over land (Seneviratne et al., 2014). Thus, the internally-driven slowdown of GSAT increase does not correspond to slowdown of warming everywhere on the Earth's surface.

Updated forcing

CMIP5 historical simulations driven by observed forcing variations ended in 2005 and were extended with RCP scenario simulations for model-observation comparisons beyond that date. Post AR5 studies based on updated external forcing show that while no net effect of updated anthropogenic aerosols is found on GSAT trends (Murphy, 2013; Gettelman et al., 2015; Oudar et al., 2018), natural forcing by moderate volcanic eruptions in the 21st century (Haywood et al., 2014; Ridley et al., 2014; Santer et al., 2014) and a prolonged solar irradiance minimum around 2009 compared to the normal 11-year cycle (Lean, 2018) yield a negative contribution to radiative forcing, which was missing in CMIP5 (Figure 2.2). This explains part of the difference between observed and CMIP5 trends, as shown based on EMIC simulations (Huber and Knutti, 2014; Ridley et al., 2014), statistical and mathematical models (Schmidt et al., 2014; Lean, 2018), and process-based climate models (Santer et al., 2014). However, in a single climate model study by Thorne et al. (2015), updating most forcings (greenhouse gas concentrations, solar irradiance, and volcanic and anthropogenic aerosols) available when the study was done makes no significant difference to the 1998-2012 GMST trend from that obtained with original CMIP5 forcing. Potential underestimation of volcanic (negative) forcing may have played a role (Outten et al., 2015). In the multi-model ensemble mean, the 1998-2012 GMST trends are almost equal in CMIP5 and CMIP6 (Cross-Chapter Box 3.1, Figure 1a), suggesting compensation by a higher transient climate response and equilibrium climate sensitivity in CMIP6 than CMIP5 (Section 7.5.6). To summarize, while there is *medium confidence* that natural forcing that was missing in CMIP5 contributed to the difference of observed and simulated GMST trends, *confidence* remains *low* in the quantitative contribution of net forcing updates.

Energy budget and heat redistribution

The early 21st century slower warming was observed in atmospheric temperatures, but the heat capacity of the atmosphere is very small compared to that of the ocean. Although there is noticeable uncertainty among observational products (Su et al., 2017a) and observation quality changes through time, global ocean heat content continued to increase during the slower surface warming period (*very high confidence*), at a rate consistent with CMIP5 and CMIP6 historical simulations (Sections 2.3.3.1, 3.5.1.3 and 7.2.2.2). There is *high confidence* that the Earth's energy imbalance was larger in the 2000s than in the 1985-1999 period (Section 7.2.2.1), consistent with accelerating ocean heat uptake in the past two decades (Section 3.5.1.3). Internal decadal variability is mainly associated with redistribution of heat within the climate system (Yan et al., 2016c; Drijfhout, 2018) while associated top of the atmosphere radiation anomalies are weak (Palmer and McNeall, 2014). Heat redistribution in the top 350 m of the Indian and Pacific Oceans has been found to be the main contributor to reduced surface warming during the slower surface warming period (Lee et al., 2015; Nieves et al., 2015; Liu et al., 2016a), consistent with the simulated signature of PDV (England et al., 2014; Maher et al., 2018a; Gastineau et al., 2019). Below 700 m, enhanced heat uptake over the slower surface warming period is observed mainly in the North Atlantic and Southern Ocean (Chen and Tung, 2014), though whether this is a response to forcing or a unique signature of the slow GMST warming has been questioned (Liu et al., 2016b).

Summary and implications

With updated observation-based GMST data sets and forcing, improved analysis methods, new modelling evidence and deeper understanding of mechanisms, there is *very high confidence* that the slower GMST and GSAT increase inferred from observations in the 1998-2012 period was a temporary event induced by internal and naturally-forced variability that partly offset the anthropogenic warming trend over this period. Global ocean heat content continued to increase throughout this period, and the slowdown was only evident in the atmosphere and at the surface (*very high confidence*). Considering all the sources of uncertainties, it is impossible to robustly identify a single cause of the early 2000s slowdown (Hedemann et al., 2017; Power et

ACCEPTED VERSION SUBJECT TO FINAL EDITING

al., 2017); rather, it should be interpreted as due to a combination of several factors (Huber and Knutti, 2014; Schmidt et al., 2014; Medhaug et al., 2017).

A major El Niño event in 2014-2016 led to three consecutive years of record annual GMST with unusually strong heat release from the Northwestern Pacific Ocean (Yin et al., 2018), which marked the end of the slower warming period (Hu and Fedorov, 2017; Su et al., 2017b; Cha et al., 2018). The past 5-year period (2016-2020) is the hottest 5-year period in the instrumental record up to 2020 (*high confidence*). This rapid warming was accompanied by a PDV shift toward its positive phase (Su et al., 2017b; Cha et al., 2018). A higher rate of warming following the 1998-2012 period is consistent with the predictions in AR5 Box 9.2 (Flato et al., 2013) and with a statistical prediction system (Sévellec and Drijfhout, 2018). Initialized decadal predictions show higher GMST trends in the early 2020s compared to uninitialized simulations (Thoma et al., 2015; Meehl et al., 2016c).

While some recent studies find that internal decadal GSAT variability may become weaker under GSAT warming, associated in part with reduced amplitude PDV (Section 4.5.3.5; Brown et al., 2017), the weakening is small under a realistic range of warming. A large volcanic eruption would temporarily cool GSAT (Cross-Chapter Box 4.1). Thus, there is *very high confidence* that reduced and increased GMST and GSAT trends at decadal timescales will continue to occur in the 21st century (Meehl et al., 2013; Roberts et al., 2015; Medhaug and Drange, 2016). However, such internal or volcanically forced decadal variations in GSAT trend have little affect on the centennial warming (England et al., 2015; Cross-Chapter Box 4.1).

[START CROSS-CHAPTER BOX 3.1, FIGURE 1 HERE]

Cross-Chapter Box 3.1, Figure 1: 15-year trends of surface global warming for 1998-2012 and 2012-2026. (a, b) GSAT and GMST trends for 1998-2012 (a) and 2012-2026 (b). Histograms are based on GSAT in historical simulations of CMIP6 (red shading, extended by SSP2-4.5) and CMIP5 (grey shading; extended by RCP4.5). Filled and open diamonds at the top represent multi-model ensemble means of GSAT and GMST trends, respectively. Diagonal lines show histograms of HadCRUT5.0.1.0. Triangles at the top of (a) represent GMST trends of Berkeley Earth, GISTEMP, Kadow et al. (2020) and NOAAGlobalTemp-Interim, and the GSAT trend of ERA5. Selected CMIP6 members whose 1998-2012 trends are lower than the HadCRUT5.0.1.0 mean trend are indicated by purple shading (a) and (b). In (a), model GMST and GSAT, and ERA5 GSAT are masked to match HadCRUT data coverage. (c-d) Trend maps of annual near-surface temperature for 1998-2012 based on HadCRUT5.0.1.0 mean (c) and composited surface air temperature trends of subsampled CMIP6 simulations (d) that are included in purple shading area in (a). In (c), cross marks indicate trends that are not significant at the 10% level based on t-tests with serial correlation taken into account. Ensemble size used for each of the histograms and the trend composite is indicated at the top right of each of panels (a,b,d). Model ensemble members are weighted with the inverse of the ensemble size of the same model, so that individual models are equally weighted. Further details on data sources and processing are available in the chapter data table (Table 3.SM.1).

[END CROSS-CHAPTER BOX 3.1, FIGURE 1 HERE]

[END CROSS-CHAPTER BOX 3.1 HERE]

3.3.2 Precipitation, Humidity and Streamflow

Paleoclimate context

A fact hindering detection and attribution studies in precipitation and other hydrological variables is the large internal variability of these fields relative to the anthropogenic signal. This low signal-to-noise ratio hinders the emergence of the anthropogenic signal from natural variability. Moreover, the sign of the change depends on location and time of the year. Paleoclimate records provide valuable context for observed trends in the 20th and 21st century and assist with the attribution of these trends to human influence (see also Section 2.3.1.3.1). By nature, hydrological proxy data represent regional conditions, but taken together can represent large-scale patterns. As an example of how paleorecords have helped assessing the origin of changes, we consider some, mainly subtropical, regions which have experienced systematic drying in recent decades (see

ACCEPTED VERSION SUBJECT TO FINAL EDITING

also Section 8.3.1.3). Paleoclimate simulations of monsoons are assessed in Section 3.3.3.2.

Records of tree ring width have provided evidence that recent prolonged dry spells in the Levant and Chile are unprecedented in the last millennium (*high confidence*) (Cook et al., 2016a; Garreaud et al., 2017). East Africa, has also been drying in recent decades (Rowell et al., 2015; Hoell et al., 2017a), a trend that is unusual in the context of the sedimentary paleorecord spanning the last millennium (Tierney et al., 2015). This may be a signature of anthropogenic forcing but cannot as of yet be distinguished from natural variability (Hoell et al., 2017b; Philip et al., 2018). Likewise, tree rings indicate that the 2012-2014 drought in the southwestern United States was exceptionally severe in the context of natural variability in the last millennium, and may have been exacerbated by the contribution of anthropogenic temperature rise (*medium confidence*) (Griffin and Anchukaitis, 2014; Williams et al., 2015). Furthermore, Williams et al. (2020) used a combination of hydrological modelling and tree-ring reconstructions to show that the period from 2000 to 2018 was the driest 19-year span in southwestern North America since the late 1500s. Nonetheless, tree rings also indicate the presence of prolonged megadroughts in western North America throughout the last millennium that were more severe than 20th and 21st century events (*high confidence*) (Cook et al., 2004, 2010, 2015). These were associated with internal variability (Coats et al., 2016; Cook et al., 2016b) and indicate that large-magnitude changes in the water cycle may occur irrespective of anthropogenic influence (see also McKitrick and Christy, 2019).

Paleoclimate records also allow for model evaluation under conditions different from present-day. AR5 concluded that models can successfully reproduce to first-order patterns of past precipitation changes during the Last Glacial Maximum (LGM) and mid-Holocene, though simulated precipitation changes during the mid-Holocene tended to be underestimated (Flato et al., 2013). Further analysis of CMIP5 models confirmed these results but has also revealed systematic offsets from the paleoclimate record (DiNezio and Tierney, 2013a; Hargreaves and Annan, 2014; Harrison et al., 2014, 2015; Bartlein et al., 2017; Scheff et al., 2017; Tierney et al., 2017a). Harrison et al. (2014) concluded that CMIP5 models do not perform better in simulating rainfall during the LGM and mid-Holocene than earlier model versions despite higher resolution and complexity. However, prescribing changes in vegetation and dust was found to improve the match to the paleoclimate record (Pausata et al., 2016; Tierney et al., 2017b) suggesting that vegetation feedbacks in the CMIP5 models may be too weak (*low confidence*) (Hopcroft et al., 2017). Brierley et al. (2020) compared the latitudinal gradient of annual precipitation changes in the European-African sector simulated by CMIP6 models for the mid-Holocene with pollen-based reconstructions and showed that models generally reproduce the direction of changes seen in the reconstructions (Figure 3.11). They do not show a robust signal in area averaged rainfall over most European regions where quantitative reconstructions exist, which is not incompatible with reconstructions. Over the Sahara/Sahel and West Africa regions, where reconstructions suggest positive anomalies during the mid-Holocene, both CMIP5 and CMIP6 models also simulate a rainfall increase, but it is much weaker (see also Section 3.3.3.2). Overall, however, large discrepancies remain between simulations and reconstructions.

Liu et al. (2018) evaluated the terrestrial moisture changes that occurred during the LGM and concluded that the multi-model median from CMIP5 is consistent with available paleo-records in some regions, but not in others. CMIP5 models accurately reproduce an increase in moisture in the western United States, related to an intensified winter storm track and decreased evaporative demand (Oster et al., 2015; Ibarra et al., 2018; Lora, 2018). On the other hand, CMIP5 models show a wide variety of responses in the tropical Indo-Pacific region, with only a few matching the pattern of change inferred from the paleoclimate record (DiNezio and Tierney, 2013b; DiNezio et al., 2018). The variable response across models is related to the effect of the exposure of the tropical shelves during glacial times, which variously intensifies or weakens convection in the rising branch of the Walker cell, depending on model parameterization (DiNezio et al., 2011). For the Last Interglacial, CMIP6 models reproduce the proxy-based increased precipitation relative to pre-industrial in the North African, South Asian and North American regions, but not in Australia (Scussolini et al., 2019).

In summary, there is *medium confidence* that CMIP5 and CMIP6 models can reproduce broad aspects of precipitation changes during paleo reference periods, but large discrepancies remain. Further assessment of model performance and comparison between CMIP5 and CMIP6 during past climates can be found in Section 3.8.2.1.

ACCEPTED VERSION SUBJECT TO FINAL EDITING

[START FIGURE 3.11 HERE]

Figure 3.11: Comparison between simulated annual precipitation changes and pollen-based reconstructions at the Mid-Holocene (6,000 years ago). The area-averaged changes over five regions (Iturbide et al., 2020) as simulated by CMIP6 models (individually identifiable, one ensemble member per model) and CMIP5 models (blue) are shown, stretching from the tropics to high-latitudes. All regions contain multiple quantitative reconstructions: their interquartile range are shown by boxes and with whiskers for their full range excluding outliers. Figure is adapted from Brierley et al. (2020). Further details on data sources and processing are available in the chapter data table (Table 3.SM.1).

[END FIGURE 3.11 HERE]

3.3.2.1 Atmospheric Water Vapour

The AR5 concluded that an anthropogenic contribution to increases in specific humidity is found with *medium confidence* at and near the surface. A levelling off of atmospheric water vapour over land in the last two decades that needed better understanding, and remaining observational uncertainties, precluded a more confident assessment (Bindoff et al., 2013). Sections 4.5.1.3 and 8.3.1.4 show that there have been significant advances in the understanding of the processes controlling land surface humidity. In particular, there has been a focus on the role of oceanic moisture transport and land-atmosphere feedbacks in explaining the observed trends in relative humidity.

Water vapour is the most important natural greenhouse gas and its amount is expected to increase in a global warming context leading to further warming. Particularly important are changes in the upper troposphere because there water vapour regulates the strength of the water-vapour feedback (Section 7.4.2.2). CMIP5 models have been shown to have a wet bias in the tropical upper troposphere and a dry bias in the lower troposphere, with the former bias and model spread being larger than the latter (Jiang et al., 2012; Tian et al., 2013). Tian et al. (2013) also showed that in comparison to the AIRS specific humidity, CMIP5 models have the well-known double intertropical convergence zone (ITCZ) bias in the troposphere from 1000 hPa to 300 hPa, especially in the tropical Pacific. Water vapour biases in models are dominated by errors in relative humidity throughout the troposphere, which are in turn closely related to errors in large scale circulation; temperature errors dominate near the tropopause (Takahashi et al., 2016). Section 7.4.2 discusses this topic in more detail for CMIP6 models. However, Schroeder et al. (2019) show that the majority of well-established water vapour records are affected by inhomogeneity issues and thus should be used with caution (see also Section 2.3.1.3.3). A comparison of trends in column water vapour path for 1998-2019 in satellite data, a reanalysis, CMIP5 and CMIP6 simulations averaged over the near-global ocean reveals that while on average model trends are higher than those in observations and reanalysis, the latter lie within the multi-model range (Figure 3.12).

[START FIGURE 3.12 HERE]

Figure 3.12: Column water vapour path trends (%/decade) for the period 1998-2019 averaged over the near-global ocean (50°S-50°N). The figure shows satellite data (RSS) and ERA5.1 reanalysis, as well as CMIP5 (sky blue) and CMIP6 (brown) historical simulations. All available ensemble members were used (see Section 3.2). Fits to the model trend probability distributions were performed with kernel density estimation. Figure is updated from Santer et al. (2007). Further details on data sources and processing are available in the chapter data table (Table 3.SM.1).

[END FIGURE 3.12 HERE]

The detection and attribution of tropospheric water vapour changes can be traced back to Santer et al. (2007),

ACCEPTED VERSION SUBJECT TO FINAL EDITING

who used estimates of the atmospheric water vapour from satellite-based Special Sensor Microwave Imager (SSM/I) and from CMIP3 historical climate simulations. They provide evidence of human-induced moistening of the troposphere, and the simulated human fingerprint pattern was detectable at the 5% level by 2002 in water vapour satellite data (from 1988 to 2006). The observed changes matched the historical simulations forced by greenhouse gas changes and other anthropogenic forcings, and not those due to natural variability alone. Then, Santer et al. (2009) repeated this study with CMIP5 models, and found that the detection and attribution conclusions were not sensitive to model quality. These results demonstrate that the human fingerprint is governed by robust and basic physical processes, such as the water vapour feedback. Finally, Chung et al. (2014) extended this line of research by focusing on the global-mean water vapour content in the upper troposphere. Using satellite-based observations and sets of CMIP5 climate simulations run under various climate-forcing options, they showed that the observed moistening trend of the upper troposphere over the 1979-2005 period could not be explained by internal variability alone, but is attributable to a combination of anthropogenic and natural forcings. This increase in water vapour is accompanied by a reduction in mid-tropospheric relative humidity and clouds in the subtropics and mid-latitude in both models and observations related to changes in the Hadley cell (Lau and Kim, 2015; also Section 3.3.3.1).

Dunn et al. (2017) confirmed earlier findings that global mean surface relative humidity increased during 1973-2000, followed by a steep decline (also reported in Willet et al., 2014) until 2013, and specific humidity correspondingly increased and then remained approximately constant (see also Section 2.3.1.3.2), with none of the CMIP5 models capturing this behaviour. They noted biases in the mean state of the CMIP5 models' surface relative humidity (and ascribe the failure to the representation of land surface processes and their response to CO_2 forcing), concluding that these biases preclude any detection and attribution assessment. On the other hand, Byrne and O'Gorman (2018) show that the positive trend in specific humidity continued in recent years and can be detected over land and ocean from 1979 to 2016. Moreover, they provide a theory suggesting that the increase in annual surface temperature and specific humidity as well as the decrease in relative humidity observed over land are linked to warming over the neighbouring ocean. They also point out that the negative trend in relative humidity over land regions is quite uncertain and requires further investigation. A recent study has also identified an anthropogenically-driven decrease in relative humidity over the NH midlatitude continents in summer during 1979-2014, which was underestimated by CMIP5 models (Douville and Plazzotta, 2017). Furthermore, in a modelling study Douville et al. (2020) showed that this decrease in boreal summer relative humidity over midlatitudes is related not only to global ocean warming, but also to the physiological effect of CO_2 on plants in the land surface model.

In summary, we assess that it is *likely* that human influence has contributed to moistening in the upper troposphere since 1979. Also, there *is medium confidence* that human influence contributed to a global increase in annual surface specific humidity, and *medium confidence* that it contributed to a decrease in surface relative humidity over midlatitude NH continents during summertime.

3.3.2.2 Precipitation

AR5 concluded that there was *medium confidence* that human influence had contributed to large-scale precipitation changes over land since 1950, including an increase in the NH mid to high latitudes. Moreover, AR5 concluded that observational uncertainties and challenges in precipitation modelling precluded a more confident assessment (Bindoff et al., 2013). Overall, they found that large-scale features of mean precipitation in CMIP5 models are in modest agreement with observations, but there are systematic errors in the tropics (Flato et al., 2013).

Since AR5, Li et al. (2016b) found that CMIP5 models simulate the large scale patterns of annual mean land precipitation and seasonality well, as well as reproducing qualitatively the observed zonal mean land precipitation trends for the period 1948-2005: models capture the drying trends in the tropics and at 45°S and the wetting trend in the NH mid-to-high latitudes, but the amplitudes of the changes are much smaller than observed. Land precipitation was found to show enhanced seasonality in observations (Chou et al., 2013), qualitatively consistent with the simulated response to anthropogenic forcing (Dwyer et al., 2014). However,

ACCEPTED VERSION SUBJECT TO FINAL EDITING

models do not appear to reproduce the zonal mean trends of seasonality over the period 1948-2005, nor the two-dimensional distributions of trends of annual precipitation and seasonality over land, but differences may be explainable by internal variability (Li et al., 2016b). However, observed trends in seasonality depend on data set used (Li et al., 2016b; Marvel et al., 2017), and Marvel et al. (2017) found that observed changes in the annual cycle phase are consistent with model estimates of forced changes. These phase changes are mainly characterized by earlier onset of the wet season on the equatorward flanks of the extratropical storm tracks, particularly in the SH. Box 8.2 assesses regional changes in water cycle seasonality.

The CMIP5 models have also been shown to adequately simulate the mean and interannual variability of the global monsoon (Section 3.3.3.2), but maintain the double ITCZ bias in the equatorial Pacific (Lee and Wang, 2014a; Tian, 2015; Ni and Hsu, 2018). Despite the ITCZ bias, CMIP5 models have been used to detect in reanalysis a southward shift in the ITCZ prior to 1975, followed by a northward shift in the ITCZ after 1975, in response to forced changes in inter-hemispheric temperature contrast (Bonfils et al., 2020; Friedman et al., 2020) (Sections 3.3.1.1 and 8.3.2.1, Figure 8.11). CMIP5 models perform better than CMIP3 models, in particular regarding the global monsoon domain and intensity (Lee and Wang, 2014b).

In observations at time scales less than a day intermittent rainfall fluctuations dominate variability, but CMIP5 models systematically underestimate them (Covey et al., 2018). Moreover, as noted in previous generation models, CMIP5 models produce rainfall too early in the day (Covey et al., 2016). Also, models overpredict precipitation frequency but have weaker intensity, although comparison with observed data sets is complex as the latter present large differences in intensity among them (Herold et al., 2016; Pendergrass and Deser, 2017; Trenberth et al., 2017). Regarding trends in precipitation intensity, models have also been shown to reproduce the compensation between increasing heavy precipitation and decreasing light to moderate rainfall (Thackeray et al., 2018), a characteristic found in the observational record (Gu and Adler, 2018). Regional performance is further assessed in Chapters 8 and the Atlas, while precipitation extremes are considered in Chapter 11.

The simulation of annual mean rainfall patterns in the CMIP6 models reveals minor improvements compared to those of CMIP5 models (Figure 3.13). The persistent biases include the double ITCZ in the tropical Pacific (seen as bands of excessive rainfall at both sides of the equatorial Pacific in Figure 3.13b,d) and the southward-shifted ITCZ in the equatorial Atlantic, which have been linked to the meridional pattern of SST bias (Zhou et al., 2020a) and the reduced sensitivity of precipitation to local SST (Good et al., 2021). Tian and Dong (2020) also found that all three generations of CMIP models share similar systematic annual mean precipitation errors in the tropics, but that the double ITCZ bias is slightly reduced in CMIP6 models in comparison to CMIP3 and CMIP5 models. They also found some improvement in the overly intense Indian ocean ITCZ and the too dry South American continent except over the Andes. Fiedler et al. (2020) identified improvements in the tropical mean spatial correlations and root mean square error of the climatology as well as in the day-to-day variability, but found little change across CMIP phases in the double ITCZ bias and diurnal cycle. The CMIP6 models reproduce better the domain and intensity of the global monsoon (see Section 3.3.3.2). Moreover, CMIP6 models better represent the storm tracks (Priestley et al., 2020; also Section 3.3.3.3), thereby reducing the precipitation biases in the North Atlantic and midlatitudes of the SH (Figure 3.13b,d). As a result, pattern correlations between simulated and observed annual mean precipitation range between 0.80 and 0.92 for CMIP6, compared to a range of 0.79 to 0.88 for CMIP5 (Bock et al., 2020). This relative improvement may be related to increased model resolution, as found when comparing biases in the mean of the HighResMIP models with the mean of the corresponding lower-resolution versions of the same models (see Figure 3.13e,f), particularly in the tropics and extratropical storm tracks. In agreement, a recent study using several coupled models showed that increasing the atmospheric resolution leads to a strong decrease in the precipitation bias in the tropical Atlantic ITCZ (Vannière et al., 2019) (see further discussion in Section 3.8.2.2). Based on these results we assess that despite some improvements, CMIP6 models still have deficiencies in simulating precipitation patterns, particularly over the tropical ocean (*high confidence*).

[START FIGURE 3.13 HERE]

ACCEPTED VERSION SUBJECT TO FINAL EDITING

Figure 3.13: Annual-mean precipitation rate (mm day^{-1}) for the period 1995–2014. (a) Multi-model (ensemble) mean constructed with one realization of the CMIP6 historical experiments from each model. (b) Multi-model mean bias, defined as the difference between the CMIP6 multi-model mean and precipitation analyses from the Global Precipitation Climatology Project (GPCP) version 2.3 (Adler et al., 2003). (c) Multi-model mean of the root mean square error calculated over all months separately and averaged with respect to the precipitation analyses from GPCP v2.3. (d) Multi-model-mean bias, calculated as the difference between the CMIP6 multi-model mean and the precipitation analyses from GPCP v2.3. Also shown is the multi-model mean bias as the difference between the multi-model mean of (e) high resolution and (f) low resolution simulations of four HighResMIP models and the precipitation analyses from GPCP v2.3. Uncertainty is represented using the advanced approach: No overlay indicates regions with robust signal, where ≥66% of models show change greater than variability threshold and ≥80% of all models agree on sign of change; diagonal lines indicate regions with no change or no robust signal, where <66% of models show a change greater than the variability threshold; crossed lines indicate regions with conflicting signal, where ≥66% of models show change greater than variability threshold and <80% of all models agree on the sign of change. For more information on the advanced approach, please refer to the Cross-Chapter Box Atlas.1. Dots in panel e) marks areas where the bias in high resolution versions of the HighResMIP models is lower in at least 3 out of 4 models than in the corresponding low resolution versions. Further details on data sources and processing are available in the chapter data table (Table 3.SM.1).

[END FIGURE 3.13 HERE]

Recent studies comparing observations and CMIP5 simulations have shown that tropical volcanic eruptions induce a significant reduction in global precipitation, particularly over the wet tropics, including the global monsoon regions (Iles and Hegerl, 2014; Paik and Min, 2017; Paik et al., 2020a). Reconstructions and modelling studies also suggest a distinct remote influence of volcanic forcing such that large volcanoes erupting in one hemisphere can enhance global monsoon precipitation in the other hemisphere (Liu et al., 2016a; Zuo et al., 2019). The climatic effect of volcanic eruptions is further assessed in Cross-Chapter Box 4.1.

An intensification of the wet-dry zonal mean patterns, consisting of the wet tropical and mid-latitude bands becoming wetter, and the dry subtopics becoming drier is expected in response to greenhouse gas and ozone changes (Section 8.2.2.1). However, detecting these changes is complicated by model errors in locating the main features of rainfall patterns. To deal with this issue, Marvel and Bonfils (2013) identified in each CMIP5 historical simulation the latitudinal peaks and troughs of the rainfall latitudinal patterns, measured the amplification and shift of these patterns in a pattern-based fingerprinting study, and found that the simultaneous amplification and shift in zonal precipitation patterns are detectable in Global Precipitation Climatology Project (GPCP) observations over the 1979-2012 period. Similarly, Bonfils et al. (2020) found that the intensification of wet-dry zonal patterns identified in CMIP5 historical simulations is detectable in reanalyses over the 1950-2014 period (see also Figure 8.11).

Based on long-term island precipitation records, Polson et al. (2016) identified significant increases in precipitation in the tropics and decreases in the subtropics, which are consistent with those simulated by the CMIP5 models. Moreover, results from Polson and Hegerl (2017) give support to an intensification of the water cycle according to the wet-gets-wetter, dry-gets-drier paradigm over tropical land areas as well. Other studies suggest that this paradigm does not necessarily hold over dry regions where moisture is limited (Greve et al., 2014; Kumar et al., 2015, see also Section 8.2.2.1). Polson and Hegerl (2017) explained this discrepancy by taking into account the seasonal and interannual movement of the regions (Allan, 2014). A follow-up study using CMIP6 models also found that the observed strengthening contrast of precipitation over wet and dry regions was detectable, although the increase was significantly larger in observations than in the multi-model mean. The change was attributed to a combination of anthropogenic and natural forcings, with anthropogenic forcings detectable in multi-signal analyses (Figure 3.14; Schurer et al. (2020)).

[START FIGURE 3.14 HERE]

ACCEPTED VERSION SUBJECT TO FINAL EDITING

Figure 3.14: Wet (a) and dry (b) region tropical mean (30°S-30°N) annual precipitation anomalies. Observed data are shown with black lines (GPCP), ERA5 reanalysis in grey, single model simulations results are shown with light blue/red lines (CMIP6), and multi-model-mean results are shown with dark blue/red lines (CMIP6). Wet and dry region annual anomalies are calculated as the running mean over 12 months relative to a 1988-2020 base period. The regions are defined as the wettest third and driest third of the surface area, calculated for the observations and for each model separately for each season (following Polson and Hegerl, 2017). Scaling factors (panels c,d) are calculated for the combination of the wet and dry region mean, where the observations, reanalysis and all the model simulations are first standardised using the mean standard deviation of the pre-industrial control simulations. Two total least squares regression methods are used: noise in variables (following Polson and Hegerl, 2017) which estimates a best estimate and a 5-95% confidence interval using the pre-industrial controls (circle and thick green line) and the pre-industrial controls with double the variance (thin green line); and a bootstrap method (DelSole et al., 2019) (5-95% confidence interval shown with a purple line and best estimate with a purple circle). Panel (c) shows results for GPCP and panel (d) for ERA5. Figure is adapted from Schurer et al. (2020). Further details on data sources and processing are available in the chapter data table (Table 3.SM.1).

[END FIGURE 3.14 HERE]

Global land precipitation has *likely* increased since the middle of the 20th century (*medium confidence*), while there is *low confidence* in trends in land data prior to 1950 and over the ocean during the satellite era due to disagreement between datasets (Section 2.3.1.3.4). Figure 3.15a shows the time evolution of the global mean land precipitation since 1950, as well as the trend during the period. Adler et al. (2017) found no significant trend in the global mean precipitation during the satellite era, consistent with model simulations (Wu et al., 2013) and physical understanding of the energy budget (Section 8.2.1). This has been suggested to be due to the negative effect of anthropogenic sulphates that opposed the positive influence of rising global mean temperatures due to greenhouse gases (Salzmann, 2016; Richardson et al., 2018). The precipitation change expected from ocean warming is also partly offset by the fast atmospheric adjustment to increasing greenhouse gases (Section 8.2.1). Over the ocean, the negligible trend may be due to the cancelling effects of CO_2 and aerosols (Richardson et al., 2018).

A gridpoint based analysis of annual precipitation trends over land regions since 1901 (Knutson and Zeng, 2018) comparing observed and simulated trends found that detectable anthropogenic increasing trends have occurred prominently over many middle to high latitude regions of the NH and subtropics of the SH. The observed trends in many cases are significantly stronger than modelled in the CMIP5 historical runs for the 1901-2010 period (though not for 1951-2010), which may be due to disagreement between observed data sets (Section 2.3.1.3.4), and/or suggest possible deficiencies in models.

The observed precipitation increase in the NH high latitudes over the period 1966-2005 was attributed to anthropogenic forcing by a study using CMIP5 models (Wan et al., 2015) supporting the AR5 assessment. Initial results from CMIP6 also support the role of anthropogenic forcing in the precipitation increase observed in NH high latitudes (see Figure 3.15c): the observed positive trend detected for the band 60°N-90°N can only be reproduced when anthropogenic forcing is included, although models tend to simulate overall a larger positive trend. A similar positive trend, but less significant, is also detected between 30°N-60°N, while in the southern mid-latitudes no trend is simulated (see Figure 3.15d, f).

[START FIGURE 3.15 HERE]

Figure 3.15: Observed and simulated time series of anomalies in zonal average annual mean precipitation. a), c)-f) Evolution of global and zonal average annual mean precipitation (mm day^{-1}) over areas of land where there are observations, expressed relative to the base-line period of 1961–1990, simulated by CMIP6 models (one ensemble member per model) forced with both anthropogenic and natural forcings (brown) and natural forcings only (green). Multi-model means are shown in thick solid lines and shading shows the 5-95% confidence interval of the individual model simulations. The data is smoothed using a low pass filter. Observations from three different data sets are included: gridded values derived from Global

ACCEPTED VERSION SUBJECT TO FINAL EDITING

Historical Climatology Network (GHCN V2) station data, updated from Zhang et al. (2007), data from the Global Precipitation Climatology Product (GPCP L3 v2.3, Huffman and Bolvin (2013)) and from the Climate Research Unit (CRU TS4.02, Harris et al. (2014)). Also plotted are boxplots showing interquartile and 5-95% ranges of simulated trends over the period for simulations forced with both anthropogenic and natural forcings (brown) and natural forcings only (blue). Observed trends for each observational product are shown as horizontal lines. Panel b) shows annual mean precipitation rate (mm day^{-1}) of GHCN V2 for the years 1950-2014 over land areas used to compute the plots. Further details on data sources and processing are available in the chapter data table (Table 3.SM.1).

[END FIGURE 3.15 HERE]

For the SH extratropics, Solman and Orlanski (2016) found that the observed summertime rainfall increase over high latitudes and decrease over mid-latitudes over the period 1979-2010 are quasi-zonally symmetric and related to changes in eddy activity. The latter were in turn found to be associated with the poleward shift of the westerlies due mostly to ozone depletion. Positive rainfall trends in the subtropics, particularly over southeastern South America (see also Section 10.4.2.2) and northern and central Australia, have been also attributed to stratospheric ozone depletion (Kang et al., 2011; Gonzalez et al., 2014) and greenhouse gases (Vera and Diaz, 2014; Saurral et al., 2019). During austral winter, wetting at high latitudes and drying at mid-latitudes are not zonally homogenous, due to both changes in eddy activity and increased lower troposphere humidity. Solman and Orlanski (2016) associated these climate changes with increases in greenhouse gas concentration levels. Recently, Blazquez and Solman (2017) have shown that CMIP5 models represent very well the dynamical forcing and the frequency of frontal precipitation in the SH winter extratropics, but the amount of precipitation due to fronts is overestimated. Chapters 10 and 11 validate in more detail the simulation of fronts in climate models (Sections 10.3.3.4.4 and 11.7.2.3).

Over the ocean, observations show coherent large-scale patterns of fresh ocean regions becoming fresher and salty ocean regions saltier across the globe, which has been related through modelling studies to changes in precipitation minus evaporation and is consistent with the wet-gets-wetter, dry-gets-drier paradigm (see Sections 3.5.2.2 and 8.2.2.1, Durack et al., 2012, 2013; Skliris et al., 2014; Durack, 2015; Hegerl et al., 2015; Levang and Schmitt, 2015; Zika et al., 2015; Grist et al., 2016; Cheng et al., 2020).

Overall, studies published since AR5 provide further evidence of an anthropogenic influence on precipitation, and therefore we now assess that it is *likely* that human influence has contributed to large-scale precipitation changes observed since the mid-20th century. New attribution studies strengthen previous findings of a detectable increase in mid to high latitude land precipitation over the NH (*high confidence*). There is *medium confidence* that human influence has contributed to a strengthening of the zonal mean wet tropics-dry subtropics contrast, and that tropical rainfall changes follow the wet-gets-wetter, dry-gets-drier paradigm. There is also *medium confidence* that ozone depletion has increased precipitation over the southern high latitudes and decreased it over southern midlatitudes during austral summer. Owing to observational uncertainties and inconsistent results between studies, we conclude that there is *low confidence* in the attribution of changes in the seasonality of precipitation.

3.3.2.3 Streamflow

Streamflow is to-date the only variable of the terrestrial water cycle with enough in-situ observations to allow for detection and attribution analysis at continental to global scales. Based on evidence from a few formal detection and attribution studies, particularly on the timing of peak streamflow, and the qualitative evaluation of studies reporting on observed and simulated trends, AR5 concluded that there is *medium confidence* that anthropogenic influence on climate has affected streamflow in some middle and high latitude regions. AR5 also noted that observational uncertainties are large and that often only a limited number of models were considered.

Section 2.3.1.3.6 assesses that there have not been significant trends in global average streamflow over the last century, though regional trends have been observed, driven in part by internal variability. Only a limited

ACCEPTED VERSION SUBJECT TO FINAL EDITING

number of studies have systematically compared observed streamflow trends at continental to global scales with changes simulated by global circulation models in a detection and attribution setting. Yang et al. (2017) did not find a significant correlation between observed runoff changes and changes simulated in CMIP5 models in most grid cells, consistent with the assessment that observed changes are dominated by internal variability. In a pan-European assessment, Gudmundsson et al. (2017) attribute the spatio-temporal pattern of decreasing streamflow in southern Europe and increasing streamflow in northern Europe to anthropogenic climate change, but also concluded that additional effects of human water withdrawals could not be excluded. Focussing on continental runoff during 1958-2004, Alkama et al. (2013) found a significant change only when using reconstructed data over all rivers, and a large uncertainty in the estimate of the global streamflow trend due to opposing changes over different continents. Gedney et al. (2014) detected the influence of aerosols on streamflow in North America and Europe, with aerosols having driven an increase in streamflow due to reduced evaporation (see Section 8.3.1.5 for details on processes). There is also evidence for a detectable anthropogenic contribution toward earlier winter-spring streamflows in the north-central US (Kam et al., 2018) and in western Canada (Najafi et al., 2017). From a model evaluation perspective, Sheffield et al. (2013) reported that CMIP5 models reproduce spatial variations in runoff in North America well, though they tend to underestimate it.

Recently, Gudmundsson et al. (2021) performed a global detection and attribution study on streamflow and found that some regions are drying and others are wetting. Moreover, the simulated streamflow trends are consistent with observations only if externally forced climate change is considered, and the simulated effects of water and land management cannot reproduce the observed trends. The effects of volcanic eruptions in driving reduced streamflow have also been detected in the wet tropics (Iles and Hegerl, 2015; Zuo et al., 2019).

In summary, there is *medium confidence* that anthropogenic climate change has altered local and regional streamflow in various parts of the world and that the associated global-scale trend pattern is inconsistent with internal variability. Moreover, human interventions and water withdrawals, while affecting streamflow, cannot explain the observed spatio-temporal trends (*medium confidence*).

[START CROSS-CHAPTER BOX 3.2 HERE]

Cross-Chapter Box 3.2: Human Influence on Large-scale Changes in Temperature and Precipitation Extremes

Contributors: Nathan Gillett (Canada), Seung-Ki Min (Republic of Korea), Krishnan Raghavan (India), Ying Sun (China), Xuebin Zhang (Canada)

Understanding how temperature and precipitation extremes have changed at large scales and the causes of these changes is an important part of our overall assessment of human influence on the climate system. Chapter 11 assesses changes in extremes and their causes, while this Cross-Chapter Box summarizes relevant assessments and supporting evidence in Chapters 8 and 11 and relates changes in extremes to mean changes on global and continental scales.

Attribution of temperature extremes

One important aspect of various indicators of temperature extremes is their connection to mean temperature at local, regional and global scales. For example, the highest daily temperature in a summer is often highly correlated with the summer mean temperature. Model projections show that changes in temperature extremes are often closely related to shifts in mean temperature (Seneviratne et al., 2016; Kharin et al., 2018). It is thus no surprise that changes in temperature extremes are consistent with warming mean temperature, with warming leading to more hot extremes and fewer cold extremes. Given the attribution of mean warming to human influence (Section 3.3.1), and the connection between changes in mean and extreme temperatures, it is to be expected that anthropogenic forcing has also influenced temperature extremes.

Chapter 11 assesses that there is *high confidence* that climate models can reproduce the mean state and

ACCEPTED VERSION SUBJECT TO FINAL EDITING

overall warming of temperature extremes observed globally and in most regions, although the magnitude of the trends may differ, and the ability of models to capture observed trends in temperature-related extremes depends on the metric evaluated, the way indices are calculated, and the time periods and spatial scales considered (Section 11.3.3). There has been widespread evidence of human influence on various aspects of temperature extremes, at global, continental, and regional scales. This includes attribution to human influence of observed changes in intensity, frequency, and duration and other relevant characteristics at global and continental scales (Section 11.3.4). The left panel of Cross-Chapter Box 3.2, Figure 1 clearly shows that long-term changes in the global mean annual maximum daily maximum temperature can be reproduced by both CMIP5 and CMIP6 models forced with the combined effect of natural and anthropogenic forcings, but cannot be reproduced by simulations under natural forcing alone. Consistent with the assessment for global mean temperature (Section 3.3.1), aerosol changes are found to have offset part of the greenhouse gas induced increase in hot extremes globally and over most continents over the 1951-2015 period (Hu et al., 2020; Seong et al., 2021), though greenhouse gas and aerosol influences are less clearly separable in observed changes in cold extremes.

Chapter 11 assesses that it is *virtually certain* that human-induced greenhouse gas forcing is the main contributor to the observed increase in the likelihood and severity of hot extremes and the observed decrease in the likelihood and severity of cold extremes on global scales, and *very likely* that this applies on most continents.

Attribution of precipitation extremes

An important piece of evidence supporting the SREX and AR5 assessment that there is *medium confidence* that anthropogenic forcing has contributed to a global scale intensification of heavy precipitation during the second half of the 20th century is the evidence for anthropogenic influence on other aspects of the global hydrological cycle. The most significant aspect of that is the increase in atmospheric moisture content associated with warming which should, in general, lead to enhanced extreme precipitation, particularly associated with enhanced convergence in tropical and extratropical cyclones (Sections 8.2.3.2, 11.4.1). Such a connection is supported by the fact that annual maximum one-day precipitation increases with global mean temperature at a rate similar to the increase in the moisture holding capacity in response to warming, both in observations and in model simulations. Additionally, models project an increase in extreme precipitation across global land regions even in areas in which total annual or seasonal precipitation is projected to decrease.

The overall performance of CMIP6 models in simulating extreme precipitation intensity and frequency is similar to that of CMIP5 models (*high confidence*), and there is *high confidence* in the ability of models to capture the large-scale spatial distribution of precipitation extremes over land (Section 11.4.3). Evidence of human influence on extreme precipitation has become stronger since the AR5. Considering changes in precipitation intensity averaged over all wet days, there is *high confidence* that daily mean precipitation intensities have increased since the mid-20th century in a majority of land regions, including Europe, North America and Asia, and it is *likely* that such an increase is mainly due to anthropogenic emissions of greenhouse gases (Section 8.3.1.3 and 11.4.4). Section 11.4.4 also finds a larger fraction of land showing enhanced extreme precipitation and a larger probability of record-breaking one-day precipitation than expected by chance, which can only be explained when anthropogenic greenhouse gas forcing is considered. The right panel of Cross-Chapter Box 3.2, Figure 1 demonstrates the consistency in global average annual maximum daily precipitation in the observations and model simulations under combined anthropogenic and natural forcing, and inconsistency with natural forcing alone. While there is more evidence in the literature to quantify the net anthropogenic influence on extreme precipitation than the influence of individual forcing components, a dominant contribution of greenhouse gas forcing to the long-term intensification of extreme precipitation on global and continental scales has recently been quantified separately from the influence of anthropogenic aerosol and natural forcings (Dong et al., 2020; Paik et al., 2020b).

Chapter 11 assesses that it is *likely* that human influence, in particular due to greenhouse gas forcing, is the main driver of the observed intensification of heavy precipitation in global land regions during recent decades (Section 11.4.4).

ACCEPTED VERSION SUBJECT TO FINAL EDITING

[START CROSS-CHAPTER BOX 3.2, FIGURE 1 HERE]

Cross-Chapter Box 3.2, Figure 1: **Comparison of observed and simulated changes in global mean temperature and precipitation extremes.** Time series of globally averaged 5-year mean anomalies of the annual maximum daily maximum temperature (TXx in °C) and annual maximum 1-day precipitation (Rx1day as standardized probability index in %) during 1953-2017 from the HadEX3 observations and the CMIP5 and CMIP6 multi-model ensembles with natural and human forcing (upper) and natural forcing only (lower). For CMIP5, historical simulations for 1953-2005 are combined with corresponding RCP4.5 scenario runs for 2006-2017. For CMIP6, historical simulations for 1953-2014 are combined with SSP2-4.5 scenario simulations for 2015-2017. Numbers in brackets represents the number of models used. The time-fixed observational mask has been applied to model data throughout the whole period. Grid cells with more than 70% data availability during 1953-2017 plus data for at least 3 years during 2013-2017 are used. Coloured lines indicate multi-model means, while shading represents 5th-95th percentile ranges, based on all available ensemble members with equal weight given to each model (Section 3.2). Anomalies are relative to 1961-1990 means. Figure is updated from Seong et al. (2021), their Figure 3 and Paik et al. (2020), their Figure 3. Further details on data sources and processing are available in the chapter data table (Table 3.SM.1).

[END CROSS-CHAPTER BOX 3.2, FIGURE 1 HERE]

[END CROSS-CHAPTER BOX 3.2 HERE]

3.3.3 Atmospheric Circulation

3.3.3.1 The Hadley and Walker Circulations

The tropical tropospheric circulation features meridional and zonal overturning circulations, called Hadley and Walker circulations. In the zonal mean, the downwelling branch of the Hadley circulation cell is located in the subtropics and is often used as an indicator of the meridional extent of the tropics. In the equatorial zonal-vertical section, the major rising branch of the Walker circulation is located over the Maritime continent with secondary ascending regions over northern South America and Africa. The zonal component of the surface trade winds over most of the equatorial Pacific and Atlantic is associated with the Walker circulation. The present section assesses the zonal-mean Hadley cell extent and the Pacific Walker circulation strength. Regional and water cycle aspects of these circulations are assessed in more detail in Section 8.3.2.

AR5 found *medium confidence* that the depletion of stratospheric ozone had contributed to Hadley cell widening in the SH in austral summer (Bindoff et al., 2013). It also noted that in contrast to a simulated weakening in response to greenhouse gas forcing, the Walker circulation had actually strengthened since the early 1990s, precluding any detection of human influence.

Hadley cell extent

Grise et al. (2019) found that a metric based on surface zonal winds, which are well constrained by surface observations, best compares reanalyses with CMIP5 models. With this method and new reanalysis products, the CMIP5 historical simulation ensembles simulate comparable mean states and variability of the subtropical edge latitude of the Hadley cells to those observed (Grise et al., 2019).

Chapter 2 assesses that there has been a *very likely* widening of the Hadley circulation since the 1980s (Section 2.3.1.4.1). The CMIP5 (Davis and Birner, 2017; Grise et al., 2018) and CMIP6 (Grise and Davis, 2020) historical simulation ensembles span the observed trend of the zonal-mean Hadley cell edges since the 1980s (Figure 3.16a-c). Studies based on CMIP5 models find a contribution from human influence to the

ACCEPTED VERSION SUBJECT TO FINAL EDITING

observed widening trend, especially in the SH (Gerber and Son, 2014a; Staten et al., 2018, 2020; Grise et al., 2019; Jebri et al., 2020), which is confirmed in CMIP6 (Figure 3.16b-c; Grise and Davis, 2020).

In the annual mean, internal variability, including Pacific Decadal Variability (PDV; Annex IV.2.6), contributed to the observed zonal-mean Hadley cell expansion since 1980 comparably with human influence (Allen et al., 2014; Allen and Kovilakam, 2017; Mantsis et al., 2017; Amaya et al., 2018; Grise et al., 2018). Indeed, the ensemble-mean expansion in historical simulations is significantly weaker than in most of the reanalyses shown in Figure 3.16a-c, while the Atmospheric Model Intercomparison Project (AMIP) simulations forced by observed SSTs (Figure 3.16a-c) show stronger trends than historical coupled simulations on average (Davis and Birner, 2017; Grise et al., 2018; Nguyen et al., 2015). The human-induced change has not yet clearly emerged out of the internal variability range in the NH expansion (Quan et al., 2018; Grise et al., 2019), whereas the trend in the annual-mean SH edge is outside the 5-95th percentile range of internal variability in CMIP6 in 3 out of the 4 reanalyses (Figure 3.16b). For the SH summer when the simulated human influence is strongest, the 1981-2000 trend in 3 out of the 4 reanalyses falls outside the 5-95th percentile range of internal variability (Grise et al., 2018, 2019; Tao et al., 2016).

In CMIP5 simulations, greenhouse gas increases and, in austral summer, stratospheric ozone depletion, contribute to the SH expansion (Gerber and Son, 2014b; Nguyen et al., 2015; Tao et al., 2016a; Kim et al., 2017b), but the ozone influence is not significant in available CMIP6 simulations (Figure 3.16b-c). Since the 2000s, the stabilization or slight recovery of stratospheric ozone (Section 2.2.5.2) is consistent with the smaller observed trends (Banerjee et al., 2020). While many CMIP5 models underrepresent the magnitude of the PDV, implying potential overconfidence on the detection of human influence on the Hadley cell expansion, this is less the case for the CMIP6 models (Section 3.7.6). However, the mechanism underlying the Hadley Cell expansion remains unclear (Staten et al., 2018, 2020), precluding a process-based validation of the simulated human influence.

Walker circulation strength

CMIP5 models reproduce the mean state of the Walker circulation with reasonable fidelity, evidenced by the spatial pattern correlations of equatorial zonal mass stream function between models and observations being larger than 0.88 (Ma and Zhou, 2016a). CMIP5 historical simulations on average simulate a significant weakening of the Pacific Walker circulation over the 20th century (DiNezio et al., 2013; Sandeep et al., 2014; Kociuba and Power, 2015), which is also seen in CMIP6 (Figure 3.16d). This weakening is accompanied by reduction of convective activity over the Maritime Continent and enhancement over the central equatorial Pacific (DiNezio et al., 2013; Sandeep et al., 2014; Kociuba and Power, 2015). In the CMIP6 simulations, greenhouse gas forcing induces this weakening (Figure 3.16d), which is consistent with theories based on radiative-convective equilibrium (Vecchi et al., 2006; Vecchi and Soden, 2007) and thermodynamic air-sea coupling (Xie et al., 2010), but inconsistent with a theory highlighting the ocean dynamical effect which suggests a strengthening in response to greenhouse gas increases (Clement et al., 1996; Seager et al., 2019; see also Section 7.4.4.2.1). Seager et al. (2019) attributed this inconsistency to equatorial Pacific SST biases in the models (Section 3.5.1.2). However, observational and reanalysis data sets disagree on the sign of trends in the Walker Circulation strength over the 1901-2010 period (Figure 3.16d,), and Section 2.3.1.4.1 assesses *low confidence* in observed long-term Walker Circulation trends. The observational uncertainty remains high in the trends since the 1950s (Tokinaga et al., 2012; L'Heureux et al., 2013), though both CMIP5 and CMIP6 historical simulations span trends of all but one observational data set (Figure 3.16e). For this period, external influence simulated in CMIP6 is insignificant due to a partial compensation of forced responses to greenhouse gases and aerosols and large internal decadal variability (Figure 3.16e). It is notable that while AMIP simulations on average show strengthening over both the periods, those simulations are forced by one reconstruction of SST, which itself is subject to uncertainty before the 1970s (Deser et al., 2010; Tokinaga et al., 2012).

Observational SST products indicate that the equatorial zonal SST gradient from the western to the eastern equatorial Pacific has strengthened since 1870 (Section 7.4.4.2.1). While CMIP5 historical simulations on average simulate a weakening, large ensemble simulations span the observed strengthening since the 1950s (Watanabe et al., 2021) suggesting an important contribution from internal variability. Coats and Karnauskas (2017) also find that the anthropogenic influence on the SST gradient is yet to emerge out of internal

ACCEPTED VERSION SUBJECT TO FINAL EDITING

variability even on centennial timescales.

Trends since the 1980s in in-situ and satellite observations and reanalyses exhibit strengthening of the Pacific Walker circulation and SST gradient (L'Heureux et al., 2013; Boisséson et al., 2014; England et al., 2014; Kociuba and Power, 2015; Ma and Zhou, 2016; Section 2.3.1.4.1; Figure 3.16f). AMIP simulations reproduce this strengthening (Boisséson et al., 2014; Ma and Zhou, 2016; Figure 3.16d), indicating a dominant role of SST changes. However, all reanalysis trends lie outside the 5-95% range of simulated CMIP6 historical Walker circulation trends over this period (Figure 3.16f), consistent with CMIP5 results (England et al., 2014; Kociuba and Power, 2015). This may be in part caused by the underestimation of the PDV magnitude especially in CMIP5 models (Kociuba and Power, 2015; Chung et al., 2019; Section 3.7.6), but also suggests a potential error in simulating the forced changes of the Walker circulation. Specifically, anthropogenic and volcanic aerosol changes over this period may have driven a strengthening (DiNezio et al., 2013; Takahashi and Watanabe, 2016a; Hua et al., 2018). This aerosol influence may be indirect via Atlantic Multidecadal Variability (AMV; Annex IV.2.7) through inter-basin teleconnections (McGregor et al., 2014; Li et al., 2015d; Chikamoto et al., 2016; Kucharski et al., 2016; Ruprich-Robert et al., 2017), which may be underestimated in models due to SST biases in the equatorial Atlantic (Section 3.5.1.2; McGregor et al., 2018). Note also the large uncertainty in aerosol influence on the Walker circulation (Kuntz and Schrag, 2016; Hua et al., 2018; Oudar et al., 2018), which is also seen in CMIP6 (Figure 3.16f).

Paleoclimate data from the Pliocene epoch suggest that there was a reduction in the zonal SST gradient in the tropical Pacific under a similar CO_2 concentration as today (Cross-Chapter Box 2.4; Section 7.4.4.2.2). Tierney et al. (2019) found that this weaker gradient compared to pre-industrial, which suggests a weaker Walker circulation, is captured by climate models under Pliocene CO_2 levels, in agreement with the CMIP6 response to greenhouse gas forcing (Figure 3.16d), though the magnitude of this effect varies strongly between models (Corvec and Fletcher, 2017).

Summary

It is *likely* that human influence has contributed to the poleward expansion of the zonal mean Hadley cell in the SH since the 1980s. This assessment is supported by studies since AR5, which consistently find human influence from greenhouse gas increases on the expansion, with additional influence from ozone depletion in austral summer. For the strong ozone depletion period of 1981-2000, human influence is detectable in the summertime poleward expansion in the SH (*medium confidence*). By contrast, there is *medium confidence* that the expansion of the zonal mean Hadley cell in the NH is within the range of internal variability, with contributions from PDV and other internal variability. The causes of the observed strengthening of the Pacific Walker circulation over the 1980-2014 period are not well understood, since the observed strengthening trend is outside the range of variability simulated in the coupled models (*medium confidence*). Large observational uncertainty, lack of understanding of the mechanism underlying the poleward Hadley cell expansion, and contradicting theories on the greenhouse gas influence and uncertainty in the aerosol influence on the Walker circulation strength, limit confidence in these assessments.

[START FIGURE 3.16 HERE]

Figure 3.16: Model evaluation and attribution of changes in Hadley cell extent and Walker circulation strength. (a-c) Trends in subtropical edge latitude of the Hadley cells in (a) the Northern Hemisphere for 1980-2014 annual mean and (b-c) Southern Hemisphere for (b) 1980-2014 annual mean and (c) 1980/81-1999/2000 December-January-February mean. Positive values indicate northward shifts. (d-f) Trends in the Pacific Walker circulation strength for (d) 1901-2010, (e) 1951-2010 and (f) 1980-2014. Positive values indicate strengthening. Based on CMIP5 historical (extended with RCP4.5), CMIP6 historical, AMIP, pre-industrial control, and single forcing simulations along with HadSLP2 and reanalyses. Pre-industrial control simulations are divided into non-overlapping segments of the same length as the other simulations. White boxes and whiskers represent mean, interquartile ranges and 5th and 95th percentiles, calculated after weighting individual members with the inverse of the ensemble of the same model, so that individual models are equally weighted (Section 3.2). The filled boxes represent the 5-95% confidence interval on the multi-model mean trends of the models with at least 3 ensemble members, with dots indicating the ensemble means of individual models. The edge latitude of the Hadley cell is defined

ACCEPTED VERSION SUBJECT TO FINAL EDITING

where the surface zonal wind velocity changes sign from negative to positive, as described in the Appendix of Grise et al. (2018). The Pacific Walker circulation strength is evaluated as the annual mean difference of sea level pressure between 5ºS-5ºN, 160ºW-80ºW and 5ºS-5ºN, 80ºE-160ºE. Further details on data sources and processing are available in the chapter data table (Table 3.SM.1).

[END FIGURE 3.16 HERE]

3.3.3.2 Global Monsoon

Monsoons are seasonal transitions of regimes in atmospheric circulation and precipitation with the annual cycle of solar insolation, in association with redistribution of moist static energy (Wang and Ding, 2008; Wang et al., 2014b; Biasutti et al., 2018). The global monsoon can be defined to encompasses all monsoon systems based on precipitation contrast in the solstice seasons (Wang and Ding, 2008; Figure 3.17). All regional monsoons are intimately connected to the global tropical atmospheric overturning by mass (Trenberth et al., 2000), momentum and energy budgets (Biasutti et al., 2018; Geen et al., 2020). Assessments of regional monsoon changes are made in Section 8.3.2.4 and Sections 10.4.2.1 and 10.6.3.

AR5 assessed that CMIP5 models simulated monsoons better than CMIP3 models but that biases remained in domains and intensity (*high confidence*) (Flato et al., 2013). There were no detection and attribution assessment statements on the decreasing trend of global monsoon precipitation over land from the 1950s to the 1980s or the increasing trend of global monsoon precipitation afterwards. In the paleoclimate context, it was determined with *high confidence* that orbital forcing produces strong interhemispheric rainfall variability evident in multiple types of proxies (Masson-Delmotte et al., 2013a).

Paleoclimate proxy evidence shows that the global monsoon has varied with orbital forcing and greenhouse gases (Section 2.3.1.4.2; Mohtadi et al., 2016; Seth et al., 2019). These large-magnitude intensifications and weakenings in the global monsoon involved in some cases orders-of-magnitude changes in precipitation locally (Harrison et al., 2014; Tierney et al., 2017c). Paleoclimate modelling and limited data from past climate states with high CO_2 suggest that precipitation intensifies in the monsoon domain under elevated greenhouse gases, providing context for present and future trends (Passey et al., 2009; Haywood et al., 2013; Zhang et al., 2013b). In model simulations of the mid-Pliocene, when globally averaged temperature was higher than present day, precipitation was larger in West African and South and East Asian monsoons than under pre-industrial conditions, consistent with proxy evidence (Zhang et al., 2015; Sun et al., 2016, 2018; Corvec and Fletcher, 2017; Li et al., 2018a). Prescott et al. (2019) and Zhang et al. (2019) find an important role for orbital forcing and CO_2 in the mid-Pliocene monsoon expansion and intensification. Models are also able to capture interhemispherically contrasting monsoon changes in the Last Interglacial in response to orbital forcing and greenhouse gases, with wetter West African and Asian monsoons and a drier South American monsoon as seen in proxies (Govin et al., 2014; Gierz et al., 2017; Pedersen et al., 2017). In overall agreement with proxy evidence, a model with transient forcing simulates wetting and drying respectively of the Southern and NH monsoons during the last deglaciation, with an important contribution from Atlantic Meridional Overturning Circulation (AMOC) slowdown (Otto-Bliesner et al., 2014; Mohtadi et al., 2016).

During the mid-Holocene, global monsoons were stronger especially in the NH with an expansion of the West African monsoon domain in response to orbital forcing (Biasutti et al., 2018; Section 2.3.1.4.2). Simulations of the mid-Holocene with CMIP5 and CMIP6 models qualitatively capture the stronger NH monsoon (Jiang et al., 2015; Brierley et al., 2020), mainly driven by atmospheric circulation changes (D'Agostino et al., 2019). However, the models underestimate the monsoon expansion found in proxy reconstructions (Perez-Sanz et al., 2014; Harrison et al., 2015; Tierney et al., 2017d), which may be linked to mean biases in the monsoon domain (Brierley et al., 2020) and may be improved by imposing vegetation and dust changes (Pausata et al., 2016). The models simulate the weaker SH monsoon during the mid-Holocene (D'Agostino et al., 2020), consistent with proxy evidence (Section 2.3.1.4.2). These studies indicate that models can qualitatively reproduce past global monsoon changes seen in proxies, though issues remain in quantitatively reproducing proxy observations. Studies of last millennium simulations show that simulated

ACCEPTED VERSION SUBJECT TO FINAL EDITING

global monsoon precipitation increases with global mean temperature, while changes in monsoon circulation and hemispheric monsoon precipitation depend on forcing sources (Liu et al., 2012; Chai et al., 2018). Compared to greenhouse gas and solar variations, volcanic forcing is more effective in changing the global monsoon precipitation over the last millennium (Chai et al., 2018).

Reproducing monsoons in terms of domain, precipitation amount, and timings of onset and retreat over the historical period also remains difficult. While CMIP5 historical simulations correctly capture global monsoon domains and intensity based on summer and winter precipitation differences, they underestimate the extent and intensity of East Asian and North American monsoons while overestimating them over the tropical western North Pacific (Lee and Wang, 2014b; Yan et al., 2016a). Wang et al. (2020) reported that CMIP6 models simulate the global monsoon domain and precipitation better (Figure 3.17a,b), albeit with biases in annual mean precipitation and the timings of onset and withdrawal of the SH monsoon. Notable inter-model differences were identified in CMIP5, with the multi-model ensemble mean outperforming individual models (Lee and Wang, 2014b). Common biases were identified across CMIP5 models in moist static energy and upper-tropospheric temperature associated with the South Asian summer monsoon, which may arise from overly smoothed model topography (Boos and Hurley, 2012). However, in atmospheric models with increasing resolution approaching 20 km, improvements in monsoon precipitation are not universal across regions and models, and overall improvements are unclear (Johnson et al., 2016; Ogata et al., 2017; Zhang et al., 2018b).

In instrumental records, global summer monsoon precipitation intensity (measured by summer precipitation averaged over the monsoon domain) decreased from the 1950s to 1980s, followed by an increase (Section 2.3.1.4.2; Figure 3.17c), arising mainly from variations in Northern Hemispheric land monsoons. A CMIP5 multi-model study by Zhang et al. (2018b) found that observed 1951-2004 trends of the global and NH summer land monsoon precipitation intensity are well captured by historical simulations, and CMIP6 models show similar results for global land summer monsoon precipitation (Figure 3.17c). However, the 1960s peak in the NH summer monsoon circulation is outside the 5th-95th percentile range of CMIP5 and CMIP6 historical simulations for two out of three reanalyses (Figure 3.17d). Modelling studies show that greenhouse gas increases act to enhance NH summer monsoon precipitation intensity (Liu et al., 2012; Polson et al., 2014; Chai et al., 2018; Zhang et al., 2018b). Since the mid-20th century, however, modelling studies show that this effect was overwhelmed by the influence of anthropogenic aerosols in CMIP5 (Polson et al., 2014; Guo et al., 2015; Zhang et al., 2018c; Giannini and Kaplan, 2019) and in CMIP6 (Zhou et al., 2020b). Weakening of the monsoon circulation and reduction of moisture availability are important in this aerosol influence (Zhou et al., 2020b). Besides these human influences, the global monsoon is sensitive to internal variability and natural forcing including ENSO and volcanic aerosols on interannual time scales and PDV and AMV on decadal to multidecadal time scales (Wang et al., 2013a, 2018; Liu et al., 2016a; Jiang and Zhou, 2019; Zuo et al., 2019); though AMV in the 20th century may have been partly driven by aerosols, see Section 3.7.7. Indeed, AMIP simulations better reproduce the observed multidecadal variations of the global monsoon precipitation and circulation (Figure 3.17c,d). Zhang et al. (2018b) find that the multi-model ensemble mean trend of global land monsoon precipitation in historical simulations, dominated by anthropogenic aerosol forcing contributions, emerges out of the 90% range of internally-driven trends in pre-industrial control simulations. However, it should be noted that CMIP5 models tend to underrepresent the PDV magnitude (Section 3.7.6), suggesting potential overconfidence on the detection of the forced signal. An observed enhancement in global summer monsoon precipitation since the 1980s is accompanied by an intensification of the NH summer monsoon circulation (Figure 3.17c,d). These trends appear to be at the extreme of the range of the CMIP6 historical simulation ensemble but well captured by AMIP simulations (Figure 3.17c,d). While the precipitation increase is consistent with greenhouse gas forcing, the circulation intensification is opposite to the simulated response to greenhouse gas forcing, and these enhancements have been attributed to PDV and AMV (Wang et al., 2013b; Kamae et al., 2017).

In summary, while greenhouse gas increases acted to enhance the global land monsoon precipitation over the 20th century (*medium confidence*), consistent with projected future enhancement (Section 4.5.1), this tendency was overwhelmed by anthropogenic aerosols from the 1950s to the 1980s, which contributed to weakening of global land summer monsoon precipitation intensity for this period (*medium confidence*). There is *medium confidence* that the intensification of global monsoon precipitation and NH summer

ACCEPTED VERSION SUBJECT TO FINAL EDITING

monsoon circulation since the 1980s is dominated by internal variability. These assessments are supported respectively by multi-model detection and attribution studies which find an important role for anthropogenic aerosols in the weakening trend, and studies that identify a role for AMV and PDV in inducing the NH summer monsoon circulation enhancement since the 1980s. Supported by multi-model simulations that are qualitatively consistent with proxy evidence, there is *high confidence* that orbital forcing contributed to stronger NH monsoon precipitation in the mid-Pliocene and mid-Holocene than pre-industrial. While CMIP5 models can capture the domain and precipitation intensity of the global monsoon, biases remain in their regional representations, and they are unsuccessful in quantitatively reproducing changes in paleo reconstructions (*high confidence*). CMIP6 models reproduce the domain and precipitation intensity of the global monsoon observed over the instrumental period better than CMIP5 models (*medium confidence*). However, CMIP5 and CMIP6 models fail to fully capture the variations of the NH summer monsoon circulation (Figure 3.17d), but there is *low confidence* to this assessment due to a lack of evidence in the literature.

[START FIGURE 3.17 HERE]

Figure 3.17: Model evaluation of global monsoon domain, intensity, and circulation. (a-b) Climatological summer-winter range of precipitation rate, scaled by annual mean precipitation rate (shading) and 850 hPa wind velocity (arrows) based on (a) GPCP and ERA5 and (b) a multi-model ensemble mean of CMIP6 historical simulations for 1979-2014. Enclosed by red lines is the monsoon domain based on the definition by Wang and Ding (2008). (c-d) 5-year running mean anomalies of (c) global land monsoon precipitation index defined as the percentage anomaly of the summertime precipitation rate averaged over the monsoon regions over land, relative to its average for 1979-2014 (the period indicated by light grey shading) and (d) the tropical monsoon circulation index defined as the vertical shear of zonal winds between 850 and 200 hPa levels averaged over 0º-20ºN, from 120ºW eastward to 120ºE in NH summer (Wang et al., 2013; m s^{-1}) in CMIP5 historical and RCP4.5 simulations, CMIP6 historical and AMIP simulations. Summer and winter are defined for individual hemispheres: May through September for NH summer and SH winter, and November through March for NH winter and SH summer. The number of models and ensembles are given in the legend. The multi-model ensemble mean and percentiles are calculated after weighting individual members with the inverse of the ensemble size of the same model, so that individual models are equally weighted irrespective of ensemble size. Further details on data sources and processing are available in the chapter data table (Table 3.SM.1).

[END FIGURE 3.17 HERE]

3.3.3.3 Extratropical Jets, Storm Tracks and Blocking

Extratropical jets are wind maxima in the upper troposphere which are often associated with storms, blocking, and weather extremes. Blocking refers to long-lived, stationary high-pressure systems that are often associated with a poleward displacement of the jet, causing cold spells in winter and heat waves in summer (e.g., Sousa et al., 2018). Sections 2.3.1.4.3, 8.3.2.7, and 11.7.2 discuss these features in more detail.

AR5 concluded that models were able to capture the general characteristics of extratropical cyclones and storm tracks, although it also noted that most models underestimated cyclone intensity, that biases in cyclone frequency were linked to biases in sea surface temperatures, and that resolution can play a significant role in the quality of the simulation of storms (Flato et al., 2013). Similarly, AR5 found with *high confidence* that simulation of blocking was improved due to increases in resolution. AR5 did not specifically assess changes in Southern-Hemisphere storm track characteristics or blocking.

Since AR5, new research using CMIP5 and CMIP6 models has confirmed that increasing the model resolution improves the simulation of cyclones and blocking in all seasons albeit with some exceptions and caveats (Zappa et al., 2013; Davini et al., 2017; Schiemann et al., 2017, 2020; Davini and D'Andrea, 2020; Priestley et al., 2020). New research also finds that model performance with respect to the simulation of cyclones and that of blocking events are correlated (Zappa et al., 2014), suggesting biases in both are aspects

ACCEPTED VERSION SUBJECT TO FINAL EDITING

of the same underlying problem in models (Figure 3.18). In the North Pacific basin the annual-mean blocking frequency is now well simulated compared to earlier evaluations, but substantial errors in the blocking frequency remain in the Euro-Atlantic sector (Dunn-Sigouin and Son, 2013; Davini and D'Andrea, 2016, 2020; Mitchell et al., 2017; Woollings et al., 2018; Figure 3.18). While there is a resolution dependence in the size of this bias, even at very high resolution blocking in the Euro-Atlantic sector remains underestimated (Schiemann et al., 2017), and there is evidence of a compensation of errors as the resolution is increased (Davini et al., 2017). Davini and D'Andrea (2020) show that while the simulation of blocking improves with increasing resolution in CMIP3, CMIP5, and CMIP6 models, other factors contribute to biases, particularly to the underestimation of Euro-Atlantic blocking (Schiemann et al., 2020). The persistence of blocking events, typically underestimated, has not improved from CMIP5 to CMIP6 (Schiemann et al., 2020). Chapter 10.3.3.3 discusses the implications of the biases discussed here for regional climate.

For the North Pacific storm track CMIP6 simulations exhibit large remaining underestimations of cyclone frequencies during summer (June to August), which for the low-resolution models have essentially remained unchanged versus CMIP5, and there is only a small resolution dependence of this bias (Priestley et al., 2020). During winter (December to February), both CMIP5 and CMIP6 models tend to place the North Pacific storm track too far equatorward (Yang et al., 2018b; Priestley et al., 2020), leading to an overestimation of cyclones between 30 and 40°N in the Pacific and an underestimation to the north of this. Both low- and high-resolution models show this pattern, but low-resolution models generally simulate fewer cyclones throughout the North Pacific (Priestley et al., 2020).

In winter, the North Atlantic storm track remains displaced to the south and east in many models (Harvey et al., 2020), leading to underestimations of cyclone frequencies near the North American coast and overestimations in the eastern North Atlantic. Higher-resolution CMIP6 models perform slightly better in this regard than low-resolution models. In summer (June to August), cyclone frequencies throughout the extratropical North Atlantic, which were substantially underestimated in CMIP5, have improved in CMIP6 high-resolution models. In low-resolution CMIP6 models, the problem is essentially unchanged (Priestley et al., 2020); this is associated with generally underestimated variability of sea level pressure in CMIP models (Harvey et al., 2020).

For the SH (not considered in AR5), (Priestley et al., 2020) find considerable improvement in the placement of the Southern Ocean storm track during summer (December to February) in CMIP6 models versus CMIP5, consistent with a more realistic annual mean surface wind maximum latitude in CMIP6 than in CMIP5 (Goyal et al., 2021). Relative to CMIP5, both low- and high-resolution CMIP6 models have increased track densities south of about 55°S and decreases between about 40 and 55°S, in better agreement with observations than CMIP5 models (Parsons et al., 2016; Patterson et al., 2019). CMIP5 models and high-resolution CMIP6 models simulate a storm track that is positioned too far equatorward, although the bias is smaller in the high-resolution models. By contrast, the low-resolution CMIP6 models simulate a storm track that is slightly too far poleward on average (Priestley et al., 2020). In winter (June to August), the biases found in CMIP5 are only slightly improved on in CMIP6, with models continuing to underestimate the broad maximum cyclone track density in the south-eastern Indian Ocean and overestimate the minimum in the south-western South Pacific (Priestley et al., 2020).

There is only one contiguous blocking region in the SH, with the blocking frequency maximizing in the South Pacific and minimizing in the southern Indian Ocean regions (Parsons et al., 2016; Patterson et al., 2019). CMIP5 simulations agree relatively well with ERA-Interim in this region regarding the distribution of blocking events (Parsons et al., 2016). Individual models exhibit considerable biases in the blocking frequency; however only in austral summer do Patterson et al. (2019) find a systematic, multi-model underestimation of the blocking frequency in and around the Tasman Sea. The blocking frequency is anticorrelated with the amplitude of the SAM. Ozone depletion, through stratosphere-troposphere coupling, may have caused an increase in the blocking frequency in the South Atlantic sector (Dennison et al., 2016); this finding requires confirmation using a multi-model approach.

In addition to inadequate resolution, blocking and storm track biases in both hemispheres also result from

ACCEPTED VERSION SUBJECT TO FINAL EDITING

mean state biases, in particular, biases related to the parameterization of orographic effects and to the misrepresentation of the Gulf Stream SST front (Anstey et al., 2013; Berckmans et al., 2013; Davini and D'Andrea, 2016b; O'Reilly et al., 2016b; Pithan et al., 2016; Schiemann et al., 2017). Overall SST biases have been suggested to have only a weak relevance to blocking (Davini and D'Andrea, 2016b).

Section 2.3.1.4.3 assesses that the total number of extratropical cyclones has *likely* increased since the 1980s in the NH (*low confidence*), but with fewer deep cyclones particularly in summer. This observed reduction in cyclone activity by about 4% per decade in the NH in summer (Chang et al., 2016; Section 2.3.1.4.3) may be associated with human-induced warming. CMIP5 historical simulations generally reproduce a reduction but underestimate its magnitude (Chang et al., 2016). Furthermore, feedback mechanisms associated with clouds may be responsible for substantial inter-model spread (Chang et al., 2016; Voigt and Shaw, 2016). In boreal winter, recent studies have suggested a potential influence of the rapid Arctic warming on observed intensification of NH storm track activity in the past few decades, while other studies question this possibility (Cross-chapter Box 10.1).

Section 2.3.1.4.3 assesses that the extratropical jets and cyclone tracks have *likely* been shifting poleward in both hemispheres since the 1980s with marked seasonality in trends (*medium confidence*). For the SH, studies using CMIP5 and other models imply that both ozone depletion and increasing greenhouse gases have caused substantial atmospheric circulation change since the 1960s when concentrations of ozone-depleting substances started to increase (Eyring et al., 2013; Iglesias-Suarez et al., 2016; Karpechko et al., 2018b; Son et al., 2018a). In particular, ozone depletion, during austral summer, has been linked to a poleward shift of the westerly jet and Southern-Hemisphere circulation zones and a southward expansion of the tropics (Kang et al., 2011), which is associated with a strengthening trend of the Southern Annular Mode (SAM; Section 3.7.2). This has been well reproduced by climate models with prescribed historical ozone concentration or interactive ozone chemistry (Gerber and Son, 2014; Son et al., 2018; Figure 3.19).

In summary, there is *low confidence* that an observed decrease in the frequency of NH summertime extratropical cyclones is linked to anthropogenic influence. In the SH, there is *high confidence* that human influence, in the form of ozone depletion, has contributed to the observed poleward shift of the jet in austral summer, while *confidence* is *low* for human influence on historical blocking activity. The *low confidence* statements are due to the limited number of studies available. The shift of the SH jet is correlated with modulations of the SAM, and justification for the associated *high confidence* statement on attribution of changes in the SAM is provided in Section 3.7.2. There is *medium confidence* in model performance regarding the simulation of the extratropical jets, storm track and blocking activity, with increased resolution sometimes corresponding to better performance, but important shortcomings remain, particularly for the Euro-Atlantic sector of the NH. Nonetheless, synthesizing across Sections 3.3.3.1-3.3.3.3, there is *high confidence* that CMIP6 models capture the general characteristics of the tropospheric large-scale circulation.

[START FIGURE 3.18 HERE]

Figure 3.18: Instantaneous Northern-Hemisphere blocking frequency (% of days) in the extended northern winter season (DJFM) for the years 1979-2000. Results are shown for ERA5 reanalysis (black), CMIP5 (blue) and CMIP6 (red) models. Coloured lines show multi-model means and shaded ranges show corresponding 5-95% ranges constructed with one realization from each model. Figure is adapted from Davini and D'Andrea (2020), their Figure 12 and following the D'Andrea et al. (1998) definition of blocking. Further details on data sources and processing are available in the chapter data table (Table 3.SM.1).

[END FIGURE 3.18 HERE]

[START FIGURE 3.19 HERE]

Figure 3.19: Long-term mean (thin black contour) and linear trend (colour) of zonal mean DJF zonal winds over 1985-2014 in the SH. Displayed are (a) ERA5 and (b) CMIP6 multi-model mean (58 CMIP6

ACCEPTED VERSION SUBJECT TO FINAL EDITING

models). The solid contours show positive (westerly) and zero long-term mean zonal wind, and the dashed contours show negative (easterly) long-term mean zonal wind. Only one ensemble member per model is included. Figure is modified from Eyring et al. (2013), their Figure 12. Further details on data sources and processing are available in the chapter data table (Table 3.SM.1).

[END FIGURE 3.19 HERE]

3.3.3.4 Sudden Stratospheric Warming Activity

Sudden stratospheric warmings (SSWs) are stratospheric weather events associated with anomalously high temperatures at high latitudes persisting from days to weeks. Section 2.3.1.4.5 discusses the definition and observational aspects of SSWs. SSWs are often associated with anomalous weather conditions, e.g. winter cold spells, in the lower atmosphere (e.g., Butler et al., 2015a; Baldwin et al., 2021).

Seviour et al. (2016) found that stratosphere-resolving CMIP5 models, on average, reproduce the observed frequency of vortex splits (one form of SSWs) but with a wide range of model-specific biases. Models that produce a better mean state of the polar vortex also tend to produce a more realistic SSW frequency (Seviour et al., 2016). The mean sea level pressure anomalies occurring in CMIP5 model simulations when an SSW is underway however differs substantially from those in reanalyses (Seviour et al., 2016). Unlike stratosphere-resolving models, models with limited stratospheric resolution, which make up more than half of the CMIP5 ensemble, underestimate the frequency of SSWs (Osprey et al., 2013; Kim et al., 2017a). Taguchi (2017) found a general underestimation in CMIP5 models of the frequency of "major" SSWs (which are associated with a break-up of the polar vortex), an aspect of an underrepresentation in those models of dynamical variability in the stratosphere. Wu and Reichler (2020) found that finer vertical resolution in the stratosphere and a model top above the stratopause tend to be associated with a more realistic SSW frequency in CMIP5 and CMIP6 models.

Some studies find an increase in the frequency of SSWs under increasing greenhouse gases (e.g. Kim et al., 2017a; Schimanke et al., 2013; Young et al., 2013). However, this behaviour is not robust across ensembles of chemistry-climate models (Mitchell et al., 2012; Ayarzagüena et al., 2018; Rao and Garfinkel, 2021). There is an absence of studies specifically focusing on simulated trends in SSWs during recent decades, and the short record and substantial decadal variability yields *low confidence* in any observed trends in the occurrence of SSW events in the NH winter (Section 2.3.1.4.5). Such an absence of a trend and large variability would also be consistent with a recent reconstruction of SSWs extending back to 1850, based on sea level pressure observations (Domeisen, 2019), although this time series has limitations as it is not based on direct observations of SSWs.

In summary, an anthropogenic influence on the frequency or other aspects of SSWs has not yet been robustly detected. There is *low confidence* in the ability of models to simulate any such trends over the historical period because of large natural interannual variability and also due to common substantial biases in the simulated mean state affecting the simulated frequency of SSWs.

3.4 Human Influence on the Cryosphere

3.4.1 Sea Ice

3.4.1.1 Arctic Sea Ice

The AR5 concluded that "anthropogenic forcings are *very likely* to have contributed to Arctic sea ice loss since 1979" (Bindoff et al., 2013), based on studies showing that models can reproduce the observed decline only when including anthropogenic forcings, and formal attribution studies. Since the beginning of the modern satellite era in 1979, NH sea ice extent has exhibited significant declines in all months with the largest reduction in September (see Figures 3.20 and 3.21 and Section 2.3.2.1.1 for more details on observed

ACCEPTED VERSION SUBJECT TO FINAL EDITING

changes). The recent Arctic sea ice loss during summer is unprecedented since 1850 (*high confidence*), but as in AR5 and SROCC there remains only *medium confidence* that the recent reduction is unique during at least past 1000 years due to sparse observations (Sections 2.3.2.1.1 and 9.3.1.1). CMIP5 models also simulate NH sea ice loss over the satellite era but with large differences among models (e.g., Massonnet et al., 2012; Stroeve et al., 2012). The envelope of simulated ice loss across model simulations encompasses the observed change, although observations fall near the low end of the CMIP5 and CMIP6 distributions of trends (Figure 3.20). CMIP6 models on average better capture the observed Arctic sea ice decline, albeit with large inter-model spread. Notz et al. (2020) found that CMIP6 models better reproduce the sensitivity of Arctic sea ice area to CO_2 emissions and global warming than earlier CMIP models although the models' underestimation of this sensitivity remains. Davy and Outten (2020) also found that CMIP6 models can simulate the seasonal cycle of Arctic sea ice extent and volume better than CMIP5 models. For the assessment of physical processes associated with changes in Arctic sea ice, see Section 9.3.1.1.

Since AR5, there have been several new detection and attribution studies on Arctic sea ice. While the attribution literature has mostly used sea ice extent (SIE), it is closely proportional to sea ice area (SIA; Notz, 2014), which is assessed in Chapters 2 and 9 and shown in Figures 3.20 and 3.21. Kirchmeier-Young et al. (2017) compared the observed time series of the September SIE over the period 1979-2012 with those from different large ensemble simulations which provide a robust sampling of internal climate variability (CanESM2, CESM1, and CMIP5) using an optimal fingerprinting technique. They detected anthropogenic signals which were separable from the response to natural forcing due to solar irradiance variations and volcanic aerosol, supporting previous findings (Figure 3.21; Kay et al., 2011; Min et al., 2008; Notz and Marotzke, 2012; Notz and Stroeve, 2016). Using selected CMIP5 models and three independently derived sets of observations, Mueller et al. (2018) detected fingerprints from greenhouse gases, natural, and other anthropogenic forcings simultaneously in the September Arctic SIE over the period 1953-2012. They further showed that about a quarter of the greenhouse gas induced decrease in SIE has been offset by an increase due to other anthropogenic forcing (mainly aerosols). Similarly, Gagné et al. (2017a) suggested that the observed increase in Arctic sea ice concentration over the 1950-1975 period was primarily due to the cooling contribution of anthropogenic aerosols forcing based on single model simulations. Gagné et al. (2017b) identified a detectable increase in Arctic SIE in response to volcanic eruptions using CMIP5 models and four observational datasets. Polvani et al. (2020) suggested that ozone depleting substances played a substantial role in the Arctic sea ice loss over the 1955-2005 period.

Differences in sea ice loss among the models (Figure 3.20) have been attributed to a number of factors (see also Section 9.3.1.1). These factors include the late 20th century simulated sea ice state (Massonnet et al., 2012), the magnitude of changing ocean heat transport (Mahlstein and Knutti, 2011), and the rate of global warming (e.g., Gregory et al., 2002; Mahlstein and Knutti, 2012; Rosenblum and Eisenman, 2017). Sea ice thermodynamic considerations indicate that the magnitude of sea ice variability and loss depends on ice thickness (Bitz, 2008; Massonnet et al., 2018) and hence the climatology simulated by different models may influence their projections of change (*medium confidence*), as indicated by the regression lines in Figure 3.20.

An important consideration in comparing Arctic sea ice loss in models and observations is the role of internal variability (*medium confidence*). Using ensemble simulations from a single model, Kay et al. (2012) suggested that internal variability could account for about half of the observed September ice loss. More recently, large ensemble simulations have been performed with many more ensemble members (Kay et al., 2015). These enable a more robust characterization of internal variability in the presence of forced anthropogenic change. Using such large ensembles, some studies discussed the influence of internal variability on Arctic sea ice trends (Swart et al., 2015). Song et al. (2016) also compared the trends in the forced and unforced simulations using multiple climate models and found that internal variability explains about 40% of the observed September sea ice melting trend, supporting previous studies (Stroeve et al., 2012). Based on the large ensembles of CESM1 and CanESM2, September Arctic sea ice extent variance first increases and then decreases as SIE declines from its pre-industrial value (Kirchmeier-Young et al., 2017; Mueller et al., 2018) consistent with previous work (Goosse et al., 2009), but neither study found a strong sensitivity of detection and attribution results to the change in variability. Further work has indicated that internally-driven summer atmospheric circulation trends with enhanced atmospheric ridges over

ACCEPTED VERSION SUBJECT TO FINAL EDITING

Greenland and the Arctic Ocean, which project on the negative phase of the North Atlantic Oscillation (Section 3.7.1), play an important role in the observed Arctic sea ice loss (Hanna et al., 2015; Ding et al., 2017). A fingerprint analysis using the CESM large ensemble suggests that this internal variability accounts for 40-50% of the observed September Arctic sea ice decline (Ding et al., 2019; England et al., 2019). Internally-generated decadal tropical variability and associated atmospheric teleconnections were suggested to have contributed to the changing atmospheric circulation in the Arctic and the associated rapid sea ice decline from 2000 to 2014 (Meehl et al., 2018).

Some recent studies evaluated the human contribution to recent record minimum SIE events in the Arctic. Analysing CMIP5 simulations, Zhang and Knutson (2013) found that the observed 2012 record low in September Arctic SIE is inconsistent with internal climate variability alone. Based on several large ensembles, Kirchmeier-Young et al. (2017) concluded that the observed 2012 SIE minimum cannot be reproduced in a simulation excluding human influence. Fučkar et al. (2016) showed that climate change contributed to the record low March Arctic SIE in 2015, which was accompanied by the record minimum SIE in the Sea of Okhotsk (Paik et al., 2017).

Based on the new attribution studies since AR5, we conclude that it is *very likely* that anthropogenic forcing mainly due to greenhouse gas increases was the main driver of Arctic sea ice loss since 1979. Increases in anthropogenic aerosols have offset part of the greenhouse gas induced Arctic sea ice loss since the 1950s (*medium confidence*). Despite large differences in the mean sea ice state in the Arctic, Arctic sea ice loss is captured by all CMIP5 and CMIP6 models. Nonetheless, large inter-model differences in the Arctic sea ice decline remain, limiting our ability to quantify forced changes and internal variability contributions.

[START FIGURE 3.20 HERE]

Figure 3.20: Mean (*x*-axis) and trend (*y*-axis) in Arctic sea ice area (SIA) in September (left) and Antarctic SIA in February (right) for 1979-2017 from CMIP5 (upper) and CMIP6 (lower) models. All individual models (ensemble means) and the multi-model mean values are compared with the observations (OSISAF, NASA Team, and Bootstrap). Solid line indicates a linear regression slope with corresponding correlation coefficient (r) and p-value provided. Note the different scales used on the y-axis for Arctic and Antarctic SIA. Results remain essentially the same when using sea ice extent (SIE) (not shown). Further details on data sources and processing are available in the chapter data table (Table 3.SM.1).

[END FIGURE 3.20 HERE]

3.4.1.2 Antarctic Sea Ice

AR5 concluded that "there is *low confidence* in the attribution of the observed increase in Antarctic SIE since 1979" (Bindoff et al., 2013) due to the limited understanding of the external forcing contribution as well as the role of internal variability. Based on a difference between the first and last decades, Antarctic sea ice cover exhibited a small increase in summer and winter over the 1979-2017 period (Section 2.3.2.1.2; Figures 3.20 and 3.21). However, these changes are not statistically significant and starting in late 2016, anomalously low sea ice area has been observed (Section 2.3.2.1.2). The mean hemispheric sea ice changes result from much larger, but partially compensating, regional changes with increases in the western Ross Sea and Weddell Sea and declines in the Bellingshausen and Amundsen Seas (Hobbs et al., 2016). Observed regional trends have been particularly large in austral autumn (see Section 2.3.2.1.2, and also Section 9.3.2.1 for more details of regional changes and related physical processes). Starting in austral spring of 2016, the ice extent decreased strongly (Turner et al., 2017) and has since remained anomalously low (Figure 3.21). This decrease has been associated with anomalous atmospheric conditions associated with teleconnections from warming in the eastern Indian Ocean and a negative Southern Annular Mode (Chenoli et al., 2017; Stuecker et al., 2017; Schlosser et al., 2018; Meehl et al., 2019; Purich and England, 2019; Wang et al., 2019a). A decadal-scale warming of the near-surface ocean that resulted from strengthened westerlies may also have contributed to and helped to sustain the sea ice loss (Meehl et al., 2019). Before satellites and on even longer time scales, very limited observational data and proxy coverage leads to *low confidence* in all

ACCEPTED VERSION SUBJECT TO FINAL EDITING

aspects of Antarctic sea-ice (Section 2.3.2.1.2; 9.3.2.1).

CMIP5 climate models generally simulate Antarctic sea ice loss over the satellite era since 1979 (Mahlstein et al., 2013; Turner et al., 2013) in contrast to the observed change, and CMIP6 models also simulate Antarctic ice loss (Roach et al., 2020; Figure 3.20 and 3.21). A number of studies have suggested that this discrepancy may be in part due to the role of internal variability in the observed change (Mahlstein et al., 2013; Polvani and Smith, 2013; Zunz et al., 2013; Meehl et al., 2016a; Turner et al., 2016), including teleconnections associated with tropical Pacific variability (Meehl et al., 2016a) and changing surface conditions resulting from multi-decadal ocean circulation variations (Singh et al., 2019). However, when the spatial pattern is considered, trends in the summer and autumn (from 1979-2005) appear outside the range of internal variability (Hobbs et al., 2015). This suggests that the models may exhibit an unrealistic simulation of the Antarctic sea ice forced response or the internal variability of the system. Discrepancies among the models in simulated sea ice variability (Zunz et al., 2013), the sea ice climatological state (Roach et al., 2018), upper ocean temperature trends (Schneider and Deser, 2018), SH westerly wind trends (Purich et al., 2016), or the sea ice response to Southern Annular Mode variations (Ferreira et al., 2014; Holland et al., 2017; Kostov et al., 2017; Landrum et al., 2017) may all play some role in explaining these differences with the observed trends. Increased fresh water fluxes caused by mass loss of the Antarctic Ice Sheet (either by melting at the front of ice shelves or via iceberg calving) have been suggested as a possible mechanism driving the multidecadal Antarctic sea ice expansion (Bintanja et al., 2015; Pauling et al., 2016) but there is a lack of consensus on this mechanism's impacts (Pauling et al., 2017). A recent study based on decadal predictability suggests that initializing the state of the Antarctic bottom water cell can reproduce the observed Antarctic sea ice increase (Zhang et al., 2017), consistent with the suggestion that multidecadal variability associated with variations in deep convection has contributed to the observed increase in Antarctic sea ice since 1979 (Latif et al., 2013; Zhang et al., 2017, 2019a) (see also Section 9.3.2.1).

There have been several studies which aimed to identify causes of the observed Antarctic SIE changes. Gagné et al. (2015) assessed the consistency of observed and simulated changes in Antarctic SIE for an extended period using recovered satellite-based estimates, and found that the observed trends since the mid-1960s are not inconsistent with model simulated trends. Studies based on the satellite period also indicate that the observed trends are largely within the range of simulated internal variability (Hobbs et al., 2016). A few distinct factors that led to the weak signal-to-noise ratio in Antarctic SIE trends have been further identified, which include large multi-decadal variability (Monselesan et al., 2015), the short observational record (e.g., Abram et al., 2013), and the limited model performance at representing the complex Antarctic climate system as discussed above (Bintanja et al., 2013; Uotila et al., 2014). The short period of comprehensive satellite observations, beginning in 1979, makes it challenging to set the observed increase between 1979 and 2015, or the subsequent decrease, in a long-term context, and to assess whether the difference in trend between observations and models, which mostly simulate long-term decreases, is systematic or a rare expression of internal variability on decadal-to-multidecadal timescales.

In conclusion, the observed small increase in Antarctic sea ice extent during the satellite era is not generally captured by global climate models, and there is *low confidence* in attributing the causes of the change.

[START FIGURE 3.21 HERE]

Figure 3.21: Seasonal evolution of observed and simulated Arctic (left) and Antarctic (right) sea ice area (SIA) over 1979–2017. SIA anomalies relative to the 1979–2000 means from observations (OBS from OSISAF, NASA Team, and Bootstrap, top) and historical (ALL, middle) and natural only (NAT, bottom) simulations from CMIP5 and CMIP6 multi-models. These anomalies were obtained by computing non-overlapping 3-year mean SIA anomalies for March (February for Antarctic SIA), June, September, and December separately. CMIP5 historical simulations are extended by using RCP4.5 scenario simulations after 2005 while CMIP6 historical simulations are extended by using SSP2-4.5 scenario simulations after 2014. CMIP5 NAT simulations end in 2012. Numbers in brackets represents the number of models used. The multi-model mean is obtained by taking the ensemble mean for each model first and then averaging over models. Grey dots indicate multi-model mean anomalies stronger than inter-model spread (beyond ± 1 standard deviation). Results remain very similar when based on sea ice extent (SIE) (not shown). Units:

ACCEPTED VERSION SUBJECT TO FINAL EDITING

10^6 km^2. Further details on data sources and processing are available in the chapter data table (Table 3.SM.1).

[END FIGURE 3.21 HERE]

3.4.2 Snow Cover

Seasonal snow cover is a defining climate feature of the northern continents. It is therefore of considerable interest that climate models correctly simulate this feature. It is discussed in more detail in Section 9.5.3, and observational aspects of snow cover are assessed in Section 2.3.2.2.

AR5 noted the strong linear correlation between NH snow cover extent (SCE) and annual-mean surface air temperature in CMIP5 models. It was assessed as *likely* that there had been an anthropogenic contribution to observed reductions in NH snow cover since 1970 (Bindoff et al., 2013). AR5 assessed that CMIP5 models reproduced key features of observed snow cover well, including the seasonal cycle of snow cover over northern regions of Eurasia and North America, but had more difficulties in more southern regions with intermittent snow cover. AR5 also found that CMIP5 models underestimate the observed reduction in spring snow cover over this period (see also Brutel-Vuilmet et al., 2013; Thackeray et al., 2016; Santolaria-Otín and Zolina, 2020; Figure 3.22). This behaviour has been linked to how the snow-albedo feedback is represented in models (Thackeray et al., 2018). The CMIP5 multi-model ensemble has been shown to represent the snow-albedo feedback more realistically than CMIP3, although models from some individual modelling centres have not improved or have even got worse (Thackeray et al., 2018). There is still a systematic overestimation of the albedo of boreal forest covered in snow (Li et al., 2016c; Thackeray et al., 2015). Consequently, the snow albedo feedback might have been overestimated by CMIP5 models (Xiao et al., 2017; Section 9.5.3).

[START FIGURE 3.22 HERE]

Figure 3.22: Time series of Northern Hemisphere March-April mean snow cover extent (SCE) from observations, CMIP5 and CMIP6 simulations. The observations (grey lines) are updated Brown-NOAA (Brown and Robinson, 2011), Mudryk et al. (2020), and GLDAS2. CMIP5 (upper) and CMIP6 (lower) simulations of the response to natural plus anthropogenic forcing are shown in orange, natural forcing only in green, and the pre-industrial control simulation range is presented in blue. 5-year mean anomalies are shown for the 1923-2017 period with the x-axis representing the centre years of each 5-year mean. CMIP5 all forcing simulations are extended by using RCP4.5 scenario simulations after 2005 while CMIP6 all forcing simulations are extended by using SSP2-4.5 scenario simulations after 2014. Shading indicates 5th-95th percentile ranges for CMIP5 and CMIP6 all and natural forcings simulations, and solid lines are ensemble means, based on all available ensemble members with equal weight given to each model (Section 3.2). The blue vertical bar indicates the mean 5th-95th percentile range of pre-industrial control simulation anomalies, based on non-overlapping segments. The numbers in brackets indicate the number of models used. Anomalies are relative to the average over 1971-2000. For models, SCE is restricted to grid cells with land fraction ≥ 50%. Greenland is excluded from the total area summation. Figure is modified from Paik et al. (2020), their Figure 1. Further details on data sources and processing are available in the chapter data table (Table 3.SM.1).

[END FIGURE 3.22 HERE]

CMIP6 models improve on CMIP5 models in producing slightly increased SCE versus CMIP5, correcting the low bias in CMIP5 mentioned above (Mudryk et al., 2020). The linear relationship noted above between GSAT and SCE also exists in CMIP6 (Mudryk et al., 2020). Like CMIP5, the CMIP6 models capture the negative trend in spring snow cover that has occurred in recent decades (Figure 3.22). However, the median CMIP6 model now produces slightly stronger post-1981 declines in the March-April mean SCE than the CMIP5 median (Mudryk et al., 2020). Until about 1980, the models produce a generally stable March-April SCE, but after that a substantial decline, reaching a loss of about 2×10^6 km^2 in 2012-2017 relative to the

ACCEPTED VERSION SUBJECT TO FINAL EDITING

1971-2000 average. Compared to earlier studies which found that models underestimate observed trends for the 1979-2005 period (Brutel-Vuilmet et al., 2013), both CMIP5 and CMIP6 models show improved agreement with the observations over the period to 2017 (Figure 3.22). One remaining concern is a failure of most CMIP6 models to correctly represent the relationship between snow cover extent and snow mass, reflecting too slow seasonal increases and decreases of SCE in the models (Mudryk et al., 2020).

Several CMIP5 and CMIP6 based studies have consistently attributed the observed NH spring SCE changes (Section 2.3.2.2) to anthropogenic influences (Rupp et al., 2013; Najafi et al., 2016; Paik and Min, 2020), with the observed changes being found to be inconsistent with natural variability alone. Similarly, spring snow thickness (Snow Water Equivalent) changes on the scale of the NH have been attributed to greenhouse gas forcing (Jeong et al., 2017). Using individual forcing simulations from multiple CMIP6 models, Paik and Min (2020) detected greenhouse gas influence in the observed decrease of early spring SCE during 1925-2019, which was found to be separable from the responses to other forcings.

In summary, it is *very likely* that anthropogenic influence contributed to the observed reductions in NH springtime snow cover since 1950. CMIP6 models better represent the seasonality and geographical distribution of snow cover than CMIP5 simulations (*high confidence*). Both CMIP5 and CMIP6 models simulate strong declines in spring-time SCE during recent years, in general agreement with observations, causing the multi-model mean decreasing trend in spring-time SCE to now better agree with observations than in earlier evaluations. Evidence has yet to emerge that interactions between vegetation and snow, found problematic in CMIP5, have indeed improved in CMIP6 models (Section 9.5.3). Such deficiencies in the representation of snow in climate models mean there is *medium confidence* in the simulation of snow cover over the northern continents in CMIP6 model simulations. The models consistently link snow extent to surface air temperature (Figure 9.24). With warming of near-surface air linked to anthropogenic influence, and particularly to greenhouse gas increases (Section 3.3.1), this provides additional evidence that reductions in snow cover are also caused by human activity.

3.4.3 Glaciers and Ice Sheets

While Chapter 9 (Sections 9.4 and 9.5) discusses process understanding for glaciers and ice sheets, as well as evaluation of global and regional-scale glacier and ice sheet models, our focus here is on the attribution of large-scale changes in glaciers and ice sheets. Land ice in the form of glaciers has been included in CMIP climate and Earth system models as components of the land surface models for many years. However, their representation is simplified and is omitted altogether in the less complex modelling systems. In CMIP3 (Meehl et al., 2007) and CMIP5 (Taylor et al., 2012) land ice area fraction, a component of land surface models, was defined as a time-independent quantity, and in most model configurations was preset at the simulation initialization as a permanent land feature. In CMIP6 considerable progress has been made in improving and evaluating the representation of modelled land ice. For glaciers, an example is the expansion of the Joint UK Land Environment Simulator (JULES) land surface model to enable elevated tiles, and hence more accurately simulate the altitudinal atmospheric effects on glaciers (Shannon et al., 2019). Moreover, standalone glacier models have now been systematically compared in GlacierMIP (Hock et al., 2019a; Marzeion et al., 2020). The Antarctic and Greenland ice sheets were absent in global climate models that pre-date CMIP6 (Eyring et al., 2016a), however some preliminary analyses that used results from CMIP5 to drive standalone ice sheet models were included in AR5 (Church et al., 2013b). For the first time in CMIP, the latest CMIP6 phase includes a coordinated effort to simulate temporally evolving ice sheets within the Ice Sheet Model Intercomparison Project (ISMIP6; Box 9.3; Nowicki et al., 2016). Our understanding of aspects of the global water storage contained in glaciers and ice sheets, and their contribution to sea-level rise, has improved since the AR5 and SROCC (Hock et al., 2019b; Meredith et al., 2019) both in models and observations (see assessment of observations and model evaluation for the Greenland Ice Sheet in Sections 2.3.2.4.1 and 9.4.1; Antarctica in Sections 2.3.2.4.2 and 9.4.2; and glaciers in Sections 2.3.2.3 and 9.5.1).

3.4.3.1 Glaciers

ACCEPTED VERSION SUBJECT TO FINAL EDITING

Glaciers are defined as perennial surface land ice masses independent of the Antarctic and Greenland ice sheets (Sections 9.5, 2.3.2.3). AR5 assessed that anthropogenic influence had *likely* contributed to the retreat of glaciers observed since the 1960s (Bindoff et al., 2013), based on a high level of scientific understanding and robust estimates of observed mass loss, internal variability, and glacier response to climatic drivers. SROCC (Hock et al., 2019b) concluded that atmospheric warming was *very likely* the primary driver of glacier recession.

Simulations of glacier mass changes under climate change rely on glacier models driven by climate model output, often in collaborative research efforts such as GlacierMIP (Hock et al., 2019a; Marzeion et al., 2020). The GlacierMIP project is a systematic coordinated modelling effort designed to further understanding of glacier loss using global models. While the low resolution and remaining biases of climate model-derived boundary forcing data is a limitation, the release of the Randolph Glacier Inventory (Pfeffer et al., 2014; RGI Consortium, 2017) has supported more sophisticated, systematic and comprehensive modelling of glaciers worldwide (Hock et al., 2019a).

A regional study considering 85 NH glacier systems concluded that there is a discernible human influence on glacier mass balance, with glacier model simulations driven by CMIP5 historical and greenhouse gas-only simulations showing a glacier mass loss, whereas those driven by natural-only forced simulations showed a net glacier growth (Hirabayashi et al., 2016). In addition, a study of the role of climate change in glacier retreat using a simple mass-balance model for 37 glaciers worldwide, concluded that observed length changes would not have occurred without anthropogenic climate change, with observed length variations exceeding those associated with internal variability by several standard deviations in many cases (Roe et al., 2017). Roe et al. (2020) used the same model to estimate that at least 85% of cumulative glacier mass loss since 1850 is attributable to anthropogenic influence. While Marzeion et al. (2014) found that anthropogenic influence contributed only 25 ± 35% of glacier mass loss for the period 1851-2010, their naturally-forced simulations exhibited a substantial negative mass balance, which Roe et al. (2020) argued is unrealistic. Moreover, Marzeion et al. (2014) estimated that anthropogenic influence contributed 69 ± 24% of glacier mass loss for the period 1991 to 2010, consistent with a progressively increasing fraction of mass loss attributable to anthropogenic influence found by Roe et al. (2020).

In summary, considering together the SROCC assessment that atmospheric warming was *very likely* the primary driver of glacier recession, the results of Roe et al. (2017, 2020) and our assessment of the dominant role of anthropogenic influence in driving atmospheric warming (Section 3.3.1), we conclude that human influence is *very likely* the main driver of the near-universal retreat of glaciers globally since the 1990s.

3.4.3.2 Ice Sheets

Greenland Ice Sheet

AR5 assessed that it is *likely* that anthropogenic forcing contributed to the surface melting of the Greenland Ice Sheet since 1993 (Bindoff et al., 2013). SROCC did not directly assess the attribution of Greenland Ice Sheet change to anthropogenic forcing, but it did assess with *medium confidence* that summer melting of the Greenland Ice Sheet has increased to a level unprecedented over at least the last 350 years, which is two-to-fivefold the pre-industrial level (see also Trusel et al.; 2018).

Section 2.3.2.4.1 assesses that Greenland ice sheet mass loss began in the latter half of the 19th century and the rate of loss has increased substantially since the turn of the 21st century (*high confidence*), and also notes that integration of proxy evidence and modelling indicates that the last time the rate of mass loss was similar to the 20th century rate was during the early Holocene. Models of Greenland Ice Sheet evolution are evaluated in detail in Section 9.4.1.2, which assesses that there is overall *medium confidence* in these models. Model evaluation of surface mass balance changes over the Greenland Ice Sheet, including regional aspects, is also assessed in Atlas.11.2.3.

Detection and attribution studies of change in the Greenland Ice Sheet remain challenging (Kjeldsen et al., 2015; Bamber et al., 2019). This is in part due to the short observational record (Shepherd et al., 2012, 2018,

ACCEPTED VERSION SUBJECT TO FINAL EDITING

2020; Bamber et al., 2018; Cazenave et al., 2018; Mouginot et al., 2019; Rignot et al., 2019) and the challenges this poses to the evaluation of modelling efforts (Section 9.4.1). The latter require not only dynamic ice sheet models, but also appropriate atmospheric and oceanic conditions to use as a boundary forcing to drive the models (Nowicki and Seroussi, 2018; Barthel et al., 2020). Nonetheless, new literature since AR5 finds that ice sheet mass balance calculations using reanalysis-driven regional model simulations of surface mass balance, are found to agree well with the observed decrease in ice sheet mass over the past twenty years (Fettweis et al., 2020; Sasgen et al., 2020a; Tedesco and Fettweis, 2020a), consistent with earlier studies (Flato et al., 2013). These studies also show that the exceptional melt events observed in 2012 and 2019 were associated with exceptional atmospheric conditions (Sasgen et al., 2020a; Tedesco and Fettweis, 2020b). These results support the finding that increased surface melting is associated with warming, although atmospheric circulation anomalies, including the summer North Atlantic Oscillation (NAO) and variations in snowfall play an important role in driving interannual variations (Sasgen et al., 2020; Tedesco and Fettweis, 2020; Section 9.4.1.1). Further, a coupled ice-sheet-climate model study found emergence of decreased surface mass balance prior to the present day in coastal locations in Greenland, which dominate the integrated surface mass balance (Fyke et al., 2014), suggesting that observed variations in surface mass balance in these regions might be expected to be distinguishable from internal variability. A CMIP6 simulation of the historical period showed stable Greenland surface mass balance up to the 1990s, after which it declined due to increased melt and runoff, consistent with a downscaled reanalysis (van Kampenhout et al., 2020). Further, all experts surveyed in a structured expert judgement exercise examining the causes of the increase in mass loss from the Greenland Ice Sheet over the last two decades (Bamber et al., 2019) concluded that external forcing was responsible for at least 50% of the mass loss. A comparison of Greenland Ice Sheet mass loss trends from observations and AR5 model projections for the period 2007-2017 found that observed surface mass balance trends were at the top of the AR5 assessed range, while mass loss due to changing ice dynamics was near the centre of the AR5 range (Slater et al., 2020), providing further evidence of consistent anthropogenically-forced mass loss trends in models and observations.

Drawing together the evidence from the continued and strengthened observed mass loss, the agreement between anthropogenically forced climate simulations and observations, and historical and paleo evidence for the unusualness of the observed rate of surface melting and mass loss, we assess that it is *very likely* that human influence has contributed to the observed surface melting of the Greenland Ice Sheet over the past two decades, and there is *medium confidence* in an anthropogenic contribution to recent overall mass loss from Greenland.

Antarctic Ice Sheet

AR5 assessed that there was *low confidence* in attributing the causes of the observed mass loss from the Antarctic ice sheet since 1993 (Bindoff et al., 2013). SROCC assessed that there is *medium agreement* but *limited evidence* of anthropogenic forcing of Antarctic mass balance through both surface mass balance and glacier dynamics. It further assessed that Antarctic ice loss is dominated by acceleration, retreat and rapid thinning of the major West Antarctic Ice Sheet outlet glaciers (*very high confidence*), driven by melting of ice shelves by warm ocean waters (*high confidence*). Based on updated observations, Chapter 2 assesses that there is *very high confidence* that the Antarctic Ice Sheet lost mass between 1992 and 2017, and that there is *medium confidence* that this mass loss has accelerated. Models of Antarctic Ice Sheet evolution are evaluated in detail in Section 9.4.2.2, which assesses that there is *medium confidence* in many ice sheet processes inAntarctic ice sheet models, but *low confidence* in the ocean forcing affecting basal melt rates. CMIP5 and CMIP6 models perform similarly in their simulation of Antarctic surface mass balance (Section 9.4.2.2, Gorte et al., 2020). Model evaluation of surface mass balance over the Antarctic Ice Sheet, including regional aspects, is also assessed in Atlas.11.1.3.

Ice discharge around the West Antarctic Ice Sheet is strongly influenced by variability in basal melt (Jenkins et al., 2018; Hoffman et al., 2019), in particular at decadal and longer time scales (Snow et al., 2017). Basal melt rate variability can be induced by wind-driven ocean current changes, which may partly be of anthropogenic origin via greenhouse gas forcing (Holland et al., 2019). Moreover, ice discharge losses from the Antarctic Ice Sheet over the 2007-2017 period are close to the centre of the model-based range projected in AR5 (Slater et al., 2020). However, expert opinion differs as to whether recent Antarctic ice loss from the

ACCEPTED VERSION SUBJECT TO FINAL EDITING

West Antarctic Ice Sheet has been driven primarily by external forcing or by internal variability, and there is no consensus (Bamber et al., 2019). Anthropogenic influence on the Antarctic surface mass balance, which is expected to partially compensate for ice discharge losses through increases in snowfall, is currently masked by strong natural variability (Previdi and Polvani, 2016; Bodart and Bingham, 2019), and observations suggest that it has been close to zero over recent years (Slater et al., 2020) (see further discussion in Section 9.4.2.1).

Overall, there is *medium agreement* but *limited evidence* of anthropogenic influence on Antarctic mass balance through changes in ice discharge.

3.5 Human Influence on the Ocean

The global ocean plays an important role in the climate system, as it is responsible for transporting and storing large amounts of heat (Sections 3.5.1 and 9.2.2.1), freshwater (Sections 3.5.2 and 9.2.2.2) and carbon (Sections 3.6.2 and 5.2.1.3) that are exchanged with the atmosphere. Therefore, accurate ocean simulation in climate models is essential for the realistic representation of the climatic response to anthropogenic warming, including rates of warming, sea level rise and carbon uptake, and the representation of coupled modes of climate variability.

Ocean model development has advanced considerably since AR5 (Section 1.5.3.1). Ongoing model developments since AR5 have focused on improving the realism of the simulated ocean in coupled models, with horizontal resolutions increasing to 10-100 km (from about 200 km in CMIP5), and increased vertical resolutions in many modelling systems of 0-1 m for near-surface levels (from the highest resolution of 10 m in CMIP5). These developments are aimed at improving the representation of the diurnal cycle and coupling to the atmosphere (e.g. Bernie et al. 2005, 2007, 2008). General improvements to simulated ocean fidelity in response to increasing resolution are expected (Hewitt et al., 2017). The effects of model resolution on the fidelity of ocean models are discussed in more detail in Sections 9.2.2 and 9.2.4.

In this section we assess the global and basin-scale properties of the simulated ocean, with a focus on evaluation of the realism of simulated ocean properties, and the detection and attribution of human-induced changes in the ocean over the period of observational coverage. Observed changes to ocean temperature (Section 2.3.3.1), salinity (Section 2.3.3.2), sea level (Section 2.3.3.3) and ocean circulation (Section 2.3.3.4) are reported in Chapter 2. A more process-based assessment of ocean changes, alongside the assessment of variability and changes in ocean properties with spatial scales smaller than ocean basin scales is presented in Chapter 9.

3.5.1 Ocean Temperature

Ocean temperature and ocean heat content are key physical variables considered for climate model evaluation and are primary indicators of a changing ocean climate. This section assesses the performance of climate models in representing the mean state ocean temperature and heat content (Section 3.5.1.1), with a particular focus on the tropical oceans given the importance of air-sea coupling in these areas (Section 3.5.1.2). This is followed by an assessment of detection and attribution studies of changes in ocean temperature and heat content (Section 3.5.1.3). Changes in global surface temperature are assessed in Section 3.3.1.1.

3.5.1.1 Sea Surface and Zonal Mean Ocean Temperature Evaluation

In CMIP3 and CMIP5 models, large SST biases were found in the mid and high latitudes (Flato et al., 2013). In CMIP6, the NH mid-latitude surface temperature biases appear to be marginally improved in the multi-model mean when contrasted to CMIP5 despite large biases remaining in a few models (Figure 3.23a, Figure 3.24). There is a decreased spread of the zonal mean SST error between 50°N and 30°S, relative to CMIP5

ACCEPTED VERSION SUBJECT TO FINAL EDITING

(Figure 3.24a). On the other hand, the Southern Ocean's warm surface temperature bias remains (Figure 3.23a; Beadling et al., 2020), and is on average larger in CMIP6 than in CMIP5 models (Figure 3.23a, Figure 3.24). This warm bias is often associated with persistent overlying atmospheric cloud biases (Hyder et al., 2018). Several other large biases also appear to remain largely unresolved in CMIP6, particularly warm biases in excess of 1°C along the equatorial eastern continental boundaries of the tropical Atlantic and Pacific Oceans (Figure 3.23a).

Overall, the simulated and observed trends in SST patterns are generally consistent for the historical period (Olonscheck et al., 2020). The CMIP6 models generally represent the observed pattern of trends better than the CMIP5 models, and observed trends fall within the range of simulated trends over a larger area for CMIP6 models than for CMIP5 models (Olonscheck et al., 2020).

The CMIP5 multi-model mean zonally averaged subsurface ocean temperature showed warm biases between 200 m and 2000 m (mid-depth) over most latitudes, with exceptions in the Southern Ocean (>60°S, 100-2000 m) and upper (0-400 m) Arctic Ocean. Cold biases were simulated near the surface (0-200 m) at most latitudes (Flato et al., 2013). CMIP6 biases are broadly consistent with those reported in CMIP5 for the near-surface (<200 m) and mid-depth (200-2000 m) ocean (Voldoire et al., 2019b; Beadling et al., 2020; Zhu et al., 2020b). The warm bias begins between 100 and 400 m depth in all three basins, however, it is most prominent in the Atlantic Ocean, with a maximum magnitude in the equatorial latitudes, as in CMIP5 (Figure 3.25). In the Pacific, the large warm biases are mostly seen in the subtropical regions (30-60°N and 30-60°S). The cool near surface tropical bias is most prominent in the Pacific Ocean and also present in the Atlantic, with a smaller magnitude (Figure 3.25). Relative to CMIP5, the most prominent difference is an increase to the mid-depth (300-2000 m) warm bias in CMIP6 relative to CMIP5, and a change in sign of the bias from cold to warm for the Southern Ocean mid-depth (>60ºS) from CMIP5 to CMIP6 (Figure 3.25). Compared to CMIP3 and CMIP5, there is improved agreement between most CMIP6 models and observations in their representation of the zonal mean temperature of the upper 100 m of the Southern Ocean (Beadling et al., 2020).

Focusing on the deep ocean (>2000 m), the CMIP6 ensemble mean shows a prominent and consistent warm bias (Figure 3.25), in all basins except the equatorial and northern Pacific, which contrasts to a cold bias seen in CMIP5 (Flato et al., 2013). We note that while an updated observational temperature dataset is used in this assessment (WOA09 was used in AR5, while WOA18, 1981-2010 is used in AR6), the deep ocean warm bias remains and is approaching double the magnitude (~0.5°C) of the equivalent CMIP5 multi-model mean bias, a feature which is particularly prominent in the Atlantic and southern Indian Oceans. Increased horizontal resolution as well as the choice of the vertical coordinate are reported to partly improve these biases in some models (Adcroft et al., 2019; Rackow et al., 2019; Hewitt et al., 2020).

Since AR5, there has been growing evidence that the representation of mean surface and deeper ocean temperatures in coupled climate models can be improved by increasing the horizontal resolution both in the ocean and the atmosphere (e.g. Small et al., 2014; Hewitt et al., 2016; Iovino et al., 2016; Roberts et al., 2019). At an ocean resolution of around 1°, which is typical of CMIP6 models, some processes are parameterized rather than explicitly resolved, leading to a compromise in their dynamical representation. An increase in the model resolution allows for processes to be explicitly resolved, and can for example, enhance the simulation of eddies, thus improving simulated vertical eddy transport, and reducing temperature drifts in the deeper ocean (Griffies et al., 2015; von Storch et al., 2016). For some models, the mean absolute error in ocean temperature below 500 m is smaller in the high resolution version compared to the low resolution version, particularly in eddy-active regions such as the North Atlantic (Rackow et al., 2019). Increasing the horizontal resolution of individual climate models often leads to an overall decrease in the surface temperature biases over regions where they persisted through earlier CMIP generations, such as the central and western equatorial Pacific, as well as the North and tropical Atlantic (Figure 3.3e; Roberts et al., 2019; Hewitt et al., 2020). Despite this, as a group the four HighResMIP models included in Figures 3.3e and 3.24 do not on average show smaller SST biases than the CMIP6 multi-model mean, demonstrating the importance of factors other than resolution in contributing to SST biases.

In summary, there is little improvement in the multi-model mean sea surface and zonal mean ocean

ACCEPTED VERSION SUBJECT TO FINAL EDITING

temperatures from CMIP5 to CMIP6 (*medium confidence*). Nevertheless, the CMIP6 models show a somewhat more realistic pattern of SST trends (*low confidence*).

[START FIGURE 3.23 HERE]

Figure 3.23: Multi-model-mean bias of (a) sea surface temperature and (b) near-surface salinity, defined as the difference between the CMIP6 multi-model mean and the climatology from the World Ocean Atlas 2018. The CMIP6 multi-model mean is constructed with one realization of 46 CMIP6 historical experiments for the period 1995–2014 and the climatology from the World Ocean Atlas 2018 is an average over all available years (1955-2017). Uncertainty is represented using the advanced approach: No overlay indicates regions with robust signal, where ≥66% of models show change greater than variability threshold and ≥80% of all models agree on sign of change; diagonal lines indicate regions with no change or no robust signal, where <66% of models show a change greater than the variability threshold; crossed lines indicate regions with conflicting signal, where ≥66% of models show change greater than the variability threshold and <80% of all models agree on sign of change. For more information on the advanced approach, please refer to the Cross-Chapter Box Atlas.1. Further details on data sources and processing are available in the chapter data table (Table 3.SM.1).

[END FIGURE 3.23 HERE]

[START FIGURE 3.24 HERE]

Figure 3.24: Biases in zonal mean and equatorial sea surface temperature (SST) in CMIP5 and CMIP6 models. CMIP6 (red), CMIP5 (blue) and HighResMIP (green) multi-model mean (a) zonally-averaged SST bias; (b) equatorial SST bias; and (c) equatorial SST compared to observed mean SST (black line) for 1979-1999. The inter-model 5th and 95th percentiles are depicted by the respective shaded range. Model climatologies are derived from the 1979-1999 mean of the historical simulations, using one simulation per model. The Hadley Centre Sea Ice and Sea Surface Temperature version 1 (HadISST) (Rayner et al., 2003) observational climatology for 1979-1999 is used as the reference for the error calculation in (a) and (b); and for observations in (c). Further details on data sources and processing are available in the chapter data table (Table 3.SM.1).

[END FIGURE 3.24 HERE]

[START FIGURE 3.25 HERE]

Figure 3.25: CMIP6 potential temperature and salinity biases for the global ocean, Atlantic, Pacific and Indian Oceans. Shown in colour are the time-mean differences between the CMIP6 historical multi-model climatological mean and observations, zonally averaged for each basin (excluding marginal and regional seas). The observed climatological values are obtained from the World Ocean Atlas 2018 (WOA18, 1981-2010; Prepared by the Ocean Climate Laboratory, National Oceanographic Data Center, Silver Spring, MD, USA), and are shown as labelled black contours for each of the basins. The simulated annual mean climatologies for 1981 to 2010 are calculated from available CMIP6 historical simulations, and the WOA18 climatology utilized synthesized observed data from 1981 to 2010. A total of 30 available CMIP6 models have contributed to the temperature panels (left column) and 28 models to the salinity panels (right column). Potential temperature units are °C and salinity units are the Practical Salinity Scale 1978 [PSS-78]. Further details on data sources and processing are available in the chapter data table (Table 3.SM.1).

[END FIGURE 3.25 HERE]

3.5.1.2 Tropical Sea Surface Temperature Evaluation

Tropical Pacific Ocean

ACCEPTED VERSION SUBJECT TO FINAL EDITING

In CMIP5, mean state biases in the tropical Pacific Ocean including the excessive equatorial cold tongue, erroneous mean thermocline depth and slope along the equator remained but were improved relative to CMIP3 (Flato et al., 2013). Misrepresentation of the interaction between the atmosphere and ocean via the Bjerknes feedback and vertical mixing parameterizations, and a bias in winds were among the suggested reasons for the persistent biases (Li et al., 2014; Zhu and Zhang, 2018). Moving to CMIP6, a reduction of the cold bias in the equatorial cold tongue in the central Pacific is found on average in the CMIP6 models (Figure 3.24b; Grose et al., 2020; Planton et al., 2020), however, this reduced bias is not statistically significant when considered across the multi-model ensemble (Planton et al., 2020). It is also noteworthy that the longitude of the 28°C isotherm is closer to observed in CMIP6 than in CMIP5, with a coincident reduction in the CMIP6 inter-model standard deviation (Grose et al., 2020). The latter result implies that there is an improvement in the representation of the tropical Pacific mean state in CMIP6 models. Comparison of biases in individual HighResMIP models with biases in lower resolution versions of the same models indicates that there is no consistent improvement in SST biases in most of the equatorial Pacific with resolution (Figure 3.3e; Bock et al., 2020).

Tropical Atlantic Ocean

Fundamental features such as the mean zonal SST gradient in the tropical Atlantic were not reproduced in CMIP5 models. Studies have proposed that weaker than observed alongshore winds, underestimation of stratocumulus clouds, coarse model resolution, and insufficient oceanic cooling due to a deeper thermocline depth and weak vertical velocities at the base of the mixed layer in the eastern basin, underpinned these tropical Atlantic SST gradient biases (Hourdin et al., 2015; Richter, 2015). The SST gradient biases still remain in CMIP6. On average the cold bias in the western part of the basin is reduced while the warm bias in the eastern part has slightly increased (Figure 3.24 b,c) (Richter and Tokinaga, 2020a). Several CMIP6 models, however, display large reductions in biases of the zonal SST gradient, such that the eastern equatorial Atlantic warm SST bias and associated westerly wind biases are mostly eliminated in these models (Richter and Tokinaga, 2020a). The high resolution (HighResMIP) CMIP6 models show a better representation of the zonal SST gradient (Figure 3.24 b,c), but some lower resolution models also perform well suggesting that resolution is not the only factor responsible for biases in Tropical Atlantic SST (Richter and Tokinaga, 2020a).

Tropical Indian Ocean

The tropical Indian Ocean mean state is reasonably well simulated both in CMIP5 and CMIP6 (Figure 3.24 b,c). However, CMIP5 models show a large spread in the thermocline depth, particularly in the equatorial part of the basin (Saji et al., 2006; Fathrio et al., 2017a), which has been linked to the parameterization of the vertical mixing and the wind structure, leading to a misrepresentation of the ventilation process in some models (Schott et al., 2009; Richter, 2015; Shikha and Valsala, 2018). A common problem with the CMIP5 models is therefore a warm bias in the subsurface, mainly at depths around the thermocline, which is also apparent in the CMIP6 models (Figure 3.25g).

In the CMIP6 multi-model mean, the western tropical Indian Ocean shows a slightly larger warm bias compared to CMIP5 (Figure 3.24 b,c), which in part could be related to excessive supply of warm water from the Red Sea (Grose et al., 2020; Semmler et al., 2020). The HighResMIP models show decreases in SST bias across the Indian Ocean with increasing resolution (Figure 3.3e; Bock et al., 2020), though as a group the SST biases in the HighResMIP models are no smaller than those of the full CMIP6 ensemble.

In summary, the structure and magnitude of multi-model mean ocean temperature biases have not changed substantially between CMIP5 and CMIP6 (*medium confidence*). Although biases remain in the latest model generation models, the broad consistency between the observed and simulated basin-scale ocean properties suggests that CMIP5 and CMIP6 models are appropriate tools for investigating ocean temperature and ocean heat content responses to forcing. This also provides *high confidence* in the utility of CMIP-class models for detection and attribution studies, for both ocean heat content (Section 3.5.1.3) and thermosteric sea level applications (Section 3.5.3).

3.5.1.3 Ocean Heat Content Change Attribution

ACCEPTED VERSION SUBJECT TO FINAL EDITING

The ocean plays an important role as the Earth's primary energy store. The AR5 and SROCC assessed that the ocean accounted for more than 90% of the Earth's energy change since the 1970s (Rhein et al., 2013; Bindoff et al., 2019). These assessments are consistent with recent studies assessed in Section 7.2 and Cross-Chapter Box 9.1, which find that 91% of the observed change in Earth's total energy from 1971 to 2018 was stored in the ocean (von Schuckmann et al., 2020). The AR5 concluded that anthropogenic forcing has *very likely* made a substantial contribution to ocean warming above 700 m, whereas below 700 m, limited measurements restricted the assessment of ocean heat content changes in AR5 and prevented a robust comparison between observations and models (Bindoff et al., 2013).

With the recent increase in ocean sampling by Argo to 2000 m (Roemmich et al., 2015; Riser et al., 2016; von Schuckmann et al., 2016) and the resulting improvements in estimates of ocean heat content (Abraham et al., 2013; Balmaseda et al., 2013; Durack et al., 2014a; Cheng et al., 2017; von Schuckmann et al., 2020), a more quantitative assessment of the global ocean heat content changes that extends into the intermediate ocean (700-2000 m) over the more recent period (from 2005 to the present) (Durack et al., 2018) can be performed. Observed ocean heat content changes are discussed in Section 2.3.3.1, where it is reported that it is *virtually certain* that the global upper ocean (0-700 m) and *very likely* that the global intermediate ocean (700-2000 m) warmed substantially from 1971 to the present. Further, ocean layer warming contributions are reported as 61% (0-700 m), 31% (700-2000 m) and 8% (>2000 m) for the 1971 to 2018 period (Table 2.7). CMIP5 model simulations replicate this partitioning fairly well for the industrial-era (1865 to 2017) throughout the upper (0-700 m, 65%), intermediate (700-2000 m, 20%) and deep (>2000 m, 15%) layers (Gleckler et al., 2016; Durack et al., 2018). The corresponding warming percentages for the multi-model mean of a subset of CMIP6 simulations over the 1850-2014 period are 58% for the upper, 21% for the intermediate, and 22% for the deep ocean layers (Figure 3.26). These results are consistent with SROCC which assessed that it is *virtually certain* that both the upper and intermediate ocean warmed from 2004 to 2016, with an increased rate of warming since 1993 (Bindoff et al., 2019). The spatial distribution of these changes for different ocean depths is assessed in Section 9.2.2.

[START FIGURE 3.26 HERE]

Figure 3.26: Global ocean heat content in CMIP6 simulations and observations. Time series of observed (black) and simulated (red) global ocean heat content anomalies with respect to 1995-2014 for the full ocean depth (left panel), upper layer - 0 to 700 m (top right panel), intermediate layer -700 to 2000 m (middle right panel), and the abyssal ocean >2000 m (bottom right panel). The best estimate observations (black solid line) for the period of 1971-2018, along with *very likely* ranges (black shading) are from Section 2.3.3.1. For the models (1860-2014), ensemble members from 15 CMIP6 models are used to calculate the multi-model mean values (red solid line) after averaging across simulations for each independent model. The *very likely* ranges in the simulations are shown in red shading. Simulation drift has been removed from all CMIP6 historical runs using a contemporaneous portion of the linear fit to each corresponding pre-industrial control run (Gleckler et al., 2012). Units are 10^{21} Joules (Zettajoules). Further details on data sources and processing are available in the chapter data table (Table 3.SM.1).

[END FIGURE 3.26 HERE]

The multi-model means of both CMIP5 and CMIP6 historical simulations forced with time varying natural and anthropogenic forcing showsrobust increases in ocean heat content in the upper (0-700 m) and intermediate (700-2000 m) ocean (*high confidence*) (Figure 3.26) (Cheng et al., 2016, 2019; Gleckler et al., 2016; Bilbao et al., 2019; Tokarska et al., 2019). Temporary (<10 years) surface and subsurface cooling during and after large volcanic eruptions are also captured in the upper-ocean, and global mean ocean heat content (Balmaseda et al., 2013). The ocean heat content increase is also reflected in the corresponding ocean thermal expansion which is a leading contributor to global mean sea level rise (Sections 3.5.3.2 and 9.2.4; Box 9.1).

For the period 1971-2014, the rate of ocean heat uptake for the global ocean in the CMIP6 models is about

ACCEPTED VERSION SUBJECT TO FINAL EDITING

6.43 [2.08-8.66] ZJ yr^{-1}, with the upper, intermediate and deeper layers respectively accounting for 68%, 16% and 16% of the full depth global heat uptake (Figure 3.26). Overall, the simulated ocean heat content changes are consistent with the updated and improved observational analyses, within the *very likely* uncertainty range defined for each (Domingues et al., 2008; Purkey and Johnson, 2010; Levitus et al., 2012; Good et al., 2013; Cheng et al., 2017; Ishii et al., 2017; Zanna et al., 2019) (see also Table 2.7, Section 2.3.3.1) as well as with the ocean components of total Earth heating assessed in Section 7.2.2.2, Table 7.1. Nevertheless, large uncertainties remain, particularly in the deeper layers due to the poor temporal and spatial sampling coverage, particularly in the Atlantic, Southern and Indian Oceans (Garry et al., 2019). The *very likely* ranges of the simulated trends for the full ocean depth and below 2000 m fall within the *very likely* range of observed uptake during the last two decades. In the intermediate layer, the multi-model ensemble mean mostly stays above (below) the observed 5^{th}-95^{th} percentile range before (after) the year 2000. For the upper ocean, some individual model realisations show a reduced ocean heat content increase during the 1970s and 1980s, which is then compensated by a greater warming than the observations from the early 1990s. These discrepancies have been linked with a temporary increase in the Southern Ocean deep water formation rate, as well as with the models' strong aerosol cooling effects and high equilibrium climate sensitivity (Andrews et al., 2019, 2020; Golaz et al., 2019; Dunne et al., 2020; Winton et al., 2020) (see also Section 7.5.6 and Box 7.2).

Nevertheless, both the observed estimates and simulations show that the rate of ocean heat uptake has doubled in the past few decades, when contrasted to the rate over the complete 20^{th} century (Figure 3.26), with over a third of the accumulated heat stored below 700 m (Cheng et al., 2016, 2019; Gleckler et al., 2016; Durack et al., 2018). The Southern Ocean shows the strongest ocean heat uptake that penetrates to deeper layers (Section 9.2.3.2), whereas ocean heat content increases in the Pacific and Indian Oceans largely occur in the upper layers (Bilbao et al., 2019).

Since AR5, the attribution of ocean heat content increases to anthropogenic forcing has been further supported by more detection and attribution studies. These studies have shown that contributions from natural forcing alone cannot explain the observed changes in ocean heat content in either the upper or intermediate ocean layers, and a response to anthropogenic forcing is clearly detectable in ocean heat content (Gleckler et al., 2016; Bilbao et al., 2019; Tokarska et al., 2019). Moreover, a response to greenhouse gas forcing is detectable independently of the response to other anthropogenic forcings (Bilbao et al., 2019; Tokarska et al., 2019), which has offset part of the greenhouse gas induced warming. Further evidence is provided by the agreement between observed and simulated changes in global thermal expansion associated with the ocean heat content increase when both natural and anthropogenic forcings are included in the simulations (Section 3.5.3), though internal variability plays a larger role in driving basin-scale thermosteric sea level trends (Bilbao et al., 2015). Over the Southern Ocean, warming is detectable over the late twentieth century and is largely attributable to greenhouse gases (Swart et al., 2018; Hobbs et al., 2021), while other anthropogenic forcings such as ozone depletion have been shown to mitigate the warming in some of the CMIP5 simulations (Swart et al., 2018; Hobbs et al., 2021). The use of the mean temperature above a fixed isotherm rather than fixed depth further strengthens a robust detection of the anthropogenic response in the upper ocean (Weller et al., 2016), and better accounting for internal variability in the upper ocean (Rathore et al., 2020), helps explain reported hemispheric asymmetry in ocean heat content change (Durack et al., 2014a).

In summary, there is strong evidence for an improved understanding of the observed global ocean heat content increase. It is *extremely likely* that human influence was the main driver of the ocean heat content increase observed since the 1970s, which extends into the deeper ocean (*very high confidence*). Updated observations, like model simulations, show that warming extends throughout the entire water column (*high confidence*).

3.5.2 Ocean Salinity

While ocean assessments have primarily focused on temperature changes, improved observational salinity products since the early 2000s have supported more assessment of long-term ocean salinity change and

ACCEPTED VERSION SUBJECT TO FINAL EDITING

variability from AR4 (Bindoff et al., 2007) to AR5 across both models and observations (Flato et al., 2013; Rhein et al., 2013). AR5 assessed that it was *very likely* that anthropogenic forcings have made a discernible contribution to surface and subsurface oceanic salinity changes since the 1960s. The SROCC augmented these insights, noting that observed high latitude freshening and warming have *very likely* made the surface ocean less dense with a stratification increase of between 2.18% and 2.42% from 1970 to 2017 (Bindoff et al., 2019). A recent observational analysis has expanded on these assessments, suggesting a very marked summertime density contrast enhancement across the mixed layer base of 6.2% to 11.6% per decade, driven by changes in temperature and salinity, which is more than six times larger than previous estimates (Sallée et al., 2021). An idealised ocean modelling study suggests that the enhanced stratification can account for a third of the salinity enhancement signal since 1990 (Zika et al., 2018). Thus, there has been an expansion of observed global- and basin-scale salinity change assessment literature since AR5, with many new studies reproducing the key patterns of long-term salinity change reported in AR5 (Rhein et al., 2013), and linking these through modelling studies to coincident changes in evaporation-precipitation patterns at the ocean surface (Sections 2.3.1, 3.3.2, 8.2.2.1 and 9.2.2).

Unlike SSTs, simulated sea surface salinity (SSS) does not provide a direct feedback to the atmosphere. However, some recent work has identified indirect radiative feedbacks through sea-salt aerosol interactions (Ayash et al., 2008; Amiri-Farahani et al., 2019; Wang et al., 2019b) that can act to strengthen tropical cyclones, and increase precipitation (Balaguru et al., 2012, 2016; Grodsky et al., 2012; Reul et al., 2014; Jiang et al., 2019). The absence of a direct feedback is one of the primary reasons why salinity simulation is difficult to constrain in ocean modelling systems, and why deviations from the observed near-surface salinity mean state between models and observations are often apparent (Durack et al., 2012; Shi et al., 2017).

3.5.2.1 Sea Surface and Depth-profile Salinity Evaluation

When compared to the routine assessment of simulated SST, simulated SSS has not received the same research attention at global- to basin-scales. For CMIP3, there was reasonable agreement between the basin-scale patterns of salinity, with a comparatively fresher Pacific when contrasted to the salty Atlantic, and basin salinity maxima features aligning well with the corresponding atmospheric evaporation minus precipitation field (Durack et al., 2012). Similar features are also reproduced in CMIP5 along with realistic variability in the upper layers, but less variability than observations at 300 m and deeper, especially in the poorly sampled Antarctic region (Pierce et al., 2012). In a regional study, only considering the Indian Ocean, CMIP5 SSS was assessed and it was shown that model biases were primarily linked to biases in the precipitation field, with ocean circulation biases playing a secondary role (Fathrio et al., 2017b). The sea surface salinity bias in CMIP6 models is shown in Figure 3.23b.

For the first time in AR5, alongside global zonal mean temperature, global zonal mean salinity bias with depth was assessed for the CMIP5 models. This showed a strong upper ocean (<300 m) negative salinity (fresh) bias of order 0.3 PSS-78, with a tendency toward a positive salinity (salty) bias (<0.25 PSS-78) in the NH intermediate layers (200-3000 m) (Flato et al., 2013). These biases are also present in CMIP6, albeit with slightly smaller magnitudes (Figure 3.25). Here we expand the global zonal mean bias assessment to consider the three independent ocean basins individually, which allows for an assessment as to which basin biases are dominating the global zonal mean. The basin with the most pronounced biases is the Atlantic, with a strong upper ocean (<300 m) fresh bias, of order 0.3 PSS-78 just like the global zonal mean, and a marked subsurface salinity bias that exceeds 0.5 PSS-78 in equatorial waters between 400–1000 m.

The Pacific Ocean shares the strongest similarity to the global bias, with a similar upper ocean (<300 m) fresh bias, of a smaller magnitude than the Atlantic, with a pronounced off-equator feature at intermediate depths (500-1500 m). Lower magnitude positive salinity biases (~0.3 PSS-78) are also present in both hemispheres between 200-3000 m, and deeper in the SH (Figure 3.25). The Indian Ocean shows similar features to the SH Pacific, with a marked upper ocean (<500 m) fresh bias of order 0.3 PSS-78, and a strong near-surface positive bias of order 0.4 PSS-78 associated with the Arabian Sea (Figure 3.25).

For the Southern Ocean in CMIP5, considerable fresh biases exist through the water column, and are most

ACCEPTED VERSION SUBJECT TO FINAL EDITING

pronounced in the ventilated layers representing the subtropical mode and intermediate water masses (Sallée et al., 2013). A fresh bias in upper and intermediate layers of comparable magnitude is also seen in CMIP6 (Figure 3.25). The structure of the biases in the CMIP6 multi-model mean (which averages across many simulations with differing subsurface geographies and differing Southern Ocean salinity biases (Beadling et al., 2020)) is similar to that evident in the CMIP5 multi-model mean, but with slightly smaller magnitudes. The Arctic Ocean also on average exhibits a surface-enhanced fresh bias in the upper ocean (Figure 3.25), which is much larger than its SH counterpart.

In summary, the structure of the salinity biases in the multi-model mean has not changed substantially between CMIP5 and CMIP6 (*medium confidence*), though there is *limited evidence* that the magnitude of subsurface biases has been reduced. This provides confidence in the utility of CMIP-class models for detection and attribution of ocean salinity.

3.5.2.2 Salinity Change Attribution

AR5 concluded that it was *very likely* that anthropogenic forcings had made a discernible contribution to surface and subsurface ocean salinity changes since the 1960s (Bindoff et al., 2013; Rhein et al., 2013). They highlighted that the spatial patterns of salinity trends, and the mean fields of salinity and evaporation minus precipitation are all similar, with an enhancement to Atlantic Ocean salinity and freshening in the Pacific and Southern Oceans. Since AR5 all subsequent work on assessing observed and modelled salinity changes has confirmed these results.

Considerable changes to observed broad- or basin-scale ocean near-surface salinity fields have been reported (see Section 2.3.3.2), and these have been linked to changes in the evaporation minus precipitation patterns at the ocean surface through model simulations, typically expressing a pattern of change where climatological mean fresh regions become fresher and corresponding salty regions becoming saltier (Durack et al., 2012, 2013; Zika et al., 2015; Lago et al., 2016; Skliris et al., 2016, 2018; Cheng et al., 2020), also broadly present in the CMIP6 multi-model mean (Figure 3.27). At basin-scales, the depth-integrated effect of mean salinity changes as captured in halosteric sea level for the top 0 to 2000 m has also been assessed based on observational products, and these results mirror near-surface patterns in the CMIP5 and CMIP6 models, with most areas that are becoming fresher at the surface exhibiting increases in halosteric sea level, and areas becoming saltier exhibiting decreases (Durack et al., 2014b; Figure 3.28). Further investigations using observations and models together have tied the long-term patterns of surface and subsurface salinity changes to coincident changes to the evaporation minus precipitation field over the ocean (Durack et al., 2012, 2013; Durack, 2015; Levang and Schmitt, 2015; Zika et al., 2015, 2018; Grist et al., 2016; Lago et al., 2016; Cheng et al., 2020), however the rate of these changes through time continues to be an active area of active research (Skliris et al., 2014; Zika et al., 2015, 2018; Cheng et al., 2020; Sallée et al., 2021).

Climate change detection and attribution assessments have considered salinity, with the first of these assessed in AR5 (Bindoff et al., 2013). Since this time, the positive detection conclusions (Stott et al., 2008; Pierce et al., 2012; Terray et al., 2012) have been supported by a number of more recent and independent assessments which have reproduced the multi-decadal basin-scale patterns of change in observations and models (Figures 3.27 and 3.28; Durack, 2015; Durack et al., 2014b; Levang and Schmitt, 2015; Skliris et al., 2016). Observed depth-integrated basin responses, contrasting the Pacific and Atlantic basins (freshening Pacific and enhanced salinity Atlantic) were also shown to be replicated in most historical (natural and anthropogenically forced) simulations, with this basin contrast absent in CMIP5 and CMIP6 natural-only simulations that exclude anthropogenic forcing (Durack et al., 2014b; Figure 3.28).

While observational sparsity considerably limits quantification of regional changes, a recent study by Friedman et al. (2017) assessed salinity changes in the Atlantic Ocean from 1896 to 2013 and confirmed the pattern of mid-to-low latitude enhanced salinity and high latitude North Atlantic freshening over this period exists even after accounting for the effects of the NAO and AMO.

Considering the bulk of evidence, it is *extremely likely* that human influence has contributed to observed

ACCEPTED VERSION SUBJECT TO FINAL EDITING

near-surface and subsurface salinity changes across the globe since the mid-20th century. All available multi-decadal assessments have confirmed that the associated pattern of change corresponds to fresh regions becoming fresher and salty regions becoming saltier (*high confidence*). CMIP5 and CMIP6 models are only able to reproduce these patterns in simulations that include greenhouse gas increases (*medium confidence*). Changes to the coincident atmospheric water cycle and ocean-atmosphere fluxes (evaporation and precipitation) are the primary drivers of the basin-scale observed salinity changes (*high confidence*). This result is supported by all available observational assessments, along with a growing number of climate modelling studies targeted at assessing ocean and water cycle changes. The basin-scale changes are consistent across models and intensify on centennial scales from the historical period through to the projections of future climate (*high confidence*).

[START FIGURE 3.27 HERE]

Figure 3.27: Maps of multi-decadal salinity trends for the near-surface ocean. Units are Practical Salinity Scale 1978 [PSS-78] decade^{-1}. (top) The best estimate (Section 2.3.3.2) observed trend (Durack and Wijffels, 2010 updated, 1950-2019). (bottom) Simulated trend from the CMIP6 historical experiment multi-model mean (1950-2014). Black contours show the climatological mean salinity in increments of 0.5 PSS-78 (thick lines 1 PSS-78). Further details on data sources and processing are available in the chapter data table (Table 3.SM.1).

[END FIGURE 3.27 HERE]

[START FIGURE 3.28 HERE]

Figure 3.28: Long-term trends in halosteric and thermosteric sea level in CMIP6 models and observations. Units are mm year^{-1}. In the right column, three observed maps of 0 to 2000 m halosteric sea level trends (right column) top from (Durack and Wijffels, 2010, 1950-2019 updated - D&W), middle from (Good et al., 2013, 1950-2019 updated- EN4), and lower from (Ishii et al., 2017, 1955-2019 updated – Ishii), and bottom, the CMIP6 historical multi-model mean (1950-2014). Red and orange colours show a halosteric contraction (enhanced salinity) and blue and green a halosteric expansion (reduced salinity). In the left column, basin-integrated halosteric (top) and thermosteric (bottom) trends for the Atlantic and Pacific, the two largest ocean basins, where Pacific anomalies are presented on the x-axis and Atlantic on the y-axis. Observational estimates are presented in black, CMIP6 historical (all forcings) simulations are shown in orange squares, with the multi-model mean shown as a dark orange diamond with a black bounding box. CMIP6 hist-nat (historical natural forcings only) simulations are shown in green squares with the multi-model mean as a dark green diamond with a black bounding box. Further details on data sources and processing are available in the chapter data table (Table 3.SM.1).

[END FIGURE 3.28 HERE]

3.5.3 Sea Level

In keeping with the scope of this chapter, this section addresses global and basin-scale sea level changes, whereas regional and local sea level changes are assessed in Section 9.6. In the AR5, the observed sea level budget was closed by considering all contributing factors including ocean warming, mass contributions from terrestrial storage, glaciers, and the Antarctic and Greenland ice sheets (Church et al., 2013a). The SROCC found that the observed global mean sea level (GMSL) rise is consistent within uncertainties with the sum of the estimated observed contributions for 1993–2015 and 2006–2015.

3.5.3.1 Sea Level Evaluation

The current generation of climate models do not fully resolve many of the components required to close the observed sea level budget, such as glaciers, ice sheets and land water storage (see Section 9.6 and Box 9.1).

ACCEPTED VERSION SUBJECT TO FINAL EDITING

Consequently, most CMIP-based analyses of sea level change have focused on thermosteric sea level changes (i.e., thermal expansion due to warming) and ocean dynamic sea level change, both of which are simulated in the CMIP5-generation of models. The improved agreement between modelled thermal expansion and observed estimates during the historical period led the SROCC to assess a *high confidence* level in the simulated thermal expansion using climate models and *high confidence* in their ability to project future thermal expansion.

Since CMIP5 models do not include all necessary components of sea level change, this gap has been bridged by using offline models (for glacier melt and ice-sheet surface mass balance) driven by reanalyses and model output. Some studies have used offline mass inputs to account for dynamic ice sheet and terrestrial contributions. Slangen et al. (2017) and Meyssignac et al. (2017) suggested including corrections to several contributions to sea level changes including to the Greenland surface mass balance and glacier contributions, based on differences between CMIP5-driven model results and reanalysis-driven results. This helps close the gap between models and observations for the 20th century globally, as well as providing better agreement with tide gauge observations in terms of interannual and multi-decadal variability at the regional scale.

In CMIP6, ice sheets (see Section 3.4.3.2 and 9.4) are included for the first time in ISMIP6 (Nowicki et al., 2016). There is also scope for new insights into terrestrial water contributions from land surface (and sub-surface) modelling in the Land Surface, Snow and Soil moisture Model Intercomparison Project (LS3MIP; van den Hurk et al., 2016). In parallel, the GlacierMIP project (Hock et al., 2019a; Marzeion et al., 2020; see Section 3.4.3.1 and 9.5) is also underway, and has provided more quantitative guidance and a comprehensive assessment of the uncertainties and best estimates of the current and future contributions of glaciers to the sea level budget.

3.5.3.2 Sea Level Change Attribution

The SROCC concluded with *high confidence* that the dominant cause of global mean sea level rise since 1970 is anthropogenic forcing. Prior to that, the AR5 had concluded that it is *very likely* that there has been a substantial contribution from anthropogenic forcings to global mean sea level rise since the 1970s. Since the AR5, several studies have identified a human contribution to observed sea level change resulting from a warming climate as manifest in thermosteric sea level change and the contribution from melting glaciers and ice sheets.

For the global mean thermosteric sea level change, Slangen et al. (2014) showed the importance of anthropogenic forcings (combined greenhouse gas and aerosol forcings) for explaining the magnitude of the observed changes between 1957-2005, considering the full depth of the ocean and natural forcings in order to capture the variability (see also Figure 3.29). Over the 1950-2005 period, Marcos and Amores (2014) found that human influence explains 87% of the 0-700 m global thermosteric sea level rise. Both thermosteric and regional dynamic patterns of sea level change in individual forcing experiments from CMIP5 were considered by Slangen et al. (2015) who showed that responses to anthropogenic forcings are significantly different from both internal variability and inter-model differences and that although greenhouse gas and anthropogenic aerosol forcings produce opposite global mean sea level responses, there are differences in response on regional scales. Based on these studies, we conclude that it is *very likely* that anthropogenic forcing was the main driver of the observed global mean thermosteric sea level change since 1970.

In an attribution study of the sea-level contributions of glaciers, Marzeion et al. (2014) found that between 1991 and 2010, the anthropogenic fraction of global glacier mass loss was 69 ±24% (see also Section 3.4.3.1). Slangen et al. (2016) considered all quantifiable components of the global mean sea level budget and showed that anthropogenically forced changes account for 69 ± 31% of the observed sea level rise over the period 1970 to 2005, whereas natural forcings combined with internal variability have a much smaller effect - only contributing 9 ± 18% of the change over the same period. These studies indicate that about 70% of the combined change in glaciers, ice sheet surface mass balance and thermal expansion since 1970 can be attributed to anthropogenic forcing, and that this percentage has increased over the course of the 20th century.

ACCEPTED VERSION SUBJECT TO FINAL EDITING

Detection studies on GMSL change in the 20th century (Becker et al., 2014; Dangendorf et al., 2015) found that observed total GMSL change in the 20th century was inconsistent with internal variability. Dangendorf et al. (2015) determined that for 1900 to 2011 at least 45% of GMSL change is human-induced. A study that developed a semi-empirical model to link sea-level change to observed GMST change concluded that at least 41% of the 20th century sea-level rise would not have happened in the absence of the century's increasing GMST and that there was a 95% probability that by 1970 GMSL was higher than that which would have occurred in the absence of increasing GMST (Kopp et al., 2016). Richter et al. (2020) compared modelled sea level change with the satellite altimeter observations from 1993 to 2015; a period short enough that internal variability can dominate the spatial pattern of change. They found that when GMSL is not removed, model simulated zonally averaged sea level trends are consistent with altimeter observations globally as well as in each ocean basin and much larger than might be expected from internal variability. Using spatial correlation, Fasullo and Nerem (2018) showed that the satellite altimeter trend pattern is already detectable.

We note that current detection and attribution studies do not yet include all processes that are important for sea-level change (see Section 9.6). However, based on the body of literature available, we conclude that the main driver of the observed GMSL rise since at least 1970 is *very likely* anthropogenic forcing.

[START FIGURE 3.29 HERE]

Figure 3.29: Simulated and observed global mean sea level change due to thermal expansion for CMIP6 models and observations relative to the baseline period 1850-1900. Historical simulations are shown in brown, natural only in green, greenhouse gas only in grey, and aerosol only in blue (multi-model means shown as thick lines, and shaded ranges between the 5th and 95th percentile). The best estimate observations (black solid line) for the period of 1971-2018, along with *very likely* ranges (black shading) are from Section 2.3.3.1 and are shifted to match the multi-model mean of the historical simulations for the 1995-2014 period. Further details on data sources and processing are available in the chapter data table (Table 3.SM.1).

[END FIGURE 3.29 HERE]

3.5.4 Ocean Circulation

Circulation of the ocean, whether it be wind or density driven, plays a prominent role in the heat and freshwater transport of the Earth system (Buckley and Marshall, 2016). Thus, its accurate representation is crucial for the realistic representation of water mass properties, and replication of observed changes driven by atmosphere-land-ocean coupling. Here, we assess the ability of CMIP models to reproduce the observed large-scale ocean circulation, along with assessment of the detection and attribution of any anthropogenically-driven changes. We also note that the process-based understanding of these circulation changes and circulation changes occurring at smaller scales are assessed in Section 9.2.3.

3.5.4.1 Atlantic Meridional Overturning Circulation (AMOC)

The Atlantic Meridional Overturning Circulation (AMOC) represents a large-scale flow of warm salty water northward at the surface and a return flow of colder water southward at depth. As such, its mean state plays an important role in transporting heat in the climate system, while its variability can act to redistribute heat (see Sections 2.3.3.4.1 and 9.2.3.1 for more details). Paleo-climatic and model evidence suggest that changes in AMOC strength have played a prominent role in past transitions between warm and cool climatic phases (e.g., Dansgaard et al., 1993; Ritz et al., 2013)

AR5 concluded that while climate models suggested that an AMOC slowdown would occur in response to anthropogenic forcing, the short direct observational AMOC record precluded it from being used to support this model finding. Chapter 2 reports with *high confidence*, a weakening of the AMOC was observed in the mid-2000s to the mid-2010s, while again also noting that the observational record was too short to determine

ACCEPTED VERSION SUBJECT TO FINAL EDITING

whether this is a significant trend or a manifestation of decadal and multi-decadal variability (Section 2.3.3.4.1). Indirect evidence of AMOC weakening since at least the 1950s is also presented, but confidence in this longer-term decrease was *low* (Section 2.3.3.4.1).

Despite the additional six years or so of observations since the AR5, the evaluation of the AMOC in models continues to be severely hampered by the geographically sparse and temporally short observational record. The longest continuous observational estimates of the AMOC are based on measurements taken at 26°N by the RAPID-MOCHA array (Smeed et al., 2018). Basic evaluation of the AMOC at 26°N shows that the CMIP5 and CMIP6 multi-model mean overturning strength is comparable with RAPID (Reintges et al., 2017; Weijer et al., 2020), but the model range is large (12-29 Sv for CMIP5, Zhang and Wang (2013); and 10-31 Sv for CMIP6, Weijer et al. (2020)) (Figure 3.30a). It is noted that deviations of AMOC strength in CMIP5 models have been related to global-scale sea surface temperature biases (Wang et al., 2014a). Both coupled and ocean-only models also underestimate the depth of the AMOC cell (Danabasoglu et al., 2014; Weijer et al., 2020; Figure 3.30a). Paleo-climatic evidence has also raised questions regarding the accuracy of the representation of the strength and depth of the modelled AMOC during past periods (Otto-Bliesner et al., 2007; Muglia and Schmittner, 2015). Overall, however, both the CMIP5 and CMIP6 model ensembles simulate the general features of the AMOC mean state reasonably well, but there is a large spread in the latitude and depth of the maximum overturning, and the maximum AMOC strength (Figure 3.30a).

The short length of the observed time-series (RAPID has measured the AMOC since 2004), sparse observations, observational uncertainties (Sinha et al., 2018), as well as significant observed variability on interannual and longer time scales, makes comparison with modelled AMOC variability challenging. RAPID observations show that the overturning at 26°N was 2.9 Sv weaker in the multi-year average of 2008-2012 relative to 2004-2008 and 2.5 Sv weaker in 2012-2017 relative to 2004-2008 (Smeed et al., 2014, 2018) (see also Section 2.3.3.4.1). As expected, this weakening was accompanied by a significant reduction in northward heat transport (Bryden et al., 2020). CMIP5 and CMIP6 models produce a forced weakening of the AMOC over the 2012-2017 period relative to 2004-2008, but at 26°N the multi-model mean response is substantially weaker than the observed AMOC decline over the same period. The discrepancy between the modelled multi-model mean (i.e. the forced response) and the RAPID observed AMOC changes has led studies to suggest that the observed weakening over 2004-2017 is largely due to internal variability (Yan et al., 2018). However, comparison of observed RAPID AMOC variability with modelled variability also reveals that most CMIP5 models appear to underestimate the interannual and decadal timescale AMOC variability (Roberts et al., 2014; Yan et al., 2018), and, although the overall variance is larger in CMIP6 than in CMIP5, similar results are found analysing the CMIP6 models (Figure 3.30b,c). It is currently unknown why most models underestimate this AMOC variability, or whether they are underestimating the internal or externally forced components. This underestimation of AMOC variability may also have potential implications for detection and attribution, the relationship between AMOC and AMV (see Section 3.7.7), and near-term predictions. There is also emerging evidence, based on analysis of freshwater transports, that the AMOC in CMIP5-era models is too stable, largely due to systematic biases in ocean salinity (Liu et al., 2017a; Mecking et al., 2017). Such a systematic bias may potentially be linked with the underestimation of both simulated AMOC internal variability through eddy-mean flow interactions that are poorly represented in standard CMIP-class model resolution (Leroux et al., 2018), and externally forced change.

As reported in Section 2.3.3.4.1, estimates of AMOC since at least 1950, which are generated from observed surface temperatures or sea surface height, suggest the AMOC weakened through the 20th century (*low confidence*) (Ezer et al., 2013; Caesar et al., 2018). Over the same period, the CMIP5 multi-model mean showed no significant net forced response in AMOC (Cheng et al., 2013). However, a significant forced change is simulated in the CMIP6 multi-model mean, where a clear increase of the AMOC is seen over the 1940-1985 period (Menary et al., 2020) (Figure 3.30e). Although there is general agreement that the influence of greenhouse gases acts to a weaken the modelled AMOC (Delworth and Dixon, 2006; Caesar et al., 2018), changes in solar, volcanic and anthropogenic aerosol emissions can lead to temporary changes in AMOC on decadal-to-multidecadal timescales (Delworth and Dixon, 2006; Menary et al., 2013; Menary and Scaife, 2014; Swingedouw et al., 2017; Undorf et al., 2018b). As such, the simulated net forced response in AMOC is often a balance between the different forcing factors (Delworth and Dixon, 2006; Menary et al., 2020) (Section 9.2.3.1). The differing AMOC response of CMIP5 and CMIP6 models during the historical

ACCEPTED VERSION SUBJECT TO FINAL EDITING

period has been associated with stronger aerosol effective radiative forcing in the CMIP6 models (Menary et al., 2020), such that the aerosol-induced AMOC increase during the 1940-1985 period overcomes the greenhouse gas induced decline (Figure 3.30e). However, models simulate a range of anthropogenic aerosol effective radiative forcing and a range of historical AMOC trends in CMIP6 (Menary et al., 2020) and there remains considerable uncertainty over the realism of the CMIP6 AMOC response during the 20th century (Figure 3.30d-f) due to disagreement among the differing lines of evidence. For example, ocean reanalysis (Jackson et al., 2019) and forced ocean model simulations (Robson et al., 2012; Danabasoglu et al., 2016), which show AMOC changes that are broadly consistent with the CMIP6 response, appear to disagree with observational estimates of AMOC over the historical period (Ezer et al., 2013; Caesar et al., 2018). It is noted, however, that the relatively short length of the forced ocean simulations and ocean reanalysis precludes a comparable assessment of 20th century trends. Furthermore, despite the similar AMOC evolution seen in forced ocean model simulations and the CMIP6 models, it is unclear whether the same underlying mechanisms are responsible for the changes.

In summary, models do not support robust assessment of the role of anthropogenic forcing in the observed AMOC weakening between the mid-2000s and the mid-2010s, which is assessed to have occurred with *high confidence* in Section 2.3.3.4.1, as the changes are outside of the range of modelled AMOC trends (regardless of whether they are forced or internally generated) in most models. Thus, we have *low confidence* that anthropogenic forcing has influenced the observed changes in AMOC strength in the post-2004 period. In addition to this, there remains considerable uncertainty over the realism of the CMIP6 AMOC response during the 20th century due to disagreement among the differing lines of observational and modelled evidence (i.e., historical AMOC estimates, ocean reanalysis, forced ocean simulations and historical CMIP6 simulations). Thus, we have *low confidence* that anthropogenic forcing has had a significant influence on changes in AMOC strength during the 1860-2014 period.

[START FIGURE 3.30 HERE]

Figure 3.30: Observed and CMIP6 simulated AMOC mean state, variability and long-term trends. (a) AMOC meridional streamfunction profiles at 26.5°N from the historical CMIP5 (1860-2004) and CMIP6 (1860-2014) simulations compared with the mean maximum overturning depth (horizontal grey line) and magnitude (vertical grey line) from the RAPID observations (2004-2018). The distributions of model ranges of AMOC maximum magnitude and depth are respectively displayed on the x- and y-axis. (b) Distributions of overlapping 8-year AMOC trends from individual CMIP6 historical simulations (pink box plots) are plotted along with the combined distributions of all available CMIP5 (blue boxplot) and CMIP6 (red boxplot) models. For reference, the observed 8-year trend calculated between 2004-2012 is also shown as a horizontal grey line (following Roberts et al., 2014) (c) Distributions of interannual AMOC variability from individual CMIP6 model historical simulations, along with the combined distributions of all available CMIP5 and CMIP6 models. Interannual variability in models and observations are estimated as annual mean (April-March) differences, and the horizontal grey line is the observed value for 2009/2010 minus 2008/2009 (following Roberts et al., 2014). (d-f) Distributions of linear AMOC trends calculated over various time periods (see panel titles) in CMIP6 simulations forced with: greenhouse gas forcing only (GHG), natural forcing only (NAT), anthropogenic aerosol forcing only (AER) and all forcing combined (Historical; HIST). (a-f) Boxes indicate 25th to 75th percentile, whiskers indicate 1st and 99th percentiles, and dots indicate outliers, while the horizontal black line is the multi-model mean trend. In (d-f) the multi-model mean trend is also written above each distribution. The multi-model distributions in (a-c) were produced with one historical ensemble member per model for which the AMOC variable was available (listed), while those in (d-f) were produced with the AMOC detection and attribution simulation data sets utilised by Menary et al. (2020). Further details on data sources and processing are available in the chapter data table (Table 3.SM.1).

[END FIGURE 3.30 HERE]

3.5.4.2 Southern Ocean Circulation

The Southern Ocean circulation provides the principal connections between the world's major ocean basins

ACCEPTED VERSION SUBJECT TO FINAL EDITING

through the circulation of the Antarctic Circumpolar Current (ACC), while also largely controlling the connection between the deep and upper layers of the global ocean circulation, through its upper and lower overturning cells.

The assessment of observations presented in Sections 2.3.3.4.2 and 9.2.3.2 reports that there is no evidence of an ACC transport change, and it is *unlikely* that the mean meridional position of the ACC has moved southward in recent decades (Section 2.3.3.4.2 and 9.2.3.2). This is despite observations of surface wind displaying an intensification and southward shift (Section 2.4.1.2). There is *low confidence* in an observed intensification of overturning in the Southern Ocean's upper ocean and there is *medium confidence* for a slowdown of the Antarctic Bottom Water circulation and commensurate Antarctic Bottom Water volume decrease since the 1990s (Section 9.2.3.2). Section 9.2.3.2 presents new evidence, since the SROCC, which assessed with *medium confidence* that the lower cell can episodically increase as a response to climatic anomalies, temporally counteracting the forced tendency for reduced bottom water formation.

The modelled strength of the ACC clearly improved from CMIP3, in which the models tended to underestimate the strength of the ACC, to CMIP5 (Meijers et al., 2012). This improvement in the realism of ACC strength continues from CMIP5 to CMIP6, with the modelled ACC strength converging toward the magnitude of observed estimates of net flow through the Drake Passage (Beadling et al., 2020). There is, however, a small number of models that still display an ACC that is much weaker than that observed, while several models also display much more pronounced ACC decadal variability than that observed (Beadling et al., 2020). The increased realism of the ACC was at least partly related to noted improvements in all metrics of the Southern Ocean's surface wind stress forcing (Beadling et al., 2020). The most notable wind stress forcing improvements were found in the strength and the latitudinal position of the zonally-averaged westerly wind stress maximum (Beadling et al., 2020; Bracegirdle et al., 2020a). While the two-cell structure of the overturning circulation appears to be well captured by CMIP5 models (Sallée et al., 2013; Russell et al., 2018), they tend to underestimate the intensity of the lower cell overturning, and overestimate the intensity of the upper cell overturning (Sallée et al., 2013). As the lower overturning cell is closely related to Antarctic Bottom Water formation and deep convection, both fields also display substantial errors in CMIP5 models (Heuzé et al., 2013, 2015). CMIP6 climate models show clear improvements compared to CMIP5 in their representation of Antarctic Bottom Water, which suggests an improved representation of the lower overturning cell (Heuzé, 2021).

Despite notable improvements of CMIP6 models compared to CMIP5 models, inherent limitations in the representation of important processes at play in the Southern Ocean's horizontal and vertical circulation remain (Section 9.2.3.2). For instance, Southern Ocean mesoscale eddies are largely parameterised in the current generation of climate models and despite their small spatial scales, they are a key element for establishing the ACC and upper overturning cell, as well as for their future evolution under changing atmospheric forcing (Kuhlbrodt et al., 2012; Downes and Hogg, 2013; Gent, 2016; Downes et al., 2018; Poulsen et al., 2018). The absence of ice-sheet coupling in the CMIP6 model suite is another important limitation, as basal meltwater and calving can influence the circulation, particularly the lower cell of the Southern Ocean (Bronselaer et al., 2018; Golledge et al., 2019; Lago and England, 2019; Jeong et al., 2020a; Moorman et al., 2020). We note that early development of global climate models with interactive ice-shelves cavities has begun and is showing potential to be developed (Jeong et al., 2020b).

In summary, while there have been improvements across successive CMIP phases (from CMIP3 to CMIP6) in the representation of the Southern Ocean circulation, such that the mean zonal and overturning circulations of the Southern Ocean are now broadly reproduced, substantial observational uncertainty and climate model challenges preclude attribution of Southern Ocean circulation changes (*high confidence*).

3.6 Human Influence on the Biosphere

3.6.1 Terrestrial Carbon Cycle

The AR5 did not make attribution statements on changes in global carbon sinks. The IPCC Special Report on

ACCEPTED VERSION SUBJECT TO FINAL EDITING

Climate Change and Land (SRCCL) assessed with *high confidence* that global vegetation photosynthetic activity has increased over the last 2-3 decades (Jia et al., 2019). That increase was attributed to direct land use and management changes, as well as to CO_2 fertilisation, nitrogen deposition, increased diffuse radiation and climate change (*high confidence*). The AR5 assessed with *high confidence* that CMIP5 Earth System Models (ESMs) simulate the global mean land and ocean carbon sinks within the range of observation-based estimates (Flato et al., 2013). The IPCC SRCCL, however, noted the remaining shortcomings of carbon cycle schemes in ESMs (Jia et al., 2019), which for example do not properly incorporate thermal responses of respiration and photosynthesis, and frequently omit representations of permafrost thaw (Comyn-Platt et al., 2018), the nitrogen cycle (Thomas et al., 2015b) and its influence on vegetation dynamics (Jeffers et al., 2015), the phosphorus cycle (Fleischer et al., 2019), and accurate implications of carbon store changes for a range of land use and land management options (Erb et al., 2018; Harper et al., 2018) (see Sections 5.2.1.4.1 and 5.4, Figure 5.24 and Table 5.4 for details).

This section considers three main large-scale indicators of climate change relevant to the terrestrial carbon cycle: atmospheric CO_2 concentration, atmosphere-land CO_2 fluxes, and leaf area index. These indicators were chosen because they have been the target of attribution studies. Other indicators, like land use and management, and wildfires, relate to human influence but are discussed in Chapter 5. Chapter 7 discusses energetic consequences of changes in the terrestrial carbon cycle in Section 7.4.2.5.2. CMIP5 and CMIP6 ESMs are most often run with prescribed observed historical changes in atmospheric CO_2 concentration and diagnose CO_2 emissions consistent with these. Such calculations require that the models simulate realistic changes in the terrestrial carbon cycle over the historical period, as changes to land carbon stores will influence the size of CO_2 emissions consistent with prescribed CO_2 pathways, and associated remaining carbon budgets (Section 5.5). Such testing of existing models is needed while also recognising there are process representations still requiring inclusion.

Since the AR5, atmospheric inversion studies have further tested or constrained models, while new datasets have been used to constrain specific parts of the terrestrial carbon cycle such as plant respiration (Huntingford et al., 2017). Figure 3.31 compares historical emissions-driven CMIP6 simulations of global mean atmospheric CO_2 concentration and net ocean and land carbon fluxes to the assessed CO_2 concentration and fluxes from the Global Carbon Project (Friedlingstein et al., 2019). For 2014, the CMIP6 models simulate a range of CO_2 concentrations centred around the observed value of 397 ppmv, with a range of 381 to 412 ppmv. GSAT anomalies simulated over the historical period are very similar in models that simulate or prescribe changes in atmospheric CO_2 concentrations (Figure 3.31b and Figure 3.4a). Most models simulate realistic temporal evolution of the global net ocean and land carbon fluxes, although model spread is larger over land (Figure 3.31c,d, see also Sections 3.6.2 and 5.4.5.2, Figure 5.24). Although literature published soon after the AR5 highlighted the importance of representing nitrogen limitation on plant growth (Peng and Dan, 2015; Thomas et al., 2015b), more recent studies note that models without nitrogen limitation can still be consistent with the latest estimates of historical carbon cycle changes (Arora et al., 2020; Meyerholt et al., 2020). Uncertainties in the photosynthetic response to atmospheric CO_2 concentrations at global scales, shifts in carbon allocation and turnover, land-use change (Hoffman et al., 2014; Wieder et al., 2019), and water limitation are also important influences on land carbon fluxes.

All models and observational estimates agree that interannual variability in net CO_2 uptake is much larger over land than over the ocean. Studies demonstrate that regional variations in both the trends and the yearly strength of the terrestrial carbon sink are considerable. Land carbon uptake is dominated by the extratropical northern latitudes (Ciais et al., 2019) (see also Section 5.4.5.3 and Figure 5.25) because the tropics may have become a net source of carbon (Baccini et al., 2017). At local to regional scales, the dominant driver of yearly sink strength variations is water availability, but at continental to global scales, temperature anomalies are the dominant driver (Section 5.2.1.4.2; Jung et al., 2017). The major role of levels of water stored in the ground in influencing land-atmosphere CO_2 exchange has also been confirmed through simultaneous analysis of satellite gravimetry and atmospheric CO_2 levels (Humphrey et al., 2018). When considered globally, simulated land and ocean carbon sinks fall within the range of observation-based estimates with *high confidence*. But there is also *high confidence* that that apparent success arises for the wrong reasons, as models underestimate the NH carbon sink, as discussed in Section 5.4.5.3.

ACCEPTED VERSION SUBJECT TO FINAL EDITING

[START FIGURE 3.31 HERE]

Figure 3.31: Evaluation of historical emission-driven CMIP6 simulations for 1850-2014. Observations (black) are compared to simulations of global mean (a) atmospheric CO_2 concentration (ppmv), with observations from the National Oceanic and Atmospheric Administration Earth System Research Laboratory (NOAA ESRL) (Dlugokencky and Tans, 2020), (b) air surface temperature anomaly (°C) with respect to the 1850-1900 mean, with observations from HadCRUT4 (Morice et al., 2012) (c) land carbon uptake (PgC yr^{-1}), (d) ocean carbon uptake (PgC yr^{-1}), both with observations from the Global Carbon Project (GCP) (Friedlingstein et al., 2019) and grey shading indicating the observational uncertainty. Land and ocean carbon uptakes are plotted using a 10-year running mean for better visibility. The ocean uptake is offset to 0 in 1850 to correct for pre-industrial riverine-induced carbon fluxes. Further details on data sources and processing are available in the chapter data table (Table 3.SM.1).

[END FIGURE 3.31 HERE]

The seasonal cycle in atmospheric CO_2, which is driven by the drawdown of carbon by photosynthesis on land during the summer and release by respiration during the winter, has increased in amplitude since the start of systematic monitoring (Figure 3.32, see also Section 2.3.4.1). This trend, which is larger at higher latitudes of the NH, was first reported by Keeling et al. (1996) and has continued. Changes in vegetation productivity have also been observed, as well as longer growing seasons (Park et al., 2016). However, a slowdown of the increasing trend has been noted, linked to a slowdown of both vegetation greening and growing-season length increases (Buermann et al., 2018; Li et al., 2018b; Wang et al., 2020b). Figure 3.32 shows that CMIP6 terrestrial carbon cycle models partially capture the increasing amplitude of the seasonal cycle of the land carbon sink, also seen in observational reconstructions. However, the identification of the human influence that contributes most strongly to these changes in the seasonal cycle is debated.

Proposed causes of the trend in the amplitude of the seasonal cycle of CO_2, and its amplification at higher latitudes, include increases in the summer productivity and/or increases in the magnitude of winter respiration of northern ecosystems (Barichivich et al., 2013; Graven et al., 2013a; Forkel et al., 2016; Wenzel et al., 2016), increases in productivity throughout the NH by CO_2 fertilisation, and increases in the productivity of agricultural crops in northern mid-latitudes (Gray et al., 2014; Zeng et al., 2014). Recent studies have attempted to quantify the different contributions by comparing atmospheric CO_2 observations with ensembles of land surface model simulations. Piao et al. (2017) found that CO_2 fertilization of photosynthesis is the main driver of the increase in the amplitude of the seasonal cycle of atmospheric CO_2 but noted that climate change drives the latitudinal differences in that increase. North of 40°N, Bastos et al. (2019) also found CO_2 fertilization to be the most likely driver, with warming at northern high latitudes contributing a decrease in amplitude, in contrast to earlier conclusions (Graven et al., 2013b; Forkel et al., 2016), and agricultural and land use changes making only a small contribution. For temperate regions of the NH, Wang et al. (2020b) found that the importance of CO_2 fertilisation is decreased by drought stress, but also found only a small contribution from agricultural and land use changes. However, many global models do not include nitrogen fertilisation, changes to crop cultivars or irrigation effects, with the latter associated with deficiencies in simulated terrestrial water cycling (Yang et al., 2018a). All these factors influence the capability of models to simulate accurately the seasonal cycle in atmosphere-land CO_2 exchanges. Model comparisons to the atmospheric CO_2 concentration record for Barrow, Alaska, suggest that models underestimate current levels of carbon fixation (Winkler et al., 2019) and have deficiencies in their phenological representation of greenness levels, particularly for autumn (Li et al., 2018c). Based on these studies and noting the uncertainty in the processes ultimately driving changes in atmospheric CO_2 seasonal cycles (Section 5.2.1.4), we assess with *medium confidence* that fertilisation by anthropogenic increases in atmospheric CO_2 concentrations is the main driver of the increase in the amplitude of the seasonal cycle of atmospheric CO_2.

Detection and attribution methods have been applied to leaf area index, which represents “greenness” and general photosynthetic productivity (see Section 2.3.4.3). Nitrogen deposition and land cover change trends remain small compared to variability, so attributing changes in leaf area index to those processes is difficult.

ACCEPTED VERSION SUBJECT TO FINAL EDITING

Using three satellite products and ten land models, Zhu et al. (2016) found increases in leaf area index (greening) over 25-50% of global vegetated areas, and they attributed 70% of this greening to CO_2 fertilisation, although they found that land use change can dominate regionally. This is consistent with the attribution study of observed greening of Mao et al. (2016), and with Mao et al. (2013) who found that CO_2 fertilisation was the dominant cause of enhanced vegetation growth, with latitudinal changes in leaf area index explained by the larger land surface warming in the NH. These conclusions are also consistent with those of Zhu et al. (2017), who found a dominant role for CO_2 fertilisation in driving leaf area index changes in an attribution study in which land models were first weighted by performance. However, Chen et al. (2019) has challenged these results by showing that greening in India and China was driven by land-use change.

Leaf area index increases attributed to CO_2 fertilisation are due to a direct raised physiological response. However, for drylands, CO_2-induced stomatal closure may act to conserve soil moisture and thereby indirectly drive higher photosynthesis through higher water use efficiency (Lu et al., 2016). In models with nitrogen deposition, there is evidence that this simulated effect also influences leaf area index trends, however because of a lack of literature based on large-scale land simulations including both nutrient limitation and crop intensification, it is not yet possible to make an attribution statement about their individual roles in leaf area index changes.

In summary, Earth system models simulate globally averaged land carbon sinks within the range of observation-based estimates (*high confidence)*, but global-scale agreement masks large regional disagreements. Based on new studies that attribute changes in atmospheric CO_2 seasonal cycle to CO_2 fertilisation, albeit counteracted by other factors, combined with the *medium confidence* that models represent the processes driving changes in the seasonal cycle, we assess that there is *medium confidence* that CO_2 fertilisation is the main driver of the increase in the amplitude of the seasonal cycle of atmospheric CO_2. Based on available literature, CO_2 fertilisation has been the main driver of the observed greening trend, but there is only *low confidence* in this assessment because of ongoing debate about the relative roles of CO_2 fertilisation, high latitude warming, and land management, and the low number of models that represent the whole suite of processes involved.

[START FIGURE 3.32 HERE]

Figure 3.32: Relative change in the amplitude of the seasonal cycle of global land carbon uptake in the historical CMIP6 simulations from 1961-2014. Net biosphere production estimates from 19 CMIP6 models (red), the data-led reconstruction JMA-TRANSCOM (Maki et al., 2010; dotted) and atmospheric CO_2 seasonal cycle amplitude changes from observations (global as dashed line, Mauna Loa Observatory (MLO) (Dlugokencky et al., 2020) in bold black). Seasonal cycle amplitude is calculated using the curve fit algorithm package from the National Oceanic and Atmospheric Administration Earth System Research Laboratory (NOAA ESRL). Relative changes are referenced to the 1961-1970 mean and for short time series adjusted to have the same mean as the model ensemble in the last 10 years. Interannual variation was removed with a 9-year Gaussian smoothing. Shaded areas show the one sigma model spread (grey) for the CMIP6 ensemble and the one sigma standard deviation of the smoothing (red) for the CO_2 MLO observations. Inset: average seasonal cycle of ensemble mean net biosphere production and its one sigma model spread for 1961-1970 (orange dashed line, light orange shading) and 2005-2014 (solid green line, green shading). Further details on data sources and processing are available in the chapter data table (Table 3.SM.1).

[END FIGURE 3.32 HERE]

3.6.2 Ocean Biogeochemical Variables

Since CMIP5, there has been a general increase in ocean horizontal and vertical grid resolution in ocean model components (Arora et al., 2020; Séférian et al., 2020). The latter of these developments is particularly significant for projections of ocean stressors as it directly affects the representation of stratification. Updates

ACCEPTED VERSION SUBJECT TO FINAL EDITING

in the representation of ocean biogeochemical processes between CMIP5 and CMIP6 have typically involved an increase in model complexity. Specific developments have been the more widespread inclusion of micronutrients, such as iron, variable stoichiometric ratios, more detailed representation of lower trophic levels including bacteria and the cycling and sinking of organic matter. CMIP6 biogeochemical model performance is generally an improvement on that of the parent CMIP5 generation of models (Séférian et al., 2020). The global representation of present-day air-sea carbon fluxes and surface chlorophyll concentrations show moderate improvements between CMIP5 and CMIP6. Similar improvements are seen in the representation of subsurface oxygen concentrations in most ocean basins, while the representation of surface macronutrient concentrations in CMIP6 is shown to have improved with respect to silicic acid but declined slightly with respect to nitrate. Model representation of the micronutrient iron has not improved substantially since CMIP5, but many more models are capable of representing iron. In addition, a comparison of the carbon concentration and carbon climate feedbacks shows no significant change between CMIP5 and CMIP6 (Arora et al., 2020).

Since AR5, research has also focused on the detection and attribution of regional patterns in ocean biogeochemical change relating to interior de-oxygenation, air-sea CO_2 flux, and ocean carbon uptake and associated acidification. Characterization of flux variability requires understanding of the suite of physical and biological processes including transport, heat fluxes, interior ventilation, biological production and gas exchange which can have very different controls on seasonal versus interannual timescales in both the North Pacific (Ayers and Lozier, 2012) and North Atlantic (Breeden and McKinley, 2016). In the Southern Ocean, models have difficulty reproducing the observed seasonal cycle and interannual variability, making attribution particularly challenging (Lovenduski et al., 2016; Mongwe et al., 2016, 2018).

The AR5 concluded that oxygen concentrations have decreased in the open ocean since 1960 and such decreases can be attributed in part to human influences with *medium confidence*. The decrease in ocean oxygen content in the upper 1000 m, between 1970-2010, is further confirmed in SROCC (*medium confidence*), with the oxygen minimum zone expanding in volume (see also Section 5.3.3.2). Observed oxygen declines over the last several decades (Stendardo and Gruber, 2012; Stramma et al., 2012; Schmidtko et al., 2017) match model estimates in the surface ocean (Oschlies et al., 2017) but are much larger than model derived estimates in the interior (Bopp et al., 2013; Cocco et al., 2013). Some of this difference has been interpreted as due to a lack of representation of coastal eutrophication in these models (Breitburg et al., 2018), but much of it remains unexplained. This disparity is particularly true in the Eastern Pacific oxygen minimum zone, where some CMIP5 models showed increasing trends whereas observations show a strong decrease (Cabré et al., 2015). However, proxy reconstructions suggest that over the last century the ocean may have in fact undergone increases in oxygen in the most oxygen poor regions (Deutsch et al., 2014). As discussed in Section 5.3.1 ocean oxygen went through wide oscillations on multi-centennial timescales through the last deglaciation, with abrupt warming resulting in loss of oxygen in subsurface waters of the North Pacific (Praetorius et al., 2015). The global upper ocean oxygen inventoryis negatively correlated with ocean heat content with a regression coefficient comparable to that found in ocean models (Ito et al., 2017). Variability and trends in the observed upper ocean oxygen concentration are mainly driven by the apparent oxygen utilization component with small contributions from oxygen solubility, suggesting that changing ocean circulation, mixing, and/or biochemical processes, rather than thermally induced solubility effects may be the main drivers of observed de-oxygenation. The spatial distribution of the ocean de-oxygenation in the interior of the ocean as well as over coastal areas are further assessed in Section 5.3.

As one of the most commonly observed surface parameters, the partial pressure of CO_2 has been the topic of considerable detection and attribution work. In North Atlantic subtropical and equatorial biomes, warming has been shown to be a significant and persistent contributor to the observed increase in the partial pressure of CO_2 since the mid-2000s with long-term warming leading to a reduction in ocean carbon uptake (Fay and McKinley, 2013), and with both the partial pressure of CO_2 and associated carbon uptake demonstrating strong predictability as a function of interannual to decadal climate state (Li et al., 2016a; Li and Ilyina, 2018). In the Southern Ocean however, detection and attribution of surface trends in the partial pressure of CO_2 has proven more elusive and dependent on methodology, with some studies suggesting that Southern Ocean carbon uptake slowed from about 1990 to 2006 and subsequently strengthened from 2007 to 2010 (Lovenduski et al., 2008; Fay et al., 2014; Ritter et al., 2017). Other studies have suggested that poor

ACCEPTED VERSION SUBJECT TO FINAL EDITING

representation of the seasonal cycle in the Southern Ocean may confound models' ability to represent changes in the partial pressure of CO_2 in the Southern Ocean (Nevison et al., 2016; Mongwe et al., 2018).

Section 5.2.1.3 assesses that both observational reconstructions based on the partial pressure of CO_2 and ocean biogeochemical models show a quasi-linear increase in the ocean sink of anthropogenic CO_2 from 1.0 ± 0.3 PgC yr^{-1} to 2.5 ± 0.6 PgC yr^{-1} between 1960–1969 and 2010–2019 in response to global CO_2 emissions *(high confidence)*. During the 1990s, the global net flux of CO_2 into the ocean is estimated to have weakened to 0.8 ± 0.5 PgC yr^{-1} while in 2000 and thereafter, it is estimated to have strengthened considerably to rates of 2.0 ± 0.5 PgC yr^{-1}, associated with changes in SST, the surface concentration of dissolved inorganic carbon and alkalinity, and decadal variations in atmospheric forcing (Landschützer et al., 2016, see also Section 5.2).

Ocean acidification is one of the most detectible metrics of environmental change and was well covered in the AR5, in which it was assessed that the uptake of anthropogenic CO_2 had *very likely* resulted in acidification of surface waters (Bindoff et al., 2013). Since then, observations and simulations of multidecadal trends in surface carbon chemistry have increased in robustness. The evidence on ocean pH decline had further strengthened in SROCC with a good agreement found between CMIP5 models and observations and an assessment that the ocean was continuing to acidify in response to ongoing carbon uptake (Bindoff et al., 2019). An observed decrease in global ocean pH is assessed in Section 2.3.3.5 to be *virtually certain* to have occurred with a rate of 0.003-0.026 $decade^{-1}$ at the surface for the past 40 years. The ocean acidification has occurred not only in the surface layer but also in the interior of the ocean (Sections 2.3.3.5 and 5.3.3). Rates have been observed to be nearly as high (between −0.015 and −0.020 $decade^{-1}$) in mode and intermediate waters of the North Atlantic through the combined effect of increased anthropogenic and remineralized carbon (Ríos et al., 2015) and acidification has been observed down to 3000 m in the deep water formation regions (Perez et al., 2018). There has also been considerable improvement in detection and attribution of anthropogenic CO_2 versus eutrophication based acidification in coastal waters (Wallace et al., 2014).

The increased evidence in recent studies supports an assessment that it is *virtually certain* that the uptake of anthropogenic CO_2 was the main driver of the observed acidification of the global ocean. The observed increase in acidification over the North Atlantic subtropical and equatorial regions since 2000 is *likely* associated in part with an increase in ocean temperature, a response which corresponds to the expected weakening of the ocean carbon sink with warming. Due to strong internal variability, systematic changes in carbon uptake in response to climate warming have not been observed in most other ocean basins at present. We further assess, consistent with AR5 and SROCC, that deoxygenation in the upper ocean is due in part to anthropogenic forcing, with *medium* confidence. There is *high confidence* that Earth system models simulate a realistic time evolution of the global mean ocean carbon sink.

3.7 Human Influence on Modes of Climate Variability

This section assesses model evaluation and attribution of changes in the modes of climate variability listed in Cross-Chapter Box 2.2, Table 2. The structure of the modes is described in Annex IV, observed changes in the modes and associated teleconnections are assessed in Sections 2.4, and the role of the modes in shaping regional climate is assessed in Section 10.1.3.2.

3.7.1 North Atlantic Oscillation and Northern Annular Mode

The Northern Annular Mode (NAM; also known as Arctic Oscillation) is an oscillation of atmospheric mass between the Arctic and northern mid-latitudes, analogous to the Southern Annular Mode (SAM; Section 3.7.2). It is the leading mode of variability of sea-level pressure in the northern extratropics but also has a clear fingerprint through the troposphere up to the lower stratosphere, with maximum expression in boreal winter (Kidston et al., 2015). The North Atlantic Oscillation (NAO) can be interpreted as the regional expression of the NAM and captures most of the related variance in the troposphere over a broad North

ACCEPTED VERSION SUBJECT TO FINAL EDITING

Atlantic/Europe domain. Indices measuring the state of the NAO correlate highly with those of the NAM, and teleconnection patterns for both modes are rather similar (Feldstein and Franzke, 2006). A detailed description of the NAM and the NAO as well as their associated teleconnection over land is given in Annex IV.2.1.

AR5 found that while models simulated correctly most of the spatial properties of the NAM, substantial inter-model differences remained in the details of the associated teleconnection patterns over land (Flato et al., 2013). AR5 reported that most models did not reproduce the observed positive trend of the NAO/NAM indices during the second half of the 20th century. It was unclear to what extent this failure reflected model shortcomings and/or if the observed trend could be simply related to pronounced internal climate variability. AR5 accordingly did not make an attribution assessment for the NAO/NAM.

New studies since the AR5 continue to find that CMIP5 models reproduce the spatial structure and magnitude of the NAM reasonably well (Lee and Black, 2013; Zuo et al., 2013; Davini and Cagnazzo, 2014; Ying et al., 2014; Ning and Bradley, 2016; Deser et al., 2017b; Gong et al., 2017) although the North Pacific SLP anomalies remain generally too strong (Zuo et al., 2013; Gong et al., 2017) and the subtropical North Atlantic lobe of SLP anomalies conversely too weak (Ning and Bradley, 2016) in many models. Such overall biases noted in both CMIP3 and CMIP5 (Davini and Cagnazzo, 2014) persist in CMIP6 historical simulations, even though the multi-model multi-member ensemble mean spatial correlation between modelled and observed NAM is slightly higher (Figure 3.33a,d,g). Regarding the NAO, the majority of CMIP5 models very successfully simulate its spatial structure (Lee et al., 2019) and its associations with extratropical jet, storm track and blocking variations over a broad North-Atlantic/Europe domain (Davini and Cagnazzo, 2014) and over land through teleconnections (Volpi et al., 2020). The good performance of the models is confirmed in CMIP6 with a marginal improvement of the averaged observation-model spatial correlation (Figure 3.33b,e,h) and better skill based on other evaluation metrics (Fasullo et al., 2020). The slight underestimation of the SLP anomalies related to the NAO centres of actions over the Azores and Greenland-Iceland-Norwegian Seas remain unchanged compared to CMIP5.

CMIP5 models with a model top within the stratosphere seriously underestimate the amplitude of the variability of the wintertime NAM expression in the stratosphere, in contrast to CMIP5 models which extend well above the stratopause (Lee and Black, 2015). However, even in the latter models, the stratospheric NAM events, and their downward influence on the troposphere, are insufficiently persistent (Charlton-Perez et al., 2013; Lee and Black, 2015). Increased vertical resolution does not show any significant added value in reproducing the structure and magnitude of the tropospheric NAM (Lee and Black, 2013) nor in the NAO predictability as assessed in a seasonal prediction context with a multi-model approach (Butler et al., 2016). On the other hand, there is mounting evidence that a correct representation of the Quasi Biennal Oscillation, extratropical stratospheric dynamics (the polar vortex and sudden stratospheric warmings), and related troposphere-stratosphere coupling, as well as their interplay with ENSO, are important for NAO/NAM timing (Scaife et al., 2016; Karpechko et al., 2017; Domeisen, 2019; Domeisen et al., 2019), in spite of underestimated troposphere-stratosphere coupling found in models compared to observations (O'Reilly et al., 2019a).

The observed trend of the NAM and NAO indices is positive in winter when calculated from the 1960s (Section 2.4.1.1) but it includes large multidecadal variability, which means that the nature of the trend should be interpreted with caution (Gillett et al., 2013). The multi-model multi-member ensemble mean of the trend estimated from historical simulations over that period is very close to zero for both CMIP5 and CMIP6 (Figure 3.33j,k and Figure 3.34a). Even if one cannot rule out that 1958-2014 was an exceptional period of variability, the observational estimates of the wintertime NAO trend lie outside the 5th-95th percentile range of the distribution of trends in the CMIP6 historical simulations, and the observed NAM trends over the same period lie above the 90th percentile. There is a tendency for the CMIP5 models to systematically underestimate the level of multidecadal versus interannual variability of the winter NAO and jet stream compared to observations (Wang et al., 2017c; Bracegirdle et al., 2018; Simpson et al., 2018). Results from CMIP6 (Figure 3.33j,k) and over the 1958-2019 period (Figure 3.34a) confirm this conclusion and seriously questions the ability of the models to simulate long-term fluctuations of the NAO/NAM, independently of its forced or internal origins.

ACCEPTED VERSION SUBJECT TO FINAL EDITING

Dedicated SST-forced stand-alone atmospheric model experiments (AMIP) suggest that ocean forcing appears to play a role in decadal variability of the NAO and associated fluctuations in the strength of the jet (Woollings et al., 2015). In particular, Atlantic and Indian Ocean SST anomalies (Fletcher and Cassou, 2015; Baker et al., 2019; Douville et al., 2019; Dhame et al., 2020) may have contributed to the long-term positive trend of the winter NAO/NAM over the 20th century, but there is only *low confidence* in such a causal relationship because of the limitation of the imposed SST approach in AMIP and the uncertainties in observed SST trends among datasets used as forcing of the atmospheric model. The representation of the NAM and NAO spatial structure is slightly improved in AMIP ensembles (Figure 3.33g,h), which also produce slightly larger trends than the historical simulations for the NAO, but not for the NAM.

When calculated over the most recent two decades, the wintertime NAM/NAO trend is weakly negative since the mid-1990s (Hanna et al., 2015). Recent studies based on observations (Gastineau and Frankignoul, 2015) and dedicated modelling experiments (Davini et al., 2015; Peings and Magnusdottir, 2016) suggest that the recent dominance of negative NAM/NAO could be partly related to the latest shift of the Atlantic Multidecadal Variability (AMV) to a warm phase (Sections 2.4.4 and 3.7.7). Some recent modelling studies also find that the Arctic sea ice decline might be partly responsible for more recurrent negative NAM/NAO (Peings and Magnusdottir, 2013; Kim et al., 2014a; Nakamura et al., 2015), while other studies do not robustly identify such responses in models (see also Cross-chapter Box 10.1).

In contrast to winter, the observed trend of the NAO index over 1958-2014 is overall negative in summer and is associated with more recurrent blocking conditions over Greenland, in particular since the mid-1990s, thus contributing to the acceleration of melting of the Arctic sea ice (Section 3.4.1.1) and Greenland ice sheet (Section 3.4.3.2) (Fettweis et al., 2013; Hanna et al., 2015; Ding et al., 2017b). The origin of the negative trend of the summer NAO has not been clearly identified, and is hypothesized to be the result of combined influences (Lim et al., 2019), though trends in summertime NAO should also be interpreted with caution because of the presence of strong multidecadal variability. The recent observed negative NAO prevalence and related blocking over Greenland is not present in any of the CMIP5 models (Hanna et al., 2018).

Regarding the influence of external forcings since pre-industrial time, AR5 noted that CMIP5 models tend to show an increase in the NAM in response to greenhouse gas increases (Bindoff et al., 2013). Based on the CMIP5 historical ensemble, Gillett and Fyfe (2013) however showed that such a trend is not significant in all seasons. A multi-model assessment of eight CMIP5 models found a NAM increase in response to greenhouse gases, but no robust influence of aerosol changes (Gillett et al., 2013). As for ozone depletion, there is no robust detectable influence on long-term trends of the NAO/NAM (Karpechko et al., 2018a) in contrast to the SAM (Section 3.7.2), but there are indications that extreme Arctic ozone depletion events and their surface expression are linked to an anomalously strong NAM episodes (Calvo et al., 2015; Ivy et al., 2017). However, the direction of causality here is not clear.

Conclusions on external forcing influences on the NAM are supported by CMIP6 results based on single forcing ensembles (Figure 3.34a). Positive trends are found in historical simulations over 1958-2019 in boreal winter and are mainly driven by greenhouse gas increases. No significant trends are simulated in response to anthropogenic aerosols, stratospheric ozone or natural forcing. Albeit weak and not statistically significant, the sign of the multi-model mean forced response due to natural forcing is consistent with the observed reduction of solar activity since the 1980s (Section 2.2.1) whose influence would have favoured the negative phase of wintertime NAM/NAO based on the fingerprint of the nearly periodical 11-year solar cycle extracted from models (Scaife et al., 2013; Andrews et al., 2015; Thiéblemont et al., 2015) or observations (Gray et al., 2016; Lüdecke et al., 2020). But such an NAO response to solar forcing remains highly uncertain and controversial, being contradicted by longer proxy records over the last millenium (Sjolte et al., 2018) and modelling evidence (Gillett and Fyfe, 2013; Chiodo et al., 2019). For all seasons and for all individual forcings, uncertainties remain in the estimation of the forced response in the NAM trend as evidenced by considerable model spread (Figure 3.34a) and because the simulated forced component has small amplitude compared to internal variability.

Despite new effort since AR5 to reconstruct the NAO beyond the instrumental record, it is still very

ACCEPTED VERSION SUBJECT TO FINAL EDITING

challenging to assess the role of external forcings in the apparent multidecadal-to-centennial variability present throughout the last millenium. Large uncertainties remain in the reconstructed NAO index that are sensitive to the types of proxies and statistical methods (Trouet et al., 2012; Ortega et al., 2015; Anchukaitis et al., 2019; Cook et al., 2019; Hernández et al., 2020; Michel et al., 2020) and reconstructed NAO variations are often not reproduced using pseudo-proxy approaches in models (Lehner et al., 2012; Landrum et al., 2013). At low frequency, it remains challenging to evaluate if the observed or reconstructed signal corresponds to an actual change in the NAO intraseasonal to interannual intrinsic properties or rather to a change in the mean background atmospheric circulation changes projecting on a specific phase of the mode. Consequently, conflicting results emerge in the attribution of reconstructed long-term variations in the NAO to solar forcing, whose influence thus remains controversial (Gómez-Navarro and Zorita, 2013; Moffa-Sánchez et al., 2014; Ortega et al., 2015; Ait Brahim et al., 2018; Sjolte et al., 2018; Xu et al., 2018). Influences from major volcanic eruptions appear to be more robust (Ortega et al., 2015; Swingedouw et al., 2017) even if some modelling experiments question the amplitude of the response, which mostly projects on the positive phase of the NAM/NAO (Bittner et al., 2016). The forced response is dependent on the strength, seasonal timing and location of the eruption but may also depend on the mean climate background state (Zanchettin et al., 2013) and/or the phases of the main modes of decadal variability such as the AMV (Section 3.7.7) (Ménégoz et al., 2018).

Finally, there is some evidence of an apparent signal-to-noise problem referred to as "paradox" in seasonal and decadal hindcasts of the NAO run over 1979-2018 (Scaife and Smith, 2018), which suggests that the NAO response to external forcing, SST or sea ice anomalies could be too weak in models. The weakness of the signal has been related to troposphere-stratosphere coupling which is too intermittent (O'Reilly et al., 2019a) and to chronic model biases in the persistence of NAO/NAM daily regimes, which is critically underestimated in coupled models (Strommen and Palmer, 2019; Zhang and Kirtman, 2019), and which does not exhibit significant improvement when model resolution is increased (Fabiano et al., 2020). Note however that the apparent signal-to-noise problem may be dependent on the period analysed over the 20th century, which questions its interpretation as a general characteristic of coupled models (Weisheimer et al., 2020).

In summary, CMIP5 and CMIP6 models are skilful in simulating the spatial features and the variance of the NAM/NAO and associated teleconnections (*high confidence*). There is *limited evidence* for a significant role for anthropogenic forcings in driving the observed multidecadal variations of the NAM/NAO from the mid 20th century. Confidence in attribution is *low* (i) because there is a large spread in the modelled forced responses which is overwhelmed anyway by internal variability, (ii) because of the apparent signal-to-noise problem and (iii) because of the chronic inability of models to produce a range of trends which encompasses the observed estimates over the last 60 years.

[START FIGURE 3.33 HERE]

Figure 3.33: Model evaluation of NAM, NAO and SAM in boreal winter. Regression of Mean Sea Level Pressure (MSLP) anomalies (in hPa) onto the normalized principal component (PC) of the leading mode of variability obtained from empirical orthogonal decomposition of the boreal winter (Dec.-Feb) MSLP poleward of 20ºN for the observed Northern Annular Mode (NAM, a), over 20ºN-80°N, 90°W-40°E for the North Atlantic Oscillation as shown by the black sector (NAO, b), and poleward of 20ºS for the Southern Annular Mode (SAM, c) for the JRA-55 reanalysis. Cross marks indicate regions where the anomalies are not significant at the 10% level based on t-test. The period used to calculate the NAO/NAM is 1958-2014 but 1979-2014 for the SAM. (d-f) Same but for the multi-model ensemble (MME) mean from CMIP6 historical simulations. Models are weighted in compositing to account for differences in their respective ensemble size. Diagonal lines stand for regions where less than 80% of the runs agree in sign. (g-i) Taylor diagram summarizing the representation of the modes in models and observations following Lee et al. (2019) for CMIP5 (light blue) and CMIP6 (red) historical runs. The reference pattern is taken from JRA-55 (a-c). The ratio of standard deviation (radial distance), spatial correlation (radial angle) and resulting root-mean-squared-errors (solid isolines) are given for individual ensemble members (crosses) and for other observational products (ERA5 and NOAA 20CRv3, black dots). Coloured dots stand for weighted multi-model mean statistics for CMIP5 (blue) and CMIP6 (light red) as well as for AMIP simulations from CMIP6 (orange). (j-l) Histograms of the trends built from all individual ensemble members and all the models (brown bars). Vertical lines in black show all the

ACCEPTED VERSION SUBJECT TO FINAL EDITING

observational estimates. The orange, light-red, and light blue lines indicate the weighted multi-model mean of CMIP6 AMIP, CMIP6 and CMIP5 historical simulations, respectively. Further details on data sources and processing are available in the chapter data table (Table 3.SM.1).

[END FIGURE 3.33 HERE]

[START FIGURE 3.34 HERE]

Figure 3.34: Attribution of observed seasonal trends in the annular modes to forcings. Simulated and observed trends in NAM indices over 1958-2019 (a) and in SAM indices over 1979-2019 (b) and over 2000-2019 (c) for boreal winter (December-February average; DJF) and summer (June-August average; JJA). The indices are based on the difference of the normalized zonally averaged monthly mean sea level pressure between 35ºN and 65ºN for the NAM and between 40ºS and 65ºS for the SAM as defined in Jianping and Wang (2003) and Gong and Wang (1999), respectively: the unit is decade^{-1}. Ensemble mean, interquartile ranges and 5th and 95th percentiles are represented by empty boxes and whiskers for pre-industrial control simulations and historical simulations. The number of ensemble members and models used for computing the distribution is given in the upper-left legend. Grey lines show observed trends from the ERA5 and JRA-55 reanalyses. Multi-model multi-member ensemble means of the forced component of the trends as well as their 5- 95% confidence intervals assessed from t-statistics, are represented by filled boxes, based on CMIP6 individual forcing simulations from DAMIP ensembles; greenhouse gases in brown, aerosols in light blue, stratospheric ozone in purple and natural forcing in green. Models with at least 3 ensemble members are used for the filled boxes, with black dots representing the ensemble means of individual models. Further details on data sources and processing are available in the chapter data table (Table 3.SM.1).

[END FIGURE 3.34 HERE]

3.7.2 Southern Annular Mode

The Southern Annular Mode (SAM) consists of a meridional redistribution of atmospheric mass around Antarctica (Figure 3.33c,f), associated with a meridional shift of the jet and surface westerlies over the Southern Ocean. SAM indices are variously defined as the difference in zonal-mean sea level pressure or geopotential height between middle and high latitudes or via a principal-component analysis (Annex IV.2.2). Observational aspects of the SAM are assessed in Section 2.4.1.2.

AR5 assessed that CMIP5 models have medium performance in reproducing the SAM with biases in pattern (Flato et al., 2013). It also concluded that the trend of the SAM toward its positive phase in austral summer since the mid-20th century is *likely* to be due in part to stratospheric ozone depletion, and there was *medium confidence* that greenhouse gases have also played a role (Bindoff et al., 2013). Based on proxy reconstructions, AR5 found with *medium confidence* that the positive SAM trend since 1950 was anomalous compared to the last 400 years (Masson-Delmotte et al., 2013b).

Additional research has shown that CMIP5 models reproduce the spatial structure of the SAM well, but tend to overestimate its variability in austral summer at interannual time scales, albeit within the observational uncertainty (Zheng et al. 2013; Schenzinger and Osprey 2015; Figure 3.33c,f,i). This is related to the models' tendency to simulate slightly more persistent SAM anomalies in summer compared to reanalyses (Schenzinger and Osprey, 2015; Bracegirdle et al., 2020b). This may be due in part to too weak a negative feedback from tropospheric planetary waves (Simpson et al., 2013). CMIP6 models show improved performance in reproducing the spatial structure and interannual variance of the SAM in summer based on Lee et al. (2019) diagnostics (Figure 3.33i), with a better match of its trend with reanalyses over 1979-2014 (Figure 3.33l), more realistic persistence and improved positioning of the westerly jet, which in CMIP5 models on average is located too far equatorward (Bracegirdle et al., 2020a; Grose et al., 2020). In CMIP5, it is also found that models which extend above the stratopause tend to simulate stronger summertime trends in the late 20th century than their counterparts with tops within the stratosphere (Rea et al., 2018a; Son et al., 2018b), though other differences between these sets of models, such as additional physical processes

ACCEPTED VERSION SUBJECT TO FINAL EDITING

operating in the stratosphere or interactive ozone chemistry, may have also affected these results (Gillett et al., 2003a; Sigmond et al., 2008; Rea et al., 2018b). At the surface, Ogawa et al. (2015) demonstrate with an atmospheric model the importance of sharp midlatitude SST gradients for stratospheric ozone depletion to affect the SAM in summer. These studies imply that the well resolved stratosphere combined with finer ocean horizontal resolution has contributed to the stronger simulated trends in CMIP6 than in CMIP5.

CMIP6 historical simulations capture the observed positive trend of summertime SAM when calculated from the 1970s to the 2010s (Figure 3.34b). Thomas et al. (2015) found that the chance for the observed 1980-2004 trend to occur only due to internal variability is less than 10% in many of the CMIP5 models, and results from CMIP6 models suggest that the chance of the 1979-2019 trend being due to internal variability could be even lower (Figure 3.34b). Although paleo-reconstructions of the SAM index are uncertain and vary in terms of long-term trends (Section 2.4.1.2), new reconstructions show that the 60-year summertime SAM trend since the mid-20th century is outside the 5th-95th percentile range of the trends in the pre-industrial variability, which matches the trend range of CMIP5 pre-industrial control simulations well (Dätwyler et al., 2018).

In general agreement with AR5, new research continues to indicate that both stratospheric ozone depletion and increasing greenhouse gases have contributed to the trend of the SAM during austral summer toward its positive phase in recent decades (Solomon and Polvani, 2016), with the ozone depletion influence dominating (Gerber and Son, 2014a; Son et al., 2018a). In CMIP6 historical simulations there are significant positive SAM trends over the 1979-2019 period in austral summer, although the contribution from ozone forcing evaluated with the four available models is not significant (Figure 3.34b). Three of these models share the same standard prescribed ozone forcing and produce significantly positive SAM trends over an extended period (1957-2019). The fourth model, MRI-ESM2-0, has the option of interactive ozone chemistry. Its ozone-only experiment is forced by prescribed ozone derived from its own historical simulations and produces a negative SAM trend associated with weak ozone depletion (Morgenstern et al., 2020). Morgenstern et al. (2014) and Morgenstern et al. (2020) find an indirect influence of greenhouse gases on the SAM via induced ozone changes in coupled chemistry-climate simulations, which differ from the prescribed ozone simulations shown in Figure 3.34b. Since ~1997, the effective abundance of ozone-depleting halogen has been decreasing in the stratosphere (WMO, 2018), leading to a stabilization or even a reversal of stratospheric ozone depletion (Sections 2.2.5.2 and 6.3.2.2). The ozone stabilisation and slight recovery since ~2000 may have caused a pause in the summertime SAM trend (Figure 3.34c; Saggioro and Shepherd, 2019; Banerjee et al., 2020), although some influence from internal variability cannot be ruled out. While some studies find an anthropogenic aerosol influence on the summertime SAM (Gillett et al., 2013; Rotstayn, 2013), recent studies with larger multi-model ensembles find that this effect is not robust (Steptoe et al., 2016; Choi et al., 2019), consistent with CMIP6 single forcing ensembles (Figure 3.34). In the CMIP5 simulations, volcanic stratospheric aerosol has a significant weakening effect on the SAM in autumn and winter (Cross-Chapter Box 4.1; Gillett and Fyfe, 2013), but there is no evidence that this effect leads to a significant multidecadal trend since the late 20th century. Beyond external forcing, Fogt et al. (2017) show a significant association of tropical SST variability with the summertime SAM trend since the mid-20th century in agreement with (Lim et al., 2016) who however demonstrate that such a teleconnection between the summertime SAM and El Niño-Southern Oscillation (Annex IV.2.3), found in observations, is missing in many CMIP5 models.

On longer time scales, last Millennium experiments from CMIP5 models fail to capture multicentennial variability evident in the reconstructions for the pre-industrial era (Abram et al., 2014; Dätwyler et al., 2018), which is also the case in those from available CMIP6 models (Figure 3.35). However there is large uncertainty among reconstructions (Section 2.4.1.2). It is therefore unclear whether this disagreement reflects this observational uncertainty, whether forcings such as variations in the imposed insolation may be too weak, whether models are insufficiently sensitive to such variations, or whether internal variability including that associated with tropical Pacific variability is underrepresented (Abram et al., 2014). The explanation could be a combination of all these factors. However, despite the aforementioned limitations of the reconstructions, Section 2.4.1.2 assesses that the recent positive trend in the SAM is *likely* unprecedented in at least the past millenium (*medium confidence*). CMIP5 and CMIP6 last-millennium simulations only capture the present anomalous state during in the final decades of the simulations which are dominated by

ACCEPTED VERSION SUBJECT TO FINAL EDITING

human influence; this state is also outside the range of simulated variability characteristic of pre-industrial times.

In summary, it is *very likely* that anthropogenic forcings have contributed to the observed trend of the summer SAM toward its positive phase since the 1970s. This assessment is supported by further model studies that confirm the human influence on the summertime SAM with improved models since AR5. While ozone depletion contributed to the trend from the 1970s to the 1990s (*medium confidence*), its influence has been small since 2000, leading to a weaker summertime SAM trend over 2000-2019 (*medium confidence*). Climate models reproduce the spatial structure of the summertime SAM observed since the late 1970s well (*high confidence*). CMIP6 models reproduce the spatiotemporal features and recent multidecadal trend of the summertime SAM better than CMIP5 models (*medium confidence*). However, there is a large spread in the intensity of the SAM response to ozone and greenhouse gas changes in both CMIP5 and CMIP6 models (*high confidence*), which limits the confidence in the assessment of the ozone contribution to the observed trends. CMIP5 and CMIP6 models do not capture multicentennial variability of the SAM found in proxy reconstructions (*low confidence*). This confidence level reflects that it is unclear whether this is due to a model or an observational shortcoming.

[START FIGURE 3.35 HERE]

Figure 3.35: Southern Annular Mode (SAM) indices in the last millennium. (a) Annual SAM reconstructions by Abram et al. (2014) and Dätwyler et al. (2018). (b) The annual-mean SAM index defined by Gong and Wang (1999) in CMIP5 and CMIP6 Last Millennium simulations extended by historical simulations. All indices are normalized with respect to 1961-1990 means and standard deviations. Thin lines and thick lines show 7-year and 70-year moving averages, respectively. Further details on data sources and processing are available in the chapter data table (Table 3.SM.1).

[END FIGURE 3.35 HERE]

3.7.3 El Niño-Southern Oscillation

The El Niño-Southern Oscillation (ENSO), which is generated via seasonally modulated interactions between the tropical Pacific ocean and atmosphere, influences severe weather, rainfall, river flow and agricultural production over large parts of the world (McPhaden et al., 2006). In fact, the remote climate influence of ENSO is so large that knowledge of its current phase and forecasts of its future phase largely underpin many seasonal rainfall and temperature forecasts worldwide (Annex IV.2.3).

AR5 noted that there have been clear improvements in the simulation of ENSO through previous generations of CMIP models (Flato et al., 2013), such that many CMIP5 models displayed behaviour that was qualitatively similar to that of the observed ENSO (Guilyardi et al., 2012). However, systematic errors were identified in the models' representation of the Tropical Pacific mean state and aspects of their interannual variability that affect quantitative comparisons. The AR5 assessment of ENSO concluded that the considerable observed inter-decadal modulations in ENSO amplitude and spatial pattern were largely consistent with unforced model simulations. Thus, there was *low confidence* in the role of a human-induced influence in these (Bindoff et al., 2013).

Observed ENSO amplitude, which is measured by the standard deviation of SST anomalies in a central equatorial Pacific region often referred to as the Nino 3.4 region, along with the lifecycle of events, are both reasonably well reproduced by most CMIP5 and CMIP6 models (Figure 3.36) (Bellenger et al., 2014; Planton et al., 2020). The average CMIP5 model ENSO amplitude is slightly lower than that observed, while the average CMIP6 model ENSO amplitude is slightly higher than observed (Figure 3.36). The ENSO amplitude of the individual models, however, is highly variable across CMIP5 and CMIP6 models with many displaying either more or less variability than observed (Stevenson, 2012; Grose et al., 2020; Planton et al., 2020).

ACCEPTED VERSION SUBJECT TO FINAL EDITING

[START FIGURE 3.36 HERE]

Figure 3.36: Life cycle of (left) El Niño and (right) La Niña events in observations (black) and historical simulations from CMIP5 (blue; extended with RCP4.5) and CMIP6 (red). An event is detected when the December ENSO index value in year zero exceeds 0.75 times its standard deviation for 1951-2010. (a, b) Composites of the ENSO index (ºC). The horizontal axis represents month relative to the reference December (the grey vertical bar), with numbers in parentheses indicating relative years. Shading and lines represent 5th-95th percentiles and multi-model ensemble means, respectively. (c, d) Mean durations (months) of El Niño and La Niña events defined as number of months in individual events for which the ENSO index exceeds 0.5 times its December standard deviation. Each dot represents an ensemble member from the model indicated on the vertical axis. The boxes and whiskers represent multi-model ensemble mean, interquartile ranges and 5th and 95th percentiles of CMIP5 and CMIP6. The CMIP5 and CMIP6 multi-model ensemble means and observational values are indicated at top right of each panel. The multi-model ensemble means and percentile values are evaluated after weighting individual members with the inverse of the ensemble size of the same model, so that individual models are equally weighted irrespective of their ensemble sizes. The ENSO index is defined as the SST anomaly averaged over the Niño 3.4 region (5ºS-5ºN, 170ºW-120ºW). All results are based on 5-month running mean SST anomalies with triangular-weights after linear detrending. Further details on data sources and processing are available in the chapter data table (Table 3.SM.1).

[END FIGURE 3.36 HERE]

ENSO events are often synchronized to the seasonal cycle in the observations, as the associated SST anomalies tend to peak in boreal winter (November-January) and be at their weakest in the boreal spring (March-April) (Harrison and Larkin, 1998; Larkin and Harrison, 2002). The majority of CMIP5 and CMIP6 models broadly reproduce the seasonality of ENSO SST variability in the central equatorial Pacific (Taschetto et al., 2014a; Abellán et al., 2017; Grose et al., 2020; Planton et al., 2020) (Figure 3.37). However, CMIP5 models, while displaying an improvement on CMIP3 models, appear to underrepresent the magnitude of the seasonal variance modulation (Bellenger et al., 2014). This under-representation of seasonal variance modulation continues in CMIP6 models, which display no statistically significant difference in this behaviour when compared to CMIP5 models (Planton et al., 2020) (Figure 3.37).

[START FIGURE 3.37 HERE]

Figure 3.37: ENSO seasonality in observations (black) and historical simulations from CMIP5 (blue; extended with RCP4.5) and CMIP6 (red) for 1951-2010. (a) Climatological standard deviation of the monthly ENSO index (SST anomaly averaged over the Niño 3.4 region; °C). Shading and lines represent 5th-95th percentiles and multi-model ensemble means, respectively. (b) Seasonality metric, which is defined for each model and each ensemble member as the ratio of the ENSO index climatological standard deviation in November-January (NDJ) to that in March-May (MAM). Each dot represents an ensemble member from the model indicated on the vertical axis. The boxes and whiskers represent the multi-model ensemble mean, interquartile ranges and 5th and 95th percentiles of CMIP5 and CMIP6 individually. The CMIP5 and CMIP6 multi-model ensemble means and observational values are indicated at the top right of the panel. The multi-model ensemble means and percentile values are evaluated after weighting individual members with the inverse of the ensemble size of the same model, so that individual models are equally weighted irrespective of their ensemble sizes. All results are based on 5-month running mean SST anomalies with triangular-weights after linear detrending. Further details on data sources and processing are available in the chapter data table (Table 3.SM.1).

[END FIGURE 3.37 HERE]

Observations show strong multi-decadal modulation of ENSO variance throughout the 20th century, with the most recent period displaying larger variability while the mid-century displayed relatively low ENSO

ACCEPTED VERSION SUBJECT TO FINAL EDITING

variability (e.g., Li et al., 2013; McGregor et al., 2013; Hope et al., 2017; Figure 2.36). As assessed in Section 2.4.2, ENSO amplitude since 1950 is higher than over the pre-industrial period from 1850 as far back as 1400 (*medium confidence*), but there is *low confidence* that it is higher than the variability over periods prior to 1400. This reported variance increase suggests that external forcing plays a role in the ENSO variance changes (Hope et al., 2017b). However, large ensembles of single model or multiple model simulations do not find strong trends in ENSO variability over the historical period, suggesting that external forcing has not yet modulated ENSO variability with a magnitude that exceeds the range of internal variability (Hope et al., 2017b; Stevenson et al., 2017; Maher et al., 2018b). This is consistent with the Chapter 2 assessment, that there is no clear evidence for a recent sustained shift in ENSO beyond the range of variability on decadal to millennial timescales (Section 2.4.2). CMIP5 and CMIP6 models show a decrease in ENSO variance in the mid-Holocene (Brown et al., 2020), though not to the extent seen in paleo-proxy records (Emile-Geay et al., 2016). This suggests that both modelled and observed ENSO respond to changes in external forcing, but not necessarily in the same manner.

Most CMIP5 and CMIP6 models are found to represent the general structure of observed SST anomalies during ENSO events well (Kim and Yu, 2012; Taschetto et al., 2014b; Brown et al., 2020; Grose et al., 2020). However, the majority of CMIP5 models display SST anomalies that: i) extend too far to the west (Taschetto et al., 2014b; Capotondi et al., 2015); and ii) have meridional widths that are too narrow (Zhang and Jin, 2012) compared to the observations. CMIP6 models display a statistically significant improvement in the longitudinal representation of ENSO SST anomalies relative to CMIP5 models (Planton et al., 2020), however, systematic biases in the zonal extent and meridional width remain in CMIP6 models (Fasullo et al., 2020; Planton et al., 2020). The ENSO phase asymmetry, where observed strong El Niño events are larger and have a shorter duration than strong La Niña events (Ohba and Ueda, 2009; Frauen and Dommenget, 2010), is also underrepresented in both CMIP5 and CMIP6 models (Zhang and Sun, 2014; Planton et al., 2020). In this instance, both CMIP5 and CMIP6 models typically display El Niño events that have a longer duration than those observed, La Niña events that have a similar duration to those observed, and there is very little asymmetry in the duration of El Niño and La Niña phases (Figure 3.36). Roberts et al. (2018) find an improvement in amplitude asymmetry in a HighResMIP model, but the underrepresentation remains.

The continuum of El Niño events are typically stratified into two types (often termed “flavours”), Central Pacific and East Pacific, where the name denotes the location of the events’ largest SST anomalies (Annex IV.2.3; Capotondi et al., 2015). As discussed in Section 2.4.2, the different types of events tend to produce distinct teleconnections and climatic impacts (e.g., Taschetto et al., 2020). The characteristics of El Niño events of these two flavours in CMIP5 were generally comparable to the observations (Taschetto et al., 2014b). CMIP6 models, however, display a statistically significant improvement in the representation of this ENSO event-to-event SST anomaly diversity when compared with CMIP5 models (Planton et al., 2020). In addition to this ENSO event diversity, the short observational record also displays an increase in the number of the Central Pacific-type events in recent decades (Ashok et al., 2007; McPhaden et al., 2011), which has also been identified as unusual in the context of the last 500-800 years based on recent paleo-climatic reconstructions (Section 2.4.2; Liu et al., 2017; Freund et al., 2019). However, the short observational record combined with observational (L’Heureux et al., 2013) and paleo-climatic reconstruction uncertainties preclude firm conclusions being made about the long-term changes in the occurrence of different El Niño event types. Initial analysis with a selected number of CMIP3 models suggested that there may be a forced component to this recent prominence of Central Pacific-type events (Yeh et al., 2009), but analysis since then suggests that this behaviour is i) consistent with that expected from internal variability (Newman et al., 2011); and ii) not apparent across the full CMIP5 ensemble of historical simulations (Taschetto et al., 2014b). Analysis of single-model large ensembles suggests that changes to ENSO event type in response to historical radiative forcing are not significant (e.g., Stevenson et al., 2017). These same results, however, also suggest that multiple forcings can have significant influences on ENSO type and that the net response will depend on the accurate representation of the balance of these forcings (Stevenson et al., 2017).

The climatic effects of ENSO outside the tropical Pacific largely arise through atmospheric teleconnections that are induced by ENSO-driven changes in deep tropical atmospheric convection and heating (Yeh et al., 2018). The teleconnections to higher latitudes are forced by waves that propagate into the extratropics (Hoskins and Karoly, 1981) and respectively excite the Pacific-North American pattern (Horel and Wallace,

ACCEPTED VERSION SUBJECT TO FINAL EDITING

1981) and Pacific-South American pattern (Karoly, 1989; Irving and Simmonds, 2016) in the Northern and Southern Hemispheres. Given the influence of these teleconnections on climate and extremes around the globe, it is important to understand how well they are reproduced in CMIP models. What has also become clear is that spatial correlations of ENSO's teleconnections calculated over relatively short periods (< 100 years) may not be the most effective way to assess these relationships (Langenbrunner and Neelin, 2013; Perry et al., 2019). This is because the spatial patterns are significantly affected by internal atmospheric variability on relatively short time scales (< 100 years) (Batehup et al., 2015; Perry et al., 2019). However, looking at simplified metrics like the agreement in the sign of the teleconnections (Langenbrunner and Neelin, 2013), regional average teleconnection strength over land (Perry et al., 2019), or a combination of both (Power and Delage, 2018a) provides a more robust depiction of the teleconnection representation. Examining sign agreement for the teleconnection patterns, ensembles of CMIP5 AMIP simulations display broad spatial regions with high sign agreement with the observations, suggesting that the model ensemble is producing useful information regarding the teleconnected precipitation signal (Langenbrunner and Neelin, 2013). Looking at regional averages of CMIP5 historical simulations, Power and Delage (2018) show that the average coupled model teleconnection pattern reproduces the sign of the observed teleconnections in the majority of the 25 regions analysed. The sign agreement between the observed teleconnection and the multi-model mean teleconnection remains strong in CMIP6 (18 out of 20 displayed regions) (Figure 3.38), and the observed DJF teleconnection strength falls within the modelled range in all of the displayed regions for temperature and precipitation. It is noted, however, that while there is broad agreement in ENSO teleconnections between CMIP6 models and observations during DJF (e.g., Fasullo et al., 2020), there are regions and seasons where the modelled teleconnection strength is outside the observed range (Chen et al., 2020).

[START FIGURE 3.38 HERE]

Figure 3.38: Model evaluation of ENSO teleconnection for 2m-temperature and precipitation in boreal winter (December-January-February). Teleconnections are identified by linear regression with the Niño 3.4 SST index based on ERSSTv5 during the period 1958-2014. Maps show observed patterns for temperature from the Berkeley Earth dataset over land and from ERSSTv5 over ocean (ºC, top) and for precipitation from GPCC over land (shading, mm day^{-1}) and GPCP worldwide (contours, period: 1979-2014). Distributions of regression coefficients (grey histograms) are provided for a subset of AR6 reference regions defined in Atlas (Section A1.3) for temperature (top) and precipitation (bottom). All fields are linearly detrended prior to computation. Multi-model multi-member ensemble means are indicated by thick vertical black lines. Blue vertical lines show three observational estimates of temperature, based on Berkeley Earth, GISTEMP and CRUTS datasets, and two observational estimates of precipitation, based on GPCC and CRUTS datasets. Further details on data sources and processing are available in the chapter data table (Table 3.SM.1).

[END FIGURE 3.38 HERE]

Most CMIP5 and CMIP6 models exhibit ENSO behaviour during the historical period that, to first order, is qualitatively similar to that of the observed ENSO. Many studies are now delving deeper into the models to understand if they are accurately producing the dynamics driving ENSO and its initiation (Jin et al., 2006; Bellenger et al., 2014; Vijayeta and Dommenget, 2017a; Bayr et al., 2019; Planton et al., 2020). For both CMIP3 and CMIP5, diagnostics of ENSO event growth appear to show that the models, while producing ENSO variability that is qualitatively similar to that observed, do not represent the balance of the underlying dynamics well. The atmospheric Bjerknes feedback is too weak in the majority of models, while the surface heat flux feedback is also too weak in the majority of models. The former restricts event growth, while the latter restricts event damping, which when combined allow most models to produce variability in a range that is consistent with the observations (Bellenger et al., 2014; Kim et al., 2014b; Vijayeta and Dommenget, 2017b; Bayr et al., 2019). Analysis of ENSO representation in a subset of CMIP6 models by Planton et al. (2020) suggests that these issues remain.

To conclude, ENSO representation in CMIP5 models displayed a significant improvement from the

ACCEPTED VERSION SUBJECT TO FINAL EDITING

representation of ENSO variability in CMIP3 models, which displayed much more intermodel spread in standard deviation, and stronger biennial periodicity (Guilyardi et al., 2012; Flato et al., 2013). In general, there has been no large step change in the representation of ENSO between CMIP5 and CMIP6, however, CMIP6 models appear to better represent some key ENSO characteristics (e.g., Brown et al., 2020; Planton et al., 2020). The instrumental record and paleo-proxy evidence through the Holocene all suggest that ENSO can display considerable modulations in amplitude, pattern and period (see also Section 2.4.2). For the period since 1850, there is also no clear evidence for a sustained shift in ENSO beyond the range of internal variability (Section 2.4.2). However, paleo-proxy evidence indicates with *medium confidence* that ENSO variability since 1950 is greater than at any time between 1400 and 1850 (Section 2.4.2). Coupled models display large changes of ENSO behaviour in the absence of external forcing changes, and little-to-no variance sensitivity to historical anthropogenic forcing. Thus, there is *low confidence* that anthropogenic forcing has led to the changes of ENSO variability inferred from paleo-proxy evidence.

Chapter 2 reports *low confidence* that the apparent change from East Pacific- to Central Pacific-type El Niño events that occurred in the last 20-30 years was representative of a long term change. While some climate models do suggest external forcing may affect the El Niño event type, most climate models suggest that what has been observed is well within the range of natural variability. Thus, there is *low confidence* that anthropogenic forcing has had an influence on the observed changes in El Niño event type.

3.7.4 Indian Ocean Basin and Dipole Modes

The Indian Ocean Basin (IOB) and Dipole (IOD) modes are the two leading modes of interannual SST variability over the tropical Indian Ocean, featuring basin-wide warming/cooling and an east-west dipole of SST anomalies, respectively (Annex IV.2.4). The IOD mode is anchored to boreal summer to autumn by the air-sea feedback, and often develops in concert with ENSO. Driven by matured ENSO events, the IOB mode peaks in boreal spring and often persists into the subsequent summer. Similar patterns of Indian Ocean SST variability also dominate its decadal and longer time scale variability (Han et al., 2014b).

AR5 concluded that models show high and medium performance in reproducing the IOB and IOD modes, respectively (*medium confidence*), with difficulty in reproducing the persistence of the IOB and the pattern and magnitude of the IOD (Flato et al., 2013). There was *low confidence* that changes in the IOD were detectable or attributable to human influence (Bindoff et al., 2013).

Since the AR5, CMIP5 model representation of these modes has been analysed in detail, finding that most of the models qualitatively reproduce the spatial and seasonal features of the IOB and IOD modes (Chu et al., 2014; Liu et al., 2014; Tao et al., 2016b). Improvements in simulating the IOB mode since CMIP3 have been identified in reduced multi-model mean bias and inter-model spread (Tao et al., 2016b). CMIP5 models overall capture the transition from the IOD to IOB modes during an ENSO event (Tao et al., 2016b). The IOB mode is forced in part through a cross-equatorial wind-evaporation-SST feedback triggered by ENSO-forced anomalous ocean Rossby waves that propagate to the shallow climatological thermocline dome in the tropical southwestern Indian Ocean (Du et al., 2009). Consistently, models with a deeper climatological thermocline dome produce a weaker and less persistent IOB mode (Li et al., 2015b; Zheng et al., 2016). The deep thermocline bias remains in the ensemble mean of CMIP5 models due to a common surface easterly wind bias over the equatorial Indian Ocean (Lee et al., 2013) associated with weaker South Asian summer monsoon circulation (Li et al., 2015c). However, the influence of this systematic bias may be compensated by other biases, resulting in a realistic IOB magnitude (Tao et al., 2016b). Halder et al. (2020) found that CMIP6 models reproduce the IOB mode reasonably well, but did not evaluate the progress since CMIP5.

By contrast, the IOD magnitude is overestimated by CMIP5 models on average, though with noticeable improvements from CMIP3 models (Liu et al., 2014). The overestimation of the IOD magnitude remains in most of 34 CMIP6 models examined in McKenna et al. (2020) with worsening on average in July and August. A too steep climatological thermocline slope along the equator due to the surface easterly wind bias in boreal summer and autumn contributes to this IOD magnitude bias through an excessively strong Bjerknes feedback in CMIP5 (Liu et al., 2014; Li et al., 2015c; Hirons and Turner, 2018). The surface easterly bias

ACCEPTED VERSION SUBJECT TO FINAL EDITING

and associated east-west SST gradient bias are not improved in CMIP6 (Long et al., 2020), suggesting that the thermocline bias also remains. McKenna et al. (2020) additionally find degradation in the positive-negative asymmetry of the IOD but an improvement in IOD frequency in a subset of CMIP6 models compared to CMIP5. In terms of teleconnections, the equatorial surface easterly wind bias also affects the IOD-associated moisture transport anomalies toward tropical eastern Africa (Hirons and Turner, 2018) where the IOD is associated with strong precipitation anomalies in boreal autumn (Annex IV.2.4). CMIP5 and CMIP6 models capture the IOD teleconnection to Southern and Central Australian precipitation although it is weaker on average than observed, with no clear improvements from CMIP5 to CMIP6 (Grose et al., 2020). Strong IOD events could also influence the NH extratropical circulation in winter and in particular the NAM (Section 3.7.1), based on interference between forced Rossby waves emerging from the Indian Ocean and climatological stationary waves (Fletcher and Cassou, 2015). The record positive phase of the NAO/NAM in winter 2019-2020 assessed over the instrumental era has been accordingly linked to the record IOD event of autumn 2019 (Hardiman et al., 2020), which has been associated with the devastating record fire season in Australia (Wang and Cai, 2020).

The observed Indian Ocean basin-average SST increase on multidecadal and centennial time scales is well represented by CMIP5 historical simulations, and has been attributed to the effects of greenhouse gases offset in part by the effects of anthropogenic aerosols mainly through aerosol-cloud interactions (Dong and Zhou, 2014; Dong et al., 2014b). The observed SST trend is larger in the western than eastern tropical Indian Ocean, which leads to an apparent upward trend of the IOD index, but this trend is statistically insignificant (Section 2.4.3). CMIP5 models capture this warming pattern, which may be associated with Walker circulation weakening over the Indian Ocean due to greenhouse gas forcing (Dong and Zhou, 2014). However, strong internal decadal IOD-like variability and observational uncertainty preclude attribution (Cai et al., 2013; Han et al., 2014c; Gopika et al., 2020). Such a positive IOD-like change in equatorial zonal SST gradient suggests an increase in the frequency of extreme positive events (Cai et al., 2014) and skewness (Cowan et al., 2015) of the IOD mode. While there is some evidence of an increase in frequency of positive IOD events during the second half of the 20th century, the current level of IOD variability is not unprecedented in a proxy reconstruction for the last millenium (Section 2.4.3, Abram et al., 2020). Besides, the IOD magnitude in the late 20th century is not significantly different between CMIP5 simulations forced by historical and natural-only forcings, though this conclusion is based on only five selected ensemble members that realistically reproduce statistical features of the IOD (Blau and Ha, 2020). While selected CMIP5 models show weakening (Thielke and Mölg, 2019) and seasonality changes (Blau and Ha, 2020) in IOD-induced rainfall anomalies in tropical eastern Africa, no comparison with observational records has been made. Likewise, while a strengthening tendency of the ENSO-IOB mode correlation and resultant intensification of the IOB mode are found in historical or future simulations in selected CMIP5 models (Hu et al., 2014; Tao et al., 2015), such a change has not been detected in observational records.

After linear detrending, Pacific decadal variability (PDV; Annex IV.2.6; Section 3.7.6) has been suggested as a driver of decadal-to-multidecadal variations in the IOB mode (Dong et al., 2016). However, correlation between the PDV and a decadal IOB index, defined from linearly detrended SST, changed from positive to negative during the 1980s (Han et al., 2014a). The increase in anthropogenic forcing and recovery from the eruptions of El Chichón in 1982 and Pinatubo in 1991 may have overwhelmed the PDV influence, and explain this change (Dong and McPhaden, 2017; Zhang et al., 2018a). However, the low statistical degrees of freedom hamper clear detection of human influence in this correlation change.

To summarize, there is *medium confidence* that changes in the interannual IOD variability in the late 20th century inferred from observations and proxy records are within the range of internal variability. There is no evidence of anthropogenic influence on the interannual IOB. On decadal-to-multidecadal time scales, there is *low confidence* that human influence has caused a reversal of the correlation between PDV and decadal variations in the IOB mode. The *low confidence* in this assessment is due to the short observational record, limited number of models used for the attribution, lack of model evaluation of the decadal IOB mode, and uncertainty in the contribution from volcanic aerosols. Nevertheless, CMIP5 models have medium overall performance in reproducing both the interannual IOB and IOD modes, with an apparently good performance in reproducing the IOB magnitude arising from compensation of biases in the formation process, and overly high IOD magnitude due to the mean state bias (*high confidence*). There is no clear improvement in the

ACCEPTED VERSION SUBJECT TO FINAL EDITING

simulation of the IOD from CMIP5 to CMIP6 models, though there is only *medium confidence* in this assessment, since only a subset of CMIP6 models have been examined. There is no evidence for performance changes in simulating the IOB from CMIP5 to CMIP6 models.

3.7.5 Atlantic Meridional and Zonal Modes

The Atlantic Zonal Mode (AZM), often referred to as the Atlantic Equatorial Mode or Atlantic Niño, and the Atlantic Meridional Mode (AMM) are the two leading basin wide patterns of interannual-to-decadal variability in the tropical Atlantic. Akin to ENSO in the Pacific, the term Atlantic Niño is broadly used to refer to years when the SSTs in the tropical eastern Atlantic basin along the cold tongue are significantly warmer than the climatological average. The AMM is characterized by anomalous cross-equatorial gradients in SST. Both modes are associated with altered strength of the ITCZ and/or latitudinal shifts in the ITCZ, which locally affect African and American monsoon systems and remotely affect Tropical Pacific and Indian Ocean variability through inter-basins teleconnections. A detailed description of both AZM and AMM, as well as their associated teleconnection over land, is given in Annex IV.2.5

AR5 mentioned the considerable difficulty in simulating both Atlantic Niño and AMM despite some improvements in CMIP5 for some models (Flato et al., 2013). Severe biases in mean state and variance for both SST and atmospheric dynamics including rainfall (e.g. a double ITCZ) as well as teleconnections were reported. AR5 highlighted the complexity of the Tropical Atlantic biases, which were explained by multiple factors both in the ocean and atmosphere.

Since AR5, further analysis of the major persistent biases in models has been reported (Xu et al., 2014; Jouanno et al., 2017; Yang et al., 2017b; Dippe et al., 2018; Lübbecke et al., 2018; Voldoire et al., 2019a). Errors in equatorial and basin wide trade winds, cloud cover and ocean vertical mixing and dynamics both locally and in remote subtropical upwelling regions, key thermodynamic ocean-atmosphere feedbacks, and tropical land-atmosphere interaction have been shown to be detrimental to the representation of both the Atlantic Niño and AMM leading to poor teleconnectivity over land (Rodríguez-Fonseca et al., 2015; Wainwright et al., 2019) and between tropical basins (Ott et al., 2015).

Despite some improvements (Richter et al., 2014; Nnamchi et al., 2015), biases in the mean state are so large that the mean east-west temperature gradient at the equator along the thermocline remains opposite to observed in two thirds of the CMIP5 models (Section 3.5.1.2), which clearly affects the simulation of the Atlantic Niño and associated dynamics (Muñoz et al., 2012; Ding et al., 2015; Deppenmeier et al., 2016). The interhemispheric SST gradient is also systematically underestimated in models with a too cold mean state in the northern part of the Tropical Atlantic ocean and too warm conditions in the Southern Atlantic basin. The seasonality is poorly reproduced and the wind-SST coupling is weaker than observed so that altogether, and despite AMM-like variability in 20th century climate simulations, AMM is not the dominant Atlantic mode in all CMIP5 models (Liu et al., 2013; Amaya et al., 2017). These biases in mean state translate into biases in modelling the mean ITCZ (Flato et al., 2013). Similar biases were found in experiments using CMIP5 models but with different climate background states, such as Last Glacial Maximum, Mid-Holocene and future scenario simulations (Brierley and Wainer, 2018). Analyses from CMIP6 show encouraging results in the representation of Atlantic Niño and AMM modes of variability in terms of amplitude and seasonality. Some models now display reduced biases in the spatial structure of the modes and related explained variance but persistent errors still remain on average in the timing of the modes and in the coupled nature of the modes, i.e. the strength of the link between ocean (SST, mixed layer depth) and atmospheric (wind) anomalies (Richter and Tokinaga, 2020b), as well as in the Indian Ocean equatorial east-west temperature gradient (Section 3.5.1.2, Figure 3.24).

There are some recent indications that increasing model resolution both vertically and horizontally, in the ocean and atmospheric component (Richter, 2015; Small et al., 2015; Harlaß et al., 2018), could partly alleviate some tropical Atlantic biases in mean state (Section 3.5.1.2), seasonality, interannual-to-decadal variability and associated teleconnectivity over land, such as with the West African monsoon (Steinig et al., 2018). Results from CMIP6 tend to confirm that increasing resolution is not the unique way to address the

ACCEPTED VERSION SUBJECT TO FINAL EDITING

biases in the Tropical Atlantic (Richter and Tokinaga, 2020b). For instance, the inclusion of a stochastic physics scheme has a nearly equivalent effect in the improvement of the mean number and the strength distribution of tropical Atlantic cyclones (Vidale et al., 2021).

Section 2.4.4 assess that there is *low confidence* in any sustained changes to the AZM and AMM variability in instrumental observations. Moreover any attribution of possible human influence on the Atlantic Modes and associated teleconnections is limited by the poor fidelity of CMIP5 and CMIP6 models in reproducing the mean tropical Atlantic climate, its seasonality and variability, despite hints of some improvement in CMIP6, as well as other sources of uncertainties related to limited process understanding in the observations (Foltz et al., 2019), the response of the tropical Atlantic climate to anthropogenic aerosol forcing (Booth et al., 2012; Zhang et al., 2013a) and the presence of strong multidecadal fluctuations related to AMV (Section 3.7.7) and cross-tropical basin interactions (Martín-Rey et al., 2018; Cai et al., 2019). The fact that most models poorly represent the climatology and variability of the tropical Atlantic combined with the short observational record makes it difficult to place the recent observed changes in the context of internal multi-annual variability versus anthropogenic forcing.

In summary, based on CMIP5 and CMIP6 results, there is no robust evidence that the observed changes in either the Atlantic Niño or AMM modes and associated teleconnections over the second half of the 20th century are beyond the range of internal variability or have been influenced by natural or anthropogenic forcing. Considering the physical processes responsible for model biases in these modes, increasing resolution in both ocean and atmosphere components may be an opportunity for progress in the simulation of the tropical Atlantic changes as evidenced by some individual model studies (Roberts et al., 2018), but this needs confirmation from a multi-model perspective.

3.7.6 Pacific Decadal Variability

Pacific decadal variability (PDV) is the generic term for the modes of variability in the Pacific Ocean that vary on decadal to interdecadal timescales. PDV and its related teleconnections encompass the Pacific Decadal Oscillation (PDO; Mantua et al. 1997; Mantua and Hare 2002; Zhang et al. 1997), and an anomalous SST pattern in the North Pacific, as well as a broader structure associated with Pacific-wide SSTs termed the Interdecadal Pacific Oscillation (IPO; Power et al. 1999; Folland et al. 2002; Henley et al. 2015). Since the PDO and IPO indices are highly correlated, this section assesses them together as the PDV (Annex IV.2.6).

AR5 mentioned an overall *limited* level of evidence for both CMIP3 and CMIP5 evaluation of the Pacific modes at interdecadal timescales, leading to *low confidence* statements about the models' performance in reproducing PDV (Flato et al., 2013) and similarly *low confidence* in the attribution of observed PDV changes to human influence (Bindoff et al., 2013).

The implication of PDV in the observed slowdown of the GMST warming rate in the early 2000s (Cross-Chapter Box 3.1) has triggered considerable research on decadal climate variability and predictability since the AR5 (Meehl et al., 2013, 2016b; England et al., 2014; Dai et al., 2015; Steinman et al., 2015; Kosaka and Xie, 2016; Cassou et al., 2018). Many studies find that the broad spatial characteristics of PDV are reasonably well represented in unforced climate models (Henley 2017; Newman et al. 2016) and in historical simulations in CMIP5 and CMIP6 (Figure 3.39), although there is sensitivity to methodology used to remove the externally-forced component of the SST (Bonfils and Santer, 2011; Xu and Hu, 2018). Compared with CMIP3 models, CMIP5 models exhibit overall slightly better performance in reproducing PDV and associated teleconnections (Polade et al., 2013; Joshi and Kucharski, 2017), and also smaller inter-model spread (Lyu et al., 2016). CMIP6 models on average show slightly improved reproduction of the PDV spatial structure than CMIP5 models (Figure 3.39a-c; Fasullo et al., 2020). SST anomalies in the subtropical South Pacific lobe are however too weak relative to the equatorial and North Pacific lobes in CMIP5 pre-industrial control and historical simulations (Henley et al., 2017), a bias that remains in CMIP6 (Figure 3.39b).

Biases in the PDV temporal properties and amplitude are present in CMIP5 (Cheung et al., 2017; Henley,

ACCEPTED VERSION SUBJECT TO FINAL EDITING

2017). While model evaluation is severely hampered by short observational records and incomplete observational coverage before satellite measurements started, the duration of PDV phases appears to be shorter in coupled models than in observations, and correspondingly the ratio of decadal to interannual variance is underestimated (Henley et al. 2017; Figure 3.39e,f). This apparent bias may be associated with overly biennial behaviour of Pacific trade wind variability and related ENSO activity, leaving too weak variability on decadal timescales (Kociuba and Power, 2015). ENSO influence on the extratropical North Pacific Ocean at decadal timescales is also very diverse among both CMIP3 and CMIP5 models, being controlled by multiple factors (Nidheesh et al., 2017). In terms of amplitude, the variance of the PDV index after decadal filtering is significantly weaker in the concatenated CMIP5 ensemble than the three observational estimates used in Figure 3.39e ($p < 0.1$ with an F-test). Consequently, the observed PDV fluctuations over the historical period often lie in the tails of the model distributions (Figure 3.39e,f). Even if one cannot rule out that the observed PDV over the instrumental era represents an exceptional period of variability, it is plausible that the tendency of the CMIP5 models to systematically underestimate the low frequency variance is due to an incomplete representation of decadal-scale mechanisms in these models. This situation is slightly improved in CMIP6 historical simulations but remains a concern (Fasullo et al., 2020). The results of McGregor et al. (2018) suggest that the underrepresentation of the magnitude stems from Atlantic mean SST bias (Section 3.5.1.2) through inter-basin coupling.

While PDV is primarily understood as an internal mode of variability (Si and Hu, 2017), there are some indications that anthropogenically induced SST changes project onto PDV and have contributed to its past evolution (Bonfils and Santer, 2011; Dong et al., 2014a; Boo et al., 2015; Xu and Hu, 2018). However, the level of evidence is *limited* because of the difficulty in correctly separating internal versus externally forced components in the observed SST variations, and because it is unclear whether the dynamics of the PDV are operative in this forced SST change pattern. Over the last two to three decades which encompass the period of slower GMST increase (Cross-Chapter Box 3.1), Smith et al. (2016) found that anthropogenic aerosols have driven part of the PDV change toward its negative phase. A similar result is shown in Takahashi and Watanabe (2016) who found intensification of the Pacific Walker circulation in response to aerosol forcing (Section 3.3.3.1). Indeed, CMIP6 models simulate a negative PDV trend since the 1980s (Figure 3.39f), which is much weaker than internal variability. However, a response to anthropogenic aerosols is not robustly identified in a large ensemble of a model (Oudar et al., 2018), across CMIP5 models (Hua et al., 2018), or in idealized model simulations (Kuntz and Schrag, 2016). Alternatively, inter-basin teleconnections associated with the warming of the North Atlantic Ocean related to the mid-1990s phase shift of the AMV (McGregor et al., 2014; Li et al., 2015d; Chikamoto et al., 2016; Kucharski et al., 2016; Ruprich-Robert et al., 2017), and also in the Indian Ocean (Luo et al., 2012; Mochizuki et al., 2016), could have favoured a delayed PDV transition to its negative phase in the 2000s. Considering the possible influence of external forcing on Indian Ocean decadal variability (Section 3.7.4) and AMV (Section 3.7.7), any such human influence on PDV would be indirect through changes in these ocean basins, and then imported to the Pacific via inter-basin coupling. However, this human influence on AMV, and how consistently the inter-basin processes affect PDV phase shifts, are uncertain. Other modelling studies find that anthropogenic aerosols can influence the PDV (Verma et al., 2019; Amiri-Farahani et al., 2020; Dow et al., 2020). It is however unclear whether and how much those forcings contributed to the observed variations of PDV. In CMIP6 models, the temporal correlation of the multi-model ensemble mean PDV index with its observational counterpart is insignificant and negligible (Figure 3.39f), suggesting that any externally-driven component in historical PDV variations was weak. Lastly, the multi-model ensemble mean computed from CMIP6 historical simulations shows slightly stronger variation than the CMIP5 counterpart, suggesting a greater simulated influence from external forcings in CMIP6. Still, the fraction of the forced signal to the total PDV is very low (Figure 3.39f), in contrast to AMV (Section 3.7.7). Consistently, Liguori et al. (2020) estimate that the variance fraction of the externally-driven to total PDV is up to only 15% in a multi-model large ensemble of historical simulations. These findings support an assessment that PDV is mostly driven by internal variability since the pre-industrial era. The sensitivity of ensemble-mean PDV trends to the ensemble size (Oudar et al., 2018), and the dominance of the ensemble spread over the ensemble mean in the 60-year trend of the equatorial Pacific zonal SST gradient in large ensemble simulations (Watanabe et al., 2021), also support this statement.

In CMIP5 last millennium simulations, there is no consistency in temporal variations of PDV across the

ACCEPTED VERSION SUBJECT TO FINAL EDITING

ensemble (Fleming and Anchukaitis, 2016). This supports the notion that PDV is internal in nature. However, this issue remains difficult to firmly conclude because paleoclimate reconstructions of PDV have too poor a level of agreement for a rigorous model evaluation in past millennia (Henley, 2017).

To conclude, there is *high confidence* that internal variability has been the main driver of the PDV since pre-industrial times, despite some modelling evidence for potential external influence. This assessment is supported by studies based on large ensemble simulations that found the dominance of internally-driven PDV, and the CMIP6-based assessment (Figure 3.39). As such, PDV is an important driver of decadal internal climate variability which limits detection of human influence on various aspects of decadal climate change on global to regional scales (*high confidence*). Model evaluation of PDV is hampered by short observational records, spatial incompleteness of observations before the satellite observation era, and poor agreement among paleoclimate reconstructions. Despite the limitations of these model-observation comparisons, CMIP5 models, on average, simulate broadly realistic spatial structures of the PDV, but with a clear bias in the South Pacific (*medium confidence*). CMIP5 models also *very likely* underestimate PDV magnitude. CMIP6 models tend to show better overall performance in spatial structure and magnitude of PDV, but there is *low confidence* in this assessment due to the lack of literature.

[START FIGURE 3.39 HERE]

Figure 3.39: Model evaluation of the Pacific Decadal Variability (PDV). (a, b) Sea surface temperature (SST) anomalies (ºC) regressed onto the Tripole Index (TPI; Henley et al., 2015) for 1900-2014 in (a) ERSSTv5 and (b) CMIP6 multi-model ensemble (MME) mean composite obtained by weighting ensemble members by the inverse of the model ensemble size. A 10-year low-pass filter was applied beforehand. Cross marks in (a) represent regions where the anomalies are not significant at the 10% level based on t-test. Diagonal lines in (b) indicate regions where less than 80% of the runs agree in sign. (c) A Taylor diagram summarizing the representation of the PDV pattern in CMIP5 (each a cross in light blue, and the weighted multi-model mean as a dot in dark blue), CMIP6 (each ensemble member is shown as a cross in red, weighted multi-model mean as a dot in orange) and observations over [40ºS-60ºN, 110ºE-70ºW]. The reference pattern is taken from ERSSTv5 and black dots indicate other observational products (HadISSTv1 and COBE-SST2). (d) Autocorrelation of unfiltered annual TPI at lag 1 year and 10-year low-pass filtered TPI at lag 10 years for observations over 1900-2014 (horizontal lines) and 115-year chunks of pre-industrial control simulations (open boxes) and individual historical simulations over 1900-2014 (filled boxes) from CMIP5 (blue) and CMIP6 (red). (e) As in (d), but standard deviation of the unfiltered and filtered TPI (ºC). Boxes and whiskers show weighted multi-model mean, interquartile ranges and 5th and 95th percentiles. (f) Time series of the 10-year low-pass filtered TPI (ºC) in ERSSTv5, HadISSTv1 and COBE-SST2 observational estimates (black) and CMIP5 and CMIP6 historical simulations. The thick red and light blue lines are the weighted multi-model mean for the historical simulations in CMIP5 and CMIP6, respectively, and the envelopes represent the 5th-95th percentile range across ensemble members. The 5-95% confidence interval for the CMIP6 multi-model mean is given in thin dashed lines. Further details on data sources and processing are available in the chapter data table (Table 3.SM.1).

[END FIGURE 3.39 HERE]

3.7.7 Atlantic Multidecadal Variability

Atlantic Multidecadal Variability (AMV) refers to a climate mode representing basin-wide multidecadal fluctuations in surface temperatures in the North Atlantic (Figure 3.40a,f), with teleconnections particularly pronounced over the adjacent continents and the Arctic. The AMV phenomenon is usually assessed through SST anomalies averaged over the entire North Atlantic basin, hereafter the AMV index, but it is associated with many physical processes including three-dimensional ocean circulation, such as AMOC fluctuations (Section 3.5.4), gyre adjustments, and salt and heat transport in the entire North Atlantic and subarctic basins. The AMV, together with the PDV, has been shown to have modulated GSAT on multi-decadal timescales since pre-industrial time (Cross Chapter-Box 3.1, Wu et al., 2019; Li et al., 2020). A detailed description of the AMV as well as its associated teleconnection over land is given in Annex IV.2.7.

ACCEPTED VERSION SUBJECT TO FINAL EDITING

In AR5, climate models suggested that the AMV was primarily internally-driven alongside some contribution from external forcings (mainly anthropogenic aerosols) over the late 20th century. But AR5 also concluded that models show medium performance in reproducing the observed AMV, with difficulties in simulating the timescale, the spatial structure and the coherency between all the physical processes involved.

Climate models analyzed since AR5 continue to simulate AMV-like variability as part of their internal variability. This statement is mostly based on CMIP5 pre-industrial control and historical simulations (Wouters et al., 2012; Schmith et al., 2014; Menary et al., 2015; Ruprich-Robert and Cassou, 2015; Brown et al., 2016b; Chen et al., 2016; Kim et al., 2018b) and is also true for the CMIP6 models (Menary et al., 2018; Voldoire et al., 2019b). Models also continue to support links to a wide array of remote climate influences through atmospheric teleconnections (Martin et al., 2013; Ruprich-Robert et al., 2017, 2018; Monerie et al., 2019; Qasmi et al., 2020; Ruggieri et al., 2020). Even if debate remains (Clement et al., 2015; Cane et al., 2017; Mann et al., 2020), there is now stronger evidence for a crucial role of oceanic dynamics in internal AMV that is primarily linked to the AMOC and its interplay with the NAO (Zhang et al., 2013a; Müller et al., 2015; O'Reilly et al., 2016a, 2019b; Delworth et al., 2017; Zhang, 2017; Kim et al., 2019; Sun et al., 2019). However, considerable diversity in the spatio-temporal properties of the simulated AMV is found in both pre-industrial control and historical CMIP5 experiments (Zhang and Wang, 2013; Wills et al., 2019). Such model diversity is presumably associated with the wide range of coupled processes associated with AMV (Baker et al., 2017; Woollings et al., 2018a) including large-scale atmospheric teleconnections and regional feedbacks relating to tropical clouds, Arctic sea ice in the subarctic basins and Saharan dust, whose relative importance and interactions across timescales are specific to each model (Brown et al., 2016; Martin et al, 2014).

Additional studies since AR5 corroborate that CMIP5-era models tend to underestimate many aspects of observed AMV and its SST fingerprint. On average, the duration of the modelled AMV episodes is too short, its magnitude is too weak and its basin-wide SST spatial structure is limited by the poor representation of the link between the tropical North Atlantic and the subpolar North Atlantic/Nordic seas (Martin et al., 2013; Qasmi et al., 2017). Such mismatches between observed and simulated AMV (Figure 3.40c-e) have been associated with intrinsic model biases in both mean state (Menary et al., 2015; Drews and Greatbatch, 2016) and variability in the ocean and overlying atmosphere. For instance, compared to available observational data CMIP5 models underestimate the ratio of decadal to interannual variability of the main drivers of AMV, namely the AMOC, NAO and related North Atlantic jet variations (Bracegirdle et al., 2018; Kim et al., 2018a; Simpson et al., 2018; Yan et al., 2018) (Section 3.7.1), which has strong implications for the simulated temporal statistics of AMV, AMV-induced teleconnections (Ault et al., 2012; Menary et al., 2015) and AMV predictability.

The increase of AMV variance in CMIP6 models (stronger magnitude and longer duration) seems to be explained by the enhanced variability in the subpolar North Atlantic SST (Figure 3.40b,c), which is particularly pronounced in some models, associated with greater variability in the AMOC (Voldoire et al., 2019a; Boucher et al., 2020; Section 3.5.4) and greater GMST multidecadal variability (Voldoire et al., 2019b; Parsons et al., 2020; Section 3.3.1) (Figure 3.40c-f). The decadal variance in SST in the subpolar North Atlantic seems now to be slightly overestimated in CMIP6 compared to observational estimates, while the AMV-related tropical SST anomalies remains weaker in line with CMIP5 (Figure 3.40b). The mechanisms producing the tropical-extratropical relationship at decadal timescales remain poorly understood despite stronger evidence since AR5 for the importance of the subpolar gyre SST anomalies in generating tropical changes through atmospheric teleconnection (Caron et al., 2015; Ruprich-Robert et al., 2017; Kim et al., 2020). Significant discrepancies remain in the simulated AMV spatial pattern when historical simulations are compared to multivariate observations (Yan et al., 2018; Robson et al., 2020).

There is additional evidence since AR5 that external forcing has been playing an important role in shaping the timing and intensity of the observed AMV since pre-industrial times (Bellomo et al., 2018; Andrews et al., 2020). The time synchronisation between observed and multi-model mean AMV SST indices is significant in both CMIP5 and CMIP6 historical simulations, while the explained variance of the forced response in CMIP6 appears stronger (Figure 3.40d-f). The competition between greenhouse gas warming

ACCEPTED VERSION SUBJECT TO FINAL EDITING

and anthropogenic sulphate aerosol cooling has been proposed to be particularly important over the latter half of the 20th century (Booth et al., 2012; Steinman et al., 2015; Murphy et al., 2017; Undorf et al., 2018a; Haustein et al., 2019). The latest observed AMV shift from the cold to the warm phase in the mid-1990s at the surface ocean is well captured in the CMIP6 forced component and may be associated with the lagged response to increased AMOC due to strong anthropogenic aerosol forcing over 1955-1985 (Menary et al., 2020) in combination with the rapid response through surface flux processes to declining aerosol forcing and increasing greenhouse gas influence since then. However, natural forcings may have also played a significant role. For instance, volcanic forcing has been shown to contribute in part to the cold phases of the AMV-related SST anomalies observed in the 20th century (Terray, 2012; Bellucci et al., 2017; Swingedouw et al., 2017; Birkel et al., 2018). Over the last millenium, natural forcings including major volcanic eruptions and fluctuations in solar activity are thought to have driven a larger fraction of the multidecadal variations in the AMV, with some interplay with internal processes (Otterå et al., 2010; Knudsen et al., 2014; Moffa-Sánchez et al., 2014; Wang et al., 2017b; Malik et al., 2018; Mann et al., 2021), but other studies question the role of natural forcings over this period (Zanchettin et al., 2014; Lapointe et al., 2020).

Model evaluation of the AMV phenomenon remains difficult because of short observational records (especially of detailed process-based observations), the lack of stationarity in the variance, spatial patterns and frequency of the AMV assessed from modelled SST (Qasmi et al., 2017), difficulties in estimating the forced signals in both historical simulations and observations (Tandon and Kushner, 2015), and because of probable interplay between internally and externally-driven processes (Watanabe and Tatebe, 2019). Furthermore, models simulate a large range of historical anthropogenic aerosol forcing (Smith et al., 2020) and questions often referred to as signal-to-noise paradox have been raised concerning the models' ability to correctly simulate the magnitude of the response of AMV-related atmospheric circulation phenomena, such as the NAO (Section 3.7.1), to both internally and externally generated changes (Scaife and Smith, 2018). Related methodological and epistemological uncertainties also call into question the relevance of the traditional basin-average SST index to assessing the AMV phenomenon (Zanchettin et al., 2014; Frajka-Williams et al., 2017; Haustein et al., 2019; Wills et al., 2019).

To summarize, results from CMIP5 and CMIP6 models together with new statistical techniques to evaluate the forced component of modelled and observed AMV, provide *robust evidence* that external forcings have modulated AMV over the historical period. In particular, anthropogenic and volcanic aerosols are thought to have played a role in the timing and intensity of the negative (cold) phase of AMV recorded from the mid-1960s to mid-1990s and subsequent warming (*medium confidence*). However, there is *low confidence* in the estimated magnitude of the human influence. The limited level of confidence is primarily explained by difficulties in accurately evaluating model performance in simulating AMV. The evaluation is severely hampered by short instrumental records but also, equally importantly, by the lack of detailed and coherent long-term process-based observations (for example of the AMOC, aerosol optical depth, surface fluxes and cloud changes), which limit our process understanding. In addition, studies often rely solely on simplistic SST indices that may be hard to interpret (Zhang et al., 2016) and may mask critical physical inconsistencies in simulations of the AMV compared to observations (Zhang, 2017).

[START FIGURE 3.40 HERE]

Figure 3.40: Model evaluation of Atlantic Multi-decadal Variability (AMV). (a, b) Sea surface temperature (SST) anomalies (ºC) regressed onto the AMV index defined as the 10-year low-pass filtered North Atlantic (0º-60°N, 80°W-0°E) area-weighted SST* anomalies over 1900-2014 in (a) ERSSTv5 and (b) the CMIP6 multi-model ensemble (MME) mean composite obtained by weighting ensemble members by the inverse of each model's ensemble size. The asterisk denotes that the global mean SST anomaly has been removed at each time step of the computation. Cross marks in (a) represent regions where the anomalies are not significant at the 10% level based on a t-test. Diagonal lines in (b) show regions where less than 80% of the runs agree in sign. (c) A Taylor diagram summarizing the representation of the AMV pattern in CMIP5 (each member is shown as a cross in light blue, and the weighted multi-model mean is shown as a dot in dark blue), CMIP6 (each member is shown as a cross in red, and the weighted multi-model mean is shown as a dot in orange) and observations over [0º-60°N, 80°W-0°E]. The reference pattern is taken from ERSSTv5 and black dots indicate other observational products (HadISSTv1 and COBE-SST2). (d)

ACCEPTED VERSION SUBJECT TO FINAL EDITING

Autocorrelation of unfiltered annual AMV index at lag 1 year and 10-year low-pass filtered AMV index at lag 10 years for observations over 1900-2014 (horizontal lines) and 115-year chunks of pre-industrial control simulations (open boxes) and individual historical simulations over 1900-2014 (filled boxes) from CMIP5 (blue) and CMIP6 (red). (e) As in (d), but showing standard deviation of the unfiltered and filtered AMV indices (ºC). Boxes and whiskers show the weighted multi-model mean, interquartile ranges and 5th and 95th percentiles. (f) Time series of the AMV index (ºC) in ERSSTv5, HadISSTv1 and COBE-SST2 observational estimates (black) and CMIP5 and CMIP6 historical simulations. The thick red and light blue lines are the weighted multi-model mean for the historical simulations in CMIP5 and CMIP6, respectively, and the envelopes represent the 5th-95th percentile range obtained from all ensemble members. The 5- 95% confidence interval for the CMIP6 multi-model mean is shown by the thin dashed line. Further details on data sources and processing are available in the chapter data table (Table 3.SM.1).

[END FIGURE 3.40 HERE]

3.8 Synthesis across Earth System Components

3.8.1 Multivariate Attribution of Climate Change

AR5 concluded that human influence on the climate system is clear (IPCC, 2013), based on observed increasing greenhouse gas concentrations in the atmosphere, positive radiative forcing, observed warming, and physical understanding of the climate system. AR5 also assessed that it was *virtually certain* that internal variability alone could not account for observed warming since 1951 (Bindoff et al., 2013). Evidence has grown since AR5 that observed changes since the 1950s in many parts of the climate system are attributable to anthropogenic influence. So far, this chapter has focused on examining individual aspects of the climate system in separate sections. The results presented in Sections 3.3 to 3.7 substantially strengthen our assessment of the role of human influence on climate since pre-industrial times. In this section we look across the whole climate system to assess to what extent a physically consistent picture of human induced change emerges across the climate system (Figure 3.41).

The observed global surface air temperature warming of 0.9-1.2°C in 2010-2019 is much greater than can be explained by internal variability (*likely* -0.2°C-0.2°C) or natural forcings (*likely* -0.1°C-0.1°C) alone, but consistent with the assessed anthropogenic warming (*likely* 0.8°C-1.3°C) (Section 3.3.1.1). Moreover it is *very likely* that human-induced greenhouse gas increases were the main driver of tropospheric warming since 1979 (Section 3.3.1.2) and *virtually certain* that greenhouse gas forcing was the main driver of the observed changes in hot and cold extremes on the global scale (Cross-Chapter Box 3.2).

As might be expected from a warming atmosphere, moisture in the troposphere has increased and precipitation patterns have changed. Human influence has *likely* contributed to the observed changes in humidity and precipitation (Section 3.3.2). It is *likely* that human influence, in particular due to greenhouse gas forcing, is the main driver of the observed intensification of heavy precipitation in global land regions during recent decades (Cross-Chapter Box 3.2). The pattern of ocean salinity changes indicate that fresh regions are becoming fresher and that salty regions are becoming saltier as a result of changes in ocean-atmosphere fluxes through evaporation and precipitation (*high confidence*) making it *extremely likely* that human influence has contributed to observed near-surface and subsurface salinity changes since the mid-20th century (Section 3.5.2.2). Taken together this evidence indicates a human influence on the water cycle.

It is *very likely* that human influence was the main driver of Arctic sea ice loss since the late 1970s (3.4.1), and *very likely* that it contributed to the observed reductions in Northern Hemisphere springtime snow cover since 1950 (3.4.2). Human influence was *very likely* the main driver of the recent global, near-universal retreat of glaciers and it is *very likely* that it contributed to the observed surface melting of the Greenland Ice Sheet over the past two decades (Sections 3.4.3). It is *extremely likely* that human influence was the main driver of the ocean heat content increase observed since the 1970s (Section 3.5.1), and *very likely* that human influence was the main driver of the observed global mean sea level rise since at least 1970 (Section 3.5.3).

ACCEPTED VERSION SUBJECT TO FINAL EDITING

Combining the evidence from across the climate system (Sections 3.3-3.7) increases the level of confidence in the attribution of observed climate change to human influence and reduces the uncertainties associated with assessments based on a single variable. From this combined evidence, it is unequivocal that human influence has warmed the global climate system.

[START FIGURE 3.41 HERE]

Figure 3.41: Summary figure showing simulated and observed changes in key large-scale indicators of climate change across the climate system, for continental, ocean basin and larger scales. Black lines show observations, brown lines and shading show the multi-model mean and 5th-95th percentile ranges for CMIP6 historical simulations including anthropogenic and natural forcing, and blue lines and shading show corresponding ensemble means and 5th-95th percentile ranges for CMIP6 natural-only simulations. Temperature time series are as in Figure 3.9, but with smoothing using a low pass filter. Precipitation time series are as in Figure 3.15 and ocean heat content as in Figure 3.26. Further details on data sources and processing are available in the chapter data table (Table 3.SM.1).

[END FIGURE 3.41 HERE]

3.8.2 Multivariate Model Evaluation

Similar to the assessment of multivariate attribution of climate change in the previous section, this section covers the performance of the models across different variables (Sections 3.8.2.1) and different classes of models (Section 3.8.2.2). Here the focus is on a system-wide assessment using integrative measures of model performance that characterize model performance using multiple diagnostic fields derived from multi-model ensembles.

3.8.2.1 Integrative Measures of Model Performance

The purpose of this section is to use multivariate analyses to address how well models simulate present-day and historical climate. For every diagnostic field considered, model performance is compared to one or multiple observational references, and the quality of the simulation is expressed as a single number, for example a correlation coefficient or a root mean square difference versus the observational reference. By simultaneously assessing different performance indices, model improvements can be quantified, similarities in behaviour between different models become apparent, and dependencies between various indices become evident (Gleckler et al., 2008; Waugh and Eyring, 2008).

AR5 found significant differences between models in the simulation of mean climate in the CMIP5 ensemble when measured against meteorological reanalyses and observations (Flato et al., 2013), see also Stouffer et al. (2017). AR5 determined that for the diagnostic fields analysed, the models usually compared similarly against two different reference datasets, suggesting that model errors were generally larger than observational uncertainties or other differences between the observational references. In agreement with previous assessments, the CMIP5 multi-model mean generally performed better than individual models (Annan and Hargreaves, 2011; Rougier, 2016). AR5 considered 13 atmospheric fields in its assessment for the instrumental period but did not assess multi-variate model performance in other climate domains (e.g., ocean, land, and sea ice). AR5 found only modest improvement regarding the simulation of climate for two periods of the Earth's history (the Last Glacial Maximum and the mid-Holocene) between CMIP5 and previous paleoclimate simulations. Similarly, for the modern period only modest, incremental progress was found between CMIP3 and CMIP5 regarding the simulation of precipitation and radiation. The representation of clouds also showed improvement, but remained a key challenge in climate modelling (Flato et al., 2013).

The type of multi-variate analysis of models presented in AR5 remains critical to building confidence for example in projections of climate change. It is expanded here to the previous-generation CMIP3 and present-

ACCEPTED VERSION SUBJECT TO FINAL EDITING

generation CMIP6 models and also to more variables and more climate domains, covering land and ocean as well as sea ice. The multi-variate evaluation of these three generations of models is performed relative to the observational datasets listed in Annex I, Table AI.1. For many of these datasets, a rigorous characterization of the observational uncertainty is not available, see discussion in Chapter 2. Here, as much as possible, multiple independent observational datasets are used. Disagreements among them would cause differences in model scoring, indicating that observational uncertainties may be substantial compared to model errors. Conversely, similar scores against different observational datasets would suggest model biases may be larger than the observational uncertainty.

An analysis of a basket of 16 atmospheric variables (Figure 3.42a) assessed across CMIP3, CMIP5, and CMIP6 models but excluding high-resolution models participating in HighResMIP, reveals the progress made between these three generations of models (Bock et al., 2020). Progress is evidenced by the increasing prevalence of blue colours (indicating a performance better than the median) for the more recent model versions. Additionally, a few CMIP6 models outperform the best-performing CMIP5 models. Progress is evident across all 16 variables. As noted in AR5, the models typically score similarly against both observational reference datasets, indicating that indeed uncertainties in these references are smaller than model biases. Several models and model families perform better compared to observational references than the median, across a majority of the climate variables assessed, and conversely some other models or model families compare more poorly against these reference datasets. Such a good correspondence across a range of diagnostic fields probing different aspects of climate enhances confidence that the improved performances reflect progress in the physical realism of these simulations. An alternative explanation, that progress is due to a cancellation of errors achieved by model tuning, appears improbable given the large number of diagnostic fields involved here. However, several instances of poor model performance (red colours in Figure 3.42) still exist in the CMIP6 ensemble. Family relationships (i.e. various degrees of shared formulations; Knutti et al., 2013) between the models are apparent, for example, the GISS, GFDL, CESM, CNRM, and HadGEM/UKESM1/ACCESS families score similarly across all atmospheric variables, both for the CMIP5 and CMIP6 generations. In the cases of CESM2 / CESM2(WACCM), CNRM-CM6-1 / CNRM-ESM2-1, NorCPM1 / NorESM2-LM, and HadGEM3-GC31-LL / UKESM1-0-LL, the high-complexity model scores as well or better than its lower-complexity counterpart, indicating that increasing complexity by adding Earth system features, which by removing constraints could be expected to degrade a model's performance, does not necessarily do so. Several high climate-sensitivity models (Section 7.5; Meehl et al., 2020), in particular CanESM5, CESM2, CESM2-WACCM, HadGEM3-GC31-LL, and UKESM1-0-LL, score well against the benchmarks. In accordance with AR5 and earlier assessments, the multi-model mean, with some notable exceptions, is better than any individual model (Annan and Hargreaves, 2011; Rougier, 2016).

Regarding model performance for the ocean and the cryosphere (Figure 3.42b), it is apparent that for many models there are substantial differences between the scores for Arctic and Antarctic sea ice concentration. This might suggest that it is not sea ice physics directly that is driving such differences in performance but rather other influences, such as differences in geography, the role of large ice shelves (which are absent in the Arctic), or large-scale ocean dynamics. As for atmospheric variables, progress is evident also across all 4 ocean and 10 land variables from CMIP5 to CMIP6.

In summary, CMIP6 models perform generally better for a basket of variables covering mean historical climate across the atmosphere, ocean, and land domains than previous-generation and older models (*high confidence*). Earth System models characterized by additional biogeochemical feedbacks often perform at least as well as related more constrained, lower-complexity models lacking these feedbacks (*medium confidence*). In many cases, the models score similarly against both observational references, indicating that model errors are usually larger than observational uncertainties (*high confidence*). Moreover, synthesizing across Sections 3.3-3.7, we assess that the CMIP6 multi-model mean captures most aspects of observed climate change well (*high confidence*).

[START FIGURE 3.42 HERE]

ACCEPTED VERSION SUBJECT TO FINAL EDITING

Figure 3.42: Relative space-time root-mean-square deviation (RMSD) calculated from the climatological seasonal cycle of the CMIP simulations (1980-1999) compared to observational datasets. (a) CMIP3, CMIP5, and CMIP6 for 16 atmospheric variables (b) CMIP5 and CMIP6 for 10 land variables and four ocean/sea-ice variables. A relative performance measure is displayed, with blue shading indicating better and red shading indicating worse performance than the median of all model results. A diagonal split of a grid square shows the relative error with respect to the reference data set (lower right triangle) and an additional data set (upper left triangle). Reference/additional datasets are from top to bottom in (a): ERA5/NCEP, GPCP-SG/GHCN, CERES-EBAF/-, CERES-EBAF/-, CERES-EBAF/-, CERES-EBAF/-, JRA-55/ERA5, ESACCI-SST/HadISST, ERA5/NCEP, ERA5/NCEP, ERA5/NCEP, ERA5/NCEP, ERA5/NCEP, ERA5/NCEP, AIRS/ERA5, ERA5/NCEP and in (b): CERES-EBAF/-, CERES-EBAF/-, CERES-EBAF/-, CERES-EBAF/-, LandFlux-EVAL/-, Landschuetzer2016/ JMA-TRANSCOM; MTE/FLUXCOM, LAI3g/-, JMA-TRANSCOM, ESACCI-SOILMOISTURE/-, HadISST/ATSR, HadISST/-, HadISST/-, ERA-Interim/-. White boxes are used when data are not available for a given model and variable. Figure is updated and expanded from Bock et al. (2020), their Figure 5 CC BY4.0 https://creativecommons.org/licenses/by/4.0/. Further details on data sources and processing are available in the chapter data table (Table 3.SM.1).

[END FIGURE 3.42 HERE]

Using centred pattern correlations (quantifying pattern similarity on a scale of -1 to 1, with 1 expressing perfect similarity and 0 no relationship) for selected fields, the AR5 documented improvements between CMIP3 and CMIP5 in surface air temperature, outgoing longwave radiation, and precipitation (Figure 9.6 of Flato et al., 2013). Little further progress between CMIP3 and CMIP5 was found for fields that were already quite well simulated in CMIP3 (such as surface air temperature and outgoing longwave). For precipitation, the spread reduced because the worst-performing models improved. The short-wave cloud radiative effect remained relatively poorly simulated with significant inter-model spread (e.g., Calisto et al., 2014). This comparison of centred pattern correlations is designed to help determine the quality of simulation of different diagnostics relative to each other, and also to examine progress between generations of models. Figure 3.43 shows the centred pattern correlations for 16 variables for CMIP3, CMIP5 and CMIP6 models. In the ensemble averages, CMIP6 performs better than CMIP5 and CMIP3 for near-surface temperature, precipitation, mean sea-level pressure, and many other variables. For the variables shown, the uncertainties in observational datasets, in particular for precipitation and northward wind at 850 hPa, remain substantial relative to mean model errors (see grey dots in Figure 3.43).

[START FIGURE 3.43 HERE]

Figure 3.43: Centred pattern correlations between models and observations for the annual mean climatology over the period 1980–1999. Results are shown for individual CMIP3 (cyan), CMIP5 (blue) and CMIP6 (red) models (one ensemble member from each model is used) as short lines, along with the corresponding ensemble averages (long lines). Correlations are shown between the models and the primary reference observational data set (from left to right: ERA5, GPCP-SG, CERES-EBAF, CERES-EBAF, CERES-EBAF, CERES-EBAF, JRA-55, ESACCI-SST, ERA5, ERA5, ERA5, ERA5, ERA5, ERA5, AIRS, ERA5). In addition, the correlation between the primary reference and additional observational data sets (from left to right: NCEP, GHCN, -, -, -, -, ERA5, HadISST, NCEP, NCEP, NCEP, NCEP, NCEP, NCEP, ERA5, NCEP) are shown (solid grey circles) if available. To ensure a fair comparison across a range of model resolutions, the pattern correlations are computed after regridding all datasets to a resolution of 4º in longitude and 5º in latitude. Figure is updated and expanded from Bock et al. (2020), their Figure 7 CC BY4.0 https://creativecommons.org/licenses/by/4.0/. Further details on data sources and processing are available in the chapter data table (Table 3.SM.1).

[END FIGURE 3.43 HERE]

In addition to the multivariate assessments of simulations of the recent historical period, simulations of selected periods of the Earth's more distant history can be used to benchmark climate models by exposing them to climate forcings that are radically different from the present and recent past (Harrison et al., 2015, 2016; Kageyama et al., 2018b; Tierney et al., 2020a). These time periods provide an out-of-sample test of

ACCEPTED VERSION SUBJECT TO FINAL EDITING

models because they are not in general used in the process of model development. They encompass a range of climate drivers, such as volcanic and solar forcing for the Last Millennium, orbital forcing for the mid-Holocene and Last Interglacial, and changes in greenhouse gases and ice sheets for the LGM, mid-Pliocene Warm Period, and early Eocene (Sections 2.2 and 2.3). These drivers led to climate changes, including in surface temperature (Section 2.3.1.1) and the hydrological cycle (Section 2.3.1.3.1), which are described by paleoclimate proxies that have been synthesised to support evaluations of models on a global and regional scale. However, the more sparse, indirect, and regionally incomplete climate information available from paleo-archives motivates a different form for the multivariate analysis of simulations available covering these periods versus the equivalent for the historical period, as described below.

AR5 found that reconstructions and simulations of past climates both show similar responses in terms of large-scale patterns of climate change, such as polar amplification (Flato et al., 2013). However, for several regional signals (e.g., the north-south temperature gradient in Europe and regional precipitation changes), the magnitude of change seen in the proxies relative to the pre-industrial period was underestimated by the models. When benchmarking CMIP5/PMIP3 models against reconstructions of the mid-Holocene and LGM, AR5 found only a slight improvement compared with earlier model versions across a range of variables. For the Last Interglacial, it was noted that the magnitude of observed annual mean warming in the NH was only reached in summer in the models. For the mid-Pliocene Warm Period, it was noted that both proxies and models showed a polar amplification of temperature compared with the pre-industrial period, but a formal model evaluation was not carried out.

Since AR5, new simulation protocols have been developed in the framework of PMIP4 (Kageyama et al., 2018b) which is further described for the mid-Holocene and the Last Interglacial by Otto-Bliesner et al. (2017), for the LGM by Kageyama et al. (2017), for the Pliocene by Haywood et al. (2016), and for the early Eocene by Lunt et al. (2017). These have resulted in new model simulations for these time periods (Brierley et al., 2020; Haywood et al., 2020; Kageyama et al., 2021a; Lunt et al., 2021; Otto-Bliesner et al., 2021). These time periods span an assessed temperature range of 20°C (Section 2.3.1.1), and for all periods the PMIP4 model ensemble mean is within 0.5°C of the assessed range of GSAT (Figure 3.44a). Those time periods for which the model ensemble mean is outside the assessed range of GSAT, the mid-Holocene and the Last Interglacial, are primarily forced by orbital changes not greenhouse gas forcing, and as a result the forcing, as well as the assessed and modelled response, are relatively close to zero in the global annual mean. During these periods, climate change therefore is a consequence of more poorly understood Earth System feedbacks acting on the response to orbital differences versus the present-day, affecting the seasonality of insolation.

Polar amplification in the LGM, mid-Pliocene Warm Period, and Early Eocene climatic optimum (EECO) simulations are assessed in Section 7.4.4. Here we focus on the mid-Holocene and the LGM, which have been a part of AMIP or CMIP through several assessment cycles, and as such serve as a reference to quantify regional model-data agreement from one IPCC assessment to another. We compare the results from 15 CMIP6 models using the PMIP4 protocol (CMIP6-PMIP4), with non-CMIP6 models using the PMIP4 protocol, with PMIP3 models, and with regional temperature and precipitation changes from proxies for the mid-Holocene (Figure 3.44b). For 6 out of 7 variables shown, the CMIP6 multi-model mean captures the correct sign of the change. For 5 out of 7 of them the CMIP6 ensemble mean is within the reconstructed range. For the other two variables (changes in the mean temperature of the warmest month over North America and in the mean annual precipitation over West Africa) nearly all PMIP4 and PMIP3 models are outside the reconstructed range. CMIP6 models show regional patterns of temperature changes similar to the PMIP3 ensemble (Brierley et al., 2020), but the slight mid-Holocene cooling in PMIP4 compared with PMIP3, probably associated with lower imposed mid-Holocene carbon dioxide concentrations (Otto-Bliesner et al., 2017), improves the regional model performance for summer and winter temperatures (Figure 3.44b). However, this cooling also results in a CMIP6 mid-Holocene GSAT that lies further from the assessed range (Figure 3.44a). All models show an expansion of the monsoon areas from the pre-industrial to the mid-Holocene simulations in the NH, but this expansion in some cases is only large enough to cancel out the bias in the pre-industrial control simulations (Brierley et al., 2020; Section 3.3.3.2). There is a slight improvement in representing the northward expansion of the West African monsoon region in PMIP4 compared with PMIP3 (Figure 3.11, Figure 3.44b).

ACCEPTED VERSION SUBJECT TO FINAL EDITING

Fourteen simulations of the LGM climate have been produced following the CMIP6-PMIP4 protocol using 11 models, 5 of which are from the latest CMIP6 generation. The multi-model-mean global cooling simulated by these models is close to that simulated by the CMIP5-PMIP3 ensemble, but the range of results is larger. The increase in the range is largely due to the inclusion of CESM2 which simulates a much larger cooling than the other PMIP4 models (Figure 3.44a). This is consistent with its larger climate sensitivity (Zhu et al., 2021) (see also Section 3.3.1.1). The other models on average also simulate slightly larger cooling, possibly a consequence of the lower ice sheet assumed in PMIP4 versus PMIP3 (Kageyama et al., 2017, 2021a). The PMIP4 multi-model mean is within the range of reconstructed regional averages for 4 out of 7 regional variables; this is unchanged from PMIP3 but for different variables (Figure 3.44c). For all fields, the results of many individual models are outside the reconstructed range. For 2 variables out of 7 (changes in the mean temperature of the warmest month and mean annual precipitation over Western Europe) no model is within the range of the reconstructions. This analysis is strengthened compared with the equivalent analysis in AR5 because it is based on larger and improved reconstructions (Cleator et al., 2020). Most CMIP6-PMIP4 models simulate slightly stronger AMOC, but no strong deepening of the AMOC (Kageyama et al., 2021a), while most other PMIP4 models simulate a strengthening and strong deepening of the AMOC, as was the case for the PMIP3 models (Muglia and Schmittner, 2015; Sherriff-Tadano et al., 2018). Only one model (CESM1.2) shows a shoaling of LGM AMOC which is consistent with reconstructions (Marzocchi and Jansen, 2017; Sherriff-Tadano et al., 2018).

17 PMIP4 models completed Last Interglacial simulations (Otto-Bliesner et al., 2021). The comparison to reconstructions is generally good, except for some discrepancies, such as for upwelling systems such as in the South East Atlantic or resulting from local melting of remnant ice sheets absent in the Last Interglacial simulation protocol. All models simulate a decrease in Arctic sea ice in summer, commensurate with increased summer insolation, while some models even simulate a large or complete loss (Guarino et al., 2020; Kageyama et al., 2021b). Sea ice reconstructions for the Central Arctic are however too uncertain to evaluate this behaviour. The Last Interglacial simulations indicate a clear relationship between simulated sea ice loss and model responses to increased greenhouse gas forcing (Kageyama et al., 2021b; Otto-Bliesner et al., 2021).

Overall, the PMIP multi-model means agree very well (within 0.5°C of the assessed range) with GSAT reconstructed from proxies across multiple time periods, spanning a range from 6°C colder than pre-industrial (Last Glacial Maximum) to 14°C warmer than pre-industrial (Early Eocene Climate Optimum) (*high confidence*). During the orbitally-forced mid-Holocene, the CMIP6 multi-model mean captures the sign of the regional changes in temperature and precipitation in most regions assessed, and there have been some regional improvements compared to AR5 (*medium confidence*). The limited number of CMIP6 simulations of the LGM hinders model evaluation of the multi-model mean, but for both LGM and mid-Holocene, models tend to underestimate the magnitude of large changes (*high confidence*). Some long-standing model-data discrepancies, such as a dry bias in North Africa in the mid-Holocene, have not improved in CMIP6 compared with PMIP3 (*high confidence*).

[START FIGURE 3.44 HERE]

Figure 3.44: Multivariate synopsis of paleoclimate model results compared to observational references. Data-model comparisons for GSAT anomalies for five PMIP4 periods and for regional features for the (b) mid-Holocene and (c) LGM periods, for PMIP3 and PMIP4 models. The results from the CMIP6 models are specified as coloured dots. In (a) the light orange shading shows the *very likely* assessed ranges presented in Section 2.3.1.1. In (b) and (c), the regions and variables are defined as follows: North America (20-50°N, 140-60°W), Western Europe (35-70°N, 10°W-30°E) and West Africa (0°-30°N, 10°W-30°E); MTCO: Mean Temperature of the Coldest Month (°C), MTWA: Mean Temperature of the Warmest Month (°C), MAP: Mean Annual Precipitation (mm/year). In (b) and (c) the ranges shown for the reconstructions (Bartlein et al. (2011) for MH and Cleator et al. (2020) for LGM) are based on the standard error given at each site: the average and associated standard deviation over each area is obtained by computing 1000 times the average of randomly drawn values from the Gaussian distributions defined at each site by the reconstruction mean and standard error; the light orange colour shows the ± 1 standard

ACCEPTED VERSION SUBJECT TO FINAL EDITING

deviation of these 1000 estimates. The dots on (b) and (c) show the average of the model output for grid points for which there are reconstructions. The ranges for the model results are based on an ensemble of 1000 averages over 50 years randomly picked in the model output time series for each region and each variable: the mean ± one standard deviation is plotted for each model. Figure is adapted from Brierley et al. (2020), their Figure S3 for the mid-Holocene and from Kageyama et al. (2021), their Figure 12 for the LGM. Further details on data sources and processing are available in the chapter data table (Table 3.SM.1).

[END FIGURE 3.44 HERE]

3.8.2.2 Process Representation in Different Classes of Models

Based on new scientific insights and newly available observations, many improvements have been made to models from CMIP5 to CMIP6, including changes in the representation of physics of the atmosphere, ocean, sea ice, and land surface. In many cases, changes in the detailed representation of cloud and aerosol processes have been implemented. The new generation of CMIP6 climate models also features increases in spatial resolution, as well as inclusion of additional Earth system processes and new components (see further details in Section 1.5.3.1 and in Tables AII.5 and AII.6). Such changes to model physics and resolution are often designed to improve the fitness-for-purpose of a model such as projecting regional aspects of climate (Section 10.3) or to more fully represent feedbacks to make the models more fit for long-term climate projections affected for example by carbon cycle feedbacks (see also Section 1.5.3.1).

Factors affecting model performance include resolution, the type of dynamical core (spectral,. finite difference or finite volume), physics parameters and parameterisations, model structure (e.g. many of the coupled HighResMIP models (Haarsma et al., 2016) use the NEMO ocean model, affecting model diversity), and the range and degree of process realism (e.g. for aerosols, atmospheric chemistry and other Earth System components). This section particularly explores the influence of model resolution and of complexity on model performance (see also Section 8.5.1).

A key advance in CMIP6 compared to CMIP5 is the presence of high-resolution models that have participated in HighResMIP. Resolution alone can significantly affect a model's performance, with some effects propagating to the global scale. Recent studies have shown that enhancing the horizontal resolution of models is seen to significantly affect aspects of large-scale circulation as well as improve the simulation of small-scale processes and extremes when compared to CMIP3 and CMIP5 models (Haarsma et al., 2016; see also Section 11.4.3), with some models approaching 10 km resolution in the atmosphere (Kodama et al., 2021) or ocean (Caldwell et al., 2019; Gutjahr et al., 2019; Roberts et al., 2019; Chang et al., 2020; Semmler et al., 2020).

As discussed in Section 3.3, CMIP6 models reproduce observed large-scale mean surface temperature patterns as well as their CMIP5 predecessors, but biases in surface temperature in the mean of HighResMIP models are smaller than those in the mean of the corresponding standard resolution CMIP6 configurations of the same models (Figure 3.3; Section 3.3.1.1). The extent and causes of improvements due to increased horizontal resolutions in the atmosphere and ocean domains depend on the model (Kuhlbrodt et al., 2018; Roberts et al., 2018, 2019; Sidorenko et al., 2019), although they typically involve better process representation (for example of ocean currents and atmospheric storms) which can lead to reduced biases in top of atmosphere radiation and cloudiness. Precipitation has likewise improved in CMIP6 versus CMIP5 models, but biases remain. The high resolution (< 25 km) class of models participating in HighResMIP compares regionally better against observations than the standard resolution CMIP6 models (of order 100 km, Figure 3.13; Section 3.3.2.2), partly because of an improved representation of orographic (mountain-induced) precipitation which constitutes a major fraction of precipitation on land, but other processes also play an important role (Vannière et al., 2019). However, there are also large parts of the tropical ocean where precipitation in high-resolution models is not improved compared to standard resolution CMIP6 models (Vannière et al., 2019).

Additionally, the representation of surface and deeper ocean mean temperature is improved in models with

ACCEPTED VERSION SUBJECT TO FINAL EDITING

higher horizontal resolution (Sections 3.5.1.1 and 3.5.1.2) with systematic improvements in coupled tropical Atlantic sea surface temperature and precipitation biases at higher resolutions (Roberts et al., 2019, single model; Vannière et al., 2019), the North Atlantic cold bias (Bock et al., 2020, multi-model; Roberts et al., 2018, 2019; Caldwell et al., 2019; all single models) as well as deep ocean biases (Small et al., 2014; Griffies et al., 2015; Caldwell et al., 2019; Gutjahr et al., 2019; Roberts et al., 2019; Chang et al., 2020, all single model studies). Atlantic ocean transports (heat and volume) are also generally improved compared to observations (Grist et al., 2018; Caldwell et al., 2019; Docquier et al., 2019; Roberts et al., 2019, 2020c; Chang et al., 2020), as well as some aspects of air-sea interactions (Wu et al., 2019a, single model; Bellucci et al., 2021, multi-model). However, warm-biased sea surface temperatures in the Southern Ocean got worse in comparison to standard resolution CMIP6 models (Bock et al., 2020). AR5 noted problems with the simulation of clouds in this region which were later attributed to a lack of supercooled liquid clouds (Bodas-Salcedo et al., 2016). Mesoscale ocean processes are critical to maintaining the Southern Ocean stratification and response to wind forcing (Marshall and Radko, 2003; Hallberg and Gnanadesikan, 2006), and their explicit representation requires even higher ocean resolution (Hallberg, 2013). Similarly, atmospheric convection remains unresolved even in the highest-resolution climate models participating in HighResMIP. However, there is also evidence of improvements in the frequency, distribution and interannual variability of tropical cyclones (Roberts et al., 2020a, 2020b), particularly in the NH (see further discussion in Section 11.7.1.3), moisture budget (Vannière et al., 2019), and interaction with the ocean (Scoccimarro et al., 2017, single model). At higher resolution the track density of tropical cyclones is increased practically everywhere where tropical cyclones occur. Modelling of some climate extremes is shown to be improved in explosively developing extra-tropical cyclones (Vries et al., 2019; Jiaxiang et al., 2020), blocking (Fabiano et al., 2020; Schiemann et al., 2020; Section 3.3.3.3) and European extreme precipitation due to a better representation of the North Atlantic storm track (Van Haren et al., 2015) and orographic boundary conditions (Schiemann et al., 2018).

In CMIP6 a number of Earth system models have increased the realism by which key biogeochemical aspects of the coupled Earth system are represented, affecting for example the carbon and nitrogen cycles, aerosols, and atmospheric chemistry (e.g., Cao et al., 2018; Gettelman et al., 2019; Lin et al., 2019; Mauritsen et al., 2019; Séférian et al., 2019; Sellar et al., 2019; Sidorenko et al., 2019; Swart et al., 2019; Dunne et al., 2020; Seland et al., 2020; Wu et al., 2020; Ziehn et al., 2020). In addition to increased process realism, the level of coupling between the physical climate and biogeochemical components of the Earth system has also been enhanced in some models (Mulcahy et al., 2020) as well as across different biogeochemical components (see Section 5.4 for a discussion and Table 5.4 for an overview). For example, the nitrogen cycle is now simulated in several ESMs (Zaehle et al., 2015; Davies-Barnard et al., 2020). This advance accounts for the fertilization effect nitrogen availability has on vegetation and carbon uptake, reducing uncertainties in the simulations of the carbon uptake responses to physical climate change (Section 3.6.1) and to CO_2 increases (Arora et al., 2020), thus improving confidence in the simulated airborne fraction of CO_2 emissions (Jones and Friedlingstein, 2020) and better constraining remaining carbon budgets (Section 5.5). Such advances also allow investigation of land-based climate mitigation options (e.g. through changes in land management and associated terrestrial carbon uptake (Mahowald et al., 2017; Pongratz et al., 2018) or interactions between different facets of the managed Earth system, such as interactions between mitigation efforts targeting climate warming and air quality (West et al., 2013)). A number of developments also explicitly target improved simulation of the past.

Further such ESM developments include: (i) Apart from the nitrogen cycle, extending terrestrial carbon cycle models to simulate interactions between the carbon cycle and other nutrient cycles, such as phosphorous, that are known to play an important role in limiting future plant uptake of CO_2 (Zaehle et al., 2015). (ii) Introducing explicit coupling between interactive atmospheric chemistry and aerosol schemes (Gettelman et al., 2019; Sellar et al., 2019), which has been shown to affect estimates of historical aerosol radiative forcing (Karset et al., 2018). Furthermore, interactive treatment of atmospheric chemistry in a full ESM supports investigation of interactions between climate and air quality mitigation efforts, such as in AerChemMIP (Collins et al., 2017) as well as interactions between stratospheric ozone recovery and global warming (Morgenstern et al., 2018). (iii) Couplings between components of Earth system models have been extended to increase their utility for studying future interactions across the full Earth system, such as between ocean biogeochemistry and cloud-aerosol processes (Mulcahy et al., 2020), vegetation and impacts

ACCEPTED VERSION SUBJECT TO FINAL EDITING

on dust production (Kok et al., 2018), production of secondary organic aerosols (SOA, Zhao et al., 2017) and Equilibrium Climate Sensitivity (ECS) whereby enhanced CO_2 fertilization of land vegetation causes changes in regional surface albedo (Andrews et al., 2019). Increased coupling between physical climate and biogeochemical processes in a single ESM, along with an increased number of interactively represented processes, such as permafrost thaw, vegetation, wildfires and continental ice sheets increases our ability to investigate the potential for abrupt and interactive changes in the Earth system (see Sections 4.7.3 and 5.4.9 and Box 5.1). Table 5.4 provides an overview of recent advances with representing the carbon cycle in ESMs.

In summary, both high-resolution and high-complexity models have been evaluated as part of CMIP6. In comparison with standard resolution CMIP6 models, higher resolution probed under the HighResMIP activity (Haarsma et al., 2016) improves aspects of the simulation of climate (particularly concerning sea surface temperature) but discrepancies remain and there are some regions, such as parts of the Southern Ocean, where currently attainable resolution produces inferior performance (*high confidence*). Such model behaviour can indicate deficiencies in model physics that are not simply associated with resolution. In several cases, high-complexity ESMs that include additional interactions and thus have potential for additional associated model errors nevertheless perform as well as their low-complexity counterparts, illustrating that interactively simulating these Earth System components as part of the climate system is now well established.

ACCEPTED VERSION
SUBJECT TO FINAL EDITING

Frequently Asked Questions

FAQ 3.1: How do we Know Humans are Responsible for Climate Change?

The dominant role of humans in driving recent climate change is clear. This conclusion is based on a synthesis of information from multiple lines of evidence, including direct observations of recent changes in Earth's climate; analyses of tree rings, ice cores, and other long-term records documenting how the climate has changed in the past; and computer simulations based on the fundamental physics that govern the climate system.

Climate is influenced by a range of factors. There are two main natural drivers of variations in climate on timescales of decades to centuries. The first is variations in the sun's activity, which alter the amount of incoming energy from the sun. The second is large volcanic eruptions, which increase the number of small particles (aerosols) in the upper atmosphere that reflect sunlight and cool the surface—an effect that can last for several years (see also FAQ 3.2). The main human drivers of climate change are increases in the atmospheric concentrations of greenhouse gases and of aerosols from burning fossil fuels, land use and other sources. The greenhouse gases trap infrared radiation near the surface, warming the climate. Aerosols, like those produced naturally by volcanoes, on average cool the climate by increasing the reflection of sunlight. Multiple lines of evidence demonstrate that human drivers are the main cause of recent climate change.

The current rates of increase of the concentration of the major greenhouse gases (carbon dioxide, methane and nitrous oxide) are unprecedented over at least the last 800,000 years. Several lines of evidence clearly show that these increases are the results of human activities. The basic physics underlying the warming effect of greenhouse gases on the climate has been understood for more than a century, and our current understanding has been used to develop the latest generation climate models (see FAQ 3.3). Like weather forecasting models, climate models represent the state of the atmosphere on a grid and simulate its evolution over time based on physical principles. They include a representation of the ocean, sea ice and the main processes important in driving climate and climate change.

Results consistently show that such climate models can only reproduce the observed warming (black line in FAQ 3.1, Figure 1) when including the effects of human activities (grey band in FAQ 3.1, Figure 1), in particular the increasing concentrations of greenhouse gases. These climate models show a dominant warming effect of greenhouse gas increases (red band, which shows the warming effects of greenhouse gases by themselves), which has been partly offset by the cooling effect of increases in atmospheric aerosols (blue band). By contrast, simulations that include only natural processes, including internal variability related to El Niño and other similar variations, as well as variations in the activity of the sun and emissions from large volcanoes (green band in FAQ 3.1, Figure 1), are not able to reproduce the observed warming. The fact that simulations including only natural processes show much smaller temperature increases indicates that natural processes alone cannot explain the strong rate of warming observed. The observed rates can only be reproduced when human influence is added to the simulations.

Moreover, the dominant effect of human activities is apparent not only in the warming of global surface temperature, but also in the pattern of warming in the lower atmosphere and cooling in the stratosphere, warming of the ocean, melting of sea ice, and many other observed changes. An additional line of evidence for the role of humans in driving climate change comes from comparing the rate of warming observed over recent decades with that which occurred prior to human influence on climate. **Evidence from tree rings and** other paleoclimate records shows that the rate of increase of global surface temperature observed over the past fifty years exceeded that which occurred in any previous 50-year period over the past 2000 years (see FAQ 2.1).

Taken together, this evidence shows that humans are the dominant cause of observed global warming over recent decades.

[START FAQ 3.1, FIGURE 1 HERE]

ACCEPTED VERSION SUBJECT TO FINAL EDITING

FAQ 3.1, Figure 1: Observed warming (1850-2018) is only reproduced in simulations including human influence. Global surface temperature changes in observations, compared to climate model simulations of the response to all human and natural forcings (grey band), greenhouse gases only (red band), aerosols and other human drivers only (blue band) and natural forcings only (green band). Solid coloured lines show the multi-model mean, and coloured bands show the 5–95% range of individual simulations.

[END FAQ 3.1, FIGURE 1 HERE]

ACCEPTED VERSION
SUBJECT TO FINAL EDITING

FAQ 3.2: What is Natural Variability and How has it Influenced Recent Climate Changes?

Natural variability refers to variations in climate that are caused by processes other than human influence. It includes variability that is internally generated within the climate system and variability that is driven by natural external factors. Natural variability is a major cause of year-to-year changes in global surface climate and can play a prominent role in trends over multiple years or even decades. But the influence of natural variability is typically small when considering trends over periods of multiple decades or longer. When estimated over the entire historical period (1850–2020), the contribution of natural variability to global surface warming of -0.23°C–0.23°C is small compared to the warming of about 1.1°C observed during the same period, which has been almost entirely attributed to the human influence.

Paleoclimatic records (indirect measurements of climate that can extend back many thousands of years) and climate models all show that global surface temperatures have changed significantly over a wide range of time scales in the past. One of these reasons is *natural variability*, which refers to variations in climate that are either *internally* generated within the climate system or *externally* driven by natural changes. Internal natural variability corresponds to a redistribution of energy within the climate system (for example via atmospheric circulation changes similar to those that drive the daily weather) and is most clearly observed as regional, rather than global, fluctuations in surface temperature. External natural variability can result from changes in the Earth's orbit, small variations in energy received from the sun, or from major volcanic eruptions. Although large orbital changes are related to global climate changes of the past, they operate on very long time scales (i.e., thousands of years). As such, they have displayed very little change over the past century and have had very little influence on temperature changes observed over that period. On the other hand, volcanic eruptions can strongly cool the Earth, but this effect is short-lived and their influence on surface temperatures typically fades within a decade of the eruption.

To understand how much of observed recent climate change has been caused by natural variability (a process referred to as attribution), scientists use climate model simulations. When only natural factors are used to force climate models, the resulting simulations show variations in climate on a wide range of time scales in response to volcanic eruptions, variations in solar activity, and internal natural variability. However, the influence of natural climate variability typically decreases as the time period gets longer, such that it only has mild effects on multi-decadal and longer trends (FAQ 3.2, Figure 1).

Consequently, over periods of a couple of decades or less, natural climate variability can dominate the human-induced surface warming trend – leading to periods with stronger or weaker warming, and sometimes even cooling (FAQ 3.2, Figure 1, left and center). Over longer periods, however, the effect of natural variability is relatively small (FAQ 3.2, Figure 1, right). For instance, over the entire historical period (1850–2019), natural variability is estimated to have caused between -0.23°C and +0.23°C of the observed surface warming of about 1.1°C. This means that the bulk of the warming has been almost entirely attributed to human activities, particularly emissions of greenhouse gases (see FAQ 3.1).

Another way to picture natural variability and human influence is to think of a person walking a dog. The path of the walker represents the human-induced warming, while their dog represents natural variability. Looking at global surface temperature changes over short periods is akin to focusing on the dog. The dog sometimes moves ahead of the owner and other times behind. This is similar to natural variability that can weaken or amplify warming on the short term. In both cases it is difficult to predict where the dog will be or how the climate will evolve in the near future. However, if we pull back and focus on the slow steady steps of the owner, the path of the dog is much clearer and more predictable, as it follows the path of its owner. Similarly, human influence on the climate is much clearer over longer time periods.

[START FAQ 3.2, FIGURE 1 HERE]

FAQ 3.2, Figure 1: Annual (left), decadal (middle) and multi-decadal (right) variations in average global surface temperature. The thick black line is an estimate of the human contribution to temperature changes, based on climate models, whereas the green lines show the combined effect of natural

ACCEPTED VERSION SUBJECT TO FINAL EDITING

variations and human-induced warming, different shadings of green represent different simulations, which can be viewed as showing a range of potential pasts. The influence of natural variability is shown by the green bars, and it decreases with longer time scales. The data is sourced from the CESM1 large ensemble.

[END FAQ 3.2, FIGURE 1 HERE]

ACCEPTED VERSION
SUBJECT TO FINAL EDITING

FAQ 3.3: Are Climate Models Improving?

Yes, climate models have improved and continue to do so, becoming better at capturing complex and small-scale processes and at simulating present-day mean climate conditions. This improvement can be measured by comparing climate simulations against historical observations. Both the current and previous generations of models show that increases in greenhouse gases cause global warming. While past warming is well simulated by the new generation models as a group, some individual models simulate past warming that is either below or above what is observed. The information about how well models simulate past warming, as well as other insights from observations and theory, are used to refine this Report's projections of global warming.

Climate models are important tools for understanding past, present and future climate change. They are sophisticated computer programs that are based on fundamental laws of physics of the atmosphere, ocean, ice, and land. Climate models perform their calculations on a three-dimensional grid made of small bricks or *grid cells* of about 100 km across. Processes that occur on scales smaller than the model grid cells (such as the transformation of cloud moisture into rain) are treated in a simplified way. This simplification is done differently in different models. Some models include more processes and complexity than others; some represent processes in finer detail (smaller grid cells) than others. Hence the simulated climate and climate change vary between models.

Climate modelling started in the 1950s and, over the years, models have become increasingly sophisticated as computing power, observations and our understanding of the climate system have advanced. The models used in the IPCC First Assessment Report published in 1990 correctly reproduced many aspects of climate (FAQ 1.1). The actual evolution of the climate since then has confirmed these early projections, when accounting for the differences between the simulated scenarios and actual emissions. Models continue to improve and get better and better at simulating the large variety of important processes that affect climate. For example, many models now simulate complex interactions between different aspects of the Earth system, such as the uptake of carbon by vegetation on land and by the ocean, and the interaction between clouds and air pollutants. While some models are becoming more comprehensive, others are striving to represent processes at higher resolution, for example to better represent the vortices and swirls in currents responsible for much of the transport of heat in the ocean.

Scientists evaluate the performance of climate models by comparing historical model simulations to observations. This evaluation includes comparison of large-scale averages as well as more detailed regional and seasonal variations. There are two important aspects to consider: (1) how models perform individually and (2) how they perform as a group. The average of many models often compares better against observations than any individual model, since errors in representing detailed processes tend to cancel each other out in multi-model averages.

As an example, FAQ 3.3 Figure 1 compares simulations from the three most recent generations of models (available around 2005, 2010 and present) with observations of three climate variables. It shows the correlation between simulated and observed patterns, where a value of 1 represents perfect agreement. Many individual models of the new generation perform significantly better, as indicated by values closer to 1. As a group, each generation out-performs the previous generation: the multi-model average (shown by the longer lines) is progressively closer to 1. The vertical extent of the colored bars indicates the range of model performance across each group. The top of the bar moves up with each generation, indicating improved performance of the best performing models from one generation to the next. In the case of precipitation, the performance of the worst performing models is similar in the two most recent model generations, increasing the spread across models.

Developments in the latest generation of climate models, including new and better representation of physical, chemical and biological processes, as well as higher resolution, have improved the simulation of many aspects of the Earth system. These simulations, along with the evaluation of the ability of the models to simulate past warming as well as the updated assessment of the temperature response to a doubling of CO_2 in the atmosphere, are used to estimate the range of future global warming (FAQ 7.3).

ACCEPTED VERSION SUBJECT TO FINAL EDITING

[START FAQ 3.3, FIGURE 1 HERE]

FAQ 3.3, Figure 1: Pattern correlations between models and observations of three different variables: surface air temperature, precipitation and sea level pressure. Results are shown for the three most recent generations of models, from the Coupled Model Intercomparison Project (CMIP): CMIP3 (orange), CMIP5 (blue) and CMIP6 (purple). Individual model results are shown as short lines, along with the corresponding ensemble average (long line). For the correlations the yearly averages of the models are compared with the reference observations for the period 1980-1999, with 1 representing perfect similarity between the models and observations. CMIP3 simulations performed in 2004-2008 were assessed in the IPCC Fourth Assessment, CMIP5 simulations performed in 2011-2013 were assessed in the IPCC Fifth Assessment, and CMIP6 simulations performed in 2018-2021 are assessed in this report.

[END FAQ 3.3, FIGURE 1 HERE]

ACCEPTED VERSION
SUBJECT TO FINAL EDITING

Acknowledgements

Graphic developers: Bettina K. Gier (Germany), Birgit Hassler (Germany), Soufiane Karmouche (Germany, Morocco), Seungmok Paik (Republic of Korea), Min-Gyu Seong (Republic of Korea)

Data providers: Leopold Haimberger (Austria), Lawrence Mudryk (Canada), Dirk Notz (Germany)

ACCEPTED VERSION
SUBJECT TO FINAL EDITING

References

Abellán, E., S. McGregor, and M.H. England, 2017: Analysis of the southward wind shift of ENSO in CMIP5 models. *Journal of Climate*, **30(7)**, 2415–2435, doi:10.1175/jcli-d-16-0326.1.

Abraham, J.P. et al., 2013: A review of global ocean temperature observations: Implications for ocean heat content estimates and climate change. *Reviews of Geophysics*, **51(3)**, 450–483, doi:10.1002/rog.20022.

Abram, N.J., E.W. Wolff, and M.A.J. Curran, 2013: A review of sea ice proxy information from polar ice cores. *Quaternary Science Reviews*, **79**, 168–183, doi:10.1016/j.quascirev.2013.01.011.

Abram, N.J. et al., 2014: Evolution of the Southern Annular Mode during the past millennium. *Nature Climate Change*, **4(7)**, 564–569, doi:10.1038/nclimate2235.

Abram, N.J. et al., 2016: Early onset of industrial-era warming across the oceans and continents. *Nature*, **536(7617)**, 411–418, doi:10.1038/nature19082.

Abram, N.J. et al., 2020: Coupling of Indo-Pacific climate variability over the last millennium. *Nature*, **579(7799)**, 385–392, doi:10.1038/s41586-020-2084-4.

Ackerley, D. et al., 2017: Evaluation of PMIP2 and PMIP3 simulations of mid-Holocene climate in the Indo-Pacific, Australasian and\\hack{\\newline} Southern Ocean regions. *Climate of the Past*, **13(11)**, 1661–1684, doi:10.5194/cp-13-1661-2017.

Adcroft, A. et al., 2019: The GFDL Global Ocean and Sea Ice Model OM4.0: Model Description and Simulation Features. *Journal of Advances in Modeling Earth Systems*, doi:10.1029/2019ms001726.

Adler, R.F., G. Gu, M. Sapiano, J.-J. Wang, and G.J. Huffman, 2017: Global precipitation: means, variations and trends during the satellite era (1979-2014). *Surv. Geophys.*, **38**, 679–699.

Adler, R.F. et al., 2003: The Version-2 Global Precipitation Climatology Project (GPCP) Monthly Precipitation Analysis (1979–Present). *Journal of Hydrometeorology*, **4(6)**, 1147–1167, doi:10.1175/1525-7541(2003)004<1147:tvgpcp>2.0.co;2.

Ait Brahim, Y. et al., 2018: Multi-decadal to centennial hydro-climate variability and linkage to solar forcing in the Western Mediterranean during the last 1000 years. *Scientific Reports*, **8(1)**, 17446, doi:10.1038/s41598-018-35498-x.

Alkama, R., L. Marchand, A. Ribes, and B. Decharme, 2013: Detection of global runoff changes: results from observations and CMIP5 experiments. *Hydrology and Earth System Sciences*, **17(7)**, 2967–2979, doi:10.5194/hess-17-2967-2013.

Allan, R.P., 2014: Dichotomy of drought and deluge. *Nat. Geosci.*, **7**, 700–701, doi:10.1038/ngeo2243.

Allen, M.R. and S.F.B. Tett, 1999a: Checking for model consistency in optimal fingerprinting. *Climate Dynamics*, **15(6)**, 419–434, doi:10.1007/s003820050291.

Allen, M.R. and S.F.B. Tett, 1999b: Checking for model consistency in optimal fingerprinting. *Climate Dynamics*, **15(6)**, 419–434, doi:10.1007/s003820050291.

Allen, M.R. and P.A. Stott, 2003: Estimating signal amplitudes in optimal fingerprinting, part I: theory. *Climate Dynamics*, **21(5)**, 477–491, doi:10.1007/s00382-003-0313-9.

Allen, M.R. et al., 2018: Framing and Context. In: *Global Warming of 1.5°C. An IPCC Special Report on the impacts of global warming of 1.5°C above pre-industrial levels and related global greenhouse gas emission pathways, in the context of strengthening the global response to the threat of climate change,* [Masson-Delmotte, V., P. Zhai, H.-O. Pörtner, D. Roberts, J. Skea, P.R. Shukla, A. Pirani, W. Moufouma-Okia, C. Péan, R. Pidcock, S. Connors, J.B.R. Matthews, Y. Chen, X. Zhou, M.I. Gomis, E. Lonnoy, T. Maycock, M. Tignor, and T. Waterfield (eds.)]. In Press, pp. 49–91.

Allen, R.J. and M. Kovilakam, 2017: The role of natural climate variability in recent tropical expansion. *Journal of Climate*, **30(16)**, 6329–6350, doi:10.1175/jcli-d-16-0735.1.

Allen, R.J., J.R. Norris, and M. Kovilakam, 2014: Influence of anthropogenic aerosols and the Pacific Decadal Oscillation on tropical belt width. *Nature Geoscience*, **7(4)**, 270–274, doi:10.1038/ngeo2091.

Amaya, D.J., M.J. DeFlorio, A.J. Miller, and S.-P. Xie, 2017: WES feedback and the Atlantic Meridional Mode: observations and CMIP5 comparisons. *Climate Dynamics*, **49(5)**, 1665–1679, doi:10.1007/s00382-016-3411-1.

Amaya, D.J., N. Siler, S.-P. Xie, and A.J. Miller, 2018: The interplay of internal and forced modes of Hadley Cell expansion: lessons from the global warming hiatus. *Climate Dynamics*, **51(1)**, 305–319, doi:10.1007/s00382-017-3921-5.

Amiri-Farahani, A., R.J. Allen, K.F. Li, and J.E. Chu, 2019: The Semidirect Effect of Combined Dust and Sea Salt Aerosols in a Multimodel Analysis. *Geophysical Research Letters*, **46(17–18)**, 10512–10521, doi:10.1029/2019gl084590.

Amiri-Farahani, A., R.J. Allen, K.F. Li, P. Nabat, and D.M. Westervelt, 2020: A La Niña-Like Climate Response to South African Biomass Burning Aerosol in CESM Simulations. *Journal of Geophysical Research: Atmospheres*, **125(6)**, doi:10.1029/2019jd031832.

Anchukaitis, K.J. et al., 2019: Coupled Modes of North Atlantic Ocean-Atmosphere Variability and the Onset of the Little Ice Age. *Geophysical Research Letters*, **46(21)**, 12417–12426, doi:10.1029/2019gl084350.

ACCEPTED VERSION SUBJECT TO FINAL EDITING

Andrews, M.B., J.R. Knight, and L.J. Gray, 2015: A simulated lagged response of the North Atlantic Oscillation to the solar cycle over the period 1960–2009. *Environmental Research Letters*, **10(5)**, 054022, doi:10.1088/1748-9326/10/5/054022.

Andrews, M.B. et al., 2020: Historical Simulations With HadGEM3-GC3.1 for CMIP6. *Journal of Advances in Modeling Earth Systems*, **12(6)**, doi:10.1029/2019ms001995.

Andrews, T. et al., 2018: Accounting for Changing Temperature Patterns Increases Historical Estimates of Climate Sensitivity. *Geophysical Research Letters*, **45(16)**, doi:10.1029/2018gl078887.

Andrews, T. et al., 2019: Forcings, feedbacks and climate sensitivity in HadGEM3-GC3. 1 and UKESM1. *Journal of Advances in Modeling Earth Systems*, **11**.

Annan, J.D. and J.C. Hargreaves, 2011: Understanding the CMIP3 Multimodel Ensemble. *Journal of Climate*, **24(16)**, 4529–4538, doi:10.1175/2011jcli3873.1.

Anstey, J.A. et al., 2013: Multi-model analysis of Northern Hemisphere winter blocking: Model biases and the role of resolution. *Journal of Geophysical Research: Atmospheres*, **118(10)**, 3956–3971, doi:10.1002/jgrd.50231.

Aquila, V. et al., 2016: Isolating the roles of different forcing agents in global stratospheric temperature changes using model integrations with incrementally added single forcings. *Journal of Geophysical Research*, **121(13)**, 8067–8082, doi:10.1002/2015jd023841.

Arora, V.K. et al., 2020: Carbon-concentration and carbon-climate feedbacks in CMIP6 models and their comparison to CMIP5 models. *Biogeosciences*, **17(16)**, 4173–4222, doi:10.5194/bg-17-4173-2020.

Ashok, K., S.K. Behera, S.A. Rao, H. Weng, and T. Yamagata, 2007: El Niño Modoki and its possible teleconnection. *Journal of Geophysical Research: Oceans*, **112(11)**, 1–27, doi:10.1029/2006jc003798.

Ault, T.R., J.E. Cole, and S. St. George, 2012: The amplitude of decadal to multidecadal variability in precipitation simulated by state-of-the-art climate models. *Geophysical Research Letters*, **39(21)**, n/a–n/a, doi:10.1029/2012gl053424.

Ayarzagüena, B. et al., 2018: No Robust Evidence of Future Changes in Major Stratospheric Sudden Warmings: A Multi-model Assessment from CCMI. *Atmospheric Chemistry and Physics Discussions*, **2018**, 1–17, doi:10.5194/acp-2018-296.

Ayash, T., S. Gong, and C.Q. Jia, 2008: Direct and Indirect Shortwave Radiative Effects of Sea Salt Aerosols. *Journal of Climate*, **21(13)**, 3207–3220, doi:10.1175/2007jcli2063.1.

Ayers, J.M. and M.S. Lozier, 2012: Unraveling dynamical controls on the North Pacific carbon sink. *Journal of Geophysical Research: Oceans*, **117(C1)**, doi:10.1029/2011jc007368.

Baccini, A. et al., 2017: Tropical forests are a net carbon source based on aboveground measurements of gain and loss. *Science*, **358(6360)**, doi:10.1126/science.aam5962.

Baker, H.S., T. Woollings, and C. Mbengue, 2017: Eddy-Driven Jet Sensitivity to Diabatic Heating in an Idealized GCM. *Journal of Climate*, **30(16)**, 6413–6431, doi:10.1175/jcli-d-16-0864.1.

Baker, H.S., T. Woollings, C.E. Forest, and M.R. Allen, 2019: The Linear Sensitivity of the North Atlantic Oscillation and Eddy-Driven Jet to SSTs. *Journal of Climate*, **32(19)**, 6491–6511, doi:10.1175/jcli-d-19-0038.1.

Balaguru, K., G.R. Foltz, L.R. Leung, and K.A. Emanuel, 2016: Global warming-induced upper-ocean freshening and the intensification of super typhoons. *Nature Communications*, **7**, doi:10.1038/ncomms13670.

Balaguru, K. et al., 2012: Ocean barrier layers' effect on tropical cyclone intensification. *Proceedings of the National Academy of Sciences of the United States of America*, **109(36)**, 14343–14347, doi:10.1073/pnas.1201364109.

Baldwin, M.P. et al., 2021: Sudden Stratospheric Warmings. *Reviews of Geophysics*, **59(1)**, e2020RG000708, doi:10.1029/2020rg000708.

Balmaseda, M.A., K.E. Trenberth, and E. Källén, 2013: Distinctive climate signals in reanalysis of global ocean heat content. *Geophysical Research Letters*, **40(9)**, 1754–1759, doi:10.1002/grl.50382.

Bamber, J.L., R.M. Westaway, B. Marzeion, and B. Wouters, 2018: The land ice contribution to sea level during the satellite era. *Environmental Research Letters*, **13(6)**, doi:10.1088/1748-9326/aac2f0.

Bamber, J.L., M. Oppenheimer, R.E. Kopp, W.P. Aspinall, and R.M. Cooke, 2019: Ice sheet contributions to future sea-level rise from structured expert judgment. *Proceedings of the National Academy of Sciences of the United States of America*, doi:10.1073/pnas.1817205116.

Banerjee, A., J.C. Fyfe, L.M. Polvani, D. Waugh, and K.-L. Chang, 2020: A pause in Southern Hemisphere circulation trends due to the Montreal Protocol. *Nature*, **579(7800)**, 544–548, doi:10.1038/s41586-020-2120-4.

Barichivich, J. et al., 2013: Large-scale variations in the vegetation growing season and annual cycle of atmospheric CO2 at high northern latitudes from 1950 to 2011. *Global Change Biology*, **19(10)**, 3167–3183, doi:10.1111/gcb.12283.

Barthel, A. et al., 2020: CMIP5 model selection for ISMIP6 ice sheet model forcing: Greenland and Antarctica. *Cryosphere*, doi:10.5194/tc-14-855-2020.

Bartlein, P.J., S.P. Harrison, and K. Izumi, 2017: Underlying causes of Eurasian midcontinental aridity in simulations of mid-Holocene climate. *Geophys. Res. Lett.*, **44(17)**, 9020–9028.

Bartlein, P.J. et al., 2011: Pollen-based continental climate reconstructions at 6 and 21 ka: A global synthesis. *Climate Dynamics*, **37(3)**, 775–802, doi:10.1007/s00382-010-0904-1.

Bastos, A. et al., 2019: Contrasting effects of CO2 fertilization, land-use change and warming on seasonal amplitude of

ACCEPTED VERSION SUBJECT TO FINAL EDITING

Northern Hemisphere CO2 exchange. *Atmospheric Chemistry and Physics*, **19(19)**, doi:10.5194/acp-19-12361-2019.

Batehup, R., S. McGregor, and A.J.E. Gallant, 2015: The influence of non-stationary teleconnections on palaeoclimate reconstructions of ENSO variance using a pseudoproxy framework. *Climate of the Past*, **11(12)**, 1733–1749, doi:10.5194/cp-11-1733-2015.

Bayr, T. et al., 2019: Error compensation of ENSO atmospheric feedbacks in climate models and its influence on simulated ENSO dynamics. *Climate Dynamics*, **53(1)**, 155–172, doi:10.1007/s00382-018-4575-7.

Beadling, R.L. et al., 2020: Representation of Southern Ocean Properties across Coupled Model Intercomparison Project Generations: CMIP3 to CMIP6. *Journal of Climate*, **33(15)**, 6555–6581, doi:10.1175/jcli-d-19-0970.1.

Becker, M., M. Karpytchev, and S. Lennartz-Sassinek, 2014: Long-term sea level trends: Natural or anthropogenic? *Geophysical Research Letters*, **41(15)**, 5571–5580, doi:10.1002/2014gl061027.

Bellenger, H., E. Guilyardi, J. Leloup, M. Lengaigne, and J. Vialard, 2014: ENSO representation in climate models: From CMIP3 to CMIP5. *Climate Dynamics*, **42(7–8)**, 1999–2018, doi:10.1007/s00382-013-1783-z.

Bellomo, K., L.N. Murphy, M.A. Cane, A.C. Clement, and L.M. Polvani, 2018: Historical forcings as main drivers of the Atlantic multidecadal variability in the CESM large ensemble. *Climate Dynamics*, **50(9)**, 3687–3698, doi:10.1007/s00382-017-3834-3.

Bellucci, A., A. Mariotti, and S. Gualdi, 2017: The Role of Forcings in the Twentieth-Century North Atlantic Multidecadal Variability: The 1940–75 North Atlantic Cooling Case Study. *Journal of Climate*, **30(18)**, 7317–7337, doi:10.1175/jcli-d-16-0301.1.

Bellucci, A. et al., 2021: Air-Sea interaction over the Gulf Stream in an ensemble of HighResMIP present climate simulations. *Climate Dynamics*, doi:10.1007/s00382-020-05573-z.

Berckmans, J., T. Woollings, M.-E. Demory, P.-L. Vidale, and M. Roberts, 2013: Atmospheric blocking in a high resolution climate model: influences of mean state, orography and eddy forcing. *Atmospheric Science Letters*, **14(1)**, 34–40, doi:10.1002/asl2.412.

Bernie, D.J., S.J. Woolnough, J.M. Slingo, and E. Guilyardi, 2005: Modeling diurnal and intraseasonal variability of the ocean mixed layer. *Journal of Climate*, **18(8)**, 1190–1202, doi:10.1175/jcli3319.1.

Bernie, D.J., E. Guilyardi, G. Madec, J.M. Slingo, and S.J. Woolnough, 2007: Impact of resolving the diurnal cycle in an ocean-atmosphere GCM. Part 1: A diurnally forced OGCM. *Climate Dynamics*, **29(6)**, 575–590, doi:10.1007/s00382-007-0249-6.

Bernie, D.J. et al., 2008: Impact of resolving the diurnal cycle in an ocean-atmosphere GCM. Part 2: A diurnally coupled CGCM. *Climate Dynamics*, **31(7–8)**, 909–925, doi:10.1007/s00382-008-0429-z.

Biasutti, M. et al., 2018: Global energetics and local physics as drivers of past, present and future monsoons. *Nature Geoscience*, **11(6)**, 392–400, doi:10.1038/s41561-018-0137-1.

Bilbao, R.A.F., J.M. Gregory, and N. Bouttes, 2015: Analysis of the regional pattern of sea level change due to ocean dynamics and density change for 1993–2099 in observations and CMIP5 AOGCMs. *Climate Dynamics*, **45(9)**, 2647–2666, doi:10.1007/s00382-015-2499-z.

Bilbao, R.A.F., J.M. Gregory, N. Bouttes, M.D. Palmer, and P. Stott, 2019: Attribution of ocean temperature change to anthropogenic and natural forcings using the temporal, vertical and geographical structure. *Climate Dynamics*, **53(9–10)**, 5389–5413, doi:10.1007/s00382-019-04910-1.

Bindoff, N.L. et al., 2007: Observations: Oceanic Climate Change and Sea Level. In: *Climate Change 2007: The Physical Science Basis. Contribution of Working Group I to the Fourth Assessment Report of the Intergovernmental Panel on Climate Change* [Solomon, S., D. Qin, M. Manning, Z. Chen, M. Marquis, K.B. Averyt, M. Tignor, and H.L. Miller (eds.)]. Cambridge University Press, Cambridge, United Kingdom and New York, NY, USA, pp. 385–432.

Bindoff, N.L. et al., 2013: Detection and attribution of climate change: From global to regional. In: *Climate Change 2013 the Physical Science Basis: Working Group I Contribution to the Fifth Assessment Report of the Intergovernmental Panel on Climate Change* [Stocker, T.F., D. Qin, G.-K. Plattner, M. Tignor, S.K. Allen, J. Boschung, A. Nauels, Y. Xia, V. Bex, and P.M. Midgley (eds.)]. Cambridge University Press, Cambridge University Press, Cambridge, United Kingdom and New York, pp. 867–952, doi:10.1017/cbo9781107415324.022.

Bindoff, N.L. et al., 2019: Changing Ocean, Marine Ecosystems, and Dependent Communities. In: *IPCC Special Report on the Ocean and Cryosphere in a Changing Climate* [Pörtner, H.-O., D.C. Roberts, V. Masson-Delmotte, P. Zhai, M. Tignor, E. Poloczanska, K. Mintenbeck, A. Alegría, M. Nicolai, A. Okem, J. Petzold, B. Rama, and N.M. Weyer (eds.)]. In Press, pp. 447–588.

Bintanja, R., G.J. van Oldenborgh, and C.A. Katsman, 2015: The effect of increased fresh water from Antarctic ice shelves on future trends in Antarctic sea ice. *Annals of Glaciology*, **56(69)**, 120–126, doi:10.3189/2015aog69a001.

Bintanja, R., G.J. van Oldenborgh, S.S. Drijfhout, B. Wouters, and C.A. Katsman, 2013: Important role for ocean warming and increased ice-shelf melt in Antarctic sea-ice expansion. *Nature Geoscience*, **6**, 376, doi:10.1038/ngeo1767.

Birkel, S.D., P.A. Mayewski, K.A. Maasch, A. Kurbatov, and B. Lyon, 2018: Evidence for a volcanic underpinning of

ACCEPTED VERSION SUBJECT TO FINAL EDITING

the Atlantic multidecadal oscillation. *npj Climate and Atmospheric Science*, **1(1)**, 24, doi:10.1038/s41612-018-0036-6.

Bittner, M., H. Schmidt, C. Timmreck, and F. Sienz, 2016: Using a large ensemble of simulations to assess the Northern Hemisphere stratospheric dynamical response to tropical volcanic eruptions and its uncertainty. *Geophysical Research Letters*, **43(17)**, 9324–9332, doi:10.1002/2016gl070587.

Bitz, C.M., 2008: Some Aspects of Uncertainty in Predicting Sea Ice Thinning. In: *Arctic Sea Ice Decline: Observations, Projections, Mechanisms, and Implications* [DeWeaver, E.T., C.M. Bitz, and L.-B. Tremblay (eds.)]. American Geophysical Union (AGU), Washington, DC, USA, pp. 63–76, doi:10.1029/180gm06.

Blau, M.T. and K.-J. Ha, 2020: The Indian Ocean Dipole and its Impact on East African Short Rains in Two CMIP5 Historical Scenarios With and Without Anthropogenic Influence. *Journal of Geophysical Research: Atmospheres*, **125(16)**, doi:10.1029/2020jd033121.

Blazquez, J. and S. Solman, 2017: Fronts and precipitation in CMIP5 models for the austral winter of the Southern Hemisphere. *Clim. Dyn.*, **50(7–8)**, 2705–2717, doi:10.1007/s00382-017-3765-z.

Bock, L. et al., 2020: Quantifying Progress Across Different CMIP Phases With the ESMValTool. *Journal of Geophysical Research: Atmospheres*, **125(21)**, doi:10.1029/2019jd032321.

Bodart, J.A. and R.J. Bingham, 2019: The Impact of the Extreme 2015–2016 El Niño on the Mass Balance of the Antarctic Ice Sheet. *Geophysical Research Letters*, doi:10.1029/2019gl084466.

Bodas-Salcedo, A. et al., 2016: Large Contribution of Supercooled Liquid Clouds to the Solar Radiation Budget of the Southern Ocean. *Journal of Climate*, **29(11)**, 4213–4228, doi:10.1175/jcli-d-15-0564.1.

Boisséson, E., M.A. Balmaseda, S. Abdalla, E. Källén, and P.A.E.M. Janssen, 2014: How robust is the recent strengthening of the Tropical Pacific trade winds? *Geophysical Research Letters*, **41(12)**, 4398–4405, doi:10.1002/2014gl060257.

Bonfils, C. and B.D. Santer, 2011: Investigating the possibility of a human component in various pacific decadal oscillation indices. *Climate Dynamics*, **37(7–8)**, 1457–1468, doi:10.1007/s00382-010-0920-1.

Bonfils, C.J.W. et al., 2020: Human influence on joint changes in temperature, rainfall and continental aridity. *Nature Climate Change*, **10(8)**, 726–731, doi:10.1038/s41558-020-0821-1.

Boo, K.-O. et al., 2015: Influence of aerosols in multidecadal SST variability simulations over the North Pacific. *Journal of Geophysical Research: Atmospheres*, **120(2)**, 517–531, doi:10.1002/2014jd021933.

Boos, W.R. and J. Hurley, 2012: Thermodynamic Bias in the Multimodel Mean Boreal Summer Monsoon. *Journal of Climate*, **26(7)**, 2279–2287, doi:10.1175/jcli-d-12-00493.1.

Booth, B.B.B., N.J. Dunstone, P.R. Halloran, T. Andrews, and N. Bellouin, 2012: Aerosols implicated as a prime driver of twentieth-century North Atlantic climate variability. *Nature*, **484(7393)**, 228–232, doi:10.1038/nature10946.

Bopp, L. et al., 2013: Multiple stressors of ocean ecosystems in the 21st century: projections with CMIP5 models. *Biogeosciences*, **10(10)**, 6225–6245, doi:10.5194/bg-10-6225-2013.

Boucher, O. et al., 2020a: Presentation and Evaluation of the IPSL-CM6A-LR Climate Model. *Journal of Advances in Modeling Earth Systems*, **12(7)**, doi:10.1029/2019ms002010.

Boucher, O. et al., 2020b: Presentation and Evaluation of the IPSL-CM6A-LR Climate Model. *Journal of Advances in Modeling Earth Systems*, **12(7)**, doi:10.1029/2019ms002010.

Bova, S., Y. Rosenthal, Z. Liu, S.P. Godad, and M. Yan, 2021: Seasonal origin of the thermal maxima at the Holocene and the last interglacial. *Nature*, **589(7843)**, 548–553, doi:10.1038/s41586-020-03155-x.

Bracegirdle, T.J., H. Lu, R. Eade, and T. Woollings, 2018: Do CMIP5 Models Reproduce Observed Low-Frequency North Atlantic Jet Variability? *Geophysical Research Letters*, **45(14)**, 7204–7212, doi:10.1029/2018gl078965.

Bracegirdle, T.J. et al., 2020a: Improvements in Circumpolar Southern Hemisphere Extratropical Atmospheric Circulation in CMIP6 Compared to CMIP5. *Earth and Space Science*, **7(6)**, e2019EA001065, doi:10.1029/2019ea001065.

Bracegirdle, T.J. et al., 2020b: Improvements in Circumpolar Southern Hemisphere Extratropical Atmospheric Circulation in CMIP6 Compared to CMIP5. *Earth and Space Science*, **7(6)**, e2019EA001065, doi:10.1029/2019ea001065.

Breeden, M.L. and G.A. McKinley, 2016: Climate impacts on multidecadal pCO2 variability in the North Atlantic: 1948–2009. *Biogeosciences*, **13(11)**, 3387–3396, doi:10.5194/bg-13-3387-2016.

Breitburg, D. et al., 2018: Declining oxygen in the global ocean and coastal waters.. *Science (New York, N.Y.)*, **359(6371)**, eaam7240, doi:10.1126/science.aam7240.

Brierley, C. and I. Wainer, 2018: Inter-annual variability in the tropical Atlantic from the Last Glacial Maximum into future climate projections simulated by CMIP5/PMIP3. *Climate of the Past*, **14(10)**, 1377–1390, doi:10.5194/cp-14-1377-2018.

Brierley, C.M. et al., 2020: Large-scale features and evaluation of the PMIP4-CMIP6 midHolocene simulations. *Climate of the Past*, **16(5)**, 1847–1872, doi:10.5194/cp-16-1847-2020.

Bronselaer, B. et al., 2018: Change in future climate due to Antarctic meltwater. *Nature*, **564(7734)**, 53–58, doi:10.1038/s41586-018-0712-z.

Brown, J.R. et al., 2020: Comparison of past and future simulations of ENSO in CMIP5/PMIP3 and CMIP6/PMIP4 models. *Climate of the Past*, **16(5)**, 1777–1805, doi:10.5194/cp-16-1777-2020.

ACCEPTED SUBJECT TO FINAL EDITING

Brown, P.T., W. Li, and S.-P. Xie, 2015: Regions of significant influence on unforced global mean surface air temperature variability in climate models. *Journal of Geophysical Research: Atmospheres*, **120(2)**, 480–494, doi:10.1002/2014jd022576.

Brown, P.T., W. Li, J.H. Jiang, and H. Su, 2016a: Spread in the magnitude of climate model interdecadal global temperature variability traced to disagreements over high-latitude oceans. *Geophysical Research Letters*, **43(24)**, 12,543–12,549, doi:10.1002/2016gl071442.

Brown, P.T., M.S. Lozier, R. Zhang, and W. Li, 2016b: The necessity of cloud feedback for a basin-scale Atlantic Multidecadal Oscillation. *Geophysical Research Letters*, **43(8)**, 3955–3963, doi:10.1002/2016gl068303.

Brown, P.T., Y. Ming, W. Li, and S.A. Hill, 2017: Change in the magnitude and mechanisms of global temperature variability with warming. *Nature Climate Change*, **7(10)**, doi:10.1038/nclimate3381.

Brutel-Vuilmet, C., M. Ménégoz, and G. Krinner, 2013: An analysis of present and future seasonal Northern Hemisphere land snow cover simulated by CMIP5 coupled climate models. *The Cryosphere*, **7(1)**, 67–80, doi:10.5194/tc-7-67-2013.

Bryden, H.L. et al., 2020: Reduction in ocean heat transport at 26°N since 2008 cools the eastern subpolar gyre of the North Atlantic Ocean. *Journal of Climate*, **33(5)**, 1677–1689, doi:10.1175/jcli-d-19-0323.1.

Buckley, M.W. and J. Marshall, 2016: Observations, inferences, and mechanisms of the Atlantic Meridional Overturning Circulation: A review. *Reviews of Geophysics*, **54(1)**, 5–63, doi:10.1002/2015rg000493.

Buermann, W. et al., 2018: Widespread seasonal compensation effects of spring warming on northern plant productivity. *Nature*, **562(7725)**, doi:10.1038/s41586-018-0555-7.

Büntgen, U. et al., 2020: Prominent role of volcanism in Common Era climate variability and human history. *Dendrochronologia*, **64**, 125757, doi:10.1016/j.dendro.2020.125757.

Butler, A.H. et al., 2015: Defining sudden stratospheric warmings. *Bulletin of the American Meteorological Society*, **96(11)**, 1913–1928.

Butler, A.H. et al., 2016: The Climate-system Historical Forecast Project: do stratosphere-resolving models make better seasonal climate predictions in boreal winter? *Quarterly Journal of the Royal Meteorological Society*, **142(696)**, 1413–1427, doi:10.1002/qj.2743.

Byrne, M.P. and P.A. O'Gorman, 2018: Trends in continental temperature and humidity directly linked to ocean warming. *Proceedings of the National Academy of Sciences*, **115**.

Cabré, A., I. Marinov, R. Bernardello, and D. Bianchi, 2015: Oxygen minimum zones in the tropical Pacific across CMIP5 models: mean state differences and climate change trends. *Biogeosciences*, **12(18)**, 5429–5454, doi:10.5194/bg-12-5429-2015.

Caesar, L., S. Rahmstorf, A. Robinson, G. Feulner, and V. Saba, 2018: Observed fingerprint of a weakening Atlantic Ocean overturning circulation. *Nature*, **556(7700)**, 191–196, doi:10.1038/s41586-018-0006-5.

Cai, W. et al., 2013: Projected response of the Indian Ocean Dipole to greenhouse warming. *Nature Geoscience*, **6**, 999, doi:10.1038/ngeo2009.

Cai, W. et al., 2014: Increased frequency of extreme Indian Ocean Dipole events due to greenhouse warming. *Nature*, **510(7504)**, 254–258, doi:10.1038/nature13327.

Cai, W. et al., 2019: Pantropical climate interactions. *Science*, **363(6430)**, eaav4236, doi:10.1126/science.aav4236.

Caldwell, P.M. et al., 2019: The DOE E3SM Coupled Model Version 1: Description and Results at High Resolution. *Journal of Advances in Modeling Earth Systems*, doi:10.1029/2019ms001870.

Calisto, M., D. Folini, M. Wild, and L. Bengtsson, 2014: Cloud radiative forcing intercomparison between fully coupled CMIP5 models and CERES satellite data. *Annales Geophysicae*, **32(7)**, 793–807, doi:10.5194/angeo-32-793-2014.

Calvo, N., L.M. Polvani, and S. Solomon, 2015: On the surface impact of Arctic stratospheric ozone extremes. *ENVIRONMENTAL RESEARCH LETTERS*, **10(9)**, doi:10.1088/1748-9326/10/9/094003.

Cane, M.A., A.C. Clement, L.N. Murphy, and K. Bellomo, 2017: Low-Pass Filtering, Heat Flux, and Atlantic Multidecadal Variability. *Journal of Climate*, **30(18)**, 7529–7553, doi:10.1175/jcli-d-16-0810.1.

Cao, J. et al., 2018: The NUIST Earth System Model~(NESM) version 3: description and preliminary evaluation. *Geoscientific Model Development*, **11(7)**, 2975–2993, doi:10.5194/gmd-11-2975-2018.

Capotondi, A. et al., 2015: Understanding ENSO Diversity. *Bulletin of the American Meteorological Society*, **96(6)**, 921–938, doi:10.1175/bams-d-13-00117.1.

Capron, E., A. Govin, R. Feng, B.L. Otto-Bliesner, and E.W. Wolff, 2017: Critical evaluation of climate syntheses to benchmark CMIP6/PMIP4 127 ka Last Interglacial simulations in the high-latitude regions. *Quaternary Science Reviews*, **168**, 137–150, doi:10.1016/j.quascirev.2017.04.019.

Caron, L.-P., L. Hermanson, and F.J. Doblas-Reyes, 2015: Multiannual forecasts of Atlantic U.S. tropical cyclone wind damage potential. *Geophysical Research Letters*, **42(7)**, 2417–2425, doi:10.1002/2015gl063303.

Cassou, C. et al., 2018: Decadal Climate Variability and Predictability: Challenges and Opportunities. *Bulletin of the American Meteorological Society*, **99(3)**, 479–490, doi:10.1175/bams-d-16-0286.1.

Cazenave, A. et al., 2018: Global sea-level budget 1993-present. *Earth System Science Data*, **10(3)**, 1551–1590, doi:10.5194/essd-10-1551-2018.

Cha, S.-C., J.-H. Moon, and Y.T. Song, 2018: A Recent Shift Toward an El Niño-Like Ocean State in the Tropical

ACCEPTED VERSION SUBJECT TO FINAL EDITING

Pacific and the Resumption of Ocean Warming. *Geophysical Research Letters*, **45(21)**, 11,885–11,894, doi:10.1029/2018gl080651.
Chai, J., F. Liu, J. Liu, and X. Shen, 2018: Enhanced Global Monsoon in Present Warm Period Due to Natural and Anthropogenic Forcings. *Atmosphere*, **9(4)**, 136, doi:10.3390/atmos9040136.
Chan, D. and Q. Wu, 2015: Attributing observed SST trends and subcontinental land warming to anthropogenic forcing during 1979-2005. *Journal of Climate*, **28(8)**, 3152–3170, doi:10.1175/jcli-d-14-00253.1.
Chang, E.K.M., C.-G. Ma, C. Zheng, and A.M.W. Yau, 2016: Observed and projected decrease in Northern Hemisphere extratropical cyclone activity in summer and its impacts on maximum temperature. *GEOPHYSICAL RESEARCH LETTERS*, **43(5)**, 2200–2208, doi:10.1002/2016gl068172.
Chang, P. et al., 2020: An Unprecedented Set of High-Resolution Earth System Simulations for Understanding Multiscale Interactions in Climate Variability and Change. *Journal of Advances in Modeling Earth Systems*, **12(12)**, e2020MS002298, doi:10.1029/2020ms002298.
Charlton-Perez, A.J. et al., 2013: On the lack of stratospheric dynamical variability in low-top versions of the CMIP5 models. *Journal of Geophysical Research: Atmospheres*, **118(6)**, 2494–2505, doi:10.1002/jgrd.50125.
Chen, C. et al., 2019: China and India lead in greening of the world through land-use management. *Nature Sustainability*, **2(2)**, doi:10.1038/s41893-019-0220-7.
Chen, H., E.K. Schneider, and Z. Wu, 2016: Mechanisms of internally generated decadal-to-multidecadal variability of SST in the Atlantic Ocean in a coupled GCM. *Climate Dynamics*, **46(5–6)**, 1517–1546, doi:10.1007/s00382-015-2660-8.
Chen, R., I.R. Simpson, C. Deser, and A.B.I.N. Wang, 2020: Model biases in the simulation of the springtime north pacific ENSO teleconnection. *Journal of Climate*, **33(23)**, 9985–10002, doi:10.1175/jcli-d-19-1004.1.
Chen, X. and K.-K. Tung, 2014: Varying planetary heat sink led to global-warming slowdown and acceleration. *Science*, **345(6199)**, 897–903, doi:10.1126/science.1254937.
Cheng, L., J. Abraham, Z. Hausfather, and K.E. Trenberth, 2019: How fast are the oceans warming? *Science*, **363(6423)**, 128–129, doi:10.1126/science.aav7619.
Cheng, L., K.E. Trenberth, M.D. Palmer, J. Zhu, and J.P. Abraham, 2016: Observed and simulated full-depth ocean heat-content changes for 1970-2005. *Ocean Science*, **12(4)**, 925–935, doi:10.5194/os-12-925-2016.
Cheng, L. et al., 2017: Improved estimates of ocean heat content from 1960 to 2015. *Science Advances*, **3(3)**, e1601545, doi:10.1126/sciadv.1601545.
Cheng, L. et al., 2020: Improved estimates of changes in upper ocean salinity and the hydrological cycle. *Journal of Climate*, **33(23)**, 10357–10381, doi:10.1175/jcli-d-20-0366.1.
Cheng, W., J.C.H. Chiang, and D. Zhang, 2013: Atlantic meridional overturning circulation (AMOC) in CMIP5 Models: RCP and historical simulations. *Journal of Climate*, **26(18)**, 7187–7197, doi:10.1175/jcli-d-12-00496.1.
Chenoli, S.N., M.Y.A. Mazuki, J. Turner, and A. Abu Samah, 2017: Historical and projected changes in the Southern Hemisphere Sub-tropical Jet during winter from the CMIP5 models. *CLIMATE DYNAMICS*, **48(1–2)**, 661–681, doi:10.1007/s00382-016-3102-y.
Cheung, A.H. et al., 2017: Comparison of low-frequency internal climate variability in CMIP5 models and observations. *Journal of Climate*, **30(12)**, 4763–4776, doi:10.1175/jcli-d-16-0712.1.
Chikamoto, Y., T. Mochizuki, A. Timmermann, M. Kimoto, and M. Watanabe, 2016: Potential tropical Atlantic impacts on Pacific decadal climate trends. *Geophysical Research Letters*, **43(13)**, 7143–7151, doi:10.1002/2016gl069544.
Chiodo, G., J. Oehrlein, L.M. Polvani, J.C. Fyfe, and A.K. Smith, 2019: Insignificant influence of the 11-year solar cycle on the North Atlantic Oscillation. *Nature Geoscience*, **12(2)**, 94–99, doi:10.1038/s41561-018-0293-3.
Choi, J., S.-W. Son, and R.J. Park, 2019: Aerosol versus greenhouse gas impacts on Southern Hemisphere general circulation changes. *Climate Dynamics*, **52(7–8)**, 4127–4142, doi:10.1007/s00382-018-4370-5.
Chou, C. et al., 2013: Increase in the range between wet and dry season precipitation. *Nature Geoscience*, **6(4)**, 263–267, doi:10.1038/ngeo1744.
Chu, J.-E. et al., 2014: Future change of the Indian Ocean basin-wide and dipole modes in the CMIP5. *Climate Dynamics*, **43(1)**, 535–551, doi:10.1007/s00382-013-2002-7.
Chung, E.-S., B.J. Soden, B.J. Sohn, and L. Shi, 2014: Upper-tropospheric moistening in response to anthropogenic warming. *Proc. Natl. Acad. Sci. U. S. A*, doi:10.1073/pnas.1409659111.
Chung, E.-S. et al., 2019: Reconciling opposing Walker circulation trends in observations and model projections. *Nature Climate Change*, **9(5)**, 405–412, doi:10.1038/s41558-019-0446-4.
Church, J.A., D. Monselesan, J.M. Gregory, and B. Marzeion, 2013a: Evaluating the ability of process based models to project sea-level change. *Environmental Research Letters*, **8(1)**, 014051, doi:10.1088/1748-9326/8/1/014051.
Church, J.A. et al., 2013b: Sea Level Change. In: *Climate Change 2013: The Physical Science Basis. Contribution of Working Group I to the Fifth Assessment Report of the Intergovernmental Panel on Climate Change* [Stocker, T.F., D. Qin, G.-K. Plattner, M. Tignor, S.K. Allen, J. Boschung, A. Nauels, Y. Xia, V. Bex, and P.M. Midgley (eds.)]. Cambridge University Press, Cambridge, United Kingdom and New York, NY, USA, pp. 1137–1216, doi:10.1017/cbo9781107415324.026.

ACCEPTED VERSION SUBJECT TO FINAL EDITING

Chylek, P., C. Folland, J.D. Klett, and M.K. Dubey, 2020: CMIP5 Climate Models Overestimate Cooling by Volcanic Aerosols. *Geophysical Research Letters*, **47(3)**, doi:10.1029/2020gl087047.
Ciais, P. et al., 2019: Five decades of northern land carbon uptake revealed by the interhemispheric CO2 gradient. *Nature*, **568(7751)**, doi:10.1038/s41586-019-1078-6.
Cleator, S.F., S.P. Harrison, N.K. Nichols, I.C. Prentice, and I. Roulstone, 2020: A new multi-variable benchmark for Last Glacial Maximum climate simulations. *Climate of the Past*, **16**, 699–712, doi:10.5194/cp-2019-55.
Clement, A. et al., 2015: The Atlantic Multidecadal Oscillation without a role for ocean circulation. *Science*, **350(6258)**, 320–324, doi:10.1126/science.aab3980.
Clement, A.C., R. Seager, M.A. Cane, and S.E. Zebiak, 1996: An Ocean Dynamical Thermostat. *Journal of Climate*, **9(9)**, 2190–2196, doi:10.1175/1520-0442(1996)009<2190:aodt>2.0.co;2.
Coats, S. and K.B. Karnauskas, 2017: Are Simulated and Observed Twentieth Century Tropical Pacific Sea Surface Temperature Trends Significant Relative to Internal Variability? *Geophysical Research Letters*, **44(19)**, 9928–9937, doi:10.1002/2017gl074622.
Coats, S. et al., 2016: Internal ocean-atmosphere variability drives megadroughts in Western North America. *Geophysical Research Letters*, **43(18)**, 9886–9894, doi:10.1002/2016gl070105.
Cocco, V. et al., 2013: Oxygen and indicators of stress for marine life in multi-model global warming projections. *Biogeosciences*, **10(3)**, 1849–1868, doi:10.5194/bg-10-1849-2013.
Collins, M. et al., 2010: The impact of global warming on the tropical Pacific Ocean and El Niño. *Nature Geoscience*, **3**, 391.
Collins, W.J. et al., 2017: AerChemMIP: quantifying the effects of chemistry and aerosols in CMIP6. *Geoscientific Model Development*, **10(2)**, 585–607, doi:10.5194/gmd-10-585-2017.
Comyn-Platt, E. et al., 2018: Carbon budgets for 1.5 and 2 °C targets lowered by natural wetland and permafrost feedbacks. *Nature Geoscience*, **11(8)**, 568–573, doi:10.1038/s41561-018-0174-9.
Cook, B.I., K.J. Anchukaitis, R. Touchan, D.M. Meko, and E.R. Cook, 2016a: Spatiotemporal drought variability in the mediterranean over the last 900 years. *Journal of Geophysical Research*, doi:10.1002/2015jd023929.
Cook, B.I. et al., 2016b: North American megadroughts in the Common Era: reconstructions and simulations. *Wiley Interdisciplinary Reviews: Climate Change*, **7(3)**, 411–432, doi:10.1002/wcc.394.
Cook, E.R., C.A. Woodhouse, C.M. Eakin, D.H. Meko, and D.W. Stahle, 2004: Long-term aridity changes in the western United States. *Science*, doi:10.1126/science.1102586.
Cook, E.R. et al., 2010: Asian monsoon failure and megadrought during the last millennium. *Science*, doi:10.1126/science.1185188.
Cook, E.R. et al., 2015: Old World megadroughts and pluvials during the Common Era. *Science Advances*, doi:10.1126/sciadv.1500561.
Cook, E.R. et al., 2019: A Euro-Mediterranean tree-ring reconstruction of the winter NAO index since 910 C.E.. *Climate Dynamics*, **53(3–4)**, 1567–1580, doi:10.1007/s00382-019-04696-2.
Corvec, S. and C.G. Fletcher, 2017: Changes to the tropical circulation in the mid-Pliocene and their implications for future climate. *Climate of the Past*, **13(2)**, 135–147, doi:10.5194/cp-13-135-2017.
Covey, C. et al., 2016: Metrics for the Diurnal Cycle of Precipitation: Toward Routine Benchmarks for Climate Models. *Journal of Climate*, **29(12)**, 4461–4471, doi:10.1175/jcli-d-15-0664.1.
Covey, C. et al., 2018: High-Frequency Intermittency in Observed and Model-Simulated Precipitation. *Geophysical Research Letters*, **45(22)**, doi:10.1029/2018gl078926.
Cowan, T., W. Cai, B. Ng, and M. England, 2015: The Response of the Indian Ocean Dipole Asymmetry to Anthropogenic Aerosols and Greenhouse Gases. *Journal of Climate*, **28(7)**, 2564–2583, doi:10.1175/jcli-d-14-00661.1.
Cowtan, K. and R.G. Way, 2014: Coverage bias in the HadCRUT4 temperature series and its impact on recent temperature trends. *Quarterly Journal of the Royal Meteorological Society*, **140(683)**, 1935–1944, doi:10.1002/qj.2297.
Crowley, T.J. and M.B. Unterman, 2013: Technical details concerning development of a 1200 yr proxy index for global volcanism. *Earth System Science Data*, **5(1)**, 187–197, doi:10.5194/essd-5-187-2013.
Crueger, T. et al., 2018: ICON-A, The Atmosphere Component of the ICON Earth System Model: II. Model Evaluation. *Journal of Advances in Modeling Earth Systems*, doi:10.1029/2017ms001233.
D'Agostino, R., J. Bader, S. Bordoni, D. Ferreira, and J. Jungclaus, 2019: Northern Hemisphere Monsoon Response to Mid-Holocene Orbital Forcing and Greenhouse Gas-Induced Global Warming. *Geophysical Research Letters*, **46(3)**, 1591–1601, doi:10.1029/2018gl081589.
D'Agostino, R. et al., 2020: Contrasting Southern Hemisphere Monsoon Response: MidHolocene Orbital Forcing versus Future Greenhouse Gas–Induced Global Warming. *Journal of Climate*, **33(22)**, 9595–9613, doi:10.1175/jcli-d-19-0672.1.
D'Andrea, F. et al., 1998: Northern Hemisphere atmospheric blocking as simulated by 15 atmospheric general circulation models in the period 1979--1988. *Climate Dynamics*, **14(6)**, 385–407, doi:10.1007/s003820050230.
Dai, A. and C.E. Bloecker, 2019: Impacts of internal variability on temperature and precipitation trends in large ensemble simulations by two climate models. *Climate Dynamics*, **52(1–2)**, 289–306, doi:10.1007/s00382-018-

ACCEPTED VERSION SUBJECT TO FINAL EDITING

4132-4.
Dai, A., J.C. Fyfe, S.P. Xie, and X. Dai, 2015: Decadal modulation of global surface temperature by internal climate variability. *Nature Climate Change*, **5(6)**, doi:10.1038/nclimate2605.
Danabasoglu, G. et al., 2014: North Atlantic Simulations in Coordinated Ocean-ice Reference Experiments phase 2 (CORE-II). Part 1: Mean States. *Ocean Modelling*, **73**, 76–107, doi:10.1016/j.ocemod.2013.10.005.
Danabasoglu, G. et al., 2016: North Atlantic simulations in Coordinated Ocean-ice Reference Experiments phase II (CORE-II). Part II: Inter-annual to decadal variability. *Ocean Modelling*, **97**, 65–90, doi:10.1016/j.ocemod.2015.11.007.
Dangendorf, S. et al., 2015: Detecting anthropogenic footprints in sea level rise. *Nature Communications*, **6(1)**, 7849, doi:10.1038/ncomms8849.
Dansgaard, W. et al., 1993: Evidence for general instability of past climate from a 250-kyr ice-core record. *Nature*, **364(6434)**, 218–220, doi:10.1038/364218a0.
Dätwyler, C. et al., 2018: Teleconnection stationarity, variability and trends of the Southern Annular Mode (SAM) during the last millennium. *Climate Dynamics*, **51(5–6)**, 2321–2339, doi:10.1007/s00382-017-4015-0.
Davies-Barnard, T. et al., 2020: Nitrogen cycling in CMIP6 land surface models: progress and limitations. *Biogeosciences*, **17(20)**, 5129–5148, doi:10.5194/bg-17-5129-2020.
Davini, P. and C. Cagnazzo, 2014: On the misinterpretation of the North Atlantic Oscillation in CMIP5 models. *Climate Dynamics*, **43(5)**, 1497–1511, doi:10.1007/s00382-013-1970-y.
Davini, P. and F. D'Andrea, 2016a: Northern Hemisphere Atmospheric Blocking Representation in Global Climate Models: Twenty Years of Improvements? *JOURNAL OF CLIMATE*, **29(24)**, 8823–8840, doi:10.1175/jcli-d-16-0242.1.
Davini, P. and F. D'Andrea, 2016b: Northern Hemisphere Atmospheric Blocking Representation in Global Climate Models: Twenty Years of Improvements? *JOURNAL OF CLIMATE*, **29(24)**, 8823–8840, doi:10.1175/jcli-d-16-0242.1.
Davini, P. and F. D'Andrea, 2020: From CMIP3 to CMIP6: Northern hemisphere atmospheric blocking simulation in present and future climate. *Journal of Climate*, **33(23)**, 10021–10038, doi:10.1175/jcli-d-19-0862.1.
Davini, P., J. Hardenberg, and S. Corti, 2015: Tropical origin for the impacts of the Atlantic Multidecadal Variability on the Euro-Atlantic climate. *Environmental Research Letters*, **10(9)**, 94010, doi:10.1088/1748-9326/10/9/094010.
Davini, P., S. Corti, F. D'Andrea, G. Rivière, and J. von Hardenberg, 2017: Improved Winter European Atmospheric Blocking Frequencies in High-Resolution Global Climate Simulations. *Journal of Advances in Modeling Earth Systems*, **9(7)**, 2615–2634, doi:10.1002/2017ms001082.
Davis, N. and T. Birner, 2017: On the Discrepancies in Tropical Belt Expansion between Reanalyses and Climate Models and among Tropical Belt Width Metrics. *Journal of Climate*, **30(4)**, 1211–1231, doi:10.1175/jcli-d-16-0371.1.
Davy, R. and S. Outten, 2020: The Arctic Surface Climate in CMIP6: Status and Developments since CMIP5. *Journal of Climate*, **33(18)**, 8047–8068, doi:10.1175/jcli-d-19-0990.1.
DelSole, T., L. Trenary, X. Yan, and M.K. Tippett, 2019: Confidence intervals in optimal fingerprinting. *Climate Dynamics*, **52(7–8)**, 4111–4126, doi:10.1007/s00382-018-4356-3.
Delworth, T.L. and K.W. Dixon, 2006: Have anthropogenic aerosols delayed a greenhouse gas-induced weakening of the North Atlantic thermohaline circulation? *Geophysical Research Letters*, **33(2)**, doi:10.1029/2005gl024980.
Delworth, T.L., F. Zeng, A. Rosati, G.A. Vecchi, and A.T. Wittenberg, 2015: A Link between the Hiatus in Global Warming and North American Drought. *Journal of Climate*, **28(9)**, 3834–3845, doi:10.1175/jcli-d-14-00616.1.
Delworth, T.L. et al., 2017: The Central Role of Ocean Dynamics in Connecting the North Atlantic Oscillation to the Extratropical Component of the Atlantic Multidecadal Oscillation. *Journal of Climate*, **30(10)**, 3789–3805, doi:10.1175/jcli-d-16-0358.1.
Dennison, F.W., A. McDonald, and O. Morgenstern, 2016: The influence of ozone forcing on blocking in the Southern Hemisphere. *Journal of Geophysical Research: Atmospheres*, **121(24)**, 14,358–14,371, doi:10.1002/2016jd025033.
Deppenmeier, A.-L., R.J. Haarsma, and W. Hazeleger, 2016: The Bjerknes feedback in the tropical Atlantic in CMIP5 models. *Climate Dynamics*, **47(7–8)**, 2691–2707, doi:10.1007/s00382-016-2992-z.
Dergiades, T., R.K. Kaufmann, and T. Panagiotidis, 2016: Long-run changes in radiative forcing and surface temperature: The effect of human activity over the last five centuries. *Journal of Environmental Economics and Management*, **76**, doi:10.1016/j.jeem.2015.11.005.
Deser, C., A.S. Phillips, and M.A. Alexander, 2010: Twentieth century tropical sea surface temperature trends revisited. *Geophysical Research Letters*, **37(10)**, n/a–n/a, doi:10.1029/2010gl043321.
Deser, C., R. Guo, and F. Lehner, 2017a: The relative contributions of tropical Pacific sea surface temperatures and atmospheric internal variability to the recent global warming hiatus. *Geophysical Research Letters*, **44(15)**, 7945–7954, doi:10.1002/2017gl074273.
Deser, C., J.W. Hurrell, and A.S. Phillips, 2017b: The role of the North Atlantic Oscillation in European climate projections. *Climate Dynamics*, **49(9)**, 3141–3157, doi:10.1007/s00382-016-3502-z.

ACCEPTED VERSION SUBJECT TO FINAL EDITING

Deutsch, C. et al., 2014: Oceanography. Centennial changes in North Pacific anoxia linked to tropical trade winds.. *Science (New York, N.Y.)*, **345(6197)**, 665–8, doi:10.1126/science.1252332.
Dhame, S., A.S. Taschetto, A. Santoso, and K.J. Meissner, 2020: Indian Ocean warming modulates global atmospheric circulation trends. *Climate Dynamics*, **55(7–8)**, 2053–2073, doi:10.1007/s00382-020-05369-1.
DiNezio, P.N. and J.E. Tierney, 2013a: The effect of sea level on glacial Indo-Pacific climate. *Nature Geoscience*, **6(6)**, 485–491, doi:10.1038/ngeo1823.
DiNezio, P.N. and J.E. Tierney, 2013b: The effect of sea level on glacial Indo-Pacific climate. *Nature Geoscience*, **6(6)**, 485–491, doi:10.1038/ngeo1823.
DiNezio, P.N., G.A. Vecchi, and A.C. Clement, 2013: Detectability of Changes in the Walker Circulation in Response to Global Warming. *Journal of Climate*, **26(12)**, 4038–4048, doi:10.1175/jcli-d-12-00531.1.
DiNezio, P.N. et al., 2011: The response of the Walker circulation to Last Glacial Maximum forcing: Implications for detection in proxies. *Paleoceanography*, **26(3)**, doi:10.1029/2010pa002083.
DiNezio, P.N. et al., 2018: Glacial changes in tropical climate amplified by the Indian Ocean. *Science Advances*, **4(12)**, eaat9658, doi:10.1126/sciadv.aat9658.
Ding, H., R.J. Greatbatch, M. Latif, and W. Park, 2015: The impact of sea surface temperature bias on equatorial Atlantic interannual variability in partially coupled model experiments. *Geophysical Research Letters*, **42(13)**, 5540–5546, doi:10.1002/2015gl064799.
Ding, Q. et al., 2017a: Influence of high-latitude atmospheric circulation changes on summertime Arctic sea ice. *Nature Climate Change*, **7(4)**, 289–295, doi:10.1038/nclimate3241.
Ding, Q. et al., 2017b: Influence of high-latitude atmospheric circulation changes on summertime Arctic sea ice. *Nature Climate Change*, **7(4)**, 289–295, doi:10.1038/nclimate3241.
Ding, Q. et al., 2019: Fingerprints of internal drivers of Arctic sea ice loss in observations and model simulations. *Nature Geoscience*, **12(1)**, 28–33, doi:10.1038/s41561-018-0256-8.
Dippe, T., R.J. Greatbatch, and H. Ding, 2018: On the relationship between Atlantic Niño variability and ocean dynamics. *Climate Dynamics*, **51(1–2)**, 597–612, doi:10.1007/s00382-017-3943-z.
Dittus, A.J. et al., 2020: Sensitivity of Historical Climate Simulations to Uncertain Aerosol Forcing. *Geophysical Research Letters*, **47(13)**, doi:10.1029/2019gl085806.
Dlugokencky, E.J. and P.P. Tans, 2020: Trends in Atmospheric Carbon Dioxide. National Oceanic and Atmospheric Administration (NOAA) Global Monitoring Laboratory (GML), Boulder, CO, USA. Retrieved from: www.esrl.noaa.gov/gmd/ccgg/trends/gl_data.html.
Dlugokencky, E.J., J.W. Mund, A.M. Crotwell, M.J. Crotwell, and K.W. Thoning, 2020: Atmospheric Carbon Dioxide Dry Air Mole Fractions from the NOAA GML Carbon Cycle Cooperative Global Air Sampling Network, 1968-2019. National Oceanic and Atmospheric Administration (NOAA) Global Monitoring Laboratory (GML), Boulder, CO, USA. Retrieved from: https://doi.org/10.15138/wkgj-f215.
Docquier, D. et al., 2019: Impact of model resolution on Arctic sea ice and North Atlantic Ocean heat transport. *Climate Dynamics*, **53(7)**, 4989–5017, doi:10.1007/s00382-019-04840-y.
Domeisen, D.I., 2019: Estimating the Frequency of Sudden Stratospheric Warming Events From Surface Observations of the North Atlantic Oscillation. *Journal of Geophysical Research: Atmospheres*, **124(6)**, 3180–3194, doi:10.1029/2018jd030077.
Domeisen, D.I.V., C.I. Garfinkel, and A.H. Butler, 2019: The Teleconnection of El Niño Southern Oscillation to the Stratosphere. *Reviews of Geophysics*, **57(1)**, 5–47, doi:10.1029/2018rg000596.
Domingues, C.M. et al., 2008: Improved estimates of upper-ocean warming and multi-decadal sea-level rise. *Nature*, **453(7198)**, 1090–1093, doi:10.1038/nature07080.
Dong, L. and T. Zhou, 2014: The Indian Ocean Sea Surface Temperature Warming Simulated by CMIP5 Models during the Twentieth Century: Competing Forcing Roles of GHGs and Anthropogenic Aerosols. *Journal of Climate*, **27(9)**, 3348–3362, doi:10.1175/jcli-d-13-00396.1.
Dong, L. and M.J. McPhaden, 2017: Why has the relationship between Indian and Pacific Ocean decadal variability changed in recent decades? *Journal of Climate*, **30(6)**, 1971–1983, doi:10.1175/jcli-d-16-0313.1.
Dong, L., T. Zhou, and X. Chen, 2014a: Changes of Pacific decadal variability in the twentieth century driven by internal variability, greenhouse gases, and aerosols. *Geophysical Research Letters*, **41(23)**, 8570–8577, doi:10.1002/2014gl062269.
Dong, L., T. Zhou, and B. Wu, 2014b: Indian Ocean warming during 1958-2004 simulated by a climate system model and its mechanism. *Climate Dynamics*, **42(1–2)**, 203–217, doi:10.1007/s00382-013-1722-z.
Dong, L. et al., 2016: The Footprint of the Inter-decadal Pacific Oscillation in Indian Ocean Sea Surface Temperatures. *Scientific Reports*, **6**, 21251, doi:10.1038/srep21251.
Dong, S. et al., 2020: Attribution of Extreme Precipitation with Updated Observations and CMIP6 Simulations. *Journal of Climate*, **34(3)**, 871–881, doi:10.1175/jcli-d-19-1017.1.
Douville, H. and M. Plazzotta, 2017: Midlatitude summer drying: and underestimated threat in CMIP5 models? *Geophys. Res. Lett.*, **44**, doi:10.1002/2017gl075353.
Douville, H., A. Ribes, and S. Tyteca, 2019: Breakdown of NAO reproducibility into internal versus externally-forced components: a two-tier pilot study. *Climate Dynamics*, **52(1–2)**, 29–48, doi:10.1007/s00382-018-4141-3.

SUBJECT TO FINAL EDITING
ACCEPTED VERSION

Douville, H. et al., 2020: Drivers of the enhanced decline of land near-surface relative humidity to abrupt 4xCO2 in CNRM-CM6-1. *Climate Dynamics*, **55**, doi:10.1007/s00382-020-05351-x.
Dow, W.J., A.C. Maycock, M. Lofverstrom, and C.J. Smith, 2020: The Effect of Anthropogenic Aerosols on the Aleutian Low. *Journal of Climate*, **34(5)**, 1725–1741, doi:10.1175/jcli-d-20-0423.1.
Downes, S.M. and A.M.C. Hogg, 2013: Southern Ocean Circulation and Eddy Compensation in CMIP5 Models. *Journal of Climate*, **26(18)**, 7198–7220, doi:10.1175/jcli-d-12-00504.1.
Downes, S.M., P. Spence, and A.M. Hogg, 2018: Understanding variability of the Southern Ocean overturning circulation in CORE-II models. *Ocean Modelling*, **123**, 98–109, doi:10.1016/j.ocemod.2018.01.005.
Drews, A. and R.J. Greatbatch, 2016: Atlantic Multidecadal Variability in a model with an improved North Atlantic Current. *Geophysical Research Letters*, **43(15)**, 8199–8206, doi:10.1002/2016gl069815.
Drijfhout, S., 2018: The relation between natural variations in ocean heat uptake and global mean surface temperature anomalies in CMIP5. *Scientific Reports*, **8(1)**, 7402, doi:10.1038/s41598-018-25342-7.
Du, Y., S.-P. Xie, G. Huang, and K. Hu, 2009: Role of Air–Sea Interaction in the Long Persistence of El Niño–Induced North Indian Ocean Warming. *Journal of Climate*, **22(8)**, 2023–2038, doi:10.1175/2008jcli2590.1.
Dunn, R.J.H., K.M. Willett, A. Ciavarella, and P.A. Stott, 2017: Comparison of land surface humidity between observations and CMIP5 models. *Earth System Dynamics*, **8(3)**, 719–747, doi:10.5194/esd-8-719-2017.
Dunne, J.P. et al., 2020: The GFDL Earth System Model Version 4.1 (GFDL-ESM 4.1): Overall Coupled Model Description and Simulation Characteristics. *Journal of Advances in Modeling Earth Systems*, **12(11)**, doi:10.1029/2019ms002015.
Dunn-Sigouin, E. and S.-W. Son, 2013: Northern Hemisphere blocking frequency and duration in the CMIP5 models. *JOURNAL OF GEOPHYSICAL RESEARCH-ATMOSPHERES*, **118(3)**, 1179–1188, doi:10.1002/jgrd.50143.
Durack, P. et al., 2018: Ocean Warming: From the Surface to the Deep in Observations and Models. *Oceanography*, **31(2)**, 41–51, doi:10.5670/oceanog.2018.227.
Durack, P.J., 2015: Ocean salinity and the global water cycle. *Oceanography*, **28(1)**, 20–31, doi:10.5670/oceanog.2015.03.
Durack, P.J. and S.E. Wijffels, 2010: Fifty-Year trends in global ocean salinities and their relationship to broad-scale warming. *Journal of Climate*, **23(16)**, 4342–4362, doi:10.1175/2010jcli3377.1.
Durack, P.J., S.E. Wijffels, and R.J. Matear, 2012: Ocean salinities reveal strong global water cycle intensification during 1950 to 2000. *Science*, **336(6080)**, 455–458, doi:10.1126/science.1212222.
Durack, P.J., S.E. Wijffels, and T.P. Boyer, 2013: Long-term salinity changes and implications for the global water cycle. *International Geophysics*, **103**, 727–757, doi:10.1016/b978-0-12-391851-2.00028-3.
Durack, P.J., S.E. Wijffels, and P.J. Gleckler, 2014a: Long-term sea-level change revisited: The role of salinity. *Environmental Research Letters*, **9(11)**, doi:10.1088/1748-9326/9/11/114017.
Durack, P.J., P.J. Gleckler, F.W. Landerer, and K.E. Taylor, 2014b: Quantifying underestimates of long-term upper-ocean warming. *Nature Climate Change*, **4(11)**, 999–1005, doi:10.1038/nclimate2389.
Dwyer, J.G., M. Biasutti, and A.H. Sobel, 2014: The effect of greenhouse gas-induced changes in SST on the annual cycle of zonal mea tropical precipitation. *J. Climate*, **27**, 4544–4565.
Emile-Geay, J. et al., 2016: Links between tropical Pacific seasonal, interannual and orbital variability during the Holocene. *Nature Geoscience*, **9(2)**, 168–173, doi:10.1038/ngeo2608.
England, M., A. Jahn, and L. Polvani, 2019: Nonuniform Contribution of Internal Variability to Recent Arctic Sea Ice Loss. *Journal of Climate*, **32(13)**, 4039–4053, doi:10.1175/jcli-d-18-0864.1.
England, M.H., J.B. Kajtar, and N. Maher, 2015: Robust warming projections despite the recent hiatus. *Nature Climate Change*, **5**, 394, doi:10.1038/nclimate2575.
England, M.H. et al., 2014: Recent intensification of wind-driven circulation in the Pacific and the ongoing warming hiatus. *Nature Climate Change*, **4(3)**, 222–227, doi:10.1038/nclimate2106.
Erb, K.H. et al., 2018: Unexpectedly large impact of forest management and grazing on global vegetation biomass. *Nature*, **553(7686)**, doi:10.1038/nature25138.
Estrada, F., P. Perron, and B. Martínez-López, 2013: Statistically derived contributions of diverse human influences to twentieth-century temperature changes. *Nature Geoscience*, **6(12)**, doi:10.1038/ngeo1999.
Eyring, V. et al., 2013: Long-term ozone changes and associated climate impacts in CMIP5 simulations. *Journal of Geophysical Research Atmospheres*, **118(10)**, 5029–5060, doi:10.1002/jgrd.50316.
Eyring, V. et al., 2016a: Overview of the Coupled Model Intercomparison Project Phase 6 (CMIP6) experimental design and organization. *Geoscientific Model Development*, **9(5)**, 1937–1958, doi:10.5194/gmd-9-1937-2016.
Eyring, V. et al., 2016b: Towards improved and more routine Earth system model evaluation in CMIP. *Earth System Dynamics*, **7(4)**, 813–830, doi:10.5194/esd-7-813-2016.
Eyring, V. et al., 2019: Taking climate model evaluation to the next level. *Nature Climate Change*, **9(2)**, 102–110, doi:10.1038/s41558-018-0355-y.
Eyring, V. et al., 2020: Earth System Model Evaluation Tool (ESMValTool) v2.0 -- an extended set of large-scale diagnostics for quasi-operational and comprehensive evaluation of Earth system models in CMIP. *Geoscientific Model Development*, **13(7)**, 3383–3438, doi:10.5194/gmd-13-3383-2020.
Ezer, T., L.P. Atkinson, W.B. Corlett, and J.L. Blanco, 2013: Gulf Stream's induced sea level rise and variability along

ACCEPTED VERSION SUBJECT TO FINAL EDITING

the U.S. mid-Atlantic coast. *Journal of Geophysical Research: Oceans*, **118(2)**, 685–697, doi:10.1002/jgrc.20091.
Fabiano, F. et al., 2020: Euro-Atlantic weather Regimes in the PRIMAVERA coupled climate simulations: impact of resolution and mean state biases on model performance. *Climate Dynamics*, **54**, 5031–5048, doi:10.1007/s00382-020-05271-w.
Fasullo, J.T. and R.S. Nerem, 2018: Altimeter-era emergence of the patterns of forced sea-level rise in climate models and implications for the future. *Proceedings of the National Academy of Sciences*, 201813233, doi:10.1073/pnas.1813233115.
Fasullo, J.T., A.S. Phillips, and C. Deser, 2020: Evaluation of Leading Modes of Climate Variability in the CMIP Archives. *Journal of Climate*, **33(13)**, 5527–5545, doi:10.1175/jcli-d-19-1024.1.
Fathrio, I., A. Manda, S. Iizuka, Y.M. Kodama, and S. Ishida, 2017a: Evaluation of CMIP5 models on sea surface salinity in the Indian Ocean. *IOP Conference Series: Earth and Environmental Science*, **54(1)**, 012039, doi:10.1088/1755-1315/54/1/012039.
Fathrio, I. et al., 2017b: Assessment of western Indian Ocean SST bias of CMIP5 models. *Journal of Geophysical Research: Oceans*, **122(4)**, 3123–3140, doi:10.1002/2016jc012443.
Fay, A.R. and G.A. McKinley, 2013: Global trends in surface ocean pCO2 from in situ data. *Global Biogeochemical Cycles*, **27(2)**, 541–557, doi:10.1002/gbc.20051.
Fay, A.R., G.A. McKinley, and N.S. Lovenduski, 2014: Southern Ocean carbon trends: Sensitivity to methods. *Geophysical Research Letters*, **41(19)**, 6833–6840, doi:10.1002/2014gl061324.
Feldstein, S.B. and C. Franzke, 2006: Are the North Atlantic Oscillation and the Northern Annular Mode Distinguishable? *Journal of the Atmospheric Sciences*, **63(11)**, 2915–2930, doi:10.1175/jas3798.1.
Ferreira, D., J. Marshall, C.M. Bitz, S. Solomon, and A. Plumb, 2014: Antarctic Ocean and Sea Ice Response to Ozone Depletion: A Two-Time-Scale Problem. *Journal of Climate*, **28(3)**, 1206–1226, doi:10.1175/jcli-d-14-00313.1.
Fettweis, X. et al., 2013: Brief communication "Important role of the mid-tropospheric atmospheric circulation in the recent surface melt increase over the Greenland ice sheet". *The Cryosphere*, **7(1)**, 241–248, doi:10.5194/tc-7-241-2013.
Fettweis, X. et al., 2020: GrSMBMIP: Intercomparison of the modelled 1980–2012 surface mass balance over the Greenland Ice sheet. *The Cryosphere*, doi:10.5194/tc-2019-321.
Fiedler, S. et al., 2020: Simulated tropical precipitation assessed across three major phases of the coupled model intercomparison project (CMIP). *Monthly Weather Review*, **148(9)**, 3653–3680, doi:10.1175/mwr-d-19-0404.1.
Flannaghan, T.J. et al., 2014: Tropical temperature trends in atmospheric general circulation model simulations and the impact of uncertainties in observed SSTs. *Journal of Geophysical Research*, **119(23)**, doi:10.1002/2014jd022365.
Flato, G. et al., 2013: Evaluation of climate models. In: *Climate Change 2013: The Physical Science Basis. Contribution of Working Group I to the Fifth Assessment Report of the Intergovernmental Panel on Climate Change* [Stocker, T.F., D. Qin, G.-K. Plattner, M. Tignor, S.K. Allen, J. Boschung, A. Nauels, Y. Xia, V. Bex, and P.M. Midgley (eds.)]. Cambridge University Press, Cambridge, United Kingdom and New York, NY, USA, pp. 741–866, doi:10.1017/cbo9781107415324.020.
Fleischer, K. et al., 2019: Amazon forest response to CO2 fertilization dependent on plant phosphorus acquisition. *Nature Geoscience*, doi:10.1038/s41561-019-0404-9.
Fleming, L.E. and K.J. Anchukaitis, 2016: North Pacific decadal variability in the CMIP5 last millennium simulations. *Climate Dynamics*, **47(12)**, 3783–3801, doi:10.1007/s00382-016-3041-7.
Fletcher, C.G. and C. Cassou, 2015: The dynamical influence of separate teleconnections from the Pacific and Indian oceans on the northern annular mode. *Journal of Climate*, **28(20)**, 7985–8002, doi:10.1175/jcli-d-14-00839.1.
Flynn, C.M. and T. Mauritsen, 2020: On the climate sensitivity and historical warming evolution in recent coupled model ensembles. *Atmospheric Chemistry and Physics*, **20(13)**, doi:10.5194/acp-20-7829-2020.
Fogt, R.L. et al., 2017: A twentieth century perspective on summer Antarctic pressure change and variability and contributions from tropical SSTs and ozone depletion. *Geophysical Research Letters*, **44(19)**, 9918–9927, doi:10.1002/2017gl075079.
Folland, C.K., J.A. Renwick, M.J. Salinger, and A.B. Mullan, 2002: Relative influences of the Interdecadal Pacific Oscillation and ENSO on the South Pacific Convergence Zone. *Geophysical Research Letters*, **29(13)**, 2–5, doi:10.1029/2001gl014201.
Folland, C.K., O. Boucher, A. Colman, and D.E. Parker, 2018: Causes of irregularities in trends of global mean surface temperature since the late 19th century. *Science Advances*, **4(6)**, doi:10.1126/sciadv.aao5297.
Foltz, G.R. et al., 2019: The Tropical Atlantic Observing System. *Frontiers in Marine Science*, **6**, doi:10.3389/fmars.2019.00206.
Forkel, M. et al., 2016: Enhanced seasonal CO2 exchange caused by amplified plant productivity in northern ecosystems. *Science*, **351(6274)**, 696–699, doi:10.1126/science.aac4971.
Frajka-Williams, E., C. Beaulieu, and A. Duchez, 2017: Emerging negative Atlantic Multidecadal Oscillation index in spite of warm subtropics. *Scientific Reports*, **7(1)**, 11224, doi:10.1038/s41598-017-11046-x.

ACCEPTED VERSION SUBJECT TO FINAL EDITING

Frauen, C. and D. Dommenget, 2010: El Niño and La Niña amplitude asymmetry caused by atmospheric feedbacks. *Geophysical Research Letters*, **37(18)**, doi:10.1029/2010gl044444.
Freund, M.B. et al., 2019: Higher frequency of Central Pacific El Niño events in recent decades relative to past centuries. *Nature Geoscience*, **12(6)**, 450–455, doi:10.1038/s41561-019-0353-3.
Friedlingstein, P. et al., 2019: Global carbon budget 2019. *Earth System Science Data*, **11(4)**, doi:10.5194/essd-11-1783-2019.
Friedman, A.R., G. Reverdin, M. Khodri, and G. Gastineau, 2017: A new record of Atlantic sea surface salinity from 1896 to 2013 reveals the signatures of climate variability and long-term trends. *Geophysical Research Letters*, **44(4)**, 1866–1876, doi:10.1002/2017gl072582.
Friedman, A.R. et al., 2020: Forced and unforced decadal behavior of the interhemispheric SST contrast during the instrumental period (1881–2012): Contextualizing the late 1960s–early 1970s shift. *Journal of Climate*, **33(9)**, doi:10.1175/jcli-d-19-0102.1.
Fučkar, N.S. et al., 2016: Record Low Northern Hemisphere Sea Ice Extent in March 2015. *Bulletin of the American Meteorological Society*, **97(12)**, S136–S140, doi:10.1175/bams-d-16-0153.1.
Fyke, J.G., M. Vizcaíno, and W.H. Lipscomb, 2014: The pattern of anthropogenic signal emergence in Greenland Ice Sheet surfacemass balance. *Geophysical Research Letters*, doi:10.1002/2014gl060735.
Gagné, M.-, N.P. Gillett, and J.C. Fyfe, 2015: Observed and simulated changes in Antarctic sea ice extent over the past 50 years. *Geophysical Research Letters*, **42(1)**, 90–95, doi:10.1002/2014gl062231.
Gagné, M.-, M.C. Kirchmeier-Young, N.P. Gillett, and J.C. Fyfe, 2017a: Arctic sea ice response to the eruptions of Agung, El Chichón, and Pinatubo. *Journal of Geophysical Research: Atmospheres*, **122(15)**, 8071–8078, doi:10.1002/2017jd027038.
Gagné, M.-, J.C. Fyfe, N.P. Gillett, I. Polyakov, and G.M. Flato, 2017b: Aerosol-driven increase in Arctic sea ice over the middle of the twentieth century. *Geophysical Research Letters*, **44(14)**, 7338–7346, doi:10.1002/2016gl071941.
Găinuşă-Bogdan, A., F. Hourdin, A.K. Traore, and P. Braconnot, 2018: Omens of coupled model biases in the CMIP5 AMIP simulations. *Climate Dynamics*, **51(7–8)**, doi:10.1007/s00382-017-4057-3.
Gan, Z. et al., 2019: The Key Role of Atlantic Multidecadal Oscillation in Minimum Temperature Over North America During Global Warming Slowdown. *Earth and Space Science*, **6(3)**, 387–397, doi:10.1029/2018ea000443.
Gao, C., A. Robock, and C. Ammann, 2008: Volcanic forcing of climate over the past 1500 years: An improved ice core-based index for climate models. *Journal of Geophysical Research: Atmospheres*, **113(D23)**, doi:10.1029/2008jd010239.
Garreaud, R.D. et al., 2017: The 2010–2015 megadrought in central Chile: impacts on regional hydroclimate and vegetation. *Hydrology and Earth System Sciences*, **21(12)**, 6307–6327, doi:10.5194/hess-21-6307-2017.
Garry, F.K. et al., 2019: Model-Derived Uncertainties in Deep Ocean Temperature Trends Between 1990 and 2010. *Journal of Geophysical Research: Oceans*, **124(2)**, 1155–1169, doi:10.1029/2018jc014225.
Gastineau, G. and C. Frankignoul, 2015: Influence of the North Atlantic SST variability on the atmospheric circulation during the twentieth century. *Journal of Climate*, **28(4)**, 1396–1416, doi:10.1175/jcli-d-14-00424.1.
Gastineau, G., A.R. Friedman, M. Khodri, and J. Vialard, 2019: Global ocean heat content redistribution during the 1998–2012 Interdecadal Pacific Oscillation negative phase. *Climate Dynamics*, **53(1–2)**, 1187–1208, doi:10.1007/s00382-018-4387-9.
Gebbie, G. and P. Huybers, 2019: The Little Ice Age and 20th-century deep Pacific cooling.. *Science (New York, N.Y.)*, **363(6422)**, 70–74, doi:10.1126/science.aar8413.
Gedney, N. et al., 2014: Detection of solar dimming and brightening effects on Northern Hemisphere river flow. *Nature Geoscience*, **7(11)**, 796-800, doi:10.1038/ngeo2263.
Geen, R., S. Bordoni, D.S. Battisti, and K. Hui, 2020: Monsoons, ITCZs and the Concept of the Global Monsoon. *Reviews of Geophysics*, doi:10.1029/2020rg000700.
Gent, P.R., 2016: Effects of Southern Hemisphere Wind Changes on the Meridional Overturning Circulation in Ocean Models. *Annual Review of Marine Science*, **8(1)**, 79–94, doi:10.1146/annurev-marine-122414-033929.
Gerber, E.P. and S.-W. Son, 2014a: Quantifying the Summertime Response of the Austral Jet Stream and Hadley Cell to Stratospheric Ozone and Greenhouse Gases. *JOURNAL OF CLIMATE*, **27(14)**, 5538–5559, doi:10.1175/jcli-d-13-00539.1.
Gerber, E.P. and S.-W. Son, 2014b: Quantifying the Summertime Response of the Austral Jet Stream and Hadley Cell to Stratospheric Ozone and Greenhouse Gases. *JOURNAL OF CLIMATE*, **27(14)**, 5538–5559, doi:10.1175/jcli-d-13-00539.1.
Gettelman, A., D.T. Shindell, and J.F. Lamarque, 2015: Impact of aerosol radiative effects on 2000–2010 surface temperatures. *Climate Dynamics*, **45(7–8)**, 2165–2179, doi:10.1007/s00382-014-2464-2.
Gettelman, A. et al., 2019: The Whole Atmosphere Community Climate Model Version 6 (WACCM6). *Journal of Geophysical Research: Atmospheres*, **124(23)**, 12380–12403, doi:10.1029/2019jd030943.
Giannini, A. and A. Kaplan, 2019: The role of aerosols and greenhouse gases in Sahel drought and recovery. *Climatic Change*, **152(3–4)**, 449–466, doi:10.1007/s10584-018-2341-9.
Gierz, P., M. Werner, and G. Lohmann, 2017: Simulating climate and stable water isotopes during the Last Interglacial

ACCEPTED VERSION SUBJECT TO FINAL EDITING

using a coupled climate-isotope model. *Journal of Advances in Modeling Earth Systems*, **9(5)**, 2027–2045, doi:10.1002/2017ms001056.
Gillett, N.P. and J.C. Fyfe, 2013: Annular mode changes in the CMIP5 simulations. *Geophysical Research Letters*, **40(6)**, 1189–1193, doi:10.1002/grl.50249.
Gillett, N.P., M.R. Allen, and K.D. Williams, 2003a: Modelling the atmospheric response to doubled CO2 and depleted stratospheric ozone using a stratosphere-resolving coupled GCM. *Quarterly Journal of the Royal Meteorological Society*, **129(589)**, 947–966, doi:10.1256/qj.02.102.
Gillett, N.P., J.C. Fyfe, and D.E. Parker, 2013: Attribution of observed sea level pressure trends to greenhouse gas, aerosol, and ozone changes. *Geophysical Research Letters*, **40(10)**, 2302–2306, doi:10.1002/grl.50500.
Gillett, N.P., F.W. Zwiers, A.J. Weaver, and P.A. Stott, 2003b: Detection of human influence on sea-level pressure. *Nature*, **422(6929)**, 292–294, doi:10.1038/nature01487.
Gillett, N.P. et al., 2016a: The Detection and Attribution Model Intercomparison Project (DAMIP v1.0) contribution to CMIP6. *Geoscientific Model Development*, **9(10)**, 3685–3697, doi:10.5194/gmd-9-3685-2016.
Gillett, N.P. et al., 2016b: The Detection and Attribution Model Intercomparison Project (DAMIP v1.0) contribution to CMIP6. *Geoscientific Model Development*, **9(10)**, 3685–3697, doi:10.5194/gmd-9-3685-2016.
Gillett, N.P. et al., 2021: Constraining human contributions to observed warming since the pre-industrial period. *Nature Climate Change*, doi:10.1038/s41558-020-00965-9.
Gleckler, P.J., K.E. Taylor, and C. Doutriaux, 2008: Performance metrics for climate models. *Journal of Geophysical Research*, **113(D6)**, D06104, doi:10.1029/2007jd008972.
Gleckler, P.J., P.J. Durack, R.J. Stouffer, G.C. Johnson, and C.E. Forest, 2016: Industrial-era global ocean heat uptake doubles in recent decades. *Nature Climate Change*, **6(4)**, 394–398, doi:10.1038/nclimate2915.
Gleckler, P.J. et al., 2012: Human-induced global ocean warming on multidecadal timescales. *Nature Climate Change*, **2(7)**, 524–529, doi:10.1038/nclimate1553.
Golaz, J.C. et al., 2019: The DOE E3SM Coupled Model Version 1: Overview and Evaluation at Standard Resolution. *Journal of Advances in Modeling Earth Systems*, doi:10.1029/2018ms001603.
Golledge, N.R. et al., 2019: Global environmental consequences of twenty-first-century ice-sheet melt. *Nature*, **566(7742)**, 65–72, doi:10.1038/s41586-019-0889-9.
Gómez-Navarro, J.J. and E. Zorita, 2013: Atmospheric annular modes in simulations over the past millennium: No long-term response to external forcing. *Geophysical Research Letters*, **40(12)**, 3232–3236, doi:10.1002/grl.50628.
Gong, D. and S. Wang, 1999: Definition of Antarctic Oscillation index. *Geophysical Research Letters*, **26(4)**, 459–462, doi:10.1029/1999gl900003.
Gong, H., L. Wang, W. Chen, X. Chen, and D. Nath, 2017: Biases of the wintertime Arctic Oscillation in CMIP5 models. *Environmental Research Letters*, **12(1)**, 14001, doi:10.1088/1748-9326/12/1/014001.
Gonzalez, P.L.M., L.M. Polvani, R. Seager, and G.J.P. Correa, 2014: Stratospheric ozone depletion: a key driver of recent precipitation trends in Southeastern South America. *Clim. Dyn.*, **42(7–8)**, 1775–1792, doi:10.1007/s00382-013-1777-x.
Good, P. et al., 2021: High sensitivity of tropical precipitation to local sea surface temperature. *Nature*, **589(7842)**, 408–414, doi:10.1038/s41586-020-2887-3.
Good, S.A., M.J. Martin, and N.A. Rayner, 2013: EN4: Quality controlled ocean temperature and salinity profiles and monthly objective analyses with uncertainty estimates. *Journal of Geophysical Research: Oceans*, **118(12)**, 6704–6716, doi:10.1002/2013jc009067.
Goosse, H., O. Arzel, C.M. Bitz, A. de Montety, and M. Vancoppenolle, 2009: Increased variability of the Arctic summer ice extent in a warmer climate. *Geophysical Research Letters*, **36(23)**, L23702, doi:10.1029/2009gl040546.
Gopika, S. et al., 2020: Aliasing of the Indian Ocean externally-forced warming spatial pattern by internal climate variability. *Climate Dynamics*, **54(1–2)**, 1093–1111, doi:10.1007/s00382-019-05049-9.
Gorte, T., J.T.M. Lenaerts, and B. Medley, 2020: Scoring Antarctic surface mass balance in climate models to refine future projections. *Cryosphere*, doi:10.5194/tc-14-4719-2020.
Govin, A., V. Varma, and M. Prange, 2014: Astronomically forced variations in western African rainfall (21°N-20°S) during the Last Interglacial period. *Geophysical Research Letters*, **41(6)**, 2117–2125, doi:10.1002/2013gl058999.
Goyal, R., A. Gupta, M. Jucker, and M.H. England, 2021: Historical and projected changes in the Southern Hemisphere surface westerlies. *Geophysical Research Letters*, **48(n/a)**, e2020GL090849, doi:10.1029/2020gl090849.
Graven, H.D. et al., 2013a: Enhanced Seasonal Exchange of CO2 by Northern Ecosystems Since 1960. *Science*, doi:10.1126/science.1239207.
Graven, H.D. et al., 2013b: Enhanced Seasonal Exchange of CO2 by Northern Ecosystems Since 1960. *Science*, doi:10.1126/science.1239207.
Gray, J.M. et al., 2014: Direct human influence on atmospheric CO2 seasonality from increased cropland productivity. *Nature*, **515**, 398.
Gray, L.J., T.J. Woollings, M. Andrews, and J. Knight, 2016: Eleven-year solar cycle signal in the NAO and

ACCEPTED VERSION SUBJECT TO FINAL EDITING

Atlantic/European blocking. *Quarterly Journal of the Royal Meteorological Society*, **142(698)**, 1890–1903, doi:10.1002/qj.2782.
Gregory, J.M. and T. Andrews, 2016: Variation in climate sensitivity and feedback parameters during the historical period. *Geophysical Research Letters*, **43(8)**, doi:10.1002/2016gl068406.
Gregory, J.M. et al., 2002: Recent and future changes in Arctic sea ice simulated by the HadCM3 AOGCM. *Geophysical Research Letters*, **29(24)**, 24–28, doi:10.1029/2001gl014575.
Greve, P. et al., 2014: Global assessment of trends in wetting and drying over land. *Nat. Geosci.*, **7**, 716–721, doi:10.1038/ngeo2247.
Griffies, S.M. et al., 2015: Impacts on ocean heat from transient mesoscale eddies in a hierarchy of climate models. *Journal of Climate*, **28(3)**, 952–977, doi:10.1175/jcli-d-14-00353.1.
Griffin, D. and K.J. Anchukaitis, 2014: How unusual is the 2012-2014 California drought? *Geophysical Research Letters*, doi:10.1002/2014gl062433.
Grise, K.M. and S.M. Davis, 2020: Hadley cell expansion in CMIP6 models. *Atmospheric Chemistry and Physics*, **20(9)**, 5249–5268, doi:10.5194/acp-20-5249-2020.
Grise, K.M., S.M. Davis, P.W. Staten, and O. Adam, 2018: Regional and Seasonal Characteristics of the Recent Expansion of the Tropics. *Journal of Climate*, **31(17)**, 6839–6856, doi:10.1175/jcli-d-18-0060.1.
Grise, K.M. et al., 2019: Recent Tropical Expansion: Natural Variability or Forced Response? *Journal of Climate*, **32(5)**, 1551–1571, doi:10.1175/jcli-d-18-0444.1.
Grist, J.P., S.A. Josey, J.D. Zika, D.G. Evans, and N. Skliris, 2016: Assessing recent air-sea freshwater flux changes using a surface temperature-salinity space framework. *Journal of Geophysical Research: Oceans*, **121(12)**, 8787–8806, doi:10.1002/2016jc012091.
Grist, J.P. et al., 2018: Increasing Atlantic Ocean Heat Transport in the Latest Generation Coupled Ocean-Atmosphere Models: The Role of Air-Sea Interaction. *Journal of Geophysical Research: Oceans*, **123(11)**, 8624–8637, doi:10.1029/2018jc014387.
Grodsky, S.A. et al., 2012: Haline hurricane wake in the Amazon/Orinoco plume: AQUARIUS/SACD and SMOS observations. *Geophysical Research Letters*, **39(20)**, 2012GL053335, doi:10.1029/2012gl053335.
Grose, M.R. et al., 2020: Insights From CMIP6 for Australia's Future Climate. *Earth's Future*, **8(5)**, doi:10.1029/2019ef001469.
Gu, G. and R.F. Adler, 2018: Precipitation Intensity Changes in the Tropics from Observations and Models. *J. Climate*, **31**, 4775–4790, doi:10.1175/jcli-d-17-0550.1.
Guan, X., J. Huang, R. Guo, and P. Lin, 2015: The role of dynamically induced variability in the recent warming trend slowdown over the Northern Hemisphere. *Scientific Reports*, **5(1)**, 12669, doi:10.1038/srep12669.
Guarino, M.-V. et al., 2020: Sea-ice-free Arctic during the Last Interglacial supports fast future loss. *Nature Climate Change*, **10(10)**, 928–932, doi:10.1038/s41558-020-0865-2.
Gudmundsson, L., S.I. Seneviratne, and X. Zhang, 2017: Anthropogenic climate change detected in European renewable freshwater resources. *Nature Climate Change*, **7**, 813, doi:10.1038/nclimate3416.
Gudmundsson, L. et al., 2021: Globally observed trends in mean and extreme river flow attributed to climate change. *Science*, **371(6534)**, 1159–1162, doi:10.1126/science.aba3996.
Guemas, V., F.J. Doblas-Reyes, I. Andreu-Burillo, and M. Asif, 2013: Retrospective prediction of the global warming slowdown in the past decade. *Nature Climate Change*, **3**, 649, doi:10.1038/nclimate1863.
Guilyardi, E. et al., 2012: A first look at ENSO in CMIP5. *Clivar Exchanges*, **17(58)**, 29–32.
Guo, L., A.G. Turner, and E.J. Highwood, 2015: Impacts of 20th century aerosol emissions on the South Asian monsoon in the CMIP5 models. *Atmospheric Chemistry and Physics*, **15(11)**, 6367–6378, doi:10.5194/acp-15-6367-2015.
Gutjahr, O. et al., 2019: Max Planck Institute Earth System Model (MPI-ESM1.2) for the High-Resolution Model Intercomparison Project (HighResMIP). *Geoscientific Model Development*, **12(7)**, 3241–3281, doi:10.5194/gmd-12-3241-2019.
Haarsma, R.J. et al., 2016: High Resolution Model Intercomparison Project (HighResMIP~v1.0) for CMIP6. *Geoscientific Model Development*, **9(11)**, 4185–4208, doi:10.5194/gmd-9-4185-2016.
Haimberger, L., C. Tavolato, and S. Sperka, 2012: Homogenization of the global radiosonde temperature dataset through combined comparison with reanalysis background series and neighboring stations. *Journal of Climate*, **25(23)**, 8108–8131, doi:10.1175/jcli-d-11-00668.1.
Halder, S., A. Parekh, J.S. Chowdary, C. Gnanaseelan, and A. Kulkarni, 2020: Assessment of CMIP6 models' skill for tropical Indian Ocean sea surface temperature variability. *International Journal of Climatology*, joc.6975, doi:10.1002/joc.6975.
Hallberg, R., 2013: Using a resolution function to regulate parameterizations of oceanic mesoscale eddy effects. *Ocean Modelling*, **72**, 92–103, doi:10.1016/j.ocemod.2013.08.007.
Hallberg, R. and A. Gnanadesikan, 2006: The role of eddies in determining the structure and response of the wind-driven Southern Hemisphere overturning: Results from the Modeling Eddies in the Southern Ocean (MESO) project. *Journal of Physical Oceanography*, **36(12)**, 2232–2252.
Han, W. et al., 2014a: Intensification of decadal and multi-decadal sea level variability in the western tropical Pacific

ACCEPTED VERSION SUBJECT TO FINAL EDITING

during recent decades. *Climate Dynamics*, **43(5)**, 1357–1379, doi:10.1007/s00382-013-1951-1.
Han, W. et al., 2014b: Indian ocean decadal variability: A review. *Bulletin of the American Meteorological Society*, **95(11)**, 1679–1703, doi:10.1175/bams-d-13-00028.1.
Han, W. et al., 2014c: Indian ocean decadal variability: A review. *Bulletin of the American Meteorological Society*, **95(11)**, 1679–1703, doi:10.1175/bams-d-13-00028.1.
Hanna, E., X. Fettweis, and R.J. Hall, 2018: Brief communication: Recent changes in summer Greenland blocking captured by none of the CMIP5 models. *The Cryosphere*, **12(10)**, 3287–3292, doi:10.5194/tc-12-3287-2018.
Hanna, E., T.E. Cropper, P.D. Jones, A.A. Scaife, and R. Allan, 2015: Recent seasonal asymmetric changes in the NAO (a marked summer decline and increased winter variability) and associated changes in the AO and Greenland Blocking Index. *International Journal of Climatology*, **35(9)**, 2540–2554, doi:10.1002/joc.4157.
Hannart, A., 2016: Integrated optimal fingerprinting: Method description and illustration. *Journal of Climate*, **29(6)**, 1977–1998, doi:10.1175/jcli-d-14-00124.1.
Hannart, A. and P. Naveau, 2018: Probabilities of causation of climate changes. *Journal of Climate*, **31(14)**, 5507–5524, doi:10.1175/jcli-d-17-0304.1.
Hannart, A., A. Ribes, and P. Naveau, 2014: Optimal fingerprinting under multiple sources of uncertainty. *Geophysical Research Letters*, **41(4)**, 1261–1268, doi:10.1002/2013gl058653.
Hardiman, S.C. et al., 2020: Predictability of European winter 2019/20: Indian Ocean dipole impacts on the NAO. *Atmospheric Science Letters*, **21(12)**, doi:10.1002/asl.1005.
Hargreaves, J.C. and J. Annan, 2014: Can we trust climate models? *WIREs Climate Change*, **5**, 435–440, doi:10.1002/wcc.288.
Harlaß, J., M. Latif, and W. Park, 2018: Alleviating tropical Atlantic sector biases in the Kiel climate model by enhancing horizontal and vertical atmosphere model resolution: climatology and interannual variability. *Climate Dynamics*, **50(7–8)**, 2605–2635, doi:10.1007/s00382-017-3760-4.
Harper, A.B. et al., 2018: Land-use emissions play a critical role in land-based mitigation for Paris climate targets. *Nature Communications*, doi:10.1038/s41467-018-05340-z.
Harris, I., P.D. Jones, T.J. Osborn, and D.H. Lister, 2014: Updated high-resolution grids of monthly climatic observations – the CRU TS3.10 Dataset. *International Journal of Climatology*, **34(3)**, 623–642, doi:10.1002/joc.3711.
Harrison, D.E. and N.K. Larkin, 1998: El Nino-Southern Oscillation sea surface temperature and wind anomalies, 1946-1993. *Reviews of Geophysics*, **36(3)**, 353–399, doi:10.1029/98rg00715.
Harrison, S.P., P.J. Bartlein, and I.C. Prentice, 2016: What have we learnt from palaeoclimate simulations? *Journal of Quaternary Science*, **31(4)**, 363–385, doi:10.1002/jqs.2842.
Harrison, S.P. et al., 2014: Climate model benchmarking with glacial and mid-Holocene climates. *Climate Dynamics*, **43(3–4)**, 671–688, doi:10.1007/s00382-013-1922-6.
Harrison, S.P. et al., 2015: Evaluation of CMIP5 palaeo-simulations to improve climate projections. *Nature Climate Change*, **5(8)**, 735–743, doi:10.1038/nclimate2649.
Harvey, B.J., P. Cook, L.C. Shaffrey, and R. Schiemann, 2020: The Response of the Northern Hemisphere Storm Tracks and Jet Streams to Climate Change in the CMIP3, CMIP5, and CMIP6 Climate Models. *Journal of Geophysical Research: Atmospheres*, **125(23)**, e2020JD032701, doi:10.1029/2020jd032701.
Hasselmann, K., 1997: Multi-pattern fingerprint method for detection and attribution of climate change. *Climate Dynamics*, **13(9)**, 601–611, doi:10.1007/s003820050185.
Hausfather, Z. et al., 2017: Assessing recent warming using instrumentally homogeneous sea surface temperature records. *Science Advances*, **3(1)**, doi:10.1126/sciadv.1601207.
Haustein, K. et al., 2017: A real-time Global Warming Index. *Scientific Reports*, **7(1)**, doi:10.1038/s41598-017-14828-5.
Haustein, K. et al., 2019: A limited role for unforced internal variability in twentieth-century warming. *Journal of Climate*, **32(16)**, 4893–4917, doi:10.1175/jcli-d-18-0555.1.
Haywood, A.M. et al., 2013: Large-scale features of Pliocene climate: Results from the Pliocene Model Intercomparison Project. *Climate of the Past*, doi:10.5194/cp-9-191-2013.
Haywood, A.M. et al., 2016: The Pliocene Model Intercomparison Project (PlioMIP) Phase 2: scientific objectives and experimental design. *Climate of the Past*, **12(3)**, 663–675, doi:10.5194/cp-12-663-2016.
Haywood, A.M. et al., 2020: The Pliocene Model Intercomparison Project Phase 2: large-scale climate features and climate sensitivity. *Climate of the Past*, **16(6)**, 2095–2123, doi:10.5194/cp-16-2095-2020.
Haywood, J.M., A. Jones, and G.S. Jones, 2014: The impact of volcanic eruptions in the period 2000-2013 on global mean temperature trends evaluated in the HadGEM2-ES climate model. *Atmospheric Science Letters*, **15(2)**, 92–96, doi:10.1002/asl2.471.
Hedemann, C., T. Mauritsen, J. Jungclaus, and J. Marotzke, 2017: The subtle origins of surface-warming hiatuses. *Nature Climate Change*, **7**, 336, doi:10.1038/nclimate3274.
Hegerl, G. and F. Zwiers, 2011: Use of models in detection and attribution of climate change. *Wiley Interdisciplinary Reviews: Climate Change*, **2(4)**, 570–591, doi:10.1002/wcc.121.
Hegerl, G.C., S. Brönnimann, A. Schurer, and T. Cowan, 2018: The early 20th century warming: Anomalies, causes,

ACCEPTED VERSION SUBJECT TO FINAL EDITING

and consequences. *Wiley Interdisciplinary Reviews: Climate Change*, **9(4)**, e522, doi:10.1002/wcc.522.
Hegerl, G.C. et al., 1996: Detecting Greenhouse-Gas-Induced Climate Change with an Optimal Fingerprint Method. *Journal of Climate*, **9**, 2281–2306, doi:10.2307/26201437.
Hegerl, G.C. et al., 2015: Challenges in quantifying changes in the global water cycle. *Bulletin of the American Meteorological Society*, **96(7)**, 1097–1115, doi:10.1175/bams-d-13-00212.1.
Hegerl, G.C. et al., 2019: Causes of climate change over the historical record. *Environmental Research Letters*, **14(12)**, 123006, doi:10.1088/1748-9326/ab4557.
Henley, B.J., 2017: Pacific decadal climate variability: Indices, patterns and tropical-extratropical interactions. *Global and Planetary Change*, **155**, 42–55, doi:10.1016/j.gloplacha.2017.06.004.
Henley, B.J. et al., 2015: A Tripole Index for the Interdecadal Pacific Oscillation. *Climate Dynamics*, **45(11–12)**, 3077–3090, doi:10.1007/s00382-015-2525-1.
Henley, B.J. et al., 2017: Spatial and temporal agreement in climate model simulations of the Interdecadal Pacific Oscillation. *Environmental Research Letters*, **12(4)**, 44011, doi:10.1088/1748-9326/aa5cc8.
Hernández, A. et al., 2020: A 2,000-year Bayesian NAO reconstruction from the Iberian Peninsula. *Scientific Reports*, **10(1)**, 14961, doi:10.1038/s41598-020-71372-5.
Herold, N., L.V. Alexander, M.G. Donat, S. Contractor, and A. Becker, 2016: How much does it rain over land? *Geophys. Res. Let.*, **43**.
Heuzé, C., 2021: Antarctic Bottom Water and North Atlantic Deep Water in CMIP6 models. *Ocean Science*, **17(1)**, 59–90, doi:10.5194/os-17-59-2021.
Heuzé, C., K.J. Heywood, D.P. Stevens, and J.K. Ridley, 2013: Southern Ocean bottom water characteristics in CMIP5 models. *Geophysical Research Letters*, **40(7)**, 1409–1414, doi:10.1002/grl.50287.
Heuzé, C., K.J. Heywood, D.P. Stevens, and J.K. Ridley, 2015: Changes in Global Ocean Bottom Properties and Volume Transports in CMIP5 Models under Climate Change Scenarios. *Journal of Climate*, **28(8)**, 2917–2944, doi:10.1175/jcli-d-14-00381.1.
Hewitt, H.T. et al., 2016: The impact of resolving the Rossby radius at mid-latitudes in the ocean: results from a high-resolution version of the Met Office GC2 coupled model. *Geoscientific Model Development*, **9(10)**, 3655–3670, doi:10.5194/gmd-9-3655-2016.
Hewitt, H.T. et al., 2017: Will high-resolution global ocean models benefit coupled predictions on short-range to climate timescales? *Ocean Modelling*, **120**, 120–136, doi:10.1016/j.ocemod.2017.11.002.
Hewitt, H.T. et al., 2020: Resolving and Parameterising the Ocean Mesoscale in Earth System Models. *Current Climate Change Reports*, 1–16, doi:10.1007/s40641-020-00164-w.
Hirabayashi, Y. et al., 2016: Contributions of natural and anthropogenic radiative forcing to mass loss of Northern Hemisphere mountain glaciers and quantifying their uncertainties. *Scientific Reports*, **6(1)**, 29723, doi:10.1038/srep29723.
Hirons, L. and A. Turner, 2018: The Impact of Indian Ocean Mean-State Biases in Climate Models on the Representation of the East African Short Rains. *Journal of Climate*, **31(16)**, 6611–6631, doi:10.1175/jcli-d-17-0804.1.
Hobbs, W.R., N.L. Bindoff, and M.N. Raphael, 2015: New Perspectives on Observed and Simulated Antarctic Sea Ice Extent Trends Using Optimal Fingerprinting Techniques. *Journal of Climate*, **28(4)**, 1543–1560, doi:10.1175/jcli-d-14-00367.1.
Hobbs, W.R., C. Roach, T. Roy, J.B. Sallée, and N. Bindoff, 2021: Anthropogenic temperature and salinity changes in the Southern ocean. *Journal of Climate*, **34(1)**, 215–228, doi:10.1175/jcli-d-20-0454.1.
Hobbs, W.R. et al., 2016: A review of recent changes in Southern Ocean sea ice, their drivers and forcings. *Global and Planetary Change*, **143**, 228–250, doi:10.1016/j.gloplacha.2016.06.008.
Hock, R. et al., 2019a: GlacierMIP-A model intercomparison of global-scale glacier mass-balance models and projections. *Journal of Glaciology*, **65(251)**, 453–467, doi:10.1017/jog.2019.22.
Hock, R. et al., 2019b: High Mountain Areas. In: *IPCC Special Report on the Ocean and Cryosphere in a Changing Climate* [Pörtner, H.-O., D.C. Roberts, V. Masson-Delmotte, P. Zhai, M. Tignor, E. Poloczanska, K. Mintenbeck, A. Alegría, M. Nicolai, A. Okem, J. Petzold, B. Rama, and N.M. Weyer (eds.)]. In Press, pp. 131–202.
Hoell, A., M. Hoerling, J. Eischeid, X.-W. Quan, and B. Liebmann, 2017a: Reconciling Theories for Human and Natural Attribution of Recent East Africa Drying. *Journal of Climate*, **30(6)**, 1939–1957, doi:10.1175/jcli-d-16-0558.1.
Hoell, A., M. Hoerling, J. Eischeid, X.-W. Quan, and B. Liebmann, 2017b: Reconciling Theories for Human and Natural Attribution of Recent East Africa Drying. *Journal of Climate*, **30(6)**, 1939–1957, doi:10.1175/jcli-d-16-0558.1.
Hoffman, F.M. et al., 2014: Causes and implications of persistent atmospheric carbon dioxide biases in Earth System Models. *Journal of Geophysical Research: Biogeosciences*, **119(2)**, 141–162, doi:10.1002/2013jg002381.
Hoffman, M.J., X. Asay-Davis, S.F. Price, J. Fyke, and M. Perego, 2019: Effect of Subshelf Melt Variability on Sea Level Rise Contribution From Thwaites Glacier, Antarctica. *Journal of Geophysical Research: Earth Surface*, doi:10.1029/2019jf005155.

ACCEPTED VERSION SUBJECT TO FINAL EDITING

Holland, M.M., L. Landrum, Y. Kostov, and J. Marshall, 2017: Sensitivity of Antarctic sea ice to the Southern Annular Mode in coupled climate models. *Climate Dynamics*, **49(5)**, 1813–1831, doi:10.1007/s00382-016-3424-9.

Holland, P.R., T.J. Bracegirdle, P. Dutrieux, A. Jenkins, and E.J. Steig, 2019: West Antarctic ice loss influenced by internal climate variability and anthropogenic forcing. *Nature Geoscience*, doi:10.1038/s41561-019-0420-9.

Hollis, C.J. et al., 2019: The DeepMIP contribution to PMIP4: methodologies for selection, compilation and analysis of latest Paleocene and early Eocene climate proxy data, incorporating version 0.1 of the DeepMIP database. *Geoscientific Model Development*, **12(7)**, 3149–3206, doi:10.5194/gmd-12-3149-2019.

Hopcroft, P.O., P.J. Valdes, A.B. Harper, and D.J. Beerling, 2017: Multi vegetation model evaluation of the Green Sahara climate regime. *Geophysical Research Letters*, doi:10.1002/2017gl073740.

Hope, P., B.J. Henley, J. Gergis, J. Brown, and H. Ye, 2017a: Time-varying spectral characteristics of ENSO over the Last Millennium. *Climate Dynamics*, **49(5–6)**, 1705–1727, doi:10.1007/s00382-016-3393-z.

Hope, P., B.J. Henley, J. Gergis, J. Brown, and H. Ye, 2017b: Time-varying spectral characteristics of ENSO over the Last Millennium. *Climate Dynamics*, **49(5–6)**, 1705–1727, doi:10.1007/s00382-016-3393-z.

Horel, J.D. and J.M. Wallace, 1981: Planetary-Scale Atmospheric Phenomena Associated with the Southern Oscillation. *Monthly Weather Review*, **109(4)**, 813–829, doi:10.1175/1520-0493(1981)109<0813:psapaw>2.0.co;2.

Hoskins, B.J. and D.J. Karoly, 1981: The Steady Linear Response of a Spherical Atmosphere to Thermal and Orographic Forcing. *Journal of the Atmospheric Sciences*, **38(6)**, 1179–1196, doi:10.1175/1520-0469(1981)038<1179:tslroa>2.0.co;2.

Hourdin, F. et al., 2015: Air moisture control on ocean surface temperature, hidden key to the warm bias enigma. *Geophysical Research Letters*, **42(24)**, 10,885–10,893, doi:10.1002/2015gl066764.

Hourdin, F. et al., 2017: The art and science of climate model tuning. *Bulletin of the American Meteorological Society*, **98(3)**, 589–602, doi:10.1175/bams-d-15-00135.1.

Hu, K. et al., 2014: Interdecadal Variations in ENSO Influences on Northwest Pacific–East Asian Early Summertime Climate Simulated in CMIP5 Models. *Journal of Climate*, **27(15)**, 5982–5998, doi:10.1175/jcli-d-13-00268.1.

Hu, S. and A. Fedorov, 2017: The extreme El Niño of 2015-2016 and the end of global warming hiatus. *Geophysical Research Letters*, **44(8)**, 3816–3824, doi:10.1002/2017gl072908.

Hu, T., Y. Sun, X. Zhang, S.K. Min, and Y.H. Kim, 2020: Human influence on frequency of temperature extremes. *Environmental Research Letters*, doi:10.1088/1748-9326/ab8497.

Hua, W., A. Dai, and M. Qin, 2018: Contributions of Internal Variability and External Forcing to the Recent Pacific Decadal Variations. *Geophysical Research Letters*, **45(14)**, 7084–7092, doi:10.1029/2018gl079033.

Huber, M. and R. Knutti, 2014: Natural variability, radiative forcing and climate response in the recent hiatus reconciled. *Nature Geoscience*, **7**, 651, doi:10.1038/ngeo2228.

Humphrey, V. et al., 2018: Sensitivity of atmospheric CO2 growth rate to observed changes in terrestrial water storage. *Nature*, **560(7720)**, 628–631, doi:10.1038/s41586-018-0424-4.

Huntingford, C., P.A. Stott, M.R. Allen, and F.H. Lambert, 2006: Incorporating model uncertainty into attribution of observed temperature change. *Geophysical Research Letters*, **33(5)**, doi:10.1029/2005gl024831.

Huntingford, C. et al., 2017: Implications of improved representations of plant respiration in a changing climate. *Nature Communications*, **8(1)**, 1602, doi:10.1038/s41467-017-01774-z.

Hyder, P. et al., 2018: Critical Southern Ocean climate model biases traced to atmospheric model cloud errors. *Nature Communications*, **9(1)**, 3625, doi:10.1038/s41467-018-05634-2.

Ibarra, D.E. et al., 2018: Warm and cold wet states in the western United States during the Pliocene-Pleistocene. *Geology*, doi:10.1130/g39962.1.

Iglesias-Suarez, F., P.J. Young, and O. Wild, 2016: Stratospheric ozone change and related climate impacts over 1850-2100 as modelled by the ACCMIP ensemble. *ATMOSPHERIC CHEMISTRY AND PHYSICS*, **16(1)**, 343–363, doi:10.5194/acp-16-343-2016.

Iles, C. and G.C. Hegerl, 2015: Systematic change in global patterns of streamflow following volcanic eruptions. *Nature Geoscience*, doi:10.1038/ngeo2545.

Iles, C. and G. Hegerl, 2017: Role of the North Atlantic Oscillation in decadal temperature trends. *Environmental Research Letters*, **12(11)**, 114010, doi:10.1088/1748-9326/aa9152.

Iles, C.E. and G.C. Hegerl, 2014: The global precipitation response to volcanic eruptions in the CMIP5 models. *Environmental Research Letters*, **9(10)**, 104012, doi:10.1088/1748-9326/9/10/104012.

Imbers, J., A. Lopez, C. Huntingford, and M. Allen, 2014: Sensitivity of Climate Change Detection and Attribution to the Characterization of Internal Climate Variability. *Journal of Climate*, **27(10)**, 3477–3491, doi:10.1175/jcli-d-12-00622.1.

Iovino, D., S. Masina, A. Storto, A. Cipollone, and V.N. Stepanov, 2016: A 1/16° eddying simulation of the global NEMO sea-ice–ocean system. *Geoscientific Model Development*, **9(8)**, 2665–2684, doi:10.5194/gmd-9-2665-2016.

IPCC, 2013: Summary for Policymakers. In: *Climate Change 2013: The Physical Science Basis. Contribution of Working Group I to the Fifth Assessment Report of the Intergovernmental Panel on Climate Change* [Stocker, T.F., D. Qin, G.K. Plattner, M. Tignor, S.K. Allen, J. Boschung, A. Nauels, Y. Xia, V. Bex, and P.M. Midgley

ACCEPTED VERSION SUBJECT TO FINAL EDITING

(eds.)]. Cambridge University Press, Cambridge, United Kingdom and New York, NY, USA, pp. 3–29, doi:10.1017/cbo9781107415324.004.

IPCC, 2018: Global Warming of 1.5°C. An IPCC Special Report on the impacts of global warming of 1.5°C above pre-industrial levels and related global greenhouse gas emission pathways, in the context of strengthening the global response to the threat of climate change,. [Masson-Delmotte, V., P. Zhai, H.-O. Pörtner, D. Roberts, J. Skea, P.R. Shukla, A. Pirani, W. Moufouma-Okia, C. Péan, R. Pidcock, S. Connors, J.B.R. Matthews, Y. Chen, X. Zhou, M.I. Gomis, E. Lonnoy, T. Maycock, M. Tignor, and T. Waterfield (eds.)]. In Press, 616 pp.

IPCC, 2019a: Climate Change and Land: an IPCC special report on climate change, desertification, land degradation, sustainable land management, food security, and greenhouse gas fluxes in terrestrial ecosystems. [Shukla, P.R., J. Skea, E.C. Buendia, V. Masson-Delmotte, H.-O. Pörtner, D.C. Roberts, P. Zhai, R. Slade, S. Connors, R. Diemen, M. Ferrat, E. Haughey, S. Luz, S. Neogi, M. Pathak, J. Petzold, J.P. Pereira, P. Vyas, E. Huntley, K. Kissick, M. Belkacemi, and J. Malley (eds.)]. In Press, 896 pp.

IPCC, 2019b: IPCC Special Report on the Ocean and Cryosphere in a Changing Climate. [Pörtner, H.-O., D.C. Roberts, V. Masson-Delmotte, P. Zhai, M. Tignor, E. Poloczanska, K. Mintenbeck, A. Alegría, M. Nicolai, A. Okem, J. Petzold, B. Rama, and N.M. Weyer (eds.)]. In Press, 755 pp.

Irving, D. and I. Simmonds, 2016: A New Method for Identifying the Pacific–South American Pattern and Its Influence on Regional Climate Variability. *Journal of Climate*, **29(17)**, 6109–6125, doi:10.1175/jcli-d-15-0843.1.

Ishii, M. et al., 2017: Accuracy of Global Upper Ocean Heat Content Estimation Expected from Present Observational Data Sets. *SOLA*, **13**, 163–167, doi:10.2151/sola.2017-030.

Ito, T., S. Minobe, M.C. Long, and C. Deutsch, 2017: Upper ocean O2 trends: 1958-2015. *Geophysical Research Letters*, **44(9)**, 4214–4223, doi:10.1002/2017gl073613.

Iturbide, M. et al., 2020: An update of IPCC climate reference regions for subcontinental analysis of climate model data: definition and aggregated datasets. *Earth System Science Data*, **12(4)**, 2959–2970, doi:10.5194/essd-12-2959-2020.

Ivy, D.J., S. Solomon, N. Calvo, and D.W.J. Thompson, 2017: Observed connections of Arctic stratospheric ozone extremes to Northern Hemisphere surface climate. *ENVIRONMENTAL RESEARCH LETTERS*, **12(2)**, doi:10.1088/1748-9326/aa57a4.

Jackson, L.C. et al., 2019: The Mean State and Variability of the North Atlantic Circulation: A Perspective From Ocean Reanalyses. *Journal of Geophysical Research: Oceans*, **n/a(n/a)**, doi:10.1029/2019jc015210.

Jebri, B. et al., 2020: Contributions of internal variability and external forcing to the recent trends in the Southeastern Pacific and Peru-Chile upwelling system. *Journal of Climate*, JCLI–D–19–0304.1, doi:10.1175/jcli-d-19-0304.1.

Jeffers, E.S., M.B. Bonsall, C.A. Froyd, S.J. Brooks, and K.J. Willis, 2015: The relative importance of biotic and abiotic processes for structuring plant communities through time. *Journal of Ecology*, doi:10.1111/1365-2745.12365.

Jenkins, A. et al., 2018: West Antarctic Ice Sheet retreat in the Amundsen Sea driven by decadal oceanic variability. *Nature Geoscience*, doi:10.1038/s41561-018-0207-4.

Jeong, D., L. Sushama, and M. Naveed Khaliq, 2017: Attribution of spring snow water equivalent (SWE) changes over the northern hemisphere to anthropogenic effects. *Climate Dynamics*, **48(11)**, 3645–3658, doi:10.1007/s00382-016-3291-4.

Jeong, H. et al., 2020a: Impacts of Ice-Shelf Melting on Water-Mass Transformation in the Southern Ocean from E3SM Simulations. *Journal of Climate*, **33(13)**, 5787–5807, doi:10.1175/jcli-d-19-0683.1.

Jeong, H. et al., 2020b: Impacts of Ice-Shelf Melting on Water-Mass Transformation in the Southern Ocean from E3SM Simulations. *Journal of Climate*, **33(13)**, 5787–5807, doi:10.1175/jcli-d-19-0683.1.

Jia, G. et al., 2019: Land–climate interactions. In: *Climate Change and Land: an IPCC special report on climate change, desertification, land degradation, sustainable land management, food security, and greenhouse gas fluxes in terrestrial ecosystems* [P.R. Shukla, J. Skea, E. Calvo Buendia, V. Masson-Delmotte, H.-O. Pörtner, D.C. Roberts, P. Zhai, R. Slade, S. Connors, R. Diemen, M. Ferrat, E. Haughey, S. Luz, S. Neogi, M. Pathak, J. Petzold, J.P. Pereira, P. Vyas, E. Huntley, K. Kissick, M. Belkacemi, and J. Malley (eds.)]. In Press, pp. 131–247.

Jia, L. and T. DelSole, 2012: Optimal Determination of Time-Varying Climate Change Signals. *Journal of Climate*, **25(20)**, 7122–7137, doi:10.1175/jcli-d-11-00434.1.

Jiang, B., D. Wang, X. Shen, J. Chen, and W. Lin, 2019: Effects of sea salt aerosols on precipitation and upper troposphere/lower stratosphere water vapour in tropical cyclone systems. *Scientific Reports*, **9(1)**, doi:10.1038/s41598-019-51757-x.

Jiang, D., Z. Tian, and X. Lang, 2015: Mid-Holocene global monsoon area and precipitation from PMIP simulations. *Climate Dynamics*, **44(9–10)**, 2493–2512, doi:10.1007/s00382-014-2175-8.

Jiang, J. and T. Zhou, 2019: Global Monsoon Responses to Decadal Sea Surface Temperature Variations during the Twentieth Century: Evidence from AGCM Simulations. *Journal of Climate*, **32(22)**, 7675–7695, doi:10.1175/jcli-d-18-0890.1.

Jiang, J.H., H. Su, and C. Zhai, 2012: Evaluation of cloud and water vapor simulations in CMIP5 climate models using

ACCEPTED VERSION SUBJECT TO FINAL EDITING

NASA "A-Train" satellite observations. *J. Geophys. Res.*, **118**, doi:10.10 29/2011jd017237.
Jianping, L. and J.X.L. Wang, 2003: A new North Atlantic Oscillation index and its variability. *Advances in Atmospheric Sciences*, **20(5)**, 661–676, doi:10.1007/bf02915394.
Jiaxiang, G. et al., 2020: Influence of model resolution on bomb cyclones revealed by HighResMIP-PRIMAVERA simulations. *Environmental Research Letters*, **15(8)**, doi:10.1088/1748-9326/ab88fa.
Jin, F.-F., S.T. Kim, and L. Bejarano, 2006: A coupled-stability index for ENSO. *Geophysical Research Letters*, **33(23)**, L23708, doi:10.1029/2006gl027221.
Johnson, S.J. et al., 2016: The resolution sensitivity of the South Asian monsoon and Indo-Pacific in a global 0.35° AGCM. *Climate Dynamics*, **46(3–4)**, 807–831, doi:10.1007/s00382-015-2614-1.
Jones, C.D. and P. Friedlingstein, 2020: Quantifying process-level uncertainty contributions to TCRE and carbon budgets for meeting Paris Agreement climate targets. *Environmental Research Letters*, **15(7)**, 74019, doi:10.1088/1748-9326/ab858a.
Jones, G.S. and J.J. Kennedy, 2017: Sensitivity of attribution of anthropogenic near-surface warming to observational uncertainty. *Journal of Climate*, **30(12)**, 4677–4691, doi:10.1175/jcli-d-16-0628.1.
Jones, G.S., P.A. Stott, and N. Christidis, 2013: Attribution of observed historical near-surface temperature variations to anthropogenic and natural causes using CMIP5 simulations. *Journal of Geophysical Research Atmospheres*, **118(10)**, 4001–4024, doi:10.1002/jgrd.50239.
Jones, G.S., P.A. Stott, and J.F.B. Mitchell, 2016: Uncertainties in the attribution of greenhouse gas warming and implications for climate prediction. *Journal of Geophysical Research*, **121(12)**, 6969–6992, doi:10.1002/2015jd024337.
Jones, P., 2016: The reliability of global and hemispheric surface temperature records. *Advances in Atmospheric Sciences*, **33(3)**, doi:10.1007/s00376-015-5194-4.
Joshi, M.K. and F. Kucharski, 2017: Impact of Interdecadal Pacific Oscillation on Indian summer monsoon rainfall: an assessment from CMIP5 climate models. *Climate Dynamics*, **48(7–8)**, 2375–2391, doi:10.1007/s00382-016-3210-8.
Jouanno, J., O. Hernandez, and E. Sanchez-Gomez, 2017: Equatorial Atlantic interannual variability and its relation to dynamic and thermodynamic processes. *Earth System Dynamics*, **8(4)**, 1061–1069, doi:10.5194/esd-8-1061-2017.
Jung, M. et al., 2017: Compensatory water effects link yearly global land CO2 sink changes to temperature. *Nature*, **541(7638)**, 516–520, doi:10.1038/nature20780.
Kadow, C., D.M. Hall, and U. Ulbrich, 2020: Artificial intelligence reconstructs missing climate information. *Nature Geoscience*, **13(6)**, 408–413, doi:10.1038/s41561-020-0582-5.
Kageyama, M. et al., 2017: The PMIP4 contribution to CMIP6 – Part 4: Scientific objectives and experimental design of the PMIP4-CMIP6 Last Glacial Maximum experiments and PMIP4 sensitivity experiments. *Geoscientific Model Development*, **10(11)**, 4035–4055, doi:10.5194/gmd-10-4035-2017.
Kageyama, M. et al., 2018a: The PMIP4 contribution to CMIP6 – Part 1: Overview and over-arching\r\nanalysis plan. *Geoscientific Model Development*, **11(3)**, 1033–1057, doi:10.5194/gmd-11-1033-2018.
Kageyama, M. et al., 2018b: The PMIP4 contribution to CMIP6 – Part 1: Overview and over-arching\r\nanalysis plan. *Geoscientific Model Development*, **11(3)**, 1033–1057, doi:10.5194/gmd-11-1033-2018.
Kageyama, M. et al., 2021a: The PMIP4-CMIP6 Last Glacial Maximum experiments: preliminary results and comparison with the PMIP3-CMIP5 simulations. *Climate of the Past* (in press).
Kageyama, M. et al., 2021b: A multi-model CMIP6-PMIP4 study of Arctic sea ice at 127 ka: sea ice data compilation and model differences. *Climate of the Past*, **17(1)**, 37–62, doi:10.5194/cp-17-37-2021.
Kageyama, M. et al., 2021c: A multi-model CMIP6-PMIP4 study of Arctic sea ice at 127 ka: sea ice data compilation and model differences. *Climate of the Past*, **17(1)**, 37–62, doi:10.5194/cp-17-37-2021.
Kam, J., T.R. Knutson, and P.C.D. Milly, 2018: Climate model assessment of changes in winter-spring streamflow timing over north America. *J. Climate*, doi:10.1175/jcli-d-17-0813.1.
Kamae, Y., X. Li, S.-P. Xie, and H. Ueda, 2017: Atlantic effects on recent decadal trends in global monsoon. *Climate Dynamics*, **49(9–10)**, 3443–3455, doi:10.1007/s00382-017-3522-3.
Kang, S.M., L.M. Polvani, J.C. Fyfe, and M. Sigmond, 2011: Impact of Polar Ozone Depletion on Subtropical Precipitation. *SCIENCE*, **332(6032)**, 951–954, doi:10.1126/science.1202131.
Karl, T.R. et al., 2015: Possible artifacts of data biases in the recent global surface warming hiatus. *Science*, **348(6242)**, 1469–1472, doi:10.1126/science.aaa5632.
Karoly, D.J., 1989: Southern Hemisphere Circulation Features Associated with El Niño–Southern Oscillation Events. *Journal of Climate*, **2(11)**, 1239–1252.
Karpechko, A.Y., A. Maycock, and et al., 2018a: Chapter 5 of Scientific Assessment of Ozone Depletion: 2018. .
Karpechko, A.Y., P. Hitchcock, D.H.W. Peters, and A. Schneidereit, 2017: Predictability of downward propagation of major sudden stratospheric warmings. *Quarterly Journal of the Royal Meteorological Society*, **143(704)**, 1459–1470, doi:10.1002/qj.3017.
Karpechko, A.Y. et al., 2018b: Stratospheric Ozone Changes and Climate. In: *Scientific Assessment of Ozone Depletion: 2018*. Global Ozone Research and Monitoring Project – Report No. 58, World Meteorological

ACCEPTED VERSION SUBJECT TO FINAL EDITING

Organization (WMO), Geneva, Switzerland, pp. 5.1–5.69.
Karset, I.H.H. et al., 2018: Strong impacts on aerosol indirect effects from historical oxidant changes. *Atmospheric Chemistry and Physics*, **18(10)**, 7669–7690.
Katzfuss, M., D. Hammerling, and R.L. Smith, 2017: A Bayesian hierarchical model for climate change detection and attribution. *Geophysical Research Letters*, **44(11)**, 5720–5728, doi:10.1002/2017gl073688.
Kaufman, D. et al., 2020: Holocene global mean surface temperature, a multi-method reconstruction approach. *Scientific Data*, **7(1)**, doi:10.1038/s41597-020-0530-7.
Kay, J.E., M.M. Holland, and A. Jahn, 2011: Inter-annual to multi-decadal Arctic sea ice extent trends in a warming world. *Geophysical Research Letters*, **38(15)**, doi:10.1029/2011gl048008.
Kay, J.E. et al., 2015: The community earth system model (CESM) large ensemble project : A community resource for studying climate change in the presence of internal climate variability. *Bulletin of the American Meteorological Society*, **96(8)**, 1333–1349, doi:10.1175/bams-d-13-00255.1.
Keeling, C.D., J.F.S. Chin, and T.P. Whorf, 1996: Increased activity of northern vegetation inferred from atmospheric CO2 measurements. *Nature*, **382**, 146.
Kharin, V. et al., 2018: Risks from Climate Extremes Change Differently from 1.5°C to 2.0°C Depending on Rarity. *Earth's Future*, doi:10.1002/2018ef000813.
Kidston, J. et al., 2015: Stratospheric influence on tropospheric jet streams, storm tracks and surface weather. *Nature Geoscience*, **8(6)**, 433–440, doi:10.1038/ngeo2424.
Kim, B.M. et al., 2014: Weakening of the stratospheric polar vortex by Arctic sea-ice loss. *Nature Communications*, **5**, 1–8, doi:10.1038/ncomms5646.
Kim, J., S.-W. Son, E.P. Gerber, and H.-S. Park, 2017: Defining Sudden Stratospheric Warming in Climate Models: Accounting for Biases in Model Climatologies. *Journal of Climate*, **30(14)**, 5529–5546, doi:10.1175/jcli-d-16-0465.1.
Kim, S.T. and J.Y. Yu, 2012: The two types of ENSO in CMIP5 models. *Geophysical Research Letters*, **39(11)**, 1–6, doi:10.1029/2012gl052006.
Kim, S.T., W. Cai, F.F. Jin, and J.Y. Yu, 2014: ENSO stability in coupled climate models and its association with mean state. *Climate Dynamics*, **42(11–12)**, 3313–3321, doi:10.1007/s00382-013-1833-6.
Kim, W.M., S.G. Yeager, and G. Danabasoglu, 2018a: Key Role of Internal Ocean Dynamics in Atlantic Multidecadal Variability During the Last Half Century. *Geophysical Research Letters*, **45(24)**, doi:10.1029/2018gl080474.
Kim, W.M., S. Yeager, and G. Danabasoglu, 2019: Atlantic Multidecadal Variability and Associated Climate Impacts Initiated by Ocean Thermohaline Dynamics. *Journal of Climate*, JCLI–D–19–0530.1, doi:10.1175/jcli-d-19-0530.1.
Kim, W.M., S. Yeager, and G. Danabasoglu, 2020: Atlantic multidecadal variability and associated climate impacts initiated by ocean thermohaline dynamics. *Journal of Climate*, **33(4)**, 1317–1334, doi:10.1175/jcli-d-19-0530.1.
Kim, W.M., S. Yeager, P. Chang, and G. Danabasoglu, 2018b: Low-Frequency North Atlantic Climate Variability in the Community Earth System Model Large Ensemble. *Journal of Climate*, **31(2)**, 787–813, doi:10.1175/jcli-d-17-0193.1.
Kim, Y.H., S.K. Min, S.W. Son, and J. Choi, 2017: Attribution of the local Hadley cell widening in the Southern Hemisphere. *Geophysical Research Letters*, **44(2)**, 1015–1024, doi:10.1002/2016gl072353.
Kirchmeier-Young, M.C., F.W. Zwiers, and N.P. Gillett, 2017: Attribution of Extreme Events in Arctic Sea Ice Extent. *Journal of Climate*, **30(2)**, 553–571, doi:10.1175/jcli-d-16-0412.1.
Kjeldsen, K.K. et al., 2015: Spatial and temporal distribution of mass loss from the Greenland Ice Sheet since AD 1900. *Nature*, **528(7582)**, 396–400, doi:10.1038/nature16183.
Knudsen, M.F., B.H. Jacobsen, M.-S. Seidenkrantz, and J. Olsen, 2014: Evidence for external forcing of the Atlantic Multidecadal Oscillation since termination of the Little Ice Age. *Nature Communications*, **5(1)**, 3323, doi:10.1038/ncomms4323.
Knutson, T.R. and F. Zeng, 2018: Model Assessment of observed precipitation trends over land regions: Detectable human influences and possible low bias in model trends. *J. Climate*, **31**, 4617–4637, doi:10.1175/jcli-d-17-0672.1.
Knutti, R., D. Masson, and A. Gettelman, 2013: Climate model genealogy: Generation CMIP5 and how we got there. *Geophysical Research Letters*, **40(6)**, 1194–1199, doi:10.1002/grl.50256.
Kociuba, G. and S.B. Power, 2015: Inability of CMIP5 models to simulate recent strengthening of the walker circulation: Implications for projections. *Journal of Climate*, **28(1)**, 20–35, doi:10.1175/jcli-d-13-00752.1.
Kodama, C. et al., 2021: The Nonhydrostatic ICosahedral Atmospheric Model for CMIP6 HighResMIP simulations (NICAM16-S): experimental design, model description, and impacts of model updates. *Geoscientific Model Development*, **14(2)**, 795–820, doi:10.5194/gmd-14-795-2021.
Kok, J.F., D.S. Ward, N.M. Mahowald, and A.T. Evan, 2018: Global and regional importance of the direct dust-climate feedback. *Nature communications*, **9(1)**, 241, doi:10.1038/s41467-017-02620-y.
Kopp, R.E. et al., 2016: Temperature-driven global sea-level variability in the Common Era. *Proceedings of the National Academy of Sciences of the United States of America*, **113(11)**, E1434–E1441,

ACCEPTED VERSION SUBJECT TO FINAL EDITING

doi:10.1073/pnas.1517056113.
Kosaka, Y. and S.-P. Xie, 2013: Recent global-warming hiatus tied to equatorial Pacific surface cooling. *Nature*, **501(7467)**, 403–407, doi:10.1038/nature12534.
Kosaka, Y. and S.-P. Xie, 2016: The tropical Pacific as a key pacemaker of the variable rates of global warming. *Nature Geoscience*, **9(9)**, doi:10.1038/ngeo2770.
Kostov, Y. et al., 2017: Fast and slow responses of Southern Ocean sea surface temperature to SAM in coupled climate models. *Climate Dynamics*, **48(5)**, 1595–1609, doi:10.1007/s00382-016-3162-z.
Kucharski, F. et al., 2016: Atlantic forcing of Pacific decadal variability. *Climate Dynamics*, **46(7)**, 2337–2351, doi:10.1007/s00382-015-2705-z.
Kuhlbrodt, T., R.S. Smith, Z. Wang, and J.M. Gregory, 2012: The influence of eddy parameterizations on the transport of the Antarctic Circumpolar Current in coupled climate models. *Ocean Modelling*, **52–53**, 1–8, doi:10.1016/j.ocemod.2012.04.006.
Kuhlbrodt, T. et al., 2018: The Low-Resolution Version of HadGEM3 GC3.1: Development and Evaluation for Global Climate. *Journal of Advances in Modeling Earth Systems*, **10(11)**, 2865–2888, doi:10.1029/2018ms001370.
Kumar, A., B. Jha, and H. Wang, 2014: Attribution of SST variability in global oceans and the role of ENSO. *Climate Dynamics*, **43(1–2)**, 209–220, doi:10.1007/s00382-013-1865-y.
Kumar, S., R.P. Allan, F.W. Zwiers, D.M. Lawrence, and P.A. Dirmeyer, 2015: Revisiting trends in wetness and dryness in the presence of internal climate variability and water limitations over land. *Geophys. Res. Lett.*, **42**, 10867–10875, doi:10.1002/2015gl066858.
Kuntz, L.B. and D.P. Schrag, 2016: Impact of Asian aerosol forcing on tropical Pacific circulation and the relationship to global temperature trends. *Journal of Geophysical Research: Atmospheres*, **121(24)**, 14,403–14,413, doi:10.1002/2016jd025430.
L'Heureux, M.L., S. Lee, and B. Lyon, 2013: Recent multidecadal strengthening of the Walker circulation across the tropical Pacific. *Nature Climate Change*, **3(6)**, 571–576, doi:10.1038/nclimate1840.
Laepple, T. and P. Huybers, 2014: Ocean surface temperature variability: Large model-data differences at decadal and longer periods. *Proceedings of the National Academy of Sciences of the United States of America*, **111(47)**, 16682–16687, doi:10.1073/pnas.1412077111.
Lago, V. and M.H. England, 2019: Projected Slowdown of Antarctic Bottom Water Formation in Response to Amplified Meltwater Contributions. *Journal of Climate*, **32(19)**, 6319–6335, doi:10.1175/jcli-d-18-0622.1.
Lago, V. et al., 2016: Simulating the role of surface forcing on observed multidecadal upper-ocean salinity changes. *Journal of Climate*, **29(15)**, 5575–5588, doi:10.1175/jcli-d-15-0519.1.
Landrum, L. et al., 2013: Last Millennium Climate and Its Variability in CCSM4. *Journal of Climate*, **26(4)**, 1085–1111, doi:10.1175/jcli-d-11-00326.1.
Landrum, L.L., M.M. Holland, M.N. Raphael, and L.M. Polvani, 2017: Stratospheric Ozone Depletion: An Unlikely Driver of the Regional Trends in Antarctic Sea Ice in Austral Fall in the Late Twentieth Century. *Geophysical Research Letters*, **44(21)**, 11,11–62,70, doi:10.1002/2017gl075618.
Landschützer, P., N. Gruber, and D.C.E. Bakker, 2016: Decadal variations and trends of the global ocean carbon sink. *Global Biogeochemical Cycles*, **30(10)**, 1396–1417, doi:10.1002/2015gb005359.
Langenbrunner, B. and J.D. Neelin, 2013: Analyzing enso teleconnections in cmip models as a measure of model fidelity in simulating precipitation. *Journal of Climate*, **26(13)**, 4431–4446, doi:10.1175/jcli-d-12-00542.1.
Lapointe, F. et al., 2020: Annually resolved Atlantic sea surface temperature variability over the past 2,900 y. *Proceedings of the National Academy of Sciences*, 202014166, doi:10.1073/pnas.2014166117.
Larkin, N.K. and D.E. Harrison, 2002: ENSO warm (El Niño) and cold (La Niña) event life cycles: Ocean surface anomaly patterns, their symmetries, asymmetries, and implications. *Journal of Climate*, **15(10)**, 1118–1140, doi:10.1175/1520-0442(2002)015<1118:ewenoa>2.0.co;2.
Latif, M., T. Martin, and W. Park, 2013: Southern ocean sector centennial climate variability and recent decadal trends. *Journal of Climate*, **26(19)**, 7767–7782, doi:10.1175/jcli-d-12-00281.1.
Lau, W.K.M. and K.-M. Kim, 2015: Robust Hadley Circulation changes and increasing global dryness due to CO2 warming from CMIP5 model projections. *Proceedings of the National Academy of Sciences*, **112(12)**, 3630–3635, doi:10.1073/pnas.1418682112.
Lauer, A. et al., 2018: Process-level improvements in CMIP5 models and their impact on tropical variability, the Southern Ocean, and monsoons. *Earth System Dynamics*, **9(1)**, 33–67, doi:10.5194/esd-9-33-2018.
Lauer, A. et al., 2020: Earth System Model Evaluation Tool (ESMValTool) v2.0 – diagnostics for emergent constraints and future projections from Earth system models in CMIP. *Geoscientific Model Development*, **13(9)**, 4205–4228, doi:10.5194/gmd-13-4205-2020.
Lean, J.L., 2018: Observation-based detection and attribution of 21st century climate change. *Wiley Interdisciplinary Reviews: Climate Change*, **9(2)**, e511, doi:10.1002/wcc.511.
Lee, J., K.R. Sperber, P.J. Gleckler, C.J.W. Bonfils, and K.E. Taylor, 2019: Quantifying the agreement between observed and simulated extratropical modes of interannual variability. *Climate Dynamics*, **52(7–8)**, 4057–4089, doi:10.1007/s00382-018-4355-4.
Lee, J.-Y. and B. Wang, 2014a: Future change of global monsoon in the CMIP5. *Clim. Dyn.*, **42**, 101–119,

SUBMITTED VERSION NOT FOR FINAL EDITING

doi:10.1007/s00382-012-1564-0.
Lee, J.-Y. and B. Wang, 2014b: Future change of global monsoon in the CMIP5. *Clim. Dyn.*, **42**, 101–119, doi:10.1007/s00382-012-1564-0.
Lee, S.K. et al., 2015: Pacific origin of the abrupt increase in Indian Ocean heat content during the warming hiatus. *Nature Geoscience*, **8(6)**, 445–449, doi:10.1038/ngeo2438.
Lee, T., D.E. Waliser, J.-L.F. Li, F.W. Landerer, and M.M. Gierach, 2013: Evaluation of CMIP3 and CMIP5 Wind Stress Climatology Using Satellite Measurements and Atmospheric Reanalysis Products. *Journal of Climate*, **26(16)**, 5810–5826, doi:10.1175/jcli-d-12-00591.1.
Lee, Y.-Y. and R.X. Black, 2013: Boreal winter low-frequency variability in CMIP5 models. *Journal of Geophysical Research: Atmospheres*, **118(13)**, 6891–6904, doi:10.1002/jgrd.50493.
Lee, Y.-Y. and R.X. Black, 2015: The Structure and Dynamics of the Stratospheric Northern Annular Mode in CMIP5 Simulations. *Journal of Climate*, **28(1)**, 86–107, doi:10.1175/jcli-d-13-00570.1.
Lehner, F., C.C. Raible, and T.F. Stocker, 2012: Testing the robustness of a precipitation proxy-based North Atlantic Oscillation reconstruction. *Quaternary Science Reviews*, **45**, 85–94, doi:10.1016/j.quascirev.2012.04.025.
Lehner, F., A.P. Schurer, G.C. Hegerl, C. Deser, and T.L. Frölicher, 2016: The importance of ENSO phase during volcanic eruptions for detection and attribution. *Geophysical Research Letters*, **43(6)**, 2851–2858, doi:10.1002/2016gl067935.
Leroux, S. et al., 2018: Intrinsic and Atmospherically Forced Variability of the AMOC: Insights from a Large-Ensemble Ocean Hindcast. *Journal of Climate*, **31(3)**, 1183–1203, doi:10.1175/jcli-d-17-0168.1.
Levang, S.J. and R.W. Schmitt, 2015: Centennial changes of the global water cycle in CMIP5 models. *Journal of Climate*, **28(16)**, 6489–6502, doi:10.1175/jcli-d-15-0143.1.
Levitus, S. et al., 2012: World ocean heat content and thermosteric sea level change (0-2000m), 1955-2010. *Geophysical Research Letters*, **39(10)**, doi:10.1029/2012gl051106.
Li, C., B. Stevens, and J. Marotzke, 2015: Eurasian winter cooling in the warming hiatus of 1998-2012. *Geophysical Research Letters*, **42(19)**, 8131–8139, doi:10.1002/2015gl065327.
Li, G., S.-P. Xie, and Y. Du, 2015a: Climate Model Errors over the South Indian Ocean Thermocline Dome and Their Effect on the Basin Mode of Interannual Variability. *Journal of Climate*, **28(8)**, 3093–3098, doi:10.1175/jcli-d-14-00810.1.
Li, G., S.-P. Xie, and Y. Du, 2015b: Monsoon-Induced Biases of Climate Models over the Tropical Indian Ocean. *Journal of Climate*, **28(8)**, 3058–3072, doi:10.1175/jcli-d-14-00740.1.
Li, G., S.-P. Xie, G. Li, and S.-P. Xie, 2014: Tropical Biases in CMIP5 Multimodel Ensemble: The Excessive Equatorial Pacific Cold Tongue and Double ITCZ Problems. *Journal of Climate*, **27(4)**, 1765–1780, doi:10.1175/jcli-d-13-00337.1.
Li, H. and T. Ilyina, 2018: Current and Future Decadal Trends in the Oceanic Carbon Uptake Are Dominated by Internal Variability. *Geophysical Research Letters*, **45(2)**, 916–925, doi:10.1002/2017gl075370.
Li, J. et al., 2013: El Niño modulations over the past seven centuries. *Nature Climate Change*, **3(9)**, 822–826, doi:10.1038/nclimate1936.
Li, L., R.W. Schmitt, C.C. Ummenhofer, and K.B. Karnauskas, 2016: Implications of North Atlantic sea surface salinity for summer precipitation over the U.S. Midwest: Mechanisms and predictive value. *Journal of Climate*, **29(9)**, 3143–3159, doi:10.1175/jcli-d-15-0520.1.
Li, X., S.-P. Xie, S.T. Gille, and C. Yoo, 2015: Atlantic-induced pan-tropical climate change over the past three decades. *Nature Climate Change*, **6(3)**, doi:10.1038/nclimate2840.
Li, X., D. Jiang, Z. Tian, and Y. Yang, 2018: Mid-Pliocene global land monsoon from PlioMIP1 simulations. *Palaeogeography, Palaeoclimatology, Palaeoecology*, **512**, 56–70, doi:10.1016/j.palaeo.2018.06.027.
Li, X. et al., 2016: Trend and seasonality of land precipitation in observations and CMIP5 model simulations. *International Journal of Climatology*, **36(11)**, 3781–3793, doi:10.1002/joc.4592.
Li, Y. et al., 2016: Evaluating biases in simulated land surface albedo from CMIP5 global climate models. *Journal of Geophysical Research*, **121(11)**, 6178–6190, doi:10.1002/2016jd024774.
Li, Z. et al., 2018a: Non-uniform seasonal warming regulates vegetation greening and atmospheric CO2 amplification over northern lands. *Environmental Research Letters*, **13(12)**, 124008, doi:10.1088/1748-9326/aae9ad.
Li, Z. et al., 2018b: Non-uniform seasonal warming regulates vegetation greening and atmospheric CO2 amplification over northern lands. *Environmental Research Letters*, **13(12)**, 124008, doi:10.1088/1748-9326/aae9ad.
Li, Z. et al., 2020: A robust relationship between multidecadal global warming rate variations and the Atlantic Multidecadal Variability. *Climate Dynamics*, **55(7–8)**, 1945–1959, doi:10.1007/s00382-020-05362-8.
Liang, Y., N.P. Gillett, and A.H. Monahan, 2020: Climate Model Projections of 21st Century Global Warming Constrained Using the Observed Warming Trend. *Geophysical Research Letters*, **47(12)**, doi:10.1029/2019gl086757.
Liguori, G., S. McGregor, J.M. Arblaster, M.S. Singh, and G.A. Meehl, 2020: A joint role for forced and internally-driven variability in the decadal modulation of global warming. *Nature Communications*, **11(1)**, doi:10.1038/s41467-020-17683-7.
Lim, E.-P. et al., 2016: The impact of the Southern Annular Mode on future changes in Southern Hemisphere rainfall.

ACCEPTED VERSION SUBJECT TO FINAL EDITING

Geophysical Research Letters, **43(13)**, 7160–7167, doi:10.1002/2016gl069453.
Lim, Y.-K., R.I. Cullather, S.M.J. Nowicki, and K.-M. Kim, 2019: Inter-relationship between subtropical Pacific sea surface temperature, Arctic sea ice concentration, and North Atlantic Oscillation in recent summers. *Scientific Reports*, **9(1)**, 3481, doi:10.1038/s41598-019-39896-7.
Lin, Y.-L. et al., 2019: The Community Integrated Earth System Model (CIESM) from Tsinghua University and its plan for CMIP6 experiments. *Advances in Climate Change Research*, **15(5)**, 545–550, doi:10.12006/j.issn.1673-1719.2019.166.
Liu, F. et al., 2016: Global monsoon precipitation responses to large volcanic eruptions. *Scientific Reports*, **6(1)**, 24331, doi:10.1038/srep24331.
Liu, H., C. Wang, S.-K. Lee, and D. Enfield, 2013: Atlantic Warm Pool Variability in the CMIP5 Simulations. *Journal of Climate*, **26(15)**, 5315–5336, doi:10.1175/jcli-d-12-00556.1.
Liu, J. et al., 2012: What drives the global summer monsoon over the past millennium? *Climate Dynamics*, **39(5)**, 1063–1072, doi:10.1007/s00382-012-1360-x.
Liu, L. et al., 2014: Indian Ocean variability in the CMIP5 multi-model ensemble: the zonal dipole mode. *Climate Dynamics*, **43(5)**, 1715–1730, doi:10.1007/s00382-013-2000-9.
Liu, S., D. Jiang, and X. Lang, 2018: A multi-model analysis of moisture changes during the last glacial maximum. *Quaternary Science Reviews*, **191**, 363–377, doi:10.1016/j.quascirev.2018.05.029.
Liu, W., S.P. Xie, and J. Lu, 2016: Tracking ocean heat uptake during the surface warming hiatus. *Nature Communications*, **7**, 1–9, doi:10.1038/ncomms10926.
Liu, W., S.-P. Xie, Z. Liu, and J. Zhu, 2017: Overlooked possibility of a collapsed Atlantic Meridional Overturning Circulation in warming climate. *Science Advances*, **3(1)**, doi:10.1126/sciadv.1601666.
Liu, Y. et al., 2017: Recent enhancement of central Pacific El Niño variability relative to last eight centuries. *Nature Communications*, **8(1)**, 15386, doi:10.1038/ncomms15386.
Ljungqvist, F.C. et al., 2019: Centennial-scale temperature change in last millennium simulations and proxy-based reconstructions. *Journal of Climate*, **32(9)**, 2441–2482, doi:10.1175/jcli-d-18-0525.1.
Long, S.-M., G. Li, K. Hu, and J. Ying, 2020: Origins of the IOD-like Biases in CMIP Multimodel Ensembles: The Atmospheric Component and Ocean–Atmosphere Coupling. *Journal of Climate*, **33(24)**, 10437–10453, doi:10.1175/jcli-d-20-0459.1.
Lora, J.M., 2018: Components and mechanisms of hydrologic cycle changes over North America at the Last Glacial Maximum. *Journal of Climate*, **31(17)**, 7035–7051, doi:10.1175/jcli-d-17-0544.1.
Lovejoy, S., 2014: Return periods of global climate fluctuations and the pause. *Geophysical Research Letters*, **41(13)**, 4704–4710, doi:10.1002/2014gl060478.
Lovenduski, N.S., N. Gruber, and S.C. Doney, 2008: Toward a mechanistic understanding of the decadal trends in the Southern Ocean carbon sink. *Global Biogeochemical Cycles*, **22(3)**, n/a–n/a, doi:10.1029/2007gb003139.
Lovenduski, N.S., G.A. McKinley, A.R. Fay, K. Lindsay, and M.C. Long, 2016: Partitioning uncertainty in ocean carbon uptake projections: Internal variability, emission scenario, and model structure. *Global Biogeochemical Cycles*, **30(9)**, 1276–1287, doi:10.1002/2016gb005426.
Lu, X., L. Wang, and M.F. McCabe, 2016: Elevated CO2 as a driver of global dryland greening. *Scientific Reports*, **6**, 20716.
Lübbecke, J.F. et al., 2018: Equatorial Atlantic variability – Modes, mechanisms, and global teleconnections. *Wiley Interdisciplinary Reviews: Climate Change*, **9(4)**, e527, doi:10.1002/wcc.527.
Lücke, L.J., G.C. Hegerl, A.P. Schurer, and R. Wilson, 2019: Effects of memory biases on variability of temperature reconstructions. *Journal of Climate*, **32(24)**, 8713–8731, doi:10.1175/jcli-d-19-0184.1.
Lüdecke, H.-J., R. Cina, H.-J. Dammschneider, and S. Lüning, 2020: Decadal and multidecadal natural variability in European temperature. *Journal of Atmospheric and Solar-Terrestrial Physics*, **205**, 105294, doi:10.1016/j.jastp.2020.105294.
Lunt, D.J. et al., 2017: The DeepMIP contribution to PMIP4: experimental designfor model simulations of the EECO, PETM, and pre-PETM (version 1.0). *Geoscientific Model Development*, **10(2)**, 889–901, doi:10.5194/gmd-10-889-2017.
Lunt, D.J. et al., 2021: DeepMIP: model intercomparison of early Eocene climatic optimum (EECO) large-scale climate features and comparison with proxy data. *Climate of the Past*, **17(1)**, 203–227, doi:10.5194/cp-17-203-2021.
Luo, B., 2018: Aerosol Radiative Forcing and SAD version v4.0.0 1850 – 2016. Retrieved from: ftp://iacftp.ethz.ch/pub_read/luo/cmip6_sad_radforcing_v4.0.0.
Luo, J.-J., W. Sasaki, and Y. Masumoto, 2012: Indian Ocean warming modulates Pacific climate change. *Proceedings of the National Academy of Sciences*, **109(46)**, 18701–18706, doi:10.1073/pnas.1210239109.
Lyu, K., X. Zhang, J.A. Church, and J. Hu, 2016: Evaluation of the interdecadal variability of sea surface temperature and sea level in the Pacific in CMIP3 and CMIP5 models. *International Journal of Climatology*, **36(11)**, 3723–3740, doi:10.1002/joc.4587.
Ma, S. and T. Zhou, 2016a: Robust Strengthening and Westward Shift of the Tropical Pacific Walker Circulation during 1979–2012: A Comparison of 7 Sets of Reanalysis Data and 26 CMIP5 Models. *Journal of Climate*, **29(9)**, 3097–3118, doi:10.1175/jcli-d-15-0398.1.

ACCEPTED VERSION
SUBJECT TO FINAL EDITING

Ma, S. and T. Zhou, 2016b: Robust Strengthening and Westward Shift of the Tropical Pacific Walker Circulation during 1979–2012: A Comparison of 7 Sets of Reanalysis Data and 26 CMIP5 Models. *Journal of Climate*, **29(9)**, 3097–3118, doi:10.1175/jcli-d-15-0398.1.

Ma, S. and T. Zhou, 2016c: Robust Strengthening and Westward Shift of the Tropical Pacific Walker Circulation during 1979–2012: A Comparison of 7 Sets of Reanalysis Data and 26 CMIP5 Models. *Journal of Climate*, **29(9)**, 3097–3118, doi:10.1175/jcli-d-15-0398.1.

Maher, N., A. Gupta, and M.H. England, 2014: Drivers of decadal hiatus periods in the 20th and 21st centuries. *Geophysical Research Letters*, **41(16)**, 5978–5986, doi:10.1002/2014gl060527.

Maher, N., M.H. England, A. Gupta, and P. Spence, 2018a: Role of Pacific trade winds in driving ocean temperatures during the recent slowdown and projections under a wind trend reversal. *Climate Dynamics*, **51(1–2)**, 321–336, doi:10.1007/s00382-017-3923-3.

Maher, N., D. Matei, S. Milinski, and J. Marotzke, 2018b: ENSO Change in Climate Projections: Forced Response or Internal Variability? *Geophysical Research Letters*, **45(20)**, doi:10.1029/2018gl079764.

Mahlstein, I. and R. Knutti, 2011: Ocean Heat Transport as a Cause for Model Uncertainty in Projected Arctic Warming. *Journal of Climate*, **24(5)**, 1451–1460, doi:10.1175/2010jcli3713.1.

Mahlstein, I. and R. Knutti, 2012: September Arctic sea ice predicted to disappear near 2°C global warming above present. *Journal of Geophysical Research: Atmospheres*, **117(D6)**, doi:10.1029/2011jd016709.

Mahlstein, I., P.R. Gent, and S. Solomon, 2013: Historical Antarctic mean sea ice area, sea ice trends, and winds in CMIP5 simulations. *Journal of Geophysical Research: Atmospheres*, **118(11)**, 5105–5110, doi:10.1002/jgrd.50443.

Mahowald, N.M. et al., 2017: Interactions between land use change and carbon cycle feedbacks. *Global Biogeochemical Cycles*, **31(1)**, 96–113.

Maki, T. et al., 2010: New technique to analyse global distributions of CO2 concentrations and fluxes from non-processed observational data. *Tellus, Series B: Chemical and Physical Meteorology*, **62(5)**, 797–809, doi:10.1111/j.1600-0889.2010.00488.x.

Malik, A., S. Brönnimann, and P. Perona, 2018: Statistical link between external climate forcings and modes of ocean variability. *Climate Dynamics*, **50(9–10)**, 3649–3670, doi:10.1007/s00382-017-3832-5.

Mann, M.E., B.A. Steinman, and S.K. Miller, 2014: On forced temperature changes, internal variability, and the AMO. *Geophysical Research Letters*, **41(9)**, doi:10.1002/2014gl059233.

Mann, M.E., B.A. Steinman, and S.K. Miller, 2020: Absence of internal multidecadal and interdecadal oscillations in climate model simulations. *Nature Communications*, **11(1)**, 49, doi:10.1038/s41467-019-13823-w.

Mann, M.E., B.A. Steinman, D.J. Brouillette, and S.K. Miller, 2021: Multidecadal climate oscillations during the past millennium driven by volcanic forcing. *Science*, **371(6533)**, 1014 LP – 1019, doi:10.1126/science.abc5810.

Mantsis, D.F., S. Sherwood, R. Allen, and L. Shi, 2017: Natural variations of tropical width and recent trends. *Geophysical Research Letters*, **44(8)**, 3825–3832, doi:10.1002/2016gl072097.

Mantua, N.J. and S.R. Hare, 2002: The Pacific Decadal Oscillation. *Journal of Oceanography*, **58(1)**, 35–44, doi:10.1023/a:1015820616384.

Mantua, N.J., S.R. Hare, Y. Zhang, J.M. Wallace, and R.C. Francis, 1997: A Pacific Interdecadal Climate Oscillation with Impacts on Salmon Production. *Bulletin of the American Meteorological Society*, **78(6)**, 1069–1080, doi:10.1175/1520-0477(1997)078<1069:apicow>2.0.co;2.

Mao, J. et al., 2013: Global latitudinal-asymmetric vegetation growth trends and their driving mechanisms: 1982-2009. *Remote Sensing*, doi:10.3390/rs5031484.

Mao, J. et al., 2016: Human-induced greening of the northern extratropical land surface. *Nature Climate Change*, **6**, 959, doi:10.1038/nclimate3056.

Marcos, M. and A. Amores, 2014: Quantifying anthropogenic and natural contributions to thermosteric sea level rise. *Geophysical Research Letters*, **41(7)**, 2502–2507, doi:10.1002/2014gl059766.

Marshall, J. and T. Radko, 2003: Residual-mean solutions for the Antarctic Circumpolar Current and its associated overturning circulation. *Journal of Physical Oceanography*, **33(11)**, 2341–2354, doi:10.1175/1520-0485(2003)033<2341:rsftac>2.0.co;2.

Martin, E.R., C. Thorncroft, and B.B.B. Booth, 2013: The Multidecadal Atlantic SST-Sahel Rainfall Teleconnection in CMIP5 Simulations. *Journal of Climate*, **27(2)**, 784–806, doi:10.1175/jcli-d-13-00242.1.

Martín-Rey, M., I. Polo, B. Rodríguez-Fonseca, T. Losada, and A. Lazar, 2018: Is There Evidence of Changes in Tropical Atlantic Variability Modes under AMO Phases in the Observational Record? *Journal of Climate*, **31(2)**, 515–536, doi:10.1175/jcli-d-16-0459.1.

Marvel, K. and C. Bonfils, 2013: Identifying external influences on global precipitation. *Proceedings of the National Academy of Sciences*, **110(48)**, 19301–19306, doi:10.1073/pnas.1314382110.

Marvel, K. et al., 2017: Observed and Projected Changes to the Precipitation Annual Cycle. *Journal of Climate*, **30(13)**, 4983–4995, doi:10.1175/jcli-d-16-0572.1.

Marvel, K. et al., 2019: Twentieth-century hydroclimate changes consistent with human influence. *Nature*, **569(7754)**, 59–65, doi:10.1038/s41586-019-1149-8.

Marzeion, B., J.G. Cogley, K. Richter, and D. Parkes, 2014: Glaciers. Attribution of global glacier mass loss to

ACCEPTED VERSION SUBJECT TO FINAL EDITING

anthropogenic and natural causes.. *Science (New York, N.Y.)*, **345(6199)**, 919–921, doi:10.1126/science.1254702.
Marzeion, B. et al., 2020: Partitioning the Uncertainty of Ensemble Projections of Global Glacier Mass Change. *Earth's Future*, **8(7)**, doi:10.1029/2019ef001470.
Marzocchi, A. and M.F. Jansen, 2017: Connecting Antarctic sea ice to deep-ocean circulation in modern and glacial climate simulations. *Geophysical Research Letters*, **44(12)**, 6286–6295, doi:10.1002/2017gl073936.
Masson-Delmotte, V. et al., 2013a: Information from Paleoclimate Archives. In: *Climate Change 2013: The Physical Science Basis. Contribution of Working Group I to the Fifth Assessment Report of the Intergovernmental Panel on Climate Change* [Stocker, T.F., D. Qin, G.-K. Plattner, M. Tignor, S.K. Allen, J. Boschung, A. Nauels, Y. Xia, V. Bex, and P.M. Midgley (eds.)]. Cambridge University Press, Cambridge, United Kingdom and New York, NY, USA, pp. 383–464, doi:10.1017/cbo9781107415324.013.
Masson-Delmotte, V. et al., 2013b: Information from Paleoclimate Archives. In: *Climate Change 2013: The Physical Science Basis. Contribution of Working Group I to the Fifth Assessment Report of the Intergovernmental Panel on Climate Change* [Stocker, T.F., D. Qin, G.-K. Plattner, M. Tignor, S.K. Allen, J. Boschung, A. Nauels, Y. Xia, V. Bex, and P.M. Midgley (eds.)]. Cambridge University Press, Cambridge, United Kingdom and New York, NY, USA, pp. 383–464, doi:10.1017/cbo9781107415324.013.
Massonnet, F. et al., 2012: Constraining projections of summer Arctic sea ice. *The Cryosphere*, **6(6)**, 1383–1394, doi:10.5194/tc-6-1383-2012.
Massonnet, F. et al., 2018: Arctic sea-ice change tied to its mean state through thermodynamic processes. *Nature Climate Change*, **8(7)**, 599–603, doi:10.1038/s41558-018-0204-z.
Mauritsen, T. and B. Stevens, 2015: Missing iris effect as a possible cause of muted hydrological change and high climate sensitivity in models. *Nature Geoscience*, **8(5)**, 346–351, doi:10.1038/ngeo2414.
Mauritsen, T. and E. Roeckner, 2020: Tuning the MPI-ESM1.2 Global Climate Model to Improve the Match With Instrumental Record Warming by Lowering Its Climate Sensitivity. *Journal of Advances in Modeling Earth Systems*, **12(5)**, doi:10.1029/2019ms002037.
Mauritsen, T. et al., 2019: Developments in the MPI-M Earth System Model version 1.2 (MPI-ESM1.2) and Its Response to Increasing CO2. *Journal of Advances in Modeling Earth Systems*, **11(4)**, doi:10.1029/2018ms001400.
Maycock, A.C. et al., 2018: Revisiting the mystery of recent stratospheric temperature trends. *Geophysical Research Letters*, doi:10.1029/2018gl078035.
McClymont, E.L. et al., 2020: Lessons from a high-CO2 world: An ocean view from ~3 million years ago. *Climate of the Past*, **16(4)**, doi:10.5194/cp-16-1599-2020.
McGregor, H.V. et al., 2015: Robust global ocean cooling trend for the pre-industrial Common Era. *Nature Geoscience*, **8(9)**, 671–677, doi:10.1038/ngeo2510.
McGregor, S., A. Timmermann, M.H. England, O. Elison Timm, and A.T. Wittenberg, 2013: Inferred changes in El Niño–Southern Oscillation variance over the past six centuries. *Climate of the Past*, **9(5)**, 2269–2284, doi:10.5194/cp-9-2269-2013.
McGregor, S., M.F. Stuecker, J.B. Kajtar, M.H. England, and M. Collins, 2018: Model tropical Atlantic biases underpin diminished Pacific decadal variability. *Nature Climate Change*, **8(6)**, 493–498, doi:10.1038/s41558-018-0163-4.
McGregor, S. et al., 2014: Recent walker circulation strengthening and pacific cooling amplified by atlantic warming. *Nature Climate Change*, **4(10)**, doi:10.1038/nclimate2330.
McKenna, S., A. Santoso, A. Gupta, A.S. Taschetto, and W. Cai, 2020: Indian Ocean Dipole in CMIP5 and CMIP6: characteristics, biases, and links to ENSO. *Scientific Reports*, **10(1)**, 11500, doi:10.1038/s41598-020-68268-9.
McKitrick, R. and J. Christy, 2018: A Test of the Tropical 200- to 300-hPa Warming Rate in Climate Models. *Earth and Space Science*, **5(9)**, 529–536, doi:10.1029/2018ea000401.
McKitrick, R. and J. Christy, 2019: Assessing changes in US regional precipitation on multiple time scales. *Journal of Hydrology*, **578**, doi:10.1016/j.jhydrol.2019.124074.
McKitrick, R. and J. Christy, 2020: Pervasive Warming Bias in CMIP6 Tropospheric Layers. *Earth and Space Science*, **7(9)**, 1–8, doi:10.1029/2020ea001281.
McPhaden, M.J., S.E. Zebiak, and M.H. Glantz, 2006: ENSO as an integrating concept in earth science. *Science*, **314(5806)**, 1740–1745, doi:10.1126/science.1132588.
McPhaden, M.J., T. Lee, and D. McClurg, 2011: El Niño and its relationship to changing background conditions in the tropical Pacific Ocean. *Geophysical Research Letters*, **38(15)**, 2–5, doi:10.1029/2011gl048275.
Mecking, J., S.S. Drijfhout, L.C. Jackson, and M.B. Andrews, 2017: The effect of model bias on Atlantic freshwater transport and implications for AMOC bi-stability. *Tellus A: Dynamic Meteorology and Oceanography*, **69(1)**, 1299910, doi:10.1080/16000870.2017.1299910.
Medhaug, I. and H. Drange, 2016: Global and regional surface cooling in a warming climate: a multi-model analysis. *Climate Dynamics*, **46(11–12)**, 3899–3920, doi:10.1007/s00382-015-2811-y.
Medhaug, I., M.B. Stolpe, E.M. Fischer, and R. Knutti, 2017: Reconciling controversies about the 'global warming hiatus'. *Nature*, **545**, 41, doi:10.1038/nature22315.

ACCEPTED VERSION SUBJECT TO FINAL EDITING

Meehl, G.A., H. Teng, and J.M. Arblaster, 2014: Climate model simulations of the observed early-2000s hiatus of global warming. *Nature Climate Change*, **4(10)**, 898–902, doi:10.1038/nclimate2357.
Meehl, G.A., A. Hu, and H. Teng, 2016a: Initialized decadal prediction for transition to positive phase of the Interdecadal Pacific Oscillation. *Nature Communications*, **7**, 1–7, doi:10.1038/ncomms11718.
Meehl, G.A., A. Hu, B.D. Santer, and S.P. Xie, 2016b: Contribution of the Interdecadal Pacific Oscillation to twentieth-century global surface temperature trends. *Nature Climate Change*, **6(11)**, 1005–1008, doi:10.1038/nclimate3107.
Meehl, G.A., J.M. Arblaster, J.T. Fasullo, A. Hu, and K.E. Trenberth, 2011: Model-based evidence of deep-ocean heat uptake during surface-temperature hiatus periods. *Nature Climate Change*, **1(7)**, 360–364, doi:10.1038/nclimate1229.
Meehl, G.A., A. Hu, J.M. Arblaster, J. Fasullo, and K.E. Trenberth, 2013: Externally Forced and Internally Generated Decadal Climate Variability Associated with the Interdecadal Pacific Oscillation. *Journal of Climate*, **26(18)**, 7298–7310, doi:10.1175/jcli-d-12-00548.1.
Meehl, G.A., J.M. Arblaster, C.M. Bitz, C.T.Y. Chung, and H. Teng, 2016c: Antarctic sea-ice expansion between 2000 and 2014 driven by tropical Pacific decadal climate variability. *Nature Geoscience*, **9(8)**, 590–595, doi:10.1038/ngeo2751.
Meehl, G.A., C.T.Y. Chung, J.M. Arblaster, M.M. Holland, and C.M. Bitz, 2018: Tropical Decadal Variability and the Rate of Arctic Sea Ice Decrease. *Geophysical Research Letters*, **45(20)**, 11,311–326,333, doi:10.1029/2018gl079989.
Meehl, G.A. et al., 2007: The WCRP CMIP3 multimodel dataset: A new era in climatic change research. *Bulletin of the American Meteorological Society*, **88(9)**, 1383–1394, doi:10.1175/bams-88-9-1383.
Meehl, G.A. et al., 2019: Sustained ocean changes contributed to sudden Antarctic sea ice retreat in late 2016. *Nature Communications*, **10(1)**, 14, doi:10.1038/s41467-018-07865-9.
Meehl, G.A. et al., 2020: Context for interpreting equilibrium climate sensitivity and transient climate response from the CMIP6 Earth system models. *Science Advances*, **6(26)**, doi:10.1126/sciadv.aba1981.
Meijers, A.J.S. et al., 2012: Representation of the Antarctic Circumpolar Current in the CMIP5 climate models and future changes under warming scenarios. *Journal of Geophysical Research: Oceans*, **117(12)**, C12008, doi:10.1029/2012jc008412.
Menary, M.B. and A.A. Scaife, 2014: Naturally forced multidecadal variability of the Atlantic meridional overturning circulation. *Climate Dynamics*, **42(5)**, 1347–1362, doi:10.1007/s00382-013-2028-x.
Menary, M.B. et al., 2013: Mechanisms of aerosol-forced AMOC variability in a state of the art climate model. *Journal of Geophysical Research: Oceans*, **118(4)**, 2087–2096, doi:10.1002/jgrc.20178.
Menary, M.B. et al., 2015: Exploring the impact of CMIP5 model biases on the simulation of North Atlantic decadal variability. *Geophysical Research Letters*, **42(14)**, 5926–5934, doi:10.1002/2015gl064360.
Menary, M.B. et al., 2018: Preindustrial Control Simulations With HadGEM3-GC3.1 for CMIP6. *Journal of Advances in Modeling Earth Systems*, 2018MS001495, doi:10.1029/2018ms001495.
Menary, M.B. et al., 2020: Aerosol-Forced AMOC Changes in CMIP6 Historical Simulations. *Geophysical Research Letters*, **47(14)**, doi:10.1029/2020gl088166.
Ménégoz, M. et al., 2018: Role of the Atlantic Multidecadal Variability in modulating the climate response to a Pinatubo-like volcanic eruption. *Climate Dynamics*, **51(5–6)**, 1863–1883, doi:10.1007/s00382-017-3986-1.
Meredith, M. et al., 2019: Polar Regions. In: *IPCC Special Report on the Ocean and Cryosphere in a Changing Climate* [Pörtner, H.-O., D.C. Roberts, V. Masson-Delmotte, P. Zhai, M. Tignor, E. Poloczanska, K. Mintenbeck, A. Alegría, M. Nicolai, A. Okem, J. Petzold, B. Rama, and N.M. Weyer (eds.)]. In Press, pp. 203–320.
Meyerholt, J., K. Sickel, and S. Zaehle, 2020: Ensemble projections elucidate effects of uncertainty in terrestrial nitrogen limitation on future carbon uptake. *Global Change Biology*, **26(7)**, doi:10.1111/gcb.15114.
Meyssignac, B. et al., 2017: Evaluating model simulations of twentieth-century sea-level rise. Part II: Regional sea-level changes. *Journal of Climate*, **30(21)**, 8565–8593, doi:10.1175/jcli-d-17-0112.1.
Michel, S. et al., 2020: Reconstructing climatic modes of variability from proxy records using ClimIndRec version 1.0. *Geoscientific Model Development*, **13(2)**, 841–858, doi:10.5194/gmd-13-841-2020.
Middlemas, E.A. and A.C. Clement, 2016: Spatial Patterns and Frequency of Unforced Decadal-Scale Changes in Global Mean Surface Temperature in Climate Models. *Journal of Climate*, **29(17)**, 6245–6257, doi:10.1175/jcli-d-15-0609.1.
Min, S.K., X. Zhang, and F. Zwiers, 2008: Human-induced Arctic moistening. *Science*, **320(5875)**, 518–520, doi:10.1126/science.1153468.
Min, S.-K., X. Zhang, F.W. Zwiers, and T. Agnew, 2008: Human influence on Arctic sea ice detectable from early 1990s onwards. *Geophysical Research Letters*, **35(21)**, doi:10.1029/2008gl035725.
Min, S.-K., X. Zhang, F.W. Zwiers, and G.C. Hegerl, 2011: Human contribution to more-intense precipitation extremes. *Nature*, **470**, 378–381, doi:10.1038/nature09763.
Mitchell, D. et al., 2017: Assessing mid-latitude dynamics in extreme event attribution systems. *CLIMATE DYNAMICS*, **48(11)**, 3889–3901, doi:10.1007/s00382-016-3308-z.
Mitchell, D.M., 2016: Attributing the forced components of observed stratospheric temperature variability to external

ACCEPTED VERSION SUBJECT TO FINAL EDITING

drivers. *Quarterly Journal of the Royal Meteorological Society*, **142(695)**, 1041–1047, doi:10.1002/qj.2707.
Mitchell, D.M., P.W. Thorne, P.A. Stott, and L.J. Gray, 2013: Revisiting the controversial issue of tropical tropospheric temperature trends. *Geophysical Research Letters*, **40(11)**, 2801–2806, doi:10.1002/grl.50465.
Mitchell, D.M., Y.T.E. Lo, W.J.M. Seviour, L. Haimberger, and L.M. Polvani, 2020: The vertical profile of recent tropical temperature trends: Persistent model biases in the context of internal variability. *Environmental Research Letters*, **15(10)**, doi:10.1088/1748-9326/ab9af7.
Mitchell, D.M. et al., 2012: The effect of climate change on the variability of the Northern Hemisphere stratospheric polar vortex. *Journal of the atmospheric sciences*, **69(8)**, 2608–2618.
Mochizuki, T., M. Kimoto, M. Watanabe, Y. Chikamoto, and M. Ishii, 2016: Interbasin effects of the Indian Ocean on Pacific decadal climate change. *Geophysical Research Letters*, **43(13)**, 7168–7175, doi:10.1002/2016gl069940.
Moffa-Sánchez, P., A. Born, I.R. Hall, D.J.R. Thornalley, and S. Barker, 2014: Solar forcing of North Atlantic surface temperature and salinity over the past millennium. *Nature Geoscience*, **7(4)**, 275–278, doi:10.1038/ngeo2094.
Mohtadi, M., M. Prange, and S. Steinke, 2016: Palaeoclimatic insights into forcing and response of monsoon rainfall. *Nature*, **533(7602)**, 191–199, doi:10.1038/nature17450.
Molteni, F., R. Farneti, F. Kucharski, and T.N. Stockdale, 2017: Modulation of air-sea fluxes by extratropical planetary waves and its impact during the recent surface warming slowdown. *Geophysical Research Letters*, **44(3)**, 1494–1502, doi:10.1002/2016gl072298.
Monerie, P.-A., J. Robson, B. Dong, D.L.R. Hodson, and N.P. Klingaman, 2019: Effect of the Atlantic Multidecadal Variability on the Global Monsoon. *Geophysical Research Letters*, **46(3)**, 1765–1775, doi:10.1029/2018gl080903.
Mongwe, N.P., M. Vichi, and P.M.S. Monteiro, 2018: The seasonal cycle of pCO2 and CO2 fluxes in the Southern Ocean: diagnosing anomalies in CMIP5 Earth system models. *Biogeosciences*, **15(9)**, 2851–2872, doi:10.5194/bg-15-2851-2018.
Monselesan, D.P., T.J. O'Kane, J.S. Risbey, and J. Church, 2015: Internal climate memory in observations and models. *Geophysical Research Letters*, **42(4)**, 1232–1242, doi:10.1002/2014gl062765.
Moorman, R., A.K. Morrison, and A. McC. Hogg, 2020: Thermal Responses to Antarctic Ice Shelf Melt in an Eddy-Rich Global Ocean–Sea Ice Model. *Journal of Climate*, **33(15)**, 6599–6620, doi:10.1175/jcli-d-19-0846.1.
Morgenstern, O. et al., 2014: Direct and ozone-mediated forcing of the Southern Annular Mode by greenhouse gases. *Geophysical Research Letters*, **41(24)**, 9050–9057, doi:10.1002/2014gl062140.
Morgenstern, O. et al., 2018: Ozone sensitivity to varying greenhouse gases and ozone-depleting substances in CCMI-1 simulations. *Atmospheric Chemistry and Physics*, **18(2)**, 1091–1114, doi:10.5194/acp-18-1091-2018.
Morgenstern, O. et al., 2020: Reappraisal of the Climate Impacts of Ozone-Depleting Substances. *Geophysical Research Letters*, **47(20)**, e2020GL088295, doi:10.1029/2020gl088295.
Morice, C.P., J.J. Kennedy, N.A. Rayner, and P.D. Jones, 2012: Quantifying uncertainties in global and regional temperature change using an ensemble of observational estimates: The HadCRUT4 data set. *Journal of Geophysical Research: Atmospheres*, **117(D8)**, doi:10.1029/2011jd017187.
Mouginot, J. et al., 2019: Forty-six years of Greenland Ice Sheet mass balance from 1972 to 2018. *Proceedings of the National Academy of Sciences*, **116(19)**, 9239 LP – 9244, doi:10.1073/pnas.1904242116.
Mudryk, L. et al., 2020: Historical Northern Hemisphere snow cover trends and projected changes in the CMIP6 multi-model ensemble. *Cryosphere*, **14(7)**, 2495–2514, doi:10.5194/tc-14-2495-2020.
Mueller, B.L., N.P. Gillett, A.H. Monahan, and F.W. Zwiers, 2018: Attribution of Arctic Sea Ice Decline from 1953 to 2012 to Influences from Natural, Greenhouse Gas, and Anthropogenic Aerosol Forcing. *Journal of Climate*, **31(19)**, 7771–7787, doi:10.1175/jcli-d-17-0552.1.
Muglia, J. and A. Schmittner, 2015: Glacial Atlantic overturning increased by wind stress in climate models. *Geophysical Research Letters*, **42(22)**, 9862–9868, doi:10.1002/2015gl064583.
Mulcahy, J.P. et al., 2020: Description and evaluation of aerosol in UKESM1 and HadGEM3-GC3.1 CMIP6 historical simulations. *Geoscientific Model Development*, **13(12)**, 6383–6423, doi:10.5194/gmd-13-6383-2020.
Müller, W.A. et al., 2015: A twentieth-century reanalysis forced ocean model to reconstruct the North Atlantic climate variation during the 1920s. *Climate Dynamics*, **44(7–8)**, 1935–1955, doi:10.1007/s00382-014-2267-5.
Muñoz, E., W. Weijer, S.A. Grodsky, S.C. Bates, and I. Wainer, 2012: Mean and variability of the tropical Atlantic Ocean in the CCSM4. *Journal of Climate*, **25(14)**, 4860–4882, doi:10.1175/jcli-d-11-00294.1.
Murphy, D.M., 2013: Little net clear-sky radiative forcing from recent regional redistribution of aerosols. *Nature Geoscience*, **6**, 258, doi:10.1038/ngeo1740.
Murphy, L.N., K. Bellomo, M. Cane, and A. Clement, 2017: The role of historical forcings in simulating the observed Atlantic multidecadal oscillation. *Geophysical Research Letters*, **44(5)**, 2472–2480, doi:10.1002/2016gl071337.
Najafi, M.R., F.W. Zwiers, and N.P. Gillett, 2016: Attribution of the spring snow cover extent decline in the Northern Hemisphere, Eurasia and North America to anthropogenic influence. *Climatic Change*, **136(3)**, 571–586, doi:10.1007/s10584-016-1632-2.
Najafi, M.R., F.W. Zwiers, and N.P. Gillett, 2017: Attribution of observed streamflow changes in key British Columbia

SUBJECT TO FINAL EDITING ACCEPTED VERSION

drainage basins. *Geophysical Research Letters*, **44(21)**, 11–12, doi:10.1002/2017gl075016.
Nakamura, T. et al., 2015: A negative phase shift of the winter AO/NAO due to the recent Arctic sea-ice reduction in late autumn. *Journal of Geophysical Research: Atmospheres*, **120(8)**, 3209–3227, doi:10.1002/2014jd022848.
Neukom, R., A.P. Schurer, N.J. Steiger, and G.C. Hegerl, 2018: Possible causes of data model discrepancy in the temperature history of the last Millennium. *Scientific Reports*, **8(1)**, 7572, doi:10.1038/s41598-018-25862-2.
Nevison, C.D. et al., 2016: Evaluating CMIP5 ocean biogeochemistry and Southern Ocean carbon uptake using atmospheric potential oxygen: Present-day performance and future projection. *Geophysical Research Letters*, **43(5)**, 2077–2085, doi:10.1002/2015gl067584.
Newman, M., S.-I. Shin, and M.A. Alexander, 2011: Natural variation in ENSO flavors. *Geophysical Research Letters*, **38(14)**, doi:10.1029/2011gl047658.
Newman, M. et al., 2016: The Pacific decadal oscillation, revisited. *Journal of Climate*, **29(12)**, 4399–4427, doi:10.1175/jcli-d-15-0508.1.
Nguyen, H., C. Lucas, A. Evans, B. Timbal, and L. Hanson, 2015: Expansion of the Southern Hemisphere hadley cell in response to greenhouse gas forcing. *Journal of Climate*, **28(20)**, 8067–8077, doi:10.1175/jcli-d-15-0139.1.
Ni, Y. and P.-C. Hsu, 2018: Inter-annual variability of global monsoon precipitation in present-day and future warming scenarios based on 33 Coupled Model Intercomparison Project Phase 5 models. *International Journal of Climatology*, **38(13)**, 4875–4890, doi:10.1002/joc.5704.
Nidheesh, A.G. et al., 2017: Influence of ENSO on the Pacific decadal oscillation in CMIP models. *Climate Dynamics*, **49(9–10)**, 3309–3326, doi:10.1007/s00382-016-3514-8.
Nieves, V., J.K. Willis, and W.C. Patzert, 2015: Recent hiatus caused by decadal shift in Indo-Pacific heating. *Science*, **349(6247)**, 532–535, doi:10.1126/science.aaa4521.
Nijsse, F.J.M.M., P.M. Cox, and M.S. Williamson, 2020: Emergent constraints on transient climate response (TCR) and equilibrium climate sensitivity (ECS) from historical warming in CMIP5 and CMIP6 models. *Earth System Dynamics*, **11(3)**, doi:10.5194/esd-11-737-2020.
Ning, L. and R.S. Bradley, 2016: NAO and PNA influences on winter temperature and precipitation over the eastern United States in CMIP5 GCMs. *Climate Dynamics*, **46(3)**, 1257–1276, doi:10.1007/s00382-015-2643-9.
Nnamchi, H.C. et al., 2015: Thermodynamic controls of the Atlantic Niño. *Nature Communications*, **6(1)**, 8895, doi:10.1038/ncomms9895.
Notz, D., 2014: Sea-ice extent and its trend provide limited metrics of model performance. *The Cryosphere*, **8(1)**, 229–243, doi:10.5194/tc-8-229-2014.
Notz, D. and J. Marotzke, 2012: Observations reveal external driver for Arctic sea-ice retreat. *Geophysical Research Letters*, **39(8)**, doi:10.1029/2012gl051094.
Notz, D. and J. Stroeve, 2016: Observed Arctic sea-ice loss directly follows anthropogenic CO2 emission. *Science*, **354(6313)**, 747–750, doi:10.1126/science.aag2345.
Notz, D. et al., 2020: Arctic Sea Ice in CMIP6. *Geophysical Research Letters*, **47(10)**, e2019GL086749, doi:10.1029/2019gl086749.
Nowicki, S. and H. Seroussi, 2018: Projections of Future Sea Level Contributions from the Greenland and Antarctic Ice Sheets: Challenges Beyond Dynamical Ice Sheet Modeling. *Oceanography*, **31(2)**, doi:10.5670/oceanog.2018.216.
Nowicki, S.M.J. et al., 2016: Ice Sheet Model Intercomparison Project (ISMIP6) contribution to CMIP6. *Geoscientific Model Development*, **9(12)**, 4521–4545, doi:10.5194/gmd-9-4521-2016.
O'Reilly, C.H., S. Minobe, and A. Kuwano-Yoshida, 2016a: The influence of the Gulf Stream on wintertime European blocking. *Climate Dynamics*, **47(5)**, 1545–1567, doi:10.1007/s00382-015-2919-0.
O'Reilly, C.H., L. Zanna, and T. Woollings, 2019a: Assessing External and Internal Sources of Atlantic Multidecadal Variability Using Models, Proxy Data, and Early Instrumental Indices. *Journal of Climate*, **32(22)**, 7727–7745, doi:10.1175/jcli-d-19-0177.1.
O'Reilly, C.H., M. Huber, T. Woollings, and L. Zanna, 2016b: The signature of low-frequency oceanic forcing in the Atlantic Multidecadal Oscillation. *Geophysical Research Letters*, **43(6)**, 2810–2818, doi:10.1002/2016gl067925.
O'Reilly, C.H., A. Weisheimer, T. Woollings, L.J. Gray, and D. MacLeod, 2019b: The importance of stratospheric initial conditions for winter North Atlantic Oscillation predictability and implications for the signal-to-noise paradox. *Quarterly Journal of the Royal Meteorological Society*, **145(718)**, 131–146, doi:10.1002/qj.3413.
Ogata, T. et al., 2017: The resolution sensitivity of the Asian summer monsoon and its inter-model comparison between MRI-AGCM and MetUM. *Climate Dynamics*, **49(9–10)**, 3345–3361, doi:10.1007/s00382-016-3517-5.
Ogawa, F., N.-E. Omrani, K. Nishii, H. Nakamura, and N. Keenlyside, 2015: Ozone-induced climate change propped up by the Southern Hemisphere oceanic front. *Geophysical Research Letters*, **42(22)**, 10,056–10,063, doi:10.1002/2015gl066538.
Ohba, M. and H. Ueda, 2009: Role of Nonlinear Atmospheric Response to SST on the Asymmetric Transition Process of ENSO. *Journal of Climate*, **22(1)**, 177–192, doi:10.1175/2008jcli2334.1.
Olonscheck, D., M. Rugenstein, and J. Marotzke, 2020: Broad Consistency Between Observed and Simulated Trends in Sea Surface Temperature Patterns. *Geophysical Research Letters*, **47(10)**, e2019GL086773,

ACCEPTED VERSION SUBJECT TO FINAL EDITING

doi:10.1029/2019gl086773.
Ortega, P. et al., 2015: A model-tested North Atlantic Oscillation reconstruction for the past millennium. *Nature*, **523(7558)**, 71–74, doi:10.1038/nature14518.
Oschlies, A. et al., 2017: Patterns of deoxygenation: sensitivity to natural and anthropogenic drivers. *Philosophical Transactions of the Royal Society A: Mathematical,\n\t\t\t\tPhysical and Engineering Sciences*, **375(2102)**, 20160325, doi:10.1098/rsta.2016.0325.
Osprey, S.M., L.J. Gray, S.C. Hardiman, N. Butchart, and T.J. Hinton, 2013: Stratospheric Variability in Twentieth-Century CMIP5 Simulations of the Met Office Climate Model: High Top versus Low Top. *Journal of Climate*, **26(5)**, 1595–1606, doi:10.1175/jcli-d-12-00147.1.
Oster, J.L., D.E. Ibarra, M.J. Winnick, and K. Maher, 2015: Steering of westerly storms over western North America at the Last Glacial Maximum. *Nature Geoscience*, doi:10.1038/ngeo2365.
Ott, I., K. Romberg, and J. Jacobeit, 2015: Teleconnections of the tropical Atlantic and Pacific Oceans in a CMIP5 model ensemble. *Climate Dynamics*, **44(11–12)**, 3043–3055, doi:10.1007/s00382-014-2394-z.
Otterå, O.H., M. Bentsen, H. Drange, and L. Suo, 2010: External forcing as a metronome for Atlantic multidecadal variability. *Nature Geoscience*, **3(10)**, 688–694, doi:10.1038/ngeo955.
Otto, F.E.L., D.J. Frame, A. Otto, and M.R. Allen, 2015: Embracing uncertainty in climate change policy. *Nature Climate Change*, **5(10)**, 917–921, doi:10.1038/nclimate2716.
Otto-Bliesner, B.L. et al., 2007: Last Glacial Maximum ocean thermohaline circulation: PMIP2 model intercomparisons and data constraints. *Geophysical Research Letters*, **34(12)**, doi:10.1029/2007gl029475.
Otto-Bliesner, B.L. et al., 2014: Coherent changes of southeastern equatorial and northern African rainfall during the last deglaciation. *Science*, **346(6214)**, 1223–1227, doi:10.1126/science.1259531.
Otto-Bliesner, B.L. et al., 2016: Climate Variability and Change since 850 CE: An Ensemble Approach with the Community Earth System Model. *Bulletin of the American Meteorological Society*, **97(5)**, 735–754, doi:10.1175/bams-d-14-00233.1.
Otto-Bliesner, B.L. et al., 2017: The PMIP4 contribution to CMIP6 – Part 2: Two interglacials, scientific objective and experimental design for Holocene and Last Interglacial simulations. *Geoscientific Model Development*, **10(11)**, 3979–4003, doi:10.5194/gmd-10-3979-2017.
Otto-Bliesner, B.L. et al., 2021: Large-scale features of Last Interglacial climate: Results from evaluating the lig127k simulations for the Coupled Model Intercomparison Project (CMIP6)-Paleoclimate Modeling Intercomparison Project (PMIP4). *Climate of the Past*, **17(1)**, doi:10.5194/cp-17-63-2021.
Oudar, T., P.J. Kushner, J.C. Fyfe, and M. Sigmond, 2018: No impact of anthropogenic aerosols on early 21st century global temperature trends in a large initial-condition ensemble. *Geophysical Research Letters*, **45**, doi:10.1029/2018gl078841.
Outten, S., P. Thorne, I. Bethke, and Seland, 2015: Investigating the recent apparent hiatus in surface temperature increases: 1. Construction of two 30-member Earth System Model ensembles. *Journal of Geophysical Research: Atmospheres*, **120(17)**, 8575–8596, doi:10.1002/2015jd023859.
Owens, M.J. et al., 2017: The Maunder minimum and the Little Ice Age: An update from recent reconstructions and climate simulations. *Journal of Space Weather and Space Climate*, **7**, doi:10.1051/swsc/2017034.
Paeth, H., F. Pollinger, and C. Ring, 2017: Detection and Attribution of Multivariate Climate Change Signals Using Discriminant Analysis and Bayesian Theorem. *Journal of Climate*, **30(19)**, 7757–7776, doi:10.1175/jcli-d-16-0850.1.
PAGES 2k Consortium, 2019: Consistent multi-decadal variability in global temperature reconstructions and simulations over the Common Era. *Nature geoscience*, **12(8)**, 643–649, doi:10.1038/s41561-019-0400-0.
PAGES 2k-PMIP3, 2015: Continental-scale temperature variability in PMIP3 simulations and PAGES 2k regional temperature reconstructions over the past millennium. *Climate of the Past*, **11(12)**, 1673–1699, doi:10.5194/cp-11-1673-2015.
Paik, S. and S.-K. Min, 2017: Climate responses to volcanic eruptions assessed from observations and CMIP5 multi-models. *Climate Dynamics*, **48(3)**, 1017–1030, doi:10.1007/s00382-016-3125-4.
Paik, S. and S.K. Min, 2020: Quantifying the anthropogenic greenhouse gas contribution to the observed spring snow-cover decline using the CMIP6 multimodel ensemble. *Journal of Climate*, **33(21)**, 9261–9269, doi:10.1175/jcli-d-20-0002.1.
Paik, S., S.-K. Min, C.E. Iles, E.M. Fischer, and A.P. Schurer, 2020a: Volcanic-induced global monsoon drying modulated by diverse El Niño responses. *Science Advances*, **6(21)**, eaba1212, doi:10.1126/sciadv.aba1212.
Paik, S. et al., 2017: Attributing Causes of 2015 Record Minimum Sea-Ice Extent in the Sea of Okhotsk. *Journal of Climate*, **30(12)**, 4693–4703, doi:10.1175/jcli-d-16-0587.1.
Paik, S. et al., 2020b: Determining the Anthropogenic Greenhouse Gas Contribution to the Observed Intensification of Extreme Precipitation. *Geophysical Research Letters*, **47(12)**, e2019GL086875, doi:10.1029/2019gl086875.
Pallotta, G. and B.D. Santer, 2020: Multi-frequency analysis of simulated versus observed variability in tropospheric temperature. *Journal of Climate*, **33(23)**, 10383–10402, doi:10.1175/jcli-d-20-0023.1.
Palmer, M.D. and D.J. McNeall, 2014: Internal variability of Earth's energy budget simulated by CMIP5 climate models. *Environmental Research Letters*, **9(3)**, 34016, doi:10.1088/1748-9326/9/3/034016.

ACCEPTED VERSION SUBJECT TO FINAL EDITING

Palmer, T. and B. Stevens, 2019: The scientific challenge of understanding and estimating climate change. *Proceedings of the National Academy of Sciences of the United States of America*, **116(49)**, doi:10.1073/pnas.1906691116.
Papalexiou, S.M., C.R. Rajulapati, M.P. Clark, and F. Lehner, 2020: Robustness of CMIP6 Historical Global Mean Temperature Simulations: Trends, Long-Term Persistence, Autocorrelation, and Distributional Shape. *Earth's Future*, **8(10)**, doi:10.1029/2020ef001667.
Park, B.J., Y.H. Kim, S.K. Min, and E.P. Lim, 2018: Anthropogenic and natural contributions to the lengthening of the summer season in the Northern Hemisphere. *Journal of Climate*, **31(17)**, doi:10.1175/jcli-d-17-0643.1.
Park, T. et al., 2016: Changes in growing season duration and productivity of northern vegetation inferred from long-term remote sensing data. *Environmental Research Letters*, doi:10.1088/1748-9326/11/8/084001.
Parsons, L.A., M.K. Brennan, R.C.J. Wills, and C. Proistosescu, 2020: Magnitudes and Spatial Patterns of Interdecadal Temperature Variability in CMIP6. *Geophysical Research Letters*, **47(7)**, doi:10.1029/2019gl086588.
Parsons, L.A. et al., 2017: Temperature and Precipitation Variance in CMIP5 Simulations and Paleoclimate Records of the Last Millennium. *Journal of Climate*, **30(22)**, 8885–8912, doi:10.1175/jcli-d-16-0863.1.
Parsons, S., J.A. Renwick, and A.J. McDonald, 2016: An Assessment of Future Southern Hemisphere Blocking Using CMIP5 Projections from Four GCMs. *Journal of Climate*, **29(21)**, 7599–7611, doi:10.1175/jcli-d-15-0754.1.
Pasini, A., U. Triacca, and A. Attanasio, 2017: Evidence for the role of the Atlantic multidecadal oscillation and the ocean heat uptake in hiatus prediction. *Theoretical and Applied Climatology*, **129(3–4)**, 873–880, doi:10.1007/s00704-016-1818-6.
Passey, B.H. et al., 2009: Strengthened East Asian summer monsoons during a period of high-latitude warmth? Isotopic evidence from Mio-Pliocene fossil mammals and soil carbonates from northern China. *Earth and Planetary Science Letters*, doi:10.1016/j.epsl.2008.11.008.
Patterson, M., T. Bracegirdle, and T. Woollings, 2019: Southern Hemisphere Atmospheric Blocking in CMIP5 and Future Changes in the Australia-New Zealand Sector. *Geophysical Research Letters*, **46(15)**, 9281–9290, doi:10.1029/2019gl083264.
Pauling, A.G., C.M. Bitz, I.J. Smith, and P.J. Langhorne, 2016: The Response of the Southern Ocean and Antarctic Sea Ice to Freshwater from Ice Shelves in an Earth System Model. *Journal of Climate*, **29(5)**, 1655–1672, doi:10.1175/jcli-d-15-0501.1.
Pauling, A.G., I.J. Smith, P.J. Langhorne, and C.M. Bitz, 2017: Time-Dependent Freshwater Input From Ice Shelves: Impacts on Antarctic Sea Ice and the Southern Ocean in an Earth System Model. *Geophysical Research Letters*, **44(20)**, 10,410–454,461, doi:10.1002/2017gl075017.
Pausata, F.S.R., G. Messori, and Q. Zhang, 2016: Impacts of dust reduction on the northward expansion of the African monsoon during the Green Sahara period. *Earth and Planetary Science Letters*, **434**, 298–307, doi:10.1016/j.epsl.2015.11.049.
Pearl, J., 2009: *Causality: models, reasoning and inference*. Cambridge University Press, Cambridge, UK, doi:10.1017/cbo9780511803161.
Pedersen, R.A., P.L. Langen, and B.M. Vinther, 2017: The last interglacial climate: comparing direct and indirect impacts of insolation changes. *Climate Dynamics*, **48(9–10)**, 3391–3407, doi:10.1007/s00382-016-3274-5.
Pederson, N., A.E. Hessl, N. Baatarbileg, K.J. Anchukaitis, and N. Di Cosmo, 2014: Pluvials, droughts, the Mongol Empire, and modern Mongolia. *Proceedings of the National Academy of Sciences*, doi:10.1073/pnas.1318677111.
Peings, Y. and G. Magnusdottir, 2013: Response of the Wintertime Northern Hemisphere Atmospheric Circulation to Current and Projected Arctic Sea Ice Decline: A Numerical Study with CAM5. *Journal of Climate*, **27(1)**, 244–264, doi:10.1175/jcli-d-13-00272.1.
Peings, Y. and G. Magnusdottir, 2016: Wintertime atmospheric response to Atlantic multidecadal variability: effect of stratospheric representation and ocean–atmosphere coupling. *Climate Dynamics*, **47(3–4)**, 1029–1047, doi:10.1007/s00382-015-2887-4.
Pendergrass, A.G. and C. Deser, 2017: Climatological characteristics of typical daily precipitation. *Journal of Climate*, **30(15)**, 5985–6003, doi:10.1175/jcli-d-16-0684.1.
Peng, J. and L. Dan, 2015: Impacts of CO2 concentration and climate change on the terrestrial carbon flux using six global climate–carbon coupled models. *Ecological modelling*, **304**, 69–83, doi:10.1016/j.ecolmodel.2015.02.016.
Perez, F.F. et al., 2018: Meridional overturning circulation conveys fast acidification to the deep Atlantic Ocean. *Nature*, **554(7693)**, 515–518, doi:10.1038/nature25493.
Perez-Sanz, A., G. Li, P. Gonzalez-Samperiz, and S.P. Harrison, 2014: Evaluation of modern and mid-Holocene seasonal precipitation of the Mediterranean and northern Africa in the CMIP5 simulations. *Clim of the Past*, **10**, 551–568, doi:10.5194/cp-10-551-2014.
Perry, S.J., S. McGregor, A. Gupta, M.H. England, and N. Maher, 2019: Projected late 21st century changes to the regional impacts of the El Niño-Southern Oscillation. *Climate Dynamics*, 1–18, doi:10.1007/s00382-019-05006-6.
Pfeffer, W.T. et al., 2014: The Randolph Glacier Inventory: a globally complete inventory of glaciers. *Journal of Glaciology*, **60(221)**, 537–552, doi:10.3189/2014jog13j176.

ACCEPTED VERSION SUBJECT TO FINAL EDITING

Philip, S. et al., 2018: Attribution analysis of the Ethiopian drought of 2015. *Journal of Climate*, doi:10.1175/jcli-d-17-0274.1.
Phillips, A.S., C. Deser, and J. Fasullo, 2014: Evaluating Modes of Variability in Climate Models. *Eos, Transactions American Geophysical Union*, **95(49)**, 453–455, doi:10.1002/2014eo490002.
Piao, S. et al., 2017: On the causes of trends in the seasonal amplitude of atmospheric CO2. *Global Change Biology*, **24(2)**, 608–616, doi:10.1111/gcb.13909.
Pierce, D.W., P.J. Gleckler, T.P. Barnett, B.D. Santer, and P.J. Durack, 2012: The fingerprint of human-induced changes in the ocean's salinity and temperature fields. *Geophysical Research Letters*, **39(21)**, n/a–n/a, doi:10.1029/2012gl053389.
Pithan, F., T.G. Shepherd, G. Zappa, and I. Sandu, 2016: Climate model biases in jet streams, blocking and storm tracks resulting from missing orographic drag. *Geophysical Research Letters*, **43(13)**, 7231–7240, doi:10.1002/2016gl069551.
Planton, Y.Y. et al., 2020: Evaluating climate models with the CLIVAR 2020 ENSO metrics package. *Bulletin of the American Meteorological Society*, 1–57, doi:10.1175/bams-d-19-0337.1.
Po-Chedley, S. et al., 2021: Natural variability can explain model-satellite differences in tropical tropospheric warming. *Proceedings of the National Academy of Sciences*, **In Press**, doi:10.1073/pnas.2020962118.
Polade, S.D., A. Gershunov, D.R. Cayan, M.D. Dettinger, and D.W. Pierce, 2013: Natural climate variability and teleconnections to precipitation over the Pacific-North American region in CMIP3 and CMIP5 models. *Geophysical Research Letters*, **40(10)**, 2296–2301, doi:10.1002/grl.50491.
Polson, D. and G.C. Hegerl, 2017: Strengthening contrast between precipitation in tropical wet and dry regions. *Geophysical Research Letters*, **44**, 365–373, doi:10.1002/2016gl071194.
Polson, D., G.C. Hegerl, and S. Solomon, 2016: Precipitation sensitivity to warming estimated from long island records. *Environmental Research Letters*, **11(7)**, 074024, doi:10.1088/1748-9326/11/7/074024.
Polson, D., M. Bollasina, G.C. Hegerl, and L.J. Wilcox, 2014: Decreased monsoon precipitation in the Northern Hemisphere due to anthropogenic aerosols. *Geophysical Research Letters*, **41**, 6023–6029, doi:10.1002/2014gl060811.
Polvani, L.M. and K.L. Smith, 2013: Can natural variability explain observed Antarctic sea ice trends? New modeling evidence from CMIP5. *Geophysical Research Letters*, **40(12)**, 3195–3199, doi:10.1002/grl.50578.
Polvani, L.M., M. Previdi, M.R. England, G. Chiodo, and K.L. Smith, 2020: Substantial twentieth-century Arctic warming caused by ozone-depleting substances. *Nature Climate Change*, **10(2)**, 130–133, doi:10.1038/s41558-019-0677-4.
Pongratz, J. et al., 2018: Models meet data: Challenges and opportunities in implementing land management in Earth system models. *Global Change Biology*, **24(4)**, 1470–1487, doi:10.1111/gcb.13988.
Poulsen, M.B., M. Jochum, and R. Nuterman, 2018: Parameterized and resolved Southern Ocean eddy compensation. *Ocean Modelling*, **124**, 1–15, doi:10.1016/j.ocemod.2018.01.008.
Power, S., T. Casey, C. Folland, A. Colman, and V. Mehta, 1999: Inter-decadal modulation of the impact of ENSO on Australia. *Climate Dynamics*, **15(5)**, 319–324, doi:10.1007/s003820050284.
Power, S., F. Delage, G. Wang, I. Smith, and G. Kociuba, 2017: Apparent limitations in the ability of CMIP5 climate models to simulate recent multi-decadal change in surface temperature: implications for global temperature projections. *Climate Dynamics*, **49(1–2)**, 53–69, doi:10.1007/s00382-016-3326-x.
Power, S.B. and F.P.D. Delage, 2018a: El Niño-Southern oscillation and associated climatic conditions around the world during the latter half of the twenty-first century. *Journal of Climate*, **31(15)**, 6189–6207, doi:10.1175/jcli-d-18-0138.1.
Power, S.B. and F.P.D. Delage, 2018b: El Niño-Southern oscillation and associated climatic conditions around the world during the latter half of the twenty-first century. *Journal of Climate*, **31(15)**, 6189–6207, doi:10.1175/jcli-d-18-0138.1.
Praetorius, S.K. et al., 2015: North Pacific deglacial hypoxic events linked to abrupt ocean warming. *Nature*, **527(7578)**, 362–366, doi:10.1038/nature15753.
Prescott, C.L., A.M. Haywood, A.M. Dolan, S.J. Hunter, and J.C. Tindall, 2019: Indian monsoon variability in response to orbital forcing during the late Pliocene. *Global and Planetary Change*, **173**, 33–46, doi:10.1016/j.gloplacha.2018.12.002.
Previdi, M. and L.M. Polvani, 2016: Anthropogenic impact on Antarctic surface mass balance, currently masked by natural variability, to emerge by mid-century. *Environmental Research Letters*, doi:10.1088/1748-9326/11/9/094001.
Priestley, M.D.K. et al., 2020: An Overview of the Extratropical Storm Tracks in CMIP6 Historical Simulations. *Journal of Climate*, **33(15)**, 6315–6343, doi:10.1175/jcli-d-19-0928.1.
Purich, A. and M.H. England, 2019: Tropical Teleconnections to Antarctic Sea Ice During Austral Spring 2016 in Coupled Pacemaker Experiments. *Geophysical Research Letters*, **46(12)**, 6848–6858, doi:10.1029/2019gl082671.
Purich, A., W. Cai, M.H. England, and T. Cowan, 2016: Evidence for link between modelled trends in Antarctic sea ice and underestimated westerly wind changes. *Nature Communications*, **7**, 10409, doi:10.1038/ncomms10409.

ACCEPTED VERSION SUBJECT TO FINAL EDITING

Purkey, S.G. and G.C. Johnson, 2010: Warming of global abyssal and deep Southern Ocean waters between the 1990s and 2000s: Contributions to global heat and sea level rise budgets. *Journal of Climate*, **23(23)**, 6336–6351, doi:10.1175/2010jcli3682.1.

Qasmi, S., C. Cassou, and J. Boé, 2017: Teleconnection Between Atlantic Multidecadal Variability and European Temperature: Diversity and Evaluation of the Coupled Model Intercomparison Project Phase 5 Models. *Geophysical Research Letters*, doi:10.1002/2017gl074886.

Qasmi, S., C. Cassou, and J. Boé, 2020: Teleconnection Processes Linking the Intensity of the Atlantic Multidecadal Variability to the Climate Impacts over Europe in Boreal Winter. *Journal of Climate*, **33(7)**, 2681–2700, doi:10.1175/jcli-d-19-0428.1.

Qian, C. and X. Zhang, 2015: Human Influences on Changes in the Temperature Seasonality in Mid- to High-Latitude Land Areas. *Journal of Climate*, **28(15)**, 5908–5921, doi:10.1175/jcli-d-14-00821.1.

Quan, X.-W., M.P. Hoerling, J. Perlwitz, and H.F. Diaz, 2018: On the Time of Emergence of Tropical Width Change. *Journal of Climate*, **31(18)**, 7225–7236, doi:10.1175/jcli-d-18-0068.1.

Rackow, T. et al., 2019: Sensitivity of deep ocean biases to horizontal resolution in prototype CMIP6 simulations with AWI-CM1.0. *Geoscientific Model Development*, **12(7)**, 2635–2656, doi:10.5194/gmd-12-2635-2019.

Rao, J. and C.I. Garfinkel, 2021: CMIP5/6 models project little change in the statistical characteristics of sudden stratospheric warmings in the 21st century. *Environmental Research Letters*, **16(3)**, 034024, doi:10.1088/1748-9326/abd4fe.

Rathore, S., N.L. Bindoff, H.E. Phillips, and M. Feng, 2020: Recent hemispheric asymmetry in global ocean warming induced by climate change and internal variability. *Nature Communications*, **11(1)**, 2008, doi:10.1038/s41467-020-15754-3.

Rayner, N.A. et al., 2003: Global analyses of sea surface temperature, sea ice, and night marine air temperature since the late nineteenth century. *Journal of Geophysical Research: Atmospheres*, **108(D14)**, doi:10.1029/2002jd002670.

Rea, G., A. Riccio, F. Fierli, F. Cairo, and C. Cagnazzo, 2018a: Stratosphere-resolving CMIP5 models simulate different changes in the Southern Hemisphere. *CLIMATE DYNAMICS*, **50(5–6)**, 2239–2255, doi:10.1007/s00382-017-3746-2.

Rea, G., A. Riccio, F. Fierli, F. Cairo, and C. Cagnazzo, 2018b: Stratosphere-resolving CMIP5 models simulate different changes in the Southern Hemisphere. *CLIMATE DYNAMICS*, **50(5–6)**, 2239–2255, doi:10.1007/s00382-017-3746-2.

Reintges, A., T. Martin, M. Latif, and N.S. Keenlyside, 2017: Uncertainty in twenty-first century projections of the Atlantic Meridional Overturning Circulation in CMIP3 and CMIP5 models. *Climate Dynamics*, **49(5)**, 1495–1511, doi:10.1007/s00382-016-3180-x.

Reul, N. et al., 2014: Multisensor observations of the Amazon-Orinoco river plume interactions with hurricanes. *Journal of Geophysical Research: Oceans*, **119(12)**, 8271–8295, doi:10.1002/2014jc010107.

RGI Consortium, 2017: Randolph Glacier Inventory – A Dataset of Global Glacier Outlines: Version 6.0. , doi:10.7265/n5-rgi-60.

Rhein, M. et al., 2013: Observations: Ocean. In: *Climate Change 2013 the Physical Science Basis: Working Group I Contribution to the Fifth Assessment Report of the Intergovernmental Panel on Climate Change* [Stocker, T.F., D. Qin, G.-K. Plattner, M. Tignor, S.K. Allen, J. Boschung, A. Nauels, Y. Xia, V. Bex, and P.M. Midgley (eds.)]. Cambridge University Press, Cambridge, United Kingdom and New York, NY, USA, pp. 255–316, doi:10.1017/cbo9781107415324.010.

Ribes, A. and L. Terray, 2013: Application of regularised optimal fingerprinting to attribution. Part II: Application to global near-surface temperature. *Climate Dynamics*, **41(11–12)**, 2837–2853, doi:10.1007/s00382-013-1736-6.

Ribes, A., J.-M. Azaïs, and S. Planton, 2009: Adaptation of the optimal fingerprint method for climate change detection using a well-conditioned covariance matrix estimate. *Climate Dynamics*, **33(5)**, 707–722, doi:10.1007/s00382-009-0561-4.

Ribes, A., S. Qasmi, and N.P. Gillett, 2021: Making climate projections conditional on historical observations. *Science Advances*, **7(4)**, eabc0671, doi:10.1126/sciadv.abc0671.

Ribes, A., F.W. Zwiers, J.-M. Azaïs, and P. Naveau, 2017: A new statistical approach to climate change detection and attribution. *Climate Dynamics*, **48(1–2)**, 367–386, doi:10.1007/s00382-016-3079-6.

Richardson, T. et al., 2018: Drivers of precipitation change: an energetic understanding. *J. CLimate*, doi:10.1175/jcli-d-17-0240.1.

Richter, I., 2015: Climate model biases in the eastern tropical oceans: causes, impacts and ways forward. *Wiley Interdisciplinary Reviews: Climate Change*, **6(3)**, 345–358, doi:10.1002/wcc.338.

Richter, I. and H. Tokinaga, 2020a: An overview of the performance of CMIP6 models in the tropical Atlantic: mean state, variability, and remote impacts. *Climate Dynamics*, **55(9–10)**, 2579–2601, doi:10.1007/s00382-020-05409-w.

Richter, I. and H. Tokinaga, 2020b: An overview of the performance of CMIP6 models in the tropical Atlantic: mean state, variability, and remote impacts. *Climate Dynamics*, **55(9–10)**, 2579–2601, doi:10.1007/s00382-020-05409-w.

ACCEPTED VERSION SUBJECT TO FINAL EDITING

Richter, I., S.P. Xie, S.K. Behera, T. Doi, and Y. Masumoto, 2014: Equatorial Atlantic variability and its relation to mean state biases in CMIP5. *Climate Dynamics*, **42(1–2)**, 171–188, doi:10.1007/s00382-012-1624-5.
Richter, K. et al., 2020: Detecting a forced signal in satellite-era sea-level change. *Environmental Research Letters*, **15(9)**, 094079, doi:10.1088/1748-9326/ab986e.
Ridley, D.A. et al., 2014: Total volcanic stratospheric aerosol optical depths and implications for global climate change. *Geophysical Research Letters*, **41**, 7763–7769, doi:10.1002/2014gl061541.
Rieger, L.A. et al., 2020: Quantifying CanESM5 and EAMv1 sensitivities to Mt. Pinatubo volcanic forcing for the CMIP6 historical experiment. *Geoscientific Model Development*, **13(10)**, 4831–4843, doi:10.5194/gmd-13-4831-2020.
Righi, M. et al., 2020: Earth System Model Evaluation Tool (ESMValTool) v2.0 – technical overview. *Geoscientific Model Development*, **13(3)**, 1179–1199, doi:10.5194/gmd-13-1179-2020.
Rignot, E. et al., 2019: Four decades of Antarctic Ice Sheet mass balance from 1979-2017. *Proceedings of the National Academy of Sciences*, **116(4)**, 1–9, doi:10.1073/pnas.1812883116.
Ríos, A.F. et al., 2015: Decadal acidification in the water masses of the Atlantic Ocean.. *Proceedings of the National Academy of Sciences of the United States of America*, **112(32)**, 9950–5, doi:10.1073/pnas.1504613112.
Risbey, J.S. et al., 2014: Well-estimated global surface warming in climate projections selected for ENSO phase. *Nature Climate Change*, **4**, 835, doi:10.1038/nclimate2310.
Risbey, J.S. et al., 2018: A fluctuation in surface temperature in historical context: reassessment and retrospective on the evidence. *Environmental Research Letters*, **13(12)**, 123008, doi:10.1088/1748-9326/aaf342.
Riser, S.C. et al., 2016: Fifteen years of ocean observations with the global Argo array. *Nature Climate Change*, **6(2)**, 145–153, doi:10.1038/nclimate2872.
Ritter, R. et al., 2017: Observation-Based Trends of the Southern Ocean Carbon Sink. *Geophysical Research Letters*, **44(24)**, 12,339–12,348, doi:10.1002/2017gl074837.
Ritz, S.P., T.F. Stocker, J.O. Grimalt, L. Menviel, and A. Timmermann, 2013: Estimated strength of the Atlantic overturning circulation during the last deglaciation. *Nature Geoscience*, **6(3)**, 208–212, doi:10.1038/ngeo1723.
Roach, L.A., S.M. Dean, and J.A. Renwick, 2018: Consistent biases in Antarctic sea ice concentration simulated by climate models. *The Cryosphere*, **12(1)**, 365–383, doi:10.5194/tc-12-365-2018.
Roach, L.A. et al., 2020: Antarctic Sea Ice in CMIP6. *Geophysical Research Letters*, **47(9)**, e2019GL086729, doi:10.1029/2019gl086729.
Roberts, C.D., L. Jackson, and D. McNeall, 2014: Is the 2004–2012 reduction of the Atlantic meridional overturning circulation significant? *Geophysical Research Letters*, **41(9)**, 3204–3210, doi:10.1002/2014gl059473.
Roberts, C.D., M.D. Palmer, D. McNeall, and M. Collins, 2015: Quantifying the likelihood of a continued hiatus in global warming. *Nature Climate Change*, **5(4)**, 337–342, doi:10.1038/nclimate2531.
Roberts, C.D. et al., 2018: Climate model configurations of the ECMWF Integrated Forecasting System (ECMWF-IFS cycle 43r1) for HighResMIP. *Geoscientific Model Development*, **11(9)**, 3681–3712, doi:10.5194/gmd-11-3681-2018.
Roberts, M.J. et al., 2019: Description of the resolution hierarchy of the global coupled HadGEM3-GC3.1 model as used in CMIP6 HighResMIP experiments. *Geoscientific Model Development*, **12(12)**, 4999–5028, doi:10.5194/gmd-12-4999-2019.
Roberts, M.J. et al., 2020a: Impact of model resolution on tropical cyclone simulation using the HighResMIP-PRIMAVERA multimodel ensemble. *Journal of Climate*, **33(7)**, 2557–2583, doi:10.1175/jcli-d-19-0639.1.
Roberts, M.J. et al., 2020b: Projected Future Changes in Tropical Cyclones Using the CMIP6 HighResMIP Multimodel Ensemble. *Geophysical Research Letters*, **47(14)**, doi:10.1029/2020gl088662.
Roberts, M.J. et al., 2020c: Sensitivity of the Atlantic Meridional Overturning Circulation to Model Resolution in CMIP6 HighResMIP Simulations and Implications for Future Changes. *Journal of Advances in Modeling Earth Systems*, **12(8)**, doi:10.1029/2019ms002014.
Robson, J., R. Sutton, K. Lohmann, D. Smith, and M.D. Palmer, 2012: Causes of the Rapid Warming of the North Atlantic Ocean in the Mid-1990s. *Journal of Climate*, **25(12)**, 4116–4134, doi:10.1175/jcli-d-11-00443.1.
Robson, J. et al., 2020: The Evaluation of the North Atlantic Climate System in UKESM1 Historical Simulations for CMIP6. *Journal of Advances in Modeling Earth Systems*, **12(9)**, doi:10.1029/2020ms002126.
Rodríguez-Fonseca, B. et al., 2015: Variability and Predictability of West African Droughts: A Review on the Role of Sea Surface Temperature Anomalies. *Journal of Climate*, **28(10)**, 4034–4060, doi:10.1175/jcli-d-14-00130.1.
Roe, G.H., M.B. Baker, and F. Herla, 2017: Centennial glacier retreat as categorical evidence of regional climate change. *Nature Geoscience*, **10(2)**, 95–99, doi:10.1038/ngeo2863.
Roe, G.H., J.E. Christian, and B. Marzeion, 2021: On the attribution of industrial-era glacier mass loss to anthropogenic climate change. *The Cryosphere* (in press), doi:10.5194/tc-2020-265.
Roemmich, D. et al., 2015: Unabated planetary warming and its ocean structure since 2006. *Nature Climate Change*, **5(3)**, 240–245, doi:10.1038/nclimate2513.
Rosenblum, E. and I. Eisenman, 2017: Sea Ice Trends in Climate Models Only Accurate in Runs with Biased Global Warming. *Journal of Climate*, **30(16)**, 6265–6278, doi:10.1175/jcli-d-16-0455.1.
Rotstayn, L.D., 2013: Projected effects of declining anthropogenic aerosols on the southern annular mode.

ACCEPTED VERSION SUBJECT TO FINAL EDITING

Environmental Research Letters, **8(4)**, 044028, doi:10.1088/1748-9326/8/4/044028.
Rougier, J., 2016: Ensemble Averaging and Mean Squared Error. *Journal of Climate*, **29(24)**, 8865–8870, doi:10.1175/jcli-d-16-0012.1.
Rowell, D.P., B.B.B. Booth, S.E. Nicholson, and P. Good, 2015: Reconciling Past and Future Rainfall Trends over East Africa. *Journal of Climate*, **28(24)**, 9768–9788, doi:10.1175/jcli-d-15-0140.1.
Ruggieri, P. et al., 2020: Atlantic Multidecadal Variability and North Atlantic Jet: a multi-model view from the Decadal Climate Prediction Project. *Journal of Climate*, 1–47, doi:10.1175/jcli-d-19-0981.1.
Rupp, D.E., P.W. Mote, N.L. Bindoff, P.A. Stott, and D.A. Robinson, 2013: Detection and attribution of observed changes in northern hemisphere spring snow cover. *Journal of Climate*, doi:10.1175/jcli-d-12-00563.1.
Ruprich-Robert, Y. and C. Cassou, 2015: Combined influences of seasonal East Atlantic Pattern and North Atlantic Oscillation to excite Atlantic multidecadal variability in a climate model. *Climate Dynamics*, **44(1–2)**, 229–253, doi:10.1007/s00382-014-2176-7.
Ruprich-Robert, Y. et al., 2017: Assessing the climate impacts of the observed atlantic multidecadal variability using the GFDL CM2.1 and NCAR CESM1 global coupled models. *Journal of Climate*, **30(8)**, 2785–2810, doi:10.1175/jcli-d-16-0127.1.
Ruprich-Robert, Y. et al., 2018: Impacts of the Atlantic Multidecadal Variability on North American Summer Climate and Heat Waves. *Journal of Climate*, **31(9)**, 3679–3700, doi:10.1175/jcli-d-17-0270.1.
Russell, J.L. et al., 2018: Metrics for the Evaluation of the Southern Ocean in Coupled Climate Models and Earth System Models. *Journal of Geophysical Research: Oceans*, **123(5)**, 3120–3143, doi:10.1002/2017jc013461.
Rypdal, K., 2018: The life and death of the recent global surface warming hiatus parsimoniously explained. *Climate*, **6(3)**, doi:10.3390/cli6030064.
Saffioti, C., E.M. Fischer, and R. Knutti, 2015: Contributions of atmospheric circulation variability and data coverage bias to the warming hiatus. *Geophysical Research Letters*, **42(7)**, 2385–2391, doi:10.1002/2015gl063091.
Saggioro, E. and T.G. Shepherd, 2019: Quantifying the Timescale and Strength of Southern Hemisphere Intraseasonal Stratosphere-troposphere Coupling. *Geophysical Research Letters*, **46(22)**, 13479–13487, doi:10.1029/2019gl084763.
Saji, N.H. et al., 2006: Tropical Indian Ocean Variability in the IPCC Twentieth-Century Climate Simulations. *Journal of Climate*, **19(17)**, 4397–4417, doi:10.1175/jcli3847.1.
Sallée, J.B. et al., 2013: Assessment of Southern Ocean water mass circulation and characteristics in CMIP5 models: Historical bias and forcing response. *Journal of Geophysical Research: Oceans*, **118(4)**, 1830–1844, doi:10.1002/jgrc.20135.
Sallée, J.-B. et al., 2021: Fifty-year changes of the world ocean's surface layer in response to climate change. *Nature* (in press).
Salzmann, M., 2016: Global warming without global mean precipitation increase? *Climate Modelling*, doi:10.1126/sciadv.1501572.
Sandeep, S., F. Stordal, P.D. Sardeshmukh, and G.P. Compo, 2014: Pacific Walker Circulation variability in coupled and uncoupled climate models. *Climate Dynamics*, **43(1–2)**, 103–117, doi:10.1007/s00382-014-2135-3.
Santer, B.D. et al., 2007: Identification of human-induced changes in atmospheric moisture content. *Proceedings of the National Academy of Sciences*, **104(39)**, 15248–15253, doi:10.1073/pnas.0702872104.
Santer, B.D. et al., 2009: Incorporating model quality information in climate change detection and attribution studies.. *Proceedings of the National Academy of Sciences of the United States of America*, doi:10.1073/pnas.0901736106.
Santer, B.D. et al., 2013: Human and natural influences on the changing thermal structure of the atmosphere. *Proceedings of the National Academy of Sciences of the United States of America*, **110(43)**, 17235–17240, doi:10.1073/pnas.1305332110.
Santer, B.D. et al., 2014: Volcanic contribution to decadal changes in tropospheric temperature. *Nature Geoscience*, **7(3)**, 185–189, doi:10.1038/ngeo2098.
Santer, B.D. et al., 2017a: Causes of differences in model and satellite tropospheric warming rates. *Nature Geoscience*, **10(7)**, 478–485, doi:10.1038/ngeo2973.
Santer, B.D. et al., 2017b: Comparing tropospheric warming in climate models and satellite data. *Journal of Climate*, **30(1)**, 373–392, doi:10.1175/jcli-d-16-0333.1.
Santer, B.D. et al., 2018: Human influence on the seasonal cycle of tropospheric temperature. *Science*, **361(6399)**, doi:10.1126/science.aas8806.
Santer, B.D. et al., 2019: Quantifying stochastic uncertainty in detection time of human-caused climate signals. *Proceedings of the National Academy of Sciences*, **116(40)**, 19821–19827, doi:10.1073/pnas.1904586116.
Santolaria-Otín, M. and O. Zolina, 2020: Evaluation of snow cover and snow water equivalent in the continental Arctic in CMIP5 models. *Climate Dynamics*, **55(11)**, 2993–3016, doi:10.1007/s00382-020-05434-9.
Sasgen, I. et al., 2020a: Return to rapid ice loss in Greenland and record loss in 2019 detected by the GRACE-FO satellites. *Communications Earth & Environment*, doi:10.1038/s43247-020-0010-1.
Sasgen, I. et al., 2020b: Return to rapid ice loss in Greenland and record loss in 2019 detected by the GRACE-FO satellites. *Communications Earth & Environment*, doi:10.1038/s43247-020-0010-1.

SUBJECT TO FINAL EDITING ACCEPTED VERSION

Saurral, R.I., F. Kucharski, and G.A. Raggio, 2019: Variations in ozone and greenhouse gases as drivers of Southern Hemisphere climate in a medium-complexity global climate model. *Climate Dynamics*, **53(11)**, 6645–6663, doi:10.1007/s00382-019-04950-7.
Scaife, A.A. and D. Smith, 2018: A signal-to-noise paradox in climate science. *npj Climate and Atmospheric Science*, **1(1)**, 28, doi:10.1038/s41612-018-0038-4.
Scaife, A.A. et al., 2013: A mechanism for lagged North Atlantic climate response to solar variability. *Geophysical Research Letters*, **40(2)**, 434–439, doi:10.1002/grl.50099.
Scaife, A.A. et al., 2016: Seasonal winter forecasts and the stratosphere. *Atmospheric Science Letters*, **17(1)**, 51–56, doi:10.1002/asl.598.
Scheff, J., R. Seager, H. Liu, and S. Coats, 2017: Are glacials dry? Consequences for paleoclimatology and for greenhouse warming. *Journal of Climate*, **30(17)**, 6593–6609, doi:10.1175/jcli-d-16-0854.1.
Schenzinger, V. and S.M. Osprey, 2015: Interpreting the nature of Northern and Southern Annular Mode variability in CMIP5 Models. *Journal of Geophysical Research: Atmospheres*, **120(21)**, 11203–11214, doi:10.1002/2014jd022989.
Schiemann, R. et al., 2017: The Resolution Sensitivity of Northern Hemisphere Blocking in Four 25-km Atmospheric Global Circulation Models. *Journal of Climate*, **30(1)**, 337–358, doi:10.1175/jcli-d-16-0100.1.
Schiemann, R. et al., 2018: Mean and extreme precipitation over European river basins better simulated in a 25km AGCM. *Hydrology and Earth System Sciences*, **22(7)**, 3933–3950, doi:10.5194/hess-22-3933-2018.
Schiemann, R. et al., 2020: Northern Hemisphere blocking simulation in current climate models: evaluating progress from the Climate Model Intercomparison Project Phase 5 to 6 and sensitivity to resolution. *Weather and Climate Dynamics*, **1**, 277–292, doi:10.5194/wcd-1-277-2020.
Schimanke, S., T. Spangehl, H. Huebener, and U. Cubasch, 2013: Variability and trends of major stratospheric warmings in simulations under constant and increasing GHG concentrations. *Climate Dynamics*, **40(7–8)**, 1733–1747, doi:10.1007/s00382-012-1530-x.
Schlosser, E., F.A. Haumann, and M.N. Raphael, 2018: Atmospheric influences on the anomalous 2016 Antarctic sea ice decay. *The Cryosphere*, **12(3)**, 1103–1119, doi:10.5194/tc-12-1103-2018.
Schlund, M., A. Lauer, P. Gentine, S.C. Sherwood, and V. Eyring, 2020: Emergent constraints on equilibrium climate sensitivity in CMIP5: do they hold for CMIP6? *Earth System Dynamics*, **11(4)**, 1233–1258, doi:10.5194/esd-11-1233-2020.
Schmidt, G.A., D.T. Shindell, and K. Tsigaridis, 2014: Reconciling warming trends. *Nature Geoscience*, **7(3)**, 158–160, doi:10.1038/ngeo2105.
Schmidt, G.A. et al., 2011: Climate forcing reconstructions for use in PMIP simulations of the last millennium (v1.0). *Geoscientific Model Development*, **4(1)**, 33–45, doi:10.5194/gmd-4-33-2011.
Schmidtko, S., L. Stramma, and M. Visbeck, 2017: Decline in global oceanic oxygen content during the past five decades. *Nature*, **542(7641)**, 335–339, doi:10.1038/nature21399.
Schmith, T., S. Yang, E. Gleeson, and T. Semmler, 2014: How Much Have Variations in the Meridional Overturning Circulation Contributed to Sea Surface Temperature Trends since 1850? A Study with the EC-Earth Global Climate Model. *Journal of Climate*, **27(16)**, 6343–6357, doi:10.1175/jcli-d-13-00651.1.
Schneider, D.P. and C. Deser, 2018: Tropically driven and externally forced patterns of Antarctic sea ice change: reconciling observed and modeled trends. *Climate Dynamics*, **50(11)**, 4599–4618, doi:10.1007/s00382-017-3893-5.
Schott, F.A., S.-P. Xie, and J.P. McCreary, 2009: Indian Ocean circulation and climate variability. *Reviews of Geophysics*, **47(1)**, RG1002, doi:10.1029/2007rg000245.
Schröder, M. et al., 2019: The GEWEX Water Vapor Assessment: Overview and Introduction to Results and Recommendations. *Remote Sensing*, **11(3)**, 251, doi:10.3390/rs11030251.
Schurer, A. et al., 2018: Estimating the transient climate response from observed warming. *Journal of Climate*, **31(20)**, 8645–8663, doi:10.1175/jcli-d-17-0717.1.
Schurer, A.P., S.F.B. Tett, and G.C. Hegerl, 2014a: Small influence of solar variability on climate over the past millennium. *Nature Geoscience*, **7(2)**, 104–108, doi:10.1038/ngeo2040.
Schurer, A.P., S.F.B. Tett, and G.C. Hegerl, 2014b: Small influence of solar variability on climate over the past millennium. *Nature Geoscience*, **7(2)**, 104–108, doi:10.1038/ngeo2040.
Schurer, A.P., G.C. Hegerl, and S.P. Obrochta, 2015: Determining the likelihood of pauses and surges in global warming. *Geophysical Research Letters*, **42(14)**, 5974–5982, doi:10.1002/2015gl064458.
Schurer, A.P., A.P. Ballinger, A.R. Friedman, and G.C. Hegerl, 2020: Human influence strengthens the contrast between tropical wet and dry regions. *Environmental Research Letters*, **15(10)**, 104026, doi:10.1088/1748-9326/ab83ab.
Schurer, A.P., G.C. Hegerl, M.E. Mann, S.F.B. Tett, and S.J. Phipps, 2013: Separating Forced from Chaotic Climate Variability over the Past Millennium. *Journal of Climate*, **26(18)**, 6954–6973, doi:10.1175/jcli-d-12-00826.1.
Scoccimarro, E. et al., 2017: Tropical Cyclone Interaction with the Ocean: The Role of High-Frequency (Subdaily) Coupled Processes. *Journal of Climate*, **30(1)**, 145–162, doi:10.1175/jcli-d-16-0292.1.
Screen, J.A., C. Deser, I. Simmonds, and R. Tomas, 2014: Atmospheric impacts of Arctic sea-ice loss, 1979--2009:

ACCEPTED VERSION SUBJECT TO FINAL EDITING

separating forced change from atmospheric internal variability. *Climate Dynamics*, **43(1)**, 333–344, doi:10.1007/s00382-013-1830-9.
Scussolini, P. et al., 2019: Agreement between reconstructed and modeled boreal precipitation of the Last Interglacial. *Science Advances*, **5(11)**, doi:10.1126/sciadv.aax7047.
Seager, R. et al., 2019: Strengthening tropical Pacific zonal sea surface temperature gradient consistent with rising greenhouse gases. *Nature Climate Change*, **9(7)**, 517–522, doi:10.1038/s41558-019-0505-x.
Séférian, R. et al., 2016: Development and evaluation of CNRM Earth system model-CNRM-ESM1. *Geoscientific Model Development*, **9(4)**, 1423–1453, doi:10.5194/gmd-9-1423-2016.
Séférian, R. et al., 2019: Evaluation of CNRM Earth System Model, CNRM-ESM2-1: Role of Earth System Processes in Present-Day and Future Climate. *Journal of Advances in Modeling Earth Systems*, **n/a(n/a)**, doi:10.1029/2019ms001791.
Séférian, R. et al., 2020: Tracking Improvement in Simulated Marine Biogeochemistry Between CMIP5 and CMIP6. *Current Climate Change Reports*, **6(3)**, 95–119, doi:10.1007/s40641-020-00160-0.
Seland et al., 2020: Overview of the Norwegian Earth System Model (NorESM2) and key climate response of CMIP6 DECK, historical, and scenario simulations. *Geoscientific Model Development*, **13(12)**, 6165–6200, doi:10.5194/gmd-13-6165-2020.
Sellar, A.A. et al., 2019: UKESM1: Description and Evaluation of the U.K. Earth System Model. *Journal of Advances in Modeling Earth Systems*, **11(12)**, 4513–4558, doi:10.1029/2019ms001739.
Semmler, T. et al., 2020: Simulations for CMIP6 With the AWI Climate Model AWI-CM-1-1. *Journal of Advances in Modeling Earth Systems*, **12(9)**, doi:10.1029/2019ms002009.
Seneviratne, S.I., M.G. Donat, B. Mueller, and L. Alexander, 2014: No pause in the increase of hot temperature extremes. *Nature Climate Change*, **4(3)**, 161–163, doi:10.1038/nclimate2145.
Seneviratne, S.I., M.G. Donat, A.J. Pitman, R. Knutti, and R.L. Wilby, 2016: Allowable CO2 emissions based on regional and impact-related climate targets. *Nature*, doi:10.1038/nature16542.
Seong, M.G., S.K. Min, Y.H. Kim, X. Zhang, and Y. Sun, 2021: Anthropogenic greenhouse gas and aerosol contributions to extreme temperature changes during 1951-2015. *Journal of Climate*, **34(3)**, 857–870, doi:10.1175/jcli-d-19-1023.1.
Seth, A. et al., 2019: Monsoon Responses to Climate Changes –Connecting Past, Present and Future. *Current Climate Change Reports*, **5(2)**, 63–79, doi:10.1007/s40641-019-00125-y.
Sévellec, F. and S.S. Drijfhout, 2018: A novel probabilistic forecast system predicting anomalously warm 2018-2022 reinforcing the long-term global warming trend. *Nature Communications*, **9(1)**, 3024, doi:10.1038/s41467-018-05442-8.
Seviour, W.J.M., L.J. Gray, and D.M. Mitchell, : Stratospheric polar vortex splits and displacements in the high-top CMIP5 climate models. *Journal of Geophysical Research: Atmospheres*, **121(4)**, 1400–1413, doi:10.1002/2015jd024178.
Seviour, W.J.M., L.J. Gray, and D.M. Mitchell, 2016: Stratospheric polar vortex splits and displacements in the high-top CMIP5 climate models. *Journal of Geophysical Research: Atmospheres*, **121(4)**, 1400–1413, doi:10.1002/2015jd024178.
Shannon, S. et al., 2019: Global glacier volume projections under high-end climate change scenarios. *The Cryosphere*, **13(1)**, 325–350, doi:10.5194/tc-13-325-2019.
Sheffield, J. et al., 2013: North American Climate in CMIP5 Experiments. Part I: Evaluation of Historical Simulations of Continental and Regional Climatology. *Journal of Climate*, **26(23)**, 9209–9245, doi:10.1175/jcli-d-12-00592.1.
Shepherd, A. et al., 2012: A reconciled estimate of ice-sheet mass balance. *Science*, **338(6111)**, 1183–1189, doi:10.1126/science.1228102.
Shepherd, A. et al., 2018: Mass balance of the Antarctic Ice Sheet from 1992 to 2017. *Nature*, **558(7709)**, 219–222, doi:10.1038/s41586-018-0179-y.
Shepherd, A. et al., 2020: Mass balance of the Greenland Ice Sheet from 1992 to 2018. *Nature*, **579(7798)**, 233–239, doi:10.1038/s41586-019-1855-2.
Shepherd, T.G., 2014: Atmospheric circulation as a source of uncertainty in climate change projections. *Nature Geoscience*, **7(10)**, 703–708, doi:10.1038/ngeo2253.
Sherriff-Tadano, S., A. Abe-Ouchi, M. Yoshimori, A. Oka, and W.-L. Chan, 2018: Influence of glacial ice sheets on the Atlantic meridional overturning circulation through surface wind change. *Climate Dynamics*, **50(7)**, 2881–2903, doi:10.1007/s00382-017-3780-0.
Sherwood, S.C. and N. Nishant, 2015: Atmospheric changes through 2012 as shown by iteratively homogenized radiosonde temperature and wind data (IUKv2). *Environmental Research Letters*, **10(5)**, doi:10.1088/1748-9326/10/5/054007.
Shi, L. et al., 2017: An assessment of upper ocean salinity content from the Ocean Reanalyses Inter-comparison Project (ORA-IP). *Climate Dynamics*, **49(3)**, 1009–1029, doi:10.1007/s00382-015-2868-7.
Shikha, S. and V. Valsala, 2018: Subsurface ocean biases in climate models and its implications in the simulated interannual variability: A case study for Indian Ocean. *Dynamics of Atmospheres and Oceans*, **84**, 55–74,

ACCEPTED VERSION SUBJECT TO FINAL EDITING

doi:10.1016/j.dynatmoce.2018.10.001.
Si, D. and A. Hu, 2017: Internally Generated and Externally Forced Multidecadal Oceanic Modes and Their Influence on the Summer Rainfall over East Asia. *Journal of Climate*, **30(20)**, 8299–8316, doi:10.1175/jcli-d-17-0065.1.
Sidorenko, D. et al., 2019: Evaluation of FESOM2.0 Coupled to ECHAM6.3: Preindustrial and HighResMIP Simulations. *Journal of Advances in Modeling Earth Systems*, **11(11)**, 3794–3815, doi:10.1029/2019ms001696.
Sigmond, M., J.F. Scinocca, and P.J. Kushner, 2008: Impact of the stratosphere on tropospheric climate change. *Geophysical Research Letters*, **35(12)**, doi:10.1029/2008gl033573.
Simmons, A.J. et al., 2014: Estimating low-frequency variability and trends in atmospheric temperature using ERA-Interim. *Quarterly Journal of the Royal Meteorological Society*, **140(679)**, 329–353, doi:10.1002/qj.2317.
Simmons, A.J. et al., 2017: A reassessment of temperature variations and trends from global reanalyses and monthly surface climatological datasets. *Quarterly Journal of the Royal Meteorological Society*, **143(702)**, 101–119, doi:10.1002/qj.2949.
Simpson, I.R., T.G. Shepherd, P. Hitchcock, and J.F. Scinocca, 2013: Southern Annular Mode Dynamics in Observations and Models. Part II: Eddy Feedbacks. *Journal of Climate*, **26(14)**, 5220–5241, doi:10.1175/jcli-d-12-00495.1.
Simpson, I.R., C. Deser, K.A. McKinnon, and E.A. Barnes, 2018: Modeled and Observed Multidecadal Variability in the North Atlantic Jet Stream and Its Connection to Sea Surface Temperatures. *Journal of Climate*, **31(20)**, 8313–8338, doi:10.1175/jcli-d-18-0168.1.
Singh, H.A., L.M. Polvani, and P.J. Rasch, 2019: Antarctic Sea Ice Expansion, Driven by Internal Variability, in the Presence of Increasing Atmospheric CO2. *Geophysical Research Letters*, **46**, doi:10.1029/2019gl083758.
Sinha, B. et al., 2018: The accuracy of estimates of the overturning circulation from basin-wide mooring arrays. *Progress in Oceanography*, **160**, 101–123, doi:10.1016/j.pocean.2017.12.001.
Sippel, S., N. Meinshausen, E.M. Fischer, E. Székely, and R. Knutti, 2020: Climate change now detectable from any single day of weather at global scale. *Nature Climate Change*, **10(1)**, 35–41, doi:10.1038/s41558-019-0666-7.
Sippel, S. et al., 2019: Uncovering the Forced Climate Response from a Single Ensemble Member Using Statistical Learning. *Journal of Climate*, **32(17)**, 5677–5699, doi:10.1175/jcli-d-18-0882.1.
Sjolte, J. et al., 2018: Solar and volcanic forcing of North Atlantic climate inferred from a process-based reconstruction. *Climate of the Past*, **14(8)**, 1179–1194, doi:10.5194/cp-14-1179-2018.
Skliris, N., J.D. Zika, G. Nurser, S.A. Josey, and R. Marsh, 2016: Global water cycle amplifying at less than the Clausius-Clapeyron rate. *Scientific Reports*, **6(1)**, 38752, doi:10.1038/srep38752.
Skliris, N., J.D. Zika, L. Herold, S.A. Josey, and R. Marsh, 2018: Mediterranean sea water budget long-term trend inferred from salinity observations. *Climate Dynamics*, 1–20, doi:10.1007/s00382-017-4053-7.
Skliris, N. et al., 2014: Salinity changes in the World Ocean since 1950 in relation to changing surface freshwater fluxes. *Climate Dynamics*, **43(3–4)**, 709–736, doi:10.1007/s00382-014-2131-7.
Slangen, A.B.A., J.A. Church, X. Zhang, and D. Monselesan, 2014: Detection and attribution of global mean thermosteric sea level change. *Geophysical Research Letters*, **41(16)**, 5951–5959, doi:10.1002/2014gl061356.
Slangen, A.B.A., J.A. Church, X. Zhang, and D.P. Monselesan, 2015: The sea level response to external forcings in historical simulations of CMIP5 climate models. *Journal of Climate*, **28(21)**, 8521–8539, doi:10.1175/jcli-d-15-0376.1.
Slangen, A.B.A. et al., 2016: Anthropogenic forcing dominates global mean sea-level rise since 1970. *Nature Climate Change*, **6(7)**, 701–705, doi:10.1038/nclimate2991.
Slangen, A.B.A. et al., 2017: Evaluating Model Simulations of Twentieth-Century Sea Level Rise. Part I: Global Mean Sea Level Change. *Journal of Climate*, **30(21)**, 8539–8563, doi:10.1175/jcli-d-17-0110.1.
Slater, T., A.E. Hogg, and R. Mottram, 2020: Ice-sheet losses track high-end sea-level rise projections. *Nature Climate Change*, doi:10.1038/s41558-020-0893-y.
Small, R.J., E. Curchitser, K. Hedstrom, B. Kauffman, and W.G. Large, 2015: The Benguela Upwelling System: Quantifying the Sensitivity to Resolution and Coastal Wind Representation in a Global Climate Model. *Journal of Climate*, **28(23)**, 9409–9432, doi:10.1175/jcli-d-15-0192.1.
Small, R.J. et al., 2014: A new synoptic scale resolving global climate simulation using the Community Earth System Model. *Journal of Advances in Modeling Earth Systems*, **6(4)**, 1065–1094, doi:10.1002/2014ms000363.
Smeed, D.A. et al., 2014: Observed decline of the Atlantic meridional overturning circulation 2004–2012. *Ocean Science*, **10(1)**, 29–38, doi:10.5194/os-10-29-2014.
Smeed, D.A. et al., 2018: The North Atlantic Ocean Is in a State of Reduced Overturning. *Geophysical Research Letters*, **45(3)**, 1527–1533, doi:10.1002/2017gl076350.
Smith, C.J. et al., 2020: Effective radiative forcing and adjustments in CMIP6 models. *Atmospheric Chemistry and Physics*, **20(16)**, 9591–9618, doi:10.5194/acp-20-9591-2020.
Smith, D.M. et al., 2016: Role of volcanic and anthropogenic aerosols in the recent global surface warming slowdown. *Nature Climate Change*, **6(10)**, 936–940, doi:10.1038/nclimate3058.
Snow, K. et al., 2017: The Response of Ice Sheets to Climate Variability. *Geophysical Research Letters*, doi:10.1002/2017gl075745.

ACCEPTED VERSION SUBJECT TO FINAL EDITING

Solman, S. and I. Orlanski, 2016a: Climate change over the extratropical southern hemisphere: the tale from an ensemble of reanalysis datasets. *J. Climate*, doi:10.1175/jcli-d-15-0588.1.
Solman, S. and I. Orlanski, 2016b: Climate change over the extratropical southern hemisphere: the tale from an ensemble of reanalysis datasets. *J. Climate*, doi:10.1175/jcli-d-15-0588.1.
Solomon, A. and L.M. Polvani, 2016: Highly Significant Responses to Anthropogenic Forcings of the Midlatitude Jet in the Southern Hemisphere. *Journal of Climate*, **29(9)**, 3463–3470, doi:10.1175/jcli-d-16-0034.1.
Son, S.-W. et al., 2018a: Tropospheric jet response to Antarctic ozone depletion: An update with Chemistry-Climate Model Initiative (CCMI) models. *ENVIRONMENTAL RESEARCH LETTERS*, **13(5)**, doi:10.1088/1748-9326/aabf21.
Son, S.-W. et al., 2018b: Tropospheric jet response to Antarctic ozone depletion: An update with Chemistry-Climate Model Initiative (CCMI) models. *ENVIRONMENTAL RESEARCH LETTERS*, **13(5)**, doi:10.1088/1748-9326/aabf21.
Song, M., L. Wei, and Z. Wang, 2016: Quantifying the contribution of natural variability to September Arctic sea ice decline. *Acta Oceanologica Sinica*, **35(5)**, 49–53, doi:10.1007/s13131-016-0854-5.
Sousa, P.M., R.M. Trigo, D. Barriopedro, P.M.M. Soares, and J.A. Santos, 2018: European temperature responses to blocking and ridge regional patterns. *Climate Dynamics*, **50(1)**, 457–477, doi:10.1007/s00382-017-3620-2.
Srivastava, A.K. and T. DelSole, 2014: Robust Forced Response in South Asian Summer Monsoon in a Future Climate. *Journal of Climate*, **27(20)**, 7849–7860, doi:10.1175/jcli-d-13-00599.1.
Staten, P.W., J. Lu, K.M. Grise, S.M. Davis, and T. Birner, 2018: Re-examining tropical expansion. *Nature Climate Change*, **8(9)**, 768–775, doi:10.1038/s41558-018-0246-2.
Staten, P.W. et al., 2020: Tropical Widening: From Global Variations to Regional Impacts. *Bulletin of the American Meteorological Society*, **101(6)**, E897–E904, doi:10.1175/bams-d-19-0047.1.
Steinig, S., J. Harlaß, W. Park, and M. Latif, 2018: Sahel rainfall strength and onset improvements due to more realistic Atlantic cold tongue development in a climate model. *Scientific Reports*, **8(1)**, 2569, doi:10.1038/s41598-018-20904-1.
Steinman, B.A., M.E. Mann, and S.K. Miller, 2015: Atlantic and Pacific multidecadal oscillations and Northern Hemisphere temperatures. *Science*, **347(6225)**, 988–991, doi:10.1126/science.1257856.
Stendardo, I. and N. Gruber, 2012: Oxygen trends over five decades in the North Atlantic. *Journal of Geophysical Research: Oceans*, **117(C11)**, n/a–n/a, doi:10.1029/2012jc007909.
Steptoe, H., L.J. Wilcox, and E.J. Highwood, 2016: Is there a robust effect of anthropogenic aerosols on the Southern Annular Mode? *Journal of Geophysical Research: Atmospheres*, **121(17)**, 10,029–10,042, doi:10.1002/2015jd024218.
Stern, D.I. and R.K. Kaufmann, 2014: Anthropogenic and natural causes of climate change. *Climatic Change*, **122(1–2)**, doi:10.1007/s10584-013-1007-x.
Stevenson, S., A. Capotondi, J. Fasullo, and B. Otto-Bliesner, 2017: Forced changes to twentieth century ENSO diversity in a last Millennium context. *Climate Dynamics*, doi:10.1007/s00382-017-3573-5.
Stevenson, S.L., 2012: Significant changes to ENSO strength and impacts in the twenty-first century: Results from CMIP5. *Geophysical Research Letters*, **39(17)**, 1–5, doi:10.1029/2012gl052759.
Stolpe, M.B., K. Cowtan, I. Medhaug, and R. Knutti, 2020: Pacific variability reconciles observed and modelled global mean temperature increase since 1950. *Climate Dynamics*, doi:10.1007/s00382-020-05493-y.
Stone, D.A. and G. Hansen, 2016: Rapid systematic assessment of the detection and attribution of regional anthropogenic climate change. *Climate Dynamics*, **47(5–6)**, 1399–1415, doi:10.1007/s00382-015-2909-2.
Stone, E.J. et al., 2016: Impact of meltwater on high-latitude early Last Interglacial climate. *Climate of the Past*, **12(9)**, 1919–1932, doi:10.5194/cp-12-1919-2016.
Stott, P.A., R.T. Sutton, and D.M. Smith, 2008: Detection and attribution of Atlantic salinity changes. *Geophysical Research Letters*, **35(21)**, L21702, doi:10.1029/2008gl035874.
Stouffer, R.J. et al., 2017: CMIP5 scientific gaps and recommendations for CMIP6. *Bulletin of the American Meteorological Society*, **98(1)**, 95–105, doi:10.1175/bams-d-15-00013.1.
Stramma, L., A. Oschlies, and S. Schmidtko, 2012: Mismatch between observed and modeled trends in dissolved upper-ocean oxygen over the last 50 yr. *Biogeosciences*, **9(10)**, 4045–4057, doi:10.5194/bg-9-4045-2012.
Stroeve, J.C. et al., 2012: Trends in Arctic sea ice extent from CMIP5, CMIP3 and observations. *Geophysical Research Letters*, **39(16)**, doi:10.1029/2012gl052676.
Strommen, K. and T.N. Palmer, 2019: Signal and noise in regime systems: A hypothesis on the predictability of the North Atlantic Oscillation. *Quarterly Journal of the Royal Meteorological Society*, **145(718)**, 147–163, doi:10.1002/qj.3414.
Stuecker, M.F., C.M. Bitz, and K.C. Armour, 2017: Conditions leading to the unprecedented low Antarctic sea ice extent during the 2016 austral spring season. *Geophysical Research Letters*, **44(17)**, 9008–9019, doi:10.1002/2017gl074691.
Su, H., X. Wu, W. Lu, W. Zhang, and X.H. Yan, 2017: Inconsistent Subsurface and Deeper Ocean Warming Signals During Recent Global Warming and Hiatus. *Journal of Geophysical Research: Oceans*, **122(10)**, 8182–8195, doi:10.1002/2016jc012481.

ACCEPTED VERSION SUBJECT TO FINAL EDITING

Su, J., R. Zhang, and H. Wang, 2017: Consecutive record-breaking high temperatures marked the handover from hiatus to accelerated warming. *Scientific Reports*, **7**, 43735, doi:10.1038/srep43735.
Suárez-Gutiérrez, L., C. Li, P.W. Thorne, and J. Marotzke, 2017: Internal variability in simulated and observed tropical tropospheric temperature trends. *Geophysical Research Letters*, **44(11)**, 5709–5719, doi:10.1002/2017gl073798.
Sun, C., J. Li, F. Kucharski, J. Xue, and X. Li, 2019: Contrasting spatial structures of Atlantic Multidecadal Oscillation between observations and slab ocean model simulations. *Climate Dynamics*, **52(3–4)**, 1395–1411, doi:10.1007/s00382-018-4201-8.
Sun, Y., T. Zhou, G. Ramstein, C. Contoux, and Z. Zhang, 2016: Drivers and mechanisms for enhanced summer monsoon precipitation over East Asia during the mid-Pliocene in the IPSL-CM5A. *Climate Dynamics*, **46(5–6)**, 1437–1457, doi:10.1007/s00382-015-2656-4.
Sun, Y. et al., 2018: Quantifying East Asian Summer Monsoon Dynamics in the ECP4.5 Scenario With Reference to the Mid-Piacenzian Warm Period. *Geophysical Research Letters*, **45(22)**, 12,523–12,533, doi:10.1029/2018gl080061.
Swart, N.C., S.T. Gille, J.C. Fyfe, and N.P. Gillett, 2018: Recent Southern Ocean warming and freshening driven by greenhouse gas emissions and ozone depletion. *Nature Geoscience*, 1, doi:10.1038/s41561-018-0226-1.
Swart, N.C., J.C. Fyfe, E. Hawkins, J.E. Kay, and A. Jahn, 2015: Influence of internal variability on Arctic sea-ice trends. *Nature Climate Change*, **5**, 86, doi:10.1038/nclimate2483.
Swart, N.C. et al., 2019: The Canadian Earth System Model version 5 (CanESM5.0.3). *Geoscientific Model Development*, **12(11)**, 4823–4873, doi:10.5194/gmd-12-4823-2019.
Swingedouw, D. et al., 2017: Impact of explosive volcanic eruptions on the main climate variability modes. *Global and Planetary Change*, **150**, 24–45, doi:10.1016/j.gloplacha.2017.01.006.
Taguchi, M., 2017: A study of different frequencies of major stratospheric sudden warmings in CMIP5 historical simulations. *Journal of Geophysical Research: Atmospheres*, **122(10)**, 5144–5156, doi:10.1002/2016jd025826.
Takahashi, C. and M. Watanabe, 2016a: Pacific trade winds accelerated by aerosol forcing over the past two decades. *Nature Climate Change*, **6(8)**, 768–772, doi:10.1038/nclimate2996.
Takahashi, C. and M. Watanabe, 2016b: Pacific trade winds accelerated by aerosol forcing over the past two decades. *Nature Climate Change*, **6(8)**, 768–772, doi:10.1038/nclimate2996.
Takahashi, H., H. Su, and J.H. Jiang, 2016: Error analysis of upper tropospheric water vapor in CMIP5 models using "A-Train" satellite observations and reanalysis data. *Climate Dynamics*, **46(9–10)**, 2787–2803, doi:10.1007/s00382-015-2732-9.
Tandon, N.F. and P.J. Kushner, 2015: Does External Forcing Interfere with the AMOC's Influence on North Atlantic Sea Surface Temperature? *Journal of Climate*, **28(16)**, 6309–6323, doi:10.1175/jcli-d-14-00664.1.
Tao, L., Y. Hu, and J. Liu, 2016: Anthropogenic forcing on the Hadley circulation in CMIP5 simulations. *Climate Dynamics*, **46(9–10)**, 3337–3350, doi:10.1007/s00382-015-2772-1.
Tao, W. et al., 2015: Interdecadal modulation of ENSO teleconnections to the Indian Ocean Basin Mode and their relationship under global warming in CMIP5 models. *International Journal of Climatology*, **35(3)**, 391–407, doi:10.1002/joc.3987.
Tao, W. et al., 2016: A study of biases in simulation of the Indian Ocean basin mode and its capacitor effect in CMIP3/CMIP5 models. *Climate Dynamics*, **46(1–2)**, 205–226, doi:10.1007/s00382-015-2579-0.
Taschetto, A.S. et al., 2014a: Cold tongue and warm pool ENSO Events in CMIP5: Mean state and future projections. *Journal of Climate*, **27(8)**, 2861–2885, doi:10.1175/jcli-d-13-00437.1.
Taschetto, A.S. et al., 2014b: Cold tongue and warm pool ENSO Events in CMIP5: Mean state and future projections. *Journal of Climate*, **27(8)**, 2861–2885, doi:10.1175/jcli-d-13-00437.1.
Taschetto, A.S. et al., 2020: ENSO atmospheric teleconnections. In: *El Niño Southern Oscillation in a Changing Climate* [McPhaden, M.J., A. Santoso, and W. Cai (eds.)]. American Geophysical Union (AGU), Washington DC, USA, pp. 309–335, doi:10.1002/9781119548164.ch14.
Taylor, K.E., R.J. Stouffer, and G.A. Meehl, 2012: An overview of CMIP5 and the experiment design. *Bulletin of the American Meteorological Society*, **93(4)**, 485–498, doi:10.1175/bams-d-11-00094.1.
Tedesco, M. and X. Fettweis, 2020a: Unprecedented atmospheric conditions (1948-2019) drive the 2019 exceptional melting season over the Greenland ice sheet. *Cryosphere*, doi:10.5194/tc-14-1209-2020.
Tedesco, M. and X. Fettweis, 2020b: Unprecedented atmospheric conditions (1948-2019) drive the 2019 exceptional melting season over the Greenland ice sheet. *Cryosphere*, doi:10.5194/tc-14-1209-2020.
Terray, L., 2012: Evidence for multiple drivers of North Atlantic multi-decadal climate variability. *Geophysical Research Letters*, **39(19)**, n/a–n/a, doi:10.1029/2012gl053046.
Terray, L. et al., 2012: Near-surface salinity as nature's rain gauge to detect human influence on the Tropical water cycle. *Journal of Climate*, **25(3)**, 958–977, doi:10.1175/jcli-d-10-05025.1.
Thackeray, C.W., C.G. Fletcher, and C. Derksen, 2015: Quantifying the skill of CMIP5 models in simulating seasonal albedo and snow cover evolution. *JOURNAL OF GEOPHYSICAL RESEARCH-ATMOSPHERES*, **120(12)**, 5831–5849, doi:10.1002/2015jd023325.
Thackeray, C.W., C.G. Fletcher, L.R. Mudryk, and C. Derksen, 2016: Quantifying the Uncertainty in Historical and

ACCEPTED VERSION SUBJECT TO FINAL EDITING

Future Simulations of Northern Hemisphere Spring Snow Cover. *Journal of Climate*, **29(23)**, 8647–8663, doi:10.1175/jcli-d-16-0341.1.

Thackeray, C.W., A.M. DeAngelis, A. Hall, D.L. Swain, and X. Qu, 2018: On the Connection Between Global Hydrologic Sensitivity and Regional Wet Extremes. *Geophysical Research Letters*, **45(20)**, 11,343–11,351, doi:10.1029/2018gl079698.

Thiéblemont, R., K. Matthes, N.-E. Omrani, K. Kodera, and F. Hansen, 2015: Solar forcing synchronizes decadal North Atlantic climate variability. *Nature Communications*, **6(1)**, 8268, doi:10.1038/ncomms9268.

Thielke, A. and T. Mölg, 2019: Observed and simulated Indian Ocean Dipole activity since the mid-19th century and its relation to East African short rains. *International Journal of Climatology*, **39(11)**, 4467–4478, doi:10.1002/joc.6085.

Thoma, M., R.J. Greatbatch, C. Kadow, and R. Gerdes, 2015: Decadal hindcasts initialized using observed surface wind stress: Evaluation and prediction out to 2024. *Geophysical Research Letters*, **42(15)**, 6454–6461, doi:10.1002/2015gl064833.

Thomas, J.L., D.W. Waugh, and A. Gnanadesikan, 2015: Southern Hemisphere extratropical circulation: Recent trends and natural variability. *Geophysical Research Letters*, **42(13)**, 5508–5515, doi:10.1002/2015gl064521.

Thomas, R.Q., E.N.J. Brookshire, and S. Gerber, 2015: Nitrogen limitation on land: how can it occur in Earth system models? *Global Change Biology*, **21(5)**, 1777–1793, doi:10.1111/gcb.12813.

Thompson, D.M., J.E. Cole, G.T. Shen, A.W. Tudhope, and G.A. Meehl, 2014: Early twentieth-century warming linked to tropical Pacific wind strength. *Nature Geoscience*, **8**, 117, doi:10.1038/ngeo2321.

Thorne, P., S. Outten, I. Bethke, and Seland, 2015: Investigating the recent apparent hiatus in surface temperature increases: 2. Comparison of model ensembles to observational estimates. *Journal of Geophysical Research: Atmospheres*, **120(17)**, 8597–8620, doi:10.1002/2014jd022805.

Tian, B., 2015: Spread of model climate sensitivity linked to double-Intertropical Convergence Zone bias. *Geophysical Research Letters*, **42(10)**, 4133–4141, doi:10.1002/2015gl064119.

Tian, B. and X. Dong, 2020: The Double-ITCZ Bias in CMIP3, CMIP5, and CMIP6 Models Based on Annual Mean Precipitation. *Geophys. Res. Let.*, **47**.

Tian, B. et al., 2013: Evaluating CMIP5 models using AIRS tropospheric air temperature and specific humidity climatology. *Journal of Geophysical Research Atmospheres*, **118(1)**, 114–134, doi:10.1029/2012jd018607.

Tierney, J.E., C.C. Ummenhofer, and P.B. DeMenocal, 2015: Past and future rainfall in the Horn of Africa. *Science Advances*, **1(9)**, e1500682, doi:10.1126/sciadv.1500682.

Tierney, J.E., F.S.R. Pausata, and P.B. deMenocal, 2017a: Rainfall regimes of the Green Sahara. *Science Advances*, **3(1)**, doi:10.1126/sciadv.1601503.

Tierney, J.E., F.S.R. Pausata, and P.B. deMenocal, 2017b: Rainfall regimes of the Green Sahara. *Science Advances*, **3(1)**, doi:10.1126/sciadv.1601503.

Tierney, J.E., F.S.R. Pausata, and P.B. deMenocal, 2017c: Rainfall regimes of the Green Sahara. *Science Advances*, **3(1)**, doi:10.1126/sciadv.1601503.

Tierney, J.E., F.S.R. Pausata, and P.B. deMenocal, 2017d: Rainfall regimes of the Green Sahara. *Science Advances*, **3(1)**, doi:10.1126/sciadv.1601503.

Tierney, J.E., A.M. Haywood, R. Feng, T. Bhattacharya, and B.L. Otto-Bliesner, 2019: Pliocene warmth consistent with greenhouse gas forcing. *Geophysical Research Letters*, **46(15)**, 9136–9144, doi:10.1029/2019gl083802.

Tierney, J.E. et al., 2020a: Past climates inform our future. *Science*, **370(6517)**, doi:10.1126/science.aay3701.

Tierney, J.E. et al., 2020b: Glacial cooling and climate sensitivity revisited. *Nature*, **584(7822)**, 569–573, doi:10.1038/s41586-020-2617-x.

Tokarska, K.B., G.C. Hegerl, A.P. Schurer, A. Ribes, and J.T. Fasullo, 2019: Quantifying human contributions to past and future ocean warming and thermosteric sea level rise. *Environmental Research Letters*, **14(7)**, doi:10.1088/1748-9326/ab23c1.

Tokarska, K.B. et al., 2020: Past warming trend constrains future warming in CMIP6 models. *Science Advances*, **6(12)**, doi:10.1126/sciadv.aaz9549.

Tokinaga, H., S.-P. Xie, C. Deser, Y. Kosaka, and Y.M. Okumura, 2012: Slowdown of the Walker circulation driven by tropical Indo-Pacific warming. *Nature*, **491**, 439, doi:10.1038/nature11576.

Toohey, M. and M. Sigl, 2017: Volcanic stratospheric sulfur injections and aerosol optical depth from 500 BCE to 1900 CE. *Earth System Science Data*, **9(2)**, 809–831, doi:10.5194/essd-9-809-2017.

Trenberth, K.E., D.P. Stepaniak, and J.M. Caron, 2000: The Global Monsoon as Seen through the Divergent Atmospheric Circulation. *Journal of Climate*, **13(22)**, 3969–3993, doi:10.1175/1520-0442(2000)013<3969:tgmast>2.0.co;2.

Trenberth, K.E., Y. Zhang, and M. Gehne, 2017: Intermittency in precipitation: duration, frequency, intensity, and amounts using hourly data.. *J. Hydrometeorol.*, **18**, 1393–1412, doi:10.1175/jhm-d-16-0263.

Trenberth, K.E., J.T. Fasullo, G. Branstator, and A.S. Phillips, 2014: Seasonal aspects of the recent pause in surface warming. *Nature Climate Change*, **4(10)**, 911–916, doi:10.1038/nclimate2341.

Triacca, U., A. Pasini, A. Attanasio, A. Giovannelli, and M. Lippi, 2014: Clarifying the roles of greenhouse gases and ENSO in recent global warming through their prediction performance. *Journal of Climate*, **27(20)**, 7903–7910,

ACCEPTED VERSION SUBJECT TO FINAL EDITING

doi:10.1175/jcli-d-13-00784.1.
Trouet, V., J.D. Scourse, and C.C. Raible, 2012: North Atlantic storminess and Atlantic Meridional Overturning Circulation during the last Millennium: Reconciling contradictory proxy records of NAO variability. *Global and Planetary Change*, **84–85**, 48–55, doi:10.1016/j.gloplacha.2011.10.003.
Trusel, L.D. et al., 2018: Nonlinear rise in Greenland runoff in response to post-industrial Arctic warming. *Nature*, doi:10.1038/s41586-018-0752-4.
Tuel, A., 2019: Explaining differences between recent model and satellite tropospheric warming rates with tropical SSTs. *Geophysical Research Letters*, **46**, 9023– 9030, doi:10.1029/2019gl083994.
Turner, J., T.J. Bracegirdle, T. Phillips, G.J. Marshall, and J. Scott Hosking, 2013: An initial assessment of antarctic sea ice extent in the CMIP5 models. *Journal of Climate*, **26(5)**, 1473–1484, doi:10.1175/jcli-d-12-00068.1.
Turner, J., J.S. Hosking, G.J. Marshall, T. Phillips, and T.J. Bracegirdle, 2016: Antarctic sea ice increase consistent with intrinsic variability of the Amundsen Sea Low. *Climate Dynamics*, **46(7)**, 2391–2402, doi:10.1007/s00382-015-2708-9.
Turner, J. et al., 2017: Unprecedented springtime retreat of Antarctic sea ice in 2016. *Geophysical Research Letters*, **44(13)**, 6868–6875, doi:10.1002/2017gl073656.
Undorf, S., M.A. Bollasina, B.B.B. Booth, and G.C. Hegerl, 2018a: Contrasting the Effects of the 1850–1975 Increase in Sulphate Aerosols from North America and Europe on the Atlantic in the CESM. *Geophysical Research Letters*, **45(21)**, 11,911–930,940, doi:10.1029/2018gl079970.
Undorf, S. et al., 2018b: Detectable Impact of Local and Remote Anthropogenic Aerosols on the 20th Century Changes of West African and South Asian Monsoon Precipitation. *Journal of Geophysical Research: Atmospheres*, **123(10)**, 4871–4889, doi:10.1029/2017jd027711.
UNFCCC, 2016: Decision 1/CP.21: Adoption of the Paris Agreement. In: *Report of the Conference of the Parties on its twenty-first session, held in Paris from 30 November to 13 December 2015. Addendum: Part two: Action taken by the Conference of the Parties at its twenty-first session*. FCCC/CP/2015/10/Add.1, United Nations Framework Convention on Climate Change (UNFCCC), pp. 1–36.
Uotila, P., P.R. Holland, T. Vihma, S.J. Marsland, and N. Kimura, 2014: Is realistic Antarctic sea-ice extent in climate models the result of excessive ice drift? *Ocean Modelling*, **79**, 33–42, doi:10.1016/j.ocemod.2014.04.004.
van den Hurk, B. et al., 2016: LS3MIP (v1.0) contribution to CMIP6: the Land Surface, Snow and Soil moisture Model Intercomparison Project – aims, setup and expected outcome. *Geoscientific Model Development*, **9(8)**, 2809–2832, doi:10.5194/gmd-9-2809-2016.
Van Haren, R., R.J. Haarsma, G.J. Van Oldenborgh, and W. Hazeleger, 2015: Resolution dependence of European precipitation in a state-of-the-art atmospheric general circulation model. *Journal of Climate*, **28(13)**, 5134–5149, doi:10.1175/jcli-d-14-00279.1.
van Kampenhout, L. et al., 2020: Present-Day Greenland Ice Sheet Climate and Surface Mass Balance in CESM2. *Journal of Geophysical Research: Earth Surface*, doi:10.1029/2019jf005318.
Vannière, B. et al., 2019: Multi-model evaluation of the sensitivity of the global energy budget and hydrological cycle to resolution. *Climate Dynamics*, **52(11)**, 6817–6846, doi:10.1007/s00382-018-4547-y.
Vecchi, G.A. and B.J. Soden, 2007: Global Warming and the Weakening of the Tropical Circulation. *Journal of Climate*, **20(17)**, 4316–4340, doi:10.1175/jcli4258.1.
Vecchi, G.A. et al., 2006: Weakening of tropical Pacific atmospheric circulation due to anthropogenic forcing. *Nature*, **441(1)**, 73–76, doi:10.1038/nature04744.
Vera, C.S. and L. Diaz, 2014: Anthropogenic influence on summer precipitation trends over South America in CMIP5 models. *Int. J. Climatol*, doi:10.1002/joc.4153.
Verma, T., R. Saravanan, P. Chang, and S. Mahajan, 2019: Tropical Pacific Ocean Dynamical Response to Short-Term Sulfate Aerosol Forcing. *Journal of Climate*, **32(23)**, 8205–8221, doi:10.1175/jcli-d-19-0050.1.
Vidale, P.L. et al., 2021: Impact of stochastic physics and model resolution on the simulation of Tropical Cyclones in climate GCMs. *Journal of Climate*, 1–85, doi:10.1175/jcli-d-20-0507.1.
Vijayeta, A. and D. Dommenget, 2017a: An evaluation of ENSO dynamics in CMIP simulations in the framework of the recharge oscillator model. *Climate Dynamics*, 1–19, doi:10.1007/s00382-017-3981-6.
Vijayeta, A. and D. Dommenget, 2017b: An evaluation of ENSO dynamics in CMIP simulations in the framework of the recharge oscillator model. *Climate Dynamics*, 1–19, doi:10.1007/s00382-017-3981-6.
Voigt, A. and T.A. Shaw, 2016: Impact of Regional Atmospheric Cloud Radiative Changes on Shifts of the Extratropical Jet Stream in Response to Global Warming. *JOURNAL OF CLIMATE*, **29(23)**, 8399–8421, doi:10.1175/jcli-d-16-0140.1.
Voldoire, A. et al., 2019a: Role of wind stress in driving SST biases in the Tropical Atlantic. *Climate Dynamics*, **53(5–6)**, 3481–3504, doi:10.1007/s00382-019-04717-0.
Voldoire, A. et al., 2019b: Evaluation of CMIP6 DECK Experiments With CNRM-CM6-1. *Journal of Advances in Modeling Earth Systems*, **11(7)**, 2177–2213, doi:10.1029/2019ms001683.
Volpi, D., L. Batté, J.-F. Guérémy, and M. Déqué, 2020: Teleconnection-based evaluation of seasonal forecast quality. *Climate Dynamics*, **55(5–6)**, 1353–1365, doi:10.1007/s00382-020-05327-x.
von Schuckmann, K. et al., 2016: An imperative to monitor Earth's energy imbalance. *Nature Climate Change*, **6(2)**,

ACCEPTED VERSION SUBJECT TO FINAL EDITING

138–144, doi:10.1038/nclimate2876.
von Schuckmann, K. et al., 2020: Heat stored in the Earth system: where does the energy go? *Earth System Science Data*, **12(3)**, 2013–2041, doi:10.5194/essd-12-2013-2020.
von Storch, J.-S., H. Haak, E. Hertwig, and I. Fast, 2016: Vertical heat and salt fluxes due to resolved and parameterized meso-scale Eddies. *Ocean Modelling*, **108**, 1–19, doi:10.1016/j.ocemod.2016.10.001.
Vries, H., S. Scher, R. Haarsma, S. Drijfhout, and A. Delden, 2019: How Gulf-Stream SST-fronts influence Atlantic winter storms. *Climate Dynamics*, **52(9)**, 5899–5909, doi:10.1007/s00382-018-4486-7.
Wainwright, C.M. et al., 2019: The impact of air–sea coupling and ocean biases on the seasonal cycle of southern West African precipitation. *Climate Dynamics*, **53(11)**, 7027–7044, doi:10.1007/s00382-019-04973-0.
Wallace, R.B., H. Baumann, J.S. Grear, R.C. Aller, and C.J. Gobler, 2014: Coastal ocean acidification: The other eutrophication problem. *Estuarine, Coastal and Shelf Science*, **148**, 1–13, doi:10.1016/j.ecss.2014.05.027.
Wan, H., X. Zhang, F. Zwiers, and S.-K. Min, 2015: Attributing northern high-latitude precipitation change over the period 1966--2005 to human influence. *Climate Dynamics*, **45(7)**, 1713–1726, doi:10.1007/s00382-014-2423-y.
Wang, B. and Q. Ding, 2008: Global monsoon: Dominant mode of annual variation in the tropics. *Dynamics of Atmospheres and Oceans*, **44(3–4)**, 165–183, doi:10.1016/j.dynatmoce.2007.05.002.
Wang, B., C. Jin, and J. Liu, 2020: Understanding Future Change of Global Monsoons Projected by CMIP6 Models. *Journal of Climate*, **33(15)**, 6471–6489, doi:10.1175/jcli-d-19-0993.1.
Wang, B. et al., 2013a: Northern Hemisphere summer monsoon intensified by mega-El Nino/southern oscillation and Atlantic multidecadal oscillation. *Proceedings of the National Academy of Sciences*, **110(14)**, 5347–5352, doi:10.1073/pnas.1219405110.
Wang, B. et al., 2013b: Northern Hemisphere summer monsoon intensified by mega-El Nino/southern oscillation and Atlantic multidecadal oscillation. *Proceedings of the National Academy of Sciences*, **110(14)**, 5347–5352, doi:10.1073/pnas.1219405110.
Wang, B. et al., 2013c: Northern Hemisphere summer monsoon intensified by mega-El Nino/southern oscillation and Atlantic multidecadal oscillation. *Proceedings of the National Academy of Sciences*, **110(14)**, 5347–5352, doi:10.1073/pnas.1219405110.
Wang, B. et al., 2018: Toward Predicting Changes in the Land Monsoon Rainfall a Decade in Advance. *Journal of Climate*, **31(7)**, 2699–2714, doi:10.1175/jcli-d-17-0521.1.
Wang, C., L. Zhang, S.-K. Lee, L. Wu, and C.R. Mechoso, 2014: A global perspective on CMIP5 climate model biases. *Nature Climate Change*, **4**, 201, doi:10.1038/nclimate2118.
Wang, C.-Y., S.-P. Xie, Y. Kosaka, Q. Liu, and X.-T. Zheng, 2017: Global influence of tropical Pacific variability with implications for global warming slowdown. *Journal of Climate*, **30(7)**, doi:10.1175/jcli-d-15-0496.1.
Wang, G. and W. Cai, 2020: Two-year consecutive concurrences of positive Indian Ocean Dipole and Central Pacific El Niño preconditioned the 2019/2020 Australian "black summer" bushfires. *Geoscience Letters*, **7(1)**, 19, doi:10.1186/s40562-020-00168-2.
Wang, G. et al., 2019: Compounding tropical and stratospheric forcing of the record low Antarctic sea-ice in 2016. *Nature Communications*, **10(1)**, 13, doi:10.1038/s41467-018-07689-7.
Wang, J. et al., 2017: Internal and external forcing of multidecadal Atlantic climate variability over the past 1,200 years. *Nature Geoscience*, **10(7)**, 512–517, doi:10.1038/ngeo2962.
Wang, K. et al., 2020: Causes of slowing-down seasonal CO2 amplitude at Mauna Loa. *Global Change Biology*, **26(8)**, doi:10.1111/gcb.15162.
Wang, P.X. et al., 2014: The global monsoon across timescales: coherent variability of regional monsoons. *Climate of the Past*, **10(6)**, 2007–2052, doi:10.5194/cp-10-2007-2014.
Wang, X., J. Li, C. Sun, and T. Liu, 2017: NAO and its relationship with the Northern Hemisphere mean surface temperature in CMIP5 simulations. *Journal of Geophysical Research: Atmospheres*, **122(8)**, 4202–4227, doi:10.1002/2016jd025979.
Wang, Z., L. Bi, B. Yi, and X. Zhang, 2019: How the Inhomogeneity of Wet Sea Salt Aerosols Affects Direct Radiative Forcing. *Geophysical Research Letters*, **46(3)**, 1805–1813, doi:10.1029/2018gl081193.
Watanabe, M. and H. Tatebe, 2019: Reconciling roles of sulphate aerosol forcing and internal variability in Atlantic multidecadal climate changes. *Climate Dynamics*, **53(7–8)**, 4651–4665, doi:10.1007/s00382-019-04811-3.
Watanabe, M., J.-L. Dufresne, Y. Kosaka, T. Mauritsen, and H. Tatebe, 2021: Enhanced warming constrained by past trends in equatorial Pacific sea surface temperature gradient. *Nature Climate Change*, **11(1)**, 33–37, doi:10.1038/s41558-020-00933-3.
Watanabe, M. et al., 2014: Contribution of natural decadal variability to global warming acceleration and hiatus. *Nature Climate Change*, **4(10)**, doi:10.1038/nclimate2355.
Waugh, D.W. and V. Eyring, 2008: Quantitative performance metrics for stratospheric-resolving chemistry-climate models. *Atmospheric Chemistry and Physics*, **8(18)**, 5699–5713, doi:10.5194/acp-8-5699-2008.
Weijer, W., W. Cheng, O.A. Garuba, A. Hu, and B.T. Nadiga, 2020: CMIP6 Models Predict Significant 21st Century Decline of the Atlantic Meridional Overturning Circulation. *Geophysical Research Letters*, **47(12)**, doi:10.1029/2019gl086075.

ACCEPTED VERSION SUBJECT TO FINAL EDITING

Weisheimer, A. et al., 2020: Seasonal Forecasts of the Twentieth Century. *Bulletin of the American Meteorological Society*, **101(8)**, E1413–E1426, doi:10.1175/bams-d-19-0019.1.
Weller, E., B.-J. Park, and S.-K. Min, 2020: Anthropogenic and natural contributions to the lengthening of the Southern Hemisphere summer season. *Journal of Climate*, doi:10.1175/jcli-d-20-0084.1.
Weller, E. et al., 2016: Multi-model attribution of upper-ocean temperature changes using an isothermal approach. *Scientific Reports*, **6(1)**, 26926, doi:10.1038/srep26926.
Wenzel, S., P.M. Cox, V. Eyring, and P. Friedlingstein, 2016: Projected land photosynthesis constrained by changes in the seasonal cycle of atmospheric CO2. *Nature*, **538(7626)**, 499–501, doi:10.1038/nature19772.
West, J.J. et al., 2013: Co-benefits of mitigating global greenhouse gas emissions for future air quality and human health. *Nature Climate Change*, **3(10)**, 885–889, doi:10.1038/nclimate2009.
Wieder, W.R. et al., 2019: Beyond Static Benchmarking: Using Experimental Manipulations to Evaluate Land Model Assumptions. *Global Biogeochemical Cycles*, **33(10)**, doi:10.1029/2018gb006141.
Willett, K.M. et al., 2014: HadISDH land surface multi-variable humidity and temperature record for climate monitoring. *Climate of the Past*, **10(6)**, 1983–2006, doi:10.5194/cp-10-1983-2014.
Williams, A.P. et al., 2015: Contribution of anthropogenic warming to California drought during 2012-2014. *Geophysical Research Letters*, doi:10.1002/2015gl064924.
Williams, A.P. et al., 2020: Large contribution from anthropogenic warming to an emerging North American megadrought. *Science*, **368(6488)**, 314–318, doi:10.1126/science.aaz9600.
Wills, R.C.J., K.C. Armour, D.S. Battisti, and D.L. Hartmann, 2019: Ocean–Atmosphere Dynamical Coupling Fundamental to the Atlantic Multidecadal Oscillation. *Journal of Climate*, **32(1)**, 251–272, doi:10.1175/jcli-d-18-0269.1.
Winkler, A.J., R.B. Myneni, G.A. Alexandrov, and V. Brovkin, 2019: Earth system models underestimate carbon fixation by plants in the high latitudes. *Nature Communications*, doi:10.1038/s41467-019-08633-z.
Winton, M. et al., 2020: Climate Sensitivity of GFDL's CM4.0. *Journal of Advances in Modeling Earth Systems*, **12(1)**, e2019MS001838, doi:10.1029/2019ms001838.
WMO, 2018: Executive Summary. In: *Scientific Assessment of Ozone Depletion: 2018*. Global Ozone Research and Monitoring Project – Report No. 58, World Meteorological Organization (WMO), Geneva, Switzerland, pp. 67.
Woollings, T. et al., 2015: Contrasting interannual and multidecadal NAO variability. *Climate Dynamics*, **45(1–2)**, 539–556, doi:10.1007/s00382-014-2237-y.
Woollings, T. et al., 2018a: Daily to Decadal Modulation of Jet Variability. *Journal of Climate*, **31(4)**, 1297–1314, doi:10.1175/jcli-d-17-0286.1.
Woollings, T. et al., 2018b: Blocking and its Response to Climate Change. *Current Climate Change Reports*, **4(3)**, 287–300, doi:10.1007/s40641-018-0108-z.
Wouters, B., S. Drijfhout, and W. Hazeleger, 2012: Interdecadal North-Atlantic meridional overturning circulation variability in EC-EARTH. *Climate Dynamics*, **39(11)**, 2695–2712, doi:10.1007/s00382-012-1366-4.
Wu, P., N. Christidis, and P. Stott, 2013: Anthropogenic impact on Earth's hydrological cycle. *Nature Clim. Change*, **3**, doi:10.1038/nclimate1932.
Wu, P. et al., 2019: The impact of horizontal atmospheric resolution in modelling air–sea heat fluxes. *Quarterly Journal of the Royal Meteorological Society*, **145(724)**, 3271–3283, doi:10.1002/qj.3618.
Wu, T., A. Hu, F. Gao, J. Zhang, and G.A. Meehl, 2019a: New insights into natural variability and anthropogenic forcing of global/regional climate evolution. *npj Climate and Atmospheric Science*, **2(1)**, 18, doi:10.1038/s41612-019-0075-7.
Wu, T. et al., 2019b: The Beijing Climate Center Climate System Model (BCC-CSM): the main progress from CMIP5 to CMIP6. *Geoscientific Model Development*, **12(4)**, 1573–1600, doi:10.5194/gmd-12-1573-2019.
Wu, T. et al., 2020: Beijing Climate Center Earth System Model version 1 (BCC-ESM1): model description and evaluation of aerosol simulations. *Geoscientific Model Development*, **13(3)**, 977–1005, doi:10.5194/gmd-13-977-2020.
Wu, Z. and T. Reichler, 2020: Variations in the Frequency of Stratospheric Sudden Warmings in CMIP5 and CMIP6 and Possible Causes. *Journal of Climate*, **33(23)**, 10305–10320, doi:10.1175/jcli-d-20-0104.1.
Xiao, L., T. Che, L. Chen, H. Xie, and L. Dai, 2017: Quantifying Snow Albedo Radiative Forcing and Its Feedback during 2003–2016. *Remote Sensing*, **9(9)**, 883, doi:10.3390/rs9090883.
Xie, S.-P. et al., 2010: Global Warming Pattern Formation: Sea Surface Temperature and Rainfall. *Journal of Climate*, **23(4)**, 966–986, doi:10.1175/2009jcli3329.1.
Xu, T., Z. Shi, and Z. An, 2018: Responses of ENSO and NAO to the external radiative forcing during the last millennium: Results from CCSM4 and MPI-ESM-P simulations. *Quaternary International*, **487**, 99–111, doi:10.1016/j.quaint.2017.12.038.
Xu, Y. and A. Hu, 2018: How Would the Twenty-First-Century Warming Influence Pacific Decadal Variability and Its Connection to North American Rainfall: Assessment Based on a Revised Procedure for the IPO/PDO. *Journal of Climate*, **31(4)**, 1547–1563, doi:10.1175/jcli-d-17-0319.1.
Xu, Z., P. Chang, I. Richter, W. Kim, and G. Tang, 2014: Diagnosing southeast tropical Atlantic SST and ocean

ACCEPTED VERSION SUBJECT TO FINAL EDITING

circulation biases in the CMIP5 ensemble. *Climate Dynamics*, **43(11)**, 3123–3145, doi:10.1007/s00382-014-2247-9.
Yan, M., B. Wang, and J. Liu, 2016: Global monsoon change during the Last Glacial Maximum: a multi-model study. *Climate Dynamics*, **47(1–2)**, 359–374, doi:10.1007/s00382-015-2841-5.
Yan, X., T. DelSole, and M.K. Tippett, 2016: What Surface Observations Are Important for Separating the Influences of Anthropogenic Aerosols from Other Forcings? *Journal of Climate*, **29(11)**, 4165–4184, doi:10.1175/jcli-d-15-0667.1.
Yan, X., R. Zhang, and T.R. Knutson, 2018: Underestimated AMOC Variability and Implications for AMV and Predictability in CMIP Models. *Geophysical Research Letters*, **45(9)**, 4319–4328, doi:10.1029/2018gl077378.
Yan, X.H. et al., 2016: The global warming hiatus: Slowdown or redistribution? *Earth's Future*, **4(11)**, 472–482, doi:10.1002/2016ef000417.
Yang, H. et al., 2017: Regional patterns of future runoff changes from Earth system models constrained by observation. *Geophysical Research Letters*, **44(11)**, 5540–5549, doi:10.1002/2017gl073454.
Yang, H. et al., 2018: Changing the retention properties of catchments and their influence on runoff under climate change. *Environmental Research Letters*, doi:10.1088/1748-9326/aadd32.
Yang, J.-C. et al., 2020: Synchronized tropical Pacific and extratropical variability during the past three decades. *Nature Climate Change*, **10(5)**, 422–427, doi:10.1038/s41558-020-0753-9.
Yang, M., X. Li, R. Zuo, X. Chen, and L. Wang, 2018: Climatology and Interannual Variability of Winter North Pacific Storm Track in CMIP5 Models. *ATMOSPHERE*, **9(3)**, doi:10.3390/atmos9030079.
Yang, Y., S.-P. Xie, L. Wu, Y. Kosaka, and J. Li, 2017: Causes of Enhanced SST Variability over the Equatorial Atlantic and Its Relationship to the Atlantic Zonal Mode in CMIP5. *Journal of Climate*, **30(16)**, 6171–6182, doi:10.1175/jcli-d-16-0866.1.
Yeh, S.-W. et al., 2009: El Niño in a changing climate. *Nature*, **461**, 511, doi:10.1038/nature08316.
Yeh, S.-W. et al., 2018: ENSO Atmospheric Teleconnections and Their Response to Greenhouse Gas Forcing. *Reviews of Geophysics*, 77–117, 110.1002/2017rg000568.
Yin, J., J. Overpeck, C. Peyser, and R. Stouffer, 2018: Big Jump of Record Warm Global Mean Surface Temperature in 2014-2016 Related to Unusually Large Oceanic Heat Releases. *Geophysical Research Letters*, **45(2)**, 1069–1078, doi:10.1002/2017gl076500.
Ying, K.-R., T.-B. Zhao, and X.-G. Zheng, 2014: Slow and Intraseasonal Modes of the Boreal Winter Atmospheric Circulation Simulated by CMIP5 Models. *Atmospheric and Oceanic Science Letters*, **7(1)**, 34–41, doi:10.3878/j.issn.1674-2834.13.0058.
Yoshimori, M. and M. Suzuki, 2019: The relevance of mid-Holocene Arctic warming to the future. *Climate of the Past*, **15(4)**, 1375–1394, doi:10.5194/cp-15-1375-2019.
Young, P.J. et al., 2013: Agreement in late twentieth century southern hemisphere stratospheric temperature trends in observations and ccmval-2, CMIP3, and CMIP5 models. *Journal of Geophysical Research Atmospheres*, **118(2)**, 605–613, doi:10.1002/jgrd.50126.
Zaehle, S., C.D. Jones, B. Houlton, J.-F. Lamarque, and E. Robertson, 2015: Nitrogen availability reduces CMIP5 projections of twenty-first-century land carbon uptake. *Journal of Climate*, **28(6)**, 2494–2511.
Zanchettin, D., O. Bothe, W. Müller, J. Bader, and J.H. Jungclaus, 2014: Different flavors of the Atlantic Multidecadal Variability. *Climate Dynamics*, **42(1–2)**, 381–399, doi:10.1007/s00382-013-1669-0.
Zanchettin, D. et al., 2013: Background conditions influence the decadal climate response to strong volcanic eruptions. *Journal of Geophysical Research: Atmospheres*, **118(10)**, 4090–4106, doi:10.1002/jgrd.50229.
Zang, C.S., S. Jochner-Oette, J. Cortés, A. Rammig, and A. Menzel, 2019: Regional trend changes in recent surface warming. *Climate Dynamics*, **52(11)**, 6463–6473, doi:10.1007/s00382-018-4524-5.
Zanna, L., S. Khatiwala, J.M. Gregory, J. Ison, and P. Heimbach, 2019: Global reconstruction of historical ocean heat storage and transport. *Proceedings of the National Academy of Sciences of the United States of America*, **116(4)**, 1126–1131, doi:10.1073/pnas.1808838115.
Zappa, G., L.C. Shaffrey, and K.I. Hodges, 2013: The ability of CMIP5 models to simulate North Atlantic extratropical cyclones. *Journal of Climate*, **26(15)**, 5379–5396, doi:10.1175/jcli-d-12-00501.1.
Zappa, G., G. Masato, L. Shaffrey, T. Woollings, and K. Hodges, 2014: Linking Northern Hemisphere blocking and storm track biases in the CMIP5 climate models. *Geophysical Research Letters*, **41(1)**, 135–139, doi:10.1002/2013gl058480.
Zeng, N. et al., 2014: Agricultural Green Revolution as a driver of increasing atmospheric CO 2 seasonal amplitude. *Nature*, **515(7527)**, 394–397, doi:10.1038/nature13893.
Zhang, L. and C. Wang, 2013: Multidecadal North Atlantic sea surface temperature and Atlantic meridional overturning circulation variability in CMIP5 historical simulations. *Journal of Geophysical Research: Oceans*, **118(10)**, 5772–5791, doi:10.1002/jgrc.20390.
Zhang, L., W. Han, and F. Sienz, 2018a: Unraveling Causes for the Changing Behavior of the Tropical Indian Ocean in the Past Few Decades. *Journal of Climate*, **31(6)**, 2377–2388, doi:10.1175/jcli-d-17-0445.1.
Zhang, L., T.L. Delworth, W. Cooke, and X. Yang, 2019: Natural variability of Southern Ocean convection as a driver of observed climate trends. *Nature Climate Change*, **9(1)**, 59–65, doi:10.1038/s41558-018-0350-3.

ACCEPTED VERSION SUBJECT TO FINAL EDITING

Zhang, L., T. Zhou, N.P. Klingaman, P. Wu, and M. Roberts, 2018b: Effect of Horizontal Resolution on the Representation of the Global Monsoon Annual Cycle in AGCMs. *Advances in Atmospheric Sciences*, **35(8)**, 1003–1020, doi:10.1007/s00376-018-7273-9.

Zhang, L. et al., 2017: Estimating Decadal Predictability for the Southern Ocean Using the GFDL CM2.1 Model. *Journal of Climate*, **30(14)**, 5187–5203, doi:10.1175/jcli-d-16-0840.1.

Zhang, R., 2017: On the persistence and coherence of subpolar sea surface temperature and salinity anomalies associated with the Atlantic multidecadal variability. *Geophysical Research Letters*, **44(15)**, 7865–7875, doi:10.1002/2017gl074342.

Zhang, R. and T.R. Knutson, 2013: The role of global climate change in the extreme low summer Arctic sea ice extent in 2012. *Bulletin of the American Meteorological Society*, **94(9)**, S23.

Zhang, R., D. Jiang, and Z. Zhang, 2015: Causes of mid-Pliocene strengthened summer and weakened winter monsoons over East Asia. *Advances in Atmospheric Sciences*, **32(7)**, 1016–1026, doi:10.1007/s00376-014-4183-3.

Zhang, R., D. Jiang, Z. Zhang, Q. Yan, and X. Li, 2019: Modeling the late Pliocene global monsoon response to individual boundary conditions. *Climate Dynamics*, **53(7–8)**, 4871–4886, doi:10.1007/s00382-019-04834-w.

Zhang, R. et al., 2013a: Have Aerosols Caused the Observed Atlantic Multidecadal Variability? *Journal of the Atmospheric Sciences*, **70(4)**, 1135–1144, doi:10.1175/jas-d-12-0331.1.

Zhang, R. et al., 2013b: Mid-Pliocene East Asian monsoon climate simulated in the PlioMIP. *Climate of the Past*, doi:10.5194/cp-9-2085-2013.

Zhang, R. et al., 2016: Comment on "The Atlantic Multidecadal Oscillation without a role for ocean circulation". *Science*, **352(6293)**, 1527–1527, doi:10.1126/science.aaf1660.

Zhang, T. and D.Z. Sun, 2014: ENSO asymmetry in CMIP5 models. *Journal of Climate*, **27(11)**, 4070–4093, doi:10.1175/jcli-d-13-00454.1.

Zhang, W. and F.F. Jin, 2012: Improvements in the CMIP5 simulations of ENSO-SSTA meridional width. *Geophysical Research Letters*, **39(23)**, 1–5, doi:10.1029/2012gl053588.

Zhang, W. and B. Kirtman, 2019: Understanding the Signal-to-Noise Paradox with a Simple Markov Model. *Geophysical Research Letters*, **46(22)**, 13308–13317, doi:10.1029/2019gl085159.

Zhang, X. et al., 2007: Detection of human influence on twentieth-century precipitation trends. *Nature*, **448(7152)**, 461–465, doi:10.1038/nature06025.

Zhang, Y., J.M. Wallace, and D.S. Battisti, 1997: ENSO-like Interdecadal Variability: 1900–93. *Journal of Climate*, **10(5)**, 1004–1020, doi:10.1175/1520-0442(1997)010<1004:eliv>2.0.co;2.

Zhang, Y., Y. Guo, W. Dong, and C. Li, 2018: What drives the decadal variation of global land monsoon precipitation over the past 50 years? *International Journal of Climatology*, **38(13)**, 4818–4829, doi:10.1002/joc.5699.

Zhao, D.F. et al., 2017: Environmental conditions regulate the impact of plants on cloud formation. *Nature Communications*, **8(1)**, 14067, doi:10.1038/ncomms14067.

Zheng, F., J. Li, R.T. Clark, and H.C. Nnamchi, 2013: Simulation and Projection of the Southern Hemisphere Annular Mode in CMIP5 Models. *Journal of Climate*, **26(24)**, 9860–9879, doi:10.1175/jcli-d-13-00204.1.

Zheng, X.-T., L. Gao, G. Li, and Y. Du, 2016: The Southwest Indian Ocean thermocline dome in CMIP5 models: Historical simulation and future projection. *Advances in Atmospheric Sciences*, **33(4)**, 489–503, doi:10.1007/s00376-015-5076-9.

Zhou, S., G. Huang, and P. Huang, 2020: Excessive ITCZ but Negative SST Biases in the Tropical Pacific Simulated by CMIP5/6 Models: The Role of the Meridional Pattern of SST Bias. *J. Climate*, **33(12)**, 5305–5316, doi:10.1175/jcli-d-19-0922.1.

Zhou, T. et al., 2020: The dynamic and thermodynamic processes dominating the reduction of global land monsoon precipitation driven by anthropogenic aerosols emission. *Science China Earth Sciences*, **63(7)**, 919–933, doi:10.1007/s11430-019-9613-9.

Zhu, F., J. Emile-Geay, G.J. Hakim, J. King, and K.J. Anchukaitis, 2020: Resolving the Differences in the Simulated and Reconstructed Temperature Response to Volcanism. *Geophysical Research Letters*, **47(8)**, e2019GL086908, doi:10.1029/2019gl086908.

Zhu, F. et al., 2019: Climate models can correctly simulate the continuum of global-average temperature variability. *Proceedings of the National Academy of Sciences*, **116(18)**, 8728–8733, doi:10.1073/pnas.1809959116.

Zhu, J. et al., 2021: Assessment of equilibrium climate sensitivity of the Community Earth System Model version 2 through simulation of the Last Glacial Maximum. *Geophysical Research Letters*, **n/a(n/a)**, e2020GL091220, doi:10.1029/2020gl091220.

Zhu, Y. and R.H. Zhang, 2018: An Argo-Derived Background Diffusivity Parameterization for Improved Ocean Simulations in the Tropical Pacific. *Geophysical Research Letters*, **45(3)**, 1509–1517, doi:10.1002/2017gl076269.

Zhu, Y., R.-H. Zhang, and J. Sun, 2020: North Pacific Upper-Ocean Cold Temperature Biases in CMIP6 Simulations and the Role of Regional Vertical Mixing. *Journal of Climate*, **33(17)**, 7523–7538, doi:10.1175/jcli-d-19-0654.1.

Zhu, Z. et al., 2016: Greening of the Earth and its drivers. *Nature Climate Change*, **6(8)**, 791–795, doi:10.1038/nclimate3004.

ACCEPTED VERSION SUBJECT TO FINAL EDITING

Zhu, Z. et al., 2017: Attribution of seasonal leaf area index trends in the northern latitudes with "optimally" integrated ecosystem models. *Global Change Biology*, **23(11)**, 4798–4813, doi:10.1111/gcb.13723.
Ziehn, T. et al., 2020: The Australian Earth System Model: ACCESS-ESM1.5. *Journal of Southern Hemisphere Earth Systems Science*, **70**, 193–214, doi:10.1071/es19035.
Zika, J.D. et al., 2015: Maintenance and broadening of the ocean's salinity distribution by the water cycle. *Journal of Climate*, **28(24)**, 9550–9560, doi:10.1175/jcli-d-15-0273.1.
Zika, J.D. et al., 2018: Improved estimates of water cycle change from ocean salinity: The key role of ocean warming. *Environmental Research Letters*, **13(7)**, 074036, doi:10.1088/1748-9326/aace42.
Zunz, V., H. Goosse, and F. Massonnet, 2013: How does internal variability influence the ability of CMIP5 models to reproduce the recent trend in Southern Ocean sea ice extent? *The Cryosphere*, **7(2)**, 451–468, doi:10.5194/tc-7-451-2013.
Zuo, J.-Q., W.-J. Li, and H.-L. Ren, 2013: Representation of the Arctic Oscillation in the CMIP5 Models. *Advances in Climate Change Research*, **4(4)**, 242–249, doi:10.3724/sp.j.1248.2013.242.
Zuo, M., T. Zhou, and W. Man, 2019: Hydroclimate Responses over Global Monsoon Regions Following Volcanic Eruptions at Different Latitudes. *Journal of Climate*, **32(14)**, 4367–4385, doi:10.1175/jcli-d-18-0707.1.

ACCEPTED VERSION
SUBJECT TO FINAL EDITING

Figures

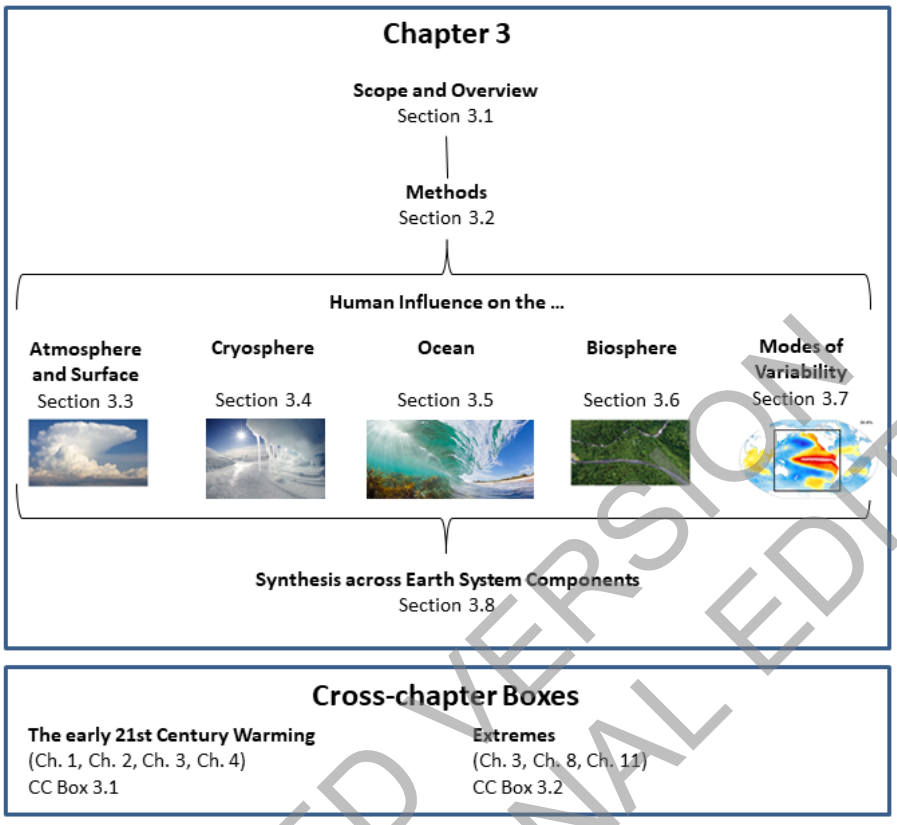


Figure 3.1: Visual Abstract for Chapter 3: Human influence on the climate syst

ACCEPTED VERSION SUBJECT TO FINAL EDITING

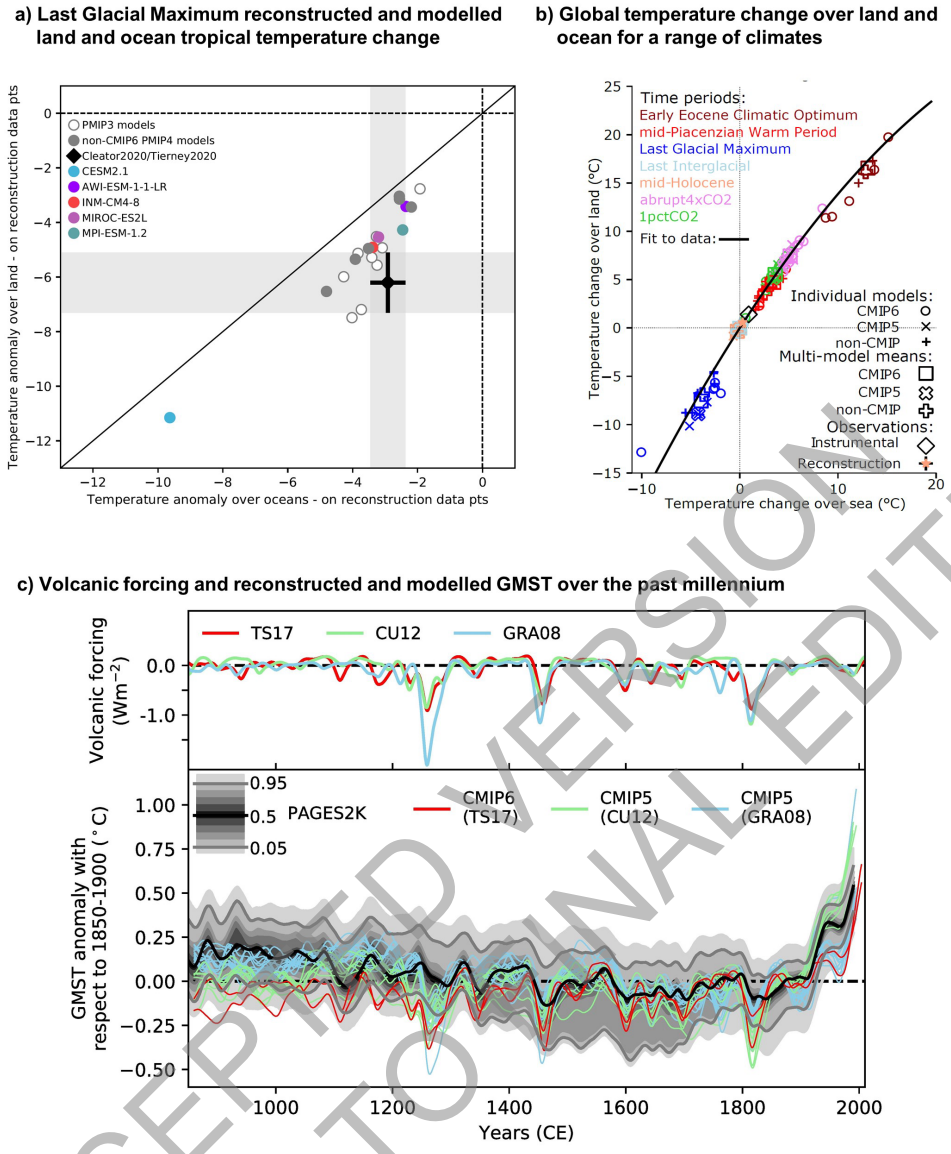


Figure 3.2: Changes in surface temperature for different paleoclimates. (a) Comparison of reconstructed and modelled surface temperature anomalies for the Last Glacial Maximum over land and ocean in the Tropics (30°N to 30°S). Land-based reconstructions are from Cleator et al., (2020). Ocean-based reconstructions are from Tierney et al. (2020). Model points are calculated as the difference between Last Glacial Maximum and pre-industrial control simulations of the PMIP3 and PMIP4 ensembles, sampled at the reconstruction data points. (b) Land-sea contrast in global mean surface temperature change for different paleoclimates. Crosses show individual model simulations from the CMIP5 and CMIP6 ensembles. Filled symbols show ensemble means and assessed values. Acronyms are LGM Last Glacial Maximum, LIG Last Inter Glacial, MPWP mid-Pliocene Warm Period, EECO Early Eocene Climatic Optimum. (c) Upper panel shows time series of volcanic radiative forcing, in W m^{-2}, as used in the CMIP5 (Gao et al., 2008; Crowley and Unterman, 2013; see also Schmidt et al., 2011) and CMIP6 (850 BCE to 1900 CE from Toohey and Sigl (2017), 1850-2015 from Luo (2018)). The forcing has been calculated from the stratospheric aerosol optical depth at 550 nm shown in Figure 2.2. Lower panel shows time series of global mean surface temperature anomalies, in K, with respect to 1850-1900 for the CMIP5 and CMIP6 past1000 simulations and their historical continuation simulations. Simulations are coloured according to the volcanic radiative forcing dataset they used. The temperature median reconstruction by PAGES 2k Consortium (2019) is shown in black, the 5-95% confidence interval by grey lines and the grey envelopes show the 1, 5, 15, 25, 35, 45, 55, 65, 75, 85, 95, and 99 percentiles. All data in both panels are band-passed, where frequencies longer than 20 years have been retained. Further details on data sources and processing are available in the chapter data table (Table 3.SM.1).

ACCEPTED VERSION SUBJECT TO FINAL EDITING

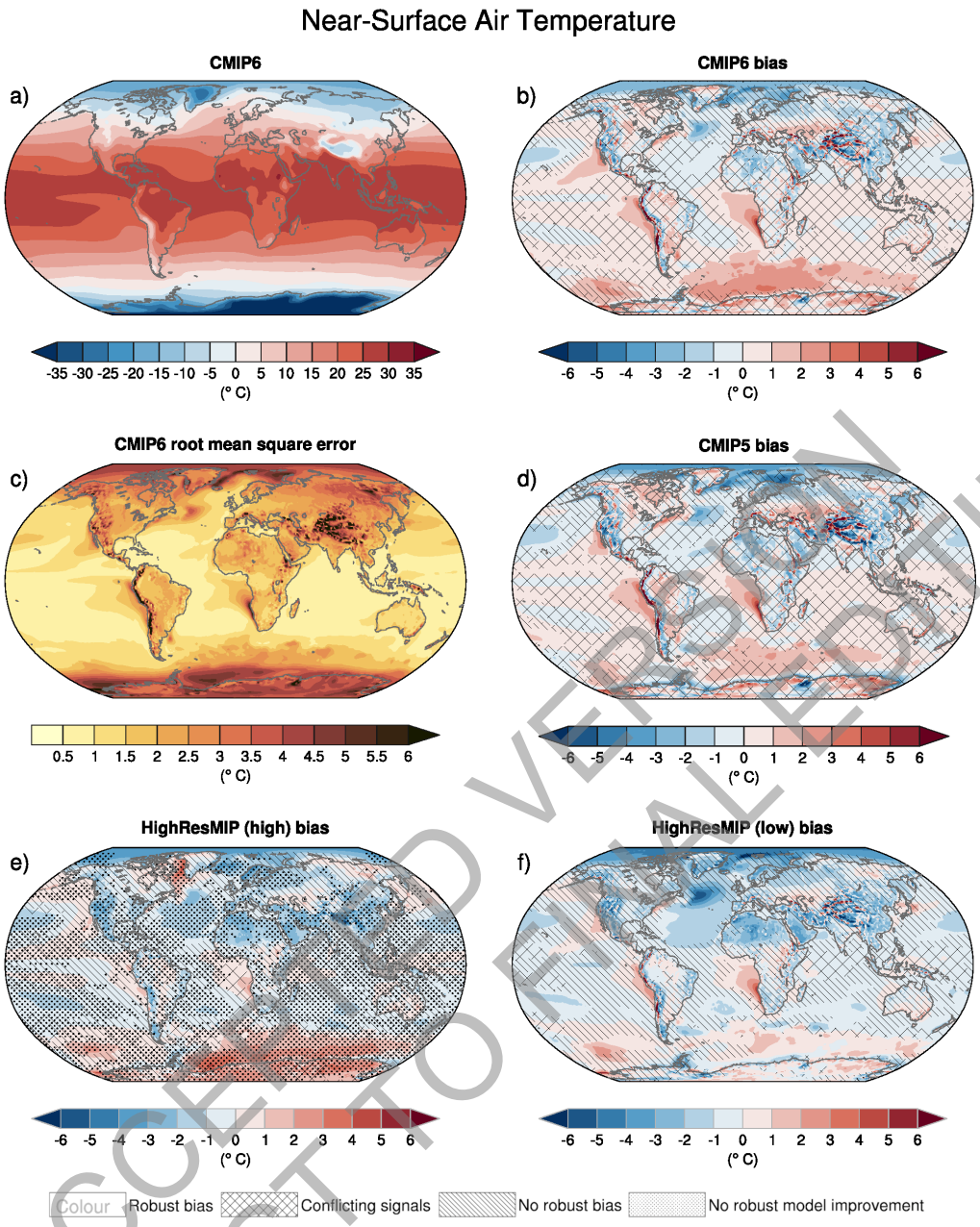
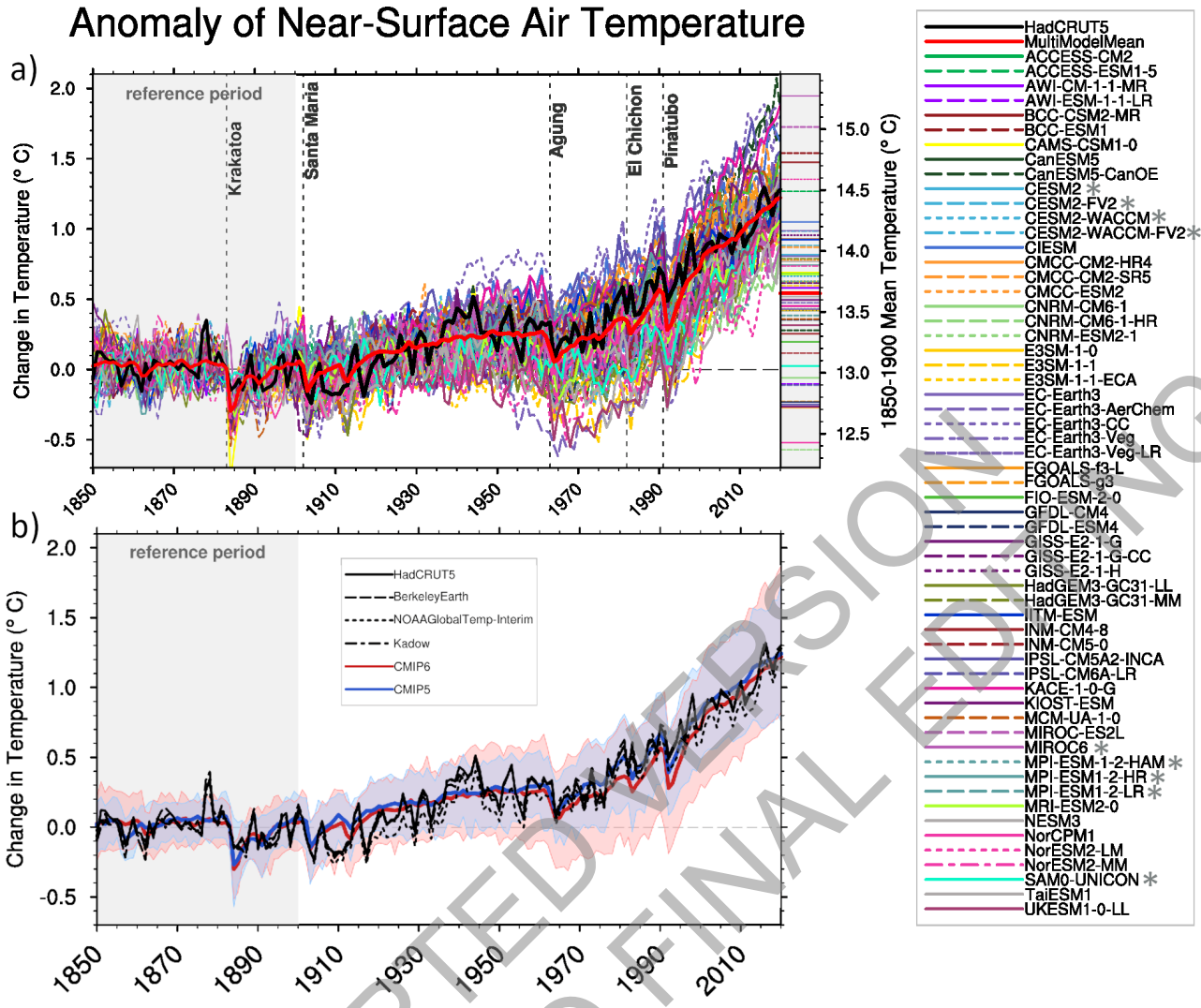


Figure 3.3: Annual-mean surface (2 m) air temperature (°C) for the period 1995–2014. (a) Multi-model (ensemble) mean constructed with one realization of the CMIP6 historical experiment from each model. (b) Multi-model mean bias, defined as the difference between the CMIP6 multi-model mean and the climatology of the Fifth generation of ECMWF atmospheric reanalyses of the global climate (ERA5). (c) Multi-model mean of the root mean square error calculated over all months separately and averaged with respect to the climatology from ERA5. (d) Multi-model-mean bias as the difference between the CMIP6 multi-model mean and the climatology from ERA5. Also shown is the multi-model mean bias as the difference between the multi-model mean of (e) high resolution and (f) low resolution simulations of four HighResMIP models and the climatology from ERA5. Uncertainty is represented using the advanced approach: No overlay indicates regions with robust signal, where ≥66% of models show change greater than variability threshold and ≥80% of all models agree on sign of change; diagonal lines indicate regions with no change or no robust signal, where <66% of models show a change greater than the variability threshold; crossed lines indicate regions with conflicting signal, where ≥66% of models show change greater than variability threshold and <80% of all models agree on sign of change. For more information on the advanced approach, please refer to the Cross-Chapter Box Atlas.1. Dots in panel e) mark areas where the bias in high resolution versions of the HighResMIP models is lower in at least 3 out of 4 models than in the corresponding low resolution versions. Further details on data sources and processing are available in the chapter data table (Table 3.SM.1).

ACCEPTED VERSION SUBJECT TO FINAL EDITING



ACCEPTED VERSION SUBJECT TO FINAL EDITING

Figure 3.4: Observed and simulated time series of the anomalies in annual and global mean near-surface air temperature (GSAT). All anomalies are differences from the 1850–1900 time-mean of each individual time series. The reference period 1850–1900 is indicated by grey shading. (a) Single simulations from CMIP6 models (thin lines) and the multi-model mean (thick red line). Observational data (thick black lines) are HadCRUT5, and are blended surface temperature (2 m air temperature over land and sea surface temperature over the ocean). All models have been subsampled using the HadCRUT5 observational data mask. Vertical lines indicate large historical volcanic eruptions. CMIP6 models which are marked with an asterisk are either tuned to reproduce observed warming directly, or indirectly by tuning equilibrium climate sensitivity. Inset: GSAT for each model over the reference period, not masked to any observations. (b). Multi-model means of CMIP5 (blue line) and CMIP6 (red line) ensembles and associated 5 to 95 percentile ranges (shaded regions). Observational data are HadCRUT5, Berkeley Earth, NOAAGlobalTemp-Interim and Kadow et al. (2020). Masking was done as in (a). CMIP6 historical simulations are extended with SSP2-4.5 simulations for the period 2015-2020 and CMIP5 simulations are extended with RCP4.5 simulations for the period 2006-2020. All available ensemble members were used (see Section 3.2). The multi-model means and percentiles were calculated solely from simulations available for the whole time span (1850-2020). Figure is updated from Bock et al. (2020), their Figures 1 and 2. / CC BY4.0 https://creativecommons.org/licenses/by/4.0/. Further details on data sources and processing are available in the chapter data table (Table 3.SM.1).

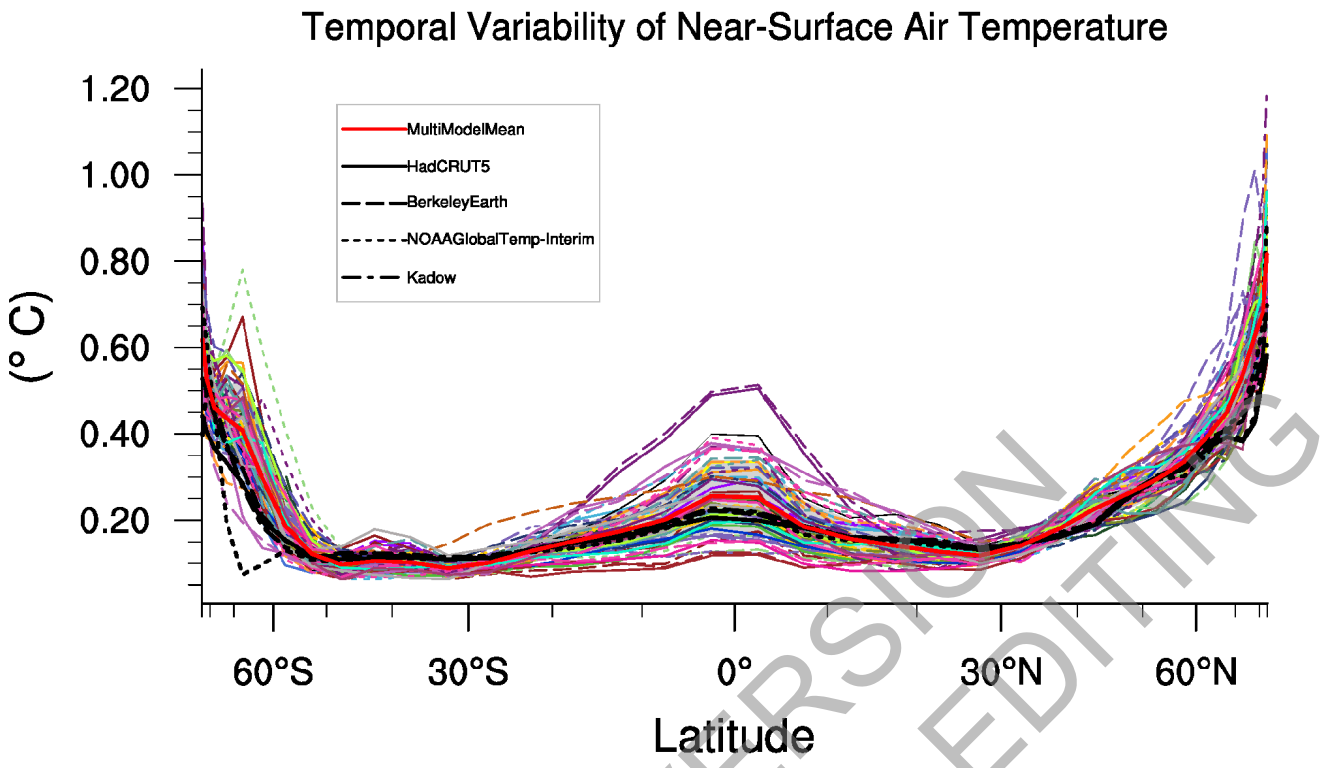
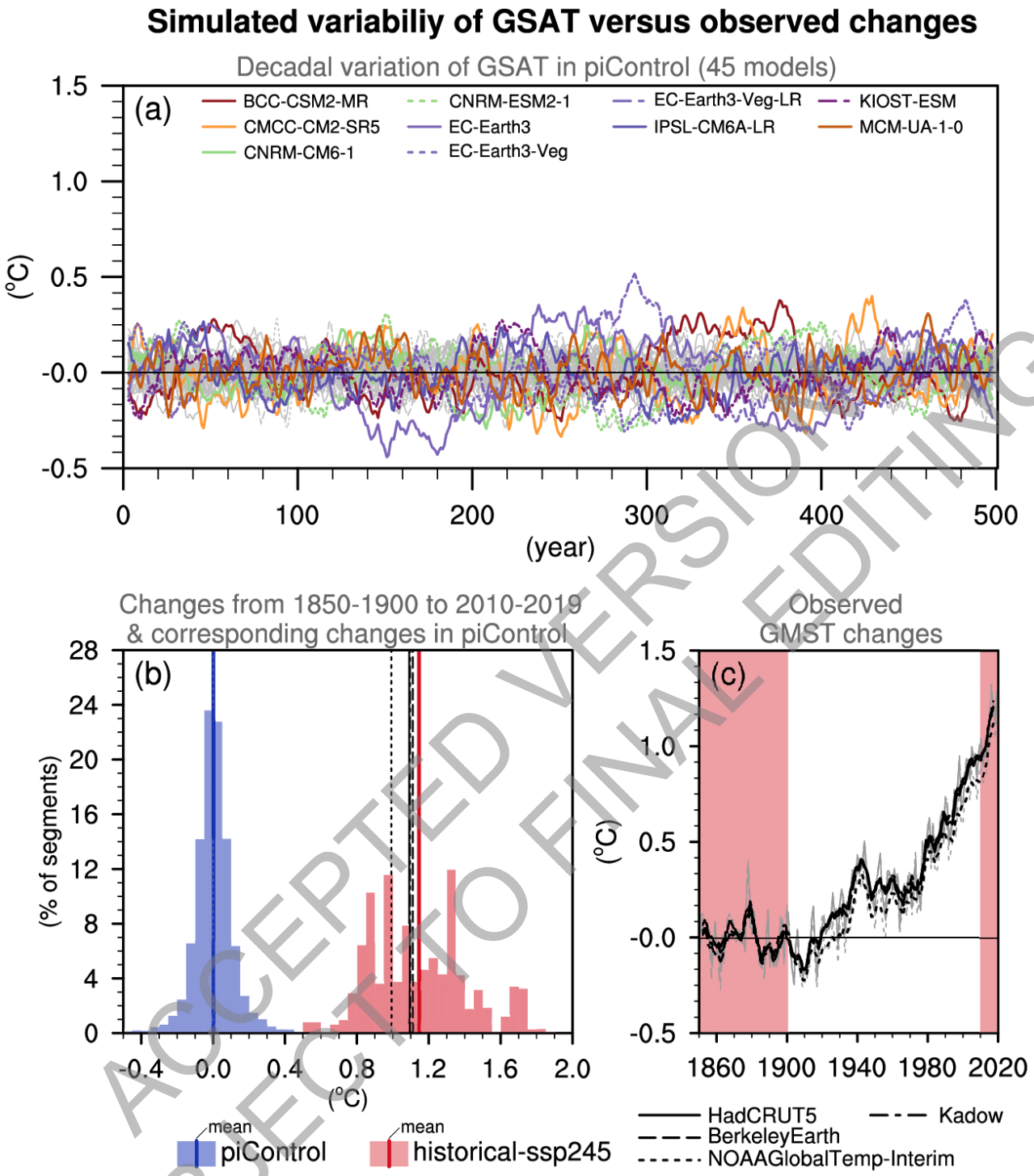


Figure 3.5: The standard deviation of annually averaged zonal-mean near-surface air temperature. This is shown for four detrended observed temperature datasets (HadCRUT5, Berkeley Earth, NOAAGlobalTemp-Interim and Kadow et al. (2020), for the years 1995-2014) and 59 CMIP6 pre-industrial control simulations (one ensemble member per model, 65 years) (after Jones et al., 2013). For line colours see the legend of Figure 3.4. Additionally, the multi-model mean (red) and standard deviation (grey shading) are shown. Observational and model datasets were detrended by removing the least-squares quadratic trend. Further details on data sources and processing are available in the chapter data table (Table 3.SM.1).

ACCEPTED VERSION SUBJECT TO FINAL EDITING



ACCEPTED VERSION SUBJECT TO FINAL EDITING

Figure 3.6: Simulated internal variability of global surface air temperature (GSAT) versus observed changes. (a) Time series of 5-year running mean GSAT anomalies in 45 CMIP6 pre-industrial control (unforced) simulations. The 10 most variable models in terms of 5-year running mean GSAT are coloured according to the legend on Figure 3.4. (b) Histograms of GSAT changes in CMIP6 historical simulations (extended by SSP2-4.5 simulations) from 1850-1900 to 2010-2019 are shown by pink shading in (c), and GSAT changes from the first 51 years average to the last 20 years average of 170-year overlapping segments of the pre-industrial control simulations shown in (a) are shown by blue shading. GMST changes in observational datasets for the same period are indicated by black vertical lines. (c) Observed GMST anomaly time series relative to the 1850-1900 average. Black lines represent the 5-year running means while grey lines show unfiltered annual time series. Further details on data sources and processing are available in the chapter data table (Table 3.SM.1).

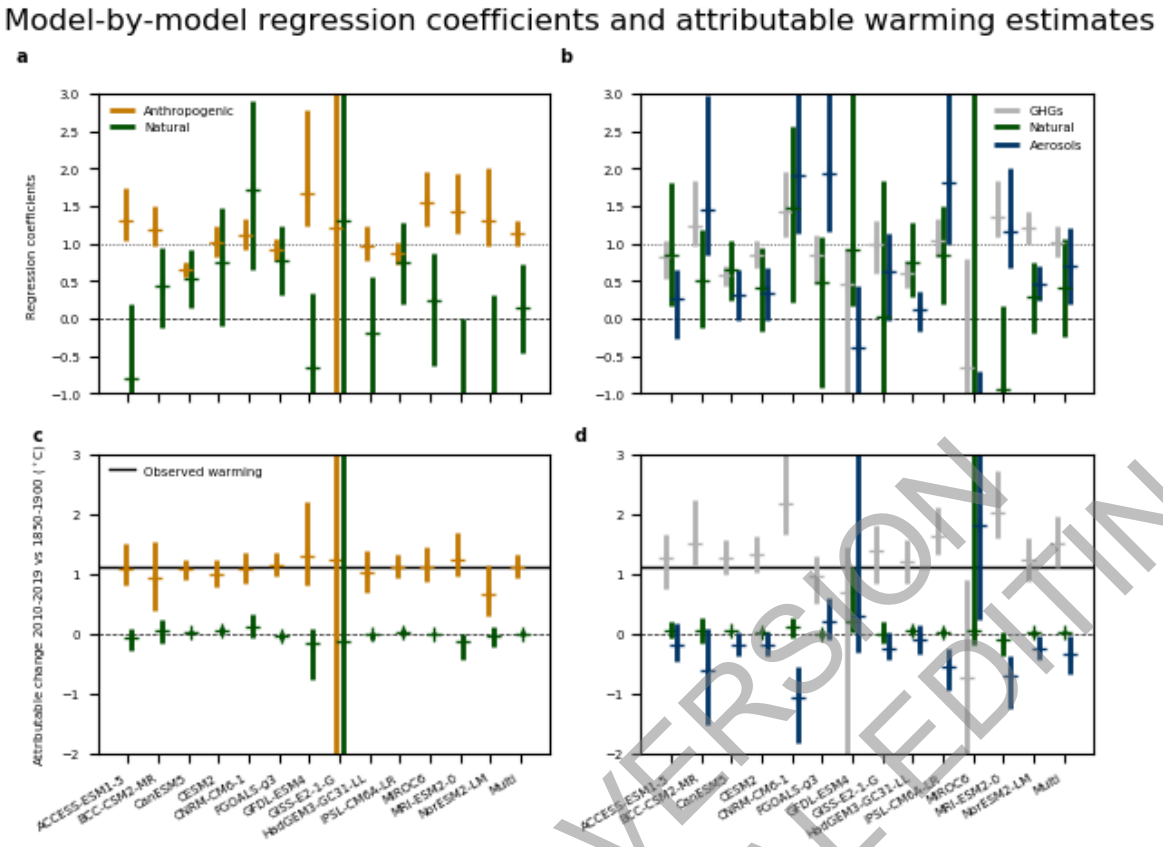


Figure 3.7: Regression coefficients and corresponding attributable warming estimates for individual CMIP6 models. Upper panels show regression coefficients based on a two-way regression (left) and three-way regression (right), of observed 5-yr mean global mean masked and blended surface temperature (HadCRUT4) onto individual model response patterns, and a multi-model mean, labelled 'Multi'. Anthropogenic, natural, greenhouse gas, and other anthropogenic (aerosols, ozone, land-use change) regression coefficients are shown. Regression coefficients are the scaling factors by which the model responses must be multiplied to best match observations. Regression coefficients consistent with one indicate a consistent magnitude response in observations and models, and regression coefficients inconsistent with zero indicate a detectable response to the forcing concerned. Lower panels show corresponding observationally-constrained estimates of attributable warming in globally-complete GSAT for the period 2010-2019, relative to 1850-1900, and the horizontal black line shows an estimate of observed warming in GSAT for this period. Figure is adapted from Gillett et al. (2021), their Extended Data Figure 3. Further details on data sources and processing are available in the chapter data table (Table 3.SM.1).

ACCEPTED VERSION SUBJECT TO FINAL EDITING

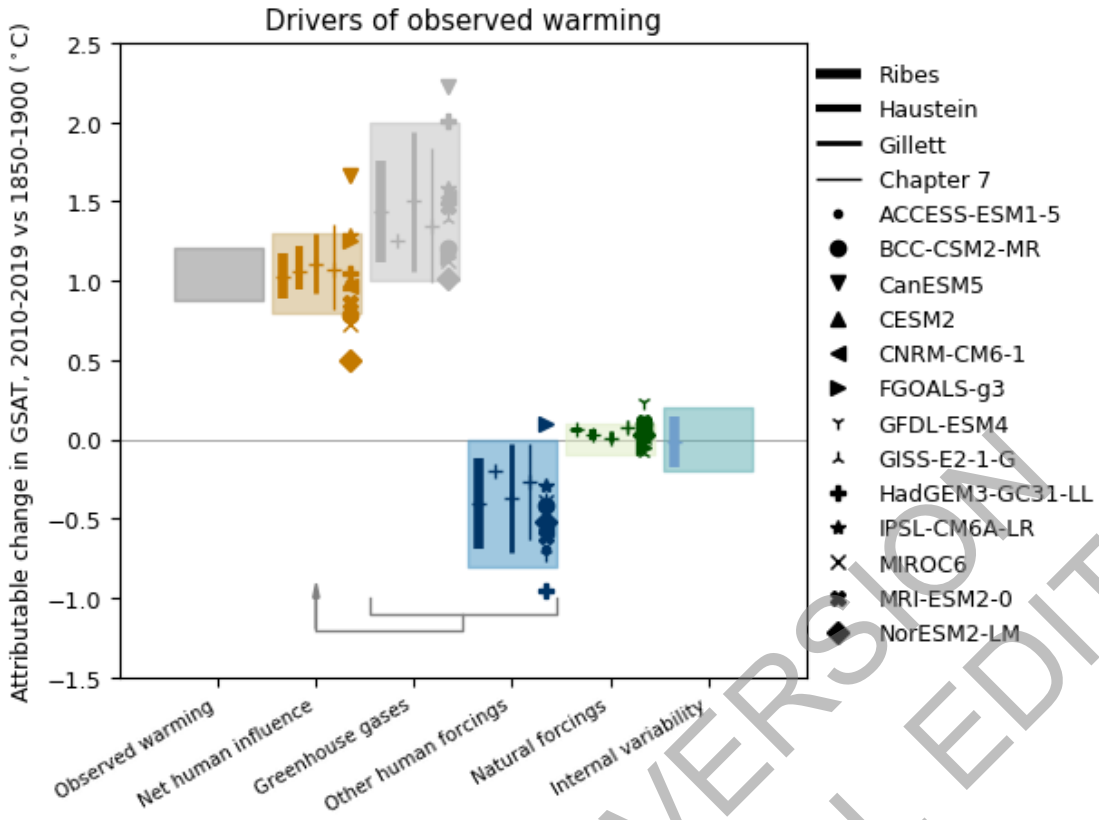


Figure 3.8: Assessed contributions to observed warming, and supporting lines of evidence. Shaded bands show assessed *likely* ranges of temperature change in GSAT, 2010-2019 relative to 1850-1900, attributable to net human influence, well-mixed greenhouse gases, other human forcings (aerosols, ozone, and land-use change), natural forcings, and internal variability, and the 5-95% range of observed warming. Bars show 5-95% ranges based on (left to right) Haustein et al. (2017), Gillett et al. (2021) and Ribes et al. (2021), and crosses show the associated best estimates. No 5-95% ranges were provided for the Haustein et al. (2017) greenhouse gas or other human forcings contributions. The Ribes et al. (2021) results were updated using a revised natural forcing time series, and the Haustein et al. (2017) results were updated using HadCRUT5. The Chapter 7 best estimates and ranges are derived using assessed forcing time series and a two-layer energy balance model as described in Section 7.3.5.3. Coloured symbols show the simulated responses to the forcings concerned in each of the models indicated. Further details on data sources and processing are available in the chapter data table (Table 3.SM.1).

ACCEPTED VERSION SUBJECT TO FINAL EDITING

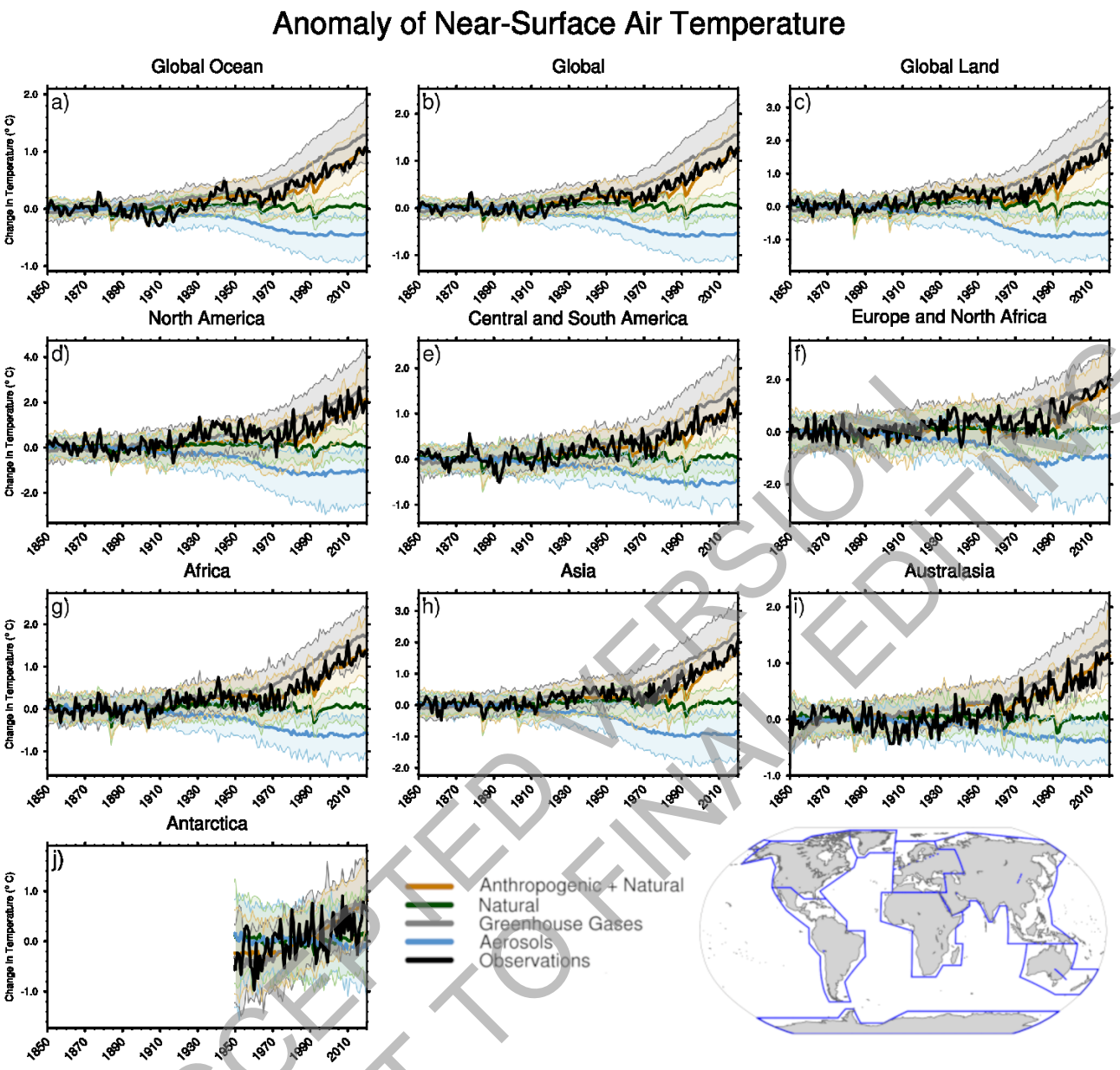


Figure 3.9: Global, land, ocean and continental annual mean near-surface air temperatures anomalies in CMIP6 models and observations. Time series are shown for CMIP6 historical anthropogenic and natural (brown), natural-only (green), greenhouse gas only (grey) and aerosol only (blue) simulations (multi-model means shown as thick lines, and shaded ranges between the 5th and 95th percentiles) and for HadCRUT5 (black). All models have been subsampled using the HadCRUT5 observational data mask. Temperatures anomalies are shown relative to 1950-2010 for Antarctica and relative to 1850–1900 for other continents. CMIP6 historical simulations are expand by the SSP2-4.5 scenario simulations. All available ensemble members were used (see Section 3.2). Regions are defined by Iturbide et al. (2020). Further details on data sources and processing are available in the chapter data table (Table 3.SM.1).

ACCEPTED VERSION SUBJECT TO FINAL EDITING

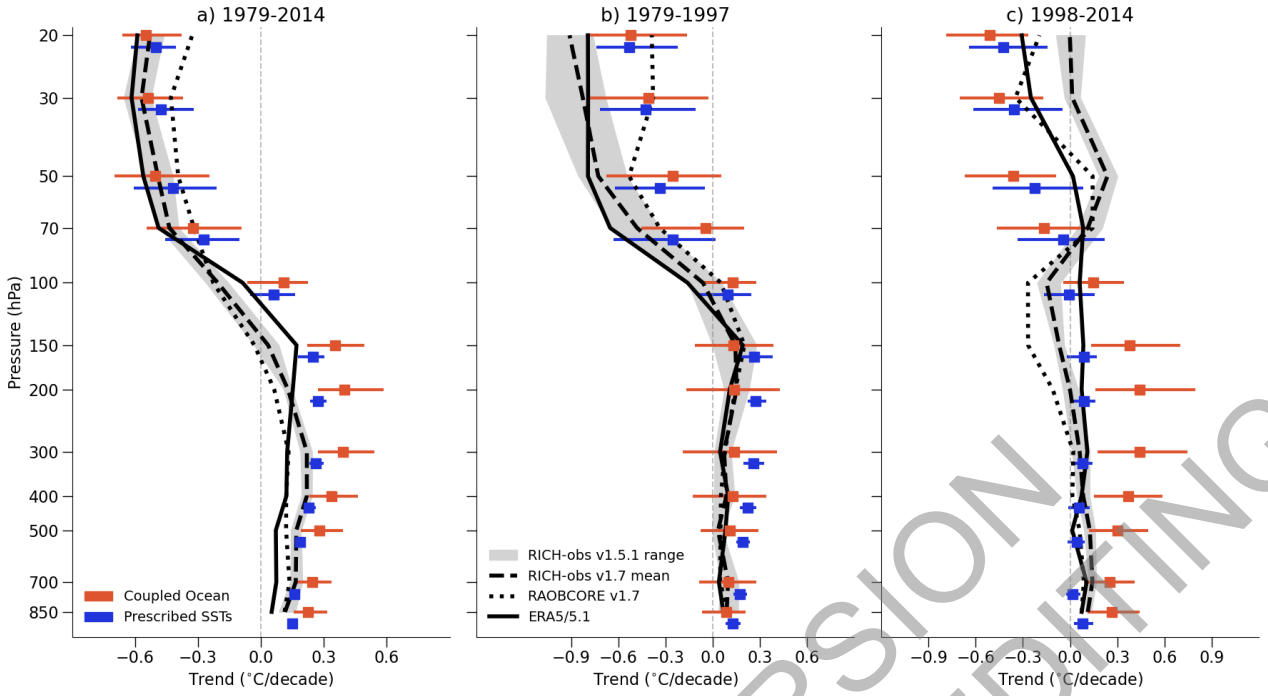
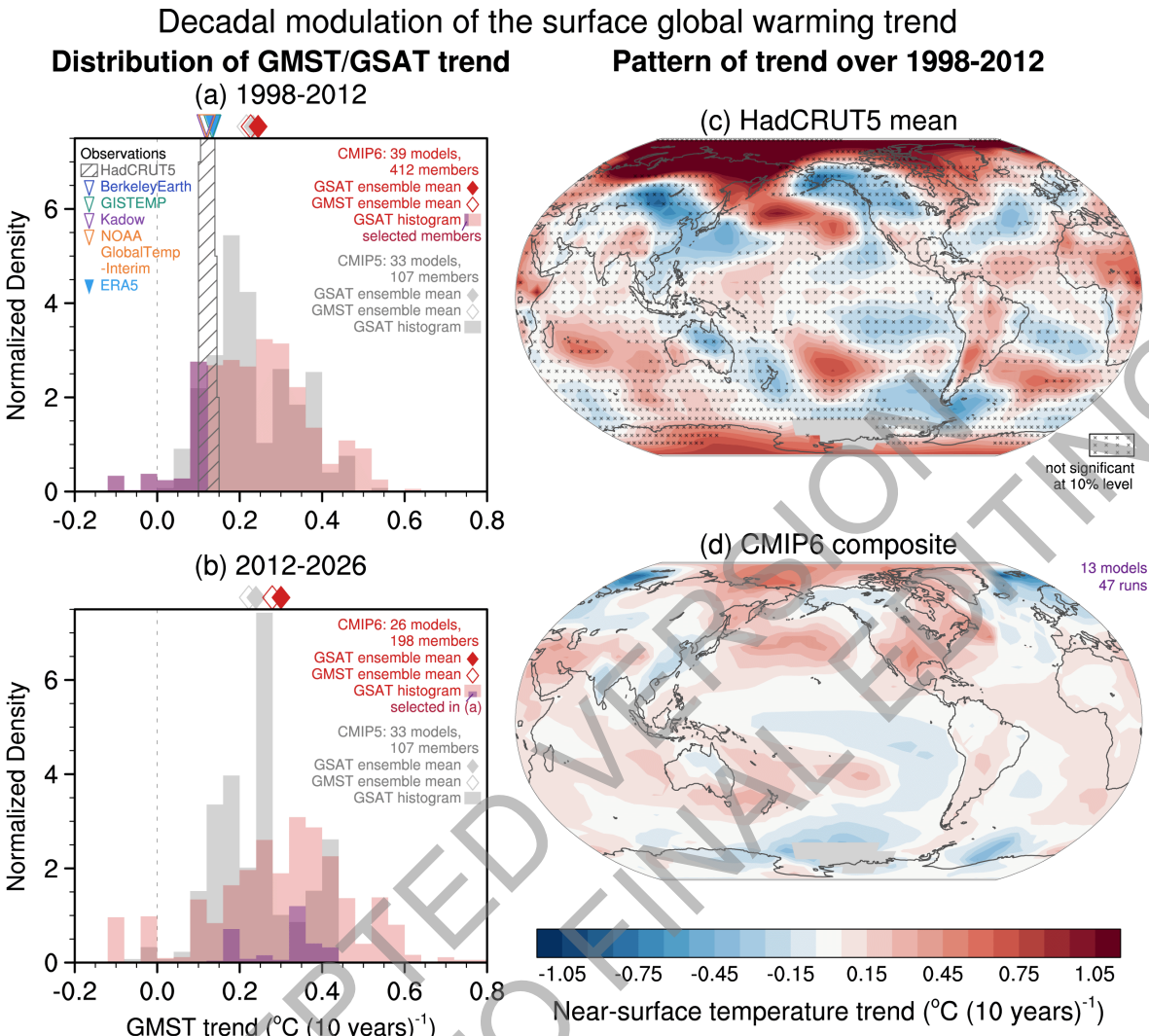


Figure 3.10: Observed and simulated tropical mean temperature trends through the atmosphere. Vertical profiles of temperature trends in the tropics (20°S-20°N) for three periods: (a) 1979-2014 (b) 1979-1997 (ozone depletion era) (c) 1998-2014 (ozone stabilisation era). The black lines show trends in the RICH 1.7 (long dashed) and RAOBCORE 1.7 (dashed) radiosonde datasets (Haimberger et al., 2012), and in the ERA5/5.1 reanalysis (solid). Grey envelopes are centred on the RICH 1.7 trends, but show the uncertainty based on 32 RICH-obs members of version 1.5.1 of the dataset, which used version 1.7.3 of the RICH software but with the parameters of version 1.5.1. ERA5 was used as reference for calculating the adjustments between 2010 and 2019, and ERA-Interim was used for the years before that. Red lines show trends in CMIP6 historical simulations from one realization of 60 models. Blue lines show trends in 46 CMIP6 models that used prescribed, rather than simulated, sea surface temperatures (SSTs). Figure is adapted from Mitchell et al. (2020), their Figure 1. Further details on data sources and processing are available in the chapter data table (Table 3.SM.1).

ACCEPTED VERSION SUBJECT TO FINAL EDITING



Cross-Chapter Box 3.1, Figure 1: ..15-year trends of surface global warming for 1998-2012 and 2012-2026. (a, b) GSAT and GMST trends for 1998-2012 (a) and 2012-2026 (b). Histograms are based on GSAT in historical simulations of CMIP6 (red shading, extended by SSP2-4.5) and CMIP5 (grey shading; extended by RCP4.5). Filled and open diamonds at the top represent multi-model ensemble means of GSAT and GMST trends, respectively. Diagonal lines show histograms of HadCRUT5.0.1.0. Triangles at the top of (a) represent GMST trends of Berkeley Earth, GISTEMP, Kadow et al. (2020) and NOAAGlobalTemp-Interim, and the GSAT trend of ERA5. Selected CMIP6 members whose 1998-2012 trends are lower than the HadCRUT5.0.1.0 mean trend are indicated by purple shading (a) and (b). In (a), model GMST and GSAT, and ERA5 GSAT are masked to match HadCRUT data coverage. (c-d) Trend maps of annual near-surface temperature for 1998-2012 based on HadCRUT5.0.1.0 mean (c) and composited surface air temperature trends of subsampled CMIP6 simulations (d) that are included in purple shading area in (a). In (c), cross marks indicate trends that are not significant at the 10% level based on t-tests with serial correlation taken into account. Ensemble size used for each of the histograms and the trend composite is indicated at the top right of each of panels (a,b,d). Model ensemble members are weighted with the inverse of the ensemble size of the same model, so that individual models are equally weighted. Further details on data sources and processing are available in the chapter data table (Table 3.SM.1).

ACCEPTED VERSION SUBJECT TO FINAL EDITING

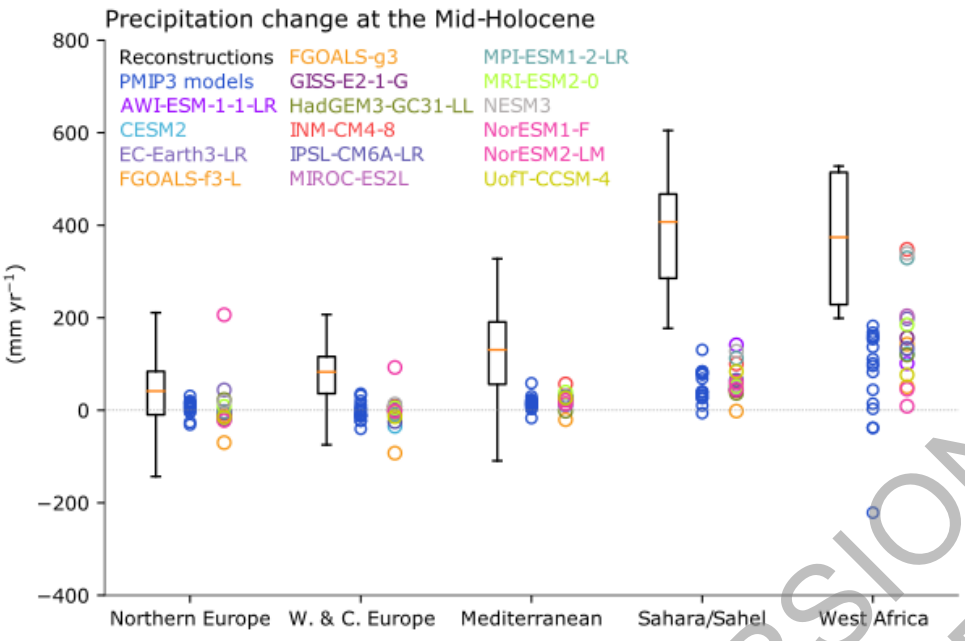


Figure 3.11: Comparison between simulated annual precipitation changes and pollen-based reconstructions at the Mid-Holocene (6,000 years ago). The area-averaged changes over five regions (Iturbide et al., 2020) as simulated by CMIP6 models (individually identifiable, one ensemble member per model) and CMIP5 models (blue) are shown, stretching from the tropics to high-latitudes. All regions contain multiple quantitative reconstructions: their interquartile range are shown by boxes and with whiskers for their full range excluding outliers. Figure is adapted from Brierley et al. (2020). Further details on data sources and processing are available in the chapter data table (Table 3.SM.1).

ACCEPTED VERSION SUBJECT TO FINAL EDITING

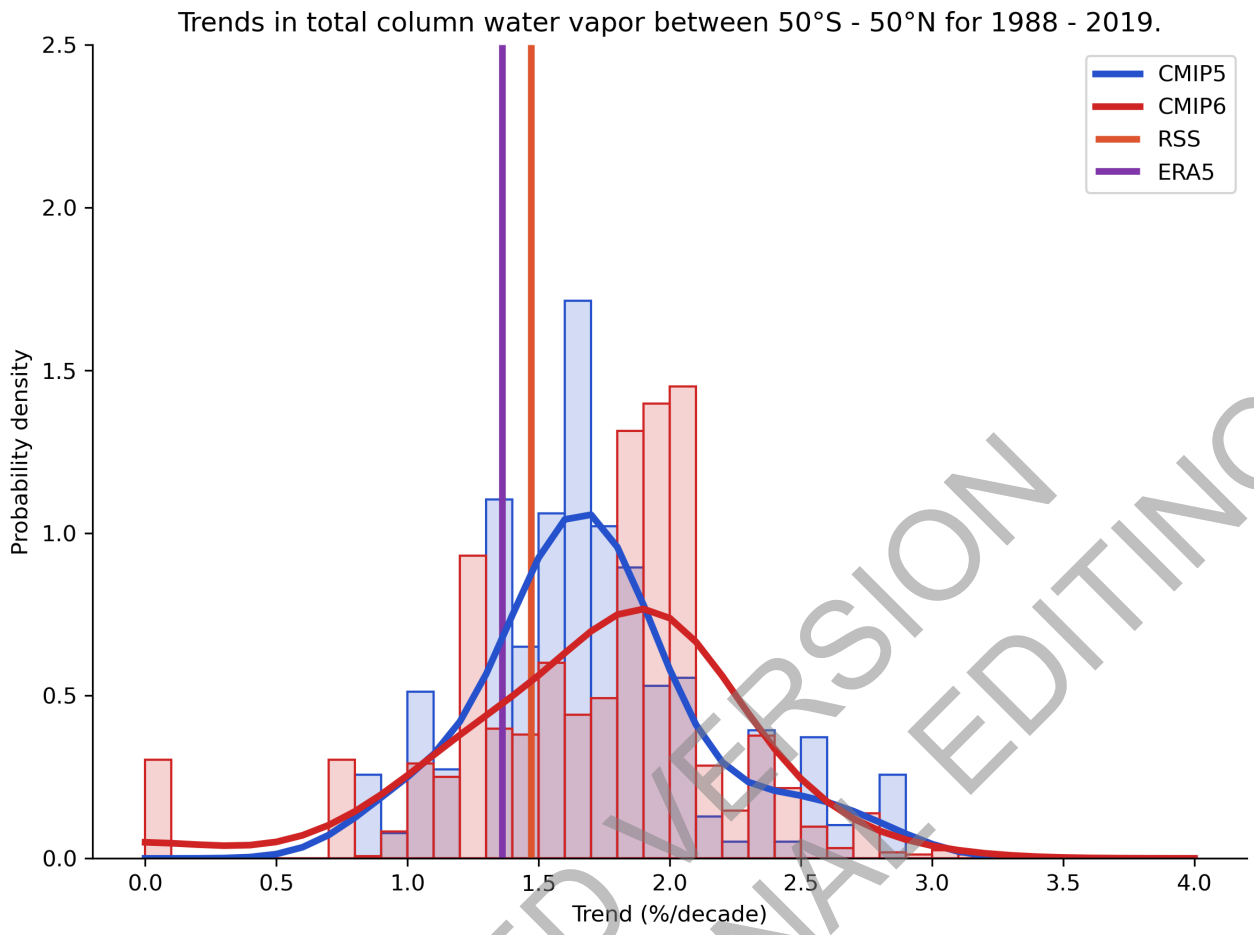


Figure 3.12: Column water vapour path trends (%/decade) for the period 1998-2019 averaged over the near-global oceans (50°S-50°N). The figure shows satellite data (RSS) and ERA5.1 reanalysis, as well as CMIP5 (sky blue) and CMIP6 (brown) historical simulations. All available ensemble members were used (see Section 3.2). Fits to the model trend probability distributions were performed with kernel density estimation. Figure is updated from Santer et al. (2007). Further details on data sources and processing are available in the chapter data table (Table 3.SM.1).

ACCEPTED VERSION SUBJECT TO FINAL EDITING

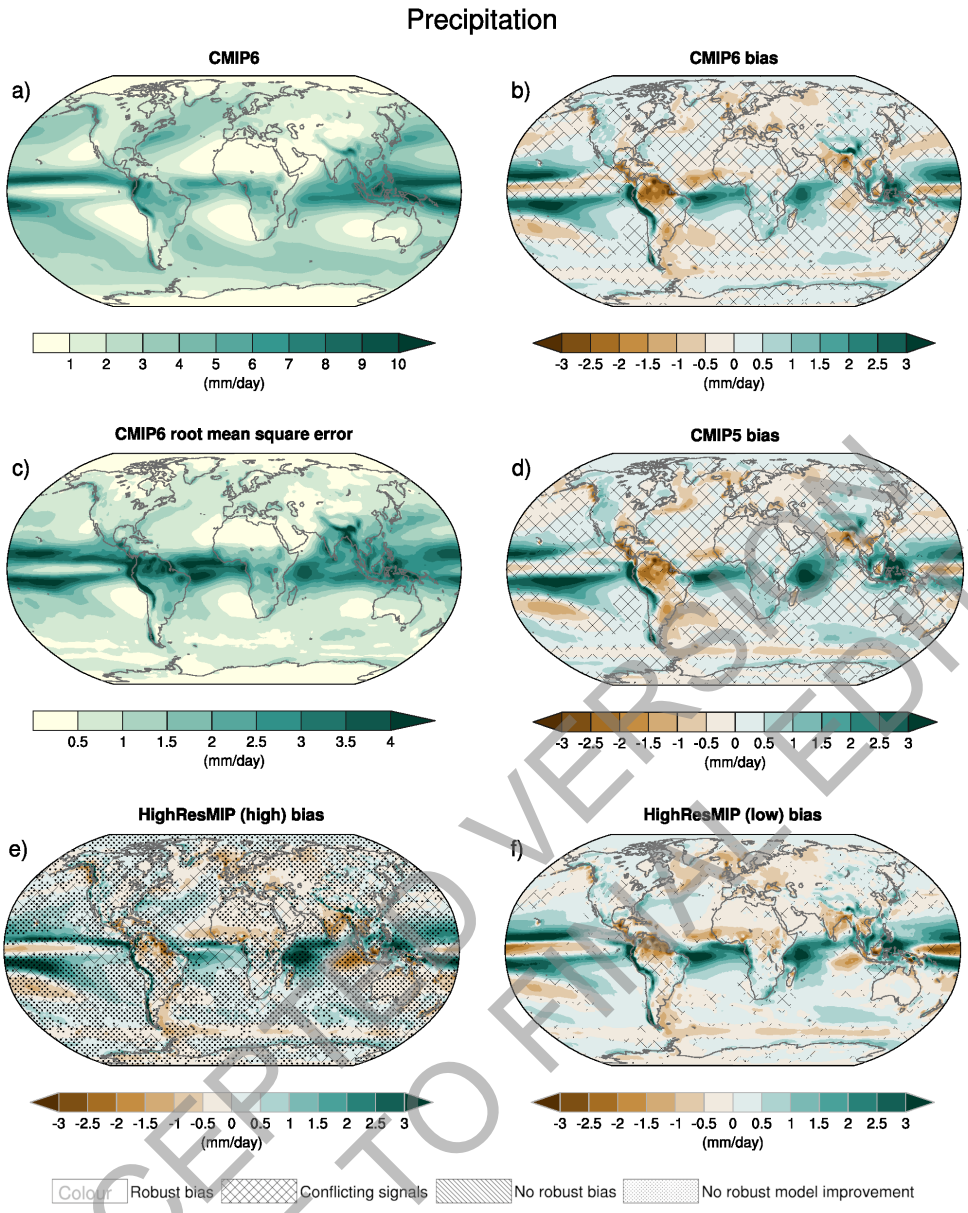


Figure 3.13: Annual-mean precipitation rate (mm day^{-1}) for the period 1995–2014. (a) Multi-model (ensemble) mean constructed with one realization of the CMIP6 historical experiments from each model. (b) Multi-model mean bias, defined as the difference between the CMIP6 multi-model mean and precipitation analyses from the Global Precipitation Climatology Project (GPCP) version 2.3 (Adler et al., 2003). (c) Multi-model mean of the root mean square error calculated over all months separately and averaged with respect to the precipitation analyses from GPCP v2.3. (d) Multi-model-mean bias, calculated as the difference between the CMIP6 multi-model mean and the precipitation analyses from GPCP v2.3. Also shown is the multi-model mean bias as the difference between the multi-model mean of (e) high resolution and (f) low resolution simulations of four HighResMIP models and the precipitation analyses from GPCP v2.3. Uncertainty is represented using the advanced approach: No overlay indicates regions with robust signal, where ≥66% of models show change greater than variability threshold and ≥80% of all models agree on sign of change; diagonal lines indicate regions with no change or no robust signal, where <66% of models show a change greater than the variability threshold; crossed lines indicate regions with conflicting signal, where ≥66% of models show change greater than variability threshold and <80% of all models agree on the sign of change. For more information on the advanced approach, please refer to the Cross-Chapter Box Atlas.1. Dots in panel e) mark areas where the bias in high resolution versions of the HighResMIP models is lower in at least 3 out of 4 models than in the corresponding low resolution versions. Further details on data sources and processing are available in the chapter data table (Table 3.SM.1).

ACCEPTED VERSION SUBJECT TO FINAL EDITING

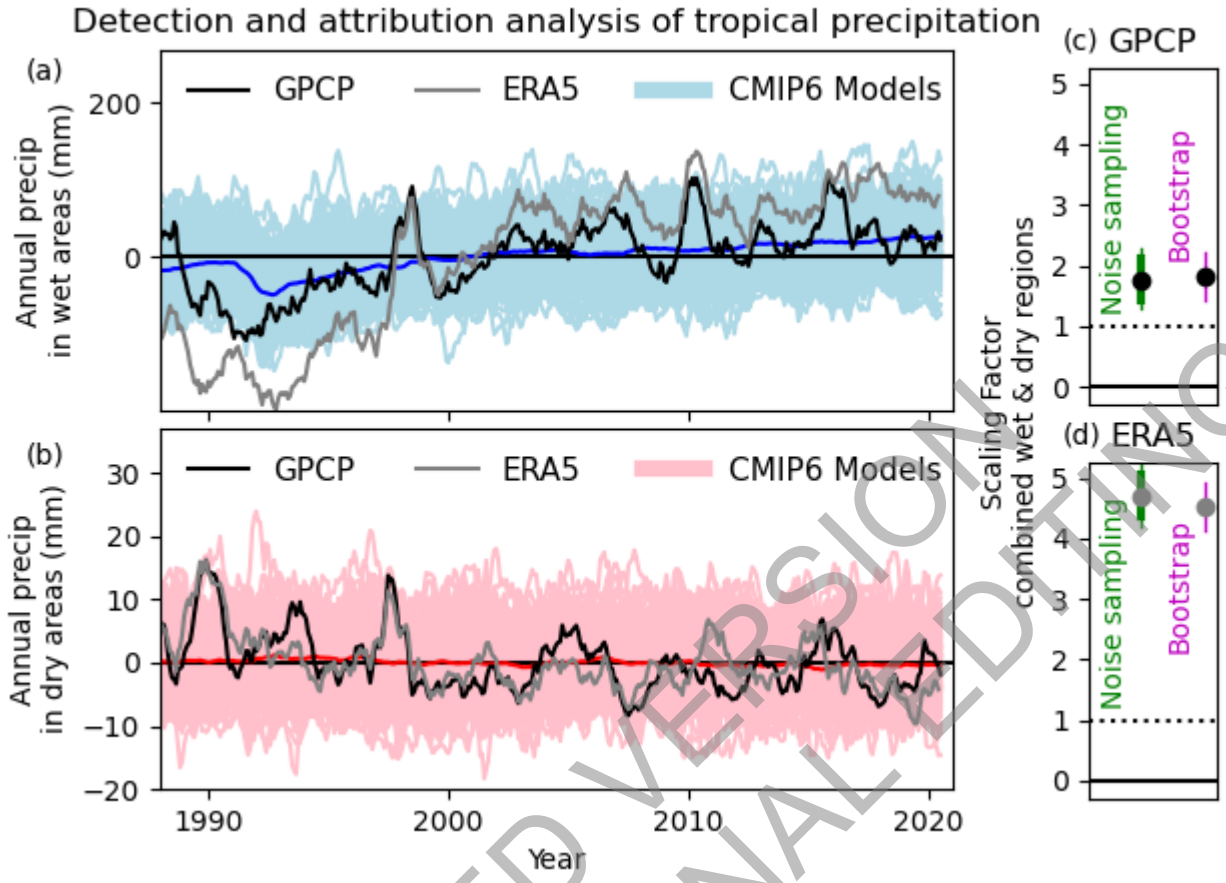


Figure 3.14: Wet (a) and dry (b) region tropical mean (30°S-30°N) annual precipitation anomalies. Observed data are shown with black lines (GPCP), ERA5 reanalysis in grey, single model simulations results are shown with light blue/red lines (CMIP6), and multi-model-mean results are shown with dark blue/red lines (CMIP6). Wet and dry region annual anomalies are calculated as the running mean over 12 months relative to a 1988-2020 based period. The regions are defined as the wettest third and driest third of the surface area, calculated for the observations and for each model separately for each season (following Polson and Hegerl, 2017). Scaling factors (panels c,d) are calculated for the combination of the wet and dry region mean, where the observations, reanalysis and all the model simulations are first standardised using the mean standard deviation of the pre-industrial control simulations. Two total least squares regression methods are used: noise in variables (following Polson and Hegerl, 2017) which estimates a best estimate and a 5-95% confidence interval using the pre-industrial controls (circle and thick green line) and the pre-industrial controls with double the variance (thin green line); and a bootstrap method (DelSole et al., 2019) (5-95% confidence interval shown with a purple line and best estimate with a purple circle). Panel (c) shows results for GPCP and panel (d) for ERA5. Figure is adapted from Schurer et al. (2020). Further details on data sources and processing are available in the chapter data table (Table 3.SM.1).

ACCEPTED VERSION SUBJECT TO FINAL EDITING

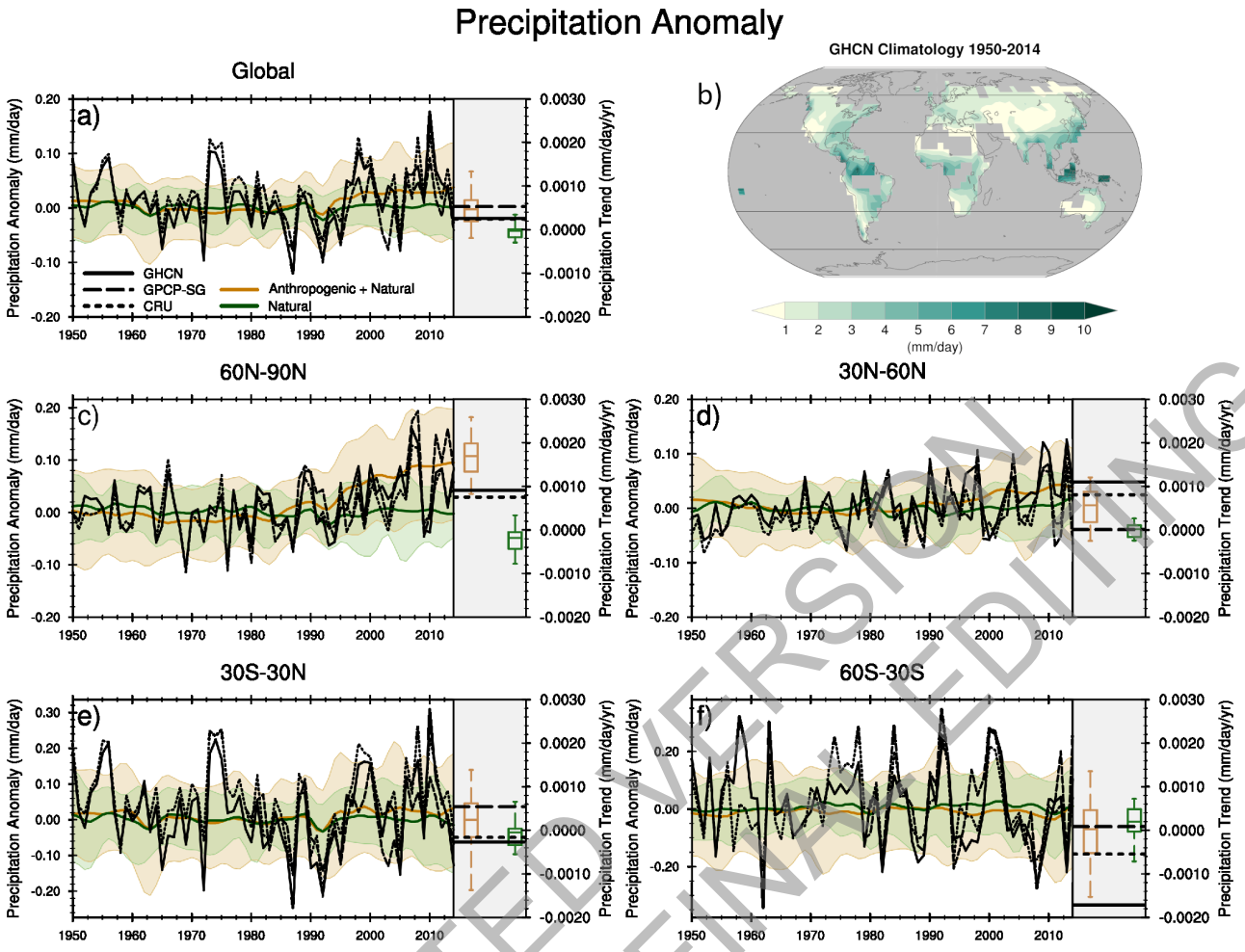
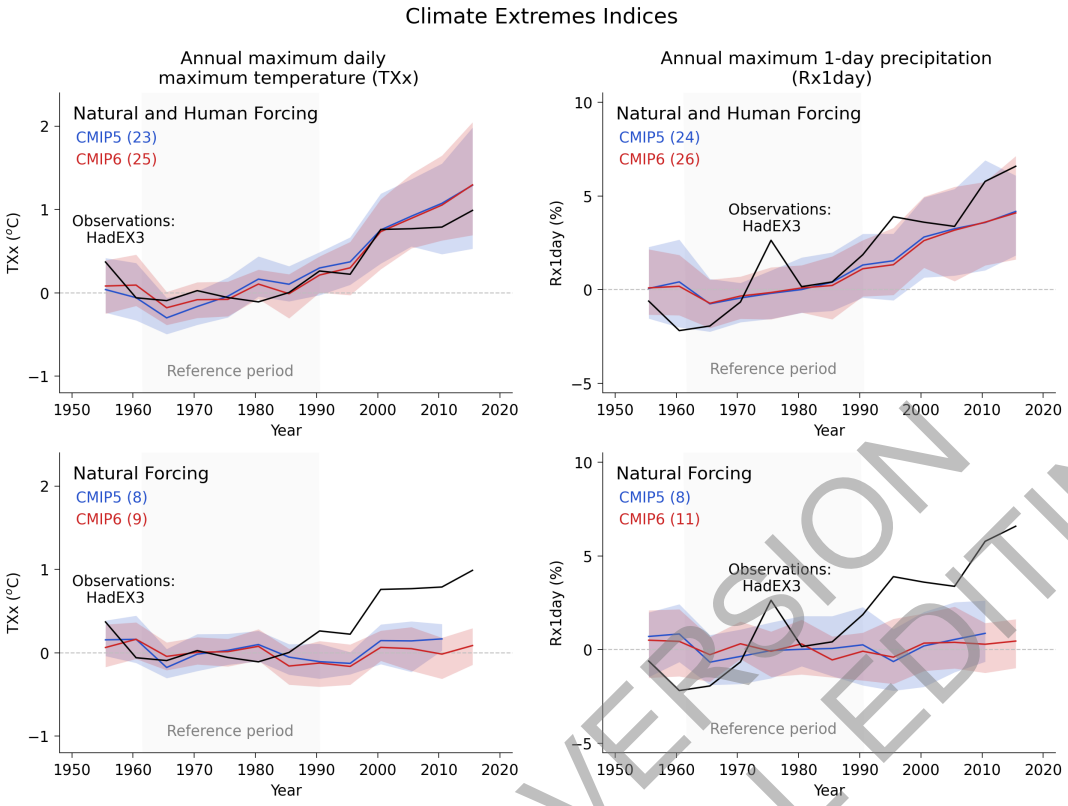


Figure 3.15: Observed and simulated time series of anomalies in zonal average annual mean precipitation. a), c)-f) Evolution of global and zonal average annual mean precipitation (mm day^{-1}) over areas of land where there are observations, expressed relative to the base-line period of 1961–1990, simulated by CMIP6 models (one ensemble member per model) forced with both anthropogenic and natural forcings (brown) and natural forcings only (green). Multi-model means are shown in thick solid lines and shading shows the 5-95% confidence interval of the individual model simulations. The data is smoothed using a low pass filter. Observations from three different data sets are included: gridded values derived from Global Historical Climatology Network (GHCN V2) station data, updated from Zhang et al. (2007), data from the Global Precipitation Climatology Product (GPCP L3 v2.3, Huffman and Bolvin (2013)) and from the Climate Research Unit (CRU TS4.02, Harris et al. (2014)). Also plotted are boxplots showing interquartile and 5-95% ranges of simulated trends over the period for simulations forced with both anthropogenic and natural forcings (brown) and natural forcings only (blue). Observed trends for each observational product are shown as horizontal lines. Panel b) shows annual mean precipitation rate (mm day^{-1}) of GHCN V2 for the years 1950-2014 over land areas used to compute the plots. Further details on data sources and processing are available in the chapter data table (Table 3.SM.1).

ACCEPTED VERSION SUBJECT TO FINAL EDITING



Cross-Chapter Box 3.2, Figure 1: Comparison of observed and simulated changes in global mean temperature and precipitation extremes. Time series of globally averaged 5-year mean anomalies of the annual maximum daily maximum temperature (TXx in °C) and annual maximum 1-day precipitation (Rx1day as standardized probability index in %) during 1953-2017 from the HadEX3 observations and the CMIP5 and CMIP6 multi-model ensembles with natural and human forcing (upper) and natural forcing only (lower). For CMIP5, historical simulations for 1953-2005 are combined with corresponding RCP4.5 scenario runs for 2006-2017. For CMIP6, historical simulations for 1953-2014 are combined with SSP2-4.5 scenario simulations for 2015-2017. Numbers in brackets represents the number of models used. The time-fixed observational mask has been applied to model data throughout the whole period. Grid cells with more than 70% data availability during 1953-2017 plus data for at least 3 years during 2013-2017 are used. Coloured lines indicate multi-model means, while shading represents 5th-95th percentile ranges, based on all available ensemble members with equal weight given to each model (Section 3.2). Anomalies are relative to 1961-1990 means. Figure is updated from Seong et al. (2021), their Figure 3 and Paik et al. (2020), their Figure 3. Further details on data sources and processing are available in the chapter data table (Table 3.SM.1).

ACCEPTED VERSION SUBJECT TO FINAL EDITING

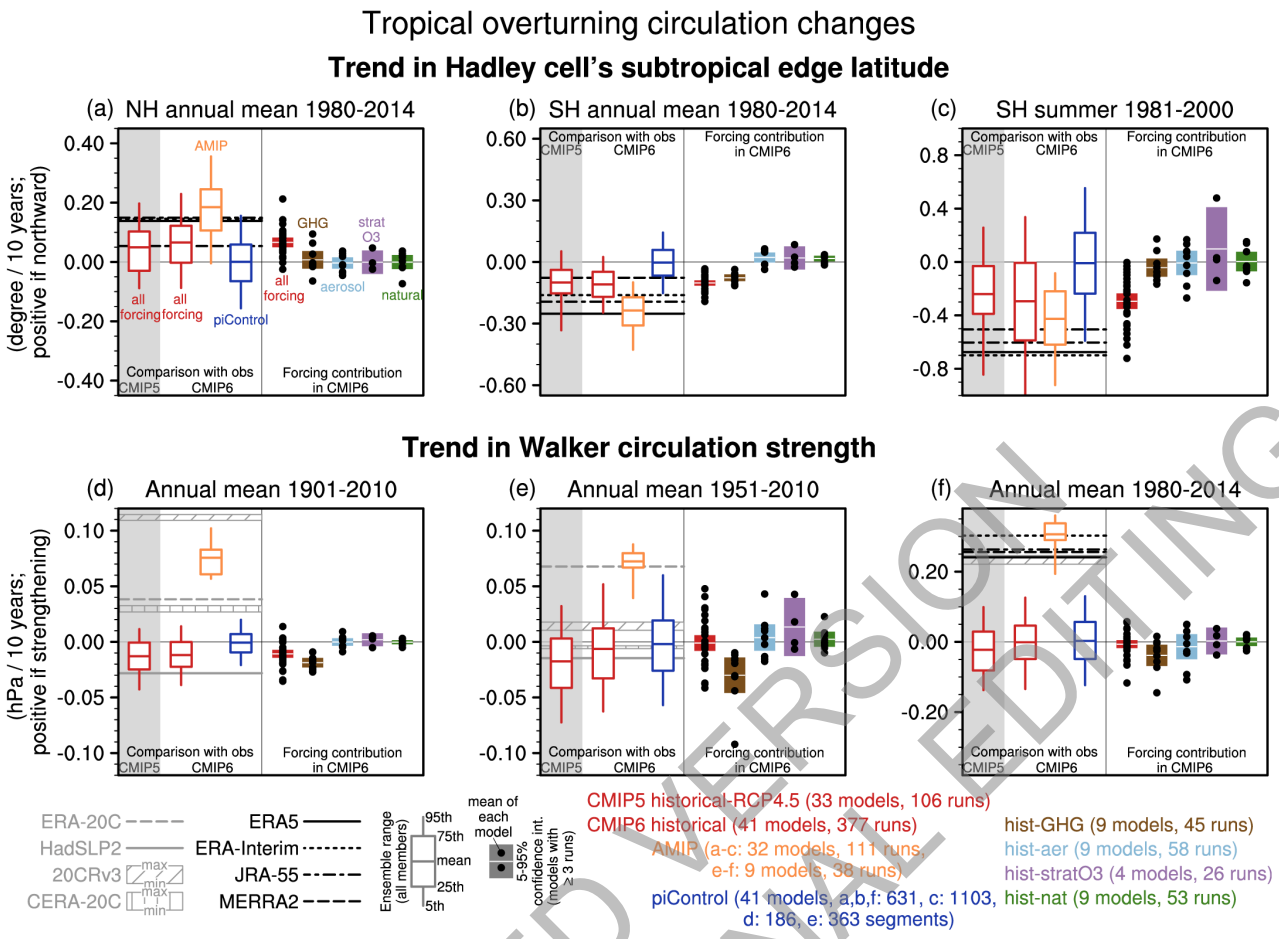


Figure 3.16: Model evaluation and attribution of changes in Hadley cell extent and Walker circulation strength. (a-c) Trends in subtropical edge latitude of the Hadley cells in (a) the Northern Hemisphere for 1980-2014 annual mean and (b-c) Southern Hemisphere for (b) 1980-2014 annual mean and (c) 1980/81-1999/2000 December-January-February mean. Positive values indicate northward shifts. (d-f) Trends in the Pacific Walker circulation strength for (d) 1901-2010, (e) 1951-2010 and (f) 1980-2014. Positive values indicate strengthening. Based on CMIP5 historical (extended with RCP4.5), CMIP6 historical, AMIP, pre-industrial control, and single forcing simulations along with HadSLP2 and reanalyses. Pre-industrial control simulations are divided into non-overlapping segments of the same length as the other simulations. White boxes and whiskers represent mean, interquartile ranges and 5th and 95th percentiles, calculated after weighting individual members with the inverse of the ensemble of the same model, so that individual models are equally weighted (Section 3.2). The filled boxes represent the 5-95% confidence interval on the multi-model mean trends of the models with at least 3 ensemble members, with dots indicating the ensemble means of individual models. The edge latitude of the Hadley cell is defined where the surface zonal wind velocity changes sign from negative to positive, as described in the Appendix of Grise et al. (2018). The Pacific Walker circulation strength is evaluated as the annual mean difference of sea level pressure between 5ºS-5ºN, 160ºW-80ºW and 5ºS-5ºN, 80ºE-160ºE. Further details on data sources and processing are available in the chapter data table (Table 3.SM.1).

ACCEPTED VERSION SUBJECT TO FINAL EDITING

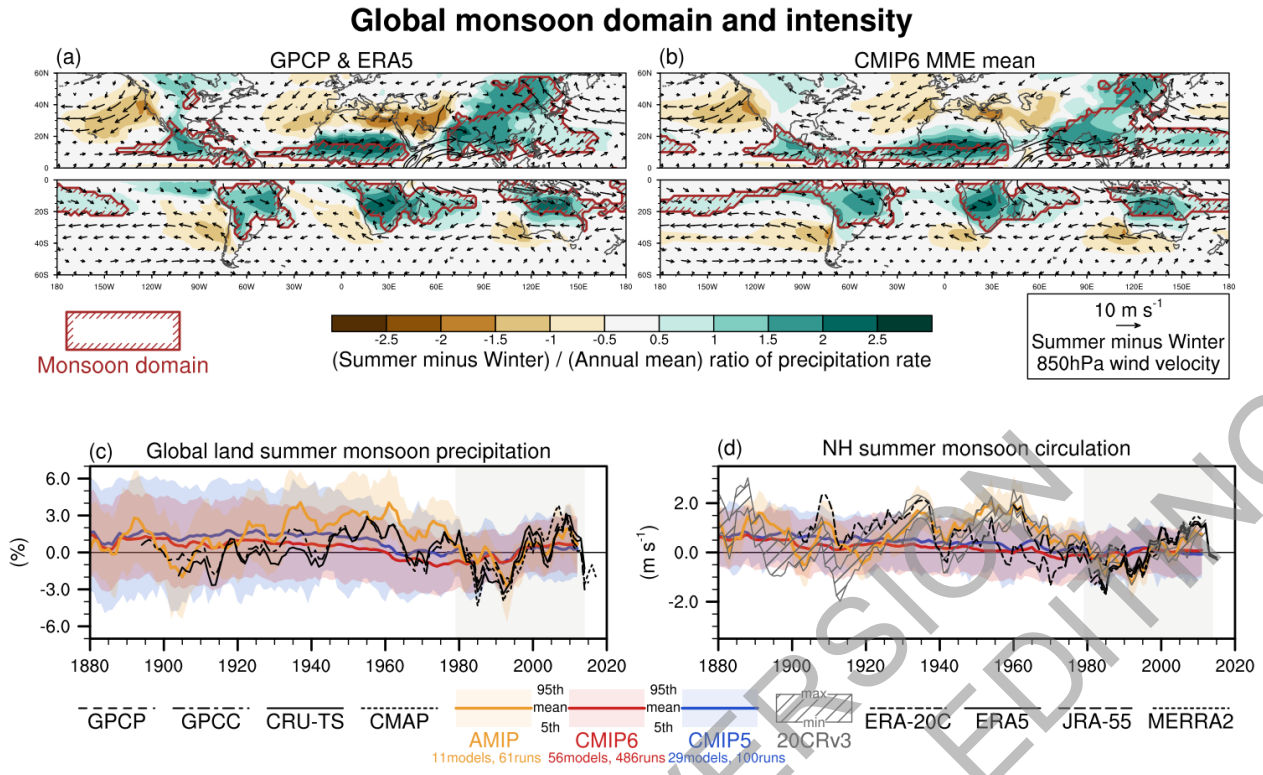


Figure 3.17: Model evaluation of global monsoon domain, intensity, and circulation. (a-b) Climatological summer-winter range of precipitation rate, scaled by annual mean precipitation rate (shading) and 850 hPa wind velocity (arrows) based on (a) GPCP and ERA5 and (b) a multi-model ensemble mean of CMIP6 historical simulations for 1979-2014. Enclosed by red lines is the monsoon domain based on the definition by Wang and Ding (2008). (c-d) 5-year running mean anomalies of (c) global land monsoon precipitation index defined as the percentage anomaly of the summertime precipitation rate averaged over the monsoon regions over land, relative to its average for 1979-2014 (the period indicated by light grey shading) and (d) the tropical monsoon circulation index defined as the vertical shear of zonal winds between 850 and 200 hPa levels averaged over 0º-20ºN, from 120ºW eastward to 120ºE in NH summer (Wang et al., 2013; m s^{-1}) in CMIP5 historical and RCP4.5 simulations, CMIP6 historical and AMIP simulations. Summer and winter are defined for individual hemispheres: May through September for NH summer and SH winter, and November through March for NH winter and SH summer. The number of models and ensembles are given in the legend. The multi-model ensemble mean and percentiles are calculated after weighting individual members with the inverse of the ensemble size of the same model, so that individual models are equally weighted irrespective of ensemble size. Further details on data sources and processing are available in the chapter data table (Table 3.SM.1).

ACCEPTED VERSION SUBJECT TO FINAL EDITING

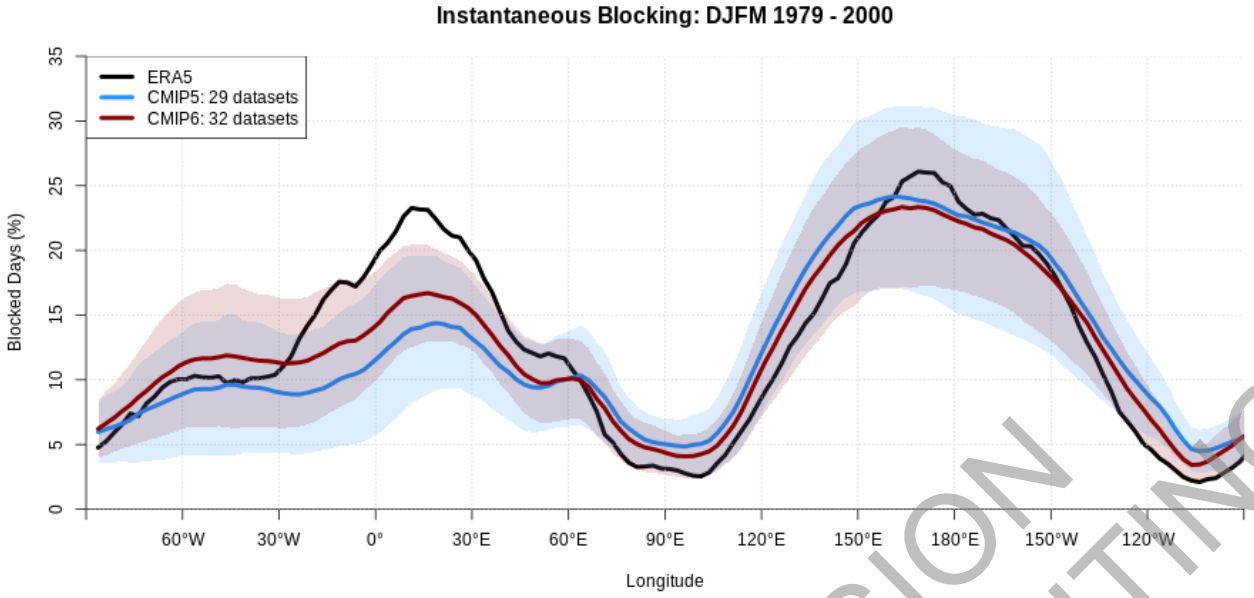


Figure 3.18: Instantaneous Northern-Hemisphere blocking frequency (% of days) in the extended northern winter season (DJFM) for the years 1979-2000. Results are shown for ERA5 reanalysis (black), CMIP5 (blue) and CMIP6 (red) models. Coloured lines show multi-model means and shaded ranges show corresponding 5-95% ranges constructed with one realization from each model. Figure is adapted from Davini and D'Andrea (2020), their Figure 12 and following the D'Andrea et al. (1998) definition of blocking. Further details on data sources and processing are available in the chapter data table (Table 3.SM.1).

ACCEPTED VERSION SUBJECT TO FINAL EDITING

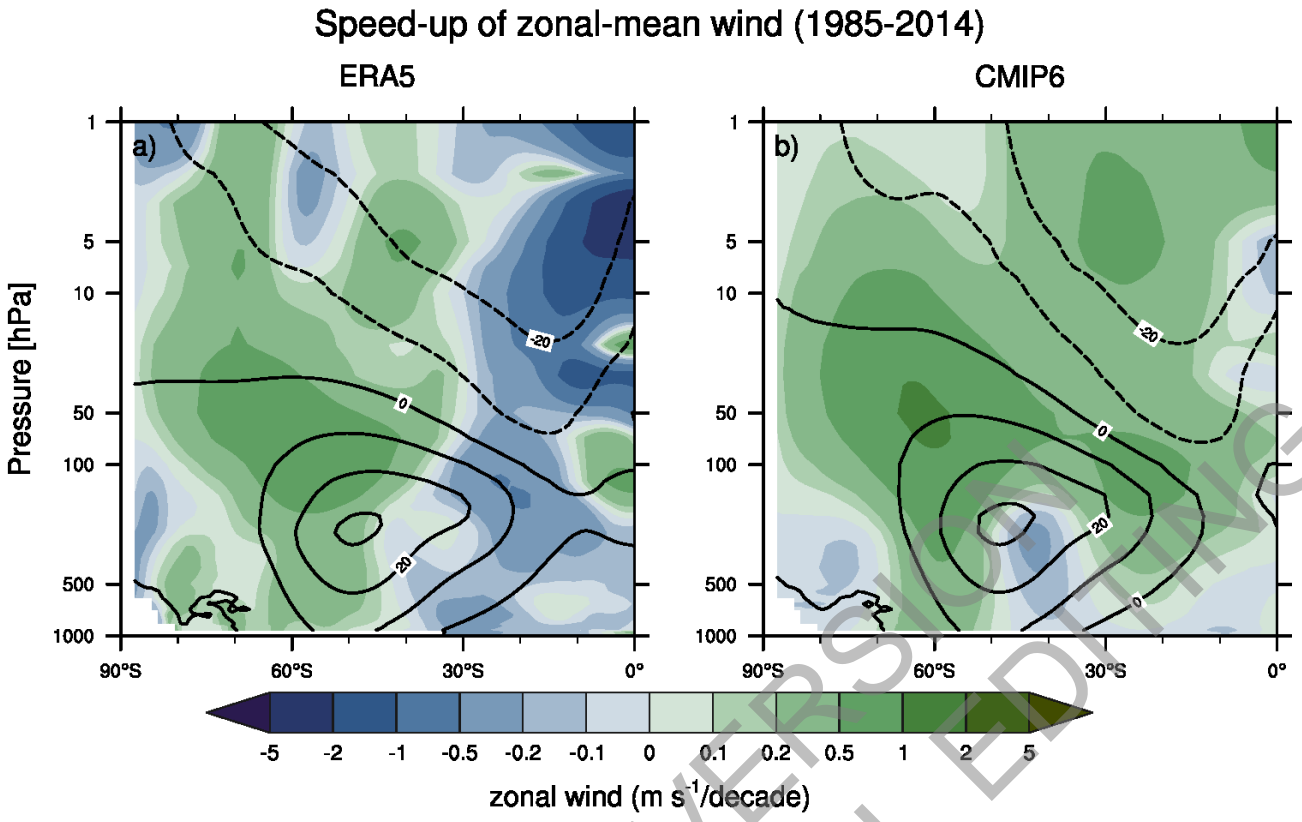


Figure 3.19: Long-term mean (thin black contour) and linear trend (colour) of zonal mean DJF zonal winds over 1985-2014 in the SH. Displayed are (a) ERA5 and (b) CMIP6 multi-model mean (58 CMIP6 models). The solid contours show positive (westerly) and zero long-term mean zonal wind, and the dashed contours show negative (easterly) long-term mean zonal wind. Only one ensemble member per model is included. Figure is modified from Eyring et al. (2013), their Figure 12. Further details on data sources and processing are available in the chapter data table (Table 3.SM.1).

ACCEPTED VERSION SUBJECT TO FINAL EDITING

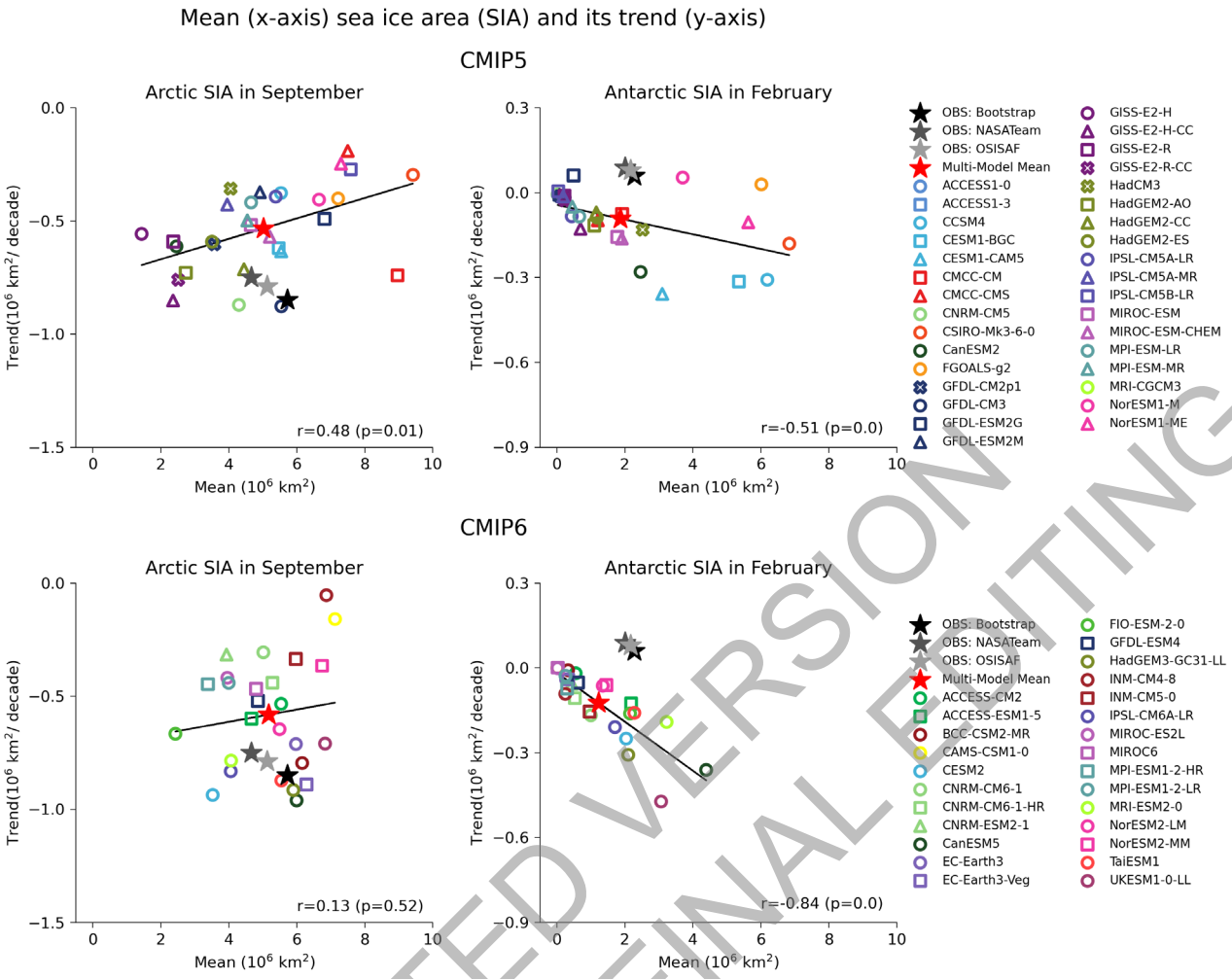


Figure 3.20: Mean (*x*-axis) and trend (*y*-axis) in Arctic sea ice area (SIA) in September (left) and Antarctic SIA in February (right) for 1979-2017 from CMIP5 (upper) and CMIP6 (lower) models. All individual models (ensemble means) and the multi-model mean values are compared with the observations (OSISAF, NASA Team, and Bootstrap). Solid line indicates a linear regression slope with corresponding correlation coefficient (r) and p-value provided. Note the different scales used on the y-axis for Arctic and Antarctic SIA. Results remain essentially the same when using sea ice extent (SIE) (not shown). Further details on data sources and processing are available in the chapter data table (Table 3.SM.1).

ACCEPTED VERSION SUBJECT TO FINAL EDITING

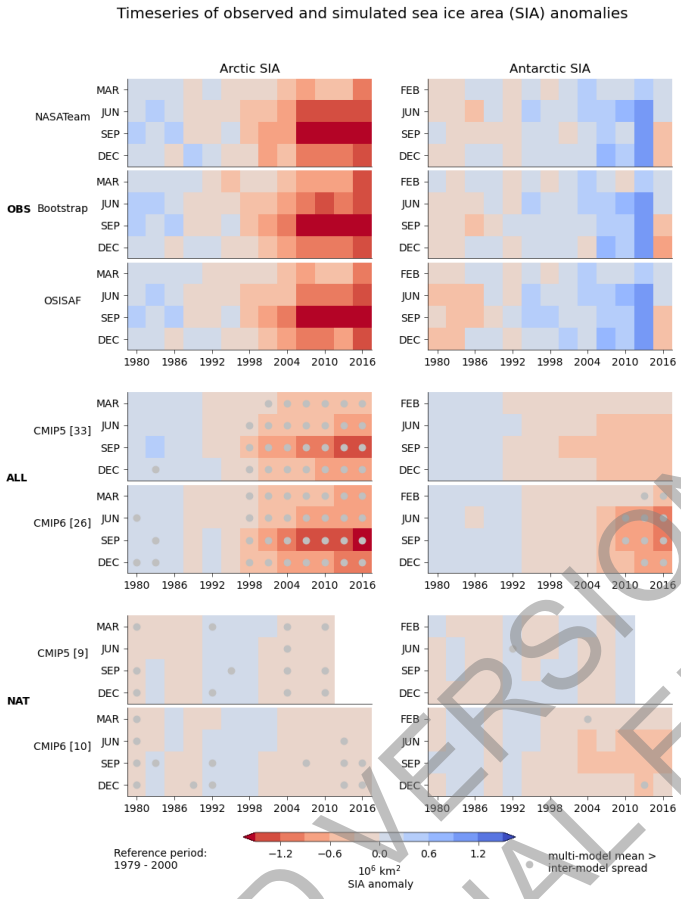


Figure 3.21: Seasonal evolution of observed and simulated Arctic (left) and Antarctic (right) sea ice area (SIA) over 1979–2017. SIA anomalies relative to the 1979–2000 means from observations (OBS from OSISAF, NASA Team, and Bootstrap, top) and historical (ALL, middle) and natural only (NAT, bottom) simulations from CMIP5 and CMIP6 multi-models. These anomalies were obtained by computing non-overlapping 3-year mean SIA anomalies for March (February for Antarctic SIA), June, September, and December separately. CMIP5 historical simulations are extended by using RCP4.5 scenario simulations after 2005 while CMIP6 historical simulations are extended by using SSP2-4.5 scenario simulations after 2014. CMIP5 NAT simulations end in 2012. Numbers in brackets represents the number of models used. The multi-model mean is obtained by taking the ensemble mean for each model first and then averaging over models. Grey dots indicate multi-model mean anomalies stronger than inter-model spread (beyond ± 1 standard deviation). Results remain very similar when based on sea ice extent (SIE) (not shown). Units: 10^6 km^2. Further details on data sources and processing are available in the chapter data table (Table 3.SM.1).

ACCEPTED VERSION SUBJECT TO FINAL EDITING

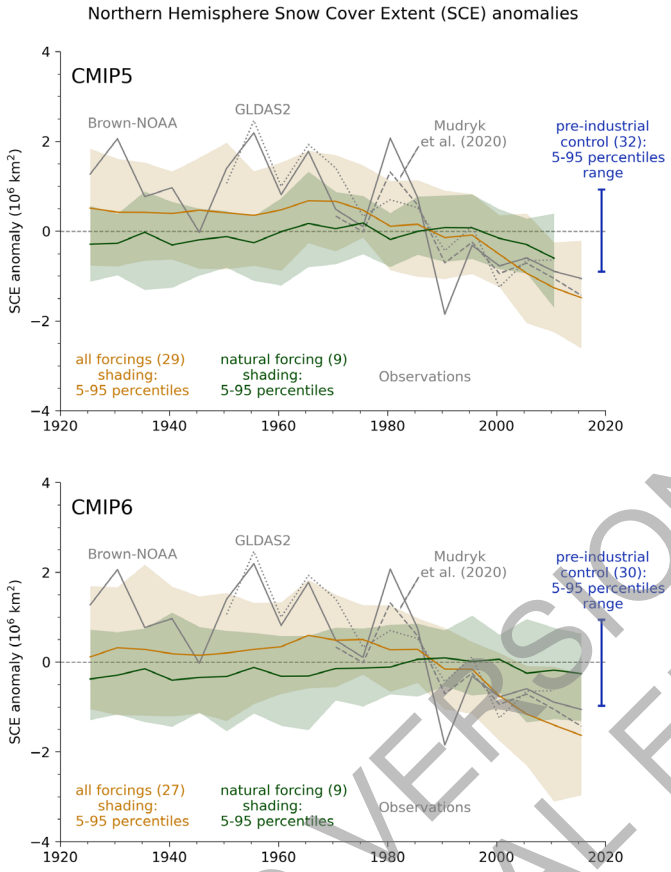


Figure 3.22: Time series of Northern Hemisphere March-April mean snow cover extent (SCE) from observations, CMIP5 and CMIP6 simulations. The observations (grey lines) are updated Brown-NOAA (Brown and Robinson, 2011), Mudryk et al. (2020), and GLDAS2. CMIP5 (upper) and CMIP6 (lower) simulations of the response to natural plus anthropogenic forcing are shown in orange, natural forcing only in green, and the pre-industrial control simulation range is presented in blue. 5-year mean anomalies are shown for the 1923-2017 period with the x-axis representing the centre years of each 5-year mean. CMIP5 all forcing simulations are extended by using RCP4.5 scenario simulations after 2005 while CMIP6 all forcing simulations are extended by using SSP2-4.5 scenario simulations after 2014. Shading indicates 5th-95th percentile ranges for CMIP5 and CMIP6 all and natural forcings simulations, and solid lines are ensemble means, based on all available ensemble members with equal weight given to each model (Section 3.2). The blue vertical bar indicates the mean 5th-95th percentile range of pre-industrial control simulation anomalies, based on non-overlapping segments. The numbers in brackets indicate the number of models used. Anomalies are relative to the average over 1971-2000. For models, SCE is restricted to grid cells with land fraction ≥ 50%. Greenland is excluded from the total area summation. Figure is modified from Paik et al. (2020), their Figure 1. Further details on data sources and processing are available in the chapter data table (Table 3.SM.1).

ACCEPTED VERSION SUBJECT TO FINAL EDITING

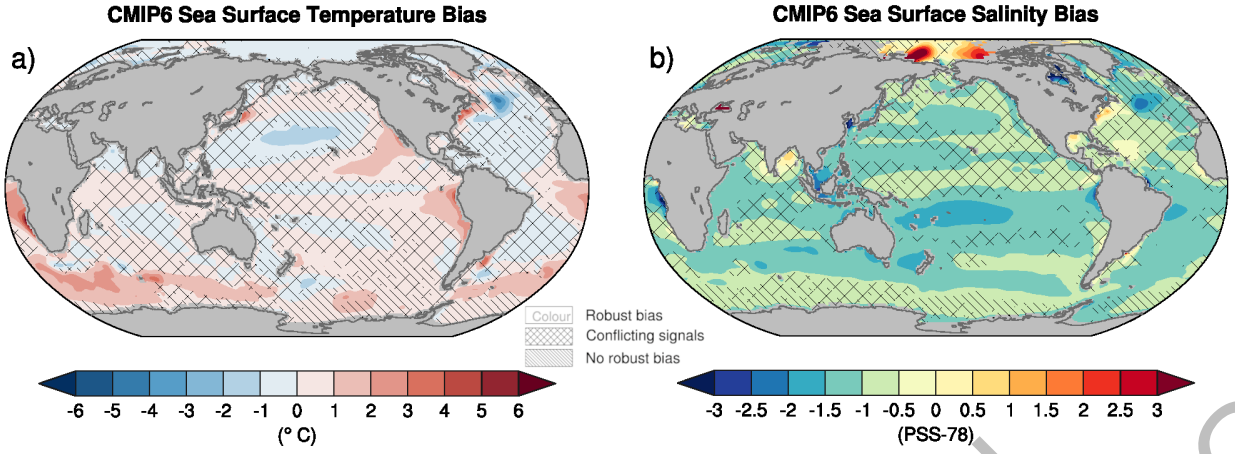


Figure 3.23: Multi-model-mean bias of (a) sea surface temperature and (b) near-surface salinity, defined as the difference between the CMIP6 multi-model mean and the climatology from the World Ocean Atlas 2018. The CMIP6 multi-model mean is constructed with one realization of 46 CMIP6 historical experiments for the period 1995–2014 and the climatology from the World Ocean Atlas 2018 is an average over all available years (1955-2017). Uncertainty is represented using the advanced approach: No overlay indicates regions with robust signal, where ≥66% of models show change greater than variability threshold and ≥80% of all models agree on sign of change; diagonal lines indicate regions with no change or no robust signal, where <66% of models show a change greater than the variability threshold; crossed lines indicate regions with conflicting signal, where ≥66% of models show change greater than the variability threshold and <80% of all models agree on sign of change. For more information on the advanced approach, please refer to the Cross-Chapter Box Atlas.1. Further details on data sources and processing are available in the chapter data table (Table 3.SM.1).

ACCEPTED VERSION SUBJECT TO FINAL EDITING

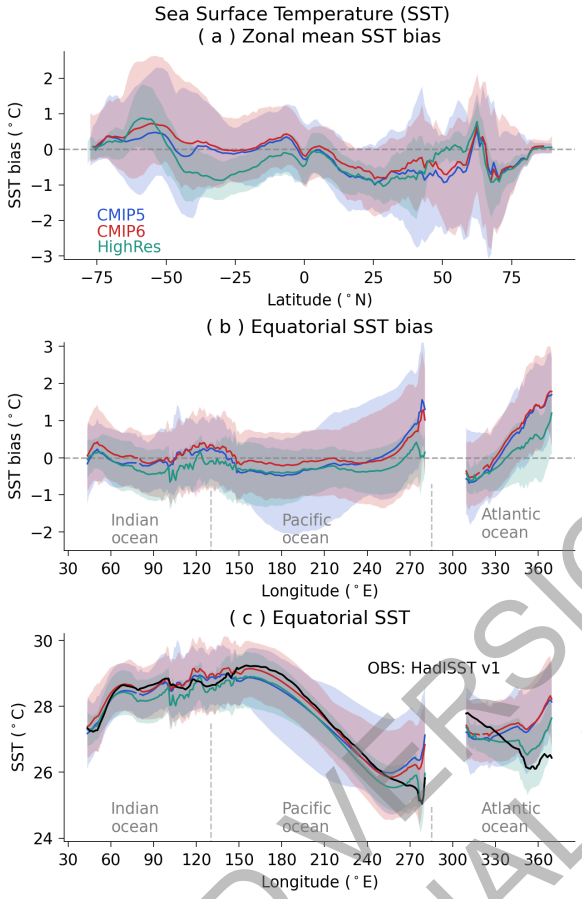


Figure 3.24: Biases in zonal mean and equatorial sea surface temperature (SST) in CMIP5 and CMIP6 models. CMIP6 (red), CMIP5 (blue) and HighResMIP (green) multi-model mean (a) zonally-averaged SST bias; (b) equatorial SST bias; and (c) equatorial SST compared to observed mean SST (black line) for 1979-1999. The inter-model 5th and 95th percentiles are depicted by the respective shaded range. Model climatologies are derived from the 1979-1999 mean of the historical simulations, using one simulation per model. The Hadley Centre Sea Ice and Sea Surface Temperature version 1 (HadISST) (Rayner et al., 2003) observational climatology for 1979-1999 is used as the reference for the error calculation in (a) and (b); and for observations in (c). Further details on data sources and processing are available in the chapter data table (Table 3.SM.1).

ACCEPTED VERSION SUBJECT TO FINAL EDITING

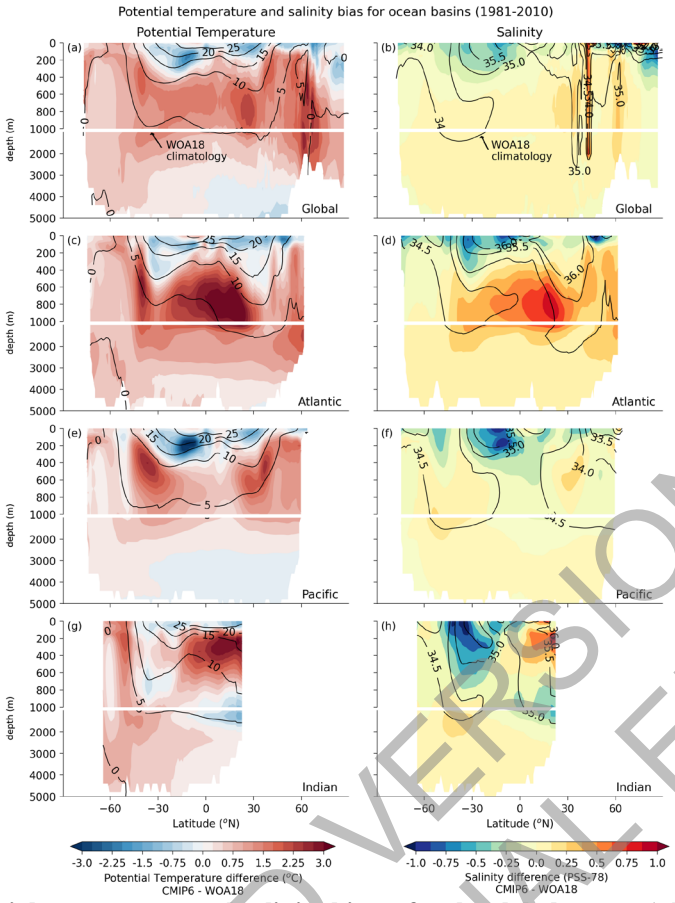


Figure 3.25: CMIP6 potential temperature and salinity biases for the global ocean, Atlantic, Pacific and Indian Oceans. Shown in colour are the time-mean differences between the CMIP6 historical multi-model climatological mean and observations, zonally averaged for each basin (excluding marginal and regional seas). The observed climatological values are obtained from the World Ocean Atlas 2018 (WOA18, 1981-2010; Prepared by the Ocean Climate Laboratory, National Oceanographic Data Center, Silver Spring, MD, USA), and are shown as labelled black contours for each of the basins. The simulated annual mean climatologies for 1981 to 2010 are calculated from available CMIP6 historical simulations, and the WOA18 climatology utilized synthesized observed data from 1981 to 2010. A total of 30 available CMIP6 models have contributed to the temperature panels (left column) and 28 models to the salinity panels (right column). Potential temperature units are °C and salinity units are the Practical Salinity Scale 1978 [PSS-78]. Further details on data sources and processing are available in the chapter data table (Table 3.SM.1).

ACCEPTED VERSION SUBJECT TO FINAL EDITING

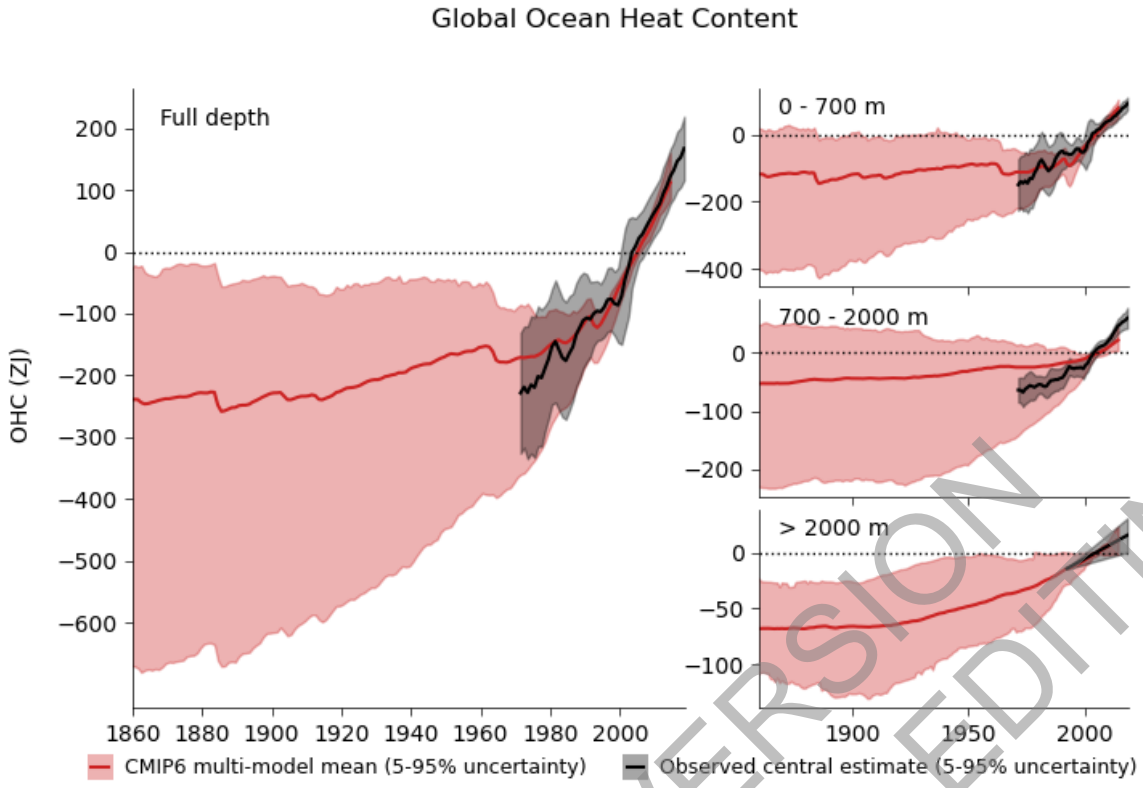


Figure 3.26: Global ocean heat content in CMIP6 simulations and observations. Time series of observed (black) and simulated (red) global ocean heat content anomalies with respect to 1995-2014 for the full ocean depth (left panel), upper layer - 0 to 700 m (top right panel), intermediate layer -700 to 2000 m (middle right panel), and the abyssal ocean >2000 m (bottom right panel). The best estimate observations (black solid line) for the period of 1971-2018, along with *very likely* ranges (black shading) are from Section 2.3.3.1. For the models (1860-2014), ensemble members from 15 CMIP6 models are used to calculate the multi-model mean values (red solid line) after averaging across simulations for each independent model. The *very likely* ranges in the simulations are shown in red shading. Simulation drift has been removed from all CMIP6 historical runs using a contemporaneous portion of the linear fit to each corresponding pre-industrial control run (Gleckler et al., 2012). Units are 10^{21} Joules (Zettajoules). Further details on data sources and processing are available in the chapter data table (Table 3.SM.1).

ACCEPTED VERSION SUBJECT TO FINAL EDITING

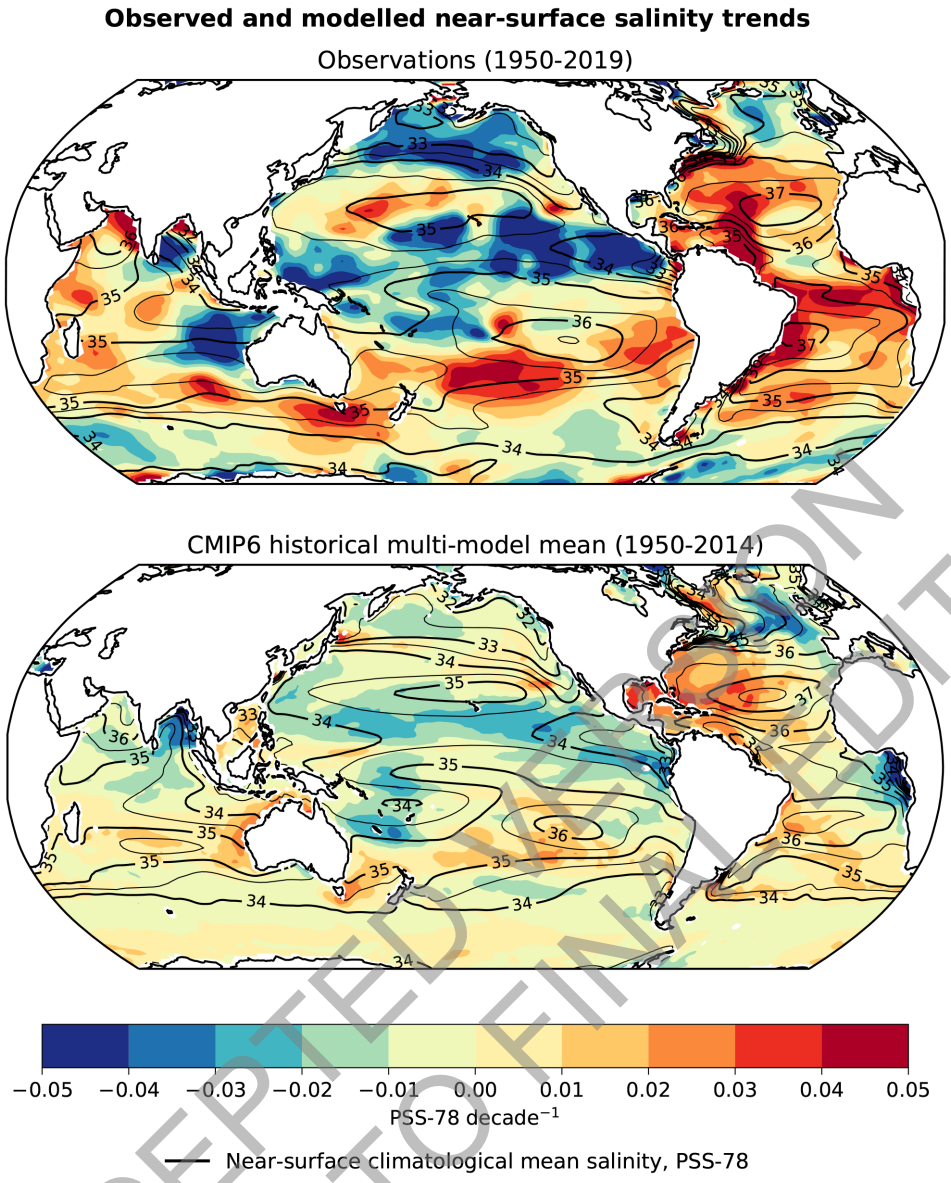


Figure 3.27: Maps of multi-decadal salinity trends for the near-surface ocean. Units are Practical Salinity Scale 1978 [PSS-78] decade^{-1}. (top) The best estimate (Section 2.3.3.2) observed trend (Durack and Wijffels, 2010 updated, 1950-2019). (bottom) Simulated trend from the CMIP6 historical experiment multi-model mean (1950-2014). Black contours show the climatological mean salinity in increments of 0.5 PSS-78 (thick lines 1 PSS-78). Further details on data sources and processing are available in the chapter data table (Table 3.SM.1).

ACCEPTED VERSION SUBJECT TO FINAL EDITING

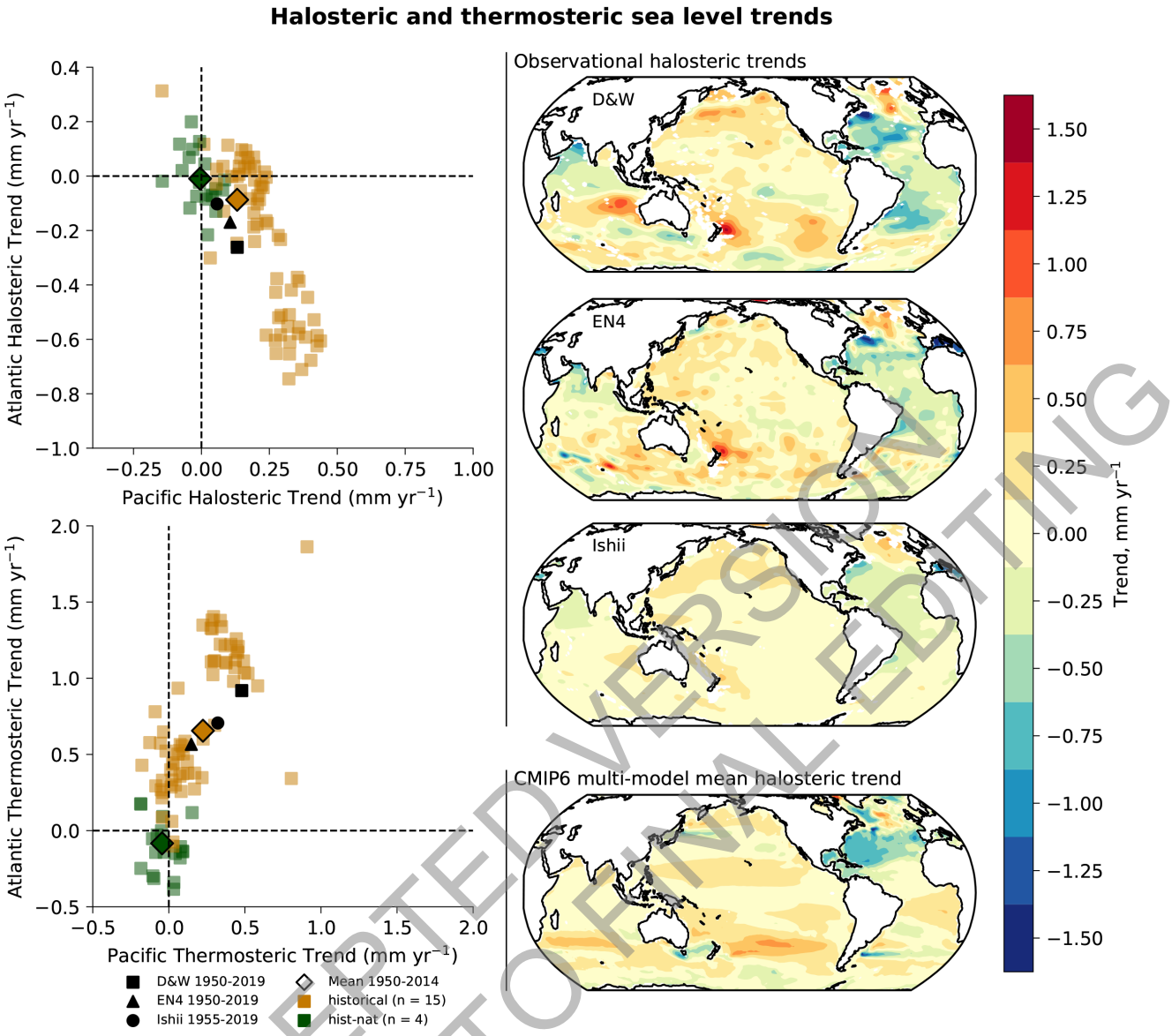


Figure 3.28: Long-term trends in halosteric and thermosteric sea level in CMIP6 models and observations. Units are mm year^{-1}. In the right column, three observed maps of 0 to 2000 m halosteric sea level trends (right column) top from (Durack and Wijffels, 2010, 1950-2019 updated - D&W), middle from (Good et al., 2013, 1950-2019 updated- EN4), and lower from (Ishii et al., 2017, 1955-2019 updated – Ishii), and bottom, the CMIP6 historical multi-model mean (1950-2014). Red and orange colours show a halosteric contraction (enhanced salinity) and blue and green a halosteric expansion (reduced salinity). In the left column, basin-integrated halosteric (top) and thermosteric (bottom) trends for the Atlantic and Pacific, the two largest ocean basins, where Pacific anomalies are presented on the x-axis and Atlantic on the y-axis. Observational estimates are presented in black, CMIP6 historical (all forcings) simulations are shown in orange squares, with the multi-model mean shown as a dark orange diamond with a black bounding box. CMIP6 hist-nat (historical natural forcings only) simulations are shown in green squares with the multi-model mean as a dark green diamond with a black bounding box. Further details on data sources and processing are available in the chapter data table (Table 3.SM.1).

ACCEPTED VERSION SUBJECT TO FINAL EDITING

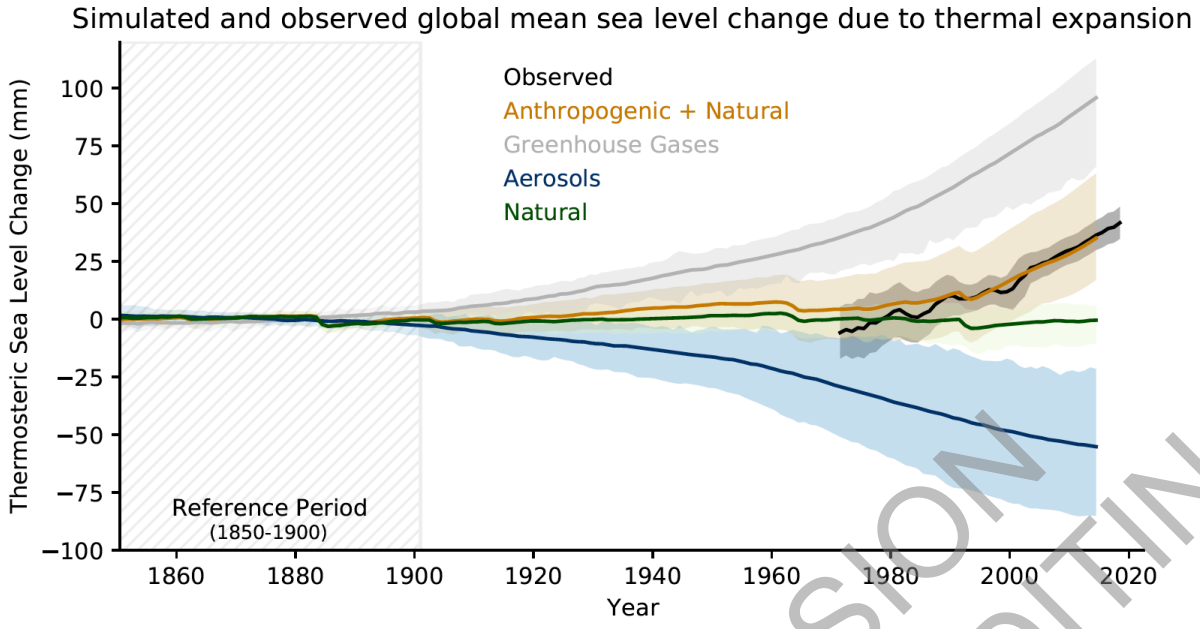


Figure 3.29: Simulated and observed global mean sea level change due to thermal expansion for CMIP6 models and observations relative to the baseline period 1850-1900. Historical simulations are shown in brown, natural only in green, greenhouse gas only in grey, and aerosol only in blue (multi-model means shown as thick lines, and shaded ranges between the 5th and 95th percentile). The best estimate observations (black solid line) for the period of 1971-2018, along with *very likely* ranges (black shading) are from Section 2.3.3.1 and are shifted to match the multi-model mean of the historical simulations for the 1995-2014 period. Further details on data sources and processing are available in the chapter data table (Table 3.SM.1).

ACCEPTED VERSION
SUBJECT TO FINAL EDITING

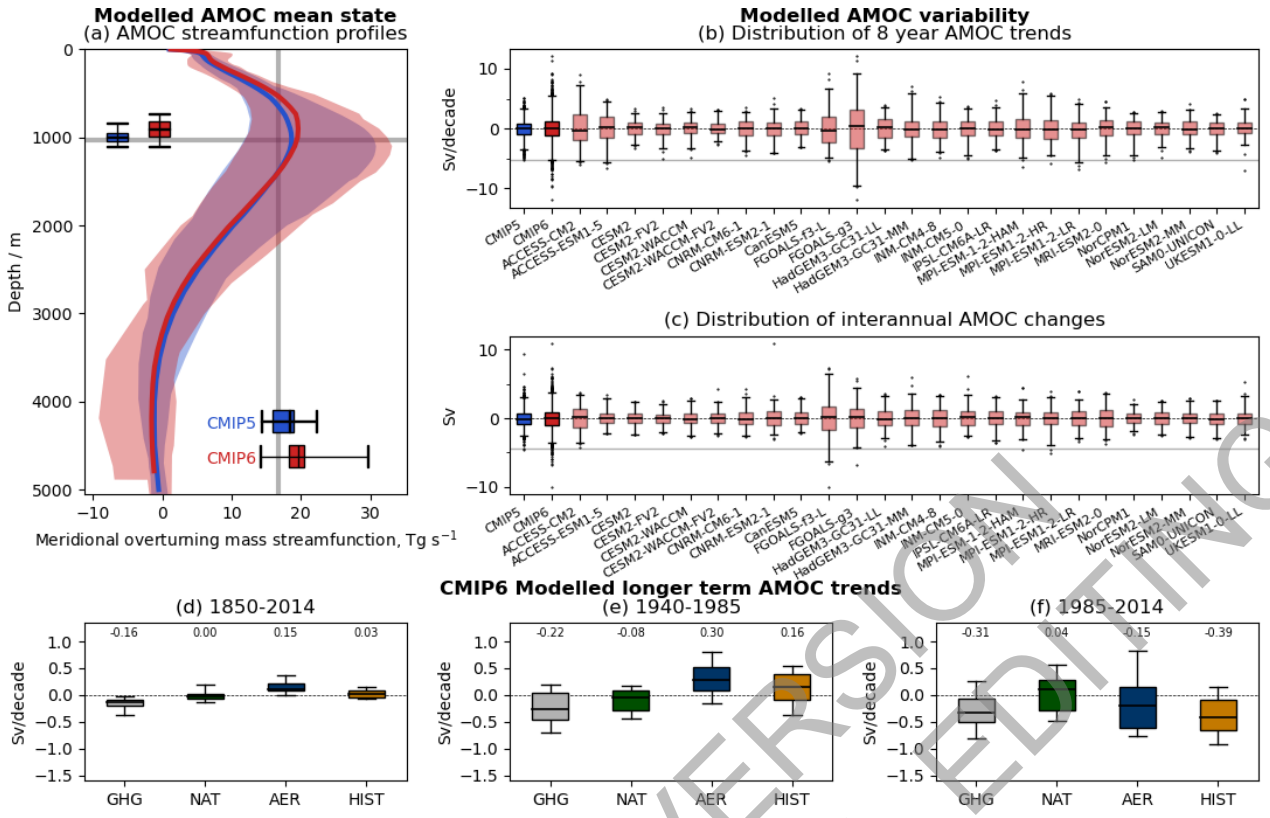


Figure 3.30: Observed and CMIP6 simulated AMOC mean state, variability and long-term trends. (a) AMOC meridional streamfunction profiles at 26.5°N from the historical CMIP5 (1860-2004) and CMIP6 (1860-2014) simulations compared with the mean maximum overturning depth (horizontal grey line) and magnitude (vertical grey line) from the RAPID observations (2004-2018). The distributions of model ranges of AMOC maximum magnitude and depth are respectively displayed on the x- and y-axis. (b) Distributions of overlapping 8-year AMOC trends from individual CMIP6 historical simulations (pink box plots) are plotted along with the combined distributions of all available CMIP5 (blue boxplot) and CMIP6 (red boxplot) models. For reference, the observed 8-year trend calculated between 2004-2012 is also shown as a horizontal grey line (following Roberts et al., 2014) (c) Distributions of interannual AMOC variability from individual CMIP6 model historical simulations, along with the combined distributions of all available CMIP5 and CMIP6 models. Interannual variability in models and observations are estimated as annual mean (April-March) differences, and the horizontal grey line is the observed value for 2009/2010 minus 2008/2009 (following Roberts et al., 2014). (d-f) Distributions of linear AMOC trends calculated over various time periods (see panel titles) in CMIP6 simulations forced with: greenhouse gas forcing only (GHG), natural forcing only (NAT), anthropogenic aerosol forcing only (AER) and all forcing combined (Historical; HIST). (a-f) Boxes indicate 25th to 75th percentile, whiskers indicate 1st and 99th percentiles, and dots indicate outliers, while the horizontal black line is the multi-model mean trend. In (d-f) the multi-model mean trend is also written above each distribution. The multi-model distributions in (a-c) were produced with one historical ensemble member per model for which the AMOC variable was available (listed), while those in (d-f) were produced with the AMOC detection and attribution simulation data sets utilised by Menary et al. (2020). Further details on data sources and processing are available in the chapter data table (Table 3.SM.1).

ACCEPTED VERSION SUBJECT TO FINAL EDITING

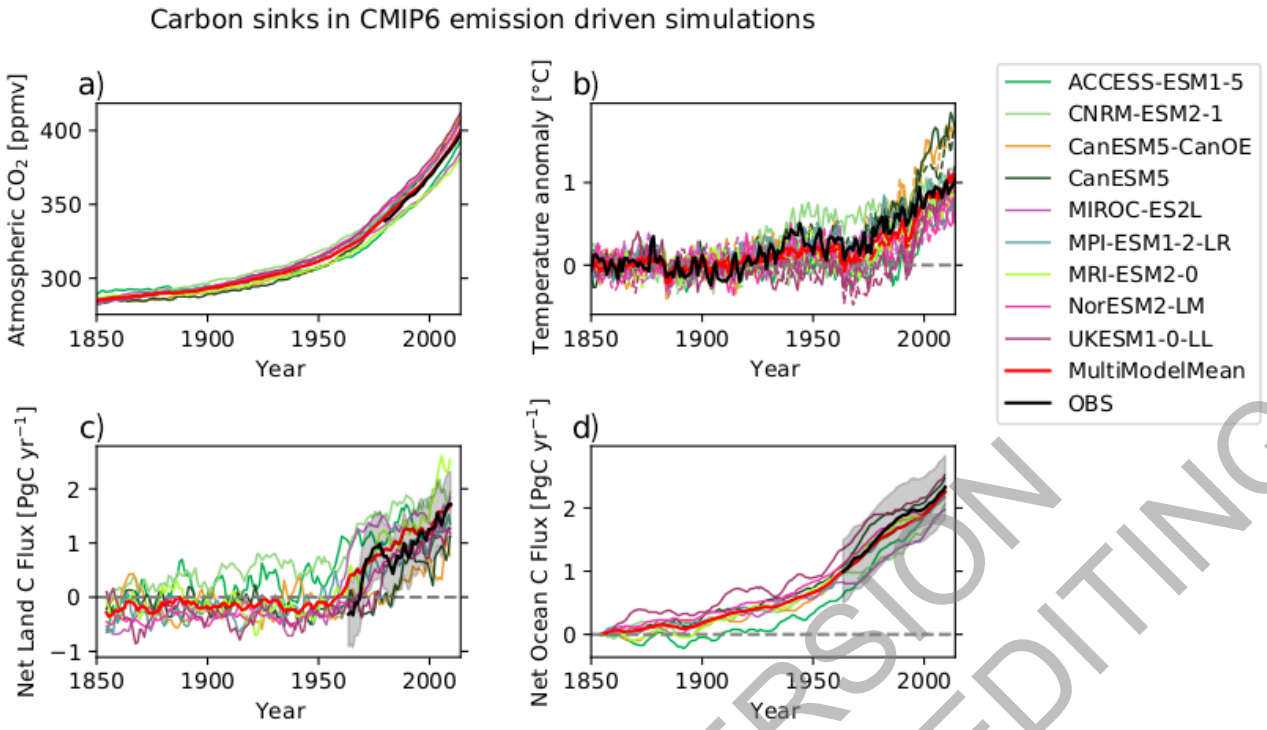


Figure 3.31: Evaluation of historical emission-driven CMIP6 simulations for 1850-2014. Observations (black) are compared to simulations of global mean (a) atmospheric CO_2 concentration (ppmv), with observations from the National Oceanic and Atmospheric Administration Earth System Research Laboratory (NOAA ESRL) (Dlugokencky and Tans, 2020), (b) air surface temperature anomaly (°C) with respect to the 1850-1900 mean, with observations from HadCRUT4 (Morice et al., 2012) (c) land carbon uptake (PgC yr^{-1}), (d) ocean carbon uptake (PgC yr^{-1}), both with observations from the Global Carbon Project (GCP) (Friedlingstein et al., 2019) and grey shading indicating the observational uncertainty. Land and ocean carbon uptakes are plotted using a 10-year running mean for better visibility. The ocean uptake is offset to 0 in 1850 to correct for pre-industrial riverine-induced carbon fluxes. Further details on data sources and processing are available in the chapter data table (Table 3.SM.1).

ACCEPTED VERSION SUBJECT TO FINAL EDITING

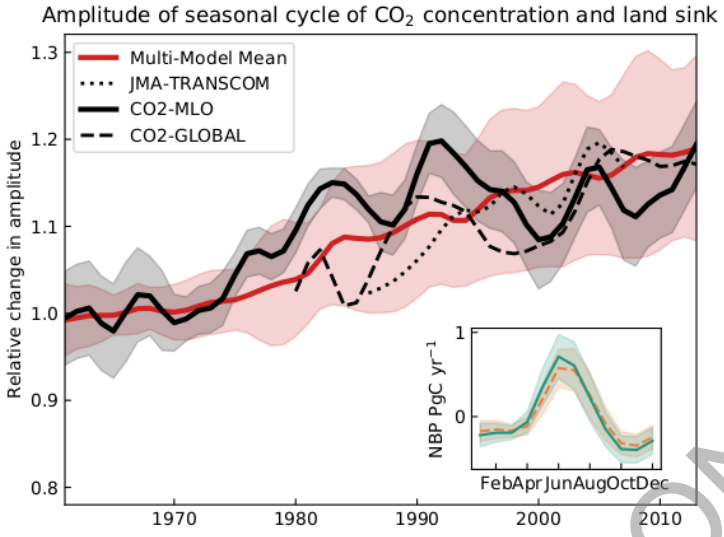
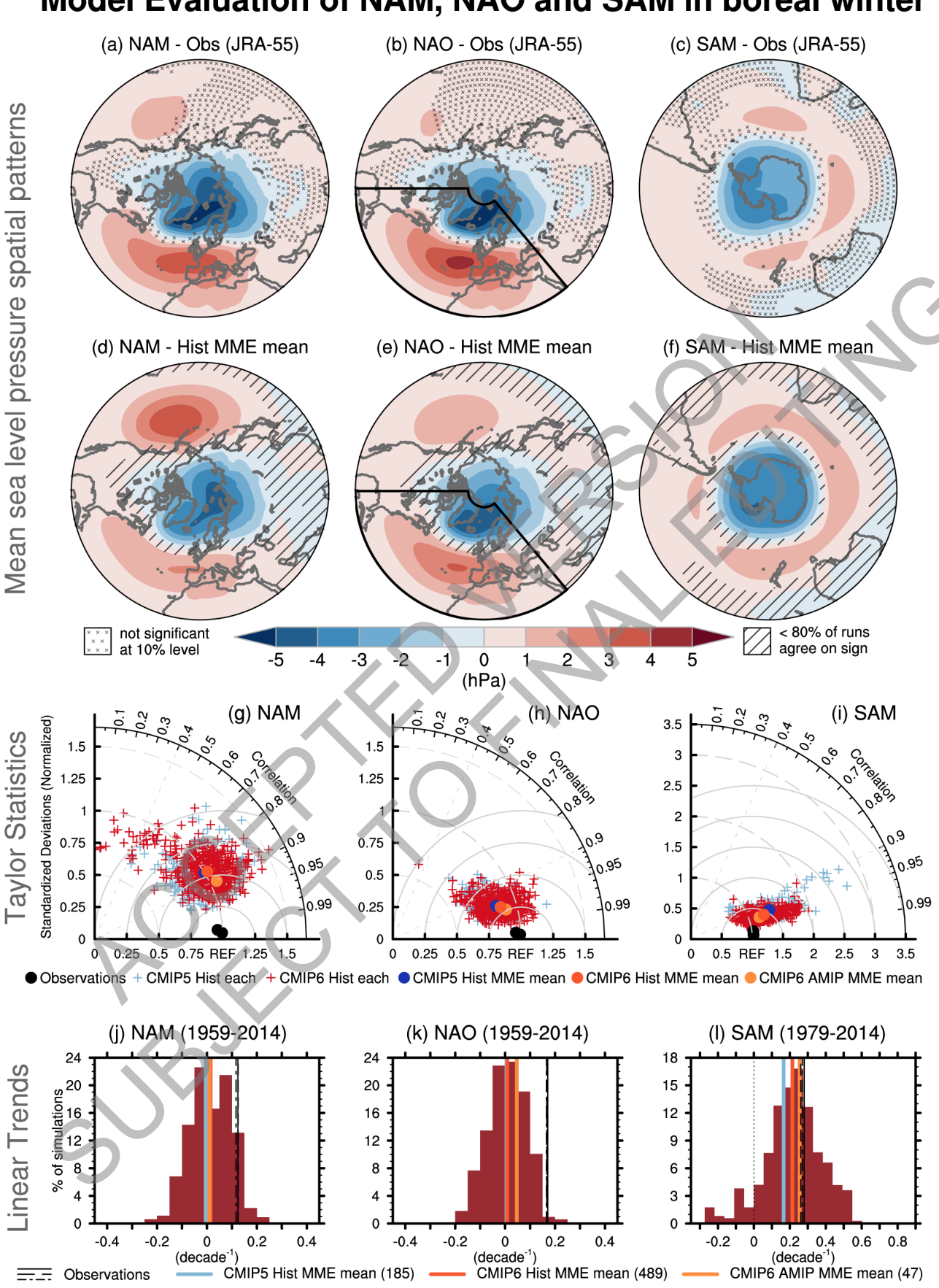


Figure 3.32: Relative change in the amplitude of the seasonal cycle of global land carbon uptake in the historical CMIP6 simulations from 1961-2014. Net biosphere production estimates from 19 CMIP6 models (red), the data-led reconstruction JMA-TRANSCOM (Maki et al., 2010; dotted) and atmospheric CO_2 seasonal cycle amplitude changes from observations (global as dashed line, Mauna Loa Observatory (MLO) (Dlugokencky et al., 2020) in bold black). Seasonal cycle amplitude is calculated using the curve fit algorithm package from the National Oceanic and Atmospheric Administration Earth System Research Laboratory (NOAA ESRL). Relative changes are referenced to the 1961-1970 mean and for short time series adjusted to have the same mean as the model ensemble in the last 10 years. Interannual variation was removed with a 9-year Gaussian smoothing. Shaded areas show the one sigma model spread (grey) for the CMIP6 ensemble and the one sigma standard deviation of the smoothing (red) for the CO_2 MLO observations. Inset: average seasonal cycle of ensemble mean net biosphere production and its one sigma model spread for 1961-1970 (orange dashed line, light orange shading) and 2005-2014 (solid green line, green shading). Further details on data sources and processing are available in the chapter data table (Table 3.SM.1).

ACCEPTED VERSION SUBJECT TO FINAL EDITING



ACCEPTED VERSION SUBJECT TO FINAL EDITING

Figure 3.33: Model evaluation of NAM, NAO and SAM in boreal winter. Regression of Mean Sea Level Pressure (MSLP) anomalies (in hPa) onto the normalized principal component (PC) of the leading mode of variability obtained from empirical orthogonal decomposition of the boreal winter (Dec.-Feb) MSLP poleward of 20ºN for the observed Northern Annular Mode (NAM, a), over 20ºN-80°N, 90°W-40°E for the North Atlantic Oscillation as shown by the black sector (NAO, b), and poleward of 20ºS for the Southern Annular Mode (SAM, c) for the JRA-55 reanalysis. Cross marks indicate regions where the anomalies are not significant at the 10% level based on t-test. The period used to calculate the NAO/NAM is 1958-2014 but 1979-2014 for the SAM. (d-f) Same but for the multi-model ensemble (MME) mean from CMIP6 historical simulations. Models are weighted in compositing to account for differences in their respective ensemble size. Diagonal lines stand for regions where less than 80% of the runs agree in sign. (g-i) Taylor diagram summarizing the representation of the modes in models and observations following Lee et al. (2019) for CMIP5 (light blue) and CMIP6 (red) historical runs. The reference pattern is taken from JRA-55 (a-c). The ratio of standard deviation (radial distance), spatial correlation (radial angle) and resulting root-mean-squared-errors (solid isolines) are given for individual ensemble members (crosses) and for other observational products (ERA5 and NOAA 20CRv3, black dots). Coloured dots stand for weighted multi-model mean statistics for CMIP5 (blue) and CMIP6 (light red) as well as for AMIP simulations from CMIP6 (orange). (j-l) Histograms of the trends built from all individual ensemble members and all the models (brown bars). Vertical lines in black show all the observational estimates. The orange, light-red, and light blue lines indicate the weighted multi-model mean of CMIP6 AMIP, CMIP6 and CMIP5 historical simulations, respectively. Further details on data sources and processing are available in the chapter data table (Table 3.SM.1).

ACCEPTED VERSION
SUBJECT TO FINAL EDITING

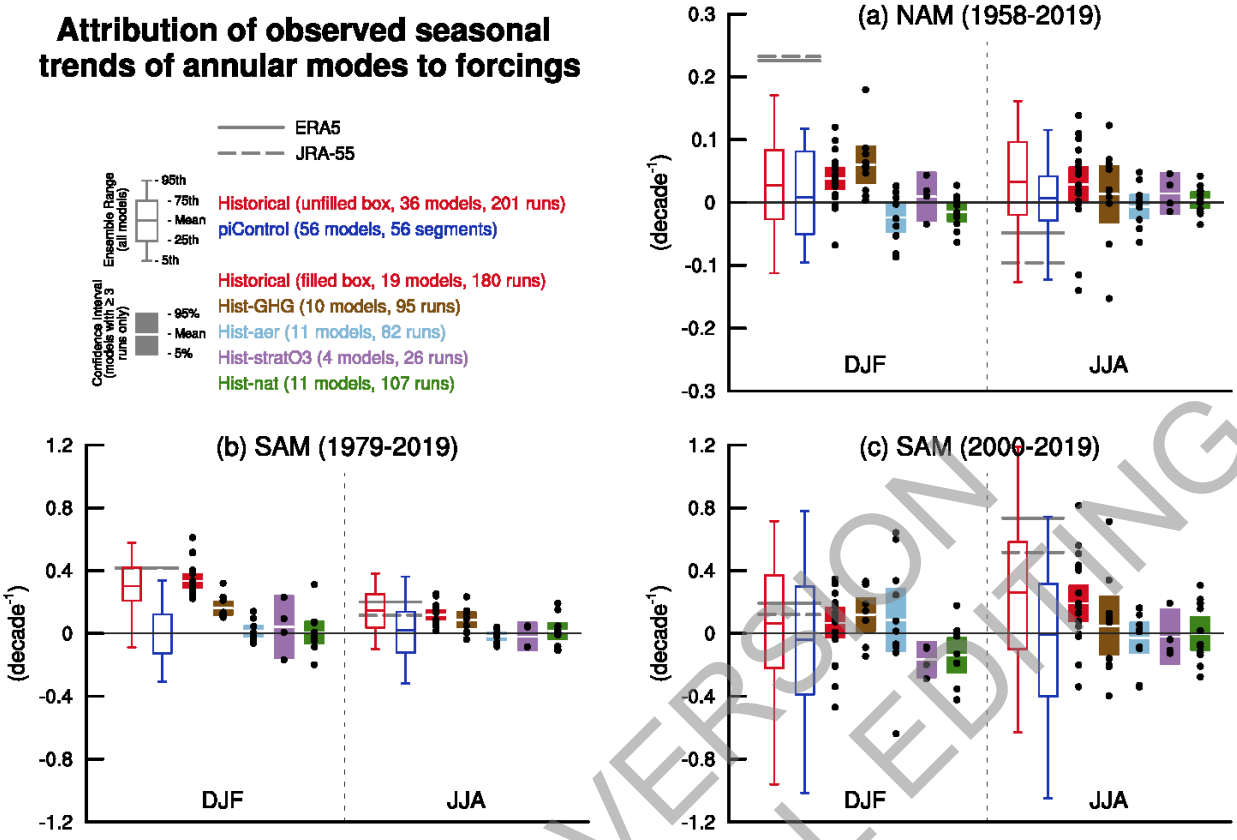


Figure 3.34: Attribution of observed seasonal trends in the annular modes to forcings. Simulated and observed trends in NAM indices over 1958-2019 (a) and in SAM indices over 1979-2019 (b) and over 2000-2019 (c) for boreal winter (December-February average; DJF) and summer (June-August average; JJA). The indices are based on the difference of the normalized zonally averaged monthly mean sea level pressure between 35ºN and 65ºN for the NAM and between 40ºS and 65ºS for the SAM as defined in Jianping and Wang (2003) and Gong and Wang (1999), respectively: the unit is decade^{-1}. Ensemble mean, interquartile ranges and 5th and 95th percentiles are represented by empty boxes and whiskers for pre-industrial control simulations and historical simulations. The number of ensemble members and models used for computing the distribution is given in the upper-left legend. Grey lines show observed trends from the ERA5 and JRA-55 reanalyses. Multi-model multi-member ensemble means of the forced component of the trends as well as their 5- 95% confidence intervals assessed from t-statistics, are represented by filled boxes, based on CMIP6 individual forcing simulations from DAMIP ensembles; greenhouse gases in brown, aerosols in light blue, stratospheric ozone in purple and natural forcing in green. Models with at least 3 ensemble members are used for the filled boxes, with black dots representing the ensemble means of individual models. Further details on data sources and processing are available in the chapter data table (Table 3.SM.1).

ACCEPTED VERSION SUBJECT TO FINAL EDITING

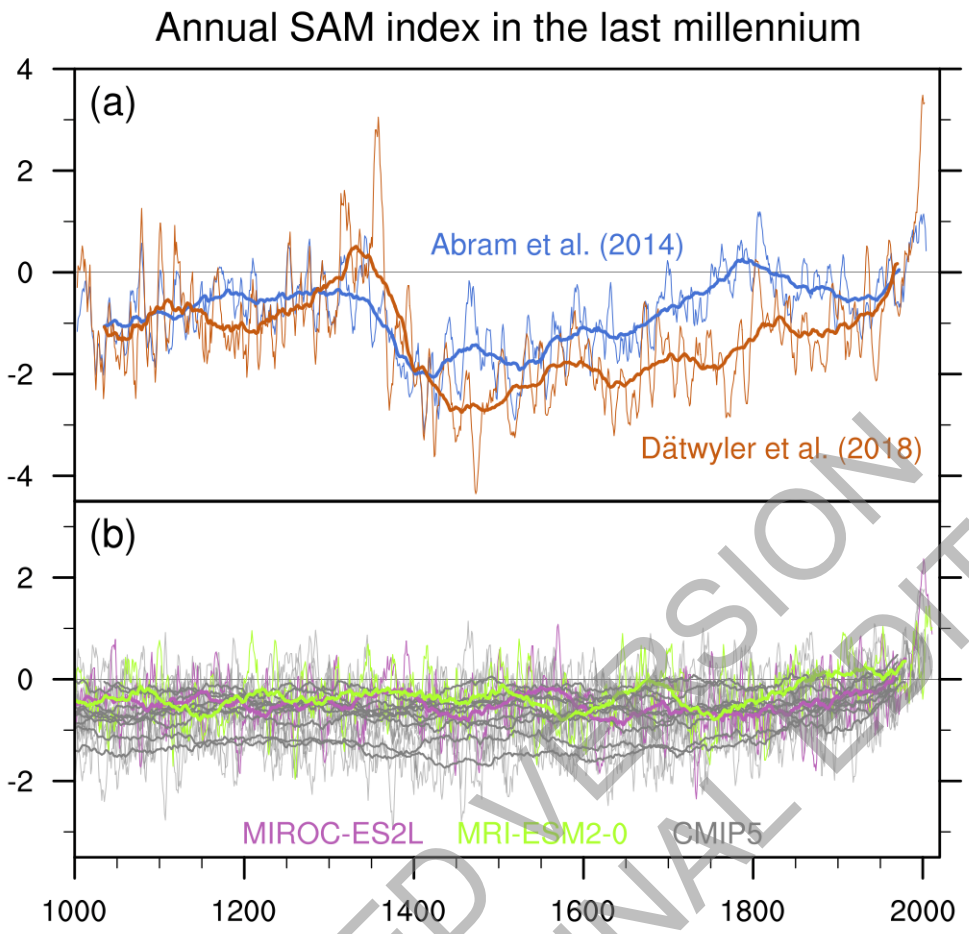


Figure 3.35: Southern Annular Mode (SAM) indices in the last millennium. (a) Annual SAM reconstructions by Abram et al. (2014) and Dätwyler et al. (2018). (b) The annual-mean SAM index defined by Gong and Wang (1999) in CMIP5 and CMIP6 Last Millennium simulations extended by historical simulations. All indices are normalized with respect to 1961-1990 means and standard deviations. Thin lines and thick lines show 7-year and 70-year moving averages, respectively. Further details on data sources and processing are available in the chapter data table (Table 3.SM.1).

ACCEPTED VERSION SUBJECT TO FINAL EDITING

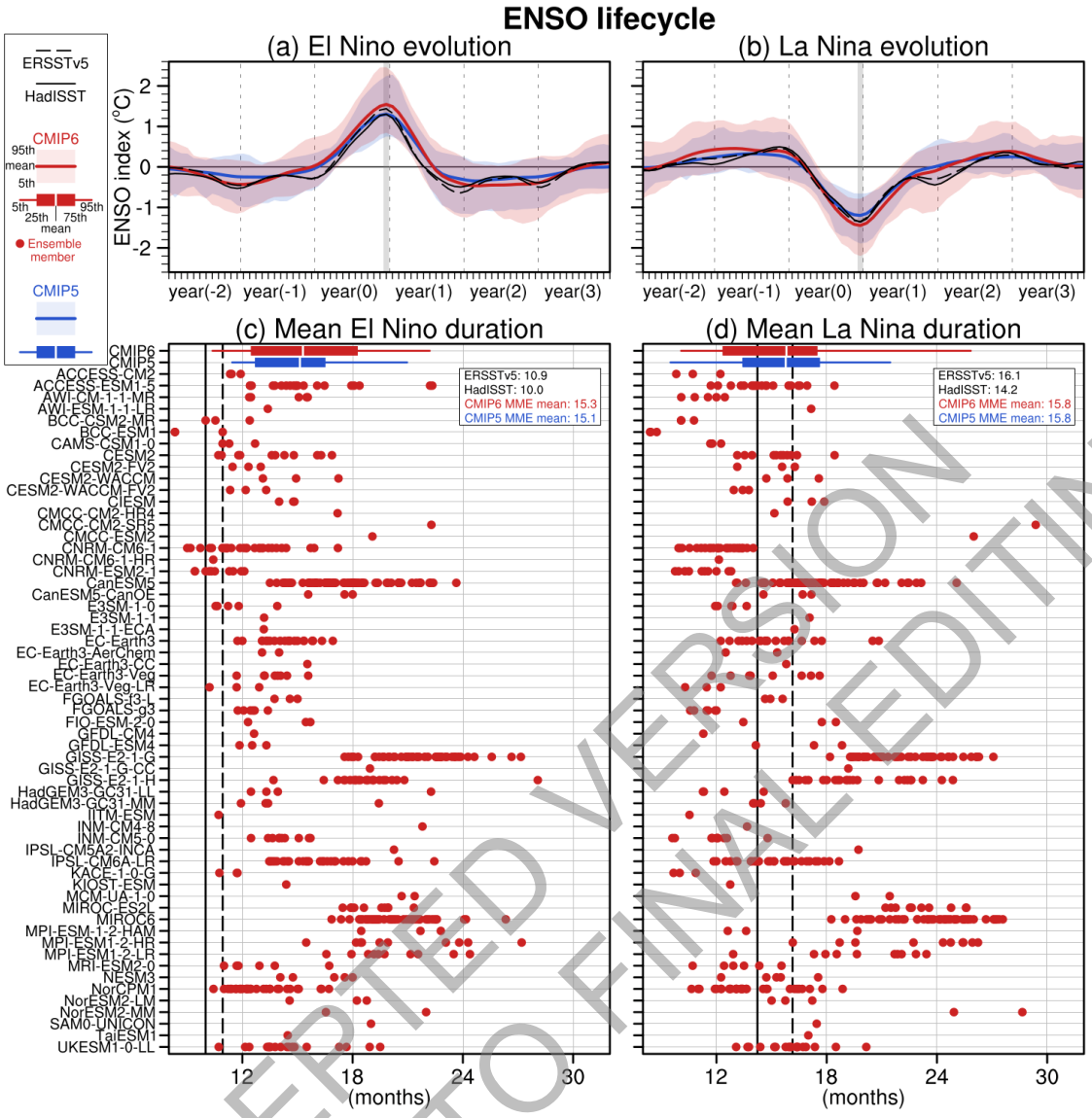


Figure 3.36: Life cycle of (left) El Niño and (right) La Niña events in observations (black) and historical simulations from CMIP5 (blue; extended with RCP4.5) and CMIP6 (red). An event is detected when the December ENSO index value in year zero exceeds 0.75 times its standard deviation for 1951-2010. (a, b) Composites of the ENSO index (ºC). The horizontal axis represents month relative to the reference December (the grey vertical bar), with numbers in parentheses indicating relative years. Shading and lines represent 5th-95th percentiles and multi-model ensemble means, respectively. (c, d) Mean durations (months) of El Niño and La Niña events defined as number of months in individual events for which the ENSO index exceeds 0.5 times its December standard deviation. Each dot represents an ensemble member from the model indicated on the vertical axis. The boxes and whiskers represent multi-model ensemble mean, interquartile ranges and 5th and 95th percentiles of CMIP5 and CMIP6. The CMIP5 and CMIP6 multi-model ensemble means and observational values are indicated at top right of each panel. The multi-model ensemble means and percentile values are evaluated after weighting individual members with the inverse of the ensemble size of the same model, so that individual models are equally weighted irrespective of their ensemble sizes. The ENSO index is defined as the SST anomaly averaged over the Niño 3.4 region (5ºS-5ºN, 170ºW-120ºW). All results are based on 5-month running mean SST anomalies with triangular-weights after linear detrending. Further details on data sources and processing are available in the chapter data table (Table 3.SM.1).

ACCEPTED VERSION SUBJECT TO FINAL EDITING

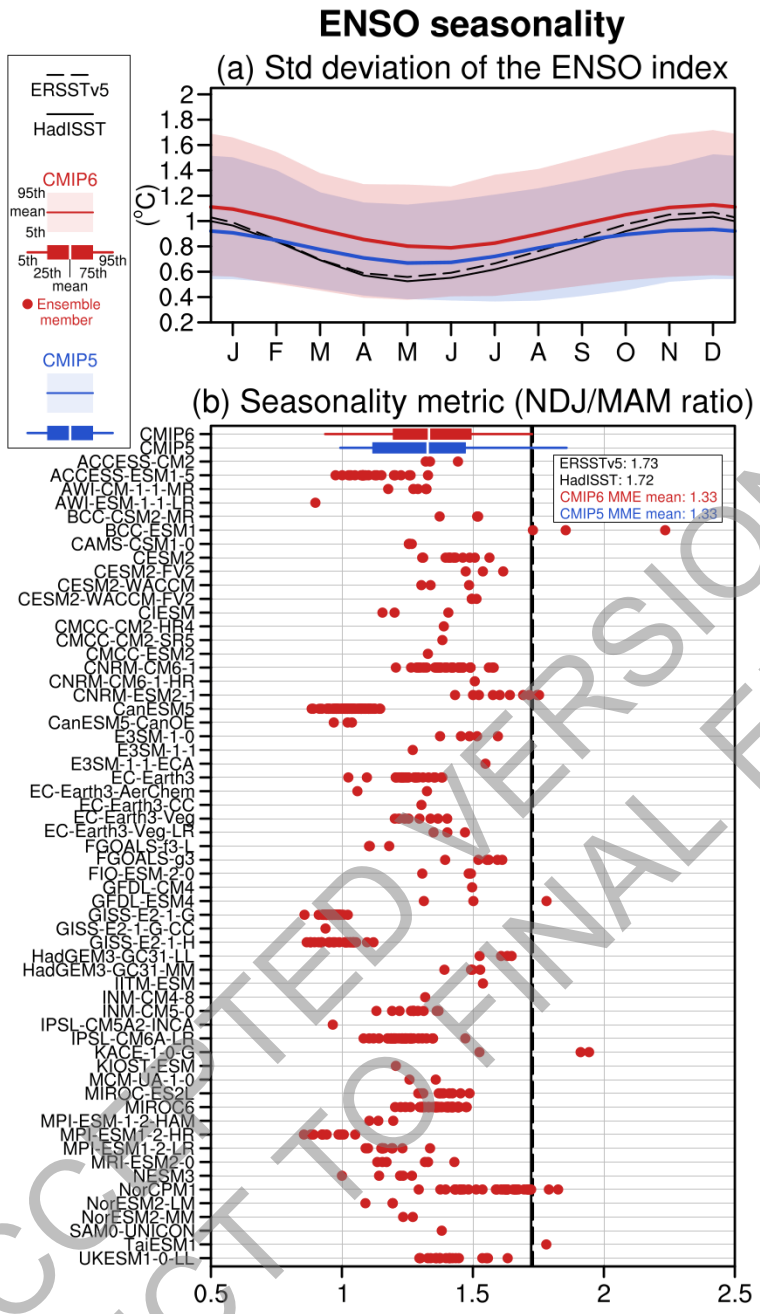


Figure 3.37: ENSO seasonality in observations (black) and historical simulations from CMIP5 (blue; extended with RCP4.5) and CMIP6 (red) for 1951-2010. (a) Climatological standard deviation of the monthly ENSO index (SST anomaly averaged over the Niño 3.4 region; °C). Shading and lines represent 5th-95th percentiles and multi-model ensemble means, respectively. (b) Seasonality metric, which is defined for each model and each ensemble member as the ratio of the ENSO index climatological standard deviation in November-January (NDJ) to that in March-May (MAM). Each dot represents an ensemble member from the model indicated on the vertical axis. The boxes and whiskers represent the multi-model ensemble mean, interquartile ranges and 5th and 95th percentiles of CMIP5 and CMIP6 individually. The CMIP5 and CMIP6 multi-model ensemble means and observational values are indicated at the top right of the panel. The multi-model ensemble means and percentile values are evaluated after weighting individual members with the inverse of the ensemble size of the same model, so that individual models are equally weighted irrespective of their ensemble sizes. All results are based on 5-month running mean SST anomalies with triangular-weights after linear detrending. Further details on data sources and processing are available in the chapter data table (Table 3.SM.1).

ACCEPTED VERSION SUBJECT TO FINAL EDITING

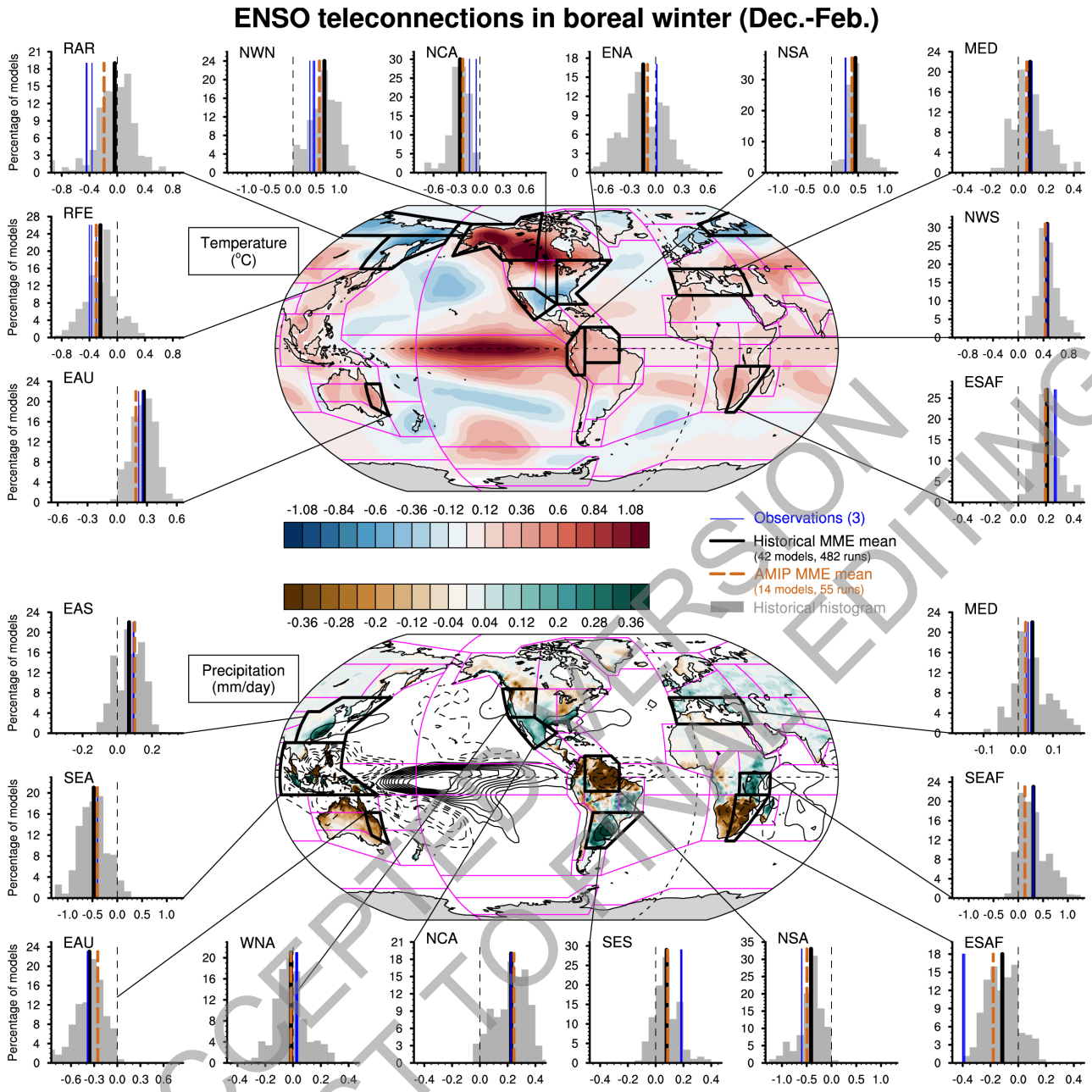


Figure 3.38: Model evaluation of ENSO teleconnection for 2m-temperature and precipitation in boreal winter (December-January-February). Teleconnections are identified by linear regression with the Niño 3.4 SST index based on ERSSTv5 during the period 1958-2014. Maps show observed patterns for temperature from the Berkeley Earth dataset over land and from ERSSTv5 over ocean (ºC, top) and for precipitation from GPCC over land (shading, mm day^{-1}) and GPCP worldwide (contours, period: 1979-2014). Distributions of regression coefficients (grey histograms) are provided for a subset of AR6 reference regions defined in Atlas (Section A1.3) for temperature (top) and precipitation (bottom). All fields are linearly detrended prior to computation. Multi-model multi-member ensemble means are indicated by thick vertical black lines. Blue vertical lines show three observational estimates of temperature, based on Berkeley Earth, GISTEMP and CRUTS datasets, and two observational estimates of precipitation, based on GPCC and CRUTS datasets. Further details on data sources and processing are available in the chapter data table (Table 3.SM.1).

ACCEPTED VERSION SUBJECT TO FINAL EDITING

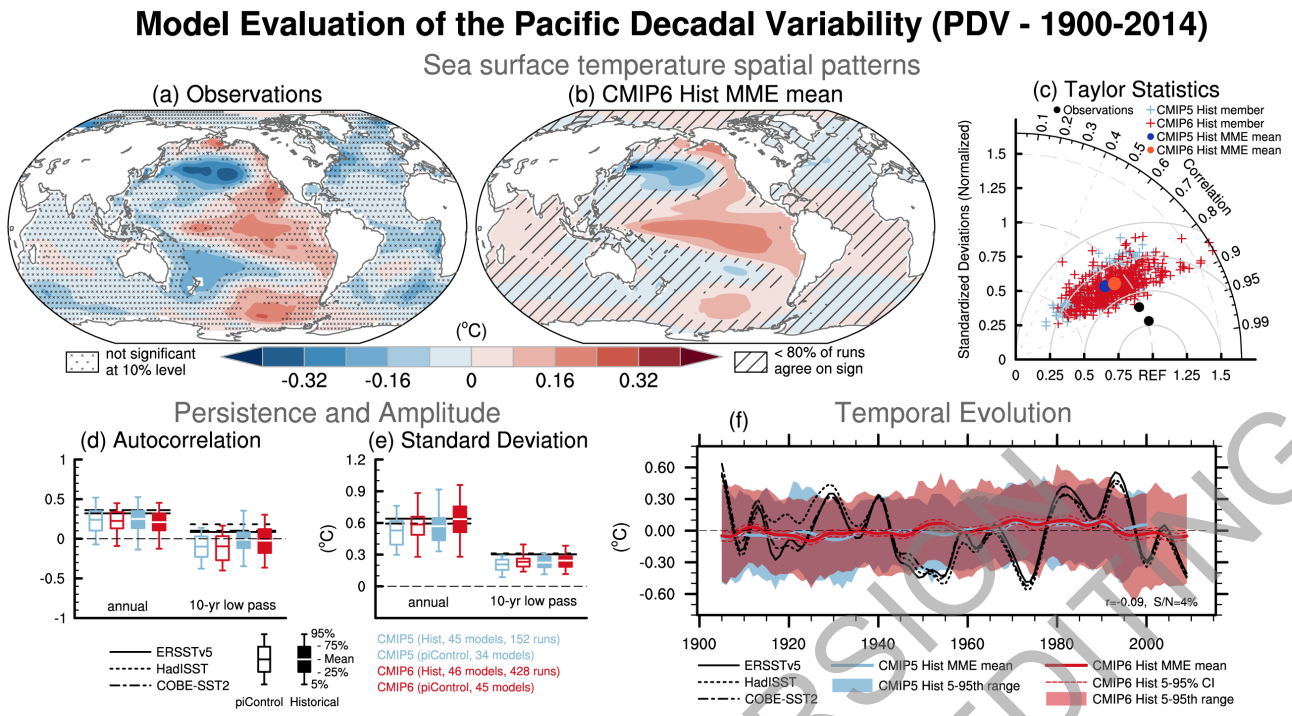


Figure 3.39: Model evaluation of the Pacific Decadal Variability (PDV). (a, b) Sea surface temperature (SST) anomalies (ºC) regressed onto the Tripole Index (TPI; Henley et al., 2015) for 1900-2014 in (a) ERSSTv5 and (b) CMIP6 multi-model ensemble (MME) mean composite obtained by weighting ensemble members by the inverse of the model ensemble size. A 10-year low-pass filter was applied beforehand. Cross marks in (a) represent regions where the anomalies are not significant at the 10% level based on t-test. Diagonal lines in (b) indicate regions where less than 80% of the runs agreein sign. (c) A Taylor diagram summarizing the representation of the PDV pattern in CMIP5 (each a cross in light blue, and the weighted multi-mode mean as a dot in dark blue), CMIP6 (each ensemble member is shown as a cross in red, weighted multi-model mean as a dot in orange) and observations over [40ºS-60ºN, 110ºE-70ºW]. The reference pattern is taken from ERSSTv5 and black dots indicate other observational products (HadISSTv1 and COBE-SST2). (d) Autocorrelation of unfiltered annual TPI at lag 1 year and 10-year low-pass filtered TPI at lag 10 years for observations over 1900-2014 (horizontal lines) and 115-year chunks of pre-industrial control simulations (open boxes) and individual historical simulations over 1900-2014 (filled boxes) from CMIP5 (blue) and CMIP6 (red). (e) As in (d), but standard deviation of the unfiltered and filtered TPI (ºC). Boxes and whiskers show weighted multi-model mdeanmean, interquartile ranges and 5th and 95th percentiles. (f) Time series of the 10-year low-pass filtered TPI (ºC) in ERSSTv5, HadISSTv1 and COBE-SST2 observational estimates (black) and CMIP5 and CMIP6 historical simulations. The thick red and light blue lines are the weighted multi-model mean for the historical simulations in CMIP5 and CMIP6, respectively, and the envelopes represent the 5th-95th percentile range across ensemble members. The 5-95% confidence interval for the CMIP6 multi-model mean is given in thin dashed lines. Further details on data sources and processing are available in the chapter data table (Table 3.SM.1).

ACCEPTED VERSION SUBJECT TO FINAL EDITING

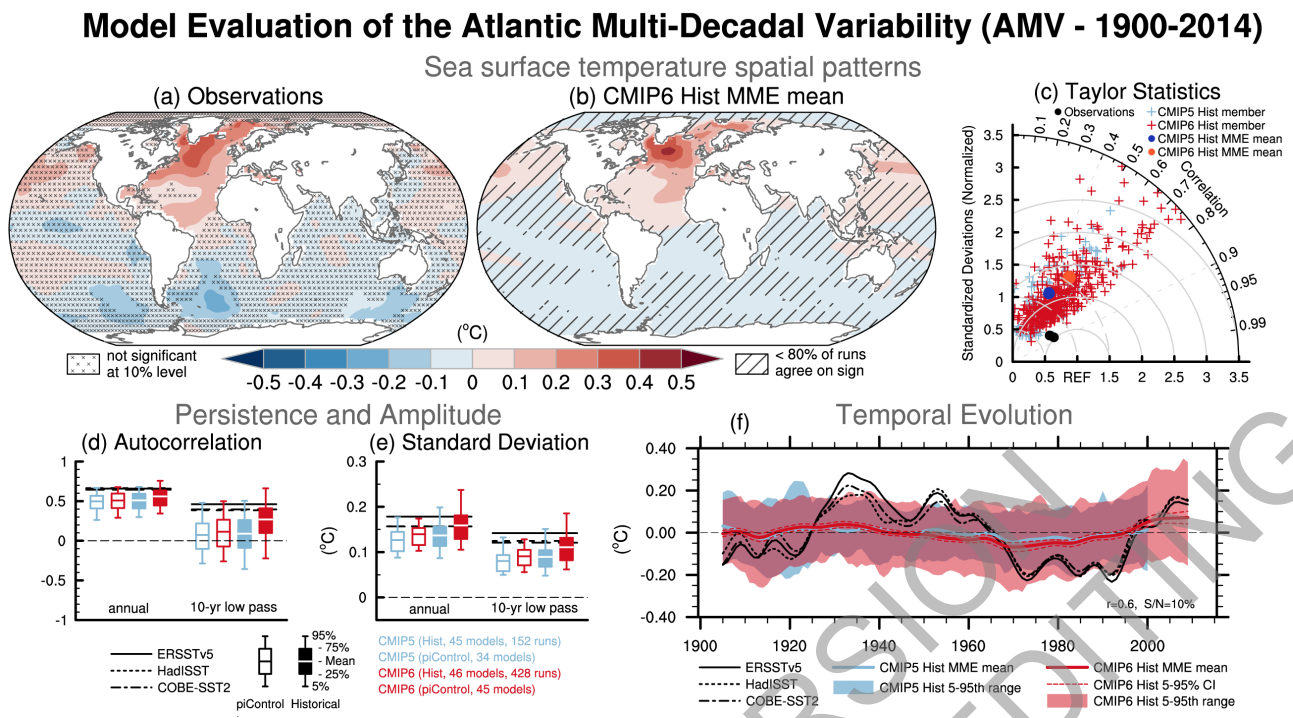


Figure 3.40: Model evaluation of Atlantic Multi-decadal Variability (AMV). (a, b) Sea surface temperature (SST) anomalies (ºC) regressed onto the AMV index defined as the 10-year low-pass filtered North Atlantic (0º-60°N, 80°W-0°E) area-weighted SST* anomalies over 1900-2014 in (a) ERSSTv5 and (b) the CMIP6 multi-model ensemble (MME) mean composite obtained by weighting ensemble members by the inverse of each model's ensemble size. The asterisk denotes that the global mean SST anomaly has been removed at each time step of the computation. Cross marks in (a) represent regions where the anomalies are not significant at the 10% level based on a t-test. Diagonal lines in (b) show regions where less than 80% of the runs agree in sign. (c) A Taylor diagram summarizing the representation of the AMV pattern in CMIP5 (each member is shown as a cross in light blue, and the weighted multi-model mean is shown as a dot in dark blue), CMIP6 (each member is shown as a cross in red, and the weighted multi-model mean is shown as a dot in orange) and observations over [0º-60°N, 80°W-0°E]. The reference pattern is taken from ERSSTv5 and black dots indicate other observational products (HadISSTv1 and COBE-SST2). (d) Autocorrelation of unfiltered annual AMV index at lag 1 year and 10-year low-pass filtered AMV index at lag 10 years for observations over 1900-2014 (horizontal lines) and 115-year chunks of pre-industrial control simulations (open boxes) and individual historical simulations over 1900-2014 (filled boxes) from CMIP5 (blue) and CMIP6 (red). (e) As in (d), but showing standard deviation of the unfiltered and filtered AMV indices (ºC). Boxes and whiskers show the weighted multi-model mean, interquartile ranges and 5th and 95th percentiles. (f) Time series of the AMV index (ºC) in ERSSTv5, HadISSTv1 and COBE-SST2 observational estimates (black) and CMIP5 and CMIP6 historical simulations. The thick red and light blue lines are the weighted multi-model mean for the historical simulations in CMIP5 and CMIP6, respectively, and the envelopes represent the 5th-95th percentile range obtained from all ensemble members. The 5- 95% confidence interval for the CMIP6 multi-model mean is shown by the thin dashed line. Further details on data sources and processing are available in the chapter data table (Table 3.SM.1).

ACCEPTED VERSION SUBJECT TO FINAL EDITING

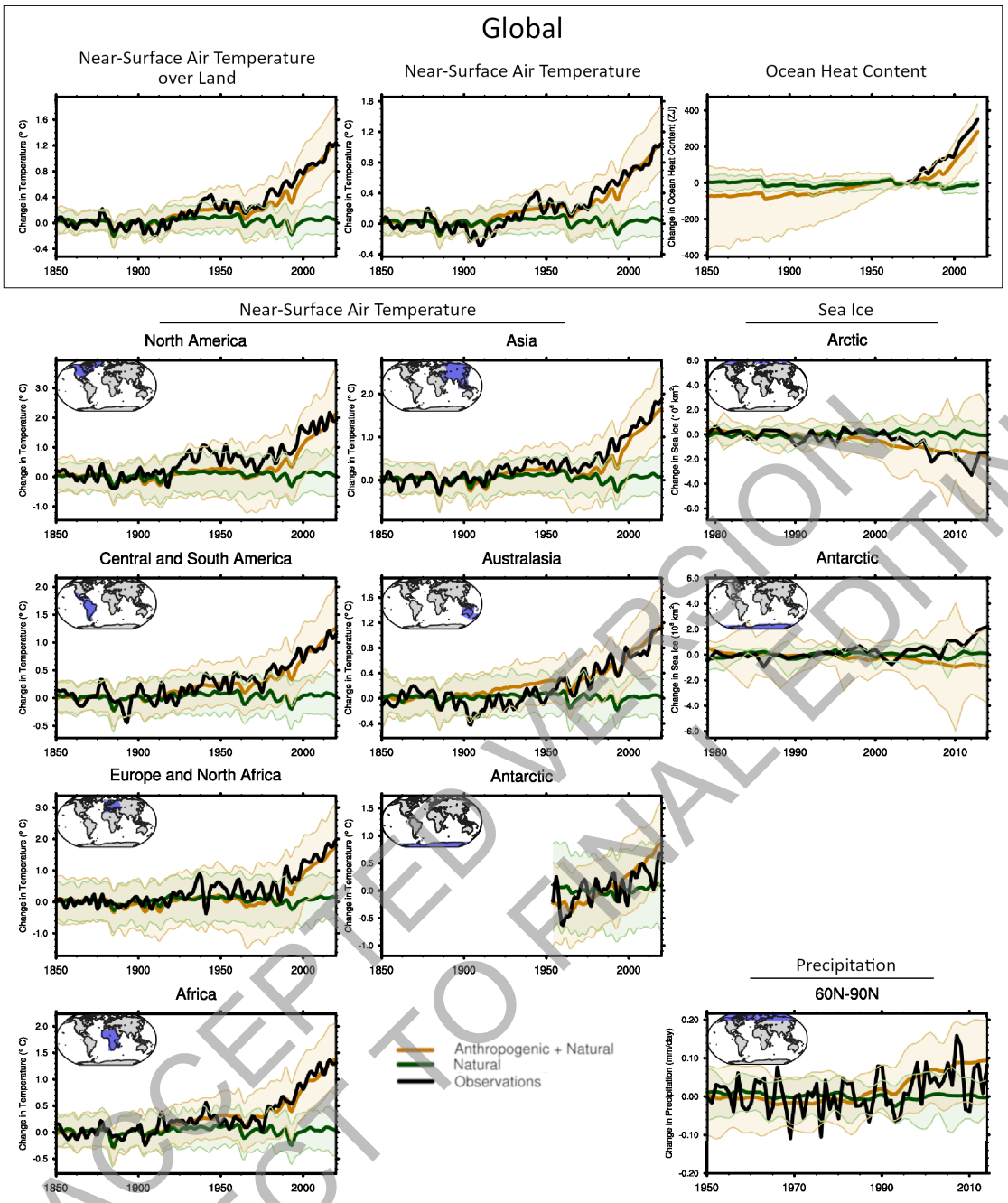
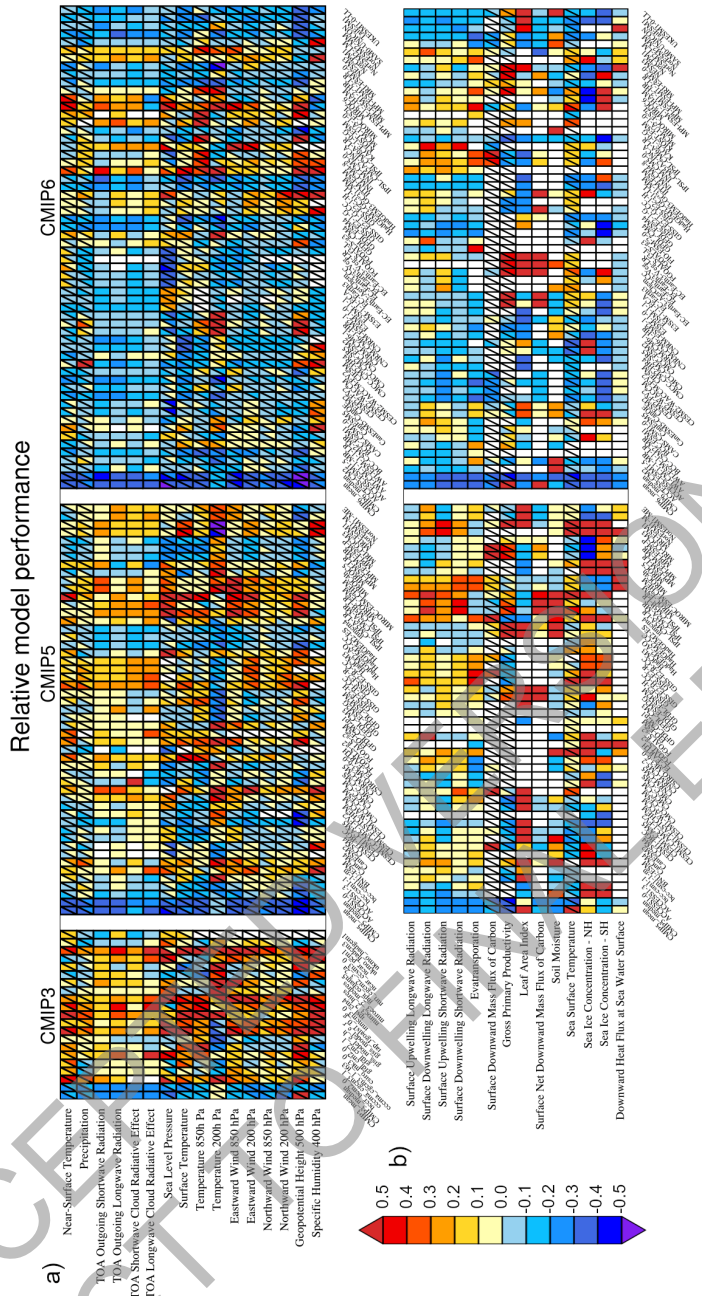


Figure 3.41: Summary figure showing simulated and observed changes in key large-scale indicators of climate change across the climate system, for continental, ocean basin and larger scales. Black lines show observations, brown lines and shading show the multi-model mean and 5th-95th percentile ranges for CMIP6 historical simulations including anthropogenic and natural forcing, and blue lines and shading show corresponding ensemble means and 5th-95th percentile ranges for CMIP6 natural-only simulations. Temperature time series are as in Figure 3.9, but with smoothing using a low pass filter. Precipitation time series are as in Figure 3.15 and ocean heat content as in Figure 3.26. Further details on data sources and processing are available in the chapter data table (Table 3.SM.1).

ACCEPTED VERSION SUBJECT TO FINAL EDITING



ACCEPTED SUBJECT TO FINAL EDITING

Figure 3.42: Relative space-time root-mean-square deviation (RMSD) calculated from the climatological seasonal cycle of the CMIP simulations (1980-1999) compared to observational datasets. (a) CMIP3, CMIP5, and CMIP6 for 16 atmospheric variables (b) CMIP5 and CMIP6 for 10 land variables and four ocean/sea-ice variables. A relative performance measure is displayed, with blue shading indicating better and red shading indicating worse performance than the median of all model results. A diagonal split of a grid square shows the relative error with respect to the reference data set (lower right triangle) and an additional data set (upper left triangle). Reference/additional datasets are from top to bottom in (a): ERA5/NCEP, GPCP-SG/GHCN, CERES-EBAF/-, CERES-EBAF/-, CERES-EBAF/-, CERES-EBAF/-, JRA-55/ERA5, ESACCI-SST/HadISST, ERA5/NCEP, ERA5/NCEP, ERA5/NCEP, ERA5/NCEP, ERA5/NCEP, ERA5/NCEP, AIRS/ERA5, ERA5/NCEP and in (b): CERES-EBAF/-, CERES-EBAF/-, CERES-EBAF/-, CERES-EBAF/-, LandFlux-EVAL/-, Landschuetzer2016/ JMA-TRANSCOM; MTE/FLUXCOM, LAI3g/-, JMA-TRANSCOM, ESACCI-SOILMOISTURE/-, HadISST/ATSR, HadISST/-, HadISST/-, ERA-Interim/-. White boxes are used when data are not available for a given model and variable. Figure is updated and expanded from Bock et al. (2020), their Figure 5 CC BY4.0 https://creativecommons.org/licenses/by/4.0/. Further details on data sources and processing are available in the chapter data table (Table 3.SM.1).

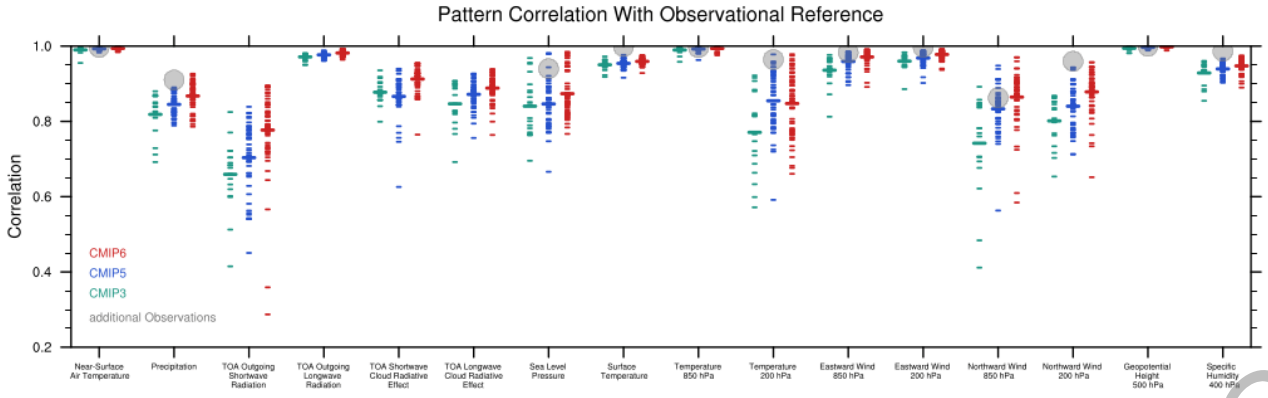


Figure 3.43: Centred pattern correlations between models and observations for the annual mean climatology over the period 1980–1999. Results are shown for individual CMIP3 (cyan), CMIP5 (blue) and CMIP6 (red) models (one ensemble member from each model is used) as short lines, along with the corresponding ensemble averages (long lines). Correlations are shown between the models and the primary reference observational data set (from left to right: ERA5, GPCP-SG, CERES-EBAF, CERES-EBAF, CERES-EBAF, CERES-EBAF, JRA-55, ESACCI-SST, ERA5, ERA5, ERA5, ERA5, ERA5, ERA5, AIRS, ERA5). In addition, the correlation between the primary reference and additional observational data sets (from left to right: NCEP, GHCN, -, -, -, -, ERA5, HadISST, NCEP, NCEP, NCEP, NCEP, NCEP, NCEP, ERA5, NCEP) are shown (solid grey circles) if available. To ensure a fair comparison across a range of model resolutions, the pattern correlations are computed after regridding all datasets to a resolution of 4º in longitude and 5º in latitude. Figure is updated and expanded from Bock et al. (2020), their Figure 7 CC BY4.0 https://creativecommons.org/licenses/by/4.0/. Further details on data sources and processing are available in the chapter data table (Table 3.SM.1

ACCEPTED VERSION SUBJECT TO FINAL EDITING

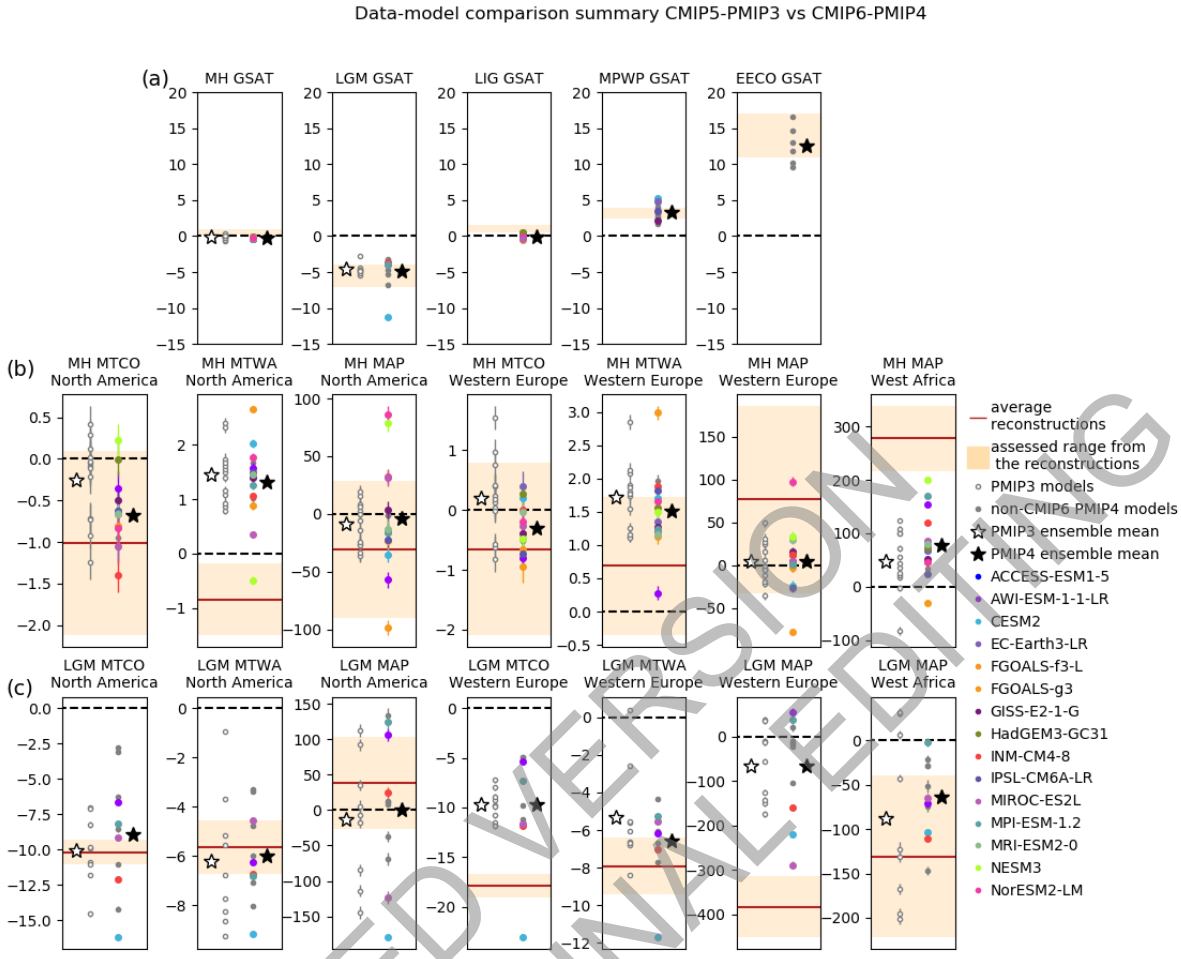
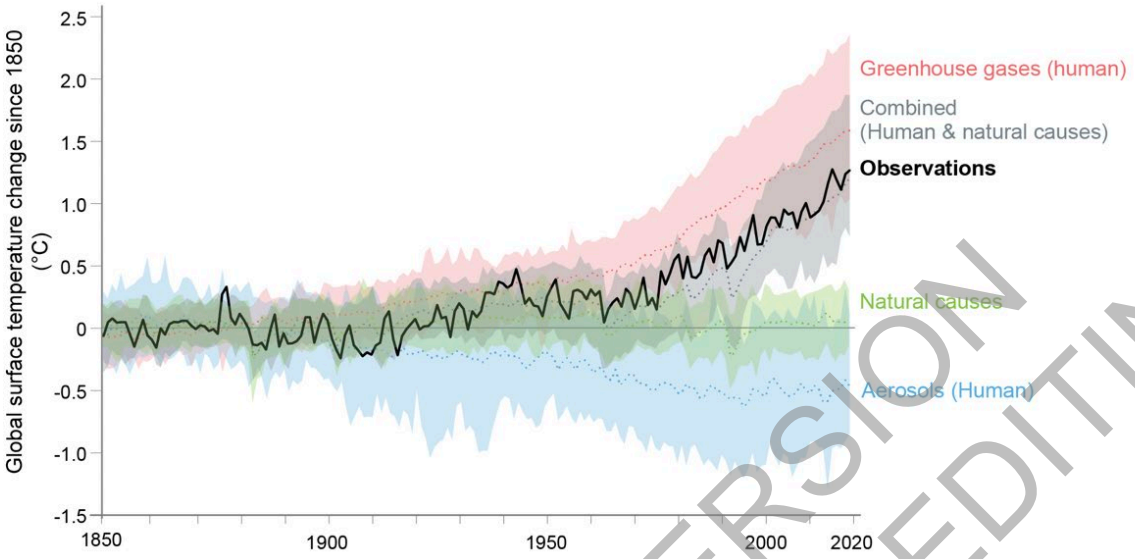


Figure 3.44: Multivariate synopsis of paleoclimate model results compared to observational references. Data-model comparisons for GSAT anomalies for five PMIP4 periods and for regional features for the (b) mid-Holocene and (c) LGM periods, for PMIP3 and PMIP4 models. The results from the CMIP6 models are specified as coloured dots. In (a) the light orange shading shows the *very likely* assessed ranges presented in Section 2.3.1.1. In (b) and (c), the regions and variables are defined as follows: North America (20-50°N, 140-60°W), Western Europe (35-70°N, 10°W-30°E) and West Africa (0°-30°N, 10°W-30°E); MTCO: Mean Temperature of the Coldest Month (°C), MTWA: Mean Temperature of the Warmest Month (°C), MAP: Mean Annual Precipitation (mm/year). In (b) and (c) the ranges shown for the reconstructions (Bartlein et al. (2011) for MH and Cleator et al. (2020) for LGM) are based on the standard error given at each site: the average and associated standard deviation over each area is obtained by computing 1000 times the average of randomly drawn values from the Gaussian distributions defined at each site by the reconstruction mean and standard error; the light orange colour shows the ± 1 standard deviation of these 1000 estimates. The dots on (b) and (c) show the average of the model output for grid points for which there are reconstructions. The ranges for the model results are based on an ensemble of 1000 averages over 50 years randomly picked in the model output time series for each region and each variable: the mean ± one standard deviation is plotted for each model. Figure is adapted from Brierley et al. (2020), their Figure S3 for the mid-Holocene and from Kageyama et al. (2021), their Figure 12 for the LGM. Further details on data sources and processing are available in the chapter data table (Table 3.SM.1).

ACCEPTED VERSION SUBJECT TO FINAL EDITING

FAQ 3.1: **How do we know humans are causing climate change?**

Observed warming (1850-2018) is only reproduced in simulations including human influence.

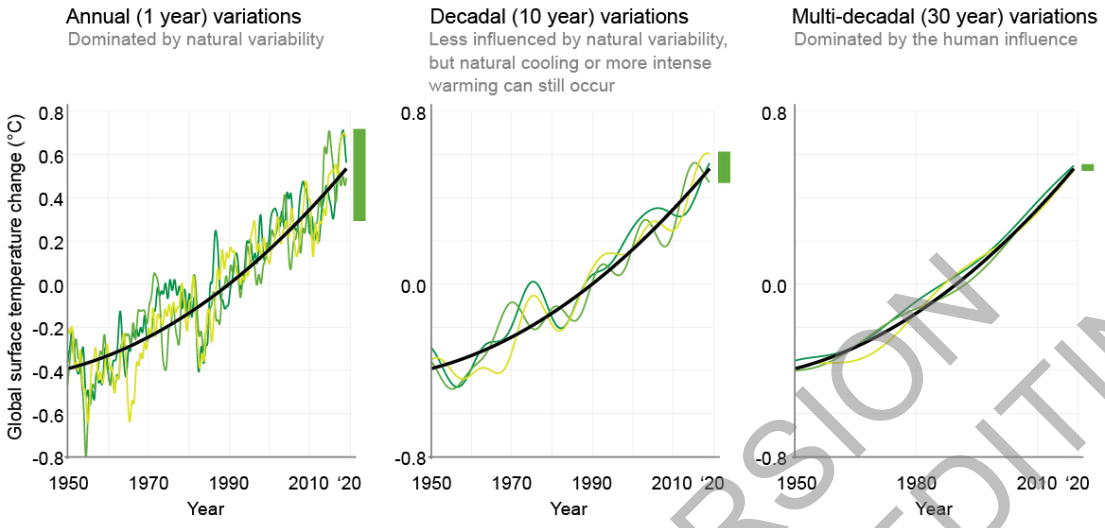


FAQ 3.1, Figure 1: Observed warming (1850-2018) is only reproduced in simulations including human influence. Global surface temperature changes in observations, compared to climate model simulations of the response to all human and natural forcings (grey band), greenhouse gases only (red band), aerosols and other human drivers only (blue band) and natural forcings only (green band). Solid coloured lines show the multi-model mean, and coloured bands show the 5–95% range of individual simulations.

ACCEPTED VERSION
SUBJECT TO FINAL EDITING

FAQ 3.2 **What is natural variability and how has it influenced recent climate changes?**

Natural variability can alter global temperature over short time scales (1 year to ~2 decades) but it has a minimal influence on longer time scales. Since 1850, **natural variability** ( ) has caused between -0.23°C and 0.23°C of global temperature change, compared to the warming of about 1.1°C **observed** ( ) over that period.

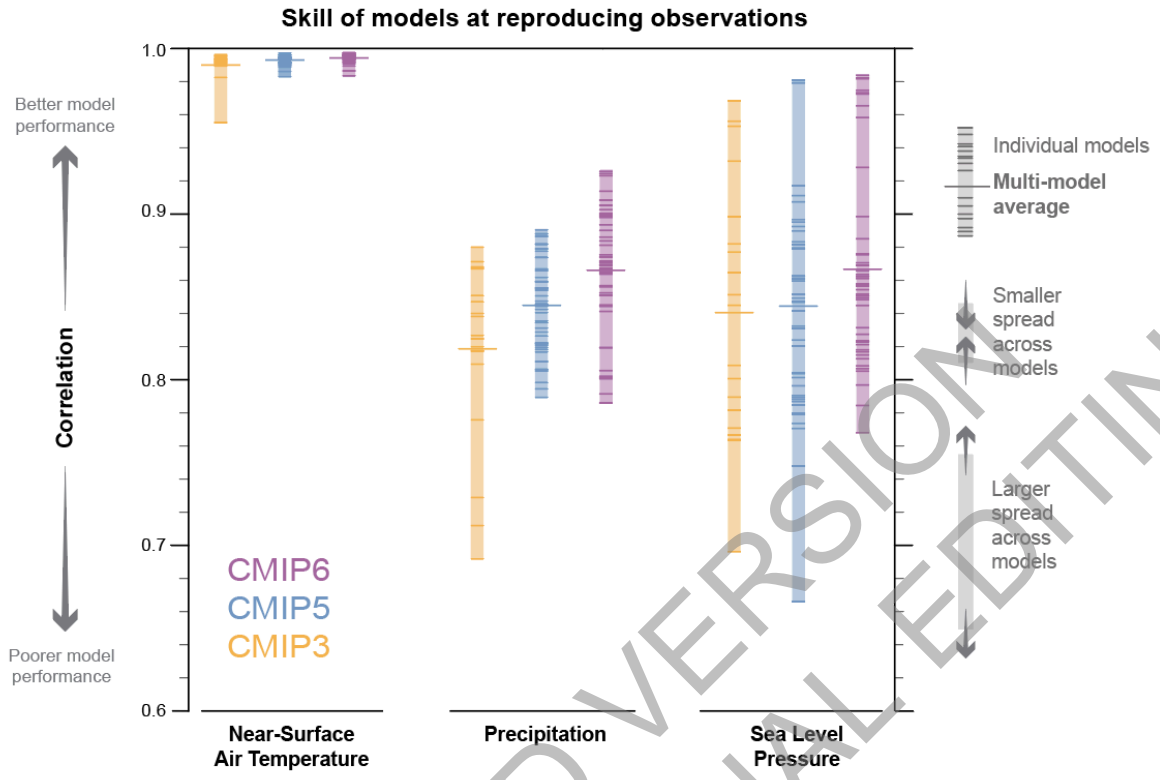


FAQ 3.2, Figure 1: Annual (left), decadal (middle) and multi-decadal (right) variations in average global surface temperature. The thick black line is an estimate of the human contribution to temperature changes, based on climate models, whereas the green lines show the combined effect of natural variations and human-induced warming, different shadings of green represent different simulations, which can be viewed as showing a range of potential pasts. The influence of natural variability is shown by the green bars, and it decreases with longer time scales. The data is sourced from the CESM1 large ensemble.

ACCEPTED VERSION
SUBJECT TO FINAL EDITING

FAQ 3.3: **Are Climate Models Improving?**

Yes, climate models have improved with increasing computer power and better understanding of climate processes.



FAQ 3.3, Figure 1: Pattern correlations between models and observations of three different variables: surface air temperature, precipitation and sea level pressure. Results are shown for the three most recent generations of models, from the Coupled Model Intercomparison Project (CMIP): CMIP3 (orange), CMIP5 (blue) and CMIP6 (purple). Individual model results are shown as short lines, along with the corresponding ensemble average (long line). For the correlations the yearly averages of the models are compared with the reference observations for the period 1980-1999, with 1 representing perfect similarity between the models and observations. CMIP3 simulations performed in 2004-2008 were assessed in the IPCC Fourth Assessment, CMIP5 simulations performed in 2011-2013 were assessed in the IPCC Fifth Assessment, and CMIP6 simulations performed in 2018-2021 are assessed in this report.

ACCEPTED VERSION SUBJECT TO FINAL EDITING

Chapter 3: Human influence on the climate system - Supplementary Material

Coordinating Lead Authors:
Veronika Eyring (Germany) and Nathan P. Gillett (Canada)

Lead Authors:
Krishna M. Achuta Rao (India), Rondrotiana Barimalala (South Africa/Madagascar), Marcelo Barreiro Parrillo (Uruguay), Nicolas Bellouin (United Kingdom/France), Christophe Cassou (France), Paul J. Durack (United States of America/Australia), Yu Kosaka (Japan), Shayne McGregor (Australia), Seung-Ki Min (Republic of Korea), Olaf Morgenstern (New Zealand/Germany), Ying Sun (China)

Contributing Authors:
Lisa Bock (Germany), Elizaveta Malinina (Canada/Russian Federation), Guðfinna Aðalgeirsdóttir (Iceland), Jonathan L. Bamber (United Kingdom), Chris Brierley (United Kingdom), Lee de Mora (United Kingdom), John P. Dunne (United States of America), John C. Fyfe (Canada), Peter J. Gleckler (United States of America), Peter Greve (Austria/Germany), Lukas Gudmundsson (Switzerland/Germany, Iceland), Karsten Haustein (United Kingdom, Germany /Germany), Ed Hawkins (United Kingdom), Benjamin J. Henley (Australia), Marika M. Holland (United States of America), Chris Huntingford (United Kingdom), Colin Jones (United Kingdom), Masa Kageyama (France), Rémi Kazeroni (Germany/France), Yeon-Hee Kim (Republic of Korea), Charles Koven (United States of America), Gerhard Krinner (France/Germany, France), Eunice Lo (United Kingdom/China), Daniel J. Lunt (United Kingdom), Sophie Nowicki (United States of America/France, United States of America), Adam S. Phillips (United States of America), Valeriu Predoi (United Kingdom), Krishnan Raghavan (India), Malcolm J. Roberts (United Kingdom), Jon Robson (United Kingdom), Lucas Ruiz (Argentina), Jean-Baptiste Sallée (France), Benjamin D. Santer (United States of America), Andrew P. Schurer (United Kingdom), Jessica Tierney (United States of America), Blair Trewin (Australia), Katja Weigel (Germany), Xuebin Zhang (Canada), Anni Zhao (United Kingdom/China), Tianjun Zhou (China)

Review Editors:
Tomas Halenka (Czech Republic), Jose A. Marengo Orsini (Brazil/Peru), Daniel Mitchell (United Kingdom)

Chapter Scientists:
Lisa Bock (Germany), Elizaveta Malinina (Canada/Russian Federation)

This Supplementary Material should be cited as:
Eyring, V., N. P. Gillett, K. M. Achuta Rao, R. Barimalala, M. Barreiro Parrillo, N. Bellouin, C. Cassou, P. J. Durack, Y. Kosaka, S. McGregor, S. Min, O. Morgenstern, Y. Sun, 2021, Human Influence on the Climate System Supplementary Material. In: *Climate Change 2021: The Physical Science Basis. Contribution of Working Group I to the Sixth Assessment Report of the Intergovernmental Panel on Climate Change* [Masson-Delmotte, V., P. Zhai, A. Pirani, S. L. Connors, C. Péan, S. Berger, N. Caud, Y. Chen, L. Goldfarb, M. I. Gomis, M. Huang, K. Leitzell, E. Lonnoy, J. B. R. Matthews, T. K. Maycock, T. Waterfield, O. Yelekçi, R. Yu and B. Zhou (eds.)]. Available from https://ipcc.ch/static/ar6/wg1.

Date: August 2021

This document is subject to copy-editing, corrigenda and trickle backs.

ACCEPTED VERSION SUBJECT TO FINAL EDITING

Table of Contents

3.SM.1 Data Table 3

References 22

ACCEPTED VERSION
SUBJECT TO FINAL EDITING

3.SM.1 Data Table

[START TABLE 3.SM.1 HERE]

Table 3.SM.1: Input Data Table. Input datasets and code used to create chapter figures

Figure number / Table number / Chapter section (for calculations)	Dataset / Code name	Type	Filename / Specificities	License type	Dataset / Code citation	Dataset / Code URL	Related publications
Figure 3.1	-	-	-	-	-	-	-
Figure 3.2	Cleator2020 (land-based reconstructions of surface temperature anomalies)	Input dataset	LGM_reconstruction.csv	Creative Commons Attribution 4.0 International	http://dx.doi.org/10.17864/1947.244	https://researchdata.reading.ac.uk/244/1/LGM_reconstruction.csv	(Cleator et al., 2020)
	Tierney2019 (land-based reconstructions of surface temperature anomalies)	Input dataset	Tierney2020_ProxyData_5x5_deltaSST.nc	Creative Commons Attribution 4.0 International		https://doi.pangaea.de/10.1594/PANGAEA.920596	(Tierney et al., 2020)
	PAGES2k temperature reconstruction	Input dataset	BHM.txt, CPS.txt, DA.txt, M08.txt, OIE.txt, PAI.txt, PCR.txt		doi.org/10.6084/m9.figshare.c.4507043.v2	https://figshare.com/collections/Global_mean_temperature_reconstructions_over_the_Common_Era/4507043	(PAGES 2k Consortium, 2019)
	Mid-Piacenzian Warm Period	Input dataset	Data_for_1a_1c_3a in supplementary information		doi: 10.5194/cp-16-2095-2020	https://doi.org/10.5194/cp-16-2095-2020	(Haywood et al., 2020)
	Figure 3.2c Code	Code				https://github.com/aschurer/IPCC_Fig3.2c	
Figure 3.3	ERA5 Reanalysis Monthly Means	Input dataset	era5_2m_temperature_*_monthly.nc		doi:10.24381/cds.68d2bb30	https://cds.climate.copernicus.eu/cdsapp#!/dataset/rean	(Hersbach et al., 2020)

ACCEPTED VERSION SUBJECT TO FINAL EDITING

						alysis-era5-land-monthly-means	
	Figure 3.3 Code	Code				Link to ESMValTool	(Bock et al., 2020)
Figure 3.4	HadCRUT5	Input dataset	HadCRUT.5.0.1.0.analysis.anomalies.ensemble_mean.nc			https://crudata.uea.ac.uk/cru/data/temperature/#datdow	(Morice et al., 2021)
	NOAAGlobalTemp v5	Input dataset	temp.ano.merg5.asc			https://www.ncei.noaa.gov/pub/data/cmb/ersst/v5/2020.grl.dat/interim.2020/	(Vose et al., 2021)
	BerkeleyEarth	Input dataset	Land_and_Ocean_LatLong1_H4.nc				(Rohde and Hausfather, 2020)
	Kadow	Input dataset	HadCRUT.5.0.1.0.anomalies.Kadow				(Kadow et al., 2020)
	Figure 3.4 Code	Code				Link to ESMValTool	(Bock et al., 2020)
Figure 3.5	HadCRUT5	Input dataset	HadCRUT.5.0.1.0.analysis.anomalies.ensemble_mean.nc			https://crudata.uea.ac.uk/cru/data/temperature/#datdow	(Morice et al., 2021)
	NOAAGlobalTemp v5	Input dataset	temp.ano.merg5.asc			https://www.ncei.noaa.gov/pub/data/cmb/ersst/v5/2020.grl.dat/interim.2020/	(Vose et al., 2021)
	BerkeleyEarth	Input dataset	Land_and_Ocean_LatLong1_H4.nc				(Rohde and Hausfather, 2020)
	Kadow	Input dataset	HadCRUT.5.0.1.0.anomalies.Kadow				(Kadow et al., 2020)
	Figure 3.5 Code	Code				Link to ESMValTool	
Figure 3.6	HadCRUT5	Input dataset	HadCRUT.5.0.1.0.analysis.anomalies.ensemble_mean.nc			https://crudata.uea.ac.uk/cru/data/temperature/#datdow	(Morice et al., 2021)

ACCEPTED VERSION SUBJECT TO FINAL EDITING

	BerkeleyEarth	Input dataset	Land_and_Ocean_LatLong1_H4.nc				(Rohde and Hausfather, 2020)
	NOAAGlobalTemp v5	Input dataset	temp.ano.merg5.asc			https://www.ncei.noaa.gov/pub/data/cmb/ersst/v5/2020.grl.dat/interim.2020/	(Vose et al., 2021)
	Kadow	Input dataset	HadCRUT.5.0.1.0.anomalies.Kadow				(Kadow et al., 2020)
	Figure 3.6 Code	Code				Link to ESMValTool	
Figure 3.7	HadCRUT4	Input dataset	HadCRUT.4.6.0.0.median.nc			https://crudata.uea.ac.uk/cru/data/temperature/#datdow	(Morice et al., 2012)
	Figure 3.7 Code	Code				Link to ESMValTool	(Gillett et al., 2021)(Gillett et al., 2021)
Figure 3.8	HadCRUT4	Input dataset	HadCRUT.4.6.0.0.median.nc			https://crudata.uea.ac.uk/cru/data/temperature/#datdow	(Morice et al., 2012)
	Figure 3.8 Code	Code				Link to ESMValTool	
Figure 3.9	HadCRUT5	Input dataset	HadCRUT.5.0.1.0.analysis.anomalies.ensemble_mean.nc			https://crudata.uea.ac.uk/cru/data/temperature/#datdow	(Morice et al., 2021)
	Figure 3.9 Code	Code				Link to ESMValTool	
Figure 3.10	RICH-obs 1.7	Input dataset	rich17obs_mean_gridded_2019.0.1979-2014_fixed2_invertlat.nc		doi:10.1175/JCLI4050.1 doi:10.1175/JCLI-D-11-00668.1	https://img.univie.ac.at/forschung/meteorologie/produkte/raobcorerich/	(Haimberger, 2007; Haimberger et al., 2012)
	RICH-obs 1.5.1	Input dataset	OBS_rich_atmos_rio*_Amon_ta_190001-201912.nc		doi:10.1175/JCLI4050.1 doi:0.1175/JCLI-D-11-00668.1	https://img.univie.ac.at/forschung/meteorologie/produkte/raobcorerich/	(Haimberger, 2007; Haimberger et al., 2012)

ACCEPTED VERSION SUBJECT TO FINAL EDITING

	RAOBCORE 1.7	Input dataset	raobcore17_gridded_2019.0.1979-2014_fixed2.nc		doi:10.1175/JCLI4050.1 doi:10.1175/JCLI-D-11-00668.1	https://img.univie.ac.at/forschung/meteorologie/produkte/raobcorerich/	(Haimberger, 2007; Haimberger et al., 2012)
	ERA5/5.1 Reanalysis Monthly Means	Input dataset	ta_monthly_era5.1_regridded_masked_1979-2014_updated_fixed.nc		doi:10.24381/cds.68d2bb30	https://cds.climate.copernicus.eu/cdsapp#!/dataset/reanalysis-era5-land-monthly-means	(Hersbach et al., 2020)
	Figure 3.10 Code	Code				Link to ESMValTool	Mitchell et al. (2020)
Figure 3.11	Reconstructions	Input dataset	map_delta_06ka_ALL_grid_2x2.nc		https://doi.org/10.1007/s00382-010-0904-1	https://static-content.springer.com/esm/art%3A10.1007%2Fs00382-010-0904-1/MediaObjects/382_2010_904_MOESM2_ESM.zip	(Bartlein et al., 2011)
	PMIP4	Input dataser			https://doi.org/10.5194/cp-2019-168	https://doi.org/10.5194/cp-2019-168	Brierley et al. (2020)
	Figure 3.11 Code	Code				https://github.com/chrisbrierley/PMIP4-midHolocene	Brierley et al. (2020)
Figure 3.12	RSS	Input dataset	tpw_v07r01_198801_202010.nc4.nc			http://www.remss.com/measurements/atmospheric-water-vapor/	(Wentz, 2013)
	ERA5.1 Reanalysis	Input dataset	era5_total_column_water_vapour_*_monthly.nc		doi:10.24381/cds.f17050d7	https://cds.climate.copernicus.eu/cdsapp#!/dataset/reanalysis-era5-single-levels-monthly-means	(Hersbach et al., 2020; Simmons et al., 2020)
	Figure 3.12 Code	Code				Link to ESMValTool	Santer et al. (2007)
Figure 3.13	Global Precipitation Climatology Project	Input dataset	pr_GPCP-SG_L3_v2.3_197901-201710.nc			https://esgf-node.llnl.gov/sear	(Huffman et al., 1997, 2009, Adler

ACCEPTED VERSION SUBJECT TO FINAL EDITING

	(GPCP) v2.3					ch/obs4mips/	et al., 2003, 2016)
	Figure 3.13 Code	Code				Link to ESMValTool	
Figure 3.14	Global Precipitation Climatology Project (GPCP) v2.3	Input dataset	pr_GPCP-SG_L3_v2.3_197901-201710.nc			https://esgf-node.llnl.gov/search/obs4mips/	(Huffman et al., 1997, 2009, Adler et al., 2003, 2016)
	ERA5 Reanalysis	Input dataset	era5_total_precipitation_*_monthly.nc			https://cds.climate.copernicus.eu/cdsapp#!/dataset/reanalysis-era5-land-monthly-means	(Hersbach et al., 2020)
	Figure 3.14 Code	Code				Link to ESMValTool	
Figure 3.15	Global Historical Climatology Network (GHCN) station data	Input dataset	precip.mon.total.nc			https://www.esrl.noaa.gov/psd/data/gridded/data.ghcngridded.html	(Zhang et al., 2007)
	Global Precipitation Climatology Project (GPCP) v2.3	Input dataset	pr_GPCP-SG_L3_v2.3_197901-201710.nc			https://esgf-node.llnl.gov/search/obs4mips/	(Huffman et al., 1997, 2009, Adler et al., 2003, 2016)
	Climate Research Unit (CRU)	Input dataset	cru_ts4.02.1901.2017.pr.dat.nc.gz			https://crudata.uea.ac.uk/cru/data/hrg/cru_ts_4.02/cruts.1811131722.v4.02/	(Harris et al., 2014)
	Figure 3.15 code	Code				Link to ESMValTool	
Figure 3.16	ERA-Interim	Input dataset	ERA-Interim_u10_monthly_*.nc, ERA-Interim_msl_monthly_*.nc			http://apps.ecmwf.int/datasets/data/interim-full-moda/	(Dee et al., 2011)
	ERA5	Input dataset	era5_10m_u_component_of_wind_*_monthly.nc, era5_mean_sea_level_pressure_*_monthly.nc		doi: 10.24381/cds.f17050d7	https://cds.climate.copernicus.eu/cdsapp#!/dataset/reanalysis-era5-single-levels-monthly-means	(Hersbach et al., 2020)
	JRA-55	Input dataset	uas_Amon_reanalysis_JRA-55_*.nc,			https://earthsyst	(Kobayashi et al.,

ACCEPTED VERSION SUBJECT TO FINAL EDITING

			psl_Amon_reanalysis_JRA-55_*.nc			emcog.org/doc/list/ana4mips/	2015)
	MERRA-2	Input dataset	uas_Amon_reanalysis_MERRA2_*.nc, psl_Amon_reanalysis_MERRA2_*.nc			https://earthsystemcog.org/doc/list/ana4mips/	(Gelaro et al., 2017)
	ERA-20C	Input dataset	msl_1900-2010.nc			https://www.ecmwf.int/en/forecasts/datasets/reanalysis-datasets/era-20c	(Poli et al., 2016)
	HadSLP2	Input dataset	hadslp2.asc, HadSLP2r_lowvar_200501-201212.nc			https://www.metoffice.gov.uk/hadobs/hadslp2/data/download.html	(Allan and Ansell, 2006)
	20CRv3	Input dataset	PRMSL_*_mnmean_mem*.nc			https://portal.nersc.gov/archive/home/projects/incite11/www/20C_Reanalysis_version_3/everymember_anal_netcdf/mnmean/PRMSL/	(Slivinski et al., 2019)
	CERA-20C	Input dataset	msl.1901-2010.ens*.nc			https://www.ecmwf.int/en/forecasts/datasets/reanalysis-datasets/cera-20c	(Laloyaux et al., 2018)
	Figure 3.16 code	Code				Link to ESMValTool	
Figure 3.17	GPCP	Input dataset	pr_GPCP-SG_L3_v2.3_197901-201710.nc			https://esgf-node.llnl.gov/search/obs4mips/	(Huffman et al., 1997, 2009, Adler et al., 2003, 2016)
	GPCC	Input dataset	full_data_monthly_v2018_05.nc			https://www.dwd.de/EN/ourservices	(Schneider et al., 2017)

ACCEPTED VERSION SUBJECT TO FINAL EDITING

						/gpcc/gpcc.html	
	CRU-TS	Input dataset	cru_ts4.02.1901.2017.pre.dat.nc			https://crudata.uea.ac.uk/cru/data/hrg/cru_ts_4.02/cruts.1811131722.v4.02/	(Harris et al., 2020)
	CMAP	Input dataset	precip.mon.mean.nc			https://psl.noaa.gov/data/gridded/data.cmap.html	(Xie and Arkin, 1997)
	20CRv3	Input dataset	UGRD200.*.mnmean_mem*.nc, UGRD850.*.mnmean_mem*.nc			https://portal.nersc.gov/archive/home/projects/incite11/www/20C_Reanalysis_version_3/everymember_anal_netcdf/mnmean/UGRD200, https://portal.nersc.gov/archive/home/projects/incite11/www/20C_Reanalysis_version_3/everymember_anal_netcdf/mnmean/UGRD850	(Slivinski et al., 2019)
	ERA-20C	Input dataset	u_1900-2010.nc			https://www.ecmwf.int/en/forecasts/datasets/reanalysis-datasets/era-20c	(Poli et al., 2016)
	ERA5	Input dataset	era5_u_component_of_wind_*_monthly.nc, era5_v_component_of_wind_*_mont		doi: 10.24381/cds.f17050d7	https://cds.climate.copernicus.eu	(Hersbach et al., 2020)

ACCEPTED VERSION SUBJECT TO FINAL EDITING

			hly.nc			/cdsapp#!/dataset/reanalysis-era5-pressure-levels-monthly-means	
	JRA-55	Input dataset	ua_Amon_reanalysis_JRA-55_*.nc			https://earthsystemcog.org/doc/list/ana4mips/	(Kobayashi et al., 2015)
	MERRA2	Input dataset	ua_Amon_reanalysis_MERRA2_*.nc			https://earthsystemcog.org/doc/list/ana4mips/	(Gelaro et al., 2017)
	Figure 3.17 Code	Code				Link to ESMValTool	
Figure 3.18	ERA5 Reanalysis Hourly	Input dataset	era5_orography_*_hourly.nc		doi:10.24381/cds.adbb2d47	https://cds.climate.copernicus.eu/cdsapp#!/dataset/reanalysis-era5-single-levels	(Hersbach et al., 2020)
	Figure 3.18 Code	Code				Link to ESMValTool	
Figure 3.19	ERA5	Input dataset	era5_u_component_of_wind_*_monthly.nc		doi:10.24381/cds.6860a573	https://cds.climate.copernicus.eu/cdsapp#!/dataset/reanalysis-era5-pressure-levels-monthly-means	(Hersbach et al., 2020; Simmons et al., 2020)
	Figure 3.19 Code	Code				Link to ESMValTool	
Figure 3.20	UHH Sea Ice Area Product	Input dataset	SeaIceArea__NorthernHemisphere__monthly__UHH__v2019_fv0.01.nc SeaIceArea__SouthernHemisphere__monthly__UHH__v2019_fv0.01.nc		doi :10.25592/uhhfdm.8559	https://www.fdr.uni-hamburg.de/record/8559#.YG5C5ehKg2w	
	Figure 3.20 Code	Code				Link to ESMValTool	
Figure 3.21	UHH Sea Ice Area Product	Input dataser	SeaIceArea__NorthernHemisphere__monthly__UHH__v2019_fv0.01.nc SeaIceArea__SouthernHemisphere__		doi :10.25592/uhhfdm.8559	https://www.fdr.uni-hamburg.de/recor	

ACCEPTED VERSION SUBJECT TO FINAL EDITING

			monthly__UHH__v2019_fv0.01.nc			d/8559#.YG5C5ehKg2w	
	Figure 3.21 Code	Code				Link to ESMValTool	
Figure 3.22	Mudryk2020	Input dataset	SCE_timeseries.nc		doi: 10.18164/cc133287-1a07-4588-b3b8-40d714edd90e	http://data.ec.gc.ca/data/climate/scientificknowledge/climate-research-publication-based-data/northern-hemisphere-blended-snow-extent-and-snow-mass-time-series/SCE_timeseries.nc	(Mudryk et al., 2020)
	GLDAS2.0	Input dataset	GLDAS_NOAH10_M.A*.020.nc4		doi: 10.5067/QN80TO7ZHFJZ	https://hydro1.gesdisc.eosdis.nasa.gov/data/GLDAS/GLDAS_NOAH10_M.2.0/	
	BR2011	Input dataset	Brown and Robinson 2011 SCE Series.xls		doi : 10.5194/tc-5-219-2011	http://www.the-cryosphere.net/5/219/2011/ tc-5-219-2011-supplement.zip.	(Brown and Robinson, 2011)
	NOAA_CDR	Input dataset	moncov.nam.txt moncov.eurasia.txt		doi: 10.7289/V5N014G9	https://climate.rutgers.edu/snowcover/table_area.php?ui_set=2	(Robinson et al., 2012)
	Figure 3.22 Code	Code				Link to ESMValTool	
Figure 3.23	WOA18	Input dataset	woa18_decav_t00_01.nc, woa18_decav_s00_01.nc			https://www.nodc.noaa.gov/OC5/woa18/woa18data.html	(Locarnini et al., 2018; Zweng et al., 2019)
	Figure 3.23 Code	Code				Link to ESMValTool	

ACCEPTED VERSION SUBJECT TO FINAL EDITING

Figure 3.24	HadISST1.1	Input dataset	HadISST_sst.nc			http://www.metoffice.gov.uk/hadobs/hadisst/data/download.html	(Rayner et al., 2003)
	Figure 3.24 Code	Code				Link to ESMValTool	
Figure 3.25	WOA18	Input dataset	woa18_decav81B0_t00_01.nc woa18_decav81B0_s00_01.nc			https://www.nodc.noaa.gov/OC5/woa18/woa18data.html	(Locarnini et al., 2018; Zweng et al., 2019)
	Figure 3.25 Code	Code				Link to ESMValTool	
Figure 3.26		Input dataset					
	Figure 3.26	Code				Link to ESMValTool	
Figure 3.27		Input dataset					
	Figure 3.27	Code				Link to ESMValTool	
Figure 3.28		Input dataset					
	Figure 3.28	Code				Link to ESMValTool	
Figure 3.29	Figure 3.29	Code				On DMS	
Figure 3.30	RAPID	Input dataset	moc_vertical.nc		doi: 10.5285/aa57e879-4cca-28b6-e053-6c86abc02de5	https://rapid.ac.uk/rapidmoc/rapid_data/datadl.php	
		Inpit dataset	Figure_AR6_DAMIP_AMOC_26N_1000m.json			https://github.com/mattofficeuk/AR6/tree/master/JSON_data	
	Figure 3.30	Code				Link to ESMValTool	
Figure 3.31	NOAA-ESRL-CO2-Globl	Input dataset				https://www.esrl.noaa.gov/gmd/ccgg/trends/gl_data.html	

ACCEPTED VERSION
SUBJECT TO FINAL EDITING

	Scripps CO2 MLO	Input dataset	monthly_in_situ_co2_mlo.csv		doi:10.3334/CDIAC/atg.035	https://scrippsco2.ucsd.edu/data/atmospheric_co2/mlo.html	
	HadCRUT5	Input dataset	HadCRUT.5.0.1.0.analysis.anomalies.ensemble_mean.nc			https://crudata.uea.ac.uk/cru/data/temperature/#datdow	(Morice et al., 2021)
	GCP	Input dataset			https://doi.org/10.18160/GCP-2019	https://icos-cp.eu/GCP/2019	(Friedlingstein et al., 2019)
	Figure 3.31 Code	Code				Link to ESMValTool	
Figure 3.32	JMA-TRANSCOM	Input dataset					(Maki et al., 2010)
	NOAA-ESRL-CO2	Input dataset			https://doi.org/10.15138/wkgj-f215	https://www.esrl.noaa.gov/gmd/dv/data/	(Dlugokencky and Tans, 2020)
	Figure 3.32 Code	Code				Link to ESMValTool	
Figure 3.33	JRA-55	Input dataset	jra55.mon.PSL.195801-201712.nc			https://jra.kishou.go.jp/JRA-55/index_en.html	(Kobayashi et al., 2015)
	ERA5	Input dataset	era5_mean_sea_level_pressure_*_monthly.nc		doi: 10.24381/cds.f17050d7	https://cds.climate.copernicus.eu/cdsapp#!/dataset/reanalysis-era5-single-levels-monthly-means	(Hersbach et al., 2020)
	20CRv3	Input dataset	prmsl.mon.mean.nc			https://psl.noaa.gov/data/gridded/data.20thC_ReanV3.monolevel.html	(Slivinski et al., 2019)
	Figure 3.33 Code	Code	recipe_ipccwg1ar6ch3_modes.yml			Link to ESMValTool	
Figure 3.34	JRA-55	Input dataset	jra55.mon.PSL.195801-201712.nc			https://jra.kishou.go.jp/JRA-	(Kobayashi et al., 2015)

ACCEPTED VERSION SUBJECT TO FINAL EDITING

						55/index_en.html	
	ERA5	Input dataset	era5_mean_sea_level_pressure_*_monthly.nc		doi: 10.24381/cds.f17050d7	https://cds.climate.copernicus.eu/cdsapp#!/dataset/reanalysis-era5-single-levels-monthly-means	(Hersbach et al., 2020)
	Figure 3.34 Code	Code	recipe_ipccwg1ar6ch3_modes.yml			Link to ESMValTool	
Figure 3.35	SAM index	Input dataset	abram2014sam.txt			ftp://ftp.ncdc.noaa.gov/pub/data/paleo/contributions_by_author/abram2014/abram2014sam.txt	(Abram et al., 2014)
	SAM index	Input dataset	Reconstructions_Annual_LC.txt			https://www1.ncdc.noaa.gov/pub/data/paleo/reconstructions/datwyler2017/	(Dätwyler et al., 2018)
	Figure 3.35 Code	Code	recipe_ar6ch3_sam_millinnium.yml			Link to ESMValTool	
Figure 3.36	ERSSTv5	Input dataset	sst.mnmean.nc			https://www.esrl.noaa.gov/psd/data/gridded/data.noaa.ersst.v5.html	(Huang et al., 2017)
	HadISST1.1	Input dataset	HadISST_sst.nc			http://www.metoffice.gov.uk/hadobs/hadisst/data/download.html	(Rayner et al., 2003)
	Figure 3.36 Code	Code	recipe_ar6ch3_enso_cmip5+6.yml			Link to ESMValTool	
Figure 3.37	ERSSTv5	Input dataset	sst.mnmean.nc			https://www.esrl.noaa.gov/psd/d	(Huang et al., 2017))

ACCEPTED VERSION SUBJECT TO FINAL EDITING

						ata/gridded/data.noaa.ersst.v5.html	
	HadISST1.1	Input dataset	HadISST_sst.nc			http://www.metoffice.gov.uk/hadobs/hadisst/data/download.html	(Rayner et al., 2003)
	Figure 3.37 Code	Code	recipe_ar6ch3_enso_cmip5+6.yml			Link to ESMValTool	
Figure 3.38	ERSSTv5	Input dataset	sst.mnmean.nc			https://www.esrl.noaa.gov/psd/data/gridded/data.noaa.ersst.v5.html	(Huang et al., 2017)
	BerkeleyEarth	Input dataset	Complete_TAVG_LatLong1.nc			http://berkeleyearth.org/data-new/	(Rohde et al., 2013)
	GISTEMP	Input dataset	gistemp250_GHCNv4.nc			https://data.giss.nasa.gov/gistemp/	(Lenssen et al., 2019)
	GPCC	Input dataset	full_data_monthly_v2018_05.nc			https://www.dwd.de/EN/ourservices/gpcc/gpcc.html	(Schneider and Deser, 2018)
	GPCP	Input dataset	precip.mon.mean.nc			https://psl.noaa.gov/data/gridded/data.gpcp.html	(Huffman et al., 1997, 2009, Adler et al., 2003, 2016)
	CRU-TS	Input dataset	cru_ts4.02.1901.2017.pre.dat.nc			https://crudata.uea.ac.uk/cru/data/hrg/cru_ts_4.02/cruts.1811131722.v4.02/	(Harris et al., 2020)
	Figure 3.38 Code	Code				Link to ESMValTool	
Figure 3.39	ERSSTv5	Input dataset	sst.mnmean.nc			https://www.esrl.noaa.gov/psd/data/gridded/data.	(Huang et al., 2017)

ACCEPTED VERSION SUBJECT TO FINAL EDITING

						noaa.ersst.v5.html	
	HadISST1.1	Input dataset	HadISST_sst.nc			http://www.metoffice.gov.uk/hadobs/hadisst/data/download.html	(Rayner et al., 2003)
	COBE-SST2	Input dataset	sst.mon.mean.nc			https://psl.noaa.gov/data/gridded/data.cobe2.html	(Hirahara et al., 2014)
	Figure 3.39 Code	Code				Link to ESMValTool	
Figure 3.40	ERSSTv5	Input dataset	sst.mnmean.nc			https://www.esrl.noaa.gov/psd/data/gridded/data.noaa.ersst.v5.html	(Huang et al., 2017)
	HadISST1.1	Input dataset	HadISST_sst.nc			http://www.metoffice.gov.uk/hadobs/hadisst/data/download.html	(Rayner et al., 2003)
	COBE-SST2	Input dataset	sst.mon.mean.nc			https://psl.noaa.gov/data/gridded/data.cobe2.html	(Hirahara et al., 2014)
	Figure 3.40 Code	Code				Link to ESMValTool	
Figure 3.41	HadCRUT5	Input dataset	HadCRUT.5.0.1.0.analysis.anomalies.ensemble_mean.nc			https://crudata.uea.ac.uk/cru/data/temperature/#datdow	(Morice et al., 2021)
	Global Historical Climatology Network (GHCN) station data	Input dataset	precip.mon.total.nc			https://www.esrl.noaa.gov/psd/data/gridded/data.ghcngridded.html	(Zhang et al., 2007)
	HadISST	Input dataset	HadISST_ice.nc.gz			http://www.metoffice.gov.uk/hadobs/hadisst/data/download.html	(Rayner et al., 2003)

ACCEPTED VERSION SUBJECT TO FINAL EDITING

	OHC assessment from Chapter 2						
	Figure 3.41 Code	Code				Link to ESMValTool	
Figure 3.42	AIRS RetStd-v5	Input dataset	hus_AIRS_L3_RetStd-v5_*.nc				(Susskind et al., 2006; Tian et al., 2013)
	CERES-EBAF	Input dataset				https://ceres.larc.nasa.gov/data/	(Loeb et al., 2012)
	ERA5	Input dataset	era5_*_*_monthly.nc		doi: 10.24381/cds.68d2bb30	https://cds.climate.copernicus.eu/cdsapp#!/dataset/reanalysis-era5-land-monthly-means	(Hersbach et al., 2020)
	ERA-Interim	Input dataset	ERA-Interim_*_monthly_*.nc hfds			http://apps.ecmwf.int/datasets/data/interim-full-moda/	(Dee et al., 2011)
	ESACCI-SST	Input dataset				ftp://anon-ftp.ceda.ac.uk/neodc/esacci/sst/data/lt/Analysis/L4/v01.1/	(Merchant et al., 2014)
	Global Historical Climatology Network (GHCN) station data	Input dataset	precip.mon.total.nc			https://www.esrl.noaa.gov/psd/data/gridded/data.ghcngridded.html	(Zhang et al., 2007)
	Global Precipitation Climatology Project (GPCP) v2.3	Input dataset	pr_GPCP-SG_L3_v2.3_197901-201710.nc			https://esgf-node.llnl.gov/search/obs4mips/	(Huffman et al., 1997, 2009, Adler et al., 2003, 2016)
	HadISST	Input dataset	HadISST_ice.nc.gz, HadISST_sst.nc.gz			http://www.metoffice.gov.uk/hadobs/hadisst/data/download.html	(Rayner et al., 2003)
	JRA-55	Input dataset	jra55.mon.PSL.195801-201712.nc			https://jra.kishou.go.jp/JRA-55/index_en.html	(Kobayashi et al., 2015)
	NCEP/NCAR	Input dataset	*.mon.mean.nc			https://psl.noaa.gov/data/gridded/dat	(Kalnay et al., 1996)

ACCEPTED VERSION SUBJECT TO FINAL EDITING

						a.ncep.reanalysis.surface.html	
	ESACCI-SOILMOISTURE	Input dataset				ftp://anon-ftp.ceda.ac.uk/neodc/esacci/soil_moisture/data/	
	JMA-TRANSCOM	Input dataset	nbp, fgco2				(Maki et al., 2010)
	FLUXCOM ANN-v1	Input dataset				http://www.bgc-jena.mpg.de/geodb/BGI/Home	
	MTE May12	Input dataset	EnsembleGPP_GL.nc			http://www.bgc-jena.mpg.de/geodb/BGI/Home	
	LAI3g	Input dataset				http://cliveg.bu.edu/modismisr/lai3g-fpar3g.html	Zhu et al., 2013
	Landschuetzer2016	Input dataset	spco2_1982-2015_MPI_SOM-FFN_v2016.nc			https://www.nodc.noaa.gov/archive/arc0105/0160558/3.3/data/0-data/	Landschützer et al., 2016
	LandFlux-EVAL	Input dataset	LandFluxEVAL.merged.89-05.monthly.all.nc			https://data.iac.ethz.ch/landflux/	Mueller et al., 2013
	ATSR	Input dataset					
	Figure 3.42 Code	Code	recipe_ipccwg1ar6ch3_modes.yml			Link to ESMValTool	
Figure 3.43	AIRS RetStd-v5	Input dataset	hus_AIRS_L3_RetStd-v5_*.nc				(Susskind et al., 2006; Tian et al., 2013)
	CERES-EBAF	Input dataset				https://ceres.larc.nasa.gov/data/	(Loeb et al., 2012)
	ERA5	Input dataset	era5_*_*_monthly.nc		doi: 10.24381/cds.68d2bb30	https://cds.climate.copernicus.eu/cdsapp#!/dataset/reanalysis-era5-land-monthly-means	(Hersbach et al., 2020)
	ESACCI-SST	Input dataset				ftp://anon-ftp.ceda.ac.uk/n	(Merchant et al., 2014)

ACCEPTED VERSION SUBJECT TO FINAL EDITING

						eodc/esacci/sst/data/lt/Analysis/L4/v01.1/	
	Global Historical Climatology Network (GHCN) station data	Input dataset	precip.mon.total.nc			https://www.esrl.noaa.gov/psd/data/gridded/data.ghcngridded.html	(Zhang et al., 2007)
	Global Precipitation Climatology Project (GPCP) v2.3	Input dataset	pr_GPCP-SG_L3_v2.3_197901-201710.nc			https://esgf-node.llnl.gov/search/obs4mips/	(Huffman et al., 1997, 2009, Adler et al., 2003, 2016)
	HadISST	Input dataset	HadISST_ice.nc.gz, HadISST_sst.nc.gz			http://www.metoffice.gov.uk/hadobs/hadisst/data/download.html	(Rayner et al., 2003)
	JRA-55	Input dataset	jra55.mon.PSL.195801-201712.nc			https://jra.kishou.go.jp/JRA-55/index_en.html	(Kobayashi et al., 2015)
	NCEP/NCAR	Input dataset	*.mon.mean.nc			https://psl.noaa.gov/data/gridded/data.ncep.reanalysis.surface.html	(Kalnay et al., 1996)
	Figure 3.43 Code	Code				Link to ESMValTool	
Figure 3.44	Bartlein et al., 2011 temperature and precipitation reconstructions for the MidHolocene climate	Input dataset	warmtemp_delta_06ka_ALL_grid_2x2.nc coldtemp_delta_06ka_ALL_grid_2x2.nc map_delta_06ka_ALL_grid_2x2.nc			https://wiki.lsce.ipsl.fr/pmip3/doku.php/pmip3:synth:bartlein:index	(Bartlein et al., 2011; Cleator et al., 2020)
	Cleator2020 (land-based reconstructions of surface temperature anomalies)	Input dataset	LGM_reconstruction.csv	Creative Commons Attribution 4.0 International	http://dx.doi.org/10.17864/1947.244	https://researchdata.reading.ac.uk/244/1/LGM_reconstruction.csv	(Cleator et al., 2020)
	Tierney2019 (land-based reconstructions of surface temperature	Input dataset	Tierney2020_ProxyData_5x5_deltaSST.nc	Creative Commons Attribution 4.0 International		https://doi.pangaea.de/10.1594/PANGAEA.920596	(Tierney et al., 2020)

ACCEPTED VERSION SUBJECT TO FINAL EDITING

	anomalies)						
	Figure 3.44 Code	Code				On DMS	
CC-Box 3.1, Figure 1	HadCRUT5	Input dataset	HadCRUT.5.0.1.0.analysis.anomalies.ensemble_mean.nc, HadCRUT.5.0.1.0.analysis.summary_series.global.monthly.nc, HadCRUT.5.0.1.0.analysis.ensemble_series.global.monthly.nc			https://www.metoffice.gov.uk/hadobs/hadcrut5/data/current/download.html	(Morice et al., 2021)
	BerkeleyEarth	Input dataset	Land_and_Ocean_LatLong1_H4.nc				(Rohde and Hausfather, 2020)
	GISTEMP	Input dataset	GLB.Ts+dSST.csv, gistemp1200_GHCNv4_ERSSTv5.nc			https://data.giss.nasa.gov/gistemp/	(Lenssen et al., 2019)
	Kadow	Input dataset	HadCRUT.5.0.1.0.anomalies.Kadow_et_al_2020_20crAI-infilled.ensemble_mean_185001-202012.nc				(Kadow et al., 2020)
	NOAAGlobalTemp-Interim	Input dataset	temp.ano.merg5.asc			https://www.ncei.noaa.gov/pub/data/cmb/ersst/v5/2020.grl.dat/interim.2020/	(Vose et al., 2021)
	ERA5	Input dataset	era5_2m_temperature_*_monthly.nc, era5_sea_surface_temperature_*_monthly.nc, era5_sea_ice_cover_*_monthly.nc		doi: 10.24381/cds.f17050d7	https://cds.climate.copernicus.eu/cdsapp#!/dataset/reanalysis-era5-single-levels-monthly-means https://cds.climate.copernicus.eu/cdsapp#!/dataset/reanalysis-era5-single-levels-monthly-means-preliminary-back-extension	(Hersbach et al., 2020)
	CC-Box 3.1, Figure 1 Code	Code				Link to ESMValTool	

ACCEPTED VERSION SUBJECT TO FINAL EDITING

CC-Box 3.2, Figure 1	HadEX3	Input dataset	HadEX3_TXx_ANN.nc			https://www.metoffice.gov.uk/hadobs/hadex3/download.html	(Dunn et al., 2020)
	HadEX3	Input dataset	HadEX3_Rx1day_ANN.nc			https://www.metoffice.gov.uk/hadobs/hadex3/download.html	(Dunn et al., 2020)
	CC-Box 3.2, Figure 1 Code	Code				Link to ESMValTool	
FAQ 3.1, Figure 1							
FAQ 3.2, Figure 1							
FAQ 3.3, Figure 1	JRA-55	Input dataset	jra55.mon.PSL.195801-201712.nc			https://jra.kishou.go.jp/JRA-55/index_en.html	(Kobayashi et al., 2015)
	ERA5	Input dataset	era5_2m_temperature_*_monthly.nc		doi: 10.24381/cds.68d2bb30	https://cds.climate.copernicus.eu/cdsapp#!/dataset/reanalysis-era5-land-monthly-means	(Hersbach et al., 2020)
	Global Precipitation Climatology Project (GPCP) v2.3	Input dataset	pr_GPCP-SG_L3_v2.3_197901-201710.nc			https://esgf-node.llnl.gov/search/obs4mips/	(Huffman et al., 1997, 2009, Adler et al., 2003, 2016)
	FAQ 3.3, Figure 1 Code	Code				Link to ESMValTool	

[END TABLE 3.SM.1 HERE]

ACCEPTED VERSION SUBJECT TO FINAL EDITING

References

Abram, N. J., Mulvaney, R., Vimeux, F., Phipps, S. J., Turner, J., and England, M. H. (2014). Evolution of the Southern Annular Mode during the past millennium. *Nat. Clim. Chang.* 4, 564–569. doi:10.1038/nclimate2235.

Adler, R. F., Huffman, G. J., Chang, A., Ferraro, R., Xie, P.-P., Janowiak, J., et al. (2003). The Version-2 Global Precipitation Climatology Project (GPCP) Monthly Precipitation Analysis (1979–Present). *J. Hydrometeorol.* 4, 1147–1167. doi:10.1175/1525-7541(2003)004<1147:TVGPCP>2.0.CO;2.

Adler, R., Sapiano, M., Huffman, G., Bolvin, D., Gu, G., Wang, J., et al. (2016). The new version 2.3 of the Global Precipitation Climatology Project (GPCP) monthly analysis product. *Univ. Maryland, April*, 1072–1084.

Allan, R., and Ansell, T. (2006). A new globally complete monthly historical gridded mean sea level pressure dataset (HadSLP2): 1850-2004. *J. Clim.* 19, 5816–5842. doi:10.1175/JCLI3937.1.

Bartlein, P. J., Harrison, S. P., Brewer, S., Connor, S., Davis, B. A. S., Gajewski, K., et al. (2011). Pollen-based continental climate reconstructions at 6 and 21 ka: A global synthesis. *Clim. Dyn.* 37, 775–802. doi:10.1007/s00382-010-0904-1.

Bock, L., Lauer, A., Schlund, M., Barreiro, M., Bellouin, N., Jones, C., et al. (2020). Quantifying Progress Across Different CMIP Phases With the ESMValTool. *J. Geophys. Res. Atmos.* 125. doi:10.1029/2019JD032321.

Brierley, C. M., Zhao, A., Harrison, S. P., Braconnot, P., Williams, C. J. R., Thornalley, D. J. R., et al. (2020). Large-scale features and evaluation of the PMIP4-CMIP6 midHolocene simulations. *Clim. Past* 16, 1847–1872. doi:10.5194/cp-16-1847-2020.

Brown, R. D., and Robinson, D. A. (2011). Northern Hemisphere spring snow cover variability and change over 1922-2010 including an assessment of uncertainty. *Cryosphere* 5, 219–229. doi:10.5194/tc-5-219-2011.

Cleator, S. F., Harrison, S. P., Nichols, N. K., Prentice, I. C., and Roulstone, I. (2020). A new multi-variable benchmark for Last Glacial Maximum climate simulations. *Clim. Past* 16, 699–712. doi:10.5194/cp-2019-55.

Dätwyler, C., Neukom, R., Abram, N. J., Gallant, A. J. E., Grosjean, M., Jacques-Coper, M., et al. (2018). Teleconnection stationarity, variability and trends of the Southern Annular Mode (SAM) during the last millennium. *Clim. Dyn.* 51, 2321–2339. doi:10.1007/s00382-017-4015-0.

Dee, D. P., Uppala, S. M., Simmons, A. J., Berrisford, P., Poli, P., Kobayashi, S., et al. (2011). The ERA-Interim reanalysis: configuration and performance of the data assimilation system. *Q. J. R. Meteorol. Soc.* 137, 553–597. doi:10.1002/qj.828.

Dlugokencky, E. J., and Tans, P. P. (2020). Trends in Atmospheric Carbon Dioxide. Available at: https://www.esrl.noaa.gov/gmd/ccgg/trends/gl_data.html.

Dunn, R. J. H., Alexander, L. V, Donat, M. G., Zhang, X., Bador, M., Herold, N., et al. (2020). Development of an Updated Global Land In Situ-Based Data Set of Temperature and Precipitation Extremes: HadEX3. *J. Geophys. Res. Atmos.* 125, e2019JD032263. doi:https://doi.org/10.1029/2019JD032263.

Friedlingstein, P., Jones, M. W., O'Sullivan, M., Andrew, R. M., Hauck, J., Peters, G. P., et al. (2019). Global carbon budget 2019. *Earth Syst. Sci. Data* 11. doi:10.5194/essd-11-1783-2019.

Gelaro, R., McCarty, W., Suárez, M. J., Todling, R., Molod, A., Takacs, L., et al. (2017). The modern-era retrospective analysis for research and applications, version 2 (MERRA-2). *J. Clim.* 30, 5419–5454. doi:10.1175/JCLI-D-16-0758.1.

Gillett, N. P., Kirchmeier-Young, M., Ribes, A., Shiogama, H., Hegerl, G. C., Knutti, R., et al. (2021). Constraining human contributions to observed warming since the pre-industrial period. *Nat. Clim. Chang.* doi:10.1038/s41558-020-00965-9.

Haimberger, L. (2007). Homogenization of radiosonde temperature time series using innovation statistics. *J. Clim.* 20, 1377–1403. doi:10.1175/JCLI4050.1.

Haimberger, L., Tavolato, C., and Sperka, S. (2012). Homogenization of the global radiosonde temperature dataset through combined comparison with reanalysis background series and neighboring stations. *J. Clim.* 25, 8108–8131. doi:10.1175/JCLI-D-11-00668.1.

Harris, I., Jones, P. D., Osborn, T. J., and Lister, D. H. (2014). Updated high-resolution grids of monthly climatic observations – the CRU TS3.10 Dataset. *Int. J. Climatol.* 34, 623–642. doi:10.1002/joc.3711.

Harris, I., Osborn, T. J., Jones, P., and Lister, D. (2020). Version 4 of the CRU TS monthly high-resolution gridded multivariate climate dataset. *Sci. Data* 7, 109. doi:10.1038/s41597-020-0453-3.

Haywood, A., Tindall, J., Dowsett, H., Dolan, A., Foley, K., Hunter, S., et al. (2020). A return to large-scale features of Pliocene climate: the Pliocene Model Intercomparison Project Phase 2. *Clim. Past Discuss.* (submitted, 1–40. doi:10.5194/cp-2019-145.

Hersbach, H., Bell, B., Berrisford, P., Hirahara, S., Horányi, A., Muñoz-Sabater, J., et al. (2020). The ERA5 global reanalysis. *Q. J. R. Meteorol. Soc.* 146, 1999–2049. doi:https://doi.org/10.1002/qj.3803.

Hirahara, S., Ishii, M., and Fukuda, Y. (2014). Centennial-Scale Sea Surface Temperature Analysis and Its Uncertainty. *J. Clim.* 27, 57–75. doi:10.1175/JCLI-D-12-00837.1.

Huang, J., Zhang, X., Zhang, Q., Lin, Y., Hao, M., Luo, Y., et al. (2017). Recently amplified arctic warming has contributed to a continual global warming trend. *Nat. Clim. Chang.* 7, 875–879. doi:10.1038/s41558-017-0009-5.

ACCEPTED VERSION SUBJECT TO FINAL EDITING

Huffman, G. J., Adler, R. F., Arkin, P., Chang, A., Ferraro, R., Gruber, A., et al. (1997). The Global Precipitation Climatology Project (GPCP) Combined Precipitation Dataset. *Bull. Am. Meteorol. Soc.* 78, 5–20. doi:10.1175/1520-0477(1997)078<0005:TGPCPG>2.0.CO;2.

Huffman, G. J., Adler, R. F., Bolvin, D. T., and Gu, G. (2009). Improving the global precipitation record: GPCP Version 2.1. *Geophys. Res. Lett.* 36. doi:https://doi.org/10.1029/2009GL040000.

Kadow, C., Hall, D. M., and Ulbrich, U. (2020). Artificial intelligence reconstructs missing climate information. *Nat. Geosci.* 13, 408–413. doi:10.1038/s41561-020-0582-5.

Kalnay, E., Kanamitsu, M., Kistler, R., Collins, W., Deaven, D., Gandin, L., et al. (1996). The NCEP/NCAR 40-Year Reanalysis Project. *Bull. Am. Meteorol. Soc.* 77, 437–472. doi:10.1175/1520-0477(1996)077<0437:TNYRP>2.0.CO;2.

Kobayashi, S., Ota, Y., Harada, Y., Ebita, A., Moriya, M., Onoda, H., et al. (2015). The JRA-55 reanalysis: General specifications and basic characteristics. *J. Meteorol. Soc. Japan. Ser. II* 93, 5–48.

Laloyaux, P., de Boisseson, E., Balmaseda, M., Bidlot, J.-R., Broennimann, S., Buizza, R., et al. (2018). CERA-20C: A Coupled Reanalysis of the Twentieth Century. *J. Adv. Model. Earth Syst.* 10, 1172–1195. doi:https://doi.org/10.1029/2018MS001273.

Landschützer, P., Gruber, N., and Bakker, D. C. E. (2016). Decadal variations and trends of the global ocean carbon sink. *Global Biogeochem. Cycles* 30, 1396–1417. doi:10.1002/2015GB005359.

Lenssen, N. J. L., Schmidt, G. A., Hansen, J. E., Menne, M. J., Persin, A., Ruedy, R., et al. (2019). Improvements in the GISTEMP Uncertainty Model. *J. Geophys. Res. Atmos.* 124, 6307–6326. doi:10.1029/2018JD029522.

Locarnini, M., Mishonov, A. V, Baranova, O. K., Boyer, T. P., Zweng, M. M., Garcia, H. E., et al. (2018). World ocean atlas 2018, volume 1: Temperature.

Loeb, N. G., Lyman, J. M., Johnson, G. C., Allan, R. P., Doelling, D. R., Wong, T., et al. (2012). Observed changes in top-of-the-atmosphere radiation and upper-ocean heating consistent within uncertainty. *Nat. Geosci.* 5, 110–113. doi:10.1038/ngeo1375.

Maki, T., Ikegami, M., Fujita, T., Hirahara, T., Yamada, K., Mori, K., et al. (2010). New technique to analyse global distributions of CO2 concentrations and fluxes from non-processed observational data. *Tellus, Ser. B Chem. Phys. Meteorol.* 62, 797–809. doi:10.1111/j.1600-0889.2010.00488.x.

Merchant, C. J., Embury, O., Roberts-Jones, J., Fiedler, E., Bulgin, C. E., Corlett, G. K., et al. (2014). Sea surface temperature datasets for climate applications from Phase 1 of the European Space Agency Climate Change Initiative (SST CCI). *Geosci. DATA J.* 1, 179–191. doi:10.1002/gdj3.20.

Mitchell, D. M., Lo, Y. T. E., Seviour, W. J. M., Haimberger, L., and Polvani, L. M. (2020). The vertical profile of recent tropical temperature trends: Persistent model biases in the context of internal variability. *Environ. Res. Lett.* 15. doi:10.1088/1748-9326/ab9af7.

Morice, C. P., Kennedy, J. J., Rayner, N. A., and Jones, P. D. (2012). Quantifying uncertainties in global and regional temperature change using an ensemble of observational estimates: The HadCRUT4 data set. *J. Geophys. Res. Atmos.* 117. doi:10.1029/2011JD017187.

Morice, C. P., Kennedy, J. J., Rayner, N. A., Winn, J. P., Hogan, E., Killick, R. E., et al. (2021). An Updated Assessment of Near-Surface Temperature Change From 1850: The HadCRUT5 Data Set. *J. Geophys. Res. Atmos.* 126, e2019JD032361. doi:https://doi.org/10.1029/2019JD032361.

Mudryk, L., Santolaria-Otín, M., Krinner, G., Ménégoz, M., Derksen, C., Brutel-Vuilmet, C., et al. (2020). Historical Northern Hemisphere snow cover trends and projected changes in the CMIP6 multi-model ensemble. *Cryosphere* 14, 2495–2514. doi:10.5194/tc-14-2495-2020.

Mueller, B., Hirschi, M., Jimenez, C., Ciais, P., Dirmeyer, P. A., Dolman, A. J., et al. (2013). Benchmark products for land evapotranspiration: LandFlux-EVAL multi-data set synthesis. *Hydrol. Earth Syst. Sci.*

PAGES 2k Consortium (2019). Consistent multi-decadal variability in global temperature reconstructions and simulations over the Common Era. *Nat. Geosci.* 12, 643–649. doi:10.1038/s41561-019-0400-0.

Poli, P., Hersbach, H., Dee, D. P., Berrisford, P., Simmons, A. J., Vitart, F., et al. (2016). ERA-20C: An Atmospheric Reanalysis of the Twentieth Century. *J. Clim.* 29, 4083–4097. doi:10.1175/JCLI-D-15-0556.1.

Rayner, N. A., Parker, D. E., Horton, E. B., Folland, C. K., Alexander, L. V., Rowell, D. P., et al. (2003). Global analyses of sea surface temperature, sea ice, and night marine air temperature since the late nineteenth century. *J. Geophys. Res.* 108, 4407. doi:10.1029/2002JD002670.

Robinson, D., David, A., Estilow, T., and Program, N. C. (2012). NOAA Climate Date Record (CDR) of Northern Hemisphere (NH) Snow Cover Extent (SCE), Version 1. *NOAA Natl. Clim. Data Cent.*, 137–142. doi:10.7289/V5N014G9.

Rohde, R. A., and Hausfather, Z. (2020). The Berkeley Earth Land/Ocean Temperature Record. *Earth Syst. Sci. Data* 12, 3469–3479. doi:10.5194/essd-12-3469-2020.

Rohde, R., Muller, R. A., Jacobsen, R., Muller, E., Perlmutter, S., Rosenfeld, A., et al. (2013). A New Estimate of the Average Earth Surface Land Temperature Spanning 1753 to 2011. *Geoinformatics Geostatistics An Overv.* 1. doi:10.4172/2327-4581.1000101.

Santer, B. D., Mears, C., Wentz, F. J., Taylor, K. E., Gleckler, P. J., Wigley, T. M. L., et al. (2007). Identification of human-induced changes in atmospheric moisture content. *Proc. Natl. Acad. Sci.* 104, 15248–15253.

ACCEPTED VERSION SUBJECT TO FINAL EDITING

doi:10.1073/pnas.0702872104.
Schneider, D. P., and Deser, C. (2018). Tropically driven and externally forced patterns of Antarctic sea ice change: reconciling observed and modeled trends. *Clim. Dyn.* 50, 4599–4618. doi:10.1007/s00382-017-3893-5.
Schneider, U., Finger, P., Meyer-Christoffer, A., Rustemeier, E., Ziese, M., and Becker, A. (2017). Evaluating the hydrological cycle over land using the newly-corrected precipitation climatology from the Global Precipitation Climatology Centre (GPCC). *Atmosphere (Basel).* 8, 52. doi:10.3390/atmos8030052.
Simmons, A., Soci, C., Nicolas, J., Bell, B., Berrisford, P., Dragani, R., et al. (2020). *Global Stratospheric Temperature Bias and Other Stratospheric Aspects of ERA5 and ERA5. 1*. European Centre for Medium Range Weather Forecasts.
Slivinski, L. C., Compo, G. P., Whitaker, J. S., Sardeshmukh, P. D., Giese, B. S., McColl, C., et al. (2019). Towards a more reliable historical reanalysis: Improvements for version 3 of the Twentieth Century Reanalysis system. *Q. J. R. Meteorol. Soc.* 145, 2876–2908. doi:10.1002/qj.3598.
Susskind, J., Barnet, C., Blaisdell, J., Iredell, L., Keita, F., Kouvaris, L., et al. (2006). Accuracy of geophysical parameters derived from Atmospheric Infrared Sounder/Advanced Microwave Sounding Unit as a function of fractional cloud cover. *J. Geophys. Res.* 111. doi:10.1029/2005JD006272.
Tian, B., Fetzer, E. J., Kahn, B. H., Teixeira, J., Manning, E., and Hearty, T. (2013). Evaluating CMIP5 models using AIRS tropospheric air temperature and specific humidity climatology. *J. Geophys. Res. Atmos.* 118, 114–134. doi:10.1029/2012JD018607.
Tierney, J. E., Zhu, J., King, J., Malevich, S. B., Hakim, G. J., and Poulsen, C. J. (2020). Glacial cooling and climate sensitivity revisited. *Nature* 584, 569–573. doi:10.1038/s41586-020-2617-x.
Vose, R. S., Huang, B., Yin, X., Arndt, D., Easterling, D. R., Lawrimore, J. H., et al. (2021). Implementing Full Spatial Coverage in NOAA's Global Temperature Analysis. *Geophys. Res. Lett.* 48, e2020GL090873. doi:10.1029/2020GL090873.
Wentz, F. J. (2013). *SSM/I version-7 calibration report*. Remote Sen.
Xie, P., and Arkin, P. A. (1997). Global precipitation: A 17-year monthly analysis based on gauge observations, satellite estimates, and numerical model outputs. *Bull. Am. Meteorol. Soc.* 78, 2539–2558.
Zhang, X., Zwiers, F. W., Hegerl, G. C., Lambert, F. H., Gillett, N. P., Solomon, S., et al. (2007). Detection of human influence on twentieth-century precipitation trends. *Nature* 448, 461–465. doi:10.1038/nature06025.
Zhu, Z., Bi, J., Pan, Y., Ganguly, S., Anav, A., Xu, L., et al. (2013). Global data sets of vegetation leaf area index (LAI)3g and fraction of photosynthetically active radiation (FPAR)3g derived from global inventory modeling and mapping studies (GIMMS) normalized difference vegetation index (NDVI3G) for the period 1981 to 2. *Remote Sens.* 5, 927–948. doi:10.3390/rs5020927.
Zweng, M. M., Seidov, D., Boyer, T., Locarnini, M., Garcia, H., Mishonov, A., et al. (2019). World ocean atlas 2018, volume 2: Salinity.

ACCEPTED VERSION
SUBJECT TO FINAL EDITING

Chapter 4: Future global climate: scenario-based projections and near-term information

Coordinating Lead Authors:
June-Yi Lee (Republic of Korea), Jochem Marotzke (Germany)

Lead Authors:
Govindasamy Bala (India/United States of America), Long Cao (China), Susanna Corti (Italy), John P. Dunne (United States of America), Francois Engelbrecht (South Africa), Erich Fischer (Switzerland), John C. Fyfe (Canada), Christopher Jones (United Kingdom), Amanda Maycock (United Kingdom), Joseph Mutemi (Kenya), Ousmane Ndiaye (Senegal), Swapna Panickal (India), Tianjun Zhou (China)

Contributing Authors:
Sebastian Milinski (Germany), Kyung-Sook Yun (Republic of Korea), Kyle Armour (United States of America), Nicolas Bellouin (United Kingdom/France), Ingo Bethke (Norway/Germany), Michael P. Byrne (United Kingdom /Ireland), Christophe Cassou (France), Deliang Chen (Sweden), Annalisa Cherchi (Italy), Hannah M. Christensen (United Kingdom), Sarah L. Connors (France/United Kingdom), Alejandro Di Luca (Australia, Canada/Argentina), Sybren S. Drijfhout (The Netherlands), Christopher G. Fletcher (Canada/United Kingdom, Canada), Piers Forster (United Kingdom), Javier García-Serrano (Spain), Nathan P. Gillett (Canada), Darrell S. Kaufmann (United States of America), David P. Keller (Germany/United States of America), Ben Kravitz (United States of America), Hongmei Li (Germany/China), Yongxiao Liang (Canada/China), Andrew H. MacDougall (Canada), Elizaveta Malinina (Canada/Russian Federation), Matthew Menary (France/United Kingdom), William J. Merryfield (Canada/United States of America), Seung-Ki Min (Republic of Korea), Zebedee R.J. Nicholls (Australia), Dirk Notz (Germany), Brodie Pearson (United States of America/United Kingdom), Matthew D. K. Priestley (United Kingdom), Johannes Quaas (Germany), Aurélien Ribes (France), Alex C. Ruane (United States of America), Jean-Baptiste Sallée (France), Emilia Sanchez-Gomez (France/Spain), Sonia I. Seneviratne (Switzerland), Aimée B. A. Slangen (The Netherlands), Chris Smith (United Kingdom), Malte F. Stuecker (United States of America/Germany), Ranjini Swaminathan (United Kingdom/India), Peter W. Thorne (Ireland/ United Kingdom), Katarzyna B. Tokarska (Switzerland/Poland), Matthew Toohey (Canada, Germany/Canada), Andrew Turner (United Kingdom), Danila Volpi (Italy), Cunde Xiao (China), Giuseppe Zappa (Italy)

Review Editors:
Krishna Kumar Kanikicharla (Qatar/India), Vladimir Kattsov (Russian Federation), Masahide Kimoto (Japan)

Chapter Scientists:
Sebastian Milinski (Germany), Kyung-Sook Yun (Republic of Korea)

This Chapter should be cited as:
Lee, J. Y., J. Marotzke, G. Bala, L. Cao, S. Corti, J. P. Dunne, F. Engelbrecht, E. Fischer, J. C. Fyfe, C. Jones, A. Maycock, J. Mutemi, O. Ndiaye, S. Panickal, T. Zhou, 2021, Future Global Climate: Scenario-Based Projections and Near-Term Information. In: *Climate Change 2021: The Physical Science Basis. Contribution of Working Group I to the Sixth Assessment Report of the Intergovernmental Panel on Climate Change* [Masson-Delmotte, V., P. Zhai, A. Pirani, S. L. Connors, C. Péan, S. Berger, N. Caud, Y. Chen, L. Goldfarb, M. I. Gomis, M. Huang, K. Leitzell, E. Lonnoy, J. B. R. Matthews, T. K. Maycock, T. Waterfield, O. Yelekçi, R. Yu and B. Zhou (eds.)]. Cambridge University Press. In Press.

Date: August 2021

This document is subject to copy-editing, corrigenda and trickle backs.

ACCEPTED VERSION SUBJECT TO FINAL EDITS

Table of Content

Executive Summary **4**

4.1 Scope and Overview of this Chapter **9**

4.2 Methodology **11**

4.2.1 Models, Model Intercomparison Projects, and Ensemble Methodologies **11**
4.2.2 Scenarios **13**
4.2.3 Sources of Near-Term Information **14**
4.2.4 Pattern Scaling **17**
4.2.5 Quantifying Various Sources of Uncertainty **18**
4.2.6 Display of Model Agreement and Spread **20**

BOX 4.1: Ensemble Evaluation and Weighting **21**

4.3 Projected Changes in Global Climate Indices in the 21st Century **24**

4.3.1 Atmosphere **25**
4.3.1.1 Surface Air Temperature **25**
4.3.1.2 Precipitation **27**
4.3.2 Cryosphere, Ocean, and Biosphere **28**
4.3.2.1 Arctic Sea Ice **28**
4.3.2.2 Global Mean Sea Level **30**
4.3.2.3 Atlantic Meridional Overturning Circulation **30**
4.3.2.4 Ocean and Land Carbon Uptake **31**
4.3.2.5 Surface Ocean pH **32**
4.3.3 Modes of Variability **32**
4.3.3.1 Northern and Southern Annular Modes **32**
4.3.3.2 El Niño-Southern Oscillation **34**
4.3.4 Synthesis Assessment of Projected Change in Global Surface Air Temperature **35**

4.4 Near-term Global Climate Changes **39**

4.4.1 Atmosphere **39**
4.4.1.1 Average Global Surface Air Temperature **39**
4.4.1.2 Spatial Patterns of Surface Warming **40**
4.4.1.3 Precipitation **40**
4.4.1.4 Global Monsoon Precipitation and Circulation **41**
4.4.2 Cryosphere, Ocean, and Biosphere **42**
4.4.2.1 Arctic Sea Ice **42**
4.4.2.2 Ocean and Land Carbon flux **43**
4.4.3 Modes of Variability **44**
4.4.3.1 Northern and Southern Annular Modes **44**
4.4.3.2 El Niño-Southern Oscillation **45**
4.4.3.3 Indian Ocean Basin and Dipole Modes. **46**
4.4.3.4 Tropical Atlantic Modes **46**
4.4.3.5 Pacific Decadal Variability **47**
4.4.3.6 Atlantic Multidecadal Variability **47**
4.4.4 Response to Short-Lived Climate Forcers and Volcanic Eruptions **48**

Cross-Chapter Box 4.1: The climate effects of volcanic eruption **51**

4.5 Mid- to Long-term Global Climate Change **53**

4.5.1 Atmosphere **53**
4.5.1.1 Near-Surface Air Temperature 53

ACCEPTED VERSION SUBJECT TO FINAL EDITS

4.5.1.2 Annual Mean Atmospheric Temperature 57
4.5.1.3 Near-Surface Relative Humidity 58
4.5.1.4 Precipitation 60
4.5.1.5 Global Monsoon Precipitation and Circulation 61
4.5.1.6 Sea Level Pressure, Large-scale Atmospheric Circulation, Storm Tracks and Blocking 62
4.5.2 Ocean 67
4.5.2.1 Ocean Temperature 67
4.5.2.2 Ocean acidification 67
4.5.3 Modes of Variability 68
4.5.3.1 Northern and Southern Annular Modes 68
4.5.3.2 El Niño-Southern Oscillation 69
4.5.3.3 Indian Ocean Basin and Dipole Modes 70
4.5.3.4 Tropical Atlantic Modes 71
4.5.3.5 Pacific Decadal Variability 71
4.5.3.6 Atlantic Multidecadal Variability 71

4.6 Implications of Climate Policy 72

4.6.1 Patterns of Climate Change for Specific Levels of Global 72
4.6.1.1 Temperature 73
4.6.1.2 Precipitation 74
4.6.1.3 Atmospheric Circulation 75
4.6.2 Climate Goals, Overshoot, and Path-Dependence 76
4.6.2.1 Climate change under overshoot 76
4.6.2.2 Consistency between Shared Socioeconomic Pathways and Representative Concentration Pathways 77
4.6.3 Climate Response to mitigation, Carbon Dioxide Removal, and Solar Radiation Modification 78
4.6.3.1 Emergence of the climate response to mitigation 79
4.6.3.2 Climate Response to Mitigation by Carbon Dioxide Removal 81
4.6.3.3 Climate Response to Solar Radiation Modification 83

4.7 Climate Change Beyond 2100 91

4.7.1 Commitment and Climate Change Beyond 2100 91
4.7.1.1 Climate change following zero emissions 91
4.7.1.2 Change in Global Climate Indices Beyond 2100 93
4.7.1.2.1 Global Surface Air Temperature 94
4.7.1.2.2 Global Land Precipitation 94
4.7.1.2.3 Arctic Sea Ice 95
4.7.2 Potential for Abrupt and Irreversible Climate Change 95

4.8 Low-Likelihood High-Warming Storylines 97

Frequently Asked Questions 102

FAQ 4.1: How Will the Climate Change over the Next Twenty Years? 102
FAQ 4.2: How Quickly Would We See the Effects of Reducing Carbon Dioxide Emissions? 102
FAQ 4.3: At a given level of global warming, what are the spatial patterns of climate change? 104

Acknowledgements 106

References 107

Figures 148

ACCEPTED VERSION SUBJECT TO FINAL EDITS

Executive Summary

This chapter assesses simulations of future global climate change, spanning time horizons from the near term (2021–2040), mid-term (2041–2060), and long term (2081–2100) out to the year 2300. Changes are assessed relative to both the recent past (1995–2014) and the 1850–1900 approximation to the pre-industrial period.

The projections assessed here are mainly based on a new range of scenarios, the Shared Socio-economic Pathways (SSPs) used in the Coupled Model Intercomparison Project Phase 6 (CMIP6). Among the SSPs, the focus is on the five scenarios SSP1-1.9, SSP1-2.6, SSP2-4.5, SSP3-7.0, and SSP5-8.5. In the SSP labels, the first number refers to the assumed shared socio-economic pathway, and the second refers to the approximate global effective radiative forcing (ERF) in 2100. Where appropriate, this chapter also assesses new results from CMIP5, which used scenarios based on Representative Concentration Pathways (RCPs). Additional lines of evidence enter the assessment, especially for change in globally averaged surface air temperature (GSAT) and global mean sea level (GMSL), while assessment for changes in other quantities is mainly based on CMIP6 results. Unless noted otherwise, the assessments assume that there will be no major volcanic eruption in the 21st century. {1.6, 4.2.2, 4.3.2, 4.3.4, 4.6.2, BOX 4.1: Cross-Chapter Box 4.1, Cross-Chapter Box 7.1, 9.6}

Temperature

Assessed future change in GSAT is, for the first time in an IPCC report, explicitly constructed by combining scenario-based projections with observational constraints based on past simulated warming, as well as an updated assessment of equilibrium climate sensitivity (ECS) and transient climate response (TCR). Climate forecasts initialized using recent observations have also been used for the period 2019–2028. The inclusion of additional lines of evidence has reduced the assessed uncertainty ranges for each scenario. {4.3.1, 4.3.4, 4.4.1, 7.5}

In the near term (2021–2040), a 1.5°C increase in the 20-year average of GSAT, relative to the average over the period 1850–1900, is *very likely* to occur in scenario SSP5-8.5, *likely* to occur in scenarios SSP2-4.5 and SSP3-7.0, and *more likely than not* to occur in scenarios SSP1-1.9 and SSP1-2.6. The threshold-crossing time is defined as the midpoint of the first 20-year period during which the average GSAT exceeds the threshold. In all scenarios assessed here except SSP5-8.5, the central estimate of crossing the 1.5°C threshold lies in the early 2030s. This is about ten years earlier than the midpoint of the *likely* range (2030–2052) assessed in the SR1.5, which assumed continuation of the then-current warming rate; this rate has been confirmed in the AR6. Roughly half of the ten-year difference between assessed crossing times arises from a larger historical warming diagnosed in AR6. The other half arises because for central estimates of climate sensitivity, most scenarios show stronger warming over the near term than was assessed as 'current' in SR1.5 (*medium confidence*). It is *more likely than not* that under SSP1-1.9, GSAT relative to 1850–1900 will remain below 1.6°C throughout the 21st century, implying a potential temporary overshoot of 1.5°C global warming of no more than 0.1°C. If climate sensitivity lies near the lower end of the assessed *very likely* range, crossing the 1.5°C warming threshold is avoided in scenarios SSP1-1.9 and SSP1-2.6 (*medium confidence*). {2.3.1, Cross-chapter Box 2.3, 3.3.1, 4.3.4, BOX 4.1:, 7.5}

By 2030, GSAT in any individual year could exceed 1.5°C relative to 1850–1900 with a likelihood between 40% and 60%, across the scenarios considered here (*medium confidence*). Uncertainty in near-term projections of annual GSAT arises in roughly equal measure from natural internal variability and model uncertainty (*high confidence*). By contrast, near-term annual GSAT levels depend less on the scenario chosen, consistent with the AR5 assessment. Forecasts initialized from recent observations simulate annual GSAT changes for the period 2019–2028 relative to the recent past that are consistent with the assessed *very likely* range (*high confidence*). {4.4.1, BOX 4.1:}

Compared to the recent past (1995–2014), GSAT averaged over the period 2081–2100 is *very likely* to be higher by 0.2°C–1.0°C in the low-emission scenario SSP1-1.9 and by 2.4°C–4.8°C in the high-emission scenario SSP5-8.5. For the scenarios SSP1-2.6, SSP2-4.5, and SSP3-7.0, the corresponding *very likely* ranges are 0.5°C–1.5°C, 1.2°C–2.6°C, and 2.0°C–3.7°C, respectively. The uncertainty ranges for the

ACCEPTED VERSION SUBJECT TO FINAL EDITS

period 2081–2100 continue to be dominated by the uncertainty in ECS and TCR (*very high confidence*). Emissions-driven simulations for SSP5-8.5 show that carbon-cycle uncertainty is too small to change the assessment of GSAT projections (*high confidence*). {4.3.1, 4.3.4, 4.6.2, 7.5}

The CMIP6 models project a wider range of GSAT change than the assessed range (*high confidence*); furthermore, the CMIP6 GSAT increase tends to be larger than in CMIP5 (*very high confidence*). About half of the increase in simulated warming has occurred because higher climate sensitivity is more prevalent in CMIP6 than in CMIP5; the other half arises from higher ERF in nominally comparable scenarios (e.g., RCP8.5 and SSP5-8.5; *medium confidence*). In SSP1-2.6 and SSP2-4.5, ERF changes also explain about half of the changes in the range of warming (*medium confidence*). For SSP5-8.5, higher climate sensitivity is the primary reason behind the upper end of the warming being higher than in CMIP5 (*medium confidence*). {4.3.1, 4.3.4, 4.6.2, 7.5.6}

While high-warming storylines – those associated with GSAT levels above the upper bound of the assessed *very likely* range – are by definition *extremely unlikely*, they cannot be ruled out. For SSP1-2.6, such a high-warming storyline implies long-term (2081–2100) warming well above, rather than well below, 2°C (*high confidence*). Irrespective of scenario, high-warming storylines imply changes in many aspects of the climate system that exceed the patterns associated with the central estimate of GSAT changes by up to more than 50% (*high confidence*). {4.3.4, 4.8}

It is *virtually certain* that the average surface warming will continue to be higher over land than over the ocean and that the surface warming in the Arctic will continue to be more pronounced than the global average over the 21st century. The warming pattern *likely* varies across seasons, with northern high latitudes warming more during boreal winter than summer (*medium confidence*). Regions with increasing or decreasing year-to-year variability of seasonal mean temperatures will *likely* increase in their spatial extent. {4.3.1, 4.5.1, 7.4.4}

It is *very likely* that long-term lower-tropospheric warming will be larger in the Arctic than in the global mean. It is *very likely* that global mean stratospheric cooling will be larger by the end of the 21st century in a pathway with higher atmospheric CO_2 concentrations. It is *likely* that tropical upper tropospheric warming will be larger than at the tropical surface, but with an uncertain magnitude owing to the effects of natural internal variability and uncertainty in the response of the climate system to anthropogenic forcing. {4.5.1, 3.3.1.2}

Precipitation

Annual global land precipitation will increase over the 21st century as GSAT increases (*high confidence*). The *likely* range of change in globally averaged annual land precipitation during 2081–2100 relative to 1995–2014 is –0.2–4.7% in the low-emission scenario SSP1-1.9 and 0.9–12.9% in the high-emission scenario SSP5-8.5, based on all available CMIP6 models. The corresponding *likely* ranges are 0.0–6.6% in SSP1-2.6, 1.5–8.3% in SSP2-4.5, and 0.5–9.6% in SSP3-7.0. {4.3.1, 4.5.1, 4.6.1, 8.4.1}

Precipitation change will exhibit substantial regional differences and seasonal contrast as GSAT increases over the 21st century (*high confidence*). As warming increases, a larger land area will experience statistically significant increases or decreases in precipitation (*medium confidence*). Precipitation will *very likely* increase over high latitudes and the tropical oceans, and *likely* increase in large parts of the monsoon region, but *likely* decrease over large parts of the subtropics in response to greenhouse gas-induced warming. Interannual variability of precipitation over many land regions will increase with global warming (*medium confidence*). {4.5.1, 4.6.1, 8.4.1}

Near-term projected changes in precipitation are uncertain, mainly because of natural internal variability, model uncertainty, and uncertainty in natural and anthropogenic aerosol forcing (*medium confidence*). In the near term, no discernible differences in precipitation changes are projected between different SSPs (*high confidence*). The anthropogenic aerosol forcing decreases in most scenarios, contributing to increases in GSAT (*medium confidence*) and global-mean land precipitation (*low*

ACCEPTED VERSION SUBJECT TO FINAL EDITS

confidence). {4.3.1, 4.4.1, 4.4.4, 8.5}

In response to greenhouse gas-induced warming, it is *likely* that global land monsoon precipitation will increase, particularly in the Northern Hemisphere, although Northern Hemisphere monsoon circulation will *likely* weaken. In the long term (2081–2100), monsoon rainfall change will feature a north–south asymmetry characterized by a greater increase in the Northern Hemisphere than in the Southern Hemisphere and an east–west asymmetry characterized by an increase in Asian-African monsoon regions and a decrease in the North American monsoon region (*medium confidence*). Near-term changes in global monsoon precipitation and circulation are uncertain due to model uncertainty and internal variability such as Atlantic Multi-decadal Variability and Pacific Decadal Variability (*medium confidence*). {4.4.1, 4.5.1, 8.4.1, 10.6.3}

It is *likely* that at least one large volcanic eruption will occur during the 21st century. Such an eruption would reduce GSAT for several years, decrease global-mean land precipitation, alter monsoon circulation, modify extreme precipitation, and change the profile of many regional climatic impact-drivers. A low-likelihood, high-impact outcome would be several large eruptions that would greatly alter the 21st century climate trajectory compared to SSP-based Earth system model projections. {Cross-Chapter Box 4.1}

Large-scale Circulation and Modes of Variability

In the near term, the forced change in Southern Annular Mode in austral summer is *likely* to be weaker than observed during the late 20th century under all five SSPs assessed. This is because of the opposing influence in the near- to mid-term from stratospheric ozone recovery and increases in other greenhouse gases on the Southern Hemisphere summertime mid-latitude circulation (*high confidence*). In the near term, forced changes in the Southern Annular Mode in austral summer are therefore *likely* to be smaller than changes due to natural internal variability. {4.3.3, 4.4.3}

In the long term, the Southern Hemisphere mid-latitude jet is *likely* to shift poleward and strengthen under SSP5-8.5 relative to 1995–2014. This is *likely* to be accompanied by an increase in the Southern Annular Mode index in all seasons relative to 1995–2014. For SSP1-2.6, CMIP6 models project no robust change in the Southern Annular Mode index in the long term. It is *likely* that wind speeds associated with extratropical cyclones will strengthen in the Southern Hemisphere storm track for SSP5-8.5. {4.5.1, 4.5.3}

The CMIP6 multi-model ensemble projects a long-term increase in the boreal wintertime Northern Annular Mode index under the high-emission scenarios of SSP3-7.0 and SSP5-8.5, but regional changes may deviate from a simple shift in the mid-latitude circulation. Substantial uncertainty and thus *low confidence* remain in projecting regional changes in Northern Hemisphere jet streams and storm tracks, especially for the North Atlantic basin in winter; this is due to large natural internal variability, the competing effects of projected upper- and lower-tropospheric temperature gradient changes, and new evidence of weaknesses in simulating past variations in North Atlantic atmospheric circulation on seasonal-to-decadal timescales. One exception is the expected decrease in frequency of atmospheric blocking events over Greenland and the North Pacific in boreal winter in SSP3-7.0 and SSP5-8.5 scenarios (*medium confidence*). {4.5.1}

Near-term predictions and projections of the sub-polar branch of the Atlantic Multi-decadal Variability (AMV) on the decadal timescale have improved in CMP6 models compared to CMIP5 (*high confidence*). This is *likely* to be related to a more accurate response to natural forcing in CMIP6 models. Initialization contributes to the reduction of uncertainty and to predicting subpolar sea surface temperature. AMV influences on the nearby regions can be predicted over lead times of 5–8 years (*medium confidence*). {4.4.3}

It is *virtually certain* that the El Niño–Southern Oscillation (ENSO) will remain the dominant mode of interannual variability in a warmer world. There is no model consensus for a systematic change in intensity of ENSO sea surface temperature (SST) variability over the 21st century in any of the SSP

ACCEPTED VERSION SUBJECT TO FINAL EDITS

scenarios assessed (*medium confidence*). However, it is *very likely* that ENSO rainfall variability, used for defining extreme El Niños and La Niñas, will increase significantly, regardless of amplitude changes in ENSO SST variability, by the second half of the 21st century in scenarios SSP2-4.5, SSP3-7.0, and SSP5-8.5. {4.3.3, 4.5.3, 8.4.2}

Cryosphere and Ocean

Under the SSP2-4.5, SSP3-7.0, and SSP5-8.5 scenarios, it is *likely* that the Arctic Ocean in September, the month of annual minimum sea ice area, will become practically ice-free (sea ice area less than 1 million km^2) averaged over 2081–2100 and all available simulations. Arctic sea ice area in March, the month of annual maximum sea ice area, also decreases in the future under each of the considered scenarios, but to a much lesser degree (in percentage terms) than in September (*high confidence*). {4.3.2}

Under the five scenarios assessed, it is *virtually certain* that global mean sea level (GMSL) will continue to rise through the 21st century. For the period 2081–2100 relative to 1995–2014, GMSL is *likely* to rise by 0.46–0.74 m under SSP3-7.0 and by 0.30–0.54 m under SSP1-2.6 (*medium confidence*). For the assessment of change in GMSL, the contribution from land-ice melt has been added offline to the CMIP6-simulated contributions from thermal expansion. {4.3.2. 9.6}

It is *very likely* that the cumulative uptake of carbon by the ocean and by land will increase through to the end of the 21st century. Carbon uptake by land shows greater increases but with greater uncertainties than for ocean carbon uptake. The fraction of emissions absorbed by land and ocean sinks will be smaller under high emission scenarios than under low emission scenarios (*high confidence*). Ocean surface pH will decrease steadily through the 21st century, except for SSP1-1.9 and SSP1-2.6 where values decrease until around 2070 and then increase slightly to 2100 (*high confidence*). {4.3.2, 5.4}

Climate Response to Emission Reduction, Carbon Dioxide Removal, and Solar Radiation Modification

If strong mitigation is applied from 2020 onward as reflected in SSP1-1.9, its effect on 20-year trends in GSAT would *likely* emerge during the near term (2021–2040), measured against an assumed non-mitigation scenario such as SSP3-7.0 and SSP5-8.5. However, the response of many other climate quantities to mitigation would be largely masked by internal variability during the near term, especially on the regional scale (*high confidence*). The mitigation benefits for these quantities would emerge only later during the 21st century (*high confidence*). During the near term, a small fraction of the surface can show cooling under all scenarios assessed here, so near-term cooling at any given location is fully consistent with GSAT increase (*high confidence*). Events of reduced and increased GSAT trends at decadal timescales will continue to occur in the 21st century but will not affect the centennial warming (*very high confidence*). {4.6.3, Cross-Chapter Box 3.1}

Because of the near-linear relationship between cumulative carbon emissions and GSAT change, the cooling or avoided warming from carbon dioxide removal (CDR) is proportional to the cumulative amount of CO_2 removed by CDR (*high confidence*). The climate system response to net negative CO_2 emissions is expected to be delayed by years to centuries. Net negative CO_2 emissions due to CDR will not reverse some climate change, such as sea level rise, at least for several centuries (*high confidence*). The climate effect of a sudden and sustained CDR termination would depend on the amount of CDR-induced cooling prior to termination and the rate of background CO_2 emissions at the time of termination (*high confidence*). {4.6.3, 5.5, 5.6}

Solar radiation modification (SRM) could offset some of the effects of anthropogenic warming on global and regional climate, but there would be substantial residual and overcompensating climate change at the regional scale and seasonal timescale (*high confidence*), and there is *low confidence* in our understanding of the climate response to SRM, specifically at the regional scale. Since the AR5, understanding of the global and regional climate response to SRM has improved, due to modelling work with more sophisticated treatment of aerosol-based SRM options and stratospheric processes. Improved modelling suggests that multiple climate goals could be met simultaneously. A sudden and sustained

ACCEPTED VERSION SUBJECT TO FINAL EDITS

termination of SRM in a high-emission scenario such as SSP5-8.5 would cause a rapid climate change (*high confidence*). However, a gradual phase-out of SRM combined with emissions reductions and CDR would *more likely than not* avoid larger rates of warming**.** {4.6.3}

Climate Change Commitment and Change Beyond 2100

Earth system modelling experiments since AR5 confirm that the zero CO_2 emissions commitment (the additional rise in GSAT after all CO_2 emissions cease) is small (*likely* less than 0.3°C in magnitude) on decadal time scales, but that it may be positive or negative. There is *low confidence* in the sign of the zero CO_2 emissions commitment. Consistent with SR1.5, the central estimate is taken as zero for assessments of remaining carbon budgets for global warming levels of 1.5°C or 2°C. {4.7.2, 5.5.2}.

Overshooting specific global warming levels such as 2°C has effects on the climate system that persist beyond 2100 (*medium confidence*). Under one scenario including a peak and decline in atmospheric CO_2 concentration (SSP5-3.4-OS), some climate metrics such as GSAT begin to decline but do not fully reverse by 2100 to levels prior to the CO_2 peak (*medium confidence*). GMSL continues to rise in all models up to 2100 despite a reduction in CO_2 to 2040 levels. {4.6.3, 4.7.1, 4.7.2}

Using extended scenarios beyond 2100, projections show *likely* warming by 2300, relative to 1850–1900, of 1.0°C–2.2°C for SSP1-2.6 and 6.6°C–14.1°C for SSP5-8.5. By 2300, warming under the SSP5-3.4-OS overshoot scenario decreases from a peak around year 2060 to a level very similar to SSP1-2.6. Precipitation over land continues to increase strongly under SSP5-8.5. GSAT projected for the end of the 23rd century under SSP2-4.5 (2.3–4.6°C) has not been experienced since the mid-Pliocene, about 3 million years ago. GSAT projected for the end of the 23rd century under SSP5-8.5 (6.6–14.1°C) overlaps with the range estimated for the Miocene Climatic Optimum (5°C–10°C) and Early Eocene Climatic Optimum (10°C–18°C), about 15 and 50 million years ago, respectively (*medium confidence*). {2.3.1.1, 4.7.1}

ACCEPTED VERSION
SUBJEC TO FINAL EDITS

4.1 Scope and Overview of this Chapter

This chapter assesses simulations of future climate change, covering both near-term and long-term global changes. The chapter assesses simulations of physical indicators of global climate change, such as global surface air temperature (GSAT), global land precipitation, Arctic sea-ice area (SIA), and global mean sea level (GMSL). Furthermore, the chapter covers indices and patterns of properties and circulation not only for mean fields but also for modes of variability that have global significance. The choice of quantities to be assessed is summarized in Cross-Chapter Box 2.2 and comprises a subset of the quantities covered in Chapters 2 and 3. This chapter provides consistent coverage from near-term to long-term global changes and provides the global reference for the later chapters covering important processes and regional change.

Essential input to the simulations assessed here is provided by future scenarios of concentrations or anthropogenic emissions of radiatively active substances; the scenarios represent possible sets of decisions by humanity, without any assessment that one set of decisions is more probable to occur than any other set (see Chapter 1, Section 1.6). As in previous assessment reports, these scenarios are used for projections of future climate using global atmosphere-ocean general circulation models (AOGCMs) and Earth system models (ESMs, see Chapter 1, Section 1.5.3); the latter include representation of various biogeochemical cycles such as the carbon cycle, the sulphur cycle, or ozone (e.g., Flato, 2011; Flato et al., 2013). This chapter thus provides a comprehensive assessment of the future global climate response to different future anthropogenic perturbations to the climate system.

Every projection assessment is conditioned on a particular forcing scenario. If sufficient evidence is available, a detailed probabilistic assessment of a physical climate outcome can be performed for each scenario separately. By contrast, there is no agreed-upon approach to assigning probabilities to forcing scenarios, to the point that it has been debated whether such an approach can even exist (e.g., Grübler and Nakicenovic, 2001; Schneider, 2001, 2002). Although there were some recent attempts to ascribe subjective probabilities to scenarios (e.g., Ho et al., 2019; Hausfather and Peters, 2020), and although 'feasibility' along different dimensions is an important concept in scenario research (see AR6 WGIII Chapter 3), the scenarios used for the model-based projections assessed in this chapter do not come with statements about their likelihood of actually unfolding in the future. Therefore, it is usually not possible to combine responses to individual scenarios into an overall probabilistic statement about expected future climate. Exceptions to this limit in the assessment are possible only under special circumstances, such as for some statements about near-term climate changes that are largely independent of the scenario chosen (e.g., Section 4.4.1). Beyond this, no combination of responses to different scenarios can be assessed in this chapter but may be possible in future assessments.

A central element of this chapter is a comprehensive assessment of the sources of uncertainty of future projections (see Chapter 1, Section 1.4.3). Uncertainty can be broken down into scenario uncertainty, model uncertainty involving model biases, uncertainty in simulated effective radiative forcing and model response, and the uncertainty arising from internal variability (Cox and Stephenson, 2007; Hawkins and Sutton, 2009). An additional source of projection uncertainty arises from possible future volcanic eruptions and future solar variability. Assessment of uncertainty relies on multi-model ensembles such as the Coupled Model Intercomparison Project Phase 6 (CMIP6, Eyring et al., 2016), single-model initial-condition large ensembles (e.g., Kay et al., 2015; Deser et al., 2020), and ensembles initialized from the observed climate state (decadal predictions, e.g., Smith et al., 2013a; Meehl et al., 2014a; Boer et al., 2016; Marotzke et al., 2016). Ensemble evaluation methods include assessment of model performance and independence (e.g., Knutti et al., 2017; Boe, 2018; Abramowitz et al., 2019); emergent and other observational constraints (e.g., Allen and Ingram, 2002; Hall and Qu, 2006; Cox et al., 2018); and the uncertainty assessment of equilibrium climate sensitivity and transient climate response in Chapter 7. Ensemble evaluation is assessed in Box 4.1 through the inclusion of lines of evidence in addition to the projection ensembles, including implications for potential model weighting.

The uncertainty assessment in this chapter builds on one particularly noteworthy advance since the IPCC

ACCEPTED VERSION SUBJECT TO FINAL EDITS

Fifth Assessment Report (AR5). Internal variability, which constitutes irreducible uncertainty over much of the time horizon considered here (Hawkins et al., 2016; Marotzke, 2019), can be better estimated in models even under a changing climate through the use of large initial-condition ensembles (Kay et al., 2015). For many climate quantities and compared to the forced climate change signal, internal variability is dominant in any individual realization – including the one that will unfold in reality – in the near term (Kirtman et al., 2013; Marotzke and Forster, 2015), is substantial in the mid-term, and is still recognizable in the long term in many quantities (Deser et al., 2012a; Marotzke and Forster, 2015). This chapter will use the strengthend information on internal variability throughout.

The expanded treatment of uncertainty allows this chapter a more comprehensive assessment of the benefits from mitigation than in previous IPCC reports, as well as the climate response to Carbon Dioxide Removal (CDR) and Solar Radiation Modification (SRM), and how to detect them against the backdrop of internal variability. Important advances have been made in the detection and attribution of mitigation, CDR, and SRM (Bürger and Cubasch, 2015; Lo et al., 2016; Ciavarella et al., 2017); exploring the 'time of emergence' (ToE; see Annex VII: Glossary) of responses to assumed emissions reductions (Tebaldi and Friedlingstein, 2013)(Samset et al., 2020) and the attribution of decadal events to forcing changes that reflect emissions reductions (Marotzke, 2019; Spring et al., 2020)(McKenna et al., 2021).

The question of the potential crossing of thresholds relative to global temperature goals (Geden and Loeschel, 2017) is intimately related to the benefits of mitigation; a prerequisite is an assessment of how robustly magnitudes of warming can be defined (Millar et al., 2017). This chapter provides an update to the IPCC Special Report on Global Warming of 1.5°C (SR1.5, Masson-Delmotte et al., 2018) and constitutes a reference point for later chapters and AR6 WGIII on the effects of mitigation, including a robust uncertainty assessment.

[START FIGURE 4.1 HERE]

Figure 4.1: Visual abstract of Chapter 4. The chapter outline and a quick guide for key topics and corresponding subsections are provided.

[END FIGURE 4.1 HERE]

The chapter is organized as follows (see Figure 4.1). After Section 4.2 on the methodologies used in the assessment, Section 4.3 assesses projected changes in key global climate indicators throughout the 21st century, relative to the period 1995–2014, which comprises the last twenty years of the historical simulations of CMIP6 (Eyring et al., 2016) and hence the most recent past simulated with the observed atmospheric composition. The global climate indicators assessed include GSAT, global land precipitation, Arctic sea-ice area (SIA), global mean sea level (GMSL), the Atlantic Meridional Overturning Circulation (AMOC), global mean ocean surface pH, carbon uptake by land and ocean, the global monsoon, the Northern and Southern Annular Modes (NAM and SAM), and the El Niño–Southern Oscillation (ENSO). Differently from the assessment for changes in other quantities only based on the range of CMIP6 projections, additional lines of evidence enter the assessment for GSAT and GMSL change. For most results and figures based on CMIP6, one realization from each model (the first of the uploaded set) is used. Section 4.3 finally synthesizes the assessment of GSAT change using multiple lines of evidence in addition to the CMIP6 projection simulations.

Section 4.4 covers near-term climate change, defined here as the period 2021–2040 and taken relative to the period 1995–2014. Section 4.4 focuses on global and large-scale climate indicators, including precipitation and circulation indices and selected modes of variability (see Cross-chapter Box 2.2 and Annex AIV), as well as on the spatial distribution of warming. The potential roles of short-lived climate forcers (SLCFs) and volcanic eruptions on near-term climate change are also discussed. Section 4.4 synthesizes information from initialized predictions and non-initialized projections for the near-term change.

ACCEPTED VERSION SUBJECT TO FINAL EDITS

Section 4.5 then covers mid-term and long-term climate change, defined here as the periods 2041–2060 and 2081–2100, respectively, again relative to the period 1995–2014. The mid-term period is thus chosen as the twenty-year period following the short-term period and straddling the mid-century point, year 2050; it is during the mid-term that differences between different scenarios are expected to emerge against internal variability. The long-term period is defined, as in the AR5, as the twenty-year period at the end of the century. Section 4.5 assesses the same set of indicators as Section 4.4, as well as changes in internal variability and in large-scale patterns, both of which are expected to emerge in the mid- to long-term. The chapter sub-division according to time slices (near term, mid-term, and long term) is thus to a large extent motivated by the different roles that internal variability plays in each period, compared to the expected forced climate-change signal.

Section 4.6 assesses the climate implications of climate policies, as simulated with climate models. First, Section 4.6 assesses patterns of climate change expected for various levels of GSAT rise including 1.5°C, 2°C, 3°C, and 4°C, compared to the approximation to the pre-industrial period 1850–1900 to facilitate immediate connection to the SR1.5 and the temperature goals specified in the Paris Agreement (UNFCCC, 2016). Section 4.6 continues with climate goals, overshoot, and path-dependence, as well as the climate response to mitigation, CDR, and SRM. Section 4.6 also covers the consistency between RCPs and SSPs.

Section 4.7 assesses very long-term changes in selected global climate indicators, from 2100 to 2300. Section 4.7 continues with climate-change commitment and the potential for irreversibility and abrupt climate change. The chapter concludes with Section 4.8 on the potential for low-probability–high-impact changes, followed by answers to three frequently asked questions (FAQs).

4.2 Methodology

4.2.1 Models, Model Intercomparison Projects, and Ensemble Methodologies

Similar to the approach used in AR5 (Flato et al., 2013), the primary lines of evidence of this chapter are comprehensive climate models (atmosphere-ocean general circulation models, AOGCMs) and Earth system models (ESMs); ESMs differ from AOGCMs by including representations of various biogeochemical cycles. We also build on results from Earth system models of intermediate complexity (EMICs, Claussen et al., 2002; Eby et al., 2013) and other types of models where appropriate. This chapter focuses on a particular set of coordinated multi-model experiments known as model intercomparison projects (MIPs). These frameworks recommend and document standards for experimental design for running AOGCMs and ESMs to minimise the chance of differences in results being misinterpreted. CMIP is an activity of the World Climate Research Programme (WCRP), and the latest phase is CMIP6 (Eyring et al., 2016). To establish robustness of results, it is vital to assess the performance of these models in terms of mean state, variability, and the response to external forcings. That evaluation has been undertaken using the CMIP6 'Diagnostic, Evaluation and Characterization of Klima' (DECK) and historical simulations in AR6 Chapter 3, which concludes that there is *high confidence* that the CMIP6 multi-model mean captures most aspects of observed climate change well (Chapter 3, Section 3.8.3.1).

This chapter draws mainly on future projections referenced both against the period 1850–1900 and the recent past, 1995–2014, performed primarily under ScenarioMIP (O'Neill et al., 2016). This allows us to assess both dimensions of integration across scenarios (Section 4.3) and global warming levels (Section 4.6) as discussed in Chapter 1, Section 1.6. Other MIPs also target future scenarios with a focus on specific processes or feedbacks and are summarised in Table 4.1.

[START TABLE 4.1 HERE]

Table 4.1: Model Intercomparison Projects (MIPs) utilized in Chapter 4.

MIP / experiment	Usage	Chapter/Section	Reference

ACCEPTED VERSION SUBJECT TO FINAL EDITS

DECK, 1%, 4 • CO_2	Diagnosing climate sensitivity	Assessed in Ch7 ECS and TCR used in GSAT assessment	(Eyring et al., 2016)
CMIP6 Historical	Evaluation, baseline	Assessed in Ch3 Used in chapter 4 to cover reference period	(Eyring et al., 2016)
ScenarioMIP	Future projections	throughout Ch.4	(O'Neill et al., 2016)
AerChemMIP	Aerosols and trace gases	4.4.4	(Collins et al., 2017)
C4MIP	CO_2 emissions driven simulations	4.3.1	(Jones et al., 2016b)
CDRMIP	Carbon Dioxide Removal	4.6.3	(Keller et al., 2018)
GeoMIP	Solar Radiation Modification	4.6.3	(Kravitz et al., 2011)
PDRMIP	Forcing dependence of precipitation	4.5.1	(Myhre et al., 2017)
SIMIP	Sea ice assessment	4.3	(Notz et al., 2016)
ZECMIP	Zero emissions commitment	4.7.1	(Jones et al., 2019a)
CMIP5	RCP scenario assessment	4.6.2, 4.7.1	(Taylor et al., 2012)

[END TABLE 4.1 HERE]

Multi-model ensembles provide the central focus of projection assessment. While single-model experiments have great value for exploring new results and theories, multi-model ensembles additionally underpin the assessment of the robustness, reproducibility, and uncertainty attributable to model internal structure and processes variability (Hawkins and Sutton, 2009) (see Section 4.2.5). Techniques underlying the combination of evaluation and weighting that are applied in this chapter are synthesized in Box 4.1.

Climate model simulations can be performed in either 'concentration-driven' or 'emissions-driven' configuration reflecting whether the CO_2 concentration is prescribed to follow a pre-defined pathway or is simulated by the Earth system models in response to prescribed emissions of CO_2 (see Box 6.4 in Ciais et al., 2013). The majority of CMIP6 experiments are conducted in concentration-driven configurations in order to enable models without a fully interactive carbon cycle to perform them, and throughout most of this chapter we present results from those simulations unless otherwise stated. Concentrations of other greenhouse gases are always prescribed. However, the SSP5-8.5 scenario has also been performed in emissions-driven configuration ('esm-ssp585') by ten ESMs, and in Section 4.3.1.1 we assess the impact on simulated climate over the 21st century.

Internal variability complicates the identification of forced climate signals, especially when considering regional climate signals over short timescales (up to a few decades), such as local trends over the satellite era (Hawkins and Sutton, 2009; Deser et al., 2012a; Xie et al., 2015; Lovenduski et al., 2016; Suárez-Gutiérrez et al., 2017). Large initial-condition ensembles, where the same model is run repeatedly under identical forcing but with initial conditions varied through small perturbations or by sampling different times of a pre-industrial control run, have substantially grown in their use since the AR5 (Deser et al., 2012a; Kay et al., 2015; Rodgers et al., 2015; Hedemann et al., 2017; Stolpe et al., 2018; Maher et al., 2019a). Such large ensembles have shown potential to quantify uncertainty due to internal variability (Hawkins et al., 2016; McCusker et al., 2016; Sigmond and Fyfe, 2016; Lehner et al., 2017; McKinnon et al., 2017; Marotzke, 2019) and thereby extract the forced signal from the internal variability, which can be calibrated against observational data to improve the reliability of probabilistic climate projections over the near and mid-term (O'Reilly et al., 2020). Moreover, they allow the investigation of forced changes in internal variability (e.g., Maher et al., 2018). A key assumption is that a given model skilfully represents internal variability; structural uncertainty is not accounted for.

A complementary approach that represents structural uncertainty in a given model is stochastic physics (Berner et al., 2017). The approach has proven useful in representing structural uncertainty on seasonal

ACCEPTED VERSION SUBJECT TO FINAL EDITS

climate timescales (Weisheimer et al., 2014; Batté and Doblas-Reyes, 2015; MacLachlan et al., 2015). Stochastic physics can markedly improve the internal variability in a given model (Dawson and Palmer, 2015; Wang et al., 2016; Christensen et al., 2017; Davini et al., 2017; Watson et al., 2017; Strømmen et al., 2018; Yang et al., 2019). Stochastic physics can also correct long-standing mean-state biases (Sanchez-Gomez et al., 2016) and can influence the predicted climate sensitivity (Christensen and Berner, 2019; Strommen et al., 2019; Meccia et al., 2020).

Perturbed-physics ensembles (Murphy et al., 2004) are also used to systematically account for parameter uncertainty in a given model. Uncertain model parameters are identified and ranges in their values selected that conform to emergent observational constraints (see Chapter 1, Section 1.5.4.2). These parameters are then changed between ensemble members to sample the effect of parameter uncertainty on climate (Piani et al., 2005; Sexton et al., 2012; Johnson et al., 2018; Regayre et al., 2018). It is possible to weight ensemble members according to some performance metric or emergent constraint (e.g., Fasullo et al., 2015; Section 1.5.4.7) to improve the ensemble distribution (see also Box 4.1).

4.2.2 Scenarios

The AR5 drew heavily on four main scenarios, known as Representative Concentration Pathways (RCPs: Meinshausen et al., 2011; van Vuuren et al., 2011), and simulation results from CMIP5 (Taylor et al., 2012, see Section 4.2.1). The RCPs were labelled by the approximate radiative forcing reached at the year 2100, going from 2.6, 4.5, 6.0 to 8.5 W m^{-2}.

This chapter draws on model simulations from CMIP6 (Eyring et al., 2016) using a new range of scenarios based on Shared Socio-economic Pathways (SSPs; O'Neill et al., 2016). The set of SSPs is described in detail in Chapter 1 (see Section 1.6) and recognizes that global radiative forcing levels can be achieved by different pathways of CO_2, non-CO_2 greenhouse gases (GHGs), aerosols (Amann et al., 2013; Rao et al., 2017), and land use; the set of SSPs therefore establishes a matrix of global forcing levels and socio-economic storylines. ScenarioMIP (O'Neill et al., 2016) identifies four priority (tier-1) scenarios that participating modelling groups are asked to perform, SSP1-2.6 for sustainable pathways, SSP2-4.5 for middle-of-the-road, SSP3-7.0 for regional rivalry, and SSP5-8.5 for fossil-fuel-rich development. This chapter focuses its assessment on these, plus the SSP1-1.9 scenario, which is directly relevant the assessment of the 1.5°C Paris Agreement goal. Further, this chapter discusses these scenarios and their extensions past 2100 in the context of the very long-term climate change in Section 4.7.1. Projections of short-lived climate forcers (SLCFs) are assessed in more detail in Chapter 6 (Section 6.7).

In presenting results and evidence, this chapter tries to be as comprehensive as possible. In tables we show multi-model mean change and 5–95% range for all five SSPs, while in time series figures we show multi-model mean change for all five SSPs but for clarity 5–95% range only for SSP1-2.6 and SSP3-7.0. Where maps are presented, due to space restrictions we focus on showing multi-model mean change for SSP1-2.6 and SSP3-7.0. SSP1-2.6 is preferred over SSP1-1.9 because the latter has far fewer simulations available. The high-end scenarios RCP8.5 or SSP5-8.5 have recently been argued to be implausible to unfold (e.g., (Hausfather and Peters, 2020); see Chapter 3 of the AR6 WGIII). However, where relevant we show results for SSP5-8.5, for example to enable backwards compatibility with AR5, for comparison between emission-driven and concentration-driven simulations, and because there is greater data availability of daily output for SSP5-8.5. When presenting low-likelihood high-warming storylines we also show results from the high-end SSP5-8.5 scenario.

ScenarioMIP simulations include advances in techniques to better harmonize with historical forcings relative to CMIP5. For example, projected changes in the solar cycle include long-term modulation rather than a repeating solar cycle (Matthes et al., 2017). Background natural aerosols are ramped down to an average historical level used in the control simulation by 2025 and background volcanic forcing is ramped up from the value at the end of the historical simulation period (2015) over 10 years to the same constant value prescribed for the piControl simulations in the DECK, and then kept fixed – both changes are intended to avoid inconsistent model treatment of unknowable natural forcing to affect the near-term projected warming.

ACCEPTED VERSION SUBJECT TO FINAL EDITS

Complete backward comparability between CMIP5 and CMIP6 scenarios cannot be established for detailed regional assessments, because the SSP scenarios include regional forcings – especially from land use and aerosols – that are different from the CMIP5 RCPs. Even at a global level, a quantitative comparison is challenging between corresponding SSP and RCP radiative forcing levels due to differing contributions to the forcing (Meinshausen et al., 2020) and evidence of differing model responses (Wyser et al., 2020) (Section 4.6.2.2). The RCP scenarios assessed in the AR5 all showed similar, rapid reductions in SLCFs and emissions of SLCF precursor species over the 21st century; the CMIP5 projections hence did not sample a wide range of possible trajectories for future SLCFs (Chuwah et al., 2013). The SSP scenarios assessed in the AR6 offer more scope to explore SLCF pathways as they sample a broader range of air quality policy options (Gidden et al., 2019) and relationships of CO_2 to non-CO_2 greenhouse gases (Meinshausen et al., 2020). Section 4.6.2.2 assesses RCP and SSP differences. Other MIPs (see Section 4.2.1) have been designed to explicitly explore some of the implications of the different socio-economic storylines for a given radiative forcing level.

4.2.3 Sources of Near-Term Information

This subsection describes the three main sources of near-term information used in Chapter 4. These are 1) the projections from the CMIP6 multi-model ensemble introduced in Section 4.2.1 (Eyring et al., 2016; O'Neill et al., 2016), 2) observationally constrained projections (Gillett et al., 2013; Stott et al., 2013), and 3) the initialized predictions contributed to CMIP6 from the Decadal Climate Prediction Project (DCPP, Boer et al., 2016). The projections under 1) and the observational constraints under 2) are used for all time horizons considered in this chapter, whereas the initialized predictions under 3) are relevant only in the near term.

Observationally constrained projections (Gillett et al., 2013, 2021; Shiogama et al., 2016; Ribes et al., 2021) use detection and attribution methods to attempt to reach consistency between observations and models and thus provide improved projections of near-term change. Notable advances have been made since the AR5, for example the ability to observationally constrain estimates of Arctic sea-ice loss for global warming of 1.5°C, 2.0°C, and 3.0°C above pre-industrial levels (Screen and Williamson, 2017; Jahn, 2018; Screen, 2018; Sigmond et al., 2018). There is *high confidence* that these approaches can reduce the uncertainties involved in such estimates.

The AR5 was the first IPCC report to assess decadal climate predictions initialized from the observed climate state (Kirtman et al., 2013), and assessed with *high confidence* that these predictions exhibit positive skill for near-term average surface temperature information, globally and over large regions, for up to ten years. Substantially more experience in producing initialized decadal predictions has been gained since the AR5; the remainder of this subsection assesses the advances made.

Because the 'memory' that potentially enables prediction of multi-year to decadal internal variability resides mainly in the ocean, some systems initialize the ocean state only (e.g., Müller et al., 2012; Yeager et al., 2018), whereas others incorporate observed information in the initial atmospheric states (e.g., Pohlmann et al., 2013; Knight et al., 2014) or other non-oceanic drivers that provide further sources of predictability (Alessandri et al., 2014; Weiss et al., 2014; Bellucci et al., 2015a).

Ocean initialization techniques generally use one of two strategies. Under full-field initialization, estimates of observed climate states are represented directly on the model grid. A potential drawback is that predictions initialized using the full-field approach tend to drift toward the biased climate preferred by the model (Smith et al., 2013a; Bellucci et al., 2015c; Sanchez-Gomez et al., 2016; Kröger et al., 2018; Nadiga et al., 2019). Such drifts can be as large as, or larger than, the climate anomaly being predicted and may therefore obscure predicted climate anomalies (Kröger et al., 2018) unless corrected for through post-processing. By contrast, anomaly initialization reduces drifts by adding observed anomalies (i.e., deviations from mean climate) to the mean model climate (Pohlmann et al., 2013; Smith et al., 2013a; Thoma et al., 2015b; Cassou et al., 2018), but has the disadvantage that the model state is then further from the real world

ACCEPTED VERSION SUBJECT TO FINAL EDITS

from the start of the prediction. For both approaches, unrealistic features in the observation data used for initialization may induce unrealistic transient behavior (Pohlmann et al., 2017; Teng et al., 2017; Nadiga et al., 2019), and non-linearity can reduce forecast skill (Chikamoto et al., 2019). As yet, neither of the initialization strategies has been clearly shown to be superior (Hazeleger et al., 2013; Magnusson et al., 2013; Smith et al., 2013a; Marotzke et al., 2016), although such comparisons may be sensitive to the model, region, and details of the initialization and forecast assessment procedures considered (Polkova et al., 2014; Bellucci et al., 2015c).

There is also a wide range of techniques employed to assimilate observed information into models in order to generate suitable initial conditions (Polkova et al., 2019). These range in complexity from simple relaxation towards observed time series of sea surface temperature (SST) (Mignot et al., 2016) or wind stress anomalies (Thoma et al., 2015a, 2015b), to relaxation toward three-dimensional ocean and sometimes atmospheric state estimates from various sources (e.g., Pohlmann et al., 2013; Knight et al., 2014; Dunstone et al., 2016), or hybrid relaxation combining surface and tri-dimensional restoring as function of ocean basins and depth (Sanchez-Gomez et al., 2016), to sophisticated data assimilation methods such as the ensemble Kalan filter (Nadiga et al., 2013; Counillon et al., 2014, 2016; Msadek et al., 2014; Karspeck et al., 2015; Brune et al., 2018; Cassou et al., 2018; Polkova et al., 2019) the four-dimensional ensemble-variational hybrid data assimilation (He et al., 2017, 2020) and the initialization of sea ice (Guemas et al., 2016; Kimmritz et al., 2018). In addition, decadal predictions necessarily consist of ensembles of forecasts to quantify uncertainty as discussed in Section 4.2.1. A common way to generate an ensemble is through sets of initial conditions containing small variations that lead to different subsequent climate trajectories. A variety of methods and assumptions has been employed to generate and filter initial-condition ensembles for decadal prediction (e.g., Marini et al., 2016; Kadow et al., 2017). As yet, there is no clear consensus as to which initialization and ensemble generation techniques are most effective, and evaluations of their comparative performance within a single modelling framework are needed (Cassou et al., 2018).

A consequence of model imperfections and resulting model systematic errors is that estimates of these errors must be removed from the prediction to isolate the predicted climate anomaly and the phase of the decadal modes of climate variability (see Annex IV, Sections AIV.2.6 and AIV.2.7 and Section 4.4.3.5 and 4.4.3.6). Because of the tendency for systematic drifts to occur following initialization, bias corrections generally depend on time since the start of the forecast, often referred to as lead time. In practice, the lead-time-dependent biases are calculated using ensemble retrospective predictions, also known as hindcasts, and recommended basic procedures for such corrections are provided in previous studies (Goddard et al., 2013; Boer et al., 2016). The biases are also dynamically corrected during hindcasts and predictions by incorporating the multi-year monthly mean analysis increments from the initialization into the initial condition at each integration step (Wang et al., 2013b). Besides mean climate as a function of lead time, further aspects of decadal predictions may be biased, such as the modes of variability (see Annex IV and Chapter 3, Section 3.7) upon which drift patterns are projecting (Sanchez-Gomez et al., 2016), and additional correction procedures have thus been proposed to remove biases in representing long-term trends (Kharin et al., 2012; Kruschke et al., 2016; Balaji et al., 2018; Pasternack et al., 2018), as well as more general dependences of drift on initial conditions (Fučkar et al., 2014; Pasternack et al., 2018; Nadiga et al., 2019).

Many skill measures exist that describe different aspects of the correspondence between predicted and observed conditions, and no single metric should be considered exclusively. Important aspects of forecast performance captured by different skill measures include: 1) the ability to predict the sign and phases of the main modes of decadal variability and their regional fingerprint through teleconnections; 2) the typical magnitude of differences between predicted and observed values, forecast reliability and resolution (Corti et al., 2012); and 3) whether the forecast ensemble appropriately represents uncertainty in the predictions. A framework for skill assessment that encompasses each of these aspects of forecast quality has been proposed (Goddard et al., 2013). A new, process-based method to assess forecast skill in decadal predictions is to analyse how well a specific mechanism is represented at each lead time (Mohino et al., 2016).

One additional aspect of forecast quality assessment is that estimated skill can be degraded by errors in observational datasets used for verification, in addition to errors in the predictions (Massonnet et al., 2016; Ferro, 2017; Karspeck et al., 2017; Juricke et al., 2018). This suggests that skill may tend to be

ACCEPTED VERSION SUBJECT TO FINAL EDITS

underestimated, particularly for climate variables whose observational uncertainties are relatively large, and that the predictions themselves may prove useful for assessing the quality of observational datasets (Massonnet, 2019).

Skill assessments have shown that initialized predictions can out-perform their uninitialized counterparts (Doblas-Reyes et al., 2013; Meehl et al., 2014; Bellucci et al., 2015b; Smith et al., 2018; Yeager et al., 2018; Smith et al., 2019b), although such comparisons are sensitive to the region and variable considered, multi-model predictions are generally more skilful than individual models (Doblas-Reyes et al., 2013; Smith et al., 2013b, 2019b). Considerable skill, especially for temperature, can be attributed to external forcings such as changes in GHG, aerosol concentrations, and volcanic eruptions. On a global scale, this contribution to skill has been found to exceed that from the prediction of internal variability except in the early stages (about one year for global SST) of the forecast (Corti et al., 2015)(Sospedra-Alfonso and Boer, 2020)(Bilbao et al., 2021), though idealized potential skill measures and observations-based studies suggest that improving the prediction of internal variability could extend this crossover to longer lead times (Boer et al., 2013; Årthun et al., 2017). In some cases, part of the skill arises from the ability of initialized predictions to capture observed transitions of major modes of climate variability (Meehl et al., 2016) such as the Pacific Decadal Variability (PDV) and the Atlantic Multidecadal Variability (AMV) (see Sections 4.4.3.5 and 4.4.3.6, and Annex IV, Sections AIV.2.6 and AIV.2.7).

Initialized predictions of near-surface temperature are particularly skilful over the North Atlantic, a region of high potential and realised predictability (Keenlyside et al., 2008; Pohlmann et al., 2009; Boer et al., 2013; Yeager and Robson, 2017). Much of this predictability is associated with the North Atlantic subpolar gyre (Wouters et al., 2013), where skill in predicting ocean conditions is typically high (Hazeleger et al., 2013; Brune and Baehr, 2020) and shifts in ocean temperature and salinity potentially affecting surface climate can be predicted up to several years in advance (Robson et al., 2012; Hermanson et al., 2014), although such assessments remain challenging due to incomplete knowledge of the state of the ocean during the hindcast evaluation periods (Menary and Hermanson, 2018). A substantial improvement of the sub-polar gyre SST prediction is found in CMIP6 models, which is attributed to a more accurate response to the AMOC-related delayed response to volcanic eruptions (Borchert et al., 2021) (see Section 4.4.3). A significant improvement GSAT prediction skill is also found over some land regions including East Asia (Monerie et al., 2018), Eurasia (Wu et al., 2019), Europe (Müller et al., 2012; Smith et al., 2019b) and the Middle East (Smith et al., 2019b).

Skill for multi-year to decadal precipitation forecasts is generally much lower than for temperature, although one exception is Sahel rainfall (Sheen et al., 2017), due to its dependence on predictable variations in North Atlantic SST through teleconnections (Martin and Thorncroft, 2014a) (Annex IV). Predictive skill on decadal timescales is found for extratropical storm-tracks and storm density (Kruschke et al., 2016; Schuster et al., 2019a), atmospheric blocking (Schuster et al., 2019b; Athanasiadis et al., 2020), the Quasi-Biennial Oscillation (QBO) (Scaife et al., 2014; Pohlmann et al., 2019) and over the tropical oceans (tropical trans-basin variability) (Chikamoto et al., 2015). In addition, decadal predictions with large ensemble sizes are able to predict multi-annual temperature (Peters et al., 2011)(Sienz et al., 2016)(Borchert et al., 2019) (Sospedra-Alfonso and Boer, 2020), precipitation (Yeager et al., 2018; Smith et al., 2019b), and atmospheric circulation (Smith et al., 2020) anomalies over certain land regions, although the ensemble-mean magnitudes are much weaker than observed. This discrepancy may be symptomatic of an apparent deficiency in climate models that causes some predictable signal, such as that associated to the North Atlantic Oscillation (NAO) (see Section AIV.2.1), to be much weaker than in nature (Eade et al., 2014; Scaife and Smith, 2018; Strommen and Palmer, 2019; Smith et al., 2020), while others, such as that linked to the Southern Annular Mode (SAM) (see Section AIV.2.2), are more consistent with observations (Byrne et al., 2019)

Evidence is accumulating that additional properties of the Earth system relating to ocean variability may be skilfully predicted on multi-annual timescales. These include levels of Atlantic hurricane activity (Smith et al., 2010; Caron et al., 2017), winter sea-ice in the Arctic (Onarheim et al., 2015; Dai et al., 2020), drought and wildfire (Chikamoto et al., 2017; Paxian et al., 2019; Solaraju-Murali et al., 2019), and variations in the ocean carbon cycle including CO_2 uptake (Li et al., 2016b, 2019; Lovenduski et al., 2019; Fransner et al., 2020) and chlorophyll (Park et al., 2019).

ACCEPTED VERSION SUBJECT TO FINAL EDITS

In summary, despite challenges (Cassou et al., 2018), there is *high confidence* that initialized predictions contribute information to near-term climate change for some regions over multiannual to decadal timescales. Furthermore, there are indications that initialized predictions can constrain near-term projections (Befort et al., 2020). The clearest improvements through initialization are seen in the North Atlantic and related phenomena such as hurricane frequency, Sahel and European rainfall. By contrast, there is *medium* or *low confidence* that uncertainty is reduced for other climate variables.

4.2.4 Pattern Scaling

Projected climate change is typically represented in this chapter for specific future periods. One important source of uncertainty in projections presented for fixed future epochs (time-slabs/time-slices) is the underlying scenario used; another is the structural uncertainty associated with model climate sensitivity. Presenting projections and associated measures of uncertainty for specific periods (see Sections 4.4 and 4.5) remains the most widely applied methodology towards informing climate change impact studies. It is becoming increasingly important from the perspective of climate change and mitigation policy, however, to present projections also as a function of the change in global mean temperature (i.e., global warming levels, GWLs). They are expressed either in terms of changes of global mean surface temperature (GMST) or GSAT (see Chapter 1, Section 1.6.2 and Cross-Chapter Box 2.3). For example, the IPCC SR1.5 (Hoegh-Guldberg et al., 2018) assessed the regional patterns of warming and precipitation change for GMST increase of 1.5°C and 2°C above 1850–1900 levels. Techniques used to represent the spatial variations in climate at a given GWL are referred to as pattern scaling.

In the 'traditional' methodology as applied in the AR5 (Collins et al., 2013), patterns of climate change in space are calculated as the product of the change in GSAT at a given point in time and a spatial pattern of change that is constant over time and the scenario under consideration, and which may or may not depend on a particular climate model (Allen and Ingram, 2002; Mitchell, 2003; Lambert and Allen, 2009; Andrews and Forster, 2010; Bony et al., 2013; Lopez et al., 2014). This approach assumes that external forcing does not affect the internal variability of the climate system, which may be regarded a stringent assumption when taking into account decadal and multi-decadal variability (Lopez et al., 2014) and the potential nonlinearity of the climate change signal. Moreover, pattern scaling is expected to have lower skill for variables with large spatial variability (Tebaldi and Arblaster, 2014). Pattern scaling also fails to capture changes in boundaries that moves poleward such as sea-ice extent and snow cover (Collins et al., 2013), and temporal frequency quantities such as frost days that decrease under warming but are bounded at zero. Spatial patterns are also expected to be different between transient and equilibrium simulations because of the long adjustment timescale of the deep ocean.

Further developments of the AR5 approach have since explored the role of aerosols in modifying regional climate responses at a specific degree of global warming and also the effect of different GCMs and scenarios on the scaled spatial patterns (Frieler et al., 2012; Levy et al., 2013). Furthermore, the modified forcing-response framework (Kamae and Watanabe, 2012, 2013; Sherwood et al., 2015), which decomposes the total climate change into fast adjustments and slow response, identifies the fast adjustment as forcing-dependent and the slow response as forcing-independent, scaling with the change in GSAT.

For precipitation change, there is near-zero fast adjustment for solar forcing but suppression during the fast-adjustment phase for CO_2 and black-carbon radiative forcing (Andrews et al., 2009; Bala et al., 2010; Cao et al., 2015). By contrast, the slow response in precipitation change is independent of the forcing. This indicates that pattern scaling is not expected to work well for climate variables that have a large fast-adjustment component. Even in such cases, pattern scaling still works for the slow response component, but a correction for the forcing-dependent fast adjustment would be necessary to apply pattern scaling to the total climate change signal. In a multi-model setting, it has been shown that temperature change patterns conform better to pattern scaling approximation than precipitation patterns (Tebaldi and Arblaster, 2014).

(Herger et al., 2015) have explored the use of multiple predictors for the spatial pattern of change at a given

ACCEPTED VERSION SUBJECT TO FINAL EDITS

degree of global warming, following the approach of Joshi et al. (2013) that explored the role of the land-sea warming ratio as a second predictor. They found that the land-sea warming contrast changes in a non-linear way with GSAT, and that it approximates the role of the rate of global warming in determining regional patterns of climate change. The inclusion of the land-sea warming contrast as the second predictor provides the largest improvement over the traditional technique. However, as pointed out by Herger et al. (2015), multiple-predictor approaches still cannot detect nonlinearities (or internal variability), such as the apparent dependence of spatial temperature variability in the mid- to high latitudes on GSAT (e.g. Screen, 2014; Fischer and Knutti, 2014).

An alternative to the traditional pattern scaling approach is the time-shift method described by Herger et al. (2015) which is applied in this chapter (also called the epoch approach, see Section 4.6.1). When applied to a transient scenario such as SSP5-8.5, a future time-slab is referenced to a particular increase in the GSAT (e.g., 1.5°C or 2°C of global warming above pre-industrial levels). The spatial patterns that result represent a direct scaling of the spatial variations of climate change at the particular level of global warming. An important advantage of this approach is that it ensures physical consistency between the different variables for which changes are presented (Herger et al., 2015). The internal variability does not have to be scaled and is consistent with the GSAT change. The time-shift method furthermore allows for a partial comparison of how the rate of increase in GSAT influences the regional spatial patterns of climate change. For example, spatial patterns of change for global warming of 2°C can be compared across the SSP2-4.5 and SSP5-8.5 scenarios. Direct comparisons can also be obtained between variations in the regional impacts of climate change for the case where global warming stabilizes at, for instance, 1.5°C or 2°C of global warming, as opposed to the case where the GSAT reaches and then exceeds the 1.5°C or 2°C thresholds (Tebaldi and Knutti, 2018). An important potential caveat is that forcing mechanisms such as aerosol radiative forcing are represented differently in different models, even for the same SSP. This may imply different regional aerosol direct and indirect effects, implying different regional climate change patterns. Hence, it is important to consider the variations in the forcing mechanisms responsible for a specific increase in GSAT towards understanding the uncertainty range associated with the variations in regional climate change. A minor practical limitation of this approach is that stabilization scenarios at 1.5°C or 2°C of global warming, such as SSP1-2.6, do not allow for spatial patterns of change to be calculated from these scenarios at higher levels of global warming, while it is possible in scenarios such as SSP5-8.5 (Herger et al., 2015).

In this chapter, the spatial patterns of change as a function of GWLs (defined in terms of the increase in the GSAT relative to 1850–1900) are thus constructed using the time-shift approach, thereby accounting for various nonlinearities and internal variability that influence the projected climate change signal. This implies a reliance on large ensemble sizes to quantify the role of uncertainties in regional responses to different degrees of global warming. The assessment in Section 4.6.1 also explores how the rate of global warming (as represented by different SSPs), aerosol effects, and transient as opposed to stabilization scenarios influence the spatial variations in climate change at specific levels of global warming.

4.2.5 Quantifying Various Sources of Uncertainty

The AR5 assessed with *very high confidence* that climate models reproduce the general features of the global-scale annual mean surface temperature increase over the historical period, including the more rapid warming in the second half of the 20th century, and the cooling immediately following large volcanic eruptions. Furthermore, because climate and Earth system models are based on physical principles, they were assessed in the AR5 to reproduce many important aspects of observed climate. Both aspects were argued to contribute to our confidence in the models' suitability for their application in quantitative future predictions and projections (Flato et al., 2013). The AR6 assesses in Chapter 3, Section 3.8.2, with *high confidence* that for most large-scale indicators of climate change, the recent mean climate simulated by the latest generation climate models underpinning this assessment has improved compared to the models assessed in the AR5, and with *high confidence* that the multi-model mean captures most aspects of observed climate change well. These assessments form the foundation of applying climate and Earth system models to the projections assessed in this chapter. Where appropriate, the assessment of projected changes is accompanied by an assessment of process understanding and model evaluation.

ACCEPTED VERSION SUBJECT TO FINAL EDITS

That said, fitness-for-purpose of the climate models used for long-term projections is fundamentally difficult to ascertain and remains an epistemological challenge (Parker, 2009; Frisch, 2015; Baumberger et al., 2017). Some literature exists comparing previous IPCC projections to what has unfolded over the subsequent decades (Cubasch et al., 2013), and recent work has confirmed that climate models since around 1970 have projected global surface warming in reasonable agreement with observations once the difference between assumed and actual forcing has been taken into account (Hausfather et al., 2020). However, the long-term perspective to the end of the 21st century or even out to 2300 takes us beyond what can be observed in time for a standard evaluation of model projections, and in this sense the assessment of long-term projections will remain fundamentally limited.

The spread across individual runs within a multi-model ensemble represents the response to a combination of different sources of uncertainties (see Chapter 1, Section 1.4.3), specifically: scenario uncertainties, climate response uncertainties (also referred to as model uncertainties) related to parametric and other structural uncertainties in the model representation of the climate system, and internal variability (e.g., Hawkins and Sutton, 2009; Kirtman et al., 2013). While the nature of these uncertainties was introduced in Section 1.4.3, this subsection assesses methods to disentangle different sources of uncertainties and quantify their contributions to the overall ensemble spread.

As discussed extensively in the AR5 (Collins et al., 2013), ensemble spread in projections performed with different climate models accounts for only part of the entire model uncertainty, even when considering the uncertainty in the radiative forcing in projections (Vial et al., 2013) and forced response. The AR5 uncertainty characterisation (Kirtman et al., 2013) followed Hawkins and Sutton (2009) and diagnosed internal variability through a high-pass temporal filter. This approach has deficiencies particularly if internal variability manifests on the multi-decadal timescales (Deser et al., 2012a; Marotzke and Forster, 2015) and is classified as (model) response uncertainty instead of internal variability. Single-model initial-condition large ensembles revealed that the AR5 approach underestimates the role of internal variability uncertainty and overestimates the role of model uncertainty (Maher et al., 2018; Stolpe et al., 2018; Lehner et al., 2020) particularly at the local scale while yielding a reasonable approximation for uncertainty separation for GSAT (Lehner et al., 2020).

Single-model initial-condition large ensembles thus represent a crucial step towards a cleaner separation of model uncertainty and internal variability than available for the AR5 (Deser et al., 2014, 2016; Saffioti et al., 2017; Sippel et al., 2019; Milinski et al., 2020; von Trentini et al., 2020; Maher et al., 2021). Novel approaches have been proposed to further quantify internal variability in multi-model ensembles (Hingray and Saïd, 2014; Evin et al., 2019; Hingray et al., 2019). For time horizons beyond the limit of decadal predictability (Branstator and Teng, 2010; Meehl et al., 2014; Marotzke et al., 2016), such as in the CMIP6 projections, the simulations are starting from random rather than assimilated initial conditions. Internal variability constitutes an uncertainty in the projection of the climate in a future period of 10 or 20 years that is irreducible, but can be precisely quantified for individual models using sufficiently large initial-condition ensembles (Fischer et al., 2013; Deser et al., 2016; Hawkins et al., 2016; Pendergrass et al., 2017; Luo et al., 2018; Dai and Bloecker, 2019; Maher et al., 2019a; Deser et al., 2020).

Uncertainties in emissions of greenhouse gases and aerosols that affect future radiative forcings are represented by selected SSP scenarios (Section 4.2.2, Section 1.6.1). In addition to emission uncertainties, SSPs represent uncertainties in land use changes (van Vuuren et al., 2011)(Ciais et al., 2013)(O'Neill et al., 2016)(Christensen et al., 2018). Additional uncertainty comes from climate carbon-cycle feedbacks and the residence time of atmospheric constituents, and are at least partly accounted for in emission-driven simulations as opposed to concentration-driven simulations (Friedlingstein et al., 2014; Hewitt et al., 2016). The climate carbon-cycle feedbacks affect the transient climate response to emissions (TCRE). Constraining this uncertainty is crucial for the assessment of remaining carbon budgets consistent with global mean temperature levels (Millar et al., 2017; Masson-Delmotte et al., 2018) and is covered in Chapter 5 of this Report. Finally, there are uncertainties in future solar and volcanic forcing (see Cross-Chapter Box 4.1)

The relative magnitude of model uncertainty and internal variability depends on the time horizon of the

ACCEPTED VERSION SUBJECT TO FINAL EDITS

projection, location, spatial and temporal aggregation, variable, and signal strength (Rowell, 2012; Fischer et al., 2013; Deser et al., 2014; Saffioti et al., 2017; Kirchmeier-Young et al., 2019). New literature published after the AR5 systematically discusses the role of different sources of uncertainty and shows that the relative contribution of internal variability is larger for short than for long projection horizons (Marotzke and Forster, 2015; Lehner et al., 2020; Maher et al., 2021), larger for high latitudes than for low latitudes, larger for land than for ocean variables, larger at station level than continental than global means, larger for annual maxima/minima than for multi-decadal means, larger for dynamic quantities (and, by implication, precipitation) than for temperature (Fischer et al., 2014).

The method introduced by Hawkins and Sutton (2009) and applied to GSAT projections reveals that by the end of the 21st century, the fraction contribution of the climate model response uncertainty to the total uncertainty is larger in CMIP6 than in CMIP5 whereas the relative contribution of scenario uncertainty is smaller (Lehner et al., 2020). This is the case even when sub-selecting pathways and scenarios that are most similar in CMIP5 and CMIP6, i.e. the range from RCP2.6 to RCP8.5 vs. SSP1-2.6 to SSP5-8-5, respectively (Lehner et al., 2020). The larger range of response uncertainty is further consistent with the larger range of TCR and GSAT warming for a comparable pathway in CMIP6 than CMIP5 (Forster et al., 2020; Tokarska et al., 2020).

Some uncertainties are not, or only partially accounted for in the CMIP6 experiments, such as uncertainties in natural forcings from solar and volcanic forcings, long-term Earth system feedbacks including land-ice feedbacks, groundwater feedbacks (Smerdon, 2017) or some long-term carbon-cycle feedbacks (Fischer et al., 2018). Where appropriate, this chapter uses results from non-CMIP ESMs or EMICs to assess the role of these feedbacks. Still other uncertainties – such as further pandemics, nuclear holocaust, global natural disaster such as tsunami or asteroid impact, or fundamental technological change such as fusion – are not accounted for at all.

4.2.6 Display of Model Agreement and Spread

Maps of multi-model mean changes provide an average estimate for the forced model climate response to a certain forcing. However, they do not include any information on the robustness of the response across models nor on the significance of the change with respect to unforced internal variability (Tebaldi et al., 2011). Models can consistently show absence of significant change, in which case they should not be expected to agree on the sign of a change (e.g., Tebaldi et al., 2011; Knutti and Sedláček, 2012; Fischer et al., 2014). If a multi-model mean map of precipitation shows no change, it is unclear whether the models consistently project insignificant changes or whether projections span both significant increases and significant decreases. Several methods have been proposed to distinguish significant conflicting signals from agreement on no significant change (Tebaldi et al., 2011; Knutti and Sedláček, 2013; McSweeney and Jones, 2013; Zappa et al., 2021). A set of different methods have been introduced in the literature to display model robustness and to put a climate change signal into the context of internal variability. AR5 Box 12.1 provides a detailed assessment of different methods of mapping model robustness and Cross-Chapter Box Atlas.1 provides an update of recent proposals including the methods used in this report.

Most methods for quantifying robustness assume that only one realization from each model is applied. There are challenges that arise from having heterogeneous multi-model ensembles with many members for some models and single members for others (Olonscheck and Notz, 2017; Evin et al., 2019). Furthermore, the methods that map model robustness usually ignore that sharing parametrizations or entire components across coupled models can lead to substantial model interdependence (Fischer et al., 2011; Kharin et al., 2012; Knutti et al., 2013, 2017; Leduc et al., 2015; Sanderson et al., 2015, 2017; Annan and Hargreaves, 2017; Boe, 2018; Abramowitz et al., 2019). This may lead to a biased estimate of model agreement if a substantial fraction of models is interdependent. The methodologies and results in these literature since AR5 are higher in quality and clarity. However, quantifying and accounting for model dependence in a robust way remains challenging (Abramowitz et al., 2019). Furthermore, absence of significant mean change in a certain climate variable does not imply absence of substantial impact, because there may be substantial change in variability, which is typically not mapped (McSweeney and Jones, 2013).

ACCEPTED VERSION SUBJECT TO FINAL EDITS

Chapter 4 uses the advanced approach, taking into account the sign and significance of the change (Cross-Chapter Box Atlas.1, approach C). Where not applicable, such as due to a lack of the necessary model output, the simple method is used taking into account only agreement on the sign of the change across the multi-model ensemble (Cross-Chapter Box Atlas.1, approach B). The advanced approach is similar to the method used in AR5 but isolates conflicting signals as proposed in (Zappa et al., 2021). It uses three mutually exclusive categories and distinguishes (a) areas with significant change and high model agreement (no overlay), (b) areas with no change or no robust change (diagonal lines), and (c) areas with significant change but low agreement (crossed lines). Category (a) marks areas where the climate change signals *likely* emerge from internal variability, where two-thirds or more of the models project changes greater than internal variability and 80% or more of the models agree on the sign of the change. Category (b) marks areas where fewer than two-thirds of the models project changes greater than internal variability, and category (c) marks areas with significant but conflicting signals, where two-thirds or more of the models project changes greater than internal variability but less than 80% agree on the sign of the change.

In this chapter variability is defined as $1.645 \cdot \sqrt{2}\,\sigma_{20yr}$, where σ_{20yr} is the standard deviation of 20-year means in the pre-industrial control simulations (see Cross-Chapter Box Atlas.1). Category (a) uses a definition very similar to the AR5 method for stippling except that the model signal is compared to its corresponding internal rather than the multi-model mean variability, to account for the substantial model differences in pre-industrial internal variability (Parsons et al., 2020). Changes smaller than internal variability can have potential impacts particularly if they persist over sustained periods such as several decades. Finally, even when changes do not exceed variability at the grid point level they may exceed variability if aggregated over catchment basins, regions, or continents (Cross-Chapter Box Atlas.1). Maps of mean changes also ignore potential changes in variability addressed by a more comprehensive assessment of changes in temperature variability (Section 4.5.1) and modes of internal variability (Sections 4.4.3).

[START BOX 4.1 HERE]

BOX 4.1: Ensemble Evaluation and Weighting

AR5 used a pragmatic approach to quantify the uncertainty in CMIP5 GSAT projections (Collins et al., 2013). The multi-model ensemble was constructed by picking one realization per model per scenario. For most quantities, the 5–95% ensemble range was used to characterize the uncertainty, but the 5–95% ensemble range was interpreted as the 17–83% (*likely*) uncertainty range. The uncertainty was thus explicitly assumed to contain sources not represented by the model range. While straightforward and clearly communicated, this approach had several drawbacks.

i) The uncertainty breakdown into scenario uncertainty, model uncertainty, and internal variability (Cox and Stephenson, 2007; Hawkins and Sutton, 2009) in the AR5 followed Hawkins and Sutton (2009) and diagnosed internal variability through a high-pass temporal filter (Kirtman et al., 2013), but it has since become clear that even multi-decadal trends contain substantial internal variability relative to the forced response in many variables (e.g., (Deser et al., 2012a; Marotzke and Forster, 2015; Deser et al., 2020; Lehner et al., 2020)); hence a more comprehensive approach is needed.

ii) The uncertainty characterization ignores observation-based information about internal climate variability during the most recent past, such as is used in initialized predictions. While this may matter little for the long-term projections (Collins et al., 2013), it is very important for the near-term future (Kirtman et al., 2013). AR5 included additional uncertainty quantification for the near-term projections (Kirtman et al., 2013), leading to a downward adjustment of assessed near-term GSAT change, which created an inconsistency in the transition from near-term to long-term GSAT assessment in the AR5.

iii) AR5 used the range of CMIP5 equilibrium climate sensitivity (ECS) side-by-side with the ECS *likely* range assessed from multiple lines of evidence (the CMIP5 ensemble, instrumental observations, and paleo-information, (Collins et al., 2013)). While the CMIP5 range in ECS and the AR5 ECS *likely* range did not differ much, the difference did create an inconsistency. Furthermore, AR5 WGIII used the assessed *likely* range for ECS in their calculations of carbon budgets (IPCC,

ACCEPTED VERSION SUBJECT TO FINAL EDITS

2014), and these uncertainties matter a great deal when assessing remaining carbon budgets consistent with limiting global warming to 1.5°C above pre-industrial levels (Millar et al., 2017, 2018a, 2018b; Schurer et al., 2018)(Rogelj et al., 2018b).

Another important consideration concerns the potential weighting of model contributions to an ensemble, based on model independence, model performance during the historical period, or both. Such model weighting (in fact, model selection) was performed in the AR5 for projections of Arctic sea ice (Collins et al., 2013), but that particular application has subsequently been shown by Notz (2015) to be contaminated by internal variability, making the resulting weighting questionable (see also Stroeve and Notz (2015)). For a general cautionary note, see Weigel et al. (2010). Approaches that take into account internal variability and model independence have been proposed since AR5 (Knutti et al., 2017; Boe, 2018; Abramowitz et al., 2019; Brunner et al., 2020).

There are hence good reasons for basing an assessment of future global climate on lines of evidence in addition to the projection simulations. However, despite some progress, no universal, robust method for weighting a multi-model projection ensemble is available, and expert judgement must be included, as it did for AR5, in the assessment of the projections. The default in this chapter follows the AR5 approach for GSAT (Collins et al., 2013) and interprets the CMIP6 5–95% ensemble range as the *likely* uncertainty range.

Additional lines of evidence enter the assessment particularly for the most important indicator of global climate change, GSAT. The CMIP6 ensemble generally shows larger projected warming by the end of the 21st century, relative to the average over the period 1995–2014, than the CMIP5 ensemble (Section 4.3.1). The warming has increased in part because of models with higher ECS in CMIP6, compared to CMIP5 (e.g., Meehl et al., 2020; Tokarska et al., 2020; Zelinka et al., 2020; Zhu et al., 2020, *high confidence*), and in part because of higher ERF in CMIP6 than in CMIP5 (e.g., Tebaldi et al., 2021, Section 4.6.2). Because change in several other important climate quantities scales with change in GSAT (Section 4.2.4), bringing in additional lines of evidence is particularly important for the GSAT assessment.

The Chapter 4 assessment uses information from the following sources:

(i) The CMIP6 multi-model ensemble (Eyring et al., 2016), augmented if appropriate by the CMIP5 ensemble (Taylor et al., 2012).

(ii) Single-model large initial-condition ensembles (e.g., Kay et al., 2015; Sigmond and Fyfe, 2016; Maher et al., 2019) and combinations of control runs with CMIP transient simulations (e.g., Thompson et al., 2015; Olonscheck and Notz, 2017) to characterize internal variability. Several analyses using multiple large ensembles have recently become available and add robustness to the results (Maher et al., 2018, 2019b, 2020; Deser et al., 2020; Lehner et al., 2020)(Maher et al., 2021).

(iii) Assessed best estimates, *likely*, and *very likely* ranges of ECS and TCR, from process understanding, warming in the instrumental record, paleoclimates, and emergent constraints (Chapter 7, Table 7.13, Table 7.14, Section 7.5). The ECS and TCR ranges are converted into GSAT ranges using as an emulator a two-layer energy balance model (EBM, e.g., Held et al., 2010) that is driven by the effective radiative forcing (ERF) assessed in Chapter 7 (see Cross-Chapter Box 7.1). Assuming for the ERF resulting from a doubling of the CO_2 concentration, $\Delta F_{2\cdot CO2}$=4.0 W m^{-2} (close to the best estimate of 3.93 W m^{-2}, Section 7.3), and using the so-called zero-layer approximation to the EBM (e.g., Marotzke and Forster, 2015; Jiménez-de-la-Cuesta and Mauritsen, 2019) permits a one-to-one translation of any pair of ECS and TCR into a pair of climate feedback parameter α and ocean heat uptake coefficient $\kappa\varepsilon$, using the simple equations $\alpha=-\Delta F_{2\cdot CO2}\ ECS^{-1}$ and $\kappa\varepsilon=\Delta F_{2\cdot CO2}\ TCR^{-1}-\Delta F_{2\cdot CO2}\ ECS^{-1}$ (e.g., Jiménez-de-la-Cuesta and Mauritsen, 2019); see Chapter 7 for a detailed discussion). The results are displayed in Box 4.1, Figure 1 and are used in the synthesis GSAT assessment in Section 4.3.4.

(iv) Model independence diagnosed a priori, based on shared model components for atmosphere, ocean, land surface, and sea ice of CMIP5 models (Boe, 2018). CMIP5 models have been re-sampled assuming that two models sharing either the atmosphere or the ocean component are effectively the same model (Maher et al., 2021). Downweighting CMIP5 models that share a

ACCEPTED VERSION SUBJECT TO FINAL EDITS

component with another has substantial influence on diagnosed model agreement on change in ENSO (Maher et al., 2021), but has negligible influence (much less than 0.1°C) on the ensemble mean and range of GSAT change over the 21st century. No corresponding diagnosis exists yet for CMIP6 models, and no weighting based on a-priori independence is applied here.

(v) Performance in simulating the past and a-posteriori independence based on comparison against observations (Knutti et al., 2017; Abramowitz et al., 2019). This approach has been applied to CMIP6-simulated GSAT and has led to a substantial reduction in model range (Liang et al., 2020, (Brunner et al., 2020), Section 4.3.4). CMIP6-simulated Arctic sea-ice area has been compared to the observed record, and models have been selected whose ensemble range across their individual realizations (Olonscheck and Notz, 2017) includes the observational range of uncertainty. A larger fraction of these selected simulations show an ice-free Arctic in September before 2050, compared to the entire CMIP6 ensemble (Notz and SIMIPCommunity, 2020, Section 4.3.2).

(vi) A linear inverse method (kriging) has combined the entire GSAT record since 1850 with the CMIP6 historical simulations to produce constrained projections for the 21st century; again the reduction in range has been substantial (Ribes et al., 2021; Section 4.3.4).

(vii) Emergent constraints (e.g., (Hall and Qu, 2006; Cox et al., 2018; Brient, 2020), which for the post-1970 warming have been applied to the CMIP5 (Jiménez-de-la-Cuesta and Mauritsen, 2019) and CMIP6 ensembles (Nijsse et al., 2020; Tokarska et al., 2020) and have likewise led to a substantial reduction in GSAT ensemble range (Section 4.3.4).

(viii) Climate predictions initialized from recent observations (e.g., Kirtman et al., 2013) and the Decadal Climate Prediction Project (DCPP) contribution to CMIP6 (Boer et al., 2016; Smith et al., 2020; Sospedra-Alfonso and Boer, 2020). Initialized predictions for the period 2019–2028 exist for eight DCPP models and are used here (Box 4.1 Figure 1, Section 4.4.1). The DCPP results have been drift-removed and referenced to the time-averaged hindcasts for 1995–2014 lead-year by lead-year, following (Kharin et al., 2012; Kruschke et al., 2016).

Box 4.1 Figure 1 shows annual-mean GSAT simulated by CMIP6 models for both the historical period and forced by scenario SSP2-4.5 until 2100, combined with various characterizations of uncertainty. First, internal variability is estimated with the 50-member ensemble simulated with CanESM5. The 5–95% ensemble range for annual-mean GSAT in CanESM5 is slightly below 0.4°C; in other CMIP6 large ensembles this range is about 0.5°C (MIROC6, IPSL-CM6A) and slightly above 0.6°C (S-LENS/EC-Earth3). The CMIP5 large ensemble MPI-GE shows a range of slightly below 0.5°C (Bengtsson and Hodges, 2019), in reasonable agreement with observed variability (Maher et al., 2019b). There is thus *high confidence* in the CMIP6-simulated level of internal variability in annual-mean GSAT, as displayed in Box 4.1, Figure 1.

Second, Section 7.5 *very likely* ECS and TCR ranges are converted into GSAT ranges with the EBM as an emulator using, in this example, SSP2-4.5 radiative forcing information. Because the ECS and TCR assessments in Section 7.5 are based on multiple lines of evidence and the EBM physics are well understood, there is likewise *high confidence* in the EBM-emulated warming. Third, the initialized-forecast ensembles from eight CMIP6 DCPP models are shown in the inset, for the period 2019–2028. During this period, the initialized forecasts are consistent, within internal variability, with the EBM-emulated range, further adding to the *high confidence* in the assessed-GSAT range.

The constrained range of GSAT change is useful for quantifying uncertainties in changes of other climate quanties that scale well with GSAT change, such as September Arctic sea-ice area, global-mean precipitation, and many climate extremes (Cross-Chapter Box 11.1). However, there are also quantities that do not scale linearly with GSAT change, such as global-mean land precipitation, atmospheric circulation, AMOC, and modes of variability, especially ENSO SST variability. Because we do not have robust scientific evidence to constrain changes in other quantities, uncertainty quantification for their changes is based on CMIP6 projections and expert judgement. For the assessment for changes in GMSL, the contribution from land-ice melt has been added offline to the CMIP6 simulated contributions from thermal expansion, consistent with Chapter 9 (see Section 9.6).

ACCEPTED VERSION SUBJECT TO FINAL EDITS

[START BOX 4.1, FIGURE 1 HERE]

Box 4.1 Figure 1: CMIP6 annual-mean GSAT simulations and various contributions to uncertainty in the projections ensemble. The figure shows anomalies relative to the period 1995–2014 (left y-axis), converted to anomalies relative to 1850–1900 (right y-axis); the difference between the y-axes is 0.85°C (Cross-Chapter Box 2.3). Shown are historical simulations with 39 CMIP6 models (grey) and projections following scenario SSP2-4.5 (dark yellow; thin lines: individual simulations; heavy line; ensemble mean; dashed lines: 5% and 95% ranges). The black curve shows the observations-based estimate (HadCRUT5, (Morice et al., 2021)). Light blue shading shows the 50-member ensemble CanESM5, such that the deviations from the CanESM5 ensemble mean have been added to the CMIP6 multi-model mean. The green curves are from the emulator and show the central estimate (solid) and *very likely* range (dashed) for GSAT. The inset shows a cut-out from the main plot and additionally in light purple for the period 2019–2028 the initialized forecasts from eight models contributing to DCPP (Boer et al., 2016); the deep-purple curve shows the average of the forecasts. Further details on data sources and processing are available in the chapter data table (Table 4.SM.1).

[END BOX 4.1, FIGURE 1 HERE]

[END BOX 4.1 HERE]

4.3 Projected Changes in Global Climate Indices in the 21st Century

This section assesses the latest simulations of representative indicators of global climate change presented as time series and tabulated values over the 21st century and across the main realms of the global climate system. In the atmospheric realm (see Section 4.3.1), we assess simulations of GSAT (see Figure 4.2a) and global land precipitation (see Figure 4.2b). Across the cryospheric, oceanic, and biospheric realms (see Section 4.3.2), we assess simulations of Arctic SIA (see Figure 4.2c), GMSL (see Figure 4.2d), the AMOC, ocean and land carbon uptake, and pH. In Section 4.3.3 we assess simulations of several indices of climate variability, namely, the indices of the NAM, SAM, and ENSO. Finally, Section 4.3.4 assesses future GSAT change based on the CMIP6 ensemble in combination with other lines of evidence. An assessment of projected changes in related global extreme indices can be found in Chapter 11.

[START FIGURE 4.2 HERE]

Figure 4.2: Selected indicators of global climate change from CMIP6 historical and scenario simulations. (a) Global surface air temperature changes relative to the 1995–2014 average (left axis) and relative to the 1850–1900 average (right axis; offset by 0.82°C, which is the multi-model mean and close to observed best estimate, Cross-Chapter Box 2.1, Table 1). (b) Global land precipitation changes relative to the 1995–2014 average. (c) September Arctic sea-ice area. (d) Global mean sea-level change (GMSL) relative to the 1995–2014 average. (a), (b) and (d) are annual averages, (c) are September averages. In (a)-(c), the curves show averages over the CMIP6 simulations, the shadings around the SSP1-2.6 and SSP3-7.0 curves show 5–95% ranges, and the numbers near the top show the number of model simulations used. Results are derived from concentration-driven simulations. In (d), the barystatic contribution to GMSL (i.e., the contribution from land-ice melt) has been added offline to the CMIP6 simulated contributions from thermal expansion (thermosteric). The shadings around the SSP1-2.6 and SSP3-7.0 curves show 5–95% ranges. The dashed curve is the *low confidence* and low likelihood outcome at the high end of SSP5-8.5 and reflects deep uncertainties arising from potential ice-sheet and ice-cliff instabilities. This curve at year 2100 indicates 1.7 m of GMSL rise relative to 1995–2014. More information on the calculation of GMSL are available in Chapter 9, and further regional details are provided in the Atlas. Further details on data sources and processing are available in the chapter data table (Table 4.SM.1).

[END FIGURE 4.2 HERE]

ACCEPTED VERSION SUBJEC TO FINAL EDITS

From the CMIP6 multi-model ensemble we consider historical simulations with observed external forcings to 2014 and extensions to 2100 based on the five high-priority scenarios. We use the first realization ('r1') contributed by each modelling group. In tabular form, we show ensemble-mean changes and uncertainties for the near-term (2021–2040), mid-term (2041–2060), and the long-term (2081–2100), relative to present-day (1995–2014) and the approximation to pre-industrial (1850–1900). Changes in precipitation over land near 1.5°C, 2.0°C, 3.0°C, and 4.0°C of global warming relative to 1850–1900 are also assessed.

4.3.1 Atmosphere

4.3.1.1 Surface Air Temperature

The AR5 assessed from CMIP5 simulations and other lines of evidence that GSAT will continue to rise over the 21st century if GHG concentrations continue increasing (Collins et al., 2013). The AR5 concluded that GSAT for 2081–2100, relative to 1986–2005 will *likely* be in the 5–95% range of 0.3°C–1.7°C under RCP2.6 and 2.6°C–4.8°C under RCP8.5. The corresponding ranges for the intermediate emission scenarios with emissions peaking around 2040 (RCP4.5) and 2060 (RCP6.0) are 1.1°C–2.6°C and 1.4°C–3.1°C, respectively. The AR5 further assessed that GSAT averaged over the period 2081–2100 are projected to *likely* exceed 1.5°C above 1850–1900 for RCP4.5, RCP6.0 and RCP8.5 (*high confidence*) and are *likely* to exceed 2°C above 1850–1900 for RCP6.0 and RCP8.5 (*high confidence*). Global surface temperature changes above 2°C under RCP2.6 were deemed *unlikely* (*medium confidence*).

Here, for continuity's sake, we assess the CMIP6 simulations of GSAT in a fashion similar to the AR5 assessment of the CMIP5 simulations. From these, we compute anomalies relative to 1995–2014 and display the evolution of ensemble means and 5–95% ranges (see Figure 4.2). We also use the ensemble mean GSAT difference between 1850–1900 and 1995–2014, 0.82°C, to provide an estimate of the changes since 1850–1900 (see the right axis on Figure 4.2). Finally, we tabulate the ensemble mean changes between 1995–2014 and 2021–2040, 2041–2060, and 2081–2100 respectively (see Figure 4.2).

The CMIP6 models show a 5–95% range of GSAT change for 2081–2100, relative to 1995–2014, of 0.6°C–2.0°C under SSP1-2.6 where CO_2 concentrations peak between 2040 and 2060 (see Table 4.2). The corresponding range under the highest overall emission scenario (SSP5-8.5) is 2.7°C–5.7°C. The ranges for the intermediate emission scenarios (SSP2-4.5 and SSP3-7.0), where CO_2 concentrations increase to 2100, but less rapidly than SSP5-8.5, are 1.4°C–3.0°C and 2.2°C–4.7°C, respectively. The range for the lowest emission scenario (SSP1-1.9) is 0.2°C–1.3°C.

In summary, the CMIP6 models show a general tendency toward larger long-term globally averaged surface warming than did the CMIP5 models, for nominally comparable scenarios (*very high confidence*). In SSP1-2.6 and SSP2-4.5, the 5–95% ranges have remained similar to the ranges in RCP2.6 and RCP4.5, respectively, but the distributions have shifted upward by about 0.3°C (*high confidence*). For SSP5-8.5 compared to RCP8.5, the 5% bound of the distribution has hardly changed, but the 95% bound and the range have increased by about 20% and 40%, respectively (*high confidence*). About half of the warming increase has occurred because of more models with higher climate sensitivity in CMIP6, compared to CMIP5; the other half of the warming increase arises from higher effective radiative forcing in nominally comparable scenarios (*medium confidence,* see Section 4.6.2).

[START TABLE 4.2 HERE]

Table 4.2: CMIP6 annual mean surface air temperature anomalies (°C). Displayed are multi-model averages and, in parentheses, the 5–95% ranges, for selected time periods, regions, and SSPs. The numbers of models used are indicated in Figure 4.2.

ACCEPTED VERSION SUBJECT TO FINAL EDITS

Units = °C	SSP1-1.9	SSP1-2.6	SSP2-4.5	SSP3-7.0	SSP5-8.5
Global: 2021–2040					
relative to 1995–2014	0.7 (0.3, 1.1)	0.7 (0.4, 1.1)	0.7 (0.4, 1.2)	0.7 (0.5, 1.2)	0.8 (0.5, 1.3)
relative to 1850–1900	1.5 (1.1, 2.2)	1.6 (1.1, 2.2)	1.6 (1.0, 2.3)	1.6 (1.0, 2.4)	1.7 (1.2, 2.4)
Global: 2041–2060					
relative to 1995–2014	0.8 (0.3, 1.5)	1.0 (0.6, 1.6)	1.3 (0.8, 1.9)	1.4 (0.9, 2.3)	1.7 (1.2, 2.5)
relative to 1850–1900	1.7 (1.1, 2.4)	1.9 (1.2, 2.7)	2.1 (1.5, 3.0)	2.3 (1.6, 3.2)	2.6 (1.8, 3.4)
Global: 2081–2100					
relative to 1995–2014	0.7 (0.2, 1.5)	1.2 (0.6, 2.0)	2.0 (1.4, 3.0)	3.1 (2.2, 4.7)	4.0 (2.7, 5.7)
relative to 1850–1900	1.5 (1.0, 2.2)	2.0 (1.3, 2.8)	2.9 (2.1, 4.0)	3.9 (2.8, 5.5)	4.8 (3.6, 6.5)
Land: 2081–2100 relative to 1995–2014	0.9 (0.3, 2.0)	1.5 (0.8, 2.6)	2.7 (1.7, 4.0)	4.1 (3.0, 6.2)	5.3 (3.5, 7.6)
Ocean: 2081–2100 relative to 1995–2014	0.6 (0.1, 1.2)	1.0 (0.5, 1.8)	1.8 (1.2, 2.7)	2.7 (1.8, 4.0)	3.4 (2.3, 4.9)
Tropics: 2081–2100 relative to 1995–2014	0.5 (0.1, 1.1)	1.0 (0.5, 1.6)	1.8 (1.2, 2.5)	2.7 (2.0, 4.0)	3.5 (2.4, 4.9)
Arctic: 2081–2100 relative to 1995–2014	2.4 (0.5, 6.6)	3.3 (0.4, 7.5)	5.4 (2.8, 10.0)	7.7 (4.5, 13.4)	10.0 (6.2, 15.2)
Antarctic: 2081–2100 relative to 1995–2014	0.5 (0.0, 1.1)	1.1 (0.1, 2.9)	1.9 (0.6, 3.2)	2.8 (1.3, 4.5)	3.6 (1.7, 5.6)

[END TABLE 4.2 HERE]

With regards to global warming levels (GWL) of 1.5°C, 2.0°C, and 3.0°C, we note that there is unanimity across all of the CMIP6 model simulations that GSAT change relative to 1850–1900 will rise above: 1) 1.5°C following SSP2-4.5, SSP3-7.0, or SSP5-8.5 (on average around 2030); 2) 2.0°C following either SSP3-7.0 or SSP5-8.5 (on average around 2043), and 3) 3.0°C following SSP5-8.5 (on average around 2062). Under SSP1-1.9, 55% and 36% of the model simulations rise above 1.5°C and 2.0°C, respectively, while for SSP1-2.6 those percentages increase to 87% and 58%, respectively. Here, the time of GSAT exceedance is determined as the first year at which 21-year running averages of GSAT exceed the given GWL. In Section 4.3.4, these values are reassessed using CMIP6 ensemble in combination with other lines of evidence.

CMIP6 models project increases in area-weighted land, ocean, tropical (30°S–30°N), Arctic (67.7°N–90°N), and Antarctic (90°S–55°S) surface air temperature (see Table 4.2). Consistent with AR5, and earlier assessments, CMIP6 models project that annual average surface air temperature will warm about 50% more over land than over the ocean, and that the Arctic will warm about more than 2.5 times the global average (see Section 4.5.1). For 2081–2100, relative to 1995–2014, the CMIP6 models show 5–95% ranges of warming over land of 0.3°C–2.0°C and 3.5°C–7.6°C following SSP1-1.9 and SSP5-8.5, respectively. The corresponding ranges for Arctic surface air temperature change are 0.5°C–6.6°C and 6.2°C–15.2°C, respectively.

The concentration-driven simulations presented above use a prescribed CO_2 pathway calculated by the MAGICC7.0 model using the CMIP6 emissions (Meinshausen et al., 2020). This is compared here with the CO_2 concentration simulated by CMIP6 ESMs in response to the SSP5-8.5 emissions (Figure 4.3). The 1995–2014 mean simulated CO_2 level is 375 ppm, very similar to the prescribed 378 ppm, but the ESM 5–95% range is 357–391 ppm. By the end of the 21st century (2081–2100), the ESM mean is 953 ppm – below the prescribed CO_2 pathway (1004 ppm), but with a large 5–95% range of 848–1045 ppm, which spans the prescribed concentration level. This result differs from CMIP5, which showed that ESMs typically simulated CO_2 concentrations higher than the prescribed concentration-driven RCP pathways. Reduced spread in CMIP6 carbon cycle feedbacks compared to CMIP5 has been postulated to be due to the inclusion of nitrogen cycle processes in about half of CMIP6 ESMs (Arora et al., 2020). This means that the CMIP6 spread in GSAT response to CO_2 emissions is dominated by climate sensitivity differences between ESMs more than by carbon cycle differences (Jones and Friedlingstein, 2020; Williams et al., 2020) (*high confidence*).

Simulated GSAT over 1995–2014, relative to 1850–1900 period, warms by very similar amounts in the two

ACCEPTED VERSION SUBJECT TO FINAL EDITS

sets of simulations: 0.82°C (0.45–1.31) in emissions-driven compared with 0.75°C (0.53–1.09) in concentration-driven simulations. By the end of the 21st century, warming in emissions-driven simulations is very similar: 4.58°C (3.53–6.70), reflecting the slightly lower CO_2 concentration simulated by the ESMs compared with warming under the prescribed CO_2 pathway of 4.69°C (3.70–6.77). This difference in model-mean response is more than an order of magnitude smaller than the 5–95% spread across model projections. The spread in CO_2 concentration, compared with the prescribed default concentration, leads to a very small increase by about 0.1°C in the spread of GSAT projections, but it is not possible to tell if this is a direct consequence of the simulation configuration or internal variability of the model simulations. These differences due to experimental configuration would be smaller still under scenarios with lower CO_2 levels, and so we assess that results from concentration-driven and emissions-driven configurations do not affect the assessment of GSAT projections (*high confidence*).

[START FIGURE 4.3 HERE]

Figure 4.3: Comparison of concentration-driven and emission-driven simulation. (a) Atmospheric CO_2 concentration, (b) GSAT from models which performed SSP5-8.5 scenario simulations in both emissions-driven (blue; *esm-ssp585*) and concentration-driven (red; *ssp585*) configurations. For concentration driven simulations, CO_2 concentration is prescribed, and follows the red line in panel (a) in all models. For emissions-driven simulations, CO_2 concentration is simulated and can therefore differ for each model, blue lines in panel (a). Further details on data sources and processing are available in the chapter data table (Table 4.SM.1).

[END FIGURE 4.3 HERE]

4.3.1.2 Precipitation

AR5 assessed from CMIP5 projections that global mean precipitation over the 21st century will increase by more than 0.05 mm day^{-1} (about 2% of global precipitation) and 0.15 mm day^{-1} (about 5% of global precipitation) under the RCP2.6 and RCP8.5 scenarios, respectively (Collins et al., 2013). These changes are generally in line with those from the CMIP6 simulations following SSP1-2.6 and SSP5-8.5 (see Table 4.3).

Unlike AR5, our focus here is on land rather than global precipitation because land precipitation has greater societal relevance. These are displayed as percent changes relative to 1995–2014 (see Figure 4.2b). Based on these results, we conclude that global land precipitation is larger during the period 2081–2100 than during the period 1995–2014, under all scenarios considered here (see Table 4.3: *high confidence*). Global land precipitation for 2081–2100, relative to 1995–2014, shows a 5–95% range of –0.2–4.7% under SSP1-1.9 and 0.9–12.9% under SSP5-8.5, respectively. The corresponding ranges under the other emission scenarios are 0.0–6.6% (SSP1-2.6), 1.5–8.3% (SSP2-4.5), and 0.5–9.6% (SSP3-7.0). A detailed assessment of hydrological sensitivity, or change in precipitation per degree warming, can be found in Chapter 8, Section 8.2.1.

For scenarios where unanimity across all of the model simulations that GSAT change relative to 1850–1900 rises above 1.5°C (SSP2-4.5, SSP3-7.0, or SSP5-8.5), the ensemble-mean change in global land precipitation from 1850–1900 until the time of exceedance is on average about 1.6%. For scenarios with unanimous global warming above 2.0°C (SSP3-7.0, or SSP5-8.5) and 3.0°C (SSP5-8.5), the ensemble-mean increase in global land precipitation for those models that do exceed 2.0°C and 3.0°C is on average about 2.6% and 4.9%, respectively. On average under SSP1-1.9 and SSP1-2.6, the global land precipitation change for simulations where global warming exceeds 1.5°C and 2.0°C will be about 1.9% and 3.0%, respectively.

[START TABLE 4.3 HERE]

Table 4.3: CMIP6 precipitation anomalies (%) relative to averages over 1995–2014 for selected future periods, regions and SSPs. Displayed are the multi-model averages across the individual models and, in

ACCEPTED VERSION SUBJECT TO FINAL EDITS

parentheses, the 5–95% ranges. Also shown are land precipitation anomalies at the time when global increase in GSAT relative to 1850–1900 exceeds 1.5°C, 2.0°C, 3.0°C, and 4.0°C, and the percentage of simulations for which such exceedances are true (to the right of the parentheses). Here, the time of GSAT exceedance is determined as the first year at which 21-year running averages of GSAT exceed the given threshold. Land precipitation percent anomalies are then computed as 21-year averages about the year of the first GSAT crossing. The numbers of models used are indicated in Figure 4.4.

Units = %	SSP1-1.9	SSP1-2.6	SSP2-4.5	SSP3-7.0	SSP5-8.5
Land: 2021–2040	2.4 (0.7, 4.1)	2.0 (–0.6, 3.6)	1.5 (–0.4, 3.6)	1.2 (–1.0, 3.4)	1.7 (–0.1, 4.1)
2041–2060	2.7 (0.6, 5.0)	2.8 (–0.4, 5.2)	2.7 (0.3, 5.2)	2.5 (–0.8, 5.1)	3.7 (–0.1, 6.9)
2081–2100	2.4 (–0.2, 4.7)	3.3 (0.0, 6.6)	4.6 (1.5, 8.3)	5.8 (0.5, 9.6)	8.3 (0.9, 12.9)
Global: 2081–2100	2.0 (0.4, 4.2)	2.9 (1.0, 5.2)	4.0 (2.3, 6.7)	4.7 (2.3, 8.2)	6.5 (3.4, 10.9)
Ocean: 2081–2100	1.9 (0.6, 4.1)	2.8 (1.1, 5.4)	3.8 (2.0, 6.8)	4.4 (2.1, 7.9)	6.0 (2.9, 10.5)
Land: ΔT > 1.5°C	2.0 (0.6, 4.4) 55	1.7 (–2.0, 6.9) 87	1.7 (–2.9, 6.2) 100	1.5 (–3.9, 6.6) 100	1.5 (–3.5, 6.4) 100
ΔT > 2.0°C	3.8 (2.4, 5.8) 36	2.2 (–2.0, 4.6) 58	2.8 (–2.2, 8.1) 97	2.4 (–4.4, 7.7) 100	2.8 (–2.8, 8.3) 100
ΔT > 3.0°C	- (-, -) 0	- (-, -) 0	4.9 (1.5, 9.6) 54	4.3 (–4.4, 11.5) 97	4.9 (–2.6, 11.0) 100
ΔT > 4.0°C	- (-, -) 0	- (-, -) 0	4.2 (1.3, 6.3) 9	5.1 (–2.5, 11.1) 57	6.4 (–3.4, 15.0) 85

[END TABLE 4.3 HERE]

Relative to 1995–2014, and across all of the scenarios considered here, CMIP6 models show greater increases in precipitation over land than either globally or over the ocean (see Table 4.3; *high confidence*). Over the Northern Hemisphere Extratropics, the 5–95% changes in precipitation over land between 1995–2014 and 2021–2040, 2041–2060, and 2081–2100, following SSP5-8.5, are 0.6–4.9%, 1.5–8.8%, and 4.7–17.2%, respectively (Figure 4.4). At the other end of scenario spectrum, SSP1-1.9, the corresponding changes are 0.6–5.4%, 0.6–7.3%, and 0.2–7.7%, respectively. By contrast, over the North Atlantic subtropics, precipitation decreases by about 10% following SSP3-7.0 and SSP5-8. There is no change in subtropical precipitation in the North Atlantic following SSP1-1.9, SSP1-2.6, or SSP2-4.5 (*high confidence*); thereby highlighting the potential limitations of pattern scaling for regional hydrological changes (see also Section 8.5.3). The reasons for the opposing changes in these two regions are assessed in Chapter 8.

[START FIGURE 4.4 HERE]

Figure 4.4: CMIP6 annual mean precipitation changes (%) from historical and scenario simulations. (a) Northern Hemisphere extratropics (30°N–90°N). (b) North Atlantic subtropics (5°N–30°N, 80°W–0°). Changes are relative to 1995–2014 averages. Displayed are multi-model averages and, in parentheses, 5–95% ranges. The numbers inside each panel are the number of model simulations. Results are derived from concentration-driven simulations. Further details on data sources and processing are available in the chapter data table (Table 4.SM.1).

[END FIGURE 4.4 HERE]

4.3.2 Cryosphere, Ocean, and Biosphere

4.3.2.1 Arctic Sea Ice

AR5 assessed from CMIP5 simulations that there will be year-round reductions of Arctic sea ice coverage by the end of this century (Collins et al., 2013). These range from 43% under RCP2.6 and 94% under RCP8.5 in September, and from 8% under RCP2.6 and 34% under RCP8.5 in March (*medium confidence*). Based on a

ACCEPTED VERSION SUBJECT TO FINAL EDITS

five-member selection of CMIP5 models, AR5 further assessed that for RCP8.5, Arctic sea-ice coverage in September will drop below 1 million km^2 and be practically ice free at some point between 2040 and 2060. SROCC further assessed that the probability of an ice-free Arctic in September for stabilized global warming of 1.5°C and 2.0°C is approximately 1% and 10–35%, respectively (IPCC, 2019).

With regards to the model selection in AR5, model evaluation studies have since identified shortcomings of the CMIP5 models to match the observed distribution of sea-ice thickness in the Arctic (Stroeve et al., 2014; Shu et al., 2015) and the observed evolution of albedo on seasonal scales (Koenigk et al., 2014). It was also found that many models' deviation from observed sea ice cover climatology cannot be explained by internal variability, whereas the models' deviation from observed sea ice cover trend (over the satellite period) can often be explained by internal variability (Olonscheck and Notz, 2017). This hinders a selection of models according to their simulated trends, which additionally has been shown to only have a weak effect on the magnitude of simulated future trends (Stroeve and Notz, 2015).

Based on results from the CMIP6 models, we conclude that on average the Arctic will become practically ice-free in September by the end of the 21st century under SSP2-4.5, SSP3-7.0, and SSP5-8.5 (see Figure 4.2c and Table 4.4; *high confidence*). Also, in the CMIP6 models, Arctic SIA in March decreases in the future, but to a much lesser degree, in percentage terms, than in September (Table 4.4; *high confidence*). A more detailed assessment of projected Arctic and also Antarctic sea ice change can be obtained in Chapter 9, Section 9.3.1.

[START TABLE 4.4 HERE]

Table 4.4: CMIP6 Arctic sea-ice area for selected months, time periods, and across five SSPs. Displayed are the multi-model averages across the individual models and, in parentheses, the 5–95% ranges. The number of models used in these calculations are shown in Figure 4.2c in Section 4.3.1.

Units = 10^6 km^2		SSP1-1.9	SSP1-2.6	SSP2-4.5	SSP3-7.0	SSP5-8.5
September:	2021–2040	2.6 (1.1, 6.5)	2.7 (0.6, 6.4)	2.8 (0.7, 6.4)	3.1 (1.1, 6.4)	2.5 (0.4, 5.8)
	2041–2060	2.2 (0.3, 6.5)	2.0 (0.2, 6.1)	1.7 (0.1, 5.6)	1.7 (0.1, 5.7)	1.2 (0.0, 5.2)
	2081–2100	2.4 (0.2, 6.2)	1.7 (0.0, 6.0)	0.8 (0.0, 4.6)	0.5 (0.0, 3.3)	0.3 (0.0, 2.2)
March:	2021–2040	14.0 (11.4, 18.7)	14.9 (11.9, 25.8)	14.9 (11.9, 23.5)	15.0 (11.7, 27.3)	14.9 (11.9, 24.7)
	2041–2060	13.8 (10.9, 18.3)	14.5 (10.9, 25.7)	14.3 (11.1, 23.3)	14.2 (10.5, 27.1)	13.9 (10.2, 24.5)
	2081–2100	13.7 (10.9, 18.5)	14.2 (10.6, 25.7)	13.1 (9.5, 22.2)	11.8 (5.4, 25.5)	9.7 (3.1, 21.6)

[END TABLE 4.4 HERE]

Studies focusing on the relationship of sea-ice extent and changes in external drivers have consistently found a much-reduced likelihood of a practically ice-free Arctic Ocean during summer for global warming of 1.5°C than for 2.0°C (Screen and Williamson, 2017; Jahn, 2018; Niederdrenk and Notz, 2018; Notz and Stroeve, 2018; Sigmond et al., 2018; Olson et al., 2019). This is shown here in a large initial-condition ensemble of observationally constrained model simulations where GSAT are stabilized at 1.5°C, 2.0°C and 3.0°C warming relative to 1850–1900 in the RCP8.5 scenario (Figure 4.5). Temperature stabilization is achieved by switching off all the anthropogenic emissions around the time that GSAT first reaches the stabilization thresholds. Simulations have been observationally constrained to correct for a model bias in simulated historical September sea-ice extent. In these simulations, Arctic sea ice coverage in September is simulated, on average, to drop below 1 million km^2 around 2040, consistent with the AR5 set of assessed models (Sigmond et al., 2018). The individual model simulations, for which there are twenty for each stabilized temperature level, show that the probability of the Arctic becoming practically ice free at the end of the 21st century is significantly higher for 2°C warming than for 1.5°C warming above 1850–1900 levels (*high confidence*).

ACCEPTED VERSION SUBJECT TO FINAL EDITS

[START FIGURE 4.5 HERE]

Figure 4.5: Arctic sea-ice extent in September in a large initial-condition ensemble of observationally-constrained simulations of an Earth system model (CanESM2). The black and red curves are average over twenty simulations following historical forcings to 2015 and RCP8.5 extensions to 2100. The coloured curves are averages over twenty simulations each after GSAT has been stabilized at the indicated degree of global mean warming relative to 1850–1900. The bars to the right are the minimum to maximum ranges over 2081–2100 (Sigmond et al., 2018). The horizontal dashed line indicates a practically ice-free Arctic. Further details on data sources and processing are available in the chapter data table (Table 4.SM.1).

[END FIGURE 4.5 HERE]

4.3.2.2 Global Mean Sea Level

AR5 assessed from CMIP5 process-based simulations that the rate of GMSL rise during the 21st century will *very likely* exceed the rate observed during 1971–2010 for all RCP scenarios due to increases in ocean warming and loss of mass from glaciers and ice sheets (Church et al., 2013). Further, AR5 concluded that for the period 2081–2100, compared to 1986–2005, GMSL rise is *likely* (*medium confidence*) to be in the 5–95% range of projections from process-based models, which give 0.26–0.55 m for RCP2.6, 0.32–0.63 m for RCP4.5, 0.33–0.63 m for RCP6.0, and 0.45–0.82 m for RCP8.5. For RCP8.5, the rise by 2100 is 0.52–0.98 m with a rate during 2081–2100 of 8–16 mm yr^{-1}.

There have been substantial modelling advances since AR5, with most sea-level projections corresponding to one of three categories: 1) central-range projections, combining scenario-conditional probability distributions for the different contributions to estimate a central range under different scenarios; 2) probabilistic projections, which explicitly consider outcomes for a wide range of likelihoods, including low-likelihood high-impact outcomes, and 3) semi-empirical projections, based on statistical relationships between past GMSL changes and climate variables, which now calibrate individual contributions and are consistent with physical-model based estimates (Chapter 9, Section 9.6.3).

Based on the assessment of the latest modelling information (see Figure 4.2d and Chapter 9, Section 9.6.3), we conclude that under the SSP3-7.0, the *likely* range of GMSL change averaged over 2081–2100 relative to 1995–2014 is 0.46–0.74 m. Under SSP1-2.6, the *likely* range over the long-term is 0.30–0.54 m. Further, in SSP2-4.5, SSP3-7.0, and SSP5-8.5, the rise in GMSL is projected to accelerate over the 21st century. A detailed assessment of the processes contributing to these projected rises and accelerations in GMSL, together with a comparison to AR5 and SROCC, can be found in Chapter 9, Section 9.6.3. Projected changes in the thermosteric component of GMSL beyond 2300 are assessed in Section 4.7.1.

In summary, it is *virtually certain* that under any one of the assessed SSPs, there will be continued rise in GMSL through the 21st century.

4.3.2.3 Atlantic Meridional Overturning Circulation

AR5 assessed from CMIP5 simulations that the AMOC will *very likely* weaken over the 21st century, and the projected weakening of the AMOC is consistent with CMIP5 projections of an increase of high-latitude temperature and high-latitude precipitation, with both effects causing the surface waters at high latitudes to become less dense and therefore more stable (Collins et al., 2013).

Based on CMIP6 models, we find that over the 21st century, AMOC strength, relative to 1995–2014, shows a multi-model mean decrease in each of the SSP scenarios but with a large spread across the individual simulations (Figure 4.6). We also note that the magnitude of the ensemble-mean strength decrease is

ACCEPTED VERSION SUBJECT TO FINAL EDITS

approximately scenario independent up to about 2060 (Weijer et al., 2020). A more detailed assessment of these projected AMOC changes, and the mechanisms involved, can be found in Chapter 9, Section 9.2.3.

In summary, we assess from the CMIP6 models that AMOC weakening over the 21st century is *very likely*; the rate of weakening is approximately independent of the emission scenario (*high confidence*).

[START FIGURE 4.6 HERE]

Figure 4.6: CMIP6 annual mean AMOC strength change in historical and scenario simulations. Changes are relative to averages from 1995–2014. The curves show ensemble averages and the shadings the 5–95% ranges across the SSP1-2.6 and SSP3-7.0 ensembles. The circles to the right of the panel show the anomalies averaged from 2081–2100 for each of the available model simulations. The numbers inside the panel are the number of model simulations. Here, the strength of the AMOC is computed as the maximum value of annual-mean ocean meridional overturning mass streamfunction in the Atlantic at 26°N. Results are from concentration-driven simulations. Further details on data sources and processing are available in the chapter data table (Table 4.SM.1).

[END FIGURE 4.6 HERE]

Based on a large initial condition ensemble of simulations with a CMIP5 model (CanESM2) with emission scenarios leading to stabilization of global warming of 1.5°C, 2.0°C, or 3.0°C relative to 1850–1900, AMOC continues to decline for 5–10 years after GSAT is effectively stabilized at the given GWL (Sigmond et al., 2020). This is followed by a recovery of AMOC strength for about the next 150 years to a level that is approximately independent of the considered stabilization scenario. These results are replicated in simulations in a CMIP6 model (CanESM5) with emissions cessation after diagnosed CO_2 emissions reach 750 Gt, 1000 Gt, or 1500 Gt. These emissions levels lead to global warming stabilization at 1.5°C, 2.0°C, or 3.0°C relative to 1850–1900. In summary, in these model simulations the AMOC recovers over several centuries after the cessation of CO_2 emissions (*medium confidence*).

4.3.2.4 Ocean and Land Carbon Uptake

AR5 concluded with *very high confidence* that ocean carbon uptake of anthropogenic CO_2 will continue under all RCPs through the 21century, with higher uptake corresponding to higher concentration pathways. The future evolution of the land carbon uptake was assessed to be much more uncertain than for ocean carbon uptake, with a majority of CMIP5 models projecting a continued cumulative carbon uptake.

Based on results from the CMIP6 models, we conclude that the flux of carbon from the atmosphere into the ocean increases continually through most of 21st century in the two highest emissions and decreases continually under the other emission scenarios (Figure 4.7a). The flux of carbon from the atmosphere to land shows a similar 21st century behaviour across the scenarios but with much higher year-to-year variation than ocean carbon flux (Figure 4.7b). A more in-depth assessment and discussion of the mechanism involved can be found in Chapter 5, Section 5.4.5.

In summary, we assess that the cumulative uptake of carbon by the ocean and by land will increase through the 21st century irrespective of the considered emission scenarios (*very high confidence*).

[START FIGURE 4.7 HERE]

Figure 4.7: CMIP6 carbon uptake in historical and scenario simulations. (a) Atmosphere to ocean carbon flux (PgC yr^{-1}). (b) Atmosphere to land carbon flux (PgC yr^{-1}). The curves show ensemble averages and the shadings show the 5–95% ranges across the SSP1-2.6 and SSP3-7.0 ensembles. The numbers inside each panel are the number of model simulations. The land uptake is taken as Net Biome Productivity (NBP)

ACCEPTED VERSION SUBJECT TO FINAL EDITS

and so includes any modelled net land-use change emissions. Results are from concentration-driven simulations. Further details on data sources and processing are available in the chapter data table (Table 4.SM.1).

[END FIGURE 4.7 HERE]

4.3.2.5 Surface Ocean pH

AR5 assessed from CMIP5 simulations that it is *virtually certain* that increasing storage of carbon by the ocean under all four RCPs through to 2100 will increase ocean acidification in the future (Ciais et al., 2013). Specifically, AR5 reported that CMIP5 models project increased ocean acidification globally to 2100 under all RCPs, and that the corresponding model mean and model spread in the decrease in surface ocean pH from 1986–2005 to 2081–2100 would be 0.065 (0.06–0.07) for RCP2.6, 0.145 (0.14–0.15) for RCP4.5, 0.203 (0.20–0.21) for RCP6.0 and 0.31 (0.30–0.32) for RCP8.5.

Based on results from the CMIP6 models we conclude that, except for the lower-emission scenarios SSP1-1.9 and SSP1-2.6, ocean surface pH decreases monotonically through the 21st century (Figure 4.8; *high confidence*).

[START FIGURE 4.8 HERE]

Figure 4.8: Global average surface ocean pH. The shadings around the SSP1-2.6 and SSP5-7.0 curves are the 5–95% ranges across those ensembles. The numbers inside each panel are the number of model simulations. Results are from concentration-driven simulations. Further details on data sources and processing are available in the chapter data table (Table 4.SM.1).

[END FIGURE 4.8 HERE]

4.3.3 Modes of Variability

4.3.3.1 Northern and Southern Annular Modes

Northern Annular Mode

The Northern Annular Mode (NAM) is the leading mode of variability in the NH extratropical atmosphere (see Annex IV, Section AIV.2.1). Throughout this chapter, we use a simple fixed latitude-based NAM index defined as the difference in SLP between 35°N and 65°N (Li and Wang, 2003; Section AIV.2.1). The NAM index computed from the latitudinal gradient in SLP is strongly correlated with variations in the latitudinal position and strength of the mid-latitude westerly jets, and with the spatial distribution of Arctic sea ice (Caian et al., 2018). Projected changes in the position and strength of the mid-latitude westerly jets, storm tracks, and atmospheric blocking in both hemispheres are assessed in Section 4.5.1.6. AR5 referred to the NAM, and its synonym the Arctic Oscillation (AO), through its regional counterpart, the North Atlantic Oscillation (NAO). Here, we use the term NAM to refer also to the AO and NAO (see Section AIV.2.1), accepting that the AO and NAO are not identical entities.

We first summarise the assessment of past NAM changes and their attribution from Chapters 2 and 3 to put into context the future projections described here. Strong positive trends for the NAM/NAO indices were observed since 1960, which have weakened since the 1990s (*high confidence*; Chapter 2, Section 2.4.1.1). The NAO variability in the instrumental record was *likely* not unusual in the millennial and multi-centennial context (Section 2.4.1.1). Climate models simulate the gross features of the NAM with reasonable fidelity, including its interannual variability, but models tend to systematically underestimate the amount of multidecadal variability of the NAM and jet stream compared to observations (Wang et al., 2017b; Bracegirdle et al., 2018; Simpson et al., 2018a); Chapter 3, Section 3.7.1), with the caveat of the observational record being relatively short to characterise decadal variability (Chiodo et al., 2019). A

ACCEPTED VERSION SUBJECT TO FINAL EDITS

realistic simulation of the stratosphere and SST variability in the tropics and northern extratropics are important for a model to realistically capture the observed NAM variability. Despite some evidence from climate model studies that anthropogenic forcings influence the NAM, the balance of evidence indicates that there is *little evidence* for a significant role for anthropogenic forcings in driving the observed multidecadal variations of the NAM over the instrumental period (Section 3.7.1).

AR5 assessed from CMIP5 simulations that the future boreal wintertime NAM is *very likely* to exhibit large natural variations and trends of similar magnitude to that observed in the past and is *likely* to become slightly more positive in the future (Collins et al., 2013). Based on CMIP6 model results displayed in Figure 4.9a, we conclude that the boreal wintertime surface NAM is more positive by the end of the 21st century under SSP3-7.0 and SSP5-8.5 (*high confidence*). For these high emission scenarios, the 5–95% range of NAM index anomalies averaged from 2081–2100 are 0.3–3.8 hPa and 0.32–5.2 hPa, respectively. On the other hand, under neither of the lowest emission scenarios, SSP1-1.9 and SSP1-2.6, does the NAM show a robust change, by the end of the 21st century (*high confidence*).

[START FIGURE 4.9 HERE]

Figure 4.9: CMIP6 simulations of boreal wintertime (DJF) Annular Mode indices. (a) NAM and (b) SAM. The NAM is defined as the difference in zonal mean SLP at 35°N and 65°N (Li and Wang, 2003) and the SAM as the difference in zonal mean SLP at 40°S and 65°S (Gong and Wang, 1999). All anomalies are relative to averages from 1995–2014. The curves show multi-model ensemble averages over the CMIP6 r1 simulations. The shadings around the SSP1-2.6 and SSP3-7.0 curves denote the 5–95% ranges of the ensembles. The numbers inside each panel are the number of model simulations. The results are for concentration-driven simulations. Further details on data sources and processing are available in the chapter data table (Table 4.SM.1).

[END FIGURE 4.9 HERE]

Significant progress has been made since AR5 in understanding the physical mechanisms responsible for changes in the NAM, although uncertainties remain. It is now clear from the literature that the NAM response, and the closely-related response of the mid-latitude storm tracks, to anthropogenic forcing in CMIP5-era climate models is determined by a 'tug-of-war' between two opposing processes (Harvey et al., 2014; Shaw et al., 2016a; Screen et al., 2018a); 1) Arctic amplification (see Section 4.5.1.1 and Chapter 7, Section 7.4.4.1), which decreases the low-level meridional temperature gradient, reduces baroclinicity on the poleward flank of the eddy-driven jet, and shifts the storm tracks equatorward and leading to a *negative* NAM (see Box 10.1; Harvey et al., 2015; Hoskins and Woollings, 2015; Peings et al., 2017; Screen et al., 2018a); 2) and enhanced warming in the tropical upper-troposphere, due to GHG increases and associated water vapour and lapse rate feedbacks, which increases the upper-level meridional temperature gradient and causes a poleward shift of the storm tracks and a *positive* NAM (Harvey et al., 2014; Vallis et al., 2015; Shaw, 2019). The large diversity in projected NAM changes in CMIP5 multi-model ensemble (Gillett and Fyfe, 2013) appears to be at least partly explained by the relative importance of these two mechanisms in particular models (Harvey et al., 2014, 2015; Vallis et al., 2015; McCusker et al., 2017; Oudar et al., 2017). Models that produce larger Arctic amplification also tend to produce larger equatorward shifts of the mid-latitude jets and associated negative NAM responses (Barnes and Polvani, 2015; Harvey et al., 2015; Zappa and Shepherd, 2017; McKenna et al., 2018; Screen et al., 2018a; Zappa et al., 2018).

Another area of progress is new understanding the role of cloud radiative effects in shaping the mid-latitude circulation response to anthropogenic forcing. Through their non-uniform distribution of radiative heating, cloud changes can modify meridional temperature gradients and alter mid-latitude circulation and the annular modes in both hemispheres (Ceppi et al., 2014; Voigt and Shaw, 2015, 2016; Ceppi and Hartmann, 2016; Ceppi and Shepherd, 2017; Lipat et al., 2018; Albern et al., 2019; Voigt et al., 2019). In addition to the effects of changing upper and lower tropospheric temperature gradients on the NAM, progress has been made since AR5 in understanding the effect of simulated changes in the strength of the stratospheric polar vortex on winter NAM projections (Manzini et al., 2014; Zappa and Shepherd, 2017; Simpson et al., 2018b).

ACCEPTED VERSION SUBJECT TO FINAL EDITS

Southern Annular Mode

The Southern Annular Mode (SAM) is the leading mode of large-scale extratropical atmospheric variability in the SH and influences most of the southern extratropics (see Annex IV, Section AIV.2.2). In its positive phase, the SAM characterizes anomalously low pressure over the polar cap and high pressure in southern mid-latitudes (Marshall, 2003). While there are some zonal asymmetries to the structure of the SAM (see Section AIV.2.2), it is more symmetric than its NH counterpart (Fyfe et al., 1999). Throughout this chapter, we use a simple fixed latitude-based SAM index defined as the difference in zonal mean SLP between 40°S and 65°S (Gong and Wang, 1999) (see Section AIV.2.2 for discussion of other SAM indices). Although the SAM is often used as a proxy for the location of the mid-latitude westerly wind belt, trends in the SAM can reflect a combination of changes in jet position, width, and strength. The changes in the SH circulation associated with the SAM influence on surface wind stress (Wang et al., 2014) and hence affect the Southern Ocean.

Over the instrumental period, there has been a robust positive trend in the SAM index, particularly since 1970 (*high confidence*; Chapter 2*,* Section 2.4.1.2). There is *medium confidence* that the recent trend in the SAM is unprecedented in the past several Centuries (Section 2.4.1.2). There is *high confidence* that stratospheric ozone depletion and GHG increases have contributed to the positive SAM trend during the late 20th century, with ozone depletion dominating in austral summer, following the peak of the Antarctic ozone hole in September–October, and GHG increases dominating in other seasons (Chapter 3, Section 3.7.2). To capture the effects of stratospheric ozone changes on the SAM, climate models must include a realistic representation of ozone variations (Section 3.7.2). In models that do not explicitly represent stratospheric ozone chemistry, which includes the majority of the CMIP6 model ensemble, an ozone dataset is prescribed. To properly capture the effects of ozone depletion and recovery on the stratosphere and surface climate, the prescribed ozone dataset must realistically capture observed stratospheric ozone trends with sufficiently high temporal resolution (Neely et al., 2014; Young et al., 2014). The CMIP6 experiment protocol recommended the use of a prescribed 4-D monthly mean ozone concentration field for models without stratospheric chemistry (Eyring et al., 2016).

AR5 assessed that the positive trend in the austral summer/autumn SAM observed since 1970 (see Section 2.4.1.2) is *likely* to weaken considerably as stratospheric ozone recovers through the mid-21st century, while in other seasons the SAM changes depend on the emission scenario, with a larger increase in SAM for higher emission scenarios. In CMIP6 models, the austral summer SAM is more positive by the end of the 21st century under SSP3-7.0 and SSP5-8.5 (Figure 4.9b). On the other hand, under SSP1-1.9 and SSP1-2.6, the SAM is projected to be less positive, especially under SSP1-1.9 where the 5–95% ranges of anomalies relative to 1995–2014 are –3.1 to 0.0 hPa averaged from 2081–2100. In summary, under the highest emission scenarios in the CMIP6 models, the SAM in the austral summer becomes more positive through the 21st century (*high confidence*).

4.3.3.2 El Niño-Southern Oscillation

ENSO is the most dominant mode of variability on interannual timescales and also the dominant source of seasonal climate predictability (Timmermann et al., 2018; see Chapter 11, Box 11.3 and Annex IV, Section AIV.2.3). AR5 assessed from CMIP5 simulations that ENSO variability will *very likely* remain the dominant mode of interannual climate variability in the future, and that associated ENSO precipitation variability on regional scales is *likely* to intensify (Christensen et al., 2013). However, they assessed there was *low confidence* in projected changes in ENSO variability in the 21st century due to a strong component of internal variability.

[START FIGURE 4.10 HERE]

Figure 4.10: Changes in amplitude of ENSO Variability. Variability of (a) SST and (b) precipitation anomalies averaged over Niño3.4 region for 1950–2014 from CMIP6 historical simulations and for 2015–2100 from

ACCEPTED VERSION SUBJECT TO FINAL EDITS

four SSPs. Thick lines stand for multi-model mean and shading is the 5–95% range across CMIP6 models for historical simulation (grey), SSP1-2.6 (blue) and SSP3-7.0 (pink), respectively. The amplitude of ENSO SST and rainfall variability is defined as the standard deviation of the detrended Niño3.4-area averaged SST and rainfall index, respectively, over 30-year running windows. The standard deviation in every single model is normalized by each model's present-day standard deviation averaged from 1995 to 2014. The number of available models is listed in parentheses. This figure is adopted from (Yun et al., 2021). Further details on data sources and processing are available in the chapter data table (Table 4.SM.1).

[END FIGURE 4.10 HERE]

Among a range of indices proposed for representing ENSO, we use the most prominent one, the Niño 3.4 index, defined as the average equatorial SST or precipitation across the central equatorial Pacific (5°S–5°N, 170°W–120°W) (see Section AIV.2.3). Here, we consider the evolution of the amplitude of Niño3.4 index for SST and precipitation over the 21st century as projected by CMIP6 models. Analysis of CMIP6 models shows there is no robust model consensus on the forced changes in the amplitude of ENSO SST variability even under the high-emission scenarios SSP3-7.0 and SSP5-8.5, but a significant increasing trend in the amplitude of ENSO precipitation variability is projected across the 21st century in the four SSPs (Figure 4.10). This is broadly consistent with results from CMIP5 models (Christensen et al., 2013)(Power et al., 2013)(Cai et al., 2015)(Chen et al., 2017)(Wengel et al., 2018), recent studies with CMIP6 models (Brown et al., 2020)(Fredriksen et al., 2020a)(Freund et al., 2020a)(Yun et al., 2021), and large initial-condition ensemble experiments (Maher et al., 2018; Zheng et al., 2018; Haszpra et al., 2020).

It is therefore *very likely* that the amplitude of ENSO rainfall variability will intensify in response to global warming over the 21st century although there is no robust consensus from CMIP6 climate models for a systematic change in amplitude of ENSO SST variability even in the high-emission scenarios of SSP3-7.0 and SSP5-8.5.

4.3.4 Synthesis Assessment of Projected Change in Global Surface Air Temperature

GSAT change is assessed using multiple lines of evidence including the CMIP6 projection simulations out to year 2100. The assessment combines CMIP6 projections driven by SSP scenarios with observational constraints on simulated past warming (Brunner et al., 2020; Liang et al., 2020; Nijsse et al., 2020; Tokarska et al., 2020; Ribes et al., 2021) (see BOX 4.1 and Figure 4.11:a,b), as well as the AR6-updated assessment of ECS and TCR in Section 7.5. The approaches of (Liang et al., 2020; Tokarska et al., 2020; Ribes et al., 2021) have first been extended to all 20-year averaging periods between 2000 and 2100. For each 20-year period, the 5%, 50%, and 95% percentile GSAT values of these three constrained CMIP6 results are averaged percentile by percentile (Figure 4.11c). Then, an emulator based on a two-layer energy balance model (e.g., Held et al., 2010) is driven by the Chapter 7-derived ERF. The emulator parameters are chosen such that the central estimate, lower bound of the *very likely* range, and upper bound of the *very likely* range of climate feedback parameter and ocean heat uptake coefficient take the values that map onto the corresponding combination of ECS (3°C, 2°C, and 5°C, respectively) and TCR (1.8°C, 1.2°C, and 2.4°C, respectively) of Section 7.5 (see Box 4.1). As a final step, the constrained-CMIP6 and the emulator-based 5%, 50%, and 95% percentile GSAT values are averaged percentile by percentile (Figure 4.11c, d; Table 4.5). Constrained CMIP6 results and the ECS- and TCR-based emulator thus contribute one-half each to the GSAT assessment. Because the emulator results and (Ribes et al., 2021) represent the forced response only, and averaging over the other two individual estimates (Liang et al., 2020; Tokarska et al., 2020) further reduces the contribution from internal variability, the assessed GSAT time series are assumed to represent purely the forced response.

Averaged over the period 2081–2100, GSAT is *very likely* to be higher than in the recent past (1995–2014) by 0.3°C–0.9°C in the low-emission scenario SSP1-1.9 and by 2.6°C–4.7°C in the high-emission scenario SSP5-8.5. For the scenarios SSP1-2.6, SSP2-4.5, and SSP3-7.0, the corresponding *very likely* ranges are 0.6°C–1.4°C, 1.3°C–2.5°C, and 2.0°C–3.8°C, respectively (Figure 4.11, Table 4.5). Because the different

ACCEPTED VERSION SUBJECT TO FINAL EDITS

approaches for estimating long-term GSAT change produce consistent results (Figure 4.11), there is *high confidence* in this assessment. These ranges of the long-term projected GSAT change generally correspond to AR5 ranges for related scenarios but the likelihood is increased to *very likely* ranges, in contrast to the *likely* ranges in AR5. Over the mid-term period 2041–2060, the *very likely* GSAT ranges of SSP1-1.9 and SSP5-8.5 are almost completely distinct (Table 4.5, *high confidence*, see also Section 4.3.1).

CMIP6 models project a wider range of GSAT change than the assessed range (*high confidence*, see Section 4.3.1). The CMIP6 models with a higher climate sensitivity simulate warming rates higher than assessed *very likely* here (see Section 4.3.1); these rates are *very unlikely* but not impossible to occur and hence cannot be excluded. The implications of these *very unlikely* warming rates for patterns of surface temperature and precipitation change are assessed in Section 4.8.

For the near term, initialized decadal forecasts constitute another line of evidence over the period 2019–2028 (see Box 4.1). The forecasts are consistent with the assessed GSAT *very likely* range (Box 4.1, Figure 1), strengthening the confidence in the near-term assessment.

[START FIGURE 4.11 HERE]

Figure 4.11: Multiple lines of evidence for GSAT changes for the long-term period, 2081–2100, relative to the average over 1995–2014, for all five priority scenarios. The unconstrained CMIP6 5–95% ranges (coloured bars) in (a) differ slightly because different authors used different subsamples of the CMIP6 archive. The constrained CMIP6 5–95% ranges (coloured bars) in (b) are smaller than the unconstrained ranges in (a) and differ because of different samples from the CMIP6 archive and because different observations and methods are used. In (c), the average of the ranges in (b) is formed (grey bars). Green bars in (c) show the emulator ranges, defined such that the best estimate, lower bound of the *very likely range*, and upper bound of the *very likely* range of climate feedback parameter and ocean heat uptake coefficient take the values that map onto the corresponding values of ECS and TCR of Section 7.5 (see BOX 4.1). The time series in (d) are constructed by taking the average of the constrained CMIP6 ranges and the emulator ranges. The y-axes on the right-hand side are shifted upward by 0.85°C, the central estimate of the observed warming for 1995–2014, relative to 1850–1900 (Cross-Chapter Box 2.3, Table 1). Further details on data sources and processing are available in the chapter data table (Table 4.SM.1).

[END FIGURE 4.11 HERE]

The assessed ranges of GSAT change can be converted to change relative to mean GSAT over the period 1850–1900 for a consistent comparison with AR5 (IPCC, 2013) and SR1.5 (Masson-Delmotte et al., 2018). GSAT was warmer in 1995–2014 (recent past) than 1850–1900 by 0.85°C [0.67–0.98°C]. GSAT diagnosed for 1986–2005 (AR5 recent past) relative to 1850–1900 is 0.08°C higher than was diagnosed in AR5, due to methodological and dataset updates (Cross-Chapter Box 2.3, Table 1).

The uncertainty in GSAT relative to 1850–1900 includes the *very likely* ranges of assessed GSAT change relative to 1995–2014 (depending on scenario and period, between 0.5°C and 2.4°C, Figure 4.11d, Table 4.5), the uncertainty in historical GSAT change from the mean over 1850–1900 to 1995–2014 (about 0.3°C, Cross-Chapter Box 2.3), and the estimate of internal variability in 20-year GSAT averages (5–95% range about 0.15°C, Box 4.1, (Maher et al., 2019a)). These uncertainties are assumed to be independent and are added in quadrature, meaning that the total uncertainty is only slightly larger than the dominating contribution by the GSAT change relative to 1995–2014 (Table 4.5). The addition is done by numerically sampling a normal distribution fitted to the 5%, 50%, and 95% percentiles of the internal variability, as well as sampling skew-normal distributions (e.g., O'Hagan and Leonard, 1976) fitted to the 5%, 50%, and 95% percentiles of both historical warming and GSAT relative to 1995–2014. The result is a joint probability distribution of GSAT change and 20-year period.

Averaged over the period 2081–2100, GSAT is *very likely* to be higher than in the period 1850–1900 by 1.0°C–1.8°C in the low-emission scenario SSP1-1.9 and by 3.3°C–5.7°C in the high-emission scenario

ACCEPTED VERSION SUBJECT TO FINAL EDITS

SSP5-8.5. For the scenarios SSP1-2.6, SSP2-4.5, and SSP3-7.0, the corresponding *very likely* ranges are 1.3°C–2.4°C, 2.1°C–3.5°C, and 2.8°C–4.6°C, respectively (Table 4.5).

Time series of assessed GSAT change are now used to assess the time when certain thresholds of GSAT increase are crossed (Table 4.5). The threshold-crossing time is defined as the midpoint of the first 20-year period during which the average GSAT exceeds the threshold. During the near term (2021–2040), a 1.5°C increase in the 20-year average of GSAT, relative to the average over the period 1850–1900, is *very likely* to occur in scenario SSP5-8.5, *likely* to occur in scenarios SSP2-4.5 and SSP3-7.0, and *more likely than not* to occur in scenarios SSP1-1.9 and SSP1-2.6. In all scenarios assessed here except SSP5-8.5, the central estimate of crossing the 1.5°C threshold lies in the early 2030s, about ten years earlier than the midpoint of the *likely* range (2030–2052) assessed in the SR1.5, which assumed continuation of the then-current warming rate. Roughly half of this ten-year difference arises from a larger historical warming diagnosed in AR6, while the other half arises because for central estimates of climate sensitivity, most scenarios show stronger warming over the near term than was estimated as 'current' in SR1.5 (*medium confidence*); this estimate has been confirmed in AR6 (Section 3.3.1). If ECS and TCR lie near the lower end of the assessed *very likely* range, crossing the 1.5°C warming threshold is avoided in scenarios SSP1-1.9 and SSP1-2.6 (*medium confidence*). It is *more likely than not* that under SSP1-1.9, GSAT relative to 1850–1900 will remain below 1.6°C throughout the 21st century, implying a potential temporary overshoot above 1.5°C of no more than 0.1°C. All statements about crossing the 1.5°C threshold assume that no major volcanic eruption occurs during the near term.

A warming level of 2°C in GSAT, relative to the period 1850–1900, is *very likely* to be crossed in the mid-term period 2041–2060 under SSP5-8.5, *likely* to be crossed in the mid-term period under SSP3-7.0, and *more likely than not* to be crossed during the mid-term period under SSP2-4.5. During the entire 21st century, a warming level of 2°C in GSAT, relative to the period 1850–1900, will be crossed under SSP5-8.5 and SSP3-7.0, will *extremely likely* be crossed under SSP2-4.5, will *unlikely* be crossed under SSP1-2.6, and will *extremely unlikely* be crossed under SSP1-1.9.

ACCEPTED VERSION
SUBJEC TO FINAL EDITS

[START TABLE 4.5 HERE]

Table 4.5: Assessment results for 20-year averaged GSAT change, based on multiple lines of evidence. The change is displayed in °C relative to the 1995–2014 and 1850–1900 reference periods for selected time periods (near term 2021–2040, mid-term 2041–2060, and long term 2081–2100), and as the time when certain temperature thresholds are crossed, relative to the period 1850–1900. The recent reference period 1995–2014 was higher in GSAT than the period 1850–1900 by 0.85°C [0.67–0.98°C], (Cross-Chapter Box 2.3). The entries give both the central estimate and, in parentheses, the *very likely* (5–95%) range. An entry n.c. means that the global warming threshold is not crossed during the period 2021–2100.

	SSP1-1.9	SSP1-2.6	SSP2-4.5	SSP3-7.0	SSP5-8.5
Near term, 2021–2040 relative to 1995–2014 relative to 1850–1900	 0.6 (0.4, 0.9) 1.5 (1.2, 1.7)	 0.6 (0.4, 0.9) 1.5 (1.2, 1.8)	 0.7 (0.4, 0.9) 1.5 (1.2, 1.8)	 0.7 (0.4, 0.9) 1.5 (1.2, 1.8)	 0.8 (0.5, 1.0) 1.6 (1.3, 1.9)
Mid-term, 2041–2060 relative to 1995–2014 relative to 1850–1900	 0.7 (0.4, 1.1) 1.6 (1.2, 2.0)	 0.9 (0.5, 1.3) 1.7 (1.3, 2.2)	 1.1 (0.8, 1.6) 2.0 (1.6, 2.5)	 1.3 (0.9, 1.7) 2.1 (1.7, 2.6)	 1.5 (1.1, 2.1) 2.4 (1.9, 3.0)
Long term, 2081–2100 relative to 1995–2014 relative to 1850–1900	 0.6 (0.2, 1.0) 1.4 (1.0, 1.8)	 0.9 (0.5, 1.5) 1.8 (1.3, 2.4)	 1.8 (1.2, 2.6) 2.7 (2.1, 3.5)	 2.8 (2.0, 3.7) 3.6 (2.8, 4.6)	 3.5 (2.4, 4.8) 4.4 (3.3, 5.7)
1.5°C, relative to 1850–1900	2025–2044 (2013–2032, n.c.)	2023–2042 (2012–2031, n.c.)	2021–2040 (2012–2031, 2037–2056)	2021–2040 (2013–2032, 2033–2052)	2018–2037 (2011–2030, 2029–2048)
2°C, relative to 1850–1900	n.c. (n.c., n.c.)	n.c. (2031–2050, n.c.)	2043–2062 (2028–2047, 2075–2094)	2037–2056 (2026–2045, 2053–2072)	2032–2051 (2023–2042, 2044–2063)
3°C, relative to 1850–1900	n.c. (n.c., n.c.)	n.c. (n.c., n.c.)	n.c. (2061–2080, n.c.)	2066–2085 (2050–2069, n.c.)	2055–2074 (2042–2061, 2074–2093)
4°C, relative to 1850–1900	n.c. (n.c., n.c.)	n.c. (n.c., n.c.)	n.c. (n.c., n.c.)	n.c. (2070–2089, n.c.)	2075–2094 (2058–2077, n.c.)

[END TABLE 4.5 HERE]

ACCEPTED VERSION SUBJECT TO FINAL EDITS

4.4 Near-term Global Climate Changes

This section assesses changes in large-scale climate over the period 2021–2040 and includes information from both projections and initialized decadal predictions. The structure is similar to Section 4.3. Unless noted otherwise, the assessment assumes that there will be no major volcanic eruption in the near term. The climatic effects of volcanic eruptions are assessed in Section 4.4.4 and Cross-Chapter Box 4.1; Section 4.4.4 also assesses the climate effects of short-lived climate forcers.

4.4.1 Atmosphere

4.4.1.1 Average Global Surface Air Temperature

AR5 assessed that it is *likely* that GSAT will increase in the range 0.3°C–0.7°C over the period 2016–2035 relative to 1986–2005 (*medium confidence*), and that there were not large differences in the GSAT change among different RCPs in this period (Kirtman et al., 2013). AR5 further assessed that it is *more likely than not* that the mean GSAT for the period 2016–2035 will be more than 1°C above the mean for 1850–1900, and it is *very unlikely* that it will be more than 1.5°C above the 1850–1900 mean (*medium confidence*). It was shown that in the period 2016–2035, differences in GSAT across RCP scenarios for a single climate model are typically smaller than differences between climate models under a single RCP scenario, indicating that model structural uncertainty is larger than scenario uncertainty over that period (Hawkins and Sutton, 2009).

Near-term (2021–2040) GSAT changes relative to 1995–2014 exhibit only minor dependence on SSP scenario, consistent with AR5 (Table 4.5). Averaged over the twenty years of the near term and across all scenarios, GSAT is *very likely* to be higher than over 1995–2014 by 0.4°C–1.0°C (Table 4.5), with most of the uncertainty arising from that in ECS and TCR (*high confidence*, e.g., Lehner et al., 2020, Section 4.3.4). The assessed near-term warming is thus larger than in AR5 by 0.1°C to 0.2°C. This upward revision has the same magnitude as the ad-hoc downward adjustment to near-term projected GSAT change that was performed in AR5 ((Kirtman et al., 2013); see Box 4.1).

Averaged near-term GSAT is *as likely as not* at least 1.5°C higher than during 1850–1900, across the five SSP scenarios used here (Table 4.5, see Section 4.3.4). This much higher likelihood of near-term warming reaching 1.5°C than in AR5 arises both because surface warming has continued since AR5 (the period 1995–2014 was warmer by 0.16°C than 1986–2005, Cross-Chapter Box 2.3, Table 1), and because of methodological and dataset updates (the AR6 assessment of 1986–2005 GSAT change relative to 1850–1900 is 0.08°C higher than in the AR5; Cross-Chapter Box 2.3, Table 1).

For annual-mean GSAT, uncertainty in near-term projections arises in roughly equal measure from internal variability and model uncertainty (*high confidence*, Box 4.1). Forecasts initialized from recent observations simulate GSAT changes for the period 2019–2028 relative to the recent past that are consistent with the assessed *very likely* range in annual-mean GSAT (Box 4.1, Figure 1, Table 4.5, *high confidence*). Because annual mean GSAT shows a higher level of internal variability than the 20-year mean, individual years are expected to cross the 1.5°C earlier than the assessed GSAT does. For example, Smith et al. (2018) apply a multi-model decadal-forecast ensemble to assess the likelihood that global warming of 1.5°C higher than over 1850–1900 will be temporarily exceeded in the near future.

When we repeat the uncertainty quantification for GSAT as in Section 4.3.4 but with the corresponding higher level of internal variability for annual instead of 20-year averages added in quadrature, we can estimate the likelihood that an individual year would cross the GSAT 1.5°C threshold. By 2030, GSAT in any individual year could exceed 1.5°C relative to 1850–1900 with a likelihood between 40 and 60 percent, across the scenarios considered here (*medium confidence*).

ACCEPTED VERSION SUBJECT TO FINAL EDITS

4.4.1.2 Spatial Patterns of Surface Warming

Consistent with AR5 and earlier assessments, Figure 4.12 shows for SSP1-2.6 and SSP3-7.0 that the largest warming occurs at high latitudes, particularly in boreal winter in the Arctic (see Section 4.5.1.1), and larger warming over land than over the ocean (see also Section 4.5.1.1). In both scenarios, the increase in seasonal mean surface temperatures over many NH land regions exceeds 1°C relative to 1995–2014. In the near term, the two scenarios show surface temperature changes that are similar in magnitude. The trajectories for well-mixed GHGs, and as a consequence the effective radiative forcing, in the scenarios have not yet diverged that much (O'Neill et al., 2016; Riahi et al., 2017). Based on the currently available CMIP6 models, regions that do not show robust warming in the near-term include the northern North Atlantic, parts of India, parts of North America and Eurasia in winter, and the subtropical eastern Pacific in the Southern Hemisphere.

[START FIGURE 4.12 HERE]

Figure 4.12: Near-term change of seasonal mean surface temperature. Displayed are projected spatial patterns of CMIP6 multi-model mean change (°C) in (top) DJF and (bottom) JJA near-surface air temperature for 2021–2040 from SSP1-2.6 and SSP3-7.0 relative to 1995–2014. The number of models used is indicated in the top right of the maps. No overlay indicates regions where the change is robust and *likely* emerges from internal variability, that is, where at least 66% of the models show a change greater than the internal-variability threshold (see Section 4.2.6) and at least 80% of the models agree on the sign of change. Diagonal lines indicate regions with no change or no robust significant change, where fewer than 66% of the models show change greater than the internal-variability threshold. Crossed lines indicate areas of conflicting signals where at least 66% of the models show change greater than the internal-variability threshold but fewer than 80% of all models agree on the sign of change. Further details on data sources and processing are available in the chapter data table (Table 4.SM.1).

[END FIGURE 4.12 HERE]

The ERF patterns from aerosols and well-mixed GHGs are distinct (Chapter 7), and warming patterns therefore depend on the precise mix of forcing agents in the scenarios. The spatial efficacies – the change in surface temperature per unit ERF – for CO_2, sulphate and black carbon aerosols and solar forcing have been recently evaluated in climate models (Modak et al., 2016; Duan et al., 2018; Modak et al., 2018a; Modak and Bala, 2019; Richardson et al., 2019). On average, the spatial patterns of near-surface warming are largely similar for different external drivers (Xie et al., 2013; Richardson et al., 2019; Samset et al., 2020), despite the patterns of forcing being different and large spread across different models (Richardson et al., 2019).

Internal variability in near-surface temperature change is large in many regions, particularly in mid-latitudes and polar regions (Hawkins and Sutton, 2012). Projections from individual realizations can therefore exhibit divergent regional responses in the near-term in areas where the amplitude of a forced signal is relatively small compared to internal variability (Deser et al., 2012b, 2014, 2016).

4.4.1.3 Precipitation

AR5 assessed that zonal mean precipitation will *very likely* increase in high and some of the mid latitudes and will *more likely than not* decrease in the subtropics. AR5 further assessed that the near-term changes in precipitation are largely uncertain at regional scales, and much of the non-robustness in near-term projections is attributable to internal variability and model uncertainty.

The mean patterns of seasonal precipitation change in CMIP6 models are consistent with AR5, increasing at high latitudes, over oceanic regions, and in wet regions over the tropics; and decreasing in dry regions including large parts of the subtropics (Figure 4.13). The magnitude of projected changes in precipitation in the near term, especially on regional scales is small compared to the magnitude of internal variability

ACCEPTED VERSION SUBJECT TO FINAL EDITS

(Hawkins and Sutton, 2011, 2016; Hoerling et al., 2011; Deser et al., 2012b; Power et al., 2012) (see Section 10.4.3). Analyses of CMIP5, CMIP6, and single-model large-ensemble simulations show that for the uncertainty in near-term precipitation projections, model uncertainty and internal variability dominate while the scenario uncertainty is very small (Lehner et al., 2020)(also see Section 8.5). Based on large ensembles of climate change experiments, it was shown that internal variability decreases over time for both temperature and precipitation on decadal scales (Zhang and Delworth, 2018; Tebaldi et al., 2021). The precipitation projections from CMIP6 models shows larger model uncertainty associated with the higher average transient climate response (Lehner et al., 2020).

The 'wet get wetter, dry get drier' paradigm, which has been used to explain the global precipitation pattern responding to global warming (Held and Soden, 2006a), might not hold, especially over subtropical land regions (Greve et al., 2014; Feng and Zhang, 2015; Greve and Seneviratne, 2015). Over the tropical oceans, precipitation changes are largely driven by the pattern of SST changes (He et al., 2018), and in the subtropics, precipitation response is driven primarily by the fast adjustment to CO_2 forcing (He and Soden, 2017). In addition to the response to GHG forcing, forcing from natural and anthropogenic aerosols exert impacts on regional patterns of precipitation (Ramanathan et al., 2005; Bollasina et al., 2011; Polson et al., 2014; Krishnan et al., 2016; Liu et al., 2018b; Shawki et al., 2018) (also see Section 10.3.1). The large uncertainties in near-term regional precipitation projections arise due to the interplay between internal variability and anthropogenic external forcing (Endo et al., 2018; Wang et al., 2021). Uncertainties in future aerosol emission scenarios contribute to uncertinites in regional precipitation projections (Wilcox et al., 2020). Aerosol changes induce a drying in the SH tropical band compensated by wetter conditions in the NH counterpart (Acosta Navarro et al., 2017). The spatially uneven distribution of the aerosol forcing may also induce changes in tropical precipitation caused by shifts in the mean location of the intertropical convergence zone (ITCZ) (Hwang et al., 2013; Ridley et al., 2015; Voigt et al., 2017). Because of the large uncertainty in the aerosol radiative forcing and the dynamical response to the aerosol forcing there is *medium confidence* in the impacts of aerosols on near-term projected changes in precipitation. Precipitation changes in the near term show seasonal amplification, precipitation increase in the rainy season and decrease in the dry season (Fujita et al., 2019).

[START FIGURE 4.13 HERE]

Figure 4.13: Near-term change of seasonal mean precipitation. Displayed are projected spatial patterns of CMIP6 multi-model mean change (%) in (top) DJF and (bottom) JJA precipitation from SSP1-2.6 and SSP3-7.0 in 2021–2040 relative to 1995–2014. The number of models used is indicated in the top right of the maps. No overlay indicates regions where the change is robust and *likely* emerges from internal variability, that is, where at least 66% of the models show a change greater than the internal-variability threshold (see Section 4.2.6) and at least 80% of the models agree on the sign of change. Diagonal lines indicate regions with no change or no robust significant change, where fewer than 66% of the models show change greater than the internal-variability threshold. Crossed lines indicate areas of conflicting signals where at least 66% of the models show change greater than the internal-variability threshold but fewer than 80% of all models agree on the sign of change. Further details on data sources and processing are available in the chapter data table (Table 4.SM.1).

[END FIGURE 4.13 HERE]

Consistent with AR5, we conclude that projected changes of seasonal mean precipitation in the near term will increase at high latitudes. Near-term projected changes in precipitation are uncertain mainly because of natural internal variability, model uncertainty, and uncertainty in natural and anthropogenic aerosol forcing (*medium confidence*).

4.4.1.4 Global Monsoon Precipitation and Circulation

ACCEPTED VERSION SUBJECT TO FINAL EDITS

The global monsoon is a forced response of the coupled atmosphere-land-ocean system to the annual cycle of solar insolation and characterized by a seasonal reversal of circulation and a seasonal alternation of dry and wet conditions (see Chapter 8, Section 8.3.2, Figure 8.11; Annex V). The global monsoon concept helps to dissect the mechanisms and controlling factors of monsoon variability at various temporal-spatial scales (Wang and Ding, 2008; Wang et al., 2017c).

[START FIGURE 4.14 HERE]

Figure 4.14: Time series of global land monsoon precipitation and Northern Hemisphere summer monsoon (NHSM) circulation index anomalies. (a) Global land monsoon precipitation index anomalies (Unit: %) defined as the area-weighted mean precipitation rate in the global land monsoon domain defined by Wang et al. (2013) for the CMIP6 historical simulation for 1950–2014 and five SSPs 2015–2100. (b) Anomalies in NHSM circulation index (Unit: m s^{-1}), defined as the vertical shear of zonal winds between 850 and 200 hPa averaged in a zone stretching from Mexico eastward to the Philippines (0°–20°N, 120°W–120°E) (Wang et al., 2013a) in the CMIP6 historical simulation and five SSPs. One realization is averaged from each model. Anomalies are shown relative to the present-day (1995–2014) mean. The curves show averages over the simulations, the shadings around the SSP1-2.6 and SSP5-8.5 curves show 5–95% ranges, and the numbers near the top show the number of model simulations used. Further details on data sources and processing are available in the chapter data table (Table 4.SM.1).

[END FIGURE 4.14 HERE]

In AR5, there was no specific assessment on global monsoon changes in the near term, but information can be derived from CMIP5 projections of the spatial patterns of precipitation change. While the basic pattern of wet regions including global monsoon regions tending to get wetter and dry regions tending to get drier is apparent, large response uncertainty is evident in the substantial spread in the magnitude of projected change simulated by different simulations. Over the global land monsoon regions, model uncertainty and internal variability together explain 99.7% of the fraction of total variance (Zhou et al. 2020), near-term projected multi-model mean precipitation changes are almost everywhere smaller than the estimated standard deviation of internal variability (Figure 4.13).

The global land monsoon precipitation index, defined as the area-weighted precipitation rate in the global land monsoon domain, tends to increase in the near term under all five core SSPs (Figure 4.14a) (Chen et al., 2020), but changes are small compared to the intermodel spread in the historical period. The Northern Hemisphere summer monsoon circulation index, defined as the vertical shear of zonal winds between 850 and 200 hPa averaged in a zone stretching from Mexico eastward to the Philippines (0°–20°N, 120°W–120°E), tends to decrease under four of the five SSP scenarios (Figure 4.14b), potentially offsetting monsoon precipitation increase. Projected changes in the global monsoon circulation are also uncertain influenced by internal variability and structural differences across models. In the near-term, for CMIP6 projections (Figure 4.14a), the multi-model mean (5–95% range) of global land monsoon precipitation change is 1.9% (–0.4–4.9%), 1.6% (–1.0–5.2%), 1.3% (–1.7–3.7%), and 1.9% (–0.8–5.2%) under SSP1-2.6, SSP2-4.5, SSP3-7.0, and SSP5-8.5, respectively.

In summary, we assess that near-term changes in global monsoon precipitation and circulation will be affected by the combined effects of model uncertainty and internal variability, which together are larger than the forced signal (*medium confidence*).

4.4.2 Cryosphere, Ocean, and Biosphere

4.4.2.1 Arctic Sea Ice

AR5 assessed that for RCP8.5, Arctic sea-ice coverage in September will drop below 1 million km^2, or become practically ice-free, at some point between 2040 and 2060 (Collins et al., 2013). Since AR5, there

ACCEPTED VERSION SUBJECT TO FINAL EDITS

has been substantial progress in understanding the response of Arctic sea ice to near-term changes in external forcing. In particular, it is *very likely* that different trajectories of the near-term evolution of anthropogenic forcing cause distinctly different likelihood ranges for very low sea-ice coverage to occur over the next two decades (Notz and Stroeve, 2018). For example, there is an *unlikely* drop of September Arctic sea-ice coverage to below 1 million km^2 before 2040 for RCP 2.6, and a *likely* drop of September Arctic sea-ice coverage to below 1 million km^2 before 2040 for RCP 8.5 (*medium confidence* given the single study). The much higher likelihood of a practically sea-ice free Arctic Ocean during summer before 2040 in RCP8.5 compared to RCP2.6 is consistent with related studies assessed in SROCC that find a substantially increased likelihood of an ice-free Arctic Ocean for 2.0°C compared to 1.5°C mean global warming relative to pre-industrial levels (Screen and Williamson, 2017; Jahn, 2018; Niederdrenk and Notz, 2018; Notz and Stroeve, 2018; Sigmond et al., 2018; Olson et al., 2019).

Based on results from CMIP6 models, we conclude that Arctic SIA will decrease in September in the near term (Figure 4.15, *high confidence*). In the case of 10-year trends ending in the near term, 79% of the simulations considered across all of the core SSPs project decreasing Arctic sea-ice area in September. Due to less of an influence from internal variability, this number rises to 98% in the case of 30-year trends. A more detailed assessment of near-term Arctic sea-ice changes can be found in Chapter 9, Section 9.3.1. A detailed assessment of Antarctic sea ice changes is in Chapter 9, Section 9.3.2.

[START FIGURE 4.15 HERE]

Figure 4.15: CMIP6 linear trends in September Arctic sea-ice area for 10-year, 20-year, and 30-year periods ending in 2021–2040 following five SSPs. Plotted are the 5–95% ranges across the ensembles of simulations. The numbers at the top of the plot are the number of model simulations in each SSP ensemble. The numbers near the bottom of the plot indicate the percentage of simulations across all the SSPs with decreasing sea-ice area. Results are from concentration-driven simulations. Further details on data sources and processing are available in the chapter data table (Table 4.SM.1).

[END FIGURE 4.15 HERE]

4.4.2.2 Ocean and Land Carbon flux

Ocean carbon flux is both a key feature of the physical ocean in mitigating the rise of atmospheric CO_2 and a driver of changes in the ocean biosphere, including changes in ocean acidity. Based on results from CMIP6 models, we conclude that SSP2-4.5, SSP3-7.0, and SSP5-8.5 all clearly lead to increasing 10-, 20-, and 30-year trends in ocean carbon flux over the near term (Figure 4.16, *high confidence*). Increasing trends in ocean carbon flux are less obvious in the lower-emission scenarios. Ensemble-mean trends in land carbon flux over the near term are generally increasing, but these are *unlikely* to be detected given a large component of terrestrial variability combined with model uncertainty. A more detailed assessment is in Chapter 5 Section 5.2.1.

In summary, it is *likely* that ocean carbon flux will increase in the near term under the higher emission scenarios, while a large component of terrestrial variability makes it is *unlikely* that an increase in land carbon flux will be detected over this period.

[START FIGURE 4.16 HERE]

Figure 4.16: CMIP6 trends in ocean and land carbon flux for 10-year, 20-year, and 30-year periods ending in 2021–2040. (a) Ocean carbon flux. (b) Land carbon flux. Plotted are the 5–95% ranges across the ensembles of simulations, for five SSPs. The numbers at the top of the plots are the number of model simulations in each SSP ensemble. Unites are PgC yr^{-1} per decade. Further details on data sources and processing are available in the chapter data table (Table 4.SM.1).

ACCEPTED VERSION SUBJECT TO FINAL EDITS

[END FIGURE 4.16 HERE]

4.4.3 Modes of Variability

This subsection assesses the near-term evolution of the large-scale modes of climate variability. Assessment of the physical mechanisms and the individual feedbacks involved in the future change of each mode and their role on future regional climate variability are provided in Sections 8.4.2, 9.2.3, 10.1.3 and Cross-Chapter Box 10.1.

4.4.3.1 Northern and Southern Annular Modes

The Northern Annular Mode

AR5 assessed from CMIP5 simulations that there is only *medium confidence* in near-term projections of a northward shift of NH storm track and westerlies, and an associated increase in the NAM index, because of the large response uncertainty and the potentially large influence of internal variability. A tendency in the near term towards a slightly more positive NAM in the three highest emission scenarios during boreal fall, winter, and spring is apparent in Figure 4.17a. However, in general the projected near-term multi-model mean change in the NAM is small in magnitude compared to the inter-model and/or multi-realization variability within the ensemble (Figure 4.17a and Deser et al., 2012; Barnes and Polvani, 2015; Deser et al., 2017).

[START FIGURE 4.17 HERE]

Figure 4.17: CMIP6 Annular Mode index change (hPa) from 1995–2014 to 2021–2040. (a) NAM and (b) SAM. The NAM is defined as the difference in zonal mean sea-level pressure (SLP) at 35°N and 65°N (Li and Wang, 2003) and the SAM as the difference in zonal mean SLP at 40°S and 65°S (Gong and Wang, 1999). The shadings are the 5–95% ranges across the simulations. The numbers near the top of each panel are the numbers of model simulations in each SSP ensemble. Further details on data sources and processing are available in the chapter data table (Table 4.SM.1).

[END FIGURE 4.17 HERE]

On seasonal to interannual timescales, there is new evidence since AR5 that initialized predictions show lower potential predictability for the boreal winter NAO than the correlation skill with respect to observations (Eade et al., 2014; Baker et al., 2018; Scaife and Smith, 2018; Athanasiadis et al., 2020). This has been referred to in the literature as a 'signal-to-noise paradox' and means that very large ensembles of predictions are needed to isolate the predictable component of the NAO. While the processes that contribute to predictability of the winter NAO on seasonal timescales may be distinct from the processes that drive multi-decadal trends, there is emerging evidence that initialized predictions also underrepresent the predictability of the winter NAO on decadal timescales (Smith et al., 2019b). Post-processing and aggregation of initialized predictions may therefore reveal significant skill for predicting the winter NAO on decadal timescales (Smith et al., 2020). Considering these new results since AR5, in the near-term it is *likely* that any anthropogenic forced signal in the NAM will be of comparable magnitude or smaller than natural internal variability in the NAM (*medium confidence*).

The Southern Annular Mode

AR5 assessed that it is *likely* that increases in GHGs and the projected recovery of the Antarctic ozone hole will be the principal drivers of future SAM trends and that the positive trend in austral summer/autumn SAM observed over the past several decades (AR5 Chapter 2, Section 2.4.1.2) is *likely* to weaken considerably as stratospheric ozone recovers through to the mid-21st century. The effects of ozone depletion and recovery on the SH circulation primarily occur in austral summer, while GHGs influence the SH circulation year round

ACCEPTED VERSION SUBJECT TO FINAL EDITS

(Gillett and Fyfe, 2013; Grise and Polvani, 2014b) and are therefore *likely* to be the dominant driver of projected circulation changes outside of austral summer (Gillett and Fyfe, 2013; Barnes et al., 2014; Solomon and Polvani, 2016). Based on current scenarios specifying future atmospheric decline of ozone depleting substances (World Meteorological Organization, 2011), chemistry-climate models project the Antarctic ozone hole in October to recover by around 2060 (Dhomse et al., 2018)(World Meteorological Organization, 2014)(WMO, 2018). Observational evidence since AR5 shows the onset of Antarctic ozone hole recovery (Solomon et al., 2016; WMO, 2018) that has been attributed to a pause in the summer SAM trend over the past couple of decades (Saggioro and Shepherd, 2019; Banerjee et al., 2020). In austral summer, ozone recovery and increasing GHGs will have opposing effects on the SAM over the next several decades (Barnes et al., 2014).

Since AR5, there have been advances in understanding the role of internal climate variability for projected near-term SH circulation trends (Solomon and Polvani, 2016). A large initial-condition ensemble following the RCP4.5 emission scenario shows a monotonic positive SAM trend in austral winter. In austral summer, the SAM trend over the first half of the 21st century is weaker compared to the strongly positive trend observed and simulated over the late 20th century. In that model, the number of realizations required to identify a detectable change in decadal mean austral winter SAM index from a year 2000 reference state decreased to below five by around 2025–2030 (Solomon and Polvani, 2016). However, in DJF the same criterion is not met until the second half of the 21st century, owing to the near-term opposing effects of ozone recovery and GHGs on the austral-summer SAM. In austral summer, forced changes in the SAM index in the near-term are therefore *likely* to be smaller than changes due to internal variability (Figure 4.17:b; Barnes et al., 2014; Solomon and Polvani, 2016).

CMIP6 models show a tendency in the near-term towards a more positive SAM index especially in the austral winter (JJA; Figure 4.17b). In all seasons, the differences between the central estimates of the change in the SAM index for each SSP are much smaller than the inter-model ensemble spread. The number of CMIP6 realizations in Figure 4.17b is larger than the suggested threshold of five realizations needed to detect a significant near-term change in decadal-mean austral winter SAM index for a single CMIP5 model (Solomon and Polvani, 2016), and yet the 5–95% intervals on the CMIP6 ensemble spread encompass zero for all core SSPs. This suggests both internal variability and model uncertainty contribute to the CMIP6 ensemble spread in near-term SAM index changes. Based on these results, it is *more likely than not* that in the near-term under all assessed SSP scenarios the SAM index would become more positive than in present-day in austral autumn, winter and spring.

An influence of forcing agents other than stratospheric ozone and GHGs, such as anthropogenic aerosols, on SAM changes over the historical period has been reported in some climate models (Rotstayn, 2013), but the response across a larger set of CMIP5 models is not robust (Steptoe et al., 2016) and depends on how tropospheric temperature response to aerosols (Choi et al., 2019). This gives *low confidence* in the potential influence of anthropogenic aerosols on the SAM in the future.

4.4.3.2 El Niño-Southern Oscillation

AR5 assessed that it is *very likely* that the ENSO will remain the dominant mode of interannual variability in the future but did not specify its change in near term. A subset of CMIP5 models that simulate the ENSO Bjerknes index most realistically show an increase of ENSO SST amplitude in the near-term future and decline thereafter (Kim et al., 2014). However, detection of robust near-term changes of ENSO SST variability in response to anthropogenic forcing is difficult to achieve due to pronounced unforced low-frequency modulations of ENSO (Wittenberg, 2009; Maher et al., 2018; Wengel et al., 2018). Figure 4.10 in Section 4.3.3.2 using CMIP6 models also shows no robust change in ENSO SST variability in the near term.

While there is no strong model consensus on the change in amplitude of ENSO SST variability, the amplitude of ENSO-associated rainfall variability *likely* increases (Power et al., 2013; Cai et al., 2015). Analysis of CMIP6 models shows a slight increasing trend in amplitude of rainfall variability over Niño3.4 region in the near term attributable to mean moisture increase, regardless of changes in ENSO SST

ACCEPTED VERSION SUBJECT TO FINAL EDITS

variability (Figure 4.10) However, there are no distinguishable changes in the rainfall variability among four SSPs with significant model spread in the near term. Hence, no robust change in amplitude of ENSO SST and rainfall variability is expected in the near term although the rainfall variability slightly increases (*medium confidence*).

4.4.3.3 Indian Ocean Basin and Dipole Modes.

Important modes of interannual climate variability with pronounced climate impacts in the Africa-Indo-Pacific areas of the globe are the Indian Ocean Dipole (IOD), which is closely related to- and often coincides with ENSO phases (Stuecker et al., 2017), and the Indian Ocean Basin (IOB) mode, which is often described as a capacitor effect in response to ENSO (Xie et al., 2009; Du et al., 2013) and can feed back onto ENSO evolution (Cai et al., 2019a). IOD and IOB are extensively described in Annex IV, Section AIV2.4.

The projected climate mean state changes in the tropical Indian Ocean resemble a positive IOD state, with faster warming in the west compared to the east. This mean state change will potentially lead to a reduction in the amplitude of IOD events, albeit with no robust change in IOD frequency (Cai et al., 2014b). There is no robust evidence yet suggesting a cessation of IOD variability or a significant change in the IOB mode in the near-term.

4.4.3.4 Tropical Atlantic Modes

Interannual variability of the tropical Atlantic can be described in terms of two main climate modes: the Atlantic Equatorial Mode and the Atlantic Meridional Mode (AMM) (Annex IV, Section AIV2.5). The Atlantic Equatorial Mode, also commonly referred to as the Atlantic Niño or Atlantic Zonal Mode, is associated with SST anomalies near the equator, peaking in the eastern basin, while the AMM is characterized by an inter-hemispheric gradient of SST and wind anomalies. Both modes are associated with changes in the ITCZ and related winds and exert a strong influence on the climate in adjacent and remote regions.

Despite considerable improvements in CMIP5 with respect to CMIP3, most CMIP5 models have difficulties in simulating the mean climate of the tropical Atlantic (Mohino et al., 2019) and are not able to correctly simulate the main aspects of Tropical Atlantic Variability (TAV) and associated impacts. This is presumably the main reason why there is a lack of specific studies dealing with near-term changes in tropical Atlantic modes. Nevertheless, AR5 reported that the ocean is more predictable than continental areas at the decadal timescale (Kirtman et al., 2013). In particular, the predictability in the tropical oceans is mainly associated with decadal variations of the external forcing component. Since the AMV affects the tropical Atlantic, near-term variations of the AMV can modulate the Equatorial Mode and the AMM as well as associated impacts.

There are no specific studies focusing on near-term changes in tropical Atlantic modes; nevertheless, decadal predictions show that although the North Atlantic stands out in most CMIP5 models as the primary region where skill might be improved because of initialization, encouraging results have also been found in the tropical Atlantic (Meehl et al., 2014). The effect of initialization in the tropical Atlantic is not only visible in surface temperature but also in the subsurface ocean (Corti et al., 2015). In particular, initialization improves the skill via remote ocean conditions in the North Atlantic subpolar gyre and tropical Pacific, which influence the tropical Atlantic through atmospheric teleconnections (Dunstone et al., 2011; Vecchi et al., 2014; García-Serrano et al., 2015a). Improvements of some aspects of climate prediction systems (initialization techniques, large ensembles, increasing model resolution) have also led to skill improvements over the tropical Atlantic (Pohlmann et al., 2013; Monerie et al., 2017; Yeager and Robson, 2017).

Recent studies have shown that the AMV can modulate not only the characteristics of the Atlantic Niños, but also their inter-basin teleconnections (Indian and Pacific). In particular, the Atlantic Niño–ENSO relationship is strongest during negative AMV phases (Martín-Rey et al., 2014; Losada and Rodríguez-Fonseca, 2016) when equatorial Atlantic SST variability is enhanced (Martín-Rey et al., 2017; Lübbecke et

ACCEPTED VERSION SUBJECT TO FINAL EDITS

al., 2018).

Based on CMIP5 and available CMIP6 results, we conclude that there is a lack of studies on the near-term evolution of TAV and associated teleconnections for a comprehensive assessment. However, some studies show that despite severe model biases there are skilful predictions in the mean state of tropical Atlantic surface temperature several years ahead (*medium confidence*), though skill in simulated variability has not been assessed yet. Decadal changes in the Atlantic Niño spatial configuration and associated teleconnections might be modulated by the AMV, but there is *limited evidence* and therefore *low confidence* in these results.

4.4.3.5 Pacific Decadal Variability

Climate variability of the Pacific Ocean on decadal and interdecadal timescales is described in terms of a number of quasi-oscillatory SST patterns such as the Pacific Decadal Oscillation (PDO) (Mantua et al., 1997) and the Interdecadal Pacific Oscillation (IPO) (Folland, 2002), which are referred to as the Pacific Decadal Variability (PDV) (Newman et al., 2016). PDV comprises an inter-hemispheric pattern that varies at decadal-to-interdecadal timescales (see Chapter 3, Figure 3.35). However, although the spatial domains to derive the IPO and PDO indices differ, and despite uncertainty related to trend removal and time-filtering (Newman et al., 2016; Tung et al., 2019), the IPO and PDO are highly correlated in time and they will be assessed together as the PDV (see Annex IV, Section AIV.2.6).

AR5 assessed that near-term predictions of PDV (then referred to as PDO or IPO) were largely model dependent (Mochizuki et al., 2012; van Oldenborgh et al., 2012), not robust to sampling of initialization start-dates, overall not statistically significant, and worse than persistence (Doblas-Reyes et al., 2013), although some studies showed positive skill for PDV (Mochizuki et al., 2010; Chikamoto et al., 2013). The CMIP5 decadal-prediction ensemble yielded no prediction skill of SST over the key PDV centres of action in the Pacific Ocean, both at 2–5 year and 6–9 year forecast averages (Doblas-Reyes et al., 2013; Guemas et al., 2013; Boer and Sospedra-Alfonso, 2019).

Since AR5, the processes causing the multi-decadal variability in the Pacific Ocean have become better understood (Newman et al., 2016)(Henley, 2017). However, the relative importance of tropical and extratropical processes underlying PDV remains unclear; although it seems to be stochastically driven rather than self-excited (Liu, 2012; Liu and Di Lorenzo, 2018), the South Pacific being a key region for the tropical branch of PDV (Chung et al., 2019; Liguori and Di Lorenzo, 2019).

Because PDV represents not one, but many dynamical processes, it represents a challenge as a target for near-term climate predictions and projections. The new generation of decadal forecast systems keeps showing poor (Shaffrey et al., 2017) to moderate (Smith et al., 2019b) multi-year prediction skill for PDV, although the potential for forecasting capabilities is demonstrated in case studies (Meehl and Teng, 2012; Meehl et al., 2014). For the near-term, a transition of PDV from the negative phase (1999–2012) towards a positive phase is predicted in the coming years (2013-2022) (Meehl et al., 2016).

The PDV has been shown to influence the pace of global warming (see Cross Chapter Box 3.1), but the extent to which PDV is externally forced or internally generated (Mann et al., 2020) remains an open question, and there is still no robust evidence. Thus, there is *low confidence* on how the PDV will evolve in the near-term (Bordbar et al., 2019).

4.4.3.6 Atlantic Multidecadal Variability

The Atlantic Multi-decadal Variability (AMV) is a large-scale climate mode accounting for the main fluctuations in North Atlantic SST on multi-decadal timescales (Annex IV, Section AIV.2.7). The AMV influences air temperatures and precipitation over adjacent and remote continents, and its undulations can partially explain the observed variations in the NH mean temperatures (Steinman et al., 2015). The origin of this variability is still uncertain. Ocean dynamics (e.g., changes in the AMOC), external forcing, and local

ACCEPTED VERSION SUBJECT TO FINAL EDITS

atmospheric forcing all seem to play a role (Menary et al., 2015; Ruprich-Robert and Cassou, 2015; Brown et al., 2016; Cassou et al., 2018; Wills et al., 2019). Recent studies have discussed that the ocean dynamics play an active role in generating AMV (Oelsmann et al., 2020) and its interplay with the NAO (Vecchi et al., 2017; Zhang et al., 2019a; Kim et al., 2020), although natural and anthropogenic external forcing might be crucial in modulating its amplitude and timing (Bellucci et al., 2017)(Bellomo et al., 2018; Andrews et al., 2020; Borchert et al., 2021)(Mann et al., 2021) (see Section 3.7.7 and Section AIV.2.7).

AR5 assessed with high confidence that initialized predictions can improve the skill for temperature over the North Atlantic, in particular in the sub-polar branch of AMV, compared to the projections, for the first five years (see WGI AR5 Figures 11.3 and 11.4). However, non-initialized predictions showed positive correlation over the same time-range as well, consistent with the notion that part of this variability is caused by external forcing (see Chapter 3 Section 3.7.7).

Since AR5, near-term initialized predictions, both multi-model (Bellucci et al., 2015a; Garcia-Serrano et al., 2015b; Smith et al., 2019b) and single-model ensembles (Marotzke et al., 2016)(Simpson et al., 2018c)(Yeager et al., 2018)(Hermanson et al., 2020)(Bilbao et al., 2021), confirm substantial skill in hindcasting North-Atlantic SST anomalies on a time range of 8–10 years. On the same time range, (Borchert et al., 2021) show a substantial improvement in the prediction of the subpolar gyre SST (the northern component of the AMV) in CMIP6 models compared to CMIP5, in both initialized and non-initialized simulations. The higher skill can be attributed to a more accurate response in CMIP6 models to natural forcing, possibly originating from the AMOC-related delayed response to volcanic eruptions, which contribute to the SST variations in the subpolar gyre (Hermanson et al., 2020).

Initialization contributes to the reduction of uncertainty and to predicting subpolar SST amplitude (Borchert et al., 2021). Yet, skill in predicting the AMV is not always translated into equally successful predictions of temperature and precipitation over the nearby land and ocean regions (Langehaug et al., 2017). This might be related to systematic model errors in the simulation of the spatial and temporal structure of the AMV and too weak associated teleconnections (see Section 3.7.7), and also to the larger noise in regional land variables compared to the AMV index. However, AMV predictions can be used as proxies to predict other variables such as precipitation over Western Europe and Eurasia and SAT over Mediterranean, northern Europe and northeast Asia (Årthun et al., 2018; Borchert et al., 2019; Ruggieri et al., 2021) whose relationship with North Atlantic SST is robust in observations, but not well captured in climate models.

Encouraging results about the prediction of land precipitation linked to the warm AMV phase (see Chapter 3 Section 3.7.7 and Annex IV, Figure AIV.2.7) on a 2-9 year timescale are reported in the multi-model study by (Smith et al., 2019b). Positive correlations with observations are found in the Sahel, South America, the Maritime Continent. Analyses from large-ensemble decadal prediction systems such as the community Earth system model decadal prediction large ensemble (CESM-DPLE) (Yeager et al., 2018) show an improvement with respect to the CMIP5 decadal hindcasts (Martin and Thorncroft, 2014b) in forecasting Sahel precipitation over three to seven years, which is consistent with the current understanding of AMV impact over Africa (Mohino et al., 2016; Smith et al., 2019b). CESM-DPLE predicts drought conditions over the Sahel through 2020, which is compatible with a shift towards a negative phase of AMV as a result of a weakening of the AMOC, advocated by a number of studies (Hermanson et al., 2014; Robson et al., 2014; Yeager et al., 2015).

In summary, the *confidence* in the predictions of AMV and its effects is *medium*. However, there is *high confidence* that the AMV skill over 5–8-year lead times is improved by using initialized predictions, compared to non-initialized simulations.

4.4.4 Response to Short-Lived Climate Forcers and Volcanic Eruptions

Mitigation of SLCFs affects future climate projections and could alter the time of emergence of anthropogenic climate change signals. AR5 assessed that emission reductions aimed at decreasing local air pollution could have a near-term warming impact on climate (*high confidence*) (Kirtman et al., 2013).

ACCEPTED VERSION SUBJECT TO FINAL EDITS

Because of their shorter lifetimes, reductions in emissions of SLCF species mainly influence near-term GSAT trends (Chalmers et al., 2012; Shindell et al., 2017; Shindell and Smith, 2019), but on decadal timescales the near-term response to even very large reductions in SLCFs may be difficult to detect in the presence of large internal climate variability (Samset et al., 2020). The changes in SLCF emissions during the COVID-19 pandemic has resulted in a small net radiative forcing without a discernible impact on GSAT (Cross-Chapter Box 6.1). SLCF mitigation also leads to a higher GSAT in the mid- to long-term (Smith and Mizrahi, 2013; Stohl et al., 2015; Hienola et al., 2018) and can influence peak warming during the 21st century (Hienola et al., 2018; Rogelj et al., 2014). This section focuses on the total effect of SLCF changes on GSAT projections in the SSP scenarios. A more detailed breakdown of the separate climate effects of SLCF species and precursor species can be found in Sections 6.7.2 and 6.7.3.

A model experiment based on the SSP3-7.0 scenario with aerosols, their precursors, and non-methane tropospheric ozone precursors set to SSP1-1.9 abundances (SSP3-7.0-lowSLCF-highCH4; Collins et al., 2017) shows a projected multi-model mean GSAT anomaly that is higher by 0.22ºC at mid-century (2045-2054) compared to SSP3-7.0 (Figure 4.18:; Allen et al., 2020), but this difference is smaller than the intermodel spread of the SSP3-7.0 projections based on the CMIP6 models. Note the SSP3-7.0-lowSLCF-highCH4 experiment does not perturb methane from SSP3-7.0 concentrations. A modified SSP3-7.0-lowSLCF-lowCH4 scenario that also includes methane mitigation shows a lower GSAT by mid-century compared to SSP3-7.0 (Allen et al., 2021).

[START FIGURE 4.18 HERE]

Figure 4.18: Influence of SLCFs on projected GSAT change. Change is shown relative to the 1995–2014 average (left axis) and relative to the 1850–1900 average (right axis). The comparison is for CMIP6 models for the AerChemMIP (Collins et al., 2017) SSP3-7.0-lowSLCF-highCH4 experiment (note in the original experiment protocol this is called SSP3-7.0-lowNTCF), where concentrations of short-lived species are reduced compared to reference SSP3-7.0 scenario. The curves show averages over the r1 simulations contributed to the CMIP6 exercise, the shadings around the SSP3-7.0 curve shows 5–95% ranges and the numbers near the top show the number of model simulations. Further details on data sources and processing are available in the chapter data table (Table 4.SM.1).

[END FIGURE 4.18 HERE]

Building on CMIP6 results for the effects of reducing SLCF emissions from a baseline of SSP3-7.0, the overall contribution of SLCFs to GSAT changes in the marker SSPs are now quantified using a simple climate model emulator. For consistency with Section 6.7.2 and Figure 6.22, the basket of SLCF compounds considered includes aerosols, ozone, methane, black carbon on snow and hydrofluorocarbons (HFCs) with lifetimes of less than 50 years. In the five marker SSPs considered, the net effect of SLCFs contributes to a higher GSAT in the near, mid- and long term (Table 4.6, Section 6.7.2). In the SSP1-1.9 and SSP1-2.6 scenarios, SLCFs contribute to a higher GSAT by a central estimate of around 0.3 °C compared to 1995–2014 across the three-time horizons. In the long-term, the 0.3 °C warming due to SLCFs in SSP1-2.6 can be compared to the assessed *very likely* GSAT change for this period of 0.5–1.5 °C (Section 4.3.4; Table 4.5). The SSP2-4.5, SSP3-7.0 and SSP5-8.5 scenarios all show a larger SLCF effect on GSAT in the long term relative to the near term. In SSP3-7.0, the long-term warming due to SLCFs by 0.7 °C can be compared with the assessed *very likely* GSAT anomaly for this period of 2.0–3.7 °C (Section 4.3.4). In summary, it is *very likely* that changes in SLCFs contribute to an overall warmer GSAT over the near, mid- and long term in the five SSP scenarios considered (Table 4.6, Section 6.7.2; Figure 6.22).

[START TABLE 4.6 HERE]

Table 4.6: The net effect of SLCFs on GSAT change. Changes in 20-year averaged GSAT relative to 1995–2014 for 2021–2040, 2041–2060, and 2081–2100 for the five marker SSP scenarios. Values give the median and, in parentheses, the 5–95% range calculated from a 2,237-member ensemble of the two-layer

ACCEPTED VERSION SUBJECT TO FINAL EDITS

emulator that is driven with the ERF projections, including uncertainties, described in Chapter 7 Supplementary Material 7.SM.1.4. The ensemble is constrained to assessed ranges of ECS, TCR, ocean heat content change, GSAT response, and carbon cycle metrics (Section 7.3.5; Chapter 7 Supplementary Material 7.SM.2.2). The GSAT contribution of individual forcer responses use the difference between parallel runs of the constrained two-layer model with all anthropogenic forcing and all anthropogenic forcing with the component of interest (e.g. methane) removed (Chapter 7 Supplementary Material 7.SM.2.3). Values are given to 1 decimal place.

Units = °C	SSP1-1.9	SSP1-2.6	SSP2-4.5	SSP3-7.0	SSP5-8.5
Near term (2021–2040)	0.2 (0.1, 0.3)	0.2 (0.1, 0.3)	0.2 (0.1, 0.3)	0.2 (0.1, 0.3)	0.3 (0.2, 0.4)
Mid-term (2041–2060)	0.2 (0.0, 0.4)	0.2 (0.0, 0.4)	0.3 (0.2, 0.4)	0.3 (0.2, 0.4)	0.5 (0.3, 0.7)
Long term (2081–2100)	0.1 (-0.1, 0.4)	0.2 (0.0, 0.4)	0.3 (0.1, 0.6)	0.5 (0.4, 0.8)	0.7 (0.4, 1.0)

[END TABLE 4.6 HERE]

In addition to effects on GSAT, SLCFs affect other aspects of the global climate system (Section 6.7.2). The additional warming at high northern latitudes associated with projected reductions in aerosol emissions over the 21st century leads to a more rapid reduction in Arctic sea-ice extent in the RCP scenarios (Gagné et al., 2015). Furthermore, mitigation of non-methane SLCFs in the SSP3-7.0-lowSLCF-highCH4 scenario causes an increase in global mean precipitation, with larger regional changes in southern and eastern Asia (Allen et al., 2020).

The main uncertainties in climate effects of SLCFs in the future come from: (i) the uncertainty in anthropogenic aerosol ERF (Section 7.3.3); (ii) uncertainty in the relative emissions of different SLCFs that have warming and cooling effects in the current climate (Section 6.2); and (iii) physical uncertainty including the efficacy of the climate response to SLCFs compared to long-lived GHGs (Marvel et al., 2016; Richardson et al., 2019). One example of physical uncertainty is that the shortwave radiative forcing from methane was neglected in previous calculations (Etminan et al., 2016; Collins et al., 2018), which affects understanding of present-day and future methane ERF (Modak et al., 2018b). Another example of physical uncertainty is projected changes in lightning-NO_x production, which contributes to future ozone radiative forcing (Banerjee et al., 2014, 2018; Finney et al., 2018).

Another factor that could substantially alter projections in the near-term would be the occurrence of a large explosive volcanic eruption, or even a decadal to multi-decadal sequence of small-to-moderate volcanic eruptions as witnessed over the early 21st century (Santer et al., 2014; Cross-Chapter Box 4.1). An eruption similar to the last large tropical eruption, Mount Pinatubo in the Philippines in June 1991, is expected to cause substantial Northern Hemisphere (NH) cooling, peaking between 0.09°C and 0.38°C and lasting for three to five years, as indicated by climate model simulations over the past millennium (e.g., Jungclaus et al., 2010). Phase 3 of Paleoclimate Modelling Intercomparison Project (PMIP3) simulated a significant NH cooling in response to individual volcanic events (peaks between 0.1°C and 0.5°C, depending on model, during the first year after the eruption) that lasts for three to five years. On a regional scale, the double volcanic events that occurred in 536 and 540 CE resulted in a cooling of 2°C (Büntgen et al., 2016a; Toohey et al., 2016a).

Since AR5, there has been growing progress in understanding the climate impacts of volcanic eruptions. Volcanic forcing is regarded as the dominant driver of forced variability in preindustrial surface air temperature (Schurer et al., 2013a, 2014). Large eruptions in the tropics and high latitudes were primary drivers of interannual-to-decadal temperature variability in the Northern Hemisphere during the past 2,500 years, with cooling persisting for up to ten years after some of the largest eruptive episodes (Sigl et al., 2015). Repeated clusters of volcanic eruptions can induce a net negative radiative forcing that results in a centennial and global scale cooling trend via a decline in mixed-layer oceanic heat content (McGregor et al.,

ACCEPTED VERSION SUBJECT TO FINAL EDITS

2015). The response to multi-decadal changes in volcanic forcing (representing clusters of eruptions) shows similar cooling in both simulations and reconstructions of NH temperature. Volcanic eruptions generally result in decreased global precipitation for up to a few years following the eruption (Iles and Hegerl, 2014, 2015; Man et al., 2014), with climatologically wet regions drying and climatologically dry regions wetting (*medium confidence*), which is opposite to the response under global warming (Held and Soden, 2006b; Iles et al., 2013; Zuo et al., 2019a, 2019b). El Niño-like warming appears after large volcanic eruptions that is seen in both observations (Adams et al., 2003; McGregor et al., 2010a; Khodri et al., 2017) and climate model simulations (Ohba et al., 2013; Pausata et al., 2015; Colose et al., 2016; Stevenson et al., 2016; Khodri et al., 2017; Predybaylo et al., 2017; Zuo et al., 2018). The large tropical eruptions are coincident with positive Indian Ocean Dipole events (Maher et al., 2015).

In AR5, uncertainty due to future volcanic activity was not considered in the assessment of the CMIP5 21st century climate projections (Taylor et al., 2012; O'Neill et al., 2016). Since AR5, there has been considerable progress in quantifying the impacts of volcanic eruptions on decadal climate prediction and longer-term climate projections (Meehl et al., 2015; Swingedouw et al., 2015, 2017; Timmreck et al., 2016; Bethke et al., 2017; Illing et al., 2018). By exploring 60 possible volcanic futures under RCP4.5, it has been demonstrated that the inclusion of time-varying volcanic forcing may enhance climate variability on annual-to-decadal timescales (Bethke et al., 2017). Consistent with a tropospheric cooling response, the change in ensemble spread in the volcanic cases is skewed towards lower GSAT relative to the non-volcanic cases (Cross-Chapter Box 4.1 Figure 1). In these simulations with multiple volcanic forcing futures there is: 1) an increase in the frequency of extremely cold individual years; 2) an increased likelihood of decades with negative GSAT trend (decades with negative GSAT trends become 50% more commonplace); 3) later anthropogenic signal emergence (the mean time at which the signal of global warming emerges from the noise of natural climate variability is delayed almost everywhere) (*high confidence*); and 4) a 10% overall reduction in global land monsoon precipitation and a 20% overall increase in the ensemble spread (Man et al., 2021).

[START Cross-Chapter Box 4.1 HERE]

Cross-Chapter Box 4.1: The climate effects of volcanic eruption

Contributing Authors: Sarah Connors (France/UK), Amanda Maycock (UK), Peter Thorne (Ireland/UK), Nicolas Bellouin (UK/ France), Ingo Bethke (Norway), Deliang Chen (Sweden), Annalisa Cherchi (Italy), Alejandro Di Luca (Australia/Argentina), Piers Forster (UK), Nathan Gillett (Canada), Darrell Kaufmann (USA), June-Yi Lee (Republic of Korea), Elizaveta Malinina (Canada), Seung-Ki Min (Republic of Korea), Johannes Quaas (Germany), Alex C. Ruane (USA), Jean-Baptiste Sallée (France), Sonia I. Seneviratne (Switzerland), Chris Smith (UK), , Matthew Toohey (Canada), Andrew Turner (UK), Cunde Xiao (China), Tianjun Zhou (China).

Before the industrial period, explosive volcanic eruptions were the largest source of forced climate variability globally on interannual to centennial timescales (Section 2.2). While usually omitted from scenarios used for future climate projections, as they are unpredictable, volcanic eruptions have the potential to influence future climate on multi-annual to decadal timescales and affect many climatic impact drivers (as defined in Sections 12.1, 12.3). Since AR5, more comprehensive paleo evidence and observations, as well as improved modelling have advanced understanding of the climate response to past volcanic eruptions. Building on multiple chapter assessments, this box synthesizes how volcanic eruptions affect climate and considers implications of possible future events.

How frequent are volcanic eruptions?

Proxy records show that large volcanic eruptions with effective radiative forcing (ERF) more negative than –1 W m^{-2} occurred on average twice a century throughout the last 2500 years, the most recent being Pinatubo in 1991 (Section 2.2.2). About eight larger eruptions (ERF stronger than –5 Wm^{-2}) also occurred during this period (Figure 2.2), notably Tambora~1815 and Samalas~1257. A Samalas-type eruption may occur 1–2 times per millennium on average (Newhall et al., 2018). Typically, three in every four centuries have

ACCEPTED VERSION SUBJECT TO FINAL EDITS

experienced at least one eruption stronger than –1 W m^{-2} (Pinatubo or larger). The volcanic aerosol burden was 14% lower during the 20th century compared to the average of the preceding 24 centuries (Section 2.2.2), whereas the 13th century was among the most volcanically active, with four eruptions exceeding that of Pinatubo-1991 (Sigl et al., 2015).

Past climate responses to volcanic activity

Major eruptions drive a range of climate system responses for several years depending upon whether the eruption occurs in the tropics (stratospheric aerosol dispersion into both hemispheres) or the extra-tropics (dispersion into the hemisphere of eruption) owing to the Brewer-Dobson circulation. The climatic response also depends on the effective injection height, sulphur mass injected, and time of year of the eruption (Marshall et al., 2019, 2020). These factors determine the total mass, lifetime and optical properties of volcanic aerosol in the stratosphere and influence the stratospheric aerosol optical depth (sAOD). The ERF from volcanic stratospheric aerosol is assessed to be –20 ± 5 W m^{-2} per unit sAOD (Section 7.3.4.6).

Due to the direct radiative effect of volcanic stratospheric aerosols, large volcanic eruptions lead to an overall **decrease of GSAT**, which can extend to multi-decadal or century timescales in the case of clustered volcanism (Section 3.3.1.1, Schurer et al., 2013; McGregor et al., 2015; Sigl et al., 2015; Kobashi et al., 2017; Zambri et al., 2017; Brönnimann et al., 2019; Neukom et al., 2019). Large eruptions also increase the frequency of extremely cold individual years and the likelihood of cooling trends occurring in individual decades (Cross-chapter Box 3.1, Section 4.4.4, Paik and Min, 2018). Re-dating of ice core chronologies now confirms that the coldest decades of the past ~2000 years are the outcome of volcanic eruptions (Sigl et al., 2015; Büntgen et al., 2016b; Toohey et al., 2016b; Neukom et al., 2019). CMIP5 and CMIP6 models reproduce the decreased GSAT that follows periods of intense volcanism. New reconciliations between simulations and proxy-based reconstructions of past eruptions have been achieved through better Earth System Model representation of volcanic plume chemical compositions (Legrande et al., 2016; Marshall et al., 2020; Zhu et al., 2020a). Yet, remaining disagreements reflect differences in the volcanic forcing datasets used in the simulations (*medium confidence*) (Section 3.3.1.1, Figure 3.2c).

Although incomplete, proxy records show large impacts upon contemporary society from eruptions such as 1257 Samalas and 1815 Tambora, the latter resulting in 'the year without a summer' with multiple harvest failures across the NH (e.g., Raible et al., 2016). Comparing CMIP5 multi-model simulations with observations has improved understanding of the hydrological responses to 20th-century eruptions, particularly global land monsoon drying, and associated uncertainties (Section 3.3.2.2). Global-mean land **precipitation** decreases for up to a few years following the eruption, with climatologically wet regions drying and dry regions wetting (Section 3.3.2.2, Section 4.4.4). Changes in **monsoon** circulations occur with a general weakening of tropical precipitation (Section 8.5.2.3) and a decrease in extreme precipitation over global monsoon regions (Section 11.4.4). Monsoon precipitation in one hemisphere tends to be enhanced by eruptions occurring in the other hemisphere or reduced if they occur in the same hemisphere (Section 3.3.2.2; 8.5.2.3). Volcanic eruptions have been linked to the onset of **El Niño** followed by **La Niña** although this connection remains contentious (Adams et al., 2003; Bradley et al., 2003; McGregor et al., 2010b; Khodri et al., 2017; Liu et al., 2018a; Sun et al., 2019; Paik et al., 2020; Predybaylo et al., 2020). Volcanic activity could drive short-term (1-3 year) positive changes in the **annual SAM** index through modulations in the extratropical temperature gradient and wave driving of the polar stratosphere (Yang and Xiao, 2018). In the **cryosphere**, Arctic sea-ice extent increases for years to decades (Gagné et al., 2017b), and modelling indicates that sea-ice/ocean feedbacks can prolong cooling long after volcanic aerosols are removed (Miller et al., 2012). On annual timescales, the **ocean** buffers the atmospheric response to volcanic eruptions by storing the cooling in the ocean subsurface, then feeding it back to the atmosphere. Large eruptions affect ocean heat content and thermosteric sea level over decadal-to-centennial scales (Section 9.2.2.1).

Potential implications on 21st century projections

Given the unpredictability of individual eruptions, volcanic forcing is prescribed as a constant background loading in CMIP6 models (Eyring et al., 2016). This means the effects of potential large volcanic eruptions are largely absent from model projections, and few studies have addressed the potential implications on 21st

ACCEPTED VERSION SUBJECT TO FINAL EDITS

century warming. One study considered future scenarios with hypothetical volcanic eruptions consistent with levels of CE volcanic activity (Bethke et al., 2017) under RCP4.5 and found that climate projections could be substantially altered (Cross Chapter Box 4.1 Figure 1). Although temporary, close to pre-industrial level temperatures could be experienced globally for a few years after a 1257 Samalas-sized eruption. Several other key climate indicators are also changed substantially, consistent with evidence from past events. (Bethke et al., 2017) suggest that an eruption early in the 21st century could delay the timing of crossing 1.5°C global warming by several years. Clustered eruptions would have substantial impact upon GSAT evolution throughout the century (Cross-Chapter Box 4.1 Figure 1), and could have far-reaching implications, as observed for past eruptions. For near-term response options, decadal prediction models can update 21st-century projections once a volcanic eruption occurs (Timmreck et al., 2016).

Summary

It is *likely* that at least one large eruption will occur during the 21st century. Such an eruption would reduce GSAT for several years, decrease global-mean land precipitation, alter monsoon circulation, modify extreme precipitation, and change the profile of many regional climatic impact-drivers. A low likelihood high impact outcome would be several large eruptions that would greatly alter the 21st century climate trajectory compared to SSP-based ESM projections.

[START CROSS-CHAPTER BOX 4.1, FIGURE 1 HERE]

Cross-Chapter Box 4.1, Figure 1: Potential impact of volcanic eruption on future global temperature change. CMIP5 projections of possible 21st-century futures under RCP4.5 after a 1257 Samalas magnitude volcanic eruption in 2044, from (Bethke et al., 2017). a, Volcanic ERF of the most volcanically active ensemble member, estimated from SAOD. b, Annual-mean GSAT. Ensemble mean (solid) of future projections including volcanoes (blue) and excluding volcanoes (red) with 5–95% range (shading) and ensemble minima/maxima (dots); evolution of the most volcanically active member (black). Data created using a SMILE approach with NorESM1 in its CMIP5 configuration. See Section 2.2.2 and Section 4.4.4 for more details. Further details on data sources and processing are available in the chapter data table (Table 4.SM.1).

[END CROSS-CHAPTER BOX 4.1, FIGURE 1 HERE]

[END Cross-Chapter Box 4.1 HERE]

4.5 Mid- to Long-term Global Climate Change

4.5.1 Atmosphere

This section assesses how the global atmospheric indicators assessed in Section 4.3 manifest themselves in large-scale spatial patterns of atmospheric change in the mid-term (2041–2060) and long term (2081–2100). The patterns of change in any given future period represent a combination of unforced internal variability and a forced response including their interaction (Deser et al., 2016). The role of internal variability is much larger at the local to regional scale than in the global mean projections. We here assess multi-model mean patterns based on CMIP6 models without any weighting or emergent constraints. The mean represents an estimate of the forced response and is a more homogeneous pattern than the 20-year mean change patterns in any individual model realization (Knutti et al., 2010).

4.5.1.1 Near-Surface Air Temperature

Patterns of near-surface air temperature changes show widespread warming by 2041–2060 and 2081–2100

ACCEPTED VERSION SUBJECT TO FINAL EDITS

(Figure 4.19) for all SSPs relative to 1995–2014. The area fraction experiencing warming increases with the level of global mean warming. As GSAT continues to increase, it is *very likely* that by the middle and the end of the 21st century most of the global land and ocean areas will be warmer than in 1995–2014 (*high confidence*) (see also Section 4.3.1.1).

[START FIGURE 4.19 HERE]

Figure 4.19: Mid- and long-term change of annual mean surface temperature. Displayed are projected spatial patterns of multi-model mean change in annual mean near-surface air temperature (°C) in 2041–2060 and 2081–2100 relative to 1995–2014 for (top) SSP1-2.6 and (bottom) SSP3-7.0. The number of models used is indicated in the top right of the maps. No overlay indicates regions where the change is robust and *likely* emerges from internal variability, that is, where at least 66% of the models show a change greater than the internal-variability threshold (see Section 4.2.6) and at least 80% of the models agree on the sign of change. Diagonal lines indicate regions with no change or no robust significant change, where fewer than 66% of the models show change greater than the internal-variability threshold. Crossed lines indicate areas of conflicting signals where at least 66% of the models show change greater than the internal-variability threshold but fewer than 80% of all models agree on the sign of change. Further details on data sources and processing are available in the chapter data table (Table 4.SM.1).

[END FIGURE 4.19 HERE]

The multi-model mean temperature change pattern (Figure 4.19) shows some robust key characteristics that are independent of the time horizon and scenario, such as a land-ocean warming contrast, amplified warming over the Arctic region, assessed below, or the comparatively small warming or even cooling in the North Atlantic subpolar gyre (see Section 9.2.1.1). Changes in aerosol concentrations and land use and land management can furthermore have a direct imprint on the regional warming pattern (Bright et al., 2017; Kasoar et al., 2018). Note that the global average of the pattern shown in Figure 4.19 corresponds to CMIP6 multi-model mean GSAT warming (see Section 4.3.1) and is thus somewhat warmer than the warming pattern consistent with the central estimate of the GSAT range assessed in Section 4.3.4. Since the regional mean warming scales well with global warming levels independent of the emission scenario (see Section 4.2.4), the key characteristics of the spatial pattern assessed here are largely independent of the difference between CMIP6 multi-model global mean and assessed global GSAT change.

Land–Ocean Warming Contrast

It is *virtually certain* that future average warming will be higher over land than over the ocean. SRCCL, Section 2.2.1 (Jia et al., 2019b) assessed that it is certain that land temperatures have increased more than global mean temperatures since the pre-industrial period. This so-called land-ocean warming contrast is a striking feature of observed trends (Lambert and Chiang, 2007; Byrne and O'Gorman, 2018) and projected changes in surface-air temperature (Sutton et al., 2007; Joshi and Gregory, 2008; Dong et al., 2009; Lambert et al., 2011; Drost et al., 2012; Bayr and Dommenget, 2013; Byrne and O'Gorman, 2013b; Izumi et al., 2013; Joshi et al., 2013). Between 1979 and 2016, average temperature over land increased by 42% more than over the ocean (Byrne and O'Gorman, 2018). A similar warming contrast is found in CMIP5 projections though with large differences across models and latitudes (Sutton et al., 2007; Drost et al., 2012; Byrne and O'Gorman, 2013b; Joshi et al., 2013), which is also consistent with paleoclimate evidence (Izumi et al., 2013; Schmidt et al., 2014). The ratio of land-to-ocean warming is greater than one for almost all regions (*high confidence*) and is larger for dry subtropical continents (about 1.5) than for moist regions in the tropics and mid-latitudes (about 1.2) (Byrne and O'Gorman, 2013a).

Since AR5, a robust physical understanding of the warming contrast been developed. A simple theory based on atmospheric dynamics and moisture transport shows that surface-air temperature and relative humidity over land are strongly coupled, and demonstrates that the warming contrast occurs because air over land is drier than over the ocean (Joshi et al., 2008; Byrne and O'Gorman, 2013a, 2013b, 2018). The warming contrast causes land relative humidity to decrease (Byrne and O'Gorman, 2016, 2018; Chadwick et al., 2016) and this feeds back on and strengthens the warming contrast. Differences in land relative humidity responses

ACCEPTED VERSION SUBJECT TO FINAL EDITS

across models are the primary cause of uncertainty in the land-ocean warming contrast (Byrne and O'Gorman, 2013b). These land relative humidity changes are ultimately controlled by moisture transport between the land and ocean boundary layers (Byrne and O'Gorman, 2016; Chadwick et al., 2016) and are also sensitive to characteristics of land surfaces that are challenging to model, including stomatal conductance and soil moisture (Berg et al., 2016; Zarakas et al., 2020).

Polar Amplification

It is *very likely* that under all SSPs the warming in the Arctic will be more pronounced than in the global average over the 21st century. Since AR5 the understanding of the physical mechanisms driving polar amplification has improved.

The Arctic surface is projected to warm more than the global average over the 21st century, with annual-average Arctic warming of about 3°C (SSP1-2.6), 10°C (SSP3-7.0) and 12°C in (SSP5-8.5) by 2081–2100 relative to 1995–2014 (Figure 4.19). This phenomenon, known as polar or Arctic amplification, is a ubiquitous feature of the response to GHG forcing simulated by climate models (Manabe and Wetherald, 1975; Manabe and Stouffer, 1980; Manabe and Wetherald, 1980; Robock, 1983; Hansen et al., 1984; Manabe et al., 1991; Holland and Bitz, 2003; Winton, 2006; Pithan and Mauritsen, 2014) and has been observed over recent decades concurrent with Arctic sea-ice loss (Serreze and Barry, 2011) (Chapter 2 Section 2.3.2.1). Based on robust scientific understanding and agreement across multiple lines of evidence (Chapter 7 Section 7.4.4.1), there is *high confidence* that the rate of Arctic surface warming will continue to exceed the global average over the 21st century.

A variety of mechanisms contribute to Arctic amplification (see Chapter 7 Section 7.4.4.1.1). While surface-albedo feedbacks associated with the loss of sea ice and snow have long been known to play important roles (Arrhenius, 1896; Manabe and Stouffer, 1980; Robock, 1983; Hall, 2004), it is now recognized that temperature (lapse-rate and Planck) feedbacks also contribute to Arctic amplification through a less efficient longwave radiative damping to space with warming at high latitudes (Winton, 2006; Pithan and Mauritsen, 2014; Goosse et al., 2018; Stuecker et al., 2018). Increases in poleward atmospheric latent heat transport and oceanic heat transport also contribute to Arctic warming (Holland and Bitz, 2003; Bitz et al., 2006; Lee et al., 2011, 2017; Alexeev and Jackson, 2013; Marshall et al., 2014, 2015; Woods and Caballero, 2016; Singh et al., 2017; Nummelin et al., 2017; Oldenburg et al., 2018; Merlis and Henry, 2018; Armour et al., 2019)(Beer et al., 2020). Projected reduction in the strength of the AMOC over the 21st century is expected to reduce Arctic warming, but even a strong AMOC reduction would not eliminate Arctic amplification entirely (Liu et al., 2017, 2018d; Wen et al., 2018) (*medium confidence*).

There remains substantial uncertainty in the magnitude of projected Arctic amplification (Smith et al., 2020), with the Arctic warming ranging from two to four times the global average in models (Holland and Bitz, 2003; Nummelin et al., 2017). This uncertainty primarily stems from different representations of polar surface-albedo, lapse-rate, and cloud feedbacks, and from different projected poleward energy transport changes (Holland and Bitz, 2003; Crook et al., 2011; Mahlstein and Knutti, 2011; Pithan and Mauritsen, 2014; Bonan et al., 2018). The magnitude of Arctic amplification may also depend on the mix of radiative forcing agents (Najafi et al., 2015; Sand et al., 2016; Stjern et al., 2019) such as the contribution of ozone depleting substances (Polvani et al., 2020). Tropospheric aerosol emissions tend to reduce simulated Arctic warming over the middle of the 20th century (Gagné et al., 2017a) and consequently aerosol emission reductions in observations and SSP scenarios enhance simulated Arctic warming over recent and future decades (Gagné et al., 2015; Acosta Navarro et al., 2016; Wobus et al., 2016; Wang et al., 2018) (also see Chapter 6 Section 6.4.3).

Climate models project weakly polar amplified warming in the SH under transient warming (Figure 4.19). Model simulations (Hall, 2004; Danabasoglu and Gent, 2009; Li et al., 2013) and paleoclimate proxies indicate polar amplification in both hemispheres near equilibrium, but generally with less warming in the Antarctic than the Arctic (Chapter 7, Section 7.4.4.1.2). The primary driver of delayed warming of the southern high latitudes is the upwelling in the Southern Ocean and associated ocean heat uptake that is then transported away from Antarctica by northward flowing surface waters (Froelicher et al., 2015; Marshall et al., 2015; Armour et al., 2016; Liu et al., 2018c), although asymmetries in feedbacks between the poles also

ACCEPTED VERSION SUBJECT TO FINAL EDITS

play a role (Chapter 7, Section 7.4.4.1.1). Changes in westerly surface winds over the Southern Ocean have the potential to affect the rate of sea-surface warming, but there is currently *low confidence* in even the sign of the effect based on a diverse range of climate model responses to wind changes (Marshall et al., 2014; Ferreira et al., 2015; Kostov et al., 2017; Seviour et al., 2019). A substantial increase in freshwater input to the ocean from the Antarctic ice sheet could further slow the emergence of SH polar amplification by cooling the Southern Ocean surface (Bronselaer et al., 2018; Golledge et al., 2019; Schloesser et al., 2019), but this process is not represented in current climate models which lack dynamic ice sheets. Thus, while there is *high confidence* that the SH high latitudes will warm by more than the tropics on centennial timescales, there is *low confidence* that such a feature will emerge this century (Chapter 7, Section 7.4.4.1).

Seasonal Warming Patterns

The warming pattern shows distinct seasonal characteristics. The majority of models show a stronger hemispheric winter than summer warming over land poleward of about 55°N and 55°S (Figure 4.20) and thereby a reduced amplitude of the temperature cycle (Dwyer et al., 2012; Donohoe and Battisti, 2013). On the other hand, over most of the subtropics and mid-latitudinal land regions except for parts of Asia, models project stronger warming in hemispheric summer than winter (Donohoe and Battisti, 2013; Santer et al., 2018), leading to an amplification of the seasonal cycle. This phenomenon has been studied particularly in the case of the amplified summer warming over the Mediterranean region (Seager et al., 2014a; Kröner et al., 2017; Brogli et al., 2019).

[START FIGURE 4.20 HERE]

Figure 4.20: Difference of surface temperature change between JJA and DJF. Displayed are spatial patterns of multi-model mean difference in projected warming in JJA minus warming in DJF in 2081–2100 relative to 1995–2014 for (left) SSP1-2.6 and (right) SSP3-7.0. Diagonal lines mark areas where fewer than 80% of the models agree on the sign of change, and no overlay where at least 80% of the models agree. Further details on data sources and processing are available in the chapter data table (Table 4.SM.1).

[END FIGURE 4.20 HERE]

Changes in Temperature Variability

It has long been recognized that along with mean temperatures also variance and skewness of the temperature distribution may be changing (Gregory and Mitchell, 1995; Mearns et al., 1997). By amplifying or dampening changes in the tail of temperature distribution such changes are potentially highly relevant to extremes (Chapter11, Section 11.3.1) and pose a serious challenge to adaptation measures. Changes in temperature variability can occur from diurnal to multi-decadal timescales and from the local to the global scale with potentially even opposing signals in different seasons and at the different spatial scales

Changes in GSAT variability are poorly understood. Based on model experiments it has been suggested that unforced variability of GSAT tends to decrease in a warmer world as a result of reduced albedo variability in high latitudes resulting from melting snow and sea ice (Huntingford et al., 2013; Brown et al., 2017), but *confidence* remains *low* and an observed change has not been detected. An assessment of changes in global temperature variability is inherently challenging due to the interplay of unforced internal variability and forced changes.

Changes in tropical temperature variability may arise from changes in the amplitude of ENSO (see Section 4.5.3.2). Over the extratropics, several studies have identified robust large-scale patterns of changes in variability of annual and particularly seasonal mean temperature, including (a) a reduction in mid- to high-latitude winter temperature variability and (b) an increase in summer temperature variability over land in the tropics and subtropics (Huntingford et al., 2013; Holmes et al., 2016)(Figure 4.21). The multi-ensemble average across seven single-model initial-condition large ensembles projects a consistent reduction in year-to-year DJF variability around about 50-70°N and JJA variability around 55°–70°S along the edge of the sea ice- and snow-covered region (Figure 4.21). There is growing evidence that year-to-year and day-to-day

ACCEPTED VERSION SUBJECT TO FINAL EDITS

temperature variability decreases in winter over northern mid- to high-latitudes (Fischer et al., 2011; De Vries et al., 2012; Screen, 2014; Schneider et al., 2015; Holmes et al., 2016; Borodina et al., 2017; Tamarin-Brodsky et al., 2020) which implies that the lowest temperatures rise more than the respective climatological mean temperatures (*medium confidence*). Over the Northern Hemisphere, reduced high-latitude temperature variability is associated with disproportionally large warming in source region of cold-air advection due to Arctic amplification and land-sea contrast (De Vries et al., 2012; Screen, 2014; Holmes et al., 2016). It has further been argued that a reduction in snow and sea-ice coverage from partly to completely snow- and ice-free ocean and land surface would substantially reduce cold-season temperature variability (Gregory and Mitchell, 1995; Fischer et al., 2011; Borodina et al., 2017) and lead to a shortening of the cold season and earlier onset of the warm season (Cassou and Cattiaux, 2016). Mid-latitudinal winter temperature variability is further affected by a complex interplay of a multitude of processes including potential changes in atmospheric circulation, but there is *low confidence* in the dominant contribution of Arctic warming compared to other drivers (see Cross-Chapter Box 10.1).

[START FIGURE 4.21 HERE]

Figure 4.21: Percentage change in interannual variability of (top) JJA and (bottom) DJF mean temperature averaged across seven large initial condition ensembles. Average changes across seven single-model initial-condition large ensembles are shown for RCP8.5 in 2081–2100 (and where not available for 2080–2099) relative to 1995–2014. Standard deviations are calculated across all members of the large ensembles for every given year to avoid inflation due to the underlying trend and then averaged across the period. Changes are averaged across the ensembles MPI-GE (100 members, (Maher et al., 2019a)), CanESM2, 50 members (Kirchmeier-Young et al., 2017)), NCAR-CESM (30 members, (Kay et al., 2015)), GFDL-CM3, 20 members, (Rodgers et al., 2015)), GFDL-ESM2M (30 members, (Sun et al., 2018)), CSIRO-Mk3-6-0 (30 members, (Jeffrey et al., 2013)), EC-EARTH (16 members, (Hazeleger et al., 2010)), see (Deser et al., 2020). Diagonal lines indicate areas with low model agreement where fewer than 80% of the models agree on the sign of the change, and no overlay areas with high model agreement where at least 80% of the models agree on the sign of the change. Further details on data sources and processing are available in the chapter data table (Table 4.SM.1).

[END FIGURE 4.21 HERE]

In JJA, the multi-model average projects an increase in year-to-year JJA variability over Central Europe and North America (Figure 4.21). In particular an increase in daily to interannual summer temperature variability has been projected over central Europe as a result of larger year-to-year variability in soil moisture conditions varying between a wet and dry regime and leading to enhanced land-atmosphere interaction (Seneviratne et al., 2006; Fischer et al., 2012; Holmes et al., 2016). Furthermore, the amplified warming in the source regions of warm-air advection due to land-ocean warming contrast and amplified Mediterranean warming (Seager et al., 2014a; Brogli et al., 2019), may lead to disproportionally strong warming of the hottest days and summers and thereby increased variability. Enhanced temperature variability is further projected over some land regions in the subtropics and tropics (Bathiany et al., 2018).

In summary, there is *medium confidence* that continued warming will regionally lead to increased and decreased year-to-year temperature variability in the extratropics and there is *medium confidence* that year-to-year temperature variability will decrease over parts of the mid- to high- latitudes of the winter hemisphere.

4.5.1.2 Annual Mean Atmospheric Temperature

Section 12.4.3.2 of the AR5 assessed that there is *high confidence* in the overall pattern of projected end of 21st century tropospheric temperature change and that it is *very likely* that some of the largest warming will occur in the northern high latitudes. They further assessed that proportionately larger warming is *likely* to occur in the tropical upper troposphere than at the tropical surface, but with *medium confidence* owing to the

ACCEPTED VERSION SUBJECT TO FINAL EDITS

relatively large observational uncertainties and contradictory analyses regarding model accuracy in simulating tropical upper tropospheric temperature trends.

[START FIGURE 4.22 HERE]

Figure 4.22: Long-term change of annual and zonal mean atmospheric temperature. Displayed are multi-model mean change in annual and zonal mean atmospheric temperature (°C) in 2081–2100 relative to 1995–2014 for (left) SSP1-2.6 and (right) SSP5-8.5. The number of models used is indicated in the top right of the maps. Diagonal lines indicate regions where less than 80% of the models agree on the sign of the change and no overlay where 80% or more of the models agree on the sign of the change. Further details on data sources and processing are available in the chapter data table (Table 4.SM.1).

[END FIGURE 4.22 HERE]

CMIP6 projections show warming throughout the troposphere by the end of this century and a mix of warming and cooling in the stratosphere depending on the emission scenario (Figure 4.22). The patterns of tropospheric temperature change are highly consistent with those derived from earlier generations of climate models as assessed in AR5, AR4 and TAR. In SSP1-2.6, the multi-model mean warming remains below 3°C everywhere in the troposphere except near the surface in the Arctic; this is similar to the findings in AR5 based on CMIP5 models for RCP2.6. In SSP3-7.0, the zonal mean tropospheric warming is also largest in the tropical upper troposphere, reaching more than 5 °C, and near the surface in the Arctic where warming exceeds 8°C (Figure 4.22). It is *likely* that the warmer projected GSAT in the unconstrained CMIP6 model ensemble contributes to larger warming in the tropical upper troposphere and in the Arctic lower troposphere. This assessment is based on the understanding of polar amplification assessed in Chapter 7, Section 7.4.4.1, and at low latitudes is based on the understanding of moist convective processes as well as the relationship between CMIP5- and CMIP6-simulated surface temperatures and tropical upper tropospheric warming over the historical period (Section 3.3.1.2).

Projected stratospheric temperature trends are determined by a balance between the major radiative drivers from ozone recovery, rising CO_2 and other greenhouse gases (including stratospheric water vapour) (Maycock, 2016), as well as future changes in the Brewer Dobson circulation, which can alter the latitudinal pattern of stratospheric temperature trends (Fu et al., 2015, 2019). In the lower stratosphere, the CMIP6 models project a weak cooling in the inner tropics in SSP1-2.6 and a warming at other latitudes (Figure 4.22). There is enhanced lower stratospheric warming over the Antarctic pole owing to the effects of ozone hole recovery on polar temperatures (Maycock, 2016; Solomon et al., 2017). The projected strengthening of the Brewer Dobson circulation in the future (Hardiman et al., 2014) also affects stratospheric temperature trends, with adiabatic cooling at low latitudes and warming in middle and high latitudes (Fu et al., 2015, 2019). In SSP3-7.0, there is widespread cooling across much of the stratosphere, as expected from the higher GHG emissions, with a smaller warming in the Antarctic lower stratosphere. Owing to the importance of ozone recovery for the radiative balance of the stratosphere, future global and local stratospheric temperature trends do not scale with projected GSAT change.

In summary, new results since AR5 do not generally alter the understanding of projected zonal mean atmospheric temperature changes. There is *high confidence* in the overall pattern of projected tropospheric temperature changes given its robustness across many generations of climate models. It is further *very likely* that projected long-term tropospheric warming will be larger than the global mean in the Arctic lower troposphere. It is *likely* that tropical upper tropospheric warming will be larger than at the tropical surface, however with an uncertain magnitude owing to the potentially large role of natural internal variability and differences across models in the simulated free tropospheric temperature response to a given forcing scenario (Section 3.3.1.2). It is *very likely* that global mean stratospheric cooling will be larger by the end of the 21st century in a pathway with higher atmospheric CO_2 concentrations.

4.5.1.3 Near-Surface Relative Humidity

ACCEPTED VERSION SUBJECT TO FINAL EDITS

AR5 contrasted future changes in near-surface relative humidity (RH) over land and ocean, concluding with *medium confidence* that reductions in near-surface RH over many land areas are *likely*. The decrease in near-surface RH over most land areas is associated with the larger warming rates over land than over the ocean and is termed the last-saturation-temperature constraint, as explained in AR5.

Since AR5, significant effort has been devoted to understanding the mechanisms for the decrease in near-surface land RH under global warming, and the relevance of RH changes for the land–sea warming contrast and the water cycle. For the near-surface RH decrease over land, both the moisture transport from the ocean and land-atmosphere feedback processes contribute. For changes in specific humidity over land, the moisture transport from the ocean is dominant while the role of evapotranspiration is secondary (Byrne and O'Gorman, 2016; Chadwick et al., 2016). Nevertheless, the changes in near-surface land RH are also strongly influenced by evapotranspiration, which is suppressed by the drying of soils and plant responses to increasing CO_2 related to stomatal closure under climate change (Byrne and O'Gorman, 2015; Berg et al., 2016; Chadwick et al., 2016; Swann et al., 2016; Lemordant et al., 2018). The combination of oceanic and continental influences can explain the spatially diverse trends in the near-surface RH over land in the observations for the recent decades, with a generally dominant negative trend at the global scale (Vicente-Serrano et al., 2018). There is a strong feedback between the near-surface land RH decrease and land-ocean warming contrast under future warming projections (see Section 4.5.1.1).

Changes in land RH can modulate the response of the water cycle to global warming (Chadwick et al., 2013; Byrne and O'Gorman, 2015). Most CMIP5 models project higher precipitation associated with higher near-surface RH and temperature under climate change (Lambert et al., 2017). Over land, the spatial gradients of fractional changes in near-surface RH contribute to a drying tendency in precipitation minus evapotranspiration with warming, which partly explains why the 'wet-gets-wetter, dry-gets-drier' principle does not hold over land (Byrne and O'Gorman, 2015). Terrestrial aridity is projected to increase over land, as manifested by a decrease in the ratio of precipitation to potential evapotranspiration, in which the decrease in near-surface land RH has a contribution of about 35% in CMIP5 models under doubled CO_2 forcing (Fu and Feng, 2014). The aridity can be further amplified by the feedbacks of projected drier soils on land surface temperature, RH, and precipitation (Berg et al., 2016).

The CMIP6 multi-model ensemble projects general decreases in near-surface relative humidity over a large fraction of land areas, but moderate increases over the ocean (Figure 4.23). The projected changes depend on emission scenario and season. Changes in near-surface RH under SSP1-2.6 are insignificant compared to natural variability. Under SSP3-7.0, during boreal summer, significant decreases relative to natural variability are projected in continental Europe and the Middle East, North America, South America and South Africa.

In summary, there is *medium confidence* that continued warming will lead to decreased near-surface relative humidity over a large fraction of land areas, but moderate increases over the ocean. There is *high confidence* that near-surface relative humidity will decrease over parts of the tropical and subtropical latitudes over land.

[START FIGURE 4.23 HERE]

Figure 4.23: Long-term changes in seasonal mean relative humidity. Displayed are projected spatial patterns of multi-model mean change (%) in seasonal (top) DJF and (bottom) JJA mean near-surface relative humidity in 2081–2100 relative to 1995–2014, for (left) SSP1-2.6 and (right) SSP3-7.0. The number of models used is indicated in the top right of the maps. No overlay indicates regions where the change is robust and *likely* emerges from internal variability, that is, where at least 66% of the models show a change greater than the internal-variability threshold (see Section 4.2.6) and at least 80% of the models agree on the sign of change. Diagonal lines indicate regions with no change or no robust significant change, where fewer than 66% of the models show change greater than the internal-variability threshold. Crossed lines indicate areas of conflicting signals where at least 66% of the models show change greater than the internal-variability threshold but fewer than 80% of all models agree on the sign of change. Further details on data sources and processing are available in the chapter data table (Table 4.SM.1).

ACCEPTED VERSION SUBJECT TO FINAL EDITS

[END FIGURE 4.23 HERE]

4.5.1.4 Precipitation

AR5 assessed that changes in mean precipitation in a warmer world will exhibit substantial spatial variation and the contrast of mean precipitation between dry and wet regions and between dry and wet seasons will increase over most of globe as temperature increase. The general pattern of change indicates that high latitude land masses are *likely* to experience greater amounts of precipitation due to the increased specific humidity of the warmer troposphere as well as increased transport of water vapour from the tropics by the end of this century under the RCP8.5 scenario. Many mid-latitude and subtropical arid and semi-arid regions will *likely* experience less precipitation and many moist mid-latitude regions will *likely* experience more precipitation by the end of this century under the RCP8.5 scenario.

Since AR5, progress has been achieved in understanding changes in patterns and rates of precipitation with GSAT rise. The projected precipitation changes can be decomposed into a part that is related to atmospheric circulation referred to as dynamical component and a part related to water vapour changes, the thermodynamic component. Based on process understanding and modelling (Fläschner et al., 2016; Samset et al., 2016), global mean precipitation will *very likely* increase by 1–3% per °C of GSAT warming (see Section 8.2.1). The increase in atmospheric water vapour is a robust change under global warming, the sensitivity of global precipitation change to warming is smaller (2% $°C^{-1}$) as compared to water vapour change (7% $°C^{-1}$) (Held and Soden, 2006a). Global energy balance places a strong constraint on the global mean precipitation (Allen and Ingram, 2002; Pendergrass and Hartmann, 2014; Myhre et al., 2018; Siler et al., 2019). Tropospheric radiative cooling constrains global precipitation (Pendergrass and Hartmann, 2014), leading to a slow SST-dependent response and a forcing-dependent rapid adjustment. Rapid adjustments account for large regional differences in hydrological sensitivity across multiple drivers (Samset et al., 2016; Myhre et al., 2017). The rapid regional precipitation response to increased CO_2 is robust across models, implying that the uncertainty in long-term changes is mainly associated with the response to SST-mediated feedbacks (Richardson et al., 2016). Precipitation response to fast adjustments and slow temperature-driven responses are assessed in detail in Chapter 8 Section 8.2.1.

The thermodynamic response to global warming is associated with a wet-get-wetter mechanism, with enhanced moisture flux leading to subtropical dry regions getting drier and tropical and mid-latitude wet regions getting wetter (Held and Soden, 2006a; Chou et al., 2009). Recent studies suggest that the dry-get-drier argument does not hold, especially over subtropical land regions (Greve et al., 2014; Feng and Zhang, 2015; Greve and Seneviratne, 2015). The discrepancy may be partly arising due to differences in model climatologies and by change in the location of wet and dry regions (Polson and Hegerl, 2017). Over the 21st century, significant rate of precipitation change is associated with a spatial stabilization and intensification of moistening and drying patterns (Chavaillaz et al., 2016a). In the tropics, weakening of circulation leads to a wet-gets-drier and dry-gets-wetter pattern (Chadwick et al., 2013). Climate model agreement for precipitation change in the tropics is lower than for other regions (Knutti and Sedláček, 2013; McSweeney and Jones, 2013). Sources of inter-model uncertainty in regional rainfall projections arise from circulation changes (Kent et al., 2015; Chadwick, 2016) and spatial shifts in convection and convergence, associated with SST pattern change and land–sea thermal contrast change (Kent et al., 2015; Chadwick et al., 2017) with a secondary contribution from the response to direct CO_2 forcing (Chadwick, 2016). Factors governing changes in large-scale precipitation patterns are assessed in detail in Section 8.2.2 and Section 10.4.1.

Long-term multi-model mean change in seasonal precipitation (JJA and DJF) from CMIP6 models (Figure 4.24) shows substantial regional differences and seasonal contrast. Changes in seasonal precipitation under SSP1-2.6 are small compared to internal variability. Consistent with the AR5, patterns of precipitation change show v*ery likely* increase in the high latitudes especially during local winter and over tropical oceanoceans under SSP3-7.0 (*high confidence*). CMIP6 projections show an increase in precipitation over larger parts of the monsoon regions and decreases in many subtropical regions including the Mediterranean, southern Africa and southwest Australia (*medium confidence*). The large-scale patterns of precipitation

ACCEPTED VERSION SUBJECT TO FINAL EDITS

shown in Figure 4.24 are consistent with the patterns presented in Section 8.4.1.3. Precipitation changes exhibit strong seasonal characteristics (Box 8.2), and, in many regions, the sign of the precipitation changes varies with season. Precipitation variability is projected to increase over a majority of global land area, as assessed in Chapter 8 Section 8.4.1.3.3, over a wide range of timescales in response to warming (Pendergrass et al., 2017).

[START FIGURE 4.24 HERE]

Figure 4.24: Long-term change of seasonal mean precipitation. Displayed are projected spatial patterns of multi-model mean change (%) in (top) DJF and (bottom) JJA mean precipitation in 2081–2100 relative to 1995–2014, for (left) SSP1-2.6 and (right) SSP3-7.0. The number of models used is indicated in the top right of the maps. No map overlay indicates regions where the change is robust and *likely* emerges from internal variability, that is, where at least 66% of the models show a change greater than the internal-variability threshold (see Section 4.2.6) and at least 80% of the models agree on the sign of change. Diagonal lines indicate regions with no change or no robust significant change, where fewer than 66% of the models show change greater than the internal-variability threshold. Crossed lines indicate areas of conflicting signals where at least 66% of the models show change greater than the internal-variability threshold but fewer than 80% of all models agree on the sign of change. Further details on data sources and processing are available in the chapter data table (Table 4.SM.1).

[END FIGURE 4.24 HERE]

Most of the projected changes in precipitation exhibit a sharp contrast between land and ocean (see Sections 8.2.1 and 8.4.1). Temperature-driven intensification of land-mean precipitation during the 20th century has been masked by fast precipitation responses to anthropogenic sulphate and volcanic forcing (Allen and Ingram, 2002; Richardson et al., 2018b). Based on the Precipitation Driver and Response Model Intercomparison Project (PDRMIP), land-mean precipitation is expected to increase more rapidly with the projected decrease in sulphate forcing and continued warming, contributing to increase global mean precipitation (Table 4.3) and will be clearly observable by the mid-21st century based on RCP4.5 and RCP8.5 scenarios (Richardson et al., 2018b).

Consistent with the findings of AR5, a gradual increase in global mean precipitation is projected over the 21st century with an increase of approximately 2.9% (1.0–5.2%) under SSP1-2.6 and 4.7% (2.3–8.2%) under SSP3-7.0 during 2081–2100 relative to 1995–2014. The corresponding increase in annual mean global land precipitation is 3.3% (0–6.6%), in the SSP1-2.6 and 5.8% (0.5–9.6%) in the SSP3-7.0. (See also Table 4.3). CMIP6 models show greater increases in precipitation over land than either globally or over the ocean (*high confidence*).

Based on the assessment of CMIP6 models, we conclude that it is *very likely* that, in the long term, global mean land and global mean ocean precipitation will increase with increasing GSAT. Annual mean and global mean precipitation will *very likely* increase by 1–3% per °C GSAT warming. The patterns of precipitation change will exhibit substantial regional differences and seasonal contrast as GSAT increases over the 21st century (*high confidence*). Precipitation will *very likely* increase over high latitudes and the tropical ocean and *likely* increase in large parts of the monsoon regions, but *likely* decrease over the subtropics, including Mediterranean, southern Africa and southwest Australia, in response to GHG-induced warming.

4.5.1.5 Global Monsoon Precipitation and Circulation

AR5 assessed changes of the global monsoon in the context of long-term trends across the 21st century and the change by 2081–2100. AR5 showed growing evidence of improved skill of climate models in reproducing the climatological features of the global monsoon. Taken together with identified model agreement on future changes, the global monsoon precipitation, aggregated over all regional monsoon regions, is *likely* to strengthen in the 21st century with increases in its area and intensity, while the monsoon

ACCEPTED VERSION SUBJECT TO FINAL EDITS

circulation weakens. In all RCP scenarios, the global monsoon area is *very likely* to increase, and the global monsoon precipitation intensity is *likely* to increase, resulting in a *very likely* increase in the global monsoon total precipitation, by 2081–2100 (Kitoh et al., 2013).

Since AR5, there has been progress in understanding physical mechanisms for the projected changes in global monsoon and quantifying the sources of uncertainty in projections. The increase in global monsoon precipitation under warming is primarily attributed to the increase of moisture convergence, which comes mainly from the thermodynamic effect due to increasing atmospheric moisture but is partly offset by reduced convergence (Zhang et al., 2019b; Chen et al., 2020). The dynamic effect, such as monsoon circulation changes, dominates regional differences in the projected monsoon precipitation changes (Chen et al., 2020). Specifically, NH monsoon precipitation will increase more strongly than its SH counterpart, due to an increase in hemispheric temperature difference between the NH and SH, enhancement of the Hadley circulation, and atmospheric moistening, countered by stabilization of the troposphere (Lee and Wang, 2014). The seasonality of global monsoon rainfall is projected to enhance in response to warming, featuring a greater wet-dry season contrast (Lee and Wang 2014; Zhang et al. 2019). In addition, the interannual variability of global monsoon rainfall is projected to intensify mainly over land, with a strengthened relationship between global monsoon and ENSO (Hsu et al., 2013; Wang et al., 2020, 2021).

For the uncertainty in mean monsoon precipitation projections, the model uncertainty is the dominant contributor throughout the century and explains more than 70% of the inter-model variance during near term, mid-term, and long term. The contribution of internal variability is only important at the beginning in early decades, while scenario uncertainty becomes important at the end of the 21st century. The sources of uncertainty for the mean and extreme monsoon precipitation mainly differ in the long-term projection, when the contribution of scenario uncertainty is comparable to the model uncertainty for extreme precipitation (Zhou et al., 2020). Although the magnitude of internal variability differs between CMIP5 models and single-model initial-condition large ensembles, the impact is only evident in the beginning decades. For the mid- and long term, the magnitude difference does not alter that model uncertainty is the dominant source of uncertainty in the projections of global land monsoon precipitation (Zhou et al., 2020).

Based on the projections of changes in precipitation from CMIP6 under the four SSPs, the global monsoon precipitation is *likely* to strengthen in the 21st century with increases in its intensity, while NH summer monsoon circulation weakens (Figure 4.14). Global land monsoon precipitation will *likely* increase by 1.3–2.4 % per °C GSAT warming among the four scenarios considered here. In the long term, the multi-model mean change (5–95% range of the available 41 projections) of global land monsoon precipitation index is 2.9% (–0.8–7.8%), 3.7% (–2.5–8.6%), 3.77% (–3.2–8.1%), and 5.7% (–2.8–12.3%) under SSP1–2.6, SSP2–4.5, SSP3–7.0, and SSP5–8.5, respectively. This enhancement is caused by thermodynamic responses due to increased moisture, which is partly offset by dynamic responses due to a weakened circulation (Chen et al., 2020). The patterns of monsoon rainfall changes in the mid- to long-term include a North–South asymmetry characterized by greater increase in the NH than the SH, and an East–West asymmetry characterized by enhanced Asian-African monsoons and weakened North American monsoon (*medium confidence*) (Lee and Wang, 2014; Mohtadi et al., 2016; Pascale et al., 2017; Wang et al., 2021).

Based on the assessment of CMIP6 models, we conclude that it is *likely* that, in the mid- to long term, the global land monsoon precipitation will increase with GSAT rise despite a weakened monsoon circulation. The global land monsoon precipitation will *likely* increase by 1.3–2.4 % per °C GSAT warming among the four scenarios. Monsoon precipitation responses depend on region and emission scenario (*high confidence*).

4.5.1.6 Sea Level Pressure, Large-scale Atmospheric Circulation, Storm Tracks and Blocking

This subsection provides a global overview of long-term changes in atmospheric dynamical features that is complementary to the regional assessment of links to the hydrological cycle in Chapter 8, Section 8.4.2, and assessment of the connections to extreme events in Chapter 11, Section 11.7.2.

Sea level pressure

ACCEPTED VERSION SUBJECT TO FINAL EDITS

AR5 assessed that mean sea level pressure is projected to decrease in high latitudes and to increase in mid-latitudes. Such a pattern is associated with a poleward shift in the storm track and an increase in the annular mode index. This broad pattern is also found in CMIP6 models (Figure 4.25). Under SSP1-2.6, the pattern in sea level pressure change resembles that for SSP3-7.0, but the amplitudes are small compared to internal variability in 20-year means (Figure 4.25). One exception is found in the SH mid-latitudes, where pressure robustly increases in SSP3-7.0 in both austral summer and winter, but shows no robust change in SSP1-2.6. This is *likely* attributable to the larger GHG forcing in SSP3-7.0 compared to SSP1-2.6, which contributes to a poleward shift of the SH mid-latitude circulation and becomes relatively more important than the effect of ozone recovery which drives an equatorward shift in the circulation (Barnes and Polvani, 2013; Barnes et al., 2014; Bracegirdle et al., 2020b) (see Section 4.5.3.1 on the Southern Annular Mode). The poleward shift in SH mid-latitude circulation in SSP3-7.0 *likely* contributes to the wetting trend at high southern latitudes (Figure 4.25).

As was found in AR5, several regional sea level pressure features stand out from the zonal-mean change. Sea level pressure markedly decreases in northeastern North America and northeastern Asia in boreal winter. In boreal summer, sea level pressure robustly decreases in the Mediterranean and the Middle-East, a decrease that has been linked to a large-scale heat low forced by the amplified warming of the region (Haarsma et al., 2009). It is *likely* that sea level pressure will increase across the southwestern North America and Central America in boreal summer under SSP3-7.0 due to an intensification of the eastern North Pacific subtropical summer high (Li et al., 2012) and a weakening of the North American monsoon (Wang et al., 2020)(Pascale et al., 2017)(see Section 4.5.1.5). These changes in circulation are connected to drying across the eastern subtropical Pacific and Central America regions (Figure 4.24:).

[START FIGURE 4.25 HERE]

Figure 4.25: Long-term change of seasonal mean sea level pressure. Displayed are projected spatial patterns of multi-model mean change in (top) DJF and (bottom) JJA mean sea level pressure (hPa) in 2081–2100 relative to 1995–2014, for (left) SSP1-2.6 and (right) SSP3-7.0. The number of models used is indicated in the top right of the maps. No overlay indicates regions where the change is robust and *likely* emerges from internal variability, that is, where at least 66% of the models show a change greater than the internal-variability threshold (see Section 4.2.6) and at least 80% of the models agree on the sign of change. Diagonal lines indicate regions with no change or no robust significant change, where fewer than 66% of the models show change greater than the internal-variability threshold. Crossed lines indicate areas of conflicting signals where at least 66% of the models show change greater than the internal-variability threshold but fewer than 80% of all models agree on the sign of change. Further details on data sources and processing are available in the chapter data table (Table 4.SM.1).

[END FIGURE 4.25 HERE]

Zonal wind and westerly jets

Storm tracks and mid-latitude westerly jets are dynamically related aspects of mid-latitude circulation. AR5 assessed that a poleward shift of the SH westerlies and storm track is *likely* by the end of the 21st century under RCP8.5 (*medium confidence*). In contrast, *low confidence* was assessed for the storm-track response in the NH.

Under both SSP1-2.6 and SSP3-7.0 there is a strengthening and lifting of the subtropical jets in both hemispheres (Figure 4.26), consistent with the response to large-scale tropospheric warming found in earlier generations of climate models (Collins et al., 2013). In the SH, GHG emissions tend to force a poleward shift of the jet, but this is opposed, particularly in austral summer, by the stratospheric ozone hole recovery (Barnes and Polvani, 2013; Barnes et al., 2014; Bracegirdle et al., 2020b). Consistent with sea level pressure changes, CMIP6 models project a strengthening and poleward shift of the SH jet in austral summer and winter under SSP3-7.0, but smaller and non-robust changes in SH mid-latitude zonal winds under SSP1-2.6

ACCEPTED VERSION SUBJECT TO FINAL EDITS

(Figure 4.26, see also Section 4.5.3.1). CMIP6 models show an improved simulation of the SH jet stream latitude (Bracegirdle et al., 2020a; Curtis et al., 2020). This has been linked to a reduction in the projected poleward shift of the SH jet in austral summer compared to the CMIP5 models (Curtis et al., 2020; Goyal et al., 2021), although differences in the pattern of SST response may also play a role (Wood et al., 2020). In the NH extratropics, the changes in lower tropospheric zonal mean zonal winds by the end of the century are generally smaller than in the SH. In boreal winter, there is a weak poleward shift of the NH zonal mean westerly jet maximum in SSP3-7.0.

CMIP5 and CMIP6 models show a strong seasonal and regional dependence in the response to climate change of NH westerlies (Barnes and Polvani, 2013; Grise and Polvani, 2014b; Simpson et al., 2014; Zappa et al., 2015; Harvey et al., 2020; Oudar et al., 2020). CMIP5 projections indicate a poleward shift of the westerlies in the North Atlantic in boreal summer, while the North Pacific jet weakens in this season (Simpson et al., 2014; Davini and D'Andrea, 2020; Harvey et al., 2020). There is a poleward shift in the westerlies in both the North Pacific and North Atlantic in Autumn (Barnes and Polvani, 2013; Simpson et al., 2014). However, the shift of the westerlies is more uncertain in the other seasons particularly in the North Atlantic in winter (Simpson et al., 2014; Zappa and Shepherd, 2017). Here, the circulation response is not well described as a simple shift, since the North Atlantic jet tends to be squeezed on both its equatorward and poleward flanks, together with an eastward extension into Europe (Li et al., 2018; Peings et al., 2018; Simpson et al., 2019b; Harvey et al., 2020; Oudar et al., 2020). Simulations indicate that most of the changes in winter storminess over the Euro-Atlantic region will occur only after exceeding the 1.5°C warming level (Barcikowska et al., 2018).

[START FIGURE 4.26 HERE]

Figure 4.26: Long-term change of zonal mean zonal wind. Dispayed are multi-model mean change in (left) boreal winter (DJF) and (right) austral winter (JJA) zonal mean zonal wind (m s^{-1}) in 2081–2100 for (top) SSP1-2.6 and (right) SSP3-7.0 relative to 1995–2014. The 1995–2014 climatology is shown in contours with spacing 10 m s^{-1}. Crossed lines indicate regions where less than 80% of the models agree on the sign of the change and no overlay where at least 80% of the models agree on the sign of the change. Further details on data sources and processing are available in the chapter data table (Table 4.SM.1).

[END FIGURE 4.26 HERE]

Progress since AR5 has improved understanding of the climate change aspects that can drive these different, and potentially opposite, responses in the mid-latitude jets and storm tracks. A poleward shift of the jets and storm tracks is expected in response to an increase in the atmospheric stratification and in the upper-tropospheric equator-to-pole meridional temperature gradient, while it is opposed by the decrease in the meridional temperature gradient in the lower troposphere associated with the polar amplification of global warming (Harvey et al., 2014; Shaw et al., 2016b). Recent analyses have identified additional climate aspects that can drive mid-latitude jet changes, including patterns in sea surface warming (Mizuta et al., 2014; Langenbrunner et al., 2015; Ceppi et al., 2018; Wood et al., 2020), land-sea warming contrast (Shaw and Voigt, 2015), loss of sea ice (Zappa et al., 2018)(Deser et al., 2015)(Harvey et al., 2015)(Screen et al., 2018b), and changes in the strength of the stratospheric polar vortex (Simpson et al., 2018b)(Manzini et al., 2014)(Grise and Polvani, 2017)(Ceppi and Shepherd, 2019a). From an energetics perspective, the uncertainty in the response of the jet streams depends on the response of clouds, their non-spatially uniform radiative feedbacks shaping the meridional profile of warming (Ceppi et al., 2014; Voigt and Shaw, 2015, 2016; Ceppi and Hartmann, 2016; Ceppi and Shepherd, 2017; Lipat et al., 2018; Albern et al., 2019; Voigt et al., 2019). Climate models seem to underestimate the forced component of the year-to-year variability in the atmospheric circulation, particularly in the North Atlantic sector (Scaife and Smith, 2018), which suggests some relevant dynamical processes may not be well represented. Whether and how this may affect long-term projections is unknown. In conclusion, due to the influence from competing dynamical drivers and the absence of observational evidence, there is *medium confidence* in a projected poleward shift of the NH zonal-mean low-level westerlies in autumn and summer and *low confidence* in the other seasons. There is also overall *low confidence* in projected regional changes in the NH low-level westerlies, particularly for the

ACCEPTED VERSION SUBJECT TO FINAL EDITS

North Atlantic basin in boreal winter.

The anthropogenic forced signal in extratropical atmospheric circulation may well be small compared to internal variability (Deser et al., 2012b, 2014) and, as assessed in AR5, there is generally low agreement across models in many aspects of regional atmospheric circulation change particularly in the NH (Shepherd, 2014). The latter means that, in some regions, a multi-model average perspective of atmospheric circulation change represents a small residual after averaging over large intermodel spread. This is in strong contrast to thermodynamic aspects of climate change, such as surface temperature change, for which model results are generally highly consistent (see, e.g., Figure 4.19). Furthermore, models share systematic biases in some aspects of extratropical atmospheric circulation such as mid-latitude jets, which can have complex implications for understanding forced changes (Simpson and Polvani, 2016a). Given these issues, an emerging field of research since AR5 has focused on the development of 'storylines' for regional atmospheric circulation change (Shepherd, 2019). The storyline approach is grounded in the identification of a set of physical predictors of atmospheric circulation change, such as those described above (Harvey et al., 2014; Manzini et al., 2014; Shepherd et al., 2018), which act together to determine a specific outcome in theprojected atmospheric circulation change. The consequences of multi-model spread in the physical predictors of atmospheric circulation change can be investigated, conditioned on a specified level of global warming (Zappa and Shepherd, 2017; Zappa, 2019; Mindlin et al., 2020) (also see Chapter 1, Section 1.4.4.2).

Storm tracks

As stated in AR5, the number of extratropical cyclones (ETC) composing the storm tracks is projected to weakly decline in future projections, but by no more than a few percent change. The reduction is mostly located on the equatorward flank of the storm tracks, which is associated with the Hadley cell expansion and a poleward shift in the mean genesis latitude of ETCs (Tamarin-Brodsky and Kaspi, 2017). Furthermore, the poleward propagation of individual ETCs is expected to increase with warming (Graff and LaCasce, 2014; Tamarin-Brodsky and Kaspi, 2017), thus contributing to a poleward shift in the mid-latitude transient-eddy kinetic energy. The increased poleward propagation results from the strengthening of the upper tropospheric jet and increased cyclone-associated precipitation (Tamarin-Brodsky and Kaspi, 2017), which are robust aspects of climate change.

In the NH boreal winter, CMIP6 models show a northward shift of the ETC density in the North Pacific, a tripolar pattern in the North Atlantic, and a weakening of the Mediterranean storm track (Figure 4.27a). CMIP6 models show overall *low agreement* on changes in ETC density in the North Atlantic in boreal winter (Figure 4.27a). A poleward shift of the storm track is evident in the SH (Figure 4.27b), particularly in the Indian and Pacific Ocean sectors. CMIP6 models still feature long-standing biases in the representation of storm tracks, such as a too zonal winter storm track into Europe, though different measures of storm track activity indicate some improvements compared to the previous generations of models (Harvey et al., 2020; Priestley et al., 2020)

Regarding the dynamical intensity of the storm tracks (see also Chapter 11, Section 11.7.2), the number of ETCs associated with intense surface wind speeds and undergoing explosive pressure deepening are projected to strongly decrease in the NH winter (Seiler and Zwiers, 2016; Chang, 2018). The weakening of surface winds of ETCs in the NH is attributed to the reduced low-level baroclinicity from SST and sea ice changes (Harvey et al., 2014; Seiler and Zwiers, 2016; Wang et al., 2017a). There are, however, regional exceptions such as in the northern North Pacific, where explosive and intense ETCs are projected to increase in association with the poleward shift of the jet and increased upper-level baroclinicity (Seiler and Zwiers, 2016). Eddy kinetic energy and intense cyclone activity is also projected to decrease in the NH summer in association with a weakening of the jet (Lehmann et al., 2014; Chang et al., 2016). However, climate models tend to have too weak explosive cyclones (Seiler and Zwiers, 2016; Priestley et al., 2020), though this bias seems to be reduced in high-resolution simulations (Jiaxiang et al., 2020). Furthermore, models may not fully capture the contribution of the future increase in mesoscale latent heating to cyclone intensification (Li et al., 2014; Pfahl et al., 2015; Willison et al., 2015; Michaelis et al., 2017). In conclusion, there is only *medium confidence* in the projected decrease in the frequency of intense NH ETCs.

ACCEPTED VERSION SUBJECT TO FINAL EDITS

In contrast to the NH, the SH shows an increase in the frequency of intense ETCs in CMIP5 models (Chang, 2017), and there is *high confidence* that wind speeds associated with ETCs are expected to intensify in the SH storm track for high emission scenarios. These changes in intensity are accompanied by an overall southward shift of the SH winter storm track (Figure 4.27b) due to the poleward shift in the upper-level jet and the increase in the meridional SST gradient linked to the slower warming of the Southern Ocean (Grieger et al., 2014) .

Regardless of dynamical intensity changes, there is *high confidence* that the number of ETCs associated with extreme precipitation is projected to increase with warming, due to the increase moisture-loading capacity of the atmosphere (Yettella and Kay, 2017; Hawcroft et al., 2018) (see also Chapter 8, Section 8.4.2).

[START FIGURE 4.27 HERE]

Figure 4.27: Changes in extratropical storm track density. Displayed are projected spatial pattern of multi-model mean change of extratropical storm track density in winter (NH DJF and SH JJA) in 2080–2100 for SSP5-8.5 relative to 1979–2014 based on 13 CMIP6 models. Diagonal lines indicate regions where fewer than 80% of the models agree on the sign of the change and no overlay where at least 80% of the models agree on the sign of change. Units are number density per 5 degree spherical cap per month. Further details on data sources and processing are available in the chapter data table (Table 4.SM.1).

[END FIGURE 4.27 HERE]

Atmospheric blocking

Blocking is associated with a class of quasi-stationary high-pressure weather systems in the middle and high latitudes that disrupt the prevailing westerly flow. These events can persist for extended periods, such as a week or longer, and can cause long-lived extreme weather conditions, from heat waves in summer to cold spells in winter (see Chapter 11, Section 11.7.2 for a detailed discussion of these features and Chapter 3, Section 3.3.3.3 for the assessment of blocking biases in models simulations). AR5 assessed with *medium confidence* that the frequency of blocking would not increase under enhanced GHG concentrations, while changes in blocking intensity and persistence remained uncertain.

CMIP5 projections suggest that the response of blocking frequency to climate change might be quite complex (Dunn-Sigouin et al., 2013; Masato et al., 2013). An eastward shift of winter blocking activity in the NH is indicated (Masato et al., 2013; Kitano and Yamada, 2016; Lee and Ahn, 2017; Matsueda and Endo, 2017) while during boreal summer, blocking frequency tends to decrease in mid-latitudes (Matsueda and Endo, 2017), with the exception of the eastern Europe–western Russia region (Masato et al., 2013). The projected decrease of blocking in boreal summer partially contrasts with the observed increase in Greenland blocking (Hanna et al., 2018; Davini and D'Andrea, 2020). However, as shown in Woollings et al. (2018), the spatial distribution and the magnitude of the suggested changes are sensitive to the blocking detection methods (Schwierz et al., 2004; Barriopedro et al., 2010; Davini et al., 2012). In the SH, blocking frequency is projected to decrease in the Pacific sector during austral spring and summer. However, seasonal and regional changes are not totally consistent across the models (Parsons et al., 2016), and, as assessed in Section 3.3.3.3, model biases might affect their response.

To better understand the uncertainty in future blocking activity, a process-oriented approach has been proposed that aims to link blocking responses to different features of the global warming pattern. Upper-level tropical warming might be the key factor leading to a reduced blocking, because of the strengthening of zonal winds (Kennedy et al., 2016). The more controversial influence of near-surface Arctic warming might lead to an increased blocking frequency (Mori et al., 2014; Francis and Vavrus, 2015) (see Chapter 10, Box 10.1).

Figure 4.28 shows a clear decrease in blocking activity over Greenland and North Pacific for SSP7.0 and SSP8.5. Models with the largest decrease in blocking frequency in boreal winter are those showing the smallest frequency bias during the historical period (Davini and D'Andrea, 2020). In conclusion, there is

ACCEPTED VERSION SUBJECT TO FINAL EDITS

medium confidence that the frequency of atmospheric blocking events over Greenland and the North Pacific will decrease in boreal winter in the SSP3-7.0 and SSP5-8.5 scenarios.

[START FIGURE 4.28 HERE

Figure 4.28: Projected wintertime atmospheric blocking frequencies. Box plot showing December-to-March atmospheric blocking frequencies from historical simulations over 1995–2014 and projections over 2081–2100, over (a) the Central European region (20°W–20°E, 45°N–65°N), (b) the Greenland region (65°W–20°W, 62.5°N–72.5°N), (c) the North Pacific region (130°E–150°W, 60°N–75°N). Values show the percentage of blocked days per season following the (Davini et al., 2012) index. Median values are the thick black horizontal bar. The lower whiskers extend from the first quartile to the smallest value in the ensemble, and the upper whiskers extend from the third quartile to the largest value. The whiskers are limited to an upper bound that is 1.5 times the interquartile range (the distance between the third and first quartiles). Black dots show outliers from the whiskers. The numbers below each bar report the number of models included. Observationally based values are obtained as the average of the ERA-Interim Reanalysis, the JRA-55 Reanalysis and the NCEP/NCAR Reanalysis. Adapted from (Davini and D'Andrea, 2020). Further details on data sources and processing are available in the chapter data table (Table 4.SM.1).

[END FIGURE 4.28 HERE]

4.5.2 Ocean

4.5.2.1 Ocean Temperature

Projections of long-term ocean thermal properties are assessed comprehensively in Chapter 9, Sections 9.2.1.1 and 9.2.2.1 and are not covered here to avoid unnecessary overlap.

4.5.2.2 Ocean acidification

The model-simulated long-term trend of ocean acidification is assessed in Section 4.3.2.5 and Chapter 5, Section 5.3.4.1. It is *virtually certain* that surface ocean acidification will continue in response to the rise in atmospheric CO_2, and continued penetration of anthropogenic CO_2 from the surface to the deep ocean will acidify the ocean interior (Figure 4.29). By the end of this century, under SSP3-7.0, a pH reduction of about 0.3 is found at a few hundred meters depth of the global ocean, with stronger acidification in the interior North Atlantic and the mid-to-high-latitude Southern Ocean. At a depth of about 1 km, a pH reduction of about 0.1 is found.

Projections with CMIP6 ESMs (Kwiatkowski et al., 2020) show a surface pH decline of -0.16 ± 0.002 (± 1 standard deviation) under SSP1-2.6 and -0.44 ± 0.005 under SSP5-8.5 from 1870–1899 to 2080–2099. The high-latitude oceans, in particular the Arctic, show greater decline in pH and accelerated acidification (Terhaar et al., 2020). For the same period, model-projected bottom-water pH decline is -0.018 ± 0.001 under SSP1-2.6 and -0.030 ± 0.002 under SSP5-8.5. The projected large scale surface ocean acidification will be primarily determined by the pathway of atmospheric CO_2, with weak dependence on change in climate (Hurd et al., 2018) (see also Section 5.3.4.1) (*high confidence*). However, for a given atmospheric CO_2 scenario, uncertainty in projected ocean acidification increases with ocean depth because of model-simulated differences in ocean circulation that transports anthropogenic CO_2 from the surface to bottom ocean (Kwiatkowski et al., 2020) (*high confidence*). For example, projected surface pH fully separates between SSPs scenarios before 2050, but some overlap across SSPs is still found for projected bottom-water pH in 2080 (Kwiatkowski et al., 2020).

[START FIGURE 4.29 HERE]

ACCEPTED VERSION SUBJECT TO FINAL EDITS

Figure 4.29: Long-term change of annual and zonal ocean pH. Displayed are multi-model mean change in annual and zonal ocean pH in 2081–2100 relative to the mean of 1995–2014 for SSP1-2.6 and SSP3-7.0, respectively. Eleven CMIP6 model results are used. Diagonal lines indicate regions where fewer than 80% of the models agree on the sign of the change and no overlay where at least 80% of the models agree on the sign of change. Further details on data sources and processing are available in the chapter data table (Table 4.SM.1).

[END FIGURE 4.29 HERE]

4.5.3 Modes of Variability

4.5.3.1 Northern and Southern Annular Modes

The Northern Annular Mode

AR5 assessed from CMIP5 simulations that the future boreal wintertime NAM is *very likely* to exhibit natural variability and forced trends of similar magnitude to that observed in the historical period and is *likely* to become slightly more positive in the future. Considerable uncertainty is related to physical mechanisms to explain the observed and projected changes in the NAM, but NAM trends are clearly closely connected to projected shifts in the mid-latitude jets and storm tracks.

NAM projections from climate models analysed since AR5 reveal broadly similar results the late 21st century. CMIP6 models show a positive ensemble-mean trend in most seasons and the higher emission scenarios that is comparable to between-model or between-realization variability (Figure 4.30a). The NAM generally becomes more positive by the end of the century except in boreal summer (JJA) when there is no change in the NAM in these simulations. In boreal winter (DJF) under SSP5-8.5, the central estimate is an increase in the NAM by almost 3 hPa in the long-term compared to 1995–2014. This can be compared to a multi-model mean interannual standard deviation in the winter NAM index of 3.4 hPa during the period 1850–1900. We conclude with *high confidence* that in the mid- to long-term, the boreal wintertime surface NAM is more positive under SSP3-7.0 and SSP5-8.5, while under SSP1-1.9 and SSP1-2.6, the NAM does not show any robust change.

The Southern Annular Mode

AR5 assessed it is *likely* that the evolution of the SAM over the 21st century will be primarily determined by the interplay between the effects of ozone recovery and changing GHG concentrations and influence the SAM in opposing ways. Owing to the relative effects of these two drivers, CMIP5 model SAM and SH circulation projections differed markedly across forcing scenarios and across seasons (Barnes and Polvani, 2013; Barnes et al., 2014). CMIP5 models simulated a weak negative SAM trend in austral summer for RCP4.5 by the end of the century (Zheng et al., 2013a), while for RCP8.5 they simulated a weak positive SAM trend in austral summer (Zheng et al., 2013a). A substantial fraction of the spread in CMIP5 projections of the end of century SH summer jet shift under RCP8.5 may be attributable to differences in the simulated change in break-up of the stratospheric polar vortex, with models that produce a later break-up date showing a larger summertime poleward jet shift (Ceppi and Shepherd, 2019b). For RCP2.6, the effect of ozone recovery on the SAM has been found to dominate over that of GHGs in austral summer (Eyring et al., 2013). In austral winter, the poleward shift of the SH circulation in CMIP5 models, and the associated increase in the SAM index, tends to be larger, on average, in higher forcing scenarios though with substantial inter-model spread (Barnes et al., 2014). New research since the AR5 shows that the previous theory for the apparent relationship across models between the annual mean climatological SH jet position and the amplitude of forced SH jet shift (Kidston and Gerber, 2010) does not hold at seasonal timescales (Simpson and Polvani, 2016b).

In most seasons, the SAM becomes more positive by the end of the century relative to 1995–2014 under SSP2-4.5, SSP3-7.0, and SSP5-8.5 (Figure 4.30b). Conversely, under SSP1-1.9 and SSP1-2.6, in most seasons the SAM index does not show a robust change compared to 1995–2014 except in austral summer when it becomes significantly more negative. The greatest change in the SAM occurs in austral winter,

ACCEPTED VERSION SUBJECT TO FINAL EDITS

where CMIP6 models show an ensemble-mean increase in the SAM index of almost 5 hPa in SSP5-8.5. This can be compared to a multi-model mean interannual standard deviation in the austral winter SAM index of 4.0 hPa during 1850–1900. In conclusion, there is *high confidence* that in high emission scenarios (SSP3-7.0 and SSP5-8.5) the SAM becomes more positive in all seasons, while in the lowest scenario (SSP1-1.9) there is a robust decrease in austral summer.

[START FIGURE 4.30 HERE]

Figure 4.30: CMIP6 Annular Mode index change from 1995–2014 to 2081–2100: (a) NAM and (b) SAM. The NAM is defined as the difference in zonal mean SLP at 35°N and 65°N (Li and Wang, 2003) and the SAM as the difference in zonal mean SLP at 40°S and 65°S (Gong and Wang, 1999). The shadings are the 5–95% ranges across the simulations. The numbers near the top are the numbers of model simulations in each SSP ensemble. Further details on data sources and processing are available in the chapter data table (Table 4.SM.1).

[END FIGURE 4.30 HERE]

4.5.3.2 El Niño-Southern Oscillation

AR5 assessed that it is *very likely* that ENSO will remain the dominant mode of interannual variability in the future. Moreover, due to increased moisture availability, the associated precipitation variability on regional scales was assessed to *likely* intensify. An eastward shift in the patterns of temperature and precipitation variations in the North Pacific and North America related to El Niño and La Niña teleconnections was projected with *medium confidence*. The stability of teleconnections to other regional implications including those in Central and South America, the Caribbean, parts of Africa, most of Asia, Australia and most Pacific Islands were assessed to be uncertain (Christensen et al., 2013).

There is no consensus on changes in amplitude of ENSO SST variability across CMIP iterations. The main factors driving the diversity of ENSO SST amplitude change in climate models are internal variability, SST mean warming pattern, and model systematic biases. First, pronounced low-frequency modulations of ENSO exist even in unforced control simulations due to internal variability, which leads a large uncertainty in quantifying future ENSO changes (Wittenberg, 2009; Vega-Westhoff and Sriver, 2017; Zheng et al., 2018). Second, ENSO characteristics depend on the climate mean state of the tropical Pacific; however, ENSO can also influence the mean state through nonlinear processes (Cai et al., 2015; Timmermann et al., 2018). The response of the tropical Pacific mean state to anthropogenic forcing is characterized by a faster warming on the equator compared to the off-equatorial region, a faster warming of the eastern equatorial Pacific compared to the central tropical Pacific (e.g., El Niño-like mean SST warming, see Chapter 7, Section 7.4.4.2), and a weakening of the Walker circulation in most models. Those models with a El Niño-like warming tend to project a strengthening of ENSO SST variability whereas models with a La Niña-like warming tend to project a weakening of variability (Zheng et al., 2016; Kohyama and Hartmann, 2017; Wang et al., 2017b; Cai et al., 2018a; Fredriksen et al., 2020b). Third, how to take model biases into account leads to different ENSO changes. (Kim et al., 2014) suggested that a subset of CMIP5 models that simulate linear ENSO stability realistically exhibit a decrease in ENSO amplitude by the second half of the 21st century. However, an increase of ENSO SST variability has been projected when considering biases in ENSO pattern simulation by different models (Zheng et al., 2016; Cai et al., 2018a). This highlights the importance of constraining tropical Pacific mean state changes in order to enhance confidence in the projected response of ENSO.

There is also no robust consensus on changes in ENSO diversity. Several studies suggest that an increase in Eastern Pacific (EP)-ENSO events tends to be projected particularly in the models with an El Niño-like warming (Zheng et al., 2016; Cai et al., 2018a; Fredriksen et al., 2020a). However, Freund et al. (2020) suggested that models with a El Niño-like mean warming show a tendency toward more Central Pacific (CP) events but fewer EP events compared to models with an La Niña-like warming in both CMIP5 and CMIP6 models.

ACCEPTED VERSION SUBJECT TO FINAL EDITS

Even though there is *limited agreement* in simulated changes in ENSO SST variability, the majority of models project an increase in amplitude of ENSO rainfall variability attributable to the increase in mean SST and moisture in CMIP5 (Power et al., 2013; Watanabe et al., 2014; Huang and Xie, 2015) and CMIP6 (Yun et al., 2021). It is *likely* that extreme El Niño events, accompanied by the eastern equatorial Pacific rainfall exceeding the 5mm day^{-1} rainfall threshold, will increase in intensity (Cai et al., 2014a, 2017). However, it has also been suggested that historical model biases over the equatorial Pacific cold tongue in CMIP5 may lead to the greater precipitation mean change and amplification of extreme ENSO-associated rainfall in CMIP5 (Stevenson et al., 2021).

There is *limited* intermodel *agreement* on future changes in ENSO teleconnections largely depending on changes in the mean state and changes in ENSO properties (Yeh et al., 2018a). Many CMIP5 and CMIP6 models project that the centres of the extratropical teleconnection over North Pacific and North America will shift eastward in association with an eastward shift in tropical convective anomalies (Yeh et al., 2018b; Fredriksen et al., 2020a). There is an indication that tropical cyclones will become more frequent during future El Niño events (and less frequent during future La Niña events) by the end of the 21st century (Chand et al., 2017), thus contributing to the projected increase in ENSO-associated hydroclimate impacts.

While CMIP6 models show no robust change in ENSO SST amplitude in the mid- and long-term period across all four SSPs, a robust increase in ENSO rainfall amplitude is found particularly in SSP2-4.5, SSP3-7.0, and SSP5-8.5 (Figure 4.10). The changes in ENSO rainfall amplitude in the long-term future (2081–2100) relative to the recent past (1995–2014) are statistically significant at the 95% confidence.

To conclude, the forced change in ENSO SST variability is highly uncertain in CMIP5 and CMIP6 models (*medium confidence*). However, it is *very likely* that ENSO-related rainfall variability will increase significantly regardless of ENSO amplitude changes in the mid- and long-term future. It is *likely* that the pattern of ENSO teleconnection over the North Pacific and North America will shift eastward.

4.5.3.3 Indian Ocean Basin and Dipole Modes

In the mid- to long-term, projected climate mean state changes in the tropical Indian Ocean are expected to resemble a positive IOD state, with faster warming in the west compared to the east (Cai et al., 2013; Zheng et al., 2013b). However, it was argued that this projected mean state change could be due to the large mean state biases in the simulated current climate and potentially not a realistic outcome (Li et al., 2016a). Mean state biases also lead to lack of consensus on projected equatorial Indian Ocean SST variability and equatorial modes of climate variability independent of the IOD (DiNezio et al., 2020). If mean state change will indeed resemble a positive IOD state, however, this would lead to a reduction in the amplitude difference between positive and negative IOD events, but with no robust change in IOD frequency (Cai et al., 2013). For a small subset of CMIP5 models that simulate IOD events best, a slight increase in IOD frequency was found under the CMIP5 RCP4.5 scenario (Chu et al., 2014) .

However, it was also found that the frequency of extreme positive IOD events, which exhibit the largest climate impacts, might increase by a factor of about three under the CMIP5 RCP8.5 scenario (Cai et al., 2014b). Partially consistent with the above result, a more recent study by (Cai et al., 2021) based on CMIP5 RCP8.5 and CMIP6 SSP5-8.5 simulations shows a robust increased SST variability of large positive IOD events, but a decreased variability of moderate IOD events. An approximate doubling of these extreme positive IOD events was still found for global warming of 1.5°C warming above pre-industrial levels, without a projected decline thereafter (Cai et al., 2018b). These results depend, however, on the realism of the projected mean state change in the Indian Ocean (Li et al., 2016a).

To conclude, the forced change in IOD in mid- and long-term future remains uncertain due to limited lines of evidence and its dependence on model mean biases. However, there is *low confidence* that the frequency of extreme positive IOD events will increase under the high-emission scenario of SSP5-8.5.

ACCEPTED VERSION SUBJECT TO FINAL EDITS

4.5.3.4 *Tropical Atlantic Modes*

AR5 assessed that there is *low confidence* in projected changes of the TAV because of the general failure of climate models to simulate main aspects of this variability such as the northward displaced ITCZ. The models that best represent the Atlantic meridional mode (AMM) show a weakening for future climate conditions. However, model biases in representation of Altantic Niños strongly limit an assessment of future changes.

Long-term changes in TAVs and associated teleconnections are expected as a result of global warming, but large uncertainties exist due to the models' systematic underestimation of the connection between PDV and Indo-Pacific SST variations (Lübbecke et al., 2018; Cai et al., 2019b). Observational analyses show large discrepancies in SST and trade winds strength (Servain et al., 2014; Mohino and Losada, 2015). Single-model sensitivity experiments show that Atlantic Niño characteristics at the end of 21st century remain consistent with those of the 20th century, though changes in the climatological SSTs can lead to changes in the associated teleconnections (Mohino and Losada, 2015).

The weakening of the AMOC expected from global warming (see Section 4.3.2.3) has been suggested to have an influence on the mean background state of tropical-Atlantic surface conditions, thereby enhancing equatorial Atlantic variability and resulting in a stronger tropical Atlantic–ENSO teleconnection (Svendsen et al., 2014) (see Chapter 3 Section 3.7.5 for a detailed discussion). A recent multi-model study, based on CMIP5, concluded that the TAV-Pacific teleconnection will weaken under global warming due to the increased thermal stability of the atmosphere (Jia et al., 2019a). However, there is still a clear lack of model studies, and hence no robust evidence on the long-term evolution of TAV and associated teleconnections.

4.5.3.5 *Pacific Decadal Variability*

AR5 assessed that there is *low confidence* in projections of future changes in Pacific decadal variability (PDV) due to the inability of CMIP5 models to represent the connection between PDV and Indo-Pacific SST variations. Because the PDV appears to encompass the combined effects of different dynamical processes operating at different timescales, representation of PDV in climate models remains a challenge (see Chapter 3, Section 3.7.6) and its long-term evolution under climate change uncertain.

In addition to uncertainty from the future evolution of the mechanisms that determined the PDV, it is also unclear how the background state in the Pacific Ocean will change due to time-varying radiative forcing, and how this change will interact with variability at interannual and low-frequency timescales (Fedorov et al., 2020). Recent research suggests that the PDV will have a weaker amplitude and higher frequency with global warming (Zhang and Delworth, 2016; Xu and Hu, 2017; Geng et al., 2019). The former appears to be associated with a decrease in SST variability and the meridional gradient over the Kuroshio-Oyashio region, with a reduction in North Pacific wind stress and meandering of the subpolar/subtropical gyre interplay (Zhang and Delworth, 2016). The latter is hypothesized to rely on the enhanced ocean stratification and shallower mixed layers of a warmer climate, which would increase the phase speed of the westward-propagating oceanic waves, hence shortening the decadal-interdecadal component (Goodman and Marshall, 1999; Zhang and Delworth, 2016; Xu and Hu, 2017). The weakening of the PDV in a warmer climate may reduce the internal variability of global mean surface temperature, to which PDV seems associated (Zhang et al., 1997; Kosaka and Xie, 2016; Geng et al., 2019). Thus, a weaker and higher frequency PDV could reduce the contribution of internal variability to the GSAT trend and eventually lead to a reduced probability of surface-warming hiatus events.

In summary, based on CMIP5, there is *medium confidence* that a weaker and higher frequency PDV is expected under global warming.

4.5.3.6 *Atlantic Multidecadal Variability*

ACCEPTED VERSION SUBJECT TO FINAL EDITS

Based on paleoclimate reconstructions and model simulations, AR5 assessed that AMV is *unlikely* to change its behaviour in the future. However, AMV fluctuations over the coming decades are *likely* to influence regional climate, enhancing or offsetting some of the effects of global warming.

Recent proxy-derived reconstructions of AMV-related signals show persistent multi-decadal variability over the last three centuries (Kilbourne et al., 2014; Svendsen et al., 2014; Moore et al., 2017), up to the last millennium (Chylek et al., 2011; Zhou et al., 2016; Wang et al., 2017b) and beyond (Knudsen et al., 2011). This implies that in the past AMV properties were little affected by large climatic excursions.

AMV long-term changes under future warming scenarios have been so far scarcely investigated. A study on the CMIP5 multi-model simulations under RCP8.5 scenario by (Villamayor et al., 2018) found no substantial differences in the simulated SST patterns (and in the related tropical rainfall response) when RCP8.5, historical and piControl simulations are compared. Such results suggest that the AMV is not expected to change under global warming. A more recent single-model large ensemble study (Hand et al., 2020) shows a pronounced change in the AMV pattern under global warming linked to a strong reduction of the mean AMOC and its variability. However, since a superposition of multiple processes controls the AMV, as extensively discussed in Annex IV, Section AIV.2.7, in Chapter 3 (Section 3.7.7), and in Chapter 9 (Section 9.2.3.1), the length of the RCP8.5 simulations might be not sufficient to properly evaluate the respective weight and interplay of internal components and influences from external forcing on AMV projections.

In conclusion, on the basis of paleoclimate reconstructions and CMIP5 model simulations, there is *low confidence* that the AMV is not expected to change in the future.

4.6 Implications of Climate Policy

4.6.1 Patterns of Climate Change for Specific Levels of Global

This subsection provides an assessment of changes in climate at 1.5°C, 2°C, 3°C, and 4°C of global warming relative to the period 1850–1900 (see Chapter 1, Section 1.6.2), in particular a discussion of the regional patterns of change in temperature (Section 4.6.1.1), precipitation (Section 4.6.1.2), and aspects of atmospheric circulation (Section 4.6.1.3). An assessment of changes in extreme weather events as a function of different levels of global warming is provided in Chapter 11, while corresponding analyses of regional climate change are provided in Chapter 12 and in Atlas. This section builds upon assessments from AR5 (Bindoff et al., 2013; Christensen et al., 2013; Collins et al., 2013; Hartmann et al., 2013) and SR1.5 (SR1.5; Hoegh-Guldberg et al., 2018), as well as new literature related to projections of climate at 1.5°C, 2°C, and higher levels of global warming above pre-industrial levels.

Several methodologies have been applied to estimate the spatial patterns of climate change associated with a given level of global warming. These include performing model simulations under stabilisation scenarios designed to achieve a specific level of global warming, the analysis of epochs identified within transient simulations that systematically exceed different thresholds of global warming (e.g. Dosio et al., 2018; Hoegh-Guldberg et al., 2018), Kjellström et al., 2018; Mitchell et al., 2017), and analysis based on statistical methodologies that include empirical scaling relationships (ESR) (Dosio and Fischer, 2018)(Schleussner et al., 2017)(Seneviratne et al., 2018) and statistical pattern scaling (e.g., Kharin et al., 2018). These different methodologies are assessed in some detail in Section 4.2.5 (see also James et al., 2017) and generally provide qualitatively consistent results regarding changes in the spatial patterns of temperature and rainfall means and extremes (see Chapter 11) at different levels of global warming.

In this subsection, we present the projected patterns of climate change obtained following the epoch approach (also called the time-shift method, see Section 4.2.4) under the Tier 1 SSPs (SSP1-2.6, SSP2-4.5, SSP3-7.0 and SSP5-8.5). For each model simulation considered under each of these SSPs, 20-year moving averages of the global average atmospheric surface temperature are first constructed, then this time series is used to detect the first year during when GSAT exceeds the 1.5°C, 2°C, 3°C and 4°C thresholds with respect

ACCEPTED VERSION SUBJECT TO FINAL EDITS

to the 1850–1900 (Cross-Chapter Box 11.1). The temperature thresholds are not exceeded in all the model simulations across the Tier 1 SSPs, that is, decreasing numbers of simulations are available for the analysis of patterns of change as the temperature threshold increases. For each simulation within which a given temperature threshold is exceeded, a 20-year global climatology is subsequently constructed to represent that level of global warming, centred on the year for which the threshold was first exceeded. The composite of all such climatologies across the Tier 1 SSPs and model simulations constitute the spatial patterns of change for a given temperature threshold. Some of the complexities of scaling patterns of climate change with different levels of global warming are also discussed in the following sections. These include overshoot versus stabilization scenarios and limitations of pattern scaling for strong mitigation and stabilization scenarios (Tebaldi and Arblaster, 2014). At least for the case of annual mean temperature and precipitation, strong evidence exists that even for strong mitigation and stabilization scenarios, patterns of change at lower levels of warming scale similarly to those reconstructed from transient simulations using either standard pattern-correlation or time-shift methodologies (Tebaldi and Knutti, 2018).

Pattern scaling performance based on scenario experiments is generally better for near-surface temperature than for precipitation (Ishizaki et al., 2013). For precipitation, rapid adjustments due to different forcing agents must be accounted for (Richardson et al., 2016). Possible non-linear responses to different forcing levels are also important (Good et al., 2015, 2016). Pattern scaling does not work as well at high forcing levels (Osborn et al., 2018). It is also important to distinguish the forced response from internal variability when comparing similar warming levels (Suarez-Gutierrez et al., 2018). The purpose of this section is not to repeat the analysis for all the variables considered in Sections 4.4 and 4.5, but rather to show a selected number of key variables that are important from the perspective of understanding the response of the physical climate system to different levels of warming.

4.6.1.1 Temperature

Global warming of 1.5°C implies higher mean temperatures compared to 1850–1900, with generally higher warming over land compared to ocean areas (*virtually certain*) and larger warming in high latitudes compared to low latitudes (Figure 4.31). In addition, global warming of 2°C versus 1.5°C results in robust increases in the mean temperatures in almost all locations, both on land and in the ocean (*virtually certain*), with subsequent further warming at almost all locations at higher levels of global warming (*virtually certain*) (Hoegh-Guldberg et al., 2018). For each particular level of global warming, relatively larger mean warming is projected for land regions (*virtually certain*, see Figure 4.31; Christensen et al., 2013; Collins et al., 2013; Seneviratne et al., 2016). The projected changes at 1.5°C and 2°C global warming are consistent with observed historical global trends in temperature and their attribution to anthropogenic forcing (see Chapter 3), as well as with observed changes under the recent global warming of 0.5°C (Hoegh-Guldberg et al., 2018; Schleussner et al., 2017). That is, spatial patterns of temperature changes associated with the 0.5°C difference in GMST warming between 1991–2010 and 1960–1979 (Schleussner et al., 2017; SR1.5) are consistent with projected changes under 1.5°C and 2°C of global warming.

The largest increase in annual mean temperature is found in the high latitudes of the Northern Hemisphere (NH) across all levels of global warming (*virtually certain*; Figure 4.31). This phenomenon peaks in the Arctic and is known as Arctic amplification, with the underlying physical mechanisms assessed in detail in Section 4.5.1 and Chapter 7, Section 7.4.4.1. For the CMIP6 ensemble average considered here, Arctic annual mean temperatures warm by a factor of 2.3, 2.5, 2.4 and 2.4 for 1.5°C, 2°C, 3°C and 4°C of global warming, respectively. That is, Arctic warming scales approximately linearly with GSAT. Generally, when Arctic amplification is considered across individual models, warming occurs at a factor of 2–4 times the global level of warming. It is *unlikely* that warming in the SH high latitudes in the 21st century will exceed the change in GSAT, or that it will substantially exceed warming in the tropics, for GSAT change ranging between 1.5°C and 4°C (Figure 4.31, Table 4.2). Correspondingly, there is *low confidence* of Antarctic amplification occurring under transient, 21st century low mitigation scenarios (Table 4.2; Chapter 7, Section 7.4.4.1). The Antarctic continent is projected to warm at a higher rate than the mid-latitude Southern Ocean, however, at all levels of global warming (Figure 4.31). The relevant physical mechanisms that reduce the amplitude of polar amplification over Antarctica compared to the Arctic are assessed in detail in Section

ACCEPTED VERSION SUBJECT TO FINAL EDITS

4.5.1 and Chapter 7, Section 7.4.4.1. In the SH the strongest warming over land is to occur, at any given level of global warming, over the subtropical areas of South America, southern Africa and Australia (*high confidence*). The relatively strong warming in subtropical southern Africa may be attributed to strong soil-moisture–temperature coupling and projected increased dryness under enhanced subsidence (Engelbrecht et al., 2015; Vogel et al., 2017). Across the globe, in the tropics, subtropics, and mid- to high latitudes, temperatures tend to scale linearly with the level of increase in GSAT and patterns of change are largely scenario independent *(high confidence)*.

[START FIGURE 4.31 HERE]

Figure 4.31: Projected spatial patterns of change in annual average near-surface temperature (°C) at different levels of global warming. Displayed are (a–d) spatial patterns of change in annual average near-surface temperature at 1.5°C, 2°C, 3°C, and 4°C of global warming relative to the period 1850–1900 and (e–g) spatial patterns of differences in temperature change at 2°C, 3°C, and 4°C of global warming compared to 1.5°C of global warming. The number of models used is indicated in the top right of the maps. No overlay indicates regions where the change is robust and *likely* emerges from internal variability, that is, where at least 66% of the models show a change greater than the internal-variability threshold (see Section 4.2.6) and at least 80% of the models agree on the sign of change. Diagonal lines indicate regions with no change or no robust significant change, where fewer than 66% of the models show change greater than the internal-variability threshold. Crossed lines indicate areas of conflicting signals where at least 66% of the models show change greater than the internal-variability threshold but fewer than 80% of all models agree on the sign of change. Values were assessed from a 20-year period at a given warming level, based on model simulations under the Tier-1 SSPs of CMIP6. Further details on data sources and processing are available in the chapter data table (Table 4.SM.1).

[END FIGURE 4.31 HERE]

4.6.1.2 Precipitation

While global mean precipitation increases as GSAT rises with the *very likely* range of 1–3% per 1°C (*high confidence*, see Sections 8.2.1 and 8.4.1), patterns of precipitation change do not scale as linearly with GSAT increase. Nevertheless, common features of precipitation change in the multi-model mean across scenarios still exist for different levels of global warming (Figure 4.32). Precipitation will *very likely* increase in the high latitudes and over tropical regions, and *likely* increase in large parts of the monsoon region, but *likely* decrease over the subtropical regions, including the Mediterranean, southern Africa, parts of Australia and South America at all four levels of global warming. The increases and decreases in precipitation will amplify at higher levels of global warming (*high confidence*) (Figure 4.32). Changes in extreme precipitation events under different levels of global warming are assessed in Chapter 11.

[START FIGURE 4.32 HERE]

Figure 4.32: Projected spatial patterns of change in annual average precipitation (expressed as a percentage change) at different levels of global warming. Displayed are (a–d) spatial patterns of change in annual precipitation at 1.5°C, 2°C, 3°C, and 4°C of global warming reletive to the period 1850–1900. No map overlay indicates regions where the change is robust and *likely* emerges from internal variability, that is, where at least 66% of the models show a change greater than the internal-variability threshold (see Section 4.2.6) and at least 80% of the models agree on the sign of change. Diagonal lines indicate regions with no change or no robust significant change, where fewer than 66% of the models show change greater than the internal-variability threshold. Crossed lines indicate areas of conflicting signals where at least 66% of the models show change greater than the internal-variability threshold but fewer than 80% of all models agree on the sign of change. Values were assessed from a 20-year period at a given warming level, based on model simulations under the Tier-1 SSPs of CMIP6. Further details on data sources and processing are available in the chapter data table (Table 4.SM.1).

ACCEPTED VERSION SUBJECT TO FINAL EDITS

[END FIGURE 4.32 HERE]

SR1.5 stated *low confidence* regarding changes in global monsoons at 1.5°C versus 2°C of global warming, as well as differences in monsoon responses at 1.5°C versus 2°C. Generally, statistically significant changes in regional annual average precipitation are expected at a global mean warming of 2.5°C–3°C or more (Tebaldi et al., 2015). Over the Austral-winter rainfall regions of south-western South America, South Africa and Australia, projected decreases in mean annual rainfall show high agreement across models and a strong climate change signal even under 1.5°C of global warming, with further amplification of the signal at higher levels of global warming (Mindlin et al., 2020) (*high confidence*). This is a signal evident in observed rainfall trends over these regions (see Chapter 2, Section 2.3.1.3, and Chapter 8, Section 8.3.1.6). Also, over the Asian monsoon regions, increases in rainfall will occur at 1.5°C and 2°C of global warming (Chevuturi et al., 2018). At warming levels of 1.5°C and 2°C, the changes in global monsoons are strongly dependent on the modelling strategies used, such as fully coupled transient, fully coupled quasi-equilibrium, and atmosphere-only quasi-equilibrium simulations. In particular, the differences of regional monsoon changes among model setups are dominated by strategy choics such as transient versus quasi-equilibrium set-up, prescription of SST, and treatment of aerosols (Zhang and Zhou, 2021).

[START FIGURE 4.33 HERE]

Figure 4.33: Area fraction of significant precipitation change at 1.5°C, 2°C, 3°C, and 4°C of global warming. Range of land fraction (top) and global area fraction (bottom) with significant precipitation increase (left-hand side) and decrease (right-hand side) in the projected annual precipitation change (%) at levels of global warming compared to the period 1850–1900. Values were assessed from a 20-year period at a given warming level from SSP1-2.6, SSP3-7.0 and SSP5-8.5 in CMIP6. The solid line illustrates the CMIP6-multi model mean and the shaded band is the 5–95% range across models that reach a given level of warming. Further details on data sources and processing are available in the chapter data table (Table 4.SM.1).

[END FIGURE 4.33 HERE]

The global and land area fractions with significant precipitation changes with global warming are shown in Figure 4.33. It is *virtually certain* that average warming will be higher over land. As warming increases, a larger global and land area will experience statistically significant increases or decreases in precipitation (*medium confidence*). The increase of the area fraction with significant precipitation increase is larger over land than over the ocean, but the increase of the area fraction with significant precipitation decrease is larger over the ocean than over land (Figure 4.33). Precipitation variability in most climate models increases over the global land area in response to warming (Pendergrass et al., 2017).

In summary, based on the assessment of CMIP6 models, there is *high confidence* that global mean precipitation will increase with increase in global mean surface temperature. Precipitation will *very likely* increase in the high latitudes and over tropical regions, *likely* increase in large parts of the monsoon region, but will *likely* decrease over the subtropical regions. There is *high confidence* that increases and decreases in precipitation will amplify over higher levels of global warming . As warming increases, there is *medium confidence* that a larger land area will experience statistically significant increases or decreases in precipitation.

4.6.1.3 Atmospheric Circulation

AR5 reported that the application of pattern scaling to extract information on variables other than surface temperature and precipitation was relatively unexplored. Since AR5, new studies have examined the relationship between projections of mid-latitude atmospheric circulation and GSAT both in terms of interpreting spread in responses across the CMIP5 multi-model ensemble (Grise and Polvani, 2014a, 2016)

ACCEPTED VERSION SUBJECT TO FINAL EDITS

and to investigate variations in the circulation response as a function of GSAT change over time within a given forcing experiment (Grise and Polvani, 2017; Ceppi et al., 2018).

At a fixed time horizon, the CMIP5 multi-model spread in GSAT explains only a small fraction of the spread in the shift of the NH mid-latitude circulation due to an abrupt quadrupling in CO_2 (Grise and Polvani, 2016). The fraction of model spread explained by GSAT in the shift of the SH circulation is larger, but still fairly small (Grise and Polvani, 2014a, 2016). At a fixed time horizon and for a given emission scenario, CMIP5 multi-model spread in storm track shifts, and the closely related mid-latitude jets, can be better explained by multi-model spread in lower and upper level meridional temperature gradients than by GSAT (Harvey et al., 2014; Grise and Polvani, 2016).

The transient response of the mid-latitude jets to forcing in the North Atlantic, North Pacific and Southern Hemisphere behaves nonlinearly with GSAT (Grise and Polvani, 2017; Ceppi et al., 2018). This is a consequence of the time-dependence of the relationship between radiative forcing and GSAT and the temporal evolution of SST patterns (Ceppi et al., 2018), with a potential seasonal component in the SH associated with polar stratospheric temperature changes (Grise and Polvani, 2017). Consequently, the epoch approach applied to a transient simulation of the 21st century will overestimate the mid-latitude circulation response in a stabilized climate. Dedicated time slice experiments simulating stabilized climates are therefore required to assess differences in mid-latitude circulation at given levels of global warming (Li et al., 2018). A further complication in the SH is the competing influences of ozone recovery and increasing GHG concentrations on the austral-summer mid-latitude circulation during the first half the 21st century (Barnes and Polvani, 2013; Barnes et al., 2014). Using transient 21st century experiments to diagnose changes in SH mid-latitude circulation at different levels of warming therefore confounds the effects of ozone recovery and GHG increases (Ceppi et al., 2018). Given these various limitations, we do not apply epoch analysis to assess mid-latitude atmospheric circulation changes and related annular modes of variability.

4.6.2 Climate Goals, Overshoot, and Path-Dependence

Many scenarios aiming at limiting warming by 2100 to 1.5°C involve overshoot – ERF temporarily exceeds a certain level before peaking and declining again (see also Annex VII: Glossary). To quantify the implications of any such overshoot, this subsection assesses reversibility of climate due to temporary overshoot of GSAT levels during the 21st century, and implications for the use of carbon budgets. It also assesses differences in climate outcomes under different pathways, with a focus on comparing the SSPs used in CMIP6 with the RCPs used in CMIP5.

4.6.2.1 Climate change under overshoot

The SR1.5 (IPCC, 2018) concluded with *high confidence* that overshoot trajectories 'result in higher impacts and associated challenges compared to pathways that limit global warming to 1.5°C with no or limited overshoot'. The degree and duration of overshoot affects the risks and impacts likely to be experienced (Hoegh-Guldberg et al., 2018) and the emissions pathway required to achieve it (Akimoto et al., 2018). Consequences such as on ice sheets and climatic extremes have been found to be greater at 2°C of global warming than at 1.5°C (Schleussner et al., 2016; Hoegh-Guldberg et al., 2018) but even on recovery to lower temperatures, these effects may not reverse. Overshoot has been found to lead to irreversible changes in thermosteric sea-level (Tokarska and Zickfeld, 2015; Palter et al., 2018; Tachiiri et al., 2019), AMOC (Palter et al., 2018), ice-sheets, and permafrost carbon (Section 4.7.2, Chapter 5, Section 5.4.9) and to long-lasting effects on ocean heat (Tsutsui et al., 2006a). Abrupt changes and tipping points are not well understood, but the higher the warming level and the longer the duration of overshoot, the greater the risk of unexpected changes (see sections 4.7.2). Non-reversal of the hydrological cycle has also been found in some studies with an increase in global precipitation following CO_2 decrease being attributed to a build-up of ocean heat (Wu et al., 2010), and to a fast atmospheric adjustment to CO_2 radiative forcing (Cao et al., 2011a).

Global temperature is expected to remain approximately constant if emissions of CO_2 were to cease (Section

ACCEPTED VERSION SUBJECT TO FINAL EDITS

4.7.1.1), and so reductions in GSAT are only possible in the event of net negative global CO_2 emissions. We assess here results from an overshoot scenario (SSP5-3.4-OS; O'Neill et al., 2016), which explores the implications of a peak and decline in forcing during the 21st century. Reversibility under more extreme and idealised carbon dioxide removal (CDR) scenarios is assessed in Section 4.6.3. In SSP5-3.4-OS, CO_2 peaks at 571 ppm in the year 2062 and reverts to 497 ppm by 2100 – approximately the same level as in 2040. SSP5-3.4-OS has strong net negative emissions of CO_2, exceeding those in SSP1-2.6 and SSP1-1.9 from 2070 onwards and reaching –5.5 PgC yr^{-1} (–20 $GtCO_2$ yr^{-1}) by 2100. While this causes global mean temperature to decline, changes in climate have not fully reversed by 2100 under this reversal of CO_2 concentration (Figure 4.34). Quantities are compared for 2081–2100 relative to a 20-year period (2034–2053) of the same average CO_2. Differences between these two periods of the same CO_2 are: GSAT: 0.28±0.30°C (mean ± standard deviation); global land precipitation: 0.026±0.011 mm/day; September Arctic sea-ice area: –0.32±0.53 million km^2; thermosteric sea-level: 12±0.8 cm. As assessed in Section 9.3.1.1, Arctic sea-ice area is linearly reversible with GSAT. Although these climate quantities are not fully reversible, the overshoot scenario results in reduced climate change compared with stabilisation or continued increase in greenhouse gases (Tsutsui et al., 2006b; Palter et al., 2018; Tachiiri et al., 2019) (*high confidence*).

[START FIGURE 4.34 HERE]

Figure 4.34: Simulated changes in climate indices for SSP5-3.4-OS plotted against atmospheric CO_2 concentration (ppm) from 480 up to 571 and back to 496 by 2100. (a) Global surface air temperature change; (b) Global land precipitation change; (c) September Arctic sea-ice area change; (d) Global thermosteric sea-level change. Plotted changes are relative to the 2034–2053 mean which has same CO_2 as 2081–2100 mean (shaded grey bar). Red lines denote changes during the period up to 2062 when CO_2 is rising, blue lines denote changes after 2062 when CO_2 is decreasing again. Thick line is multi model mean; thin lines and shading show individual models and complete model range. Numbers in square brackets indicate number of models used in each panel. Further details on data sources and processing are available in the chapter data table (Table 4.SM.1).

[END FIGURE 4.34 HERE]

The transient climate response to cumulative carbon (CO_2) emissions, TCRE, allows climate policy goals to be associated with remaining carbon budgets as global temperature increase is near-linear with cumulative emissions (Section 5.5). Research since AR5 has shown that the concept of near-linearity of climate change to cumulative carbon emissions holds for measures other than just GSAT, such as regional climate (Leduc et al., 2016) or extremes (Harrington et al., 2016)(Seneviratne et al., 2016). However, ocean heat and carbon uptake do exhibit path dependence, leading to deviation from the TCRE relationship for levels of overshoot above 300 PgC (Zickfeld et al., 2016; Tokarska et al., 2019). Sea-level rise, loss of ice-sheets, and permafrost carbon release may not reverse under overshoot and recovery of GSAT and cumulative emissions (Section 4.7). TCRE remains a valuable concept to assess climate policy goals and how to achieve them but given the non-reversibility of different climate metrics with CO_2 and GSAT reductions, it has limitations associated with evaluating the climate response under overshoot scenarios and CO_2 removal (*medium confidence*).

4.6.2.2 Consistency between Shared Socioeconomic Pathways and Representative Concentration Pathways

As CMIP5 and CMIP6 employed different scenario sets (RCPs and SSPs, respectively – see Section 1.6.1.1, Cross-Chapter Box 1.4), we assess how much of the differences in projections are due to the scenario change and how much due to model changes. CMIP6-simulated GSAT increases tend to be larger than in CMIP5, for nominally comparable scenarios ((Tebaldi et al., 2021), see Section 4.3.1).

The radiative forcing labels on SSP and RCP scenarios is approximate and enables the multiple climate

ACCEPTED VERSION SUBJECT TO FINAL EDITS

forcings within the scenario to be characterised by a single number. While the scenarios are similar in terms of the stratospheric adjusted radiative forcing (Tebaldi et al., 2021), they differ more in their effective radiative forcing (ERF). The combination of component forcings (CO_2, non-CO_2 greenhouse gases, aerosols) within the scenario also differ (Meinshausen et al., 2020). The ERF levels in the RCP and SSP scenarios have been calculated by sampling uncertainty in forcing from a range of different GHG species and aerosols (see 7.SM.1.4 for details). Figure 4.35 shows the time evolution and 2081–2100 mean across the families of scenarios and how this affects projections of GSAT. That the ERFs differ between corresponding SSP and RCP scenarios makes comparison between CMIP6 and CMIP5 projections challenging (Tebaldi et al., 2021). (Wyser et al., 2020) find the EC-Earth3-Veg model exhibits stronger radiative forcing and substantially greater warming under SSP5-8.5 than RCP8.5, and similar, but smaller additional warmings for SSP2-4.5 and SSP1-2.6 compared with RCP4.5 and RCP2.6, respectively. In addition to the global response, climate can vary regionally due to non-CO_2 components of forcing (Samset et al., 2016; Richardson et al., 2018b, 2018a).

Emulators (Cross-Chapter Box 7.1) can be used to aid understanding of differences between generations of scenarios. AR5 (Collins et al., 2013) explored the differences between CMIP3 and CMIP5 (their Figure 12.40). Here we use an emulator calibrated to AR6 assessed GSAT ranges, thus eliminating the effect of differences in the model ensembles, to analyse the differences between SSP and RCP scenarios. MAGICC7.5 in its WGIII-calibrated setup (see Cross Chapter Box 7.1) projects differences in 2081–2100 mean warming between the RCP2.6 and SSP1-2.6 scenarios of around 0.2°C, between RCP4.5 and SSP2-4.5 of around 0.3°C and between RCP8.5 and SSP5-8.5 of around 0.3°C (Figure 4.35b). The SSP scenarios also have a wider 5–95% range simulated by MAGICC7.5 explaining about half of the increased range seen when comparing CMIP5 and CMIP6 models. Higher climate sensitivity is, though, the primary reason behind the upper end of the warming for SSP5-8.5 reaching 1.5°C higher than the CMIP5 results. Compared with the differences between the CMIP5 and CMIP6 multi-model ensembles for the same scenario pairs (Table A6 in Tebaldi et al., 2021), the higher ERFs of the SSP scenarios contribute approximately half of the warmer CMIP6 SSP outcomes (*medium confidence*).

In summary, there is *medium confidence* that about half of the warming increase in CMIP6 compared to CMIP5 is due to higher climate sensitivity in CMIP6 models; the other half arises from higher ERF in nominally comparable scenarios (e.g., RCP8.5 and SSP5-8.5).

[START FIGURE 4.35 HERE]

Figure 4.35: Comparison of RCPs and SSPs run by a single emulator to estimate scenario differences. Time series with 5–95% ranges and medians of (a) effective radiative forcings, calculated as described in Annex 7.A.1; and (b) GSAT projections relative to 1850–1900 for the RCP and SSP scenarios from MAGICC 7.5. Note that the nameplate radiative forcing level refers to stratospheric adjusted radiative forcings in AR5-consistent settings (Tebaldi et al., 2021) while ERFs may differ. MAGICC7.5 is here run in the recommended setup for WGIII, prescribing observed GHG concentrations for the historical period and switching to emission-driven runs in 2015. Further details on data sources and processing are available in the chapter data table (Table 4.SM.1).

[END FIGURE 4.35 HERE]

4.6.3 Climate Response to mitigation, Carbon Dioxide Removal, and Solar Radiation Modification

Most strong-mitigation scenarios assume – in addition to emissions reductions – some form of carbon dioxide removal (CDR) – anthropogenic activities that remove CO_2 from the atmosphere and durably store it in geological, terrestrial, or ocean reservoirs, or in products (see Annex VII: Glossary). SR1.5 (Rogelj et al., 2018b) assessed that all pathways that limit warming to 1.5°C by 2100 with no or limited overshoot use CDR. In the SSP class of scenarios, SSP1-1.9 is characterized by a rapid decline of net CO_2 emissions to zero by 2050 and net negative CO_2 emissions in the second half of this century (O'Neill et al., 2016; Rogelj et al., 2018a), implying the use of CDR. The term 'net CO_2 emissions' refers to the difference between

ACCEPTED VERSION SUBJECT TO FINAL EDITS

anthropogenic CO_2 emissions and removal by CDR options, and 'net negative CO_2 emissions' imply a scenario where CO_2 removal exceeds emissions (van Vuuren et al., 2011) (van Vuuren et al., 2016). The terms 'negative emissions' and 'net negative emissions' refer to and include all GHGs (see Annex VII: Glossary).

Climate change can be also offset by solar radiation modification (SRM) measures that modify the Earth's radiation budget to reduce global warming (see Annex VII: Glossary). CDR and SRM approaches have been together referred to as 'geoengineering' or 'climate engineering' in the literature (The Royal Society, 2009; NRC, 2015a, 2015b; Schäfer et al., 2015). However, following SR1.5 (de Coninck et al., 2018), these terms inconsistently used in the literature, so that CDR and SRM are explicitly differentiated here. SRM contrasts with climate mitigation because it introduces a 'mask' to the climate change problem by altering the Earth's radiation budget, rather than attempting to address the root cause of the problem, which is the increase in GHGs in the atmosphere.

Section 4.6.3.1 assesses the emergence of the climate response to mitigation, which is reflected by the difference between high- and low-emission scenarios. Section 4.6.3.2 then assesses the climate response to mitigation through CDR options, usually assumed against the background of some emission scenario; note that the CDR options themselves are assessed in Chapter 5 (Section 5.6.2). Section 4.6.3.3 assesses the climate system response to SRM options. The biogeochemical implications of CDR and SRM are assessed in Chapter 5 (Sections 5.6.2 and 5.6.3, respectively). The importance of CDR for reaching net zero or negative CO_2 emissions in mitigation pathways is assessed in the AR6 WGIII report (Chapters 3, 4, 6, 7 and 12). The risks for and impacts on human and natural systems due to SRM are assessed in the AR6 WGII report (Chapter 16), and the international governance issues related to SRM and CDR are assessed in the AR6 WGIII report (Chapter 14).

4.6.3.1 Emergence of the climate response to mitigation

Reducing GHG emissions will eventually slow and limit the degree of climate change relative to high-emission scenarios such as SSP5-8.5 (*very high confidence*). Even when CO_2 emissions are reduced, however, atmospheric CO_2 concentrations continue to increase as long as emissions exceed removal by sinks (Millar et al., 2017). Surface warming would likewise initially continue under scenarios of decreasing emissions, resulting in a substantial lag between a peak in CO_2 emissions and peak warming (Ricke and Caldeira, 2014; Zickfeld and Herrington, 2015) (*high confidence*). The lag between peak emissions and warming depends on the emissions history prior to the peak and also on the rate of the subsequent emissions reductions (Matthews, 2010; Ricke and Caldeira, 2014; Zickfeld and Herrington, 2015).

In addition to the lag between peak emissions and peak warming, the climate response to reduced emissions would be overlain by internal variability, which can amplify or attenuate the forced response. The resulting masking of differences between scenarios is illustrated in Figure 4.36 for GSAT trends over 2021–2040 (Maher et al., 2020). The overall trends conform to expectations in that most simulations show warming almost everywhere, especially under scenario RCP8.5 (Figure 4.36 bottom row). But any individual grid point can in principle show no warming or even cooling, even under RCP 8.5, over the near term (Figure 4.36 middle row). The magnitude of pointwise maximum and minimum temperature trends can be as large as 0.5°C per year (Figure 4.36 top and middle rows), exceeding possible trends in the global mean by one order of magnitude. While it is only a small fraction of the surface that simultaneously can show cooling, cooling at any given location is fully consistent with globally averaged surface warming over the near term (*high confidence*, since the findings of (Maher et al., 2020) are consistent across six different large initial-condition ensembles).

[START FIGURE 4.36 HERE]

Figure 4.36: Masking of climate response to mitigation by internal variability in the near term. Near-term (2021–2040) pointwise maximum (top row) and pointwise minimum (middle row) surface air

ACCEPTED VERSION SUBJECT TO FINAL EDITS

temperature trends in the large initial-condition ensemble from MPI (left and centre columns), and CESM (right column) models in the RCP2.6 (left column) and RCP8.5 scenarios (centre and right columns). The percentage of ensemble members with a warming trend in the near term is shown in the bottom panels. Figure modified from (Maher et al., 2020). Further details on data sources and processing are available in the chapter data table (Table 4.SM.1).

[END FIGURE 4.36 HERE]

An important development since AR5 has been the quantification of when the climate response to mitigation can be expected to emerge from the background noise of internal variability (illustrated in Figure 4.36; see Section 1.4.2.2, see also Annex VII: Glossary). A basic ambiguity arises because once mitigation measures are in place, it is no longer possible to observe what the climate would have been without these measures, and any statement about emergence of the response to mitigation is contingent upon the assumed strength of mitigation in relation to an assumed ('counterfactual') no-mitigation scenario. Still, there is *high agreement* on the emergence of the climate response to mitigation across a number of independent studies using different models and different statistical approaches.

Among global quantities, emergence of the response to differing CO_2 emissions – representing differences between low- and high-emission scenarios – is first expected to arise in global-mean CO_2 concentrations, about 10 years after emission pathways have started diverging (Tebaldi and Friedlingstein, 2013; Peters et al., 2017; Schwartzman and Keeling, 2020; Spring et al., 2020) (*high confidence*). In these studies, emergence is generally defined as the time at which the global mean concentration first differs between mitigation and non-mitigation scenarios by more than two standard deviations of internal variability, although there are some methodological differences.

Emergence in GSAT would be delayed further, owing to the inertia in the climate system. Although not investigating emergence as defined here in AR6, (Tebaldi et al., 2021) used 20-year running-mean GSAT and compared pairwise either model-by-model or between CM IP6 ensemble means from the core set of five scenarios assessed in this chapter. Differences by more than 0.1°C showed up in most cases in the near term, with only some of the individual models and the comparisons of the closest scenarios showing a delay until the mid-term. Taking internal variability explicitly into account, (Tebaldi and Friedlingstein, 2013) and (Samset et al., 2020) found emergence of mitigation benefits in GSAT changes about 25–30 years after RCP2.6 emissions diverge from the higher-emissions trajectories in RCP4.5 and RCP8.5. Consistently, (Marotzke, 2019) found about one-third likelihood that a trend reduction in GSAT, over the period 2021–2035 relative to 2005–2020, would be attributable to the emissions reductions implied by the difference between RCP2.6 and RCP4.5. Emergence of the GSAT response to mitigation of individual short-lived climate forcers (SLCFs) would likewise not occur until several decades after emissions trajectories diverge, owing to the relatively small influence of individual SLCFs on the total ERF (Samset et al., 2020), see also Section 4.4.4 and Figure 4.18.

In contrast to the earlier studies, emergence in GSAT within the near- term has recently been found by (McKenna et al., 2021) who investigated the likelihood that under the SSP scenarios GSAT trends will exceed the largest historical observed 20-year trends. They found that under scenario SSP1-1.9, the 20-year GSAT trends would *likely* be lower than in SSP3-7.0 and SSP5-8.5 within the near term. This earlier diagnosed time of emergence compared to (Marotzke, 2019), while using a similar statistical approach, presumably arose because of the longer-period trends (20 rather than 15 years) and the larger difference between emissions trajectories considered (*medium confidence*). Using 20-year temperature anomalies relative to 1995–2014 instead of 20-year trends yielded a low probability of emergence (McKenna et al., 2021), consistent with the AR5 (Collins et al., 2013; Kirtman et al., 2013), (Tebaldi and Friedlingstein, 2013) (Samset et al., 2020). It is not yet understood why GSAT trends appear to show faster emergence of mitigation benefits, compared to GSAT anomalies.

Emergence of mitigation benefits has been studied much less for quantities other than globally and annually averaged CO_2 concentration and surface temperature. Boreal-winter temperatures are more challenging for emergence, due to larger variability in boreal winter and adding a decade to the time of emergence, whereas

ACCEPTED VERSION SUBJECT TO FINAL EDITS

emergence times for boreal-summer averages are similar to the annual temperature averages (Tebaldi and Friedlingstein, 2013). Emergence happens later at the regional scale, with a median time of emergence of 30–45 years after emission paths separate in RCP2.6 relative to RCP4.5 and RCP8.5; a stricter requirement of 95% confidence level instead of median induces a delay of several decades, bringing time of emergence toward the end of the 21st century at regional scales (Tebaldi and Friedlingstein, 2013).

Attribution to emissions reductions, for the case of RCP2.6 relative to RCP4.5, is not substantially more likely for 2021–2035 trends in upper-2000m OHC than for GSAT (Marotzke, 2019), although OHC change is thought to be less susceptible to internal variability. Furthermore, (Marotzke, 2019) found only around 10% likelihood of mitigation-benefit emergence during 2021–2035 for change in AMOC and September Arctic sea-ice area. (Tebaldi and Wehner, 2018) showed that the differences in temperature extremes between RCP4.5 and RCP8.5 over all land areas become statistically significant by 2050. The seemingly contrasting result of (Ciavarella et al., 2017) that mitigation benefits arise earlier for climate extremes poses no contradiction, because (Ciavarella et al., 2017) did not look at emergence as defined here but at the extremes of a distribution, which differ between scenarios already at a time when the distributions are still largely overlapping.

In summary, if strong mitigation is applied from 2020 onward as reflected in SSP1-1.9, its effect on 20-year trends in GSAT would *likely* emerge during the near term, measured against an assumed non-mitigation scenario such as SSP3-7.0 and SSP5-8.5. However, the response of many other climate quantities to mitigation would be largely masked by internal variability during the near term, especially on the regional scale (*high confidence*). The mitigation benefits for these quantities would emerge only later during the 21st century (*high confidence*). During the near term, a small fraction of the surface can show cooling under all scenarios assessed here, so near-term cooling at any given location is fully consistent with globally averaged surface warming (*high confidence*).

4.6.3.2 Climate Response to Mitigation by Carbon Dioxide Removal

CDR options include afforestation, soil carbon sequestration, bioenergy with carbon capture and storage (BECCS), wet land restoration, ocean fertilization, ocean alkalinisation, enhanced terrestrial weathering and direct air capture and storage (see Chapter 5, Section 5.6.2 and Table 5.9 for a more complete discussion). Chapter 8 (Section 8.4.3) assesses the implications of CDR for water cycle changes. The potential of different CDR options in terms of the amount of CO_2 removed per year from the atmosphere, costs, co-benefits and side effects of the CDR approaches are assessed in the SR1.5 (de Coninck et al., 2018), the AR6 WGIII report (see Chapters 7 and 12), and in several review papers (Fuss et al., 2018; Lawrence et al., 2018; Nemet et al., 2018). In the literature, CDR options are also referred to as 'negative CO_2 emission technologies'.

Deployment of CDR will lead to a reduction in atmospheric CO_2 levels only if uptake by sinks exceeds net CO_2 emissions. Hence, there could be a substantial delay between the initiation of CDR and net CO_2 emissions turning negative (van Vuuren et al., 2016), and the time to reach net negative CO_2 emissions and the evolution of atmospheric CO_2 and climate thereafter would depend on the combined pathways of anthropogenic CO_2 emissions, CDR, and natural sinks. The cooling (or avoided warming) due to CDR would be proportional to the cumulative amount of CO_2 removed from the atmosphere by CDR (Tokarska and Zickfeld, 2015; Zickfeld et al., 2016), as implied by the near-linear relationship between cumulative carbon emissions and GSAT change (see Section 5.5)

Emission pathways that limit globally averaged warming to 1.5°C or 2°C by the year 2100 assume the use of CDR approaches in combination with emission reductions to follow net negative CO_2 emissions trajectory in the second half of this century. For instance, in SR1.5, all analysed pathways limiting warming to 1.5°C by 2100 with no or limited overshoot include the use of CDR to some extent to offset anthropogenic CO_2 emissions and the median of CO_2 removal across all scenarios was 730 $GtCO_2$ in the 21st century (Rogelj et al., 2018b) (Rickels et al., 2018). Affordable and environmentally and socially acceptable CDR options at scale well before 2050 are an important element of 1.5°C-consistent pathways especially in overshoot

ACCEPTED VERSION SUBJECT TO FINAL EDITS

scenarios (de Coninck et al., 2018). The required scale of removal by CDR can vary from 1–2 $GtCO_2$ per year from 2050 onwards to as much as 20 $GtCO_2$ p`er year (Waisman et al., 2019). In the SSP class of scenarios, net CO_2 emissions turn negative from around 2050 in SSP1-1.9 and around 2070 in SSP1-2.6 and in the overshoot scenario SSP5-3.4-OS (O'Neill et al., 2016). Thus, CDR would play a pivotal role in limiting climate warming to 1.5°C or 2°C (Minx et al., 2018). In stark contrast, however, two extensive reviews (Lawrence et al., 2018; Nemet et al., 2018) conclude that it is implausible that any CDR technique can be implemented at scale that is needed by 2050.

When CDR is applied continuously and at scales as large as currently deemed possible, under RCP8.5 as the background scenario, the widely discussed CDR options such as afforestation, ocean iron fertilization and surface ocean alkalinisation are individually expected to be relatively ineffective, with limited (8%) warming reductions relative to the scenario with no CDR option (Keller et al., 2014). Hence, the potential role that CDR will play in lowering the temperature in high-emission scenarios is limited (*medium confidence*). The challenges involved in comparing the climatic effects of various CDR options has also been recognized in recent studies (Sonntag, 2018; Mengis et al., 2019). For instance, due to compensating processes such as biogeophysical effects of afforestation (warming from albedo decrease when croplands are converted to forests) more carbon is expected to be removed from the atmosphere by afforestation than by ocean alkalinisation to reach the same global mean cooling.

[START FIGURE 4.37 HERE]

Figure 4.37: Delayed climate response to CDR-caused net negative CO_2 emissions. Multi-model simulated response in global and annual mean climate variables for a ramp-up followed by ramp-down of CO_2. Atmospheric CO_2 increases from the pre-industrial level at a rate of 1% yr^{-1} to 4 • CO_2, then decreases at the same rate to the pre-industrial level and then remains constant. The ramp-down phase represents the period of net negative CO_2 emissions. a) normalized ensemble mean anomaly of key variables as a function of year, including atmospheric CO_2, surface air temperature, precipitation, thermosteric sea-level rise (see Glossary), global sea-ice area, Northern Hemisphere sea-ice area in September, and Atlantic meridional overturning circulation (AMOC); b) surface air temperature; c) precipitation; d) September Arctic sea-ice area; e) AMOC; f) thermostatic sea level; 5-year running means are shown for all variables except the sea-level rise. In b–f, red lines represent the phase of CO_2 ramp-up, blue lines represent the phase of CO_2 ramp-down, brown lines represent the period after CO_2 has returned to pre-industrial level, and black lines represent the multi-model mean. For all of the segments in b–f, the solid coloured lines are CMIP6 models, and the dashed lines are other models (i.e., EMICs, CMIP5 era models). Vertical dashed lines indicate peak CO_2 and when CO_2 again reaches pre-industrial value. The number of CMIP6 and non-CMIP6 models used is indicated in each panel. The time series for the multi-model means (b–f) and the normalized anomalies (a) are terminated when data from all models are not available, in order to avoid the discontinuity in the time series. Further details on data sources and processing are available in the chapter data table (Table 4.SM.1).

[END FIGURE 4.37 HERE]

The climate response to CDR-caused net negative CO_2 emissions has been studied in Earth system models by prescribing idealized ramp-down of CO_2 concentrations (Zickfeld et al., 2016) (MacDougall, 2013a) (Schwinger and Tjiputra, 2018), CO_2 concentrations of RCP scenarios that have net negative CO_2 emissions (Jones et al., 2016c), and idealized net negative CO_2 emission scenarios (Tokarska and Zickfeld, 2015). The Carbon Dioxide Removal Model Intercomparison Project (CDRMIP) uses multiple ESMs to explore the climate response, effectiveness of CO_2 removal, and challenges of CDR options (Keller et al., 2018). Idealized CDRMIP simulations increase CO_2 concentrations at 1% per year from the level in the pre-industrial control run (piControl) to 4 • CO_2 and subsequently decrease at the same rate to the piControl level. This section assesses the lag in climate response to CDR-caused negative emission; climate 'reversibility' is assessed in Section 4.7.2. The ramp-down phase, though unrealistic, represents the 'net negative CO_2 emission' phase.

ACCEPTED VERSION SUBJECT TO FINAL EDITS

Figure 4.37: illustrates the first results from CDRMIP (Keller et al., 2018). Other studies that use similar (Zickfeld et al., 2016) (Schwinger and Tjiputra, 2018)(Jeltsch-Thömmes et al., 2020) or other idealized scenarios (MacDougall, 2013a) or more realistic net negative CO_2 emission scenarios such as RCP2.6 (Jones et al., 2016c) and scenarios that limit warming to 2°C or less after different levels of overshoot (Tokarska and Zickfeld, 2015) arrive at similar conclusions. Changes in key climate variables substantially lag behind the decline in CO_2 (Figure 4.37). The precipitation increase at the beginning of the ramp-down phase agrees with the increase in precipitation for an abrupt decline in CO_2 (Cao et al., 2011b). Notwithstanding a decline in atmospheric CO_2, global mean thermosteric sea level would continue to rise. When atmospheric CO_2 returns to the piControl level, global mean thermosteric sea level is higher than its value at peak CO_2 (Figure 4.37), and it is *likely* that thermosteric global sea level would not return to piControl levels for over 1000 years after atmospheric CO_2 is restored to piControl concentrations (Tokarska and Zickfeld, 2015; Ehlert and Zickfeld, 2018). Therefore, there is *high confidence* that sea-level rise will not be reversed by CDR at least for several centuries (see also Chapter 9, Section 9.6.3.5). A comparison of different models shows recovery of AMOC intensity during net negative CO_2 emissions, but the results are model dependent – strengthening with an overshoot in most models (Jackson et al., 2014;) and strengthening but not reaching the initial state in some models (Sgubin et al., 2015). The overall lag in response is qualitatively similar to the lagged climate system response in the overshoot scenario SSP5-34-OS where CO_2 rises until 2062 and decreases thereafter (Figure 4.34) The lag in climate response to CDR causes hysteresis between key climate variables such as temperature, precipitation, AMOC and sea level, and atmosphere CO_2 with the hysteresis characteristics dependent on the rate of CDR and climate sensitivity (MacDougall, 2013b) (Jeltsch-Thömmes et al., 2020).

Termination of CDR refers to a sudden and sustained discontinuation of CDR deployment (see Section 4.6.3.3 for termination effects of SRM). The literature on the termination effects of CDR is limited, mostly considering scenarios where CDR implementation is explicit and does not result in net negative CO_2 emissions (Keller et al., 2014; González et al., 2018). In simulations where CDR is applied on the RCP8.5 scenario at scales as large as currently deemed possible, the increase in global mean warming rates following CDR termination are relatively small in comparison to SRM termination (Keller et al., 2014). The exception is artificial ocean upwelling where surface cooling is mainly caused by bringing cold water from the deep ocean; upon termination this causes larger rates of surface warming (Oschlies et al., 2010). When background emissions are as high as in RCP8.5, termination of a large global-scale application of CDR such as ocean alkalinisation for multiple decades could also result in large regional warming rates (up to 0.15°C per year) that are comparable to those caused by termination of SRM (González et al. 2018). In such cases, large amounts of CO_2 would be removed from the atmosphere before termination, and termination would cause a temporal trajectory of atmospheric CO_2 that is parallel to the high-emission scenario but from an atmosphere with much lower CO_2 levels. Because CO_2 radiative forcing is a logarithmic function of CO_2 concentration, large regional warming rates are simulated in such terminations. Thus, there is *high confidence* that the climate effect of CDR termination would depend on the amount CO_2 removed by CDR prior to termination and the rate of background CO_2 emissions at the time of termination. See also Chapter 5, Table 5.9 that summarizes the termination effects of individual CDR options.

In summary, there is *high confidence* that, due to the near-linear relationship between cumulative carbon emissions and GSAT change, cooling or avoided warming due to a CDR option would depend on the cumulative amount of CO_2 removed by that CDR option. The climate system response to the deployment of CDR is expected to be delayed by years (e.g., in temperature, precipitation, sea-ice extent) to centuries (e.g., sea level and AMOC) (*high confidence*). The climate response to a sudden and sustained CDR termination would depend on the amount of CDR-induced cooling prior to termination and the rate of background CO_2 emissions at the time of termination (*high confidence*).

4.6.3.3 Climate Response to Solar Radiation Modification

Most SRM approaches, including stratospheric aerosol injection (SAI), marine cloud brightening (MCB), and surface albedo enhancements (Table 4.7), aim to cool the Earth by deflecting more solar radiation to space. Although cirrus cloud thinning (CCT) aims to cool the planet by increasing the longwave emission to

ACCEPTED VERSION SUBJECT TO FINAL EDITS

space, it is included in the portfolio of SRM options (Table 4.7) for consistency with AR5 (Boucher et al., 2013) and SR1.5 (de Coninck et al., 2018). Other approaches such as injection of sulphate aerosols into the Arctic troposphere and sea-ice albedo enhancements for moderating *regional* warming have also been suggested (MacCracken, 2016) (Field et al., 2018). As noted in SR1.5 (de Coninck et al., 2018), SRM is only considered as a potential supplement to deep mitigation, for example in overshoot scenarios (MacMartin et al., 2018).

[START TABLE 4.7 HERE]

Table 4.7: A summary of the various SRM approaches.

SRM approach	Proposed mechanism and associated uncertainties of the SRM approach	Global mean negative radiative forcing potential and characteristics	Key climate and environmental effects	References
Stratospheric Aerosol Injection (SAI)	Injection of aerosols or their precursor gases into the stratosphere to scatter sunlight back to space; Aerosol types such as sulphates, calcium carbonate, and titanium dioxide have been proposed; large uncertainties associated with type of aerosol, aerosol radiative properties, microphysics, chemistry, stratospheric processes, and temporal and spatial strategy of aerosol injection	1–8 W m^{-2}, depending on the amount and pattern of injection, and transport and growth of injected particles; compared to other SRM approaches, radiative forcing could be more homogenously distributed.	Change in temperature and precipitation pattern; precipitation reduction in some monsoon regions; decrease in direct and increase in diffuse sunlight at surface; stratospheric heating and changes to stratospheric dynamics and chemistry; potential delay in ozone hole recovery; changes in surface UV radiation; changes in crop yields	(Visioni et al., 2017; Tilmes et al., 2018b; Simpson et al., 2019a)
Marine cloud brightening (MCB)	Injection of sea salt or other types of aerosols to increase the albedo of marine stratocumulus clouds; regional option to reduce SST in hurricane formation regions and in coral reef areas; large uncertainties associated with cloud microphysics and aerosol–cloud-radiation interactions.	1–5 W m^{-2}, depending on the scale and amount of sea salt injection; heterogeneous radiative forcing	Change in land-sea contrast and precipitation patterns	(Latham et al., 2012)(Latham et al., 2014) (Ahlm et al., 2017) (Stjern et al., 2018)
Cirrus cloud thinning (CCT)	Inject ice nuclei in the upper troposphere to reduce the lifetime and optical thickness of cirrus clouds to allow more longwave radiation to escape to space; large uncertainties associated with cirrus cloud formation processes, cirrus microphysics, and interaction with aerosol	1-2 W m^{-2}, depending on cirrus microphysical response and seeding strategy; heterogeneous radiative forcing; loss in cirrus clouds could also cause significant shortwave forcing regionally; risk of overseeding and consequent warming	Changes in temperature and precipitation pattern; increase in solar radiation reaching surface	(Storelvmo and Herger, 2014; Jackson et al., 2016; Gasparini et al., 2020)
Surface-based albedo modification	Increase ocean albedo by creating microbubbles; add reflective material to incease desert albedo; paint the roof of buildings white to increase roof reflectivity; increase albedo of agriculture land via no-till farming or modifying crop albedo, add reflective material to increase sea ice albedo	Radiative forcing of a few W m^{-2} might be achieved via increase in ocean and desert albedo, but the large-scale implementation is not feasible; less than 0.5 W m^{-2} for white roof and crop albedo enhancement; heterogeneous radiative forcing.	Change in land-sea contrast and precipitation pattern for ocean and desert albedo increase; more localized effect for white roofs, no-till farming, and crop albedo modification.	(Evans et al., 2010; Davin et al., 2014; Zhang et al., 2016; Field et al., 2018; Kravitz et al., 2018)

ACCEPTED VERSION SUBJECT TO FINAL EDITS

[END TABLE 4.7 HERE]

AR5 assessed the climate response to, as well as risks and side effects of, several SRM options (Boucher et al., 2013) and concluded with *high confidennce* that SRM, if practicable, could substantially offset a global temperature rise and partially offset some other impacts of global warming, but the compensation for the climate change caused by GHGs would be imprecise. AR5 furthermore concluded that models consistently suggest that SRM would generally reduce climate differences compared to a world with elevated GHG concentrations and no SRM; however, there would also be residual regional differences in climate (e.g., temperature and rainfall) when compared to a climate without elevated GHGs. AR5 concluded with *high confidence* that scaling SRM to substantial levels would carry the risk that if the SRM were terminated for any reason, surface temperatures would increase rapidly (within a decade or two) to values consistent with the GHG forcing (Boucher et al., 2013).

SR1.5 (de Coninck et al., 2018) assessed SRM in terms of its potential to limit warming to below 1.5°C in temporary overshoot scenarios and the associated impacts. It concluded that SAI could limit warming to below 1.5°C but that the climate response to SAI is uncertain and varies across climate models. Overall, the assessment concluded that the combined uncertainties related to SRM approaches, including technological maturity, limited physical understanding of the response to SRM, potential impacts, and challenges of governance, constrain potential deployment of SRM in the near future.

This subsection assesses the global and large-scale physical climate system response to SRM based on theoretical and modelling studies. There is no mature technology today to implement any of the SRM options assessed here. A short summary of the SRM options, including the proposed mechanism of each SRM approach, radiative forcing potential, and key climate and environmental effects, is listed in Table 4.7 Chapter 5 (Section 5.6.3) assesses the biogeochemical implications of SRM, Chapter 6 (Section 6.3.6) assesses the potential ERF of the aerosol-based SRM options and Chapter 8 (Section 8.6.3) assesses the abrupt water cycle changes in response to initiation or termination of SRM. The risks to human and natural systems, impacts of SRM, ethics, and perceptions are assessed in the WGII report (Chapter 16). Governance issues associated with SRM research and deployment are assessed in the WGII and WGIII Reports. The assessment of technical feasibility and engineering aspects of SRM is beyond the scope of this report.

The AR5 assessed SRM modelling mainly based on idealized simulations that used solar constant reductions. Since then, more in-depth investigations into specific SRM approaches have been conducted with more sophisticated treatment of aerosol–cloud–radiative interactions and stratospheric dynamics and chemistry underlying SAI, MCB, and CCT. Another major development since AR5 is the investigation into whether multiple climate policy goals may be met by optimally designed SRM strategies, including large-ensemble SAI simulations using multiple injection locations. There are large uncertainties in important SRM-related processes such as aerosol microphysics and aerosol-cloud-radiation interaction and hence the level of understanding is low.

As assessed in SR1.5 (de Coninck et al., 2018), most of the knowledge about SRM is based on idealized model simulations and some natural analogues. In addition to single-model studies, more results from the coordinated modelling work of Geoengineering Model Intercomparison Project (GeoMIP) have become available. GeoMIP was initiated at the time of AR5 (Kravitz et al., 2011) (Kravitz et al., 2013a) and is now in its second phase under the framework of CMIP6 (GEOMIP6, Kravitz et al., 2015). However, studies based on GeoMIP6 data are currently limited and hence the assessment on climate response to SRM here is derived mostly from GeoMIP literature together with studies with single models.

Simple calculations and climate modelling studies show that about 2% extra solar irradiance reflected away from Earth or a 1 percentage point increase in planetary albedo (0.31 to 0.32) would suffice to offset global mean warming from a doubling of the CO_2 concentration (The Royal Society, 2009)(Kravitz et al., 2013a) (Kravitz et al., 2021). To offset the same amount of CO_2-induced GSAT increase, different levels of ERF are

ACCEPTED VERSION SUBJECT TO FINAL EDITS

required for different methods of SRM (Schmidt et al., 2012; Russotto and Ackerman, 2018)(Modak et al., 2016)(Chiodo and Polvani, 2016)(Duan et al., 2018) (Krishnamohan et al., 2019)(Zhao et al., 2020).

As assessed in AR5 (Boucher et al., 2013), abruptly introducing SRM to fully offset global warming reduces temperature toward 1850–1900 values with an e-folding time of only about 5 years (Matthews and Caldeira, 2007). A more realistic approach would be a slow ramp-up of SRM to offset further warming (MacCracken, 2016) (Tilmes et al., 2016). Modelling studies have consistently shown that SRM has the potential to offset some effects of increasing GHGs on global and regional climate, including the melting of Arctic sea ice (Moore et al., 2014) (Berdahl et al., 2014) and mountain glaciers (Zhao et al., 2017), weakening of Atlantic meridional overturning circulation (AMOC) (Cao et al., 2016; Hong et al., 2017) (Tilmes et al., 2020), changes in extremes of temperature and precipitation (Curry et al., 2014) (Ji et al., 2018)(Muthyala et al., 2018), and changes in frequency and intensity of tropical cyclone (Moore et al., 2015) (Jones et al., 2017).

The climate response to SRM depends greatly on the characteristics of SRM implementation approaches. There could be substantial residual or overcompensating climate change at both the global and regional scales and seasonal timescales (Irvine et al., 2016) (Kravitz et al., 2014) (Fasullo et al., 2018) (McCusker et al., 2015) (Gertler et al., 2020) (Jiang et al., 2019). This is because the climate response to SRM options is different from the response to GHG increase (Figure 4.38). For instance, when global mean warming is offset by a uniform reduction in incoming sunlight, there is residual warming in the high latitudes and overcooling in the tropics (Kravitz et al., 2013a; Kalidindi et al., 2015), and a reduction in tropical mean rainfall (Tilmes et al., 2013). In simulations of stratospheric SO_2 injection, SRM diminishes the amplitude of the seasonal cycle of temperature at many high-latitude locations, with warmer winters and cooler summers (Jiang et al., 2019). Further, the rates of response could differ between surface temperature and slow components in the climate system such as sea-level rise (Irvine et al., 2012; Jones et al., 2018). SRM implemented at a moderate intensity, for example by offsetting half of the global warming, has the potential to reduce negative effects such as reduced precipitation that are associated with fully offsetting global mean warming (Irvine et al., 2019) (Irvine and Keith, 2020).

For the same amount of global mean cooling achieved, the pattern of climate response would depend on SRM characteristics (Niemeier et al., 2013)(Muri et al., 2018)(Duan et al., 2018). This is illustrated in Figure 4.38 for temperature and precipitation change relative to a high-CO_2 world for scenarios of CO_2 reduction, solar irradiance reduction, SAI, and MCB. The pattern differences for different methods are much larger for precipitation than for temperature. The pattern of climate change resulting from SRM is also different from that resulting from CO_2 reduction (Figure 4.38). It is *virtually certain* that SRM approaches would not be able to precisely offset the GHG-induced anthropogenic climate change at global and regional scales.

Because of different sensitivity of precipitation change to CO_2 and solar forcings (Myhre et al., 2017), if shortwave-based SRM is used to fully offset GHG-induced global mean warming, there would be a overcompensation of GHG-induced increase in global mean precipitation (Kravitz et al., 2013a; Tilmes et al., 2013; Irvine et al., 2016). Further, regional SRM approaches such as aerosol injections into the Arctic stratosphere are *likely* to remotely influence on tropical monsoon precipitation by shifting the mean position of ITCZ (Nalam et al., 2018). However, the shift could be avoided by simultaneously cooling the southern hemisphere (MacCracken et al., 2013; Kravitz et al., 2016; Nalam et al., 2018). The SRM response of precipitation minus evapotranspiration (P–E) is found to be smaller than that of precipitation because of reduction in both precipitation and evapotranspiration (Tilmes et al., 2013; Nalam et al., 2018; Irvine et al., 2019). Thus, global mean soil moisture could be effectively maintained, though with significant regional variability (Cheng et al., 2019).

The Geoengineering Large Ensemble Project (GLENS) has investigated achieving multiple climate policy goals by adjusting the rate of stratospheric SO_2 injection at four different latitudes. GSAT, the inter-hemispheric temperature difference, and the equator-to-pole temperature gradient could be maintained simultaneously at the year-2020 level under RCP 8.5 (Tilmes et al., 2018a). The possibility of using SAI to simultaneously stabilize non-temperature metrics such as tropical precipitation and Arctic sea-ice extent is also explored (Lee et al., 2020). Furthermore, the potential of achieving multiple climate policy goals by combining two SRM approaches is also examined in a few modelling studies, with *low confidence* in the

ACCEPTED VERSION SUBJECT TO FINAL EDITS

outcome of combining various approaches and the related climate response (Boucher et al., 2017; Cao et al., 2017).

[START FIGURE 4.38 HERE]

Figure 4.38: Multi-model response per degree global mean cooling in temperature and precipitation in response to CO_2 forcing and SRM forcing. Top row shows the response to a CO_2 decrease, calculated as the difference between pre-industrial control simulation and abrupt 4 • CO_2 simulations where the CO_2 concentration is quadrupled abruptly from the pre-industrial level (11-model average); second row shows the response to a globally uniform solar reduction, calculated as the difference between GeoMIP experiment G1 and abrupt 4 • CO_2 (11-model average); third row shows the response to stratospheric sulphate aerosol injection, calculated as the difference between GeoMIP experiment G4 (a continuous injection of 5Tg SO_2 per year at one point on the equator into the lower stratosphere against the RCP4.5 background scenario) and RCP4.5 (6-model average); and bottom row shows the response to marine cloud brightening, calculated as the difference between GeoMIP experiment G4cdnc (increase cloud droplet concentration number in marine low cloud by 50% over the global ocean against RCP4.5 background scenario) and RCP4.5 (8-model average). All differences (average of years 11–50 of simulation) are normalized by the global mean cooling in each scenario, averaged over years 11–50. Diagonal lines represent regions where fewer than 80% of the models agree on the sign of change. The values of correlation represent the spatial correlation of each SRM-induced temperature and precipitation change pattern with the pattern of change caused by a reduction of atmospheric CO_2. RMS (root mean square) is calculated based on the fields shown in the maps (normalized by global mean cooling). Further details on data sources and processing are available in the chapter data table (Table 4.SM.1).

[END FIGURE 4.38 HERE]

Stratospheric aerosol injection (SAI)

Most research has focused on SIA, the injection of sulphate particles or its precursor gases such as SO_2, which would then be oxidized to H_2SO_4. Injection of other types of aerosol particles, such as calcite ($CaCO_3$), titanium dioxide (TiO_2), aluminium oxide (Al_2O_3), and engineered nanoparticles has also been proposed (Keith, 2010)(Ferraro et al., 2011)(Pope et al., 2012)(Keith et al., 2016)(Jones et al., 2016a)(Weisenstein et al., 2015), but are much less studied compared to sulphate injection. The natural analogue for sulphate aerosol injection is major volcanic eruptions (see Cross-Chapter Box 4.1), While volcanic eruptions are not perfect analogues for SAI (Robock et al., 2013; Plazzotta et al., 2018a; Duan et al., 2019), studies on climate impacts of past volcanic eruptions can inform on the potential impact of stratospheric sulphate injection. For example, emergent constraints (see Chapter 1 and 5) that relate the climate system response to volcanic eruptions can be used to reduce uncertainty of the land surface temperature response to SAI (Plazzotta et al., 2018b).

The cooling potential of SAI using sulphate aerosols depends on many factors (Visioni et al., 2017) including the amount of injection (Niemeier and Timmreck, 2015), aerosol microphysics (Krishnamohan et al., 2020), the spatial and temporal pattern of injection (Tilmes et al., 2017), response of stratospheric dynamics and chemistry (Richter Jadwiga et al., 2018), and aerosol effect on cirrus clouds (Visioni et al., 2018). A negative radiative forcing of a few W m^{-2} (ranging from 1 to 8 W m^{-2}) could be achieved depending on the amount and location of SO_2 injected into the stratosphere (Pitari et al., 2014)(Aquila et al., 2014)(Niemeier and Timmreck, 2015)(Kleinschmitt et al., 2018a)(Kleinschmitt et al., 2018a)(Kravitz et al., 2017)(Tilmes et al., 2018a). The simulated efficacy of SAI by emission of SO_2 (radiative forcing per mass of injection rate) generally decreases with the increase in injection rate because of the growth of larger particles (about 0.5 microns) through condensation and coagulation reducing the mass scattering efficiency (Niemeier and Timmreck, 2015; Kleinschmitt et al., 2018b). However, efficacy changes little for total injection rate up to about 25 Tg Syr^{-1} when SO_2 is injected at multiple locations simultaneously (Kravitz et al., 2017)(Tilmes et al., 2018a). Differences in model representation of aerosol microphysics, evolution of particle size, stratospheric dynamics and chemistry, and aerosol microphysics-radiation-circulation interactions all contribute to the uncertainty in simulated cooling efficiency of SAI. Compared to sulphate aerosols, injection of non-sulphate particles would result in different cooling efficacy, but understanding is limited (Weisenstein

ACCEPTED VERSION SUBJECT TO FINAL EDITS

et al., 2015)(Pope et al., 2012)(Jones et al., 2016a).

Earlier modelling studies focused on the effect of equatorial sulphate injection that tends to overcool the tropics and undercool the poles. Compared to equatorial injection, off-equatorial injection at multiple locations shows a closer resemblance to the baseline climate in many aspects, including temperature, precipitation, and sea ice coverage (Kravitz et al., 2019). However, significant regional and seasonal residual and overcompensating climate change is reported, including regional shifts in precipitation, continued warming of polar oceans, and shifts in the seasonal cycle of snow depth and sea ice cover (Simpson et al., 2019a)(Fasullo et al., 2018)(Jiang et al., 2019). By appropriately adjusting the amount, latitude, altitude, and timing of the aerosol injection, modelling studies suggest that SAI is conceptually able to achieve some desired combination of radiative forcing and climate response (*medium confidence*) (Dai et al., 2018)(MacMartin et al., 2017)(Visioni et al., 2020b)(Lee et al., 2020).

There is large uncertainty in the stratospheric response to SAI, and the change in stratospheric dynamics and chemistry would depend on the amount, size, type, location, and timing of injection. There is *high confidence* that aerosol-induced stratospheric heating will play an important role in surface climate change (Simpson et al., 2019a) by altering the effective radiative forcing (Krishnamohan et al., 2019), lower stratosphere stability (Ferraro and Griffiths, 2016), quasi-biennial oscillation (QBO) (Aquila et al., 2014) (Niemeier and Schmidt, 2017)(Kleinschmitt et al., 2018a), polar vortexes (Visioni et al., 2020a), and North Atlantic Oscillation (Jones et al., 2021). Model simulations indicate stronger polar jets and weaker storm tracks and a poleward shift of the tropospheric mid-latitude jets in response to stratospheric sulphate injections in the tropics (Ferraro et al., 2015)(Richter Jadwiga et al., 2018), as the meridional temperature gradient is increased in the lower stratosphere by the aerosol-induced heating. The aerosol-induced warming would also offset some of the GHG-induced stratospheric cooling. Compared to equatorial injection, off-equatorial injection is *likely* to result in reduced change in stratospheric heating, circulation, and QBO (Richter Jadwiga et al., 2018)(Kravitz et al., 2019). Stratospheric ozone response to sulphate injection is uncertain depending on the amount, altitude, and location of injection (WMO, 2018). It is *likely* that sulphate injection would cause a reduction in polar column ozone concentration and delay the recovery of Antarctic ozone hole (Pitari et al., 2014)(Richter Jadwiga et al., 2018)(Tilmes et al., 2018b), which would have implications for UV radiation and surface ozone (Pitari et al., 2014)(Richter Jadwiga et al., 2018)(Tilmes et al., 2018b)(Xia et al., 2017). Injection of non-sulphate aerosols is *likely* to result in less stratospheric heating and ozone loss (Keith et al., 2016)(Weisenstein et al., 2015)(Pope et al., 2012). One side effect of SAI is increased sulphate deposition at surface. A recent modelling study indicates that to maintain global temperature at 2020 levels under RCP 8.5, increased sulphate deposition from stratospheric sulphate injection could be globally balanced by the projected decrease in tropospheric anthropogenic SO_2 emission, but the spatial distribution of sulphate deposition would move from low to high latitudes (Visioni et al., 2020c).

Marine cloud brightening (MCB)

MCB involves injecting small aerosols such as sea salt into the base of marine stratocumulus clouds where the aerosols act as cloud condensation nuclei (CCN). In the absence of other changes, an increase in CCN would produce higher cloud droplet number concentration with reduced droplet sizes, increasing cloud albedo. Increased droplet concentration may also increase cloud water content and optical thickness, but recent studies suggest that liquid water path response to anthropogenic aerosols is weak due to the competing effects of suppressed precipitation and enhanced cloud water evaporation (Toll et al., 2019). An analogue for MCB are reflective, persistent 'ship tracks' observed after the passage of a sea-going vessel emitting combustion aerosols into susceptible clouds (Chen et al., 2012) (Christensen and Stephens, 2011) (Gryspeerdt et al., 2019). A recent study (Diamond et al., 2020) found a substantial increase in cloud reflectivity from shipping in southeast Atlantic basin, suggesting that a regional-scale test of MCB in stratocumulus-dominated regions could be successful.

Modelling studies suggest that MCB has the potential to achieve a negative forcing of about 1 to 5 W m^{-2}, depending on the deployment area and strategies of cloud seeding (Partanen et al., 2012) (Stjern et al., 2018)(Alterskjær et al., 2013) (Ahlm et al., 2017) (Hill and Ming, 2012). Regional applications of MCB has also been suggested for offsetting severe impacts from tropical cyclones whose genesis is associated with

ACCEPTED VERSION SUBJECT TO FINAL EDITS

higher SST (MacCracken, 2016) (Latham et al., 2014) and for protecting coral reefs from higher SST (Latham et al., 2013). However, such regional approaches also involve large uncertainties in the magnitude of the responses and consequences.

Several modelling studies suggest that the direct scattering effect by injected particles might also play an important role in the cooling effect of MCB, but the relative contribution of aerosol–cloud and aerosol–cloud–radiation effect is uncertain (Partanen et al., 2012) (Ahlm et al., 2017) (Kravitz et al., 2013b). Relative to the high-GHG climate, it is *likely* that MCB would increase precipitation over tropical land due to the inhomogeneous forcing pattern of MCB over ocean and land (*medium confidence*) (Alterskjær et al., 2013) (Ahlm et al., 2017)(Stjern et al., 2018) (Niemeier et al., 2013) (Muri et al., 2018) (Bala et al., 2011). Because of the high level of uncertainty associated with cloud microphysics and aerosol–cloud–radiation interaction (See also Chapter 7, Section 7.3), the climate response to MCB is as uncertain. Results from global climate models are subject to large uncertainty because of different treatment of cloud microphysics and inadequate representation of sub-grid aerosol and cloud processes (Stjern et al., 2018) (Stuart et al., 2013) (Alterskjær and Kristjánsson, 2013) (Connolly et al., 2014). Sea salt deposition over land (Muri et al., 2015) and the effect of sea salt emission on atmospheric chemistry (Horowitz et al., 2020) are some of the potential side effects of MCB.

Cirrus Cloud Thinning (CCT)

Cirrus clouds trap more outgoing thermal radiation than they reflect incoming solar radiation and thus have an overall warming effect on the climate system (Mitchell and Finnegan, 2009). The aim of CCT is to reduce cirrus cloud optical depth by increasing the heterogeneous nucleation via seeding cirrus clouds with an optimal concentration of ice nucleating particles, which might cause larger ice crystals and rapid fallout, resulting in reduced lifetime and coverage of cirrus clouds (Muri et al., 2014), (Gasparini et al., 2017; Lohmann and Gasparini, 2017; Gruber et al., 2019a). CCT aims to achieve the opposite effect of contrails that increase cirrus cover and cause a small positive ERF (Chapter 7, Section 7.3). A high-resolution modelling study of CCT over a limited area of the Arctic suggested that cirrus seeding causes a decrease in ice crystal number concentration and a reduction in mixed-phase cloud cover, both of which cause a cooling effect (Gruber et al., 2019b).

Under present-day climate, cirrus clouds exerts a net positive radiative forcing of about 5 W m^{-2} (Gasparini and Lohmann, 2016)(Hong et al., 2016), indicating a maximum cooling potential of the same magnitude if all cirrus cloud were removed from the climate system. However, modelling results show a much smaller cooling effect of CCT. For the optimal ice nuclei seeding concentration and globally non-uniform seeding strategy, a net negative cloud radiative forcing of about 1 to 2 W m^{-2} is achieved (Storelvmo and Herger, 2014) (Gasparini et al., 2020). A few studies find that no seeding strategy could achieve a significant cooling effect, owing to complex microphysical mechanisms limiting robust climate responses to cirrus seeding (Penner et al., 2015; Gasparini and Lohmann, 2016). A higher than optimal concentration of ice nucleating particles could also result in over-seeding that increases rather than decreases cirrus optical thickness (Storelvmo et al., 2013) (Gasparini and Lohmann, 2016). Thus, there is *low confidence* in the cooling effect of CCT, due to limited understanding of cirrus microphysics, its interaction with aerosols, and the complexity of seeding strategy.

Relative to the high-GHG climate and for the same amount of global cooling, CCT is simulated to cause an increase in global precipitation compared to shortwave-based SRM options such as SAI and MCB (Muri et al., 2018) (Duan et al., 2018) because of the opposing effects of CCT and increased CO_2 on outgoing longwave radiation (Kristjánsson et al., 2015) (Jackson et al., 2016). Combining SAI and CCT has suggested that GHG-induced changes in global mean temperature and precipitation can be simultaneously offset (Cao et al., 2017), but there is *low confidence* in the applicability of this result to the real world owing to the large uncertainty in simulating aerosol forcing and the complex cirrus microphysical processes.

Surface-based albedo modification

Surface-based albedo modification could, in principle, achieve a negative radiative forcing of a few W m^{-2} by enhancing the albedo of the ocean surface (Kravitz et al., 2018)(Gabriel et al., 2017). However, the technology does not exist today to increase ocean albedo at large scale. An increase in crop albedo or roof

ACCEPTED VERSION SUBJECT TO FINAL EDITS

albedo in urban areas could help to reduce warming in densely populated and important agricultural regions, but the effect would be limited to local scales and ineffective at counteracting global warming (Crook et al., 2015a) (Zhang et al., 2016). Large changes in desert albedo could in principle result in substantial global cooling, but would severely alter the hydrological cycle (Crook et al., 2015a).

In addition to above-mentioned SRM methods, a number of local intervention methods have been proposed to limit the loss of cryosphere, such as applying reflective materials over sea ice (Field et al., 2018), pumping seawater on top of the ice surface (Desch et al., 2017) (Zampieri and Goessling, 2019), depositing massive amount of snow over ice sheets (Feldmann et al., 2019), and blocking warm seawater from reaching glaciers (Moore et al., 2018a). The stabilization of ice sheets through local intervention methods would reduce sea level commitment (Section 9.6.3.5). However, these methods are subject to large uncertainty concerning their feasibility and effectiveness, and their effects would be largely localized.

Detectability of climate response to SRM

Internal variability could mask the response to SRM-related forcing in the near term (see also Section 4.6.3.1). A detection of the global scale climate system response to stratospheric sulphate aerosol injection will *likely* require a forcing of the size produced by the 1991 Mount Pinatubo eruption (Robock et al., 2010). In model simulations of where 5 Tg SO_2 is injected into the stratosphere continuously (roughly one fourth of the 1991 Pinatubo eruption per year) under RCP 4.5, it is shown that, relative to the high-GHG world without SRM, the effect of SRM on global temperature and precipitation is detectable after one to two decades (Bürger and Cubasch, 2015; Lo et al., 2016) which is similar to the timescale for the emergence of GSAT trends due to strong mitigation (Section 4.6.3.1). The detection time is sensitive to detection methods and filtering techniques (Lo et al. 2016). An analysis using GLENS simulation (MacMartin et al., 2019) compares response in temperature, precipitation, and precipitation minus evapotranspiration (P-E) between a climate state with GHG-induced 1.5° C global mean temperature change and that with the same global mean temperature but under RCP4.5 emissions and a limited deployment of SO_2 injection. It is found that at grid-scale, difference in climate response between these two climate states are not detectable by the end of this century. However, for higher emission scenarios of the RCP8.5 and correspondingly larger SRM deployment for maintaining the same global mean temperature change of 1.5°C, the regional differences are detectable before the end of the century. In addition to surface temperature and precipitation, observations of aerosol burden and temperature in the stratosphere via the deployment of stratospheric aerosol observing system might facilitate the detection of climate response to SAI.

Climate response to termination of SRM

A hypothetical, sudden and sustained termination of SRM in a world with high GHG concentrations has been simulated to cause climate rebound effects such as rapid increase in global temperature, precipitation, and sea level, and rapid reduction in sea-ice area (Crook et al., 2015; Jones et al., 2013; McCusker et al., 2014; Muri et al., 2018). Model simulations also show reduced precipitation over land areas in the first few years following termination, indicating general drying that would exacerbate the effects of rapid warming (McCusker et al., 2014). A sudden and sustained termination of SRM is also expected to weaken carbon sinks, accelerating atmospheric CO_2 accumulation and warming (Tjiputra et al., 2016) (Muri et al., 2018) (Plazzotta et al., 2019). A gradual phase-out of SRM combined with mitigation and CDR could reduce the large warming rates from sudden SRM termination (MacMartin et al., 2014) (Keith and MacMartin, 2015; Tilmes et al., 2016), though this would be limited by how rapidly emission reductions can be scaled up (Ekholm and Korhonen, 2016).

Synthesis of the climate response to SRM

Modelling studies have consistently shown that SRM has the potential to offset some effect of increasing GHGs on global and regional climate (*high confidence*), but there would be substantial residual or overcompensating climate change at the regional scale and seasonal timescale (*high confidence*). Large uncertainties associated with aerosol–cloud–radiation interactions persist in our understanding of climate response to aerosol-based SRM options. For the same amount of global mean cooling, different SRM options would cause different patterns of climate change (*medium confidence*). Modelling studies suggest that it is conceptually possible to achieve multiple climate policy goals by optimally designed SRM strategies.

ACCEPTED VERSION SUBJECT TO FINAL EDITS

The effect of SRM options on global temperature and precipitation response would detectable after one or two decades, which is similar to the timescale for the detection of strong mitigation. There is *high confidence* that a sudden and sustained termination of a high level of SRM against a high-GHG background would cause a rapid increase in temperature at a rate that far exceeds that projected for climate change without SRM. However, a gradual phase-out of SRM combined with mitigation and CDR would *more likely than not* avoid large rates of warming**.**

4.7 Climate Change Beyond 2100

This section assesses changes in climate beyond 2100. An advance since AR5 is the availability of ESM results for scenarios beyond 2100 and for much longer stabilisation simulations compared with analysis predominantly based on Earth system models of intermediate complexity (EMICs) at the time of AR5 (e.g. Eby et al., 2013; Zickfeld et al., 2013). Long-term commitment of sea-level rise due to thermal expansion and ice-sheet loss is assessed in Chapter 9 (9.6.3.5; figure 9.0). Here we assess projections of GSAT, global precipitation, and Arctic sea ice. Uncertainties relating to potential long-term changes in AMOC are treated in 9.2.3.1.

On multi-century timescales it is common to explore changes that are due to long-term commitment.Here we differentiate between:

- *Committed emissions due to infrastructure*. Infrastructure that causes greenhouse gas emissions cannot be changed straight away leading to a commitment from existing infrastructure that some emissions will continue for a number of years into the future (Davis and Socolow, 2014; Smith et al., 2019a). Further consideration of this aspect of commitment will be assessed by WGIII.
- *Climate response to constant emissions*. Some of the scenario extensions beyond 2100 make assumptions about constant emissions (either positive or negative). Section 4.7.1 will assess changes in climate under scenario extensions beyond 2100.
- *Committed climate change to constant atmospheric composition*. There is widespread literature on how the climate continues to change after stabilisation of radiative forcing. This includes diagnosing the long-term climate response to a doubling of CO_2 (ECS, Chapter 7). Since AR5, more GCMs have run stabilised forcing simulations for many centuries allowing new insights into their very long-term behaviour (Section 7.4.3).
- *Committed response to zero emissions*. How climate would continue to evolve if all emissions ceased. SR1.5 assessed changes in climate if emissions of all greenhouse gases and aerosols ceased. Section 4.7.2 assesses new results considering cessation of CO_2-only emissions which forms a significant term in calculating remaining carbon budgets.
- *Irreversibility*. Some changes do not revert if the forcing is removed, leaving a committed change to the system. Section 4.7.2 assesses changes in the Earth system which may be irreversible.
- *Abrupt changes*. If a tipping point in the climate system is passed, then some elements may continue to respond if the forcing which caused them is removed. Section 4.7.2 assesses the potential for abrupt changes in the Earth system.

4.7.1 Commitment and Climate Change Beyond 2100

4.7.1.1 Climate change following zero emissions

The zero emissions commitment (ZEC) is the the climate change commitment that would result, in terms of projected GSAT, from setting carbon dioxide (CO_2) emissions to zero. It is determined by both inertia in physical climate system components (ocean, cryosphere, land surface) and carbon cycle inertia (see Annex VII). In its widest sense it refers to emissions of all compounds including greenhouses gases, aerosols and their pre-cursors. A specific sub-category of zero emissions commitment is the zero CO_2 emissions commitment, which refers to the climate system response to a cessation of anthropogenic CO_2 emissions

ACCEPTED VERSION SUBJECT TO FINAL EDITS

excluding the impact of non-CO_2 forcers. Assessment of remaining carbon budgets requires an assessment of zero CO_2 emissions commitment as well as of the transient climate response to cumulative carbon emissions (TCRE, Chapter 5 Section 5.5.2).

There is an offset of continued warming following cessation of emissions by continued CO_2 removal by natural sinks (e.g. Joos et al., 2013; Matthews and Caldeira, 2008; Solomon et al., 2009; Ricke and Caldeira, 2014) (*high confidence*). Some models continue warming by up to 0.5°C after emissions cease at 2°C of warming (Frölicher & Paynter, 2015; Frölicher et al., 2014; Williams et al., 2017), while others simulate little to no additional warming (Nohara et al., 2015). In SR1.5, the available evidence indicated that past CO_2 emissions do not commit to substantial further warming (Allen et al., 2018). A ZEC close to zero was thus applied for the computation of the remaining carbon budget for the (Rogelj et al., 2018b). However, the available literature consisted of simulations from a small number of models using a variety of experimental designs, with some simulations showing a complex evolution of temperature following cessation of emissions (e.g., Frölicher & Paynter, 2015; Frölicher et al., 2014).

Here we draw on new simulations to provide an assessment of ZEC using multiple ESMs (Jones et al., 2019b) and EMICs (MacDougall et al., 2020). Figure 4.39 shows results from 20 models that simulate the evolution of CO_2 and the GSAT response following cessation of CO_2 emissions for an experiment where 1000 PgC is emitted during a 1% per year CO_2 increase. All simulations show a strong reduction in atmospheric CO_2 concentration following cessation of CO_2 emissions in agreement with previous studies and basic theory that natural carbon sinks will persist. Therefore, there is *very high confidence* that atmospheric CO_2 concentrations would decline for decades if CO_2 emissions cease. Temperature evolution in the 100 years following cessation of emissions varies by model and across timescales, with some models showing declining temperature, others having ZEC close to zero, and others showing continued warming following cessation of emissions (Figure 4.39). The GSAT response depends on the balance of carbon sinks and ocean heat uptake (MacDougall et al., 2020). The 20-year average GSAT change 50 years after the cessation of emissions (ZEC_{50}) is summarised in Table 4.8. The mean value of ZEC_{50} is –0.079°C, with 5–95% range –0.34 to 0.28 °C. There is no strong relationship between ZEC_{50} and modelled climate sensitivity (neither ECS nor TCR; MacDougall et al., 2020). It is therefore *likely* that the absolute magnitude of ZEC_{50} is less than 0.3 °C, but we assess *low confidence* in the sign of ZEC on 50-year timescales. This is small compared with natural variability in GSAT.

[START FIGURE 4.39 HERE]

Figure 4.39: Zero Emissions Commitment (ZEC). Changes in (a) atmospheric CO_2 concentration and (b) evolution of GSAT following cessation of CO_2 emissions branched from the 1% per year experiment after emission of 1000 PgC (Jones et al., 2019a). ZEC is the temperature anomaly relative to the estimated temperature at the year of cessation. ZEC_{50} is the 20-year mean GSAT change centred on 50 years after the time of cessation (see Table 4.8) – this period is marked with the vertical dotted lines. Multi-model mean is shown as thick black line, individual model simulations are in grey. Further details on data sources and processing are available in the chapter data table (Table 4.SM.1).

[END FIGURE 4.39 HERE]

[START TABLE 4.8 HERE]

Table 4.8: The 20-year average GSAT change 50 years after the cessation of emission (ZEC_{50}). Displayed are ZEC_{50} estimated from eleven ESMs (top) and nine EMICs (bottom).

MODEL	ZEC_{50} (°C)
ACCESS-ESM1.5	0.01
CANESM5	-0.14
CESM2	-0.31
CNRM-ESM2-1	0.06
GFDL-ESM2M	-0.27

ACCEPTED VERSION SUBJECT TO FINAL EDITS

GFDL-ESM4	-0.21
GISS-E2-1-G	-0.15
MIROC-ES2L	-0.08
MPI-ESM1.2-LR	-0.27
NORESM2-LM	-0.33
UKESM1-0-LL	0.28
BERN3D-LPX	0.01
DCESS1.0	0.06
CLIMBER-2	-0.07
IAPRAS	0.28
LOVECLIM 1.2	-0.04
MESM	0.01
MIROC-LITE	-0.06
PLASM-GENIE	-0.36
UVIC ESCM 2.10	0.03

[END TABLE 4.8 HERE]

4.7.1.2 Change in Global Climate Indices Beyond 2100

This subsection assesses changes in global climate indices out to 2300 using extensions of the SSP scenarios (Meinshausen et al., 2020) and literature based on extensions to the RCP scenarios from CMIP5 (Meinshausen et al., 2011), which differ from the SSPs despite similar labelling of global radiative forcing levels (Section 4.6.2). Meinshausen et al. (2020) describe the extensions to the SSP scenarios, which differ slightly from the ScenarioMIP documentation (O'Neill et al., 2016). A simplified approach across scenarios reduces emissions such that after 2100, land use CO_2 emissions are reduced to zero by 2150; any net negative fossil CO_2 emissions are reduced to zero by 2200, and positive fossil CO_2 emissions are reduced to zero by 2250. Non-CO_2 fossil fuel emissions are also reduced to zero by 2250 while land-use-related non-CO_2 emissions are held constant at 2100 levels. The extensions are created up to the year 2500, but ESM simulations have only been requested, as part of the CMIP6 protocol, to run to 2300. As a result, unlike the RCP8.5 extension, SSP5-8.5 sees a decline in CO_2 concentration after 2250, but the radiative forcing level is similar, reaching approximately 12 Wm^{-2} during most of the extension. Both SSP1-2.6 and SSP5-3.4-OS decrease radiative forcing after 2100. SSP5-3.4-OS is designed to return to the same level of forcing as SSP1-2.6 during the first half of the 22nd century. Because relatively few CMIP6 ESMs have submitted results beyond 2100, GSAT projections using the MAGICC7 emulator (see Cross-Chapter Box 7.1) are also shown here.

Changes in climate at 2300 have impacts and commitments beyond this timeframe (*high confidence*). Sea-level rise may exceed 2 m on millennial timescales even when warming is limited to 1.5–2°C, and tens of meters for higher warming levels (Chapter 9, Section 9.6.3.5, Table 9.10). Randerson et al. (2015) showed increasing importance on carbon cycle feedbacks of slow ocean processes, Mahowald et al. (2017) showed the long-lasting legacy of land-use effects and Moore et al., (2018) show how changes in Southern Ocean winds affect nutrients and marine productivity well beyond 2300. Clark et al. (2016) show that physical and biogeochemical impacts of 21st century emissions have a potential committed legacy of at least 10,000 years.

[START FIGURE 4.40 HERE]

Figure 4.40: Simulated climate changes up to 2300 under the extended SSP scenarios. Displayed are (a) projected GSAT change, relative to 1850–1900, from CMIP6 models (individual lines) and MAGICC7 (shaded plumes), (b) as (a) but zoomed in to show low-emission scenarios, (c) global land precipitation change, and (d) September Arctic sea-ice area. Further details on data sources and processing are available in the chapter data table (Table 4.SM.1).

[END FIGURE 4.40 HERE]

ACCEPTED VERSION SUBJECT TO FINAL EDITS

4.7.1.2.1 Global Surface Air Temperature

Both CMIP6 and CMIP5 results show that global temperature beyond 2100 is strongly dependent on scenario, and the difference in GSAT projections between high- and low-emission scenarios continues to increase (*high confidence*). Under the extended RCP2.6 (Caesar et al., 2013) and SSP1-2.6 scenarios, where CO_2 concentration and radiative forcing continue to decline beyond 2100, GSAT stabilises during the 21st century before decreasing and remaining below 2°C until 2300 except in some of the very high climate-sensitivity ESMs, which project GSAT to stay above 2°C by 2300 (Figure 4.40). Under RCP8.5, regional temperature changes above 20°C have been reported in multiple models over high-latitude land areas (Caesar et al., 2013; Randerson et al., 2015b). Non-CO_2 forcing and feedbacks remain important by 2300 (*high confidence*). Randerson et al. (2015) found that 1.6°C of warming by 2300 came from non-CO_2 forcing alone in RCP8.5, and Rind et al. (2018) show that regional forcing from aerosols can have notable effects on ocean circulation on centennial timescales. High latitude warming led to longer growing seasons and increased vegetation growth in the CESM1 model (Liptak et al., 2017), and Burke et al. (2017) found that carbon release from permafrost areas susceptible to this warming may amplify future climate change by up to 17% by 2300.

Too few CMIP6 models performed the extension simulations to allow a robust assessment of GSAT projection, and some of those which did had higher than average climate sensitivity values. Therefore, we base our assessment of GSAT projections (Table 4.9) on the MAGICC7 emulator calibrated against assessed GSAT to 2100 (Section 4.3.4, Cross-Chapter Box 7.1). Because the emulator approach has not been evaluated in depth up to 2300 in the same way as it has up to 2100 (Cross-Chapter Box 7.1) we account for possible additional uncertainty by assessing the 5–95% range from MAGICC as *likely* instead of *very likely*. It is therefore *likely* that GSAT will exceed 2°C above that of the period 1850–1900 at the year 2300 in the extended SSP scenarios SSP2-4.5, SSP3-7.0 and SSP5-8.5 (Figure 4.40). For SSP1-2.6 and SSP1-1.9, mean warming at 2300 is 1.5°C and 0.9°C respectively. GSAT differences between SSP5-3.4-overshoot and SSP1-2.6 peak during the 21st century but decline to less than about 0.25°C after 2150 (*medium confidence*).

To place the temperature projections for the end of the 23rd century into the context of paleo temperatures, GSAT under SSP2-4.5 (2.3°C–4.6°C) has not been experienced since the Mid Pliocene, about 3 million years ago. GSAT projected for the end of the 23rd century under SSP5-8.5 (6.6°C–14.1°C) overlaps with the range estimated for the Miocene Climatic Optimum (5-10°C) and Early Eocene Climatic Optimum (10°C–18°C), about 15 and 50 million years ago, respectively (*medium confidence;* Chapter 2).

[START TABLE 4.9 HERE]

Table 4.9: Change of global surface air temperature at 2300. Displayed are the median and 5–95% range of GSAT change at 2300 relative to 1850–1900 for the six scenarios used with MAGICC7.

Scenario	Median (°C)	5–95% range (°C)
SSP5-8.5	9.6	6.6–14.1
SSP3-7.0	8.2	5.7–11.8
SSP2-4.5	3.3	2.3–4.6
SSP5-3.4-OS	1.6	1.1–2.2
SSP1-2.6	1.5	1.0–2.2
SSP1-1.9	0.9	0.6– .4

[END TABLE 4.9 HERE]

4.7.1.2.2 Global Land Precipitation

Global land precipitation will continue to increase in line with GSAT under high emission scenarios (*medium confidence*). Precipitation changes over land show larger variability and a less clear signal than global total precipitation. Caesar et al. (2013) showed that under the CMIP5 extension simulations, HadGEM2-ES projected global land precipitation to remain roughly the same in RCP2.6, to increase by

ACCEPTED VERSION SUBJECT TO FINAL EDITS

about 4% in RCP4.5 and to increase by about 7% in RCP8.5. Their results showed global precipitation increasing linearly with temperature while radiative forcing increases, but then more quickly if forcing is stabilised or reduced. This backs up findings of an intensification of the hydrological cycle following CO_2 decrease which has been attributed to a build-up of ocean heat (Wu et al., 2010), and to a fast atmospheric adjustment to CO_2 radiative forcing (Cao et al., 2011a). Figure 4.40 shows that global land precipitation increases in CMIP6 models until 2300 for SSP5-8.5 but stabilises in SSP1-2.6 and SSP5-3.4-OS. SSP1-2.6 and SSP5-3.4-OS are not distinguishable in behaviour of projected global land precipitation after 2100.

4.7.1.2.3 Arctic Sea Ice

Chapter 9 assesses with *high confidence* that on decadal and longer timescales, Arctic summer sea-ice area will remain highly correlated with global mean temperature until the summer sea ice has vanished (Section 9.3.1.1). This means that Arctic sea ice will continue to decline in scenarios of continued warming but will begin to recover in scenarios where GSAT begins to decrease. Under the CMIP5 extension simulations, minimum (September) Arctic sea-ice area began to recover for most models under RCP2.6 out to 2300, while RCP4.5 and RCP8.5 extensions became ice-free in September (Hezel et al., 2014; Bathiany et al., 2016). They also found increasingly strong winter responses under continued warming such that under the RCP8.5 extension, the Arctic became ice-free nearly year-round by 2300. Consistent with the assessment in Section 9.3.1.1 that Arctic sea-ice area is correlated with GSAT, CMIP6 projections to 2300 show partial sea ice recovery by 2300 in SSP1-2.6 in line with GSAT (Figure 4.40), with one model (MRI-ESM2-0) showing near complete recovery to present-day values. SSP1-2.6 and SSP5-3.4-OS are not distinguishable in behaviour of Arctic sea-ice in these models after 2100. SSP5-8.5 remains ice-free in September up to 2300.

4.7.2 Potential for Abrupt and Irreversible Climate Change

Similar to AR5 and SROCC, AR6 defines an abrupt climate change as a large-scale abrupt change in the climate system that takes place over a few decades or less, persists (or is anticipated to persist) for at least a few decades and causes substantial impacts in human and/or natural systems (Annex VII: Glossary). Further, AR6 considers such a perturbed state of a dynamical system as irreversible on a given timescale, if the recovery timescale from this state due to natural processes takes substantially longer than the timescale of interest (Annex VII: Glossary). The AR6 adopts the related definition of a tipping point as a critical threshold beyond which a system reorganizes, often abruptly and/or irreversibly, and a tipping element as a component of the Earth system that is susceptible to a tipping point (Annex VII: Glossary). Tipping points may involve global or regional climate changes from one stable state to another stable state or to changes that occur faster than the rate of change of forcing (Alley et al., 2003) and include shifts from one equilibrium state to another and other responses of the climate system to external forcing (see Section 1.2.4.2 in Chapter 1). While reversibility has been defined alternatively in the literature with respect to the response specifically to idealized CO_2 forcing and generally GSAT change, AR6 considers both definitions synonymous, because it has been widely demonstrated that the GSAT change is reversible in models with respect to CO_2 with a several-year lag (Boucher et al., 2012).

Abrupt and irreversible changes in the climate system are assessed across multiple chapters in AR6. This section provides a cross-chapter synthesis of these assessments as an update to the AR5 Table 12.4 and SROCC Table 6.1. Understanding of abrupt climate change and irreversibility has advanced considerably since AR5 with many of the projected changes in proposed Tipping Elements having grown more confident (Table 4.10). Many aspects of the physical climate changes induced by GHG warming previously demonstrated to be reversible in a single model have been confirmed in multiple models (Boucher et al., 2012; Tokarska and Zickfeld, 2015) with others such as sea-level rise or terrestrial ecosystems confirmed to continue to respond on long timescales (Clark et al., 2016; Zickfeld et al., 2017; Pugh et al., 2018).

The Carbon Dioxide Removal Model Intercomparison Project (CDR-MIP) (Keller et al., 2018) comprises a set of 1% ramp-up ramp-down simulations aimed at establishing a multi-model assessment of reversibility of Earth system components. Preliminary results from CDRMIP are presented in Section 4.6.3. Results from the SSP5-3.4-Overshoot scenario and other quantities of climate change at the same CO_2 level before and

ACCEPTED VERSION SUBJECT TO FINAL EDITS

after overshoot are assessed in Section 4.6.2. Forcing reversal is followed by reversal of ocean surface and land temperature along with land and ocean precipitation, snow cover, and Arctic sea ice with a lag of a few years to decades (Table 4.10). Other tipping elements have much longer timescales of reversibility from decades to millennia. (Drijfhout et al., 2015) provided an assessment of 13 regional mechanisms of abrupt change, finding abrupt changes in sea ice, oceanic flows, land ice, and terrestrial ecosystem response, although with little consistency among the models. The potential for abrupt changes in ice sheets, the AMOC, tropical forests, and ecosystem responses to ocean acidification were also recently reviewed by (Good et al., 2018). They found that some degree of irreversible loss of the West Antarctic Ice Sheet (WAIS) may have already begun, that tropical forests are adversely affected by drought, and rapid development of aragonite undersaturation at high latitudes affecting calcifying organisms.

New since AR5 is the fundamental recognition in SRCCL and in this Report (Chapter 5) that projected changes in forests strongly depend on the human disturbance and that tropical forest dieback in the absence of disturbance is largely driven by the increased potential for drought, while that in boreal forests includes both thermal and hydrological factors (Drijfhout et al., 2015). For some proposed tipping elements, the role of seasonal change has become better understood. For example, the lack of a tipping point in the reduction of summer Arctic sea-ice area (Stroeve and Notz, 2015) has been further substantiated. The role of abrupt change at the edges (Bathiany et al., 2020) has also been clarified, as has been the importance of distinguishing summer from winter mechanisms and associated abruptness, because ice area reduces gradually in summer, but not necessarily in winter (Bathiany et al., 2016). For other tipping elements including AMOC (Section 9.2.3.1), mixed layer depth (9.2.1.3), and sea-level rise (9.6.3.5), an increase in the diversity of model structure and sensitivity to multiple factors has led to a better understanding of the complexity of the problem, with some increase in assessed uncertainty and an assessed deep uncertainty (see Annex VII: Glossary) related to projected sea-level rise with global warming levels above 3°C (Section 9.6.3.5). In still other cases such as Antarctic Sea Ice (Section 9.3.2) and Southern Ocean Meridional Overturning Circulation (MOC; Section 9.2.3.1), uncertainty remains high. Finally, it has also been postulated that models may be prone to being too stable (Valdes, 2011) based on the limitations of models as well as other lines of evidence such paleo-evidence of abrupt events (Dakos et al., 2008; Klus et al., 2018; Sime et al., 2019).

[START TABLE 4.10 HERE]

Table 4.10: Cross-chapter assessment updating AR5 and SROCC of components in the Earth system that have been proposed as susceptible to tipping points/abrupt change, irreversibility, projected 21st century change, and overall change in assessment from previous IPCC reports. Also provided are confidence levels and, in parentheses, the main section(s) of this report in which proposed tipping elements are assessed.

Earth System Component/Tipping Element	Potential Abrupt Climate Change?	Irreversibility if forcing reversed (timescales indicated)	Projected 21st century change under continued warming	Change in Assessment
Global Monsoon (4.5.1.5; 8.6)	Yes under AMOC collapse, *medium confidence*	Reversible within years to decades, *Medium confidence*	*Medium confidence* in global monsoon increase; *Medium confidence* in Asian-African strengthening and North American weakening	More lines of evidence than AR5
Tropical Forest (5.4.8; 8.6.2)	Yes, *Low confidence*	Irreversible for multi-decades, *Medium confidence*	*Medium confidence* of increasing vegetation carbon storage depending on human disturbance	More confident rates than AR5
Boreal Forest (5.4.8)	Yes, *Low confidence*	Irreversible for multi-decades, *Medium confidence*	*Medium confidence* in offsetting lower latitude dieback and poleward extension depending on human disturbance	More confident rates than AR5
Permafrost Carbon (5.4.8)	Yes, *High confidence*	Irreversible for centuries, *High confidence*	*Virtually certain* decline in frozen carbon; *Low confidence* in net carbon change	More confident rates than SROCC

ACCEPTED VERSION SUBJECT TO FINAL EDITS

Arctic Summer Sea Ice (4.3.2; 4.6.2.1; 9.3.1)	No, *high confidence*	Reversible within years to decades, *High confidence*	*Likely complete loss*	More specificity than SROCC
Arctic Winter Sea Ice (4.3.2; 9.3.1)	Yes, *High confidence*	Reversible within years to decades, *High confidence*	*High confidence* in moderate winter declines	More specificity than SROCC
Antarctic Sea Ice (9.3.2)	*Yes, Low confidence*	Unknown, *Low confidence*	*Low confidence* in moderate winter and summer declines	Improved CMIP6 simulation
Greenland Ice Sheet (9.4.1)	No, *High confidence*	Irreversible for millennia, *High confidence*	*Virtually certain* mass loss under all scenarios	More lines of evidence than SROCC
West Antarctic Ice Sheet and Shelves (9.4.2; Box 9.4)	*Yes, High confidence*	Irreversible for decades to millennia, *High confidence*	*Likely* mass loss under all scenarios; *Deep uncertainty* in projections for above 3°C	Added deep uncertainty at GWL > 3°C
Global Ocean Heat Content (4.5.2.1; 4.6.2.1; 9.2.2; CCBox 7.1)	No, *High confidence*	Irreversible for centuries, *Very high confidence*	*Very high confidence* oceans will continue to warm	Better consistency with ECS/TCR
Global Sea-Level Rise (4.6.2.1; 4.6.3.2; 9.6.3.5; Box 9.4)	Yes, *High confidence*	Irreversible for centuries, *Very high confidence*	*Very high confidence* in continued rise; *Deep uncertainty* in projections for above 3°C	Added deep uncertainty at GWL > 3°C
AMOC (4.6.3.2; 8.6.1; 9.2.3.1)	Yes, *Medium confidence*	Reversible within centuries, *High confidence*	*Very likely decline; Medium confidence of no collapse*	More lines of evidence than SROCC
Southern MOC (9.2.3.2)	Yes, *Medium confidence*	Reversible within decades to centuries, *Low confidence*	*Medium confidence* in decrease in strength	More lines of evidence than SROCC
Ocean Acidification (4.3.2.5; 5.4.2 ; 5.4.4)	Yes, *High confidence*	Reversible at surface; irreversible for centuries to millennia at depth, *Very high confidence*	*Virtually certain* to continue with increasing CO_2; Likely polar aragonite undersaturation	More lines of evidence than SROCC
Ocean Deoxygenation (5.3.3.2)	Yes, *High confidence*	Reversible at surface; irreversible for centuries to millennia at depth, *Medium confidence*	*Medium confidence* in deoxygenation rates and increased hypoxia	Improved CMIP6 simulation

[END TABLE 4.10 HERE]

4.8 Low-Likelihood High-Warming Storylines

Previous IPCC assessments have primarily assessed the projected *likely* range of changes (e.g., (Collins et al., 2013), see also BOX 1.1). The focus on the *likely* range partly results from the design of model intercomparison projects that are not targeted to systematically assess the upper and lower bounds of projections, which in principle would require a systematic sampling of structural and parametric model uncertainties. The upper and lower bounds of model projections may further be sensitive to the missing representation of processes and to deep uncertainties about aspects of the climate system (Section 1.2.3.1).

However, a comprehensive risk assessment requires taking into account also high potential levels of warming whose likelihood is low, but potential impacts on society and ecosystems are high (Xu and Ramanathan, 2017a; Sutton, 2018). Climate-related risks have been argued to increase with increasing levels of global warming even if their likelihood decreases (O'Neill et al., 2017). Thus, it has recently been argued that an assessment that is too narrowly focused on the *likely* range potentially ignores the changes in the physical climate system associated with the highest risks ((Sutton, 2018), see Section 1.4.4.1).

ACCEPTED VERSION SUBJECT TO FINAL EDITS

Given that the CMIP experiments can be considered ensembles of opportunity that are not designed for probabilistic assessments, alternative approaches such as physically plausible high-impact scenarios (Sutton, 2018) or storylines have been suggested to investigate the tail of the distribution (Lenderink et al., 2014; Zappa and Shepherd, 2017; Kjellström et al., 2018; Shepherd et al., 2018) (see Section 1.4.4). Such storylines informed by a combination of process understanding, model evidence, and paleo information can be used for risk assessment and adaptation planning to test how well adaptation strategies would cope if the impacts of climate change were more severe than suggested by the *likely* model range (see Chapter 1 Section 1.4.4). Note that by definition the lower bound of the *likely* model range (see Box 4.1) is equally likely as the upper bound. However, low-warming storylines are not specifically assessed in this section to focus on storylines associated with highest risks. This section further focuses on storylines of high and very high global warming levels along with their manifestation in global patterns of temperature and precipitation changes. However, this does not account for the largest potential changes at regional levels, which would require taking into account storylines of regional changes dependent on changes in atmospheric circulation, land-atmosphere interactions, and regional to local feedbacks.

This section adopts an approach suggested in Sutton (2018). Since changes in temperature and precipitation tend to increase with the level of warming (Section 4.6.1), low-likelihood high-warming storylines are here illustrated for a level of warming consistent with the upper bound of the assessed *very likely* range (see Section 4.3.4) and for a level of warming above the *very likely* range. ECS and TCR are the dominant sources of uncertainty in projections of future warming under moderate to strong emission scenarios (Section 7.5.7). Thus, a very high level of warming may occur if ECS and TCR are close to or above the upper bound of the assessed *very likely* range, which, to agree with historical trends, would require a strong historical aerosol cooling and/or strong SST pattern effects, combined with strong positive cloud feedback and substantial biases in paleoclimate temperature reconstructions, each of which are assessed as either *unlikely* or *very unlikely*, though not ruled out (Section 7.5.5).

For SSP1-2.6, the warming consistent with the upper bound of the assessed *very likely* range corresponds to a warming of 1.5°C in 2081–2100 relative to 1995–2014 and 2.4°C relative to 1850–1900 (Section 4.3.4), a warming well above the 2°C warming level even in SSP1-2.6. Based on different lines of evidence, Figure 4.41 illustrates by how much such a low-likelihood high-warming storyline exceeds the warming pattern consistent with the assessed best estimate GSAT warming of 0.9°C relative to 1995–2014. The first estimate (Figure 4.41, second row) is based on the assumption that the multi-model mean temperature pattern scales linearly with global mean warming. While linear scaling provides an appropriate approximation for changes in temperatures patterns at lower levels of warming (Section 4.2.4), this assumption cannot easily be tested for an extrapolation to higher levels of warming. Thus, a second estimate (Figure 4.41, third row) is based on the average of the five models that simulate a GSAT warming most consistent with the upper bound of the assessed *very likely* range (see Box 4.1 and Section 4.3.4; note some of the models share components). The two estimates for the annual mean temperature pattern for a low-likelihood high-warming storyline consistently show a warming pattern that substantially exceeds the best estimate warming pattern in most regions except around the North Atlantic and the parts of the Arctic. Pattern scaling suggests more than 50% warming above the best estimate, with 2–3°C warming over much of Eurasia and North America and more than 4°C warming relative to 1995–2014 over the Arctic (Figure 4.41c). The other approach based on five models shows less warming than the best estimate and even larger area of cooling in the North Atlantic but more warming than the best estimate over much of the tropical Pacific, Atlantic, around Antarctica and other the land regions (Figure 4.41e).

For the high-emission scenarios SSP3-7.0 and SSP5-8.5, a high-warming storyline is associated with wide-spread warming that exceeds the already high best-estimate warming by another 35–50%. For SSP5-8.5, this corresponds to a warming of 1°C–3°C in addition to the best estimate over most land regions, which implies more than 6°C relative to 1995–2014 over most extra-tropical land regions and Amazonia. Over large parts of the Arctic, annual mean temperatures increase by more than 10°C relative to 1995–2014 in such a high-warming storyline under SSP5-8.5. The two lines of evidence yield more consistent patterns for SSP5-8.5 than for SSP1-2.6, but there are substantial differences concerning whether the strongest warming above the best estimate occurs over the tropics or extratropical land regions.

ACCEPTED VERSION SUBJECT TO FINAL EDITS

While individual models project even stronger warming over extratropical land regions (Figure 4.41 bottom row), their projected GSAT warming exceeds the assessed *very likely* 5–95% range and thus correspond to an *extremely unlikely* (below 5% likelihood) storyline. While all the models consistent with such a storyline tend to overestimate the observed warming trend over the historical period (Brunner et al., 2020; Liang et al., 2020; Nijsse et al., 2020; Tokarska et al., 2020; Ribes et al., 2021), some of them show a good representation of several aspects of the present-day climate (Andrews et al., 2019; Sellar et al., 2019; Swart et al., 2019). Such a very high-warming storyline implies widespread warming of more than 1.5°C and 3°C above the best-estimate warming pattern under SSP1-2.6 and SSP5-8.5, respectively. Under SSP1-2.6, this corresponds to more than 3°C warming relative to 1995–2014 over land regions in the northern mid- to high latitudes and more than 6°C in the Arctic (Figure 4.41g). Under SSP5-8.5, such a very high-warming storyline implies more than 8°C warming over parts of Amazonia and more than 6°C over most other tropical land regions (Figure 4.41h).

[START FIGURE 4.41 HERE]

Figure 4.41: High-warming storylines for changes in annual mean temperature. (a, b) Changes in 2081–2100 relative to 1995–2014 consistent with the assessed best GSAT estimate (0.9°C and 3.5°C relative to 1995–2014 for SSP1-2.6 and SSP5-8.5, respectively). The CMIP6 multi-model mean is linearly pattern-scaled to the best GSAT estimate. (c–h) Annual mean warming above the best estimate (relative to panels a and b, respectively, note the different colour bar) in a high and very high-warming storyline for 2081–2100. (c, d) Multi-model mean warming pattern scaled to very high GSAT level corresponding to the upper bound of the assessed *very likely* range (4.8°C for SSP5-8.5 and 1.5°C for SSP1-2.6, see Section 4.3.4). (e, f) Average of five models with high GSAT warming nearest to the upper estimate of the *very likely* range (CESM2, CESM2-WACCM, CNRM-CM6-1, CNRM-CM6-1-HR, EC-Earth3 for SSP1-2.6 and ACCESS-CM2, CESM2, CESM2-WACCM, CNRM-CM6-1, CNRM-CM6-1-HRfor SSP5-8.5), (g, h) Average of four and five models, respectively (ACCESS-CM2, HadGEM3-GC31-LL, HadGEM3-GC31-MM, UKESM1-0-LL for SSP1-2.6 and CanESM5, CanESM5-CanOE, HadGEM3-GC31-LL: HadGEM3-GC31-MM, UKESM1-0-LL for SSP5-8.5) projecting very high GSAT warming exceeding the *very likely* range. Further details on data sources and processing are available in the chapter data table (Table 4.SM.1).

[END FIGURE 4.41 HERE]

High-warming storylines are *very likely* also associated with substantial changes in the hydrological cycle due to strong thermodynamic changes, which can be amplified or offset by dynamical changes (Emori and Brown, 2005; Seager et al., 2014b; Chavaillaz et al., 2016b; Kröner et al., 2017; Chen et al., 2019). Here the assessment of the hydrological cycle in high-warming storylines is limited to changes in annual mean precipitation, but changes in seasonal mean precipitation can be even stronger due to enhanced seasonality in many regions (Chapter 8, Box 8.2).

Quantifying precipitation changes associated with high-warming storylines is challenging since models show the largest changes in precipitation over different regions (Sections 4.5.1 and 4.6.1). In some areas, models project opposing signals in different seasons or a combination of decreasing mean and increasing extreme precipitation (Kendon et al., 2014; Ban et al., 2015; Giorgi et al., 2016; Pendergrass et al., 2017). Models with the most pronounced GSAT warming are not necessarily associated with the strongest precipitation response in all regions, in part due to projected changes in atmospheric dynamics (Madsen et al., 2017; Zappa and Shepherd, 2017; Li et al., 2018).

Different alternative estimates of changes in annual mean precipitation patterns consistent with high-warming levels are compared here. The first estimate (Figure 4.42b) is based on a linear pattern scaling of the multi-model mean precipitation pattern for SSP5-8.5 (Figure 4.42a) to be consistent with the upper bound of the assessed *very likely* GSAT range (see above). This estimate is reasonably consistent with the average response of the five models with GSAT warming most consistent with the upper bound of the *very likely* warming range (Figure 4.42c) except for Australia. Both estimates show about 30–40% larger changes

ACCEPTED VERSION SUBJECT TO FINAL EDITS

in annual mean precipitation than the response pattern consistent with the best GSAT estimate. In a high-warming storyline, widespread increases of more than 30% occur in many regions north of 50°N and over parts of the tropics. Around the Mediterranean and other parts of the subtropics, a high-warming storyline is associated with a reduction in annual mean precipitation of more than 30% depending on the season.

Both the multi-model mean and the pattern-scaled responses show a smoother pattern than in individual simulations (Tebaldi and Knutti, 2007; Knutti et al., 2010), because the multi-model mean filters out internal variability and because model differences in the location of the largest change tend to cancel. Individual model simulations show opposing signs in precipitation change such as over parts of Australia, the west coast of North America, parts of West Africa and India (Figure 4.42d), which tend to offset in the multi-model mean response. The spatial probability distribution of precipitation changes shows that areas of strong precipitation increase or decrease occur in all models (Figure 4.42g, see also Section 4.6.1). However, due to the spatial smoothing, the multi-model mean response shows a lower area fraction of drying than most of the individual models (Tebaldi and Knutti, 2007; Knutti et al., 2010). The five models with GSAT warming consistent with a high-warming storyline and the two models projecting GSAT warming exceeding the *very likely* GSAT warming range show a much larger area fraction of drying and somewhat larger fraction of strong precipitation increases than the multi-model mean (Figure 4.42 b–d).

The high-warming storyline shown in Figure 4.42b, c does not correspond to an upper or lower estimate of annual precipitation increase and decrease over individual locations, which in many regions may differ in the sign of the response (Figure 4.42e, f) due to differences in the model response and internal variability (Madsen et al., 2017). Figure 4.42e, f illustrates upper and lower local estimates corresponding to the 5–95% model range of local uncertainties as opposed to the global-warming storylines. Note, however, that Figure 4.42e, f does not show a physically plausible global precipitation response pattern, because information at the different grid points is taken from different model simulations.

Again, the manifestation of changes in the hydrological cycle for a high-warming storyline is not limited to precipitation, but would substantially affect other variables such as soil moisture, runoff, atmospheric humidity, and evapotranspiration. The changes are also not limited to annual mean precipitation but may be stronger or weaker for individual seasons and for precipitation extremes and dry spells.

While this assessment is limited to temperature and precipitation, such a high-warming storyline would manifest itself also in other climate variables (Sanderson et al., 2011) assessed in this chapter such as Arctic sea ice, atmospheric circulation changes, and sea-level rise (Ramanathan and Feng, 2008; Xu and Ramanathan, 2017b; Steffen et al., 2018).

In summary, while high-warming storylines – those associated with global warming levels above the upper bound of the assessed *very likely* range – are by definition *extremely unlikely*, they cannot be ruled out. For SSP1-2.6, such a high-warming storyline implies warming well above rather than well below 2°C (*high confidence*). Irrespective of scenario, high-warming storylines imply changes in many aspects of the climate system that exceed the patterns associated with the best estimate of GSAT changes by up to more than 50% (*high confidence*).

[START FIGURE 4.42 HERE]

Figure 4.42: High-warming storylines for changes in annual mean precipitation. (a) Estimates for annual mean precipitation changes in 2081–2100 relative 1995–2014, consistent with the best GSAT estimate derived by linearly scaling the CMIP6 multi-model mean changes to a GSAT change of 3.5°C. (b, c) Estimates for annual mean precipitation changes in 2081–2100 relative 1995–2014 in a storyline representing a physically plausible high-global-warming level. (b) Multi-model mean precipitation scaled to high-global-warming level (corresponding to 4.8°C, the upper bound of the *very likely* range, see Section 4.3.4). (c) Average of five models with GSAT warming nearest to the high level of warming (ACCESS-CM2, CESM2, CESM2-WACCM, CNRM-CM6-1, CNRM-CM6-1-HR) (d) Annual mean precipitation changes in four of the five individual model simulations averaged in (c). (e, f) Local upper estimate (95% quantile across models) and lower estimate (5% quantile across models) at each grid point. Information at

ACCEPTED VERSION SUBJECT TO FINAL EDITS

individual grid points comes from different model simulations and illustrates local uncertainty range but should not be interpreted as a pattern. (g) Area fraction of changes in annual mean precipitation 2081–2100 relative to 1995–2014 for all CMIP6 model simulations (thin black lines), models shown in (c) (red lines), and models showing very high warming above the models shown in (c). The grey range illustrates the 5–95% range across CMIP6 models and the solid black line the area fraction of the multi-model mean pattern shown in (a). Further details on data sources and processing are available in the chapter data table (Table 4.SM.1).

[END FIGURE 4.42 HERE]

ACCEPTED VERSION
SUBJEC TO FINAL EDITS

Frequently Asked Questions

FAQ 4.1: How Will the Climate Change over the Next Twenty Years?

The parts of the climate system that have shown clear increasing or decreasing trends in recent decades will continue these trends for at least the next twenty years. Examples include changes in global surface temperature, Arctic sea ice cover, and global average sea level. However, over a period as short as twenty years, these trends are substantially influenced by natural climate variability, which can either amplify or attenuate the trend expected from the further increase in greenhouse gas concentrations.

Twenty years are a long time by human standards but a short time from a climate point of view. Emissions of greenhouse gases will continue over the next twenty years, as assumed in all the scenarios considered in this report, albeit with varying rates. These emissions will further increase concentrations of greenhouse gases in the atmosphere (see FAQ 4.2), leading to continued trends in global surface warming and other parts of the climate system, including Arctic sea ice and global average sea level (see FAQ 9.2). FAQ 4.1, Figure 1 shows that both global surface temperature rise and the shrinking of sea ice in the Arctic will continue, with little difference between high- and low-emission scenarios over the next 20 years (that is, between the red and blue lines).

However, these expected trends will be overlain by natural climate variability (see FAQ 3.2). First, a major volcanic eruption might occur, such as the 1991 eruption of Mt. Pinatubo on the Philippines; such an eruption might cause a global surface cooling of a few tenths of a degree Celsius lasting several years. Second, both atmosphere and ocean show variations that occur spontaneously, without any external influence. These variations range from localized weather systems to continent- and ocean-wide patterns and oscillations that change over months, years, or decades. Over a period of twenty years, natural climate variability strongly influences many climate quantities, when compared to the response to the increase in greenhouse gas concentrations from human activities. The effect of natural variability is illustrated by the very different trajectories that individual black, red or blue lines can take in FAQ 4.1, Figure 1. Whether natural variability would amplify or attenuate the human influence cannot generally be predicted out to twenty years into the future. Natural climate variability over the next twenty years thus constitutes an uncertainty that at best can be quantified accurately but that cannot be reduced.

Locally, the effect of natural variability would be much larger still. Simulations (not shown here) indicate that, locally, a cooling trend over the next twenty year cannot be ruled out, even under the high-emission scenario – at a small number of locations on Earth, but these might lie anywhere. Globally, though, temperatures would rise under all scenarios.

In summary, while the direction of future change is clear for the two important climate quantities shown here – the global surface temperature and the Arctic sea-ice area in September – the magnitude of the change is much less clear because of natural variability.

[START FAQ 4.1, FIGURE 1 HERE]

FAQ 4.1, Figure 1: Simulations over the period 1995–2040, encompassing the recent past and the next twenty years, of two important indicators of global climate change, (top) global surface temperature, and (bottom), the area of Arctic sea ice in September. Both quantities are shown as deviations from the average over the period 1995–2014. The black curves are for the historical period ending in 2014; the blue curves represent a low-emission scenario (SSP1-2.6) and the red curves one high-emission scenario (SSP3-7.0).

[END FAQ 4.1, FIGURE 1 HERE]

FAQ 4.2: How Quickly Would We See the Effects of Reducing Carbon Dioxide Emissions?

ACCEPTED VERSION SUBJECT TO FINAL EDITS

The effects of substantial reductions in carbon dioxide emissions would not be apparent immediately, and the time required to detect the effects would depend on the scale and pace of emissions reductions. Under the lower-emission scenarios considered in this report, the increase in atmospheric carbon dioxide concentrations would slow visibly after about five to ten years, while the slowing down of global surface warming would be detectable after about twenty to thirty years. The effects on regional precipitation trends would only become apparent after several decades.

Reducing emissions of carbon dioxide (CO_2) – the most important greenhouse gas emitted by human activities – would slow down the rate of increase in atmospheric CO_2 concentration. However, concentrations would only begin to decrease when net emissions approach zero, that is, when most or all of the CO_2 emitted into the atmosphere each year is removed by natural and human processes (see FAQ 5.1, FAQ 5.3). This delay between a peak in emissions and a decrease in concentration is a manifestation of the very long lifetime of CO_2 in the atmosphere; part of the CO_2 emitted by humans remains in the atmosphere for centuries to millennia.

Reducing the rate of increase in CO_2 concentration would slow down global surface warming within a decade. But this reduction in the rate of warming would initially be masked by natural climate variability and might not be detected for a few decades (see FAQ 1.2, FAQ 3.2, FAQ 4.1). Detecting whether surface warming has indeed slowed down would thus be difficult in the years right after emissions reductions begin.

The time needed to detect the effect of emissions reductions is illustrated by comparing low- and high-emission scenarios (FAQ 4.2, Figure 1). In the low-emission scenario (SSP1-2.6), CO_2 emissions level off after 2015 and begin to fall in 2020, while they keep increasing throughout the 21st century in the high-emission scenario (SSP3-7.0). The uncertainty arising from natural internal variability in the climate system is represented by simulating each scenario ten times with the same climate model but starting from slightly different initial states back in 1850 (thin lines). For each scenario, the differences between individual simulations are caused entirely by simulated natural internal variability. The average of all simulations represents the climate response expected for a given scenario. The climate history that would actually unfold under each scenario would consist of this expected response combined with the contribution from natural internal variability and the contribution from potential future volcanic eruptions (the latter effect is not represented here).

FAQ 4.2, Figure 1 shows that the atmospheric CO_2 concentrations differ noticeably between the two scenarios about five to ten years after the emissions have begun to diverge in year 2015. In contrast, the difference in global surface temperatures between the two scenarios does not become apparent until later – about two to three decades after the emissions histories have begun to diverge in this example. This time would be longer if emissions were reduced more slowly than in the low-emission scenario illustrated here and shorter in the case of stronger reductions. Detection would take longer for regional quantities and for precipitation changes, which vary more strongly from natural causes. For instance, even in the low-emission scenario, the effect of reduced CO_2 emissions would not become visible in regional precipitation until late in the 21st century.

In summary, it is only after a few decades of reducing CO_2 emissions that we would clearly see global temperatures starting to stabilise. By contrast, short-term reductions in CO_2 emissions, such as during the COVID-19 pandemic, do not have detectable effects on either CO_2 concentration or global temperature. Only sustained emission reductions over decades would have a widespread effect across the climate system.

[START FAQ 4.2, FIGURE 1 HERE]

FAQ 4.2, Figure 1: Observing the benefits of emission reductions. (top) Carbon dioxide (CO_2) emissions, (middle) CO_2 concentration in the atmosphere and (bottom) effect on global surface temperature for two scenarios: a low-emission scenario (SSP1-2.6, blue) and a high-emission scenario (SSP3-7.0). In the low-emission scenario, CO_2 emissions begin to decrease in 2020 whereas they keep increasing throughout the 21st

ACCEPTED VERSION SUBJECT TO FINAL EDITS

century in the high-emission scenario. The thick lines are the average of the ten individual simulations (thin line) for each scenario. Differences between individual simulations reflect natural variability.

[END FAQ 4.2, FIGURE 1 HERE]

FAQ 4.3: At a given level of global warming, what are the spatial patterns of climate change?

As the planet warms, climate change does not unfold uniformly across the globe, but some patterns of regional change show clear, direct and consistent relationships to increases in global surface temperature. The Arctic warms more than other regions, land areas warm more than the ocean surface, and the Northern Hemisphere more than the Southern Hemisphere. Precipitation increases over high latitudes, tropics and large parts of the monsoon regions, but decreases over the subtropics. For cases like these, we can infer the direction and magnitude of some regional changes – particularly temperature and precipitation changes – for any given level of global warming.

The intensity of climate change will depend on the level of global warming. It is possible to identify certain patterns of regional climate change that occur consistently, but increase in amplitude, across increasing levels of global warming. Such robust spatial patterns of climate change are largely independent of the specific scenario (and pathway in time) that results in a given level of global warming. That is, as long as different scenarios result in the same global warming level, irrespective of the time when this level is attained in each scenario, we can infer the patterns of regional change that would result from this warming. When patterns of changes are robust, regional consequences can be assessed for all levels of global warming, for all future time periods, and for all scenarios. Temperature and precipitation show such robust patterns of changes that are particularly striking.

The high latitudes of the Northern Hemisphere are projected to warm the most, by two to four times the level of global warming – a phenomenon referred to as Arctic amplification (FAQ 4.3 Figure 1, left). Several processes contribute to this high rate of warming, including increases in the absorption of solar radiation due to the loss of reflective sea ice and snow in a warmer world. In the Southern Hemisphere, Antarctica is projected to warm faster than the mid-latitude Southern Ocean, but the Southern Hemisphere high latitudes are projected to warm at a reduced amplitude compared to the level of global warming (FAQ 4.3 Figure 1, left). An important reason for the relatively slower warming of the Southern Hemisphere high latitudes is the upwelling of Antarctic deep waters that drives a large surface heat uptake in the Southern Ocean.

The warming is generally stronger over land than over the ocean, and in the Northern Hemisphere compared to the Southern Hemisphere, and with less warming over the central subpolar North Atlantic and the southernmost Pacific. The differences are the result of several factors, including differences in how land and ocean areas absorb and retain heat, the fact that there is more land area in the Northern Hemisphere than in the Southern Hemisphere, and the influence of ocean circulation. In the Southern Hemisphere, robust patterns of relatively high warming are projected for subtropical South America, southern Africa, and Australia. The relatively strong warming in subtropical southern Africa arises from strong interactions between soil moisture and temperature and from increased solar radiation as a consequence of enhanced subsidence.

Precipitation changes are also proportional to the level of global warming (FAQ 4.3 Figure 1, right), although uncertainties are larger than for the temperature change. In the high latitudes of both the Southern and Northern Hemispheres, increases in precipitation are expected as the planet continues to warm, with larger changes expected at higher levels of global warming (FAQ 4.3 Figure 1, right). The same holds true for the projected precipitation increases over the tropics and large parts of the monsoon regions. General drying is expected over the subtropical regions, particularly over the Mediterranean, southern Africa and parts of Australia, South America, and southwest North America, as well as over the subtropical Atlantic and parts of the subtropical Indian and Pacific Oceans. Increases in precipitation over the tropics and decreases over the subtropics amplify with higher levels of global warming.

ACCEPTED VERSION SUBJECT TO FINAL EDITS

Some regions that are already dry and warm, such as southern Africa and the Mediterranean, are expected to become progressively drier and drastically warmer at higher levels of global warming.

In summary, climate change will not affect all the parts of the globe evenly. Rather, distinct regional patterns of temperature and precipitation change can be identified, and these changes are projected to amplify as the level of global warming increases.

[START FAQ 4.3, FIGURE 1 HERE]

FAQ 4.3, Figure 1: Regional changes in temperature (left) and precipitation (right) are proportional to the level of global warming, irrespective of the scenario through which the level of global warming is reached. Surface warming and precipitation change are shown relative to the 1850–1900 climate, and for time periods over which the globally averaged surface warming is 1.5°C (top) and 3°C (bottom), respectively. Changes presented here are based on thirty-one CMIP6 models using the high-emission scenario SSP3-7.0.

[END FAQ 4.3, FIGURE 1 HERE]

ACCEPTED VERSION
SUBJEC TO FINAL EDITS

Acknowledgements

The authors are deeply grateful to the WGI Bureau and Technical Support Unit for their support throughout the writing process. Special thanks go to Anna Pirani, Sarah Connors, Clotilde Pean, and Elisabeth Lonnoy for their organisational support. Special thanks go to Michael Sigmond, Sophie Berger, Paolo Davini, Melissa Gomis and Tom Maycock for their contributions to figures and FAQs. We acknowledge outstanding contributions from our two chapter scientists, Sebastian Milinski and Kyung-Sook Yun. We thank Ziming Chen for contributing the analysis of CMIP6 models. Finally, we would like to thank all reviewers for their constructive comments.

ACCEPTED VERSION
SUBJEC TO FINAL EDITS

References

Abramowitz, G. et al., 2019: ESD Reviews: Model dependence in multi-model climate ensembles: weighting, sub-selection and out-of-sample testing. *Earth Syst. Dynam.*, **10(1)**, 91–105, doi:10.5194/esd-10-91-2019.

Acosta Navarro, J.C. et al., 2016: Amplification of Arctic warming by past air pollution reductions in Europe. *Nature Geoscience*, **9(4)**, 277–281, doi:10.1038/ngeo2673.

Acosta Navarro, J.C. et al., 2017: Future Response of Temperature and Precipitation to Reduced Aerosol Emissions as Compared with Increased Greenhouse Gas Concentrations. *Journal of Climate*, **30(3)**, 939–954, doi:10.1175/jcli-d-16-0466.1.

Adams, J.B., M.E. Mann, and C.M. Ammann, 2003: Proxy evidence for an El Niño-like response to volcanic forcing. *Nature*, **426(6964)**, 274–278, doi:10.1038/nature02101.

Ahlm, L. et al., 2017: Marine cloud brightening – as effective without clouds. *Atmospheric Chemistry and Physics*, **17(21)**, 13071–13087, doi:10.5194/acp-17-13071-2017.

Akimoto, K., F. Sano, and T. Tomoda, 2018: GHG emission pathways until 2300 for the 1.5°C temperature rise target and the mitigation costs achieving the pathways. *Mitigation and Adaptation Strategies for Global Change*, **23(6)**, 839–852, doi:10.1007/s11027-017-9762-z.

Albern, N., A. Voigt, and J.G. Pinto, 2019: Cloud-Radiative Impact on the Regional Responses of the Midlatitude Jet Streams and Storm Tracks to Global Warming. *Journal of Advances in Modeling Earth Systems*, **11(7)**, 1940–1958, doi:10.1029/2018ms001592.

Alessandri, A. et al., 2014: Multi-scale enhancement of climate prediction over land by increasing the model sensitivity to vegetation variability in EC-Earth. *Journal of Climate*, **49(4)**, 8563–8577, doi:10.1007/s00382-016-3372-4.

Alexeev, V.A. and C.H. Jackson, 2013: Polar amplification: is atmospheric heat transport important? *Climate Dynamics*, **41(2)**, 533–547, doi:10.1007/s00382-012-1601-z.

Allen, M.R. and W.J. Ingram, 2002: Constraints on future changes in climate and the hydrologic cycle. *Nature*, **419(6903)**, 224–232, doi:10.1038/nature01092.

Allen, M.R. et al., 2018: Framing and Context. In: *Global Warming of 1.5°C. An IPCC Special Report on the impacts of global warming of 1.5°C above pre-industrial levels and related global greenhouse gas emission pathways, in the context of strengthening the global response to the threat of climate change,* [Masson-Delmotte, V., P. Zhai, H.-O. Pörtner, D. Roberts, J. Skea, P.R. Shukla, A. Pirani, W. Moufouma-Okia, C. Péan, R. Pidcock, S. Connors, J.B.R. Matthews, Y. Chen, X. Zhou, M.I. Gomis, E. Lonnoy, T. Maycock, M. Tignor, and T. Waterfield (eds.)]. In Press, pp. 49–91.

Allen, R.J. et al., 2020: Climate and air quality impacts due to mitigation of non-methane near-term climate forcers. *Atmospheric Chemistry and Physics*, **20(16)**, 9641–9663, doi:10.5194/acp-20-9641-2020.

Allen, R.J. et al., 2021: Significant climate benefits from near-term climate forcer mitigation in spite of aerosol reductions. *Environmental Research Letters*, **16(3)**, 034010, doi:10.1088/1748-9326/abe06b.

Alley, R.B. et al., 2003: Abrupt Climate Change. *Science*, **299(5615)**, 2005–2010, doi:10.1126/science.1081056.

Alterskjær, K. and J.E. Kristjánsson, 2013: The sign of the radiative forcing from marine cloud brightening depends on both particle size and injection amount. *Geophysical Research Letters*, **40(1)**, 210–215, doi:10.1029/2012gl054286.

Alterskjær, K. et al., 2013: Sea-salt injections into the low-latitude marine boundary layer: The transient response in three Earth system models. *Journal of Geophysical Research: Atmospheres*, **118(21)**, 12,112–195,206, doi:10.1002/2013jd020432.

Amann, M., Z. Klimont, and F. Wagner, 2013: Regional and Global Emissions of Air Pollutants: Recent Trends and Future Scenarios. *Annual Review of Environment and Resources*, **38(1)**, 31–55, doi:10.1146/annurev-environ-052912-173303.

Andrews, M.B. et al., 2020: Historical Simulations With HadGEM3-GC3.1 for CMIP6. *Journal of Advances in Modeling Earth Systems*, **12(6)**, doi:10.1029/2019ms001995.

Andrews, T. and P.M. Forster, 2010: The transient response of global-mean precipitation to increasing carbon dioxide levels. *Environmental Research Letters*, **5(2)**, 1–6, doi:10.1088/1748-9326/5/2/025212.

Andrews, T., P.M. Forster, and J.M. Gregory, 2009: A surface energy perspective on climate change. *Journal of Climate*, **22(10)**, 2557–2570, doi:10.1175/2008jcli2759.1.

Andrews, T. et al., 2019: Forcings, Feedbacks, and Climate Sensitivity in HadGEM3-GC3.1 and UKESM1. *Journal of Advances in Modeling Earth Systems*, **11(12)**, 4377–4394, doi:10.1029/2019ms001866.

Annan, J.D. and J.C. Hargreaves, 2017: On the meaning of independence in climate science. *Earth System Dynamics*, **8**, 211–224, doi:10.5194/esd-8-211-2017.

Aquila, V., C.I. Garfinkel, P.A. Newman, L.D. Oman, and D.W. Waugh, 2014: Modifications of the quasi-biennial oscillation by a geoengineering perturbation of the stratospheric aerosol layer. *Geophysical Research Letters*, **41(5)**, 1738–1744, doi:10.1002/2013gl058818.

Armour, K.C., N. Siler, A. Donohoe, and G.H. Roe, 2019: Meridional Atmospheric Heat Transport Constrained by Energetics and Mediated by Large-Scale Diffusion. *Journal of Climate*, **32(12)**, 3655–3680, doi:10.1175/jcli-d-

ACCEPTED VERSION SUBJECT TO FINAL EDITS

18-0563.1.
Armour, K.C., J. Marshall, J.R. Scott, A. Donohoe, and E.R. Newsom, 2016: Southern Ocean warming delayed by circumpolar upwelling and equatorward transport. *Nature Geoscience*, **9**, 549–554, doi:10.1038/ngeo2731.
Arora, V.K. et al., 2020: Carbon–concentration and carbon–climate feedbacks in CMIP6 models and their comparison to CMIP5 models. *Biogeosciences*, **17(16)**, 4173–4222, doi:10.5194/bg-17-4173-2020.
Arrhenius, S., 1896: On the influence of carbonic acid in the air upon the temperature of the ground. *The London, Edinburgh, and Dublin Philosophical Magazine and Journal of Science*, **41(251)**, 237–276, doi:10.1080/14786449608620846.
Årthun, M., K.E. W., T. Eldevik, and K.N. S., 2018: Time Scales and Sources of European Temperature Variability. *Geophysical Research Letters*, **45(8)**, 3597–3604, doi:10.1002/2018gl077401.
Årthun, M. et al., 2017: Skillful prediction of northern climate provided by the ocean. *Nature Communications*, **8(1)**, 15875, doi:10.1038/ncomms15875.
Athanasiadis, P.J. et al., 2020: Decadal predictability of North Atlantic blocking and the NAO. *npj Climate and Atmospheric Science*, **3(1)**, doi:10.1038/s41612-020-0120-6.
Baker, L.H., L.C. Shaffrey, R.T. Sutton, A. Weisheimer, and A.A. Scaife, 2018: An Intercomparison of Skill and Overconfidence/Underconfidence of the Wintertime North Atlantic Oscillation in Multimodel Seasonal Forecasts. *Geophysical Research Letters*, **45(15)**, 7808–7817, doi:10.1029/2018gl078838.
Bala, G., K. Caldeira, and R. Nemani, 2010: Fast versus slow response in climate change: Implications for the global hydrological cycle. *Climate Dynamics*, **35(2–3)**, 423–434, doi:10.1007/s00382-009-0583-y.
Bala, G. et al., 2011: Albedo enhancement of marine clouds to counteract global warming: impacts on the hydrological cycle. *Climate Dynamics*, **37(5)**, 915–931, doi:10.1007/s00382-010-0868-1.
Balaji, V. et al., 2018: Requirements for a global data infrastructure in support of CMIP6. *Geoscientific Model Development*, **11(9)**, 3659–3680, doi:10.5194/gmd-11-3659-2018.
Ban, N., J. Schmidli, and C. Schär, 2015: Heavy precipitation in a changing climate: Does short-term summer precipitation increase faster? *Geophysical Research Letters*, **42(4)**, 1165–1172, doi:10.1002/2014gl062588.
Banerjee, A., A.C. Maycock, and J.A. Pyle, 2018: Chemical and climatic drivers of radiative forcing due to changes in stratospheric and tropospheric ozone over the 21st century. *Atmospheric Chemistry and Physics*, **18(4)**, 2899–2911, doi:10.5194/acp-18-2899-2018.
Banerjee, A., J.C. Fyfe, L.M. Polvani, D. Waugh, and K.-L. Chang, 2020: A pause in Southern Hemisphere circulation trends due to the Montreal Protocol. *Nature*, **579(7800)**, 544–548, doi:10.1038/s41586-020-2120-4.
Banerjee, A. et al., 2014: Lightning NOx, a key chemistry-climate interaction: Impacts of future climate change and consequences for tropospheric oxidising capacity. *Atmospheric Chemistry and Physics*, **14(18)**, 9871–9881, doi:10.5194/acp-14-9871-2014.
Barcikowska, M.J. et al., 2018: Euro-Atlantic winter storminess and precipitation extremes under 1.5°C vs. 2°C warming scenarios. *Earth System Dynamics*, **9(2)**, 679–699, doi:10.5194/esd-9-679-2018.
Barnes, E.A. and L. Polvani, 2013: Response of the Midlatitude Jets, and of Their Variability, to Increased Greenhouse Gases in the CMIP5 Models. *Journal of Climate*, **26(18)**, 7117–7135, doi:10.1175/jcli-d-12-00536.1.
Barnes, E.A. and L.M. Polvani, 2015: CMIP5 projections of arctic amplification, of the North American/North Atlantic circulation, and of their relationship. *Journal of Climate*, **28**, 5254–5271, doi:10.1175/jcli-d-14-00589.1.
Barnes, E.A., N.W. Barnes, and L.M. Polvani, 2014: Delayed southern hemisphere climate change induced by stratospheric ozone recovery, as projected by the CMIP5 models. *Journal of Climate*, **27**, 852–867, doi:10.1175/jcli-d-13-00246.1.
Barriopedro, D., R. Garcia-Herrera, and R.M. Trigo, 2010: Application of blocking diagnosis methods to General Circulation Models. Part I: a novel detection scheme. *Climate Dynamics*, **35(7–8)**, 1373–1391, doi:10.1007/s00382-010-0767-5.
Bathiany, S., J. Hidding, and M. Scheffer, 2020: Edge Detection Reveals Abrupt and Extreme Climate Events. *Journal of Climate*, **33(15)**, 6399–6421, doi:10.1175/jcli-d-19-0449.1.
Bathiany, S., V. Dakos, M. Scheffer, and T.M. Lenton, 2018: Climate models predict increasing temperature variability in poor countries. *Science Advances*, **4(5)**, eaar5809, doi:10.1126/sciadv.aar5809.
Bathiany, S., D. Notz, T. Mauritsen, G. Raedel, and V. Brovkin, 2016: On the potential for abrupt Arctic winter sea ice loss. *Journal of Climate*, **29(7)**, 2703–2719, doi:10.1175/jcli-d-15-0466.1.
Batté, L. and F.J. Doblas-Reyes, 2015: Stochastic atmospheric perturbations in the EC-Earth3 global coupled model: impact of SPPT on seasonal forecast quality. *Climate Dynamics*, **45(11)**, 3419–3439, doi:10.1007/s00382-015-2548-7.
Baumberger, C., R. Knutti, and G. Hirsch Hadorn, 2017: Building confidence in climate model projections: an analysis of inferences from fit. *Wiley Interdisciplinary Reviews: Climate Change*, **8(3)**, e454, doi:10.1002/wcc.454.
Bayr, T. and D. Dommenget, 2013: The Tropospheric Land–Sea Warming Contrast as the Driver of Tropical Sea Level Pressure Changes. *Journal of Climate*, **26(4)**, 1387–1402, doi:10.1175/jcli-d-11-00731.1.
Beer, E., I. Eisenman, and T.J.W. Wagner, 2020: Polar Amplification Due to Enhanced Heat Flux Across the Halocline. *Geophysical Research Letters*, **47(4)**, doi:10.1029/2019gl086706.
Befort, D.J., C.H. O'Reilly, and A. Weisheimer, 2020: Constraining Projections Using Decadal Predictions.

ACCEPTED VERSION SUBJECT TO FINAL EDITS

Geophysical Research Letters, **47(18)**, e2020GL087900, doi:10.1029/2020gl087900.
Bellomo, K., L.N. Murphy, M.A. Cane, A.C. Clement, and L.M. Polvani, 2018: Historical forcings as main drivers of the Atlantic multidecadal variability in the CESM large ensemble. *Climate Dynamics*, **50(9)**, 3687–3698, doi:10.1007/s00382-017-3834-3.
Bellucci, A., A. Mariotti, and S. Gualdi, 2017: The Role of Forcings in the Twentieth-Century North Atlantic Multidecadal Variability: The 1940–75 North Atlantic Cooling Case Study. *Journal of Climate*, **30(18)**, 7317–7337, doi:10.1175/jcli-d-16-0301.1.
Bellucci, A. et al., 2015a: Advancements in decadal climate predictability: The role of nonoceanic drivers. *Reviews of Geophysics*, **53(2)**, 165–202, doi:10.1002/2014rg000473.
Bellucci, A. et al., 2015b: Advancements in decadal climate predictability: The role of nonoceanic drivers. *Reviews of Geophysics*, **53(2)**, 165–202, doi:10.1002/2014rg000473.
Bellucci, A. et al., 2015c: An assessment of a multi-model ensemble of decadal climate predictions. *Climate Dynamics*, **44(9–10)**, 2787–2806, doi:10.1007/s00382-014-2164-y.
Bengtsson, L. and K.I. Hodges, 2019: Can an ensemble climate simulation be used to separate climate change signals from internal unforced variability? *Climate Dynamics*, **52(5–6)**, 3553–3573, doi:10.1007/s00382-018-4343-8.
Berdahl, M. et al., 2014: Arctic cryosphere response in the geoengineering model intercomparison project G3 and G4 scenarios. *Journal of Geophysical Research*, **119(3)**, 1308–1321, doi:10.1002/2013jd020627.
Berg, A. et al., 2016: Land–atmosphere feedbacks amplify aridity increase over land under global warming. *Nature Climate Change*, **6(9)**, 869–874, doi:10.1038/nclimate3029.
Berner, J. et al., 2017: Stochastic Parameterization: Toward a New View of Weather and Climate Models. *Bulletin of the American Meteorological Society*, **98(3)**, 565–588, doi:10.1175/bams-d-15-00268.1.
Bethke, I. et al., 2017: Potential volcanic impacts on future climate variability. *Nature Climate Change*, **7(11)**, 799–805, doi:10.1038/nclimate3394.
Bilbao, R. et al., 2021: Assessment of a full-field initialized decadal climate prediction system with the CMIP6 version of EC-Earth. *Earth System Dynamics*, **12(1)**, 173–196, doi:10.5194/esd-12-173-2021.
Bindoff, N.L. et al., 2013: Detection and Attribution of Climate Change: from Global to Regional. In: *Climate Change 2013: The Physical Science Basis. Contribution of Working Group I to the Fifth Assessment Report of the Intergovernmental Panel on Climate Change* [Stocker, T.F., D. Qin, G.-K. Plattner, M. Tignor, S.K. Allen, J. Boschung, A. Nauels, Y. Xia, V. Bex, and P.M. Midgley (eds.)]. Cambridge University Press, Cambridge, United Kingdom and New York, NY, USA, pp. 867–952, doi:10.1017/cbo9781107415324.022.
Bitz, C.M., P.R. Gent, R.A. Woodgate, M.M. Holland, and R. Lindsay, 2006: The influence of sea ice on ocean heat uptake in response to increasing CO2. *Journal of Climate*, **19(11)**, 2437–2450, doi:10.1175/jcli3756.1.
Boe, J., 2018: Interdependency in multimodel climate projections: Component replication and result similarity. *Geophysical Research Letters*, **45(6)**, 2771–2779, doi:10.1002/2017gl076829.
Boer, G.J. and R. Sospedra-Alfonso, 2019: Assessing the skill of the Pacific Decadal Oscillation (PDO) in a decadal prediction experiment. *Climate Dynamics*, **53(9)**, 5763–5775, doi:10.1007/s00382-019-04896-w.
Boer, G.J., V. Kharin, and W.J. Merryfield, 2013: Decadal predictability and forecast skill. *Climate Dynamics*, **41(7–8)**, 1817–1833, doi:10.1007/s00382-013-1705-0.
Boer, G.J. et al., 2016: The Decadal Climate Prediction Project (DCPP) contribution to CMIP6. *Geoscientific Model Development*, **9(10)**, 3751–3777, doi:10.5194/gmd-9-3751-2016.
Bollasina, M.A., Y. Ming, and V. Ramaswamy, 2011: Anthropogenic Aerosols and the Weakening of the South Asian Summer Monsoon. *Science*, **334(6055)**, 502 – 505, doi:10.1126/science.1204994.
Bonan, D.B., K.C. Armour, G.H. Roe, N. Siler, and N. Feldl, 2018: Sources of Uncertainty in the Meridional Pattern of Climate Change. *Geophysical Research Letters*, **45**, 9131–9140, doi:10.1029/2018gl079429.
Bony, S. et al., 2013: Robust direct effect of carbon dioxide on tropical circulation and regional precipitation. *Nature Geoscience*, **6(6)**, 447–451, doi:10.1038/ngeo1799.
Borchert, L.F. et al., 2019: Decadal Predictions of the Probability of Occurrence for Warm Summer Temperature Extremes. *Geophysical Research Letters*, **46(23)**, 14042–14051, doi:10.1029/2019gl085385.
Borchert, L.F. et al., 2021: Improved Decadal Predictions of North Atlantic Subpolar Gyre SST in CMIP6. *Geophysical Research Letters*, **48(3)**, e2020GL091307, doi:10.1029/2020gl091307.
Bordbar, M.H. et al., 2019: Uncertainty in near-term global surface warming linked to tropical Pacific climate variability. *Nature Communications*, **10(1)**, 1990, doi:10.1038/s41467-019-09761-2.
Borodina, A., E.M. Fischer, and R. Knutti, 2017: Emergent constraints in climate projections: A case study of changes in high-latitude temperature variability. *Journal of Climate*, **30**, 3655–3670, doi:10.1175/jcli-d-16-0662.1.
Boucher, O., C. Kleinschmitt, and G. Myhre, 2017: Quasi-Additivity of the Radiative Effects of Marine Cloud Brightening and Stratospheric Sulfate Aerosol Injection. *Geophysical Research Letters*, **44(21)**, 11,111–158,165, doi:10.1002/2017gl074647.
Boucher, O. et al., 2012: Reversibility in an Earth System model in response to CO2 concentration changes. *Environmental Research Letters*, **7(2)**, 024013, doi:10.1088/1748-9326/7/2/024013.
Boucher, O. et al., 2013: Clouds and Aerosols. In: *Climate Change 2013: The Physical Science Basis. Contribution of Working Group I to the Fifth Assessment Report of the Intergovernmental Panel on Climate Change* [Stocker,

ACCEPTED VERSION SUBJECT TO FINAL EDITS

T.F., D. Qin, G.-K. Plattner, M. Tignor, S.K. Allen, J. Boschung, A. Nauels, Y. Xia, V. Bex, and P.M. Midgley (eds.)]. Cambridge University Press, Cambridge, United Kingdom and New York, NY, USA, pp. 571–657, doi:10.1017/cbo9781107415324.016.

Bracegirdle, T.J., H. Lu, R. Eade, and T. Woollings, 2018: Do CMIP5 Models Reproduce Observed Low-Frequency North Atlantic Jet Variability? *Geophysical Research Letters*, **45(14)**, 7204–7212, doi:10.1029/2018gl078965.

Bracegirdle, T.J. et al., 2020a: Improvements in Circumpolar Southern Hemisphere Extratropical Atmospheric Circulation in CMIP6 Compared to CMIP5. *Earth and Space Science*, **7(6)**, e2019EA001065, doi:10.1029/2019ea001065.

Bracegirdle, T.J. et al., 2020b: Twenty first century changes in Antarctic and Southern Ocean surface climate in CMIP6. *Atmospheric Science Letters*, **21(9)**, e984, doi:10.1002/asl.984.

Bradley, R.S., K.R. Briffa, J. Cole, M.K. Hughes, and T.J. Osborn, 2003: The Climate of the Last Millennium. In: *Paleoclimate, Global Change and the Future* [Alverson, K.D., T.F. Pedersen, and R.S. Bradley (eds.)]. Global Change – The IGBP Series, Springer, Berlin and Heidelberg, Germany, pp. 105–141, doi:10.1007/978-3-642-55828-3_6.

Branstator, G. and H.Y. Teng, 2010: Two limits of initial-value decadal predictability in a CGCM. *Journal of Climate*, **23(23)**, 6292–6311, doi:10.1175/2010jcli3678.1.

Brient, F., 2020: Reducing Uncertainties in Climate Projections with Emergent Constraints: Concepts, Examples and Prospects. *Advances in Atmospheric Sciences*, **37(1)**, 1–15, doi:10.1007/s00376-019-9140-8.

Bright, R.M. et al., 2017: Local temperature response to land cover and management change driven by non-radiative processes. *Nature Climate Change*, **7(4)**, 296–302, doi:10.1038/nclimate3250.

Brogli, R., N. Kröner, S.L. Sørland, D. Lüthi, and C. Schär, 2019: The Role of Hadley Circulation and Lapse-Rate Changes for the Future European Summer Climate. *Journal of Climate*, **32(2)**, 385–404, doi:10.1175/jcli-d-18-0431.1.

Brönnimann, S. et al., 2019: Last phase of the Little Ice Age forced by volcanic eruptions. *Nature Geoscience*, **12(8)**, 650–656, doi:10.1038/s41561-019-0402-y.

Bronselaer, B. et al., 2018: Change in future climate due to Antarctic meltwater. *Nature*, **564**, 55–58, doi:10.1038/s41586-018-0712-z.

Brown, J.R. et al., 2020: Comparison of past and future simulations of ENSO in CMIP5/PMIP3 and CMIP6/PMIP4 models. *Climate of the Past*, **16(5)**, 1777–1805, doi:10.5194/cp-16-1777-2020.

Brown, P.T., M.S. Lozier, R. Zhang, and W. Li, 2016: The necessity of cloud feedback for a basin-scale Atlantic Multidecadal Oscillation. *Geophysical Research Letters*, **43(8)**, 3955–3963, doi:10.1002/2016gl068303.

Brown, P.T., Y. Ming, W. Li, and S.A. Hill, 2017: Change in the magnitude and mechanisms of global temperature variability with warming. *Nature Climate Change*, **7(10)**, 743–748, doi:10.1038/nclimate3381.

Brune, S. and J. Baehr, 2020: Preserving the coupled atmosphere–ocean feedback in initializations of decadal climate predictions. *WIREs Climate Change*, **11(3)**, e637, doi:10.1002/wcc.637.

Brune, S., A. Düsterhus, H. Pohlmann, W.A. Müller, and J. Baehr, 2018: Time dependency of the prediction skill for the North Atlantic subpolar gyre in initialized decadal hindcasts. *Climate Dynamics*, **51(5)**, 1947–1970, doi:10.1007/s00382-017-3991-4.

Brunner, L. et al., 2020: Reduced global warming from CMIP6 projections when weighting models by performance and independence. *Earth System Dynamics*, **11(4)**, 995–1012, doi:10.5194/esd-11-995-2020.

Büntgen, U. et al., 2016a: Cooling and societal change during the Late Antique Little Ice Age from 536 to around 660 AD. *Nature Geoscience*, **9(3)**, 231–236, doi:10.1038/ngeo2652.

Büntgen, U. et al., 2016b: Cooling and societal change during the Late Antique Little Ice Age from 536 to around 660 AD. *Nature Geoscience*, **9(3)**, 231–236, doi:10.1038/ngeo2652.

Bürger, G. and U. Cubasch, 2015: The detectability of climate engineering. *Journal of Geophysical Research*, **120(22)**, 11,404–11,418, doi:10.1002/2015jd023954.

Burke, E.J. et al., 2017: Quantifying uncertainties of permafrost carbon–climate feedbacks. *Biogeosciences*, **14(12)**, 3051–3066, doi:10.5194/bg-14-3051-2017.

Byrne, M.P. and P.A. O'Gorman, 2013a: Land–Ocean Warming Contrast over a Wide Range of Climates: Convective Quasi-Equilibrium Theory and Idealized Simulations. *Journal of Climate*, **26(12)**, 4000–4016, doi:10.1175/jcli-d-12-00262.1.

Byrne, M.P. and P.A. O'Gorman, 2013b: Link between land-ocean warming contrast and surface relative humidities in simulations with coupled climate models. *Geophysical Research Letters*, **40**, 5223–5227, doi:10.1002/grl.50971.

Byrne, M.P. and P.A. O'Gorman, 2015: The Response of Precipitation Minus Evapotranspiration to Climate Warming: Why the "Wet-Get-Wetter, Dry-Get-Drier" Scaling Does Not Hold over Land. *Journal of Climate*, **28(20)**, 8078–8092, doi:10.1175/jcli-d-15-0369.1.

Byrne, M.P. and P.A. O'Gorman, 2016: Understanding Decreases in Land Relative Humidity with Global Warming: Conceptual Model and GCM Simulations. *Journal of Climate*, **29(24)**, 9045–9061, doi:10.1175/jcli-d-16-0351.1.

Byrne, M.P. and P.A. O'Gorman, 2018: Trends in continental temperature and humidity directly linked to ocean warming. *Proceedings of the National Academy of Sciences*, **115(19)**, 4863–4868, doi:10.1073/pnas.1722312115.

ACCEPTED VERSION SUBJECT TO FINAL EDITS

Byrne, N.J., T.G. Shepherd, and I. Polichtchouk, 2019: Subseasonal-to-Seasonal Predictability of the Southern Hemisphere Eddy-Driven Jet During Austral Spring and Early Summer. *Journal of Geophysical Research: Atmospheres*, **124(13)**, 6841–6855, doi:10.1029/2018jd030173.
Caesar, J. et al., 2013: Response of the HadGEM2 Earth System Model to future greenhouse gas emissions pathways to the year 2300. *Journal of Climate*, **26(10)**, 3275–3284, doi:10.1175/jcli-d-12-00577.1.
Cai, W., G. Wang, A. Santoso, X. Lin, and L. Wu, 2017: Definition of Extreme El Niño and Its Impact on Projected Increase in Extreme El Niño Frequency. *Geophysical Research Letters*, **44(21)**, doi:10.1002/2017gl075635.
Cai, W. et al., 2013: Projected response of the Indian Ocean Dipole to greenhouse warming. *Nature Geoscience*, **6**, 997–1007, doi:10.1038/ngeo2009.
Cai, W. et al., 2014a: Increasing frequency of extreme El Niño events due to greenhouse warming. *Nature Climate Change*, **4(2)**, 111–116, doi:10.1038/nclimate2100.
Cai, W. et al., 2014b: Increased frequency of extreme Indian Ocean Dipole events due to greenhouse warming. *Nature*, **510**, 254–258, doi:10.1038/nature13327.
Cai, W. et al., 2015: ENSO and greenhouse warming. *Nature Climate Change*, **5(9)**, 849–859, doi:10.1038/nclimate2743.
Cai, W. et al., 2018a: Increased variability of eastern Pacific El Niño under greenhouse warming. *Nature*, **564(7735)**, 201–206, doi:10.1038/s41586-018-0776-9.
Cai, W. et al., 2018b: Stabilised frequency of extreme positive Indian Ocean Dipole under 1.5 °C warming. *Nature Communications*, **9(1)**, 1419, doi:10.1038/s41467-018-03789-6.
Cai, W. et al., 2019a: Pantropical climate interactions. *Science*, **363(6430)**, eaav4236, doi:10.1126/science.aav4236.
Cai, W. et al., 2019b: Pantropical climate interactions. *Science*, **363(6430)**, eaav4236, doi:10.1126/science.aav4236.
Cai, W. et al., 2021: Opposite response of strong and moderate positive Indian Ocean Dipole to global warming. *Nature Climate Change*, **11(1)**, 27–32, doi:10.1038/s41558-020-00943-1.
Caian, M., T. Koenigk, R. Döscher, and A. Devasthale, 2018: An interannual link between Arctic sea-ice cover and the North Atlantic Oscillation. *Climate Dynamics*, **50(1–2)**, 423–441, doi:10.1007/s00382-017-3618-9.
Cao, L., G. Bala, and K. Caldeira, 2011a: Why is there a short-term increase in global precipitation in response to diminished CO2 forcing? *Geophysical Research Letters*, **38(6)**, doi:10.1029/2011gl046713.
Cao, L., G. Bala, and K. Caldeira, 2011b: Why is there a short-term increase in global precipitation in response to diminished CO2 forcing? *Geophysical Research Letters*, **38(6)**, doi:10.1029/2011gl046713.
Cao, L., G. Bala, M. Zheng, and K. Caldeira, 2015: Fast and slow climate responses to CO2 and solar forcing: A linear multivariate regression model characterizing transient climate change. *Journal of Geophysical Research*, **120(23)**, 12,037–12,053, doi:10.1002/2015jd023901.
Cao, L., L. Duan, G. Bala, and K. Caldeira, 2016: Simulated long-term climate response to idealized solar geoengineering. *Geophysical Research Letters*, **43(5)**, 2209–2217, doi:10.1002/2016gl068079.
Cao, L., L. Duan, G. Bala, and K. Caldeira, 2017: Simultaneous stabilization of global temperature and precipitation through cocktail geoengineering. *Geophysical Research Letters*, **44(14)**, 7429–7437, doi:10.1002/2017gl074281.
Caron, L.-P. et al., 2017: How Skillful are the Multiannual Forecasts of Atlantic Hurricane Activity? *Bulletin of the American Meteorological Society*, **99(2)**, 403–413, doi:10.1175/bams-d-17-0025.1.
Cassou, C. and J. Cattiaux, 2016: Disruption of the European climate seasonal clock in a warming world. *Nature Climate Change*, **6(6)**, 589–594, doi:10.1038/nclimate2969.
Cassou, C. et al., 2018: Decadal Climate Variability and Predictability: Challenges and Opportunities. *Bulletin of the American Meteorological Society*, **99(3)**, 479–490, doi:10.1175/bams-d-16-0286.1.
Ceppi, P. and D.L. Hartmann, 2016: Clouds and the Atmospheric Circulation Response to Warming. *Journal of Climate*, **29(2)**, 783–799, doi:10.1175/jcli-d-15-0394.1.
Ceppi, P. and T.G. Shepherd, 2017: Contributions of Climate Feedbacks to Changes in Atmospheric Circulation. *Journal of Climate*, **30(22)**, 9097–9118, doi:10.1175/jcli-d-17-0189.1.
Ceppi, P. and T.G. Shepherd, 2019a: The Role of the Stratospheric Polar Vortex for the Austral Jet Response to Greenhouse Gas Forcing. *Geophysical Research Letters*, **46(12)**, 6972–6979, doi:10.1029/2019gl082883.
Ceppi, P. and T.G. Shepherd, 2019b: The Role of the Stratospheric Polar Vortex for the Austral Jet Response to Greenhouse Gas Forcing. *Geophysical Research Letters*, **46(12)**, 6972–6979, doi:10.1029/2019gl082883.
Ceppi, P., M.D. Zelinka, and D.L. Hartmann, 2014: The response of the Southern Hemispheric eddy-driven jet to future changes in shortwave radiation in CMIP5. *Geophysical Research Letters*, **41(9)**, 3244–3250, doi:10.1002/2014gl060043.
Ceppi, P., G. Zappa, T.G. Shepherd, and J.M. Gregory, 2018: Fast and Slow Components of the Extratropical Atmospheric Circulation Response to CO2 Forcing. *Journal of Climate*, **31(3)**, 1091–1105, doi:10.1175/jcli-d-17-0323.1.
Chadwick, R., 2016: Which aspects of CO2forcing and SST warming cause most uncertainty in projections of tropical rainfall change over land and ocean? *Journal of Climate*, **29(7)**, 2493–2509, doi:10.1175/jcli-d-15-0777.1.
Chadwick, R., I. Boutle, and G. Martin, 2013: Spatial Patterns of Precipitation Change in CMIP5: Why the Rich Do Not Get Richer in the Tropics. *Journal of Climate*, **26(11)**, 3803–3822, doi:10.1175/jcli-d-12-00543.1.
Chadwick, R., P. Good, and K.M. Willett, 2016: A simple moisture advection model of specific humidity change over

ACCEPTED VERSION SUBJECT TO FINAL EDITS

land in response to SST warming. *J. Climate*, **29**, 7613–7632, doi:10.1175/jcli-d-16-0241.1.
Chadwick, R., H. Douville, and C.B. Skinner, 2017: Timeslice experiments for understanding regional climate projections: applications to the tropical hydrological cycle and European winter circulation. *Climate Dynamics*, **49(9–10)**, 3011–3029, doi:10.1007/s00382-016-3488-6.
Chalmers, N., E.J. Highwood, E. Hawkins, R. Sutton, and L.J. Wilcox, 2012: Aerosol contribution to the rapid warming of near-term climate under RCP 2.6. *Geophysical Research Letters*, **39(17)**, 2–7, doi:10.1029/2012gl052848.
Chand, S.S., K.J. Tory, H. Ye, and K.J.E. Walsh, 2017: Projected increase in El Niño-driven tropical cyclone frequency in the Pacific. *Nature Climate Change*, **7**, 123–127, doi:10.1038/nclimate3181.
Chang, E.K.M., 2017: Projected Significant Increase in the Number of Extreme Extratropical Cyclones in the Southern Hemisphere. *Journal of Climate*, **30(13)**, 4915–4935, doi:10.1175/jcli-d-16-0553.1.
Chang, E.K.M., C.-G. Ma, C. Zheng, and A.M.W. Yau, 2016: Observed and projected decrease in Northern Hemisphere extratropical cyclone activity in summer and its impacts on maximum temperature. *Geophysical Research Letters*, **43(5)**, 2200–2208, doi:10.1002/2016gl068172.
Chang, E.K.-M., 2018: CMIP5 Projected Change in Northern Hemisphere Winter Cyclones with Associated Extreme Winds. *Journal of Climate*, **31(16)**, 6527–6542, doi:10.1175/jcli-d-17-0899.1.
Chavaillaz, Y., S. Joussaume, S. Bony, and P. Braconnot, 2016a: Spatial stabilization and intensification of moistening and drying rate patterns under future climate change. *Climate Dynamics*, **47(3)**, 951–965, doi:10.1007/s00382-015-2882-9.
Chavaillaz, Y., S. Joussaume, S. Bony, and P. Braconnot, 2016b: Spatial stabilization and intensification of moistening and drying rate patterns under future climate change. *Climate Dynamics*, **47(3)**, 951–965, doi:10.1007/s00382-015-2882-9.
Chen, G. et al., 2019: Thermodynamic and Dynamic Mechanisms for Hydrological Cycle Intensification over the Full Probability Distribution of Precipitation Events. *Journal of the Atmospheric Sciences*, **76(2)**, 497–516, doi:10.1175/jas-d-18-0067.1.
Chen, L., T. Li, Y. Yu, and S.K. Behera, 2017: A possible explanation for the divergent projection of ENSO amplitude change under global warming. *Climate Dynamics*, **49(11–12)**, 3799–3811, doi:10.1007/s00382-017-3544-x.
Chen, Y.-C. et al., 2012: Occurrence of lower cloud albedo in ship tracks. *Atmospheric Chemistry and Physics*, **12(17)**, 8223–8235, doi:10.5194/acp-12-8223-2012.
Chen, Z. et al., 2020: Global Land Monsoon Precipitation Changes in CMIP6 Projections. *Geophysical Research Letters*, **47(14)**, doi:10.1029/2019gl086902.
Cheng, W. et al., 2019: Soil Moisture and Other Hydrological Changes in a Stratospheric Aerosol Geoengineering Large Ensemble. *Journal of Geophysical Research: Atmospheres*, **124(23)**, 12773–12793, doi:10.1029/2018jd030237.
Chevuturi, A., N.P. Klingaman, A.G. Turner, and S. Hannah, 2018: Projected Changes in the Asian-Australian Monsoon Region in 1.5°C and 2.0°C Global-Warming Scenarios. *Earth's Future*, **6(3)**, 339–358, doi:10.1002/2017ef000734.
Chikamoto, Y., A. Timmermann, M.J. Widlansky, M.A. Balmaseda, and L. Stott, 2017: Multi-year predictability of climate, drought, and wildfire in southwestern North America. *Scientific Reports*, **7(1)**, 6568, doi:10.1038/s41598-017-06869-7.
Chikamoto, Y., A. Timmermann, M.J. Widlansky, S. Zhang, and M.A. Balmaseda, 2019: A Drift-Free Decadal Climate Prediction System for the Community Earth System Model. *Journal of Climate*, **32(18)**, 5967–5995, doi:10.1175/jcli-d-18-0788.1.
Chikamoto, Y. et al., 2013: An overview of decadal climate predictability in a multi-model ensemble by climate model MIROC. *Climate Dynamics*, **40(5–6)**, 1201–1222, doi:10.1007/s00382-012-1351-y.
Chikamoto, Y. et al., 2015: Skilful multi-year predictions of tropical trans-basin climate variability. *Nature Communications*, **6(1)**, 6869, doi:10.1038/ncomms7869.
Chiodo, G. and L.M. Polvani, 2016: Reduction of Climate Sensitivity to Solar Forcing due to Stratospheric Ozone Feedback. *Journal of Climate*, **29(12)**, 4651–4663, doi:10.1175/jcli-d-15-0721.1.
Chiodo, G., J. Oehrlein, L.M. Polvani, J.C. Fyfe, and A.K. Smith, 2019: Insignificant influence of the 11-year solar cycle on the North Atlantic Oscillation. *Nature Geoscience*, **12(2)**, 94–99, doi:10.1038/s41561-018-0293-3.
Choi, J., S.W. Son, and R.J. Park, 2019: Aerosol versus greenhouse gas impacts on Southern Hemisphere general circulation changes. *Climate Dynamics*, **52(7–8)**, 4127–4142, doi:10.1007/s00382-018-4370-5.
Chou, C., J.D. Neelin, C.-A. Chen, and J.-Y. Tu, 2009: Evaluating the "Rich-Get-Richer" Mechanism in Tropical Precipitation Change under Global Warming. *Journal of Climate*, **22(8)**, 1982–2005, doi:10.1175/2008jcli2471.1.
Christensen, H.M. and J. Berner, 2019: From reliable weather forecasts to skilful climate response: A dynamical systems approach. *Quarterly Journal of the Royal Meteorological Society*, **145(720)**, 1052–1069, doi:10.1002/qj.3476.
Christensen, H.M., J. Berner, D.R.B. Coleman, and T.N. Palmer, 2017: Stochastic parameterization and El Niño-southern oscillation. *Journal of Climate*, **30**, 17–38, doi:10.1175/jcli-d-16-0122.1.
Christensen, J.H. et al., 2013: Climate Phenomena and their Relevance for Future Regional Climate Change. In:

ACCEPTED VERSION SUBJECT TO FINAL EDITS

Climate Change 2013: The Physical Science Basis. Contribution of Working Group I to the Fifth Assessment Report of the Intergovernmental Panel on Climate Change [Stocker, T.F., D. Qin, G.-K. Plattner, M. Tignor, S.K. Allen, J. Boschung, A. Nauels, Y. Xia, V. Bex, and P.M. Midgley (eds.)]. Cambridge University Press, Cambridge, United Kingdom and New York, NY, USA, pp. 1217–1308, doi:10.1017/cbo9781107415324.028.

Christensen, M.W. and G.L. Stephens, 2011: Microphysical and macrophysical responses of marine stratocumulus polluted by underlying ships: Evidence of cloud deepening. *Journal of Geophysical Research*, **116(D3)**, D03201, doi:10.1029/2010jd014638.

Christensen, P., K. Gillingham, and W. Nordhaus, 2018: Uncertainty in forecasts of long-run economic growth. *Proceedings of the National Academy of Sciences of the United States of America*, doi:10.1073/pnas.1713628115.

Chu, J.-E. et al., 2014: Future change of the Indian Ocean basin-wide and dipole modes in the CMIP5. *Climate Dynamics*, **43(1–2)**, 535–551, doi:10.1007/s00382-013-2002-7.

Chung, C.T.Y., S.B. Power, A. Sullivan, and F. Delage, 2019: The role of the South Pacific in modulating Tropical Pacific variability. *Scientific Reports*, **9(1)**, 18311, doi:10.1038/s41598-019-52805-2.

Church, J. et al., 2013: Sea Level Change. In: *Climate Change 2013: The Physical Science Basis. Contribution of Working Group I to the Fifth Assessment Report of the Intergovernmental Panel on Climate Change* [Stocker, T.F., D. Qin, G.-K. Plattner, M. Tignor, S.K. Allen, J. Boschung, A. Nauels, Y. Xia, V. Bex, and P.M. Midgley (eds.)]. Cambridge University Press, Cambridge, United Kingdom and New York, NY, USA, pp. 1137–1216, doi:10.1017/cbo9781107415324.026.

Chuwah, C. et al., 2013: Implications of alternative assumptions regarding future air pollution control in scenarios similar to the Representative Concentration Pathways. *Atmospheric Environment*, **79**, 787–801, doi:10.1016/j.atmosenv.2013.07.008.

Chylek, P., C.K. Folland, H.A. Dijkstra, G. Lesins, and M.K. Dubey, 2011: Ice-core data evidence for a prominent near 20 year time-scale of the Atlantic Multidecadal Oscillation. *Geophysical Research Letters*, **38(13)**, doi:10.1029/2011gl047501.

Ciais, P. et al., 2013: Carbon and Other Biogeochemical Cycles. In: *Climate Change 2013: The Physical Science Basis. Contribution of Working Group I to the Fifth Assessment Report of the Intergovernmental Panel on Climate Change* [Stocker, T.F., D. Qin, G.-K. Plattner, M. Tignor, S.K. Allen, J. Boschung, A. Nauels, Y. Xia, V. Bex, and P.M. Midgley (eds.)]. Cambridge University Press, Cambridge, United Kingdom and New York, NY, USA, pp. 465–570, doi:10.1017/cbo9781107415324.015.

Ciavarella, A., P. Stott, and J. Lowe, 2017: Early benefits of mitigation in risk of regional climate extremes. *Nature Climate Change*, **7(5)**, 326–330, doi:10.1038/nclimate3259.

Clark, P.U. et al., 2016: Consequences of twenty-first-century policy for multi-millennial climate and sea-level change. *Nature Climate Change*, **6**, 360–369, doi:10.1038/nclimate2923.

Claussen, M. et al., 2002: Earth system models of intermediate complexity: closing the gap in the spectrum of climate system models. *Climate Dynamics*, **18(7)**, 579–586, doi:10.1007/s00382-001-0200-1.

Collins, M. et al., 2013: Long-term Climate Change: Projections, Commitments and Irreversibility. In: *Climate Change 2013: The Physical Science Basis. Contribution of Working Group I to the Fifth Assessment Report of the Intergovernmental Panel on Climate Change* [Stocker, T.F., D. Qin, G.-K. Plattner, M. Tignor, S.K. Allen, J. Boschung, A. Nauels, Y. Xia, V. Bex, and P.M. Midgley (eds.)]. Cambridge University Press, Cambridge, United Kingdom and New York, NY, USA, pp. 1029–1136, doi:10.1017/cbo9781107415324.024.

Collins, W.D., D.R. Feldman, C. Kuo, and N.H. Nguyen, 2018: Large regional shortwave forcing by anthropogenic methane informed by Jovian observations. *Science Advances*, **4(9)**, 1–10, doi:10.1126/sciadv.aas9593.

Collins, W.J. et al., 2017: AerChemMIP: quantifying the effects of chemistry and aerosols in CMIP6. *Geoscientific Model Development*, **10(2)**, 585–607, doi:10.5194/gmd-10-585-2017.

Colose, C.M., A.N. LeGrande, and M. Vuille, 2016: The influence of volcanic eruptions on the climate of tropical South America during the last millennium in an isotope-enabled general circulation model. *Climate of the Past*, **12(4)**, 961–979, doi:10.5194/cp-12-961-2016.

Connolly, P.J., G.B. McFiggans, R. Wood, and A. Tsiamis, 2014: Factors determining the most efficient spray distribution for marine cloud brightening. *Philosophical Transactions of the Royal Society A: Mathematical, Physical and Engineering Sciences*, **372(2031)**, 20140056, doi:10.1098/rsta.2014.0056.

Corti, S., A. Weisheimer, T.N. Palmer, F.J. Doblas-Reyes, and L. Magnusson, 2012: Reliability of decadal predictions. *Geophysical Research Letters*, **39**, L21712, doi:10.1029/2012gl053354.

Corti, S. et al., 2015: Impact of initial conditions versus external forcing in decadal climate predictions: A sensitivity experiment. *Journal of Climate*, **28**, 4454–4470, doi:10.1175/jcli-d-14-00671.1.

Counillon, F. et al., 2014: Seasonal-to-decadal predictions with the ensemble Kalman filter and the Norwegian Earth System Model: a twin experiment. *Tellus A: Dynamic Meteorology and Oceanography*, **66(1)**, 21074, doi:10.3402/tellusa.v66.21074.

Counillon, F. et al., 2016: Flow-dependent assimilation of sea surface temperature in isopycnal coordinates with the Norwegian Climate Prediction Model. *Tellus A: Dynamic Meteorology and Oceanography*, **68(1)**, 32437, doi:10.3402/tellusa.v68.32437.

ACCEPTED VERSION SUBJECT TO FINAL EDITS

Cox, P. and D. Stephenson, 2007: A Changing Climate for Prediction. *Science*, **317(5835)**, 207–208, doi:10.1126/science.1145956.
Cox, P.M., C. Huntingford, and M.S. Williamson, 2018: Emergent constraint on equilibrium climate sensitivity from global temperature variability. *Nature*, **553(7688)**, 319–322, doi:10.1038/nature25450.
Crook, J.A., P.M. Forster, and N. Stuber, 2011: Spatial patterns of modeled climate feedback and contributions to temperature response and polar amplification. *Journal of Climate*, **24**, 3575–3592, doi:10.1175/2011jcli3863.1.
Crook, J.A., L.S. Jackson, S.M. Osprey, and P.M. Forster, 2015a: A comparison of temperature and precipitation responses to different earth radiation management geoengineering schemes. *Journal of Geophysical Research*, **120(18)**, 9352–9373, doi:10.1002/2015jd023269.
Crook, J.A., L.S. Jackson, S.M. Osprey, and P.M. Forster, 2015b: A comparison of temperature and precipitation responses to different earth radiation management geoengineering schemes. *Journal of Geophysical Research*, **120(18)**, 9352–9373, doi:10.1002/2015jd023269.
Cubasch, U. et al., 2013: Introduction. In: *Climate Change 2013: The Physical Science Basis. Contribution of Working Group I to the Fifth Assessment Report of the Intergovernmental Panel on Climate Change* [Stocker, T.F., D. Qin, G.-K. Plattner, M. Tignor, S.K. Allen, J. Boschung, A. Nauels, Y. Xia, V. Bex, and P.M. Midgley (eds.)]. Cambridge University Press, Cambridge, United Kingdom and New York, NY, USA, pp. 119–158, doi:10.1017/cbo9781107415324.007.
Curry, C.L. et al., 2014: A multimodel examination of climate extremes in an idealized geoengineering experiment. *Journal of Geophysical Research: Atmospheres*, **119(7)**, 3900–3923, doi:10.1002/2013jd020648.
Curtis, P.E., P. Ceppi, and G. Zappa, 2020: Role of the mean state for the Southern Hemispheric jet stream response to CO2 forcing in CMIP6 models. *Environmental Research Letters*, **15(6)**, 064011, doi:10.1088/1748-9326/ab8331.
Dai, A. and C.E. Bloecker, 2019: Impacts of internal variability on temperature and precipitation trends in large ensemble simulations by two climate models. *Climate Dynamics*, **52(1–2)**, 289–306, doi:10.1007/s00382-018-4132-4.
Dai, P. et al., 2020: Seasonal to decadal predictions of regional Arctic sea ice by assimilating sea surface temperature in the Norwegian Climate Prediction Model. *Climate Dynamics*, **54(9–10)**, 3863–3878, doi:10.1007/s00382-020-05196-4.
Dai, Z., D.K. Weisenstein, and D.W. Keith, 2018: Tailoring Meridional and Seasonal Radiative Forcing by Sulfate Aerosol Solar Geoengineering. *Geophysical Research Letters*, **45(2)**, 1030–1039, doi:10.1002/2017gl076472.
Dakos, V. et al., 2008: Slowing down as an early warning signal for abrupt climate change. *Proceedings of the National Academy of Sciences*, **105(38)**, 14308–14312, doi:10.1073/pnas.0802430105.
Danabasoglu, G. and P.R. Gent, 2009: Equilibrium climate sensitivity: Is it accurate to use a slab ocean model? *Journal of Climate*, **22**, 2494–2499, doi:10.1175/2008jcli2596.1.
Davin, E.L., S.I. Seneviratne, P. Ciais, A. Olioso, and T. Wang, 2014: Preferential cooling of hot extremes from cropland albedo management. *Proceedings of the National Academy of Sciences of the United States of America*, **111(27)**, 9757–9761, doi:10.1073/pnas.1317323111.
Davini, P. and F. D'Andrea, 2020: From CMIP3 to CMIP6: Northern Hemisphere Atmospheric Blocking Simulation in Present and Future Climate. *Journal of Climate*, **33(23)**, 10021–10038, doi:10.1175/jcli-d-19-0862.1.
Davini, P., C. Cagnazzo, S. Gualdi, and A. Navarra, 2012: Bidimensional Diagnostics, Variability, and Trends of Northern Hemisphere Blocking. *Journal of Climate*, **25(19)**, 6496–6509, doi:10.1175/jcli-d-12-00032.1.
Davini, P. et al., 2017: Climate SPHINX: Evaluating the impact of resolution and stochastic physics parameterisations in the EC-Earth global climate model. *Geoscientific Model Development*, **10**, 1383–1402, doi:10.5194/gmd-10-1383-2017.
Davis, S.J. and R.H. Socolow, 2014: Commitment accounting of CO2emissions. *Environmental Research Letters*, **9(8)**, 84018, doi:10.1088/1748-9326/9/8/084018.
Dawson, A. and T.N. Palmer, 2015: Simulating weather regimes: impact of model resolution and stochastic parameterization. *Climate Dynamics*, **44(7–8)**, 2177–2193, doi:10.1007/s00382-014-2238-x.
de Coninck, H. et al., 2018: Strengthening and Implementing the Global Response Supplementary Material. In: *Global Warming of 1.5°C. An IPCC Special Report on the impacts of global warming of 1.5°C above pre-industrial levels and related global greenhouse gas emission pathways, in the context of strengthening the global response to the threat of climate change,* [Masson-Delmotte, V., P. Zhai, H.-O. Pörtner, D. Roberts, J. Skea, P.R. Shukla, A. Pirani, W. Moufouma-Okia, C. Péan, R. Pidcock, S. Connors, J.B.R. Matthews, Y. Chen, X. Zhou, M.I. Gomis, E. Lonnoy, T. Maycock, M. Tignor, and T. Waterfield (eds.)]. In Press, pp. 4SM: 1–82.
De Vries, H., R.J. Haarsma, and W. Hazeleger, 2012: Western European cold spells in current and future climate. *Geophysical Research Letters*, **39**, L04706, doi:10.1029/2011gl050665.
Desch, S.J. et al., 2017: Arctic ice management. *Earth's Future*, **5(1)**, 107–127, doi:10.1002/2016ef000410.
Deser, C., R.A. Tomas, and L. Sun, 2015: The Role of Ocean–Atmosphere Coupling in the Zonal-Mean Atmospheric Response to Arctic Sea Ice Loss. *Journal of Climate*, **28(6)**, 2168–2186, doi:10.1175/jcli-d-14-00325.1.
Deser, C., L. Terray, and A.S. Phillips, 2016: Forced and internal components of winter air temperature trends over North America during the past 50 years: Mechanisms and implications. *Journal of Climate*, **29**, 2237–2258, doi:10.1175/jcli-d-15-0304.1.

ACCEPTED VERSION SUBJECT TO FINAL EDITS

Deser, C., J.W. Hurrell, and A.S. Phillips, 2017: The role of the North Atlantic Oscillation in European climate projections. *Climate Dynamics*, **49(9–10)**, 3141–3157, doi:10.1007/s00382-016-3502-z.

Deser, C., R. Knutti, S. Solomon, and A.S. Phillips, 2012a: Communication of the role of natural variability in future North American climate. *Nature Climate Change*, **2(11)**, 775–779, doi:10.1038/nclimate1562.

Deser, C., A. Phillips, V. Bourdette, and H. Teng, 2012b: Uncertainty in climate change projections: the role of internal variability. *Climate Dynamics*, **38(3)**, 527–546, doi:10.1007/s00382-010-0977-x.

Deser, C., A.S. Phillips, M.A. Alexander, and B. Smoliak, 2014: Projecting North American climate over the next 50 years: Uncertainty due to internal variability. *Journal of Climate*, **27(6)**, 2271–2296, doi:10.1175/jcli-d-13-00451.1.

Deser, C. et al., 2020: Insights from Earth system model initial-condition large ensembles and future prospects. *Nature Climate Change*, **10(4)**, 277–286, doi:10.1038/s41558-020-0731-2.

Dhomse, S.S. et al., 2018: Estimates of ozone return dates from Chemistry-Climate Model Initiative simulations. *Atmospheric Chemistry and Physics*, **18(11)**, 8409–8438, doi:10.5194/acp-18-8409-2018.

Diamond, M.S., H.M. Director, R. Eastman, A. Possner, and R. Wood, 2020: Substantial Cloud Brightening From Shipping in Subtropical Low Clouds. *AGU Advances*, **1(1)**, e2019AV000111, doi:10.1029/2019av000111.

DiNezio, P.N., M. Puy, K. Thirumalai, F.-F. Jin, and J.E. Tierney, 2020: Emergence of an equatorial mode of climate variability in the Indian Ocean. *Science Advances*, **6(19)**, doi:10.1126/sciadv.aay7684.

Doblas-Reyes, F.J. et al., 2013: Initialized near-term regional climate change prediction. *Nature Communications*, **4**, 1715, doi:10.1038/ncomms2704.

Dong, B., J.M. Gregory, and R.T. Sutton, 2009: Understanding land-sea warming contrast in response to increasing greenhouse gases. Part I: Transient adjustment. *J. Climate*, **22**, 3079–3097.

Donohoe, A. and D.S. Battisti, 2013: The Seasonal Cycle of Atmospheric Heating and Temperature. *Journal of Climate*, **26(14)**, 4962–4980, doi:10.1175/jcli-d-12-00713.1.

Dosio, A. and E.M. Fischer, 2018: Will Half a Degree Make a Difference? Robust Projections of Indices of Mean and Extreme Climate in Europe Under 1.5°C, 2°C, and 3°C Global Warming. *Geophysical Research Letters*, **45(2)**, 935–944, doi:10.1002/2017gl076222.

Dosio, A., L. Mentaschi, E.M. Fischer, and K. Wyser, 2018: Extreme heat waves under 1.5°C and 2°C global warming. *Environmental Research Letters*, **13(5)**, 054006, doi:10.1088/1748-9326/aab827.

Drijfhout, S. et al., 2015: Catalogue of abrupt shifts in Intergovernmental Panel on Climate Change climate models.. *Proceedings of the National Academy of Sciences of the United States of America*, **112(43)**, E5777–E5786, doi:10.1073/pnas.1511451112.

Drost, F., D. Karoly, and K. Braganza, 2012: Communicating global climate change using simple indices: an update. *Climate Dynamics*, **39(3–4)**, 989–999, doi:10.1007/s00382-011-1227-6.

Du, Y. et al., 2013: Indian Ocean Variability in the CMIP5 Multimodel Ensemble: The Basin Mode. *Journal of Climate*, **26(18)**, 7240–7266, doi:10.1175/jcli-d-12-00678.1.

Duan, L., L. Cao, G. Bala, and K. Caldeira, 2018: Comparison of the Fast and Slow Climate Response to Three Radiation Management Geoengineering Schemes. *Journal of Geophysical Research: Atmospheres*, **123(21)**, 1,11,912–980, doi:10.1029/2018jd029034.

Duan, L., L. Cao, G. Bala, and K. Caldeira, 2019: Climate Response to Pulse Versus Sustained Stratospheric Aerosol Forcing. *Geophysical Research Letters*, **46(15)**, 8976–8984, doi:10.1029/2019gl083701.

Dunn-Sigouin, E., S.-W. Son, and H. Lin, 2013: Evaluation of Northern Hemisphere Blocking Climatology in the Global Environment Multiscale Model. *Monthly Weather Review*, **141(2)**, 707–727, doi:10.1175/mwr-d-12-00134.1.

Dunstone, N. et al., 2016: Skilful predictions of the winter North Atlantic Oscillation one year ahead. *Nature Geoscience*, **9(11)**, 809–814, doi:10.1038/ngeo2824.

Dunstone, N.J., D.M. Smith, and R. Eade, 2011: Multi-year predictability of the tropical Atlantic atmosphere driven by the high latitude North Atlantic Ocean. *Geophysical Research Letters*, **38(14)**, L14701, doi:10.1029/2011gl047949.

Dwyer, J.G., M. Biasutti, and A.H. Sobel, 2012: Projected Changes in the Seasonal Cycle of Surface Temperature. *Journal of Climate*, **25(18)**, 6359–6374, doi:10.1175/jcli-d-11-00741.1.

Eade, R. et al., 2014: Do seasonal-to-decadal climate predictions underestimate the predictability of the real world? *Geophysical Research Letters*, **41(15)**, 5620–5628, doi:10.1002/2014gl061146.

Eby, M. et al., 2013: Historical and idealized climate model experiments: an intercomparison of Earth system models of intermediate complexity. *Climate of the Past*, **9(3)**, 1111–1140, doi:10.5194/cp-9-1111-2013.

Ehlert, D. and K. Zickfeld, 2018: Irreversible ocean thermal expansion under carbon dioxide removal. *Earth Syst. Dynam*, **9**, 197–210, doi:10.5194/esd-9-197-2018.

Ekholm, T. and H. Korhonen, 2016: Climate change mitigation strategy under an uncertain Solar Radiation Management possibility. *Climatic Change*, **139(3)**, 503–515, doi:10.1007/s10584-016-1828-5.

Emori, S. and S.J. Brown, 2005: Dynamic and thermodynamic changes in mean and extreme precipitation under changed climate. *Geophysical Research Letters*, **32(17)**, doi:10.1029/2005gl023272.

Engelbrecht, F. et al., 2015: Projections of rapidly rising surface temperatures over Africa under low mitigation.

ACCEPTED VERSION SUBJECT TO FINAL EDITS

Environmental Research Letters, **10(8)**, 085004, doi:10.1088/1748-9326/10/8/085004.
Etminan, M., G. Myhre, E.J. Highwood, and K.P. Shine, 2016: Radiative forcing of carbon dioxide, methane, and nitrous oxide: A significant revision of the methane radiative forcing. *Geophysical Research Letters*, **43(24)**, 12,614–12,623, doi:10.1002/2016gl071930.
Evans, J.R.G., E.P.J. Stride, M.J. Edirisinghe, D.J. Andrews, and R.R. Simons, 2010: Can oceanic foams limit global warming? *Climate Research*, **42(2)**, 155–160, doi:10.3354/cr00885.
Evin, G. et al., 2019: Partitioning uncertainty components of an incomplete ensemble of climate projections using data augmentation. *Journal of Climate*, **32(8)**, 2423–2440, doi:10.1175/jcli-d-18-0606.1.
Eyring, V. et al., 2013: Long-term ozone changes and associated climate impacts in CMIP5 simulations. *Journal of Geophysical Research: Atmospheres*, **118(10)**, 5029–5060, doi:10.1002/jgrd.50316.
Eyring, V. et al., 2016: Overview of the Coupled Model Intercomparison Project Phase 6 (CMIP6) experimental design and organization. *Geoscientific Model Development*, **9(5)**, 1937–1958, doi:10.5194/gmd-9-1937-2016.
Fasullo, J.T., B.M. Sanderson, and K.E. Trenberth, 2015: Recent Progress in Constraining Climate Sensitivity With Model Ensembles. *Current Climate Change Reports*, **1(4)**, 268–275, doi:10.1007/s40641-015-0021-7.
Fasullo, J.T. et al., 2018: Persistent polar ocean warming in a strategically geoengineered climate. *Nature Geoscience*, **11(12)**, 910–914, doi:10.1038/s41561-018-0249-7.
Fedorov, A., S. Hu, A.T. Wittenberg, A.F.Z. Levine, and C. Deser, 2020: ENSO Low-Frequency Modulation and Mean State Interactions. In: *El Niño Southern Oscillation in a Changing Climate* [McPhaden, M., A. Santoso, and W. Cai (eds.)]. American Geophysical Union (AGU), Washington, DC, USA, pp. 173–198, doi:10.1002/9781119548164.ch8.
Feldmann, J., A. Levermann, and M. Mengel, 2019: Stabilizing the West Antarctic Ice Sheet by surface mass deposition. *Science Advances*, **5(7)**, doi:10.1126/sciadv.aaw4132.
Feng, H. and M. Zhang, 2015: Global land moisture trends: drier in dry and wetter in wet over land. *Scientific Reports*, **5(1)**, 18018, doi:10.1038/srep18018.
Ferraro, A.J. and H.G. Griffiths, 2016: Quantifying the temperature-independent effect of stratospheric aerosol geoengineering on global-mean precipitation in a multi-model ensemble. *Environmental Research Letters*, **11(3)**, 034012, doi:10.1088/1748-9326/11/3/034012.
Ferraro, A.J., E.J. Highwood, and A.J. Charlton-Perez, 2011: Stratospheric heating by potential geoengineering aerosols. *Geophysical Research Letters*, **38(24)**, 1–6, doi:10.1029/2011gl049761.
Ferraro, A.J., A.J. Charlton-Perez, and E.J. Highwood, 2015: Stratospheric dynamics and midlatitude jets under geoengineering with space mirrors and sulfate and titania aerosols. *Journal of Geophysical Research: Atmospheres*, **120(2)**, 414–429, doi:10.1002/2014jd022734.
Ferreira, D., J. Marshall, C.M. Bitz, S. Solomon, and A. Plumb, 2015: Antarctic ocean and sea ice response to ozone depletion: A two-time-scale problem. *Journal of Climate*, **28(3)**, 1206–1226, doi:10.1175/jcli-d-14-00313.1.
Ferro, C.A.T., 2017: Measuring forecast performance in the presence of observation error. *Quarterly Journal of the Royal Meteorological Society*, **143(708)**, 2665–2676, doi:10.1002/qj.3115.
Field, L. et al., 2018: Increasing Arctic Sea Ice Albedo Using Localized Reversible Geoengineering. *Earth's Future*, **6(6)**, 882–901, doi:10.1029/2018ef000820.
Finney, D.L. et al., 2018: A projected decrease in lightning under climate change. *Nature Climate Change*, **8(3)**, 210–213, doi:10.1038/s41558-018-0072-6.
Fischer, E.M. and R. Knutti, 2014: Heated debate on cold weather. *Nature Climate Change*, **4(7)**, 537–538, doi:10.1038/nclimate2286.
Fischer, E.M., D.M. Lawrence, and B.M. Sanderson, 2011: Quantifying uncertainties in projections of extremes-a perturbed land surface parameter experiment. *Climate Dynamics*, **37(7–8)**, 1381–1398, doi:10.1007/s00382-010-0915-y.
Fischer, E.M., J. Rajczak, and C. Schär, 2012: Changes in European summer temperature variability revisited. *Geophysical Research Letters*, **39**, L19702, doi:10.1029/2012gl052730.
Fischer, E.M., U. Beyerle, and R. Knutti, 2013: Robust spatially aggregated projections of climate extremes. *Nature Climate Change*, **3**, 1033–1038, doi:10.1038/nclimate2051.
Fischer, E.M., J. Sedláček, E. Hawkins, and R. Knutti, 2014: Models agree on forced response pattern of precipitation and temperature extremes. *Geophysical Research Letters*, **41(23)**, 8554–8562, doi:10.1002/2014gl062018.
Fischer, H. et al., 2018: Palaeoclimate constraints on the impact of 2°C anthropogenic warming and beyond. *Nature Geoscience*, **11**, 474–485, doi:10.1038/s41561-018-0146-0.
Fläschner, D., T. Mauritsen, and B. Stevens, 2016: Understanding the intermodel spread in global-mean hydrological sensitivity. *Journal of Climate*, **29(2)**, 801–817, doi:10.1175/jcli-d-15-0351.1.
Flato, G. et al., 2013: Evaluation of Climate Models. In: *Climate Change 2013: The Physical Science Basis. Contribution of Working Group I to the Fifth Assessment Report of the Intergovernmental Panel on Climate Change* [Stocker, T.F., D. Qin, G.-K. Plattner, M. Tignor, S.K. Allen, J. Boschung, A. Nauels, Y. Xia, V. Bex, and P.M. Midgley (eds.)]. Cambridge University Press, Cambridge, United Kingdom and New York, NY, USA, pp. 741–866, doi:10.1017/cbo9781107415324.020.
Flato, G.M., 2011: Earth system models: an overview. *Wiley Interdisciplinary Reviews: Climate Change*, **2(6)**, 783–

ACCEPTED VERSION SUBJECT TO FINAL EDITS

800, doi:10.1002/wcc.148.
Folland, C.K., 2002: Relative influences of the Interdecadal Pacific Oscillation and ENSO on the South Pacific Convergence Zone. *Geophysical Research Letters*, **29(13)**, 1643, doi:10.1029/2001gl014201.
Forster, P.M., A.C. Maycock, C.M. McKenna, and C.J. Smith, 2020: Latest climate models confirm need for urgent mitigation. *Nature Climate Change*, **10(1)**, 7–10, doi:10.1038/s41558-019-0660-0.
Francis, J.A. and S.J. Vavrus, 2015: Evidence for a wavier jet stream in response to rapid Arctic warming. *Environmental Research Letters*, **10(1)**, 014005, doi:10.1088/1748-9326/10/1/014005.
Fransner, F. et al., 2020: Ocean Biogeochemical Predictions – Initialization and Limits of Predictability. *Frontiers in Marine Science*, **7**, 386, doi:10.3389/fmars.2020.00386.
Fredriksen, H.-B., J. Berner, A.C. Subramanian, and A. Capotondi, 2020a: How Does El Niño–Southern Oscillation Change Under Global Warming – A First Look at CMIP6. *Geophysical Research Letters*, **47(22)**, doi:10.1029/2020gl090640.
Fredriksen, H.-B., J. Berner, A.C. Subramanian, and A. Capotondi, 2020b: How Does El Niño–Southern Oscillation Change Under Global Warming – A First Look at CMIP6. *Geophysical Research Letters*, **47(22)**, doi:10.1029/2020gl090640.
Freund, M.B., J.R. Brown, B.J. Henley, D.J. Karoly, and J.N. Brown, 2020a: Warming Patterns Affect El Niño Diversity in CMIP5 and CMIP6 Models. *Journal of Climate*, **33(19)**, 8237–8260, doi:10.1175/jcli-d-19-0890.1.
Freund, M.B., J.R. Brown, B.J. Henley, D.J. Karoly, and J.N. Brown, 2020b: Warming Patterns Affect El Niño Diversity in CMIP5 and CMIP6 Models. *Journal of Climate*, **33(19)**, 8237–8260, doi:10.1175/jcli-d-19-0890.1.
Friedlingstein, P. et al., 2014: Uncertainties in CMIP5 climate projections due to carbon cycle feedbacks. *Journal of Climate*, **27(2)**, 511–526, doi:10.1175/jcli-d-12-00579.1.
Frieler, K., M. Meinshausen, M. Mengel, N. Braun, and W. Hare, 2012: A scaling approach to probabilistic assessment of regional climate change. *Journal of Climate*, **25(9)**, 3117–3144, doi:10.1175/jcli-d-11-00199.1.
Frisch, M., 2015: Predictivism and old evidence: a critical look at climate model tuning. *European Journal for Philosophy of Science*, **5(2)**, 171–190, doi:10.1007/s13194-015-0110-4.
Froelicher, T.L. et al., 2015: Dominance of the Southern Ocean in anthropogenic carbon and heat uptake in CMIP5 models. *Journal of Climate*, **28(2)**, 862–886, doi:10.1175/jcli-d-14-00117.1.
Frölicher, T.L. and D.J. Paynter, 2015: Extending the relationship between global warming and cumulative carbon emissions to multi-millennial timescales. *Environmental Research Letters*, **10(7)**, 075002, doi:10.1088/1748-9326/10/7/075002.
Frölicher, T.L., M. Winton, and J.L. Sarmiento, 2014: Continued global warming after CO2 emissions stoppage. *Nature Climate Change*, **4(1)**, 40–44, doi:10.1038/nclimate2060.
Fu, Q. and S. Feng, 2014: Responses of terrestrial aridity to global warming. *Journal of Geophysical Research: Atmospheres*, **119(13)**, 7863–7875, doi:10.1002/2014jd021608.
Fu, Q., P. Lin, S. Solomon, and D.L. Hartmann, 2015: Observational evidence of strengthening of the Brewer-Dobson circulation since 1980. *Journal of Geophysical Research Atmospheres*, **120**, 10,214–10,228, doi:10.1038/175238c0.
Fu, Q., S. Solomon, H.A. Pahlavan, and P. Lin, 2019: Observed changes in Brewer–Dobson circulation for 1980–2018. *Environmental Research Letters*, **14(11)**, 114026, doi:10.1088/1748-9326/ab4de7.
Fučkar, N.S., D. Volpi, V. Guemas, and F.J. Doblas-Reyes, 2014: A posteriori adjustment of near-term climate predictions: Accounting for the drift dependence on the initial conditions. *Geophysical Research Letters*, **41(14)**, 5200–5207, doi:10.1002/2014gl060815.
Fujita, M. et al., 2019: Precipitation Changes in a Climate With 2-K Surface Warming From Large Ensemble Simulations Using 60-km Global and 20-km Regional Atmospheric Models. *Geophysical Research Letters*, **46(1)**, 435–442, doi:10.1029/2018gl079885.
Fuss, S. et al., 2018: Negative emissions-Part 2: Costs, potentials and side effects. *Environmental Research Letters*, **13(6)**, 063002, doi:10.1088/1748-9326/aabf9f.
Fyfe, J.C., G.J. Boer, and G.M. Flato, 1999: The Arctic and Antarctic oscillations and their projected changes under global warming. *Geophysical Research Letters*, **26(11)**, 1601–1604, doi:10.1029/1999gl900317.
Gabriel, C.J., A. Robock, L. Xia, B. Zambri, and B. Kravitz, 2017: The G4Foam Experiment: global climate impacts of regional ocean albedo modification. *Atmospheric Chemistry and Physics*, **17(1)**, 595–613, doi:10.5194/acp-17-595-2017.
Gagné, M., M.C. Kirchmeier-Young, N.P. Gillett, and J.C. Fyfe, 2017: Arctic sea ice response to the eruptions of Agung, El Chichón, and Pinatubo. *Journal of Geophysical Research*, **122(15)**, 8071–8078, doi:10.1002/2017jd027038.
Gagné, M.-, N.P. Gillett, and J.C. Fyfe, 2015: Impact of aerosol emission controls on future Arctic sea ice cover. *Geophysical Research Letters*, **42(20)**, 8481–8488, doi:10.1002/2015gl065504.
Gagné, M.-, J.C. Fyfe, N.P. Gillett, I. Polyakov, and G.M. Flato, 2017: Aerosol-driven increase in Arctic sea ice over the middle of the twentieth century. *Geophysical Research Letters*, **44(14)**, 7338–7346, doi:10.1002/2016gl071941.
García-Serrano, J., V. Guemas, and F.J. Doblas-Reyes, 2015a: Added-value from initialization in predictions of Atlantic

ACCEPTED VERSION SUBJECT TO FINAL EDITS

multi-decadal variability. *Climate Dynamics*, **44(9–10)**, 2539–2555, doi:10.1007/s00382-014-2370-7.
García-Serrano, J., V. Guemas, and F.J. Doblas-Reyes, 2015b: Added-value from initialization in predictions of Atlantic multi-decadal variability. *Climate Dynamics*, **44(9–10)**, 2539–2555, doi:10.1007/s00382-014-2370-7.
Gasparini, B. and U. Lohmann, 2016: Why cirrus cloud seeding cannot substantially cool the planet. *Journal of Geophysical Research: Atmospheres*, **121(9)**, 4877–4893, doi:10.1002/2015jd024666.
Gasparini, B., Z. McGraw, T. Storelvmo, and U. Lohmann, 2020: To what extent can cirrus cloud seeding counteract global warming? *Environmental Research Letters*, **15(5)**, 54002, doi:10.1088/1748-9326/ab71a3.
Gasparini, B., S. Münch, L. Poncet, M. Feldmann, and U. Lohmann, 2017: Is increasing ice crystal sedimentation velocity in geoengineering simulations a good proxy for cirrus cloud seeding? *Atmospheric Chemistry and Physics*, **17(7)**, 4871–4885, doi:10.5194/acp-17-4871-2017.
Geden, O. and A. Loeschel, 2017: Define limits for temperature overshoot targets. *Nature Geoscience*, **10(12)**, 881–882, doi:10.1038/s41561-017-0026-z.
Geng, T., Y. Yang, and L. Wu, 2019: On the Mechanisms of Pacific Decadal Oscillation Modulation in a Warming Climate. *Journal of Climate*, **32(5)**, 1443–1459, doi:10.1175/jcli-d-18-0337.1.
Gertler, C.G. et al., 2020: Weakening of the Extratropical Storm Tracks in Solar Geoengineering Scenarios. *Geophysical Research Letters*, **47(11)**, e2020GL087348, doi:10.1029/2020gl087348.
Gidden, M.J. et al., 2019: Global emissions pathways under different socioeconomic scenarios for use in CMIP6: a dataset of harmonized emissions trajectories through the end of the century. *Geosci. Model Dev.*, **12(4)**, 1443–1475, doi:10.5194/gmd-12-1443-2019.
Gillett, N.P. and J.C. Fyfe, 2013: Annular mode changes in the CMIP5 simulations. *Geophysical Research Letters*, **40(6)**, 1189–1193, doi:10.1002/grl.50249.
Gillett, N.P., V.K. Arora, D. Matthews, and M.R. Allen, 2013: Constraining the Ratio of Global Warming to Cumulative CO2 Emissions Using CMIP5 Simulations. *Journal of Climate*, **26(18)**, 6844–6858, doi:10.1175/jcli-d-12-00476.1.
Gillett, N.P. et al., 2021: Constraining human contributions to observed warming since the pre-industrial period. *Nature Climate Change*, **11(3)**, 207–212, doi:10.1038/s41558-020-00965-9.
Giorgi, F. et al., 2016: Enhanced summer convective rainfall at Alpine high elevations in response to climate warming. *Nature Geoscience*, **9(8)**, 584–589, doi:10.1038/ngeo2761.
Goddard, L. et al., 2013: A verification framework for interannual-to-decadal predictions experiments. *Climate Dynamics*, **40(1–2)**, 245–272, doi:10.1007/s00382-012-1481-2.
Golledge, N.R. et al., 2019: Global environmental consequences of twenty-first-century ice-sheet melt. *Nature*, **566(7742)**, 65–72, doi:10.1038/s41586-019-0889-9.
Gong, D. and S. Wang, 1999: Definition of Antarctic Oscillation index. *Geophysical Research Letters*, **26(4)**, 459–462, doi:10.1029/1999gl900003.
González, M.F., T. Ilyina, S. Sonntag, and H. Schmidt, 2018: Enhanced Rates of Regional Warming and Ocean Acidification After Termination of Large-Scale Ocean Alkalinization. *Geophysical Research Letters*, **45(14)**, 7120–7129, doi:10.1029/2018gl077847.
Good, P. et al., 2015: Nonlinear regional warming with increasing CO2 concentrations. *Nature Climate Change*, **5**, 138–142, doi:10.1038/nclimate2498.
Good, P. et al., 2016: Large differences in regional precipitation change between a first and second 2 K of global warming. *Nature Communications*, **7**, 13667, doi:10.1038/ncomms13667.
Good, P. et al., 2018: Recent progress in understanding climate thresholds. *Progress in Physical Geography: Earth and Environment*, **42(1)**, 24–60, doi:10.1177/0309133317751843.
Goodman, J. and J. Marshall, 1999: A Model of Decadal Middle-Latitude Atmosphere–Ocean Coupled Modes. *Journal of Climate*, **12(2)**, 621–641, doi:10.1175/1520-0442(1999)012<0621:amodml>2.0.co;2.
Goosse, H. et al., 2018: Quantifying climate feedbacks in polar regions. *Nature Communications*, **9(1)**, 1919, doi:10.1038/s41467-018-04173-0.
Goyal, R., A. Sen Gupta, M. Jucker, and M.H. England, 2021: Historical and Projected Changes in the Southern Hemisphere Surface Westerlies. *Geophysical Research Letters*, **48**, e2020GL090849, doi:10.1029/2020gl090849.
Graff, L.S. and J.H. LaCasce, 2014: Changes in Cyclone Characteristics in Response to Modified SSTs. *Journal of Climate*, **27(11)**, 4273–4295, doi:10.1175/jcli-d-13-00353.1.
Gregory, J.M. and J.F.B. Mitchell, 1995: Simulation of daily variability of surface temperature and precipitation over europe in the current and 2 × CO2 climates using the UKMO climate model. *Quarterly Journal of the Royal Meteorological Society*, **121(526)**, 1451–1476, doi:10.1002/qj.49712152611.
Greve, P. and S.I. Seneviratne, 2015: Assessment of future changes in water availability and aridity. *Geophysical Research Letters*, **42(13)**, 5493–5499, doi:10.1002/2015gl064127.
Greve, P. et al., 2014: Global assessment of trends in wetting and drying over land. *Nature Geoscience*, **7(10)**, 716–721, doi:10.1038/ngeo2247.
Grieger, J., G.C. Leckebusch, M.G. Donat, M. Schuster, and U. Ulbrich, 2014: Southern Hemisphere winter cyclone activity under recent and future climate conditions in multi-model AOGCM simulations. *International Journal of*

ACCEPTED VERSION SUBJECT TO FINAL EDITS

Climatology, **34(12)**, 3400–3416, doi:10.1002/joc.3917.
Grise, K.M. and L.M. Polvani, 2014a: Is climate sensitivity related to dynamical sensitivity? A Southern Hemisphere perspective. *Geophys. Res. Lett.*, **41**, 534–540, doi:10.1002/2013gl058466.
Grise, K.M. and L.M. Polvani, 2014b: The response of midlatitude jets to increased CO2: Distinguishing the roles of sea surface temperature and direct radiative forcing. *Geophysical Research Letters*, **41(19)**, 6863–6871, doi:10.1002/2014gl061638.
Grise, K.M. and L.M. Polvani, 2016: Is climate sensitivity related to dynamical sensitivity? *Journal of Geophysical Research Atmospheres*, **121**, 5159–5176, doi:10.1002/2015jd024687.
Grise, K.M. and L.M. Polvani, 2017: Understanding the Time Scales of the Tropospheric Circulation Response to Abrupt CO 2 Forcing in the Southern Hemisphere: Seasonality and the Role of the Stratosphere. *Journal of Climate*, **30(21)**, 8497–8515, doi:10.1175/jcli-d-16-0849.1.
Gruber, S. et al., 2019a: A Process Study on Thinning of Arctic Winter Cirrus Clouds With High-Resolution ICON-ART Simulations. *Journal of Geophysical Research: Atmospheres*, **124(11)**, 5860–5888, doi:10.1029/2018jd029815.
Gruber, S. et al., 2019b: A Process Study on Thinning of Arctic Winter Cirrus Clouds With High-Resolution ICON-ART Simulations. *Journal of Geophysical Research: Atmospheres*, **124(11)**, 5860–5888, doi:10.1029/2018jd029815.
Grübler, A. and N. Nakicenovic, 2001: Identifying dangers in an uncertain climate. *Nature*, **412(6842)**, 15, doi:10.1038/35083752.
Gryspeerdt, E., T.W.P. Smith, E. O'Keeffe, M.W. Christensen, and F.W. Goldsworth, 2019: The Impact of Ship Emission Controls Recorded by Cloud Properties. *Geophysical Research Letters*, **46(21)**, 12547–12555, doi:10.1029/2019gl084700.
Guemas, V. et al., 2013: The Indian Ocean: The Region of Highest Skill Worldwide in Decadal Climate Prediction. *Journal of Climate*, **26(3)**, 726–739, doi:10.1175/jcli-d-12-00049.1.
Guemas, V. et al., 2016: A review on Arctic sea-ice predictability and prediction on seasonal to decadal time-scales. *Quarterly Journal of the Royal Meteorological Society*, **142**, 546–561, doi:10.1002/qj.2401.
Haarsma, R.J., F. Selten, B. Hurk, W. Hazeleger, and X. Wang, 2009: Drier Mediterranean soils due to greenhouse warming bring easterly winds over summertime central Europe. *Geophysical Research Letters*, **36(4)**, doi:10.1029/2008gl036617.
Hall, A., 2004: The Role of Surface Albedo Feedback in Climate. *Journal of Climate*, **17(7)**, 1550–1568, doi:10.1175/1520-0442(2004)017<1550:trosaf>2.0.co;2.
Hall, A. and X. Qu, 2006: Using the current seasonal cycle to constrain snow albedo feedback in future climate change. *Geophysical Research Letters*, **33(3)**, L03502, doi:10.1029/2005gl025127.
Hand, R., J. Bader, D. Matei, R. Ghosh, and J.H. Jungclaus, 2020: Changes of Decadal SST Variations in the Subpolar North Atlantic under Strong CO2 Forcing as an Indicator for the Ocean Circulation's Contribution to Atlantic Multidecadal Variability. *Journal of Climate*, **33(8)**, 3213–3228, doi:10.1175/jcli-d-18-0739.1.
Hanna, E., X. Fettweis, and R.J. Hall, 2018: Brief communication: Recent changes in summer Greenland blocking captured by none of the CMIP5 models. *The Cryosphere*, **12(10)**, 3287–3292, doi:10.5194/tc-12-3287-2018.
Hansen, J. et al., 1984: Climate sensitivity: Analysis of feedback mechanisms. In: *Climate Processes and Climate Sensitivity* [Hansen, J.E. and T. Takahashi (eds.)]. American Geophysical Union (AGU), Washington, DC, USA, pp. 130–163, doi:10.1029/gm029p0130.
Hardiman, S.C., N. Butchart, and N. Calvo, 2014: The morphology of the Brewer-Dobson circulation and its response to climate change in CMIP5 simulations. *Quarterly Journal of the Royal Meteorological Society*, **140(683)**, 1958–1965, doi:10.1002/qj.2258.
Harrington, L.J. et al., 2016: Poorest countries experience earlier anthropogenic emergence of daily temperature extremes. *Environmental Research Letters*, **11(5)**, 055007, doi:10.1088/1748-9326/11/5/055007.
Hartmann, D.L. et al., 2013: Observations: Atmosphere and Surface. In: *Climate Change 2013: The Physical Science Basis. Contribution of Working Group I to the Fifth Assessment Report of the Intergovernmental Panel on Climate Change* [Stocker, T.F., D. Qin, G.-K. Plattner, M. Tignor, S.K. Allen, J. Boschung, A. Nauels, Y. Xia, V. Bex, and P.M. Midgley (eds.)]. Cambridge University Press, Cambridge, United Kingdom and New York, NY, USA, pp. 159–254, doi:10.1017/cbo9781107415324.008.
Harvey, B.J., L.C. Shaffrey, and T.J. Woollings, 2014: Equator-to-pole temperature differences and the extra-tropical storm track responses of the CMIP5 climate models. *Climate Dynamics*, **43(5–6)**, 1171–1182, doi:10.1007/s00382-013-1883-9.
Harvey, B.J., L.C. Shaffrey, and T.J. Woollings, 2015: Deconstructing the climate change response of the Northern Hemisphere wintertime storm tracks. *Climate Dynamics*, **45(9–10)**, 2847–2860, doi:10.1007/s00382-015-2510-8.
Harvey, B.J., P. Cook, L.C. Shaffrey, and R. Schiemann, 2020: The Response of the Northern Hemisphere Storm Tracks and Jet Streams to Climate Change in the CMIP3, CMIP5, and CMIP6 Climate Models. *Journal of Geophysical Research: Atmospheres*, **125(23)**, e2020JD032701, doi:10.1029/2020jd032701.
Haszpra, T., M. Herein, and T. Bódai, 2020: Investigating ENSO and its teleconnections under climate change in an ensemble view – a new perspective. *Earth System Dynamics*, **11(1)**, 267–280, doi:10.5194/esd-11-267-2020.

ACCEPTED VERSION SUBJECT TO FINAL EDITS

Hausfather, Z. and G.P. Peters, 2020: Emissions – the 'business as usual' story is misleading. *Nature*, **577**, 618–620, doi:10.1038/d41586-020-00177-3.
Hausfather, Z., H.F. Drake, T. Abbott, and G.A. Schmidt, 2020: Evaluating the performance of past climate model projections. *Geophysical Research Letters*, **47(1)**, e2019GL085378, doi:10.1029/2019gl085378.
Hawcroft, M., E. Walsh, K. Hodges, and G. Zappa, 2018: Significantly increased extreme precipitation expected in Europe and North America from extratropical cyclones. *Environmental Research Letters*, **13(12)**, 124006, doi:10.1088/1748-9326/aaed59.
Hawkins, E. and R. Sutton, 2009: The Potential to Narrow Uncertainty in Regional Climate Predictions. *Bulletin of the American Meteorological Society*, **90(8)**, 1095–1108, doi:10.1175/2009bams2607.1.
Hawkins, E. and R. Sutton, 2011: The potential to narrow uncertainty in projections of regional precipitation change. *Climate Dynamics*, **37(1)**, 407–418, doi:10.1007/s00382-010-0810-6.
Hawkins, E. and R. Sutton, 2012: Time of emergence of climate signals. *Geophysical Research Letters*, **39(1)**, L01702, doi:10.1029/2011gl050087.
Hawkins, E. and R. Sutton, 2016: Connecting Climate Model Projections of Global Temperature Change with the Real World. *Bulletin of the American Meteorological Society*, **97(6)**, 963–980, doi:10.1175/bams-d-14-00154.1.
Hawkins, E., R.S. Smith, J.M. Gregory, and D.A. Stainforth, 2016: Irreducible uncertainty in near-term climate projections. *Climate Dynamics*, **46(11)**, 3807–3819, doi:10.1007/s00382-015-2806-8.
Hazeleger, W. et al., 2010: EC-Earth. *Bulletin of the American Meteorological Society*, **91(10)**, 1357–1364, doi:10.1175/2010bams2877.1.
Hazeleger, W. et al., 2013: Multiyear climate predictions using two initialization strategies. *Geophysical Research Letters*, **40(9)**, 1794–1798, doi:10.1002/grl.50355.
He, J. and B.J. Soden, 2017: A re-examination of the projected subtropical precipitation decline. *Nature Climate Change*, **7(1)**, 53–57, doi:10.1038/nclimate3157.
He, J. et al., 2018: Precipitation Sensitivity to Local Variations in Tropical Sea Surface Temperature. *Journal of Climate*, **31(22)**, 9225–9238, doi:10.1175/jcli-d-18-0262.1.
He, Y. et al., 2017: Reduction of initial shock in decadal predictions using a new initialization strategy. *Geophysical Research Letters*, **44(16)**, 8538–8547, doi:10.1002/2017gl074028.
He, Y. et al., 2020: A new DRP-4DVar-based coupled data assimilation system for decadal predictions using a fast online localization technique. *Climate Dynamics*, **54(7–8)**, 3541–3559, doi:10.1007/s00382-020-05190-w.
Hedemann, C., T. Mauritsen, J. Jungclaus, and J. Marotzke, 2017: The subtle origins of surface-warming hiatuses. *Nature Climate Change*, **7(5)**, 336–339, doi:10.1038/nclimate3274.
Held, I.M. and B.J. Soden, 2006a: Robust responses of the hydrological cycle to global warming. *Journal of Climate*, **19(21)**, 5686–5699, doi:10.1175/jcli3990.1.
Held, I.M. and B.J. Soden, 2006b: Robust Responses of the Hydrological Cycle to Global Warming. *Journal of Climate*, **19(21)**, 5686–5699, doi:10.1175/jcli3990.1.
Held, I.M. et al., 2010: Probing the Fast and Slow Components of Global Warming by Returning Abruptly to Preindustrial Forcing. *Journal of Climate*, **23(9)**, 2418–2427, doi:10.1175/2009jcli3466.1.
Henley, B.J., 2017: Pacific decadal climate variability: Indices, patterns and tropical-extratropical interactions. *Global and Planetary Change*, **155**, 42–55, doi:10.1016/j.gloplacha.2017.06.004.
Herger, N., B.M. Sanderson, and R. Knutti, 2015: Improved pattern scaling approaches for the use in climate impact studies. *Geophysical Research Letters*, **42(9)**, 3486–3494, doi:10.1002/2015gl063569.
Hermanson, L. et al., 2014: Forecast cooling of the Atlantic subpolar gyre and associated impacts. *Geophysical Research Letters*, **41(14)**, 5167–5174, doi:10.1002/2014gl060420.
Hermanson, L. et al., 2020: Robust Multiyear Climate Impacts of Volcanic Eruptions in Decadal Prediction Systems. *Journal of Geophysical Research: Atmospheres*, **125(9)**, doi:10.1029/2019jd031739.
Hewitt, A.J. et al., 2016: Sources of Uncertainty in Future Projections of the Carbon Cycle. *Journal of Climate*, **29(20)**, 7203–7213, doi:10.1175/jcli-d-16-0161.1.
Hezel, P.J., T. Fichefet, and F. Massonnet, 2014: Modeled Arctic sea ice evolution through 2300 in CMIP5 extended RCPs. *The Cryosphere*, **8(4)**, 1195–1204, doi:10.5194/tc-8-1195-2014.
Hienola, A. et al., 2018: The impact of aerosol emissions on the 1.5°C pathways. *Environmental Research Letters*, **13(4)**, 044011, doi:10.1088/1748-9326/aab1b2.
Hill, S. and Y. Ming, 2012: Nonlinear climate response to regional brightening of tropical marine stratocumulus. *Geophysical Research Letters*, **39(15)**, L15707, doi:10.1029/2012gl052064.
Hingray, B. and M. Saïd, 2014: Partitioning Internal Variability and Model Uncertainty Components in a Multimember Multimodel Ensemble of Climate Projections. *Journal of Climate*, **27(17)**, 6779–6798, doi:10.1175/jcli-d-13-00629.1.
Hingray, B., J. Blanchet, G. Evin, and J.P. Vidal, 2019: Uncertainty component estimates in transient climate projections: Precision of estimators in a single time or time series approach. *Climate Dynamics*, **53(5–6)**, 2501–2516, doi:10.1007/s00382-019-04635-1.
Ho, E., D. Budescu, V. Bosetti, D.P. van Vuuren, and K. Keller, 2019: Not all carbon dioxide emission scenarios are equally likely: a subjective expert assessment. *Climatic Change*, **155(4)**, 545–561, doi:10.1007/s10584-019-

ACCEPTED VERSION SUBJECT TO FINAL EDITS

02500-y.
Hoegh-Guldberg, O. et al., 2018: Impacts of 1.5°C Global Warming on Natural and Human Systems. In: *Global Warming of 1.5°C. An IPCC Special Report on the impacts of global warming of 1.5°C above pre-industrial levels and related global greenhouse gas emission pathways, in the context of strengthening the global response to the threat of climate change,* [Masson-Delmotte, V., P. Zhai, H.-O. Pörtner, D. Roberts, J. Skea, P.R. Shukla, A. Pirani, W. Moufouma-Okia, C. Péan, R. Pidcock, S. Connors, J.B.R. Matthews, Y. Chen, X. Zhou, M.I. Gomis, E. Lonnoy, T. Maycock, M. Tignor, and T. Waterfield (eds.)]. In Press, pp. 175–311.
Hoerling, M. et al., 2011: On North American Decadal Climate for 2011–20. *Journal of Climate*, **24(16)**, 4519–4528, doi:10.1175/2011jcli4137.1.
Holland, M.M. and C.M. Bitz, 2003: Polar amplification of climate change in coupled models. *Climate Dynamics*, **21(3–4)**, 221–232, doi:10.1007/s00382-003-0332-6.
Holmes, C.R., T. Woollings, E. Hawkins, and H. de Vries, 2016: Robust Future Changes in Temperature Variability under Greenhouse Gas Forcing and the Relationship with Thermal Advection. *Journal of Climate*, **29(6)**, 2221–2236, doi:10.1175/jcli-d-14-00735.1.
Hong, Y., G. Liu, and J.-L.F. Li, 2016: Assessing the Radiative Effects of Global Ice Clouds Based on CloudSat and CALIPSO Measurements. *Journal of Climate*, **29(21)**, 7651–7674, doi:10.1175/jcli-d-15-0799.1.
Hong, Y. et al., 2017: Impact of the GeoMIP G1 sunshade geoengineering experiment on the Atlantic meridional overturning circulation. *Environmental Research Letters*, **12(3)**, doi:10.1088/1748-9326/aa5fb8.
Horowitz, H.M. et al., 2020: Effects of Sea Salt Aerosol Emissions for Marine Cloud Brightening on Atmospheric Chemistry: Implications for Radiative Forcing. *Geophysical Research Letters*, **47(4)**, e2019GL085838, doi:10.1029/2019gl085838.
Hoskins, B. and T. Woollings, 2015: Persistent Extratropical Regimes and Climate Extremes. *Current Climate Change Reports*, **1(3)**, 115–124, doi:10.1007/s40641-015-0020-8.
Hsu, P.-, T. Li, H. Murakami, and A. Kitoh, 2013: Future change of the global monsoon revealed from 19 CMIP5 models. *Journal of Geophysical Research: Atmospheres*, **118(3)**, 1247–1260, doi:10.1002/jgrd.50145.
Huang, P. and S.-P. Xie, 2015: Mechanisms of change in ENSO-induced tropical Pacific rainfall variability in a warming climate. *Nature Geoscience*, **8(12)**, 922–926, doi:10.1038/ngeo2571.
Huntingford, C., P.D. Jones, V.N. Livina, T.M. Lenton, and P.M. Cox, 2013: No increase in global temperature variability despite changing regional patterns. *Nature*, **500(7462)**, 327–330, doi:10.1038/nature12310.
Hurd, C.L., A. Lenton, B. Tilbrook, and P.W. Boyd, 2018: Current understanding and challenges for oceans in a higher-CO2 world. *Nature Climate Change*, **8(8)**, 686–694, doi:10.1038/s41558-018-0211-0.
Hwang, Y.-T., D.M.W. Frierson, and S.M. Kang, 2013: Anthropogenic sulfate aerosol and the southward shift of tropical precipitation in the late 20th century. *Geophysical Research Letters*, **40(11)**, 2845–2850, doi:10.1002/grl.50502.
Iles, C.E. and G.C. Hegerl, 2014: The global precipitation response to volcanic eruptions in the CMIP5 models. *Environmental Research Letters*, **9(10)**, 104012, doi:10.1088/1748-9326/9/10/104012.
Iles, C.E. and G.C. Hegerl, 2015: Systematic change in global patterns of streamflow following volcanic eruptions. *Nature Geoscience*, **8**, 838–842, doi:10.1038/ngeo2545.
Iles, C.E., G.C. Hegerl, A.P. Schurer, and X. Zhang, 2013: The effect of volcanic eruptions on global precipitation. *Journal of Geophysical Research: Atmospheres*, **118(16)**, 8770–8786, doi:10.1002/jgrd.50678.
Illing, S., C. Kadow, H. Pohlmann, and C. Timmreck, 2018: Assessing the impact of a future volcanic eruption on decadal predictions. *Earth System Dynamics*, **9(2)**, doi:10.5194/esd-9-701-2018.
IPCC, 2013: Climate Change 2013: The Physical Science Basis. Contribution of Working Group I to the Fifth Assessment Report of the Intergovernmental Panel on Climate Change. In: [Stocker, T.F., D. Qin, G.-K. Plattner, M. Tignor, S.K. Allen, J. Boschung, A. Nauels, Y. Xia, V. Bex, and P.M. Midgley (eds.)]. Cambridge University Press, Cambridge, United Kingdom and New York, NY, USA, pp. 1535, doi:10.1017/cbo9781107415324.
IPCC, 2014: Climate Change 2014: Mitigation of Climate Change. Contribution of Working Group III to the Fifth Assessment Report of the Intergovernmental Panel on Climate Change. [Edenhofer, O., R. Pichs-Madruga, Y. Sokona, E. Farahani, S. Kadner, K. Seyboth, A. Adler, I. Baum, S. Brunner, P. Eickemeier, B. Kriemann, J. Savolainen, S. Schlömer, C. Stechow, T. Zwickel, and J.C. Minx (eds.)]. Cambridge University Press, Cambridge, United Kingdom and New York, NY, USA, 1435 pp., doi:10.1017/cbo9781107415416.
IPCC, 2018: Summary for Policymakers. In: *Global Warming of 1.5°C. An IPCC Special Report on the impacts of global warming of 1.5°C above pre-industrial levels and related global greenhouse gas emission pathways, in the context of strengthening the global response to the threat of climate change,* [Masson-Delmotte, V., P. Zhai, H.-O. Pörtner, D. Roberts, J. Skea, P.R. Shukla, A. Pirani, W. Moufouma-Okia, C. Péan, R. Pidcock, S. Connors, J.B.R. Matthews, Y. Chen, X. Zhou, M.I. Gomis, E. Lonnoy, T. Maycock, M. Tignor, and T. Waterfield (eds.)]. In Press, pp. 3–24.
IPCC, 2019: IPCC Special Report on the Ocean and Cryosphere in a Changing Climate. [Pörtner, H.-O., D.C. Roberts, V. Masson-Delmotte, P. Zhai, M. Tignor, E. Poloczanska, K. Mintenbeck, A. Alegria, M. Nicolai, A. Okem, J. Petzold, B. Rama, and N.M. Weyer (eds.)]. In Press, 755 pp.

ACCEPTED VERSION SUBJECT TO FINAL EDITS

Irvine, P. et al., 2019: Halving warming with idealized solar geoengineering moderates key climate hazards. *Nature Climate Change*, **9(4)**, 295–299, doi:10.1038/s41558-019-0398-8.
Irvine, P.J. and D.W. Keith, 2020: Halving warming with stratospheric aerosol geoengineering moderates policy-relevant climate hazards. *Environmental Research Letters*, **15(4)**, 44011, doi:10.1088/1748-9326/ab76de.
Irvine, P.J., R.L. Sriver, and K. Keller, 2012: Tension between reducing sea-level rise and global warming through solar-radiation management. *Nature Climate Change*, **2(2)**, 97–100, doi:10.1038/nclimate1351.
Irvine, P.J., B. Kravitz, M.G. Lawrence, and H. Muri, 2016: An overview of the Earth system science of solar geoengineering. *Wiley Interdisciplinary Reviews: Climate Change*, **7(6)**, 815–833, doi:10.1002/wcc.423.
Ishizaki, Y. et al., 2013: Dependence of Precipitation Scaling Patterns on Emission Scenarios for Representative Concentration Pathways. *Journal of Climate*, **26(22)**, 8868–8879, doi:10.1175/jcli-d-12-00540.1.
Izumi, K., P.J. Bartlein, and S.P. Harrison, 2013: Consistent large-scale temperature responses in warm and cold climates. *Geophysical Research Letters*, **40**, 1817–1823, doi:10.1002/grl.50350.
Jackson, L.C., N. Schaller, R.S. Smith, M.D. Palmer, and M. Vellinga, 2014: Response of the Atlantic meridional overturning circulation to a reversal of greenhouse gas increases. *Climate dynamics*, **42(11–12)**, 3323–3336.
Jackson, L.S., J.A. Crook, and P.M. Forster, 2016: An intensified hydrological cycle in the simulation of geoengineering by cirrus cloud thinning using ice crystal fall speed changes. *Journal of Geophysical Research: Atmospheres*, **121(12)**, 6822–6840, doi:10.1002/2015jd024304.
Jahn, A., 2018: Reduced probability of ice-free summers for 1.5 °C compared to 2 °C warming. *Nature Climate Change*, **8(5)**, 409–413, doi:10.1038/s41558-018-0127-8.
James, R., R. Washington, C.-F. Schleussner, J. Rogelj, and D. Conway, 2017: Characterizing half-a-degree difference: a review of methods for identifying regional climate responses to global warming targets. *Wiley Interdisciplinary Reviews: Climate Change*, **8(2)**, e457, doi:10.1002/wcc.457.
Jeffrey, S. et al., 2013: Australia's CMIP5 submission using the CSIRO-Mk3.6 model. *Australian Meteorological and Oceanographic Journal*, **63(1)**, 1–14, doi:10.22499/2.6301.001.
Jeltsch-Thömmes, A., T.F. Stocker, and F. Joos, 2020: Hysteresis of the Earth system under positive and negative CO2 emissions. *Environmental Research Letters*, **15(12)**, 124026, doi:10.1088/1748-9326/abc4af.
Ji, D. et al., 2018: Extreme temperature and precipitation response to solar dimming and stratospheric aerosol geoengineering. *Atmospheric Chemistry and Physics*, **18(14)**, 10133–10156, doi:10.5194/acp-18-10133-2018.
Jia, F. et al., 2019: Weakening Atlantic Niño–Pacific connection under greenhouse warming. *Science Advances*, **5(8)**, eaax4111, doi:10.1126/sciadv.aax4111.
Jia, G. et al., 2019: Land–climate interactions. In: *Climate Change and Land: an IPCC special report on climate change, desertification, land degradation, sustainable land management, food security, and greenhouse gas fluxes in terrestrial ecosystems* [Shukla, P.R., J. Skea, E.C. Buendia, V. Masson-Delmotte, H.-O. Pörtner, D.C. Roberts, P. Zhai, R. Slade, S. Connors, R. Diemen, M. Ferrat, E. Haughey, S. Luz, S. Neogi, M. Pathak, J. Petzold, J.P. Pereira, P. Vyas, E. Huntley, K. Kissick, M. Belkacemi, and J. Malley (eds.)]. In Press, pp. 131–247.
Jiang, J. et al., 2019: Stratospheric Sulfate Aerosol Geoengineering Could Alter the High-Latitude Seasonal Cycle. *Geophysical Research Letters*, **46(23)**, 14153–14163, doi:10.1029/2019gl085758.
Jiaxiang, G. et al., 2020: Influence of model resolution on bomb cyclones revealed by HighResMIP-PRIMAVERA simulations. *Environmental Research Letters*, **15(8)**, 084001, doi:10.1088/1748-9326/ab88fa.
Jiménez-de-la-Cuesta, D. and T. Mauritsen, 2019: Emergent constraints on Earth's transient and equilibrium response to doubled CO2 from post-1970s global warming. *Nature Geoscience*, **12(11)**, 902–905, doi:10.1038/s41561-019-0463-y.
Johnson, J.S. et al., 2018: The importance of comprehensive parameter sampling and multiple observations for robust constraint of aerosol radiative forcing. *Atmospheric Chemistry and Physics*, **18(17)**, 13031–13053, doi:10.5194/acp-18-13031-2018.
Jones, A. et al., 2013: The impact of abrupt suspension of solar radiation management (termination effect) in experiment G2 of the Geoengineering Model Intercomparison Project (GeoMIP). *Journal of Geophysical Research Atmospheres*, **118(17)**, 9743–9752, doi:10.1002/jgrd.50762.
Jones, A. et al., 2021: North Atlantic Oscillation response in GeoMIP experiments G6solar and G6sulfur: why detailed modelling is needed for understanding regional implications of solar radiation management. *Atmospheric Chemistry and Physics*, **21(2)**, 1287–1304, doi:10.5194/acp-21-1287-2021.
Jones, A.C., J.M. Haywood, and A. Jones, 2016: Climatic impacts of stratospheric geoengineering with sulfate, black carbon and titania injection. *Atmospheric Chemistry and Physics*, **16(5)**, 2843–2862, doi:10.5194/acp-16-2843-2016.
Jones, A.C. et al., 2017: Impacts of hemispheric solar geoengineering on tropical cyclone frequency. *Nature Communications*, **8(1)**, 1382, doi:10.1038/s41467-017-01606-0.
Jones, A.C. et al., 2018: Regional Climate Impacts of Stabilizing Global Warming at 1.5 K Using Solar Geoengineering. *Earth's Future*, **6(2)**, 230–251, doi:10.1002/2017ef000720.
Jones, C.D. and P. Friedlingstein, 2020: Quantifying process-level uncertainty contributions to TCRE and carbon budgets for meeting Paris Agreement climate targets. *Environmental Research Letters*, **15(7)**, 074019,

ACCEPTED VERSION SUBJECT TO FINAL EDITS

doi:10.1088/1748-9326/ab858a.
Jones, C.D. et al., 2016a: C4MIP – The Coupled Climate–Carbon Cycle Model Intercomparison Project: experimental protocol for CMIP6. *Geoscientific Model Development*, **9(8)**, 2853–2880, doi:10.5194/gmd-9-2853-2016.
Jones, C.D. et al., 2016b: Simulating the Earth system response to negative emissions. *Environmental Research Letters*, **11(9)**, 095012, doi:10.1088/1748-9326/11/9/095012.
Jones, C.D. et al., 2019a: The Zero Emissions Commitment Model Intercomparison Project (ZECMIP) contribution to C4MIP: quantifying committed climate changes following zero carbon emissions. *Geoscientific Model Development*, **12(10)**, 4375–4385, doi:10.5194/gmd-12-4375-2019.
Jones, C.D. et al., 2019b: The Zero Emissions Commitment Model Intercomparison Project (ZECMIP) contribution to C4MIP: quantifying committed climate changes following zero carbon emissions. *Geoscientific Model Development*, **12(10)**, 4375–4385, doi:10.5194/gmd-12-4375-2019.
Joos, F. et al., 2013: Carbon dioxide and climate impulse response functions for the computation of greenhouse gas metrics: a multi-model analysis. *Atmospheric Chemistry and Physics*, **13(5)**, 2793–2825, doi:10.5194/acp-13-2793-2013.
Joshi, M. and J. Gregory, 2008: Dependence of the land-sea contrast in surface climate response on the nature of the forcing. *Geophysical Research Letters*, **35(24)**, L24802, doi:10.1029/2008gl036234.
Joshi, M.M., F.H. Lambert, and M.J. Webb, 2013: An explanation for the difference between twentieth and twenty-first century land–sea warming ratio in climate models. *Climate Dynamics*, **41(7–8)**, 1853–1869, doi:10.1007/s00382-013-1664-5.
Joshi, M.M., J.M. Gregory, M.J. Webb, D.M.H. Sexton, and T.C. Johns, 2008: Mechanisms for the land/sea warming contrast exhibited by simulations of climate change. *Climate Dynamics*, **30(5)**, 455–465, doi:10.1007/s00382-007-0306-1.
Jungclaus, J.H. et al., 2010: Climate and carbon-cycle variability over the last millennium. *Climate of the Past*, **6(5)**, 723–737, doi:10.5194/cp-6-723-2010.
Juricke, S., D. MacLeod, A. Weisheimer, L. Zanna, and T.N. Palmer, 2018: Seasonal to annual ocean forecasting skill and the role of model and observational uncertainty. *Quarterly Journal of the Royal Meteorological Society*, **144(715)**, 1947–1964, doi:10.1002/qj.3394.
Kadow, C., S. Illing, I. Kröner, U. Ulbrich, and U. Cubasch, 2017: Decadal climate predictions improved by ocean ensemble dispersion filtering. *Journal of Advances in Modeling Earth Systems*, **9(2)**, 1138–1149, doi:10.1002/2016ms000787.
Kalidindi, S., G. Bala, A. Modak, and K. Caldeira, 2015: Modeling of solar radiation management: a comparison of simulations using reduced solar constant and stratospheric sulphate aerosols. *Climate Dynamics*, **44(9–10)**, 2909–2925, doi:10.1007/s00382-014-2240-3.
Kamae, Y. and M. Watanabe, 2012: On the robustness of tropospheric adjustment in CMIP5 models. *Geophysical Research Letters*, **39(23)**, L23808, doi:10.1029/2012gl054275.
Kamae, Y. and M. Watanabe, 2013: Tropospheric adjustment to increasing CO2: Its timescale and the role of land-sea contrast. *Climate Dynamics*, **41(11–12)**, 3007–3024, doi:10.1007/s00382-012-1555-1.
Karspeck, A., S. Yeager, G. Danabasoglu, and H. Teng, 2015: An evaluation of experimental decadal predictions using CCSM4. *Climate Dynamics*, **44(3)**, 907–923, doi:10.1007/s00382-014-2212-7.
Karspeck, A.R. et al., 2017: Comparison of the Atlantic meridional overturning circulation between 1960 and 2007 in six ocean reanalysis products. *Climate Dynamics*, **49(3)**, 957–982, doi:10.1007/s00382-015-2787-7.
Kasoar, M., D. Shawki, and A. Voulgarakis, 2018: Similar spatial patterns of global climate response to aerosols from different regions. *npj Climate and Atmospheric Science*, **1(1)**, 12, doi:10.1038/s41612-018-0022-z.
Kay, J.E. et al., 2015: The Community Earth System Model (CESM) Large Ensemble Project: A Community Resource for Studying Climate Change in the Presence of Internal Climate Variability. *Bulletin of the American Meteorological Society*, **96(8)**, 1333–1349, doi:10.1175/bams-d-13-00255.1.
Keenlyside, N.S., M. Latif, J. Jungclaus, L. Kornblueh, and E. Roeckner, 2008: Advancing decadal-scale climate prediction in the North Atlantic sector. *Nature*, **453(7191)**, 84–88, doi:10.1038/nature06921.
Keith, D.W., 2010: Photophoretic levitation of engineered aerosols for geoengineering. *Proceedings of the National Academy of Sciences*, **107(38)**, 16428–16431, doi:10.1073/pnas.1009519107.
Keith, D.W. and D.G. MacMartin, 2015: A temporary, moderate and responsive scenario for solar geoengineering. *Nature Climate Change*, **5(3)**, 201–206, doi:10.1038/nclimate2493.
Keith, D.W., D.K. Weisenstein, J.A. Dykema, and F.N. Keutsch, 2016: Stratospheric solar geoengineering without ozone loss. *Proceedings of the National Academy of Sciences*, **113(52)**, 14910–14914, doi:10.1073/pnas.1615572113.
Keller, D.P., E.Y. Feng, and A. Oschlies, 2014: Potential climate engineering effectiveness and side effects during a high carbon dioxide-emission scenario. *Nature Communications*, **5(1)**, 3304, doi:10.1038/ncomms4304.
Keller, D.P. et al., 2018: The Carbon Dioxide Removal Model Intercomparison Project (CDRMIP): rationale and experimental protocol for CMIP6. *Geoscientific Model Development*, **11(3)**, 1133–1160, doi:10.5194/gmd-11-1133-2018.
Kendon, E.J. et al., 2014: Heavier summer downpours with climate change revealed by weather forecast resolution

ACCEPTED VERSION SUBJECT TO FINAL EDITS

model. *Nature Climate Change*, **4(7)**, 570–576, doi:10.1038/nclimate2258.
Kennedy, D., T. Parker, T. Woollings, B. Harvey, and L. Shaffrey, 2016: The response of high-impact blocking weather systems to climate change. *Geophysical Research Letters*, **43(13)**, 7250–7258, doi:10.1002/2016gl069725.
Kent, C., R. Chadwick, and D.P. Rowell, 2015: Understanding Uncertainties in Future Projections of Seasonal Tropical Precipitation. *Journal of Climate*, **28(11)**, 4390–4413, doi:10.1175/jcli-d-14-00613.1.
Kharin, V., G.J. Boer, W.J. Merryfield, J.F. Scinocca, and W.-S. Lee, 2012: Statistical adjustment of decadal predictions in a changing climate. *Geophysical Research Letters*, **39(19)**, doi:10.1029/2012gl052647.
Kharin, V. et al., 2018: Risks from Climate Extremes Change Differently from 1.5°C to 2.0°C Depending on Rarity. *Earth's Future*, **6(5)**, 704–715, doi:10.1002/2018ef000813.
Khodri, M. et al., 2017: Tropical explosive volcanic eruptions can trigger El Ninõ by cooling tropical Africa. *Nature Communications*, **8(1)**, 1–12, doi:10.1038/s41467-017-00755-6.
Kidston, J. and E.P. Gerber, 2010: Intermodel variability of the poleward shift of the austral jet stream in the CMIP3 integrations linked to biases in 20th century climatology. *Geophysical Research Letters*, **37(9)**, 1–5, doi:10.1029/2010gl042873.
Kilbourne, K.H., M.A. Alexander, and J.A. Nye, 2014: A low latitude paleoclimate perspective on Atlantic multidecadal variability. *Journal of Marine Systems*, **133**, 4–13, doi:10.1016/j.jmarsys.2013.09.004.
Kim, S.T. et al., 2014: Response of El Niño sea surface temperature variability to greenhouse warming. *Nature Climate Change*, **4(9)**, 786–790, doi:10.1038/nclimate2326.
Kim, W.M., S. Yeager, and G. Danabasoglu, 2020: Atlantic Multidecadal Variability and Associated Climate Impacts Initiated by Ocean Thermohaline Dynamics. *Journal of Climate*, **33(4)**, 1317–1334, doi:10.1175/jcli-d-19-0530.1.
Kimmritz, M. et al., 2018: Optimising assimilation of sea ice concentration in an Earth system model with a multicategory sea ice model. *Tellus A: Dynamic Meteorology and Oceanography*, **70(1)**, 1–23, doi:10.1080/16000870.2018.1435945.
Kirchmeier-Young, M.C., F.W. Zwiers, and N.P. Gillett, 2017: Attribution of Extreme Events in Arctic Sea Ice Extent. *Journal of Climate*, **30(2)**, 553–571, doi:10.1175/jcli-d-16-0412.1.
Kirchmeier-Young, M.C., H. Wan, X. Zhang, and S.I. Seneviratne, 2019: Importance of Framing for Extreme Event Attribution: The Role of Spatial and Temporal Scales. *Earth's Future*, **7(10)**, 1192–1204, doi:10.1029/2019ef001253.
Kirtman, B. et al., 2013: Near-term climate change: projections and predictability. In: *Climate Change 2013: The Physical Science Basis. Contribution of Working Group I to the Fifth Assessment Report of the Intergovernmental Panel on Climate Change* [Stocker, T.F., D. Qin, G.-K. Plattner, M. Tignor, S.K. Allen, J. Boschung, A. Nauels, Y. Xia, V. Bex, and P.M. Midgley (eds.)]. Cambridge University Press, Cambridge, United Kingdom and New York, NY, USA, pp. 953–1028, doi:10.1017/cbo9781107415324.023.
Kitano, Y. and T.J. Yamada, 2016: Relationship between atmospheric blocking and cold day extremes in current and RCP8.5 future climate conditions over Japan and the surrounding area. *Atmospheric Science Letters*, **17(11)**, 616–622, doi:10.1002/asl.711.
Kitoh, A. et al., 2013: Monsoons in a changing world: A regional perspective in a global context. *Journal of Geophysical Research: Atmospheres*, **118(8)**, 3053–3065, doi:10.1002/jgrd.50258.
Kjellström, E. et al., 2018: European climate change at global mean temperature increases of 1.5 and 2°C above pre-industrial conditions as simulated by the EURO-CORDEX regional climate models. *Earth System Dynamics*, **9(2)**, 459–478, doi:10.5194/esd-9-459-2018.
Kleinschmitt, C., O. Boucher, and U. Platt, 2018a: Sensitivity of the radiative forcing by stratospheric sulfur geoengineering to the amount and strategy of the SO2 injection studied with the LMDZ-S3A model. *Atmospheric Chemistry and Physics*, **18(4)**, 2769–2786, doi:10.5194/acp-18-2769-2018.
Kleinschmitt, C., O. Boucher, and U. Platt, 2018b: Sensitivity of the radiative forcing by stratospheric sulfur geoengineering to the amount and strategy of the SO2 injection studied with the LMDZ-S3A model. *Atmospheric Chemistry and Physics*, **18(4)**, 2769–2786, doi:10.5194/acp-18-2769-2018.
Klus, A., M. Prange, V. Varma, L.B. Tremblay, and M. Schulz, 2018: Abrupt cold events in the North Atlantic Ocean in a transient Holocene simulation. *Climate of the Past*, **14(8)**, 1165–1178, doi:10.5194/cp-14-1165-2018.
Knight, J.R. et al., 2014: Predictions of Climate Several Years Ahead Using an Improved Decadal Prediction System. *Journal of Climate*, **27(20)**, 7550–7567, doi:10.1175/jcli-d-14-00069.1.
Knudsen, M.F., M.-S. Seidenkrantz, B.H. Jacobsen, and A. Kuijpers, 2011: Tracking the Atlantic Multidecadal Oscillation through the last 8,000 years. *Nature Communications*, **2(1)**, 178, doi:10.1038/ncomms1186.
Knutti, R. and J. Sedláček, 2013: Robustness and uncertainties in the new CMIP5 climate model projections. *Nature Climate Change*, **3(4)**, 369–373, doi:10.1038/nclimate1716.
Knutti, R., D. Masson, and A. Gettelman, 2013: Climate model genealogy: Generation CMIP5 and how we got there. *Geophysical Research Letters*, **40(6)**, 1194–1199, doi:10.1002/grl.50256.
Knutti, R., R. Furrer, C. Tebaldi, J. Cermak, and G. Meehl, 2010: Challenges in Combining Projections from Multiple Climate Models. *Journal of Climate*, **23(10)**, 2739–2758, doi:10.1175/2009jcli3361.1.
Knutti, R. et al., 2017: A climate model projection weighting scheme accounting for performance and interdependence.

ACCEPTED VERSION SUBJECT TO FINAL EDITS

Geophysical Research Letters, **44(4)**, 1909–1918, doi:10.1002/2016gl072012.
Kobashi, T. et al., 2017: Volcanic influence on centennial to millennial Holocene Greenland temperature change. *Scientific Reports*, **7(1)**, 1–10, doi:10.1038/s41598-017-01451-7.
Koenigk, T., A. Devasthale, and K.G. Karlsson, 2014: Summer arctic sea ice albedo in CMIP5 models. *Atmospheric Chemistry and Physics*, **14(4)**, 1987–1998, doi:10.5194/acp-14-1987-2014.
Kohyama, T. and D.L. Hartmann, 2017: Nonlinear ENSO Warming Suppression (NEWS). *Journal of Climate*, **30(11)**, 4227–4251, doi:10.1175/jcli-d-16-0541.1.
Kosaka, Y. and S.-P. Xie, 2016: The tropical Pacific as a key pacemaker of the variable rates of global warming. *Nature Geoscience*, **9(9)**, 669–673, doi:10.1038/ngeo2770.
Kostov, Y. et al., 2017: Fast and slow responses of Southern Ocean sea surface temperature to SAM in coupled climate models. *Climate Dynamics*, **48(5–6)**, 1595–1609, doi:10.1007/s00382-016-3162-z.
Kravitz, B., D.G. MacMartin, H. Wang, and P.J. Rasch, 2016: Geoengineering as a design problem. *Earth System Dynamics*, **7(2)**, 469–497, doi:10.5194/esd-7-469-2016.
Kravitz, B. et al., 2011: The Geoengineering Model Intercomparison Project (GeoMIP). *Atmospheric Science Letters*, **12(2)**, 162–167, doi:10.1002/asl.316.
Kravitz, B. et al., 2013a: Climate model response from the Geoengineering Model Intercomparison Project (GeoMIP). *Journal of Geophysical Research Atmospheres*, **118(15)**, 8320–8332, doi:10.1002/jgrd.50646.
Kravitz, B. et al., 2013b: Sea spray geoengineering experiments in the geoengineering model intercomparison project (GeoMIP): Experimental design and preliminary results. *Journal of Geophysical Research: Atmospheres*, **118(19)**, 11,175–11,186, doi:10.1002/jgrd.50856.
Kravitz, B. et al., 2014: A multi-model assessment of regional climate disparities caused by solar geoengineering. *Environmental Research Letters*, **9(7)**, doi:10.1088/1748-9326/9/7/074013.
Kravitz, B. et al., 2015: The Geoengineering Model Intercomparison Project Phase 6 (GeoMIP6): simulation design and preliminary results. *Geoscientific Model Development*, **8(10)**, 3379–3392, doi:10.5194/gmd-8-3379-2015.
Kravitz, B. et al., 2017: First Simulations of Designing Stratospheric Sulfate Aerosol Geoengineering to Meet Multiple Simultaneous Climate Objectives. *Journal of Geophysical Research: Atmospheres*, **122(23)**, 12,616–12,634, doi:10.1002/2017jd026874.
Kravitz, B. et al., 2018: The climate effects of increasing ocean albedo: an idealized representation of solar geoengineering. *Atmospheric Chemistry and Physics*, **18(17)**, 13097–13113, doi:10.5194/acp-18-13097-2018.
Kravitz, B. et al., 2019: Comparing Surface and Stratospheric Impacts of Geoengineering With Different SO2 Injection Strategies. *Journal of Geophysical Research: Atmospheres*, **124(14)**, 7900–7918, doi:10.1029/2019jd030329.
Kravitz, B. et al., 2021: Comparing different generations of idealized solar geoengineering simulations in the Geoengineering Model Intercomparison Project (GeoMIP). *Atmospheric Chemistry and Physics*, **21(6)**, 4231–4247, doi:10.5194/acp-21-4231-2021.
Krishnamohan, K.-P.S.-P., G. Bala, L. Cao, L. Duan, and K. Caldeira, 2019: Climate system response to stratospheric sulfate aerosols: sensitivity to altitude of aerosol layer. *Earth System Dynamics*, **10(4)**, 885–900, doi:10.5194/esd-10-885-2019.
Krishnamohan, K.S., G. Bala, L. Cao, L. Duan, and K. Caldeira, 2020: The Climatic Effects of Hygroscopic Growth of Sulfate Aerosols in the Stratosphere. *Earth's Future*, **8(2)**, e2019EF001326, doi:10.1029/2019ef001326.
Krishnan, R. et al., 2016: Deciphering the desiccation trend of the South Asian monsoon hydroclimate in a warming world. *Climate Dynamics*, **47(3)**, 1007–1027, doi:10.1007/s00382-015-2886-5.
Kristjánsson, J.E., H. Muri, and H. Schmidt, 2015: The hydrological cycle response to cirrus cloud thinning. *Geophysical Research Letters*, **42(24)**, 10807–10815, doi:10.1002/2015gl066795.
Kröger, J. et al., 2018: Full-field initialized decadal predictions with the MPI Earth system model: an initial shock in the North Atlantic. *Climate Dynamics*, **51**, 2593–2608, doi:10.1007/s00382-017-4030-1.
Kröner, N. et al., 2017: Separating climate change signals into thermodynamic, lapse-rate and circulation effects: theory and application to the European summer climate. *Climate Dynamics*, **48(9–10)**, 3425–3440, doi:10.1007/s00382-016-3276-3.
Kruschke, T. et al., 2016: Probabilistic evaluation of decadal prediction skill regarding Northern Hemisphere winter storms. *Meteorologische Zeitschrift*, **25(6)**, 721–738, doi:10.1127/metz/2015/0641.
Kwiatkowski, L. et al., 2020: Twenty-first century ocean warming, acidification, deoxygenation, and upper-ocean nutrient and primary production decline from CMIP6 model projections. *Biogeosciences*, **17(13)**, 3439–3470, doi:10.5194/bg-17-3439-2020.
Lambert, F.H. and J.C.H. Chiang, 2007: Control of land-ocean temperature contrast by ocean heat uptake. *Geophysical Research Letters*, **34(13)**, L13704, doi:10.1029/2007gl029755.
Lambert, F.H. and M.R. Allen, 2009: Are changes in global precipitation constrained by the tropospheric energy budget? *Journal of Climate*, **22(3)**, 499–517, doi:10.1175/2008jcli2135.1.
Lambert, F.H., M.J. Webb, and M.M. Joshi, 2011: The Relationship between Land–Ocean Surface Temperature Contrast and Radiative Forcing. *Journal of Climate*, **24(13)**, 3239–3256, doi:10.1175/2011jcli3893.1.
Lambert, F.H., A.J. Ferraro, and R. Chadwick, 2017: Land–Ocean Shifts in Tropical Precipitation Linked to Surface Temperature and Humidity Change. *Journal of Climate*, **30(12)**, 4527–4545, doi:10.1175/jcli-d-16-0649.1.

ACCEPTED VERSION SUBJECT TO FINAL EDITS

Langehaug, H.R., D. Matei, T. Eldevik, K. Lohmann, and Y. Gao, 2017: On model differences and skill in predicting sea surface temperature in the Nordic and Barents Seas. *Climate Dynamics*, **48(3–4)**, 913–933, doi:10.1007/s00382-016-3118-3.

Langenbrunner, B., J.D. Neelin, B.R. Lintner, and B.T. Anderson, 2015: Patterns of Precipitation Change and Climatological Uncertainty among CMIP5 Models, with a Focus on the Midlatitude Pacific Storm Track. *Journal of Climate*, **28(19)**, 7857–7872, doi:10.1175/jcli-d-14-00800.1.

Latham, J., J. Kleypas, R. Hauser, B. Parkes, and A. Gadian, 2013: Can marine cloud brightening reduce coral bleaching? *Atmospheric Science Letters*, **14(4)**, 214–219, doi:10.1002/asl2.442.

Latham, J. et al., 2012: Marine cloud brightening. *Philosophical Transactions of the Royal Society A: Mathematical, Physical and Engineering Sciences*, **370(1974)**, 4217–4262, doi:10.1098/rsta.2012.0086.

Latham, J. et al., 2014: Marine cloud brightening: regional applications. *Philosophical Transactions of the Royal Society A: Mathematical, Physical and Engineering Sciences*, **372(2031)**, 20140053, doi:10.1098/rsta.2014.0053.

Lawrence, M.G. et al., 2018: Evaluating climate geoengineering proposals in the context of the Paris Agreement temperature goals. *Nature Communications*, **9(1)**, 3734, doi:10.1038/s41467-018-05938-3.

Leduc, M., H.D. Matthews, and R. De Elía, 2015: Quantifying the limits of a linear temperature response to cumulative CO2 emissions. *Journal of Climate*, **28(24)**, 9955–9968, doi:10.1175/jcli-d-14-00500.1.

Leduc, M., H.D. Matthews, and R. de Elía, 2016: Regional estimates of the transient climate response to cumulative CO2 emissions. *Nature Climate Change*, **6(5)**, 474–478, doi:10.1038/nclimate2913.

Lee, D.Y. and J.-B. Ahn, 2017: Future change in the frequency and intensity of wintertime North Pacific blocking in CMIP5 models. *International Journal of Climatology*, **37(5)**, 2765–2781, doi:10.1002/joc.4878.

Lee, H.J. et al., 2017: Impact of Poleward Moisture Transport from the North Pacific on the Acceleration of Sea Ice Loss in the Arctic since 2002. *Journal of Climate*, **30(17)**, 6757–6769, doi:10.1175/jcli-d-16-0461.1.

Lee, J.Y. and B. Wang, 2014: Future change of global monsoon in the CMIP5. *Climate Dynamics*, **42(1–2)**, 101–119, doi:10.1007/s00382-012-1564-0.

Lee, S., T. Gong, N. Johnson, S.B. Feldstein, and D. Pollard, 2011: On the Possible Link between Tropical Convection and the Northern Hemisphere Arctic Surface Air Temperature Change between 1958 and 2001. *Journal of Climate*, **24(16)**, 4350–4367, doi:10.1175/2011jcli4003.1.

Lee, W., D. MacMartin, D. Visioni, and B. Kravitz, 2020: Expanding the design space of stratospheric aerosol geoengineering to include precipitation-based objectives and explore trade-offs. *Earth System Dynamics*, **11(4)**, 1051–1072, doi:10.5194/esd-11-1051-2020.

Legrande, A.N., K. Tsigaridis, and S.E. Bauer, 2016: Role of atmospheric chemistry in the climate impacts of stratospheric volcanic injections. *Nature Geoscience*, **9(9)**, 652–655, doi:10.1038/ngeo2771.

Lehmann, J., D. Coumou, K. Frieler, A. Eliseev, and A. Levermann, 2014: Future changes in extratropical storm tracks and baroclinicity under climate change. *Environmental Research Letters*, **9(8)**, 084002, doi:10.1088/1748-9326/9/8/084002.

Lehner, F., C. Deser, and L. Terray, 2017: Toward a new estimate of "Time of Emergence" of anthropogenic warming: Insights from dynamical adjustment and a large initial-condition model ensemble. *Journal of Climate*, **30(19)**, 7739–7756, doi:10.1175/jcli-d-16-0792.1.

Lehner, F. et al., 2020: Partitioning climate projection uncertainty with multiple large ensembles and CMIP5/6. *Earth System Dynamics*, **11(2)**, 491–508, doi:10.5194/esd-11-491-2020.

Lemordant, L., P. Gentine, A.S. Swann, B.I. Cook, and J. Scheff, 2018: Critical impact of vegetation physiology on the continental hydrologic cycle in response to increasing CO2. *Proceedings of the National Academy of Sciences*, **115(16)**, 4093–4098, doi:10.1073/pnas.1720712115.

Lenderink, G. et al., 2014: Preparing local climate change scenarios for the Netherlands using resampling of climate model output. *Environmental Research Letters*, **9(11)**, 115008, doi:10.1088/1748-9326/9/11/115008.

Levy, H. et al., 2013: The roles of aerosol direct and indirect effects in past and future climate change. *Journal of Geophysical Research: Atmospheres*, **118(10)**, 4521–4532, doi:10.1002/jgrd.50192.

Li, C., J.-S. von Storch, and J. Marotzke, 2013: Deep-ocean heat uptake and equilibrium climate response. *Climate Dynamics*, **40(5–6)**, 1071–1086, doi:10.1007/s00382-012-1350-z.

Li, C. et al., 2018: Midlatitude atmospheric circulation responses under 1.5 and 2.0°C warming and implications for regional impacts. *Earth System Dynamics*, **9(2)**, 359–382, doi:10.5194/esd-9-359-2018.

Li, G., S.-P. Xie, and Y. Du, 2016: A Robust but Spurious Pattern of Climate Change in Model Projections over the Tropical Indian Ocean. *Journal of Climate*, **29(15)**, 5589–5608, doi:10.1175/jcli-d-15-0565.1.

Li, H., T. Ilyina, W.A. Müller, and F. Sienz, 2016: Decadal predictions of the North Atlantic CO2 uptake. *Nature Communications*, **7**, 10.1038/ncomms11076, doi:10.1038/ncomms11076.

Li, H., T. Ilyina, W.A. Müller, and P. Landschützer, 2019: Predicting the variable ocean carbon sink. *Science Advances*, **5(4)**, eaav6471, doi:10.1126/sciadv.aav6471.

Li, J. and J.X.L. Wang, 2003: A modified zonal index and its physical sense. *Geophysical Research Letters*, **30(12)**, doi:10.1029/2003gl017441.

Li, W., L. Li, M. Ting, and Y. Liu, 2012: Intensification of Northern Hemisphere subtropical highs in a warming

ACCEPTED VERSION SUBJECT TO FINAL EDITS

climate. *Nature Geoscience*, **5(11)**, 830–834, doi:10.1038/ngeo1590.
Liang, Y., N.P. Gillett, and A.H. Monahan, 2020: Climate Model Projections of 21st Century Global Warming Constrained Using the Observed Warming Trend. *Geophysical Research Letters*, **47(12)**, e2019GL086757, doi:10.1029/2019gl086757.
Liguori, G. and E. Di Lorenzo, 2019: Separating the North and South Pacific Meridional Modes Contributions to ENSO and Tropical Decadal Variability. *Geophysical Research Letters*, **46(2)**, 906–915, doi:10.1029/2018gl080320.
Lipat, B.R., A. Voigt, G. Tselioudis, and L.M. Polvani, 2018: Model uncertainty in cloud-circulation coupling, and cloud-radiative response to increasing CO2, linked to biases in climatological circulation. *Journal of Climate*, **31(24)**, 10013–10020, doi:10.1175/jcli-d-17-0665.1.
Liptak, J., G. Keppel-Aleks, and K. Lindsay, 2017: Drivers of multi-century trends in the atmospheric CO2 mean annual cycle in a prognostic ESM. *Biogeosciences*, **14(6)**, 1383–1401, doi:10.5194/bg-14-1383-2017.
Liu, F. et al., 2018: How Do Tropical, Northern Hemispheric, and Southern Hemispheric Volcanic Eruptions Affect ENSO Under Different Initial Ocean Conditions? *Geophysical Research Letters*, **45(23)**, 13,041–13,049, doi:10.1029/2018gl080315.
Liu, L. et al., 2018: A PDRMIP Multimodel Study on the Impacts of Regional Aerosol Forcings on Global and Regional Precipitation. *Journal of Climate*, **31(11)**, 4429–4447, doi:10.1175/jcli-d-17-0439.1.
Liu, W., S.-P. Xie, Z. Liu, and J. Zhu, 2017: Overlooked possibility of a collapsed Atlantic Meridional Overturning Circulation in warming climate. *Science Advances*, **3(1)**, e1601666, doi:10.1126/sciadv.1601666.
Liu, W., J. Lu, S.-P. Xie, and A. Fedorov, 2018: Southern Ocean Heat Uptake, Redistribution, and Storage in a Warming Climate: The Role of Meridional Overturning Circulation. *Journal of Climate*, **31(12)**, 4727–4743, doi:10.1175/jcli-d-17-0761.1.
Liu, Y. et al., 2018: Climate response to the meltwater runoff from Greenland ice sheet: evolving sensitivity to discharging locations. *Climate Dynamics*, **51(5–6)**, 1733–1751, doi:10.1007/s00382-017-3980-7.
Liu, Z., 2012: Dynamics of Interdecadal Climate Variability: A Historical Perspective. *Journal of Climate*, **25(6)**, 1963–1995, doi:10.1175/2011jcli3980.1.
Liu, Z. and E. Di Lorenzo, 2018: Mechanisms and Predictability of Pacific Decadal Variability. *Current Climate Change Reports*, **4(2)**, 128–144, doi:10.1007/s40641-018-0090-5.
Lo, Y.T.E., A.J. Charlton-Perez, F.C. Lott, and E.J. Highwood, 2016: Detecting sulphate aerosol geoengineering with different methods. *Scientific Reports*, **6**, 1–10, doi:10.1038/srep39169.
Lohmann, U. and B. Gasparini, 2017: A cirrus cloud climate dial? *Science*, **357(6348)**, 248–249, doi:10.1126/science.aan3325.
Lopez, A., E.B. Suckling, and L.A. Smith, 2014: Robustness of pattern scaled climate change scenarios for adaptation decision support. *Climatic Change*, **122(4)**, 555–566, doi:10.1007/s10584-013-1022-y.
Losada, T. and B. Rodríguez-Fonseca, 2016: Tropical atmospheric response to decadal changes in the Atlantic Equatorial Mode. *Climate Dynamics*, **47(3–4)**, 1211–1224, doi:10.1007/s00382-015-2897-2.
Lovenduski, N.S., S.G. Yeager, K. Lindsay, and M.C. Long, 2019: Predicting near-term variability in ocean carbon uptake. *Earth System Dynamics*, **10(1)**, 45–57, doi:10.5194/esd-10-45-2019.
Lovenduski, N.S., G.A. McKinley, A.R. Fay, K. Lindsay, and M.C. Long, 2016: Partitioning uncertainty in ocean carbon uptake projections: Internal variability, emission scenario, and model structure. *Global Biogeochemical Cycles*, **30(9)**, 1276–1287, doi:10.1002/2016gb005426.
Lübbecke, J.F. et al., 2018: Equatorial Atlantic variability-Modes, mechanisms, and global teleconnections. *Wiley Interdisciplinary Reviews: Climate Change*, **9(4)**, e527, doi:10.1002/wcc.527.
Luo, D., X. Chen, A. Dai, and I. Simmonds, 2018: Changes in Atmospheric Blocking Circulations Linked with Winter Arctic Warming: A New Perspective. *Journal of Climate*, **31(18)**, 7661–7678, doi:10.1175/jcli-d-18-0040.1.
MacCracken, M.C., 2016: The rationale for accelerating regionally focused climate intervention research. *Earth's Future*, **4(12)**, 649–657, doi:10.1002/2016ef000450.
MacCracken, M.C., H.J. Shin, K. Caldeira, and G.A. Ban-Weiss, 2013: Climate response to imposed solar radiation reductions in high latitudes. *Earth System Dynamics*, **4(2)**, 301–315, doi:10.5194/esd-4-301-2013.
MacDougall, A.H., 2013a: Reversing climate warming by artificial atmospheric carbon-dioxide removal: Can a Holocene-like climate be restored? *Geophysical Research Letters*, **40(20)**, 5480–5485.
MacDougall, A.H., 2013b: Reversing climate warming by artificial atmospheric carbon-dioxide removal: Can a Holocene-like climate be restored? *Geophysical Research Letters*, **40(20)**, 5480–5485.
MacDougall, A.H. et al., 2020: Is there warming in the pipeline? A multi-model analysis of the Zero Emissions Commitment from CO2. *Biogeosciences*, **17(11)**, 2987–3016, doi:10.5194/bg-17-2987-2020.
MacLachlan, C. et al., 2015: Global Seasonal forecast system version 5 (GloSea5): a high-resolution seasonal forecast system. *Quarterly Journal of the Royal Meteorological Society*, **141(689)**, 1072–1084, doi:10.1002/qj.2396.
MacMartin, D.G., K. Caldeira, and D.W. Keith, 2014: Solar geoengineering to limit the rate of temperature change. *Philosophical Transactions of the Royal Society A: Mathematical, Physical and Engineering Sciences*, **372(2031)**, 20140134, doi:10.1098/rsta.2014.0134.
MacMartin, D.G., K.L. Ricke, and D.W. Keith, 2018: Solar geoengineering as part of an overall strategy for meeting the 1.5°C Paris target. *Philosophical Transactions of the Royal Society A: Mathematical, Physical and*

ACCEPTED VERSION SUBJECT TO FINAL EDITS

Engineering Sciences, **376(2119)**, 20160454, doi:10.1098/rsta.2016.0454.
MacMartin, D.G. et al., 2017: The Climate Response to Stratospheric Aerosol Geoengineering Can Be Tailored Using Multiple Injection Locations. *Journal of Geophysical Research: Atmospheres*, **122(23)**, 12,574–12,590, doi:10.1002/2017jd026868.
MacMartin, D.G. et al., 2019: Timescale for Detecting the Climate Response to Stratospheric Aerosol Geoengineering. *Journal of Geophysical Research: Atmospheres*, **124(3)**, 1233–1247, doi:10.1029/2018jd028906.
Madsen, M.S., P.L. Langen, F. Boberg, and J.H. Christensen, 2017: Inflated Uncertainty in Multimodel-Based Regional Climate Projections. *Geophysical Research Letters*, **44(22)**, 11,606–11,613, doi:10.1002/2017gl075627.
Magnusson, L., M. Alonso-Balmaseda, S. Corti, F. Molteni, and T. Stockdale, 2013: Evaluation of forecast strategies for seasonal and decadal forecasts in presence of systematic model errors. *Climate Dynamics*, **41(9–10)**, 2393–2409, doi:10.1007/s00382-012-1599-2.
Maher, N., F. Lehner, and J. Marotzke, 2020: Quantifying the role of internal variability in the temperature we expect to observe in the coming decades. *Environmental Research Letters*, **15(5)**, 054014, doi:10.1088/1748-9326/ab7d02.
Maher, N., S.B. Power, and J. Marotzke, 2021: More accurate quantification of model-to-model agreement in externally forced climatic responses over the coming century. *Nature Communications*, **12(1)**, 788, doi:10.1038/s41467-020-20635-w.
Maher, N., S. McGregor, M.H. England, and A. Gupta, 2015: Effects of volcanism on tropical variability. *Geophysical Research Letters*, **42(14)**, 6024–6033, doi:10.1002/2015gl064751.
Maher, N., D. Matei, S. Milinski, and J. Marotzke, 2018: ENSO Change in Climate Projections: Forced Response or Internal Variability? *Geophysical Research Letters*, **45(20)**, 11,390–11,398, doi:10.1029/2018gl079764.
Maher, N. et al., 2019a: The Max Planck Institute Grand Ensemble: Enabling the Exploration of Climate System Variability. *Journal of Advances in Modeling Earth Systems*, **11(7)**, 2050–2069, doi:10.1029/2019ms001639.
Maher, N. et al., 2019b: The Max Planck Institute Grand Ensemble: Enabling the Exploration of Climate System Variability. *Journal of Advances in Modeling Earth Systems*, **11(7)**, 2050–2069, doi:10.1029/2019ms001639.
Mahlstein, I. and R. Knutti, 2011: Ocean Heat Transport as a Cause for Model Uncertainty in Projected Arctic Warming. *Journal of Climate*, **24(5)**, 1451–1460, doi:10.1175/2010jcli3713.1.
Mahowald, N.M. et al., 2017: Interactions between land use change and carbon cycle feedbacks. *Global Biogeochemical Cycles*, **31(1)**, 96–113, doi:10.1002/2016gb005374.
Man, W., T. Zhou, and J.H. Jungclaus, 2014: Effects of Large Volcanic Eruptions on Global Summer Climate and East Asian Monsoon Changes during the Last Millennium: Analysis of MPI-ESM Simulations. *Journal of Climate*, **27(19)**, 7394–7409, doi:10.1175/jcli-d-13-00739.1.
Man, W. et al., 2021: Potential influences of volcanic eruptions on future global land monsoon precipitation changes. *Earth's Future*, doi:10.1029/2020ef001803.
Manabe, S. and R.T. Wetherald, 1975: The Effects of Doubling the CO2 Concentration on the climate of a General Circulation Model. *Journal of the Atmospheric Sciences*, **32(1)**, 3–15, doi:10.1175/1520-0469(1975)032<0003:teodtc>2.0.co;2.
Manabe, S. and R.J. Stouffer, 1980: Sensitivity of a global climate model to an increase of CO2 concentration in the atmosphere. *Journal of Geophysical Research*, **85(C10)**, 5529–5554, doi:10.1029/jc085ic10p05529.
Manabe, S. and R.T. Wetherald, 1980: On the Distribution of Climate Change Resulting from an Increase in CO2 Content of the Atmosphere. *Journal of the Atmospheric Sciences*, **37(1)**, 99–118, doi:10.1175/1520-0469(1980)037<0099:otdocc>2.0.co;2.
Manabe, S., R.J. Stouffer, M.J. Spelman, and K. Bryan, 1991: Transient Responses of a Coupled Ocean–Atmosphere Model to Gradual Changes of Atmospheric CO2. Part I. Annual Mean Response. *Journal of Climate*, **4(8)**, 785–818, doi:10.1175/1520-0442(1991)004<0785:troaco>2.0.co;2.
Mann, M.E., B.A. Steinman, and S.K. Miller, 2020: Absence of internal multidecadal and interdecadal oscillations in climate model simulations. *Nature Communications*, **11(1)**, 49, doi:10.1038/s41467-019-13823-w.
Mann, M.E., B.A. Steinman, D.J. Brouillette, and S.K. Miller, 2021: Multidecadal climate oscillations during the past millennium driven by volcanic forcing. *Science*, **371(6533)**, 1014–1019, doi:10.1126/science.abc5810.
Mantua, N.J., S.R. Hare, Y. Zhang, J.M. Wallace, and R.C. Francis, 1997: A Pacific Interdecadal Climate Oscillation with Impacts on Salmon Production. *Bulletin of the American Meteorological Society*, **78(6)**, 1069–1079, doi:10.1175/1520-0477(1997)078<1069:apicow>2.0.co;2.
Manzini, E. et al., 2014: Northern winter climate change: Assessment of uncertainty in CMIP5 projections related to stratosphere-troposphere coupling. *Journal of Geophysical Research: Atmospheres*, **119(13)**, 7979–7998, doi:10.1002/2013jd021403.
Marini, C., I. Polkova, A. Köhl, and D. Stammer, 2016: A Comparison of Two Ensemble Generation Methods Using Oceanic Singular Vectors and Atmospheric Lagged Initialization for Decadal Climate Prediction. *Monthly Weather Review*, **144(7)**, 2719–2738, doi:10.1175/mwr-d-15-0350.1.
Marotzke, J., 2019: Quantifying the irreducible uncertainty in near-term climate projections. *Wiley Interdisciplinary Reviews: Climate Change*, **10(1)**, e563, doi:10.1002/wcc.563.
Marotzke, J. and P.M. Forster, 2015: Forcing, feedback and internal variability in global temperature trends. *Nature*, **517(7536)**, 565–570, doi:10.1038/nature14117.

ACCEPTED VERSION SUBJECT TO FINAL EDITS

Marotzke, J. et al., 2016: MiKlip: A national research project on decadal climate prediction. *Bulletin of the American Meteorological Society*, **97(12)**, 2379–2394, doi:10.1175/bams-d-15-00184.1.
Marshall, G.J., 2003: Trends in the Southern Annular Mode from Observations and Reanalyses. *Journal of Climate*, **16(24)**, 4134–4143, doi:10.1175/1520-0442(2003)016<4134:titsam>2.0.co;2.
Marshall, J. et al., 2014: The ocean's role in polar climate change: asymmetric Arctic and Antarctic responses to greenhouse gas and ozone forcing. *Philosophical Transactions of the Royal Society A: Mathematical, Physical and Engineering Sciences*, **372(2019)**, 20130040–20130040, doi:10.1098/rsta.2013.0040.
Marshall, J. et al., 2015: The ocean's role in the transient response of climate to abrupt greenhouse gas forcing. *Climate Dynamics*, **44(7–8)**, 2287–2299, doi:10.1007/s00382-014-2308-0.
Marshall, L. et al., 2019: Exploring How Eruption Source Parameters Affect Volcanic Radiative Forcing Using Statistical Emulation. *Journal of Geophysical Research: Atmospheres*, **124(2)**, 964–985, doi:10.1029/2018jd028675.
Marshall, L.R. et al., 2020: Large Variations in Volcanic Aerosol Forcing Efficiency Due to Eruption Source Parameters and Rapid Adjustments. *Geophysical Research Letters*, **47(19)**, e2020GL090241, doi:10.1029/2020gl090241.
Martin, E.R. and C. Thorncroft, 2014a: Sahel rainfall in multimodel CMIP5 decadal hindcasts. *Geophysical Research Letters*, **41(6)**, 2169–2175, doi:10.1002/2014gl059338.
Martin, E.R. and C.D. Thorncroft, 2014b: The impact of the AMO on the West African monsoon annual cycle. *Quarterly Journal of the Royal Meteorological Society*, **140(678)**, 31–46, doi:10.1002/qj.2107.
Martín-Rey, M., B. Rodríguez-Fonseca, I. Polo, and F. Kucharski, 2014: On the Atlantic–Pacific Niños connection: a multidecadal modulated mode. *Climate Dynamics*, **43(11)**, 3163–3178, doi:10.1007/s00382-014-2305-3.
Martín-Rey, M., I. Polo, B. Rodríguez-Fonseca, T. Losada, and A. Lazar, 2017: Is There Evidence of Changes in Tropical Atlantic Variability Modes under AMO Phases in the Observational Record? *Journal of Climate*, **41(7)**, 3071–3089, doi:10.1007/s00382-015-2471-y.
Marvel, K., G.A. Schmidt, R.L. Miller, and L.S. Nazarenko, 2016: Implications for climate sensitivity from the response to individual forcings. *Nature Climate Change*, **6(4)**, 386–389, doi:10.1038/nclimate2888.
Masato, G., B.J. Hoskins, and T. Woollings, 2013: Winter and Summer Northern Hemisphere Blocking in CMIP5 Models. *Journal of Climate*, **26(18)**, 7044–7059, doi:10.1175/jcli-d-12-00466.1.
Masson-Delmotte, V. et al., 2018: Global warming of 1.5°C An IPCC Special Report. *Report of the Intergovernmental Panel on Climate Change*, **265**, 37–46.
Massonnet, F., 2019: Climate Models as Guidance for the Design of Observing Systems: the Case of Polar Climate and Sea Ice Prediction. *Current Climate Change Reports*, **5(4)**, 334–344, doi:10.1007/s40641-019-00151-w.
Massonnet, F., O. Bellprat, V. Guemas, and F.J. Doblas-Reyes, 2016: Using climate models to estimate the quality of global observational data sets. *Science*, **354(6311)**, 452–455, doi:10.1126/science.aaf6369.
Matsueda, M. and H. Endo, 2017: The robustness of future changes in Northern Hemisphere blocking: A large ensemble projection with multiple sea surface temperature patterns. *Geophysical Research Letters*, **44(10)**, 5158–5166, doi:10.1002/2017gl073336.
Matthes, K. et al., 2017: Solar forcing for CMIP6 (v3.2). *Geoscientific Model Development*, **10(6)**, 2247–2302, doi:10.5194/gmd-10-2247-2017.
Matthews, H.D., 2010: Can carbon cycle geoengineering be a useful complement to ambitious climate mitigation? *Carbon Management*, **1(1)**, 135–144, doi:10.4155/cmt.10.14.
Matthews, H.D. and K. Caldeira, 2007: Transient climate carbon simulations of planetary geoengineering. *Proceedings of the National Academy of Sciences*, **104(24)**, 9949–9954, doi:10.1073/pnas.0700419104.
Matthews, H.D. and K. Caldeira, 2008: Stabilizing climate requires near-zero emissions. *Geophysical Research Letters*, **35(4)**, L04705, doi:10.1029/2007gl032388.
Maycock, A.C., 2016: The contribution of ozone to future stratospheric temperature trends. *Geophysical Research Letters*, **43(9)**, 4609–4616, doi:10.1002/2016gl068511.
McCusker, K.E., D.S. Battisti, and C.M. Bitz, 2015: Inability of stratospheric sulfate aerosol injections to preserve the West Antarctic Ice Sheet. *Geophysical Research Letters*, **42(12)**, 4989–4997, doi:10.1002/2015gl064314.
McCusker, K.E., J.C. Fyfe, and M. Sigmond, 2016: Twenty-five winters of unexpected Eurasian cooling unlikely due to Arctic sea-ice loss. *Nature Geoscience*, **9(11)**, 838–842, doi:10.1038/ngeo2820.
McCusker, K.E., K.C. Armour, C.M. Bitz, and D.S. Battisti, 2014: Rapid and extensive warming following cessation of solar radiation management. *Environmental Research Letters*, **9(2)**, 024005, doi:10.1088/1748-9326/9/2/024005.
McCusker, K.E. et al., 2017: Remarkable separability of circulation response to Arctic sea ice loss and greenhouse gas forcing. *Geophysical Research Letters*, **44(15)**, 7955–7964, doi:10.1002/2017gl074327.
McGregor, H. et al., 2015: Robust global ocean cooling trend for the pre-industrial Common Era. *Nature Geoscience*, **8(9)**, doi:10.1038/ngeo2510.
McGregor, S., A. Timmermann, and O. Timm, 2010a: A unified proxy for ENSO and PDO variability since 1650. *Climate of the Past*, **6(1)**, 1–17, doi:10.5194/cp-6-1-2010.
McGregor, S., A. Timmermann, and O. Timm, 2010b: A unified proxy for ENSO and PDO variability since 1650. *Climate of the Past*, **6(1)**, 1–17, doi:10.5194/cp-6-1-2010.

ACCEPTED VERSION SUBJECT TO FINAL EDITS

McKenna, C.M., T.J. Bracegirdle, E.F. Shuckburgh, P.H. Haynes, and M.M. Joshi, 2018: Arctic Sea Ice Loss in Different Regions Leads to Contrasting Northern Hemisphere Impacts. *Geophysical Research Letters*, **45(2)**, 945–954, doi:10.1002/2017gl076433.

McKenna, C.M., A.C. Maycock, P.M. Forster, C.J. Smith, and K.B. Tokarska, 2021: Stringent mitigation substantially reduces risk of unprecedented near-term warming rates. *Nature Climate Change*, **11(2)**, 126–131, doi:10.1038/s41558-020-00957-9.

McKinnon, K.A., A. Poppick, E. Dunn-Sigouin, and C. Deser, 2017: An "Observational Large Ensemble" to Compare Observed and Modeled Temperature Trend Uncertainty due to Internal Variability. *Journal of Climate*, **30(19)**, 7585–7598, doi:10.1175/jcli-d-16-0905.1.

McSweeney, C.F. and R.G. Jones, 2013: No consensus on consensus: the challenge of finding a universal approach to measuring and mapping ensemble consistency in GCM projections. *Climatic Change*, **119(3–4)**, 617–629, doi:10.1007/s10584-013-0781-9.

Mearns, L.O., C. Rosenzweig, and R. Goldberg, 1997: Mean and variance change in climate scenarios: Methods, agricultural applications, and measures of uncertainty. *Climatic Change*, **35(4)**, 367–396, doi:10.1023/a:1005358130291.

Meccia, V.L., F. Fabiano, P. Davini, and S. Corti, 2020: Stochastic Parameterizations and the Climate Response to External Forcing: An Experiment With EC-Earth. *Geophysical Research Letters*, **47(3)**, e2019GL085951, doi:10.1029/2019gl085951.

Meehl, G.A. and H. Teng, 2012: Case studies for initialized decadal hindcasts and predictions for the Pacific region. *Geophysical Research Letters*, **39(22)**, n/a–n/a, doi:10.1029/2012gl053423.

Meehl, G.A., A. Hu, and H. Teng, 2016: Initialized decadal prediction for transition to positive phase of the Interdecadal Pacific Oscillation. *Nature Communications*, **7(1)**, 11718, doi:10.1038/ncomms11718.

Meehl, G.A., H. Teng, N. Maher, and M.H. England, 2015: Effects of the Mount Pinatubo eruption on decadal climate prediction skill of Pacific sea surface temperatures. *Geophysical Research Letters*, **42(24)**, 10,840–10,846, doi:10.1002/2015gl066608.

Meehl, G.A. et al., 2014: Decadal climate prediction an update from the trenches. *Bulletin of the American Meteorological Society*, **95(2)**, 243–267, doi:10.1175/bams-d-12-00241.1.

Meehl, G.A. et al., 2020: Context for interpreting equilibrium climate sensitivity and transient climate response from the CMIP6 Earth system models. *Science Advances*, **6(26)**, eaba1981, doi:10.1126/sciadv.aba1981.

Meinshausen, M. et al., 2011: The RCP greenhouse gas concentrations and their extensions from 1765 to 2300. *Climatic Change*, **109(1–2)**, 213–241, doi:10.1007/s10584-011-0156-z.

Meinshausen, M. et al., 2020: The shared socio-economic pathway (SSP) greenhouse gas concentrations and their extensions to 2500. *Geoscientific Model Development*, **13(8)**, 3571–3605, doi:10.5194/gmd-13-3571-2020.

Menary, M.B. and L. Hermanson, 2018: Limits on determining the skill of North Atlantic Ocean decadal predictions. *Nature Communications*, **9(1)**, 1694, doi:10.1038/s41467-018-04043-9.

Menary, M.B. et al., 2015: Exploring the impact of CMIP5 model biases on the simulation of North Atlantic decadal variability. *Geophysical Research Letters*, **42(14)**, 5926–5934, doi:10.1002/2015gl064360.

Mengis, N., D.P. Keller, W. Rickels, M. Quaas, and A. Oschlies, 2019: Climate engineering-induced changes in correlations between Earth system variables – implications for appropriate indicator selection. *Climatic Change*, **153(3)**, 305–322, doi:10.1007/s10584-019-02389-7.

Merlis, T.M. and M. Henry, 2018: Simple Estimates of Polar Amplification in Moist Diffusive Energy Balance Models. *Journal of Climate*, **31(15)**, 5811–5824, doi:10.1175/jcli-d-17-0578.1.

Mignot, J. et al., 2016: Decadal prediction skill in the ocean with surface nudging in the IPSL-CM5A-LR climate model. *Climate Dynamics*, **47(3–4)**, 1225–1246, doi:10.1007/s00382-015-2898-1.

Milinski, S., N. Maher, and D. Olonscheck, 2020: How large does a large ensemble need to be? *Earth System Dynamics*, **11(4)**, 885–901, doi:10.5194/esd-11-885-2020.

Millar, R.J. et al., 2017: Emission budgets and pathways consistent with limiting warming to 1.5 degrees C. *Nature Geoscience*, **10(10)**, 741–748, doi:10.1038/ngeo3031.

Millar, R.J. et al., 2018a: Author Correction: Emission budgets and pathways consistent with limiting warming to 1.5°C (Nature Geoscience (2017) DOI: 10.1038/ngeo3031). *Nature Geoscience*, **11(6)**, 454–455, doi:10.1038/s41561-018-0153-1.

Millar, R.J. et al., 2018b: Reply to 'Interpretations of the Paris climate target'. *Nature Geoscience*, **11(4)**, 222, doi:10.1038/s41561-018-0087-7.

Miller, G.H. et al., 2012: Abrupt onset of the Little Ice Age triggered by volcanism and sustained by sea-ice/ocean feedbacks. *Geophysical Research Letters*, **39(2)**, 1–5, doi:10.1029/2011gl050168.

Mindlin, J. et al., 2020: Storyline description of Southern Hemisphere midlatitude circulation and precipitation response to greenhouse gas forcing. *Climate Dynamics*, **54(9–10)**, 4399–4421, doi:10.1007/s00382-020-05234-1.

Minx, J.C. et al., 2018: Negative emissions-Part 1: Research landscape and synthesis. *Environmental Research Letters*, **13(6)**, 063001, doi:10.1088/1748-9326/aabf9b.

Mitchell, D. et al., 2017: Half a degree additional warming, prognosis and projected impacts (HAPPI): background and experimental design. *Geoscientific Model Development*, **10(2)**, 571–583, doi:10.5194/gmd-10-571-2017.

ACCEPTED VERSION SUBJECT TO FINAL EDITS

Mitchell, D.L. and W. Finnegan, 2009: Modification of cirrus clouds to reduce global warming. *Environmental Research Letters*, **4(4)**, 045102, doi:10.1088/1748-9326/4/4/045102.
Mitchell, T.D., 2003: Pattern Scaling: An Examination of the Accuracy of the Technique for Describing Future Climates. *Climatic Change*, **60(3)**, 217–242, doi:10.1023/a:1026035305597.
Mizuta, R. et al., 2014: Classification of CMIP5 Future Climate Responses by the Tropical Sea Surface Temperature Changes. *SOLA*, **10(0)**, 167–171, doi:10.2151/sola.2014-035.
Mochizuki, T. et al., 2010: Pacific decadal oscillation hindcasts relevant to near-term climate prediction. *Proceedings of the National Academy of Sciences*, **107(5)**, 1833–1837, doi:10.1073/pnas.0906531107.
Mochizuki, T. et al., 2012: Decadal Prediction Using a Recent Series of MIROC Global Climate Models. *Journal of the Meteorological Society of Japan*, **90A**, 373–383, doi:10.2151/jmsj.2012-a22.
Modak, A. and G. Bala, 2019: Efficacy of black carbon aerosols: the role of shortwave cloud feedback. *Environmental Research Letters*, **14(8)**, 084029, doi:10.1088/1748-9326/ab21e7.
Modak, A., G. Bala, L. Cao, and K. Caldeira, 2016: Why must a solar forcing be larger than a CO2 forcing to cause the same global mean surface temperature change? *Environmental Research Letters*, **11(4)**, 044013, doi:10.1088/1748-9326/11/4/044013.
Modak, A., G. Bala, K. Caldeira, and L. Cao, 2018a: Does shortwave absorption by methane influence its effectiveness? *Climate Dynamics*, **51(9–10)**, 3653–3672, doi:10.1007/s00382-018-4102-x.
Modak, A., G. Bala, K. Caldeira, and L. Cao, 2018b: Does shortwave absorption by methane influence its effectiveness? *Climate Dynamics*, **51(9–10)**, 3653–3672, doi:10.1007/s00382-018-4102-x.
Mohino, E. and T. Losada, 2015: Impacts of the Atlantic Equatorial Mode in a warmer climate. *Climate Dynamics*, **45(7–8)**, 2255–2271, doi:10.1007/s00382-015-2471-y.
Mohino, E., N. Keenlyside, and H. Pohlmann, 2016: Decadal prediction of Sahel rainfall: where does the skill (or lack thereof) come from? *Climate Dynamics*, **47(11)**, 3593–3612, doi:10.1007/s00382-016-3416-9.
Mohino, E., B. Rodríguez-Fonseca, C.R. Mechoso, T. Losada, and I. Polo, 2019: Relationships among Intermodel Spread and Biases in Tropical Atlantic Sea Surface Temperatures. *Journal of Climate*, **32(12)**, 3615–3635, doi:10.1175/jcli-d-18-0846.1.
Mohtadi, M., M. Prange, and S. Steinke, 2016: Palaeoclimatic insights into forcing and response of monsoon rainfall. *Nature*, **533(7602)**, 191–199, doi:10.1038/nature17450.
Monerie, P.-A., J. Robson, B. Dong, and N. Dunstone, 2018: A role of the Atlantic Ocean in predicting summer surface air temperature over North East Asia? *Climate Dynamics*, **51(1)**, 473–491, doi:10.1007/s00382-017-3935-z.
Monerie, P.-A. et al., 2017: Decadal prediction skill using a high-resolution climate model. *Climate Dynamics*, **49(9–10)**, 3527–3550, doi:10.1007/s00382-017-3528-x.
Moore, G.W.K., J. Halfar, H. Majeed, W. Adey, and A. Kronz, 2017: Amplification of the Atlantic Multidecadal Oscillation associated with the onset of the industrial-era warming. *Scientific Reports*, **7(1)**, 40861, doi:10.1038/srep40861.
Moore, J.C., R. Gladstone, T. Zwinger, and M. Wolovick, 2018: Geoengineer polar glaciers to slow sea-level rise. *Nature*, **555(7696)**, 303–305, doi:10.1038/d41586-018-03036-4.
Moore, J.C. et al., 2014: Arctic sea ice and atmospheric circulation under the GeoMIP G1 scenario. *Journal of Geophysical Research: Atmospheres*, **119(2)**, 567–583, doi:10.1002/2013jd021060.
Moore, J.C. et al., 2015: Atlantic hurricane surge response to geoengineering.. *Proceedings of the National Academy of Sciences of the United States of America*, **112(45)**, 13794–9, doi:10.1073/pnas.1510530112.
Moore, J.K. et al., 2018: Sustained climate warming drives declining marine biological productivity. *Science*, **359(6380)**, 1139–1143, doi:10.1126/science.aao6379.
Mori, M., M. Watanabe, H. Shiogama, J. Inoue, and M. Kimoto, 2014: Robust Arctic sea-ice influence on the frequent Eurasian cold winters in past decades. *Nature Geoscience*, **7(12)**, 869–873, doi:10.1038/ngeo2277.
Morice, C.P. et al., 2021: An Updated Assessment of Near-Surface Temperature Change From 1850: The HadCRUT5 Data Set. *Journal of Geophysical Research: Atmospheres*, **126(3)**, e2019JD032361, doi:10.1029/2019jd032361.
Msadek, R., G.A. Vecchi, M. Winton, and R.G. Gudgel, 2014: Importance of initial conditions in seasonal predictions of Arctic sea ice extent. *Geophysical Research Letters*, **41(14)**, 5208–5215, doi:10.1002/2014gl060799.
Müller, W.A. et al., 2012: Forecast skill of multi-year seasonal means in the decadal prediction system of the Max Planck Institute for Meteorology. *Geophysical Research Letters*, **39(22)**, doi:10.1029/2012gl053326.
Muri, H., U. Niemeier, and J.E. Kristjánsson, 2015: Tropical rainforest response to marine sky brightening climate engineering. *Geophysical Research Letters*, **42(8)**, 2951–2960, doi:10.1002/2015gl063363.
Muri, H., J.E. Kristjansson, T. Storelvmo, and M.A. Pfeffer, 2014: The climatic effects of modifying cirrus clouds in a climate engineering framework. *Journal of Geophysical Research: Atmospheres*, **119(7)**, 4174–4191, doi:10.1002/2013jd021063.
Muri, H. et al., 2018: Climate response to aerosol geoengineering: A multimethod comparison. *Journal of Climate*, **31(16)**, 6319–6340, doi:10.1175/jcli-d-17-0620.1.
Murphy, J.M. et al., 2004: Quantification of modelling uncertainties in a large ensemble of climate change simulations. *Nature*, **430(7001)**, 768–772, doi:10.1038/nature02771.
Muthyala, R., G. Bala, and A. Nalam, 2018: Regional Scale Analysis of Climate Extremes in an SRM Geoengineering

ACCEPTED VERSION SUBJECT TO FINAL EDITS

Simulation, Part 1:Precipitation Extremes. *Current Science*, **114(05)**, 1024–1035, doi:10.18520/cs/v114/i05/1024-1035.
Myhre, G. et al., 2017: PDRMIP: A Precipitation Driver and Response Model Intercomparison Project-Protocol and Preliminary Results. *Bulletin of the American Meteorological Society*, **98(6)**, 1185–1198, doi:10.1175/bams-d-16-0019.1.
Myhre, G. et al., 2018: Sensible heat has significantly affected the global hydrological cycle over the historical period. *Nature Communications*, **9(1)**, 1922, doi:10.1038/s41467-018-04307-4.
Nadiga, B.T., W.R. Casper, and P.W. Jones, 2013: Ensemble-based global ocean data assimilation. *Ocean Modelling*, **72**, 210–230, doi:10.1016/j.ocemod.2013.09.002.
Nadiga, B.T., T. Verma, W. Weijer, and N.M. Urban, 2019: Enhancing Skill of Initialized Decadal Predictions Using a Dynamic Model of Drift. *Geophysical Research Letters*, **46(16)**, 9991–9999, doi:10.1029/2019gl084223.
Najafi, M.R., F.W. Zwiers, and N.P. Gillett, 2015: Attribution of Arctic temperature change to greenhouse-gas and aerosol influences. *Nature Climate Change*, **5(3)**, 246–249, doi:10.1038/nclimate2524.
Nalam, A., G. Bala, and A. Modak, 2018: Effects of Arctic geoengineering on precipitation in the tropical monsoon regions. *Climate Dynamics*, **50(9–10)**, 3375–3395, doi:10.1007/s00382-017-3810-y.
Neely, R.R., D.R. Marsh, K.L. Smith, S.M. Davis, and L.M. Polvani, 2014: Biases in southern hemisphere climate trends induced by coarsely specifying the temporal resolution of stratospheric ozone. *Geophysical Research Letters*, **41(23)**, 8602–8610, doi:10.1002/2014gl061627.
Nemet, G.F. et al., 2018: Negative emissions-Part 3: Innovation and upscaling. *Environmental Research Letters*, **13(6)**, 063003, doi:10.1088/1748-9326/aabff4.
Neukom, R. et al., 2019: Consistent multidecadal variability in global temperature reconstructions and simulations over the Common Era. *Nature Geoscience*, **12(8)**, 643–649, doi:10.1038/s41561-019-0400-0.
Newhall, C., S. Self, and A. Robock, 2018: Anticipating future Volcanic Explosivity Index (VEI) 7 eruptions and their chilling impacts. *Geosphere*, **14(2)**, 572–603, doi:10.1130/ges01513.1.
Newman, M. et al., 2016: The Pacific Decadal Oscillation, Revisited. *Journal of Climate*, **29(12)**, 4399–4427, doi:10.1175/jcli-d-15-0508.1.
Niederdrenk, A.L. and D. Notz, 2018: Arctic Sea Ice in a 1.5°C Warmer World. *Geophysical Research Letters*, **45(4)**, 1963–1971, doi:10.1002/2017gl076159.
Niemeier, U. and C. Timmreck, 2015: What is the limit of climate engineering by stratospheric injection of SO2? *Atmospheric Chemistry and Physics*, **15(16)**, 9129–9141, doi:10.5194/acp-15-9129-2015.
Niemeier, U. and H. Schmidt, 2017: Changing transport processes in the stratosphere by radiative heating of sulfate aerosols. *Atmospheric Chemistry and Physics*, **17(24)**, 14871–14886, doi:10.5194/acp-17-14871-2017.
Niemeier, U., H. Schmidt, K. Alterskjær, and J.E. Kristjánsson, 2013: Solar irradiance reduction via climate engineering: Impact of different techniques on the energy balance and the hydrological cycle. *Journal of Geophysical Research: Atmospheres*, **118(21)**, 11,905–911,917, doi:10.1002/2013jd020445.
Nijsse, F.J.M.M., P.M. Cox, and M.S. Williamson, 2020: Emergent constraints on transient climate response (TCR) and equilibrium climate sensitivity (ECS) from historical warming in CMIP5 and CMIP6 models. *Earth System Dynamics*, **11(3)**, 737–750, doi:10.5194/esd-11-737-2020.
Nohara, D. et al., 2015: Examination of a climate stabilization pathway via zero-emissions using Earth system models. *Environmental Research Letters*, **10(9)**, 095005, doi:10.1088/1748-9326/10/9/095005.
Notz, D., 2015: How well must climate models agree with observations? *Philosophical Transactions of the Royal Society A: Mathematical, Physical and Engineering Sciences*, **373(2052)**, 20140164, doi:10.1098/rsta.2014.0164.
Notz, D. and J. Stroeve, 2018: The Trajectory Towards a Seasonally Ice-Free Arctic Ocean. *Current Climate Change Reports*, **4(4)**, 407–416, doi:10.1007/s40641-018-0113-2.
Notz, D. and SIMIP Community, 2020: Arctic Sea Ice in CMIP6. *Geophysical Research Letters*, **47(10)**, e2019GL086749, doi:10.1029/2019gl086749.
Notz, D. et al., 2016: The CMIP6 Sea-Ice Model Intercomparison Project (SIMIP): understanding sea ice through climate-model simulations. *Geoscientific Model Development*, **9(9)**, 3427–3446, doi:10.5194/gmd-9-3427-2016.
NRC, 2015a: *Climate Intervention: Carbon Dioxide Removal and Reliable Sequestration*. National Research Council (NRC). The National Academies Press, Washington, DC, USA, 154 pp., doi:10.17226/18805.
NRC, 2015b: *Climate Intervention: Reflecting Sunlight to Cool Earth*. National Research Council (NRC). The National Academies Press, Washington, DC, USA, 260 pp., doi:10.17226/18988.
Nummelin, A., C. Li, and P.J. Hezel, 2017: Connecting ocean heat transport changes from the midlatitudes to the Arctic Ocean. *Geophysical Research Letters*, **44**, 1899–1908, doi:10.1002/2016gl071333.
O'Hagan, A. and T.O.M. Leonard, 1976: Bayes estimation subject to uncertainty about parameter constraints. *Biometrika*, **63(1)**, 201–203, doi:10.1093/biomet/63.1.201.
O'Neill, B.C. et al., 2016: The Scenario Model Intercomparison Project (ScenarioMIP) for CMIP6. *Geoscientific Model Development*, **9(9)**, 3461–3482, doi:10.5194/gmd-9-3461-2016.
O'Neill, B.C. et al., 2017: IPCC reasons for concern regarding climate change risks. *Nature Climate Change*, **7(1)**, 28–37, doi:10.1038/nclimate3179.

ACCEPTED VERSION SUBJECT TO FINAL EDITS

O'Reilly, C.H., D.J. Befort, and A. Weisheimer, 2020: Calibrating large-ensemble European climate projections using observational data. *Earth System Dynamics*, **11(4)**, 1033–1049, doi:10.5194/esd-11-1033-2020.
Oelsmann, J., L. Borchert, R. Hand, J. Baehr, and J.H. Jungclaus, 2020: Linking Ocean Forcing and Atmospheric Interactions to Atlantic Multidecadal Variability in MPI-ESM1.2. *Geophysical Research Letters*, **47(10)**, e2020GL087259, doi:10.1029/2020gl087259.
Ohba, M., H. Shiogama, T. Yokohata, and M. Watanabe, 2013: Impact of strong tropical volcanic eruptions on enso simulated in a coupled gcm. *Journal of Climate*, **26(14)**, 5169–5182, doi:10.1175/jcli-d-12-00471.1.
Oldenburg, D., K.C. Armour, L.A.A. Thompson, and C.M. Bitz, 2018: Distinct Mechanisms of Ocean Heat Transport Into the Arctic Under Internal Variability and Climate Change. *Geophysical Research Letters*, **45(15)**, 7692–7700, doi:10.1029/2018gl078719.
Olonscheck, D. and D. Notz, 2017: Consistently Estimating Internal Climate Variability from Climate Model Simulations. *Journal of Climate*, **30(23)**, 9555–9573, doi:10.1175/jcli-d-16-0428.1.
Olson, R., S.-I. An, Y. Fan, J.P. Evans, and L. Caesar, 2018: North Atlantic observations sharpen meridional overturning projections. *Climate Dynamics*, **50(11–12)**, 4171–4188, doi:10.1007/s00382-017-3867-7.
Olson, R. et al., 2019: A novel method to test non-exclusive hypotheses applied to Arctic ice projections from dependent models. *Nature Communications*, **10(1)**, 3016, doi:10.1038/s41467-019-10561-x.
Onarheim, I.H., T. Eldevik, M. Årthun, R.B. Ingvaldsen, and L.H. Smedsrud, 2015: Skillful prediction of Barents Sea ice cover. *Geophysical Research Letters*, **42(13)**, 5364–5371, doi:10.1002/2015gl064359.
Osborn, T.J., C.J. Wallace, J.A. Lowe, and D. Bernie, 2018: Performance of Pattern-Scaled Climate Projections under High-End Warming. Part I: Surface Air Temperature over Land. *Journal of Climate*, **31(14)**, 5667–5680, doi:10.1175/jcli-d-17-0780.1.
Oschlies, A., M. Pahlow, A. Yool, and R.J. Matear, 2010: Climate engineering by artificial ocean upwelling: Channelling the sorcerer's apprentice. *Geophysical Research Letters*, **37(4)**, 1–5, doi:10.1029/2009gl041961.
Oudar, T., J. Cattiaux, and H. Douville, 2020: Drivers of the Northern Extratropical Eddy-Driven Jet Change in CMIP5 and CMIP6 Models. *Geophysical Research Letters*, **47(8)**, e2019GL086695, doi:10.1029/2019gl086695.
Oudar, T. et al., 2017: Respective roles of direct GHG radiative forcing and induced Arctic sea ice loss on the Northern Hemisphere atmospheric circulation. *Climate Dynamics*, **49(11–12)**, 3693–3713, doi:10.1007/s00382-017-3541-0.
Paik, S. and S.K. Min, 2018: Assessing the impact of volcanic eruptions on climate extremes using CMIP5 models. *Journal of Climate*, **31(14)**, 5333–5349, doi:10.1175/jcli-d-17-0651.1.
Paik, S., S.K. Min, C.E. Iles, E.M. Fischer, and A.P. Schurer, 2020: Volcanic-induced global monsoon drying modulated by diverse El Ninõ responses. *Science Advances*, **6(21)**, 1–9, doi:10.1126/sciadv.aba1212.
Palter, J.B., T.L. Frölicher, D. Paynter, and J.G. John, 2018: Climate, ocean circulation, and sea level changes under stabilization and overshoot pathways to 1.5 K warming. *Earth System Dynamics*, **9(2)**, 817–828, doi:10.5194/esd-9-817-2018.
Park, J.-Y., C.A. Stock, J.P. Dunne, X. Yang, and A. Rosati, 2019: Seasonal to multiannual marine ecosystem prediction with a global Earth system model. *Science*, **365(6450)**, 284–288, doi:10.1126/science.aav6634.
Parker, W.S., 2009: II-Wendy S. Parker: Confirmation and adequacy-for-Purpose in Climate Modelling. *Aristotelian Society Supplementary Volume*, **83(1)**, 233–249, doi:10.1111/j.1467-8349.2009.00180.x.
Parsons, L.A., M.K. Brennan, R.C.J. Wills, and C. Proistosescu, 2020: Magnitudes and Spatial Patterns of Interdecadal Temperature Variability in CMIP6. *Geophysical Research Letters*, **47(7)**, e2019GL086588, doi:10.1029/2019gl086588.
Parsons, S., J.A. Renwick, and A.J. McDonald, 2016: An Assessment of Future Southern Hemisphere Blocking Using CMIP5 Projections from Four GCMs. *Journal of Climate*, **29(21)**, 7599–7611, doi:10.1175/jcli-d-15-0754.1.
Partanen, A.-I. et al., 2012: Direct and indirect effects of sea spray geoengineering and the role of injected particle size. *Journal of Geophysical Research: Atmospheres*, **117(D2)**, D02203, doi:10.1029/2011jd016428.
Pascale, S. et al., 2017: Weakening of the North American monsoon with global warming. *Nature Climate Change*, **7(11)**, 806–812, doi:10.1038/nclimate3412.
Pasternack, A. et al., 2018: Parametric decadal climate forecast recalibration (DeFoReSt 1.0). *Geoscientific Model Development*, **11(1)**, 351–368, doi:10.5194/gmd-11-351-2018.
Pausata, F.S.R., L. Chafik, R. Caballero, and D.S. Battisti, 2015: Impacts of high-latitude volcanic eruptions on ENSO and AMOC. *Proceedings of the National Academy of Sciences of the United States of America*, **112(45)**, 13784–13788, doi:10.1073/pnas.1509153112.
Paxian, A. et al., 2019: User-oriented global predictions of the GPCC drought index for the next decade. *Meteorologische Zeitschrift*, **28(1)**, 3–21, doi:10.1127/metz/2018/0912.
Peings, Y., J. Cattiaux, S. Vavrus, and G. Magnusdottir, 2017: Late twenty-first-century changes in the midlatitude atmospheric circulation in the CESM large ensemble. *Journal of Climate*, **30(15)**, 5943–5960, doi:10.1175/jcli-d-16-0340.1.
Peings, Y., J. Cattiaux, S.J. Vavrus, and G. Magnusdottir, 2018: Projected squeezing of the wintertime North-Atlantic jet. *Environmental Research Letters*, **13(7)**, 74016, doi:10.1088/1748-9326/aacc79.
Pendergrass, A.G. and D.L. Hartmann, 2014: The Atmospheric Energy Constraint on Global-Mean Precipitation

ACCEPTED VERSION SUBJECT TO FINAL EDITS

Change. *Journal of Climate*, **27(2)**, 757–768, doi:10.1175/jcli-d-13-00163.1.
Pendergrass, A.G., R. Knutti, F. Lehner, C. Deser, and B.M. Sanderson, 2017: Precipitation variability increases in a warmer climate. *Scientific Reports*, **7(1)**, 17966, doi:10.1038/s41598-017-17966-y.
Penner, J.E., C. Zhou, and X. Liu, 2015: Can cirrus cloud seeding be used for geoengineering? *Geophysical Research Letters*, **42(20)**, 8775–8782, doi:10.1002/2015gl065992.
Peters, G.P., B. Aamaas, T. Berntsen, and J.S. Fuglestvedt, 2011: The integrated global temperature change potential (iGTP) and relationships between emission metrics. *Environmental Research Letters*, **6(4)**, 044021, doi:10.1088/1748-9326/6/4/044021.
Peters, G.P. et al., 2017: Towards real-time verification of CO2 emissions. *Nature Climate Change*, **7(12)**, 848–850, doi:10.1038/s41558-017-0013-9.
Piani, C., D.J. Frame, D.A. Stainforth, and M.R. Allen, 2005: Constraints on climate change from a multi-thousand member ensemble of simulations. *Geophysical Research Letters*, **32(23)**, L23825, doi:10.1029/2005gl024452.
Pitari, G. et al., 2014: Stratospheric ozone response to sulfate geoengineering: Results from the geoengineering model intercomparison project (GeoMip). *Journal of Geophysical Research*, **119(5)**, 2629–2653, doi:10.1002/2013jd020566.
Pithan, F. and T. Mauritsen, 2014: Arctic amplification dominated by temperature feedbacks in contemporary climate models. *Nature Geoscience*, **7(3)**, 181–184, doi:10.1038/ngeo2071.
Plazzotta, M., R. Séférian, and H. Douville, 2019: Impact of Solar Radiation Modification on Allowable CO2 Emissions: What Can We Learn From Multimodel Simulations? *Earth's Future*, **7(6)**, 664–676, doi:10.1029/2019ef001165.
Plazzotta, M., R. Séférian, H. Douville, B. Kravitz, and J. Tjiputra, 2018a: Land Surface Cooling Induced by Sulfate Geoengineering Constrained by Major Volcanic Eruptions. *Geophysical Research Letters*, **45**, 5663–5671, doi:10.1029/2018gl077583.
Plazzotta, M., R. Séférian, H. Douville, B. Kravitz, and J. Tjiputra, 2018b: Land Surface Cooling Induced by Sulfate Geoengineering Constrained by Major Volcanic Eruptions. *Geophysical Research Letters*, **45**, 5663–5671, doi:10.1029/2018gl077583.
Pohlmann, H., J. Kröger, R.J. Greatbatch, and W.A. Müller, 2017: Initialization shock in decadal hindcasts due to errors in wind stress over the tropical Pacific. *Climate Dynamics*, **49(7–8)**, 2685–2693, doi:10.1007/s00382-016-3486-8.
Pohlmann, H., J.H. Jungclaus, A. Köhl, D. Stammer, and J. Marotzke, 2009: Initializing Decadal Climate Predictions with the GECCO Oceanic Synthesis: Effects on the North Atlantic. *Journal of Climate*, **22(14)**, 3926–3938, doi:10.1175/2009jcli2535.1.
Pohlmann, H. et al., 2013: Improved forecast skill in the tropics in the new MiKlip decadal climate predictions. *Geophysical Research Letters*, **40(21)**, 5798–5802, doi:10.1002/2013gl058051.
Pohlmann, H. et al., 2019: Realistic Quasi-Biennial Oscillation Variability in Historical and Decadal Hindcast Simulations Using CMIP6 Forcing. *Geophysical Research Letters*, **46(23)**, 14118–14125, doi:10.1029/2019gl084878.
Polkova, I., A. Köhl, and D. Stammer, 2014: Impact of initialization procedures on the predictive skill of a coupled ocean–atmosphere model. *Climate Dynamics*, **42(11–12)**, 3151–3169, doi:10.1007/s00382-013-1969-4.
Polkova, I. et al., 2019: Initialization and Ensemble Generation for Decadal Climate Predictions: A Comparison of Different Methods. *Journal of Advances in Modeling Earth Systems*, **11(1)**, 149–172, doi:10.1029/2018ms001439.
Polson, D. and G.C. Hegerl, 2017: Strengthening contrast between precipitation in tropical wet and dry regions. *Geophysical Research Letters*, **44(1)**, 365–373, doi:10.1002/2016gl071194.
Polson, D., M. Bollasina, G.C. Hegerl, and L.J. Wilcox, 2014: Decreased monsoon precipitation in the Northern Hemisphere due to anthropogenic aerosols. *Geophysical Research Letters*, **41(16)**, 6023–6029, doi:10.1002/2014gl060811.
Polvani, L.M., M. Previdi, M.R. England, G. Chiodo, and K.L. Smith, 2020: Substantial twentieth-century Arctic warming caused by ozone-depleting substances. *Nature Climate Change*, **10(2)**, 130–133, doi:10.1038/s41558-019-0677-4.
Pope, F.D. et al., 2012: Stratospheric aerosol particles and solar-radiation management. *Nature Climate Change*, **2(10)**, 713–719, doi:10.1038/nclimate1528.
Power, S., F. Delage, C. Chung, G. Kociuba, and K. Keay, 2013: Robust twenty-first-century projections of El Niño and related precipitation variability. *Nature*, **502(7472)**, 541–545, doi:10.1038/nature12580.
Power, S.B., F. Delage, R. Colman, and A. Moise, 2012: Consensus on Twenty-First-Century Rainfall Projections in Climate Models More Widespread than Previously Thought. *Journal of Climate*, **25(11)**, 3792–3809, doi:10.1175/jcli-d-11-00354.1.
Predybaylo, E., G.L. Stenchikov, A.T. Wittenberg, and F. Zeng, 2017: Impacts of a pinatubo-size volcanic eruption on ENSO. *Journal of Geophysical Research*, **122(2)**, 925–947, doi:10.1002/2016jd025796.
Predybaylo, E., G. Stenchikov, A.T. Wittenberg, and S. Osipov, 2020: El Niño/Southern Oscillation response to low-latitude volcanic eruptions depends on ocean pre-conditions and eruption timing. *Communications Earth &*

ACCEPTED VERSION SUBJECT TO FINAL EDITS

Environment, **1(1)**, 1–13, doi:10.1038/s43247-020-0013-y.
Priestley, M.D.K. et al., 2020: An Overview of the Extratropical Storm Tracks in CMIP6 Historical Simulations. *Journal of Climate*, **33(15)**, 6315–6343, doi:10.1175/jcli-d-19-0928.1.
Pugh, T.A.M. et al., 2018: A Large Committed Long-Term Sink of Carbon due to Vegetation Dynamics. *Earth's Future*, **6(10)**, 1413–1432, doi:10.1029/2018ef000935.
Raible, C.C. et al., 2016: Tambora 1815 as a test case for high impact volcanic eruptions: Earth system effects. *Wiley Interdisciplinary Reviews: Climate Change*, **7(4)**, 569–589, doi:10.1002/wcc.407.
Ramanathan, V. and Y. Feng, 2008: On avoiding dangerous anthropogenic interference with the climate system: Formidable challenges ahead. *Proceedings of the National Academy of Sciences*, **105(38)**, 14245–14250, doi:10.1073/pnas.0803838105.
Ramanathan, V. et al., 2005: Atmospheric brown clouds: Impacts on South Asian climate and hydrological cycle. *Proceedings of the National Academy of Sciences*, **102(15)**, 5326–5333, doi:10.1073/pnas.0500656102.
Randerson, J.T. et al., 2015a: Multicentury changes in ocean and land contributions to the climate-carbon feedback. *Global Biogeochemical Cycles*, **29(6)**, 744–759, doi:10.1002/2014gb005079.
Randerson, J.T. et al., 2015b: Multicentury changes in ocean and land contributions to the climate-carbon feedback. *Global Biogeochemical Cycles*, **29(6)**, 744–759, doi:10.1002/2014gb005079.
Rao, S. et al., 2017: Future air pollution in the Shared Socio-economic Pathways. *Global Environmental Change*, **42**, 346–358, doi:10.1016/j.gloenvcha.2016.05.012.
Regayre, L.A. et al., 2018: Aerosol and physical atmosphere model parameters are both important sources of uncertainty in aerosol ERF. *Atmospheric Chemistry and Physics*, **18(13)**, 9975–10006, doi:10.5194/acp-18-9975-2018.
Riahi, K. et al., 2017: The Shared Socioeconomic Pathways and their energy, land use, and greenhouse gas emissions implications: An overview. *Global Environmental Change*, **42**, 153–168, doi:10.1016/j.gloenvcha.2016.05.009.
Ribes, A., S. Qasmi, and N.P. Gillett, 2021: Making climate projections conditional on historical observations. *Science Advances*, **7(4)**, eabc0671, doi:10.1126/sciadv.abc0671.
Richardson, T.B., P.M. Forster, T. Andrews, and D.J. Parker, 2016: Understanding the Rapid Precipitation Response to CO2 and Aerosol Forcing on a Regional Scale. *Journal of Climate*, **29(2)**, 583–594, doi:10.1175/jcli-d-15-0174.1.
Richardson, T.B. et al., 2018a: Drivers of Precipitation Change: An Energetic Understanding. *Journal of Climate*, **31(23)**, 9641–9657, doi:10.1175/jcli-d-17-0240.1.
Richardson, T.B. et al., 2018b: Carbon Dioxide Physiological Forcing Dominates Projected Eastern Amazonian Drying. *Geophysical Research Letters*, **45(6)**, 2815–2825, doi:10.1002/2017gl076520.
Richardson, T.B. et al., 2019: Efficacy of Climate Forcings in PDRMIP Models. *Journal of Geophysical Research: Atmospheres*, **124(23)**, 12824–12844, doi:10.1029/2019jd030581.
Richter Jadwiga, H. et al., 2018: Stratospheric Response in the First Geoengineering Simulation Meeting Multiple Surface Climate Objectives. *Journal of Geophysical Research: Atmospheres*, **123(11)**, 5762–5782, doi:10.1029/2018jd028285.
Ricke, K.L. and K. Caldeira, 2014: Maximum warming occurs about one decade after a carbon dioxide emission. *Environmental Research Letters*, **9(12)**, 124002, doi:10.1088/1748-9326/9/12/124002.
Rickels, W., F. Reith, D. Keller, A. Oschlies, and M.F. Quaas, 2018: Integrated Assessment of Carbon Dioxide Removal. *Earth's Future*, **6(3)**, 565–582, doi:10.1002/2017ef000724.
Ridley, H.E. et al., 2015: Aerosol forcing of the position of the intertropical convergence zone since ad 1550. *Nature Geoscience*, **8(3)**, 195–200, doi:10.1038/ngeo2353.
Rind, D. et al., 2018: Multicentury Instability of the Atlantic Meridional Circulation in Rapid Warming Simulations With GISS ModelE2. *Journal of Geophysical Research: Atmospheres*, **123(12)**, 6331–6355, doi:10.1029/2017jd027149.
Robock, A., 1983: Ice and Snow Feedbacks and the Latitudinal and Seasonal Distribution of Climate Sensitivity. *Journal of the Atmospheric Sciences*, **40(4)**, 986–997, doi:10.1175/1520-0469(1983)040<0986:iasfat>2.0.co;2.
Robock, A., L. Oman, and G. Stenchikov, 2008: Regional climate responses to geoengineering with tropical and Artic SO2 injections. *Journal of Geophysical Research*, **113**, 1–15, doi:10.1029/2008jd010050.
Robock, A., M. Bunzl, B. Kravitz, and G.L. Stenchikov, 2010: A Test for Geoengineering? *Science*, **327(5965)**, 530–531, doi:10.1126/science.1186237.
Robock, A., D.G. MacMartin, R. Duren, and M.W. Christensen, 2013: Studying geoengineering with natural and anthropogenic analogs. *Climatic Change*, **121(3)**, 445–458, doi:10.1007/s10584-013-0777-5.
Robson, J., R. Sutton, and D. Smith, 2014: Decadal predictions of the cooling and freshening of the North Atlantic in the 1960s and the role of ocean circulation. *Climate Dynamics*, **42(9)**, 2353–2365, doi:10.1007/s00382-014-2115-7.
Robson, J.I., R.T. Sutton, and D.M. Smith, 2012: Initialized decadal predictions of the rapid warming of the North Atlantic Ocean in the mid 1990s. *Geophysical Research Letters*, **39(19)**, L19713, doi:10.1029/2012gl053370.
Rodgers, K.B., J. Lin, and T.L. Frölicher, 2015: Emergence of multiple ocean ecosystem drivers in a large ensemble suite with an Earth system model. *Biogeosciences*, **12(11)**, 3301–3320, doi:10.5194/bg-12-3301-2015.

ACCEPTED VERSION SUBJECT TO FINAL EDITS

Rogelj, J. et al., 2014: Disentangling the effects of CO2 and short-lived climate forcer mitigation. *Proceedings of the National Academy of Sciences*, **111(46)**, 16325–16330, doi:10.1073/pnas.1415631111.

Rogelj, J. et al., 2018a: Scenarios towards limiting global mean temperature increase below 1.5 °c. *Nature Climate Change*, **8(4)**, 325–332, doi:10.1038/s41558-018-0091-3.

Rogelj, J. et al., 2018b: Mitigation Pathways Compatible with 1.5°C in the Context of Sustainable Development Supplementary Material. In: *Global Warming of 1.5°C. An IPCC Special Report on the impacts of global warming of 1.5°C above pre-industrial levels and related global greenhouse gas emission pathways, in the context of strengthening the global response to the threat of climate change,* [Masson-Delmotte, V., P. Zhai, H.-O. Pörtner, D. Roberts, J. Skea, P.R. Shukla, A. Pirani, W. Moufouma-Okia, C. Péan, R. Pidcock, S. Connors, J.B.R. Matthews, Y. Chen, X. Zhou, M.I. Gomis, E. Lonnoy, T. Maycock, M. Tignor, and T. Waterfield (eds.)]. In Press, pp. 2SM: 1–50.

Rotstayn, L.D., 2013: Projected effects of declining anthropogenic aerosols on the southern annular mode. *Environmental Research Letters*, **8(4)**, 044028, doi:10.1088/1748-9326/8/4/044028.

Rowell, D.P., 2012: Sources of uncertainty in future changes in local precipitation. *Climate Dynamics*, **39(7–8)**, 1929–1950, doi:10.1007/s00382-011-1210-2.

Ruggieri, P. et al., 2021: Atlantic Multidecadal Variability and North Atlantic Jet: A Multimodel View from the Decadal Climate Prediction Project. *Journal of Climate*, **34(1)**, 347–360, doi:10.1175/jcli-d-19-0981.1.

Ruprich-Robert, Y. and C. Cassou, 2015: Combined influences of seasonal East Atlantic Pattern and North Atlantic Oscillation to excite Atlantic multidecadal variability in a climate model. *Climate Dynamics*, **44(1–2)**, 229–253, doi:10.1007/s00382-014-2176-7.

Russotto, R.D. and T.P. Ackerman, 2018: Changes in clouds and thermodynamics under solar geoengineering and implications for required solar reduction. *Atmos. Chem. Phys.*, **18(16)**, 11905–11925, doi:10.5194/acp-18-11905-2018.

Saffioti, C., E.M. Fischer, and R. Knutti, 2017: Improved Consistency of Climate Projections over Europe after Accounting for Atmospheric Circulation Variability. *Journal of Climate*, **30(18)**, 7271–7291, doi:10.1175/jcli-d-16-0695.1.

Saggioro, E. and T.G. Shepherd, 2019: Quantifying the Timescale and Strength of Southern Hemisphere Intraseasonal Stratosphere-troposphere Coupling. *Geophysical Research Letters*, **46(22)**, 13479–13487, doi:10.1029/2019gl084763.

Samset, B.H., J.S. Fuglestvedt, and M.T. Lund, 2020: Delayed emergence of a global temperature response after emission mitigation. *Nature Communications*, **11(1)**, 3261, doi:10.1038/s41467-020-17001-1.

Samset, B.H. et al., 2016: Fast and slow precipitation responses to individual climate forcers: A PDRMIP multimodel study. *Geophysical Research Letters*, **43(6)**, 2782–2791, doi:10.1002/2016gl068064.

Sanchez-Gomez, E., C. Cassou, Y. Ruprich-Robert, E. Fernandez, and L. Terray, 2016: Drift dynamics in a coupled model initialized for decadal forecasts. *Climate Dynamics*, **46(5–6)**, 1819–1840, doi:10.1007/s00382-015-2678-y.

Sand, M. et al., 2016: Response of Arctic temperature to changes in emissions of short-lived climate forcers. *Nature Climate Change*, **6(3)**, 286–289, doi:10.1038/nclimate2880.

Sanderson, B.M., R. Knutti, and P. Caldwell, 2015: Addressing Interdependency in a Multimodel Ensemble by Interpolation of Model Properties. *Journal of Climate*, **28(13)**, 5150–5170, doi:10.1175/jcli-d-14-00361.1.

Sanderson, B.M., M. Wehner, and R. Knutti, 2017: Skill and independence weighting for multi-model assessments. *Geoscientific Model Development*, **10(6)**, 2379–2395, doi:10.5194/gmd-10-2379-2017.

Sanderson, B.M. et al., 2011: The response of the climate system to very high greenhouse gas emission scenarios. *Environmental Research Letters*, **6(3)**, 034005, doi:10.1088/1748-9326/6/3/034005.

Santer, B.D. et al., 2014: Volcanic contribution to decadal changes in tropospheric temperature. *Nature Geoscience*, **7(3)**, 185–189, doi:10.1038/ngeo2098.

Santer, B.D. et al., 2018: Human influence on the seasonal cycle of tropospheric temperature. *Science*, **361(6399)**, eaas8806, doi:10.1126/science.aas8806.

Scaife, A.A. and D. Smith, 2018: A signal-to-noise paradox in climate science. *npj Climate and Atmospheric Science*, **1(1)**, 28, doi:10.1038/s41612-018-0038-4.

Scaife, A.A. et al., 2014: Predictability of the quasi-biennial oscillation and its northern winter teleconnection on seasonal to decadal timescales. *Geophysical Research Letters*, **41(5)**, 1752–1758, doi:10.1002/2013gl059160.

Schäfer, S., M. Lawrence, H. Stelzer, W. Born, S. Low, S. Schäfer, M. Lawrence, H. Stelzer, W. Born, S. Low, P. Adriázola, G. Betz, O. Boucher, S. Haszeldine, J. Haywood, P. Irvine, J.- Kristjansson, M. Lawrence, T. Lenton, H. Muri, A. Oschlies, A. Proelss, T. Rayner, W. Rickels, L. Ruthner, S. Schäfer, J. Scheffran, H. Schmidt, V. Scott, H. Stelzer, N. Vaughan, M. Watson, A. Aaheim, A. Carius, P. Devine-right, A.T. Gullberg, K. Houghton, F. Herrmann, D. Keith, T. Kruger, D. Parr, K. Redgwell, A. Robock, D. Santillo, and P. Suarez (eds.), 2015: *The European Transdisciplinary Assessment of Climate Engineering (EuTRACE): Removing Greenhouse Gases from the Atmosphere and Reflecting Sunlight away from Earth*. Funded by the European Union's Seventh Framework Programme under Grant Agreement 306993, Institute for Advanced Sustainability Studies (IASS), Potsdam, Germany, 170 pp., doi:10.2312/iass.2015.024.

ACCEPTED VERSION SUBJECT TO FINAL EDITS

Schleussner, C.-F., P. Pfleiderer, and E.M. Fischer, 2017: In the observational record half a degree matters. *Nature Climate Change*, **7(7)**, 460–462, doi:10.1038/nclimate3320.
Schleussner, C.-F. et al., 2016: Differential climate impacts for policy-relevant limits to global warming: the case of 1.5°C and 2°C. *Earth System Dynamics*, **7(2)**, 327–351, doi:10.5194/esd-7-327-2016.
Schloesser, F., T. Friedrich, A. Timmermann, R.M. DeConto, and D. Pollard, 2019: Antarctic iceberg impacts on future Southern Hemisphere climate. *Nature Climate Change*, **9(9)**, 672–677, doi:10.1038/s41558-019-0546-1.
Schmidt, G.A. et al., 2014: Using palaeo-climate comparisons to constrain future projections in CMIP5. *Climate of the Past*, **10(1)**, 221–250, doi:10.5194/cp-10-221-2014.
Schmidt, H. et al., 2012: Solar irradiance reduction to counteract radiative forcing from a quadrupling of CO2: Climate responses simulated by four earth system models. *Earth System Dynamics*, **3(1)**, 63–78, doi:10.5194/esd-3-63-2012.
Schneider, S.H., 2001: What is 'dangerous' climate change? *Nature*, **411(6833)**, 17–19, doi:10.1038/35075167.
Schneider, S.H., 2002: Can we estimate the likelihood of climatic changes at 2100? *Climatic Change*, **52(4)**, 441–451, doi:10.1023/a:1014276210717.
Schneider, T., T. Bischoff, and H. Płotka, 2015: Physics of Changes in Synoptic Midlatitude Temperature Variability. *Journal of Climate*, **28(6)**, 2312–2331, doi:10.1175/jcli-d-14-00632.1.
Schurer, A.P., S.F.B. Tett, and G.C. Hegerl, 2014: Small influence of solar variability on climate over the past millennium. *Nature Geoscience*, **7(2)**, 104–108, doi:10.1038/ngeo2040.
Schurer, A.P., G.C. Hegerl, M.E. Mann, S.F.B. Tett, and S.J. Phipps, 2013a: Separating Forced from Chaotic Climate Variability over the Past Millennium. *Journal of Climate*, **26(18)**, doi:10.1175/jcli-d-12-00826.1.
Schurer, A.P., G.C. Hegerl, M.E. Mann, S.F.B. Tett, and S.J. Phipps, 2013b: Separating Forced from Chaotic Climate Variability over the Past Millennium. *Journal of Climate*, **26(18)**, doi:10.1175/jcli-d-12-00826.1.
Schurer, A.P. et al., 2018: Interpretations of the Paris climate target. *Nature Geoscience*, **11(4)**, 220–221, doi:10.1038/s41561-018-0086-8.
Schuster, M. et al., 2019a: Improvement in the decadal prediction skill of the North Atlantic extratropical winter circulation through increased model resolution. *Earth System Dynamics*, **10(4)**, 901–917, doi:10.5194/esd-10-901-2019.
Schuster, M. et al., 2019b: Improvement in the decadal prediction skill of the North Atlantic extratropical winter circulation through increased model resolution. *Earth System Dynamics*, **10(4)**, 901–917, doi:10.5194/esd-10-901-2019.
Schwartzman, A. and R.F. Keeling, 2020: Achieving atmospheric verification of CO2 emissions. *Nature Climate Change*, **10(5)**, 416–417, doi:10.1038/s41558-020-0735-y.
Schwierz, C., M. Croci-Maspoli, and H.C. Davies, 2004: Perspicacious indicators of atmospheric blocking. *Geophysical Research Letters*, **31(6)**, n/a–n/a, doi:10.1029/2003gl019341.
Schwinger, J. and J. Tjiputra, 2018: Ocean Carbon Cycle Feedbacks Under Negative Emissions. *Geophysical Research Letters*, **45(10)**, 5062–5070, doi:10.1029/2018gl077790.
Screen, J.A., 2014: Arctic amplification decreases temperature variance in northern mid- to high-latitudes. *Nature Climate Change*, **4(7)**, 577–582, doi:10.1038/nclimate2268.
Screen, J.A., 2018: Arctic sea ice at 1.5 and 2°C. *Nature Climate Change*, **8(5)**, 362–363, doi:10.1038/s41558-018-0137-6.
Screen, J.A. and D. Williamson, 2017: Ice-free Arctic at 1.5°C? *Nature Climate Change*, **7(4)**, 230–231, doi:10.1038/nclimate3248.
Screen, J.A., T.J. Bracegirdle, and I. Simmonds, 2018a: Polar Climate Change as Manifest in Atmospheric Circulation. *Current Climate Change Reports*, **4(4)**, 383–395, doi:10.1007/s40641-018-0111-4.
Screen, J.A. et al., 2018b: Consistency and discrepancy in the atmospheric response to Arctic sea-ice loss across climate models. *Nature Geoscience*, **11(3)**, 155–163, doi:10.1038/s41561-018-0059-y.
Seager, R. et al., 2014a: Causes of Increasing Aridification of the Mediterranean Region in Response to Rising Greenhouse Gases. *Journal of Climate*, **27(12)**, 4655–4676, doi:10.1175/jcli-d-13-00446.1.
Seager, R. et al., 2014b: Dynamical and Thermodynamical Causes of Large-Scale Changes in the Hydrological Cycle over North America in Response to Global Warming. *Journal of Climate*, **27(20)**, 7921–7948, doi:10.1175/jcli-d-14-00153.1.
Seiler, C. and F.W. Zwiers, 2016: How will climate change affect explosive cyclones in the extratropics of the Northern Hemisphere? *Climate Dynamics*, **46(11–12)**, 3633–3644, doi:10.1007/s00382-015-2791-y.
Sellar, A.A. et al., 2019: UKESM1: Description and Evaluation of the U.K. Earth System Model. *Journal of Advances in Modeling Earth Systems*, **11(12)**, 4513–4558, doi:10.1029/2019ms001739.
Seneviratne, S.I., D. Lüthi, M. Litschi, and C. Schär, 2006: Land–atmosphere coupling and climate change in Europe. *Nature*, **443(7108)**, 205–209, doi:10.1038/nature05095.
Seneviratne, S.I., M.G. Donat, A.J. Pitman, R. Knutti, and R.L. Wilby, 2016: Allowable CO2 emissions based on regional and impact-related climate targets. *Nature*, **529(7587)**, 477–483, doi:10.1038/nature16542.
Seneviratne, S.I. et al., 2018: Climate extremes, land–climate feedbacks and land-use forcing at 1.5°C. *Philosophical Transactions of the Royal Society A: Mathematical, Physical and Engineering Sciences*, **376(2119)**, 20160450,

ACCEPTED VERSION SUBJECT TO FINAL EDITS

doi:10.1098/rsta.2016.0450.
Serreze, M.C. and R.G. Barry, 2011: Processes and impacts of Arctic amplification: A research synthesis. *Global and Planetary Change*, **77(1–2)**, 85–96, doi:10.1016/j.gloplacha.2011.03.004.
Servain, J., G. Caniaux, Y.K. Kouadio, M.J. McPhaden, and M. Araujo, 2014: Recent climatic trends in the tropical Atlantic. *Climate Dynamics*, **43(11)**, 3071–3089, doi:10.1007/s00382-014-2168-7.
Seviour, W.J.M. et al., 2019: The Southern Ocean Sea Surface Temperature Response to Ozone Depletion: A Multimodel Comparison. *Journal of Climate*, **32(16)**, 5107–5121, doi:10.1175/jcli-d-19-0109.1.
Sexton, D.M.H., J.M. Murphy, M. Collins, and M.J. Webb, 2012: Multivariate probabilistic projections using imperfect climate models part I: outline of methodology. *Climate Dynamics*, **38(11–12)**, 2513–2542, doi:10.1007/s00382-011-1208-9.
Sgubin, G., D. Swingedouw, S. Drijfhout, S. Hagemann, and E. Robertson, 2015: Multimodel analysis on the response of the AMOC under an increase of radiative forcing and its symmetrical reversal. *Climate Dynamics*, **45(5–6)**, 1429–1450, doi:10.1007/s00382-014-2391-2.
Shaffrey, L.C. et al., 2017: Decadal predictions with the HiGEM high resolution global coupled climate model: description and basic evaluation. *Climate Dynamics*, **48(1–2)**, 297–311, doi:10.1007/s00382-016-3075-x.
Shaw, T.A., 2019: Mechanisms of Future Predicted Changes in the Zonal Mean Mid-Latitude Circulation. *Current Climate Change Reports*, **5(4)**, 345–357, doi:10.1007/s40641-019-00145-8.
Shaw, T.A. and A. Voigt, 2015: Tug of war on summertime circulation between radiative forcing and sea surface warming. *Nature Geoscience*, **8(7)**, 560–566, doi:10.1038/ngeo2449.
Shaw, T.A. et al., 2016a: Storm track processes and the opposing influences of climate change. *Nature Geoscience*, **9(9)**, 656–664, doi:10.1038/ngeo2783.
Shaw, T.A. et al., 2016b: Storm track processes and the opposing influences of climate change. *Nature Geoscience*, **9(9)**, 656–664, doi:10.1038/ngeo2783.
Shawki, D., A. Voulgarakis, A. Chakraborty, M. Kasoar, and J. Srinivasan, 2018: The South Asian Monsoon Response to Remote Aerosols: Global and Regional Mechanisms. *Journal of Geophysical Research: Atmospheres*, **123(20)**, 11,511–585,601, doi:10.1029/2018jd028623.
Sheen, K.L. et al., 2017: Skilful prediction of Sahel summer rainfall on inter-annual and multi-year timescales. *Nature Communications*, **8(1)**, 14966, doi:10.1038/ncomms14966.
Shepherd, T.G., 2014: Atmospheric circulation as a source of uncertainty in climate change projections. *Nature Geoscience*, **7(10)**, 703–708, doi:10.1038/ngeo2253.
Shepherd, T.G., 2019: Storyline approach to the construction of regional climate change information. *Proceedings of the Royal Society A: Mathematical, Physical and Engineering Sciences*, **475(2225)**, 20190013, doi:10.1098/rspa.2019.0013.
Shepherd, T.G. et al., 2018: Storylines: an alternative approach to representing uncertainty in physical aspects of climate change. *Climatic Change*, **151(3–4)**, 555–571, doi:10.1007/s10584-018-2317-9.
Sherwood, S.C. et al., 2015: Adjustments in the Forcing-Feedback Framework for Understanding Climate Change. *Bulletin of the American Meteorological Society*, **96(2)**, 217–228, doi:10.1175/bams-d-13-00167.1.
Shindell, D. and C.J. Smith, 2019: Climate and air-quality benefits of a realistic phase-out of fossil fuels. *Nature*, **573(7774)**, 408–411, doi:10.1038/s41586-019-1554-z.
Shindell, D. et al., 2017: A climate policy pathway for near- and long-term benefits. *Science*, **356(6337)**, 493–494, doi:10.1126/science.aak9521.
Shiogama, H. et al., 2016: Predicting future uncertainty constraints on global warming projections. *Scientific Reports*, **6(1)**, 18903, doi:10.1038/srep18903.
Shu, Q., Z. Song, and F. Qiao, 2015: Assessment of sea ice simulations in the CMIP5 models. *The Cryosphere*, **9(1)**, 399–409, doi:10.5194/tc-9-399-2015.
Sienz, F., W.A. Müller, and H. Pohlmann, 2016: Ensemble size impact on the decadal predictive skill assessment. *Meteorologische Zeitschrift*, **25(6)**, 645–655, doi:10.1127/metz/2016/0670.
Sigl, M. et al., 2015: Timing and climate forcing of volcanic eruptions for the past 2,500 years. *Nature*, **523(7562)**, 543–549, doi:10.1038/nature14565.
Sigmond, M. and J.C. Fyfe, 2016: Tropical Pacific impacts on cooling North American winters. *Nature Climate Change*, **6(10)**, 970–974, doi:10.1038/nclimate3069.
Sigmond, M., J.C. Fyfe, and N.C. Swart, 2018: Ice-free Arctic projections under the Paris Agreement. *Nature Climate Change*, **8(5)**, 404–408, doi:10.1038/s41558-018-0124-y.
Sigmond, M., J.C. Fyfe, O.A. Saenko, and N.C. Swart, 2020: Ongoing AMOC and related sea-level and temperature changes after achieving the Paris targets. *Nature Climate Change*, **10(7)**, 672–677, doi:10.1038/s41558-020-0786-0.
Siler, N., G.H. Roe, K.C. Armour, and N. Feldl, 2019: Revisiting the surface-energy-flux perspective on the sensitivity of global precipitation to climate change. *Climate Dynamics*, **52(7)**, 3983–3995, doi:10.1007/s00382-018-4359-0.
Sime, L.C., P.O. Hopcroft, and R.H. Rhodes, 2019: Impact of abrupt sea ice loss on Greenland water isotopes during the last glacial period.. *Proceedings of the National Academy of Sciences of the United States of America*,

ACCEPTED VERSION SUBJECT TO FINAL EDITS

116(10), 4099–4104, doi:10.1073/pnas.1807261116.
Simpson, I.R. and L.M. Polvani, 2016a: Revisiting the relationship between jet position, forced response, and annular mode variability in the southern midlatitudes. *Geophysical Research Letters*, **43(6)**, 2896–2903, doi:10.1002/2016gl067989.
Simpson, I.R. and L.M. Polvani, 2016b: Revisiting the relationship between jet position, forced response, and annular mode variability in the southern midlatitudes. *Geophysical Research Letters*, **43(6)**, 2896–2903, doi:10.1002/2016gl067989.
Simpson, I.R., T.A. Shaw, and R. Seager, 2014: A Diagnosis of the Seasonally and Longitudinally Varying Midlatitude Circulation Response to Global Warming. *Journal of the Atmospheric Sciences*, **71(7)**, 2489–2515, doi:10.1175/jas-d-13-0325.1.
Simpson, I.R., C. Deser, K.A. McKinnon, and E.A. Barnes, 2018a: Modeled and observed multidecadal variability in the North Atlantic jet stream and its connection to sea surface temperatures. *Journal of Climate*, **31(20)**, 8313–8338, doi:10.1175/jcli-d-18-0168.1.
Simpson, I.R., C. Deser, K.A. McKinnon, and E.A. Barnes, 2018b: Modeled and observed multidecadal variability in the North Atlantic jet stream and its connection to sea surface temperatures. *Journal of Climate*, **31(20)**, 8313–8338, doi:10.1175/jcli-d-18-0168.1.
Simpson, I.R., C. Deser, K.A. McKinnon, and E.A. Barnes, 2018c: Modeled and observed multidecadal variability in the North Atlantic jet stream and its connection to sea surface temperatures. *Journal of Climate*, **31(20)**, 8313–8338, doi:10.1175/jcli-d-18-0168.1.
Simpson, I.R., S.G. Yeager, K.A. McKinnon, and C. Deser, 2019a: Decadal predictability of late winter precipitation in western Europe through an ocean–jet stream connection. *Nature Geoscience*, **12(8)**, 613–619, doi:10.1038/s41561-019-0391-x.
Simpson, I.R. et al., 2019b: The Regional Hydroclimate Response to Stratospheric Sulfate Geoengineering and the Role of Stratospheric Heating. *Journal of Geophysical Research: Atmospheres*, **124(23)**, 12587–12616, doi:10.1029/2019jd031093.
Singh, H.A., P.J. Rasch, and B.E.J. Rose, 2017: Increased Ocean Heat Convergence Into the High Latitudes With CO2 Doubling Enhances Polar-Amplified Warming. *Geophysical Research Letters*, **44(20)**, 10,583–10,591, doi:10.1002/2017gl074561.
Sippel, S. et al., 2019: Uncovering the forced climate response from a single ensemble member using statistical learning. *Journal of Climate*, doi:10.1175/jcli-d-18-0882.1.
Smerdon, B.D., 2017: A synopsis of climate change effects on groundwater recharge. *Journal of Hydrology*, **555**, 125–128, doi:10.1016/j.jhydrol.2017.09.047.
Smith, C.J. et al., 2019: Current fossil fuel infrastructure does not yet commit us to 1.5°C warming. *Nature Communications*, **10(1)**, 101, doi:10.1038/s41467-018-07999-w.
Smith, D.M., R. Eade, and H. Pohlmann, 2013a: A comparison of full-field and anomaly initialization for seasonal to decadal climate prediction. *Climate Dynamics*, **41(11–12)**, 3325–3338, doi:10.1007/s00382-013-1683-2.
Smith, D.M. et al., 2010: Skilful multi-year predictions of Atlantic hurricane frequency. *Nature Geoscience*, **3(12)**, 846–849, doi:10.1038/ngeo1004.
Smith, D.M. et al., 2013b: Real-time multi-model decadal climate predictions. *Climate Dynamics*, **41(11–12)**, 2875–2888, doi:10.1007/s00382-012-1600-0.
Smith, D.M. et al., 2018: Predicted Chance That Global Warming Will Temporarily Exceed 1.5°C. *Geophysical Research Letters*, **45(21)**, 11,895–11,903, doi:10.1029/2018gl079362.
Smith, D.M. et al., 2019: Robust skill of decadal climate predictions. *npj Climate and Atmospheric Science*, **2(1)**, 13, doi:10.1038/s41612-019-0071-y.
Smith, D.M. et al., 2020: North Atlantic climate far more predictable than models imply. *Nature*, **583(7818)**, 796–800, doi:10.1038/s41586-020-2525-0.
Smith, S.J. and A. Mizrahi, 2013: Near-term climate mitigation by short-lived forcers. *Proceedings of the National Academy of Sciences*, **110(35)**, 14202–14206, doi:10.1073/pnas.1308470110.
Solaraju-Murali, B., L.-P. Caron, N. Gonzalez-Reviriego, and F.J. Doblas-Reyes, 2019: Multi-year prediction of European summer drought conditions for the agricultural sector. *Environmental Research Letters*, **14(12)**, 124014, doi:10.1088/1748-9326/ab5043.
Solomon, A. and L.M. Polvani, 2016: Highly Significant Responses to Anthropogenic Forcings of the Midlatitude Jet in the Southern Hemisphere. *Journal of Climate*, **29(9)**, 3463–3470, doi:10.1175/jcli-d-16-0034.1.
Solomon, S., G.-K. Plattner, R. Knutti, and P. Friedlingstein, 2009: Irreversible climate change due to carbon dioxide emissions. *Proceedings of the National Academy of Sciences*, **106(6)**, 1704–1709, doi:10.1073/pnas.0812721106.
Solomon, S. et al., 2016: Antarctic ozone layer. *Science*, **353(6296)**, 269–274.
Solomon, S. et al., 2017: Mirrored changes in Antarctic ozone and stratospheric temperature in the late 20th versus early 21st centuries. *Journal of Geophysical Research: Atmospheres*, **122(16)**, 8940–8950, doi:10.1002/2017jd026719.
Sonntag, S., 2018: Quantifying effects and side-effects of climate engineering on the Earth system. *Earth's Future*, **6**,

ACCEPTED VERSION SUBJECT TO FINAL EDITS

doi:10.1002/eft2.285.
Sospedra-Alfonso, R. and G.J. Boer, 2020: Assessing the Impact of Initialization on Decadal Prediction Skill. *Geophysical Research Letters*, **47(4)**, e2019GL086361, doi:10.1029/2019gl086361.
Spring, A., T. Ilyina, and J. Marotzke, 2020: Inherent uncertainty disguises attribution of reduced atmospheric CO2 growth to CO2 emission reductions for up to a decade. *Environmental Research Letters*, **15(11)**, 114058, doi:10.1088/1748-9326/abc443.
Steffen, W. et al., 2018: Trajectories of the Earth System in the Anthropocene. *Proceedings of the National Academy of Sciences*, **115(33)**, 8252–8259, doi:10.1073/pnas.1810141115.
Steinman, B.A., M.E. Mann, and S.K. Miller, 2015: Atlantic and Pacific multidecadal oscillations and Northern Hemisphere temperatures. *Science*, **347(6225)**, 988–991, doi:10.1126/science.1257856.
Steptoe, H., L.J. Wilcox, and E.J. Highwood, 2016: Is there a robust effect of anthropogenic aerosols on the Southern Annular Mode? *Journal of Geophysical Research: Atmospheres*, **121(17)**, 10,029–10,042, doi:10.1002/2015jd024218.
Stevenson, S., B. Otto-Bliesner, J. Fasullo, and E. Brady, 2016: "El Niño Like" hydroclimate responses to last millennium volcanic eruptions. *Journal of Climate*, **29(8)**, 2907–2921, doi:10.1175/jcli-d-15-0239.1.
Stevenson, S., A.T. Wittenberg, J. Fasullo, S. Coats, and B. Otto-Bliesner, 2021: Understanding Diverse Model Projections of Future Extreme El Niño. *Journal of Climate*, **34(2)**, 449–464, doi:10.1175/jcli-d-19-0969.1.
Stjern, C.W. et al., 2018: Response to marine cloud brightening in a multi-model ensemble. *Atmospheric Chemistry and Physics*, **18(2)**, 621–634, doi:10.5194/acp-18-621-2018.
Stjern, C.W. et al., 2019: Arctic Amplification Response to Individual Climate Drivers. *Journal of Geophysical Research: Atmospheres*, **124(13)**, 6698–6717, doi:10.1029/2018jd029726.
Stohl, A. et al., 2015: Evaluating the climate and air quality impacts of short-lived pollutants. *Atmospheric Chemistry and Physics*, **15(18)**, 10529–10566, doi:10.5194/acp-15-10529-2015.
Stolpe, M.B., I. Medhaug, J. Sedláček, and R. Knutti, 2018: Multidecadal Variability in Global Surface Temperatures Related to the Atlantic Meridional Overturning Circulation. *Journal of Climate*, **31(7)**, 2889–2906, doi:10.1175/jcli-d-17-0444.1.
Storelvmo, T. and N. Herger, 2014: Cirrus cloud susceptibility to the injection of ice nuclei in the upper troposphere. *Journal of Geophysical Research: Atmospheres*, **119(5)**, 2375–2389, doi:10.1002/2013jd020816.
Storelvmo, T. et al., 2013: Cirrus cloud seeding has potential to cool climate. *Geophysical Research Letters*, **40(1)**, 178–182, doi:10.1029/2012gl054201.
Stott, P., P. Good, G. Jones, N. Gillett, and E. Hawkins, 2013: The upper end of climate model temperature projections is inconsistent with past warming. *Environmental Research Letters*, **8(1)**, 014024, doi:10.1088/1748-9326/8/1/014024.
Stroeve, J. and D. Notz, 2015: Insights on past and future sea-ice evolution from combining observations and models. *Global and Planetary Change*, **135**, 119–132, doi:10.1016/j.gloplacha.2015.10.011.
Stroeve, J., A. Barrett, M. Serreze, and A. Schweiger, 2014: Using records from submarine, aircraft and satellites to evaluate climate model simulations of Arctic sea ice thickness. *The Cryosphere*, **8(5)**, 1839–1854, doi:10.5194/tc-8-1839-2014.
Strommen, K. and T.N. Palmer, 2019: Signal and noise in regime systems: A hypothesis on the predictability of the North Atlantic Oscillation. *Quarterly Journal of the Royal Meteorological Society*, **145(718)**, 147–163, doi:10.1002/qj.3414.
Strommen, K., P.A.G. Watson, and T.N. Palmer, 2019: The Impact of a Stochastic Parameterization Scheme on Climate Sensitivity in EC-Earth. *Journal of Geophysical Research: Atmospheres*, **124(23)**, 12726–12740, doi:10.1029/2019jd030732.
Strømmen, K., H.M. Christensen, J. Berner, and T.N. Palmer, 2018: The impact of stochastic parametrisations on the representation of the Asian summer monsoon. *Climate Dynamics*, **50(5–6)**, 2269–2282, doi:10.1007/s00382-017-3749-z.
Stuart, G.S. et al., 2013: Reduced efficacy of marine cloud brightening geoengineering due to in-plume aerosol coagulation: parameterization and global implications. *Atmospheric Chemistry and Physics*, **13(20)**, 10385–10396, doi:10.5194/acp-13-10385-2013.
Stuecker, M.F. et al., 2017: Revisiting ENSO/Indian Ocean Dipole phase relationships. *Geophysical Research Letters*, **44(5)**, 2481–2492, doi:10.1002/2016gl072308.
Stuecker, M.F. et al., 2018: Polar amplification dominated by local forcing and feedbacks. *Nature Climate Change*, **8(12)**, 1076–1081, doi:10.1038/s41558-018-0339-y.
Suarez-Gutierrez, L., C. Li, W.A. Müller, and J. Marotzke, 2018: Internal variability in European summer temperatures at 1.5 °C and 2 °C of global warming. *Environmental Research Letters*, **13(6)**, 064026, doi:10.1088/1748-9326/aaba58.
Suárez-Gutiérrez, L., C. Li, P.W. Thorne, and J. Marotzke, 2017: Internal variability in simulated and observed tropical tropospheric temperature trends. *Geophysical Research Letters*, **44**, 5709–5719, doi:10.1002/2017gl073798.
Sun, L., M. Alexander, and C. Deser, 2018: Evolution of the Global Coupled Climate Response to Arctic Sea Ice Loss during 1990–2090 and Its Contribution to Climate Change. *Journal of Climate*, **31(19)**, 7823–7843,

ACCEPTED VERSION SUBJECT TO FINAL EDITS

doi:10.1175/jcli-d-18-0134.1.
Sun, W. et al., 2019: A "La Niña-like" state occurring in the second year after large tropical volcanic eruptions during the past 1500 years. *Climate Dynamics*, **52(12)**, 7495–7509, doi:10.1007/s00382-018-4163-x.
Sutton, R.T., 2018: ESD Ideas: a simple proposal to improve the contribution of IPCC WGI to the assessment and communication of climate change risks. *Earth System Dynamics*, **9(4)**, 1155–1158, doi:10.5194/esd-9-1155-2018.
Sutton, R.T., B. Dong, and J.M. Gregory, 2007: Land/sea warming ratio in response to climate change: IPCC AR4 model results and comparison with observations. *Geophysical Research Letters*, **34(2)**, L02701, doi:10.1029/2006gl028164.
Svendsen, L., S. Hetzinger, N. Keenlyside, and Y. Gao, 2014: Marine-based multiproxy reconstruction of Atlantic multidecadal variability. *Geophysical Research Letters*, **41(4)**, 1295–1300, doi:10.1002/2013gl059076.
Swann, A.L.S., F.M. Hoffman, C.D. Koven, and J.T. Randerson, 2016: Plant responses to increasing CO2 reduce estimates of climate impacts on drought severity. *Proceedings of the National Academy of Sciences*, **113(36)**, 10019–10024, doi:10.1073/pnas.1604581113.
Swart, N.C. et al., 2019: The Canadian Earth System Model version 5 (CanESM5.0.3). *Geoscientific Model Development*, **12(11)**, 4823–4873, doi:10.5194/gmd-12-4823-2019.
Swingedouw, D. et al., 2015: Bidecadal North Atlantic ocean circulation variability controlled by timing of volcanic eruptions. *Nature Communications*, **6(1)**, doi:10.1038/ncomms7545.
Swingedouw, D. et al., 2017: Impact of explosive volcanic eruptions on the main climate variability modes. *Global and Planetary Change*, **150**, 24–45, doi:10.1016/j.gloplacha.2017.01.006.
Tachiiri, K., D. Silva Herran, X. Su, and M. Kawamiya, 2019: Effect on the Earth system of realizing a 1.5°C warming climate target after overshooting to the 2°C level. *Environmental Research Letters*, **14(12)**, 124063, doi:10.1088/1748-9326/ab5199.
Tamarin-Brodsky, T. and Y. Kaspi, 2017: Enhanced poleward propagation of storms under climate change. *Nature Geoscience*, **10(12)**, 908–913, doi:10.1038/s41561-017-0001-8.
Tamarin-Brodsky, T., K. Hodges, B.J. Hoskins, and T.G. Shepherd, 2020: Changes in Northern Hemisphere temperature variability shaped by regional warming patterns. *Nature Geoscience*, **13(6)**, 414–421, doi:10.1038/s41561-020-0576-3.
Taylor, K.E., R.J. Stouffer, and G.A. Meehl, 2012: An Overview of CMIP5 and the Experiment Design. *Bulletin of the American Meteorological Society*, **93(4)**, 485–498, doi:10.1175/bams-d-11-00094.1.
Tebaldi, C. and R. Knutti, 2007: The use of the multi-model ensemble in probabilistic climate projections. *Philosophical Transactions of the Royal Society A: Mathematical, Physical and Engineering Sciences*, **365(1857)**, 2053–2075, doi:10.1098/rsta.2007.2076.
Tebaldi, C. and P. Friedlingstein, 2013: Delayed detection of climate mitigation benefits due to climate inertia and variability. *Proceedings National Academy of Sciences (USA)*, **110(43)**, 17229–17234, doi:10.1073/pnas.1300005110.
Tebaldi, C. and J.M. Arblaster, 2014: Pattern scaling: Its strengths and limitations, and an update on the latest model simulations. *Climatic Change*, **122(3)**, 459–471, doi:10.1007/s10584-013-1032-9.
Tebaldi, C. and R. Knutti, 2018: Evaluating the accuracy of climate change pattern emulation for low warming targets. *Environmental Research Letters*, **13(5)**, 055006, doi:10.1088/1748-9326/aabef2.
Tebaldi, C. and M.F. Wehner, 2018: Benefits of mitigation for future heat extremes under RCP4.5 compared to RCP8.5. *Climatic Change*, **146(3–4)**, 349–361, doi:10.1007/s10584-016-1605-5.
Tebaldi, C., J.M. Arblaster, and R. Knutti, 2011: Mapping model agreement on future climate projections. *Geophysical Research Letters*, **38(23)**, L23701, doi:10.1029/2011gl049863.
Tebaldi, C., B. O'Neill, and J.-F. Lamarque, 2015: Sensitivity of regional climate to global temperature and forcing. *Environmental Research Letters*, **10(7)**, 74001, doi:10.1088/1748-9326/10/7/074001.
Tebaldi, C. et al., 2021: Climate model projections from the Scenario Model Intercomparison Project (ScenarioMIP) of CMIP6. *Earth System Dynamics*, **12(1)**, 253–293, doi:10.5194/esd-12-253-2021.
Teng, H., G.A. Meehl, G. Branstator, S. Yeager, and A. Karspeck, 2017: Initialization Shock in CCSM4 Decadal Prediction Experiments. *Past Global Changes Magazine*, **25(1)**, 41–46, doi:10.22498/pages.25.1.41.
Terhaar, J., L. Kwiatkowski, and L. Bopp, 2020: Emergent constraint on Arctic Ocean acidification in the twenty-first century. *Nature*, **582(7812)**, 379–383, doi:10.1038/s41586-020-2360-3.
The Royal Society, 2009: *Geoengineering the climate: science, governance and uncertainty*. RS Policy document 10/09, The Royal Society, London, UK, 82 pp.
Thoma, M., R. Gerdes, R.J. Greatbatch, and H. Ding, 2015a: Partially coupled spin-up of the MPI-ESM: implementation and first results. *Geoscientific Model Development*, **8(1)**, 51–68, doi:10.5194/gmd-8-51-2015.
Thoma, M., R.J. Greatbatch, C. Kadow, and R. Gerdes, 2015b: Decadal hindcasts initialized using observed surface wind stress: Evaluation and prediction out to 2024. *Geophysical Research Letters*, **42(15)**, 6454–6461, doi:10.1002/2015gl064833.
Thompson, D.W.J., E.A. Barnes, C. Deser, W.E. Foust, and A.S. Phillips, 2015: Quantifying the Role of Internal Climate Variability in Future Climate Trends. *Journal of Climate*, **28(16)**, 6443–6456, doi:10.1175/jcli-d-14-

ACCEPTED VERSION SUBJECT TO FINAL EDITS

00830.1.
Tilmes, S., B.M. Sanderson, and B.C. O'Neill, 2016: Climate impacts of geoengineering in a delayed mitigation scenario. *Geophysical Research Letters*, **43(15)**, 8222–8229, doi:10.1002/2016gl070122.
Tilmes, S., A. Jahn, J.E. Kay, M. Holland, and J.- Lamarque, 2014: Can regional climate engineering save the summer Arctic sea ice? *Geophysical Research Letters*, **41(3)**, 880–885, doi:10.1002/2013gl058731.
Tilmes, S. et al., 2013: The hydrological impact of geoengineering in the Geoengineering Model Intercomparison Project (GeoMIP). *Journal of Geophysical Research Atmospheres*, **118(19)**, 11036–11058, doi:10.1002/jgrd.50868.
Tilmes, S. et al., 2017: Sensitivity of aerosol distribution and climate response to stratospheric SO2 injection locations. *Journal of Geophysical Research: Atmospheres*, **122(23)**, 12,591–12,615, doi:10.1002/2017jd026888.
Tilmes, S. et al., 2018a: CESM1(WACCM) Stratospheric Aerosol Geoengineering Large Ensemble Project. *Bulletin of the American Meteorological Society*, **99(11)**, 2361–2371, doi:10.1175/bams-d-17-0267.1.
Tilmes, S. et al., 2018b: Effects of Different Stratospheric SO2 Injection Altitudes on Stratospheric Chemistry and Dynamics. *Journal of Geophysical Research: Atmospheres*, **123(9)**, 4654–4673, doi:10.1002/2017jd028146.
Tilmes, S. et al., 2020: Reaching 1.5 and 2.0°C global surface temperature targets using stratospheric aerosol geoengineering. *Earth System Dynamics*, **11(3)**, 579–601, doi:10.5194/esd-11-579-2020.
Timmermann, A. et al., 2018: El Niño–Southern Oscillation complexity. *Nature*, **559(7715)**, 535–545, doi:10.1038/s41586-018-0252-6.
Timmreck, C., H. Pohlmann, S. Illing, and C. Kadow, 2016: The impact of stratospheric volcanic aerosol on decadal-scale climate predictions. *Geophysical Research Letters*, **43(2)**, 834–842, doi:10.1002/2015gl067431.
Tjiputra, J.F., A. Grini, and H. Lee, 2016: Impact of idealized future stratospheric aerosol injection on the large-scale ocean and land carbon cycles. *Journal of Geophysical Research: Biogeosciences*, **121(1)**, 2–27, doi:10.1002/2015jg003045.
Tokarska, K.B. and K. Zickfeld, 2015: The effectiveness of net negative carbon dioxide emissions in reversing anthropogenic climate change. *Environmental Research Letters*, **10(9)**, 094013, doi:10.1088/1748-9326/10/9/094013.
Tokarska, K.B., K. Zickfeld, and J. Rogelj, 2019: Path Independence of Carbon Budgets When Meeting a Stringent Global Mean Temperature Target After an Overshoot. *Earth's Future*, **7(12)**, 1283–1295, doi:10.1029/2019ef001312.
Tokarska, K.B. et al., 2020: Past warming trend constrains future warming in CMIP6 models. *Science Advances*, **6(12)**, eaaz9549, doi:10.1126/sciadv.aaz9549.
Toll, V., M. Christensen, J. Quaas, and N. Bellouin, 2019: Weak average liquid-cloud-water response to anthropogenic aerosols. *Nature*, **572(7767)**, 51–55, doi:10.1038/s41586-019-1423-9.
Toohey, M., K. Krüger, M. Sigl, F. Stordal, and H. Svensen, 2016a: Climatic and societal impacts of a volcanic double event at the dawn of the Middle Ages. *Climatic Change*, **136(3–4)**, 401–412, doi:10.1007/s10584-016-1648-7.
Toohey, M., K. Krüger, M. Sigl, F. Stordal, and H. Svensen, 2016b: Climatic and societal impacts of a volcanic double event at the dawn of the Middle Ages. *Climatic Change*, **136(3–4)**, 401–412, doi:10.1007/s10584-016-1648-7.
Tsutsui, J. et al., 2006a: Long-term climate response to stabilized and overshoot anthropogenic forcings beyond the twenty-first century. *Climate Dynamics*, **28(2–3)**, 199–214, doi:10.1007/s00382-006-0176-y.
Tsutsui, J. et al., 2006b: Long-term climate response to stabilized and overshoot anthropogenic forcings beyond the twenty-first century. *Climate Dynamics*, **28(2–3)**, 199–214, doi:10.1007/s00382-006-0176-y.
Tung, K.-K., X. Chen, J. Zhou, and K.-F. Li, 2019: Interdecadal variability in pan-Pacific and global SST, revisited. *Climate Dynamics*, **52(3)**, 2145–2157, doi:10.1007/s00382-018-4240-1.
UNFCCC, 2016: *Decision 1/CP.21: Adoption of the Paris Agreement*. FCCC/CP/2015/10/Add.1, United Nations Framework Convention on Climate Change (UNFCCC), 1–36 pp.
Valdes, P., 2011: Built for stability. *Nature Geoscience*, **4(7)**, 414–416, doi:10.1038/ngeo1200.
Vallis, G.K., P. Zurita-Gotor, C. Cairns, and J. Kidston, 2015: Response of the large-scale structure of the atmosphere to global warming. *Quarterly Journal of the Royal Meteorological Society*, **141(690)**, 1479–1501, doi:10.1002/qj.2456.
van Oldenborgh, G.J., F.J. Doblas-Reyes, B. Wouters, and W. Hazeleger, 2012: Decadal prediction skill in a multi-model ensemble. *Climate Dynamics*, **38(7–8)**, 1263–1280, doi:10.1007/s00382-012-1313-4.
van Vuuren, D.P. et al., 2011: The representative concentration pathways: an overview. *Climatic Change*, **109(1–2)**, 5–31, doi:10.1007/s10584-011-0148-z.
van Vuuren, D.P. et al., 2016: Carbon budgets and energy transition pathways. *Environmental Research Letters*, **11(7)**, 75002, doi:10.1088/1748-9326/11/7/075002.
Vecchi, G.A., T.L. Delworth, and B. Booth, 2017: Origins of Atlantic decadal swings. *Nature*, **548(7667)**, 284–285, doi:10.1038/nature23538.
Vecchi, G.A. et al., 2014: On the Seasonal Forecasting of Regional Tropical Cyclone Activity. *Journal of Climate*, **27(21)**, 7994–8016, doi:10.1175/jcli-d-14-00158.1.
Vega-Westhoff, B. and R.L. Sriver, 2017: Analysis of ENSO's response to unforced variability and anthropogenic forcing using CESM. *Scientific Reports*, **7(1)**, 18047, doi:10.1038/s41598-017-18459-8.

ACCEPTED VERSION SUBJECT TO FINAL EDITS

Vial, J., J.-L. Dufresne, and S. Bony, 2013: On the interpretation of inter-model spread in CMIP5 climate sensitivity estimates. *Climate Dynamics*, **41(11–12)**, 3339–3362, doi:10.1007/s00382-013-1725-9.
Vicente-Serrano, S.M.M. et al., 2018: Recent changes of relative humidity: regional connections with land and ocean processes. *Earth System Dynamics*, **9(2)**, 915–937, doi:10.5194/esd-9-915-2018.
Villamayor, J., T. Ambrizzi, and E. Mohino, 2018: Influence of decadal sea surface temperature variability on northern Brazil rainfall in CMIP5 simulations. *Climate Dynamics*, **51(1)**, 563–579, doi:10.1007/s00382-017-3941-1.
Visioni, D., G. Pitari, and V. Aquila, 2017: Sulfate geoengineering: a review of the factors controlling the needed injection of sulfur dioxide. *Atmospheric Chemistry and Physics*, **17(6)**, 3879–3889, doi:10.5194/acp-17-3879-2017.
Visioni, D., G. Pitari, G. di Genova, S. Tilmes, and I. Cionni, 2018: Upper tropospheric ice sensitivity to sulfate geoengineering. *Atmospheric Chemistry and Physics*, **18(20)**, 14867–14887, doi:10.5194/acp-18-14867-2018.
Visioni, D. et al., 2020a: Reduced Poleward Transport Due to Stratospheric Heating Under Stratospheric Aerosols Geoengineering. *Geophysical Research Letters*, **47(17)**, e2020GL089470, doi:10.1029/2020gl089470.
Visioni, D. et al., 2020b: Seasonally Modulated Stratospheric Aerosol Geoengineering Alters the Climate Outcomes. *Geophysical Research Letters*, **47(12)**, e2020GL088337, doi:10.1029/2020gl088337.
Visioni, D. et al., 2020c: What goes up must come down: impacts of deposition in a sulfate geoengineering scenario. *Environmental Research Letters*.
Vogel, M.M. et al., 2017: Regional amplification of projected changes in extreme temperatures strongly controlled by soil moisture-temperature feedbacks. *Geophysical Research Letters*, **44(3)**, 1511–1519, doi:10.1002/2016gl071235.
Voigt, A. and T.A. Shaw, 2015: Circulation response to warming shaped by radiative changes of clouds and water vapour. *Nature Geoscience*, **8(2)**, 102–106, doi:10.1038/ngeo2345.
Voigt, A. and T.A. Shaw, 2016: Impact of regional atmospheric cloud radiative changes on shifts of the extratropical jet stream in response to global warming. *Journal of Climate*, **29(23)**, 8399–8421, doi:10.1175/jcli-d-16-0140.1.
Voigt, A., N. Albern, and G. Papavasileiou, 2019: The atmospheric pathway of the cloud-radiative impact on the circulation response to global warming: Important and uncertain. *Journal of Climate*, **32(10)**, 3051–3067, doi:10.1175/jcli-d-18-0810.1.
Voigt, A. et al., 2017: Fast and slow shifts of the zonal-mean intertropical convergence zone in response to an idealized anthropogenic aerosol. *Journal of Advances in Modeling Earth Systems*, **9(2)**, 870–892, doi:10.1002/2016ms000902.
von Trentini, F., E.E. Aalbers, E.M. Fischer, and R. Ludwig, 2020: Comparing interannual variability in three regional single-model initial-condition large ensembles (SMILEs) over Europe. *Earth System Dynamics*, **11(4)**, 1013–1031, doi:10.5194/esd-11-1013-2020.
Waisman, H., H. De Coninck, and J. Rogelj, 2019: Key technological enablers for ambitious climate goals: insights from the IPCC special report on global warming of 1.5°C. *Environmental Research Letters*, **14(11)**, 111001, doi:10.1088/1748-9326/ab4c0b.
Wang, B. and Q. Ding, 2008: Global monsoon: Dominant mode of annual variation in the tropics. *Dynamics of Atmospheres and Oceans*, **44(3–4)**, 165–183, doi:10.1016/j.dynatmoce.2007.05.002.
Wang, B., C. Jin, and J. Liu, 2020: Understanding Future Change of Global Monsoons Projected by CMIP6 Models. *Journal of Climate*, **33(15)**, 6471–6489, doi:10.1175/jcli-d-19-0993.1.
Wang, B. et al., 2013a: Northern Hemisphere summer monsoon intensified by mega-El Niño/southern oscillation and Atlantic multidecadal oscillation. *Proceedings of the National Academy of Sciences*, **110(14)**, 5347 LP – 5352, doi:10.1073/pnas.1219405110.
Wang, B. et al., 2013b: Preliminary evaluations of FGOALS-g2 for decadal predictions. *Advances in Atmospheric Sciences*, **30(3)**, 674–683, doi:10.1007/s00376-012-2084-x.
Wang, B. et al., 2021: Monsoons Climate Change Assessment. *Bulletin of the American Meteorological Society*, **102(1)**, E1–E19, doi:10.1175/bams-d-19-0335.1.
Wang, G., W. Cai, and A. Purich, 2014: Trends in Southern Hemisphere wind-driven circulation in CMIP5 models over the 21st century: Ozone recovery versus greenhouse forcing. *Journal of Geophysical Research: Oceans*, **119(5)**, 2974–2986, doi:10.1002/2013jc009589.
Wang, J., H.-M. Kim, and E.K.M. Chang, 2017a: Changes in Northern Hemisphere Winter Storm Tracks under the Background of Arctic Amplification. *Journal of Climate*, **30(10)**, 3705–3724, doi:10.1175/jcli-d-16-0650.1.
Wang, J. et al., 2017b: Internal and external forcing of multidecadal Atlantic climate variability over the past 1,200 years. *Nature Geoscience*, **10(7)**, 512–517, doi:10.1038/ngeo2962.
Wang, P.X. et al., 2017: The global monsoon across time scales: Mechanisms and outstanding issues. *Earth-Science Reviews*, **174**, 84–121, doi:10.1016/j.earscirev.2017.07.006.
Wang, Y., G.J. Zhang, and G.C. Craig, 2016: Stochastic convective parameterization improving the simulation of tropical precipitation variability in the NCAR CAM5. *Geophysical Research Letters*, **43(12)**, 6612–6619, doi:10.1002/2016gl069818.
Wang, Y. et al., 2018: Elucidating the Role of Anthropogenic Aerosols in Arctic Sea Ice Variations. *Journal of Climate*, **31(1)**, 99–114, doi:10.1175/jcli-d-17-0287.1.

ACCEPTED VERSION SUBJECT TO FINAL EDITS

Watanabe, M., Y. Kamae, and M. Kimoto, 2014: Robust increase of the equatorial Pacific rainfall and its variability in a warmed climate. *Geophysical Research Letters*, **41(9)**, 3227–3232, doi:10.1002/2014gl059692.

Watson, P.A.G. et al., 2017: The impact of stochastic physics on tropical rainfall variability in global climate models on daily to weekly time scales. *Journal of Geophysical Research: Atmospheres*, **122(11)**, 5738–5762, doi:10.1002/2016jd026386.

Weigel, A.P., R. Knutti, M.A. Liniger, and C. Appenzeller, 2010: Risks of Model Weighting in Multimodel Climate Projections. *Journal of Climate*, **23(15)**, 4175–4191, doi:10.1175/2010jcli3594.1.

Weijer, W., W. Cheng, O.A. Garuba, A. Hu, and B.T. Nadiga, 2020: CMIP6 Models Predict Significant 21st Century Decline of the Atlantic Meridional Overturning Circulation. *Geophysical Research Letters*, **47**, e2019GL086075, doi:10.1029/2019gl086075.

Weisenstein, D., D. Keith, and J. Dykema, 2015: Solar geoengineering using solid aerosol in the stratosphere. *Atmospheric Chemistry and Physics*, **15**, 11835–11859, doi:10.5194/acp-15-11835-2015.

Weisheimer, A., S. Corti, T. Palmer, and F. Vitart, 2014: Addressing model error through atmospheric stochastic physical parametrizations: impact on the coupled ECMWF seasonal forecasting system. *Philosophical Transactions of the Royal Society A: Mathematical, Physical and Engineering Sciences*, **372(2018)**, 20130290, doi:10.1098/rsta.2013.0290.

Weiss, M. et al., 2014: Contribution of Dynamic Vegetation Phenology to Decadal Climate Predictability. *Journal of Climate*, **27(22)**, 8563–8577, doi:10.1175/jcli-d-13-00684.1.

Wen, Q., J. Yao, K. Döös, and H. Yang, 2018: Decoding Hosing and Heating Effects on Global Temperature and Meridional Circulations in a Warming Climate. *Journal of Climate*, **31(23)**, 9605–9623, doi:10.1175/jcli-d-18-0297.1.

Wengel, C., D. Dommenget, M. Latif, T. Bayr, and A. Vijayeta, 2018: What Controls ENSO-Amplitude Diversity in Climate Models? *Geophysical Research Letters*, **45(4)**, 1989–1996, doi:10.1002/2017gl076849.

Wilcox, L.J. et al., 2020: Accelerated increases in global and Asian summer monsoon precipitation from future aerosol reductions. *Atmospheric Chemistry and Physics*, **20(20)**, 11955–11977, doi:10.5194/acp-20-11955-2020.

Williams, R.G., P. Ceppi, and A. Katavouta, 2020: Controls of the transient climate response to emissions by physical feedbacks, heat uptake and carbon cycling. *Environmental Research Letters*, **15(9)**, 940–941, doi:10.1088/1748-9326/ab97c9.

Williams, R.G., V. Roussenov, T.L. Frölicher, and P. Goodwin, 2017: Drivers of Continued Surface Warming After Cessation of Carbon Emissions. *Geophysical Research Letters*, **44(20)**, 10,610–633,642, doi:10.1002/2017gl075080.

Wills, R.C.J., K.C. Armour, D.S. Battisti, and D.L. Hartmann, 2019: Ocean–Atmosphere Dynamical Coupling Fundamental to the Atlantic Multidecadal Oscillation. *Journal of Climate*, **32(1)**, 251–272, doi:10.1175/jcli-d-18-0269.1.

Winton, M., 2006: Amplified Arctic climate change: What does surface albedo feedback have to do with it? *Geophysical Research Letters*, **33(3)**, L03701, doi:10.1029/2005gl025244.

Wittenberg, A.T., 2009: Are historical records sufficient to constrain ENSO simulations? *Geophysical Research Letters*, **36(12)**, L12702, doi:10.1029/2009gl038710.

WMO, 2011: *Scientific Assessment of Ozone Depletion: 2010*. Global Ozone Research and Monitoring Project – Report No. 52, World Meteorological Organization (WMO), Geneva, Switzerland, 516 pp.

WMO, 2018: *Scientific Assessment of Ozone Depletion: 2018*. Global Ozone Research and Monitoring Project – Report No. 58, World Meteorological Organization (WMO), Geneva, Switzerland, 588 pp.

Wobus, C., M. Flanner, M.C. Sarofim, M.C.P. Moura, and S.J. Smith, 2016: Future Arctic temperature change resulting from a range of aerosol emissions scenarios. *Earth's Future*, **4(6)**, 270–281, doi:10.1002/2016ef000361.

Wood, T., C.M. McKenna, A. Chrysanthou, and A.C. Maycock, 2020: Role of sea surface temperature patterns for the Southern Hemisphere jet stream response to CO2 forcing. *Environmental Research Letters*, **16(1)**, doi:10.1088/1748-9326/abce27.

Woods, C. and R. Caballero, 2016: The Role of Moist Intrusions in Winter Arctic Warming and Sea Ice Decline. *Journal of Climate*, **29(12)**, 4473–4485, doi:10.1175/jcli-d-15-0773.1.

Woollings, T. et al., 2018: Blocking and its Response to Climate Change. *Current Climate Change Reports*, **4(3)**, 287–300, doi:10.1007/s40641-018-0108-z.

World Meteorological Organization, 2014: Scientific Assessment of Ozone Depletion: 2014. , 416.

Wouters, B., W. Hazeleger, S. Drijfhout, G.J. Oldenborgh, and V. Guemas, 2013: Multiyear predictability of the North Atlantic subpolar gyre. *Geophysical Research Letters*, **40(12)**, 3080–3084, doi:10.1002/grl.50585.

Wu, B., T. Zhou, C. Li, W.A. Müller, and J. Lin, 2019: Improved decadal prediction of Northern-Hemisphere summer land temperature. *Climate Dynamics*, **53(3)**, 1357–1369, doi:10.1007/s00382-019-04658-8.

Wu, P., R. Wood, J. Ridley, and J. Lowe, 2010: Temporary acceleration of the hydrological cycle in response to a CO2 rampdown. *Geophysical Research Letters*, **37(12)**, L12705, doi:10.1029/2010gl043730.

Wu, P., L. Jackson, A. Pardaens, and N. Schaller, 2011: Extended warming of the northern high latitudes due to an overshoot of the Atlantic meridional overturning circulation. *Geophysical Research Letters*, **38(24)**, L24704, doi:10.1029/2011gl049998.

ACCEPTED VERSION SUBJECT TO FINAL EDITS

Wyser, K., E. Kjellström, T. Koenigk, H. Martins, and R. Döscher, 2020: Warmer climate projections in EC-Earth3-Veg: The role of changes in the greenhouse gas concentrations from CMIP5 to CMIP6. *Environmental Research Letters*, **15(5)**, 054020, doi:10.1088/1748-9326/ab81c2.

Xia, L., P.J. Nowack, S. Tilmes, and A. Robock, 2017: Impacts of stratospheric sulfate geoengineering on tropospheric ozone. *Atmospheric Chemistry and Physics*, **17(19)**, 11913–11928, doi:10.5194/acp-17-11913-2017.

Xie, S.-P., B. Lu, and B. Xiang, 2013: Similar spatial patterns of climate responses to aerosol and greenhouse gas changes. *Nature Geoscience*, **6(10)**, 828–832, doi:10.1038/ngeo1931.

Xie, S.-P. et al., 2009: Indian Ocean Capacitor Effect on Indo–Western Pacific Climate during the Summer following El Niño. *Journal of Climate*, **22(3)**, 730–747, doi:10.1175/2008jcli2544.1.

Xie, S.-P. et al., 2015: Towards predictive understanding of regional climate change. *Nature Climate Change*, **5(10)**, 921–930, doi:10.1038/nclimate2689.

Xu, Y. and A. Hu, 2017: How Would the Twenty-First-Century Warming Influence Pacific Decadal Variability and Its Connection to North American Rainfall: Assessment Based on a Revised Procedure for the IPO/PDO. *Journal of Climate*, **31(4)**, 1547–1563, doi:10.1175/jcli-d-17-0319.1.

Xu, Y. and V. Ramanathan, 2017a: Well below 2°C: Mitigation strategies for avoiding dangerous to catastrophic climate changes. *Proceedings of the National Academy of Sciences*, **114(39)**, 10315–10323, doi:10.1073/pnas.1618481114.

Xu, Y. and V. Ramanathan, 2017b: Well below 2°C: Mitigation strategies for avoiding dangerous to catastrophic climate changes. *Proceedings of the National Academy of Sciences*, **114(39)**, 10315–10323, doi:10.1073/pnas.1618481114.

Yang, C., H.M. Christensen, S. Corti, J. von Hardenberg, and P. Davini, 2019: The impact of stochastic physics on the El Niño Southern Oscillation in the EC-Earth coupled model. *Climate Dynamics*, **53(5–6)**, 2843–2859, doi:10.1007/s00382-019-04660-0.

Yang, J. and C. Xiao, 2018: The evolution and volcanic forcing of the southern annular mode during the past 300 years. *International Journal of Climatology*, **38(4)**, 1706–1717, doi:10.1002/joc.5290.

Yeager, S.G. and J.I. Robson, 2017: Recent Progress in Understanding and Predicting Atlantic Decadal Climate Variability. *Current Climate Change Reports*, **3(2)**, 112–127, doi:10.1007/s40641-017-0064-z.

Yeager, S.G., A.R. Karspeck, and G. Danabasoglu, 2015: Predicted slowdown in the rate of Atlantic sea ice loss. *Geophysical Research Letters*, **42(24)**, 10,704–10,713, doi:10.1002/2015gl065364.

Yeager, S.G. et al., 2018: Predicting Near-Term Changes in the Earth System: A Large Ensemble of Initialized Decadal Prediction Simulations Using the Community Earth System Model. *Bulletin of the American Meteorological Society*, **99(9)**, 1867–1886, doi:10.1175/bams-d-17-0098.1.

Yeh, S.-W. et al., 2018a: ENSO Atmospheric Teleconnections and Their Response to Greenhouse Gas Forcing. *Reviews of Geophysics*, **56(1)**, 185–206, doi:10.1002/2017rg000568.

Yeh, S.-W. et al., 2018b: ENSO Atmospheric Teleconnections and Their Response to Greenhouse Gas Forcing. *Reviews of Geophysics*, **56(1)**, 185–206, doi:10.1002/2017rg000568.

Yettella, V. and J.E. Kay, 2017: How will precipitation change in extratropical cyclones as the planet warms? Insights from a large initial condition climate model ensemble. *Climate Dynamics*, **49(5–6)**, 1765–1781, doi:10.1007/s00382-016-3410-2.

Young, P.J., S.M. Davis, B. Hassler, S. Solomon, and K.H. Rosenlof, 2014: Modeling the climate impact of Southern Hemisphere ozone depletion: The importance of the ozone data set. *Geophysical Research Letters*, **41(24)**, 9033–9039, doi:10.1002/2014gl061738.

Yun, K.-S. et al., 2021: Increasing ENSO–rainfall variability due to changes in future tropical temperature–rainfall relationship. *Communications Earth & Environment*, **2(1)**, 43, doi:10.1038/s43247-021-00108-8.

Zambri, B., A.N. LeGrande, A. Robock, and J. Slawinska, 2017: Northern Hemisphere winter warming and summer monsoon reduction after volcanic eruptions over the last millennium. *Journal of Geophysical Research*, **122(15)**, 7971–7989, doi:10.1002/2017jd026728.

Zampieri, L. and H.F. Goessling, 2019: Sea Ice Targeted Geoengineering Can Delay Arctic Sea Ice Decline but not Global Warming. *Earth's Future*, **7(12)**, 1296–1306, doi:10.1029/2019ef001230.

Zappa, G., 2019: Regional Climate Impacts of Future Changes in the Mid–Latitude Atmospheric Circulation: a Storyline View. *Current Climate Change Reports*, **5(4)**, 358–371, doi:10.1007/s40641-019-00146-7.

Zappa, G. and T.G. Shepherd, 2017: Storylines of Atmospheric Circulation Change for European Regional Climate Impact Assessment. *Journal of Climate*, **30(16)**, 6561–6577, doi:10.1175/jcli-d-16-0807.1.

Zappa, G., B.J. Hoskins, and T.G. Shepherd, 2015: Improving Climate Change Detection through Optimal Seasonal Averaging: The Case of the North Atlantic Jet and European Precipitation. *Journal of Climate*, **28(16)**, 6381–6397, doi:10.1175/jcli-d-14-00823.1.

Zappa, G., F. Pithan, and T.G. Shepherd, 2018: Multimodel Evidence for an Atmospheric Circulation Response to Arctic Sea Ice Loss in the CMIP5 Future Projections. *Geophysical Research Letters*, **45(2)**, 1011–1019, doi:10.1002/2017gl076096.

Zappa, G., E. Bevacqua, and T.G. Shepherd, 2021: Communicating potentially large but non-robust changes in multi-model projections of future climate. *International Journal of Climatology*, joc.7041, doi:10.1002/joc.7041.

ACCEPTED VERSION SUBJECT TO FINAL EDITS

Zarakas, C.M., A.L.S. Swann, M.M. Laguë, K.C. Armour, and J.T. Randerson, 2020: Plant Physiology Increases the Magnitude and Spread of the Transient Climate Response to CO2 in CMIP6 Earth System Models. *Journal of Climate*, **33(19)**, 8561–8578, doi:10.1175/jcli-d-20-0078.1.

Zelinka, M.D. et al., 2020: Causes of Higher Climate Sensitivity in CMIP6 Models. *Geophysical Research Letters*, **47(1)**, e2019GL085782, doi:10.1029/2019gl085782.

Zhang, H. and T.L. Delworth, 2018: Robustness of anthropogenically forced decadal precipitation changes projected for the 21st century. *Nature Communications*, **9(1)**, 1150, doi:10.1038/s41467-018-03611-3.

Zhang, J., K. Zhang, J. Liu, and G. Ban-Weiss, 2016: Revisiting the climate impacts of cool roofs around the globe using an Earth system model. *Environmental Research Letters*, **11(8)**, 84014, doi:10.1088/1748-9326/11/8/084014.

Zhang, L. and T.L. Delworth, 2016: Simulated Response of the Pacific Decadal Oscillation to Climate Change. *Journal of Climate*, **29(16)**, 5999–6018, doi:10.1175/jcli-d-15-0690.1.

Zhang, R. et al., 2019: A Review of the Role of the Atlantic Meridional Overturning Circulation in Atlantic Multidecadal Variability and Associated Climate Impacts. *Reviews of Geophysics*, **57(2)**, 316–375, doi:10.1029/2019rg000644.

Zhang, W. and T. Zhou, 2021: The Effect of Modeling Strategies on Assessments of Differential Warming Impacts of 0.5°C. *Earth's Future*, **9(4)**, e2020EF001640, doi:10.1029/2020ef001640.

Zhang, W., T. Zhou, L. Zhang, and L. Zou, 2019: Future Intensification of the Water Cycle with an Enhanced Annual Cycle over Global Land Monsoon Regions. *Journal of Climate*, **32(17)**, 5437–5452, doi:10.1175/jcli-d-18-0628.1.

Zhang, Y., J.M. Wallace, and D.S. Battisti, 1997: ENSO-like Interdecadal Variability: 1900–93. *Journal of Climate*, **10(5)**, 1004–1020, doi:10.1175/1520-0442(1997)010<1004:eliv>2.0.co;2.

Zhao, L., Y. Yang, W. Cheng, D. Ji, and J.C. Moore, 2017: Glacier evolution in high-mountain Asia under stratospheric sulfate aerosol injection geoengineering. *Atmospheric Chemistry and Physics*, **17(11)**, 6547–6564, doi:10.5194/acp-17-6547-2017.

Zhao, M., L. Cao, L. Duan, G. Bala, and K. Caldeira, 2020: Climate more responsive to marine cloud brightening than ocean albedo modification: A model study. *Journal of Geophysical Research: Atmospheres*, **125(n/a)**, e2020JD033256, doi:10.1029/2020jd033256.

Zheng, F., J. Li, R.T. Clark, and H.C. Nnamchi, 2013: Simulation and Projection of the Southern Hemisphere Annular Mode in CMIP5 Models. *Journal of Climate*, **26(24)**, 9860–9879, doi:10.1175/jcli-d-13-00204.1.

Zheng, X.-T., C. Hui, and S.-W. Yeh, 2018: Response of ENSO amplitude to global warming in CESM large ensemble: uncertainty due to internal variability. *Climate Dynamics*, **50(11–12)**, 4019–4035, doi:10.1007/s00382-017-3859-7.

Zheng, X.-T., S.-P. Xie, L.-H. Lv, and Z.-Q. Zhou, 2016: Intermodel Uncertainty in ENSO Amplitude Change Tied to Pacific Ocean Warming Pattern. *Journal of Climate*, **29(20)**, 7265–7279, doi:10.1175/jcli-d-16-0039.1.

Zheng, X.-T. et al., 2013: Indian Ocean Dipole Response to Global Warming in the CMIP5 Multimodel Ensemble. *Journal of Climate*, **26(16)**, 6067–6080, doi:10.1175/jcli-d-12-00638.1.

Zhou, J., K.-K. Tung, and K.-F. Li, 2016: Multi-decadal variability in the Greenland ice core records obtained using intrinsic timescale decomposition. *Climate Dynamics*, **47(3)**, 739–752, doi:10.1007/s00382-015-2866-9.

Zhou, T., J. Lu, W. Zhang, and Z. Chen, 2020: The Sources of Uncertainty in the Projection of Global Land Monsoon Precipitation. *Geophysical Research Letters*, **47(15)**, e2020GL088415, doi:10.1029/2020gl088415.

Zhu, F., J. Emile-Geay, G.J. Hakim, J. King, and K.J. Anchukaitis, 2020: Resolving the Differences in the Simulated and Reconstructed Temperature Response to Volcanism. *Geophysical Research Letters*, **47(8)**, 1–12, doi:10.1029/2019gl086908.

Zhu, J., C.J. Poulsen, and B.L. Otto-Bliesner, 2020: High climate sensitivity in CMIP6 model not supported by paleoclimate. *Nature Climate Change*, **10(5)**, 378–379, doi:10.1038/s41558-020-0764-6.

Zickfeld, K. and T. Herrington, 2015: The time lag between a carbon dioxide emission and maximum warming increases with the size of the emission. *Environmental Research Letters*, **10(3)**, 31001, doi:10.1088/1748-9326/10/3/031001.

Zickfeld, K., A.H. MacDougall, and H.D. Matthews, 2016: On the proportionality between global temperature change and cumulative CO2 emissions during periods of net negative CO2 emissions. *Environmental Research Letters*, **11(5)**, 055006, doi:10.1088/1748-9326/11/5/055006.

Zickfeld, K., S. Solomon, and D.M. Gilford, 2017: Centuries of thermal sea-level rise due to anthropogenic emissions of short-lived greenhouse gases. *Proceedings of the National Academy of Sciences*, **114(4)**, 657–662, doi:10.1073/pnas.1612066114.

Zickfeld, K. et al., 2013: Long-Term Climate Change Commitment and Reversibility: An EMIC Intercomparison. *Journal of Climate*, **26(16)**, 5782–5809, doi:10.1175/jcli-d-12-00584.1.

Zuo, M., T. Zhou, and W. Man, 2019a: Hydroclimate Responses over Global Monsoon Regions Following Volcanic Eruptions at Different Latitudes. *Journal of Climate*, **32(14)**, doi:10.1175/jcli-d-18-0707.1.

Zuo, M., T. Zhou, and W. Man, 2019b: Wetter Global Arid Regions Driven by Volcanic Eruptions. *Journal of Geophysical Research: Atmospheres*, **124(24)**, doi:10.1029/2019jd031171.

ACCEPTED VERSION SUBJECT TO FINAL EDITS

Zuo, M., W. Man, T. Zhou, and Z. Guo, 2018: Different Impacts of Northern, Tropical, and Southern Volcanic Eruptions on the Tropical Pacific SST in the Last Millennium. *Journal of Climate*, **31(17)**, 6729–6744, doi:10.1175/jcli-d-17-0571.1.

ACCEPTED VERSION
SUBJEC TO FINAL EDITS

Figures

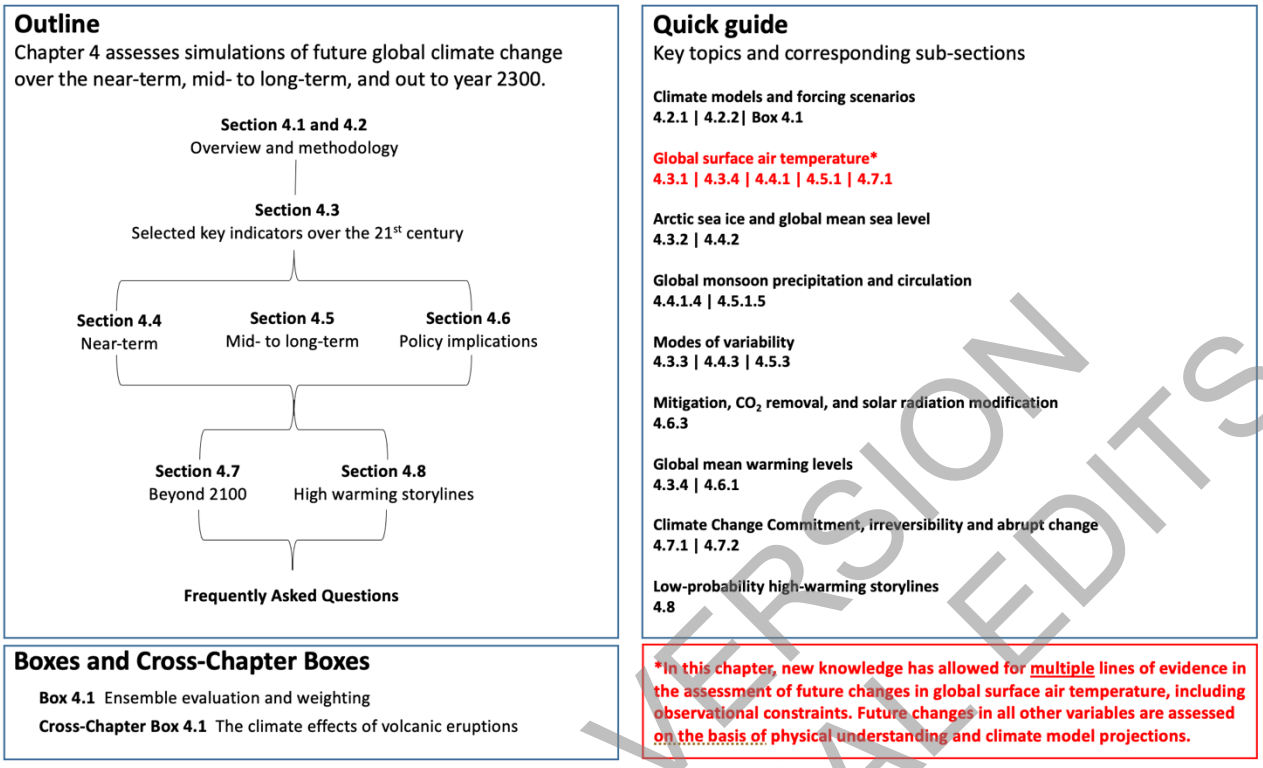
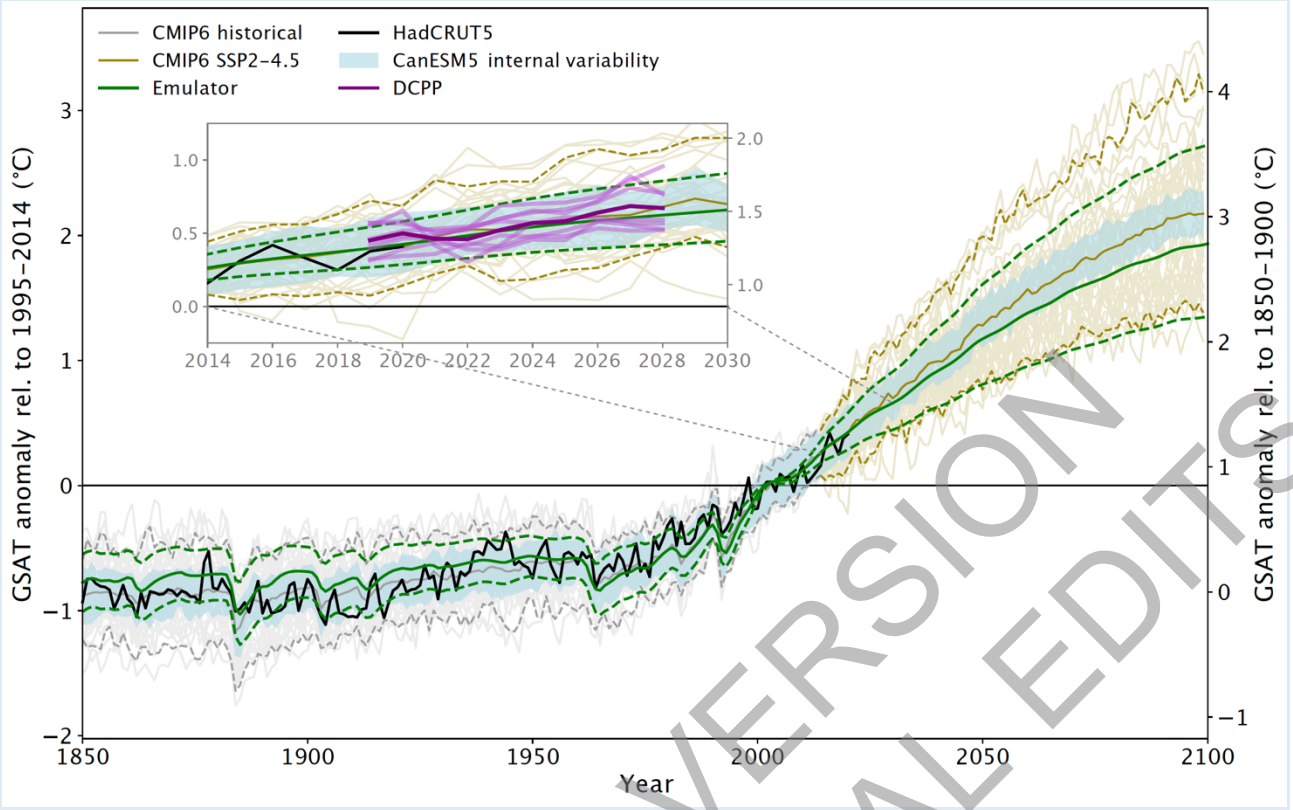


Figure 4.1: Visual abstract of Chapter 4. The chapter outline and a quick guide for key topics and corresponding subsections are provided.

ACCEPTED VERSION
SUBJEC TO FINAL EDITS



Box 4.1 Figure 1: CMIP6 annual-mean GSAT simulations and various contributions to uncertainty in the projections ensemble. The figure shows anomalies relative to the period 1995–2014 (left y-axis), converted to anomalies relative to 1850–1900 (right y-axis); the difference between the y-axes is 0.85°C (Cross-Chapter Box 2.3). Shown are historical simulations with 39 CMIP6 models (grey) and projections following scenario SSP2-4.5 (dark yellow; thin lines: individual simulations; heavy line; ensemble mean; dashed lines: 5% and 95% ranges). The black curve shows the observations-based estimate (HadCRUT5, (Morice et al., 2021)). Light blue shading shows the 50-member ensemble CanESM5, such that the deviations from the CanESM5 ensemble mean have been added to the CMIP6 multi-model mean. The green curves are from the emulator and show the central estimate (solid) and *very likely* range (dashed) for GSAT. The inset shows a cut-out from the main plot and additionally in light purple for the period 2019–2028 the initialized forecasts from eight models contributing to DCPP (Boer et al., 2016); the deep-purple curve shows the average of the forecasts. Further details on data sources and processing are available in the chapter data table (Table 4.SM.1).

ACCEPTED VERSION SUBJECT TO FINAL EDITS

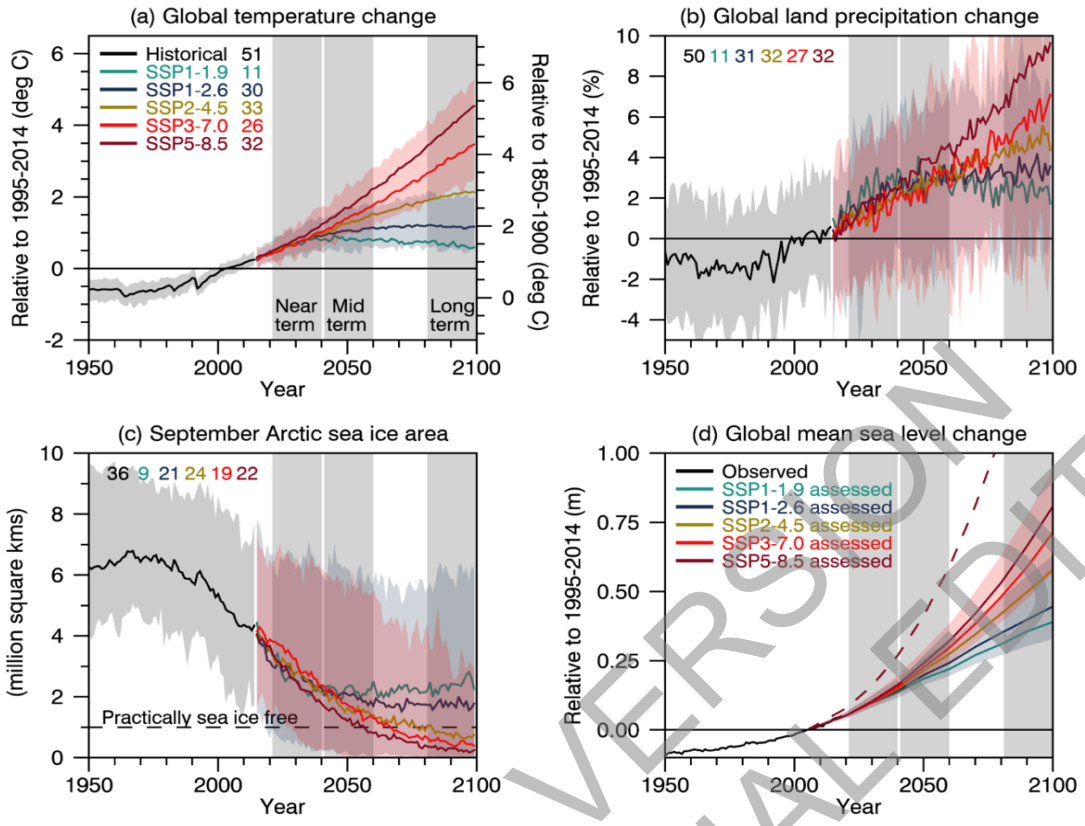


Figure 4.2: Selected indicators of global climate change from CMIP6 historical and scenario simulations. (a) Global surface air temperature changes relative to the 1995–2014 average (left axis) and relative to the 1850–1900 average (right axis; offset by 0.82°C, which is the multi-model mean and close to observed best estimate, Cross-Chapter Box 2.1, Table 1). (b) Global land precipitation changes relative to the 1995–2014 average. (c) September Arctic sea-ice area. (d) Global mean sea-level change (GMSL) relative to the 1995–2014 average. (a), (b) and (d) are annual averages, (c) are September averages. In (a)-(c), the curves show averages over the CMIP6 simulations, the shadings around the SSP1-2.6 and SSP3-7.0 curves show 5–95% ranges, and the numbers near the top show the number of model simulations used. Results are derived from concentration-driven simulations. In (d), the barystatic contribution to GMSL (i.e., the contribution from land-ice melt) has been added offline to the CMIP6 simulated contributions from thermal expansion (thermosteric). The shadings around the SSP1-2.6 and SSP3-7.0 curves show 5–95% ranges. The dashed curve is the *low confidence* and low likelihood outcome at the high end of SSP5-8.5 and reflects deep uncertainties arising from potential ice-sheet and ice-cliff instabilities. This curve at year 2100 indicates 1.7 m of GMSL rise relative to 1995–2014. More information on the calculation of GMSL are available in Chapter 9, and further regional details are provided in the Atlas. Further details on data sources and processing are available in the chapter data table (Table 4.SM.1).

ACCEPTED VERSION SUBJECT TO FINAL EDITS

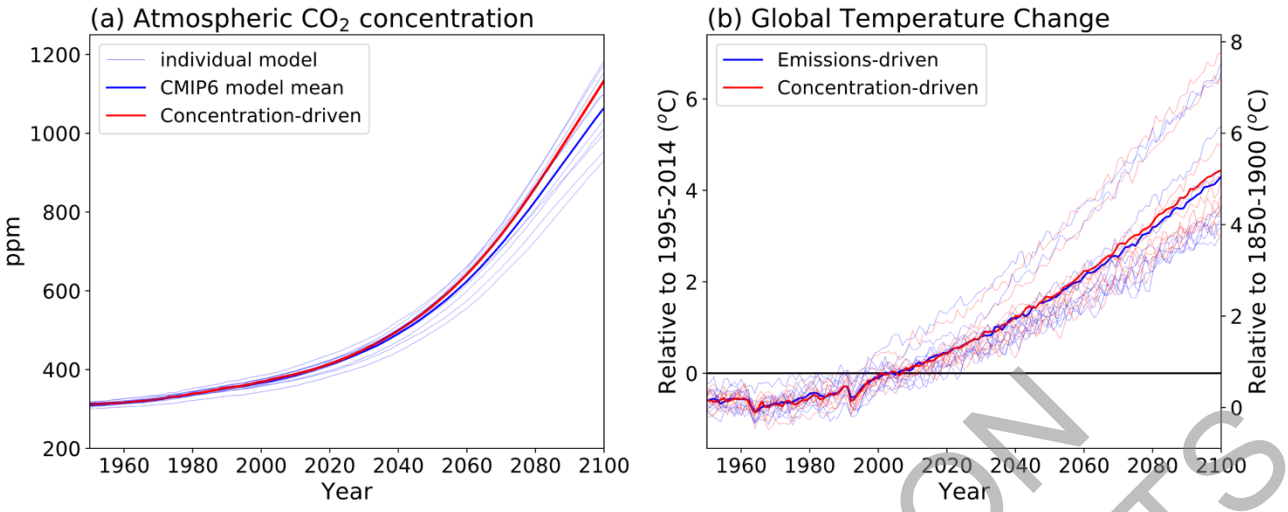


Figure 4.3: Comparison of concentration-driven and emission-driven simulation. (a) Atmospheric CO_2 concentration, (b) GSAT from models which performed SSP5-8.5 scenario simulations in both emissions-driven (blue; *esm-ssp585*) and concentration-driven (red; *ssp585*) configurations. For concentration driven simulations, CO_2 concentration is prescribed, and follows the red line in panel (a) in all models. For emissions-driven simulations, CO_2 concentration is simulated and can therefore differ for each model, blue lines in panel (a). Further details on data sources and processing are available in the chapter data table (Table 4.SM.1).

ACCEPTED VERSION SUBJEC TO FINAL EDITS

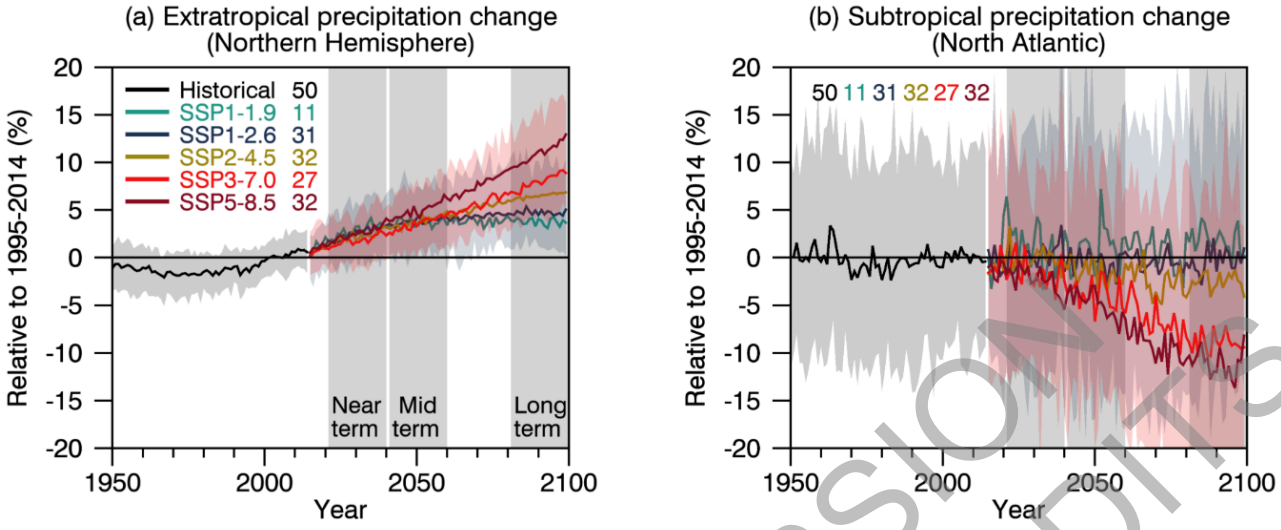


Figure 4.4: CMIP6 annual mean precipitation changes (%) from historical and scenario simulations. (a) Northern Hemisphere extratropics (30°N–90°N). (b) North Atlantic subtropics (5°N–30°N, 80°W–0°). Changes are relative to 1995–2014 averages. Displayed are multi-model averages and, in parentheses, 5–95% ranges. The numbers inside each panel are the number of model simulations. Results are derived from concentration-driven simulations. Further details on data sources and processing are available in the chapter data table (Table 4.SM.1).

ACCEPTED VERSION
SUBJEC TO FINAL EDITS

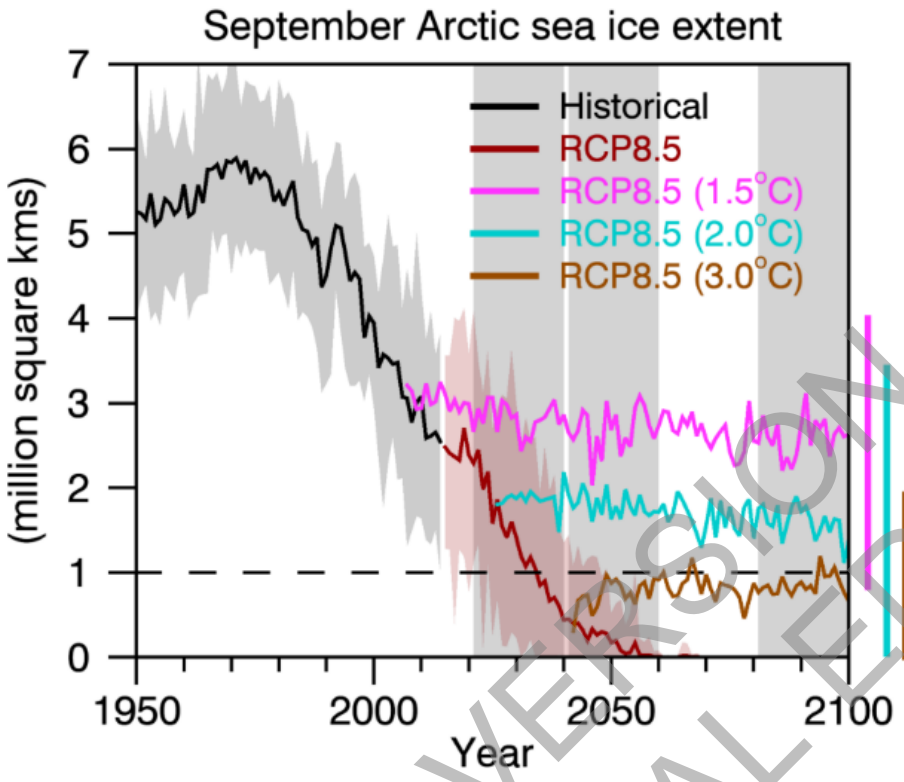


Figure 4.5: **Arctic sea-ice extent in September in a large initial-condition ensemble of observationally-constrained simulations of an Earth system model (CanESM2).** The black and red curves are average over twenty simulations following historical forcings to 2015 and RCP8.5 extensions to 2100. The coloured curves are averages over twenty simulations each after GSAT has been stabilized at the indicated degree of global mean warming relative to 1850–1900. The bars to the right are the minimum to maximum ranges over 2081–2100 (Sigmond et al., 2018). The horizontal dashed line indicates a practically ice-free Arctic. Further details on data sources and processing are available in the chapter data table (Table 4.SM.1).

ACCEPTED VERSION SUBJEC TO FINAL EDITS

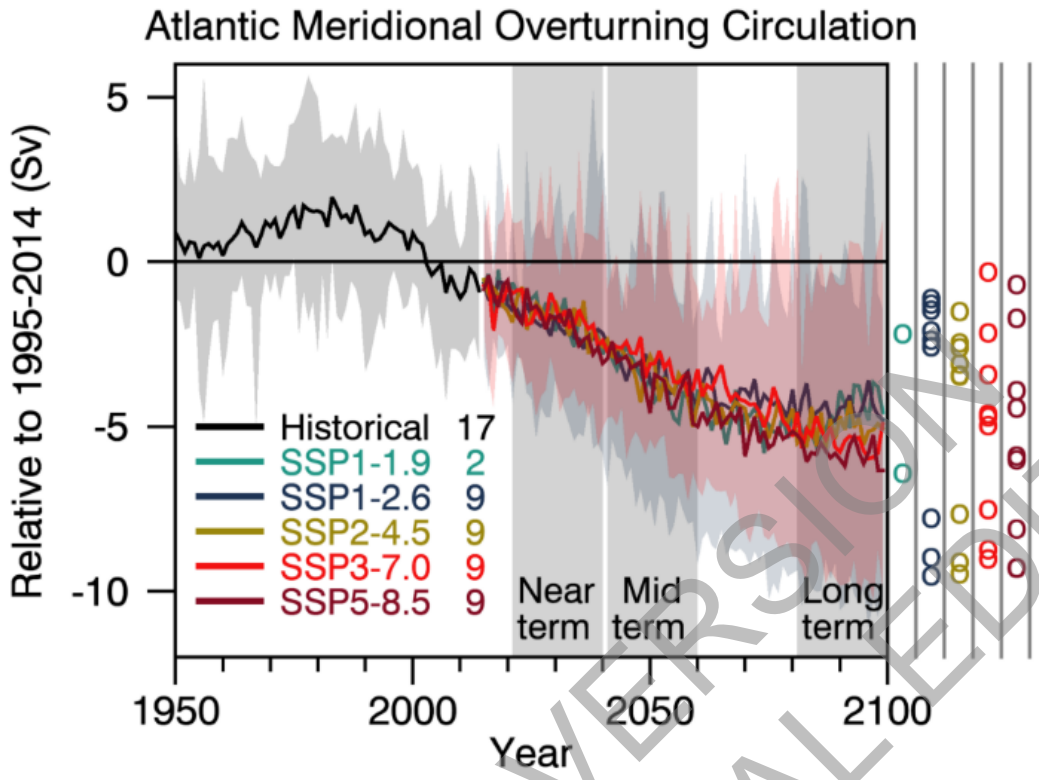


Figure 4.6: **CMIP6 annual mean AMOC strength change in historical and scenario simulations**. Changes are relative to averages from 1995–2014. The curves show ensemble averages and the shadings the 5–95% ranges across the SSP1-2.6 and SSP3-7.0 ensembles. The circles to the right of the panel show the anomalies averaged from 2081–2100 for each of the available model simulations. The numbers inside the panel are the number of model simulations. Here, the strength of the AMOC is computed as the maximum value of annual-mean ocean meridional overturning mass streamfunction in the Atlantic at 26°N. Results are from concentration-driven simulations. Further details on data sources and processing are available in the chapter data table (Table 4.SM.1).

ACCEPTED VERSION SUBJEC TO FINAL EDITS

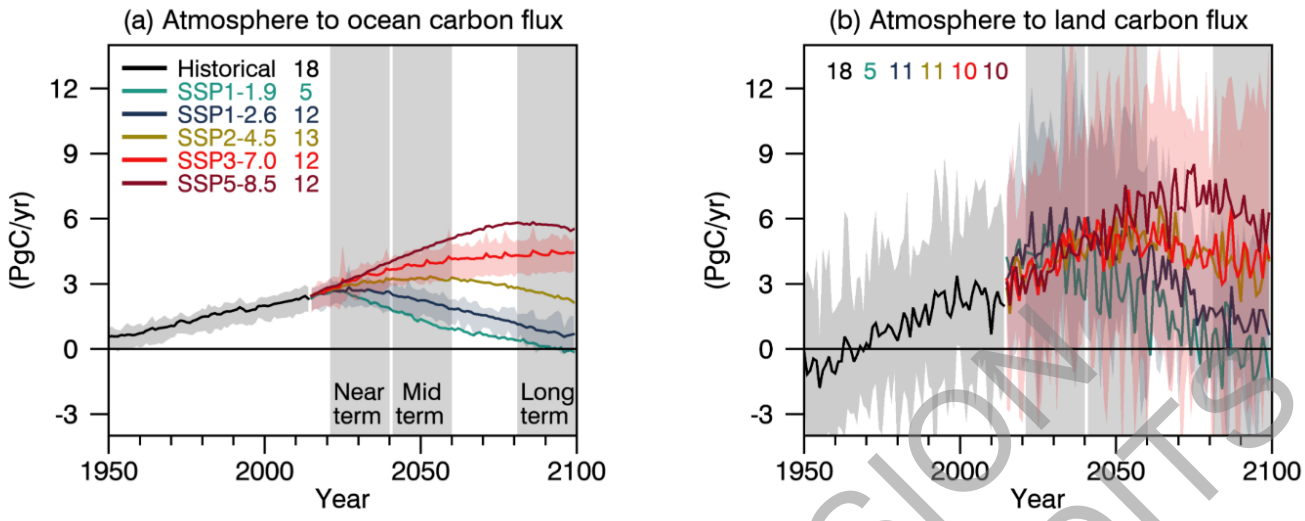


Figure 4.7: **CMIP6 carbon uptake in historical and scenario simulations.** (a) Atmosphere to ocean carbon flux (PgC yr^{-1}). (b) Atmosphere to land carbon flux (PgC yr^{-1}). The curves show ensemble averages and the shadings show the 5–95% ranges across the SSP1-2.6 and SSP3-7.0 ensembles. The numbers inside each panel are the number of model simulations. The land uptake is taken as Net Biome Productivity (NBP) and so includes any modelled net land-use change emissions. Results are from concentration-driven simulations. Further details on data sources and processing are available in the chapter data table (Table 4.SM.1).

ACCEPTED VERSION SUBJEC TO FINAL EDITS

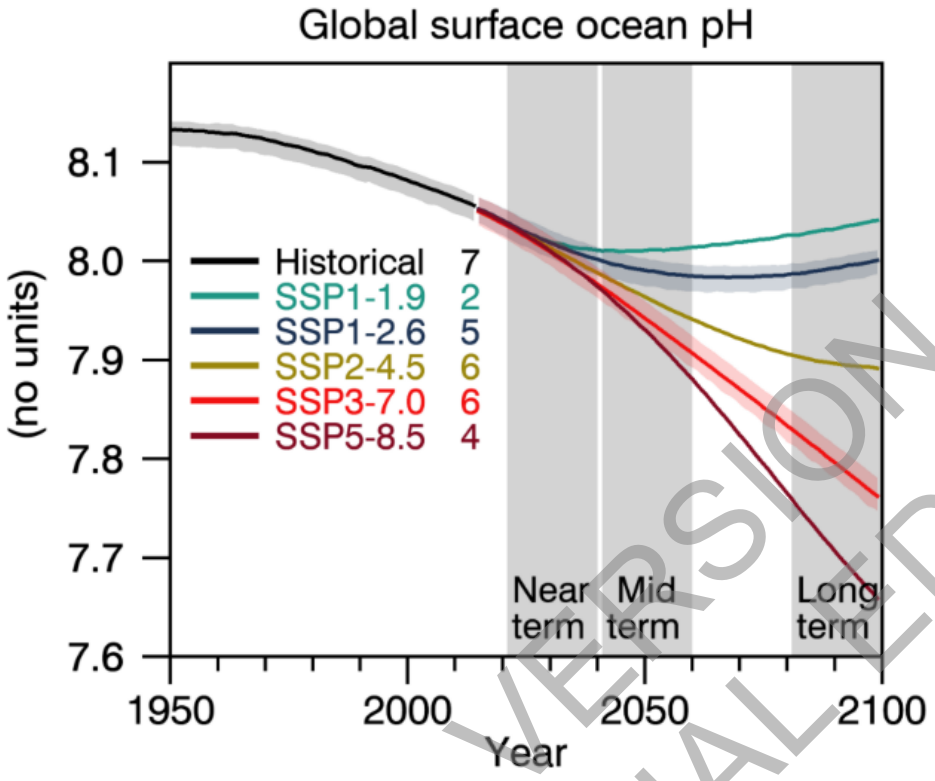


Figure 4.8: **Global average surface ocean pH**. The shadings around the SSP1-2.6 and SSP5-7.0 curves are the 5–95% ranges across those ensembles. The numbers inside each panel are the number of model simulations. Results are from concentration-driven simulations. Further details on data sources and processing are available in the chapter data table (Table 4.SM.1).

ACCEPTED VERSION SUBJEC TO FINAL EDITS

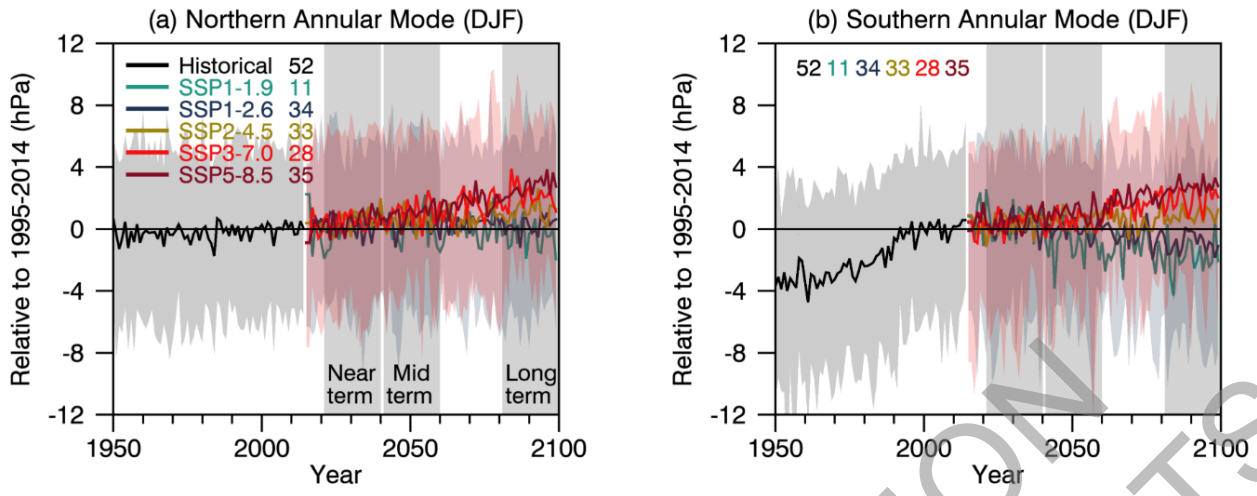


Figure 4.9: **CMIP6 simulations of boreal wintertime (DJF) Annular Mode indices.** (a) NAM and (b) SAM. The NAM is defined as the difference in zonal mean SLP at 35°N and 65°N (Li and Wang, 2003) and the SAM as the difference in zonal mean SLP at 40°S and 65°S (Gong and Wang, 1999). All anomalies are relative to averages from 1995–2014. The curves show multi-model ensemble averages over the CMIP6 r1 simulations. The shadings around the SSP1-2.6 and SSP3-7.0 curves denote the 5–95% ranges of the ensembles. The numbers inside each panel are the number of model simulations. The results are for concentration-driven simulations. Further details on data sources and processing are available in the chapter data table (Table 4.SM.1).

ACCEPTED VERSION SUBJEC TO FINAL EDITS

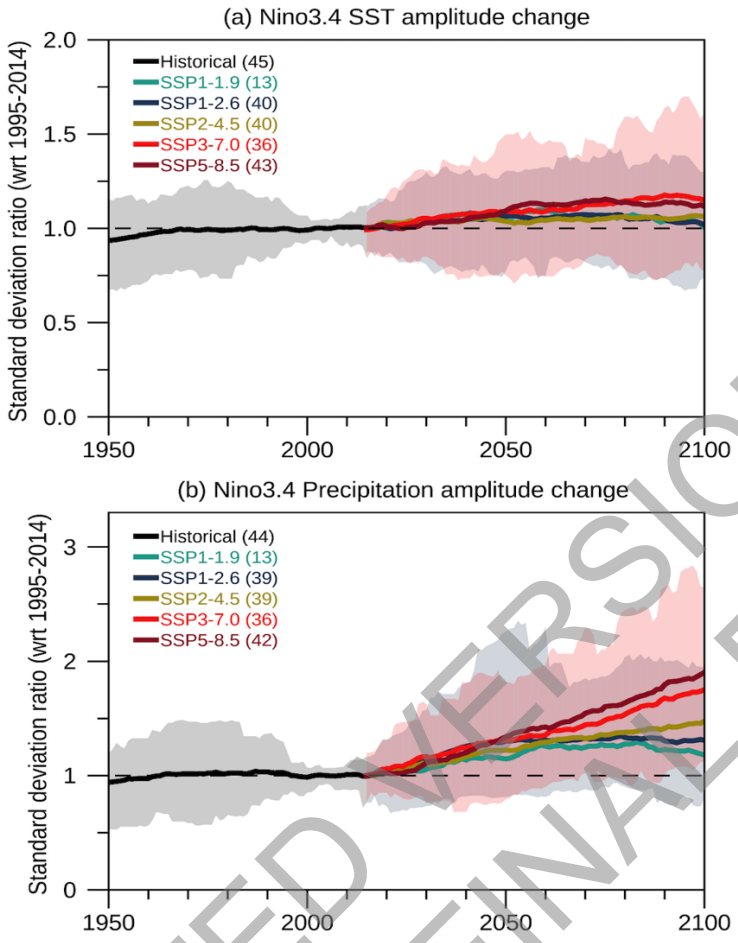


Figure 4.10: Changes in amplitude of ENSO Variability. Variability of (a) SST and (b) precipitation anomalies averaged over Niño3.4 region for 1950–2014 from CMIP6 historical simulations and for 2015–2100 from four SSPs. Thick lines stand for multi-model mean and shading is the 5–95% range across CMIP6 models for historical simulation (grey), SSP1-2.6 (blue) and SSP3-7.0 (pink), respectively. The amplitude of ENSO SST and rainfall variability is defined as the standard deviation of the detrended Niño3.4-area averaged SST and rainfall index, respectively, over 30-year running windows. The standard deviation in every single model is normalized by each model's present-day standard deviation averaged from 1995 to 2014. The number of available models is listed in parentheses. This figure is adopted from (Yun et al., 2021). Further details on data sources and processing are available in the chapter data table (Table 4.SM.1).

ACCEPTED VERSION SUBJECT TO FINAL EDITS

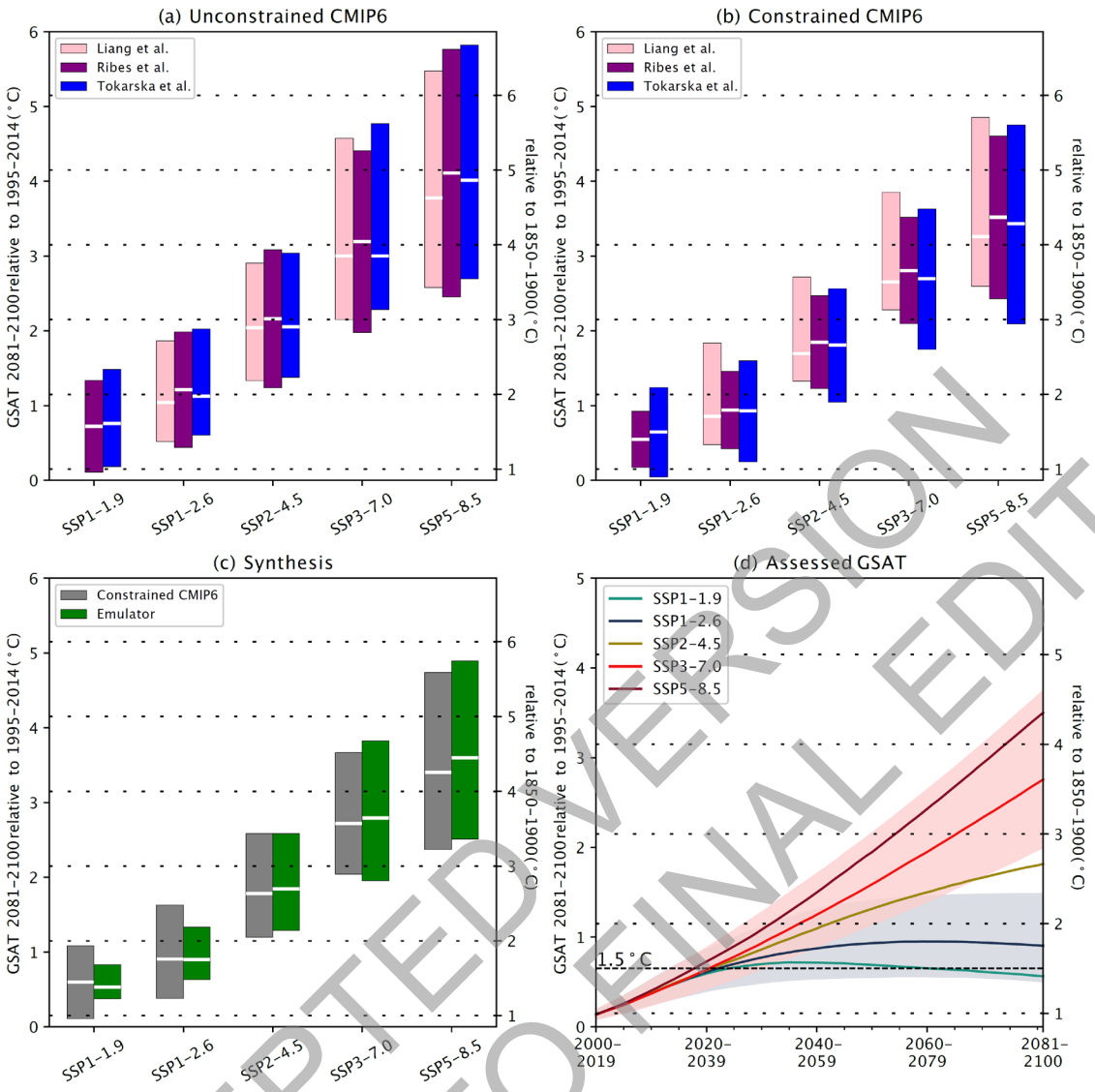


Figure 4.11: Multiple lines of evidence for GSAT changes for the long-term period, 2081–2100, relative to the average over 1995–2014, for all five priority scenarios. The unconstrained CMIP6 5–95% ranges (coloured bars) in (a) differ slightly because different authors used different subsamples of the CMIP6 archive. The constrained CMIP6 5–95% ranges (coloured bars) in (b) are smaller than the unconstrained ranges in (a) and differ because of different samples from the CMIP6 archive and because different observations and methods are used. In (c), the average of the ranges in (b) is formed (grey bars). Green bars in (c) show the emulator ranges, defined such that the best estimate, lower bound of the *very likely range*, and upper bound of the *very likely* range of climate feedback parameter and ocean heat uptake coefficient take the values that map onto the corresponding values of ECS and TCR of Section 7.5 (see BOX 4.1). The time series in (d) are constructed by taking the average of the constrained CMIP6 ranges and the emulator ranges. The y-axes on the right-hand side are shifted upward by 0.85°C, the central estimate of the observed warming for 1995–2014, relative to 1850–1900 (Cross-Chapter Box 2.3, Table 1). Further details on data sources and processing are available in the chapter data table (Table 4.SM.1).

ACCEPTED VERSION SUBJECT TO FINAL EDITS

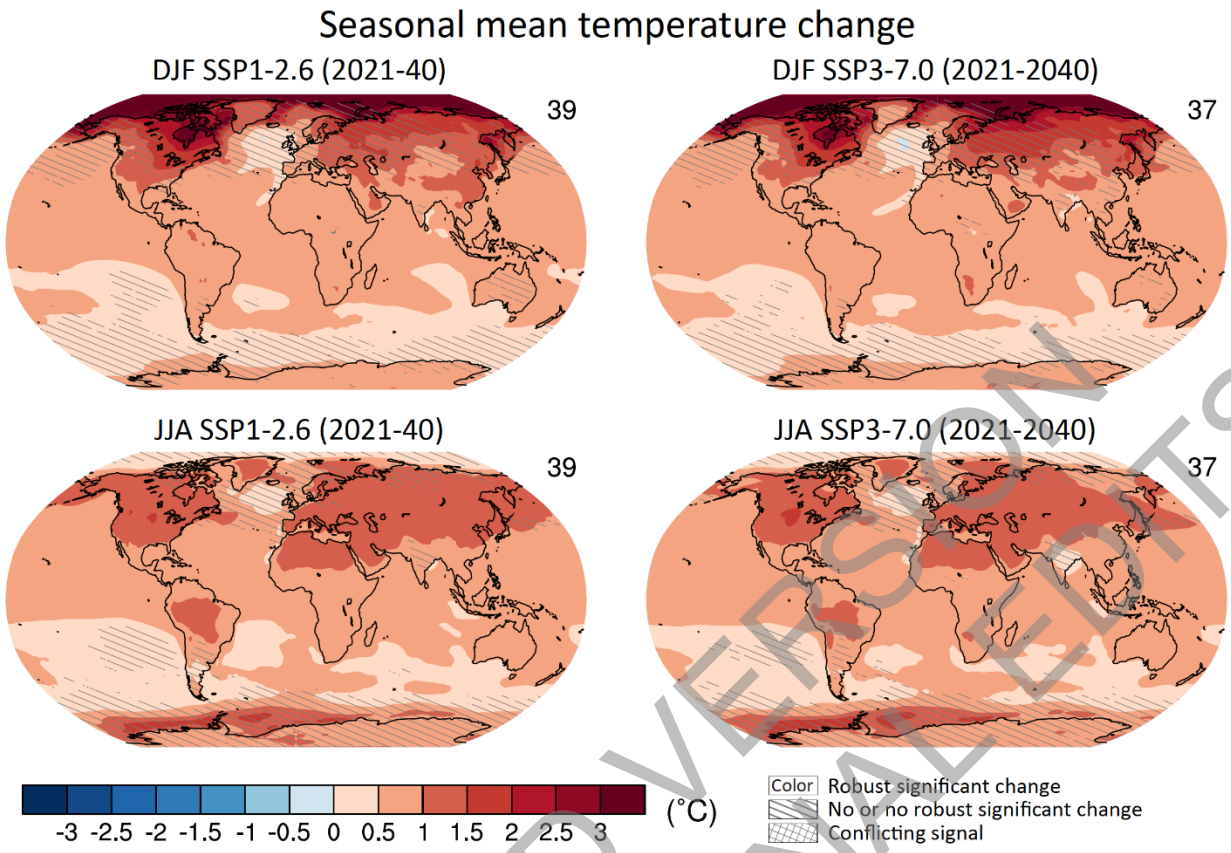


Figure 4.12: Near-term change of seasonal mean surface temperature. Displayed are projected spatial patterns of CMIP6 multi-model mean change (°C) in (top) DJF and (bottom) JJA near-surface air temperature for 2021–2040 from SSP1-2.6 and SSP3-7.0 relative to 1995–2014. The number of models used is indicated in the top right of the maps. No overlay indicates regions where the change is robust and *likely* emerges from internal variability, that is, where at least 66% of the models show a change greater than the internal-variability threshold (see Section 4.2.6) and at least 80% of the models agree on the sign of change. Diagonal lines indicate regions with no change or no robust significant change, where fewer than 66% of the models show change greater than the internal-variability threshold. Crossed lines indicate areas of conflicting signals where at least 66% of the models show change greater than the internal-variability threshold but fewer than 80% of all models agree on the sign of change. Further details on data sources and processing are available in the chapter data table (Table 4.SM.1).

ACCEPTED VERSION SUBJECT TO FINAL EDITS

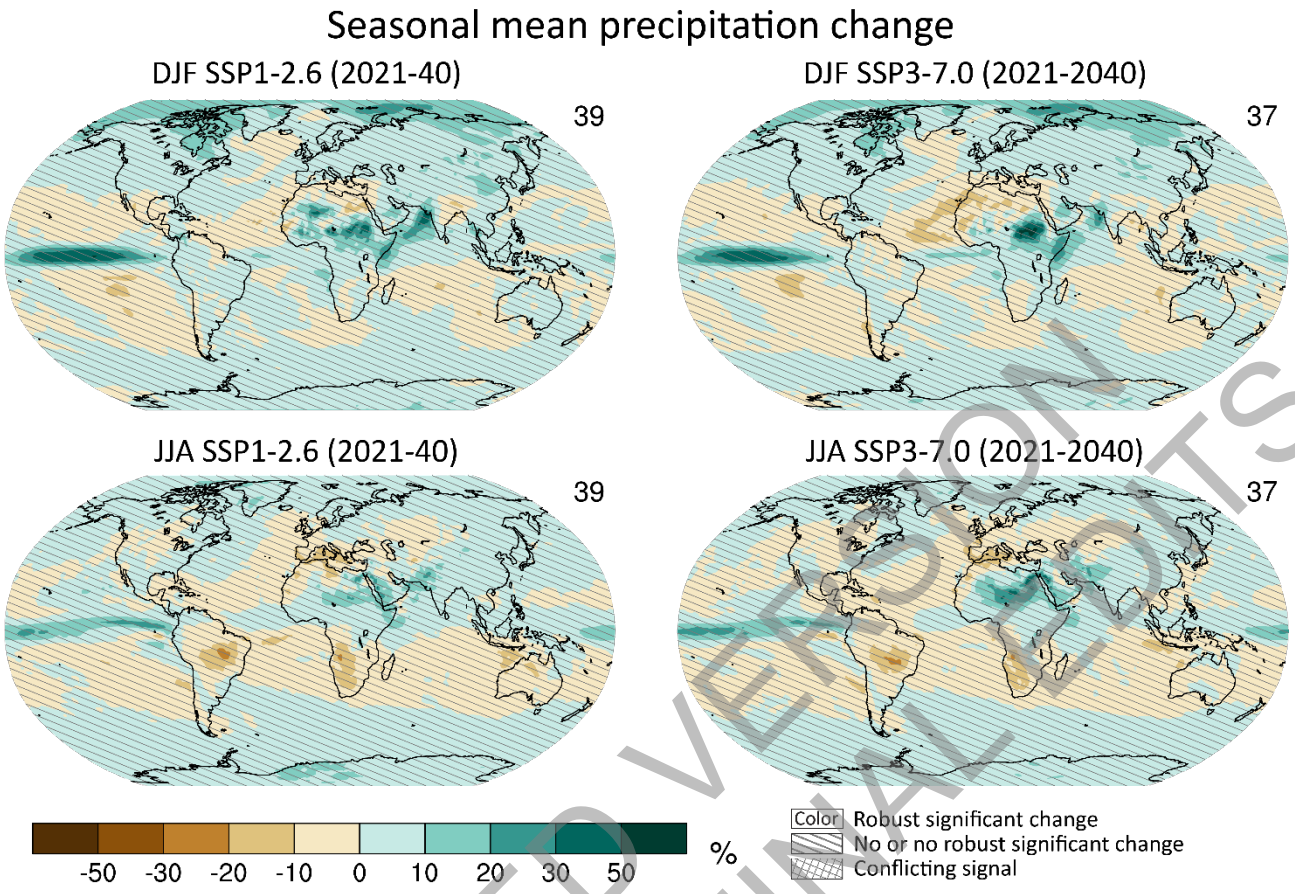


Figure 4.13: Near-term change of seasonal mean precipitation. Displayed are projected spatial patterns of CMIP6 multi-model mean change (%) in (top) DJF and (bottom) JJA precipitation from SSP1-2.6 and SSP3-7.0 in 2021–2040 relative to 1995–2014. The number of models used is indicated in the top right of the maps. No overlay indicates regions where the change is robust and *likely* emerges from internal variability, that is, where at least 66% of the models show a change greater than the internal-variability threshold (see Section 4.2.6) and at least 80% of the models agree on the sign of change. Diagonal lines indicate regions with no change or no robust significant change, where fewer than 66% of the models show change greater than the internal-variability threshold. Crossed lines indicate areas of conflicting signals where at least 66% of the models show change greater than the internal-variability threshold but fewer than 80% of all models agree on the sign of change. Further details on data sources and processing are available in the chapter data table (Table 4.SM.1).

ACCEPTED VERSION SUBJECT TO FINAL EDITS

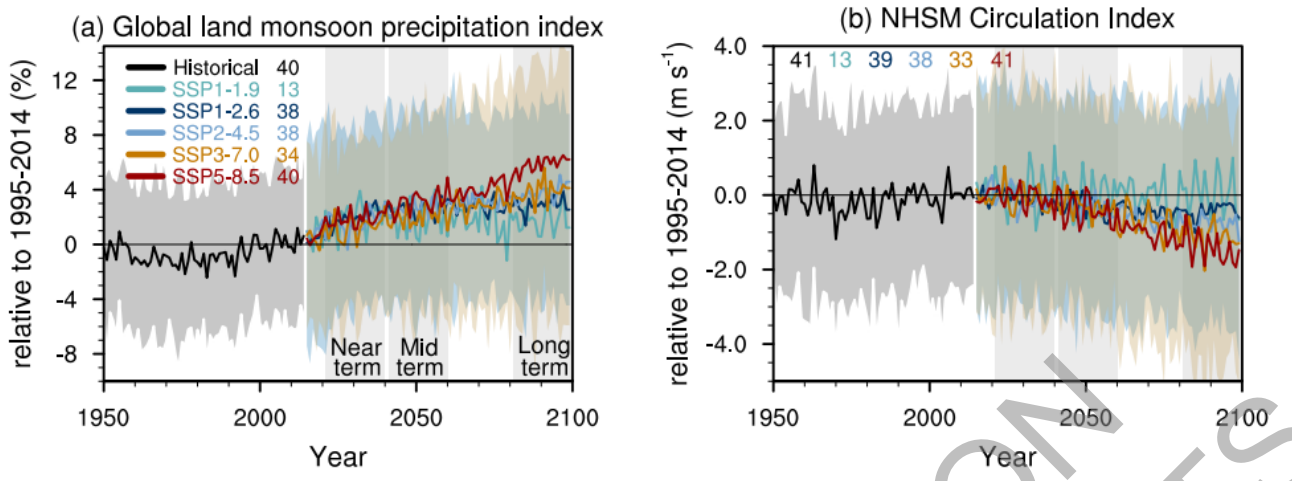


Figure 4.14: Time series of global land monsoon precipitation and Northern Hemisphere summer monsoon (NHSM) circulation index anomalies. (a) Global land monsoon precipitation index anomalies (Unit: %) defined as the area-weighted mean precipitation rate in the global land monsoon domain defined by Wang et al. (2013) for the CMIP6 historical simulation for 1950–2014 and five SSPs 2015–2100. (b) Anomalies in NHSM circulation index (Unit: m s^{-1}), defined as the vertical shear of zonal winds between 850 and 200 hPa averaged in a zone stretching from Mexico eastward to the Philippines (0°–20°N, 120°W–120°E) (Wang et al., 2013) in the CMIP6 historical simulation and five SSPs. One realization is averaged from each model. Anomalies are shown relative to the present-day (1995–2014) mean. The curves show averages over the simulations, the shadings around the SSP1-2.6 and SSP5-8.5 curves show 5–95% ranges, and the numbers near the top show the number of model simulations used. Further details on data sources and processing are available in the chapter data table (Table 4.SM.1).

ACCEPTED VERSION SUBJEC TO FINAL EDITS

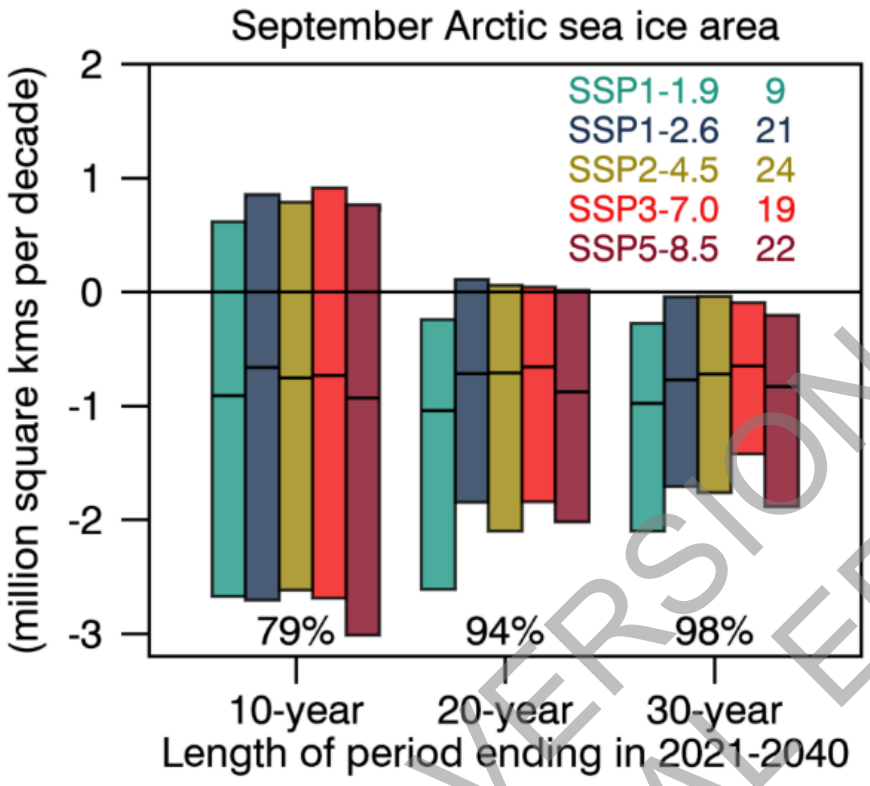


Figure 4.15: CMIP6 linear trends in September Arctic sea-ice area for 10-year, 20-year, and 30-year periods ending in 2021–2040 following five SSPs. Plotted are the 5–95% ranges across the ensembles of simulations. The numbers at the top of the plot are the number of model simulations in each SSP ensemble. The numbers near the bottom of the plot indicate the percentage of simulations across all the SSPs with decreasing sea-ice area. Results are from concentration-driven simulations. Further details on data sources and processing are available in the chapter data table (Table 4.SM.1).

ACCEPTED VERSION
SUBJEC TO FINAL EDITS

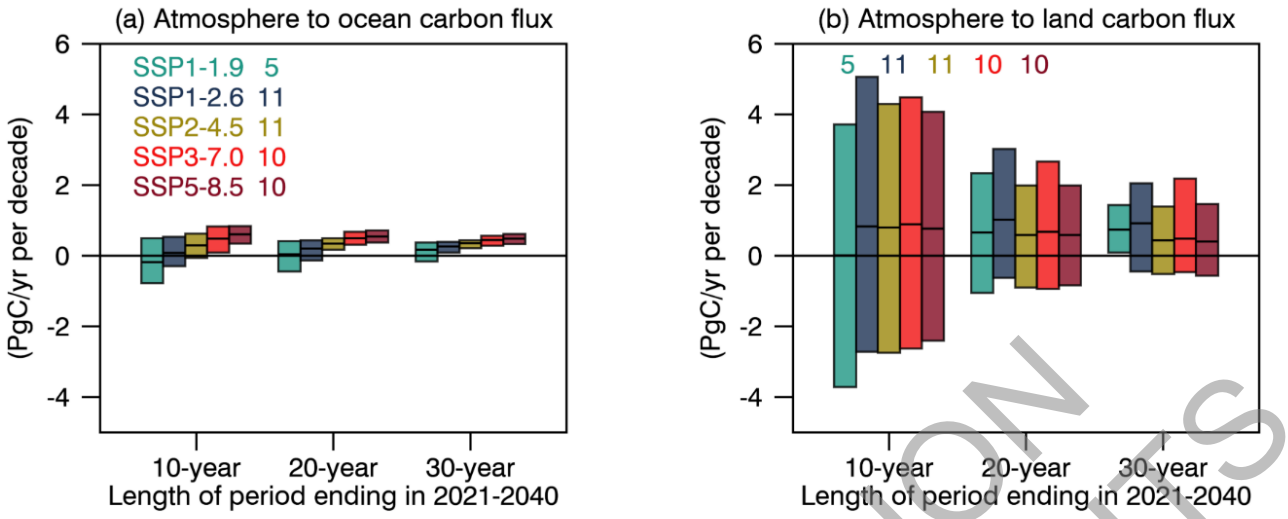


Figure 4.16: CMIP6 trends in ocean and land carbon flux for 10-year, 20-year, and 30-year periods ending in 2021–2040. (a) Ocean carbon flux. (b) Land carbon flux. Plotted are the 5–95% ranges across the ensembles of simulations, for five SSPs. The numbers at the top of the plots are the number of model simulations in each SSP ensemble. Unites are Pg C yr^{-1} per decade. Further details on data sources and processing are available in the chapter data table (Table 4.SM.1).

ACCEPTED VERSION
SUBJEC TO FINAL EDITS

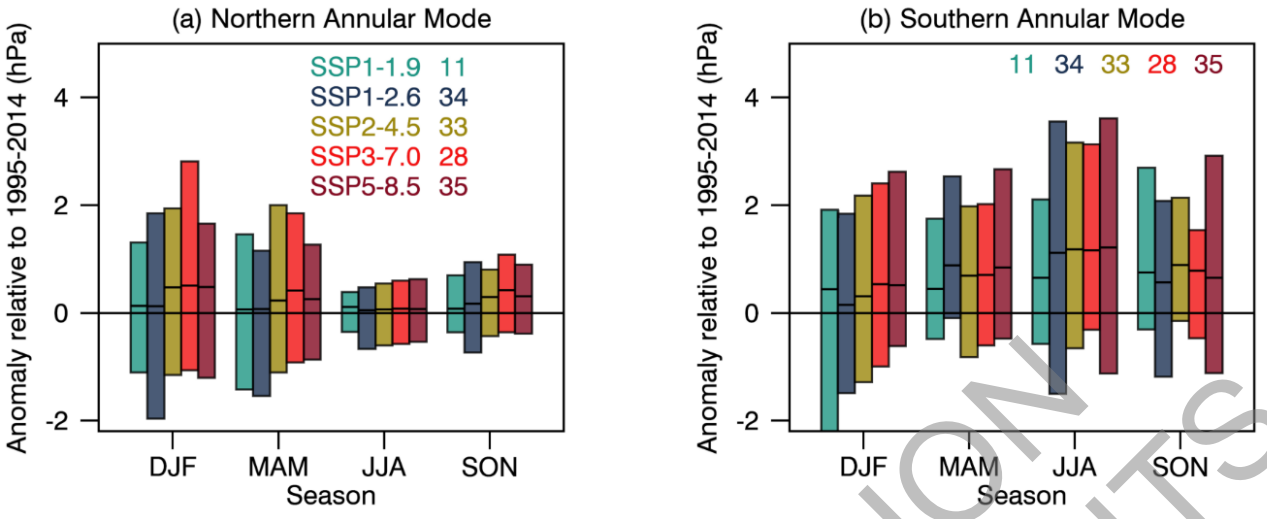


Figure 4.17: CMIP6 Annular Mode index change (hPa) from 1995–2014 to 2021–2040. (a) NAM and (b) SAM. The NAM is defined as the difference in zonal mean sea-level pressure (SLP) at 35°N and 65°N (Li and Wang, 2003) and the SAM as the difference in zonal mean SLP at 40°S and 65°S (Gong and Wang, 1999). The shadings are the 5–95% ranges across the simulations. The numbers near the top of each panel are the numbers of model simulations in each SSP ensemble. Further details on data sources and processing are available in the chapter data table (Table 4.SM.1).

ACCEPTED VERSION
SUBJEC TO FINAL EDITS

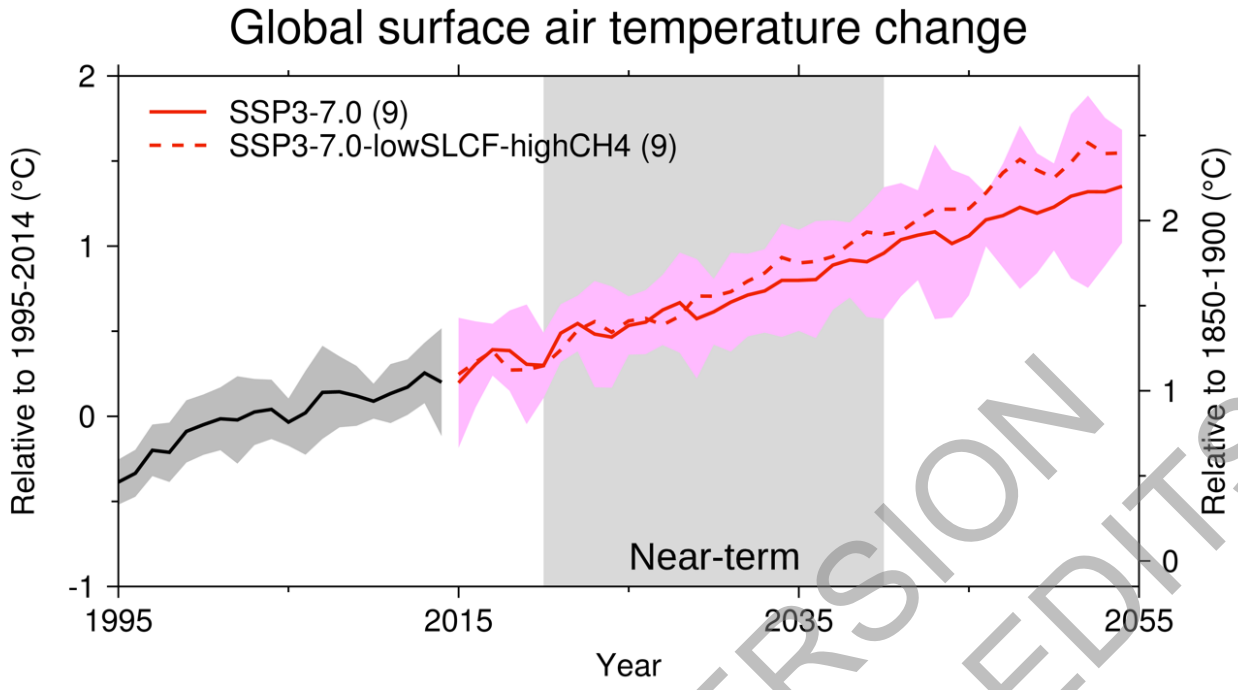
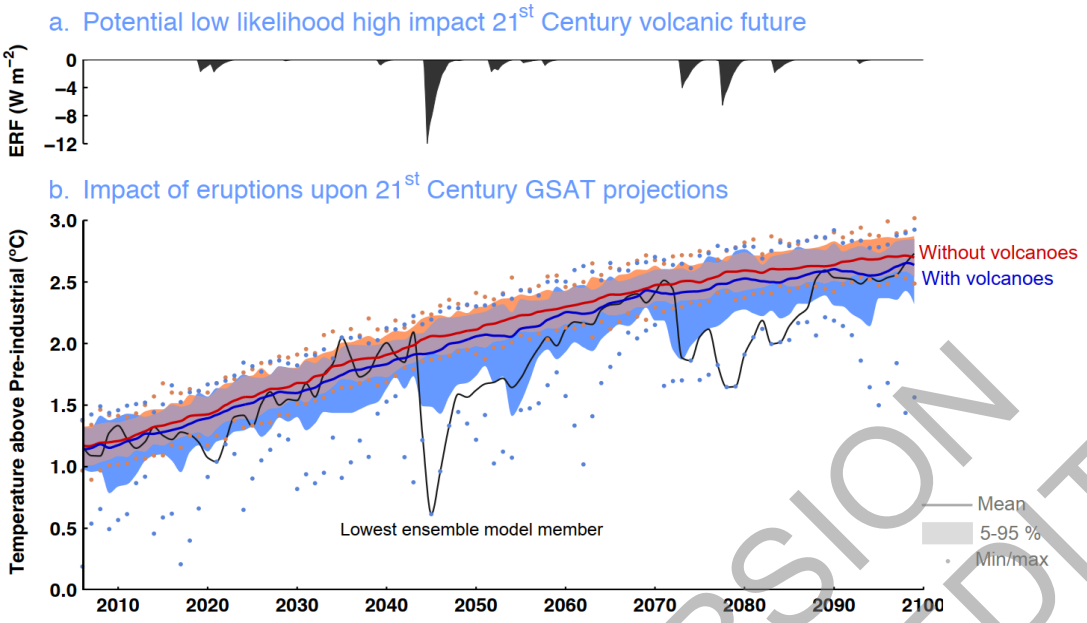


Figure 4.18: Influence of SLCFs on projected GSAT change. Change is shown relative to the 1995–2014 average (left axis) and relative to the 1850–1900 average (right axis). The comparison is for CMIP6 models for the AerChemMIP (Collins et al., 2017) SSP3-7.0-lowSLCF-highCH4 experiment (note in the original experiment protocol this is called SSP3-7.0-lowNTCF), where concentrations of short-lived species are reduced compared to reference SSP3-7.0 scenario. The curves show averages over the r1 simulations contributed to the CMIP6 exercise, the shadings around the SSP3-7.0 curve shows 5–95% ranges and the numbers near the top show the number of model simulations. Further details on data sources and processing are available in the chapter data table (Table 4.SM.1).

ACCEPTED VERSION SUBJEC TO FINAL EDITS



Cross-Chapter Box 4.1, Figure 1: Potential impact of volcanic eruption on future global temperature change. CMIP5 projections of possible 21st-century futures under RCP4.5 after a 1257 Samalas magnitude volcanic eruption in 2044, from Bethke et al. (2017). a, Volcanic ERF of the most volcanically active ensemble member, estimated from SAOD. b, Annual-mean GSAT. Ensemble mean (solid) of future projections including volcanoes (blue) and excluding volcanoes (red) with 5–95% range (shading) and ensemble minima/maxima (dots); evolution of the most volcanically active member (black). Data created using a SMILE approach with NorESM1 in its CMIP5 configuration. See Section 2.2.2 and Section 4.4.4 for more details. Further details on data sources and processing are available in the chapter data table (Table 4.SM.1).

ACCEPTED VERSION SUBJEC TO FINAL EDITS

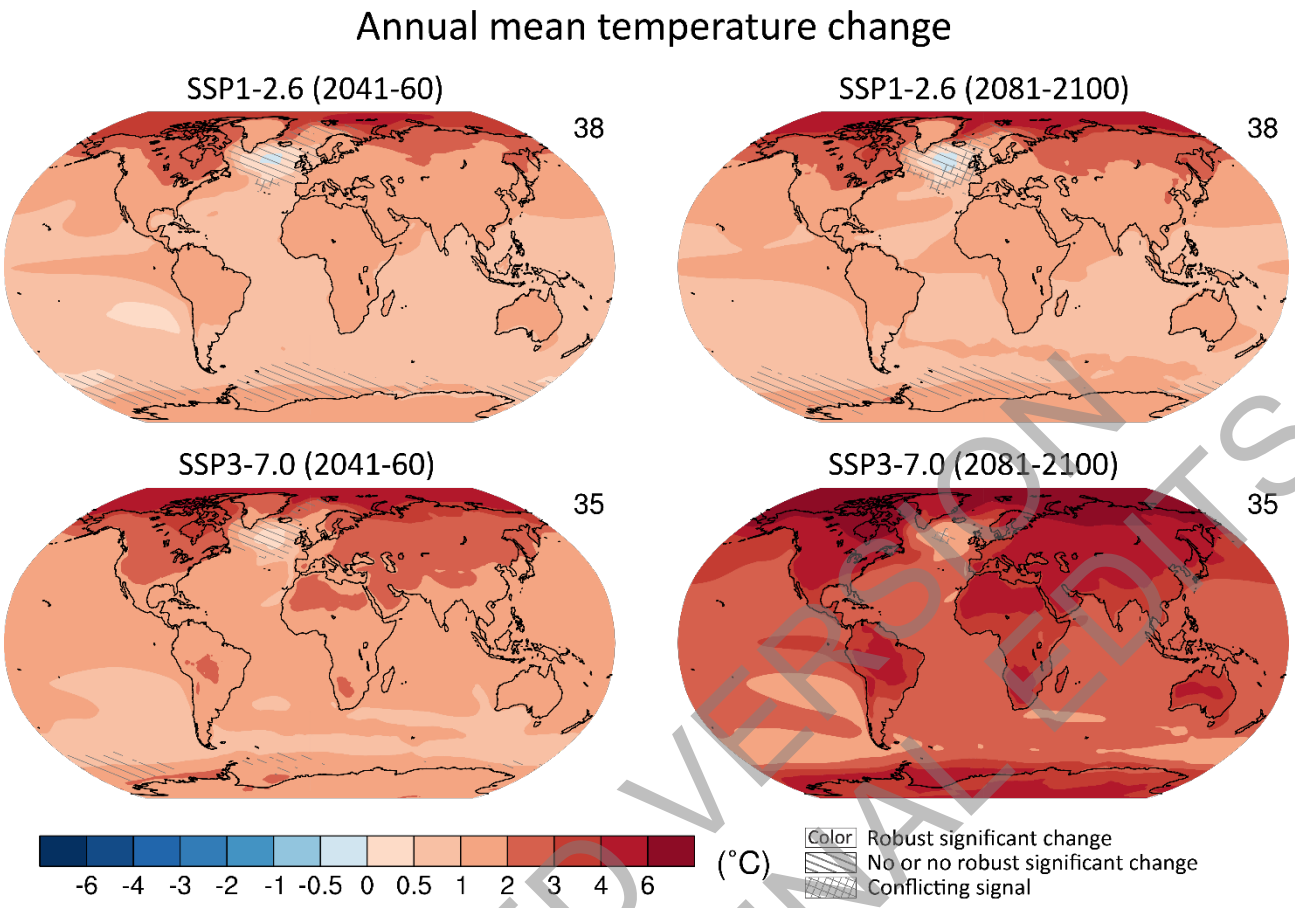


Figure 4.19: Mid- and long-term change of annual mean surface temperature. Displayed are projected spatial patterns of multi-model mean change in annual mean near-surface air temperature (°C) in 2041–2060 and 2081–2100 relative to 1995–2014 for (top) SSP1-2.6 and (bottom) SSP3-7.0. The number of models used is indicated in the top right of the maps. No overlay indicates regions where the change is robust and *likely* emerges from internal variability, that is, where at least 66% of the models show a change greater than the internal-variability threshold (see Section 4.2.6) and at least 80% of the models agree on the sign of change. Diagonal lines indicate regions with no change or no robust significant change, where fewer than 66% of the models show change greater than the internal-variability threshold. Crossed lines indicate areas of conflicting signals where at least 66% of the models show change greater than the internal-variability threshold but fewer than 80% of all models agree on the sign of change. Further details on data sources and processing are available in the chapter data table (Table 4.SM.1).

ACCEPTED VERSION SUBJECT TO FINAL EDITS

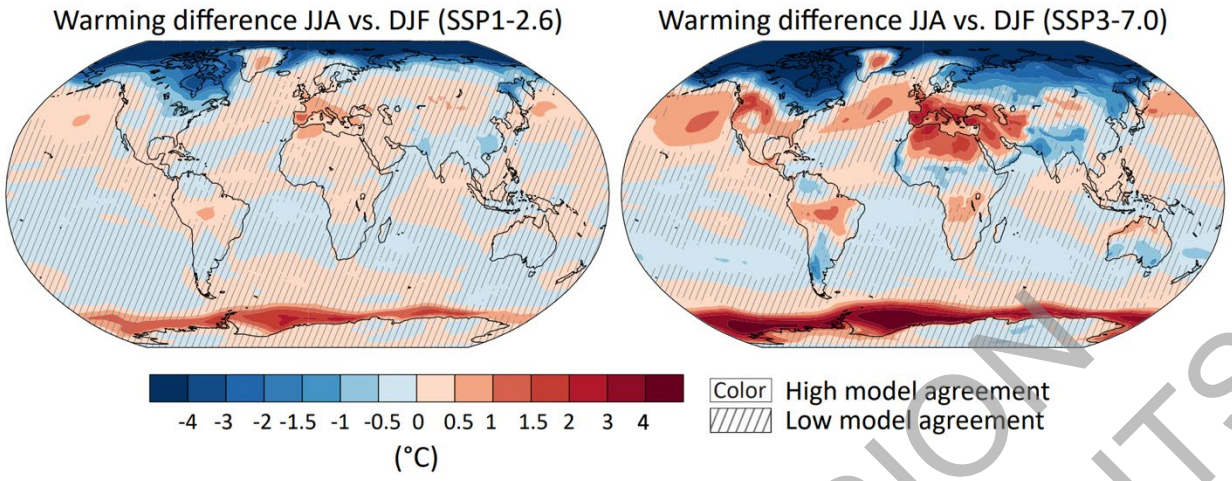


Figure 4.20: Difference of surface temperature change between JJA and DJF. Displayed are spatial patterns of multi-model mean difference in projected warming in JJA minus warming in DJF in 2081–2100 relative to 1995–2014 for (left) SSP1-2.6 and (right) SSP3-7.0. Diagonal lines mark areas where fewer than 80% of the models agree on the sign of change, and no overlay where at least 80% of the models agree. Further details on data sources and processing are available in the chapter data table (Table 4.SM.1).

ACCEPTED VERSION SUBJEC TO FINAL EDITS

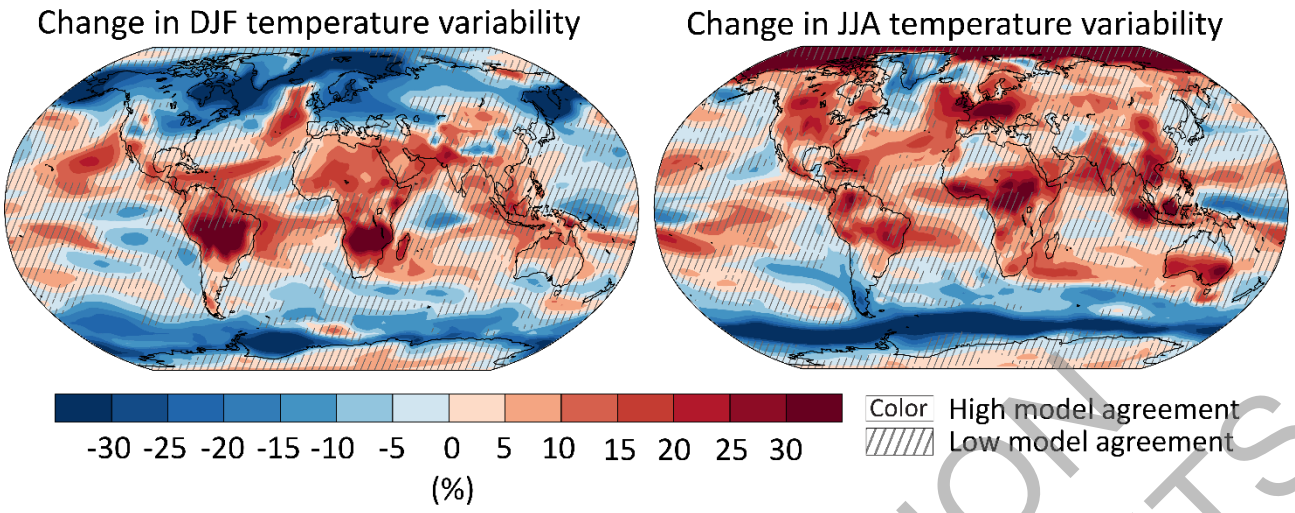


Figure 4.21: Percentage change in interannual variability of (top) JJA and (bottom) DJF mean temperature averaged across seven large initial condition ensembles. Average changes across seven single-model initial-condition large ensembles are shown for RCP8.5 in 2081–2100 (and where not available for 2080–2099) relative to 1995–2014. Standard deviations are calculated across all members of the large ensembles for every given year to avoid inflation due to the underlying trend and then averaged across the period. Changes are averaged across the ensembles MPI-GE (100 members, (Maher et al., 2019)), CanESM2, 50 members (Kirchmeier-Young et al., 2017)), NCAR-CESM (30 members, (Kay et al., 2015)), GFDL-CM3, 20 members, (Rodgers et al., 2015)), GFDL-ESM2M (30 members, (Sun et al., 2018)), CSIRO-Mk3-6-0 (30 members, (Jeffrey et al., 2013)), EC-EARTH (16 members, (Hazeleger et al., 2010)), see (Deser et al., 2020). Diagonal lines indicate areas with low model agreement where fewer than 80% of the models agree on the sign of the change, and no overlay areas with high model agreement where at least 80% of the models agree on the sign of the change. Further details on data sources and processing are available in the chapter data table (Table 4.SM.1).

ACCEPTED VERSION
SUBJEC TO FINAL EDITS

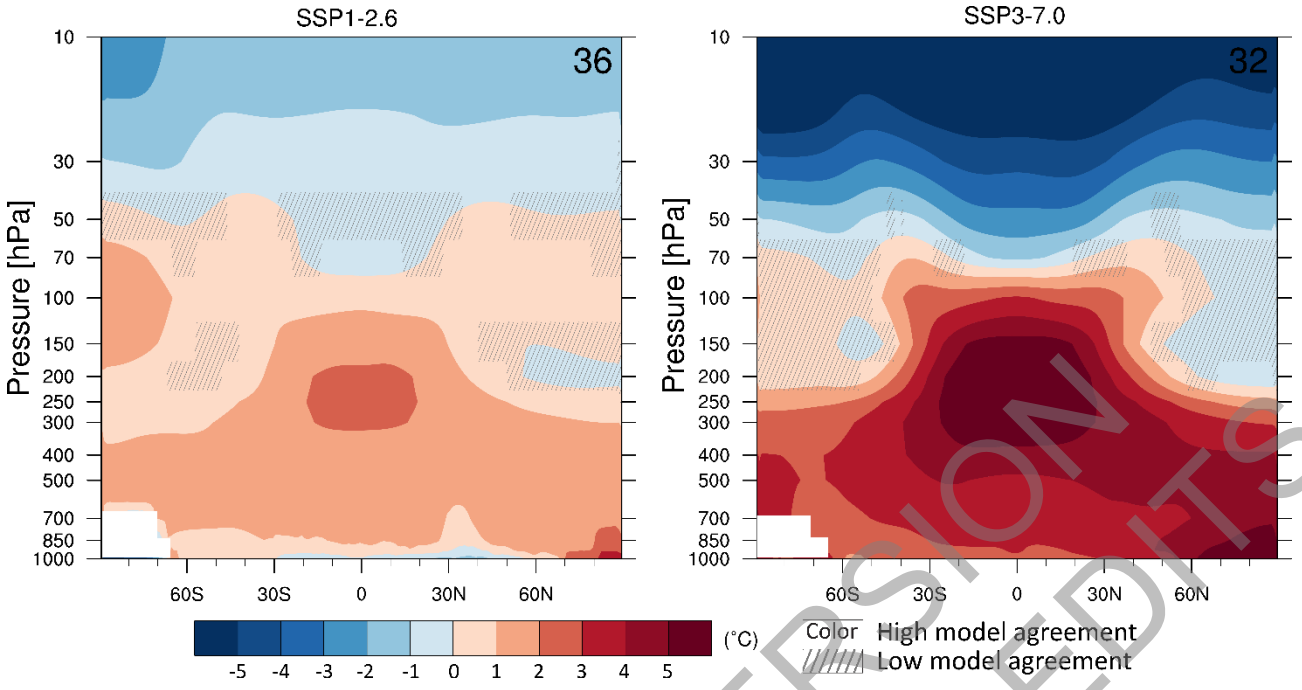


Figure 4.22: Long-term change of annual and zonal mean atmospheric temperature. Displayed are multi-model mean change in annual and zonal mean atmospheric temperature (°C) in 2081–2100 relative to 1995–2014 for (left) SSP1-2.6 and (right) SSP5-8.5. The number of models used is indicated in the top right of the maps. Diagonal lines indicate regions where less than 80% of the models agree on the sign of the change and no overlay where 80% or more of the models agree on the sign of the change. Further details on data sources and processing are available in the chapter data table (Table 4.SM.1).

ACCEPTED VERSION SUBJEC TO FINAL EDITS

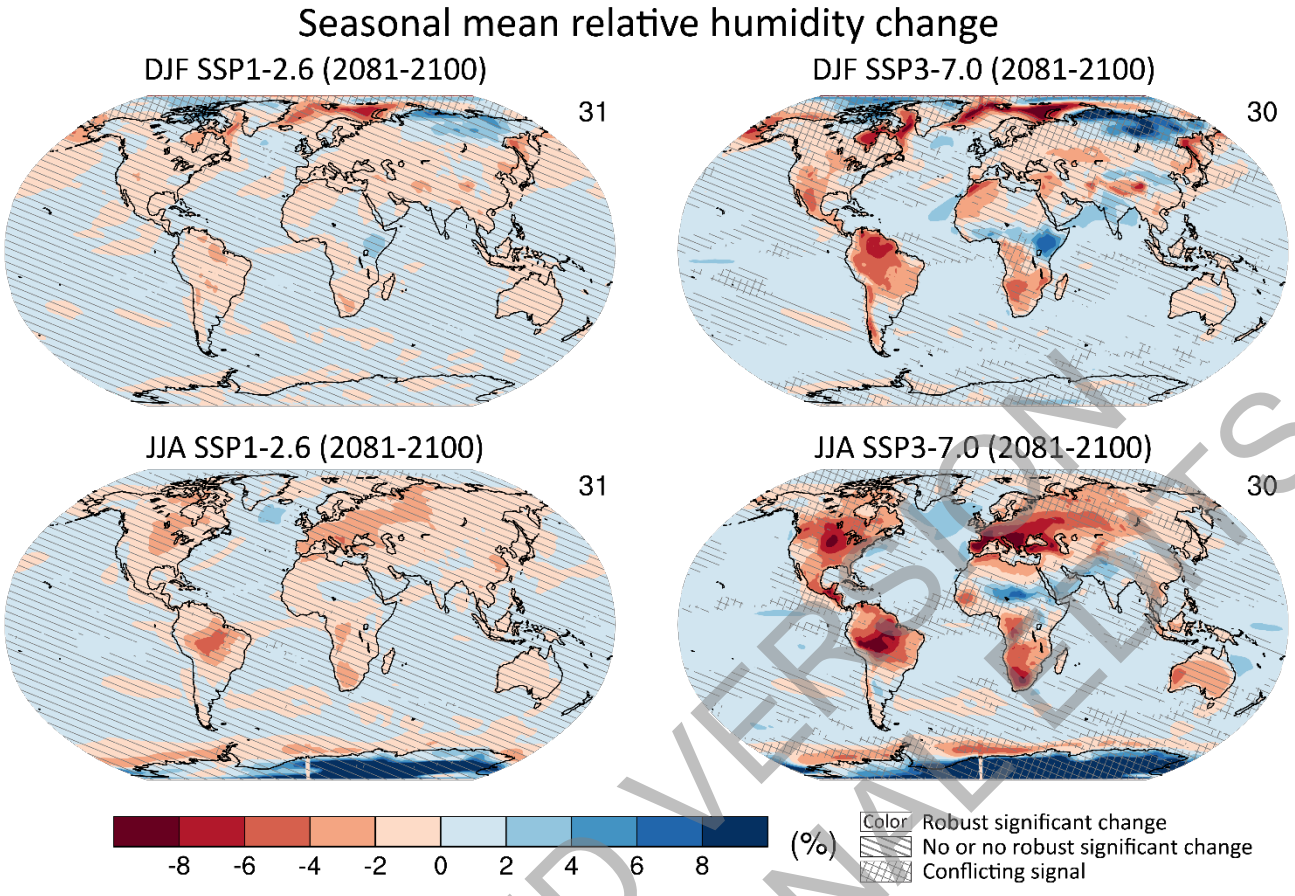


Figure 4.23: Long-term changes in seasonal mean relative humidity. Displayed are projected spatial patterns of multi-model mean change (%) in seasonal (top) DJF and (bottom) JJA mean near-surface relative humidity in 2081–2100 relative to 1995–2014, for (left) SSP1-2.6 and (right) SSP3-7.0. The number of models used is indicated in the top right of the maps. No overlay indicates regions where the change is robust and *likely* emerges from internal variability, that is, where at least 66% of the models show a change greater than the internal-variability threshold (see Section 4.2.6) and at least 80% of the models agree on the sign of change. Diagonal lines indicate regions with no change or no robust significant change, where fewer than 66% of the models show change greater than the internal-variability threshold. Crossed lines indicate areas of conflicting signals where at least 66% of the models show change greater than the internal-variability threshold but fewer than 80% of all models agree on the sign of change. Further details on data sources and processing are available in the chapter data table (Table 4.SM.1).

ACCEPTED VERSION SUBJECT TO FINAL EDITS

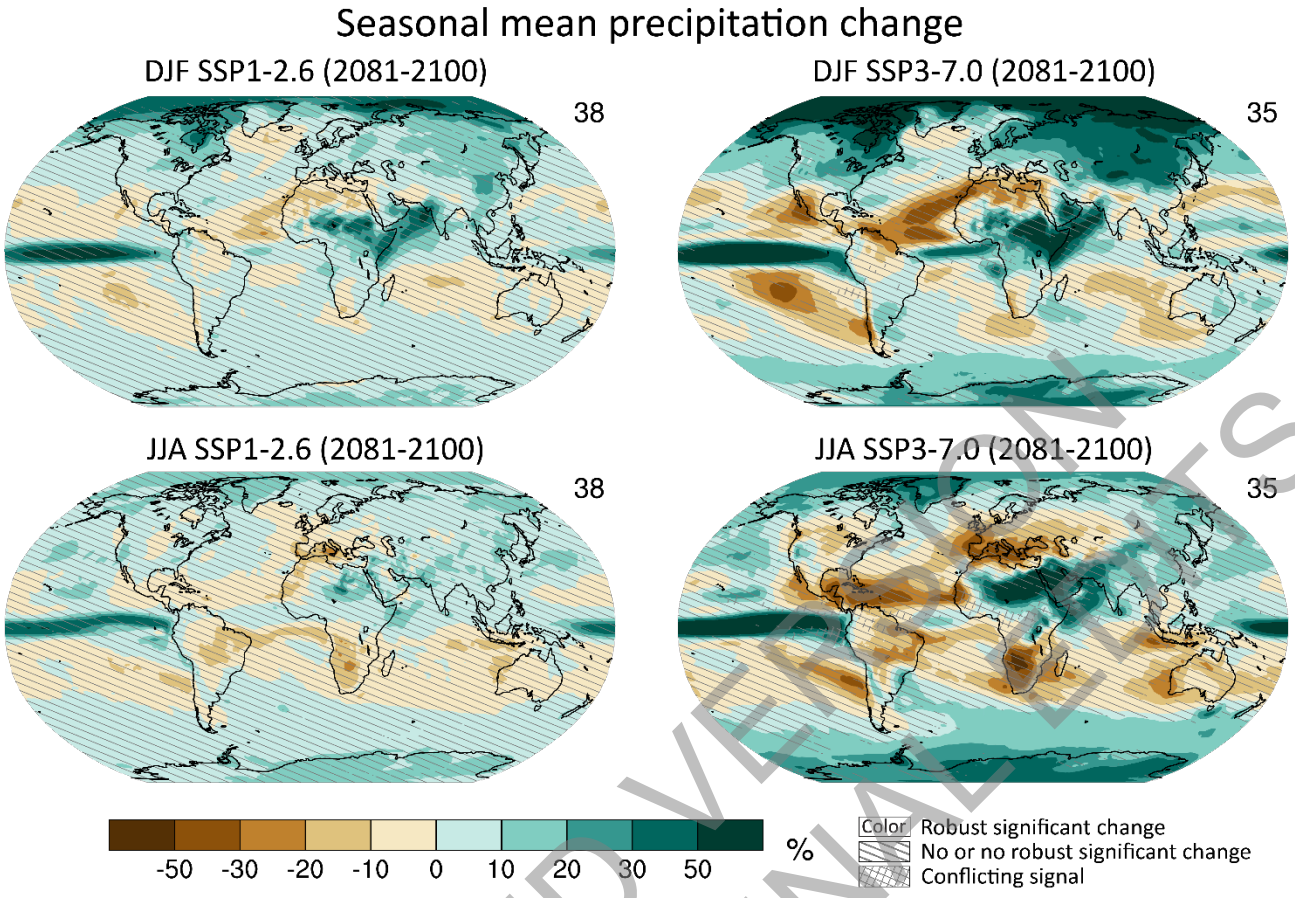


Figure 4.24: Long-term change of seasonal mean precipitation. Displayed are projected spatial patterns of multi-model mean change (%) in (top) DJF and (bottom) JJA mean precipitation in 2081–2100 relative to 1995–2014, for (left) SSP1-2.6 and (right) SSP3-7.0. The number of models used is indicated in the top right of the maps. No map overlay indicates regions where the change is robust and *likely* emerges from internal variability, that is, where at least 66% of the models show a change greater than the internal-variability threshold (see Section 4.2.6) and at least 80% of the models agree on the sign of change. Diagonal lines indicate regions with no change or no robust significant change, where fewer than 66% of the models show change greater than the internal-variability threshold. Crossed lines indicate areas of conflicting signals where at least 66% of the models show change greater than the internal-variability threshold but fewer than 80% of all models agree on the sign of change. Further details on data sources and processing are available in the chapter data table (Table 4.SM.1).

ACCEPTED VERSION SUBJECT TO FINAL EDITS

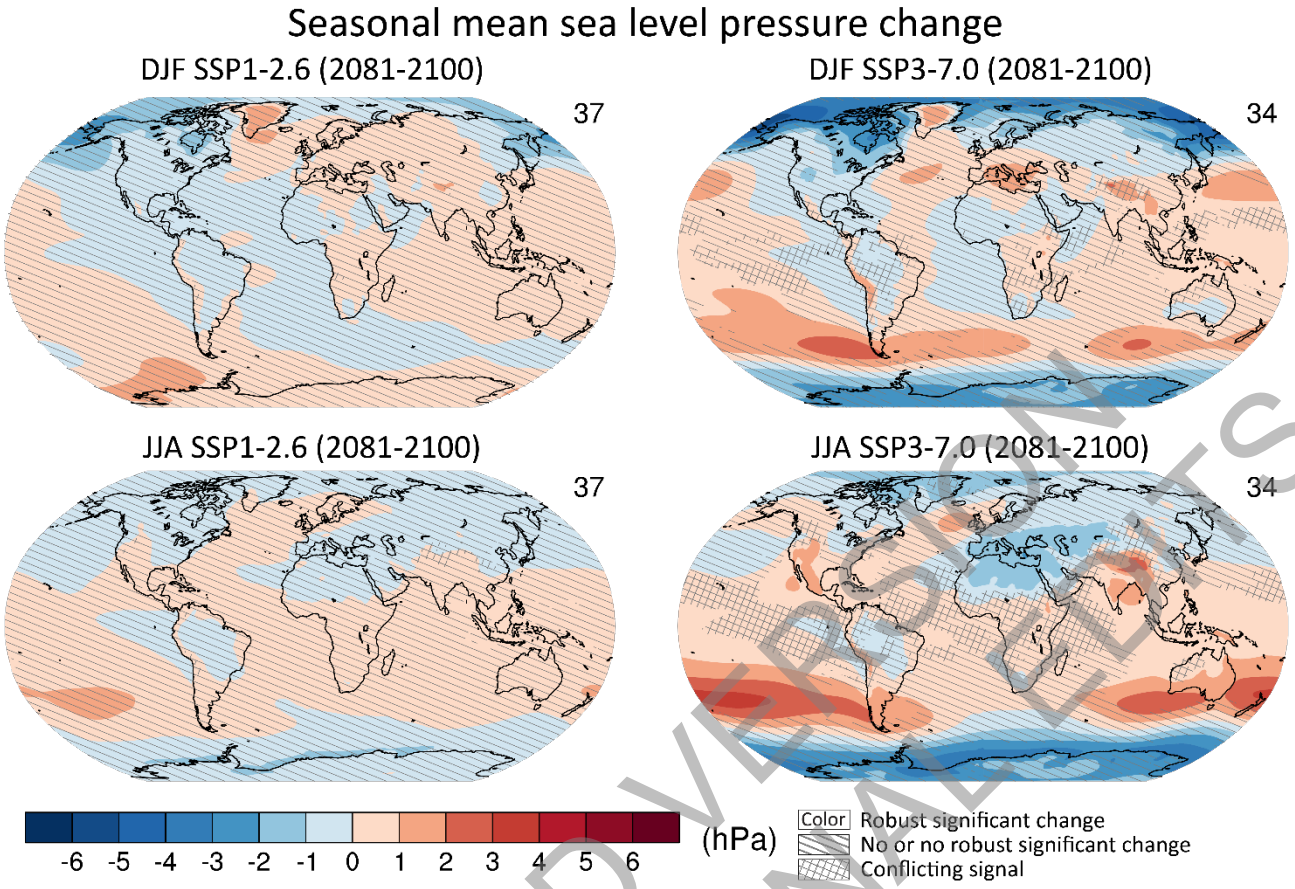


Figure 4.25: Long-term change of seasonal mean sea level pressure. Displayed are projected spatial patterns of multi-model mean change in (top) DJF and (bottom) JJA mean sea level pressure (hPa) in 2081–2100 relative to 1995–2014, for (left) SSP1-2.6 and (right) SSP3-7.0. The number of models used is indicated in the top right of the maps. No overlay indicates regions where the change is robust and *likely* emerges from internal variability, that is, where at least 66% of the models show a change greater than the internal-variability threshold (see Section 4.2.6) and at least 80% of the models agree on the sign of change. Diagonal lines indicate regions with no change or no robust significant change, where fewer than 66% of the models show change greater than the internal-variability threshold. Crossed lines indicate areas of conflicting signals where at least 66% of the models show change greater than the internal-variability threshold but fewer than 80% of all models agree on the sign of change. Further details on data sources and processing are available in the chapter data table (Table 4.SM.1).

ACCEPTED VERSION SUBJECT TO FINAL EDITS

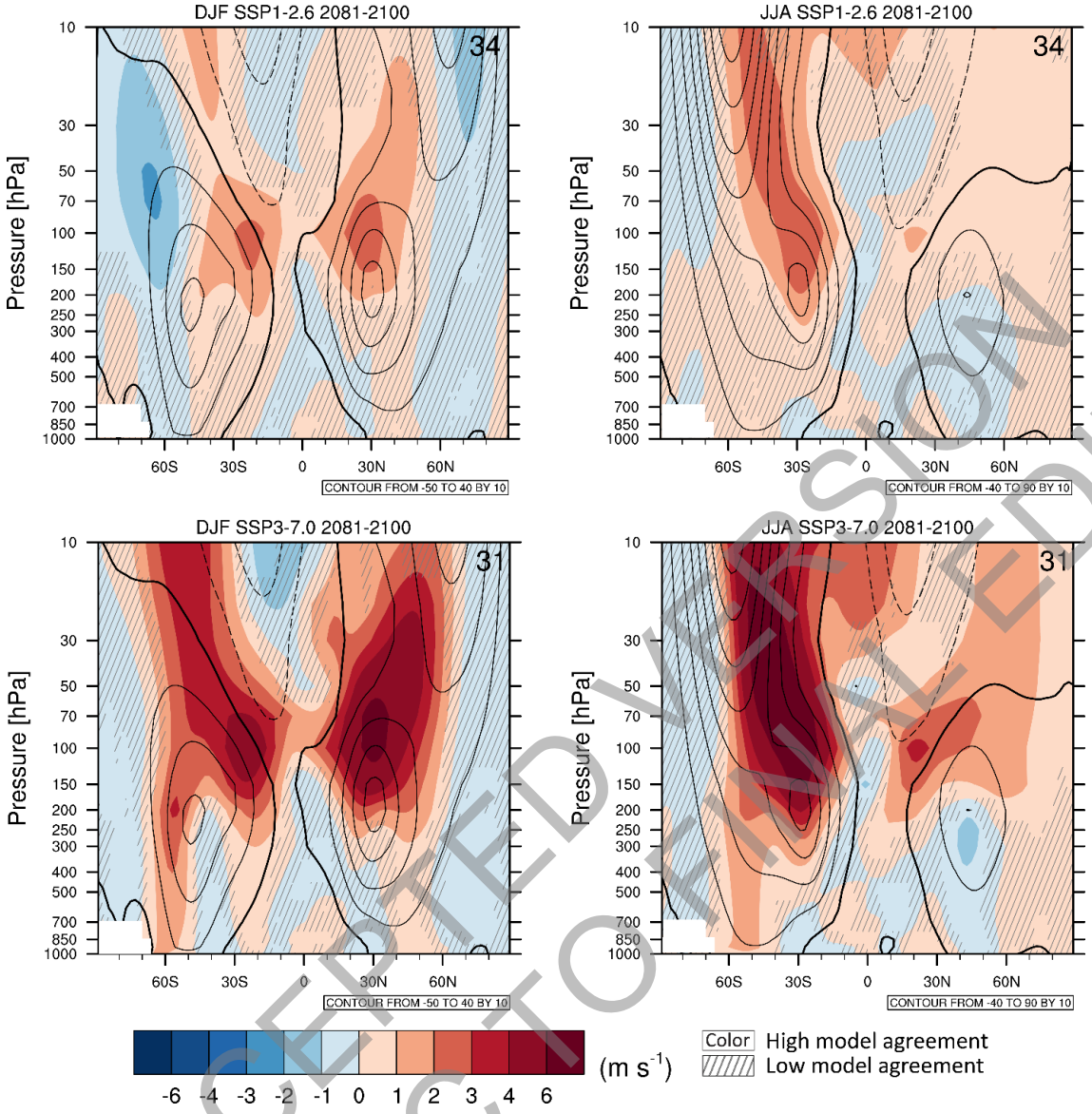


Figure 4.26: Long-term change of zonal mean zonal wind. Dispayed are multi-model mean change in (left) boreal winter (DJF) and (right) austral winter (JJA) zonal mean zonal wind (m s^{-1}) in 2081–2100 for (top) SSP1-2.6 and (right) SSP3-7.0 relative to 1995–2014. The 1995–2014 climatology is shown in contours with spacing 10 m s^{-1}. Diagonal lines indicate regions where less than 80% of the models agree on the sign of the change and no overlay where at least 80% of the models agree on the sign of the change. Further details on data sources and processing are available in the chapter data table (Table 4.SM.1).

ACCEPTED VERSION SUBJECT TO FINAL EDITS

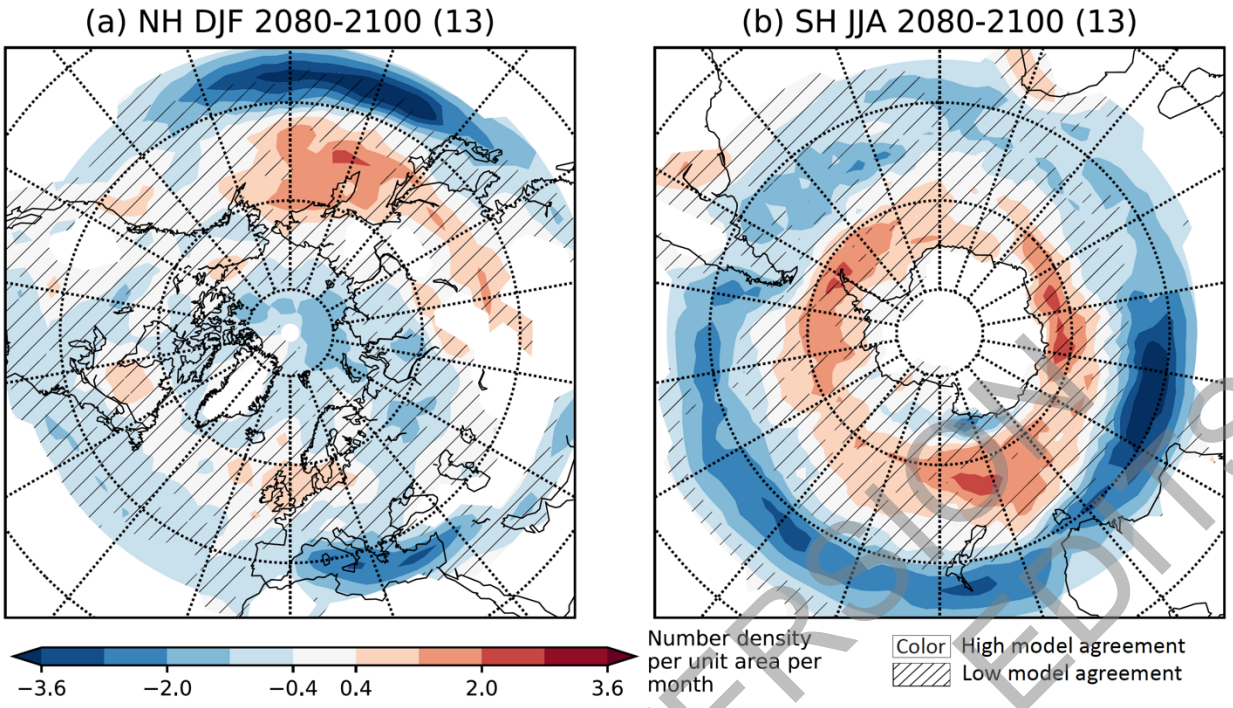


Figure 4.27: Changes in extratropical storm track density. Displayed are projected spatial pattern of multi-model mean change of extratropical storm track density in winter (NH DJF and SH JJA) in 2080–2100 for SSP5-8.5 relative to 1979–2014 based on 13 CMIP6 models. Diagonal lines indicate regions where fewer than 80% of the models agree on the sign of the change and no overlay where at least 80% of the models agree on the sign of change. Units are number density per 5 degree spherical cap per month. Further details on data sources and processing are available in the chapter data table (Table 4.SM.1).

ACCEPTED VERSION SUBJEC TO FINAL EDITS

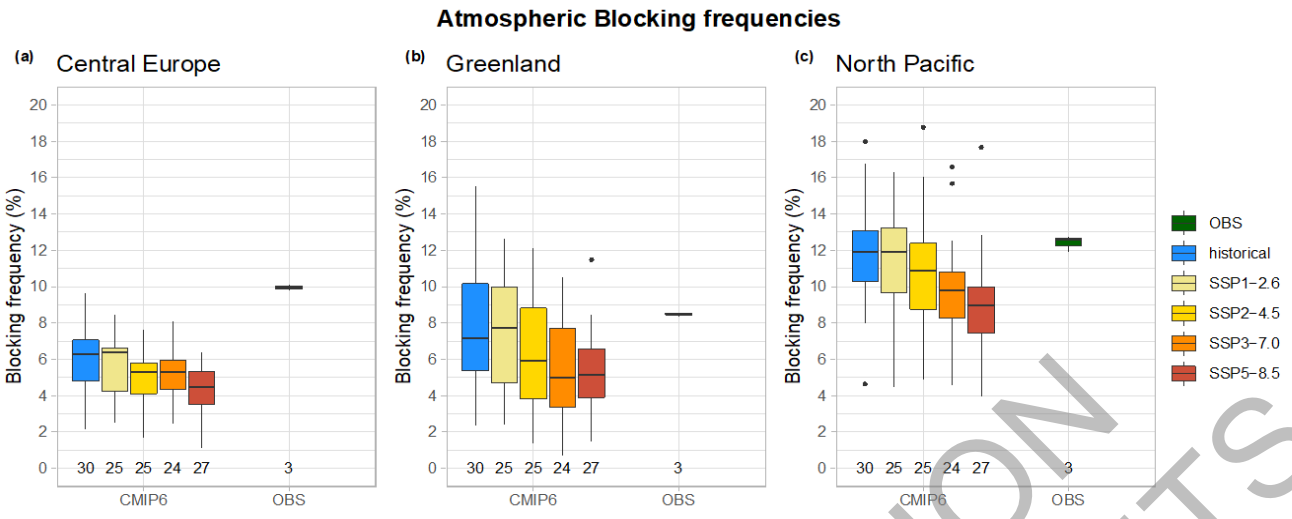


Figure 4.28: Projected wintertime atmospheric blocking frequencies. Box plot showing December-to-March atmospheric blocking frequencies from historical simulations over 1995–2014 and projections over 2081–2100, over (a) the Central European region (20°W–20°E, 45°N–65°N), (b) the Greenland region (65°W–20°W, 62.5°N–72.5°N), (c) the North Pacific region (130°E–150°W, 60°N–75°N). Values show the percentage of blocked days per season following the (Davini et al., 2012) index. Median values are the thick black horizontal bar. The lower whiskers extend from the first quartile to the smallest value in the ensemble, and the upper whiskers extend from the third quartile to the largest value. The whiskers are limited to an upper bound that is 1.5 times the interquartile range (the distance between the third and first quartiles). Black dots show outliers from the whiskers. The numbers below each bar report the number of models included. Observationally based values are obtained as the average of the ERA-Interim Reanalysis, the JRA-55 Reanalysis and the NCEP/NCAR Reanalysis. Adapted from (Davini and D'Andrea, 2020). Further details on data sources and processing are available in the chapter data table (Table 4.SM.1).

ACCEPTED VERSION SUBJEC TO FINAL EDITS

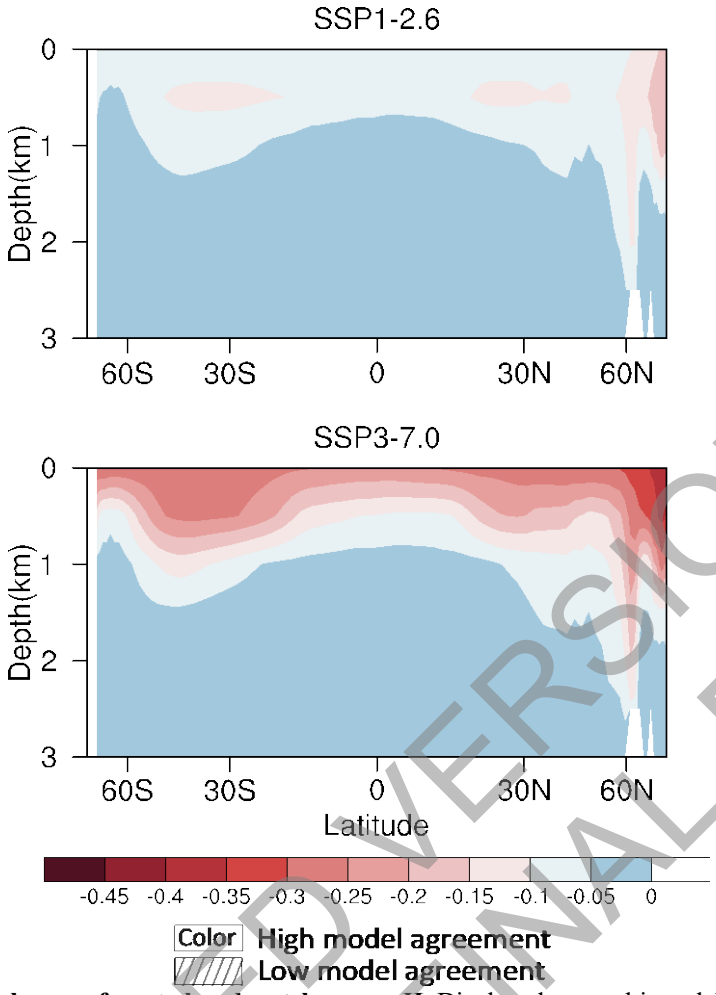


Figure 4.29: Long-term change of annual and zonal ocean pH. Displayed are multi-model mean change in annual and zonal ocean pH in 2081–2100 relative to the mean of 1995–2014 for SSP1-2.6 and SSP3-7.0, respectively. Eleven CMIP6 model results are used. Diagonal lines indicate regions where fewer than 80% of the models agree on the sign of the change and no overlay where at least 80% of the models agree on the sign of change. Further details on data sources and processing are available in the chapter data table (Table 4.SM.1).

ACCEPTED VERSION
SUBJEC TO FINAL EDITS

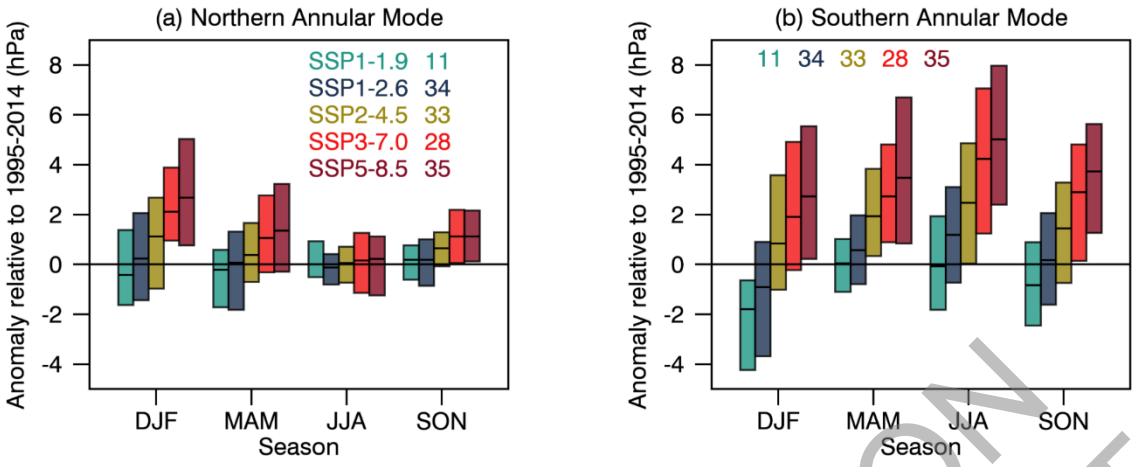


Figure 4.30: CMIP6 Annular Mode index change from 1995–2014 to 2081–2100: (a) NAM and (b) SAM. The NAM is defined as the difference in zonal mean SLP at 35°N and 65°N (Li and Wang, 2003) and the SAM as the difference in zonal mean SLP at 40°S and 65°S (Gong and Wang, 1999). The shadings are the 5–95% ranges across the simulations. The numbers near the top are the numbers of model simulations in each SSP ensemble. Further details on data sources and processing are available in the chapter data table (Table 4.SM.1).

ACCEPTED VERSION
SUBJEC TO FINAL EDITS

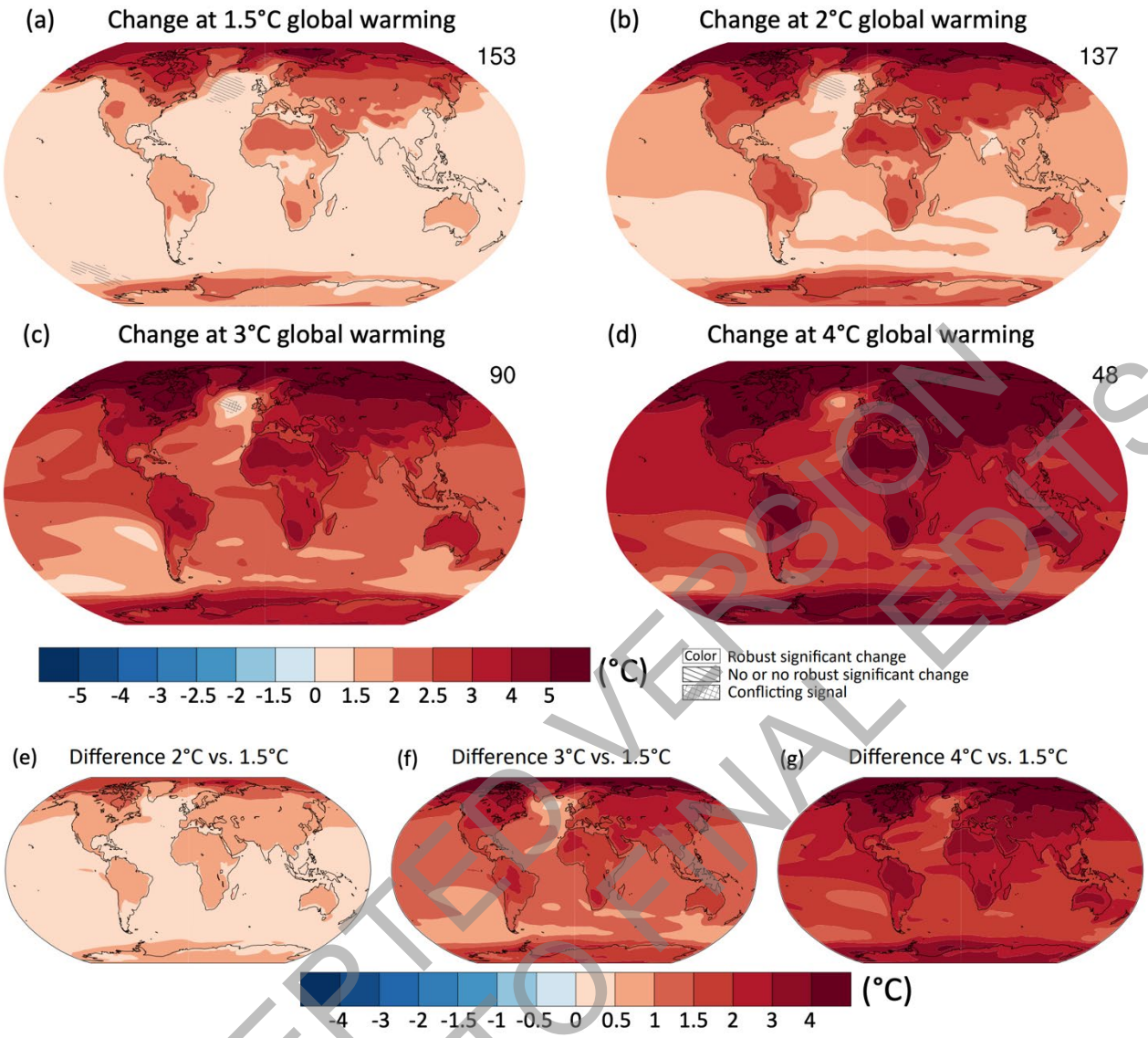


Figure 4.31: Projected spatial patterns of change in annual average near-surface temperature (°C) at different levels of global warming. Displayed are (a–d) spatial patterns of change in annual average near-surface temperature at 1.5°C, 2°C, 3°C, and 4°C of global warming relative to the period 1850–1900 and (e–g) spatial patterns of differences in temperature change at 2°C, 3°C, and 4°C of global warming compared to 1.5°C of global warming. The number of models used is indicated in the top right of the maps. No overlay indicates regions where the change is robust and *likely* emerges from internal variability, that is, where at least 66% of the models show a change greater than the internal-variability threshold (see Section 4.2.6) and at least 80% of the models agree on the sign of change. Diagonal lines indicate regions with no change or no robust significant change, where fewer than 66% of the models show change greater than the internal-variability threshold. Crossed lines indicate areas of conflicting signals where at least 66% of the models show change greater than the internal-variability threshold but fewer than 80% of all models agree on the sign of change. Values were assessed from a 20-year period at a given warming level, based on model simulations under the Tier-1 SSPs of CMIP6. Further details on data sources and processing are available in the chapter data table (Table 4.SM.1).

ACCEPTED VERSION SUBJECT TO FINAL EDITS

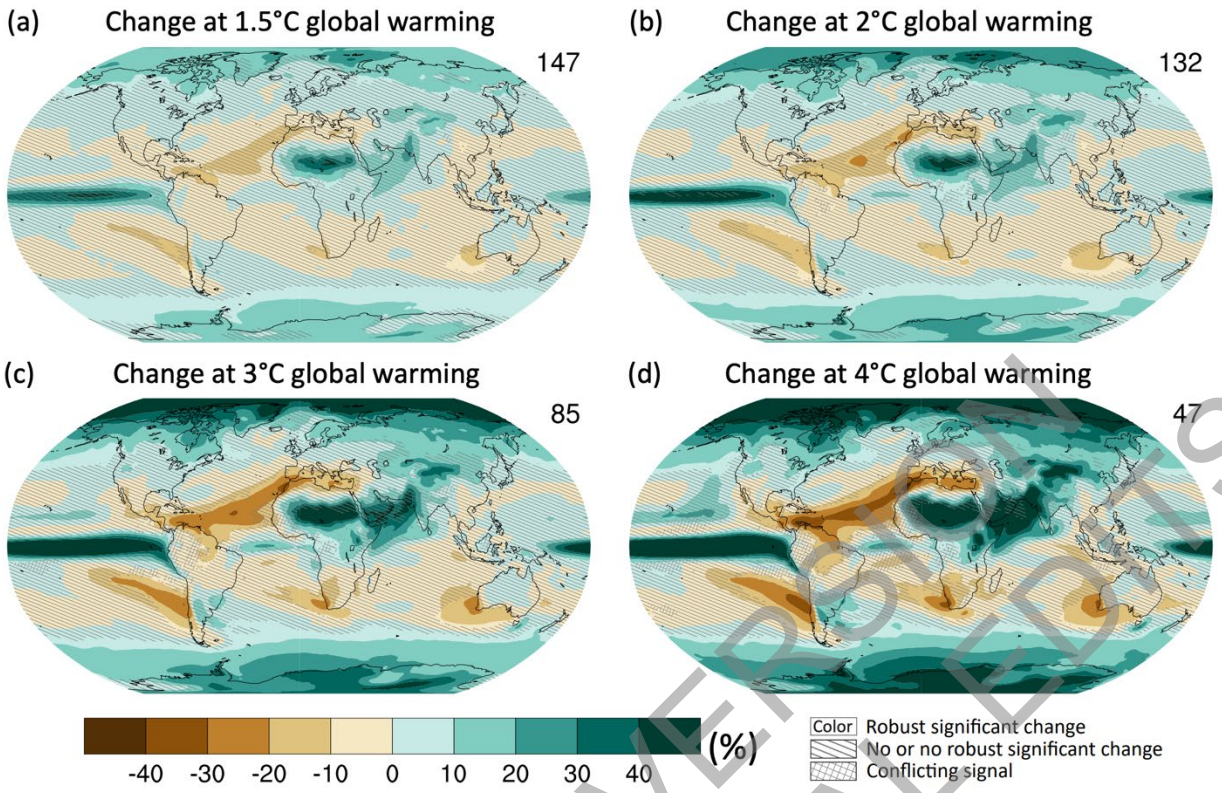


Figure 4.32: Projected spatial patterns of change in annual average precipitation (expressed as a percentage change) at different levels of global warming. Displayed are (a–d) spatial patterns of change in annual precipitation at 1.5°C, 2°C, 3°C, and 4°C of global warming reletive to the period 1850–1900. No map overlay indicates regions where the change is robust and *likely* emerges from internal variability, that is, where at least 66% of the models show a change greater than the internal-variability threshold (see Section 4.2.6) and at least 80% of the models agree on the sign of change. Diagonal lines indicate regions with no change or no robust significant change, where fewer than 66% of the models show change greater than the internal-variability threshold. Crossed lines indicate areas of conflicting signals where at least 66% of the models show change greater than the internal-variability threshold but fewer than 80% of all models agree on the sign of change. Values were assessed from a 20-year period at a given warming level, based on model simulations under the Tier-1 SSPs of CMIP6. Further details on data sources and processing are available in the chapter data table (Table 4.SM.1).

ACCEPTED VERSION SUBJECT TO FINAL EDITS

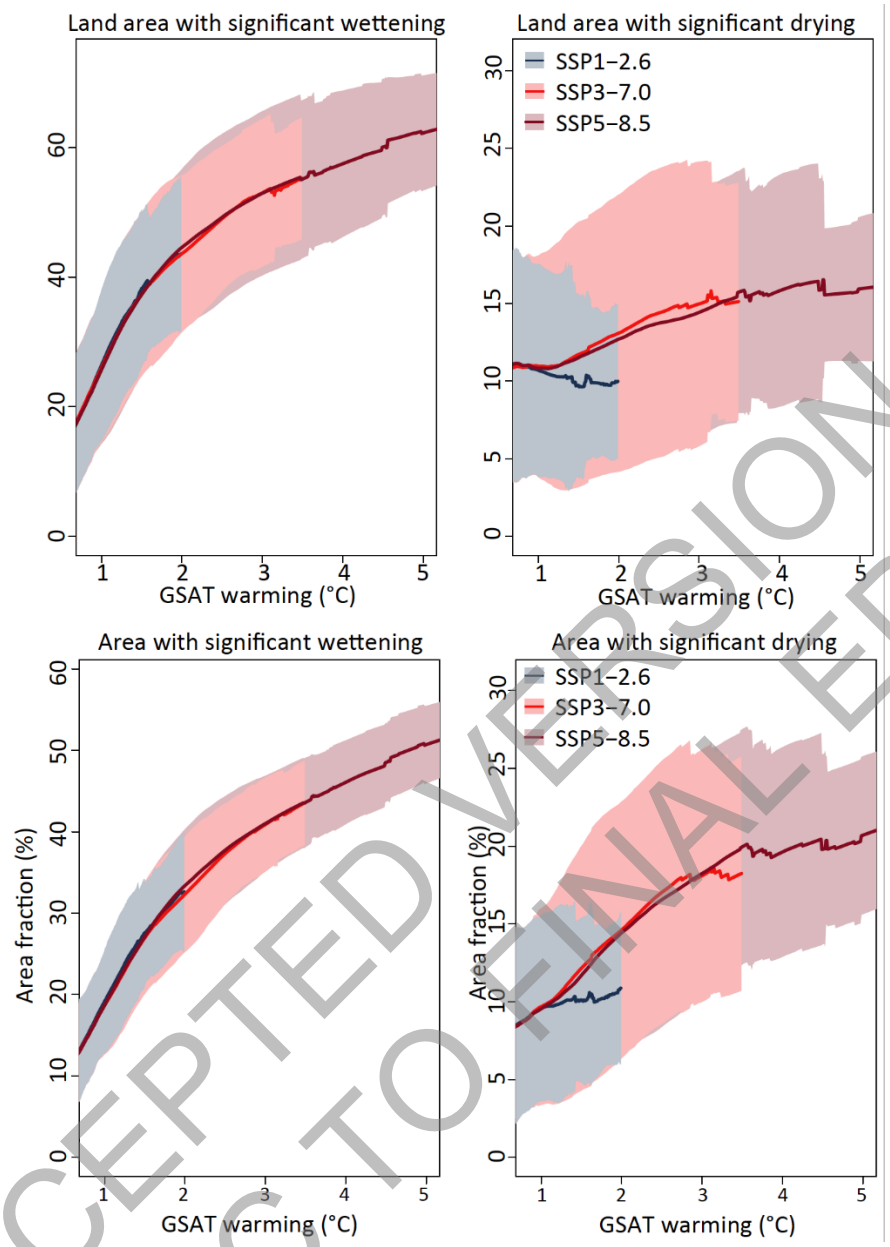


Figure 4.33: Area fraction of significant precipitation change at 1.5°C, 2°C, 3°C, and 4°C of global warming. Range of land fraction (top) and global area fraction (bottom) with significant precipitation increase (left-hand side) and decrease (right-hand side) in the projected annual precipitation change (%) at levels of global warming compared to the period 1850–1900. Values were assessed from a 20-year period at a given warming level from SSP1-2.6, SSP3-7.0 and SSP5-8.5 in CMIP6. The solid line illustrates the CMIP6-multi model mean and the shaded band is the 5–95% range across models that reach a given level of warming. Further details on data sources and processing are available in the chapter data table (Table 4.SM.1).

ACCEPTED VERSION SUBJECT TO FINAL EDITS

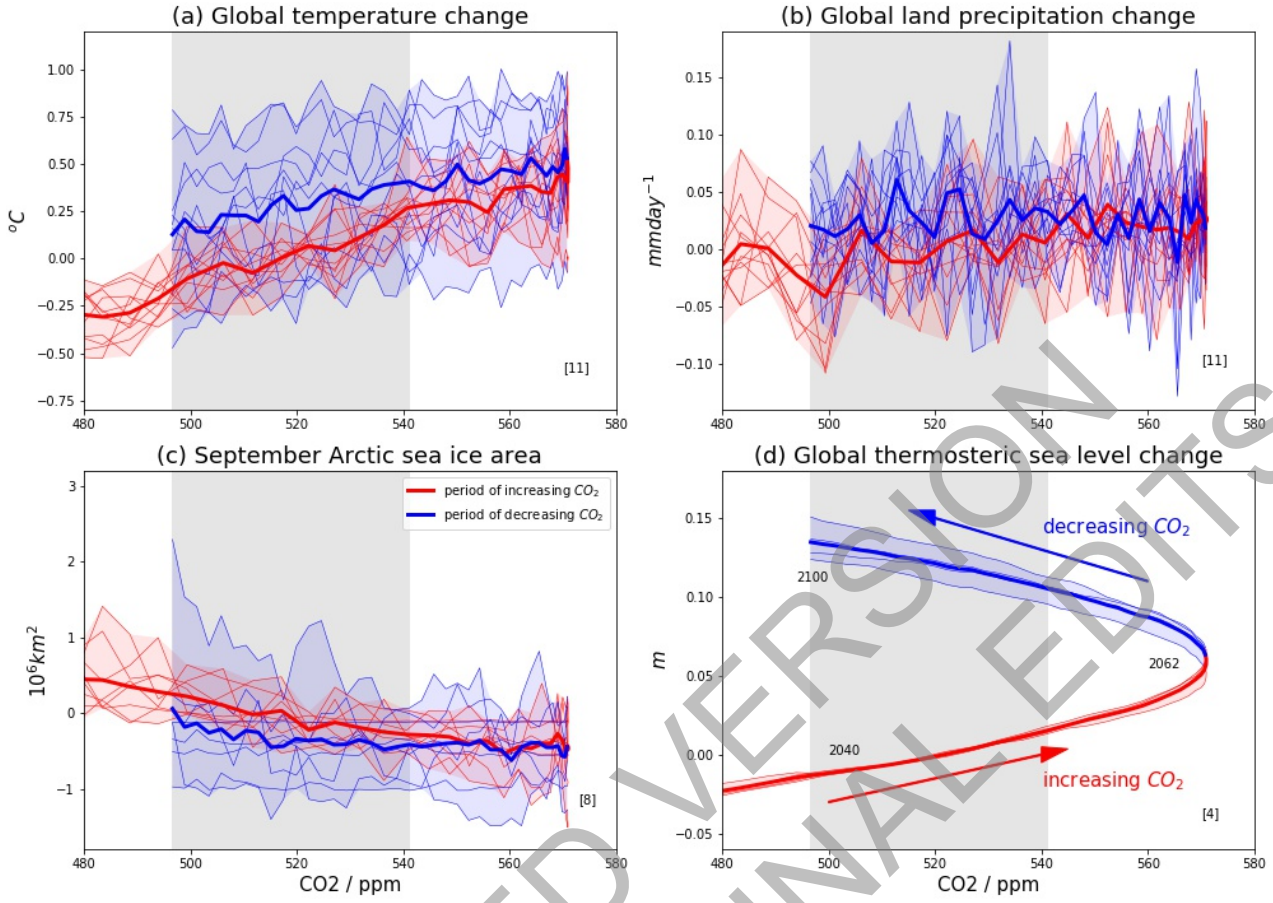


Figure 4.34: Simulated changes in climate indices for SSP5-3.4-OS plotted against atmospheric CO_2 concentration (ppm) from 480 up to 571 and back to 496 by 2100. (a) Global surface air temperature change; (b) Global land precipitation change; (c) September Arctic sea-ice area change; (d) Global thermosteric sea-level change. Plotted changes are relative to the 2034–2053 mean which has same CO_2 as 2081–2100 mean (shaded grey bar). Red lines denote changes during the period up to 2062 when CO_2 is rising, blue lines denote changes after 2062 when CO_2 is decreasing again. Thick line is multi model mean; thin lines and shading show individual models and complete model range. Numbers in square brackets indicate number of models used in each panel. Further details on data sources and processing are available in the chapter data table (Table 4.SM.1).

ACCEPTED VERSION SUBJECT TO FINAL EDITS

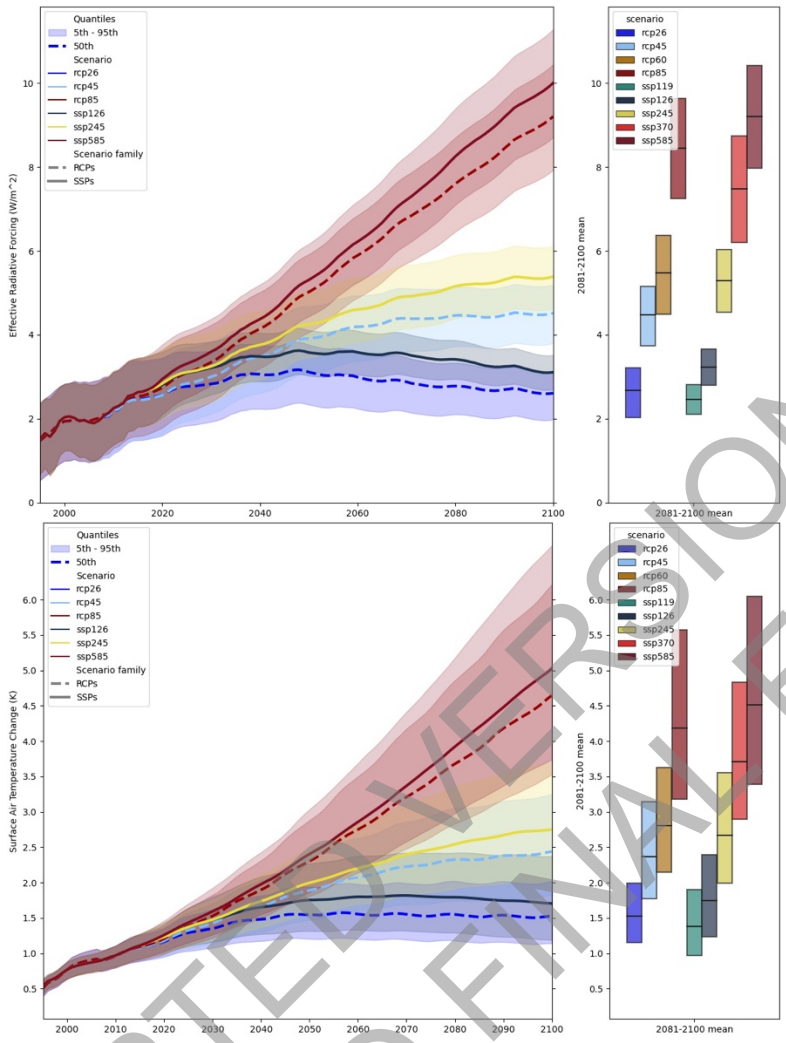


Figure 4.35: Comparison of RCPs and SSPs run by a single emulator to estimate scenario differences. Time series with 5–95% ranges and medians of (a) effective radiative forcings, calculated as described in Annex 7.A.1; and (b) GSAT projections relative to 1850–1900 for the RCP and SSP scenarios from MAGICC 7.5. Note that the nameplate radiative forcing level refers to stratospheric adjusted radiative forcings in AR5-consistent settings (Tebaldi et al., 2021) while ERFs may differ. MAGICC7.5 is here run in the recommended setup for WGIII, prescribing observed GHG concentrations for the historical period and switching to emission-driven runs in 2015. Further details on data sources and processing are available in the chapter data table (Table 4.SM.1).

ACCEPTED VERSION SUBJECT TO FINAL EDITS

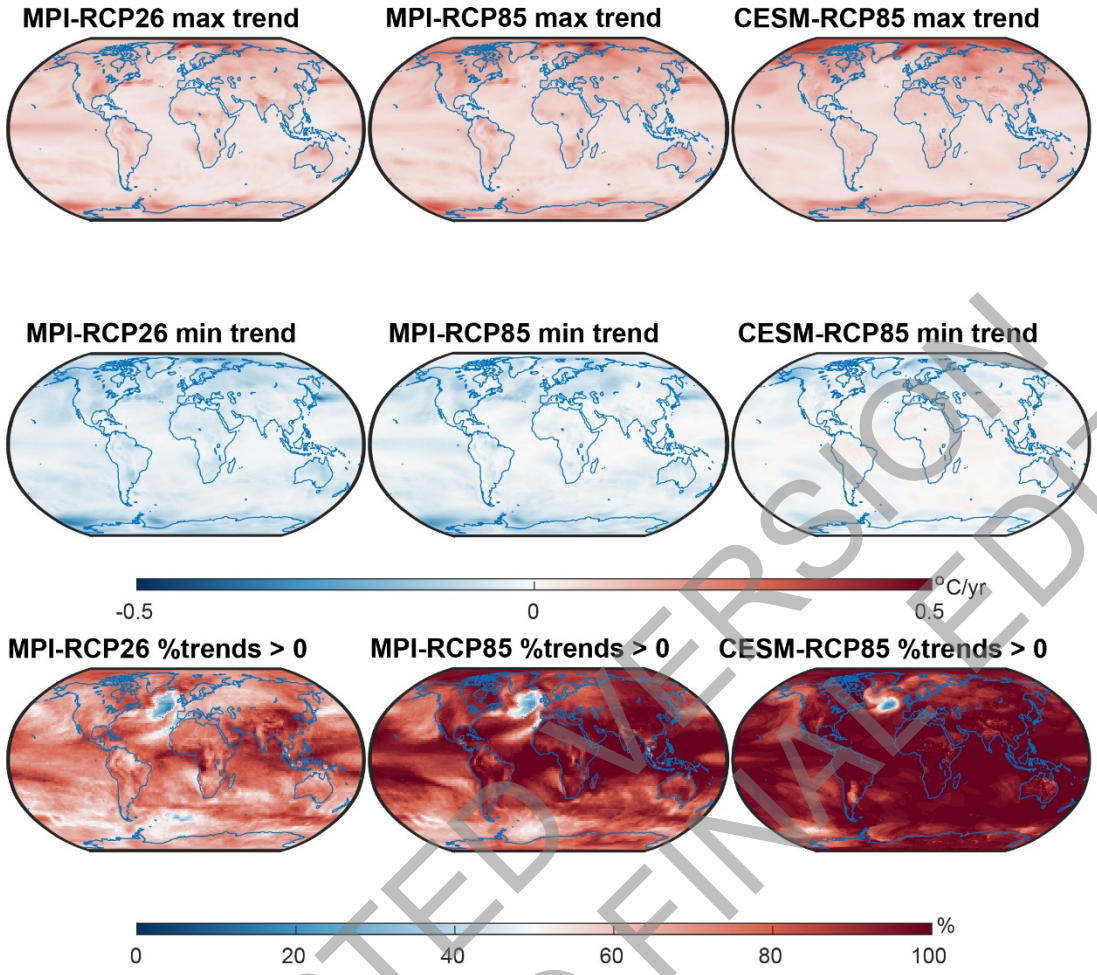


Figure 4.36: Masking of climate response to mitigation by internal variability in the near term. Near-term (2021–2040) pointwise maximum (top row) and pointwise minimum (middle row) surface air temperature trends in the large initial-condition ensemble from MPI (left and centre columns), and CESM (right column) models in the RCP2.6 (left column) and RCP8.5 scenarios (centre and right columns). The percentage of ensemble members with a warming trend in the near term is shown in the bottom panels. Figure modified from (Maher et al., 2020). Further details on data sources and processing are available in the chapter data table (Table 4.SM.1).

ACCEPTED VERSION SUBJECT TO FINAL EDITS

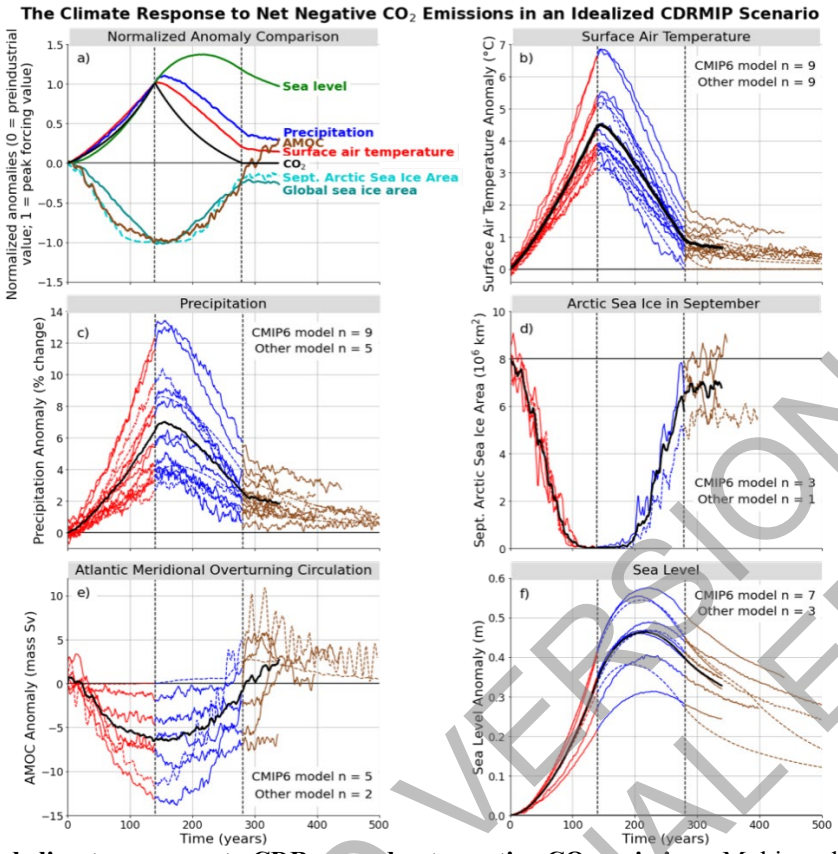
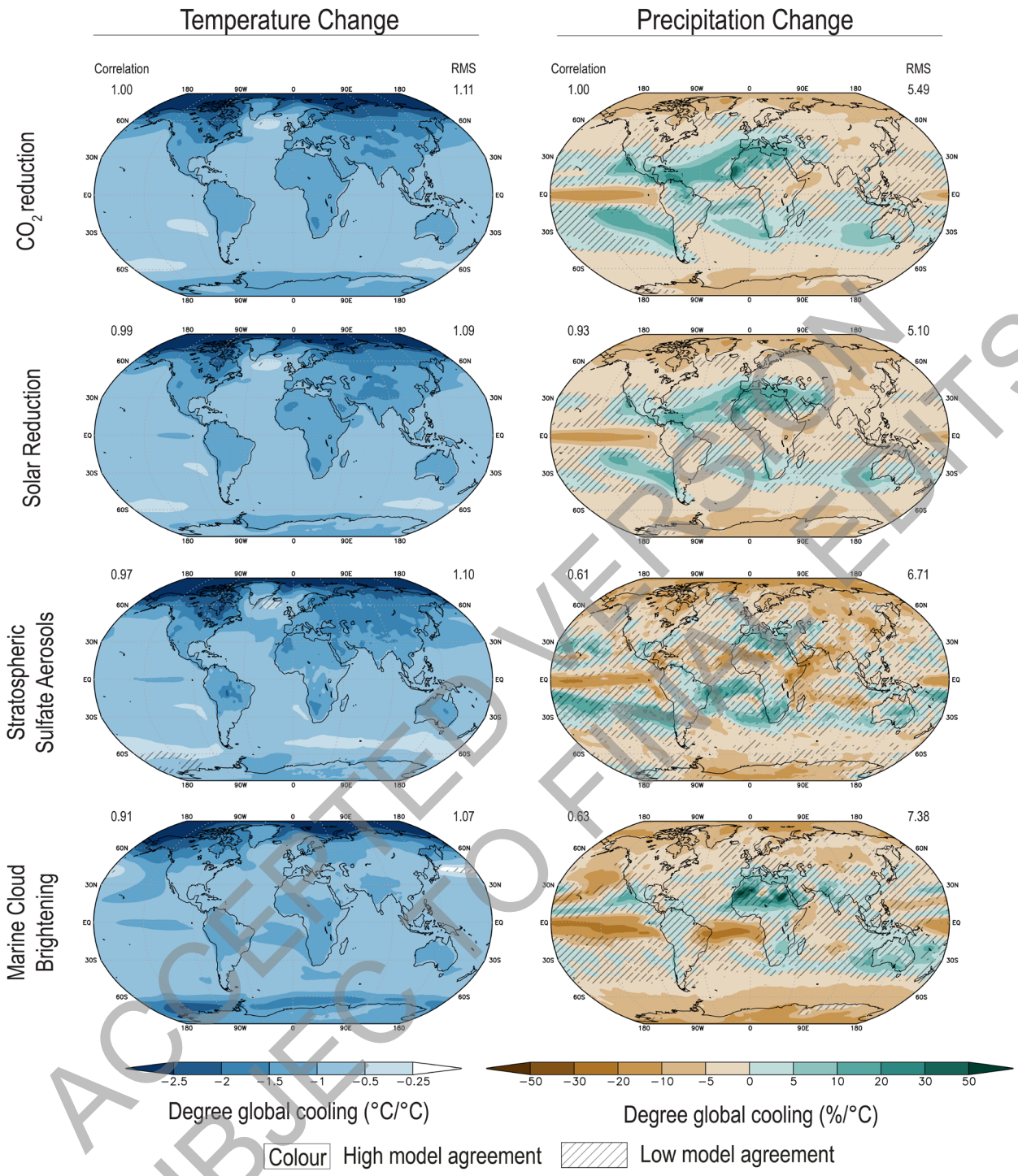


Figure 4.37: Delayed climate response to CDR-caused net negative CO_2 emissions. Multi-model simulated response in global and annual mean climate variables for a ramp-up followed by ramp-down of CO_2. Atmospheric CO_2 increases from the pre-industrial level at a rate of 1% yr^{-1} to 4×CO_2, then decreases at the same rate to the pre-industrial level and then remains constant. The ramp-down phase represents the period of net negative CO_2 emissions. a) normalized ensemble mean anomaly of key variables as a function of year, including atmospheric CO_2, surface air temperature, precipitation, thermosteric sea-level rise (see Glossary), global sea-ice area, Northern Hemisphere sea-ice area in September, and Atlantic meridional overturning circulation (AMOC); b) surface air temperature; c) precipitation; d) September Arctic sea-ice area; e) AMOC; f) thermostatic sea level; 5-year running means are shown for all variables except the sea-level rise. In b–f, red lines represent the phase of CO_2 ramp-up, blue lines represent the phase of CO_2 ramp-down, brown lines represent the period after CO_2 has returned to pre-industrial level, and black lines represent the multi-model mean. For all of the segments in b–f, the solid coloured lines are CMIP6 models, and the dashed lines are other models (i.e., EMICs, CMIP5 era models). Vertical dashed lines indicate peak CO_2 and when CO_2 again reaches pre-industrial value. The number of CMIP6 and non-CMIP6 models used is indicated in each panel. The time series for the multi-model means (b–f) and the normalized anomalies (a) are terminated when data from all models are not available, in order to avoid the discontinuity in the time series. Further details on data sources and processing are available in the chapter data table (Table 4.SM.1).

ACCEPTED VERSION SUBJECT TO FINAL EDITS



ACCEPTED VERSION SUBJECT TO FINAL EDITS

Figure 4.38: Multi-model response per degree global mean cooling in temperature and precipitation in response to CO_2 forcing and SRM forcing. Top row shows the response to a CO_2 decrease, calculated as the difference between pre-industrial control simulation and abrupt4 • CO_2 simulations where the CO_2 concentration is quadrupled abruptly from the pre-industrial level (11-model average); second row shows the response to a globally uniform solar reduction, calculated as the difference between GeoMIP experiment G1 and abrupt4 • CO_2 (11-model average); third row shows the response to stratospheric sulphate aerosol injection, calculated as the difference between GeoMIP experiment G4 (a continuous injection of 5Tg SO_2 per year at one point on the equator into the lower stratosphere against the RCP4.5 background scenario) and RCP4.5 (6-model average); and bottom row shows the response to marine cloud brightening, calculated as the difference between GeoMIP experiment G4cdnc (increase cloud droplet concentration number in marine low cloud by 50% over the global ocean against RCP4.5 background scenario) and RCP4.5 (8-model average). All differences (average of years 11–50 of

simulation) are normalized by the global mean cooling in each scenario, averaged over years 11–50. Diagonal lines represent regions where fewer than 80% of the models agree on the sign of change. The values of correlation represent the spatial correlation of each SRM-induced temperature and precipitation change pattern with the pattern of change caused by a reduction of atmospheric CO_2. RMS (root mean square) is calculated based on the fields shown in the maps (normalized by global mean cooling). Further details on data sources and processing are available in the chapter data table (Table 4.SM.1).

ACCEPTED VERSION
SUBJEC TO FINAL EDITS

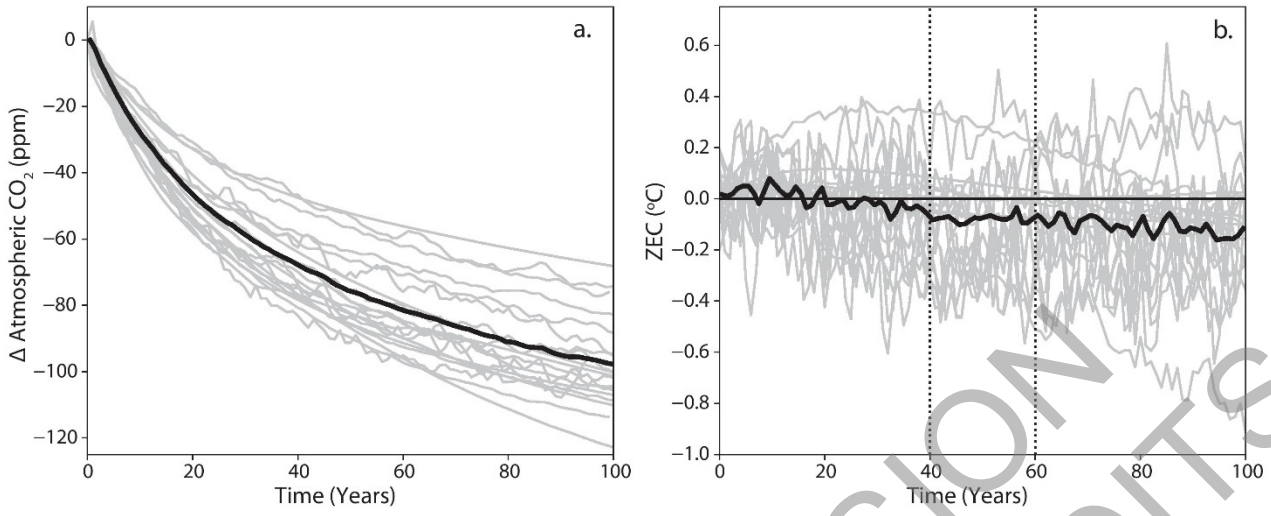


Figure 4.39: Zero Emissions Commitment (ZEC). Changes in (a) atmospheric CO_2 concentration and (b) evolution of GSAT following cessation of CO_2 emissions branched from the 1% per year experiment after emission of 1000 PgC (Jones et al., 2019). ZEC is the temperature anomaly relative to the estimated temperature at the year of cessation. ZEC_{50} is the 20-year mean GSAT change centred on 50 years after the time of cessation (see Table 4.8) – this period is marked with the vertical dotted lines. Multi-model mean is shown as thick black line, individual model simulations are in grey. Further details on data sources and processing are available in the chapter data table (Table 4.SM.1).

ACCEPTED VERSION
SUBJEC TO FINAL EDITS

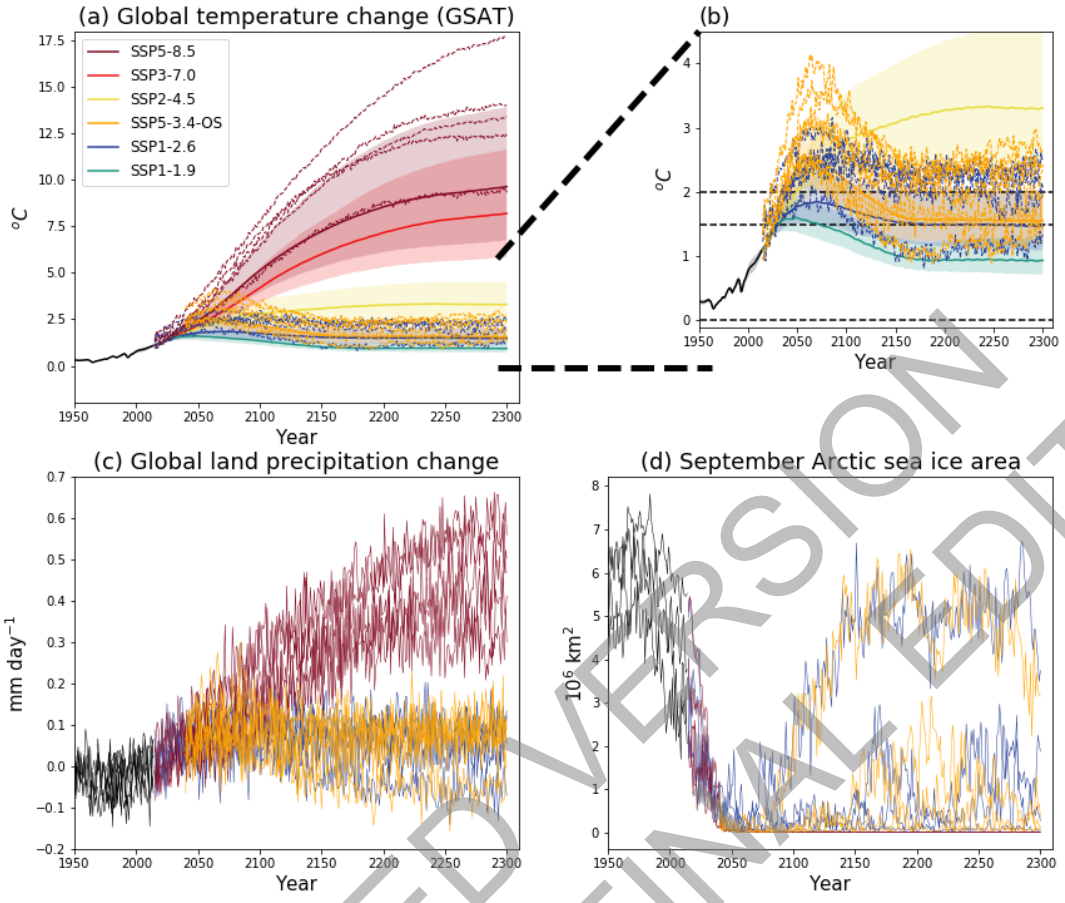


Figure 4.40: Simulated climate changes up to 2300 under the extended SSP scenarios. Displayed are (a) projected GSAT change, relative to 1850–1900, from CMIP6 models (individual lines) and MAGICC7 (shaded plumes), (b) as (a) but zoomed in to show low-emission scenarios, (c) global land precipitation change, and (d) September Arctic sea-ice area. Further details on data sources and processing are available in the chapter data table (Table 4.SM.1).

ACCEPTED VERSION SUBJEC TO FINAL EDITS

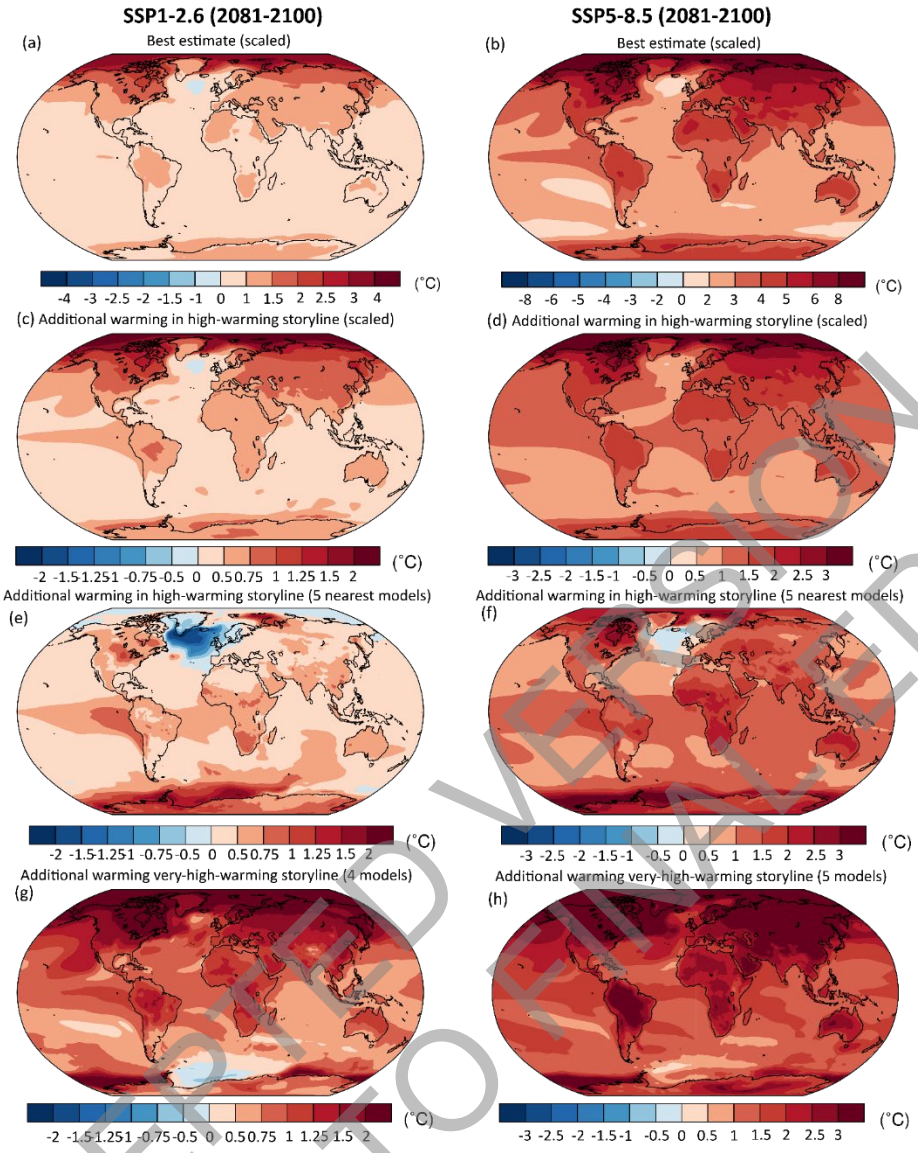


Figure 4.41: High-warming storylines for changes in annual mean temperature. (a, b) Changes in 2081–2100 relative to 1995–2014 consistent with the assessed best GSAT estimate (0.9°C and 3.5°C relative to 1995–2014 for SSP1-2.6 and SSP5-8.5, respectively). The CMIP6 multi-model mean is linearly pattern-scaled to the best GSAT estimate. (c–h) Annual mean warming above the best estimate (relative to panels a and b, respectively, note the different colour bar) in a high and very high-warming storyline for 2081–2100. (c, d) Multi-model mean warming pattern scaled to very high GSAT level corresponding to the upper bound of the assessed *very likely* range (4.8°C for SSP5-8.5 and 1.5°C for SSP1-2.6, see Section 4.3.4). (e, f) Average of five models with high GSAT warming nearest to the upper estimate of the *very likely* range (CESM2, CESM2-WACCM, CNRM-CM6-1, CNRM-CM6-1-HR, EC-Earth3 for SSP1-2.6 and ACCESS-CM2, CESM2, CESM2-WACCM, CNRM-CM6-1, CNRM-CM6-1-HRfor SSP5-8.5), (g, h) Average of four and five models, respectively (ACCESS-CM2, HadGEM3-GC31-LL, HadGEM3-GC31-MM, UKESM1-0-LL for SSP1-2.6 and CanESM5, CanESM5-CanOE, HadGEM3-GC31-LL: HadGEM3-GC31-MM, UKESM1-0-LL for SSP5-8.5) projecting very high GSAT warming exceeding the *very likely* range. Further details on data sources and processing are available in the chapter data table (Table 4.SM.1).

ACCEPTED VERSION SUBJECT TO FINAL EDITS

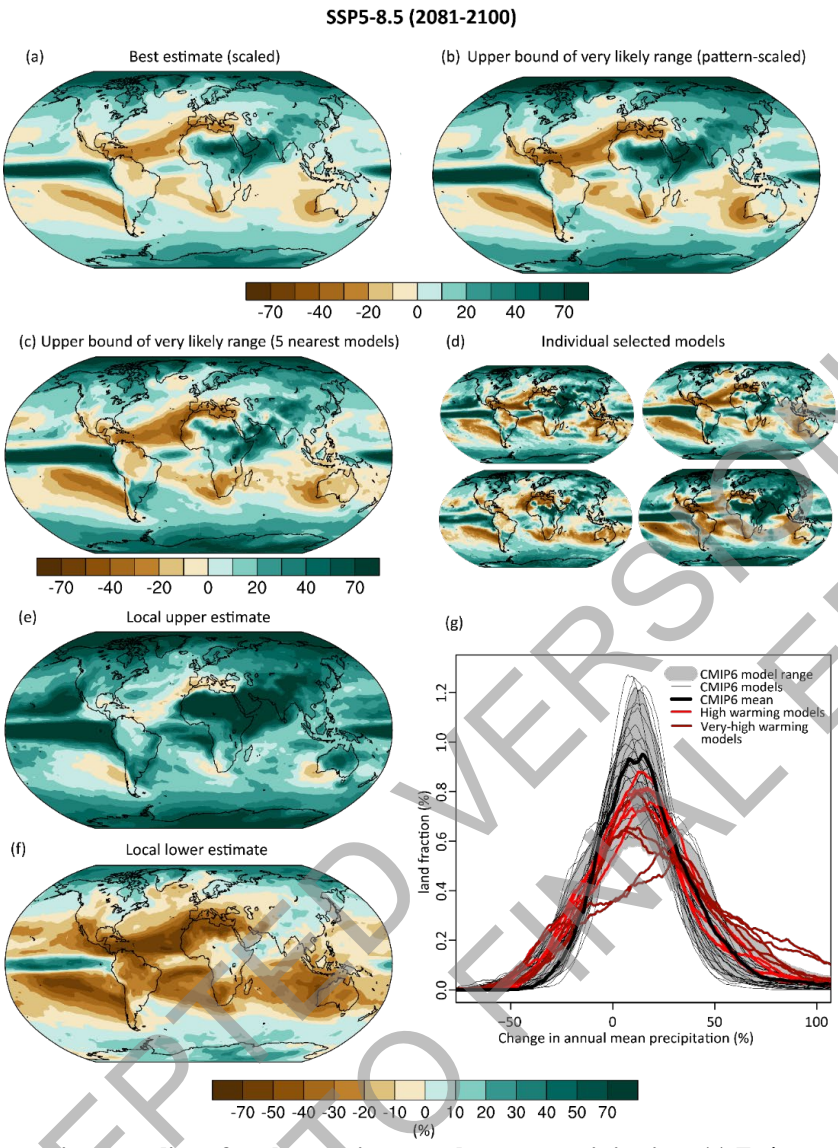
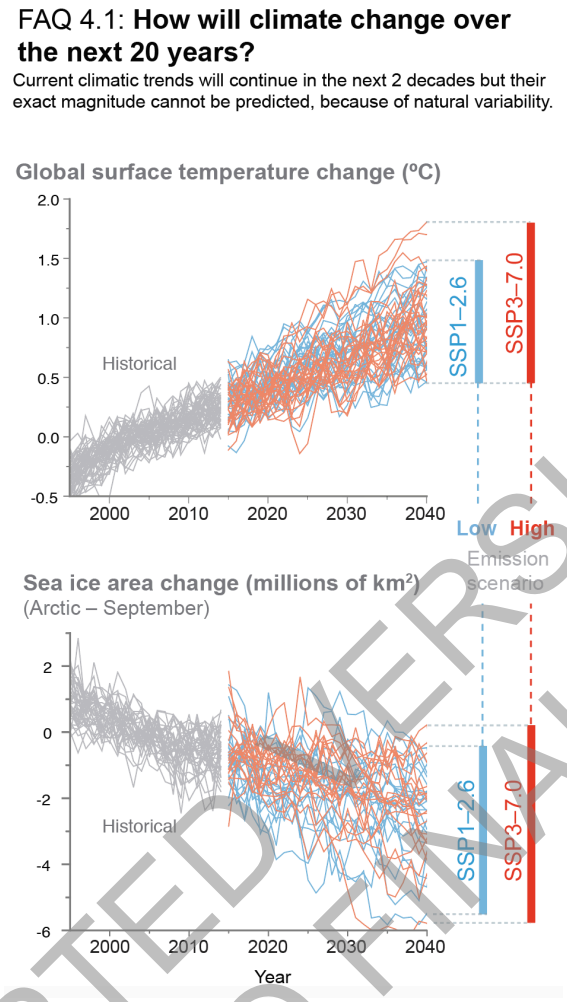


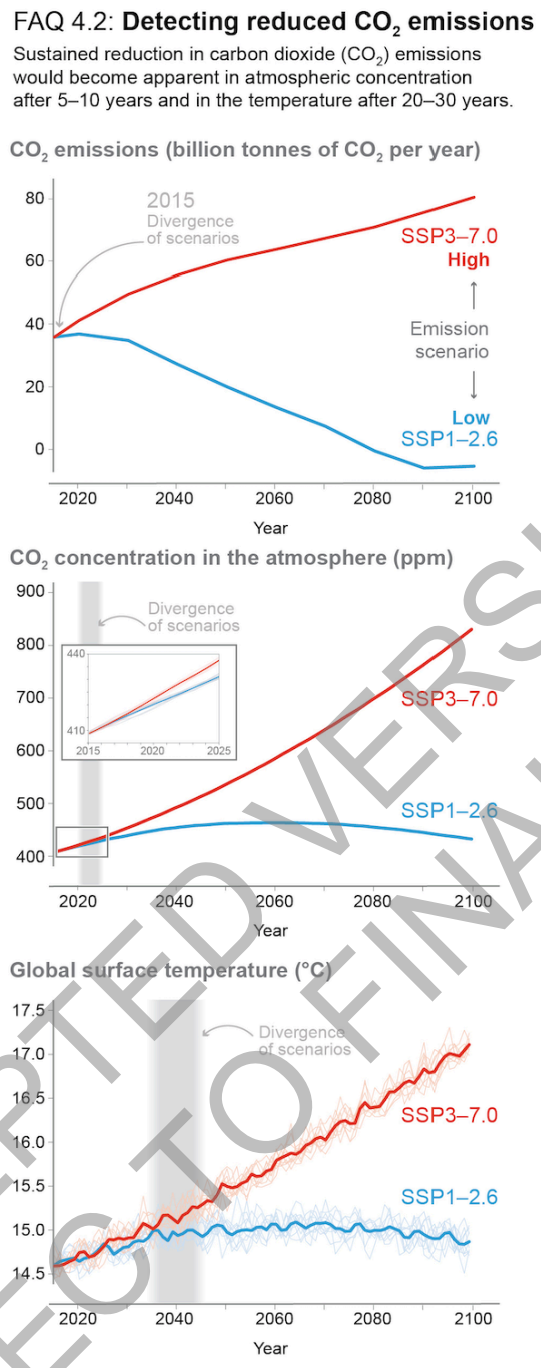
Figure 4.42: High-warming storylines for changes in annual mean precipitation. (a) Estimates for annual mean precipitation changes in 2081–2100 relative 1995–2014, consistent with the best GSAT estimate derived by linearly scaling the CMIP6 multi-model mean changes to a GSAT change of 3.5°C. (b, c) Estimates for annual mean precipitation changes in 2081–2100 relative 1995–2014 in a storyline representing a physically plausible high-global-warming level. (b) Multi-model mean precipitation scaled to high-global-warming level (corresponding to 4.8°C, the upper bound of the *very likely* range, see Section 4.3.4). (c) Average of five models with GSAT warming nearest to the high level of warming (ACCESS-CM2, CESM2, CESM2-WACCM, CNRM-CM6-1, CNRM-CM6-1-HR) (d) Annual mean precipitation changes in four of the five individual model simulations averaged in (c). (e, f) Local upper estimate (95% quantile across models) and lower estimate (5% quantile across models) at each grid point. Information at individual grid points comes from different model simulations and illustrates local uncertainty range but should not be interpreted as a pattern. (g) Area fraction of changes in annual mean precipitation 2081–2100 relative to 1995–2014 for all CMIP6 model simulations (thin black lines), models shown in (c) (red lines), and models showing very high warming above the models shown in (c). The grey range illustrates the 5–95% range across CMIP6 models and the solid black line the area fraction of the multi-model mean pattern shown in (a). Further details on data sources and processing are available in the chapter data table (Table 4.SM.1).

ACCEPTED VERSION SUBJECT TO FINAL EDITS



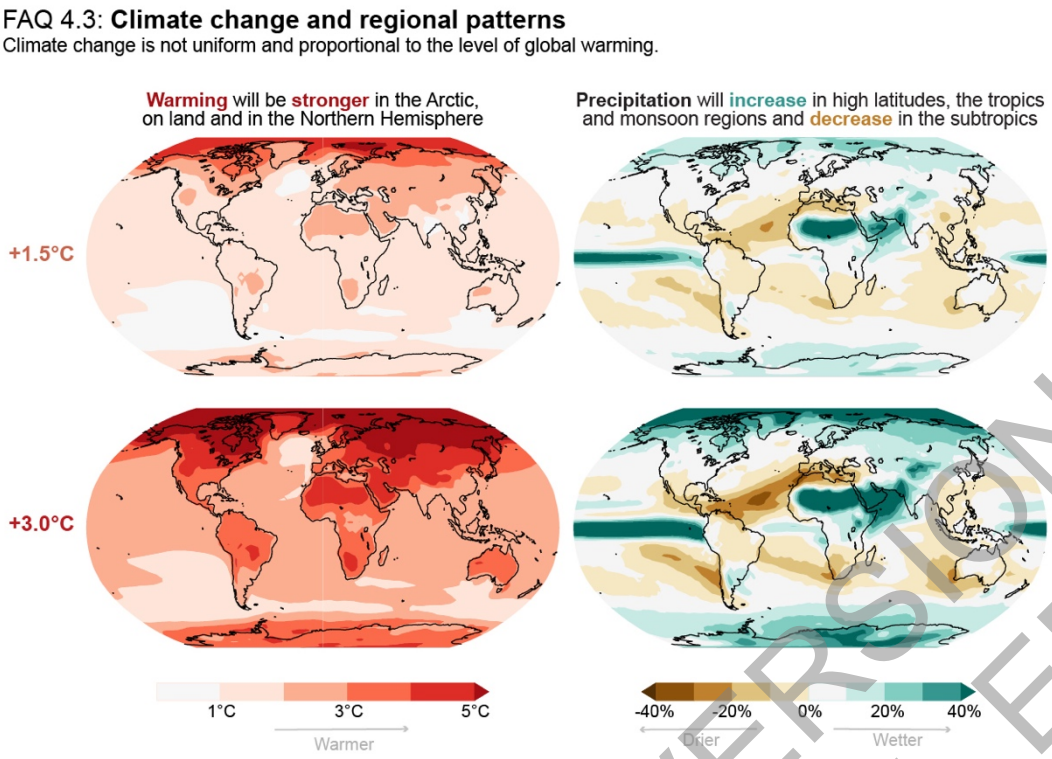
FAQ 4.1, Figure 1: Simulations over the period 1995–2040, encompassing the recent past and the next twenty years, of two important indicators of global climate change. (top) global surface temperature, and (bottom), the area of Arctic sea ice in September. Both quantities are shown as deviations from the average over the period 1995–2014. The black curves are for the historical period ending in 2014; the blue curves represent a low-emission scenario (SSP1-2.6) and the red curves one high-emission scenario (SSP3-7.0).

ACCEPTED VERSION SUBJECT TO FINAL EDITS



FAQ 4.2, Figure 1: Observing the benefits of emission reductions. (top) Carbon dioxide (CO_2) emissions, (middle) CO_2 concentration in the atmosphere and (bottom) effect on global surface temperature for two scenarios: a low-emission scenario (SSP1-2.6, blue) and a high-emission scenario (SSP3-7.0). In the low-emission scenario, CO_2 emissions begin to decrease in 2020 whereas they keep increasing throughout the 21st century in the high-emission scenario. The thick lines are the average of the ten individual simulations (thin line) for each scenario. Differences between individual simulations reflect natural variability.

ACCEPTED VERSION SUBJECT TO FINAL EDITS



FAQ 4.3, Figure 1: Regional changes in temperature (left) and precipitation (right) are proportional to the level of global warming, irrespective of the scenario through which the level of global warming is reached. Surface warming and precipitation change are shown relative to the 1850–1900 climate, and for time periods over which the globally averaged surface warming is 1.5°C (top) and 3°C (bottom), respectively. Changes presented here are based on thirty-one CMIP6 models using the high-emission scenario SSP3-7.0.

ACCEPTED VERSION SUBJEC TO FINAL EDITS

Chapter 4: Future global climate: scenario-based projections and near-term information - Supplementary Material

Coordinating Lead Authors:
June-Yi Lee (Republic of Korea), Jochem Marotzke (Germany)

Lead Authors:
Govindasamy Bala (India/United States of America), Long Cao (China), Susanna Corti (Italy), John P. Dunne (United States of America), Francois Engelbrecht (South Africa), Erich Fischer (Switzerland), John C. Fyfe (Canada), Christopher Jones (United Kingdom), Amanda Maycock (United Kingdom), Joseph Mutemi (Kenya), Ousmane Ndiaye (Senegal), Swapna Panickal (India), Tianjun Zhou (China)

Contributing Authors:
Sebastian Milinski (Germany), Kyung-Sook Yun (Republic of Korea), Kyle Armour (United States of America), Nicolas Bellouin (United Kingdom/France), Ingo Bethke (Norway/Germany), Michael P. Byrne (United Kingdom /Ireland), Christophe Cassou (France), Deliang Chen (Sweden), Annalisa Cherchi (Italy), Hannah M. Christensen (United Kingdom), Sarah L. Connors (France/United Kingdom), Alejandro Di Luca (Australia, Canada/Argentina), Sybren S. Drijfhout (The Netherlands), Christopher G. Fletcher (Canada/United Kingdom, Canada), Piers Forster (United Kingdom), Javier García-Serrano (Spain), Nathan P. Gillett (Canada), Darrell S. Kaufmann (United States of America), David P. Keller (Germany/United States of America), Ben Kravitz (United States of America), Hongmei Li (Germany/China), Yongxiao Liang (Canada/China), Andrew H. MacDougall (Canada), Elizaveta Malinina (Canada/Russian Federation), Matthew Menary (France/United Kingdom), William J. Merryfield (Canada/United States of America), Seung-Ki Min (Republic of Korea), Zebedee R.J. Nicholls (Australia), Dirk Notz (Germany), Brodie Pearson (United States of America/United Kingdom), Matthew D. K. Priestley (United Kingdom), Johannes Quaas (Germany), Aurélien Ribes (France), Alex C. Ruane (United States of America), Jean-Baptiste Sallée (France), Emilia Sanchez-Gomez (France/Spain), Sonia I. Seneviratne (Switzerland), Aimée B. A. Slangen (The Netherlands), Chris Smith (United Kingdom), Malte F. Stuecker (United States of America/Germany), Ranjini Swaminathan (United Kingdom/India), Peter W. Thorne (Ireland/ United Kingdom), Katarzyna B. Tokarska (Switzerland/Poland), Matthew Toohey (Canada, Germany/Canada), Andrew Turner (United Kingdom), Danila Volpi (Italy), Cunde Xiao (China), Giuseppe Zappa (Italy)

Review Editors:
Krishna Kumar Kanikicharla (Qatar/India), Vladimir Kattsov (Russian Federation), Masahide Kimoto (Japan)

Chapter Scientists:
Sebastian Milinski (Germany), Kyung-Sook Yun (Republic of Korea)

This Supplementary Material should be cited as:
Lee, J. Y., J. Marotzke, G. Bala, L. Cao, S. Corti, J. P. Dunne, F. Engelbrecht, E. Fischer, J. C. Fyfe, C. Jones, A. Maycock, J. Mutemi, O. Ndiaye, S. Panickal, T. Zhou, 2021, Future Global Climate: Scenario-Based Projections and Near-Term Information Supplementary Material. In: *Climate Change 2021: The Physical Science Basis. Contribution of Working Group I to the Sixth Assessment Report of the Intergovernmental Panel on Climate Change* [Masson-Delmotte, V., P. Zhai, A. Pirani, S. L. Connors, C. Péan, S. Berger, N. Caud, Y. Chen, L. Goldfarb, M. I. Gomis, M. Huang, K. Leitzell, E. Lonnoy, J.B.R. Matthews, T. K. Maycock, T. Waterfield, O. Yelekçi, R. Yu and B. Zhou (eds.)]. Available from https://ipcc.ch/static/ar6/wg1.

Date: August 2021

This document is subject to copy-editing, corrigenda and trickle backs

4.SM.1 Data Table

[START TABLE 4.SM.1 HERE]

Table 4.SM.1: Input Data Table. Input datasets and code used to create chapter figures.

Figure number / Table number / Chapter section (for calculations)	**Dataset / Code name**	**Type**	**Filename / Specificities**	**License type**	**Dataset / Code citation**	**Dataset / Code URL**	**Related publications / Software used**	**Notes** [Can add info on data processing, e.g., reference period conversion]
Figure 4.2d	Global mean sea-level (GMSL) change	Input dataset	Annual GMSL time series, 1950-2100					Emulator-based time series from Chapter 9
Figure 4.5	AMOC change	Input dataset					(Sigmond et al., 2018)	
Figure 4.28	ECMWF ERA-Interim Reanalysis	Input dataset	Daily, DJF, 1986-2005, zg 500hPa	CC BY-SA 4.0		http://apps.ecmwf.int/datasets/data/interim-full-moda/	(Dee et al., 2011)	
	NCEP/NCAR Reanalysis	Input dataset	Daily, DJF, 1986-2005, zg 500hPa	CC BY-SA 4.0		https://psl.noaa.gov/data	(Kalnay et al., 1996)	
	JRA55 Reanalysis	Input dataset	Daily, DJF, 1986-2005, zg 500hPa	CC BY-SA 4.0		https://jra.kishou.go.jp/JRA-55/index_en.html	(Kobayashi et al., 2015)	
Figure 4.35	GSAT data : MAGICC AR6-WG1 calibration SSP and RCP experiments (including 2300 extension)	Code				https://gitlab.com/magicc/wg1-ar6-plots/-/blob/master/notebooks/010-magicc-runs/110_ssps_and_rcps.ipynb	(Meinshausen et al., 2009, 2011, 2020)	Cross-chapter Box 7.1
	ERF data	Code		MIT (as part of Chris Smith's		https://github.com/chrisroadmap/		Chapter 7.SM.1.4

ACCEPTED VERSION SUBJECT TO FINAL EDITING

				AR6 repository)		ar6/blob/main/notebooks/070_chapter7_fig7.4.ipynb		
Figure 4-39	Zero Emissions Commitment from CO2	Input dataset				http://terra.seos.uvic.ca/ZEC/Data/	(MacDougall et al., 2020)	
	CMIP6 CMIP and C4MIP simulation	Input dataset	CMIP6.CMIP.NOAA-GFDL.GFDL-ESM4.1pctCO2.r1i1p1f1.Amon.tas.gr1.v20180701	CC BY-SA 4.0		https://esgf-node.llnl.gov/search/cmip6/		
			CMIP6.C4MIP.NOAA-GFDL.GFDL-ESM4.esm-1pct-brch-1000PgC.r1i1p1f1.Amon.co2.gr1.v20180701					
			CMIP6.C4MIP.NOAA-GFDL.GFDL-ESM4.esm-1pct-brch-1000PgC.r1i1p1f1.Amon.tas.gr1.v20180701					
Figure 4-40	MAGICC AR6-WG1 calibration SSP and RCP experiments (including 2300 extension)	Code				https://gitlab.com/magicc/wg1-ar6-plots/-/blob/master/notebooks/010-magicc-runs/110_ssps_and_rcps.ipynb	Meinshausen et al., 2009, 2011, 2020)	Cross-chapter Box 7.1
Box Figure 4.1	HadCRUT5	Input dataset		CC BY-SA 4.0		https://crudata.uea.ac.uk/cru/data/temperature/#datdow	(Morice et al., 2021)	
Cross-Chapter Box Figure 4.1	Volcanic ERF and annual mean GSAT	Input dataset	Cross Chapter Box Fig 4.1_ERF data Cross Chapter Box Fig			DMS	(Bethke et al., 2017)	

ACCEPTED VERSION SUBJECT TO FINAL EDITING

			4.1_GMSTvolc data Cross Chapter Box Fig 4.1_GMSTzero data					
	Re-plotting Figure 2 from Bethke et al. 2017	Code	Cross Chapter Box Fig 4.1_code.m			DMS		

[END TABLE 4.SM.1 HERE]

ACCEPTED VERSION
SUBJECT TO FINAL EDITING

References

Bethke, I., Outten, S., Otterå, O. H. H., Hawkins, E., Wagner, S., Sigl, M., et al. (2017). Potential volcanic impacts on future climate variability. *Nat. Clim. Chang.* 7, 799–805. doi:10.1038/nclimate3394.

Dee, D. P., Uppala, S. M., Simmons, A. J., Berrisford, P., Poli, P., Kobayashi, S., et al. (2011). The ERA-Interim reanalysis: configuration and performance of the data assimilation system. *Q. J. R. Meteorol. Soc.* 137, 553–597. doi:10.1002/qj.828.

Kalnay, E., Kanamitsu, M., Kistler, R., Collins, W., Deaven, D., Gandin, L., et al. (1996). The NCEP/NCAR 40-Year Reanalysis Project. *Bull. Am. Meteorol. Soc.* 77, 437–471. doi:10.1175/1520-0477(1996)077<0437:TNYRP>2.0.CO;2.

Kobayashi, S., Ota, Y., Harada, Y., Ebita, A., Moriya, M., Onoda, H., et al. (2015). The JRA-55 Reanalysis: General Specifications and Basic Characteristics. *J. Meteorol. Soc. Japan. Ser. II* 93, 5–48. doi:10.2151/jmsj.2015-001.

MacDougall, A. H., Frölicher, T. L., Jones, C. D., Rogelj, J., Matthews, H. D., Zickfeld, K., et al. (2020). Is there warming in the pipeline? A multi-model analysis of the Zero Emissions Commitment from CO2. *Biogeosciences* 17, 2987–3016. doi:10.5194/bg-17-2987-2020.

Meinshausen, M., Meinshausen, N., Hare, W., Raper, S. C. B., Frieler, K., Knutti, R., et al. (2009). Greenhouse-gas emission targets for limiting global warming to 2°C. *Nature* 458, 1158–1162. doi:10.1038/nature08017.

Meinshausen, M., Nicholls, Z. R. J., Lewis, J., Gidden, M. J., Vogel, E., Freund, M., et al. (2020). The shared socio-economic pathway (SSP) greenhouse gas concentrations and their extensions to 2500. *Geosci. Model Dev.* 13, 3571–3605. doi:10.5194/gmd-13-3571-2020.

Meinshausen, M., Raper, S. C. B., and Wigley, T. M. L. (2011). Emulating coupled atmosphere-ocean and carbon cycle models with a simpler model, MAGICC6 – Part 1: Model description and calibration. *Atmos. Chem. Phys.* 11, 1417–1456. doi:10.5194/acp-11-1417-2011.

Morice, C. P., Kennedy, J. J., Rayner, N. A., Winn, J. P., Hogan, E., Killick, R. E., et al. (2021). An Updated Assessment of Near-Surface Temperature Change From 1850: The HadCRUT5 Data Set. *J. Geophys. Res. Atmos.* 126, e2019JD032361. doi:10.1029/2019JD032361.

Sigmond, M., Fyfe, J. C., and Swart, N. C. (2018). Ice-free Arctic projections under the Paris Agreement. *Nat. Clim. Chang.* 8, 404–408. doi:10.1038/s41558-018-0124-y.

ACCEPTED VERSION
SUBJECT TO FINAL EDITING

Chapter 5: Global Carbon and other Biogeochemical Cycles and Feedbacks

Coordinating Lead Authors:
Josep G. Canadell (Australia), Pedro M.S. Monteiro (South Africa)

Lead Authors:
Marcos H. Costa (Brazil), Leticia Cotrim da Cunha (Brazil), Peter M. Cox (United Kingdom), Alexey V. Eliseev (Russian Federation), Stephanie Henson (United Kingdom), Masao Ishii (Japan), Samuel Jaccard (Switzerland), Charles Koven (United States of America), Annalea Lohila (Finland), Prabir K. Patra (Japan/India), Shilong Piao (China), Joeri, Rogelj (United Kingdom/Belgium), Stephen Syampungani (Zambia), Sönke Zaehle (Germany), Kirsten Zickfeld (Canada/Germany)

Contributing Authors:
Georgii A. Alexandrov (Russian Federation), Govindasamy Bala (India/ United States of America), Laurent Bopp (France), Lena Boysen (Germany), Long Cao (China), Naveen Chandra (Japan/India), Philippe Ciais (France), Sergey N. Denisov (Russian Federation), Frank J. Dentener (EU, The Netherlands), Hervé Douville (France), Amanda Fay (United States of America), Piers Forster (United Kingdom), Baylor Fox-Kemper (United States of America), Pierre Friedlingstein (United Kingdom), Weiwei Fu (United States of America /China), Sabine Fuss (Germany), Véronique Garçon (France), Bettina Gier (Germany), Nathan P. Gillett (Canada), Luke Gregor (Switzerland/South Africa), Karsten Haustein (United Kingdom /Germany), Vanessa Haverd (Australia), Jian He (United States of America /China), Helene T. Hewitt (United Kingdom), Forrest M. Hoffman (United States of America), Tatiana Ilyina (Germany), Robert Jackson (United States of America), Christopher Jones (United Kingdom), David P. Keller (Germany/ United States of America), Lester Kwiatkowski (France/ United Kingdom), Robin D. Lamboll (United Kingdom/United States of America, United Kingdom), Xin Lan (United States of America/China), Charlotte Laufkötter (Switzerland/Germany), Corinne Le Quéré (United Kingdom), Andrew Lenton (Australia), Jared Lewis (Australia/New Zealand), Spencer Liddicoat (United Kingdom), Laura Lorenzoni (United States of America/Venezuela), Nicole Lovenduski (United States of America), Andrew H. MacDougall (Canada), Sabine Mathesius (Canada/Germany), Damon H. Matthews (Canada), Malte Meinshausen (Australia/Germany), Igor I. Mokhov (Russian Federation), Vaishali Naik (United States of America), Zebedee R. J. Nicholls (Australia), Intan Suci Nurhati (Indonesia), Michael O'Sullivan (United Kingdom), Glen Peters (Norway), Julia Pongratz (Germany), Benjamin Poulter (United States of America), Jean-Baptiste Sallée (France), Marielle Saunois (France), Edward A.G. Schuur (United States of America), Sonia I. Seneviratne (Switzerland), Ann Stavert (Australia), Parvadha Suntharalingam (United Kingdom/United States of America), Kaoru Tachiiri (Japan), Jens Terhaar (Switzerland/Germany), Rona Thompson (Norway, Luxembourg/New Zealand), Hanqin Tian (United States of America), Jocelyn Turnbull (New Zealand), Sergio M. Vicente-Serrano (Spain), Xuhui Wang (China), Rik Wanninkhof (United States of America), Phil Williamson (United Kingdom),

Review Editors:
Victor Brovkin (Germany/Russian Federation), Richard A. Feely (United States of America)

Chapter Scientist:
Alice D. Lebehot (South Africa/France)

ACCEPTED VERSION SUBJECT TO FINAL EDITS

This Chapter should be cited as:
Josep G. Canadell, J. G., P. M. S. Monteiro, M. H. Costa, L. Cotrim da Cunha, P. M. Cox, A. V. Eliseev, S. Henson, M. Ishii, S. Jaccard, C. Koven, A. Lohila, P. K. Patra, S. Piao, J. Rogelj, S. Syampungani, S. Zaehle, K. Zickfeld, 2021, Global Carbon and other Biogeochemical Cycles and Feedbacks. In: *Climate Change 2021: The Physical Science Basis. Contribution of Working Group I to the Sixth Assessment Report of the Intergovernmental Panel on Climate Change* [Masson-Delmotte, V., P. Zhai, A. Pirani, S. L. Connors, C. Péan, S. Berger, N. Caud, Y. Chen, L. Goldfarb, M. I. Gomis, M. Huang, K. Leitzell, E. Lonnoy, J.B.R. Matthews, T. K. Maycock, T. Waterfield, O. Yelekçi, R. Yu and B. Zhou (eds.)]. Cambridge University Press. In Press.

Date: August 2021

This document is subject to copy-editing, corrigenda and trickle backs.

ACCEPTED VERSION
SUBJECT TO FINAL EDITS

Table of content

Executive Summary **6**

5.1 Introduction **11**

5.1.1 The Physical and Biogeochemical Processes in Carbon-Climate feedbacks 12

5.1.2 Paleo Trends and Feedbacks 14

5.1.2.1 Cenozoic Proxy CO_2 Record 14

5.1.2.2 Glacial-Interglacial Greenhouse Gases Records 15

5.1.2.3 Holocene Changes 18

5.2 Historical Trends, Variability and Budgets of CO2, CH4, and N2O **19**

5.2.1 CO_2: Trends, Variability and Budget 19

5.2.1.1 Anthropogenic CO_2 Emissions 19

5.2.1.2 Atmosphere 21

5.2.1.3 Ocean Carbon Fluxes and Storage 23

5.2.1.3.1 Ocean Carbon Fluxes and Storage: Global Multi-Decadal Trends 24

5.2.1.3.2 Ocean Carbon Fluxes and Storage: Regional – Global Variability 26

5.2.1.4 Land CO_2 Fluxes: Historical and Contemporary Variability and Trends 27

5.2.1.4.1 Trend in Land-Atmosphere CO2 Exchange 27

5.2.1.4.2 Interannual variability in land-atmosphere CO_2 exchange 29

Cross-Chapter Box 5.1: Interactions between the carbon and water cycles, particularly under drought conditions **30**

5.2.1.5 CO_2 Budget 32

5.2.2 CH_4: Trends, Variability and Budget 34

5.2.2.1 Atmosphere 34

5.2.2.2 Anthropogenic CH_4 emissions 35

5.2.2.3 Land Biospheric Emissions and Sinks 37

5.2.2.4 Ocean and Inland Water Emissions and Sinks 38

5.2.2.5 CH_4 Budget 39

Cross-Chapter Box 5.2: Drivers of atmospheric methane changes during 1980–2019 ..... **39**

5.2.3 N_2O: Trends, Variability and Budget 41

5.2.3.1 Atmosphere 42

5.2.3.2 Anthropogenic N_2O Emissions 43

5.2.3.3 Emissions from Ocean, Inland Water Bodies and Estuaries 44

5.2.3.4 Emissions and Sinks in Non-Agricultural Land 44

ACCEPTED VERSION SUBJECT TO FINAL EDITS

5.2.3.5 N_2O budget 45
5.2.4 The Relative Importance of CO2, CH4, and N2O 47

5.3 Ocean Acidification and Deoxygenation 48
5.3.1 Paleoclimate Context 48
5.3.1.1 Paleocene-Eocene Thermal Maximum 48
5.3.1.2 Last Deglacial Transition 49
5.3.2 Historical Trends and Spatial Characteristics in the Upper Ocean 50
5.3.2.1 Reconstructed Centennial Ocean Acidification Trends 50
5.3.2.2 Observations of Ocean Acidification over the Recent Decades 51
5.3.3 Ocean Interior Change 52
5.3.3.1 Ocean Memory – Acidification in the Ocean Interior 52
5.3.3.2 Ocean Deoxygenation and its Implications for GHGs 53
5.3.4 Future Projections for Ocean Acidification 54
5.3.4.1 Future Projections with Earth System Models 54
5.3.4.2 Reversal of Ocean Acidification by Carbon Dioxide Removal 56
5.3.5 Coastal Ocean Acidification and Deoxygenation 56
5.3.5.1 Drivers 56
5.3.5.2 Spatial Characteristics 57

5.4 Biogeochemical Feedbacks on Climate Change 58
5.4.1 Direct CO_2 Effect on Land Carbon Uptake 59
5.4.2 Direct CO_2 Effects on Projected Ocean Carbon Uptake 60
5.4.3 Climate Effect on Land Carbon Uptake 61
5.4.3.1 Plant Physiology 61
5.4.3.2 Fire and Other Disturbances 61
5.4.3.3 Soil Carbon 62

BOX 5.1: Permafrost Carbon and Feedbacks to Climate 63

5.4.4 Climate Effects on Future Ocean Carbon Uptake 67
5.4.4.1 Physical Drivers of Future Ocean Carbon Uptake and Storage 67
5.4.4.2 Biological Drivers of Future Ocean Carbon Uptake 67
5.4.5 Carbon Cycle Projections in Earth System Models 69
5.2.1.1 Evaluation of the Contemporary Carbon Cycle in Concentration-Driven Runs 70
5.4.5.1 Evaluation of Historical Carbon Cycle Simulations in Concentration-Driven Runs 71
5.4.5.2 Evaluation of Latitudinal Distribution of Simulated Carbon Sinks 71
5.4.5.3 Coupled Climate-Carbon Cycle Projections 72

ACCEPTED VERSION
SUBJECT TO FINAL EDITS

5.4.5.4 Linear Feedback Analysis 73
5.4.6 Emergent constraints to reduce uncertainties in projections 75
5.4.7 Climate Feedbacks from CH4 and N2O 76
5.4.8 Combined Biogeochemical Climate Feedback 77
5.4.9 Abrupt Changes and Tipping Points 78
5.4.9.1 Assessment of biogeochemical tipping points 79
5.4.9.1.1 Forest Dieback 79
5.4.9.1.2 Biogenic Emissions Following Permafrost Thaw 80
5.4.9.1.3 Methane Release from Clathrates 80
5.4.9.2 Abrupt Changes Detected in ESM Projections 81
5.4.10 Long Term Response past 2100 81
5.4.11 Near-Term Prediction of Ocean and Land Carbon Sinks 82

5.5 Remaining Carbon Budgets 83
5.5.1 Transient Climate Response to Cumulative Emissions of carbon dioxide (TCRE) 83
5.5.1.1 Contributing Physical Processes and Theoretical Frameworks 83

Cross-Chapter Box 5.3: The Ocean Carbon-Heat Nexus and Climate Change Commitment 84

5.5.1.2 Assessment of Limits of the TCRE Concept 87
5.5.1.2.1 Sensitivity to amount of cumulative CO_2 emissions 87
5.5.1.2.2 Sensitivity to the Rate of CO_2 Emissions 88
5.5.1.2.3 Reversibility and Earth System Feedbacks 88
5.5.1.3 Estimates of TCRE 89
5.5.1.4 Combined assessment of TCRE 91
5.5.2 Remaining Carbon Budget Assessment 91
5.5.2.1 Framework and Earlier Approaches 91
5.5.2.2 Assessment of Individual Components 93
5.5.2.2.1 TCRE 93
5.5.2.2.2 Historical Warming 93
5.5.2.2.3 Non-CO2 Warming Contribution 94
5.5.2.2.4 Adjustments due to the Zero-Emission Commitment (ZEC) 95
5.5.2.2.5 Adjustments for Other not Represented Feedbacks 95
5.5.2.3 Remaining Carbon Budget 95

BOX 5.2: Implications of methodological advancements in estimating the remaining carbon budget since AR5 97

5.6 Biogeochemical Implications of Carbon Dioxide Removal and Solar Radiation Modification 99

ACCEPTED VERSION SUBJECT TO FINAL EDITS

5.6.1 Introduction 99
5.6.2 Biogeochemical Responses to Carbon Dioxide Removal (CDR) 99
5.6.2.1 Global Carbon Cycle Responses to CDR 102

BOX 5.3: Carbon cycle response to CO_2 removal from the atmosphere 102

5.6.2.1.1 Carbon Cycle Response to Instantaneous CDR 103
5.6.2.1.2 Carbon Cycle Response Over Time in Scenarios with CDR 103
5.6.2.1.3 Removal Effectiveness of CDR 104
5.6.2.1.4 Symmetry of Carbon Cycle Response to Positive and Negative CO_2 Emissions 105
5.6.2.2 Effects of Specific CDR Methods on Biogeochemical Cycles and Climate 106
5.6.2.2.1 Land-based Biological CDR Methods 106
5.6.2.2.2 Ocean-based Biological CDR Methods 109
5.6.2.2.3 Geochemical CDR Methods 109
5.6.2.2.4 Chemical CDR methods 110
5.6.2.2.5 Methane removal 110
5.6.3 Biogeochemical responses to Solar Radiation Modification (SRM) 111
5.6.3.1 Effects of SRM on the Carbon Cycle 111
5.6.3.2 Consequences of SRM and its termination on atmospheric CO2 burden 113
5.6.3.3 Consequences of SRM on other Biogeochemical Cycles 113
5.6.3.4 Synthesis of biogeochemical responses to SRM 113

5.7 Final Remarks 113

Frequently Asked Questions 116
FAQ 5.1: Is the natural removal of carbon from the atmosphere weakening? 116
FAQ 5.2: Can thawing permafrost substantially increase global warming? 118
FAQ 5.3: Could climate change be reversed by removing carbon dioxide from the atmosphere? 120
FAQ 5.4: What are carbon budgets? 122

References 124

Figures 177

ACCEPTED VERSION
SUBJECT TO FINAL EDITS

Executive Summary

It is unequivocal that emissions of the well-mixed greenhouse gases (GHG) carbon dioxide (CO_2), methane (CH_4) and nitrous oxide (N_2O) from human activities are the main driver of increases in atmospheric GHG concentrations since the pre-industrial period. The accumulation of GHGs in the atmosphere is determined by the balance between anthropogenic emissions, anthropogenic removals, and physical-biogeochemical source and sink dynamics on land and in the ocean. This chapter assesses how physical and biogeochemical processes of the carbon and nitrogen cycles affect the variability and trends of GHGs in the atmosphere as well as ocean acidification and deoxygenation. It identifies physical and biogeochemical feedbacks that have affected or could affect future rates of GHG accumulation in the atmosphere, and therefore, influence climate change and its impacts. This chapter also assesses the remaining carbon budget to limit global warming within various goals, as well as the large-scale consequences of carbon dioxide removal (CDR) and solar radiation modification (SRM) on biogeochemical cycles {Figures 5.1, 5.2}.

The Human Perturbation of the Carbon and Biogeochemical cycles

Global mean concentrations for well-mixed GHGs (CO_2, CH_4 and N_2O) in 2019 correspond to increases of about 47%, 156%, and 23%, respectively, above the levels in 1750 (representative of the pre-industrial) (*high confidence*). Current atmospheric concentrations of the three GHGs are higher than at any point in the last 800,000 years, and in 2019 reached 409.9 ppm of CO_2, 1866.3 ppb of CH_4, and 332.1 ppb of N_2O (*very high confidence*). Current CO_2 concentrations in the atmosphere are also unprecedented in the last 2 million years (*high confidence*). In the past 60 Myr, there have been periods in Earth's history when CO_2 concentrations were significantly higher than at present, but multiple lines of evidence show that the rate at which CO_2 has increased in the atmosphere during 1900–2019 is at least 10 times faster than at any other time during the last 800,000 years (*high confidence*), and 4-5 times faster than during the last 56 million years (*low confidence*). {5.1.1, 2.2.3; Figures 5.3, 5.4; Cross-Chapter Box 2.1}

Contemporary Trends of Greenhouse Gases

It is unequivocal that the increase of CO_2, CH_4, and N_2O in the atmosphere over the industrial era is the result of human activities (*very high confidence*). This assessment is based on multiple lines of evidence including atmospheric gradients, isotopes, and inventory data. During the last measured decade, global average annual anthropogenic emissions of CO_2, CH_4, and N_2O, reached the highest levels in human history at 10.9 ± 0.9 PgC yr^{-1} (2010–2019), 335–383 Tg CH_4 yr^{-1} (2008–2017), and 4.2–11.4 TgN yr^{-1} (2007–2016), respectively (*high confidence*). {5.2.1, 5.2.2, 5.2.3, 5.2.4; Figures 5.6, 5.13, 5.15}.

The CO_2 emitted from human activities during the decade of 2010–2019 (decadal average 10.9 ± 0.9 PgC yr^{-1}) was distributed between three Earth system components: 46% accumulated in the atmosphere (5.1 ± 0.02 PgC yr^{-1}), 23% was taken up by the ocean (2.5 ± 0.6 PgC yr^{-1}) and 31% was stored by vegetation in terrestrial ecosystems (3.4 ± 0.9 PgC yr^{-1}) (*high confidence*). Of the total anthropogenic CO_2 emissions, the combustion of fossil fuels was responsible for 81–91%, with the remainder being the net CO_2 flux from land-use change and land management (e.g., deforestation, degradation, regrowth after agricultural abandonment or peat drainage). {5.2.1.2, 5.2.1.5; Table 5.1; Figures 5.5, 5.7, 5.12}

Over the past six decades, the average fraction of anthropogenic CO_2 emissions that has accumulated in the atmosphere (referred to as the airborne fraction) has remained nearly constant at approximately 44%. The ocean and land sinks of CO_2 have continued to grow over the past six decades in response to increasing anthropogenic CO_2 emissions (*high confidence)*. Interannual and decadal variability of the regional and global ocean and land sinks indicate that these sinks are sensitive to climate conditions and therefore to climate change (*high confidence*). {5.2.1.1, 5.2.1.3, 5.2.1.4.2; Figures 5.7, 5.8, 5.10}

Recent observations show that ocean carbon processes are starting to change in response to the growing ocean sink, and these changes are expected to contribute significantly to future weakening of the ocean sink under medium- to high-emission scenarios. However, the effects of these changes is not

ACCEPTED VERSION SUBJECT TO FINAL EDITS

yet reflected in a weakening trend of the contemporary (1960–2019) ocean sink (*high confidence*). {5.1.2, 5.2.1.3, 5.3.2.1; Figures 5.8, 5.20; Cross-Chapter Box 5.3}

Atmospheric concentration of CH_4 grew at an average rate of 7.6 ± 2.7 ppb yr^{-1} for the last decade (2010–2019), with a faster growth of 9.3 ± 2.4 ppb yr^{-1} over the last six years (2014–2019) (*high confidence*). The multi-decadal growth trend in atmospheric CH_4 is dominated by anthropogenic activities (*high confidence*), and the growth since 2007 is largely driven by emissions from both fossil fuels and agriculture (dominated by livestock) sectors (*medium confidence)*. The interannual variability is dominated by El Niño–Southern Oscillation cycles, during which biomass burning and wetland emissions, as well as loss by reaction with tropospheric hydroxyl radical OH play an important role. {5.2.2; Figures 5.13, 5.14; Table 5.2; Cross-Chapter Box 5.2}

Atmospheric concentration of N_2O grew at an average rate of 0.85 ± 0.03 ppb yr^{-1} between 1995 and 2019, with a further increase to 0.95 ± 0.04 ppb yr^{-1} in the most recent decade (2010–2019). This increase is dominated by anthropogenic emissions, which have increased by 30% between the 1980s and the most recent observational decade (2007–2016) (*high confidence*). Increased use of nitrogen fertilizer and manure contributed to about two-thirds of the increase during the 1980–2016 period, with the fossil fuels/industry, biomass burning, and wastewater accounting for much of the rest (*high confidence*). {5.2.3; Figures 5.15, 5.16, 5.17}

Ocean Acidification and Ocean Deoxygenation

Ocean acidification is strengthening as a result of the ocean continuing to take up CO_2 from human-caused emissions (*very high confidence*). This CO_2 uptake is driving changes in seawater chemistry that result in the decrease of pH and associated reductions in the saturation state of calcium carbonate, which is a constituent of skeletons or shells of a variety of marine organisms. These trends of ocean acidification are becoming clearer globally, with a *very likely* rate of decrease in pH in the ocean surface layer of 0.016 to 0.020 per decade in the subtropics and 0.002 to 0.026 per decade in subpolar and polar zones since the 1980s. Ocean acidification has spread deeper in the ocean, surpassing 2000 m depth in the northern North Atlantic and in the Southern Ocean. The greater projected pH declines in CMIP6 models are primarily a consequence of higher atmospheric CO_2 concentrations in the Shared Socio-economic Pathways (SSPs) scenarios than their CMIP5-RCP analogues {5.3.2.2, 5.3.3.1; 5.3.4.1; Figures 5.20, 5.21}

Ocean deoxygenation is projected to continue to increase with ocean warming (*high confidence*). Earth system models (ESMs) project a 32–71% greater subsurface (100–600 m) oxygen decline, depending on scenario, than reported in the Special Report on the Ocean and Cryosphere (SROCC) for the period 2080–2099. This is attributed to the effect of larger surface warming in CMIP6 models, which increases ocean stratification and reduces ventilation (*medium confidence*). There is *low confidence* in the projected reduction of oceanic N_2O emissions under high emission scenarios because of greater oxygen losses simulated in ESMs in CMIP6, uncertainties in the process of oceanic N_2O emissions, and a limited number of modelling studies available {5.3.3.2; 7.5}

Future Projections of Carbon Feedbacks on Climate Change

Oceanic and terrestrial carbon sinks are projected to continue to grow with increasing atmospheric concentrations of CO_2, but the fraction of emissions taken up by land and ocean is expected to decline as the CO_2 concentration increases (*high confidence*). ESMs suggest approximately equal global land and ocean carbon uptake for each of the SSPs scenarios. However, the range of model projections is much larger for the land carbon sink. Despite the wide range of model responses, uncertainty in atmospheric CO_2 by 2100 is dominated by future anthropogenic emissions rather than uncertainties related to carbon–climate feedbacks (*high confidence*). {5.4.5; Figure 5.25, 5.26}

Increases in atmospheric CO_2 lead to increases in land carbon storage through CO_2 fertilization of photosynthesis and increased water use efficiency (*high confidence*). However, the overall change in land carbon also depends on land-use change and on the response of vegetation and soil to continued warming

ACCEPTED VERSION SUBJECT TO FINAL EDITS

and changes in the water cycle, including increased droughts in some regions that will diminish the sink capacity. Climate change alone is expected to increase land carbon accumulation in the high latitudes (not including permafrost), but also to lead to a counteracting loss of land carbon in the tropics (*medium confidence*, Figure 5.25). More than half of the latest CMIP6 ESMs include nutrient limitations on the carbon cycle, but these models still project increasing tropical land carbon (*medium confidence*) and increasing global land carbon (*high confidence*) through the 21st century. {5.4.1, 5.4.3, 5.4.5; Figure 5.27; Cross-Chapter Box 5.1}

Future trajectories of the ocean CO_2 sink are strongly emissions-scenario dependent (*high confidence*). Emission scenarios SSP4-6.0 and SSP5-8.5 lead to warming of the surface ocean and large reductions of the buffering capacity, which will slow the growth of the ocean sink after 2050. Scenario SSP1-2.6 limits further reductions in buffering capacity and warming, and the ocean sink weakens in response to the declining rate of increasing atmospheric CO_2. There is *low confidence* in how changes in the biological pump will influence the magnitude and direction of the ocean carbon feedback. {5.4.2, 5.4.4, Cross-Chapter Box 5.3}

Beyond 2100, land and ocean may transition from being a carbon sink to a source under either very high emissions or net negative emissions scenarios, but for different reasons. Under very high emissions scenarios such as SSP5-8.5, ecosystem carbon losses due to warming lead the land to transition from a carbon sink to a source (*medium confidence*), while the ocean is expected to remain a sink (*high confidence*). For scenarios in which CO_2 concentration stabilizes, land and ocean carbon sinks gradually take up less carbon as the increase in atmospheric CO_2 slows down. In scenarios with moderate net negative CO_2 emissions and CO_2 concentrations declining during the 21st century (e.g., SSP1-2.6), the land sink transitions to a net source in decades to a few centuries after CO_2 emissions become net negative, while the ocean remains a sink (*low confidence*). Under scenarios with large net negative CO_2 emissions and rapidly declining CO_2 concentrations (e.g., SSP5-3.4-OS (overshoot)), both land and ocean switch from a sink to a transient source during the overshoot period (*medium confidence*). {5.4.10, 5.6.2.1.2; Figures 5.30, 5.33}

Thawing terrestrial permafrost will lead to carbon release (*high confidence*), but there is *low confidence* in the timing, magnitude and the relative roles of CO_2 versus CH_4 as feedback processes. CO_2 release from permafrost is projected to be 3–41 PgC per 1ºC of global warming by 2100, based on an ensemble of models. However, the incomplete representation of important processes such as abrupt thaw, combined with weak observational constraints, only allow *low confidence* in both the magnitude of these estimates and in how linearly proportional this feedback is to the amount of global warming. It is *very unlikely* that gas clathrates in terrestrial and subsea permafrost will lead to a detectable departure from the emissions trajectory during this century. {5.4.9; Box 5.1}

The net response of natural CH_4 and N_2O sources to future warming will be increased emissions (*medium confidence*). Key processes include increased CH_4 emissions from wetlands and permafrost thaw, as well as increased soil N_2O emissions in a warmer climate, while ocean N_2O emissions are projected to decline at centennial time scale. The magnitude of the responses of each individual process and how linearly proportional these feedbacks are to the amount of global warming is known with *low confidence* due to incomplete representation of important processes in models combined with weak observational constraints. Models project that over the 21st century the combined feedback of 0.02–0.09 W m^{-2} $°C^{-1}$ is comparable to the effect of a CO_2 release of 5-18 PgCeq $°C^{-1}$ (*low confidence*). {5.4.7, 5.4.8; Figure 5.29}

The response of biogeochemical cycles to the anthropogenic perturbation can be abrupt at regional scales, and irreversible on decadal to century time scales (*high confidence*). The probability of crossing uncertain regional thresholds (e.g., high severity fires, forest dieback) increases with climate change (*high confidence*). Possible abrupt changes and tipping points in biogeochemical cycles lead to additional uncertainty in 21st century GHG concentrations, but these are *very likely* to be smaller than the uncertainty associated with future anthropogenic emissions (*high confidence*). {5.4.9}

Remaining Carbon Budgets to Climate Stabilization

There is a near-linear relationship between cumulative CO_2 emissions and the increase in global mean

ACCEPTED VERSION SUBJECT TO FINAL EDITS

surface air temperature (GSAT) caused by CO_2 over the course of this century for global warming levels up to at least 2°C relative to pre-industrial (*high confidence*). Halting global warming would thus require global net anthropogenic CO_2 emissions to become zero. The ratio between cumulative CO_2 emissions and the consequent GSAT increase, which is called the transient climate response to cumulative emissions of CO_2 (TCRE), *likely* falls in the 1.0°C–2.3°C per 1000 PgC range. The narrowing of this range compared to AR5 is due to a better integration of evidence across the science in this assessment. Beyond this century, there is *low confidence* that the TCRE remains an accurate predictor of temperature changes in scenarios of very low or net negative CO_2 emissions because of uncertain Earth system feedbacks that can result in further warming or a path-dependency of warming as a function of cumulative CO_2 emissions. {5.4, 5.5.1}

Mitigation requirements over this century for limiting maximum warming to specific levels can be quantified using a carbon budget that relates cumulative CO_2 emissions to global mean temperature increase (*high confidence*). For the period 1850–2019, a total of 655 ± 65 PgC (2390 ± 240 $GtCO_2$) of anthropogenic CO_2 has been emitted. Remaining carbon budgets (starting from 1 January 2020) for limiting warming to 1.5°C, 1.7°C, and 2.0°C are 140 PgC (500 $GtCO_2$), 230 PgC (850 $GtCO_2$) and 370 PgC (1350 $GtCO_2$), respectively, based on the 50th percentile of TCRE. For the 67th percentile, the respective values are 110 PgC (400 $GtCO_2$), 190 PgC (700 $GtCO_2$) and 310 PgC (1150 $GtCO_2$). These remaining carbon budgets may vary by an estimated ± 60 PgC (220 $GtCO_2$) depending on how successfully future non-CO_2 emissions can be reduced. Since AR5 and SR1.5, estimates have undergone methodological improvements, resulting in larger, yet consistent estimates. {5.5.2, 5.6; Figure 5.31; Table 5.8}

Several factors affect the precise value of remaining carbon budgets, including estimates of historical warming, future emissions from thawing permafrost, and variations in projected non-CO_2 warming. Remaining carbon budget estimates can increase or decrease by 150 PgC (550 $GtCO_2$, *likely* range) due to uncertainties in the level of historical warming, and by an additional ± 60 PgC (±220 GtCO, *likely* range) due to geophysical uncertainties surrounding the climate response to non-CO_2 emissions such as CH_4, N_2O, and aerosols. Permafrost thaw is included in the estimates together with other feedbacks that are often not captured by models. Despite the large uncertainties surrounding the quantification of the effects of additional Earth system feedback processes, such as emissions from wetlands and permafrost thaw, these feedbacks represent identified additional amplifying risk factors that scale with additional warming and mostly increase the challenge of limiting warming to specific temperature thresholds. These uncertainties do not change the basic conclusion that global CO_2 emissions would need to decline to at least net zero to halt global warming. {5.4, 5.5.2}

Biogeochemical Implications of Carbon Dioxide Removal and Solar Radiation Modification

Land- and ocean-based carbon dioxide removal (CDR) methods have the potential to sequester CO_2 from the atmosphere, but the benefits of this removal would be partially offset by CO_2 release from land and ocean carbon stores (*very high confidence*). The fraction of CO_2 removed that remains out of the atmosphere, a measure of CDR effectiveness, decreases slightly with increasing amount of removal (*medium confidence*) and decreases strongly if CDR is applied at lower CO_2 concentrations (*medium confidence*). {5.6.2.1; Figures 5.32, 5.33, 5.34}

The century-scale climate–carbon cycle response to a CO_2 removal from the atmosphere is not always equal and opposite to the response to a CO_2 emission (*medium confidence*). For simultaneously cumulative CO_2 emissions and removals of greater than or equal to 100 PgC, CO_2 emissions are 4 ± 3% more effective at raising atmospheric CO_2 than CO_2 removals are at lowering atmospheric CO_2. The asymmetry originates from state-dependencies and non-linearities in carbon cycle processes and implies that an extra amount of CDR is required to compensate for a positive emission of a given magnitude to attain the same change in atmospheric CO_2. The net effect of this asymmetry on the global surface temperature is poorly constrained due to *low agreement* between models (*low confidence*). {5.6.2.1; Figure 5.35}

Wide-ranging side-effects of CDR methods have been identified that can either weaken or strengthen the carbon sequestration and cooling potential of these methods and affect the achievement of

ACCEPTED VERSION SUBJECT TO FINAL EDITS

sustainable development goals (*high confidence*). Biophysical and biogeochemical side-effects of CDR methods are associated with changes in surface albedo, the water cycle, emissions of CH_4 and N_2O, ocean acidification and marine ecosystem productivity (*high confidence*). These side-effects and associated Earth system feedbacks can decrease carbon uptake and/or change local and regional climate, and in turn limit the CO_2 sequestration and cooling potential of specific CDR methods (*medium confidence*). Deployment of CDR, particularly on land, can also affect water quality and quantity, food production and biodiversity, with consequences for the achievement of related sustainable development goals (*high confidence*). These effects are often highly dependent on local context, management regime, prior land use, and scale of deployment (*high confidence*). A wide range of co-benefits are obtained with methods that seek to restore natural ecosystems or improve soil carbon (*high confidence*). The biogeochemical effects of terminating CDR are expected to be small for most CDR methods (*medium confidence*). {5.6.2.2; Figure 5.36; Cross-Chapter Box 5.1}

Solar radiation modification (SRM) would increase the global land and ocean CO_2 sinks (*medium confidence*) but would not stop CO_2 from increasing in the atmosphere, thus exacerbating ocean acidification under continued anthropogenic emissions (*high confidence*). SRM acts to cool the planet relative to unmitigated climate change, which would increase the land sink by reducing plant and soil respiration and slow the reduction of ocean carbon uptake due to warming (*medium confidence*). SRM would not counteract or stop ocean acidification (*high confidence*). The sudden and sustained termination of SRM would rapidly increase global warming, with the return of positive and negative effects on the carbon sinks (*very high confidence*) {4.6.3; 5.6.3}

ACCEPTED VERSION
SUBJECT TO FINAL EDITS

5.1 Introduction

The physical and biogeochemical controls of greenhouse gases (GHGs) is a central motivation for this chapter, which identifies biogeochemical feedbacks that have led or could lead to a future acceleration, slowdown or abrupt transitions in the rate of GHG accumulation in the atmosphere, and therefore of climate change. A characterisation of the trends and feedbacks lead to improved quantification for the remaining carbon budgets for climate stabilisation, and the responses of the carbon cycle to atmospheric CO_2 removal, which is embedded in many of the mitigation scenarios, to achieve the goals of the Paris Agreement.

Changes in the abundance of well-mixed GHGs (carbon dioxide (CO_2), methane (CH_4) and nitrous oxide (N_2O)) in the atmosphere play a large role in determining the Earth's radiative properties and its climate in the past, the present and the future (Chapters 2, 4, 6 and 7). Since 1950, the increase in atmospheric GHGs has been the dominant cause of the human-induced climate change (Section 3.3). While the main driver of changes in atmospheric GHGs over the past 200 years relate to the direct emissions from human activities, the net accumulation of GHGs in the atmosphere is controlled by biogeochemical source-sink dynamics of carbon that exchange between multiple reservoirs on land, oceans and atmosphere. The combustion of fossil fuels and land use change for the period 1750–2019 have released an estimated 700 ± 75 PgC (1 PgC = 10^{15} g of carbon) to the atmosphere of which less than half remains in the atmosphere today (Sections 5.2.1.2; 5.2.1.5) (Friedlingstein et al., 2020). This underscores the central role of terrestrial and ocean CO_2 sinks in regulating its atmospheric concentration (Ballantyne et al., 2012; Li et al., 2016c; Le Quéré et al., 2018a; Ciais et al., 2019; Gruber et al., 2019a; Friedlingstein et al., 2020).

The chapter covers three dominant GHGs in the human perturbation of the Earth's radiation budget for which high quality records exist: carbon dioxide (CO_2), methane (CH_4) and nitrous oxide (N_2O) (Figure 5.1).

Section 5.1 (this section) provides the time context on how unique current and future scenarios of GHGs atmospheric concentrations and growth rates are in the Earth's history. It also introduces the main processes involved in carbon-climate feedbacks followed by an assessment of what can be learned from the paleo record towards a better understanding of contemporary and future GHGs-climate dynamics and their response to different mitigation trajectories.

Section 5.2 covers the state of the carbon cycle and other biogeochemical cycles, and global budgets of CO_2, CH_4 and N_2O for the industrial era (since 1750). The section emphasises the last 60-year period for which high-resolution observations are available and the most recent decade for comprehensive GHGs budgets. Significant advances have taken place since the IPCC fifth assessment report (AR5), particularly in constraining the annual to decadal variability of the ocean and land carbon sources and sinks, and in revealing about the sensitivity of carbon pools to current and future climate changes. There has been an important increase in modelling capability of the three GHGs both for land and oceans, atmospheric and ocean observations, and remote sensing products that has enabled to constrain the causes of the observed trends and variability.

Section 5.3 builds on SROCC covering the change in ocean acidification due to oceanic CO_2 uptake across the paleo, historical periods and future projections using CMIP6, with consequences for marine life (assessed in sixth assessment report (AR6) working group II (WGII)) and biogeochemical cycles. The section also assesses changes in deoxygenation of the oceans due to warming, increased stratification of the surface ocean and slowing of the meridional overturning circulation.

Section 5.4 covers the future projections of biogeochemical cycles and their feedbacks to the climate system fully utilising the database of the concentration-driven coupled model intercomparison project phase 6 (CMIP6). Since AR5, Earth system models (ESMs) have made progress towards including more complex carbon cycle and associated biogeochemical processes that enable exploring a range of possible future carbon-climate feedbacks and their influences on the climate system. The section addresses uncertainties and limits of our models to predict future dynamics for GHG emissions trajectories, as well as new understanding on processes involved in carbon-climate feedbacks and the possibility for rapid and abrupt

ACCEPTED VERSION SUBJECT TO FINAL EDITS

changes brought by non-linear dynamics.

Section 5.5 covers the development of the total and remaining carbon budgets to climate stabilisation targets and the associated transient climate response to cumulative CO_2 emissions. The section shows the progress made since the AR5 (IPCC, 2013a) and the 1.5°C Special Report (IPCC, 2018a), particularly on key components required to estimate the remaining carbon budget, including the transient response to cumulative emissions of CO_2, the zero emission commitment, the projected non-CO_2 warming, and the unrepresented Earth system feedbacks.

Section 5.6 assesses the impacts of carbon dioxide removal and solar radiation modification for the purpose of climate mitigation on the global carbon cycle building from the assessment in the IPCC Special Report on Climate Change and Land (SRCCL). It includes an overview of the major carbon dioxide removal options and potential collateral biogeochemical effects beyond those intended climate mitigation strategies. The potential capacity to deliver atmospheric reductions and the socio-economic feasibility of such options are assessed in detail in AR6 working group III (WGIII).

Finally, Section 5.7 highlights the knowledge gaps as limits to the assessment, which would have strengthened this assessment had those gaps not existed.

[START FIGURE 5.1 HERE]

Figure 5.1: Visual abstract for Chapter 5.

[END FIGURE 5.1 HERE]

5.1.1 The Physical and Biogeochemical Processes in Carbon-Climate feedbacks

The influence of anthropogenic CO_2 emissions and emission scenarios on the carbon – climate system is primarily driving the ocean and terrestrial sinks as major negative feedbacks (β) that determine the atmospheric CO_2 levels, that then drive climate feedbacks through radiative forcing (γ) (Figure 5.2) (Friedlingstein et al., 2006; Jones et al., 2013b; Jones and Friedlingstein, 2020). Biogeochemical feedbacks follow as an outcome of both carbon and climate forcing on the physics and the biogeochemical processes of the ocean and terrestrial carbon cycles (Figure 5.2) (Katavouta et al., 2018; Williams et al., 2019; Jones and Friedlingstein, 2020). Together, these carbon-climate feedbacks can amplify or suppress climate change by altering the rate at which CO_2 builds up in the atmosphere through changes in the land and ocean sources and sinks (Figure 5.2) (Jones et al., 2013b; Raupach et al., 2014; Williams et al., 2019). These changes depend on the, often non-linear, interaction of the drivers (CO_2 and climate) and processes in the ocean and land as well as the emission scenarios (Figure 5.2; Sections 5.4 and 5.6) (Raupach et al., 2014; Schwinger et al., 2014; Williams et al., 2019). There is *high confidence* that carbon-climate feedbacks and their century scale evolution play a critical role in two linked climate metrics that have significant climate and policy implications: (i) the fraction of anthropogenic CO_2 emissions that remains in the atmosphere, the so-called airborne fraction of CO_2 (AF) (Figure 5.2, Section 5.2.1.2, Figure 5.7, FAQ 5.1), and (ii) the quasi-linear trend characteristic of the transient temperature response to cumulative CO_2 emissions (TCRE) (MacDougall, 2016; Williams et al., 2016; Jones and Friedlingstein, 2020; Section 5.5) and other GHGs (CH_4 and N_2O). This chapter assesses the implications of these issues from a carbon cycle processes perspective (Figure 5.2) in Sections 5.2 (historical and contemporary), 5.3 (changing carbonate chemistry), 5.4 (future projections), 5.5 (remaining carbon budget) and 5.6 (response to carbon dioxide removal and solar radiation modification).

The airborne fraction is an important constraint for adjustments in carbon-climate feedbacks and reflects the partitioning of CO_2 emissions between reservoirs by the negative feedbacks, which for the decade 2010–2019 were 31% on land and 23% in the ocean and also dominated the historical period (Figure 5.2; Table 5.1) (Friedlingstein et al., 2020). During the period 1959–2019, the airborne fraction has largely followed the

ACCEPTED VERSION SUBJECT TO FINAL EDITS

growth in anthropogenic CO_2 emissions with a mean of 44% and a large interannual variability (Ballantyne et al., 2012; Ciais et al., 2019; Friedlingstein et al., 2020) (Section 5.2.1.2; Table 5.1). The negative feedback to CO_2 concentrations is associated with its impact on the air-sea and air-land CO_2 exchange through strengthening of partial pressure of CO_2 (pCO_2) gradients as well as the internal processes that enhance uptake. Two of these key processes are the buffering capacity of the ocean and the CO_2 fertilisation effect on gross primary production (Section 5.4.1–5.4.4).

Positive and negative climate and carbon feedbacks involve, (i) fast processes on land and oceans at time scales from minutes to years such as photosynthesis, soil respiration, net primary production, shallow ocean physics and air-sea fluxes, and (ii) slower processes taking decades to millennia such as changing ocean buffering capacity, ocean ventilation, vegetation dynamics, permafrost changes, peat formation and decomposition (Figure 5.2) (Ciais et al., 2013; Forzieri et al., 2017; Williams et al., 2019). Depending on the particular combination of driver process and response dynamics, they behave as positive or negative feedbacks that amplify or dampen the magnitude and rates of climate change, respectively (Cox et al., 2000; Friedlingstein et al., 2003, 2006; Hauck and Völker, 2015; Williams et al., 2019); red and turquoise arrows in Figure 5.2; Section 5.2.1.5; Table 5.1).

Carbon cycle feedbacks co-exist with climate (heat and moisture) feedbacks (Cross-Chapter Boxes 5.1 and 5.3), which together drive contemporary (Section 5.2) and future (Section 5.4) carbon-climate feedbacks (Williams et al., 2019). The excess heat generated by radiative forcing from increasing concentration of atmospheric CO_2 and other GHGs is mostly taken up by the ocean (> 90%) and the residual balance partitioned between atmospheric, terrestrial and ice melting (Cross-Chapter Box 9.2; Frölicher et al., 2015). The combined effect of these two large scale negative feedbacks of CO_2 and heat are reflected in the TCRE (Section 5.5; Cross-Chapter Box 5.3), which points to a quasi-linear and quasi-emission-path independent relationship between cumulative emissions of CO_2 and global warming, which is used as the basis to estimate the remaining carbon budget (Section 5.5) (MacDougall and Friedlingstein, 2015; MacDougall, 2017; Bronselaer and Zanna, 2020; Jones and Friedlingstein, 2020). There is still *low confidence* on the relative roles and importance of the ocean and terrestrial carbon processes on TCRE variability and uncertainty on centennial time scales (MacDougall, 2016; MacDougall et al., 2017; Williams et al., 2017a; Katavouta et al., 2018, 2019; Jones and Friedlingstein, 2020) (Sections 5.5.1.1, 5.5.1.2).

[START FIGURE 5.2 HERE]

Figure 5.2: Key compartments, processes and pathways that govern historical and future CO_2 concentrations and carbon–climate feedbacks through the coupled earth system. The anthropogenic CO_2 emissions, including land use change, are partitioned via negative feedbacks (turquoise dotted arrows) between the ocean (23%), the land (31%) and the airborne fraction (46%) of anthropogenic CO_2 that sets the changing CO_2 concentration in the atmosphere (2010–2019, Table 5.1). This regulates most of the radiative forcing that creates the heat imbalance that drives the climate feedbacks to the ocean (blue) and land (green). Positive feedbacks (red arrows) result from processes in the ocean and on land (red text). Positive feedbacks are influenced by both carbon-concentration and carbon-climate feedbacks simultaneously. Additional biosphere processes have been included but these have an as yet uncertain feedback impact (blue-dotted arrows). CO_2 removal from the atmosphere into the ocean, land and geological reservoirs, necessary for negative emissions, has been included (grey arrows). Although this schematic is built around CO_2, the dominant GHG, some of the same processes also influence the fluxes of CH_4 and N_2O and the strength of the positive feedbacks from the terrestrial and ocean systems.

[END FIGURE 5.2 HERE]

The combined effects of climate and CO_2 concentration feedbacks on the global carbon cycle are projected by ESMs to modify both the processes and natural reservoirs of carbon on a regional and global scale that may result in positive feedbacks (red arrows in Figure 5.2), which could weaken the major terrestrial and ocean sinks and disrupt both the airborne fraction and TCRE under medium to high emission scenarios (Figure 5.25; Section 5.4.5).

ACCEPTED VERSION SUBJECT TO FINAL EDITS

5.1.2 Paleo Trends and Feedbacks

Paleoclimatic proxy records extend beyond the variability of recent decadal climate oscillations and thus provide an independent perspective on feedbacks between climate and carbon cycle dynamics. These past changes according to reconstructions were slower than the current anthropogenic ones, so they cannot provide an unequivocal comparison. Nonetheless, they can help appraise sensitivities and point toward potentially dominant mechanisms of change (Tierney et al., 2020) on (sub)centennial to (multi)millennial timescales.

AR5 (WGI, Chapter 5) concluded with *medium confidence* that atmospheric CO_2 concentrations reached 350–450 ppm during the mid-Pliocene (3.3–3.0 Ma), and possibly 1000 ppm during the Early Eocene (52–48 Ma). AR5 (WGI, Chapter 5) also concluded with *very high confidence* that the current rates of CO_2, CH_4 and N_2O rise in atmospheric concentrations were unprecedented with respect to the ice core record covering the last deglacial transition (LDT, 18–11 ka) and with *medium confidence* that the rate of change of the reconstructed GHG rise was also unprecedented compared to the lower resolution of the records of the past 800 kyr.

5.1.2.1 Cenozoic Proxy CO_2 Record

Quantifying past changes in the rate of CO_2 accumulation in the atmosphere based on reconstructions using marine sediment proxies is complex as age model uncertainties, assumptions and shortcomings underlying proxy applications and sedimentary processes conspire to alter and confound rate estimates (Ajayi et al., 2020). Indeed, differential sediment mixing and bioturbation contribute to smooth and attenuate proxy records (Hupp and Kelly, 2020), thereby tending to underestimate maximum rates of change (Kemp et al., 2015). Considering the extent to which uncertainties can affect sediment-based rate estimates and notwithstanding recent effort in minimizing their inherent contribution, there is generally *low to medium confidence* in quantifying rates of change on timescale less than a decade back thousands of years, and less than a millennium back millions of years in the past based on marine sediments.

In the past, atmospheric CO_2 concentrations reached much higher levels than present day (see Cross-Chapter Box 2.1; Figure 5.3). In particular, the Paleocene-Eocene thermal maximum (PETM), 55.9–55.7 Ma (Figure 5.3), provides some level of comparison with the current and projected anthropogenic increase in CO_2 emissions (Chapter 2). Atmospheric CO_2 concentrations increased from about 900 to around 2000 ppm in 3–20 kyr as a result of geological carbon release to the ocean-atmosphere system (Zeebe et al., 2016; Gutjahr et al., 2017; Cui and Schubert, 2018; Kirtland Turner, 2018). There is *low to medium confidence* in evaluations of the total amount of carbon released during the PETM, as proxy data constrained estimates vary from around 3000 to more than 7000 PgC, with methane hydrates, volcanic emissions, terrestrial and/or marine organic carbon, or some combination thereof, as the probable sources of carbon (Zeebe et al., 2009; Cui et al., 2011; Gutjahr et al., 2017; Luo et al., 2016; Jones et al., 2019; Elling et al., 2020; Haynes & Hönisch, 2020). Methane emissions related to hydrate/permafrost thawing and fossil carbon oxidation may have acted as positive feedbacks (Lunt et al., 2011; Armstrong McKay and Lenton, 2018; Lyons et al., 2019), as the inferred increase in atmospheric CO_2 can only account for approximately half of the reported warming (Zeebe et al., 2009). The estimated, time-integrated carbon input is broadly similar to the RCP8.5 extension scenario, although CO_2 emission rates (0.3–1.5 Pg yr^{-1}) and by inference the rate of CO_2 accumulation in the atmosphere (4–42 ppm per century) during the PETM were at least 4–5 lower than during the modern era (from 1995 to 2014, Table 2.1) (Zeebe et al., 2016; Gingerich, 2019).

[START FIGURE 5.3 HERE]

Figure 5.3: Atmospheric CO_2 concentrations and growth rates for the past 60 million years and projections to 2100. (a) CO_2 concentrations. Concentrations data for the period 60 Myr to the time prior to 800 Kyr (left

ACCEPTED VERSION SUBJECT TO FINAL EDITS

column) are shown as the LOESS Fit and 68% range (data from Chapter 2) (Foster et al., 2017). Concentrations from 1750 and projections through 2100 are taken from Shared Socioeconomic Pathways of IPCC AR6 (Meinshausen et al., 2017). (b) Growth rates are shown as the time derivative of the concentration time series. Inserts in (b) show growth rates at the scale of the sampling resolution. Further details on data sources and processing are available in the chapter data table (Table 5.SM.6).

[END FIGURE 5.1 HERE]

The last 50 Myr have been characterised by a gradual decline in atmospheric CO_2 levels at a rate of ~16 ppm Myr^{-1} (Foster et al., 2017; Gutjahr et al., 2017) (Figure 5.3). The exact cause of this long-term change in CO_2 remains uncertain, but may be related to an imbalance between long-term sources of CO_2 (volcanic outgassing) and long-term sinks (organic carbon burial and silicate weathering).

The most recent time interval when atmospheric CO_2 concentration was as high as 1000 ppm (i.e. similar to the end-of 21st century projection for the high-end emission scenario RCP8.5) was around 33.5 Ma, prior to the Eocene-Oligocene transition (Zhang et al., 2013; Anagnostou et al., 2016). Atmospheric CO_2 levels then reached a critical threshold (1000–750 ppm, (DeConto et al., 2008)) to allow for the development of permanent regional ice-sheets on Antarctica, associated with changes in Southern Ocean hydrography, which would have increased deep ocean CO_2 storage (Leutert et al., 2020).

The most recent interval characterised by atmospheric CO_2 levels similar to modern (i.e. 360–420 ppm) was the Mid-Pliocene warm period (MPWP; 3.3–3.0 Myr, (Martínez-Botí et al., 2015a; de la Vega et al., 2020)) (Chapter 2). The relatively high atmospheric CO_2 concentration during the MPWP are related to vigorous ocean circulation and a rather inefficient marine biological carbon pump (Burls et al., 2017), which would have reduced deep ocean carbon storage. After the MPWP, atmospheric CO_2 concentrations declined gradually at a rate of 30 ppm Myr^{-1} (de la Vega et al., 2020) (Figure 5.3), as an increase in ocean stratification led to enhanced ocean carbon storage, allowing for major, sustained advances in northern hemisphere ice sheets, 2.7 Ma (Sigman et al., 2004; DeConto et al., 2008).

5.1.2.2 Glacial-Interglacial Greenhouse Gases Records

The Antarctic ice core record covering the past 800 kyr provides an important archive to explore the carbon-climate feedbacks prior to anthropogenic perturbations (Brovkin et al., 2016). Polar ice cores represent the only climatic archive from which past GHG concentrations can be directly measured. Major GHGs, CH_4, N_2O and CO_2 generally co-vary on orbital timescales (Loulergue et al., 2008; Lüthi et al., 2008; Schilt et al., 2010) (Chapter 2), with consistently higher atmospheric concentrations during warm intervals of the past, pointing to a strong sensitivity to climate (Figure 5.4). Modelling work suggests that the carbon cycle contributed to globalise and amplify changes in orbital forcing, which are pacing glacial-interglacial climate oscillations (Ganopolski and Brovkin, 2017), with ocean biogeochemistry and physics, terrestrial vegetation, peatland, permafrost and exchanges with the lithosphere including chemical weathering, volcanic activity, sediment burial and marine calcium carbonate compensation all playing a role in modulating the concentration of atmospheric GHGs.

Since AR5, the number of ice core records and the temporal resolution of their data for the last 800 kyr have improved, in particular for the last 60 kyr. Additionally, the advent of isotopic measurements on GHGs extracted from air trapped in ice, allows for more robust source apportionments and inventory assessments. The ensuing discussion will thus mainly focus on these two specific aspects.

Major pre-industrial sources of CH_4 comprise wetlands (including subglacial environments) and biomass burning (Bock et al., 2010, 2017; Lamarche-Gagnon et al., 2019; Kleinen et al., 2020). Pre-industrial atmospheric N_2O concentrations were regulated by microbial production in marine and terrestrial environments and by photochemical removal in the stratosphere (Schilt et al., 2014; Battaglia and Joos, 2018; Fischer et al., 2019). Pre-industrial atmospheric CO_2 concentrations were largely regulated by

ACCEPTED VERSION SUBJECT TO FINAL EDITS

exchange with exogenic terrestrial and ocean carbon reservoirs. The imbalance between geological sources and sinks in the ocean-atmosphere-land biosphere system additionally plays an important role in modulating the air-sea partitioning of the active carbon inventory on multi-millennial timescales (Cartapanis et al., 2018).

[START FIGURE 5.4 HERE]

Figure 5.4: Atmospheric concentrations of CO_2, CH_4 and N_2O in air bubbles and clathrate crystals in ice cores (800,000 BCE to 1990 CE). Note the variable x-axis range and tick mark intervals for the 3 columns. Ice core data is over-plotted by atmospheric observations from 1958 to present for CO_2, from 1984 for CH_4 and from 1994 for N_2O. The time-integrated, millennial-scale linear growth rates for different time periods (800,000–0 BCE, 0–1900 CE and 1900–2017 CE) are given in each panel. For the BCE period, mean rise and fall rates are calculated for the individual slopes between the peaks (interglacials) and troughs (glacial periods), which are given in the panels in left column. The data for BCE period are used from the Vostok, EPICA, Dome C and WAIS ice cores (Petit et al., 1999; Monnin, 2001; Pépin et al., 2001; Raynaud et al., 2005; Siegenthaler et al., 2005; Loulergue et al., 2008; Lüthi et al., 2008; Schilt et al., 2010a). The data after 0–yr CE are taken mainly from Law Dome ice core analysis (MacFarling Meure et al., 2006). The surface observations for all species are taken from NOAA cooperative research network (Dlugokencky and Tans, 2019), where ALT, MLO and SPO stand for Alert (Canada), Mauna Loa Observatory, and South Pole Observatory, respectively. BCE = before current era, CE = current era. Further details on data sources and processing are available in the chapter data table (Table 5.SM.6).

[END FIGURE 5.4 HERE]

Model-based estimates indicate that wetland CH_4 emissions were reduced by 24–40% during the Last Glacial Maximum (LGM) when compared to pre-industrial, while CH_4 emissions related to biomass burning (wildfires) decreased by 35–75% (Valdes, et al., 2005; Hopcroft et al., 2017; Kleinen et al., 2020). N_2O emissions decreased by about 30% during the LGM based on data-constrained model estimates (Schilt et al., 2014; Fischer et al., 2019b) owing to a combination of a weaker hydrological cycle and a generally better ventilated intermediate depth ocean relative to present, reducing (de)nitrification processes (Galbraith and Kienast, 2013; Fischer et al., 2019b).

During past ice ages, generally colder and drier climate conditions contributed to a substantial decline of the land biosphere carbon inventory, in particular in boreal peatlands (–300 PgC) (Treat et al., 2019). Estimates assessing the glacial decrease in the global terrestrial biosphere C stock vary between –300 and –600 PgC (Ciais et al., 2012; Peterson et al., 2014; Menviel et al., 2017; Kleinen et al., 2020), possibly –850 PgC when accounting for ocean-sediment interactions and burial (Jeltsch-Thömmes et al., 2019), a considerable contraction when compared to the modern land biosphere stock. The large range of estimates reflects a yet limited understanding on how glacially perturbed nutrient fluxes and soil dynamics, as well as largely exposed shelf areas in the tropics as a result of lowered sea-level, altered carbon cycle dynamics. Recent estimates suggest deep-sea CO_2 storage during the last ice age exceeded modern values by as much as 750 – 950 PgC (Skinner et al., 2015; Buchanan et al., 2016; Skinner et al., 2017; Anderson et al., 2019; Gottschalk et al., 2020). A combination of increased CO_2 solubility associated with 2–3°C lower mean oceanic temperatures (Bereiter et al., 2018), increased oceanic residence time of CO_2 (Skinner et al., 2017), altered oceanic alkalinity (Yu et al., 2010a; Cartapanis et al., 2018), and a generally more efficient marine biological carbon pump (BCP) (Galbraith and Jaccard, 2015; Yu et al., 2019; Galbraith and Skinner, 2020) enhanced the partition CO_2 into the ocean interior, although the relative contribution of each mechanism remains a matter of debate. Recent observationally constrained Earth system model results highlight that air-sea disequilibrium amplifies the effect of cooling and iron fertilisation on glacial carbon storage (Khatiwala et al., 2019).

Ice core observations combined with model-based estimates thus reveal with *high confidence* that both terrestrial and marine CH_4 and N_2O emissions were reduced under glacial climate conditions. Multiple lines of evidence indicate with *high confidence* that enhanced storage of remineralised CO_2 in the ocean interior,

ACCEPTED VERSION SUBJECT TO FINAL EDITS

owing to a combination of synergistic mechanisms, was sufficient to balance the removal of carbon from the atmosphere and the terrestrial biosphere reservoirs combined during the last ice age.

Vegetation regrowth and increased precipitation in wetland regions associated with the mid-deglacial Northern Hemisphere warming (referred to as the Bølling/Allerød (B/A) warm interval, 14.7–12.7 ka), in particular in the (sub)tropics, accounts for large increases in both CH_4 and N_2O emissions to the atmosphere (Schilt et al., 2014; Baumgartner et al., 2014; Bock et al., 2017; Fischer et al., 2019). Specifically, changes in CH_4 sources were steered by variations in vegetation productivity, source size area, temperatures and precipitation as modulated by insolation, local sea-level changes and monsoon intensity (Bock et al., 2017; Kleinen et al., 2020). Changes in the CH_4 atmospheric sink term probably only played a secondary role in modulating atmospheric CH_4 inventories across the LDT (Hopcroft et al., 2017; Kleinen et al., 2020) Geological emissions, related to the destabilisation of fossil (radiocarbon-dead) CH_4 sources buried in continental margins as a result of sudden warming appear small (Bock et al., 2017; Petrenko et al., 2017; Dyonisius et al., 2020). Stable isotope analysis on N_2O extracted from Antarctic and Greenland ice reveal that marine and terrestrial emissions increased by 0.7 ± 0.3 and 1.7 ± 0.3 TgN, respectively, across the LDT (Fischer et al., 2019b). During abrupt Northern Hemisphere warmings, terrestrial emissions responded rapidly to the northward displacement of the Intertropical Convergence Zone (ITCZ) associated with the resumption of the Atlantic meridional overturning circulation (AMOC) (Fischer et al., 2019b). About 90% of these step increases occurred rapidly, possibly in less than 200 years (Fischer et al., 2019b). In contrast, marine emissions increased more gradually, modulated by global ocean circulation reorganisation.

The gradual increase in atmospheric CO_2 across the LDT was punctuated by three centennial 10–13 ppm increments, coeval with 100–200 ppb increases in CH_4 (Marcott et al., 2014), reminiscent of similar oscillations reported for the last ice age associated with transient warming events (Dansgaard/Oeschger (DO) events) (Ahn and Brook, 2014; Rhodes et al., 2017; Bauska et al., 2018) as well as previous deglacial transitions (Nehrbass-Ahles et al., 2020). The rate of change in atmospheric CO_2 accumulation during these transient events exceed the averaged deglacial growth rates by at least 50% (Table 2.1, Figure 5.4). The early deglacial release of remineralised carbon from the ocean abyss coincided with the resumption of Southern Ocean overturning circulation (Skinner et al., 2010; Schmitt et al., 2012; Ferrari et al., 2014; Gottschalk et al., 2016, 2020; Jaccard et al., 2016; Rae et al., 2018; Moy et al., 2019) and the concomitant reduction in the global efficiency of the marine BCP, associated, in part, with dwindling iron fertilisation (Hain et al., 2010; Martinez-Garcia et al., 2014; Jaccard et al., 2016) The two subsequent pulses, centred 14.8 and 12.9 ka, are associated with enhanced air-sea gas exchange in the Southern Ocean (Li et al., 2020a), iron fertilisation in the South Atlantic and North Pacific (Lambert et al., 2021) and rapid increase in soil respiration owing to the resumption of AMOC and associated southward migration of the ITCZ (Bauska et al., 2016; Marcott et al., 2014). Indeed, rapid warming of high northern latitudes contributed to thaw permafrost, possibly liberating labile organic carbon to the atmosphere (Köhler et al., 2014; Crichton et al., 2016; Winterfeld et al., 2018; Meyer et al., 2019). Ocean surface pH reconstructions indicate that the ocean was oversaturated with respect to the atmosphere during the early, mid-LDT (Martínez-Botí et al., 2015b; Shao et al., 2019; Shuttleworth et al., 2021), suggesting that ocean sources may have been larger than terrestrial sources then. Over the course of the LDT, the decrease in northern hemisphere permafrost carbon stocks has been more than compensated by an increase in the carbon stocks of mineral soils, peatland and vegetation (Lindgren et al., 2018; Jeltsch-Thömmes et al., 2019). The land biosphere was on average a net sink for atmospheric carbon and accumulated several hundred Gt of carbon over the LDT.

Detailed investigations reveal that Antarctic air temperatures and more generally Southern Hemisphere (30°S–60°S) proxy temperature reconstructions led the rise in pCO_2 at the onset of the LDT, 18 ka ago, by several hundred years (Shakun et al., 2012; Chowdhry Beeman et al., 2019). Atmospheric CO_2, on the other hand, led reconstructed global average temperature by several centuries (Shakun et al., 2012), corroborating the importance of CO_2 as an amplifier of orbitally-driven warming. The phasing between Antarctic air temperature and atmospheric GHG concentration changes was nearly synchronous, yet variable, during the LDT, owing to the complex nature of the mechanisms modulating the global carbon cycle (Chowdhry Beeman et al., 2019). Mean ocean temperature reconstructions, based on noble gas extracted from Antarctic ice are closely correlated with Antarctic air temperature and pCO_2 records, emphasising the role the Southern Ocean is playing in modulating global climate variability (Bereiter et al., 2018; Baggenstos et al., 2019).

ACCEPTED VERSION SUBJECT TO FINAL EDITS

Enhanced mid-ocean ridge magmatism and/or hydrothermal activity modulated by sea-level rise has recently been hypothesised to have contributed to the deglacial CO_2 rise (Crowley et al., 2015; Lund et al., 2016; Huybers and Langmuir, 2017; Stott et al., 2019b). While geological carbon release may have affected the ocean's radiocarbon budget (Ronge et al., 2016; Rafter et al., 2019; Stott et al., 2019a), model results suggest however that the potential contribution of geological carbon sources to the atmosphere remained small (Roth and Joos, 2012; Hasenclever et al., 2017).

Simulations of Earth models of intermediate complexity (EMIC) with coupled glacial-interglacial climate and the carbon cycle were able to reproduce first-order changes in the atmospheric CO_2 content for the first time in recent years (Ganopolski and Brovkin, 2017; Khatiwala et al., 2019). The most important processes accounting for the full deglacial CO_2 amplitude in the models include solubility changes, changes in oceanic circulation and marine carbonate chemistry. The effect of the terrestrial carbon cycle, variable volcanic outgassing and the temperature dependence on the oceanic remineralisation length scale contribute less than 15 ppm CO_2 between the glacial and interglacial intervals of the cycles. However, details in the simulated response of the marine carbon cycle and atmospheric CO_2 concentrations to changes in ocean circulation depend to a large degree on model parametrisation (Gottschalk et al., 2019).

Independent paleoclimatic evidence suggests with *high confidence* that marine and terrestrial CH_4 and N_2O emissions are highly sensitive to climate on (sub)centennial timescales. Limited, yet internally consistent ice core measurements indicate with *medium confidence* that pulsed geologic CH_4 release from continental margins associated with warming remained negligible across the LDT. Multiple lines of evidence suggest with *high confidence* that CO_2 was released from the ocean interior on centennial timescales during the LDT in response to or associated with warming, contributing to the transition out of the last glacial stage to the current interglacial period.

Multiple lines of evidence inferred from marine sediment proxies indicate with *low to medium confidence* that the millennial rates of CO_2 concentration change in the atmosphere during the last 56 Myr were at least 4-5 times lower than during the last century (Figure 5.3). In spite of uncertainties in ice core reconstructions related to delayed enclosure of air bubbles, which tend to smooth the records, there is *high confidence* that the rates of atmospheric CO_2 and CH_4 change during the last century were at least 10 and 5 times faster, respectively, than the maximum centennial growth rate averages of those gases during the last 800 kyr (Fig. 5.4).

5.1.2.3 Holocene Changes

Atmospheric GHG concentrations were much less variable during the pre-industrial Holocene (from 11.7 ka to 1750). Atmospheric CH_4 concentrations decreased at the beginning of the Holocene, consistent with a general weakening of boreal sources (Yang et al., 2017; Beck et al., 2018) and further decline during the Mid-Holocene owing to a reduction in Southern Hemisphere emissions concomitant with a southward shift of the ITCZ (Singarayer et al., 2011; Beck et al., 2018). Atmospheric CH_4 concentrations increased about 5 ka, which prompted the hypothesis of an early anthropogenic influence, related to land use changes in southeast Asia (Ruddiman et al., 2016). However, stable isotope compositions on CH_4 extracted from Greenland and Antarctic ice (Beck et al., 2018) reveal that natural emissions located in the southern tropics were responsible for the rise in atmospheric CH_4 concentrations, in line with model simulations (Singarayer et al., 2011) thus disputing the early anthropogenic influence on the global CH_4 budget. Atmospheric N_2O concentrations increased slightly (20 ppb) across the Holocene, associated with a gradual decline in its nitrogen stable isotope composition (Fischer et al., 2019b). The combined signal is consistent with a small increase in terrestrial emissions, offset by a reduction in marine emissions (Schilt et al., 2010b; Fischer et al., 2019b).

The early Holocene decrease in CO_2 concentration by about 5 ppm (Schmitt et al., 2012) has been attributed to post-glacial regrowth in terrestrial biomass and a gradual increase in peat reservoirs over the Holocene, resulting in the sequestration of several hundred PgC (Yu et al., 2010; Nichols and Peteet, 2019). Peat

ACCEPTED VERSION SUBJECT TO FINAL EDITS

accumulation rates in boreal and temperate regions were higher under warmer summer conditions in the early to middle Holocene (Loisel et al., 2014; Stocker et al., 2017). The 20 ppm gradual increase of atmospheric CO_2 starting 7 ka has been attributed to a decrease in natural terrestrial biomass due to climate change, carbonate compensation and enhanced shallow water carbonate deposition (Menviel and Joos, 2012; Brovkin et al., 2016b), consistent with stable carbon isotope measurements on CO_2 extracted from Antarctic ice (Elsig et al., 2009; Schmitt et al., 2012). These isotopic measurements do not support an early anthropogenic influence on atmospheric CO_2 due to land use change and forest clearing (Ruddiman et al., 2016). Recent paleoceanographic evidence suggests that remineralised carbon outgassing associated with increased Southern Ocean circulation and upwelling (Studer et al., 2018), possibly promoted by stronger Southern Hemisphere westerly winds (Saunders et al., 2018), could have additionally contributed to the late Holocene increase in atmospheric CO_2 concentrations. However, the role of these mechanisms remained insignificant in transient Holocene ESM simulations (Brovkin et al., 2019). Overall, as in AR5 (WGI, Chapter 5), there is *medium confidence* in the key drivers of the CO_2 increase between the early Holocene and the beginning of the industrial era yet there is *low confidence* to the relative contributions of these drivers due to insufficient quantitative constraints on particular processes.

5.2 Historical Trends, Variability and Budgets of CO2, CH4, and N2O

This section assesses the trends and variability in atmospheric accumulation of the three main GHGs (CO_2, CH_4 and N_2O), their ocean and terrestrial sources and sinks as well as their budgets during the Industrial Era (1750–2019). Emphasis is placed on the more recent contemporary period (1959–2019) where understanding is increasingly better constrained by atmospheric, ocean and land observations. The section also assesses our increased understanding of the anthropogenic forcing and processes driving the trends, as well as how variability at the seasonal to decadal scales provide insights on the mechanism governing long-term trends and emerging biogeochemical-climate feedbacks with their regional characteristics.

5.2.1 CO_2: Trends, Variability and Budget

5.2.1.1 Anthropogenic CO_2 Emissions

There are two anthropogenic sources of CO_2: fossil emissions and net emissions (including removals) resulting from land use change and land management (also shown in this chapter as LULUCF: land-use, land-use change, and forestry, termed forestry and other land use (FOLU) in previous IPCC reports). Fossil CO_2 emissions include the combustion of the fossil fuels coal, oil and gas covering all sectors of the economy (electricity, transport, industrial, and buildings), fossil carbonates such as in cement manufacturing, and other industrial processes such as the production of chemicals and fertilisers (Figure 5.5a). Fossil CO_2 emissions are estimated by combining economic activity data and emission factors, with different levels of methodological complexity (tiers) or approaches (e.g., IPCC Guidelines for National Greenhouse Gas Inventories). Several organisations or groups provide estimates of fossil CO_2 emissions, with each dataset having slightly different system boundaries, methods, activity data, and emission factors (Andrew, 2020). Datasets cover different time periods, which can dictate the datasets and methods that are used for a particular application. The data reported here is from an annually updated data source that combines multiple sources to maximise temporal coverage (Friedlingstein et al., 2020). The uncertainty in global fossil CO_2 emissions is estimated to be ±5% (1 standard deviation).

Fossil CO_2 emissions have grown continuously since the beginning of the industrial era (Figure 5.5) with short intermissions due to global economic crises or social instability (Peters et al., 2012; Friedlingstein et al., 2020). In the most recent decade (2010–2019), fossil CO_2 emissions reached an average 9.6 ± 0.5 PgC yr^{-1} and were responsible for 86% of all anthropogenic CO_2 emissions during. In 2019, fossil CO_2 emissions were estimated to be 9.9 ± 0.5 PgC yr^{-1} excluding carbonation (Friedlingstein et al., 2020) the highest on record. These estimates excluding the cement carbonation sink of around 0.2 PgC yr^{-1}. Fossil CO_2 emissions grew at 0.9% yr^{-1} in the 1990s, increasing to 3.0% per year in the 2000s, and reduced to 1.2% from 2010 to

ACCEPTED VERSION SUBJECT TO FINAL EDITS

2019. The slower growth in fossil CO_2 emissions in the last decade is due to a slowdown in growth from coal use. CO_2 emissions from coal use grew at 4.8% yr^{-1} in the 2000s, but they slowed to 0.4% yr^{-1} in the 2010s. CO_2 emissions from oil use grew steadily at 1.1% yr^{-1} in both the 2000s and 2010s. CO_2 emissions from gas use grew at 2.5% yr^{-1} in the 2000s and 2.4% yr^{-1} in 2010s, but is showing signs of accelerated growth of 3% yr^{-1} since 2015 (Peters et al., 2020a). Direct CO_2 emissions from carbonates in cement production are around 4% of total fossil CO_2 emissions, and grew at 5.8% yr^{-1} in the 2000s but a slower 2.4% yr^{-1} in the 2010s. The uptake of CO_2 in cement infrastructure (carbonation) offsets about one half of the carbonate emissions from current cement production (Friedlingstein et al., 2020). These results are robust across the different fossil CO_2 emission datasets, despite minor differences in levels and rates as expected given the reported uncertainties (Andrew, 2020). During 2020, the COVID-19 pandemic led to a rapid, temporary decline in fossil CO_2 emissions, estimated to be around 7% based on a synthesis of four estimates. (Forster et al., 2020; Friedlingstein et al., 2020; Le Quéré et al., 2020; Liu et al., 2020c) (Cross-Chapter Box 6.1).

[START FIGURE 5.5 HERE]

Figure 5.5: Global anthropogenic CO_2 emissions. (a) Historical trends of anthropogenic CO_2 emission (fossil fuels and net land use change, including land management, called LULUCF flux in the main text) for the period 1870 to 2019, with 'others' representing flaring, emissions from carbonates during cement manufacture. Data sources: (Boden et al., 2017; IEA, 2017; Andrew, 2018; BP, 2018; Le Quéré et al., 2018a; Friedlingstein et al., 2020). (b) The net land use change CO_2 flux (PgC yr^{-1}) as estimated by three bookkeeping models and 16 Dynamic Global Vegetation Models (DGVMs) for the global annual carbon budget 2019 (Friedlingstein et al., 2020). The three bookkeeping models are from Hansis et al., (2015); Houghton and Nassikas, (2017); Gasser et al., (2020) and are all updated to 2019; their average is used to determine the net land use change flux in the annual global carbon budget (black line). The DGVM estimates are the result of differencing a simulation with and without land use changes run under observed historical climate and CO_2, following the Trendy v9 protocol; they are used to provide an uncertainty range to the bookkeeping estimates (Friedlingstein et al., 2020). All estimates are unsmoothed annual data. Estimates differ in process comprehensiveness of the models and in definition of flux components included in the net land use change flux. Further details on data sources and processing are available in the chapter data table (Table 5.SM.6).

[END FIGURE 5.5 HERE]

The global net flux from land use change and land management is composed of carbon fluxes from land use conversions, land management and changes therein (Pongratz et al., 2018) and is equivalent to the LULUCF fluxes from the agriculture, forestry and other land use (AFOLU) sector (Jia et al., 2019). It thus consists of gross emissions (loss of biomass and soil carbon in clearing or logging, harvested product decay, emissions from peat drainage and burning, degradation) and gross removals (CO_2 uptake in natural vegetation re-growing after harvesting or agricultural abandonment, afforestation). The LULUCF flux relates to direct human interference with terrestrial vegetation, as opposed to the natural carbon fluxes occurring due to interannual variability or trends in environmental conditions (in particular climate, CO_2, and nutrient deposition) (Houghton, 2013).

Progress since AR5 and the SRCCL (IPCC, 2019a) allows more accurate estimates of gross and net fluxes due to availability of more models, model advancement in terms of inclusiveness of land-use practices (see below), and advanced land use forcings (Ciais et al., 2013; Goldewijk et al., 2017; Hurtt et al., 2020). In addition, important terminological discrepancies were resolved. First, synergistic effects of land use change and environmental changes-have been identified as a key reason for the large discrepancies between model estimates of the LULUCF flux, explaining up to 50% of differences (Pongratz et al., 2014; Stocker and Joos, 2015; Gasser et al. 2020). Another reason for discrepancies relates to natural fluxes being considered as part of the LULUCF flux when occurring on managed land in the United Nation Framework Convention on Climate Change (UNFCCC) national greenhouse gas inventories; these fluxes are considered part of the natural terrestrial sink in global vegetation models and excluded in bookkeeping models (Grassi et al., 2018). LULUCF fluxes following national GHG inventories or FAO datasets, including recent estimates (Tubiello

ACCEPTED VERSION SUBJECT TO FINAL EDITS

et al., 2021), are thus excluded from our global assessment, but their comparison against the academic approach is available elsewhere (at the global scale (Jia et al., 2019) and European level (Petrescu et al., 2020).

Land-use-related component fluxes can be verified by the growing databases of global satellite-based biomass observations in combination with information on remotely-sensed land cover change, but differ from bookkeeping and modelling with Dynamic Global Vegetation Models (DGVMs) in excluding legacy emissions from pre-satellite-era land use change and land management, and neglecting soil carbon changes, and often focus on gross deforestation, not regrowth (Jia et al., 2019).

For the decade 2010–2019, average emissions were estimated at 1.6 ± 0.7 PgC yr^{-1} (mean ± standard deviation, 1 sigma) (Friedlingstein et al., 2020). A *likely* general upward trend since 1850 is reversed during the second part of the 20th century (Figure 5.5b). Trends since the 1980s have *low confidence* because they differ between estimates, which is related inter alia to Houghton and Nassikas (2017) using a different land use forcing than Hansis et al. (2015) and the DGVMs. Higher emissions estimates are expected from DGVMs run under transient environmental conditions compared to bookkeeping estimates, because the DGVM estimate includes the loss of additional sink capacity. Because the transient setup requires a reference simulation without land use change to separate anthropogenic fluxes from natural land fluxes, LULUCF estimates by DGVMs include the sink forests would have developed in response to environmental changes on areas that in reality have been cleared (Pongratz et al., 2014). The agricultural areas that replaced these forests have a reduced residence time of carbon, lacking woody material, and thus provide a substantially smaller additional sink over time (Gitz and Ciais, 2003). The loss of additional sink capacity is growing in particular with atmospheric CO_2 and increases DGVM-based LULUCF flux estimates relative to bookkeeping estimates over time (Figure 5.5).

Gross emissions are on average 2–3 times larger than the net flux from LULUCF, increasing from an average of 3.5 ± 1.2 PgC yr^{-1} for the decade of the 1960s to an average of 4.4 ± 1.6 PgC yr^{-1} during 2010–2019 (Friedlingstein et al., 2020). Gross removals partly balance these gross emissions to yield as the sum the net flux from LULUCF and increase from -2.0 ± 0.7 PgC yr^{-1} for the 1960s to -2.9 ± 1.2 PgC yr^{-1} during 2010-2019. These large gross fluxes show the relevance of land management such as harvesting or rotational agriculture and the large potential to reduce emissions by halting deforestation and degradation.

More evidence on the pre-industrial LULUCF flux has emerged since AR5 in the form of new estimates of cumulative carbon losses until today and of a better understanding of natural carbon cycle processes over the Holocene (Ciais et al., 2013). Cumulative carbon losses by land use activities since the start of agriculture and forestry (pre-industrial and industrial era) have been estimated at 116 PgC based on global compilations of carbon stocks for soils (Sanderman et al., 2017) with about 70 PgC of this occurring prior to 1750, and for vegetation as 447 PgC (inner quartiles of 42 calculations: 375–525 PgC) (Erb et al., 2018). Emissions prior to 1750 can be estimated by subtracting the post-1750 LULUCF flux from Table 5.1 from the combined soil and vegetation losses until today; they would then amount to 328 (161–501) PgC assuming error ranges are independent. A share of 353 (310–395) PgC from prior to 1800 has indirectly been suggested as the difference between net biosphere flux and terrestrial sink estimates, which is compatible with ice-core records due to a low airborne fraction of anthropogenic emissions in pre-industrial times (Erb et al., 2018) (see also Section 5.1.2.3). *Low confidence* is assigned to pre-industrial emissions estimates.

Since AR5, evidence emerged that the LULUCF flux might have been underestimated as DGVMs include anthropogenic land cover change, but often ignore land management practices not associated with a change in land cover; land management is more widely captured by bookkeeping models through use of observation-based carbon densities (Ciais et al., 2013; Pongratz et al., 2018). Sensitivity studies show that practices such as wood and crop harvesting increase global net LULUCF emissions (Arneth et al., 2017) and explain about half of the cumulative loss in biomass (Erb et al., 2018).

5.2.1.2 Atmosphere

ACCEPTED VERSION SUBJECT TO FINAL EDITS

Atmospheric CO_2 concentration measurements in remote locations began in 1957 at the South Pole Observatory (SPO) and in 1958 at Mauna Loa Observatory (MLO), Hawaii, USA (Keeling, 1960) (Figure 5.6a). Since then, measurements have been extended to multiple locations around the world (Bacastow et al., 1980; Conway et al., 1994; Nakazawa et al., 1997). In addition, high density global observations of total column CO_2 measurements have been made since 2009 by dedicated greenhouse gases observing satellites (Yoshida et al., 2013; O'Dell et al., 2018). Annual mean CO_2 growth rates are observed to be 1.56 ± 0.18 ppm yr^{-1} (average and range from 1 standard deviation of annual values) over the 61 years of atmospheric measurements (1959–2019), with the rate of CO_2 accumulation almost tripling from an average of 0.82 ± 0.29 ppm yr^{-1} during the decade of 1960–1969 to 2.39 ± 0.37 ppm yr^{-1} during the decade of 2010–2019 (Chapter 2). The latter agrees well with that derived for total column (XCO_2) measurements by the greenhouse gases observing satellite (GOSAT) (Figure 5.6b). The interannual oscillations in monthly-mean CO_2 growth rates (Figure 5.6b) show close relationship with the El Niño southern oscillation (ENSO) cycle (Figure 5.6b) due to the ENSO-driven changes in terrestrial and ocean CO_2 sources and sinks on the Earth's surface (Section 5.2.1.4).

Multiple lines of evidence unequivocally establish the dominant role of human activities in the growth of atmospheric CO_2. First, the systematic increase in the difference between the MLO and SPO records (Figure 5.6a) is caused primarily by the increase in emissions from fossil fuel combustion in industrialised regions that are situated predominantly in the northern hemisphere (Ciais et al., 2019). Second, measurements of the stable carbon isotope in the atmosphere ($\delta^{13}C–CO_2$) are more negative over time because CO_2 from fossil fuels extracted from geological storage is depleted in ^{13}C (Rubino et al., 2013; Keeling et al., 2017) (Figure 5.6c). Third, measurements of the $\delta(O_2/N_2)$ ratio show a declining trend because for every molecule of carbon burned, 1.17 to 1.98 molecules of oxygen (O_2) is consumed (Ishidoya et al., 2012; Keeling and Manning, 2014) (Figure 5.6d). These three lines of evidence confirm unambiguously that the atmospheric increase of CO_2 is due to an oxidative process (i.e. combustion). Fourth, measurements of radiocarbon ($^{14}C–CO_2$) at sites around the world (Levin et al., 2010; Graven et al., 2017; Turnbull et al., 2017) show a continued long-term decrease in the $^{14}C/^{12}C$ ratio. Fossil fuels are devoid of ^{14}C and therefore fossil-fuel-derived CO_2 additions decrease the atmospheric $^{14}C/^{12}C$ ratio (Suess, 1955).

[START FIGURE 5.6 HERE]

Figure 5.6: Time series of CO_2 concentrations and related measurements in ambient air. (a) concentration time series and MLO-SPO difference, (b) growth rates, (c) ^{14}C and ^{13}C isotopes, and (d) O_2/N_2 ratio. The data for Mauna Loa Observatory (MLO) and South Pole Observatory (SPO) are taken from the Scripps Institution of Oceanography (SIO)/University of California, San Diego (Keeling et al., 2001). The global mean CO_2 are taken from NOAA cooperative network (as in Chapter 2), and GOSAT monthly-mean XCO_2 time series are taken from National Institute for Environmental Studies (Yoshida et al., 2013). CO_2 growth rates are calculated as the time derivative of deseasonalised time series (Nakazawa et al., 1997). The $\Delta(O_2/N2)$ are expressed in per meg units (= $(FF/M)\times10^6$, where FF = moles of O_2 consumed by fossil-fuel burning, M = 3.706×10^{19}, total number of O_2 molecules in the atmosphere (Keeling and Manning, 2014). The $^{14}CO_2$ time series at Barring Head, Wellington, New Zealand (BHD) is taken from GNS Science and NIWA (Turnbull et al., 2017). The multivariate ENSO index (MEI) is shown as the shaded background in panel (b; warmer shade indicates El Niño). Further details on data sources and processing are available in the chapter data table (Table 5.SM.6).

[END FIGURE 5.6 HERE]

Over the past six decades, the fraction of anthropogenic CO_2 emissions that has accumulated in the atmosphere (referred to as airborne fraction) has remained near constant at approximately 44% (Figure 5.7) (Ballantyne et al., 2012; Ciais et al., 2019; Gruber et al., 2019b; Friedlingstein et al., 2020). This suggests that the land and ocean CO_2 sinks have continued to grow at a rate consistent with the growth rate of anthropogenic CO_2 emissions, albeit with large inter-annual and sub-decadal variability dominated by the land sinks (Figure 5.7).

ACCEPTED VERSION SUBJECT TO FINAL EDITS

Since AR5, an alternative observable diagnostic to the airborne fraction has been proposed to understand the trends in land and ocean sinks in response to its driving atmospheric CO_2 concentrations (Raupach et al., 2014; Bennedsen et al., 2019). It is the sink rate which is defined as the combined ocean and land sink flux per unit of atmospheric excess of CO_2 above pre-industrial levels (Raupach et al., 2014). The sink rate has declined over the past six decades, which indicates that the combined ocean and land sinks are not growing as fast as the growth in atmospheric CO_2 (Raupach et al., 2014; Bennedsen et al., 2019). Possible explanations for the sink rate decline are that the land and/or ocean CO_2 sinks are no longer responding linearly with CO_2 concentrations or that anthropogenic emissions are slower than exponential (Gloor et al., 2010; Raupach et al., 2014; Bennedsen et al., 2019) (Figure 5.7; Sections 5.2.1.3, 5.2.1.4). In addition, both diagnostics are influenced by major climate modes (e.g. ENSO) and volcanic eruptions that contribute to high interannual variability (Gloor et al., 2010; Frölicher et al., 2013; Raupach et al., 2014), suggesting high sensitivity to future climate change. Uncertain land use change fluxes (Section 5.2.1.2) influence the robustness of the trends. Based on the AF, it is concluded with *medium confidence* that both ocean and land CO_2 sinks have grown consistent with the rising of anthropogenic emissions. Further research is needed to understand the drivers of changes in the CO_2 sink rate.

[START FIGURE 5.7 HERE]

Figure 5.7: Airborne fraction and anthropogenic (fossil fuel and land use change) CO_2 emissions. Data as in Section 5.2.1.1. The multivariate ENSO index (shaded) and the major volcanic eruptions are marked along the x-axis. Further details on data sources and processing are available in the chapter data table (Table 5.SM.6).

[END FIGURE 5.7 HERE]

5.2.1.3 Ocean Carbon Fluxes and Storage

Since AR5 and the Special Report on Ocean and the Cryosphere (SROCC), major advances in globally coordinated ocean CO_2 observations (Surface Ocean CO_2 Atlas - SOCAT and Global Ocean Data Analysis Project - GLODAP), the harmonisation of ocean and coastal observations based products, atmospheric and oceanic inversion models and forced global ocean biogeochemical models (GOBMs) have increased the level of confidence in the assessment of trends and variability of air-sea fluxes and storage of CO_2 in the ocean during the historical period (1960–2018) (Ciais et al., 2013; Bakker et al., 2016; Landschützer et al., 2020, 2016; Bindoff et al., 2019; Tohjima et al., 2019; DeVries et al., 2019; Gregor et al., 2019; Gruber et al., 2019c, 2019a; Olsen et al., 2020; Friedlingstein et al., 2020; Hauck et al., 2020) (See also Supplementary Materials 5.SM.1). A major advance since SROCC is that for the first time all 6 published observational product fluxes, used in this assessment, are made more comparable using a common ocean and sea-ice cover area, integration of climatological coastal fluxes scaled to increasing atmospheric CO_2 and an ensemble mean of ocean fluxes calculated from three re-analysis wind products (Landschützer et al., 2014, 2020; Rödenbeck et al., 2014; Zeng et al., 2014; Denvil-Sommer et al., 2019; Gregor et al., 2019; Iida et al., 2020) Supplementary Materials 5.SM.2). From a process point of view, the ocean uptake of anthropogenic carbon is a two-step set of abiotic processes that involves the exchange of CO_2, first across the air-sea boundary into the surface mixed layer, followed by its transport into the ocean interior where it is stored for decades to millennia, depending on the depth of storage (Gruber et al., 2019a), Two definitions of air-sea fluxes of CO_2 are used in this assessment for both observational products and models: S_{ocean} is the global mean ocean CO_2 sink and F_{net} denotes the net spatially varying CO_2 fluxes (Hauck et al., 2020). Adjustment of the mean global F_{net} for the pre-industrial sea-to-air CO_2 flux associated with land-to-ocean carbon flux term makes F_{net} comparable to S_{ocean} (Jacobson et al., 2007; Resplandy et al., 2018a; Hauck et al., 2020).

There are multiple lines of observational and modelling evidence that support with *high confidence* the finding that in the historical period air-sea fluxes and storage of anthropogenic CO_2 are largely influenced by atmospheric CO_2 concentrations, physical ocean processes and physico-chemical carbonate chemistry, which determines the unique properties of CO_2 in sea water (Wanninkhof et al., 2014; DeVries et al., 2017; Gruber

ACCEPTED VERSION SUBJECT TO FINAL EDITS

et al., 2019, 2019a; Hauck et al., 2020; McKinley et al., 2017; 2020; Chapter 9, Cross-Chapter Box 5.3). Here we assess three different approaches (Figures 5.8a, 5.8b and 5.9) that together provide *high confidence* that during the historical period (1960–2018) the ocean carbon sink (S_{ocean}) and its associated ocean carbon storage have grown in response to global anthropogenic CO_2 emissions (Gruber et al., 2019c; Hauck et al., 2020; McKinley et al., 2020).

5.2.1.3.1 Ocean Carbon Fluxes and Storage: Global Multi-Decadal Trends

In the first assessment approach, the mean global multidecadal (1960–2019) trends in the ocean sink (S_{ocean}) for CO_2 show a high degree of coherence across the 9 GOBMs and 6 pCO_2-based observational product reconstructions (1987–2018), which despite a temporary slowdown (or "hiatus") in the 1990s, is also quasi-linear over that period (Figure 5.8a) (Gregor et al., 2019; Hauck et al., 2020). This coherence between the GOBMs and observations-based reconstructions (1987–2018; r^2=0.85) provides *high confidence* that the ocean sink (S_{ocean} in Section 5.2.1.5) evaluated from GOBMs (1960–2019) grew quasi-linearly from 1.0 ± 0.3 PgC yr^{-1} to 2.5 ± 0.6 PgC yr^{-1} between the decades 1960–1969 and 2010–2019 in response to global CO_2 emissions (Figure 5.8a; Table 5.1; Hauck et al., 2020; Friedlingstein et al., 2020). The cumulative ocean CO_2 uptake (105 ± 20 PgC) is 23% of total anthropogenic CO_2 emissions (450 ± 50 PgC) for the same period (Friedlingstein et al., 2020). Notwithstanding the *high confidence* in the magnitude of the annual to decadal trends for S_{ocean} this assessment is moderated to *medium confidence* by the *low confidence* in the currently inadequately constrained uncertainties in the pre-industrial land-to-ocean carbon flux, the uncertain magnitude of winter outgassing from the Southern Ocean, and the uncertain effect of the ocean surface cool-skin, the effect of data sparsity, differences between wind products and the uncertain contribution from the changing land-ocean continuum on global and regional fluxes (Jacobson et al., 2007; Resplandy et al., 2018a; Roobaert et al., 2018; Bushinsky et al., 2019; Gloege et al., 2020; Hauck et al., 2020; Watson et al., 2020). However, both GOBMs and pCO_2-based observational products independently reveal a slowdown or "hiatus" of the ocean sink in the 1990s, which provides a valuable constraint for model verification and leads to greater confidence in the model outputs (Figure 5.8a) (Landschützer et al., 2016; Gregor et al., 2018; DeVries et al., 2019; Hauck et al., 2020). A number of studies point to the role of the Southern Ocean in the global "1990s-hiatus" in air-sea CO_2 fluxes but provide different process-based explanations linking ocean temperature, mixing and MOC responses to variability in large scale climate systems, wind stress and volcanic activity as well as the sensitivity of the air-sea CO_2 flux to small changes in the atmospheric forcing from anthropogenic CO_2 (Landschützer et al., 2016; DeVries et al., 2017; Bronselaer et al., 2018; Gregor et al., 2018; Gruber et al., 2019c; Keppler and Landschützer, 2019; McKinley et al., 2020; Nevison et al., 2020). Data sparsity in the Southern Ocean could also be a factor amplifying the global decadal perturbation of the 1990s (Gloege et al., 2020). Therefore, while there is *high confidence* in the 1990's-hiatus of the global ocean sink for anthropogenic CO_2 and that the Southern Ocean makes an observable contribution to it, there is still *low confidence* in the attribution for the processes behind the 1990s-hiatus (5.2.1.3.2). Observed increases in the amplitude of the seasonal cycle of ocean pCO_2 and reductions in the mean global buffering capacity provide *high confidence* that growing CO_2 sink is also beginning to drive observable large-scale changes in ocean carbonate chemistry (Jiang et al., 2019). However, there is *medium confidence* that these changes, which depending on the emissions scenario could drive future ocean feedbacks, are still too small to emerge from the historical multi-decadal observed growth rate of S_{ocean} (Figure 5.8a; Sections 5.1.2; 5.3.2, 5.4.2; SROCC 5.2.2.3.2) (Bates et al., 2014; Sutton et al., 2016; Fassbender et al., 2017; Landschützer et al., 2018; Jiang et al., 2019). A recent model-based study suggests that re-emergence of previously stored anthropogenic CO_2 is both changing the buffering capacity of the mixed layer and reducing the ocean sink for anthropogenic CO_2 during the historical period (Rodgers et al., 2020). This trend is not reflected in observations-based products (Figure 5.8), so we attribute a *low confidence*.

The second assessment approach makes use of 6 independent methods to constrain the mean decadal ocean sink over the period 1990–2019 (Figure 5.8b). This provides a multi-decadal advance on the 1990–1999 decadal constraint from (Denman et al., 2007) that have been widely used as a model constraint for GOBMs used for the global carbon budget (Hauck et al., 2020). The *medium confidence* attributed of this assessment of the global multi-decadal trend (Figure 5.8a) is further supported by the broad agreement in magnitude and trend of the decadal mean ocean CO_2 uptake with assessments that also include additional observations-based, independent methods such as ocean CO_2 inversion and atmospheric CO_2 and O_2/N_2 measurements

ACCEPTED VERSION SUBJECT TO FINAL EDITS

(Figure 5.8b; Supplementary Materials Tables 5.SM.1 and 5.SM.2).

[START FIGURE 5.8 HERE]

Figure 5.8: Multi-decadal trends for the ocean sink of CO_2. (a): The multi-decadal (1960–2019) trends in the annual ocean sink (S_{ocean}) reconstructed from 9 Global Ocean Biogeochemical Models (GOBM) forced with observed atmospheric re-analysis products (Hauck et al., 2020), 6 observationally-based gap-filling products that reconstructed spatial and temporal variability in the ocean CO_2 flux from sparse observations of surface ocean pCO_2 (Supplementary Materials 5.SM.2). The trends in S_{ocean} were calculated from the mean annual global GOBM outputs and the observational products were used to provide confidence in the GOBM assessments (r^2=0.85). Thick lines represent the multi-model mean. Observationally-based products have been corrected for pre-industrial river carbon fluxes (0.62 PgC yr^{-1}) based on the average of estimates from Jacobson et al., (2007) and Resplandy et al. (2018). (b): Mean decadal constraints and their confidence intervals for global ocean sink (S_{ocean}) of anthropogenic CO_2 using multiple independent or quasi-independent lines of evidence or methods for the period 1990–2019 (See Supplementary Materials Tables 5.SM.1 and 5.SM.2 for magnitudes, uncertainties and published sources). Further details on data sources and processing are available in the chapter data table (Table 5.SM.6).

[END FIGURE 5.8 HERE]

Here we provide a third comparative assessment approach depicting the spatial coherence of ocean air-sea fluxes and storage rates of CO_2 as well as a quantitative assessment of both fluxes for the same period (1994–2007) (Figure 5.9). Observation-based pCO_2 flux products show that emissions of natural CO_2 occur mostly in the tropics and high latitude Southern Ocean, and that the uptake and storage of anthropogenic CO_2 occur predominantly in the mid-latitudes (Figure 5.9; Chapter 9; Cross-Chapter Box 5.3). Strong ocean CO_2 sink regions are those in the mid-latitudes associated with the cooling of poleward flowing sub-tropical surface waters as well as equatorward flowing sub-polar surface waters both of which contribute to the formation of Mode, Intermediate and Deep water masses that transport anthropogenic CO_2 into the ocean interior on time scales of decades to centuries in both hemispheres (Figure 5.9) (DeVries, 2014; Gruber et al., 2019a; Wu et al., 2020; Chapter 9.2.2.3). The mean decadal scale magnitude and uncertainties of S_{ocean} from net air sea fluxes (F_{net}) were calculated from an ensemble of 6 observational based product reconstructions (Figure 5.9a) and the storage rates in the ocean interior derived from multiple ocean interior CO_2 data sets (Gruber et al., 2019a) (Figure 5.9b). The cumulative CO_2 stored in the ocean interior from 1800 to 2007 has been estimated at 140 ±18 PgC (Gruber et al., 2019a). As reported in SROCC (Section 5.2.2.3.1; IPCC, 2019b), the net ocean CO_2 storage between 1994–2007 was 29 ± 4 PgC, which corresponds to a mean storage of 26 ± 5% of anthropogenic CO_2 emissions for that period (Gruber et al., 2019a). The resulting net annual storage rate of anthropogenic CO_2, equivalent to S_{ocean} for the period mid-1994–mid-2007 is 2.2 ± 0.3 $PgCyr^{-1}$, which is in very close agreement with the top-down air-sea flux estimate of S_{ocean} of 2.1 ± 0.5 PgC yr^{-1} from GOBMs and 1.9 ± 0.3PgC yr^{-1} from pCO_2-based observational products with the steady river carbon flux correction of 0.62PgCy-1 for the same time period (Gruber et al., 2019b; Hauck et al., 2020). This close agreement between these independent ocean CO_2 sink estimates derived from air-sea fluxes and storage rates in the ocean interior support the *medium confidence* assessment that the ocean anthropogenic carbon storage rates continue to be determined by the ocean sink (S_{ocean}) in response to growing CO_2 emissions (McKinley et al., 2020) (Figure 5.9).

[START FIGURE 5.9 HERE]

Figure 5.9: Comparative regional characteristics of the mean decadal (1994–2007) sea-air CO_2 flux (F_{net}) and ocean storage of anthropogenic CO_2. (a) regional sink–source characteristics for contemporary ocean air-sea CO_2 fluxes (F_{net}) derived from the ensemble of 6 observation-based products using SOCATv6 observational data set (Bakker et al., 2020; Landschützer et al., 2014; Rödenbeck et al., 2014; Zeng et al., 2014; Denvil-Sommer et al., 2019; Gregor et al., 2019; Iida et al., 2020). Warm colours depict outgassing fluxes and black contours characterise the the five basin-scale biomes aggregated from the original 17

ACCEPTED VERSION SUBJECT TO FINAL EDITS

from Fay and McKinley (2014) and adjusted by Gregor et al., (2019) also used to calculate the regional variability in flux anomalies (Supplementary Materials Figure 5.SM.1); and (b) the regional characteristics of the storage fluxes of CO_2 in the ocean interior for the same period (Gruber et al., 2019a). The dots reflect ocean areas where the 1-sigma standard deviation of Fnet from the 6 observation product is larger than the magnitude of the mean. This reflects source-sink transition areas where the mean Fnet is small and more strongly influenced by spatial and temporal variability across the products. Further details on data sources and processing are available in the chapter data table (Table 5.SM.6).

[END FIGURE 5.9 HERE]

5.2.1.3.2 Ocean Carbon Fluxes and Storage: Regional – Global Variability

The intent of this assessment is to show how global variability can be regionally forced (Gregor et al., 2019; Landschützer et al., 2019; Hauck et al., 2020). Since AR5 and SROCC, advances in global ocean CO_2 flux products, GOBMs and atmospheric inversion models have strengthened the confidence in the assessment of how ocean regions influence mean global variability and trends of ocean CO_2 air-sea fluxes (F_{net}; see Supplementary Materials Figure 5.SM.1) (Ciais et al., 2013; Landschützer et al., 2014, 2015; Rödenbeck et al., 2014; McKinley et al., 2017; Bindoff et al., 2019; Gregor et al., 2019; Friedlingstein et al., 2020; Hauck et al., 2020). The coherence in the regional variability of the anomalies in F_{net} from 3 independent lines of evidence support with *high confidence* that the non-steady state global interannual-decadal variability of F_{net} has clear regional influences (Gregor et al., 2019; Landschützer et al., 2019). The tropical oceans contribute the most to the global mean interannual variability (Supplementary Materials Figure 5.SM.1d). The high latitude oceans, particularly the Southern Ocean, contribute the most to the global-scale decadal variability (Supplementary Materials Figure 5.SM5.1b, c; (Landschützer et al., 2016, 2019; Gregor et al., 2019; Gruber et al., 2019c; Hauck et al., 2020). The influence of the Southern Ocean on the global mean decadal variability and the 1990's hiatus is supported by the highest regional-global correlation coefficients (Supplementary Materials Figures 5.SM.1a, c). In contrast, the Equatorial oceans' influence on global mean F_{net} has a low correlation because, notwithstanding the coherence in interannual variability, it does not show the same global mean trend of strengthening sink in response to growing global emissions (Supplementary Materials Figure 5.SM.1d; (Gregor et al., 2019). All regions, except the Equatorial ocean, contribute to varying extents to the multidecadal trend of growth in the global ocean sink (Supplementary Materials Figure 5.SM.1). Data sparseness in the high latitudes and the relatively short length of the observational records leads to *low confidence* in the attribution of the processes that link regional-global variability to climate (Landschützer et al., 2019; Gloege et al., 2020).

Regional decadal-scale anomalies in the variability of ocean CO_2 storage have also emerged, probably associated with changes in the meridional overturning circulation (MOC), which may influence the global variability in F_{net} (DeVries et al., 2017); Chapter 9). In the interior of the Indian and Pacific sectors of the Southern Ocean, and the North Atlantic, the increase in the CO_2 inventory from 1994 to 2007 was about 20% smaller than expected from the atmospheric CO_2 increase during the same period and the anthropogenic CO_2 inventory in 1994 (Sabine, 2004; Gruber et al., 2019a). There is *medium confidence* that the ocean CO_2 inventory strengthened again in the decade 2005–2015 (DeVries et al., 2017). In the North Atlantic, a low rate of anthropogenic CO_2 storage at 1.9 ± 0.4 PgC per decade during the time period of 1989–2003 increased to 4.4 ± 0.9 PgC per decade during 2003–2014, associated with changing ventilation patterns driven by the North Atlantic Oscillation (Woosley et al., 2016). In the Pacific sector of the Southern Ocean, the rate of anthropogenic CO_2 storage also increased from 8.8 ± 1.1 (1σ) PgC per decade during 1995–2005 to 11.7 ± 1.1 PgC per decade during 2005–2015 (Carter et al., 2019). However, in the Subantarctic Mode Water of the Atlantic sector of the Southern Ocean, the storage rate of the anthropogenic CO_2 was rather lower after 2005 than before (Tanhua et al., 2017; Bindoff et al., 2019; Section 9.2.3.2). These changes have been predominantly ascribed to the impact of changes in the MOC on the transport of anthropogenic CO_2 into the ocean interior due to regional climate variability, in addition to the increase in the atmospheric CO_2 concentration (Wanninkhof et al., 2010; Pérez et al., 2013; DeVries et al., 2017, 2019; Gruber et al., 2019b; McKinley et al., 2020) (Section 9.2.3.1). However, the low frequency of carbon observations in the interior of the vast ocean leads to *medium confidence* in the assessment of temporal variability in the rate of regional ocean CO_2 storage and its controlling mechanisms.

ACCEPTED VERSION SUBJECT TO FINAL EDITS

In summary, multiple lines of both observational and modelling evidence provide *high confidence* that the finding that the ocean sink for anthropogenic CO_2 has increased quasi-linearly over the past 60 years in response to growing global emissions of anthropogenic CO_2 with a mean fraction of 23% of total emissions. The *high confidence* assessment is moderated to *medium confidence* because of a number of as yet to be adequately unconstrained ocean CO_2 flux terms. Observed changes in the variability of ocean pCO_2 and observed reductions in the mean global buffering capacity provide *high confidence* that the growing CO_2 sink is also beginning to drive observable large-scale changes in ocean carbonate chemistry. However, there is *medium confidence* that these changes, which depending on the emissions scenario could drive future ocean feedbacks, are still too small to emerge from the historical multi-decadal observed growth rate of S_{ocean}.

5.2.1.4 Land CO_2 Fluxes: Historical and Contemporary Variability and Trends

5.2.1.4.1 Trend in Land-Atmosphere CO2 Exchange

The global net land CO_2 sink is assessed to have grown over the past six decades (Ciais et al., 2019; Le Quéré et al., 2018a; Sarmiento et al., 2010; Friedlingstein et al., 2019) (*high confidence*). Estimated as the residual from the mass balance budget of fossil fuel CO_2 emissions minus atmospheric CO_2 growth and the ocean CO_2 sink, the global net land CO_2 sink (including both land CO_2 sink and net land use change emission) increased from 0.3 ± 0.6 PgC yr^{-1} during the 1960s to 1.8 ± 0.8 PgC yr^{-1} during 2010s (Friedlingstein et al., 2020). An increasing global net land CO_2 sink since 1980s (Figure 5.10) was consistently suggested both by atmospheric inversions (e.g. Peylin et al., 2013) and by Dynamic Global Vegetation Models (e.g. Sitch et al., 2015; Friedlingstein et al., 2019). The northern hemisphere contributes more to the net increase in the land CO_2 sink compared to the southern hemisphere (Ciais et al., 2019), and boreal and temperate forests probably contribute the most (Tagesson et al., 2020). Attributing an increased net land CO_2 sink to finer regional scales remains challenging, but inversions of satellite-based column CO_2 products that have emerged since AR5 are a promising tool to further constrain regional land-atmosphere CO_2 exchange (Ciais et al., 2013; Houweling et al., 2015; Reuter et al., 2017; O'Dell et al., 2018; Palmer et al., 2019a).

Carbon uptake by vegetation photosynthesis exerts a first-order control over the net land CO_2 sink. Several lines of evidence show enhanced vegetation photosynthesis over the past decades (*medium to high confidence*) (Figure 5.10), including increasing satellite-derived vegetation greenness (e.g. Mao et al., 2016; Zhu et al., 2016; Jia et al., 2019; See also Chapter 2) and satellite-derived photosynthesis indicators (e.g. Badgley et al., 2017; Zhang et al., 2018b), change in atmospheric concentration of carbonyl sulphide (Campbell et al., 2017), enhanced seasonal CO_2 amplitude (Graven et al., 2013; Forkel et al., 2016). observation-driven inference of increasing photosynthesis CO_2 uptake based mostly on enhanced water use efficiency (Cheng et al., 2017), and DGVM simulated increase of photosynthesis CO_2 uptake (Anav et al., 2015).

Substantial progress has been made since AR5 on attributing change of the global net land CO_2 sink. Increasing global net land CO_2 sink since the 1980s is mainly driven by the fertilisation effect from rising atmospheric CO_2 concentrations (Schimel et al., 2015; Sitch et al., 2015; Fernández-Martínez et al., 2019; O'Sullivan et al., 2019; Tagesson et al., 2020; Walker et al., 2020) (*medium confidence*). Increasing nitrogen deposition (de Vries et al., 2009; Devaraju et al., 2016; Huntzinger et al., 2017) or the synergy between increasing nitrogen deposition and atmospheric CO_2 concentration (O'Sullivan et al., 2019) could have also contributed to the increasing global net land CO_2 sink. The effects of climate change alone on the global net land CO_2 sink is so divergent that even the signs of the effects are not the same across DGVMs (e.g. Huntzinger et al., 2017).

Lower fire emission of CO_2 and enhanced vegetation carbon uptake due to reduced global burned area have contributed to the increasing global net land CO_2 sink in the recent decade (Arora and Melton, 2018; Yin et al., 2020) (*low to medium confidence*). Satellite observations reveal a declining trend in global burned area by about 20% over past two decades (Andela et al., 2017; Earl and Simmonds, 2018; Forkel et al., 2019b; Jones et al., 2020), a trend most pronounced in regions like northern Africa (Forkel et al., 2019; Zubkova et

ACCEPTED VERSION SUBJECT TO FINAL EDITS

al., 2019; Bowman et al., 2020; Jones et al., 2020) and Mediterranean Europe (Turco et al., 2016). However, burned area trends are highly heterogeneous regionally with increasing trends reported in regions like western United States (Holden et al., 2018a; Abatzoglou et al., 2019) and southeastern Australia (Canadell et al., 2020). Some regions (e.g. Amazon basin and Australia) experienced record-breaking fire events in 2019 and 2020 (e.g. Boer et al., 2020), whose effects on burned area trends remain to be explored. The burned area trends were primarily attributed to both human-induced climate change and human activities (Jolly et al., 2015; Andela et al., 2017; Holden et al., 2018b; Turco et al., 2018; Teckentrup et al., 2019; Bowman et al., 2020), as well as changing frequency of lightning in the boreal region (Veraverbeke et al., 2017). In addition to changes in the burned area, fire dynamics could affect trend in land-atmosphere CO_2 exchange indirectly through increasing concentration of air pollutants (Yue and Unger, 2018; Lasslop et al., 2019; see Section 6.3.4 for impacts of ozone and aerosol on the carbon cycle).

Significant uncertainties remain on land CO_2 sink partition of processes due to challenges in reconciling multiple-scale evidence from experiments to the globe (Fatichi et al., 2019; Walker et al., 2020), due to large spatial and inter-model differences in diagnosing dominant driving factors affecting the net land CO_2 sink (Huntzinger et al., 2017; Fernández-Martínez et al., 2019), and due to model deficiency in process representations (He et al., 2016). Nitrogen dynamics, a major gap in DGVMs identified in AR5, have now been incorporated in about half of the DGVMs contributing to the carbon budget of the Global Carbon Project (GCP) (see Le Quéré et al., (2018a) for model characteristics) and a growing number of ESMs (Arora et al., 2020). However, as the representations of carbon-nitrogen interactions vary greatly among models, large uncertainties remain on how nitrogen cycling regulates the response of ecosystem carbon uptake to higher atmospheric CO_2 (Davies-Barnard et al., 2020; Walker et al., 2015; Wieder et al., 2019; Meyerholt et al., 2020; see Section 5.4.1). Fire modules have been incorporated into 10 of 16 DGVMs contributing to the global carbon budget (Le Quéré et al., 2018a), and a growing number of models have representations of human ignitions and fire suppression processes (Rabin et al., 2017; Teckentrup et al., 2019). There are also growing DGVM developments to include management practices (Pongratz et al., 2018b) and the effects of secondary forest regrowth (Pugh et al., 2019a), though models still under represent intensively managed ecosystems, such as croplands and managed forests (Guanter et al., 2014; Thurner et al., 2017). Processes that have not yet played a significant role in the land CO_2 sink of the past decades but can grow in importance, include permafrost (Section 5.4) and peatlands dynamics (Dargie et al., 2017; Gibson et al., 2019), have also been incorporated in some DGVMs (Koven et al., 2015a; Burke et al., 2017a; Guimberteau et al., 2018). Growing numbers and varieties of Earth observations are being jointly used to drive and benchmark models, helping further identify key processes missing or mechanisms poorly represented in the current generation of DGVMs (e.g. Collier et al., 2018).

[START FIGURE 5.10 HERE]

Figure 5.10: Trends of the net land CO_2 sink and related vegetation observations during 1980–2019. (a) Net land CO_2 sink. The residual net land CO_2 sink is estimated from the global CO_2 mass balance (fossil fuel emission minus atmospheric CO_2 growth rate and ocean CO_2 sink). Inversions indicate the net land CO_2 sink estimated by an ensemble of four atmospheric inversions. Dynamic Global Vegetation Models (DGVMs) indicate the mean net land CO_2 sink estimated by 17 dynamic global vegetation models driven by climate change, rising atmospheric CO_2, land use change and nitrogen deposition change (for carbon-nitrogen models). The positive values indicate net CO_2 uptake from the atmosphere. (b) Normalised difference vegetation index (NDVI). The anomaly of global area-weighted NDVI observed by AVHRR and MODIS satellite sensors. AVHRR data are accessible during 1982–2016 and MODIS data are accessible during 2000–2018. (c) Near-infrared reflectance of vegetation (NIRv) and contiguous solar-induced chlorophyll fluorescence (CSIF). The standardised anomaly of area-weighted NIRv during 2001-2018 (Badgley et al., 2017) and CSIF during 2000-2018 (Zhang et al., 2018). (d) Gross primary production (GPP). The GPP from Cheng et al. (2017), DGVMs and MODIS GPP product (MOD17A3). GPP from Cheng et al. (2017) is based on an analytical model driven by climate change, rising atmospheric CO_2, AVHRR leaf area index datasets and evapotranspiration datasets. GPP from DGVMs is the ensemble mean global GPP estimated by the same 17 DGVMs that provide the net land CO_2 sink estimates. Shaded area indicates 1–σ inter-model spread except for atmospheric inversions, whose ranges were used due to limited number of models. Further details on data sources and processing are available in the chapter data table (Table 5.SM.6).

ACCEPTED VERSION SUBJECT TO FINAL EDITS

[END FIGURE 5.10 HERE]

5.2.1.4.2 Interannual variability in land-atmosphere CO_2 exchange

AR5 stated that the interannual variability of the atmospheric CO_2 growth rate is dominated by tropical land ecosystems. A set of new satellite measurements applied to assess the variability of the tropical land carbon balance since AR5 (Ciais et al., 2013) confirm this statement, including satellite column CO_2 measurements, estimating recent anomalous land-atmosphere CO_2 exchange induced by El Niño at continental scale (e.g. Liu et al., 2017; Palmer et al., 2019), and L-band vegetation optical depth, estimating tropical above-ground biomass carbon stock changes (Fan et al., 2019). In addition, based on medium evidence and medium agreement between studies with DGVMs and atmospheric inversions, semi-arid ecosystems over the tropical zones have a larger contribution to interannual variability in global land-atmosphere CO_2 exchange than moist tropical forest ecosystems (Poulter et al., 2014; Ahlstrom et al., 2015; Piao et al., 2020) (*low to medium confidence*).

Understanding the mechanisms driving interannual variability in the carbon cycle has the potential to provide insights into whether and to what extent the carbon cycle can affect the climate (carbon-climate feedback), with particular interests over the highly climate-sensitive tropical carbon cycle (e.g. Cox et al., 2013a; Fang et al., 2017; Humphrey et al., 2018; Jung et al., 2017a; Malhi et al., 2018; Wang et al., 2014; see Section 5.4). Consistent findings from studies with atmospheric inversions, satellite observations and DGVMs (e.g. Malhi et al., 2018; Rödenbeck et al., 2018) lead to *high confidence* that the tropical net land CO_2 sink is reduced under warmer and drier conditions, particularly during El Niño events. Interannual variations in tropical land-atmosphere CO_2 exchange are significantly correlated with anomalies of tropical temperature, water availability and terrestrial water storage (Wang et al., 2014; Jung et al., 2017; Humphrey et al., 2018; Piao et al., 2020), whose relative contribution are difficult to separate due to covariations between these climatic factors. At continental scale, the dominant climatic driver of interannual variations of tropical land-atmosphere CO_2 exchange was temperature variations (Figure 5.11; Piao et al., 2020), which could partly result from the spatial compensation of the water availability effects on land-atmospheric CO_2 exchange (Jung et al., 2017).

[START FIGURE 5.11 HERE]

Figure 5.11: Interannual variation in detrended anomalies of the net land CO_2 sink and land surface air temperature during 1980–2019. Correlation coefficients between the net land CO_2 sink anomalies and temperature anomalies are show on the right bar plots. The net land CO_2 sink is estimated by four atmospheric inversions (blue) and fifteen Dynamic Global Vegetation Models (DGVMs) (green), respectively (Friedlingstein et al., 2020). Solid blue and green lines show model mean detrended anomalies of the net land CO_2 sink. The ensemble mean of DGVMs is bounded by the 1–σ inter-model spread in each large latitude band (North 30°N–90°N, Tropics 30°S–30°N, South 90°S–30°S) and the globe. The ensemble mean of atmospheric inversions is bounded by model spread. For each latitudinal band, the anomalies of the net land CO_2 sink and temperature (orange) were obtained by removing the long-term trend and seasonal cycle. A 12-month running mean was applied to reduce high-frequency noise. The bars in the right panels show correlation coefficients between the net land CO_2 sink anomalies and temperature anomalies for each region. Two asterisks indicate $P<0.01$, and one indicates $P<0.05$. Grey shaded area shows the intensity of El Niño southern oscillation (ENSO) as defined by the Niño 3.4 index. Two volcanic eruptions (El Chichón eruption and Pinatubo eruption) are indicated with light blue dashed lines. Temperature data are from the Climatic Research Unit (CRU), University of East Anglia (Harris et al., 2014). Anomalies were calculated following Patra et al. (2005), but using 12-month low-pass filter and detrended to obtain interannual variations. Further details on data sources and processing are available in the chapter data table (Table 5.SM.6).

[END FIGURE 5.11 HERE]

[START CROSS-CHAPTER BOX 5.1]

ACCEPTED VERSION SUBJECT TO FINAL EDITS

Cross-Chapter Box 5.1: Interactions between the carbon and water cycles, particularly under drought conditions

Contributors: Josep G Canadell (Australia), Philippe Ciais (France), Hervé Douville (France), Sabine Fuss (Germany), Robert B Jackson (USA), Annalea Lohila (Finland), Shilong Piao (China), Sonia I. Seneviratne (Switzerland), Sergio M. Vicente-Serrano (Spain), Sönke Zaehle (Germany)

This box presents an assessment of interactions between the carbon and water cycles that influence the dynamics of the biosphere and its interaction with the climate system. It also highlights carbon-water trade-offs arising from the use of land-based climate mitigation options. Individual aspects of the interactions between the carbon and water cycles are addressed in separate chapters (Sections 5.2.1, 5.4.1, 8.2.3, 8.3.1, 8.4.1, 11.6). The influence of wetlands and dams on methane emissions is assessed elsewhere (Sections 5.2.2, 5.4.7, 8.3.1), as well as the consequences of permafrost thawing (Box 5.1, Section 9.5.2) and/or increased flooding (Sections 8.4.1, 11.5, 12.4) on wetland extent in the northern high latitudes and wet tropics.

Does elevated CO_2 alleviate the impacts of drought?

Increasing atmospheric CO_2 concentration enhances leaf photosynthesis and drives a partial closure of leaf stomata, leading to higher water-use efficiency (WUE) at the leaf, canopy to ecosystem scales (Norby and Zak, 2011; De Kauwe et al., 2013; Fatichi et al., 2016; Knauer et al., 2017; Mastrotheodoros et al., 2017). Since AR5 (Box 6.3), a growing body of evidence from tree-ring and carbon isotopes further confirms an increase of plant water-use efficiency over decadal to centennial time scales, with some evidence for a stronger enhancement of photosynthesis compared to stomatal reductions (Frank et al., 2015; Guerrieri et al., 2019; Adams et al., 2020).

Multiple lines of evidence suggest that WUE has increased in near proportionality to atmospheric CO_2 (*high confidence*), at a rate generally consistent with Earth System Models (ESMs), despite variation in the WUE response to CO_2 (De Kauwe et al., 2013; Frank et al., 2015; Keeling et al., 2017; Lavergne et al., 2019; Walker et al., 2020). Both field-scale CO_2 enrichment experiments and process models show the effect of physiologically induced water savings, particularly under water limiting conditions (De Kauwe et al., 2013; Farrior et al., 2015; Lu et al., 2016; Roy et al., 2016). Plants can also benefit from reduced drought stress due to enhanced CO_2 without ecosystems-scale water savings (Jiang et al., 2021). This increased WUE offsets to some extent the effects of enhanced vapor pressure deficit (VPD) on plant transpiration (Bobich et al., 2010; Creese et al., 2014; Jiao et al., 2019), but will have limited effect on ameliorating plant water stress during extreme drought events (Xu et al., 2016; Menezes-Silva et al., 2019; Liu et al., 2020b), when leaf stomata is governed primarily by soil moisture (Roy et al., 2016).

Leaf stomata closure can have large effects on land freshwater availability because of reduced plant transpiration leading in some regions to higher soil moisture and runoff (Roderick et al., 2015; Milly and Dunne, 2016; Yang et al., 2019c). However, increased water availability is often not realized because other CO_2 physiological effects that enhance ecosystem evapotranspiration might offset the gains. These effects include plant growth and leaf area expansion (Ainsworth and Long, 2005; Ukkola et al., 2016; McDermid et al., 2021), lengthening of the vegetative growing season (Frank et al., 2015; Lian et al., 2021), and the effects of stomatal closure on near-surface atmosphere that leads to increased air temperature and vapor-pressure deficits (Berg et al., 2016; Vogel et al., 2018; Zhou et al., 2019; Grossiord et al., 2020).

ESMs show no consensus about the net hydrological response to physiological CO_2 effects. Some studies show water savings as a consequence of the CO_2 effects on leaf stomata closure (Swann et al., 2016; Lemordant et al., 2018), while other studies show that increased leaf area offsets the gains from increased WUE (Mankin et al., 2019). However, these projections are subject to ESM uncertainties to quantify transpiration (Lian et al., 2021), among them the correct representations of plant hydraulic architecture such as changes in xylem anatomical properties and deep rooting (Nie et al., 2013; Liu et al., 2020b).

ACCEPTED VERSION SUBJECT TO FINAL EDITS

In conclusion, it is *very likely* that elevated CO_2 leads to increased WUE at the leaf level concurrent with enhanced photosynthesis. Increased CO_2 concentrations alleviate the effects of water deficits on plant productivity (*medium confidence*) but there is *low confidence* on its role under extreme drought conditions. There is *low confidence* that increased WUE by vegetation will substantially reduce global plant transpiration and diminish the frequency and severity of soil moisture and streamflow deficits associated with the radiative effect of higher CO_2 concentrations.

How does drought affect the terrestrial CO_2 sink?

Water availability controls the spatial distribution of photosynthesis (gross primary productivity, GPP) over a larger part of the globe (Beer et al., 2010) and, at local scale, drought decreases GPP more than respiration (Schwalm et al., 2012) over most ecosystem types. This makes water availability a major climatic driver of variability in net ecosystem exchange (Jung et al., 2017; Humphrey et al., 2018). In addition to suppressing photosynthesis, field evidence suggests that droughts reduce the land CO_2 sink also through increasing forest mortality and promoting wildfire (Allen et al., 2015; Brando et al., 2019; Abram et al., 2021).

At the global scale, interannual variability in the atmospheric CO_2 growth rate and global-scale terrestrial water storage from satellite shows that a lower global net land CO_2 sink is associated with below-average terrestrial water storage (Humphrey et al., 2018). Atmospheric inversions based on surface and satellite column CO_2 measurements show significant carbon release during drought events in pan-tropic areas (Phillips et al., 2009; Gatti et al., 2014; Liu et al., 2017a; Palmer et al., 2019a). Regional extreme droughts in the mid-latitudes also lead to decreased GPP and land CO_2 sink (Ciais et al., 2005; Wolf et al., 2016; Peters et al., 2020b; Flach et al., 2021). Droughts cannot be compensated by equivalent wet anomalies because of the non-linear response of the terrestrial carbon uptake to soil moisture (Green et al., 2019).

Uncertainties remain on the magnitude of sensitivity of the land carbon fluxes to droughts. Global studies indicate stronger control of soil moisture to variations in satellite proxies of GPP than VPD (Stocker et al., 2019; Liu et al., 2020b). However, given that VPD increases exponentially with atmospheric warming, some studies suggest that the importance of VPD in stomatal regulation will become increasingly more important under warmer climate (Novick et al., 2016; Grossiord et al., 2020). It is difficult to isolate the relative contributions of warmer temperature, higher VPD and lower soil moisture. This is because land-atmosphere feedbacks cause a simultaneous increase of plant evaporative demand and of root zone water deficit impairing plant root uptake (Berg et al., 2016). These physiological responses can be further compounded by drought legacies (Anderegg et al., 2015), changes in structure and population dynamics due to forest mortality (McDowell et al., 2020), disturbances associated with drought (fire, insects damage) (Anderegg et al., 2020) and possible trade-offs between resistance and resilience (Li et al., 2020b). Nonetheless, ESMs suggest that increased drought effects under very high levels of global warming (ca. 4°C at the end of the 21st century) contribute to the reduced efficiency of the land sink (Green et al., 2019).

In conclusion, there is *high confidence* that the global net land CO_2 sink is reduced on interannual scale when regional-scale reductions in water availability associated with droughts occur, particularly in tropical regions. There is also *high confidence* that the global land sink will become less efficient due to soil moisture limitations and associated drought conditions in some regions for high emission scenarios, specially under global warming above 4°C. However, there is *low confidence* on how these water cycle feedbacks will play out in lower emission scenarios (at 2°C global warming or lower) due to uncertainties in regional rainfall changes and the balance between the CO_2 fertilisation effect, through WUE, and the radiative impacts of greenhouse gases.

What are the limits of carbon dioxide removal from a water cycle perspective?

Carbon dioxide removal (CDR) options based on terrestrial carbon sinks will require the appropriation of significant amounts of water at the landscape level. Most mitigation pathways that seek to limit global warming to 1.5°C or less than 2°C require the removal of about 30 to 300 GtC from the atmosphere by 2100 (Rogelj et al., 2018b). Bioenergy with carbon capture and storage (BECCS), and afforestation/reforestation are the dominant CDR options used in climate stabilisation scenarios implying large requirements for land and water (Section 5.6; (Beringer et al., 2011; Boysen et al., 2017b; Fajardy and Mac Dowell, 2017; Jans et

ACCEPTED VERSION SUBJECT TO FINAL EDITS

al., 2018; Séférian et al., 2018b; Yamagata et al., 2018; Stenzel et al., 2019). A review of freshwater requirements for irrigating biomass plantations shows a range between 15 and 1250 km^3 per GtC^{-1} of biomass harvest. This is equivalent to a water requirement of 99–8250 km^3 for the median BECCS deployment of around 3.3 $GtCyr^{-1}$ (Smith et al., 2016) in <2°C-scenarios (Stenzel et al., 2021), assuming that biomass is converted to electricity which is substantially less efficient than to heat. These large ranges are the result of different assumptions about the type of biomass and yield improvements, management, and land availability. The use of alternative feedstocks, such as wastes, residues and algae, would lead to smaller water requirements (Smith et al., 2019).

Most of the water consumed in BECCS is used to grow the feedstock, with carbon capture and storage constituting a smaller portion across all crops (Rosa et al., 2020), with an estimated evaporative loss of 260 $km^3\ yr^{-1}$ for 3.3 GtC yr^{-1} (Smith et al., 2016). The same authors also estimate water use for CDR through afforestation at 1040 $km^3\ yr^{-1}$ for 3.3 GtC yr^{-1}, including interception and transpiration and adjusted for the original land cover's water use.

The impacts of different CDR options on the water cycle depend crucially on regional climate, prior land cover, and scale of deployment (Trabucco et al., 2008). Extensive irrigation for afforestation in drier areas will have larger downstream impacts than in wetter regions with the difference in water use between the afforested landscapes and its previous vegetation determining the level of potential impacts on evapotranspiration and runoff (Jackson et al., 2005; Teuling et al., 2017). Afforestation and reforestation sometimes enhances precipitation through atmospheric feedbacks such as increased convection, at least in the tropics (Ellison et al., 2017) and the increase in precipitation can in some regions even cancel out the increased evapotranspiration (Li et al., 2018).

In conclusion, extensive deployment of BECCS and afforestation/reforestation will require larger amounts of freshwater resources than used by the previous vegetation, altering the water cycle at regional scales (*high confidence*). Consequences of high water consumption on downstream uses, biodiversity, and regional climate depend on prior land cover, background climate conditions, and scale of deployment (*high confidence*). Therefore, a regional approach is required to determine the efficacy and sustainability of CDR projects.

[END CROSS-CHAPTER BOX 5.1]

5.2.1.5 CO_2 Budget

The global CO_2 budget (Figure 5.12) encompasses all natural and anthropogenic CO_2 sources and sinks. Table 5.1 shows the perturbation of the global carbon mass balance between reservoirs since the beginning of the industrial era, circa 1750.

Since AR5 (Ciais et al., 2013), a number of improvements have led to a more constrained carbon budget presented here. Some new additions include: (i) the use of independent estimates for the residual carbon sink on natural terrestrial ecosystems (Le Quéré et al., 2018a), (ii) improvements in the estimates of emissions from cement production (Andrew, 2019) and the sink associated with cement carbonation (Cao et al., 2020), (iii) improved and new emission estimates from forestry and other land use (Hansis et al., 2015; Gasser et al., 2020), (iv) the use of ocean observation-based sink estimates and a revised river flux partition between hemisphere (Friedlingstein et al., 2020); and (v) the expansion of constraints from atmospheric inversions, both based on surface networks and the use of satellite retrievals.

The budget, based on the annual assessment by the GCP (Friedlingstein et al., 2020), uses independent estimates of all major flux components: fossil fuel and carbonate emissions (E_{FOS}), CO_2 fluxes from Forestry and other Land Use (E_{LULUCF}), the growth rate of CO_2 in the atmosphere (G_{atm}), and the ocean (S_{ocean}) and natural land (S_{land}) CO_2 sinks. An imbalance term (B_{Imb}) is required to ensure mass balance of the source and sinks that have been independently estimated: $E_{FOS} + E_{LULUCF} = G_{atm} + S_{ocean} + S_{land.} + B_{Imb.}$ All estimates are reported with 1 standard deviation (±1σ, 1 sigma) representing a likelihood of 68%.

ACCEPTED VERSION SUBJECT TO FINAL EDITS

Over the past decade (2010–2019), 10.9 ± 0.9 PgC yr^{-1} were emitted from human activities which were distributed between three Earth system components: 46% accumulated in the atmosphere (5.1 ± 0.02 PgC yr^{-1}), 23% was taken up by the ocean (2.5 ± 0.6 PgC yr^{-1}) and 31% was stored by vegetation in terrestrial ecosystems (3.4 ± 0.9 PgC yr^{-1}) (Table 5.1). There is a budget imbalance of 0.1 PgCyr^{-1} which is within the uncertainties of the other terms. Over the industrial era (1750–2019), the total cumulative CO_2 fossil fuel and industry emissions were 445 ± 20 PgC, and the LULUCF flux (=net land use change in Figure 5.12) was 240 ± 70 PgC (*medium confidence*). The equivalent total emissions (685 ± 75 PgC) was distributed between the atmosphere (285 ± 5 PgC), oceans (170 ± 20 PgC) and land (230 ± 60 PgC) (Table 5.1), with a budget imbalance of 20 PgC.

This budget (Table 5.1) does not explicitly account for source/sink dynamics due to carbon cycling in the land–ocean aquatic continuum comprising freshwaters, estuaries, and coastal areas. Natural and anthropogenic transfers of carbon from soils to freshwater systems are significant (2.4–5.1 PgC yr^{-1}) (Regnier et al., 2013a; Drake et al., 2018). Some of the carbon is buried in freshwater bodies (0.15 PgC) (Mendonça et al., 2017), and a significant proportion returns to the atmosphere via outgassing from lakes, rivers and estuaries (Raymond et al., 2013; Regnier et al., 2013a; Lauerwald et al., 2015). The net export of carbon from the terrestrial domain to the open oceans is estimated to be 0.80 PgC yr^{-1} (*medium confidence)*, based on the average of (Jacobson et al., 2007; Resplandy et al., 2018b) and corrected to account for 0.2 PgC buried in ocean floor sediments. These terms are included in Figure 5.12. Inclusion of other smaller fluxes could further constrain the carbon budget (Ito, 2019; Friedlingstein et al., 2020).

[START FIGURE 5.12 HERE]

Figure 5.12: Global carbon (CO_2) budget (2010-2019). Yellow arrows represent annual carbon fluxes (in PgC yr^{-1}) associated with the natural carbon cycle estimated for the time prior to the industrial era, around 1750. Pink arrows represent anthropogenic fluxes averaged over the period 2010–2019. The rate of carbon accumulation in the atmosphere is equal to net land-use change emissions, including land management (called LULUCF in the main text) plus fossil fuel emissions, minus land and ocean net sinks (plus a small budget imbalance, Table 5.1). Circles with yellow numbers represent pre-industrial carbon stocks in PgC. Circles with pink numbers represent anthropogenic changes to these stocks (cumulative anthropogenic fluxes) since 1750. Anthropogenic net fluxes are reproduced from Friedlingstein et al., (2020). The relative change of *gross photosynthesis* since pre-industrial times is based on 15 DGVMs used in Friedlingstein et al., (2020). The corresponding emissions by *Total respiration and fire* are those required to match the *net land flux*, exclusive of net land-use change emissions which are accounted for separately. The cumulative change of anthropogenic carbon in the terrestrial reservoir is the sum of carbon cumulatively lost by net land use change emissions, and net carbon accumulated since 1750 in response to environmental drivers (warming, rising CO_2, nitrogen deposition). The adjusted gross natural ocean-atmosphere CO_2 flux was derived by rescaling the value in figure 1 of (Sarmiento and Gruber, 2002) of 70 PgC/yr by the revised estimate of the bomb ^{14}C inventory in the ocean. The original bomb ^{14}C inventoy yielded an average global gas transfer velocity of 22 cm/hr; the revised estimate is 17cm/h leading to 17/22*70=54. Dissolved organic carbon reservoir and fluxes from (Hansell et al., 2009). Dissolved inorganic carbon exchanges between surface and deep ocean, subduction and obduction from (Levy et al., 2013) Levy et al. 2013. Export production and flux from (Boyd et al., 2019). NPP and remineralisation in surface layer of the ocean from (Kwiatkowski et al., 2020; Séférian et al., 2020). Deep ocean reservoir from (Keppler et al., 2020). Note that the mass balance of the two ocean carbon stocks *surface ocean* and *intermediate and deep ocean* includes a yearly accumulation of anthropogenic carbon (not shown). Fossil fuel reserves are from (BGR, 2019); fossil fuel resources are 11,490 PgC for coal, 6,780 PgC for oil, and 365 PgC for natural gas. Permafrost region stores are from (Hugelius et al., 2014; Strauss et al., 2017; Mishra et al., 2021) (see also Box 5.1) and soil carbon stocks outside of permafrost region from Batjes, (2016); Jackson et al., (2017). Biomass stocks (range of seven estimates) are from Erb et al., (2018). Sources for the fluxes of the continuum land-to-ocean are provided in main text and adjusted within the ranges of the various assessment to balance the budget (section 5.2.1.5).

[END FIGURE 5.12 HERE]

[START TABLE 5.1 HERE]

ACCEPTED VERSION SUBJECT TO FINAL EDITS

Table 5.1: Global anthropogenic CO_2 budget accumulated since the industrial revolution (onset in 1750) and averaged over the 1980s, 1990s, 2000s, and 2010s. By convention, a negative ocean or land to atmosphere CO_2 flux is equivalent to a gain of carbon by these reservoirs. The table does not include natural exchanges (e.g. rivers, weathering) between reservoirs. Uncertainties represent the 68% confidence interval (Friedlingstein et al., 2020).

	1750–2019 Cumulative (PgC)	1850-2019 Cumulative (PgC)	1980–1989 Mean Annual Growth Rate (PgC yr^{-1})	1990–1999 Mean Annual Growth Rate (PgC yr^{-1})	2000–2009 Mean Annual Growth Rate (PgC yr^{-1})	2010–2019 Mean Annual Growth Rate (PgC yr^{-1})
Emissions						
Fossil fuel combustion and cement production	445 ± 20	445 ± 20	5.4 ± 0.3	6.3 ± 0.3	7.7 ± 0.4	9.4 ± 0.5
Net land use change	240 ± 70	210 ± 60	1.3 ± 0.7	1.4 ± 0.7	1.4 ± 0.7	1.6 ± 0.7
Total emissions	685 ± 75	655 ± 65	6.7 ± 0.8	7.7 ± 0.8	9.1 ± 0.8	10.9 ± 0.9
Partition						
Atmospheric increase	285 ± 5	265 ± 5	3.4 ± 0.02	3.2 ± 0.02	4.1 ± 0.02	5.1 ± 0.02
Ocean sink[c]	170 ± 20	160 ± 20	1.7 ± 0.4	2.0 ± 0.5	2.1 ± 0.5	2.5 ± 0.6
Terrestrial sink	230 ± 60	210 ± 55	2.0 ± 0.7	2.6 ± 0.7	2.9 ± 0.8	3.4 ± 0.9
Budget imbalance	0	20	–0.4	–0.1	0	–0.1

[END TABLE 5.1 HERE]

5.2.2 CH_4: Trends, Variability and Budget

Methane is a much more powerful greenhouse gas than CO_2 (Chapter 7) and participates in tropospheric air chemistry (Chapter 6). The CH_4 variability in the atmosphere is mainly the result of the net balance between the sources and sinks on the Earth's surface and chemical losses in the atmosphere. Atmospheric transport evens out the regional CH_4 differences between different parts of the Earth's atmosphere. The steady-state lifetime is estimated to be 9.1 ± 0.9 (Chapter 6, Section 3.1). About 90% of the loss of atmospheric CH_4 occurs in the troposphere by reaction with hydroxyl (OH) radical, 5% by bacterial soil oxidation, and the rest 5% by chemical reactions with OH, excited state oxygen (O^1D), and atomic chlorine (Cl) in the stratosphere (Saunois et al., 2020). Methane has large emissions from both natural and anthropogenic origins, but a clear demarcation of their nature is difficult because of the use and conversions of the natural ecosystem for human activities. The largest natural sources are from wetlands, freshwater and geological process, while the largest anthropogenic emissions are from enteric fermentation and manure treatment, landfills and waste treatment, rice cultivation and fossil fuel exploitation (Table 5.2). In the past two centuries, CH_4 emissions have nearly doubled, predominantly human driven since 1900, and persistently exceeded the losses (*virtually certain*), thereby increasing the atmospheric abundance as evidenced from the ice core and firn air measurements (Ferretti et al., 2005; Ghosh et al., 2015).

This section discusses both bottom-up and top-down estimates of emissions and sinks. Bottom-up estimates are based on empirical upscaling of point measurements, emission inventories and dynamical model simulations, while top-down estimates refer to those constrained by atmospheric measurements and chemistry-transport models in inversion systems. Since the AR5, a larger suite of atmospheric inversions using both in situ and remote sensing measurement have led to better understanding of the regional CH_4 sources (Cross-Chapter Box 5.2). New ice core measurements of ^{14}C-CH_4 are used for estimating the geological sources of CH_4 (Table 5.2). Compared to the IPCC SRCCL (IPCC, 2019a; Jia et al., 2019), we provide a whole atmospheric sources-sinks budget consisting of all emissiones and losses.

5.2.2.1 Atmosphere

Since the start of direct measurements of CH_4 in the atmosphere in the 1970s (Figure 5.13), the highest

ACCEPTED VERSION SUBJECT TO FINAL EDITS

growth rate was observed from 1977 to 1986 at 18 ± 4 ppb yr^{-1} (multi-year mean and 1 standard deviation) (Rice et al., 2016). This rapid CH_4 growth followed the green revolution with increased crop-production and a fast rate of industrialisation that caused rapid increases in CH_4 emissions from ruminant animals, rice cultivation, landfills, oil and gas industry and coal mining (Ferretti et al., 2005; Ghosh et al., 2015; Crippa et al., 2020). Due to increases in oil prices in the early 1980s, emissions from gas flaring declined significantly (Stern and Kaufmann, 1996). This explains the first reduction in CH_4 growth rates from 1985 to 1990 (Steele et al., 1992; Chandra et al., 2021). Further reductions in emission occurred following the Mt Pinatubo eruption in 1991 that triggered a reduction in CH_4 growth rate through a decrease in wetland emissions driven by lower surface temperatures due to the scattering aerosols (Bândă et al., 2016; Chandra et al., 2021). In the late 1990s through 2006 there was a temporary pause in the CH_4 growth rate, with higher confidence on its causes than the in AR5: emission from the oil and gas sectors declined by about 10 Tg yr^{-1} through the 1990s, and atmospheric CH_4 loss steadily increased (Dlugokencky et al., 2003; Simpson et al., 2012; Crippa et al., 2020; Höglund-Isaksson et al., 2020; Chandra et al., 2021). Methane growth rate began to increase again at 7 ± 3 ppb yr^{-1} during 2007–2016, the causes of which are highly debated since the AR5 (Rigby et al., 2008; Dlugokencky et al., 2011; Dalsøren et al., 2016; Nisbet et al., 2016; Patra et al., 2016; Schaefer et al., 2016; Schwietzke et al., 2016; Turner et al., 2017; Worden et al., 2017; He et al., 2020); studies disagree on the relative contribution of thermogenic, pyrogenic and biogenic emission processes and variability in tropospheric OH concentration. The renewed CH_4 increase is accompanied by a reversal of $\delta^{13}C$ trend to more negative values post 2007; opposite to what occurred in the 200 years prior (Ferretti et al., 2005; Ghosh et al., 2015; Schaefer et al., 2016; Schwietzke et al., 2016; Nisbet et al., 2019), suggesting an increasing contribution from animal farming, landfills and waste, and a slower increase in emissions from fossil fuel exploitation since the early 2000s (Patra et al., 2016; Jackson et al., 2020; Chandra et al., 2021). A comprehensive assessment of the CH_4 growth rates over the past 4 decades is presented in the Cross-Chapter Box 5.2.

[START FIGURE 5.13 HERE]

Figure 5.13: Time series of CH_4 concentrations, growth rates and isotopic composition. a) CH_4 concentrations, b) CH_4 growth rates, c) δ^{13}-CH_4. Data from selected site networks operated by NOAA (Dlugokencky et al., 2003), AGAGE (Prinn et al., 2018) and PDX (Portland State University) (Rice et al., 2016). To maintain clarity, data from many other measurement networks are not included here, and all measurements are shown in WMO X2004ACH_4 global calibration standard. Global mean values of XCH_4 (total-column), retrieved from radiation spectra measured by the greenhouse gases observation satellite (GOSAT) are shown in panels (a) and (b). Cape Grim Observatory (CGO; 41°S, 145°E) and Trinidad Head (THD; 41°N, 124°W) data are taken from the AGAGE network, NOAA global and northern hemispheric (NH) means for $\delta^{13}C$ are calculated from 10 and 6 sites, respectively. The PDX data adjusted to NH (period: 1977–2000) are merged with THD (period: 2001–2019) for CH_4 concentration and growth rate analysis, and PDX and NOAA NH means of $\delta^{13}C$ data are used for joint interpretation of long-term trends analysis. The multivariate ENSO index (MEI) is shown in panel (b). Further details on data sources and processing are available in the chapter data table (Table 5.SM.6).

[END FIGURE 5.13 HERE]

5.2.2.2 Anthropogenic CH_4 emissions

The positive gradient between CH_4 at Cape Grim, Australia (41°S) and Trinidad Head, USA (41°N), and the bigger difference between Trinidad Head and global mean CH_4 compared to that between global mean CH_4 and Cape Grim, strongly suggest that the northern hemisphere is the dominant origin of anthropogenic CH_4 emissions (Figure 5.13). The loss rate of CH_4 in troposphere does not produce a large positive north-south hemispheric gradient in CH_4 due to parity in hemispheric mean OH concentration (Patra et al., 2014) or in the case of greater OH concentrations in the northern than the southern hemisphere as simulated by the chemistry-climate models (Naik et al., 2013). Coal mining contributed about 35% of the total CH_4 emissions from all fossil fuel related sources. Top-down estimates of fossil fuel emissions (106 Tg yr^{-1}) are smaller than bottom-up estimates (115 Tg yr^{-1}) during 2008–2017 (Table 5.2). Inventory-based estimates suggest that

ACCEPTED VERSION SUBJECT TO FINAL EDITS

CH_4 emissions from coal mining increased by 17 Tg yr^{-1} between the periods 2002–2006 and 2008–2012, with a dominant contribution from China (Peng et al., 2016; Crippa et al., 2020; Höglund-Isaksson et al., 2020). Furthermore, top-down estimates suggest emissions from China's coal mines have continued to grow at a slower rate after 2010 (Miller et al., 2019; Chandra et al., 2021). Emissions from oil and gas extraction and use decreased in the 1980s and 1990s, but increased in the 2000s and 2010s (Dlugokencky et al., 1994; Stern and Kaufmann, 1996; Howarth, 2019; Crippa et al., 2020). The attribution to multiple CH_4 source using spatially aggregated atmospheric $\delta^{13}C$ data remained underdetermined to infer the global total emissions from the fossil fuel industry, biomass burning and agriculture (Rice et al., 2016; Schaefer et al., 2016; Schwietzke et al., 2016; Worden et al., 2017; Thompson et al., 2018).

In the agriculture and waste sectors (Table 5.2), livestock production has the largest emission source (109 Tg yr^{-1} in 2008–2017) dominated by enteric fermentation by about 90%. Methane is formed during the storage of manure, when anoxic conditions are developed (Hristov et al., 2013). Emissions from enteric fermentation and manure have increased gradually from about 87 Tg yr^{-1} in 1990–1999 to 109 Tg yr^{-1} in 2008–2017 mainly due to the increase in global total animal numbers. Methane production in livestock rumens (cattle, goats, sheep, water buffalo) are affected by the type, amount and quality of feeds, energy consumption, animal size, health and growth rate, meat and milk production rate, and temperature (Broucek, 2014; Williams et al., 2015; IPCC SRCCL 5.4.3). Waste management and landfills produced 64 Tg yr^{-1} in 2008–2017, with global emissions increasing steadily since the 1970s and despite significant declines in US, western Europe and Japan (Crippa et al., 2020; Höglund-Isaksson et al., 2020).

Emissions from rice cultivation decreased from about 45 Tg yr^{-1} in the 1980s to about 29 Tg yr^{-1} in the 2000-2009 but increased again slightly to 31 Tg yr^{-1} during 2008–2017 based inventories data. However, ecosystem models showed a gradual increase with time due to climate change (*limited evidence, low agreement*) (Crippa et al., 2020; Höglund-Isaksson et al., 2020; Ito, 2020).

Biomass burning and biofuel consumption (including both natural and anthropogenic processes) caused at least 30 Tg yr^{-1} emissions during 2008–2017 and constituted up to about 5% of global anthropogenic CH_4 emissions. Methane emissions from open biomass burning decreased during the past two decades mainly due to reduction of burning in savanna, grassland and shrubland (van der Werf et al., 2017; Worden et al., 2017). There is recent evidence from the tropics that fire occurrence is non-linearly related to precipitation, implying that severe droughts will increase CH_4 emissions from fires, particularly from the degraded peatlands (Field et al., 2016).

[START TABLE 5.2 HERE]

Table 5.2: **Global CH_4 budget.** Sources and sinks of CH_4 for the two recent decades from bottom–up and top-down estimations (in Tg CH_4 yr^{-1}). The data are updated from (Saunois et al., 2020), for the bottom-up anthropogenic emissions (FAO, 2019; US EPA, 2019; Crippa et al., 2020; Höglund-Isaksson et al., 2020), top-down geological emissions (Schwietzke et al., 2016; Petrenko et al., 2017; Hmiel et al., 2020), and top-down sinks from 7 selected inverse models. The means (min-max) with outliers removed from both the range and the means are given. Outliers defined as >75th percentile + 3 × the interquartile range or < 25th percentile – 3 × the interquartile range. The top-down budget imbalances are calculated for each model separately and averaged. Note also the round-off error for the sources and sinks, which sometimes leads to last digit mismatch in the sums. For detailed information on datasets, see further details on data table 5.SM.6.

Tg CH_4 yr^{-1}	2000–2009				2008–2017			
	Top-Down		Bottom-up		Top-Down		Bottom-up	
SOURCES								
Natural sources	215	(176–243)	369	(245–484)	215	(183–248)	371	(245–488)
Wetlands	180	(153–196)	147	(102-178)	180	(159–199)	149	(102–182)
Other Sources	35	(21–47)	222	(143–306)	36	(21–49)	222	(143–306)

ACCEPTED VERSION SUBJECT TO FINAL EDITS

Freshwater (lakes and rivers)							159	(117-212)
Wild animals							2	(1-3)
Termites							9	(3-15)
Geological (land and oceans)					23	(0-71)	45	(18-65)
Other oceanic (sea-air flux and hydrates)							6	(4-10)
Permafrost (excl. lakes and wetlands)							1	(0-1)
Anthropogenic sources	332	(312–347)	330	(309–350)	357	(336–375)	356	(335–383)
Agriculture & Waste	206	(198–219)	195	(185–212)	221	(209–238)	208	(192–230)
Enteric fermentation & Manure			103	(101–107)			109	(106–115)
Landfills & waste			60	(53–70)			64	(55–77)
Rice			29	(23–34)			31	(25–37)
Fossil fuels	101	(71–151)	100	(94–108)	106	(81–131)	115	(114–116)
Coal			29	(26–33)			38	(36–39)
Oil and gas			65	(60–72)			70	(68–73)
Transport			3	(1–8)			5	(1–11)
Industry			3	(0–6)			3	(1–5)
Biomass burning & biofuels	29	(23–35)	32	(24–44)	30	(22–36)	30	(22–39)
Biomass burning			19	(15–32)			17	(14–26)
Biofuels			10	(8–12)			10	(8–13)
SINKS								
Total chemical loss	511	(502–515)	595	(489–749)	514	(474–529)	602	(496–754)
Tropospheric OH			553	(476–677)			560	(483–682)
Stratospheric loss			31	(12–37)			31	(12–37)
Tropospheric Cl			11	(1–35)			11	(1–35)
Soil uptake	34	(27–41)	30	(11–49)	37	(27–43)	30	(11–49)
Sum of sources	548	(524–560)	699	(554–834)	576	(550–589)	727	(581–872)
Sum of sinks	546	(533–556)	625	(500–798)	551	(501–572)	632	(507–803)
Imbalance	7	(4–11)	74		21	(18-26)	95	
Atmospheric growth rate (ppb yr^{-1})	2 ± 4				7 ± 3			

[END TABLE 5.2 HERE]

5.2.2.3 Land Biospheric Emissions and Sinks

Freshwater wetlands are the single largest global natural source of CH_4 into the atmosphere, accounting for about 26% of the total CH_4 source (*robust evidence, medium agreement*). Progress has been made since AR5 (Ciais et al., 2013) in better constraining freshwater lake and river emissions and reducing double counting with wetland emissions. Bottom-up and top-down estimates for 2008–2017 are 149 and 180 Tg yr^{-1}, respectively, with a top-down uncertainty range of 159–199 Tg yr^{-1} (Table 5.2). The large uncertainties stem from challenges in mapping wetland area and temporal dynamics, and in scaling methane production, transport and consumption processes, that are measured with small chambers or flux towers, to landscape estimates (Pham-Duc et al., 2017). Both the top-down and bottom-up estimates presented in Table 5.2 indicate little increase in wetland CH_4 emissions during the last three decades, with the new estimates being slightly smaller than in AR5 due to updated wetland maps and ecosystem model simulations (Melton et al., 2013; Poulter et al., 2017). The wetland emissions show strong interannual variability due to the changes in inundated land area, air temperature and microbial activity (Bridgham et al., 2013). Present terrestrial ecosystem model simulated CH_4 emission variability does not produce strong correlation with the ENSO cycle (Cross-Chapter Box 5.2, Figure 2), although observation evidence is emerging for lower CH_4 emissions during El Niños and greater emissions during the La Niña (Pandey et al., 2017).

Trees in upland and wetland forests contribute to CH_4 emissions by abiotic production in the canopy, by the methanogenesis taking place in the stem, and by conducting CH_4 from soil into the atmosphere (Covey and

ACCEPTED VERSION SUBJECT TO FINAL EDITS

Megonigal, 2019). There is emerging evidence of the important role of trees in transporting and conducting CH_4 from soils into the atmosphere especially in tropics (Pangala et al., 2017), whereas direct production of CH_4 by vegetation only has a minor contribution (*limited evidence, high agreement*) (Bruhn et al., 2012; Covey and Megonigal, 2019). The contribution of trees in transporting CH_4 may further widen the gap between the bottom-up and top-down estimates in the global budget, particularly needing a reassessment of emissions in the tropics and in forested wetlands of temperate and boreal regions (Pangala et al., 2017; Jeffrey et al., 2019; Welch et al., 2019; Sjögersten et al., 2020).

Microbial methane uptake by soil comprises up to 5% (30 Tg yr^{-1}) of the total CH_4 sink in 2008–2017 (Table 5.2). There is evidence from experimental and modelling studies of increasing soil microbial uptake due to increasing temperature (Yu et al., 2017), although evidence for decreasing CH_4 consumption, possibly linked to precipitation changes, also exist (Ni and Groffman, 2018). The estimate of global methane loss by microbial oxidation in upland soils has been lowered marginally by 4 Tg yr^{-1}, compared to 34 Tg yr^{-1} in AR5, for the period 2000–2009. Termites, an infraorder of insects (Isoptera) found in almost all landmasses, emitted about 9 Tg yr^{-1} of CH_4 in 2000–2009, and increased emissions from the insects and other anthropods are projected (Brune, 2018).

5.2.2.4 Ocean and Inland Water Emissions and Sinks

In AR5, the ocean CH_4 emissions were reported together with geological emissions summing up to 54 (33–75) Tg yr^{-1}. Coastal oceans, fjords and mud volcanos are major source of CH_4 in the marine environment, but CH_4 flux measurements are sparse. Saunois et al. (2020) estimate that the oceanic budget, including biogenic, geological and hydrate emissions from coastal and open ocean, is 6 (range 4–10) Tg yr^{-1} for the 2000s, which is in good agreement with an air-sea flux measurement-based estimate of 6–12 Tg yr^{-1} (Weber et al., 2019). When estuaries are included, the total oceanic budget is 9–22 Tg yr^{-1}, with a mean value of 13 Tg yr^{-1}. A recent synthesis suggests that CH_4 emissions from shallow coastal ecosystems, particularly from mangroves, can be as high as 5–6 Tg yr^{-1} (Al-Haj and Fulweiler, 2020). The reservoir emissions, including coastal wetlands and tidal flats, contribute up to 13 Tg yr^{-1} (Borges and Abril, 2011; Deemer et al., 2016). Methane seepage from the Arctic shelf, possibly triggered by the loss of geological storage due to warming and thawing of permafrost and hydrate decomposition, has a wide estimated range of 0.0–17 Tg yr^{-1} (Shakhova et al., 2010, 2014, 2017; Berchet et al., 2016); advanced eddy covariance measurements put the best estimate at just about 3 Tg yr^{-1} from the East Siberian Arctic shelf (Thornton et al., 2020). The current flux is expected to be a mix of pre-industrial and climate change-driven fluxes, CH_4 seepage is anticipated to increase in a warmer world (Dean et al., 2018).

All geological sources around the world, including the coastal oceans and fjords, are estimated to emit CH_4 in the range of 35–76 Tg yr^{-1} (Etiope et al., 2019). There is evidence that the ventilation of geological CH_4 is *likely* to be smaller than 15 Tg yr^{-1} (Petrenko et al., 2017; Hmiel et al., 2020). A lower geological CH_4 ventilation will reduce the gap between bottom-up estimations and that are used in top-down models (Table 5.2), but widen the gap in the ratio of fossil-fuel derived sources to the biogenic sources for matching the $\Delta^{14}C$-CH_4 observations.

Inland water (lakes, rivers, streams, ponds, estuaries) emissions are proportionally the largest source of uncertainty in the CH_4 budget. Since AR5 (Ciais et al., 2013), the inland water CH_4 source has been revised from 8–73 Tg yr^{-1} (1980s) to 117–212 Tg yr^{-1} (2000s) with the availability of more observational data and improved areal estimates (Bastviken et al., 2011; Deemer et al., 2016; Stanley et al., 2016; DelSontro et al., 2018; Saunois et al., 2020). A large spatial and temporal variation in lake and river CH_4 fluxes (Wik et al., 2016; Crawford et al., 2017; Natchimuthu et al., 2017) and uncertainties in the global area of them (Allen and Pavelsky, 2018), together with a relatively small number of observations, varying measurement methods, for example those neglecting ebullition, varying upscaling methods and lack of appropriate process make the bottom-up CH_4 emission estimate uncertain (Sanches et al., 2019; Engram et al., 2020; Zhang et al., 2020a). Accordingly, there is no clear accounting of inland waters in top-down budgets, which is the main reason for the large gap in bottom-up and top-down estimates of "other sources" in the CH_4 budget (Table 5.2). Despite recent progress in separating wetlands from inland waters, there is double-counting in

ACCEPTED VERSION SUBJECT TO FINAL EDITS

the bottom-up estimates of their emissions (Thornton et al., 2016). Although there is evidence that regional human activities and warming both increase inland water CH_4 emissions (Beaulieu et al., 2019), the increase in the decadal emissions since AR5 (Ciais et al., 2013) rather reflect improvements in the estimate (*medium confidence)*, due to updates in the datasets and new upscaling approaches (Saunois et al., 2020).

5.2.2.5 CH_4 Budget

A summary of top-down and bottom-up estimations of CH_4 emissions and sinks for the period 2008–2017 is presented in Figure 5.14 (details in Table 5.2 and the associated text for the emissions). In addition to 483-682 Tg yr^{-1} loss of CH_4 in the troposphere by reaction with OH, 1–35 Tg yr^{-1} of CH_4 loss is estimated to occur in the lower troposphere due to Cl but are not included in the top-down models as shown in Table 5.2 (Hossaini et al., 2016; Gromov et al., 2018; Wang et al., 2019b). The decadal mean CH_4 burden/imbalance have increased at the rate of 30, 12, 7 and 21 Tg yr^{-1} in the 1980s (1980–1989), 1990s (1990–1999), 2000s (2000–2009) and the most recent decade (2008–2017), respectively (*virtually certain*), as can be estimated from observed atmospheric growth rate (Cross-Chapter Box 5.2, Figure 1).

Recent analysis using $\Delta^{14}C\text{-}CH_4$ in ice samples suggest that CH_4 emissions from fossil fuels exploitation are responsible for 30% of total CH_4 emissions (Lassey et al., 2007; Hmiel et al., 2020), which is largely inconsistent with sectorial budgets where fossil fuel emissions add up to 20% only (Ciais et al., 2013). However, recent model simulations produce fairly consistent $\delta^{13}C\text{-}CH_4$ values and trends as observed in the atmospheric samples using 20% fossil fuel emission fraction (Ghosh et al., 2015; Warwick et al., 2016; Fujita et al., 2020; Strode et al., 2020). Further research is needed in order to clarify relative roles of CH_4 emissions from fossil fuel exploitation and freshwater components. A key challenge is to accommodate higher estimated emissions from these two components without a major increase in the sinks for explaining the carbon and hydrogen isotopes variabilities at the same time.

[START FIGURE 5.14 HERE]

Figure 5.14: Global methane (CH_4) budget (2008–2017). Values and data sources as in Table 5.2 (in $TgCH_4$). The atmospheric stock is calculated from mean CH_4 concentration, multiplying a factor of 2.75 ± 0.015 Tg ppb^{-1}, which accounts for the uncertainties in global mean CH_4 (Chandra et al., 2021). Further details on data sources and processing are available in the chapter data table (Table 5.SM.6).

[END FIGURE 5.14 HERE]

[START CROSS-CHAPTER BOX 5.2]

Cross-Chapter Box 5.2: Drivers of atmospheric methane changes during 1980–2019

Contributors: Prabir K. Patra (Japan/India), Josep G. Canadell (Australia), Frank Dentener (EU, Netherlands), Xin Lan (USA), Vaishali Naik (USA)

The atmospheric methane (CH_4) growth rate has varied widely over the past three decades, and the causes of which have been extensively studied since AR5. The mean growth rate decreased from 15 ± 5 ppb yr^{-1} in the 1980s to 0.48 ± 3.2 ppb yr^{-1} during 2000–2006 (the so-called quasi-equilibrium phase) and returned to an average rate of 7.6 ± 2.7 ppb yr^{-1} in the past decade (2010–2019) (based on data in Figure 5.14). Atmospheric CH_4 grew faster (9.3 ± 2.4 ppb yr^{-1}) over the last six years (2014–2019) – a period with prolonged El Niño conditions, which contributed to high CH_4 growth rates consistent with behaviour during previous El Niño events (Figure 5.14b). Because of large uncertainties in both the emissions and sinks of CH_4, it has been challenging to quantify accurately the methane budget and ascribe reasons for the growth over 1980-2019. In the context of CH_4 emissions mitigation, it is critical to understand if the changes in growth rates are caused by emissions from human activities or by natural processes responding to changing

ACCEPTED VERSION SUBJECT TO FINAL EDITS

climate. If CH_4 continues to grow at rates similar to those observed over the past decade, it will contribute to decadal scale climate change and hinder the achievement of the long-term temperature goals of the Paris Agreement (Nisbet et al., 2019)(7.3.2.2).

Cross-Chapter Box 5.2 Figure 1 shows the decadal CH_4 budget derived from the Global Carbon Project (GCP)-CH_4 synthesis for 1980s, 1990s and 2000s (Kirschke et al., 2013), and for 2010–2017 (Saunois et al., 2020). The imbalance of the sources and sinks estimated by atmospheric inversions (red bars) can be used to explain the changes in CH_4 concentration increase rates between the decades (Table 5.2).

[START CROSS-CHAPTER BOX 5.2, FIGURE 1 HERE]

Cross-Chapter Box 5.2, Figure 1: **Methane sources and sinks for four decades from atmospheric inversions with the budget imbalance** (source-sink; red bars) (plotted on the left y-axis). Top-down analysis from (Kirschke et al., 2013; Saunois et al., 2020), The global CH_4 concentration seen in the black line (plotted on the right y-axis), representing NOAA observed global monthly mean atmospheric CH_4 in dry-air mole fractions for 1983–2019 (Chapter 2, Annex III. Natural sources include emissions from natural wetlands, lakes and rivers, geological sources, wild animals, termites, wildfires, permafrost soils, and oceans. Anthropogenic sources include emissions from enteric fermentation and manure, landfills, waste and wastewater, rice cultivation, coal mining, oil and gas industry, biomass and biofuel burning. The top-down total sink is determined from global mass balance includes chemical losses due to reactions with hydroxyl (OH), atomic chlorine (Cl), and excited atomic oxygen (O^1D), and oxidation by bacteria in aerobic soils (Table 5.2). Further details on data sources and processing are available in the chapter data table (Table 5.SM.6).

[END CROSS-CHAPTER BOX 5.2, FIGURE 1 HERE]

Since AR5, many studies have discussed the role of different source categories in explaining the increase in CH_4 growth rate since 2007 and a coincident decrease of $\delta^{13}C$–CH_4 and δD–CH_4 isotopes (ref. Figure 5.13; Rice et al., 2016). Both ^{13}C and D are enriched in mass-weighted average source signatures for CH_4 emissions from thermogenic sources (e.g. coal mining, oil and gas industry) and pyrogenic (biomass burning) sources, and depleted in biogenic (e.g. wetlands, rice paddies, enteric fermentation, landfill and waste) sources. Proposed hypotheses for CH_4 growth (2007–2017) are inconclusive and vary from a concurrent decrease in thermogenic and increase in wetland and other biogenic emissions (Nisbet et al., 2016; Schwietzke et al., 2016), increase in from emissions agriculture in the tropics (Schaefer et al., 2016), a concurrent reduction in pyrogenic and increase in thermogenic emissions (Worden et al., 2017), or emission increase from biogenic sources and a slower increase in emissions from thermogenic sources compared to inventory emissions (Patra et al., 2016; Thompson et al., 2018; Jackson et al., 2020; Chandra et al., 2021).

A few studies have emphasised the role of chemical destruction by OH, the primary sink of methane, in driving changes in the growth of atmospheric methane abundance, in particular after 2006 (Rigby et al., 2017; Turner et al., 2017). Studies applying three-dimensional atmospheric inversion (McNorton et al., 2018), simple multi-species inversion (Thompson et al., 2018), as well as empirical method using a variety of observational constraints based on OH chemistry (Nicely et al., 2018; Patra et al., 2021), do not find trends in OH large enough to explain the methane changes post-2006. On the contrary, global chemistry-climate models based on fundamental principles of atmospheric chemistry and known emission trends of anthropogenic non-methane SLCFs simulate an increase in OH over this period (Zhao et al., 2019; Stevenson et al., 2020) (see Section 6.2.3). These contrasting lines of evidence suggest that OH changes may have had a small moderating influence on methane growth since 2007 (*low confidence*).

Cross-Chapter Box 5.2 Figure 2 shows that modelled wetland emission anomalies for all regions did not exhibit statistically significant trends (*high agreement between models, medium evidence*). Thus, the inter-decadal difference of total CH_4 emissions derived from inversion models and wetland emissions, arises

ACCEPTED VERSION SUBJECT TO FINAL EDITS

mainly from anthropogenic activities. The timeseries of regional emissions suggest that progress towards atmospheric CH_4 quasi-equilibrium was primarily driven by reductions in anthropogenic (fossil fuel exploitation) emissions in Europe, Russia and temperate North America over 1988–2000. In the global totals, emissions equalled loss in the early 2000s. The growth since 2007 is driven by increasing agricultural emissions from East Asia (1997–2017), West Asia (2005–2017), Brazil (1988–2017) and Northern Africa (2005–2017), and fossil fuel exploitations in temperate North America (2010–2017) (Lan et al., 2019; Crippa et al., 2020; Höglund-Isaksson et al., 2020; Jackson et al., 2020; Chandra et al., 2021).

[START CROSS-CHAPTER BOX 5.2, FIGURE 2 HERE]

Cross-Chapter Box 5.2, Figure 2: Anomalies in global and regional methane (CH_4) emissions for 1988–2017. Map in the centre shows mean CH_4 emission for 2010–2016. Multi-model mean (line) and 1-σ standard deviations (shaded) for 2000–2017 are shown for 9 surface CH_4 and 10 satellite XCH_4 inversions, and 22 wetland models or model variants that participated in GCP-CH_4 budget assessment (Saunois et al., 2020). The results for the period before 2000 are available from two inversions, 1) using 19 sites (Chandra et al., 2021; also used for the 2010-2016 mean emission map) and for global totals (Bousquet et al., 2006). The long-term mean values for 2010-2016 (common for all GCP–CH_4 inversions), as indicated within each panel separately, is subtracted from the annual-mean time series for the calculation of anomalies for each region. Further details on data sources and processing are available in the chapter data table (Table 5.SM.6).

[END CROSS-CHAPTER BOX 5.2, FIGURE 2 HERE]

Evidence from emission inventories at country level and regional scale inverse modelling that CH_4 growth rate variability during the 1988 through 2017 is closely linked to anthropogenic activities (*medium agreement*). Isotopic composition observations and inventory data suggest that concurrent emission changes from both fossil fuels and agriculture are playing roles in the resumed CH_4 growth since 2007 (*high confidence*). Shorter-term decadal variability is predominantly driven by the influence of El Niño Southern Oscillation on emissions from wetlands and biomass burning (Cross-Chapter Box 5.2 Figure 2), and loss due to OH variations (*medium confidence*), but lacking quantitative contribution from each of the sectors. By synthesising all available information regionally from a-priori (bottom-up) emissions, satellite and surface observations, including isotopic information, and inverse modelling (top-down), the capacity to track and explain changes in and drivers of natural and anthropogenic CH_4 regional and global emissions has been improved since the AR5, but fundamental uncertainties related to OH variations remain unchanged.

[END CROSS-CHAPTER BOX 5.2]

5.2.3 N_2O: Trends, Variability and Budget

In natural ecosystems, nitrous oxide (N_2O) is primarily produced as a by-product during the remineralisation of organic matter via the primary processes of nitrification and denitrification (Butterbach-Bahl et al., 2013; Voss et al., 2013). The net N_2O production is highly sensitive to local environmental conditions such as temperature, oxygen concentrations, pH and the concentrations of ammonium and nitrate, amongst others, causing strong variability of N_2O emissions in time and space even at small scales. Changes in the atmospheric abundance of N_2O result largely from the balance of the net N_2O sources on land and ocean, and the photochemical destruction of N_2O in the stratosphere.

Since AR5 (WGI, 6.4.3), improved understanding of N_2O sources allows for a more comprehensive assessement of the global N_2O budget (Table 5.3). This progress is based on extended atmospheric observations (Francey et al., 2003; Elkins et al., 2018; Prinn et al., 2018), improved atmospheric N_2O inversions (Saikawa et al., 2014; Thompson et al., 2019), updated and expanded inventories of N_2O sources

ACCEPTED VERSION SUBJECT TO FINAL EDITS

(Janssens-Maenhout et al., 2017; Winiwarter et al., 2018), as well as improved bottom-up estimate of freshwater, ocean and terrestrial sources (Martinez-Rey et al., 2015; Landolfi et al., 2017; Buitenhuis et al., 2018a; Lauerwald et al., 2019; Maavara et al., 2019; Tian et al., 2019).

The human perturbation of the natural nitrogen cycle through the use of synthetic fertilisers and manure, as well as nitrogen deposition resulting from land-based agriculture and fossil fuel burning has been the largest driver of the increase in atmospheric N_2O of 31.0 ± 0.5 parts per billion (ppb) (10%) between 1980 and 2019 (*robust evidence, high agreement*) (Tian et al., 2020). The long atmospheric lifetime of N_2O implies that it will take more than a century before atmospheric abundances stabilise after the stabilisation of global emissions. The rise of atmospheric N_2O is of concern, not only because of its contribution to the anthropogenic radiative forcing (see Chapter 7), but also because of the importance of N_2O in stratospheric ozone loss (Ravishankara et al., 2009; Fleming et al., 2011; Wang et al., 2014a).

5.2.3.1 Atmosphere

The tropospheric abundance of N_2O was 332.1 ± 0.4 ppb in 2019 (Figure 5.15), which is 23% higher than pre-industrial levels of 270.1 ± 6.0 ppb (*robust evidence, high agreement*). Current estimates are based on atmospheric measurements with high accuracy and density (Francey et al., 2003; Elkins et al., 2018; Prinn et al., 2018), and pre-industrial estimates are based on multiple ice-core records (see Section 2.2.3.2.3). The average annual tropospheric growth rate was 0.85 ± 0.03 ppb yr^{-1} during the period 1995 to 2019 (Figure 5.15a). The atmospheric growth rate increased by about 20% between the decade of 2000 to 2009 and the most recent decade of 2010 to 2019 (0.95 ± 0.04 ppb yr^{-1}) (*robust evidence, high agreement*). The growth rate in 2010–2019 was also higher than during 1970–2000 (0.6–0.8 ppb yr^{-1} (Ishijima et al., 2007)) and the thirty-year period prior to 2011 (0.73 ± 0.03 ppb yr^{-1}), as reported by AR5. New evidence since AR5 (WGI, 6.4.3) confirms that in the tropics and sub-tropics, large inter-annual variations in the atmospheric growth rate are negatively correlated with the multivariate ENSO index (MEI) and associated anomalies in land and ocean fluxes (Ji et al., 2019; Thompson et al., 2019; Yang et al., 2020c) (Figure 5.15a).

As assessed by SRCCL (IPCC, 2019a), combined firn, ice, air and atmospheric measurements show that the $^{15}N/^{14}N$ isotope ratio (*robust evidence, high agreement*) as well as the predominant position of the ^{15}N atom in atmospheric N_2O (*limited evidence, low agreement*) in N_2O has changed since 1940 (Figure 5.15b, c) whereas they were relatively constant in the pre-industrial period (Ishijima et al., 2007; Park et al., 2012; Prokopiou et al., 2017, 2018). SRCCL concluded that this change indicates a shift in the nitrogen-substrate available for de-nitrification, and the relative contribution of nitrification to the global N_2O source (*robust evidence, high agreement*), which are associated with increased fertiliser use in agriculture (Park et al., 2012; Snider et al., 2015; Prokopiou et al., 2018).

Since AR5 (WGI, 6.4.3), the mean atmospheric lifetime of N_2O has been revised to 116 ± 9 years (Prather et al., 2015). The small negative feedback of the N_2O lifetime to increasing atmospheric N_2O results in a slightly lower residence time (109 ± 10 years) of N_2O perturbations compared with that assessed by AR5 (118–131 years) (Prather et al., 2015). The dominant N_2O loss occurs through photolysis and oxidation by O(1D) radicals in the Stratosphere and amounts to approximately 13.1 (12.4–13.6) TgN yr^{-1} (Minschwaner et al., 1993; Prather et al., 2015; Tian et al., 2020).

[START FIGURE 5.15 HERE]

Figure 5.15: Changes in atmospheric nitrous oxide (N_2O) and its isotopic composition since 1940. (a) Atmospheric N_2O abundance (parts per billion, ppb) and growth rate (ppb yr^{-1}), (b) $\delta^{15}N$ of atmospheric N_2O, and (c) alpha-site ^{15}N–N_2O. Estimate are based on direct atmospheric measurements in the AGAGE , CSIRO, and NOAA networks (Prinn et al., 2000, 2018; Francey et al., 2003; Hall et al., 2007; Elkins et al., 2018), archived air samples from Cape Grim, Australia (Park et al., 2012), and firn air from NGRIP Greenland and H72 Antarctica (Ishijima et al., 2007), Law Dome Antarctica (Park et al., 2012), as well as a collection of firn ice samples from Greenland (Prokopiou et al., 2017, 2018). Shading in (a) is based on the multivariate ENSO index, with red indicating El Niño conditions (Wolter and Timlin, 1998). Further

ACCEPTED VERSION SUBJECT TO FINAL EDITS

details on data sources and processing are available in the chapter data table (Table 5.SM.6).

[END FIGURE 5.15 HERE]

5.2.3.2 Anthropogenic N_2O Emissions

AR5 (WGI, 6.4.3) and SRCCL (2.3.3) concluded that agriculture is the largest anthropogenic source of N_2O emissions. Since SRCCL (2.3.3), a new synthesis of inventory-based and modelling studies shows that the widespread use of synthetic fertilisers and manure on cropland and pasture, manure management and aquaculture resulted in 3.8 (2.5–5.8) TgN yr^{-1} (average 2007–2016) (*robust evidence, high agreement*) (Table 5.3) (Winiwarter et al., 2018; FAO, 2019; Janssens-Maenhout et al., 2019; Tian et al., 2020). Observations from field-measurements (Song et al., 2018), inventories (Wang et al., 2020) and atmospheric inversions (Thompson et al., 2019) further corroborate the assessment of the SRCCL that there is a non-linear relationship between N_2O emissions and nitrogen input, implying an increasing fraction of fertiliser lost as N_2O with larger fertiliser excess (*medium evidence, high agreement*). Several studies using complementary methods indicate that agricultural N_2O emissions have increased by more than 45% since the 1980s (*high confidence*) (Davidson, 2009; Janssens-Maenhout et al., 2017; Winiwarter et al., 2018; Tian et al., 2020) (Figure 5.16, Table 5.3), mainly due to the increased use of nitrogen fertiliser and manure. N_2O emissions from aquaculture are amongst the fastest rising contributors of N_2O emissions, but their overall magnitude is still small in the overall N_2O budget (Tian et al., 2020).

[START FIGURE 5.16 HERE]

Figure 5.16: Decadal mean nitrous oxide (N_2O) emissions for 2007–2016 and its change since 1850 based on process-model projections. The total effect including that from anthropogenic nitrogen additions (atmospheric deposition, manure addition, fertiliser use and land-use) is evaluated against the background flux driven by changes in atmospheric CO_2 concentration, and climate change. Fluxes are derived from the N_2O Model Intercomparison Project ensemble of terrestrial biosphere models (Tian et al., 2019) and three ocean biogeochemical models (Landolfi et al., 2017; Battaglia and Joos, 2018a; Buitenhuis et al., 2018b). Further details on data sources and processing are available in the chapter data table (Table 5.SM.6).

[END FIGURE 5.16 HERE]

The principal non-agricultural anthropogenic sources of N_2O are industry, specifically chemical processing, wastewater, and the combustion of fossil fuels (Table 5.3). Industrial emissions of N_2O mainly due to nitric and adipic acid production have decreased in North America and Europe since the wide-spread installation of abatement technologies in the 1990s (Pérez-Ramírez et al., 2003; Lee et al., 2011; Janssens-Maenhout et al., 2019). There is still considerable uncertainty in industrial emissions from other regions of the world with contrasting trends between inventories (Thompson et al., 2019). Globally, industrial emissions and emissions from fossil fuel combustion by stationary sources, such as power plants, as well as smaller emissions from mobile sources (e.g. road transport and aviation) have remained nearly constant between1980s and 2007-2016 (*moderate evidence, medium agreement*) (Janssens-Maenhout et al., 2017; Winiwarter et al., 2018; Tian et al., 2020). Wastewater N_2O emissions, including those from domestic and industrial sources have increased from 0.2 (0.1–0.3) TgN yr^{-1} to 0.35 (0.2–0.5) TgN yr^{-1} between the 1980s and 2007–2016 (Tian et al., 2020).

Biomass burning from crop residue burning, grassland, savannah and forest fires, as well as biomass burnt in household stoves, releases N_2O during the combustion of organic matter. Updated inventories since AR5 (WGI, 6.4.3) result in a lower range of the decadal mean emissions of 0.6 (0.5–0.8) TgN yr^{-1} (van der Werf et al., 2017; Tian et al., 2020). The attribution of grassland, savannah or forest fires to natural or anthropogenic origins is uncertain, preventing a separation of the biomass burning source into natural and anthropogenic.

ACCEPTED VERSION SUBJECT TO FINAL EDITS

5.2.3.3 Emissions from Ocean, Inland Water Bodies and Estuaries

Since AR5 (WGI, 6.4.3), new estimates of the global ocean N_2O source derived from ocean biogeochemistry models are 3.4 (2.5–4.3) TgN yr^{-1} for the period 2007-2016 (Manizza et al., 2012; Suntharalingam et al., 2012; Martinez-Rey et al., 2015; Landolfi et al., 2017; Buitenhuis et al., 2018a; Tian et al., 2020) (Figure 5.16). This is slightly lower than climatological estimates from empirically based-methods and surface ocean data syntheses (Bianchi et al., 2012; Yang et al., 2020c). Nitrous oxide processes in coastal upwelling zones continue to be poorly represented in global estimates of marine N_2O emissions (Kock et al., 2016), but may account for an additional 0.2 to 0.6 TgN yr^{-1} of the global ocean source (Seitzinger et al., 2000; Nevison et al., 2004).

In the oxic ocean (> 97% of ocean volume), nitrification is believed to be the primary N_2O source (Freing et al., 2012). In sub-oxic ocean zones (see Section 5.3), where denitrification prevails, higher N_2O yields and turnover rates make these regions potentially significant sources of N_2O (Arévalo-Martínez et al., 2015; Babbin et al., 2015; Ji et al., 2015). The relative proportion of ocean N_2O from oxygen-minimum zones is highly uncertain (Zamora et al., 2012). Estimates derived from in situ sampling, particularly in the eastern tropical Pacific, suggest significant fluxes from these regions, and potentially accounting for up to 50% of the global ocean source (Codispoti, 2010; Arévalo-Martínez et al., 2015; Babbin et al., 2015). However, recent global-scale analyses estimate lower contributions (4 to 7%, Battaglia and Joos, 2018; Buitenhuis et al., 2018). Further investigation is required to reconcile these estimates and provide improved constraints on the N_2O source from low-oxygen zones.

Atmospheric deposition of anthropogenic N on oceans can stimulate marine productivity and influence ocean emissions of N_2O. New ocean model analyses since AR5 (WGI, 6.4.3), suggest a relatively modest global potential impact of 0.01–0.32 TgN yr^{-1} (pre-industrial to present-day) equivalent to 0.5–3.3% of the global ocean N_2O source (Suntharalingam et al., 2012; Jickells et al., 2017; Landolfi et al., 2017). However, larger proportionate impacts are predicted in nitrogen-limited coastal and inland waters down-wind of continental pollution outflow, such as the Northern Indian Ocean (Jickells et al., 2017; Suntharalingam et al., 2019).

Inland waters and estuaries are generally sources of N_2O as a result of nitrification and denitrification of dissolved inorganic nitrogen, however, they can serve as N_2O sinks in specific conditions (Webb et al., 2019). Since AR5 (WGI, 6.4.3), improved emission factors including their spatio-temporal scaling, and consideration of transport within the aquatic system allow to better constrain these emissions (Murray et al., 2015; Hu et al., 2016; Lauerwald et al., 2019; Maavara et al., 2019; Kortelainen et al., 2020; Yao et al., 2020). Despite uncertainties because of the side-effects of canals and reservoirs on nutrient cycling, these advances permit to attribute a fraction of inland water N_2O emissions to anthropogenic sources (Tian et al., 2020), which contributes to the increased anthropogenic share of the global N_2O source in this report compared to AR5 (Ciais et al., 2013). As indirect consequence of agricultural nitrogen-use and waste-water treatment, the anthropogenic emissions from inland waters have increased by about a quarter (0.1 TgN yr^{-1}) between the 1980s and 2007–2016 (Tian et al., 2020).

5.2.3.4 Emissions and Sinks in Non-Agricultural Land

Soils are the largest natural source of N_2O, arising primarily from nitrogen processing associated with microbial nitrification and denitrification (Butterbach-Bahl et al., 2013; Snider et al., 2015) (Table 5.3). Under some conditions, soils can also act as a net sink of N_2O, but this effect is small compared to the overall source (Schlesinger, 2013). Since AR5 (WGI, 6.4.3), improved global process-based models (Tian et al., 2019) suggest a present-day source of 6.7 (5.3–8.1) TgN yr^{-1} (2007–2016 average), which is consistent with the estimate in AR5. Process-based models and inventory-based methods show that increased N deposition has enhanced terrestrial N_2O emissions by 0.8 (0.4–1.4 TgN yr^{-1}) relative to approximately pre-industrial times, and by 0.2 (0.1–0.2) TgN yr^{-1} between the 1980s and 2007–2016 (*limited evidence, medium agreement*) (Figure 5.16) (Tian et al., 2019). This estimate is at the high end of the range reported in AR5 (WGI, 6.4.3). Model projections further show that global warming has led to increased soil N_2O emissions of

ACCEPTED VERSION SUBJECT TO FINAL EDITS

0.8 (0.3–1.3) TgN yr^{-1} since approximately pre-industrial times, of which about half occurred since the 1980s (*limited evidence, high agreement)* (Tian et al., 2019, 2020).

SRCCL assessed that deforestation and other forms of land-use change significantly alter terrestrial N_2O emissions through emission pulses following conversions, resulting generally in long-term reduced emissions in unfertilised ecosystems (*medium evidence, high agreement*). This conclusion is supported by a recent study demonstrating that the deforestation-pulse effect is offset by the effect of reduced area of mature tropical forests (Tian et al., 2020).

Uncertainties remain in process-based models with respect to their ability to capture the complicated responses of terrestrial N_2O emissions to rain pulses, freeze-thaw cycles and the net consequences of elevated levels of CO_2 accurately (Tian et al., 2019). Emerging literature suggests that permafrost thaw may contribute significantly to arctic N_2O emissions (Voigt et al., 2020), but these processes are not yet adequately represented in models and upscaling to large-scale remains a significant challenge.

5.2.3.5 N_2O budget

[START FIGURE 5.17 HERE]

Figure 5.17: Global nitrous oxide (N_2O) budget (2007–2016). Values and data sources as in Table 5.3. The atmospheric stock is calculated from mean N_2O concentration, multiplying a factor of 4.79 ± 0.05 Tg ppb^{-1} (Prather et al., 2012). Pool sizes for the other reservoirs are largely unknown. Further details on data sources and processing are available in the chapter data table (Table 5.SM.6).

[END FIGURE 5.17 HERE]

The synthesis of bottom-up estimates of N_2O sources (Sections 5.2.3.2–5.2.3.4; Figure 5.17) yields a global source of 17.0 (12.2–23.5) TgN yr^{-1} for the years 2007–2016 (Table 5.3). This estimate is comparable to AR5, but the uncertainty range has been reduced primarily due to improved estimates of ocean and anthropogenic N_2O sources. Since AR5 (WGI, 6.4.3), improved capacity to estimate N_2O sources from atmospheric N_2O measurements by inverting models of atmospheric transport provides a new and independent constraint for the global N_2O budget (Saikawa et al., 2014; Thompson et al., 2019; Tian et al., 2020). The decadal mean source derived from these inversions is remarkably consistent with the bottom-up global N_2O budget for the same period, however, the split between land and ocean sources based on atmospheric inversions is less well constrained, yielding a smaller land source of 11.3 (10.2–13.2) TgN yr^{-1} and a larger ocean source of 5.7 (3.4–7.2) TgN yr^{-1}, respectively, compared to bottom-up estimates.

Supported by multiple studies and extensive observational evidence (Sections 5.2.3.2–5.2.3.4; Figure 5.17), anthropogenic emissions contributed about 40% (7.3; uncertainty range: 4.2–11.4 TgN yr^{-1}) to the total N_2O source in 2007–2016 (*high confidence)*. This estimate is larger than in AR5 (WGI, 6.4.3) due to a larger estimated effect of nitrogen deposition on soil N_2O emission and the explicit consideration of the role of anthropogenic nitrogen in determining inland water and estuary emissions.

Based on bottom-up estimates, anthropogenic emissions from agricultural nitrogen use, industry and other indirect effects have increased by 1.7 (1.0–2.7) TgN yr^{-1} between the decades 1980–1989 and 2007–2016, and are the primary cause of the increase in the total N_2O source (*high confidence)*. Atmospheric inversions indicate that changes in surface emissions rather than in the atmospheric transport or sink of N_2O are the cause for the increased atmospheric growth rate of N_2O (*robust evidence, high agreement*) (Thompson et al., 2019). However, the increase of 1.6 (1.4–1.7) TgN yr^{-1} in global emissions between 2000–2005 and 2010–2015 based on atmospheric inversions is somewhat larger than bottom-up estimates over the same period, primarily because of differences in the estimates of land-based emissions.

ACCEPTED VERSION SUBJECT TO FINAL EDITS

[START TABLE 5.3 HERE]

Table 5.3: Global N_2O budget (units TgN yr^{-1}) averaged over the 1980s, 1990s, 2000s as well as the recent decade starting in 2007. Uncertainties represent the assessed range of source/sink estimates. All numbers are reproduced from (Tian et al., 2020) based on a compilation of inventories, bottom-up models, as well as atmospheric inversions. For detailed information on datasets, see Data Table 5.SM.6.

		AR6 1980–1989	AR6 1990–1999	AR6 2000–2009	AR6 (2007–2016)	AR5 (2006/2011)
Bottom-up budget						
Anthropogenic Sources						
	Fossil Fuel combustion and Industry	0.9 (0.8–1.1)	0.9 (0.9–1.0)	1,0 (0.8–1.0)	1.0 (0.8–1.1)	0.7 (0.2–1.8)
	Agriculture (incl. Aquaculture)	2.6 (1.8–4.1)	3.0 (2.1–4.8)	3.4 (2.3–5.2)	3.8 (2.5–5.8)	4.1 (1.7–4.8)
	Biomass and biofuel burning	0.7 (0.7–0.7)	0.7 (0.6–0.8)	0.6 (0.6–0.6)	0.6 (0.5–0.8)	0.7 (0.2–1.0)
	Wastewater	0.2 (0.1–0.3)	0.3 (0.2–0.4)	0.3 (0.2–0.4)	0.4 (0.2–0.5)	0.2 (0.1–0.3)
	Inland water, estuaries, coastal zones	0.4 (0.2–0.5)	0.4 (0.2–0.5)	0.4 (0.2–0.6)	0.5 (0.2–0.7)	
	Atmospheric nitrogen deposition on ocean	0.1 (0.1–0.2)	0.1 (0.1–0.2)	0.1 (0.1–0.2)	0.1 (0.1–0.2)	0.2 (0.1–0.4)
	Atmospheric nitrogen deposition on land	0.6 (0.3–1.2)	0.7 (0.4–1.4)	0.7 (0.4–1.3)	0.8 (0.4–1.4)	0.4 (0.3–0.9)
	Other indirect effects from CO_2, climate and land-use change	0.1 (-0.4–0.7)	0.1 (-0.5–0.7)	0.2 (-0.4–0.9)	0.2 (-0.6–1.1)	
	Total Anthropogenic	**5.6 (3.6–8.7)**	**6.2 (3.9–9.6)**	**6.7 (4.1–10.3)**	**7.3 (4.2–11.4)**	**6.3 (2.6–9.2)**
Natural Sources and Sinks						
	Rivers, estuaries, and coastal zones	0.3 (0.3–0.4)	0.3 (0.3–0.4)	0.3 (0.3–0.4)	0.3 (0.3–0.4)	0.6 (0.1–2.9)
	Open oceans	3.6 (3.0–4.4)	3.5 (2.8–4.4)	3.5 (2.7–4.3)	3.4 (2.5–4.3)	3.8 (1.8–9.4)
	Soils under natural vegetation	5.6 (4.9–6.6)	5.6 (4.9–6.5)	5.6 (5.0–6.5)	5.6 (4.9–6.5)	6.6 (3.3–9.0)
	Atmospheric chemistry	0.4 (0.2–1.2)	0.4 (0.2–1.2)	0.4 (0.2–1.2)	0.4 (0.2–1.2)	0.6 (0.3–1.2)
	Surface sink	-0.01 (-0.3–0)	-0.01 (-0.3–0)	-0.01 (-0.3–0)	-0.01 (-0.3–0)	-0.01 (-1–0)
	Total natural	**9.9 (8.5–12.2)**	**9.8 (8.3–12.1)**	**9.8 (8.2–12.0)**	**9.7 (8.0–12.0)**	**11.6 (5.5–23.5)**
Total bottom-up source		**15.5 (12.1–20.9)**	**15.9 (12.2–21.7)**	**16.4 (12.3–22.4)**	**17.0 (12.2–23.5)**	**17.9 (8.1–30.7)**
Observed growth rate				**3.7 (3.7–3.7)**	**4.5 (4.3–4.6)**	**3.6 (3.5–3.8)**
Inferred stratospheric sink				**12.9 (12.2-13.5)**	**13.1 (12.4–13.6)**	14.3 (4.3–28.7)
Atmospheric inversion						
	Atmospheric loss			12.1 (11.4–13.3)	12.4 (11.7–13.3)	
	Total source			15.9 (15.1–16.9)	16.9 (15.9–17.7)	
	Imbalance			3.6 (2.2–5.7)	4.2 (2.4–6.4)	

[END TABLE 5.3 HERE]

ACCEPTED VERSION SUBJECT TO FINAL EDITS

5.2.4 The Relative Importance of CO2, CH4, and N2O

The total influence of anthropogenic greenhouse gases (GHGs) on the Earth's radiative balance is driven by the combined effect of those gases, and the three most important were discussed separately in the previous sections. This section compares the balance of the sources and sinks of these three gases and their regional net flux contributions to the radiative forcing. CO_2 has multiple residence times in the atmosphere from one year to many thousands of years (Box 6.1 in Ciais et al. (2013)), and N_2O has a mean lifetime of 116 years. They are both long-lived GHGs, while CH_4 has a lifetime of 9.0 years and is considered a short-lived GHGs (see Chapter 2 for lifetime of GHGs, Chapter 6 for CH_4 chemical lifetime, and Chapter 7 for effective radiative forcing of all GHGs).

Figure 5.18 shows the contribution to radiative forcing of CO_2, CH_4, N_2O, and the halogenated species since the 1900s and the more recent decades. For the period 1960–2019, the relative contribution to the total effective radiative forcing (ERF) was 63% for CO_2, 11% for CH_4, 6% for N_2O, and 17% for the halogenated species (Chapter 7; Figure 5.18). The systematic decline in the relative contribution to ERF for CH_4 since 1850 is caused by slower increase rate of CH_4 in the recent decades, at 6, 10 and 5 ppb yr^{-1} during 1850-2019, 1960–2019 and 2000–2019, respectively, in comparison with the increasing rate of CO_2 (at 0.7, 1.6 and 2.2 ppm yr^{-1}, respectively) and N_2O (at 0.4, 0.7 and 0.9 ppb yr^{-1}, respectively) (Figure 5.4). Owing to the shorter lifetime of CH_4, the effect of reduction in emission increase rate on the ERF increase is evident at inter-decadal timescales.

[START FIGURE 5.18 HERE]

Figure 5.18: Contributions of carbon dioxide (CO_2), methane (CH_4), nitrous oxide (N_2O) and halogenated species to the total effective radiative forcing (ERF) increase since 1850 and 1960, and for 2000 to 2009. ERF data are taken from Annex III (based on calculations from Chapter 7). Note that the sum of the ERFs exceeds 100% because there are negative ERFs due to aerosols and clouds. Further details on data sources and processing are available in the chapter data table (Table 5.SM.6).

[END FIGURE 5.18 HERE]

Atmospheric abundance of GHGs is proportional to their emissions-loss budgets in the Earth's environment. There are multiple metrics to evaluate the relative importance of different GHGs for the global atmospheric radiation budget and the socioeconomic impacts (Section 7.6). Metrics for weighting emissions are further developed in the AR6 of IPCC WGIII. Figure 5.19 shows the regional emissions of the three main GHGs. For East Asia, Europe, Temperate North America and West Asia, the most dominant GHG source is CO_2 (*high confidence*) (Figure 5.19), while for East Asia, South Asia, Southeast Asia, Tropical South America, Temperate North America and Central Africa is CH_4 (Figure 5.19). The N_2O emissions are dominant in regions with intense use of nitrogen fertilisers in agriculture. Only boreal North America showed net sinks of CO_2, while close to flux neutrality is observed for North Asia, Southern Africa, and Australasia. Persistent emission of CO_2 is observed for Tropical and South America, northern Africa, and southeast Asia (*medium confidence*). The *medium confidence* arises from large uncertainties in the estimated non-fossil fuel CO_2 fluxes over these regions due to the lack of high-quality atmospheric measurements.

[START FIGURE 5.19 HERE]

Figure 5.19: Regional distributions of net fluxes of carbon dioxide (CO_2), methane (CH_4), nitrous oxide (N_2O) on the Earth's surface. The region divisions, shown as the shaded map, are made based on ecoclimatic characteristics of the land. The fluxes include those from anthropogenic activities and natural causes that result from responses to anthropogenic greenhouse gases and climate change (feedbacks) as in the three budgets shown in Sections 5.2.1.5, 5.2.2.5, and 5.2.3.5. The CH_4 and N_2O emissions are weighted by

ACCEPTED VERSION SUBJECT TO FINAL EDITS

arbitrary factors of 50 and 500, respectively, for depiction by common y-axes. Fluxes are shown as the mean of the inverse models as available from (Thompson et al., 2019; Friedlingstein et al., 2020; Saunois et al., 2020). Further details on data sources and processing are available in the chapter data table (Table 5.SM.6).

[END FIGURE 5.19 HERE]

5.3 Ocean Acidification and Deoxygenation

The surface ocean has absorbed a quarter of all anthropogenic CO_2 emissions mainly through physical-chemical processes (McKinley et al., 2016; Gruber et al., 2019b; Friedlingstein et al., 2020). Once dissolved in seawater, CO_2 reacts with water and forms carbonic acid. In turn carbonic acid dissociates, leading to a decrease in the concentration of carbonate (CO_3^{-2}) ions, and increasing both bicarbonate (HCO_3^-) and hydrogen (H^+) ion concentration, which has caused a shift in the carbonate chemistry towards a less basic state, commonly referred to as ocean acidification (Caldeira and Wickett, 2003; Orr et al., 2005; Doney et al., 2009). Although the societal concern for this problem is relatively recent (about the last 20 years), the physical-chemical basis for the ocean absorption (sink) of atmospheric CO_2 has been discussed much earlier by Revelle and Suess (1957). The AR5 and SROCC assessments were of *robust evidence* that the H^+ ion concentration is increasing in the surface ocean, thereby reducing seawater pH (= - log[H^+]) (Orr et al., 2005; Feely et al., 2009; Ciais et al., 2013; Bindoff et al., 2019; Chapter 2, Section 2.3.4.1), and there is *high confidence* that ocean acidification is impacting marine organisms (Bindoff et al., 2019).

Ocean oxygen decline, or deoxygenation, is driven by changes in ocean ventilation and solubility (Bindoff et al., 2019). It is *virtually certain* that anthropogenic forcing has made a substantial contribution to the ocean heat content increase over the historical period (Bindoff et al., 2019; IPCC, 2019c) (Chapter 9, Section 2.3.3.1), strengthening upper water column stratification. Ocean warming decreases the solubility of dissolved oxygen in seawater, and it contributes to about 15% of the dissolved oxygen decrease in the oceans according to estimates based on solubility and the recent SROCC assessment (*medium confidence*), especially in sub-surface waters, between 100–600 m depth (Helm et al., 2011; Schmidtko et al., 2017; Breitburg et al., 2018; Oschlies et al., 2018) (SROCC, Section 5.3.1). Stratification reduces the ventilation flux into the ocean interior, contributing to most of the remaining ocean deoxygenation (Schmidtko et al., 2017; Breitburg et al., 2018) (Section 3.6.2). Deoxygenation may enhance the emissions of nitrous oxide, especially from oxygen minimum zones (OMZs) or hypoxic coastal areas (Breitburg et al., 2018; Oschlies et al., 2018). Since SROCC (Bindoff et al., 2019), CMIP6 model simulation results agree with the reported 2% loss (4.8 ± 2.1 Pmoles O_2) in total dissolved oxygen in the upper ocean layer (100–600 m) for the 1970–2010 period (Helm et al., 2011; Ito et al., 2017; Schmidtko et al., 2017; Kwiatkowski et al., 2020) (Section 2.3.4.2). The response of marine organisms to the coupled effects of ocean warming, acidification and deoxygenation occur at different metabolic levels on different groups, and include respiratory stress and reduction of thermal tolerance by organisms (Gruber, 2011; Bindoff et al., 2019; IPCC, 2019c; Kawahata et al., 2019). An assessment of these effects on marine biota is found in WGII AR6 Chapter 2.

This section assesses past events of ocean acidification and deoxygenation (Section 5.3.1), the historical trends and spatial variability for the upper ocean (Section 5.3.2) and the ocean interior (Section 5.3.3). Future projections for ocean acidification and the drivers in the coastal ocean are assessed in Sections 5.3.4 and 5.3.5, respectively.

5.3.1 Paleoclimate Context

5.3.1.1 Paleocene-Eocene Thermal Maximum

The Paleocene-Eocene thermal maximum (PETM) was an episode of global warming exceeding pre-industrial temperatures by 4°C–8°C (McInerney and Wing, 2011; Dunkley Jones et al., 2013) that occurred 55.9–55.7 Ma. The PETM involved a large pulse of geologic CO_2 released into the ocean-atmosphere

ACCEPTED VERSION SUBJECT TO FINAL EDITS

system in 3–20 kyr (Zeebe et al., 2016; Gutjahr et al., 2017; Kirtland Turner et al., 2017; Kirtland Turner, 2018; Gingerich, 2019) (5.2.1.1). In response to carbon emissions during the PETM, observationally-constrained model simulations report an increase in atmospheric CO_2 concentrations ranging from about 900 ppm to >2000 ppm (Gutjahr et al., 2017; Cui & Schubert, 2018; Anagnostou et al., 2020) (Chapter 2). The PETM thus provides a test for our understanding of the ocean's response to the increase in carbon (and heat) emissions over geologically short timescales.

A limited number of independent proxy records indicate that the PETM was associated with a surface ocean pH decline ranging from 0.15 to 0.30 units (Gutjahr et al., 2017; Penman et al., 2014; Babila et al., 2018). It was also accompanied by a rapid (<10 ka) shallowing of the carbonate saturation horizon, resulting in the widespread dissolution of sedimentary carbonate, followed by a gradual (100 kyr) recovery (Zachos et al., 2005; Bralower et al., 2018). The remarkable similarity among sedimentary records spanning a wide range of ecosystems suggests with *medium confidence* that the perturbation in the ocean carbonate saturation was global (Babila et al., 2018) and directly resulted from elevated atmospheric CO_2 levels. The degree of acidification is similar to the 0.4 pH unit decrease projected for the end of the 21st century under RCP8.5 (Gattuso et al., 2015) and is estimated to have occurred at a rate about one order of magnitude slower than the current rate of ocean acidification (Zeebe et al., 2016). There is *low confidence* in the inferred rates of ocean acidification inherent to the range of uncertainties affecting rates estimates based on marine sediments (Section 5.1.2.1).

Recent model outputs as well as globally distributed geochemical data reveal with *medium confidence* widespread ocean deoxygenation during the PETM (Dickson et al., 2012; Winguth et al., 2012; Dickson et al., 2014; Chang et al., 2018; Remmelzwaal et al., 2019), with parts of the ocean potentially becoming drastically oxygen-depleted (anoxic) (Yao et al., 2018; Clarkson et al., 2021). Deoxygenation affected the surface ocean globally (including the Arctic Ocean) (Sluijs et al., 2006), due to vertical and lateral expansion of Oxygen Minimum Zones (OMZs) (Zhou et al., 2014) that resulted from warming and related changes in ocean stratification. Expansion of OMZs may have stimulated N_2O production through water-column (de)nitrification (Junium et al., 2018). The degree to which N_2O production impacted PETM warming, however, has not yet been established.

The feedbacks associated with recovery from the PETM are uncertain, yet could include drawdown associated with silicate weathering (Zachos et al., 2005) and regrowth of terrestrial and marine organic carbon stocks (Bowen and Zachos, 2010; Gutjahr et al., 2017).

5.3.1.2 Last Deglacial Transition

The Last deglacial transition (LDT) is the best documented climatic transition in the past associated with a substantial atmospheric CO_2 rise ranging from 190 to 265 ppm between 18–11 ka (Marcott et al., 2014). The amplitude of the deglacial CO_2 rise is thus on the order of magnitude of the increase undergone since the industrial revolution.

Boron isotope ($\delta^{11}B$) data suggest a 0.15–0.05 unit decrease in sea-surface pH (Hönisch and Hemming, 2005; Henehan et al., 2013) across the LDT, an average rate of decline of about 0.002 units per century compared with the current rate of more than 0.1 units per century (Bopp et al., 2013; Gattuso et al., 2015). Planktonic foraminiferal shell weights decreased by 40% to 50% (Barker & Elderfield, 2002), and coccolith mass decreased by about 25% (Beaufort et al., 2011) across the LDT. Independent proxy reconstructions thus highlight with *high confidence* that pH values decreased as atmospheric CO_2 concentrations increased across the LDT. There is however *low confidence* in the inferred rate of ocean acidification owing to multiple sources of uncertainties affecting rates estimates based on marine sediments (Section 5.1.2.1). Geochemical and micropaleontological evidence suggest that intermediate-depth OMZs almost vanished during the LGM (Jaccard et al., 2014). However, multiple lines of evidence suggest with *medium confidence* that the deep (>1500 m) ocean became depleted in O_2 (concentrations were possibly lower than 50 µmol kg^{-1}) globally (Jaccard and Galbraith, 2012; Hoogakker et al., 2015, 2018, Gottschalk et al., 2016, 2020; Anderson et al., 2019) as a combined result of sluggish ventilation of the ocean subsurface (Gottschalk et al.,

ACCEPTED VERSION SUBJECT TO FINAL EDITS

2016, 2020; Skinner et al., 2017) and a generally more efficient marine biological carbon pump (Buchanan et al., 2016; Yamamoto et al., 2019; Galbraith and Skinner, 2020).

During the LDT, deep ocean ventilation increased as Antarctic bottom water (AABW) (Skinner et al., 2010; Gottschalk et al., 2016; Jaccard et al., 2016) and subsequently the Atlantic meridional overturning circulation (McManus et al., 2004; Lippold et al., 2016) resumed, transferring previously sequestered remineralised carbon from the ocean interior to the upper ocean and eventually the atmosphere (Skinner et al., 2010; Galbraith and Jaccard, 2015; Gottschalk et al., 2016; Ronge et al., 2016; Sikes et al., 2016; Rae et al., 2018; Ronge et al., 2020), contributing to the deglacial CO_2 rise. Intermediate depths lost oxygen as a result of sluggish ventilation and increasing temperatures (decreasing saturation) as the world emerged from the last Glacial period OMZs underwent a large volumetric increase at the beginning of the Bølling-Allerød (B/A), a northern-hemisphere wide warming event, 14.7 ka (Jaccard and Galbraith, 2012; Praetorius et al., 2015) with deleterious consequences for benthic ecosystems (e.g. Moffitt et al., 2015). These observations indicate with *high confidence* that the rate of warming, affecting the solubility of oxygen and upper water column stratification, coupled with changes in subsurface ocean ventilation impose a direct control on the degree of ocean deoxygenation, implying a high sensitivity of ocean oxygen loss to warming. The expansion of OMZs contributed to a widespread increase in water column (de)nitrification (Galbraith et al., 2013), which contributed substantially to enhanced marine N_2O emissions (Schilt et al., 2014; Fischer et al., 2019). Nitrogen stable isotope measurements on N_2O extracted from ice cores suggest that approximately one third (on the order of 0.7 ± 0.3 TgN yr^{-1}) of the deglacial increase in N_2O emissions relates to oceanic sources (Schilt et al., 2014; Fischer et al., 2019).

5.3.2 Historical Trends and Spatial Characteristics in the Upper Ocean

5.3.2.1 Reconstructed Centennial Ocean Acidification Trends

Ocean pH timeseries are are based on the reconstruction of coral boron isotope ratios ($\delta^{11}B$). A majority of coral $\delta^{11}B$ data have been generated from the western Pacific region with a few records from the Atlantic Ocean. Biweekly resolution paleo-pH records show monsoonal variation of about 0.5 pH unit in the South China Sea (Liu et al., 2014). Interannual ocean pH variability in the range of 0.07–0.16 pH unit characterises southwest Pacific corals that are attributed to ENSO (Wu et al., 2018a) and river runoff (D'Olivo et al., 2015). Decadal (10, 22 and 48-year) ocean pH variations in the southwest Pacific have been linked to the Interdecadal Pacific Oscillation, causing variations of up to 0.30 pH unit in the Great Barrier Reef (Pelejero et al., 2005; Wei et al., 2009) but weaker (about 0.08 pH unit) in the open ocean (Wu et al., 2018a). Decadal variations in the South China Sea ocean pH changes of 0.10–0.20 also have been associated with the variation in the East Asian monsoon (Liu et al., 2014; Wei et al., 2015), as a weakening of the Asian winter monsoon leads to sluggish water circulation within the reefs, building up localised CO_2 concentration in the water due to calcification and respiration.

Since the beginning of the industrial period in the mid-19th century, coral $\delta^{11}B$-derived ocean pH has decreased by 0.06–0.24 pH unit in the South China Sea (Liu et al., 2014; Wei et al., 2015) and 0.12 pH unit in the southwest Pacific (Wu et al., 2018a). Since the mid-20th century, a distinct feature of coral $\delta^{11}B$ records relates to ocean acidification trends, albeit having a wide-range of values: 0.12–0.40 pH unit in the great barrier reef (Wei et al., 2009; D'Olivo et al., 2015), 0.05–0.08 pH unit in the northwest Pacific (Shinjo et al., 2013) and 0.04–0.09 pH unit in the Atlantic Ocean (Goodkin et al., 2015; Fowell et al., 2018). Concurrent coral carbon isotopic ($\delta^{13}C$) measurements infer ocean uptake of anthropogenic CO_2 from the combustion of fossil fuel, based on the lower abundance of ^{13}C in fossil fuel carbon. Western Pacific coral records show depleted $\delta^{13}C$ trends since the late 19th century that are more prominent since the mid-20th century (*high confidence*) (Pelejero, 2005; Wei et al., 2009; Shinjo et al., 2013; Liu et al., 2014; Kubota et al., 2017; Wu et al., 2018).

Overall, many of the records show a highly variable seawater pH underlaying strong imprints of internal climate variability (*high confidence*), and in most instances superimposed on a decreasing $\delta^{11}B$ trend that is indicative of anthropogenic ocean acidification in recent decades (*medium confidence*). The robustness of

ACCEPTED VERSION SUBJECT TO FINAL EDITS

seawater pH reconstructions is currently limited by the uncertainty on the calibration of the $\delta^{11}B$ proxy in different tropical coral species.

5.3.2.2 Observations of Ocean Acidification over the Recent Decades

SROCC (Section 5.2.2.3) indicated it is *virtually certain* that the ocean has undergone acidification globally in response to ocean CO_2 uptake and concluded that pH in open ocean surface water has changed by a *virtually certain* range of –0.017 to –0.027 pH units per decade since the late 1980s. Since SROCC, continued observations of seawater carbonate chemistry at ocean time series stations and compiled shipboard studies providing temporally resolved and methodologically consistent datasets have further strengthened the evidence of the progress of acidification across all regions of the oceans (Jiang et al., 2019) (Figure 5.20; Supplementary Material Table 5.SM.3) (Section 2.3.3.5).

In the subtropical open oceans, decreases in pH have been reported with a *very likely* range of rate from –0.016 to –0.019 pH units per decade since 1980s, which equate to approximately 4 % increase in hydrogen ion concentration ($[H^+]$) per decade. Accordingly, the saturation state Ω ($=[Ca^{2+}][CO_3^{2-}]/K_{sp}$) of seawater with respect to calcium carbonate mineral aragonite has been declining at rates ranging from –0.07 to –0.12 per decade (González-Dávila et al., 2010; Feely et al., 2012; Bates et al., 2014; Takahashi et al., 2014; Ono et al., 2019; Bates and Johnson, 2020) (Supplementary Material Table 5.SM.3). These rates are consistent with the rates expected from the transient equilibration with increasing atmospheric CO_2 concentrations, but the variability of rate in decadal time-scale has also been detected with *robust evidence* (Ono et al., 2019; Bates and Johnson, 2020). In the tropical Pacific, its central and eastern upwelling zones exhibited a faster pH decline of –0.022 to –0.026 pH unit per decade due to increased upwelling of CO_2-rich sub-surface waters in addition to anthropogenic CO_2 uptake (Sutton et al., 2014; Lauvset et al., 2015). By contrast, warm pool in the western tropical Pacific exhibited slower pH decline of –0.010 to –0.013 pH unit per decade (Supplementary Material Table 5.SM.3) (Lauvset et al., 2015; Ishii et al., 2020). Observational and modeling studies (Nakano et al., 2015; Ishii et al., 2020) consistently suggest that slower acidification in this region is attributable to the anthropogenic CO_2 taken up in the extra-tropics around a decade ago and transported to the tropics via shallow meridional overturning circulations.

In open subpolar and polar zones, the *very likely* range (–0.003 to –0.026 pH unit per decade) and uncertainty (up to 0.010) observed in pH decline are larger than in the subtropics, reflecting the complex interplay between physical and biological forcing mechanisms (Olafsson et al., 2009; Midorikawa et al., 2012; Bates et al., 2014; Takahashi et al., 2014; Lauvset et al., 2015; Wakita et al., 2017). Nevertheless, the *high agreement* of pH decline among these available time-series studies leads to *high confidence* in the trend of acidification in these zones. In the Arctic Ocean, a temporally limited time series of carbonate chemistry measurements prevents drawing robust conclusions on ocean acidification trends. However, the carbonate saturation state Ω is generally low, and observational studies show with *robust evidence* that the recent extensive melting of sea ice leading to enhanced air-sea CO_2 exchange, large freshwater inputs, together with river discharge and glacial drainage, as well as the degradation of terrestrial organic matter in seawater, result in the decline of Ω of aragonite to undersaturation (Bates et al., 2009; Chierici and Fransson, 2009; Yamamoto-Kawai et al., 2009; Azetsu-Scott et al., 2010; Robbins et al., 2013; Fransson et al., 2015; Semiletov et al., 2016; Anderson et al., 2017; Qi et al., 2017; Zhang et al., 2020; Beaupré-Laperrière et al., 2020) (SROCC Section 3.2.1.2.4, IPCC, (2019b)). The low saturation state of aragonite (Ω~1) has also been observed in surface waters of the Antarctic coastal zone associated with freshwater input from glacier (Mattsdotter Björk et al., 2014) and with upwelling of deep water (Hauri et al., 2015) as well as along eastern boundary upwelling systems (Feely et al., 2016a).

Overall, in agreement with SROCC, it is *virtually certain* from these observational studies that ocean surface waters undergo acidification globally with the CO_2 increase in the atmosphere. These sustained measurements over the past decades and campaign studies of ocean carbonate chemistry also highlight with *robust evidence* that trends of acidification have been modulated by the variability and changes in physical and chemical states of ocean including those affected by the warming of the cryosphere, requiring their improved understandings.

ACCEPTED VERSION SUBJECT TO FINAL EDITS

[START FIGURE 5.20 HERE]

Figure 5.20: Multi-decadal trends of pH (Total Scale) in surface layer at various sites of the oceans and a global distribution of annual mean pH adjusted to the year 2000. Time-series data of pH are from Dore et al., 2009; Olafsson et al., 2009; González-Dávila et al., 2010; Bates et al., 2014b; Takahashi et al., 2014; Wakita et al., 2017; Merlivat et al., 2018; Ono et al., 2019; and Bates and Johnson, 2020. Global distribution of annual mean pH have been evaluated from data of surface ocean pCO_2 measurements (Bakker et al., 2016; Jiang et al., 2019). Acronyms in panels: KNOT and K2 - Western Pacific subarctic gyre time-series; HOT - Hawaii Ocean Time-series; BATS - Bermuda Atlantic Time-series Study; DYFAMED - Dynamics of Atmospheric Fluxes in the Mediterranean Sea; ESTOC - European Station for Time-series in the Ocean Canary Islands; CARIACO - Carbon Retention in a Colored Ocean Time-series. Further details on data sources and processing are available in the chapter data table (Table 5.SM.6).

[END FIGURE 5.20 HERE]

5.3.3 Ocean Interior Change

5.3.3.1 Ocean Memory – Acidification in the Ocean Interior

Advances in observations and modelling for ocean physics and biogeochemistry and established knowledge of ocean carbonate chemistry show with *very high confidence* that anthropogenic CO_2 taken up into the ocean surface layer is further spreading into the ocean interior through ventilation processes including vertical mixing, diffusion, subduction and meridional overturning circulations (Sallée et al., 2012; Bopp et al., 2015; Nakano et al., 2015; Iudicone et al., 2016; Toyama et al., 2017; Perez et al., 2018; Gruber et al., 2019b) (Sections 2.3.3.5, 5.2.1.3 and 9.2.2.3) and is causing acidification in the ocean interior. The net change in oxygen consumptions by aerobic respiration of marine organisms further influences acidification by releasing CO_2 (Chen et al., 2017; Breitburg et al., 2018; Robinson, 2019) (Section 5.3.3.2).

Basin-wide and global syntheses of ocean interior carbon observations for the past decades show that the extent of acidification due to anthropogenic CO_2 invasion tends to diminish with depth (*very high confidence*) (Woosely et al., 2016;; Lauvset et al., 2020) (Carter et al., 2017a)(Figure 5.21; Section 5.2.1.3.3). The regions of deep convection such as subpolar North Atlantic and Southern Ocean present the deepest acidification detections below 2000 m (*medium confidence*). Mid-latitudinal zones within the subtropical cells and tropical regions present a relatively deep and shallow detection, respectively. A pH decrease has also been observed on the Antarctic continental shelf (Hauck et al., 2010; Williams et al., 2015). Acidification is also underway in the subsurface to intermediate layers of the Arctic Ocean due to the inflow of ventilated waters from the North Atlantic and the North Pacific (Qi et al., 2017; Ulfsbo et al., 2018).

[START FIGURE 5.21 HERE]

Figure 5.21: Spread of ocean acidification from the surface into the interior of ocean since pre-industrial times. (a) map showing the three transects used to create the cross sections shown in (b) and (c); vertical sections of the changes in (b) pH and (c) saturation state of aragonite (Ω_{arag}) between 1800–2002 due to anthropogenic CO_2 invasion (colour). Contour lines are their contemporary values in 2002. The red transect begins in the Nordic Seas and then follows the GO-SHIP lines A16 southward in the Atlantic Ocean, SR04 and S04P westward in the Southern Ocean, and P16 northward in the Pacific Ocean. The purple line follows the GO-SHIP line I09 southward in the Indian Ocean. The green line on the smaller inset crosses the Arctic Ocean from the Bering Strait to North Pole along 175°W and from the North Pole to the Fram Strait along 5°E (Lauvset et al., 2020). Further details on data sources and processing are available in the chapter data table (Table 5.SM.6).

[END FIGURE 5.21 HERE]

ACCEPTED VERSION SUBJECT TO FINAL EDITS

A significant increase in acidification resulting from net metabolic CO_2 release coupled with ocean circulation changes has been shown with *high confidence* in large swathes of intermediate waters both in the Pacific and Atlantic oceans (Byrne et al., 2010; Carter et al., 2017; Chu et al., 2016; Dore et al., 2009; Rios et a., 2015; Lauvset et al., 2020). For example, ocean circulation contributes a pH change of –0.013 ± 0.013 to the overall observed change of –0.029 ± 0.014 for 1993–2013 at depths around 1000 m at 30°S–40°S in the South Atlantic ocean (Ríos et al., 2015). Long-term repeated observations in the North Pacific show a decline in dissolved oxygen (–4.0 μmol kg^{-1} per decade at maximum) being sustained in the intermediate water since the 1980s (Takatani et al., 2012; Sasano et al., 2015), and thus the amplification of acidification associated with the weakening ventilation is thought to have been occurring persistently. In contrast, for the North Pacific subtropical mode water, large decadal variability in pH and aragonite saturation state with amplitudes of about 0.02 and about 0.1, respectively, are superimposed on secular declining trends due to anthropogenic CO_2 invasion (Oka et al., 2019). This is associated with the variability in ventilation due to the approximately 50% variation in the formation volume of the mode water that is forced remotely by the Pacific decadal oscillation (Qiu et al., 2014; Oka et al., 2015).

These trends of acidification in the ocean interior leads to *high confidence* in shoaling of the saturation horizons of calcium carbonate minerals where $\Omega = 1$. In the Pacific Ocean where the aragonite saturation horizon is shallower (a few hundred meters to 1200 m; Figure 5.21c), the rate of its shoaling is on the order of 1–2 m yr^{-1} (Feely et al., 2012; Ross et al., 2020). In contrast, shoaling rates of 4 m yr^{-1} to 1710 m for 1984–2008 and of 10–15 m yr^{-1} to 2250 m for 1991–2016 have been observed in the Iceland sea and the Irminger sea, respectively (Olafsson et al., 2009; Perez et al., 2018).

In summary, ocean acidification is spreading into the ocean interior. Its rates at depths are controlled by the ventilation of the ocean interior as well as anthropogenic CO_2 uptake at the surface, thereby diminishing with depth (*very high confidence*) (Figure 5.21). Variability in ocean circulation modulates the trend of ocean acidification at depths through the changes in ventilation and their impacts on metabolic CO_2 content, but there are large knowledge gaps of ventilation changes leading to *low confidence* in their impacts in many ocean regions (Sections 9.2.2.3 and 9.3.2; Section 5.3.3.2).

5.3.3.2 Ocean Deoxygenation and its Implications for GHGs

As summarised in SROCC (Section 5.2.2.4), there is a growing consensus that between 1970–2010 the open ocean has *very likely* lost 0.5–3.3% of its dissolved oxygen in the upper 1000 m depth (Helm et al., 2011; Ito et al., 2017; Schmidtko et al., 2017; Bindoff et al., 2019) (Section 2.3.3.6). Regionally, the equatorial and North Pacific, the Southern Ocean and the South Atlantic have shown the greatest oxygen loss of up to 30 mol m^{-2} per decade (Schmidtko et al., 2017). Warming – via solubility reduction and circulation changes –, mixing and respiration are considered the major drivers with 50% of the oxygen loss for the upper 1000 m of the global oceans attributable to the solubility reduction (Schmidtko et al., 2017). Climate variability also modifies the oxygen loss on interannual and decadal timescales especially for the tropical ocean OMZs (Deutsch et al., 2011, 2014; Llanillo et al., 2013) and the North Pacific subarctic zone (Whitney et al., 2007; Sasano et al., 2018; Cummins and Ross, 2020). However, quantifying the oxygen decline and variability and attributing them to processes in different regions remains challenging (Oschlies et al., 2018; Levin, 2018). ESMs in coupled model intercomparison project phase 5 (CMIP5) and CMIP6 corroborate the decline in ocean oxygen, and project a continuing and accelerating decline with a strong impact of natural climate variability under high emission scenarios (Bopp et al., 2013; Kwiatkowski et al., 2020; Long et al., 2016). However, CMIP5 models did not reproduce observed patterns for oxygen changes in the tropical thermocline and generally simulated only about half the oxygen loss inferred from observations (Oschlies et al., 2018). CMIP6 models have more realistic simulated mean state of ocean biogeochemistry than CMIP5 models due to improved ocean physical processes and better representation of biogeochemical processes (Séférian et al., 2020). They also exhibit enhanced ocean warming as a result of an increase in the equilibrium climate sensitivity (ECS) of CMIP6 relative to CMIP5 models, which contributes to increased stratification and reduced subsurface ventilation (4.3.1, 4.3.4, 5.3.3.2, 7.4.2, 7.5.6, 9.2.1, TS2.4). Consequently, CMIP6 model

ACCEPTED VERSION SUBJECT TO FINAL EDITS

ensembles not only reproduce the ocean deoxygenation trend of −0.30 to −1.52 mmol m^{-3} per decade between 1970–2010 reported in SROCC (Section 5.2.2.4) with a *very likely* range, but also project 32–71 % greater subsurface (100–600 m) oxygen decline relative to their RCP analogues in CMIP5, reaching to the *likely* range of decline of 6.4 ± 2.9 mmol m^{-3} under SSP1–2.6 and 13.3 ± 5.3 mmol m^{-3} under SSP5–8.5, from 1870–1899 to 2080–2099. However, they also exhibit enhanced surface ocean warming as a result of an increased climate sensitivity (ECS), which contributes to greater reduction in subsurface ventilation. Consequently, CMIP6 model ensembles now reproduce the recent observed historical ocean deoxygenation trend of −0.30 to −1.52 mmol m^{-3} per decade between 1970–2010 reported in SROCC (Section 5.2.2.4) within 90% confidence range, but project 32–71 % greater subsurface (100–600m) oxygen decline relative to their RCP analogues in CMIP5, reaching to the *likely* range of decline of 6.4 ± 2.9 mmol m^{-3} under SSP1–2.6 and 13.3 ± 5.3 mmol m^{-3} under SSP5–8.5, from 1870–1899 to 2080–2099 due to increased warming (Kwiatkowski et al., 2020). It is concluded that the oxygen content of subsurface ocean is projected to transition to historically unprecedented condition with decline over the 21st century (*medium confidence*).

In oxygen-depleted waters, microbial processes (denitrification and anammox, i.e. anaerobic ammonium oxidation) (Kuypers et al., 2005; Codispoti, 2007; Gruber and Galloway, 2008) remove fixed nitrogen, and thus when upwelled waters reach the photic zone, primary production becomes nitrogen-limited (Tyrrell and Lucas, 2002). However, in other oceanic regions, increased water-column stratification due to warming may reduce the amount of N_2O reaching the surface and thereby decrease N_2O flux to the atmosphere. Landolfi et al. (2017) suggest that by 2100, under the RCP8.5 scenario, total N_2O production in the ocean may decline by 5% and N_2O emissions be reduced by 24% relative to the pre-industrial era due to decreased organic matter export and anthropogenic driven changes in ocean circulation and atmospheric N_2O concentrations. Projected oxygen loss in the ocean is thought to result in an ocean-climate feedback through changes in the natural emission of greenhouse gases (*low confidence*).

The areas with relatively rapid oxygen decrease include OMZs in the tropical oceans, where oxygen content has been decreasing at a rate of 0.9 to 3.4 μmol kg^{-1} per decade in the thermocline for the past five decades (Stramma et al., 2008). Low oxygen, low pH and shallow aragonite saturation horizons in the OMZs of the eastern boundary upwelling regions co-occur, affecting ecosystem structure (Chavez et al., 2008) and function in the water column, including the presently unbalanced nitrogen cycle (Paulmier and Ruiz-Pino, 2009). The coupling between upwelling, productivity, and oxygen depletion feeds back to biological productivity and the role of these regions as sinks or sources of climate active gases. When OMZ waters upwell and impinge on the euphotic zone, they release significant quantities of greenhouse gases, including N_2O (0.81–1.35 TgN yr^{-1}), CH_4 (0.27–0.38 $TgCH_4$ yr^{-1}), and CO_2 (yet to be quantified) to the atmosphere, exacerbating global warming (Paulmier et al., 2008; Naqvi et al., 2010; Kock et al., 2012; Arévalo-Martínez et al., 2015; Babbin et al., 2015a; Farías et al., 2015). Modelling projections suggest a global decrease of 4 to 12% in oceanic N_2O emissions (from 3.71–4.03 TgN yr^{-1} to 3.54–3.56 TgN yr^{-1}) from 2005 to 2100 under RCP8.5, despite a tendency to increased N_2O production in the OMZs, associated primarily with denitrification (Martinez-Rey et al., 2015). It is difficult to single out the contribution of nitrification and denitrification which can occur simultaneously. A rigorous separation of these two processes would require more mechanistic parameterisations that have been hindered by the still large conceptual and parametric uncertainties (Babbin et al., 2015; Trimmer et al., 2016; Landolfi et al., 2017). Furthermore, the correlation between N_2O and oxygen varies with microorganisms present, nutrient concentrations, and other environmental variables (Voss et al., 2013).

In summary, total oceanic N_2O emissions were projected to decline by 4–12% from 2005–2100 (Martinez-Rey et al., 2015) and by 24% from the pre-industrial era to 2100 (Landolfi et al., 2017) under RCP8.5. However, there is *low confidence* in the reduction in N_2O emission to the atmosphere, because of large conceptual and parametric uncertainties, a limited number of modelling studies that explored this process, and greater oxygen losses simulated in CMIP6 models than in CMIP5 models (Kwiatkowski et al., 2020).

5.3.4 Future Projections for Ocean Acidification

5.3.4.1 Future Projections with Earth System Models

ACCEPTED VERSION SUBJECT TO FINAL EDITS

Projections with CMIP5 ESMs, reported in AR5 (Section 6.4.4) and SROCC (Section 5.2.2.3; (IPCC, 2019b)), showed changes in global mean surface ocean pH from 1870–1899 to 2080–2099 of -0.14 ± 0.001 (inter-model standard deviation) under RCP2.6 and –0.38 ±0.005 under RCP8.5 with pronounced regional variability (Bopp et al., 2013; Hurd et al., 2018). They also projected faster pH declines in mode waters below seasonal mixed layers (Resplandy et al., 2013; Watanabe and Kawamiya, 2017) as has been observed in the Atlantic (Salt et al., 2015) and in the Pacific (Carter et al., 2019), because of the net CO_2 release by respiration and lowering CO_2 buffering capacity of seawater. In these CO_2 concentration-driven simulations, the level of acidification in the surface ocean is primarily determined by atmospheric CO_2 concentration and regional seawater carbonate chemistry, thereby providing consistent projections across models. New projections with CMIP6 ESMs show greater surface pH decline of -0.16 ± 0.002 under the SSP1–2.6 and –0.44 ± 0.005 under SSP5–8.5 from 1870–1899 to 2080–2099 (Kwiatkowski et al., 2020) (Section 4.3.2.5; Cross-Chapter Box 5.3). The greater pH declines in CMIP6 are primarily a consequence of higher atmospheric CO_2 concentrations in SSPs than their CMIP5-RCP analogues (Kwiatkowski et al., 2020). Ocean acidification is also projected to occur with *high confidence* in the abyssal bottom waters in regions such as the northern North Atlantic and the Southern Ocean (Sulpis et al., 2019), with the rates of global mean pH decline of –0.018 ±0.001 under SSP1–2.6 and –0.030 ± 0.002 under SSP5–8.5 from 1870–1899 to 2080–2099 in CMIP6 (Kwiatkowski et al., 2020).

In surface ocean, changes in the amplitude of seasonal variations in pH are also projected to occur with *high confidence.* ESMs in CMIP6 s show +73 ± 12% increase in the amplitude of seasonal variation in hydrogen ion concentration ($[H^+]$) but 10 ±5% decrease in the seasonal variation in pH (= -log $[H^+]$) from 1995–2014 to 2080–2099 under SSP5–8.5. The simultaneous amplification of $[H^+]$ and attenuation of pH seasonal cycles is counterintuitive but is the consequence of greater increase in the annual mean $[H^+]$ due to anthropogenic CO_2 invasion than the corresponding increase in its seasonal amplitude. These changes are consistent with the amplification/attenuation of the seasonal variation of +81 ±16% for $[H^+]$ and –16 ± 7% for pH from 1990–1999 to 2090–2099 under RCP8.5 in CMIP5 (Kwiatkowski and Orr, 2018).

The signal of ocean acidification in surface ocean is large and is projected to emerge beyond the range of natural variability within the time scale of a decade in all ocean basins (Schlunegger et al., 2019). There is *high agreement* among modelling studies that the largest pH decline and large-scale undersaturation of aragonite in surface seawater start to occur first in polar oceans (Orr et al., 2005; Steinacher et al., 2009; Hurd et al., 2018; Jiang et al., 2019). Under SSP5–8.5, the largest surface pH decline, exceeding 0.45 between 1995–2014 and 2080–2099, occurs in the Arctic Ocean (Kwiatkowski et al., 2020). The freshwater input from sea-ice melt is an additional factor leading to a faster decline of aragonite saturation level than expected from the anthropogenic CO_2 uptake (Yamamoto et al., 2012). The increase in riverine and glacial discharges that provide terrigenous carbon, nutrients and alkalinity as well as freshwater are the other factors modifying the rate of acidification in the Arctic Ocean. However, their impacts have been projected in a limited number of studies with extensive knowledge gaps and model simplifications leading to *low confidence* in their impacts (Terhaar et al., 2019; Hopwood et al., 2020). In the Southern Ocean, the aragonite undersaturation starts in 2030 in RCP8.5, and the area that experiences aragonite undersaturation for at least one month per year by 2100 is projected to be more than 95%. Under RCP2.6, short periods (< 1 month) of aragonite undersaturation are expected to be found in less than 2% to the area during this century (Sasse et al., 2015; Hauri et al., 2016; Negrete-García et al., 2019). These long term projections are modified at interannual timescales by large-scale climate modes (Ríos et al., 2015) such as the El Niño southern oscillation and the southern annular mode (Conrad and Lovenduski, 2015). In other regions, acidification trends are influenced by a range of processes such as changes in ocean circulation, temperature, salinity, carbon cycling, and the structure of the marine ecosystem. As, at present, models do not resolve fine-scale variability of these processes, current projections do not fully capture the changes that the marine environment will experience in the future (Takeshita et al., 2015; Turi et al., 2016).

Overall, with the rise of atmospheric CO_2, the physics of CO_2 transfer across the air-sea interface, the carbonate chemistry in seawater, the trends of ocean acidification being observed in the past decades (Section 5.3.3.2) and modelling studies described in this section, it is *virtually certain* that ocean acidification will continue to grow. However, the magnitude and sign of many of ocean carbon-climate

ACCEPTED VERSION SUBJECT TO FINAL EDITS

feedbacks are still poorly constrained (Matear and Lenton, 2014; Matear and Lenton, 2018), leading to *low confidence* in their significant and long-lasting impacts on ocean acidification.

5.3.4.2 Reversal of Ocean Acidification by Carbon Dioxide Removal

Reversing the increase in atmospheric CO_2 concentrations through negative emissions (Section 5.6) will reverse ocean acidification at the sea surface but will not result in rapid amelioration of ocean acidification in the deeper ocean (Section 5.3.3.2). The ocean's uptake of atmospheric CO_2 will start to decrease as atmospheric CO_2 decreases (Mathesius et al., 2015; Tokarska and Zickfeld, 2015) (Sections 5.4.5, 5.4.10; 5.6.2.1) However, because of the long timescales of the ocean turnover that transfers CO_2 from the upper to the deep ocean, excess carbon will continue to accumulate in the deep ocean even after a decrease in atmospheric CO_2 (Cao et al., 2014; Mathesius et al., 2015; Tokarska and Zickfeld, 2015; Li et al., 2020). There is thus *high confidence* that CO_2 emissions leave a long-term legacy in ocean acidification, and are therefore irreversible at multi-human generational scales, even with aggressive atmospheric CO_2 removal.

5.3.5 Coastal Ocean Acidification and Deoxygenation

The coastal ocean, from the shore line to the isobath of 200 m, is highly heterogeneous due to the complex interplay between physical, biogeochemical and anthropogenic factors (Gattuso et al., 1998; Chen and Borges, 2009; Dürr et al., 2011; Laruelle et al., 2014; McCormack et al., 2016). These areas, according to SROCC (Bindoff et al., 2019) are, with *high confidence*, already affected by ocean acidification and deoxygenation. This section assesses the drivers and spatial variability of acidification and deoxygenation based on new observations and data products.

5.3.5.1 Drivers

Observations and data products including models (Astor et al., 2013; Bakker et al., 2016; Kosugi et al., 2016; Vargas et al., 2016; Laruelle et al., 2017, 2018; Orselli et al., 2018; Roobaert et al., 2019; Cai et al., 2020; Sun et al., 2020a) confirm the strong spatial and temporal variability in the coastal ocean surface carbonate chemistry and sea-air CO_2 fluxes *(high agreement, robust evidence)*. The anthropogenic CO_2-induced acidification is either mitigated or enhanced through biological processes; primary production removes dissolved CO_2 from the surface, and respiration adds CO_2 and consumes oxygen in the subsurface layers. The relative intensity of these processes is controlled by natural or anthropogenic eutrophication. Other drivers of variability include biological community composition, freshwater input from rivers or ice-melting, sea-ice cover and calcium carbonate precipitation/dissolution dynamics, coastal upwelling and regional circulation, and seasonal surface cooling (Fransson et al., 2015, 2017; Feely et al., 2018; Roobaert et al., 2019; Cai et al., 2020; Hauri et al., 2020; Monteiro et al., 2020b; Sun et al., 2020a). Near-shore surface waters are often supersaturated with CO_2, regardless of the latitude, especially in highly populated areas receiving substantial amounts of domestic and industrial sewage (Chen and Borges, 2009). Nevertheless, thermal or haline stratified eutrophic coastal areas may act as net atmospheric CO_2 sinks (Chou et al., 2013; Cotovicz Jr. et al., 2015a). Continental shelves, excluding near-shore areas, act as CO_2 sinks at a rate of 0.2 ± 0.02 PgC yr^{-1} (Laruelle et al., 2014; Roobaert et al., 2019), considering ice-free areas only. Under increasing atmospheric CO_2 and eutrophication, such ecosystems would be more vulnerable to ecological and seawater chemistry changes, impacting local economy.

Since AR5, (Ciais et al., 2013) and in agreement with SROCC (IPCC, 2019b), there is now *high agreement (robust evidence)* that coastal ocean acidification, whether induced only by increasing atmospheric CO_2 or exacerbated by eutrophication or upwelling, has negative effects on specific groups of marine organisms such as reef-building corals, crabs, pteropods, and sessile fauna (Dupont et al., 2010; Bindoff et al., 2019; Bednaršek et al., 2020; Osborne et al., 2020), WGII AR6 Chapter 3), especially when combined with stressors such as temperature and deoxygenation, and potentially increased bioavailability of toxic elements such as arsenic and copper (Millero et al., 2009; Boyd et al., 2015; Breitburg et al., 2018).

ACCEPTED VERSION SUBJECT TO FINAL EDITS

Since SROCC (Bindoff et al., 2019), there is further evidence that anthropogenic eutrophication via continental runoff and atmospheric nutrient deposition, and ocean warming are *very likely* the main drivers of deoxygenation in coastal areas (Levin and Breitburg, 2015; Levin et al., 2015; Royer et al., 2016; Breitburg et al., 2018; Cocquempot et al., 2019; Fagundes et al., 2020; Limburg et al., 2020a). Increasing intensity and frequency of wind-driven upwelling is responsible for longer and more intense coastal hypoxia, fuelled by organic matter degradation from primary production *(medium to high agreement, medium evidence)* (Rabalais et al., 2010; Bakun et al., 2015; Varela et al., 2015; Fennel and Testa, 2019; Limburg et al., 2020a). Locally, submarine groundwater discharge may enhance the eutrophication state (*low agreement, limited evidence*, (Luijendijk et al., 2020)). Since AR5 (Ciais et al., 2013) and SROCC (Bindoff et al., 2019) new observations and model studies confirm the trends in increasing coastal hypoxia caused by eutrophication, ocean warming and changes in circulation (Claret et al., 2018; Dussin et al., 2019; Limburg et al., 2020a), as well as the ubiquitous impacts on marine organisms and fisheries (Carstensen and Conley, 2019; Fennel and Testa, 2019; Osma et al., 2020); WGII Chapter 3). Following open ocean deoxygenation trends, since the 1950s more than 700 coastal regions are being reported as hypoxic (dissolved oxygen concentration <2 mg O_2 L^{-1}) (Limburg et al., 2020a). Additionally, deoxygenation or increasing severe hypoxic periods in coastal areas may enhance the sea-to-air fluxes of N_2O and CH_4 especially through microbial-mediated processes in the water column-sediment interface *(medium agreement)* (Middelburg and Levin, 2009; Naqvi et al., 2010b; Farías et al., 2015; Limburg et al., 2020a).

5.3.5.2 Spatial Characteristics

There is *high agreement (robust evidence)* that heterogeneity implies different responses of coastal regions to increasing atmospheric CO_2, decreasing seawater pH and calcium carbonate saturation state, and deoxygenation (Duarte et al., 2013; Regnier et al., 2013b; Breitburg et al., 2018; Laruelle et al., 2018; Carstensen and Duarte, 2019).

There is *high agreement* that long time series of observations utilising standard methods are needed to distinguish the climate change signal in seawater carbonate chemistry from the natural variability of coastal sites (Duarte et al., 2013; Salisbury and Jönsson, 2018; IOC, 2019; Sutton et al., 2019; Tilbrook et al., 2019; Turk et al., 2019). Despite increasing availability of data and sea-air CO_2 flux budgets for the coastal ocean (Sections 5.3.5.1, 5.2.3.1), additional long-term observations are required to constrain the global time of emergence of coastal acidification. There is *high agreement* (*medium evidence*) that, for the coastal subtropical to temperate northeast Pacific and northwest Atlantic, the mean time of emergence for acidification is above two decades (Sutton et al., 2019; Turk et al., 2019).

Observations and models predict for the northeast Pacific coastal upwelling area an expansion and intensification of low-pH deep water intrusions *(high agreement, robust evidence)* (Hauri et al., 2013; Feely et al., 2016b; Cai et al., 2020). There, areas such as the California Current System are naturally exposed to intrusions of low-pH, high pCO_{2sea} deep waters from remineralisation processes and anthropogenic CO_2 intrusion (Feely et al., 2008, 2010, 2018; Chan et al., 2019; Lilly et al., 2019; Cai et al., 2020).The eastern Pacific coastal upwelling displays seasonality in subsurface aragonite undersaturation as a consequence of the interplay between anthropogenic CO_2, respiration and intrusion of upwelling waters (Feely et al., 2008, 2010, 2016, 2018; Hauri et al., 2013; Vargas et al., 2016; Chan et al., 2019; Lilly et al., 2019). The coastal southeast Pacific, upwelling combined with low-pH, low-alkalinity, organic matter-rich river inputs display extreme temporal variability in surface seawater pCO_2 and low aragonite saturation (Vargas et al., 2016; Osma et al., 2020).

Temperate, non-upwelling coastal areas along the northwest Atlantic display a trend of decreasing seawater pH, mainly attributed to the combined effects of decreasing seawater buffering capacity and eutrophication (*high agreement, robust evidence*). Observations show an increasing north to south gradient of aragonite saturation state (Sutton et al., 2016; Fennel et al., 2019; Cai et al., 2020). Low alkalinity and total inorganic carbon concentration, combined with an ocean signal of acidification, diminishes the buffering capacity along the decreasing salinity gradient from the ocean to the coast. Models suggest that in this area the

ACCEPTED VERSION SUBJECT TO FINAL EDITS

aragonite saturation is seasonally controlled by nutrient availability and primary production, supporting that eutrophication is the main driver for exacerbating acidification.(Cai et al., 2017, 2020). The coastal Gulf of Mexico is facing a parallel increase in bottom water acidification and deoxygenation off the Mississippi Delta driven by eutrophication (Cai et al., 2011; Laurent et al., 2017; Fennel et al., 2019).

Many coastal tropical are under heavy anthropogenic eutrophication induced by the effluents from large cities or receive large riverine inputs of freshwater, nutrients, and organic matter (such as Amazon, Mississippi, Orinoco, Congo, Mekong, or Changjiang rivers). Under strong eutrophication, often sub-surface and bottom waters present pH values lower than average surface open ocean (about 8.0) because increased respiration decreases pH *(high agreement, robust evidence)*, despite a net atmospheric CO_2 sink in shallow and vertically stratified coastal areas (Koné et al., 2009; Wallace et al., 2014; Cotovicz Jr. et al., 2015b; Cotovicz et al., 2018; Fennel and Testa, 2019; Lowe et al., 2019) (Section 5.3.5.1).

There is *medium evidence* from observations and models that the coastal northwestern Antarctic Peninsula (Southern Ocean) will experience calcium carbonate undersaturation by 2060, considering that anthropogenic emissions reach an atmospheric CO_2 concentration of about 500 pm at that date (Lencina-Avila et al., 2018; Monteiro et al., 2020a). The synergies among warming, meltwater, sea-air CO_2 equilibrium and circulation may, to some extent, offset the coastal ocean acidification trends in Antarctica (Henley et al., 2020). In the coastal western Arctic Ocean, there is increasing *robust evidence* that ocean acidification is driven by sea-air CO_2 fluxes and sea-ice melt and increasing intrusions since the 1990s of low-alkalinity Pacific water, lowering aragonite saturation state (Qi et al., 2017, 2020; Cross et al., 2018). The Bering Sea (northeastern Pacific) shows decreasing trends in calcium carbonate saturation, associated to the increasing atmospheric CO_2 uptake combined with riverine freshwater and carbon inputs *(high agreement, robust evidence)* (Pilcher et al., 2019; Sun et al., 2020a).

The spatial distribution of hypoxic areas is highly heterogeneous in the coastal ocean, and there is *high agreement, robust evidence* that more severe hypoxia or anoxia is often associated to highly populated coastal areas, or local circulation and upwelling, and seasonal stratification lead to an accumulation of organic matter in subsurface waters (Ciais et al., 2013; Rabalais et al., 2014; Li et al., 2016b; Breitburg et al., 2018; Bindoff et al., 2019) (SROCC Chapter 5; IPCC, (2019b)). The causes and trends of coastal deoxygenation can only be assessed by making available long-term time series combined to regional modelling (Fennel and Testa, 2019), as in the California current system (Wang et al., 2017), the East China Sea (Chen et al., 2007; Qian et al., 2017), the Namibian or along the northwestern Atlantic shelves (Claret et al., 2018). Other coastal upwelling sites such as the Arabian Sea display seasonal hypoxia but no worsening trends (Gupta et al., 2016).

The Baltic Sea is the largest semi-enclosed sea where hypoxia is reported to have happened before the 1950s (Carstensen et al., 2014; Rabalais et al., 2014; Łukawska-Matuszewska et al., 2019). The frequency and volume of seawater inflow from the North Sea decreased after 1950, leading to an expansion of hypoxic areas from 40,000 to 60,000 km² in combination with increasing eutrophication (Carstensen et al., 2014). From the available observations, there is *robust evidence* that many areas in the Baltic Sea are experiencing deoxygenation despite efforts to reduce nutrient loads (Lennartz et al., 2014; Jokinen et al., 2018).

There is *medium agreement (medium evidence)* that just by reducing anthropogenic nutrient inputs may lead to less severe coastal hypoxic conditions, as observed in the coastal north-western Adriatic Sea (Djakovac et al. (2015). However, low-oxygen sediments may remain a long-term source of phosphorus and ammonium to the water column, fuelling primary production (Jokinen et al., 2018; Fennel and Testa, 2019; Limburg et al., 2020b).

5.4 Biogeochemical Feedbacks on Climate Change

This section covers biogeochemical feedbacks on climate change, which represent one of the largest sources of uncertainty in climate change projections. The relevant processes are discussed (Sections 5.4.1 to 5.4.4), prior to discussing the simulation and projection of the carbon cycle in Earth system models (Section 5.4.5),

ACCEPTED VERSION SUBJECT TO FINAL EDITS

emergent constraints on future projections (Section 5.4.7), non-CO_2 feedbacks (Section 5.4.7), and possible biogeochemical abrupt changes (Section 5.4.8).

5.4.1 Direct CO_2 Effect on Land Carbon Uptake

AR5 (WGI, Box 6.3) and SRCCL (IPCC, 2019a) concluded with *high confidence* that rising atmospheric CO_2 increases leaf-level photosynthesis. This effect is represented in all ESMs. New studies since AR5 add evidence that the leaf-level CO_2 fertilisation is modulated by acclimation of photosynthesis to long-term CO_2 exposure, growth temperature, seasonal drought, and nutrient availability, but these effects are not yet routinely represented in ESMs (Smith and Dukes, 2013; Baig et al., 2015; Kelly et al., 2016; Drake et al., 2017; Jiang et al., 2020a). Cross-Chapter Box 5.1 assesses multiple lines of evidence, which suggest that the ratio of plant CO_2 uptake to water loss (plant water-use efficiency; WUE) increases in near proportionality to atmospheric CO_2. Despite advances in the regional coverage of field experiments, observations of the consequences of CO_2 fertilisation at ecosystem level are still scarce, in particular from outside the temperate zone (Song et al., 2019a). New syntheses since AR5 corroborate that the effect of elevated CO_2 on plant growth and ecosystem carbon storage is generally positive (*high confidence*), but is modulated by temperature, water and nutrient availability (Reich et al., 2014; Obermeier et al., 2017; Peñuelas et al., 2017; Hovenden et al., 2019; Song et al., 2019a). Plant carbon allocation, changes in plant community composition, disturbance, and natural plant mortality are important processes affecting the magnitude of the response, but are currently poorly represented in models (De Kauwe et al., 2014; Friend et al., 2014; Reich et al., 2018; Walker et al., 2019a; Yu et al., 2019), and thus contribute strongly to uncertainty in ESM projections (Arora et al., 2020).

Field studies with elevated CO_2 have demonstrated that the initial stimulation of above-ground growth may decline if insufficient nutrients such as nitrogen or phosphorus are available (Finzi et al., 2007; Norby et al., 2010; Hungate et al., 2013; Reich and Hobbie, 2013; Talhelm et al., 2014; Terrer et al., 2018). Model-data syntheses have demonstrated that the ability to capture the observed long-term effect of elevated CO_2 depends on the ability of models to predict the effect of vegetation on soil biogeochemistry (Zaehle et al., 2014; Koven et al., 2015; Medlyn et al., 2015; Walker et al., 2015). Meta-analyses of CO_2 manipulation experiments point to increased soil microbial activity and accelerated turnover of soil organic matter (van Groenigen et al., 2017) as a result of increased below-ground carbon allocation by plants (Song et al., 2019b), and increased root exudation or mycorrhizal activity due to enhanced plant nutrient requirements under elevated CO_2 (Drake et al., 2011; Terrer et al., 2016; Meier et al., 2017). These effects are not considered in most ESMs. One global model that attempts to represent these processes suggests that elevated CO_2 related carbon accumulation is reduced in soils but increased in vegetation relative to more conventional models (Sulman et al., 2019).

Our understanding of the effects of phosphorus limitation is less developed than for nitrogen, but a growing body of literature suggests it is as important, particularly in regions with highly weathered soils (Wang et al., 2018; Terrer et al., 2019; Du et al., 2020). CO_2 experiments collectively show that soil phosphorus is an important constraint on the CO_2 fertilisation effect on plant biomass (Terrer et al., 2019; Jiang et al., 2020a). Indeed, a free-air CO_2 enrichment experiment in a phosphorus-limited mature forest ecosystem did not find an increase in biomass production despite increases in photosynthesis after four years of CO_2 exposure (Jiang et al., 2020b). The lack of free-air CO_2 enrichment experiments in phosphorus-limited tropical forests limits our understanding on the role of phosphorus availability in constraining the CO_2 fertilisation effect globally (Norby et al., 2016; Fleischer et al., 2019). Models accounting for the effects of phosphorus availability, in addition to nitrogen, generally show an even stronger reduction of the response of ecosystem carbon storage to elevated CO_2 (Goll et al., 2012; Zhang et al., 2014; Yang et al., 2019b). Insufficient data and uncertainties in the process formulation cause large uncertainty in the magnitude of this effect (Medlyn et al., 2016; Fleischer et al., 2019).

Consistent with AR5 (WGI, Section 6.4.2), the CO_2 fertilisation effect is the dominant cause for the projected increase in land carbon uptake between 1860 and 2100 in ESMs (Figures 5.26, 5.27; Table 5.5; Arora et al., 2020). In the CMIP6 ensemble, the increase of land carbon storage due to CO_2 fertilisation is a global

ACCEPTED VERSION SUBJECT TO FINAL EDITS

phenomenon but is strongest in the tropics (Figure 5.26). The resulting increase of productivity is a key driver of increases in vegetation and soil carbon storage. However, consistent with earlier findings (Todd-Brown et al., 2013; Friend et al., 2014; Hajima et al., 2014), processes affecting vegetation carbon-use efficiency and turnover such as allocation changes, mortality, and vegetation structural changes, as well as the pre-industrial soil carbon turnover time, also play an important role (Arora et al., 2020).

As a major advance since AR5 (WGI, Section 6.4.2), 6 out of 11 models in the C^4MIP-CMIP6 ensemble account for nitrogen cycle dynamics over land (Table 5.4). On average, these models exhibit a 25–30% lower CO_2 fertilisation effect on land carbon storage, compared to models that do not (Figures 5.29, Table 5.5). The only model in the C^4MIP-CMIP6 ensemble that explicitly represents the effect of P availability on plant growth suggests the lowest C storage response to increasing CO_2 (Arora et al., 2020). The lower CO_2 effect due to decreased nutrient availability is generally consistent with analyses of the implicit nutrient limitation in CMIP5 simulations (Wieder et al., 2015; Zaehle et al., 2015) and independent assessments by stand-alone land models (Zaehle et al., 2010; Wårlind et al., 2014; Zhang et al., 2014; Goll et al., 2017; Meyerholt et al., 2020a). The simulated effects are generally consistent with expectations based on independent observations (Walker et al., 2020). However, the magnitude of nutrient feedbacks in these models is poorly constrained by observations, owing to the limited geographic distribution of available observations and the uncertain scaling of results obtained from manipulation experiments to transient system dynamics (Song et al., 2019a; Wieder et al., 2019; Meyerholt et al., 2020a).

Our understanding of the various biological processes, which affect the strength of the CO_2 fertilisation effect on photosynthesis and its impact on carbon storage in vegetation and soils, in particular regarding the limitations imposed by nitrogen and phosphorus availability, has developed since AR5 (WGI, Box 6.2). Based on consistent behaviour across all CMIP6 ESMs, there is *high confidence* that CO_2 fertilisation of photosynthesis acts as an important negative feedback on anthropogenic climate change, by reducing the rate at which CO_2 accumulates in the atmosphere. Since AR5 (WGI, Box 6.2), an increasing number of CMIP6 ESMs account for nutrient cycles and the consistent results found in their model projections suggests with *high confidence* that limited nutrient availability will limit the CO_2 fertilisation effect (Arora et al., 2020). The magnitude of both the direct CO_2 effect on land carbon uptake, and its limitation by nutrients, remains uncertain (*low confidence*).

5.4.2 Direct CO_2 Effects on Projected Ocean Carbon Uptake

In AR5 (WGI, Section 6.4.2) there was *high agreement* that CMIP5 ESMs project continued ocean CO_2 uptake through to 2100, with higher uptake corresponding to higher concentration or emission pathways. There has been no significant change in the magnitude of the sensitivity of ocean carbon uptake to increasing atmospheric CO_2, or in the inter-model spread, between the CMIP5 and CMIP6 era (Arora et al., 2020). The analysis from both emissions and concentration driven CMIP5 models projections show that the ocean sink stops growing beyond 2050 across all emission scenarios (Section 5.4.5.3). CMIP6 models also show a similar time-evolution of global ocean CO_2 uptake to CMIP5 models over the 21st century (Figure 5.25) with decreasing net ocean CO_2 uptake ratio to anthropogenic CO_2 emissions under SSP5–8.5.

The projected weakening of ocean carbon uptake is driven by a combination of decreasing carbonate buffering capacity and warming which are positive feedbacks under weak to no mitigation scenarios (SSP4 and 5). In high mitigation scenarios (SSP1–2.6), weakening ocean carbon uptake is driven by decreasing emissions (Cross-Chapter Box 5.3). The detailed understanding of carbonate chemistry in seawater that has accumulated over more than half a century (e.g. Egleston et al., 2010; Revelle & Suess, 1957), provides *high confidence* that the excess CO_2 dissolved in seawater leads to a nonlinear reduction of the CO_2 buffering capacity, that is smaller dissolved inorganic carbon (DIC) increase with respect to pCO_2 increase along with the increase in cumulative ocean CO_2 uptake. Recent studies (Katavouta et al., 2018; Jiang et al., 2019; Arora et al., 2020; Rodgers et al., 2020) suggest with *medium confidence* that the decrease in the ocean CO_2 uptake ratio to anthropogenic CO_2 emission under low to no mitigation scenarios over the 21st century is predominantly attributable to the ocean carbon-concentration feedback through the reduction of the seawater CO_2 buffering capacity but with contributions from physical drivers such as warming and wind stress

ACCEPTED VERSION SUBJECT TO FINAL EDITS

(*medium confidence*) and biological drivers (*low confidence*) (Sections 5.2.1.3.3, 5.4.4).

Projected increases in ocean DIC due to anthropogenic CO_2 uptake amplify the sensitivity of carbonate system variables to perturbations of DIC in the surface ocean, for example via the amplitude of the seasonal cycle of pCO_2, which impact the mean annual air-sea fluxes (Fassbender et al., 2018; Hauck et al., 2015; Landschützer et al., 2018; SROCC Section 5.2.2.3). A larger amplification of the surface ocean pCO_2 seasonality occurs in the subtropics where pCO_2 seasonality is dominated by temperature seasonality, with the summer increase in the difference in pCO_2 between surface water and the overlying atmosphere reaching 3µatm per decade between 1990 and 2030 under RCP8.5 (Schlunegger et al., 2019; Rodgers et al., 2020). In contrast, the impact of biological production on the seasonal cycle of pCO_2 in summer in the Southern Ocean strengthens the drawdown of CO_2 (Hauck et al., 2015).

Overall, there is *medium confidence* on three outcomes in the ocean from projected CO_2 uptake under medium to high CO_2 concentration scenarios: (i) a strengthening positive feedback, which impacts on the airborne fraction via the reduction of the ocean CO_2 buffering capacity due to cumulative ocean CO_2 uptake, which reduces the net ocean CO_2 uptake ratio to anthropogenic CO_2 emission (Katavouta et al., 2018; Arora et al., 2020; Rodgers et al., 2020); (ii) an amplification of the seasonal cycle of CO_2 variables, which impact both the ocean sink and ocean acidification (Hauck et al., 2015); (iii) a decrease in the aragonite and calcite saturation levels in the ocean which negatively impacts the calcification rates of marine organisms (*high confidence*) and which forms a negative feedback on the uptake of CO_2 (McNeil and Sasse, 2016) (Cross-Chapter Box 5.3).

5.4.3 Climate Effect on Land Carbon Uptake

AR5 assessed with *medium confidence*, that future climate change will decrease land carbon uptake relative to the case with constant climate, but with a poorly-constrained magnitude (WGI, Chapter 6, Executive Summary). Ongoing uncertainty in the magnitude and geographic pattern of the feedbacks (Section 5.4.5), continues to support a *medium confidence* assessment that future climate change will decrease land carbon uptake relative to the case with constant climate.

5.4.3.1 Plant Physiology

Plant productivity is highly dependent on local climate. In cold environments, warming has generally led to an earlier onset of the growing season, and with it an increase in early-season vegetation productivity (e.g. Forkel et al., 2016). However, this trend is affected by adverse effects of climate variability, and other emerging limitations on vegetation production by water, energy and nutrients, which may gradually reduce the effects of warming (Piao et al., 2017; Buermann et al., 2018; Liu et al., 2019). At centennial timescales, boreal forest expansion may act as a climate-driven carbon sink (Pugh et al., 2018).

In tropical and temperate environments, temperature simultaneously affects the metabolic rates of photosynthetic processes within leaf tissues as well as the vapor pressure deficit that drives transpiration, its control by leaf stomata, and the resulting soil and plant tissue water content. Thus the direct effect of warming on photosynthesis can be positive, negative, or invariant depending on environmental context (Lin et al., 2012; Yamori et al., 2014; Smith and Dukes, 2017; Grossiord et al., 2020). Observations and models suggest that the vapour pressure deficit effects are stronger than direct temperature effects on enzyme activities (Smith et al., 2020), and that acclimation of photosynthetic optimal temperature may mitigate productivity losses of tropical forests under climate change (Kattge and Knorr, 2007; Tan et al., 2017; Kumarathunge et al., 2019). Some models have begun to include these acclimation responses, both in photosynthesis and autotrophic respiration (Lombardozzi et al., 2015; Smith et al., 2015; Huntingford et al., 2017; Mercado et al., 2018).

5.4.3.2 Fire and Other Disturbances

ACCEPTED VERSION SUBJECT TO FINAL EDITS

SRCCL assessed that climate change is playing an increasing role in determining wildfire regimes alongside human activity (*medium confidence*), with future climate variability expected to enhance the recurrence and severity of wildfires in many biomes, such as tropical rainforests (*high confidence*). Projections of increased fire weather in a warmer climate are widespread (Section 12.3.2.8) and may drive increased fire frequency and severity in several regions, including Arctic and boreal ecosystems (Gauthier et al., 2015; Walker et al., 2019b), Mediterranean-type ecosystems (Turco et al., 2014; Jin et al., 2015), degraded tropical forests (Aragão et al., 2018), and tropical forest-savanna transition zones (Lehmann et al., 2014).

Wildfire is included in some CMIP6 ESMs (Table 5.4) and is thus only partially represented in estimates of carbon-climate feedbacks from these models. The CMIP5 ESMs that include fire project 8–58% increases of fire carbon emissions under future scenarios, with higher emissions under higher-warming scenarios; the ensemble spread is driven by differing factors such as population density, fire management, and other land-use processes (Kloster and Lasslop, 2017). Fire dynamics in CMIP6 models, as evaluated in land-only configurations of CMIP6-generation land surface models, also show large variations but better agreement with observations (Teckentrup et al., 2019; Hantson et al., 2020; Lasslop et al., 2020).

Climate change also drives changes to vegetation composition and ecosystem carbon storage through other disturbances such as forest dieback that lead to biome shifts in tropical forests (Cox et al., 2004; Jones et al., 2009; Brando et al., 2014; Le Page et al., 2017; Zemp et al., 2017), and temperate and boreal regions (Joos et al., 2001; Lucht et al., 2006; Scheffer et al., 2012; Lasslop et al., 2016). AR5 assessed that large-scale loss of tropical forests due to climate change is *unlikely* (WGI, Section 6.4.9). Newer ecosystem modelling approaches that include a greater degree of ecosystem heterogeneity and diversity show a reduced sensitivity of such forest dieback-type changes (Levine et al., 2016; Sakschewski et al., 2016), supporting the AR5 assessment (Section 5.4.8). Beyond such biome shifts, observations of tropical forests also show that increasing tree mortality rates within tropical forests may reduce carbon turnover times and storage (Brienen et al., 2015), that increased tree mortality rates in tropical forests and elsewhere are expected with increased temperatures and vapor pressure deficit (Cross-chapter Box 5.1; (Allen et al., 2015; McDowell et al., 2018; Grossiord et al., 2020), and that these processes are not well represented in ESMs (Powell et al., 2013; Fisher et al., 2018). An ensemble of land models that include ecological processes such as forest demography shows that changes to mortality may be a more important driver of carbon dynamics than changes to productivity (Friend et al., 2014).

Overall, climate change will force widespread increases in fire weather throughout the world (Section 12.3.2.8). Because of incomplete inclusion of fire in ESMs, a separate compilation of fire-driven carbon-climate feedback estimates (Eliseev et al., 2014a; Harrison et al., 2018) (section 5.4.8). There is *low agreement* in magnitude and *medium agreement* in sign, which alongside other literature (Jones et al., 2020), leads to an assessment of *medium confidence* that fire represents a positive carbon-climate feedback, but *very low confidence* in the magnitude of that feedback. Other disturbances such as tree mortality will increase across several ecosystems (*medium agreement*) with decreased vegetation carbon (*medium confidence*). However, the lack of model agreement and lack of key process representation in ESMs lead to a *low confidence* assessment in the projected magnitude of this feedback.

5.4.3.3 Soil Carbon

Changes to soil carbon stocks in response to climate change are a potentially strong positive feedback (Cox et al., 2000). Since the AR5 (WGI, Section 6.4.2), there has been progress made in understanding soil carbon dynamics, and associated feedbacks. These include: (i) an increased understanding of and ability to quantify high latitude soil carbon feedbacks (Box 5.1); (ii) increased understanding of the causes responsible for soil carbon persistence on long timescales, particularly the interactions between decomposers and soil organic matter and mineral assemblages (Kleber et al., 2007; Schmidt et al., 2011; Luo et al., 2016); and (iii) increased understanding of soil carbon dynamics in subsurface layers (Hicks Pries et al., 2017; Balesdent et al., 2018).

ACCEPTED VERSION SUBJECT TO FINAL EDITS

CMIP6 ESMs predict losses of soil carbon with warming, which are larger than climate-driven vegetation carbon losses (Arora et al., 2020). As in CMIP5 (Todd-Brown et al., 2013), there is also a large CMIP6 ensemble spread in climate-driven soil carbon changes, partially driven by a large spread in the current soil carbon stocks predicted by the models. In CMIP5 ESMs, much of the soil carbon losses with warming can be traced to decreased carbon inputs, with a weaker contribution from changing soil carbon lifetimes due to faster decomposition rates (Koven et al., 2015a), which may be an artefact of the lack of permafrost carbon (Box 5.1). Isotopic constraints suggest that CMIP5 ESMs systematically overestimated the transient sensitivity of soil ^{14}C responses to atmospheric ^{14}C changes, implying that the models respond too quickly to changes in either inputs or turnover times and that the soil contribution to all feedbacks may thus be weaker than currently projected (He et al., 2016). Using natural gradients of soil carbon turnover as a constraint on long-term responses to warming suggests that both CMIP5 and CMIP6 ESMs may systematically underestimate the temperature sensitivity at high latitudes, and may overestimate the temperature sensitivity in the tropics (Koven et al., 2017; Wieder et al., 2018; Varney et al., 2020), although experimental soil warming in tropical forests suggest high sensitivity of decomposition to warming in those regions as well (Nottingham et al., 2020).

Peat soils, where thick organic layers build up due to saturated and anoxic conditions, represent another possible source of carbon to the atmosphere. Peats could dry, and decompose or burn as a result of climate change in both high (Chaudhary et al., 2020) and tropical (Cobb et al., 2017) latitudes, and in combination with anthropogenic drainage of peatlands (Warren et al., 2017). Peat carbon dynamics are not included in the majority of CMIP6 ESMs.

Soil microbial dynamics shift in response to temperature, giving rise to complex longer-term trophic effects that are more complex than the short-term sensitivity of decomposition to temperature. Such responses are observed in response to long-term warming experiments (Melillo et al., 2017). While most CMIP6 ESMs do not include microbial dynamics, simplified global soil models that do include such dynamics show greater uncertainty in projections of soil C changes, despite agreeing more closely with current observations, than the linear models used in most ESMs (Wieder et al., 2013; Guenet et al., 2018).

In nutrient limited ecosystems, prolonged soil warming can induce a fertilisation effect through increased decomposition, which increases nutrient availability and thereby vegetation productivity (Melillo et al., 2011). Models that include this process tend to show a weaker carbon-climate feedback than those that do not (Thornton et al., 2009; Zaehle et al., 2010; Wårlind et al., 2014; Meyerholt et al., 2020b). In CMIP6, 6 out of 11 ESMs include a representation of the nitrogen cycle, and the mean of those models predicts a weaker carbon-climate feedback than the overall ensemble mean (Arora et al., 2020) (Section 5.4.8). These models only partly account for the interactions of nutrient effects with other processes such as shifts of vegetation zones under climate changes (Sakaguchi et al., 2016) leading to either changes in species composition or changes in plant tissue nutrient to carbon ratios (Thomas et al., 2015; Achat et al., 2016; Du et al., 2019).

The *high agreement* and multiple lines of evidence that warming increases decomposition rates lead to *high confidence* that warming will overall result in carbon losses relative to a constant climate and contribute to the positive carbon-climate feedback (Section 5.4.8). However, the widespread in ESM projections and lack of model representation of key processes that may amplify or mitigate soil carbon losses on longer timescales (including microbial dynamics, permafrost, peatlands, and nutrients) lead to *low confidence* in the magnitude of global soil carbon losses with warming.

[START BOX 5.1 HERE]

BOX 5.1: Permafrost Carbon and Feedbacks to Climate

What is permafrost carbon and why should we be concerned about it?

Soils in the Arctic and other cold regions contain perennially frozen layers, known as permafrost. Soils in the

ACCEPTED VERSION SUBJECT TO FINAL EDITS

northern permafrost region store a large amount of organic carbon, estimated at 1460–1600 PgC across both surface soils and deeper deposits (Hugelius et al., 2014; Strauss et al., 2017; Mishra et al., 2021). Of that carbon, permafrost soils and deposits store 1070–1360 PgC, of which 300–400 PgC are in the first meter, and the rest at depth. The remaining 280–340 Pg C are in permafrost-free soils within the permafrost region. These carbon deposits have accumulated over thousands of years due to the slow rates of organic matter decomposition in frozen and/or waterlogged soil layers, but these frozen soils are highly decomposable upon thaw (Schädel et al., 2014).

Is permafrost carbon already thawing and emitting greenhouse gases?

The permafrost region was a historic carbon sink over centuries to millennia (*high confidence*) (Loisel et al., 2014; Lindgren et al., 2018). Currently though, thawing soils due to anthropogenic warming are losing carbon from the decomposition of old frozen organic matter, as found via ^{14}C signature of respiration at sites undergoing rapid permafrost thaw (Hicks Pries et al., 2013), of dissolved organic carbon in rivers draining watersheds with permafrost thaw (Vonk et al., 2015; Wild et al., 2019), and of CH_4 produced in thawing lakes (Walter Anthony et al., 2016).

Despite accumulating evidence of increased carbon losses, it is difficult to scale up site- and ecosystem-level measurements to assess the net carbon balance over the entire permafrost region, due to the high spatial heterogeneity, the strong seasonal cycles and the difficulty in monitoring these regions consistently across the year. SROCC assessed with *high confidence* both that ecosystems in the permafrost region act as carbon sinks during the summer growing season, and that wintertime carbon losses are significant, consistent with a multi-decadal small increase in CO_2 emissions during early winter at Barrow, Alaska (Sweeney et al., 2016; Webb et al., 2016; Meredith et al., 2019). These findings have been further strengthened by recent comprehensive synthesis of in-situ wintertime flux observations that show large carbon losses during the non-growing season (Natali et al., 2019). Increased autumn and winter respiration are a key large-scale fingerprint of top-down permafrost thaw predicted by ecosystem models (Parazoo et al., 2018). However, the length of these wintertime observational records is too short to unequivocally determine whether winter carbon losses are higher now than they used to be. One study inferred a multi-year net CO_2 source for the tundra in Alaska (Commane et al., 2017), which is equivalent to 0.3 PgC yr^{-1} when scaled up to the northern permafrost region (*low confidence*) (Meredith et al., 2019).

Since the AR5, evidence of a more active carbon cycle in the northern high latitude regions has also been observed through the increased amplitude of CO_2 seasonal cycles. However, the relative roles of local sources versus influence from mid-latitudes makes it difficult to infer changes to Arctic ecosystems from these observations (Graven et al., 2013; Forkel et al., 2016; Takata et al., 2017; Bruhwiler et al., 2021). Estimates of CO_2 fluxes with atmospheric inversion models showed an enhanced seasonal cycle amplitude but no significant trends in annual total fluxes, in agreement with flux tower measurements over one decade (2004–2013) (Welp et al., 2016; Takata et al., 2017).

In addition to CO_2, CH_4 emissions from the northern permafrost region contribute to the global methane budget, but evidence as to whether these emissions have increased from thawing permafrost is mixed. SROCC assigned *low confidence* to the degree of recent additional methane emissions from diverse sources throughout the permafrost region. These include observed regional lake area change, which suggest a 1.6–5 Tg CH_4 yr^{-1} increase over the last 50 years (Walter Anthony et al., 2016), ice-capped geological sources (Walter Anthony et al., 2012; Kohnert et al., 2017), and shallow Arctic Ocean shelves. The shallow subsea emissions are particularly uncertain due to both the wide range of estimates (3 Tg CH_4 yr^{-1}(Thornton et al., 2016a) to 17 Tg CH_4 yr^{-1} (Shakhova et al., 2014)), and the lack of a baseline with which to infer any changes; the upper half of this range in flux estimates is, however, inconsistent with the atmospheric inversions constrained by the pan-Arctic CH_4 concentration measurements (Berchet et al., 2016).

Atmospheric measurements and inversions performed at the global and regional scales do not show any detectable trends in annual mean CH_4 emissions from the permafrost region over the past 30 years (Jackson et al., 2020; Saunois et al., 2020; Bruhwiler et al., 2021), consistent with atmospheric measurements in Alaska that showed no significant annual trends despite significant increase in air temperature (Sweeney et

ACCEPTED VERSION SUBJECT TO FINAL EDITS

al., 2016). Atmospheric inversions and biospheric models do not show any clear trends in CH_4 emission for wetland regions of the high latitudes during the period 2000–2016 (Patra et al., 2016; Poulter et al., 2017; Jackson et al., 2020; Saunois et al., 2020). Large uncertainties on wetland extent and limited data constraints place *low confidence* in these modeling approaches.

SROCC also assessed with *high confidence* that methane fluxes have been under-observed due to their high variability at multiple scales in both space and time, and that there is a persistent mismatch between top-down and bottom-up methane budgets, with emissions calculated by upscaling ground observations typically higher than emissions inferred from large-scale atmospheric observations (Thornton et al., 2016b).

In conclusion, there is *high confidence* that the permafrost region has acted as a historic carbon sink over centuries to millennia and *high confidence* that some permafrost regions are currently net sources of CO_2. There is *robust evidence* that some CH_4 emissions sources and for some regions have increased over the past decades (*medium confidence*). For the northern permafrost-wide region, no multi-decadal trend has been detected on CO_2 and CH_4 fluxes but given the low resolution and sparse observations of current observations and modeling sytems, we place *low confidence* in this statement.

Since AR5, there have been new studies showing that permafrost thaw also leads to N_2O release from soil (Abbott and Jones, 2015; Karelin et al., 2017; Wilkerson et al., 2019), a previously unaccounted source. However, this release is unquantified at the pan-Arctic scale.

What does the paleo record tell us about how much emissions to expect?

Large areas of Alaska and Siberia are underlain by frozen, glacial-age, ice- and carbon-rich deposits, and many of these areas show evidence of thermokarst processes during Holocene warm periods. Rapid warming of high northern latitudes contributed to permafrost thaw, liberating labile organic carbon to the atmosphere (Köhler et al., 2014; Crichton et al., 2016; Winterfeld et al., 2018; Meyer et al., 2019), supporting the vulnerability of these areas to further warming (Strauss et al., 2013, 2017).

Radiogenic and stable isotopic measurements on CH_4 trapped in Antarctic ice support the view that CH_4 emissions from fossil carbon reservoirs, including permafrost and methane hydrates, in response to the deglacial warming remained small. Mass-balance calculations reveal that geological CH_4 emissions have not exceeded 19 Tg yr^{-1}, highlighting that the deglacial increase in CH_4 emissions were predominantly related to contemporary methane emissions from tropical wetlands and seasonally inundated floodplains (Bock et al., 2017; Petrenko et al., 2017; Dyonisius et al., 2020). Isotopic constraints on CO_2 losses from permafrost with warming after the Last Glacial Maximumm (LGM) are weaker than for CH_4. While the biosphere as a whole held less carbon during LGM than the preindustrial, that change in stocks was smaller than the change in plant productivity, and so carbon losses at high latitudes may have been offset by increased tropical productivity in response to warming during the last deglacial transition (LDT) (Ciais et al., 2012b). There is also paleoclimate evidence for processes that mitigate carbon losses with warming on longer timescales, such as longer-term carbon accumulation in lake deposits following thermokarst thaw (Walter Anthony et al., 2014), and long-term accumulation of carbon in permafrost soils following LDT carbon loss (Lindgren et al., 2018), particularly in peatlands which accumulated carbon at a slow but persistent rate in warm paleoclimates (Treat et al., 2019).

In conclusion, several independent lines of evidence indicate that permafrost thaw did not release vast quantities of fossil CH_4 associated with the transient warming events of the LDT, suggesting that large emissions of CH_4 from old carbon sources will not to occur in response to future warming (*medium confidence*).

How much emissions do we expect in the future?

Near-surface permafrost is projected to decrease significantly under future global warming scenarios (*high confidence,* Section 9.5.2), thus creating the potential for releasing CO_2 and CH_4 to the atmosphere, and act as a positive carbon-climate feedback.

ACCEPTED VERSION SUBJECT TO FINAL EDITS

The processes that govern permafrost carbon loss are grouped into gradual and abrupt mechanisms. Gradual processes include the deepening of the seasonally-thawed active layer into perennially-frozen permafrost layers and lengthening of the thawed season within the active layer, which increases the amount of organic carbon that is thawed and the duration of thaw. Abrupt thaw processes include ice-wedge polygon degradation, hillslope collapse, thermokarst lake expansion and draining, all of which are processes largely occurring in regions with very high soil carbon content (Olefeldt et al., 2016a, 2016b). Abrupt thaw processes can contribute up to half of the total net greenhouse gas release from permafrost loss, the rest attributed to gradual thaw (Schneider von Deimling et al., 2015; Turetsky et al., 2020). Increased fire frequency and severity (Hu et al., 2010) also contributes to abrupt emissions and the removal of the insulating cover which leads to an acceleration of permafrost thaw (Genet et al., 2013). Ecological feedbacks can both mitigate and amplify carbon losses: nutrient release from increased organic matter decomposition can drive vegetation growth that partially offsets soil carbon losses (Salmon et al., 2016), but also lead to biophysical feedbacks that further amplify warming (Myers-Smith et al., 2011).

Through CMIP5, Earth system models (ESMs) had not included permafrost carbon dynamics. This remains largely true in CMIP6, with most models not representing permafrost carbon processes, a small number representing the active-layer thickening effect on decomposition (Table 5.4), and no ESMs representing thermokarst or fire-permafrost-carbon interactions. The CMIP6 ensemble mean predicts a negative carbon-climate feedback in the permafrost region. However, those that do include permafrost carbon show a positive carbon-climate feedback in the permafrost region (Figure 5.27). Given the current limited ESM capacity to assess permafrost feedbacks, estimates in this report are based on published permafrost-enabled land surface model results.

SROCC assessed that warming under a high emission scenario (RCP8.5 or similar) would result in a loss of permafrost carbon by 2100 of 10s to 100s of PgC, with a maximum estimate of 240 PgC and a best estimate of 92 ± 17 PgC (Meredith et al., 2019) (SROCC, Figure 3.11). Under lower emissions scenarios, Schneider von Deimling et al., (2015) estimated permafrost feedbacks of 20–58 PgC of CO_2 by 2100 under a RCP2.6 scenario, and 28–92 PgC of CO_2 under a RCP4.5 scenario.

This new assessment, based on studies included in or published since SROCC (Schaefer et al., 2014; Koven et al., 2015c; Schneider von Deimling et al., 2015; Schuur et al., 2015; MacDougall and Knutti, 2016a; Gasser et al., 2018; Yokohata et al., 2020), estimates that the permafrost CO_2 feedback per degree of global warming (Figure 5.29) is 18 (3.1–41, 5th–95th percentile range) PgC $^{o}C^{-1}$. The assessment is based on a wide range of scenarios evaluated at 2100, and an assessed estimate of the permafrost CH_4-climate feedback at 2.8 (0.7–7.3 5th–95th percentile range) Pg Ceq $^{o}C^{-1}$ (Figure 5.29). This feedback affects the remaining carbon budgets for climate stabilisation and is included in their assessment (Section 5.5.2).

Beyond 2100, models suggest that the magnitude of the permafrost carbon feedback strengthens considerably over the period 2100–2300 under a high-emissions scenario (Schneider von Deimling et al., 2015; McGuire et al., 2018). Schneider von Deimling et al., (2015) estimated that thawing permafrost could release 20–40 PgC of CO_2 in the period from 2100 to 2300 under a RCP2.6 scenario, and 115–172 PgC of CO_2 under a RCP8.5 scenario. The multi-model ensemble in (McGuire et al., 2018) project a much wider range of permafrost soil carbon losses of 81–642 PgC (mean 314 PgC) for an RCP8.5 scenario from 2100 to 2300, and of a gain of 14 PgC to a loss of 54 PgC (mean loss of 17 PgC) for an RCP4.5 scenario over the same period.

Methane release from permafrost thaw (including abrupt thaw) under high-warming RCP8.5 scenario has been estimated at 836–2614 Tg CH_4 over the 21st century and 2800–7400 Tg CH_4 from 2100–2300 (Schneider von Deimling et al., 2015), and as 5300 Tg CH_4 over the 21st century and 16000 Tg CH_4 from 2100–2300 (Turetsky et al., 2020). For RCP4.5, these numbers are 538–2356 Tg CH_4 until 2100 and 2000-6100 Tg CH_4 from 2100–2300 (Schneider von Deimling et al., 2015), and 4100 Tg CH_4 until 2100 and 10000 Tg CH_4 from 2100–2300 (Turetsky et al., 2020).

A key uncertainty is whether permafrost carbon feedbacks scale roughly linearly with warming (Koven et

ACCEPTED VERSION SUBJECT TO FINAL EDITS

al., 2015c), or instead scale at a greater (MacDougall and Knutti, 2016b; McGuire et al., 2018) or smaller rate (e.g. CH_4 emissions estimated by Turetsky et al., (2020a)). It also remains unclear whether the permafrost carbon pool represents a coherent global tipping element of the Earth system with a single abrupt threshold (Drijfhout et al., 2015) at a given level of global warming, or a local scale tipping point without abrupt thresholds when aggregated across the pan-Arctic region as is suggested by recent model results (e.g. (Koven et al., 2015b; McGuire et al., 2018)).

In conclusion, thawing terrestrial permafrost will lead to carbon release under a warmer world (*high confidence*). However, there is *low confidence* on the timing, magnitude and linearity of the permafrost climate feedback owing to the wide range of published estimates and the incomplete knowledge and representation in models of drivers and relationships. It is projected that CO_2 released from permafrost will be 18 (3.1–41) PgC per 1°C by 2100 with the relative contribution of CO_2 vs CH_4 remaining poorly constrained. Permafrost carbon feedbacks are included among the underrepresented feedbacks quantified in Figure 5.29.

[END BOX 5.1 HERE]

5.4.4 Climate Effects on Future Ocean Carbon Uptake

5.4.4.1 Physical Drivers of Future Ocean Carbon Uptake and Storage

The principal contribution to increasing global ocean carbon is the air-sea flux of CO_2, which changes the DIC inventory (Section 5.4.2) (Arora et al., 2020). The processes that influence the variability and trends of the ocean carbon-heat nexus are assessed in Cross-Chapter Box 5.3. Climate has three important impacts on the ocean uptake of anthropogenic CO_2: (i) ocean warming reduces the solubility of CO_2, which increases pCO_2 and increases the stratification of the mixed layer with both acting as positive feedbacks weakening the ocean sink (Arora et al., 2020; Cross-Chapter Box 5.3; 9.2.1); (ii) changing the temporal and spatial characteristics of wind stress and storm alters mixing – entrainment in the mixed layer and across the bottom of the mixed layer (Bronselaer et al., 2018) and (iii) both warming and wind stress influence the large scale MOC circulation which modifies the rate of ventilation, storage or outgassing of ocean carbon in the ocean interior (Section 5.2.3.1; Gruber et al., 2019; Arora et al., 2020). The land-to-ocean riverine flux and the carbon burial in ocean sediments also play a minor role (*low confidence*) (Arora et al., 2020). Based on *high agreement* of projections by coupled climate models, there is *high confidence* that the resultant climate-carbon cycle feedbacks are positive but the extent of the weakening the ocean sink is scenario dependent (Arora et al., 2020).

Regionally, the Southern Ocean is a major sink of anthropogenic CO_2 (Figure 5.8a), although challenges in modelling its circulation and Antarctic sea ice transport (Section 3.4.1.2; Section 9.2.3.2; Section 9.3.2) generate uncertainty in the response of its sink to future carbon-climate feedbacks. Increased freshwater input may cause a slowdown of the lower overturning circulation, leading to increased Southern Ocean biological carbon storage (Ito et al., 2015); alternatively, increased winds may intensify the overturning circulation, reducing the net CO_2 sink in the Southern Ocean (Bronselaer et al., 2018; Saunders et al., 2018). On centennial timescales, there is thus *low confidence* in the overall effect of intensifying winds in the Southern Ocean on CO_2 uptake.

5.4.4.2 Biological Drivers of Future Ocean Carbon Uptake

While physical drivers control the present-day anthropogenic carbon sink, biological processes are responsible for the majority of the vertical gradient in DIC (natural carbon storage). A small fraction of the organic carbon fixed by primary production (PP) reaches the sea floor, where it can be stored in sediments on geological timescales, making the biological carbon pump (BCP) an important mechanism for very long-term CO_2 storage. Projected reductions in ocean ventilation (Section 9.2.1.4) would lengthen residence time and lead to DIC accumulating in the deep ocean due to organic carbon remineralisation.

ACCEPTED VERSION SUBJECT TO FINAL EDITS

Since AR5 (Section 6.3.2.5.6), progress has been made in understanding the biological drivers of ocean carbon uptake in both coupled climate models and observations (SROCC Section 5.2.2.6). Here we focus on potential feedbacks between biological processes and climate. In CMIP5 models, the direction of modelled PP in response to increased atmospheric CO_2 concentration and climate warming was unclear (Taucher and Oschlies, 2011; Laufkoetter et al., 2015). This remains the case in the CMIP6 models; indeed, inter-model uncertainty has increased in CMIP6 models, compared to CMIP5. The projected global multi-model mean change in PP in 13 models run under the SSP5−8.5 scenario project is −3 ± 9% (2080–2099 mean values relative to 1870–1899 ± the inter-model standard deviation; Kwiatkowski et al., 2020). Under the low-emission, high-mitigation scenario SSP1−2.6, the global change in PP is −0.56 ± 4%. Observations in the contemporary period provide little direct constraint on the modelled responses of PP to climate change, partly due to insufficiently long records (Henson et al., 2016). However, there is some indication of an emergent constraint on changes in tropical PP based on interannual variability derived from remote sensing (Kwiatkowski et al., 2017b; Section 5.4.6).

In CMIP5 models run under RCP8.5, particulate organic carbon (POC) export flux is projected to decline by 1–12% by 2100 (Taucher and Oschlies 2011; Laufkoetter et al. 2015). Similar values are predicted in 18 CMIP6 models, with declines of 2.5–21.5% (median –14%) or 0.2–2 GtC (median –0.8 GtC) between 1900 and 2100 under the SSP5–8.5 scenario. The mechanisms driving these changes vary widely between models due to differences in parameterisation of particle formation, remineralisation and plankton community structure.

Ocean warming reduces the vertical supply of nutrients to the upper ocean due to increasing stratification (Section 9.2.1.4) but may also act to alleviate seasonal light limitation. The projected effect is to decrease PP at low latitudes and increase PP at high latitudes (Kwiatkowski et al., 2020). Future changes to dust deposition due to desertification (Mahowald et al., 2017), alterations to the nitrogen cycle (Section 5.3.3.2; SROCC Section 5.2.3.1.2), and reducing sea ice cover (Ardyna and Arrigo, 2020) all have the potential to alter PP regionally. Higher ocean temperatures tend to result in higher metabolic rates, although respiration may increase more rapidly than PP (Boscolo-Galazzo et al., 2018; Brewer, 2019; Cavan et al., 2019). Ocean warming and reduced PP are expected to result in lower zooplankton abundance, and the expansion of OMZs may reduce the ability of zooplankton to remineralise POC, thus increasing the efficiency of the BCP and forming a negative climate feedback (Cavan et al., 2017). Increased microbial respiration due to warming may result in greater quantities of organic carbon transferred into the dissolved organic carbon pool (Jiao et al., 2014; Legendre et al., 2015; Roshan and DeVries, 2017) which, while increasing the residence time of carbon in the ocean, would ultimately reduce the sedimentary burial and hence sequestration on geologic time scales (Olivarez Lyle and Lyle, 2006).

Most models project that smaller phytoplankton are favoured in future ocean conditions (*medium confidence*; Cabré et al., 2015; Fu et al., 2016; Flombaum et al., 2020) driven by warming water and/or changing nutrient availability, which would alter the magnitude and efficiency of the BCP by altering the sinking speed, respiration rate and aggregation/fragmentation of sinking particles. There is *low confidence* in the sign of the resulting feedback: regions in which small phytoplankton dominate may have a more efficient pump, although the total amount of organic carbon reaching the sea floor is lower (Herndl and Reinthaler, 2013; Bach et al., 2016; Richardson, 2019). Alternatively, an increase in small phytoplankton could result in a less efficient pump, due either to a greater fraction of PP being processed through the upper ocean microbial loop (Jiao et al., 2014) or generation of slower sinking particles (Guidi et al., 2009; Leung et al., 2021). Variable phytoplankton stoichiometry is predicted to increase the amount of carbon stored via the BCP relative to the amount of PP, so that fixed stoichiometry models (as in CMIP5) may underestimate cumulative ocean carbon uptake to 2100 by 0.5–3.5% (2–15 PgC) (RCP8.5 scenario; Kwiatkowski et al., 2018). Other climate effects such as deoxygenation or ocean acidification could also result in alterations to the magnitude and efficiency of the BCP (Krumhardt et al., 2019; Raven et al., 2021; Taucher et al., 2021).

Based on *high agreement* across multiple lines of evidence and physical understanding there is thus *high confidence* that feedbacks to climate will arise from alterations to the magnitude and efficiency of the BCP changing PP, and the depth of remineralisation. However, the complexity of the mechanisms involved in the

ACCEPTED VERSION SUBJECT TO FINAL EDITS

export and remineralisation of POC result in *low confidence* in the magnitude and sign of biological feedbacks to climate. Nevertheless, improved model representation of PP and the BCP is required (which requires better observational constraints), as the contribution of biological processes to CO_2 uptake is expected to become more significant with continued climate change (Hauck et al., 2015).

5.4.5 Carbon Cycle Projections in Earth System Models

This section summarises future projections of land and ocean carbon sinks from the latest ESMs. ESMs are the basis for century timescale projections (Chapter 4), and for detection and attribution studies (Chapter 3). These models aim to simulate the evolution of the carbon sources and sinks on land and in the ocean, in addition to the physical components of the climate system. ESMs include interactions between many of the processes and feedbacks described in Sections 5.4.1 to 5.4.4.

ESMs are now integral to the coupled model intercomparison project. Model output data from CMIP5 was analysed in the AR5, while data from CMIP6 forms the basis for the analysis presented in this subsection. The CMIP5 ESMs discussed in AR5 (WGI, Section 6.4.2) produced a wide range of projections of future CO_2 (Friedlingstein et al., 2014) primarily associated with different magnitudes of carbon-climate and carbon-concentration feedbacks (Arora et al., 2013), but also exacerbated by differences in the simulation of the net carbon release from land-use change (Brovkin et al., 2013). A key deficiency of almost all CMIP5 ESMs was the neglect of nutrient limitations on CO_2-fertilisation of land plant photosynthesis (Zaehle et al., 2015) (see Section 5.4.1).

Some CMIP6 models considered in this report now include nitrogen limitations on land vegetation growth, along with many other added processes compared to CMIP5. Table 5.4 summarises characteristics of the land and ocean carbon cycle models used in CMIP6 ESMs (Arora et al., 2020). In CMIP6, most ocean carbon cycle models (8 of 11) track three or more limiting nutrients (most often nitrogen, phosphorus, silicon, iron), and represent two or more phytoplankton types. More than half of the land carbon cycle models (6 of 11) now include an interactive nitrogen cycle, and almost half (5 of 11) represent forest fires. However, even for CMIP6, very few models explicitly represent vegetation dynamics (3 of 11) or permafrost carbon (2 of 11). Despite these remaining limitations, the carbon cycle components of CMIP6 represent an advance on those in CMIP5 as they represent additional important processes (e.g. nitrogen-limitations on the land carbon sink, iron-limitations on ocean ecosystems).

[START TABLE 5.4 HERE]

Table 5.4: Properties of the CMIP6 Earth system models (ESMs), focussing on the land and ocean carbon cycle components of these models (Arora et al., 2020). Characteristics listed under each ESM are: number of vegetation carbon pools (Veg C pools), number of soil and litter carbon pools (Dead C pools), number of Plant Functional Types (PFTs), whether forest fire is represented (Fire), whether vegetation dynamics is represented (Dynamic Veg), whether permafrost carbon is represented (Permafrost C), whether the nitrogen cycle is represented (Nitrogen cycle), the number of phytoplankton types (Phytoplankton), the number of zooplankton types (Zooplankton), and the list of ocean nutrients represented (Nutrients).

Modelling group	**CSIRO**	**BCC**	**CCCma**	**CESM**	**CNRM**	**GFDL**	**IPSL**	**JAMSETC**	**MPI**	**NorESM2-LM**	**UK**
ESM	ACCESS-ESM1.5	BCC-CSM2-MR	CanESM5	CESM2	CNRM-ESM2-1	GFDL-ESM4	IPSL-CM6A-LR	MIROC-ES2L	MPI-ESM1.2-LR	NorESM2-LM	UKESM1-0-LL
Land carbon/biogeochemistry component											
Model name	CABLE2.4 CASA-CNP	BCC-AVIM2	CLASS-CTEM	CLM5	ISBA-CTRIP	LM4p1	ORCHIDEE (2)	MATSIRO (phys) VISIT-e (BGC)	JSBACH3.2	CLM5	JULES-ES-1.0
Veg C pools	3	3	3	22	6	6	8	3	3	3	3
Dead C pools	6	8	2	7	7	4	3	6	18	7	4
PFTS	13	16	9	22	16	6	15	13	13	21	13

ACCEPTED VERSION SUBJECT TO FINAL EDITS

Fire	No	No	No	Yes	Yes	Yes	No	No	Yes	Yes	No
Dynamic Veg	No	No	No	No	No	Yes	No	No	Yes	No	Yes
Permafrost C	No	No	No	Yes	No	No	No	No	No	Yes	No
Nitrogen cycle	Yes	No	No	Yes	No	No	No	Yes	Yes	Yes	Yes
Ocean carbon/biogeochemistry component											
Model name	WOMBAT	MOM4 L40	CMOC (biol)	MARBL	PISCESv2-gas	COBALTv2	PISCES-v2	OECO2	HAMOCC6	HAMOCC5.1	MEDUSA-2.1
Phytoplankton	1	0	1	3	2	2	2	2	2	1	2
Zooplankton	1	0	1	1	2	3	2	1	1	1	2
Limiting Nutrients	P, Fe	P	N	N, P, Si, Fe	N, P, Si, Fe	N, P, Si, Fe	N, P, Si, Fe	N, P, Fe	N, P, Si, FE	N, P, Si, Fe	N, Si, Fe

[END TABLE 5.4 HERE]

ESMs can be driven by anthropogenic CO_2 emissions ('emissions-driven' runs), in which case atmospheric CO_2 concentration is a predicted variable; or by prescribed time-varying atmospheric concentrations ('concentration-driven' runs). In concentration-driven runs, simulated land and ocean carbon sinks respond to the prescribed atmospheric CO_2 and resulting changes in climate, but do not feed back through changes in the atmospheric CO_2 concentration. Concentration-driven runs are used to diagnose the carbon emissions consistent with the SSPs and other prescribed concentration scenarios (Section 5.5). In this subsection we specifically analyse results from concentration-driven ESM projections.

5.2.1.1 Evaluation of the Contemporary Carbon Cycle in Concentration-Driven Runs

Models need to be compared to as wide an array of observational benchmarks as possible in order to have confidence in their projections. This is particularly the case for highly-uncertain land carbon cycle feedbacks (Arora et al., 2013; Friedlingstein et al., 2014b). Land models within ESMs can be compared to multiple different datasets of processes such as gross carbon uptake, physical predictions such as leaf area and carbon stocks which influence carbon fluxes and are diagnostic of carbon turnover times, as well as linkages between carbon and water cycles and other aspects of the terrestrial carbon cycle. To provide these multiple orthogonal constraints, a model benchmarking system, the international land model benchmarking (ILAMB), has been developed (Collier et al., 2018).

Figure 5.22 shows an overview set of land (Figure 5.22a) and ocean (Figure 5.22b) benchmarks applied to both the CMIP5 and CMIP6 historical simulations. There is good evidence of an improvement in model performance from CMIP5 (in yellow) to CMIP6 (in green), in both the land and ocean, based on these benchmarks. The mean of the CMIP6 land models outperform or perform equivalently to the mean of the CMIP5 land models on all available metrics.

[START FIGURE 5.22 HERE]

Figure 5.22: Overview scores for CMIP5 (left hand side of table) and CMIP6 (right hand side of table) Earth system models (ESMs), for multiple benchmarks against different datasets. (a) Benchmarking of ESM land models, (b) benchmarking of ocean models. Scores are relative to other models within each benchmark row, with positive scores indicating a better agreement with observations. Models included are only those from institutions that participated in both CMIP5 and CMIP6 carbon cycle experiments, in order to trace changes from one ensemble to the next. CMIP5 models are labels in yellow and CMIP6 in green, with the multi-model ensemble means labelled in white. Further details on data sources and processing are available in the chapter data table (Table 5.SM.6).

[END FIGURE 5.22 HERE]

ACCEPTED VERSION SUBJECT TO FINAL EDITS

5.4.5.1 Evaluation of Historical Carbon Cycle Simulations in Concentration-Driven Runs

This section evaluates concentration-driven historical simulations of changes in land and ocean cumulative carbon uptake, against observation-based estimates from GCP (Le Quéré et al., 2018a). For each model, common historical land-use changes were prescribed (Jones et al., 2016a).

Figure 5.23 shows global annual mean values from CMIP6 concentration-driven runs for 1850 to 2014. The ocean carbon cycle models reproduce historical carbon uptake well, with the model range for the global ocean carbon sink in 2014 (2.3–2.7 GtC yr^{-1}) clustering around the central GCP estimate of 2.6 ± 0.5 GtC yr^{-1}. Simulated cumulative ocean carbon uptake (1850–2014) ranges from 110 to 166 GtC, with a model mean of 131 ± 17 PgC which is lower than the GCP estimate of 150 ± 25 GtC (Figure 5.23a). This suggests that CMIP6 models may slightly underestimate historical ocean carbon uptake (Watson et al., 2020).

The land carbon cycle components of historical ESM simulations show a larger range, with simulated cumulative land carbon uptake (1850–2014) spanning the range from –47 to +21 GtC, compared to the GCP estimate of –12 ± 50 GtC (Figure 5.22b). This range is due in part to the complications of simulating the difference between carbon uptake by intact ecosystems and the direct release of carbon due to land-use change (Hajima et al., 2020a). There is *high confidence* that the land continues to dominate the overall uncertainty in the projected response of the global carbon cycle to climate change.

[START FIGURE 5.23 HERE]

Figure 5.23: CMIP6 Earth system model (ESM) concentration-driven historical simulations for 1850 to 2014, compared to observation-based estimates from the global carbon project (GCP). Panel (a) cumulative ocean carbon uptake from 1850 (PgC); (b) cumulative land carbon uptake from 1850 (PgC). Only models that simulate both land and ocean carbon fluxes are shown here. Further details on data sources and processing are available in the chapter data table (Table 5.SM.6).

[END FIGURE 5.23 HERE]

5.4.5.2 Evaluation of Latitudinal Distribution of Simulated Carbon Sinks

This distinction between the relatively high fidelity with which the ocean carbon sink is simulated, and the much wider range of simulations of the land carbon sink, is also evident in the zonal distribution of the sinks (Figure 5.24). We compare the ESM simulations to estimates from three atmospheric inversion models: CAMS (Chevallier et al., 2005), CT 2017 (Peters et al., 2007) and MIROC-ATM4 (Saeki and Patra, 2017). The ocean carbon cycle components of CMIP6 ESMs are able to simulate the tropical CO_2 source and mid-latitude CO_2 sink, with relatively small model spread (Figure 5.24a). The CMIP6 ensemble (red wedge) simulates a larger ocean carbon sink at 50°N and a weaker sink in the Southern Ocean, than the inversion estimate, but with some evidence of a reduction in these residual errors compared to CMIP5 (blue wedge). The spread in inversion fluxes arises primarily from differences in the atmospheric CO_2 measurement networks and from transport model uncertainties.

It has been previously noted that AR5 models tended to overestimate land-uptake in the tropics and underestimate uptake in the northern mid-latitudes, compared to inversion estimates. The inclusion of nitrogen limitations on CO_2-fertilisation within CMIP6 models was expected to reduce this discrepancy (Anav et al., 2013). There is indeed some evidence that the CMIP6 ensemble (red wedge in Figure 5.24b) captures the northern land carbon sink more clearly than CMIP5 (blue wedge in Figure 5.24b), but there remains a tendency for the ESMs to place more of the global land carbon sink in the tropics than the mid-latitudes, compared to the inversion estimates. Based on a consistent signal across CMIP6 ESMs, there is *medium confidence* that land carbon cycle models continue to underestimate the northern hemisphere land carbon sink, when compared to estimates from atmospheric inversion (Ciais et al., 2019).

ACCEPTED VERSION SUBJECT TO FINAL EDITS

[START FIGURE 5.24 HERE]

Figure 5.24: Comparison of modelled zonal distribution of contemporary carbon sinks against atmospheric inversion estimates for 2000–2009, (a) ocean carbon uptake; (b) net land uptake. Latitude runs from 90°S (i.e. –90°N) to 90°N. Positive uptake represents a carbon sink to ocean/land while negative uptake represents a carbon source. The land uptake is taken as Net Biome Productivity (NBP) and so includes net land-use change emissions. The bands show the mean ±1 standard deviation across the available inversions (black bands, 3 models), CMIP5 Earth system models (ESMs) (blue bands, 12 models for the ocean, 12 models for the land), and CMIP6 ESMs (red bands, 11 models for ocean, 10 models for land). Further details on data sources and processing are available in the chapter data table (Table 5.SM.6).

[END FIGURE 5.24 HERE]

5.4.5.3 Coupled Climate-Carbon Cycle Projections

Land and ocean carbon uptake are driven primarily by increases in atmospheric CO_2 (Figure 5.25). As a result, the evolution of land and ocean carbon sinks differs significantly between the SSP scenarios. Under scenarios which have greater increases in atmospheric CO_2 (such as SSP5–8.5 and SSP3–7.0) the absolute values of the sinks are larger, but the fraction of implied emissions taken-up by the sinks declines through the 21st century. By contrast, scenarios that assume CO_2 stabilisation in the 21st century (such as SSP1–2.6 or SSP2–4.5), have smaller absolute sinks but these sinks take-up an increasing fraction of the implied emissions (Figure 5.25d). These general principles apply to both the ocean and land carbon sinks.

The concentration-driven CMIP6 ESMs agree well on the evolution of the global ocean carbon sink through the 21st century for four SSP scenarios (Figure 5.26b). The 5-year ensemble mean ocean sink declines to 0.6 ± 0.2 GtC yr^{-1} by 2100 under SSP1–2.6, and peaks around 2080 at 5.4 ± 0.4 GtC yr^{-1} under SSP5–8.5. Cumulative ocean carbon uptake from 1850 is projected to saturate at approximately 290 ± 30 GtC under SSP1–2.6, and to reach 520 ± 40 GtC by 2100 under SSP5–8.5 (Figure 5.25e).

The ensemble mean changes in land and ocean sinks are qualitatively similar, but the land shows much higher interannual variability in carbon uptake (Figure 5.25c) and also a much larger spread in the model projections of cumulative land carbon uptake (Figure 5.25f). The 5-year ensemble mean net land carbon sink is projected to decline to 0.4 ± 1.0 GtC yr^{-1} by 2100 under SSP1–2.6, and to reach around 5.6 ± 3.7 GtC yr^{-1} under SSP5–8.5 (Figure 5.25b). Cumulative net land carbon uptake from 1850 is projected to saturate at approximately 150 ± 35 GtC under SSP1–2.6, and to reach 310 ± 130 GtC by 2100 under SSP5–8.5. Significant uncertainty remains in the future of the global land carbon sink, but there has been a notable reduction in the model spread from CMIP5 to CMIP6.

[START FIGURE 5.25 HERE]

Figure 5.25: Modelled evolution of the global land and ocean carbon sinks for 1850 to 2100 in concentration-driven CMIP6 Earth system model (ESM) scenario runs (SSP1–2.6: blue; SSP2–4.5: skyblue; SSP3–7.0: yellow; SSP5–8.5: red): (a) prescribed atmospheric CO_2 concentrations; (b) 5-year running mean ocean carbon sink (GtC yr^{-1}); (c) 5-year running mean net land carbon sink (GtC yr^{-1}); (d) inferred cumulative sink fraction of emissions from 1850; (e) change in ocean carbon storage from 1850 (GtC); (f) change in land carbon storage from 1850 (GtC). Thick lines represent the ensemble mean of the listed ESM runs, and the error bars represents ± one standard deviation about that mean. The grey wedges represent estimates from the global carbon project (GCP), assuming uncertainties in the annual mean ocean and net land carbon sinks of 0.5 GtC yr^{-1} and 1 GtC yr^{-1} respectively, and uncertainties in the changes in carbon stores (ocean, land and cumulative total emissions) of 25 GtC. The net land carbon sink is taken as net biome productivity (NBP) and so includes any modelled net land-use change emissions. Further details on data sources and processing are available in the chapter data table (Table 5.SM.6).

ACCEPTED VERSION SUBJECT TO FINAL EDITS

[END FIGURE 5.25 HERE]

Geographical patterns of carbon changes for four SSP scenarios are shown in Figure 5.26, with cleared areas (no diagonal lines) showing agreement on the sign of the change by at least 80% of the models. In all scenarios the ocean sink is strongest in the Southern Ocean and North Atlantic. The land carbon sink occurs primarily where there are present-day forests. In the mid- and high northern latitudes, a carbon sink is projected as a result of the combined impacts of increasing CO_2 and warming (see Section 5.4.5.5). Changes in land carbon storage in the tropics also depend strongly on the assumed rate of deforestation which varies in magnitude across the SSPs, from relatively low rates in SSP1–2.6 to relatively high rates in SSP3–7.0.

[START FIGURE 5.26 HERE]

Figure 5.26: Maps of net carbon changes under four Shared Socioeconomic Pathway (SSP) scenarios, as evaluated from nine CMIP6 Earth system models. Uncertainty is represented using the simple approach (see Cross-Chapter Box Atlas.1 for more information): No overlay indicates regions with high model agreement, where ≥80% of models agree with the ensemble mean on the sign of change; diagonal lines indicate regions with low model agreement, where <80% of models agree with the ensemble mean on the sign of change. On land, this is calculated as the time integral of NBP, for the ocean it is the time-integral of air-sea CO_2 gas flux anomalies relative to the pre-industrial. Further details on data sources and processing are available in the chapter data table (Table 5.SM.6).

[END FIGURE 5.26 HERE]

In summary, oceanic and terrestrial carbon sinks are projected to continue to grow with increasing atmospheric concentrations of CO_2, but the fraction of emissions that is taken up by land and ocean is expected to decline as the CO_2 concentration increases (*high confidence*). In the ensemble mean, ESMs suggest approximately equal global land and ocean carbon uptake for each of the SSP scenarios. However, the range of model projections is much larger for the land carbon sink. Despite the wide range of model responses, uncertainty in atmospheric CO_2 by 2100 is dominated by future anthropogenic emissions rather than carbon-climate feedbacks (*high confidence*).

5.4.5.4 Linear Feedback Analysis

In order to diagnose the causes of the varying time-evolution of carbon sinks, the traditional linear feedback approach is adopted (Friedlingstein et al., 2003), as used previously to analyse C^{4}MIP (Friedlingstein et al., 2006) and CMIP5 models (Arora et al., 2013). Changes in land carbon storage (ΔC_L) and changes in ocean carbon storage (ΔC_o) are decomposed into contributions arising from warming (ΔT) and increases in CO_2 (ΔCO_2):

$$\Delta C_L = \beta_L \, \Delta CO_2 + \gamma_L \, \Delta T$$

$$\Delta C_o = \beta_o \, \Delta CO_2 + \gamma_o \, \Delta T$$

where β_L (β_o) and γ_L (γ_o) are coefficients that represent the sensitivity of land (ocean) carbon storage to changes in CO_2 and global mean temperature respectively. This feedback formalism is one of several that have been proposed for analysing climate-carbon cycle feedbacks (Lade et al., 2018).

This quasi-equilibrium framework is scenario dependent because of the timescales associated with land and ocean carbon uptake, as discussed in AR5 (WGI, Box 6.4). However, it is retained here for traceability with AR5. This approach has been used to define a number of emergent constraints on carbon cycle feedbacks (Section 5.4.6) and to reconstruct the transient climate response to emissions (TCRE) (Jones and Friedlingstein, 2020), as in Section 5.5. In order to minimise the confounding effect of the scenario

ACCEPTED VERSION SUBJECT TO FINAL EDITS

dependence, β and γ values are diagnosed from idealised runs in which a 1% per year increase in atmospheric CO_2 concentration is prescribed, as for AR5 (WGI, Box 6.4) (Arora et al., 2013). Values of β are calculated from 'biogeochemical' runs in which the prescribed CO_2 increases do not affect climate, and these are then used to isolate γ values in fully-coupled runs in which both climate and CO_2 change (Friedlingstein et al., 2003).

Table 5.5 shows the global land and global ocean values of β and γ for each of the CMIP6 ESMs (Arora et al., 2020). Also shown in the last two rows are the ensemble mean and standard deviation across the ensemble, for CMIP6 and CMIP5. In both ensembles, the largest uncertainties are in the sensitivity of land carbon storage to CO_2 (β_L) and the sensitivity of land carbon storage to temperature (γ_L). The more widespread modelling of nitrogen limitations in CMIP6 was expected to lead to reductions in both of these feedback parameters. There is indeed some evidence for that with ensemble mean γ_L moving from –58 ± 38 GtC K^{-1} to –33 ± 33 GtC K^{-1}. Between CMIP5 and CMIP6, there are also reductions in ensemble mean β_o (0.82 to 0.77 GtC ppm^{-1}), β_L (0.93 to 0.89 GtC K^{-1}) and γ_o (–17.3 to –16.9 GtC K^{-1}), but these are progressively less significant compared to the model spread in each case.

[START TABLE 5.5 HERE]

Table 5.5: Diagnosed global feedback parameters for CMIP6 ESMs based on 4 x CO_2 runs (Arora et al., 2020). The last two rows show the mean and standard deviation cross the CMIP6 and CMIP5 models, respectively.

	Land Feedback Factors		Ocean Feedback Factors	
Model Name	**β_L (PgC ppm^{-1})**	**γ_L (PgC K^{-1})**	**β_o (PgC ppm^{-1})**	**γ_o (PgC K^{-1})**
ACCESS-ESM1.5	0.37	-21.1	0.90	-23.8
CanESM5	1.28	16.0	0.77	-14.7
CESM2	0.90	-21.6	0.71	-10.9
CNRM-ESM2-1	1.36	-83.1	0.70	-9.4
IPSL-CM6A-LR	0.62	-8.7	0.76	-13.0
MIROC-ES2L	1.12	-69.6	0.73	-22.3
MPI-ESM1.2-LR	0.71	-5.2	0.77	-20.1
NOAA-GFDL-ESM4	0.93	-80.1	0.84	-21.7
NorESM2-LM	0.85	-21.0	0.78	-19.6
UKESM1-0-LL	0.75	-38.4	0.75	-14.1
CMIP6 Model Mean	**0.89 ± 0.30**	**-33.3 ± 33.8**	**0.77 ± 0.06**	**-16.9 ± 5.1**
CMIP5 Model Mean	**0.93 ± 0.49**	**-57.9 ± 38.2**	**0.82 ± 0.07**	**-17.3 ± 3.8**

[END TABLE 5.5 HERE]

In these idealised 1% per year CO_2 runs, the CMIP6 models show reasonable agreement on the patterns of carbon uptake and also on the separate impacts of CO_2 increase and climate change (Figure 5.27). For the ensemble mean, increasing atmospheric CO_2 increases carbon uptake by the oceans, especially in the

Southern Ocean and the North Atlantic Ocean; and on the land, especially in tropical and boreal forests (*β,* Figure 5.27a). Climate change further enhances land carbon storage in the boreal zone but has a compensating negative impact on the carbon sink in tropical and subtropical lands, and in the North Atlantic

ACCEPTED VERSION SUBJECT TO FINAL EDITS

Ocean (γ, Figure 5.27b). Overall, the ensemble mean of the CMIP6 ESMs models indicates increasing carbon storage with CO_2 in almost all locations (Figure 5.27c).

[START FIGURE 5.27 HERE]

Figure 5.27: Maps of carbon-concentration and carbon-climate feedback terms, as well as net carbon changes under the idealised 1% per year CO_2 scenario, as evaluated from CMIP6 Earth system models (ESMs). Shown are the model means from nine CMIP6 ESMs. Uncertainty is represented using the simple approach (see Cross-Chapter Box Atlas.1 for more information): No overlay indicates regions with high model agreement, where ≥80% of models agree with the ensemble mean on the sign of change; diagonal lines indicate regions with low model agreement, where <80% of models agree with the ensemble mean on the sign of change. Also shown are zonal-mean latitude profiles of land (green) and ocean (blue) feedbacks. On the land, the zonal mean feedback for the mean of the ensemble of models that include nitrogen is shown as dashed lines, and carbon-only models as dash-dotted lines, and the carbon-climate feedback from one permafrost-carbon enabled ESM is shown as a dotted line carbon changes are calculated as the difference between carbon stocks at different times on land and for the ocean as the time integral of atmosphere-ocean CO_2 flux anomalies relative to the pre-industrial. The denominator for gamma here is the global mean surface air temperature. Further details on data sources and processing are available in the chapter data table (Table 5.SM.6).

[END FIGURE 5.27 HERE]

5.4.6 Emergent constraints to reduce uncertainties in projections

Emergent constraints are based on relationships between observable aspects of the current or past climate (such as trends or variability), and uncertain aspects of future climate change (such as the strength of particular feedbacks). These relationships are evident across an ensemble of models. When combined with an observational estimate of the trend or variability in the real climate, such emergent relationships can yield 'emergent constraints' on future climate change (Hall et al., 2019). At the time of the AR5 (WGI, 9.8.3), there had been relatively few applications of the technique to constrain carbon cycle sensitivities, but there have been many studies published since (see for example summary in Cox, (2019)). Figure 5.28 shows some key published emergent constraints on the carbon cycle in ESMs.

[START FIGURE 5.28 HERE]

Figure 5.28: Examples of emergent constraints on the carbon cycle in Earth system models (ESMs), reproduced from previously published studies: (a) projected global mean atmospheric CO_2 concentration by 2060 under the RCP8.5 emissions scenario against the simulated CO_2 in 2010 (Friedlingstein et al., 2014b; Hoffman et al., 2014); (b) sensitivity of tropical land carbon to warming (γ_{LT}) against the sensitivity of the atmospheric CO_2 growth-rate to tropical temperature variability (Cox et al., 2013b; Wenzel et al., 2014); (c) sensitivity of extratropical (30°N–90°N) gross primary production to a doubling of atmospheric CO_2 against the sensitivity of the amplitude of the CO_2 seasonal cycle at Kumkahi, Hawaii to global atmospheric CO_2 concentration (Wenzel et al., 2016); (d) change in high-latitude (30°N–90°N) gross primary production versus trend in high-latitude leaf area index or 'greenness' (Winkler et al., 2019); (e) sensitivity of the primary production of the Tropical ocean to climate change versus its sensitivity to ENSO-driven temperature variability (Kwiatkowski et al., 2017); (f) global ocean carbon sink in the 2090s versus the current-day carbon sink in the Southern Ocean. In each case, a red-dot represents a single ESM projection, the grey bar represents the emergent relationship between the y-variable and the x-variable, the blue bar represents the observational estimate of the x-axis variable, and the green bar represents the resulting emergent constraint on the y-axis variable. The thicknesses represent ± one standard error in each case. Figure after Cox, (2019). Further details on data sources and processing are available in the chapter data table (Table 5.SM.6).

ACCEPTED VERSION SUBJECT TO FINAL EDITS

[END FIGURE 5.28 HERE]

5.4.7 Climate Feedbacks from CH4 and N2O

Sources and sinks of CH_4 and N_2O respond both directly and indirectly to atmospheric CO_2 concentration and climate change, and thereby give rise to additional biogeochemical feedbacks in the climate system, which may amplify or attenuate climate-carbon cycle feedbacks (Gasser et al., 2017; Lade et al., 2018; Denisov et al., 2019). Many of these of feedbacks are only partially understood, and thus were only partially addressed in AR5 (WGI, Sections 6.3.3, 6.3.4, 6.4.7). Since AR5, a growing body of estimates from ESMs, as well as independent modelling and observation-based studies, enable improved estimates of the associated feedbacks.

The goal of this section is to assess the climate feedback parameters α, as it is defined in Section 7.4.1.1, for CH_4 and N_2O biogeochemical feedbacks. The strength of the feedbacks is estimated in a linear framework (Gregory et al., 2009), using the radiative forcing equations for CO_2, CH_4 and N_2O (Etminan et al., 2016). In addition to estimates from ESMs, the feedback parameter α is estimated from independent estimates of surface emission climate sensitivities and atmospheric box models, following (Arneth et al., 2010; Thornhill et al., 2020). These assessed feedback parameters are used in Section 7.4.2.5.

CH_4 feedbacks may arise from changing wetland emissions (including rice farming) and from sources that are expected to grow under climate change (e.g. related to permafrost thaw, fires, and freshwater bodies). CH_4 emissions from wetlands and landfills generally increase with warming due to enhanced decomposition with higher temperatures, thereby potentially providing a positive CH_4 feedback on climate (Dean et al., 2018). The contribution of wetlands to interannual variability of atmospheric CH_4 is shaped by the different impacts of temperature and precipitation anomalies on wetland emissions (e.g. during El Niño episodes) and therefore the relationship between climate anomalies and the wetland contribution to the CH_4 growth rate is complex (Pison et al., 2013; Nisbet et al., 2016; Zhang et al., 2020b). As assessed by SROCC (IPCC, 2019b), there is *high agreement* across model simulations that wetlands CH_4 emissions will increase in the 21st century, but *low agreement* in the magnitude of the change (Denisov et al., 2013; Shindell et al., 2013a; Stocker et al., 2013a; Zhang et al., 2017; Koffi et al., 2020). Climate change increases wetland emissions (Gedney, 2004; Volodin, 2008; Ringeval et al., 2011; Denisov et al., 2013; Shindell et al., 2013a; Gedney et al., 2019) and gives rise to an estimated wetland CH_4-climate feedback of 0.03 ± 0.01 W m^{-2} $°C^{-1}$ (mean ± 1 standard deviation; *limited evidence, high agreement*) (Arneth et al., 2010; Shindell et al., 2013b; Stocker et al., 2013a; Zhang et al., 2017). The effect of rising CO_2 on productivity, and therefore on the substrate for methanogenesis, can further increase the projected increase in wetland CH_4 emissions (Ringeval et al., 2011; Melton et al., 2013). Model projections accounting for the combined effects of CO_2 and climate change suggest a potentially larger climate feedback (0.01–0.16 W m^{-2} $°C^{-1}$; *limited evidence, limited agreement*) (Gedney et al., 2019; Thornhill et al., 2020). Methane release from wetlands depends on the nutrient availability for methanogenic and methanotrophic microorganisms that can further modify this feedback (Stepanenko et al., 2016; Donis et al., 2017; Beaulieu et al., 2019). Methane emissions from thermokarst ponds and wetlands resulting from permafrost thaw, is estimated to contribute an additional CH_4-climate feedback of 0.01 [0.003–0.04, 5–95th percentile range] W m^{-2} $°C^{-1}$ (*limited evidence, moderate agreement*).

Methane release from wildfires may increase by a up to a factor of 1.5 during the 21st century (Eliseev et al., 2014a, 2014b; Kloster and Lasslop, 2017). However, given the contemporary estimate for CH_4 from wildfires of no more than 16 $TgCH_4$ yr^{-1} (van der Werf et al., 2017; Saunois et al., 2020), this feedback is small, adding no more than 40 ppb to the atmospheric CH_4 by the end of the 21st century (*medium confidence*). Methane emissions from pan-Arctic freshwater bodies is also estimated to increase by 16 $TgCH_4$ yr^{-1} in the 21st century (Tan and Zhuang, 2015). Emissions from subsea and permafrost methane hydrates are not expected to change substantially in the 21st century (Section 5.4.8).

Land biosphere models show *high agreement* that long-term warming will increase N_2O release from terrestrial ecosystems (Xu-Ri et al., 2012; Stocker et al., 2013b; Zaehle, 2013a; Tian et al., 2019). A positive land N_2O climate feedback is consistent with paleo-evidence based on reconstructed and modelled emissions

ACCEPTED VERSION SUBJECT TO FINAL EDITS

during the last deglacial period (Schilt et al., 2014; Fischer et al., 2019b; Joos et al., 2020). The response of terrestrial N_2O emissions to atmospheric CO_2 increase and associated warming is dependent on nitrogen availability (van Groenigen et al., 2011; Butterbach-Bahl et al., 2013; Tian et al., 2019). Model-based estimates do not account for the potentially strong emission increases in Boreal and Arctic ecosystems associated with future warming and permafrost thaw (Elberling et al., 2010; Voigt et al., 2017). There is *medium confidence* that the land N_2O climate feedback is positive, but *low confidence* in the magnitude (0.02 ± 0.01 W m^{-2} °C^{-1}).

Climate change will also affect N_2O production in the ocean (Codispoti, 2010; Freing et al., 2012; Bopp et al., 2013; Rees et al., 2016; Breider et al., 2019). Model projections in the 21st century show a 4–12% decrease in ocean N_2O emissions under RCP8.5 due to a combination of factors including increased ocean stratification, decreases in ocean productivity, and the impact of increasing atmospheric N_2O abundance on the air-sea flux, corresponding to an ocean N_2O climate feedback of –0.008 ± 0.002 W m^{-2} °C^{-1} (*high agreement, limited evidence*) (Martinez-Rey et al., 2015; Landolfi et al., 2017; Battaglia and Joos, 2018). On millennial timescales, the ocean N_2O climate feedback may be positive, owing to ocean deoxygenation and long-term increases in remineralisation (Battaglia and Joos, 2018b).

Based-on these studies, there is medium confidence that the combined climate feedback parameter for CH_4 and N_2O is positive, but there is low confidence in the magnitude of the estimate (0.05 (0.02–0.09) W m^{-2} °C^{-1}, 5–95th percentile range).

5.4.8 Combined Biogeochemical Climate Feedback

This section assesses the magnitude of the combined biogeochemical feedback in the climate system (Figure 5.29) by integrating evidence from: carbon-cycle projections represented in Earth system models (Section 5.4.5.5), independent estimates of CO_2 emissions due to permafrost thaw (Box 5.1) and fire (Section 5.4.3.2), natural CH_4 and N_2O emissions (Section 5.4.7), and aerosol and atmospheric chemistry (Section 6.3.6). We derive a physical climate feedback parameter α, as defined in Section 7.4.1.1, for CO_2-based feedbacks using the linear framework proposed by Gregory et al. (2009), using the radiative forcing equations for CO_2 (Etminan et al., 2016).

[START FIGURE 5.29 HERE]

Figure 5.29: Estimates of the biogeochemical climate feedback parameter (α). The parameter α (W m^{-2} °C^{-1}) for a feedback variable x is defined as $\alpha_x = \frac{\partial N}{\partial x}\frac{dx}{dT}$ where $\frac{\partial N}{\partial x}$ is the change in TOA energy balance in response to a change in x induced by a change in surface temperature (T), as in Section 7.4.1.1. (a) Synthesis of biogeochemical feedbacks from panels (b) and (c). Red (blue) bars correspond to positive (negative) feedbacks increasing (decreasing) radiative forcing at the top of the atmosphere. Bars denote the mean and the error bar represents the 5–95th percentile range of the estimates; (b) carbon-cycle feedbacks as estimated by coupled carbon-cycle climate models in the CMIP5 (Arora et al., 2013) and CMIP6 (Arora et al., 2020) ensembles, where dots represent single model estimates, and filled (open) circles are those estimates which do (not) include the representation of a terrestrial nitrogen cycle; (c) Estimates of other biogeochemical feedback mechanisms based on various modelling studies. Dots represent single estimates, and coloured bars denote the mean of these estimates with no weighting being made regarding the likelihood of any single estimate, and error bars the 5–95th percentile range derived from these estimates. Results in panel (c) have been compiled from (a) Section 5.4.3.2 (Eliseev et al., 2014a; Harrison et al., 2018); (b) Section 5.4.3.3 (Schneider von Deimling et al., 2012; Burke et al., 2013, 2017b, Koven et al., 2015c, 2015b; MacDougall and Knutti, 2016b; Gasser et al., 2018; Kleinen and Brovkin, 2018), where the estimates from Burke et al. have been constrained as assessed in their study (c) Section 5.4.7 (Schneider von Deimling et al., 2012, 2015; Koven et al., 2015c; Turetsky et al., 2020); (d) Section 5.4.7 (Arneth et al., 2010; Denisov et al., 2013; Shindell et al., 2013a; Stocker et al., 2013a; Zhang et al., 2017); (f) Section 5.4.7 (Xu-Ri et al., 2012; Zaehle, 2013; Stocker et al., 2013; Tian et al., 2019); (g) Section 5.4.7 (Martinez-Rey et al., 2015; Landolfi et al., 2017; Battaglia and Joos, 2018). (h) Section 6.3, Table 6.9 mean and the 5–95th percentile range the assessed feedback parameter. Further details on data

ACCEPTED VERSION SUBJECT TO FINAL EDITS

sources and processing are available in the chapter data table (Table 5.SM.6).

[END FIGURE 5.29 HERE]

The climate feedback parameter for CO_2 (–1.13 ± 0.45 W m^{-2} °$C^{-1,}$ mean and 1 standard-deviation range) is dominated by the contribution of the CO_2-induced increase of ocean and land carbon storage (–1.46 ± 0.41 W m^{-2} °C^{-1}, corresponding to a β_{L+O} of 1.66 ± 0.31 PgC ppm^{-1}), with smaller contributions from the carbon cycle's response to climate (0.24 ± 0.17 W m^{-2} °C^{-1}, corresponding to γ_{L+O} of –50 ± 34 PgC °C^{-1}), and emissions from permafrost thaw (0.09 [0.02–0.20] W m^{-2} °C^{-1}, corresponding to γ of –18 [3–41] PgC °C^{-1}, mean and 5–95th percentile range) (Figure 5.29a). This estimate does not include an estimate of the fire-related CO_2 feedback (range: 0.01–0.06 W m^{-2} °C^{-1}), as only limited evidence was available to inform its assessment. The sum (mean and 5–95th percentile range) of feedbacks from natural emissions of CH_4 including permafrost thaw, and N_2O (0.05 [0.02–0.09] W m^{-2} °C^{-1}), and feedbacks from aerosol and atmospheric chemistry (–0.20 [–0.41 to 0.01] W m^{-2} °C^{-1}) leads to an estimate of the non-CO_2 biogeochemical feedback parameter of –0.15 [–0.36 to 0.06] W m^{-2} °C^{-1}. There is *low confidence* in the estimate of the non-CO_2 biogeochemical feedbacks, due to the large range in the estimates of α for some individual feedbacks (Figure 5.29c), which can be attributed to the diversity in how models account for these feedbacks, limited process-level understanding, and the existence of known feedbacks for which there is not sufficient evidence to assess the feedback strength.

CO_2 and non-CO_2 biogeochemical feedbacks are an important component of the assessment of TCRE and the remaining carbon budget (Section 5.5). The feedbacks of the carbon cycle of CO_2 and climate are implicitly taken account in the TCRE assessment, because they are represented in the various underlying lines of evidence. Other feedback contributions, such as the non-CO_2 biogeochemical feedback, can be converted into a carbon-equivalent feedback term (γ; Section 5.4.5.5, 7.6) by reverse application of the linear feedback approximation (Gregory et al., 2009). The contributions of non-CO_2 biogeochemical feedbacks combine to a linear feedback term of 30 ± 27 PgCeq °C^{-1} (1 standard deviation range, 111 ± 98 Gt CO_2eq °C^{-1}), including a feedback term of –11 (–18 to –5) PgCeq °C^{-1} (5th–95th percentile range, –40 (–62 to –18) Gt CO_2eq °C^{-1}) from natural CH_4 and N_2O sources. The biogeochemical feedback from permafrost thaw leads to a combined linear feedback term of –21 ± 12 PgCeq °C^{-1} (1 standard deviation range –77 ± 44 Gt CO2eq °C^{-1}). For the integration of these feedbacks in the assessment of the remaining carbon budget (Section 5.5.2), two individual non-CO_2 feedbacks (tropospheric ozone, and methane lifetime) are captured in the AR6-calibrated emulators (Box 7.1). Excluding those two contributions, the resulting combined linear feedback term for application in Section 5.5.2 is assessed at a reduction of 7 ± 27 PgCeq °C^{-1} (1 standard deviation range, –26 ± 97 PgCeq °C^{-1}). For the same reasons as for the feedback terms expressed in W m^{-2} °C^{-1} (see above), there is overall *low confidence* in the magnitude of these feedbacks.

5.4.9 Abrupt Changes and Tipping Points

The applicability of the linear feedback framework (Section 5.4.5.5) suggests that large-scale biogeochemical feedbacks are approximately linear in the forcing from changes in CO_2 and climate. Nevertheless, regionally the biosphere is known to be capable of producing abrupt changes or even 'tipping points' (Higgins and Scheiter, 2012; Lasslop et al., 2016). Abrupt change is defined as a change in the system that is substantially faster than the typical rate of the changes in its history (Chapter 1, Section 1.4.5). A related matter is a tipping point: a critical threshold beyond which a system reorganizes, often abruptly and/or irreversibly. Possible abrupt changes in the Earth system include those related to ecosystems and biogeochemistry (Lenton et al., 2008; Steffen et al., 2018): tropical and boreal forest dieback; and release of greenhouse gases from permafrost and methane clathrates (Table 5.6). It is not currently possible to carry out a full assessment of proposed abrupt changes and tipping points in the biogeochemical cycles. In this section we therefore focus instead on estimating upper limits on the possible impact of abrupt changes on the evolution of atmospheric GHGs out to 2100, for comparison to the impact of direct anthropogenic emissions.

ACCEPTED VERSION SUBJECT TO FINAL EDITS

[START TABLE 5.6 HERE]

Table 5.6: Examples of possible biogeochemical abrupt changes and tipping points in the Earth system. The fourth and sixth comments provide upper estimates of the impact of each example on the evolution of atmospheric GHGs in the 21st century. These upper estimates are therefore *very unlikely* but provide a useful comparison to the impact of direct anthropogenic emissions (currently 2.5 ppm yr^{-1}).

Abrupt change/Tipping point	Key region(s)	Probability to occur in the 21st century	Maximum carbon dioxide or methane release in the 21st century	Principal development timescale	Maximum CO_2 or CH_4 rate of change over the 21st century	(Ir)reversibility
Tropical forests dieback (Section 5.4.9.1.1)	Amazon watershed	low	<200 PgC as CO_2 (Section 5.4.8.1.1; *medium confidence*)	multi-decadal	CO_2: <0.5 ppm yr^{-1}	irreversible at multi-decadal scale (*medium confidence*)
Boreal forests dieback (Section 5.4.9.1.1, 5.4.3.2)	boreal Eurasia and North America	low	<27 Pg (Section 5.4.8.1.1; *medium confidence*)	multi-decadal	small (*low confidence*)	irreversible at multi-decadal scale (*medium confidence*)
Biogenic emissions from permafrost thaw (Section 5.4.9.1.2)	pan-Arctic	high	up to 240 PgC of CO_2 and up to 5300 Tg of CH_4 (Section 5.4.8.1.2; *low confidence*)	multi-decadal	CO_2: ≤1 ppm yr^{-1} CH_4: ≤10 ppb yr^{-1}	irreversible at centennial timescales (*high confidence*)
Methane release from clathrates (Section 5.4.9.1.3)	oceanic shelf	very low	*very likely* small (Section 5.4.9.1.3)	multi-millennium	CH_4: ≤0.2 ppb yr^{-1}	irreversible at multi-millennium timescales (*medium confidence*)

[END TABLE 5.6 HERE]

ACCEPTED VERSION SUBJECT TO FINAL EDITS

5.4.9.1 Assessment of biogeochemical tipping points

5.4.9.1.1 Forest Dieback

Published examples of abrupt biogeochemical changes in models include tropical rain forest dieback (Cox et al., 2004; Jones et al., 2009; Brando et al., 2014; Le Page et al., 2017; Zemp et al., 2017), and temperate and boreal forest dieback (Joos et al., 2001; Lucht et al., 2006; Scheffer et al., 2012; Lasslop et al., 2016) (see also Section 5.4.3). Such transitions may be related to (i) large-scale changes in mean climate conditions crossing particular climate thresholds (Joos et al., 2001; Cox et al., 2004; Lucht et al., 2006; Hirota et al., 2011; Scheffer et al., 2012; Le Page et al., 2017; Zemp et al., 2017), (ii) temperature and precipitation extremes (Staver et al., 2011; Higgins and Scheiter, 2012; Scheffer et al., 2012; Pavlov, 2015; Zemp et al., 2017), or (iii) possible enhancement and intermittency in fire activity (Staver et al., 2011; Higgins and Scheiter, 2012; Lasslop et al., 2016; Brando et al., 2020). Simulated changes in forest cover are a combination of the effects of CO_2 on photosynthesis and water-use efficiency (Section 5.4.1), and the effects of climate change on photosynthesis, respiration and disturbance (Section 5.4.3). In ESMs, direct CO_2 effects tend to enhance forest growth, but the impacts of climate change vary between being predominantly negative in the tropics and predominantly positive in the boreal zone (Figure 5.27).

Most ESMs project continuing carbon accumulation in tropical forests as a result of direct CO_2 effects overwhelming the negative effects of climate change (Huntingford et al., 2013; Drijfhout et al., 2015;

Boulton et al., 2017). In the real world, forests may be less vulnerable to climate changes than those modelled in ESMs because of the greater plant trait diversity which confers additional resilience (Reyer et al., 2015; Levine et al., 2016; Sakschewski et al., 2016), and also because of possible acclimation of vegetation to warming (Good et al., 2011, 2013; Lloret et al., 2012; Mercado et al., 2018). Contrary, forests may be more vulnerable in the real world due to indirect climate change effects such as insect outbreaks and diseases not considered here (Section 5.4.3.2) or model limitations in representing the effects disturbances such as wildfire and droughts. In general, forests are most vulnerable when climate change is combined with increased rates of direct deforestation (Nobre et al., 2016; Le Page et al., 2017).

In order to estimate an upper limit on the impact of Amazon forest dieback on atmospheric CO_2, we consider the *very unlikely* limiting case of negligible direct-CO_2 effects (Section 5.4.1). Emergent constraint approaches (Section 5.4.6) may be used to estimate an overall loss of tropical land carbon due to climate change alone, of around 50 PgC per ^{o}C of tropical warming (Cox et al., 2013b; Wenzel et al., 2014). This implies an upper limit to the release of tropical land carbon of <200 PgC over the 21st century (assuming tropical warming of <4^{o}C, and no CO_2-fertilisation), which translates to $dCO_2/dt < 0.5$ ppm yr^{-1}.

Boreal forest dieback is not expected to change the atmospheric CO_2 concentration substantially because forest loss at the south is partly compensated by (i) temperate forest invasion into the previous boreal area and (ii) boreal forest gain at the north (Friend et al., 2014; Kicklighter et al., 2014; Schaphoff et al., 2016) (*medium confidence*). An upper estimate of this magnitude, based on statistical modelling of climate change alone, is of 27 Pg vegetation C loss in the southern boreal forest, which is roughly balanced by gains in the northern zone (Koven, 2013). Carbon release from vegetation and soil due to wildfires in boreal regions (Eliseev et al., 2014b; Turetsky et al., 2015; Walker et al., 2019a) is also not expected to change this estimate substantially because of its small present-day value of about 0.2 PgC yr^{-1} (van der Werf et al., 2017), and because of *likely* increases in precipitation in boreal regions (Chapter 4, Section 4.5.1).

5.4.9.1.2 Biogenic Emissions Following Permafrost Thaw

There is large uncertainty in release of GHGs from permafrost in the 21st century with the largest of these estimates implying tens to hundreds of gigatons of carbon released in the form of CO_2 (Box 5.1) and methane emissions up to 100 TgCH$_4$ yr^{-1} (Box 5.1). A carbon dioxide release of such magnitude would lead to an increase in the CO_2 accumulation rate in the atmosphere of ≤1 ppm yr^{-1}. These emissions develop at multi-decadal timescale. Assuming a CH_4 lifetime in the atmosphere of the order of 10 years and the associated feedback parameter of 1.34 ± 0.04 (Chapter 6, Section 6.2.2.1), this would increase the atmospheric methane content by about 500 ppb over the century, corresponding to a rate of ≤10 ppb yr^{1}. Irrespective of its origin, additional methane accumulation of such a magnitude is not expected to modify the temperature response to anthropogenic emissions by more than a few tens of °C cent (Gedney, 2004; Eliseev et al., 2008; Denisov et al., 2013). Emissions from the permafrost are assessed in Box 5.1.

5.4.9.1.3 Methane Release from Clathrates

The total global clathrate reservoir is estimated to contain 1500–2000 PgC (Archer et al., 2009; Ruppel and Kessler, 2017), held predominantly in ocean sediments with only an estimated 20 PgC in and under permafrost (Ruppel, 2015). The present-day methane release from shelf clathrates is <10 TgCH$_4$ yr^{-1} (Kretschmer et al., 2015; Saunois et al., 2020). Despite polar amplification (Chapter 7), substantial releases from the permafrost-embedded subsea clathrates is *very unlikely* (Minshull et al., 2016; Malakhova and Eliseev, 2017, 2020). This is consistent with an overall small release of methane from the shelf clathrates during the last deglacial despite large reorganisations in climate state (Bock et al., 2017; Petrenko et al., 2017; Dyonisius et al., 2020). The long timescales associated with clathrate destabilisation makes it *unlikely* that CH_4 release from the ocean to the atmosphere will deviate markedly from the present-day value through the 21st century (Hunter et al., 2013), corresponding to no more than additional 20 ppb of atmospheric methane (i.e. <0.2 ppb yr^{-1}). Another possible source of CH_4 are gas clathrates in deeper terrestrial permafrost and below it (Buldovicz et al., 2018; Chuvilin et al., 2018), which may have caused recent craters in the north of Russia (Arzhanov et al., 2016, 2020; Arzhanov and Mokhov, 2017; Kizyakov et al., 2017, 2018). Land clathrates are formed at depths >200 m (Ruppel and Kessler, 2017; Malakhova and Eliseev,

ACCEPTED VERSION SUBJECT TO FINAL EDITS

2020), which precludes a substantial response to global warming over the next few centuries and associated emissions.

Thus, it is *very unlikely* that CH_4 emissions from clathrates will substantially warm the climate system over the next few centuries.

5.4.9.2 Abrupt Changes Detected in ESM Projections

Projecting abrupt changes is intrinsically difficult, because by definition abrupt changes occur in a small region of the parameter and/or forcing space. At the time of the AR5 there was no available systematic study of abrupt changes or tipping points in ESMs. An analysis of ESMs since the AR5 has identified a number of abrupt changes in the CMIP5 ensemble (Drijfhout et al., 2015; Bathiany et al., 2020). These include abrupt changes in tropical forests and high-latitude greening, permafrost thaw, and vegetation composition change (Bathiany et al., 2020). Most modelled abrupt changes were detected in boreal and tundra regions, with few models showing Amazon forest dieback (Bathiany et al., 2020).

Based on the evidence presented in this section, we conclude that abrupt changes and tipping points in the biogeochemical cycles lead to additional uncertainty in 21st century GHG concentrations changes, but these are *very likely* to be small compared to the uncertainty associated with future anthropogenic emissions (*high confidence*).

5.4.10 Long Term Response past 2100

AR5 assessed with *very high confidence* that the carbon cycle in the ocean and on land will continue to respond to climate change and rising atmospheric CO_2 concentrations created during the 21st century (WGI, Chapter 6, Executive Summary). Since AR5, experiments with the CESM1 model under the RCP8.5 extension scenario out to 2300, suggest that both land and ocean carbon-climate feedbacks strengthen in time, land and ocean carbon-concentration feedbacks weaken, and the relative importance of ocean sinks versus land sinks increases (Randerson et al., 2015). Under high emissions scenarios, this relative strengthening of land carbon-climate feedbacks leads the terrestrial biosphere to shift from sink to source at some point after 2100 in all of the CMIP5 ESMs and CMIP5-era EMICs (Tokarska et al., 2016). The strengthening of land and ocean carbon-climate feedbacks projected beyond 2100 under high emissions scenarios offsets the declining climate sensitivity to incremental increases of CO_2, leading to a net strengthening of carbon cycle feedbacks, as measured by the gain parameter, from one century to the next (Randerson et al., 2015).

Figure 5.30 shows carbon cycle changes to 2300 under three SSP scenarios with long-term extensions: SSP5–8.5, SSP5–3.4–overshoot, and SSP1–2.6, for four CMIP6 ESMs and one EMIC. Under all three scenarios, all five models project a reversal of the terrestrial carbon cycle from a sink to a source. However, the reasons for these reversals under very high emissions and low/negative emissions are very different. Under the SSP5–8.5 scenario, the terrestrial carbon-climate feedback is projected to strengthen, while the carbon-concentration feedbacks weaken after emissions peak at 2100, which together drives the land to become a net carbon source after 2100 (Tokarska et al., 2016). The difference in both timing and magnitude of this transition across the ensemble, leads to an assessment of *medium confidence* in the likelihood and *low confidence* in the timing and strength, of the land transitioning from a net sink to a net source under such a scenario. Based on *high agreement* across all available models, we assess with *high confidence* that the ocean sink strength would weaken but not reverse under a long-term high-emissions scenario. In the SSP5–3.4–overshoot scenario, both the terrestrial and ocean reservoirs act as transient carbon sources during the overshoot period, when net anthropogenic CO_2 emissions are negative and CO_2 concentrations are falling, and then revert to near-zero (land) or weak sink (ocean) fluxes after stabilisation of atmospheric CO_2. The SSP1–2.6 scenario, characterised by lower peak CO_2 concentrations, a smaller overshoot, and much less carbon loss from land use change, shows instead a relaxation towards a neutral biosphere on land and a sustained weak sink in the ocean (see also Section 5.6.2.2.1.2).

ACCEPTED VERSION SUBJECT TO FINAL EDITS

[START FIGURE 5.30 HERE]

Figure 5.30: Trajectories of carbon cycle dynamics for models beyond 2100. Shown are three scenarios, SSP5–8.5, SSP5–3.4–overshoot, and SSP1–2.6, from four ESMs (CanESM5, UKESM1, CESM2-WACCM, IPSL-CM6a-LR) and one EMIC (UVIC-ESCM, (Mengis et al., 2020)) for which extensions beyond 2100 are available. Solid lines represent the median flux value across the ensemble, and shading represents 15th–85th percentiles across the ensemble. Further details on data sources and processing are available in the chapter data table (Table 5.SM.6).

[END FIGURE 5.30 HERE]

5.4.11 Near-Term Prediction of Ocean and Land Carbon Sinks

The IPCC AR5 (WGI, Section 11.3.2) assessed near-term climate predictability based on ESMs initialised from the observed climate state. Since the AR5, a growing number of prediction systems have been developed based on ESMs that include the ocean and land carbon cycle components. Predictability of key physical climate variables (assessed in Chapter 4) provides a platform to establish predictive skill for interannual variations in the strength of the natural carbon sinks in response to internal climate variability. In most systems the carbon cycle components are only indirectly initialised and respond to the initialised climate variations (Li et al., 2019). This subsection synthesises information on predictability of the land and ocean carbon sinks using both the idealised potential predictability and the actual predictability skill measures.

Longer-term memory residing in the ocean enables predictability of the ocean carbon sink (McKinley et al., 2017; Li and Ilyina, 2018). The predictive horizon of the globally integrated air-sea CO_2 fluxes has been assessed in perfect-model frameworks that are based on an idealised ensemble of simulations in which each ensemble member serves as a verification, while no observations are assessed. Perfect-model studies provide an estimate of the upper range of potential predictability for the integrated air-sea CO_2 fluxes of about 2 years globally and up to a decade in some regions (Séférian et al., 2018a; Spring and Ilyina, 2020). Evidence is also emerging for predictive skill of the global air-sea CO_2 fluxes of up to 6 years based-on prediction systems initialised with observed physical climate states (Li et al., 2019), with a potential for even longer-term regional predictability in some regions including the North Atlantic and subpolar Southern Ocean (Li et al., 2016a; Lovenduski et al., 2019b).

Models suggest that predictability of the air-sea CO_2 flux is related to predictability of ocean biogeochemical state variables such as dissolved inorganic carbon (DIC) and total alkalinity (TA) (Lovenduski et al., 2019b), as well as the mixed layer depth (Li et al., 2016a). Temperature variations largely control shorter-term predictability of the ocean carbon sink, while longer term predictability is related to non-thermal drivers such as ocean circulation and biology (Li et al., 2019). Although there is a substantial spatial heterogeneity, initialised predictions suggest stronger multi-year variations of the air-sea CO_2 flux and generally tend to outperform uninitialized simulations on the global scale (Li et al., 2019). The predictive skill of air-sea CO_2 flux shows a consistent spatial pattern in different models despite the wide range of techniques used to assimilate observational information (Regnier et al., 2013a). ESM-based prediction systems also demonstrate predictability of other marine biogeochemical properties such as net primary production (Séférian et al., 2014; Yeager et al., 2018; Park et al., 2019) and seawater pH (Brady et al., 2020).

Seasonal predictability of air-land CO_2 flux up to 6–8 months is driven by the state of ENSO (Zeng et al., 2008; Betts et al., 2018). Fewer land carbon initialised predictions are available from decadal prediction systems, yet they tend to outperform the uninitialized simulations in capturing the major year-to-year variations as indicated by higher correlations with the Global Carbon Budget estimates. There is growing evidence that potential predictive skill of air-land CO_2 flux is maintained out to a lead-time of 2 years (Lovenduski et al., 2019a); this predictability horizon is also supported by perfect model studies (Séférian et al., 2018a; Spring and Ilyina, 2020). The origins of this interannual predictability are not yet fully

ACCEPTED VERSION SUBJECT TO FINAL EDITS

understood. However, they seem to be associated with the oscillatory behaviour of ENSO (Séférian et al., 2014) and the predictability of terrestrial ecosystem drivers such as ecosystem respiration and gross primary production (Lovenduski et al., 2019b). Initialised simulations suggest that observed variability in the land carbon sink is improved through initialisation of prediction systems with the observed state of the physical climate.

The predictability horizon of variations in atmospheric CO_2 growth-rate are not yet fully established in the literature. However, predictive skill of the land and ocean carbon sinks show a potential to establish predictability of variations in atmospheric CO_2 up to 2 years in advance in the initialised prediction systems with an upper bound of up to 3 years in a perfect-model study (Spring and Ilyina, 2020); this skill is primarily limited by the terrestrial carbon sink predictability.

5.5 Remaining Carbon Budgets

Science at the time of the IPCC AR5 established a near-linear relationship between cumulative emissions of CO_2 and the resulting global warming (Allen et al., 2009; Matthews et al., 2009; Meinshausen et al., 2009; Zickfeld et al., 2009; Collins et al., 2013; Stocker et al., 2013;). The amount of global warming per unit of cumulated CO_2 emissions is called the transient climate response to cumulative emissions of carbon dioxide (TCRE). This TCRE relationship is now used to estimate the amount of CO_2 emissions that would be consistent with limiting global warming to specific levels (Allen et al., 2009; Matthews et al., 2009; Meinshausen et al., 2009; Zickfeld et al., 2009; Matthews et al., 2012; Collins et al., 2013; Stocker et al., 2013; Knutti and Rogelj, 2015; Rogelj et al., 2016; Goodwin et al., 2018; Rogelj et al., 2019). The remainder of CO_2 emissions that would be in line with limiting global warming to a specific temperature level (while accounting for all other factors affecting global warming) can be estimated with help of the TCRE and is referred to as the remaining carbon budget (Rogelj et al., 2019; Matthews et al., 2020). Section 5.5.1 first assesses the TCRE as one of the core concepts underlying the notion of a remaining carbon budget and Section 5.5.2 then integrates this with the assessment of other contributing factors from across this assessment to provide a consolidated assessment following the approach of the IPCC SR1.5 (Rogelj et al., 2018b). The historical carbon budget of CO_2 already emitted is assessed in Section 5.2.1.5.

5.5.1 Transient Climate Response to Cumulative Emissions of carbon dioxide (TCRE)

5.5.1.1 Contributing Physical Processes and Theoretical Frameworks

The processes that translate emissions of CO_2 into a change in global temperature (terrestrial and oceanic carbon uptake, radiative forcing from CO_2, and ocean heat uptake) are governed by complex mechanisms that all evolve in time (Gregory et al., 2009) (Sections 3.5, 4.3, 4.5, 5.4, and 7.3, Cross-Chapter Box 5.3). Starting with an initial description in AR5 (Collins et al., 2013a; Stocker et al., 2013c) a body of literature has since expanded the understanding of physical mechanisms from which a simple proportional relationship between cumulative emissions of CO_2 and change in global temperature (expressed in either global mean surface temperature, GMST or global mean surface air temperature, GSAT) arises.

Studies have focused on two key features of the TCRE relationship: (i) why the relationship is nearly constant in time (Goodwin et al., 2015; MacDougall and Friedlingstein, 2015; Williams et al., 2016; Ehlert et al., 2017; Katavouta et al., 2018); and (ii) why and under which conditions the relationship is independent on the historical rate (or pathway) of CO_2 emissions (MacDougall, 2017; Seshadri, 2017).

There is increased confidence in the near-constancy of TCRE because of the variety of methods that have been used to examine this relationship: sensitivity studies with Earth system models of EMICs (Herrington and Zickfeld, 2014; Ehlert et al., 2017); theory-based equations used to examine Earth system model (ESM) and EMIC output (Goodwin et al., 2015; Williams et al., 2016, 2017c); and simple analytical models that capture aspects of the TCRE relationship (MacDougall and Friedlingstein, 2015). All studies agree that the near-constancy of the TCRE arises from compensation between the diminishing sensitivity of radiative

ACCEPTED VERSION SUBJECT TO FINAL EDITS

forcing to CO_2 at higher atmospheric concentration, and the diminishing ability of the ocean to take up heat and carbon at higher cumulative emissions (Allen et al., 2009; Matthews et al., 2009; Frölicher and Paynter, 2015; Goodwin et al., 2015; Gregory et al., 2015; MacDougall and Friedlingstein, 2015; MacDougall, 2016; Tokarska et al., 2016; Ehlert et al., 2017).

The question whether and under which conditions the TCRE relationship is independent of the historical rate of CO_2 emissions (also referred to as 'pathway independence of TCRE') has been examined by using simple mathematically-tractable models (MacDougall, 2017; Seshadri, 2017). Based on the assumption that the cumulative fraction of carbon taken up by the terrestrial biosphere is constant, and that the climate feedback parameter and ocean heat uptake efficacy do not change in time, both studies agree that pathway independence is sensitive to the rate of CO_2 emissions, such that pathway independence is expected to breakdown at both very high and very low absolute CO_2 emission rates (MacDougall, 2017; Seshadri, 2017). Note that in pathways with strongly declining emissions, the cumulative sink fraction by the combined terrestrial biosphere and ocean is expected to increase (see Figure 5.25 in Section 5.4.5). The studies also agree that no similar relationship analogous to TCRE can be expected for short-lived non-CO_2 forcers, for which the annual emissions are a closer proxy for the implied warming (Collins et al., 2013a); Sections 6.4, 7.6. MacDougall, (2017) suggests that two additional constraints are required to create pathway independence: first, the transport of heat and carbon into the deep ocean should be governed by processes with similar timescales; and second, the ratio of the net change in the atmospheric carbon pool to the net change in the ocean carbon pool should be close to the ratio of the enhanced longwave radiation to space (i.e. the radiative response of the surface) to ocean heat uptake. If these ratios are identical then TCRE would be completely path independent (MacDougall, 2017). If the ratios are close but not identical, TCRE would be only approximately path independent over a wide range of cumulative emissions (MacDougall, 2017) (Cross-Chapter Box 5.3).

The land carbon cycle does not appear to play a fundamental role in the origin of the linearity and path-independence of TCRE (Goodwin et al., 2015; MacDougall and Friedlingstein, 2015; Ehlert et al., 2017), but, in contrast to the ocean sink, dominates the uncertainty in the magnitude of TCRE by modulating the cumulative airborne fraction of carbon (Goodwin et al., 2015; Williams et al., 2016; Katavouta et al., 2018; Jones and Friedlingstein, 2020). Some terrestrial carbon cycle feedbacks (such as the permafrost carbon feedback, Section 5.4.8, Box 5.1) have the potential to alter both the linearity and pathway independence of TCRE, if such feedbacks significantly contribute carbon to the atmosphere (MacDougall and Friedlingstein, 2015) (Section 5.5.1.2.3, Section 5.4.8, Box 5.1). A recent study also shows how the value of TCRE can depend on the effect of ocean ventilation modulating ocean heat uptake (Katavouta et al., 2019).

[START CROSS-CHAPTER BOX 5.3]

Cross-Chapter Box 5.3: The Ocean Carbon-Heat Nexus and Climate Change Commitment

Contributors: Pedro M.S. Monteiro (South Africa), Jean-Baptiste Sallée (France), Piers Foster (UK), Baylor Fox-Kemper (USA), Helen Hewitt (UK), Masao Ishii (Japan), Joeri Rogelj (Belgium), Kirsten Zickfeld (Canada/Germany)

Context

In the past 60 years the ocean has taken up and stored 23 ± 5% of anthropogenic carbon emissions (*medium confidence*; Section 5.2.1.3) as well as more than 90% of the heat that has accumulated in the Earth system (referred to as excess heat) since the 1970s (Sections 7.2.2, 9.2.2, 9.2.3; Box 7.2;) (Frölicher et al., 2015; Talley et al., 2016; Gruber et al., 2019a; Hauck et al., 2020). The interplay between heat and CO_2 uptake by the ocean has not only played a major role in slowing the rate of global warming but provides a first order influence in determining the unique properties of a metric of the coupled climate-carbon cycle response, transient climate response to cumulative carbon emissions (TCRE), which is critical to setting the future remaining carbon emissions budget (Sections 5.5.1.3, 5.5.4). This role of the ocean in the uptake of heat and anthropogenic CO_2 and related feedbacks is what we term here the "Ocean Heat-Carbon Nexus". The ocean

ACCEPTED VERSION SUBJECT TO FINAL EDITS

processes behind this nexus are important in shaping and understanding the near-linear relationship between cumulative CO_2 emissions and global warming (TCRE) as well as the uncertainties in future projections of TCRE properties (Zickfeld et al., 2016; Bronselaer and Zanna, 2020; Jones and Friedlingstein, 2020), its path independence (MacDougall, 2017), and the warming commitment after cessation of greenhouse gas emissions (ZEC) (Zickfeld et al., 2016; Ehlert and Zickfeld, 2017; Section 5.5.2). In this box, we assess the role of the ocean and its physical and chemical thermodynamic processes that shape these striking characteristics.

The role of the ocean in setting the coupled climate-carbon cycle response is threefold: firstly, the ocean and land carbon sinks together set the airborne fraction (AF) of CO_2 in the atmosphere, which sets the radiative forcing that drives the additional heat in the atmosphere most of which is taken up by the ocean (Katavouta et al., 2019; Williams et al., 2019; Sections 7.2, 9.2). However, the land carbon sink does not appear to play an important role in determining the linearity and path-independence of TCRE (Section 5.5.1.1; Goodwin et al., 2015; MacDougall and Friedlingstein, 2015; Ehlert et al., 2017). Secondly, the ocean sets the thermal response through ocean heat uptake (Section 9.2; Frölicher et al., 2015; Bronselaer and Zanna, 2020). Thirdly, there is a feedback within the ocean heat-carbon nexus as ocean warming, particularly under low or no mitigation scenarios weakens the ocean sink of CO2, which influences the AF, and hence the radiative forcing (Williams et al., 2019) (Box 7.1). The near-linear relationship between cumulative CO_2 emissions and global warming (TCRE) is thought to arise to a large extent from the compensation between the decreasing ability of the ocean to take up heat and CO_2 at higher cumulative CO_2 emissions, pointing to similar processes that determine ocean uptake of heat and carbon (Goodwin et al., 2015; MacDougall and Friedlingstein, 2015; Williams et al., 2016; Zickfeld et al., 2016; Ehlert et al., 2017; Section 5.5.1.1).

Processes the drive the Ocean Carbon - Heat Nexus and its change

The air-sea flux of heat and all gases across the ocean interface is driven by a common set of complex and difficult to observe turbulent diffusion and mixing processes (Wanninkhof et al., 2009; Wanninkhof, 2014; Cronin et al., 2019; Watson et al., 2020; Sections 5.2.1.3; 9.2.1.2). These processes are typically simplified into widely verified expressions that link the flux to wind stress, the solubility and the gradient across the air-sea interface (*medium confidence*). Because the ocean has a higher heat capacity than the atmosphere (heat capacity of the upper 100 m of the ocean is about 30 times larger than the heat capacity of the atmosphere), the partitioning of heat between the atmosphere and the ocean is primarily influenced by the temperature differences between air and seawater. Similarly, the unique seawater carbonate buffering capacity, enables CO_2 to be stored in the ocean as dissolved salts, rather than just as dissolved gas, which increases the capacity of seawater to store CO_2 by two orders of magnitude beyond the solubility of CO_2 gas and approximate the partitioning ratio of heat between the atmosphere and the ocean (Zeebe and Wolf-Gladrow, 2009; Bronselaer and Zanna, 2020; Section 9.2.2.1). The role of the biological carbon pump in influencing the ocean sink of anthropogenic carbon into the ocean interior is assessed to be minimal during the historical period but this may change, particularly in regional contexts, by 2100 (*medium confidence*) (Laufkötter et al., 2015; Kwiatkowski et al., 2020). Its role is important in the natural or pre-industrial carbon cycle (*medium confidence*) (Henson et al., 2016).

Under climate change, the buffering capacity of the ocean decreases (increasing Revelle Factor), which reflects a decreasing capacity for the ocean to take up additional anthropogenic CO_2 and store it in the DIC reservoir (Egleston et al., 2010). In contrast to CO_2, there is no physical limitation that would reduce the ability of surface ocean temperature to equilibrate with the atmospheric temperature. However, both carbon and heat fluxes depend on air-sea heat fluxes that depend on gradients of characteristics at the air-sea interface. These gradients at the air-sea interface respond to ocean dynamics, such as the volume of the surface mixed-layer that equilibrates with the atmosphere, and ocean circulation that can flush the surface layer with water-masses that have not equilibrated with the atmosphere for a long time. Limited recent evidence has suggested that the effect of small-scale dynamics absent in climate and earth system models might be locally important in this regard (Bachman and Klocker, 2020). In summary, changes in heat and carbon uptake by the ocean rely on a combination of unique chemical and shared physical processes any of which have the potential to disrupt the coherence of heat and CO_2 change in the ocean.

ACCEPTED VERSION SUBJECT TO FINAL EDITS

Spatial pattern of air-sea fluxes and storage

Large scale regional and global ocean circulation shape the spatial pattern of the uptake and storage of both CO_2 and heat (see Figure 5.8 for carbon; Figure 9.6 for heat observations; Section 9.2; (Frölicher et al., 2015; Bronselaer and Zanna, 2020). This coherence of spatial patterns driven by the large-scale ocean circulation has three aspects: firstly, notwithstanding interannual - decadal variability in heat and CO_2 uptake, there is a spatial coherence of the temporally integrated uptake at the air-sea boundary, particularly in the Southern Ocean (Cross-Chapter Box 5.3, Figure 1; Talley et al., 2016; Keppler and Landschützer, 2019; Auger et al., 2021). Secondly, the importance of the meridional overturning circulation in the subsequent storage of both heat and CO_2 in mode, intermediate and deep waters of the ocean interior (Section 9.2). Of particular note are the roles of the North Atlantic Ocean (Section 9.2.3.1) and the Southern Ocean (Section 9.2.3.2) in linking the spatial pattern of air-sea fluxes, the storage of heat and carbon, and ultimately in understanding and predicting the sensitivity of the carbon – heat nexus to climate change (Frölicher et al., 2015; Thomas et al., 2018; Wu et al., 2019).

[START CROSS-CHAPTER BOX 5.3, FIGURE 1 HERE]

Cross-Chapter Box 5.3, Figure 1: CMIP6 multi-model mean of changes in zonally integrated (a) carbon and (b) heat storage in ocean between the pre-industrial and the modern period. Carbon corresponds to dissolved inorganic carbon. Data are shown for the upper 2000m. The modern period is 1995–2014. Adapted from (Frölicher et al., 2015))

[END CROSS-CHAPTER BOX 5.3, FIGURE 1 HERE]

The role of the large-scale circulation in shaping these fluxes is to (i) flush the ocean surface layer with deep waters that are relatively cold and with weak or no anthropogenic CO_2 and heat content because they have been isolated from the atmosphere for centuries, and (ii) transport the anthropogenic CO_2 and heat at depth, away from the atmosphere (Frölicher et al., 2015; Marshall et al., 2015; Armour et al., 2016). For instance, in the Southern Ocean upwelled water-masses uptake large amount of anthropogenic CO_2 and heat (Cross-Chapter Box 5.3, Figure 1), which are then exported northward by the circulation to be stored at depth in the Southern Hemisphere subtropical gyres (Cross-Chapter Box 5.3, Figure 1; Figure 9.7). In the North Atlantic, the signature of the Atlantic meridional overturning circulation (AMOC) is also clearly visible, with large amounts of heat and carbon being stored beneath the North Atlantic subtropical gyre at 1 km depth (Cross-Chapter Box 5.3, Figure 1). In summary, the net air-sea fluxes of anthropogenic CO_2 and heat depend on large-scale circulation, which is associated with upper ocean stratification, mixed-layer depth, and water-mass formation, transport and mixing (Sections 9.1; 9.2; 9.3).

Changes in ocean processes and impact on the ocean carbon-heat nexus

Future projections of the ocean carbon-heat nexus in the second half of the 21st century, particularly those under weak or no mitigation scenarios, are characterized by the strengthening of the two largest positive feedbacks: weakening surface ocean CO_2 buffering capacity (increasing Revelle Factor) and warming that further reduces CO_2 solubility and strengthens ocean stratification, which reduces exchange between the ocean surface and interior (Jiang et al., 2019; Bronselaer and Zanna, 2020). These are offset by a growing but scenario-dependent negative feedback from increasing carbon and heat air sea fluxes towards the ocean, due to increased atmospheric temperature and CO_2 concentrations (Talley et al., 2016; Jiang et al., 2019; McKinley et al., 2020). The Southern Ocean (SO) in particular is one of the regions where the projected feedback can be largest and where inter-model differences are strongest (Roy et al., 2011; Frölicher et al., 2015; Hewitt et al., 2016; Mongwe et al., 2018). These projected trends in ocean carbonate chemistry (5.4.2), together with surface ocean warming (Section 9.2.1.1), explain the slow down and long-term reduction of the ocean sink for anthropogenic CO_2 even as emissions continue to rise beyond 2050 under weak to no mitigation scenarios (Section 5.4: Figure 5.25; Technical Summary TS Box 7 and Figure 2.7.1). Projected change in the North Atlantic and Southern Ocean overturning circulation also impact air-sea fluxes of heat

ACCEPTED VERSION SUBJECT TO FINAL EDITS

and carbon. The *very likely* decline in AMOC in the 21st century for all shared socioeconomic pathways (SSP) scenarios (Section 9.2.3.1) tends to reduce heat and carbon uptake translating in a positive feedback. In contrast, in the Southern Ocean, the future 21st century projected increase in upper ocean overturning circulation (*low confidence*) due to increasing wind forcing projected for all scenarios, except those with large mitigation (SSP1–2.6), translate in a negative feedback with increasing heat and carbon uptake and storage despite the increasing stratification and outgassing of natural CO_2 in the upwelling zone (Sections 9.2.3.2; 5.2.1.3).

In summary, a combination of unique chemical properties of seawater carbonate combined with shared physical ocean processes explain the coherence and scaling in the uptake and storage of both CO_2 and heat in the ocean, which is the basis for the carbon-heat nexus (*high confidence*). In this way the processes of the ocean carbon – heat nexus help understand the quasi-linear and path independence of properties of TCRE, which forms the basis for the ZEC (Section 5.5) (*medium confidence*). Future projections under low or no mitigation indicate with *high confidence* that carbon chemistry and warming will strengthen the positive feedback to climate change by reducing ocean carbon uptake, and *medium confidence* that ocean circulation may partially compensate that positive feedback by slightly increasing anthropogenic carbon storage. Increasing ocean warming and stratification may decrease exchanges between the surface and subsurface ocean, which could reduce the path independence of TCRE, though this effect can be partially counterbalanced regionally by increasing circulation associated with increasing winds (*low confidence*).

[END CROSS-CHAPTER BOX 5.3]

5.5.1.2 Assessment of Limits of the TCRE Concept

5.5.1.2.1 Sensitivity to amount of cumulative CO_2 emissions

AR5 indicated that the concept of a constant ratio of cumulative emissions of CO_2 to temperature was applicable to scenarios with increasing cumulative CO_2 emissions up to 2000 PgC (Collins et al., 2013a). Recent analyses have added confidence to this insight (Herrington and Zickfeld, 2014; Steinacher and Joos, 2016) and have also shown some evidence of a potentially larger window of constant TCRE (Leduc et al., 2015; Tokarska et al., 2016). Using an analytical approach, MacDougall and Friedlingstein (2015) quantified a window of constant TCRE – defined as the range in cumulative emissions over which the TCRE remains within 95% of its maximum value – as between 360 to 1560 PgC. However, models with a more sophisticated ocean representation suggest that TCRE could also remain constant for considerably larger quantities of cumulative emissions, up to at least 3000 PgC (Leduc et al., 2015; Tokarska et al., 2016). Beyond this upper limit, studies are inconclusive with some suggesting that TCRE will decrease (Leduc et al., 2015) and others indicating that the linearity would hold up to as much as 5000 PgC (Tokarska et al., 2016).

As cumulative emissions increase, weakening land and ocean carbon sinks increase the airborne fraction of CO_2 emissions (see Section 5.4.5, Figure 5.25), but each unit increase in atmospheric CO_2 has a smaller effect on global temperature owing to the logarithmic relationship between CO_2 and its radiative forcing (Matthews et al., 2009; Etminan et al., 2016). At high values of cumulative emissions, some models simulate less warming per unit CO_2 emitted, suggesting that the saturation of CO_2 radiative forcing becomes more important than the effect of weakened carbon sinks (Herrington and Zickfeld, 2014; Leduc et al., 2015). The behaviour of carbon sinks at high emissions levels remains uncertain, as models used to assess the limits of the TCRE show a large spread in net land carbon balance (Section 5.4.5) and most estimates did not include the effect of permafrost carbon feedbacks (Sections 5.5.1.2.3, 5.4). The latter would tend to further increase the airborne fraction at high cumulative emissions levels, and could therefore extend the window of linearity to higher total amounts of emissions (MacDougall et al., 2015). Leduc et al. (2016) suggested further that a declining strength of snow and sea-ice feedbacks in a warmer world would also contribute to a smaller TCRE at high amounts of cumulative emissions. On the other hand, Tokarska et al. (2016) suggested that a large decrease in TCRE for high cumulative emissions is only associated with some EMICs; in the four ESMs analysed in their study, the TCRE remained approximately constant up to 5000 PgC, owing to stronger declines in the efficiency of ocean heat uptake in ESMs compared to EMICs.

ACCEPTED VERSION SUBJECT TO FINAL EDITS

Overall, there is *high agreement* between multiple lines of evidence (*robust evidence*) resulting in *high confidence* that TCRE remains constant for the domain of increasing cumulative CO_2 emissions until at least 1500 PgC, with *medium confidence* of it remaining constant up to 3000 PgC because of less agreement across available lines of evidence.

5.5.1.2.2 Sensitivity to the Rate of CO_2 Emissions

Global average temperature increase responds over a timescale of about 10 years following the emission of a 100 PgC pulse of CO_2 (Joos et al., 2013; Ricke and Caldeira, 2014), with larger emission pulses associated with longer timescales and smaller pulses with shorter ones (Joos et al., 2013; Matthews and Solomon, 2013; Zickfeld and Herrington, 2015). This behaviour is confirmed in other studies, including those that calculate the temperature response to an instantaneous doubling or quadrupling of atmospheric CO_2 (Matthews et al., 2009; Gillett et al., 2013; Herrington and Zickfeld, 2014; Leduc et al., 2015; Hajima et al., 2020b). These findings suggest that the TCRE is sensitive to the rate of emissions, but studies assessing this sensitivity have found diverging results. For example, an increase in TCRE and its surrounding uncertainty was reported for experiments that imply a gradual decline in annual CO_2 emissions (Tachiiri et al., 2019). These studies suggest that in most cases TCRE would be expected to increase in scenarios with decreasing annual emissions rates. This increase in TCRE for annual CO_2 emissions declining towards zero can be the result of the zero emissions commitment (ZEC) which is the amount of warming projected to occur following a complete cessation of emissions (see Chapter 4, Section 4.7.2 for its assessment), as well as Earth system processes that are unrepresented in current TCRE estimates (Section 5.5.2.2.4) and other factors. When using TCRE to estimate CO_2 emissions consistent with a specific maximum warming level these factors have to be taken into account (see Figure 5.31). Combined with recent literature on the ZEC (MacDougall et al., 2020) and emissions pathways (Huppmann et al., 2018) and noting the lack of literature that disentangles these various contributions, there is *medium evidence* and *high agreement* resulting in *medium confidence* that TCRE remains a good predictor of CO_2-induced warming when applied in the context of emission reduction pathways, provided that ZEC and long-term Earth system feedbacks are adequately accounted for when emissions decline towards zero (see also next section).

5.5.1.2.3 Reversibility and Earth System Feedbacks

There are relatively few studies that have assessed how the TCRE is expected to change in scenarios of declining emissions followed by net negative annual CO_2 emissions. Conceptually, the literature suggests that the small lag of about a decade between CO_2 emissions and temperature change (Ricke and Caldeira, 2014; Zickfeld and Herrington, 2015) would result in more warming at a given amount of cumulative emissions in a scenario where that emission level is first exceeded and then returned to by deploying negative emissions (referred to as an "overshoot", as is often the case in scenarios that aim to limit radiative forcing in 2100 to 2.6 or 1.9 W/m^2 (Riahi et al., 2017; Rogelj et al., 2018a). Zickfeld et al. (2016) showed this to hold across a range of scenarios with positive emissions followed by negative emissions, whereby the TCRE increased by about 10% across the transition from positive to negative emissions as a result of the thermal and carbon inertia of the deep ocean. However, CMIP6 results for the SSP5–3.4-overshoot scenario show diverging trends across various ESMs (see Section 5.4.10, Figure 5.30). In an idealised CO_2-concentration-driven setting Tachiiri et al. (2019) also reported an increase in TCRE. Exploring pathways with emissions rates and overshoots closer to mitigation pathways considered over the 21st century (in this case up to about 300 PgC), a recent emission-driven EMIC experiment showed pathway independence of TCRE (Tokarska et al., 2019b). Furthermore, also in absence of net negative emissions, warming would not necessarily remain perfectly constant on timescales of centuries and millennia, but could both decrease or increase (Frölicher and Paynter, 2015; Williams et al., 2017b; Hajima et al., 2020b). These additional changes in global mean temperature increase at various timescales are known as the ZEC (Jones et al., 2019; MacDougall et al., 2020), assessed in Section 4.7.2, and have to be integrated when using TCRE to estimate warming or remaining carbon budgets in overshoot scenarios.

The AR5-assessed (Collins et al., 2013b) TCRE range was based in part on the ESMs available at the time, which did not include some potentially important Earth system feedbacks. Since then, a number of studies

ACCEPTED VERSION SUBJECT TO FINAL EDITS

have assessed the importance of permafrost carbon feedbacks in particular on remaining carbon budgets (MacDougall et al., 2015; MacDougall and Friedlingstein, 2015; Burke et al., 2017; Gasser et al., 2018; Lowe and Bernie, 2018), a development highlighted and assessed in the IPCC Special Report on Global Warming of 1.5°C (Rogelj et al., 2018b). MacDougall and Friedlingstein (2015) reported a TCRE increase of about 15% when including permafrost carbon feedbacks. The overall linearity of the TCRE during the 21st century was not affected, but they also found that permafrost carbon feedbacks caused an increase in TCRE on multi-century timescales under declining CO_2 emission rates. In addition, other processes that are not or only partially considered in individual or all ESMs could cause a further increase or decrease of TCRE (Matthews et al., 2020). These are discussed in detail in Section 5.4, but their quantitative effects on TCRE have not yet been explored by the literature.

Whether TCRE remains an accurate predictor of CO_2-induced warming when annual CO_2 emissions reach zero and are followed by net carbon-dioxide removal (also referred to as TCRE reversibility) therefore hinges on contributions of slow components of the climate system that cause unrealised warming from past CO_2 emissions. Such slow components can arise from either physical climate (i.e., ocean heat uptake) or carbon cycle (i.e., ocean carbon uptake and permafrost carbon release) processes. The combined effect of these processes determines the magnitude and sign of the ZEC (MacDougall et al., 2020), which in turn impacts TCRE reversibility. As discussed in Section 4.7.2, recent model estimates of the ZEC suggest a range of ±0.19°C centred on zero (MacDougall et al., 2020). This suggests *limited agreement* among models as to the reversibility of the TCRE in response to net-negative CO_2 emissions. Furthermore, most models used for ZEC assessments to date do not represent permafrost carbon processes, although understanding their contribution is essential to isolate the TCRE contribution. There is therefore *limited evidence* that quantifies the impact of permafrost carbon feedbacks on the reversibility of TCRE, leading to *low confidence* that the TCRE remains an accurate predictor of temperature changes in scenarios of net-negative CO_2 emissions on timescales of more than a half a century.

5.5.1.3 Estimates of TCRE

IPCC AR5 (Collins et al., 2013a) assessed TCRE *likely* to fall in the range of 0.8–2.5°C per 1000 PgC (or per exagrams of carbon, EgC^{-1}) for cumulative emissions up to 2000 PgC, based on multiple lines of evidence. These include estimates based on Earth system models of varying complexity (Matthews et al., 2009; Gillett et al., 2013; Zickfeld et al., 2013), simple climate modelling approaches (Allen et al., 2009; Rogelj et al., 2012) or observational constraints and attributable warming (Gillett et al., 2013).

Since IPCC AR5, new studies have further expanded the evidence base for estimating the value of TCRE. These studies rely on ESMs or EMICs, observational constraints and concepts of attributable warming, or theoretically derived equations (see Table 5.7 for an overview). Several studies have endeavoured to partition the uncertainty in the value of TCRE into constituent sources. For example, TCRE can be decomposed into terms of TCR and the airborne fraction of anthropogenic CO_2 emissions over time (Allen et al., 2009; Matthews et al., 2009). These two terms are assessed individually (see Section 5.4 and Chapter 7, respectively) and allow the integration of evidence assessed elsewhere in the report into the assessment of TCRE (Section 5.5.1.4). Further studies use a variety of methods including analysing CMIP5 (Williams et al., 2017c) or CMIP6 (Arora et al., 2020; Jones and Friedlingstein, 2020) output, conducting perturbed parameter experiments with a single model (MacDougall et al., 2017), Monte-Carlo methods applied to a simple climate model (Spafford and Macdougall, 2020), or observations and estimates of the contribution of CO_2 and non-CO_2 forcers (Matthews et al., 2021). All of the studies agree that uncertainty in climate sensitivity (either Equilibrium Climate Sensitivity (ECS) or Transient Climate Response (TCR)) is amongst the most important contribution to uncertainty in TCRE, with uncertainty in the strength of the land carbon feedback and ocean heat uptake or ventilation having also been identified as crucial to uncertainty in TCRE (Matthews et al., 2009; Gillett et al., 2013; Ehlert et al., 2017; MacDougall et al., 2017; Williams et al., 2017b, 2020; Katavouta et al., 2019; Arora et al., 2020; Jones and Friedlingstein, 2020; Spafford and Macdougall, 2020). Finally, internal variability has been shown to affect the maximum accuracy of TCRE estimates by ±0.1°C per 1000 PgC (5–95% range) (Tokarska et al., 2020).

ACCEPTED VERSION SUBJECT TO FINAL EDITS

[START TABLE 5.7 HERE]

Table 5.7: Overview of estimates of studies estimating the transient response to cumulative emissions (TCRE) of CO_2. GSAT = Global mean surface air temperature increase, SAT = surface air temperature (e.g. over land only), SST = sea surface temperature, ECS = equilibrium climate sensitivity. Studies that do not isolate the CO_2-induced warming contribution in their TCRE estimates are not included.

Study	TCRE Range (°C per 1000 PgC)	Notes
Studies available at the time of IPCC AR5		
(Matthews et al., 2009)	1–2.1	5 to 95% range; GSAT; C^4MIP model range
(Allen et al., 2009)	1.4–2.5	5 to 95% range; blended global mean SAT and SSTs (no infilling of coverage gaps); simple model
(Zickfeld et al., 2009)	1.5	Best estimate; GSAT, EMIC
(Williams et al., 2012)	0.8–1.9	Range consistent with 2 to 4.5 °C ECS; GSAT
(Rogelj et al., 2012)	About 1–2	5 to 95% range; historical constraint on GMST increase, but other constraints on GSAT increase MAGICC model calibrated to C^4MIP model range and 2–4.5°C *likely* ECS
(Zickfeld et al., 2013)	1.4–2.5; mean: 1.9	Model range; GSAT, EMICs
(Eby et al., 2013)	1.1–2.1; mean: 1.6	Model range; GSAT, EMICs
(Gillett et al., 2013)	0.8–2.4	Model range; GSAT, CMIP5 ESMs
(Gillett et al., 2013)	0.7–2.0	5 to 95% range; blended global mean SAT and SSTs; observationally constrained estimates of historical warming and emissions
IPCC AR5 (Collins et al., 2013a)	0.8–2.5	Assessed *likely* range; multiple lines of evidence; mixed definition of global average temperature increase
Studies published since IPCC AR5		
(Tachiiri et al., 2015)	0.3–2.4	5 to 95% range; blended global mean SAT and SSTs; JUMP-LCM model perturbed physics ensemble (EMIC)
(Tachiiri et al., 2015)	1.1–1.7	5 to 95% range; blended global mean SAT and SSTs; observationally constrained JUMP-LCM perturbed physics ensemble
(Goodwin et al., 2015)	1.1 ± 0.5	5 to 95% range; theoretically derived TCRE equation constrained by surface warming, radiative forcing, and historic ocean and land carbon uptake from IPCC AR5
(Millar et al., 2017b)	1.0–2.5	5 to 95% range; blended global mean SAT and SSTs (HadCRUT4); observationally constrained probabilistic setup of simple climate model
(Steinacher and Joos, 2016)	1.0–2.7; median: 1.7	5 to 95% range; GSAT, observationally constrained BERN3D-LPJ EMIC
(MacDougall et al., 2017)	0.9–2.5; mean: 1.7	5 to 95% range; GSAT, emulation of 23 CMIP5 ESMs
(Ehlert et al., 2017)	1.2–2.1	Model range; GSAT, UVIC EMIC with varying ocean mixing parameters
(Williams et al., 2017c)	1.4–2.1; mean: 1.8	1-sigma range; GSAT, diagnosed from 10 CMIP5 ESMs
(Millar and Friedlingstein, 2018)	0.9–2.6; best estimate: 1.3	5 to 95% range; blended global mean SAT and SSTs (Cowtan and Way, 2014); detection attribution with observational constraints
(Millar and Friedlingstein, 2018)	best estimate: 1.5	Blended global mean SAT and SSTs (Berkeley Earth); detection attribution with observational constraints
(Millar and Friedlingstein, 2018)	best estimate: 1.2	Blended global mean SAT and SSTs (Cowtan and Way, 2014); detection attribution with observational constraints, with updated historical CO_2 emissions (Le Quéré et al., 2018b)
(Smith et al., 2018a)	1.0–2.2	5 to 95% range; blended global mean SAT and SSTs (Cowtan and Way, 2014); observationally constrained probabilistic setup of simple climate model
(Matthews et al., 2021)	1.0–2.2; median: 1.5	5 to 95% range; blended global mean SAT and SSTs; human-induced warming (Haustein et al., 2017) based on an average of three full coverage datasets; observationally constrained estimate using the current non-CO_2 fraction of total anthropogenic forcing
(Arora et al., 2020)	1.3–2.4; mean: 1.8; median: 1.65	Model range; GSAT, diagnosed CO_2 emissions in CMIP6 ESMs
(Williams et al., 2020)	1.2–2.1; mean: 1.6	1-sigma range; GSAT, diagnosed CO_2 emissions in 9 CMIP6 ESMs
(Jones and Friedlingstein, 2020)	1.2–2.7; median: 1.8	5 to 95% range; GSAT; Estimate based on decomposition presented in (Jones and Friedlingstein, 2020) with ranges of carbon cycle feedback parameters from CMIP6 (Arora et al., 2020), see Section 5.4.
(Spafford and Macdougall, 2020)	1.1–2.9; mean: 1.9; median: 1.8	5 to 95% range; ratio of land SAT and SST; probabilistic assessment of with a zero-dimensional ocean diffusive model
Cross-AR6 lines of evidence		
Transient Climate Response (TCR) and Airborne	1.0–2.3; median: 1.6	5 to 95% range; GSAT; TCR–AF decomposition-based estimate using the assessed range of TCR (Section 7.5, 1.8°C median with 0.4°C 1-sigma

ACCEPTED VERSION SUBJECT TO FINAL EDITS

Fraction (AF)		range) and an airborne fraction of 53 ± 6% (1-sigma range)
Overall assessment		
IPCC AR6	1.0–2.3; best estimate: 1.65	*Likely* range; GSAT; Based on combination of cross-AR6 lines of evidence (Section 5.5.1.4); normally distributed

[END TABLE 5.7 HERE]

5.5.1.4 Combined assessment of TCRE

Studies differ in how they define TCRE, in the methods they use, and their assumptions, such as the assumed climate sensitivity distribution or the choice of metrics of global temperature change (e.g. GMST or GSAT, see Table 5.7). This makes TCRE estimates from individual studies difficult to compare. The combined assessment of TCRE therefore takes advantage of the well-established decomposition of TCRE in two factors: the transient climate response (TCR) and the airborne fraction (Section 5.5.1.3). This provides a TCRE assessment range for CO_2-induced warming at the time of doubling CO_2 concentrations that builds on the broader Working Group 1 assessment. Expert judgment based on the airborne fraction range found in CMIP6 models (Arora et al., 2020; Jones and Friedlingstein, 2020) suggest a value of 53% with a 1-sigma range of ±6%, which is double the sigma range based on the spread of CMIP6 models only. Combining this range with the AR6 TCR assessment (Section 7.5, best estimate 1.8°C, 1.4–2.2°C *likely* and 1.2–2.4°C *very likely* range) results in a 5–95% range of 1.0–2.3°C per 1000 PgC. Based on expert judgment that accounts for the incomplete coverage of all Earth system components, this result in a consolidated assessment that TCRE would fall *likely* in the range of 1.0–2.3°C per 1000 PgC, with a best estimate of 1.65°C per 1000 PgC. Warming here reflects the human-induced GSAT increase and assumes a normal distribution. Some studies using observational constraints support a lognormal shape for the TCRE distribution (Spafford and Macdougall, 2020), but such a distribution is currently not supported by the combined assessment of TCR and airborne fraction. Finally, this assessed TCRE range needs to be considered in combination with the ZEC (Section 4.7.2) when estimating the CO_2-induced warming of low-emissions scenarios.

5.5.2 Remaining Carbon Budget Assessment

Estimates of remaining carbon budgets consistent with holding global warming below a specific temperature threshold depend on a range of factors which are increasingly being studied and quantified. These factors include (i) well-understood methodological and definitional choices (Friedlingstein et al., 2014a; Rogelj et al., 2016, 2018b) (see Sections 5.5.2.1 and Section 5.5.2.2), and (ii) a set of contributing factors such as historical warming, the TCRE and its limitations, the ZEC (the amount of warming projected to occur following a complete cessation of emissions, see Section 4.7.2), as well as contributions of non-CO_2 climate forcers (Section 5.5.2.2) (Rogelj et al., 2015a, 2015b; MacDougall and Friedlingstein, 2015; Simmons and Matthews, 2016; MacDougall, 2016; Ehlert et al., 2017; Matthews et al., 2017, 2021; Millar et al., 2017a; Tokarska et al., 2018; Goodwin et al., 2018; Mengis et al., 2018; Pfleiderer et al., 2018; Cain et al., 2019). These contributing factors are integrated in an overarching assessment of remaining carbon budgets for limiting global average warming to levels ranging from 1.5°C to 2.5°C relative to pre-industrial levels provided in Section 5.5.2.3. Box 5.2 provides an overview of the methodological advances since AR5 (Collins et al., 2013b).

5.5.2.1 Framework and Earlier Approaches

The IPCC AR6 Glossary (Annex VII) defines remaining carbon budgets as the maximum amount of cumulative net global anthropogenic CO_2 emissions expressed from a recent specified date that would result in limiting global warming to a given level with a given probability, taking into account the effect of other anthropogenic climate forcers, consistent with their assessment in the IPCC SR1.5 (Rogelj et al., 2018b). Studies, however, apply a variety of definitions that result in published remaining carbon budget estimates informing to cumulative emissions at the time when global-mean temperature increase would reach, exceed,

ACCEPTED VERSION SUBJECT TO FINAL EDITS

avoid, or peak at a given warming level with a given probability, for example (Collins et al., 2013a; Stocker et al., 2013c; Clarke et al., 2014; Friedlingstein et al., 2014a; IPCC, 2014; Rogelj et al., 2016; Millar et al., 2017a). This section provides an assessment of remaining carbon budgets consistent with the AR6 Glossary definition (Annex VII). Given that some feedbacks are time dependent, the values in this section apply to limiting warming over the 21st century, consistent with recent studies highlighting the usefulness of time-limited carbon budgets (Sanderson, 2020). Irrespective of the exact definition of the remaining carbon budget, the finding that higher cumulative CO_2 emissions lead to higher temperatures implies that annual net CO_2 emissions have to decline to close to zero in order to halt global warming, whether at 1.5°C, 2°C or another level (Allen et al., 2018).

Two approaches were used in AR5 to determine carbon budgets (Collins et al., 2013; Stocker et al., 2013; Clarke et al., 2014; IPCC, 2014; Rogelj et al., 2016). Working group I (WGI) reported threshold exceedance budgets (TEB) that correspond to the amount of cumulative CO_2 emissions at the time a specific temperature threshold is exceeded with a given probability in a particular greenhouse-gas and aerosol (pre-cursor) emission scenario (Collins et al., 2013a; IPCC, 2013b; Stocker et al., 2013c). WGI also reported TEBs for the hypothetical case that only CO_2 would be emitted by human activities (Collins et al., 2013a; IPCC, 2013b; Stocker et al., 2013c). AR5 Working group III used threshold avoidance budgets (TAB) that correspond to the cumulative CO_2 emissions over a given time period of a subset of greenhouse-gas and aerosol (precursor) emission scenarios in which global-mean temperature increase stays below a specific temperature threshold with at least a given probability (Clarke et al., 2014). The AR5 synthesis report used TABs defined until the time of peak warming over the 21st century (IPCC, 2014). Drawbacks have been identified for both TEBs and TABs (Rogelj et al., 2016). TABs provide an estimate of the cumulative CO_2 emissions under pathways that have as a common characteristic that they do not exceed a specific global warming threshold. The actual level of maximum warming can however vary between pathways, leading to an unnecessary and poorly constrained spread in TAB estimates (Rogelj et al., 2016). The TAB approach does therefore typically not result in accurate projections of the remaining carbon budget. On the other hand, a drawback of TEBs is that they provide an estimate of the cumulative CO_2 emissions at the time global warming crosses a given threshold of interest in a specific emissions scenario, for example, most of the standard scenarios used in climate change research such as the RCPs or SSP-based scenarios exceed global warming of 1.5°C or 2°C (see Cross-Chapter Box 1.5) (Collins et al., 2013a; Stocker et al., 2013c; Friedlingstein et al., 2014a; Millar et al., 2017a). Because of potential variations in non-CO_2 warming at that point in time or potential lags of about a decade in CO_2 warming (Joos et al., 2013; Ricke and Caldeira, 2014; Zickfeld and Herrington, 2015; Rogelj et al., 2015a, 2016, 2018) TEBs also do not provide a precise estimate of the remaining carbon budget for limiting warming to a specific level.

Since the publication of AR5 (Collins et al., 2013b), several new approaches have been proposed that provide a solution to the identified limitations of TABs and TEBs. Most of these approaches indirectly rely on the concept of TCRE (Section 5.5.1), for example, because they estimate modelled cumulative CO_2 emissions until a temperature threshold is crossed and use this budget to infer insights for pathways which attempt to limit warming to below this threshold and thus need to follow a different path (Friedlingstein et al., 2014; Matthews et al., 2017; Millar et al., 2017; Goodwin et al., 2018; Tokarska and Gillett, 2018). In this report, the assessment framework of the IPCC SR1.5 for remaining carbon budgets is applied (Rogelj et al., 2018b, 2019). This framework allows to integrate multiple lines of evidence to assess the contributions of five components that together result in a consolidated assessment of the remaining carbon budget (historical warming, TCRE, non-CO_2 warming, the ZEC, and adjustments due to additional Earth system feedbacks, see Section 5.5.2.2). It builds on the advances in estimating remaining carbon budgets or related quantities that have been published since AR5 (Rogelj et al., 2015a; Haustein et al., 2017; Matthews et al., 2017, 2021; Millar et al., 2017a; Gasser et al., 2018; Lowe and Bernie, 2018; Tokarska et al., 2018; Nicholls et al., 2020).

Recent studies suggest further changes to this framework by including non-linear adjustments to the TCRE contribution (Nicholls et al., 2020), or including non-CO_2 forcers in different ways by accounting for their different forcing effects (Matthews et al., 2021). Figure 5.31 provides a conceptual schematic of how the various individually assessed contributions are combined into a consolidated assessment of the remaining carbon budget. Together with estimates of historical CO_2 emissions to date (Section 5.2.1), these remaining carbon budgets provide the overall amount of cumulative CO_2 emissions consistent with limiting global

ACCEPTED VERSION SUBJECT TO FINAL EDITS

warming to specific levels. A comparison with the approach applied in AR5 (Collins et al., 2013; Clarke et al., 2014) is available in the IPCC SR1.5 Section 2.2.2 (Rogelj et al., 2018b) as well as Box 5.2.

[START FIGURE 5.31 HERE]

Figure 5.31: Illustration of relationship between cumulative emissions of carbon dioxide (CO_2) and global mean surface air temperature increase (left) and conceptual schematic of the assessment of the remaining carbon budget from its constituting components (right). Carbon budgets consistent with various levels of additional warming are provided in Table 5.8 and should not be read from the illustrations in either panel. Left-hand panel: Historical data (thin black line data) shows historical CO_2 emissions as reported in (Friedlingstein et al., 2020) together with the assessed global mean surface air temperature increase from 1850–1900 as assessed in Chapter 2 (Box 2.3, GSAT). The orange-brown range with its central line shows the estimated human-induced share of historical warming (Haustein et al., 2017). The vertical orange-brown line shows the assessed range of historical human-induced warming for the 2010–2019 period relative to 1850–1900 (Chapter 3). The grey cone shows the assessed range for the transient climate response to cumulative emissions of carbon dioxide (TCRE) assessed to fall *likely* in the 1.0–2.3 °C per 1000 PgC range (Section 5.5.1.4), starting from 2015. Thin coloured lines show CMIP6 simulations for the five scenarios of the AR6 core set (SSP1–1.9, green; SSP1–2.6, blue; SSP2–4.5, yellow; SSP3–7.0, red; SSP5–8.5, maroon), starting from 2015. Diagnosed carbon emissions (Arora et al., 2020) are complemented with estimated land-use change emissions for each respective scenario (Gidden et al., 2018). Coloured areas show the Chapter 4 assessed *very likely* range of GSAT projections and thick coloured central lines the median estimate, for each respective scenario, relative to the original scenario emissions (Riahi et al., 2017; Gidden et al., 2018; Rogelj et al., 2018a). Right-hand panel: schematic illustration of assessment of remaining carbon budget based on multiple lines of evidence. The remaining allowable warming is estimated by combining the global warming limit of interest with the assessed historical human induced warming (Section 5.5.2.2.2), the assessed future potential non-CO_2 warming contribution (Section 5.5.2.2.3) and the ZEC (Section 5.5.2.2.4). Note that contributions in the right-hand panel are illustrative and contributions are not to scale. For example, the central ZEC estimate was assessed to be zero. The remaining allowable warming (vertical blue bar) is subsequently combined with the assessed TCRE (Sections 5.5.1.4 and 5.5.2.2.1) and contribution of unrepresented Earth system feedbacks in models used to estimate ZEC and TCRE (Section 5.5.2.2.5) to provide an assessed estimate of the remaining carbon budget (horizontal blue bar, Table 5.8). Further details on data sources and processing are available in the chapter data table (Table 5.SM.6).

[END FIGURE 5.31 HERE]

5.5.2.2 Assessment of Individual Components

Remaining carbon budgets are assessed through the combination of five separate components (Forster et al., 2018; Rogelj et al., 2018b). Each component is discussed and assessed separately in the sections below, based on all available lines of evidence. Box 5.1 details the differences compared to AR5 and SR1.5 estimates (Collins et al., 2013b) (Rogelj et al., 2018b).

5.5.2.2.1 TCRE

The first and central component for estimating remaining carbon budgets is the TCRE. Based on the assessment in Section 5.5.1.4, an assessed *likely* range for TCRE of 1.0–2.3°C per 1000 PgC with a normal distribution is used.

5.5.2.2.2 Historical Warming

Advances in methods to estimate remaining carbon budgets have shown the importance of applying an as accurate as possible estimate of historical warming to date (Millar et al., 2017a; Tokarska and Gillett, 2018). This becomes particularly important when assessing remaining carbon budgets for global warming levels that are relatively close to present-day warming, such as a 1.5°C or 2°C levels (Rogelj et al., 2018b). Also

ACCEPTED VERSION SUBJECT TO FINAL EDITS

the definition of global average temperature by which historical warming is estimated is shown to be important (see Cross-Chapter Box 2.3) (Cowtan and Way, 2014; Allen et al., 2018; Pfleiderer et al., 2018; Richardson et al., 2018; Tokarska et al., 2019a), as is the correct isolation of human-induced global warming (Haustein et al., 2017; Allen et al., 2018) to remove the effect of internal variability. Based on the assessment in Section 3.3 (Table 3.1), we here apply an assessed best-estimate historical warming estimate expressed in global average surface air temperatures (GSAT) of 1.07°C (0.8–1.3°C, *likely* range) between 1850–1900 and 2010–2019. This choice implies global coverage and is consistent with AR5 where carbon budgets were reported in GSAT (Collins et al., 2013a; Stocker et al., 2013c), the SR1.5 where GSAT was the central metric for remaining carbon budgets (Rogelj et al., 2018b) and recent studies that highlight how GSAT enables an easy translation with AR5 (Tokarska et al., 2019a). The use of other historical reference periods (Cross-Chapter Box 1.2) or temperature metrics and updated data products (Cross-Chapter Box 2.3) can result in a different estimated historical warming and thus a changed remaining carbon budget.

5.5.2.2.3 Non-CO2 Warming Contribution

Non-CO_2 emissions contribute either cumulatively (N_2O, and other long-lived climate forcers) or in proportion to their annual emissions (CH_4 and other short-lived climate forcers) to global warming, and thus also affect estimates of remaining carbon budgets by reducing the amount of warming that could still result from CO_2 emissions (Meinshausen et al., 2009; Friedlingstein et al., 2014a; Knutti and Rogelj, 2015; Rogelj et al., 2015a, 2016, Williams et al., 2017c, 2016; Matthews et al., 2017; Collins et al., 2018; Mengis et al., 2018; Tokarska et al., 2018; Zickfeld et al., 2021). The size of this contribution has been estimated both implicitly (Meinshausen et al., 2009; Friedlingstein et al., 2014a; Rogelj et al., 2016; Matthews et al., 2017; Mengis et al., 2018; Tokarska et al., 2018) and explicitly (Rogelj et al., 2015a, 2018b; Collins et al., 2018; Matthews et al., 2021) by varying the assumptions of non-CO_2 emissions and associated warming. Internally consistent evolutions of future CO_2 and non-CO_2 emissions allow to derive non-CO_2 warming contributions consistent with global CO_2 emissions reaching net zero levels and therewith capping maximum future CO_2 emissions (Smith and Mizrahi, 2013; Clarke et al., 2014; Huppmann et al., 2018; Rogelj et al., 2018b; Matthews et al., 2021). Pathways that reflect such development typically show a stabilisation or decline in non-CO_2 radiative forcing and warming at and after the time of global CO_2 emissions reaching net zero levels, as illustrated in the scenario database underlying the IPCC SR1.5 (Huppmann et al., 2018; Rogelj et al., 2018b).

The impact of non-CO_2 emissions on remaining carbon budgets is assessed with emulators (Meinshausen et al., 2009; Millar et al., 2017a; Gasser et al., 2018; Goodwin et al., 2018; Rogelj et al., 2018b; Smith et al., 2018a; Matthews et al., 2021) that incorporate synthesised climate and carbon-cycle knowledge (Cross-Chapter Box 7.1). The estimated implied non-CO_2 warming can subsequently be applied to reduce the remaining allowable warming for estimating the remaining carbon budget (see Figure 5.31) (Rogelj et al., 2018b, 2019). Alternative methods estimate the non-CO_2 fraction of total anthropogenic forcing (Matthews et al., 2021), or do not correct for non-CO_2 warming directly. The latter methods instead consider CO_2 and non-CO_2 warming together to define a CO_2 forcing equivalent carbon budget from which eventual non-CO_2 contributions expressed in CO_2-forcing-equivalent emissions have to be subtracted to obtain a remaining carbon budget (Jenkins et al., 2018; Matthews et al., 2020). These studies also use emulators to invert a specified evolution of non-CO_2 forcing to a corresponding amount of equivalent CO_2 emissions (Matthews et al., 2020), or alternatively use empirical relationships linking changes in non-CO_2 greenhouse gas emissions to warming (Cain et al., 2019). Methods to express non-CO_2 emissions in CO_2 equivalence are assessed in Section 7.6, yet their applicability and related uncertainties for remaining carbon budgets have not yet been covered in-depth in the literature.

Application of the SR1.5 method (Forster et al., 2018; Rogelj et al., 2018b) with AR6-calibrated emulators (Box 7.1) suggests a median additional non-CO_2 warming contribution at the time global CO_2 emissions reach net zero levels of about 0.1–0.2°C relative to 2010–2019. Uncertainty surrounding this range due to geophysical uncertainties such as non-CO_2 forcing uncertainties and TCR is of the order of ±0.1°C. Differences in the choices of mitigation strategies considered in low-emission scenarios (Huppmann et al., 2018) result in a potential additional variation around the central range of at least ±0.1°C (spread across scenarios, referred to as non-CO_2 scenario uncertainty in Table 5.8).

ACCEPTED VERSION SUBJECT TO FINAL EDITS

5.5.2.2.4 Adjustments due to the Zero-Emission Commitment (ZEC)

Use of TCRE for estimating remaining carbon budgets needs to consider the ZEC, the potential additional warming after a complete cessation of net CO_2 emissions. Based on the ZEC assessment presented in Section 4.7.2, the ZEC's central value is taken to be zero with a *likely* range of ±0.19°C, noting that it might either increase or decrease after half a century. ZEC uncertainty is assessed for a time frame of half a century, as this most appropriately reflects the time between the time stringent mitigation pathways reach net zero CO_2 emissions and the end of the century. For shorter time horizons, a similar central zero value applies, but with a smaller range (MacDougall et al., 2020). Experiments that ramped up and down emissions following a bell-shaped trajectory (MacDougall and Knutti, 2016a) show that when annual CO_2 emissions decline to zero at a pace consistent with those currently assumed in mitigation scenarios (Huppmann et al., 2018; Rogelj et al., 2018b), the ZEC will already be realised to a large degree at the time of reaching net zero CO_2 emissions (MacDougall et al., 2020).

5.5.2.2.5 Adjustments for Other not Represented Feedbacks

Section 5.5.1.2 highlighted recent literature describing potential impacts of Earth system feedbacks that have typically not been included in standard ESMs (Schneider von Deimling et al., 2015; MacDougall and Friedlingstein, 2015; Schädel et al., 2016; Burke et al., 2017; Mahowald et al., 2017; Comyn-Platt et al., 2018; Gasser et al., 2018; Lowe and Bernie, 2018), the most important of which is carbon release from thawing permafrost. The IPCC SR1.5 estimated unrepresented Earth system processes to result in a reduction of remaining carbon budgets of up to 100 $GtCO_2$ over the course of this century, and more thereafter (Rogelj et al., 2018b). Here this assessment is updated based on the Earth system feedback assessment of Section 5.4.8 and synthesised in Figure 5.29 by applying the reverse method by (Gregory et al., 2009).

The assessment in Section 5.4 and Box 5.1 highlights the different nature, magnitude and uncertainties surrounding additional Earth system feedback. The remaining carbon budgets reported in Table 5.8 account for these feedbacks, including corrections due to permafrost CO_2 and CH_4 feedbacks as well as those due to aerosol and atmospheric chemistry (Section 5.4.8). Two of these additional feedbacks (tropospheric ozone and methane lifetime feedbacks) are included in the projections of non-CO_2 warming carried out with AR6-calibrated emulators (Box 7.1). The remainder of these independent Earth system feedbacks combine to a feedback of about 7 ± 27 PgC K^{-1} (1-sigma range, or 26 ± 97 $GtCO_2$ $°C^{-1}$). Overall, Section 5.4.8 assessed there to be *low confidence* in the exact magnitude of these feedbacks and they represent identified additional amplifying factors that scale with additional warming and mostly increase the challenge of limiting global warming to or below specific temperature levels.

5.5.2.3 Remaining Carbon Budget

The combination of the five components assessed in Sections 5.5.2.2.1–5.5.2.2.5 allows for an overall assessment of the remaining carbon budget in line with different levels of global average warming, as documented in the IPCC SR1.5 (Rogelj et al., 2018b). The overall assessment of remaining carbon budgets (Table 5.8) reflects the uncertainty in TCRE quantification and provides estimates of the uncertainties surrounding the contributions of each of the respective further components. A formal combination of all uncertainties is not possible because they are not all independent or because they represent choices rather than probabilistic uncertainties (Matthews et al., 2021). In light of all uncertainties related to TCRE, non-CO_2 forcing and response, the level of non-CO_2 mitigation, and historical warming, there is a small probability that the remaining carbon budget for limiting warming to 1.5°C since the 1850–1900 period is effectively zero. However, applying best estimate values for all but uncertainties in Earth system feedbacks and TCRE, the remaining carbon budgets in line with the Paris Agreement are generally small yet not zero (see Table 5.8).

There is *robust evidence* supporting the concept of TCRE as well as *high confidence* in the range of historical human-induced warming. Combined with the assessed uncertainties in the Earth system's response

ACCEPTED VERSION SUBJECT TO FINAL EDITS

to non-CO_2 emissions and less well-established quantification of some of the effect of non-linear Earth system feedbacks, this leads to *medium confidence* being assigned to the assessed remaining carbon budget estimates while noting the identified and assessed uncertainties and potential variations. The reported values are applicable to warming and cumulative emissions over the 21st century. For climate stabilisation beyond the 21st century this confidence would decline to *very low confidence* due to uncertainties in Earth system feedbacks and the ZEC.

For estimates of total carbon budgets in line with limiting global warming to a specific level, an estimate of historical CO_2 emissions should be added to the remaining carbon budget values reported in Table 5.8. Historical CO_2 emissions between 1850 and 2019 have been estimated at about 655 ± 65 PgC (1-sigma range, or 2390 ± 240 $GtCO_2$, see Table 5.1), while since 1 January 2015, an additional 57 PgC (210 $GtCO_2$) has been emitted until the end of 2019 (Friedlingstein et al., 2020).

[START TABLE 5.8 HERE]

Table 5.8: The assessed remaining carbon budget and corresponding uncertainties. Assessed estimates are provided for additional human-induced warming expressed as global average surface air temperature since the recent past (2010–2019), which *likely* amounted to 0.8 to 1.3 with a best estimate of 1.07°C relative to 1850–1900 (Table 3.1 in Chapter 3).

Additional warming since 2010–2019 *(1)	Warming since 1850–1900 *(1)	Remaining carbon budget*(2) starting from 1 January 2020 and subject to variations and uncertainties quantified in the columns on the right					Scenario variation	Geophysical uncertainties			
°C	°C	Percentiles of TCRE*(3)*(4) *PgC ($GtCO_2$)*					Non-CO_2 scenario variation *(5)	Non-CO_2 forcing and response uncertainty *(6)	Historical temperature uncertainty *(1)	ZEC uncertainty *(7)	Recent emissions uncertainty*(8)
		17th	*33rd*	*50th*	*67th*	*83rd*	*PgC ($GtCO_2$)*	*PgC ($GtCO_2$)*	*PgC ($GtCO_2$)*	*PgC ($GtCO_2$)*	*PgC ($GtCO_2$)*
0.23	1.3	*100 (400)*	*60 (250)*	*40 (150)*	*30 (100)*	*10 (50)*	Values can vary by at least ±60 PgC (±220 $GtCO_2$) due to choices related to non-CO_2 emissions mitigation	Values can vary by at least ±60 PgC (±220 $GtCO_2$) due to uncertainty in the warming reponse to future non-CO_2 emissions	±150 PgC (±550 $GtCO_2$)	±115 PgC (±420 $GtCO_2$)	±6 PgC (±20 $GtCO_2$)
0.33	1.4	*180 (650)*	*120 (450)*	*90 (350)*	*70 (250)*	*50 (200)*					
0.43	1.5	*250 (900)*	*180 (650)*	*140 (500)*	*110 (400)*	*80 (300)*					
0.53	1.6	*330 (1200)*	*230 (850)*	*180 (650)*	*150 (550)*	*110 (400)*					
0.63	1.7	*400 (1450)*	*290 (1050)*	*230 (850)*	*190 (700)*	*150 (550)*					
0.73	1.8	*470 (1750)*	*350 (1250)*	*280 (1000)*	*230 (850)*	*180 (650)*					
0.83	1.9	*550 (2000)*	*400 (1450)*	*320 (1200)*	*270 (1000)*	*120 (800)*					
0.93	2	*620 (2300)*	*460 (1700)*	*370 (1350)*	*310 (1150)*	*250 (900)*					
1.03	2.1	*700 (2550)*	*510 (1900)*	*420 (1500)*	*560 (1250)*	*280 (1050)*					
1.13	2.2	*770 (2850)*	*570 (2100)*	*460 (1700)*	*390 (1400)*	*310 (1150)*					
1.23	2.3	*850 (3100)*	*630 (2300)*	*510 (1850)*	*430 (1550)*	*350 (1250)*					
1.33	2.4	*920 (3350)*	*680 (2500)*	*550 (2050)*	*470 (1700)*	*380 (1400)*					

*(1) Human-induced global surface air temperature increase between 1850–1900 and 2010–2019 is assessed at 0.8–1.3°C (*likely* range; Chapter 3) with a best estimate of 1.07°C. Warming here reflects GSAT, as TCRE and other estimates are GSAT based. Combined with a central estimate of TCRE (1.65 °C EgC^{-1}) the uncertainty in historical human-induced GSAT warming results in a potential variation of remaining carbon budgets of ±150 PgC or ±550 $GtCO_2$.

*(2) Historical CO_2 emissions between 1850 and 2019 have been estimated at about 655 ± 65 PgC (1-sigma range, or 2390 ± 240 $GtCO_2$, see Table 5.1). Note that 57 PgC (210 $GtCO_2$) have been emitted from the middle of the 2010-2019 reference period (2015) until the end of 2019 (Friedlingstein et al., 2020).

*(3) TCRE: transient climate response to cumulative emissions of carbon, assessed to fall *likely* between 1.0–2.3 °C EgC^{-1} with a normal distribution. PgC values are rounded to the nearest 10; $GtCO_2$ values to the nearest 50. For comparison, assuming a lognormal distribution with a 1.0–2.3 °C EgC^{-1} central 66% range instead of a normal distribution would increase remaining carbon budgets at the 17th, 33rd, 50th, 67th, and 83rd percentile with 3%, 10%, 12%, 9%, 2%, respectively. Future non-CO_2 contributions in these remaining carbon budget estimates are based on the scenarios assessed in the IPCC SR1.5 report and estimated as the median quantile regression of non-CO_2 warming since 2010–2019 relative to total additional warming since 2010–2019 at the time scenarios reach net-zero CO_2 emissions (Forster et al., 2018; Huppmann et al., 2018; Rogelj et al., 2018b).

*(4) Additional Earth system feedbacks are included in the remaining carbon budget estimates as discussed in Section 5.5.2.2.5. The tropospheric ozone and methane lifetime contributions are included through the non-CO_2 warming projections by the AR6-calibrated MAGICC emulator, while the remaining feedbacks are assessed totalling a combined feedback of magnitude 7 ± 27 PgC K^{-1} (1-sigma range, or 26 ± 97 $GtCO_2$ $°C^{-1}$).

*(5) Variations due to different scenario assumptions related to the future evolution of non-CO_2 emissions in mitigation scenarios reaching net zero CO_2 emissions (Huppmann et al., 2018; Rogelj et al., 2018b) of at least ±0.1°C (spread across scenarios). Combined with a central estimate of TCRE (1.65 °C EgC^{-1}) this results in at least ±60 PgC or ±220 $GtCO_2$. This spread reflects the variation in the underlying scenario ensemble but is not a formal likelihood. WGIII will reassess the potential for non-CO_2 mitigation based on literature since the SR1.5.

*(6) Remaining carbon budget variation due to geophysical uncertainty in forcing and temperature response of non-CO_2 emissions of the order of ±0.1°C, very largely range (5–95%) of non-CO_2 response (Section 5.5.2.2.3). Combined with a central estimate of TCRE (1.65 °C EgC^{-1}) this results in at least ±60 PgC or ±220 $GtCO_2$.

*(7) The variation due to the ZEC is estimated for a central TCRE value of 1.65 °C EgC^{-1} and a 1-sigma ZEC range of 0.19°C. In real-world pathways, the magnitude of this effect will depend on the pace of CO_2 emissions reductions to net zero.

SUBJECT TO FINAL EDITS
ACCEPTED VERSION

*(8) Historical emissions uncertainty reflects the ±10% uncertainty in the historical emissions estimate since 1 January 2015.

[END TABLE 5.8 HERE]

[START BOX 5.2 HERE]

BOX 5.2: Implications of methodological advancements in estimating the remaining carbon budget since AR5

Methodological advancements since the IPCC AR5 (Collins et al., 2013; IPCC, 2013; Clarke et al., 2014; IPCC, 2014; Stocker et al., 2013) result in an updated and strengthened assessment of remaining carbon budgets. Methods and approaches at the time of AR5 are described in Section 5.5.2.1. Since AR5, strengths and weaknesses of various approaches have been more clearly articulated in the literature (e.g., in (Rogelj et al., 2016; Millar et al., 2017a; Tokarska and Gillett, 2018; Matthews et al., 2020)), resulting in a new consolidated framework applied in SR1.5 (Rogelj et al., 2018b, 2019) that is also used in AR6. This framework incorporates five methodological advancements compared to AR5, the implications of which are discussed in this box.

First, publications since AR5 applied methods that limit the effect of uncertainties in historical, diagnosed emissions in coupled Earth system models on estimates of the remaining carbon budget (Millar et al., 2017a; Tokarska and Gillett, 2018). These new methods express remaining carbon budget estimates relative to a recent reference period instead of relative to pre-industrial (Millar et al., 2017a; Tokarska et al., 2019a). Estimates of the full carbon budget since pre-industrial can still be obtained by adding estimates of historical CO_2 emissions (Table 5.1) to estimates in Table 5.8. This methodological update resulted, all other aspects being equal, in median estimates of remaining carbon budgets being about 350–450 $GtCO_2$ larger compared to AR5 (IPCC, 2014; Millar et al., 2017a).

At the time of the AR5, CMIP5 (Taylor et al., 2012) provided global mean surface air temperature (GSAT) projections for the representative concentration pathways (Meinshausen et al., 2011b), which were used to determine carbon budgets while taking into account the effects of non-CO_2 forcers (Stocker et al., 2013c). Their use came with two recognised limitations: first, the model spread of the CMIP5 ensemble represents an ensemble of opportunity with limited statistical value (Tebaldi and Knutti, 2007); and second, the evolution of non-CO_2 emissions as a function of cumulative CO_2 emissions can differ markedly between high and low emissions pathways (Meinshausen et al., 2011a; Rogelj et al., 2016; Friedlingstein et al., 2014; Matthews et al., 2017). Solutions to these two limitations have been published since AR5 and represent the second and third methodological improvement compared to AR5.

The reliance on an ensemble of opportunity (i.e. a serendipitous collection of scenario data from a variety of sources and studies) is avoided by methodologically separating the assessment of future warming contributions of non-CO_2 emissions from the spread in TCRE (Rogelj et al., 2018b, 2019) (see Section 5.5.2). This facilitates the explicit representation of TCRE uncertainty by a formal distribution, in this case a normal distribution with a 1.0–2.3°C PgC^{-1} 1–sigma range (Section 5.5.1.4). The effect of this methodological advance can be estimated from a direct comparison of the frequency distribution of TCRE in CMIP5 models that were used in AR5 and the formal TCRE distribution used in AR6, but is limited in precision. For estimates of the remaining carbon budget in line with limiting warming to 1.5°C or 2°C relative to pre-industrial levels, this improvement is estimated to lead to a reduction of budgets of the order of about 100 $GtCO_2$ between AR5 and AR6.

The third methodological improvement is a more direct estimation of the warming contribution of non-CO_2 emissions, consistent with pathways that bring global CO_2 emissions down to net zero. Instead of deriving this contribution implicitly from the CMIP5 ensemble, climate emulators (Meinshausen et al., 2011c; Schwarber et al., 2018; Smith et al., 2018b) that are calibrated to the combined AR6 assessment (Cross-Chapter Box 7.1) are used to estimate the non-CO_2 contribution across a wide variety of stringent mitigation

ACCEPTED VERSION SUBJECT TO FINAL EDITS

scenarios (Huppmann et al., 2018). The specific relative effect of this advance compared to AR5 is not calculable because CMIP5 data does not isolate non-CO_2 from CO_2-induced warming.

The fourth and fifth methodological advancements are to explicitly account for the zero-emission commitment (ZEC, Section 5.5.2.2.4) and adjust estimates for Earth system feedbacks that are typically not represented in Earth System models (Section 5.5.2.2.5). The central estimate of the assessed ZEC used in SR1.5 and AR6 is zero (Sections 4.7.2). ZEC uncertainties are reported separately (Table 5.8), and the additional consideration of ZEC therefore does result in a better understanding but not in a net shift of central estimates of the remaining carbon budget compared to AR5. Furthermore, AR5 did not explicitly account for Earth system feedbacks not represented in Earth system models. SR1.5 assessed that they could reduce the remaining carbon budgets by about 100 $GtCO_2$ over centennial timescales. This assessment has been updated in AR6, including a wider range of biogeochemical feedbacks and new evidence (Section 5.5.2.2.5). Some of these feedbacks are captured in the estimation of non-CO_2 warming (see below), while the combined effect of remaining positive and negative feedbacks is assessed to reduce the remaining carbon budget estimates by 7 ± 27 PgC K^{-1} (1-sigma range, or 26 ± 97 $GtCO_2$ $°C^{-1}$) compared to AR5.

Between SR1.5 and AR6, each of the five components described in Section 5.5.2.1 and Figure 5.32 have been re-assessed (see Sections 5.5.2.2.1 to 5.5.2.2.5). Their updated assessments in turn affect the assessment of the remaining carbon budget. The new and narrower assessment of TCRE in AR6 compared to SR1.5 (*likely* range of 1.0–2.3°C EgC^{-1} compared to 0.8–2.5°C EgC^{-1}, respectively, with the same central estimate) leads to no change in median estimates and about a 50 and 100 $GtCO_2$ increase in remaining carbon budgets estimates at the 67th percentile in AR6 compared to SR1.5 for 1.5°C and 2°C of global warming, respectively.

For historical warming, SR1.5 used GSAT increase between 1850–1900 and 2006–2015 of 0.97°C as its main starting point, while also providing values for other temperature metrics. Remaining carbon budgets were expressed starting from 1 January 2018 by accounting for historical emissions emitted from 1 January 2011 until the end of 2017. AR6 uses anthropogenic (human-induced) warming until the 2010–2019 period, which is assessed at the 0.8-1.3°C range, with a best estimate of 1.07°C (Table 3.1), and subsequently accounts for historical emissions from 1 January 2015 until the end of 2019 to express remaining carbon budget estimates from 1 January 2020 onwards. The human-induced warming between the 1850–1900 and 2006–2015 periods used in SR1.5 was assessed by AR6 at 0.97°C (Table 3.1). In a like-with-like comparison, the combined effect of data and methodological updates in historical warming estimates thus results in no shift in estimated remaining carbon budgets between SR1.5 and AR6. However, the emissions of the years passed since SR1.5 reduce the remaining carbon budget by about 85 $GtCO_2$. Note that AR6 also updated its GSAT assessment for total warming between the 1850–1900 and 2006–2015 periods, reporting 0.94°C of warming. On a like-with-like basis, this would have resulted in slightly larger remaining carbon budgets compared to SR1.5 (Cross-Chapter Box 2.3).

The non-CO_2 contribution to future warming in emissions scenarios (Huppmann et al., 2018) is re-assessed with AR6-calibrated emulators, in this case MAGICC7 (Meinshausen et al., 2009, 2011a, 2020) (Cross-Chapter Box 7.1). The re-assessment of non-CO_2 warming with MAGICC7 results in a relationship that closely matches the average relationship applied in SR1.5 (shown in Section 2.SM.1.1.2 in (Forster et al., 2018)), and does therefore not change estimates of the remaining carbon budget relative to SR1.5. The median ZEC assessment remained the same between SR1.5 and AR6, and therefore also does not change the median remaining carbon budget estimates. Finally, as indicated above, AR6 expanded the assessment of Earth system feedbacks compared to SR1.5 and included it in its central remaining carbon budget estimates. Some feedbacks are accounted for through the non-CO_2 warming estimate (Section 5.5.2.2.5), while the remainder combines to reduce the median remaining carbon budget estimates for 1.5°C and 2°C of warming by about 10 to 20 $GtCO_2$, respectively, compared to SR1.5.

All methodological improvements and new evidence combined result in median and 67th percentile remaining carbon budget estimates for limiting warming to 1.5°C being about 300–350 $GtCO_2$ larger compared to an assessment that would use the evidence and methods available at the time of the AR5. For limiting warming to 2°C, the difference is about 400–500 $GtCO_2$. Since SR1.5, fewer key advancements had

ACCEPTED VERSION SUBJECT TO FINAL EDITS

to be integrated. In a like-with-like comparison, the combined effects of all AR6 updates result in median remaining carbon budget estimates for limiting warming to 1.5°C and 2°C being the same and about 60 $GtCO_2$ smaller, respectively, in AR6 compared to SR1.5. At the 67th percentile, remaining carbon budget estimates for limiting warming to 1.5°C and 2°C are about 40 to 60 $GtCO_2$ larger, respectively, mainly as a result of a narrower assessed TCRE range.

[END BOX 5.2 HERE]

5.6 Biogeochemical Implications of Carbon Dioxide Removal and Solar Radiation Modification

5.6.1 Introduction

Carbon dioxide removal (CDR) refers to anthropogenic activities that seek to remove CO_2 from the atmosphere and durably store it in geological, terrestrial or ocean reservoirs, or in products (Glossary, Annex VII). CO_2 is removed from the atmosphere by enhancing biological or geochemical carbon sinks or by direct capture of CO_2 from air and storage. Solar radiation modification (SRM), on the other hand, refers to the intentional, planetary-scale modification of the Earth's radiative budget with the aim of limiting global warming. Most proposed SRM methods involve reducing the amount of incoming solar radiation reaching the surface, but others also act on the longwave radiation budget by reducing optical thickness and cloud lifetime (Glossary, Annex VII). SRM does not fall within the IPCC definitions of mitigation and adaptation (Glossary, Annex VII). CDR and SRM are referred to as 'geoengineering' in some of the literature and are considered separately in this report.

This section assesses the implications of CDR and SRM for biogeochemical cycles. CDR has received growing interest as an important mitigation option in emission scenarios consistent with meeting the Paris Agreement climate goals (SR1.5, SRCCL). The climate effects of CDR and SRM are assessed in Chapter 4, and a detailed assessment of the socio-economic dimensions of these options is presented in AR6 WGIII, Chapters 7 and 12.

5.6.2 Biogeochemical Responses to Carbon Dioxide Removal (CDR)

The scope of this section is to assess the general and methods-specific effects of CDR on the global carbon cycle and other biogeochemical cycles. The focus is on Earth system feedbacks that either amplify or reduce carbon sequestration potentials of specific CDR methods, and determine their effectiveness in reducing atmospheric CO_2 and mitigating climate change. Technical carbon sequestration potentials of CDR methods are assessed on a qualitative scale; a comprehensive quantitative assessment is left to the AR6 Working Group III report (Chapters 7 and 12). Biogeochemical and biophysical side effects of CDR methods are assessed here while the co-benefits and trade-offs for biodiversity, water and food production are briefly discussed for completeness, but a comprehensive assessment is left to WGII (Chapters 2 and 5) and WGIII (Chapters 7 and 12). The assessment in this chapter emphasises literature published since the AR5 WGI report (Chapter 6) for the assessment of the global carbon cycle response to CDR, and literature published since the IPCC SR1.5 (Chapter 4; IPCC, 2018), SRCCL (Chapter 6, IPCC, 2019) and SROCC (Bindoff et al., 2019) for the assessment of potentials and side effects of specific CDR methods. Emerging literature on deliberate methane removal is also briefly discussed.

In this chapter, CDR methods are categorised by the carbon cycle processes that result in CO_2 removal: (i) enhanced net biological production and storage by land ecosystems, (ii) enhanced net biological production and storage in the open and coastal ocean, (iii) enhanced geochemical processes on land and in the ocean, and (iv) direct air capture and storage by chemical processes. A subset of CDR methods that restore or sustainably manage natural or modified ecosystems while providing human well-being and biodiversity benefits are also referred to as natural or nature-based solutions (see Glossary, Annex VII) (Griscom et al., 2017, 2020; Fargione et al., 2018). CDR methods commonly discussed in the literature are summarised in Table 5.9. Other CDR options have been suggested, but there is insufficient literature for an assessment.

ACCEPTED VERSION SUBJECT TO FINAL EDITS

These include ocean biomass burial, ocean downwelling, removal of CO_2 from seawater with storage, and cloud alkalinisation (Keller et al., 2018a; GESAMP, 2019).

[START TABLE 5.9 HERE]

Table 5.9: Characteristics of carbon dioxide removal (CDR) methods. Termination effects refer to the possible effects of a hypothetical, sudden and sustained termination of the CDR method.

Category	Methods (subsection where the method is assessed)	Nature of CO_2 Removal Process / Storage Form	Description	Time scale of carbon storage	Factors that affect carbon storage time scale	Termination effects
Enhanced biological production and storage on land (in vegetation, soils or geologic formations)	Afforestation, reforestation and forest management (5.6.2.2.1)	Biological / Organic	Store carbon in trees and soils by planting, restoring or managing forests	Decades to centuries (Cooper, 1983)	Disturbances (e.g., fires, pests), extreme weather	None
	Soil carbon sequestration (5.6.2.2.1)	Biological / Organic	Use agricultural management practices to improve soil carbon storage	Decades to centuries (Dignac et al., 2017)	Soil and crop management.	None
	Biochar (5.6.2.2.1)	Biological / Organic	Burn biomass at high temperature under anoxic conditions to form biochar and add to soils	Decades to centuries (Campbell et al., 2018)	Fire	None
	Peatland restoration (5.6.2.2.1)	Biological / Organic	Store carbon in soil by creating or restoring peatlands	Decades to centuries (Harenda et al., 2018)	Peatland drainage, fire, drought, land use change	None
	Bioenergy with carbon capture and storage (BECCS) (5.6.2.2.1)	Biological / Inorganic	Production of energy from plant biomass combined with carbon capture and storage	Potentially permanent (analogous to DACCS) (Szulczewski et al., 2012)	Leakage	None
Enhanced biological production and storage in coastal and open ocean	Ocean fertilisation (5.6.2.2.2)	Biological / organic	Fertilise upper ocean with micro (Fe) and macronutrients (N, P) to increase phytoplankton photosynthesis and biomass and deep ocean carbon storage through the biological	Decades to millennia (Oschlies et al., 2010; Robinson et al., 2014)	Ocean stratification and circulation (Robinson et al., 2014); efficiency of carbon sequestration in deep ocean(Yoon et al., 2018)	Uncertain (Keller et al., 2014)

ACCEPTED VERSION SUBJECT TO FINAL EDITS

			pump			
	Artificial ocean upwelling (5.6.2.2.2)	Biological / organic	Pump nutrient-rich deep ocean water to the surface to increase carbon uptake and storage through the biological pump.	Centuries to millennia (Oschlies et al., 2010b)	Ocean circulation; DIC content of upwelled waters (Oschlies et al., 2010c)	Warming beyond temperatures experienced if artificial ocean upwelling had not been deployed (Keller et al., 2014)
	Restoration of vegetated coastal ecosystems ("blue carbon") (5.6.2.2.2)	Biological / organic	Manage coastal ecosystems to increase net primary production and store carbon in sediments	Decades to centuries if functional integrity of ecosystem maintained (Mcleod et al., 2011)	Land use change of coastal ecosystems; extreme weather (e.g., heatwaves); sea level change (NASEM, 2019)	None
Enhanced geochemical processes on land and in ocean	Enhanced weathering (5.6.2.2.3)	Geochemical / inorganic	Spread alkaline minerals on land to chemically remove atmospheric CO_2 in reactions that form solid minerals (carbonates and silicates) that are stored in soils or in the ocean	10,000 to 10^6 years (Fuss et al., 2018)	Storage in soils or ocean (Fuss et al., 2018)	None
	Ocean alkalinisation (5.6.2.2.3)	Geochemical / inorganic	Increased CO_2 uptake via increased alkalinity by deposition of alkaline minerals (e.g. olivine).	10,000 to 100,000 years (Keller, 2019)	Carbonate chemistry; ocean stratification and circulation (Keller, 2019)	Higher rates of warming and acidification than if alkalinisation not begun (under a high emissions scenario) (González et al., 2018)
Chemical	Direct air carbon capture with storage (DACCS) (5.6.2.2.4)	Chemical / inorganic	Direct removal of CO_2 from air through chemical adsorption, absorption or mineralisation, and storage underground,	Potentially permanent	Leakage	None

ACCEPTED VERSION SUBJECT TO FINAL EDITS

			in deep ocean or in long-lasting usable materials			

[END TABLE 5.9 HERE]

5.6.2.1 Global Carbon Cycle Responses to CDR

This subsection assesses evidence about the response of the global carbon cycle to CDR from idealised model simulations which assume that CO_2 is removed from the atmosphere directly and stored permanently in the geologic reservoir, which is analogous to direct air carbon capture with carbon storage (DACCS; Table 5.9). The carbon cycle response to specific land and ocean-based CDR methods is assessed in Section 5.6.2.2.2. At the time of AR5 there were very few studies about the global carbon cycle response to CDR. Based on these studies and general understanding of the carbon cycle, AR5 WGI Chapter 6 assessed that it is *virtually certain* that deliberate removal of CO_2 from the atmosphere will be partially offset by outgassing of CO_2 from the ocean and land carbon sinks. *Low confidence* was placed on any quantification of effects. Since the WGI AR5 (Chapter 6), several studies have investigated the carbon cycle response to CDR in idealised "pulse" removal simulations, whereby a specified amount of CO_2 is removed instantly from the atmosphere, and scenario simulations with CO_2 emissions and removals following a plausible trajectory. In addition, a dedicated carbon dioxide removal model intercomparison project (CDRMIP) (Keller et al., 2018b) was initiated, which includes a range of CDR experiments from idealised simulations to simulations of deployment of specific CDR methods (afforestation and ocean alkalinisation).

This subsection assesses three aspects of the climate-carbon cycle response to CDR: the time-dependent behaviour of CO_2 fluxes in scenarios with CDR, the effectiveness of CDR in drawing down atmospheric CO_2 and cooling global mean temperature, and the symmetry of the climate-carbon cycle response to positive and negative CO_2 emissions.

[START BOX 5.3 HERE]

BOX 5.3: Carbon cycle response to CO_2 removal from the atmosphere

During the industrial era, CO_2 emitted by the combustion of fossil fuels and land-use change has been redistributed between atmosphere, land, and ocean carbon reservoirs due to carbon cycle processes (Box 5.3 Figure 1b; Figure 5.13). Over the past decade (2010–2019), 46% of the emitted CO_2 remained in the atmosphere, 23% was taken up by the ocean and 31% by the terrestrial biosphere (Section 5.2.1.5). When carbon dioxide removal (CDR) is applied during periods in which human activities are net CO_2 sources to the atmosphere and the amount of emissions removed by CDR is smaller than the net source (net positive CO_2 emissions), CDR acts to reduce the net emissions (Box 5.3 Figure 1c). In this scenario part of the CO_2 emissions into the atmosphere is removed by the land and ocean sinks, as has been the case historically.

When CDR removes more CO_2 emissions than human activities emit (net negative CO_2 emissions), and atmospheric CO_2 declines, the land and ocean sinks initially continue to take up CO_2 from the atmosphere. This because carbon sinks, particularly the ocean, exhibit inertia and continue to respond to the prior trajectory of rising atmospheric CO_2 concentration. After some time, which is determined by the magnitude of the removal and the rate and amount of CO_2 emissions prior to the CDR application, land and ocean carbon reservoirs begin to release CO_2 to the atmosphere making CDR less effective (Box 5.3 Figure 1d).

[START BOX 5.3, FIGURE 1 HERE]

Box 5.3, Figure 1: Schematic representation of carbon fluxes between atmosphere, land, ocean and geological

ACCEPTED VERSION SUBJECT TO FINAL EDITS

reservoirs. Different system conditions are shown: (a) an unperturbed Earth system; and changes in carbon fluxes for (b) an Earth system perturbed by fossil-fuel CO_2 emissions, (c) an Earth system in which fossil-fuel CO_2 emissions are partially offset by CDR, (d) an Earth system in which CDR exceeds CO_2 emissions from fossil fuels ("net negative" CO_2 emissions). Carbon fluxes depicted in (a) (solid and dashed black lines) also occur in (b)-(d). The question mark in the land-to-ocean carbon flux perturbation in (c) and (d) indicates that the effect of CDR on this flux is unknown. Note that box sizes do not scale with the size of carbon reservoirs. Adapted from (Keller et al., 2018a). Further details on data sources and processing are available in the chapter data table (Table 5.SM.6).

[END BOX 5.3, FIGURE 1 HERE]

[END BOX 5.3 HERE]

5.6.2.1.1 Carbon Cycle Response to Instantaneous CDR

Idealised "pulse" removal Earth system model simulations are useful for understanding the carbon cycle response to CDR. Figure 5.32 illustrates the response of atmospheric CO_2, land and ocean carbon sinks to an instantaneous CO_2 removal applied from a pre-industrial equilibrium state. Following CO_2 removal from the atmosphere, the atmospheric CO_2 concentration declines rapidly at first and then rebounds (Figure 5.32 a). This rebound is due to CO_2 release by the terrestrial biosphere and the ocean in response to declining atmospheric CO_2 levels (Figure 5.32 b, c) (Collins et al., 2013a). For the model simulations shown in Figure 5.32, 23 ± 6% (mean ± 1 standard deviation) of the 100 PgC removed remains out of the atmosphere 80–100 years after the instantaneous removal. The remainder is offset by CO_2 outgassing from the land (49 ± 12%) and ocean (29 ± 7%). While the direction of the CO_2 flux is robust across models, the relative contribution of the outgassing from land and ocean reservoirs to the atmospheric CO_2 rebound after removal varies. These results corroborate the *high confidence* placed by WGI AR5 Chapter 6 on the partial compensation of CO_2 removal from the atmosphere by CO_2 outgassing from the land and ocean. Due to disagreement between models, the magnitude of this outgassing and in the relative contribution of land and ocean fluxes remains *low confidence*.

[START FIGURE 5.32 HERE]

Figure 5.32: Carbon cycle response to instantaneous carbon dioxide (CO_2) removal from the atmosphere. (a) Atmospheric CO_2 concentration, (b) change in land carbon reservoir, (c) change in ocean carbon reservoir. Results are shown for simulations with seven CMIP6 Earth system models and the UVic ESCM model of intermediate complexity forced with 100 PgC instantaneously removed from the atmosphere. The 'pulse' removal is applied from a model state in equilibrium with a pre-industrial atmospheric CO_2 concentration (CDRMIP experiment CDR-pi-pulse; Keller et al., 2018b). Changes in land and ocean carbon reservoirs are calculated relative to a pre-industrial control simulation. Data for the UVic ESCM is from Zickfeld et al. (2021). Further details on data sources and processing are available in the chapter data table (Table 5.SM.6).

[END FIGURE 5.32 HERE]

5.6.2.1.2 Carbon Cycle Response Over Time in Scenarios with CDR

Since WGI AR5 (Chapter 6), studies with ESMs have explored the land and ocean carbon sink response to scenarios with CO_2 emissions gradually declining during the 21st century. As CDR and other mitigation activities are ramped up, CO_2 emissions in these scenarios reach net zero and, as removals exceed emissions, become net negative. Studies exploring the carbon sink response to such scenarios (e.g. RCP2.6, SSP1–2.6) show that when net CO_2 emissions are positive, but start to decline, uptake of CO_2 by the land and ocean begins to weaken (compare land and ocean CO_2 fluxes in panels (a) and (b) of Figure 5.33) (Tokarska and Zickfeld, 2015; Jones et al., 2016b). During the first decades after CO_2 emissions become net negative, both the ocean and land carbon sinks continue to take up CO_2, albeit at a lower rate. For the land carbon sink, the sink-to-source transition occurs decades to a century after CO_2 emissions become net negative (Figure

ACCEPTED VERSION SUBJECT TO FINAL EDITS

5.33c). The ocean remains a sink of CO_2 for centuries after emissions become net negative (Figure 5.33c-e; Section 5.4.9; Figure 5.30). Whether the transition to source occurs at all, the timing of the transition and the magnitude of the CO_2 source are determined by the magnitude of the removal and the rate and amount of net CO_2 emissions prior to emissions becoming net negative (*medium confidence*) (Tokarska and Zickfeld, 2015; Jones et al., 2016b). For scenarios with large amounts of CO_2 removal such as SSP5–3.4–overshoot the land source is larger than for SSP1–2.6 and the ocean also turns into a source (Section 5.4.10, Figure 5.30). While the qualitative response to scenarios with net-negative emissions is largely robust across models, the timing of the sink-to-source transition and the magnitude of the CO_2 source vary between models, particularly for the land sink. Due to *limited agreement* between models there is *low confidence* in the timing of the sink-to-source transition and the magnitude of the CO_2 source in scenarios with net-negative CO_2 emissions.

[START FIGURE 5.33 HERE]

Figure 5.33: Carbon sink response in a scenario with net carbon dioxide (CO_2) removal from the atmosphere. Shown are CO_2 flux components from concentration-driven Earth system model simulations during different emission stages of SSP1–2.6 and its long-term extension. (a) Large net positive CO_2 emissions, (b) small net positive CO_2 emissions, (c) – (d) net negative CO_2 emissions, (e) net zero CO_2 emissions. Positive flux components act to raise the atmospheric CO_2 concentration, whereas negative components act to lower the CO_2 concentration. Net CO_2 emissions, land and ocean CO_2 fluxes represent the multi-model mean and standard deviation (error bar) of four ESMs (CanESM5, UKESM1, CESM2-WACCM, IPSL-CM6a-LR) and one EMIC (UVic ESCM; (Mengis et al., 2020)). Net CO_2 emissions are calculated from concentration-driven Earth system model simulations as the residual from the rate of increase in atmospheric CO_2 and land and ocean CO_2 fluxes. Fluxes are accumulated over each 50-year period and converted to concentration units (ppm). Further details on data sources and processing are available in the chapter data table (Table 5.SM.6).

[END FIGURE 5.33 HERE]

5.6.2.1.3 Removal Effectiveness of CDR

It is well understood that land and ocean carbon fluxes are sensitive to the level of atmospheric CO_2 and climate change and differ under different future scenarios (Section 5.4). It is therefore important to establish to what extent the removal effectiveness of CDR – here defined as the fraction of total CO_2 removed remaining out of the atmosphere – is dependent on the scenario from which CDR is applied. Different metrics have been proposed to quantify the removal effectiveness of CDR (Tokarska and Zickfeld, 2015; Jones et al., 2016b; Zickfeld et al., 2016). One is the airborne fraction of cumulative CO_2 emissions (AF), defined in the same way as for positive emissions (i.e. as the fraction of total CO_2 emissions remaining in the atmosphere), with its use extended to periods of declining and net negative CO_2 emissions. This metric, however, has not proven to be useful to quantify the removal effectiveness of CDR in simulations where CDR is applied from a trajectory of increasing atmospheric CO_2 concentration, as it measures the carbon cycle response to CDR as well as to the prior atmospheric CO_2 trajectory (Tokarska and Zickfeld, 2015; Jones et al., 2016b). A more useful metric is the perturbation airborne fraction (PAF) (Jones et al., 2016b), which measures the airborne fraction of the perturbation (in this case the CO_2 removal) relative to a reference scenario (Tokarska and Zickfeld, 2015; Jones et al., 2016b). The advantage of this metric is that it isolates the response to a CO_2 removal from the response to atmospheric CO_2 prior to the point in time the removal is applied. A disadvantage is that the PAF cannot be calculated from a single model simulation but requires a reference simulation relative to which the effect of the CO_2 removal can be evaluated. When CDR is applied from an equilibrium state, the PAF and AF are equivalent measures.

In scenario simulations and idealised simulations with instantaneous CO_2 removals applied from an equilibrium state, the removal effectiveness of CDR is found to be slightly dependent on the rate and amount of CDR (Tokarska and Zickfeld, 2015; Jones et al., 2016b; Zickfeld et al., 2021), and to be strongly dependent on the emission scenario from which CDR is applied (Jones et al., 2016b; Zickfeld et al., 2021). The fraction of CO_2 removed remaining out of the atmosphere decreases slightly for larger removals and decreases strongly when CDR is applied from a lower background atmospheric CO_2 concentration (Figure

ACCEPTED VERSION SUBJECT TO FINAL EDITS

5.34), due to state dependencies and climate-carbon cycle feedbacks that lead to a stronger overall response to CO_2 removal (Zickfeld et al., 2021). Based on the *high agreement* between studies we assess with *medium confidence* that the removal effectiveness of CDR is only slightly dependent on the rate and magnitude of removal and is smaller at lower background atmospheric CO_2 concentrations. Simulations with Earth system models of EMIC with instantaneous CO_2 removal from different equilibrium initial states suggest that the smaller removal effectiveness of CDR at lower background CO_2 levels results in greater cooling per unit CO_2 removed (Zickfeld et al., 2021). However, there is *low confidence* in the robustness of this result as climate sensitivity has been shown to exhibit opposite state dependence in EMICs and ESMs (Section 7.4.3.1).

[START FIGURE 5.34 HERE]

Figure 5.34: Removal effectiveness of carbon dioxide removal (CDR). (a) Fraction of CO_2 remaining out of the atmosphere for idealised model simulations with CDR applied instantly (pulse removals) from climate states in equilibrium with different atmospheric CO_2 concentration levels (1 to 4 times the pre-industrial atmospheric CO_2 concentration; shown on the horizontal axis). The fraction is calculated 100 years after pulse removal. The black triangle and error bar indicate the multi-model mean and standard deviation for the seven Earth system models shown in Figure 5.32 forced with a 100 PgC pulse removal. Other symbols illustrate results with the UVic ESCM model of intermediate complexity for different magnitudes of pulse removals (triangles: –100 PgC; circles: –500 PgC; squares: –1000 PgC). Data for the UVic ESCM is from (Zickfeld et al., 2021). (b) Perturbation airborne fraction (see text for definition) for model simulations where CDR is applied from four RCPs (shown on the horizontal axis in terms of their cumulative CO_2 emissions during 2020–2099). Symbols indicate results for four CDR scenarios, which differ in terms of the magnitude and rate of CDR (see Jones et al. (2016b) for details). Results are based on simulations with the Hadley Centre Simple Climate-Carbon Model and are shown for the year 2100. Data from Jones et al. (2016b). Further details on data sources and processing are available in the chapter data table (Table 5.SM.6).

[END FIGURE 5.34 HERE]

5.6.2.1.4 Symmetry of Carbon Cycle Response to Positive and Negative CO_2 Emissions

It is commonly assumed that the climate-carbon cycle response to a negative CO_2 emission (i.e. removal from the atmosphere) is equal in magnitude and opposite in sign to the response to a positive CO_2 emission of equal magnitude, that is, symmetric. If the response were symmetric, a positive CO_2 emission could be offset by a negative emission. This subsection assesses the symmetry in the coupled climate-carbon cycle response in model simulations with positive and negative CO_2 emission pulses applied from a pre-industrial climate state. Simulations with seven CMIP6 ESMs and the UVic ESCM model of intermediate complexity suggest that the carbon cycle response is asymmetric for pulse emissions/removals of ±100 PgC (Figure 5.35). For all models, the fraction of CO_2 remaining in the atmosphere after an emission is larger than the fraction of CO_2 remaining out of the atmosphere after a removal (by 4 ± 3%; mean ± standard deviation). In other words, an emission of CO_2 into the atmosphere is more effective at raising atmospheric CO_2 than an equivalent CO_2 removal is at lowering it. Sensitivity experiments with the UVic ESCM suggest that the asymmetry increases for larger amounts of emissions/removals and is insensitive to the background atmospheric CO_2 concentration from which the emissions/removals are applied (Figure 5.35). This asymmetry in the atmospheric CO_2 response originates from asymmetries in the land and ocean carbon fluxes due to nonlinearities in the carbon cycle response to CO_2 and temperature (Section 5.4) (Zickfeld et al., 2021). Given *medium evidence* and *high agreement*, there is *medium confidence* in the sign of the asymmetry of the carbon cycle response to positive and negative CO_2 emissions. The sign of the symmetry of the temperature response, on the other hand, differs between models, with three out of seven examined ESMs showing a smaller temperature response to a 100 PgC CO_2 emission than to an equivalent CO_2 removal. Therefore, there is *low confidence* in the sign of the asymmetry of the temperature response to positive and negative CO_2 emissions.

ACCEPTED VERSION SUBJECT TO FINAL EDITS

[START FIGURE 5.35 HERE]

Figure 5.35: Asymmetry in the atmospheric carbon dioxide (CO_2) response to CO_2 emissions and removals. Shown are the fractions of total CO_2 emissions remaining in the atmosphere (right-hand side) and CO_2 removals remaining out of the atmosphere (left-hand side) 80–100 after a pulse emission/removal. Triangles and green circles denote results for seven Earth system models (ESMs) and the UVic ESCM model of intermediate complexity forced with ±100 PgC pulses applied from a pre-industrial state ($1\times CO_2$) (CDRMIP experiment CDR-pi-pulse; Keller et al. (2018b)). Yellow circles and diamonds indicate UVic ESCM results for CO_2 emissions/removals applied at 1.5 times ($1.5\times CO_2$) and 2 times ($2\times CO_2$) the pre-industrial CO_2 concentration, respectively. Pulses applied from a $2\times CO_2$ state span the magnitude ±100 PgC to ±500 PgC. UVic ESCM data is from (Zickfeld et al., 2021). Further details on data sources and processing are available in the chapter data table (Table 5.SM.6).

[END FIGURE 5.35 HERE]

5.6.2.2 Effects of Specific CDR Methods on Biogeochemical Cycles and Climate

WGI AR5 Chapter 6 discussed the CDR methods, their implications and unintended side effects on carbon cycle and climate, including their time scales and potentials. Since then, three IPCC special reports (SR) have been published. First, SR15 Chapter 4 (IPCC, 2018a) assessed the potentials and current understanding, including the side effects, of BECCS, afforestation/reforestation, soil carbon sequestration, biochar, enhanced weathering, ocean alkalinisation, DACCS and ocean fertilisation. Second, SRCCL Chapter 6 (IPCC, 2019a) assessed the potentials, co-benefits and trade-offs of land-based mitigation options. It assessed with *high confidence* that land-based CDR options do not sequester carbon indefinitely, except for peatland restoration. Multiple co-benefits were identified in the deployment of CDR options, many of them with a potential to make positive contributions to sustainable development, enhancement of ecosystem functions and services and other societal goals. However, their potential was concluded to be context specific and limits to their contribution to global mitigation, such as competition for land, were identified. The third report, SROCC Chapter 5 (IPCC, 2019b), assessed the potential of marine options for climate change mitigation. It concluded that the feasibility of open ocean fertilisation and alkalinisation approaches were negligible, due to their inconclusive influence on ocean carbon storage on long timescales, due to the unintended side effects on marine ecosystems, and the associated governance challenges. The assessment of the benefits of blue carbon ecosystems concluded that they could contribute only minimally to atmospheric CO_2 reduction globally but emphasised that the benefits of protection and restoration of coastal blue carbon extend beyond climate mitigation (SROCC Section 5.5.12).

5.6.2.2.1 Land-based Biological CDR Methods

Biological CDR methods, introduced in Table 5.9, seek to increase carbon storage on land by enhancing net primary productivity and/or reducing CO_2 sources to the atmosphere.

Forest-based methods include afforestation, reforestation, and forest management (Table 5.9). Building on previous work that emphasized the global potentials of various options, more recent advances have focused on the limits of those global potentials in light of ecological and climate risks that can threaten the long-term permanence of carbon stocks (Boysen et al., 2017b; Anderegg et al., 2020). Some of those risks arise from droughts, fires, insect outbreaks, diseases, erosion, and other disturbances (Thompson et al., 2009).

Sustainable forest management can help to manage some of these vulnerabilities, while in some cases, it can increase and maintain forest sinks through harvest, transfer of carbon to wood products and their use to store carbon and substitute emissions-intensive construction materials (Churkina et al., 2020). Forest genomics techniques can increase the success of both reforestation and conservation initiatives, accelerating breeding for tree health and productivity (Isabel et al., 2020).

In response to increasing risks to permanence of carbon stocks of some types of afforestation practices and the competition for land, there has been an increasing recognition that secondary forest regrowth and

ACCEPTED VERSION SUBJECT TO FINAL EDITS

restoration of degraded forests and non-forest ecosystems can play a large role in carbon sequestration (*high confidence*). The rational for this focus builds on their high carbon stocks and rates of sequestration (Griscom et al., 2017; Lewis et al., 2019; Maxwell et al., 2019; Pugh et al., 2019b), high resilience to disturbances (Dymond et al., 2014; Messier et al., 2019), and more additional benefits such as enhanced biodiversity (Strassburg et al., 2020).

The global sequestration potential of forestation varies substantially depending on the scenario-assumptions of available land and of background climate (WGIII AR6 Section 7.5). Afforestation of native grasslands, savannas, and open-canopy woodlands leads to the undesirable loss of unique natural ecosystems with rich biodiversity, carbon storage and other ecosystem services (Veldman et al., 2015; IBPES, 2018). Comprehensive approaches to assess the effectiveness of land-based carbon removal options need to be based on the whole carbon cycle covering both carbon stocks and flows, and establishing the links between human activities and their impacts on the biosphere and atmosphere (Keith et al., 2021).

A range of mechanisms could enhance CO_2 sequestration of forest-based methods under future scenarios, including CO_2 fertilisation, soil carbon enrichment due to enhanced litter input, or the northward shift of the tree-line in future climate projection (Bathiany et al., 2010; Sonntag et al., 2015; Boysen et al., 2017; Harper et al., 2018). There is *low confidence* in the net direction of feedbacks of afforestation on global mean temperature. The feedbacks are highly region dependent. For instances, afforestation at high latitudes would decrease albedo and increase local warming, while at low latitudes, the cooling effect of enhanced evapotranspiration could exceed the warming effect due to albedo decrease (Pearson et al. 2013; Zhang et al. 2013; Jia et al. 2019, SRCCL Section 2.6.1). Both afforestation and reforestation affect the hydrological cycle through increased VOC emissions and cloud albedo (Teuling et al., 2017; Kalliokoski et al., 2020), enhanced precipitation (Ellison et al., 2017) and increased transpiration, with potential effects on runoff and, especially in dry areas, on water supply (Farley et al., 2005; Smith et al., 2016; Krause et al., 2017; Teuling et al., 2019) (Figure 5.36, Cross-Chapter Box 5.1). Forest-based methods can either raise or lower N_2O emissions, depending on tree species, previous land use, soil type and climatic factors (*low confidence)* (Benanti et al., 2014; Chen et al., 2019; McDaniel et al., 2019) (Figure 5.36, Supplementary Materials, Table 5.SM.4) . Afforestation will decrease biodiversity if native species are replaced by monocultures (*high confidence)*, while there is *medium confidence* that biodiversity is improved when forests are introduced into land areas with degraded soils or intensive monocultures, or where native species are re-introduced into managed land (Hua et al., 2016; Williamson, P., & Bodle, 2016; Smith et al., 2018c; Holl and Brancalion, 2020) (Figure 5.36, Supplementary Materials Table 5.SM.4).

Soil carbon losses from human agriculture accounted for about 116 PgC in the last 12,000 years (Sanderman et al., 2017), (Section 5.2.1.2). With best management practices, two-thirds of these losses may be recoverable, setting a theoretical maximum of 77 PgC that can be sequestered in soils. Methods to increase soil carbon content may be applied to the restoration of marginal or degraded land (Paustian et al., 2016; Smith, 2016), but may also be used in traditional agricultural lands. A simple practice is to increase the input of carbon to the soil by selecting appropriate varieties or species with greater root mass (Kell, 2011) or higher yields and NPP (Burney et al., 2010). In addition, improved agricultural practices also increase soil carbon content. These include the use of crop rotation cycles, increase the amount of crop residues, use of crop cover to prevent periods of bare soil (Poeplau and Don, 2015; Griscom et al., 2017), optimisation of grazing (Henderson et al., 2015) and residue management (Wilhelm et al., 2004), use of irrigation (Campos et al., 2020), employment of low-tillage or no-tillage (Sun et al., 2020b), agroforestry, and cropland nutrient recycling, and avoid grassland conversion management (Paustian et al., 2016; Fargione et al., 2018). With *medium confidence,* methods which seek soil carbon sequestration will diminish N_2O emissions and nutrient leaching, and improve soil fertility and biological activity (Tonitto et al., 2006; Fornara et al., 2011; Paustian et al., 2016a; Smith et al., 2016; SRCCL 2.6.1.3, IPCC, 2019a; Figure 5.36). However, if improved soil carbon sequestration practices involve higher fertilisation rates, N_2O emissions would increase (Gu et al., 2017). Some soil carbon sequestration methods, such as cover crops and crop diversity, can increase biodiversity (*medium confidence*) (Paustian et al., 2016; Smith et al., 2018).

Biochar is produced by burning biomass at high temperatures under anoxic conditions (pyrolysis) and can, when added to soils, increase soil carbon stocks and fertility for decades to centuries (Woolf et al., 2010;

ACCEPTED VERSION SUBJECT TO FINAL EDITS

Lehmann et al., 2015). Biochar application improves many soil qualities and increase crop yield (*medium confidence*) (Ye et al., 2020; SRCCL Chapter 4.9.5), particularly in already degraded or weathered soils (Woolf et al., 2010; Lorenz and Lal, 2014; Jeffery et al., 2016), increases soil water holding capacity (*medium confidence*) (Karhu et al., 2011; Liu et al., 2016; Fischer et al., 2019a; Verheijen et al., 2019) and evapotranspiration (*low confidence)* (Fischer et al., 2019). The use of biochar reduces nutrient losses (*low confidence*) (Woolf et al., 2010), enhances fertiliser nitrogen use efficiency and improves the bioavailability of phosphorus (Clough et al., 2013; Shen et al., 2016; Liu et al., 2017b; Figure 5.36). Biochar addition may decrease CH_4 emissions in inundated and acid soils such as rice fields (*low confidence*) (Jeffery et al., 2016; Huang et al., 2019; Wang et al., 2019a; Yang et al., 2019a). In non-inundated, neutral soils CH_4 uptake from the atmosphere is suppressed after biochar application (*low confidence*) (Jeffery et al., 2016), and soil N_2O emissions decline (*medium confidence*) (Cayuela et al., 2014; Kammann et al., 2017). Potential risks of introducing harmful contaminants into the soil environment are not well understood (Lorenz and Lal, 2014). With *low confidence*, application of biochar can have co-benefits for soil microbial biodiversity (Smith et al., 2018), while the potential trade-offs for biodiversity are due to land requirements (Tisserant and Cherubini, 2019).

Peatlands are less extensive than forests, croplands and grazing lands, yet per unit area, they hold high carbon stocks (Griscom et al., 2017). Peatland restoration relies on back-conversion or building of high-carbon-density soils through flooding, that is rewetting (Leifeld et al., 2019). High water level and anoxic conditions are prerequisites for restoring by returning drained and/or degraded peatlands back to their natural state as CO_2 sinks, but restoration also results in enhanced CH_4 emissions which are similar or higher than the pre-drainage fluxes (*high confidence)* (Koskinen et al., 2016; Wilson et al., 2016a; Hemes et al., 2019; Renou-Wilson et al., 2019; Holl et al., 2020). In a multi-decadal timeframe, the reduction in CO_2 emissions from rewetting more than compensates for the initial increase in radiative forcing due to enhanced CH_4 emissions (Günther et al., 2020). Rewetting drained peatlands will decrease N_2O emissions (*medium confidence*) (Wilson et al., 2016b; Liu et al., 2020a; Tiemeyer et al., 2020). Restored wetlands and peatlands act as buffer zones that provide infiltration and nutrient retention and offer protection to water quality (Daneshvar et al., 2017; Lundin et al., 2017), particularly in nutrient-loaded agricultural catchments. Peatland restoration can also recover much of the original biodiversity (*medium confidence*) (Meli et al., 2014; Smith et al. 2018).

The concept of bioenergy with carbon capture and storage (BECCS) rests on the premise that bioenergy production is carbon neutral, that is as much CO_2 is sequestered when growing biomass as feedstock as is released by its combustion. If these emissions are also captured and stored, the net effect is removal of CO_2 from the atmosphere (Fuss et al., 2018). Sequestration potentials from BECCS depend strongly on the feedstock, climate, and management practices (Beringer et al., 2011; Kato & Yamagata, 2014; Heck et al., 2016; Smith et al., 2016; Krause et al., 2017). If woody bioenergy plants replace marginal land, net carbon uptake increases, enriching soil carbon (Don et al., 2012; Heck et al., 2016; Boysen et al., 2017a,b). On the other hand, replacing carbon-rich ecosystems with herbaceous bioenergy plants could deplete soil-carbon stocks and reduce the additional sink capacity of standing forests (Don et al., 2012; Harper et al., 2018). Furthermore, wood-based BECCS may not be carbon negative in the first decades, initially emitting more CO_2 than sequestering (Sterman et al., 2018). BECCS has several trade-offs to deal with, including possible threats to water supply and soil nutrient deficiencies (*medium confidence*) (Smith et al., 2016; Krause et al., 2017; de Coninck et al., 2018; Heck et al., 2018; Roy et al., 2018) (SRCCL Chapters 2 and 6, Cross-Chapter Box 5.1). Deployment of BECCS at the scales envisioned by many 1.5–2.0°C mitigation scenarios could threaten biodiversity and require large land areas, competing with afforestation, reforestation and food security (Smith et al. 2018; Anderson and Peters 2016). Additional risks and side effects are related to geologic carbon storage (Fuss et al., 2018) (see also Section 5.6.2.2.4).

In conclusion, land-based CDR methods that rely on enhanced net biological uptake and storage of carbon, have a wide range of biogeochemical and biophysical side effects, which can directly or indirectly strengthen or weaken the climate mitigation effect of a given method, or affect water quality and quantity, food supply and biodiversity (Figure 5.36). With the exception of a weakening of ocean carbon sequestration, there is *low confidence* in the Earth system feedbacks of these methods. Most methods are associated with a range of biogeochemical and biophysical side effects and co-benefits and trade-offs, but these are often highly

ACCEPTED VERSION SUBJECT TO FINAL EDITS

dependent on local context, management regime, prior land use, and scale (*high confidence*). Highest co-benefits are obtained with methods that seek to restore natural ecosystems and improve soil carbon sequestration (Figure 5.36) while highest trade-off possibilities (symmetry with the highest cobenefits) offs occurs for re/afforestation with monocultures and BECCS, again with strong dependence on scale and context (*medium confidence*).

5.6.2.2.2 Ocean-based Biological CDR Methods

Both ocean biological and physical processes drive the CO_2 exchange between the ocean and atmosphere. However, the ocean physical processes that remove CO_2 from the atmosphere, such as large-scale circulation, cannot be feasibly altered, so ocean CDR methods focus on increasing the productivity of ocean ecosystems, and subsequent sequestration of carbon (GESAMP, 2019). There has been no change to the assessment of SROCC (Section 5.5.1): there is *low confidence* that nutrient addition to the open ocean, either through artificial ocean upwelling or iron fertilisation, could contribute to climate mitigation, due to its inconclusive effect on carbon sequestration and risks of adverse side effects on marine ecosystems (Figure 5.36; Table 5.9; Supplementary Materials Text 5.SM.3; Supplementary Materials Table 5.SM.4; WGIII, Section 12.3; Gattuso et al., 2018; Boyd and Vivian, 2019; Feng et al., 2020). In addition, ocean fertilisation is currently prohibited by the London Protocol (Dixon et al., 2014; GESAMP, 2019).

Restoration of vegetated coastal ecosystems (sometimes referred to as 'blue carbon' – see Glossary, Annex VII) refers to the potential for increasing carbon sequestration by plant growth and burial of organic carbon in the soil of coastal wetlands (including salt marshes and mangroves) and seagrass ecosystems. Wider usage of the term blue carbon occurs in the literature, for example including seaweeds (macroalgae), shelf sea sediments and open ocean carbon exchanges. However, such systems are less amenable to management, with many uncertainties relating to the permanence of their carbon stores (Windham-Myers et al., 2018; Lovelock and Duarte, 2019; SROCC Section 5.5.1.1).

Coastal wetlands and seagrass meadows store significant amounts of carbon and are among the most productive ecosystems per unit area (Griscom et al., 2017, 2020; Ortega et al., 2019; Serrano et al., 2019). These rates could be reduced in the future, since these habitats are vulnerable to changing conditions, such as temperature, salinity, sediment supply, storm severity and continued coastal development (National Academies of Sciences and Medicine, 2019; Bindoff et al., 2019). These ecosystems are under threat from anthropogenic conversion and degradation and are being lost at rates between 0.7% and 7% per annum with consequent CO_2 emissions (e.g. Atwood et al., 2017; Howard et al., 2017; Hamilton and Friess, 2018; Sasmito et al., 2019). Although sea level rise might lead to greater carbon sequestration in coastal wetlands (Rogers et al., 2019), there is *high confidence* that the frequency and intensity of marine heatwaves will increase (Cross-Chapter Box 9.1; Frölicher and Laufkötter, 2018; Laufkötter et al., 2020),which poses a more immediate threat to the integrity of coastal carbon stocks (Smale et al., 2019). Blue carbon restoration seeks to increase the rate of carbon sequestration, although restoration may be challenging, because of on-going use of coastal land for human settlement, conversion to agriculture and aquaculture, shoreline hardening and port development.

Biogeochemical factors affecting reliable quantification of the climatic benefits of coastal vegetation include the variable production of CH_4 and N_2O by such ecosystems (Adams et al., 2012; Rosentreter et al., 2018; Keller, 2019), uncertainties regarding the provenance of the carbon that they accumulate (Macreadie et al., 2019), and the release of CO_2 by biogenic carbonate formation in seagrass ecosystems (Kennedy et al., 2018). Whilst coastal habitat restoration potentially provides significant mitigation of national emissions for some countries (Taillardat et al., 2018; Serrano et al., 2019), the global sequestration potential of blue carbon approaches is <0.02 PgC yr^{-1} (*medium confidence*) (Figure 5.36; SROCC Section 5.5.1.2; Griscom et al., 2017; Gattuso et al., 2018; National Academies of Sciences and Medicine, 2019).

5.6.2.2.3 Geochemical CDR Methods

Enhanced weathering (EW) is based on naturally occurring weathering processes of silicate and carbonate rocks, removing CO_2 from the atmosphere. Weathering is accelerated by spreading ground rocks on soils,

ACCEPTED VERSION SUBJECT TO FINAL EDITS

coasts or oceans. EW increases the alkalinity and pH of natural waters, helps dampen ocean acidification and increases ocean carbon uptake (Beerling et al., 2018). The dissolution of minerals stimulates biological productivity of croplands (Hartmann et al., 2013; Beerling et al., 2018), but can also liberate toxic trace metals (such as Ni, Cr, Cu) into soil or water bodies (Keller et al. 2018; Strefler et al. 2018). EW can also contribute to freshwater salinisation as a result of increased salt inputs and cation exchange in watersheds, and so adversely affecting drinking water quality (*low confidence*) (Kaushal et al., 2018). With a *medium confidence*, amendment of soils with minerals will have lower N_2O emissions (Blanc-Betes et al.; Kantola et al., 2017) but will not have a marked effect on evapotranspiration or albedo (Fuss et al., 2018; de Oliveira Garcia et al., 2020). The mining of minerals can cause adverse impacts on biodiversity, however the use of waste materials such as concrete demolition or steel slags for EW can reduce the need for mining (Renforth, 2019). The spreading of minerals on land has a neutral impact on biodiversity (Smith et al. 2018)

Ocean alkalinisation, via the deposition of alkaline minerals (e.g. olivine) or their dissociation products (e.g. quicklime) at the ocean surface, can increase surface total alkalinity and thus increase CO_2 uptake and storage (see Glossary, Annex VII; Supplementary Material Text 5.SM.3; WGIII Section 12.3; GESAMP 2019; Keller 2019). Ocean alkalinisation ameliorates somewhat surface ocean acidification (*high confidence*; Hauck et al., 2016; Tran et al., 2020), there are also negative side effects on the marine ecosystem, most of which are poorly understood or quantified (Bach et al., 2019; Figure 5.36; Supplementary Materials Table 5.SM.4). Although ocean alkalinisation could potentially sequester large amounts of carbon ($\geq$1 PgC yr^{-1}; Figure 5.36; Supplementary Materials Table 5.SM.5) there is no new evidence to revisit the SROCC (Section 5.5.1.2.4) conclusion that there is *low confidence* that ocean alkalinisation is a viable climate mitigation approach.

5.6.2.2.4 Chemical CDR methods

Direct air carbon capture with carbon storage (DACCS) is a combination of two techniques, direct capture of CO_2 from ambient air (DAC) and carbon storage. DAC entails contacting the air, capturing the CO_2 on a liquid solvent or solid sorbent, and regenerating the solvent or sorbent. Different DAC methods have been proposed, which differ by the chemical process used to capture the CO_2 and to recover it from the sorbent or solvent (NASEM, 2019). The captured CO_2 may be either stored geologically as a high-pressure gas or sequestered by a mineral carbonation process. Storage is potentially permanent in both pressurised gas and mineral form (Fuss et al., 2018). DACCS has significant requirements of energy and, depending on the type of technology, water and materials (Smith et al., 2016; NASEM, 2019). Compared to other CDR methods it has a small land footprint (Smith et al., 2016; NASEM, 2019). Side effects of DACCS include CO_2-depleted air leaving the air contactor, which could have adverse effects on crop and ecosystem productivity, and VOC emissions (NASEM, 2019). Additional risks and side effects are related to the high pressure at which CO_2 is stored in geologic formations (Fuss et al., 2018). DACCS is assessed in detail in WGIII Section 12.3.

5.6.2.2.5 Methane removal

Proposals to remove CH_4 from the atmosphere are emerging (de Richter et al., 2017; Jackson et al., 2019). CH_4 removal methods seek to capture CH_4 directly from ambient air similarly to DACCS for CO_2 using for example zeolite trapping, but instead of storing it CH_4 would be chemically oxidized to CO_2 (Jackson et al., 2019). Methane can be also removed microbially by supporting naturally occurring processes, for example by enhancing the soil microbial uptake through afforestation (Wu et al., 2018b) or by directing the venting air from a cow barn into the soil bed of a nearby greenhouse, utilising microbial CH_4 oxidation (Nisbet et al., 2020). Microbial CH_4 oxidation could also be utilized for removal of CH_4 leaked from point sources by building biocatalytic polymers which include methane-oxidizing enzymes (Blanchette et al., 2016). Methane removal is, however, still in its infancy and the available literature is insufficient for an assessment.

[START FIGURE 5.36 HERE]

Figure 5.36: Characteristics of carbon dioxide removal (CDR) methods, ordered according to the time scale of carbon storage. The first column shows biogeophysical (for open-ocean methods) or technical (for all

ACCEPTED VERSION SUBJECT TO FINAL EDITS

other methods) sequestration potentials (i.e. the sequestration potentials constrained by biological, geophysical, geochemical limits and thermodynamics and, for technical potentials, availability of technologies and practices; technical potentials for some methods also consider social or environmental factors if these represent strong barriers for deployment; see Glossary, Annex VII), classified into low (< 0.3 $GtCO_2$ yr^{-1}), moderate (0.3−3 $GtCO_2$ yr^{-1}) and large (>3 $GtCO_2$ yr^{-1}) (details underlying this classification are provided in Supplementary Materials Table 5.SM.5). The other columns show Earth system feedbacks that deployment of a given CDR method would have on carbon sequestration and climate, along with biogeochemical, biophysical, and other side effects of a given method. Earth system feedbacks do not include the direct effect of CO_2 sequestration on atmospheric CO_2, only secondary effects. For Earth system feedbacks, the colours indicate whether the feedbacks strengthen or weaken carbon sequestration and the climate cooling effect of a given CDR method. For biogeochemical and biophysical side effects the colours indicate whether the deployment of a CDR method increases or decreases the magnitude of the effect, whereas for co-benefits and trade-offs the colour indicates whether deployment of a CDR method results in beneficial (co-benefits) or adverse side-effects (trade-offs) for water quality and quantity, food production and biodiversity. The details and references underlying the Earth system feedback and side-effect assessment are provided in Supplementary Materials Table 5.SM.4. Further details on data sources and processing are available in the chapter data table (Table 5.SM.6).

[END FIGURE 5.36 HERE]

5.6.3 Biogeochemical responses to Solar Radiation Modification (SRM)

This section assesses the possible consequences of solar radiation modification (SRM) on the biosphere and global biogeochemical cycles. The SRM options (Table 4.6) and the physical climate response to SRM is assessed in detail in Chapter 4 (Section 4.6.3). Chapter 6 (Section 6.3.6) assesses the potential effective radiative forcing of aerosol-based SRM options and Chapter 8 (Section 8.6.3) assesses the abrupt water cycle changes in response to initiation or termination of SRM. Most literature on the biogeochemical responses to SRM focuses on stratospheric aerosol injection (SAI), and only a few studies have investigated the biogeochemical responses to marine cloud brightening (MCB) and cirrus cloud thinning (CCT). At the time of AR5, there were only a few studies on the biogeochemical responses to SRM. The main assessment of AR5 (Ciais et al., 2013) was that SRM will not interfere with the direct biogeochemical effects of increased CO_2 such as ocean acidification and CO_2 fertilisation effect but could affect the carbon cycle through climate-carbon feedbacks. Overall, AR5 concluded that the level of confidence on the effects of SRM on carbon and other biogeochemical cycles is *very low* (Ciais et al., 2013). Since AR5, more modelling work has been conducted to examine various aspects of the global biogeochemical cycle responses to SRM.

5.6.3.1 Effects of SRM on the Carbon Cycle

Relative to a high-GHG world without SRM, SRM would affect the carbon cycles through changes in sunlight, climate (e.g. temperature, precipitation, soil moisture, ocean circulation), and atmospheric chemistry (e.g. ozone) (Cao, 2018) (Section 4.6.3.3). Net SRM effects on the carbon cycle, relative to a world without SRM, depend on the change of individual factors, and interactions among them.

SRM-mediated sunlight changes directly affect the carbon cycle. In particular, SAI would reduce the sunlight reaching the Earth's surface, but also increase the fraction of sunlight that is diffuse. These changes in the quantity and quality of the sunlight have opposing effects on the photosynthesis of land plants. On their own, reductions in photosynthetically active radiation (PAR) will reduce photosynthesis. However, diffuse light is more effective than direct light in accessing the light-limited leaves within plant canopies, leading to the so-called 'diffuse-radiation' fertilisation effect (Mercado et al., 2009). The estimated balance between the negative impacts of reducing PAR and the positive impacts of increasing diffuse fraction differ between models (Kalidindi et al., 2015; Xia et al., 2016; Yang et al., 2020a) and across different ecosystems. The change in the absolute amount of direct and diffuse radiation could also depend on the height of the additional sulphate aerosol layer in the stratosphere and the hygroscopic growth of aerosols (Krishnamohan et al., 2019, 2020) .

ACCEPTED VERSION SUBJECT TO FINAL EDITS

SRM-mediated cooling also affects the terrestrial carbon cycle. Relative to a high-GHG world without SRM, the simulated responses of net primary production (NPP) to SRM differ widely between models, such that even the sign of global mean change is uncertain (Glienke et al., 2015). SRM-induced cooling would decrease NPP at high latitudes by reducing the length of the growing season (Glienke et al., 2015). At low latitudes, the NPP response to SRM-induced cooling is sensitive to the effect of nitrogen limitation (Duan et al., 2020; Glienke et al., 2015;). SRM-induced cooling tends to increase NPP in models without the nitrogen cycle because of reduced heat stress. However, in models including the nitrogen cycle, this is counteracted by reductions in NPP because of reductions in nitrogen mineralisation and nitrogen availability (Glienke et al., 2015). SRM-induced changes in the hydrological cycle (Section 8.6.3), including changes in evapotranspiration, precipitation, and soil moisture, also pose strong constraints on the vegetation response (Dagon and Schrag, 2019). For the same amount of global mean cooling, different SRM options, such as SAI, MCB, and CCT, would have different effects on GPP and NPP because of different spatial patterns of temperature available sunlight, and hydrological cycle changes (Section 4.6.3.3) (Duan et al., 2020). Modelling studies show that SRM-induced cooling would reduce plant and soil respiration (Tjiputra et al., 2016; Cao and Jiang, 2017; Muri et al., 2018; Yang et al., 2020b). Thus, despite the large uncertainty in modelled NPP response, existing modelling studies consistently show that relative to a high-CO_2 world without SRM, SRM would increase the global land carbon sink (*high confidence*).

Based on available evidence, SRM with elevated CO_2 would increase global mean NPP and carbon storage on land, relative to an unperturbed climate mainly because of CO_2 fertilisation of photosynthesis (Glienke et al., 2015; Tjiputra et al., 2016; Dagon and Schrag, 2019; Duan et al., 2020; Yang et al., 2020b) (*high confidence*). However, the amount of increase is uncertain as it depends on the extent to which CO_2 fertilisation of land plants is limited by nutrient availability.

[START FIGURE 5.37 HERE]

Figure 5.37: Cumulative carbon dioxide (CO_2) uptake by land and ocean carbon sinks in response to stratospheric sulfur dioxide (SO_2) injection. Results are shown for a scenario with 50-year (2020−2069) continuous stratospheric SO_2 injection at a rate of 5 Tg per year appplied to a RCP4.5 baseline scenario (GeoMIP experiment G4; Kravitz et al., (2011)), followed by termination in year 2070. Anomalies are shown relative to RCP4.5 for the multimodel ensemble mean and for each of six ESMs over the 50-year period of stratospheric SO_2 injection (left), and over 20 years after termination of SO_2 injection (right). Adapted from Plazzotta et al. (2019). Further details on data sources and processing are available in the chapter data table (Table 5.SM.6).

[END FIGURE 5.37 HERE]

Relative to a high-CO_2 world without SRM, SRM would also have compensating effects on crop yields. SRM is expected to have a positive impact on crop yields by diminishing heat stress (Pongratz et al., 2012). However, reductions in light availability will produce a counteracting reduction in crop yields, especially if the crop type does not benefit appreciably from diffuse-light fertilisation (Proctor et al., 2018). The balance between these effects varies markedly across crop types and regions, from projected increases in maize production in China (Xia et al., 2014) to reductions in groundnut yields in parts of India (Yang et al., 2016). Because of these diverging results from a limited set of studies, there is overall *low confidence* in the effect of SRM on crop yields.

Consistent with the AR5 assessment, there is *high confidence* that SRM would not mitigate CO_2-induced ocean acidification (Ciais et al., 2013). Some studies even suggest an acceleration of deep-ocean acidification as a result of ocean circulation change (Tjiputra et al., 2016; Lauvset et al., 2017). There are large differences in the simulated spatial pattern of ocean NPP change in response to SRM, which depends strongly on the SRM method that is considered (Partanen et al., 2016; Lauvset et al., 2017).

ACCEPTED VERSION SUBJECT TO FINAL EDITS

5.6.3.2 Consequences of SRM and its termination on atmospheric CO2 burden

Modelling studies consistently show that relative to a high-CO_2 world without SRM, SRM-induced cooling (Section 4.6.3.3) would reduce plant and soil respiration, and also reduce the negative effects of warming on ocean carbon uptake (Tjiputra et al., 2016; Xia et al., 2016; Cao and Jiang, 2017; Jiang et al., 2018; Muri et al., 2018; Sonntag et al., 2018; Plazzotta et al., 2019; Yang et al., 2020b). A multi-model study (Plazzotta et al., 2019) indicates that relative to a high-CO_2 concentration world without SRM, statospheric SO_2 injection increases the allowable CO_2 emission by enhancing CO_2 uptake by both land and ocean (Figure 5.37). As a result of enhanced global carbon uptake, SRM would reduce the burden of atmospheric CO_2 (*high confidence*). However, the amount of SRM-induced reduction in atmospheric CO_2 depends on the future emission scenario and modelled oceanic and terrestrial carbon sinks, which differ widely between models (Tjiputra et al., 2016; Xia et al., 2016; Cao and Jiang, 2017; Muri et al., 2018). Models that include the terrestrial nitrogen cycle usually report a much smaller reduction of atmospheric CO_2 in response to SRM than models without the nitrogen cycle mainly because nitrogen limitation leads to a weaker terrestrial carbon sink (Tjiputra et al., 2016; Muri et al., 2018; Yang et al., 2020b). Large scale application of SAI is found to reduce the rate of release of CO_2 and CH_4 from permafrost thaw (Lee et al., 2019; Chen et al., 2020).

A hypothetical, sudden and sustained termination of SRM would cause a rapid increase in global warming that poses great risks to biodiversity (Jones et al., 2013a; McCusker et al., 2014; Trisos et al., 2018) (Section 4.6.3.3). A sudden and sustained termination of SRM would also weaken carbon sinks, accelerating atmospheric CO_2 accumulation and inducing further warming (Figure 5.37) (Matthews and Caldeira, 2007; Tjiputra et al., 2016; Muri et al., 2018; Plazzotta et al., 2019). However, a scenario with gradual phase-out of SRM under emission reduction could reduce the large negative effect of sudden SRM termination (MacMartin et al., 2014; Keith and MacMartin, 2015; Tilmes et al., 2016), though this would be limited by how rapidly emission reductions can be scaled-up (Ekholm and Korhonen, 2016).

5.6.3.3 Consequences of SRM on other Biogeochemical Cycles

SAI is found to reduce global average surface ozone concentration (Xia et al., 2017) mainly as a result of aerosol-induced reduction in stratospheric ozone at polar regions, resulting in reduced transport of ozone from the stratosphere (Pitari et al., 2014; Tilmes et al., 2018). The reduction in surface ozone, together with alteration to UV radiation, would have important implications for vegetation response (Xia et al., 2017). A modelling study shows that sea salt aerosol injection for MCB would reduce OH concentration and increase CH_4 lifetime, and hence, have potential implications for surface ozone pollution (Horowitz et al., 2020). It has also been reported that the use of SAI to limit global mean warming from 2°C to 1.5°C would reduce fire weather in many areas (Burton et al., 2018).

5.6.3.4 Synthesis of biogeochemical responses to SRM

SRM would alter the global carbon cycle through SRM-induced climate effect such as changes in sunlight, temperature, precipitation, and ocean circulation. Compared to high-CO_2 world without SRM, SRM would enhance the net uptake of CO_2 by the terrestrial biosphere and ocean, thus acting to reduce atmospheric CO_2 (*high confidence*). SRM would also affect surface ozone, UV radiation, and atmospheric chemistry. Due to complex interplays between SRM-induced changes in direct and diffuse sunlight, temperature, the coupling of water-carbon-nitrogen cycles, and atmospheric chemistry, there is large uncertainty in the overall response of the terrestrial biosphere response to SRM. Thus, the level of *confidence* on the effect of SRM on carbon and other biogeochemical cycles is *low*.

5.7 Final Remarks

Key research developments to further strengthen the confidence levels in AR7.

ACCEPTED VERSION SUBJECT TO FINAL EDITS

Contemporary Greenhouse Gases Trends and Attribution

- Further constrain the CO_2, CH_4 and N_2O fluxes from land use, land use change and forestry (including gross fluxes), and fossil fuels. Improving spatial resolution and representations of land management, such as forestry, grazing and cropping.
- Improve representation of the variability and trends in the transport of carbon through the land to ocean continuum, which has implications for partitioning of the land and ocean CO_2 sinks.
- Improve understanding of the controls over the airborne franction and sinks rates, their trends, and future dynamics.
- Fill gaps in space and time for ocean CO_2 and ancillary physical and biogeochemical observations at the ocean surface and interior to reduce the biases and uncertainties in the variability and trends for air-sea fluxes and inventory changes, particularly for the Arctic and the Southern Ocean.
- Reduce uncertainties in wetland CH_4 emissions, which is largest source term in the global CH_4 budget and proportionally have the largest uncertainty, in order to better understand future CH_4-climate feedbacks.
- Reduce uncertainties in atmospheric transport models used to estimate regional sources and sinks of greenhouse gases as independent evidence from that of ground and inventory estimates.

Ocean Acidification and Deoxygenation

- Improve observations for the interplay between carbonate chemistry and a variety of biogeochemical and physical processes including eutrophication and freshwater inflow in coastal zones to increase the robustness of future assessments of ocean acidification.
- Improve our understanding of changes in water mass ventilation associated with climate change and variability to gain further insights into future trends in ocean acidification and deoxygenation in the ocean interior.

Biogeochemical Feedbacks on Climate Change

- Improve understanding and representation in Earth system models (ESMs) of changes in land carbon storage and associated carbon-climate feedbacks including better treatment of the CO_2 fertilisation, nutrient-limitations, soil organic matter stabilisation and turnover; land use change; large-scale and fine-scale permafrost carbon; plant growth, mortality, and competition dynamics; plant hydraulics; and disturbance processes.
- Improve observations and process understanding of CH_4 and N_2O source responses to climate, specifically from wetlands and permafrost thaw.
- Improve observations and process understanding of ocean N_2O source responses to oxygen loss and climate particularly in the oxygen minimum zones of the tropical oceans and eastern boundary upwelling regions.
- Improve understanding of the sensitivity of ocean carbon-climate feedbacks to physical processes that are not yet resolved by the ocean domain in ESMs.
- Improve understanding of the processes affecting the efficiency, climate sensitivity and emerging feedbacks in the ocean carbon cycle via the biological carbon pump to constrain future global ocean feedbacks.

Remaining Carbon Budget to Climate Stabilisation

- Improve understanding of both the sign and magnitude of a possible zero emissions commitment (ZEC). The ZEC affects estimates of carbon budgets derived from the TCRE, but not TCRE itself. ZEC is particularly relevant once global CO_2 emissions decline towards net zero.
- Better constrain of the airborne fraction to reduce the spread in TCRE assessment.
- Accounting for timescales of Earth system feedbacks over time for increased accuracy of mitigation needs once global CO_2 emissions reach near-zero levels.

Carbon Dioxide Removal (CDR) and Solar Radiation Modification

- Run large-scale and long-term experiments and assessments to explore regional feasibility of CDR methods, that they present an actual and verifiable negative regional carbon balance, and that they do not result in adverse unintended consequences.

ACCEPTED VERSION SUBJECT TO FINAL EDITS

- Improve understanding of the effectiveness of CDR methods to lower atmospheric CO_2 and reduce warming taking into account Earth system feedbacks.

ACCEPTED VERSION
SUBJECT TO FINAL EDITS

Frequently Asked Questions

FAQ 5.1: Is the natural removal of carbon from the atmosphere weakening?

For decades, about half of the carbon dioxide (CO_2) that human activities have emitted to the atmosphere has been taken up by natural carbon sinks in vegetation, soils and oceans. These natural sinks of CO_2 have thus roughly halved the rate at which atmospheric CO_2 concentrations have increased, and therefore slowed down global warming. However, observations show that the processes underlying this uptake are beginning to respond to increasing CO_2 in the atmosphere and climate change in a way that will weaken nature's capacity to take up CO_2 in the future. Understanding of the magnitude of this change is essential for projecting how the climate system will respond to future emissions and emission reduction-efforts.

Direct observations of CO_2 concentrations in the atmosphere, which began in 1958, show that the atmosphere has only retained roughly half of the CO_2 emitted by human activities due to the combustion of fossil fuels and land-use change such as deforestation (FAQ 5.1, Figure 1). Natural carbon cycle processes on land and in the oceans have taken up the remainder of these emissions. These land and ocean removals or 'sinks' have grown largely in proportion to the increase in CO_2 emissions, taking up 31% (land) and 23% (ocean) of the emissions in 2010–2019, respectively (FAQ 5.1, Figure 1). Therefore, the average proportion of yearly CO_2 emissions staying in the atmosphere has remained roughly stable at 44 % over the last six decades despite continuously increasing CO_2 emissions from human activities.

On land, it is mainly the vegetation that captures CO_2 from the atmosphere through *plant photosynthesis,* which ultimately accumulates both in vegetation and soils. As more CO_2 accumulates in the atmosphere, plant carbon capture increases through the so-called *CO_2 fertilisation effect* in regions where plant growth is not limited by, for instance, nutrient availability. Climate change affects the processes responsible for the uptake and release of CO_2 on land in multiple ways. Land CO_2 uptake is generally increased by longer growing seasons due to global warming in cold regions and by nitrogen deposition in nitrogen-limited regions. Respiration by plants and soil organisms, natural disturbances such as fires, and human activities such as deforestation all release CO_2 back into the atmosphere. The combined effect of climate change on these processes is to weaken the future land sink. In particular, extreme temperatures and droughts as well as permafrost thaw (see FAQ 5.2) tend to reduce the land sink regionally.

In the ocean, several factors control how much CO_2 is captured: the difference in CO_2 partial pressure between the atmosphere and the surface ocean; wind speeds at the ocean surface; the chemical composition of seawater (that is, its *buffering capacity*), which affects how much CO_2 can be taken up; and the use of CO_2 in photosynthesis by seawater microalgae. The CO_2-enriched surface ocean water is transported to the deep ocean in specific zones around the globe (such as the Northern Atlantic and the Southern Ocean), effectively storing the CO_2 away from the atmosphere for many decades to centuries. The combined effect of warmer surface ocean temperatures on these processes is to weaken the future ocean CO_2 sink.

The ocean carbon sink is better quantified than the land sink thanks to direct ocean and atmospheric carbon observations. The land carbon sink is more challenging to monitor globally, because it varies widely even regionally. There is currently no direct evidence that the natural sinks are slowing down, because observable changes in the fraction of human emissions stored on land or in oceans are small compared to year-to-year and decadal variations of these sinks. Nevertheless, it is becoming more obvious that atmospheric and climate changes are affecting the processes controlling the land and ocean sinks.

Since both the land and ocean sinks respond to the rise in atmospheric CO_2 and to human-induced global warming, the absolute amount of CO_2 taken up by land and ocean will be affected by future CO_2 emissions. This also implies that if countries manage to strongly reduce global CO_2 emissions, or even remove CO_2 from the atmosphere, these sinks will take up less CO_2 because of the reduced human perturbation of the carbon cycle. Under future high-warming scenarios, it is expected that the global ocean and land sinks will stop growing in the second half of the century as climate change increasingly affects them. Thus, both the total amount of CO_2 emitted to the atmosphere and the responses of the natural CO_2 sinks will determine what efforts are required to limit global warming to a certain level (see FAQ 5.4), underscoring how

ACCEPTED VERSION SUBJECT TO FINAL EDITS

important it is to understand the evolution of these natural CO_2 sinks.

[START FAQ 5.1, FIGURE 1 HERE]

FAQ 5.1, Figure 1: Atmospheric CO2 and natural carbon sinks. (Top) Global emissions of CO2 from human activities and the growth rate of CO2 in the atmosphere, (middle) the net land and ocean CO2 removal ("natural sinks"), as well as (bottom) the fraction of CO2 emitted by human activities remaining in atmosphere from 1960 to 2019. Lines are the five years running mean, error-bars denote the uncertainty of the mean estimate. See Table 5.SM.6 for more information on the data underlying this figure.

[END FAQ 5.1, FIGURE 1 HERE]

ACCEPTED VERSION
SUBJECT TO FINAL EDITS

FAQ 5.2: Can thawing permafrost substantially increase global warming?

In the Arctic, large amounts of organic carbon are stored in permafrost – ground that remains frozen throughout the year. If significant areas of permafrost thaw as the climate warms, some of that carbon may be released into the atmosphere in the form of carbon dioxide or methane, resulting in additional warming. Projections from models of permafrost ecosystems suggest that future permafrost thaw will lead to some additional warming – enough to be important, but not enough to lead to a 'runaway warming' situation, where permafrost thaw leads to a dramatic, self-reinforcing acceleration of global warming.

The Arctic is the biggest climate-sensitive carbon pool on Earth, storing twice as much carbon in its frozen soils, or *permafrost*, than is currently stored in the atmosphere. As the Arctic region warms faster than anywhere else on earth, there are concerns that this warming could release greenhouse gases to the atmosphere and therefore significantly amplify climate change.

The carbon in the permafrost has built up over thousands of years, as dead plants have been buried and accumulated within layers of frozen soil, where the cold prevents the organic material from decomposing. As the Arctic warms and soils thaw, the organic matter in these soils begins to decompose rapidly and return to the atmosphere as either carbon dioxide or methane, which are both important greenhouse gases. Permafrost can also thaw abruptly in a given place, due to melting ice in the ground reshaping Arctic landscapes, lakes growing and draining, and fires burning away insulating surface soil layers. Thawing of permafrost carbon has already been observed in the Arctic, and climate models project that much of the shallow permafrost (<3 m depth) throughout the Arctic would thaw under moderate to high amounts of global warming (2°C–4°C).

While permafrost processes are complex, they are beginning to be included in models that represent the interactions between the climate and the carbon cycle. The projections from these permafrost carbon models show a wide range in the estimated strength of a carbon–climate vicious circle, from both carbon dioxide and methane, equivalent to 14–175 billion tonnes of carbon dioxide released per 1°C of global warming. By comparison, in 2019, human activities have released about 40 billion tonnes of carbon dioxide into the atmosphere. This has two implications. First, the extra warming caused by permafrost thawing is strong enough that it must be considered when estimating the total amount of remaining emissions permitted to stabilise the climate at a given level of global warming (i.e., the remaining carbon budget, see FAQ 5.4). Second, the models do not identify any one amount of warming at which permafrost thaw becomes a 'tipping point' or threshold in the climate system that would lead to a runaway global warming. However, models do project that emissions would continuously increase with warming, and that this trend could last for hundreds of years.

Permafrost can also be found in other cold places (e.g., mountain ranges), but those places contain much less carbon than in the Arctic. For instance, the Tibetan plateau contains about 3% as much carbon as is stored in the Arctic. There is also concern about carbon frozen in shallow ocean sediments. These deposits are known as *methane hydrates* or *clathrates*, which are methane molecules locked within a cage of ice molecules. They formed as frozen soils that were flooded when sea levels rose after the last ice age. If these hydrates thaw, they may release methane that can bubble up to the surface. The total amount of carbon in permafrost-associated methane hydrates is much less than the carbon in permafrost soils. Global warming takes millennia to penetrate into the sediments beneath the ocean, which is why these hydrates are still responding to the last deglaciation. As a result, only a small fraction of the existing hydrates could be destabilised during the coming century. Even when methane is released from hydrates, most of it is expected to be consumed and oxidised into carbon dioxide in the ocean before reaching the atmosphere. The most complete modelling of these processes to date suggests a release to the atmosphere at a rate of less than 2% of current human-induced methane emissions.

Overall, thawing permafrost in the Arctic appears to be an important additional source of heat-trapping gases to the atmosphere, more so than undersea hydrates. Climate and carbon cycle models are beginning to consider permafrost processes. While these models disagree on the exact amount of the heat-trapping gases that will be released into the atmosphere, they agree (i) that the amount of such gases released from

ACCEPTED VERSION SUBJECT TO FINAL EDITS

permafrost will increase with the amount of global warming, and (ii) that the warming effect of thawing permafrost is significant enough to be considered in estimates of the remaining carbon budgets for limiting future warming.

[START FAQ 5.2, FIGURE 1 HERE]

FAQ 5.2, Figure 1: The Arctic permafrost is a big pool of carbon that is sensitive to climate change. (left) Quantity of carbon stored in the permafrost, to 3 m depth (NCSCDv2 dataset) and (right) area of permafrost vulnerable to abrupt thaw (Circumpolar Thermokarst Landscapes dataset).

[END FAQ 5.2, FIGURE 1 HERE]

ACCEPTED VERSION
SUBJECT TO FINAL EDITS

FAQ 5.3: Could climate change be reversed by removing carbon dioxide from the atmosphere?

Deliberate removal of carbon dioxide (CO_2) from the atmosphere could reverse (i.e. change the direction of) some aspects of climate change. However, this will only happen if it results in a net reduction in the total amount of CO_2 in the atmosphere, that is, if deliberate removals are larger than emissions. Some climate change trends, such as the increase in global surface temperature, would start to reverse within a few years. Other aspects of climate change would take decades (e.g., permafrost thawing) or centuries (e.g., acidification of the deep ocean) to reverse, and some, such as sea level rise, would take centuries to millennia to change direction.

The term *negative carbon dioxide (CO_2) emissions* refers to the removal of CO_2 from the atmosphere by deliberate human activities, in addition to the removals that occur naturally, and is often used as synonymous with *carbon dioxide removal*. Negative CO_2 emissions can compensate for the release of CO_2 into the atmosphere by human activities. They could be achieved by strengthening natural CO_2 sequestration processes on land (e.g., by planting trees or through agricultural practices that increase the carbon content of soils) and/or in the ocean (e.g., by restoration of coastal ecosystems) or by removing CO_2 directly from the atmosphere. If CO_2 removals are greater than human-caused CO_2 emissions globally, emissions are said to be *net negative*. It should be noted that CO_2 removal technologies are not yet ready or unable to achieve the scale of removal that would be required to compensate for current levels of emissions, and most have undesired side effects.

In the absence of deliberate CO_2 removal, the CO_2 concentration in the atmosphere (a measure of the amount of CO_2 in the atmosphere) results from a balance between human-caused CO_2 release and the removal of CO_2 by natural processes on land and in the ocean (natural 'carbon sinks') (see FAQ 5.1). If CO_2 release exceeds removal by carbon sinks, the CO_2 concentration in the atmosphere would increase; if CO_2 release equals removal, the atmospheric CO_2 concentration would stabilise; and if CO_2 removal exceeds release, the CO_2 concentration would decline. This applies in the same way to *net* CO_2 emissions that is, the sum of human-caused releases and deliberate removals.

If the CO_2 concentration in the atmosphere starts to go down, the Earth's climate would respond to this change (FAQ 5.3, Figure 1). Some parts of the climate system take time to react to a change in CO_2 concentration, so a decline in atmospheric CO_2 as a result of net negative emissions would not lead to immediate reversal of all climate change trends. Recent studies have shown that global surface temperature starts to decline within a few years following a decline in atmospheric CO_2, although the decline would not be detectable for decades due to natural climate variability (see FAQ 4.2). Other consequences of human-induced climate change such as reduction in permafrost area would take decades, and yet others such as warming, acidification and oxygen loss of the deep ocean would take centuries to reverse following a decline in the atmospheric CO_2 concentration. Sea level would continue to rise for many centuries to millennia, even if large deliberate CO_2 removals were successfully implemented.

A class of future scenarios that is receiving increasing attention, particularly in the context of ambitious climate goals such as the global warming limits of 1.5°C or 2°C included in the Paris Agreement, are so-called 'overshoot' scenarios. In these scenarios, a slow rate of reductions in emissions in the near term is compensated by net negative CO_2 emissions in the later part of this century, which results in a temporary breach or 'overshoot' of a given warming level. Due to the delayed reaction of several climate system components, it follows that the temporary overshoot would result in additional climate changes compared to a scenario that reaches the goal without overshoot. These changes would take decades to many centuries to reverse, with the reversal taking longer for scenarios with larger overshoot.

Removing more CO_2 from the atmosphere than is emitted into it would indeed begin to reverse some aspects of climate change, but some changes would still continue in their current direction for decades to millennia. Approaches capable of large-scale removal of CO_2 are still in the state of research and development or unproven at the scales of deployment necessary to achieve a net reduction in atmospheric CO_2 levels. CO_2 removal approaches, particularly those deployed on land, can have undesired side-effects on water, food production and biodiversity.

ACCEPTED VERSION SUBJECT TO FINAL EDITS

[START FAQ 5.3, FIGURE 1 HERE]

FAQ 5.3, Figure 1: Changes in aspects of climate change in response to a peak and decline in the atmospheric CO_2 concentration (top panel). The vertical grey dashed line indicates the time of peak CO_2 concentration in all panels. It is shown that the reversal of global surface warming lags the decrease in the atmospheric CO_2 concentration by a few years, the reversal of permafrost area decline lags the decrease in atmospheric CO_2 by decades, and ocean thermal expansion continues for several centuries. Note that the quantitative information in the figure (i.e., numbers on vertical axes) is not to be emphasized as it results from simulations with just one model and will be different for other models. The qualitative behaviour, however, can be expected to be largely model independent.

[END FAQ 5.3, FIGURE 1 HERE]

ACCEPTED VERSION
SUBJECT TO FINAL EDITS

FAQ 5.4: What are carbon budgets?

There are several types of carbon budgets. Most often, the term refers to the total net amount of carbon dioxide (CO_2) that can still be emitted by human activities while limiting global warming to a specified level (e.g., 1.5ºC or 2ºC above pre-industrial levels). This is referred to as the 'remaining carbon budget'. Several choices and value judgments have to be made before it can be unambiguously estimated. When the remaining carbon budget is combined with all past CO_2 emissions to date, a 'total carbon budget' compatible with a specific global warming limit can also be defined. A third type of carbon budget is the 'historical carbon budget', which is a scientific way to describe all past and present sources and sinks of CO_2.

The term *remaining carbon budget* is used to describe the total net amount of CO_2 that human activities can still release into the atmosphere while keeping global warming to a specified level, like 1.5°C or 2°C relative to pre-industrial temperatures. Emissions of CO_2 from human activities are the main cause of global warming. A remaining carbon budget can be defined because of the specific way CO_2 behaves in the Earth system. That is, global warming is roughly linearly proportional to the total net amount of CO_2 emissions that are released into the atmosphere by human activities – also referred to as cumulative anthropogenic CO_2 emissions. Other greenhouse gases behave differently and have to be accounted for separately.

The concept of a remaining carbon budget implies that to stabilize global warming at any particular level, global emissions of CO_2 need to be reduced to net zero levels at some point. Net zero CO_2 emissions describes a situation in which all the anthropogenic emissions of CO_2 are counterbalanced by deliberate anthropogenic removals so that on average no CO_2 is added or removed from the atmosphere by human activities. Atmospheric CO_2 concentrations in such a situation would gradually decline to a long-term stable level as excess CO_2 in the atmosphere is taken up ocean and land sinks (see FAQ 5.1). The concept of a remaining carbon budget also means that if CO_2 emissions reductions are delayed, deeper and faster reductions are needed later to stay within the same budget. If the remaining carbon budget is exceeded, this will result in either higher global warming or a need to actively remove CO_2 from the atmosphere to reduce global temperatures back down to the desired level (see FAQ 5.3).

Estimating the size of remaining carbon budgets depends on a set of choices. These choices include (1) the global warming level that is chosen as a limit (for example, 1.5°C or 2°C relative to pre-industrial levels), (2) the probability with which we want to ensure that warming is held below that limit (for example, a one-in-two, two-in-three, or higher chance), and (3) how successful we are in limiting emissions of other greenhouse gases that affect the climate, such as methane or nitrous oxide. These choices can be informed by science but ultimately represent subjective choices. Once they have been made, we can combine knowledge about how much our planet has warmed already, about the amount of warming per cumulative tonne of CO_2, and about the amount of warming that is still expected once global net CO_2 emissions are brought down to zero to estimate the remaining carbon budget for a given temperature goal. For example, to limit global warming to 1.5°C above pre-industrial levels with either a one-in-two (50%) or two-in-three (67%) chance, the remaining carbon budgets amount to 500 and 400 billion tonnes of CO_2, respectively, from 1 January 2020 onward (FAQ 5.4, Figure 1). Currently, human activities are emitting around 40 billion tonnes of CO_2 into the atmosphere in a single year.

The remaining carbon budget depends on how much the world has already warmed to date. This past warming is caused by historical emissions, which are estimated by looking at the *historical carbon budget* – a scientific way to describe all past and present sources and sinks of CO_2. It describes how the CO_2 emissions from human activities have redistributed across the various CO_2 reservoirs of the Earth system. These reservoirs are the ocean, the land vegetation, and the atmosphere (into which CO_2 was emitted). The share of CO_2 that is not taken up by the ocean or the land, and that thus increases the concentration of CO_2 in the atmosphere, causes global warming. The historical carbon budget tells us that of the about 2560 billion tonnes of CO_2 that were released into the atmosphere by human activities between the years 1750 and 2019, about a quarter were absorbed by the ocean (causing ocean acidification) and about a third by the land vegetation. About 45% of these emissions remain in the atmosphere (see FAQ 5.1). Adding these historical CO_2 emissions to estimates of remaining carbon budgets allows one to estimate the *total carbon budget*

ACCEPTED VERSION SUBJECT TO FINAL EDITS

consistent with a specific global warming level.

In summary, determining a remaining carbon budget – that is, how much CO_2 can be released into the atmosphere while stabilizing global temperature below a chosen level – is well understood but relies on a set of choices. What is clear, however, is that for limiting warming below 1.5°C or 2°C the remaining carbon budget from 2020 onwards is much smaller than the total CO_2 emissions released to date.

[START FAQ 5.4, FIGURE 1]

FAQ 5.4, Figure 1: Various types of carbon budgets. Historical cumulative CO_2 emissions determine to a large degree how much the world has warmed to date, while the remaining carbon budget indicates how much CO_2 could still be emitted while keeping warming below specific temperature thresholds. Several factors limit the precision with which the remaining carbon budget can be estimated, and estimates therefore need to specify the probability with which they aim at limiting warming to the intended target level (e.g., limiting warming to 1.5°C with a 67% probability).

[END FAQ 5.4, FIGURE 1]

ACCEPTED VERSION
SUBJECT TO FINAL EDITS

References

Abatzoglou, J.T., A.P. Williams, and R. Barbero, 2019: Global Emergence of Anthropogenic Climate Change in Fire Weather Indices. *Geophysical Research Letters*, **46(1)**, 326–336, doi:10.1029/2018gl080959.

Abbott, B.W. and J.B. Jones, 2015: Permafrost collapse alters soil carbon stocks, respiration, CH4, and N2O in upland tundra. *Global Change Biology*, **21(12)**, 4570–4587, doi:10.1111/gcb.13069.

Abram, N.J. et al., 2021: Connections of climate change and variability to large and extreme forest fires in southeast Australia. *Communications Earth & Environment*, **2(1)**, 8, doi:10.1038/s43247-020-00065-8.

Achat, D.L., L. Augusto, A. Gallet-Budynek, and D. Loustau, 2016: Future challenges in coupled C–N–P cycle models for terrestrial ecosystems under global change: a review. *Biogeochemistry*, **131(1–2)**, 173–202, doi:10.1007/s10533-016-0274-9.

Adams, C.A., J.E. Andrews, and T. Jickells, 2012: Nitrous oxide and methane fluxes vs. carbon, nitrogen and phosphorous burial in new intertidal and saltmarsh sediments. *Science of The Total Environment*, **434**, 240–251, doi:10.1016/j.scitotenv.2011.11.058.

Adams, M.A., T.N. Buckley, and T.L. Turnbull, 2020: Diminishing CO2-driven gains in water-use efficiency of global forests. *Nature Climate Change*, **10(5)**, 466–471, doi:10.1038/s41558-020-0747-7.

Ahlstrom, A. et al., 2015: The dominant role of semi-arid ecosystems in the trend and variability of the land CO2 sink. *Science*, **348(6237)**, 895–899, doi:10.1126/science.aaa1668.

Ahn, J. and E.J. Brook, 2014: Siple Dome ice reveals two modes of millennial CO2 change during the last ice age. *Nature Communications*, **5(1)**, 3723, doi:10.1038/ncomms4723.

Ainsworth, E.A. and S.P. Long, 2005: What have we learned from 15 years of free-air CO2 enrichment (FACE)? A meta-analytic review of the responses of photosynthesis, canopy properties and plant production to rising CO2. *New Phytologist*, **165(2)**, 351–372, doi:10.1111/j.1469-8137.2004.01224.x.

Ajayi, S. et al., 2020: Evaluation of Paleocene-Eocene Thermal Maximum Carbon Isotope Record Completeness – An Illustration of the Potential of Dynamic Time Warping in Aligning Paleo-Proxy Records. *Geochemistry, Geophysics, Geosystems*, **21(3)**, e2019GC008620, doi:10.1029/2019gc008620.

Al-Haj, A.N. and R.W. Fulweiler, 2020: A synthesis of methane emissions from shallow vegetated coastal ecosystems. *Global Change Biology*, **26(5)**, 2988–3005, doi:10.1111/gcb.15046.

Allen, C.D., D.D. Breshears, and N.G. McDowell, 2015: On underestimation of global vulnerability to tree mortality and forest die-off from hotter drought in the Anthropocene. *Ecosphere*, **6(8)**, art129, doi:10.1890/es15-00203.1.

Allen, G.H. and T.M. Pavelsky, 2018: Global extent of rivers and streams. *Science*, **361(6402)**, 585–588, doi:10.1126/science.aat0636.

Allen, M.R. et al., 2009: Warming caused by cumulative carbon emissions towards the trillionth tonne. *Nature*, **458(7242)**, 1163–1166, doi:10.1038/nature08019.

Allen, M.R. et al., 2018: Framing and Context. In: *Global Warming of 1.5°C. An IPCC Special Report on the impacts of global warming of 1.5°C above pre-industrial levels and related global greenhouse gas emission pathways, in the context of strengthening the global response to the threat of climate change,* [Masson-Delmotte, V., P. Zhai, H.-O. Pörtner, D. Roberts, J. Skea, P.R. Shukla, A. Pirani, W. Moufouma-Okia, C. Péan, R. Pidcock, S. Connors, J.B.R. Matthews, Y. Chen, X. Zhou, M.I. Gomis, E. Lonnoy, T. Maycock, M. Tignor, and T. Waterfield (eds.)]. In Press, pp. 49–92.

Anagnostou, E. et al., 2016: Changing atmospheric CO2 concentration was the primary driver of early Cenozoic climate. *Nature*, **533(7603)**, 380–384, doi:10.1038/nature17423.

Anav, A. et al., 2013: Evaluating the Land and Ocean Components of the Global Carbon Cycle in the CMIP5 Earth System Models. *Journal of Climate*, **26(18)**, 6801–6843, doi:10.1175/jcli-d-12-00417.1.

Anav, A. et al., 2015: Spatiotemporal patterns of terrestrial gross primary production: A review. *Reviews of Geophysics*, **53(3)**, 785–818, doi:10.1002/2015rg000483.

Andela, N. et al., 2017: A human-driven decline in global burned area. *Science*, **1356**, 1356–1362, doi:10.1126/science.aal4108.

Anderegg, W.R.L. et al., 2015: Tropical nighttime warming as a dominant driver of variability in the terrestrial carbon sink. *Proceedings of the National Academy of Sciences*, **112(51)**, 201521479, doi:10.1073/pnas.1521479112.

Anderegg, W.R.L. et al., 2020: Climate-driven risks to the climate mitigation potential of forests. *Science*, doi:10.1126/science.aaz7005.

Anderson, K. and G. Peters, 2016: The trouble with negative emissions. *Science*, **354(6309)**, 182 LP – 183, doi:10.1126/science.aah4567.

Anderson, R.F. et al., 2019: Deep-Sea Oxygen Depletion and Ocean Carbon Sequestration During the Last Ice Age. *Global Biogeochemical Cycles*, **33(3)**, 301–317, doi:10.1029/2018gb006049.

Andrew, R.M., 2018: Global CO2 emissions from cement production. *Earth System Science Data*, **10(1)**, 195–217, doi:10.5194/essd-10-195-2018.

Andrew, R.M., 2019: Global CO2 emissions from cement production, 1928–2018. *Earth System Science Data*, **11(4)**,

ACCEPTED VERSION SUBJECT TO FINAL EDITS

1675–1710, doi:10.5194/essd-11-1675-2019.
Andrew, R.M., 2020: A comparison of estimates of global carbon dioxide emissions from fossil carbon sources. *Earth System Science Data*, **12(2)**, 1437–1465, doi:10.5194/essd-12-1437-2020.
Aragão, L.E.O.C. et al., 2018: 21st Century drought-related fires counteract the decline of Amazon deforestation carbon emissions. *Nature Communications*, **9(1)**, 536, doi:10.1038/s41467-017-02771-y.
Archer, D., B. Buffett, and V. Brovkin, 2009: Ocean methane hydrates as a slow tipping point in the global carbon cycle. *Proceedings of the National Academy of Sciences*, **106(49)**, 20596–20601, doi:10.1073/pnas.0800885105.
Ardyna, M. and K.R. Arrigo, 2020: Phytoplankton dynamics in a changing Arctic Ocean. *Nature Climate Change*, **10(10)**, 892–903, doi:10.1038/s41558-020-0905-y.
Arévalo-Martínez, D.L., A. Kock, C.R. Löscher, R.A. Schmitz, and H.W. Bange, 2015: Massive nitrous oxide emissions from the tropical South Pacific Ocean. *Nature Geoscience*, **8(7)**, 530–533, doi:10.1038/ngeo2469.
Armour, K.C., J. Marshall, J.R. Scott, A. Donohoe, and E.R. Newsom, 2016: Southern Ocean warming delayed by circumpolar upwelling and equatorward transport. *Nature Geoscience*, **9(7)**, 549–554, doi:10.1038/ngeo2731.
Arneth, A. et al., 2010: Terrestrial biogeochemical feedbacks in the climate system. *Nature Geoscience*, **3(8)**, 525–532, doi:10.1038/ngeo905.
Arneth, A. et al., 2017: Historical carbon dioxide emissions caused by land-use changes are possibly larger than assumed. *Nature Geoscience*, **10(2)**, 79–84, doi:10.1038/ngeo2882.
Arora, V.K. and J.R. Melton, 2018: Reduction in global area burned and wildfire emissions since 1930s enhances carbon uptake by land. *Nature Communications*, **9(1)**, 1326, doi:10.1038/s41467-018-03838-0.
Arora, V.K. et al., 2013: Carbon–concentration and carbon–climate feedbacks in CMIP5 Earth system models. *Journal of Climate*, **26(15)**, 5289–5314, doi:10.1175/jcli-d-12-00494.1.
Arora, V.K. et al., 2020: Carbon–concentration and carbon–climate feedbacks in CMIP6 models and their comparison to CMIP5 models. *Biogeosciences*, **17(16)**, 4173–4222, doi:10.5194/bg-17-4173-2020.
Arzhanov, M.M. and I.I. Mokhov, 2017: Stability of continental relic methane hydrates for the holocene climatic optimum and for contemporary conditions. *Doklady Earth Sciences*, **476(2)**, 1163–1167, doi:10.1134/s1028334x17100026.
Arzhanov, M.M., I.I. Mokhov, and S.N. Denisov, 2016: Impact of regional climatic change on the stability of relic gas hydrates. *Doklady Earth Sciences*, **468(2)**, 616–618, doi:10.1134/s1028334x1606009x.
Arzhanov, M.M., V. Malakhova, and I.I. Mokhov, 2020: Modeling thermal regime and evolution of the methane hydrate stability zone of the Yamal peninsula permafrost. *Permafrost and Periglacial Processes*, **31(4)**, 487–496, doi:10.1002/ppp.2074.
Astor, Y.M. et al., 2013: Interannual variability in sea surface temperature and fCO2 changes in the Cariaco Basin. *Deep Sea Research Part II: Topical Studies in Oceanography*, –, doi:10.1016/j.dsr2.2013.01.002.
Atwood, T.B. et al., 2017: Global patterns in mangrove soil carbon stocks and losses. *Nature Climate Change*, **7(7)**, 523–528, doi:10.1038/nclimate3326.
Auger, M., R. Morrow, E. Kestenare, J.-B. Sallée, and R. Cowley, 2021: Southern Ocean in-situ temperature trends over 25 years emerge from interannual variability. *Nature Communications*, **12(1)**, 514, doi:10.1038/s41467-020-20781-1.
Azetsu-Scott, K. et al., 2010: Calcium carbonate saturation states in the waters of the Canadian Arctic Archipelago and the Labrador Sea. *Journal of Geophysical Research*, **115(C11)**, C11021, doi:10.1029/2009jc005917.
Babbin, A.R., D. Bianchi, A. Jayakumar, and B.B. Ward, 2015: Rapid nitrous oxide cycling in the suboxic ocean. *Science*, **348(6239)**, 1127–1129, doi:10.1126/science.aaa8380.
Babila, T.L. et al., 2018: Capturing the global signature of surface ocean acidification during the Palaeocene–Eocene Thermal Maximum. *Philosophical Transactions of the Royal Society A: Mathematical, Physical and Engineering Sciences*, **376(2130)**, 20170072, doi:10.1098/rsta.2017.0072.
Bacastow, R.B. et al., 1980: Atmospheric carbon dioxide, the Southern oscillation, and the weak 1975 El Nino. *Science*, **210(4465)**, 66–68, doi:10.1126/science.210.4465.66.
Bach, L.T., S.J. Gill, R.E.M. Rickaby, S. Gore, and P. Renforth, 2019: CO2 Removal With Enhanced Weathering and Ocean Alkalinity Enhancement: Potential Risks and Co-benefits for Marine Pelagic Ecosystems. *Frontiers in Climate*, **1**, doi:10.3389/fclim.2019.00007.
Bach, L.T. et al., 2016: Influence of plankton community structure on the sinking velocity of marine aggregates. *Global Biogeochemical Cycles*, **30(8)**, 1145–1165, doi:10.1002/2016gb005372.
Bachman, S.D. and A. Klocker, 2020: Interaction of jets and submesoscale dynamics leads to rapid ocean ventilation. *Journal of Physical Oceanography*, **50(10)**, 2873–2883, doi:10.1175/jpo-d-20-0117.1.
Badgley, G., C.B. Field, and J.A. Berry, 2017: Canopy near-infrared reflectance and terrestrial photosynthesis. *Science Advances*, **3(3)**, doi:10.1126/sciadv.1602244.
Baggenstos, D. et al., 2019: Earth's radiative imbalance from the Last Glacial Maximum to the present. *Proceedings of the National Academy of Sciences*, **116(30)**, 14881–14886, doi:10.1073/pnas.1905447116.
Baig, S., B.E. Medlyn, L.M. Mercado, and S. Zaehle, 2015: Does the growth response of woody plants to elevated CO2increase with temperature? A model-oriented meta-analysis. *Global Change Biology*, **21(12)**, 4303–4319,

ACCEPTED VERSION SUBJECT TO FINAL EDITS

doi:10.1111/gcb.12962.
Bakker, D.C.E. et al., 2016: A multi-decade record of high-quality fCO2 data in version 3 of the Surface Ocean CO2 Atlas (SOCAT). *Earth System Science Data*, **8(2)**, 383–413, doi:10.5194/essd-8-383-2016.
Bakun, A. et al., 2015: Anticipated Effects of Climate Change on Coastal Upwelling Ecosystems. *Current Climate Change Reports*, **1(2)**, 85–93, doi:10.1007/s40641-015-0008-4.
Balesdent, J. et al., 2018: Atmosphere–soil carbon transfer as a function of soil depth. *Nature*, **559(7715)**, 599–602, doi:10.1038/s41586-018-0328-3.
Ballantyne, A. et al., 2017: Accelerating net terrestrial carbon uptake during the warming hiatus due to reduced respiration. *Nature Climate Change*, **7(2)**, 148–152, doi:10.1038/nclimate3204.
Ballantyne, A.P., C.B. Alden, J.B. Miller, P.P. Tans, and J.W.C. White, 2012: Increase in observed net carbon dioxide uptake by land and oceans during the past 50 years. *Nature*, **488(7409)**, 70–72, doi:10.1038/nature11299.
Bândă, N. et al., 2016: Can we explain the observed methane variability after the Mount Pinatubo eruption? *Atmospheric Chemistry and Physics*, **16(1)**, 195–214, doi:10.5194/acp-16-195-2016.
Barker, S. and H. Elderfield, 2002: Foraminiferal Calcification Response to Glacial-Interglacial Changes in Atmospheric CO2. *Science*, **297(5582)**, 833–836, doi:10.1126/science.1072815.
Bastviken, D., L.J. Tranvik, J.A. Downing, P.M. Crill, and A. Enrich-Prast, 2011: Freshwater Methane Emissions Offset the Continental Carbon Sink. *Science*, **331(6013)**, 50–50, doi:10.1126/science.1196808.
Bates, N. et al., 2014: A Time-Series View of Changing Ocean Chemistry Due to Ocean Uptake of Anthropogenic CO2 and Ocean Acidification. *Oceanography*, **27(1)**, 126–141, doi:10.5670/oceanog.2014.16.
Bates, N.R. and R.J. Johnson, 2020: Acceleration of ocean warming, salinification, deoxygenation and acidification in the surface subtropical North Atlantic Ocean. *Communications Earth & Environment*, **1(1)**, 33, doi:10.1038/s43247-020-00030-5.
Bates, N.R., J.T. Mathis, and L.W. Cooper, 2009: Ocean acidification and biologically induced seasonality of carbonate mineral saturation states in the western Arctic Ocean. *Journal of Geophysical Research*, **114(C11)**, C11007, doi:10.1029/2008jc004862.
Bathiany, S., J. Hidding, and M. Scheffer, 2020: Edge Detection Reveals Abrupt and Extreme Climate Events. *Journal of Climate*, **33(15)**, 6399–6421, doi:10.1175/jcli-d-19-0449.1.
Bathiany, S., M. Claussen, V. Brovkin, T. Raddatz, and V. Gayler, 2010: Combined biogeophysical and biogeochemical effects of large-scale forest cover changes in the MPI earth system model. *Biogeosciences*, **7(5)**, 1383–1399, doi:10.5194/bg-7-1383-2010.
Batjes, N.H., 2016: Harmonized soil property values for broad-scale modelling (WISE30sec) with estimates of global soil carbon stocks. *Geoderma*, **269**, 61–68, doi:10.1016/j.geoderma.2016.01.034.
Battaglia, G. and F. Joos, 2018a: Hazards of decreasing marine oxygen: the near-term and millennial-scale benefits of meeting the Paris climate targets. *Earth System Dynamics*, **9(2)**, 797–816, doi:10.5194/esd-9-797-2018.
Battaglia, G. and F. Joos, 2018b: Marine N2O emissions from nitrification and denitrification constrained by modern observations and projected in multimillennial global warming simulations. *Global Biogeochemical Cycles*, **32(1)**, 92–121, doi:10.1002/2017gb005671.
Bauska, T.K. et al., 2018: Controls on Millennial-Scale Atmospheric CO 2 Variability During the Last Glacial Period. *Geophysical Research Letters*, **45(15)**, 7731–7740, doi:10.1029/2018gl077881.
Beaufort, L. et al., 2011: Sensitivity of coccolithophores to carbonate chemistry and ocean acidification. *Nature*, **476(7358)**, 80–83, doi:10.1038/nature10295.
Beaulieu, J.J., T. DelSontro, and J.A. Downing, 2019: Eutrophication will increase methane emissions from lakes and impoundments during the 21st century. *Nature Communications*, **10(1)**, 1375, doi:10.1038/s41467-019-09100-5.
Beck, J. et al., 2018: Bipolar carbon and hydrogen isotope constraints on the Holocene methane budget. *Biogeosciences*, **15(23)**, 7155–7175, doi:10.5194/bg-15-7155-2018.
Bednaršek, N. et al., 2020: Exoskeleton dissolution with mechanoreceptor damage in larval Dungeness crab related to severity of present-day ocean acidification vertical gradients. *Science of The Total Environment*, **716**, 136610, doi:10.1016/j.scitotenv.2020.136610.
Beer, C. et al., 2010: Terrestrial Gross Carbon Dioxide Uptake: Global Distribution and Covariation with Climate. *Science*, **329(5993)**, 834–838, doi:10.1126/science.1184984.
Beerling, D.J. et al., 2018: Farming with crops and rocks to address global climate, food and soil security. *Nature Plants*, **4(3)**, 138–147, doi:10.1038/s41477-018-0108-y.
Benanti, G., M. Saunders, B. Tobin, and B. Osborne, 2014: Contrasting impacts of afforestation on nitrous oxide and methane emissions. *Agricultural and Forest Meteorology*, **198–199**, 82–93, doi:10.1016/j.agrformet.2014.07.014.
Bennedsen, M., E. Hillebrand, and S. Jan Koopman, 2019: Trend analysis of the airborne fraction and sink rate of anthropogenically released CO2. *Biogeosciences*, **16(18)**, 3651–3663, doi:10.5194/bg-16-3651-2019.
Berchet, A. et al., 2016: Atmospheric constraints on the methane emissions from the East Siberian Shelf. *Atmospheric Chemistry and Physics*, **16(6)**, 4147–4157, doi:10.5194/acp-16-4147-2016.
Bereiter, B., S. Shackleton, D. Baggenstos, K. Kawamura, and J. Severinghaus, 2018: Mean global ocean temperatures

ACCEPTED VERSION SUBJECT TO FINAL EDITS

during the last glacial transition. *Nature*, **553(7686)**, 39–44, doi:10.1038/nature25152.
Berg, A. et al., 2016: Land-atmosphere feedbacks amplify aridity increase over land under global warming. *Nature Climate Change*, **6(9)**, 869–874, doi:10.1038/nclimate3029.
Beringer, T., W. Lucht, and S. Schaphoff, 2011: Bioenergy production potential of global biomass plantations under environmental and agricultural constraints. *GCB Bioenergy*, **3(4)**, 299–312, doi:10.1111/j.1757-1707.2010.01088.x.
Betts, R.A. et al., 2018: A successful prediction of the record CO2 rise associated with the 2015/2016 El Niño. *Philosophical Transactions of the Royal Society B: Biological Sciences*, **373(1760)**, 20170301, doi:10.1098/rstb.2017.0301.
BGR, 2019: Data and developments concerning German and Global energy supplies. .
Bianchi, D., J.P. Dunne, J.L. Sarmiento, and E.D. Galbraith, 2012: Data-based estimates of suboxia, denitrification, and N2O production in the ocean and their sensitivities to dissolved O2. *Global Biogeochemical Cycles*, **26(2)**, GB2009, doi:10.1029/2011gb004209.
Bindoff, N.L. et al., 2019: Changing Ocean, Marine Ecosystems, and Dependent Communities. In: *IPCC Special Report on the Ocean and Cryosphere in a Changing Climate* [Pörtner, H.-O., D.C. Roberts, V. Masson-Delmotte, P. Zhai, M. Tignor, E. Poloczanska, K. Mintenbeck, A. Alegría, M. Nicolai, A. Okem, J. Petzold, B. Rama, and N.M. Weyer (eds.)]. In Press, pp. 447–588.
Blanc-Betes, E. et al., : In silico assessment of the potential of basalt amendments to reduce N2O emissions from bioenergy crops. *GCB Bioenergy*, **n/a(n/a)**, doi:10.1111/gcbb.12757.
Blanchette, C.D. et al., 2016: Printable enzyme-embedded materials for methane to methanol conversion. *Nature Communications*, **7(1)**, 11900, doi:10.1038/ncomms11900.
Bobich, E.G., G.A. Barron-Gafford, K.G. Rascher, and R. Murthy, 2010: Effects of drought and changes in vapour pressure deficit on water relations of Populus deltoides growing in ambient and elevated CO2. *Tree Physiology*, **30(7)**, 866–875, doi:10.1093/treephys/tpq036.
Bock, M. et al., 2010: Hydrogen isotopes preclude marine hydrate CH4 emissions at the onset of Dansgaard-Oeschger events.. *Science*, **328(5986)**, 1686–9, doi:10.1126/science.1187651.
Bock, M. et al., 2017: Glacial/interglacial wetland, biomass burning, and geologic methane emissions constrained by dual stable isotopic CH 4 ice core records. *Proceedings of the National Academy of Sciences*, **114(29)**, E5778–E5786, doi:10.1073/pnas.1613883114.
Boden, T.A., G. Marland, and R.J. Andres, 2017: Global, Regional, and National Fossil-Fuel CO2 Emissions (1751 – 2014) (V. 2017). Carbon Dioxide Information Analysis Center (CDIAC), Oak Ridge National Laboratory (ORNL), Oak Ridge, TN, USA. Retrieved from: https://cdiac.ess-dive.lbl.gov/trends/emis/overview.html.
Boer, M.M., V. Resco de Dios, and R.A. Bradstock, 2020: Unprecedented burn area of Australian mega forest fires. *Nature Climate Change*, **10(3)**, 171–172, doi:10.1038/s41558-020-0716-1.
Bopp, L., M. Lévy, L. Resplandy, and J.B. Sallée, 2015: Pathways of anthropogenic carbon subduction in the global ocean. *Geophysical Research Letters*, **42(15)**, 6416–6423, doi:10.1002/2015gl065073.
Bopp, L. et al., 2013: Multiple stressors of ocean ecosystems in the 21st century: projections with CMIP5 models. *Biogeosciences*, **10(10)**, 6225–6245, doi:10.5194/bg-10-6225-2013.
Borges, A.V. and G. Abril, 2011: Carbon Dioxide and Methane Dynamics in Estuaries. In: *Treatise on Estuarine and Coastal Science* [Wolanski, E. and D. McLusky (eds.)]. Academic Press, Waltham, MA, USA, pp. 119–161, doi:10.1016/b978-0-12-374711-2.00504-0.
Boscolo-Galazzo, F., K.A. Crichton, S. Barker, and P.N. Pearson, 2018: Temperature dependency of metabolic rates in the upper ocean: A positive feedback to global climate change? *Global and Planetary Change*, **170**, 201–212, doi:10.1016/j.gloplacha.2018.08.017.
Boulton, C.A., B.B.B. Booth, and P. Good, 2017: Exploring uncertainty of Amazon dieback in a perturbed parameter Earth system ensemble. *Global Change Biology*, **23(12)**, 5032–5044, doi:10.1111/gcb.13733.
Bousquet, P. et al., 2006: Contribution of anthropogenic and natural sources to atmospheric methane variability. *Nature*, **443(7110)**, 439–443, doi:10.1038/nature05132.
Bowen, G.J. and J.C. Zachos, 2010: Rapid carbon sequestration at the termination of the Palaeocene–Eocene Thermal Maximum. *Nature Geoscience*, **3(12)**, 866–869, doi:10.1038/ngeo1014.
Bowman, D.M.J.S. et al., 2017: Human exposure and sensitivity to globally extreme wildfire events. *Nature Ecology and Evolution*, doi:10.1038/s41559-016-0058.
Bowman, D.M.J.S. et al., 2020: Vegetation fires in the Anthropocene. *Nature Reviews Earth & Environment*, **1(10)**, 500–515, doi:10.1038/s43017-020-0085-3.
Boyd, P. and C. Vivian, 2019: Should we fertilize oceans or seed clouds? No one knows. *Nature*, **570(7760)**, 155–157, doi:10.1038/d41586-019-01790-7.
Boyd, P.W., S.T. Lennartz, D.M. Glover, and S.C. Doney, 2015: Biological ramifications of climate-change-mediated oceanic multi-stressors. *Nature Climate Change*, **5(1)**, 71–79, doi:10.1038/nclimate2441.
Boyd, P.W., H. Claustre, M. Levy, D.A. Siegel, and T. Weber, 2019: Multi-faceted particle pumps drive carbon sequestration in the ocean. *Nature*, **568(7752)**, 327–335, doi:10.1038/s41586-019-1098-2.
Boysen, L.R., W. Lucht, and D. Gerten, 2017a: Trade-offs for food production, nature conservation and climate limit

ACCEPTED VERSION SUBJECT TO FINAL EDITS

the terrestrial carbon dioxide removal potential. *Global Change Biology*, **23(10)**, 4303–4317, doi:10.1111/gcb.13745.
Boysen, L.R. et al., 2017b: The limits to global-warming mitigation by terrestrial carbon removal. *Earth's Future*, **5(5)**, 463–474, doi:10.1002/2016ef000469.
BP, 2018: *BP Statistical Review of World Energy June 2018*. BP, London, UK, 53 pp.
Brady, R.X., N.S. Lovenduski, S.G. Yeager, M.C. Long, and K. Lindsay, 2020: Skillful multiyear predictions of ocean acidification in the California Current System. *Nature Communications*, **11(1)**, 2166, doi:10.1038/s41467-020-15722-x.
Bralower, T.J. et al., 2018: Evidence for shelf acidification during the onset of the Paleocene-Eocene thermal maximum. *Paleoceanography and Paleoclimatology*, **33(12)**, 1408–1426, doi:10.1029/2018pa003382.
Brando, P.M. et al., 2014: Abrupt increases in Amazonian tree mortality due to drought-fire interactions. *Proceedings of the National Academy of Sciences*, **111(17)**, 6347–6352, doi:10.1073/pnas.1305499111.
Brando, P.M. et al., 2019: Droughts, Wildfires, and Forest Carbon Cycling: A Pantropical Synthesis. *Annual Review of Earth and Planetary Sciences*, **47**, 555–581, doi:10.1146/annurev-earth-082517-010235.
Brando, P.M. et al., 2020: The gathering firestorm in southern Amazonia. *Science Advances*, **6(2)**, doi:10.1126/sciadv.aay1632.
Breider, F. et al., 2019: Response of N2O production rate to ocean acidification in the western North Pacific. *Nature Climate Change*, **9(12)**, 954–958, doi:10.1038/s41558-019-0605-7.
Breitburg, D. et al., 2018: Declining oxygen in the global ocean and coastal waters. *Science*, **359(6371)**, eaam7240, doi:10.1126/science.aam7240.
Brewer, P.G., 2019: The Molecular Basis for Understanding the Impacts of Ocean Warming. *Reviews of Geophysics*, **57(3)**, 1112–1123, doi:10.1029/2018rg000620.
Bridgham, S.D., H. Cadillo-Quiroz, J.K. Keller, and Q. Zhuang, 2013: Methane emissions from wetlands: biogeochemical, microbial, and modeling perspectives from local to global scales. *Global Change Biology*, **19(5)**, 1325–1346, doi:10.1111/gcb.12131.
Brienen, R.J.W. et al., 2015: Long-term decline of the Amazon carbon sink. *Nature*, **519(7543)**, 344–348, doi:10.1038/nature14283.
Brienen, R.J.W. et al., 2017: Tree height strongly affects estimates of water-use efficiency responses to climate and CO2 using isotopes. *Nature Communications*, **8(1)**, 288, doi:10.1038/s41467-017-00225-z.
Bronselaer, B. and L. Zanna, 2020: Heat and carbon coupling reveals ocean warming due to circulation changes. *Nature*, **584(7820)**, 227–233, doi:10.1038/s41586-020-2573-5.
Bronselaer, B., L. Zanna, D.R. Munday, and J. Lowe, 2018: Southern Ocean carbon-wind stress feedback. *Climate Dynamics*, **51(7–8)**, 2743–2757, doi:10.1007/s00382-017-4041-y.
Broucek, J., 2014: Production of Methane Emissions from Ruminant Husbandry: A Review. *Journal of Environmental Protection*, **05(15)**, 1482–1493, doi:10.4236/jep.2014.515141.
Brovkin, V., A. Ganopolski, D. Archer, and G. Munhoven, 2012: Glacial CO2 cycle as a succession of key physical and biogeochemical processes. *Climate of the Past*, **8(1)**, 251–264, doi:10.5194/cp-8-251-2012.
Brovkin, V. et al., 2013: Effect of anthropogenic land-use and land-cover changes on climate and land carbon storage in CMIP5 projections for the twenty-first century. *Journal of Climate*, **26(18)**, 6859–6881, doi:10.1175/jcli-d-12-00623.1.
Brovkin, V. et al., 2016a: Comparative carbon cycle dynamics of the present and last interglacial. *Quaternary Science Reviews*, **137**, 15–32, doi:10.1016/j.quascirev.2016.01.028.
Brovkin, V. et al., 2016b: Comparative carbon cycle dynamics of the present and last interglacial. *Quaternary Science Reviews*, **137**, 15–32, doi:10.1016/j.quascirev.2016.01.028.
Brovkin, V. et al., 2019: What was the source of the atmospheric CO2 increase during the Holocene? *Biogeosciences*, **16(13)**, 2543–2555, doi:10.5194/bg-16-2543-2019.
Bruhn, D., I.M. Møller, T.N. Mikkelsen, and P. Ambus, 2012: Terrestrial plant methane production and emission. *Physiologia Plantarum*, **144(3)**, 201–209, doi:10.1111/j.1399-3054.2011.01551.x.
Bruhwiler, L., F.J.W. Parmentier, P. Crill, M. Leonard, and P.I. Palmer, 2021: The Arctic Carbon Cycle and Its Response to Changing Climate. *Current Climate Change Reports*, 14–34, doi:10.1007/s40641-020-00169-5.
Brune, A., 2018: Methanogenesis in the Digestive Tracts of Insects and Other Arthropods. In: *Biogenesis of Hydrocarbons* [Stams, A. and D. Sousa (eds.)]. Springer, Cham, Switzerland, pp. 1–32, doi:10.1007/978-3-319-53114-4_13-1.
Buchanan, P.J. et al., 2016: The simulated climate of the Last Glacial Maximum and insights into the global marine carbon cycle. *Climate of the Past*, **12(12)**, 2271–2295, doi:10.5194/cp-12-2271-2016.
Buermann, W. et al., 2018: Widespread seasonal compensation effects of spring warming on northern plant productivity. *Nature*, **562(7725)**, 110–114, doi:10.1038/s41586-018-0555-7.
Buitenhuis, E.T., P. Suntharalingam, and C. Le Quéré, 2018a: Constraints on global oceanic emissions of N2O from observations and models. *Biogeosciences*, **15(7)**, 2161–2175, doi:10.5194/bg-15-2161-2018.
Buitenhuis, E.T., P. Suntharalingam, and C. Le Quéré, 2018b: Constraints on global oceanic emissions of N2O from observations and models. *Biogeosciences*, **15(7)**, 2161–2175, doi:10.5194/bg-15-2161-2018.

ACCEPTED VERSION SUBJECT TO FINAL EDITS

Buldovicz, S.N. et al., 2018: Cryovolcanism on the Earth: prigin of a spectacular crater in the Yamal peninsula (Russia). *Scientific Reports*, **8(1)**, 13534, doi:10.1038/s41598-018-31858-9.

Burke, E.J., C.D. Jones, and C.D. Koven, 2013: Estimating the permafrost-carbon climate response in the CMIP5 climate models using a simplified approach. *Journal of Climate*, **26(14)**, 4897–4909, doi:10.1175/jcli-d-12-00550.1.

Burke, E.J., S.E. Chadburn, and A. Ekici, 2017a: A vertical representation of soil carbon in the JULES land surface scheme (vn4.3_permafrost) with a focus on permafrost regions. *Geoscientific Model Development*, **10(2)**, 959–975, doi:10.5194/gmd-10-959-2017.

Burke, E.J. et al., 2017b: Quantifying uncertainties of permafrost carbon–climate feedbacks. *Biogeosciences*, **14(12)**, 3051–3066, doi:10.5194/bg-14-3051-2017.

Burls, N.J. et al., 2017: Active Pacific meridional overturning circulation (PMOC) during the warm Pliocene. *Science Advances*, **3(9)**, e1700156, doi:10.1126/sciadv.1700156.

Burney, J.A., S.J. Davis, and D.B. Lobell, 2010: Greenhouse gas mitigation by agricultural intensification. *Proceedings of the National Academy of Sciences*, **107(26)**, 12052–12057, doi:10.1073/pnas.0914216107.

Burton, C., R.A. Betts, C.D. Jones, and K. Williams, 2018: Will Fire Danger Be Reduced by Using Solar Radiation Management to Limit Global Warming to 1.5°C Compared to 2.0°C? *Geophysical Research Letters*, **45(8)**, 3644–3652, doi:10.1002/2018gl077848.

Bushinsky, S.M. et al., 2019: Reassessing Southern Ocean Air-Sea CO 2 Flux Estimates With the Addition of Biogeochemical Float Observations. *Global Biogeochemical Cycles*, **33(11)**, 1370–1388, doi:10.1029/2019gb006176.

Butterbach-Bahl, K., E.M. Baggs, M. Dannenmann, R. Kiese, and S. Zechmeister-Boltenstern, 2013: Nitrous oxide emissions from soils: how well do we understand the processes and their controls? *Philosophical Transactions of the Royal Society B: Biological Sciences*, **368(1621)**, 20130122–20130122, doi:10.1098/rstb.2013.0122.

Byrne, R.H., S. Mecking, R.A. Feely, and X. Liu, 2010: Direct observations of basin-wide acidification of the North Pacific Ocean. *Geophysical Research Letters*, **37(2)**, L02601, doi:10.1029/2009gl040999.

Cabré, A., I. Marinov, and S. Leung, 2015: Consistent global responses of marine ecosystems to future climate change across the IPCC AR5 earth system models. *Climate Dynamics*, **45(5–6)**, 1253–1280, doi:10.1007/s00382-014-2374-3.

Cai, W.-J. et al., 2011: Acidification of subsurface coastal waters enhanced by eutrophication. *Nature Geoscience*, **4(11)**, 766–770, doi:10.1038/ngeo1297.

Cai, W.-J. et al., 2017: Redox reactions and weak buffering capacity lead to acidification in the Chesapeake Bay. *Nature Communications*, **8(1)**, 369, doi:10.1038/s41467-017-00417-7.

Cai, W.-J. et al., 2020: Controls on surface water carbonate chemistry along North American ocean margins. *Nature Communications*, **11(1)**, 2691, doi:10.1038/s41467-020-16530-z.

Cain, M. et al., 2019: Improved calculation of warming-equivalent emissions for short-lived climate pollutants. *npj Climate and Atmospheric Science*, **2(29)**, doi:10.1038/s41612-019-0086-4.

Caldeira, K. and M.E. Wickett, 2003: Anthropogenic carbon and ocean pH. *Nature*, **425(6956)**, 365–365, doi:10.1038/425365a.

Campbell, J.E. et al., 2017: Large historical growth in global terrestrial gross primary production. *Nature*, **544(7648)**, 84–87, doi:10.1038/nature22030.

Campbell, J.L., J. Sessions, D. Smith, and K. Trippe, 2018: Potential carbon storage in biochar made from logging residue: Basic principles and Southern Oregon case studies. *PLoS ONE*, **13(9)**, doi:10.1371/journal.pone.0203475.

Campos, R., G.F. Pires, and M.H. Costa, 2020: Soil Carbon Sequestration in Rainfed and Irrigated Production Systems in a New Brazilian Agricultural Frontier. *Agriculture* , **10(5)**, doi:10.3390/agriculture10050156.

Canadell, J.G., C.P.M. Meyer, G. Cook, A. Dowdy, and R. Peter, 2020: Multi-decadal increase of forest burned area in Australia is linked to climate change. .

Cao, L., 2018: The effects of solar radiation management on the carbon cycle. *Current Climate Change Reports*.

Cao, L. and J. Jiang, 2017: Simulated Effect of Carbon Cycle Feedback on Climate Response to Solar Geoengineering. *Geophysical Research Letters*, **44(24)**, 12,484–12,491, doi:10.1002/2017gl076546.

Cao, L., H. Zhang, M. Zheng, and S. Wang, 2014: Response of ocean acidification to a gradual increase and decrease of atmospheric CO2. *Environmental Research Letters*, **9(2)**, 024012, doi:10.1088/1748-9326/9/2/024012.

Cao, Z. et al., 2020: The sponge effect and carbon emission mitigation potentials of the global cement cycle. *Nature Communications*, **11(1)**, 1–9, doi:10.1038/s41467-020-17583-w.

Carstensen, J. and D.J. Conley, 2019: Baltic Sea Hypoxia Takes Many Shapes and Sizes. *Limnology and Oceanography Bulletin*, **28(4)**, 125–129, doi:10.1002/lob.10350.

Carstensen, J. and C.M. Duarte, 2019: Drivers of pH variability in coastal ecosystems. *Environmental Science & Technology*, **53(8)**, 4020–4029, doi:10.1021/acs.est.8b03655.

Carstensen, J., J.H. Andersen, B.G. Gustafsson, and D.J. Conley, 2014: Deoxygenation of the Baltic Sea during the last century. *Proceedings of the National Academy of Sciences*, **111(15)**, 5628–5633, doi:10.1073/pnas.1323156111.

ACCEPTED VERSION SUBJECT TO FINAL EDITS

Cartapanis, O., E.D. Galbraith, D. Bianchi, and S.L. Jaccard, 2018: Carbon burial in deep-sea sediment and implications for oceanic inventories of carbon and alkalinity over the last glacial cycle. *Climate of the Past*, **14(11)**, 1819–1850, doi:10.5194/cp-14-1819-2018.

Carter, B.R. et al., 2017a: Two decades of Pacific anthropogenic carbon storage and ocean acidification along Global Ocean Ship-based Hydrographic Investigations Program sections P16 and P02. *Global Biogeochemical Cycles*, **31(2)**, 306–327, doi:10.1002/2016gb005485.

Carter, B.R. et al., 2017b: Two decades of Pacific anthropogenic carbon storage and ocean acidification along Global Ocean Ship-based Hydrographic Investigations Program sections P16 and P02. *Global Biogeochemical Cycles*, **31(1)**, 306–327, doi:10.1002/2016gb005485.

Carter, B.R. et al., 2019: Pacific anthropogenic carbon between 1991 and 2017. *Global Biogeochemical Cycles*, **33(5)**, 597–617, doi:10.1029/2018gb006154.

Cavan, E.L., S.A. Henson, and P.W. Boyd, 2019: The Sensitivity of Subsurface Microbes to Ocean Warming Accentuates Future Declines in Particulate Carbon Export. *Frontiers in Ecology and Evolution*, **6**, doi:10.3389/fevo.2018.00230.

Cavan, E.L., S.A. Henson, A. Belcher, and R. Sanders, 2017: Role of zooplankton in determining the efficiency of the biological carbon pump. *Biogeosciences*, **14(1)**, 177–186, doi:10.5194/bg-14-177-2017.

Cayuela, M.L. et al., 2014: Biochar's role in mitigating soil nitrous oxide emissions: A review and meta-analysis. *Agriculture, Ecosystems & Environment*, **191**, 5–16, doi:10.1016/j.agee.2013.10.009.

Chan, F., J. Barth, K. Kroeker, J. Lubchenco, and B. Menge, 2019: The dynamics and impact of ocean acidification and hypoxia: insights from sustained investigations in the northern California current large marine ecosystem. *Oceanography*, **32(3)**, 62–71, doi:10.5670/oceanog.2019.312.

Chandra, N. et al., 2021: Emissions from the Oil and Gas Sectors, Coal Mining and Ruminant Farming Drive Methane Growth over the Past Three Decades. *Journal of the Meteorological Society of Japan. Ser. II*, **99(2)**, doi:10.2151/jmsj.2021-015.

Chaudhary, N. et al., 2020: Modelling past and future peatland carbon dynamics across the pan-Arctic. *Global Change Biology*, **26(7)**, 4119–4133, doi:10.1111/gcb.15099.

Chavez, F.P., A. Bertrand, R. Guevara-Carrasco, P. Soler, and J. Csirke, 2008: The northern Humboldt Current System: Brief history, present status and a view towards the future. *Progress in Oceanography*, **79(2–4)**, 95–105, doi:10.1016/j.pocean.2008.10.012.

Chen, C.-C., G.-C. Gong, and F.-K. Shiah, 2007: Hypoxia in the East China Sea: One of the largest coastal low-oxygen areas in the world. *Marine Environmental Research*, **64(4)**, 399–408, doi:10.1016/j.marenvres.2007.01.007.

Chen, C.-T.A. et al., 2017: Deep oceans may acidify faster than anticipated due to global warming. *Nature Climate Change*, **7(12)**, 890–894, doi:10.1038/s41558-017-0003-y.

Chen, C.-T.A.A. and A.V. Borges, 2009: Reconciling opposing views on carbon cycling in the coastal ocean: Continental shelves as sinks and near-shore ecosystems as sources of atmospheric CO2. *Deep Sea Research Part II: Topical Studies in Oceanography*, **56(8–10)**, 578–590, doi:10.1016/j.dsr2.2009.01.001.

Chen, P. et al., 2019: Effects of afforestation on soil CH4 and N2O fluxes in a subtropical karst landscape. *Science of The Total Environment*, 135974, doi:10.1016/j.scitotenv.2019.135974.

Chen, Y., A. Liu, and J.C. Moore, 2020: Mitigation of Arctic permafrost carbon loss through stratospheric aerosol geoengineering. *Nature Communications*, **11(1)**, 2430, doi:10.1038/s41467-020-16357-8.

Cheng, L. et al., 2017: Recent increases in terrestrial carbon uptake at little cost to the water cycle. *Nature Communications*, **8(1)**, 110, doi:10.1038/s41467-017-00114-5.

Chevallier, F. et al., 2005: Inferring CO2 sources and sinks from satellite observations: Method and application to TOVS data. *Journal of Geophysical Research*, **110(D24)**, D24309, doi:10.1029/2005jd006390.

Chierici, M. and A. Fransson, 2009: Calcium carbonate saturation in the surface water of the Arctic Ocean: undersaturation in freshwater influenced shelves. *Biogeosciences*, **6(11)**, 2421–2431, doi:10.5194/bg-6-2421-2009.

Chou, W.-C., G.-C. Gong, W.-J. Cai, and C.-M. Tseng, 2013: Seasonality of CO2 in coastal oceans altered by increasing anthropogenic nutrient delivery from large rivers: evidence from the Changjiang–East China Sea system. *Biogeosciences*, **10(6)**, 3889–3899, doi:10.5194/bg-10-3889-2013.

Chowdhry Beeman, J. et al., 2019: Antarctic temperature and CO 2 : Near-synchrony yet variable phasing during the last deglaciation. *Climate of the Past*, **15(3)**, 913–926, doi:10.5194/cp-15-913-2019.

Chu, S.N., Z.A. Wang, S.C. Doney, G.L. Lawson, and K.A. Hoering, 2016: Changes in anthropogenic carbon storage in the Northeast Pacific in the last decade. *Journal of Geophysical Research: Oceans*, **121(7)**, 4618–4632, doi:10.1002/2016jc011775.

Churkina, G. et al., 2020: Buildings as a global carbon sink. *Nature Sustainability*, **3(4)**, 269–276, doi:10.1038/s41893-019-0462-4.

Chuvilin, E., B. Bukhanov, D. Davletshina, S. Grebenkin, and V. Istomin, 2018: Dissociation and self-preservation of gas hydrates in permafrost. *Geosciences*, **8(12)**, 431, doi:10.3390/geosciences8120431.

Ciais, P. et al., 2005: Europe-wide reduction in primary productivity caused by the heat and drought in 2003. *Nature*, **437(7058)**, 529–533, doi:10.1038/nature03972.

ACCEPTED VERSION SUBJECT TO FINAL EDITS

Ciais, P. et al., 2012a: Large inert carbon pool in the terrestrial biosphere during the Last Glacial Maximum. *Nature Geoscience*, **5(1)**, 74–79, doi:10.1038/ngeo1324.
Ciais, P. et al., 2012b: Large inert carbon pool in the terrestrial biosphere during the Last Glacial Maximum. *Nature Geoscience*, **5(1)**, 74–79, doi:10.1038/ngeo1324.
Ciais, P. et al., 2013: Carbon and Other Biogeochemical Cycles. In: *Climate Change 2013: The Physical Science Basis. Contribution of Working Group I to the Fifth Assessment Report of the Intergovernmental Panel on Climate Change* [Stocker, T.F., D. Qin, G.-K. Plattner, M. Tignor, S.K. Allen, J. Boschung, A. Nauels, Y. Xia, V. Bex, and P.M. Midgley (eds.)]. Cambridge University Press, Cambridge, United Kingdom and New York, NY, USA, pp. 465–570, doi:10.1017/cbo9781107415324.015.
Ciais, P. et al., 2019: Five decades of northern land carbon uptake revealed by the interhemispheric CO2 gradient. *Nature*, **568(7751)**, 221–225, doi:10.1038/s41586-019-1078-6.
Claret, M. et al., 2018: Rapid coastal deoxygenation due to ocean circulation shift in the northwest Atlantic. *Nature Climate Change*, **8(10)**, 868–872, doi:10.1038/s41558-018-0263-1.
Clarke, L. et al., 2014: Assessing transformation pathways. In: *Climate Change 2014: Mitigation of Climate Change. Contribution of Working Group III to the Fifth Assessment Report of the Intergovernmental Panel on Climate Change* [Edenhofer, O., R. Pichs-Madruga, Y. Sokona, E. Farahani, S. Kadner, K. Seyboth, A. Adler, I. Baum, S. Brunner, P. Eickemeier, B. Kriemann, J. Savolainen, S. Schlömer, C. von Stechow, T. Zwickel, and J.C. Minx (eds.)]. Cambridge University Press, Cambridge, United Kingdom and New York, NY, USA, pp. 413–510, doi:10.1017/cbo9781107415416.012.
Clarkson, M.O. et al., 2021: Upper limits on the extent of seafloor anoxia during the PETM from uranium isotopes. *Nature Communications*, **12(1)**, 399, doi:10.1038/s41467-020-20486-5.
Clough, T., L. Condron, C. Kammann, and C. Müller, 2013: A review of biochar and soil nitrogen dynamics. *Agronomy*, **3(2)**, 275–293, doi:10.3390/agronomy3020275.
Cobb, A.R. et al., 2017: How temporal patterns in rainfall determine the geomorphology and carbon fluxes of tropical peatlands. *Proceedings of the National Academy of Sciences*, **114(26)**, E5187—E5196, doi:10.1073/pnas.1701090114.
Cocquempot, L. et al., 2019: Coastal Ocean and Nearshore Observation: A French Case Study. *Frontiers in Marine Science*, **6**, 324, doi:10.3389/fmars.2019.00324.
Codispoti, L.A., 2007: An oceanic fixed nitrogen sink exceeding 400 Tg N a^{−1} vs the concept of homeostasis in the fixed-nitrogen inventory. *Biogeosciences*, **4(2)**, 233–253, doi:10.5194/bg-4-233-2007.
Codispoti, L.A., 2010: Interesting Times for Marine N2O. *Science*, **327(5971)**, 1339–1340, doi:10.1126/science.1184945.
Collier, N. et al., 2018: The International Land Model Benchmarking (ILAMB) System: Design, Theory, and Implementation. *Journal of Advances in Modeling Earth Systems*, **10(11)**, 2731–2754, doi:10.1029/2018ms001354.
Collins, M. et al., 2013: Long-term Climate Change: Projections, Commitments and Irreversibility. In: *Climate Change 2013: The Physical Science Basis. Contribution of Working Group I to the Fifth Assessment Report of the Intergovernmental Panel on Climate Change* [Stocker, T.F., D. Qin, G.-K. Plattner, M. Tignor, S.K. Allen, J. Boschung, A. Nauels, Y. Xia, V. Bex, and P.M. Midgley (eds.)]. Cambridge University Press, Cambridge, United Kingdom and New York, NY, USA, pp. 1029–1136, doi:10.1017/cbo9781107415324.024.
Collins, W.J. et al., 2013: Global and regional temperature-change potentials for near-term climate forcers. *Atmospheric Chemistry and Physics*, **13(5)**, 2471–2485, doi:10.5194/acp-13-2471-2013.
Collins, W.J. et al., 2018: Increased importance of methane reduction for a 1.5 degree target. *Environmental Research Letters*, **13(5)**, 054003, doi:10.1088/1748-9326/aab89c.
Commane, R. et al., 2017: Carbon dioxide sources from Alaska driven by increasing early winter respiration from Arctic tundra. *Proceedings of the National Academy of Sciences*, **114(21)**, 5361–5366.
Comyn-Platt, E. et al., 2018: Carbon budgets for 1.5 and 2°C targets lowered by natural wetland and permafrost feedbacks. *Nature Geoscience*, **11(8)**, 568–573, doi:10.1038/s41561-018-0174-9.
Conrad, C.J. and N.S. Lovenduski, 2015: Climate-driven variability in the Southern Ocean carbonate system. *Journal of Climate*, **28(13)**, 5335–5350, doi:10.1175/jcli-d-14-00481.1.
Conway, T.J. et al., 1994: Evidence for interannual variability of the carbon cycle from the National Oceanic and Atmospheric Administration/Climate monitoring and diagnostics laboratory global air sampling network. *Journal of Geophysical Research*, **99(D11)**, 22831, doi:10.1029/94jd01951.
Cooper, C.F., 1983: Carbon storage in managed forests.. *Canadian Journal of Forest Research*, doi:10.1139/x83-022.
Cotovicz, L.C. et al., 2018: Predominance of phytoplankton-derived dissolved and particulate organic carbon in a highly eutrophic tropical coastal embayment (Guanabara Bay, Rio de Janeiro, Brazil). *Biogeochemistry*, **137(1–2)**, 1–14, doi:10.1007/s10533-017-0405-y.
Cotovicz Jr., L.C., B.A. Knoppers, N. Brandini, S.J. Costa Santos, and G. Abril, 2015a: A strong CO2 sink enhanced by eutrophication in a tropical coastal embayment (Guanabara Bay, Rio de Janeiro, Brazil). *Biogeosciences*, **12(20)**, 6125–6146, doi:10.5194/bg-12-6125-2015.
Cotovicz Jr., L.C., B.A. Knoppers, N. Brandini, S.J. Costa Santos, and G. Abril, 2015b: A strong CO2 sink enhanced by

ACCEPTED VERSION SUBJECT TO FINAL EDITS

eutrophication in a tropical coastal embayment (Guanabara Bay, Rio de Janeiro, Brazil). *Biogeosciences*, **12(20)**, 6125–6146, doi:10.5194/bg-12-6125-2015.
Covey, K.R. and J.P. Megonigal, 2019: Methane production and emissions in trees and forests. *New Phytologist*, **222(1)**, 35–51, doi:10.1111/nph.15624.
Cowtan, K. and R.G. Way, 2014: Coverage bias in the HadCRUT4 temperature series and its impact on recent temperature trends. *Quarterly Journal of the Royal Meteorological Society*, **140(683)**, 1935–1944, doi:10.1002/qj.2297.
Cox, P.M., 2019: Emergent constraints on climate-carbon cycle feedbacks. *Current Climate Change Reports*, **5(4)**, 275–281, doi:10.1007/s40641-019-00141-y.
Cox, P.M., R.A. Betts, C.D. Jones, S.A. Spall, and I.J. Totterdell, 2000: Acceleration of global warming due to carbon-cycle feedbacks in a coupled climate model. *Nature*, **408(6809)**, 184–187, doi:10.1038/35041539.
Cox, P.M. et al., 2004: Amazonian forest dieback under climate-carbon cycle projections for the 21st century. *Theoretical and Applied Climatology*, **78(1–3)**, 137–156, doi:10.1007/s00704-004-0049-4.
Cox, P.M. et al., 2013a: Sensitivity of tropical carbon to climate change constrained by carbon dioxide variability. *Nature*, **494(7437)**, 341–344, doi:10.1038/nature11882.
Cox, P.M. et al., 2013b: Sensitivity of tropical carbon to climate change constrained by carbon dioxide variability. *Nature*, **494(7437)**, 341–344, doi:10.1038/nature11882.
Crawford, J.T. et al., 2017: Spatial heterogeneity of within-stream methane concentrations. *Journal of Geophysical Research: Biogeosciences*, **122(5)**, 1036–1048, doi:10.1002/2016jg003698.
Creese, C., S. Oberbauer, P. Rundel, and L. Sack, 2014: Are fern stomatal responses to different stimuli coordinated? Testing responses to light, vapor pressure deficit, and CO2 for diverse species grown under contrasting irradiances. *New Phytologist*, **204(1)**, 92–104, doi:10.1111/nph.12922.
Crichton, K.A., N. Bouttes, D.M. Roche, J. Chappellaz, and G. Krinner, 2016: Permafrost carbon as a missing link to explain CO2 changes during the last deglaciation. *Nature Geoscience*, **9(9)**, 683–686, doi:10.1038/ngeo2793.
Crippa, M. et al., 2020: High resolution temporal profiles in the Emissions Database for Global Atmospheric Research. *Scientific Data*, **7(1)**, 121, doi:10.1038/s41597-020-0462-2.
Cronin, M.F. et al., 2019: Air-sea fluxes with a focus on heat and momentum. *Frontiers in Marine Science*, **6(JUL)**, 430, doi:10.3389/fmars.2019.00430.
Cross, J.N., J.T. Mathis, R.S. Pickart, and N.R. Bates, 2018: Formation and transport of corrosive water in the Pacific Arctic region. *Deep Sea Research Part II: Topical Studies in Oceanography*, **152**, 67–81, doi:10.1016/j.dsr2.2018.05.020.
Crowley, J.W., R.F. Katz, P. Huybers, C.H. Langmuir, and S.-H. Park, 2015: Glacial cycles drive variations in the production of oceanic crust. *Science*, **347(6227)**, 1237–1240, doi:10.1126/science.1261508.
Cui, Y. et al., 2011: Slow release of fossil carbon during the Palaeocene–Eocene Thermal Maximum. *Nature Geoscience*, **4(7)**, 481–485, doi:10.1038/ngeo1179.
D'Olivo, J.P., M.T. McCulloch, S.M. Eggins, and J. Trotter, 2015: Coral records of reef-water pH across the central Great Barrier Reef, Australia: assessing the influence of river runoff on inshore reefs. *Biogeosciences*, **12(4)**, 1223–1236, doi:10.5194/bg-12-1223-2015.
Dagon, K. and D.P. Schrag, 2019: Quantifying the effects of solar geoengineering on vegetation. *Climatic Change*, **153(1–2)**, 235–251, doi:10.1007/s10584-019-02387-9.
Dalsøren, S.B. et al., 2016: Atmospheric methane evolution the last 40 years. *Atmospheric Chemistry and Physics*, **16(5)**, 3099–3126, doi:10.5194/acp-16-3099-2016.
Daneshvar, F. et al., 2017: Evaluating the significance of wetland restoration scenarios on phosphorus removal. *Journal of Environmental Management*, **192**, 184–196, doi:10.1016/j.jenvman.2017.01.059.
Dargie, G.C. et al., 2017: Age, extent and carbon storage of the central Congo Basin peatland complex. *Nature*, **542(7639)**, doi:10.1038/nature21048.
Davidson, E.A., 2009: The contribution of manure and fertilizer nitrogen to atmospheric nitrous oxide since 1860. *Nature Geoscience*, **2(9)**, 659–662, doi:10.1038/ngeo608.
Davies-Barnard, T. et al., 2020: Nitrogen cycling in CMIP6 land surface models: progress and limitations. *Biogeosciences*, **17(20)**, 5129–5148, doi:10.5194/bg-17-5129-2020.
de Coninck, H. et al., 2018: Strengthening and Implementing the Global Response. In: *Global Warming of 1.5°C. An IPCC Special Report on the impacts of global warming of 1.5°C above pre-industrial levels and related global greenhouse gas emission pathways, in the context of strengthening the global response to the threat of climate change,* [Masson-Delmotte, V., P. Zhai, H.-O. Pörtner, D. Roberts, J. Skea, P.R. Shukla, A. Pirani, W. Moufouma-Okia, C. Péan, R. Pidcock, S. Connors, J.B.R. Matthews, Y. Chen, X. Zhou, M.I. Gomis, E. Lonnoy, T. Maycock, M. Tignor, and T. Waterfield (eds.)]. In Press, pp. 313–444.
De Kauwe, M.G. et al., 2013: Forest water use and water use efficiency at elevated CO2 : a model-data intercomparison at two contrasting temperate forest FACE sites. *Global Change Biology*, **19(6)**, 1759–1779, doi:10.1111/gcb.12164.
De Kauwe, M.G. et al., 2014: Where does the carbon go? A model-data intercomparison of vegetation carbon allocation and turnover processes at two temperate forest free-air CO2 enrichment sites. *New Phytologist*, **203(3)**, 883–

ACCEPTED VERSION SUBJECT TO FINAL EDITS

899, doi:10.1111/nph.12847.
de la Vega, E., T.B. Chalk, P.A. Wilson, R.P. Bysani, and G.L. Foster, 2020: Atmospheric CO2 during the Mid-Piacenzian Warm Period and the M2 glaciation. *Scientific Reports*, **10(1)**, 11002, doi:10.1038/s41598-020-67154-8.
de Oliveira Garcia, W. et al., 2020: Impacts of enhanced weathering on biomass production for negative emission technologies and soil hydrology. *Biogeosciences*, **17(7)**, 2107–2133, doi:10.5194/bg-17-2107-2020.
de Richter, R., T. Ming, P. Davies, W. Liu, and S. Caillol, 2017: Removal of non-CO2 greenhouse gases by large-scale atmospheric solar photocatalysis. *Progress in Energy and Combustion Science*, **60**, 68–96, doi:10.1016/j.pecs.2017.01.001.
de Vries, W. et al., 2009: The impact of nitrogen deposition on carbon sequestration by European forests and heathlands. *Forest Ecology and Management*, **258(8)**, 1814–1823, doi:10.1016/j.foreco.2009.02.034.
Dean, J.F. et al., 2018: Methane feedbacks to the global climate system in a warmer world. *Reviews of Geophysics*, **56(1)**, 207–250, doi:10.1002/2017rg000559.
DeConto, R.M. et al., 2008: Thresholds for Cenozoic bipolar glaciation. *Nature*, **455(7213)**, 652–656, doi:10.1038/nature07337.
DeConto, R.M. et al., 2012: Past extreme warming events linked to massive carbon release from thawing permafrost. *Nature*, **484(7392)**, 87–91, doi:10.1038/nature10929.
Deemer, B.R. et al., 2016: Greenhouse Gas Emissions from Reservoir Water Surfaces: A New Global Synthesis. *BioScience*, **66(11)**, 949–964, doi:10.1093/biosci/biw117.
DelSontro, T., J.J. Beaulieu, and J.A. Downing, 2018: Greenhouse gas emissions from lakes and impoundments: Upscaling in the face of global change. *Limnology and Oceanography Letters*, **3(3)**, 64–75, doi:10.1002/lol2.10073.
Denisov, S.N., A. Eliseev, and I.I. Mokhov, 2013: Climate change in IAP RAS global model taking account of interaction with methane cycle under anthropogenic scenarios of RCP family. *Russian Meteorology and Hydrology*, **38(11)**, 741–749, doi:10.3103/s1068373913110034.
Denisov, S.N., A. Eliseev, and I.I. Mokhov, 2019: Contribution of Natural and Anthropogenic Emissions of CO2 and CH4 to the Atmosphere from the Territory of Russia to Global Climate Changes in the Twenty-first Century. *Doklady Earth Sciences*, **488(1)**, 1066–1071, doi:10.1134/s1028334x19090010.
Denman, K.L. et al., 2007: Couplings Between Changes in the Climate System and Biogeochemistry. In: *Climate Change 2007: The Physical Science Basis. Contribution of Working Group I to the Fourth Assessment Report of the Intergovernmental Panel on Climate Change* [Solomon, S., D. Qin, M. Manning, Z. Chen, M. Marquis, K.B. Averyt, M. Tignor, and H.L. Miller (eds.)]. Cambridge University Press, Cambridge, United Kingdom and New York, NY, USA, pp. 499–588.
Denvil-Sommer, A., M. Gehlen, M. Vrac, and C. Mejia, 2019: LSCE-FFNN-v1: a two-step neural network model for the reconstruction of surface ocean pCO2 over the global ocean. *Geoscientific Model Development*, **12(5)**, 2091–2105, doi:10.5194/gmd-12-2091-2019.
Deutsch, C., H. Brix, T. Ito, H. Frenzel, and L.A. Thompson, 2011: Climate-Forced Variability of Ocean Hypoxia. *Science*, **333(6040)**, 336–339, doi:10.1126/science.1202422.
Deutsch, C. et al., 2014: Centennial changes in North Pacific anoxia linked to tropical trade winds. *Science*, **345(6197)**, 665–668, doi:10.1126/science.1252332.
Devaraju, N., G. Bala, K. Caldeira, and R. Nemani, 2016: A model based investigation of the relative importance of CO2-fertilization, climate warming, nitrogen deposition and land use change on the global terrestrial carbon uptake in the historical period. *Climate Dynamics*, doi:10.1007/s00382-015-2830-8.
DeVries, T., 2014: The oceanic anthropogenic CO2 sink: Storage, air-sea fluxes, and transports over the industrial era. *Global Biogeochemical Cycles*, **28(7)**, 631–647, doi:10.1002/2013gb004739.
DeVries, T., M. Holzer, and F. Primeau, 2017: Recent increase in oceanic carbon uptake driven by weaker upper-ocean overturning. *Nature*, **542(7640)**, 215–218, doi:10.1038/nature21068.
DeVries, T. et al., 2019: Decadal trends in the ocean carbon sink. *Proceedings of the National Academy of Sciences*, **116(24)**, 11646, doi:10.1073/pnas.1900371116.
Dickson, A.J., A.S. Cohen, and A.L. Coe, 2012: Seawater oxygenation during the Paleocene-Eocene Thermal Maximum. *Geology*, **40(7)**, 639–642, doi:10.1130/g32977.1.
Dignac, M.F. et al., 2017: Increasing soil carbon storage: mechanisms, effects of agricultural practices and proxies. A review. *Agronomy for Sustainable Development*, doi:10.1007/s13593-017-0421-2.
Dixon, T., J. Garrett, and E. Kleverlaan, 2014: Update on the London Protocol – Developments on Transboundary CCS and on Geoengineering. *Energy Procedia*, **63**, 6623–6628, doi:10.1016/j.egypro.2014.11.698.
Djakovac, T., N. Supić, F. Bernardi Aubry, D. Degobbis, and M. Giani, 2015: Mechanisms of hypoxia frequency changes in the northern Adriatic Sea during the period 1972–2012. *Journal of Marine Systems*, **141**, 179–189, doi:10.1016/j.jmarsys.2014.08.001.
Dlugokencky, E. and P. Tans, 2019: Trends in atmospheric carbon dioxide. National Oceanic and Atmospheric Administration, Earth System Research Laboratory (NOAA/ESRL). Retrieved from: www.esrl.noaa.gov/gmd/ccgg/trends/global.html.

ACCEPTED VERSION SUBJECT TO FINAL EDITS

Dlugokencky, E.J., E.G. Nisbet, R. Fisher, and D. Lowry, 2011: Global atmospheric methane: budget, changes and dangers. *Philosophical Transactions of the Royal Society A: Mathematical, Physical and Engineering Sciences*, **369(1943)**, 2058–2072, doi:10.1098/rsta.2010.0341.

Dlugokencky, E.J. et al., 1994: A dramatic decrease in the growth rate of atmospheric methane in the northern hemisphere during 1992. *Geophysical Research Letters*, **21(1)**, 45–48, doi:10.1029/93gl03070.

Dlugokencky, E.J. et al., 2003: Atmospheric methane levels off: Temporary pause or a new steady-state? *Geophysical Research Letters*, **30(19)**, 1992, doi:10.1029/2003gl018126.

Don, A. et al., 2012: Land-use change to bioenergy production in Europe: implications for the greenhouse gas balance and soil carbon. *GCB Bioenergy*, **4(4)**, 372–391, doi:10.1111/j.1757-1707.2011.01116.x.

Doney, S.C. et al., 2009: Mechanisms governing interannual variability in upper-ocean inorganic carbon system and air–sea CO2 fluxes: Physical climate and atmospheric dust. *Deep Sea Research Part II: Topical Studies in Oceanography*, **56(8–10)**, 640–655, doi:10.1016/j.dsr2.2008.12.006.

Donis, D. et al., 2017: Full-scale evaluation of methane production under oxic conditions in a mesotrophic lake. *Nature Communications*, **8(1)**, 1661, doi:10.1038/s41467-017-01648-4.

Dore, J.E., R. Lukas, D.W. Sadler, M.J. Church, and D.M. Karl, 2009: Physical and biogeochemical modulation of ocean acidification in the central North Pacific. *Proceedings of the National Academy of Sciences*, **106(30)**, 12235–12240, doi:10.1073/pnas.0906044106.

Drake, B.L., D.T. Hanson, T.K. Lowrey, and Z.D. Sharp, 2017: The carbon fertilization effect over a century of anthropogenic CO2 emissions: higher intracellular CO2 and more drought resistance among invasive and native grass species contrasts with increased water use efficiency for woody plants in the US Southwes. *Global Change Biology*, **23(2)**, 782–792, doi:10.1111/gcb.13449.

Drake, J.E. et al., 2011: Increases in the flux of carbon belowground stimulate nitrogen uptake and sustain the long-term enhancement of forest productivity under elevated CO2. *Ecology Letters*, **14(4)**, 349–357, doi:10.1111/j.1461-0248.2011.01593.x.

Drake, J.E. et al., 2018: Three years of soil respiration in a mature eucalypt woodland exposed to atmospheric CO2 enrichment. *Biogeochemistry*, **139(1)**, 85–101, doi:10.1007/s10533-018-0457-7.

Drijfhout, S. et al., 2015: Catalogue of abrupt shifts in Intergovernmental panel on climate change climate models. *Proceedings of the National Academy of Sciences*, **112(43)**, E5777–E5786, doi:10.1073/pnas.1511451112.

Du, C., X. Wang, M. Zhang, J. Jing, and Y. Gao, 2019: Effects of elevated CO2 on plant C-N-P stoichiometry in terrestrial ecosystems: A meta-analysis. *Science of The Total Environment*, **650**, 697–708, doi:10.1016/j.scitotenv.2018.09.051.

Du, E. et al., 2020: Global patterns of terrestrial nitrogen and phosphorus limitation. *Nature Geoscience*, **13(3)**, 221–226, doi:10.1038/s41561-019-0530-4.

Duan, L., L. Cao, G. Bala, and K. Caldeira, 2020: A Model-Based Investigation of Terrestrial Plant Carbon Uptake Response to Four Radiation Modification Approaches. *Journal of Geophysical Research: Atmospheres*, **125(9)**, e2019JD031883, doi:10.1029/2019jd031883.

Duarte, C.M. et al., 2013: Is Ocean Acidification an Open-Ocean Syndrome? Understanding Anthropogenic Impacts on Seawater pH. *Estuaries and Coasts*, **36(2)**, 221–236, doi:10.1007/s12237-013-9594-3.

Dunkley Jones, T. et al., 2013: Climate model and proxy data constraints on ocean warming across the Paleocene–Eocene Thermal Maximum. *Earth-Science Reviews*, **125**, 123–145, doi:10.1016/j.earscirev.2013.07.004.

Dupont, S., N. Dorey, and M. Thorndyke, 2010: What meta-analysis can tell us about vulnerability of marine biodiversity to ocean acidification? *Estuarine, Coastal and Shelf Science*, **89(2)**, 182–185, doi:10.1016/j.ecss.2010.06.013.

Dürr, H.H. et al., 2011: Worldwide typology of nearshore coastal systems: defining the estuarine filter of river inputs to the oceans. *Estuaries and Coasts*, **34(3)**, 441–458, doi:10.1007/s12237-011-9381-y.

Dussin, R., E.N. Curchitser, C.A. Stock, and N. Van Oostende, 2019: Biogeochemical drivers of changing hypoxia in the California Current Ecosystem. *Deep Sea Research Part II: Topical Studies in Oceanography*, **169–170**, 104590, doi:10.1016/j.dsr2.2019.05.013.

Dymond, C.C. et al., 2014: Diversifying managed forests to increase resilience. *Canadian Journal of Forest Research*, **44(10)**, 1196–1205, doi:10.1139/cjfr-2014-0146.

Dyonisius, M.N. et al., 2020: Old carbon reservoirs were not important in the deglacial methane budget. *Science*, **367(6480)**, 907–910, doi:10.1126/science.aax0504.

Earl, N. and I. Simmonds, 2018: Spatial and temporal variability and trends in 2001–2016 global fire activity. *Journal of Geophysical Research: Atmospheres*, doi:10.1002/2017jd027749.

Eby, M. et al., 2013: Historical and idealized climate model experiments: an intercomparison of Earth system models of intermediate complexity. *Climate of the Past*, **9(3)**, 1111–1140, doi:10.5194/cp-9-1111-2013.

Egleston, E.S., C.L. Sabine, and F.M.M. Morel, 2010: Revelle revisited: Buffer factors that quantify the response of ocean chemistry to changes in DIC and alkalinity. *Global Biogeochemical Cycles*, **24(1)**, doi:10.1029/2008gb003407.

Ehlert, D. and K. Zickfeld, 2017: What determines the warming commitment after cessation of CO2 emissions? *Environmental Research Letters*, **12(1)**, 015002, doi:10.1088/1748-9326/aa564a.

ACCEPTED VERSION SUBJECT TO FINAL EDITS

Ehlert, D., K. Zickfeld, M. Eby, and N. Gillett, 2017: The sensitivity of the proportionality between temperature change and cumulative CO2 emissions to ocean mixing. *Journal of Climate*, **30(8)**, 2921–2935, doi:10.1175/jcli-d-16-0247.1.

Ekholm, T. and H. Korhonen, 2016: Climate change mitigation strategy under an uncertain Solar Radiation Management possibility. *Climatic Change*, **139(3)**, 503–515, doi:10.1007/s10584-016-1828-5.

Elberling, B., H.H. Christiansen, and B.U. Hansen, 2010: High nitrous oxide production from thawing permafrost. *Nature Geoscience*, **3(5)**, 332–335, doi:10.1038/ngeo803.

Eliseev, A., I.I. Mokhov, and A. Chernokulsky, 2014a: An ensemble approach to simulate CO2 emissions from natural fires. *Biogeosciences*, **11(12)**, 3205–3223, doi:10.5194/bg-11-3205-2014.

Eliseev, A., I.I. Mokhov, and A. Chernokulsky, 2014b: Influence of ground and peat fires on CO2 emissions into the atmosphere. *Doklady Earth Sciences*, **459(2)**, 1565–1569, doi:10.1134/s1028334x14120034.

Eliseev, A., I.I. Mokhov, M.M. Arzhanov, P.F. Demchenko, and S.N. Denisov, 2008: Interaction of the methane cycle and processes in wetland ecosystems in a climate model of intermediate complexity. *Izvestiya, Atmospheric and Oceanic Physics*, **44(2)**, 139–152, doi:10.1134/s0001433808020011.

Elkins, J.W. et al., 2018: Combined Nitrous Oxide data from the NOAA/ESRL Global Monitoring Division. National Oceanic and Atmospheric Administration, Earth System Research Laboratory (NOAA/ESRL). Retrieved from: www.esrl.noaa.gov/gmd/hats/combined/n2o.html.

Ellison, D. et al., 2017: Trees, forests and water: Cool insights for a hot world. *Global Environmental Change*, **43**, 51–61, doi:10.1016/j.gloenvcha.2017.01.002.

Elsig, J. et al., 2009: Stable isotope constraints on Holocene carbon cycle changes from an Antarctic ice core. *Nature*, **461(7263)**, 507–510, doi:10.1038/nature08393.

Engram, M. et al., 2020: Remote sensing northern lake methane ebullition. *Nature Climate Change*, **10(6)**, 511–517, doi:10.1038/s41558-020-0762-8.

Erb, K.-H. et al., 2018: Unexpectedly large impact of forest management and grazing on global vegetation biomass. *Nature*, **553(7686)**, 73–76, doi:10.1038/nature25138.

Etiope, G., G. Ciotoli, S. Schwietzke, and M. Schoell, 2019: Gridded maps of geological methane emissions and their isotopic signature. *Earth System Science Data*, **11(1)**, 1–22, doi:10.5194/essd-11-1-2019.

Etminan, M., G. Myhre, E.J.J. Highwood, and K.P.P. Shine, 2016: Radiative forcing of carbon dioxide, methane, and nitrous oxide: A significant revision of the methane radiative forcing. *Geophysical Research Letters*, **43(24)**, 12,614–12,623, doi:10.1002/2016gl071930.

Fagundes, M. et al., 2020: Downscaling global ocean climate models improves estimates of exposure regimes in coastal environments. *Scientific Reports*, **10(1)**, 14227, doi:10.1038/s41598-020-71169-6.

Fajardy, M. and N. Mac Dowell, 2017: Can BECCS deliver sustainable and resource efficient negative emissions? *Energy and Environmental Science*, **10(6)**, 1389–1426, doi:10.1039/c7ee00465f.

Fan, L. et al., 2019: Satellite-observed pantropical carbon dynamics. *Nature Plants*, doi:10.1038/s41477-019-0478-9.

Fang, Y. et al., 2017: Global land carbon sink response to temperature and precipitation varies with ENSO phase. *Environmental Research Letters*, **12(6)**, 064007, doi:10.1088/1748-9326/aa6e8e.

FAO, 2019: FAOSTAT: Emissions – Agriculture, Emissions – Land Use, Trade (Crops and livestock products), Population, Agri-Environmental Indicators (Livestock Manure). The Food and Agriculture Organization of the United Nations (FAO), Rome, Italy. Retrieved from: www.fao.org/faostat/en/#data.

Fargione, J.E. et al., 2018: Natural climate solutions for the United States. *Science Advances*, **4(11)**, eaat1869, doi:10.1126/sciadv.aat1869.

Farías, L., V. Besoain, and S. García-Loyola, 2015: Presence of nitrous oxide hotspots in the coastal upwelling area off central Chile: an analysis of temporal variability based on ten years of a biogeochemical time series. *Environmental Research Letters*, **10(4)**, 044017, doi:10.1088/1748-9326/10/4/044017.

Farley, K.A., E.G. Jobbagy, and R.B. Jackson, 2005: Effects of afforestation on water yield: a global synthesis with implications for policy. *Global Change Biology*, **11(10)**, 1565–1576, doi:10.1111/j.1365-2486.2005.01011.x.

Farrior, C.E., I. Rodriguez-Iturbe, R. Dybzinski, S.A. Levin, and S.W. Pacala, 2015: Decreased water limitation under elevated CO2 amplifies potential for forest carbon sinks. *Proceedings of the National Academy of Sciences*, **112(23)**, 7213–7218, doi:10.1073/pnas.1506262112.

Fassbender, A.J., C.L. Sabine, and H.I. Palevsky, 2017: Nonuniform ocean acidification and attenuation of the ocean carbon sink. *Geophysical Research Letters*, **44(16)**, 8404–8413, doi:10.1002/2017gl074389.

Fassbender, A.J. et al., 2018: Seasonal carbonate chemistry variability in marine surface waters of the US Pacific Northwest. *Earth System Science Data*, **10(3)**, doi:10.5194/essd-10-1367-2018.

Fatichi, S., C. Pappas, J. Zscheischler, and S. Leuzinger, 2019: Modelling carbon sources and sinks in terrestrial vegetation. *New Phytologist*, **221(2)**, 652–668, doi:10.1111/nph.15451.

Fatichi, S. et al., 2016: Partitioning direct and indirect effects reveals the response of water-limited ecosystems to elevated CO2. *Proceedings of the National Academy of Sciences of the United States of America*, **113(45)**, 12757–12762, doi:10.1073/pnas.1605036113.

Fay, A.R. and G.A. McKinley, 2014: Global open-ocean biomes: mean and temporal variability. *Earth System Science Data*, **6(2)**, 273–284, doi:10.5194/essd-6-273-2014.

ACCEPTED VERSION SUBJECT TO FINAL EDITS

Feely, R., S. Doney, and S. Cooley, 2009: Ocean Acidification: Present Conditions and Future Changes in a High-CO2 World. *Oceanography*, **22(4)**, 36–47, doi:10.5670/oceanog.2009.95.
Feely, R.A., C.L. Sabine, J.M. Hernandez-Ayon, D. Ianson, and B. Hales, 2008: Evidence for upwelling of corrosive "acidified" water onto the continental shelf. *Science*, **320(5882)**, 1490–1492, doi:10.1126/science.1155676.
Feely, R.A. et al., 2010: The combined effects of ocean acidification, mixing, and respiration on pH and carbonate saturation in an urbanized estuary. *Estuarine, Coastal and Shelf Science*, **88(4)**, 442–449, doi:10.1016/j.ecss.2010.05.004.
Feely, R.A. et al., 2012: Decadal changes in the aragonite and calcite saturation state of the Pacific Ocean. *Global Biogeochemical Cycles*, **26(3)**, 2011GB004157, doi:10.1029/2011gb004157.
Feely, R.A. et al., 2016a: Chemical and biological impacts of ocean acidification along the west coast of North America. *Estuarine, Coastal and Shelf Science*, **183**, 260–270, doi:10.1016/j.ecss.2016.08.043.
Feely, R.A. et al., 2016b: Chemical and biological impacts of ocean acidification along the west coast of North America. *Estuarine, Coastal and Shelf Science*, **183**, 260–270, doi:10.1016/j.ecss.2016.08.043.
Feely, R.A. et al., 2018: The combined effects of acidification and hypoxia on pH and aragonite saturation in the coastal waters of the California current ecosystem and the northern Gulf of Mexico. *Continental Shelf Research*, **152**, 50–60, doi:10.1016/j.csr.2017.11.002.
Feng, E.Y., B. Su, and A. Oschlies, 2020: Geoengineered Ocean Vertical Water Exchange Can Accelerate Global Deoxygenation. *Geophysical Research Letters*, **47(16)**, e2020GL088263, doi:10.1029/2020gl088263.
Fennel, K. and J.M. Testa, 2019: Biogeochemical controls on coastal hypoxia. *Annual Review of Marine Science*, **11(1)**, 105–130, doi:10.1146/annurev-marine-010318-095138.
Fennel, K. et al., 2019: Carbon cycling in the North American coastal ocean: a synthesis. *Biogeosciences*, **16(6)**, 1281–1304, doi:10.5194/bg-16-1281-2019.
Fernández-Martínez, M. et al., 2019: Global trends in carbon sinks and their relationships with CO2 and temperature. *Nature Climate Change*, **9(1)**, 73–79, doi:10.1038/s41558-018-0367-7.
Ferrari, R. et al., 2014: Antarctic sea ice control on ocean circulation in present and glacial climates. *Proceedings of the National Academy of Sciences*, **111(24)**, 8753–8758, doi:10.1073/pnas.1323922111.
Ferretti, D.F. et al., 2005: Unexpected changes to the global methane budget over the past 2000 years.. *Science (New York, N.Y.)*, **309(5741)**, 1714–7, doi:10.1126/science.1115193.
Field, R.D. et al., 2016: Indonesian fire activity and smoke pollution in 2015 show persistent nonlinear sensitivity to El Niño-induced drought. *Proceedings of the National Academy of Sciences*, **113(33)**, 9204–9209, doi:10.1073/pnas.1524888113.
Fine, M., H. Zibrowius, and Y. Loya, 2001: Oculina patagonica : a non-lessepsian scleractinian coral invading the Mediterranean Sea. *Marine Biology*, **138(6)**, 1195–1203, doi:10.1007/s002270100539.
Finzi, A.C. et al., 2007: Increases in nitrogen uptake rather than nitrogen-use efficiency support higher rates of temperate forest productivity under elevated CO2. *Proceedings of the National Academy of Sciences*, **104(35)**, 14014–14019, doi:10.1073/pnas.0706518104.
Fischer, B.M.C. et al., 2019: Improving agricultural water use efficiency with biochar – A synthesis of biochar effects on water storage and fluxes across scales.. *The Science of the total environment*, **657**, 853–862, doi:10.1016/j.scitotenv.2018.11.312.
Fischer, H. et al., 2019: N2O changes from the Last Glacial Maximum to the preindustrial – Part 1: Quantitative reconstruction of terrestrial and marine emissions using N2O stable isotopes in ice cores. *Biogeosciences*, **16(20)**, 3997–4021, doi:10.5194/bg-16-3997-2019.
Fisher, R.A. et al., 2018: Vegetation demographics in Earth System Models: A review of progress and priorities. *Global Change Biology*, **24(1)**, 35–54, doi:10.1111/gcb.13910.
Flach, M. et al., 2021: Vegetation modulates the impact of climate extremes on gross primary production. *Biogeosciences*, **18(1)**, 39–53, doi:10.5194/bg-18-39-2021.
Fleischer, K. et al., 2019: Amazon forest response to CO2 fertilization dependent on plant phosphorus acquisition. *Nature Geoscience*, **12(9)**, 736–741, doi:10.1038/s41561-019-0404-9.
Fleming, E.L., C.H. Jackman, R.S. Stolarski, and A.R. Douglass, 2011: A model study of the impact of source gas changes on the stratosphere for 1850–2100. *Atmospheric Chemistry and Physics*, **11(16)**, 8515–8541, doi:10.5194/acp-11-8515-2011.
Flombaum, P., W.-L. Wang, F.W. Primeau, and A.C. Martiny, 2020: Global picophytoplankton niche partitioning predicts overall positive response to ocean warming. *Nature Geoscience*, **13(2)**, 116–120, doi:10.1038/s41561-019-0524-2.
Forkel, M. et al., 2016: Enhanced seasonal CO2 exchange caused by amplified plant productivity in northern ecosystems. *Science*, **351(6274)**, 696–699, doi:10.1126/science.aac4971.
Forkel, M. et al., 2019: Recent global and regional trends in burned area and their compensating environmental controls. *Environmental Research Communications*, doi:10.1088/2515-7620/ab25d2.
Fornara, D.A. et al., 2011: Increases in soil organic carbon sequestration can reduce the global warming potential of long-term liming to permanent grassland. *Global Change Biology*, **17(5)**, 1925–1934, doi:10.1111/j.1365-2486.2010.02328.x.

ACCEPTED VERSION SUBJECT TO FINAL EDITS

Forster, P. et al., 2018: Mitigation Pathways Compatible with 1.5°C in the Context of Sustainable Development Supplementary Material. In: *Global Warming of 1.5°C. An IPCC Special Report on the impacts of global warming of 1.5°C above pre-industrial levels and related global greenhouse gas emission pathways, in the context of strengthening the global response to the threat of climate change,* [Masson-Delmotte, V., P. Zhai, H.-O. Pörtner, D. Roberts, J. Skea, P.R. Shukla, A. Pirani, W. Moufouma-Okia, C. Péan, R. Pidcock, S. Connors, J.B.R. Matthews, Y. Chen, X. Zhou, M.I. Gomis, E. Lonnoy, T. Maycock, M. Tignor, and T. Waterfield (eds.)]. In Press, pp. 2SM: 1–50.

Forster, P.M. et al., 2020: Current and future global climate impacts resulting from COVID-19. *Nature Climate Change*, **10(10)**, 913–919, doi:10.1038/s41558-020-0883-0.

Forzieri, G., R. Alkama, D.G. Miralles, and A. Cescatti, 2017: Satellites reveal contrasting responses of regional climate to the widespread greening of Earth. *Science*, **356(6343)**, 1180–1184, doi:10.1126/science.aal1727.

Foster, G.L., D.L. Royer, and D.J. Lunt, 2017: Future climate forcing potentially without precedent in the last 420 million years. *Nature Communications*, **8**, 14845, doi:10.1038/ncomms14845.

Fowell, S.E. et al., 2018: Historical trends in pH and carbonate biogeochemistry on the belize mesoamerican barrier reef system. *Geophysical Research Letters*, **45(7)**, 3228–3237, doi:10.1002/2017gl076496.

Francey, R.J. et al., 2003: The CSIRO (Australia) measurement of greenhouse gases in the global atmosphere. In: [Toru, S. and S. Kazuto (eds.)]. WMO TD No. 1138, World Meteorological Organization (WMO), Geneva, Switzerland, pp. 97–111.

Frank, D.C. et al., 2015: Water-use efficiency and transpiration across European forests during the Anthropocene. *Nature Climate Change*, **5(6)**, 579–583, doi:10.1038/nclimate2614.

Fransson, A. et al., 2015: Effect of glacial drainage water on the CO2 system and ocean acidification state in an Arctic tidewater-glacier fjord during two contrasting years. *Journal of Geophysical Research: Oceans*, **120(4)**, 2413–2429, doi:10.1002/2014jc010320.

Fransson, A. et al., 2017: Effects of sea-ice and biogeochemical processes and storms on under-ice water fCO2 during the winter-spring transition in the high Arctic Ocean: Implications for sea-air CO2 fluxes. *Journal of Geophysical Research: Oceans*, **122(7)**, 5566–5587, doi:10.1002/2016jc012478.

Freing, A., D.W.R. Wallace, and H.W. Bange, 2012: Global oceanic production of nitrous oxide. *Philosophical Transactions of the Royal Society B: Biological Sciences*, **367(1593)**, 1245–1255, doi:10.1098/rstb.2011.0360.

Friedlingstein, P., J.-L. Dufresne, P.M. Cox, and P. Rayner, 2003: How positive is the feedback between climate change and the carbon cycle? *Tellus B*, **55(2)**, 692–700, doi:10.1034/j.1600-0889.2003.01461.x.

Friedlingstein, P. et al., 2006: Climate–Carbon Cycle Feedback Analysis: Results from the C 4 MIP Model Intercomparison. *Journal of Climate*, **19(14)**, 3337–3353, doi:10.1175/jcli3800.1.

Friedlingstein, P. et al., 2014a: Persistent growth of CO2 emissions and implications for reaching climate targets. *Nature Geoscience*, **7(10)**, 709–715, doi:10.1038/ngeo2248.

Friedlingstein, P. et al., 2014b: Uncertainties in CMIP5 climate projections due to carbon cycle feedbacks. *Journal of Climate*, **27(2)**, 511–526, doi:10.1175/jcli-d-12-00579.1.

Friedlingstein, P. et al., 2019: Global Carbon Budget 2019. *Earth System Science Data*, **11(4)**, 1783–1838, doi:10.5194/essd-11-1783-2019.

Friedlingstein, P. et al., 2020: Global Carbon Budget 2020. *Earth System Science Data*, **12(4)**, 3269–3340, doi:10.5194/essd-12-3269-2020.

Friend, A.D. et al., 2014: Carbon residence time dominates uncertainty in terrestrial vegetation responses to future climate and atmospheric CO2. *Proceedings of the National Academy of Sciences*, **111(9)**, 3280–3285, doi:10.1073/pnas.1222477110.

Frölicher, T.L. and D.J. Paynter, 2015: Extending the relationship between global warming and cumulative carbon emissions to multi-millennial timescales. *Environmental Research Letters*, **10(7)**, 075002, doi:10.1088/1748-9326/10/7/075002.

Frölicher, T.L. and C. Laufkötter, 2018: Emerging risks from marine heat waves. *Nature Communications*, **9(1)**, 650, doi:10.1038/s41467-018-03163-6.

Frölicher, T.L., F. Joos, C.C. Raible, and J.L. Sarmiento, 2013: Atmospheric CO2 response to volcanic eruptions: The role of ENSO, season, and variability. *Global Biogeochemical Cycles*, **27(1)**, 239–251, doi:10.1002/gbc.20028.

Frölicher, T.L. et al., 2015: Dominance of the Southern Ocean in Anthropogenic Carbon and Heat Uptake in CMIP5 Models. *Journal of Climate*, **28(2)**, 862–886, doi:10.1175/jcli-d-14-00117.1.

Frolking, S.T.E.V.E. and N.I.G.E.L.T. Roulet, 2007: Holocene radiative forcing impact of northern peatland carbon accumulation and methane emissions. *Global Change Biology*, **13(5)**, 1079–1088, doi:10.1111/j.1365-2486.2007.01339.x.

Fu, W., J.T. Randerson, and J.K. Moore, 2016: Climate change impacts on net primary production (NPP) and export production (EP) regulated by increasing stratification and phytoplankton community structure in the CMIP5 models. *Biogeosciences*, **13(18)**, 5151–5170, doi:10.5194/bg-13-5151-2016.

Fujita, R. et al., 2020: Global and Regional CH4 Emissions for 1995–2013 Derived From Atmospheric CH4, δ13C-CH4 , and δD-CH4 Observations and a Chemical Transport Model. *Journal of Geophysical Research: Atmospheres*, **125(14)**, doi:10.1029/2020jd032903.

ACCEPTED VERSION SUBJECT TO FINAL EDITS

Fuss, S. et al., 2018: Negative emissions – Part 2: Costs, potentials and side effects. *Environmental Research Letters*, **13(6)**, 063002, doi:10.1088/1748-9326/aabf9f.
Galbraith, E.D. and M. Kienast, 2013: The acceleration of oceanic denitrification during deglacial warming. *Nature Geoscience*, **6(7)**, 579–584, doi:10.1038/ngeo1832.
Galbraith, E.D. and S.L. Jaccard, 2015: Deglacial weakening of the oceanic soft tissue pump: global constraints from sedimentary nitrogen isotopes and oxygenation proxies. *Quaternary Science Reviews*, **109**, 38–48, doi:10.1016/j.quascirev.2014.11.012.
Galbraith, E.D. and L.C. Skinner, 2020: The biological pump during the Last Glacial Maximum. *Annual Review of Marine Science*, **12(1)**, 559–586, doi:10.1146/annurev-marine-010419-010906.
Ganopolski, A. and V. Brovkin, 2017: Simulation of climate, ice sheets and CO2 evolution during the last four glacial cycles with an Earth system model of intermediate complexity. *Climate of the Past*, **13(12)**, 1695–1716, doi:10.5194/cp-13-1695-2017.
Gasser, T. et al., 2017: Accounting for the climate–carbon feedback in emission metrics. *Earth System Dynamics*, **8(2)**, 235–253, doi:10.5194/esd-8-235-2017.
Gasser, T. et al., 2018: Path-dependent reductions in CO2 emission budgets caused by permafrost carbon release. *Nature Geoscience*, **11(11)**, 830–835, doi:10.1038/s41561-018-0227-0.
Gasser, T. et al., 2020: Historical CO2 emissions from land use and land cover change and their uncertainty. *Biogeosciences*, **17(15)**, 4075–4101, doi:10.5194/bg-17-4075-2020.
Gatti, L. et al., 2014: Drought sensitivity of Amazonian carbon balance revealed by atmospheric measurements. *Nature*, **506(7486)**, 76–80, doi:10.1038/nature12957.
Gattuso, J.-P., M. Frankignoulle, and R. Wollast, 1998: Carbon and carbonate metabolism in coastal aquatic ecosystems. *Annual Review of Ecology and Systematics*, **29(1)**, 405–434, doi:10.1146/annurev.ecolsys.29.1.405.
Gattuso, J.-P. et al., 2015: Contrasting futures for ocean and society from different anthropogenic CO2 emissions scenarios. *Science*, **349(6243)**, aac4722–1, aac47722–10, doi:10.1126/science.aac4722.
Gattuso, J.-P. et al., 2018: Ocean Solutions to Address Climate Change and Its Effects on Marine Ecosystems. *Frontiers in Marine Science*, **5**, 337, doi:10.3389/fmars.2018.00337.
Gauthier, S., P. Bernier, T. Kuuluvainen, A.Z. Shvidenko, and D.G. Schepaschenko, 2015: Boreal forest health and global change. *Science*, **349(6250)**, 819 LP – 822, doi:10.1126/science.aaa9092.
Gedney, N., 2004: Climate feedback from wetland methane emissions. *Geophysical Research Letters*, **31(20)**, L20503, doi:10.1029/2004gl020919.
Gedney, N., C. Huntingford, E. Comyn-Platt, and A. Wiltshire, 2019: Significant feedbacks of wetland methane release on climate change and the causes of their uncertainty. *Environmental Research Letters*, **14(8)**, 84027, doi:10.1088/1748-9326/ab2726.
Genet, H. et al., 2013: Modeling the effects of fire severity and climate warming on active layer thickness and soil carbon storage of black spruce forests across the landscape in interior Alaska. *Environmental Research Letters*, **8(4)**, 45016, doi:10.1088/1748-9326/8/4/045016.
GESAMP, 2019: High level review of a wide range of proposed marine geoengineering techniques. , 144.
Ghosh, A. et al., 2015: Variations in global methane sources and sinks during 1910–2010. *Atmospheric Chemistry and Physics*, **15(5)**, 2595–2612, doi:10.5194/acp-15-2595-2015.
Gibson, C.M., C. Estop-Aragonés, M. Flannigan, D.K. Thompson, and D. Olefeldt, 2019: Increased deep soil respiration detected despite reduced overall respiration in permafrost peat plateaus following wildfire. *Environmental Research Letters*, **14(12)**, doi:10.1088/1748-9326/ab4f8d.
Gidden, M.J. et al., 2018: Global emissions pathways under different socioeconomic scenarios for use in CMIP6: a dataset of harmonized emissions trajectories through the end of the century. *Geoscientific Model Development Discussions*, 1–42, doi:10.5194/gmd-2018-266.
Gillett, N.P., V.K. Arora, D. Matthews, and M.R. Allen, 2013: Constraining the ratio of global warming to cumulative CO2 emissions using CMIP5 simulations. *Journal of Climate*, **26(18)**, 6844–6858, doi:10.1175/jcli-d-12-00476.1.
Gingerich, P.D., 2019: Temporal Scaling of Carbon Emission and Accumulation Rates: Modern Anthropogenic Emissions Compared to Estimates of PETM Onset Accumulation. *Paleoceanography and Paleoclimatology*, 1–7, doi:10.1029/2018pa003379.
Gitz, V. and P. Ciais, 2003: Amplifying effects of land-use change on future atmospheric CO2 levels. *Global Biogeochemical Cycles*, **17(1)**, 1–15, doi:10.1029/2002gb001963.
Glienke, S., P.J. Irvine, and M.G. Lawrence, 2015: The impact of geoengineering on vegetation in experiment G1 of the GeoMIP. *Journal of Geophysical Research: Atmospheres*, **120(19)**, 10,196–10,213, doi:10.1002/2015jd024202.
Gloege, L. et al., 2020: Quantifying errors in observationally-based estimates of ocean carbon sink variability. , doi:10.1002/essoar.10502036.2.
Gloor, M., J.L. Sarmiento, and N. Gruber, 2010: What can be learned about carbon cycle climate feedbacks from the CO2 airborne fraction? *Atmospheric Chemistry and Physics*, **10(16)**, 7739–7751, doi:10.5194/acp-10-7739-

ACCEPTED VERSION SUBJECT TO FINAL EDITS

2010.
Goldewijk, K.K., A. Beusen, J. Doelman, and E. Stehfest, 2017: Anthropogenic land use estimates for the Holocene - HYDE 3.2. *Earth System Science Data*, **9(2)**, 927–953, doi:10.5194/essd-9-927-2017.
Goll, D.S. et al., 2012: Nutrient limitation reduces land carbon uptake in simulations with a model of combined carbon, nitrogen and phosphorus cycling. *Biogeosciences*, **9(9)**, 3547–3569, doi:10.5194/bg-9-3547-2012.
Goll, D.S. et al., 2017: Carbon–nitrogen interactions in idealized simulations with JSBACH (version 3.10). *Geoscientific Model Development*, **10(5)**, 2009–2030, doi:10.5194/gmd-10-2009-2017.
González, M.F., T. Ilyina, S. Sonntag, and H. Schmidt, 2018: Enhanced rates of regional warming and ocean acidification after termination of large-scale ocean alkalinization. *Geophysical Research Letters*, **45(14)**, 7120–7129, doi:10.1029/2018gl077847.
González-Dávila, M., J.M. Santana-Casiano, M.J. Rueda, and O. Llinás, 2010: The water column distribution of carbonate system variables at the ESTOC site from 1995 to 2004. *Biogeosciences*, **7(10)**, 3067–3081, doi:10.5194/bg-7-3067-2010.
Good, P., C. Jones, J. Lowe, R. Betts, and N. Gedney, 2013: Comparing tropical forest projections from two denerations of Hadley Centre Earth System Models, HadGEM2-ES and HadCM3LC. *Journal of Climate*, **26(2)**, 495–511, doi:10.1175/jcli-d-11-00366.1.
Good, P. et al., 2011: Quantifying environmental drivers of future tropical forest extent. *Journal of Climate*, **24(5)**, 1337–1349, doi:10.1175/2010jcli3865.1.
Goodkin, N.F. et al., 2015: Ocean circulation and biogeochemistry moderate interannual and decadal surface water pH changes in the Sargasso Sea. *Geophysical Research Letters*, **42(12)**, 4931–4939, doi:10.1002/2015gl064431.
Goodwin, P., R.G. Williams, and A. Ridgwell, 2015: Sensitivity of climate to cumulative carbon emissions due to compensation of ocean heat and carbon uptake. *Nature Geoscience*, **8(1)**, 29–34, doi:10.1038/ngeo2304.
Goodwin, P. et al., 2018: Pathways to 1.5°C and 2°C warming based on observational and geological constraints. *Nature Geoscience*, **11(2)**, 102–107, doi:10.1038/s41561-017-0054-8.
Gottschalk, J. et al., 2016: Biological and physical controls in the Southern Ocean on past millennial-scale atmospheric CO2 changes. *Nature Communications*, **7(1)**, 11539, doi:10.1038/ncomms11539.
Gottschalk, J. et al., 2019: Mechanisms of millennial-scale atmospheric CO2 change in numerical model simulations. *Quaternary Science Reviews*, **220**, 30–74, doi:10.1016/j.quascirev.2019.05.013.
Gottschalk, J. et al., 2020: Glacial heterogeneity in Southern Ocean carbon storage abated by fast South Indian deglacial carbon release. *Nature Communications*, **11(1)**, 6192, doi:10.1038/s41467-020-20034-1.
Govindasamy, B., S. Thompson, P.B. Duffy, K. Caldeira, and C. Delire, 2002: Impact of geoengineering schemes on the terrestrial biosphere. *Geophysical Research Letters*, **29(22)**, 18–1–18–4, doi:10.1029/2002gl015911.
Grassi, G. et al., 2018: Reconciling global-model estimates and country reporting of anthropogenic forest CO2 sinks. *Nature Climate Change*, **8(10)**, 914–920, doi:10.1038/s41558-018-0283-x.
Graven, H. et al., 2017: Compiled records of carbon isotopes in atmospheric CO2 for historical simulations in CMIP6. *Geoscientific Model Development*, **10(12)**, 4405–4417, doi:10.5194/gmd-10-4405-2017.
Graven, H.D. et al., 2013: Enhanced Seasonal Exchange of CO2 by Northern Ecosystems Since 1960. *Science*, **341(6150)**, 1085–1089, doi:10.1126/science.1239207.
Green, J.K. et al., 2019: Large influence of soil moisture on long-term terrestrial carbon uptake. *Nature*, **565(7740)**, 476–479, doi:10.1038/s41586-018-0848-x.
Gregor, L., S. Kok, and P.M.S. Monteiro, 2018: Interannual drivers of the seasonal cycle of CO2 in the Southern Ocean. *Biogeosciences*, **15(8)**, 2361–2378, doi:10.5194/bg-15-2361-2018.
Gregor, L., A.D. Lebehot, S. Kok, and P.M. Scheel Monteiro, 2019: A comparative assessment of the uncertainties of global surface ocean CO2 estimates using a machine-learning ensemble (CSIR-ML6 version 2019a) – have we hit the wall? *Geoscientific Model Development*, **12(12)**, 5113–5136, doi:10.5194/gmd-12-5113-2019.
Gregory, J.M., T. Andrews, and P. Good, 2015: The inconstancy of the transient climate response parameter under increasing CO2. *Philosophical Transactions of the Royal Society A: Mathematical, Physical and Engineering Sciences*, **373(2054)**, 20140417, doi:10.1098/rsta.2014.0417.
Gregory, J.M., C.D. Jones, P. Cadule, and P. Friedlingstein, 2009: Quantifying Carbon Cycle Feedbacks. *Journal of Climate*, **22(19)**, 5232–5250, doi:10.1175/2009jcli2949.1.
Griscom, B.W. et al., 2017: Natural climate solutions. *Proceedings of the National Academy of Sciences*, **114(44)**, 11645–11650, doi:10.1073/pnas.1710465114.
Griscom, B.W. et al., 2020: National mitigation potential from natural climate solutions in the tropics. *Philosophical Transactions of the Royal Society B: Biological Sciences*, **375(1794)**, 20190126, doi:10.1098/rstb.2019.0126.
Gromov, S., C.A.M. Brenninkmeijer, and P. Jöckel, 2018: A very limited role of tropospheric chlorine as a sink of the greenhouse gas methane. *Atmospheric Chemistry and Physics*, **18(13)**, 9831–9843, doi:10.5194/acp-18-9831-2018.
Grossiord, C. et al., 2020: Plant responses to rising vapor pressure deficit. *New Phytologist*, **226(6)**, 1550–1566, doi:10.1111/nph.16485.
Gruber, N., 2011: Warming up, turning sour, losing breath: ocean biogeochemistry under global change. *Philosophical Transactions of the Royal Society A: Mathematical, Physical and Engineering Sciences*, **369(1943)**, 1980–

ACCEPTED VERSION SUBJECT TO FINAL EDITS

1996, doi:10.1098/rsta.2011.0003.
Gruber, N. and J.N. Galloway, 2008: An Earth-system perspective of the global nitrogen cycle. *Nature*, **451(7176)**, 293–296, doi:10.1038/nature06592.
Gruber, N., P. Landschützer, and N.S. Lovenduski, 2019a: The variable Southern Ocean carbon sink. *Annual Review of Marine Science*, **11(1)**, 159–186, doi:10.1146/annurev-marine-121916-063407.
Gruber, N. et al., 2019b: The oceanic sink for anthropogenic CO 2 from 1994 to 2007. *Science*, **363(6432)**, 1193–1199, doi:10.1126/science.aau5153.
Gruber, N. et al., 2019c: The oceanic sink for anthropogenic CO2 from 1994 to 2007. *Science*, **363(6432)**, 1193–1199, doi:10.1126/science.aau5153.
Gu, J. et al., 2017: Trade-off between soil organic carbon sequestration and nitrous oxide emissions from winter wheat-summer maize rotations: Implications of a 25-year fertilization experiment in Northwestern China. *Science of The Total Environment*, **595**, 371–379, doi:10.1016/j.scitotenv.2017.03.280.
Guanter, L. et al., 2014: Global and time-resolved monitoring of crop photosynthesis with chlorophyll fluorescence. *Proceedings of the National Academy of Sciences*, **111(14)**, E1327–E1333, doi:10.1073/pnas.1320008111.
Guenet, B. et al., 2018: Impact of priming on global soil carbon stocks. *Global Change Biology*, **24(5)**, 1873–1883, doi:10.1111/gcb.14069.
Guerrieri, R. et al., 2019: Disentangling the role of photosynthesis and stomatal conductance on rising forest water-use efficiency. *Proceedings of the National Academy of Sciences of the United States of America*, **116(34)**, 16909–16914, doi:10.1073/pnas.1905912116.
Guidi, L. et al., 2009: Effects of phytoplankton community on production, size, and export of large aggregates: A world-ocean analysis. *Limnology and Oceanography*, **54(6)**, 1951–1963, doi:10.4319/lo.2009.54.6.1951.
Guimberteau, M. et al., 2018: ORCHIDEE-MICT (v8.4.1), a land surface model for the high latitudes: model description and validation. *Geoscientific Model Development*, **11(1)**, 121–163, doi:10.5194/gmd-11-121-2018.
Günther, A. et al., 2020: Prompt rewetting of drained peatlands reduces climate warming despite methane emissions. *Nature Communications*, **11(1)**, 1644, doi:10.1038/s41467-020-15499-z.
Gupta, G.V.M. et al., 2016: Evolution to decay of upwelling and associated biogeochemistry over the southeastern Arabian Sea shelf. *Journal of Geophysical Research: Biogeosciences*, **121(1)**, 159–175, doi:10.1002/2015jg003163.
Gutjahr, M. et al., 2017: Very large release of mostly volcanic carbon during the Palaeocene–Eocene Thermal Maximum. *Nature*, **548(7669)**, 573–577, doi:10.1038/nature23646.
Hain, M.P., D.M. Sigman, and G.H. Haug, 2010: Carbon dioxide effects of Antarctic stratification, North Atlantic Intermediate Water formation, and subantarctic nutrient drawdown during the last ice age: Diagnosis and synthesis in a geochemical box model. *Global Biogeochemical Cycles*, **24(4)**, GB4023, doi:10.1029/2010gb003790.
Hajima, T., K. Tachiiri, A. Ito, and M. Kawamiya, 2014: Uncertainty of concentration–terrestrial carbon feedback in Earth System Models*. *Journal of Climate*, **27(9)**, 3425–3445, doi:10.1175/jcli-d-13-00177.1.
Hajima, T. et al., 2020a: Development of the MIROC-ES2L Earth system model and the evaluation of biogeochemical processes and feedbacks. *Geoscientific Model Development*, **13(5)**, 2197–2244, doi:10.5194/gmd-13-2197-2020.
Hajima, T. et al., 2020b: Millennium time-scale experiments on climate-carbon cycle with doubled CO2 concentration. *Progress in Earth and Planetary Science*, **7(1)**, 1–19, doi:10.1186/s40645-020-00350-2.
Hall, A., P. Cox, C. Huntingford, and S. Klein, 2019: Progressing emergent constraints on future climate change. *Nature Climate Change*, **9(4)**, 269–278, doi:10.1038/s41558-019-0436-6.
Hall, B.D., G.S. Dutton, and J.W. Elkins, 2007: The NOAA nitrous oxide standard scale for atmospheric observations. *Journal of Geophysical Research*, **112(D9)**, D09305, doi:10.1029/2006jd007954.
Hamilton, S.E. and D.A. Friess, 2018: Global carbon stocks and potential emissions due to mangrove deforestation from 2000 to 2012. *Nature Climate Change*, **8(3)**, 240–244, doi:10.1038/s41558-018-0090-4.
Hansell, D.A., C.A. Carlson, D.J. Repeta, and R. Schlitzer, 2009: Dissolved organic matter in the ocean a controversy stim ulates new insights. *Oceanography*, **22(SPL.ISS. 4)**, 202–211, doi:10.5670/oceanog.2009.109.
Hansis, E., S.J. Davis, and J. Pongratz, 2015: Relevance of methodological choices for accounting of land use change carbon fluxes. *Global Biogeochemical Cycles*, **29(8)**, 1230–1246, doi:10.1002/2014gb004997.
Hantson, S. et al., 2020: Quantitative assessment of fire and vegetation properties in simulations with fire-enabled vegetation models from the Fire Model Intercomparison Project. *Geoscientific Model Development*, **13(7)**, 3299–3318, doi:10.5194/gmd-13-3299-2020.
Harenda, K.M., M. Lamentowicz, M. Samson, and B.H. Chojnicki, 2018: The role of peatlands and their carbon storage function in the context of climate change. In: *Interdisciplinary Approaches for Sustainable Development Goals: Economic Growth, Social Inclusion and Environmental Protection* [Zielinski, T., I. Sagan, and W. Surosz (eds.)]. Springer, Cham, Switzerland, pp. 169–187, doi:10.1007/978-3-319-71788-3_12.
Harper, A.B. et al., 2018: Land-use emissions play a critical role in land-based mitigation for Paris climate targets. *Nature Communications*, **9(1)**, 2938, doi:10.1038/s41467-018-05340-z.
Harris, I., P.D. Jones, T.J. Osborn, and D.H. Lister, 2014: Updated high-resolution grids of monthly climatic

ACCEPTED VERSION SUBJECT TO FINAL EDITS

observations – the CRU TS3.10 Dataset. *International Journal of Climatology*, **34(3)**, 623–642, doi:10.1002/joc.3711.
Harrison, S.P. et al., 2018: The biomass burning contribution to climate–carbon-cycle feedback. *Earth System Dynamics*, **9(2)**, 663–677, doi:10.5194/esd-9-663-2018.
Hartmann, J. et al., 2013: Enhanced chemical weathering as a geoengineering strategy to reduce atmospheric carbon dioxide, supply nutrients, and mitigate ocean acidification. *Reviews of Geophysics*, **51(2)**, 113–149, doi:10.1002/rog.20004.
Hauck, J. and C. Völker, 2015: Rising atmospheric CO2 leads to large impact of biology on Southern Ocean CO2 uptake via changes of the Revelle factor. *Geophysical Research Letters*, **42(5)**, 1459–1464, doi:10.1002/2015gl063070.
Hauck, J., P. Köhler, D. Wolf-Gladrow, and C. Völker, 2016: Iron fertilisation and century-scale effects of open ocean dissolution of olivine in a simulated CO2 removal experiment. *Environmental Research Letters*, **11(2)**, 024007, doi:10.1088/1748-9326/11/2/024007.
Hauck, J., M. Hoppema, R.G.J. Bellerby, C. Völker, and D. Wolf-Gladrow, 2010: Data-based estimation of anthropogenic carbon and acidification in the Weddell Sea on a decadal timescale. *Journal of Geophysical Research*, **115(C3)**, C03004, doi:10.1029/2009jc005479.
Hauck, J. et al., 2015: On the Southern Ocean CO2 uptake and the role of the biological carbon pump in the 21st century. *Global Biogeochemical Cycles*, **29(9)**, 1451–1470, doi:10.1002/2015gb005140.
Hauck, J. et al., 2020: Consistency and Challenges in the Ocean Carbon Sink Estimate for the Global Carbon Budget. *Frontiers in Marine Science*, **7**, 852, doi:10.3389/fmars.2020.571720.
Hauri, C., T. Friedrich, and A. Timmermann, 2016: Abrupt onset and prolongation of aragonite undersaturation events in the Southern Ocean. *Nature Climate Change*, **6(2)**, 172–176, doi:10.1038/nclimate2844.
Hauri, C. et al., 2013: Spatiotemporal variability and long-term trends of ocean acidification in the California Current System. *Biogeosciences*, **10(1)**, 193–216, doi:10.5194/bg-10-193-2013.
Hauri, C. et al., 2015: Two decades of inorganic carbon dynamics along the West Antarctic Peninsula. *Biogeosciences*, **12(22)**, 6761–6779, doi:10.5194/bg-12-6761-2015.
Hauri, C. et al., 2020: A regional hindcast model simulating ecosystem dynamics, inorganic carbon chemistry, and ocean acidification in the Gulf of Alaska. *Biogeosciences*, **17(14)**, 3837–3857, doi:10.5194/bg-17-3837-2020.
Haustein, K. et al., 2017: A real-time Global Warming Index. *Scientific Reports*, **7(1)**, 15417, doi:10.1038/s41598-017-14828-5.
He, J., V. Naik, L.W. Horowitz, E. Dlugokencky, and K. Thoning, 2020: Investigation of the global methane budget over 1980–2017 using GFDL-AM4.1. *Atmospheric Chemistry and Physics*, **20(2)**, 805–827, doi:10.5194/acp-20-805-2020.
He, Y. et al., 2016: Radiocarbon constraints imply reduced carbon uptake by soils during the 21st century. *Science*, **353(6306)**, 1419 LP – 1424, doi:10.1126/science.aad4273.
Heck, V., D. Gerten, W. Lucht, and L.R. Boysen, 2016: Is extensive terrestrial carbon dioxide removal a 'green' form of geoengineering? A global modelling study. *Global and Planetary Change*, **137**, 123–130, doi:10.1016/j.gloplacha.2015.12.008.
Heck, V., D. Gerten, W. Lucht, and A. Popp, 2018: Biomass-based negative emissions difficult to reconcile with planetary boundaries. *Nature Climate Change*, **8(2)**, 151–155, doi:10.1038/s41558-017-0064-y.
Helm, K.P., N.L. Bindoff, and J.A. Church, 2011: Observed decreases in oxygen content of the global ocean. *Geophysical Research Letters*, **38(23)**, L23602, doi:10.1029/2011gl049513.
Hemes, K.S. et al., 2019: Assessing the carbon and climate benefit of restoring degraded agricultural peat soils to managed wetlands. *Agricultural and Forest Meteorology*, **268**, 202–214, doi:10.1016/j.agrformet.2019.01.017.
Henderson, B.B. et al., 2015: Greenhouse gas mitigation potential of the world's grazing lands: Modeling soil carbon and nitrogen fluxes of mitigation practices. *Agriculture, Ecosystems & Environment*, **207**, 91–100, doi:10.1016/j.agee.2015.03.029.
Henley, S.F. et al., 2020: Changing Biogeochemistry of the Southern Ocean and Its Ecosystem Implications. *Frontiers in Marine Science*, **7**, 581, doi:10.3389/fmars.2020.00581.
Henson, S.A., C. Beaulieu, and R. Lampitt, 2016: Observing climate change trends in ocean biogeochemistry: when and where. *Global Change Biology*, **22(4)**, 1561–1571, doi:10.1111/gcb.13152.
Herndl, G.J. and T. Reinthaler, 2013: Microbial control of the dark end of the biological pump. *Nature Geoscience*, **6(9)**, 718–724, doi:10.1038/ngeo1921.
Herrington, T. and K. Zickfeld, 2014: Path independence of climate and carbon cycle response over a broad range of cumulative carbon emissions. *Earth System Dynamics*, **5(2)**, 409–422, doi:10.5194/esd-5-409-2014.
Hewitt, H.T. et al., 2016: The impact of resolving the Rossby radius at mid-latitudes in the ocean: Results from a high-resolution version of the Met Office GC2 coupled model. *Geoscientific Model Development*, **9(10)**, 3655–3670, doi:10.5194/gmd-9-3655-2016.
Hicks Pries, C.E., E.A.G. Schuur, and K.G. Crummer, 2013: Thawing permafrost increases old soil and autotrophic respiration in tundra: Partitioning ecosystem respiration using δ13C and Δ14C. *Global Change Biology*, **19(2)**, 649–661, doi:10.1111/gcb.12058.

ACCEPTED VERSION SUBJECT TO FINAL EDITS

Hicks Pries, C.E., C. Castanha, R.C. Porras, and M.S. Torn, 2017: The whole-soil carbon flux in response to warming. *Science*, **355(6332)**, 1420 LP – 1423, doi:10.1126/science.aal1319.
Higgins, S.I. and S. Scheiter, 2012: Atmospheric CO2 forces abrupt vegetation shifts locally, but not globally. *Nature*, **488(7410)**, 209–212, doi:10.1038/nature11238.
Hirota, M., M. Holmgren, E.H. Van Nes, and M. Scheffer, 2011: Global resilience of tropical forest and savanna to critical transitions. *Science*, **334(6053)**, 232–235, doi:10.1126/science.1210657.
Hmiel, B. et al., 2020: Preindustrial 14CH4 indicates greater anthropogenic fossil CH4 emissions. *Nature*, **578(7795)**, 409–412, doi:10.1038/s41586-020-1991-8.
Hoffman, F.M. et al., 2014: Causes and implications of persistent atmospheric carbon dioxide biases in Earth System Models. *Journal of Geophysical Research: Biogeosciences*, **119(2)**, 141–162, doi:10.1002/2013jg002381.
Höglund-Isaksson, L., A. Gómez-Sanabria, Z. Klimont, P. Rafaj, and W. Schöpp, 2020: Technical potentials and costs for reducing global anthropogenic methane emissions in the 2050 timeframe – results from the GAINS model. *Environmental Research Communications*, **2(2)**, 025004, doi:10.1088/2515-7620/ab7457.
Holden, Z.A. et al., 2018a: Decreasing fire season precipitation increased recent western US forest wildfire activity. *Proceedings of the National Academy of Sciences of the United States of America*, doi:10.1073/pnas.1802316115.
Holden, Z.A. et al., 2018b: Decreasing fire season precipitation increased recent western US forest wildfire activity. *Proceedings of the National Academy of Sciences of the United States of America*, doi:10.1073/pnas.1802316115.
Holl, D., E.-M. Pfeiffer, and L. Kutzbach, 2020: Comparison of eddy covariance CO2 and CH4 fluxes from mined and recently rewetted sections in a northwestern German cutover bog. *Biogeosciences*, **17(10)**, 2853–2874, doi:10.5194/bg-17-2853-2020.
Holl, K.D. and P.H.S. Brancalion, 2020: Tree planting is not a simple solution. *Science*, **368(6491)**, 580–581, doi:10.1126/science.aba8232.
Hönisch, B. and N.G. Hemming, 2005: Surface ocean pH response to variations in pCO2 through two full glacial cycles. *Earth and Planetary Science Letters*, **236(1–2)**, 305–314, doi:10.1016/j.epsl.2005.04.027.
Hoogakker, B.A.A., H. Elderfield, G. Schmiedl, I.N. McCave, and R.E.M. Rickaby, 2015: Glacial–interglacial changes in bottom-water oxygen content on the Portuguese margin. *Nature Geoscience*, **8(1)**, 40–43, doi:10.1038/ngeo2317.
Hoogakker, B.A.A. et al., 2018: Glacial expansion of oxygen-depleted seawater in the eastern tropical Pacific. *Nature*, **562(7727)**, 410–413, doi:10.1038/s41586-018-0589-x.
Hopcroft, P.O., P.J. Valdes, F.M. O'Connor, J.O. Kaplan, and D.J. Beerling, 2017: Understanding the glacial methane cycle. *Nature Communications*, **8**, doi:10.1038/ncomms14383.
Hopwood, M.J. et al., 2020: Review article: How does glacier discharge affect marine biogeochemistry and primary production in the Arctic? *The Cryosphere*, **14(4)**, 1347–1383, doi:10.5194/tc-14-1347-2020.
Horowitz, H.M. et al., 2020: Effects of Sea Salt Aerosol Emissions for Marine Cloud Brightening on Atmospheric Chemistry: Implications for Radiative Forcing. *Geophysical Research Letters*, **47(4)**, e2019GL085838, doi:10.1029/2019gl085838.
Hossaini, R. et al., 2016: A global model of tropospheric chlorine chemistry: Organic versus inorganic sources and impact on methane oxidation. *Journal of Geophysical Research: Atmospheres*, **121(23)**, 14,271–14,297, doi:10.1002/2016jd025756.
Houghton, R.A., 2013: Keeping management effects separate from environmental effects in terrestrial carbon accounting. *Global Change Biology*, **19(9)**, 2609–2612, doi:10.1111/gcb.12233.
Houghton, R.A. and A.A. Nassikas, 2017: Global and regional fluxes of carbon from land use and land cover change 1850-2015. *Global Biogeochemical Cycles*, **31(3)**, 456–472, doi:10.1002/2016gb005546.
Houweling, S. et al., 2015: An intercomparison of inverse models for estimating sources and sinks of CO2 using GOSAT measurements. *Journal of Geophysical Research: Atmospheres*, **120(10)**, 5253–5266, doi:10.1002/2014jd022962.
Hovenden, M.J. et al., 2019: Globally consistent influences of seasonal precipitation limit grassland biomass response to elevated CO2. *Nature Plants*, **5(2)**, 167–173, doi:10.1038/s41477-018-0356-x.
Howard, J. et al., 2017: The potential to integrate blue carbon into MPA design and management. *Aquatic Conservation: Marine and Freshwater Ecosystems*, **27**, 100–115, doi:10.1002/aqc.2809.
Howarth, R.W., 2019: Ideas and perspectives: is shale gas a major driver of recent increase in global atmospheric methane? *Biogeosciences*, **16(15)**, 3033–3046, doi:10.5194/bg-16-3033-2019.
Hristov, A.N. et al., 2013: SPECIAL TOPICS - Mitigation of methane and nitrous oxide emissions from animal operations: I. A review of enteric methane mitigation options1. *Journal of Animal Science*, **91(11)**, 5045–5069, doi:10.2527/jas.2013-6583.
Hu, F.S. et al., 2010: Tundra burning in Alaska: Linkages to climatic change and sea ice retreat. *Journal of Geophysical Research: Biogeosciences*, **115(G4)**, doi:10.1029/2009jg001270.
Hu, M., D. Chen, and R.A. Dahlgren, 2016: Modeling nitrous oxide emission from rivers: a global assessment. *Global Change Biology*, **22(11)**, 3566–3582, doi:10.1111/gcb.13351.

ACCEPTED VERSION SUBJECT TO FINAL EDITS

Hua, F. et al., 2016: Opportunities for biodiversity gains under the world's largest reforestation programme. *Nature Communications*, **7(1)**, 12717, doi:10.1038/ncomms12717.
Huang, Y. et al., 2019: Methane and Nitrous Oxide Flux after Biochar Application in Subtropical Acidic Paddy Soils under Tobacco-Rice Rotation. *Scientific Reports*, **9(1)**, 17277, doi:10.1038/s41598-019-53044-1.
Hugelius, G. et al., 2014: Estimated stocks of circumpolar permafrost carbon with quantified uncertainty ranges and identified data gaps. *Biogeosciences*, **11(23)**, 6573–6593, doi:10.5194/bg-11-6573-2014.
Humphrey, V. et al., 2018: Sensitivity of atmospheric CO2 growth rate to observed changes in terrestrial water storage. *Nature*, **560(7720)**, 628–631, doi:10.1038/s41586-018-0424-4.
Hungate, B.A. et al., 2013: Cumulative response of ecosystem carbon and nitrogen stocks to chronic CO2 exposure in a subtropical oak woodland. *New Phytologist*, **200(3)**, 753–766, doi:10.1111/nph.12333.
Hunter, S.J., D.S. Goldobin, A.M. Haywood, A. Ridgwell, and J.G. Rees, 2013: Sensitivity of the global submarine hydrate inventory to scenarios of future climate change. *Earth and Planetary Science Letters*, **367**, 105–115, doi:10.1016/j.epsl.2013.02.017.
Huntingford, C. et al., 2013: Simulated resilience of tropical rainforests to CO2-induced climate change. *Nature Geoscience*, **6(4)**, 268–273, doi:10.1038/ngeo1741.
Huntingford, C. et al., 2017: Implications of improved representations of plant respiration in a changing climate. *Nature Communications*, **8(1)**, 1602, doi:10.1038/s41467-017-01774-z.
Huntzinger, D.N. et al., 2017: Uncertainty in the response of terrestrial carbon sink to environmental drivers undermines carbon-climate feedback predictions. *Scientific Reports*, **7(1)**, 4765, doi:10.1038/s41598-017-03818-2.
Hupp, B. and D.C. Kelly, 2020: Delays, Discrepancies, and Distortions: Size-Dependent Sediment Mixing and the Deep-Sea Record of the Paleocene-Eocene Thermal Maximum From ODP Site 690 (Weddell Sea). *Paleoceanography and Paleoclimatology*, **35(11)**, doi:10.1029/2020pa004018.
Huppmann, D., J. Rogelj, E. Kriegler, V. Krey, and K. Riahi, 2018: A new scenario resource for integrated 1.5°C research. *Nature Climate Change*, **8(12)**, 1027–1030, doi:10.1038/s41558-018-0317-4.
Hurd, C.L., A. Lenton, B. Tilbrook, and P.W. Boyd, 2018: Current understanding and challenges for oceans in a higher-CO2 world. *Nature Climate Change*, **8(8)**, 686–694, doi:10.1038/s41558-018-0211-0.
Hurtt, G.C. et al., 2020: Harmonization of global land use change and management for the period 850–2100 (LUH2) for CMIP6. *Geoscientific Model Development*, **13(11)**, 5425–5464, doi:10.5194/gmd-13-5425-2020.
Huybers, P. and C.H. Langmuir, 2017: Delayed CO2 emissions from mid-ocean ridge volcanism as a possible cause of late-Pleistocene glacial cycles. *Earth and Planetary Science Letters*, **457**, 238–249, doi:10.1016/j.epsl.2016.09.021.
Montanarella, L., R. Scholes, and A. Brainich (eds.), 2018: *The IPBES assessment report on land degradation and restoration*. Secretariat of the Intergovernmental Science-Policy Platform on Biodiversity and Ecosystem Services (IPBES), 744 pp., doi:10.5281/zenodo.3237392.
IEA, 2017: *CO2 Emissions from Fuel Combustion 2017*. International Energy Agency (IEA), Paris, France, 529 pp., doi:10.1787/co2_fuel-2017-en.
Iida, Y., Y. Takatani, A. Kojima, and M. Ishii, 2020: Global trends of ocean CO2 sink and ocean acidification: an observation-based reconstruction of surface ocean inorganic carbon variables. *Journal of Oceanography*, doi:10.1007/s10872-020-00571-5.
IOC, 2019: *Indicator Methodology for 14.3.1*. Intergovernmental Oceanographic Commission (IOC), Paris, France, 17 pp.
IPCC, 2013a: Climate Change 2013: The Physical Science Basis. Contribution of Working Group I to the Fifth Assessment Report of the Intergovernmental Panel on Climate Change. , 1535, doi:10.1017/cbo9781107415324.004.
IPCC, 2013b: Summary for Policymakers. In: *Climate Change 2013: The Physical Science Basis. Contribution of Working Group I to the Fifth Assessment Report of the Intergovernmental Panel on Climate Change* [Stocker, T.F., D. Qin, G.-K. Plattner, M. Tignor, S.K. Allen, J. Boschung, A. Nauels, Y. Xia, V. Bex, and P.M. Midgley (eds.)]. Cambridge University Press, Cambridge, United Kingdom and New York, NY, USA, pp. 3–29, doi:10.1017/cbo9781107415324.004.
IPCC, 2014: Climate Change 2014: Synthesis Report. Contribution of Working Groups I, II and III to the Fifth Assessment Report of the Intergovernmental Panel on Climate Change. [Core Writing Team, R.K. Pachauri, and L.A. Meyer (eds.)]. IPCC, Geneva, Switzerland, 151 pp.
IPCC, 2018a: Global Warming of 1.5°C. An IPCC Special Report on the impacts of global warming of 1.5°C above pre-industrial levels and related global greenhouse gas emission pathways, in the context of strengthening the global response to the threat of climate change,. [Masson-Delmotte, V., P. Zhai, H.-O. Pörtner, D. Roberts, J. Skea, P.R. Shukla, A. Pirani, W. Moufouma-Okia, C. Péan, R. Pidcock, S. Connors, J.B.R. Matthews, Y. Chen, X. Zhou, M.I. Gomis, E. Lonnoy, T. Maycock, M. Tignor, and T. Waterfield (eds.)]. In Press, 616 pp.
IPCC, 2018b: Summary for Policymakers. In: *Global Warming of 1.5°C. An IPCC Special Report on the impacts of global warming of 1.5°C above pre-industrial levels and related global greenhouse gas emission pathways, in the context of strengthening the global response to the threat of climate change,* [Masson-Delmotte, V., P.

ACCEPTED VERSION SUBJECT TO FINAL EDITS

Zhai, H.-O. Pörtner, D. Roberts, J. Skea, P.R. Shukla, A. Pirani, W. Moufouma-Okia, C. Péan, R. Pidcock, S. Connors, J.B.R. Matthews, Y. Chen, X. Zhou, M.I. Gomis, E. Lonnoy, T. Maycock, M. Tignor, and T. Waterfield (eds.)]. In Press, pp. 3–24.

IPCC, 2019a: Climate Change and Land: an IPCC special report on climate change, desertification, land degradation, sustainable land management, food security, and greenhouse gas fluxes in terrestrial ecosystems. [Shukla, P.R., J. Skea, E.C. Buendia, V. Masson-Delmotte, H.-O. Pörtner, D.C. Roberts, P. Zhai, R. Slade, S. Connors, R. Diemen, M. Ferrat, E. Haughey, S. Luz, S. Neogi, M. Pathak, J. Petzold, J.P. Pereira, P. Vyas, E. Huntley, K. Kissick, M. Belkacemi, and J. Malley (eds.)]. In Press, 896 pp.

IPCC, 2019b: IPCC Special Report on the Ocean and Cryosphere in a Changing Climate. [Pörtner, H.-O., D.C. Roberts, V. Masson-Delmotte, P. Zhai, M. Tignor, E. Poloczanska, K. Mintenbeck, A. Alegría, M. Nicolai, A. Okem, J. Petzold, B. Rama, and N.M. Weyer (eds.)]. In Press, 755 pp.

IPCC, 2019c: Summary for Policymakers. In: *IPCC Special Report on the Ocean and Cryosphere in a Changing Climate* [Pörtner, H.-O., D.C. Roberts, V. Masson-Delmotte, P. Zhai, M. Tignor, E. Poloczanska, K. Mintenbeck, M. Nicolai, A. Okem, J. Petzold, B. Rama, and N. Weyer (eds.)]. In Press, pp. 3–35.

Isabel, N., J.A. Holliday, and S.N. Aitken, 2020: Forest genomics: Advancing climate adaptation, forest health, productivity, and conservation. *Evolutionary Applications*, **13(1)**, 3–10, doi:10.1111/eva.12902.

Ishidoya, S. et al., 2012: Time and space variations of the O2/N2 ratio in the troposphere over Japan and estimation of the global CO2 budget for the period 2000–2010. *Tellus B: Chemical and Physical Meteorology*, **64(1)**, 18964, doi:10.3402/tellusb.v64i0.18964.

Ishii, M. et al., 2011: Ocean acidification off the south coast of Japan: A result from time series observations of CO2 parameters from 1994 to 2008. *Journal of Geophysical Research*, **116(C6)**, C06022, doi:10.1029/2010jc006831.

Ishii, M. et al., 2020: Ocean Acidification From Below in the Tropical Pacific. *Global Biogeochemical Cycles*, **34(8)**, e2019GB006368, doi:10.1029/2019gb006368.

Ishijima, K. et al., 2007: Temporal variations of the atmospheric nitrous oxide concentration and its δ15N and δ18O for the latter half of the 20th century reconstructed from firn air analyses. *Journal of Geophysical Research*, **112(D3)**, D03305, doi:10.1029/2006jd007208.

Ito, A., 2017: Solar radiation management and ecosystem functional responses. *Climatic Change*, **142(1–2)**, 53–66, doi:10.1007/s10584-017-1930-3.

Ito, A., 2019: Disequilibrium of terrestrial ecosystem CO2 budget caused by disturbance-induced emissions and non-CO2 carbon export flows: A global model assessment. *Earth System Dynamics*, **10(4)**, 685–709, doi:10.5194/esd-10-685-2019.

Ito, A., 2020: Bottom-up evaluation of the regional methane budget of northern lands from 1980 to 2015. *Polar Science*, 100558, doi:10.1016/j.polar.2020.100558.

Ito, T., S. Minobe, M.C. Long, and C. Deutsch, 2017: Upper ocean O2 trends: 1958-2015. *Geophysical Research Letters*, **44(9)**, 4214–4223, doi:10.1002/2017gl073613.

Ito, T. et al., 2015: Sustained growth of the Southern Ocean carbon storage in a warming climate. *Geophysical Research Letters*, **42(11)**, 4516–4522, doi:10.1002/2015gl064320.

Iudicone, D. et al., 2016: The formation of the ocean's anthropogenic carbon reservoir. *Scientific Reports*, **6(1)**, 35473, doi:10.1038/srep35473.

Jaccard, S., E. Galbraith, T. Frölicher, and N. Gruber, 2014: Ocean (de)oxygenation across the last deglaciation: insights for the future. *Oceanography*, **27(1)**, 26–35, doi:10.5670/oceanog.2014.05.

Jaccard, S.L. and E.D. Galbraith, 2012: Large climate-driven changes of oceanic oxygen concentrations during the last deglaciation. *Nature Geoscience*, **5(2)**, 151–156, doi:10.1038/ngeo1352.

Jaccard, S.L., E.D. Galbraith, A. Martínez-García, and R.F. Anderson, 2016: Covariation of deep Southern Ocean oxygenation and atmospheric CO2 through the last ice age. *Nature*, **530(7589)**, 207–210, doi:10.1038/nature16514.

Jaccard, S.L. et al., 2009: Subarctic Pacific evidence for a glacial deepening of the oceanic respired carbon pool. *Earth and Planetary Science Letters*, **277(1–2)**, 156–165, doi:10.1016/j.epsl.2008.10.017.

Jackson, R.B., E.I. Solomon, J.G. Canadell, M. Cargnello, and C.B. Field, 2019: Methane removal and atmospheric restoration. *Nature Sustainability*, **2(6)**, 436–438, doi:10.1038/s41893-019-0299-x.

Jackson, R.B. et al., 2005: Atmospheric science: Trading water for carbon with biological carbon sequestration. *Science*, **310(5756)**, 1944–1947, doi:10.1126/science.1119282.

Jackson, R.B. et al., 2017: The ecology of soil carbon: pools, vulnerabilities, and biotic and abiotic controls. *Annual Review of Ecology, Evolution, and Systematics*, **48(1)**, 419–445, doi:10.1146/annurev-ecolsys-112414-054234.

Jackson, R.B. et al., 2020: Increasing anthropogenic methane emissions arise equally from agricultural and fossil fuel sources. *Environmental Research Letters*, **15(7)**, 071002, doi:10.1088/1748-9326/ab9ed2.

Jacobson, A.R., S.E. Mikaloff Fletcher, N. Gruber, J.L. Sarmiento, and M. Gloor, 2007: A joint atmosphere-ocean inversion for surface fluxes of carbon dioxide: 1. Methods and global-scale fluxes. *Global Biogeochemical Cycles*, **21(1)**, doi:10.1029/2005gb002556.

Jans, Y., G. Berndes, J. Heinke, W. Lucht, and D. Gerten, 2018: Biomass production in plantations: Land constraints

ACCEPTED VERSION SUBJECT TO FINAL EDITS

increase dependency on irrigation water. *GCB Bioenergy*, **10(9)**, 628–644, doi:10.1111/gcbb.12530.
Janssens-Maenhout, G. et al., 2017: EDGAR v4.3.2 Global Atlas of the three major Greenhouse Gas Emissions for the period 1970-2012. *Earth System Science Data Discussions*, **(in prep)**, 1–55, doi:10.5194/essd-2017-79.
Janssens-Maenhout, G. et al., 2019: EDGAR v4.3.2 Global atlas of the three major greenhouse gas emissions for the period 1970-2012. *Earth System Science Data*, **11(3)**, 959–1002, doi:10.5194/essd-11-959-2019.
Jeffery, S., F.G.A. Verheijen, C. Kammann, and D. Abalos, 2016: Biochar effects on methane emissions from soils: A meta-analysis. *Soil Biology and Biochemistry*, **101**, 251–258, doi:10.1016/j.soilbio.2016.07.021.
Jeffrey, L.C. et al., 2019: Are methane emissions from mangrove stems a cryptic carbon loss pathway? Insights from a catastrophic forest mortality. *New Phytologist*, **224(1)**, 146–154, doi:10.1111/nph.15995.
Jeltsch-Thömmes, A., G. Battaglia, O. Cartapanis, S.L. Jaccard, and F. Joos, 2019: Low terrestrial carbon storage at the Last Glacial Maximum: constraints from multi-proxy data. *Climate of the Past*, **15(2)**, 849–879, doi:10.5194/cp-15-849-2019.
Jenkins, S., R.J. Millar, N. Leach, and M.R. Allen, 2018: Framing Climate Goals in Terms of Cumulative CO2-Forcing-Equivalent Emissions. *Geophysical Research Letters*, **45(6)**, 2795–2804, doi:10.1002/2017gl076173.
Ji, Q., A.R. Babbin, A. Jayakumar, S. Oleynik, and B.B. Ward, 2015: Nitrous oxide production by nitrification and denitrification in the Eastern Tropical South Pacific oxygen minimum zone. *Geophysical Research Letters*, **42(24)**, 10,755–10,764, doi:10.1002/2015gl066853.
Ji, Q. et al., 2019: Investigating the effect of El Niño on nitrous oxide distribution in the eastern tropical South Pacific. *Biogeosciences*, **16(9)**, 2079–2093, doi:10.5194/bg-16-2079-2019.
Jia, G. et al., 2019: Land–climate interactions. In: *Climate Change and Land: an IPCC special report on climate change, desertification, land degradation, sustainable land management, food security, and greenhouse gas fluxes in terrestrial ecosystems.* [Shukla, P.R., J. Skea, E.C. Buendia, V. Masson-Delmotte, H.-O. Pörtner, D.C. Roberts, P. Zhai, R. Slade, S. Connors, R. Diemen, M. Ferrat, E. Haughey, S. Luz, S. Neogi, M. Pathak, J. Petzold, J.P. Pereira, P. Vyas, E. Huntley, K. Kissick, M. Belkacemi, and J. Malley (eds.)]. In Press, pp. 131–248.
Jiang, J., H. Zhang, and L. Cao, 2018: Simulated effect of sunshade solar geoengineering on the global carbon cycle. *Science China Earth Sciences*, **61(9)**, 1306–1315, doi:10.1007/s11430-017-9210-0.
Jiang, L.-Q., B.R. Carter, R.A. Feely, S.K. Lauvset, and A. Olsen, 2019: Surface ocean pH and buffer capacity: past, present and future. *Scientific Reports*, **9(1)**, 18624, doi:10.1038/s41598-019-55039-4.
Jiang, M., J.W.G. Kelly, B.J. Atwell, D.T. Tissue, and B.E. Medlyn, 2021: Drought by CO2 interactions in trees: a test of the water savings mechanism. *New Phytologist*, doi:10.1111/nph.17233.
Jiang, M. et al., 2020a: Low phosphorus supply constrains plant responses to elevated CO 2 : A meta-analysis. *Global Change Biology*, **26(10)**, 5856–5873, doi:10.1111/gcb.15277.
Jiang, M. et al., 2020b: The fate of carbon in a mature forest under carbon dioxide enrichment. *Nature*, **580(7802)**, 227–231, doi:10.1038/s41586-020-2128-9.
Jiao, N. et al., 2014: Mechanisms of microbial carbon sequestration in the ocean – future research directions. *Biogeosciences*, **11(19)**, 5285–5306, doi:10.5194/bg-11-5285-2014.
Jiao, X.C., X.M. Song, D.L. Zhang, Q.J. Du, and J.M. Li, 2019: Coordination between vapor pressure deficit and CO2 on the regulation of photosynthesis and productivity in greenhouse tomato production. *Scientific Reports*, **9(1)**, 1–10, doi:10.1038/s41598-019-45232-w.
Jickells, T.D. et al., 2017: A reevaluation of the magnitude and impacts of anthropogenic atmospheric nitrogen inputs on the ocean. *Global Biogeochemical Cycles*, **31(2)**, 289–305, doi:10.1002/2016gb005586.
Jin, Y. et al., 2015: Identification of two distinct fire regimes in Southern California: implications for economic impact and future change. *Environmental Research Letters*, **10(9)**, 94005, doi:10.1088/1748-9326/10/9/094005.
Jokinen, S.A. et al., 2018: A 1500-year multiproxy record of coastal hypoxia from the northern Baltic Sea indicates unprecedented deoxygenation over the 20th century. *Biogeosciences*, **15(13)**, 3975–4001, doi:10.5194/bg-15-3975-2018.
Jolly, W.M. et al., 2015: Climate-induced variations in global wildfire danger from 1979 to 2013. *Nature Communications*, doi:10.1038/ncomms8537.
Jones, A. et al., 2013: The impact of abrupt suspension of solar radiation management (termination effect) in experiment G2 of the Geoengineering Model Intercomparison Project (GeoMIP). *Journal of Geophysical Research: Atmospheres*, **118(17)**, 9743–9752, doi:10.1002/jgrd.50762.
Jones, C., J. Lowe, S. Liddicoat, and R. Betts, 2009: Committed terrestrial ecosystem changes due to climate change. *Nature Geoscience*, **2(7)**, 484–487, doi:10.1038/ngeo555.
Jones, C. et al., 2013: Twenty-First-Century Compatible CO2 Emissions and Airborne Fraction Simulated by CMIP5 Earth System Models under Four Representative Concentration Pathways. *Journal of Climate*, **26(13)**, 4398–4413, doi:10.1175/jcli-d-12-00554.1.
Jones, C.D. and P. Friedlingstein, 2020: Quantifying process-level uncertainty contributions to TCRE and carbon budgets for meeting Paris Agreement climate targets. *Environmental Research Letters*, **15(7)**, 074019, doi:10.1088/1748-9326/ab858a.
Jones, C.D. et al., 2016a: C4MIP - The Coupled Climate–Carbon Cycle Model Intercomparison Project: experimental

ACCEPTED VERSION SUBJECT TO FINAL EDITS

protocol for CMIP6. *Geoscientific Model Development*, **9(8)**, 2853–2880, doi:10.5194/gmd-9-2853-2016.
Jones, C.D. et al., 2016b: Simulating the earth system response to negative emissions. *Environmental Research Letters*, **11(9)**, 095012, doi:10.1088/1748-9326/11/9/095012.
Jones, C.D. et al., 2019: The Zero Emissions Commitment Model Intercomparison Project (ZECMIP) contribution to C4MIP: quantifying committed climate changes following zero carbon emissions. *Geoscientific Model Development*, **12(10)**, 4375–4385, doi:10.5194/gmd-12-4375-2019.
Jones, M.W. et al., 2020: Human activities modulate regional fire trends despite the upwards pressure of global climate change. .
Joos, F. et al., 2001: Global warming feedbacks on terrestrial carbon uptake under the Intergovernmental Panel on Climate Change (IPCC) emission scenarios. *Global Biogeochemical Cycles*, **15(4)**, 891–907, doi:10.1029/2000gb001375.
Joos, F. et al., 2013: Carbon dioxide and climate impulse response functions for the computation of greenhouse gas metrics: a multi-model analysis. *Atmospheric Chemistry and Physics*, **13(5)**, 2793–2825, doi:10.5194/acp-13-2793-2013.
Joos, F. et al., 2020: N2O changes from the Last Glacial Maximum to the preindustrial – Part 2: terrestrial N2O emissions and carbon–nitrogen cycle interactions. *Biogeosciences*, **17(13)**, 3511–3543, doi:10.5194/bg-17-3511-2020.
Jung, M. et al., 2017: Compensatory water effects link yearly global land CO2 sink changes to temperature. *Nature*, **541(7638)**, 516–520, doi:10.1038/nature20780.
Junium, C.K., A.J. Dickson, and B.T. Uveges, 2018: Perturbation to the nitrogen cycle during rapid Early Eocene global warming. *Nature Communications*, **9(1)**, 3186, doi:10.1038/s41467-018-05486-w.
Kalidindi, S., G. Bala, A. Modak, and K. Caldeira, 2015: Modeling of solar radiation management: a comparison of simulations using reduced solar constant and stratospheric sulphate aerosols. *Climate Dynamics*, **44(9–10)**, 2909–2925, doi:10.1007/s00382-014-2240-3.
Kalliokoski, T. et al., 2020: Mitigation Impact of Different Harvest Scenarios of Finnish Forests That Account for Albedo, Aerosols, and Trade-Offs of Carbon Sequestration and Avoided Emissions. *Frontiers in Forests and Global Change*, **3**, 112, doi:10.3389/ffgc.2020.562044.
Kammann, C. et al., 2017: Biochar as a Tool to teduce the Agricultural Greenhouse-gas Burden – Knowns, Unknowns and Future Research Needs. *Journal of Environmental Engineering and Landscape Management*, **25(2)**, 114–139, doi:10.3846/16486897.2017.1319375.
Kantola, I.B., M.D. Masters, D.J. Beerling, S.P. Long, and E.H. DeLucia, 2017: Potential of global croplands and bioenergy crops for climate change mitigation through deployment for enhanced weathering. *Biology Letters*, **13(4)**, 20160714, doi:10.1098/rsbl.2016.0714.
Karelin, D. et al., 2017: Human footprints on greenhouse gas fluxes in cryogenic ecosystems. *Doklady Earth Sciences*, **477(2)**, 1467–1469, doi:10.1134/s1028334x17120133.
Karhu, K., T. Mattila, I. Bergström, and K. Regina, 2011: Biochar addition to agricultural soil increased CH4 uptake and water holding capacity – Results from a short-term pilot field study. *Agriculture, Ecosystems & Environment*, **140(1)**, 309–313, doi:10.1016/j.agee.2010.12.005.
Katavouta, A., R.G. Williams, and P. Goodwin, 2019: The Effect of Ocean Ventilation on the Transient Climate Response to Emissions. *Journal of Climate*, **32(16)**, 5085–5105, doi:10.1175/jcli-d-18-0829.1.
Katavouta, A., R.G. Williams, P. Goodwin, and V. Roussenov, 2018: Reconciling Atmospheric and Oceanic Views of the Transient Climate Response to Emissions. *Geophysical Research Letters*, **45(12)**, 6205–6214, doi:10.1029/2018gl077849.
Kato, E. and Y. Yamagata, 2014: BECCS capability of dedicated bioenergy crops under a future land-use scenario targeting net negative carbon emissions. *Earth's Future*, **2(9)**, 421–439, doi:10.1002/2014ef000249.
Kattge, J. and W. Knorr, 2007: Temperature acclimation in a biochemical model of photosynthesis: a reanalysis of data from 36 species. *Plant, Cell & Environment*, **30(9)**, 1176–1190, doi:10.1111/j.1365-3040.2007.01690.x.
Kaushal, S.S. et al., 2018: Freshwater salinization syndrome on a continental scale. *Proceedings of the National Academy of Sciences*, **115(4)**, E574–E583, doi:10.1073/pnas.1711234115.
Kawahata, H. et al., 2019: Perspective on the response of marine calcifiers to global warming and ocean acidification – Behavior of corals and foraminifera in a high CO2 world "hot house". *Progress in Earth and Planetary Science*, **6(1)**, 5, doi:10.1186/s40645-018-0239-9.
Keeling, C.D., 1960: The Concentration and Isotopic Abundances of Carbon Dioxide in the Atmosphere. *Tellus*, **12(2)**, 200–203, doi:10.1111/j.2153-3490.1960.tb01300.x.
Keeling, C.D., T.P. Whorf, M. Wahlen, and J. van der Plicht, 2001: *Exchanges of Atmospheric CO2 and 13CO2 with the Terrestrial Biosphere and Oceans from 1978 to 2000. I. Global Aspects*. SIO Reference No. 01–06, Scripps Institution of Oceanography, University of California San Diego, San Diego, CA, USA, 28 pp.
Keeling, R.F. and A.C. Manning, 2014: Studies of Recent Changes in Atmospheric O2 Content. In: *Treatise on Geochemistry (Second Edition)* [Holland, H.D. and K.K. Turekian (eds.)]. Elsevier, pp. 385–404, doi:10.1016/b978-0-08-095975-7.00420-4.
Keeling, R.F. et al., 2017: Atmospheric evidence for a global secular increase in carbon isotopic discrimination of land

ACCEPTED VERSION SUBJECT TO FINAL EDITS

photosynthesis. *Proceedings of the National Academy of Sciences*, **114(39)**, 10361–10366, doi:10.1073/pnas.1619240114.
Keenan, T.F. et al., 2016: Recent pause in the growth rate of atmospheric CO2 due to enhanced terrestrial carbon uptake. *Nature Communications*, **7(1)**, 13428, doi:10.1038/ncomms13428.
Keith, D.W. and D.G. MacMartin, 2015: A temporary, moderate and responsive scenario for solar geoengineering. *Nature Climate Change*, **5(3)**, 201–206, doi:10.1038/nclimate2493.
Keith, H. et al., 2021: Evaluating nature-based solutions for climate mitigation and conservation requires comprehensive carbon accounting. *Science of the Total Environment*, **769**, 144341, doi:10.1016/j.scitotenv.2020.144341.
Kell, D.B., 2011: Breeding crop plants with deep roots: their role in sustainable carbon, nutrient and water sequestration. *Annals of Botany*, **108(3)**, 407–418, doi:10.1093/aob/mcr175.
Keller, D.P., 2019: Marine climate engineering. In: *Handbook on Marine Environment Protection: Science, Impacts and Sustainable Management* [Salomon, M. and T. Markus (eds.)]. Springer, Cham, Switzerland, pp. 261–276, doi:10.1007/978-3-319-60156-4_13.
Keller, D.P., E.Y. Feng, and A. Oschlies, 2014: Potential climate engineering effectiveness and side effects during a high carbon dioxide-emission scenario. *Nature Communications*, **5(1)**, 3304, doi:10.1038/ncomms4304.
Keller, D.P. et al., 2018a: The Effects of Carbon Dioxide Removal on the Carbon Cycle. *Current Climate Change Reports*, **4(3)**, 250–265, doi:10.1007/s40641-018-0104-3.
Keller, D.P. et al., 2018b: The Carbon Dioxide Removal Model Intercomparison Project (CDRMIP): rationale and experimental protocol for CMIP6. *Geoscientific Model Development*, **11(3)**, 1133–1160, doi:10.5194/gmd-11-1133-2018.
Keller, J., 2018: Greenhouse gases. In: *A Blue Carbon Primer, The State of Coastal Wetland Carbon Science, Practice and Policy* [Windham-Myers, L., S. Crooks, and Troxler (eds.)]. CRC Press, Boca Raton, FL, USA, pp. 93–106.
Kelly, J.W.G., R.A. Duursma, B.J. Atwell, D.T. Tissue, and B.E. Medlyn, 2016: Drought × CO2 interactions in trees: a test of the low-intercellular CO2 concentration (C_i) mechanism. *New Phytologist*, **209(4)**, 1600–1612, doi:10.1111/nph.13715.
Kemp, D.B., K. Eichenseer, and W. Kiessling, 2015: Maximum rates of climate change are systematically underestimated in the geological record. *Nature Communications*, **6(1)**, 8890, doi:10.1038/ncomms9890.
Kennedy, H., J. Fourqueran, and S. Papadimitriou, 2018: The calcium carbonate cycle in seagrass ecosystems. In: *A Blue Carbon Primer. The State of Coastal Wetland Carbon Science, Practice and Policy* [Windham-Myers, L., S. Crooks, and T. Troxler (eds.)]. CRC Press, Boca Raton, FL, USA, pp. 107–119, doi:10.1201/9780429435362.
Keppler, L. and P. Landschützer, 2019: Regional Wind Variability Modulates the Southern Ocean Carbon Sink. *Scientific Reports*, **9(1)**, 7384, doi:10.1038/s41598-019-43826-y.
Keppler, L., P. Landschützer, N. Gruber, S.K. Lauvset, and I. Stemmler, 2020: Seasonal Carbon Dynamics in the Near-Global Ocean. *Global Biogeochemical Cycles*, **34(12)**, doi:10.1029/2020gb006571.
Khatiwala, S., A. Schmittner, and J. Muglia, 2019: Air-sea disequilibrium enhances ocean carbon storage during glacial periods. *Science Advances*, **5(6)**, eaaw4981, doi:10.1126/sciadv.aaw4981.
Khatiwala, S. et al., 2013: Global ocean storage of anthropogenic carbon. *Biogeosciences*, **10(4)**, 2169–2191, doi:10.5194/bg-10-2169-2013.
Kicklighter, D.W. et al., 2014: Potential influence of climate-induced vegetation shifts on future land use and associated land carbon fluxes in Northern Eurasia. *Environmental Research Letters*, **9(3)**, 35004, doi:10.1088/1748-9326/9/3/035004.
Kirschke, S. et al., 2013: Three decades of global methane sources and sinks. *Nature Geoscience*, **6(10)**, 813–823, doi:10.1038/ngeo1955.
Kizyakov, A. et al., 2017: Comparison of gas emission crater geomorphodynamics on Yamal and Gydan Peninsulas (Russia), based on repeat very-high-resolution stereopairs. *Remote Sensing*, **9(10)**, 1023, doi:10.3390/rs9101023.
Kizyakov, A. et al., 2018: Microrelief associated with gas emission craters: remote-sensing and field-based study. *Remote Sensing*, **10(5)**, 677, doi:10.3390/rs10050677.
Kleber, M., P. Sollins, and R. Sutton, 2007: A conceptual model of organo-mineral interactions in soils: self-assembly of organic molecular fragments into zonal structures on mineral surfaces. *Biogeochemistry*, **85(1)**, 9–24, doi:10.1007/s10533-007-9103-5.
Kleinen, T. and V. Brovkin, 2018: Pathway-dependent fate of permafrost region carbon. *Environmental Research Letters*, **13(9)**, 094001, doi:10.1088/1748-9326/aad824.
Kleinen, T., U. Mikolajewicz, and V. Brovkin, 2020: Terrestrial methane emissions from the Last Glacial Maximum to the preindustrial period. *Climate of the Past*, **16(2)**, 575–595, doi:10.5194/cp-16-575-2020.
Kloster, S. and G. Lasslop, 2017: Historical and future fire occurrence (1850 to 2100) simulated in CMIP5 Earth System Models. *Global and Planetary Change*, **150**, 58–69, doi:10.1016/j.gloplacha.2016.12.017.
Kluber, L.A. et al., 2014: Multistate assessment of wetland restoration on CO2 and N2O emissions and soil bacterial

ACCEPTED VERSION SUBJECT TO FINAL EDITS

communities. *Applied Soil Ecology*, **76**, 87–94, doi:10.1016/j.apsoil.2013.12.014.
Knauer, J. et al., 2017: The response of ecosystem water-use efficiency to rising atmospheric CO2 concentrations: sensitivity and large-scale biogeochemical implications. *New Phytologist*, **213(4)**, 1654–1666, doi:10.1111/nph.14288.
Knutti, R. and J. Rogelj, 2015: The legacy of our CO2 emissions: a clash of scientific facts, politics and ethics. *Climatic Change*, **133(3)**, 361–373, doi:10.1007/s10584-015-1340-3.
Kock, A., D.L. Arévalo-Martínez, C.R. Löscher, and H.W. Bange, 2016: Extreme N2O accumulation in the coastal oxygen minimum zone off Peru. *Biogeosciences*, **13(3)**, 827–840, doi:10.5194/bg-13-827-2016.
Kock, A., J. Schafstall, M. Dengler, P. Brandt, and H.W. Bange, 2012: Sea-to-air and diapycnal nitrous oxide fluxes in the eastern tropical North Atlantic Ocean. *Biogeosciences*, **9(3)**, 957–964, doi:10.5194/bg-9-957-2012.
Koffi, E.N., P. Bergamaschi, R. Alkama, and A. Cescatti, 2020: An observation-constrained assessment of the climate sensitivity and future trajectories of wetland methane emissions. *Science Advances*, **6(15)**, doi:10.1126/sciadv.aay4444.
Köhler, P., G. Knorr, and E. Bard, 2014: Permafrost thawing as a possible source of abrupt carbon release at the onset of the Bølling/Allerød. *Nature Communications*, **5(1)**, 5520, doi:10.1038/ncomms6520.
Kohnert, K., A. Serafimovich, S. Metzger, J. Hartmann, and T. Sachs, 2017: Strong geologic methane emissions from discontinuous terrestrial permafrost in the Mackenzie Delta, Canada. *Scientific Reports*, **7(1)**, 5828, doi:10.1038/s41598-017-05783-2.
Koné, Y.J.M., G. Abril, K.N. Kouadio, B. Delille, and A. Borges, 2009: Seasonal Variability of Carbon Dioxide in the Rivers and Lagoons of Ivory Coast (West Africa). *Estuaries and Coasts*, **32(2)**, 246–260, doi:10.1007/s12237-008-9121-0.
Kortelainen, P. et al., 2020: Lakes as nitrous oxide sources in the boreal landscape. *Global Change Biology*, **26(3)**, 1432–1445, doi:10.1111/gcb.14928.
Koskinen, M., L. Maanavilja, M. Nieminen, K. Minkkinen, and E. Tuittila, 2016: High methane emissions from restored Norway spruce swamps in southern Finland over one growing season. *Mires and Peat*, **17(02)**, 1–13, doi:10.19189/map.2015.omb.202.
Kosugi, N., D. Sasano, M. Ishii, K. Enyo, and S. Saito, 2016: Autumn CO 2 chemistry in the Japan Sea and the impact of discharges from the Changjiang River. *Journal of Geophysical Research: Oceans*, n/a–n/a, doi:10.1002/2016jc011838.
Koven, C.D., 2013: Boreal carbon loss due to poleward shift in low-carbon ecosystems. *Nature Geoscience*, **6(6)**, 452–456, doi:10.1038/ngeo1801.
Koven, C.D., D.M. Lawrence, and W.J. Riley, 2015a: Permafrost carbon-climate feedback is sensitive to deep soil carbon decomposability but not deep soil nitrogen dynamics. *Proceedings of the National Academy of Sciences*, **112(12)**, 201415123, doi:10.1073/pnas.1415123112.
Koven, C.D., G. Hugelius, D.M. Lawrence, and W.R. Wieder, 2017: Higher climatological temperature sensitivity of soil carbon in cold than warm climates. *Nature Climate Change*, **7(11)**, 817–822, doi:10.1038/nclimate3421.
Koven, C.D. et al., 2015b: Controls on terrestrial carbon feedbacks by productivity versus turnover in the CMIP5 Earth System Models. *Biogeosciences*, **12(17)**, 5211–5228, doi:10.5194/bg-12-5211-2015.
Koven, C.D. et al., 2015c: A simplified, data-constrained approach to estimate the permafrost carbon–climate feedback. *Philosophical Transactions of the Royal Society A: Mathematical, Physical and Engineering Sciences*, **373(2054)**, 20140423, doi:10.1098/rsta.2014.0423.
Krause, A. et al., 2017: Global consequences of afforestation and bioenergy cultivation on ecosystem service indicators. *Biogeosciences*, **14(21)**, 4829–4850, doi:10.5194/bg-14-4829-2017.
Kravitz, B. et al., 2011: The Geoengineering Model Intercomparison Project (GeoMIP). *Atmospheric Science Letters*, **12(2)**, 162–167, doi:10.1002/asl.316.
Kraxner, F. et al., 2013: Global bioenergy scenarios – Future forest development, land-use implications, and trade-offs. *Biomass and Bioenergy*, **57**, 86–96, doi:10.1016/j.biombioe.2013.02.003.
Kretschmer, K., A. Biastoch, L. Rüpke, and E. Burwicz, 2015: Modeling the fate of methane hydrates under global warming. *Global Biogeochemical Cycles*, **29(5)**, 610–625, doi:10.1002/2014gb005011.
Krishnamohan, K.-P.S.-P., G. Bala, L. Cao, L. Duan, and K. Caldeira, 2019: Climate system response to stratospheric sulfate aerosols: sensitivity to altitude of aerosol layer. *Earth System Dynamics*, **10(4)**, 885–900, doi:10.5194/esd-10-885-2019.
Krishnamohan, K.S., G. Bala, L. Cao, L. Duan, and K. Caldeira, 2020: The Climatic Effects of Hygroscopic Growth of Sulfate Aerosols in the Stratosphere. *Earth's Future*, **8(2)**, e2019EF001326, doi:10.1029/2019ef001326.
Krumhardt, K.M. et al., 2019: Coccolithophore Growth and Calcification in an Acidified Ocean: Insights From Community Earth System Model Simulations. *Journal of Advances in Modeling Earth Systems*, **11(5)**, 1418–1437, doi:10.1029/2018ms001483.
Kubota, K., Y. Yokoyama, T. Ishikawa, A. Suzuki, and M. Ishii, 2017: Rapid decline in pH of coral calcification fluid due to incorporation of anthropogenic CO2. *Scientific Reports*, **7(1)**, 7694, doi:10.1038/s41598-017-07680-0.
Kumarathunge, D.P. et al., 2019: Acclimation and adaptation components of the temperature dependence of plant photosynthesis at the global scale. *New Phytologist*, **222(2)**, 768–784, doi:10.1111/nph.15668.

ACCEPTED VERSION SUBJECT TO FINAL EDITS

Kuypers, M.M.M. et al., 2005: From The Cover: Massive nitrogen loss from the Benguela upwelling system through anaerobic ammonium oxidation. *Proceedings of the National Academy of Sciences*, **102(18)**, 6478–6483, doi:10.1073/pnas.0502088102.

Kwiatkowski, L. and J.C. Orr, 2018: Diverging seasonal extremes for ocean acidification during the twenty-first century. *Nature Climate Change*, **8(2)**, 141–145, doi:10.1038/s41558-017-0054-0.

Kwiatkowski, L., O. Aumont, L. Bopp, and P. Ciais, 2018: The impact of variable phytoplankton stoichiometry on projections of primary production, food quality, and carbon uptake in the global ocean. *Global Biogeochemical Cycles*, **32(4)**, 516–528, doi:10.1002/2017gb005799.

Kwiatkowski, L. et al., 2017: Emergent constraints on projections of declining primary production in the tropical oceans. *Nature Climate Change*, **7(5)**, 355–358, doi:10.1038/nclimate3265.

Kwiatkowski, L. et al., 2020: Twenty-first century ocean warming, acidification, deoxygenation, and upper-ocean nutrient and primary production decline from CMIP6 model projections. *Biogeosciences*, **17(13)**, 3439–3470, doi:10.5194/bg-17-3439-2020.

Lade, S.J. et al., 2018: Analytically tractable climate-carbon cycle feedbacks under 21st century anthropogenic forcing. *Earth System Dynamics*, **9(2)**, 507–523, doi:10.5194/esd-9-507-2018.

Lambert, F. et al., 2021: Regional patterns and temporal evolution of ocean iron fertilization and CO2 drawdown during the last glacial termination. *Earth and Planetary Science Letters*, **554**, doi:10.1016/j.epsl.2020.116675.

Lan, X. et al., 2019: Long-Term Measurements Show Little Evidence for Large Increases in Total U.S. Methane Emissions Over the Past Decade. *Geophysical Research Letters*, **46(9)**, 4991–4999, doi:10.1029/2018gl081731.

Landolfi, A., C.J. Somes, W. Koeve, L.M. Zamora, and A. Oschlies, 2017: Oceanic nitrogen cycling and N2 flux perturbations in the Anthropocene. *Global Biogeochemical Cycles*, **31(8)**, 1236–1255, doi:10.1002/2017gb005633.

Landschützer, P., N. Gruber, and D.C.E. Bakker, 2016: Decadal variations and trends of the global ocean carbon sink. *Global Biogeochemical Cycles*, **30(10)**, 1396–1417, doi:10.1002/2015gb005359.

Landschützer, P., T. Ilyina, and N.S. Lovenduski, 2019: Detecting Regional Modes of Variability in Observation-Based Surface Ocean p CO 2. *Geophysical Research Letters*, **46(5)**, 2670–2679, doi:10.1029/2018gl081756.

Landschützer, P., N. Gruber, D.C.E. Bakker, and U. Schuster, 2014: Recent variability of the global ocean carbon sink. *Global Biogeochemical Cycles*, **28(9)**, 927–949, doi:10.1002/2014gb004853.

Landschützer, P., G.G. Laruelle, A. Roobaert, and P. Regnier, 2020: A uniform pCO2 climatology combining open and coastal oceans. *Earth System Science Data*, **12(4)**, 2537–2553, doi:10.5194/essd-12-2537-2020.

Landschützer, P., N. Gruber, D.C.E. Bakker, I. Stemmler, and K.D. Six, 2018: Strengthening seasonal marine CO2 variations due to increasing atmospheric CO2. *Nature Climate Change*, **8(2)**, 146–150, doi:10.1038/s41558-017-0057-x.

Landschützer, P. et al., 2015: The reinvigoration of the Southern Ocean carbon sink. *Science*, **349(6253)**, 1221–1224, doi:10.1126/science.aab2620.

Laruelle, G.G., R. Lauerwald, B. Pfeil, and P. Regnier, 2014: Regionalized global budget of the CO2 exchange at the air-water interface in continental shelf seas. *Global Biogeochemical Cycles*, **28(11)**, 1199–1214, doi:10.1002/2014gb004832.

Laruelle, G.G. et al., 2017: Global high-resolution monthly CO2 climatology for the coastal ocean derived from neural network interpolation. *Biogeosciences*, **14(19)**, 4545–4561, doi:10.5194/bg-14-4545-2017.

Laruelle, G.G. et al., 2018: Continental shelves as a variable but increasing global sink for atmospheric carbon dioxide. *Nature Communications*, **9(1)**, 454, doi:10.1038/s41467-017-02738-z.

Lassey, K.R., D.M. Etheridge, D.C. Lowe, A.M. Smith, and D.F. Ferretti, 2007: Centennial evolution of the atmospheric methane budget: what do the carbon isotopes tell us? *Atmospheric Chemistry and Physics*, **7(8)**, 2119–2139, doi:10.5194/acp-7-2119-2007.

Lasslop, G., V. Brovkin, C.H. Reick, S. Bathiany, and S. Kloster, 2016: Multiple stable states of tree cover in a global land surface model due to a fire-vegetation feedback. *Geophysical Research Letters*, **43(12)**, 6324–6331, doi:10.1002/2016gl069365.

Lasslop, G., A.I. Coppola, A. Voulgarakis, C. Yue, and S. Veraverbeke, 2019: Influence of Fire on the Carbon Cycle and Climate. *Current Climate Change Reports*, **5(2)**, doi:10.1007/s40641-019-00128-9.

Lasslop, G. et al., 2020: Global ecosystems and fire: Multi-model assessment of fire-induced tree-cover and carbon storage reduction. *Global Change Biology*, **26(9)**, 5027–5041, doi:10.1111/gcb.15160.

Lauerwald, R., G.G. Laruelle, J. Hartmann, P. Ciais, and P.A.G. Regnier, 2015: Spatial patterns in CO2 evasion from the global river network. *Global biogeochemical cycles*, 534–554.

Lauerwald, R. et al., 2019: Natural Lakes Are a Minor Global Source of N2O to the Atmosphere. *Global Biogeochemical Cycles*, **33(12)**, 1564–1581, doi:10.1029/2019gb006261.

Laufkoetter, C. et al., 2015: Drivers and uncertainties of future global marine primary production in marine ecosystem models. *Biogeosciences*, **12(23)**, 6955–6984, doi:10.5194/bg-12-6955-2015.

Laufkötter, C., J. Zscheischler, and T. Frölicher, 2020: High-impact marine heatwaves attributable to human-induced global warming. *Science*, **369(6511)**, 1621–1625, doi:10.1126/science.aba0690.

ACCEPTED VERSION SUBJECT TO FINAL EDITS

Laufkötter, C. et al., 2015: Drivers and uncertainties of future global marine primary production in marine ecosystem models. *Biogeosciences*, **12(23)**, 6955–6984, doi:10.5194/bg-12-6955-2015.
Laurent, A. et al., 2017: Eutrophication-induced acidification of coastal waters in the northern Gulf of Mexico: Insights into origin and processes from a coupled physical-biogeochemical model. *Geophysical Research Letters*, **44(2)**, 946–956, doi:10.1002/2016gl071881.
Lauvset, S.K., J. Tjiputra, and H. Muri, 2017: Climate engineering and the ocean: effects on biogeochemistry and primary production. *Biogeosciences*, **14(24)**, 5675–5691, doi:10.5194/bg-14-5675-2017.
Lauvset, S.K. et al., 2020: Processes driving global interior ocean pH distribution. *Global Biogeochemical Cycles*, 2019GB006229, doi:10.1029/2019gb006229.
Lavergne, A. et al., 2019: Observed and modelled historical trends in the water-use efficiency of plants and ecosystems. *Global Change Biology*, gcb.14634, doi:10.1111/gcb.14634.
Le Page, Y. et al., 2017: Synergy between land use and climate change increases future fire risk in Amazon forests. *Earth System Dynamics*, **8(4)**, 1237–1246, doi:10.5194/esd-8-1237-2017.
Le Quéré, C. et al., 2018a: Global Carbon Budget 2018. *Earth System Science Data*, **10(4)**, 2141–2194, doi:10.5194/essd-10-2141-2018.
Le Quéré, C. et al., 2018b: Global Carbon Budget 2017. *Earth System Science Data*, **10(1)**, 405–448, doi:10.5194/essd-10-405-2018.
Le Quéré, C. et al., 2020: Temporary reduction in daily global CO2 emissions during the COVID-19 forced confinement. *Nature Climate Change*, **10(7)**, 647–653, doi:10.1038/s41558-020-0797-x.
Leduc, M., H.D. Matthews, and R. de Elía, 2015: Quantifying the limits of a linear temperature response to cumulative CO2 emissions. *Journal of Climate*, **28(24)**, 9955–9968, doi:10.1175/jcli-d-14-00500.1.
Leduc, M., H.D. Matthews, and R. de Elía, 2016: Regional estimates of the transient climate response to cumulative CO2 emissions. *Nature Climate Change*, **6(5)**, 474–478, doi:10.1038/nclimate2913.
Lee, H. et al., 2019: The Response of Permafrost and High-Latitude Ecosystems Under Large-Scale Stratospheric Aerosol Injection and Its Termination. *Earth's Future*, **7(6)**, 605–614, doi:10.1029/2018ef001146.
Lee, S.-J., I.-S. Ryu, B.-M. Kim, and S.-H. Moon, 2011: A review of the current application of N2O emission reduction in CDM projects. *International Journal of Greenhouse Gas Control*, **5(1)**, 167–176, doi:10.1016/j.ijggc.2010.07.001.
Legendre, L., R.B. Rivkin, M.G. Weinbauer, L. Guidi, and J. Uitz, 2015: The microbial carbon pump concept: Potential biogeochemical significance in the globally changing ocean. *Progress in Oceanography*, **134**, 432–450, doi:10.1016/j.pocean.2015.01.008.
Lehmann, C.E.R. et al., 2014: Savanna vegetation-fire-climate relationships differ among continents. *Science*, **343(6170)**, 548 LP – 552, doi:10.1126/science.1247355.
Lehmann, J. et al., 2015: Persistence of biochar in soil. In: *Biochar for Environmental Management: Science, Technology and Implementation (Second Edition)* [Lehmann, J. and S. Joseph (eds.)]. Routledge, London, UK, pp. 233—80, doi:10.4324/9780203762264.
Leifeld, J., C. Wüst-Galley, and S. Page, 2019: Intact and managed peatland soils as a source and sink of GHGs from 1850 to 2100. *Nature Climate Change*, **9(12)**, 945–947, doi:10.1038/s41558-019-0615-5.
Lemordant, L., P. Gentine, A.S. Swann, B.I. Cook, and J. Scheff, 2018: Critical impact of vegetation physiology on the continental hydrologic cycle in response to increasing CO2. *Proceedings of the National Academy of Sciences of the United States of America*, **115(16)**, 4093–4098, doi:10.1073/pnas.1720712115.
Lencina-Avila, J.M. et al., 2018: Past and future evolution of the marine carbonate system in a coastal zone of the Northern Antarctic Peninsula. *Deep Sea Research Part II: Topical Studies in Oceanography*, **149(SI)**, 193–205, doi:10.1016/j.dsr2.2017.10.018.
Lennartz, S.T. et al., 2014: Long-term trends at the Boknis Eck time series station (Baltic Sea), 1957–2013: does climate change counteract the decline in eutrophication? *Biogeosciences*, **11(22)**, 6323–6339, doi:10.5194/bg-11-6323-2014.
Lenton, T.M. et al., 2008: Tipping elements in the Earth's climate system. *Proceedings of the National Academy of Sciences*, **105(6)**, 1786–1793, doi:10.1073/pnas.0705414105.
Leung, S.W., T. Weber, J.A. Cram, and C. Deutsch, 2021: Variable particle size distributions reduce the sensitivity of global export flux to climate change. *Biogeosciences*, **18(1)**, 229–250, doi:10.5194/bg-18-229-2021.
Leutert, T.J., A. Auderset, A. Martínez-García, S. Modestou, and A.N. Meckler, 2020: Coupled Southern Ocean cooling and Antarctic ice sheet expansion during the middle Miocene. *Nature Geoscience*, **13(9)**, 634–639, doi:10.1038/s41561-020-0623-0.
Levin, I. et al., 2010: Observations and modelling of the global distribution and long-term trend of atmospheric 14CO2. *Tellus B: Chemical and Physical Meteorology*, **62(1)**, 26–46, doi:10.1111/j.1600-0889.2009.00446.x.
Levin, L.A., 2018: Manifestation, drivers, and emergence of open ocean deoxygenation. *Annual Review of Marine Science*, **10(1)**, 229–260, doi:10.1146/annurev-marine-121916-063359.
Levin, L.A. and D.L. Breitburg, 2015: Linking coasts and seas to address ocean deoxygenation. *Nature Climate Change*, **5(5)**, 401–403, doi:10.1038/nclimate2595.
Levin, L.A. et al., 2015: Comparative biogeochemistry–ecosystem–human interactions on dynamic continental margins.

ACCEPTED VERSION SUBJECT TO FINAL EDITS

Journal of Marine Systems, **141**, 3–17, doi:10.1016/j.jmarsys.2014.04.016.
Levine, N.M. et al., 2016: Ecosystem heterogeneity determines the ecological resilience of the Amazon to climate change. *Proceedings of the National Academy of Sciences*, **113(3)**, 793–797, doi:10.1073/pnas.1511344112.
Levy, M. et al., 2013: Physical pathways for carbon transfers between the surface mixed layer and the ocean interior. *Global Biogeochemical Cycles*, **27(4)**, 1001–1012, doi:10.1002/gbc.20092.
Lewis, S.L., C.E. Wheeler, E.T.A. Mitchard, and A. Koch, 2019: Regenerate natural forest to store carbon. *Nature*, **568(7750)**, 25–28, doi:10.1038/d41586-019-01026-8.
Li, H. and T. Ilyina, 2018: Current and future decadal trends in the oceanic carbon uptake are dominated by internal variability. *Geophysical Research Letters*, **45(2)**, 916–925, doi:10.1002/2017gl075370.
Li, H., T. Ilyina, W.A. Müller, and F. Sienz, 2016: Decadal predictions of the North Atlantic CO2 uptake. *Nature Communications*, **7(1)**, 11076, doi:10.1038/ncomms11076.
Li, H., T. Ilyina, W.A. Müller, and P. Landschützer, 2019: Predicting the variable ocean carbon sink. *Science Advances*, **5(4)**, eaav6471, doi:10.1126/sciadv.aav6471.
Li, M. et al., 2016: What drives interannual variability of hypoxia in Chesapeake Bay: Climate forcing versus nutrient loading? *Geophysical Research Letters*, **43(5)**, 2127–2134, doi:10.1002/2015gl067334.
Li, T. et al., 2020: Rapid shifts in circulation and biogeochemistry of the Southern Ocean during deglacial carbon cycle events. *Science Advances*, **6(42)**, 1–10, doi:10.1126/sciadv.abb3807.
Li, W. et al., 2016: Reducing uncertainties in decadal variability of the global carbon budget with multiple datasets. *Proceedings of the National Academy of Sciences*, **113(46)**, 13104–13108, doi:10.1073/pnas.1603956113.
Li, W. et al., 2018: Temporal response of soil organic carbon after grassland-related land-use change. *Global Change Biology*, **24(10)**, 4731–4746, doi:10.1111/gcb.14328.
Li, X. et al., 2020: Temporal trade-off between gymnosperm resistance and resilience increases forest sensitivity to extreme drought. *Nature Ecology and Evolution*, **4(8)**, 1075–1083, doi:10.1038/s41559-020-1217-3.
Lian, X. et al., 2021: Multifaceted characteristics of dryland aridity changes in a warming world. *Nature Reviews Earth & Environment*, doi:10.1038/s43017-021-00144-0.
Lilly, L.E. et al., 2019: Biogeochemical Anomalies at Two Southern California Current System Moorings During the 2014–2016 Warm Anomaly-El Niño Sequence. *Journal of Geophysical Research: Oceans*, **124(10)**, 6886–6903, doi:10.1029/2019jc015255.
Limburg, K.E., D. Breitburg, D.P. Swaney, and G. Jacinto, 2020a: Ocean Deoxygenation: A Primer. *One Earth*, **2(1)**, 24–29, doi:10.1016/j.oneear.2020.01.001.
Limburg, K.E., D. Breitburg, D.P. Swaney, and G. Jacinto, 2020b: Ocean Deoxygenation: A Primer. *One Earth*, **2(1)**, 24–29, doi:10.1016/j.oneear.2020.01.001.
Lin, Y.-S., B.E. Medlyn, and D.S. Ellsworth, 2012: Temperature responses of leaf net photosynthesis: the role of component processes. *Tree Physiology*, **32(2)**, 219–231, doi:10.1093/treephys/tpr141.
Lindgren, A., G. Hugelius, and P. Kuhry, 2018: Extensive loss of past permafrost carbon but a net accumulation into present-day soils. *Nature*, **560(7717)**, 219–222, doi:10.1038/s41586-018-0371-0.
Lippold, J. et al., 2016: Deep water provenance and dynamics of the (de)glacial Atlantic meridional overturning circulation. *Earth and Planetary Science Letters*, **445**, 68–78, doi:10.1016/j.epsl.2016.04.013.
Liu, C. et al., 2016: Biochar increased water holding capacity but accelerated organic carbon leaching from a sloping farmland soil in China. *Environmental Science and Pollution Research*, **23(2)**, 995–1006, doi:10.1007/s11356-015-4885-9.
Liu, H., N. Wrage-Mönnig, and B. Lennartz, 2020: Rewetting strategies to reduce nitrous oxide emissions from European peatlands. *Communications Earth & Environment*, **1(1)**, 17, doi:10.1038/s43247-020-00017-2.
Liu, J. et al., 2017: Contrasting carbon cycle responses of the tropical continents to the 2015-2016 El Nino. *Science*, **358(6360)**, doi:10.1126/science.aam5690.
Liu, L. et al., 2020: Soil moisture dominates dryness stress on ecosystem production globally. *Nature Communications*, **11(1)**, 1–9, doi:10.1038/s41467-020-18631-1.
Liu, Y. et al., 2014: Acceleration of modern acidification in the South China Sea driven by anthropogenic CO2. *Scientific Reports*, **4(1)**, 5148, doi:10.1038/srep05148.
Liu, Z. et al., 2017: Effects of biochar application on nitrogen leaching, ammonia volatilization and nitrogen use efficiency in two distinct soils. *Journal of soil science and plant nutrition*, **17(2)**, 515–528, doi:10.4067/s0718-95162017005000037.
Liu, Z. et al., 2019: Global divergent responses of primary productivity to water, energy, and {CO} 2. *Environmental Research Letters*, **14(12)**, 124044, doi:10.1088/1748-9326/ab57c5.
Liu, Z. et al., 2020: Near-real-time monitoring of global CO2 emissions reveals the effects of the COVID-19 pandemic. *Nature Communications*, **11(1)**, 5172, doi:10.1038/s41467-020-18922-7.
Llanillo, P.J., J. Karstensen, J.L. Pelegrí, and L. Stramma, 2013: Physical and biogeochemical forcing of oxygen and nitrate changes during El Niño/El Viejo and La Niña/La Vieja upper-ocean phases in the tropical eastern South Pacific along 86° W. *Biogeosciences*, **10(10)**, 6339–6355, doi:10.5194/bg-10-6339-2013.
Lloret, F., A. Escudero, J.M. Iriondo, J. Martínez-Vilalta, and F. Valladares, 2012: Extreme climatic events and vegetation: the role of stabilizing processes. *Global Change Biology*, **18(3)**, 797–805, doi:10.1111/j.1365-

ACCEPTED VERSION SUBJECT TO FINAL EDITS

2486.2011.02624.x.
Loisel, J. et al., 2014: A database and synthesis of northern peatland soil properties and Holocene carbon and nitrogen accumulation. *The Holocene*, **24(9)**, 1028–1042, doi:10.1177/0959683614538073.
Lombardozzi, D.L., G.B. Bonan, N.G. Smith, J.S. Dukes, and R.A. Fisher, 2015: Temperature acclimation of photosynthesis and respiration: A key uncertainty in the carbon cycle-climate feedback. *Geophysical Research Letters*, **42(20)**, 8624–8631, doi:10.1002/2015gl065934.
Long, M.C., C. Deutsch, and T. Ito, 2016: Finding forced trends in oceanic oxygen. *Global Biogeochemical Cycles*, **30(2)**, 381–397, doi:10.1002/2015gb005310.
Lorenz, K. and R. Lal, 2014: Biochar application to soil for climate change mitigation by soil organic carbon sequestration. *Journal of Plant Nutrition and Soil Science*, **177(5)**, 651–670, doi:10.1002/jpln.201400058.
Loulergue, L. et al., 2008: Orbital and millennial-scale features of atmospheric CH4 over the past 800,000 years. *Nature*, **453(7193)**, 383–386, doi:10.1038/nature06950.
Lovelock, C.E. and C.M. Duarte, 2019: Dimensions of Blue Carbon and emerging perspectives. *Biology Letters*, **15(3)**, 20180781, doi:10.1098/rsbl.2018.0781.
Lovenduski, N.S., S.G. Yeager, K. Lindsay, and M.C. Long, 2019a: Predicting near-term variability in ocean carbon uptake. *Earth System Dynamics*, **10(1)**, 45–57, doi:10.5194/esd-10-45-2019.
Lovenduski, N.S., G.B. Bonan, S.G. Yeager, K. Lindsay, and D.L. Lombardozzi, 2019b: High predictability of terrestrial carbon fluxes from an initialized decadal prediction system. *Environmental Research Letters*, **14(12)**, 124074, doi:10.1088/1748-9326/ab5c55.
Lowe, A.T., J. Bos, and J. Ruesink, 2019: Ecosystem metabolism drives pH variability and modulates long-term ocean acidification in the Northeast Pacific coastal ocean. *Scientific Reports*, **9(1)**, 963, doi:10.1038/s41598-018-37764-4.
Lowe, J.A. and D. Bernie, 2018: The impact of Earth system feedbacks on carbon budgets and climate response. *Philosophical Transactions of the Royal Society A: Mathematical, Physical and Engineering Sciences*, **376(2119)**, 20170263, doi:10.1098/rsta.2017.0263.
Lu, X., L. Wang, and M.F. McCabe, 2016: Elevated CO2 as a driver of global dryland greening. *Scientific Reports*, **6**, 1–7, doi:10.1038/srep20716.
Lucht, W., S. Schaphoff, T. Erbrecht, U. Heyder, and W. Cramer, 2006: Terrestrial vegetation redistribution and carbon balance under climate change. *Carbon Balance and Management*, **1(1)**, 6, doi:10.1186/1750-0680-1-6.
Luijendijk, E., T. Gleeson, and N. Moosdorf, 2020: Fresh groundwater discharge insignificant for the world's oceans but important for coastal ecosystems. *Nature Communications*, **11(1)**, 1260, doi:10.1038/s41467-020-15064-8.
Łukawska-Matuszewska, K., B. Graca, O. Brocławik, and T. Zalewska, 2019: The impact of declining oxygen conditions on pyrite accumulation in shelf sediments (Baltic Sea). *Biogeochemistry*, **142(2)**, 209–230, doi:10.1007/s10533-018-0530-2.
Lund, D.C. et al., 2016: Enhanced East Pacific Rise hydrothermal activity during the last two glacial terminations. *Science*, **351(6272)**, 478–482, doi:10.1126/science.aad4296.
Luo, Y. et al., 2016: Toward more realistic projections of soil carbon dynamics by Earth system models. *Global Biogeochemical Cycles*, **30(1)**, 40–56, doi:10.1002/2015gb005239.
Lüthi, D. et al., 2008: High-resolution carbon dioxide concentration record 650,000–800,000 years before present. *Nature*, **453(7193)**, 379–382, doi:10.1038/nature06949.
Maavara, T. et al., 2019: Nitrous oxide emissions from inland waters: Are IPCC estimates too high? *Global Change Biology*, **25(2)**, 473–488, doi:10.1111/gcb.14504.
MacDougall, A.H., 2016: The Transient Response to Cumulative CO2 Emissions: a Review. *Current Climate Change Reports*, **2(1)**, 39–47, doi:10.1007/s40641-015-0030-6.
MacDougall, A.H., 2017: The oceanic origin of path-independent carbon budgets. *Scientific Reports*, **7(1)**, 10373, doi:10.1038/s41598-017-10557-x.
MacDougall, A.H. and P. Friedlingstein, 2015: The origin and limits of the near proportionality between climate warming and cumulative CO2 emissions. *Journal of Climate*, **28(10)**, 4217–4230, doi:10.1175/jcli-d-14-00036.1.
MacDougall, A.H. and R. Knutti, 2016a: Enhancement of non-CO2 radiative forcing via intensified carbon cycle feedbacks. *Geophysical Research Letters*, **43(11)**, 5833–5840, doi:10.1002/2016gl068964.
MacDougall, A.H. and R. Knutti, 2016b: Projecting the release of carbon from permafrost soils using a perturbed parameter ensemble modelling approach. *Biogeosciences*, **13(7)**, 2123–2136, doi:10.5194/bg-13-2123-2016.
MacDougall, A.H., N.C. Swart, and R. Knutti, 2017: The uncertainty in the transient climate response to cumulative CO2 emissions arising from the uncertainty in physical climate parameters. *Journal of Climate*, **30(2)**, 813–827, doi:10.1175/jcli-d-16-0205.1.
MacDougall, A.H., K. Zickfeld, R. Knutti, and H.D. Matthews, 2015: Sensitivity of carbon budgets to permafrost carbon feedbacks and non-CO2 forcings. *Environmental Research Letters*, **10(12)**, 125003, doi:10.1088/1748-9326/10/12/125003.
MacDougall, A.H. et al., 2020: Is there warming in the pipeline? A multi-model analysis of the Zero Emissions Commitment from CO2. *Biogeosciences*, **17(11)**, 2987–3016, doi:10.5194/bg-17-2987-2020.

ACCEPTED VERSION SUBJECT TO FINAL EDITS

MacFarling Meure, C. et al., 2006: Law Dome CO2 , CH4 and N2O ice core records extended to 2000 years BP. *Geophysical Research Letters*, **33(14)**, L14810, doi:10.1029/2006gl026152.
MacMartin, D.G., K. Caldeira, and D.W. Keith, 2014: Solar geoengineering to limit the rate of temperature change. *Philosophical Transactions of the Royal Society A: Mathematical, Physical and Engineering Sciences*, **372(2031)**, 20140134, doi:10.1098/rsta.2014.0134.
Macreadie, P.I. et al., 2019: The future of Blue Carbon science. *Nature Communications*, **10(1)**, 3998, doi:10.1038/s41467-019-11693-w.
Mahowald, N.M. et al., 2017: Aerosol deposition impacts on land and ocean carbon cycles. *Current Climate Change Reports*, **3(1)**, 16–31, doi:10.1007/s40641-017-0056-z.
Malakhova, V. and A. Eliseev, 2017: The role of heat transfer time scale in the evolution of the subsea permafrost and associated methane hydrates stability zone during glacial cycles. *Global and Planetary Change*, **157**, 18–25, doi:10.1016/j.gloplacha.2017.08.007.
Malakhova, V. and A. Eliseev, 2020: Uncertainty in temperature and sea level datasets for the Pleistocene glacial cycles: Implications for thermal state of the subsea sediments. *Global and Planetary Change*, **192**, 103249, doi:10.1016/j.gloplacha.2020.103249.
Malhi, Y., L. Rowland, L.E.O.C. Aragão, and R.A. Fisher, 2018: New insights into the variability of the tropical land carbon cycle from the El Niño of 2015/2016. *Philosophical Transactions of the Royal Society B: Biological Sciences*, **373(1760)**, 20170298, doi:10.1098/rstb.2017.0298.
Manizza, M., R.F. Keeling, and C.D. Nevison, 2012: On the processes controlling the seasonal cycles of the air–sea fluxes of O2 and N2O: A modelling study. *Tellus B: Chemical and Physical Meteorology*, **64(1)**, 18429, doi:10.3402/tellusb.v64i0.18429.
Mankin, J.S., R. Seager, J.E. Smerdon, B.I. Cook, and A.P. Williams, 2019: Mid-latitude freshwater availability reduced by projected vegetation responses to climate change. *Nature Geoscience*, **12(12)**, 983–988, doi:10.1038/s41561-019-0480-x.
Mao, J. et al., 2016: Human-induced greening of the northern extratropical land surface. *Nature Climate Change*, **6(10)**, 959–963, doi:10.1038/nclimate3056.
Marcott, S.A. et al., 2014: Centennial-scale changes in the global carbon cycle during the last deglaciation. *Nature*, **514(7524)**, 616–619, doi:10.1038/nature13799.
Marshall, J. et al., 2015: The ocean's role in the transient response of climate to abrupt greenhouse gas forcing. *Climate Dynamics*, **44(7–8)**, 2287–2299, doi:10.1007/s00382-014-2308-0.
Martínez-Botí, M.A. et al., 2015a: Plio-Pleistocene climate sensitivity evaluated using high-resolution CO2 records. *Nature*, **518(7537)**, 49–54, doi:10.1038/nature14145.
Martínez-Botí, M.A. et al., 2015b: Boron isotope evidence for oceanic carbon dioxide leakage during the last deglaciation. *Nature*, **518(7538)**, 219–222, doi:10.1038/nature14155.
Martinez-Garcia, A. et al., 2014: Iron Fertilization of the Subantarctic Ocean During the Last Ice Age. *Science*, **343(6177)**, 1347–1350, doi:10.1126/science.1246848.
Martinez-Rey, J., L. Bopp, M. Gehlen, A. Tagliabue, and N. Gruber, 2015: Projections of oceanic N2O emissions in the 21st century using the IPSL Earth system model. *Biogeosciences*, **12(13)**, 4133–4148, doi:10.5194/bg-12-4133-2015.
Mastrotheodoros, T. et al., 2017: Linking plant functional trait plasticity and the large increase in forest water use efficiency. *Journal of Geophysical Research: Biogeosciences*, **122(9)**, 2393–2408, doi:10.1002/2017jg003890.
Matear, R.J. and A. Lenton, 2014: Quantifying the impact of ocean acidification on our future climate. *Biogeosciences*, **11(14)**, 3965–3983, doi:10.5194/bg-11-3965-2014.
Mathesius, S., M. Hofmann, K. Caldeira, and H.J. Schellnhuber, 2015: Long-term response of oceans to CO2 removal from the atmosphere. *Nature Climate Change*, **5(12)**, 1107–1113, doi:10.1038/nclimate2729.
Matthews, H.D. and K. Caldeira, 2007: Transient climate carbon simulations of planetary geoengineering. *Proceedings of the National Academy of Sciences*, **104(24)**, 9949–9954, doi:10.1073/pnas.0700419104.
Matthews, H.D. and S. Solomon, 2013: Irreversible does not mean unavoidable. *Science*, **340(6131)**, 438–439, doi:10.1126/science.1236372.
Matthews, H.D., S. Solomon, and R. Pierrehumbert, 2012: Cumulative carbon as a policy framework for achieving climate stabilization. *Philosophical Transactions of the Royal Society A: Mathematical, Physical and Engineering Sciences*, **370(1974)**, 4365–4379, doi:10.1098/rsta.2012.0064.
Matthews, H.D., N.P. Gillett, P.A. Stott, and K. Zickfeld, 2009: The proportionality of global warming to cumulative carbon emissions. *Nature*, **459(7248)**, 829–832, doi:10.1038/nature08047.
Matthews, H.D. et al., 2017: Estimating carbon budgets for ambitious climate targets. *Current Climate Change Reports*, **3(1)**, 69–77, doi:10.1007/s40641-017-0055-0.
Matthews, H.D. et al., 2020: Opportunities and challenges in using remaining carbon budgets to guide climate policy. *Nature Geoscience*, 1–13, doi:10.1038/s41561-020-00663-3.
Matthews, H.D. et al., 2021: An integrated approach to quantifying uncertainties in the remaining carbon budget. *Communications Earth & Environment*, **2(1)**, 1–11, doi:10.1038/s43247-020-00064-9.
Mattsdotter Björk, M., A. Fransson, A. Torstensson, and M. Chierici, 2014: Ocean acidification state in western

ACCEPTED VERSION SUBJECT TO FINAL EDITS

Antarctic surface waters: controls and interannual variability. *Biogeosciences*, **11(1)**, 57–73, doi:10.5194/bg-11-57-2014.
Maxwell, S.L. et al., 2019: Degradation and forgone removals increase the carbon impact of intact forest loss by 626%. *Science Advances*, **5(10)**, eaax2546, doi:10.1126/sciadv.aax2546.
McCormack, C.G. et al., 2016: Key impacts of climate engineering on biodiversity and ecosystems, with priorities for future research. *Journal of Integrative Environmental Sciences*, **13(2–4)**, 1–26, doi:10.1080/1943815x.2016.1159578.
McCusker, K.E., K.C. Armour, C.M. Bitz, and D.S. Battisti, 2014: Rapid and extensive warming following cessation of solar radiation management. *Environmental Research Letters*, **9(2)**, doi:10.1088/1748-9326/9/2/024005.
McDaniel, M.D., D. Saha, M.G. Dumont, M. Hernández, and M.A. Adams, 2019: The effect of land-use change on soil CH4 and N2O fluxes: a global meta-analysis. *Ecosystems*, **22(6)**, 1424–1443, doi:10.1007/s10021-019-00347-z.
McDermid, S.S. et al., 2021: Disentangling the Regional Climate Impacts of Competing Vegetation Responses to Elevated Atmospheric CO2. *Journal of Geophysical Research: Atmospheres*, **126(5)**, 1–23, doi:10.1029/2020jd034108.
McDowell, N. et al., 2018: Drivers and mechanisms of tree mortality in moist tropical forests. *New Phytologist*, **219(3)**, 851–869, doi:10.1111/nph.15027.
McDowell, N.G. et al., 2020: Soil moisture dominates dryness stress on ecosystem production globally. *Nature Climate Change*, **6(1)**, 1–9, doi:10.1038/s41467-020-18631-1.
McGuire, A.D. et al., 2018: Dependence of the evolution of carbon dynamics in the northern permafrost region on the trajectory of climate change. *Proceedings of the National Academy of Sciences*, **115(15)**, 3882–3887, doi:10.1073/pnas.1719903115.
McKinley, G.A., A.R. Fay, N.S. Lovenduski, and D.J. Pilcher, 2017: Natural Variability and Anthropogenic Trends in the Ocean Carbon Sink. *Annual Review of Marine Science*, **9(1)**, 125–150, doi:10.1146/annurev-marine-010816-060529.
McKinley, G.A., A.R. Fay, Y.A. Eddebbar, L. Gloege, and N.S. Lovenduski, 2020: External Forcing Explains Recent Decadal Variability of the Ocean Carbon Sink. *AGU Advances*, **1(2)**, doi:10.1029/2019av000149.
McKinley, G.A. et al., 2016: Timescales for detection of trends in the ocean carbon sink. *Nature*, **530(7591)**, 469–472, doi:10.1038/nature16958.
Mcleod, E. et al., 2011: A blueprint for blue carbon: toward an improved understanding of the role of vegetated coastal habitats in sequestering CO2. *Frontiers in Ecology and the Environment*, **9(10)**, 552–560, doi:10.1890/110004.
McManus, J.F., R. Francois, J.-M. Gherardi, L.D. Keigwin, and S. Brown-Leger, 2004: Collapse and rapid resumption of Atlantic meridional circulation linked to deglacial climate changes. *Nature*, **428(6985)**, 834–837, doi:10.1038/nature02494.
McNeil, B.I. and T.P. Sasse, 2016: Future ocean hypercapnia driven by anthropogenic amplification of the natural CO2 cycle. *Nature*, **529(7586)**, 383–386, doi:10.1038/nature16156.
McNorton, J. et al., 2018: Attribution of recent increases in atmospheric methane through 3-D inverse modelling. *Atmos. Chem. Phys.*, **18(24)**, 18149–18168, doi:10.5194/acp-18-18149-2018.
Medlyn, B.E. et al., 2015: Using ecosystem experiments to improve vegetation models. *Nature Climate Change*, **5(6)**, 528–534, doi:10.1038/nclimate2621.
Medlyn, B.E. et al., 2016: Using models to guide field experiments: a priori predictions for the CO2 response of a nutrient- and water-limited native Eucalypt woodland. *Global Change Biology*, **22(8)**, 2834–2851, doi:10.1111/gcb.13268.
Meier, I.C., A.C. Finzi, and R.P. Phillips, 2017: Root exudates increase N availability by stimulating microbial turnover of fast-cycling N pools. *Soil Biology and Biochemistry*, **106**, 119–128, doi:10.1016/j.soilbio.2016.12.004.
Meinshausen, M., S.C.B. Raper, and T.M.L. Wigley, 2011a: Emulating coupled atmosphere-ocean and carbon cycle models with a simpler model, MAGICC6 – Part 1: Model description and calibration. *Atmospheric Chemistry and Physics*, **11(4)**, 1417–1456, doi:10.5194/acp-11-1417-2011.
Meinshausen, M., T.M.L. Wigley, and S.C.B. Raper, 2011b: Emulating atmosphere-ocean and carbon cycle models with a simpler model, MAGICC6 – Part 2: Applications. *Atmospheric Chemistry and Physics*, **11(4)**, 1457–1471, doi:10.5194/acp-11-1457-2011.
Meinshausen, M. et al., 2009: Greenhouse-gas emission targets for limiting global warming to 2°C. *Nature*, **458(7242)**, 1158–1162, doi:10.1038/nature08017.
Meinshausen, M. et al., 2011c: The RCP greenhouse gas concentrations and their extensions from 1765 to 2300. *Climatic Change*, **109(1–2)**, 213–241, doi:10.1007/s10584-011-0156-z.
Meinshausen, M. et al., 2017: Historical greenhouse gas concentrations for climate modelling (CMIP6). *Geoscientific Model Development*, **10(5)**, 2057–2116, doi:10.5194/gmd-10-2057-2017.
Meinshausen, M. et al., 2020: The shared socio-economic pathway (SSP) greenhouse gas concentrations and their extensions to 2500. *Geoscientific Model Development*, **13(8)**, 3571–3605, doi:10.5194/gmd-13-3571-2020.
Meli, P., J.M. Rey Benayas, P. Balvanera, and M. Martínez Ramos, 2014: Restoration enhances wetland biodiversity and ecosystem service supply, but results are context-dependent: a meta-analysis. *PloS one*, **9(4)**, e93507–

ACCEPTED VERSION SUBJECT TO FINAL EDITS

e93507, doi:10.1371/journal.pone.0093507.
Melillo, J.M. et al., 2011: Soil warming, carbon-nitrogen interactions, and forest carbon budgets. *Proceedings of the National Academy of Sciences*, **108(23)**, 9508–9512, doi:10.1073/pnas.1018189108.
Melillo, J.M. et al., 2017: Long-term pattern and magnitude of soil carbon feedback to the climate system in a warming world. *Science*, **358(6359)**, 101–105, doi:10.1126/science.aan2874.
Melton, J.R. et al., 2013: Present state of global wetland extent and wetland methane modelling: conclusions from a model inter-comparison project (WETCHIMP). *Biogeosciences*, **10(2)**, 753–788, doi:10.5194/bg-10-753-2013.
Mendonça, R. et al., 2017: Organic carbon burial in global lakes and reservoirs. *Nature Communications*, **8(1)**, 1–6, doi:10.1038/s41467-017-01789-6.
Menezes-Silva, P.E. et al., 2019: Different ways to die in a changing world: Consequences of climate change for tree species performance and survival through an ecophysiological perspective. *Ecology and Evolution*, **9(20)**, 11979–11999, doi:10.1002/ece3.5663.
Mengis, N., A.-I. Partanen, J. Jalbert, and H.D. Matthews, 2018: 1.5°C carbon budget dependent on carbon cycle uncertainty and future non-CO2 forcing. *Scientific Reports*, **8(1)**, 5831, doi:10.1038/s41598-018-24241-1.
Mengis, N. et al., 2020: Evaluation of the University of Victoria Earth System Climate Model version 2.10 (UVic ESCM 2.10). *Geoscientific Model Development*, **13(9)**, 4183–4204, doi:10.5194/gmd-13-4183-2020.
Menviel, L. and F. Joos, 2012: Toward explaining the Holocene carbon dioxide and carbon isotope records: Results from transient ocean carbon cycle-climate simulations. *Paleoceanography*, **27(1)**, PA1207, doi:10.1029/2011pa002224.
Mercado, L.M. et al., 2009: Impact of changes in diffuse radiation on the global land carbon sink. *Nature*, **458(7241)**, 1014–1017, doi:10.1038/nature07949.
Mercado, L.M. et al., 2018: Large sensitivity in land carbon storage due to geographical and temporal variation in the thermal response of photosynthetic capacity. *New Phytologist*, **218(4)**, 1462–1477, doi:10.1111/nph.15100.
Meredith, M. et al., 2019: Polar Regions. In: *IPCC Special Report on the Ocean and Cryosphere in a Changing Climate* [Pörtner, H.-O., D.C. Roberts, V. Masson-Delmotte, P. Zhai, M. Tignor, E. Poloczanska, K. Mintenbeck, A. Alegría, M. Nicolai, A. Okem, J. Petzold, B. Rama, and N.M. Weyer (eds.)]. In Press, pp. 203–320.
Merlivat, L. et al., 2018: Increase of dissolved inorganic carbon and decrease in pH in near-surface waters in the Mediterranean Sea during the past two decades. *Biogeosciences*, **15(18)**, 5653–5662, doi:10.5194/bg-15-5653-2018.
Messier, C. et al., 2019: The functional complex network approach to foster forest resilience to global changes. *Forest Ecosystems*, **6(1)**, 21, doi:10.1186/s40663-019-0166-2.
Meyerholt, J., K. Sickel, and S. Zaehle, 2020a: Ensemble projections elucidate effects of uncertainty in terrestrial nitrogen limitation on future carbon uptake. *Global Change Biology*, **26(7)**, 3978–3996, doi:10.1111/gcb.15114.
Meyerholt, J., K. Sickel, and S. Zaehle, 2020b: Ensemble projections elucidate effects of uncertainty in terrestrial nitrogen limitation on future carbon uptake. *Global Change Biology*, **26(7)**, 3978–3996, doi:10.1111/gcb.15114.
Middelburg, J.J. and L.A. Levin, 2009: Coastal hypoxia and sediment biogeochemistry. *Biogeosciences*, **6(7)**, 1273–1293, doi:10.5194/bg-6-1273-2009.
Midorikawa, T.A.K.A.S.H.I. et al., 2010: Decreasing pH trend estimated from 25-yr time series of carbonate parameters in the western North Pacific. *Tellus B: Chemical and Physical Meteorology*, **62(5)**, 649–659, doi:10.1111/j.1600-0889.2010.00474.x.
Millar, R.J. and P. Friedlingstein, 2018: The utility of the historical record for assessing the transient climate response to cumulative emissions. *Philosophical Transactions of the Royal Society A: Mathematical, Physical and Engineering Sciences*, **376(2119)**, 20160449, doi:10.1098/rsta.2016.0449.
Millar, R.J., Z.R. Nicholls, P. Friedlingstein, and M.R. Allen, 2017a: A modified impulse-response representation of the global near-surface air temperature and atmospheric concentration response to carbon dioxide emissions. *Atmospheric Chemistry and Physics*, **17(11)**, 7213–7228, doi:10.5194/acp-17-7213-2017.
Millar, R.J. et al., 2017b: Emission budgets and pathways consistent with limiting warming to 1.5°C. *Nature Geoscience*, **10(10)**, 741–747, doi:10.1038/ngeo3031.
Miller, S.M. et al., 2019: China's coal mine methane regulations have not curbed growing emissions. *Nature Communications*, **10(1)**, 303, doi:10.1038/s41467-018-07891-7.
Millero, F., R. Woosley, B. DiTrolio, and J. Waters, 2009: Effect of Ocean Acidification on the Speciation of Metals in Seawater. *Oceanography*, **22(4)**, 72–85, doi:10.5670/oceanog.2009.98.
Milly, P.C.D. and K.A. Dunne, 2016: Potential evapotranspiration and continental drying. *Nature Climate Change*, **6(10)**, 946–949, doi:10.1038/nclimate3046.
Minschwaner, K., R.J. Salawitch, and M.B. McElroy, 1993: Absorption of solar radiation by O2: Implications for O3 and lifetimes of N2O, CFCl3, and CF2Cl2. *Journal of Geophysical Research*, **98(D6)**, 10543, doi:10.1029/93jd00223.
Minshull, T.A., H. Marín-Moreno, D.I. Armstrong McKay, and P.A. Wilson, 2016: Mechanistic insights into a hydrate contribution to the Paleocene-Eocene carbon cycle perturbation from coupled thermohydraulic simulations.

ACCEPTED VERSION SUBJECT TO FINAL EDITS

Geophysical Research Letters, **43(16)**, 8637–8644, doi:10.1002/2016gl069676.
Mishra, U. et al., 2021: Spatial heterogeneity and environmental predictors of permafrost region soil organic carbon stocks. *Science Advances*, **7(9)**, eaaz5236, doi:10.1126/sciadv.aaz5236.
Moffitt, S.E., T.M. Hill, P.D. Roopnarine, and J.P. Kennett, 2015: Response of seafloor ecosystems to abrupt global climate change. *Proceedings of the National Academy of Sciences*, **112(15)**, 4684–4689, doi:10.1073/pnas.1417130112.
Mongwe, N.P., M. Vichi, and P.M.S. Monteiro, 2018: The seasonal cycle of pCO2 and CO2 fluxes in the Southern Ocean: diagnosing anomalies in CMIP5 Earth system models. *Biogeosciences*, **15(9)**, 2851–2872, doi:10.5194/bg-15-2851-2018.
Monnin, E., 2001: Atmospheric CO2 Concentrations over the Last Glacial Termination. *Science*, **291(5501)**, 112–114, doi:10.1126/science.291.5501.112.
Monteiro, T., R. Kerr, and E.C. Machado, 2020a: Seasonal variability of net sea-air CO2 fluxes in a coastal region of the northern Antarctic Peninsula. *Scientific Reports*, **10(1)**, 14875, doi:10.1038/s41598-020-71814-0.
Monteiro, T., R. Kerr, I.B.M. Orselli, and J.M. Lencina-Avila, 2020b: Towards an intensified summer CO2 sink behaviour in the Southern Ocean coastal regions. *Progress in Oceanography*, **183**, 102267, doi:10.1016/j.pocean.2020.102267.
Mora, C. et al., 2013: Biotic and human vulnerability to projected changes in ocean biogeochemistry over the 21st Century. *PLoS Biology*, **11(10)**, e1001682, doi:10.1371/journal.pbio.1001682.
Moy, A.D. et al., 2019: Varied contribution of the Southern Ocean to deglacial atmospheric CO2 rise. *Nature Geoscience*, **12(12)**, 1006–1011, doi:10.1038/s41561-019-0473-9.
Muri, H. et al., 2018: Climate response to aerosol geoengineering: A multimethod comparison. *Journal of Climate*, **31(16)**, 6319–6340, doi:10.1175/jcli-d-17-0620.1.
Murray, R.H., D. Erler, and B.D. Eyre, 2015: Nitrous oxide fluxes in estuarine environments: response to global change. *Global Change Biology*, **21(9)**, 3219–3245, doi:10.1111/gcb.12923.
Myers-Smith, I.H. et al., 2011: Shrub expansion in tundra ecosystems: dynamics, impacts and research priorities. *Environmental Research Letters*, **6(4)**, 45509, doi:10.1088/1748-9326/6/4/045509.
Naik, V. et al., 2013: Preindustrial to present-day changes in tropospheric hydroxyl radical and methane lifetime from the Atmospheric Chemistry and Climate Model Intercomparison Project (ACCMIP). *Atmospheric Chemistry and Physics*, **13(10)**, 5277–5298, doi:10.5194/acp-13-5277-2013.
Nakano, H., M. Ishii, K.B. Rodgers, H. Tsujino, and G. Yamanaka, 2015: Anthropogenic CO2 uptake, transport, storage, and dynamical controls in the ocean imposed by the meridional overturning circulation: A modeling study. *Global Biogeochemical Cycles*, **29(10)**, 1706–1724, doi:10.1002/2015gb005128.
Nakazawa, T., S. Morimoto, S. Aoki, and M. Tanaka, 1997: Temporal and spatial variations of the carbon isotopic ratio of atmospheric carbon dioxide in the western Pacific region. *Journal of Geophysical Research: Atmospheres*, **102(D1)**, 1271–1285, doi:10.1029/96jd02720.
Naqvi, S.W.A. et al., 2010a: Marine hypoxia/anoxia as a source of CH4 and N2O. *Biogeosciences*, **7(7)**, 2159–2190, doi:10.5194/bg-7-2159-2010.
Naqvi, S.W.A. et al., 2010b: Marine hypoxia/anoxia as a source of CH4 and N2O. *Biogeosciences*, **7(7)**, 2159–2190, doi:10.5194/bg-7-2159-2010.
NASEM, 2019: *Negative Emissions Technologies and Reliable Sequestration: A Research Agenda*. National Academies of Sciences, Engineering, and Medicine (NASEM). The National Academies Press, Washington, DC, USA, 510 pp., doi:10.17226/25259.
Natali, S.M. et al., 2019: Large loss of CO2 in winter observed across the northern permafrost region. *Nature Climate Change*, **9(11)**, 852–857, doi:10.1038/s41558-019-0592-8.
Natchimuthu, S., M.B. Wallin, L. Klemedtsson, and D. Bastviken, 2017: Spatio-temporal patterns of stream methane and carbon dioxide emissions in a hemiboreal catchment in Southwest Sweden. *Scientific Reports*, **7(1)**, 39729, doi:10.1038/srep39729.
Negrete-García, G., N.S. Lovenduski, C. Hauri, K.M. Krumhardt, and S.K. Lauvset, 2019: Sudden emergence of a shallow aragonite saturation horizon in the Southern Ocean. *Nature Climate Change*, **9(4)**, 313–317, doi:10.1038/s41558-019-0418-8.
Nehrbass-Ahles, C. et al., 2020: Abrupt CO2 release to the atmosphere under glacia and early interglacial climate conditions. *Science*, **369(6506)**, 1000–1005, doi:10.1126/science.aay8178.
Nevison, C.D., T.J. Lueker, and R.F. Weiss, 2004: Quantifying the nitrous oxide source from coastal upwelling. *Global Biogeochemical Cycles*, **18(1)**, GB1018, doi:10.1029/2003gb002110.
Nevison, C.D. et al., 2020: Southern Annular Mode Influence on Wintertime Ventilation of the Southern Ocean Detected in Atmospheric O ₂ and CO ₂ Measurements. *Geophysical Research Letters*, **47(4)**, e2019GL085667, doi:10.1029/2019gl085667.
Ni, X. and P.M. Groffman, 2018: Declines in methane uptake in forest soils. *Proceedings of the National Academy of Sciences*, **115(34)**, 8587–8590, doi:10.1073/pnas.1807377115.
Nicely, J.M. et al., 2018: Changes in global tropospheric OH expected as a result of climate change over the last several decades. *Journal of Geophysical Research: Atmospheres*, **123(18)**, 10,774–10,795, doi:10.1029/2018jd028388.

ACCEPTED VERSION SUBJECT TO FINAL EDITS

Nicholls, Z.R.J., R. Gieseke, J. Lewis, A. Nauels, and M. Meinshausen, 2020: Implications of non-linearities between cumulative CO2 emissions and CO2-induced warming for assessing the remaining carbon budget. *Environmental Research Letters*, **15(7)**, 074017, doi:10.1088/1748-9326/ab83af.

Nie, M., M. Lu, J. Bell, S. Raut, and E. Pendall, 2013: Altered root traits due to elevated CO2: A meta-analysis. *Global Ecology and Biogeography*, **22(10)**, 1095–1105, doi:10.1111/geb.12062.

Nisbet, E.G. et al., 2016: Rising atmospheric methane: 2007-2014 growth and isotopic shift. *Global Biogeochemical Cycles*, **30(9)**, 1356–1370, doi:10.1002/2016gb005406.

Nisbet, E.G. et al., 2019: Very strong atmospheric methane growth in the 4 years 2014–2017: implications for the Paris Agreement. *Global Biogeochemical Cycles*, **33**, 2018GB006009, doi:10.1029/2018gb006009.

Nisbet, E.G. et al., 2020: Methane Mitigation: Methods to Reduce Emissions, on the Path to the Paris Agreement. *Reviews of Geophysics*, **58(1)**, e2019RG000675, doi:10.1029/2019rg000675.

Nobre, C.A. et al., 2016: Land-use and climate change risks in the Amazon and the need of a novel sustainable development paradigm. *Proceedings of the National Academy of Sciences*, **113(39)**, 10759–10768, doi:10.1073/pnas.1605516113.

Norby, R.J. and D.R. Zak, 2011: Ecological Lessons from Free-Air CO2 Enrichment (FACE) Experiments. *Annual Review of Ecology, Evolution, and Systematics*, **42(1)**, 181–203, doi:10.1146/annurev-ecolsys-102209-144647.

Norby, R.J., J.M. Warren, C.M. Iversen, B.E. Medlyn, and R.E. McMurtrie, 2010: CO2 enhancement of forest productivity constrained by limited nitrogen availability. *Proceedings of the National Academy of Sciences*, **107(45)**, 19368–19373, doi:10.1073/pnas.1006463107.

Norby, R.J. et al., 2016: Model-data synthesis for the next generation of forest free-air CO2 enrichment (FACE) experiments. *New Phytologist*, **209(1)**, 17–28, doi:10.1111/nph.13593.

Nottingham, A.T., P. Meir, E. Velasquez, and B.L. Turner, 2020: Soil carbon loss by experimental warming in a tropical forest. *Nature*, **584(7820)**, 234–237, doi:10.1038/s41586-020-2566-4.

Novick, K.A., C.F. Miniat, and J.M. Vose, 2016: Drought limitations to leaf-level gas exchange: Results from a model linking stomatal optimization and cohesion-tension theory. *Plant Cell and Environment*, **39(3)**, 583–596, doi:10.1111/pce.12657.

O'Dell, C.W. et al., 2018: Improved retrievals of carbon dioxide from Orbiting Carbon Observatory-2 with the version 8 ACOS algorithm. *Atmospheric Measurement Techniques*, **11(12)**, 6539–6576, doi:10.5194/amt-11-6539-2018.

O'Sullivan, M. et al., 2019: Have synergies between nitrogen deposition and atmospheric CO2 driven the recent enhancement of the terrestrial carbon sink? *Global Biogeochemical Cycles*, **33(2)**, 163–180, doi:10.1029/2018gb005922.

Obermeier, W.A. et al., 2017: Reduced CO2 fertilization effect in temperate C3 grasslands under more extreme weather conditions. *Nature Climate Change*, **7(2)**, 137–141, doi:10.1038/nclimate3191.

Oka, E. et al., 2015: Decadal variability of Subtropical Mode Water subduction and its impact on biogeochemistry. *Journal of Oceanography*, **71(4)**, 389–400, doi:10.1007/s10872-015-0300-x.

Oka, E. et al., 2019: Remotely forced decadal physical and biogeochemical variability of North Pacific Subtropical Mode Water over the last 40 years. *Geophysical Research Letters*, **46(3)**, 1555–1561, doi:10.1029/2018gl081330.

Olafsson, J. et al., 2009: Rate of Iceland Sea acidification from time series measurements. *Biogeosciences*, **6(11)**, 2661–2668, doi:10.5194/bg-6-2661-2009.

Olefeldt, D. et al., 2016a: Circumpolar distribution and carbon storage of thermokarst landscapes. *Nature Communications*, **7(1)**, 13043, doi:10.1038/ncomms13043.

Olefeldt, D. et al., 2016b: Arctic Circumpolar Distribution and Soil Carbon of Thermokarst Landscapes, 2015. , doi:10.3334/ornldaac/1332.

Olivarez Lyle, A. and M.W. Lyle, 2006: Missing organic carbon in Eocene marine sediments: Is metabolism the biological feedback that maintains end-member climates? *Paleoceanography*, **21(2)**, n/a–n/a, doi:10.1029/2005pa001230.

Olsen, A. et al., 2020: An updated version of the global interior ocean biogeochemical data product, GLODAPv2.2020. *Earth System Science Data*, **12(4)**, 3653–3678, doi:10.5194/essd-12-3653-2020.

Ono, H. et al., 2019: Acceleration of ocean acidification in the Western North Pacific. *Geophysical Research Letters*, **46(n/a)**, 13161–13169, doi:10.1029/2019gl085121.

Orr, J.C. et al., 2005: Anthropogenic ocean acidification over the twenty-first century and its impact on calcifying organisms. *Nature*, **437(7059)**, 681–686, doi:10.1038/nature04095.

Orselli, I.B.M. et al., 2018: How fast is the Patagonian shelf-break acidifying? *Journal of Marine Systems*, **178**, 1–14, doi:10.1016/j.jmarsys.2017.10.007.

Ortega, A. et al., 2019: Important contribution of macroalgae to oceanic carbon sequestration. *Nature Geoscience*, **12(9)**, 748–754, doi:10.1038/s41561-019-0421-8.

Osborne, E.B., R.C. Thunell, N. Gruber, R.A. Feely, and C.R. Benitez-Nelson, 2020: Decadal variability in twentieth-century ocean acidification in the California Current Ecosystem. *Nature Geoscience*, **13(1)**, 43–49, doi:10.1038/s41561-019-0499-z.

ACCEPTED VERSION SUBJECT TO FINAL EDITS

Oschlies, A., W. Koeve, W. Rickels, and K. Rehdanz, 2010a: Side effects and accounting aspects of hypothetical large-scale Southern Ocean iron fertilization. *Biogeosciences*, **7(12)**, 4017–4035, doi:10.5194/bg-7-4017-2010.
Oschlies, A., M. Pahlow, A. Yool, and R.J. Matear, 2010b: Climate engineering by artificial ocean upwelling: Channelling the sorcerer's apprentice. *Geophysical Research Letters*, **37(4)**, doi:10.1029/2009gl041961.
Oschlies, A., M. Pahlow, A. Yool, and R.J. Matear, 2010c: Climate engineering by artificial ocean upwelling: Channelling the sorcerer's apprentice. *Geophysical Research Letters*, **37(4)**, doi:10.1029/2009gl041961.
Oschlies, A., P. Brandt, L. Stramma, and S. Schmidtko, 2018: Drivers and mechanisms of ocean deoxygenation. *Nature Geoscience*, **11(7)**, 467–473, doi:10.1038/s41561-018-0152-2.
Osma, N. et al., 2020: Response of Phytoplankton Assemblages From Naturally Acidic Coastal Ecosystems to Elevated pCO2. *Frontiers in Marine Science*, **7**, 323, doi:10.3389/fmars.2020.00323.
Palmer, P.I. et al., 2019a: Net carbon emissions from African biosphere dominate pan-tropical atmospheric CO2 signal. *Nature Communications*, doi:10.1038/s41467-019-11097-w.
Palmer, P.I. et al., 2019b: Net carbon emissions from African biosphere dominate pan-tropical atmospheric CO2 signal. *Nature Communications*, doi:10.1038/s41467-019-11097-w.
Panchuk, K., A. Ridgwell, and L.R. Kump, 2008: Sedimentary response to Paleocene-Eocene Thermal Maximum carbon release: A model-data comparison. *Geology*, **36(4)**, 315, doi:10.1130/g24474a.1.
Pandey, S. et al., 2017: Enhanced methane emissions from tropical wetlands during the 2011 La Niña. *Scientific Reports*, **7(1)**, 45759, doi:10.1038/srep45759.
Pangala, S.R. et al., 2017: Large emissions from floodplain trees close the Amazon methane budget. *Nature*, **552(7684)**, 230–234, doi:10.1038/nature24639.
Parazoo, N.C., C.D. Koven, D.M. Lawrence, V. Romanovsky, and C.E. Miller, 2018: Detecting the permafrost carbon feedback: talik formation and increased cold-season respiration as precursors to sink-to-source transitions. *The Cryosphere*, **12(1)**, 123–144, doi:10.5194/tc-12-123-2018.
Park, J.-Y., C.A. Stock, J.P. Dunne, X. Yang, and A. Rosati, 2019: Seasonal to multiannual marine ecosystem prediction with a global Earth system model. *Science*, **365(6450)**, 284–288, doi:10.1126/science.aav6634.
Park, S. et al., 2012: Trends and seasonal cycles in the isotopic composition of nitrous oxide since 1940. *Nature Geoscience*, **5(4)**, 261–265, doi:10.1038/ngeo1421.
Partanen, A.-I., D.P. Keller, H. Korhonen, and H.D. Matthews, 2016: Impacts of sea spray geoengineering on ocean biogeochemistry. *Geophysical Research Letters*, **43(14)**, 7600–7608, doi:10.1002/2016gl070111.
Patra, P.K., M. Ishizawa, S. Maksyutov, T. Nakazawa, and G. Inoue, 2005: Role of biomass burning and climate anomalies for land-atmosphere carbon fluxes based on inverse modeling of atmospheric CO2. *Global Biogeochemical Cycles*, doi:10.1029/2004gb002258.
Patra, P.K. et al., 2014: Observational evidence for interhemispheric hydroxyl-radical parity. *Nature*, **513(7517)**, 219–223, doi:10.1038/nature13721.
Patra, P.K. et al., 2016: Regional methane emission estimation based on observed atmospheric concentrations (2002-2012). *Journal of the Meteorological Society of Japan. Ser. II*, **94(1)**, 91–113, doi:10.2151/jmsj.2016-006.
Patra, P.K. et al., 2021: Methyl Chloroform continues to constrain the hydroxyl (OH) variability in the troposphere. *Journal of Geophysical Research: Atmospheres*, **126(4)**, e2020JD033862, doi:10.1029/2020jd033862.
Paulmier, A. and D. Ruiz-Pino, 2009: Oxygen minimum zones (OMZs) in the modern ocean. *Progress in Oceanography*, **80(3–4)**, 113–128, doi:10.1016/j.pocean.2008.08.001.
Paustian, K. et al., 2016: Climate-smart soils. *Nature*, **532(7597)**, 49–57, doi:10.1038/nature17174.
Pavlov, I.N., 2015: Biotic and abiotic factors as causes of coniferous forests dieback in Siberia and Far East. *Contemporary Problems of Ecology*, **8(4)**, 440–456, doi:10.1134/s1995425515040125.
Pearson, R.G. et al., 2013: Shifts in Arctic vegetation and associated feedbacks under climate change. *Nature Climate Change*, **3(7)**, 673–677, doi:10.1038/nclimate1858.
Pelejero, C. et al., 2005: Preindustrial to Modern Interdecadal Variability in Coral Reef pH. *Science*, **309(5744)**, 2204–2207, doi:10.1126/science.1113692.
Peng, S. et al., 2016: Inventory of anthropogenic methane emissions in mainland China from 1980 to 2010. *Atmospheric Chemistry and Physics*, **16(22)**, 14545–14562, doi:10.5194/acp-16-14545-2016.
Penman, D.E., B. Hönisch, R.E. Zeebe, E. Thomas, and J.C. Zachos, 2014: Rapid and sustained surface ocean acidification during the Paleocene-Eocene Thermal Maximum. *Paleoceanography*, **29(5)**, 357–369, doi:10.1002/2014pa002621.
Peñuelas, J. et al., 2017: Shifting from a fertilization-dominated to a warming-dominated period. *Nature Ecology & Evolution*, **1(10)**, 1438–1445, doi:10.1038/s41559-017-0274-8.
Pépin, L., D. Raynaud, J.-M. Barnola, and M.F. Loutre, 2001: Hemispheric roles of climate forcings during glacial-interglacial transitions as deduced from the Vostok record and LLN-2D model experiments. *Journal of Geophysical Research: Atmospheres*, **106(D23)**, 31885–31892, doi:10.1029/2001jd900117.
Perez, F.F. et al., 2018: Meridional overturning circulation conveys fast acidification to the deep Atlantic Ocean. *Nature*, **554(7693)**, 515–518, doi:10.1038/nature25493.
Pérez-Ramírez, J., F. Kapteijn, K. Schöffel, and J.A. Moulijn, 2003: Formation and control of N2O in nitric acid production. *Applied Catalysis B: Environmental*, **44(2)**, 117–151, doi:10.1016/s0926-3373(03)00026-2.

ACCEPTED VERSION SUBJECT TO FINAL EDITS

Peters, G.P. et al., 2012: Rapid growth in CO2 emissions after the 2008–2009 global financial crisis. *Nature Climate Change*, **2(1)**, 2–4, doi:10.1038/nclimate1332.
Peters, G.P. et al., 2020: Carbon dioxide emissions continue to grow amidst slowly emerging climate policies. *Nature Climate Change*, **10**, 2–10.
Peters, W., A. Bastos, P. Ciais, and A. Vermeulen, 2020: A historical, geographical and ecological perspective on the 2018 European summer drought: Perspective on the 2018 European drought. *Philosophical Transactions of the Royal Society B: Biological Sciences*, **375(1810)**, doi:10.1098/rstb.2019.0505.
Peters, W. et al., 2007: An atmospheric perspective on North American carbon dioxide exchange: CarbonTracker. *Proceedings of the National Academy of Sciences*, **104(48)**, 18925–18930, doi:10.1073/pnas.0708986104.
Peterson, C.D., L.E. Lisiecki, and J. Stern, 2014: Deglacial whole-ocean δ13C change estimated from 480 benthic foraminiferal records. *Paleoceanography*, **29(6)**, 549–563, doi:10.1002/2013pa002552.
Petit, J.R. et al., 1999: Climate and atmospheric history of the past 420,000 years from the Vostok ice core, Antarctica. *Nature*, **399(6735)**, 429–436, doi:10.1038/20859.
Petrenko, V. et al., 2017: Minimal geological methane emissions during the Younger Dryas–Preboreal abrupt warming event. *Nature*, **548(7668)**, 443–446, doi:10.1038/nature23316.
Petrescu, A.M.R. et al., 2020: European anthropogenic AFOLU greenhouse gas emissions: a review and benchmark data. *Earth System Science Data*, **12(2)**, 961–1001, doi:10.5194/essd-12-961-2020.
Peylin, P. et al., 2013: Global atmospheric carbon budget: results from an ensemble of atmospheric CO2 inversions. *Biogeosciences*, **10(10)**, 6699–6720, doi:10.5194/bg-10-6699-2013.
Pfleiderer, P., C.-F. Schleussner, M. Mengel, and J. Rogelj, 2018: Global mean temperature indicators linked to warming levels avoiding climate risks. *Environmental Research Letters*, **13(6)**, 064015, doi:10.1088/1748-9326/aac319.
Pham-Duc, B., C. Prigent, F. Aires, and F. Papa, 2017: Comparisons of global terrestrial surface water datasets over 15 years. *Journal of Hydrometeorology*, **18(4)**, 993–1007, doi:10.1175/jhm-d-16-0206.1.
Phillips, O.L. et al., 2009: Drought Sensitivity of the Amazon Rainforest. , **323**, 1344–1347.
Piao, S. et al., 2017: Weakening temperature control on the interannual variations of spring carbon uptake across northern lands. *Nature Climate Change*, **7(5)**, 359–363, doi:10.1038/nclimate3277.
Piao, S. et al., 2020: Interannual variation of terrestrial carbon cycle: Issues and perspectives. *Global Change Biology*, **26(1)**, doi:10.1111/gcb.14884.
Pilcher, D.J. et al., 2019: Modeled Effect of Coastal Biogeochemical Processes, Climate Variability, and Ocean Acidification on Aragonite Saturation State in the Bering Sea. *Frontiers in Marine Science*, **5**, 508, doi:10.3389/fmars.2018.00508.
Pison, I., B. Ringeval, P. Bousquet, C. Prigent, and F. Papa, 2013: Stable atmospheric methane in the 2000s: key-role of emissions from natural wetlands. *Atmospheric Chemistry and Physics*, **13(23)**, 11609–11623, doi:10.5194/acp-13-11609-2013.
Pitari, G. et al., 2014: Stratospheric ozone response to sulfate geoengineering: Results from the Geoengineering Model Intercomparison Project (GeoMIP). *Journal of Geophysical Research: Atmospheres*, **119(5)**, 2629–2653, doi:10.1002/2013jd020566.
Plazzotta, M., R. Séférian, and H. Douville, 2019: Impact of solar radiation modification on allowable CO2 emissions: what can we learn from multimodel simulations? *Earth's Future*, **7(6)**, 664–676, doi:10.1029/2019ef001165.
Poeplau, C. and A. Don, 2015: Carbon sequestration in agricultural soils via cultivation of cover crops – A meta-analysis. *Agriculture, Ecosystems & Environment*, **200**, 33–41, doi:10.1016/j.agee.2014.10.024.
Pongratz, J., D.B. Lobell, L. Cao, and K. Caldeira, 2012: Crop yields in a geoengineered climate. *Nature Climate Change*, **2(2)**, 101–105, doi:10.1038/nclimate1373.
Pongratz, J., C.H. Reick, R.A. Houghton, and J.I. House, 2014: Terminology as a key uncertainty in net land use and land cover change carbon flux estimates. *Earth System Dynamics*, **5(1)**, 177–195, doi:10.5194/esd-5-177-2014.
Pongratz, J. et al., 2018: Models meet data: Challenges and opportunities in implementing land management in Earth system models. *Global Change Biology*, **24(4)**, 1470–1487, doi:10.1111/gcb.13988.
Poulter, B. et al., 2014: Contribution of semi-arid ecosystems to interannual variability of the global carbon cycle. *Nature*, **509(7502)**, 600–603, doi:10.1038/nature13376.
Poulter, B. et al., 2017: Global wetland contribution to 2000–2012 atmospheric methane growth rate dynamics. *Environmental Research Letters*, **12(9)**, 094013, doi:10.1088/1748-9326/aa8391.
Powell, T.L. et al., 2013: Confronting model predictions of carbon fluxes with measurements of Amazon forests subjected to experimental drought. *New Phytologist*, **200(2)**, 350–365, doi:10.1111/nph.12390.
Praetorius, S.K. et al., 2015: North Pacific deglacial hypoxic events linked to abrupt ocean warming. *Nature*, **527(7578)**, 362–366, doi:10.1038/nature15753.
Prather, M.J., C.D. Holmes, and J. Hsu, 2012: Reactive greenhouse gas scenarios: Systematic exploration of uncertainties and the role of atmospheric chemistry. *Geophysical Research Letters*, **39(9)**, L09803, doi:10.1029/2012gl051440.
Prather, M.J. et al., 2015: Measuring and modeling the lifetime of nitrous oxide including its variability. *Journal of Geophysical Research: Atmospheres*, **120(11)**, 5693–5705, doi:10.1002/2015jd023267.

ACCEPTED VERSION SUBJECT TO FINAL EDITS

Prinn, R.G. et al., 2000: A history of chemically and radiatively important gases in air deduced from ALE/GAGE/AGAGE. *Journal of Geophysical Research: Atmospheres*, **105(D14)**, 17751–17792, doi:10.1029/2000jd900141.

Prinn, R.G. et al., 2018: History of chemically and radiatively important atmospheric gases from the Advanced Global Atmospheric Gases Experiment (AGAGE). *Earth System Science Data*, **10(2)**, 985–1018, doi:10.5194/essd-10-985-2018.

Proctor, J., S. Hsiang, J. Burney, M. Burke, and W. Schlenker, 2018: Estimating global agricultural effects of geoengineering using volcanic eruptions. *Nature*, **560(7719)**, 480–483, doi:10.1038/s41586-018-0417-3.

Prokopiou, M. et al., 2017: Constraining N2O emissions since 1940 using firn air isotope measurements in both hemispheres. *Atmospheric Chemistry and Physics*, **17(7)**, 4539–4564, doi:10.5194/acp-17-4539-2017.

Prokopiou, M. et al., 2018: Changes in the Isotopic Signature of Atmospheric Nitrous Oxide and Its Global Average Source During the Last Three Millennia. *Journal of Geophysical Research: Atmospheres*, **123(18)**, 10,757–10,773, doi:10.1029/2018jd029008.

Pugh, T.A.M. et al., 2018: A Large Committed Long-Term Sink of Carbon due to Vegetation Dynamics. *Earth's Future*, **6(10)**, 1413–1432, doi:10.1029/2018ef000935.

Pugh, T.A.M. et al., 2019a: Role of forest regrowth in global carbon sink dynamics. *Proceedings of the National Academy of Sciences*, **116(10)**, 4382–4387, doi:10.1073/pnas.1810512116.

Pugh, T.A.M. et al., 2019b: Role of forest regrowth in global carbon sink dynamics. *Proceedings of the National Academy of Sciences*, **116(10)**, 4382–4387, doi:10.1073/pnas.1810512116.

Qi, D. et al., 2017: Increase in acidifying water in the western Arctic Ocean. *Nature Climate Change*, **7(3)**, 195–199, doi:10.1038/nclimate3228.

Qi, D. et al., 2020: Coastal acidification induced by biogeochemical processes driven by sea-ice melt in the western Arctic ocean. *Polar Science*, **23**, 100504, doi:10.1016/j.polar.2020.100504.

Qian, W. et al., 2017: Non-local drivers of the summer hypoxia in the East China Sea off the Changjiang Estuary. *Estuarine, Coastal and Shelf Science*, **198**, 393–399, doi:10.1016/j.ecss.2016.08.032.

Rabalais, N. et al., 2014: Eutrophication-driven deoxygenation in the coastal ocean. *Oceanography*, **27(1)**, 172–183, doi:10.5670/oceanog.2014.21.

Rabalais, N.N. et al., 2010: Dynamics and distribution of natural and human-caused hypoxia. *Biogeosciences*, **7(2)**, 585–619, doi:10.5194/bg-7-585-2010.

Rabin, S.S. et al., 2017: The Fire Modeling Intercomparison Project (FireMIP), phase 1: experimental and analytical protocols with detailed model descriptions. *Geoscientific Model Development*, **10(3)**, 1175–1197, doi:10.5194/gmd-10-1175-2017.

Rae, J.W.B. et al., 2018: CO2 storage and release in the deep Southern Ocean on millennial to centennial timescales. *Nature*, **562(7728)**, 569–573, doi:10.1038/s41586-018-0614-0.

Rafter, P.A. et al., 2019: Anomalous >2000 year old surface ocean radiocarbon age as evidence for deglacial geologic carbon release. *Geophysical Research Letters*, 2019GL085102, doi:10.1029/2019gl085102.

Randerson, J.T. et al., 2015: Multicentury changes in ocean and land contributions to the climate-carbon feedback. *Global Biogeochemical Cycles*, **29(6)**, 744–759, doi:10.1002/2014gb005079.

Raupach, M.R. et al., 2014: The declining uptake rate of atmospheric CO2 by land and ocean sinks. *Biogeosciences*, **11(13)**, 3453–3475, doi:10.5194/bg-11-3453-2014.

Raven, M.R., R.G. Keil, and S.M. Webb, 2021: Microbial sulfate reduction and organic sulfur formation in sinking marine particles. *Science*, **371(6525)**, 178–181, doi:10.1126/science.abc6035.

Ravishankara, A.R., J.S. Daniel, and R.W. Portmann, 2009: Nitrous Oxide (N2O): The Dominant Ozone-Depleting Substance Emitted in the 21st Century. *Science*, **326(5949)**, 123–125, doi:10.1126/science.1176985.

Raymond, P.A. et al., 2013: Global carbon dioxide emissions from inland waters. *Nature*, **503(7476)**, 355–359, doi:10.1038/nature12760.

Raynaud, D. et al., 2005: The record for marine isotopic stage 11. *Nature*, **436(7047)**, 39–40, doi:10.1038/43639b.

Rayner, P.J. et al., 2015: Recent changes in the global and regional carbon cycle: analysis of first-order diagnostics. *Biogeosciences*, **12(3)**, 835–844, doi:10.5194/bg-12-835-2015.

Rees, A.P., I.J. Brown, A. Jayakumar, and B.B. Ward, 2016: The inhibition of N2O production by ocean acidification in cold temperate and polar waters. *Deep Sea Research Part II: Topical Studies in Oceanography*, **127**, 93–101, doi:10.1016/j.dsr2.2015.12.006.

Regnier, P. et al., 2013a: Anthropogenic perturbation of the carbon fluxes from land to ocean. *Nature Geoscience*, **6(8)**, 597–607, doi:10.1038/ngeo1830.

Regnier, P. et al., 2013b: Anthropogenic perturbation of the carbon fluxes from land to ocean. *Nature Geoscience*, **6(8)**, 597–607, doi:10.1038/ngeo1830.

Reich, P.B. and S.E. Hobbie, 2013: Decade-long soil nitrogen constraint on the CO2 fertilization of plant biomass. *Nature Climate Change*, **3(3)**, 278–282, doi:10.1038/nclimate1694.

Reich, P.B., S.E. Hobbie, and T.D. Lee, 2014: Plant growth enhancement by elevated CO2 eliminated by joint water and nitrogen limitation. *Nature Geoscience*, **7(12)**, 920–924, doi:10.1038/ngeo2284.

Reich, P.B., S.E. Hobbie, T.D. Lee, and M.A. Pastore, 2018: Unexpected reversal of C3 versus C4 grass response to

ACCEPTED VERSION SUBJECT TO FINAL EDITS

elevated CO2 during a 20-year field experiment. *Science*, **360(6386)**, 317–320, doi:10.1126/science.aas9313.
Renforth, P., 2019: The negative emission potential of alkaline materials. *Nature Communications*, **10(1)**, 1401, doi:10.1038/s41467-019-09475-5.
Renou-Wilson, F. et al., 2019: Rewetting degraded peatlands for climate and biodiversity benefits: Results from two raised bogs. *Ecological Engineering*, **127**, 547–560, doi:10.1016/j.ecoleng.2018.02.014.
Resplandy, L., L. Bopp, J.C. Orr, and J.P. Dunne, 2013: Role of mode and intermediate waters in future ocean acidification: Analysis of CMIP5 models. *Geophysical Research Letters*, **40(12)**, 3091–3095, doi:10.1002/grl.50414.
Resplandy, L. et al., 2018a: Revision of global carbon fluxes based on a reassessment of oceanic and riverine carbon transport. *Nature Geoscience*, **11(7)**, 504–509, doi:10.1038/s41561-018-0151-3.
Resplandy, L. et al., 2018b: Revision of global carbon fluxes based on a reassessment of oceanic and riverine carbon transport. *Nature Geoscience*, **11(7)**, 504–509, doi:10.1038/s41561-018-0151-3.
Reuter, M. et al., 2017: How Much CO2 Is Taken Up by the European Terrestrial Biosphere? *Bulletin of the American Meteorological Society*, **98(4)**, 665–671, doi:10.1175/bams-d-15-00310.1.
Revelle, R.O.G.E.R. and H.A.N.S.E. Suess, 1957: Carbon Dioxide Exchange Between Atmosphere and Ocean and the Question of an Increase of Atmospheric CO2 during the Past Decades. *Tellus*, **9(1)**, 18–27, doi:10.1111/j.2153-3490.1957.tb01849.x.
Reyer, C.P.O. et al., 2015: Forest resilience and tipping points at different spatio-temporal scales: Approaches and challenges. *Journal of Ecology*, **103(1)**, 5–15, doi:10.1111/1365-2745.12337.
Rhodes, R.H. et al., 2017: Atmospheric methane variability: Centennial-scale signals in the Last Glacial Period. *Global Biogeochemical Cycles*, **31**, 575–590, doi:10.1002/2016gb005570.
Riahi, K. et al., 2017: The Shared Socioeconomic Pathways and their energy, land use, and greenhouse gas emissions implications: An overview. *Global Environmental Change*, **42**, 153–168, doi:10.1016/j.gloenvcha.2016.05.009.
Rice, A.L. et al., 2016: Atmospheric methane isotopic record favors fossil sources flat in 1980s and 1990s with recent increase. *Proceedings of the National Academy of Sciences*, **113(39)**, 10791–10796, doi:10.1073/pnas.1522923113.
Richardson, M., K. Cowtan, and R.J. Millar, 2018: Global temperature definition affects achievement of long-term climate goals. *Environmental Research Letters*, **13(5)**, 054004, doi:10.1088/1748-9326/aab305.
Richardson, T.L., 2019: Mechanisms and Pathways of Small-Phytoplankton Export from the Surface Ocean. *Annual Review of Marine Science*, **11(1)**, 57–74, doi:10.1146/annurev-marine-121916-063627.
Ricke, K.L. and K. Caldeira, 2014: Maximum warming occurs about one decade after a carbon dioxide emission. *Environmental Research Letters*, **9(12)**, 124002, doi:10.1088/1748-9326/9/12/124002.
Rigby, M. et al., 2008: Renewed growth of atmospheric methane. *Geophysical Research Letters*, **35(22)**, L22805, doi:10.1029/2008gl036037.
Rigby, M. et al., 2017: Role of atmospheric oxidation in recent methane growth. *Proceedings of the National Academy of Sciences of the United States of America*, **114(21)**, 5373–5377, doi:10.1073/pnas.1616426114.
Ringeval, B. et al., 2011: Climate-CH4 feedback from wetlands and its interaction with the climate-CO2 feedback. *Biogeosciences*, **8(8)**, 2137–2157, doi:10.5194/bg-8-2137-2011.
Ríos, A.F. et al., 2015: Decadal acidification in the water masses of the Atlantic Ocean. *Proceedings of the National Academy of Sciences*, **112(32)**, 9950–9955, doi:10.1073/pnas.1504613112.
Robinson, C., 2019: Microbial respiration, the engine of ocean deoxygenation. *Frontiers in Marine Science*, **5**, 533, doi:10.3389/fmars.2018.00533.
Robinson, J. et al., 2014: How deep is deep enough? Ocean iron fertilization and carbon sequestration in the Southern Ocean. *Geophysical Research Letters*, **41(7)**, 2489–2495, doi:10.1002/2013gl058799.
Rödenbeck, C., S. Zaehle, R. Keeling, and M. Heimann, 2018: History of El Niño impacts on the global carbon cycle 1957–2017: a quantification from atmospheric CO2 data. *Philosophical Transactions of the Royal Society B: Biological Sciences*, **373(1760)**, 20170303, doi:10.1098/rstb.2017.0303.
Rödenbeck, C. et al., 2014: Interannual sea–air CO2 flux variability from an observation-driven ocean mixed-layer scheme. *Biogeosciences*, **11(17)**, 4599–4613, doi:10.5194/bg-11-4599-2014.
Roderick, M.L., P. Greve, and G. Farquharm, 2015: On the assessment of aridity with changes in atmospheric CO2. *Water Resources Research*, **51**, 5450–5463.
Rodgers, K.B. et al., 2020: Reemergence of Anthropogenic Carbon Into the Ocean's Mixed Layer Strongly Amplifies Transient Climate Sensitivity. *Geophysical Research Letters*, **47(18)**, doi:10.1029/2020gl089275.
Rogelj, J., M. Meinshausen, and R. Knutti, 2012: Global warming under old and new scenarios using IPCC climate sensitivity range estimates. *Nature Climate Change*, **2(4)**, 248–253, doi:10.1038/nclimate1385.
Rogelj, J., M. Meinshausen, M. Schaeffer, R. Knutti, and K. Riahi, 2015a: Impact of short-lived non-CO2 mitigation on carbon budgets for stabilizing global warming. *Environmental Research Letters*, **10(7)**, 075001, doi:10.1088/1748-9326/10/7/075001.
Rogelj, J., P.M. Forster, E. Kriegler, C.J. Smith, and R. Séférian, 2019: Estimating and tracking the remaining carbon budget for stringent climate targets. *Nature*, **571(7765)**, 335–342, doi:10.1038/s41586-019-1368-z.

ACCEPTED VERSION SUBJECT TO FINAL EDITS

Rogelj, J. et al., 2015b: Mitigation choices impact carbon budget size compatible with low temperature goals. *Environmental Research Letters*, **10(7)**, 075003, doi:10.1088/1748-9326/10/7/075003.
Rogelj, J. et al., 2016: Differences between carbon budget estimates unravelled. *Nature Climate Change*, **6(3)**, 245–252, doi:10.1038/nclimate2868.
Rogelj, J. et al., 2018a: Scenarios towards limiting global mean temperature increase below 1.5°C. *Nature Climate Change*, **8(4)**, 325–332, doi:10.1038/s41558-018-0091-3.
Rogelj, J. et al., 2018b: Mitigation Pathways Compatible with 1.5°C in the Context of Sustainable Development. In: *Global Warming of 1.5°C. An IPCC Special Report on the impacts of global warming of 1.5°C above pre-industrial levels and related global greenhouse gas emission pathways, in the context of strengthening the global response to the threat of climate change,* [Masson-Delmotte, V., P. Zhai, H.-O. Pörtner, D. Roberts, J. Skea, P.R. Shukla, A. Pirani, W. Moufouma-Okia, C. Péan, R. Pidcock, S. Connors, J.B.R. Matthews, Y. Chen, X. Zhou, M.I. Gomis, E. Lonnoy, T. Maycock, M. Tignor, and T. Waterfield (eds.)]. In Press, pp. 93–174.
Rogers, K. et al., 2019: Wetland carbon storage controlled by millennial-scale variation in relative sea-level rise. *Nature*, **567(7746)**, 91–95, doi:10.1038/s41586-019-0951-7.
Ronge, T.A. et al., 2016: Radiocarbon constraints on the extent and evolution of the South Pacific glacial carbon pool. *Nature Communications*, **7(1)**, 11487, doi:10.1038/ncomms11487.
Roobaert, A., G.G. Laruelle, P. Landschützer, and P. Regnier, 2018: Uncertainty in the global oceanic CO2 uptake induced by wind forcing: quantification and spatial analysis. *Biogeosciences*, **15(6)**, 1701–1720, doi:10.5194/bg-15-1701-2018.
Roobaert, A. et al., 2019: The spatiotemporal dynamics of the sources and sinks of CO2 in the global coastal ocean. *Global Biogeochemical Cycles*, **33(12)**, 2019GB006239, doi:10.1029/2019gb006239.
Rosa, L., J.A. Reimer, M.S. Went, and P. D'Odorico, 2020: Hydrological limits to carbon capture and storage. *Nature Sustainability*, **3(8)**, 658–666, doi:10.1038/s41893-020-0532-7.
Rosentreter, J.A., D.T. Maher, D. Erler, R.H. Murray, and B.D. Eyre, 2018: Methane emissions partially offset "blue carbon" burial in mangroves. *Science Advances*, **4(6)**, eaao4985, doi:10.1126/sciadv.aao4985.
Roshan, S. and T. DeVries, 2017: Efficient dissolved organic carbon production and export in the oligotrophic ocean. *Nature Communications*, **8(1)**, 2036, doi:10.1038/s41467-017-02227-3.
Roth, R. and F. Joos, 2012: Model limits on the role of volcanic carbon emissions in regulating glacial–interglacial CO2 variations. *Earth and Planetary Science Letters*, **329–330**, 141–149, doi:10.1016/j.epsl.2012.02.019.
Roy, J. et al., 2016: Elevated CO2 maintains grassland net carbon uptake under a future heat and drought extreme. *Proceedings of the National Academy of Sciences of the United States of America*, **113(22)**, 6224–6229, doi:10.1073/pnas.1524527113.
Roy, J. et al., 2018: Sustainable Development, Poverty Eradication and Reducing Inequalities. In: *Global Warming of 1.5°C. An IPCC Special Report on the impacts of global warming of 1.5°C above pre-industrial levels and related global greenhouse gas emission pathways, in the context of strengthening the global response to the threat of climate change,* [Masson-Delmotte, V., P. Zhai, H.-O. Pörtner, D. Roberts, J. Skea, P.R. Shukla, A. Pirani, W. Moufouma-Okia, C. Péan, R. Pidcock, S. Connors, J.B.R. Matthews, Y. Chen, X. Zhou, M.I. Gomis, E. Lonnoy, T. Maycock, M. Tignor, and T. Waterfield (eds.)]. In Press, pp. 445–538.
Roy, T. et al., 2011: Regional impacts of climate change and atmospheric CO2 on future ocean carbon uptake: A multimodel linear feedback analysis. *Journal of Climate*, **24(9)**, 2300–2318, doi:10.1175/2010jcli3787.1.
Royer, S.-J. et al., 2016: A high-resolution time-depth view of dimethylsulphide cycling in the surface sea. *Scientific Reports*, **6**, 32325, doi:10.1038/srep32325.
Rubino, M. et al., 2013: A revised 1000 year atmospheric δ 13 C-CO2 record from Law Dome and South Pole, Antarctica. *Journal of Geophysical Research: Atmospheres*, **118(15)**, 8482–8499, doi:10.1002/jgrd.50668.
Ruddiman, W.F. et al., 2016: Late Holocene climate: Natural or anthropogenic? *Reviews of Geophysics*, **54(1)**, 93–118, doi:10.1002/2015rg000503.
Ruppel, C., 2015: Permafrost-Associated Gas Hydrate: Is It Really Approximately 1 % of the Global System? *Journal of Chemical & Engineering Data*, **60(2)**, 429–436, doi:10.1021/je500770m.
Ruppel, C.D. and J.D. Kessler, 2017: The interaction of climate change and methane hydrates. *Reviews of Geophysics*, **55(1)**, 126–168, doi:10.1002/2016rg000534.
Sabine, C.L., 2004: The oceanic sink for anthropogenic CO2. *Science*, **305(5682)**, 367–371, doi:10.1126/science.1097403.
Saeki, T. and P.K. Patra, 2017: Implications of overestimated anthropogenic CO2 emissions on East Asian and global land CO2 flux inversion. *Geoscience Letters*, **4(1)**, 9, doi:10.1186/s40562-017-0074-7.
Saikawa, E. et al., 2014: Global and regional emissions estimates for N2O. *Atmospheric Chemistry and Physics*, **14(9)**, 4617–4641, doi:10.5194/acp-14-4617-2014.
Sakaguchi, K., X. Zeng, L.R. Leung, and P. Shao, 2016: Influence of dynamic vegetation on carbon-nitrogen cycle feedback in the Community Land Model (CLM4). *Environmental Research Letters*, **11(12)**, 124029, doi:10.1088/1748-9326/aa51d9.
Sakschewski, B. et al., 2016: Resilience of Amazon forests emerges from plant trait diversity. *Nature Climate Change*,

ACCEPTED VERSION SUBJECT TO FINAL EDITS

6(11), 1032–1036, doi:10.1038/nclimate3109.
Salisbury, J.E. and B.F. Jönsson, 2018: Rapid warming and salinity changes in the Gulf of Maine alter surface ocean carbonate parameters and hide ocean acidification. *Biogeochemistry*, **141(3)**, 401–418, doi:10.1007/s10533-018-0505-3.
Sallée, J.-B., R.J. Matear, S.R. Rintoul, and A. Lenton, 2012: Localized subduction of anthropogenic carbon dioxide in the Southern Hemisphere oceans. *Nature Geoscience*, **5(8)**, 579–584, doi:10.1038/ngeo1523.
Salmon, V.G. et al., 2016: Nitrogen availability increases in a tundra ecosystem during five years of experimental permafrost thaw. *Global Change Biology*, **22(5)**, 1927–1941, doi:10.1111/gcb.13204.
Salt, L.A., S.M.A.C. van Heuven, M.E. Claus, E.M. Jones, and H.J.W. de Baar, 2015: Rapid acidification of mode and intermediate waters in the southwestern Atlantic Ocean. *Biogeosciences*, **12(5)**, 1387–1401, doi:10.5194/bg-12-1387-2015.
Sanches, L.F., B. Guenet, C.C. Marinho, N. Barros, and F. de Assis Esteves, 2019: Global regulation of methane emission from natural lakes. *Scientific Reports*, **9(1)**, 255, doi:10.1038/s41598-018-36519-5.
Sanderman, J., T. Hengl, and G.J. Fiske, 2017: Soil carbon debt of 12,000 years of human land use. *Proceedings of the National Academy of Sciences*, **114(36)**, 9575 LP – 9580, doi:10.1073/pnas.1706103114.
Sanderman, J., T. Hengl, and G.J. Fiske, 2018: Correction for Sanderman et al., Soil carbon debt of 12,000 years of human land use. *Proceedings of the National Academy of Sciences*, **115(7)**, E1700–E1700, doi:10.1073/pnas.1800925115.
Sanderson, B.M., 2020: The role of prior assumptions in carbon budget calculations. *Earth Syst. Sci. Data Discuss.*, **11(2)**, 563–577, doi:10.5194/esd-11-563-2020.
Sarmiento, J.L. and N. Gruber, 2002: Sinks for anthropogenic carbon. *Physics Today*, **55(8)**, 30–36.
Sarmiento, J.L. et al., 2010: Trends and regional distributions of land and ocean carbon sinks. *Biogeosciences*, **7(8)**, 2351–2367, doi:10.5194/bg-7-2351-2010.
Sarnthein, M., B. Schneider, and P.M. Grootes, 2013: Peak glacial 14C ventilation ages suggest major draw-down of carbon into the abyssal ocean. *Climate of the Past*, **9(6)**, 2595–2614, doi:10.5194/cp-9-2595-2013.
Sasano, D. et al., 2015: Multidecadal trends of oxygen and their controlling factors in the western North Pacific. *Global Biogeochemical Cycles*, **29(7)**, 935–956, doi:10.1002/2014gb005065.
Sasano, D. et al., 2018: Decline and Bidecadal Oscillations of Dissolved Oxygen in the Oyashio Region and Their Propagation to the Western North Pacific. *Global Biogeochemical Cycles*, **32(6)**, 909–931, doi:10.1029/2017gb005876.
Sasmito, S.D. et al., 2019: Effect of land-use and land-cover change on mangrove blue carbon: A systematic review. *Global Change Biology*, **25(12)**, 4291–4302, doi:10.1111/gcb.14774.
Sasse, T.P., B.I. McNeil, R.J. Matear, and A. Lenton, 2015: Quantifying the influence of CO2 seasonality on future aragonite undersaturation onset. *Biogeosciences*, **12(20)**, 6017–6031, doi:10.5194/bg-12-6017-2015.
Saunders, K.M. et al., 2018: Holocene dynamics of the Southern Hemisphere westerly winds and possible links to CO2 outgassing. *Nature Geoscience*, **11(9)**, 650–655, doi:10.1038/s41561-018-0186-5.
Saunois, M. et al., 2020: The Global Methane Budget 2000–2017. *Earth System Science Data*, **12(3)**, 1561–1623, doi:10.5194/essd-12-1561-2020.
Schädel, C. et al., 2014: Circumpolar assessment of permafrost C quality and its vulnerability over time using long-term incubation data. *Global Change Biology*, **20(2)**, 641–652, doi:10.1111/gcb.12417.
Schädel, C. et al., 2016: Potential carbon emissions dominated by carbon dioxide from thawed permafrost soils. *Nature Climate Change*, **6(10)**, 950–953, doi:10.1038/nclimate3054.
Schaefer, H. et al., 2016: A 21st-century shift from fossil-fuel to biogenic methane emissions indicated by 13CH4. *Science*, **352(6281)**, 80–84, doi:10.1126/science.aad2705.
Schaefer, K., H. Lantuit, V.E. Romanovsky, E.A.G. Schuur, and R. Witt, 2014: The impact of the permafrost carbon feedback on global climate. *Environmental Research Letters*, **9(8)**, 85003, doi:10.1088/1748-9326/9/8/085003.
Schaphoff, S., C.P.O. Reyer, D. Schepaschenko, D. Gerten, and A. Shvidenko, 2016: Tamm Review: Observed and projected climate change impacts on Russia's forests and its carbon balance. *Forest Ecology and Management*, **361**, 432–444, doi:10.1016/j.foreco.2015.11.043.
Scheffer, M., M. Hirota, M. Holmgren, E.H. Van Nes, and F.S. Chapin, 2012: Thresholds for boreal biome transitions. *Proceedings of the National Academy of Sciences*, **109(52)**, 21384–21389, doi:10.1073/pnas.1219844110.
Schilt, A. et al., 2010a: Glacial–interglacial and millennial-scale variations in the atmospheric nitrous oxide concentration during the last 800,000 years. *Quaternary Science Reviews*, **29(1–2)**, 182–192, doi:10.1016/j.quascirev.2009.03.011.
Schilt, A. et al., 2010b: Atmospheric nitrous oxide during the last 140,000years. *Earth and Planetary Science Letters*, **300(1–2)**, 33–43, doi:10.1016/j.epsl.2010.09.027.
Schilt, A. et al., 2014: Isotopic constraints on marine and terrestrial N2O emissions during the last deglaciation. *Nature*, **516(7530)**, 234–237, doi:10.1038/nature13971.
Schimel, D., B.B. Stephens, and J.B. Fisher, 2015: Effect of increasing CO2 on the terrestrial carbon cycle.. *Proceedings of the National Academy of Sciences of the United States of America*, **112(2)**, 436–441, doi:10.1073/pnas.1407302112.

ACCEPTED VERSION SUBJECT TO FINAL EDITS

Schlesinger, W.H., 2013: An estimate of the global sink for nitrous oxide in soils. *Global Change Biology*, **19(10)**, 2929–2931, doi:10.1111/gcb.12239.
Schlunegger, S. et al., 2019: Emergence of anthropogenic signals in the ocean carbon cycle. *Nature Climate Change*, **9(9)**, 719–725, doi:10.1038/s41558-019-0553-2.
Schmidt, M.W.I. et al., 2011: Persistence of soil organic matter as an ecosystem property. *Nature*, **478(7367)**, 49–56, doi:10.1038/nature10386.
Schmidtko, S., L. Stramma, and M. Visbeck, 2017: Decline in global oceanic oxygen content during the past five decades. *Nature*, **542(7641)**, 335–339, doi:10.1038/nature21399.
Schmitt, J. et al., 2012: Carbon Isotope Constraints on the Deglacial CO2 Rise from Ice Cores. *Science*, **336(6082)**, 711–714, doi:10.1126/science.1217161.
Schneider von Deimling, T. et al., 2012: Estimating the near-surface permafrost-carbon feedback on global warming. *Biogeosciences*, **9(2)**, 649–665, doi:10.5194/bg-9-649-2012.
Schneider von Deimling, T. et al., 2015: Observation-based modelling of permafrost carbon fluxes with accounting for deep carbon deposits and thermokarst activity. *Biogeosciences*, **12(11)**, 3469–3488, doi:10.5194/bg-12-3469-2015.
Schuur, E.A.G. et al., 2015: Climate change and the permafrost carbon feedback. *Nature*, **520(7546)**, 171–179, doi:10.1038/nature14338.
Schwalm, C.R. et al., 2012: Reduction in carbon uptake during turn of the century drought in western North America. *Nature Geoscience*, **5(8)**, 551–556, doi:10.1038/ngeo1529.
Schwarber, A.K., S.J. Smith, C.A. Hartin, B.A. Vega-Westhoff, and R. Sriver, 2018: Evaluating Climate Emulation: Unit Testing of Simple Climate Models. *Earth System Dynamics Discussions*, 1–13, doi:10.5194/esd-2018-63.
Schwietzke, S. et al., 2016: Upward revision of global fossil fuel methane emissions based on isotope database. *Nature*, **538(7623)**, 88–91, doi:10.1038/nature19797.
Schwinger, J. et al., 2014: Nonlinearity of Ocean Carbon Cycle Feedbacks in CMIP5 Earth System Models. *Journal of Climate*, **27(11)**, 3869–3888, doi:10.1175/jcli-d-13-00452.1.
Séférian, R., S. Berthet, and M. Chevallier, 2018a: Assessing the decadal predictability of land and ocean carbon uptake. *Geophysical Research Letters*, **45(5)**, 2455–2466, doi:10.1002/2017gl076092.
Séférian, R., M. Rocher, C. Guivarch, and J. Colin, 2018b: Constraints on biomass energy deployment in mitigation pathways: The case of water scarcity. *Environmental Research Letters*, **13(5)**, doi:10.1088/1748-9326/aabcd7.
Séférian, R. et al., 2014: Multiyear predictability of tropical marine productivity. *Proceedings of the National Academy of Sciences*, **111(32)**, 11646–11651, doi:10.1073/pnas.1315855111.
Séférian, R. et al., 2020: Tracking Improvement in Simulated Marine Biogeochemistry Between CMIP5 and CMIP6. *Current Climate Change Reports*, **6(3)**, 95–119, doi:10.1007/s40641-020-00160-0.
Seitzinger, S.P., C. Kroeze, and R. Styles, 2000: Global distribution of N2O emissions from aquatic systems: natural emissions and anthropogenic effects. *Chemosphere - Global Change Science*, **2(3–4)**, 267–279, doi:10.1016/s1465-9972(00)00015-5.
Serrano, O. et al., 2019: Australian vegetated coastal ecosystems as global hotspots for climate change mitigation. *Nature Communications*, **10(1)**, 4313, doi:10.1038/s41467-019-12176-8.
Seshadri, A.K., 2017: Origin of path independence between cumulative CO2 emissions and global warming. *Climate Dynamics*, **49(9–10)**, 3383–3401, doi:10.1007/s00382-016-3519-3.
Shakhova, N. et al., 2010: Extensive methane venting to the atmosphere from sediments of the East Siberian Arctic shelf. *Science*, **327(5970)**, 1246–1250, doi:10.1126/science.1182221.
Shakhova, N. et al., 2014: Ebullition and storm-induced methane release from the East Siberian Arctic Shelf. *Nature Geoscience*, **7(1)**, 64–70, doi:10.1038/ngeo2007.
Shakhova, N. et al., 2017: Current rates and mechanisms of subsea permafrost degradation in the East Siberian Arctic Shelf. *Nature Communications*, **8**, 15872, doi:10.1038/ncomms15872.
Shakun, J.D. et al., 2012: Global warming preceded by increasing carbon dioxide concentrations during the last deglaciation. *Nature*, **484(7392)**, 49–54, doi:10.1038/nature10915.
Shao, J. et al., 2019: Atmosphere-Ocean CO2 Exchange Across the Last Deglaciation From the Boron Isotope Proxy. *Paleoceanography and Paleoclimatology*, **34(10)**, 1650–1670, doi:10.1029/2018pa003498.
Shen, Q., M. Hedley, M. Camps Arbestain, and M.U.F. Kirschbaum, 2016: Can biochar increase the bioavailability of phosphorus? *Journal of soil science and plant nutrition*, **16(ahead)**, 0–0, doi:10.4067/s0718-95162016005000022.
Shindell, D.T. et al., 2013a: Interactive ozone and methane chemistry in GISS-E2 historical and future climate simulations. *Atmospheric Chemistry and Physics*, **13(5)**, 2653–2689, doi:10.5194/acp-13-2653-2013.
Shindell, D.T. et al., 2013b: Interactive ozone and methane chemistry in GISS-E2 historical and future climate simulations. *Atmospheric Chemistry and Physics*, **13(5)**, 2653–2689, doi:10.5194/acp-13-2653-2013.
Shinjo, R., R. Asami, K.-F. Huang, C.-F. You, and Y. Iryu, 2013: Ocean acidification trend in the tropical North Pacific since the mid-20th century reconstructed from a coral archive. *Marine Geology*, **342**, 58–64, doi:10.1016/j.margeo.2013.06.002.
Shuttleworth, R. et al., 2020: Early deglacial CO2 release from the Sub-Antarctic Atlantic and Pacific oceans. *Earth*

ACCEPTED VERSION SUBJECT TO FINAL EDITS

and Planetary Science Letters, 116649, doi:10.1016/j.epsl.2020.116649.
Shuttleworth, R. et al., 2021: Early deglacial CO2 release from the Sub-Antarctic Atlantic and Pacific oceans. *Earth and Planetary Science Letters*, **554**, doi:10.1016/j.epsl.2020.116649.
Siegenthaler, U. et al., 2005: EPICA Dome C carbon dioxide concentrations from 650 to 391 kyr BP. PANGAEA. Retrieved from: https://doi.pangaea.de/10.1594/pangaea.728136.
Sigman, D.M., S.L. Jaccard, and G.H. Haug, 2004: Polar ocean stratification in a cold climate. *Nature*, **428(6978)**, 59–63, doi:10.1038/nature02357.
Simmons, C.T. and H.D. Matthews, 2016: Assessing the implications of human land-use change for the transient climate response to cumulative carbon emissions. *Environmental Research Letters*, **11(3)**, 035001, doi:10.1088/1748-9326/11/3/035001.
Simpson, I.J. et al., 2012: Long-term decline of global atmospheric ethane concentrations and implications for methane. *Nature*, **488(7412)**, 490–494, doi:10.1038/nature11342.
Singarayer, J.S., P.J. Valdes, P. Friedlingstein, S. Nelson, and D.J. Beerling, 2011: Late Holocene methane rise caused by orbitally controlled increase in tropical sources. *Nature*, **470(7332)**, 82–86, doi:10.1038/nature09739.
Sitch, S. et al., 2015: Recent trends and drivers of regional sources and sinks of carbon dioxide. *Biogeosciences*, **12(3)**, 653–679, doi:10.5194/bg-12-653-2015.
Sjögersten, S. et al., 2020: Methane emissions from tree stems in neotropical peatlands. *New Phytologist*, **225(2)**, 769–781, doi:10.1111/nph.16178.
Skinner, L.C., S. Fallon, C. Waelbroeck, E. Michel, and S. Barker, 2010: Ventilation of the Deep Southern Ocean and Deglacial CO2 Rise. *Science*, **328(5982)**, 1147–1151, doi:10.1126/science.1183627.
Skinner, L.C. et al., 2017: Radiocarbon constraints on the glacial ocean circulation and its impact on atmospheric CO2. *Nature Communications*, **8**, 16010, doi:10.1038/ncomms16010.
Sluijs, A. et al., 2006: Subtropical Arctic Ocean temperatures during the Palaeocene/Eocene thermal maximum. *Nature*, **441(7093)**, 610–613, doi:10.1038/nature04668.
Smale, D.A. et al., 2019: Marine heatwaves threaten global biodiversity and the provision of ecosystem services. *Nature Climate Change*, **9(4)**, 306–312, doi:10.1038/s41558-019-0412-1.
Smith, C.J. et al., 2018a: FAIR v1.3: a simple emissions-based impulse response and carbon cycle model. *Geoscientific Model Development*, **11(6)**, 2273–2297, doi:10.5194/gmd-11-2273-2018.
Smith, C.J. et al., 2018b: FAIR v1.3: a simple emissions-based impulse response and carbon cycle model. *Geoscientific Model Development*, **11(6)**, 2273–2297, doi:10.5194/gmd-11-2273-2018.
Smith, M.N. et al., 2020: Empirical evidence for resilience of tropical forest photosynthesis in a warmer world. *Nature Plants*.
Smith, N.G. and J.S. Dukes, 2013: Plant respiration and photosynthesis in global-scale models: incorporating acclimation to temperature and CO2. *Global Change Biology*, **19(1)**, 45–63, doi:10.1111/j.1365-2486.2012.02797.x.
Smith, N.G. and J.S. Dukes, 2017: Short-term acclimation to warmer temperatures accelerates leaf carbon exchange processes across plant types. *Global Change Biology*, **23(11)**, 4840–4853, doi:10.1111/gcb.13735.
Smith, N.G., S.L. Malyshev, E. Shevliakova, J. Kattge, and J.S. Dukes, 2015: Foliar temperature acclimation reduces simulated carbon sensitivity to climate. *Nature Climate Change*, **6**, 407, doi:10.1038/nclimate2878.
Smith, P., 2016: Soil carbon sequestration and biochar as negative emission technologies. *Global Change Biology*, **22(3)**, 1315–1324, doi:10.1111/gcb.13178.
Smith, P., J. Price, A. Molotoks, R. Warren, and Y. Malhi, 2018: Impacts on terrestrial biodiversity of moving from a 2°C to a 1.5°C target. *Philosophical Transactions of the Royal Society A: Mathematical,Physical and Engineering Sciences*, **376(2119)**, 20160456, doi:10.1098/rsta.2016.0456.
Smith, P. et al., 2016: Biophysical and economic limits to negative CO2 emissions. *Nature Climate Change*, **6(1)**, 42–50, doi:10.1038/nclimate2870.
Smith, P. et al., 2019: Land-Management Options for Greenhouse Gas Removal and Their Impacts on Ecosystem Services and the Sustainable Development Goals. *Annual Review of Environment and Resources*, **44(1)**, 255–286, doi:10.1146/annurev-environ-101718-033129.
Smith, S.J. and A. Mizrahi, 2013: Near-term climate mitigation by short-lived forcers. *Proceedings of the National Academy of Sciences*, **110(35)**, 14202–14206, doi:10.1073/pnas.1308470110.
Smith, W.K., M. Zhao, and S.W. Running, 2012: Global bioenergy capacity as constrained by observed biospheric productivity rates. *BioScience*, **62(10)**, 911–922, doi:10.1525/bio.2012.62.10.11.
Snider, D.M., J.J. Venkiteswaran, S.L. Schiff, and J. Spoelstra, 2015: From the Ground Up: Global Nitrous Oxide Sources are Constrained by Stable Isotope Values. *PLOS ONE*, **10(3)**, e0118954, doi:10.1371/journal.pone.0118954.
Song, J. et al., 2019a: A meta-analysis of 1,119 manipulative experiments on terrestrial carbon-cycling responses to global change. *Nature Ecology & Evolution*, **3(9)**, 1309–1320, doi:10.1038/s41559-019-0958-3.
Song, J. et al., 2019b: A meta-analysis of 1,119 manipulative experiments on terrestrial carbon-cycling responses to global change. *Nature Ecology & Evolution*, **3(9)**, 1309–1320, doi:10.1038/s41559-019-0958-3.
Song, X. et al., 2018: Nitrous Oxide Emissions Increase Exponentially When Optimum Nitrogen Fertilizer Rates Are

ACCEPTED VERSION SUBJECT TO FINAL EDITS

Exceeded in the North China Plain. *Environmental Science & Technology*, **52(21)**, 12504–12513, doi:10.1021/acs.est.8b03931.
Sonntag, S., J. Pongratz, C. Reick, and H. Schmidt, 2015: Carbon sequestration potential and climatic effects of reforestation in an Earth system model. , **17**, 13707.
Sonntag, S. et al., 2018: Quantifying and Comparing Effects of Climate Engineering Methods on the Earth System. *Earth's Future*, **6(2)**, 149–168, doi:10.1002/2017ef000620.
Spafford, L. and A.H. Macdougall, 2020: Quantifying the probability distribution function of the transient climate response to cumulative CO2 emissions. *Environmental Research Letters*, **15(3)**, doi:10.1088/1748-9326/ab6d7b.
Spring, A. and T. Ilyina, 2020: Predictability Horizons in the Global Carbon Cycle Inferred From a Perfect-Model Framework. *Geophysical Research Letters*, **47(9)**, doi:10.1029/2019gl085311.
Stanley, E.H. et al., 2016: The ecology of methane in streams and rivers: patterns, controls, and global significance. *Ecological Monographs*, **86(2)**, 146–171, doi:10.1890/15-1027.
Staver, A.C., S. Archibald, and S.A. Levin, 2011: The global extent and determinants of savanna and forest as alternative biome states. *Science*, **334(6053)**, 230–232, doi:10.1126/science.1210465.
Steele, L.P. et al., 1992: Slowing down of the global accumulation of atmospheric methane during the 1980s. *Nature*, **358(6384)**, 313–316, doi:10.1038/358313a0.
Steffen, W. et al., 2018: Trajectories of the Earth System in the Anthropocene. *Proceedings of the National Academy of Sciences*, **115(33)**, 8252–8259, doi:10.1073/pnas.1810141115.
Steinacher, M. and F. Joos, 2016: Transient Earth system responses to cumulative carbon dioxide emissions: linearities, uncertainties, and probabilities in an observation-constrained model ensemble. *Biogeosciences*, **13(4)**, 1071–1103, doi:10.5194/bg-13-1071-2016.
Steinacher, M., F. Joos, T.L. Frölicher, G.-K. Plattner, and S.C. Doney, 2009: Imminent ocean acidification in the Arctic projected with the NCAR global coupled carbon cycle-climate model. *Biogeosciences*, **6(4)**, 515–533, doi:10.5194/bg-6-515-2009.
Stenzel, F., P. Greve, and S. Tramberend, 2021: increase water stress more than climate change. *Nature Communications*, 1–9, doi:10.1038/s41467-021-21640-3.
Stenzel, F., D. Gerten, C. Werner, and J. Jägermeyr, 2019: Freshwater requirements of large-scale bioenergy plantations for limiting global warming to 1.5°C. *Environmental Research Letters*, **14(8)**, 084001, doi:10.1088/1748-9326/ab2b4b.
Stepanenko, V. et al., 2016: LAKE 2.0: a model for temperature, methane, carbon dioxide and oxygen dynamics in lakes. *Geoscientific Model Development*, **9(5)**, 1977–2006, doi:10.5194/gmd-9-1977-2016.
Sterman, J.D., L. Siegel, and J.N. Rooney-Varga, 2018: Does replacing coal with wood lower CO2 emissions? Dynamic lifecycle analysis of wood bioenergy. *Environmental Research Letters*, **13(1)**, 15007, doi:10.1088/1748-9326/aaa512.
Stern, D.I. and R.K. Kaufmann, 1996: Estimates of global anthropogenic methane emissions 1860–1993. *Chemosphere*, **33(1)**, 159–176, doi:10.1016/0045-6535(96)00157-9.
Stevenson, D.S. et al., 2020: Trends in global tropospheric hydroxyl radical and methane lifetime since 1850 from AerChemMIP. *Atmos. Chem. Phys.*, **20(21)**, 12905–12920, doi:10.5194/acp-20-12905-2020.
Stocker, B.D. and F. Joos, 2015: Quantifying differences in land use emission estimates implied by definition discrepancies. *Earth System Dynamics*, **6(2)**, 731–744, doi:10.5194/esd-6-731-2015.
Stocker, B.D., Z. Yu, C. Massa, and F. Joos, 2017: Holocene peatland and ice-core data constraints on the timing and magnitude of CO 2 emissions from past land use. *Proceedings of the National Academy of Sciences*, **114(7)**, 1492–1497, doi:10.1073/pnas.1613889114.
Stocker, B.D. et al., 2013a: Multiple greenhouse-gas feedbacks from the land biosphere under future climate change scenarios. *Nature Climate Change*, **3(7)**, 666–672, doi:10.1038/nclimate1864.
Stocker, B.D. et al., 2013b: Multiple greenhouse-gas feedbacks from the land biosphere under future climate change scenarios. *Nature Climate Change*, **3(7)**, 666–672, doi:10.1038/nclimate1864.
Stocker, B.D. et al., 2019: Drought impacts on terrestrial primary production underestimated by satellite monitoring. *Nature Geoscience*, **12(4)**, 264–270, doi:10.1038/s41561-019-0318-6.
Stocker, T.F. et al., 2013: Technical Summary. In: *Climate Change 2013: The Physical Science Basis. Contribution of Working Group I to the Fifth Assessment Report of the Intergovernmental Panel on Climate Change* [Stocker, T.F., D. Qin, G.-K. Plattner, M. Tignor, S.K. Allen, A. Boschung, A. Nauels, Y. Xia, V. Bex, and P.M. Midgley (eds.)]. Cambridge University Press, Cambridge, United Kingdom and New York, NY, USA, pp. 33–115, doi:10.1017/cbo9781107415324.005.
Stott, L. et al., 2019: CO2 release from pockmarks on the chatham rise-bounty trough at the glacial termination. *Paleoceanography and Paleoclimatology*, 2019PA003674, doi:10.1029/2019pa003674.
Stott, L.D., K.M. Harazin, and N.B. Quintana Krupinski, 2019: Hydrothermal carbon release to the ocean and atmosphere from the eastern equatorial Pacific during the last glacial termination. *Environmental Research Letters*, **14(2)**, 025007, doi:10.1088/1748-9326/aafe28.
Stramma, L., G.C. Johnson, J. Sprintall, and V. Mohrholz, 2008: Expanding oxygen-minimum zones in the tropical

ACCEPTED VERSION SUBJECT TO FINAL EDITS

oceans. *Science*, **320(5876)**, 655–658, doi:10.1126/science.1153847.
Strassburg, B.B.N. et al., 2020: Global priority areas for ecosystem restoration. *Nature*, **586(7831)**, 724–729, doi:10.1038/s41586-020-2784-9.
Strauss, J. et al., 2013: The deep permafrost carbon pool of the Yedoma region in Siberia and Alaska. *Geophysical Research Letters*, **40(23)**, 6165–6170, doi:10.1002/2013gl058088.
Strauss, J. et al., 2017: Deep Yedoma permafrost: A synthesis of depositional characteristics and carbon vulnerability. *Earth-Science Reviews*, **172**, 75–86, doi:10.1016/j.earscirev.2017.07.007.
Strefler, J., T. Amann, N. Bauer, E. Kriegler, and J. Hartmann, 2018: Potential and costs of carbon dioxide removal by enhanced weathering of rocks. *Environmental Research Letters*, **13(3)**, 34010, doi:10.1088/1748-9326/aaa9c4.
Strode, S.A. et al., 2020: Strong sensitivity of the isotopic composition of methane to the plausible range of tropospheric chlorine. *Atmospheric Chemistry and Physics*, **20(14)**, 8405–8419, doi:10.5194/acp-20-8405-2020.
Studer, A.S. et al., 2018: Increased nutrient supply to the Southern Ocean during the Holocene and its implications for the pre-industrial atmospheric CO2 rise. *Nature Geoscience*, **11(10)**, 756–760, doi:10.1038/s41561-018-0191-8.
Suess, H.E., 1955: Radiocarbon Concentration in Modern Wood. *Science*, **122(3166)**, 415–417, doi:10.1126/science.122.3166.415-a.
Sulman, B.N. et al., 2019: Diverse mycorrhizal associations enhance terrestrial C storage in a global model. *Global Biogeochemical Cycles*, **33(4)**, 501–523, doi:10.1029/2018gb005973.
Sulpis, O. et al., 2019: Reduced CaCO3 Flux to the Seafloor and Weaker Bottom Current Speeds Curtail Benthic CaCO3 Dissolution Over the 21st Century. *Global Biogeochemical Cycles*, **33(12)**, 1654–1673, doi:10.1029/2019gb006230.
Sun, H. et al., 2020: Surface seawater partial pressure of CO2 variability and air-sea CO2 fluxes in the Bering Sea in July 2010. *Continental Shelf Research*, **193**, 104031, doi:10.1016/j.csr.2019.104031.
Sun, W. et al., 2020: Climate drives global soil carbon sequestration and crop yield changes under conservation agriculture. *Global Change Biology*, **26(6)**, 3325–3335, doi:10.1111/gcb.15001.
Suntharalingam, P. et al., 2012: Quantifying the impact of anthropogenic nitrogen deposition on oceanic nitrous oxide. *Geophysical Research Letters*, **39(7)**, L07605, doi:10.1029/2011gl050778.
Suntharalingam, P. et al., 2019: Anthropogenic nitrogen inputs and impacts on oceanic N2O fluxes in the northern Indian Ocean: The need for an integrated observation and modelling approach. *Deep Sea Research Part II: Topical Studies in Oceanography*, **166**, 104–113, doi:10.1016/j.dsr2.2019.03.007.
Suthhof, A., V. Ittekkot, and B. Gaye-Haake, 2001: Millennial-scale oscillation of denitrification intensity in the Arabian Sea during the Late Quaternary and its potential influence on atmospheric N2O and global climate. *Global Biogeochemical Cycles*, **15(3)**, 637–649, doi:10.1029/2000gb001337.
Sutton, A.J. et al., 2014: Natural variability and anthropogenic change in equatorial Pacific surface ocean pCO2 and pH. *Global Biogeochemical Cycles*, **28(2)**, 131–145, doi:10.1002/2013gb004679.
Sutton, A.J. et al., 2016: Using present-day observations to detect when anthropogenic change forces surface ocean carbonate chemistry outside preindustrial bounds. *Biogeosciences*, **13(17)**, 5065–5083, doi:10.5194/bg-13-5065-2016.
Sutton, A.J. et al., 2019: Autonomous seawater CO2 and pH time series from 40 surface buoys and the emergence of anthropogenic trends. *Earth System Science Data*, **11(1)**, 421–439, doi:10.5194/essd-11-421-2019.
Swann, A.L.S., F.M. Hoffman, C.D. Koven, and J.T. Randerson, 2016: Plant responses to increasing CO 2 reduce estimates of climate impacts on drought severity. *Proceedings of the National Academy of Sciences*, **113(36)**, 10019–10024, doi:10.1073/pnas.1604581113.
Sweeney, C. et al., 2016: No significant increase in long-term CH 4 emissions on North Slope of Alaska despite significant increase in air temperature. *Geophysical Research Letters*, **43(12)**, 6604–6611, doi:10.1002/2016gl069292.
Szulczewski, M.L., C.W. MacMinn, H.J. Herzog, and R. Juanes, 2012: Lifetime of carbon capture and storage as a climate-change mitigation technology. *Proceedings of the National Academy of Sciences of the United States of America*, doi:10.1073/pnas.1115347109.
Tachiiri, K., T. Hajima, and M. Kawamiya, 2015: Increase of uncertainty in transient climate response to cumulative carbon emissions after stabilization of atmospheric CO2 concentration. *Environmental Research Letters*, **10(12)**, 125018, doi:10.1088/1748-9326/10/12/125018.
Tachiiri, K., T. Hajima, and M. Kawamiya, 2019: Increase of the transient climate response to cumulative carbon emissions with decreasing CO2 concentration scenarios. *Environmental Research Letters*, doi:10.1088/1748-9326/ab57d3.
Tagesson, T. et al., 2020: Recent divergence in the contributions of tropical and boreal forests to the terrestrial carbon sink. *Nature Ecology and Evolution*, **4(2)**, doi:10.1038/s41559-019-1090-0.
Taillardat, P., D.A. Friess, and M. Lupascu, 2018: Mangrove blue carbon strategies for climate change mitigation are most effective at the national scale. *Biology Letters*, **14(10)**, 20180251, doi:10.1098/rsbl.2018.0251.
Takahashi, T. et al., 2014: Climatological distributions of pH, pCO2, total CO2, alkalinity, and CaCO3 saturation in the

ACCEPTED VERSION SUBJECT TO FINAL EDITS

global surface ocean, and temporal changes at selected locations. *Marine Chemistry*, **164**, 95–125, doi:10.1016/j.marchem.2014.06.004.
Takata, K. et al., 2017: Reconciliation of top-down and bottom-up CO2 fluxes in Siberian larch forest. *Environmental Research Letters*, **12(12)**, doi:10.1088/1748-9326/aa926d.
Takatani, Y., D. Sasano, T. Nakano, T. Midorikawa, and M. Ishii, 2012: Decrease of dissolved oxygen after the mid-1980s in the western North Pacific subtropical gyre along the 137°E repeat section. *Global Biogeochemical Cycles*, **26(2)**, GB2013, doi:10.1029/2011gb004227.
Takeshita, Y. et al., 2015: Including high-frequency variability in coastal ocean acidification projections. *Biogeosciences*, **12(19)**, 5853–5870, doi:10.5194/bg-12-5853-2015.
Talhelm, A.F. et al., 2014: Elevated carbon dioxide and ozone alter productivity and ecosystem carbon content in northern temperate forests. *Global Change Biology*, **20(8)**, 2492–2504, doi:10.1111/gcb.12564.
Talley, L.D. et al., 2016: Changes in Ocean Heat, Carbon Content, and Ventilation: A Review of the First Decade of GO-SHIP Global Repeat Hydrography. *Annual Review of Marine Science*, **8(1)**, 185–215, doi:10.1146/annurev-marine-052915-100829.
Tan, Z. and Q. Zhuang, 2015: Arctic lakes are continuous methane sources to the atmosphere under warming conditions. *Environmental Research Letters*, **10(5)**, 054016, doi:10.1088/1748-9326/10/5/054016.
Tan, Z.-H. et al., 2017: Optimum air temperature for tropical forest photosynthesis: mechanisms involved and implications for climate warming. *Environmental Research Letters*, **12(5)**, 054022, doi:10.1088/1748-9326/aa6f97.
Tanhua, T. et al., 2017: Temporal changes in ventilation and the carbonate system in the Atlantic sector of the Southern Ocean. *Deep Sea Research Part II: Topical Studies in Oceanography*, **138**, 26–38, doi:10.1016/j.dsr2.2016.10.004.
Taucher, J. and A. Oschlies, 2011: Can we predict the direction of marine primary production change under global warming? *Geophysical Research Letters*, **38(2)**, L02603, doi:10.1029/2010gl045934.
Taucher, J. et al., 2021: Changing carbon-to-nitrogen ratios of organic-matter export under ocean acidification. *Nature Climate Change*, **11(1)**, 52–57, doi:10.1038/s41558-020-00915-5.
Taylor, K.E., R.J. Stouffer, and G.A. Meehl, 2012: An Overview of CMIP5 and the Experiment Design. *Bulletin of the American Meteorological Society*, **93(4)**, 485–498, doi:10.1175/bams-d-11-00094.1.
Tebaldi, C. and R. Knutti, 2007: The use of the multi-model ensemble in probabilistic climate projections. *Philosophical Transactions of the Royal Society A: Mathematical, Physical and Engineering Sciences*, **365(1857)**, 2053–2075, doi:10.1098/rsta.2007.2076.
Teckentrup, L. et al., 2019: Response of simulated burned area to historical changes in environmental and anthropogenic factors: a comparison of seven fire models. *Biogeosciences*, **16(19)**, 3883–3910, doi:10.5194/bg-16-3883-2019.
Terhaar, J., J.C. Orr, C. Ethé, P. Regnier, and L. Bopp, 2019: Simulated Arctic Ocean Response to Doubling of Riverine Carbon and Nutrient Delivery. *Global Biogeochemical Cycles*, **33(8)**, 1048–1070, doi:10.1029/2019gb006200.
Terrer, C., S. Vicca, B.A. Hungate, R.P. Phillips, and I.C. Prentice, 2016: Mycorrhizal association as a primary control of the CO2 fertilization effect. *Science*, **353(6294)**, 72–74, doi:10.1126/science.aaf4610.
Terrer, C. et al., 2018: Ecosystem responses to elevated CO2 governed by plant-soil interactions and the cost of nitrogen acquisition. *New Phytologist*, **217(2)**, 507–522, doi:10.1111/nph.14872.
Terrer, C. et al., 2019: Nitrogen and phosphorus constrain the CO2 fertilization of global plant biomass. *Nature Climate Change*, **9(9)**, 684–689, doi:10.1038/s41558-019-0545-2.
Teuling, A.J. et al., 2017: Observational evidence for cloud cover enhancement over western European forests. *Nature Communications*, **8(1)**, 14065, doi:10.1038/ncomms14065.
Teuling, A.J. et al., 2019: Climate change, reforestation/afforestation, and urbanization impacts on evapotranspiration and streamflow in Europe. *Hydrology and Earth System Sciences*, **23(9)**, 3631–3652, doi:10.5194/hess-23-3631-2019.
Thomas, J., D. Waugh, and A. Gnanadesikan, 2018: Relationship between ocean carbon and heat multidecadal variability. *Journal of Climate*, **31(4)**, 1467–1482, doi:10.1175/jcli-d-17-0134.1.
Thomas, R.Q., E.N.J. Brookshire, and S. Gerber, 2015: Nitrogen limitation on land: how can it occur in Earth system models? *Global Change Biology*, **21(5)**, 1777–1793, doi:10.1111/gcb.12813.
Thompson, I., B. Mackey, S. Mcnulty, and A. Mosseler, 2009: Forest Resilience, Biodiversity, and Climate Change. A Synthesis of the Biodiversity/Resilience/Stability Relationship in Forest Ecosystems. *Technical Series no. 43*, 67.
Thompson, R.L. et al., 2018: Variability in Atmospheric Methane From Fossil Fuel and Microbial Sources Over the Last Three Decades. *Geophysical Research Letters*, **45(20)**, 11,499–11,508, doi:10.1029/2018gl078127.
Thompson, R.L. et al., 2019: Acceleration of global N2O emissions seen from two decades of atmospheric inversion. *Nature Climate Change*, **9(12)**, 993–998, doi:10.1038/s41558-019-0613-7.
Thornhill, G. et al., 2020: Climate-driven chemistry and aerosol feedbacks in CMIP6 Earth system models. *Atmospheric Chemistry and Physics*, 1–36, doi:10.5194/acp-2019-1207.

ACCEPTED VERSION SUBJECT TO FINAL EDITS

Thornton, B.F., M. Wik, and P.M. Crill, 2016a: Double-counting challenges the accuracy of high-latitude methane inventories. *Geophysical Research Letters*, **43(24)**, 12,569–12,577, doi:10.1002/2016gl071772.
Thornton, B.F., M.C. Geibel, P.M. Crill, C. Humborg, and C.-M. Mörth, 2016b: Methane fluxes from the sea to the atmosphere across the Siberian shelf seas. *Geophysical Research Letters*, **43(11)**, 5869–5877, doi:10.1002/2016gl068977.
Thornton, B.F. et al., 2020: Shipborne eddy covariance observations of methane fluxes constrain Arctic sea emissions. *Science Advances*, **6(5)**, eaay7934, doi:10.1126/sciadv.aay7934.
Thornton, P.E. et al., 2009: Carbon-nitrogen interactions regulate climate-carbon cycle feedbacks: results from an atmosphere-ocean general circulation model. *Biogeosciences*, **6(10)**, 2099–2120, doi:10.5194/bg-6-2099-2009.
Thurner, M. et al., 2017: Evaluation of climate-related carbon turnover processes in global vegetation models for boreal and temperate forests. *Global Change Biology*, **23(8)**, 3076–3091, doi:10.1111/gcb.13660.
Tian, H. et al., 2019: Global soil nitrous oxide emissions since the preindustrial era estimated by an ensemble of terrestrial biosphere models: Magnitude, attribution, and uncertainty. *Global Change Biology*, **25(2)**, 640–659, doi:10.1111/gcb.14514.
Tian, H. et al., 2020: A comprehensive quantification of global nitrous oxide sources and sinks. *Nature*, **586(7828)**, 248–256, doi:10.1038/s41586-020-2780-0.
Tiemeyer, B. et al., 2020: A new methodology for organic soils in national greenhouse gas inventories: Data synthesis, derivation and application. *Ecological Indicators*, **109**, 105838, doi:10.1016/j.ecolind.2019.105838.
Tierney, J.E. et al., 2020: Past climates inform our future. *Science (New York, N.Y.)*, **370(6517)**, doi:10.1126/science.aay3701.
Tilbrook, B. et al., 2019: An Enhanced Ocean Acidification Observing Network: From People to Technology to Data Synthesis and Information Exchange. *Frontiers in Marine Science*, **6**, 337, doi:10.3389/fmars.2019.00337.
Tilmes, S., B.M. Sanderson, and B.C. O'Neill, 2016: Climate impacts of geoengineering in a delayed mitigation scenario. *Geophysical Research Letters*, **43(15)**, 8222–8229, doi:10.1002/2016gl070122.
Tilmes, S. et al., 2018: Effects of Different Stratospheric SO2Injection Altitudes on Stratospheric Chemistry and Dynamics. *Journal of Geophysical Research: Atmospheres*, **123(9)**, 4654–4673, doi:10.1002/2017jd028146.
Tisserant, A. and F. Cherubini, 2019: Potentials, Limitations, Co-Benefits, and Trade-Offs of Biochar Applications to Soils for Climate Change Mitigation. *Land*, **8(12)**, doi:10.3390/land8120179.
Tjiputra, J.F., A. Grini, and H. Lee, 2016: Impact of idealized future stratospheric aerosol injection on the large-scale ocean and land carbon cycles. *Journal of Geophysical Research: Biogeosciences*, **121(1)**, 2–27, doi:10.1002/2015jg003045.
Todd-Brown, K.E.O. et al., 2013: Causes of variation in soil carbon simulations from CMIP5 Earth system models and comparison with observations. *Biogeosciences*, **10(3)**, 1717–1736, doi:10.5194/bg-10-1717-2013.
Tohjima, Y., H. Mukai, T. Machida, Y. Hoshina, and S.-I. Nakaoka, 2019: Global carbon budgets estimated from atmospheric O2/N2 and\nCO2 observations in the western Pacific region over a 15-year period. *Atmospheric Chemistry and Physics*, **19(14)**, 9269–9285, doi:10.5194/acp-19-9269-2019.
Tokarska, K.B. and K. Zickfeld, 2015: The effectiveness of net negative carbon dioxide emissions in reversing anthropogenic climate change. *Environmental Research Letters*, **10(9)**, 094013, doi:10.1088/1748-9326/10/9/094013.
Tokarska, K.B. and N.P. Gillett, 2018: Cumulative carbon emissions budgets consistent with 1.5°C global warming. *Nature Climate Change*, **8(4)**, 296–299, doi:10.1038/s41558-018-0118-9.
Tokarska, K.B., K. Zickfeld, and J. Rogelj, 2019a: Path independence of carbon budgets when meeting a stringent global mean temperature target after an overshoot. *Earth's Future*, 2019EF001312, doi:10.1029/2019ef001312.
Tokarska, K.B., N.P. Gillett, A.J. Weaver, V.K. Arora, and M. Eby, 2016: The climate response to five trillion tonnes of carbon. *Nature Climate Change*, **6(9)**, 851–855, doi:10.1038/nclimate3036.
Tokarska, K.B., N.P. Gillett, V.K. Arora, W.G. Lee, and K. Zickfeld, 2018: The influence of non-CO2 forcings on cumulative carbon emissions budgets. *Environmental Research Letters*, **13(3)**, 034039, doi:10.1088/1748-9326/aaafdd.
Tokarska, K.B. et al., 2019b: Recommended temperature metrics for carbon budget estimates, model evaluation and climate policy. *Nature Geoscience*, **12(12)**, 964–971, doi:10.1038/s41561-019-0493-5.
Tokarska, K.B. et al., 2020: Uncertainty in carbon budget estimates due to internal climate variability. *Environmental Research Letters*, doi:10.1088/1748-9326/abaf1b.
Tonitto, C., M.B. David, and L.E. Drinkwater, 2006: Replacing bare fallows with cover crops in fertilizer-intensive cropping systems: A meta-analysis of crop yield and N dynamics. *Agriculture, Ecosystems & Environment*, **112(1)**, 58–72, doi:10.1016/j.agee.2005.07.003.
Toyama, K. et al., 2017: Large reemergence of anthropogenic carbon into the ocean's surface mixed layer sustained by the ocean's overturning circulation. *Journal of Climate*, **30(21)**, 8615–8631, doi:10.1175/jcli-d-16-0725.1.
Trabucco, A., R.J. Zomer, D.A. Bossio, O. van Straaten, and L. Verchot, 2008: Climate change mitigation through afforestation/reforestation: A global analysis of hydrologic impacts with four case studies. *Agriculture, Ecosystems and Environment*, **126(1–2)**, 81–97, doi:10.1016/j.agee.2008.01.015.

ACCEPTED VERSION SUBJECT TO FINAL EDITS

Tran, G.T., A. Oschlies, and D.P. Keller, 2020: Comparative Assessment of Climate Engineering Scenarios in the Presence of Parametric Uncertainty. *Journal of Advances in Modeling Earth Systems*, **12(4)**, doi:10.1029/2019ms001787.
Treat, C.C. et al., 2019: Widespread global peatland establishment and persistence over the last 130,000 y. *Proceedings of the National Academy of Sciences*, **116(11)**, 4822–4827, doi:10.1073/pnas.1813305116.
Trimmer, M. et al., 2016: Nitrous oxide as a function of oxygen and archaeal gene abundance in the North Pacific. *Nature Communications*, **7(1)**, 13451, doi:10.1038/ncomms13451.
Trisos, C.H. et al., 2018: Potentially dangerous consequences for biodiversity of solar geoengineering implementation and termination. *Nature Ecology and Evolution*, doi:10.1038/s41559-017-0431-0.
Tubiello, F. et al., 2021: Carbon Emissions and Removals by Forests: New Estimates 1990–2020. *Earth System Science Data* (in press), doi:10.5194/essd-2020-203.
Turco, M., M.-C. Llasat, J. von Hardenberg, and A. Provenzale, 2014: Climate change impacts on wildfires in a Mediterranean environment. *Climatic Change*, **125(3)**, 369–380, doi:10.1007/s10584-014-1183-3.
Turco, M. et al., 2016: Decreasing fires in mediterranean Europe. *PLoS ONE*, **11(3)**, doi:10.1371/journal.pone.0150663.
Turco, M. et al., 2018: Exacerbated fires in Mediterranean Europe due to anthropogenic warming projected with non-stationary climate-fire models. *Nature Communications*, doi:10.1038/s41467-018-06358-z.
Turetsky, M.R. et al., 2015: Global vulnerability of peatlands to fire and carbon loss. *Nature Geoscience*, **8(1)**, 11–14, doi:10.1038/ngeo2325.
Turetsky, M.R. et al., 2020: Carbon release through abrupt permafrost thaw. *Nature Geoscience*, **13(2)**, 138–143, doi:10.1038/s41561-019-0526-0.
Turetsky, M.R. et al., 2021: Abrupt thaw amplifies the permafrost carbon feedback through upland erosion and methane hotspots. *Nature Geosciences* (in press).
Turi, G., Z. Lachkar, N. Gruber, and M. Münnich, 2016: Climatic modulation of recent trends in ocean acidification in the California Current System. *Environmental Research Letters*, **11(1)**, 014007, doi:10.1088/1748-9326/11/1/014007.
Turk, D. et al., 2019: Time of Emergence of Surface Ocean Carbon Dioxide Trends in the North American Coastal Margins in Support of Ocean Acidification Observing System Design. *Frontiers in Marine Science*, **6**, 91, doi:10.3389/fmars.2019.00091.
Turnbull, J.C. et al., 2017: Sixty years of radiocarbon dioxide measurements at Wellington, New Zealand: 1954–2014. *Atmospheric Chemistry and Physics*, **17(23)**, 14771–14784, doi:10.5194/acp-17-14771-2017.
Turner, A.J., C. Frankenberg, P.O. Wennberg, and D.J. Jacob, 2017: Ambiguity in the causes for decadal trends in atmospheric methane and hydroxyl. *Proceedings of the National Academy of Sciences*, **114(21)**, 5367–5372, doi:10.1073/pnas.1616020114.
Turner, S.K., 2018: Constraints on the onset duration of the Paleocene–Eocene Thermal Maximum. *Philosophical Transactions of the Royal Society A: Mathematical, Physical and Engineering Sciences*, **376(2130)**, 20170082, doi:10.1098/rsta.2017.0082.
Tyrrell, T. and M.I. Lucas, 2002: Geochemical evidence of denitrification in the Benguela upwelling system. *Continental Shelf Research*, **22(17)**, 2497–2511, doi:10.1016/s0278-4343(02)00077-8.
Ukkola, A.M. et al., 2016: Reduced streamflow in water-stressed climates consistent with CO2 effects on vegetation. *Nature Climate Change*, **6(1)**, 75–78, doi:10.1038/nclimate2831.
Ulfsbo, A. et al., 2018: Rapid Changes in Anthropogenic Carbon Storage and Ocean Acidification in the Intermediate Layers of the Eurasian Arctic Ocean: 1996–2015. *Global Biogeochemical Cycles*, **32(9)**, 1254–1275, doi:10.1029/2017gb005738.
US EPA, 2019: *Global Non-CO2 Greenhouse Gas Emission Projections & Mitigation Potential: 2015-2050*. EPA-430-R-19-010, United States Environmental Protection Agency (US EPA), Office of Atmospheric Programs (6207A), Washington DC, USA, 78 pp.
Valdes, Paul J., Beerling, David J., Johnson, C.E., 2005: The ice age methane budget. *Geophysical Research Letters*, **32(2)**, L02704, doi:10.1029/2004gl021004.
van der Sleen, P. et al., 2015: No growth stimulation of tropical trees by 150 years of CO2 fertilization but water-use efficiency increased. *Nature Geoscience*, **8(1)**, 24–28, doi:10.1038/ngeo2313.
van der Werf, G.R. et al., 2017: Global fire emissions estimates during 1997–2016. *Earth System Science Data*, **9(2)**, 697–720, doi:10.5194/essd-9-697-2017.
van Groenigen, K.J., C.W. Osenberg, and B.A. Hungate, 2011: Increased soil emissions of potent greenhouse gases under increased atmospheric CO2. *Nature*, **475(7355)**, 214–216, doi:10.1038/nature10176.
van Groenigen, K.J. et al., 2017: Faster turnover of new soil carbon inputs under increased atmospheric CO2. *Global Change Biology*, **23(10)**, 4420–4429, doi:10.1111/gcb.13752.
Varela, R., I. Álvarez, F. Santos, M. DeCastro, and M. Gómez-Gesteira, 2015: Has upwelling strengthened along worldwide coasts over 1982-2010? *Scientific Reports*, **5**, 10016, doi:10.1038/srep10016.
Vargas, C.A. et al., 2016: Influences of riverine and upwelling waters on the coastal carbonate system off Central Chile and their ocean acidification implications. *Journal of Geophysical Research: Biogeosciences*, **121(6)**, 1468–1483, doi:10.1002/2015jg003213.

ACCEPTED VERSION SUBJECT TO FINAL EDITS

Varney, R.M. et al., 2020: A spatial emergent constraint on the sensitivity of soil carbon turnover to global warming. *Nature Communications*, **11(1)**, 5544, doi:10.1038/s41467-020-19208-8.
Veldman, J.W. et al., 2015: Where tree planting and forest expansion are bad for biodiversity and ecosystem services. *BioScience*, **65(10)**, 1011–1018, doi:10.1093/biosci/biv118.
Veraverbeke, S. et al., 2017: Lightning as a major driver of recent large fire years in North American boreal forests. *Nature Climate Change*, doi:10.1038/nclimate3329.
Verheijen, F.G.A. et al., 2019: The influence of biochar particle size and concentration on bulk density and maximum water holding capacity of sandy vs sandy loam soil in a column experiment. *Geoderma*, **347**, 194–202, doi:10.1016/j.geoderma.2019.03.044.
Vogel, M.M., J. Zscheischler, and S.I. Seneviratne, 2018: Varying soil moisture-atmosphere feedbacks explain divergent temperature extremes and precipitation projections in central Europe. *Earth System Dynamics*, **9(3)**, 1107–1125, doi:10.5194/esd-9-1107-2018.
Voigt, C. et al., 2017: Increased nitrous oxide emissions from Arctic peatlands after permafrost thaw. *Proceedings of the National Academy of Sciences*, **114(24)**, 6238–6243, doi:10.1073/pnas.1702902114.
Voigt, C. et al., 2020: Nitrous oxide emissions from permafrost-affected soils. *Nature Reviews Earth & Environment*, **1(8)**, 420–434, doi:10.1038/s43017-020-0063-9.
Volodin, E.M., 2008: Methane cycle in the INM RAS climate model. *Izvestiya, Atmospheric and Oceanic Physics*, **44(2)**, 153–159, doi:10.1134/s0001433808020023.
Vonk, J.E. et al., 2015: Reviews and syntheses: Effects of permafrost thaw on Arctic aquatic ecosystems. *Biogeosciences*, **12(23)**, 7129–7167, doi:10.5194/bg-12-7129-2015.
Voss, M. et al., 2013: The marine nitrogen cycle: recent discoveries, uncertainties and the potential relevance of climate change. *Philosophical Transactions of the Royal Society B: Biological Sciences*, **368(1621)**, 20130121, doi:10.1098/rstb.2013.0121.
Wakita, M., A. Nagano, T. Fujiki, and S. Watanabe, 2017: Slow acidification of the winter mixed layer in the subarctic western North Pacific. *Journal of Geophysical Research: Oceans*, **122(8)**, 6923–6935, doi:10.1002/2017jc013002.
Walker, A.P. et al., 2015: Predicting long-term carbon sequestration in response to CO2 enrichment: How and why do current ecosystem models differ? *Global Biogeochemical Cycles*, **29(4)**, 476–495, doi:10.1002/2014gb004995.
Walker, A.P. et al., 2019: Decadal biomass increment in early secondary succession woody ecosystems is increased by CO2 enrichment. *Nature Communications*, **10(1)**, 454, doi:10.1038/s41467-019-08348-1.
Walker, A.P. et al., 2020: Integrating the evidence for a terrestrial carbon sink caused by increasing atmospheric CO2. *New Phytologist*, nph.16866, doi:10.1111/nph.16866.
Walker, X.J. et al., 2019: Increasing wildfires threaten historic carbon sink of boreal forest soils. *Nature*, **572(7770)**, 520–523, doi:10.1038/s41586-019-1474-y.
Wallace, R.B., H. Baumann, J.S. Grear, R.C. Aller, and C.J. Gobler, 2014: Coastal ocean acidification: The other eutrophication problem. *Estuarine, Coastal and Shelf Science*, **148(0)**, 1–13, doi:10.1016/j.ecss.2014.05.027.
Walter Anthony, K. et al., 2016: Methane emissions proportional to permafrost carbon thawed in Arctic lakes since the 1950s. *Nature Geoscience*, **9(9)**, 679–682, doi:10.1038/ngeo2795.
Walter Anthony, K.M., P. Anthony, G. Grosse, and J. Chanton, 2012: Geologic methane seeps along boundaries of Arctic permafrost thaw and melting glaciers. *Nature Geoscience*, **5(6)**, 419–426, doi:10.1038/ngeo1480.
Walter Anthony, K.M. et al., 2014: A shift of thermokarst lakes from carbon sources to sinks during the Holocene epoch. *Nature*, **511(7510)**, 452–456, doi:10.1038/nature13560.
Wang, Q. et al., 2020: Data-driven estimates of global nitrous oxide emissions from croplands. *National Science Review*, **7(2)**, 441–452, doi:10.1093/nsr/nwz087.
Wang, S. et al., 2019: A 2-year study on the effect of biochar on methane and nitrous oxide emissions in an intensive rice–wheat cropping system. *Biochar*, **1(2)**, 177–186, doi:10.1007/s42773-019-00011-8.
Wang, W. et al., 2014: Stratospheric ozone depletion from future nitrous oxide increases. *Atmospheric Chemistry and Physics*, **14(23)**, 12967–12982, doi:10.5194/acp-14-12967-2014.
Wang, X. et al., 2014: A two-fold increase of carbon cycle sensitivity to tropical temperature variations. *Nature*, **506(7487)**, 212–215, doi:10.1038/nature12915.
Wang, X. et al., 2019: The role of chlorine in global tropospheric chemistry. *Atmospheric Chemistry and Physics*, **19(6)**, 3981–4003, doi:10.5194/acp-19-3981-2019.
Wang, Y., I. Hendy, and T.J. Napier, 2017: Climate and anthropogenic controls of coastal deoxygenation on interannual to centennial timescales. *Geophysical Research Letters*, **44(22)**, 11,528–11,536, doi:10.1002/2017gl075443.
Wang, Y. et al., 2018: GOLUM-CNP v1.0: a data-driven modeling of carbon, nitrogen and phosphorus cycles in major terrestrial biomes. *Geoscientific Model Development*, **11(9)**, 3903–3928, doi:10.5194/gmd-11-3903-2018.
Wanninkhof, R., 2014: Relationship between wind speed and gas exchange over the ocean revisited. *Limnology and Oceanography: Methods*, **12(6)**, 351–362, doi:10.4319/lom.2014.12.351.
Wanninkhof, R., W.E. Asher, D.T. Ho, C. Sweeney, and W.R. McGillis, 2009: Advances in Quantifying Air-Sea Gas Exchange and Environmental Forcing. *Annual Review of Marine Science*, **1(1)**, 213–244, doi:10.1146/annurev.marine.010908.163742.

ACCEPTED VERSION SUBJECT TO FINAL EDITS

Wårlind, D., B. Smith, T. Hickler, and A. Arneth, 2014: Nitrogen feedbacks increase future terrestrial ecosystem carbon uptake in an individual-based dynamic vegetation model. *Biogeosciences*, **11(21)**, 6131–6146, doi:10.5194/bg-11-6131-2014.

Warren, M., S. Frolking, Z. Dai, and S. Kurnianto, 2017: Impacts of land use, restoration, and climate change on tropical peat carbon stocks in the twenty-first century: implications for climate mitigation. *Mitigation and Adaptation Strategies for Global Change*, **22(7)**, 1041–1061, doi:10.1007/s11027-016-9712-1.

Warwick, N.J. et al., 2016: Using δ13C-CH4 and δD-CH4 to constrain Arctic methane emissions. *Atmospheric Chemistry and Physics*, **16(23)**, 14891–14908, doi:10.5194/acp-16-14891-2016.

Watanabe, M. and M. Kawamiya, 2017: Remote effects of mixed layer development on ocean acidification in the subsurface layers of the North Pacific. *Journal of Oceanography*, **73(6)**, 771–784, doi:10.1007/s10872-017-0431-3.

Watson, A.J. et al., 2020: Revised estimates of ocean-atmosphere CO2 flux are consistent with ocean carbon inventory. *Nature Communications*, doi:10.1038/s41467-020-18203-3.

Webb, E.E. et al., 2016: of Sustained Tundra Warming. *Journal of Geophysical Research: Biogeosciences*, 249–265, doi:10.1002/2014jg002795.received.

Webb, J.R. et al., 2019: Widespread nitrous oxide undersaturation in farm waterbodies creates an unexpected greenhouse gas sink. *Proceedings of the National Academy of Sciences*, 201820389, doi:10.1073/pnas.1820389116.

Weber, T., N.A. Wiseman, and A. Kock, 2019: Global ocean methane emissions dominated by shallow coastal waters. *Nature Communications*, **10(1)**, 4584, doi:10.1038/s41467-019-12541-7.

Wei, G., M.T. McCulloch, G. Mortimer, W. Deng, and L. Xie, 2009: Evidence for ocean acidification in the Great Barrier Reef of Australia. *Geochimica et Cosmochimica Acta*, **73(8)**, 2332–2346, doi:10.1016/j.gca.2009.02.009.

Wei, G. et al., 2015: Decadal variability in seawater pH in the West Pacific: Evidence from coral δ1 B records. *Journal of Geophysical Research: Oceans*, **120(11)**, 7166–7181, doi:10.1002/2015jc011066.

Welch, B., V. Gauci, and E.J. Sayer, 2019: Tree stem bases are sources of CH4 and N2O in a tropical forest on upland soil during the dry to wet season transition. *Global Change Biology*, **25(1)**, 361–372, doi:10.1111/gcb.14498.

Welp, L.R. et al., 2016: Increasing summer net CO₂ uptake in high northern ecosystems inferred from atmospheric inversions and comparisons to remote-sensing NDVI. *Atmospheric Chemistry and Physics*, **16(14)**, 9047–9066, doi:10.5194/acp-16-9047-2016.

Wenzel, S., P.M. Cox, V. Eyring, and P. Friedlingstein, 2014: Emergent constraints on climate-carbon cycle feedbacks in the CMIP5 Earth system models. *Journal of Geophysical Research: Biogeosciences*, **119(5)**, 794–807, doi:10.1002/2013jg002591.

Wenzel, S., P.M. Cox, V. Eyring, and P. Friedlingstein, 2016: Projected land photosynthesis constrained by changes in the seasonal cycle of atmospheric CO2. *Nature*, **538(7626)**, 499–501, doi:10.1038/nature19772.

Whitney, F.A., H.J. Freeland, and M. Robert, 2007: Persistently declining oxygen levels in the interior waters of the eastern subarctic Pacific. *Progress in Oceanography*, **75(2)**, 179–199, doi:10.1016/j.pocean.2007.08.007.

Wieder, W.R., G.B. Bonan, and S.D. Allison, 2013: Global soil carbon projections are improved by modelling microbial processes. *Nature Climate Change*, **3(10)**, 909–912, doi:10.1038/nclimate1951.

Wieder, W.R., C.C. Cleveland, W.K. Smith, and K. Todd-Brown, 2015: Future productivity and carbon storage limited by terrestrial nutrient availability. *Nature Geoscience*, **8(6)**, 441–444, doi:10.1038/ngeo2413.

Wieder, W.R. et al., 2018: Carbon cycle confidence and uncertainty: Exploring variation among soil biogeochemical models. *Global Change Biology*, **24(4)**, 1563–1579, doi:10.1111/gcb.13979.

Wieder, W.R. et al., 2019: Beyond Static Benchmarking: Using Experimental Manipulations to Evaluate Land Model Assumptions. *Global Biogeochemical Cycles*, **33(10)**, 1289–1309, doi:10.1029/2018gb006141.

Wik, M., R.K. Varner, K.W. Anthony, S. MacIntyre, and D. Bastviken, 2016: Climate-sensitive northern lakes and ponds are critical components of methane release. *Nature Geoscience*, **9(2)**, 99–105, doi:10.1038/ngeo2578.

Wild, B. et al., 2019: Rivers across the Siberian Arctic unearth the patterns of carbon release from thawing permafrost. *Proceedings of the National Academy of Sciences*, **116(21)**, 10280–10285, doi:10.1073/pnas.1811797116.

Wilhelm, W.W., J.M.F. Johnson, J.L. Hatfield, W.B. Voorhees, and D.R. Linden, 2004: Crop and Soil Productivity Response to Corn Residue Removal. *Agronomy Journal*, **96(1)**, 1–17, doi:10.2134/agronj2004.1000.

Wilkerson, J. et al., 2019: Permafrost nitrous oxide emissions observed on a landscape scale using the airborne eddy-covariance method. *Atmospheric Chemistry and Physics*, **19(7)**, 4257–4268, doi:10.5194/acp-19-4257-2019.

Williams, N.L. et al., 2015: Quantifying anthropogenic carbon inventory changes in the Pacific sector of the Southern Ocean. *Marine Chemistry*, **174**, 147–160, doi:10.1016/j.marchem.2015.06.015.

Williams, N.L. et al., 2017: Calculating surface ocean pCO2 from biogeochemical Argo floats equipped with pH: An uncertainty analysis. *Global Biogeochemical Cycles*, **31(3)**, 591–604, doi:10.1002/2016gb005541.

Williams, R.G., A. Katavouta, and P. Goodwin, 2019: Carbon-cycle feedbacks operating in the climate system. *Current Climate Change Reports*, doi:10.1007/s40641-019-00144-9.

Williams, R.G., P. Ceppi, and A. Katavouta, 2020: Controls of the transient climate response to emissions by physical feedbacks, heat uptake and carbon cycling. *Environmental Research Letters*, **15(9)**, 0940c1, doi:10.1088/1748-

ACCEPTED VERSION SUBJECT TO FINAL EDITS

9326/ab97c9.
Williams, R.G., P. Goodwin, A. Ridgwell, and P.L. Woodworth, 2012: How warming and steric sea level rise relate to cumulative carbon emissions. *Geophysical Research Letters*, **39(19)**, n/a–n/a, doi:10.1029/2012gl052771.
Williams, R.G., P. Goodwin, V.M. Roussenov, and L. Bopp, 2016: A framework to understand the transient climate response to emissions. *Environmental Research Letters*, **11(1)**, 015003, doi:10.1088/1748-9326/11/1/015003.
Williams, R.G., V. Roussenov, T.L. Frölicher, and P. Goodwin, 2017a: Drivers of continued surface warming after cessation of carbon emissions. *Geophysical Research Letters*, **44(20)**, 10,633–10,642, doi:10.1002/2017gl075080.
Williams, R.G., V. Roussenov, P. Goodwin, L. Resplandy, and L. Bopp, 2017b: Sensitivity of Global Warming to Carbon Emissions: Effects of Heat and Carbon Uptake in a Suite of Earth System Models. *Journal of Climate*, **30(23)**, 9343–9363, doi:10.1175/jcli-d-16-0468.1.
Williamson, P., & Bodle, R., 2016: Update on climate geoengineering in relation to the convention on biological diversity: potential impacts and regulatory framework.. , 158.
Wilson, D. et al., 2016a: Greenhouse gas emission factors associated with rewetting of organic soils. *Mires and Peat*, **17(04)**, 1–28, doi:10.19189/map.2016.omb.222.
Wilson, D. et al., 2016b: Multiyear greenhouse gas balances at a rewetted temperate peatland. *Global Change Biology*, **22(12)**, 4080–4095, doi:10.1111/gcb.13325.
Windham-Myers, L., S. Crooks, and T. Troxler (eds.), 2018: *A Blue Carbon Primer: The State of Coastal Wetland Carbon Science, Practice and Policy*. CRC Press, Boca Raton, FL, USA, 507 pp., doi:10.1201/9780429435362.
Winguth, A.M.E., E. Thomas, and C. Winguth, 2012: Global decline in ocean ventilation, oxygenation, and productivity during the Paleocene-Eocene Thermal Maximum: Implications for the benthic extinction. *Geology*, **40(3)**, 263–266, doi:10.1130/g32529.1.
Winiwarter, W., L. Höglund-Isaksson, Z. Klimont, W. Schöpp, and M. Amann, 2018: Technical opportunities to reduce global anthropogenic emissions of nitrous oxide. *Environmental Research Letters*, **13(1)**, 014011, doi:10.1088/1748-9326/aa9ec9.
Winkler, A.J., R.B. Myneni, G.A. Alexandrov, and V. Brovkin, 2019: Earth system models underestimate carbon fixation by plants in the high latitudes. *Nature Communications*, **10(1)**, 885, doi:10.1038/s41467-019-08633-z.
Wolf, S. et al., 2016: Warm spring reduced carbon cycle impact of the 2012 US summer drought. *Proceedings of the National Academy of Sciences of the United States of America*, **113(21)**, 5880–5885, doi:10.1073/pnas.1519620113.
Wolter, K. and M.S. Timlin, 1998: Measuring the strength of ENSO events: How does 1997/98 rank? *Weather*, **53(9)**, 315–324, doi:10.1002/j.1477-8696.1998.tb06408.x.
Woolf, D., J.E. Amonette, F.A. Street-Perrott, J. Lehmann, and S. Joseph, 2010: Sustainable biochar to mitigate global climate change. *Nature Communications*, **1(1)**, 56, doi:10.1038/ncomms1053.
Woosley, R.J., F.J. Millero, and R. Wanninkhof, 2016: Rapid anthropogenic changes in CO2 and pH in the Atlantic Ocean: 2003-2014. *Global Biogeochemical Cycles*, **30(1)**, 70–90, doi:10.1002/2015gb005248.
Worden, J.R. et al., 2017: Reduced biomass burning emissions reconcile conflicting estimates of the post-2006 atmospheric methane budget. *Nature Communications*, **8(1)**, 2227, doi:10.1038/s41467-017-02246-0.
Wu, H.C. et al., 2018: Surface ocean pH variations since 1689 CE and recent ocean acidification in the tropical South Pacific. *Nature Communications*, **9(1)**, 2543, doi:10.1038/s41467-018-04922-1.
Wu, J. et al., 2018: Afforestation enhanced soil CH4 uptake rate in subtropical China: Evidence from carbon stable isotope experiments. *Soil Biology and Biochemistry*, **118**, 199–206, doi:10.1016/j.soilbio.2017.12.017.
Wu, Y., M.P. Hain, M.P. Humphreys, S. Hartman, and T. Tyrrell, 2019: What drives the latitudinal gradient in open-ocean surface dissolved inorganic carbon concentration? *Biogeosciences*, **16(13)**, 2661–2681, doi:10.5194/bg-16-2661-2019.
Xia, L., A. Robock, S. Tilmes, and R.R. Neely III, 2016: Stratospheric sulfate geoengineering could enhance the terrestrial photosynthesis rate. *Atmospheric Chemistry and Physics*, **16(3)**, 1479–1489, doi:10.5194/acp-16-1479-2016.
Xia, L., P.J. Nowack, S. Tilmes, and A. Robock, 2017: Impacts of stratospheric sulfate geoengineering on tropospheric ozone. *Atmospheric Chemistry and Physics*, **17(19)**, 11913–11928, doi:10.5194/acp-17-11913-2017.
Xia, L. et al., 2014: Solar radiation management impacts on agriculture in China: A case study in the Geoengineering Model Intercomparison Project (GeoMIP). *Journal of Geophysical Research: Atmospheres*, **119(14)**, 8695–8711, doi:10.1002/2013jd020630.
Xu, Z., Y. Jiang, B. Jia, and G. Zhou, 2016: Elevated-CO2 response of stomata and its dependence on environmental factors. *Frontiers in Plant Science*, **7**, 1–15, doi:10.3389/fpls.2016.00657.
Xu-Ri, I.C. Prentice, R. Spahni, and H.S. Niu, 2012: Modelling terrestrial nitrous oxide emissions and implications for climate feedback. *New Phytologist*, **196(2)**, 472–488, doi:10.1111/j.1469-8137.2012.04269.x.
Yamagata, Y. et al., 2018: Estimating water–food–ecosystem trade-offs for the global negative emission scenario (IPCC-RCP2.6). *Sustainability Science*, **13(2)**, 301–313, doi:10.1007/s11625-017-0522-5.
Yamamoto, A., A. Abe-Ouchi, R. Ohgaito, A. Ito, and A. Oka, 2019: Glacial CO2 decrease and deep-water

ACCEPTED VERSION SUBJECT TO FINAL EDITS

deoxygenation by iron fertilization from glaciogenic dust. *Climate of the Past*, **15(3)**, 981–996, doi:10.5194/cp-15-981-2019.

Yamamoto-Kawai, M., F.A. McLaughlin, E.C. Carmack, S. Nishino, and K. Shimada, 2009: Aragonite undersaturation in the Arctic ocean: effects of ocean acidification and sea ice melt. *Science*, **326(5956)**, 1098–1100, doi:10.1126/science.1174190.

Yamori, W., K. Hikosaka, and D.A. Way, 2014: Temperature response of photosynthesis in C3, C4, and CAM plants: temperature acclimation and temperature adaptation. *Photosynthesis Research*, **119(1)**, 101–117, doi:10.1007/s11120-013-9874-6.

Yang et al., 2019: Biochar improved rice yield and mitigated CH4 and N2O emissions from paddy field under controlled irrigation in the Taihu Lake Region of China. *Atmospheric Environment*, **200**, 69–77, doi:10.1016/j.atmosenv.2018.12.003.

Yang, C.-E. et al., 2020a: Assessing terrestrial biogeochemical feedbacks in a strategically geoengineered climate. *Environmental Research Letters*, **15(10)**, 104043, doi:10.1088/1748-9326/abacf7.

Yang, C.-E. et al., 2020b: Assessing terrestrial biogeochemical feedbacks in a strategically geoengineered climate. *Environmental Research Letters*, **15(10)**, 104043, doi:10.1088/1748-9326/abacf7.

Yang, H. et al., 2016: Potential negative consequences of geoengineering on crop production: A study of Indian groundnut. *Geophysical Research Letters*, **43(22)**, 11,711–786,795, doi:10.1002/2016gl071209.

Yang, J.-W., J. Ahn, E.J. Brook, and Y. Ryu, 2017: Atmospheric methane control mechanisms during the early Holocene. *Climate of the Past*, **13(9)**, 1227–1242, doi:10.5194/cp-13-1227-2017.

Yang, S. et al., 2020: Global reconstruction reduces the uncertainty of oceanic nitrous oxide emissions and reveals a vigorous seasonal cycle. *Proceedings of the National Academy of Sciences*, **117(22)**, 11954–11960, doi:10.1073/pnas.1921914117.

Yang, X. et al., 2019: The Effects of Phosphorus Cycle Dynamics on Carbon Sources and Sinks in the Amazon Region: A Modeling Study Using ELM v1. *Journal of Geophysical Research: Biogeosciences*, **124(12)**, 3686–3698, doi:10.1029/2019jg005082.

Yang, Y., M.L. Roderick, S. Zhang, T.R. McVicar, and R.J. Donohue, 2019: Hydrologic implications of vegetation response to elevated CO2 in climate projections. *Nature Climate Change*, **9(1)**, 44–48, doi:10.1038/s41558-018-0361-0.

Yao, W., A. Paytan, and U.G. Wortmann, 2018: Large-scale ocean deoxygenation during the Paleocene-Eocene Thermal Maximum. *Science*, **361(6404)**, 804–806, doi:10.1126/science.aar8658.

Yao, Y. et al., 2020: Increased global nitrous oxide emissions from streams and rivers in the Anthropocene. *Nature Climate Change*, **10(2)**, 138–142, doi:10.1038/s41558-019-0665-8.

Ye, L. et al., 2020: Biochar effects on crop yields with and without fertilizer: A meta-analysis of field studies using separate controls. *Soil Use and Management*, **36(1)**, 2–18, doi:10.1111/sum.12546.

Yeager, S.G. et al., 2018: Predicting near-term changes in the Earth system: a large ensemble of initialized decadal prediction simulations using the community Earth system model. *Bulletin of the American Meteorological Society*, **99(9)**, 1867–1886, doi:10.1175/bams-d-17-0098.1.

Yin, Y. et al., 2020: Fire decline in dry tropical ecosystems enhances decadal land carbon sink. *Nature Communications*, **11(1)**, doi:10.1038/s41467-020-15852-2.

Yokohata, T. et al., 2020: Future projection of greenhouse gas emissions due to permafrost degradation using a simple numerical scheme with a global land surface model. *Progress in Earth and Planetary Science*, **7(1)**, 56, doi:10.1186/s40645-020-00366-8.

Yoon, J.-E. et al., 2018: Reviews and syntheses: Ocean iron fertilization experiments – past, present, and future looking to a future Korean Iron Fertilization Experiment in the Southern Ocean (KIFES) project. *Biogeosciences*, **15(19)**, 5847–5889, doi:10.5194/bg-15-5847-2018.

Yoshida, Y. et al., 2013: Improvement of the retrieval algorithm for GOSAT SWIR XCO2 and XCH4 and their validation using TCCON data. *Atmospheric Measurement Techniques*, **6(6)**, 1533–1547, doi:10.5194/amt-6-1533-2013.

Yu, J. et al., 2010: Loss of carbon from the Deep Sea since the last glacial maximum. *Science*, **330(6007)**, 1084–1087, doi:10.1126/science.1193221.

Yu, K. et al., 2019: Pervasive decreases in living vegetation carbon turnover time across forest climate zones. *Proceedings of the National Academy of Sciences*, **116(49)**, 24662–24667, doi:10.1073/pnas.1821387116.

Yu, L., Y. Huang, W. Zhang, T. Li, and W. Sun, 2017: Methane uptake in global forest and grassland soils from 1981 to 2010. *Science of The Total Environment*, **607–608**, 1163–1172, doi:10.1016/j.scitotenv.2017.07.082.

Yue, X. and N. Unger, 2018: Fire air pollution reduces global terrestrial productivity. *Nature Communications*, doi:10.1038/s41467-018-07921-4.

Zachos, J.C., 2005: Rapid acidification of the ocean during the Paleocene-Eocene Thermal Maximum. *Science*, **308(5728)**, 1611–1615, doi:10.1126/science.1109004.

Zaehle, S., 2013a: Terrestrial nitrogen-carbon cycle interactions at the global scale. *Philosophical Transactions of the Royal Society B: Biological Sciences*, **368(1621)**, 20130125–20130125, doi:10.1098/rstb.2013.0125.

Zaehle, S., 2013b: Terrestrial nitrogen-carbon cycle interactions at the global scale. *Philosophical Transactions of the*

ACCEPTED VERSION SUBJECT TO FINAL EDITS

Royal Society B: Biological Sciences, **368(1621)**, 20130125–20130125, doi:10.1098/rstb.2013.0125.
Zaehle, S., P. Friedlingstein, and A.D. Friend, 2010: Terrestrial nitrogen feedbacks may accelerate future climate change. *Geophysical Research Letters*, **37(1)**, L01401, doi:10.1029/2009gl041345.
Zaehle, S., C.D. Jones, B. Houlton, J.-F. Lamarque, and E. Robertson, 2015: Nitrogen Availability Reduces CMIP5 Projections of Twenty-First-Century Land Carbon Uptake. *Journal of Climate*, **28(6)**, 2494–2511, doi:10.1175/jcli-d-13-00776.1.
Zaehle, S. et al., 2014: Evaluation of 11 terrestrial carbon-nitrogen cycle models against observations from two temperate free-air CO2 Enrichment studies. *New Phytologist*, **202(3)**, 803–822, doi:10.1111/nph.12697.
Zamora, L.M. et al., 2012: Nitrous oxide dynamics in low oxygen regions of the Pacific: insights from the MEMENTO database. *Biogeosciences*, **9(12)**, 5007–5022, doi:10.5194/bg-9-5007-2012.
Zeebe, R.E. and D.A. Wolf-Gladrow, 2009: Carbon Dioxide, Dissolved (Ocean). In: *Encyclopedia of Paleoclimatology and Ancient Environments* [Gornitz, V. (ed.)]. Encyclopedia of Earth Sciences Series, Springer, Dordrecht, The Netherlands, pp. 1037–1039, doi:10.1007/978-1-4020-4411-3_30.
Zeebe, R.E., J.C. Zachos, and G.R. Dickens, 2009: Carbon dioxide forcing alone insufficient to explain Palaeocene–Eocene Thermal Maximum warming. *Nature Geoscience*, **2(8)**, 576–580, doi:10.1038/ngeo578.
Zeebe, R.E., A. Ridgwell, and J.C. Zachos, 2016: Anthropogenic carbon release rate unprecedented during the past 66 million years. *Nature Geoscience*, **9(4)**, 325–329, doi:10.1038/ngeo2681.
Zemp, D.C. et al., 2017: Self-amplified Amazon forest loss due to vegetation-atmosphere feedbacks. *Nature Communications*, **8**, 14681, doi:10.1038/ncomms14681.
Zeng, J., Y. Nojiri, P. Landschützer, M. Telszewski, and S. Nakaoka, 2014: A Global Surface Ocean f CO 2 Climatology Based on a Feed-Forward Neural Network. *Journal of Atmospheric and Oceanic Technology*, **31(8)**, 1838–1849, doi:10.1175/jtech-d-13-00137.1.
Zeng, N. et al., 2008: Dynamical prediction of terrestrial ecosystems and the global carbon cycle: A 25-year hindcast experiment. *Global Biogeochemical Cycles*, **22(4)**, n/a–n/a, doi:10.1029/2008gb003183.
Zhang, L. et al., 2020: Significant methane ebullition from alpine permafrost rivers on the East Qinghai–Tibet Plateau. *Nature Geoscience*, **13(5)**, 349–354, doi:10.1038/s41561-020-0571-8.
Zhang, Q., Y.P. Wang, R.J. Matear, A.J. Pitman, and Y.J. Dai, 2014: Nitrogen and phosphorous limitations significantly reduce future allowable CO 2 emissions. *Geophysical Research Letters*, **41(2)**, 632–637, doi:10.1002/2013gl058352.
Zhang, W. et al., 2013: Tundra shrubification and tree-line advance amplify arctic climate warming: results from an individual-based dynamic vegetation model. *Environmental Research Letters*, **8(3)**, 34023, doi:10.1088/1748-9326/8/3/034023.
Zhang, X., X. Xu, G. Jia, B. Poulter, and Z. Zhang, 2020: Hiatus of wetland methane emissions associated with recent La Niña episodes in the Asian monsoon region. *Climate Dynamics*, **54(9)**, 4095–4107, doi:10.1007/s00382-020-05219-0.
Zhang, Y., J. Joiner, S. Hamed Alemohammad, S. Zhou, and P. Gentine, 2018: A global spatially contiguous solar-induced fluorescence (CSIF) dataset using neural networks. *Biogeosciences*, **15(19)**, doi:10.5194/bg-15-5779-2018.
Zhang, Y.G., M. Pagani, Z. Liu, S.M. Bohaty, and R. DeConto, 2013: A 40-million-year history of atmospheric CO2. *Philosophical Transactions of the Royal Society A: Mathematical, Physical and Engineering Sciences*, **371(2001)**, 20130096–20130096, doi:10.1098/rsta.2013.0096.
Zhang, Z. et al., 2017: Emerging role of wetland methane emissions in driving 21st century climate change. *Proceedings of the National Academy of Sciences*, **114(36)**, 9647–9652, doi:10.1073/pnas.1618765114.
Zhao, Y. et al., 2019: Inter-model comparison of global hydroxyl radical (OH) distributions and their impact on atmospheric methane over the 2000–2016 period. *Atmos. Chem. Phys*, **19**, 13701–13723, doi:10.5194/acp-2019-281.
Zhou, S. et al., 2019: Land–atmosphere feedbacks exacerbate concurrent soil drought and atmospheric aridity. *Proceedings of the National Academy of Sciences of the United States of America*, **116(38)**, 18848–18853, doi:10.1073/pnas.1904955116.
Zhou, X., E. Thomas, R.E.M. Rickaby, A.M.E. Winguth, and Z. Lu, 2014: I/Ca evidence for upper ocean deoxygenation during the PETM. *Paleoceanography*, **29(10)**, 964–975, doi:10.1002/2014pa002702.
Zhu, Z. et al., 2016: Greening of the Earth and its drivers. *Nature Climate Change*, **6(8)**, 791–795, doi:10.1038/nclimate3004.
Zickfeld, K. and T. Herrington, 2015: The time lag between a carbon dioxide emission and maximum warming increases with the size of the emission. *Environmental Research Letters*, **10(3)**, 031001, doi:10.1088/1748-9326/10/3/031001.
Zickfeld, K., A.H. MacDougall, and H.D. Matthews, 2016: On the proportionality between global temperature change and cumulative CO2 emissions during periods of net negative CO2 emissions. *Environmental Research Letters*, **11(5)**, 055006, doi:10.1088/1748-9326/11/5/055006.
Zickfeld, K., M. Eby, H.D. Matthews, and A.J. Weaver, 2009: Setting cumulative emissions targets to reduce the risk of dangerous climate change. *Proceedings of the National Academy of Sciences*, **106(38)**, 16129–16134,

ACCEPTED VERSION
SUBJECT TO FINAL EDITS

doi:10.1073/pnas.0805800106.
Zickfeld, K., D. Azevedo, S. Mathesius, and H.D. Matthews, 2021: Asymmetry in the climate-carbon cycle response to positive and negative CO2 emissions. , **accepted**.
Zickfeld, K. et al., 2013: Long-term climate change commitment and reversibility: An EMIC intercomparison. *Journal of Climate*, **26(16)**, 5782–5809, doi:10.1175/jcli-d-12-00584.1.
Ziegler, M., P. Diz, I.R. Hall, and R. Zahn, 2013: Millennial-scale changes in atmospheric CO2 levels linked to the Southern Ocean carbon isotope gradient and dust flux. *Nature Geoscience*, **6(6)**, 457–461, doi:10.1038/ngeo1782.
Zubkova, M., L. Boschetti, J.T. Abatzoglou, and L. Giglio, 2019: Changes in Fire Activity in Africa from 2002 to 2016 and Their Potential Drivers. *Geophysical Research Letters*, **46(13)**, doi:10.1029/2019gl083469.

ACCEPTED VERSION
SUBJECT TO FINAL EDITS

Figures

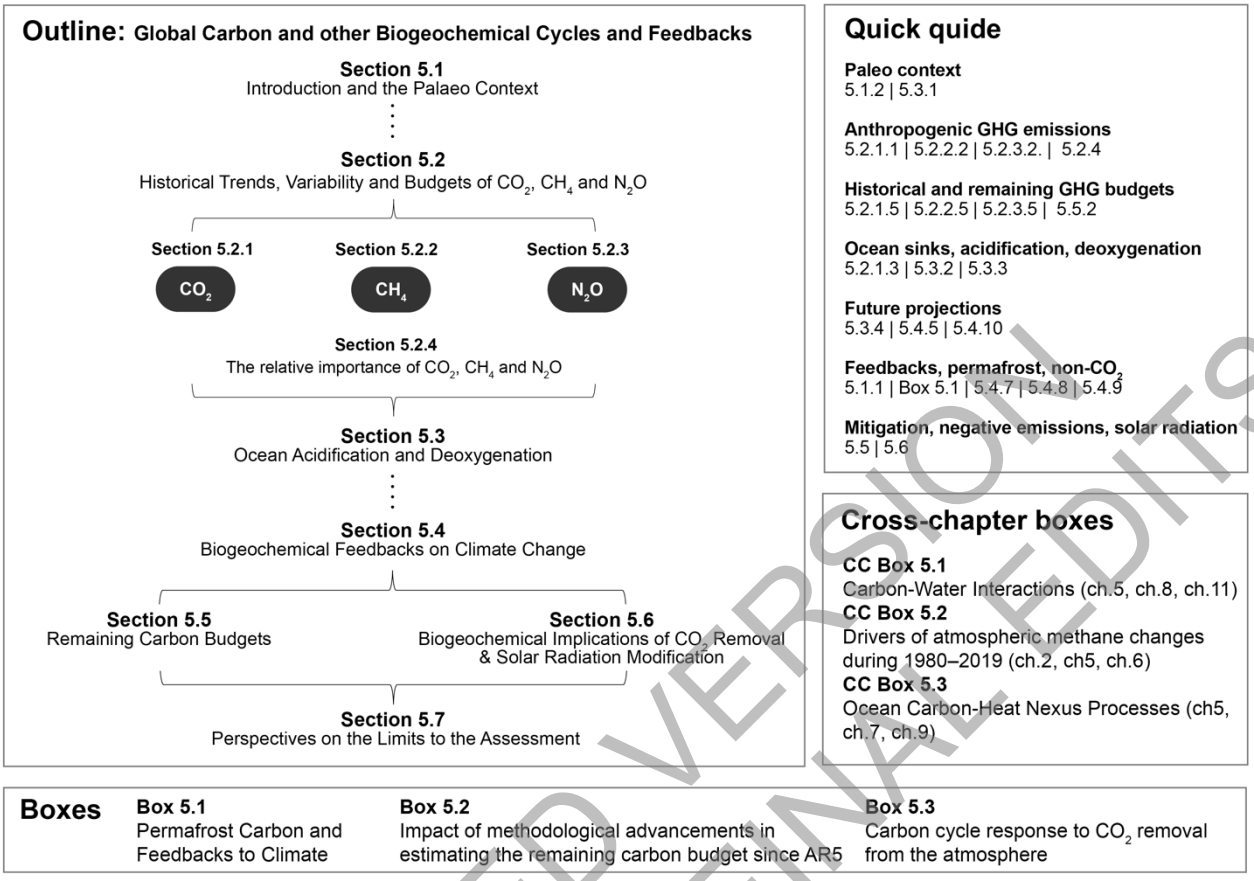


Figure 5.1: Visual abstract for Chapter 5

ACCEPTED VERSION
SUBJECT TO FINAL EDITS

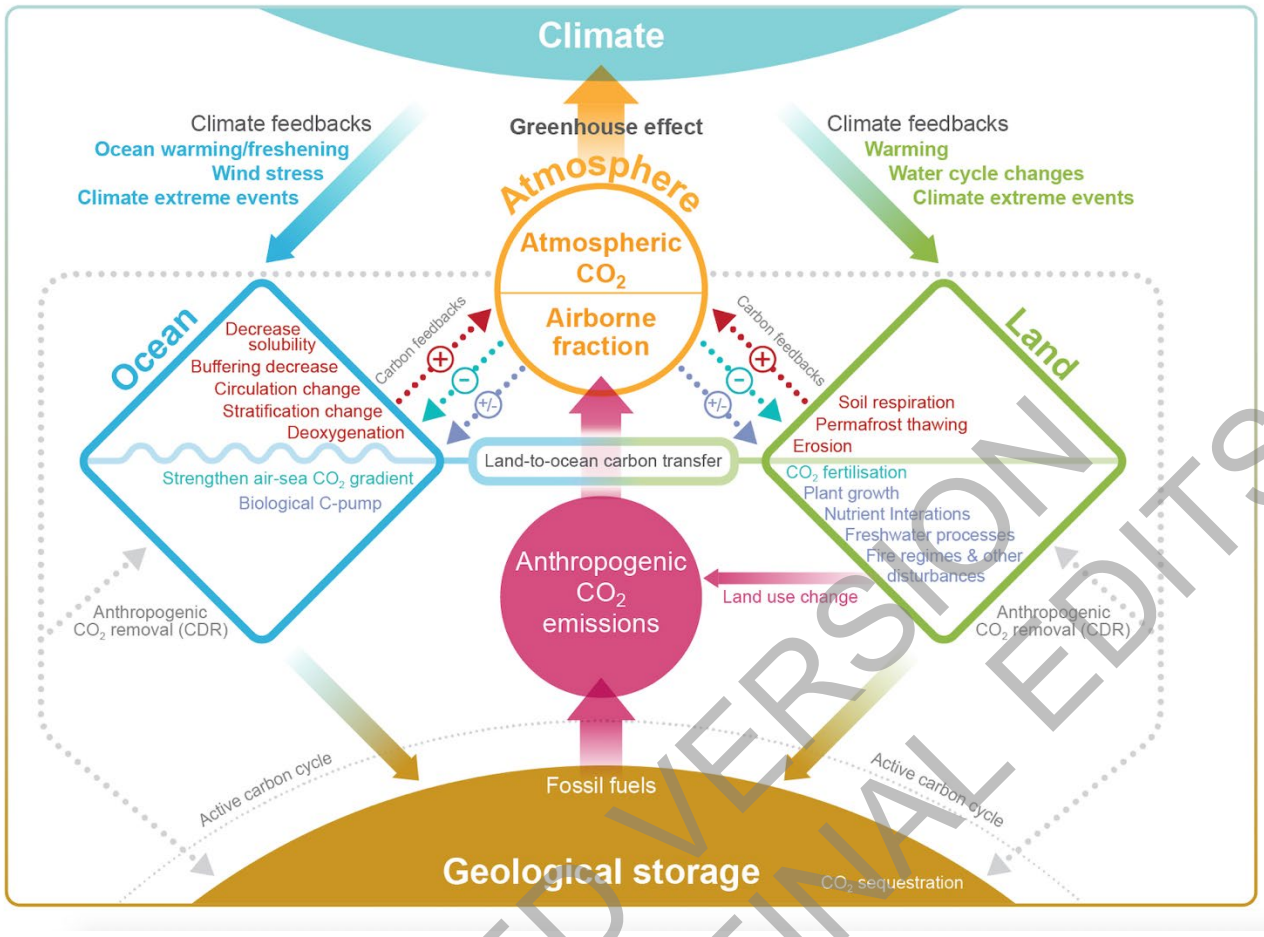


Figure 5.2: Key compartments, processes and pathways that govern historical and future CO_2 concentrations and carbon–climate feedbacks through the coupled earth system. The anthropogenic CO_2 emissions, including land use change, are partitioned via negative feedbacks (turquoise dotted arrows) between the ocean (23%), the land (31%) and the airborne fraction (46%) of anthropogenic CO_2 that sets the changing CO_2 concentration in the atmosphere (2010–2019, Table 5.1). This regulates most of the radiative forcing that creates the heat imbalance that drives the climate feedbacks to the ocean (blue) and land (green). Positive feedbacks (red arrows) result from processes in the ocean and on land (red text). Positive feedbacks are influenced by both carbon-concentration and carbon-climate feedbacks simultaneously. Additional biosphere processes have been included but these have an as yet uncertain feedback impact (blue-dotted arrows). CO_2 removal from the atmosphere into the ocean, land and geological reservoirs, necessary for negative emissions, has been included (grey arrows). Although this schematic is built around CO_2, the dominant GHG, some of the same processes also influence the fluxes of CH_4 and N_2O and the strength of the positive feedbacks from the terrestrial and ocean systems.

ACCEPTED VERSION SUBJECT TO FINAL EDITS

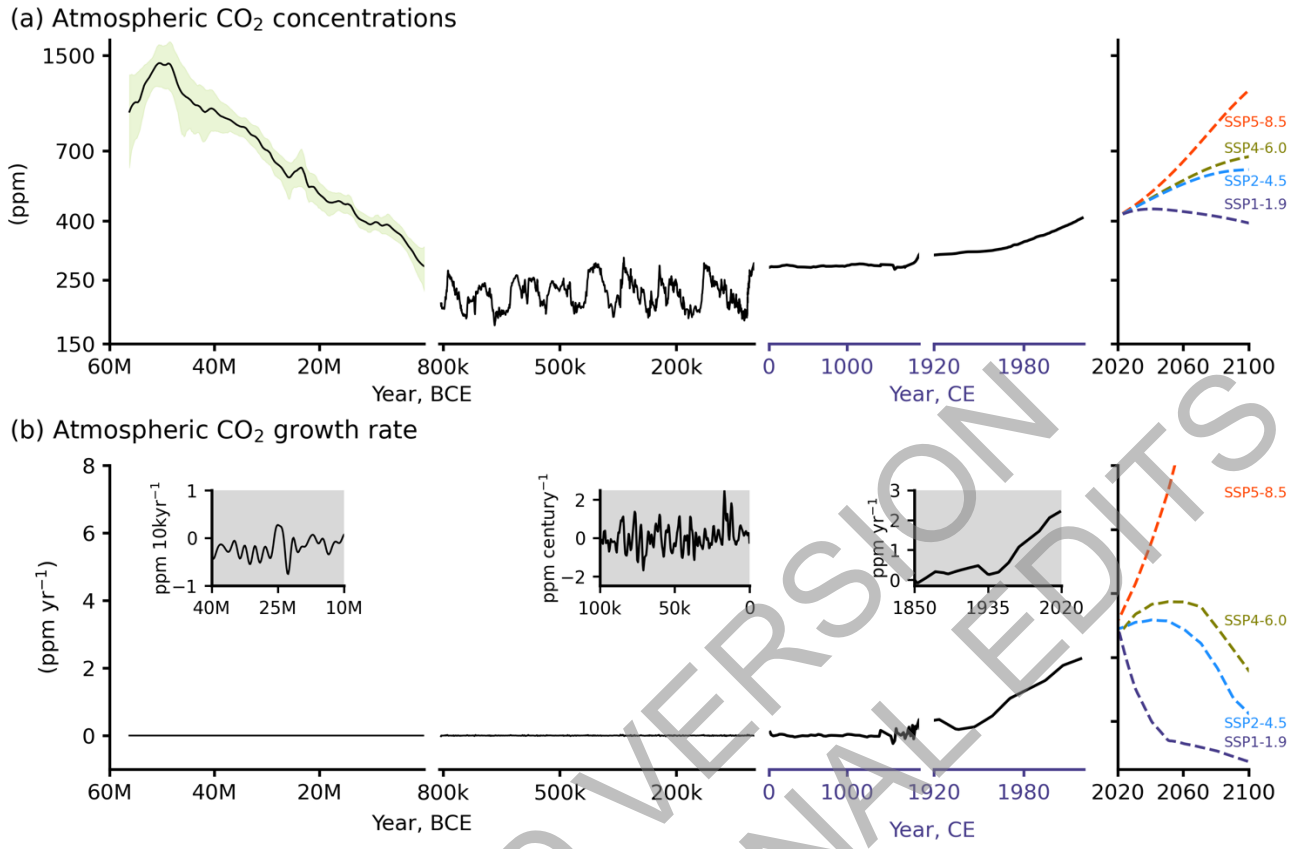


Figure 5.3: Atmospheric CO_2 concentrations and growth rates for the past 60 million years and projections to 2100. (a) CO_2 concentrations. Concentrations data for the period 60 Myr to the time prior to 800 Kyr (left column) are shown as the LOESS Fit and 68% range (data from Chapter 2) (Foster et al., 2017). Concentrations from 1750 and projections through 2100 are taken from Shared Socioeconomic Pathways of IPCC AR6 (Meinshausen et al., 2017). (b) Growth rates are shown as the time derivative of the concentration time series. Inserts in (b) show growth rates at the scale of the sampling resolution. Further details on data sources and processing are available in the chapter data table (Table 5.SM.6).

ACCEPTED VERSION SUBJECT TO FINAL EDITS

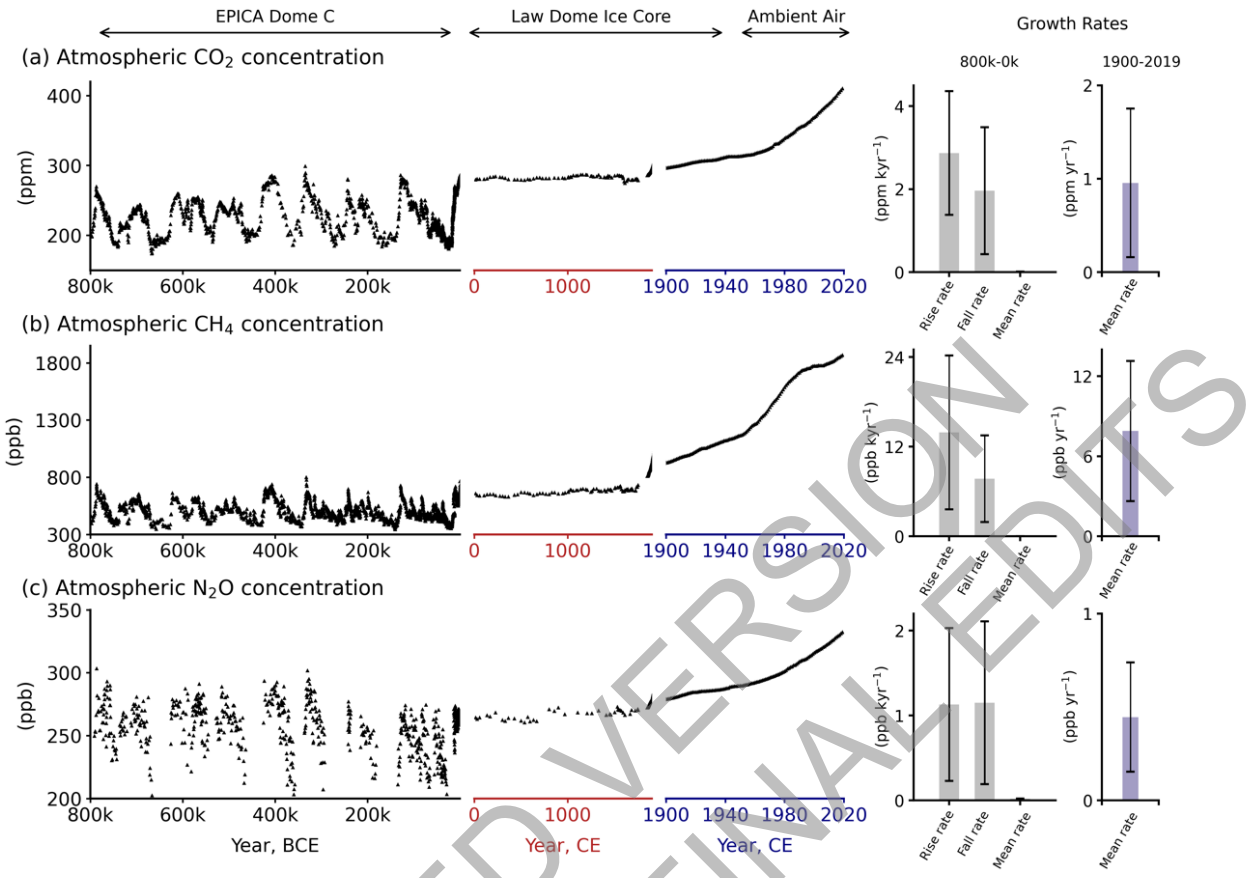


Figure 5.4: Atmospheric concentrations of CO_2, CH_4 and N_2O in air bubbles and clathrate crystals in ice cores (800,000 BCE to 1990 CE). Note the variable x-axis range and tick mark intervals for the 3 columns. Ice core data is over-plotted by atmospheric observations from 1958 to present for CO_2, from 1984 for CH_4 and from 1994 for N_2O. The time-integrated, millennial-scale linear growth rates for different time periods (800,000–0 BCE, 0–1900 CE and 1900–2017 CE) are given in each panel. For the BCE period, mean rise and fall rates are calculated for the individual slopes between the peaks (interglacials) and troughs (ice ages), which are given in the panels in left column. The data for BCE period are used from the Vostok, EPICA, Dome C and WAIS ice cores (Petit et al., 1999; Monnin, 2001; Pépin et al., 2001; Raynaud et al., 2005; Siegenthaler et al., 2005; Loulergue et al., 2008; Lüthi et al., 2008; Schilt et al., 2010a). The data after 0–yr CE are taken mainly from Law Dome ice core analysis (MacFarling Meure et al., 2006). The surface observations for all species are taken from NOAA cooperative research network (Dlugokencky and Tans, 2019), where ALT, MLO and SPO stand for Alert (Canada), Mauna Loa Observatory, and South Pole Observatory, respectively. BCE = before current era, CE = current era. Further details on data sources and processing are available in the chapter data table (Table 5.SM.6).

ACCEPTED VERSION SUBJECT TO FINAL EDITS

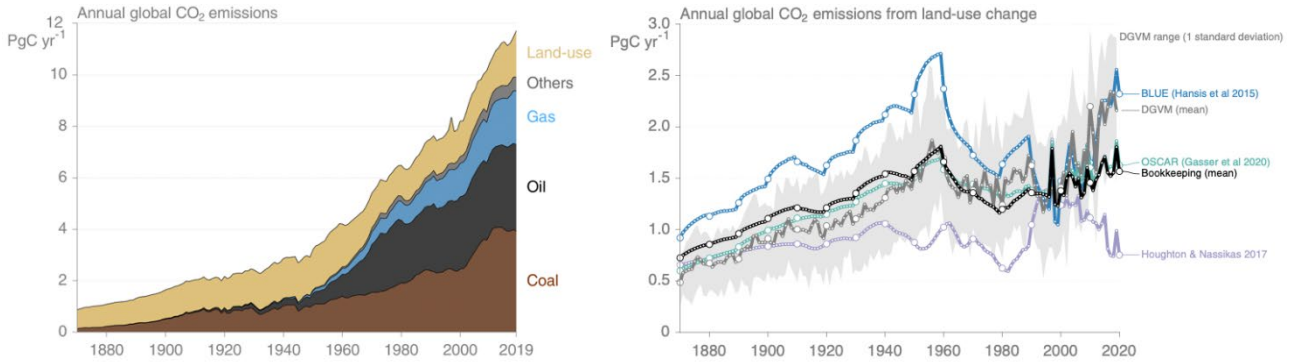


Figure 5.5: **Global anthropogenic CO_2 emissions**. (a) Historical trends of anthropogenic CO_2 emission (fossil fuels and net land use change, including land management, called LULUCF flux in the main text) for the period 1870 to 2019, with 'others' representing flaring, emissions from carbonates during cement manufacture. Data sources: (Boden et al., 2017; IEA, 2017; Andrew, 2018; BP, 2018; Le Quéré et al., 2018; Friedlingstein et al., 2020). (b) The net land use change CO_2 flux (PgC yr^{-1}) as estimated by three bookkeeping models and 16 Dynamic Global Vegetation Models (DGVMs) for the global annual carbon budget 2019 (Friedlingstein et al., 2020). The three bookkeeping models are from Hansis et al., 2015; Houghton and Nassikas, 2017; (Gasser et al., 2020) and are all updated to 2019; their average is used to determine the net land use change flux in the annual global carbon budget (black line). The DGVM estimates are the result of differencing a simulation with and without land use changes run under observed historical climate and CO_2, following the Trendy v9 protocol; they are used to provide an uncertainty range to the bookkeeping estimates (Friedlingstein et al., 2020). All estimates are unsmoothed annual data. Estimates differ in process comprehensiveness of the models and in definition of flux components included in the net land use change flux. Further details on data sources and processing are available in the chapter data table (Table 5.SM.6).

ACCEPTED VERSION SUBJECT TO FINAL EDITS

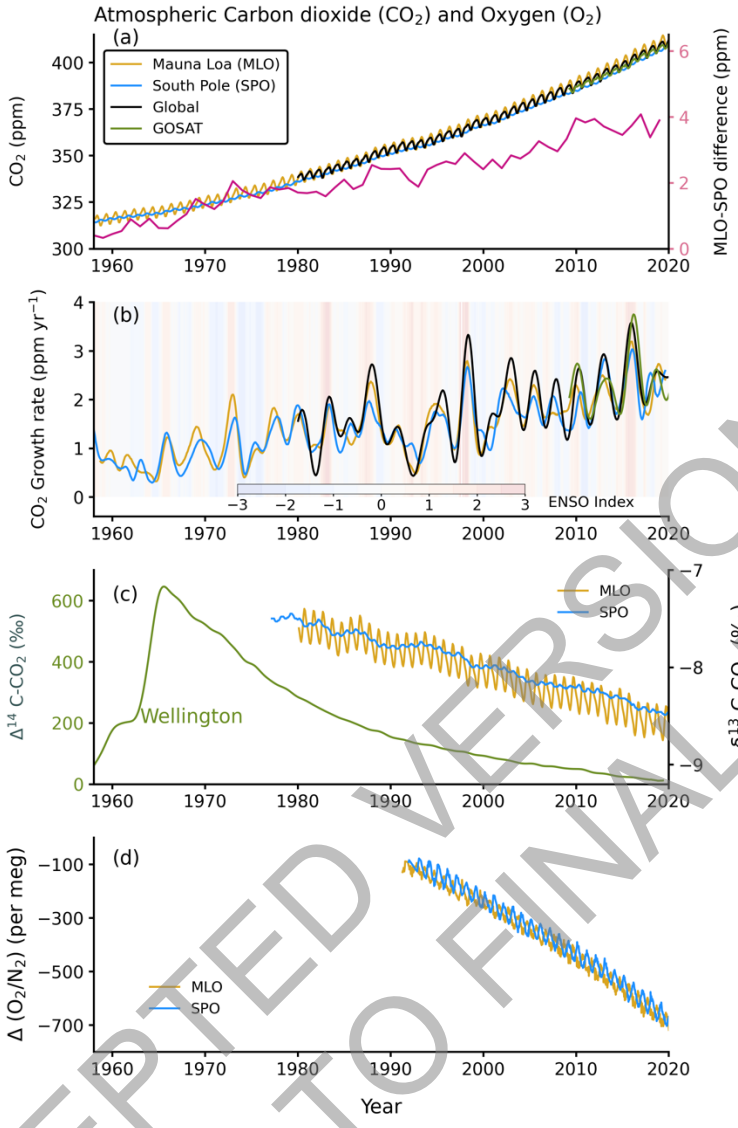


Figure 5.6: **Time series of CO_2 concentrations and related measurements in ambient air**. (a) concentration time series and MLO-SPO difference, (b) growth rates, (c) ^{14}C and ^{13}C isotopes, and (d) O_2/N_2 ratio. The data for Mauna Loa Observatory (MLO) and South Pole Observatory (SPO) are taken from the Scripps Institution of Oceanography (SIO)/University of California, San Diego (Keeling et al., 2001). The global mean CO_2 are taken from NOAA cooperative network (as in Chapter 2), and GOSAT monthly-mean XCO_2 time series are taken from National Institute for Environmental Studies (Yoshida et al., 2013). CO_2 growth rates are calculated as the time derivative of deseasonalised time series (Nakazawa et al., 1997). The $\Delta(O_2/N2)$ are expressed in per meg units (= $(FF/M)\times10^6$, where FF = moles of O_2 consumed by fossil-fuel burning, M = 3.706×10^{19}, total number of O_2 molecules in the atmosphere (Keeling and Manning, 2014).The $^{14}CO_2$ time series at Barring Head, Wellington, New Zealand (BHD) is taken from GNS Science and NIWA (Turnbull et al., 2017). The multivariate ENSO index (MEI) is shown as the shaded background in panel (b; warmer shade indicates El Niño). Further details on data sources and processing are available in the chapter data table (Table 5.SM.6).

ACCEPTED VERSION SUBJECT TO FINAL EDITS

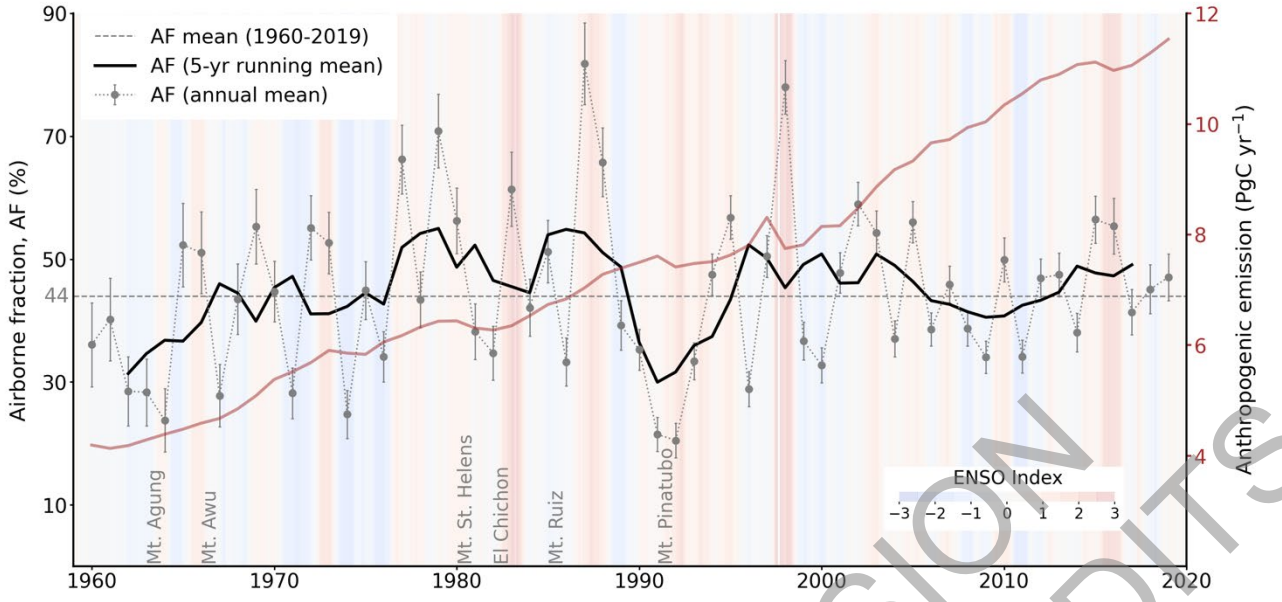


Figure 5.7: **Airborne fraction and anthropogenic (fossil fuel and land use change) CO_2 emissions**. Data as in Section 5.2.1.1. The multivariate ENSO index (shaded) and the major volcanic eruptions are marked along the x-axis. Further details on data sources and processing are available in the chapter data table (Table 5.SM.6).

ACCEPTED VERSION
SUBJECT TO FINAL EDITS

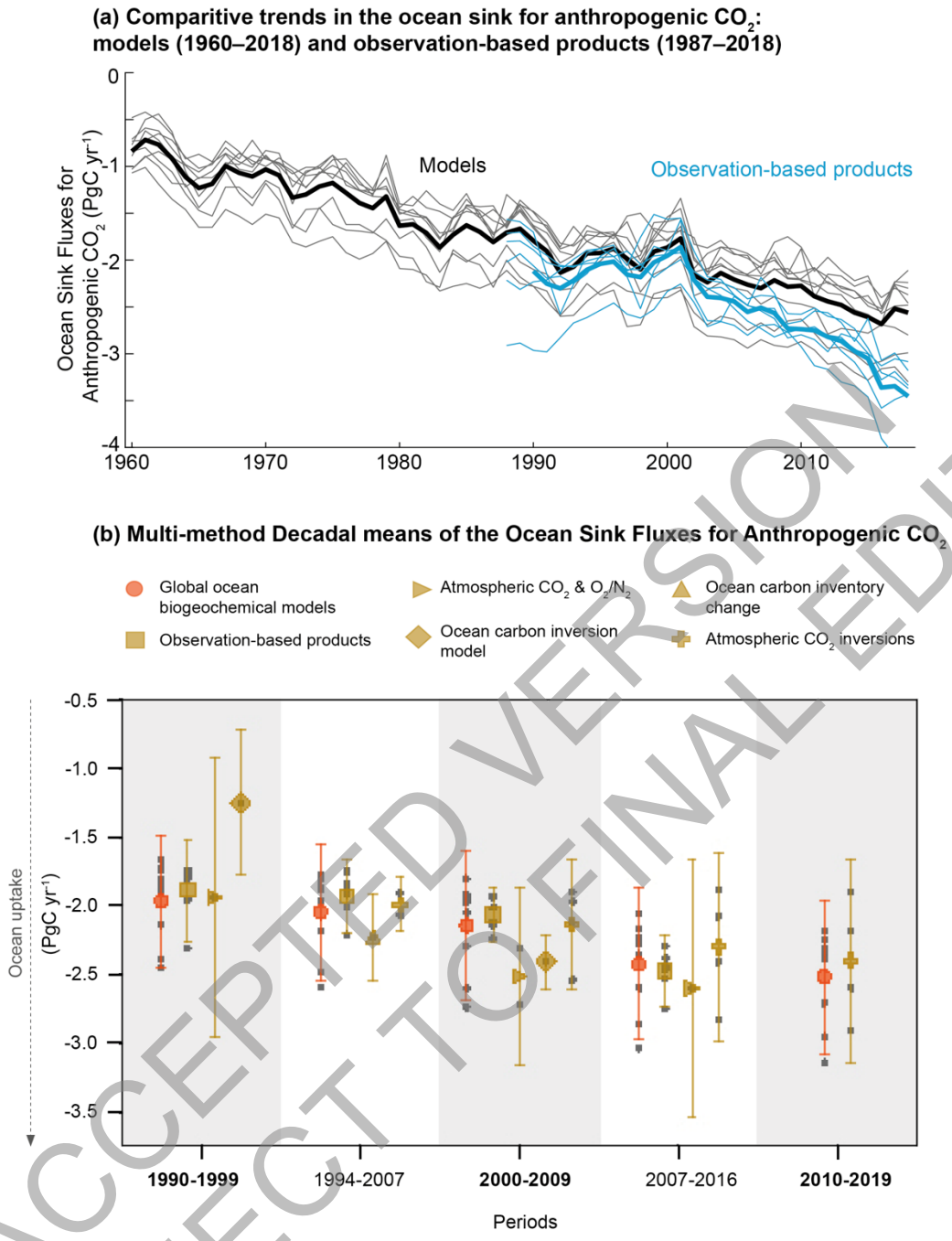


Figure 5.8: Multi-decadal trends for the ocean sink of CO_2. (a): The multi-decadal (1960–2019) trends in the annual ocean sink (S_{ocean}) reconstructed from 9 Global Ocean Biogeochemical Models (GOBM) forced with observed atmospheric re-analysis products (Hauck et al., 2020), 6 observationally-based gap-filling products that reconstructed spatial and temporal variability in the ocean CO_2 flux from sparse observations of surface ocean pCO_2 (Supplementary Materials 5.SM.2). The trends in S_{ocean} were calculated from the mean annual global GOBM outputs and the observational products were used to provide confidence in the GOBM assessments (r^2=0.85). Thick lines represent the multi-model mean. Observationally-based products have been corrected for pre-industrial river carbon fluxes (0.62 $PgC\ yr^{-1}$) based on the average of estimates from Jacobson et al., (2007) and Resplandy et al. (2018). (b): Mean decadal constraints and their confidence intervals for global ocean sink (S_{ocean}) of anthropogenic CO_2 using multiple independent or quasi-independent lines of evidence or methods for the period 1990–2019 (See Supplementary Materials Tables 5.SM.1 and 5.SM.2 for magnitudes, uncertainties and published sources). Further details on data sources and processing are available in the chapter data table (Table 5.SM.6).

ACCEPTED VERSION SUBJECT TO FINAL EDITS

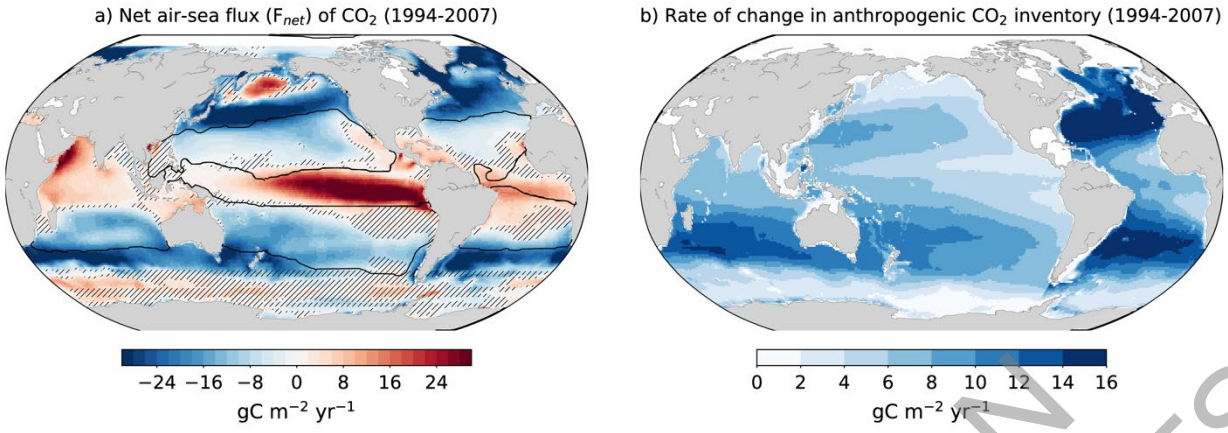


Figure 5.9: Comparative regional characteristics of the mean decadal (1994–2007) sea-air CO_2 flux (F_{net}) and ocean storage of anthropogenic CO_2. (a) regional sink–source characteristics for contemporary ocean air-sea CO_2 fluxes (F_{net}) derived from the ensemble of 6 observation-based products using SOCATv6 observational data set (Bakker et al., 2020; Landschützer et al., 2014; Rödenbeck eta l., 2014; Zeng et al., 2014; Denvil-Sommer et al., 2019; Gregor et al., 2019; Iida et al., 2020) Warm colours depict outgassing fluxes and black contours characterise the super-biomes defined from Fay and McKinley (2014) and adjusted by Gregor et al., (2019) also used to calculate the variability in regional flux anomalies (Supplementary Materials Figure 5.SM.1); and (b) the regional characteristics of the storage fluxes of CO_2 in the ocean interior for the same period (Gruber et al., 2019a). The dots reflect ocean areas where the 1-sigma standard deviation of Fnet from the 6 observation product is larger than the magnitude of the mean. This reflects source-sink transition areas where the mean Fnet is small and more strongly influenced by spatial and temporal variability across the products. Further details on data sources and processing are available in the chapter data table (Table 5.SM.6).

ACCEPTED VERSION
SUBJECT TO FINAL EDITS

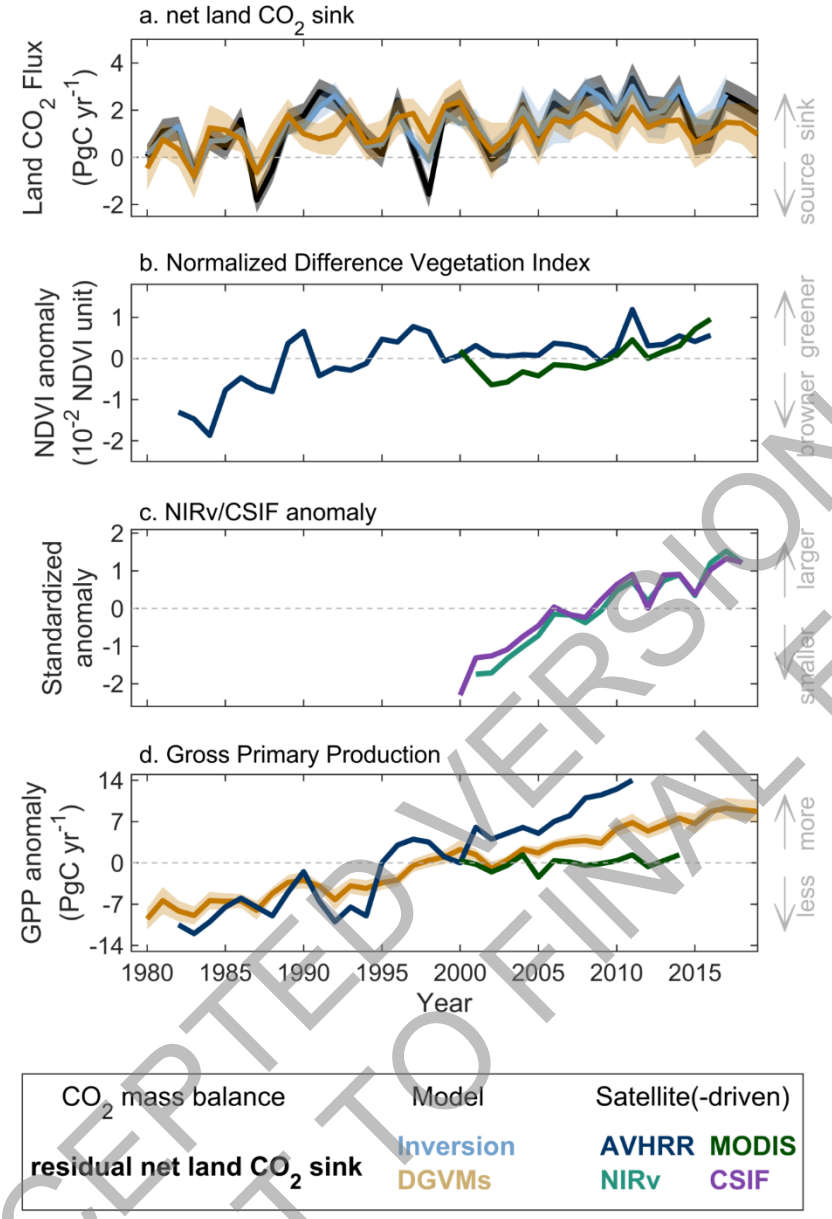


Figure 5.10: Trends of the net land CO_2 sink and related vegetation observations during 1980–2019. (a) Net land CO_2 sink. The residual net land CO_2 sink is estimated from the global CO_2 mass balance (fossil fuel emission minus atmospheric CO_2 growth rate and ocean CO_2 sink). Inversions indicate the net land CO_2 sink estimated by an ensemble of four atmospheric inversions. Dynamic Global Vegetation Models (DGVMs) indicate the mean net land CO_2 sink estimated by 17 dynamic global vegetation models driven by climate change, rising atmospheric CO_2, land use change and nitrogen deposition change (for carbon-nitrogen models). The positive values indicate net CO_2 uptake from the atmosphere. (b) Normalised difference vegetation index (NDVI). The anomaly of global area-weighted NDVI observed by AVHRR and MODIS satellite sensors. AVHRR data are accessible during 1982–2016 and MODIS data are accessible during 2000–2018. (c) Near-infrared reflectance of vegetation (NIRv) and contiguous solar-induced chlorophyll fluorescence (CSIF). The standardised anomaly of area-weighted NIRv during 2001-2018 (Badgley et al., 2017) and CSIF during 2000-2018 (Zhang et al., 2018). (d) Gross primary production (GPP). The GPP from Cheng et al. (2017), DGVMs and MODIS GPP product (MOD17A3). GPP from Cheng et al. (2017) is based on an analytical model driven by climate change, rising atmospheric CO_2, AVHRR leaf area index datasets and evapotranspiration datasets. GPP from DGVMs is the ensemble mean global GPP estimated by the same 17 DGVMs that provide the net land CO_2 sink estimates. Shaded area indicates 1–σ inter-model spread except for atmospheric inversions, whose ranges were used due to limited number of models. Further details on data sources and processing are available in the chapter data table (Table 5.SM.6).

ACCEPTED VERSION SUBJECT TO FINAL EDITS

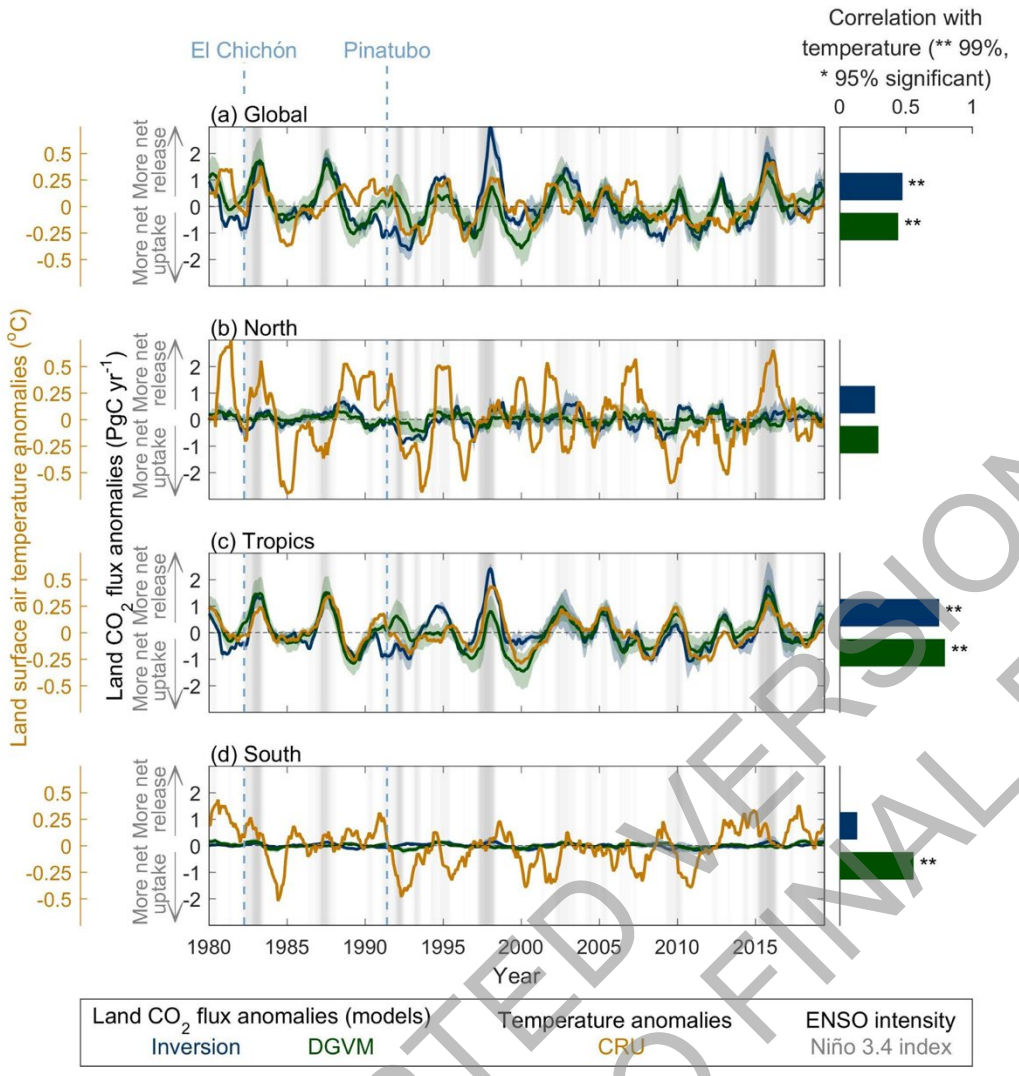


Figure 5.11: Interannual variation in detrended anomalies of the net land CO_2 sink and land surface air temperature during 1980–2019. Correlation coefficients between the net land CO_2 sink anomalies and temperature anomalies are show on the right bar plots. The net land CO_2 sink is estimated by four atmospheric inversions (blue) and fifteen Dynamic Global Vegetation Models (DGVMs) (green), respectively (Friedlingstein et al., 2020). Solid blue and green lines show model mean detrended anomalies of the net land CO_2 sink. The ensemble mean of DGVMs is bounded by the 1–σ inter-model spread in each large latitude band (North 30°N–90°N, Tropics 30°S–30°N, South 90°S–30°S) and the globe. The ensemble mean of atmospheric inversions is bounded by model spread. For each latitudinal band, the anomalies of the net land CO_2 sink and temperature (orange) were obtained by removing the long-term trend and seasonal cycle. A 12-month running mean was taken to reduce high-frequency noise. The bars in the right panels show correlation coefficients between the net land CO_2 sink anomalies and temperature anomalies for each region. Two asterisks indicate P<0.01, and one indicates P<0.05. Grey shaded area shows the intensity of El Niño southern oscillation (ENSO) as defined by the Niño 3.4 index. Two volcanic eruptions (El Chichón eruption and Pinatubo eruption) are indicated with light blue dashed lines. Temperature data are from the Climatic Research Unit (CRU), University of East Anglia (Harris et al., 2014). Anomalies were calculated following Patra et al. (2005), but using 12-month low-pass filter and detrended to obtain interannual variations. Further details on data sources and processing are available in the chapter data table (Table 5.SM.6).

ACCEPTED VERSION SUBJECT TO FINAL EDITS

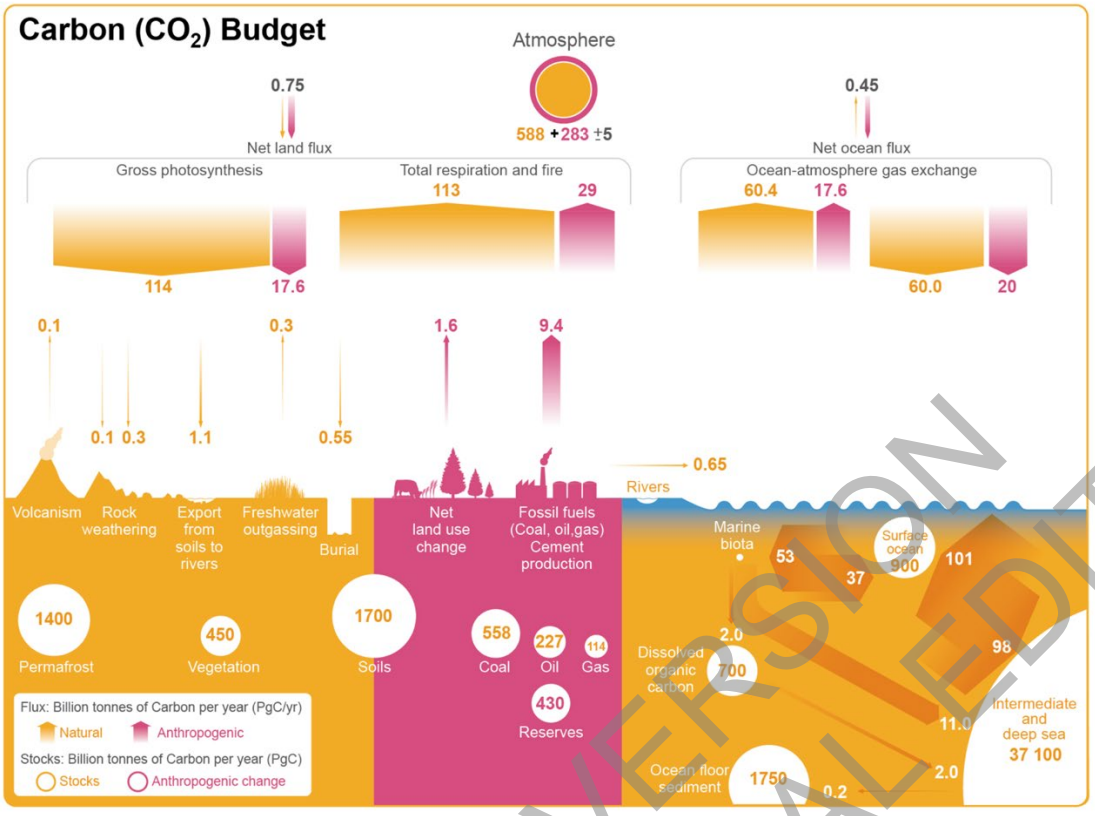


Figure 5.12: Global carbon (CO_2) budget (2010-2019). Yellow arrows represent annual carbon fluxes (in PgC yr^{-1}) associated with the natural carbon cycle estimated for the time prior to the industrial era, around 1750. Pink arrows represent anthropogenic fluxes averaged over the period 2010–2019. The rate of carbon accumulation in the atmosphere is equal to net land-use change emissions, including land management (called LULUCF in the main text) plus fossil fuel emissions, minus land and ocean net sinks (plus a small budget imbalance, Table 5.1). Circles with yellow numbers represent pre-industrial carbon stocks in PgC. Circles with pink numbers represent anthropogenic changes to these stocks (cumulative anthropogenic fluxes) since 1750. Anthropogenic net fluxes are reproduced from Friedlingstein et al., (2020). The relative change of *gross photosynthesis* since pre-industrial times is based on 15 DGVMs used in Friedlingstein et al., (2020). The corresponding emissions by *Total respiration and fire* are those required to match the *net land flux*, exclusive of net land-use change emissions which are accounted for separately. The cumulative change of anthropogenic carbon in the terrestrial reservoir is the sum of carbon cumulatively lost by net land use change emissions, and net carbon accumulated since 1750 in response to environmental drivers (warming, rising CO_2, nitrogen deposition). The adjusted gross natural ocean-atmosphere CO_2 flux was derived by rescaling the value in figure 1 of (Sarmiento and Gruber, 2002) of 70 PgC/yr by the revised estimate of the bomb ^{14}C inventory in the ocean. The original bomb ^{14}C inventoy yielded an average global gas transfer velocity of 22 cm/hr; the revised estimate is 17cm/h leading to 17/22*70=54. Dissolved organic carbon reservoir and fluxes from (Hansell et al., 2009). Dissolved inorganic carbon exchanges between surface and deep ocean, subduction and obduction from (Levy et al., 2013) Levy et al. 2013. Export production and flux from (Boyd et al., 2019). NPP and remineralisation in surface layer of the ocean from (Kwiatkowski et al., 2020; Séférian et al., 2020). Deep ocean reservoir from (Keppler et al., 2020). Note that the mass balance of the two ocean carbon stocks *surface ocean* and *intermediate and deep ocean* includes a yearly accumulation of anthropogenic carbon (not shown). Fossil fuel reserves are from (BGR, 2019); fossil fuel resources are 11,490 PgC for coal, 6,780 PgC for oil, and 365 PgC for natural gas. Permafrost region stores are from (Hugelius et al., 2014; Strauss et al., 2017; Mishra et al., 2021) (see also Box 5.1) and soil carbon stocks outside of permafrost region from Batjes, (2016); Jackson et al., (2017). Biomass stocks (range of seven estimates) are from Erb et al., (2018). Sources for the fluxes of the continuum land-to-ocean are provided in main text and adjusted within the ranges of the various assessment to balance the budget (section 5.2.1.5).

ACCEPTED VERSION SUBJECT TO FINAL EDITS

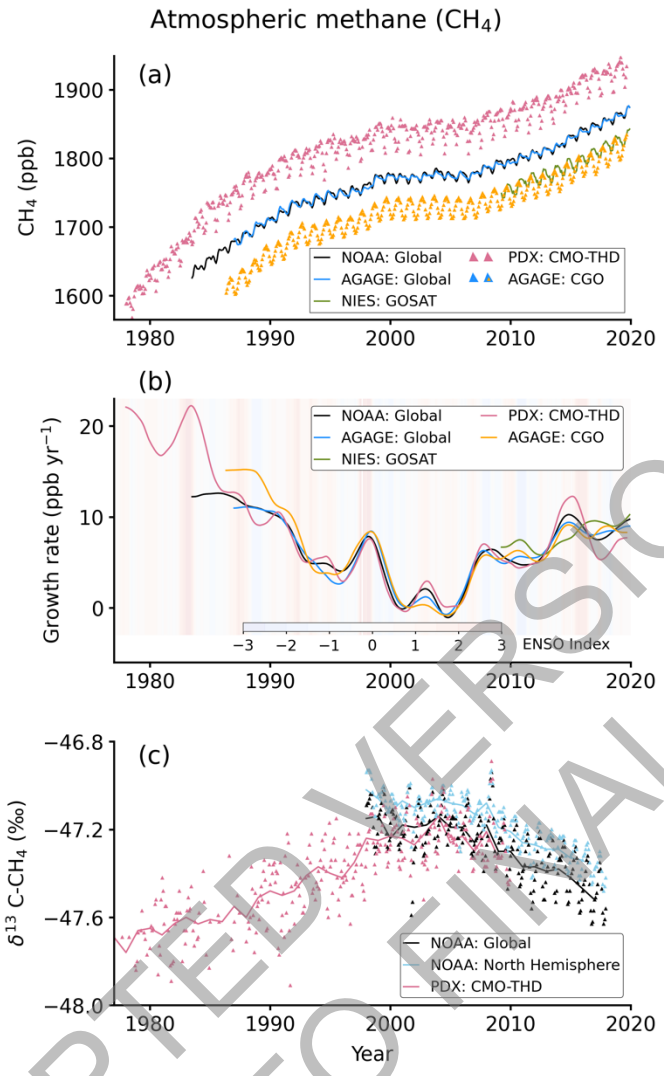


Figure 5.13: Time series of CH_4 concentrations, growth rates and isotopic composition. a) CH_4 concentrations, b) CH_4 growth rates, c) δ^{13}-CH_4. Data from selected site networks operated by NOAA (Dlugokencky et al., 2003), AGAGE (Prinn et al., 2018) and PDX (Portland State University) (Rice et al., 2016). To maintain clarity, data from many other measurement networks are not included here, and all measurements are shown in WMO X2004ACH_4 global calibration standard. Global mean values of XCH_4 (total-column), retrieved from radiation spectra measured by the greenhouse gases observation satellite (GOSAT) are shown in panels (a) and (b). Cape Grim Observatory (CGO; 41°S, 145°E) and Trinidad Head (THD; 41°N, 124°W) data are taken from the AGAGE network, NOAA global and northern hemispheric (NH) means for δ^{13}C are calculated from 10 and 6 sites, respectively. The PDX data adjusted to NH (period: 1977–2000) are merged with THD (period: 2001–2019) for CH_4 concentration and growth rate analysis, and PDX and NOAA NH means of δ^{13}C data are used for joint interpretation of long-term trends analysis. The multivariate ENSO index (MEI) is shown in panel (b). Further details on data sources and processing are available in the chapter data table (Table 5.SM.6).

ACCEPTED VERSION SUBJECT TO FINAL EDITS

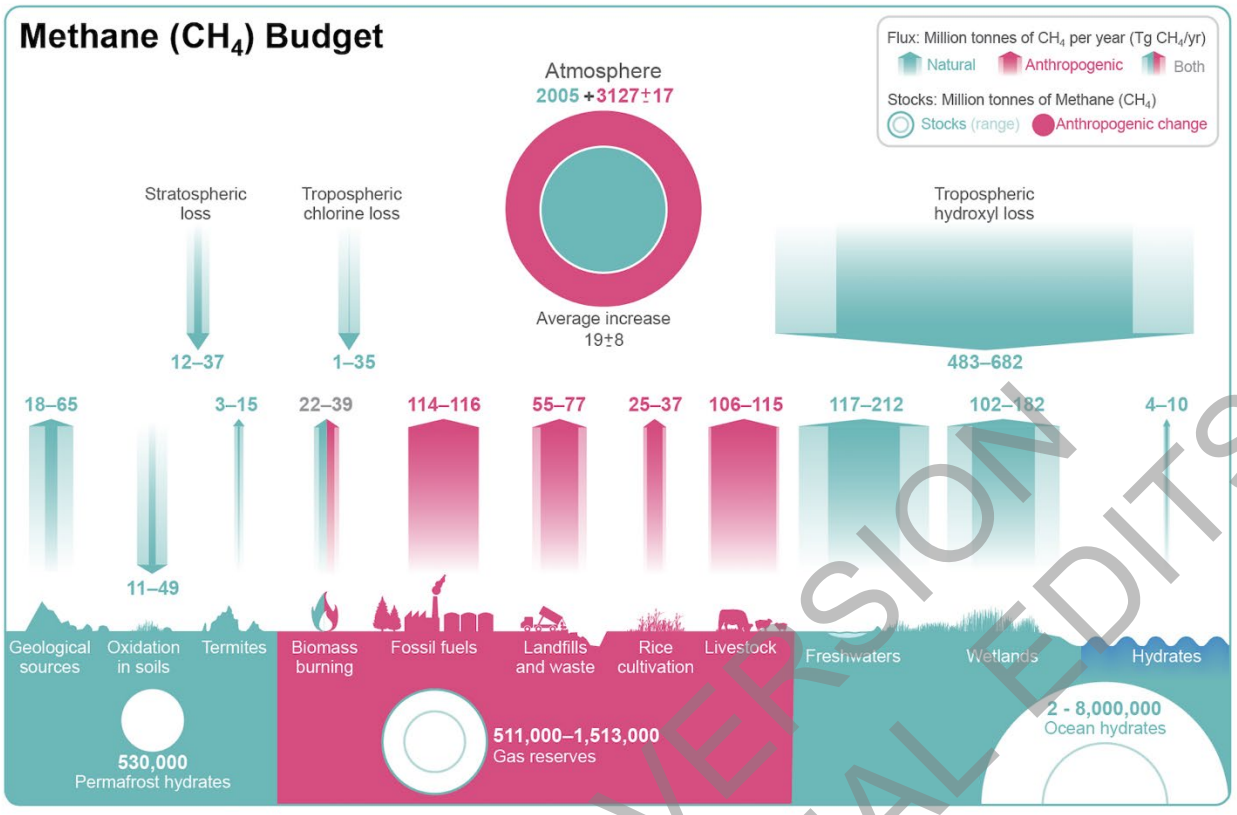
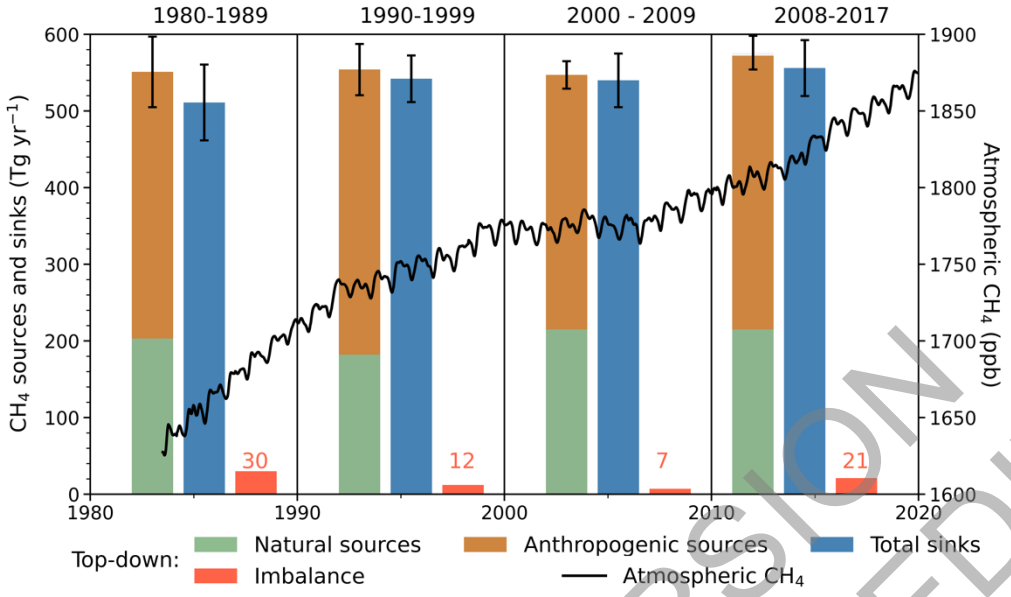


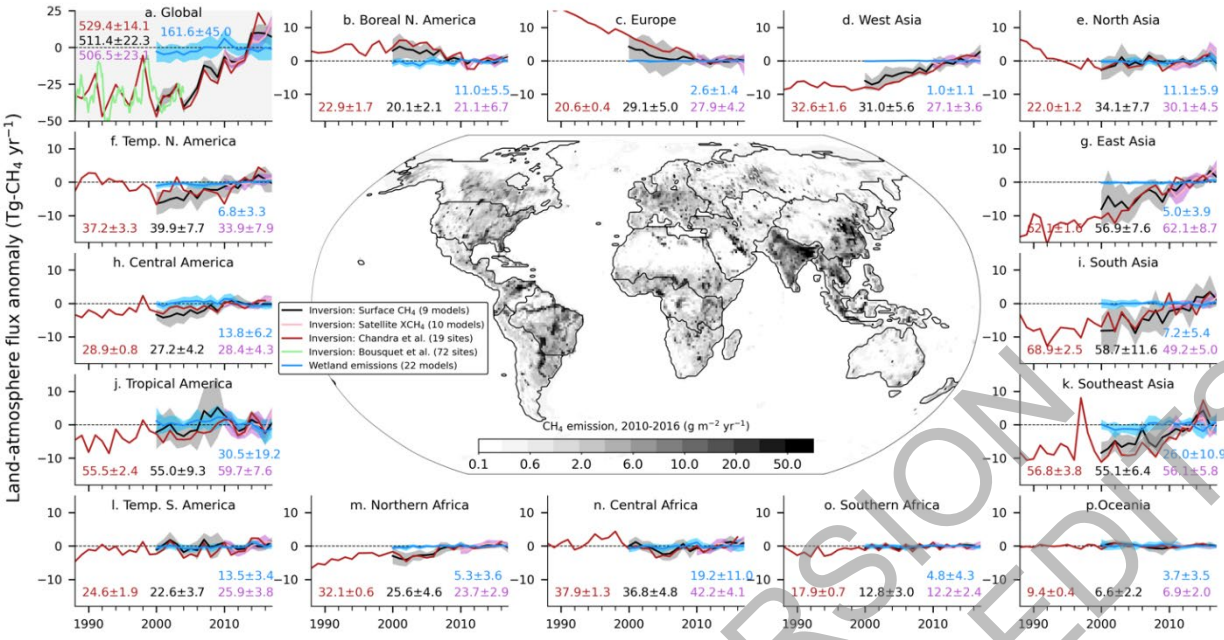
Figure 5.14: Global methane (CH_4) budget (2008–2017). Values and data sources as in Table 5.2 (in TgCH_4). The atmospheric stock is calculated from mean CH_4 concentration, multiplying a factor of 2.75 ± 0.015 Tg ppb^{-1}, which accounts for the uncertainties in global mean CH_4 (Chandra et al., 2021). Further details on data sources and processing are available in the chapter data table (Table 5.SM.6).

ACCEPTED VERSION SUBJECT TO FINAL EDITS



Cross-Chapter Box 5.2, Figure 1: **Methane sources and sinks for four decades from atmospheric inversions with the budget imbalance** (source-sink; red bars) (plotted on the left y-axis). Top-down analysis from (Kirschke et al., 2013; Saunois et al., 2020), The global CH_4 concentration seen in the black line (plotted on the right y-axis), representing NOAA observed global monthly mean atmospheric CH_4 in dry-air mole fractions for 1983–2019 (Chapter 2, Annex V). Natural sources include emissions from natural wetlands, lakes and rivers, geological sources, wild animals, termites, wildfires, permafrost soils, and oceans. Anthropogenic sources include emissions from enteric fermentation and manure, landfills, waste and wastewater, rice cultivation, coal mining, oil and gas industry, biomass and biofuel burning. The top-down total sink is determined from global mass balance includes chemical losses due to reactions with hydroxyl (OH), atomic chlorine (Cl), and excited atomic oxygen (O^1D), and oxidation by bacteria in aerobic soils (Table 5.2). Further details on data sources and processing are available in the chapter data table (Table 5.SM.6).

ACCEPTED VERSION SUBJECT TO FINAL EDITS



Cross-Chapter Box 5.2, Figure 2: Anomalies in global and regional methane (CH_4) emissions for 1988–2017. Map in the centre shows mean CH_4 emission for 2010–2016 . Multi-model mean (line) and 1-σ standard deviations (shaded) for 2000–2017 are shown for 9 surface CH_4 and 10 satellite XCH_4 inversions, and 22 wetland models or model variants that participated in GCP-CH_4 budget assessment (Saunois et al., 2020). The results for the period before 2000 are available from two inversions, 1) using 19 sites (Chandra et al., 2021; also used for the 2010-2016 mean emission map) and for global totals (Bousquet et al., 2006). The long-term mean values for 2010-2016 (common for all GCP–CH_4 inversions), as indicated within each panel separately, is subtracted from the annual-mean time series for the calculation of anomalies for each region. Further details on data sources and processing are available in the chapter data table (Table 5.SM.6).

ACCEPTED VERSION SUBJECT TO FINAL EDITS

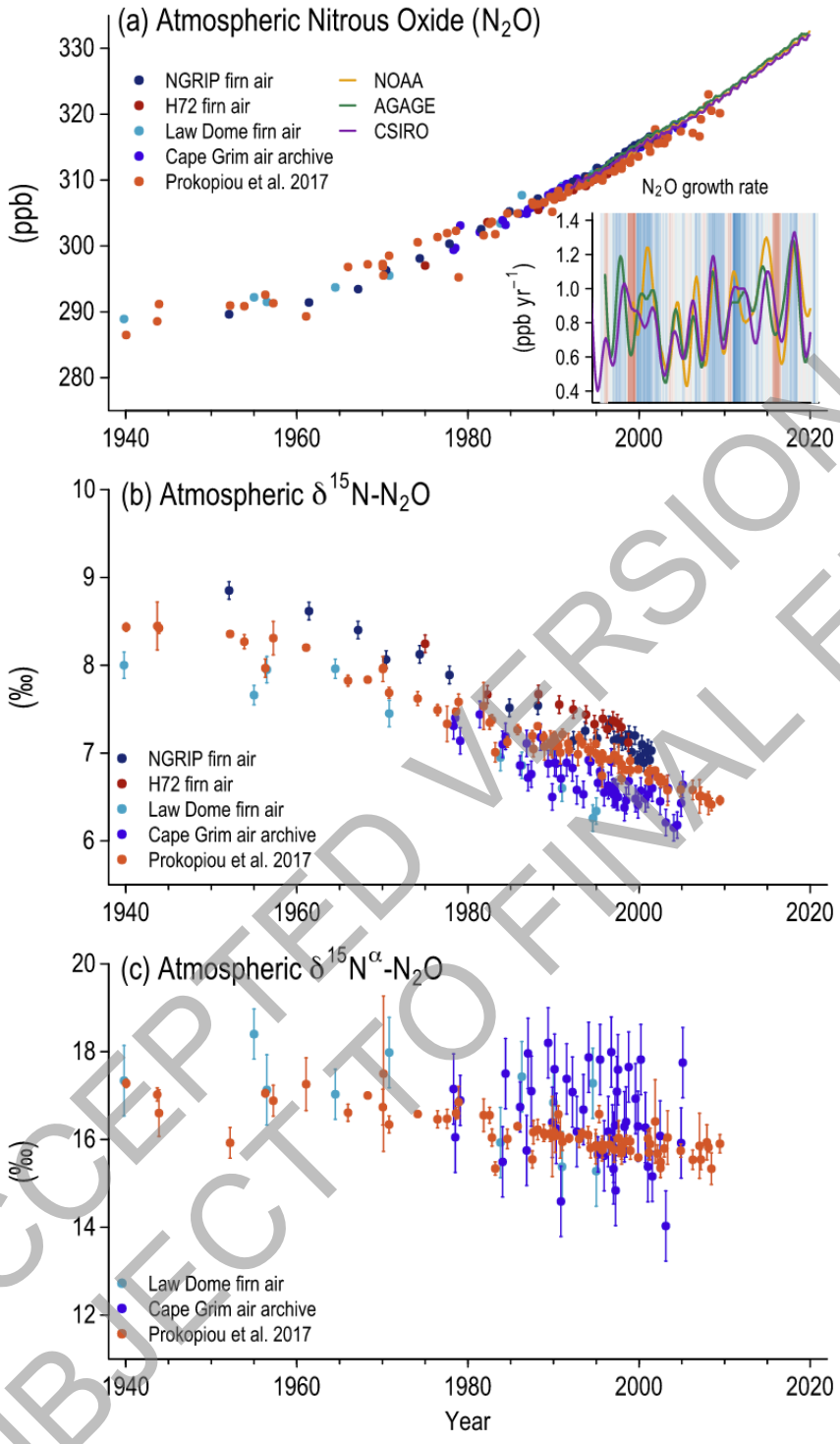


Figure 5.15: Changes in atmospheric nitrous oxide (N_2O) and its isotopic composition since 1940. (a) Atmospheric N_2O abundance (parts per billion, ppb) and growth rate (ppb yr^{-1}), (b) $\delta^{15}N$ of atmospheric N_2O, and (c) alpha-site ^{15}N–N_2O. Estimate are based on direct atmospheric measurements in the AGAGE , CSIRO, and NOAA networks (Prinn et al., 2000, 2018; Francey et al., 2003; Hall et al., 2007; Elkins et al., 2018), archived air samples from Cape Grim, Australia (Park et al., 2012), and firn air from NGRIP Greenland and H72 Antarctica (Ishijima et al., 2007), Law Dome Antarctica (Park et al., 2012), as well as a collection of firn ice samples from Greenland (Prokopiou et al., 2017, 2018). Shading in (a) is based on the multivariate ENSO index, with red indicating El Niño conditions (Wolter and Timlin, 1998). Further details on data sources and processing are available in the chapter data table (Table 5.SM.6).

ACCEPTED VERSION SUBJECT TO FINAL EDITS

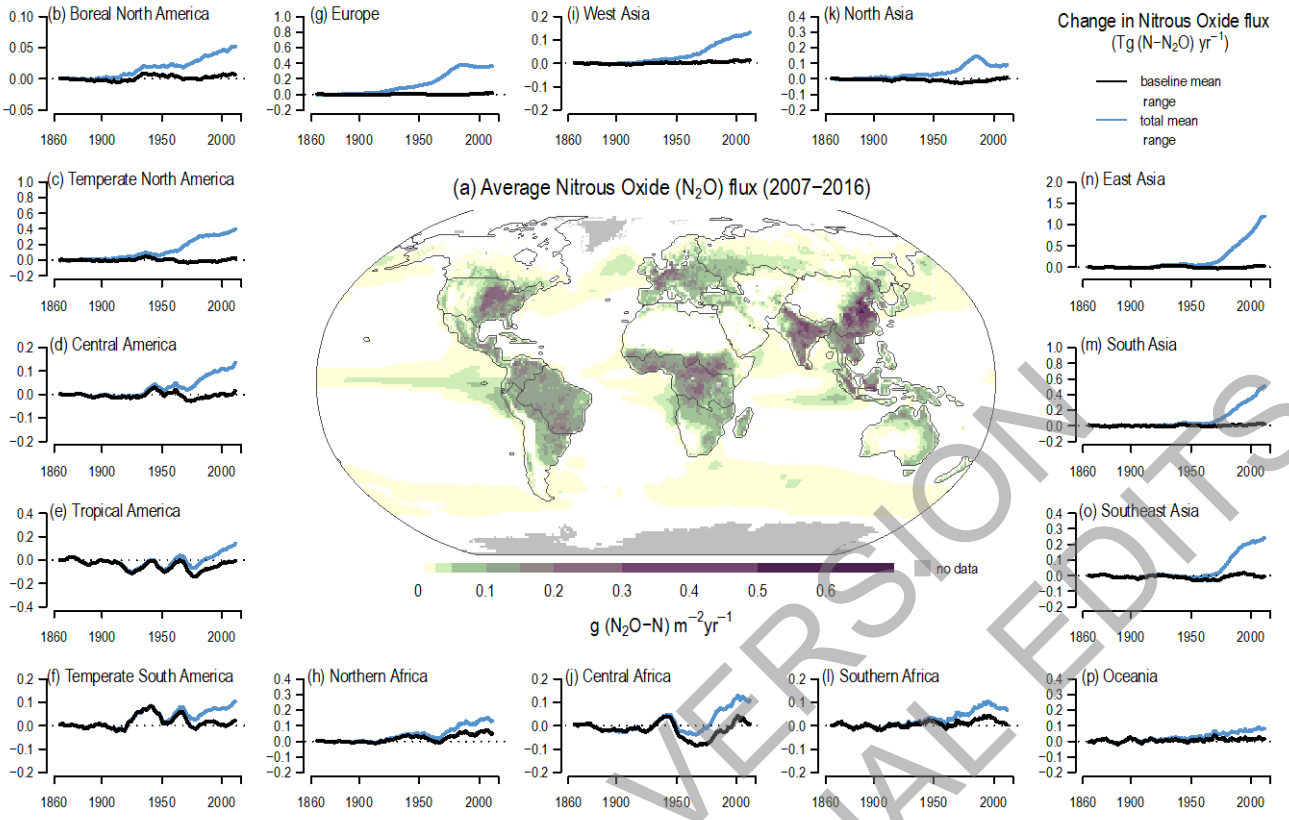


Figure 5.16: Decadal mean nitrous oxide (N_2O) emissions for 2007–2016 and its change since 1850 based on process-model projections. The total effect including that from anthropogenic nitrogen additions (atmospheric deposition, manure addition, fertiliser use and land-use) is evaluated against the background flux driven by changes in atmospheric CO_2 concentration, and climate change. Fluxes are derived from the N_2O Model Intercomparison Project ensemble of terrestrial biosphere models (Tian et al., 2019) and three ocean biogeochemical models (Landolfi et al., 2017; Battaglia and Joos, 2018a; Buitenhuis et al., 2018). Further details on data sources and processing are available in the chapter data table (Table 5.SM.6).

ACCEPTED VERSION SUBJECT TO FINAL EDITS

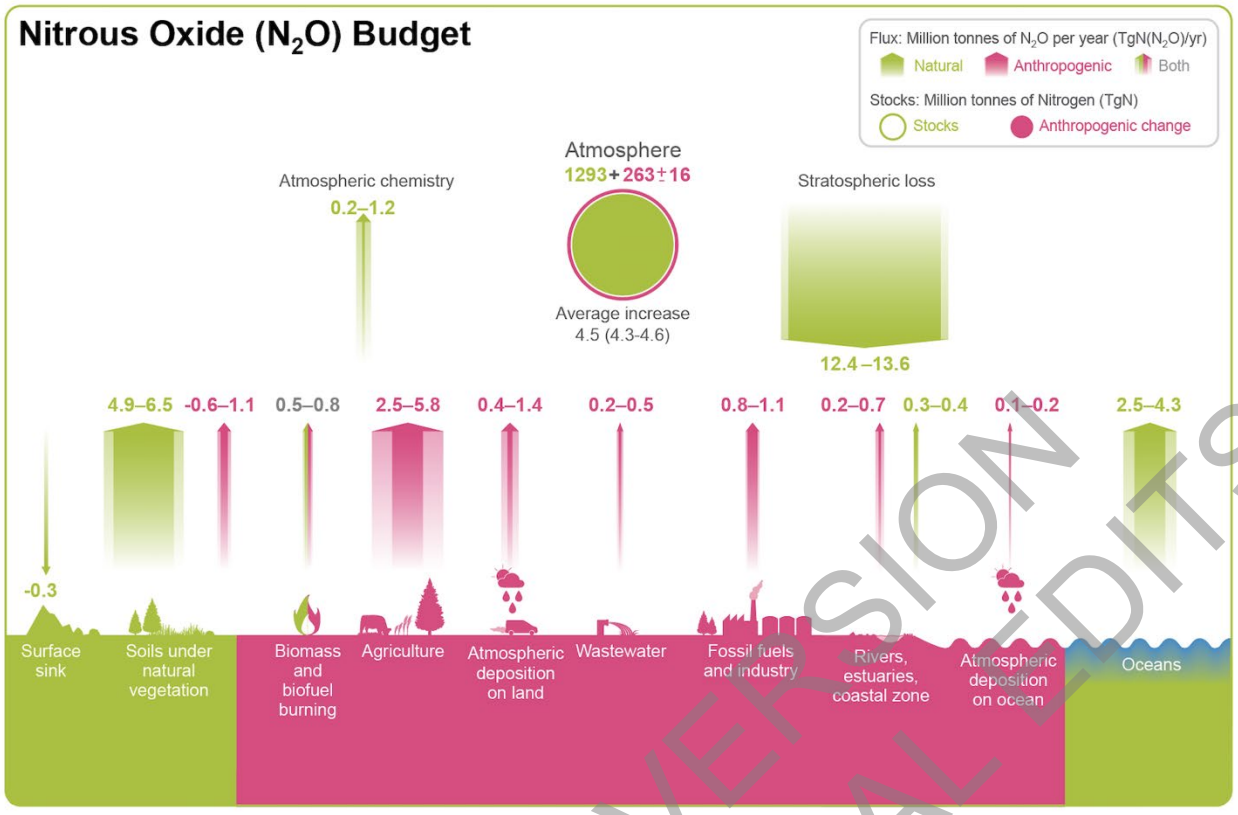


Figure 5.17: Global nitrous oxide (N_2O) budget (2007–2016). Values and data sources as in Table 5.3. The atmospheric stock is calculated from mean N_2O concentration, multiplying a factor of 4.79 ± 0.05 Tg ppb^{-1} (Prather et al., 2012). Pool sizes for the other reservoirs are largely unknown. Further details on data sources and processing are available in the chapter data table (Table 5.SM.6).

ACCEPTED VERSION SUBJECT TO FINAL EDITS

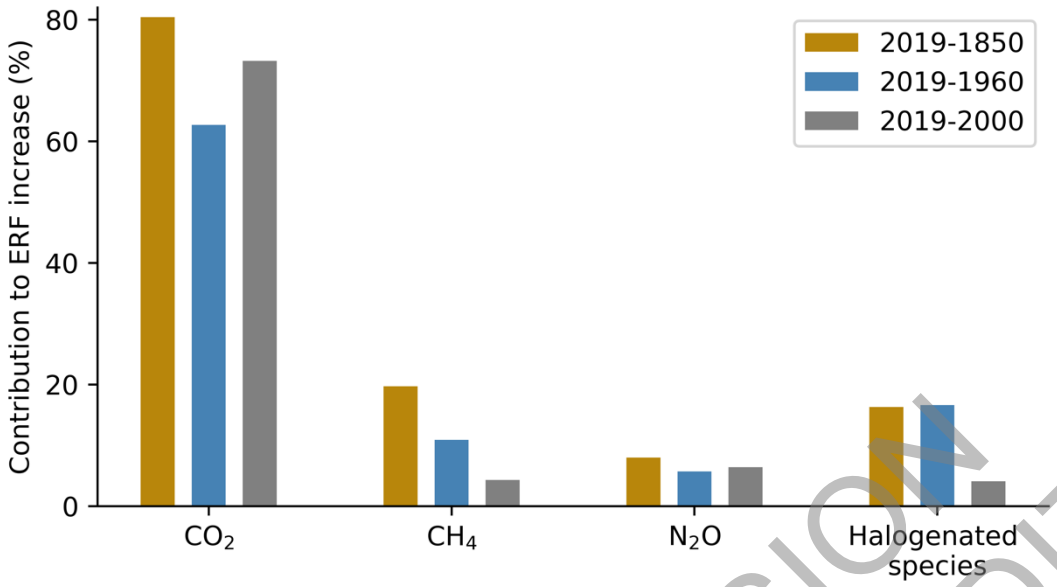


Figure 5.18: Contributions of carbon dioxide (CO_2), methane (CH_4), nitrous oxide (N_2O) and halogenated species to the total effective radiative forcing (ERF) increase since 1850 and 1960, and for 2000 to 2009. ERF data are taken from Annex 5 (based on calculations from Chapter 7). Note that the sum of the ERFs exceeds 100% because there are negative ERFs due to aerosols and clouds. Further details on data sources and processing are available in the chapter data table (Table 5.SM.6).

ACCEPTED VERSION SUBJECT TO FINAL EDITS

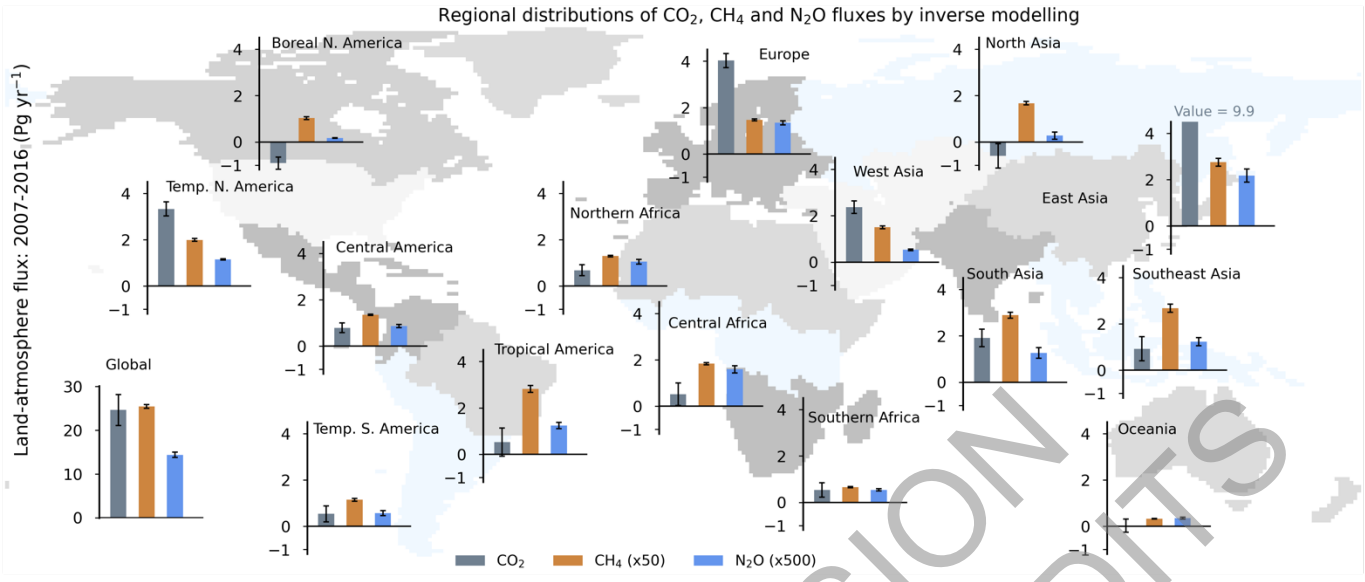


Figure 5.19: Regional distributions of net fluxes of carbon dioxide (CO_2), methane (CH_4), nitrous oxide (N_2O) on the Earth's surface. The region divisions, shown as the shaded map, are made based on ecoclimatic characteristics of the land. The fluxes include those from anthropogenic activities and natural causes that result from responses to anthropogenic greenhouse gases and climate forcing (feedbacks) as in the three budgets shown in Sections 5.2.1.5, 5.2.2.5, and 5.2.3.5. The CH_4 and N_2O emissions are weighted by arbitrary factors of 50 and 500, respectively, for depiction by common y-axes. Fluxes are shown as the mean of the inverse models as available from (Thompson et al., 2019; Friedlingstein et al., 2020; Saunois et al., 2020). Further details on data sources and processing are available in the chapter data table (Table 5.SM.6).

ACCEPTED VERSION SUBJECT TO FINAL EDITS

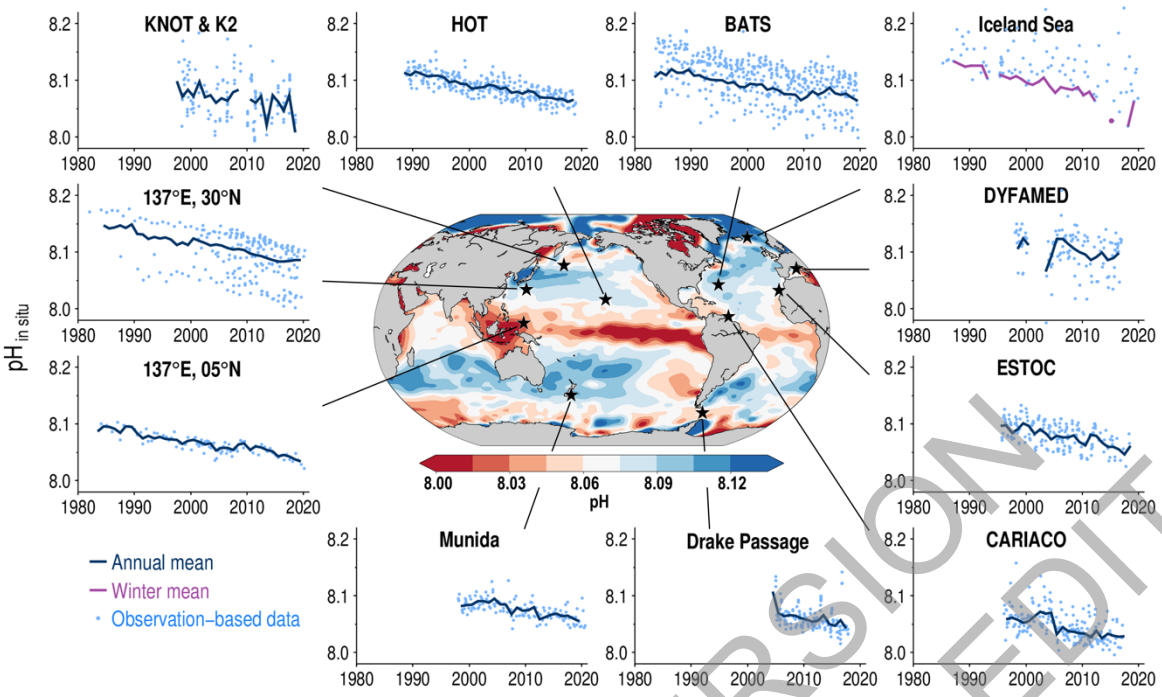


Figure 5.20: Multi-decadal trends of pH (Total Scale) in surface layer at various sites of the oceans and a global distribution of annual mean pH adjusted to the year 2000. Time-series data of pH are from Dore et al., 2009; Olafsson et al., 2009; González-Dávila et al., 2010; Bates et al., 2014b; Takahashi et al., 2014; Wakita et al., 2017; Merlivat et al., 2018; Ono et al., 2019; and Bates and Johnson, 2020. Global distribution of annual mean pH have been evaluated from data of surface ocean pCO_2 measurements (Bakker et al., 2016; Jiang et al., 2019). Acronyms in panels: KNOT and K2 - Western Pacific subarctic gyre time-series; HOT - Hawaii Ocean Time-series; BATS - Bermuda Atlantic Time-series Study; DYFAMED - Dynamics of Atmospheric Fluxes in the Mediterranean Sea; ESTOC - European Station for Time-series in the Ocean Canary Islands; CARIACO - Carbon Retention in a Colored Ocean Time-series. Further details on data sources and processing are available in the chapter data table (Table 5.SM.6).

ACCEPTED VERSION SUBJECT TO FINAL EDITS

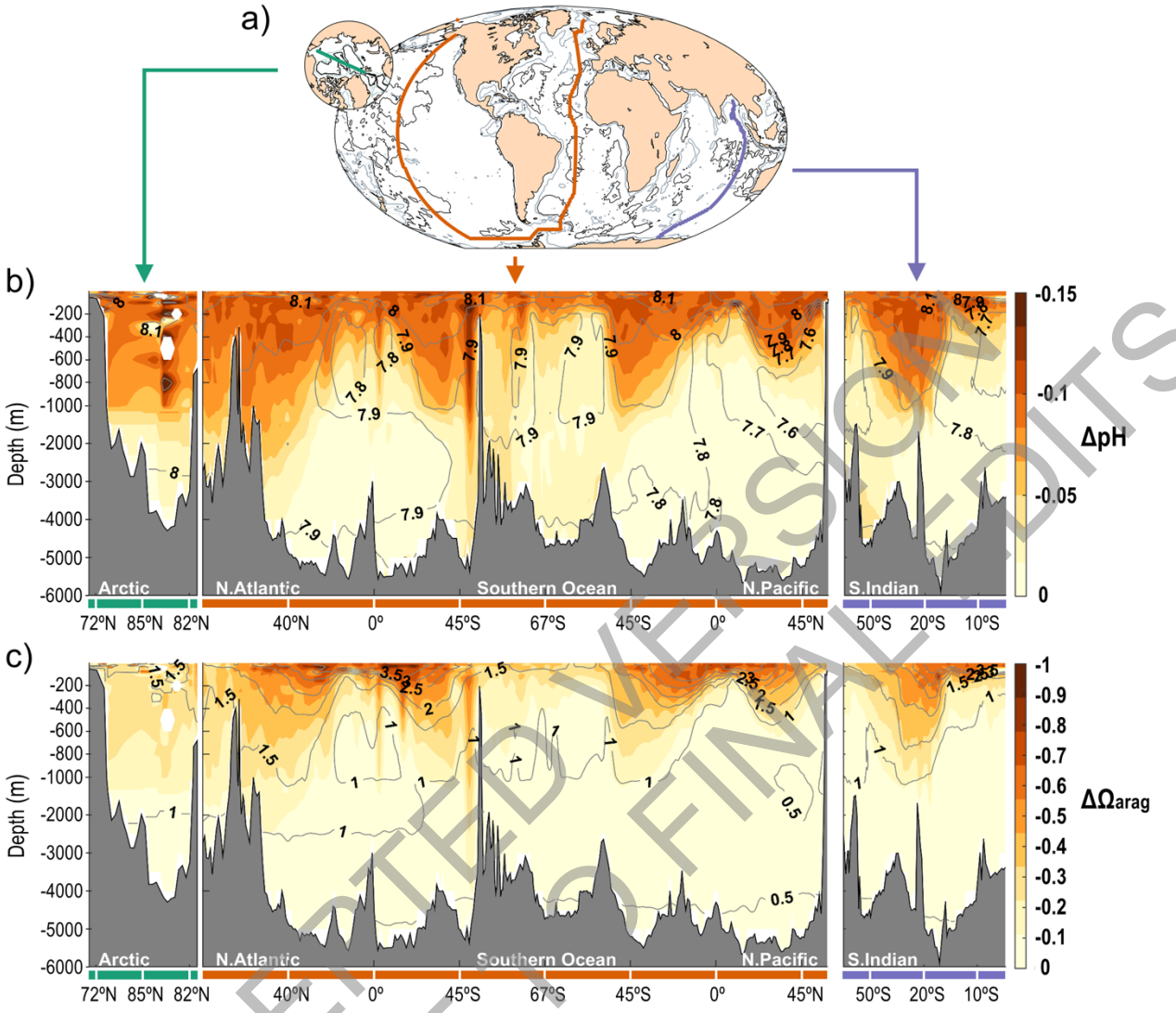
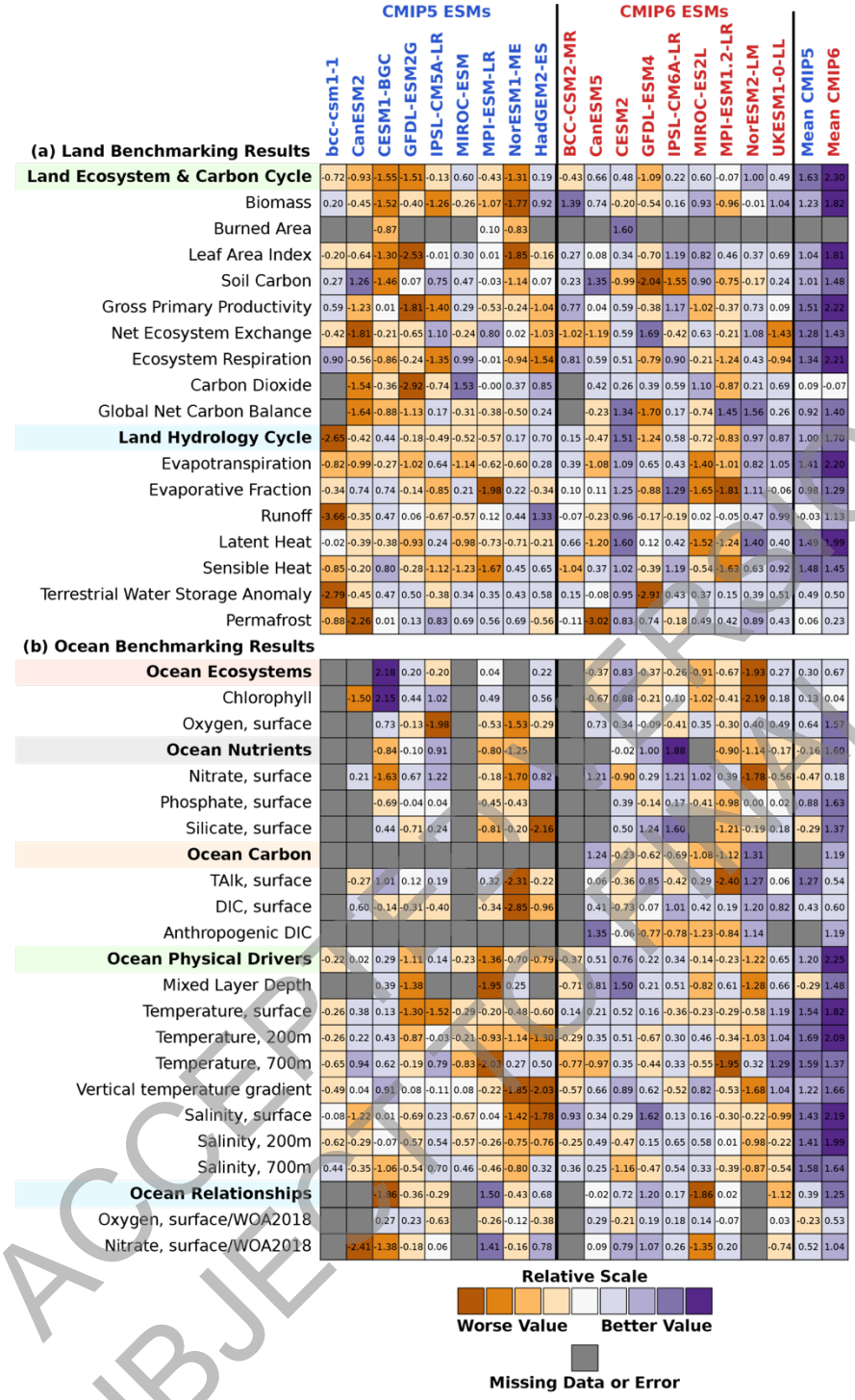


Figure 5.21: Spread of ocean acidification from the surface into the interior of ocean since pre-industrial times. (a) map showing the three transects used to create the cross sections shown in (b) and (c); vertical sections of the changes in (b) pH and (c) saturation state of aragonite (Ω_{arag}) between 1800–2002 due to anthropogenic CO_2 invasion (colour). Contour lines are their contemporary values in 2002. The red transect begins in the Nordic Seas and then follows the GO-SHIP lines A16 southward in the Atlantic Ocean, SR04 and S04P westward in the Southern Ocean, and P16 northward in the Pacific Ocean. The purple line follows the GO-SHIP line I09 southward in the Indian Ocean. The green line on the smaller inset crosses the Arctic Ocean from the Bering Strait to North Pole along 175°W and from the North Pole to the Fram Strait along 5°E (Lauvset et al., 2020). Further details on data sources and processing are available in the chapter data table (Table 5.SM.6).

ACCEPTED VERSION SUBJECT TO FINAL EDITS



ACCEPTED VERSION SUBJECT TO FINAL EDITS

Figure 5.22: Overview scores for CMIP5 (left hand side of table) and CMIP6 (right hand side of table) Earth system models (ESMs), for multiple benchmarks against different datasets. (a) Benchmarking of ESM land models, (b) benchmarking of ocean models. Scores are relative to other models within each benchmark row, with positive scores indicating a better agreement with observations. Models included are only those from institutions that participated in both CMIP5 and CMIP6 carbon cycle experiments, in order to trace changes from one ensemble to the next. CMIP5 models are labels in yellow and CMIP6 in green, with the multi-model ensemble means labelled in white. Further details on data sources and processing are available in the chapter data table (Table 5.SM.6).

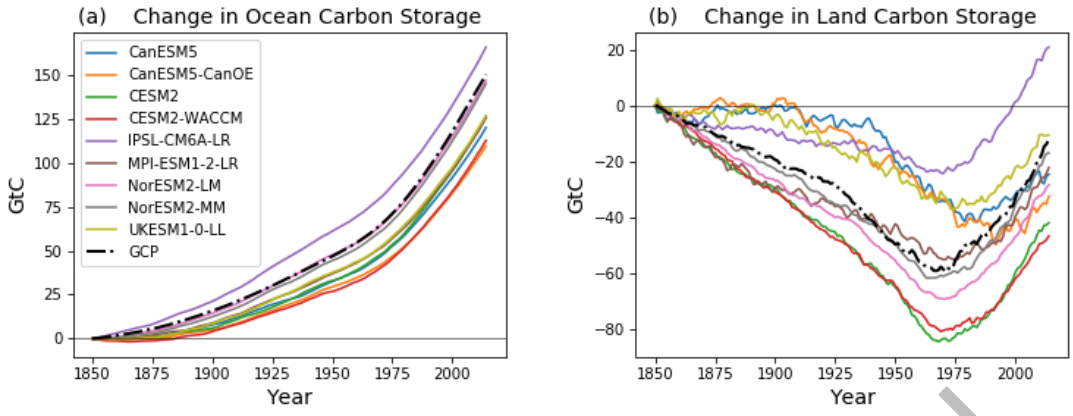


Figure 5.23: CMIP6 Earth system model (ESM) concentration-driven historical simulations for 1850 to 2014, compared to observation-based estimates from the global carbon project (GCP). Panel (a) cumulative ocean carbon uptake from 1850 (PgC); (b) cumulative land carbon uptake from 1850 (PgC). Only models that simulate both land and ocean carbon fluxes are shown here. Further details on data sources and processing are available in the chapter data table (Table 5.SM.6).

ACCEPTED VERSION
SUBJECT TO FINAL EDITS

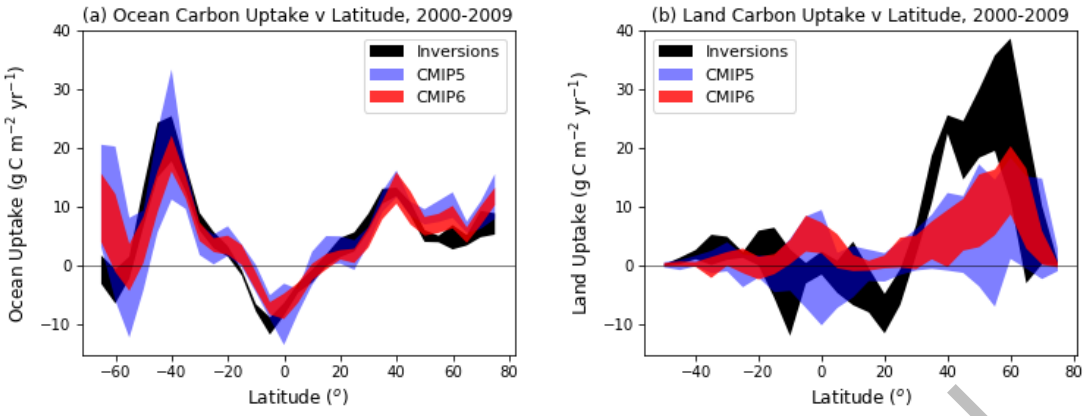


Figure 5.24: Comparison of modelled zonal distribution of contemporary carbon sinks against atmospheric inversion estimates for 2000–2009, (a) ocean carbon uptake; (b) net land uptake. Latitude runs from 90°S (i.e. –90°N) to 90°N. Positive uptake represents a carbon sink to ocean/land while negative uptake represents a carbon source. The land uptake is taken as Net Biome Productivity (NBP) and so includes net land-use change emissions. The bands show the mean ±1 standard deviation across the available inversions (black bands, 3 models), CMIP5 Earth system models (ESMs) (blue bands, 12 models for the ocean, 12 models for the land), and CMIP6 ESMs (red bands, 11 models for ocean, 10 models for land). Further details on data sources and processing are available in the chapter data table (Table 5.SM.6).

ACCEPTED VERSION
SUBJECT TO FINAL EDITS

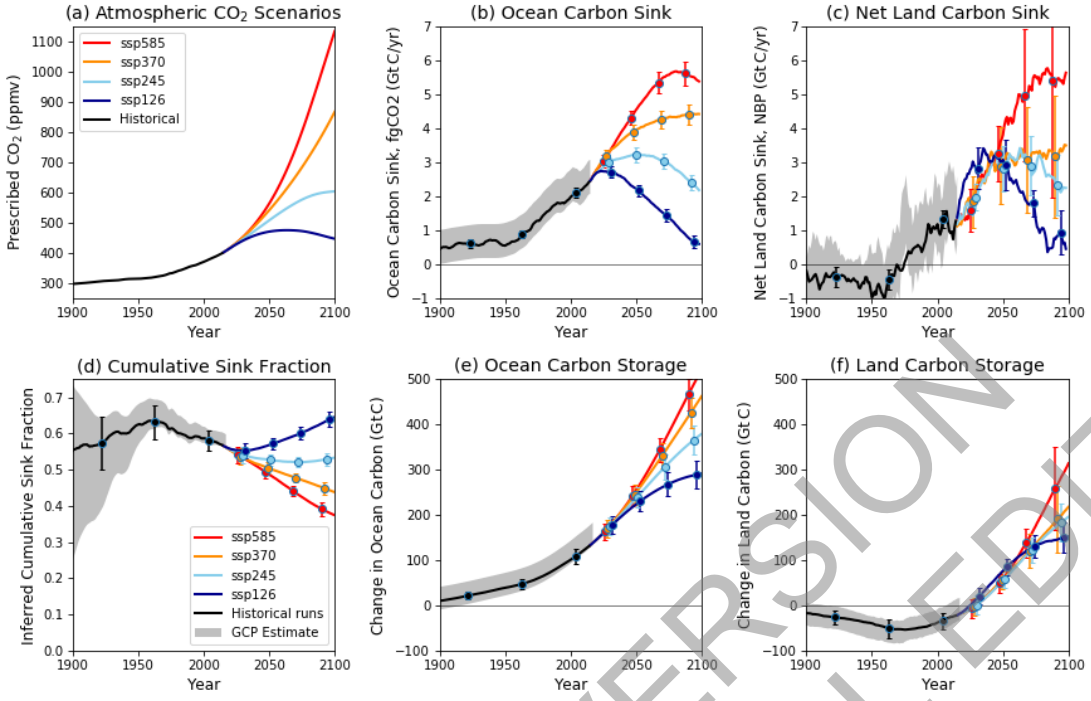


Figure 5.25: Modelled evolution of the global land and ocean carbon sinks for 1850 to 2100 in concentration-driven CMIP6 Earth system model (ESM) scenario runs (SSP1–2.6: blue; SSP2–4.5: skyblue; SSP3–7.0: yellow; SSP5–8.5: red): (a) prescribed atmospheric CO_2 concentrations; (b) 5-year running mean ocean carbon sink (GtC yr^{-1}); (c) 5-year running mean net land carbon sink (GtC yr^{-1}); (d) inferred cumulative sink fraction of emissions from 1850; (e) change in ocean carbon storage from 1850 (GtC); (f) change in land carbon storage from 1850 (GtC). Thick lines represent the ensemble mean of the listed ESM runs, and the error bars represents ± one standard deviation about that mean. The grey wedges represent estimates from the global carbon project (GCP), assuming uncertainties in the annual mean ocean and net land carbon sinks of 0.5 GtC yr^{-1} and 1 GtC yr^{-1} respectively, and uncertainties in the changes in carbon stores (ocean, land and cumulative total emissions) of 25 GtC. The net land carbon sink is taken as net biome productivity (NBP) and so includes any modelled net land-use change emissions. Further details on data sources and processing are available in the chapter data table (Table 5.SM.6).

ACCEPTED VERSION SUBJECT TO FINAL EDITS

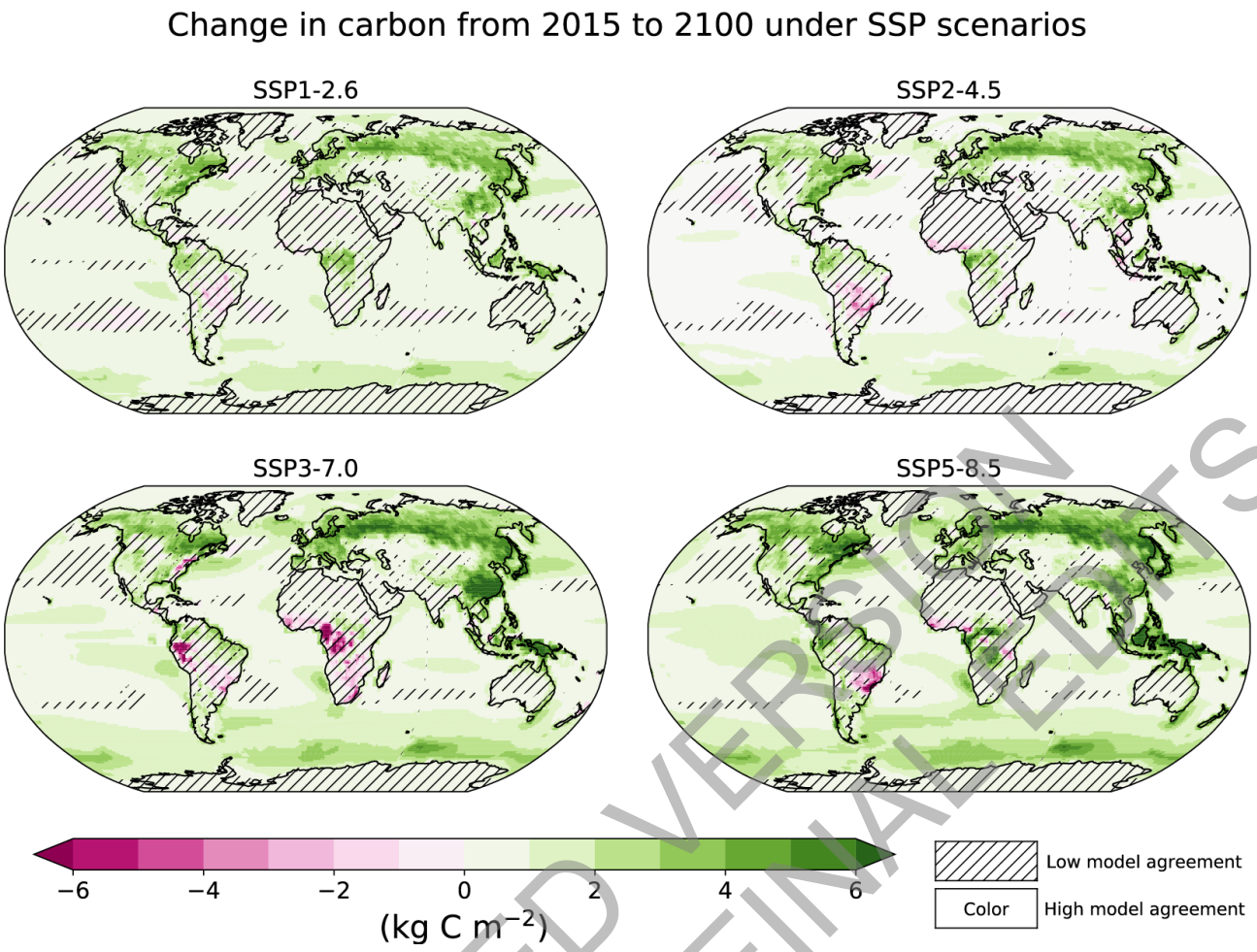


Figure 5.26: Maps of net carbon changes under four Shared Socioeconomic Pathway (SSP) scenarios, as evaluated from nine CMIP6 Earth system models. Uncertainty is represented using the simple approach (see Cross-Chapter Box Atlas.1 for more information): No overlay indicates regions with high model agreement, where ≥80% of models agree with the ensemble mean on the sign of change; diagonal lines indicate regions with low model agreement, where <80% of models agree with the ensemble mean on the sign of change. On land, this is calculated as the time integral of NBP, for the ocean it is the time-integral of air-sea CO_2 gas flux anomalies relative to the pre-industrial. Further details on data sources and processing are available in the chapter data table (Table 5.SM.6).

ACCEPTED VERSION SUBJECT TO FINAL EDITS

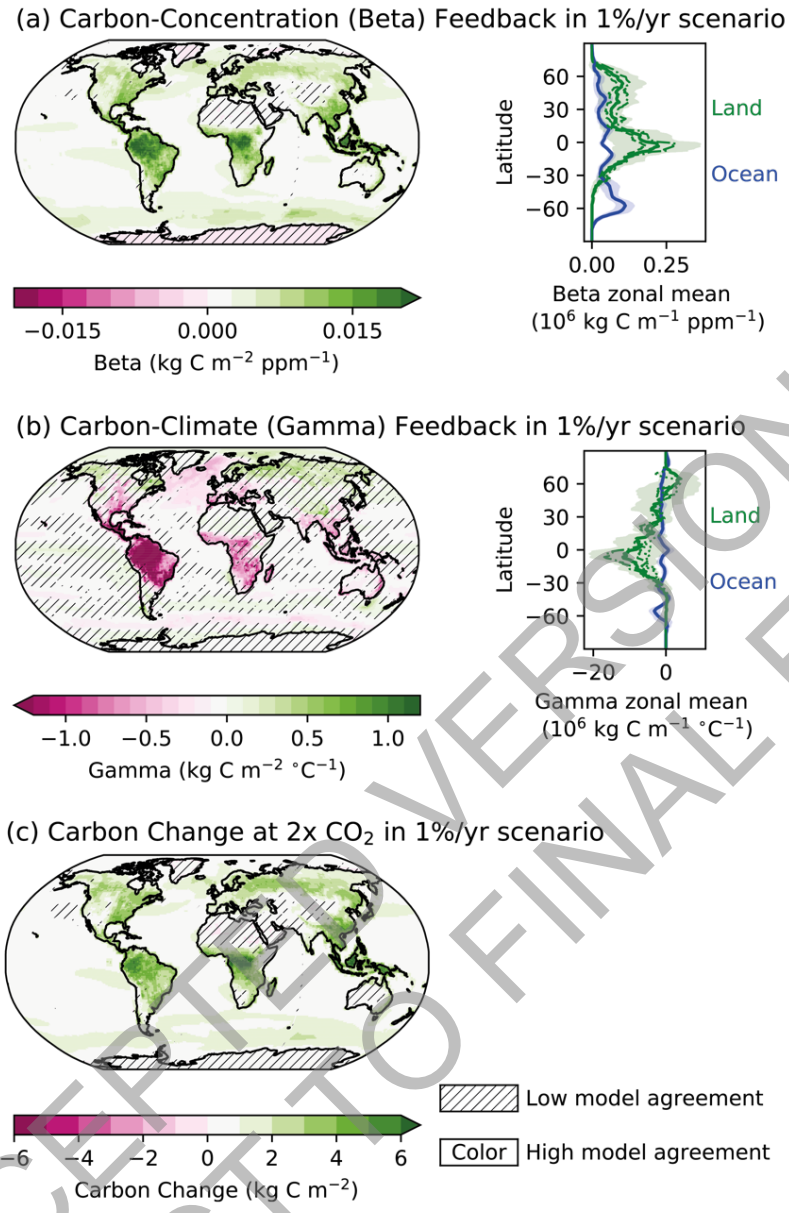


Figure 5.27: Maps of carbon-concentration and carbon-climate feedback terms, as well as net carbon changes under the idealised 1% per year CO_2 scenario, as evaluated from CMIP6 Earth system models (ESMs). Shown are the model means from nine CMIP6 ESMs. Uncertainty is represented using the simple approach (see Cross-Chapter Box Atlas.1 for more information): No overlay indicates regions with high model agreement, where ≥80% of models agree with the ensemble mean on the sign of change; diagonal lines indicate regions with low model agreement, where <80% of models agree with the ensemble mean on the sign of change. Also shown are zonal-mean latitude profiles of land (green) and ocean (blue) feedbacks. On the land, the zonal mean feedback for the mean of the ensemble of models that include nitrogen is shown as dashed lines, and carbon-only models as dash-dotted lines, and the carbon-climate feedback from one permafrost-carbon enabled ESM is shown as a dotted line carbon changes are calculated as the difference between carbon stocks at different times on land and for the ocean as the time integral of atmosphere-ocean CO_2 flux anomalies relative to the pre-industrial. The denominator for gamma here is the global mean surface air temperature. Further details on data sources and processing are available in the chapter data table (Table 5.SM.6).

ACCEPTED VERSION SUBJECT TO FINAL EDITS

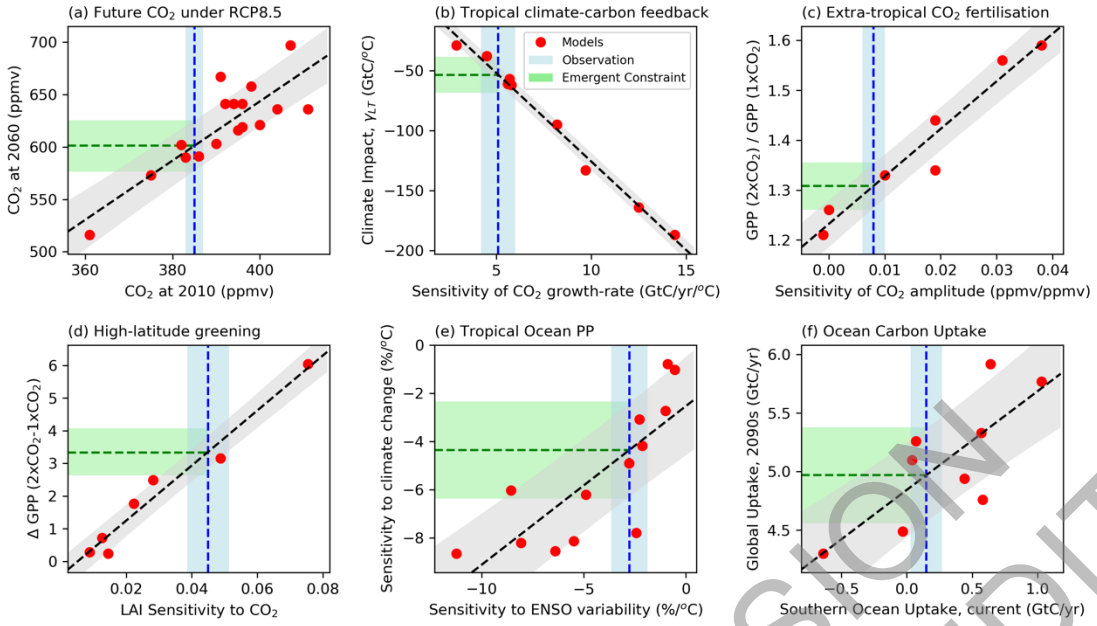


Figure 5.28: Examples of emergent constraints on the carbon cycle in Earth system models (ESMs), reproduced from previously published studies: (a) projected global mean atmospheric CO_2 concentration by 2060 under the RCP8.5 emissions scenario against the simulated CO_2 in 2010 (Friedlingstein et al., 2014; Hoffman et al., 2014); (b) sensitivity of tropical land carbon to warming (γ_{LT}) against the sensitivity of the atmospheric CO_2 growth-rate to tropical temperature variability (Cox et al., 2013; Wenzel et al., 2014); (c) sensitivity of extratropical (30°N–90°N) gross primary production to a doubling of atmospheric CO_2 against the sensitivity of the amplitude of the CO_2 seasonal cycle at Kumkahi, Hawaii to global atmospheric CO_2 concentration (Wenzel et al., 2016); (d) change in high-latitude (30°N–90°N) gross primary production versus trend in high-latitude leaf area index or 'greenness' (Winkler et al., 2019); (e) sensitivity of the primary production of the Tropical ocean to climate change versus its sensitivity to ENSO-driven temperature variability (Kwiatkowski et al., 2017); (f) global ocean carbon sink in the 2090s versus the current-day carbon sink in the Southern Ocean. In each case, a red-dot represents a single ESM projection, the grey bar represents the emergent relationship between the y-variable and the x-variable, the blue bar represents the observational estimate of the x-axis variable, and the green bar represents the resulting emergent constraint on the y-axis variable. The thicknesses represent ± one standard error in each case. Figure after Cox, (2019). Further details on data sources and processing are available in the chapter data table (Table 5.SM.6).

ACCEPTED VERSION SUBJECT TO FINAL EDITS

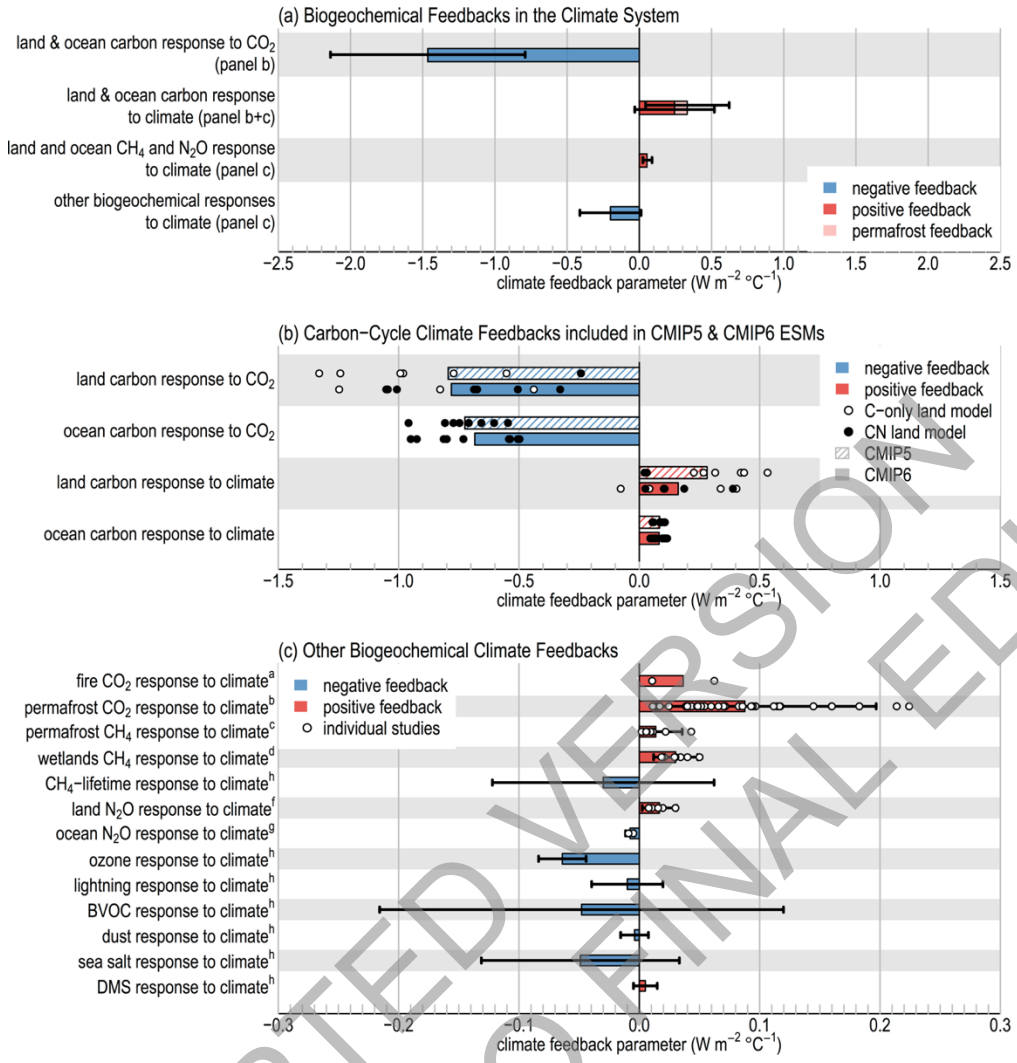


Figure 5.29: Estimates of the biogeochemical climate feedback parameter (α). The parameter α (W m^{-2} °C^{-1}) for a feedback variable x is defined as $\alpha_x = \frac{\partial N}{\partial x}\frac{dx}{dT}$ where $\frac{\partial N}{\partial x}$ is the change in TOA energy balance in response to a change in x induced by a change in surface temperature (T), as in Section 7.4.1.1. (a) Synthesis of biogeochemical feedbacks from panels (b) and (c). Red (blue) bars correspond to positive (negative) feedbacks increasing (decreasing) radiative forcing at the top of the atmosphere. Bars denote the mean and the error bar represents the 5–95th percentile range of the estimates; (b) carbon-cycle feedbacks as estimated by coupled carbon-cycle climate models in the CMIP5 (Arora et al., 2013) and CMIP6 (Arora et al., 2020) ensembles, where dots represent single model estimates, and filled (open) circles are those estimates which do (not) include the representation of a terrestrial nitrogen cycle; (c) Estimates of other biogeochemical feedback mechanisms based on various modelling studies. Dots represent single estimates, and coloured bars denote the mean of these estimates with no weighting being made regarding the likelihood of any single estimate, and error bars the 5–95th percentile range derived from these estimates. Results in panel (c) have been compiled from (a) Section 5.4.3.2 (Eliseev et al., 2014; Harrison et al., 2018); (b) Section 5.4.3.3 (Schneider von Deimling et al., 2012; Burke et al., 2013; Koven et al., 2015b, 2015a; MacDougall and Knutti, 2016; Burke et al., 2017; Gasser et al., 2018; Kleinen and Brovkin, 2018), where the estimates from Burke et al. have been constrained as assessed in their study (c) Section 5.4.7 (Schneider von Deimling et al., 2012; Koven et al., 2015b; Schneider von Deimling et al., 2015; Turetsky et al., 2020); (d) Section 5.4.7 (Arneth et al., 2010; Denisov et al., 2013; Shindell et al., 2013; Stocker et al., 2013; Zhang et al., 2017); (f) Section 5.4.7 (Xu-Ri et al., 2012; Zaehle, 2013; Stocker et al., 2013; Tian et al., 2019); (g) Section 5.4.7 (Martinez-Rey et al., 2015; Landolfi et al., 2017; Battaglia and Joos, 2018). (h) Section 6.3, Table 6.9 mean and the 5–95th percentile range the assessed feedback parameter. Further details on data sources and processing are available in the chapter data table (Table 5.SM.6).

ACCEPTED VERSION SUBJECT TO FINAL EDITS

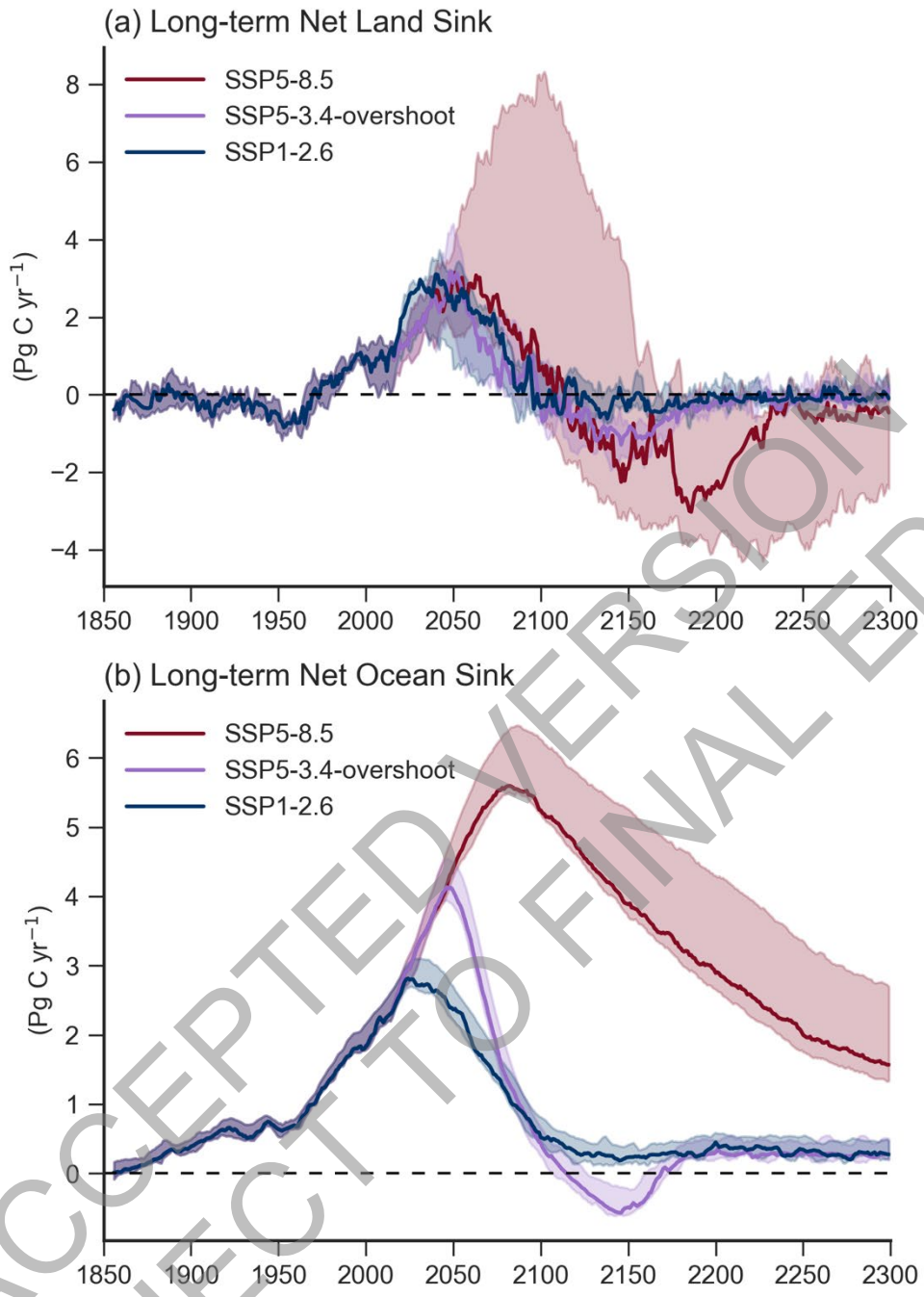
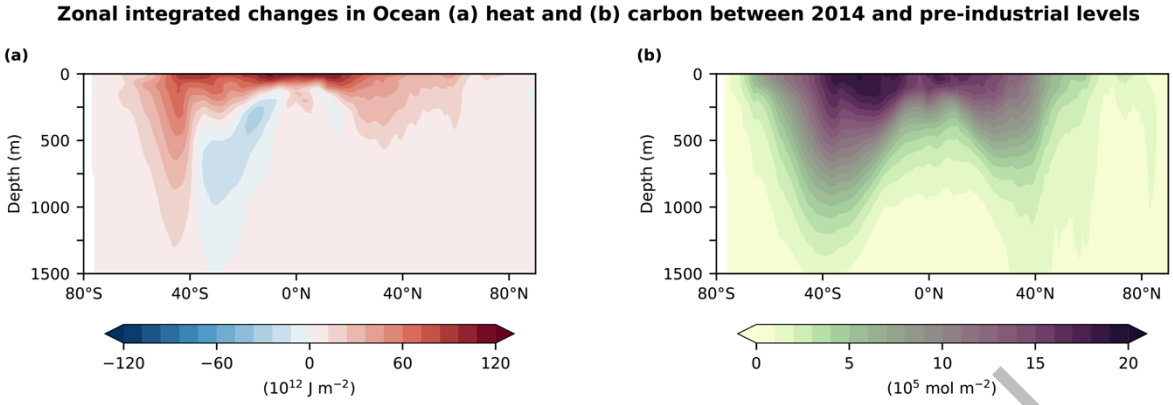


Figure 5.30: Trajectories of carbon cycle dynamics for models beyond 2100. Shown are three scenarios, SSP5–8.5, SSP5–3.4–overshoot, and SSP1–2.6, from four ESMs (CanESM5, UKESM1, CESM2-WACCM, IPSL-CM6a-LR) and one EMIC (UVIC-ESCM, (Mengis et al., 2020)) for which extensions beyond 2100 are available. Solid lines represent the median flux value across the ensemble, and shading represents 15th–85th percentiles across the ensemble. Further details on data sources and processing are available in the chapter data table (Table 5.SM.6).

ACCEPTED VERSION SUBJECT TO FINAL EDITS



Cross-Chapter Box 5.3, Figure 1: CMIP6 multi-model mean of changes in zonally integrated (a) carbon and (b) heat storage in ocean between the pre-industrial and the modern period. Carbon corresponds to dissolved inorganic carbon. Data are shown for the upper 2000m. The modern period is 1995–2014. Adapted from (Frölicher et al., 2015))

ACCEPTED VERSION
SUBJECT TO FINAL EDITS

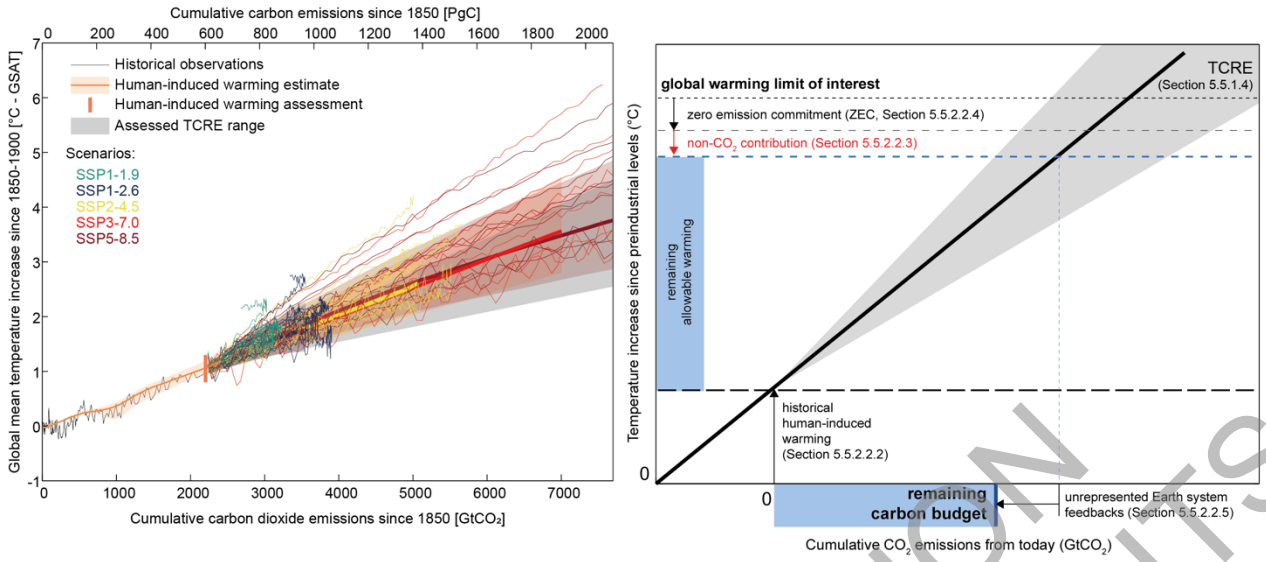
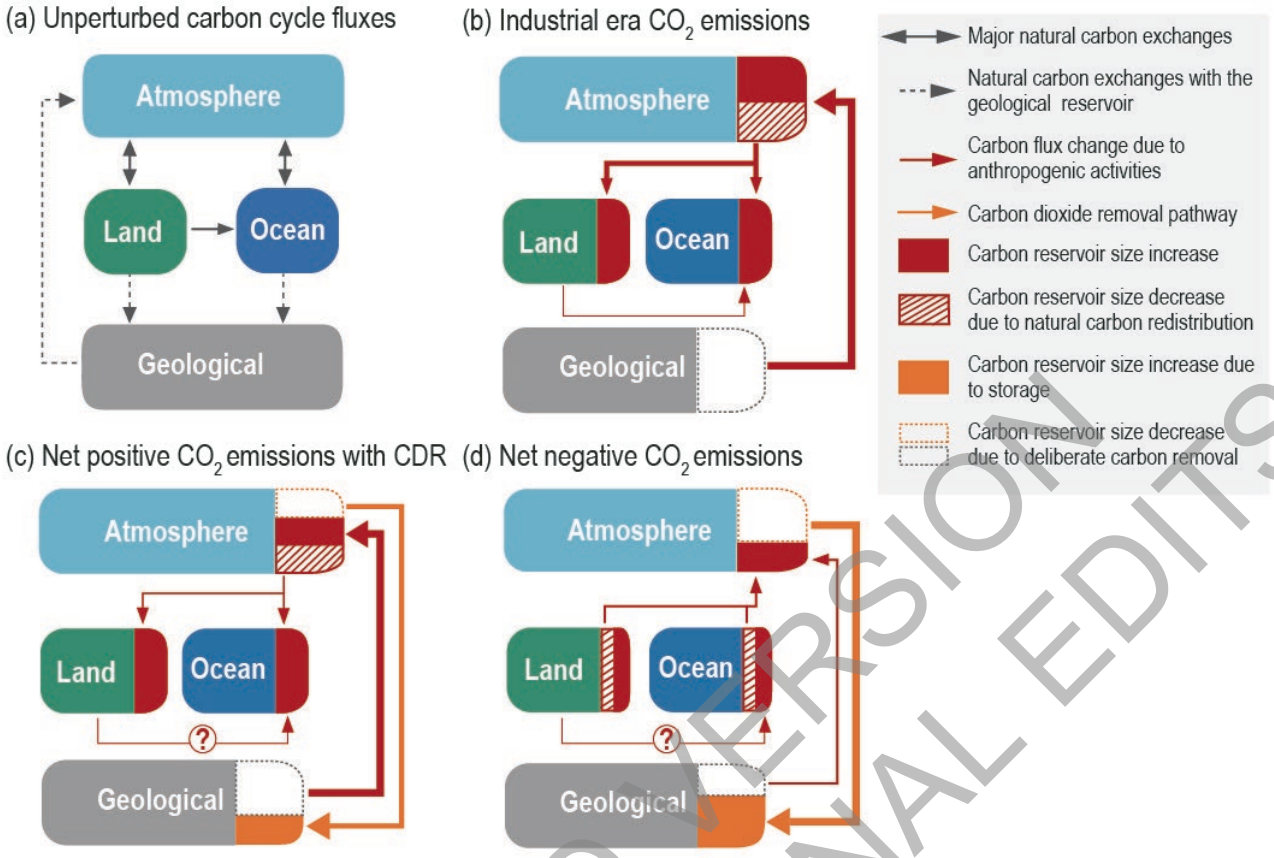


Figure 5.31: Illustration of relationship between cumulative emissions of carbon dioxide (CO_2) and global mean surface air temperature increase (left) and conceptual schematic of the assessment of the remaining carbon budget from its constituting components (right). Carbon budgets consistent with various levels of additional warming are provided in Table 5.8 and should not be read from the illustrations in either panel. Left-hand panel: Historical data (thin black line data) shows historical CO_2 emissions as reported in (Friedlingstein et al., 2020) together with the assessed global mean surface air temperature increase from 1850–1900 as assessed in Chapter 2 (Box 2.3, GSAT). The orange-brown range with its central line shows the estimated human-induced share of historical warming (Haustein et al., 2017). The vertical orange-brown line shows the assessed range of historical human-induced warming for the 2010–2019 period relative to 1850–1900 (Chapter 3). The grey cone shows the assessed range for the transient climate response to cumulative emissions of carbon dioxide (TCRE) assessed to fall *likely* in the 1.0–2.3 °C per 1000 PgC range (Section 5.5.1.4), starting from 2015. Thin coloured lines show CMIP6 simulations for the five scenarios of the AR6 core set (SSP1–1.9, green; SSP1–2.6, blue; SSP2–4.5, yellow; SSP3–7.0, red; SSP5–8.5, maroon), starting from 2015. Diagnosed carbon emissions (Arora et al., 2020) are complemented with estimated land-use change emissions for each respective scenario (Gidden et al., 2018). Coloured areas show the Chapter 4 assessed *likely* range of GSAT projections and thick coloured central lines the median estimate, for each respective scenario, relative to the original scenario emissions (Riahi et al., 2017; Gidden et al., 2018; Rogelj et al., 2018). Right-hand panel: schematic illustration of assessment of remaining carbon budget based on multiple lines of evidence. The remaining allowable warming is estimated by combining the global warming limit of interest with the assessed historical human induced warming (Section 5.5.2.2.2), the assessed future potential non-CO_2 warming contribution (Section 5.5.2.2.3) and the ZEC (Section 5.5.2.2.4). The remaining allowable warming (vertical blue bar) is subsequently combined with the assessed TCRE (Sections 5.5.1.4 and 5.5.2.2.1) and contribution of unrepresented Earth system feedbacks (Section 5.5.2.2.5) to provide an assessed estimate of the remaining carbon budget (horizontal blue bar, Table 5.8). Further details on data sources and processing are available in the chapter data table (Table 5.SM.6).

ACCEPTED VERSION SUBJECT TO FINAL EDITS



Box 5.3, Figure 1: Schematic representation of carbon fluxes between atmosphere, land, ocean and geological reservoirs. Different system conditions are shown: (a) an unperturbed Earth system; and changes in carbon fluxes for (b) an Earth system perturbed by fossil-fuel CO_2 emissions, (c) an Earth system in which fossil-fuel CO_2 emissions are partially offset by CDR, (d) an Earth system in which CDR exceeds CO_2 emissions from fossil fuels ("net negative" CO_2 emissions). Carbon fluxes depicted in (a) (solid and dashed black lines) also occur in (b)-(d). The question mark in the land-to-ocean carbon flux perturbation in (c) and (d) indicates that the effect of CDR on this flux is unknown. Note that box sizes do not scale with the size of carbon reservoirs. Adapted from (Keller et al., 2018a). Further details on data sources and processing are available in the chapter data table (Table 5.SM.6).

ACCEPTED VERSION SUBJECT TO FINAL EDITS

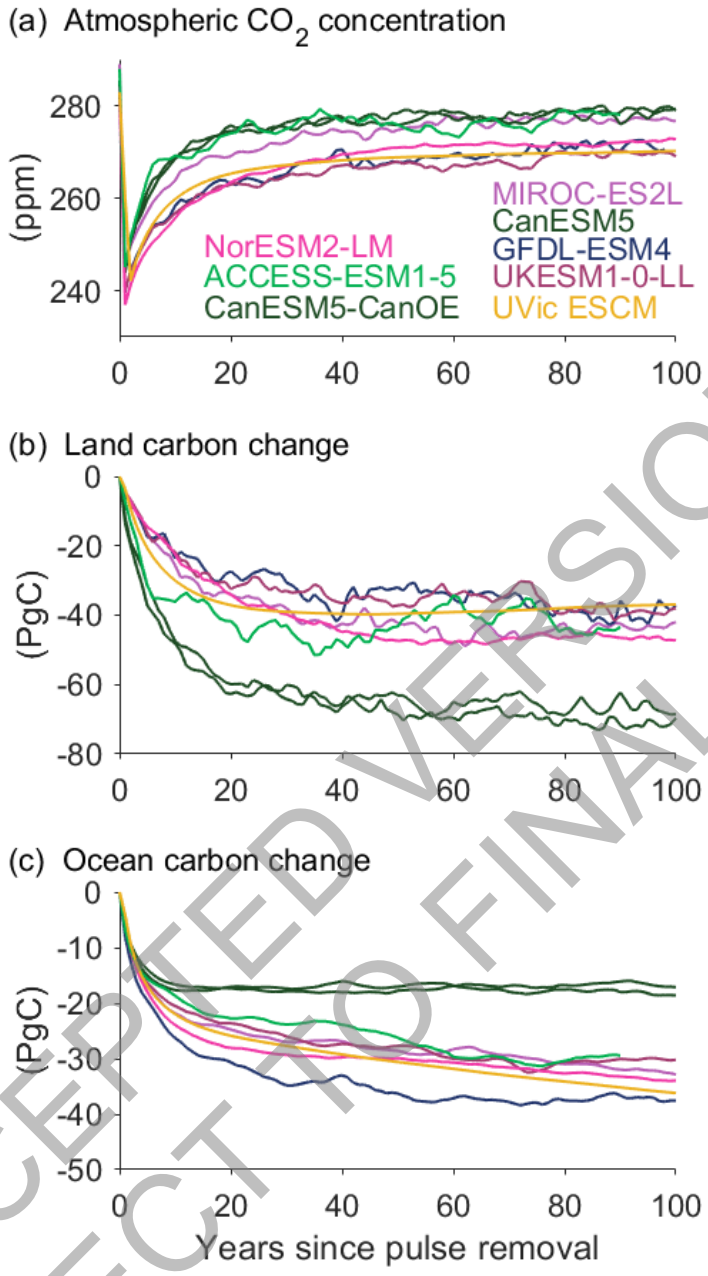


Figure 5.32: Carbon cycle response to instantaneous carbon dioxide (CO_2) removal from the atmosphere. (a) Atmospheric CO_2 concentration, (b) change in land carbon reservoir, (c) change in ocean carbon reservoir. Results are shown for simulations with seven CMIP6 Earth system models and the UVic ESCM model of intermediate complexity forced with 100 PgC instantaneously removed from the atmosphere. The 'pulse' removal is applied from a model state in equilibrium with a pre-industrial atmospheric CO_2 concentration (CDRMIP experiment CDR-pi-pulse; Keller et al., 2018b). Changes in land and ocean carbon reservoirs are calculated relative to a pre-industrial control simulation. Data for the UVic ESCM is from Zickfeld et al. (2021). Further details on data sources and processing are available in the chapter data table (Table 5.SM.6).

ACCEPTED VERSION SUBJECT TO FINAL EDITS

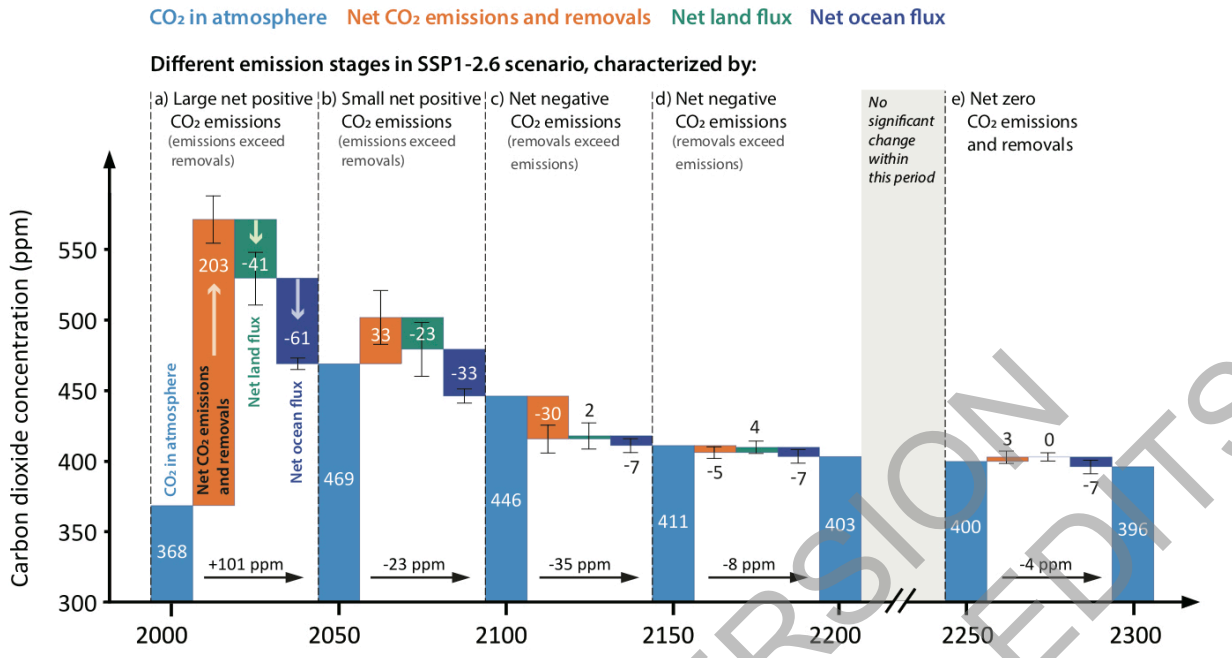


Figure 5.33: Carbon sink response in a scenario with net carbon dioxide (CO_2) removal from the atmosphere. Shown are CO_2 flux components from concentration-driven Earth system model simulations during different emission stages of SSP1–2.6 and its long-term extension. (a) Large net positive CO_2 emissions, (b) small net positive CO_2 emissions, (c) – (d) net negative CO_2 emissions, (e) net zero CO_2 emissions. Positive flux components act to raise the atmospheric CO_2 concentration, whereas negative components act to lower the CO_2 concentration. Net CO_2 emissions, land and ocean CO_2 fluxes represent the multi-model mean and standard deviation (error bar) of four ESMs (CanESM5, UKESM1, CESM2-WACCM, IPSL-CM6a-LR) and one EMIC (UVic ESCM; (Mengis et al., 2020)). Net CO_2 emissions are calculated from concentration-driven Earth system model simulations as the residual from the rate of increase in atmospheric CO_2 and land and ocean CO_2 fluxes. Fluxes are accumulated over each 50-year period and converted to concentration units (ppm). Further details on data sources and processing are available in the chapter data table (Table 5.SM.6).

ACCEPTED VERSION SUBJECT TO FINAL EDITS

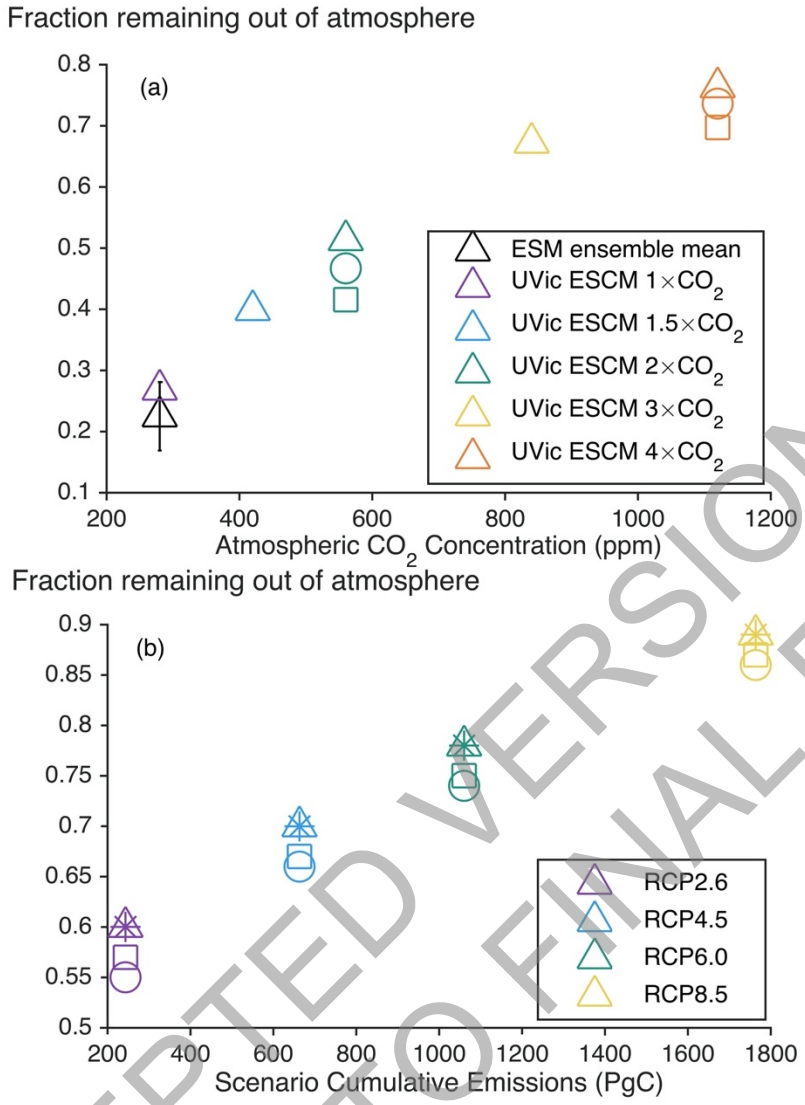


Figure 5.34: Removal effectiveness of carbon dioxide removal (CDR). (a) Fraction of CO_2 remaining out of the atmosphere for idealised model simulations with CDR applied instantly (pulse removals) from climate states in equilibrium with different atmospheric CO_2 concentration levels (1 to 4 times the pre-industrial atmospheric CO_2 concentration; shown on the horizontal axis). The fraction is calculated 100 years after pulse removal. The black triangle and error bar indicate the multi-model mean and standard deviation for the seven Earth system models shown in Figure 5.32 forced with a 100 PgC pulse removal. Other symbols illustrate results with the UVic ESCM model of intermediate complexity for different magnitudes of pulse removals (triangles: –100 PgC; circles: –500 PgC; squares: –1000 PgC). Data for the UVic ESCM is from (Zickfeld et al., 2021). (b) Perturbation airborne fraction (see text for definition) for model simulations where CDR is applied from four RCPs (shown on the horizontal axis in terms of their cumulative CO_2 emissions during 2020–2099). Symbols indicate results for four CDR scenarios, which differ in terms of the magnitude and rate of CDR (see Jones et al. (2016b) for details). Results are based on simulations with the Hadley Centre Simple Climate-Carbon Model and are shown for the year 2100. Data from Jones et al. (2016b). Further details on data sources and processing are available in the chapter data table (Table 5.SM.6).

ACCEPTED VERSION SUBJECT TO FINAL EDITS

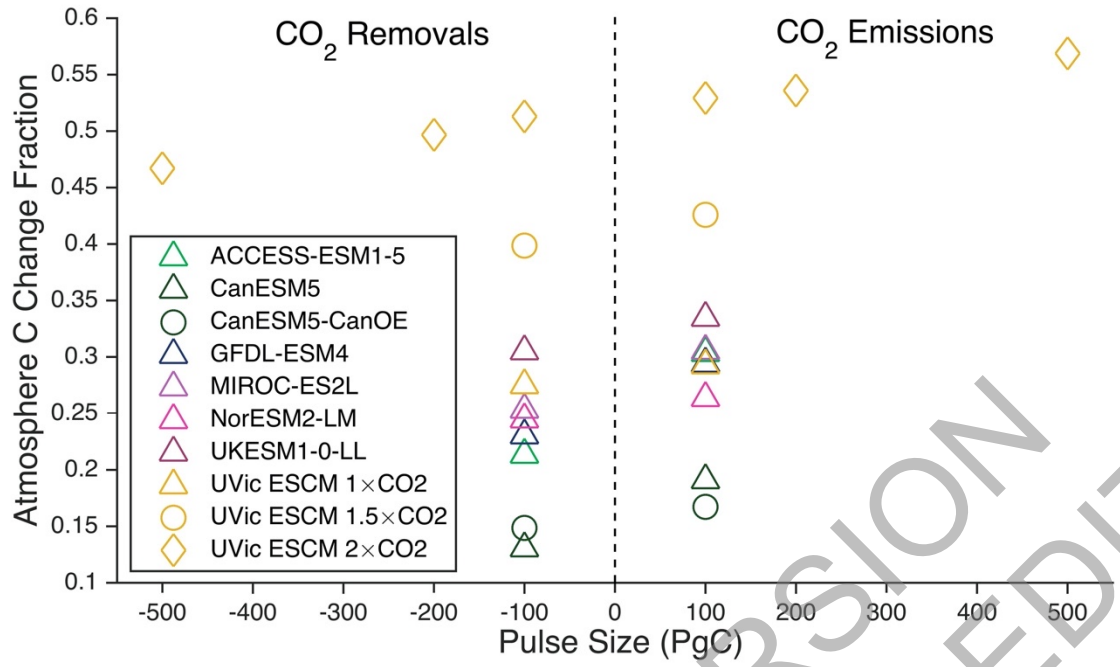


Figure 5.35: Asymmetry in the atmospheric carbon dioxide (CO_2) response to CO_2 emissions and removals. Shown are the fractions of total CO_2 emissions remaining in the atmosphere (right-hand side) and CO_2 removals remaining out of the atmosphere (left-hand side) 80–100 after a pulse emission/removal. Triangles and green circles denote results for seven Earth system models (ESMs) and the UVic ESCM model of intermediate complexity forced with ±100 PgC pulses applied from a pre-industrial state ($1\times CO_2$) (CDRMIP experiment CDR-pi-pulse; Keller et al. (2018b)). Yellow circles and diamonds indicate UVic ESCM results for CO_2 emissions/removals applied at 1.5 times ($1.5\times CO_2$) and 2 times ($2\times CO_2$) the pre-industrial CO_2 concentration, respectively. Pulses applied from a $2\times CO_2$ state span the magnitude ±100 PgC to ±500 PgC. UVic ESCM data is from (Zickfeld et al., 2021). Further details on data sources and processing are available in the chapter data table (Table 5.SM.6).

ACCEPTED VERSION SUBJECT TO FINAL EDITS

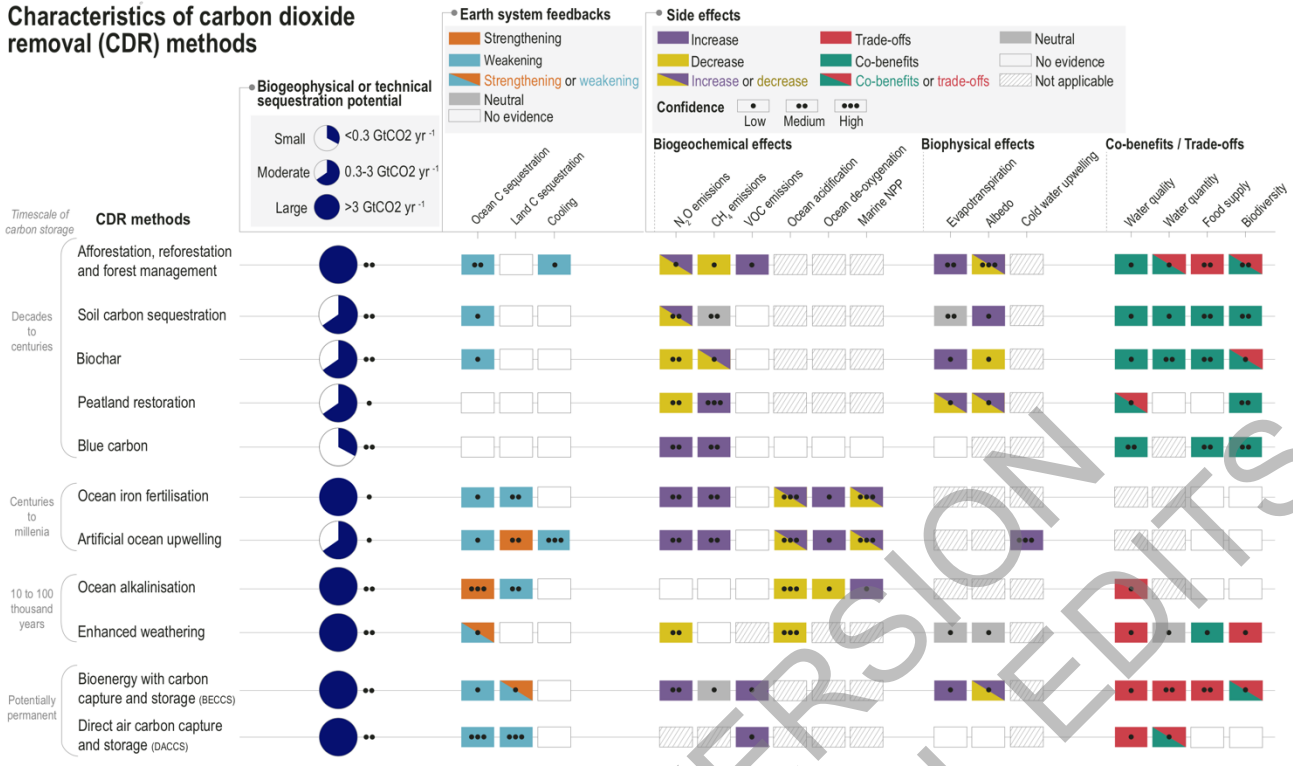


Figure 5.36: Characteristics of carbon dioxide removal (CDR) methods, ordered according to the time scale of carbon storage. The first column shows biogeophysical (for open-ocean methods) or technical (for all other methods) sequestration potentials (i.e. the sequestration potentials constrained by biological, geophysical, geochemical limits and thermodynamics and, for technical potentials, availability of technologies and practices; technical potentials for some methods also consider social or environmental factors if these represent strong barriers for deployment; see Glossary), classified into low (< 0.3 $GtCO_2$ yr^{-1}), moderate (0.3–3 $GtCO_2$ yr^{-1}) and large (>3 $GtCO_2$ yr^{-1}) (details underlying this classification are provided in Supplementary Materials Table 5.SM.5). The other columns show Earth system feedbacks that deployment of a given CDR method would have on carbon sequestration and climate, along with biogeochemical, biophysical, and other side effects of a given method. Earth system feedbacks do not include the direct effect of CO_2 sequestration on atmospheric CO_2, only secondary effects. For Earth system feedbacks, the colours indicate whether the feedbacks strengthen or weaken carbon sequestration and the climate cooling effect of a given CDR method. For biogeochemical and biophysical side effects the colours indicate whether the deployment of a CDR method increases or decreases the magnitude of the effect, whereas for co-benefits and trade-offs the colour indicates whether deployment of a CDR method results in beneficial (co-benefits) or adverse side-effects (trade-offs) for water quality and quantity, food production and biodiversity. The details and references underlying the Earth system feedback and side-effect assessment are provided in Supplementary Materials Table 5.SM.4. Further details on data sources and processing are available in the chapter data table (Table 5.SM.6).

ACCEPTED VERSION SUBJECT TO FINAL EDITS

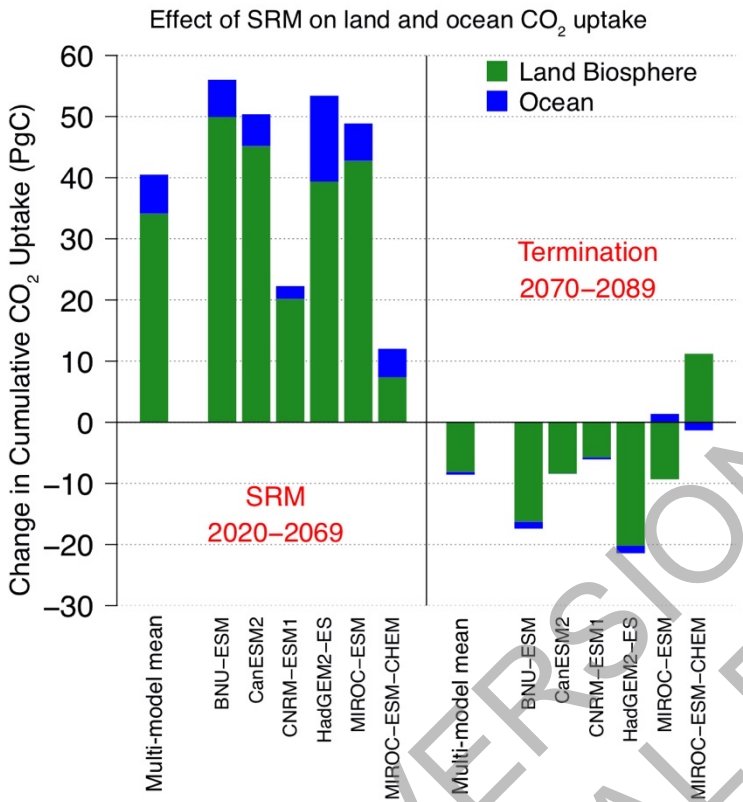
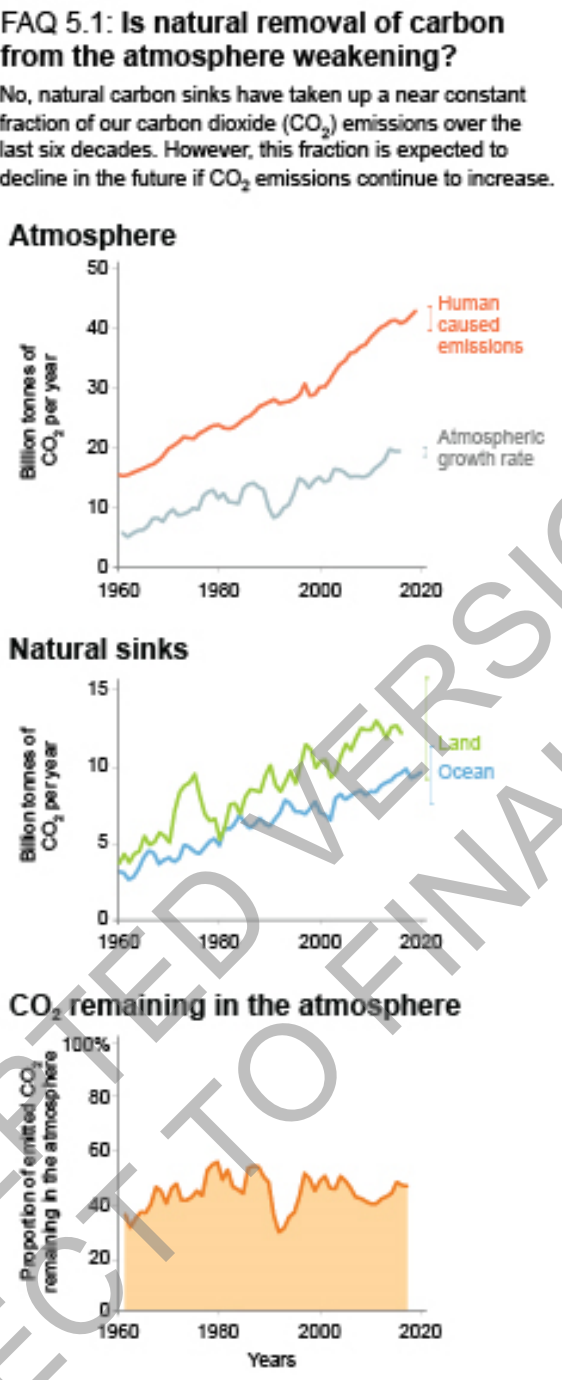


Figure 5.37: Cumulative carbon dioxide (CO_2) uptake by land and ocean carbon sinks in response to stratospheric sulfur dioxide (SO_2) injection. Results are shown for a scenario with 50-year (2020−2069) continuous stratospheric SO_2 injection at a rate of 5 Tg per year appplied to a RCP4.5 baseline scenario (GeoMIP experiment G4: Kravitz et al., (2011)), followed by termination in year 2070. Anomalies are shown relative to RCP4.5 for the multimodel ensemble mean and for each of six ESMs over the 50-year period of stratospheric SO_2 injection (left), and over 20 years after termination of SO_2 injection (right). Adapted from Plazzotta et al. (2019). Further details on data sources and processing are available in the chapter data table (Table 5.SM.6).

ACCEPTED VERSION
SUBJECT TO FINAL EDITS

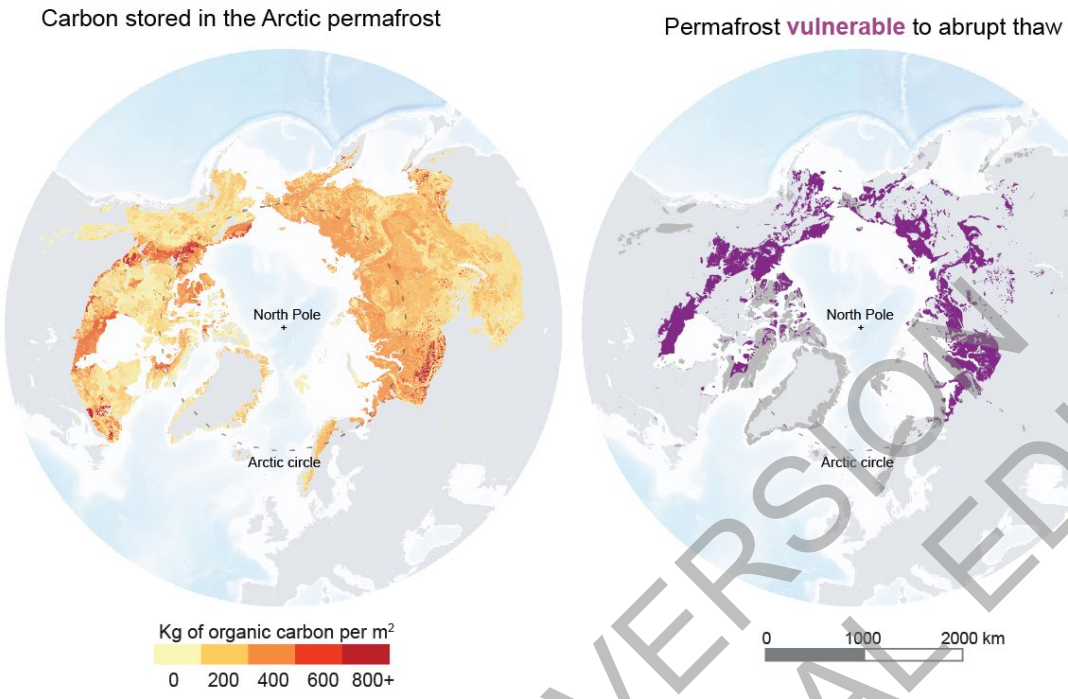


FAQ 5.1, Figure 1: Atmospheric CO2 and natural carbon sinks. (Top) Global emissions of CO2 from human activities and the growth rate of CO2 in the atmosphere, (middle) the net land and ocean CO2 removal ("natural sinks"), as well as (bottom) the fraction of CO2 emitted by human activities remaining in atmosphere from 1960 to 2019. Lines are the five years running mean, error-bars denote the uncertainty of the mean estimate. See Table 5.SM.6 for more information on the data underlying this figure.

ACCEPTED VERSION SUBJECT TO FINAL EDITS

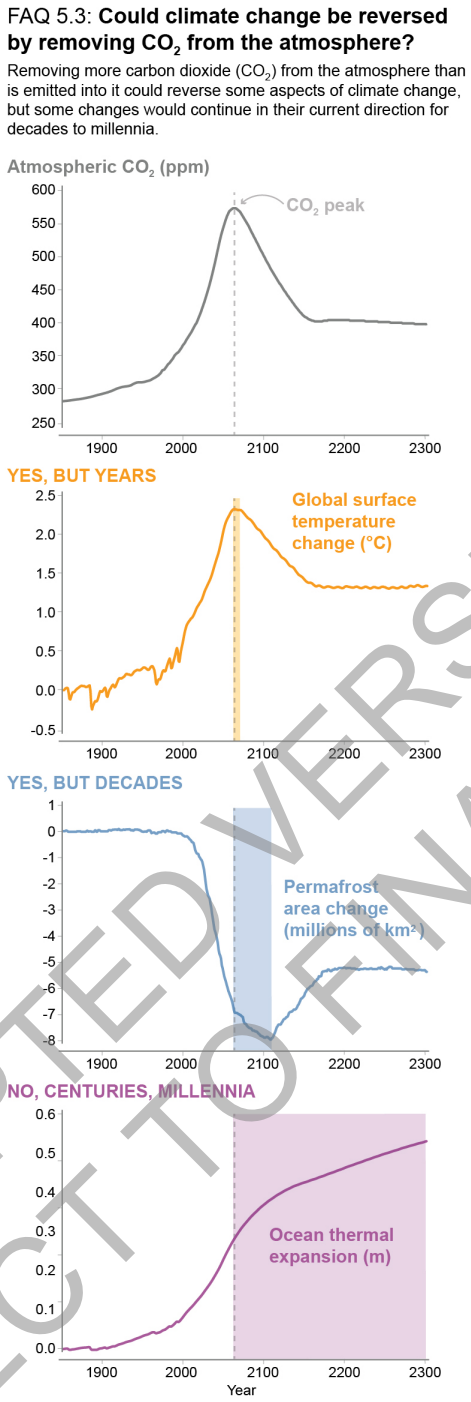
FAQ5.2: **Can thawing permafrost substantially increase global temperatures?**

The thawing of frozen ground in the Arcrtic will release carbon that will amplify global warming but this will not lead to runaway warming.



FAQ 5.2, Figure 1: The Arctic permafrost is a big pool of carbon that is sensitive to climate change. (left) Quantity of carbon stored in the permafrost, to 3 m depth (NCSCDv2 dataset) and (right) area of permafrost vulnerable to abrupt thaw (Circumpolar Thermokarst Landscapes dataset).

ACCEPTED VERSION SUBJECT TO FINAL EDITS



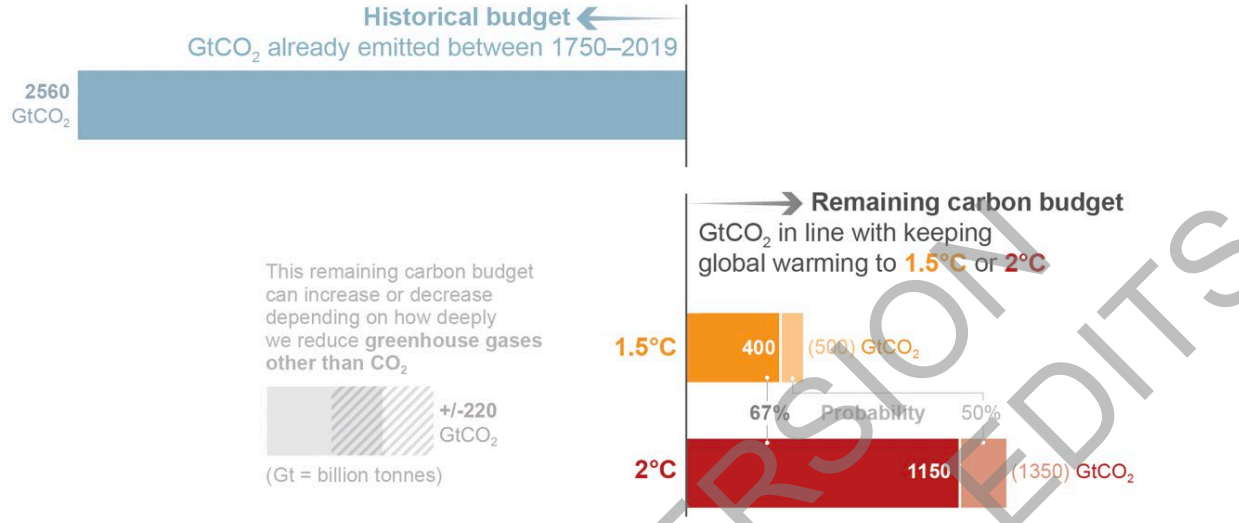
ACCEPTED VERSION SUBJECT TO FINAL EDITS

FAQ 5.3, Figure 1: Changes in aspects of climate change in response to a peak and decline in the atmospheric CO_2 concentration (top panel). The vertical grey dashed line indicates the time of peak CO_2 concentration in all panels. It is shown that the reversal of global surface warming lags the decrease in the atmospheric CO_2 concentration by a few years, the reversal of permafrost area decline lags the decrease in atmospheric CO_2 by decades, and ocean thermal expansion continues for several centuries. Note that the quantitative information in the figure (i.e., numbers on vertical axes) is not to be emphasized as it results from simulations with just one model and will be different for other models. The qualitative behaviour, however, can be expected to be largely model independent.

1

FAQ 5.4: **What are Carbon Budgets?**

The term carbon budget is used in several ways. Most often the term refers to the total net amount of carbon dioxide (CO_2) that can still be emitted by human activities while limiting global warming to a specified level.



2

3 **FAQ 5.4, Figure 1: Various types of carbon budgets.** Historical cumulative CO_2 emissions determine to a large
4 degree how much the world has warmed to date, while the remaining carbon budget
5 indicates how much CO_2 could still be emitted while keeping warming below specific
6 temperature thresholds. Several factors limit the precision with which the remaining
7 carbon budget can be estimated, and estimates therefore need to specify the probability
8 with which they aim at limiting warming to the intended target level (e.g., limiting
9 warming to 1.5°C with a 67% probability).

10

ACCEPTED VERSION SUBJECT TO FINAL EDITS

Chapter 5: Global Carbon and other Biogeochemical Cycles and Feedbacks – Supplementary Material

Coordinating Lead Authors:
Josep G. Canadell (Australia), Pedro M.S. Monteiro (South Africa)

Lead Authors:
Marcos H. Costa (Brazil), Leticia Cotrim da Cunha (Brazil), Peter M. Cox (United Kingdom), Alexey V. Eliseev (Russian Federation), Stephanie Henson (United Kingdom), Masao Ishii (Japan), Samuel Jaccard (Switzerland), Charles Koven (United States of America), Annalea Lohila (Finland), Prabir K. Patra (Japan/India), Shilong Piao (China), Joeri, Rogelj (United Kingdom/Belgium), Stephen Syampungani (Zambia), Sönke Zaehle (Germany), Kirsten Zickfeld (Canada/Germany)

Contributing Authors:
Georgii A. Alexandrov (Russian Federation), Govindasamy Bala (India/ United States of America), Laurent Bopp (France), Lena Boysen (Germany), Long Cao (China), Naveen Chandra (Japan/India), Philippe Ciais (France), Sergey N. Denisov (Russian Federation), Frank J. Dentener (EU, The Netherlands), Hervé Douville (France), Amanda Fay (United States of America), Piers Forster (United Kingdom), Baylor Fox-Kemper (United States of America), Pierre Friedlingstein (United Kingdom), Weiwei Fu (United States of America /China), Sabine Fuss (Germany), Véronique Garçon (France), Bettina Gier (Germany), Nathan P. Gillett (Canada), Luke Gregor (Switzerland/South Africa), Karsten Haustein (United Kingdom /Germany), Vanessa Haverd (Australia), Jian He (United States of America /China), Helene T. Hewitt (United Kingdom), Forrest M. Hoffman (United States of America), Tatiana Ilyina (Germany), Robert Jackson (United States of America), Christopher Jones (United Kingdom), David P. Keller (Germany/ United States of America), Lester Kwiatkowski (France/ United Kingdom), Robin D. Lamboll (United Kingdom/United States of America, United Kingdom), Xin Lan (United States of America/China), Charlotte Laufkötter (Switzerland/Germany), Corinne Le Quéré (United Kingdom), Andrew Lenton (Australia), Jared Lewis (Australia/New Zealand), Spencer Liddicoat (United Kingdom), Laura Lorenzoni (United States of America/Venezuela), Nicole Lovenduski (United States of America), Andrew H. MacDougall (Canada), Sabine Mathesius (Canada/Germany), Damon H. Matthews (Canada), Malte Meinshausen (Australia/Germany), Igor I. Mokhov (Russian Federation), Vaishali Naik (United States of America), Zebedee R. J. Nicholls (Australia), Intan Suci Nurhati (Indonesia), Michael O'Sullivan (United Kingdom), Glen Peters (Norway), Julia Pongratz (Germany), Benjamin Poulter (United States of America), Jean-Baptiste Sallée (France), Marielle Saunois (France), Edward A.G. Schuur (United States of America), Sonia I. Seneviratne (Switzerland), Ann Stavert (Australia), Parvadha Suntharalingam (United Kingdom/United States of America), Kaoru Tachiiri (Japan), Jens Terhaar (Switzerland/Germany), Rona Thompson (Norway, Luxembourg/New Zealand), Hanqin Tian (United States of America), Jocelyn Turnbull (New Zealand), Sergio M. Vicente-Serrano (Spain), Xuhui Wang (China), Rik Wanninkhof (United States of America), Phil Williamson (United Kingdom),

Review Editors:
Victor Brovkin (Germany/Russian Federation), Richard A. Feely (United States of America)

Chapter Scientist:
Alice D. Lebehot (South Africa/France)

ACCEPTED VERSION SUBJECT TO FINAL EDITS

This Supplementary Material should be cited as:
Josep G. Canadell, J. G., P. M. S. Monteiro, M. H. Costa, L. Cotrim da Cunha, P. M. Cox, A. V. Eliseev, S. Henson, M. Ishii, S. Jaccard, C. Koven, A. Lohila, P. K. Patra, S. Piao, J. Rogelj, S. Syampungani, S. Zaehle, K. Zickfeld, 2021, Global Carbon and other Biogeochemical Cycles and Feedbacks Supplementary Material. In: *Climate Change 2021: The Physical Science Basis. Contribution of Working Group I to the Sixth Assessment Report of the Intergovernmental Panel on Climate Change* [Masson-Delmotte, V., P. Zhai, A. Pirani, S. L. Connors, C. Péan, S. Berger, N. Caud, Y. Chen, L. Goldfarb, M. I. Gomis, M. Huang, K. Leitzell, E. Lonnoy, J.B.R. Matthews, T. K. Maycock, T. Waterfield, O. Yelekçi, R. Yu and B. Zhou (eds.)]. Available from https://ipcc.ch/static/ar6/wg1.

Date: August 2021

This document is subject to copy-edit, corrigenda and trickle backs.

ACCEPTED VERSION
SUBJECT TO FINAL EDITS

1 **Table of Contents**

2

3 5.SM.1 Assessment of recent advances in observational and modelling methodologies 3
4 5.SM.2 SeaFlux method: a 4 step methodological approach to address the first order inconsistencies
5 between the ocean six (6) CO_2 flux observational based products used in Chapter 5 (5.2.3.1) 3
6 5.SM.3 Biogeophysical sequestration potential of ocean-based CDR methods 7
7 5.SM.4 Data Table 20
8 References 39

9

10

ACCEPTED VERSION
SUBJECT TO FINAL EDITS

5.SM.1 Assessment of recent advances in observational and modelling methodologies

Since AR5 three major advances have had a decisive impact on the levels of confidence of the trends and the variability of both air-sea fluxes of CO_2 and its storage in the ocean interior. These are (i) the new observations and observational-based products for decadal variability in ocean uptake fluxes and ocean storage, (ii) the observational-based product changes in amplitude of the seasonal cycle of surface ocean pCO_2 (the partial pressure of CO_2 expressed in μatm) in response to changing ocean carbonate chemistry, and (iii) spatially-resolved pCO_2 seasonal climatologies for the global coastal ocean (Gruber et al., 2019a; (Rödenbeck et al., 2015; Landschützer et al., 2016, 2018); Laruelle et al., 2017). These advances were made possible by the simultaneous global coordination of observations and data quality control through the surface ocean CO_2 atlas (SOCAT) and Lamont-Doherty Earth observatory (LDEO) as well as the rapid adoption of a large variety of interpolation techniques for the surface layer and their inter-comparison to constrain uncertainties and biases (Rödenbeck et al., 2015; Bakker et al., 2016; Landschützer et al., 2016; McKinley et al., 2017; Gregor et al., 2019; Gruber et al., 2019b).

Advances in the multiple methods of interpolating surface ocean pCO_2 observations provide a *medium to high confidence* in the air-sea fluxes of CO_2 over most of the ocean (Rödenbeck et al., 2015; Landschützer et al., 2016; Gregor et al., 2019). However, there is *low confidence* in those fluxes for important regions such as the Southern Ocean, the Arctic, South Pacific as well as coastal oceans (Laruelle et al., 2017; Gregor et al., 2019; Gruber et al., 2019c); while these regions remain temporally and spatially under sampled the development and deployment of carbon and biogeochemically enabled Argo autonomous floats is starting to close those gaps (Williams et al., 2017; Gray et al., 2018; Claustre et al., 2020).

Similarly, for anthropogenic carbon storage in the ocean interior (i.e. below the mixed layer) the global ocean ship-based hydrographic investigations programme (GO-SHIP) coupled to the global ocean data analysis project for carbon (GLODAPv2) were central to supporting the advances in characterising changes to the storage in the ocean interior by generating a new consistent, quality-controlled, global dataset, allowing the decadal variability in ocean carbon storage to be quantified (Lauvset et al., 2016; Olsen et al., 2016; Clement and Gruber, 2018; Gruber et al., 2019b). There is *high confidence* that a significant advance since AR5 and SROCC is the improved characterization of the variability of the ocean CO_2 storage trends in space and time, which has notable decadal and regional scale variability (Tanhua et al., 2017; Gruber et al., 2019b) (SROCC Chapters 3 and 5).

Since it is also unequivocal that anthropogenic CO_2 taken up from the atmosphere into the ocean surface layer is further transported into the ocean interior through ocean ventilation processes including vertical mixing, diffusion, subduction and meridional overturning circulations (Sallée et al., 2012; Nakano et al., 2015; Bopp et al., 2015; Iudicone et al., 2016; Toyama et al., 2017), the trends as well as the spatial and temporal variability were assessed in an integrated way for both the air-sea flux and storage of anthropogenic CO_2.

5.SM.2 SeaFlux method: a 4 step methodological approach to address the first order inconsistencies between the ocean six (6) CO_2 flux observational based products used in Chapter 5 (5.2.3.1)

Contributors: Amanda Fay and Luke Gregor

Methods

The SeaFlux method is based on six published and widely used observation-based products of surface ocean partial pressure (of CO_2 (pCO_2) and spans years 1988–2018 (Gregor and Fay, 2021). These six include three neural network derived products (MPI-SOMFFN, CMEMS-FFNN, NIES-FNN), a mixed layer scheme product (JENA-MLS), a multiple linear regression (JMA-MLR), and a machine learning ensemble (CSIR-ML6) (Supplementary Materials Table 5.SM.1). These products are included as they have been regularly updated to extend their time period and incorporate additional data that comes with each annual release of the SOCAT database.

ACCEPTED VERSION SUBJECT TO FINAL EDITS

Surface pCO_2 observations play a key role in constraining the global ocean carbon sink. This is because variations in surface ocean pCO_2 is the driving force governing the exchange of CO_2 across the air-sea interface, which is commonly described through a bulk formula (Garbe et al., 2014; Wanninkhof, 2014):

$$\text{Flux} = k_w \cdot sol \cdot (pCO_2 - pCO_2^{atm}) \cdot (1 - ice) \quad (1)$$

where k_w is the gas transfer velocity, *sol* is the solubility of CO_2 in seawater, in units mol m^{-3} μatm^{-1}, pCO_2 is the partial pressure of surface ocean CO_2 in µatm, and pCO^{atm} in units of µatm represents the partial pressure of atmospheric CO_2 in the marine boundary layer. Finally, to account for the seasonal ice cover in high latitudes the fluxes are weighted by 1 minus the ice fraction (*ice*), *i.e.* the open ocean fraction.

All of these methods provide full three-dimensional fields (latitude, longitude, time) of the sea surface partial pressure of CO_2 (pCO_2) and the air-sea CO_2 flux. In their original form each product may utilise different choices for the inputs to Equation 1. In this work recompute the fluxes using the following inputs to the bulk parameterization approach Equation 1: k_w is the gas transfer velocity, *sol* is the solubility of CO_2 in seawater, in units mol m^{-3} μatm^{-1}, calculated using the formulation by Weiss, (1974), EN4 salinity (Good et al., 2013), Operational Sea Surface Temperature and Sea Ice Analysis (OSTIA) sea surface temperature (Good et al., 2020), and European Centre for Medium- Range Weather Forecasts (ECMWF) ERA5 sea level pressure (Hersbach et al., 2020); *ice* is the sea ice fraction from OSTIA (Good et al., 2020); pCO_2 is the partial pressure of oceanic CO_2 in µatm for each observation-based product after filling, and pCO_2^{atm} is the dry air mixing ratio of atmospheric CO_2 (xCO_2) from the ESRL surface marine boundary layer CO_2 product available at https://www.esrl.noaa.gov/gmd/ccgg/mbl/data.php (Dlugokencky and Tans, 2020) multiplied by ERA5 sea level pressure (Hersbach et al., 2020) at monthly resolution, and applying the water vapor correction according to Dickson et al. (2007).

Flux is defined positive upward, that is CO_2 release from the ocean into the atmosphere is positive, and uptake by the ocean is negative. In the following sections we discuss the three steps that have the greatest impact on the inconsistencies between unadjusted flux calculations in the six pCO_2 products and the approach that we utilise for the SeaFlux ensemble product.

Step 1: Area filling

Machine learning methods aim to maximise the utility of the existing in situ observations by extrapolation using various proxy variables for processes influencing changes in ocean pCO_2. Extrapolation with these independently observed variables is possible due to the nonlinear relationship between pCO_2 in the surface ocean and the proxies that drive these changes.

However, not all of the proxy variables have complete global ocean coverage for all months, so the resulting pCO_2 products are limited by the extent of the proxy variables. Additionally, in coastal regions there is the potential that different relationships of pCO_2 are expected than in the open ocean, thus limiting the extrapolations. In contrast, the mixed layer scheme (utilised by the JENA-MLS product) does not suffer from such missing areas but does not distinguish between coastal and open ocean. While the area extent of the available air-sea flux estimates varies between products, there are consistent patterns; nearly all products cover the open ocean, whereas larger differences exist in the coverage of coastal regions, shelf seas, marginal seas and the Arctic Ocean. To account for differing area coverage, past studies (Friedlingstein et al., 2019, 2020; Hauck et al., 2020) have adjusted simply by scaling based on the percent of the total ocean area covered by each observation-based product. This does not account for the fact that some areas have CO_2 flux densities that are higher or lower than the global average. Thus, the magnitude of the adjustment by area-scaling is likely an underestimate (McKinley et al., 2020). One specific example is the northern high latitudes where coverage by the six products varies substantially. Similarly, three products provide estimates in marginal seas such as the Mediterranean while the other three products have no reported pCO_2 values here. Shutler et al., (2016) report that subtle differences in regional definitions can cause differences of >10% in the calculated net fluxes.

ACCEPTED VERSION SUBJECT TO FINAL EDITS

To address the inconsistent spatial coverage in products we utilise a newly released open and coastal merged climatology product (MPI-ULB-SOMFFN; Landschützer et al., 2020b) that is a blend of the coastal ocean SOMFFN mapping method (Laruelle et al., 2017) and the open ocean equivalent (MPI-SOMFFN; Landschützer et al., 2020a), but which now includes missing coastal ocean regions, marginal seas and the full Arctic Ocean. For each observationally-based product, we fill missing grid cells with a scaled value based on this global-coverage climatology. The scaling accounts for year-to- year changes in pCO_2 in the missing areas (given that the extended MPI-ULB-SOMFFN product is a monthly climatology centred on year 2006) and is obtained as follows. To extend the open and coastal merged monthly climatology (MPI-ULB-SOMFFN) to 1988–2018, we calculate a global scaling factor based on the product-based ensemble mean pCO_2 for regions which are covered consistently by all six pCO_2 products. We first mask all pCO_2 products to a common sea mask before taking an ensemble mean (pCO_2^{ens}). Next, we divide this ensemble mean by the MPI-ULB-SOMFFN climatology (pCO_2^{clim}) at monthly 1° by 1° resolution (Equation 2). The monthly scaling factor ($sf\,pCO_2$) is calculated by taking the mean over the spatial dimensions.

The scaling factor calculation can be represented as:

$$sf_{pCO_2} = mean_{x,y}\left(\frac{pCO_2^{ens}}{pCO_2^{clim}}\right) \qquad (2)$$

where $sfpCO_2$ is the one-dimensional scaling factor (time dimension), pCO_2^{ens} is the ensemble mean of all pCO_2 products at three-dimension, monthly 1° by 1° resolution, pCO_2^{clim} is the MPI-ULB-SOMFFN climatology, also at three-dimension but limited to just one climatological year. The *x* and *y* indicate that we take the area-weighted average over longitude (*x*) and latitude (*y*) resulting in the monthly scaling value. If a product mean is exactly equal to the climatology mean, the scaling factor is 1. Value ranges from 0.91 to 1.06 over the 31-year time period. The one-dimensional scaling factor is then multiplied by the MPI-ULB-SOMFFN climatology for each spatial point resulting in a three-dimensional scaled filling map. These values are then used to fill in missing grid cells in each observation-based product. Globally, the adjustments are all less than 20% of the total flux, with the mean adjustment for the six products at 9%. In the Northern Hemisphere however, the filling process can drive adjustments of up to 35%. As expected, the observationally-based products with more complete spatial coverage tend to have smaller flux adjustments, however the impact on the final CO_2 flux depends on the ΔpCO_2 and wind speed of the areas being filled. The only product that does not change during this adjustment process is the JENA-MLS mixed layer scheme-based product (Rödenbeck et al., 2013) which is produced with full spatial coverage and therefore needs no spatial filling.

Our approach is not without its own assumptions and limitations. We rely on a single estimate of the missing pCO_2 in coastal ocean regions, marginal seas, and the full Arctic Ocean, given that this is the only publicly available product currently existing. Nevertheless, the fact that common missing areas along coastal regions and marginal seas are reconstructed using specific coastal observations provides a step forward from the linear-scaling approach currently used by the Global Carbon Budget (Friedlingstein et al., 2019, 2020). Further confidence is provided by previous research showing that climatological relevant signals, i.e. mean state and seasonality, are well reconstructed by the MPI-SOMFFN method.

Furthermore, our scaled filling methodology assumes that pCO_2 in the missing ocean regions is increasing at the same rate as the common area of open-ocean pCO_2 used to calculate the scaling factor. Research from coastal ocean regions and shelf seas reveal that, in spite of a large spatial heterogeneity, this is a reasonable first order approximation (Laruelle et al., 2017). While our approach has a constant scaling factor for the missing ocean areas regardless of latitude we acknowledge that this could be improved with increased understanding.

Step 2: Wind product selection

180 Historical wind speed observations (including measurements from satellites and moored buoys) are aggregated and extrapolated through modelling and data assimilation systems to create global wind reanalyses. These reanalyses are required to compute air-sea gas exchange. Air-sea flux is commonly parameterised as a function of the gradient of CO_2 between the ocean and the atmosphere with wind speed

ACCEPTED VERSION SUBJECT TO FINAL EDITS

modulating the rate of the gas exchange (Equation 1). Each of these wind reanalyses has strengths and weaknesses, specifically on regional and seasonal scales (Chaudhuri et al., 2014; Ramon et al., 2019) but all are considered reasonable options by the community (Roobaert et al., 2018). We use three wind reanalysis products for completeness: the Cross-Calibrated Multi-Platform v2 (CCMP2, (Atlas et al., 2011)), the Japanese 55-year Reanalysis (JRA-55, KOBAYASHI et al., 2015) and the European Centre for Medium-Range Weather Forecasts (ECMWF) ERA5 (Hersbach et al., 2020). The wind speed (U10) is calculated at the native resolution of each wind product from the u- and v-components of wind.

Step 3: Calculation of gas exchange coefficient

We employ the quadratic windspeed dependence of the gas transfer velocity (Wanninkhof, 1992) and calculate the piston velocity (*kw*) for each of the wind reanalysis products as:

$$k_W = a \cdot \langle U^2 \rangle \cdot \left(Sc/_{660}\right)^{-0.5} \quad (3)$$

where the units of k_W are in cm h^{-1}, *Sc* is the dimensionless Schmidt number, and $\langle U^2 \rangle$ denotes the second moment of average 10-m height winds (m s^{-1}). We choose the quadratic dependence of the gas transfer velocity as it is widely accepted and used in the literature (Wanninkhof, 1992). Observational and modelling studies have often suggested that different parametrizations could be more appropriate under specific conditions (Fairaill et al., 2000; Nightingale et al., 2000; McGillis et al., 2001; Krakauer et al., 2006); however, recent direct carbon dioxide flux measurements made in the high latitude Southern Ocean confirm that even in this high wind environment, a quadratic parameterization fits the observations best (Butterworth and Miller, 2016). Future updates of the SeaFlux product will include options for other parameterizations. We calculate the square of the wind speed at the native resolution of each wind product and then average it to 1° by 1° monthly resolution. The order of this calculation is important as information is lost when resampling data to lower resolutions because of the concavity of the quadratic function. For example, if the second moment were calculated from time-averaged wind speeds, it would result in an underestimate of the gas transfer velocity (Sarmiento and Gruber 2006; (Sweeney et al., 2007). The resulting second moment is equivalent to $\langle U^2 \rangle = U_{mean}^2 + U_{std}^2$ where U_{mean} and U_{std} are the temporal mean and standard deviation calculated from the native temporal resolution of U.

In addition to the choice of wind parameterization, large differences in flux can result due to the scaling coefficient of gas transfer (*a*) that is applied when calculating the global mean piston velocity. This constant originates from the gas exchange process studies (Krakauer et al., 2006; Sweeney et al., 2007; Müller et al., 2008; Naegler, 2009) utilise observations of radiocarbon data from the GEOSECS and WOCE/JGOFS expeditions (Key et al., 2004). The ^{14}C released from nuclear bomb testing (hence bomb-^{14}C) in the mid twentieth century has since been taken up by the ocean. The number of bomb-^{14}C atoms in the ocean, relative to the pre-bomb ^{14}C, can thus be used as a constraint on the long-term rate of exchange of carbon between the atmosphere and the ocean. A probability distribution of wind speed is used to optimise the coefficient of gas transfer based on these observed natural and bomb ^{14}C invasion rates. This coefficient must be individually calculated and is not consistent for each wind product. Further, the gas transfer velocity used by the different pCO_2 mapping products are not scaled to the same bomb-^{14}C estimate. The range of the different bomb-^{14}C estimates is within the range of the uncertainty from the associated studies (Naegler, 2009), but the choice would introduce inconsistency that is easily addressed here.

We scale the gas transfer velocity to a bomb-^{14}C flux estimate of 16.5 cm hr^{-1} as recommended by Naegler, (2009). The coefficient (*a*) is calculated for each wind product via a cost function which optimises the coefficient of gas transfer

$$a = k_W \cdot \langle U^2 \rangle^{-1} \cdot \left(Sc/_{660}\right)^{0.5} \cdot (1 - ice) \quad (4)$$

where parameters are as defined in Equation 3. The units of the coefficient a are (cm h^{-1}) (m s^{-1})$^{-2}$. Global winds from the wind speed products differ and therefore even with the same bomb-^{14}C observations the scaled coefficient (a) can have a 40% range (Wanninkhof, 2014). By determining the optimal a coefficient

ACCEPTED VERSION SUBJECT TO FINAL EDITS

for each of the reanalysis winds, uncertainty in the global fluxes can be decreased. Our scaled coefficients correspond well with the estimate of Wanninkhof, (2014) who uses the CCMP wind product to estimate a as 0.251. Differences in the coefficient will also result from the time period considered and definition of global area and ice fraction applied in the calculation.

This scaling of the gas exchange coefficient (a) for each wind product is an essential, and an inconsistently applied step, that has large implications for air-sea flux estimates. Without individual scaling, and instead utilising a set value for the gas transfer coefficient (a) regardless of wind product, our results show that calculated global fluxes could be as high as 9% different depending on which pCO_2 and wind reanalysis product considered (Roobaert et al., 2018).

Step 4: Further parameters for flux calculation

The remaining parameters of Equation 1 are the solubility of CO_2 in seawater (*sol*), the atmospheric partial pressure of CO_2 (pCO_2^{atm}), and the area weighting to account for sea ice cover. While the choices of products used for these parameters can also result in differences in flux estimates, the impacts are much smaller as compared with the parameters discussed above.

Atmospheric pCO_2 is calculated as the product of surface xCO_2 and sea level pressure corrected for the contribution of water vapor pressure. The choice of the sea level pressure product, or absence of the water vapor correction can have small, but not insignificant, impact on the calculated fluxes. Additionally, some products utilise the output of an atmospheric CO_2 inversion product (e.g. CarboScope, (Rödenbeck et al., 2013), CAMS CO_2 inversion) (Chevallier, 2013) which can introduce differences in the flux estimate outside of the sources related to a product's surface ocean pCO_2 mapping method. Importantly, we do not advocate that our estimate of pCO_2^{atm} is an improvement over other estimates thereof, rather we provide an estimate of pCO_2^{atm} that has few assumptions and leads to a methodologically consistent estimate of ΔpCO_2. We maintain the same philosophy in our estimates of solubility of CO_2 in seawater and sea-ice area weighting and therefore we do not elaborate on them here.

5.SM.3 Biogeophysical sequestration potential of ocean-based CDR methods

Ocean fertilisation (OF) aims to boost primary production and subsequently organic carbon export by seeding the ocean surface with nutrients, typically in iron-limited areas such as the Southern Ocean or North Pacific. Iron fertilisation experiments have been inconclusive on whether deep-sea carbon sequestration is enhanced (Boyd et al., 2007; Yoon et al., 2018), with only one observing an increase in the biological pump below 1000 m (Smetacek et al., 2012), suggesting that the effectiveness of ocean fertilisation is low (*medium confidence*). Model simulations (Oschlies et al., 2010; Keller et al., 2014) suggest that if ocean fertilisation is applied continuously in the Southern Ocean under high CO_2 emission scenarios, CO_2 sequestration rates are initially between 2 and 4 PgC yr^{-1}, but then decrease to 0.4 to 1 PgC yr^{-1} after the initial decade, with an 80-year cumulative carbon uptake of 73 to 90 PgC. Taking the sequestration rates from these model simulations to constitute an upper limit, we assess the maximum biogeophysical sequestration potential of iron fertilization to be 1 PgC yr^{-1} (*low confidence*). Increased productivity in the fertilised areas would result in decreased productivity in unfertilised regions (Oschlies et al., 2010b). The carbonate counter pump could also reduce iron fertilisation-induced carbon sequestration by 6–32% (Salter et al., 2014).

Artificial ocean upwelling (AOUpw) brings nutrient-rich water to the ocean surface to alleviate nutrient limitation of (near-) surface phytoplankton growth and thus boost primary production and subsequent ocean CO_2 uptake. For AOUpw to be effective at increasing ocean carbon storage, the increased primary production has to result in increased transfer of organic carbon into the deep ocean. AOUpw also returns previously-sequestered dissolved inorganic carbon to the surface ocean, thus increasing surface water pCO_2 and decreasing (or potentially negating) atmospheric CO_2 drawdown stimulated by the additional nutrient input. In model simulations (Oschlies, 2010; Keller et al., 2014) where AOUpw is applied continuously and at the largest feasible scales, atmospheric CO_2 removal is up to 4.3 PgC yr^{-1} during the first decade, and decreases afterwards to 0.9 to 1.5 PgC yr^{-1} (average), with an 80-year cumulative CO_2 removal of 80 to 140

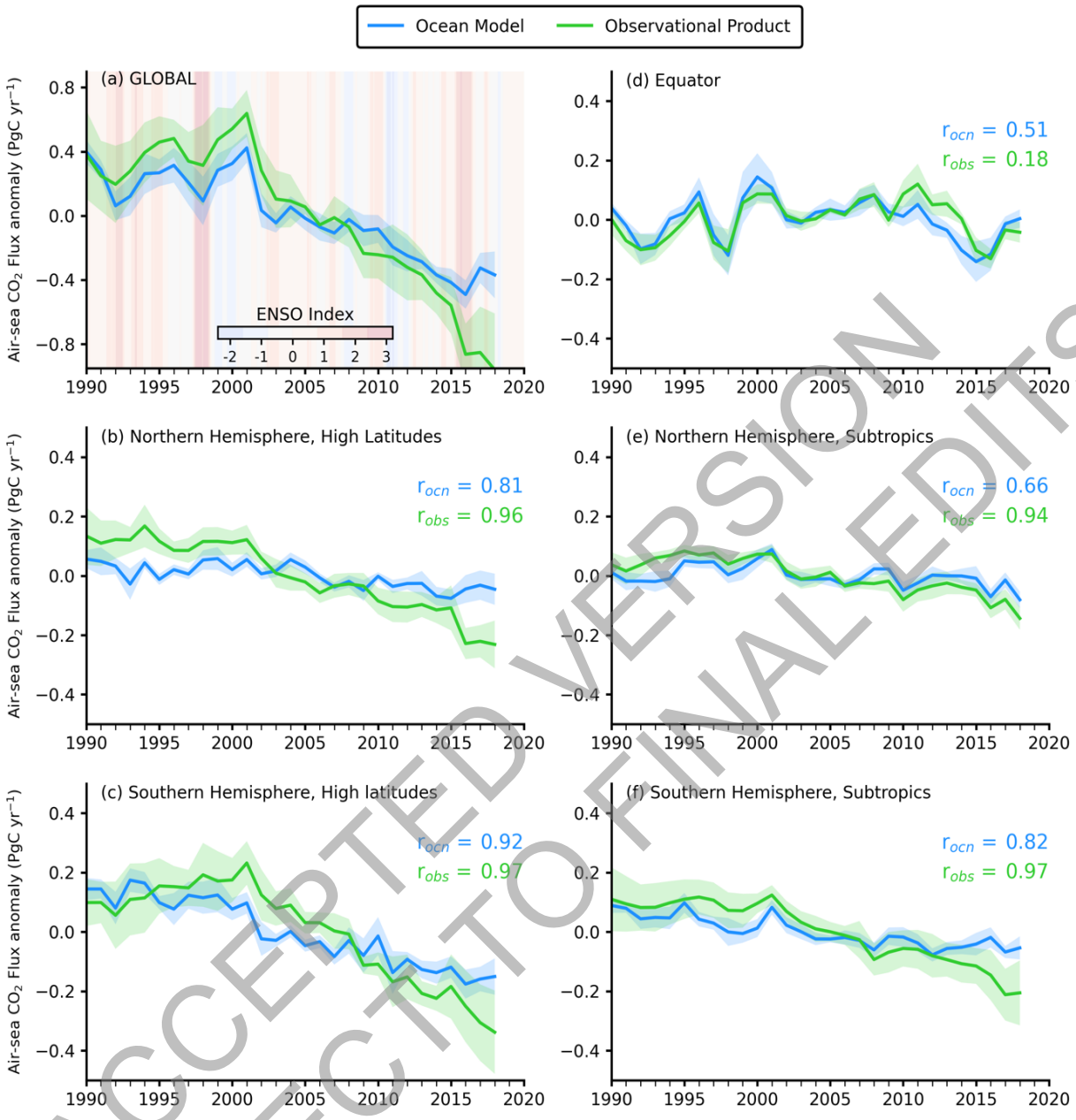
ACCEPTED VERSION SUBJECT TO FINAL EDITS

PgC. 50–80% of this removal results from cooling-induced enhancement of the terrestrial carbon sink (Keller et al., 2014). Removing terrestrial CO_2 removal from the total cumulative CO_2 removal yields cumulative ocean CO_2 removal of 16 to 70 PgC over 80 years, or 0.2 to 0.9 PgC yr^{-1} (*low confidence*).

Ocean alkalinisation, via the deposition of alkaline minerals (e.g. olivine) or their dissociation products (e.g. quicklime) at the ocean surface, can increase surface total alkalinity and thus increase CO_2 uptake and storage. Modelling studies suggest that massive additions of alkalinity (114 Pmol by the end of the century) in high CO_2 emission scenarios could increase ocean uptake by up to 27 PgC yr^{-1} by the end of the century (cumulative atmospheric CDR of up to 905 PgC), and permanently keep it there (100 ka residence time; Renforth & Henderson, 2017) even if additions were stopped (González et al., 2016; Feng et al., 2017; Sonntag et al., 2018). Taking the sequestration rates from these model simulations to constitute an upper limit, we assess the maximum biogeophysical sequestration potential of ocean alkalinisation to be 10 PgC yr^{-1} *(medium confidence*).

ACCEPTED VERSION
SUBJECT TO FINAL EDITS

[START FIGURE 5.SM.1 HERE]



ACCEPTED VERSION SUBJECT TO FINAL EDITS

Figure 5.SM.1: A comparative assessment of the contribution made by 5 regional ocean biomes (panels b-f) to the temporal variability characteristics of the global mean air-sea CO_2 flux anomalies for the period 1990–2018 using ensembles of global ocean biogeochemical models (GOBMs; 9 time series), observation-based products (6 time series) (Gregor et al., 2019; Supplementary Material 5.SM.2) (based on the SOCATv6 observational data (Bakker et al., 2020). Numbers in the top right of panels (b) to (f) indicate the correlation between the regional mean time series of the different models and the global mean time series (panel a). The 5 regional super-biomes (boundaries in Figure 5.9a) were derived by aggregation of the original 17 biomes of Fay and McKinley (2014).

[END FIGURE 5.SM.1 HERE]

[START TABLE 5.SM.1 HERE]

Table 5.SM.1: Decadal mean for the global ocean sink (S_{ocean}) for anthropogenic CO_2 (PgC yr^{-1}) from global ocean biogeochemistry models, pCO_2 observation-based data products, and atmospheric CO_2 inverse models. The uncertainty range for the mean of each approach is 90% confidence intervals. The range of ocean CO_2 uptake for each models or products represents interannual variability.

Methods	1990-1999		2000-2009		2009-2018		2010-2019		Citation
Global ocean biogeochemistry models	**-1.96**	**± 0.48**	**-2.14**	**± 0.54**	**-2.48**	**± 0.56**	**-2.51**	**± 0.56**	
CESM-ETH	-1.81	± 0.26	-1.98	± 0.37	-2.30	± 0.26	-2.35	± 0.29	Doney et al., 2009
CSIRO	-2.45	± 0.27	-2.74	± 0.40	-3.10	± 0.24	-3.14	± 0.23	Law et al., 2017
FESOM-1.4-REcoM2	-1.73	± 0.22	-1.80	± 0.34	-2.13	± 0.36	-2.18	± 0.30	Hauck et al., 2020
MPIOM-HAMOCC6	-1.67	± 0.19	-1.94	± 0.26	-2.23	± 0.26	-2.25	± 0.26	Paulsen et al., 2017
NEMO3.6-PISCESv2-gas (CNRM)	-1.90	± 0.27	-1.92	± 0.27	-2.27	± 0.22	-2.31	± 0.25	Berthet et al., 2019
NEMO-PlankTOM5	-2.14	± 0.25	-2.29	± 0.27	-2.67	± 0.23	-2.71	± 0.20	Buitenhuis et al., 2013
MICOM-HAMOCC (NorESM-OCv1.2)	-2.39	± 0.20	-2.60	± 0.24	-2.91	± 0.28	-2.95	± 0.24	Schwinger et al., 2016
MOM6-COBALT (Princeton)	-1.74	± 0.23	-1.97	± 0.43	-2.35	± 0.24	-2.39	± 0.20	Liao et al., 2020
NEMO-PISCES (IPSL)	-1.85	± 0.26	-2.05	± 0.32	-2.35	± 0.31	-2.35	± 0.31	Aumont et al., 2015
p*CO_2 observation-based data products	**-1.89**	**± 0.37**	**-2.06**	**± 0.20**	**-2.62**	**± 0.32**			
MPI_SOMFFN	-1.74	± 0.23	-1.93	± 0.38	-2.54	± 0.11			Landschützer et al., 2014
JENA_MLS	-1.96	± 0.23	-2.12	± 0.31	-2.52	± 0.19			Rödenbeck et al., 2014
LSCE_FFNN2	-1.77	± 0.05	-1.94	± 0.18	-2.46	± 0.28			Denvil-Sommer et al., 2019
CSIR_ML6	-1.74	± 0.08	-2.01	± 0.24	-2.57	± 0.20			Gregor et al., 2019
NIES_NN	-1.80	± 0.10	-2.14	± 0.26	-3.00	± 0.44			Zeng et al., 2014
JMA_MLR	-2.31	± 0.16	-2.24	± 0.17	-2.66	± 0.29			Iida et al., 2020
Atmospheric CO_2 inverse models*			**-2.13**	**± 0.47**	**-2.36**	**± 0.72**	**-2.40**	**± 0.74**	
MIROC4-lr2020			-1.97	± 0.27	-1.91	± 0.45	-1.90	± 0.45	Saeki and Patra, 2017
MIROC4-gcp2020			-1.90	± 0.30	-2.10	± 0.27	-2.18	± 0.31	Saeki and Patra, 2017
CAMS2020			-2.12	± 0.11	-2.54	± 0.23	-2.60	± 0.24	Chevallier et al., 2005
CTE2020			-2.54	± 0.46	-2.88	± 0.29	-2.91	± 0.26	van der Laan-Luijkx et al., 2017
Previous IPCC assessment reports									
TAR	-1.7	± 0.8							Prentice et al., 2001
AR4	-2.2	± 0.7							Denman et al., 2007
AR5	-2.2	± 0.7	-2.3	± 0.7					Ciais et al., 2013

ACCEPTED VERSION SUBJECT TO FINAL EDITS

***** Pre-industrial sea-to-air CO_2 flux associated with land-to-ocean carbon flux of +0.62 PgC year^{-1} (Jacobson et al., 2007; Resplandy et al., 2018) has been subtracted from original flux estimates.

[END TABLE 5.SM.1 HERE]

[START TABLE 5.SM.2 HERE]

Table 5.SM.2: Decadal means for the global ocean sink (S_{ocean}) for anthropogenic CO_2 (PgC yr^{-1}) from methods additional to those show in Table 5.SM.1. The uncertainty ranges presented here are 90% confidence intervals otherwise specified.

Methods	Citation	Period	Sea-to-air flux		Global ocean biogeochemistry models		pCO_2 observation-based data products	Atmospheric CO_2 inverse models
Ocean interior carbon inventory change	Gruber et al., 2019a	1994-2007	-2.23 ± 0.31		-2.05	± 0.50	-1.93 ± 0.27	-1.99 ± 0.20
Ocean interior CFC inventory change	McNeil et al., 2003	1980-1989	-1.6 ± 0.4	*	-1.71	± 0.48		
		1990-1999	-2.0 ± 0.4	*	-1.96	± 0.48	-1.89 ± 0.37	
Ocean interior $\Delta^{14}C$ change and GOBMs	Graven et al., 2012	1990-2007	-2.0 ± 0.3	*	-2.03	± 0.50	-1.94 ± 0.30	
Ocean inverse model	Gloor et al., 2003	1990	-1.80 ± 0.40	*	-1.79	± 0.54	-1.87 ± 0.60	
	Mikaloff Fletcher et al., 2006; Gruber et al., 2009	1995-2000	-2.2 ± 0.41		-1.94	± 0.47	-1.81 ± 0.34	-2.02 ± 0.04
	DeVries et al., 2017	1990-1999	-1.25 ± 0.53		-1.96	± 0.48	-1.89 ± 0.37	
		2000-2014	-2.41 ± 0.20		-2.24	± 0.55	-2.20 ± 0.19	-2.21 ± 0.35
Joint atmosphere-ocean inversion	Jacobson et al., 2007	1992-1996	-2.1 ± 0.2		-1.99	± 0.45	-1.88 ± 0.33	
Deconvolution atm. $\delta^{13}C$ and CO_2	Joos et al., 1999	1985-1995	-2.0 ± 1.3		-1.84	± 0.49		
Atmospheric O_2/N_2 ratio & $\delta^{13}C$	Battle et al., 2000	1991-1997	-2.0 ± 0.6	*	-1.97	± 0.47	-1.90 ± 0.35	
Air-sea $\delta^{13}C$ disequilibrium	Gruber and Keeling, 2001	1985-1995	-1.5 ± 0.9	*	-1.84	± 0.49		
Atmospheric O_2/N_2 ratio	Bender et al., 2005	1994-2002	-1.70 ± 0.50	*	-1.95	± 0.48	-1.81 ± 0.31	-2.01 ± 0.06
	Keeling and Manning, 2014	1990-2000	-1.94 ± 1.02		-1.95	± 0.48	-1.87 ± 0.36	
		1993-2003	-2.20 ± 0.94		-1.98	± 0.48	-1.85 ± 0.30	-1.96 ± 0.13
		2000-2010	-2.72 ± 0.99		-2.16	± 0.54	-2.09 ± 0.19	-2.12 ± 0.31
	Tohjima et al., 2019	1991-2011	-2.45 ± 0.96		-2.09	± 0.51	-2.02 ± 0.24	
		1999-2003	-2.20 ± 1.20		-1.99	± 0.52	-1.82 ± 0.33	-2.06 ± 0.11
		2004-2008	-1.97 ± 1.02		-2.22	± 0.57	-2.18 ± 0.19	-2.17 ± 0.45

ACCEPTED VERSION SUBJECT TO FINAL EDITS

2009-2013	-2.65 ± 1.44	-2.37 ± 0.56	-2.43 ± 0.24	-2.26 ± 0.48
2012-2016	-3.05 ± 1.49	-2.55 ± 0.57	-2.63 ± 0.33	-2.40 ± 0.39

[END TABLE 5.SM.2 HERE]

[START TABLE 5.SM.3 HERE]

Table 5.SM.3: Compiled information on the rates of pH change and aragonite saturation state (Ω_{arag}) change from various time series, ship reoccupations and moorings.

Station, region	Study period	pH change (per decade)	Uncer-tainty	Ω_{arag} change (per decade)	Uncer-tainty	Study type	Citation
North Atlantic							
Iceland Sea (winter) (68°N, 12.67°W)	1985-2008	-0.024	±0.002	-0.072	±0.007	Time series	Olafsson et al., 2009
	1985-2010	-0.014	±0.005	-0.018	±0.027		Bates et al., 2014
Irminger Sea (64.3°N, 28°W)	1983-2004	-0.026	±0.006	-0.08	±0.04	Time series	Bates et al., 2014
Subpolar Gyre	1981-2007	-0.022	±0.004			Merged ship occupations	Lauvset and Gruber, 2014
NA-SPSS	1991-2011	-0.02	±0.004			Merged ship occupations	Lauvset et al., 2015
NA-STSS	1991-2011	-0.018	±0.003			Merged ship occupations	Lauvset et al., 2015
BATS (32°N, 64°W)	1983-2010	-0.018	±0.002	-0.11	±0.01	Time series	Takahashi et al., 2014
	1983-2012	-0.017	±0.001	-0.095	±0.007		Bates et al., 2014
	1983-2020	-0.019	±0.001	-0.09	±0.01		Bates and Johnson, 2020
ESTOC (29.04°N, 15.50°W)	1995-2004	-0.017	±0.003			Time series	González-Dávila et al., 2010
	1995-2011	-0.018	±0.002	-0.115	±0.023		Bates et al., 2014
	1996-2010	-0.02	±0.004	-0.1	±0.02		Takahashi et al., 2014
NA-STPS	1991-2011	-0.011	±0.002			Merged ship occupations	Lauvset et al., 2015
CARIACO (10.50°N, 64.66°W)	1995-2012	-0.025	±0.004	-0.066	±0.028	Time series	Bates et al., 2014
Mediterranean							
Dyfamed (43.42°N, 7.87°E)	1995-2011	-0.03	±0.01			Time series	Yao et al., 2016

ACCEPTED VERSION SUBJECT TO FINAL EDITS

GIFT, Gibraltar	2012-2015	-0.044	±0.006			Time series	Flecha et al., 2019
Equatorial Atlantic							
A-EQU	1991-2011	-0.016	±0.003			Merged ship occupations	Lauvset et al., 2015
South Atlantic							
SA-STPS	1991-2011	-0.011	±0.005			Merged ship occupations	Lauvset et al., 2015
Atlantic Meridional Transect (50S-50N)	1995-2013	-0.013	±0.009			Merged ship occupations	Kitidis et al., 2017
North Pacific							
NP-SPSS	1983-2011 1991-2011	-0.003 0.013	±0.005 ±0.005			Merged ship occupations	Lauvset et al., 2015
Papa (50°N, 145°W)	2007-2014	-0.01	±0.005	0.1	0.04	Mooring	Sutton et al., 2017
K2 (47°N, 160°E) (Winter)	1999-2015	-0.025 -0.008	±0.01 ±0.004	-0.12	0.05	Time series	Wakita et al., 2017
NP-STSS	1991-2011	-0.01	±0.005			Merged ship occ	Lauvset et al., 2015
HOT (22.75°N, 158°W)	1988-2007 1988-2009 1988-2011	-0.019 -0.018 -0.016	±0.002 ±0.001 ±0.001	-0.08 -0.084	±0.01 ±0.011	Time series	Dore et al., 2009 Takahashi et al., 2014 Bates et al., 2014
WHOTS (23°N, 158°W)	2004-2013	-0.02	±0.003	-0.2	±0.02	Mooring	Sutton et al., 2017
KEO (32°N, 144°E)	2007-2014	-0.01	±0.005	-0.1	±0.02	Mooring	Sutton et al., 2017
137°E Line 33°N-34°N	1994-2008	-0.020	±0.007	-0.12	±0.05	Merged ship occupations	Ishii et al., 2011
137°E Line 26°N-30°N	1983-2017	-0.0193	±0.0008	-0.121	±0.005	Merged ship occupations	Ono et al., 2019
137°E Line 20°N-22°N		-0.0171	±0.0007	-0.113	±0.004		
137°E Line 11°N-18°N		-0.0136	±0.0007	-0.09	±0.005		
137°E Line 5°N-10°N		-0.0124	±0.0008	-0.081	±0.005		
NP-STPS	1983-2011 1991-2011	-0.016 -0.019	±0.002 ±0.002			Merged ship occupations	Lauvset et al., 2015
Equatorial Pacific							
WP-EQU	1983-2011 1991-2011	-0.01 -0.012	±0.002 ±0.002			Merged ship occupations	Lauvset et al., 2015
Warm Pool in 130°E-180°	1985-2016	-0.013	±0.001	-0.083	±0.007	Merged ship occupations	Ishii et al., 2020

ACCEPTED VERSION SUBJECT TO FINAL EDITS

EP-EQU		1983-2011 1991-2011	-0.023 -0.026	±0.003 ±0.002			Merged ship occupations	Lauvset et al., 2015
TAO	0°, 155°W 0°, 140°W 0°, 125°W	1997-2011 2004-2011 2004-2011	-0.022 -0.018 -0.026	±0.003 ±0.004 ±0.005			Moorings	Sutton et al., 2014
South Pacific								
Munida (45.833°S, 171.5°E)		1998-2011	-0.013	±0.003	-0.085	±0.026	Time series	Bates et al., 2014
SP-STPS		1983-2011 1991-2011	-0.019 -0.022	±0.002 ±0.003			Merged ship occupations	Lauvset et al., 2015
Stratus (20°S, 86°W)		2006-2015	-0.02	±0.003	-0.1	±0.03	Merged ship occupations	Sutton et al., 2017
Indian Ocean								
East Eq. Indian (90°E-95°E)		1962-2012	-0.016	±0.001	-0.095	±0.005	Merged ship occupations	Xue et al., 2014
IO-STPS		1987-2011 1991-2011	-0.024 -0.027	±0.004 ±0.005			Merged ship occupations	Lauvset et al., 2015
Southern Ocean								
140°E-160°E	North of STF SAZ PFZ PZ	1969-2003	-0.011 -0.011 -0.013 -0.020	±0.004 ±0.004 ±0.003 ±0.003			Merged ship occupations	Midorikawa et al., 2012
Drake Passage	SAZ PZ	2002-2012	-0.023 -0.015	±0.007 ±0.008	-0.09 -0.06	±0.05 ±0.05	Merged ship occupations	Takahashi et al., 2014
SO-STSS		1983-2011 1991-2011	-0.006 -0.004	±0.004 ±0.004			Merged ship occupations	Lauvset et al., 2015
SO-SPSS		1983-2011 1991-2011	-0.02 -0.021	±0.002 ±0.002			Merged ship occupations	Lauvset et al., 2015
PAL-LTER, west Antarctic Peninsula		1993-2012	0.02	±0.02	0.01	±0.1	Time series	Hauri et al., 2015
SO-ICE		1991-2011	-0.002	±0.004			Merged ship occupations	Lauvset et al., 2015

[END TABLE 5.SM.3 HERE]

ACCEPTED VERSION SUBJECT TO FINAL EDITS

[START TABLE 5.SM.4 HERE]

Table 5.SM.4: Explanation and references of earth system feedbacks, biogeochemical and biophysical impacts, and trade-offs and co-benefits of the carbon dioxide removal (CDR) methods as presented in Figure 5.37.

CDR Method	Earth system feedbacks on CO_2 sequestration potential and temperature	Biogeochemical and biophysical effects	Trade-offs and co-benefits related to water quantity and quality, food supply, biodiversity (BD)
Afforestation, reforestation and forest management	Weakens ocean C sequestration through decreased [CO_2] (Keller et al., 2018; Sonntag et al., 2018); decrease in albedo due to afforestation weakens the effect of CO_2 removal on surface air temperature (Sonntag et al., 2018); may shift the location of the Intertropical Convergence Zone and hence precipitation in the monsoon regions (Devaraju et al., 2015a)	Increased emissions of biogenic volatile organic compounds (BVOC) (Krause et al., 2017, SRCCL Sections 2.5.2.1, 2.6.1.2), decreased and increased surface temperature, in tropics and boreal region, respectively, due to changes in albedo, evapotranspiration and surface roughness (SRCCL Section 2.5.2.1; Fuss et al., 2018; Griscom et al., 2017; Pongratz et al., 2010; Jackson et al., 2008; Bright et al., 2015; Devaraju et al., 2015); decreased (Chen et al., 2019; Zhou et al., 2019; Deng et al., 2019) or increased (Benanti et al., 2014) N_2O emissions; increased CH_4 uptake (Chen et al., 2019; Nisbet et al., 2020)	Threatened water supply in dry areas regional climate, initial land cover, and scale of deployment (Farley et al., 2005; Mengis et al., 2019); improved water quality due to higher soil water retention and filtering capacity (Smith et al., 2019); affects food supply through competition for land (Smith et al., 2018b); decreased BD if not adopted wisely, increased BD if monocultures are replaced by native species (Smith et al., 2018; Williamson & Bodle, 2016); potentially negative impacts on food security due to land requirements (Smith et al., 2020).
Soil carbon sequestration	Weakens ocean C sequestration through decreased [CO_2] (Keller et al., 2018)	Decreased or increased N_2O emissions, depending on management strategy, fertilization, land-use, use of cover crops (Smith et al., 2016; Gu et al., 2017; Fuss et al., 2018b) Small or negligible impact on soil CH_4 flux (Smith et al., 2008); Albedo increase by no-till farming (Davin et al., 2014)	Reduced nutrient losses, increased biological activity (Fornara et al., 2011; Paustian et al., 2016; Tonitto et al., 2006; (Fuss et al., 2018b; Smith, 2016), improved soil water holding capacity (Paustian et al., 2019), positive impact on food security due to increased yield (Smith et al., 2020); no impact or increased BD, depending on method (Paustian et al., 2016; Smith et al., 2018b)
Biochar	Weakens ocean C sequestration through decreased [CO_2] (Keller et al., 2018)	Decreased N_2O emissions (Cayuela et al., 2014; Kammann, 2017), decreased CH_4 uptake in non-inundated soils (Jeffery et al., 2016); decreased CH_4 emissions in inundated soils such as rice fields (Jeffery et al., 2016; Yang et al., 2019; Wang et al., 2019; Huang et al., 2019), local warming related to darkened surface (Genesio et al., 2012; Zhang et al., 2018; Jia et al., 2019, SRCCL); VOC's	Improved soil fertility and productivity, reduced nutrient losses, enhanced fertiliser N use efficiency (Clough et al., 2013; Liu et al., 2017; Shen et al., 2016, Woolf et al., 2010); improved soil water holding capacity (Karhu et al., 2011; Verheijen et al., 2019; C. Liu et al., 2016; Bock et al., 2017; Fischer et al., 2019); no impact or increased BD (Smith et al., 2018); adverse impacts on BD due to land

ACCEPTED VERSION SUBJECT TO FINAL EDITS

		produced when preparing biochar can be toxic to plants and animals (Buss and Mašek, 2016)	requirements of feedstock (12.3.3, WGIII); benefits for food security due to improved yields (Smith et al., 2020)
Peatland restoration	no evidence	Enhanced CH_4 emission (Vanselow-Algan et al., 2015; Wilson et al., 2016; Renou-Wilson et al., 2019; Hemes et al., 2019; Holl et al., 2020); suppressed N_2O emissions (Wilson et al., 2016; Liu et al., 2020; Tiemeyer et al., 2020); increased (Koskinen et al., 2017) or decreased (Singh et al., 2019) leaching of nutrients; surface cooling due to higher evapotranspiration (Hemes et al., 2018; Helbig et al., 2020; Worrall et al., 2019)	Increased nutrient infiltration and retention to increase water quality (Daneshvar et al., 2017; Kluber et al., 2014; Lundin et al., 2017); protection from fire, increased BD (Meli et al., 2014; Smith et al., 2018b)
Restoration of vegetated coastal ecosystems (‘blue carbon’)	no evidence	Emission of CH_4 and N_2O, and biogenic calcification may partly offset benefits (Rosentreter et al., 2018; Keller, 2019; Kennedy et al., 2019)	Provision of very wide range of ecosystem services (biodiversity support recreation and tourism; fishery habitats; improved water quality, and flood and erosion protection) (Bindoff et al., 2019)
Ocean fertilisation	Carbonate counter pump could decrease C sequestration (Salter et al., 2014); Weakens terrestrial C storage (Keller et al., 2018)	Enhanced subsurface ocean acidification (Cao and Caldeira, 2010; Williamson et al., 2012a; Oschlies, 2009); Increased suboxic zone extent in fertilised areas; Shrinkage of suboxic zones outside fertilised areas (Oschlies, 2009; Keller et al., 2014); Increased production of N_2O and CH_4 (Jin and Gruber, 2003; Lampitt et al., 2008)	Perturbation to marine ecosystems via reorganisation of community structure, including possibly toxic algal blooms (Oschlies et al., 2010a; Williamson et al., 2012)
Artificial ocean upwelling	Cooling effect; increases terrestrial C storage (Oschlies et al., 2010b; Keller et al., 2014; Kwiatkowski et al., 2015); Returns previously sequestered C to ocean surface, decreasing or potentially negating CO_2 drawdown (Bauman et al., 2014; Kwiatkowski et al., 2015)	Enhanced subsurface ocean acidification (Cao and Caldeira, 2010; Oschlies et al., 2010c; Williamson et al., 2012a); Increased suboxic zone extent in fertilised areas (Keller et al., 2014; Feng et al., 2020); alters ocean temperature, salinity, circulation (Keller et al., 2014b); alters Earth’s heat and water budget (Keller et al., 2014); increased production of N_2O and CH_4 (Jin and Gruber, 2003; Lampitt et al., 2008; Williamson et al., 2012a)	Perturbation to marine ecosystems via reorganisation of community structure, including possibly toxic algal blooms (Oschlies et al., 2010a; Williamson et al., 2012)
Ocean alkalinisation	Increased ocean C storage through enhanced primary production through addition of iron and silicic acid from olivine dissolution (Köhler	Decreased ocean acidification (surface waters only); decreased de-oxygenation (González and Ilyina, 2016)	Release of toxic trace metals from some deposited minerals (Hartmann et al., 2013) Perturbation to marine ecosystems via

ACCEPTED VERSION SUBJECT TO FINAL EDITS

	et al., 2013; Hauck et al., 2016); Lowers terrestrial carbon storage (González and Ilyina, 2016; Sonntag et al., 2018)		reorganisation of community structure (González and Ilyina, 2016; González et al., 2018)
Enhanced weathering - terrestrial	Will initially reduce the ocean CO_2 sequestration, but after enough weathering products are transported into ocean to increase alkalinity, will increase ocean CO_2 sequestration (Keller et al., 2018)	Decreased N_2O emissions (Blanc-Betes et al; Kantola et al., 2017); reduced ocean acidification (Beerling et al., 2018)	Soil fertilisation and stimulated biological production (Hartmann et al., 2013); can liberate toxic trace metals into soil or water bodies (Keller et al., 2018); can decrease drinking water quality by causing freshwater salinization (Kaushal et al., 2018); increases alkalinity and pH of natural waters (Beerling et al., 2018); adverse impact on BD from mining (Smith et al., 2018)
BECCS	Weakens ocean C sequestration through decreased [CO_2] (Keller et al. 2018); Can weaken or strengthen land C sequestration depending on whether bioenergy crops replace marginal land or carbon-rich ecosystems (Don et al., 2012; Heck et al., 2016; Boysen et al., 2017a,b) (Harper et al., 2018)	Increased N_2O emissions related to land-use or if fertilized (Creutzig et al., 2015; Smith et al., 2016); local warming due to decreased albedo depending on the type of bioenergy crop (Smith et al., 2016); VOC emissions (Krause et al., 2017)	Threatened water supply (Farley et al., 2005; Smith et al., 2016, Cross-chapter box 5.1); threatened food supply through competition for land (Smith et al., 2019); soil nutrient deficiency; decreased BD depending on scale and previous land-use (Smith et al., 2018; Creutzig et al., 2019; Heck et al., 2018); see DACCS for storage-related side effects
Direct air carbon capture and storage (DACCS)	Weakens ocean and land C sequestration through decreased [CO_2] (Tokarska and Zickfeld, 2015; Jones et al., 2016; Zickfeld et al., 2021)	No evidence or not applicable	Perturbation of marine ecosystems through leakage of CO_2 from submarine storage (Molari et al., 2018); potentially decreased BD due to land and water requirements (Williamson, P., & Bodle, 2016); water use or production (Fuss et al., 2018; NASEM, 2019); VOC emissions in solid-sorbent systems (NASEM, 2019); Storage related: pollution of drinking water; seismic activity, leaks (Fuss et al., 2018)

[END TABLE 5.SM.4 HERE]

ACCEPTED VERSION SUBJECT TO FINAL EDITS

[START TABLE 5.SM.5 HERE]

Table 5.SM.5: Carbon dioxide removal (CDR) Potentials: Details underlying sequestration potentials classification shown in Figure 5.37.

CDR Method	Technical/ biogeophysical sequestration potential class*	Confidence level	Technical/ biogeophysical sequestration potential median and range**	Sequestration potential category	Data source
Afforestation, reforestation and forest management	Large	Medium (large evidence, medium agreement)	Afforestation, reforestation: 3.7 (0.5–10) $GtCO_2e\ yr^{-1}$; forest management 1.8 (1–2.1) $GtCO_2e\ yr^{-1}$	Technical potential; estimates also consider environmental and social factors	Median and range calculated based on technical and sustainable potentials from (Roe et al., 2019a)
Soil carbon sequestration	Moderate	Medium (large evidence, medium agreement)	Croplands: 1.6 (0.4–6.8) $GtCO_2e\ yr^{-1}$; Pasture lands: 0.7 (0.15–2.6) $GtCO_2e\ yr^{-1}$	Technical potential; estimates also consider environmental and social factors	Median and range calculated based on technical and sustainable potentials from (Roe et al., 2019b)
Biochar	Moderate	Medium (medium evidence, medium agreement)	1.1 (0.1–4.9) $GtCO_2e\ yr^{-1}$	Technical potential; estimates also consider environmental and social factors	Median and range calculated based on technical and sustainable potentials from (Roe et al., 2019b)
Peatland restoration	Moderate	Low (low evidence)	0.7 (0.6–0.8) $GtCO_2e\ yr^{-1}$	Technical potential; estimates also consider environmental and social factors	Median and range calculated based on technical and sustainable potentials from (Roe et al., 2019b)
Restoration of vegetated coastal ecosystems (‘blue carbon’)	Low	Low (low evidence)	0.2–0.7 $GtCO_2\ yr^{-1}$ (0.05–0.2 $GtC\ yr^{-1}$); 0.2–0.8 $GtCO_2\ yr^{-1}$	Technical potential; estimates also consider environmental and social factors	SROCC Ch 5 (IPCC, 2019); Range calculated based on technical and sustainable potentials from (Roe et al., 2019b)
Ocean iron fertilization	Large	Low (medium evidence, low agreement)	<3.7 $GtCO_2\ yr^{-1}$ (<1 $GtC\ yr^{-1}$); 3.7 $GtCO_2\ yr^{-1}$ (1 $GtC\ yr^{-1}$); 3.7 (0–44) $GtCO_2\ yr^{-1}$	Biogeophysical potential	Supplementary Material 5.SM3; (GESAMP, 2019) Table 4.4; median and range based on global studies considered in (Fuss et al., 2018)

ACCEPTED VERSION SUBJECT TO FINAL EDITS

Artificial ocean upwelling	Moderate	Low (low evidence)	0.7–3.3 $GtCO_2\ yr^{-1}$ (0.2–0.9 GtC yr^{-1}); <0.7 $GtCO_2\ yr^{-1}$ (< 0.2 GtC/yr)	Biogeophysical potential	Supplementary Material 5.SM3; (GESAMP, 2019) Table 4.4
Ocean alkalinization	Large	Medium (medium evidence, medium agreement)	<37 $GtCO_2\ yr^{-1}$ (<10 GtC yr^{-1}); 3.7 $GtCO_2\ yr^{-1}$ (1 GtC yr^{-1}); 1–99 $GtCO_2\ yr^{-1}$	Biogeophysical potential	Supplementary Material 5.SM3; (GESAMP, 2019) Table 4.4; full range (Fuss et al., 2018)
Enhanced weathering	Large	Medium (medium evidence, low agreement)	3.7 (1–95) $GtCO_2\ yr^{-1}$	Technical potential	Median and range based on global studies considered in (Fuss et al., 2018)
BECCS	Large	Medium (medium evidence, medium agreement)	4.6 (0.4–11.3) $GtCO_2\ yr^{-1}$	Technical potential; estimates also consider environmental and social factors	Median and range calculated based on technical and sustainable potentials from (Roe et al., 2019b)
DACCS	Large	Medium (low evidence, large agreement)	5–40 $GtCO_2\ yr^{-1}$	Technical potential	Full range (Fuss et al., 2018)

*Potentials classes: Low <0.3 $GtCO_2\ yr^{-1}$; Moderate 0.3–3 $GtCO_2\ yr^{-1}$; Large >3 $GtCO_2\ yr^{-1}$; classification based on *median* potentials estimate

**WGIII will present an update of these estimates based on more recent literature

[END TABLE 5.SM.5 HERE]

ACCEPTED VERSION SUBJECT TO FINAL EDITS

5.SM.4 Data Table

[START TABLE 5.SM.6 HERE]

Table 5.SM.6: Input Data Table. Input datasets and code used to create chapter figures

Figure number / Table number / Chapter section (for calculations)	Dataset / Code name	Type	Filename / Specificities	License type	Dataset / Code citation	Dataset / Code URL	Related publications / Software used	Notes [Can add info on data processing, e.g., reference period conversion]
Figure 5.3 (a)	CO2, 60M year BCE	proxy CO2 reconstructions based on marine and terrestrial archives		Published	Chapter 2, AR6		(Foster et al., 2017)	
	CO2, 800k year BCE	ice air-bubble measurement	Ch2_ice_core.xlsx	Published	Chapter 2, AR6		(Bereiter et al., 2015)	
	CO2, 1-1749 year CE	ice air-bubble measurement		Published	Chapter 2, AR6		(Rubino et al., 2019)	
	CO2, 1750-2019	air-bubble & ambient air measurement	LLGHG_history_AR6_v9_updated.xlsx		Chapter 2, AR6		(Meinshausen et al., 2017)	Updated from Meinshausen et al. (2017) by Jinho Anh
	CO2, 2020-2100	model output		Published				
Figure 5.3 (b)	CO2, 60M year BCE	proxy CO2 reconstructions based on marine and terrestrial archives			Chapter 5, AR6		Python 3.8, for growth rate calculation	
	CO2, 800k year BCE	ice air-bubble measurement			Chapter 5, AR6		Python 3.8, for growth rate calculation	
	CO2, 1-1749 year CE	ice air-bubble measurement			Chapter 5, AR6		Python 3.8, for growth rate calculation	
	CO2, 1750-2019	air-bubble & ambient air			Chapter 5, AR6		Python 3.8, for growth rate	

ACCEPTED VERSION SUBJECT TO FINAL EDITS

		measurement					calculation	
	CO2, 2020-2100	model output			Chapter 5, AR6		Python 3.8, for growth rate calculation	
Figure 5.4 (a)	CO2, 800k year BCE	ice air-bubble measurement	Ch2_ice_core.xlsx		Chapter 2, AR6		(Foster et al., 2017) (Bereiter et al., 2015)	
	CO2, 1-1749 year CE	ice air-bubble measurement			Chapter 2, AR6		(Rubino et al., 2019)	
	CO2, 1750-2019	air-bubble & ambient air measurement	LLGHG_history_AR6_v9_updated.xlsx		Chapter 2, AR6		(Meinshausen et al., 2017)	Updated from Meinshausen et al. (2017) by Jinho Anh
					Chapter 5, AR6		Python 3.8, for growth rate calculation	
Figure 5.4 (b)	CH4, 800k year BCE	ice air-bubble measurement	Ch2_ice_core.xlsx		Chapter 2, AR6		(Loulergue et al., 2008)	
	CH4, 1-1749 year CE	ice air-bubble measurement			Chapter 2, AR6		(Rubino et al., 2019)	
	CH4, 1750-2019	air-bubble & ambient air measurement	LLGHG_history_AR6_v9_updated.xlsx		Chapter 2, AR6		(Meinshausen et al., 2017)	Updated from Meinshausen et al. (2017) by Jinho Anh
					Chapter 5, AR6		Python 3.8, for growth rate calculation	
Figure 5.4 (c)	N2O, 800k year BCE	ice air-bubble measurement	Ch2_ice_core.xlsx		Chapter 2, AR6		(Schilt et al., 2010)	
	N2O, 1-1749 year CE	ice air-bubble measurement			Chapter 2, AR6		(Rubino et al., 2019)	
	N2O, 1750-2019	air-bubble & ambient air measurement	LLGHG_history_AR6_v9_updated.xlsx		Chapter 2, AR6		(Meinshausen et al., 2017)	Updated from Meinshausen et al. (2017) by Jinho Anh
					Chapter 5, AR6		Python 3.8, for growth rate calculation	
Figure 5.5 (a)	Annual global CO2 (Land-use)	model-based estimation		Published			(Friedlingstein et al., 2020)	

ACCEPTED VERSION SUBJECT TO FINAL EDITS

	emissions							
	Annual global CO2 (fossil-fuel) emissions	emission inventory		Published			(Friedlingstein et al., 2020)	
Figure 5.5 (b)	Annual global CO2 emissions from land-use change	DGVM range					(Friedlingstein et al., 2020)	
	Annual global CO2 emissions from land-use change	DGVM mean					(Friedlingstein et al., 2020)	
	Annual global CO2 emissions from land-use change	BLUE					(Hansis et al., 2015)	
	Annual global CO2 emissions from land-use change	OSCAR					(Gasser et al., 2020)	
	Annual global CO2 emissions from land-use change	Bookkeeping					(Houghton and Nassikas, 2017)	
Figure 5.6 (a)	CO2, Mauna Loa	ambient air	monthly_flask_co2_mlo.csv		SIO/UCSD	Scripps CO2 Program (http://scrippsco2.ucsd.edu)	(Keeling et al., 2001)	
	CO2, South Pole	ambient air	monthly_flask_co2_spo.csv		SIO/UCSD	Scripps CO2 Program (http://scrippsco2.ucsd.edu)	(Keeling et al., 2001)	
	CO2, Global	Global, marine background air	co2_mm_gl.txt		GMD/NOAA	NOAA	(Conway et al., 1994)	
	CO2, GOSAT	total column dry air mole fractions	whole-atmosphere-monthly-mean_co2_january_2021.txt		NIES	NIES, https://www.gosat.nies.go.jp/en/recent-global-co2.html	(Yoshida et al., 2013)	

ACCEPTED VERSION SUBJECT TO FINAL EDITS

Figure 5.6 (b)	CO2, Mauna Loa	ambient air			Chapter 5, AR6		(Nakazawa et al., 1997)	Python 3.8, Nakazawa et al. (1997) for growth rate calculation
	CO2, South Pole	ambient air			Chapter 5, AR6		(Nakazawa et al., 1997)	Python 3.8, Nakazawa et al. (1997) for growth rate calculation
	CO2, Global	Global, marine background air			Chapter 5, AR6		(Nakazawa et al., 1997)	Python 3.8, Nakazawa et al. (1997) for growth rate calculation
	CO2, GOSAT	total column dry air mole fractions			Chapter 5, AR6		(Nakazawa et al., 1997)	Python 3.8, Nakazawa et al. (1997) for growth rate calculation
Figure 5.6 (c)	d13C-CO2 Mauna Loa	ambient air	monthly_flask_c13_mlo		SIO/UCSD	Scripps CO2 Program (http://scrippsco2.ucsd.edu)	(Keeling et al., 2001)	
	d13C-CO2 South Pole	ambient air	monthly_flask_c13_spo		SIO/UCSD	Scripps CO2 Program (http://scrippsco2.ucsd.edu)	(Keeling et al., 2001)	
	D14C-CO2 Wellington	ambient air	BHD_14CO2_datasets_20210309.xlsx		GNS Science/NIWA		(Turnbull et al., 2017)	
Figure 5.6 (d)	O2/N2 Mauna Loa	ambient air	mloav.csv		SIO/UCSD	Scripps O2 Program (http://scrippso2.ucsd.edu)	(Keeling and Manning, 2014)	
	O2/N2 South Pole	ambient air	spoav.csv		SIO/UCSD	Scripps O2 Program (http://scrippso2.ucsd.edu)	(Keeling and Manning, 2014)	
Figure 5.7	Anthropogenic		Dataset2020_Glo		GCP-CO2		(Friedlingstein et	

ACCEPTED VERSION SUBJECT TO FINAL EDITS

	emission, Fossil Fuel		bal_Budget_v1.0.xlsx				al., 2020)	
	Anthropogenic emission, Landuse change		Dataset2020_Global_Budget_v1.0.xlsx		GCP-CO2		(Friedlingstein et al., 2020)	
	CO2, 1750-2019	ambient air measurement	LLGHG_history_AR6_v9_updated.xlsx		Chapter 2, AR6		(Meinshausen et al., 2017)	Updated from Meinshausen et al. (2017) by Jinho Anh
	ENSO Index		meiv2.data				(Wolter and Timlin, 2011)	
Figure 5.8 (b)	CESM-ETH	Global ocean biogeochemistry model output	Global_Carbon_Budget_2020v1.0.xlsx		(Friedlingstein et al., 2020)	https://www.icos-cp.eu/science-and-impact/global-carbon-budget/2020	(Doney et al., 2009b)	
	CSIRO	Global ocean biogeochemistry model output	Global_Carbon_Budget_2020v1.0.xlsx		(Friedlingstein et al., 2020)	https://www.icos-cp.eu/science-and-impact/global-carbon-budget/2020	(Law et al., 2017)	
	FESOM-1.4-REcoM2	Global ocean biogeochemistry model output	Global_Carbon_Budget_2020v1.0.xlsx		(Friedlingstein et al., 2020)	https://www.icos-cp.eu/science-and-impact/global-carbon-budget/2020	(Hauck et al., 2020)	
	MPIOM-HAMOCC6	Global ocean biogeochemistry model output	Global_Carbon_Budget_2020v1.0.xlsx		(Friedlingstein et al., 2020)	https://www.icos-cp.eu/science-and-impact/global-carbon-budget/2020	(Paulsen et al., 2017)	
	NEMO3.6-PISCESv2-gas (CNRM)	Global ocean biogeochemistry model output	Global_Carbon_Budget_2020v1.0.xlsx		(Friedlingstein et al., 2020)	https://www.icos-cp.eu/science-and-impact/global-	(Berthet et al., 2019)	

ACCEPTED VERSION SUBJECT TO FINAL EDITS

						carbon-budget/2020		
	NEMO-PlankTOM5	Global ocean biogeochemistry model output	Global_Carbon_Budget_2020v1.0.xlsx		(Friedlingstein et al., 2020)	https://www.icos-cp.eu/science-and-impact/global-carbon-budget/2020	(Buitenhuis et al., 2013)	
	MICOM-HAMOCC (NorESM-OCv1.2)	Global ocean biogeochemistry model output	Global_Carbon_Budget_2020v1.0.xlsx		(Friedlingstein et al., 2020)	https://www.icos-cp.eu/science-and-impact/global-carbon-budget/2020	(Schwinger et al., 2016)	
	MOM6-COBALT (Princeton)	Global ocean biogeochemistry model output	Global_Carbon_Budget_2020v1.0.xlsx		(Friedlingstein et al., 2020)	https://www.icos-cp.eu/science-and-impact/global-carbon-budget/2020	(Liao et al., 2020)	
	NEMO-PISCES (IPSL)	Global ocean biogeochemistry model output	Global_Carbon_Budget_2020v1.0.xlsx		(Friedlingstein et al., 2020)	https://www.icos-cp.eu/science-and-impact/global-carbon-budget/2020	(Aumont et al., 2015)	
	MPI_SOMFFN	Observation-based data product	ipcc_socom_flux_annual_20191206.csv				(Landschützer et al., 2014)	
	JENA_MLS	Observation-based data product	ipcc_socom_flux_annual_20191206.csv				(Rödenbeck et al., 2014)	
	LSCE_FFNN2	Observation-based data product	ipcc_socom_flux_annual_20191206.csv				(Denvil-Sommer et al., 2019)	
	CSIR_ML6	Observation-based data product	ipcc_socom_flux_annual_20191206.csv				(Gregor et al., 2019)	
	NIES_NN	Observation-based data	ipcc_socom_flux_annual_201912				(Zeng et al., 2014)	

ACCEPTED VERSION SUBJECT TO FINAL EDITS

		product	06.csv					
	JMA_MLR	Observation-based data product	ipcc_socom_flux_annual_20191206.csv				(Iida et al., 2020)	
	MIROC4-lr2020	Data of atmospheric CO2 inversion					(Saeki and Patra, 2017)	
	MIROC4-gcp2020	Data of atmospheric CO2 inversion					(Saeki and Patra, 2017)	
	CAMS2020	Data of atmospheric CO2 inversion					(Chevallier et al., 2005)	
	CTE2020	Data of atmospheric CO2 inversion					(van der Laan-Luijkx et al., 2017)	
	The oceanic sink for anthropogenic CO2 from 1994 to 2007 - the data (NCEI Accession 0186034)	Observation-based data product	inv_dcant_emlr_cstar_gruber_94-07_vs1.nc		(Gruber et al., 2019b)	https://www.ncei.noaa.gov/access/ocean-carbon-data-system/oceans/ndp_100/ndp100.html	(Gruber et al., 2019b)	
	Global decadal variability of the oceanic CO2 sink.	Data of global ocean inverse model			(DeVries et al., 2017)		(DeVries et al., 2017)	
	Global carbon budget based on trends in dAPO from three stations in the Scripps O2 network,	Data of global carbon budget from atmospheric O2/N2 and CO2 measurements			(Keeling and Manning, 2014)		(Keeling and Manning, 2014)	
	Global carbon budgets estimated from APO variations in the western	Data of global carbon budget from atmospheric O2/N2 and CO2			(Tohjima et al., 2019)		(Tohjima et al., 2019)	

ACCEPTED VERSION SUBJECT TO FINAL EDITS

	Pacific region	measurements						
Figure 5.9 (a)	pCO2 observation-based sea-air CO2 flux products	sea-air CO2 exchange	FCO2DatProd_mean.nc		Fay and Gregor sysnthesis	sea-air CO2 flux synthesis	(Landschützer et al., 2014; Rödenbeck et al., 2014; Zeng et al., 2014; Bakker et al., 2016; Denvil-Sommer et al., 2019; Gregor et al., 2019; Iida et al., 2020)	
Figure 5.9 (b)	Anthropogenic CO2 inventory	Ocean CO2	inv_dcant_emlr_cstar_gruber_94-07_vs1.nc				(Gruber et al., 2019b)	
Figure 5.10 (a)	Global net land CO2 sink	Data derived from global carbon budget	Global_Carbon_Budget_2020v1.0.xlsx		(Friedlingstein et al., 2020)		(Friedlingstein et al., 2020)	
	CarbonTracker-Europe	atmospheric CO2 inversion			(van der Laan-Luijkx et al., 2017)		(van der Laan-Luijkx et al., 2017)	
	Jena CarboScope	atmospheric CO2 inversion			(Rödenbeck et al., 2018)		(Rödenbeck et al., 2018)	
	Copernicus Atmosphere Monitoring Service (CAMS)	atmospheric CO2 inversion			(Chevallier et al., 2005)		(Chevallier et al., 2005)	
	MIROC4-ACTM	atmospheric CO2 inversion			(Patra et al., 2018)		(Patra et al., 2018)	
Figure 5.10 (b)	AVHRR NDVI	satellite data			(Tucker et al., 2005)		(Tucker et al., 2005)	
	MODIS NDVI	satellite data			Didan et al., 2015		Didan, K.. MOD13C2 MODIS/Terra Vegetation Indices Monthly L3 Global 0.05Deg CMG V006. 2015, distributed by	10.5067/MODIS/MOD13C2.006

ACCEPTED VERSION SUBJECT TO FINAL EDITS

							NASA EOSDIS Land Processes DAAC	
Figure 5.10 (c)	NIRv	satellite data			(Badgley et al., 2017)		(Badgley et al., 2017)	
	CSIF	satellite data			(Zhang et al., 2018b)		(Zhang et al., 2018b)	
Figure 5.10 (d)	WEC GPP	data-driven GPP product			(Cheng et al., 2017)		(Cheng et al., 2017)	
	MODIS GPP	satellite-based GPP product			Running et al., 2019		Running, S., M. Zhao. MOD17A3HGF MODIS/Terra Net Primary Production Gap-Filled Yearly L4 Global 500 m SIN Grid V006. 2019, distributed by NASA EOSDIS Land Processes DAAC	10.5067/MODIS/MOD17A3HGF.006
Figure 5.11	CarbonTracker-Europe	atmospheric CO2 inversion			van der Laan-Luijkx et al., 2017		(van der Laan-Luijkx et al., 2017)	
	Jena CarboScope	atmospheric CO2 inversion			Rödenbeck et al., 2018		(Rödenbeck et al., 2018)	
	Copernicus Atmosphere Monitoring Service (CAMS)	atmospheric CO2 inversion			Chevallier et al., 2005		(Chevallier et al., 2005)	
	MIROC4-ACTM	atmospheric CO2 inversion			Patra et al., 2018		(Patra et al., 2018)	
	Nino 3.4 index	sea surface temperature reanalysis			(Rayner, 2003)		(Rayner, 2003)	
	CRU	gridded temperature			(Harris et al., 2014)		(Harris et al., 2014)	

ACCEPTED VERSION SUBJECT TO FINAL EDITS

		observation						
Figure 5.13 (a)	CH4, Global	NOAA: Global			NOAA		(Dlugokencky et al., 2003)	
	CH4, Global	AGAGE: Global			AGAGE		(Prinn et al., 2018)	
	XCH4, GOSAT	NIES: GOSAT; total column dry air mole fractions	whole-atmosphere-monthly-mean_ch4_january_2021.txt		NIES	NIES, https://www.gosat.nies.go.jp/en/recent-global-ch4.html	(Yoshida et al., 2013)	
	CH4, CMO-THD	PDX: CMO-THD			Portland State University	PDX	(Rice et al., 2016)	
	CH4, CGO	AGAGE: CGO					(Prinn et al., 2018)	
Figure 5.13 (b)	CH4, Global CH4, Global XCH4, GOSAT CH4, CMO-THD CH4, CGO				Chapter 5, AR6		Python 3.8, (Nakazawa et al., 1997) for growth rate calculation	
Figure 5.13 (c)	d13C-CH4, NOAA				NOAA	ftp://aftp.cmdl.noaa.gov/data/trace_gases/ch4c13/flask/	White, J.W.C., B.H. Vaughn, and S.E. Michel (2018), University of Colorado, Institute of Arctic and Alpine Research (INSTAAR), Stable Isotopic Composition of Atmospheric Methane (13C) from the NOAA ESRL Carbon	

ACCEPTED VERSION SUBJECT TO FINAL EDITS

							Cycle Cooperative Global Air Sampling Network, 1998-2017, Version: 2018-09-24.	
	d13C-CH4, PDX	PDX: CMO-THD			Portland State University	PDX	(Rice et al., 2016)	
Cross-Chapter Box 5.1 Figure 1	CH4, sources/sinks	GCP-CH4			GCP-CH4		(Kirschke et al., 2013)	
	CH4, sources/sinks	GCP-CH4	WG1 AR6, Table 5.2		GCP-CH4		(Saunois et al., 2020)	
	CH4, concentration	NOAA: Global			NOAA		(Dlugokencky et al., 2003)	
Cross-Chapter Box 5.1 Figure 2	LMDz	CH4 inversion			GCP-CH4		(Bousquet et al., 2006)	
	TM5-4DVAR	CH4 inversion			GCP-CH4		(Bergamaschi et al., 2013)	
	CTE-CH4	CH4 inversion			GCP-CH4		(Tsuruta et al., 2017)	
	MIROC4-ACTM	CH4 inversion			GCP-CH4		(Chandra et al., 2021)	
	LMDzPyVAR	CH4 inversion			GCP-CH4		(Yin et al., 2015)	
	NICAM-TM	CH4 inversion			GCP-CH4		(Niwa et al., 2017)	
	NIES-TM-Flexpart	CH4 inversion			GCP-CH4		(Wang et al., 2019a)	
	NIES-TM-GELCA	CH4 inversion			GCP-CH4		(Ishizawa et al., 2016)	
	TOMCAT	CH4 inversion			GCP-CH4		(McNorton et al., 2018)	
	GCP-WETLAND mean	Land ecosystem model			GCP-CH4		(Saunois et al., 2020)	
Figure 5.15 (a)	NOAA atmospheric N2O network	input dataset	n2o_gbl_mean_grate_noaa.txt			https://www.esrl.noaa.gov/gmd/dv/data/	Elkins, J. W., Dlugokencky, E., Hall, B., Dutton,	https://www.esrl.noaa.gov/gmd/hats/combined/N2

ACCEPTED VERSION SUBJECT TO FINAL EDITS

	dataset						G., Nance, D., and Mondeel, D. J. (2018). Combined Nitrous Oxide data from the NOAA/ESRL Global Monitoring Division. Earth Syst. Res. Lab. (ESRL), Natl. Ocean. Atmos. Adm. Available at: https://www.esrl.noaa.gov/gmd/hats/combined/N2O.html [Accessed January 24, 2019].	O.html
	AGAGE atmospheric N2O network dataset	input dataset	n2o_gbl_mean_grate_agage.txt			https://agage2.eas.gatech.edu/data_archive/agage/	(Prinn et al., 2018)	
	CSIRO atmospheric N2O network dataset	input dataset	n2o_gbl_mean_grate_csiro.txt			https://gaw.kishou.go.jp/	(Francey et al., 2003) Available at: http://hdl.handle.net/102.100.100/194315?index=1.	
	Archived air sampes from Cape Grim	input dataset	N2O_isotope_CGAA_Park_2012.csv				(Park et al., 2012)	
	firn air data set Law Dome	input dataset	N2O_isotope_LD_Park_2012.csv				(Park et al., 2012)	
	firn air data set	input dataset	N2O_isotope_N			https://ads.nipr.a	(Ishijima et al.,	

ACCEPTED VERSION SUBJECT TO FINAL EDITS

	NGRIP		GRIP_Ishijima_2007.csv			c.jp/data/search/list/1	2007)	
	firn air data set H72	input dataset	N2O_isotope_H72_Ishijima_2007.csv			https://ads.nipr.ac.jp/data/search/list/1	(Ishijima et al., 2007)	
	firn ice data set Greenland	input dataset	N2O_isotope_BRK_Prokopiou.csv				(Prokopiou et al., 2017)	
	firn ice data set Greenland	input dataset	N2O_isotope_DC_Prokopiou.csv				(Prokopiou et al., 2017)	
	firn ice data set Greenland	input dataset	N2O_isotope_DML_Prokopiou.csv				(Prokopiou et al., 2017)	
	firn ice data set Greenland	input dataset	N2O_isotope_NGR_SB_Prokopiou.csv				(Prokopiou et al., 2017)	
	firn ice data set Greenland	input dataset	N2O_isotope_NEEM_09_Prokopiou.csv				(Prokopiou et al., 2017)	
	firn ice data set Greenland	input dataset	N2O_isotope_NEEM_EU_Prokopiou.csv				(Prokopiou et al., 2017)	
	Multivariate Enso Index	input dataset	noaa_mei_index_1979_2020.txt			https://psl.noaa.gov/enso/mei	(Wolter and Timlin, 1998)	
Figure 5.15 (b)	Archived air sampes from Cape Grim	input dataset	N2O_isotope_CGAA_Park_2012.csv				(Park et al., 2012)	
	firn air data set Law Dome	input dataset	N2O_isotope_LD_Park_2012.csv				(Park et al., 2012)	
	firn air data set NGRIP	input dataset	N2O_isotope_NGRIP_Ishijima_2007.csv				(Ishijima et al., 2007)	
	firn air data set H72	input dataset	N2O_isotope_H72_Ishijima_2007.csv				(Ishijima et al., 2007)	
	firn ice data set Greenland	input dataset	N2O_isotope_BRK_Prokopiou.c				(Prokopiou et al., 2017)	

ACCEPTED VERSION SUBJECT TO FINAL EDITS

			sv					
	firn ice data set Greenland	input dataset	N2O_isotope_DC_Prokopiou.csv				(Prokopiou et al., 2017)	
	firn ice data set Greenland	input dataset	N2O_isotope_DML_Prokopiou.csv				(Prokopiou et al., 2017)	
	firn ice data set Greenland	input dataset	N2O_isotope_NGR_SB_Prokopiou.csv				(Prokopiou et al., 2017)	
	firn ice data set Greenland	input dataset	N2O_isotope_NEEM_09_Prokopiou.csv				(Prokopiou et al., 2017)	
	firn ice data set Greenland	input dataset	N2O_isotope_NEEM_EU_Prokopiou.csv				(Prokopiou et al., 2017)	
Figure 5.15 (c)	Archived air sampes from Cape Grim	input dataset	N2O_isotope_CGAA_Park_2012.csv				(Park et al., 2012)	
	firn air data set H72	input dataset	N2O_isotope_H72_Ishijima_2007.csv				(Ishijima et al., 2007)	
	firn ice data set Greenland	input dataset	N2O_isotope_BRK_Prokopiou.csv				(Prokopiou et al., 2017)	
	firn ice data set Greenland	input dataset	N2O_isotope_DC_Prokopiou.csv				(Prokopiou et al., 2017)	
	firn ice data set Greenland	input dataset	N2O_isotope_DML_Prokopiou.csv				(Prokopiou et al., 2017)	
	firn ice data set Greenland	input dataset	N2O_isotope_NGR_SB_Prokopiou.csv				(Prokopiou et al., 2017)	
	firn ice data set Greenland	input dataset	N2O_isotope_NEEM_09_Prokopiou.csv				(Prokopiou et al., 2017)	
	firn ice data set Greenland	input dataset	N2O_isotope_NEEM_EU_Prokopiou.csv				(Prokopiou et al., 2017)	
Figure 5.17 (a)	land mean N2O	model simulation	N2O_emission_d	IPCC data	GCP-N2O-		(Tian et al.,	

ACCEPTED VERSION SUBJECT TO FINAL EDITS

	flux (2007-2016 average)		ensity_IPCC_0716.txt	agreement available	budget		2020)	
	baseline mean & range	model simulation	ocean_mean_0716.txt	IPCC data agreement available	GCP-N2O-budget		(Tian et al., 2020)	
Figure 5.17 (b-p)	total mean & range	model simulation	IPCC_NMPI_all_forcing.xlsx	IPCC data agreement available	NMIP		(Tian et al., 2019)	
	baseline mean & range	model simulation	IPCC_NMPI_co2_climate.xlsx	IPCC data agreement available	NMIP		(Tian et al., 2019)	
Figure 5.18	Effective Radiative Forcing	input dataset	AR6_ERF_all.xlsx		Chapter 7, AR6		Forster, P., et al., Chapter 7, AR6, 2021	
Figure 5.19	CarbonTracker-Europe	CO2 inversion			GCP-CO2		(van der Laan-Luijkx et al., 2017)	contact: wouter.peters@wur.nl, ingrid.luijkx@wur.nl
	Jena Carboscope	CO2 inversion			GCP-CO2		(Rödenbeck et al., 2018)	contact: Christian.Roedenbeck@bgc-jena.mpg.de
	CAMS	CO2 inversion			GCP-CO2		(Chevallier et al., 2005)	contact: frederic.chevallier@lsce.ipsl.fr
	MIROC4-ACTM	CO2 inversion			GCP-CO2		(Patra et al., 2018)	contact: prabir@jamstec.go.jp, naveennegi@jamstec.go.jp
	NISMON-CO2	CO2 inversion			GCP-CO2		(Niwa et al., 2017)	contact: niwa.yosuke@nies.go.jp
	LMDz	CH4 inversion			GCP-CH4		(Bousquet et al., 2006)	
	TM5-4DVAR	CH4 inversion			GCP-CH4		(Bergamaschi et al., 2013)	
	CTE-CH4	CH4 inversion			GCP-CH4		(Tsuruta et al., 2017)	

ACCEPTED VERSION SUBJECT TO FINAL EDITS

	MIROC4-ACTM	CH4 inversion			GCP-CH4		(Chandra et al., 2021)	
	LMDzPyVAR	CH4 inversion			GCP-CH4		(Yin et al., 2015)	
	NICAM-TM	CH4 inversion			GCP-CH4		(Niwa et al., 2017)	
	NIES-TM-Flexpart	CH4 inversion			GCP-CH4		(Wang et al., 2019a)	
	NIES-TM-GELCA	CH4 inversion			GCP-CH4		(Ishizawa et al., 2016)	
	TOMCAT	CH4 inversion			GCP-CH4		(McNorton et al., 2018)	
	INVICAT	N2O inversion			GCP-N2O		(Thompson et al., 2019)	C.Wilson@leeds.ac.uk (Chris Wilson)
	PyVAR-1	N2O inversion			GCP-N2O		rlt@nilu.no (Rona Thompson)	
	PyVAR-2	N2O inversion			GCP-N2O		rlt@nilu.no (Rona Thompson)	
	MIRO4-ACTM	N2O inversion			GCP-N2O		prabir@jamstec.go.jp (Prabir Patra)	
	GEOS-Chem	N2O inversion			GCP-N2O		(Tian et al., 2020)	kcw@umn.edu (Kelly Wells)
Figure 5.20	Global surface ocean pH, acidity, and Revelle Factor on a 1x1 degree global grid from 1770 to 2100 (NCEI Accession 0206289)	observation-based dataset	Surface_pH_1770_2000.nc		(Jiang et al., 2019)	https://www.ncei.noaa.gov/data/oceans/ncei/ocads/data/0206289/Surface_pH_1770_2100	(Jiang et al., 2019)	
	Annual mean seasonally-detrended surface ocean pH	observation-based dataset	annual_mean_pH_seosonally_detrended.xlsx					

ACCEPTED VERSION SUBJECT TO FINAL EDITS

	at time-series sites							
	Time-series data of surface ocean pH at 137E	observation-based dataset	137E_surface_carbon.xlsx			https://www.data.jma.go.jp/gmd/kaiyou/db/vessel_obs/data-report/html/ship/ship_e	(Ono et al., 2019)	
	Time-series data of surface ocean pH at stations KNOT and K2	observation-based dataset	KNOT_ML.csv, K2_ML.csv			https://www.ncei.noaa.gov/access/ocean-carbon-data-system/oceans/Moorings/K2.html	(Wakita et al., 2017)	
	Time-series data of surface ocean pH at station ALOHA	observation-based dataset	HOT_surface_CO2.txt		(Dore et al., 2009b)	https://hahana.soest.hawaii.edu/hot/products/HOT_surface_CO2.txt	(Dore et al., 2009b)	
	Time-series data of surface ocean pH at the BATS site	observation-based dataset	43247_2020_30_MOESM2_ESM.xlsx		(Bates and Johnson, 2020)	https://www.nature.com/articles/s43247-020-00030-5#Sec22	(Bates and Johnson, 2020)	
	Time-series data of surface ocean pH in the Iceland Sea	observation-based dataset	IcelandSea.exc.csv, IcelandSea_LN6_2014-2019.csv			https://www.ncei.noaa.gov/access/ocean-carbon-data-system/oceans/Moorings/Iceland_Sea.html	(Olafsson et al., 2009)	
	Time-series data of surface ocean pH at the DYFAMED site	observation-based dataset	DYFAMED_surface_pH.csv			https://www.ncei.noaa.gov/access/ocean-carbon-data-system/oceans/Coastal/DYFAMED.html	(Merlivat et al., 2018)	
	Time-series data of surface ocean pH at the ESTOC site	observation-based dataset	ESTOC_TS_Data_1995-2016.csv			https://www.ncei.noaa.gov/access/ocean-carbon-data-	(González-Dávila et al., 2010)	

ACCEPTED VERSION SUBJECT TO FINAL EDITS

						system/oceans/Coastal/ESTOC.html		
	Time-series data of surface ocean pH at the CARIACO site	observation-based dataset	CARIACO_surface_pH.csv			http://imars.marine.usf.edu/CAR-legacy/Master.txt	(Bates et al., 2014)	
	Time-series data of surface ocean pH at the Drake Passage	observation-based dataset	DrakePass_pH_Omega_LDEO_030519.PRT.xlsx		(Takahashi et al., 2014)	https://www.ldeo.columbia.edu/res/pi/CO2/carbondioxide/pages/pCO2data.html	(Takahashi et al., 2014)	
	Time-series data of surface ocean pH at the Munida site	observation-based dataset	MunidaTimeSeries210106.csv			https://marinedata.niwa.co.nz/nzoa-on-map/	(Bates et al., 2014)	
Figure 5.21	GLODAPv2 Mapped Data Product	observation-based dataset	GLODAPv2.2016b_MappedClimatologies.tar.gz		(Lauvset et al., 2016)	https://www.glodap.info/index.php/mapped-data-product/	(Lauvset et al., 2020)	
					(Olsen et al., 2016)	https://doi.org/10.5194/essd-8-297-2016		
Figure 5.31	IPCC AR6 assessed historical GSAT time series (Chapter 2)							
	Global Carbon Budget 2020	Input Dataset	2020_Global_Budget_v1.0.xlsx			10.18160/gcp-2020	(Friedlingstein et al., 2020)	
FAQ 5.1	Global Carbon Budget 2020	Input Dataset	2020_Global_Budget_v1.0.xlsx			10.18160/gcp-2020	(Friedlingstein et al., 2020)	
FAQ 5.2	Northern Circumpolar Soil Carbon Database version 2 (NCSCDv2)	Input Dataset			(Hugelius et al., 2013)	https://bolin.su.se/data/ncscd/		
	Circumpolar Thermokarst Landscapes	Input Dataset			(Olefeldt et al., 2016)			

ACCEPTED VERSION SUBJECT TO FINAL EDITS

	Database							

[END TABLE 5.SM.6 HERE]

ACCEPTED VERSION
SUBJECT TO FINAL EDITS

References

Atlas, R., Hoffman, R. N., Ardizzone, J., Leidner, S. M., Jusem, J. C., Smith, D. K., et al. (2011). A Cross-calibrated, Multiplatform Ocean Surface Wind Velocity Product for Meteorological and Oceanographic Applications. *Bull. Am. Meteorol. Soc.* 92, 157–174. doi:10.1175/2010BAMS2946.1.

Aumont, O., Ethé, C., Tagliabue, A., Bopp, L., and Gehlen, M. (2015). PISCES-v2: an ocean biogeochemical model for carbon and ecosystem studies. *Geosci. Model Dev.* 8, 2465–2513. doi:10.5194/gmd-8-2465-2015.

Badgley, G., Field, C. B., and Berry, J. A. (2017). Canopy near-infrared reflectance and terrestrial photosynthesis. *Sci. Adv.* 3. doi:10.1126/sciadv.1602244.

Bakker, D. C. E., Pfeil, B., Landa, C. S., Metzl, N., O'Brien, K. M., Olsen, A., et al. (2016). A multi-decade record of high-quality fCO2 data in version 3 of the Surface Ocean CO2 Atlas (SOCAT). *Earth Syst. Sci. Data* 8, 383–413. doi:10.5194/essd-8-383-2016.

Bates, N., Astor, Y., Church, M., Currie, K., Dore, J., Gonaález-Dávila, M., et al. (2014). A Time-Series View of Changing Ocean Chemistry Due to Ocean Uptake of Anthropogenic CO2 and Ocean Acidification. *Oceanography* 27, 126–141. doi:10.5670/oceanog.2014.16.

Bates, N. R., and Johnson, R. J. (2020). Acceleration of ocean warming, salinification, deoxygenation and acidification in the surface subtropical North Atlantic Ocean. *Commun. Earth Environ.* 1, 33. doi:10.1038/s43247-020-00030-5.

Battle, M., Bender, M. L., Tans, P. P., White, J. W. C., Ellis, J. T., Conway, T., et al. (2000). Global Carbon Sinks and Their Variability Inferred from Atmospheric O₂ and δ¹³C. *Science (80-.).* 287, 2467. doi:10.1126/science.287.5462.2467.

Bauman, S., Costa, M., Fong, M., House, B., Perez, E., Tan, M., et al. (2014). Augmenting the Biological Pump: The Shortcomings of Geoengineered Upwelling. *Oceanography* 27, 17–23. doi:10.5670/oceanog.2014.79.

Beerling, D. J., Leake, J. R., Long, S. P., Scholes, J. D., Ton, J., Nelson, P. N., et al. (2018). Farming with crops and rocks to address global climate, food and soil security. *Nat. Plants* 4, 138–147. doi:10.1038/s41477-018-0108-y.

Benanti, G., Saunders, M., Tobin, B., and Osborne, B. (2014). Contrasting impacts of afforestation on nitrous oxide and methane emissions. *Agric. For. Meteorol.* 198–199, 82–93. doi:10.1016/j.agrformet.2014.07.014.

Bender, M. L., Ho, D. T., Hendricks, M. B., Mika, R., Battle, M. O., Tans, P. P., et al. (2005). Atmospheric O2/N2 changes, 1993–2002: Implications for the partitioning of fossil fuel CO2 sequestration. *Global Biogeochem. Cycles* 19. doi:https://doi.org/10.1029/2004GB002410.

Bereiter, B., Eggleston, S., Schmitt, J., Nehrbass-Ahles, C., Stocker, T. F., Fischer, H., et al. (2015). Revision of the EPICA Dome C CO2 record from 800 to 600-kyr before present. *Geophys. Res. Lett.* 42, 542–549. doi:10.1002/2014GL061957.

Bergamaschi, P., Houweling, S., Segers, A., Krol, M., Frankenberg, C., Scheepmaker, R. A., et al. (2013). Atmospheric CH 4 in the first decade of the 21st century: Inverse modeling analysis using SCIAMACHY satellite retrievals and NOAA surface measurements. *J. Geophys. Res. Atmos.* 118, 7350–7369. doi:10.1002/jgrd.50480.

Berthet, S., Séférian, R., Bricaud, C., Chevallier, M., Voldoire, A., and Ethé, C. (2019). Evaluation of an Online Grid-Coarsening Algorithm in a Global Eddy-Admitting Ocean Biogeochemical Model. *J. Adv. Model. Earth Syst.* 11, 1759–1783. doi:10.1029/2019MS001644.

Bindoff, N. L., Cheung, W. W. L., Kairo, J. G., Arístegui, J., Guinder, V. A., Hallberg, R., et al. (2019). "Changing Ocean, Marine Ecosystems, and Dependent Communities," in *IPCC Special Report on the Ocean and Cryosphere in a Changing Climate*, eds. H.-O. Pörtner, D. C. Roberts, V. Masson-Delmotte, P. Zhai, M. Tignor, E. Poloczanska, et al. (In Press), 447–588. Available at: https://www.ipcc.ch/srocc/chapter/chapter-5.

Blanc-Betes, E., Kantola, I. B., Gomez-Casanovas, N., Hartman, M. D., Parton, W. J., Lewis, A. L., et al. In silico assessment of the potential of basalt amendments to reduce N2O emissions from bioenergy crops. *GCB Bioenergy* n/a. doi:10.1111/gcbb.12757.

Bock, M., Schmitt, J., Beck, J., Seth, B., Chappellaz, J., and Fischer, H. (2017). Glacial/interglacial wetland, biomass burning, and geologic methane emissions constrained by dual stable isotopic CH 4 ice core records. *Proc. Natl. Acad. Sci.* 114, E5778–E5786. doi:10.1073/pnas.1613883114.

Bousquet, P., Ciais, P., Miller, J. B., Dlugokencky, E. J., Hauglustaine, D. A., Prigent, C., et al. (2006). Contribution of anthropogenic and natural sources to atmospheric methane variability. *Nature* 443, 439–443. doi:10.1038/nature05132.

Boyd, P. W., Jickells, T., Law, C. S., Blain, S., Boyle, E. A., Buesseler, K. O., et al. (2007). Mesoscale Iron Enrichment Experiments 1993-2005: Synthesis and Future Directions. *Science (80-.).* 315, 612–617. doi:10.1126/science.1131669.

Boysen, L. R., Lucht, W., and Gerten, D. (2017). Trade-offs for food production, nature conservation and climate limit the terrestrial carbon dioxide removal potential. *Glob. Chang. Biol.* 23, 4303–4317. doi:10.1111/gcb.13745.

ACCEPTED VERSION SUBJECT TO FINAL EDITS

Buitenhuis, E. T., Hashioka, T., and Quéré, C. Le (2013). Combined constraints on global ocean primary production using observations and models. *Global Biogeochem. Cycles* 27, 847–858. doi:10.1002/gbc.20074.

Buss, W., and Mašek, O. (2016). High-VOC biochar—effectiveness of post-treatment measures and potential health risks related to handling and storage. *Environ. Sci. Pollut. Res.* 23, 19580–19589. doi:10.1007/s11356-016-7112-4.

Butterworth, B. J., and Miller, S. D. (2016). Air-sea exchange of carbon dioxide in the Southern Ocean and Antarctic marginal ice zone. *Geophys. Res. Lett.* 43, 7223–7230. doi:10.1002/2016GL069581.

Cao, L., and Caldeira, K. (2010). Can ocean iron fertilization mitigate ocean acidification? *Clim. Change* 99, 303–311. doi:10.1007/s10584-010-9799-4.

Cayuela, M. L., van Zwieten, L., Singh, B. P., Jeffery, S., Roig, A., and Sánchez-Monedero, M. A. (2014). Biochar's role in mitigating soil nitrous oxide emissions: A review and meta-analysis. *Agric. Ecosyst. Environ.* 191, 5–16. doi:10.1016/j.agee.2013.10.009.

Chandra, N., Patra, P. K., Bisht, J. S. H., Ito, A., Umezawa, T., Saigusa, N., et al. (2021). Emissions from the Oil and Gas Sectors, Coal Mining and Ruminant Farming Drive Methane Growth over the Past Three Decades. *J. Meteorol. Soc. Japan. Ser. II* 99. doi:10.2151/jmsj.2021-015.

Chaudhuri, A. H., Ponte, R. M., and Nguyen, A. T. (2014). A Comparison of Atmospheric Reanalysis Products for the Arctic Ocean and Implications for Uncertainties in Air–Sea Fluxes. *J. Clim.* 27, 5411–5421. doi:10.1175/JCLI-D-13-00424.1.

Chen, P., Zhou, M., Wang, S., Luo, W., Peng, T., Zhu, B., et al. (2019). Effects of afforestation on soil CH4 and N2O fluxes in a subtropical karst landscape. *Sci. Total Environ.*, 135974. doi:https://doi.org/10.1016/j.scitotenv.2019.135974.

Cheng, L., Zhang, L., Wang, Y.-P., Canadell, J. G., Chiew, F. H. S., Beringer, J., et al. (2017). Recent increases in terrestrial carbon uptake at little cost to the water cycle. *Nat. Commun.* 8, 110. doi:10.1038/s41467-017-00114-5.

Chevallier, F. (2013). On the parallelization of atmospheric inversions of CO2 surface fluxes within a variational framework. *Geosci. Model Dev.* 6, 783–790. doi:10.5194/gmd-6-783-2013.

Chevallier, F., Fisher, M., Peylin, P., Serrar, S., Bousquet, P., Bréon, F.-M., et al. (2005). Inferring CO2 sources and sinks from satellite observations: Method and application to TOVS data. *J. Geophys. Res.* 110, D24309. doi:10.1029/2005JD006390.

Ciais, P., Sabine, C., Bala, G., Bopp, L., Brovkin, V., Canadell, J., et al. (2013). "Carbon and Other Biogeochemical Cycles," in *Climate Change 2013: The Physical Science Basis. Contribution of Working Group I to the Fifth Assessment Report of the Intergovernmental Panel on Climate Change*, eds. T. F. Stocker, D. Qin, G.-K. Plattner, M. Tignor, S. K. Allen, J. Boschung, et al. (Cambridge, United Kingdom and New York, NY, USA: Cambridge University Press), 465–570. doi:10.1017/CBO9781107415324.015.

Claustre, H., Johnson, K. S., and Takeshita, Y. (2020). Observing the global ccean with biogeochemical-argo. *Ann. Rev. Mar. Sci.* 12. doi:10.1146/annurev-marine-010419-010956.

Clement, D., and Gruber, N. (2018). The eMLR(C*) method to determine decadal changes in the global ocean storage of anthropogenic CO2. *Global Biogeochem. Cycles* 32, 654–679. doi:10.1002/2017GB005819.

Clough, T., Condron, L., Kammann, C., and Müller, C. (2013). A review of biochar and soil nitrogen dynamics. *Agronomy* 3, 275–293. doi:10.3390/agronomy3020275.

Conway, T. J., Tans, P. P., Waterman, L. S., Thoning, K. W., Kitzis, D. R., Masarie, K. A., et al. (1994). Evidence for interannual variability of the carbon cycle from the National Oceanic and Atmospheric Administration/Climate Monitoring and Diagnostics Laboratory Global Air Sampling Network. *J. Geophys. Res.* 99, 22831. doi:10.1029/94JD01951.

Creutzig, F., Breyer, C., Hilaire, J., Minx, J., Peters, G. P., and Socolow, R. (2019). The mutual dependence of negative emission technologies and energy systems. *Energy Environ. Sci.* 12, 1805–1817. doi:10.1039/C8EE03682A.

Creutzig, F., Ravindranath, N. H., Berndes, G., Bolwig, S., Bright, R., Cherubini, F., et al. (2015). Bioenergy and climate change mitigation: an assessment. *GCB Bioenergy* 7, 916–944. doi:10.1111/gcbb.12205.

Daneshvar, F., Nejadhashemi, A. P., Adhikari, U., Elahi, B., Abouali, M., Herman, M. R., et al. (2017). Evaluating the significance of wetland restoration scenarios on phosphorus removal. *J. Environ. Manage.* 192, 184–196. doi:10.1016/j.jenvman.2017.01.059.

Davin, E. L., Seneviratne, S. I., Ciais, P., Olioso, A., and Wang, T. (2014). Preferential cooling of hot extremes from cropland albedo management. *Proc. Natl. Acad. Sci.* 111, 9757–9761. doi:10.1073/pnas.1317323111.

Deng, N., Wang, H., Hu, S., and Jiao, J. (2019). Effects of Afforestation Restoration on Soil Potential N2O Emission and Denitrifying Bacteria After Farmland Abandonment in the Chinese Loess Plateau. *Front. Microbiol.* 10, 262. doi:10.3389/fmicb.2019.00262.

Denman, K. L., Brasseur, G. P., Chidthaisong, A., Ciais, P., Cox, P. M., Dickinson, R. E., et al. (2007). "Couplings Between Changes in the Climate System and Biogeochemistry," in *Climate Change 2007: The Physical Science Basis. Contribution of Working Group I to the Fourth Assessment Report of the Intergovernmental Panel on Climate*

ACCEPTED VERSION SUBJECT TO FINAL EDITS

Change, eds. S. Solomon, D. Qin, M. Manning, Z. Chen, M. Marquis, K. B. Averyt, et al. (Cambridge, United Kingdom and New York, NY, USA: Cambridge University Press), 499–588. Available at: https://www.ipcc.ch/report/ar4/wg1.

Denvil-Sommer, A., Gehlen, M., Vrac, M., and Mejia, C. (2019). LSCE-FFNN-v1: a two-step neural network model for the reconstruction of surface ocean pCO2 over the global ocean. *Geosci. Model Dev.* 12, 2091–2105. doi:10.5194/gmd-12-2091-2019.

Devaraju, N., Bala, G., and Modak, A. (2015a). Effects of large-scale deforestation on precipitation in the monsoon regions: Remote versus local effects. *Proc. Natl. Acad. Sci.* 112, 3257–3262. doi:10.1073/pnas.1423439112.

Devaraju, N., Bala, G., and Nemani, R. (2015b). Modelling the influence of land-use changes on biophysical and biochemical interactions at regional and global scales. *Plant. Cell Environ.* 38, 1931–1946. doi:10.1111/pce.12488.

DeVries, T., Holzer, M., and Primeau, F. (2017). Recent increase in oceanic carbon uptake driven by weaker upper-ocean overturning. *Nature* 542, 215–218. doi:10.1038/nature21068.

Dlugokencky, E. J., Houwelling, S., Bruhwiler, L., Masarie, K. A., Lang, P. M., Miller, J. B., et al. (2003). Atmospheric methane levels off: Temporary pause or a new steady-state? *Geophys. Res. Lett.* 30, 1992. doi:10.1029/2003GL018126.

Dlugokencky, E., and Tans, P. . (2020). Trends in atmospheric carbon dioxide, National Oceanic and Atmospheric Administration. *Earth Syst. Res. Lab.*

Don, A., Osborne, B., Hastings, A., Skiba, U., Carter, M. S., Drewer, J., et al. (2012). Land-use change to bioenergy production in Europe: implications for the greenhouse gas balance and soil carbon. *GCB Bioenergy* 4, 372–391. doi:10.1111/j.1757-1707.2011.01116.x.

Doney, S. C., Lima, I., Feely, R. A., Glover, D. M., Lindsay, K., Mahowald, N., et al. (2009a). Mechanisms governing interannual variability in upper-ocean inorganic carbon system and air–sea CO2 fluxes: Physical climate and atmospheric dust. *Deep Sea Res. Part II Top. Stud. Oceanogr.* 56, 640–655. doi:10.1016/j.dsr2.2008.12.006.

Doney, S. C., Lima, I., Feely, R. A., Glover, D. M., Lindsay, K., Mahowald, N., et al. (2009b). Mechanisms governing interannual variability in upper-ocean inorganic carbon system and air–sea CO2 fluxes: Physical climate and atmospheric dust. *Deep Sea Res. Part II Top. Stud. Oceanogr.* 56, 640–655. doi:https://doi.org/10.1016/j.dsr2.2008.12.006.

Dore, J. E., Lukas, R., Sadler, D. W., Church, M. J., and Karl, D. M. (2009a). Physical and biogeochemical modulation of ocean acidification in the central North Pacific. *Proc. Natl. Acad. Sci.* 106, 12235–12240. doi:10.1073/PNAS.0906044106.

Dore, J. E., Lukas, R., Sadler, D. W., Church, M. J., and Karl, D. M. (2009b). Physical and biogeochemical modulation of ocean acidification in the central North Pacific. *Proc. Natl. Acad. Sci.* 106, 12235–12240. doi:10.1073/pnas.0906044106.

Fairaill, C. W., Hare, J. E., Edson, J. B., and McGillis, W. (2000). Parameterization and Micrometeorological Measurement of Air–Sea Gas Transfer. *Boundary-Layer Meteorol.* 96, 63–106. doi:10.1023/A:1002662826020.

Farley, K. A., Jobbagy, E. G., and Jackson, R. B. (2005). Effects of afforestation on water yield: a global synthesis with implications for policy. *Glob. Chang. Biol.* 11, 1565–1576. doi:10.1111/j.1365-2486.2005.01011.x.

Fay, A. R., and McKinley, G. A. (2014). Global open-ocean biomes: mean and temporal variability. *Earth Syst. Sci. Data* 6, 273–284. doi:10.5194/essd-6-273-2014.

Feng, E. Y., Koeve, W., Keller, D. P., and Oschlies, A. (2017). Model-based assessment of the CO2 sequestration potential of coastal ocean alkalinization. *Earth's Futur.* 5, 1252–1266. doi:10.1002/2017EF000659.

Feng, E. Y., Su, B., and Oschlies, A. (2020). Geoengineered Ocean Vertical Water Exchange Can Accelerate Global Deoxygenation. *Geophys. Res. Lett.* 47, e2020GL088263. doi:10.1029/2020GL088263.

Fischer, B. M. C., Manzoni, S., Morillas, L., Garcia, M., Johnson, M. S., and Lyon, S. W. (2019). Improving agricultural water use efficiency with biochar – A synthesis of biochar effects on water storage and fluxes across scales. *Sci. Total Environ.* 657, 853–862. doi:10.1016/j.scitotenv.2018.11.312.

Flecha, S., Pérez, F. F., Murata, A., Makaoui, A., and Huertas, I. E. (2019). Decadal acidification in Atlantic and Mediterranean water masses exchanging at the Strait of Gibraltar. *Sci. Rep.* 9, 15533. doi:10.1038/s41598-019-52084-x.

Fornara, D. A., Steinbeiss, S., McNamara, N. P., Gleixner, G., Oakley, S., Poulton, P. R., et al. (2011). Increases in soil organic carbon sequestration can reduce the global warming potential of long-term liming to permanent grassland. *Glob. Chang. Biol.* 17, 1925–1934. doi:10.1111/j.1365-2486.2010.02328.x.

Foster, G. L., Royer, D. L., and Lunt, D. J. (2017). Future climate forcing potentially without precedent in the last 420 million years. *Nat. Commun.* 8, 14845. doi:10.1038/ncomms14845.

Francey, R. J., Steele, L. P., Spencer, D. A., Langenfelds, R. L., Law, R. M., Krummel, P. B., et al. (2003). "The CSIRO (Australia) measurement of greenhouse gases in the global atmosphere," in WMO TD No. 1138., eds. S. Toru and S.

ACCEPTED VERSION SUBJECT TO FINAL EDITS

Kazuto (Geneva, Switzerland: World Meteorological Organization (WMO)), 97–111. Available at: https://library.wmo.int/index.php?lvl=notice_display&id=11080#.YHA_RtV1DIU.

Friedlingstein, P., Jones, M. W., O'Sullivan, M., Andrew, R. M., Hauck, J., Peters, G. P., et al. (2019). Global Carbon Budget 2019. *Earth Syst. Sci. Data* 11, 1783–1838. doi:10.5194/essd-11-1783-2019.

Friedlingstein, P., O'Sullivan, M., Jones, M. W., Andrew, R. M., Hauck, J., Olsen, A., et al. (2020). Global Carbon Budget 2020. *Earth Syst. Sci. Data* 12, 3269–3340. doi:10.5194/essd-12-3269-2020.

Fuss, S., Lamb, W. F., Callaghan, M. W., Hilaire, J., Creutzig, F., Amann, T., et al. (2018). Negative emissions – Part 2: Costs, potentials and side effects. *Environ. Res. Lett.* 13, 063002. doi:10.1088/1748-9326/aabf9f.

Garbe, C. S., Rutgersson, A., Boutin, J., de Leeuw, G., Delille, B., Fairall, C. W., et al. (2014). "Transfer across the air-sea interface," in *Ocean-Atmosphere Interactions of Gases and Particles* (Springer Berlin Heidelberg), 55–112. doi:10.1007/978-3-642-25643-1_2.

Gasser, T., Crepin, L., Quilcaille, Y., Houghton, R. A., Ciais, P., and Obersteiner, M. (2020). Historical CO2 emissions from land use and land cover change and their uncertainty. *Biogeosciences* 17, 4075–4101. doi:10.5194/bg-17-4075-2020.

Genesio, L., Miglietta, F., Lugato, E., Baronti, S., Pieri, M., and Vaccari, F. P. (2012). Surface albedo following biochar application in durum wheat. *Environ. Res. Lett.* 7, 014025. doi:10.1088/1748-9326/7/1/014025.

GESAMP (2019). High level review of a wide range of proposed marine geoengineering techniques.

Gloor, M., Gruber, N., Sarmiento, J., Sabine, C. L., Feely, R. A., and Rödenbeck, C. (2003). A first estimate of present and preindustrial air-sea CO2 flux patterns based on ocean interior carbon measurements and models. *Geophys. Res. Lett.* 30, 10-1-10–4. doi:https://doi.org/10.1029/2002GL015594.

González-Dávila, M., Santana-Casiano, J. M., Rueda, M. J., and Llinás, O. (2010). The water column distribution of carbonate system variables at the ESTOC site from 1995 to 2004. *Biogeosciences* 7, 3067–3081. doi:10.5194/bg-7-3067-2010.

González, M. F., and Ilyina, T. (2016). Impacts of artificial ocean alkalinization on the carbon cycle and climate in Earth system simulations. *Geophys. Res. Lett.* 43, 6493–6502. doi:10.1002/2016GL068576.

González, M. F., Ilyina, T., Sonntag, S., and Schmidt, H. (2018). Enhanced rates of regional warming and ocean acidification after termination of large-scale ocean alkalinization. *Geophys. Res. Lett.* 45, 7120–7129. doi:10.1029/2018GL077847.

Good, S. A., Martin, M. J., and Rayner, N. A. (2013). EN4: Quality controlled ocean temperature and salinity profiles and monthly objective analyses with uncertainty estimates. *J. Geophys. Res. Ocean.* 118, 6704–6716. doi:10.1002/2013JC009067.

Good, S., Fiedler, E., Mao, C., Martin, M. J., Maycock, A., Reid, R., et al. (2020). The Current Configuration of the OSTIA System for Operational Production of Foundation Sea Surface Temperature and Ice Concentration Analyses. *Remote Sens.* 12, 720. doi:10.3390/rs12040720.

Graven, H. D., Gruber, N., Key, R., Khatiwala, S., and Giraud, X. (2012). Changing controls on oceanic radiocarbon: New insights on shallow-to-deep ocean exchange and anthropogenic CO2 uptake. *J. Geophys. Res. Ocean.* 117. doi:https://doi.org/10.1029/2012JC008074.

Gray, A. R., Johnson, K. S., Bushinsky, S. M., Riser, S. C., Russell, J. L., Talley, L. D., et al. (2018). Autonomous biogeochemical Ffoats detect significant carbon dioxide outgassing in the high-latitude Southern Ocean. *Geophys. Res. Lett.* 45, 9049–9057. doi:10.1029/2018GL078013.

Gregor, L., and Fay, A. R. (2021). SeaFlux data set: Air-sea CO2 fluxes for surface pCO2 data products using a standardised approach. Zenodo. *SeaFlux data set Air-sea CO2 fluxes Surf. pCO2 data Prod. using a Stand. approach. Zenodo*. doi:/10.5281/zenodo.4133802, 2021.

Gregor, L., Lebehot, A. D., Kok, S., and Scheel Monteiro, P. M. (2019). A comparative assessment of the uncertainties of global surface ocean CO2 estimates using a machine-learning ensemble (CSIR-ML6 version 2019a) – have we hit the wall? *Geosci. Model Dev.* 12, 5113–5136. doi:10.5194/gmd-12-5113-2019.

Griscom, B. W., Adams, J., Ellis, P. W., Houghton, R. A., Lomax, G., Miteva, D. A., et al. (2017). Natural climate solutions. *Proc. Natl. Acad. Sci.* 114, 11645–11650. doi:10.1073/pnas.1710465114.

Gruber, N., Clement, D., Carter, B. R., Feely, R. A., van Heuven, S., Hoppema, M., et al. (2019a). The oceanic sink for anthropogenic CO 2 from 1994 to 2007. *Science (80-.).* 363, 1193–1199. doi:10.1126/science.aau5153.

Gruber, N., Clement, D., Carter, B. R. R., Feely, R. A. A., van Heuven, S., Hoppema, M., et al. (2019b). The oceanic sink for anthropogenic CO2 from 1994 to 2007. *Science (80-.).* 363, 1193–1199. doi:10.1126/science.aau5153.

Gruber, N., Gloor, M., Mikaloff Fletcher, S. E., Doney, S. C., Dutkiewicz, S., Follows, M. J., et al. (2009). Oceanic sources, sinks, and transport of atmospheric CO2. *Global Biogeochem. Cycles* 23. doi:https://doi.org/10.1029/2008GB003349.

Gruber, N., and Keeling, C. D. (2001). An improved estimate of the isotopic air-sea disequilibrium of CO2: Implications for the oceanic uptake of anthropogenic CO2. *Geophys. Res. Lett.* 28, 555–558.

ACCEPTED VERSION SUBJECT TO FINAL EDITS

doi:https://doi.org/10.1029/2000GL011853.
Gruber, N., Landschützer, P., and Lovenduski, N. S. (2019c). The variable Southern Ocean carbon sink. *Ann. Rev. Mar. Sci.* 11, 159–186. doi:10.1146/annurev-marine-121916-063407.
Gu, J., Yuan, M., Liu, J., Hao, Y., Zhou, Y., Qu, D., et al. (2017). Trade-off between soil organic carbon sequestration and nitrous oxide emissions from winter wheat-summer maize rotations: Implications of a 25-year fertilization experiment in Northwestern China. *Sci. Total Environ.* 595, 371–379. doi:10.1016/j.scitotenv.2017.03.280.
Hansis, E., Davis, S. J., and Pongratz, J. (2015). Relevance of methodological choices for accounting of land use change carbon fluxes. *Global Biogeochem. Cycles*. doi:10.1002/2014GB004997.
Harper, A. B., Powell, T., Cox, P. M., House, J., Huntingford, C., Lenton, T. M., et al. (2018). Land-use emissions play a critical role in land-based mitigation for Paris climate targets. *Nat. Commun.* 9, 2938. doi:10.1038/s41467-018-05340-z.
Harris, I., Jones, P. D., Osborn, T. J., and Lister, D. H. (2014). Updated high-resolution grids of monthly climatic observations – the CRU TS3.10 Dataset. *Int. J. Climatol.* 34, 623–642. doi:10.1002/joc.3711.
Hartmann, J., West, A. J., Renforth, P., Köhler, P., De La Rocha, C. L., Wolf-Gladrow, D. A., et al. (2013). Enhanced chemical weathering as a geoengineering strategy to reduce atmospheric carbon dioxide, supply nutrients, and mitigate ocean acidification. *Rev. Geophys.* 51, 113–149. doi:10.1002/rog.20004.
Hauck, J., Köhler, P., Wolf-Gladrow, D., and Völker, C. (2016). Iron fertilisation and century-scale effects of open ocean dissolution of olivine in a simulated CO2 removal experiment. *Environ. Res. Lett.* 11, 024007. doi:10.1088/1748-9326/11/2/024007.
Hauck, J., Zeising, M., Le Quéré, C., Gruber, N., Bakker, D. C. E., Bopp, L., et al. (2020). Consistency and Challenges in the Ocean Carbon Sink Estimate for the Global Carbon Budget. *Front. Mar. Sci.* 7, 852. doi:10.3389/fmars.2020.571720.
Hauri, C., Doney, S. C., Takahashi, T., Erickson, M., Jiang, G., and Ducklow, H. W. (2015). Two decades of inorganic carbon dynamics along the West Antarctic Peninsula. *Biogeosciences* 12, 6761–6779. doi:10.5194/bg-12-6761-2015.
Heck, V., Gerten, D., Lucht, W., and Boysen, L. R. (2016). Is extensive terrestrial carbon dioxide removal a 'green' form of geoengineering? A global modelling study. *Glob. Planet. Change* 137, 123–130. doi:10.1016/j.gloplacha.2015.12.008.
Heck, V., Gerten, D., Lucht, W., and Popp, A. (2018). Biomass-based negative emissions difficult to reconcile with planetary boundaries. *Nat. Clim. Chang.* 8, 151–155. doi:10.1038/s41558-017-0064-y.
Helbig, M., Waddington, J. M., Alekseychik, P., Amiro, B., Aurela, M., Barr, A. G., et al. (2020). The biophysical climate mitigation potential of boreal peatlands during the growing season. *Environ. Res. Lett.* 15. doi:10.1088/1748-9326/abab34.
Hemes, K. S., Chamberlain, S. D., Eichelmann, E., Anthony, T., Valach, A., Kasak, K., et al. (2019). Assessing the carbon and climate benefit of restoring degraded agricultural peat soils to managed wetlands. *Agric. For. Meteorol.* 268, 202–214. doi:10.1016/j.agrformet.2019.01.017.
Hemes, K. S., Eichelmann, E., Chamberlain, S. D., Knox, S. H., Oikawa, P. Y., Sturtevant, C., et al. (2018). A Unique Combination of Aerodynamic and Surface Properties Contribute to Surface Cooling in Restored Wetlands of the Sacramento-San Joaquin Delta, California. *J. Geophys. Res. Biogeosciences* 123, 2072–2090. doi:https://doi.org/10.1029/2018JG004494.
Hersbach, H., Bell, B., Berrisford, P., Hirahara, S., Horányi, A., Muñoz-Sabater, J., et al. (2020). The ERA5 global reanalysis. *Q. J. R. Meteorol. Soc.* 146, 1999–2049. doi:10.1002/qj.3803.
Holl, D., Pfeiffer, E.-M., and Kutzbach, L. (2020). Comparison of eddy covariance CO2 and CH4 fluxes from mined and recently rewetted sections in a northwestern German cutover bog. *Biogeosciences* 17, 2853–2874. doi:10.5194/bg-17-2853-2020.
Houghton, R. A., and Nassikas, A. A. (2017). Global and regional fluxes of carbon from land use and land cover change 1850-2015. *Global Biogeochem. Cycles* 31, 456–472. doi:10.1002/2016GB005546.
Huang, Y., Wang, C., Lin, C., Zhang, Y., Chen, X., Tang, L., et al. (2019). Methane and Nitrous Oxide Flux after Biochar Application in Subtropical Acidic Paddy Soils under Tobacco-Rice Rotation. *Sci. Rep.* 9, 17277. doi:10.1038/s41598-019-53044-1.
Hugelius, G., Bockheim, J. G., Camill, P., Elberling, B., Grosse, G., Harden, J. W., et al. (2013). A new data set for estimating organic carbon storage to 3 m depth in soils of the northern circumpolar permafrost region. *Earth Syst. Sci. Data* 5, 393–402. doi:10.5194/essd-5-393-2013.
Iida, Y., Takatani, Y., Kojima, A., and Ishii, M. (2020). Global trends of ocean CO2 sink and ocean acidification: an observation-based reconstruction of surface ocean inorganic carbon variables. *J. Oceanogr.* doi:10.1007/s10872-020-00571-5.
IPCC (2019). IPCC Special Report on the Ocean and Cryosphere in a Changing Climate. , eds. H.-O. Pörtner, D. C.

ACCEPTED VERSION SUBJECT TO FINAL EDITS

Roberts, V. Masson-Delmotte, P. Zhai, M. Tignor, E. Poloczanska, et al. In Press Available at: https://www.ipcc.ch/report/srocc.

Ishii, M., Kosugi, N., Sasano, D., Saito, S., Midorikawa, T., and Inoue, H. Y. (2011). Ocean acidification off the south coast of Japan: A result from time series observations of CO2 parameters from 1994 to 2008. *J. Geophys. Res.* 116, C06022. doi:10.1029/2010JC006831.

Ishii, M., Rodgers, K. B., Inoue, H. Y., Toyama, K., Sasano, D., Kosugi, N., et al. (2020). Ocean Acidification From Below in the Tropical Pacific. *Global Biogeochem. Cycles* 34, e2019GB006368. doi:10.1029/2019GB006368.

Ishijima, K., Sugawara, S., Kawamura, K., Hashida, G., Morimoto, S., Murayama, S., et al. (2007). Temporal variations of the atmospheric nitrous oxide concentration and its δ15N and δ18O for the latter half of the 20th century reconstructed from firn air analyses. *J. Geophys. Res.* 112, D03305. doi:10.1029/2006JD007208.

Ishizawa, M., Mabuchi, K., Shirai, T., Inoue, M., Morino, I., Uchino, O., et al. (2016). Inter-annual variability of summertime CO 2 exchange in Northern Eurasia inferred from GOSAT XCO 2. *Environ. Res. Lett.* 11, 105001. doi:10.1088/1748-9326/11/10/105001.

Jacobson, A. R., Mikaloff Fletcher, S. E., Gruber, N., Sarmiento, J. L., and Gloor, M. (2007). A joint atmosphere-ocean inversion for surface fluxes of carbon dioxide: 1. Methods and global-scale fluxes. *Global Biogeochem. Cycles* 21. doi:10.1029/2005GB002556.

Jeffery, S., Verheijen, F. G. A., Kammann, C., and Abalos, D. (2016). Biochar effects on methane emissions from soils: A meta-analysis. *Soil Biol. Biochem.* 101, 251–258. doi:10.1016/j.soilbio.2016.07.021.

Jia, G., Shevliakova, E., Artaxo, P., Noblet-Ducoudré, N. De, Houghton, R., House, J., et al. (2019). "Land–climate interactions," in *Climate Change and Land: an IPCC special report on climate change, desertification, land degradation, sustainable land management, food security, and greenhouse gas fluxes in terrestrial ecosystems.*, eds. P. R. Shukla, J. Skea, E. C. Buendia, V. Masson-Delmotte, H.-O. Pörtner, D. C. Roberts, et al. (In Press), 131–248. Available at: https://www.ipcc.ch/srccl/chapter/chapter-2.

Jiang, L.-Q., Carter, B. R., Feely, R. A., Lauvset, S. K., and Olsen, A. (2019). Surface ocean pH and buffer capacity: past, present and future. *Sci. Rep.* 9, 18624. doi:10.1038/s41598-019-55039-4.

Jin, X., and Gruber, N. (2003). Offsetting the radiative benefit of ocean iron fertilization by enhancing N 2 O emissions. *Geophys. Res. Lett.* 30, 2249. doi:10.1029/2003GL018458.

Jones, C. D., Ciais, P., Davis, S. J., Friedlingstein, P., Gasser, T., Peters, G. P., et al. (2016). Simulating the earth system response to negative emissions. *Environ. Res. Lett.* 11, 095012. doi:10.1088/1748-9326/11/9/095012.

Joos, F., Meyer, R., Bruno, M., and Leuenberger, M. (1999). The variability in the carbon sinks as reconstructed for the last 1000 years. *Geophys. Res. Lett.* 26, 1437–1440. doi:https://doi.org/10.1029/1999GL900250.

Kammann, C., Ippoloto, J., Hagemann, N., Borchard, N., Cayuela, M. L., Estavillo, J. M., et al. (2017). Biochar as a Tool to teduce the Agricultural Greenhouse-gas Burden – Knowns, Unknowns and Future Research Needs. *J. Environ. Eng. Landsc. Manag.* 25, 114–139. doi:10.3846/16486897.2017.1319375.

Kantola, I. B., Masters, M. D., Beerling, D. J., Long, S. P., and DeLucia, E. H. (2017). Potential of global croplands and bioenergy crops for climate change mitigation through deployment for enhanced weathering. *Biol. Lett.* 13, 20160714. doi:10.1098/rsbl.2016.0714.

Karhu, K., Mattila, T., Bergström, I., and Regina, K. (2011). Biochar addition to agricultural soil increased CH4 uptake and water holding capacity – Results from a short-term pilot field study. *Agric. Ecosyst. Environ.* 140, 309–313. doi:https://doi.org/10.1016/j.agee.2010.12.005.

Kaushal, S. S., Likens, G. E., Pace, M. L., Utz, R. M., Haq, S., Gorman, J., et al. (2018). Freshwater salinization syndrome on a continental scale. *Proc. Natl. Acad. Sci.* 115, E574–E583. doi:10.1073/pnas.1711234115.

Keeling, C. D., Whorf, T. P., Wahlen, M., and van der Plicht, J. (2001). Exchanges of Atmospheric CO2 and 13CO2 with the Terrestrial Biosphere and Oceans from 1978 to 2000. I. Global Aspects. San Diego, CA, USA: Scripps Institution of Oceanography, University of California San Diego Available at: https://escholarship.org/uc/item/09v319r9.

Keeling, R. F., and Manning, A. C. (2014). "Studies of Recent Changes in Atmospheric O2 Content," in *Treatise on Geochemistry (Second Edition)*, eds. H. D. Holland and K. K. Turekian (Elsevier), 385–404. doi:10.1016/B978-0-08-095975-7.00420-4.

Keller, D. P., Feng, E. Y., and Oschlies, A. (2014a). Potential climate engineering effectiveness and side effects during a high carbon dioxide-emission scenario. *Nat. Commun.* 5, 3304. doi:10.1038/ncomms4304.

Keller, D. P., Feng, E. Y., and Oschlies, A. (2014b). Potential climate engineering effectiveness and side effects during a high carbon dioxide-emission scenario. *Nat. Commun.* 5, 3304. doi:10.1038/ncomms4304.

Keller, D. P., Lenton, A., Littleton, E. W., Oschlies, A., Scott, V., and Vaughan, N. E. (2018). The Effects of Carbon Dioxide Removal on the Carbon Cycle. *Curr. Clim. Chang. Reports* 4, 250–265. doi:10.1007/s40641-018-0104-3.

Key, R. M., Kozyr, A., Sabine, C. L., Lee, K., Wanninkhof, R., Bullister, J. L., et al. (2004). A global ocean carbon climatology: Results from Global Data Analysis Project (GLODAP). *Global Biogeochem. Cycles* 18, GB4031.

ACCEPTED VERSION SUBJECT TO FINAL EDITS

doi:10.1029/2004GB002247.
Kirschke, S., Bousquet, P., Ciais, P., Saunois, M., Canadell, J. G., Dlugokencky, E. J., et al. (2013). Three decades of global methane sources and sinks. *Nat. Geosci.* 6, 813–823. doi:10.1038/ngeo1955.
Kitidis, V., Brown, I., Hardman-Mountford, N., and Lefèvre, N. (2017). Surface ocean carbon dioxide during the Atlantic Meridional Transect (1995–2013); evidence of ocean acidification. *Prog. Oceanogr.* 158, 65–75. doi:https://doi.org/10.1016/j.pocean.2016.08.005.
Kluber, L. A., Miller, J. O., Ducey, T. F., Hunt, P. G., Lang, M., and S. Ro, K. (2014). Multistate assessment of wetland restoration on CO2 and N2O emissions and soil bacterial communities. *Appl. Soil Ecol.* 76, 87–94. doi:10.1016/j.apsoil.2013.12.014.
Kobayashi, S., OTA, Y., HARADA, Y., EBITA, A., MORIYA, M., ONODA, H., et al. (2015). The JRA-55 Reanalysis: General Specifications and Basic Characteristics. *J. Meteorol. Soc. Japan. Ser. II* 93, 5–48. doi:10.2151/jmsj.2015-001.
Köhler, P., Abrams, J. F., Völker, C., Hauck, J., and Wolf-Gladrow, D. A. (2013). Geoengineering impact of open ocean dissolution of olivine on atmospheric CO2, surface ocean pH and marine biology. *Environ. Res. Lett.* 8, 014009. doi:10.1088/1748-9326/8/1/014009.
Koskinen, M., Tahvanainen, T., Sarkkola, S., Menberu, M. W., Laurén, A., Sallantaus, T., et al. (2017). Restoration of nutrient-rich forestry-drained peatlands poses a risk for high exports of dissolved organic carbon, nitrogen, and phosphorus. *Sci. Total Environ.* 586, 858–869. doi:10.1016/j.scitotenv.2017.02.065.
Krakauer, N. Y., Randerson, J. T., Primeau, F. W., Gruber, N., and Menemenlis, D. (2006). Carbon isotope evidence for the latitudinal distribution and wind speed dependence of the air–sea gas transfer velocity. *Tellus B Chem. Phys. Meteorol.* 58, 390–417. doi:10.1111/j.1600-0889.2006.00223.x.
Krause, A., Pugh, T. A. M., Bayer, A. D., Doelman, J. C., Humpenöder, F., Anthoni, P., et al. (2017). Global consequences of afforestation and bioenergy cultivation on ecosystem service indicators. *Biogeosciences* 14, 4829–4850. doi:10.5194/bg-14-4829-2017.
Kraxner, F., Nordström, E.-M., Havlík, P., Gusti, M., Mosnier, A., Frank, S., et al. (2013). Global bioenergy scenarios – Future forest development, land-use implications, and trade-offs. *Biomass and Bioenergy* 57, 86–96. doi:10.1016/j.biombioe.2013.02.003.
Kwiatkowski, L., Ricke, K. L., and Caldeira, K. (2015). Atmospheric consequences of disruption of the ocean thermocline. *Environ. Res. Lett.* 10, 034016. doi:10.1088/1748-9326/10/3/034016.
Lampitt, R. ., Achterberg, E. ., Anderson, T. ., Hughes, J. ., Iglesias-Rodriguez, M. ., Kelly-Gerreyn, B. ., et al. (2008). Ocean fertilization: a potential means of geoengineering? *Philos. Trans. R. Soc. A Math. Phys. Eng. Sci.* 366, 3919–3945. doi:10.1098/rsta.2008.0139.
Landschützer, P., Gruber, N., and Bakker, D. C. E. (2016). Decadal variations and trends of the global ocean carbon sink. *Global Biogeochem. Cycles* 30, 1396–1417. doi:10.1002/2015GB005359.
Landschützer, P., Gruber, N., and Bakker, D. C. E. (2020a). An observation-based global monthly gridded sea surface pCO2 product from 1982 onward and its monthly climatology (NCEI Accession 0160558). *NOAA Natl. Centers Environ. Inf.*, Version 5.5. doi:10.7289/v5z899n6.
Landschützer, P., Gruber, N., Bakker, D. C. E., and Schuster, U. (2014). Recent variability of the global ocean carbon sink. *Global Biogeochem. Cycles* 28, 927–949. doi:10.1002/2014GB004853.
Landschützer, P., Gruber, N., Bakker, D. C. E., Stemmler, I., and Six, K. D. (2018). Strengthening seasonal marine CO2 variations due to increasing atmospheric CO2. *Nat. Clim. Chang.* 8, 146–150. doi:10.1038/s41558-017-0057-x.
Landschützer, P., Laruelle, G. G., Roobaert, A., and Regnier, P. (2020b). A uniform pCO2 climatology combining open and coastal oceans. *Earth Syst. Sci. Data* 12, 2537–2553. doi:10.5194/essd-12-2537-2020.
Laruelle, G. G., Landschützer, P., Gruber, N., Tison, J.-L., Delille, B., and Regnier, P. (2017). Global high-resolution monthly CO2 climatology for the coastal ocean derived from neural network interpolation. *Biogeosciences* 14, 4545–4561. doi:10.5194/bg-14-4545-2017.
Lauvset, S. K., Carter, B. R., Perez, F. F., Jiang, L. -Q., Feely, R. A., Velo, A., et al. (2020). Processes driving global interior ocean pH distribution. *Global Biogeochem. Cycles*, 2019GB006229. doi:10.1029/2019GB006229.
Lauvset, S. K., and Gruber, N. (2014). Long-term trends in surface ocean pH in the North Atlantic. *Mar. Chem.* 162, 71–76. doi:https://doi.org/10.1016/j.marchem.2014.03.009.
Lauvset, S. K., Gruber, N., Landschützer, P., Olsen, A., and Tjiputra, J. (2015). Trends and drivers in global surface ocean pH over the past 3 decades. *Biogeosciences* 12, 1285–1298. doi:10.5194/bg-12-1285-2015.
Lauvset, S. K., Key, R. M., Olsen, A., van Heuven, S., Velo, A., Lin, X., et al. (2016). A new global interior ocean mapped climatology: the 1° × 1° GLODAP version 2. *Earth Syst. Sci. Data* 8, 325–340. doi:10.5194/essd-8-325-2016.
Law, R. M., Ziehn, T., Matear, R. J., Lenton, A., Chamberlain, M. A., Stevens, L. E., et al. (2017). The carbon cycle in the Australian Community Climate and Earth System Simulator (ACCESS-ESM1) – Part 1: Model description and pre-

ACCEPTED VERSION SUBJECT TO FINAL EDITS

industrial simulation. *Geosci. Model Dev.* 10, 2567–2590. doi:10.5194/gmd-10-2567-2017.
Liao, E., Resplandy, L., Liu, J., and Bowman, K. W. (2020). Amplification of the Ocean Carbon Sink During El Niños: Role of Poleward Ekman Transport and Influence on Atmospheric CO2. *Global Biogeochem. Cycles* 34, e2020GB006574. doi:https://doi.org/10.1029/2020GB006574.
Liu, C., Wang, H., Tang, X., Guan, Z., Reid, B. J., Rajapaksha, A. U., et al. (2016). Biochar increased water holding capacity but accelerated organic carbon leaching from a sloping farmland soil in China. *Environ. Sci. Pollut. Res.* 23, 995–1006. doi:10.1007/s11356-015-4885-9.
Liu, H., Wrage-Mönnig, N., and Lennartz, B. (2020). Rewetting strategies to reduce nitrous oxide emissions from European peatlands. *Commun. Earth Environ.* 1, 17. doi:10.1038/s43247-020-00017-2.
Liu, Z., He, T., Cao, T., Yang, T., Meng, J., and Chen, W. (2017). Effects of biochar application on nitrogen leaching, ammonia volatilization and nitrogen use efficiency in two distinct soils. *J. soil Sci. plant Nutr.* 17, 515–528. doi:10.4067/S0718-95162017005000037.
Loulergue, L., Schilt, A., Spahni, R., Masson-Delmotte, V., Blunier, T., Lemieux, B., et al. (2008). Orbital and millennial-scale features of atmospheric CH4 over the past 800,000 years. *Nature* 453, 383–386. doi:10.1038/nature06950.
Lundin, L., Nilsson, T., Jordan, S., Lode, E., and Strömgren, M. (2017). Impacts of rewetting on peat, hydrology and water chemical composition over 15 years in two finished peat extraction areas in Sweden. *Wetl. Ecol. Manag.* 25, 405–419. doi:10.1007/s11273-016-9524-9.
Marcellin Yao, K., Marcou, O., Goyet, C., Guglielmi, V., Touratier, F., and Savy, J.-P. (2016). Time variability of the north-western Mediterranean Sea pH over 1995–2011. *Mar. Environ. Res.* 116, 51–60. doi:https://doi.org/10.1016/j.marenvres.2016.02.016.
McGillis, W. R., Edson, J. B., Hare, J. E., and Fairall, C. W. (2001). Direct covariance air-sea CO 2 fluxes. *J. Geophys. Res. Ocean.* 106, 16729–16745. doi:10.1029/2000JC000506.
McKinley, G. A., Fay, A. R., Eddebbar, Y. A., Gloege, L., and Lovenduski, N. S. (2020). External Forcing Explains Recent Decadal Variability of the Ocean Carbon Sink. *AGU Adv.* 1. doi:10.1029/2019AV000149.
McKinley, G. A., Fay, A. R., Lovenduski, N. S., and Pilcher, D. J. (2017). Natural Variability and Anthropogenic Trends in the Ocean Carbon Sink. *Ann. Rev. Mar. Sci.* 9, 125–150. doi:10.1146/annurev-marine-010816-060529.
McNeil, B. I., Matear, R. J., Key, R. M., Bullister, J. L., and Sarmiento, J. L. (2003). Anthropogenic CO₂ Uptake by the Ocean Based on the Global Chlorofluorocarbon Data Set. *Science (80-.).* 299, 235. doi:10.1126/science.1077429.
McNorton, J., Wilson, C., Gloor, M., Parker, R. J., Boesch, H., Feng, W., et al. (2018). Attribution of recent increases in atmospheric methane through 3-D inverse modelling. *Atmos. Chem. Phys.* 18, 18149–18168. doi:10.5194/acp-18-18149-2018.
Meinshausen, M., Vogel, E., Nauels, A., Lorbacher, K., Meinshausen, N., Etheridge, D. M., et al. (2017). Historical greenhouse gas concentrations for climate modelling (CMIP6). *Geosci. Model Dev.* 10, 2057–2116. doi:10.5194/gmd-10-2057-2017.
Meli, P., Rey Benayas, J. M., Balvanera, P., and Martínez Ramos, M. (2014). Restoration enhances wetland biodiversity and ecosystem service supply, but results are context-dependent: a meta-analysis. *PLoS One* 9, e93507–e93507. doi:10.1371/journal.pone.0093507.
Mengis, N., Keller, D. P., Rickels, W., Quaas, M., and Oschlies, A. (2019). Climate engineering–induced changes in correlations between Earth system variables—implications for appropriate indicator selection. *Clim. Change* 153, 305–322. doi:10.1007/s10584-019-02389-7.
Merlivat, L., Boutin, J., Antoine, D., Beaumont, L., Golbol, M., and Vellucci, V. (2018). Increase of dissolved inorganic carbon and decrease in pH in near-surface waters in the Mediterranean Sea during the past two decades. *Biogeosciences* 15, 5653–5662. doi:10.5194/bg-15-5653-2018.
Midorikawa, T., Ishii, M., Kosugi, N., Sasano, D., Nakano, T., Saito, S., et al. (2012). Recent deceleration of oceanic pCO2 increase in the western North Pacific in winter. *Geophys. Res. Lett.* 39, n/a-n/a. doi:10.1029/2012GL051665.
Mikaloff Fletcher, S. E., Gruber, N., Jacobson, A. R., Doney, S. C., Dutkiewicz, S., Gerber, M., et al. (2006). Inverse estimates of anthropogenic CO2 uptake, transport, and storage by the ocean. *Global Biogeochem. Cycles* 20. doi:https://doi.org/10.1029/2005GB002530.
Molari, M., Guilini, K., Lott, C., Weber, M., de Beer, D., Meyer, S., et al. (2018). CO2 leakage alters biogeochemical and ecological functions of submarine sands. *Sci. Adv.* 4, eaao2040. doi:10.1126/sciadv.aao2040.
Müller, S. A., Joos, F., Plattner, G.-K., Edwards, N. R., and Stocker, T. F. (2008). Modeled natural and excess radiocarbon: Sensitivities to the gas exchange formulation and ocean transport strength. *Global Biogeochem. Cycles* 22, n/a-n/a. doi:10.1029/2007GB003065.
Naegler, T. (2009). Reconciliation of excess 14 C-constrained global CO 2 piston velocity estimates. *Tellus B Chem. Phys. Meteorol.* 61, 372–384. doi:10.1111/j.1600-0889.2008.00408.x.

ACCEPTED VERSION
SUBJECT TO FINAL EDITS

Nakano, H., Ishii, M., Rodgers, K. B., Tsujino, H., and Yamanaka, G. (2015). Anthropogenic CO2 uptake, transport, storage, and dynamical controls in the ocean imposed by the meridional overturning circulation: A modeling study. *Global Biogeochem. Cycles* 29, 1706–1724. doi:10.1002/2015GB005128.

Nakazawa, T., Morimoto, S., Aoki, S., and Tanaka, M. (1997). Temporal and spatial variations of the carbon isotopic ratio of atmospheric carbon dioxide in the western Pacific region. *J. Geophys. Res. Atmos.* 102, 1271–1285. doi:10.1029/96JD02720.

NASEM (2019). Negative Emissions Technologies and Reliable Sequestration: A Research Agenda. Washington, DC, USA: National Academies of Sciences, Engineering, and Medicine (NASEM). The National Academies Press doi:10.17226/25259.

Nightingale, P. D., Malin, G., Law, C. S., Watson, A. J., Liss, P. S., Liddicoat, M. I., et al. (2000). In situ evaluation of air-sea gas exchange parameterizations using novel conservative and volatile tracers. *Global Biogeochem. Cycles* 14, 373–387. doi:10.1029/1999GB900091.

Nisbet, E. G., Fisher, R. E., Lowry, D., France, J. L., Allen, G., Bakkaloglu, S., et al. (2020). Methane Mitigation: Methods to Reduce Emissions, on the Path to the Paris Agreement. *Rev. Geophys.* 58, e2019RG000675. doi:https://doi.org/10.1029/2019RG000675.

Niwa, Y., Tomita, H., Satoh, M., Imasu, R., Sawa, Y., Tsuboi, K., et al. (2017). A 4D-Var inversion system based on the icosahedral grid model (NICAM-TM 4D-Var v1.0) – Part 1: Offline forward and adjoint transport models. *Geosci. Model Dev.* 10, 1157–1174. doi:10.5194/gmd-10-1157-2017.

Olafsson, J., Olafsdottir, S. R., Benoit-Cattin, A., Danielsen, M., Arnarson, T. S., and Takahashi, T. (2009). Rate of Iceland Sea acidification from time series measurements. *Biogeosciences* 6, 2661–2668. doi:10.5194/bg-6-2661-2009.

Olefeldt, D., Goswami, S., Grosse, G., Hayes, D. J., Hugelius, G., Kuhry, P., et al. (2016). Arctic Circumpolar Distribution and Soil Carbon of Thermokarst Landscapes, 2015. doi:10.3334/ORNLDAAC/1332.

Olsen, A., Key, R. M., van Heuven, S., Lauvset, S. K., Velo, A., Lin, X., et al. (2016). The Global Ocean Data Analysis Project version 2 (GLODAPv2) – an internally consistent data product for the world ocean. *Earth Syst. Sci. Data* 8, 297–323. doi:10.5194/essd-8-297-2016.

Ono, H., Kosugi, N., Toyama, K., Tsujino, H., Kojima, A., Enyo, K., et al. (2019). Acceleration of ocean acidification in the Western North Pacific. *Geophys. Res. Lett.* 46, 13161–13169. doi:10.1029/2019GL085121.

Oschlies, A. (2009). Impact of atmospheric and terrestrial CO2 feedbacks on fertilization-induced marine carbon uptake. *Biogeosciences* 6, 1603–1613. doi:10.5194/bg-6-1603-2009.

Oschlies, A., Koeve, W., Rickels, W., and Rehdanz, K. (2010a). Side effects and accounting aspects of hypothetical large-scale Southern Ocean iron fertilization. *Biogeosciences* 7, 4017–4035. doi:10.5194/bg-7-4017-2010.

Oschlies, A., Pahlow, M., Yool, A., and Matear, R. J. (2010b). Climate engineering by artificial ocean upwelling: Channelling the sorcerer's apprentice. *Geophys. Res. Lett.* 37. doi:10.1029/2009GL041961.

Oschlies, A., Pahlow, M., Yool, A., and Matear, R. J. (2010c). Climate engineering by artificial ocean upwelling: Channelling the sorcerer's apprentice. *Geophys. Res. Lett.* 37, L04701. doi:10.1029/2009GL041961.

Park, S., Croteau, P., Boering, K. A., Etheridge, D. M., Ferretti, D., Fraser, P. J., et al. (2012). Trends and seasonal cycles in the isotopic composition of nitrous oxide since 1940. *Nat. Geosci.* 5, 261–265. doi:10.1038/ngeo1421.

Patra, P. K., Takigawa, M., Watanabe, S., Chandra, N., Ishijima, K., and Yamashita, Y. (2018). Improved Chemical Tracer Simulation by MIROC4.0-based Atmospheric Chemistry-Transport Model (MIROC4-ACTM). *SOLA* 14, 91–96. doi:10.2151/sola.2018-016.

Paulsen, H., Ilyina, T., Six, K. D., and Stemmler, I. (2017). Incorporating a prognostic representation of marine nitrogen fixers into the global ocean biogeochemical model HAMOCC. *J. Adv. Model. Earth Syst.* 9, 438–464. doi:10.1002/2016MS000737.

Paustian, K., Larson, E., Kent, J., Marx, E., and Swan, A. (2019). Soil C Sequestration as a Biological Negative Emission Strategy. *Front. Clim.* 1, 8. doi:10.3389/fclim.2019.00008.

Paustian, K., Lehmann, J., Ogle, S., Reay, D., Robertson, G. P., and Smith, P. (2016). Climate-smart soils. *Nature* 532, 49–57. doi:10.1038/nature17174.

Pongratz, J., Reick, C. H., Raddatz, T., and Claussen, M. (2010). Biogeophysical versus biogeochemical climate response to historical anthropogenic land cover change. *Geophys. Res. Lett.* 37, L08702. doi:10.1029/2010GL043010.

Prentice, I. C., Farquhar, G. D., Fasham, M. J. R., Goulden, M. L., Heimann, M., Jaramillo, V. J., et al. (2001). "The carbon cycle and atmospheric carbon dioxide.," in *Climate change 2001: The scientific basis. Contribution of Working Group I to the Third Assessment Report of the Intergovernmental Panel on Climate Change (IPCC).*, eds. J. T. Houghton, Y. Ding, D. J. Griggs, M. Noguer, P. J. van der Linden, X. Dai, et al. (Cambridge University Press, Cambridge, United Kingdom and New York, NY, USA), 183–237.

Prinn, R. G., Weiss, R. F., Arduini, J., Arnold, T., DeWitt, H. L., Fraser, P. J., et al. (2018). History of chemically and radiatively important atmospheric gases from the Advanced Global Atmospheric Gases Experiment (AGAGE). *Earth*

ACCEPTED VERSION SUBJECT TO FINAL EDITS

Syst. Sci. Data 10, 985–1018. doi:10.5194/essd-10-985-2018.
Prokopiou, M., Martinerie, P., Sapart, C. J., Witrant, E., Monteil, G., Ishijima, K., et al. (2017). Constraining N2O emissions since 1940 using firn air isotope measurements in both hemispheres. *Atmos. Chem. Phys.* 17, 4539–4564. doi:10.5194/acp-17-4539-2017.
Ramon, J., Lledó, L., Torralba, V., Soret, A., and Doblas-Reyes, F. J. (2019). What global reanalysis best represents near-surface winds? *Q. J. R. Meteorol. Soc.* 145, 3236–3251. doi:10.1002/qj.3616.
Rayner, N. A. (2003). Global analyses of sea surface temperature, sea ice, and night marine air temperature since the late nineteenth century. *J. Geophys. Res.* 108, 4407. doi:10.1029/2002JD002670.
Renforth, P., and Henderson, G. (2017). Assessing ocean alkalinity for carbon sequestration. *Rev. Geophys.* 55, 636–674. doi:10.1002/2016RG000533.
Renou-Wilson, F., Moser, G., Fallon, D., Farrell, C. A., Müller, C., and Wilson, D. (2019). Rewetting degraded peatlands for climate and biodiversity benefits: Results from two raised bogs. *Ecol. Eng.* 127, 547–560. doi:10.1016/j.ecoleng.2018.02.014.
Resplandy, L., Keeling, R. F., Rödenbeck, C., Stephens, B. B., Khatiwala, S., Rodgers, K. B., et al. (2018). Revision of global carbon fluxes based on a reassessment of oceanic and riverine carbon transport. *Nat. Geosci.* 11, 504–509. doi:10.1038/s41561-018-0151-3.
Rice, A. L., Butenhoff, C. L., Teama, D. G., Röger, F. H., Khalil, M. A. K., and Rasmussen, R. A. (2016). Atmospheric methane isotopic record favors fossil sources flat in 1980s and 1990s with recent increase. *Proc. Natl. Acad. Sci.* 113, 10791–10796. doi:10.1073/pnas.1522923113.
Rödenbeck, C., Bakker, D. C. E., Gruber, N., Iida, Y., Jacobson, A. R., Jones, S., et al. (2015). Data-based estimates of the ocean carbon sink variability – first results of the Surface Ocean pCO2 Mapping intercomparison (SOCOM). *Biogeosciences* 12, 7251–7278. doi:10.5194/bg-12-7251-2015.
Rödenbeck, C., Bakker, D. C. E., Metzl, N., Olsen, A., Sabine, C., Cassar, N., et al. (2014). Interannual sea–air CO2 flux variability from an observation-driven ocean mixed-layer scheme. *Biogeosciences* 11, 4599–4613. doi:10.5194/bg-11-4599-2014.
Rödenbeck, C., Keeling, R. F., Bakker, D. C. E., Metzl, N., Olsen, A., Sabine, C., et al. (2013). Global surface-ocean pCO2 and sea–air CO2 flux variability from an observation-driven ocean mixed-layer. *Ocean Sci.* 9, 193–216. doi:10.5194/os-9-193-2013.
Rödenbeck, C., Zaehle, S., Keeling, R., and Heimann, M. (2018). How does the terrestrial carbon exchange respond to inter-annual climatic variations? A quantification based on atmospheric CO₂ data. *Biogeosciences* 15, 2481–2498. doi:10.5194/bg-15-2481-2018.
Roe, S., Streck, C., Obersteiner, M., Frank, S., Griscom, B., Drouet, L., et al. (2019a). Contribution of the land sector to a 1.5 °C world. *Nat. Clim. Chang.* 9, 817–828. doi:10.1038/s41558-019-0591-9.
Roe, S., Streck, C., Obersteiner, M., Frank, S., Griscom, B., Drouet, L., et al. (2019b). Contribution of the land sector to a 1.5 °C world. *Nat. Clim. Chang.* 9, 817–828. doi:10.1038/s41558-019-0591-9.
Roobaert, A., Laruelle, G. G., Landschützer, P., and Regnier, P. (2018). Uncertainty in the global oceanic CO2 uptake induced by wind forcing: quantification and spatial analysis. *Biogeosciences* 15, 1701–1720. doi:10.5194/bg-15-1701-2018.
Rosentreter, J. A., Maher, D. T., Erler, D. V., Murray, R. H., and Eyre, B. D. (2018). Methane emissions partially offset "blue carbon" burial in mangroves. *Sci. Adv.* 4, eaao4985. doi:10.1126/sciadv.aao4985.
Rubino, M., Etheridge, D. M., Thornton, D. P., Howden, R., Allison, C. E., Francey, R. J., et al. (2019). Revised records of atmospheric trace gases CO2, CH4, N2O, and 13C over the last 2000 years from Law Dome, Antarctica. *Earth Syst. Sci. Data* 11, 473–492. doi:10.5194/essd-11-473-2019.
Saeki, T., and Patra, P. K. (2017). Implications of overestimated anthropogenic CO2 emissions on East Asian and global land CO2 flux inversion. *Geosci. Lett.* 4, 9. doi:10.1186/s40562-017-0074-7.
Sallée, J.-B., Matear, R. J., Rintoul, S. R., and Lenton, A. (2012). Localized subduction of anthropogenic carbon dioxide in the Southern Hemisphere oceans. *Nat. Geosci.* 5, 579–584. doi:10.1038/ngeo1523.
Salter, I., Schiebel, R., Ziveri, P., Movellan, A., Lampitt, R., and Wolff, G. A. (2014). Carbonate counter pump stimulated by natural iron fertilization in the Polar Frontal Zone. *Nat. Geosci.* 7, 885–889. doi:10.1038/ngeo2285.
Saunois, M., Stavert, A. R., Poulter, B., Bousquet, P., Canadell, J. G., Jackson, R. B., et al. (2020). The Global Methane Budget 2000–2017. *Earth Syst. Sci. Data* 12, 1561–1623. doi:10.5194/essd-12-1561-2020.
Schilt, A., Baumgartner, M., Schwander, J., Buiron, D., Capron, E., Chappellaz, J., et al. (2010). Atmospheric nitrous oxide during the last 140,000years. *Earth Planet. Sci. Lett.* 300, 33–43. doi:10.1016/j.epsl.2010.09.027.
Schwinger, J., Goris, N., Tjiputra, J. F., Kriest, I., Bentsen, M., Bethke, I., et al. (2016). Evaluation of NorESM-OC (versions 1 and 1.2), the ocean carbon-cycle stand-alone configuration of the Norwegian Earth System Model

ACCEPTED VERSION
SUBJECT TO FINAL EDITS

(NorESM1). *Geosci. Model Dev.* 9, 2589–2622. doi:10.5194/gmd-9-2589-2016.
Shen, Q., Hedley, M., Camps Arbestain, M., and Kirschbaum, M. U. . (2016). Can biochar increase the bioavailability of phosphorus? *J. soil Sci. plant Nutr.* 16, 0–0. doi:10.4067/S0718-95162016005000022.
Shutler, J. D., Land, P. E., Piolle, J.-F., Woolf, D. K., Goddijn-Murphy, L., Paul, F., et al. (2016). FluxEngine: A Flexible Processing System for Calculating Atmosphere–Ocean Carbon Dioxide Gas Fluxes and Climatologies. *J. Atmos. Ocean. Technol.* 33, 741–756. doi:10.1175/JTECH-D-14-00204.1.
Singh, N. K., Gourevitch, J. D., Wemple, B. C., Watson, K. B., Rizzo, D. M., Polasky, S., et al. (2019). Optimizing wetland restoration to improve water quality at a regional scale. *Environ. Res. Lett.* 14, 64006. doi:10.1088/1748-9326/ab1827.
Smetacek, V., Klaas, C., Strass, V. H., Assmy, P., Montresor, M., Cisewski, B., et al. (2012). Deep carbon export from a Southern Ocean iron-fertilized diatom bloom. *Nature* 487, 313–319. doi:10.1038/nature11229.
Smith, P. (2016). Soil carbon sequestration and biochar as negative emission technologies. *Glob. Chang. Biol.* 22, 1315–1324. doi:10.1111/gcb.13178.
Smith, P., Adams, J., Beerling, D. J., Beringer, T., Calvin, K. V., Fuss, S., et al. (2019). Land-Management Options for Greenhouse Gas Removal and Their Impacts on Ecosystem Services and the Sustainable Development Goals. *Annu. Rev. Environ. Resour.* 44, 255–286. doi:10.1146/annurev-environ-101718-033129.
Smith, P., Calvin, K., Nkem, J., Campbell, D., Cherubini, F., Grassi, G., et al. (2020). Which practices co-deliver food security, climate change mitigation and adaptation, and combat land degradation and desertification? *Glob. Chang. Biol.* 26, 1532–1575. doi:https://doi.org/10.1111/gcb.14878.
Smith, P., Davis, S. J., Creutzig, F., Fuss, S., Minx, J., Gabrielle, B., et al. (2016). Biophysical and economic limits to negative CO2 emissions. *Nat. Clim. Chang.* 6, 42–50. doi:10.1038/nclimate2870.
Smith, P., Martino, D., Cai, Z., Gwary, D., Janzen, H., Kumar, P., et al. (2008). Greenhouse gas mitigation in agriculture. *Philos. Trans. R. Soc. B Biol. Sci.* 363, 789–813. doi:10.1098/rstb.2007.2184.
Smith, P., Price, J., Molotoks, A., Warren, R., and Malhi, Y. (2018). Impacts on terrestrial biodiversity of moving from a 2°C to a 1.5°C target. *Philos. Trans. R. Soc. A Math. Eng. Sci.* 376, 20160456. doi:10.1098/rsta.2016.0456.
Smith, W. K., Zhao, M., and Running, S. W. (2012). Global bioenergy capacity as constrained by observed biospheric productivity rates. *Bioscience* 62, 911–922. doi:10.1525/bio.2012.62.10.11.
Sonntag, S., Ferrer González, M., Ilyina, T., Kracher, D., Nabel, J. E. M. S., Niemeier, U., et al. (2018). Quantifying and Comparing Effects of Climate Engineering Methods on the Earth System. *Earth's Futur.* 6, 149–168. doi:10.1002/2017EF000620.
Sutton, A. J., Feely, R. A., Sabine, C. L., McPhaden, M. J., Takahashi, T., Chavez, F. P., et al. (2014). Natural variability and anthropogenic change in equatorial Pacific surface ocean pCO2 and pH. *Global Biogeochem. Cycles* 28, 131–145. doi:10.1002/2013GB004679.
Sutton, A. J., Wanninkhof, R., Sabine, C. L., Feely, R. A., Cronin, M. F., and Weller, R. A. (2017). Variability and trends in surface seawater pCO2 and CO2 flux in the Pacific Ocean. *Geophys. Res. Lett.* 44, 5627–5636. doi:10.1002/2017GL073814.
Sweeney, C., Gloor, E., Jacobson, A. R., Key, R. M., McKinley, G., Sarmiento, J. L., et al. (2007). Constraining global air-sea gas exchange for CO 2 with recent bomb 14 C measurements. *Global Biogeochem. Cycles* 21, GB2015. doi:10.1029/2006GB002784.
Takahashi, T., Sutherland, S. C., Chipman, D. W., Goddard, J. G., Ho, C., Newberger, T., et al. (2014). Climatological distributions of pH, pCO2, total CO2, alkalinity, and CaCO3 saturation in the global surface ocean, and temporal changes at selected locations. *Mar. Chem.* 164, 95–125. doi:10.1016/j.marchem.2014.06.004.
Tanhua, T., Hoppema, M., Jones, E. M., Stöven, T., Hauck, J., Dávila, M. G., et al. (2017). Temporal changes in ventilation and the carbonate system in the Atlantic sector of the Southern Ocean. *Deep Sea Res. Part II Top. Stud. Oceanogr.* 138, 26–38. doi:10.1016/j.dsr2.2016.10.004.
Thompson, R. L., Lassaletta, L., Patra, P. K., Wilson, C., Wells, K. C., Gressent, A., et al. (2019). Acceleration of global N2O emissions seen from two decades of atmospheric inversion. *Nat. Clim. Chang.* 9, 993–998. doi:10.1038/s41558-019-0613-7.
Tian, H., Xu, R., Canadell, J. G., Thompson, R. L., Winiwarter, W., Suntharalingam, P., et al. (2020). A comprehensive quantification of global nitrous oxide sources and sinks. *Nature* 586, 248–256. doi:10.1038/s41586-020-2780-0.
Tian, H., Yang, J., Xu, R., Lu, C., Canadell, J. G., Davidson, E. A., et al. (2019). Global soil nitrous oxide emissions since the preindustrial era estimated by an ensemble of terrestrial biosphere models: Magnitude, attribution, and uncertainty. *Glob. Chang. Biol.* 25, 640–659. doi:10.1111/gcb.14514.
Tiemeyer, B., Freibauer, A., Borraz, E. A., Augustin, J., Bechtold, M., Beetz, S., et al. (2020). A new methodology for organic soils in national greenhouse gas inventories: Data synthesis, derivation and application. *Ecol. Indic.* 109, 105838. doi:https://doi.org/10.1016/j.ecolind.2019.105838.
Tohjima, Y., Mukai, H., Machida, T., Hoshina, Y., and Nakaoka, S.-I. (2019). Global carbon budgets estimated from

ACCEPTED VERSION SUBJECT TO FINAL EDITS

atmospheric O2/N2 andCO2 observations in the western Pacific region over a 15-year period. *Atmos. Chem. Phys.* 19, 9269–9285. doi:10.5194/acp-19-9269-2019.
Tokarska, K. B., and Zickfeld, K. (2015). The effectiveness of net negative carbon dioxide emissions in reversing anthropogenic climate change. *Environ. Res. Lett.* 10, 094013. doi:10.1088/1748-9326/10/9/094013.
Tonitto, C., David, M. B., and Drinkwater, L. E. (2006). Replacing bare fallows with cover crops in fertilizer-intensive cropping systems: A meta-analysis of crop yield and N dynamics. *Agric. Ecosyst. Environ.* 112, 58–72. doi:10.1016/j.agee.2005.07.003.
Toyama, K., Rodgers, K. B., Blanke, B., Iudicone, D., Ishii, M., Aumont, O., et al. (2017). Large reemergence of anthropogenic carbon into the ocean's surface mixed layer sustained by the ocean's overturning circulation. *J. Clim.* 30, 8615–8631. doi:10.1175/JCLI-D-16-0725.1.
Tsuruta, A., Aalto, T., Backman, L., Hakkarainen, J., van der Laan-Luijkx, I. T., Krol, M. C., et al. (2017). Global methane emission estimates for 2000–2012 from CarbonTracker Europe-CH₄ v1.0. *Geosci. Model Dev.* 10, 1261–1289. doi:10.5194/gmd-10-1261-2017.
Tucker, C. J., Pinzon, J. E., Brown, M. E., Slayback, D. A., Pak, E. W., Mahoney, R., et al. (2005). An extended AVHRR 8-km NDVI dataset compatible with MODIS and SPOT vegetation NDVI data. *Int. J. Remote Sens.* 26, 4485–4498. doi:10.1080/01431160500168686.
Turnbull, J. C., Mikaloff Fletcher, S. E., Ansell, I., Brailsford, G. W., Moss, R. C., Norris, M. W., et al. (2017). Sixty years of radiocarbon dioxide measurements at Wellington, New Zealand: 1954–2014. *Atmos. Chem. Phys.* 17, 14771–14784. doi:10.5194/acp-17-14771-2017.
van der Laan-Luijkx, I. T., van der Velde, I. R., van der Veen, E., Tsuruta, A., Stanislawska, K., Babenhauserheide, A., et al. (2017). The CarbonTracker Data Assimilation Shell (CTDAS) v1.0: implementation and global carbon balance 2001–2015. *Geosci. Model Dev.* 10, 2785–2800. doi:10.5194/gmd-10-2785-2017.
Vanselow-Algan, M., Schmidt, S. R., Greven, M., Fiencke, C., Kutzbach, L., and Pfeiffer, E.-M. (2015). High methane emissions dominated annual greenhouse gas balances 30 years after bog rewetting. *Biogeosciences* 12, 4361–4371. doi:10.5194/bg-12-4361-2015.
Verheijen, F. G. A., Zhuravel, A., Silva, F. C., Amaro, A., Ben-Hur, M., and Keizer, J. J. (2019). The influence of biochar particle size and concentration on bulk density and maximum water holding capacity of sandy vs sandy loam soil in a column experiment. *Geoderma* 347, 194–202. doi:10.1016/j.geoderma.2019.03.044.
Wakita, M., Nagano, A., Fujiki, T., and Watanabe, S. (2017). Slow acidification of the winter mixed layer in the subarctic western North Pacific. *J. Geophys. Res. Ocean.* 122, 6923–6935. doi:10.1002/2017JC013002.
Wang, F., Maksyutov, S., Tsuruta, A., Janardanan, R., Ito, A., Sasakawa, M., et al. (2019a). Methane Emission Estimates by the Global High-Resolution Inverse Model Using National Inventories. *Remote Sens.* 11, 2489. doi:10.3390/rs11212489.
Wang, S., Ma, S., Shan, J., Xia, Y., Lin, J., and Yan, X. (2019b). A 2-year study on the effect of biochar on methane and nitrous oxide emissions in an intensive rice–wheat cropping system. *Biochar* 1, 177–186. doi:10.1007/s42773-019-00011-8.
Wanninkhof, R. (1992). Relationship between wind speed and gas exchange over the ocean. *J. Geophys. Res.* 97, 7373. doi:10.1029/92JC00188.
Wanninkhof, R. (2014). Relationship between wind speed and gas exchange over the ocean revisited. *Limnol. Oceanogr. Methods* 12, 351–362. doi:10.4319/lom.2014.12.351.
Weiss, R. F. (1974). Carbon dioxide in water and seawater: the solubility of a non-ideal gas. *Mar. Chem.* 2, 203–215. doi:10.1016/0304-4203(74)90015-2.
Williams, N. L., Juranek, L. W., Feely, R. A., Johnson, K. S., Sarmiento, J. L., Talley, L. D., et al. (2017). Calculating surface ocean pCO2 from biogeochemical Argo floats equipped with pH: An uncertainty analysis. *Global Biogeochem. Cycles* 31, 591–604. doi:10.1002/2016GB005541.
Williamson, P., & Bodle, R. (2016). Update on climate geoengineering in relation to the convention on biological diversity: potential impacts and regulatory framework. Montreal.
Williamson, P., Wallace, D. W. R., Law, C. S., Boyd, P. W., Collos, Y., Croot, P., et al. (2012). Ocean fertilization for geoengineering: A review of effectiveness, environmental impacts and emerging governance. *Process Saf. Environ. Prot.* 90, 475–488. doi:10.1016/j.psep.2012.10.007.
Wilson, D., Blain, D., Couwenberg, J., Evans, C.D., Murdiyarso, D., Page, S.E., Renou-Wilson, F., Rieley, J.O., Sirin, A., Strack, M. & Tuittila, E.-S. (2016). Greenhouse gas emission factors associated with rewetting of organic soils. *Mires Peat* 17, 1–28. doi:10.19189/MaP.2016.OMB.222.
Wilson, D., Farrell, C. A., Fallon, D., Moser, G., Müller, C., and Renou-Wilson, F. (2016). Multiyear greenhouse gas balances at a rewetted temperate peatland. *Glob. Chang. Biol.* 22, 4080–4095. doi:10.1111/gcb.13325.
Wolter, K., and Timlin, M. S. (1998). Measuring the strength of ENSO events: How does 1997/98 rank? *Weather* 53, 315–

ACCEPTED VERSION SUBJECT TO FINAL EDITS

324. doi:10.1002/j.1477-8696.1998.tb06408.x.
Wolter, K., and Timlin, M. S. (2011). El Niño/Southern Oscillation behaviour since 1871 as diagnosed in an extended multivariate ENSO index (MEI.ext). *Int. J. Climatol.* 31, 1074–1087. doi:10.1002/joc.2336.
Woolf, D., Amonette, J. E., Street-Perrott, F. A., Lehmann, J., and Joseph, S. (2010). Sustainable biochar to mitigate global climate change. *Nat. Commun.* 1, 56. doi:10.1038/ncomms1053.
Worrall, F., Boothroyd, I. M., Gardner, R. L., Howden, N. J. K., Burt, T. P., Smith, R., et al. (2019). The Impact of Peatland Restoration on Local Climate: Restoration of a Cool Humid Island. *J. Geophys. Res. Biogeosciences* 124, 1696–1713. doi:https://doi.org/10.1029/2019JG005156.
Xue, L., Yu, W., Wang, H., Jiang, L.-Q., Feng, L., Gao, L., et al. (2014). Temporal changes in surface partial pressure of carbon dioxide and carbonate saturation state in the eastern equatorial Indian Ocean during the 1962–2012 period. *Biogeosciences* 11, 6293–6305. doi:10.5194/bg-11-6293-2014.
Yang, shihong, Xiao, Y., Sun, X., Ding, J., Jiang, Z., and Xu, J. (2019). Biochar improved rice yield and mitigated CH4 and N2O emissions from paddy field under controlled irrigation in the Taihu Lake Region of China. *Atmos. Environ.* 200, 69–77. doi:10.1016/j.atmosenv.2018.12.003.
Yin, Y., Chevallier, F., Ciais, P., Broquet, G., Fortems-Cheiney, A., Pison, I., et al. (2015). Decadal trends in global CO emissions as seen by MOPITT. *Atmos. Chem. Phys.* 15, 13433–13451. doi:10.5194/acp-15-13433-2015.
Yoshida, Y., Kikuchi, N., Morino, I., Uchino, O., Oshchepkov, S., Bril, A., et al. (2013). Improvement of the retrieval algorithm for GOSAT SWIR XCO2 and XCH4 and their validation using TCCON data. *Atmos. Meas. Tech.* 6, 1533–1547. doi:10.5194/amt-6-1533-2013.
Zeng, J., Nojiri, Y., Landschützer, P., Telszewski, M., and Nakaoka, S. (2014). A Global Surface Ocean f CO 2 Climatology Based on a Feed-Forward Neural Network. *J. Atmos. Ocean. Technol.* 31, 1838–1849. doi:10.1175/JTECH-D-13-00137.1.
Zhang, Y., Hu, X., Zou, J., Zhang, D., Chen, W., Liu, Y., et al. (2018a). Response of surface albedo and soil carbon dioxide fluxes to biochar amendment in farmland. *J. Soils Sediments* 18, 1590–1601. doi:10.1007/s11368-017-1889-8.
Zhang, Y., Joiner, J., Hamed Alemohammad, S., Zhou, S., and Gentine, P. (2018b). A global spatially contiguous solar-induced fluorescence (CSIF) dataset using neural networks. *Biogeosciences* 15. doi:10.5194/bg-15-5779-2018.
Zhou, M., Wang, X., Ke, Y., and Zhu, B. (2019). Effects of afforestation on soil nitrous oxide emissions in a subtropical montane agricultural landscape: A 3-year field experiment. *Agric. For. Meteorol.* 266–267, 221–230. doi:https://doi.org/10.1016/j.agrformet.2019.01.003.
Zickfeld, K., Azevedo, D., Mathesius, S., and Matthews, H. D. (2021). Asymmetry in the climate-carbon cycle response to positive and negative CO2 emissions. accepted.

ACCEPTED VERSION
SUBJECT TO FINAL EDITS

Chapter 6: Short-lived climate forcers

Coordinating Lead Authors:
Vaishali Naik (United States of America), Sophie Szopa (France)

Lead Authors:
Bhupesh Adhikary (Nepal), Paulo Artaxo (Brazil), Terje Berntsen (Norway), William D. Collins (United States of America), Sandro Fuzzi (Italy), Laura Gallardo (Chile), Astrid Kiendler-Scharr (Germany/Austria), Zbigniew Klimont (Austria/Poland), Hong Liao (China), Nadine Unger (United Kingdom/United States of America), Prodromos Zanis (Greece)

Contributing Authors:
Wenche Aas (Norway), Dimitris Akritidis (Greece), Robert J. Allen (United States of America), Nicolas Bellouin (United Kingdom/France), Sophie Berger (France/Belgium), Sara M. Blichner (Norway), Josep G. Canadell (Australia), William Collins (United Kingdom), Owen R. Cooper (United States of America), Frank J. Dentener (EU/The Netherlands), Sarah Doherty (United States of America), Jean-Louis Dufresne (France), Sergio Henrique Faria (Spain/Brazil), Piers Forster (United Kingdom), Tzung-May Fu (China), Jan S. Fuglestvedt (Norway), John C. Fyfe (Canada), Aristeidis K. Georgoulias (Greece), Matthew J. Gidden (Austria/ United States of America), Nathan P. Gillett (Canada), Paul Ginoux (United States of America), Paul T. Griffiths (United Kingdom), Jian He (United States of America/China), Christopher Jones (United Kingdom), Svitlana Krakovska (Ukraine), Chaincy Kuo (United States of America), David S. Lee (United Kingdom), Maurice Levasseur (Canada), Martine Lizotte (Canada), Thomas K. Maycock (United States of America), Jean-François Müller (Belgium), Helène Muri (Norway), Lee T. Murray (United States of America), Zebedee R. J. Nicholls (Australia), Jurgita Ovadnevaite (Ireland/Lithuania), Prabir K. Patra (Japan/India), Fabien Paulot (United States of America/France, United States of America), Pallav Purohit (Austria/India), Johannes Quaas (Germany), Joeri Rogelj (United Kingdom /Belgium), Bjørn H. Samset (Norway), Chris Smith (United Kingdom), Izuru Takayabu (Japan), Marianne Tronstad Lund (Norway),Alexandra P. Tsimpidi (Germany/Greece), Steven Turnock United Kingdom), Rita Van Dingenen (Italy/Belgium), Hua Zhang (China), Alcide Zhao (United Kingdom/China)

Review Editors:
Yugo Kanaya (Japan), Michael J. Prather (United States of America), Noureddine Yassaa (Algeria)

Chapter Scientist:
Chaincy Kuo (United States of America)

This Chapter should be cited as:
Naik, V., S. Szopa, B. Adhikary, P. Artaxo, T. Berntsen, W. D. Collins, S. Fuzzi, L. Gallardo, A. Kiendler Scharr, Z. Klimont, H. Liao, N. Unger, P. Zanis, 2021, Short-Lived Climate Forcers. In: *Climate Change 2021: The Physical Science Basis. Contribution of Working Group I to the Sixth Assessment Report of the Intergovernmental Panel on Climate Change* [Masson-Delmotte, V., P. Zhai, A. Pirani, S. L. Connors, C. Péan, S. Berger, N. Caud, Y. Chen, L. Goldfarb, M. I. Gomis, M. Huang, K. Leitzell, E. Lonnoy, J. B. R. Matthews, T. K. Maycock, T. Waterfield, O. Yelekçi, R. Yu and B. Zhou (eds.)]. Cambridge University Press. In Press.

Date: August 2021

This document is subject to copy-editing, corrigenda and trickle backs.

ACCEPTED VERSION SUBJECT TO FINAL EDITING

Executive Summary 4
6.1 Introduction 9
6.1.1 Importance of SLCFs for climate and air quality 9
6.1.2 Treatment of SLCFs in previous assessments 11
6.1.3 Chapter Roadmap 12
6.2 Global and regional temporal evolution of SLCF emissions 13
6.2.1 Anthropogenic sources 13
6.2.2 Emissions by natural systems 16
6.2.2.1 Lightning NO_x 17
6.2.2.2 NO_x emissions by soils 17
6.2.2.3 Vegetation emissions of organic compounds 17
6.2.2.4 Land emissions of dust particles 19
6.2.2.5 Oceanic emissions of marine aerosols and precursors 19
6.2.2.6 Open biomass burning emissions 20
6.3 Evolution of Atmospheric SLCF abundances 21
BOX 6.1: Atmospheric abundance of SLCFs: from process level studies to global chemistry-climate models 21
6.3.1 Methane (CH_4) 23
6.3.2 Ozone (O_3) 25
6.3.2.1 Tropospheric ozone 25
6.3.2.2 Stratospheric ozone 27
6.3.3 Precursor Gases 28
6.3.3.1 Nitrogen Oxides (NO_x) 28
6.3.3.2 Carbon Monoxide (CO) 29
6.3.3.3 Non-Methane Volatile Organic Compounds (NMVOCs) 31
6.3.3.4 Ammonia (NH_3) 32
6.3.3.5 Sulphur Dioxide (SO_2) 33
6.3.4 Short-lived Halogenated Species 34
6.3.5 Aerosols 35
6.3.5.1 Sulphate (SO_4^{2-}) 36
6.3.5.2 Ammonium (NH_4^+), and Nitrate Aerosols (NO_3^-) 38
6.3.5.3 Carbonaceous Aerosols 39
6.3.6 Implications of SLCF abundances for Atmospheric Oxidizing Capacity 41
6.4 SLCF radiative forcing and climate effects 44
6.4.1 Historical Estimates of Regional Short-lived Climate Forcing 44
6.4.2 Emission-based Radiative Forcing and effect on GSAT 46
6.4.3 Climate responses to SLCFs 49
6.4.4 Indirect radiative forcing through effects of SLCFs on the carbon cycle 51
6.4.5 Non-CO_2 biogeochemical feedbacks 52

ACCEPTED VERSION SUBJECT TO FINAL EDITING

6.4.6 ERF by aerosols in proposed Solar Radiation Modification 55
6.5 Implications of changing climate on AQ 57
6.5.1 Effect of climate change on surface O_3 57
6.5.2 Impact of climate change on particulate matter 59
6.5.3 Impact of climate change on extreme pollution 60
6.6 Air Quality and Climate response to SLCF mitigation 61
6.6.1 Implications of lifetime on temperature response time horizon 62
6.6.2 Attribution of temperature and air pollution changes to emission sectors and regions 63
6.6.2.1 Agriculture 63
6.6.2.2 Residential and Commercial cooking, heating 63
6.6.2.3 Transportation 64
6.6.2.3.1 Aviation 64
6.6.2.3.2 Shipping 65
6.6.2.3.3 Land transportation 65
6.6.2.3.4 GSAT response to emission pulse of current emissions 66
6.6.2.3.5 Source attribution of regional air pollution 67
6.6.3 Past and current SLCF reduction policies and future mitigation opportunities 69
6.6.3.1 Climate response to past AQ policies 70
6.6.3.2 Recently decided SLCF relevant global legislation 70
6.6.3.3 Assessment of SLCF mitigation strategies and opportunities 71
BOX 6.2: SLCF Mitigation and Sustainable Development Goals (SDG) opportunities 73
6.7 Future projections of Atmospheric Composition and Climate response in SSP scenarios 77
6.7.1 Projections of Emissions and Atmospheric Abundances 77
6.7.1.1 SLCF Emissions and atmospheric abundances 77
6.7.1.2 Future evolution of surface ozone and PM concentrations 81
6.7.2 Evolution of future climate in response to SLCF emissions 83
6.7.2.1 Effects of SLCFs on ERF and climate response 83
6.7.2.2 Effect of regional emissions of SLCFs on GSAT 85
6.7.3 Effect of SLCFs mitigation in SSP scenarios 86
6.8 Perspectives 89
Frequently Asked Questions 90
References 93
Figures 128

ACCEPTED VERSION
SUBJECT TO FINAL EDITING

Executive Summary

Short-lived climate forcers (SLCFs) affect climate and are, in most cases, also air pollutants. They include aerosols (sulphate, nitrate, ammonium, carbonaceous aerosols, mineral dust and sea spray), which are also called particulate matter (PM), and chemically reactive gases (methane, ozone, some halogenated compounds, nitrogen oxides, carbon monoxide, non-methane volatile organic compounds, sulphur dioxide and ammonia). Except for methane and some halogenated compounds whose lifetimes are about a decade or more, SLCFs abundances are highly spatially heterogeneous since they only persist in the atmosphere from a few hours to a couple of months. SLCFs are either radiatively active or influence the abundances of radiatively active compounds through chemistry (chemical adjustments), and their climate effect occurs predominantly in the first two decades after their emission or formation. They can have either a cooling or warming effect on climate, and they also affect precipitation and other climate variables. Methane and some halogenated compounds are included in climate treaties, unlike the other SLCFs that are nevertheless indirectly affected by climate change mitigation since many of them are often co-emitted with CO_2 in combustion processes. This chapter assesses the changes, in the past and in a selection of possible futures of the emissions and abundances of individual SLCFs primarily on a global and continental scale, and how these changes affect the Earth's energy balance through radiative forcing and feedback in the climate system. The attribution of climate and air-quality changes to emission sectors and regions, and the effects of SLCF mitigations defined for various environmental purposes, are also assessed.

Recent Evolution in SLCF Emissions and Abundances

Over the last decade (2010–2019), strong shifts in the geographical distribution of emissions have led to changes in atmospheric abundances of highly variable SLCFs (*high confidence*). Evidence from satellite and surface observations show strong regional variations in trends of ozone (O_3), aerosols and their precursors (*high confidence*). In particular, tropospheric columns of nitrogen dioxide (NO_2) and sulphur dioxide (SO_2) continued to decline over North America and Europe (*high confidence*) and to increase over South Asia (*medium confidence*), but have declined over East Asia (*high confidence*). Global carbon monoxide (CO) abundance has continued to decline (*high confidence*). The concentrations of hydrofluorocarbons (HFCs) are increasing (*high confidence*). Global carbonaceous aerosol budgets and trends remain poorly characterized due to limited observations, but sites representative of background conditions have reported multi-year declines in black carbon (BC) over several regions of the Northern Hemisphere. {6.2, 6.3, 2.2.4, 2.2.5, 2.2.6}

There is no significant trend in the global mean tropospheric concentration of hydroxyl (OH) radical – the main sink for many SLCFs, including methane (CH_4) – from 1850 up to around 1980 (*low confidence*) but OH has remained stable or exhibited a positive trend since the 1980s (*medium confidence)*. Global OH cannot be measured directly and is inferred from Earth system and climate chemistry models (ESMs, CCMs) constrained by emissions and from observationally constrained inversion methods. There is conflicting information from these methods for the 1980–2014 period. ESMs and CCMs concur on a positive trend since 1980 (about a 9% increase over 1980–2014) and there is *medium confidence* that this trend is mainly driven by increases in global anthropogenic nitrogen oxide (NO_x) emissions and decreases in anthropogenic CO emissions. The observation-constrained methods suggest either positive trends or the absence of trends based on *limited evidence and medium agreement.* Future changes in global OH, in response to SLCF emissions and climate change, will depend on the interplay between multiple offsetting drivers of OH. {6.3.6 and Cross-Chapter Box 5.1}

Effect of SLCFs on Climate and Biogeochemical Cycles

Over the historical period, changes in aerosols and their ERF have primarily contributed to a surface cooling, partly masking the greenhouse gas driven warming (*high confidence*). Radiative forcings induced by aerosol changes lead to both local and remote temperature responses (*high confidence*). The temperature response preserves the South-North gradient of the aerosol ERF – hemispherical asymmetry- but is more uniform with latitude and is strongly amplified towards the Arctic (*medium confidence*). {6.4.1, 6.4.3}

Since the mid-1970s, trends in aerosols and their precursor emissions have led to a shift from an

ACCEPTED VERSION SUBJECT TO FINAL EDITING

increase to a decrease of the magnitude of the negative globally-averaged net aerosol ERF (*high confidence*). However, the timing of this shift varies by continental-scale region and has not occured for some finer regional scales. The spatial and temporal distribution of the net aerosol ERF from 1850 to 2014 is highly heterogeneous, with stronger magnitudes in the Northern Hemisphere (*high confidence*). {6.4.1}

For forcers with short lifetimes (e.g., months) and not considering chemical adjustments, the response in surface temperature occurs strongly as soon as a sustained change in emissions is implemented, and that response continues to grow for a few years, primarily due to thermal inertia in the climate system (*high confidence*). Near its maximum, the response slows down but will then take centuries to reach equilibrium (*high confidence*). For SLCFs with longer lifetimes (e.g., a decade), a delay equivalent to their lifetimes is appended to the delay due to thermal inertia (*high confidence*). {6.6.1}

Over the 1750-2019 period, changes in SLCF emissions, especially of CH_4, NO_x and SO_2, have substantial effects on effective radiative forcing (ERF) (*high confidence*). The net global emissions-based ERF of NO_x is negative and that of non-methane volatile organic compounds (NMVOCs) is positive, in agreement with the AR5 assessment (*high confidence*). For methane, the emission-based ERF is twice as high as the abundance-based ERF (*high confidence*) attributed to chemical adjustment mainly via ozone production. SO_2 emission changes make the dominant contribution to the ERF from aerosol–cloud interactions (*high confidence*). Over the 1750-2019 period, the contributions from the emitted compounds to GSAT changes broadly match their contributions to the ERF (*high confidence*). Since a peak in emissions-induced SO_2 ERF has already occurred recently and since there is a delay in the full GSAT response, changes in SO_2 emissions have a slightly larger contribution to GSAT change than for CO_2 emissions, relative to their respective contributions to ERF. {6.4.2, 6.6.1 and 7.3.5}

Reactive nitrogen, ozone and aerosols affect terrestrial vegetation and the carbon cycle through deposition and effects on large scale radiation (*high confidence*). However, the magnitude of these effects on the land carbon sink, ecosystem productivity and hence their indirect CO_2 forcing remain uncertain due to the difficulty in disentangling the complex interactions between the individual effects. As such, these effects are assessed to be of second order in comparison to the direct CO_2 forcing (*high confidence*), but effects of ozone on terrestrial vegetation could add a substantial (positive) forcing compared with the direct ozone forcing (*low confidence*). {6.4.5}

Climate feedbacks induced from changes in emissions, abundances or lifetimes of SLCFs mediated by natural processes or atmospheric chemistry are assessed to have an overall cooling effect (*low confidence*), that is, a total negative feedback parameter, of -0.20 [-0.41 to +0.01] W m^{-2} $°C^{-1}$. These non-CO_2 biogeochemical feedbacks are estimated from ESMs, which have advanced since AR5 to include a consistent representation of biogeochemical cycles and atmospheric chemistry. However, process-level understanding of many chemical and biogeochemical feedbacks involving SLCFs, particularly natural emissions, is still emerging, resulting in *low confidence* in the magnitude and sign of most of SLCF climate feedback parameter. {6.2.2, 6.4.5}

Future Projections for Air Quality Considering Shared Socio-economic Pathways (SSPs)

Future air quality (in term of surface ozone and PM concentrations) on global to local scales will be primarily driven by changes in precursor emissions as opposed to climate change (*high confidence*) and climate change is projected to have mixed effects. A warmer climate is expected to reduce surface O_3 in regions remote from pollution sources (*high confidence*) but is expected to increase it by a few parts per billion over polluted regions, depending on ozone precursor levels (*medium to high confidence*). Future climate change is expected to have mixed effects, positive or negative, with an overall low effect, on global surface PM and more generally on the aerosol global burden (*medium confidence*), but stronger effects are not excluded in regions prone to specific meteorological conditions (*low confidence*). Overall, there is *low confidence* in the response of surface ozone and PM to future climate change due to the uncertainty in the response of the natural processes (e.g., stratosphere–troposphere exchange, natural precursor emissions, particularly including biogenic volatile organic compounds, wildfire-emitted precursors, land and marine aerosols, and lightning NO_x) to climate change. {6.3, 6.5}

ACCEPTED VERSION SUBJECT TO FINAL EDITING

The SSPs span a wider range of SLCF emissions than the Representative Concentration Pathways, representing better the diversity of future options in air pollution management (*high confidence*). In the SSPs, the socio-economic assumptions and climate mitigation ambition primarily drive future emissions, but the SLCF emission trajectories are also steered by varying levels of air pollution control originating from the SSP narratives, independently from climate mitigation. Consequently, SSPs consider a large variety of regional ambition and effectiveness in implementing air pollution legislation and result in wider range of future air pollution levels and SLCF-induced climate effects. {6.7.1}

Air pollution projections range from strong reductions in global surface ozone and PM (e.g., SSP1-2.6, with strong mitigation of both air pollution and climate change) to no improvement and even degradation (e.g., SSP3-7.0 without climate change mitigation and with only weak air pollution control) (*high confidence*). Under the SSP3-7.0 scenario, PM levels are projected to increase until 2050 over large parts of Asia, and surface ozone pollution is projected to worsen over all continental areas through 2100 (*high confidence*). Without climate change mitigation but with stringent air pollution control (SSP5-8.5), PM levels decline through 2100, but high methane levels hamper the decline in global surface ozone at least until 2080 (*high confidence*). {6.7.1}

Future Projections of the Effect of SLCFs on GSAT in the Core SSPs

In the next two decades, it is *very likely* that the SLCF emission changes in the WG1 core set of SSPs will cause a warming relative to 2019, whatever the SSPs, in addition to the warming from long-lived greenhouse gases. The net effect of SLCF and HFC changes on GSAT across the SSPs is a *likely* warming of 0.06°C–0.35°C in 2040 relative to 2019. Warming over the next two decades is quite similar across the SSPs due to competing effects of warming (methane, ozone) and cooling (aerosols) SLCFs. For the scenarios with the most stringent climate and air pollution mitigations (SSP1-1.9 and SSP1-2.6), the *likely* near-term warming from the SLCFs is predominantly due to sulphate aerosol reduction, but this effect levels off after 2040. In the absence of climate change policies and with weak air pollution control (SSP3-7.0), the *likely* near-term warming due to changes in SLCFs is predominantly due to increases in methane, ozone and HFCs, with smaller contributions from changes in aerosols. SSP5-8.5 has the highest SLCF-induced warming rates due to warming from methane and ozone increases and reduced aerosols due to stronger air pollution control compared to the SSP3-7.0 scenario. {6.7.3}

At the end of the century, the large diversity of GSAT response to SLCFs among the scenarios robustly covers the possible futures, as the scenarios are internally consistent and span a range from very high to very low emissions. In the scenarios without climate change mitigation (SSP3-7.0, SSP5-8.5,) the *likely* range of the estimated warming due to SLCFs in 2100 relative to 2019 is 0.4°C–0.9°C {6.7.3, 6.7.4}. In SSP3-7.0 there is a near-linear warming due to SLCFs of 0.08°C per decade, while for SSP5-8.5 there is a more rapid warming in the first half of the century. For the scenarios considering the most stringent climate and air pollution mitigations (SSP1-1.9 and SSP1-2.6), the reduced warming from reductions in methane, ozone and HFCs partly balances the warming from reduced aerosols, and the overall SLCF effect is a *likely* increase in GSAT of 0.0°C–0.3°C in 2100, relative to 2019. The SSP2-4.5 scenario (with moderate climate and air pollution mitigations) results in a *likely* warming in 2100 due to the SLCFs of 0.2°C–0.5°C, with the largest warming from reductions in aerosols. {6.7.3}

Potential Effects of SLCF Mitigation

Over time scales of 10 to 20 years, the global temperature response to a year's worth of current emissions of SLCFs is at least as large as that due to a year's worth of CO_2 emissions (*high confidence*). Sectors producing the largest SLCF-induced warming are those dominated by CH_4 emissions: fossil fuel production and distribution, agriculture and waste management (*high confidence*). On these time scales, SLCFs with cooling effects can significantly mask the CO_2 warming in the case of fossil fuel combustion for energy and land transportation, or completely offset the CO_2 warming and lead to an overall net cooling in the case of industry and maritime shipping (prior to the implementation of the revised fuel-sulphur limit policy for shipping in 2020) (*medium confidence*). Ten years after a one-year pulse of present-day aviation emissions, SLCFs induce strong, but short-lived warming contributions to the GSAT response

ACCEPTED VERSION SUBJECT TO FINAL EDITING

(*medium confidence*), while CO_2 both gives a warming effect in the near term and dominates the long-term warming impact (*high-confidence*). {6.6.1, 6.6.2}

The effects of the SLCFs decay rapidly over the first few decades after pulse emission. Consequently, on time scales longer than about 30 years, the net long-term global temperature effects of sectors and regions are dominated by CO_2 (*high confidence*). The global mean temperature response following a climate mitigation measure that affects emissions of both short- and long-lived climate forcers depends on their atmospheric decay times, how fast and for how long the emissions are reduced, and the inertia in the climate system. For the SLCFs including methane, the rate of emissions drives the long-term global temperature effect, as opposed to CO_2 for which the long-term global temperature effect is controlled by the cumulative emissions. About 30 years or more after a one-year emission pulse occurs, the sectors contributing the most to global warming are industry, fossil fuel combustion for energy and land transportation, essentially through CO_2 (*high confidence*). Current emissions of SLCFs, CO_2 and N_2O from East Asia and North America are the largest regional contributors to additional net future warming on both short- (*medium confidence*) and long-time scales (*high confidence*). {6.6.1, 6.6.2}

At present, emissions from the residential and commercial sectors (fossil and biofuel use for cooking and heating) and the energy sector (fossil fuel production, distribution and combustion) contribute the most to the world population's exposure to anthropogenic fine PM (*high confidence*), whereas emissions from the energy and land transportation sectors contribute the most to ozone exposure (*medium to high confidence*). The contribution of different emission sectors to PM varies across regions, with the residential sector being the most important in South Asia and Africa, agricultural emissions dominating in Europe and North America, and industry and energy production dominating in Central and East Asia, Latin America and Middle East. Energy and industry are important $PM_{2.5}$ contributors in most regions, except Africa (*high confidence*). Source contributions to surface ozone concentrations are similar for all regions. {6.6.2}

Assuming implementation and efficient enforcement of both the Kigali Amendment to the Montreal Protocol on Ozone Depleting Substances and current national plans limit emissions (as in SSP1-2.6), the effects of HFCs on GSAT, relative to 2019, would remain below +0. 02°C from 2050 onwards versus about +0.04–0.08°C in 2050 and +0.1–0.3°C in 2100 considering only national HFC regulations decided prior to the Kigali Amendment (as in SSP5-8.5) (*medium confidence*). Further improvements in the efficiency of refrigeration and air-conditioning equipment during the transition to low-global-warming-potential refrigerants would bring additional GHG reductions (*medium confidence*) resulting in benefits for climate change mitigation and to a lesser extent for air quality due to reduced air pollutant emissions from power plants. {6.6.3, 6.7.3}

Future changes in SLCFs are expected to cause an additional warming. This warming is stable after 2040 in scenarios leading to lower global air pollution as long as methane emissions are also mitigated, but the overall warming induced by SLCF changes is higher in scenarios in which air quality continues to deteriorate (induced by growing fossil fuel use and limited air pollution control) (*high confidence*). If a strong air pollution control resulting in reductions in anthropogenic aerosols and non-methane ozone precursors was considered in SSP3-7.0, it would lead to a *likely* additional near-term global warming of 0.08 [0.00–0.10] °C in 2040. An additional concomitant methane mitigation (consistent with SSP1's stringent climate mitigation policy implemented in the SSP3 world) would not only alleviate this warming but would turn this into a cooling of 0.07 with a *likely* range of [-0.02 to 0.14] °C (compared with SSP3-7.0 in 2040). Across the SSPs, the collective reduction of CH_4, ozone precursors and HFCs can make a difference of GSAT of 0.2 with a *very likely* range of [0.1–0.4] °C in 2040 and 0.8 with a *very likely* range of [0.5–1.3] °C at the end of the 21st century (comparing SSP3-7.0 and SSP1-1.9), which is substantial in the context of the Paris Agreement. Sustained methane mitigation, wherever it occurs, stands out as an option that combines near- and long-term gains on surface temperature (*high confidence*) and leads to air quality benefits by reducing surface ozone levels globally (*high confidence*). {6.6.3, 6.7.3, 4.4.4}

Rapid decarbonization strategies lead to air quality improvements but are not sufficient to achieve, in the near term, air quality guidelines set for fine PM by the World Health Organization (WHO),

ACCEPTED VERSION SUBJECT TO FINAL EDITING

especially in parts of Asia and in some other highly polluted regions (*high confidence*). Additional CH_4 and BC mitigation would contribute to offsetting the additional warming associated with SO_2 reductions that would accompany decarbonization (*high confidence*). Strong air pollution control as well as strong climate change mitigation, implemented separately, lead to large reductions in exposure to air pollution by the end of the century (*high confidence*). Implementation of air pollution controls, relying on the deployment of existing technologies, leads more rapidly to air quality benefits than climate change mitigation, which requires systemic changes. However, in both cases, significant parts of the population are projected to remain exposed to air pollution exceeding the WHO guidelines. Additional policies envisaged to attain Sustainable Development Goals (SDG) (e.g., access to clean energy, waste management) bring complementary SLCF reduction. Only strategies integrating climate, air quality, and developments goals are found to effectively achieve multiple benefits. {6.6.3, 6.7.3, Box 6.2}

Implications of COVID-19 Restrictions for Emissions, Air Quality and Climate

Emissions reductions associated with COVID-19 containment led to a discernible temporary improvement of air quality in most regions, but changes to global and regional climate are undetectable above internal variability. Global anthropogenic NO_x emissions decreased by a maximum of about by 35% in April 2020 (*medium confidence*). There is *high confidence* that, with the exception of surface ozone, these emission reductions have contributed to improved air quality in most regions of the world. Global fossil CO_2 emissions decreased by 7% (with a range of 5.8% to 13.0%) in 2020 relative to 2019, largely due to reduced emissions from the transportation sector (*medium confidence*). Overall, the net ERF, relative to ongoing trends, from COVID-19 restrictions was likely small and positive for 2020 (less than 0.2 W m^{-2}), thus temporarily adding to the total anthropogenic climate influence, with positive forcing from aerosol changes dominating over negative forcings from CO_2, NO_x and contrail cirrus changes. Consistent with this small net radiative forcing, and against a large component of internal variability, Earth system model simulations show no detectable effect on global or regional surface temperature or precipitation (*high confidence*). {Cross-Chapter Box 6.1}

ACCEPTED VERSION
SUBJECT TO FINAL EDITING

6.1 Introduction

Short lived climate forcers (SLCFs) are a set of chemically and physically reactive compounds with atmospheric lifetimes typically shorter than two decades but differing in terms of physiochemical properties and environmental effects. SLCFs can be classified as direct or indirect, with direct SLCFs exerting climate effects through their radiative forcing and indirect SLCFs being precursors of direct climate forcers. Direct SLCFs include methane (CH_4), ozone (O_3), short lived halogenated compounds, such as hydrofluorocarbons (HFCs), hydrochlorofluorocarbons (HCFCs), and aerosols. Indirect SLCFs include nitrogen oxides (NO_x), carbon monoxide (CO), non-methane volatile organic compounds (NMVOCs), sulphur dioxide (SO_2), and ammonia (NH_3). Aerosols consist of sulphate (SO_4^{2-}), nitrate (NO_3^-), ammonium (NH_4^+), carbonaceous aerosols (e.g., black carbon (BC), organic aerosols (OA)), mineral dust, and sea spray (see Table 6.1) and can be present as internal or external mixtures and at sizes from nano-meters to tens of micro-meters. SLCFs can be emitted directly from natural systems and anthropogenic sources (primary) or can be formed by reactions in the atmosphere (secondary) (Figure 6.1).

6.1.1 Importance of SLCFs for climate and air quality

The atmospheric lifetime determines the spatial and temporal variability, with most SLCFs showing high variability, except CH_4 and many HCFCs and HFCs that are also well mixed (as a consequence CH_4 is discussed together with other well-mixed GHGs in Chapters 2, 5, and 7). In contrast to well-mixed greenhouse gases, such as CO_2, CH_4 and some HFCs, the radiative forcing effects of most of the SLCFs are largest at regional scales and climate effects predominantly occur in the first two decades after their emissions or formation. However, changes in their emissions can also induce long-term climate effects, for instance by altering some biogeochemical cycles. Therefore, the temporal evolution of radiative effects of SLCFs follows that of emissions, i.e., when SLCF emissions decline to zero their atmospheric abundance and radiative effects decline towards zero. The total influence of individual SLCF emissions on radiative forcing and climate account for their effects on the abundances of other forcers through chemistry (chemical adjustments).

SLCFs can affect climate by interacting with radiation or by perturbing other components of the climate system (e.g., the cryosphere and carbon cycle through deposition, or the water cycle through modifications of cloud properties via cloud condensation nuclei or ice nuclei). SLCFs can have either net warming or cooling effects on climate. In addition to altering the Earth's radiative balance, many SLCFs are also air pollutants with adverse effects on human health and ecosystems. SLCFs are of interest for climate policies (e.g., CH_4, HFCs), and are regulated as air pollutants (e.g., aerosols, O_3) or because of their deleterious influence on stratospheric ozone (e.g., HCFCs). The list of SLCFs assessed in this chapter and their effects are provided in Table 6.1.

[START FIGURE 6.1 HERE]

Figure 6.1: Sources and processes leading to atmospheric short-lived climate forcer (SLCF) burden and their interactions with the climate system. Both direct and indirect SLCFs and the role of atmospheric processes for the lifetime of SLCFs are depicted. Anthropogenic emission sectors illustrated are fossil fuel exploration, distribution and use, biofuel production and use, waste, transport, industry, agricultural sources, and open biomass burning. Emissions from natural systems include those from open biomass burning, vegetation, soil, oceans, lightning, and volcanoes. SLCFs interact with solar or terrestrial radiation, surface albedo, and cloud or precipitation system. The radiative forcing due to individual SLCF can be either positive or negative. Climate change induces changes in emissions from most natural systems as well as from some anthropogenic emission sectors (e.g. agriculture) leading to a climate feedback (purple arrows). Climate change also influences atmospheric chemistry processes, such as chemical reaction rates or via circulation changes, thus affecting atmospheric composition leading to a climate feedback. Air pollutants influence emissions from terrestrial vegetation, including agriculture (the grey arrow).

ACCEPTED VERSION SUBJECT TO FINAL EDITING

[END FIGURE 6.1 HERE]

[START TABLE 6.1 HERE]

Table 6.1: Overview of SLCFs of interest for Chapter 6. For each SLCF, its source types, lifetime in the atmosphere, and associated radiatively active agent is given. Source type can be primary (emitted from source categories) and/or secondary (formed through atmospheric oxidation mechanisms in the atmosphere). Unless otherwise noted, the stated lifetime refers to tropospheric lifetime*. Climate effect of increased SLCFs is indicated as "+" for warming and "-" for cooling. "Direct" is used for SLCFs exerting climate effects through their radiative forcing and "Indirect" for SLCFs which are precursors affecting the atmospheric burden of other climatically active compounds. Other processes through which SLCFs affect climate are listed where applicable. The World Health Organization (WHO) guidelines for air quality (AQ) are given, where applicable, to show which SLCFs are regulated for air quality purposes.

Compounds	**Source Type[a]**	**Lifetime**	**Direct**	**Indirect**	**Climate Forcing**	**Other effects on climate**	**WHO AQ guidelines[b]**
CH_4	Primary	~9 years ~12 years (perturbation time)	CH_4	O_3, H_2O, CO_2	+		No[c]
O_3	Secondary	Hours - weeks	O_3	CH_4, secondary organic aerosols, sulphates	+	Ecosystem	100 μg m^{-3} 8-hour mean
NO_x (= NO + NO_2)	Primary	Hours - days		O_3, nitrates, CH_4	+/-	Ecosystem	40 μg m^{-3} annual mean 200 μg m^{-3} 1-hour mean
CO	Primary + Secondary	1-4 months		O_3, CH_4	+		No
NMVOCs	Primary + Secondary	Hours - months		O_3, CH_4, organic aerosols	+/-		No
SO_2	Primary	Days (trop.) to weeks (strat.)		sulphates, nitrates, O_3	-		20 μg m^{-3} 24-hour mean 500 μg m^{-3} 10-minute mean
NH_3	Primary	Hours		Ammonium Sulphate, Ammonium Nitrate	-	Ecosystem	No
HCFCs	Primary	Months – years	HCFCs	Stratospheric O_3	+/-		No[c]
HFCs	Primary	Days – years	HFCs		+		No[c]
Halons and Methylbromide	Primary	Years	Halons and Methylbromide	Stratospheric O_3	+/-		No[c]
Very Short-Lived halogenated Species (VSLSs)	Primary	less than 0.5 year		Stratospheric O_3	-		No[c]
Sulphates	Secondary	Minutes – weeks	Sulphates		-	Cloud	as part of PM[d]
Nitrates	Secondary	Minutes – weeks	Nitrates		-	Cloud	as part of PM[d]
Carbonaceous aerosols	Primary + Secondary	Minutes to Weeks	BC, OA		+/ -	Cryo, Cloud	as part of PM[d]

ACCEPTED VERSION SUBJECT TO FINAL EDITING

Sea spray	Primary	day to week	Sea spray		-	Cloud	as part of PM[d]
Mineral dust	Primary	Minutes to Weeks	Mineral dust		-	Cryo, Cloud	as part of PM[d]

[*] For lifetimes reported it in this table, it is assumed that the compounds are uniformly mixed throughout the troposphere, however, this assumption is unlikely for compounds with lifetimes < 1 year and therefore, the reported values should be viewed as approximations (Prather et al., 2001).
[a] Source types can be primary (emitted from source categories) and/or secondary (formed by reactions in the atmosphere). Cryo: effect on planetary albedo through deposition on snow and ice; [b] Krzyzanowski and Cohen (2008) ; [c] regulated through Kyoto/Montreal protocol; [d] For Particulate Matter with diameter < 2.5 µm ($PM_{2.5}$): 10 µg m^{-3} annual mean or 25 µg m^{-3} 24 hour mean (99th percentile) and for Particulate Matter with diameter < 10 µm (PM_{10}): 20 µg m^{-3} annual mean or 50 µ µg m^{-3} 24 hour mean (99th percentile)

[END TABLE 6.1 HERE]

As depicted in Figure 6.1, emissions of SLCFs are governed by anthropogenic activities and sources from natural systems (see Section 6.2 for details). Atmospheric chemistry in this context is both a source and a sink of SLCFs. For instance, O_3 and secondary aerosols are exclusively formed through atmospheric mechanisms (Section 6.3.2 and 6.3.5 respectively). The hydroxyl (OH) radical, the most important oxidizing agent in the troposphere, acts as a sink for SLCFs by reacting with them, and thereby, influencing their lifetime (Section 6.3.6). Through SLCF radiative forcing and feedbacks (see Section 6.4), key climate parameters, such as temperature, hydrological cycle, and weather patterns are perturbed. Climate change also influences air quality (Section 6.5). As depicted in Figure 6.1, SLCFs affect both climate and air quality, hence SLCF mitigation has linkages to both the issues (Section 6.6). Socio-economic narratives including air quality policies determine future projections of SLCFs in the five core Socioeconomic Pathways (SSPs): SSP1-1.9, SSP1-2.6, SSP2-4.5, SSP3-7.0, and SSP5-8.5 (described in Chapter 1), and in addition, a subset of SSP3 scenarios allows to isolate the effect of various SLCF mitigation trajectories on climate and air quality (Section 6.7).

6.1.2 Treatment of SLCFs in previous assessments

Although O_3, aerosols and their precursors have been considered in previous IPCC assessment reports, AR5 considered SLCFs as a specific category of climate relevant compounds but referred to them as near-term climate forcers (NTCFs) (Myhre et al., 2013). In AR5, the linkages between air quality and climate change were also considered in a more detailed and quantitative way than in previous reports (Kirtman et al., 2013; Myhre et al., 2013).

AR5 WGI assessed radiative forcings for short-lived gases, aerosols, aerosol precursors and aerosol cloud interactions (ERFaci) as well as the evolution of confidence level in the forcing mechanisms from SAR to AR5. Whereas the forcing mechanisms for ozone and aerosol-radiation interactions were estimated to be characterised with *high confidence*, the ones induced by aerosols through other processes remained of *very low* to *low confidence*. AR5 also reported that forcing agents such as aerosols and ozone changes are highly heterogeneous spatially and temporally and these patterns affect global and regional temperature responses as well as other aspects of climate response such as the hydrologic cycle (Myhre et al., 2013).

AR5 WGI also evaluated the air quality-climate interaction through the projected trends of surface O_3 and $PM_{2.5}$. Kirtman et al. (2013) concluded with *high confidence* that the response of air quality to climate-driven changes is more uncertain than the response to emission-driven changes, and also that locally higher surface temperatures in polluted regions will trigger regional feedbacks in chemistry and local emissions that will increase peak levels of O_3 and $PM_{2.5}$ (*medium confidence*).

In the Special Report on Global Warming of 1.5 °C (SR15)(Allen et al., 2018a), Rogelj et al., (2018a) state

ACCEPTED VERSION SUBJECT TO FINAL EDITING

that the evolution of CH_4 and SO_2 emissions strongly influences the chances of limiting warming to 1.5°C, and that, considering mitigation scenarios to limit warming to 1.5 or 2°C, a weakening of aerosol cooling would add to future warming in the near term, but can be tempered by reductions in methane emissions (*high confidence*). In addition, as some SLCFs are co-emitted alongside CO_2, especially in the energy and transport sectors, low CO_2 scenarios, relying on decline of fossil fuel use, can result in strong abatement of some cooling and warming SLCFs (Rogelj et al., 2018a).

On the other hand, specific reductions of the warming SLCFs (CH_4 and BC) would, in the short term, contribute significantly to the efforts of limiting warming to 1.5°C. Reductions of BC and CH_4 would have substantial co-benefits improving air quality and therefore limit effects on human health and agricultural yields. This would, in turn, enhance the institutional and socio-cultural feasibility of such actions in line with the United Nations' Sustainable Development Goals (Coninck et al., 2018).

Following SR15, the IPCC Special Report Climate Change and Land (SRCCL)(IPCC, 2019a) took into consideration the emissions on land of three major SLCFs: mineral dust, carbonaceous aerosols (BC and OA) and BVOCs (Jia et al., 2019). The SRCCL concluded that: i) there is no agreement about the direction of future changes in mineral dust emissions; ii) fossil fuel and biomass burning, and SOA from natural BVOC emissions are the main global sources of carbonaceous aerosols whose emissions are expected to increase in the near future due to possible increases in open biomass burning and increase in SOA from oxidation of BVOCs (*medium confidence*); iii) BVOCs are emitted in large amounts by forests and they are rapidly oxidised in the atmosphere to form less volatile compounds that can condense and form SOA, and in a warming planet, BVOC emissions are expected to increase but magnitude is unknown and will depend on future land use change, in addition to climate (*limited evidence, medium agreement*).

Finally, the IPCC Special Report on the Ocean and Cryosphere in a Changing Climate (SROCC)(IPCC, 2019b) discussed the effects of BC deposition on snow and glaciers, concluding that there is *high confidence* that darkening of snow through the deposition of BC and other light absorbing particles enhances snow melt in the Arctic (Meredith et al., 2019), but that there is *limited evidence* and *low agreement* that long-term changes in glacier mass of high mountain areas are linked to light absorbing particles (Hock et al., 2019).

6.1.3 Chapter Roadmap

Figure 6.2 presents the Chapter 6 roadmap.

Specific aspects of SLCFs can also be found in other chapters of this report: the evolution of ozone, HFCs, aerosols as well as long term evolution of methane, dust, volcanic aerosols are discussed in Chapter 2, near-term climate projections and SLCFs are discussed in Chapter 4, the global budget of methane is addressed in Chapter 5, aerosol-cloud and aerosol-precipitation interactions are treated in Chapters 7 and 8, respectively, the global radiative forcing of SLCFs is assessed in Chapter 7, some aspects of downscaling methodology in climate modelling concerning SLCFs are discussed in Chapter 10. The WGII report assesses how climate change affects air pollution and impacts on human health and the WGIII report assesses the role of SLCFs in abatement strategies and their cost effectiveness, the implications of mitigation efforts on air pollution as well as the articulation between air pollution policies and GHG mitigation.

This chapter discusses air quality from a global point of view with focus on surface ozone and particulate matter surface concentrations. Local and indoor air pollution, as well as effect of air pollution on health, are beyond the scope of this chapter. This assessment is mainly based on results and studies relying on global models or observation datasets operated through global networks or from satellites. Global chemistry-climate models allow to quantify the changes in background concentrations such as surface ozone due to large scale changes in climate or CH_4 by considering comprehensively the physiochemical processes (see Box 6.1). In addition, climate effects are often non-linear responses to concentrations which already respond non-linearly to emissions, with per mass unit effects often larger in pristine than in polluted regions, justifying the relevance of global models. However, specific aspects of urban air quality cannot be captured by global models and require high resolution modelling which reproduce the temporal and spatial variability of

ACCEPTED VERSION SUBJECT TO FINAL EDITING

emissions and abundances necessary to precisely account for the non-linearity of the chemistry and the sensitivity of local air pollution to its drivers. Consequently, the sectoral analysis in Section 6.6 and the mitigation effects in Section 6.7 cannot be directly applied for local air quality planning.

Due to their short lifetimes, SLCF trends and effects are strongly related to the localisation and evolution of the emission sources. To better link the drivers of emission evolution and SLCFs, Chapter 6 makes use of regions defined by the WGIII in most of the analysis. An exception is made for the effect of SLCFs on the climate, for which analysis relies on WGI Atlas regions.

[START FIGURE 6.2 HERE]

Figure 6.2: Chapter roadmap. See Section 6.1.3 for additional description of the chapter.

[END FIGURE 6.2 HERE]

6.2 Global and regional temporal evolution of SLCF emissions

SLCF emissions originate from a variety of sources driven by anthropogenic activities and natural processes. The natural sources include vegetation, soil, fire, lightning, volcanoes, and oceans. Changes in SLCF emissions from natural systems occur either due to human activities, such as land-use change, or due to global changes. Their sensitivity to climate change thus induces a climate feedback (see Section 6.4.6 for a quantification of these feedbacks). This section reviews the current understanding of historical emissions for anthropogenic, natural, and open biomass burning sources. A detailed discussion of methane sources, sinks, trends and their evaluation are provided in Chapter 5; Section 5.2.2.

6.2.1 Anthropogenic sources

Estimates of global anthropogenic SLCF emissions and their historical evolution that were used in AR5 (CMIP5) (Lamarque et al., 2010) have been revised for use in CMIP6 (Hoesly et al., 2018). The update considered new data and assessment of the impact of the environmental policies, primarily regarding air pollution control (Wang et al., 2014c, 2014b; Montzka et al., 2015; Crippa et al., 2016; Turnock et al., 2016; Klimont et al., 2017a; Zanatta et al., 2017; Prinn et al., 2018). Additionally, Hoesly et al. (2018) have extended estimates of anthropogenic emissions back to 1750 and developed an updated and new set of spatial proxies allowing for more differentiated (source sector-wise) gridding of emissions (Feng et al., 2020). The CMIP6 emission inventory has been developed with the Community Emissions Data System (CEDS) that improves upon existing inventories with a more consistent and reproducible methodology, similar to approaches used in, for example, EDGAR (Crippa et al., 2016) and GAINS model (Amann et al., 2011; Klimont et al., 2017b; Höglund-Isaksson et al., 2020) where emissions of all compounds are consistently estimated using the same emission drivers and propagating individual components (activity data and emission factors) separately to capture fuel and technology trends affecting emission trajectories over time. This contrasts the approach used to establish historical emissions for CMIP5 where different data sets available at the time were combined. The CMIP6 exercise is based on the first release of CEDS emission dataset (version 2017-05-18, sometimes referred to hereafter as CMIP6 emissions) whose main features regarding SLCFs are described hereafter. The CEDS has been and will be regularly updated and extended; the recent update of CEDS (Hoesly et al., 2019) and consequences for this assessment is discussed when necessary. Some details on how SLCF emissions have been represented in scenarios used by IPCC assessments can be found in Chapter 1 (see Chapter 1, Section 1.6.1 and Cross Chapter Box 1.4).

For most of the SLCF species, the global and regional anthropogenic emission trends developed for CMIP6 for the period 1850 to 2000 are not substantially different from those used in CMIP5 (Figures 6.18 & 6.19) despite the different method used to derive them. Hoesly et al. (2018, CEDS) developed an independent time series capturing trends in fuel use, technology, and level of control, whereas CMIP5 combined different

ACCEPTED VERSION SUBJECT TO FINAL EDITING

emission data sets. However, for the period after 1990, the CMIP6 dataset shows for all species, except for SO_2 and CO and since 2011 for NO_x, a different trend than CMIP5, i.e., continued strong growth of emissions driven primarily by developments in Asia (Figure 6.19). The unprecedented growth of East and South Asian emissions since 2000 changed the global landscape of emissions making Asia the dominant SLCF source region (Figures 6.3, 6.19). The Representative Concentration Pathways (RCP) scenarios used in AR5 started from the year 2000 (van Vuuren et al., 2011) and did not represent well the development of SLCF emissions until 2015. The CEDS inventory (Hoesly et al., 2018) includes improved representation of these trends and the estimate for 2014. These findings have been largely supported by several independent emission inventory studies and remote sensing data analysis, however, for the last decade the decline of Asian emissions of SO_2 and NO_x appears underestimated while growth of BC and OC emissions in Asia and Africa seems overestimated in CMIP6, compared to most recent regional evaluations (Klimont et al., 2017b; Zheng et al., 2018b; e.g., Elguindi et al., 2020; Kanaya et al., 2020; McDuffie et al., 2020), which are largely considered in the updated release of the CEDS (Hoesly et al., 2019). Consequently, global CMIP6 anthropogenic emissions for 2015 are likely overestimated by about 10% for SO_2 and NO_x and about 15% for BC and OC.

For SO_2, independent emission inventories and observational evidence show that on a global scale strong growth of Asian emissions has been countered by reduction in North America and Europe (Reis et al., 2012; Amann et al., 2013; Crippa et al., 2016; Aas et al., 2019). Since about 2006, also Chinese emissions declined by nearly 70% by 2017 (Silver et al., 2018; Zheng et al., 2018b; Mortier et al., 2020; Tong et al., 2020) (*high confidence*). The estimated reduction in China contrasts continuing strong growth of SO_2 emissions in South Asia (Figure 6.19). In 2014, over 80% of anthropogenic SO_2 emissions originated from power plants and industry with Asian sources contributing more than 50% of total (Figure 6.3).

Global emissions of NO_x have been growing in spite of the successful reduction of emissions in North America, Europe, Japan, Korea (Crippa et al., 2016; Turnock et al., 2016; Miyazaki et al., 2017; Jiang et al., 2018a) partly driven by continuous efforts to strengthen the emission standards for road vehicles in most countries (Figure 6.18 & 6.19). In many regions, an increase in vehicle fleet as well as non-compliance with emission standards (Anenberg et al., 2017, 2019; Jonson et al., 2017; Jiang et al., 2018a), growing aviation (Grewe et al., 2019; Lee et al., 2021) and demand for energy, and consequently large number of new fossil fuel power plants, have been overcompensating these reductions. Since about 2011, global NO_x emissions appear to have stabilized or slightly declined (*medium confidence*) but the global rate of decline has been underestimated in CEDS, as recent data suggest that emission reductions in China were larger than included in CEDs. (Figure 6.19 and Hoesly et al. (2018)). Recent bottom up emission estimates (Zheng et al., 2018b) largely confirm what has been shown in satellite data (Liu et al., 2016a; Miyazaki et al., 2017; Silver et al., 2018); a strong decline of NO_2 column over Eastern China (*high confidence*) (see Section 6.3.3.1). At a global level, the estimated CEDS CO emission trends are comparable to NO_x, which has been confirmed by several inverse modelling studies (see Section 6.3.3.2). Transport sector (including international shipping and aviation) was the largest anthropogenic source of NO_x (about 50% of total) and contributed also over 25% of CO emissions in 2014, and Asia represented half and North America and Europe about 20% of global total NO_x and CO (Figure 6.3).

Oil production-distribution and transport sector have dominated anthropogenic NMVOC emissions for most of the 20th century (Hoesly et al., 2018) and still represent a large share (Figure 6.3). Efforts to control transport emissions (i.e. increasing stringency of vehicle emission limits) were largely offset by fast growth of emissions from chemical industries and solvent use as well as from fossil fuel production and distribution, resulting in continued growth of global anthropogenic NMVOC emissions since 1900 (Figure 6.18) (*high confidence)*. Since AR5, there is *high confidence* that motor vehicle NMVOC emissions have sharply decreased in North America and Europe in the last decades (Rossabi and Helmig, 2018), i.e., by about an order of magnitude in major U.S. cities since 1990 (Bishop and Haugen, 2018; McDonald et al., 2018). Increasing (since 2008) oil and gas extraction activities in North America lead to a strong growth of NMVOC emissions (*high confidence*) as shown by analysis of ethane columns data (Franco et al., 2016), but absolute emission amounts remain uncertain (Pétron et al., 2014; Tzompa-Sosa et al., 2019). In East Asia, there is *medium confidence* in a decreasing trend of motor vehicle emissions, suggested by ambient measurements in Beijing since 2002 (Wang et al., 2015) and by bottom-up estimates (Zheng et al., 2018b),

ACCEPTED VERSION SUBJECT TO FINAL EDITING

and decrease of residential heating emissions due to declining coal and biofuel use since 2005 (Zheng et al., 2018b; Li et al., 2019b). However, total anthropogenic NMVOC emissions have increased steadily in China since the mid-20th century, largely due to growing importance of the solvent use and industrial sectors (Sun et al., 2018; Zheng et al., 2018b; Li et al., 2019b) (*medium evidence, high agreement*). Resulting changes in the NMVOC speciated emissions might be underestimated in the current regional and global inventories. For example, in the U.S., a recent study suggested an emergent shift in urban NMVOC sources from transportation to chemical products (i.e. household chemicals, personal care products, solvents, etc.), which is not in accordance with emission inventories currently used (McDonald et al., 2018). In many European regions and cities, wood burning has been increasingly used for residential heating, partly for economic reasons and because it is considered CO_2-neutral (Athanasopoulou et al., 2017); in situ measurements in several cities, including Paris, suggest that wood burning explains up to half the NMVOC emissions during winter (Kaltsonoudis et al., 2016; Languille et al., 2020). Due to the vast heterogeneity of sources and components of VOCs, uncertainty in regional emissions and trends is higher than for most other components.

Emissions of carbonaceous aerosols (BC, OC) have been steadily increasing and their emissions have almost doubled since 1950 (Hoesly et al., 2018) (*medium confidence*). Before 1950, North America and Europe contributed about half of the global total but successful introduction of diesel particulate filters on road vehicles (Fiebig et al., 2014; Robinson et al., 2015; Klimont et al., 2017a) and declining reliance on solid fuels for heating brought in large reductions (Figure 6.19) (*high confidence*). Currently, global carbonaceous aerosol emissions originate primarily from Asia and Africa (Bond et al., 2013; Hoesly et al., 2018; Elguindi et al., 2020; McDuffie et al., 2020), representing about 80% of global total (Figure 6.3) (*high confidence*). Consideration, in CMIP6, of emissions from kerosene lamps and gas flaring, revised estimates for open burning of waste, regional coal consumption, and new estimates for Russia (Stohl et al., 2013; Huang et al., 2015; Huang and Fu, 2016; Kholod et al., 2016; Conrad and Johnson, 2017; Evans et al., 2017; Klimont et al., 2017a) resulted in over 15% higher global emissions of OC and BC than in the CMIP5 estimates for the first decade of the 21st Century (Figure 6.18). The continued increase of BC emissions over East Asia after 2005, estimated in CMIP6 (Figure 6.19), has been, however, questioned recently as a steady decline of BC concentrations was measured in the air masses flowing out from east coast of China (Kanaya et al., 2020), which has been also estimated in recent regional bottom-up and top-down inventories (Zheng et al., 2018a; Elguindi et al., 2020; McDuffie et al., 2020). Since AR5, confidence in emission estimates and trends in North America and Europe has increased but high uncertainties remain for Asia and Africa that dominate global emissions. Size distribution of emitted species, of importance for climate and health impacts, remains uncertain and CEDS inventory does not provide such information. Overall, a factor two uncertainty in global estimates of BC and OC emissions remains, with post 2005 emissions overestimated in Asia (*high confidence*) and Africa (*medium confidence*).

Bottom up global emission estimates of CH_4 (Lamarque et al., 2010; Hoesly et al., 2018; Janssens-Maenhout et al., 2019; Höglund-Isaksson et al., 2020) for the last two decades are higher than top down assessments (e.g., Saunois et al., 2016, 2020) but trends from the two methods are similar and indicate continued growth (*high confidence*). Larger discrepancies exist at the sectoral and regional levels, notably for coal mining (Peng et al., 2016; Miller et al., 2019) and oil and gas sector due to growth of unconventional production and higher loss estimates (Franco et al., 2016; Alvarez et al., 2018; Dalsøren et al., 2018) (see also Section 5.2.2).

Agricultural production (livestock and mineral nitrogen fertilizer application) is the primarily source of ammonia in the atmosphere with more than half of present day emissions originating in Asia (Hoesly et al., 2018; Figure 6.3, EC-JRC / PBL, 2020; Vira et al., 2020). NH_3 emissions are estimated to have grown strongly since 1850, especially since 1950 driven by continuously increasing livestock production, widespread application of mineral nitrogen fertilizers and lack of action to control ammonia (Erisman et al., 2008; Riddick et al., 2016; Hoesly et al., 2018; Fowler et al., 2020) (*high confidence*). The trends estimated in CMIP5 and CMIP6 are similar, while in absolute terms CMIP6 has somewhat higher emissions as it includes emissions from wastewater and human waste that were largely missing in CMIP5 (Hoesly et al., 2018). CMIP6 has improved spatial and temporal distribution of emissions (e.g., Lamarque et al., 2013a) relying on the EDGAR v4.3 and Paulot et al. (2014), but important uncertainties remain for regionally-specific temporal patterns (Riddick et al., 2016; Liu et al., 2019; Feng et al., 2020; Vira et al., 2020). The continuing increase in global NH_3 emissions is driven primarily by growing livestock and crop production in

ACCEPTED VERSION SUBJECT TO FINAL EDITING

Asia while emissions in the US and Europe remain about constant or slightly decline in the last decade (Hoesly et al., 2018). Recent satellite and ground observations support trends estimated in CMIP6 dataset (Section 6.3.3.4).

To summarize, there are significant differences in spatial and temporal emission patterns of SLCFs across global regions (Figure 6.18). Until the 1950s, the majority of SLCF emissions associated with fossil fuel use (SO_2, NO_x, NMVOCs, CO) and about half of BC and OC originated from North America and Europe (Lamarque et al., 2010; Hoesly et al., 2018). Since the 1990s a large redistribution of emission was associated with strong economic growth in Asia and declining emissions in North America and Europe due to air quality legislation and declining capacity of energy intensive industry, and currently more than 50% of anthropogenic emissions of each SLCF species (including CH_4 and NH_3) originates from Asia (Amann et al., 2013; Bond et al., 2013; Fiore et al., 2015; Crippa et al., 2016, 2018; Klimont et al., 2017a; Hoesly et al., 2018) (Figure 6.3). The dominance of Asia for SLCF emissions is corroborated by growing remote sensing capacity that has been providing independent evaluation of estimated pollution trends in the last decade (Duncan et al., 2013; Lamsal et al., 2015; Luo et al., 2015; Fioletov et al., 2016; Geddes et al., 2016; Irie et al., 2016; Krotkov et al., 2016; Wen et al., 2018).

Since AR5, the quality and completeness of activity and emission factor data and applied methodology, including spatial allocation together with independent satellite-derived observations, have improved, raising confidence in methods used to derive emissions. There is *high confidence* in the sign of global trends of SLCF emissions until the year 2000. However, only *medium confidence* for the rate of change in the two last decades owing primarily to uncertainties in actual application of reduction technologies in fast growing economies of Asia. At a regional level, bottom-up derived SLCF emission trends and magnitudes in regions with strong economic growth and changing air quality regulation are highly uncertain and better constrained with top-down methods (Section 6.3). For most SLCF species, there is *high confidence* in trends and magnitudes for affluent OECD regions where accurate and detailed information about drivers of emissions exists; *medium* confidence is assessed for regional emissions of NH_3, CH_4 and NMVOC.

[START FIGURE 6.3 HERE]

Figure 6.3: Relative regional and sectoral contributions to the present day (year 2014) anthropogenic emissions of Short Lived Climate Forcers (SLCFs). Emission data are from the Community Emissions Data System (CEDS) (Hoesly et al., 2018). Emissions are aggregated into the following sectors: fossil fuel production and distribution (coal mining, oil and gas production, upstream gas flaring, gas distribution networks), fossil fuel combustion for energy (power plants), residential and commercial (fossil and biofuel use for cooking and heating), industry (combustion and production processes, solvent use loses from production and end use), land transportation (road and off-road vehicles), shipping (including international shipping), aviation (including international aviation), agriculture (livestock and crop production), waste management (solid waste, including landfills and open trash burning, residential and industrial waste water), and other. Further details on data sources and processing are available in the chapter data table (Table 6.SM.1).

[END FIGURE 6.3 HERE]

6.2.2 Emissions by natural systems

This section assesses our current understanding of SLCF emissions by natural systems. Many naturally occurring emission processes in the Earth System have been perturbed by the growing influence of human activities either directly (e.g., deforestation, agriculture) or via human-induced atmospheric CO_2 increase and climate change and can therefore not be considered as purely natural emissions. The temporal evolution and spatial distribution of natural SLCF emissions are highly variable and their estimates rely on models with rather uncertain parameterizations for production mechanisms. For some SLCFs, the natural processes by which emissions occur are also not well-understood. In the following sections, we assess the level of confidence in present-day SLCF emissions by natural systems, in their perturbation since preindustrial and

ACCEPTED VERSION SUBJECT TO FINAL EDITING

their sensitivity to future changes. When available, the assessment also includes estimates from CMIP6 model ensemble. Note that volcanic SO_2 emissions are discussed in Section 2.2.2.

6.2.2.1 Lightning NO_x

Lightning contributes ~10% of the total NO_x emissions (Murray, 2016). Since lightning NO_x (LNO_x) is predominantly released in the upper troposphere, it has a disproportionately large impact on O_3 and OH, and on the lifetime of CH_4 compared with surface NO_x emissions. Whereas the global spatial and temporal distribution of lightning flashes can be characterized thanks to satellite-borne and ground sensors (DuplicateVirts, 2013; Cecil et al., 2014), constraining the amount of NO_x produced per flash (Miyazaki et al., 2014; Medici et al., 2017; Nault et al., 2017; Marais et al., 2018; Allen et al., 2019a; Bucsela et al., 2019) and its vertical allocation (Koshak et al., 2014; Medici et al., 2017) has been more elusive. Atmospheric Chemistry and Climate Model Intercomparison Project (ACCMIP) models in CMIP5 used a range of LNO_x between 1.2 to 9.7 TgN $year^{-1}$ (Lamarque et al., 2013c). In CMIP6, the corresponding LNO_x range is between 3.2 to 7.6 TgN $year^{-1}$ (Griffiths et al., 2020). All CMIP6 models (as well as most models included in the CMIP5, Young et al., 2013) apply a parameterization that relates cloud-top-height to lightning intensity (Price and Rind, 1992), projecting an increase in LNO_x in a warmer world in the range 0.27 to 0.61 Tg(N) yr^{-1} per °C (Thornhill et al., 2021a). However, models using parameterizations based on convection (Grewe et al., 2001), updraft mass flux (Allen and Pickering, 2002), or ice flux (Finney et al., 2016a) show either much less sensitivity or a negative response (Finney et al., 2016b, 2018; Clark et al., 2017).
In summary, the total present-day global lightning NO_x emissions are still estimated to be within a factor of 2. There is *high confidence* that LNO_x are perturbed by climate change however there is *low confidence* in the sign of the change due to fundamental uncertainties in parameterizations.

6.2.2.2 NO_x emissions by soils

Soil NO_x (SNO_x) emissions occur in connection with complex biogenic/microbial nitrification and denitrification processes (Ciais et al., 2013), which in turn are sensitive – in a non-linear manner – to temperature, precipitation, soil moisture, carbon and nutrient content and the biome itself (e.g., Hudman et al., 2012). Global SNO_x estimates, based on observationally constrained chemistry-transport model and vegetation model studies, show a broad range between 4.7 and 16.8 TgN/yr (Young et al., 2018). This estimate is generally larger than the current source strength used in CMIP6 simulations, which is prescribed using an early empirical estimate, typically scaled to about 5 TgN/yr (Yienger and Levy, 1995)
Under warmer climate, the overall nitrogen fixation in non-agricultural ecosystems is expected to be 40% larger than in 2000, due to increased enzyme activity with growing temperatures, but the emission rates of NO (and N_2O) is expected to be dominated by changes in precipitation patterns and evapotranspiration fluxes (Fowler et al., 2015). Current earth system models (ESM) incorporate biophysical and biogeochemical processes only to a limited extent (Jia et al., 2019), precluding adequate climate sensitivity studies for SNO_x. Hence, while the current strength source of soil NO_x has been better constrained over the last decade, adequate representations of SNO_x and how it escapes from the canopy are still missing in ESM to provide quantitative estimates of climate driven changes in SNO_x.

6.2.2.3 Vegetation emissions of organic compounds

A wide range of BVOCs are emitted from vegetation with the dominant compounds being isoprene and monoterpenes but also including sesquiterpenes, alkenes, alcohols, aldehydes and ketones. The photo-oxidation of BVOC emissions plays a fundamental role in atmospheric composition by controlling the regional and global budgets of ozone and organic aerosols, and impacting the lifetime of methane and other reactive components (Arneth et al., 2010b; Heald and Spracklen, 2015). Substantial uncertainty exists across different modelling frameworks for estimates of global total BVOC emissions and individual compound emissions (Messina et al., 2016). Global isoprene emission estimates differ by a factor of 2 from 300-600 Tg(C) yr^{-1} and global monoterpene emission estimates by a factor of 5 from 30-150 Tg(C) yr^{-1} (Messina et al., 2016). A main driver of the uncertainty ranges is the choice of assignment of PFT-specific basal emission

ACCEPTED VERSION SUBJECT TO FINAL EDITING

rates in the model, however, the smaller uncertainty range for isoprene than for monoterpenes is not fully understood (Arneth et al., 2008). The evaluation of global BVOC emissions is challenging because of poor measurement data coverage in many regions and the lack of year-round measurements (Unger et al., 2013). Several observational approaches have been developed in the past few years to improve understanding of BVOC emissions including indirect methods such as the measurement of the OH loss rate in forested environments (Yang et al., 2016) and application of the variability in satellite formaldehyde concentrations (Palmer et al., 2006; Barkley et al., 2013; Stavrakou et al., 2014). Direct space-borne isoprene retrievals using infrared (IR) radiance measurements have very recently become available (Fu et al., 2019; Wells et al., 2020). Collectively these approaches have identified weaknesses in the ability of the parameterizations in global models to reproduce BVOC emissions hotspots (Wells et al., 2020). However, none of the current observational approaches have yet been able to reduce the uncertainty ranges in global emission estimates.

At the plant level, BVOC emission rates and composition depend strongly on plant species with plants tending to emit either isoprene or monoterpenes but not both. Photosynthetic activity is a main driver of isoprene and monoterpene production. Therefore, radiation and temperature, along with leaf water status, phenological state and atmospheric CO_2 mixing ratio, affect emissions directly (on the leaf-scale) and indirectly (via plant productivity) (Guenther et al., 2012; Loreto et al., 2014; Niinemets et al., 2014). CO_2 directly influences the isoprene synthesis process, with inhibition under increasing atmospheric CO_2 (Rosenstiel et al., 2003; Possell et al., 2005; Wilkinson et al., 2009). Direct CO_2 inhibition has been observed for some monoterpene compounds (Loreto et al., 2001; Llorens et al., 2009). Severe/long-term water stress may reduce emissions whilst mild/short-term water stress may temporarily amplify or maintain BVOC emissions to protect plants against on-going stress (Peñuelas and Staudt, 2010; Potosnak et al., 2014; Genard-Zielinski et al., 2018). Furthermore, observations in the Amazon, indicate the chemical composition of monoterpene emissions could also change under elevated temperature conditions (Jardine et al., 2016). In addition, all these processes are investigated over short-time scales but the long-term response of BVOC emissions depends on how the vegetation itself responds to the altered climate state (including temperature and water stress).

Global BVOC emissions are highly sensitive to environmental change including changes in climate, atmospheric CO_2 and vegetation composition and cover changes in natural and managed lands. Recent global modelling studies agree that global isoprene emissions have declined since the preindustrial driven predominantly by anthropogenic LULCC with results converging on a 10-25% loss of isoprene emissions globally between 1850 and present day (Lathière et al., 2010; Unger, 2013, 2014; Acosta Navarro et al., 2014; Heald and Geddes, 2016a; Hantson et al., 2017; Hollaway et al., 2017; Scott et al., 2017). The historical evolution of monoterpene and sesquiterpene emissions is less well studied and there is no robust consensus on even the sign of the change (Acosta Navarro et al., 2014; Hantson et al., 2017). Future global isoprene and monoterpene emissions depend strongly on the climate and land-use scenarios considered (Hantson et al., 2017; Szogs et al., 2017). BVOC emissions will be sensitive to future land-based climate change mitigation strategies including afforestation and bioenergy, with impacts of bioenergy depending on the choice of crops (Szogs et al., 2017).

Most CMIP6 models use overly simplistic parameterizations and project an increase in global BVOC emissions in response to warming temperatures (Turnock et al., 2020). This good agreement actually reflects the lack of diversity in BVOC emission parametrizations in global models that do not fully account for the complex processes influencing emissions discussed above.

Overall, we assess that historical global isoprene emissions declined between the preindustrial and present day by 10-25% *low confidence*) but historical changes in global monoterpenes and sesquiterpenes are too uncertain to provide an assessment. Future changes in BVOCs depend strongly on the evolution of climate and land-use and are strongly sensitive to land-based climate change mitigation strategies. However, the net response of BVOC emissions is uncertain due to complexity of processes, hard to constrain observationally, considered with various degrees of details in models.

ACCEPTED VERSION SUBJECT TO FINAL EDITING

6.2.2.4 Land emissions of dust particles

The emission of dust particles into the atmosphere results from a natural process, namely saltation bombardment of the soil by large wind-blown particles such as sand grains and from disintegration of saltating particle clusters (Kok et al., 2012). The occurrence and intensity of dust emissions are controlled by soil properties, vegetation, and near-surface wind, making dust emissions sensitive to changes in climate, and land-use and land cover (Jia et al., 2019). In addition, dust can be directly emitted through human activities, such as agriculture, off-road vehicles, building construction, mining, and indirectly emitted through hydrological changes due to human actions such water diversion for irrigation (e.g. Ginoux et al., 2012). Estimates of the anthropogenic fraction of global dust vary from less than 10% to over 60% suggesting that human contribution to the global dust budget is quite uncertain (Ginoux et al., 2012; Stanelle et al., 2014; Xi and Sokolik, 2016). Reconstruction of global dust (deposition) from paleo records indicate factor of 2 to 4 changes between the different climate regimes in the glacial and interglacial periods (see Section 2.2.6). An extremely limited number of studies have explored the evolution of global dust sources since preindustrial times (Mahowald et al., 2010; Stanelle et al., 2014). A modelling study estimated a 25% increase in global dust emissions between the late nineteenth century to present due to agricultural land expansion and climate change (Stanelle et al., 2014). CMIP5 models were unable to capture the observed variability of annual and longer time scales in North African dust emissions (Evan et al., 2014), however more recent ESMs with process-based dust emission schemes that account for changes in vegetation and climate in a more consistent manner better match the observations (Kok et al., 2014; Evans et al., 2016). Feedbacks between the global dust cycle and the climate system (see Section 6.4.6) could account for a substantial fraction of the total aerosol feedbacks in the climate system with an order of magnitude enhancement on regional scale (Kok et al., 2018). In summary, there is *high confidence* that atmospheric dust source and loading are sensitive to changes in climate and land use, however, there is *low confidence* in quantitative estimates of dust emission response to climate change.

6.2.2.5 Oceanic emissions of marine aerosols and precursors

Oceans are a significant source of marine aerosols that influence climate directly by scattering and absorbing solar radiation or indirectly through the formation of cloud condensation nuclei (CCN) and ice nucleating particles (INP). Marine aerosols consist of primary sea spray particles and secondary aerosols produced by the oxidation of emitted precursors, such as dimethylsulphide (DMS) and numerous other BVOCs. Sea spray particles, composed of sea-salt and primary organic aerosols (POA), are produced by wind induced wave breaking as well as direct mechanical disruption of waves. The understanding of sea spray emissions has increased substantially over the last five years, however, the knowledge of formation pathways and factors influencing their emissions continue to have large uncertainties (Forestieri et al., 2018; Saliba et al., 2019). The emission rate of sea-spray particles is predominantly controlled by wind speed. Since AR5, the influence of other factors, including sea surface temperature, wave history and salinity is increasingly evident (Callaghan et al., 2014; Grythe et al., 2014; Ovadnevaite et al., 2014; Salter et al., 2014; Barthel et al., 2019). Marine POA, often the dominant submicron component of sea spray, are emitted as a result of oceanic biological activity, however the biological processes by which these particles are produced remain poorly characterized contributing to large uncertainties in global marine POA emission estimates (Tsigaridis et al., 2014; Burrows et al., 2018; Cravigan et al., 2020; Hodzic et al., 2020). Furthermore, particle size and chemical composition of sea spray particles and how these evolve in response to changing climate factors and dynamic oceanic biology continue to have large uncertainties.

DMS, the largest natural source of sulphur in the atmosphere, is produced by marine phytoplankton and is transferred from ocean water to the atmosphere due to wind-induced mixing of surface water. DMS oxidizes to produce sulphate aerosols and contributes to the formation of CCN. Since AR5, the range in global DMS flux estimates reduced from 10-40 Tg S $year^{-1}$ to 9 to 34 Tg S $year^{-1}$ with a *very likely* range of 18-24 Tg S $year^{-1}$ based on sea-surface measurements and satellite observations (Lana et al., 2011). DMS production, and consequently emissions, have been shown to respond to multiple stressors, including climate warming, eutrophication, and ocean acidification. However, large uncertainties in process-based understanding of the mechanisms controlling DMS emissions, from physiological to ecological, limit our knowledge of past

ACCEPTED VERSION SUBJECT TO FINAL EDITING

variations and our capacity to predict future changes.

Overall, there is *low confidence* in the magnitude and changes in marine aerosol emissions in response to shifts in climate and marine ecosystem processes.

6.2.2.6 Open biomass burning emissions

Open biomass burning (including forest, grassland, peat fires and agricultural waste burning) represent about 30%, 10%, 15% and 40% of present-day global emissions of CO, NO_x, BC, and OC, respectively (van Marle et al., 2017; Hoesly et al., 2018). Wildfires also play an important role in several atmospheric chemistry–climate feedback mechanisms (Bowman et al., 2009; Fiore et al., 2012) and fire events occurring near populated areas induce severe air pollution episodes (Marlier et al., 2020; Rooney et al., 2020; Yu et al., 2020).

For the last two decades, model-based emission estimates are constrained by remote sensing capacity to detect active fires and area burned. In AR5, biomass burning emissions were derived from a satellite product (Lamarque et al., 2010). Since then, improvements in detection of small fires has enhanced the agreement with higher-resolution and ground-based data on burned area in several regions (Randerson et al., 2012; Mangeon et al., 2015) especially for areas subjected to agricultural waste burning (Chuvieco et al., 2016, 2019). The updated emission factors and contribution of forest versus savannah fires lead to significantly higher global emissions of NO_x and lower emissions of OC and CO in CMIP6, compared with CMIP5. A recent compilation and assessment of emission factors (Andreae, 2019) indicates that the emission factors from Akagi et al. (2011), primarily used to produce the CMIP6 datasets, differ within ±50% for CO, OC, BC, and NO_x, depending on the biome, and would imply, for example, up to 10-30% higher OC and BC emissions from tropical forest fires.

The historical (pre-satellite era) dataset for CMIP6 considers advances in knowledge of past fire dynamics (new fire proxy datasets, such as charcoal in sediments or levoglucosan in ice-cores) and visibility records from weather stations (Marlon et al., 2016; van Marle et al., 2017). At a global level, CMIP5 and CMIP6 emission trends are similar, however, there are substantial differences at the regional level, especially for the United States, South America (south of Amazonia), and southern hemisphere Africa (van Marle et al., 2017).

Globally, the CMIP5 estimates (Lamarque et al., 2010), indicated gradual decline of open biomass burning emission from 1920 to about 1950 and then steady, and stronger than CMIP6, increase towards 2000. In contrast, CMIP6 biomass burning emissions (van Marle et al., 2017) increase only slightly over 1750 to 2015 and peak during the 1990s after which they decrease gradually consistently, with the assessment of fire trends in Chapter 5. Therefore, the CMIP6 evolution has a smaller difference between pre-industrial and present emissions than CMIP5, resulting in a lower radiative forcing of biomass burning SLCFs, leading to possibly lower effect on climate (van Marle et al., 2017).

Climate warming, especially through change in temperature and precipitation, will generally increase the risk of fire (Jia et al., 2019, see also Chapter 12) and can also affect the fire injection and plume height (Veira et al., 2016), but occurrence of fires and their emissions in the future strongly depends on anthropogenic factors such as population density, land use and fire management (Veira et al., 2016). Consequently, future emissions vary widely with increases and decreases amongst the SSP scenarios due to different land use change scenarios.

In summary, there has been an improvement in the knowledge of biomass burning emissions by reducing key uncertainties highlighted in AR5. However, systematic assessment of remaining uncertainties is limited, with a lower limit of uncertainties due to emission factors of 30 %, and larger uncertainties due to burning activity estimates, especially at regional level. Overall, a *medium confidence* in current global biomass burning SLCF emissions and their evolution over the satellite era is assessed. There is *low*-to-*medium confidence* in pre-industrial to the 1980s of biomass SLCF emissions, which rely on incorporation of several proxy data, with limited spatial representativeness. Nevertheless, uncertainties in absolute value of pre-

ACCEPTED VERSION SUBJECT TO FINAL EDITING

industrial emissions remain high, limiting confidence of radiative forcing estimates.

6.3 Evolution of Atmospheric SLCF abundances

This section assesses the evolution of atmospheric abundance[1] of SLCFs since AR5 based on observations and modelling, our knowledge of SLCFs burden and distribution, and our understanding of the trends over longer time scales. In addition to emissions (section 6.2), atmospheric chemistry (gas and aqueous chemistry), deposition (including wet and dry removal), and transport processes play a major role in determining the atmospheric distribution, budget and lifetime of SLCFs. The distribution and lifetime of SLCFs are further influenced by the modulation of chemical and physical processes in response to a changing climate. Therefore, the time evolution of atmospheric abundance of SLCFs is characterized by many complex non-linear interactions occurring at varying temporal and spatial scales. For this assessment, global scale, long-term measurements are employed only for a few gaseous SLCFs while for most short-lived species regional-scale observations and global models are relied upon.

[START BOX 6.1 HERE]

BOX 6.1: Atmospheric abundance of SLCFs: from process level studies to global chemistry-climate models

Changes in the atmospheric distribution of SLCFs determine their radiative forcing, and climate and air quality impacts. This box provides an overview of how process level understanding of the distribution and evolution of chemical compounds is derived and where uncertainties come from.

Process-level understanding of tropospheric gas and aerosol chemistry developed through laboratory and simulation chamber experiments as well as quantum chemical theory is used to generate chemical mechanisms. Atmospheric simulation chambers are designed to identify the chemical pathways and quantify reaction kinetics in isolation from atmospheric transport, deposition and emission processes. Ideally the chemical regimes studied, are representative for ambient atmospheric complexity and concentrations (e.g., McFiggans et al., 2019). Recently, quantum chemical theory has advanced to a level that it can provide kinetic and product information in a parameter range not possible with laboratory experiments (Vereecken et al., 2015). Iterative and interlinked use of simulation chamber and quantum chemical theory has led to improved knowledge of chemical mechanisms (Fuchs et al., 2013a; Nguyen et al., 2010; Peeters et al., 2009, 2014). For application in chemistry climate models (CCMs), the chemical mechanisms need to be computationally efficient, requiring simplifications. Such simplifications include reduced hydrocarbon representations, the application of lumping techniques (one compound or a chemical structure representing a family of compounds, for example, as done for parameterizing SOA formation) and/or the implementation of artificial operators representing key steps of the chemistry (Emmerson and Evans, 2009; Xia et al., 2009; Stockwell et al., 2020). Additionally, aerosol microphysical processes (nucleation, coagulation, condensation, evaporation, and sedimentation) that determine the evolution of aerosol number concentrations and size particle distribution are represented in parameterised forms in global models with varying levels of complexity (Mann et al., 2014).

A wide range of in situ and remotely sensed observations are used to characterise atmospheric chemical composition. Measurements made routinely as part of long-term monitoring programmes are particularly useful for assessing long-term trends and variability, and spatial distributions (as in Section 2.2, Section 6.3, and Section 7.3.3) while intensive field campaigns provide a more comprehensive view of atmospheric composition at a specific location for a limited time facilitating an improved process-level understanding. Retrieval of atmospheric concentrations from satellites, in particular, has been tremendously useful for providing global continuous coverage, although the retrievals themselves depend on prior information of atmospheric composition usually derived from models. Over the last decade or so, observations of

[1] The word ‘concentration’ is used to denote abundances in terms of mixing ratio for most species unless specified

ACCEPTED VERSION SUBJECT TO FINAL EDITING

atmospheric concentrations have been combined with information from global chemistry-climate models to produce global assimilation and forecasting systems with the purpose of producing chemical reanalysis or improving model inputs (i.e., emissions or boundary conditions) and forecasts (Miyazaki et al., 2015; Randles et al., 2017; Inness et al., 2019).

Global three-dimensional CCMs (Box 6.1, Figure 1) represent the full coupling of chemistry with climate physics (e.g., Morgenstern et al. 2017) with different levels of complexity (e.g, interactive aerosols with or without tropospheric and/or stratospheric chemistry). Methane concentrations are typically prescribed or constrained to observations while emissions of other SLCFs (or their precursors) are either prescribed or calculated interactively in the current generation of CCMs (Collins et al., 2017). CCMs, now part of Earth System Models (ESMs), are applied extensively to simulate the distribution and evolution of chemical compounds on a variety of spatial and temporal scales to improve current knowledge, make future projections and investigate global scale chemistry-climate interactions and feedbacks (see also Chapter 3 Section 3.8.2.2). CCMs are also used to interpret observations to disentangle the processes that drive observed variability and trends. Some aspects of air quality, such as diurnal peaks or local threshold violations, strong gradient in chemical regimes and coupling between processes cannot be captured by relatively coarse spatial resolution (> 50 km) global CCMs (Markakis et al., 2014) and necessitate subsequent downscaling modelling exercises.

The skill of CCMs is typically assessed by their ability to reproduce observed abundance, and trends and variability of chemical compounds. However, uncertainty remains large because of observation limitations (errors and uncertainties, spatial and temporal coverage), model parameterizations (e.g., chemical mechanisms, photolysis schemes, parameterizations for mixing and convective transport, and deposition), model input parameters (e.g., reaction rate constants, emissions) and an incomplete understanding of the physical and chemical processes that determine SLCF distributions (Brasseur and Jacob, 2017; Young et al., 2018). CCMs can therefore not capture every aspect of atmospheric chemical composition, but are expected to represent, as faithfully as possible, the sensitivity of chemical compounds to their drivers (e.g., anthropogenic emissions). Models are evaluated in multiple ways to identify their strengths and weaknesses in explaining the evolution of SLCF abundances. For example, CCM simulations are performed in the nudged or offline meteorology mode, that is, driven by observed or reanalysed meteorology rather than in the free-running mode, for consistent comparison of modelled chemical composition with observations for a specific time period (Dameris and Jöckel, 2013). Although, caution is exercised as nudging can alter the model climate resulting in unintentional impacts on the simulated atmospheric physics and/or chemistry (Orbe et al., 2018; Chrysanthou et al., 2019). Chemical mechanisms implemented in CCMs are evaluated and intercompared to assess their skill in capturing relevant chemistry features (e.g., Brown-Steiner et al. 2018). The multi-model ensemble approach, employed for evaluating climate models, has been particularly useful for characterizing errors in CCM simulations of SLCFs related to structural uncertainty and internal variability (Naik et al., 2013b; Shindell et al., 2013; Turnock et al., 2020; Young et al., 2013). However, as discussed in BOX 4.1, this approach is unable to capture the full uncertainty range.

This assessment draws upon results from single model studies and recent multi-model intercomparisons (e.g., AeroCom, CCMI), in particular those endorsed by CMIP6, which then allows for the full consideration of robustness and uncertainty due to model structures and processes. Based on the collective information provided in this body of literature, the CMIP6 multimodel ensemble is largely fit-for-purpose of evaluating the influence of SLCFs on radiative forcing, climate and non-CO_2 biogeochemical feedbacks. Additionally, CMIP6 models are fit for capturing global air pollution response to changes in emissions and meteorology but have difficulty in simulating the mean state (Turnock et al., 2020). The set of CMIP6 simulations has been used to update the relations between emissions and surface temperature at the heart of the emulators (Cross-Chapter box 7.1) and update emission metrics (Section 7.6). Emulators and emission metrics are used in this chapter (Sections 6.5 and 6.7) to assess more specifically the effect of the individual SLCFs for each sector and region which would be of prohibitive computing cost with CCMs. CCMs are also used to build global source-receptor models which use relations between surface concentrations and emissions. Such a model is used to assess the impact of various mitigation on air quality (Sections 6.5 and 6.7.)

ACCEPTED VERSION SUBJECT TO FINAL EDITING

[START BOX 6.1, FIGURE 1 HERE]

Box 6.1, Figure 1: Knowledge exchange between laboratory/theoretical studies, observations and global chemistry-climate models to inform our understanding of short-lived climate forcers (SLCFs).

[END BOX 6.1, FIGURE 1 HERE]

[END BOX 6.1 HERE]

6.3.1 Methane (CH_4)

The global mean surface mixing ratio of methane has increased by 156% since 1750 (see Section 2.2.3.4; Annex III). Since AR5, the methane mixing ratio has increased by about 3.5% from 1803±2 ppb in 2011 to 1866±3 ppb in 2019 (see Section 2.2.3.3.2) largely driven by anthropogenic activities as assessed in Chapter 5 (Section 5.2.2 and Cross-Chapter Box 5.2).

An assessment of the global methane budget is provided in Chapter 5, while this section assesses methane atmospheric lifetime and perturbation time (Prather et al., 2001). AR5 based its assessment of methane lifetime on (Prather et al., 2012). The methane lifetime due to tropospheric OH, the primary sink of methane, was assessed to be 11.2 ± 1.3 years constrained by surface observations of methyl chloroform (MCF), and lifetimes due to stratospheric loss[2], tropospheric halogen loss and soil uptake were assessed to be 150 ± 50 years, 200 ± 100 years, 120 ± 24 years, respectively (Myhre et al., 2013b). Considering the full range of individual lifetimes, the total methane lifetime was assessed in AR5 to be 9.25 ± 0.6 years.

The global chemical methane sink, essentially due to tropospheric OH, required to calculate the chemical lifetime is estimated by either bottom-up global CCMs and ESMs (BU) or top-down observational inversion methods (TD). BU global models represent the coupled chemical processes and feedbacks that determine the chemical sinks but show large diversity in their estimates, particularly the tropospheric OH sink (Zhao et al., 2019b; Stevenson et al., 2020). TD inversion methods, on the contrary, provide independent observational constraints on methane sink due to tropospheric OH over large spatio-temporal scales, but are prone to observational uncertainties and do not account for the chemical feedbacks on OH (Prather and Holmes, 2017; Naus et al., 2019). The central estimate of mean chemical methane loss over the period 2008-2017 varies from 602 [minimum and maximum range of 507-803] Tg yr^{-1} from BU chemistry-climate models in the Chemistry Climate Modeling Initiative (CCMI) to 514 [474-529] Tg yr^{-1} from TD inverse modelling (also see section 5.2.2 and Table 5.2). The smaller range in TD estimate (11%) results from the use of a common climatological mean OH distribution (Saunois et al., 2020; Zhao et al., 2020a) while the larger range in BU estimate (49%) reflects the diversity in OH concentrations from different chemical mechanisms implemented in the global models (Zhao et al., 2019b). See Section 6.3.3 for further discussion on the conflicting information on OH from CCMs/ESMs and TD inversion approaches. Further work is required to reconcile differences between BU and TD estimates of the chemical methane sink.

[START TABLE 6.2HERE]

Table 6.2: Methane lifetime due to chemical losses, soil uptake, and total atmospheric lifetime based on CMIP6 multi-model analysis, and bottom-up and top-down methane budget estimates in Table 5.2. Bottom-up and top-down methane lifetimes are calculated using the central estimates of the respective sinks for the mean 2008-2017 period in Table 5.2 together with mean 2008-2017 global methane concentration of 1815 ppb (see Annex III) converted to methane burden using a fill-factor of 2.75 Tg/ppb from Prather et al., (2012). Values in parentheses show the minimum and maximum range.

[2] Prather et al (2012) report lifetime due to stratospheric loss and soil uptake as 120 ± 24 years and 150 ± 50 years, respectively, and they were inadvertently swapped in AR5 with no effect on the total methane lifetime.

ACCEPTED VERSION SUBJECT TO FINAL EDITING

Study	Total Chemical Lifetime (yr)	Soil Lifetime (yr)	Total Atmospheric Lifetime (yr)	Number of models/inversions
(Stevenson et al., 2020)[a]	8.3 (8.1-8.6)[b]	160	8.0 (7.7-8.2)	3 CMIP6 ESMs
Bottom-up (based on Table 5.2)	8.3 (6.2-9.8)	166 (102-453)	8.0 (6.3-10.0)	7 CCMI CCMs/CTMs
Top-down (based on Table 5.2)	9.7 (9.4-10.5)	135 (116-185)	9.1 (8.7-10.0)	7 inversion systems
AR6 assessed value [c]	9.7 ± 1.1	135 ± 44	9.1 ± 0.9	Based on Top-down with uncertainty estimate from AR5

[a] mean over 2005-2014
[b] does not include lifetime due to tropospheric halogen loss
[c] uncertainties indicate ± 1-standard deviation

[END TABLE 6.2HERE]

The present-day BU methane chemical lifetime shows a larger spread than that in the TD estimates (Table 6.2) in line with the spread seen in the sink estimates. The spread in the methane lifetime calculated by three CMIP6 ESMs is narrower and is enclosed within the spread of the BU CCMI model ensemble. Based on the consideration that the small imbalance in total methane sources versus sinks derived from TD estimates is close to the observed atmospheric methane growth rate (see Table 5.2), the TD values are assessed to be the best estimates for this assessment. The relative uncertainty (1-sigma) is taken to be the same as that in AR5, i.e., 11.8%, 33% and 10% for chemical, soil and total lifetime, respectively. The central estimate of the total atmospheric methane lifetime assessed here is the same as that in the AR5.

The methane perturbation lifetime (τ_{pert}) is defined as the e-folding time it takes for methane burden to decay back to its initial value after being perturbed by a change in methane emissions. Perturbation lifetime is longer than the total atmospheric lifetime of methane as an increase in methane emissions decreases tropospheric OH which in turn decreases the lifetime and therefore the methane burden (Prather, 1994; Fuglestvedt et al., 1996; Holmes et al., 2013; Holmes, 2018). Since perturbation lifetime relates changes in emissions to changes in burden, it is used to determine the emissions metrics assessed in Chapter 7 Section 7.6. The perturbation lifetime is related to the atmospheric lifetime as $\tau_{pert} = f * \tau_{total}$ where f is the feedback factor and is calculated as $f = 1/(1-s)$, where $s = - \delta (\ln \tau_{total})/ \delta (\ln[CH_4])$ (Prather et al., 2001). Since there are no observational constraints for either τ_{pert} or f, these quantities are derived from CCMs or ESMs. AR5 used f = 1.34 ± 0.06 based on a combination of multimodel (mostly CTMs and a few CCMs) estimates (Holmes et al., 2013). A recent model study explored new aspects of methane feedbacks finding that the strength of the feedback, typically treated as a constant, varies in space and time but will in all likelihood remain within 10% over the 21st century (Holmes, 2018). For this assessment, the value of f is assessed to be 1.30±0.07 based on a six member ensemble of AerChemMIP ESMs (Thornhill et al., 2021b). This f value is slightly smaller but within the range of the AR5 value. This results in an overall perturbation methane lifetime of 11.8 ± 1.8 years, within the range of the AR5 value of 12.4 ± 1.4 years. The methane perturbation lifetime assessed here is used in the calculation of emission metrics in Section 7.6.

ACCEPTED VERSION SUBJECT TO FINAL EDITING

6.3.2 Ozone (O_3)

6.3.2.1 Tropospheric ozone

About ten percent of the total atmospheric ozone column resides in the troposphere. The ozone forcing on climate strongly depends on its vertical and latitudinal distribution in troposphere. The lifetime of ozone in the troposphere ranges from a few hours in polluted urban regions to up to few months in the upper troposphere. Observed tropospheric ozone concentrations range from less than 10 ppb over the tropical Pacific Ocean to as much as 100 ppb in the upper troposphere and more than 100 ppb downwind of major ozone precursor emissions regions. An ensemble of five CMIP6 models including whole atmospheric chemistry and interactive ozone has been shown to simulate consistently the present-day ozone distribution (N-S and latitudinal gradients) and its seasonal variability when compared with observations from sondes, background surface stations and satellite products (Griffiths et al., 2020). The biases, whose magnitude is similar to AR5, are lower than 15% against climatological seasonal cycle from ozonesondes with an overestimate in the Northern Hemisphere and an underestimate in the Southern Hemisphere (Griffiths et al., 2020). The CMIP6 multimodel ensemble estimate of the global mean lifetime of ozone for present day conditions is 25.5 ± 2.2 days (Griffiths et al., 2020) which is within the range of previous multi-model estimates (Stevenson et al., 2006; Young et al., 2013), indicating a *high level of confidence*.

AR5 assessed the tropospheric ozone burden to be 337±23 Tg for year 2000 based on the ACCMIP ensemble of model simulations (Myhre et al., 2013b). Multiple satellites products, ozonesondes and CCMs are used to estimate tropospheric ozone burden (Table 6.3). Satellite products provide lower-bound values as they exclude regions under polar night conditions (Gaudel et al., 2018). The tropospheric ozone burden values from multi-model exercises are within the range of the observational estimates despite different definitions of the tropopause for multi-model estimates which can lead to differences of about 10% on the ozone burden model estimates (Griffiths et al., 2020). Weighted by their number of members, CMIP6 and CCMI multimodel estimates and observational estimates of tropospheric ozone burden about year 2010, lead to an assessment of the tropospheric ozone burden of 347±28 Tg for 2010.

The tropospheric ozone budget is controlled by chemical production and loss, by STE, and by deposition at the Earth's surface, whose magnitude are calculated by CCMs (Table 6.3). Despite the high agreement of the model ensemble mean with observational estimates in present-day tropospheric ozone burden, the values of individual budget terms can vary widely across models in CMIP6 consistent with previous model intercomparison experiments (Young et al., 2018). Furthermore, single-model studies have shown that the halogen chemistry, which is typically neglected from model chemistry schemes in CCMs, may have a notable impact on the ozone budget, as halogens, particularly of marine origin, take part in efficient ozone loss catalytic cycles in the troposphere (Saiz-Lopez et al., 2012; Sarwar et al., 2015; Sherwen et al., 2016).

[START TABLE 6.3 HERE]

Table 6.3: Global tropospheric ozone budget terms and burden based on multi-model estimates and observations for present conditions. All uncertainties quoted as 1 σ. Values of tropospheric ozone burden with asterisk indicate average over the latitudinal zone 60ºN- 60ºS.

Period	Burden (Tg)	Production Tg yr^{-1}	Loss Tg yr^{-1}	Deposition Tg yr^{-1}	STE Tg yr^{-1}	Number of Models / Reference
	Models					
~ 2000 time slice (1995–2004)	347± 30	5283 ± 1798	4108 ± 486	1075 ± 514	626 ± 781	CMIP6[a] (5 Earth System Models) (Griffiths et al., 2020)
~2010 time slice (2005–2014)	356 ± 31	5530 ± 1909	4304± 535	1102 ± 538	628 ± 804	
~ 2000	341±31					

ACCEPTED VERSION SUBJECT TO FINAL EDITING

	(309±31)*					CCMI[b] (9 models) (Archibald et al., 2020)
2010	345±30 (314±29)*					
~ 2000	340 ± 34	4937 ± 656	4442 ± 570	996 ± 203	535 ± 161	TOAR[c] (based on 32-49 models participating in intermodel comparisons and single model studies) (Young et al., 2018)
	Observations					
2010–2014	338 ± 6					TOST[d], IASI[e]-FORLI, and IASI-SOFRID (Gaudel et al., 2018)
2010–2014	302 ± 12*					TOST, IASI-FORLI, IASI-SOFRID, OMI[f]/MLS, OMI-SAO and OMI-RAL (Gaudel et al., 2018)

[a]CMIP6: Coupled Model Intercomparison Project Phase 6; [b]CCMI: Chemistry-Climate Model Initiative;[c] TOAR Tropospheric Ozone Assessment Report; [d] TOST Trajectory-mapped Ozonesonde dataset for the Stratosphere and Troposphere; [e] IASI Infrared Atmospheric Sounding Interferometer; [f] OMI Ozone Monitoring Instrument.

[END TABLE 6.3 HERE]

Because of the heterogeneous distribution of ozone, limited observations or proxies do not provide accurate information about the global preindustrial abundance, posing a challenge to the estimation of the historical evolution of tropospheric ozone. Therefore, global CCMs complemented by observations are relied upon for estimating the long-term changes in tropospheric ozone. AR5 concluded that anthropogenic changes in ozone precursor emissions are unequivocally responsible for the increase between 1850 and present (Myhre et al., 2013b). Based on limited isotopic evidence, Chapter 2 assesses that the global tropospheric ozone increased by less than 40% between 1850 and 2005 (*low confidence*) (see Section 2.2.5.3). The CMIP6 models are in line with this increase of tropospheric ozone with an ensemble mean value of 109± 25 Tg (model range) from 1850-1859 to 2005-2014 (Figure 6.4). This increase is higher than the AR5 value of 100 ± 25 Tg from 1850 to 2010 due to higher ozone precursor emissions in CMIP6. However, the AR5 and CMIP6 value are close when considering the reported uncertainties. The uncertainties are equivalent in CMIP6 and AR5 despite enhanced inclusion of coupled processes in the CMIP6 ESMs (e.g. biogenic VOC emissions or interactive stratospheric ozone chemistry).

[START FIGURE 6.4 HERE]

Figure 6.4: Time evolution of global annual mean tropospheric ozone burden (in Tg) from 1850 to 2100. Multi-model means for CMIP6 historical experiment (1850-2014) from UKESM1-LL-0, CESM2-WACCM, MRI-ESM2-0, GISS-E2.1-G and GFDL-ESM4 and for ScenarioMIP SSP3-7.0 experiment (2015-2100) are represented with their intermodel standard deviation (±1 σ , shaded areas). Observation based global tropospheric ozone burden estimate (from Table 6.3) is for 2010-2014. Tropospheric Ozone Assessment Report (TOAR) multi-model mean value (from Table 6.3) is for 2000 with a ±1 σ error-bar. Atmospheric Chemistry and Climate Model Intercomparison Project (ACCMIP) multi-model means are for 1850, 1930, 1980 and 2000 time-slices with ±1 σ error-bars. The troposphere is masked by the tropopause pressure calculated in each model using the WMO thermal tropopause definition. Further details on data sources and processing are available in the chapter data table (Table 6.SM.1).

[END FIGURE 6.4 HERE]

ACCEPTED VERSION SUBJECT TO FINAL EDITING

Since the mid-20th century, the CMIP6 model ensemble shows a higher global trend (Figure 6.4). Since mid-1990s, the trends are better documented by observations (see also Section 2.2.5.3) and indicate spatial heterogeneity. In particular, in-situ observations at remote surface sites and in the lower free troposphere indicate positive trends that are far more common than negative trends, especially in the northern tropics and across southern and eastern Asia (Figure 6.5). The CMIP6 ensemble and observations largely agree in the magnitude of the global positive trend since 1997 (0.82±0.13 Tg yr^{-1} in the model ensemble; 0.70±0.15 Tg yr^{-1} in ozonesonde dataset; 0.83± 0.85 Tg yr^{-1} in the satellite ensemble) and qualitatively reproduce positive trends in Southern Hemisphere (Griffiths et al., 2020). More analyses are needed for evaluation in other parts of the world to assess the skill of the recent ensemble based on CMIP6 emissions.

[START FIGURE 6.5 HERE]

Figure 6.5: Decadal tropospheric ozone trends since 1994. Trends are shown at 28 remote and regionally representative surface sites (Cooper et al., 2020) and in 11 regions of the lower free troposphere (650 hPa, ca. 3.5 km) as measured by In-Service Aircraft for a Global Observing System (IAGOS) above Europe, northeastern USA, southeastern USA, western North America, northeast China, South East Asia, southern India, Persian Gulf, Malaysia/Indonesia, Gulf of Guinea and northern South America (Gaudel et al., 2020). High elevation surface sites are >1500 m above sea level. All trends end with the most recently available year but begin in 1995 or 1994. The sites and datasets are the same as those used in Figure 2.8, further details on data sources and processing are available in the Chapter 2 data table (Table 2.SM.1).

[END FIGURE 6.5 HERE]

In summary, there is *high confidence* in the estimated present-day (about 2010) global tropospheric ozone burden based on an ensemble of models and observational estimates (347±28 Tg), but there is *medium confidence* among the individual models for their estimates of the tropospheric ozone related budget terms. Evidence from successive multi-model intercomparisons and the limited isotopic evidence agree on the magnitude of the increase of the tropospheric ozone burden from 1850 to present-day in response to anthropogenic changes in ozone precursor emissions corroborating AR5 findings. This increase is assessed to be 109±25 Tg (*medium confidence*). CMIP6 model ensemble shows a constant global increase since the mid-20th century whose rate is consistent with that derived from observations since the mid-1990s.

6.3.2.2 Stratospheric ozone

Ninety percent of total-column ozone resides in the stratosphere. The chemical lifetime of ozone in the stratosphere ranges from less than a day in the upper stratosphere to several months in the lower stratosphere (Bekki and Lefevre, 2009). Global stratospheric ozone trends based on observations are assessed in Chapter 2 (Section 2.2.5.2). CMIP6 model ensemble shows that global total ozone column (TCO) has slightly changed from 1850 to 1960 (Keeble et al., 2021). The rapid decline in the 1970s and 1980s due to halogenated ODSs (as assessed in Chapter 2 Section 2.2.5.2 from observations) until the end of the 1990s followed by a slight increase since then is captured by the models (Keeble et al., 2021). Overall the observed climatology patterns and annual cycle amplitudes, are well represented in the CMIP6 ensemble mean. CMIP6 ensemble overestimates the observed TCO values by up to 6% (10-20 DU) globally in the NH and SH mid-latitudes, and in the tropics, but the trend in these regions is well captured between 1960 and 2014. However, there is poor agreement between the individual CMIP6 models in the pre-industrial and throughout the historical period, with model TCO values spread across a range of ~60 DU. The global stratospheric ozone column decreased by 14.3±8.7 DU from 1850 to 2014 (Keeble et al., 2021).

Model simulations attribute about half of the observed upper stratospheric ozone increase after 2000 to the decline of ODS since the late 1990s while the other half of the ozone increase is attributed to the slowing of gas-phase ozone destruction cycles due to cooling of the upper stratosphere by increasing GHGs (Aschmann et al., 2014; Oberländer-Hayn et al., 2015).

ACCEPTED VERSION SUBJECT TO FINAL EDITING

In summary, global stratospheric ozone column has decreased from pre-industrial to present-day in response to the ODS-induced ozone rapid decline in the 1970s and 1980s followed by slow, and still incomplete, recovery. There is *medium confidence* that global stratospheric ozone column has changed by 14.3±8.7 DU between 1850 and 2014.

6.3.3 Precursor Gases

6.3.3.1 Nitrogen Oxides (NO_x)

The distribution of tropospheric NO_x is highly variable in space and time owing to its short lifetime coupled with highly heterogeneous emission and sink patterns. NO_x undergoes chemical processing, including the formation of nitric acid (HNO_3), nitrate (NO_3^-), organic nitrates (e.g, alkyl nitrate, peroxyacyl nitrate), and atmospheric transport, and deposition. Despite challenges in retrieving quantitative information from satellite observations (Duncan et al., 2014; Lin et al., 2015; Lorente et al., 2017; Silvern et al., 2018), improved accuracy and resolution of satellite-derived tropospheric NO_2 columns over the past two decades have advanced understanding of the global distribution, long-term trends, and source attribution of NO_x. Long-term average tropospheric NO_2 column based on multiple satellites born instruments (Figure 6.6a) reveals highest NO_2 levels over the most populated, urbanized, and industrialised regions of the world corresponding to high NO_x emission source regions (Krotkov et al., 2016; Georgoulias et al., 2019). Enhanced but highly variable NO_2 columns are also associated with biomass burning regions as well as areas influenced by lightning activity (Miyazaki et al., 2014; Tanimoto et al., 2015).

Observational constraints derived from isotopic composition of atmospheric nitrate inferred from ice cores provide evidence of increasing anthropogenic NO_x sources since pre-industrial times (Hastings et al., 2009; Geng et al., 2014). Global NO_x emission trends in bottom-up inventories (Section 6.2.1) as well as model simulations of nitrogen deposition (Lamarque et al., 2013b) are in qualitative agreement with these observational constraints. CMIP6 ESMs exhibit stable NO_x burden until early 1900s and then a sharp increase driven by a factor of three increase in emissions, however the magnitude of this increase remains uncertain due to poor observational constraints on pre-industrial concentrations of NO_x (Griffiths et al., 2020).

AR5 reported NO_2 decreases by 30-50% in Europe and North America and increases by more than a factor of two in Asia over the 1996 to 2011 based on satellite observations (Hartmann et al., 2013). Extension of this analysis covering time period up to 2015 reveals that NO_2 has continued to decline over the USA, western Europe, and Japan (Schneider et al., 2015; Duncan et al., 2016; Krotkov et al., 2016) because of effective fossil fuel NO_x emission controls (Section 6.2), although this rate of decline has slowed down post-2011 (Jiang et al., 2018b). Satellite observations also reveal a 32% decline in NO_2 column over China after peaking in 2011 (see Figure 6.6b) consistent with declining NO_x emissions (Section 6.2) due to the implementation of emission control strategies (de Foy et al., 2016; Irie et al., 2016; Liu et al., 2016a). Over South Asia, tropospheric NO_2 levels have grown rapidly with increases of 50% during 2005 to 2015 largely driven by hotspot areas in India experiencing rapid expansion of the power sector (Duncan et al., 2016; Krotkov et al., 2016). Further analysis indicates that many parts of India have also undergone a reversal in NO_2 trends since 2011 that has been attributed to a combination of factors, including a slowdown in economic growth, implementation of cleaner technologies, non-linear NO_x chemistry, and meteorological variability (Georgoulias et al., 2019). Satellite data reveals spatially heterogeneous NO_2 trends over the Middle East with an overall increase over 2005-2010 and a decrease over large parts of the region after 2011-2012. The reasons for trend reversal within individual areas are diverse, including warfare, imposed sanctions, and air quality controls (Lelieveld et al., 2015a; Georgoulias et al., 2019). Satellite-derived tropospheric NO_2 levels over Africa and Latin America do not show a clear trend; both increasing and decreasing trends are observed over large agglomerations in these regions since the early 2000s (Schneider et al., 2015; Duncan et al., 2016).

In summary, global tropospheric NO_x abundance has increased from 1850 to 2015 (*high confidence*). Satellite observations of tropospheric NO_x indicate strong regional variations in trends over 2005-2015.

ACCEPTED VERSION SUBJECT TO FINAL EDITING

There is *high confidence* that NO_2 has declined over the USA and western Europe since the mid 1990s and increased over China until 2011. NO_2 trends have reversed (declining) over China beginning in 2012 and NO_2 has increased over South Asia by 50% since 2005 (*medium confidence*).

[START FIGURE 6.6 HERE]

Figure 6.6: Long term climatological mean (a) and time evolution (b) of tropospheric nitrogen dioxide (NO_2) vertical column density. Values come from the merged GOME/SCIAMACHY/GOME-2 (TM4NO2A version 2.3) dataset for the period 1996-2016 (Georgoulias et al., 2019). Time evolution of NO_2 column shown in panel (b) is normalized to the fitted 1996 levels for the 10 regions shown as boxes in panel (a). Further details on data sources and processing are available in the chapter data table (Table 6.SM.1).

[END FIGURE 6.6 HERE]

6.3.3.2 Carbon Monoxide (CO)

About half of the atmospheric CO burden is due to its direct emissions and the remainder is due to atmospheric oxidation of methane and NMVOCs. Reaction with OH is the primary sink of CO with a smaller contribution from dry deposition.

Since AR5, advances in satellite retrievals (e.g. Worden et al., 2013; Warner et al., 2014; Buchholz et al., 2021a), ground based column observations (e.g. Zeng et al., 2012; Té et al., 2016), airborne platforms (e.g. Cohen et al., 2018; Petetin et al., 2018), surface measurement networks (e.g., Andrews et al., 2014; Petron et al., 2019; Prinn et al., 2018; Schultz et al., 2015) and assimilation products (e.g., Deeter et al., 2017; Flemming et al., 2017; Zheng et al., 2019) have resulted in better characterization of the present day atmospheric CO distribution. Typical annual mean surface CO concentrations range from ~120 ppb in the Northern Hemisphere to ~40 ppb in the Southern Hemisphere (Petron et al., 2019). The sub-regional patterns in CO reflect the distribution of emission sources. Seasonal hotspots are linked to areas of biomass burning in tropical South America, equatorial Africa, Southeast Asia, and Australia. A study using data assimilation techniques estimates a global mean CO burden of 356 ± 27 Tg over the 2002-2013 period (Gaubert et al., 2017).

Global models generally capture the global spatial distribution of the observed CO concentrations but have regional biases of up to 50% (e.g., Emmons et al., 2020; Horowitz et al., 2020). Despite updated emissions datasets, the global multi-model and single model simulations persistently underestimate observed CO concentrations at northern high- and mid-latitudes as well as in the Southern Hemisphere but with smaller biases compared with that in the Northern Hemisphere (Monks et al., 2015b; Naik et al., 2013b; Stein et al., 2014; Strode et al., 2015). Models are biased high in the tropics, particularly over highly polluted areas in India and Eastern Asia (Strode et al., 2016; Yarragunta et al., 2017).

Estimates of global CO burden simulated by global models generally fall within the range of that derived from data assimilation techniques, though the spread across the models is large (Myriokefalitakis et al., 2016; Naik et al., 2013b; Stein et al., 2014; Zeng et al., 2015). There is a large diversity in model simulated CO budget driven by uncertainties in CO sources and sinks, particularly those related to in situ production from NMVOCs and loss due to reaction with OH (Stein et al., 2014; Zeng et al., 2015; Myriokefalitakis et al., 2016). Global CO budget analysis from a multimodel ensemble for more recent years including results from the CMIP6 model runs are not yet available.

Reconstructions of CO concentrations based on limited ice core samples in the Northern Hemisphere high latitudes suggest CO mole fractions of about 145 ppb in the 1950s, which rose by 10-15 ppb in the mid-1970s, and then declined by about 30 ppb to about 130 ppb by 2008 (Petrenko et al., 2013). The negative trends since the 1990s are often attributed to emission regulations from road transportation in North America and Europe. Due to limited observations prior to the satellite era, our knowledge on long-term global CO

ACCEPTED VERSION SUBJECT TO FINAL EDITING

trends are estimated using models. An increase of global CO burden of about 50% for the year 2000 relative to 1850 is found in CMIP6 (Griffiths et al., 2020).

AR5 reported a global CO decline of about 1% yr^{-1} based on satellite data from 2002-2010, but biases in instruments rendered low confidence in this trend. AR5 also indicated a small CO decrease from in situ networks but did not provide quantitative estimates. New analysis of CO trends performed since AR5 and based on different observational platforms and assimilation products show a decline globally and over most regions during the last one to two decades with varying amplitudes partly depending on the period of analysis (Table 6.4). Inversion based analysis attribute the global CO decline during the past two decades to decreases in anthropogenic and biomass burning CO emissions despite probable increase in atmospheric CO chemical production (Gaubert et al., 2017; Jiang et al., 2017; Zheng et al., 2019). Furthermore, (Buchholz et al., 2021) report a slowdown in global CO decline in 2010-2018 compared to 2002-2010, although the magnitude and sign of this change in the trend varies regionally. Global models prescribed with emissions inventories developed prior to the CMIP6 inventory capture the declining observed CO trends over North America and Europe but not over East Asia (Strode et al., 2016). CMIP6 models driven by CMIP6 emissions simulate a negative trend in global CO burden over the 1990-2020 period (Griffiths et al., 2020), however the simulated trends have not yet been evaluated against observations.

In summary, our understanding of present day global CO distribution has increased since AR5 with newer and improved observations and reanalysis. There is *high confidence* that global CO burden is declining since 2000. Evidence from observational CO reanalysis suggests this decline to be driven by reductions in anthropogenic CO emissions, however this is yet to be corroborated by global ESM studies with the most recent emission inventories.

[START TABLE 6.4 HERE]

Table 6.4: Summary of the global CO trends based on model estimates and observations.

Analysis period	Trends : Regions	Reference/Methodology
Global / Hemispheric		
2003 to 2015	-0.86 % yr^{-1}	(Flemming et al., 2017) Model assimilating MOPITT
2002 to 2013	-1.4% yr^{-1}	(Gaubert et al., 2017) Model assimilating MOPITT
2002-2018	-0.50±0.3% yr^{-1}: 60°N – 60°S (MOPITT) -0.56±0.3% yr^{-1}; -0.61±0.2% yr^{-1}: 0°-60°N -0.35±-0.3% yr^{-1}; -0.33±0.3% yr^{-1}: 0°-60°S	(Buchholz et al., 2021) Satellite Observations MOPITT; AIRS
2000-2017	-0.32±0.05% yr^{-1}	(Zheng et al., 2019) Satellite Observations MOPITT
2003-2014	~ 0.5 to -2.5 ppb yr^{-1}: Northern Hemisphere ~ 0 to -0.5 ppb yr^{-1}: Southern Hemisphere	(Flemming et al., 2017) NOAA Carbon Cycle Cooperative Global Air Sampling Network
2001-2013	-0.80 ppb yr^{-1} to -2.19 ppb yr^{-1}: Northern Hemisphere (Upper Troposphere / Tropopause Layer)	(Cohen et al., 2018) IAGOS Airborne
Pacific / Tropic		
2004-2013 (Spring Mean)	-2.9 ± 2.6 ppb yr^{-1} : Mauna Loa (19.54°N, 155.58°W)	(Gratz et al., 2015) Ground based

ACCEPTED VERSION SUBJECT TO FINAL EDITING

2004-2013 (Spring Mean)	-2.6 ± 1.8 ppb yr^{-1}: Sand Island Midway (28.21°N, 177.38°W)	(Gratz et al., 2015) Ground based
Europe		
1996-2006	-0.45±0.16 %yr^{-1}: Jungfraujoch (46.6°N 8.0°E) -1.00±0.24 %yr^{-1}: Zugspitze (47.4°N 11.0°E) -0.62±0.19 %yr^{-1}: Harestua (60.2°N 10.8°E) 0.61±0.16 %yr^{-1}: Kiruna (67.8°N 20.4°E)	(Angelbratt et al., 2011) Ground based
2001-2011 May-Sep	-3.1±0.30 ppb yr^{-1}: Pico Mt.Obs (38.47 °N 28.40 °W) -1.4±0.20 ppb yr^{-1}: Mace Head, Ireland	(Kumar et al., 2013) Ground based
2002-2018	-0.89 ±0.1 %yr^{-1}: Europe (45°-55°N 0°-15°E)	(Buchholz et al., 2021) Satellite Observations MOPITT
North America		
2001-2010	-2.5 ppb yr^{-1}: Thompson Farm (43.11 °N 70.95 °W) -2.3 ppb yr-1: Mt. Washington (44.27 °N 71.30 °W) +2.8 ppb yr^{-1}: Castle Springs (43.75 °N 71.35 °W) -3.5 ppb yr^{-1}: Pack Monadnock (42.86 °N 71.88 °W) -2.8 ppb yr^{-1}: Whiteface Mountain (44.40 °N 73.90 °W) -4.3 ppb yr^{-1}: Pinnacle State Park (42.09 °N 77.21 °W)	(Zhou et al., 2017) Ground based
2004-2013 (Spring Mean)	-3.2 ± 2.9 ppb yr^{-1} : Mt. Bachelor Observatory	(Gratz et al., 2015) Ground based
2004-2012 (Spring Mean)	-2.8 ± 1.8 ppb yr^{-1}: Shemya Island (55.21°N, 162.72°W)	(Gratz et al., 2015) Ground based
2002-2018	-0.85 ± 0.1%yr^{-1}: Eastern USA (35°-40°N, -95° to -75°E)	(Buchholz et al., 2021) Satellite Observations MOPITT
Asia		
2005-2018	-0.46±0.14 % yr^{-1}: East Asia	(Zheng et al., 2018a) WDCGG Ground based
2005-2018	-0.41±0.09 % yr^{-1}: East Asia	(Zheng et al., 2018a) MOPITT
2002-2018	-1.18 ± 0.3 %yr^{-1}: (N.E. China 30°-40°, 110°-123°E) -0.28±0. : (N. India 20°-30°N 70°-95°E)	(Buchholz et al., 2021) Satellite Observations MOPITT

[END TABLE 6.4 HERE]

6.3.3.3 Non-Methane Volatile Organic Compounds (NMVOCs)

NMVOCs encompass thousands of compounds with lifetimes from hours to days to months and abundances and chemical composition highly variable with respect to space, time. Although the biogenic source (Section 6.2.2) dominates the global NMVOC budget, anthropogenic activities are the main driver of long-term trends in the abundance of many compounds.

Information on the global distribution of individual NMVOCs is scarce, except for the less reactive

ACCEPTED VERSION SUBJECT TO FINAL EDITING

compounds having lifetimes of several days to months. Based on measurements from polar firn air samples and ground-based networks, AR5 reported that the abundances of the predominantly anthropogenic light alkanes (C_2-C_5) increased until 1980 and declined afterwards. The decline was attributed to air quality emission controls and to fugitive emission decreases following the collapse of the Soviet Union (Simpson et al., 2012). Since AR5, scarce ground-based measurements have shown that the decline in C_2-C_3 alkanes ended around 2008 and their abundances are since growing again, which is primarily attributed to increasing North American emissions (see Section 6.2.1). Furthermore, since AR5 the evolution of ethane levels during the past millennium was made accessible by analysis of ice core samples (Nicewonger et al., 2016). The large observed interpolar ratio of ethane in preindustrial times (3.9) corroborates a large geologic source of ethane previously put forward by (Etiope and Ciccioli, 2009), and narrows down its likely global magnitude (Nicewonger et al., 2018) (*low to medium confidence*). The incorporation of geologic emissions in CCMs is not yet systematic though a one-model study has shown improved agreement of the results with observations (Dalsøren et al., 2018).

Formaldehyde is a short-lived high-yield product of NMVOC oxidation and formaldehyde column data from satellite instruments can therefore inform on trends in anthropogenic NMVOC abundances over very industrialized region. AR5 reported significant positive trends in HCHO between 1997 and 2009 over north-eastern China (4% yr^{-1}) and negative trends over north-eastern U.S. cities. Since AR5, there is *robust evidence* and *high agreement* of an upward trend of HCHO over eastern China, though large regional disparities exist in the trends (De Smedt et al., 2015; Shen et al., 2019) with possible negligible or decreasing trend over Beijing and the Pearl River Delta. In other world regions, in particular North America, there is *limited to medium evidence* for significant changes in the HCHO columns, except in regions where the trend is particularly strong, e.g. the Houston area (-2.2% yr^{-1} over 2005-2014) and the Alberta oil sands (+3.8% yr^{-1}) (Zhu et al., 2017). Over the north-eastern U.S., even the sign of the trend differs between studies (De Smedt et al., 2015; Zhu et al., 2017) for reasons that are unclear.

In summary, after a decline between 1980 and 2008, abundances of light NMVOCs have increased again over the Northern Hemisphere due to extraction of oil and gas in North America (*high confidence*). Trends in satellite HCHO observations, used as a proxy of anthropogenic NMVOC over industrialised areas, show a significant positive trend over Eastern China (*high confidence*) but also indicate large regional disparities in the magnitude of the trends over China and even in their signs over North America.

6.3.3.4 Ammonia (NH_3)

Ammonia is the most abundant alkaline gas in the atmosphere. Its present-day source is dominated by livestock and crop production (section 6.2). Ammonia reacts with nitric acid and sulphuric acid to produce ammonium sulphate and ammonium nitrate, which contribute to the aerosol burden (see section 6.3.5.2), promotes aerosol nucleation by stabilizing sulphuric acid clusters (Kirkby et al., 2011) and contributes to nitrogen deposition (see section 6.4.4) (Sheppard et al., 2011; Flechard et al., 2020). Trends in NH_3 were not assessed in AR5.

Considerable expansion of satellite (Clarisse et al., 2009; Shephard and Cady-Pereira, 2015; Warner et al., 2016) and ground-based observations (Miller et al., 2014; Li et al., 2016; Pan et al., 2018) has improved our understanding of the spatial distribution and seasonal to inter-annual variability of ammonia, and advanced its representations in models (e.g., Zhu et al., 2015). Regionally, peak NH_3 concentrations are observed over large agricultural (e.g., Northern India, US Midwest and Central Valley) and biomass burning regions, in good qualitative agreement with emission inventories (Van Damme et al., 2015, Van Damme et al., 2018). However, several large agricultural and industrial hotspots have been found to be missing or greatly underestimated in emission inventories (Van Damme et al., 2018). NH_3 exhibits a strong vertical gradient, with a maximum in the boundary layer (Schiferl et al., 2016) and can be transported into the upper troposphere and lower stratosphere (UTLS), particularly in the Asian Monsoon region, as indicated by observations (Froyd et al., 2009; Höpfner et al., 2016, 2019) and theoretical considerations (Ge et al., 2018). There is a large range in the present-day NH_3 burden (from 0.04 to 0.7 TgN) simulated by CCMs, highlighting deficiencies in the process-level representation of NH_3 in current global models (Bian et al.,

ACCEPTED VERSION SUBJECT TO FINAL EDITING

2017). The underestimate of surface NH_3 concentrations (Bian et al., 2017) further highlights such deficiencies and the limitations in comparing site-specific observations with relatively coarse-resolution models.

Observations show that NH_3 concentration has been increasing in recent decades in the USA (Butler et al., 2016; Warner et al., 2016; Yu et al., 2018), western Europe (van Zanten et al., 2017; Warner et al., 2017, Wichink Kruit et al., 2017; Tang et al., 2018b), and China (Warner et al., 2017; Liu et al., 2018). This trend has been attributed to a combination of increasing ammonia emissions (Sutton et al., 2013; Fowler et al., 2015) and decreases in the chemical reaction of NH_3 with nitric and sulphuric acids associated with reductions in SO_2 and NO_x emissions whose rate depends on the region (Warner et al., 2017; Yao and Zhang, 2019). Over longer time scales, CCMs simulate an increase of the NH_3 burden by a factor of 2 to 7 since preindustrial conditions (Xu and Penner, 2012; Hauglustaine et al., 2014).

In summary, progress has been made in the understanding of the spatio-temporal distribution of ammonia, though representation of NH_3 remains rather unsatisfactory due to process-level uncertainties. Evidence from observations and models suggests that ammonia concentrations have been increasing over the recent decades due to emissions and chemistry. There is *high confidence* that the global NH_3 burden has increased considerably from preindustrial to present-day although the magnitude of the increase remains uncertain.

6.3.3.5 Sulphur Dioxide (SO_2)

AR5 did not assess trends in SO_2 concentrations. Trends in SO_2 abundances are consistent with the overall anthropogenic emission changes as presented in Section 6.2 and Figure 6.18. Long-term surface-based in situ observations in North America and Europe show reductions of more than 80% since the measurements began around 1980 (Table 6.5). Europe had the largest reductions in the first part of the period while the highest reduction came later in North America. Observed trends are qualitatively reproduced by global and regional models over North America and Europe over the period 1990-2015 for which emission changes are well quantified (Table 6.5) (Aas et al., 2019).

In situ observations over other parts of the world are scattered. However, the limited in-situ observations in East Asia indicate an increase in atmospheric SO_2 up to around 2005 and then a decline (Aas et al., 2019). This is confirmed by satellite observations (Krotkov et al., 2016), which further reveal a rapid decline in SO_2 since 2012 to 2013 (Krotkov et al., 2016; Zheng et al., 2018b). In India, on the other hand, the SO_2 levels have doubled over 2005 to 2015 (Krotkov et al., 2016).

In summary, surface and satellite observations indicate strong regional variations in trends of atmospheric SO_2 abundance. The SO_2 concentrations in North America and Europe have declined over 1980 to 2015 with slightly stronger reductions in North America (70 ± 20%) than over Europe (58 ± 32%) over 2000-2015, though Europe had larger reductions than the US in the prior decade (1990-2000). In Asia, the SO_2 trends are more scattered, though there is *medium confidence* that there was a strong increase up to around 2005, followed by a steep decline in China, while over India, the concentrations are increasing steadily.

[START TABLE 6.5 HERE]

Table 6.5: Summary of changes or trends in atmospheric abundance of sulphur dioxide (SO_2) and sulphate (SO_4^{2-}) aerosols based on in situ and satellite observations.

Analysis period	Trends in SO_2	Trends in particulate SO_4^{2-}	Reference
Global Models/Assimilated models			

ACCEPTED VERSION SUBJECT TO FINAL EDITING

1990-2000	-8.54 ± 1.40 % yr^{-1} (EU, 43 sites) -2.63 ± 0.30 % yr^{-1} (NA, 53 sites)	-5.23 ±1.17% yr^{-1} (EU, 41 sites) -1.94 ±0.43% yr^{-1} (NA 101 sites)	(Aas et al., 2019)
2000-2015	-0.41 ± 0.92 % yr^{-1} (EA, 19 sites) -4.86 ± 1.31 % yr^{-1} (EU, 47 sites) -4.40 ± 0.93 % yr^{-1} (NA, 77 sites)	0.02 ±0.91% yr^{-1} (EA, 13 sites) -3.26 ±0.85% yr^{-1} (EU, 36 sites) -3.18 ±0.66% yr^{-1} (NA, 218 sites)	(Aas et al., 2019)
Ground based in situ observations			
1980-1990	-5.03 ± 2.04 % yr^{-1} (EU, 20 sites) -2.5 % yr^{-1} (US)	-2.56 ± 3.10% yr^{-1} (EU, 16 sites) -1.80 ± 4.09% yr^{-1} (US SO_4^{2-} in precipitation, 78 sites)	(Aas et al., 2019) US EPA[a]
1990-2000	-7.56 ± 1.81 % yr^{-1} (EU, 43 sites) -3.27 ± 1.69 % yr^{-1} (NA, 53 sites)	-5.16 ± 2.11% yr^{-1} (EU, 41 sites) -2.08 ± 1.44% yr^{-1} (NA, 101 sites)	(Aas et al., 2019)
2000-2015	-0.14 ± 5.32 % yr^{-1} (EA, 19 sites) -3.89 ± 2.16 % yr^{-1} (EU, 47 sites) -4.69 ± 1.35 % yr^{-1} (NA, 77 sites)	2.68 ± 9.41% yr^{-1} (EA, 13 sites) -2.67 ± 2.03% yr^{-1} (EU, 36 sites) -3.15 ± 1.30% yr^{-1} (NA, 218 sites)	(Aas et al., 2019)
Change based on satellite observations			
2005-2015	ca -80% (Eastern US)		(Krotkov et al., 2016)
2005-2015	ca -60% (Eastern EU)		(Krotkov et al., 2016)
2005-2015	200 ± 50 % (India)		(Krotkov et al., 2016)
2005 (and 2012) - 2015	ca -50 % (The North China Plain)		(Krotkov et al., 2016)

[a] https://www.epa.gov/air-trends/sulfur-dioxide-trends

[END TABLE 6.5 HERE]

6.3.4 Short-lived Halogenated Species

The halogenated species are emitted in the atmosphere in the form of the synthetically produced chlorofluorocarbons (CFCs), halons, hydrochlorofluorocarbons (HCFCs), hydrofluorocarbons (HFCs) and others. Their historical global abundances are provided in Annex III and discussed in Chapter 2 (Section 2.2.4, Table 2.3). In summary, for the period 2011-2019, the abundance of total chlorine from HCFCs has continued to increase in the atmosphere with decreased growth rates, total tropospheric bromine from halons and methyl bromide continued to decrease while abundances of most currently measured HFCs increased significantly, consistent with expectations based on the ongoing transition away from the use of ODSs. Here, emphasis is given on the very short-lived halogenated species (VSLSs). The trends for these species were not discussed in IPCC AR5.

VSLSs are halogenated substances with atmospheric lifetimes less than 0.5 year. While longer-lived ODSs account for most of the present day stratospheric halogen loading, there is *robust evidence* that VSLSs contribute to stratospheric bromine and chlorine (Carpenter et al., 2014; Hossaini et al., 2015; Leedham Elvidge et al., 2015b) thus also contributing to stratospheric ozone depletion.

Of the atmospheric VSLSs, brominated and iodinated species are predominantly of oceanic origin, while chlorinated species have significant additional anthropogenic sources (Carpenter et al., 2014; Hossaini et al., 2015). Global mean chlorine from the VSLSs has increased in the troposphere from about 91 ppt in 2012 to about 110 ppt in 2016 (Engel et al., 2018). This increase is mostly due to dichloromethane (CH_2Cl_2), a species that has predominantly anthropogenic sources reflected by 3-times higher concentrations in the Northern Hemisphere than in the Southern Hemisphere (Hossaini et al., 2017). The upward dichloromethane

ACCEPTED VERSION SUBJECT TO FINAL EDITING

trend is corroborated by upper tropospheric aircraft data over the period 1998-2014 (Leedham Elvidge et al., 2015a; Oram et al., 2017). The observations from the surface networks show that the abundance of dichloromethane continued to increase until 2019 (Annex III), although the accuracy of global abundance of VSLSs is limited by the limited coverage by networks. No long-term change of the bromine containing VSLSs have been observed (Engel et al., 2018).

6.3.5 Aerosols

This section assesses trends in atmospheric distribution of aerosols and improvements in relevant physical and chemical processes. The observed large-scale temporal evolution of aerosols is assessed in Section 2.2.6. Since AR5, long term measurements of aerosol mass concentrations from regional global surface networks have continued to expand and provide information on the distribution and trends in aerosols (Figure 6.7). There is large spatial variability in aerosol mass concentration, expressed as $PM_{2.5}$, dominant aerosol type and aerosol composition, consistent with the findings in AR5.

[START FIGURE 6.7 HERE]

Figure 6.7: Distribution of $PM_{2.5}$ composition mass concentration (in µg m^{-3}) for the major $PM_{2.5}$ aerosol components. Those aerosol components are sulphate, nitrate, ammonium, sodium, chloride, organic carbon, and elemental carbon. The central world map depicts the intermediate level regional breakdown of observations (10 regions) following the IPCC Sixth Assessment Report Working Group III (AR6 WGIII). Monthly averaged $PM_{2.5}$ aerosol component measurements are from: (i) the Environmental Protection Agency (EPA) network which include 211 monitor sites primarily in urban areas of North America during 2000-2018 (Solomon et al., 2014) (ii) the Interagency Monitoring of Protected Visual Environments (IMPROVE) network during 2000-2018 over 198 monitoring sites representative of the regional haze conditions over North America, (iii) the European Monitoring and Evaluation Programme (EMEP) network over 70 monitoring in Europe and (eastern) Eurasia during 2000-2018, (iv) the Acid Deposition Monitoring Network in East Asia (EANET) network with 39 (18 remote, 10 rural, 11 urban) sites in Eurasia, Eastern Asia, South-East Asia and Developing Pacific, and Asia-Pacific Developed during 2001-2017, (v) the global Surface Particulate Matter Network (SPARTAN) during 2013-2019 with sites primarily in highly populated regions around the world (i.e, North America, Latin America and Caribbean, Africa, Middle East, Southern Asia, Eastern Asia, South-Eastern Asia and Developing Pacific) (Snider et al., 2015, 2016), and (vii) individual observational field campaign averages over Latin America and Caribbean, Africa, Europe, Eastern Asia, and Asia-Pacific Developed (Celis et al., 2004; Feng et al., 2006; Mariani and de Mello, 2007; Molina et al., 2007, 2010; Bourotte et al., 2007; Fuzzi et al., 2007; Mkoma, 2008; Favez et al., 2008; Aggarwal and Kawamura, 2009; Mkoma et al., 2009; Li et al., 2010; Martin et al., 2010; Radhi et al., 2010; Weinstein et al., 2010; de Souza et al., 2010; Batmunkh et al., 2011; Pathak et al., 2011; Gioda et al., 2011; Zhang et al., 2012a; Zhao et al., 2013; Cho and Park, 2013; Wang et al., 2019; Kuzu et al., 2020). Further details on data sources and processing are available in the chapter data table (Table 6.SM.1).

[END FIGURE 6.7 HERE]

Remote sensing instruments provide a larger-scale view of aerosol distributions and trends than ground-based monitoring networks by retrieving the Aerosol optical depth (AOD), which is indirectly related to aerosol mass concentrations. AOD is the column-integrated aerosol mass extinction at a given wavelength, and is therefore relevant to the estimation of the radiative forcing of aerosol-radiation interactions (Section 7.3.3.1). Models participating in Phase III of the AeroCom intercomparison project were found to underestimate present-day AOD by about 20% (Gliß et al., 2020), although different remote sensing estimates obtain different estimates of global mean AOD. Gliß et al. (2020) also highlight the considerable diversity in the simulated contribution of various aerosol types to total AOD. However, models simulate regional trends in AODs that agree well, when expressed as percentage change, with ground- (Gliß et al., 2020; Mortier et al., 2020) and satellite-based (Cherian and Quaas, 2020a; Gliß et al., 2020) observations. AOD trends simulated by CMIP6 models are more consistent with satellite-derived trends than CMIP5

ACCEPTED VERSION SUBJECT TO FINAL EDITING

models for several subregions, thanks to improved emission estimates (Cherian and Quaas, 2020b).

All CMIP6 models simulate a positive trend in global mean AOD since 1850, with a strong increase after the 1950s coinciding with the massive increase in anthropogenic SO_2 emissions (Figure 6.8). Global mean AOD increases have slowed since 1980, or even reversed in some models, as a result of a compensation between SO_2 emission decreases over the United States and Europe in response to air quality controls since the mid-1980s and increases over Asia. Since the mid-2000s, global mean AOD stabilized driven by soaring emissions in South Asia, and declining emissions in East Asia (section 6.2.1). Trends post ~2010 are difficult to assess from CMIP6 models since the historical simulations end at 2014. Nevertheless, the strong decline in anthropogenic SO_2 emissions over East Asia since 2011 is underestimated in the CMIP6 emission database (Hoesly et al., 2018) indicating that the observed AOD change over East Asia may not be captured accurately by CMIP6 models (Wang et al., 2021). While all CMIP6 models simulate increase of AOD between 1850 and 2014 there is strong inter-model diversity in the simulated AOD change since 1850 ranging from 0.01 (15%) to 0.08 (53%) in 2014. Some models therefore lie outside the 68% confidence interval of 0.02 (15%) to 0.04 (or 30%) for global AOD change in 2005-2015 compared to 1850 estimated by (Bellouin et al., 2020) based on observational and model (excluding CMIP6) lines of evidence. In addition to the horizontal distribution of aerosols documented by AOD, their number size distribution, vertical distribution, optical properties, hygroscopicity, ability to act as CCN, chemical composition, mixing state and morphology are key elements to assess their climate effect (see Section 6.4.).

[START FIGURE 6.8 HERE]

Figure 6.8: Time evolution of changes in global mean aerosol optical depth (AOD) at 550 nm. Year of reference is 1850. Data shown from individual Coupled Model Intercomparison Project Phase 6 (CMIP6) historical simulations. Each time series corresponds to the ensemble mean of realizations done by each model. Simulation results from years including major volcanic eruptions, e.g. Novarupta (1912) and Pinatubo (1991), are excluded from the analysis for models encompassing the contribution of stratospheric volcanic aerosols to total AOD. Further details on data sources and processing are available in the chapter data table (Table 6.SM.1).

[END FIGURE 6.8 HERE]

6.3.5.1 Sulphate (SO_4^{2-})

Sulphate aerosols (or sulphate containing aerosols) are emitted directly or formed in the atmosphere by gas and aqueous phase oxidation of precursor sulphur gases, including SO_2, DMS, and carbonyl sulphide (OCS), emitted from anthropogenic and natural sources (Section 6.2). Sulphate aerosols influence climate forcing directly by either scattering solar radiation or absorbing longwave radiation, and indirectly by influencing cloud micro- and macrophysical properties and precipitation (Boucher et al., 2013; Myhre et al., 2013b). Additionally, sulphate aerosols and sulphate deposition have a large impact on air quality and ecosystems (Reis et al., 2012). The majority of sulphate particles are formed in the troposphere, however, SO_2 and other longer-lived natural precursors, such as OCS, transported into the stratosphere contribute to the background stratospheric aerosol layer (Kremser et al., 2016). SO_2 emissions from volcanic eruptions are a significant source of stratospheric sulphate loading (see Chapter 2 for reconstruction of stratospheric aerosol optical depth and Chapter 7 for radiative forcing of volcanic aerosols). Furthermore, studies suggest contributions from anthropogenic SO_2 emissions transported into the stratosphere with a consequent impact on radiative forcing (Myhre et al., 2004; Yu et al., 2016). However there is significant uncertainty in the relative importance of this stratospheric sulphate source (Kremser et al., 2016).

Process understanding of sulphate production pathways from SO_2 emissions has seen some progress since AR5. More specifically, many global climate models now have a more complete description of chemical reactions such that oxidant levels s (including ozone) are better described, include a pH-dependence of SO_2 oxidation (e.g., Bauer et al., 2020; Kirkevåg et al., 2018), and implement explicit descriptions of ammonium and nitrate aerosol components, which may influence the partitioning of sulphate (Bian et al., 2017; Lund et

ACCEPTED VERSION SUBJECT TO FINAL EDITING

al., 2018). The pH influences the heterogeneous chemistry as well as the physical properties of the aerosols, and this topic has been a subject of growing interest since AR5 (Cheng et al., 2016; Freedman et al., 2019; Nenes et al., 2020). Increases in cloudwater pH have been shown to significantly increase the radiative forcing of sulphates (Turnock et al., 2019).

Sulphate is removed from the atmosphere by dry deposition and wet scavenging, and these processes depend on the characteristics of the Earth's surface, and the intensity, frequency and amount of precipitation (Boucher et al., 2013). Even though there have been some improvements since AR5, model representation of wet scavenging and related cloud processes, and atmospheric transport remains a key source of uncertainty in the simulated aerosol distribution and lifetime with further consequences for the sulphate forcing estimates (Kristiansen et al., 2016; Lund et al., 2018a). There are also still relatively large uncertainties in the emission height used in models affecting the simulated aerosol distribution (Yang et al., 2019).

Based on long-term surface-based in situ observations, AR5 reported strong decline in sulphate aerosols in Europe and the USA over 1990 to 2009, with the largest decreases occurring before 2000 in Europe and post 2000 in the USA. Since AR5, atmospheric measurements in conjunction with model results have provided insights into the spatial and temporal distribution of sulphate and sulphur deposition (Vet et al., 2014; Tan et al., 2018; Aas et al., 2019). The *in situ* observations in North America and Europe reveal substantial reduction since the measurements started around 1980, though the trends have not been linear through this period (Table 6.5). Several regional studies agree with these trend estimates for Europe (Banzhaf et al., 2015b; Theobald et al., 2019) and North America (Sickles II and Shadwick, 2015; Paulot et al., 2016a). Further, the concentrations of primary emitted SO_2 (Section 6.3.3.5) show greater decreases than secondary sulphate aerosols over these regions due to a combination of higher oxidation rate (hence more SO_2 converted to SO_4^{2-}) and increased dry deposition rate of SO_2 (Fowler et al., 2009; Banzhaf et al., 2015). In situ observations over other parts of the world are scattered (see Figure 6.7), and the lack of observations makes it too uncertain to quantify regional representative trends (Hammer et al., 2018). However, limited in-situ observations in East Asia indicate an increase in atmospheric sulphate up to around 2005 and then a decline (Aas et al., 2019) which is confirmed by satellite observations of SO_2 (Section 6.3.3.5). In India, on the other hand satellite observations indicate a rapid increase in the SO_2 levels (Krotkov et al., 2016), and long-term measurements of sulphate in precipitation in India further provide evidence of an increasing trend from 1980 to 2010 (Bhaskar and Rao, 2017; Aas et al., 2019). Further improvements in global trend assessments are expected with new integrated reanalysis products from the Earth-system data assimilation projects (Randles et al., 2017; Inness et al., 2019).

Indirect evidence of decadal trends in the atmospheric loading of sulphur are provided by Alpine ice cores, mainly influenced by European sources (Engardt et al., 2017), and ice cores from Svalbard (Samyn et al., 2012) and Greenland (Patris et al., 2002; Iizuka et al., 2018) influenced by sources in Europe and North America. These show similar patterns with a weak increase from the end of the 19th century up to around 1950 followed by a steep increase up to around 1980, and then a significant decrease over the next two decades. This general trend is consistent with the emissions of SO_2 in North America and Europe (Hoesly et al., 2018; Figures 6.18; 6.19).

Global and regional models qualitatively reproduce observed trends over North America and Europe for the period 1990-2015 for which emission changes are generally well quantified (Aas et al., 2019; Mortier et al., 2020), building confidence in the relationship between emissions, concentration, deposition and radiative forcing derived from these models. Though, the models seem to systematically underestimate sulphate (Bian et al., 2017; Lund et al., 2018a) and AOD (Lund et al., 2018a; Gliß et al., 2020), and there are quite large differences in the models' distribution of the concentration fields of sulphate driven by differences in the representation of photochemical production and sinks of aerosols. One global model study also highlighted biases in simulated sulphate trends over the 2001-2015 period over eastern China due to uncertainties in the CEDS anthropogenic SO_2 emissions trends (Paulot et al., 2018).

In summary, there is *high confidence* that the global tropospheric sulphate burden increased from 1850 to around 2005, but there are large regional differences in the magnitude. Sulphate aerosol concentrations in North America and Europe have declined over 1980 to 2015 with slightly stronger reductions in North

ACCEPTED VERSION SUBJECT TO FINAL EDITING

America (47%) than over Europe (40%) over 2000-2015, though Europe had larger reductions in the prior decade (1990-2000), 52% and 21% respectively for Europe and North America. In Asia, the trends are more scattered, though there is *medium confidence* that there was a strong increase up to around 2005, followed by a steep decline in China, while over India, the concentrations are increasing steadily.

6.3.5.2 Ammonium (NH_4^+), and Nitrate Aerosols (NO_3^-)

Ammonium sulphate and ammonium nitrate aerosols are formed when NH_3 reacts with nitric acid (HNO_3) and sulphuric acid (H_2SO_4) produced in the atmosphere by the oxidation of NO_x and SO_2, respectively. Ammonium nitrate is formed only after H_2SO_4 is fully neutralized. NH_4^+ and NO_3^- aerosols produced via these gas-to-particle reactions are a major fraction of fine-mode particles (with diameter < 1μm) affecting air quality and climate. Coarse-mode nitrate, formed by the heterogeneous reaction of nitric acid with dust and sea salt, dominates the overall global nitrate burden, but has little radiative effect (Hauglustaine et al., 2014; Bian et al., 2017). Trends in ammonium (NH_4^+) and nitrate (NO_3^-) were not assessed in AR5.

Global model present-day estimates of the global NH_4^+ burden range from 0.1 to 0.6 TgN (Bian et al., 2017). Models generally simulate surface NH_4^+ concentrations better than surface NH_3 concentrations (Bian et al., 2017), which reflects its thermodynamic control by SO_4^{2-} rather than NH_3 (Shi et al., 2017). The concomitant increases of NH_3, SO_2, and NO_x emissions (see Section 6.2) have led to a factor of 3 to 9 increase in the simulated NH_4^+ burden from 1850 to 2000 (Hauglustaine et al., 2014; Lund et al., 2018a), driven primarily by ammonium sulphate (70-90%). The increases in the NH_3 and NH_4^+ burdens are indirectly supported by the observed increase of NH_4^+ concentration in ice cores in mid to high latitudes (Kang et al., 2002; Kekonen et al., 2005; Lamarque et al., 2013a; Iizuka et al., 2018).

Ammonium nitrate is semi-volatile, which results in complex spatial and temporal patterns in its concentrations (Putaud et al., 2010; Hand et al., 2012a; Zhang et al., 2012b) reflecting variations in its precursors, NH_3 and HNO_3, as well as SO_4^{2-}, non-volatile cations, temperature and relative humidity (Nenes et al., 2020). High relative humidity and low temperature as well as elevated fine particulate matter loading (Huang et al., 2014; Petit et al., 2015; Li et al., 2016; Sandrini et al., 2016) favour nitrate production. Measurements reveal high contribution of NO_3^- to surface $PM_{2.5}$ (>30%) in regions with elevated regional NO_x and NH_3 emissions, such as the Paris area (Beekmann et al., 2015; Zhang et al., 2019), northern Italy (Masiol et al., 2015; Ricciardelli et al., 2017), Salt Lake City (Kuprov et al., 2014; Franchin et al., 2018), the North China Plains (Guo et al., 2014; Chen et al., 2016), and New Delhi (Pant et al., 2015). Recent observations also show that ammonium nitrate contributes to the Asian tropopause aerosol layer (Vernier et al., 2018; Höpfner et al., 2019). Model diversity in simulating present-day global fine-mode NO_3^- burden is large with two multimodel intercomparison studies reporting estimates in the range of 0.14-1.88 Tg and 0.08-0.93 Tg, respectively (Bian et al., 2017; Gliß et al., 2021). Models differ in their estimates of the global tropospheric nitrate burden by up to a factor of 13 with differences remain nearly the same across CMIP5 and CMIP6 generation of models (Bian et al., 2017; Gliß et al., 2021). While regional patterns in the concentration of fine-mode NO_3^- are qualitatively captured by models, the simulation of fine-mode NO_3^- is generally worse than that of NH_4^+ or SO_4^{2-} (Bian et al., 2017). This can be partly attributed to the semi-volatile nature of ammonium nitrate and biases in the simulation of its precursors (Heald et al., 2014; Paulot et al., 2016), including the sub-grid scale heterogeneity in NO_x and NH_3 emissions (Zakoura and Pandis, 2018).

Models indicate that the burden of fine-mode NO_3^- has increased by a factor of 2-5 from 1850 to 2000 (Xu and Penner, 2012; Hauglustaine et al., 2014; Lund et al., 2018a), an increase that has accelerated between 2001 and 2015 (Lund et al., 2018a; Paulot et al., 2018). The sensitivity of NO_3^- to changes in NH_3, SO_4^{2-}, and HNO_3 is determined primarily by aerosol pH, temperature, and aerosol liquid water (Guo et al., 2016, 2018; Weber et al., 2016; Nenes et al., 2020). In regions, where aerosol pH is high, changes in NO_3^- follow changes in NO_x emissions, consistent with the observed increase of ammonium nitrate in Northern China from 2000 to 2015 (Wen et al., 2018) and its decrease in the US Central Valley (Pusede et al., 2016). In contrast, the decrease in SO_2 emissions in the US Southeast has caused little change in NO_3^- from 1998 to 2014 as nitric acid largely remains in the gas phase due to highly acidic aerosols (Weber et al., 2016; Guo et al., 2018).

ACCEPTED VERSION SUBJECT TO FINAL EDITING

In summary, there is *high confidence* that the NH_4^+ and NO_3^- burdens have increased from preindustrial to present-day, although the magnitude of the increase is uncertain especially for NO_3^-. The sensitivity of NH_4^+ and NO_3^- to changes in NH_3, H_2SO_4, and HNO_3 is well understood theoretically. However, it remains challenging to represent in models in part because of uncertainties in the simulation of aerosol pH and only a minority of ESMs consider nitrate aerosols in CMIP6.

6.3.5.3 Carbonaceous Aerosols

Carbonaceous aerosols are black carbon (BC)[3], which is soot made almost purely of carbon, and organic aerosols[4] (OA), which also contain hydrogen and oxygen and can be of both primary (POA) or secondary (SOA) origin. BC and a fraction of OA called Brown Carbon (BrC) absorb solar radiation. The various components of carbonaceous aerosols have different optical properties, so the knowledge of their partition, mixing, coating and ageing is essential to assess their climate effect (see Section 7.3.3.1.2).

Carbonaceous aerosols receive attention in the scientific and policy arena due to their radiative forcing, and their sizeable contribution to PM in an air quality context (Rogelj et al., 2014b; Harmsen et al., 2015; Shindell et al., 2016; Haines et al., 2017a; Myhre et al., 2017). BC exerts a positive ERF, but the ERF of carbonaceous aerosol as a whole is negative (Bond et al., 2013; Thornhill et al., 2021b). On average, carbonaceous aerosols accounts for 50 to 70% of PM with diameter lower than 1 µm in polluted and pristine areas (Zhang et al., 2007; Carslaw et al., 2010; Andreae et al., 2015; Monteiro dos Santos et al., 2016; Chen et al., 2017).

An extensive review on BC (Bond et al., 2013) discussed limitations in inferring its atmospheric abundance and highlighted inconsistencies between different terminology and related measurement techniques (Petzold et al., 2013; Sharma et al., 2017). Due to a lack of global observations, AR5 only reported declining total carbonaceous aerosol trends from USA and declining BC trend from the Arctic based on data available up to 2008. Since AR5, the number of observation sites has grown worldwide (see also Figure 6.7) but datasets suitable for global trend analyses remain limited (Reddington et al., 2017; Laj et al., 2020). Locally, studies based on observations from rural and background sites have reported decreasing surface carbonaceous aerosol trends in the Arctic, Europe, USA, Japan and India (Table 6.6). Increases in carbonaceous aerosol concentrations in some rural sites of the Western USA have been associated with wildfires (Hand et al., 2013; Malm et al., 2017). Long-term OA observations are scarce, so their trends outside of the USA are difficult to assess. Ice-core analysis have provided insight into carbonaceous aerosol trends predating the satellite and observation era over the Northern Hemisphere (Section 2.2.6, Figure 2.9b).

[START TABLE 6.6 HERE]

Table 6.6: Summary of the regional carbonaceous aerosol trends at background observation sites.

Species	Analysis period	Change/Trends	References
BC	1990-2009	Arctic Sites (Alert, Barrow, Ny-Alesund)) $-2\%\ yr^{-1}$	(Sharma et al., 2013a)
	1970-2010	Finland (Kevo remote site) $-1.8\%\ yr^{-1}$	(Dutkiewicz et al., 2014)
	2005-2014	Germany (rural site) $-2\%\ yr^{-1}$	(Kutzner et al., 2018)

[3] The terms EC and BC are operationally defined on the basis of the methodology used for their quantification, i.e., thermal refractivity and light absorption, respectively, and often used interchangeably.

[4] The carbon mass fraction of OA is termed as OC, conversion factor between 1.4 to 1.6 from OC to OA are typically assumed

ACCEPTED VERSION SUBJECT TO FINAL EDITING

	2009-2016	United Kingdom (Harwell rural site) −8% yr^{-1}	(Singh et al., 2018)
	2009-2019	Japan (Fukue Island) −5.8 ± 1.5% yr^{-1}	(Kanaya et al., 2020)
	2009-2015	India (Darjeeling mountain site) −5% yr^{-1}	(Sarkar et al., 2019)
OA	2001-2015	USA (IMPROVE sites east of 100°W) −2% yr^{-1}	(Malm et al., 2017)
Total Carbon (EC+OC)	1990-2010	USA (IMPROVE sites) Western USA: −4 to −5% yr^{-1} Eastern USA: −1 to −2% yr^{-1}	(Hand et al., 2013)
	2002-2010	Spain (Montseny rural site) −5% yr^{-1}	(Querol et al., 2013)

[END TABLE 6.6 HERE]

Knowledge of carbonaceous aerosol atmospheric abundance continues to rely on global models due to a lack of global scale observations. For BC, models agree within a factor of two with measured surface mass concentrations in Europe and North America, but underestimate concentrations at the Arctic surface by one to two orders or magnitude, especially in winter and spring (Lee et al., 2013a; Lund et al., 2018a). For OA, AeroCom models underestimate surface mass concentrations by a factor 2 over urban areas, as their low horizontal resolution prevents them for resolving local pollution peaks (Tsigaridis et al., 2014; Lund et al., 2018a). Models agree within a factor of two with OA surface concentrations measured at remote sites, where surface concentrations are more spatially uniform (Tsigaridis et al., 2014).

Lifetimes in models are estimated to 5.5 days ±35% for BC and 6.0 days ±29% for OA (median ± 1 standard deviation) according to an ensemble of 14 models (Gliß et al., 2021). Disagreement in simulated lifetime leads to horizontal and vertical variations in predicted carbonaceous aerosol concentrations, with implications for radiative forcing (Lund et al., 2018b) (Samset et al., 2013). Airborne campaigns have provided valuable vertical profile measurements of carbonaceous aerosol concentrations (Schwarz et al., 2013; Freney et al., 2018; Hodgson et al., 2018; Morgan et al., 2019; Schulz et al., 2019; Zhao et al., 2019a). Compared to those measurements, models tend to transport BC too high in the atmosphere, suggesting that lifetimes are not larger than 5.5 days (Samset et al., 2013; Lund et al., 2018b). Newly developed size-dependent wet scavenging parameterisation for BC (Taylor et al., 2014; Schroder et al., 2015; Ohata et al., 2016; Zhang et al., 2017a; Ding et al., 2019; Moteki et al., 2019; Motos et al., 2019) may lead to decreased BC lifetimes and improve agreement with observed vertical profiles.

Simulated BC burdens show a large spread among models (Gliß et al., 2021), despite using harmonised primary emissions, because of differences in BC removal efficiency linked to different treatment of ageing and mixing, particularly in strong source regions. The multi-model median BC burden for the year 2010 from Gliß et al. (2021), based on 14 AeroCom models, is 0.131 ± 0.047 Tg (median ± standard deviation). That range encompasses values reported by independent single model estimates (Huang et al., 2013; Lee et al., 2013b; Sharma et al., 2013b; Wang et al., 2014a; Tilmes et al., 2019).

Simulated OA burdens also show a large spread among global models, with Gliß et al. (2021) reporting a multi-model median of 1.91 ±0.65 Tg for the year 2010. This large spread reflects the wide range in the complexity of the OA parameterizations, particularly for SOA formation, as well as in the primary OA emissions (Tsigaridis et al., 2014; Gliß et al., 2021). The uncertainties are particularly large in model estimates of SOA production rates, which vary between 10 and 143 Tg yr^{-1} (Tsigaridis et al., 2014; Hodzic et

ACCEPTED VERSION SUBJECT TO FINAL EDITING

al., 2016; Tilmes et al., 2019). While the level of complexity in the representation of OA in global models has increased since AR5 (Shrivastava et al., 2017; Hodzic et al., 2020) limitations in process level understanding of the formation, aging and removal of organic compounds lead to uncertainties in the global model predictions of global OA burden and distribution as well as the relative contribution of POA and SOA to OA. Jo et al. (2016) estimated that BrC contributes about 20% of total OA burden. That would give BrC a burden similar to that of BC (*low confidence*), enhancing the overall forcing exerted by carbonaceous aerosol absorption (Zhang et al., 2020).

In summary, the lack of global scale observations of carbonaceous aerosol, its complex atmospheric chemistry, and the large spread in its simulated global budget and burdens means that there is only *low confidence* in the quantification of the present-day atmospheric distribution of individual components of carbonaceous aerosols. Global trends in carbonaceous aerosols cannot be characterised due to limited observations, but sites representative of background conditions have reported multi-year declines in BC over several regions of the Northern Hemisphere.

6.3.6 Implications of SLCF abundances for Atmospheric Oxidizing Capacity

The atmospheric oxidising capacity is determined primarily by tropospheric hydroxyl (OH) radical and to a smaller extent by NO_3 radical, ozone, hydrogen peroxide (H_2O_2) and halogen radicals. OH is the main sink for many SLCFs, including methane, halogenated compounds (HCFCs and HFCs), CO and NMVOCs, controlling their lifetimes and consequently their abundance and climate influence. OH initiated oxidation of methane, CO and NMVOCs in the presence of NO_x leads to the production of tropospheric ozone. OH also contributes to the formation of aerosols from oxidation of SO_2 to sulphate and VOCs to secondary organic aerosols. The evolution of atmospheric oxidising capacity of the Earth driven by human activities and natural processes is, therefore, of significance for climate and air quality concerns.

The main source of tropospheric OH is the photoexcitation of tropospheric ozone that creates an electronically excited oxygen atom which reacts with water vapour producing OH. A secondary source of importance for global OH is the recycling of peroxy radicals formed by the reaction of OH with reduced and partly oxidized species, including methane, CO and NMVOCs. In polluted air, NO_x emissions control the secondary OH production, while in pristine air it occurs via other mechanisms involving, in particular, isoprene (Lelieveld et al., 2016; Wennberg et al., 2018). Knowledge of the effect of isoprene oxidation on OH recycling has evolved tremendously over the past decade facilitating mechanistic explanation of elevated OH concentrations observed in locations characterised by low NO_x levels (Hofzumahaus et al., 2009; Paulot et al., 2009; Peeters et al., 2009, 2014; Fuchs et al., 2013). Since AR5, inclusion of improved chemical mechanisms in some CTMs suggest advances in understanding of the global OH budget, however these improvements have yet to be incorporated in CMIP6-generation ESMs.

As a result of the complex photochemistry, tropospheric OH abundance is sensitive to changes in SLCF emissions as well as climate. Increases in methane, CO, NMVOCs reduce OH while increases in water vapour and temperature, incoming solar radiation, NO_x and tropospheric ozone enhance OH. The OH level thus responds to climate change and climate variability via its sensitivity to temperature and water vapour as well as the influence of climate on natural emissions (e.g., wetland methane emissions, lightning NO_x, BVOCs, fire emissions) with consequent feedbacks on climate (Section 6.4.5). Climate modes of variability, like ENSO, also contribute to OH variability via changes in lightning NO_x emissions and deep convection (Turner et al., 2018), and fire emissions (Rowlinson et al., 2019).

Global scale OH observations are non-existent because of its extremely short lifetime (~1 s) and therefore global OH abundance and its time variations are either inferred from atmospheric measurements of methyl chloroform (MCF) (Prinn et al., 2018 and references therein) or derived from global atmospheric chemistry models (Lelieveld et al., 2016). AR5 reported small interannual OH variations in the 2000s based on atmospheric inversions of MCF observations (within ±5%) and global CCMs and CTMs (within ±3%) (Ciais et al., 2013).

ACCEPTED VERSION SUBJECT TO FINAL EDITING

Since AR5, there is much closer agreement in the estimates of interannual variations in global mean OH derived from atmospheric inversions, empirical reconstruction, and global CCMs and ESMs with an estimate of 2 to 3% over the 1980 to 2015 period (Table 6.7). While the different methodologies agree on the occurrence of small inter-annual variations, there is much debate over longer term global OH trend. Two studies using multi-box model inversions of MCF and methane observations suggest large positive and negative trends since 1990s in global mean OH (Rigby et al., 2017; Turner et al., 2017), however, both find that observational constraints are weak such that a wide range of multi-annual OH variations are possible. Indeed, (Naus et al., 2019) find an overall positive global OH trend over the past two decades (Table 6.7) after accounting for uncertainties and biases in atmospheric MCF and CH_4 inversions confirming the weakness in observational constraints for deriving OH trends. Global ESMs, CCMs and CTMs exhibit stabilized or increasing global OH after 1980 contrary to the lack of trend derived from some atmospheric inversions and empirical reconstructions (Table 6.7). In particular, a three member ensemble of ESMs participating in the AerChemMIP/CMIP6 agrees that global OH has increased since 1980 by around 9% (Figure 6.9) with an associated reduction in methane lifetime (Stevenson et al., 2020). This positive OH trend is in agreement with the ~7% OH increase derived by assimilating global-scale satellite observations of CO over the 2002-2013 period (with CO declining trends) into a CCM (Gaubert et al., 2017; see section 6.3.4). Multi-model sensitivity analysis suggests that increasing OH since 1980 is predominantly driven by changes in anthropogenic SLCF emissions with complementary influence of increasing NO_x and decreasing CO emissions (Stevenson et al., 2020).

Over paleo time scales, proxy-based observational constraints from CH_4 and formaldehyde suggest tropospheric OH to be a factor of 2 to 4 lower in the last glacial maximum (LGM) relative to preindustrial levels, though these estimates are highly uncertain (Alexander and Mickley, 2015). Global models, in contrast, exhibit no change in tropospheric OH (and consequently in methane lifetime) at the LGM relative to the preindustrial (Murray et al., 2014; Quiquet et al., 2015), however the sign and magnitude of OH changes are sensitive to model predictions of changes in natural emissions, including lightning NO_x and BVOCs, and model representation of isoprene oxidation chemistry (Achakulwisut et al., 2015; Hopcroft et al., 2017).

Regarding change since preindustrial era, at the time of the AR5, ensemble mean of 17 global models participating in ACCMIP indicated little change in tropospheric OH from 1850 to 2000. This was due to the competing and finally offsetting changes in factors enhancing or reducing OH with a consequent small decline in methane lifetime (Naik et al., 2013; Voulgarakis et al., 2013). However, there was large diversity in both the sign and magnitude of past OH changes across the individual models attributed to disparate implementation of chemical and physical processes (Nicely et al., 2017; Wild et al., 2020). Analysis of historical simulations from three CMIP6 ESMs indicates little change in global mean OH from 1850 to about 1980 (Stevenson et al., 2020). However, there is no observational evidence of changes in global OH since 1850 up to early 1980s to evaluate the ESMs.

In summary, global mean tropospheric OH does not show a significant trend from 1850 up to around 1980 (*low confidence*). There is conflicting information from global models constrained by emissions versus observationally constrained inversion methods over the 1980-2014 period. A positive trend since 1980 (about 9 % increase over 1980-2014) is a robust feature among ESMs and CCMs and there is *medium confidence* that this trend is mainly driven by increases in global anthropogenic NO_x emissions and decreases in CO emissions. There is *limited evidence* and *medium agreement* for positive trends or absence of trends inferred from observation-constrained methods. Overall, there is *medium confidence* that global mean OH has remained stable or exhibited a positive trend since the 1980s.

ACCEPTED VERSION SUBJECT TO FINAL EDITING

[START TABLE 6.7 HERE]

Table 6.7: Summary of global OH trends and interannual variability from studies post 2010.

Reference	Time period	OH trends and IAV	Approach
Inversion and empirical methods based on observations			
(Montzka et al., 2011)	1998-2007	2.3±1.3% (IAV)	3D inversion
(Ciais et al., 2013)	2000s	<±5% (IAV)	AR5 based on inversions
(McNorton et al., 2016)	1993-2011	±2.3% (IAV)	Box model inversion
(Rigby et al., 2017)	1980-2014	10% increase from the late 1990s to 2004; 10% decrease from 2004 to 2014	Box model inversion
(Turner et al., 2017)	1983-2015	~7% increase in 1991-2001; 7% decrease in 2003-2016	Box model inversion
(Nicely et al., 2018)	1980-2015	1.6% (IAV)	Empirical reconstruction
(McNorton et al., 2018)	2003-2015	1.8±0.4% decrease	3D inversion
(Naus et al., 2019)	1994-2015	3.8±3.2% increase	Box model inversion
(Patra et al., 2021)	1996-2015	2-3% IAV, no trend	3D inversion
Global CTMs, CCMs and ESMs			
(John et al., 2012)	1860-2005 1980-2000	6% decrease ~3% increase	CCM
(Holmes et al., 2013)	1997-2009	0.7–1.1% (IAV)	Multi-model CTMs
(Ciais et al., 2013)	2000s	<±3 % (IAV)	AR5 based on CCMs
(Murray et al., 2013)	1998–2006	increasing trend	3D CTM
(Naik et al., 2013)	1980-2000 1850-2000	3.5±2.2 % increase −0.6 ± 8.8%	Multi-model CCMs/CTMs
(Murray et al., 2014)	1770s-1990s	5.3% increase	CCM
(Dalsøren et al., 2016)	1970-2012	8% increase	3D CTM
(Gaubert et al., 2017)	2002-2013	7% increase	CCM with assimilated satellite CO observations
(Zhao et al., 2019b)	1960-2010 1980-2000	1.9 ± 1.2 % (IAV) 4.6 ± 2.4 % increase	Multimodel CCMs/CTMs
(Stevenson et al., 2020)	1980-2014 1850-1980	9% increase no trend	Multimodel ESMs

[END TABLE 6.7 HERE]

[START FIGURE 6.9 HERE]

Figure 6.9: Time evolution of global annual mean tropospheric hydroxyl (OH) over the historical period, expressed as a percentage anomaly relative to the mean over 1998-2007. a) Results from three CMIP6 models, including UKESM1-0LL (green), GFDL-ESM4 (blue), and CESM2-WACCM (red), are shown; the shaded light green and light red bands show mean over multiple ensemble members for UKESM1-0LL (3) and CESM2-WACCM (3) models, respectively with the multi-model mean anomalies shown in thick black line. b) multimodel mean OH anomalies for 1980-2015 period compared with those derived

ACCEPTED VERSION SUBJECT TO FINAL EDITING

from observational-based inversions from (Montzka et al., 2011; Rigby et al., 2017; Turner et al., 2017; Nicely et al., 2018; Naus et al., 2019; Patra et al., 2021) in the zoomed box. Further details on data sources and processing are available in the chapter data table (Table 6.SM.1).

[END FIGURE 6.9 HERE]

6.4 SLCF radiative forcing and climate effects

The radiative forcing on the climate system introduced by SLCFs is distinguished from that of LLGHGs by the diversity of forcing mechanisms for SLCFs, and the challenges of constraining these mechanisms via observations and of inferring their global forcings from available data. Chapter 7 assesses the global estimates of ERFs due to SLCF abundance changes. This section assesses the characteristics (e.g., spatial patterns, temporal evolution) of forcings, climate response and feedbacks due to SLCFs relying primarily on results from CMIP6 models. Additionally, the ERFs for several aerosol-based forms of solar radiation modification (SRM) are discussed in Section 6.4.6.

Forcing and climate response due to changes in SLCFs are typically estimated from global models that vary in their representation of the various chemical, physical, and radiative processes (see Box 6.1) affecting the causal chain from SLCF emissions to climate response (Figure 6.2). The AR5 noted that the representation of aerosol processes varied greatly in CMIP5 models and that it remained unclear what level of sophistication is required to properly quantify aerosol effects on climate (Boucher et al., 2013). Since the AR5, (Ekman, 2014) found that the CMIP5 models with the most complex representations of aerosol impacts on cloud microphysics had the largest reduction in biases in surface temperature trends. CMIP6-generation CCMs that simulate aerosol and cloud size distributions better represent the effect of a volcanic eruption on lower atmosphere clouds than a model with aerosol-mass only (Malavelle et al., 2017). This highlights the need for skillful simulation of conditions underlying aerosol-cloud interactions, such as the distribution, transport and properties of aerosol species, in addition to the interactions themselves (see Chapter 7). In advance of CMIP6, representations of aerosol processes and aerosol-cloud interactions in ESMs have generally become more comprehensive (Gliß et al., 2021; Meehl et al., 2020; Thornhill et al., 2021b; see also Section 1.5), with enhanced links to aerosol emissions and gas-phase chemistry. Many CMIP6 models (see Annex II Table AII.5) now simulate aerosol number size distribution, in addition to mass distribution, which is a prerequisite for accurately simulating number concentrations of cloud condensation nuclei (CCN) (Bellouin et al., 2013) while some CMIP6 models use prescribed aerosol optical properties to constrain aerosol forcing (e.g., Stevens et al., 2017). Hence, the range of complexity in aerosol modeling noted in CMIP5 is still present in the CMIP6 ensemble. Although simulated CCN have been compared to surface (Fanourgakis et al., 2019) and aircraft (Reddington et al., 2017) measurements, with mixed results, the lack of global coverage limits confidence in the evaluations. Evaluations of aerosol optical depths have been more wide ranging (section 6.3.5; Gliß et al., 2021) but are less relevant to aerosol-cloud interactions as they do not allow to evaluate vertical profiles, aerosol-cloud overlap regions, aerosol type or number. Nevertheless, biases in simulated patterns and trends in aerosol optical depths, alongside biases in cloud fractions (Vignesh et al., 2020), likely affect quantifications of the aerosol-cloud interactions.

In summary, CMIP6 models generally represent more processes that drive aerosol-cloud interactions than the previous generation of climate models, but there is only *medium confidence* that those enhancements improve their fitness for the purpose of simulating radiative forcing of aerosol-cloud interactions because only a few studies have identified the level of sophistication required to do so. In addition, the challenge of representing the small-scale processes involved in aerosol-cloud interactions, and a lack of relevant model-data comparisons, does not allow to quantitatively assess the progress of the models from CMIP5 to CMIP6 in simulating the underlying conditions relevant for aerosol-cloud interactions at this time.

6.4.1 Historical Estimates of Regional Short-lived Climate Forcing

The highly heterogeneous distribution of SLCF abundances (section 6.3) translates to strong heterogeneity in

ACCEPTED VERSION SUBJECT TO FINAL EDITING

the spatial pattern and temporal evolution of forcing and climate responses due to SLCFs. This section assesses the spatial patterns of the current forcing due to aerosols and their historical evolution by region.

In AR5, the confidence in the spatial patterns of aerosol and ozone forcing was lower than that for the global mean because of the large spread in the regional distribution simulated by global models, and was assessed as 'medium'. The AR5 assessment was based on aerosol and ozone RFs and aerosol ERFs (with fixed SSTs) from ACCMIP and a small sample of CMIP5 experiments (Myhre et al., 2013b; Shindell et al., 2013). For this assessement, the spatial distribution of aerosol ERF (ERF_{AER}) due to human-induced changes in aerosol concentrations over 1850-2014 is quantified based on results from a 7 member ensemble of CMIP6 ESMs including interactive gas and aerosol chemistry analysed in AerChemMIP. There is insufficient information to estimate the spatial patterns of ozone ERF from CMIP6, however, the spatial patterns in SLCF ERF are dominated by that from aerosol ERF over most regions (e.g., Shindell et al., 2015). The ERF_{AER} includes contributions from both direct aerosol-radiation (ERF_{ari}) and indirect aerosol-cloud interactions (ERF_{aci}) (see Section 7.3.3) and is computed as the difference between radiative fluxes from simulations with time-evolving aerosol and their precuror emissions and identical simulations but with these emissions held at their 1850 levels (Collins et al., 2017). Both the simulations are driven by time-evolving SSTs and sea ice from the respective coupled model historical simulation and therefore differ from ERFs computed using fixed pre-industrial SST and sea-ice fields (Section 7.3.1), but the effect of this difference is generally small (Forster et al., 2016). A correction for land surface temperature change (Section 7.3.1) is not available from these data to explicitly quantify the contribution from adjustments. The ESMs included here used the CMIP6 anthropogenic and biomass burning emissions for ozone and aerosol precursors but varied in their representation of natural emissions, chemistry and climate characteristics contributing to spread in the simulated concentrations (also see section 6.3) and resulting forcings, partly reflecting uncertainties in the successive processes (Thornhill et al., 2021b).

The geographical distribution of the ensemble mean ERF_{AER} over the 1850-2014 period is highly heterogeneous (Figure 6.10a) in agreement with AR5. Negative ERF_{AER} is greatest over and downwind of most industrialized regions in the Northern Hemisphere and to some extent over tropical biomass burning regions, with robust signals. Largest negative forcing occurs over East Asia and South Asia, followed by Europe and North America, reflecting the changes in anthropogenic aerosol emissions in the recent decades (Section 6.2). Positive ERF_{AER} over high albedo areas, including cryosphere, deserts and clouds, also found in AR5 and attributed to absorbing aerosols, are not robust across the small CMIP6 ensemble applied here. Regionally aggregated shortwave (SW) and longwave (LW) components of the ERF_{AER} exhibit similar large variability across regions (Figure 6.10b). The SW flux changes come from aerosol-radiation and aerosol-cloud interactions while the small positive LW flux changes come from aerosol-cloud interactions (related to liquid water path changes (Section 7.3.2.2). These spatial patterns in ERF_{AER} are similar to the patterns reported in AR5.

Time evolution of 20 year means of regional net ERF_{AER} shows that the regions are divided into two groups depending on whether the mean ERF_{AER} attains its negative peak value in the 1970s to 1980s (e.g., Europe, North America) or in the late 1990s to 2000s (e.g., Asia, South America) (Figure 6.11). Qualitatively, this shift in the distribution of ERF_{AER} trends is consistent with the regional long-term trends in aerosol precursor emissions (Section 6.21; Figures 6.18 and 6.19) and their abundances (Section 6.3). However, at finer regional scales, there are regions where sulphate aerosols are still following an upward trend (e.g., South Asia; see Section 6.3.5) implying that the trends in ERF_{AER} may not have shifted for these regions. The continental scale ERF_{AER} trends are also in line with the satellite-observed AOD trends assessed in Section 2.2.6. Global mean ERF_{AER} reaches maximum negative values in the mid-1970s and its magnitude gradually decreases thereafter. This weakening of the negative forcing since 1990 agrees with findings by who attribute this to a reduction in global mean SO_2 emissions combined with an increase in global BC (Myhre et al., 2017). Uncertainties in model simulated aerosol ERF distribution and trends can result from intermodel variations in the representation of aerosol-cloud interactions and aerosol microphysical processes as also demonstrated by Bauer et al., (2020).

In summary, the spatial and temporal distribution of the net aerosol ERF from 1850 to 2014 is highly heterogeneous (*high confidence*). Globally, there has been a shift from increase to decrease of the negative

ACCEPTED VERSION SUBJECT TO FINAL EDITING

net aerosol ERF driven by trends in aerosol and their precursor emissions (*high confidence*). However, the timing of this shift varies by continental-scale region and has not occured for some finer regional scales.

[START FIGURE 6.10 HERE].

Figure 6.10: Multi-model mean Effective radiative forcings (ERFs) due to aerosol changes between 1850 and recent-past (1995-2014). Panel (a) shows the spatial distribution of the net ERF with area-weighted global mean ERF shown at the lower right corner. Uncertainty is represented using the advanced approach: No overlay indicates regions with robust signal, where ≥66% of models show change greater than variability threshold and ≥80% of all models agree on sign of change; diagonal lines indicate regions with no change or no robust signal, where <66% of models show a change greater than the variability threshold; crossed lines indicate regions with conflicting signal, where ≥66% of models show change greater than variability threshold and <80% of all models agree on sign of change. For more information on the advanced approach, please refer to the Cross-Chapter Box Atlas.1. Panel (b) shows the mean shortwave and longwave ERF for each of the 14 regions defined in the Atlas. Violins in panel (b) show the distribution of values over regions where ERFs are significant. ERFs are derived from the difference between top of the atmosphere (TOA) radiative fluxes for Aerosol Chemistry Model Intercomparison Project (AerChemMIP) experiments histSST and histSST-piAer (Collins et al., 2017) averaged over 1995-2014 (Box 1.4, Chapter 1). The results come from 7 Earth System Models: MIROC6, MPI-I-ESM-1-2-HAM, MRI-ESM2-0, GFDL-ESM4, GISS-E2-1-G, NorESM2-LM, and UKESM-0-LL. These data can be seen in the Interactive Atlas. Further details on data sources and processing are available in the chapter data table (Table 6.SM.1).

[END FIGURE 6.10 HERE]

[START FIGURE 6.11 HERE]

Figure 6.11: Time evolution of 20-year multi-model mean averages of the annual area-weighted mean regional net Effective Radiative Forcings (ERFs) due to aerosols. Each of the 14 major regions in the Atlas are shown, as well as the global mean, using the models and model experiments as in Figure 6.10. Further details on data sources and processing are available in the chapter data table (Table 6.SM.1).

[END FIGURE 6.11 HERE]

6.4.2 Emission-based Radiative Forcing and effect on GSAT

The ERFs attributable to emissions versus concentrations for several SLCFs including ozone and methane are different. A concentration change, used to assess the abundance-based ERF, results from the changes in emissions of multiple species and subsequent chemical reactions. The corollary is that the perturbation of a single emitted compound can induce subsequent chemical reactions and affect the concentrations of several climate forcers (chemical adjustments), this is what is accounted for in emission-based ERF. Due to non-linear chemistry (cf. Section 6.3) and non-linear aerosol-cloud interactions (section 7.3.3.2), the ERF attributed to the individual species cannot be precisely defined, and can only be estimated through model simulations. For example, the ERF attributed to methane emissions, which includes indirect effects through ozone formation and oxidation capacity with feedbacks on the methane lifetime, depend non-linearly on the concentrations of NO_x, CO and VOCs. This means that the results from the model simulations depend to some extent on the chosen methodology. In AR5 (based on Shindell et al., 2009; Stevenson et al., 2013) the attribution was done by removing the anthropogenic emissions of individual species one-by-one from a control simulation for present day conditions. Further, only the radiative forcings, and not the ERF (mainly including the effect of aerosol-cloud interactions) were attributed to the emitted compounds.

Since AR5, the emission estimates have been revised and extended for CMIP6 (Hoesly et al., 2018), the models have been further developed, the period has been extended (1750-2019, vs 1750-2011 in AR5) and the experimental setup for the model simulations has changed (Collins et al., 2017) making a direct

ACCEPTED VERSION SUBJECT TO FINAL EDITING

comparison of results difficult. Figure 6.13 shows the global and annual mean ERF attributed to emitted compounds over the period 1750-2019 based on AerChemMIP simulations (Thornhill et al., 2021b) where anthropogenic emissions or concentrations of individual species were perturbed from 1850 levels to 2014 levels (methodology described in Supplementary Material 6.SM.1).

[START FIGURE 6.12 HERE]

Figure 6.12: Contribution to effective radiative forcing (ERF) (left) and global mean surface air temperature (GSAT) change (right) from component emissions between 1750 to 2019 based on CMIP6 models (Thornhill et al., 2021b). ERFs for the direct effect of well-mixed greenhouse gases (WMGHGs) are from the analytical formulae in section 7.3.2, H_2O (strat) is from Table 7.8. ERFs for other components are multi-model means from Thornhill et al. (2021b) and are based on ESM simulations in which emissions of one species at a time are increased from 1850 to 2014 levels. The derived emission-based ERFs are rescaled to match the concentration-based ERFs in Figure 7.6. Error bars are 5-95% and for the ERF account for uncertainty in radiative efficiencies and multi-model error in the means. ERF due to aerosol-radiation (ERFari) and cloud effects are calculated from separate radiation calls for clear-sky and aerosol free conditions (Ghan, 2013; Thornhill et al., 2021b). "Cloud" includes cloud adjustments (semi-direct effect) and indirect aerosol-cloud interactions (ERFaci). The aerosol components (SO_2, organic carbon, black carbon) are scaled to sum to -0.22 W m^{-2} for ERFari and -0.84 W m^{-2} for "cloud" (section 7.3.3). For GSAT estimates, time series (1750-2019) for the ERFs have been estimated by scaling with concentrations for WMGHGs and with historical emissions for SLCFs. The time variation of ERFaci for aerosols is from Chapter 7. The global mean temperature response is calculated from the ERF time series using an impulse response function (see Cross-Chapter Box 7.1) with a climate feedback parameter of -1.31 W m^{-2} $°C^{-1}$. Further details on data sources and processing are available in the chapter data table (Table 6.SM.1).

[END FIGURE 6.12 HERE]

The ERF based on primary CO_2 emissions is slightly lower than the abundance-based estimate (section 7.3.2.1) because the abundance-based ERF combines the effect of primary CO_2 emissions and a small additional secondary contribution from atmospheric oxidation of CH_4, CO, and VOCs (4%) of fossil origin, consistent with AR5 findings.

Ozone depleting substances, such as N_2O and halocarbons, cause a reduction in stratospheric ozone, which affects ozone and OH production in the troposphere through radiation UV changes (and thus affect methane). They also have indirect effects on aerosols and clouds (Karset et al., 2018) since changes in oxidants induce changes in the oxidation of aerosol precursors.

The net ERF from N_2O emissions is estimated to be 0.24 (0.13 to 0.34) W m^{-2}, which is very close to the abundance-based estimate of 0.21 W m^{-2} (Section 7.3.2.3). The indirect contributions from N_2O are relatively minor with negative (methane lifetime) and positive (ozone and clouds) effects nearly compensating each other. Emissions of halogenated compounds, including CFCs and HCFCs, were assessed as very likely causing a net positive ERF in the AR5. However recent studies (Morgenstern et al., 2020; O'Connor et al., 2021; Thornhill et al., 2021b) find strong adjustments in Southern Hemisphere aerosols and clouds such that the *very likely* range in the emission based ERF for CFC+HCFCs+HFCs now also include negative values.

For methane emissions, in addition to their direct effect, there are indirect positive ERFs from methane enhancing its own lifetime, causing ozone production, enhancing stratospheric water vapor, and influencing aerosols and the lifetimes of HCFCs and HFCs (Myhre et al., 2013b; O'Connor et al., 2021). The ERF from methane emissions is considerably higher than the ERF estimate resulting from its abundance change. The central estimate with the *very likely* range is 1.21 (0.90 to 1.51) W m^{-2} for emission-based estimate versus 0.54 W m^{-2} for abundance-based estimate (cf. section 7.3.5). The abundance-based ERF estimate for CH_4 results from contributions of its own emissions and the effects of several other compounds, some decreasing CH_4 lifetime, notably NO_x, which importantly reduce the CH_4 abundance-based ERF. Emissions of CO and

ACCEPTED VERSION SUBJECT TO FINAL EDITING

NMVOCs both indirectly contribute to a positive ERF through enhancing ozone production in the troposphere and increasing the methane lifetime. For CO and NMVOCs of fossil origin there is also a 0.07 W m^{-2} contribution to CO_2 from their oxidation. The *very likely* total ERF of CO and NMVOCs emissions is estimated to 0.45 (0.22 to 0.67) W m^{-2}.

NO_x causes a positive ERF through enhanced tropospheric ozone production and a negative ERF through enhanced OH concentrations that reduce the methane lifetime. There is also a small negative ERF contribution through formation of nitrate aerosols, although only 3 of the AerChemMIP models include nitrate aerosols. The best estimate of the net ERF from changes in anthropogenic NO_x emissions is -0.29 (-0.57 to 0.0) W m^{-2}. The magnitude is somewhat greater than the AR5 estimate (-0.15 (-0.34 to + 0.02) W m^{-2}) but with similar level of uncertainty. The difference between AR6 and AR5 estimates is possibly due to the different modeling protocols (see Supplementary Material 6.SM.1).

Anthropogenic emissions of SO_2 lead to formation of sulphate aerosols and a negative ERF through aerosol-radiation and aerosol-cloud interactions. The emission-based ERF_{aci}, which was not previously considered in AR5, is now included. The estimated ERF is thus considerably more negative than the AR5 estimate with a radiative forcing of -0.4 W m^{-2}, despite the decline of ERF due to aerosols since 2011 (Figure 6.12, Section 7.3.3.1.3). SO_2 emissions are estimated to contribute to a negative ERF of -0.90 (-0.24 to -1.56) W m^{-2}, with -0.22 W m^{-2} from aerosol-radiation interactions and -0.68 W m^{-2} from aerosol-cloud interactions. Emissions of NH_3 lead to formation of ammonium-nitrate aerosols with an estimated ERF of -0.03 W m^{-2}.

The best estimate for the ERF due to emissions of BC is reduced from the AR5, and is now estimated to be 0.063 (-0.28 to 0.42) W m^{-2} with an uncertainty also including negative values. As discussed in Section 7.3.3.1.2, a significant portion of the positive BC forcing from aerosol-radiation interactions is offset by negative atmospheric adjustments due to cloud changes as well as lapse rate and atmospheric water vapor changes, resulting in a smaller positive net ERF for BC compared with AR5. The large range in the forcing estimate stems from variation in the magnitude and sign of atmospheric adjustments across models and is related to the differences in the model treatment of different processes affecting BC (e.g., ageing, mixing) and its interactions with clouds and cryosphere (Thornhill et al., 2021b and Section 7.3.3.). The emission-based ERF for organic carbon aerosols is -0.20 (-0.03 to -0.41) W m^{-2}, a weaker estimate compared with AR5 attributed to stronger absorption by OC (section 7.3.3.1.2).

The emission-based contributions to GSAT change (Figure 6.12) were not assessed in AR5, but with the ERF from aerosol-cloud interactions attributed to the emitted compounds there is now a better foundation for this assessment. The contribution to emissions-based ERF at 2019 (left panel in figure 6.12) is scaled by the historical emissions (over the period 1750 to 2019) of each compound to reconstruct the historical time series of ERF. An impulse response function (see Cross-Chapter Box 7.1 and Supplementary Material 7.SM5.2) is then applied to obtain the contribution of SLCF emissions to the GSAT response. Due to the non-linear chemical and physical processes described above relating emissions to ERF, and the additional non-linear relations between ERF and GSAT, these emission-based estimates of GSAT responses strongly depend on the methodology applied to estimate ERF and GSAT (see Supplementary Material 6.SM.2). Therefore, the relative contribution of each compound through its primary emissions versus secondary formation or destruction (e.g. for methane emissions its ozone versus methane contributions), by construction (omitting the non-linear processes), will be equal for ERF and GSAT. Uncertainties in the GSAT response are estimated using the assessed range of the ECS from Chapter 7 of this report. For most of the SLCFs the uncertainty in the GSAT response is dominated by the uncertainty in the relationship between emissions and the ERF.

The contributions from the emitted compounds to GSAT broadly follow their contributions to the ERF, mainly because their evolution over the past decades have been relatively similar and slow enough compared to their lifetimes to be reflected similarly in their ERF and GSAT despite the delay of the GSAT response to ERF changes (see Section 6.6.1). However, for some SLCFs, e.g. SO_2, that have been reduced globally, their contribution to GSAT change is slightly higher compared with that of CO_2 than their relative contribution to ERF because the peak in their ERF change has already occurred (see Section 6.4.1) whereas the peak of their GSAT effect started to decline recently (see also Figure 7.9). This is due to the inertia of the climate system

ACCEPTED VERSION SUBJECT TO FINAL EDITING

delaying the full response of GSAT to a change in forcing (Figure 6.15).

In summary, emissions of SLCFs, especially CH_4, NO_x and SO_2, have substantial effects on effective radiative forcing (ERF) (*high confidence*). The net global emissions-based ERF of NO_x is negative and that of NMVOCs is positive, in agreement with the AR5 assessment (*high confidence*). For methane, the emission-based ERF is twice as high as the abundance-based ERF (*high confidence*). SO_2 emissions make the dominant contribution to the ERF associated with the aerosol–cloud interaction (*high confidence*)**.** The contributions from the emitted compounds to GSAT broadly follow their contributions to the ERF (*high confidence*). However, due to the inertia of the climate system delaying the full GSAT response to a change in forcing, the contribution to GSAT change due to SO_2 emission is slightly higher compared with that due to CO_2 emissions (than their relative contributions to ERF) because the peak in emission-induced SO_2 ERF has already occurred.

6.4.3 Climate responses to SLCFs

This section briefly discusses the climate response to SLCFs, in particular to changes in aerosols, and gathers complementary information and assessments from Chapters 3, 7, 8, and 10.

Warming or cooling atmospheric aerosols, such as BC and sulphate, can affect temperature and precipitation in distinct ways by modifying the shortwave and longwave radiation, the lapse rate of the troposphere, and influencing cloud microphysical properties (see Box 8.1 and Section 10.1.4.1.4). An important distinction between scattering and absorbing aerosols is the opposing nature of their influences on circulation, clouds, and precipitation, besides surface temperature as evident from the contrasting regional climate responses to regional aerosol emissions (e.g., Lewinschal et al., 2019; Sand et al., 2020; also see Chapters 8 and 10).

On the global scale, as assessed in Chapter 3, anthropogenic aerosols have *likely* cooled GSAT since 1850–1900 driven by the negative aerosol forcing, while it is *extremely likely* that human-induced stratospheric ozone depletion has primarily driven stratospheric between 1979 and the mid-1990s. Multiple modelling studies support the understanding that present-day emissions of SO_2, precursor for sulphate aerosols, are the dominant driver of near-surface air temperature in comparison to BC or OC even though, for some regions, BC forcing plays a key role (Baker et al., 2015; Samset et al., 2016; Stjern et al., 2017; Zanis et al., 2020)**.** Further, there is *high confidence* that the aerosol-driven cooling has led to detectable large-scale water cycle changes since at least the mid-20th century as assessed in Chapter 8. The overall effect of surface cooling from anthropogenic aerosols is to reduce global precipitation and alter large-scale atmospheric circulation patterns (*high confidence*), primarily driven by the cooling effects of sulphate aerosols (Section 8.2.1). In addition, there is *high confidence* that darkening of snow through the deposition of black carbon and other light absorbing particles enhances snow melt (SROCC Chapter 3, see also Section 7.3.4.3).

In AR5, there was low confidence in the overall understanding of climate response to spatially varying patterns of forcing, though there was medium to high confidence in some regional climate responses, such as the damped warming of the NH and shifting of the ITCZ from aerosols, and positive feedbacks enhancing the local response from high-latitude snow and ice albedo changes. Since AR5, the relationship between inhomogeneous forcing and climate response is better understood providing further evidence of the climate influence of SLCFs (aerosols and ozone in particular) on global to regional scales (Collins et al., 2013; Shindell et al., 2015; Aamaas et al., 2017; Kasoar et al., 2018; Persad and Caldeira, 2018; Wilcox et al., 2019) which differ from the relatively homogeneous spatial influence from LLGHGs.

Large geographical variations in aerosol ERFs (section 6.4.1) affect global and regional temperature responses (Shindell et al., 2015, Myhre et al., 2013a). A multimodel CMIP6 ensemble mean results (Figure 6.13) show cooling over almost all areas of the globe in response to increases of aerosol and their precursor emissions from 1850 to recent past (1995–2014). While the ERF has hotspots, the temperature response is more evenly distributed in line with the results of CMIP5 models including the temperature response to ozone changes (Shindell et al 2015). The ensemble mean global mean surface temperature decreases by 0.66±0.51 °C while decreasing by 0.97±0.54 °C for Northern Hemisphere and 0.34±0.2 °C for Southern

ACCEPTED VERSION SUBJECT TO FINAL EDITING

Hemisphere. The zonal mean temperature response is negative at all latitudes (high confidence) and becomes more negative with increasing latitude, with a maximum ensemble mean decrease of around 2.7 °C at Northern polar latitudes. The zonal mean response is not directly proportional to the zonal mean forcing, especially in the Arctic where the temperature response is cooling while the local ERF is positive (6.10). This is consistent with prior studies showing that the Arctic, in particular, is highly sensitive to forcing at NH midlatitudes (e.g., Sand et al., 2013b; Shindell and Faluvegi, 2009) and with results from CMIP5 models (Shindell et al., 2015) (more on Arctic below). Thus, there is *high confidence* that the temperature response to aerosols is more asymmetric than the response to WMGHGs and negative at all latitudes.

The asymmetric aerosol and greenhouse gas forcing on regional scale climate responses have also been assessed to lead to contrasting effects on precipitation in Chapter 8. The asymmetric historical radiative forcing due to aerosols led to a southward shift in the tropical rain belt (*high confidence*) and contributed to the Sahel drought from the 1970s to the 1980s (*high confidence*). Furthermore, the asymmetry of the forcing led to contrasting effects in monsoon precipitation changes over West Africa, South Asia and East Asia over much of the mid-20th century due to GHG-induced precipitation increases counteracted by anthropogenic aerosol-induced decreases (*high confidence*) (see Section 8.3, Box 8.1).

The Arctic region is warming considerably faster than the rest of the globe (Atlas 5.9.2.2) and, generally, studies indicate that this amplification of the temperature response toward the Arctic has important contribution from local and remote aerosol forcing (Stjern et al., 2017; Westervelt et al., 2018). Several studies indicate that changes in long-range transport of sulphate and BC from northern midlatitudes can potentially explain a significant fraction of Arctic warming since 1980s (e.g., Breider et al., 2017; Navarro et al., 2016; Ren et al., 2020). Modeling studies show that changes in midlatitude aerosols have influenced Arctic climate by changing the radiative balance through aerosol-radiation and aerosol-cloud interactions and enhancing poleward heat transport (Navarro et al., 2016; Ren et al., 2020b). Idealized aerosol perturbation studies have shed further light on the sensitivity of Arctic temperature response to individual aerosol species. Studies show relatively large responses in the Arctic to BC perturbations and reveal the importance of remote BC forcing by rapid adjustments (Sand et al., 2013a; Stjern et al., 2017; Liu et al., 2018; Yang et al., 2019a). Perturbations in SO_2 emissions over major emitting regions in the Northern Hemisphere have been shown to produce largest Arctic temperature responses (Kasoar et al., 2018; Lewinschal et al., 2019).

The effects of changes in aerosols on local and remote changes in temperature, circulation and precipitation are sensitive to a number of model uncertainties affecting aerosol sources, transformation, and resulting climate effects. Therefore, regional climate effects in global model studies must be interpreted with caution. When investigating the climate response to regional aerosol emissions, such uncertainties are likely to be confounded even further by the variability between models in regional climate and circulation patterns, leading to greater intermodel spread at regional scales than at a global scale (Baker et al., 2015; Kasoar et al., 2016).

In summary, over the historical period, changes in aerosols and their ERF have primarily contributed to cool the surface temperature partly masking the human-induced warming (*high confidence*). Radiative forcings induced by aerosol changes lead to both local and remote changes in temperature (*high confidence*). The temperature response preserves hemispheric asymmetry of the ERF but is more latitudinally uniform with strong amplification of the temperature response towards the Arctic (*medium confidence*).

[START FIGURE 6.13 HERE]

Figure 6.13: Multi-model mean surface air temperature response due to aerosol changes between 1850 and recent-past (1995-2014). Calculation is based on the difference between CMIP6 'historical' and AerChemMIP 'hist-piAer' experiments, where a) is the spatial pattern of the annual mean surface air temperature response, and b) is the mean zonally averaged response. Model means are derived from years 1995-2014. Uncertainty is represented using the advanced approach: No overlay indicates regions with robust signal, where ≥66% of models show change greater than variability threshold and ≥80% of all models agree on sign of change; diagonal lines indicate regions with no change or no robust signal, where <66% of models show a change greater than the variability threshold; crossed lines indicate regions with

ACCEPTED VERSION SUBJECT TO FINAL EDITING

conflicting signal, where ≥66% of models show change greater than variability threshold and <80% of all models agree on sign of change. For more information on the advanced approach, please refer to the Cross-Chapter Box Atlas.1. AerChemMIP models MIROC6, MRI-ESM2-0, NorESM2-LM, GFDL-ESM4, GISS-E2-1-G, UKESM1-0-LL are used in the analysis. Further details on data sources and processing are available in the chapter data table (Table 6.SM.1).

[END FIGURE 6.13 HERE]

6.4.4 Indirect radiative forcing through effects of SLCFs on the carbon cycle

Deposition of reactive nitrogen (Nr) (i.e. NH_3 and NO_x) increases the plant productivity and carbon sequestration in N-limited forests and grasslands, and also in open and coastal waters and open ocean. Such inadvertent fertilization of the biosphere can lead to eutrophication and reduction in biodiversity in terrestrial and aquatic ecosystems. AR5 assessed that it is *likely* that Nr deposition over land currently increases natural CO_2 sinks, in particular in forests, but the magnitude of this effect varies between regions (Ciais et al., 2013). Increasing Nr deposition or the synergy between increasing Nr deposition and atmospheric CO_2 concentration could have contributed to the increasing global net land CO_2 sink [Section 5.2.1.4.1].

Ozone uptake itself damages photosynthesis and reduces plant growth with consequences for the carbon and water cycles (Ainsworth et al., 2012; Emberson et al., 2018). AR5 concluded there was robust evidence of the effect of ozone on plant physiology and subsequent alteration of the carbon storage but considered insufficient quantification of and a lack of systematic incorporation of the ozone effect in carbon-cycle models as a limitation to assess the terrestrial carbon balance (Ciais et al., 2013). Since AR5 several more ESMs have incorporated interactive ozone-vegetation damage resulting in an increase in evidence to support the influence of ozone on the land carbon cycle. The new modelling studies tend to focus on ozone effects on plant productivity rather than the land carbon storage and agree that ozone-induced gross-primary productivity (GPP) losses are largest today in eastern USA, Europe and eastern China ranging from 5-20% on the regional scale (Yue and Unger, 2014; Lombardozzi et al., 2015; Yue et al., 2017; Oliver et al., 2018) (*low confidence*). There is *medium evidence* and *high agreement* based on observational studies and models that ozone-vegetation interactions further influence the climate system, including water and carbon cycles by affecting stomatal control over plant transpiration of water vapour between the leaf surface and atmosphere (Arnold et al., 2018; Hoshika et al., 2015; Lombardozzi et al., 2013; Sun et al., 2012; VanLoocke et al., 2012; Wittig et al., 2007). While some modelling studies suggest that the unintended Nr deposition fertilization effect in forests may potentially offset the ozone-induced carbon losses (Felzer et al., 2007; de Vries et al., 2017), complex interactions have been observed between ozone and Nr deposition to ecosystems that have not yet been included in ESMs. For some plants, the effects of increasing ozone on root biomass become more pronounced as Nr deposition increased, and the beneficial effects of Nr on root development were lost at higher ozone treatments (Mills et al., 2016). Reducing uncertainties in ozone vegetation damage effects on the carbon cycle requires improved information on the sensitivity of different plant species to ozone, and measurements of ozone dose-response relationships for tropical plants, which are currently lacking. Surface ozone effect on the land carbon sink and indirect CO_2 forcing, therefore, remains uncertain. Collins et al. (2010) showed that adding in the effects of surface ozone on vegetation damage and reduced uptake of CO_2 added about 10 % to the methane emission metrics and could change the sign of the NO_x metrics. However, this estimate has to be considered as an upper limit due to limitation of the paramaterization used by Sitch et al. (2007) considering more recent knowledge and is thus not included in the current metrics (Section 7.6.1.3).

Tropospheric aerosols influence the land and ocean ecosystem productivity and the carbon cycle through changing physical climate and meteorology (Jones, 2003; Cox et al., 2008; Mahowald, 2011; Unger et al., 2017) and through changing deposition of nutrients including nitrogen, sulphur, iron and phosphorous (Mahowald et al., 2017; Kanakidou et al., 2018). There is *high evidence* and *high agreement* from field (Oliveira et al., 2007; Cirino et al., 2014; Rap et al., 2015; Wang et al., 2018c) and modelling (Mercado et al., 2009; Strada and Unger, 2016; Lu et al., 2017; Yue et al., 2017) studies that aerosols affect plant productivity through increasing the diffuse fraction of downward shortwave radiation although the

ACCEPTED VERSION SUBJECT TO FINAL EDITING

magnitude and importance to the global land carbon sink is controversial. At large-scales the dominant effect of aerosols on the carbon cycle is *likely* a global cooling effect of the climate (Jones, 2003; Mahowald, 2011; Unger et al., 2017) (*medium confidence*). We assess that these interactions between aerosols and the carbon cycle are currently too uncertain to constrain quantitatively the indirect CO_2 forcing.

In summary, reactive nitrogen, ozone and aerosols affect terrestrial vegetation and carbon cycle through deposition and effects on large scale radiation (*high confidence*) but the magnitude of these effects on the land carbon sink, ecosystem productivity and indirect CO_2 forcing remain uncertain due to the difficulty in disentangling the complex interactions between the effects. As such we assess it to be of second order in comparison to the direct CO_2 forcing (*high confidence*) but, at least for ozone, it could add a substantial (positive) forcing compared with its direct forcing (*low confidence*).

6.4.5 Non-CO_2 biogeochemical feedbacks

Climate change-induced changes in atmospheric composition and forcing due to perturbations in natural processes constitute an Earth system feedback amplifying (positive feedback) or diminishing (negative feedback) the initial climate perturbation (Ciais et al., 2013; Heinze et al., 2019). Quantification of these biogeochemical feedbacks is important to allow for better estimate of the expected effects of emission reduction policies for mitigating climate change and the effect on the allowable global carbon budget (Lowe and Bernie, 2018). Biogeochemical feedbacks due to changes in carbon-cycle are assessed in Section 5.4.5, while physical and biophysical climate feedbacks are assessed in Section 7.4.2. Additionally, non-CO_2 biogeochemical feedbacks due to climate driven changes in methane sources and N_2O sources and sinks are assessed in Section 5.4.7. The goal of this section is to estimate the feedback parameter (α as defined in section 7.4.1.1) from climate-induced changes in atmospheric abundances or lifetimes of SLCFs mediated by natural processes or atmospheric chemistry. These non-CO_2 biogeochemical feedbacks act on time scales of years to decades and have important implications for climate sensitivity and emission abatement policies. The feedback parameter is quantified entirely from ESMs that expand the complexity of CCMs by coupling the physical climate and atmospheric chemistry to land and ocean biogeochemistry. In AR5, α for non-CO_2 biogeochemical feedbacks was estimated from an extremely limited set of modeling studies with much less confidence associated with the estimate. Since AR5, ESMs have advanced to include more feedback processes facilitating a relatively more robust assessment of α. CMIP6 ESMs participating in AerChemMIP performed coordinated sets of experiments (Collins et al., 2017) facilitating the consistent estimation of α (Thornhill et al., 2021a) and we rely on this multi-model analysis for the best estimates (Table 6.9). Considering the consistent methodology, the assessed central values and 5-95% ranges for α are based on the AerChemMIP estimates. The full range of model uncertainty is not captured in AerChemMIP because of the relatively small ensemble size therefore estimates from studies using other models or with different protocols are discussed to reinforce or critique these values.

Climate-Sea-spray feedback: Sea-spray emissions from ocean surfaces influence climate directly or indirectly through the formation of CCN as discused in Section 6.2.1.2. They are sensitive to sea-surface temperature, sea ice extent, as well as wind speed and are therefore expected to feedback on climate (Struthers et al., 2013). However, there are large uncertainties in the strength of climate feedback from sea-spray aerosols because of the diversity in the model representation of emissions (many represent sea-salt emissions only) and their functional dependence on environmental factors noted above, in situ atmospheric chemical and physical processes affecting the sea-spray lifetime, and aerosol-cloud interactions (Struthers et al., 2013; Soares et al., 2016; Nazarenko et al., 2017). Additional work is needed to identify how sea-spray and POA emissions respond to shifts in ocean biology and chemistry in response to warming, ocean acidification, and changes in circulation patterns (Burrows et al., 2018) and affect CCN and INP formation (DeMott et al., 2016). AerChemMIP models, representing only the sea-salt emissions, agree that the sea-salt-climate feedback is negative, however there is a large range in the feedback parameter indicating large uncertainties (Table 6.9).

Climate-DMS feedback: Dimethyl sulphide (DMS) is produced by marine phytoplankton and is emitted to the atmosphere where it can lead to the subsequent formation of sulphate aerosol and CCN (see Section

ACCEPTED VERSION SUBJECT TO FINAL EDITING

6.2.1.2). Changes in DMS emissions from ocean could feedback on climate through their response to changes in temperature, solar radiation, ocean mixed-layer depth, sea-ice extent, wind-speed, nutrient recycling or shifts in marine ecosystems due to ocean acidification and climate change, or atmospheric processing of DMS into CCN (Heinze et al., 2019). Models with varying degrees of representation of the relevant biogeochemical processes and effects on DMS fluxes produce diverging estimates of changes in DMS emission strength under climate change resulting in large uncertainties in the DMS–sulphate–cloud albedo feedback (Bopp et al., 2004; Kloster et al., 2007; Gabric et al., 2013). In AR5, the climate-DMS feedback parameter was estimated to be -0.02 W m^{-2} °C^{-1} based on a single model. Since AR5, new modeling studies using empirical relationships between pH and total DMS production find that global DMS emissions decrease due to combined ocean acidification and climate change leading to a strong positive climate feedback (Six et al., 2013; Schwinger et al., 2017). However, another study argues for a much weaker positive feedback globally due to complex and compensating regional changes in marine ecosystems (Wang et al., 2018b). The AerChemMIP multimodel analysis suggests small positive feedback (Table 6.9), consistent with these recent studies, but with large uncertainties in the magnitude of α.

Climate-dust feedback: Mineral dust is the most abundant aerosol type in the atmosphere, when considering aerosol mass, and affects the climate system by interacting with both longwave and shortwave radiation as well as contributing to the formation of CCN and INP. Because dust emissions are sensitive to climate variability (e.g., through changes in the extent of arid land) (Section 6.2.1.2), it has been hypothesized that the climate-dust feedback could be an important feedback loop in the climate system. Since AR5, an improved understanding of the shortwave absorption properties of dust as well as a consensus that dust particles are larger than previously thought has led to a revised understanding that the magnitude of radiative forcing due to mineral dust is small (Kok et al., 2017; Ryder et al., 2018). A recent study notes that global models underestimate the amount of coarse dust in the atmosphere and accounting for this limitation raises the possibility that dust emissions warm the climate system (Adebiyi and Kok, 2020). Model predictions of dust emissions in response to future climate change range from an increase (Woodward et al., 2005) to a decrease (Mahowald and Luo, 2003), thus leading to high uncertainties on the sign of the climate-dust feedback. Since the AR5, Kok et al. (2018) estimated the direct dust-climate feedback parameter, from changes in the dust direct radiative effect only, to be in the range –0.04 to +0.02 W m^{-2} °C^{-1}. The assessed central value and the 5-95%range of climate-dust feedback parameter based on AerChemMIP ensemble (Table 6.9) is within the range of the published estimate, however both the magnitude and sign of α are model-dependent.

Climate-ozone feedback: Changes in ozone concentrations in response to projected climate change have been shown to lead to a potential climate-atmospheric chemistry feedback. Chemistry-climate models consistently project a decrease in lower tropical stratospheric ozone levels due to enhanced upwelling of ozone poor tropospheric air associated with surface warming driven strengthening of the Brewer-Dobson circulation (Bunzel and Schmidt, 2013). Further, models project an increase in middle and extratropical stratospheric ozone due to increased downwelling through the strengthened Brewer-Dobson circulation (Bekki et al., 2013; Dietmüller et al., 2014). These stratospheric ozone changes induce a net negative global mean ozone radiative feedback (Dietmüller et al., 2014). Tropospheric ozone shows a range of responses to climate with models generally agreeing that warmer climate will lead to decreases in the tropical lower troposphere owing to increased water vapour and increases in the sub-tropical to mid-latitude upper troposphere due to increases in lightning and stratosphere-to-troposphere transport (Stevenson et al., 2013). A small positive feedback is estimated from climate-induced changes in global mean tropospheric ozone (Dietmüller et al., 2014) while a small negative feedback is estimated by (Heinze et al., 2019) based on the model results of (Stevenson et al., 2013). Additionally, these ozone feedbacks induce a change in stratospheric water vapor amplifying the feedback due to stratospheric ozone (Stuber et al., 2001). Since AR5, several modeling studies have estimated the intensity of meteorology driven ozone feedbacks on climate from either combined tropospheric and stratospheric ozone changes or separately with contrasting results. One study suggests no change (Marsh et al., 2016), while other studies report reductions of equilibrium climate sensitivity ranging from 7-8% (Dietmüller et al., 2014; Muthers et al., 2014) to 20% (Nowack et al., 2015). The estimate of this climate-ozone feedback parameter is very strongly model dependent with values ranging from -0.13 to -0.01 W m^{-2} °C^{-1} though there is agreement that it is negative. The assessed central value and the 5-95% range of climate-ozone feedback parameter based on

ACCEPTED VERSION SUBJECT TO FINAL EDITING

AerChemMIP ensemble is within the range of these published estimates but closer to the lower bound. This climate-ozone feedback factor does not include the feedback on ozone from lightning changes which is discussed separately below.

Climate-BVOC feedback: BVOCs, such as isoprene and terpenes, are produced by land vegetation and marine plankton (Section 6.2.1.2). Once in the atmosphere, BVOCs and their oxidation products lead to the formation of secondary organic aerosols (SOA) exerting a negative forcing, and increased ozone concentrations and methane lifetime exerting a positive forcing. BVOC emissions are suggested to lead to a climate feedback in part because of their strong temperature dependence observed under present-day conditions (Kulmala et al., 2004; Arneth et al., 2010a). Their response to future changes in climate and CO_2 levels remains uncertain (see Section 6.2.2.3. Estimates of the climate-BVOC feedback parameter are typically based on global models which vary in their level of complexity of emissions parameterization, BVOC speciation, the mechanism of SOA formation and the interaction with ozone chemistry (Thornhill et al., 2021a). Since AR5, observational studies (Paasonen et al. 2013) and models (Scott et al. 2018) estimate the feedback due to biogenic SOA (via changes in BVOC emissions) to be in the range of about –0.06 to -0.01 W m^{-2} °C^{-1}. The assessed central estimate of the climate-BVOC feedback parameter based on the AerChemMIP ensemble suggests that climate-induced increases in SOA from BVOCs will lead to a strong cooling effect that will outweigh the warming from increased ozone and methane lifetime, however the uncertainty is large (Thornhill et al., 2021a).

Climate-Lightning NO_x feedback: As discussed in Section 6.2.1.2, climate change influences lightning NO_x emissions. Increases in lightning NO_x emissions will not only increase tropospheric ozone and decrease methane lifetime but also increase the formation of sulphate and nitrate aerosols, via oxidant changes, offsetting the positive forcing from ozone. The response of lightning NO_x to climate change remains uncertain and is highly dependent on the parameterization of lightning in ESMs (Finney et al., 2016b; Clark et al., 2017) (also see section 6.2.1.2). AerChemMIP multi-model ensemble mean estimate a net negative climate feedback from increases in lightning NO_x in a warming world (Thornhill et al., 2021a). All AerChemMIP models use a cloud-top height lightning parameterization that predicts increases in lightning with warming. However, a positive climate-lightning NO_x feedback cannot be ruled out because of the dependence of the response to lightning parameterizations as discussed in section 6.2.2.1.

Climate-CH_4 Lifetime feedback: Warmer and wetter climate will lead to increases in OH and oxidation rates leading to reduced atmospheric methane lifetime – a negative feedback (Naik et al., 2013; Voulgarakis et al., 2013). Furthermore, since OH is in turn removed by methane, the climate-methane lifetime feedback will be amplified (Prather, 1996) (also see section 6.3.1). Based on the multimodel results of Voulgarakis et al. (2013), α for climate-methane lifetime is estimated to be -0.030 ± 0.01 W m^{-2} °C^{-1} by Heinze et al., (2019). The assessed central value of α based on the AerChemMIP ensemble is within the range of this estimate but with greater uncertainty (Thornhill et al., 2021a).

Climate-Fire feedback: Wildfires are a major source of SLCF emissions (section 6.2.2.6). Climate change has the potential to enhance fire activity (see Sections 5.4.3.2, Chapter 12.4) thereby enhancing SLCF emissions leading to feedbacks. Climate driven increases in fire could potentially lead to offsetting feedback from increased ozone and decreased methane lifetime (due to increases in OH) leaving the feedback from aerosols to dominate with an uncertain net effect (e.g., Landry et al., 2015). AR5 assessment of climate-fire feedbacks included a value of α due to fire aerosols to be in the range of -0.03 to + 0.06 W m^{-2} °C^{-1} based on Arneth et al. (2010). A recent study estimates climate feedback due to fire aerosols to be greater than that due to BVOCs, with a value of α equal to -0.15 (-0.24 to -0.05) W m^{-2} °C^{-1} (Scott et al., 2018). Clearly, the assessment of fire related non-CO_2 biogeochemical feedbacks is very uncertain because of limitations in the process understanding of the interactions between climate, vegetation and fire dynamics, and atmospheric chemistry and their representation in the current generation ESMs. Some AerChemMIP ESMs include the representation of fire dynamics but do not activate their interaction with atmospheric chemistry. Given the large uncertainty and lack of information from AerChemMIP ESMs, we do not include a quantitative assessment of climate-fire feedback for AR6.

In summary, climate-driven changes in emissions, atmospheric abundances or lifetimes of SLCFs are

ACCEPTED VERSION SUBJECT TO FINAL EDITING

assessed to have an overall cooling effect, i.e., a negative feedback parameter of -0.20 W m^{-2} °C^{-1} with a 5-95% range of -0.41 to + 0.01 W m^{-2} °C^{-1}, thereby reducing climate sensitivity (see Section 7.4.2.5.1). This net feedback parameter is obtained by summing the assessed estimates for the individual feedback given in Table 6.8. *Confidence* in the magnitude and the sign of most of the individual as well as the total non-CO_2 biogeochemical feedbacks remains *low* as evident from the large range in the value of α. This large uncertainty is attributed to the diversity in model representation of the relevant chemical and biogeochemical processes based on limited process-level understanding.

[START TABLE 6.8 HERE]

Table 6.8: Assessed central estimates and the *very likely* ranges (5-95%) of non-CO_2 biogeochemical feedback parameter (α_x) based on the AerChemMIP ensemble estimates (Thornhill et al., 2021a). As in Section 7.4.1.1, α_x (W m^{-2} °C^{-1}) for a feedback variable x is defined as $\alpha_x = \frac{\partial N}{\partial x}\frac{dx}{dT}$ where $\frac{\partial N}{\partial x}$ is the change in TOA energy balance in response to a change in x induced by a change in surface temperature (T). The 5-95% range is calculated as mean ± standard deviation * 1.645 for each feedback. The level of confidence in these estimates is *low* owing to the large model spread. Published estimates of α are also shown for comparison.

Non-CO_2 Biogeochemical Climate Feedback (x)	**# of AerChemMIP Models**	**Assessed Central Estimate and Very Likely Range of Feedback Parameter (α_x) W m^{-2} °C^{-1}**	**Published estimates of α_x W m^{-2} °C^{-1}**
Sea-salt	6	-0.049 (-0.13 to +0.03)	-0.08 (Paulot et al., 2020)
DMS	3	0.005 (0.0 to 0.01)	-0.02 (Ciais et al., 2013)
Dust	6	-0.004 (-0.02 to +0.01)	-0.04 to +0.02 (Kok et al., 2018)
Ozone	4	-0.064 (-0.08 to -0.04)	-0.015 (Dietmüller et al., 2014), -0.06 (Muthers et al., 2014, stratospheric ozone changes only), -0.01 (Marsh et al., 2016, stratospheric ozone changes only), -0.13 (Nowack et al., 2015, stratospheric ozone and water vapor changes), -0.007 ± 0.009 (Heinze et al., 2019, tropospheric ozone changes only)
BVOC	4	-0.05 (-0.22 to +0.12)	-0.06 (Scott et al., 2017, aerosol effects only), -0.01 (Paasonen et al., 2013; indirect aerosol effects only), 0-0.06 (Ciais et al., 2013)
Lightning	4	-0.010 (-0.04 to +0.02)	
Methane lifetime	4	-0.030 (-0.12 to +0.06)	-0.30 ± 0.01 (Heinze et al., 2019)
Total non-CO_2 Biogeochemical Feedbacks assessed in this chapter		-0.200 (-0.41 to +0.01)	0.0 ± 0.15 (Sherwood et al., 2020)

[END TABLE 6.8 HERE]

6.4.6 ERF by aerosols in proposed Solar Radiation Modification

Solar radiation modification (SRM, see also Sections 4.6.3.3, 8.6.3) have the potential to exert a significant ERF on the climate, mainly by affecting the SW component of the radiation budget (e.g. Caldeira et al., 2013; Lawrence et al., 2018; National Academy of Sciences, 2015). The possible ways and the extent to

ACCEPTED VERSION SUBJECT TO FINAL EDITING

which the most commonly discussed options may affect radiative forcing is addressed in this section. Side-effects of SRM on stratospheric ozone and changes in atmospheric transport due to radiative heating of the lower stratosphere are discussed in Section 4.6.3.3.

Stratospheric aerosol injections have the potential to achieve a high negative global ERF, with maximum ERFs ranging from -2 to -5 W m^{-2} (Niemeier and Timmreck, 2015; Weisenstein et al., 2015; Niemeier and Schmidt, 2017; Kleinschmitt et al., 2018). The magnitude of the maximum achievable ERF depends on the chosen aerosol type and mixture, internal structure and size, or precursor gas (e.g. SO_2), as well as the injection strategy; latitude, altitude, magnitude, and season of injections, plume dispersal, model representation of aerosol microphysics, and ambient aerosol concentrations (Rasch et al., 2008; Robock et al., 2008; Pierce et al., 2010; Weisenstein et al., 2015; Laakso et al., 2017; Macmartin et al., 2017; Dai et al., 2018; Kleinschmitt et al., 2018; Vattioni et al., 2019; Visioni et al., 2019). For sulphur, the radiative forcing efficiency is of around -0.1 to -0.4 W m^{-2} / (TgS yr^{-1}) (Niemeier and Timmreck, 2015; Weisenstein et al., 2015; Niemeier and Schmidt, 2017). Different manufactured aerosols, such as ZrO_2, TiO_2, and Al_2O_3, have different ERF efficiencies compared to sulphate (Ferraro et al., 2011; Weisenstein et al., 2015; Dykema et al., 2016; Jones et al., 2016). The aerosol size distribution influences the optical properties of an aerosol layer, and hence the ERF efficiency, which also depends on the dispersion, transport, and residence time of the aerosols.

For marine cloud brightening (MCB), seeded aerosols may affect both cloud microphysical and macrophysical properties (see also Section 7.3.3.2). By principle, MCB relies on ERF_{aci} through the so-called Twomey effect (Twomey, 1977), but ERF_{ari} may be of equal magnitude as shown in studies that consider spraying of sea salt outside tropical marine cloud areas (Jones and Haywood, 2012; Partanen et al., 2012; Alterskjær and Kristjánsson, 2013; Ahlm et al., 2017). The maximum negative ERF estimated from modelling is within the range of -0.8 to -5.4 W m^{-2} (Latham et al., 2008; Rasch et al., 2009; Jones et al., 2011; Partanen et al., 2012; Alterskjær and Kristjánsson, 2013). For dry sea salt, the ERF efficiency is estimated to be within the range of -3 to -10 W m^{-2} / (Pg yr^{-1}), when emitted over tropical oceans in ESMs in the Geoengineering Intercomparison Project (GeoMIP) (Ahlm et al., 2017). Cloud resolving models reveal complex behaviour and response of stratocumulus clouds to seeding, in that the ERF efficiency depends on meteorological conditions, and the ambient aerosol composition, where lower background particle concentrations may increase the ERF_{aci} efficiency (Wang et al., 2011). Seeding could suppress precipitation formation and drizzle, and hence increase the lifetime of clouds, preserving their cooling effect (Ferek et al., 2000). In contrast, cloud lifetime could be decreased by making the smaller droplets more susceptible to evaporation. Modelling studies have shown that a positive ERF_{aci} (warming) could also result from seeding clouds with too large aerosols (Pringle et al., 2012; Alterskjær and Kristjánsson, 2013). These processes, and the combination of these, are not well understood, and may have a limited representation in models, or counteracting errors (Mülmenstädt and Feingold, 2018), lending *low to medium confidence* to the ERF estimates.

Modelled ERF_{aci} associated with cirrus cloud thinning (CCT) cover a wide range in the literature, and the maximum are of the order of -0.8 to -3.5 W m^{-2}, though they are of *low confidence*, with some studies using more simplified representations (Mitchell and Finnegan, 2009; Storelvmo et al., 2013; Kristjánsson et al., 2015; Jackson et al., 2016; Muri et al., 2018; Gasparini et al., 2020). ERF_{aci} for CCT is mainly affected by particle seeding concentrations, with an optimum around 20 L^{-1}, according to limited evidence from models (Storelvmo et al., 2013). Seeding leading to higher particle concentrations could lead to a warming (Storelvmo et al., 2013; Penner et al., 2015; Gasparini and Lohmann, 2016). The lack of representation of processes related to, for example, heterogeneous and homogeneous freezing and their prevalence, is a dominant source of uncertainty in ERF estimates, in addition to less research activity.

In summary, the aerosol and cloud microphysics involved with SRM are not well understood, with a varying degree of lack of representation of relevant processes in models. ERF of up to several W m^{-2} is reported in the literature, with SAI at the higher end and CCT with lower potentials, though it remains a challenge to establish ERF potentials and efficacies with confidence. Modelling studies have been published with more sophisticated treatment of SRM since AR5, but the uncertainties, such as cloud-aerosol radiation interactions, remain large (*high confidence*).

ACCEPTED VERSION SUBJECT TO FINAL EDITING

6.5 Implications of changing climate on AQ

Air pollutants can be impacted by climate change through physical changes affecting meterorological conditions, chemical changes affecting their lifetimes, and biological changes affecting their natural emissions (Kirtman et al., 2013). Changes in meteorology affect air quality directly through modifications of atmospheric transport patterns (e.g., occurrence and length of atmospheric blocking episodes, ventilation of the polluted boundary layer), extent of mixing layer and stratosphere-troposphere exchange (STE) for surface ozone (Von Schneidemesser et al., 2015), and through modifications of the rate of reactions that generate secondary species in the atmosphere. Changing precipitation patterns in a future climate also influence the wet removal efficiency, in particular for atmospheric aerosols (Hou et al., 2018). Processes at play in non-CO_2 biogeochemical feedbacks (Section 6.4.5) are also involved in the perturbation of atmospheric pollutants (see Section 6.2.2).

This section relies on observational studies performed by analysing correlation between specific meteorological conditions projected to occur more frequently in the future and surface pollutants, and global and regional scale modelling studies considering solely climate change in the future. We also assess the surface ozone and $PM_{2.5}$ changes based on CMIP6 models analysed in AerChemMIP, considering climate change in isolation with emissions in 2050 from SSP3-7.0 scenario (see Section 6.7.1). Air quality being highly variable in space and time, the use of regional atmospheric chemistry models is necessary to characterise the effect of future climate on air quality properly. However, difficulties for such assessment arise from the need for long simulations that include complex chemistry-natural system interactions with high computational cost, in addition to the difficulty related to the regionalisation of climate change (see Section 10.3.1.2). Changes in the occurrence of weather patterns influencing air pollution (e.g., anticyclonic stagnation conditions, transport pathways from pollution sources, convection) due to climate change are assessed in Chapters 4 and 11.

6.5.1 Effect of climate change on surface O_3

AR5 assessed with high confidence that (Kirtman et al., 2013), in unpolluted regions, higher water vapour abundances and temperatures in a warmer climate would enhance ozone chemical destruction, leading to lower baseline[5] surface ozone levels. In polluted regions, AR5 assessed with medium confidence that higher surface temperatures will trigger regional feedbacks in chemistry and local emissions that will increase surface ozone and intensity of surface O_3 peaks.

The response of surface ozone to climate induced Earth system changes is complex due to counteracting effects. Studies considering the individual effects of climate driven changes in specific precursor emissions or processes show increases in surface ozone under warmer atmosphere for some processes. This is indeed the case for enhanced STE and stratospheric ozone recovery (Sekiya and Sudo, 2014; Banerjee et al., 2015; Hess et al., 2015; Meul et al., 2018; Morgenstern et al., 2018; Akritidis et al., 2019) or the increase of soil NO_x emissions (Wu et al., 2008; Romer et al., 2018), which can each lead to 1 to 2 ppb increase in surface ozone. Other processes, in particular deposition or those related to emissions from natural systems (see section 6.2.2) are expected to play a key role in future surface ozone and even occurrence of pollution events (e.g. in the case of wildfires) but their effects are difficult to quantify in isolation.

Since the AR5, several studies have investigated the net effect of climate change on surface ozone, based on either global or regional model projections. A systematic and quantitative comparison of the ozone change, however, is difficult due to the variety of models with different complexities in the representation of natural emissions, chemical mechanisms, and physical processes as well as the surface O_3 metrics applied for analysis. Processes like temperature-, CO_2-sensitive BVOC emissions, deposition, and branching ratio in isoprene nitrates chemistry have been shown to be particularly sensitive (Squire et al., 2015; Val Martin et al., 2015; Schnell et al., 2016; Pommier et al., 2018). More robust protocol are now used more commonly

[5] Baseline ozone is defined as the observed ozone at a site when it is not influenced by recent, locally emitted or anthropogenically produced pollution (Jaffe et al., 2018).

ACCEPTED VERSION SUBJECT TO FINAL EDITING

comprising, notably, longer simulations necessary to separate change from interannual variability (Lacressonnière et al., 2016; Garcia-Menendez et al., 2017) (Barnes et al., 2016). However, the amplitude of climate change penalty on ozone over polluted regions may be different in high-resolution (regional and urban-scale) models in comparison to coarse resolution global models as a number of controlling processes are resolution-dependent including e.g local emissions, sensitivity to the chemical regime (VOC limited versus NO_x limited) (Lauwaet et al., 2014; Markakis et al., 2014, 2016).

Consistent with AR5 findings, global surface ozone concentration decreases by up to -1.2 to 2.3 ppb for annual mean due to the dominating role of ozone destruction by water vapor are found in four member ensemble of CMIP6 ESM for surface warmings of 1.5 to 2.5 °C (Figure 6.14). This decrease is driven by the ozone decrease over oceans, especially in the tropics (decrease of 1 ppb to 5 ppb) and large parts of the continental unpolluted regions. The sensitivity of annual mean surface ozone to the level of surface warming over these remote areas varies spatially from -0.2 to -2 ppb $^{o}C^{-1}$ (see Figure 6.SM.1 in the Supplementary Material)

Over ozone producing regions of the world, such as in North America, Europe, and East Asia, AR5 and post AR5 model studies project a general increase of surface ozone levels (climate change penalty on ozone) in a future warmer climate particularly during summertime (Fu and Tian, 2019). However, in current regional models, using more robust protocols, this increase of surface ozone, attributable to climate change is of lower magnitude than in previous estimates (Lacressonnière et al., 2016; Garcia-Menendez et al., 2017). Climate change enhances the efficiency of precursor emissions to generate surface ozone in polluted regions, (Schnell et al., 2016) and thus the magnitude of this effect will depend on the emissions considered in the study (present or future, and mitigated or not) (Colette et al., 2015; Fiore et al., 2015).

Considering anthropogenic emissions of precursors globally higher than the current emissions (SSP3-7.0 in 2050, see Figure 6.20), the CMIP6 ensemble confirms the surface O_3 penalty due to climate change over regions close to anthropogenic pollution sources or close to natural emission sources of ozone precursors (e.g. biomass burning areas), with a penalty of a few ppb for the annual mean, proportional to warming levels (Figure 6.14). This rate ranges regionally from 0.2 to 2 ppb $^{o}C^{-1}$ (see Figure 6.SM.1 in Supplementary Material). The CMIP6 ESMs show this consistently for South East Asia (in line with Hong et al., (2019) and Schnell et al. (2016)) and for India (in line with (Pommier et al., 2018) as well as in parts of Africa and South America, close to enhanced BVOC emissions (at least 3 out 4 ESMs agree on the sign of change). The results are mixed in polluted regions of Europe and US because of lower anthropogenic precursor emissions which leads to a very low sensitivity of surface ozone to climate change (-0.5 ppb $°C^{-1}$ to 0.5 ppb $°C^{-1}$) (see Figure 6.SM.1 in Supplementary Material) and thus the ESMs can disagree on sign of changes for a given warming level. This heterogeneity in the results is also found in regional studies over North America (Gonzalez-Abraham et al., 2015; Val Martin et al., 2015; Schnell et al., 2016; He et al., 2018; Nolte et al., 2018; Rieder et al., 2018) or over Europe (Colette et al., 2015; Lacressonnière et al., 2016; Schnell et al., 2016; Fortems-Cheiney et al., 2017).

Overall, warmer climate is expected to reduce surface ozone in unpolluted regions as a result of greater water vapor abundance accelerating ozone chemical loss (*high confidence*). Over regions with high anthropogenic and/or natural ozone precursor emissions, there is prevailing evidence that climate change will introduce a surface O_3 penalty increasing with increasing warming levels (with a magnitude ranging regionally from 0.2 to 2 ppb $°C^{-1}$) (*medium confidence to high confidence*). Yet, there are uncertainties in processes affected in a warmer climate which can impact and modify future baseline and regional/local surface ozone levels. The response of surface ozone to future climate change through stratosphere-troposphere exchange, soil NO_x emissions and wildfires is positive (*medium confidence)*. In addition, there is *low confidence* in the magnitude of effect of climate change on surface ozone through biosphere interactions (natural CH_4, non-methane BVOC emissions and ozone deposition) and lighting NO_x emissions.

ACCEPTED VERSION SUBJECT TO FINAL EDITING

[START FIGURE 6.14 HERE]

Figure 6.14: Multi-model annual mean change in surface ozone (O_3) (ppb) concentrations at different warming levels. Changes are shown for a) 1.0°C, b) 1.5°C, c) 2.0°C and d) 2.5°C increase in global mean surface air temperature. CMIP6 models include GFDL-ESM4, GISS-E2-1-G, MRI-ESM2-0 and UKESM1-0-LL. For each model the change in surface O3 is calculated as difference between the ssp370SST and ssp370pdSST experiments in the year when the difference in the global mean surface air temperature between the experiments exceeds the temperature threshold. The difference is calculated as a 20-year mean in surface O_3 around the year when the temperature threshold in each model is exceeded. The multi-model change in global annual mean surface O_3 concentrations with ± 1 σ are shown within parenthesis. Uncertainty is represented using the simple approach: No overlay indicates regions with high model agreement, 3 out of 4 models agree on sign of change; diagonal lines indicate regions with low model agreement, where 3 out of 4 models agree on sign of change. For more information on the simple approach, please refer to the Cross-Chapter Box Atlas.1. Further details on data sources and processing are available in the chapter data table (Table 6.SM.1).

[END FIGURE 6.14 HERE]

6.5.2 Impact of climate change on particulate matter

Changes in concentration and chemistry of particulate matter (PM) in a changing climate depend in a complex manner on the response of the multiple interactions of changes in emissions, chemical processes, deposition and other factors (e.g., temperature, precipitation, circulation patterns). These changes are difficult to assess and, at the time of AR5, *no confidence level* was attached to the overall impact of climate change on $PM_{2.5}$ (Kirtman et al., 2013). Possible changes induced by climate change may concern both atmospheric concentration levels and chemical composition.

Higher temperatures increase the reaction rate of gaseous SO_2 to particulate sulphate conversion but also favour evaporation of particulate ammonium nitrate (Megaritis et al., 2013). Also, higher temperatures are expected to affect BVOC emissions (e.g. Pacifico et al., 2012) that would influence SOA concentrations, although this effect has been questioned by more recent evidence (Wang et al., 2018a; Zhao et al., 2019c). More generally, climate change will also affect dust concentration levels in the atmosphere (see Section 6.2.2.4) and the occurrence of forest fires, both very large sources of aerosols to the global troposphere (see Section 6.2.1.2.3).

Wet deposition constitutes the main sink for atmospheric PM (Allen et al., 2016b, 2019b; Xu and Lamarque, 2018). In particular, precipitation frequency has a higher effect on PM wet deposition than precipitation intensity (Hou et al., 2018). PM is also sensitive to wind speed and atmospheric stability conditions emphasising the importance of stagnation episodes and low planetary boundary layer heights for increasing PM atmospheric concentrations (Porter et al., 2015).

At the global scale, depending on its magnitude, the warming leads either to a small increase in global mean PM concentration levels (ca. 0.21 μg m^{-3} in 2100 for RCP8.5), mainly controlled by sulphate and organic aerosols or a small decrease (-0.06 μg m^{-3} for RCP2.6), Westervelt et al. (2016) and Xu and Lamarque (2018). On the other hand, Xu and Lamarque (2018) and Allen et al. (2016c, 2019b) found an increase of aerosol burden and PM surface concentration throughout the 21st Century, attributed to a decrease in wet removal flux despite the overall projected increase in global precipitation, on the ground of an expected shift of future precipitation towards more frequent heavy events. Based only on three models, the CMIP6 ensemble shows that for most land areas, there is low agreement between models on the sign of climate change on annual mean $PM_{2.5}$ (see Figure 6.SM.2 in Supplementary Material).

Due to the typical atmospheric lifetime of PM in the atmosphere, of the order of a few days, most studies dealing with the future PM concentration levels have a regional character and concern mainly Europe (Megaritis et al., 2013; Lacressonnière et al., 2016, 2017; Lemaire et al., 2016; Cholakian et al., 2019), the US (Penrod et al., 2014; Fiore et al., 2015; Gonzalez-Abraham et al., 2015; Shen et al., 2017; He et al., 2018;

ACCEPTED VERSION SUBJECT TO FINAL EDITING

Nolte et al., 2018), South and East Asia (Jiang et al., 2013; Nguyen et al., 2019) and India (Pommier et al., 2018). No studies are available for other areas of the world.

Changes in the chemical composition of PM as a result of future climate change can also be an important issue for the effects of PM on human health and the environment, but only a few sparse data are available in the literature on this and the results are, as yet, inconclusive (Im et al., 2012; Jiang et al., 2013; Megaritis et al., 2013; Gonzalez-Abraham et al., 2015; Gao et al., 2018; He et al., 2018; Cholakian et al., 2019).

Overall, there is *medium confidence* (*medium evidence, high agreement*) in a small effect, positive or negative, on PM global burden due to climate change.

6.5.3 Impact of climate change on extreme pollution

Extreme air pollution is identified as the concentration of an air pollutant that is above a given threshhold value (high concentration or a high percentile) as the sensitivity of peak values to meteorological conditions can be different from sensitivity of the median or mean (Porter et al., 2015). AR5 assessed with medium confidence that uniformly higher temperatures in polluted environments will trigger regional feedbacks in chemistry and local emissions that will increase peak ozone and PM pollution, but assessed low confidence in projecting changes in meteorological blocking associated with these extreme episodes.

Meteorological conditions, such as heat waves, temperature inversions, and atmospheric stagnation episodes favor air quality extremes and are influenced by changing climate (Fiore et al., 2015). The body of literature on the connection between climate change and extreme anthropogenic pollution episodes is essentially based on correlation and regression applied to observation reanalysis but the metrics and methodologies differ making quantitative comparisons difficult. Many emission processes in the natural systems are sensitive to temperature, and burst of emissions as a reponse to extreme weather, as in the case of wildfires in dry conditions (Bondur et al., 2020; Xie et al., 2020) can occur which would then add to the risk of extreme air pollution but are not sufficiently constrained to be quantitatively assessed.

Since AR5, published studies provide augmented evidence for the connections between extreme ozone and PM pollution events and high temperatures, especially long-lasting heat waves, whose frequency is increasing due to a warming climate (Lelieveld et al., 2014; Porter et al., 2015; Hou and Wu, 2016; Schnell and Prather, 2017; Zhang et al., 2017b) (Sun et al., 2017) Jing et al., 2017. However, relationship between air pollution and individual meteorological parameters is exaggerated because of covariation on synoptic time scales (Fiore et al., 2015). For example, heatwaves are often associated with clear-skies and stagnation, making clear attribution to specific meteorological variable complicated. In Asia, future changes in winter conditions have also been shown to favour more particulate pollution (Cai et al., 2017), and (Zou et al. (2017). The relationship between the occurrence of stagnation episodes and high concentrations of ozone and $PM_{2.5}$ has been shown to be regionally and metric dependant (Oswald et al., 2015; Sun et al., 2017; Kerr and Waugh, 2018; Schnell et al., 2018; Garrido-Perez et al., 2019).

The increase of heatwaves frequency, duration and intensity is extremely likely on all continents for different future warming levels (Chapter 11, see Table 11.2 and Section 11.3.5). However, there is low confidence in projected changes in storm tracks, jets, and blocking and thus their influence in extreme temperatures in mid-latitudes (See Section 11.3.1).

In conclusion, there is still *medium confidence* that climate driven changes in meterorological conditions, such as heatwaves or stagnations, will favour extreme air pollution episodes over highly polluted areas, however the relationship between these meteorological conditions and high concentrations of ozone and $PM_{2.5}$ have been shown to be regionally and metric dependant.

ACCEPTED VERSION SUBJECT TO FINAL EDITING

6.6 Air Quality and Climate response to SLCF mitigation

LLGHG emission reductions are typically motivated by climate mitigation policies, whereas SLCF reductions mostly result from air pollution control, climate policies (see FAQ6.2) as well as policies focusing on achieving UN Sustainable Development Goals (SDGs) (see Box 6.2). The management of several SLCFs (BC, CH_4, tropospheric O_3, and HFCs) is considered in the literature as a fast-response, near-term measure to curb climate change, while reduction of emissions of LLGHGs is an essential measure for mitigating long-term climate warming (Shindell et al., 2012a, 2017a; Shoemaker et al., 2013; Rogelj et al., 2014b; Lelieveld et al., 2019). Note that the term short-lived climate pollutants (SLCPs) refering only to warming SLCFs has been used within the policy arena. The SR 1.5 report states that limiting warming to 1.5°C to achieve Paris Agreement goals, implies net zero CO_2 emissions around 2050 and concurrent deep reductions in emissions of non-CO_2 forcers, particularly methane (Rogelj et al., 2018a). In addition, several SLCFs are key air pollutants or precursors of fine particulate matter (PM2.5) and tropospheric O3 and therefore subject to control driven by air quality targets.

Policies addressing either SLCFs or LLGHGs reduction, often prioritize mitigation of specific anthropogenic sources, such as energy production, industry, transportation, agriculture, waste management, and residential fuel use. Choice of the targetted sector and chosen measures will determine the ratios of emitted SLCFs and LLGHGs. These changes in emissions of co-emitted species will result in diverse responses driven by complex chemical and physical processes and resulting climate perturbations (see Section 6.5). The understanding of the co-benefits through sectoral mitigation efforts (as well as potential negative impacts) is essential to inform policy making.

The discussion of targeted SLCF policies and their role in climate change mitigation ranges from critical evaluation of the climate co-benefits (Smith and Mizrahi, 2013; Pierrehumbert, 2014; Rogelj et al., 2014b; Strefler et al., 2014; Allen et al., 2016a), modelling the potential of dedicated BC and CH_4 reductions in association with or without climate policy (Harmsen et al., 2019; Smith et al., 2020), individual or multi-component mitigation in relation to natural variability (Samset et al., 2020), warning about the risk of diversion of resources from LLGHGs, especially CO_2, policies (e.g., Shoemaker et al., 2013), to seeing it as an opportunity to strengthen commitment and accelerate action on LLGHGs (Victor et al., 2015; Aakre et al., 2018).

Over the last decade, research on air quality-climate interactions and feedbacks has brought new attention of policy communities on the possibility of win-win mitigation policies that could both improve air quality and mitigate climate change, possibly also reducing the cost of interventions (Anenberg et al., 2012; Shindell et al., 2012a, 2017a, Schmale et al., 2014a, 2014b; Sadiq et al., 2017; Fay et al., 2018; Harmsen et al., 2020). Haines et al. (2017a) and Shindell et al. (2017a) connect the measures to mitigate SLCFs with the achievements of some of the SDGs. Indeed, most studies on co-benefits to date focus on the impacts of climate mitigation strategies, in particular to meet Nationally Determined Contributions (NDCs) and/or specific global temperature targets, on air quality and human health (West et al., 2013; Zhang et al., 2016; Rao et al., 2016; Shindell et al., 2016, 2017a; Chang et al., 2017; Haines et al., 2017a; Xie et al., 2018; Li et al., 2018a; Markandya et al., 2018; Williams et al., 2018; Lelieveld et al., 2019). Such co-benefits of climate mitigation for air quality and human health can offset the costs of the climate measures (Saari et al., 2015; Li et al., 2018a). A growing number of studies analyse the co-benefits of current and planned air quality policies on LLGHGs and global and regional climate change impacts (Lund et al., 2014a; Akimoto et al., 2015; Lee et al., 2016; Maione et al., 2016; Peng et al., 2017).

This section assesses the effects of mitigating SLCFs, motivated by various objectives, discussing temperature response time, temperature and air quality attribution of SLCFs sources, and chosen mitigation approach. The effects of the measures, to contain the spread of COVID-19 in 2020, on air quality (AQ) and climate are discussed in cross-chapter Box 6.1 at the end of this section.

ACCEPTED VERSION SUBJECT TO FINAL EDITING

6.6.1 Implications of lifetime on temperature response time horizon

The effect over time on GSAT following a mitigation effort affecting emissions of LLGHGs or SLCFs depends on the lifetimes of the LLGHGs and SLCFs, their radiative efficiencies, how fast the emissions are reduced, how long reductions last (limited time or sustained reduction), and the inertia of the climate system itself. Mitigation of SLCFs are often implemented through new legislation or technology standards for the different emission sectors and components, implying that reductions are sustained over time.

It is often perceived that the full climatic response following mitigation of SLCFs will occur almost immediately. However the inertia of the climate system strongly modifies the short-term and long-term response. SLCFs with lifetimes shorter than the time scales for interhemisheric mixing (1-2 years) can cause a more spatially heterogeneous forcing than LLGHGs and thus different regional patterns of the climate response (see Sections 6.4.3). The temporal response in GSAT to a radiative forcing can be quantified using linear impulse response functions (see Cross Chapter box 7.1), (Olivié and Peters, 2013; Geoffroy et al., 2013; Smith et al., 2018). Figure 6.15 shows the GSAT response for sustained step reduction in emissions of idealised SLCFs with different lifetimes. The response is relative to a baseline with constant emissions, so effects of emissions before the step reduction is not shown. For SLCFs with lifetimes shorter than a few years, the concentrations quickly reach a new steady state and the response time is primarily governed by the thermal inertia and thus the time scales of the climate system. For compounds with lifetime on the order of 10 years (for example methane), there is about a 10-year delay in the response during the first decades, compared to compounds with lifetimes less than one year. However on longer time scales the response is determined solely by the time scales of the climate system itself. For CO_2 (dashed line in Figure 6.15) the temporal response is very different due to the long time scale for mixing into the deep ocean and therefore a substantial fraction of atmospheric CO_2 is only removed on millenium time scales. This means that for SLCFs including methane, the rate of emissions drives the long term stabilisation, as opposed to CO_2 where the long term effect is controlled by cumulative emissions (Allen et al., 2018b). Methods to compare rates of SLCF emission with cumulative CO_2 emissions are discussed in chapter 7, section 7.6.1.4.

[START FIGURE 6.15 HERE]

Figure 6.15: Global mean surface air temperature (GSAT) response to an abrupt reduction in emissions (at time t=0) of idealized climate forcing agents with different lifetimes. All emissions are cut to give a radiative forcing of -1 W m^{-2} at steady state (except for CO_2). In other words, if the yearly emissions are E0 before the reduction, they will have a fixed lower value $E_{year>0}$ = (E0 - ΔE) for all succeeding years. For comparison, the GSAT response to a sustained reduction in CO_2 emissions resulting in an RF of -1 W m^{-2} in year 100 is included (dashed line). The temperature response is calculated using an impulse response function (see Cross-Chapter Box 7.1) with a climate feedback parameter of -1.31 W m^{-2} °C^{-1}. Further details on data sources and processing are available in the chapter data table (Table 6.SM.1).

[END FIGURE 6.15 HERE]

As a consequence, in idealized ESM studies that assume an instantaneous removal of all anthropogenic or fossil fuel-related emissions, a rapid change in aerosol levels occurs leading to large increases in GSAT with the rate of warming lasting for several years. Similarly, the thermal inertia causes the pulse emissions (Figure 6.16) of SLCFs to have a significant effect on surface temperature even after 10 years.

In summary, for SLCFs with short lifetime (e.g. months), the response in surface temperature occurs strongly as soon as a sustained change in emissions is implemented and continues to grow for a few years, primarily due to thermal inertia in the climate system (*high confidence*). Near its maximum, the response slows down but will then take centuries to reach equilibrium (*high confidence*). For SLCF with longer lifetimes (e.g. a decade), a delay equivalent to their lifetimes comes in addition to the delay due the thermal inertia (*high confidence*).

ACCEPTED VERSION SUBJECT TO FINAL EDITING

6.6.2 Attribution of temperature and air pollution changes to emission sectors and regions

Assessment of the temperature response to source emission sectors is important for identifying priority mitigation measures and designing efficient mitigation strategies.

Temperature effects of emissions can be quantified for the historical contribution to the present temperature impact (see 6.4.2), for idealized one-year pulses of emissions or for continued (sustained) emissions at present levels and for changes during a specific time period, for emissions from future scenarios with various hypotheses, giving complementary information to feed mitigation strategies. AR5 assessed the net global temperature impact of source emission sectors from a one-year pulse (single year worth) of year 2008 emissions and found that the largest contributors to warming on 50-100 year time scales are the energy, industrial and on-road transportation sectors. Sectors that emit large amounts of methane (agriculture and waste management) and black carbon (residential biofuel) are important contributors to warming over short time horizons up to 20 years. Below, we discuss the effect on ERFs, temperature and air pollution of selected key sectors estimated to have large non-CO_2 forcing, including agriculture, residential and commercial, and transport (aviation, shipping, land transportation).

6.6.2.1 Agriculture

According to the SRCCL assessment (Jia et al., 2019), agriculture, forestry and other land use (AFOLU) is a significant net source of GHG emissions (*high confidence*), with more than half of these emissions attributed to non-CO_2 GHGs from agriculture. With respect to SLCFs, agricultural activities are major global sources of CH_4 and NH_3 (Section 6.2.1). The agriculture sector exerts strong near term warming due to large CH_4 emission that is slightly offset by a small cooling from secondary inorganic aerosols formed notably from the NH_3 emission (Heald and Geddes, 2016b; Lund et al., 2020). For present day emissions, agriculture is the 2nd largest contributor to warming on short time scales but with a small persisting effect on surface temperature (+0.0012±0.00028°C) after a pulse of current emissions (Lund et al., 2020 and Figure 6.16, see detailed description in 6.6.2.3.4). Aerosols produced from agricultural emissions, released after nitrogen fertilizer application and from animal husbandry, influence surface air quality and make an important contribution to surface $PM_{2.5}$ in many densely populated areas (Lelieveld et al., 2015b; Bauer et al., 2016) and Figure 6.17.

6.6.2.2 Residential and Commercial cooking, heating

The residential and commercial sector is associated with SLCF emissions of carbonaceous aerosol, CO and VOCs, SO_2 and NO_x and can be split by fuel type (biofuel or fossil fuel) where residential fossil fuel is also associated with CO_2 and CH_4 emissions (Section 6.2.1). The impacts of residential CO and VOC emissions are warming and SO_2 and NO_x are net cooling. However, the net sign of the global radiative effects of carbonaceous aerosols from the residential sector and solid fuel cookstove emissions (warming or cooling) is not well constrained based on evidence from recent global atmospheric modelling studies. Estimates of global residential sector direct aerosol-radiation effects range from -20 to +60 mW m^{-2} (Kodros et al., 2015) and -66 to +21 mW m^{-2} (Butt et al., 2016); and aerosol-cloud effects range from -20 to +10 mWm^{-2} (Kodros et al., 2015) and -52 to -16 mW m^{-2} (Butt et al., 2016). Uncertainties are due to assumptions about the aerosol emission masses, size distribution, aerosol optical properties and mixing states (see Section 6.3.5.3). Allowing BC to act as an INP in a global model leads to a much larger global forcing estimate from -275 to +154 mW m^{-2} with large uncertainty range due to uncertainty in the plausible range of maximum freezing efficiency of BC (Huang et al., 2018). The net sign of the impacts of carbonaceous aerosols from residential burning on radiative forcing and climate (warming or cooling) is ambiguous. The residential biofuel sector is a major concern for indoor air quality (Bonjour et al., 2013). In addition, several atmospheric modelling studies find that this sector is also important for outdoor air quality and even a dominant source of population-weighted outdoor $PM_{2.5}$ in India and China (Lelieveld et al., 2015b; Silva et al., 2016a; Spracklen et al., 2018, Figure 6.17; Reddington et al., 2019).

ACCEPTED VERSION SUBJECT TO FINAL EDITING

The net climate impact of the residential sector is warming in the near term of +0.0018±0.00084°C for fossil fuel use and +0.0014±0.0012°C for biofuel use, and +0.0017±0.00017°C and +0.0001±0.000079°C, respectively over a 100 years horizon, after a one year pulse of current emissions (Lund et al., 2020), due to the effects of BC, CH_4, CO and VOCs which adds to that of CO_2 but the uncertainty in the net sign of carbonaceous aerosol impacts challenges overall quantitative understanding of this sector and leads to *low confidence* in this assessment. Residential sector emissions are an important source of indoor and outdoor air pollution in Asia and globally (*high confidence*).

6.6.2.3 Transportation

6.6.2.3.1 Aviation

Aviation is associated with a range of SLCFs from emissions of NO_x, aerosol particles, and NO_x, alongside its emissions of water vapour and CO_2. The largest SLCF effects are those from the formation of persistent condensation trails (contrails) and NO_x emissions. Persistent contrails are ice crystal clouds, formed around aircraft soot particles (and water vapour from the engine), when the ambient cold and ice-supersaturated atmosphere, which can spread and form contrail cirrus clouds. The 'net NO_x' effect arises from the formation of tropospheric O_3, counterbalanced by the destruction of ambient CH_4 and associated cooling effects of reductions in stratospheric water vapour and background O_3. AR5 assessed the radiative forcing from persistent linear contrails to be +0.01 (+0.005 to +0.03) W m^{-2} for year 2011, with a medium confidence (Boucher et al., 2013). The combined linear contrail and their subsequent evolution to contrail cirrus radiative forcing from aviation was assessed to be +0.05 (+0.02 to +0.15) W m^{-2}, with a low confidence. An additional forcing of +0.003 W m^{-2} due to emissions of water vapour in the stratosphere by aviation was also reported (Boucher et al., 2013). The aviation sector was also estimated to lead to a net surface warming at 20 and 100 years horizons following a one year pulse emission. This net temperature response was determined by similar contributions from contrails and contrail cirrus and CO_2 over a 20 year time horizon, and dominated by CO_2 in a 100 years perspective (Figure 8.34 AR5: Myhre et al., 2013).

Our assessment builds on Lee et al. (2020a). Their study consists of an updated, comprehensive assessment of aviation climate forcing in terms of RF and ERF based on a large number of studies and the most recent air traffic and fuel use datasets available (for 2018), new calculations and the normalization of values from published modeling studies, and combining the resulting best estimates via a Monte-Carlo analysis. Lee et al. (2020a), reports a net aviation ERF for year 2018 emissions of +0.101 W m^{-2} (5–95% likelihood range of 0.055–0.145) with major contributions from contrail cirrus (0.057 W m^{-2}), CO_2 (0.034 W m^{-2}), and NO_x (0.017 W m^{-2}). Contrails and aviation-induced cirrus yields the largest individual positive ERF term, whose confidence level is similarly assessed to Lee et al. (2020a), as 'low' by Chapter 7 (Section 7.3.4.2) due to potential missing processes, followed by CO_2 and NO_x emissions (Lee et al., 2020a). The formation and emission of sulphate aerosol yields a negative (cooling) term. SLCF forcing terms contribute about 8 times more than CO_2 to the uncertainty in the aviation net ERF in 2018 (Lee et al., 2020a). The largest uncertainty in assessing aviation climate effects is on the interactions of BC and sulphate aerosols on cirrus and mixed phase clouds, for which no best estimates of the ERFs were provided (Lee et al., 2020a).

One of the most significant changes between AR5 and AR6 in terms of aviation SLCFs is the explicit calculation of a contrail cirrus ERF found to be 35% of the corresponding RF Bickel et al. (2020), which has confirmed studies indicating smaller efficacy of linear contrails Ponater et al. (2005) and Rap et al. (2010). The net-NO_x term is generally agreed to be a positive RF in the present day, although attribution in a non-linear chemical system is problematic (Grewe et al., 2019) but Skowron et al. (2021) point out that the sign of net NO_x term is dependent on background conditions and could be negative under certain future scenarios.

The best estimate ERFs from aviation (Lee et al., 2020b) have been used to calculate aviation-specific Absolute Global Temperature change Potential (AGTP) using the method described in (Lund et al., 2020) and subsequently compute the effect of one-year pulse of aviation emissions on global-mean surface temperature on a 10- and 100-year time horizon (Figure 6.16, see 6.6.2.3.4). The effect of contrail-cirrus is most important for the estimated net GSAT response after the first decade, followed by similar warming contributions from NO_x and CO_2 emissions. At a 20-year time horizon, the net contribution from aviation to

ACCEPTED VERSION SUBJECT TO FINAL EDITING

GSAT has switched from positive to a small negative effect (see 6.SM.4). This is due to the combination of rapidly decaying contrail-cirrus warming and the complex time variation of the net temperature response to NO_x emissions, which changes sign between 10 and 20 years due to the balance between the positive short-lived ozone forcing and negative forcing from changes in CH_4 and CH_4-induced changes in ozone and stratospheric water vapour. The net GSAT response to aviation emissions has previously been estimated to be positive on a 20-year time horizon (Chapter 8 AR5; Lund et al., 2017). This difference in net GSAT after 20 years in AR5 compared to AR6 results primarily from a shorter time scale of the climate response in the underlying AGTP calculations in Lund et al. (2020), which means the initial, strong impacts of the most short-lived SLFCs, including the warming by contrail-cirrus decay faster, in turn giving the net NO_x effect a relatively higher importance after 20 years. On longer time horizons, the net GSAT response switches back to positive, as CO_2 becomes the dominating warming contribution.

In summary, the net aviation ERF is assessed to be +0.1 W m^{-2} (±0.045) for the year 2018 (*low confidence)*. This confidence level is largely a result of the fact that the SLCF-related terms which counts for more than half (66% of the net aviation ERF) are the most uncertain terms. The climate response to SLCF-related aviation terms exhibits substantial spatiotemporal heterogeneity in characteristics (*high confidence*). Overall, cirrus and contrail cirrus warming, as well as NO_x-induced ozone increase, induce strong, but short-lived warming contributions to the GSAT response ten years after a one-year pulse of present-day aviation emissions (*medium confidence*), while CO_2 both gives a warming effect in the near term and dominates the long-term warming impact (*high-confidence*).

6.6.2.3.2 Shipping

Quantifying the effects of shipping on climate is particularly challenging because (i) the sulphate cooling impact is dominated by aerosol cloud interactions and (ii) ship emissions contain NO_x, SO_x and BC, which lead to mixed particles. Previous estimates of the sulphate radiative effects from present day shipping span the range -47 to -8 mW m^{-2} (direct radiative effect) and -600 to -38 mW m^{-2} (indirect radiative effects) (Balkanski et al., 2010; Eyring et al., 2010; Lauer et al., 2007; Lund et al., 2012). Partanen et al. (2013) reported a global mean ERF for year 2010 shipping aerosol emissions of -390 mW m^{-2}. The temperature change has been shown to be highly sensitive to the choice of aerosol-cloud parameterization (Lund et al., 2012). One year of global present-day shipping emissions, not considering impact of recent low sulphur fuel regulation (IMO, 2016), are estimated to cause net cooling in the near term (-0.0024±0.0025°C) and slight warming (+0.00033±0.00015°C) on a 100-year horizon (Lund et al., 2020).

Shipping is also of importance for air pollution in coastal areas along the major trade routes, especially in Europe and Asia (Corbett et al., 2007; Liu et al., 2016b, Figure 6.17; Jonson et al., 2020). Jonson et al. (2020) estimated that shipping is responsible for 10% or more of the controllable $PM_{2.5}$ concentrations and depositions of oxidised nitrogen and sulphur for many coastal countries. Widespread introduction of low-sulphur fuels in shipping from 2020 (IMO, 2016) will lead to improved air quality and reduction in premature mortality and morbidy (Sofiev et al., 2018).

In summary, one year of present-day global shipping emissions (i.e., without the implementation of the 2020 clean fuel standards) cause a net global cooling (-0.0024±0.0025°C) on 10-20 year time horizons (*high confidence*) but its magnitude is of *low confidence*.

6.6.2.3.3 Land transportation

The on-road and off-road transportation sectors have a net warming impact on climate over all time scales (Berntsen and Fuglestvedt, 2008; Fuglestvedt et al., 2008; Unger et al., 2010; Lund et al., 2020). One year pulse of present day emissions has a small net global temperature effect on short time-scales (+0.0011±0.0045°C), predominantly driven by CO_2 and BC warming offset by NO_x-induced cooling through CH_4 lifetime reductions (Lund et al., 2020).

The vehicle tailpipe emission profiles of diesel and gasoline are distinctly different. Diesel air pollutant emissions are dominated by BC and NO_x whereas petrol air pollutant emissions are dominated by CO and

ACCEPTED VERSION SUBJECT TO FINAL EDITING

NMVOCs, especially when distribution and upstream losses are considered. Thus, net radiative effect of the on-road vehicle fleets depends upon the share of different fuels used, in particular gasoline and diesel (Lund et al., 2014b; Huang et al., 2020b). The net SLCF for year 2010 emissions from the global diesel vehicle fleet have been estimated to be +28 mW m^{-2} (Lund et al., 2014b). Huang et al. (2020b) estimated net global radiative effects of SLCFs (including aerosols, O_3, and CH_4) from the gasoline and diesel vehicle fleets in year 2015 at +13.6 and +9.4 mW m^{-2}, respectively, with similar fractional contributions of SLCFs to the total global climate impact including CO_2 on the 20-year time scale (14-15%).

There is a consensus that on-road transportation sector emissions, including gasoline and diesel, are important anthropogenic contributors to elevated surface O_3 and $PM_{2.5}$ concentrations (Chambliss et al., 2014; Lelieveld et al., 2015b; Silva et al., 2016a, Figure 6.17; Anenberg et al., 2019). At a global-scale, land transportation has been estimated to be the dominant contributor to surface ozone concentrations in populated areas (Silva et al., 2016b) and O_3-induced vegetation damages (Section 6.4.4) (Unger et al., 2020). Furthermore, it is now well established that real world diesel NO_x emission rates are substantially higher, the so-called "excess NO_x", in all regional markets than in laboratory tests worsening air quality (Anenberg et al., 2017; Jonson et al., 2017; Chossière et al., 2018) and contributing to slightly larger warming on the scale of years and smaller warming at the decadal scale (Tanaka et al., 2018). Excess NO_x emissions from key global diesel markets are estimated at 4.6 Tg a^{-1} in 2015, with annual mean O_3 and $PM_{2.5}$ increases of 1 ppb and 1μg m^{-3} across large-regions of Europe, India and China (Anenberg et al., 2017).

In summary, the present-day global land-based transport pulse emissions cause a net global warming on all time scales (*high confidence*) and are detrimental to air quality (*high confidence*).

6.6.2.3.4 GSAT response to emission pulse of current emissions

Figure 6.16 presents the GSAT response to an idealized pulse of year 2014 emissions of individual SLCF and LLGHG. The GSAT response is calculated for 11 sectors and 10 regions accounting for best available knowledge and geographical dependence of the forcing efficacy of different SLCFs (Lund et al., 2020). Two time horizons are shown (10 and 100 year) to represent near- and long-term effects (and 20 year horizon is presented in Figure 6.SM.3). Other time horizon choices may affect the relative importance, and even sign in the case of the NO_x effect, of the temperature response from some of the SLCFs, or be more relevant for certain applications. GSAT response is calculated using the concept of AGTP (see Section 7.6.2.2). Further details of the AGTP emulator applied in Figure 6.16 are provided in (Lund et al., 2020) and 6.SM.4 (see also Section 7.6.1.2, cross-chapter Box 7.1 and 7.SM.7.2). As discussed in Lund et al. (2020), the AGTP framework is primarily designed to study relative importance of individual emissions and sources, but the absolute magnitude of temperature responses should be interpreted with care due to the linearity of the AGTP, which does not necessarily capture all the non-linear effects of SLCFs emissions on temperature.

Differences in the mix of emissions result in net effects on GSAT that vary substantially, in both magnitude and sign, between sectors and regions. SLCFs contribute substantially to the GSAT effects of sectors on short time horizons (10-20 years) but CO_2 dominates on longer time horizons (Figure 6.16). As the effect of the SLCFs decays rapidly over the first few decades after emission, the net long-term temperature effect is predominantly determined by CO_2. N_2O adds a small contribution to the long-term effect of agriculture. CO_2 emissions cause an important contribution to near-term warming that is not always fully acknowledged in discussions of LLGHGs and SLCFs (Lund et al., 2020).

The global sectoral ranking for near- and long-term global temperature effects is similar to the AR5 assessment despite regional reductions in aerosol precursor emissions between 2008 and 2014. This report has applied updated climate policy metrics for SLCFs and treatment of aerosol-cloud interactions for SO_2, BC and OC (Lund et al., 2020). By far the largest 10-year GSAT effects are from the energy production (fossil fuel mining and distribution), agriculture and waste management (*high confidence*). CH_4 is the dominant contributor in the energy production, agriculture, and waste management sectors. On the 10-year time horizon, other net warming sectors are residential fossil fuel and energy combustion (dominated by CO_2) and aviation and residential biofuel (dominated by SLCFs and cloud) (*medium confidence*). The total residential and commercial sector including biofuel and fossil fuels is the 4th most warming economic sector

ACCEPTED VERSION SUBJECT TO FINAL EDITING

globally on short time horizons of 10-20 years. The energy combustion sector has considerable cooling from high emissions of SO_2 that result in a relatively small net GSAT temperature effect on short time horizons, despite the high CO_2 emissions from this activity. On the 10-year time horizon, global emissions from industry and shipping cause a net cooling effect despite a considerable warming from CO_2 emissions. On the 100-year time horizon, the net effects of agriculture and waste management are small, while energy combustion is the largest individual contributor to warming due to its high CO_2 emissions. The second largest driver of long-term temperature change is industry, demonstrating the importance of non-CO_2 emissions for shaping relative weight over different time frames. Transport contributes a small net warming on the 10-year time horizon that increases by a factor of three on the 100-year time horizon. In contrast, aviation sector contribution to warming shrinks by about a factor of three between the 10- and 100-year time horizons. Results for the 20-year time horizon are provided in the Supplementary Material 6.SM.4. Compared to the 10-year time horizon, there are some changes in ranking, especially of sectors and regions with a strong SO_2 contribution, which decays substantially between 10 and 20 years. Aviation is the sector with most distinct difference between 10 and 20 year time horizons such that the net GSAT effect after 20 years becomes small but negative due to a switch in sign for the NO_x AGTP for this sector and these two time horizons related to the stronger short-lived ozone response than other sectors.

In terms of source regions, the largest contributions to net short-term warming are caused by emissions in Eastern Asia, Latin America and North America, followed by Africa, Eastern Europe and West-Central Asia and South East Asia (*medium confidence*). However, the relative contributions from individual species vary. In East Asia, North America, Europe and South Asia the effect of current emissions of cooling and warming SLCFs approximately balance in the near term and these regions cause comparable net warming effects on 10- and 100-year time horizons (Figure 6.16). In Latin America, Africa and South East Asia and Developing Pacific, CH_4 and BC emissions are currently high while emissions of CO_2 and cooling aerosols are low compared to other regions, resulting in a net warming effect after 10 years that is substantially higher than that of CO_2 alone.

Overall, the global sectors that contribute the largest warming on short time scales are the CH_4-dominated sources, i.e., energy production (fossil fuel mining and distribution), agriculture and waste management (*high confidence*). On short time scales, other net warming sectors are residential fossil fuel and energy combustion (dominated by CO_2) and aviation and residential biofuel (dominated by SLCFs) (*medium confidence*). On short-time scales, global emissions from industry and shipping cause a net cooling effect despite a considerable warming from CO_2 emissions (*high confidence*). On longer time horizons, the sectors that contribute the largest warming are energy combustion and industry due to the large CO_2 emissions (*high confidence*).

6.6.2.3.5 Source attribution of regional air pollution

The attribution of present-day surface $PM_{2.5}$ and O_3 concentrations to sectors and regions (Figure 6.17) is based on 2014 CMIP6 emissions used in the TM5-FASST model (Van Dingenen et al., 2018) that has been widely applied to analyse air quality in regional and global scenarios (Van Dingenen et al., 2009; Rao et al., 2016, 2017; Vandyck et al., 2018; e.g., Harmsen et al., 2020). Regions with largest year 2014 population-weighted annual average surface $PM_{2.5}$ concentrations are South Asia, East Asia, and Middle East. The dominant anthropogenic source of ambient $PM_{2.5}$ in South Asia is residential and commercial sector (biomass and coal fuel-based cooking and heating) with secondary contributions from energy and industry. In East Asia, the main anthropogenic sources of ambient $PM_{2.5}$ are energy, industry and residential sources. Natural sources, predominantly dust, are the most important $PM_{2.5}$ source in the Middle East, Africa and Eurasia, contributing about 40-70% of ambient annual average concentrations (Figure 6.17). Agriculture is an important contributor to ambient $PM_{2.5}$ in Europe and North America, while open biomass burning is a major contributor in South East Asia and Developing Pacific, North America as well as Latin America. These results are consistent with several global and regional studies, where contribution of emission sources to ambient $PM_{2.5}$ or premature mortality was estimated at different scales (Guttikunda et al., 2014; Lelieveld et al., 2015b; e.g., Amann et al., 2017; Qiao et al., 2018; Venkataraman et al., 2018; Wu et al., 2018).

Natural sources contribute more than 50% to surface ozone in all regions except South Asia and South East

ACCEPTED VERSION SUBJECT TO FINAL EDITING

Asia. South Asia, East Asia and the Middle East experience the highest surface ozone levels of all regions. For ozone, the anthropogenic sectoral attribution is more uniform across regions than for $PM_{2.5}$, except for South and Southeast Asia where land transportation plays are larger role and East Asia with most significant contribution from energy and industry. Land transportation and energy are the most important contributors to ozone across many of the regions, with smaller contributions from agriculture, biomass burning, waste management and industry. Open biomass burning is not a major contributor to surface ozone, except for Africa, Latin America and South East Asia where its contribution is estimated at about 5-10% of anthropogenic sources. Relative importance of natural and anthropogenic emission sources on surface ozone have been assessed in several studies (Uherek et al., 2010; Zare et al., 2014; Mertens et al., 2020; Unger et al., 2020) and the results are comparable with the estimates of the TM5-FASST used here.

Residential and commercial cooking and heating is among the most important anthropogenic sources of ambient $PM_{2.5}$, except Middle East and Asia-Pacific Developed (*high confidence*) and agriculture is the dominant source in Europe and North America (*medium confidence*). Energy and industry are important $PM_{2.5}$ contributors in most regions, except Africa (*high confidence*). Energy and land transportation are the major anthropogenic sources of ozone across many world regions (*medium to high confidence*).

[START FIGURE 6.16 HERE]

Figure 6.16: Global-mean surface temperature response 10 and 100 years following one year of present-day (year 2014) emissions. The temperature response is broken down by individual species and shown for total anthropogenic emissions (top), sectoral emissions (left) and regional emissions (right). Sectors and regions are sorted by (high-to-low) net temperature effect on the 10-year time scale. Error bars in the top panel show uncertainty (5-95% interval) in net temperature effect due to uncertainty in radiative forcing only (calculated using a Monte Carlo approach and best estimate uncertainties from the literature - see Lund et al. (Lund et al., 2020) for details). CO2 emissions are excluded from open biomass burning and residential biofuel use due to their unavailability in CEDS and uncertainties around non-sustainable emission fraction. Emissions for 2014 originate from the Community Emissions Data System (CEDS) (Hoesly et al., 2018), except for HFCs which are from Purohit et al. (2020), open biomass burning from van Marle et al. (2017), and aviation H2O which is from Lee et al.(2020b). The split of fossil fuel production and distribution and combustion for energy and residential and commercial fuel use into fossil fuel and biofuel components obtained from the GAINS model (ECLIPSE version 6b dataset). Open biomass burning emissions are not included for the regions. Emission are aggregated into fossil fuel production and distribution (coal mining, oil and gas production, upstream gas flaring, gas distribution networks), agriculture (livestock and crop production), fossil fuel combustion for energy (power plants), industry (combustion and production processes, solvent use loses from production and end use), residential and commercial (fossil fuel use for cooking and heating as well is HFCs leakage from A/C and refrigeration), waste management (solid waste, incl. landfills and open trash burning, residential and industrial waste water), land transportation (road and off-road vehicles, and HFC leakage from A/C and refrigeration equipment), residential and commercial (biofuels use for cooking and heating), open biomass burning (forest, grassland, savannah fires, and agricultural waste burning), shipping (incl. international shipping), and aviation (incl. international aviation). Further details on data sources and processing are available in the chapter data table (Table 6.SM.1).

[END FIGURE 6.16 HERE]

[START FIGURE 6.17 HERE]

Figure 6.17: Emission source-sector attribution of regional population weighted mean concentrations of $PM_{2.5}$ and ozone for present day emissions (year 2014). Regional concentrations and source apportionment calculated with the TM5-FASST model (Van Dingenen et al., 2018) for the 2014 emission data from the Community Emissions Data System (CEDS) (Hoesly et al., 2018) and van Marle et al.(2017) for open biomass burning. $PM_{2.5}$ dust and seasalt are monthly mean climatological average over 2010-2018 from CAMS global reanalysis (EAC4) (Inness et al., 2019), generated using Copernicus Climate Change Service information [January 2020]. Anthropogenic sectors are similar to those in Figures 6.3 and 6.16 except grouping of fossil fuel production, distribution and combustion for energy under “Energy” and

ACCEPTED VERSION SUBJECT TO FINAL EDITING

grouping of use of fossil fuel and biofuel use for cooking and heating under "Residential and Commercial". Further details on data sources and processing are available in the chapter data table (Table 6.SM.1).

[END FIGURE 6.17 HERE]

6.6.3 Past and current SLCF reduction policies and future mitigation opportunities

Several SLCF emission reduction strategies have been explored in the literature or are already pursued as part of the environmental and development policies, including air quality, waste management, energy poverty, and climate change. The effects of various policies and strategies have been addressed in a limited number of modelling studies having different objectives and range from assessment of specific policies and their regional effects (UNEP and WMO, 2011; Shindell et al., 2012a, 2017a, AMAP, 2015a, 2015b; Haines et al., 2017a; UNEP and CCAC, 2018; Harmsen et al., 2019; UNEP, 2019) to large-scale global scenario studies with varying level of SLCF control (Sand et al., 2016; e.g., Rogelj et al., 2018b; Shindell and Smith, 2019). They could be grouped into:

- Projections of future SLCF emissions compatible with the climate mitigation trajectories investigated in the climate model intercomparison projects (respective RCP or SSP scenarios): In such scenarios, when climate change mitigation is considered, it is associated with strong decrease of CO_2 emissions, largely relying on fossil fuel use reduction, the co-emitted SLCFs from combustion and methane from production and distribution of fossil fuels will be reduced proportionally. Depending on carbon price and climate mitigation target, further reduction of methane from waste and agriculture will also be part of such scenarios. Limitations of RCP scenarios, where continuous strengthening of air quality legislation was assumed and therefore lack of futures where global and regional air quality deteriorates, for the analysis of air quality and potential for mitigation of SLCFs have been discussed in literature (e.g., Amann et al., 2013; Von Schneidemesser et al., 2015). SSP scenarios consider various levels of air pollution control, in accordance with their socioeconomic narrative, and thus cover a wider span of SLCF trajectories (Section 6.7). The economical cost of implementation of these scenarios and their co-benefits on air quality and SDGs are assessed in WGIII (Chapter 3) reports.

- Projections of SLCF emissions assuming strong reduction of all air pollutants in the absence of climate mitigation (e.g., the SSP3-LowSLCF scenario); the latter is an idealized simulation of a very ambitious air quality policy where maximum technical potential of existing end-of-pipe technologies is explored in the SSP3-7.0 scenario. Methane reduction can also be part of such sensitivity analysis although methane reductions have not historically been motivated by air pollution concerns.

- Projection of emissions targeting air quality or other development priorities: Anthropogenic emissions source-structure and the level of exposure to pollution and subsequent effects vary significantly from one region to another (section 6.3.2). Therefore, the air quality policy, regional climate impact concerns as well as development priorities, and consequently the level of mitigation of particular SLCF species, will differ regionally and source-wise with respect to the emissions sources, influence of intercontinental transport of pollution, and spatial physical heterogeneities (Lund et al., 2014b; AMAP, 2015a; Sand et al., 2016; Turnock et al., 2016; Sofiev et al., 2018; WMO, 2018). This is also the case at a finer local and regional scale where priorities and scope for SLCF mitigation will differ (e.g., Amann et al., 2017; UNEP, 2019).

- Projections exploring mitigation potential for a particular source or SLCF: These studies focus on the assessment of SLCF reduction potential that can be realised with either existing and proven technologies or extend the scope to include transformational changes needed to achieve further reduction (UNEP and WMO, 2011; Stohl et al., 2015; Velders et al., 2015; Purohit and Höglund-Isaksson, 2017; e.g., Gómez-Sanabria et al., 2018; UNEP, 2019; Höglund-Isaksson et al., 2020; Purohit et al., 2020) – several of these studies are subsequently used for parameterization of the

ACCEPTED VERSION SUBJECT TO FINAL EDITING

models used to develop emission scenarios (e.g., IAM models used in the IPCC process).

In the following subsections, we assess the SLCF mitigation and its effects as identified in regional and global studies evaluating past and current air quality and other SLCF regulations (Sections 6.6.3.1, 6.6.3.2, 6.6.3.3). Development policies, independent from the CMIP6 assessment framework, including peer-reviewed studies and initiatives like UNEP, analysing win-win climate, air quality and SDG motivated strategies are discussed in Section 6.6.3.4. Note that sensitivity studies where impacts of complete removal of particular species are analysed (e.g., Samset et al., 2018) are used sparingly in this assessment. While such analysis can be useful for assessing the effect of a zero-emission commitment (see Chapter 4.7.1.1), they do not correspond to a realistic SLCF mitigation strategy with plausible pace of implementation and removal of co-emitted species (Shindell and Smith, 2019). Discussion of climate and air quality implications of SLCF reductions in SSP scenarios is provided in section 6.7.

6.6.3.1 Climate response to past AQ policies

Air quality policies emerged several decades ago focusing on emission mitigation first driven by local then by regional scale air quality and ecosystem damage concerns, that is, health impacts and acidification and eutrophication. They have made it possible to reduce or limit pollution exposure in many megacities or highly populated regions e.g. in Los Angeles, Mexico City, Houston in North America (Parrish et al., 2011), Santiago in Chile (Gallardo et al., 2018), São Paulo in Brazil (Andrade et al., 2017), Europe (Reis et al., 2012; Crippa et al., 2016; Serrano et al., 2019), and over East Asia during the last decade (Silver et al., 2018; Zheng et al., 2018b). However, very few studies have quantified the impact of these policies on climate. AR5 concluded that air quality control will have consequences on climate including strong regional variability, however, no estimates of impacts of specific air quality policy were available. Since AR5, few studies have provided estimates of climate relevant indicators affected by significant air pollutant burden changes due to air quality policy in selected regions. Turnock et al. (2016) estimated that the strong decrease in NO_x, SO_2 and $PM_{2.5}$ emissions in Europe, induced by air quality policies resulting in implementation of abatement measures since the 1970s, have caused a surface warming of +0.45±0.11°C and increase of precipitation +13±0.8 mm yr^{-1} over Europe, compared to the scenario without such policies. While the temperature increase is likely overestimated since the impact of increase in ammonium nitrate was not considered in this study, the simulated European all-sky TOA radiative effect of the European air pollutant mitigation over the period 1970-2009 is 2.5 times the change in global mean CO_2 radiative forcing over the same period (Myhre et al., 2013b). Other studies found that the recent measures to reduce pollution over China have induced a decrease of aerosols and increase of ozone over east China (Li et al., 2019a, 2020a) resulting in an overall warming effect mainly due to the dominant effect of sulphate reductions in the period 2012-2017 (Dang and Liao, 2019).

6.6.3.2 Recently decided SLCF relevant global legislation

International shipping emissions regulation: from January 2020, a new global standard, proposed by the International Maritime Organisation, limits the sulphur content in marine fuels to 0.5% against previous 3.5% (IMO, 2016). This legislation is considered in the SSP5 and SSP2-4.5 and with a delay of few years in SSP3-LowSLCF, SSP1-1.9, and SSP1-2.6, and in other SSP emission scenarios achieved by mid 21st century. This global measure aims to reduce the formation of sulphate (and consequently $PM_{2.5}$) and largely reduce the health exposure to $PM_{2.5}$ especially over India, East China and coastal areas of Africa and the Middle East (Sofiev et al., 2018). Sofiev et al. (2018) used a high spatial and temporal resolution chemistry-climate model and estimated a net total ERF of +71 mW m^{-2} associated with this measure and due to lower direct aerosol cooling (-3.9 mW m^{-2}) and lower cloud albedo (-67 mW m^{-2}). This value, which correponds to 80% decrease of the cooling effect of shipping induced by about 8 Tg of SO_2 of avoided emissions, is consistent with older estimates which considered similar reduction of emitted sulphur. However, there is considerable uncertainty in the indirect forcing since small changes in aerosols, acting as CCNs in clean environment, can have disproportionally large effects on the radiative balance. Since sulphate is by far the largest component of the radiative forcing (Fuglestvedt et al., 2008) and of surface temperature effect (Figure

ACCEPTED VERSION SUBJECT TO FINAL EDITING

6.16) due to ship emissions over short time scale, limiting the co-emitted SLCFs can not offset the warming by sulphur reductions. The reduction of sulphur emission from shipping is assessed to lead to a slight warming mainly due to aerosol-cloud interactions (*medium evidence, medium agreement*).

Kigali Amendment (UNEP, 2016): With the adoption of the Kigali Amendment to the Montreal Protocol (UN, 1987) in 2016, parties agreed to the phasedown of HFCs, substances that are not ozone depleting but are climate forcing agents (Papanastasiou et al., 2018). Baseline scenarios, in the absence of controls or only pre-Kigali national legislation, projected increased use and emissions of HFCs. All recent baseline projections are significantly higher than those used in the Representative Concentration Pathways (RCP) scenarios ((Meinshausen et al., 2011) and Figure 6.18). There is *low confidence* that the high baseline (assuming absence of controls, lack of technical progress, and high growth) as developed in Velders et al. (2009), resulting in additional warming of about 0.5°C by 2100 (Xu et al., 2013; WMO, 2018), is plausible. Evolution of HFC emissions along the baselines consistent with Velders et al. (2009) and Velders et al (2015) would result in a global average warming, due to HFCs, relative to 2000, of about 0.1-0.12°C by 2050 and 0.35–0.5°C and 0.28–0.44°C by 2100, respectively (Xu et al., 2013). The baseline implementation considered in SSP5-8.5 (see Section 6.7.1.1) is comparable to the lower bound of projections by Velders et al. (2015) (Figure 6.18) and several other studies (Gschrey et al., 2011; Purohit and Höglund-Isaksson, 2017; EPA, 2019; Purohit et al., 2020) and result in additional warming of 0.15-0.3°C by 2100 (Figure 6.22) (*medium confidence*).

Efficient implementation of the Kigali Amendment and national and regional regulations has been projected to reduce global average warming in 2050 by 0.05°–0.07°C (Klimont et al., 2017c; WMO, 2018) and by 0.2–0.4°C in 2100 compared with the baseline (see Figure 2.20 of WMO, 2018). Analysis of SSP scenarios based on an emulator (Section 6.7.3) shows a comparable mitigation potential of about 0.02–0.07°C in 2050 and about 0.1–0.3°C in 2100 (Figure 6.22, SSP5-8.5 versus SSP1-2.6). Furthermore, the energy efficiency improvements of cooling equipment alongside the transition to low global warming potential alternative refrigerants for refrigeration and air-conditioning equipment could potentially increase the climate benefits from the HFC phasedown under the Kigali Amendment (Shah et al., 2015; Höglund-Isaksson et al., 2017; Purohit and Höglund-Isaksson, 2017; WMO, 2018). Purohit et al (2020) estimated that depending on the expected rate of technological development, improving energy efficiency of stationary cooling technologies, and compliance with Kigali Amendment could bring future global electricity-savings of more than 20% of expected world's electricity consumption beyond 2050 or cumulative reduction of about 75-275 Gt CO_2eq over the period 2018-2100 (*medium confidence*). This could potentially double the climate benefits of the HFC phase-down of the Kigali Amendment as well as result in small air quality improvements due to reduced air pollutant emissions from power sector, i.e., 8-16% reduction of $PM_{2.5}$, SO_2, NO_x (Purohit et al., 2020).

6.6.3.3 Assessment of SLCF mitigation strategies and opportunities

There is a consensus in the literature that mitigation of SLCF emissions plays a central role in simultaneous mitigation of climate change, air quality, and other development goals including SDG targets (UNEP and WMO, 2011; Shindell et al., 2012b, 2017a, Rogelj et al., 2014b, 2018b; AMAP, 2015a; Haines et al., 2017a; Klimont et al., 2017c; UNEP and CCAC, 2018; McCollum et al., 2018; Rafaj et al., 2018; UNEP, 2019). There is less agreement in the literature with respect to the actual mitigation potential (or its potential rate of implementation), necessary policies to trigger successful implementation, and resulting climate impacts. Most studies agree that climate policies, especially those aiming to keep warming below 1.5-2°C, trigger large SLCF mitigation co-benefits, (e.g., Rogelj et al., 2014b, 2018b), however, discussion of practical implementation of respective policies and SDGs has only started (Haines et al., 2017a). Note that mitigation scenarios outside of the SSP framework are assessed here while those within the SSPs are assessed in Section 6.7.3.

Focusing on air quality, specifically addressing aerosol SLCFs, by introducing best available technology reducing $PM_{2.5}$, SO_2, NO_x in most Asian countries within the 2030-2050 time frame (a strategy that has indeed shown reduction in $PM_{2.5}$ exposure in China) comes, in many regions, short of national regulatory

ACCEPTED VERSION SUBJECT TO FINAL EDITING

$PM_{2.5}$ concentration standards (often set at 35 μg m^{-3} for annual mean) (UNEP, 2019). Similarly, global studies (Rafaj et al., 2018; Amann et al., 2020) shows that strengthening current air quality policies, addressing primarily aerosols and their precursors, will not allow to achieve WHO air quality guidelines (annual average concentration of $PM_{2.5}$ below 10 μg m^{-3}) in many regions.

A multi-model study (four ESMs and six CTMs) found a consistent response to removal of SO_2 emissions that resulted in a global mean surface temperature increase of 0.69°C (0.4-0.84°C), while mixed results for a global BC-focused deep SLCF reduction, excluding SO_2 and CH_4 mitigation which remain like in the baseline (see ECLIPSE in Figure 6.18), concluding about -0.022°C temperature reduction for the decade 2041-2050; this is derived from their estimate that mitigation of the non-CH_4 species contributed only about 10% of the global temperature reduction for the strategy where also CH_4 mitigation was included (-0.22°C ±0.07°C) (Stohl et al., 2015). These results are consistent with studies analysing similar strategies using emulators (Smith and Mizrahi, 2013; e.g., Rogelj et al., 2014b). Stohl et al. (2015) analysed also the impact of BC-focused mitigation on air quality, estimating large scale regional reduction in $PM_{2.5}$ mean concentration from about 2% in Europe to 20% over India for the decade 2041-2050.

Local response to global reduction can be higher than the global temperature response in particular for regions subjected to rapid changes. Hence, mitigation of rapid warming in the Arctic has been subject to increasing number of studies (Sand et al., 2013a, 2016; Jiao et al., 2014; AMAP, 2015b, 2015a; Mahmood et al., 2016; Christensen et al., 2019). Considering maximum technical mitigation potential for CH_4 globally and an idealized strategy reducing key global anthropogenic sources of BC (about 80% reduction by 2030 and sustained thereafter) and precursors of O_3 was estimated to jointly bring a reduction of Arctic warming, averaged over the 2041-2050 period, between 0.2 and 0.6°C (AMAP, 2015a; Sand et al., 2016). Stohl et al. (2015) have estimated that a global SLCF mitigation strategy (excluding further reduction of SO_2) would lead to about twice as high temperature reduction (-0.44°C (-0.39 to -0.49°C)) in the Arctic than the global response to such mitigation.

While there is robust evidence that air-quality policies, resulting in reduction of aerosols and ozone, can be beneficial for human health but can lead to 'disbenefits' for near-term climate change, such trade-offs in response to climate mitigation policies is less certain (Shindell and Smith, 2019). Recent studies show that very ambitious but plausible gradual phasing out of fossil-fuels in 1.5°C compatible pathways with little or no overshoot, lead to a near-term future warming of less than 0.1°C, when considering associated emission reduction of both warming and cooling species. This suggests that there may not be a strong conflict, at least at the global scale, between climate and air-quality benefits in the case of a worldwide transition to clean energy (Shindell and Smith, 2019; Smith et al., 2019). However, at the regional scale, the changes in spatially variable emission and abundance changes might result in different responses including implications for precipitation, monsoon, etc. (Chapter 8), especially over South Asia (e.g., Wilcox et al., 2020).

Decarbonization of energy supply and end use sectors is among key pillars of any ambitious climate mitigation strategy and it would result in improved air quality owing to associated reduction of co-emitted SLCF emissions (McCollum et al., 2013; Rogelj et al., 2014b; e.g., Braspenning Radu et al., 2016; Rao et al., 2016; Stechow et al., 2016; Lelieveld et al., 2019; Shindell and Smith, 2019). Regional studies (Lee et al., 2016; Shindell et al., 2016; Chen et al., 2018; Li et al., 2018b), where significant CO_2 reductions were assumed for 2030 and 2050, show consistently reduction of $PM_{2.5}$ and ozone concentrations resulting in important health benefits. However, these improvements are not sufficient to bring $PM_{2.5}$ levels in agreement with the WHO air quality guideline in several regions. Amann et al. (2020) and UNEP (2019) highlight that only combination of strong air quality, development, and climate policies, including societal transformations, could pave the way towards achievement of such target at a regional and global level.

At a global level, Rao et al. (2016) showed that climate policies, compatible with Copenhagen pledges and a long-term CO_2 target of 450 ppm, result in important air quality benefits, reducing the share of global population exposed to $PM_{2.5}$ levels above the WHO Tier 1 standard (35 μg m^{-3}) in 2030 from 21% to 5%. The impacts are similar to a strong air quality policy but still leaving large parts of population, especially in Asia and Africa, exposed to levels well above WHO air quality guideline level of 10 μg m^{-3}. The latter can be partly alleviated by combining such climate policy with strong air quality policy. Shindell et al. (2018)

ACCEPTED VERSION SUBJECT TO FINAL EDITING

analysed more ambitious climate mitigation scenarios than Rao et al. (2016) and highlighted the opportunities to improve air quality and avert societal effect associated with warmer climate by accelerated decarbonization strategies. Most climate mitigation strategies compatible with limiting global warming to well below 2°C, rely on future negative CO_2 emissions postponing immediate reduction. Alternatively, a faster decarbonization could allow to achieve a 2°C goal without negative CO_2 emissions and with currently known and effectively applied emission control technologies would have also immediate and significant air quality benefits, reducing premature deaths worldwide (Shindell et al., 2018). For a 2°C compatible pathway, Vandyck et al. (2018) estimated 5% and 15% reduction in premature mortality due to $PM_{2.5}$ in 2030 and 2050, respectively, compared to reference scenarios.

There is robust evidence that reducing atmospheric CH_4 will benefit climate and improve air quality through near-surface O_3 reduction (Fiore et al., 2015; Shindell et al., 2017b) and wide agreement that strategies reducing CH_4 offer larger (and less uncertain) climate benefits than policies addressing BC (Smith and Mizrahi, 2013; Rogelj et al., 2014b, 2018b; Stohl et al., 2015; e.g., Christensen et al., 2019; Shindell and Smith, 2019). SR1.5 (Rogelj et al., 2018b) highlighted the importance of CH_4 mitigation in limiting warming to 1.5 ºC in addition to net zero CO_2 emission by 2050. Implementation of the identified maximum technical mitigation (MTFR) potential for CH_4 globally, estimated at nearly 50% reduction (or 205 Tg CH_4 in 2050) of anthropogenic emissions from the baseline, would lead to a reduction in warming, calculated as the differences between the baseline and MTFR scenario, for the 2036-2050 period of about 0.20±0.02°C globally (AMAP, 2015b). Plausible levels of methane mitigation, achieved with proven technologies, can increase the feasibility of achieving the Paris Agreement goal through slightly slowing down the pace of CO_2 reductions (but not changing the final CO_2 reduction goal) while this benefit is enhanced by the indirect effects of methane mitigation on ozone levels (Collins et al., 2018). Adressing methane mitigation appears even more important in view of recently observed growth in atmospheric concentrations that is linked to increasing anthropogenic emissions (see Section 5.1.1.).

Neither ambitious climate change policy nor air quality abatement policy can automatically yield co-benefits without integrated policies aimed at co-beneficial solutions (Zusman et al., 2013; Schmale et al., 2014b; Melamed et al., 2016), particularly in the energy generation and transport sectors (Rao et al., 2013; Thompson et al., 2016; Shindell et al., 2018; Vandyck et al., 2018). Integrated policies are necessary to yield multiple benefits of mitigating climate change, improving air quality, protecting human health, and achieving several Sustainable Development Goals.

[START BOX 6.2 HERE]

BOX 6.2: SLCF Mitigation and Sustainable Development Goals (SDG) opportunities

Striving to achieve air quality and climate targets will bring significant SLCFs reductions. These reductions contribute first and foremost to attainment of SDGs targeting improved human health and sustainable cities (SDG 3 and 11), specifically related to PM exposure (goals 3.9 and 11.6) (Lelieveld, 2017; Amann et al., 2020) but also access to affordable and clean energy, responsible consumption and production, climate, as well as reducing nutrient losses and consequently protect biodiversity (SDG 7, 12, 13, 14, and 15) (UNEP, 2019; Amann et al., 2020). Furthermore, declining SLCF emissions will result in reduced crop losses (SDG 2; zero hunger) due to decrease of ozone exposure (Feng and Kobayashi, 2009; Ainsworth et al., 2012; Emberson et al., 2018).

However, the design of suitable policies addressing these SDGs can be difficult because of the complexity linking emissions to impacts on human health, ecosystem, equity, infrastructure, and costs. Beyond the fact that several species are co-emitted, interlinkage between species, for example through atmospheric chemistry, can weaken the benefit of emissions reduction efforts. An illustration lies in the recent (2013-2017) reduction of aerosols over China (Silver et al., 2018; Zheng et al., 2018b) resulting from the strategy to improve air quality ("Clean Air Action"), has successfully reduced the level of $PM_{2.5}$ but has led to a concurrent increase in surface ozone, partly due to declining heterogeneous interactions of O_3 precursors with aerosols (Li et al., 2019a; Yu et al., 2019). This side effect on ozone has been addressed since then by

ACCEPTED VERSION SUBJECT TO FINAL EDITING

amending the legislation to target NMVOC sources, especially solvent use. Complex interactions between anthropogenic and biogenic vapours are also at play and reduction of certain SLCFs could possibly promote new particle formation from organic vapours (e.g., Lehtipalo et al., 2018). Finally, a recent example of this complexity is the mixed effects on ozone pollution induced by NO_x decrease during the COVID-19 pandemic (see Cross-Chapter Box 6.1). Thus, the climate and air pollution effects of policies depend strongly on choice of regulated compounds and the degree of reduction. Such policies have to be informed by strong science support, including for example multi-model analyses, e.g., HTAP (UNECE, 2010), AMAP (AMAP, 2015a, 2015b), based on global and regional CCMs, essential to capture the complexity and inform the policy development process.

In addition, pursuing SDG objectives, apparently decoupled from air pollution, such as improved waste management, access to clean energy, or improved agricultural practices, would also stimulate and lead to mitigation of SLCFs (Box 6.2, Figure 1). Amann et al. (2020) shows that a global strategy to achieve the WHO air quality guidelines, cannot only rely on air pollution control but also on a combination of SDG aligned policies. Such actions would include energy efficiency improvements, increased use of renewables, reduction of CH_4 from waste management and agriculture, and CO_2 and CH_4 due to lower fossil fuel consumption, resulting in climate co-benefits. Consideration of SDGs including local air quality co-benefits, creates an opportunity to support and gain acceptance for ambitious climate mitigation (Jakob and Steckel, 2016; Stechow et al., 2016; Vandyck et al., 2018). Such near-term policies targeting SDGs and air quality would enable longer term transformations necessary to achieve climate goals (Chapter 17, WGIII).

[END BOX 6.2 HERE]

In summary, there is *high confidence* that effective decarbonization strategies could lead to air quality improvements but are not sufficient to achieve, in the near term, air quality WHO guideline values set for fine particulate matter), especially in parts of Asia and in some highly polluted regions. Additional policies (e.g., access to clean energy, waste management) envisaged to attain Sustainable Development Goals (SDG) bring complementary SLCF reduction (*high confidence)*. Sustained methane mitigation, wherever it occurs, stands out as an option that combines near and long-term gains on surface temperature (*high confidence)* and leads to air pollution benefit by reducing globally the surface ozone level (*high confidence).*

[START CROSS-CHAPTER BOX 6.1 HERE]

Cross-Chapter Box 6.1: Implications of COVID-19 restrictions for emissions, air quality and climate

Coordinators:
Astrid Kiendler-Scharr (Germany/Austria), John C. Fyfe (Canada)

Contributors:
Josep G. Canadell (Australia), Sergio Henrique Faria (Spain/Brazil), Piers Forster (UK), Sandro Fuzzi (Italy), Nathan P. Gillett (Canada), Christopher Jones (UK), Zbigniew Klimont (Austria/Poland), Svitlana Krakovska (Ukraine), Prabir Patra (Japan/India), Joeri Rogelj (Austria/Belgium), Bjørn Samset (Norway), Sophie Szopa (France), Izuru Takayabu (Japan), Hua Zhang (China)

In response to the outbreak of COVID-19 (officially the severe acute respiratory syndrome–coronavirus 2 or SARS-CoV-2), which was declared a pandemic on March 11 2020 by the World Health Organization (WHO), regulations were imposed by many countries to contain the spread of COVID-19. Restrictions were implemented on the movement of people, such as closing borders or requiring the majority of population to stay at home, for periods of several months. This Cross Chapter Box assess the influence of the COVID-19 containment on short-lived climate forcers (SLCFs) and long-lived greenhouse gases (LLGHGs) and related implications for the climate. Note that this assessment was developed late in the AR6 WGI process and is based on the available emerging literature.

ACCEPTED VERSION SUBJECT TO FINAL EDITING

Emissions

Global fossil CO_2 emissions are estimated to have declined by 7% (*medium confidence*) in 2020 compared to 2019 emissions, with estimates ranging from 5.8% to 13.0% based on various combinations of data on energy production and consumption, economic activity and proxy activity data for emissions and economic activity and proxy activity data for emissions and their drivers (Forster et al., 2020; Friedlingstein et al., 2020; Le Quéré et al., 2020; Liu et al., 2020). However, the concentration of atmospheric CO_2 continued to grow in 2020 compared to previous years (Dlugokencky and Tans, 2021). Given the large natural inter-annual variability of CO_2 (Section 5.2.1), and the small expected impact of emissions in the CO_2 growth rate, there were no observed changes in CO2 concentration that could be attributed to COVID-19 containment (Chevallier et al., 2020; Tohjima et al., 2020).

Global daily CO_2 emissions from fossil fuel sources had a maximum decline of 17% in early April, compared with the mean 2019 levels, and coinciding with the global peak pandemic lockdown (Le Quéré et al., 2020). The reductions in CO_2 emissions in 2020 were dominated by the drop in emissions from surface transport followed, in order of absolute emission reductions, by industry, power, and aviation (Le Quéré et al., 2020; Liu et al., 2020). Residential emissions showed little change (Liu et al., 2020) or rose slightly (Forster et al., 2020; Le Quéré et al., 2020). Aviation had the biggest relative drop in activity accounting. CO_2 emissions due to land-use (based on early and uncertain evidence on deforestation and forest fires) were higher than average in 2020 (Amador-Jiménez et al., 2020).

Using similar methodologies, (Forster et al., 2020) assembled activity data and emissions estimates for other greenhouse gases and aerosols and their precursors. Anthropogenic NO_x emissions, which are largely from the transport sector, are estimated to have decreased by a maximum of 35% in April (*medium confidence*). Species whose emissions are dominated by other sectors, such as CH_4 and NH_3 from agriculture, saw smaller reductions.

Abundances and air quality

Owing to the short atmospheric lifetimes of SLCFs relevant to air quality, changes in their concentrations were detected within few days after lockdowns had been implemented (e.g., Bauwens et al., 2020b; Gkatzelis et al., 2021; Shi et al., 2021; Venter et al., 2020b). The COVID-19 driven economic slowdown has illustrated how complex the relationship is between emissions and air pollutant concentrations due to non-linearity in the atmospheric chemistry leading to secondary compound formation (see also Section 6.1 and Box 6.1) (Kroll et al., 2020).

Several studies have examined the effect of COVID-19 containment on air quality, showing that multi-year datasets with proper statistical/modelling analysis are required to discriminate the effect of meteorology from that of emission reduction (Dhaka et al., 2020; Li et al., 2020b; Wang et al., 2020; Zhao et al., 2020b) . Accounting for meteorological influences and with increasing stringency index, the median observed change in NO_2 decreased from -13% to -48%, and in $PM_{2.5}$ decreased from -10% to -33%, whereas the median change in O_3 increased from 0% to 4% (Gkatzelis et al., 2021). The latter can be explained by the decrease of NO emissions that titrate ozone in specific highly polluted areas, leading to the observed increase in surface O_3 concentration in cities (Huang et al., 2020a; Le et al., 2020; Sicard et al., 2020).

The temporary decrease of $PM_{2.5}$ concentrations should be put in perspective of the sustained reduction (estimated at 30% to 70%), which could be achieved by implementing policies addressing air quality and climate change (see Section 6.6.3). Such sustained reductions can lead to multiple benefits and simultaneously achieve several SDGs (Section 6.6.3). These policies would also result in reduction of ground-level ozone by up to 20% (see Section 6.7.1.3).

Except for ozone, temporary improvement of air quality during lockdown periods was observed in most regions of the world (*high confidence*), resulting from a combination of inter-annual meteorological variability and impact of COVID-19 containment measures (*high confidence*). Estimated air pollution

ACCEPTED VERSION SUBJECT TO FINAL EDITING

reductions associated with lockdown periods are lower than what can be expected from integrated mitigation policy leading to lasting reductions (*medium confidence*).

Radiative forcings

COVID-19 related emission changes primarily exerted effective radiative forcing (ERF) through reduced emission rates of CO_2 and methane, altered abundance of short-lived climate forcers (SLCFs), notably O_3, NO_2 and aerosols, and through other changes in anthropogenic activities, notably a reduction in the formation of aviation-induced cirrus clouds.

Forster et al. (2020) combined the FaIR emulator (see Cross-Chapter Box 7.1) with emission changes for a range of species, relative to a continuation of Nationally Determined Contributions (Rogelj et al., 2017). They found a negative ERF from avoided CO_2 emissions that strengthens through 2020, to -0.01 Wm^{-2}. During the spring lockdown, they found a peak positive ERF of 0.1 Wm^{-2} from loss of aerosol-induced cooling, and a peak negative ERF of -0.04 Wm^{-2} from reductions in tropospheric ozone (from reduced photochemical production via NO_x). Overall, they estimated a net ERF of +0.05 Wm^{-2} for spring 2020, declining to +0.025 Wm^{-2} by the end of the year.

Gettelman et al. (2021) extended Forster et al. (2020) results using two ESMs, and found a spring peak aerosol-induced ERF ranging from 0.12 to 0.3 Wm^{-2}, depending on the aerosol parameterization. They also estimated an ERF of -0.04 Wm^{-2} from loss of contrail warming. Overall, they report a peak ERF of 0.04 to 0.2 Wm^{-2}, and a subsequent decline to around half the peak value.

Two independent ESM studies, Weber et al. (2020) and Yang et al. (2020), found consistent results in time evolution and component contributions, but included fewer forcing components.

The available studies are in broad agreement on the sign and magnitude of contributions to ERF from COVID-19 related emission changes during 2020. The peak global mean ERF, in spring 2020, was [0.025-0.2] Wm^{-2} (*medium confidence*), composed by a positive forcing from aerosol-climate interactions of [0.1-0.3] Wm^{-2}, and negative forcings from CO_2 (-0.01 Wm^{-2}), NO_x (-0.04 Wm^{-2}) and contrail cirrus (-0.04 Wm^{-2}) (*low evidence, medium agreement*). By the end of 2020, the ERF was at half the peak value (*medium confidence*).

Climate responses

Changes in atmospheric composition due to COVID-19 emissions reductions are not thought to have caused a detectable change in global temperature or rainfall in 2020 (*high confidence*). A large ensemble of Earth System Model (ESM) simulations show an ensemble average reduction in Aerosol Optical Depth (AOD) in some regions, notably eastern and southern Asia (Fyfe et al., 2021). This result is supported by observational studies finding decreases in optical depth in 2020 (Gkatzelis et al., 2021; Ming et al., 2021; van Heerwaarden et al., 2021), which may have contributed to observed increases in solar irradiance (van Heerwaarden et al., 2021) or solar clear-sky reflection (Ming et al., 2021).

Model simulations of the response to COVID-19 emissions reductions indicate a small warming of global surface air temperature (GSAT) due to a decrease in sulphate aerosols (Forster et al., 2020; Fyfe et al., 2021), balanced by cooling due to an ozone decrease (Forster et al., 2020; Weber et al., 2020), black carbon decrease (Weber et al., 2020) and CO_2 decrease. It is noted that observational studies report little SO_2 change, at least locally near the surface (Shi et al., 2021) and do not correlate with emission inventory based changes (Gkatzelis et al., 2021). One study suggests a small net warming while another using idealized simulations suggests a small cooling (Weber et al., 2020). Simulated GSAT and rainfall changes are unlikely to be detectable in observations (Samset et al., 2020; Fyfe et al., 2021) (*high confidence*).

Multi-model ESM simulations based on a realistic COVID-19 containment forcing scenario (Forster et al., 2020) indicate a model mean reduction in regional AOD but no discernible response in GSAT (Cross-Chapter Box 6.1 Figure 1).

ACCEPTED VERSION SUBJECT TO FINAL EDITING

Scenarios of future emissions following COVID-19 disruption have been examined under a range of hypothetical assumptions (Forster et al., 2020).

[START CROSS-CHAPER BOX 6.1, FIGURE 1 HERE]

Cross-Chapter Box 6.1, Figure 1: **Emission reductions and their effect on aerosols and climate in response to COVID-19.** Estimated reductions in emissions of CO_2, SO_2 and NO_x are shown in panel (a) based on reconstructions using activity data (updated from Forster et al., 2020). Eight Earth System Models (ESMs) performed multiple ensemble simulations of the response to COVID-19 emissions reductions forced with these assumed emission reductions up till August 2020 followed by a constant continuation near the August value to the end of 2020. Emission reductions were applied relative to the SSP2-4.5 scenario. Panel (b) shows ESM simulated AOD at 550nm (only seven models reported this variable). Panel (c) shows ESM simulated GSAT anomalies during 2020; curves denote the ensemble mean result for each model with shading used for ±1 standard deviation for each model. ESM data from these simulations ("ssp245-covid") is archived on the Earth System Grid CMIP6 database. Uncertainty is represented using the simple approach: No overlay indicates regions with high model agreement, where ≥80% of models agree on sign of change; diagonal lines indicate regions with low model agreement, where <80% of models agree on sign of change. For more information on the simple approach, please refer to the Cross-Chapter Box Atlas.1.

[END CROSS-CHAPER BOX 6.1, FIGURE 1 HERE]

[END CROSS-CHAPTER BOX 6.1 HERE]

6.7 Future projections of Atmospheric Composition and Climate response in SSP scenarios

This section assesses the 21st century projections of SLCF emissions, abundances, and responses in terms of climate and air quality following the SSPs (Riahi et al., 2017; Gidden et al., 2019) (also see Chapter 1, Cross-Chapter Box 1.5, and Section 1.6.1.3). The future evolution of atmospheric abundances and the resulting climate and AQ responses is driven mainly by anthropogenic emissions and by natural emissions modulated by chemical, physical and biological processes as discussed in Sections 6.2 and 6.3. Like the RCP scenarios used in AR5, the SSP emission scenarios consider only direct anthropogenic (including biomass burning) emissions and do not project natural emission changes due to climate or land-use changes; ESMs intrinsically consider these biogeochemical feedbacks to varying degrees (Section 6.4.5). We rely on future projections based on CMIP6 ESMs with comprehensive representation of chemistry, aerosol microphysics, and biospheric processes that participated in the ScenarioMIP (O'Neill et al., 2016) and AerChemMIP (Collins et al., 2017). However, due to high computational costs of running coupled ESMs, they cannot be used for quantifying the contributions from individual species, regions and sectors and across the scenarios. Therefore, reduced complexity models (see Box 1.3 and Cross-Chapter Box 7.1), which represent chemistry and complex ESM interactions in parameterized forms updated since the AR5, are also applied here.

6.7.1 Projections of Emissions and Atmospheric Abundances

6.7.1.1 SLCF Emissions and atmospheric abundances

The trajectory of future SLCF emissions is driven by the evolution of socioeconomic drivers described in 1.6.1.1 but dedicated, SSP-specific, air pollution policy storylines can change the regional and global trends (Rao et al., 2017). Additionally, assumptions about urbanization (Jiang and O'Neill, 2017) will affect spatial distribution of emissions and consequently air quality.

ACCEPTED VERSION SUBJECT TO FINAL EDITING

Growing urbanization worldwide has strongly modified the spatial distribution and intensity of SLCF emissions. The effect and extent of urbanization on air pollution and other emissions species are captured within Integrated Assessment Models (IAM) at varying levels of complexity. In most cases, models use a combination of proxies and assumptions of end-use efficiency and technological improvement assumptions to estimate emissions species arising from rural-to-urban migration and population growth within cities, utilizing quantifications of urbanization for the SSPs (Jiang and O'Neill, 2017). In addition, spatial patterns of future rural and urban population growth, migration, and decline have been quantified for the SSPs using a gravity model (Jiang and O'Neill, 2017). However, linking these spatial patterns with IAM regional emissions pathways is still an ongoing area of study and has not yet been represented in spatial emissions estimates provided by IAMs (Riahi et al., 2017; Gidden et al., 2019; Feng et al., 2020). As described in Feng et al. (2020), spatial emissions estimates derived for CMIP6 are largely a product of existing spatial patterns of population, but do not vary dynamically in future patterns. To the extend urbanization is accounted for in gridded emissions, IAM native region resolution (varying, for example, from 11 world regions to more than 30, depending on the model) provides urbanization-based dynamics. Despite the interest of studying the effect of well planned, densely populated urban centres, which can help to maximize the benefits of agglomeration, by providing proximity to infrastructure and services, opportunity for energy saving, and provide a frame for air quality control, IAM realizations of SSPs are not sufficient to assess this effect. The opportunities and risks associated with this rapid urbanization for SLCF emissions and air quality are analysed in the Chapter 6 of the WGII report and Chapter 8 of the WGIII report.

All the RCP trajectories started in 2005 relying on the assumption that economic growth will bring rapid strengthening of air pollution legislation effectively reducing emissions of non-methane SLCFs (e.g., Chuwah et al., 2013). While in the long term such trends are expected if more ambitious air pollution control goes on par with the economic growth. The near term developments, however, might be much more diverse across the regions and species as has been observed in the last three decades (Amann et al., 2013; Rafaj et al., 2014; Rafaj and Amann, 2018; Ru et al., 2018), especially in several fast-growing economies, leading to the difference between CMIP6 historical estimates for the post 2000 period (Hoesly et al., 2018) and those used in RCPs (Figure 6.18). Since several SLCFs are also air pollutants, the narrow range of the RCP emissions trajectories in the future allowed for only limited analysis of near-future air quality (Amann et al., 2013; Chuwah et al., 2013; Von Schneidemesser et al., 2015). However, the range of storylines in the SSPs lead to a wider range of assumed pollution control policies in the SSPs (Rao et al., 2017; Riahi et al., 2017). In SSP1 and SSP5, strong air quality policies are assumed to minimize adverse effects of pollution on population and ecosystems. In SSP2, a medium pollution control, with lower than current policy targets, is considered. Only weak, regionally varied, air pollution policies are applied in the SSP3 and SSP4. Additional climate policies introduced to reach defined radiative forcing targets will also affect SLCF emissions. The SSP SLCF emission trajectories (Rao et al., 2017; Gidden et al., 2019) assume a long term coupling of economic growth and specific emission indicators, such as, sectoral emission densities. The pace of change varies across regions and SSPs resulting in a wider range of future air pollutants evolution **(**Figure 6.18**)** reflecting the differences in assumed level of air pollution controls across the regions (Figure 6.19). At the end of the century, the SSP scenarios range is about four times that of RCP for SO_2 and NO_x, two to four times for BC and NMVOC, and up to three times for CO and OC, while indicating slightly smaller range than RCPs for CH_4 (Figure 6.20). The originally developed SSP scenarios (Rao et al., 2017) have been harmonized with the CMIP6 historical emissions (Hoesly et al., 2018) and include updated SO_2 emissions to account for the recent decline in China (Gidden et al., 2019).

All SSP scenarios (Figure 6.18), except SSP3-7.0, project decline in global total emissions for all SLCFs by the end of the 21st century, except for ammonia and for HFCs where Kigali Amendment is not included (see Section 6.6.3.2). Similar to RCPs, ammonia emissions continue to increase in most SSPs, except SSP1 and SSP2, accounting for the expected growth in food demand and a general lack of effective policies targeting agricultural emissions. Additionally, mitigation potential for NH_3 is generally smaller than for other species owing to fugitive and widely distributed sources (Pinder et al., 2006; Klimont and Winiwarter, 2015; Mohankumar Sajeev et al., 2018; Sajeev et al., 2018). Most significant changes of SLCF emissions in the near and long term compared to present day are expected for SO_2 owing to ever more stringent (and enforced) legislation in China's power sector, extended recently to industrial sources (Zheng et al., 2018b; Tong et al., 2020), declining coal use in most SSPs, recently announced stricter emission limits for power

ACCEPTED VERSION SUBJECT TO FINAL EDITING

sector in India, and reduction of sulphur content of oil fuel used in international shipping from 2020 (IMO, 2016). For the lower forcing targets (e.g., SSP1-2.6), the SO_2 trajectories are similar to the RCPs resulting in over 50% to 90% decline by 2050 and 2100, respectively, while for the scenarios with no climate policies, the SSPs show large spread even at the end of the century.

[START FIGURE 6.18 HERE]

Figure 6.18: Global anthropogenic and biomass burning short-lived climate forcer (SLCF) and carbon dioxide (CO_2) emissions from 1850 to 2100 and HFC emissions from 1990 to 2100. Emissions for the Coupled Model Intercomparison Project Phase 6 (CMIP6) for the period 1850-2014 are based on Hoesly et al. (2018) and van Marle et al. (2017), emissions for CMIP5 for the period 1850-2005 are from Lamarque et al. (2010), CO_2 emissions are from EDGAR database (Crippa et al., 2020); CH_4 and HFCs are from (Crippa et al., 2019); and air pollutants are from (EC-JRC / PBL, 2020), Höglund-Isaksson (2012) and Klimont et al. (2017b) for ECLIPSE. Projections originate from the Shared Socio-Economic Pathway (SSP) database (Riahi et al., 2017; Rogelj et al., 2018a; Gidden et al., 2019), Representative Concentration Pathway (RCP) database (van Vuuren et al., 2011), GAINS (CLE – current legislation baseline, KA – Kigali Amendment, MTFR – maximum technical mitigation potential) for HFCs (Purohit et al., 2020), Velders et al. (2015), ECLIPSE (Stohl et al., 2015). Further details on data sources and processing are available in the chapter data table (Table 6.SM.1).

[END FIGURE 6.18 HERE]

[START FIGURE 6.19 HERE]

Figure 6.19: Regional anthropogenic and biomass burning short-lived climate forcer (SLCF) emissions from 1850 to 2100. Emissions for the Coupled Model Intercomparison Project Phase 6 (CMIP6) for the period 1850-2014 are based on Hoesly et al. (2018) and van Marle et al. (2017) and emissions for CMIP5 for the period 1850-2005 are from Lamarque et al. (2010). Projections originate from the Shared Socio-Economic Pathway (SSP) database (Riahi et al., 2017; Rogelj et al., 2018a; Gidden et al., 2019) and Representative Concentration Pathway (RCP) database (van Vuuren et al., 2011). Further details on data sources and processing are available in the chapter data table (Table 6.SM.1).

[END FIGURE 6.19 HERE]

Until mid-century, SSP3-7.0 and SSP5-8.5 scenarios project no reduction in NO_x emissions at the global level with decline in most OECD countries and East Asia, driven by existing legislation in power, industry, and transportation, e.g., Tong et al. (2020), and continued increase in the rest of the world (Figure 6.18 and 6.19). Towards the end of the century, similar trends continue in SSP3-7.0 while emissions in SSP5 decline strongly owing to faster technological progress and stronger air quality action (Rao et al., 2017; Riahi et al., 2017). By 2100, the 'Regional Rivalry' (SSP3) scenario emissions of NO_x (and most other SLCFs, except ammonia) are typically twice as high as next highest SSP projection, both at the global (Figure 6.18) and regional level (Figure 6.19). In emission pathways consistent with Paris Agreement goals, NO_x drops, compared to 2015, by 50% in SSP1-2.6 and by 65% in SSP1-1.9 by 2050, and by 2100 is reduced by about 70%, resulting in global emission levels comparable to 1950s and below the RCP range. Similar reductions are projected in climate mitigation pathways at the regional level, except Africa (less than 50% decline) due to high share of biomass emissions as well as strong growth in population and fossil fuel use. The trends in anthropogenic and biomass burning emissions for other ozone precursors (NMVOC, CO) are similar to that of NO_x.

An additional scenario, based on the SSP3-7.0, has been designed specifically to assess the effect of a strong SLCF emission abatement and is called SSP3-7.0-lowNTCF in the literature (Collins et al., 2017; Gidden et al., 2019). It has been applied in the modelling studies (e.g., AerChemMIP) with or without consideration of additional CH_4 reduction and we refer here to these scenarios, respectively, as SSP3-7.0-lowSLCF-lowCH_4 or SSP3-7.0-lowSLCF-highCH_4. In these scenarios, aerosols, their precursors, and non-methane tropospheric

ACCEPTED VERSION SUBJECT TO FINAL EDITING

ozone precursors are mitigated by applying the same emission factors as in SSP1-1.9.

For global methane emissions, the range is similar for SSPs and RCPs over the entire century (Figure 6.18), with highest projections in SSP3-7.0 (slightly below RCP8.5) estimating doubling of the current emissions and a reduction of about 75% by 2100 in scenarios consistent with 1.5-2°C targets; similar as in RCP2.6. At the regional level, the evolution of CH_4 emissions in climate mitigation scenarios is comparable to RCPs but there are significant differences for some regions with respect to high-emission scenarios. Especially, projection for East Asia differ significantly, the highest SSP3-7.0 is about half of the highest RCP by 2100 (Figure 6.19) which is due to much lower projections of coal use in China driven largely by the last decade efforts to combat poor air quality. At the same time, the SSP scenarios without climate mitigation project faster growth in CH_4 emissions in Africa, Middle East, and Latin America (Figure 6.19) driven by developments in agriculture, oil and gas sectors, and, especially in Africa, waste management. There are significant differences in the assessment and feasibility of rapid CH_4 mitigation. Höglund-Isaksson et al. (2020) review most recent studies and assess feasibility of rapid widespread mitigation, concluding that significant (over 50%) reductions are attainable but feasibility of such reductions could be constrained in the short term due to locked capital. This might have implications for near term evolution assumed in, for example, SSP1-1.9 or SSP3-lowSLCF-lowCH_4, where emissions drop very quickly due to fast decarbonization and reductions in agriculture. Such high reduction potential in agriculture has been also assumed in other studies (Lucas et al., 2007; Harmsen et al., 2019) but is questioned by Höglund-Isaksson et al. (2020) who indicate that widespread implementation (within decades) of policies bringing about institutional and behavioural changes would be important for transition towards very low CH_4 emissions from livestock production.

Global emissions of carbonaceous aerosols are projected to decline in all SSP scenarios (Figure 6.18) except SSP3-7.0. In that scenario, which also has much higher emissions than any of the RCPs, about half of the anthropogenic BC originates from cooking and heating on solid fuels, mostly in Asia and Africa (Figure 6.19), where only limited progress in access to clean energy is achieved. Slow progress in improving waste management, high coal use in energy and industry, and no further progress in controlling diesel engines in Asia, Africa, and Latin America contributes most of the remaining emissions resulting in about 90% of anthropogenic BC emitted in non-OECD world by 2100 in SSP3-7.0. Similar picture emerges for OC but with larger importance of waste management sector and biomass burning and lower impact of transportation and industry developments. Since scenarios compliant with Paris Agreement goals (SSP1-1.9 or SSP1-2.6; see Section 1.6.1) include a widespread access to clean energy already by 2050, the global and regional emissions of BC decline by 70-75% by 2050 and 80% by 2100. The decline in residential sector (about 90% by 2050 and over 95% by 2100) is accompanied by a strong reduction in transport (over 98%) and decarbonization of industry and energy sector. About 50% of remaining BC emissions in SSP1-1.9 or SSP1-2.6 is projected to originate from waste and open biomass burning of which open burning of residues represent a significant part. Some studies suggest this might be pessimistic as, for example, efficient waste management (consistent with SDG goals) could potentially eliminate open burning of solid waste (Gómez-Sanabria et al., 2018), which accounts for over 30% of BC emissions in SSP1-1.9 in 2050 or 2100.

The SSP scenarios draw on the HFCs projections developed by Velders et al. (2015) considering, in climate mitigation scenarios, the provisions of the Kigali Amendment (2016) to the Montreal Protocol leading to phasedown of HFCs (Papanastasiou et al., 2018) (see Section 6.6.3.2). The SSP scenarios without climate mitigation (e.g, SSP3-7.0, SSP5-8.5) show a range of 3.2-5.3 Gt CO_2-eq yr^{-1} in 2050 and about 4-7.2 Gt CO_2-eq yr^{-1} by 2100 while in deep climate mitigation scenarios (e.g., SSP1-1.9), consistent with the 1.5-2°C targets, they are expected to drop to 0.1-0.3 and 0.1-0.35 GtCO_2-eq yr^{-1}, respectively (Figure 6.19). In SSP1-1.9, the extent of reduction and its pace is more ambitious than current estimates of the effect of fully implemented and enforced Kigali Amendment (Figure 6.19) (Höglund-Isaksson et al., 2017; Purohit and Höglund-Isaksson, 2017). The best representation of the HFC emission trajectories in the SSP framework compliant with the Kigali Amendment is the SSP1-2.6 and the baseline (including only pre-Kigali national legislation; 6.6.3) is best represented by SSP5-8.5 (see Figure 6.19). However, since HFC emissions in SSPs were developed shortly after the Kigali Amendment had been agreed, none of these projections represents accurately the HFC emission trajectory corresponding to the phase-out emission levels agreed to in the Kigali Amendment (Meinshausen et al., 2020), leading to *medium confidence* in the assessment of the

ACCEPTED VERSION SUBJECT TO FINAL EDITING

benefits of the Kigali Amendment when using SSP projections for HFCs.

The SSP SLCF trajectories reflect the effect of recent legislation and assumed evolution thereof in the longer term, however, they do not necessarily reflect the full mitigation potential for several SLCFs, within particular SSPs (Figure 6.18), that could be achieved with air quality or SDG targeted policies (Amann et al., 2013; Rogelj et al., 2014a; Haines et al., 2017b; Klimont et al., 2017c; Rafaj and Amann, 2018; Shindell et al., 2018; Tong et al., 2020). Such policies could bring more rapid mitigation of SLCFs, independent of the climate strategy (also see Section 6.6.3).

The projections of future SLCF abundances typically follow their emissions trajectories except for SLCFs that are formed from precursor reactions (e.g., tropospheric ozone) or are influenced by biogeochemical feedbacks (See 6.2.2 and 6.4.5). According to multi-model CMIP6 simulations, total column ozone (reflecting mostly stratospheric ozone) is projected to return to 1960s values by the middle of the 21st century under the SSP2-4.5, SSP3-7.0, SSP4-3.4, SSP4-6.0 and SSP5-8.5 scenarios (Keeble et al., 2021). ESMs project increasing tropospheric ozone burden over the 2015-2100 period for the SSP3-7.0 scenario (Figure 6.4) (Griffiths et al., 2020), there is, however, a large spread in the magnitude of this increase reflecting structural uncertainties associated with the model representation of processes that influence tropospheric ozone. Sources of uncertainties in SLCF abundance projections include scenario uncertainties, or parametric and structural uncertainties in the model representation of the processes affecting simulated abundances with implications for radiative forcing and air quality. The evolution of methane abundances in SSP scenarios, for example, is derived from integrated assessment models (IAMs) which do not include the effects from biogeochemical feedbacks (e.g., climate-driven changes in wetland emissions) (Meinshausen et al., 2020) introducing uncertainty.

In summary, in SSPs, in addition to the socio-economic development and climate mitigation policies shaping the GHG emission trajectories, the SLCF emission trajectories are also steered by varying levels of air pollution control originating from SSP narratives and independent from climate mitigation. Consequently, SSPs span a wider range of SLCF emissions than considered in the RCPs, better covering the diversity of future options in air pollution management and SLCF-induced climate effects (*high confidence*). In addition to SSP-driven emissions, the future evolution of SLCFs abundance is also sensitive to chemical and biogeochemical feedbacks involving SLCFs, particularly natural emissions, whose magnitude and sign are poorly constrained.

6.7.1.2 Future evolution of surface ozone and PM concentrations

The projection of air quality relevant abundances (surface ozone and $PM_{2.5}$) under the SSP scenarios are assessed here. Future changes in global and regional annual mean surface ozone and $PM_{2.5}$ driven by the evolution of emissions as well as climate change have been quantified by CMIP6 models analysed in AerChemMIP (Allen et al., 2020; Turnock et al., 2020; Allen et al., 2021).

[START FIGURE 6.20 HERE]

Figure 6.20: Projected changes in regional annual mean surface ozone (O_3) (ppb) from 2015 to 2100 in different shared socio-economic pathways (SSPs). Each panel represents values averaged over the corresponding land area (except for Global) shown on the map in Figure 6.7. Solid colored lines and shading indicate the multi-model mean and ±1 σ across the available CMIP6 models (Turnock et al., 2020; Allen et al., 2021) for each scenario. Changes are relative to annual mean values calculated over the period 2005-2014 from the historical experiment as indicated in the top left of each regional panel along with ±1 σ. For each model all available ensemble members are averaged before being used to calculate the multi-model mean. Ozone changes are also displayed in the Interactive Atlas. Further details on data sources and processing are available in the chapter data table (Table 6.SM.1).

[END FIGURE 6.20 HERE]

ACCEPTED VERSION SUBJECT TO FINAL EDITING

Surface ozone increases continuously until 2050 across most regions in SSP3-7.0 and SSP5-8.5, (Turnock et al., 2020), particularly over Eastern Asia, Southern Asia, Middle East, Africa and South East Asia and developping Pacific where this increase can reach and even exceed 5ppb for annual mean averaged over land areas (Figure 6.20). After 2050, surface ozone concentrations decrease in SSP5-8.5, reaching levels below there 2005-2014 levels in most regions but and level off or continue to increase under SSP3-7.0.This increase in surface ozone in the SSP5-8.5 scenario occurs despite emissions decrease of several ozone precursors because of is due to CH_4 emissions increase until about 2080 in the absence of climate mitigation. Ozone decreases over all regions in response to strong emissions mitigation in SSP1-1.9 and SSP1-2.6 (Turnock et al., 2020), with decreases of 5 to10 ppb as soon as 2030 in North America, Europe, Eurasia, Eastern Asia, Middle East and Southern Asia in their annual means over land areas . In most regions surface ozone is reduced slightly or remains near present day values in the middle of the road scenario, SSP2-4.5. In 2100, the largest differences in surface ozone changes across the scenarios occur for the Middle East, Southern Asia and Eastern Asia with differences ranging up to 40 ppb between SSP3-7.0 and SSP1-1.9 at the end of the century. Despite discrepancies in the magnitude of changes, especially over North America, Europe, Eurasia, Eastern Asia and Southern Asia, the models are in high agreement regarding the signs of the changes with are thus assessed as of *high confidence*.

The strong abatement of ozone precursor emissions (except those of CH_4) (SSP3-7.0-lowSLCF-highCH_4) lead to a decrease of global average surface ozone by 15% (6 ppb) between 2015 and 2055 (Allen et al., 2020) and ozone decreases in all regions except Southern Asia. However, this decrease is two times larger when CH_4 emissions are abated simultaneously (SSP3-7.0-lowSLCF-lowCH_4), underlying the importance of methane emission reduction as an important lever to reduce ozone pollution (*high confidence*) (see also 6.6.4).

[START FIGURE 6.21 HERE]

Figure 6.21: Future changes in regional 5-year mean surface $PM_{2.5}$ from 2015 to 2100 in different shared socio-economic pathways (SSPs). $PM_{2.5}$ stands for micrograms per cubic meter of aerosols with diameter less than 2.5 μm and is calculated by summing up individual aerosol mass components from each model as: black carbon + particulate organic matter + sulphate + 0.25 * sea salt + 0.1 * dust. Since not all CMIP6 models reported nitrate aerosol, it is not included here. See Figure 6.20 for further details. $PM_{2.5}$ changes are also displayed in the Interactive Atlas. Further details on data sources and processing are available in the chapter data table (Table 6.SM.1).

[END FIGURE 6.21 HERE]

A decrease in surface $PM_{2.5}$ concentrations is estimated for SSP1-1.9, SSP1-2.6 and SSP2-4.5 (Turnock et al., 2020) (Figure 6.21). A decrease in $PM_{2.5}$, is also projected in SSP5-8.5 which does not consider any climate mitigation but has a strong air pollution control. The decrease is largest in the regions with the highest 2005-2014 mean concentrations (Middle East, South Asia and East Asia). Under the SSP3-7.0 scenario, $PM_{2.5}$ is predicted to increase or remain at near present-day values across Asia; regions where present-day concentrations are currently the highest. There is large model spread over regions with large natural aerosol sources, for example, in North Africa, where dust sources are important. The mitigation of non-methane SLCFs in the SSP3-7.0-lowSLCF-highCH_4 scenario is predicted to reduce $PM_{2.5}$ by 25% (in 2055, relative to the SSP3-7.0 scenario) over global land surface areas (Allen et al., 2020).

The magnitude of the annual mean change in surface ozone and $PM_{2.5}$ for all the SSPs (accounting for both emission and climate change) is greater than that expected from climate change in isolation (Turnock et al., 2020). The uncertainty in the projections comes from how natural emissions will respond to climate change. However, multiple lines of evidence (along with those from Sections 6.2.2, 6.5, and 6.7.1) provide *high confidence* (compared to *medium* in AR5) that changes in emissions, and in particular human-induced emissions, will drive future air pollution levels rather than physical climate change.

In summary, future air pollution levels are strongly driven by precursor emission trajectories in the SSPs

ACCEPTED VERSION SUBJECT TO FINAL EDITING

with substantial reductions in global surface ozone and PM (when air pollution and climate change are both strongly mitigated, e.g., SSP1-2.6) to no improvement and even degradation (when no climate change mitigation and only weak air pollution control are considered, SSP3-7.0) (*high confidence*). In the latter case, PM levels are estimated to increase until 2050 over large parts of Asia and surface ozone pollution worsens over all continental areas throughout the whole century (*high confidence*). In scenarios without climate change mitigation but with strong air pollution control (SSP5-8.5), high methane levels hamper the decline in global surface ozone in the near term and only PM levels decrease (*high confidence*).

6.7.2 Evolution of future climate in response to SLCF emissions

6.7.2.1 Effects of SLCFs on ERF and climate response

This section assesses how the different spatial and temporal evolution of SLCF emissions in the SSPs affects the future global and regional ERFs, and GSAT and precipitation responses. In CMIP6, only a very limited set of simulations (all based on the SSP3-7.0 scenario) have been carried out with coupled ESMs to specifically address the future role of SLCFs (Collins et al., 2017), see also Sections 4.3 and 4.4. Note that the ScenarioMIP simulations (Section 4.3) include the SLCF emissions (as shown in Figures 6.18 and 6.19), however they cannot be used to quantify the effect of individual forcers. Coupled ESMs can in principle be used for this through a series of sensitivity simulations (e.g. Allen et al., 2020, 2021), but the amount of computer time required has made this approach prohibitive across the full SSP range. Therefore, to quantify the contribution from emissions of individual forcers spanning the range of the SSP scenarios to GSAT response, the analysis is mainly based on estimates using a two-layer emulator configuration derived from the medians of MAGICC7 and FaIRv1.6.2 (see Section 1.5.3.4, Cross Chapter Box 7.1, and Supplementary Material 7.SM5.2). The contribution from SLCFs to changes in GSAT have been calculated based on the global mean ERF for the various components as assessed in section 7.3.5, using the two-layer emulator for the climate response (Cross Chapter Box 7.1 and Supplementary Material 7.SM5.2).

The projections of GSAT for a broad group of forcing agents (aerosols, methane, tropospheric ozone, and HFCs with lifetimes lower than 50 years) for the SSP scenarios shows how much of the future warming or cooling (relative to 2019) can be attributed to the SLCFs (Figure 6.22). Note that during the first two decades, some of these changes in GSAT are due to emissions before 2019, in particular for the longer lived SLCFs such as methane and HFCs (see also Figure 6.15). The scenarios SSP3-7.0-lowSLCF-highCH_4 and SSP3-7.0-lowSLCF-lowCH_4 are special cases of the SSP3-7.0 scenario with strong, but realistic, reductions in non-methane SLCFs and all SLCFs respectively (Gidden et al., 2019).

As discussed in sections 6.2, 6.3 and 6.4, there are uncertainties relating emissions of SLCFs to changes in abundance (see Box 6.2) and further to ERF, in particular for aerosols and tropospheric ozone. Furthermore there are uncertainties related to the climate sensitivity, i.e., the relation between ERF and change in GSAT. Uncertainties in the ERF are assessed in Chapter 7 and calibrated impulse response function includes also the assessed range (see Box 7.1). There are also uncertainties related to the efficacies of the different SLCFs and time scales for the response, in particular for regional emissions (Schwarber et al., 2019; Yang et al., 2019b) that cannot be accounted for with the simple models used here.

[START FIGURE 6.22 HERE]

Figure 6.22: Time evolution of the effects of short-lived climate forcers (SLCFs) and hydrofluorocarbons (HFCs) on global surface air temperature (GSAT) across the WGI core set of Shared Socio-Economic Pathways (SSPs). Effects of net aerosols, methane, tropospheric ozone and HFCs (with lifetimes <50years), relative to year 2019 and to year 1750. The GSAT changes are based on the assessed historic and future evolution of Effective Radiative Forcing (Section 7.3.5). The temperature responses to the ERFs are calculated with an impulse response function with an equilibrium climate sensitivity of 3.0°C for a doubling of atmospheric CO2 (feedback parameter of -1.31 W m-2 °C-1, see CC-Box 7.1). Uncertainties are 5-95% ranges. The vertical bars to the right in each panel show the uncertainties for the GSAT change between 2019 and 2100. Further details on data sources and processing are available in the

ACCEPTED VERSION SUBJECT TO FINAL EDITING

chapter data table (Table 6.SM.1).

[END FIGURE 6.22 HERE]

Historical emissions have been updated until 2019 (see Supplementary Material of Chapter 7, 7.SM.1.3.1) and used for ERF for calculating GSAT in Figure 6.22. Year 2019 has been chosen as the base year to be consistent with the attributed temperature changes since 1750 (Figure 7.8). The warming attributed to SLCFs (methane, ozone and aerosols) over the last decade (Figure 7.8) constitutes about 30% of the peak SLCF driven warming in the most stringent scenarios (SSP1), in good agreement with Shindell and Smith (2019), and supported by the recent observed decline in AOD (Section 2.2.6).

From 2019 and until about 2040, SLCFs and HFCs will contribute to increase GSAT in the WG1 core set of SSP scenarios, with a *very likely* range of 0.04-0.41°C relative to 2019. The warming is most pronounced in the strong mitigation scenarios (i.e., SSP1-1.9 and SSP1-2.6) due to rapid cuts in aerosols. In the scenario SSP3-7.0, there is no reduction of aerosols until mid-century and it is the increases in methane and ozone that give a net warming in 2040. The warming is similar in magnitude to the SSP1-scenarios, in which the reduction in aerosols is the main driver. Contributions to warming from methane, ozone, aerosols and HFCs make SSP5-8.5 the scenario with the highest warming in 2040 and throughout the century.

After about 2040, it is *likely* that across the scenarios the net effect of the removal of aerosols is a further increase in GSAT. However, their contribution to the rate of change decreases towards the end of the century (from up to 0.2°C per decade before 2040 to about 0.03 °C per decade). After 2040, the changes in methane, HFCs and tropospheric ozone become equally important as the changes in the aerosols for the GSAT trends. In the low emission scenarios (SSP1-1.9 and SSP1-2.6), the contribution to warming from the SLCFs peaks around 2040 with a *very likely* range of 0.04°C-0.34°C. After the peak, the reduced warming from reductions in methane and ozone dominates, giving a best total estimate warming induced by SLCF and HFC changes of 0.12°C and 0.14°C respectively, in 2100, with a *very likely* range of -0.07°C to + 0.45°C (Figure 6.22). However, in the longer term towards the end of the century there are very significant differences between the scenarios. In SSP3-7.0 there is a near linear warming due to SLCFs of 0.08°C per decade, while for SSP5-8.5 there is a more rapid early warming. In SSP3-7.0, the limited reductions in aerosols, but a steady increase in methane, HFCs and ozone lead to a nearly linear contribution to GSAT reaching a best estimate of 0.5°C in 2100. Contributions from methane and ozone decrease towards 2100 in SSP5-8.5, however the warming from HFCs still increase and the SSP5-8.5 has the largest SLCF and HFC warming in 2100 with a best estimate of of 0.6°C. In the SSP2-4.5 scenario, a reduction in aerosols contributes to about 0.3°C warming in 2100, while contributions from ozone and methane in this scenario are small.

The simplified approach used to estimate the contributions to GSAT in Figure 6.22 have been supplemented with ESM simulations driven by the two versions of the SSP3-7.0-lowSLCF scenario (Section 6.7.1.1). Results from five CMIP6 ESMs with fully interactive atmospheric chemistry and aerosols for the high-methane scenario show (Allen et al., 2020, 2021) that these reductions in emissions of air pollutants would lead to additional increase in GSAT by 2055 relative to 2015 compared to the standard SSP3-7.0 scenario, with a best estimate of 0.23 ± 0.05°C, and a corresponding increase in global mean precipitation of 1.3 ± 0.17% (note that uncertainties from the work of Allen et al here and elsewhere are reported as twice standard deviation). Including methane mitigation (SSP3-7.0-lowSLCF-lowCH_4) would lead to a small increase in global precipitation (0.7 ± 0.1 %) by mid-century despite a decrease in GSAT (see 6.7.3), which is related to the higher sensitivity of precipitation to sulphate aerosols than greenhouse gases (Allen et al., 2021) (also see Section 8.2.1).

Regionally inhomogeneous ERFs can lead to regionally dependent responses (see section 6.4.3). Mitigation of non-methane SLCFs over the period 2015 to 2055 (SSP3-7.0-lowSLCF-highCH_4 versus SSP3-7.0) will lead to positive ERF over land regions (Allen et al., 2020). There are large regional differences in the ERF from no significant trend over Northern Africa to about 0.5 W m^{-2} $decade^{-1}$ for South Asia. The differences are mainly driven by differences in the reductions of sulphate aerosols. There is not a strong correspondence between regional warming and the ERF trends. As expected, the sensitivity (temperature change per unit

ACCEPTED VERSION SUBJECT TO FINAL EDITING

ERF) increases towards higher latitudes due to climate feedbacks and teleconnections. Regionally, the warming rates are higher over continental regions, with highest increase in temperatures for Central and Northern Asia and the Arctic in 2055 relative to 2015. The models agree on increasing global mean trend in precipitation due to SLCFs, however precipitation trends over land are more uncertain (Allen et al., 2020), in agreement with the relationship between aerosol and precipitation trends assessed in Chapter 8.

ESM estimates of future concentrations of various SLCFs vary considerably even when using the same future emission scenarios which is related to sources of model structural uncertainty in the several physical, chemical and natural emission model parameterisations. The general uncertainties in understanding and representing chemical and physical processes governing the life cycle of SLCFs (see Box 6.1) necessarily also applies to simulations of future concentrations and ERF. In addition, how the models are able to simulate climate changes (i.e., circulation and precipitation) that affects the dispersion and removal of SLCFs constitute a structural uncertainty in the models. Also SLCF related climate feedbacks (e.g., NO_x from lightning or BVOCs from vegetation) (Section 6.4.5) add to the uncertainty.

In the near term (2035-2040), it is *unlikely* that differences in the socio-economic developments (as embedded in the SSPs) can lead to a discernible difference in the net effect of changes of SLCFs on GSAT. This is because the intermodel spread in the estimated net effect of SLCFs on GSAT is as large as difference between the scenarios due to compensating effects of change in emissions leading to cooling and warming. However, in the longer term there is *high confidence* that the net warming of the SLCFs will be lower in the mitigation scenarios (SSP1-1.9 and SSP1-2.6 that include reductions in methane emissions) than in the high-emission scenarios (SSP3-7.0 and SSP5-8.5).

6.7.2.2 Effect of regional emissions of SLCFs on GSAT

For SLCFs with lifetimes shorter than typical mixing times in the atmosphere (days to weeks), the effects on secondary forcing agents (e.g. tropospheric ozone, sulphate and nitrate aerosols) depend on where and when the emissions occur due to non-linear chemical and physical processes. Also, the effective radiative forcing following a change in concentrations depends on the local conditions (see Sections 6.2, 6.3 and 6.4). While the emulators used for GSAT projections shown in figure 6.22 do not take the regional perspective into account, the set of simulations performed within the Hemispheric Transport of Air Pollutants phase two (HTAP2) project (Galmarini et al., 2017) allows for this perspective. The results from the chemistry-transport model OsloCTM3 taking part in in HTAP-2 have been used by Lund et al. (2020) to derive regional specific absolute global warming potentials (AGTPs, cf. (Aamaas et al., 2016)) for each emitted SLCF and each HTAP-2 region. With this set of AGTPs Lund et al. (2020) estimate the transient response in GSAT to the regional anthropogenic emissions. There are important differences in the contributions to GSAT in 2040 and 2100 (relative to 2020) between the regions and scenarios mainly due to the differences in mixture of emitted SLCFs (Figure 6.23). There is overall good agreement between the total net contribution from all regions to GSAT and the estimate based on global ERF and the two-layer emulator (Figure 6.22).

In the low and medium emission scenarios (SSP1-2.6 and SSP2-4.5), the warming effects of the SLCFs on GSAT are dominated by emissions in North America, Europe, and East Asia (Figure 6.23). In SSP1-2.6 the emissions of all SLCFs in all regions decrease and the net effect of the changes in SLCFs from all of these three regions is an increase in GSAT of about 0.02°C (per region) in 2040 and about 0.04°C in 2100. For SSP2-4.5 emissions of most SLCFs continue to increase in South Asia (see Figure 6.19), leading to a net cooling in the near term (-0.03°C in 2040), while in 2100, North America, Europe, East and South Asia all contribute to a warming, most pronounced from East Asia (0.05°C). In the SSP3-7.0 scenario the net effect of SLCFs in all regions is an enhanced warming towards the end of the century. Methane then becomes the dominant SLCF, and Africa is the region contributing the most to predicted global warming in 2100 (0.24°C). In SSP5-8.5, methane emissions increase in North America, Europe and Africa, while there is a decrease in the Asian regions. For North America and Europe, the methane increase combined with a reduction in aerosol leads to highest net contribution to GSAT in this scenario (0.06 and 0.04°C in 2100, respectively). The high growth in methane makes Africa the region with the largest contribution to future

ACCEPTED VERSION SUBJECT TO FINAL EDITING

warming by SLCFs (0.18°C in 2100 versus 2020) in this scenario.

[START FIGURE 6.23 HERE]

Figure 6.23: Contribution from regional emissions of short-lived climate forcers (SLCFs) to changes in global surface air temperature (GSAT) in 2040 (upper row) and 2100 (lower row), relative to 2020 for four Shared Socio-economic Pathways (SSP). Adapted from (Lund et al., 2020). NOx, CO, and VOC account for the impact through changes in ozone and methane, NOx additionally includes the impact through formation of nitrate aerosols. BC, SO_2 and OC accounts for the direct aerosol effect (aerosol-radiation interactions), as well as an estimate of the semi-direct effect for BC due to rapid adjustments and indirect effect (aerosol-cloud interactions) of sulfate aerosols. Regions are the same as shown in the map in Figure 6.7. Further details on data sources and processing are available in the chapter data table (Table 6.SM.1).

[END FIGURE 6.23 HERE]

6.7.3 Effect of SLCFs mitigation in SSP scenarios

Air quality policies lead to a decrease in emissions of both warming and cooling SLCFs. Here we assess the contribution of SLCFs to the total warming (including also the long-lived climate forcers) in the case of stringent SLCF mitigation to improve air quality in scenarios with continued high use of fossil fuels (e.g., SSP3-7.0-lowSLCF and SSP5-8.5). Conversely, we also assess the effect on air quality of strategies aiming to mitigate air pollution or climate change under the SSP3-7.0 framework (using the SSP3-7.0-lowSLCF-lowCH_4, SSP3-7.0-lowSLCF-highCH_4 and SSP3-3.4 scenarios).

As illustrated in Figure 6.24 (Section 6.7.2.2) and in Figure 2.2 of SR1.5 (Rogelj et al., 2018a), the total aerosol ERF change in stringent mitigation pathways is expected to be dominated by the effects from the phase-out of SO_2 contributing to a warming. Recent emission inventories and observations of trends in AOD (see Section 2.2.6 and 6.2.1) show that it is *very likely* that there have been reductions in global SO_2 emissions and in aerosol burdens over the last decade. Here, we use 2019 as the reference year rather than the 'Recent Past' defined as the average over 1995–2014 (Section 4.1) in order to exclude the recent emission reductions when discussing the different possible futures.

The role of the different SLCFs, and also the net of all the SLCFs relative to the total warming in the scenarios, is quite different across the SSP scenarios varying with the summed levels of climate change mitigation and air pollution control (Figure 6.24). In the scenario without climate change mitigation but with strong air pollution control (SSP5-8.5) all the SLCFs (CH_4, aerosols, tropospheric O_3) and the HFCs (with lifetimes less than 50 years) add to the warming, while in the strong climate change and air pollution mitigation scenarios (SSP1-1.9 and SSP1-2.6), the emission controls act to reduce methane, ozone and BC, and these reductions thus contribute to cooling. In all scenarios, except SSP3-7.0, emission controls lead to a reduction of the aerosols relative to 2019, causing a warming. However, the warming from aerosol reductions is stronger in the SSP1 scenarios (with best estimates of 0.21°C in 2040 and 0.4°C in 2100 in SSP1-2.6) because of higher emission reductions from stronger decrease of fossil-fuel use in these scenario than in SSP5-8.5 (0.13°C in 2040 and 0.22°C in 2100). The changes in methane abundance contribute a warming of 0.14°C in SSP5-8.5, but a cooling of 0.14°C in SSP1-2.6 by the end of the 21st century relative to 2019. Furthermore, under SSP5-8.5, HFCs induce a warming of 0.06°C with a *very likely* range of [0.04 to 0.08°C] in 2050 and 0.2 [0.1 to 0.3]°C by the end of the 21st century, relative to 2019, while under SSP1-2.6, warming due to HFCs is negligible (below 0.02°C) (*high confidence*). This assessment relies on these estimates, which are based on updated ERFs and HFC lifetimes. It is in accordance with previous estimates (Section 6.6.3.2) of the efficiency of implementation of the Kigali Amendment and national regulations. It is *very likely* that under a stringent climate and air pollution mitigation scenario (SSP1-2.6), the warming induced by changes in methane, ozone, aerosols, and HFCs towards the end of 21st century, will be very low compared with the warming they would cause under SSP5-8.5 scenario (0.14 °C in SSP1-2.6 versus 0.62 °C in SSP5-8.5).

ACCEPTED VERSION SUBJECT TO FINAL EDITING

For the SSP3-7.0-lowSLCF-highCH_4 and SSP3-7.0-lowSLCF-lowCH_4 scenarios, a five ESM ensemble has been analyzed relative to the standard SSP3-7.0 scenario (Allen et al., 2020, 2021). For SSP3-7.0-lowSLCF-highCH_4, in which the methane emissions are as in the standard SSP3-7.0 scenario, (Allen et al., 2021) found an enhanced global mean surface warming of 0.23±0.05 °C by mid-century and 0.21±0.03 °C by 2100 relative to the warming in the standard SSP3-7.0 scenario. Including also strong mitigation of methane emissions, the same models (Allen et al., 2021) find that the warming is off-set resulting in a net cooling of 0.15±0.05 °C at mid-century (2050-2059) and 0.50±0.02 °C at the end of the century (2090-2099) relative to SSP3-7.0.

There is *robust evidence* and *high agreement* that non-methane SLCFs mitigation measures, through reductions in aerosols and non-methane ozone precursors to improve air quality (SSP3-7.0-lowSLCF-highCH_4 versus SSP3-7.0), would lead to additional near-term warming with a range of 0.1°C -0.3°C. Methane mitigation which also reduces tropospheric ozone, stands out as an option that combines near and long term gains on surface temperature (*high confidence)*. With stringent but realistic methane mitigation (SSP3-7.0-lowSLCF-lowCH_4), it is *very likely* that warming (relative to SSP3-7.0) from non-methane SLCFs can be off-set (Figure 6.24 and Allen et al., 2021). Due to the slower response to the methane mitigation, this offset becomes more robust over time and it is *very likely* to be an offset after 2050. However, when comparing to present day, it is *unlikely* that that methane mitigation can fully cancel out the warming over the 21st century from reduction of non-methane cooling SLCFs.

The SSP3 storyline assumes 'regional rivalry' (see 1.6.1.1) with weak air pollution legislation and no climate mitigation and is compared here against SSP3-7.0-lowSLCF-lowCH_4 (strong air pollution control) and SSP3-3.4 (the most ambitious climate policy feasible under SSP3 narrative). In the SSP3-3.4 scenario, all emissions follow the SSP3-7.0 scenario until about 2030 and then deep and rapid cuts in fossil fuel use are imposed (Fujimori et al., 2017). In the case of climate mitigation, such as in the SSP3-3.4 scenario, the decrease of SLCFs emissions is a co-benefit from the targeted decrease of CO_2 (when SLCFs are co-emitted), but also directly targeted as in the case of methane. For SLCFs, this means that emissions of aerosols and methane increase until 2030 and are reduced fast thereafter (Fujimori et al., 2017). The effect on GSAT (relative to 2019) is shown in Figure 6.22 and 6.24. The net GSAT response to the SLCFs is dominated by the aerosols, with an initial cooling until 2030, then a fast rebound for 15 years followed by a very moderate warming reaching 0.21°C in 2100. The ozone change causes a slight cooling (up to 0.06°C), in contrast to the warming in the SSP3-7.0-lowSLCF-highCH_4 scenario in which the methane emissions increase until 2100.

[START FIGURE 6.24 HERE]

Figure 6.24: Effects of short-lived climate forcers (SLCFs) and hydrofluorocarbons (HFCs) on global surface air temperature (GSAT) across the WGI core set of Shared Socio-Economic Pathways (SSPs). Effects of net aerosols, methane, tropospheric ozone, and hydrofluorocarbons (HFCs; with lifetimes < 50 years), are compared with those of total anthropogenic forcing for 2040 and 2100 relative to year 2019. The GSAT changes are based on the assessed historic and future evolution of Effective Radiative Forcing (Section 7.3.5). The temperature responses to the ERFs are calculated with an impulse response function with an equilibrium climate sensitivity of 3.0°C for a doubling of atmospheric CO_2 (feedback parameter of -1.31 W m^{-2} °C^{-1}, see Cross-Chapter Box 7.1). Uncertainties are 5-95% ranges. The scenario total (grey bar) includes all anthropogenic forcings (long- and short-lived climate forcers, and land use changes) whereas the white points and bars show the net effects of SLCFs and HFCs and their uncertainties. Further details on data sources and processing are available in the chapter data table (Table 6.SM.1).

[END FIGURE 6.24 HERE]

To assess the effect of dedicated air quality versus climate policy on air quality, $PM_{2.5}$ and ozone indicators were estimated for three SSP3 scenarios by applying a widely used approach for the analysis of air quality implications for given emission scenarios (Rao et al., 2017; Van Dingenen et al., 2018; Vandyck et al., 2018)

ACCEPTED VERSION SUBJECT TO FINAL EDITING

and whose sensitivity of surface concentrations to emission changes is comparable to ESMs ensemble (see Supplementary Material 6.SM.5). The assessment shows that both strong air pollution control and strong climate mitigation, implemented independently, lead to large reduction of exposure to $PM_{2.5}$ and ozone by the end of the century (Figures 6.25, 6.26) (*high confidence*). However, implementation of air pollution control, relying on the deployment of existing technologies, leads to benefits more rapidly than climate mitigation (*high confidence*), which requires systemic changes and is thus implemented later in this scenario. Notably, under the underlying SSP3 context, significant parts of the population remain exposed to air quality exceeding the WHO guidelines for $PM_{2.5}$ over the whole century (*high confidence*), in particular in Africa, Eastern and Southern Asia, Middle East and for ozone only small improvement in population exposure is expected in Africa and Asia. Confidence levels here result from expert judgement on the whole chain of evidence.

[START FIGURE 6.25 HERE]

Figure 6.25: Effect of dedicated air pollution or climate policy on population-weighted $PM_{2.5}$ concentrations (µg m^{-3}) and share of population (%) exposed to different $PM_{2.5}$ levels across selected world regions. Thresholds of 10 µg m^{-3} and 35 µg m^{-3} represent the WHO air quality guideline and the WHO interim target 1, respectively; WHO (2017). Results are compared for SSP3-7.0 (no major improvement of current legislation is assumed), SSP3-LowSLCF (strong air pollution controls are assumed), and a climate mitigation scenario SSP3-3.4; details of scenario assumptions are discussed in Riahi et al. (2017) and Rao et al. (2017). Analysis performed with the TM5-FASST model (Van Dingenen et al., 2018) using emission projections from the Shared Socio-Economic Pathway (SSP) database (Riahi et al., 2017; Rogelj et al., 2018a; Gidden et al., 2019). Further details on data sources and processing are available in the chapter data table (Table 6.SM.1).

[END FIGURE 6.25 HERE]

[START FIGURE 6.26 HERE]

Figure 6.26: Effect of dedicated air pollution or climate policy on population-weighted ozone concentrations (SOMO0; ppb) and share of population (%) exposed to chosen ozone levels across ten world regions. Results are compared for SSP3-7.0 (no major improvement of current legislation is assumed), SSP3-Low NTCF (strong air pollution controls are assumed), and a climate mitigation scenario (SSP3-3.4); details of scenario assumptions are discussed in Riahi et al. (2017) and Rao et al. (2017). Analysis performed with the TM5-FASST model (Van Dingenen et al., 2018) using emission projections from the Shared Socio-Economic Pathway (SSP) database (Riahi et al., 2017; Rogelj et al., 2018a; Gidden et al., 2019). Further details on data sources and processing are available in the chapter data table (Table 6.SM.1).

[END FIGURE 6.26 HERE]

In summary, the warming induced by SLCF changes is stable after 2040 in the WG1 core set of SSP scenarios associated with lower global air pollution as long as methane emissions are also mitigated, but the overall warming induced by SLCF changes is higher in scenarios in which air quality continues to deteriorate (caused by growing fossil fuel use and limited air pollution control) (*high confidence*). In the SSP3-7.0 context, applying an additional strong air pollution control resulting in reductions in anthropogenic aerosols and non-methane ozone precursors would lead to an additional near-term global warming of 0.1°C with a *very likely* range of [-0.05 to 0.25]°C (compared with SSP3-7.0 for the same period). A simultaneous methane mitigation consistent with SSP1's stringent climate mitigation policy implemented in the SSP3 world, could entirely alleviate this warming and even lead to a cooling of 0.1°C with a *very likely* range of [-0.1 to 0.20]°C (compared with SSP3-7.0 for the same period). Across the SSPs, the reduction of CH_4, ozone precursors and HFCs can make a 0.2°C [0.1–0.4]°C difference on GSAT in 2040 and a 0.8°C [0.5–1.3]°C difference at the end of the 21st century (Figure 6.24), which is substantial in the context of the 2015 Paris

ACCEPTED VERSION SUBJECT TO FINAL EDITING

Agreement. Sustained methane mitigation, wherever it occurs, stands out as an option that combines near and long term gains on surface temperature (*high confidence)* and leads to air pollution benefit by reducing globally the surface ozone level (*high confidence)*.

Strong air pollution control as well as strong climate change mitigation, implemented independently, lead to large reduction of the exposure to air pollution by the end of the century (*high confidence*). Implementation of air pollution control, relying on the deployment of existing technologies, leads more rapidly to air quality benefits than climate change mitigation which requires systemic changes but, in both cases, significant parts of the population remain exposed to air pollution exceeding the WHO guidelines.

6.8 Perspectives

Ice-core analyses can now inform trends for more SLCFs over the last millennium (such as light NMVOCs or CO) and more proxies are available to inform about past emissions. However, preindustrial levels of SLCFs are still relatively poorly constrained. In addition, recent trends in abundances of the various types of aerosols and of NMVOCs suffer from the scarcity of observation networks in various parts of the world, in particular in the Southern Hemisphere. Such network development is necessary to record and understand the evolution of atmospheric composition.

Assessment of the future air pollution changes at the urban level require the use of high resolution model to properly account for non-linearities in chemistry, specific urban structures, local meteorology as well as temporal and spatial variations in emissions and population exposure. To assess the relevance of air pollution reduction policies, regional air quality models are necessary and are still not implemented in many developing countries. To properly apply such models, the quality of spatialized emission inventories is essential, but the production of accurate emission inventories remain a challenge for lots of rapidly growing urban areas. The emission reporting now planned in the official mandate of the Task Force on National Greenhouse Gas Inventories (TFI) can be a step in this direction if accompanied by efforts on emission spatial distribution. An integrated modelling framework associating global and high-resolution chemistry-transport models with shared protocols is missing to allow a systematic assessment of future changes on air quality at this scale.

In parallel, opportunities of progress may emerge from big data acquisition. Big data and their mining can inform practices related to emissions or can document pollution levels if associated with massive deployment of low cost sensors through citizen science. New generation satellite data will as well give access to sub-km scale air pollution observations.

A systematic emission modeling framework is needed to assess the LLGHG emission changes associated with SLCFs reductions induced by air pollution control in the SSP framework. The SLCF mediated effects of large-scale technology deployment to allow climate mitigation, such as hydrogen energy production, carbon capture and storage though amine filters or changes in agricultural practices to limit GHG emissions and/or produce bioenergy are also not considered in the emission scenarios.

Since AR5, the complexity of ESMs has increased to include many chemical and biogeochemical processes. These lasts are necessary to quantify non-CO_2 biogeochemical feedbacks on the Earth System resulting from climate driven changes in atmospheric chemistry and SLCF emissions from natural systems and, in turn, impacts of SLCFs on biogeochemical cycles. Enhanced understanding of the biological, chemical and physical processes based on experimental and observational work has facilitated advances in the ESMs. However, assessment of non-CO_2 biogeochemical feedbacks and SLCF effects on land and aquatic ecosystem productivity still remains challenging due to the multiple complex processes involved and limitations in observational constraints to evaluate the skill of ESMs in realistically simulating the processes. Advances will come from better understanding of the processes and mechanisms, in particular at the component interfaces. The development of high resolution ESMs will facilitate their evaluation against high resolution observations.

ACCEPTED VERSION SUBJECT TO FINAL EDITING

Frequently Asked Questions

FAQ 6.1: What are short-lived climate forcers and how do they affect the climate?

Short-lived climate forcers (SLCFs) are compounds such as methane and sulphate aerosols that warm or cool the Earth's climate over shorter time scales – from days to years – than greenhouse gases like carbon dioxide, whose climatic effect lasts for decades, centuries or more. Because SLCFs do not remain in the atmosphere for very long, their effects on the climate are different from one region to another and can change rapidly in response to changes in SLCF emissions. As some SLCFs also negatively affect air quality, measures to improve air quality have resulted in sharp reductions in emissions and concentrations of those SLCFs in many regions over the few last decades.

The SLCFs include gases as well as tiny particles called *aerosols*, and they can have a warming or cooling effect on the climate (FAQ 6.1, Figure 1). Warming SLCFs are either greenhouse gases (e.g., ozone or methane) or particles like black carbon (also known as soot), which warm the climate by absorbing energy and are sometimes referred to as *short-lived climate pollutants.* Cooling SLCFs, on the other hand, are mostly made of aerosol particles (e.g., sulphates, nitrates and organic aerosols) that cool down the climate by reflecting away more incoming sunlight.

Some SLCFs do not directly affect the climate but produce climate-active compounds and are referred to as precursors. SLCFs are emitted both naturally and as a result of human activities, such as agriculture or extraction of fossil fuels. Many of the human sources, particularly those based on combustion, produce SLCFs at the same time as carbon dioxide and other long-lived greenhouse gases. Emissions have increased since the start of industrialization, and humans are now the dominant source for several SLCFs and SLCF precursors, such as sulphur dioxide (which produces sulphates) and nitrogen oxides (which produce nitrates and ozone), despite strong reductions over the last few decades in some regions from efforts to improve air quality.

The climatic effect of a chemical compound in the atmosphere depends on two things: (1) how effective it is at cooling or warming the climate (its *radiative efficiency*) and (2) how long it remains in the atmosphere (its *lifetime*). Because they have high radiative efficiencies, SLCFs can have a strong effect on the climate even though they have relatively short lifetimes of up to about two decades after emission. Today, there is a balance between warming and cooling from SLCFs, but this can change in the future.

The short lifetime of SLCFs constrains their effects in both space and time. First, of all the SLCFs, methane and the short-lived halocarbons persist the longest in the atmosphere: up to two decades (FAQ 6.1, Figure 1). This is long enough to mix in the atmosphere and to spread globally. Most other SLCFs only remain in the atmosphere for a few days to weeks, which is generally too short for mixing in the atmosphere, sometimes even regionally. As a result, the SLCFs are unevenly distributed and their effects on the climate are more regional than those of longer-lived gases. Second, rapid (but sustained) changes in emissions of SLCFs can result in rapid climatic effects.

In addition to the direct warming and cooling effects, SLCFs have many other consequences for the climate system and for air quality (see FAQ 6.2). For instance, deposition of black carbon on snow darkens its surface, which subsequently absorbs more solar energy, leading to more melting and more warming. Aerosols also modify the properties of clouds, which has indirect cooling effects on the climate and causes changes in local rainfall (see FAQ 7.2). Climate models indicate that SLCFs have altered atmospheric circulation on local and even hemispheric scales (e.g., monsoons) as well as regional precipitation. For instance, recent observations show that regional weather is influenced by strong regional contrasts in the evolution of aerosol concentrations, particularly over South and East Asia.

Although policies to limit climate change and discussions of the so-called *remaining carbon budgets* primarily focus on carbon dioxide (see FAQ 5.4), SLCFs can significantly affect temperature changes. It is therefore important to understand how SLCFs work and to quantify their effects. Because reducing some of

ACCEPTED VERSION SUBJECT TO FINAL EDITING

the SLCF emissions, such as methane, can simultaneously reduce warming effects and adverse effects on air quality as well as help attaining Sustainable Development Goals, mitigation of SLCFs is often viewed as a favourable 'win-win' policy option.

[START FAQ 6.1, FIGURE 1 HERE]

FAQ 6.1, Figure 1: Main short-lived climate forcers, their sources, how long they exist in the atmosphere, and their relative contribution to global surface temperature changes between 1750 and 2019 (area of the globe). By definition, this contribution depends on the lifetime, the warming/cooling potential (radiative efficiency), and the emissions of each compound in the atmosphere. Blue indicates cooling and orange warming. Note that, between 1750 and 2019, the cooling contribution from aerosols (blue diamonds and globe) was approximately half the warming contribution from carbon dioxide.

[END FAQ 6.1, FIGURE 1 HERE]

FAQ 6.2: What are the links between limiting climate change and improving air quality?

Climate change and air quality are intimately linked. Many of the human activities that produce long-lived greenhouse gases also emit air pollutants, and many of these air pollutants are also 'short-lived climate forcers' that affect the climate. Therefore, many options for improving air quality may also serve to limit climate change and vice versa. However, some options for improving air quality cause additional climate warming, and some actions that address climate change can worsen air quality.

Climate change and air pollution are both critical environmental issues that are already affecting humanity. In 2016, the World Health Organization attributed 4.2 million deaths worldwide every year to ambient (outdoor) air pollution. Meanwhile, climate change impacts water resources, food production, human health, extreme events, coastal erosion, wildfires, and many other phenomena.

Most human activities, including energy production, agriculture, transportation, industrial processes, waste management and residential heating and cooling, result in emissions of gaseous and particulate pollutants that modify the composition of the atmosphere, leading to degradation of air quality as well as to climate change. These air pollutants are also *short-lived climate forcers* – substances that affect the climate but remain in the atmosphere for shorter periods (days to decades) than long-lived greenhouse gases like carbon dioxide (see FAQ 6.1). While this means that the issues of air pollution and climate change are intimately connected, air pollutants and greenhouse gases are often defined, investigated and regulated independently of one another in both the scientific and policy arenas.

Many sources simultaneously emit carbon dioxide and air pollutants. When we drive our fossil fuel vehicles or light a fire in the fireplace, it is not just carbon dioxide or air pollutants that are emitted, but always both. It is therefore not possible to separate emissions into two clearly distinct groups. As a result, policies aiming at addressing climate change may have benefits or side-effects for air quality, and vice versa.

For example, some short-term 'win-win' policies that simultaneously improve air quality and limit climate change include the implementation of energy efficiency measures, methane capture and recovery from solid waste management and oil and gas industry, zero-emission vehicles, efficient and clean stoves for heating and cooking, filtering of soot (particulate matter) for diesel vehicles, cleaner brick kiln technology, practices that reduce burning of agricultural waste, and the eradication of burning of kerosene for lighting.

There are, however, also 'win-lose' actions. For example, wood burning is defined as carbon neutral because a tree accumulates the same amount of carbon dioxide throughout its lifetime as is released when wood from that tree is burned. However, burning wood can also result in significant emissions of air pollutants, including carbon monoxide, nitrogen oxides, volatile organic compounds, and particulate matter, that locally

ACCEPTED VERSION SUBJECT TO FINAL EDITING

or regionally affect the climate, human health and ecosystems (FAQ 6.2, Figure 1). Alternatively, decreasing the amount of sulphate aerosols produced by power and industrial plants and from maritime transport improves air quality but results in a warming influence on the climate, because those sulphate aerosols contribute to cooling the atmosphere by blocking incoming sunlight.

Air quality and climate change represent two sides of the same coin, and addressing both issues together could lead to significant synergies and economic benefits while avoiding policy actions that mitigate one of the two issues but worsen the other.

[START FAQ 6.2, FIGURE 1 HERE]

FAQ 6.2, Figure 1: Links between actions aiming to limit climate change and actions to improve air quality. Greenhouse gases and aerosols (orange and blue) can affect directly climate. Air pollutants (bottom) can affect the human health, ecosystems and climate. All these compounds have common sources and sometimes interact with each other in the atmosphere which makes impossible to consider them separately (dotted grey arrows).

[END FAQ 6.2, FIGURE 1 HERE]

ACCEPTED VERSION
SUBJECT TO FINAL EDITING

References

Aakre, S., S. Kallbekken, R. Van Dingenen, and D.G. Victor, 2018: Incentives for small clubs of Arctic countries to limit black carbon and methane emissions. *Nature Climate Change*, doi:10.1038/s41558-017-0030-8.

Aamaas, B., T.K. Berntsen, J.S. Fuglestvedt, K.P. Shine, and N. Bellouin, 2016: Regional emission metrics for short-lived climate forcers from multiple models. *Atmospheric Chemistry and Physics*, **16(11)**, 7451–7468, doi:10.5194/acp-16-7451-2016.

Aamaas, B., T.K. Berntsen, J.S. Fuglestvedt, K.P. Shine, and W.J. Collins, 2017: Regional temperature change potentials for short-lived climate forcers based on radiative forcing from multiple models. *Atmospheric Chemistry and Physics*, **17(17)**, 10795–10809, doi:10.5194/acp-17-10795-2017.

Aas, W. et al., 2019: Global and regional trends of atmospheric sulfur. *Scientific Reports*, **9(1)**, 953, doi:10.1038/s41598-018-37304-0.

Achakulwisut, P. et al., 2015: Uncertainties in isoprene photochemistry and emissions: Implications for the oxidative capacity of past and present atmospheres and for climate forcing agents. *Atmospheric Chemistry and Physics*, **15(14)**, 7977–7998, doi:10.5194/acp-15-7977-2015.

Acosta Navarro, J.C. et al., 2014: Global emissions of terpenoid VOCs from terrestrial vegetation in the last millennium. *Journal of Geophysical Research: Atmospheres*, **119(11)**, 6867–6885, doi:10.1002/2013jd021238.

Adebiyi, A.A. and J.F. Kok, 2020: Climate models miss most of the coarse dust in the atmosphere. *Science Advances*, **6(15)**, eaaz9507, doi:10.1126/sciadv.aaz9507.

Aggarwal, S.G. and K. Kawamura, 2009: Carbonaceous and inorganic composition in long-range transported aerosols over northern Japan: Implication for aging of water-soluble organic fraction. *Atmospheric Environment*, **43(16)**, 2532–2540, doi:10.1016/j.atmosenv.2009.02.032.

Ahlm, L. et al., 2017: Marine cloud brightening - As effective without clouds. *Atmospheric Chemistry and Physics*, doi:10.5194/acp-17-13071-2017.

Ainsworth, E.A., C.R. Yendrek, S. Sitch, W.J. Collins, and L.D. Emberson, 2012: The Effects of Tropospheric Ozone on Net Primary Productivity and Implications for Climate Change. *Annual Review of Plant Biology*, **63(1)**, 637–661, doi:10.1146/annurev-arplant-042110-103829.

Akagi, S.K. et al., 2011: Emission factors for open and domestic biomass burning for use in atmospheric models. *Atmospheric Chemistry and Physics*, **11(9)**, 4039–4072, doi:10.5194/acp-11-4039-2011.

Akimoto, H. et al., 2015: SLCP co-control approach in East Asia: Tropospheric ozone reduction strategy by simultaneous reduction of NOx/NMVOC and methane. *Atmospheric Environment*, **122**, 588–595, doi:10.1016/j.atmosenv.2015.10.003.

Akritidis, D., A. Pozzer, and P. Zanis, 2019: On the impact of future climate change on tropopause folds and tropospheric ozone. *Atmospheric Chemistry and Physics Discussions*, **2019(22)**, 1–22, doi:10.5194/acp-2019-508.

Alexander, B. and L.J. Mickley, 2015: Paleo-Perspectives on Potential Future Changes in the Oxidative Capacity of the Atmosphere Due to Climate Change and Anthropogenic Emissions. *Current Pollution Reports*, **1(2)**, 57–69, doi:10.1007/s40726-015-0006-0.

Allen, D.J. and K.E. Pickering, 2002: Evaluation of lighning flash rate parametrisations for use in a global chemical transport model. *Journal of Geophysical Research*, **107(D23)(4711)**, doi:101029/2002JD002066, doi:10.1029/2002jd002066.

Allen, D.J., K.E. Pickering, E. Bucsela, N. Krotkov, and R. Holzworth, 2019: Lightning NOx Production in the Tropics as Determined Using OMI NO2 Retrievals and WWLLN Stroke Data. *Journal of Geophysical Research: Atmospheres*, **124(23)**, 13498–13518, doi:10.1029/2018jd029824.

Allen, M.R. et al., 2016: New use of global warming potentials to compare cumulative and short-lived climate pollutants. *Nature Climate Change*, **6(8)**, 773–776, doi:10.1038/nclimate2998.

Allen, M.R. et al., 2018a: Framing and Context. In: *Global Warming of 1.5°C. An IPCC Special Report on the impacts of global warming of 1.5°C above pre-industrial levels and related global greenhouse gas emission pathways, in the context of strengthening the global response to the threat of climate change*, [Masson-Delmotte, V., P. Zhai, H.-O. Pörtner, D. Roberts, J. Skea, P.R. Shukla, A. Pirani, W. Moufouma-Okia, C. Péan, R. Pidcock, S. Connors, J.B.R. Matthews, Y. Chen, X. Zhou, M.I. Gomis, E. Lonnoy, T. Maycock, M. Tignor, and T. Waterfield (eds.)]. In Press, pp. 49–91.

Allen, M.R. et al., 2018b: A solution to the misrepresentations of CO₂-equivalent emissions of short-lived climate pollutants under ambitious mitigation. *npj Climate and Atmospheric Science*, **1(1)**, 16, doi:10.1038/s41612-018-0026-8.

Allen, R.J., W. Landuyt, and S.T. Rumbold, 2016: An increase in aerosol burden and radiative effects in a warmer world. *Nature Climate Change*, **6(3)**, 269–274, doi:10.1038/nclimate2827.

Allen, R.J., T. Hassan, C.A. Randles, and H. Su, 2019: Enhanced land–sea warming contrast elevates aerosol pollution in a warmer world. *Nature Climate Change*, doi:10.1038/s41558-019-0401-4.

Allen, R.J. et al., 2020: Climate and air quality impacts due to mitigation of non-methane near-term climate forcers.

ACCEPTED VERSION SUBJECT TO FINAL EDITING

Atmospheric Chemistry and Physics, **20(16)**, 9641–9663, doi:10.5194/acp-20-9641-2020.
Allen, R.J. et al., 2021: Significant climate benefits from near-term climate forcer mitigation in spite of aerosol reductions. *Environmental Research Letters*, **16(3)**, doi:10.1088/1748-9326/abe06b.
Alterskjær, K. and J.E. Kristjánsson, 2013: The sign of the radiative forcing from marine cloud brightening depends on both particle size and injection amount. *Geophysical Research Letters*, doi:10.1029/2012gl054286.
Alvarez, R.A. et al., 2018: Assessment of methane emissions from the U.S. oil and gas supply chain. *Science*, **361(6398)**, 186 LP – 188, doi:10.1126/science.aar7204.
Amador-Jiménez, M., N. Millner, C. Palmer, R.T. Pennington, and L. Sileci, 2020: The Unintended Impact of Colombia's Covid-19 Lockdown on Forest Fires. *Environmental and Resource Economics*, doi:10.1007/s10640-020-00501-5.
Amann, M., Z. Klimont, and F. Wagner, 2013: Regional and Global Emissions of Air Pollutants: Recent Trends and Future Scenarios. *Annual Review of Environment and Resources*, **38(1)**, 31-55, doi:10.1146/annurev-environ-052912-173303.
Amann, M. et al., 2011: Cost-effective control of air quality and greenhouse gases in Europe: Modeling and policy applications. *Environmental Modelling and Software*, **26(12)**, doi:10.1016/j.envsoft.2011.07.012.
Amann, M. et al., 2017: Managing future air quality in megacities: A case study for Delhi. *Atmospheric Environment*, **161**, 99–111, doi:10.1016/j.atmosenv.2017.04.041.
Amann, M. et al., 2020: Reducing global air pollution: the scope for further policy interventions. *Philosophical Transactions of the Royal Society A: Mathematical, Physical and Engineering Sciences*, **378(2183)**, 20190331, doi:10.1098/rsta.2019.0331.
AMAP, 2015a: *AMAP Assessment 2015: Black carbon and ozone as Arctic climate forcers*. Arctic Monitoring and Assessment Programme (AMAP), Oslo, Norway, 116 pp.
AMAP, 2015b: *AMAP Assessment 2015: Methane as an Arctic climate forcer*. Arctic Monitoring and Assessment Programme (AMAP), Oslo, Norway, 139 pp.
Andrade, M.F. et al., 2017: Air quality in the megacity of São Paulo: Evolution over the last 30 years and future perspectives. *Atmospheric Environment*, **159**, 66–82, doi:10.1016/j.atmosenv.2017.03.051.
Andreae, M.O., 2019: Emission of trace gases and aerosols from biomass burning – An updated assessment. *Atmospheric Chemistry and Physics*, **19(13)**, 8523–8546, doi:10.5194/acp-19-8523-2019.
Andreae, M.O. et al., 2015: The Amazon Tall Tower Observatory (ATTO): overview of pilot measurements on ecosystem ecology, meteorology, trace gases, and aerosols. *Atmospheric Chemistry and Physics*, **15(18)**, 10723–10776, doi:10.5194/acp-15-10723-2015.
Andrews, A.E. et al., 2014: CO₂, CO, and CH₄ measurements from tall towers in the NOAA earth system research laboratory's global greenhouse gas reference network: Instrumentation, uncertainty analysis, and recommendations for future high-accuracy greenhouse gas. *Atmospheric Measurement Techniques*, doi:10.5194/amt-7-647-2014.
Anenberg, S., J. Miller, D. Henze, and R. Minjares, 2019: *A global snapshot of the air pollution-related health impacts of transportation sector emissions in 2010 and 2015*. International Council on Clean Transportation (ICCT), Washington, DC, USA, 55 pp.
Anenberg, S.C. et al., 2012: Global air quality and health co-benefits of mitigating near-term climate change through methane and black carbon emission controls. *Environmental Health Perspectives*, **120(6)**, 831–839, doi:10.1289/ehp.1104301.
Anenberg, S.C. et al., 2017: Impacts and mitigation of excess diesel-related NOx emissions in 11 major vehicle markets. *Nature*, **545(7655)**, 467–471, doi:10.1038/nature22086.
Angelbratt, J. et al., 2011: Carbon monoxide (CO) and ethane (C2H6) trends from ground-based solar FTIR measurements at six European stations, comparison and sensitivity analysis with the EMEP model. *Atmospheric Chemistry and Physics*, **11(17)**, 9253–9269, doi:10.5194/acp-11-9253-2011.
Archibald, A.T. et al., 2020: Tropospheric Ozone Assessment Report: A critical review of changes in the tropospheric ozone burden and budget from 1850-2100.. *Elem Sci Anth*.
Arneth, A., R.K. Monson, G. Schurgers, Niinemets, and P.I. Palmer, 2008: Why are estimates of global terrestrial isoprene emissions so similar (and why is this not so for monoterpenes)? *Atmospheric Chemistry and Physics*, **8(16)**, 4605–4620, doi:10.5194/acp-8-4605-2008.
Arneth, A. et al., 2010a: Terrestrial biogeochemical feedbacks in the climate system. *Nature Geoscience*, **3(8)**, 525–532, doi:10.1038/ngeo905.
Arneth, A. et al., 2010b: From biota to chemistry and climate: towards a comprehensive description of trace gas exchange between the biosphere and atmosphere. *Biogeosciences*, **7(1)**, 121–149, doi:10.5194/bg-7-121-2010.
Arnold, S.R. et al., 2018: Simulated Global Climate Response to Tropospheric Ozone-Induced Changes in Plant Transpiration. *Geophysical Research Letters*, **45(23)**, 13,13–70,79, doi:10.1029/2018gl079938.
Aschmann, J. et al., 2014: On the hiatus in the acceleration of tropical upwelling since the beginning of the 21st century. *Atmospheric Chemistry and Physics*, **14(23)**, 12803–12814, doi:10.5194/acp-14-12803-2014.
Athanasopoulou, E. et al., 2017: Changes in domestic heating fuel use in Greece: Effects on atmospheric chemistry and radiation. *Atmospheric Chemistry and Physics*, doi:10.5194/acp-17-10597-2017.

ACCEPTED VERSION SUBJECT TO FINAL EDITING

Baker, L.H. et al., 2015: Climate responses to anthropogenic emissions of short-lived climate pollutants. *Atmospheric Chemistry and Physics*, **15(14)**, 8201–8216, doi:10.5194/acp-15-8201-2015.
Balkanski, Y. et al., 2010: Direct radiative effect of aerosols emitted by transport: from road, shipping and aviation. *Atmospheric Chemistry and Physics*, **10(10)**, 4477–4489, doi:10.5194/acp-10-4477-2010.
Banerjee, A. et al., 2015: Drivers of changes in stratospheric and tropospheric ozone between year 2000 and 2100. *Atmospheric Chemistry and Physics Discussions*, **15(21)**, 30645–30691, doi:10.5194/acpd-15-30645-2015.
Banzhaf, S. et al., 2015: Dynamic model evaluation for secondary inorganic aerosol and its precursors over Europe between 1990 and 2009. *Geoscientific Model Development*, **8(4)**, 1047–1070, doi:10.5194/gmd-8-1047-2015.
Barkley, M.P. et al., 2013: Top-down isoprene emissions over tropical South America inferred from SCIAMACHY and OMI formaldehyde columns. *Journal of Geophysical Research: Atmospheres*, **118(12)**, 6849–6868, doi:10.1002/jgrd.50552.
Barnes, E.A., A.M. Fiore, and L.W. Horowitz, 2016: Detection of trends in surface ozone in the presence of climate variability. *Journal of Geophysical Research: Atmospheres*, **121(10)**, 6112–6129, doi:10.1002/2015jd024397.
Barthel, S., I. Tegen, and R. Wolke, 2019: Do new sea spray aerosol source functions improve the results of a regional aerosol model? *Atmospheric Environment*, **198**, 265–278, doi:10.1016/j.atmosenv.2018.10.016.
Bates, K.H. and D.J. Jacob, 2019: A new model mechanism for atmospheric oxidation of isoprene: Global effects on oxidants, nitrogen oxides, organic products, and secondary organic aerosol. *Atmospheric Chemistry and Physics*, **19(14)**, 9613–9640, doi:10.5194/acp-19-9613-2019.
Batmunkh, T. et al., 2011: Time-Resolved Measurements of PM2.5 Carbonaceous Aerosols at Gosan, Korea. *Journal of the Air & Waste Management Association*, **61(11)**, 1174–1182, doi:10.1080/10473289.2011.609761.
Bauer, S.E., K. Tsigaridis, and R. Miller, 2016: Significant atmospheric aerosol pollution caused by world food cultivation. *Geophysical Research Letters*, **43(10)**, 5394–5400, doi:10.1002/2016gl068354.
Bauer, S.E. et al., 2020: Historical (1850–2014) Aerosol Evolution and Role on Climate Forcing Using the GISS ModelE2.1 Contribution to CMIP6. *Journal of Advances in Modeling Earth Systems*, **12(8)**, e2019MS001978, doi:10.1029/2019ms001978.
Bauwens, M. et al., 2020: Impact of Coronavirus Outbreak on NO2 Pollution Assessed Using TROPOMI and OMI Observations. *Geophysical Research Letters*, **47(11)**, doi:10.1029/2020gl087978.
Beekmann, M. et al., 2015: In situ, satellite measurement and model evidence on the dominant regional contribution to fine particulate matter levels in the Paris megacity. *Atmospheric Chemistry and Physics*, **15**, 9577–9591, doi:10.5194/acp-15-9577-2015.
Bekki, S. and F. Lefevre, 2009: Stratospheric ozone: History and concepts and interactions with climate. 113–136 pp., doi:10.1140/epjconf/e2009-00914-y.
Bekki, S. et al., 2013: Climate impact of stratospheric ozone recovery. *Geophysical Research Letters*, **40(11)**, 2796–2800, doi:10.1002/grl.50358.
Bellouin, N. et al., 2013: Impact of the modal aerosol scheme GLOMAP-mode on aerosol forcing in the Hadley Centre Global Environmental Model. *Atmos. Chem. Phys.*, **13(6)**, 3027–3044, doi:10.5194/acp-13-3027-2013.
Bellouin, N. et al., 2020: Bounding Global Aerosol Radiative Forcing of Climate Change. *Reviews of Geophysics*, **58(1)**, e2019RG000660, doi:10.1029/2019rg000660.
Berntsen, T. and J. Fuglestvedt, 2008: Global temperature responses to current emissions from the transport sectors. *Proceedings of the National Academy of Sciences*, **105(49)**, 19154–19159, doi:10.1073/pnas.0804844105.
Bhaskar, V.V. and P.S.P. Rao, 2017: Annual and decadal variation in chemical composition of rain water at all the ten GAW stations in India. *Journal of Atmospheric Chemistry*, **74(1)**, 23–53, doi:10.1007/s10874-016-9339-3.
Bian, H. et al., 2017: Investigation of global particulate nitrate from the AeroCom phase III experiment. *Atmospheric Chemistry and Physics*, **17(21)**, 12911–12940, doi:10.5194/acp-17-12911-2017.
Bickel, M., M. Ponater, L. Bock, U. Burkhardt, and S. Reineke, 2020: Estimating the Effective Radiative Forcing of Contrail Cirrus. *Journal of Climate*, **33(5)**, 1991–2005, doi:10.1175/jcli-d-19-0467.1.
Bishop, G.A. and M.J. Haugen, 2018: The Story of Ever Diminishing Vehicle Tailpipe Emissions as Observed in the Chicago, Illinois Area. *Environmental Science and Technology*, **52(13)**, 7587–7593, doi:10.1021/acs.est.8b00926.
Bocquet, M. et al., 2015: Data assimilation in atmospheric chemistry models: Current status and future prospects for coupled chemistry meteorology models. *Atmospheric Chemistry and Physics*, **15(10)**, 5325–5358, doi:10.5194/acp-15-5325-2015.
Bond, T.C. et al., 2013: Bounding the role of black carbon in the climate system: A scientific assessment. *Journal of Geophysical Research Atmospheres*, **118(11)**, 5380–5552, doi:10.1002/jgrd.50171.
Bondur, V.G., I.I. Mokhov, O.S. Voronova, and S.A. Sitnov, 2020: Satellite Monitoring of Siberian Wildfires and Their Effects: Features of 2019 Anomalies and Trends of 20-Year Changes. *Doklady Earth Sciences*, **492(1)**, 370–375, doi:10.1134/s1028334x20050049.
Bonjour, S. et al., 2013: Solid fuel use for household cooking: Country and regional estimates for 1980-2010. *Environmental Health Perspectives*, **121(7)**, 784–790, doi:10.1289/ehp.1205987.
Bopp, L. et al., 2004: Will marine dimethylsulfide emissions amplify or alleviate global warming? A model study. *Canadian Journal of Fisheries and Aquatic Sciences*, **61(5)**, 826–835, doi:10.1139/f04-045.

ACCEPTED VERSION SUBJECT TO FINAL EDITING

Boucher, O. et al., 2013: Clouds and Aerosols. In: *Climate Change 2013 the Physical Science Basis: Working Group I Contribution to the Fifth Assessment Report of the Intergovernmental Panel on Climate Change* [Stocker, T.F., D. Qin, G.-K. Plattner, M. Tignor, S.K. Allen, J. Boschung, A. Nauels, Y. Xia, V. Bex, and P.M. Midgley (eds.)]. Cambridge University Press, Cambridge, pp. 571–658, doi:10.1017/cbo9781107415324.016.

Bourotte, C. et al., 2007: Association between ionic composition of fine and coarse aerosol soluble fraction and peak expiratory flow of asthmatic patients in São Paulo city (Brazil). *Atmospheric Environment*, **41(10)**, 2036–2048, doi:10.1016/j.atmosenv.2006.11.004.

Bowman, D.M.J.S. et al., 2009: Fire in the earth system. *Science*, **324(5926)**, 481–484, doi:10.1126/science.1163886.

Braspenning Radu, O. et al., 2016: Exploring synergies between climate and air quality policies using long-term global and regional emission scenarios. *Atmospheric Environment*, **140**, 577–591, doi:10.1016/j.atmosenv.2016.05.021.

Brasseur, G.P. and D.J. Jacob, 2017: Modeling of atmospheric chemistry. *Modeling of Atmospheric Chemistry*, 1-606, doi:10.1017/9781316544754.

Breider, T.J. et al., 2017: Multidecadal trends in aerosol radiative forcing over the Arctic: Contribution of changes in anthropogenic aerosol to Arctic warming since 1980. *Journal of Geophysical Research*, **122(6)**, 3573–3594, doi:10.1002/2016jd025321.

Brown-Steiner, B. et al., 2018: Evaluating simplified chemical mechanisms within present-day simulations of the Community Earth System Model version 1.2 with CAM4 (CESM1.2 CAM-chem): MOZART-4 vs. Reduced Hydrocarbon vs. Super-Fast chemistry. *Geosci. Model Dev.*, **11(10)**, 4155–4174, doi:10.5194/gmd-11-4155-2018.

Buchholz, R.R. et al., 2021: Air pollution trends measured from Terra: CO and AOD over industrial, fire-prone, and background regions. *Remote Sensing of Environment*, **256**, 112275, doi:10.1016/j.rse.2020.112275.

Bucsela, E.J., K.E. Pickering, D.J. Allen, R.H. Holzworth, and N.A. Krotkov, 2019: Midlatitude Lightning NOx Production Efficiency Inferred From OMI and WWLLN Data. *Journal of Geophysical Research: Atmospheres*, **124(23)**, 13475–13497, doi:10.1029/2019jd030561.

Bunzel, F. and H. Schmidt, 2013: The brewer-dobson circulation in a changing climate: Impact of the model configuration. *Journal of the Atmospheric Sciences*, **70(5)**, 1437–1455, doi:10.1175/jas-d-12-0215.1.

Burrows, S.M. et al., 2018: OCEANFILMS sea-spray organic aerosol emissions -- Part 1: implementation and impacts on clouds. 1–27 pp., doi:10.5194/acp-2018-70.

Butler, T., F. Vermeylen, C.M. Lehmann, G.E. Likens, and M. Puchalski, 2016: Increasing ammonia concentration trends in large regions of the USA derived from the NADP/AMoN network. *Atmospheric Environment*, **146**, 132–140, doi:10.1016/j.atmosenv.2016.06.033.

Butt, E.W. et al., 2016: The impact of residential combustion emissions on atmospheric aerosol, human health, and climate. *Atmospheric Chemistry and Physics*, **16(2)**, doi:10.5194/acp-16-873-2016.

Cai, W., K. Li, H. Liao, H. Wang, and L. Wu, 2017: Weather conditions conducive to Beijing severe haze more frequent under climate change. *Nature Climate Change*, **7(4)**, 257–262, doi:10.1038/nclimate3249.

Caldeira, K., G. Bala, and L. Cao, 2013: The Science of Geoengineering. *Annual Review of Earth and Planetary Sciences*, **41(1)**, 231–256, doi:10.1146/annurev-earth-042711-105548.

Callaghan, A.H., M.D. Stokes, and G.B. Deane, 2014: The effect of water temperature on air entrainment, bubble plumes, and surface foam in a laboratory breaking-wave analog. *Journal of Geophysical Research: Oceans*, **119(11)**, 7463–7482, doi:10.1002/2014jc010351.

Carpenter, L.J. et al., 2014: Update on Ozone-Depleting Substances (ODSs) and Other Gases of Interest to the Montreal Protocol, Chapter 1. In: *Scientific Assessment of Ozone Depletion: 2014*. Global Ozone Research and Monitoring Project – Report No. 55, World Meteorological Organization (WMO), Geneva, Switzerland, pp. 1.1–1.101.

Carslaw, K.S. et al., 2010: A review of natural aerosol interactions and feedbacks within the Earth system. *Atmospheric Chemistry and Physics*, **10(4)**, 1701–1737, doi:10.5194/acp-10-1701-2010.

Cecil, D.J., D.E. Buechler, and R.J. Blakeslee, 2014: Gridded lightning climatology from TRMM-LIS and OTD: Dataset description. *Atmospheric Research*, **135–136**, 404–414, doi:10.1016/j.atmosres.2012.06.028.

Celis, J.E., J.R. Morales, C.A. Zaror, and J.C. Inzunza, 2004: A study of the particulate matter PM₁₀ composition in the atmosphere of Chillán, Chile. *Chemosphere*, **54(4)**, 541–550, doi:10.1016/s0045-6535(03)00711-2.

Chambliss, S.E., R. Silva, J.J. West, M. Zeinali, and R. Minjares, 2014: Estimating source-attributable health impacts of ambient fine particulate matter exposure: Global premature mortality from surface transportation emissions in 2005. *Environmental Research Letters*, **9(10)**, 104009, doi:10.1088/1748-9326/9/10/104009.

Chang, K.M. et al., 2017: Ancillary health effects of climate mitigation scenarios as drivers of policy uptake: A review of air quality, transportation and diet co-benefits modeling studies. *Environmental Research Letters*, **12(11)**, doi:10.1088/1748-9326/aa8f7b.

Chen, D., Z. Liu, J. Fast, and J. Ban, 2016: Simulations of sulfate-nitrate-ammonium (SNA) aerosols during the extreme haze events over northern China in October 2014. *Atmospheric Chemistry and Physics*, **16(16)**, 10707–10724, doi:10.5194/acp-16-10707-2016.

ACCEPTED VERSION SUBJECT TO FINAL EDITING

Chen, K. et al., 2018: Future ozone-related acute excess mortality under climate and population change scenarios in China: A modeling study. *PLOS Medicine*, **15(7)**, e1002598.
Chen, S. et al., 2017: Direct observations of organic aerosols in common wintertime hazes in North China: Insights into direct emissions from Chinese residential stoves. *Atmospheric Chemistry and Physics*, **17(2)**, 1259–1270, doi:10.5194/acp-17-1259-2017.
Cheng, Y. et al., 2016: Reactive nitrogen chemistry in aerosol water as a source of sulfate during haze events in China. *Sci. Adv.*, **2(12)**, e1601530—e1601530, doi:10.1126/sciadv.1601530.
Cherian, R. and J. Quaas, 2020a: Trends in AOD, Clouds, and Cloud Radiative Effects in Satellite Data and CMIP5 and CMIP6 Model Simulations Over Aerosol Source Regions. *Geophysical Research Letters*, **47(9)**, e2020GL087132, doi:10.1029/2020gl087132.
Cherian, R. and J. Quaas, 2020b: Trends in AOD, Clouds, and Cloud Radiative Effects in Satellite Data and CMIP5 and CMIP6 Model Simulations Over Aerosol Source Regions. *Geophysical Research Letters*, **47(9)**, e2020GL087132, doi:10.1029/2020gl087132.
Chevallier, F. et al., 2020: Local Anomalies in the Column-Averaged Dry Air Mole Fractions of Carbon Dioxide Across the Globe During the First Months of the Coronavirus Recession. *Geophysical Research Letters*, **47(22)**, doi:10.1029/2020gl090244.
Cho, S.Y. and S.S. Park, 2013: Resolving sources of water-soluble organic carbon in fine particulate matter measured at an urban site during winter. *Environmental Science: Processes & Impacts*, **15**, 524–534, doi:10.1039/c2em30730h.
Cholakian, A., A. Colette, I. Coll, G. Ciarelli, and M. Beekmann, 2019: Future climatic drivers and their effect on PM10 components in Europe and the Mediterranean Sea. *Atmospheric Chemistry and Physics*, **19(7)**, 4459–4484, doi:10.5194/acp-19-4459-2019.
Chossière, G.P. et al., 2018: Country- and manufacturer-level attribution of air quality impacts due to excess NOx emissions from diesel passenger vehicles in Europe. *Atmospheric Environment*, **189**, 89–97, doi:10.1016/j.atmosenv.2018.06.047.
Christensen, T.R., V.K. Arora, M. Gauss, L. Höglund-Isaksson, and F.J.W. Parmentier, 2019: Tracing the climate signal: mitigation of anthropogenic methane emissions can outweigh a large Arctic natural emission increase. *Scientific Reports*, **9(1)**, 1146, doi:10.1038/s41598-018-37719-9.
Chrysanthou, A. et al., 2019: The effect of atmospheric nudging on the stratospheric residual circulation in chemistry–climate models. *Atmos. Chem. Phys.*, **19(17)**, 11559–11586, doi:10.5194/acp-19-11559-2019.
Chuvieco, E. et al., 2016: A new global burned area product for climate assessment of fire impacts. *Global Ecology and Biogeography*, **25(5)**, 619–629, doi:10.1111/geb.12440.
Chuvieco, E. et al., 2019: Historical background and current developments for mapping burned area from satellite Earth observation. *Remote Sensing of Environment*, **225**, 45–64, doi:10.1016/j.rse.2019.02.013.
Chuwah, C. et al., 2013: Implications of alternative assumptions regarding future air pollution control in scenarios similar to the Representative Concentration Pathways. *Atmospheric Environment*, **79**, 787–801, doi:10.1016/j.atmosenv.2013.07.008.
Ciais, P. et al., 2013: Carbon and other biogeochemical cycles. 465–570 pp., doi:10.1017/cbo9781107415324.015.
Cirino, G.G., R.A.F. Souza, D.K. Adams, and P. Artaxo, 2014: The effect of atmospheric aerosol particles and clouds on net ecosystem exchange in the Amazon. *Atmospheric Chemistry and Physics*, **14(13)**, 6523–6543, doi:10.5194/acp-14-6523-2014.
Civerolo, K. et al., 2010: Evaluation of an 18-year CMAQ simulation: Seasonal variations and long-term temporal changes in sulfate and nitrate. *Atmospheric Environment*, **44(31)**, 3745–3752, doi:10.1016/j.atmosenv.2010.06.056.
Clarisse, L., C. Clerbaux, F. Dentener, D. Hurtmans, and P.F. Coheur, 2009: Global ammonia distribution derived from infrared satellite observations. 479–483 pp., doi:10.1038/ngeo551.
Clark, S.K., D.S. Ward, and N.M. Mahowald, 2017: Parameterization-based uncertainty in future lightning flash density. *Geophysical Research Letters*, **44(6)**, 2893–2901, doi:10.1002/2017gl073017.
Cohen, Y. et al., 2018: Climatology and long-term evolution of ozone and carbon monoxide in the upper troposphere-lower stratosphere (UTLS) at northern midlatitudes, as seen by IAGOS from 1995 to 2013. *Atmospheric Chemistry and Physics*, **18(8)**, 5415–5453, doi:10.5194/acp-18-5415-2018.
Colette, A. et al., 2015: Is the ozone climate penalty robust in Europe? *Environmental Research Letters*, **10(8)**, 084015, doi:10.1088/1748-9326/10/8/084015.
Collins, W.J. et al., 2013: Global and regional temperature-change potentials for near-term climate forcers. *Atmospheric Chemistry and Physics*, **13(5)**, 2471–2485, doi:10.5194/acp-13-2471-2013.
Collins, W.J. et al., 2017: AerChemMIP: Quantifying the effects of chemistry and aerosols in CMIP6. *Geoscientific Model Development*, **10(2)**, 585–607, doi:10.5194/gmd-10-585-2017.
Collins, W.J. et al., 2018: Increased importance of methane reduction for a 1.5 degree target. *Environmental Research Letters*, **13(5)**, 54003, doi:10.1088/1748-9326/aab89c.
Coninck, H. et al., 2018: Strengthening and Implementing the Global Response. In: *Global warming of 1.5°C. An IPCC Special Report on the impacts of global warming of 1.5°C above pre-industrial levels and related global*

ACCEPTED VERSION SUBJECT TO FINAL EDITING

greenhouse gas emission pathways, in the context of strengthening the global response to the threat of climate change, [Masson-Delmotte, V., P. Zhai, H.O. Pörtner, D. Roberts, J. Skea, P.R. Shukla, A. Pirani, W. Moufouma-Okia, C. Péan, R. Pidcock, S. Connors, J.B.R. Matthews, Y. Chen, X. Zhou, M.I. Gomis, E. Lonnoy, T. Maycock, M. Tignor, and T. Waterfield (eds.)]. In Press, pp. 313–443.

Conrad, B.M. and M.R. Johnson, 2017: Field Measurements of Black Carbon Yields from Gas Flaring. *Environmental Science & Technology*, **51(3)**, 1893–1900, doi:10.1021/acs.est.6b03690.

Cooper, O.R. et al., 2020: Multi-decadal surface ozone trends at globally distributed remote locations. *Elem Sci Anth*, **8(1)**, 23, doi:10.1525/elementa.420.

Corbett, J.J. et al., 2007: Mortality from Ship Emissions: A Global Assessment. *Environmental Science & Technology*, **41(24)**, 8512–8518, doi:10.1021/es071686z.

Cox, P.M. et al., 2008: Increasing risk of Amazonian drought due to decreasing aerosol pollution. *Nature*, **453(7192)**, 212–215, doi:10.1038/nature06960.

Cravigan, L.T. et al., 2020: Sea spray aerosol organic enrichment, water uptake and surface tension effects. *Atmos. Chem. Phys.*, **20(13)**, 7955–7977, doi:10.5194/acp-20-7955-2020.

Crippa, M. et al., 2016: Forty years of improvements in European air quality: regional policy-industry interactions with global impacts. *Atmospheric Chemistry and Physics*, **16(6)**, 3825–3841, doi:10.5194/acp-16-3825-2016.

Crippa, M. et al., 2018: Gridded emissions of air pollutants for the period 1970--2012 within EDGAR v4.3.2. *Earth System Science Data*, **10(4)**, 1987–2013, doi:10.5194/essd-10-1987-2018.

Crippa, M. et al., 2019: *Fossil CO2 and GHG emissions of all world countries – 2019 Report*. JRC117610, Publications Office of the European Union, Luxembourg, 251 pp., doi:10.2760/687800.

Crippa, M. et al., 2020: *Fossil CO2 emissions of all world countries – 2020 Report*. JRC121460, Publications Office of the European Union, Luxembourg, 244 pp., doi:10.2760/143674.

Dai, Z., D.K. Weisenstein, and D.W. Keith, 2018: Tailoring Meridional and Seasonal Radiative Forcing by Sulfate Aerosol Solar Geoengineering. *Geophysical Research Letters*, doi:10.1002/2017gl076472.

Dalsøren, S.B. et al., 2016: Atmospheric methane evolution the last 40 years. *Atmospheric Chemistry and Physics*, **16(5)**, 3099–3126, doi:10.5194/acp-16-3099-2016.

Dalsøren, S.B. et al., 2018: Discrepancy between simulated and observed ethane and propane levels explained by underestimated fossil emissions. *Nature Geoscience*, **11(3)**, 178–184, doi:10.1038/s41561-018-0073-0.

Dameris, M. and P. Jöckel, 2013: Numerical modeling of climate-chemistry connections: Recent developments and future challenges. *Atmosphere*, **4(2)**, 132–156, doi:10.3390/atmos4020132.

Dang, R. and H. Liao, 2019: Radiative Forcing and Health Impact of Aerosols and Ozone in China as the Consequence of Clean Air Actions over 2012–2017. *Geophysical Research Letters*, **46(21)**, 12511–12519, doi:10.1029/2019gl084605.

de Foy, B., Z. Lu, and D.G. Streets, 2016: Satellite NO₂ retrievals suggest China has exceeded its NO_x reduction goals from the twelfth Five-Year Plan. *Scientific Reports*, **6**, doi:10.1038/srep35912.

De Smedt, I. et al., 2015: Diurnal, seasonal and long-term variations of global formaldehyde columns inferred from combined OMI and GOME-2 observations. *Atmospheric Chemistry and Physics*, **15(21)**, 12519–12545, doi:10.5194/acp-15-12519-2015.

de Souza, P.A., W.Z. Mello, R.L. Mariani, and S.M. Sella, 2010: Caracterização do material particulado fino e grosso e composição da fração inorgânica solúvel em água em São José dos Campos (SP). *Quimica Nova*, **33(6)**, 1247–1253.

de Vries, W., M. Posch, D. Simpson, and G.J. Reinds, 2017: Modelling long-term impacts of changes in climate, nitrogen deposition and ozone exposure on carbon sequestration of European forest ecosystems. *Science of The Total Environment*, **605–606**, 1097–1116, doi:10.1016/j.scitotenv.2017.06.132.

Deeter, M.N. et al., 2017: A climate-scale satellite record for carbon monoxide: The MOPITT Version 7 product. *Atmospheric Measurement Techniques*, **10(7)**, 2533–2555, doi:10.5194/amt-10-2533-2017.

DeMott, P.J. et al., 2016: Sea spray aerosol as a unique source of ice nucleating particles. *Proceedings of the National Academy of Sciences*, **113(21)**, 5797–5803, doi:10.1073/pnas.1514034112.

Dhaka, S.K. et al., 2020: PM2.5 diminution and haze events over Delhi during the COVID-19 lockdown period: an interplay between the baseline pollution and meteorology. *Scientific Reports*, **10(1)**, 13442, doi:10.1038/s41598-020-70179-8.

Dietmüller, S., M. Ponater, and R. Sausen, 2014: Interactive ozone induces a negative feedback in CO₂ -driven climate change simulations. *Journal of Geophysical Research*, **119(4)**, 1796–1805, doi:10.1002/2013jd020575.

Ding, S. et al., 2019: Observed Interactions Between Black Carbon and Hydrometeor During Wet Scavenging in Mixed-Phase Clouds. *Geophysical Research Letters*, doi:10.1029/2019gl083171.

Dlugokencky, E. and P. Tans, 2021: Trends in Atmospheric Carbon Dioxide, Methane and Nitrous Oxide. Global Monitoring Laboratory, National Oceanic & Atmospheric Administration Earth System Research Laboratories (NOAA/ESRL). Retrieved from: www.esrl.noaa.gov/gmd/ccgg/trends.

Duncan, B.N. et al., 2013: The observed response of Ozone Monitoring Instrument (OMI) NO₂ columns

ACCEPTED VERSION SUBJECT TO FINAL EDITING

to NO_x emission controls on power plants in the United States: 2005–2011. *Atmospheric Environment*, **81**, 102–111, doi:10.1016/j.atmosenv.2013.08.068.
Duncan, B.N. et al., 2014: Satellite data of atmospheric pollution for U.S. air quality applications: Examples of applications, summary of data end-user resources, answers to FAQs, and common mistakes to avoid. *Atmospheric Environment*, **94**, 647–662, doi:10.1016/j.atmosenv.2014.05.061.
Duncan, B.N. et al., 2016: A space-based, high-resolution view of notable changes in urban NOx pollution around the world (2005–2014). *Journal of Geophysical Research*, **121(2)**, 976–996, doi:10.1002/2015jd024121.
DuplicateMüller, N.C.J.F., T. Stavrakou, and J. Peeters, 2019: Chemistry and deposition in the model of atmospheric composition at global and regional scales using inversion techniques for trace gas emissions (magritte v1.1)-part 1: Chemical mechanism. *Geoscientific Model Development*, **12(6)**, 2307–2356, doi:10.5194/gmd-12-2307-2019.
DuplicateThornhill, N.O.C. et al., 2021: Effective Radiative forcing from emissions of reactive gases and aerosols -- a multimodel comparison. *Atmospheric Chemistry and Physics*, **21(2)**, 853–874, doi:10.5194/acp-21-853-2021.
Duplicatevan Marle, N.C. et al., 2017: Historic global biomass burning emissions for CMIP6 (BB4CMIP) based on merging satellite observations with proxies and fire models (1750--2015). *Geoscientific Model Development*, **10(9)**, 3329–3357, doi:10.5194/gmd-10-3329-2017.
DuplicateVirts, N.C., 2013: A New Ground-Based, Hourly Global Lightning Climatology (A53J-0286). 2004 pp.
Dutkiewicz, V.A. et al., 2014: Forty-seven years of weekly atmospheric black carbon measurements in the Finnish Arctic: Decrease in black carbon with declining emissions. *Journal of Geophysical Research*, **119(12)**, 7667–7683, doi:10.1002/2014jd021790.
Dykema, J.A., D.W. Keith, and F.N. Keutsch, 2016: Improved aerosol radiative properties as a foundation for solar geoengineering risk assessment. *Geophysical Research Letters*, doi:10.1002/2016gl069258.
EC-JRC / PBL, 2020: EDGAR v5.0 Global Air Pollutant Emissions. European Commission, Joint Research Centre (EC-JRC) / Netherlands Environmental Assessment Agency (PBL). Retrieved from: https://edgar.jrc.ec.europa.eu/overview.php?v=50_ap.
Ekman, A.M.L., 2014: Do sophisticated parameterizations of aerosol-cloud interactions in CMIP5 models improve the representation of recent observed temperature trends? *Journal of Geophysical Research: Atmospheres*, **119(2)**, 817–832, doi:10.1002/2013jd020511.
Elguindi, N. et al., 2020: Intercomparison of Magnitudes and Trends in Anthropogenic Surface Emissions From Bottom-Up Inventories, Top-Down Estimates, and Emission Scenarios. *Earth's Future*, **8(8)**, e2020EF001520, doi:10.1029/2020ef001520.
Emberson, L.D. et al., 2018: Ozone effects on crops and consideration in crop models. *European Journal of Agronomy*, doi:10.1016/j.eja.2018.06.002.
Emmerson, K.M. and M.J. Evans, 2009: Comparison of tropospheric gas-phase chemistry schemes for use within global models. *Atmospheric Chemistry and Physics*, **9(5)**, 1831–1845, doi:10.5194/acp-9-1831-2009.
Emmons, L.K. et al., 2020: The Chemistry Mechanism in the Community Earth System Model Version 2 (CESM2). *Journal of Advances in Modeling Earth Systems*, **12(4)**, e2019MS001882, doi:10.1029/2019ms001882.
Engardt, M., D. Simpson, M. Schwikowski, and L. Granat, 2017: Deposition of sulphur and nitrogen in Europe 1900–2050. Model calculations and comparison to historical observations. *Tellus, Series B: Chemical and Physical Meteorology*, **69(1)**, 1328945, doi:10.1080/16000889.2017.1328945.
Engel, A. et al., 2018: Update on Ozone-Depleting Substances (ODSs) and Other Gases of Interest to the Montreal Protocol, Chapter 1. In: *Scientific Assessment of Ozone Depletion: 2018*. Global Ozone Research and Monitoring Project – Report No. 58, World Meteorological Organization (WMO), Geneva, Switzerland, pp. 1.1–1.87.
EPA, 2019: *Global Non-CO2 Greenhouse Gas Emission Projections & Mitigation: 2015–2020*. EPA-430-R-19-010, United States Environmental Protection Agency (EPA), Office of Atmospheric Programs (6207A), Washington, DC, USA, 84 pp.
Erisman, J.W., M.A. Sutton, J. Galloway, Z. Klimont, and W. Winiwarter, 2008: How a century of ammonia synthesis changed the world. *Nature Geoscience*, **1(10)**, doi:10.1038/ngeo325.
Etiope, G. and P. Ciccioli, 2009: Earth's degassing: A missing ethane and propane source. *Science*, **323(5913)**, 478, doi:10.1126/science.1165904.
Evan, A.T., C. Flamant, S. Fiedler, and O. Doherty, 2014: An analysis of aeolian dust in climate models. *Geophysical Research Letters*, **41(16)**, 5996–6001, doi:10.1002/2014gl060545.
Evans, M. et al., 2017: Black carbon emissions in Russia: A critical review. *Atmospheric Environment*, **163**, 9–21, doi:10.1016/j.atmosenv.2017.05.026.
Evans, S., P. Ginoux, S. Malyshev, and E. Shevliakova, 2016: Climate-vegetation interaction and amplification of Australian dust variability. *Geophysical Research Letters*, **43(22)**, 11,823–11,830, doi:10.1002/2016gl071016.
Eyring, V. et al., 2010: Transport impacts on atmosphere and climate: Shipping. *Atmospheric Environment*, **44(37)**, 4735–4771, doi:10.1016/j.atmosenv.2009.04.059.
Fanourgakis, G.S. et al., 2019: Evaluation of global simulations of aerosol particle and cloud condensation nuclei number, with implications for cloud droplet formation. *Atmospheric Chemistry and Physics*, **19(13)**, 8591–

ACCEPTED VERSION SUBJECT TO FINAL EDITING

8617, doi:10.5194/acp-19-8591-2019.
Favez, O. et al., 2008: Seasonality of major aerosol species and their transformations in Cairo megacity. *Atmospheric Environment*, **42(7)**, 1503–1516, doi:10.1016/j.atmosenv.2007.10.081.
Fay, M. et al., 2018: Energy investment needs for fulfilling the Paris Agreement and achieving the Sustainable Development Goals. *Nature Energy*, **3(7)**, 589–599, doi:10.1038/s41560-018-0179-z.
Felzer, B.S., T. Cronin, J.M. Reilly, J.M. Melillo, and X. Wang, 2007: Impacts of ozone on trees and crops. *Comptes Rendus Geoscience*, **339(11–12)**, 784–798, doi:10.1016/j.crte.2007.08.008.
Feng, J. et al., 2006: A comparative study of the organic matter in PM2.5 from three Chinese megacities in three different climatic zones. *Atmospheric Environment*, **40(21)**, 3983–3994, doi:10.1016/j.atmosenv.2006.02.017.
Feng, L. et al., 2020: Gridded Emissions for CMIP6. *Geoscientific Model Development*, **13(2)**, 461–482, doi:10.5194/gmd-13-461-2020.
Feng, Z. and K. Kobayashi, 2009: Assessing the impacts of current and future concentrations of surface ozone on crop yield with meta-analysis. *Atmospheric Environment*, **43(8)**, 1510–1519, doi:10.1016/j.atmosenv.2008.11.033.
Ferek, R.J. et al., 2000: Drizzle suppression in ship tracks. *Journal of the Atmospheric Sciences*, doi:10.1175/1520-0469(2000)057<2707:dsist>2.0.co;2.
Ferraro, A.J., E.J. Highwood, and A.J. Charlton-Perez, 2011: Stratospheric heating by potential geoengineering aerosols. *Geophysical Research Letters*, doi:10.1029/2011gl049761.
Fiebig, M., A. Wiartalla, B. Holderbaum, and S. Kiesow, 2014: Particulate emissions from diesel engines: correlation between engine technology and emissions. *Journal of Occupational Medicine and Toxicology*, **9(1)**, 6, doi:10.1186/1745-6673-9-6.
Finney, D.L., R.M. Doherty, O. Wild, and N.L. Abraham, 2016a: The impact of lightning on tropospheric ozone chemistry using a new global lightning parametrisation. *Atmospheric Chemistry and Physics*, **16(12)**, 7507–7522, doi:10.5194/acp-16-7507-2016.
Finney, D.L., R.M. Doherty, O. Wild, P.J. Young, and A. Butler, 2016b: Response of lightning NO _x emissions and ozone production to climate change: Insights from the Atmospheric Chemistry and Climate Model Intercomparison Project. *Geophysical Research Letters*, **43(10)**, 5492–5500, doi:10.1002/2016gl068825.
Finney, D.L. et al., 2018: A projected decrease in lightning under climate change. *Nature Climate Change*, **8(3)**, 210–213, doi:10.1038/s41558-018-0072-6.
Fioletov, V.E. et al., 2016: A global catalogue of large SO₂ sources and emissions derived from the Ozone Monitoring Instrument. *Atmospheric Chemistry and Physics*, **16(18)**, 11497–11519, doi:10.5194/acp-16-11497-2016.
Fiore, A.M., V. Naik, and E.M. Leibensperger, 2015: Air Quality and Climate Connections. *Journal of the Air & Waste Management Association*, **65(6)**, 645–685, doi:10.1080/10962247.2015.1040526.
Fiore, A.M. et al., 2012: Global air quality and climate. *Chemical Society Reviews*, **41(19)**, 6663–6683, doi:10.1039/c2cs35095e.
Flechard, C.R. et al., 2020: Carbon–nitrogen interactions in European forests and semi-natural vegetation – Part 1: Fluxes and budgets of carbon, nitrogen and greenhouse gases from ecosystem monitoring and modelling. *Biogeosciences*, **17(6)**, 1583–1620, doi:10.5194/bg-17-1583-2020.
Flemming, J. et al., 2017: The CAMS interim Reanalysis of Carbon Monoxide, Ozone and Aerosol for 2003-2015. *Atmospheric Chemistry and Physics*, **17(3)**, 1945–1983, doi:10.5194/acp-17-1945-2017.
Forestieri, S.D. et al., 2018: Temperature and Composition Dependence of Sea Spray Aerosol Production. *Geophysical Research Letters*, doi:10.1029/2018gl078193.
Forster, P.M. et al., 2016: Recommendations for diagnosing effective radiative forcing from climate models for CMIP6. *Journal of Geophysical Research*, **121(20)**, 12,460–12,475, doi:10.1002/2016jd025320.
Forster, P.M. et al., 2020: Current and future global climate impacts resulting from COVID-19. *Nature Climate Change*, doi:10.1038/s41558-020-0883-0.
Fortems-Cheiney, A. et al., 2017: A 3 °c global RCP8.5 emission trajectory cancels benefits of European emission reductions on air quality. *Nature Communications*, **8(1)**, doi:10.1038/s41467-017-00075-9.
Fowler, D. et al., 2015: Effects of global change during the 21st century on the nitrogen cycle. *Atmospheric Chemistry and Physics*, **15(24)**, 13849–13893, doi:10.5194/acp-15-13849-2015.
Fowler, D. et al., 2020: A chronology of global air quality. *Philosophical Transactions of the Royal Society A: Mathematical, Physical and Engineering Sciences*, **378(2183)**, 20190314, doi:10.1098/rsta.2019.0314.
Franchin, A. et al., 2018: Airborne and ground-based observations of ammonium-nitrate-dominated aerosols in a shallow boundary layer during intense winter pollution episodes in northern Utah. *Atmospheric Chemistry and Physics*, **18(23)**, 17259–17276, doi:10.5194/acp-18-17259-2018.
Franco, B. et al., 2016: Evaluating ethane and methane emissions associated with the development of oil and natural gas extraction in North America. *Environmental Research Letters*, **11(4)**, doi:10.1088/1748-9326/11/4/044010.
Freedman, M.A., E.J.E. Ott, and K.E. Marak, 2019: Role of pH in Aerosol Processes and Measurement Challenges. *Journal of Physical Chemistry A*, **123(7)**, 1275–1284, doi:10.1021/acs.jpca.8b10676.
Freney, E. et al., 2018: Aerosol composition and the contribution of SOA formation over Mediterranean forests.

ACCEPTED VERSION SUBJECT TO FINAL EDITING

Atmospheric Chemistry and Physics, doi:10.5194/acp-18-7041-2018.
Friedlingstein, P. et al., 2020: Global Carbon Budget 2020. *Earth System Science Data*, **12(4)**, 3269–3340, doi:10.5194/essd-12-3269-2020.
Froyd, K.D. et al., 2009: Aerosol composition of the tropical upper troposphere. *Atmospheric Chemistry and Physics*, **9(13)**, 4363–4385, doi:10.5194/acp-9-4363-2009.
Fu, D. et al., 2019: Direct retrieval of isoprene from satellite-based infrared measurements. *Nature Communications*, **10(1)**, 3811, doi:10.1038/s41467-019-11835-0.
Fu, T.M. and H. Tian, 2019: Climate Change Penalty to Ozone Air Quality: Review of Current Understandings and Knowledge Gaps. *Current Pollution Reports*, **5(3)**, 159–171, doi:10.1007/s40726-019-00115-6.
Fuchs, H. et al., 2013: Experimental evidence for efficient hydroxyl radical regeneration in isoprene oxidation. *Nature Geoscience*, **6**, 1023.
Fuglestvedt, J., T. Berntsen, G. Myhre, K. Rypdal, and R.B. Skeie, 2008: Climate forcing from the transport sectors. *Proceedings of the National Academy of Sciences of the United States of America*, **105(2)**, 454–458, doi:10.1073/pnas.0702958104.
Fuglestvedt, J.S., I.S.A. Isaksen, and W.C. Wang, 1996: Estimates of indirect global warming potentials for CH₄, CO and NO_x. *Climatic Change*, **34(3–4)**, 405–437, doi:10.1007/bf00139300.
Fujimori, S. et al., 2017: SSP3: AIM implementation of Shared Socioeconomic Pathways. *Global Environmental Change*, **42**, 268–283, doi:10.1016/j.gloenvcha.2016.06.009.
Fuzzi, S. et al., 2007: Overview of the inorganic and organic composition of size-segregated aerosol in Rondônia, Brazil, from the biomass-burning period to the onset of the wet season. *Journal of Geophysical Research: Atmospheres*, **112(D1)**, doi:10.1029/2005jd006741.
Fyfe, J.C. et al., 2021: Quantifying the influence of short-term emission reductions on climate. *Science Advances*, **7(10)**, doi:10.1126/sciadv.abf7133.
Gabric, A.J., B. Qu, L. Rotstayn, and J.M. Shephard, 2013: Global simulations of the impact on contemporary climate of a perturbation to the sea-to-air flux of dimethylsulfide. *Australian Meteorological and Oceanographic Journal*, **63(3)**, 365–376, doi:10.22499/2.6303.002.
Gallardo, L. et al., 2018: Evolution of air quality in Santiago: The role of mobility and lessons from the science-policy interface. *Elementa*, **6(1)**, 38, doi:10.1525/elementa.293.
Galmarini, S. et al., 2017: Technical note: Coordination and harmonization of the multi-scale, multi-model activities HTAP2, AQMEII3, and MICS-Asia3: Simulations, emission inventories, boundary conditions, and model output formats. *Atmospheric Chemistry and Physics*, **17(2)**, 1543–1555, doi:10.5194/acp-17-1543-2017.
Gao, M. et al., 2018: Air quality and climate change, Topic 3 of the Model Inter-Comparison Study for Asia Phase III (MICS-Asia III) - Part 1: Overview and model evaluation. *Atmospheric Chemistry and Physics*, **18(7)**, 4859–4884, doi:10.5194/acp-18-4859-2018.
Garcia-Menendez, F., E. Monier, and N.E. Selin, 2017: The role of natural variability in projections of climate change impacts on U.S. ozone pollution. *Geophysical Research Letters*, **44(6)**, 2911–2921, doi:10.1002/2016gl071565.
Garrido-Perez, J.M., C. Ordóñez, R. García-Herrera, and J.L. Schnell, 2019: The differing impact of air stagnation on summer ozone across Europe. *Atmospheric Environment*, **219**, doi:10.1016/j.atmosenv.2019.117062.
Gasparini, B. and U. Lohmann, 2016: Why cirrus cloud seeding cannot substantially cool the planet. *Journal of Geophysical Research*, doi:10.1002/2015jd024666.
Gasparini, B., Z. McGraw, T. Storelvmo, and U. Lohmann, 2020: To what extent can cirrus cloud seeding counteract global warming? *Environmental Research Letters*, **15(5)**, 054002, doi:10.1088/1748-9326/ab71a3.
Gaubert, B. et al., 2017: Chemical Feedback From Decreasing Carbon Monoxide Emissions. *Geophysical Research Letters*, **44(19)**, 9985–9995, doi:10.1002/2017gl074987.
Gaudel, A. et al., 2018: Tropospheric Ozone Assessment Report: Present-day distribution and trends of tropospheric ozone relevant to climate and global atmospheric chemistry model evaluation. *Elem Sci Anth*, **6(1)**, 39, doi:10.1525/elementa.291.
Gaudel, A. et al., 2020: Aircraft observations since the 1990s reveal increases of tropospheric ozone at multiple locations across the Northern Hemisphere. *Science Advances*, **6(34)**, doi:10.1126/sciadv.aba8272.
Geddes, J.A., R. Martin, B.L. Boys, and A. van Donkelaar, 2016: Long-Term Trends Worldwide in Ambient NO(2) Concentrations Inferred from Satellite Observations. *Environmental Health Perspectives*, **124(3)**, 281–289, doi:10.1289/ehp.1409567.
Genard-Zielinski, A.-C. et al., 2018: Seasonal variations of <i>Quercus pubescens</i> isoprene emissions from an <i>in natura</i> forest under drought stress and sensitivity to future climate change in the Mediterranean area. 4711–4730 pp., doi:10.5194/bg-15-4711-2018.
Geng, L. et al., 2014: Nitrogen isotopes in ice core nitrate linked to anthropogenic atmospheric acidity change. *Proceedings of the National Academy of Sciences of the United States of America*, **111(16)**, 5808–5812, doi:10.1073/pnas.1319441111.
Geng, L. et al., 2017: Isotopic evidence of multiple controls on atmospheric oxidants over climate transitions. *Nature*, **546(7656)**, 133–136, doi:10.1038/nature22340.

ACCEPTED VERSION SUBJECT TO FINAL EDITING

Georgoulias, A.K., R.A.J. Van Der, P. Stammes, K. Folkert Boersma, and H.J. Eskes, 2019: Trends and trend reversal detection in 2 decades of tropospheric NO₂ satellite observations. *Atmospheric Chemistry and Physics*, **19(9)**, 6269–6294, doi:10.5194/acp-19-6269-2019.

Gettelman, A., R. Lamboll, C.G. Bardeen, P.M. Forster, and D. Watson-Parris, 2021: Climate Impacts of COVID-19 Induced Emission Changes. *Geophysical Research Letters*, **48(3)**, e2020GL091805, doi:10.1029/2020gl091805.

Ghan, S.J., 2013: Technical Note: Estimating aerosol effects on cloud radiative forcing. *Atmospheric Chemistry and Physics*, **13(19)**, 9971–9974, doi:10.5194/acp-13-9971-2013.

Gidden, M.J. et al., 2019: Global emissions pathways under different socioeconomic scenarios for use in CMIP6: A dataset of harmonized emissions trajectories through the end of the century. *Geoscientific Model Development*, **12(4)**, 1443–1475, doi:10.5194/gmd-12-1443-2019.

Ginoux, P., J.M. Prospero, T.E. Gill, N.C. Hsu, and M. Zhao, 2012: Global-scale attribution of anthropogenic and natural dust sources and their emission rates based on MODIS Deep Blue aerosol products. *Reviews of Geophysics*, **50(3)**, doi:10.1029/2012rg000388.

Gioda, A., B.S. Amaral, I.L.G. Monteiro, and T.D. Saint'Pierre, 2011: Chemical composition, sources, solubility, and transport of aerosol trace elements in a tropical region. *J. Environ. Monit.*, **13(8)**, 2134–2142, doi:10.1039/c1em10240k.

Gkatzelis, G.I. et al., 2021: The global impacts of COVID-19 lockdowns on urban air quality: a critical review and recommendations. *Elementa: Science of the Anthropocene*, **9(1)**, doi:10.1525/elementa.2021.00176.

Gliß, J. et al., 2020: Multi-model evaluation of aerosol optical properties in the AeroCom phase III Control experiment, using ground and space based columnar observations from AERONET, MODIS, AATSR and a merged satellite product as well as surface in-situ observations from GAW. *Atmos. Chem. Phys. Discuss.*, **2020**, 1–62, doi:10.5194/acp-2019-1214.

Gliß, J. et al., 2021: AeroCom phase III multi-model evaluation of the aerosol life cycle and optical properties using ground- and space-based remote sensing as well as surface in situ observations. *Atmospheric Chemistry and Physics*, **21(1)**, 87–128, doi:10.5194/acp-21-87-2021.

Gómez-Sanabria, A., L. Höglund-Isaksson, P. Rafaj, and W. Schöpp, 2018: Carbon in global waste and wastewater flows – its potential as energy source under alternative future waste management regimes. *Advances in Geosciences*, **45**, 105–113, doi:10.5194/adgeo-45-105-2018.

Gonzalez-Abraham, R. et al., 2015: The effects of global change upon United States air quality. *Atmospheric Chemistry and Physics*, **15(21)**, 12645–12665, doi:10.5194/acp-15-12645-2015.

Gratz, L.E., D.A. Jaffe, and J.R. Hee, 2015: Causes of increasing ozone and decreasing carbon monoxide in springtime at the Mt. Bachelor Observatory from 2004 to 2013. *Atmospheric Environment*, **109**, 323–330, doi:10.1016/j.atmosenv.2014.05.076.

Grewe, V., S. Matthes, and K. Dahlmann, 2019: The contribution of aviation NOx emissions to climate change: are we ignoring methodological flaws? *Environmental Research Letters*, **14(12)**, 121003, doi:10.1088/1748-9326/ab5dd7.

Grewe, V. et al., 2001: Origin and variability of upper tropospheric nitrogen oxides and ozone at northern mid-latitudes. *Atmospheric Environment*, **35(20)**, 3421–3433, doi:10.1016/s1352-2310(01)00134-0.

Griffiths, P.T. et al., 2020: Tropospheric ozone in CMIP6 Simulations. *Atmospheric Chemistry and Physics*, **2020**, 1–50, doi:10.5194/acp-2019-1216.

Grythe, H., J. Ström, R. Krejci, P. Quinn, and A. Stohl, 2014: A review of sea-spray aerosol source functions using a large global set of sea salt aerosol concentration measurements. *Atmospheric Chemistry and Physics*, **14(3)**, 1277–1297, doi:10.5194/acp-14-1277-2014.

Gschrey, B., W. Schwarz, C. Elsner, and R. Engelhardt, 2011: High increase of global F-gas emissions until 2050. *Greenhouse Gas Measurement and Management*, **1(2)**, 85–92, doi:10.1080/20430779.2011.579352.

Guenther, A.B. et al., 2012: The model of emissions of gases and aerosols from nature version 2.1 (MEGAN2.1): An extended and updated framework for modeling biogenic emissions. *Geoscientific Model Development*, **5(6)**, 1471–1492, doi:10.5194/gmd-5-1471-2012.

Guo, H. et al., 2016: Fine particle pH and the partitioning of nitric acid during winter in the northeastern United States. *Journal of Geophysical Research*, **121(17)**, 10355–10376, doi:10.1002/2016jd025311.

Guo, H. et al., 2018: Effectiveness of ammonia reduction on control of fine particle nitrate. *Atmospheric Chemistry and Physics*, **18(16)**, 12241–12256, doi:10.5194/acp-18-12241-2018.

Guo, S. et al., 2014: Elucidating severe urban haze formation in China. *Proceedings of the National Academy of Sciences*, **111(49)**, 17373–17378, doi:10.1073/pnas.1419604111.

Guttikunda, S.K., R. Goel, and P. Pant, 2014: Nature of air pollution, emission sources, and management in the Indian cities. *Atmospheric Environment*, **95**, 501–510, doi:10.1016/j.atmosenv.2014.07.006.

Haines, A. et al., 2017a: Short-lived climate pollutant mitigation and the Sustainable Development Goals. *Nature Climate Change*, **7(12)**, 863–869, doi:10.1038/s41558-017-0012-x.

Haines, A. et al., 2017b: Short-lived climate pollutant mitigation and the Sustainable Development Goals. *Nature Climate Change*, **7(12)**, 863–869, doi:10.1038/s41558-017-0012-x.

ACCEPTED VERSION SUBJECT TO FINAL EDITING

Hammer, M.S. et al., 2018: Insight into global trends in aerosol composition from 2005 to 2015 inferred from the OMI Ultraviolet Aerosol Index. *Atmospheric Chemistry and Physics*, **18(11)**, 8097–8112, doi:10.5194/acp-18-8097-2018.

Hand, J.L., K.A. Gebhart, B.A. Schichtel, and W.C. Malm, 2012a: Increasing trends in wintertime particulate sulfate and nitrate ion concentrations in the Great Plains of the United States (2000–2010). *Atmospheric Environment*, **55**, 107–110, doi:10.1016/j.atmosenv.2012.03.050.

Hand, J.L., B.A. Schichtel, W.C. Malm, and M.L. Pitchford, 2012b: Particulate sulfate ion concentration and SO2 emission trends in the United States from the early 1990s through 2010. *Atmospheric Chemistry and Physics*, **12(21)**, 10353–10365, doi:10.5194/acp-12-10353-2012.

Hand, J.L., B.A. Schichtel, W.C. Malm, and N.H. Frank, 2013: Spatial and temporal trends in PM_{2.5} organic and elemental carbon across the United States. *Advances in Meteorology*, **2013**, doi:10.1155/2013/367674.

Hantson, S., W. Knorr, G. Schurgers, T.A.M. Pugh, and A. Arneth, 2017: Global isoprene and monoterpene emissions under changing climate, vegetation, CO2 and land use. *Atmospheric Environment*, **155**, 35–45, doi:10.1016/j.atmosenv.2017.02.010.

Harmsen, M. et al., 2019: Taking some heat off the NDCs? The limited potential of additional short-lived climate forcers' mitigation. *Climatic Change*, doi:10.1007/s10584-019-02436-3.

Harmsen, M.J.H.M. et al., 2015: How well do integrated assessment models represent non-CO₂ radiative forcing? *Climatic Change*, **133(4)**, 565–582, doi:10.1007/s10584-015-1485-0.

Harmsen, M.J.H.M. et al., 2020: Co-benefits of black carbon mitigation for climate and air quality. *Climatic Change*, doi:10.1007/s10584-020-02800-8.

Hartmann, D.L. et al., 2013: Observations: Atmosphere and Surface. In: *Climate Change 2013 the Physical Science Basis: Working Group I Contribution to the Fifth Assessment Report of the Intergovernmental Panel on Climate Change* [Stocker, T.F., D. Qin, G.-K. Plattner, M. Tignor, S.K. Allen, J. Boschung, A. Nauels, Y. Xia, V. Bex, and P.M. Midgley (eds.)]. Cambridge University Press, Cambridge, United Kingdom and New York, NY, USA, pp. 159–254, doi:10.1017/cbo9781107415324.008.

Hastings, M.G., J.C. Jarvis, and E.J. Steig, 2009: Anthropogenic Impacts on Nitrogen Isotopes of Ice-Core Nitrate. *Science*, **324(5932)**, 1288, doi:10.1126/science.1170510.

Hauglustaine, D.A., Y. Balkanski, and M. Schulz, 2014: A global model simulation of present and future nitrate aerosols and their direct radiative forcing of climate. *Atmospheric Chemistry and Physics*, **14(20)**, 11031–11063, doi:10.5194/acp-14-11031-2014.

He, H., X.Z. Liang, and D.J. Wuebbles, 2018: Effects of emissions change, climate change and long-range transport on regional modeling of future U.S. particulate matter pollution and speciation. *Atmospheric Environment*, **179**, 166–176, doi:10.1016/j.atmosenv.2018.02.020.

Heald, C.L. and D. Spracklen, 2015: Land Use Change Impacts on Air Quality and Climate. *Chemical Reviews*, **115(10)**, 4476–4496, doi:10.1021/cr500446g.

Heald, C.L. and J.A. Geddes, 2016a: The impact of historical land use change from 1850 to 2000 on secondary particulate matter and ozone. *Atmospheric Chemistry and Physics*, **16(23)**, 14997–15010, doi:10.5194/acp-16-14997-2016.

Heald, C.L. and J.A. Geddes, 2016b: The impact of historical land use change from 1850 to 2000 on secondary particulate matter and ozone. *Atmospheric Chemistry and Physics*, **16(23)**, 14997–15010, doi:10.5194/acp-16-14997-2016.

Heald, C.L. et al., 2014: Contrasting the direct radiative effect and direct radiative forcing of aerosols. *ATMOSPHERIC CHEMISTRY AND PHYSICS*, **14(11)**, 5513–5527, doi:10.5194/acp-14-5513-2014.

Heinze, C. et al., 2019: ESD Reviews: Climate feedbacks in the Earth system and prospects for their evaluation. *Earth System Dynamics*, **10(3)**, 379–452, doi:10.5194/esd-10-379-2019.

Hess, P., D. Kinnison, and Q. Tang, 2015: Ensemble simulations of the role of the stratosphere in the attribution of northern extratropical tropospheric ozone variability. *Atmospheric Chemistry and Physics*, **15(5)**, 2341–2365, doi:10.5194/acp-15-2341-2015.

Hock, R. et al., 2019: High Mountain Areas. In: *IPCC Special Report on the Ocean and Cryosphere in a Changing Climate* [Pörtner, H.-O., D.C. Roberts, V. Masson-Delmotte, P. Zhai, M. Tignor, E. Poloczanska, K. Mintenbeck, A. Alegría, M. Nicolai, A. Okem, J. Petzold, B. Rama, and N.M. Weyer (eds.)]. In Press, pp. 131–202.

Hodgson, A.K. et al., 2018: Near-field emission profiling of tropical forest and Cerrado fires in Brazil during SAMBBA 2012. *Atmospheric Chemistry and Physics*, doi:10.5194/acp-18-5619-2018.

Hodzic, A. et al., 2016: Rethinking the global secondary organic aerosol (SOA) budget: stronger production, faster removal, shorter lifetime. *Atmos. Chem. Phys.*, **16(12)**, 7917–7941, doi:10.5194/acp-16-7917-2016.

Hodzic, A. et al., 2020: Characterization of organic aerosol across the global remote troposphere: a comparison of ATom measurements and global chemistry models. *Atmos. Chem. Phys.*, **20(8)**, 4607–4635, doi:10.5194/acp-20-4607-2020.

Hoesly, R. et al., 2019: Community Emissions Data System (Version Dec-23-2019). Retrieved from:

ACCEPTED VERSION SUBJECT TO FINAL EDITING

www.globalchange.umd.edu/ceds.
Hoesly, R.M. et al., 2018: Historical (1750-2014) anthropogenic emissions of reactive gases and aerosols from the Community Emissions Data System (CEDS). *Geoscientific Model Development*, **11(1)**, 369–408, doi:10.5194/gmd-11-369-2018.
Hofzumahaus, A. et al., 2009: Amplified trace gas removal in the troposphere.. *Science (New York, N.Y.)*, **324(5935)**, 1702–4, doi:10.1126/science.1164566.
Höglund-Isaksson, L., 2012: Global anthropogenic methane emissions 2005–2030: technical mitigation potentials and costs. *Atmospheric Chemistry and Physics*, **12(19)**, 9079–9096, doi:10.5194/acp-12-9079-2012.
Höglund-Isaksson, L., A. Gomez-Sanabria, Z. Klimont, P. Rafaj, and W. Schöpp, 2020: Technical potentials and costs for reducing global anthropogenic methane emissions in the 2050 timeframe - results from the GAINS model. *Environmental Reaserch Communication*, **2**.
Höglund-Isaksson, L. et al., 2017: Cost estimates of the Kigali Amendment to phase-down hydrofluorocarbons. *Environmental Science and Policy*, **75**, 138–147, doi:10.1016/j.envsci.2017.05.006.
Hollaway, M.J., S.R. Arnold, W.J. Collins, G. Folberth, and A. Rap, 2017: Sensitivity of midnineteenth century tropospheric ozone to atmospheric chemistry-vegetation interactions. *Journal of Geophysical Research: Atmospheres*, **122(4)**, 2452–2473, doi:10.1002/2016jd025462.
Holmes, C.D., 2018: Methane Feedback on Atmospheric Chemistry: Methods, Models, and Mechanisms. *Journal of Advances in Modeling Earth Systems*, **10(4)**, 1087–1099, doi:10.1002/2017ms001196.
Holmes, C.D., M.J. Prather, O.A. Søvde, and G. Myhre, 2013: Future methane, hydroxyl, and their uncertainties: Key climate and emission parameters for future predictions. *Atmospheric Chemistry and Physics*, **13(1)**, 285–302, doi:10.5194/acp-13-285-2013.
Hong, C. et al., 2019: Impacts of climate change on future air quality and human health in China. *Proceedings of the National Academy of Sciences of the United States of America*, **116(35)**, 17193–17200, doi:10.1073/pnas.1812881116.
Hopcroft, P.O., P.J. Valdes, F.M. O'Connor, J.O. Kaplan, and D.J. Beerling, 2017: Understanding the glacial methane cycle. *Nature Communications*, **8**, 14383, doi:10.1038/ncomms14383.
Höpfner, M. et al., 2016: First detection of ammonia (NH₃) in the Asian summer monsoon upper troposphere. *Atmospheric Chemistry and Physics*, **16(22)**, 14357–14369, doi:10.5194/acp-16-14357-2016.
Höpfner, M. et al., 2019: Ammonium nitrate particles formed in upper troposphere from ground ammonia sources during Asian monsoons. *Nature Geoscience*, **12(8)**, 608–612, doi:10.1038/s41561-019-0385-8.
Horowitz, L.W. et al., 2020: The GFDL Global Atmospheric Chemistry-Climate Model AM4.1: Model Description and Simulation Characteristics. *Journal of Advances in Modeling Earth Systems*, **12(10)**, e2019MS002032, doi:10.1029/2019ms002032.
Hoshika, Y. et al., 2015: Ozone-induced stomatal sluggishness changes carbon and water balance of temperate deciduous forests. *Scientific Reports*, **5(1)**, 9871, doi:10.1038/srep09871.
Hossaini, R. et al., 2015: Efficiency of short-lived halogens at influencing climate through depletion of stratospheric ozone. *NATURE GEOSCIENCE*, **8(3)**, 186–190, doi:10.1038/ngeo2363.
Hossaini, R. et al., 2017: The increasing threat to stratospheric ozone from dichloromethane. *Nature Communications*, **8**, 15962.
Hou, P. and S. Wu, 2016: Long-term Changes in Extreme Air Pollution Meteorology and the Implications for Air Quality. *Scientific Reports*, **6**, doi:10.1038/srep23792.
Hou, P., S. Wu, J.L. McCarty, and Y. Gao, 2018: Sensitivity of atmospheric aerosol scavenging to precipitation intensity and frequency in the context of global climate change. *Atmospheric Chemistry and Physics*, **18(11)**, 8173–8182, doi:10.5194/acp-18-8173-2018.
Huang, K. and J.S. Fu, 2016: A global gas flaring black carbon emission rate dataset from 1994 to 2012. *Scientific Data*, **3**, 160104.
Huang, K. et al., 2015: Russian anthropogenic black carbon: Emission reconstruction and Arctic black carbon simulation. *Journal of Geophysical Research: Atmospheres*, **120(21)**, 11,306–311,333, doi:10.1002/2015jd023358.
Huang, R.-J. et al., 2014: High secondary aerosol contribution to particulate pollution during haze events in China. *Nature*, **514(7521)**, 218–222, doi:10.1038/nature13774.
Huang, X. et al., 2020: Enhanced secondary pollution offset reduction of primary emissions during COVID-19 lockdown in China. *National Science Review*, doi:10.1093/nsr/nwaa137.
Huang, Y., S. Wu, M.K. Dubey, and N.H.F. French, 2013: Impact of aging mechanism on model simulated carbonaceous aerosols. *Atmospheric Chemistry and Physics*, doi:10.5194/acp-13-6329-2013.
Huang, Y., N. Unger, K. Harper, and C. Heyes, 2020: Global Climate and Human Health Effects of the Gasoline and Diesel Vehicle Fleets. *GeoHealth*, **4(3)**, doi:10.1029/2019gh000240.
Huang, Y. et al., 2018: Global radiative effects of solid fuel cookstove aerosol emissions. *Atmospheric Chemistry and Physics*, **18(8)**, 5219–5233, doi:10.5194/acp-18-5219-2018.
Hudman, R.C. et al., 2012: Steps towards a mechanistic model of global soil nitric oxide emissions: implementation and space based-constraints. *Atmospheric Chemistry and Physics*, **12(16)**, 7779–7795, doi:10.5194/acp-12-7779-

ACCEPTED VERSION SUBJECT TO FINAL EDITING

2012.
Iizuka, Y. et al., 2018: A 60 Year Record of Atmospheric Aerosol Depositions Preserved in a High-Accumulation Dome Ice Core, Southeast Greenland. *Journal of Geophysical Research: Atmospheres*, **123(1)**, 574–589, doi:10.1002/2017jd026733.
Im, U. et al., 2012: Summertime aerosol chemical composition in the Eastern Mediterranean and its sensitivity to temperature. *Atmospheric Environment*, **50**, 164–173, doi:10.1016/j.atmosenv.2011.12.044.
IMO, 2016: *Effective date of implementation of the fuel oil standard in regulation 14.1.3 of MARPOL Annex VI. Resolution MEPC 280(70) – Adopted on 28 October 2016*. MEPC 70/18/Add.1, International Maritime Organization (IMO), London, UK.
Inness, A. et al., 2019: The CAMS reanalysis of atmospheric composition. *Atmospheric Chemistry and Physics*, **19(6)**, 3515–3556, doi:10.5194/acp-19-3515-2019.
IPCC, 2019a: Climate Change and Land: an IPCC special report on climate change, desertification, land degradation, sustainable land management, food security, and greenhouse gas fluxes in terrestrial ecosystems. [Shukla, P.R., J. Skea, E.C. Buendia, V. Masson-Delmotte, H.-O. Pörtner, D.C. Roberts, P. Zhai, R. Slade, S. Connors, R. Diemen, M. Ferrat, E. Haughey, S. Luz, S. Neogi, M. Pathak, J. Petzold, J.P. Pereira, P. Vyas, E. Huntley, K. Kissick, M. Belkacemi, and J. Malley (eds.)]. In Press, 896 pp.
IPCC, 2019b: IPCC Special Report on the Ocean and Cryosphere in a Changing Climate. [Pörtner, H.-O., D.C. Roberts, V. Masson-Delmotte, P. Zhai, M. Tignor, E. Poloczanska, K. Mintenbeck, A. Alegría, M. Nicolai, A. Okem, J. Petzold, B. Rama, and N.M. Weyer (eds.)]. In Press, 755 pp., doi:www.ipcc.ch/report/srocc/.
Irie, H., T. Muto, S. Itahashi, J.- Kurokawa, and I. Uno, 2016: Turnaround of Tropospheric Nitrogen Dioxide Pollution Trends in China, Japan, and South Korea. *SOLA*, **12**, 170–174, doi:10.2151/sola.2016-035.
Jackson, L.S., J.A. Crook, and P.M. Forster, 2016: An intensified hydrological cycle in the simulation of geoengineering by cirrus cloud thinning using ice crystal fall speed changes. *Journal of Geophysical Research*, doi:10.1002/2015jd024304.
Jakob, M. and J.C. Steckel, 2016: Implications of climate change mitigation for sustainable development. *Environmental Research Letters*, **11(10)**, 104010, doi:10.1088/1748-9326/11/10/104010.
Janssens-Maenhout, G. et al., 2019: EDGAR v4.3.2 Global Atlas of the three major Greenhouse Gas Emissions for the period 1970--2012. *Earth System Science Data Discussions*, **2019**, 1–52, doi:10.5194/essd-2018-164.
Jardine, K.J. et al., 2016: Monoterpene 'thermometer' of tropical forest-atmosphere response to climate warming. *Plant, Cell & Environment*, **40(3)**, 441–452, doi:10.1111/pce.12879.
Jia, G. et al., 2019: Land–climate interactions. *Special report on climate change, desertification, land degradation, sustainable land management, food security, and greenhouse gas fluxes in terrestrial ecosystems*.
Jiang, H. et al., 2013: Projected effect of 2000–2050 changes in climate and emissions on aerosol levels in China and associated transboundary transport. *Atmospheric Chemistry and Physics*, **13(16)**, 7937–7960, doi:10.5194/acp-13-7937-2013.
Jiang, L. and B.C. O'Neill, 2017: Global urbanization projections for the Shared Socioeconomic Pathways. *Global Environmental Change*, **42**, 193–199, doi:10.1016/j.gloenvcha.2015.03.008.
Jiang, Z. et al., 2017: A 15-year record of CO emissions constrained by MOPITT CO observations. *Atmospheric Chemistry and Physics*, **17(7)**, 4565–4583, doi:10.5194/acp-17-4565-2017.
Jiang, Z. et al., 2018a: Unexpected slowdown of US pollutant emission reduction in the past decade. *Proceedings of the National Academy of Sciences of the United States of America*, **115(20)**, 5099–5104, doi:10.1073/pnas.1801191115.
Jiang, Z. et al., 2018b: Unexpected slowdown of US pollutant emission reduction in the past decade. *Proceedings of the National Academy of Sciences of the United States of America*, **115(20)**, 5099–5104, doi:10.1073/pnas.1801191115.
Jiao, C. et al., 2014: An aerocom assessment of black carbon in Arctic snow and sea ice. *Atmospheric Chemistry and Physics*, **14(5)**, 2399–2417, doi:10.5194/acp-14-2399-2014.
Jo, D.S., R.J. Park, S. Lee, S.W. Kim, and X. Zhang, 2016: A global simulation of brown carbon: Implications for photochemistry and direct radiative effect. *Atmospheric Chemistry and Physics*, **16(5)**, 3413–3432, doi:10.5194/acp-16-3413-2016.
John, J.G., A.M. Fiore, V. Naik, L.W. Horowitz, and J.P. Dunne, 2012: Climate versus emission drivers of methane lifetime against loss by tropospheric OH from 1860-2100. *Atmospheric Chemistry and Physics*, **12(24)**, 12021–12036, doi:10.5194/acp-12-12021-2012.
Jones, A. and J.M. Haywood, 2012: Sea-spray geoengineering in the HadGEM2-ES earth-system model: Radiative impact and climate response. *Atmospheric Chemistry and Physics*, doi:10.5194/acp-12-10887-2012.
Jones, A., J. Haywood, and O. Boucher, 2011: A comparison of the climate impacts of geoengineering by stratospheric SO₂ injection and by brightening of marine stratocumulus cloud. *Atmospheric Science Letters*, doi:10.1002/asl.291.
Jones, A.C., J.M. Haywood, and A. Jones, 2016: Climatic impacts of stratospheric geoengineering with sulfate, black carbon and titania injection. *Atmospheric Chemistry and Physics*, doi:10.5194/acp-16-2843-2016.
Jones, C.D., 2003: Strong carbon cycle feedbacks in a climate model with interactive CO 2 and sulphate aerosols.

ACCEPTED VERSION SUBJECT TO FINAL EDITING

Geophysical Research Letters, **30(9)**, 1479, doi:10.1029/2003gl016867.
Jonson, J.E., M. Gauss, M. Schulz, J.-P. Jalkanen, and H. Fagerli, 2020: Effects of global ship emissions on European air pollution levels. *Atmospheric Chemistry and Physics*, **20(19)**, 11399–11422, doi:10.5194/acp-20-11399-2020.
Jonson, J.E. et al., 2017: Impact of excess NO_x emissions from diesel cars on air quality, public health and eutrophication in Europe. *Environmental Research Letters*, **12(9)**, 94017, doi:10.1088/1748-9326/aa8850.
Kaltsonoudis, C., E. Kostenidou, K. Florou, M. Psichoudaki, and S.N. Pandis, 2016: Temporal variability and sources of VOCs in urban areas of the eastern Mediterranean. *Atmospheric Chemistry and Physics*, doi:10.5194/acp-16-14825-2016.
Kanakidou, M., S. Myriokefalitakis, and K. Tsigaridis, 2018: Aerosols in atmospheric chemistry and biogeochemical cycles of nutrients. *Environmental Research Letters*, **13(6)**, 063004, doi:10.1088/1748-9326/aabcdb.
Kanaya, Y. et al., 2020: Rapid reduction in black carbon emissions from China: evidence from 2009–2019 observations on Fukue Island, Japan. *Atmospheric Chemistry and Physics*, **20(11)**, 6339–6356, doi:10.5194/acp-20-6339-2020.
Kang, S. et al., 2002: Twentieth century increase of atmospheric ammonia recorded in Mount Everest ice core. *Journal of Geophysical Research Atmospheres*, **107(21)**, ACL 13–1–ACL 13–9, doi:10.1029/2001jd001413.
Karset, I.H.H. et al., 2018: Strong impacts on aerosol indirect effects from historical oxidant changes. *Atmos. Chem. Phys.*, **18(10)**, 7669–7690, doi:10.5194/acp-18-7669-2018.
Kasoar, M., D. Shawki, and A. Voulgarakis, 2018: Similar spatial patterns of global climate response to aerosols from different regions. *npj Climate and Atmospheric Science*, doi:10.1038/s41612-018-0022-z.
Kasoar, M. et al., 2016: Regional and global temperature response to anthropogenic SO₂ emissions from China in three climate models. *Atmospheric Chemistry and Physics*, **16(15)**, 9785–9804, doi:10.5194/acp-16-9785-2016.
Keeble, J., B. Hassler, A. Banerjee, and et al., 2021: Evaluating stratospheric ozone and water vapour changes in CMIP6 models from 1850-2100. *Atmos. Chem. Phys.*
Kekonen, T. et al., 2005: The 800 year long ion record from the Lomonosovfonna (Svalbard) ice core. *Journal of Geophysical Research Atmospheres*, **110(7)**, 1–11, doi:10.1029/2004jd005223.
Kerr, G.H. and D.W. Waugh, 2018: Connections between summer air pollution and stagnation. *Environmental Research Letters*, **13(8)**, 084001, doi:10.1088/1748-9326/aad2e2.
Kholod, N., M. Evans, and T. Kuklinski, 2016: Russia's black carbon emissions: Focus on diesel sources. *Atmospheric Chemistry and Physics*, **16(17)**, 11267–11281, doi:10.5194/acp-16-11267-2016.
Kirkby, J. et al., 2011: Role of sulphuric acid, ammonia and galactic cosmic rays in atmospheric aerosol nucleation. *Nature*, **476(7361)**, 429–433, doi:10.1038/nature10343.
Kirkevåg, A. et al., 2018: A production-tagged aerosol module for Earth system models, OsloAero5.3 – extensions and updates for CAM5.3-Oslo. *Geosci. Model Dev.*, **11(10)**, 3945–3982, doi:10.5194/gmd-11-3945-2018.
Kirtman, B. et al., 2013: Near-term Climate Change: Projections and Predictability. In: *Climate Change 2013: The Physical Science Basis. Contribution of Working Group I to the Fifth Assessment Report of the Intergovernmental Panel on Climate Change* [Stocker, T.F., D. Qin, G.-K. Plattner, M. Tignor, S.K. Allen, J. Boschung, A. Nauels, Y. Xia, V. Bex, and P.M. Midgley (eds.)]. Cambridge University Press, Cambridge, United Kingdom and New York, USA, pp. 953–1028, doi:10.1017/cbo9781107415324.023.
Kleinschmitt, C., O. Boucher, and U. Platt, 2018: Sensitivity of the radiative forcing by stratospheric sulfur geoengineering to the amount and strategy of the SO₂ injection studied with the LMDZ-S3A model. *Atmospheric Chemistry and Physics*, doi:10.5194/acp-18-2769-2018.
Klimont, Z. and W. Winiwarter, 2015: Estimating Costs and Potential for Reduction of Ammonia Emissions from Agriculture in the GAINS Model. In: *Costs of Ammonia Abatement and the Climate Co-Benefits (1 edition)* [Reis, S., C. Howard, and M.A. Sutton (eds.)]. Springer, Dordrecht, The Netherlands, pp. 233–261, doi:10.1007/978-94-017-9722-1_9.
Klimont, Z. et al., 2017a: Global anthropogenic emissions of particulate matter including black carbon. *Atmospheric Chemistry and Physics*, **17(14)**, 8681–8723, doi:10.5194/acp-17-8681-2017.
Klimont, Z. et al., 2017b: Global anthropogenic emissions of particulate matter including black carbon. *Atmospheric Chemistry and Physics*, **17(14)**, 8681–8723, doi:10.5194/acp-17-8681-2017.
Klimont, Z. et al., 2017c: Bridging the gap – The role of short-lived climate pollutants. In: *The Emissions Gap Report 2017*. United Nations Environment Programme (UNEP), Nairobi, Kenya, pp. 48–57.
Kloster, S. et al., 2007: Response of dimethylsulfide (DMS) in the ocean and atmosphere to global warming. *Journal of Geophysical Research: Biogeosciences*, **112(G3)**, doi:10.1029/2006jg000224.
Knorr, W., A. Arneth, and L. Jiang, 2016: Demographic controls of future global fire risk. *Nature Climate Change*, **6(8)**, 781–785, doi:10.1038/nclimate2999.
Kodros, J.K. et al., 2015: Uncertainties in global aerosols and climate effects due to biofuel emissions. *Atmospheric Chemistry and Physics*, **15(15)**, 8577–8596, doi:10.5194/acp-15-8577-2015.
Kok, J.F., E.J.R. Parteli, T.I. Michaels, and D.B. Karam, 2012: The physics of wind-blown sand and dust. *Reports on Progress in Physics*, **75(10)**, doi:10.1088/0034-4885/75/10/106901.

ACCEPTED VERSION SUBJECT TO FINAL EDITING

Kok, J.F., D.S. Ward, N.M. Mahowald, and A.T. Evan, 2018: Global and regional importance of the direct dust-climate feedback. *Nature Communications*, **9(1)**, 241, doi:10.1038/s41467-017-02620-y.
Kok, J.F. et al., 2014: An improved dust emission model - Part 1: Model description and comparison against measurements. *Atmospheric Chemistry and Physics*, **14(23)**, 13023–13041, doi:10.5194/acp-14-13023-2014.
Kok, J.F. et al., 2017: Smaller desert dust cooling effect estimated from analysis of dust size and abundance. *Nature Geoscience*, **10(4)**, 274–278, doi:10.1038/ngeo2912.
Koshak, W., H. Peterson, A. Biazar, M. Khan, and L. Wang, 2014: The NASA Lightning Nitrogen Oxides Model (LNOM): Application to air quality modeling. *Atmospheric Research*, **135–136**, 363–369, doi:10.1016/j.atmosres.2012.12.015.
Kremser, S. et al., 2016: Stratospheric aerosol – Observations, processes, and impact on climate. *Reviews of Geophysics*, **54(2)**, 278–335, doi:10.1002/2015rg000511.
Kristiansen, N.I. et al., 2016: Evaluation of observed and modelled aerosol lifetimes using radioactive tracers of opportunity and an ensemble of 19 global models. *Atmospheric Chemistry and Physics*, **16(5)**, 3525–3561, doi:10.5194/acp-16-3525-2016.
Kristjánsson, J.E., H. Muri, and H. Schmidt, 2015: The hydrological cycle response to cirrus cloud thinning. *Geophysical Research Letters*, doi:10.1002/2015gl066795.
Kroll, J.H. et al., 2020: The complex chemical effects of COVID-19 shutdowns on air quality. *Nature Chemistry*, **12(9)**, 777–779, doi:10.1038/s41557-020-0535-z.
Krotkov, N.A. et al., 2016: Aura OMI observations of regional SO₂ and NO₂ pollution changes from 2005 to 2015. *Atmospheric Chemistry and Physics*, **16(7)**, 4605–4629, doi:10.5194/acp-16-4605-2016.
Krzyzanowski, M. and A. Cohen, 2008: Update of WHO air quality guidelines. *Air Quality, Atmosphere & Health*, **1(1)**, 7–13, doi:10.1007/s11869-008-0008-9.
Kulmala, M. et al., 2004: A new feedback mechanism linking forests, aerosols, and climate. *Atmospheric Chemistry and Physics*, **4(2)**, 557–562, doi:10.5194/acp-4-557-2004.
Kumar, A. et al., 2013: Free-troposphere ozone and carbon monoxide over the North Atlantic for 2001-2011. *Atmospheric Chemistry and Physics*, doi:10.5194/acp-13-12537-2013.
Kuprov, R. et al., 2014: Composition and secondary formation of fine particulate matter in the Salt Lake Valley: Winter 2009. *Journal of the Air & Waste Management Association*, **64(8)**, 957–969, doi:10.1080/10962247.2014.903878.
Kutzner, R.D. et al., 2018: Long-term monitoring of black carbon across Germany. *Atmospheric Environment*, **185**, 41–52, doi:10.1016/j.atmosenv.2018.04.039.
Kuzu, S.L. et al., 2020: Black carbon and size-segregated elemental carbon, organic carbon compositions in a megacity: a case study for Istanbul. *Air Quality, Atmosphere & Health*, **13(7)**, 827–837, doi:10.1007/s11869-020-00839-1.
Laakso, A., H. Korhonen, S. Romakkaniemi, and H. Kokkola, 2017: Radiative and climate effects of stratospheric sulfur geoengineering using seasonally varying injection areas. *Atmospheric Chemistry and Physics*, doi:10.5194/acp-17-6957-2017.
Lacressonnière, G. et al., 2016: Impacts of regional climate change on air quality projections and associated uncertainties. *Climatic Change*, **136(2)**, 309–324, doi:10.1007/s10584-016-1619-z.
Lacressonnière, G. et al., 2017: Particulate matter air pollution in Europe in a +2°C warming world. *Atmospheric Environment*, **154**, 129–140, doi:10.1016/j.atmosenv.2017.01.037.
Laj, P. et al., 2020: A global analysis of climate-relevant aerosol properties retrieved from the network of Global Atmosphere Watch (GAW) near-surface observatories. *Atmospheric Measurement Techniques*, **13(8)**, 4353–4392, doi:10.5194/amt-13-4353-2020.
Lamarque, J.F. et al., 2010: Historical (1850-2000) gridded anthropogenic and biomass burning emissions of reactive gases and aerosols: Methodology and application. *Atmospheric Chemistry and Physics*, **10(15)**, 7017–7039, doi:10.5194/acp-10-7017-2010.
Lamarque, J.F. et al., 2013a: Multi-model mean nitrogen and sulfur deposition from the atmospheric chemistry and climate model intercomparison project (ACCMIP): Evaluation of historical and projected future changes. *Atmospheric Chemistry and Physics*, **13(16)**, 7997–8018, doi:10.5194/acp-13-7997-2013.
Lamarque, J.F. et al., 2013b: Multi-model mean nitrogen and sulfur deposition from the atmospheric chemistry and climate model intercomparison project (ACCMIP): Evaluation of historical and projected future changes. *Atmospheric Chemistry and Physics*, **13(16)**, 7997–8018, doi:10.5194/acp-13-7997-2013.
Lamarque, J.F. et al., 2013c: The atmospheric chemistry and climate model intercomparison Project (ACCMIP): Overview and description of models, simulations and climate diagnostics. *Geoscientific Model Development*, **6(1)**, 179–206, doi:10.5194/gmd-6-179-2013.
Lamsal, L.N. et al., 2015: U.S. NO₂ trends (2005–2013): EPA Air Quality System (AQS) data versus improved observations from the Ozone Monitoring Instrument (OMI). *Atmospheric Environment*, **110**, 130–143, doi:10.1016/j.atmosenv.2015.03.055.
Lana, A. et al., 2011: An updated climatology of surface dimethlysulfide concentrations and emission fluxes in the

ACCEPTED VERSION SUBJECT TO FINAL EDITING

global ocean. *Global Biogeochemical Cycles*, **25(1)**, doi:10.1029/2010gb003850.
Landry, J.-S., H.D. Matthews, and N. Ramankutty, 2015: A global assessment of the carbon cycle and temperature responses to major changes in future fire regime. *Climatic Change*, **133(2)**, 179–192, doi:10.1007/s10584-015-1461-8.
Languille, B. et al., 2020: Wood burning: A major source of Volatile Organic Compounds during wintertime in the Paris region. *Science of the Total Environment*, doi:10.1016/j.scitotenv.2019.135055.
Latham, J. et al., 2008: Global temperature stabilization via controlled albedo enhancement of low-level maritime clouds. *Philosophical Transactions of the Royal Society A: Mathematical, Physical and Engineering Sciences*, doi:10.1098/rsta.2008.0137.
Lathière, J., C.N. Hewitt, and D.J. Beerling, 2010: Sensitivity of isoprene emissions from the terrestrial biosphere to 20th century changes in atmospheric CO₂ concentration, climate, and land use. *Global Biogeochemical Cycles*, **24(1)**, doi:10.1029/2009gb003548.
Lauer, A., V. Eyring, J. Hendricks, P. Jöckel, and U. Lohmann, 2007: Global model simulations of the impact of ocean-going ships on aerosols, clouds, and the radiation budget. *Atmospheric Chemistry and Physics*, **7(19)**, 5061–5079, doi:10.5194/acp-7-5061-2007.
Lauwaet, D. et al., 2014: The effect of climate change and emission scenarios on ozone concentrations over Belgium: a high-resolution model study for policy support. *Atmospheric Chemistry and Physics*, **14(12)**, 5893–5904, doi:10.5194/acp-14-5893-2014.
Lawrence, M.G. et al., 2018: Evaluating climate geoengineering proposals in the context of the Paris Agreement temperature goals. *Nature Communications*, doi:10.1038/s41467-018-05938-3.
Le, T. et al., 2020: Unexpected air pollution with marked emission reductions during the COVID-19 outbreak in China. *Science*, **369(6504)**, 702–706, doi:10.1126/science.abb7431.
Le Quéré, C. et al., 2020: Temporary reduction in daily global CO2 emissions during the COVID-19 forced confinement. *Nature Climate Change*, **10(7)**, 647–653, doi:10.1038/s41558-020-0797-x.
Lee, D.S. et al., 2020a: The contribution of global aviation to anthropogenic climate forcing for 2000 to 2018. *Atmospheric Environment*, 117834, doi:10.1016/j.atmosenv.2020.117834.
Lee, D.S. et al., 2020b: The contribution of global aviation to anthropogenic climate forcing for 2000 to 2018. *Atmospheric Environment*, 117834, doi:10.1016/j.atmosenv.2020.117834.
Lee, D.S. et al., 2021: The contribution of global aviation to anthropogenic climate forcing for 2000 to 2018. *Atmospheric Environment*, **244**, 117834, doi:10.1016/j.atmosenv.2020.117834.
Lee, Y., D.T. Shindell, G. Faluvegi, and R.W. Pinder, 2016: Potential impact of a US climate policy and air quality regulations on future air quality and climate change. *Atmospheric Chemistry and Physics*, **16(8)**, 5323–5342, doi:10.5194/acp-16-5323-2016.
Lee, Y.H. et al., 2013a: Evaluation of preindustrial to present-day black carbon and its albedo forcing from Atmospheric Chemistry and Climate Model Intercomparison Project (ACCMIP). *Atmospheric Chemistry and Physics*, **13(5)**, 2607–2634, doi:10.5194/acp-13-2607-2013.
Lee, Y.H. et al., 2013b: Evaluation of preindustrial to present-day black carbon and its albedo forcing from Atmospheric Chemistry and Climate Model Intercomparison Project (ACCMIP). *Atmospheric Chemistry and Physics*, **13(5)**, 2607–2634, doi:10.5194/acp-13-2607-2013.
Leedham Elvidge, E.C., S.-M. Phang, W.T. Sturges, and G. Malin, 2015a: The effect of desiccation on the emission of volatile bromocarbons from two common temperate macroalgae. *Biogeosciences*, **12(2)**, 387–398, doi:10.5194/bg-12-387-2015.
Leedham Elvidge, E.C. et al., 2015b: Increasing concentrations of dichloromethane, CH2Cl2, inferred from CARIBIC air samples collected 1998–2012. *Atmospheric Chemistry and Physics*, **15(4)**, 1939–1958, doi:10.5194/acp-15-1939-2015.
Lehtipalo, K. et al., 2018: Multicomponent new particle formation from sulfuric acid, ammonia, and biogenic vapors. *Science Advances*, **4(12)**, eaau5363, doi:10.1126/sciadv.aau5363.
Lelieveld, J., 2017: Clean air in the Anthropocene. *Faraday Discussions*, **200**, 693–703, doi:10.1039/c7fd90032e.
Lelieveld, J., S. Gromov, A. Pozzer, and D. Taraborrelli, 2016: Global tropospheric hydroxyl distribution, budget and reactivity. *Atmospheric Chemistry and Physics*, **16(19)**, 12477–12493, doi:10.5194/acp-16-12477-2016.
Lelieveld, J., S. Beirle, C. Hörmann, G. Stenchikov, and T. Wagner, 2015a: Abrupt recent trend changes in atmospheric nitrogen dioxide over the Middle East. *Science Advances*, **1(7)**.
Lelieveld, J., J.S. Evans, M. Fnais, D. Giannadaki, and A. Pozzer, 2015b: The contribution of outdoor air pollution sources to premature mortality on a global scale. *Nature*, **525(7569)**, 367–371, doi:10.1038/nature15371.
Lelieveld, J. et al., 2014: Model projected heat extremes and air pollution in the eastern Mediterranean and Middle East in the twenty-first century. *Regional Environmental Change*, **14(5)**, 1937–1949, doi:10.1007/s10113-013-0444-4.
Lelieveld, J. et al., 2019: Effects of fossil fuel and total anthropogenic emission removal on public health and climate. *Proceedings of the National Academy of Sciences*, 201819989, doi:10.1073/pnas.1819989116.
Lemaire, V.E.P., A. Colette, and L. Menut, 2016: Using statistical models to explore ensemble uncertainty in climate impact studies: The example of air pollution in Europe. *Atmospheric Chemistry and Physics*, **16(4)**, 2559–

ACCEPTED VERSION SUBJECT TO FINAL EDITING

2574, doi:10.5194/acp-16-2559-2016.
Lewinschal, A. et al., 2019: Local and remote temperature response of regional SO₂ emissions. *Atmospheric Chemistry and Physics*, **19(4)**, 2385–2403, doi:10.5194/acp-19-2385-2019.
Li, H. et al., 2016: Size-Dependent Characterization of Atmospheric Particles during Winter in Beijing. *Atmosphere*, **7(3)**, doi:10.3390/atmos7030036.
Li, K. et al., 2019: Anthropogenic drivers of 2013–2017 trends in summer surface ozone in China. *Proceedings of the National Academy of Sciences of the United States of America*, doi:10.1073/pnas.1812168116.
Li, K. et al., 2020: Increases in surface ozone pollution in China from 2013 to 2019: anthropogenic and meteorological influences. *Atmospheric Chemistry and Physics*, **20(19)**, 11423–11433, doi:10.5194/acp-20-11423-2020.
Li, L. et al., 2010: Composition, source, mass closure of PM2.5 aerosols for four forests in eastern China. *Journal of Environmental Sciences*, **22(3)**, 405–412, doi:10.1016/s1001-0742(09)60122-4.
Li, L. et al., 2020: Air quality changes during the COVID-19 lockdown over the Yangtze River Delta Region: An insight into the impact of human activity pattern changes on air pollution variation. *Science of the Total Environment*, **732**, doi:10.1016/j.scitotenv.2020.139282.
Li, M. et al., 2018a: Air quality co-benefits of carbon pricing in China. *Nature Climate Change*, **8(5)**, 398–403, doi:10.1038/s41558-018-0139-4.
Li, M. et al., 2018b: Air quality co-benefits of carbon pricing in China. *Nature Climate Change*, **8(5)**, 398–403, doi:10.1038/s41558-018-0139-4.
Li, M. et al., 2019: Persistent growth of anthropogenic non-methane volatile organic compound (NMVOC) emissions in China during 1990-2017: Drivers, speciation and ozone formation potential. *Atmospheric Chemistry and Physics*, **19(13)**, 8897–8913, doi:10.5194/acp-19-8897-2019.
Lin, J.T. et al., 2015: Influence of aerosols and surface reflectance on satellite NO₂ retrieval: Seasonal and spatial characteristics and implications for NO_x emission constraints. *Atmospheric Chemistry and Physics*, **15(19)**, 11217–11241, doi:10.5194/acp-15-11217-2015.
Liu, F. et al., 2016: Recent reduction in NO_x emissions over China: synthesis of satellite observations and emission inventories. *Environmental Research Letters*, **11(11)**, doi:10.1088/1748-9326/11/11/114002.
Liu, H. et al., 2016: Health and climate impacts of ocean-going vessels in East Asia. *Nature Climate Change*, **6(11)**, 1037–1041, doi:10.1038/nclimate3083.
Liu, L. et al., 2018: A PDRMIP Multimodel Study on the Impacts of Regional Aerosol Forcings on Global and Regional Precipitation. *Journal of Climate*, **31(11)**, 4429–4447, doi:10.1175/jcli-d-17-0439.1.
Liu, L. et al., 2019: Estimating global surface ammonia concentrations inferred from satellite retrievals. *Atmospheric Chemistry and Physics*, **19(18)**, 12051–12066, doi:10.5194/acp-19-12051-2019.
Liu, Z. et al., 2020: Near-real-time monitoring of global CO2 emissions reveals the effects of the COVID-19 pandemic. *Nature Communications*, **11(1)**, 5172, doi:10.1038/s41467-020-18922-7.
Llorens, L., J. Llusià, E.H. Murchie, J. Peñuelas, and D.J. Beerling, 2009: Monoterpene emissions and photoinhibition of "living fossil" trees grown under CO2 enrichment in a simulated Cretaceous polar environment. *Journal of Geophysical Research*, **114(G1)**, G01005, doi:10.1029/2008jg000802.
Lombardozzi, D., J.P. Sparks, and G. Bonan, 2013: Integrating O$_{3}$ influences on terrestrial processes: photosynthetic and stomatal response data available for regional and global modeling. *Biogeosciences*, **10(11)**, 6815–6831, doi:10.5194/bg-10-6815-2013.
Lombardozzi, D., S. Levis, G. Bonan, P.G. Hess, and J.P. Sparks, 2015: The Influence of Chronic Ozone Exposure on Global Carbon and Water Cycles. *Journal of Climate*, **28(1)**, 292–305, doi:10.1175/jcli-d-14-00223.1.
Lorente, A. et al., 2017: Structural uncertainty in air mass factor calculation for NO₂ and HCHO satellite retrievals. *Atmospheric Measurement Techniques*, **10(3)**, 759–782, doi:10.5194/amt-10-759-2017.
Loreto, F., M. Dicke, J.-P. Schnitzler, and T.C.J. Turlings, 2014: Plant volatiles and the environment. *Plant, Cell & Environment*, **37(8)**, 1905–1908, doi:10.1111/pce.12369.
Loreto, F. et al., 2001: Monoterpene emission and monoterpene synthase activities in the Mediterranean evergreen oak Quercus ilex L. grown at elevated CO 2 concentrations. *Global Change Biology*, **7(6)**, 709–717, doi:10.1046/j.1354-1013.2001.00442.x.
Lowe, J.A. and D. Bernie, 2018: The impact of Earth system feedbacks on carbon budgets and climate response. *Philosophical Transactions of the Royal Society A: Mathematical, Physical and Engineering Sciences*, **376(2119)**, 20170263, doi:10.1098/rsta.2017.0263.
Lu, X., M. Chen, Y. Liu, D.G. Miralles, and F. Wang, 2017: Enhanced water use efficiency in global terrestrial ecosystems under increasing aerosol loadings. *Agricultural and Forest Meteorology*, **237–238**, 39–49, doi:10.1016/j.agrformet.2017.02.002.
Lucas, P.L., D.P. van Vuuren, J.G.J. Olivier, and M.G.J. den Elzen, 2007: Long-term reduction potential of non-CO2 greenhouse gases. *Environmental Science and Policy*, **10(2)**, 85–103, doi:10.1016/j.envsci.2006.10.007.
Lund, M.T., T.K. Berntsen, C. Heyes, Z. Klimont, and B.H. Samset, 2014a: Global and regional climate impacts of black carbon and co-emitted species from the on-road diesel sector. *Atmospheric Environment*, **98**, 50–58, doi:10.1016/j.atmosenv.2014.08.033.
Lund, M.T., T.K. Berntsen, C. Heyes, Z. Klimont, and B.H. Samset, 2014b: Global and regional climate impacts of

ACCEPTED VERSION SUBJECT TO FINAL EDITING

black carbon and co-emitted species from the on-road diesel sector. *Atmospheric Environment*, **98**, 50–58, doi:10.1016/j.atmosenv.2014.08.033.

Lund, M.T. et al., 2017: Emission metrics for quantifying regional climate impacts of aviation. *Earth System Dynamics*, **8(3)**, 547–563, doi:10.5194/esd-8-547-2017.

Lund, M.T. et al., 2018a: Concentrations and radiative forcing of anthropogenic aerosols from 1750 to 2014 simulated with the Oslo CTM3 and CEDS emission inventory. *Geoscientific Model Development*, **11(12)**, 4909–4931, doi:10.5194/gmd-11-4909-2018.

Lund, M.T. et al., 2018b: Short Black Carbon lifetime inferred from a global set of aircraft observations. *npj Climate and Atmospheric Science*, **1(1)**, 31, doi:10.1038/s41612-018-0040-x.

Lund, M.T. et al., 2020: A continued role of short-lived climate forcers under the Shared Socioeconomic Pathways. *Earth System Dynamics*, **11(4)**, 977–993, doi:10.5194/esd-11-977-2020.

Luo, M. et al., 2015: Satellite observations of tropospheric ammonia and carbon monoxide: Global distributions, regional correlations and comparisons to model simulations. *Atmospheric Environment*, doi:10.1016/j.atmosenv.2015.02.007.

Macmartin, D.G. et al., 2017: The climate response to stratospheric aerosol geoengineering can be tailored using multiple injection locations. *Journal of Geophysical Research: Atmospheres*, doi:10.1002/2017jd026868.

Mahmood, R. et al., 2016: Seasonality of global and arctic black carbon processes in the arctic monitoring and assessment programme models. *Journal of Geophysical Research*, **121(12)**, 7100–7116, doi:10.1002/2016jd024849.

Mahowald, N., 2011: Aerosol Indirect Effect on Biogeochemical Cycles and Climate. *Science*, **334(6057)**, 794–796, doi:10.1126/science.1207374.

Mahowald, N.M. and C. Luo, 2003: A less dusty future? *Geophysical Research Letters*, **30(17)**, doi:10.1029/2003gl017880.

Mahowald, N.M. et al., 2010: Observed 20th century desert dust variability: Impact on climateand biogeochemistry. *Atmospheric Chemistry and Physics*, **10(22)**, 10875–10893, doi:10.5194/acp-10-10875-2010.

Mahowald, N.M. et al., 2017: Aerosol Deposition Impacts on Land and Ocean Carbon Cycles. *Current Climate Change Reports*, **3(1)**, 16–31, doi:10.1007/s40641-017-0056-z.

Maione, M. et al., 2016: Air quality and climate change: Designing new win-win policies for Europe. *Environmental Science and Policy*, **65**, 48–57, doi:10.1016/j.envsci.2016.03.011.

Malavelle, F.F. et al., 2017: Strong constraints on aerosol-cloud interactions from volcanic eruptions. *Nature*, doi:10.1038/nature22974.

Malm, W.C., B.A. Schichtel, J.L. Hand, and J.L. Collett, 2017: Concurrent Temporal and Spatial Trends in Sulfate and Organic Mass Concentrations Measured in the IMPROVE Monitoring Program. *Journal of Geophysical Research: Atmospheres*, doi:10.1002/2017jd026865.

Mangeon, S., R. Field, M. Fromm, C. McHugh, and A. Voulgarakis, 2015: Satellite versus ground-based estimates of burned area: A comparison between MODIS based burned area and fire agency reports over North America in 2007. *The Anthropocene Review*, **3(2)**, 76–92, doi:10.1177/2053019615588790.

Mann, G.W. et al., 2014: Intercomparison and evaluation of global aerosol microphysical properties among AeroCom models of a range of complexity. *Atmospheric Chemistry and Physics*, **14(9)**, 4679–4713, doi:10.5194/acp-14-4679-2014.

Marais, E.A. et al., 2018: Nitrogen oxides in the global upper troposphere: Interpreting cloud-sliced NO2 observations from the OMI satellite instrument. *Atmospheric Chemistry and Physics*, **18(23)**, 17017–17027, doi:10.5194/acp-18-17017-2018.

Mariani, R.L. and W.Z. de Mello, 2007: PM2.5-10, PM2.5 and associated water-soluble inorganic species at a coastal urban site in the metropolitan region of Rio de Janeiro. *Atmospheric Environment*, **41(13)**, 2887–2892, doi:10.1016/j.atmosenv.2006.12.009.

Markakis, K. et al., 2014: Air quality in the mid-21st century for the city of Paris under two climate scenarios; From the regional to local scale. *Atmospheric Chemistry and Physics*, **14(14)**, 7323–7340, doi:10.5194/acp-14-7323-2014.

Markakis, K. et al., 2016: Mid-21st century air quality at the urban scale under the influence of changed climate and emissions – case studies for Paris and Stockholm. *Atmospheric Chemistry and Physics*, **16(4)**, 1877–1894, doi:10.5194/acp-16-1877-2016.

Markandya, A. et al., 2018: Health co-benefits from air pollution and mitigation costs of the Paris Agreement: a modelling study. *The Lancet Planetary Health*, **2(3)**, e126–e133, doi:10.1016/s2542-5196(18)30029-9.

Marlier, M.E., E.X. Bonilla, and L.J. Mickley, 2020: How Do Brazilian Fires Affect Air Pollution and Public Health? *GeoHealth*, **4(12)**, e2020GH000331, doi:10.1029/2020gh000331.

Marlon, J.R. et al., 2016: Reconstructions of biomass burning from sediment-charcoal records to improve data–model comparisons. *Biogeosciences*, **13(11)**, 3225–3244, doi:10.5194/bg-13-3225-2016.

Marsh, D.R., J.F. Lamarque, A.J. Conley, and L.M. Polvani, 2016: Stratospheric ozone chemistry feedbacks are not critical for the determination of climate sensitivity in CESM1(WACCM). *Geophysical Research Letters*, **43(8)**, 3928–3934, doi:10.1002/2016gl068344.

ACCEPTED VERSION SUBJECT TO FINAL EDITING

Martin, S.T. et al., 2010: Sources and properties of Amazonian aerosol particles. *Reviews of Geophysics*, **48(2)**, doi:10.1029/2008rg000280.
Martínez-Alonso, S. et al., 2020: 1.5 years of TROPOMI CO measurements: Comparisons to MOPITT and ATom. *Atmospheric Measurement Techniques Discussions*, **13(9)**, 1–37, doi:10.5194/amt-2020-63.
Masiol, M. et al., 2015: Spatial, seasonal trends and transboundary transport of PM_{2.5} inorganic ions in the Veneto region (Northeastern Italy). *Atmospheric Environment*, **117**, 19–31, doi:10.1016/j.atmosenv.2015.06.044.
McCollum, D. et al., 2013: Climate policies can help resolve energy security and air pollution challenges. *Climatic Change*, **119**, doi:10.1007/s10584-013-0710-y.
McCollum, D.L. et al., 2018: Connecting the sustainable development goals by their energy inter-linkages. *Environmental Research Letters*, **13(3)**, 33006, doi:10.1088/1748-9326/aaafe3.
McDonald, B.C. et al., 2018: Volatile chemical products emerging as largest petrochemical source of urban organic emissions. *Science*, **359(6377)**, 760–764, doi:10.1126/science.aaq0524.
McDuffie, E.E. et al., 2020: A global anthropogenic emission inventory of atmospheric pollutants from sector- and fuel-specific sources (1970–2017): an application of the Community Emissions Data System (CEDS). *Earth System Science Data*, **12(4)**, 3413–3442, doi:10.5194/essd-12-3413-2020.
McFiggans, G. et al., 2019: Secondary organic aerosol reduced by mixture of atmospheric vapours. *Nature*, **565(7741)**, 587–593, doi:10.1038/s41586-018-0871-y.
McNorton, J. et al., 2016: Role of OH variability in the stalling of the global atmospheric CH₄ growth rate from 1999 to 2006. *Atmospheric Chemistry and Physics*, **16(12)**, 7943–7956, doi:10.5194/acp-16-7943-2016.
McNorton, J. et al., 2018: Attribution of recent increases in atmospheric methane through 3-D inverse modelling. *Atmospheric Chemistry and Physics*, **18(24)**, 18149–18168, doi:10.5194/acp-18-18149-2018.
Medici, G., K.L. Cummins, D.J. Cecil, W.J. Koshak, and S.D. Rudlosky, 2017: The Intracloud Lightning Fraction in the Contiguous United States. *Monthly Weather Review*, **145(11)**, 4481–4499, doi:10.1175/mwr-d-16-0426.1.
Meehl, G.A. et al., 2020: Context for interpreting equilibrium climate sensitivity and transient climate response from the CMIP6 Earth system models. *Science Advances*, **6(26)**, eaba1981, doi:10.1126/sciadv.aba1981.
Megaritis, A.G., C. Fountoukis, P.E. Charalampidis, C. Pilinis, and S.N. Pandis, 2013: Response of fine particulate matter concentrations to changes of emissions and temperature in Europe. *Atmospheric Chemistry and Physics*, **13(6)**, 3423–3443, doi:10.5194/acp-13-3423-2013.
Meinshausen, M. et al., 2011: The RCP greenhouse gas concentrations and their extensions from 1765 to 2300. *Climatic Change*, **109(1–2)**, 213–241, doi:10.1007/s10584-011-0156-z.
Meinshausen, M. et al., 2020: The shared socio-economic pathway (SSP) greenhouse gas concentrations and their extensions to 2500. *Geoscientific Model Development*, **13(8)**, 3571–3605, doi:10.5194/gmd-13-3571-2020.
Melamed, M.L., J. Schmale, and E. von Schneidemesser, 2016: Sustainable policy – key considerations for air quality and climate change. *Current Opinion in Environmental Sustainability*, **23**, 85–91, doi:10.1016/j.cosust.2016.12.003.
Mercado, L.M. et al., 2009: Impact of changes in diffuse radiation on the global land carbon sink. *Nature*, **458(7241)**, 1014–1017, doi:10.1038/nature07949.
Meredith, M. et al., 2019: Polar Regions. In: *IPCC Special Report on the Ocean and Cryosphere in a Changing Climate* [Pörtner, H.-O., D.C. Roberts, V. Masson-Delmotte, P. Zhai, M. Tignor, E. Poloczanska, K. Mintenbeck, A. Alegría, M. Nicolai, A. Okem, J. Petzold, B. Rama, and N.M. Weyer (eds.)]. In Press, pp. 203–320.
Mertens, M., A. Kerkweg, V. Grewe, P. Jöckel, and R. Sausen, 2020: Attributing ozone and its precursors to land transport emissions in Europe and Germany. *Atmospheric Chemistry and Physics*, **20(13)**, 7843–7873, doi:10.5194/acp-20-7843-2020.
Messina, P. et al., 2016: Global biogenic volatile organic compound emissions in the ORCHIDEE and MEGAN models and sensitivity to key parameters. *Atmospheric Chemistry and Physics*, **16(22)**, 14169–14202, doi:10.5194/acp-16-14169-2016.
Meul, S., U. Langematz, P. Kröger, S. Oberländer-Hayn, and P. Jöckel, 2018: Future changes in the stratosphere-to-troposphere ozone mass flux and the contribution from climate change and ozone recovery. *Atmospheric Chemistry and Physics*, **18(10)**, 7721–7738, doi:10.5194/acp-18-7721-2018.
Miller, S.M. et al., 2019: China's coal mine methane regulations have not curbed growing emissions. *Nature Communications*, **10(1)**, 303, doi:10.1038/s41467-018-07891-7.
Mills, G. et al., 2016: Ozone impacts on vegetation in a nitrogen enriched and changing climate. *Environmental Pollution*, **208**, 898–908, doi:10.1016/j.envpol.2015.09.038.
Ming, Y. et al., 2021: Assessing the Influence of COVID-19 on the Shortwave Radiative Fluxes Over the East Asian Marginal Seas. *Geophysical Research Letters*, **48(3)**, e2020GL091699, doi:10.1029/2020gl091699.
Mitchell, D.L. and W. Finnegan, 2009: Modification of cirrus clouds to reduce global warming. *Environmental Research Letters*, doi:10.1088/1748-9326/4/4/045102.
Miyazaki, K., H.J. Eskes, and K. Sudo, 2015: A tropospheric chemistry reanalysis for the years 2005-2012 based on an assimilation of OMI, MLS, TES, and MOPITT satellite data. *Atmospheric Chemistry and Physics*, **15(14)**, 8315–8348, doi:10.5194/acp-15-8315-2015.

ACCEPTED VERSION SUBJECT TO FINAL EDITING

Miyazaki, K., H.J. Eskes, K. Sudo, and C. Zhang, 2014: Global lightning NO_x production estimated by an assimilation of multiple satellite data sets. *Atmospheric Chemistry and Physics*, **14(7)**, 3277–3305, doi:10.5194/acp-14-3277-2014.

Miyazaki, K. et al., 2017: Decadal changes in global surface NOx emissions from multi-constituent satellite data assimilation. *Atmospheric Chemistry and Physics*, **17(2)**, 807–837, doi:10.5194/acp-17-807-2017.

Mkoma, S., 2008: Physico-Chemical Characterisation of Atmospheric Aerosols in Tanzania, with Emphasis on the Carbonaceous Aerosol Components and on Chemical Mass Closure., Ghent University, Faculty of Sciences, Ghent, Belgium, 182 pp., doi:1854/9881.

Mkoma, S.L., W. Maenhaut, X. Chi, W. Wang, and N. Raes, 2009: Characterisation of PM₁₀ atmospheric aerosols for the wet season 2005 at two sites in East Africa. *Atmospheric Environment*, **43(3)**, 631–639, doi:10.1016/j.atmosenv.2008.10.008.

Mohankumar Sajeev, E.P., W. Winiwarter, and B. Amon, 2018: Greenhouse Gas and Ammonia Emissions from Different Stages of Liquid Manure Management Chains: Abatement Options and Emission Interactions. *Journal of Environmental Quality*, **47(1)**, 30–41, doi:10.2134/jeq2017.05.0199.

Molina, L.T. et al., 2007: Air quality in North America's most populous city – overview of the MCMA-2003 campaign. *Atmospheric Chemistry and Physics*, **7(10)**, 2447–2473, doi:10.5194/acp-7-2447-2007.

Molina, L.T. et al., 2010: An overview of the MILAGRO 2006 Campaign: Mexico City emissions and their transport and transformation. *Atmospheric Chemistry and Physics*, **10(18)**, 8697–8760, doi:10.5194/acp-10-8697-2010.

Monks, S.A. et al., 2015: Multi-model study of chemical and physical controls on transport of anthropogenic and biomass burning pollution to the Arctic. *Atmospheric Chemistry and Physics*, **15(6)**, 3575–3603, doi:10.5194/acp-15-3575-2015.

Monteiro dos Santos, D.A., J.F. Brito, J.M. Godoy, and P. Artaxo, 2016: Ambient concentrations and insights on organic and elemental carbon dynamics in São Paulo, Brazil. *Atmospheric Environment*, **144**, 226–233, doi:10.1016/j.atmosenv.2016.08.081.

Montzka, S.A. et al., 2011: Small Interannual Variability of Global Atmospheric Hydroxyl. *Science*, **331(6013)**, 67–69, doi:10.1126/science.1197640.

Montzka, S.A. et al., 2015: Recent Trends in Global Emissions of Hydrochlorofluorocarbons and Hydrofluorocarbons: Reflecting on the 2007 Adjustments to the Montreal Protocol. *The Journal of Physical Chemistry A*, **119(19)**, 4439–4449, doi:10.1021/jp5097376.

Morgan, W.T. et al., 2019: Transformation and aging of biomass burning carbonaceous aerosol over tropical South America from aircraft in-situ measurements during SAMBBA. *Atmospheric Chemistry and Physics Discussions*, doi:10.5194/acp-2019-157.

Morgenstern, O. et al., 2017: Review of the global models used within phase 1 of the Chemistry–Climate Model Initiative (CCMI). *Geosci. Model Dev.*, **10(2)**, 639–671, doi:10.5194/gmd-10-639-2017.

Morgenstern, O. et al., 2018: Ozone sensitivity to varying greenhouse gases and ozone-depleting substances in CCMI-1 simulations. *Atmospheric Chemistry and Physics*, **18(2)**, 1091–1114, doi:10.5194/acp-18-1091-2018.

Morgenstern, O. et al., 2020: Reappraisal of the climate impacts of ozone-depleting substances. *Geophysical Research Letters*, **47(e2020GL088295)**, 13, doi:10.1002/essoar.10502742.1.

Mortier, A. et al., 2020: Evaluation of climate model aerosol trends with ground-based observations over the last 2 decades – an AeroCom and CMIP6 analysis. *Atmospheric Chemistry and Physics*, **20(21)**, 13355–13378, doi:10.5194/acp-20-13355-2020.

Moteki, N., T. Mori, H. Matsui, and S. Ohata, 2019: Observational constraint of in-cloud supersaturation for simulations of aerosol rainout in atmospheric models. *npj Climate and Atmospheric Science*, doi:10.1038/s41612-019-0063-y.

Motos, G. et al., 2019: Cloud droplet activation properties and scavenged fraction of black carbon in liquid-phase clouds at the high-alpine research station Jungfraujoch (3580ma.s.l.). *Atmospheric Chemistry and Physics*, doi:10.5194/acp-19-3833-2019.

Mülmenstädt, J. and G. Feingold, 2018: The Radiative Forcing of Aerosol – Cloud Interactions in Liquid Clouds : State of the Field. , 23–40.

Muri, H. et al., 2018: Climate response to aerosol geoengineering: A multimethod comparison. *Journal of Climate*, doi:10.1175/jcli-d-17-0620.1.

Murray, L., A.M. Fiore, D.T. Shindell, V. Naik, and L.W. Horowitz, 9999: Large uncertainties in global hydroxyl projections tied to fate of reactive nitrogen and carbon. *PNAS*, **(submitted**.

Murray, L.T., 2016: Lightning NO x and Impacts on Air Quality. *Current Pollution Reports*, **2(2)**, 115–133, doi:10.1007/s40726-016-0031-7.

Murray, L.T., J.A. Logan, and D.J. Jacob, 2013: Interannual variability in tropical tropospheric ozone and OH: The role of lightning. *Journal of Geophysical Research: Atmospheres*, **118(19)**, 11,411–468,480, doi:10.1002/jgrd.50857.

Murray, L.T. et al., 2014: Factors controlling variability in the oxidative capacity of the troposphere since the Last Glacial Maximum. *Atmospheric Chemistry and Physics*, **14(7)**, 3589–3622, doi:10.5194/acp-14-3589-2014.

Muthers, S. et al., 2014: The coupled atmosphere-chemistry-ocean model SOCOL-MPIOM. *Geosci. Model Dev.*, **7(5)**,

ACCEPTED VERSION SUBJECT TO FINAL EDITING

2157–2179, doi:10.5194/gmd-7-2157-2014.
Myhre, G., T.F. Berglen, C.E.L. Myhre, and I.S.A. Isaksen, 2004: The radiative effect of the anthropogenic influence on the stratospheric sulfate aerosol layer. *Tellus B: Chemical and Physical Meteorology*, **56(3)**, 294–299, doi:10.3402/tellusb.v56i3.16431.
Myhre, G. et al., 2013a: Anthropogenic and Natural Radiative Forcing. In: *Climate Change 2013: The Physical Science Basis. Contribution of Working Group I to the Fifth Assessment Report of the Intergovernmental Panel on Climate Change* [Stocker, T.F., D. Qin, G.-K. Plattner, M. Tignor, S.K. Allen, J. Boschung, A. Nauels, Y. Xia, V. Bex, and P.M. Midgley (eds.)]. Cambridge University Press, Cambridge, United Kingdom and New York, NY, USA, pp. 659–740.
Myhre, G. et al., 2013b: Anthropogenic and Natural Radiative Forcing. In: *Climate Change 2013: The Physical Science Basis. Contribution of Working Group I to the Fifth Assessment Report of the Intergovernmental Panel on Climate Change* [Stocker, T.F., D. Qin, G.-K. Plattner, M. Tignor, S.K. Allen, J. Boschung, A. Nauels, Y. Xia, V. Bex, and P.M. Midgley (eds.)]. Cambridge University Press, Cambridge, United Kingdom and New York, NY, USA, pp. 659–740, doi:10.1017/cbo9781107415324.018.
Myhre, G. et al., 2017: Multi-model simulations of aerosol and ozone radiative forcing due to anthropogenic emission changes during the period 1990-2015. *Atmospheric Chemistry and Physics*, **17(4)**, 2709–2720, doi:10.5194/acp-17-2709-2017.
Myriokefalitakis, S. et al., 2016: Ozone and carbon monoxide budgets over the Eastern Mediterranean. *Science of the Total Environment*, **563–564**, 40–52, doi:10.1016/j.scitotenv.2016.04.061.
Naik, V. et al., 2013: Preindustrial to present-day changes in tropospheric hydroxyl radical and methane lifetime from the Atmospheric Chemistry and Climate Model Intercomparison Project (ACCMIP). *Atmospheric Chemistry and Physics*, **13(10)**, 5277–5298, doi:10.5194/acp-13-5277-2013.
Nault, B.A. et al., 2017: Lightning NO_x Emissions: Reconciling Measured and Modeled Estimates With Updated NO_x Chemistry. *Geophysical Research Letters*, **44(18)**, 9479–9488, doi:10.1002/2017gl074436.
Naus, S. et al., 2019: Constraints and biases in a tropospheric two-box model of OH. *Atmospheric Chemistry and Physics*, **19(1)**, 407–424, doi:10.5194/acp-19-407-2019.
Navarro, J.C.A. et al., 2016: Amplification of Arctic warming by past air pollution reductions in Europe. *Nature Geoscience*, **9(4)**, 277–281, doi:10.1038/ngeo2673.
Nazarenko, L. et al., 2017: Interactive nature of climate change and aerosol forcing. *Journal of Geophysical Research: Atmospheres*, **122(6)**, 3457–3480, doi:10.1002/2016jd025809.
Nenes, A., S.N. Pandis, R.J. Weber, and A. Russell, 2020: Aerosol pH and liquid water content determine when particulate matter is sensitive to ammonia and nitrate availability. *Atmos. Chem. Phys.*, **20(5)**, 3249–3258, doi:10.5194/acp-20-3249-2020.
Nguyen, G.T.H., H. Shimadera, K. Uranishi, T. Matsuo, and A. Kondo, 2019: Numerical assessment of PM_{2.5} and O₃ air quality in Continental Southeast Asia: Impacts of potential future climate change. *Atmospheric Environment*, **215**, doi:10.1016/j.atmosenv.2019.116901.
Nguyen, T.L., L. Vereecken, and J. Peeters, 2010: HOx Regeneration in the Oxidation of Isoprene III: Theoretical Study of the key Isomerisation of the Z-δ-hydroxy-peroxy Isoprene Radicals. *ChemPhysChem*, **11(18)**, 3996–4001, doi:10.1002/cphc.201000480.
Nicely, J.M. et al., 2017: Quantifying the causes of differences in tropospheric OH within global models. *Journal of Geophysical Research-Atmospheres*, **122(3)**, 1983–2007, doi:10.1002/2016jd026239.
Nicely, J.M. et al., 2018: Changes in Global Tropospheric OH Expected as a Result of Climate Change Over the Last Several Decades. *Journal of Geophysical Research: Atmospheres*, **123(18)**, 10,710–774,795, doi:10.1029/2018jd028388.
Nicewonger, M.R., K.R. Verhulst, M. Aydin, and E.S. Saltzman, 2016: Preindustrial atmospheric ethane levels inferred from polar ice cores: A constraint on the geologic sources of atmospheric ethane and methane. *Geophysical Research Letters*, **43(1)**, 214–221, doi:10.1002/2015gl066854.
Nicewonger, M.R., M. Aydin, M.J. Prather, and E.S. Saltzman, 2018: Large changes in biomass burning over the last millennium inferred from paleoatmospheric ethane in polar ice cores. *Proceedings of the National Academy of Sciences of the United States of America*, **115(49)**, 12413–12418, doi:10.1073/pnas.1807172115.
Niemeier, U. and C. Timmreck, 2015: What is the limit of climate engineering by stratospheric injection of SO₂? *Atmospheric Chemistry and Physics*, doi:10.5194/acp-15-9129-2015.
Niemeier, U. and H. Schmidt, 2017: Changing transport processes in the stratosphere by radiative heating of sulfate aerosols. *Atmospheric Chemistry and Physics*, doi:10.5194/acp-17-14871-2017.
Niinemets, S. Fares, P. Hardley, and K.J. Jardine, 2014: Bidirectional exchange of biogenic volatiles with vegetation: emission sources, reactions, breakdown and deposition. *Plant, Cell & Environment*, **37(8)**, 1790–1809, doi:10.1111/pce.12322.
Nolte, C.G., T.L. Spero, J.H. Bowden, M.S. Mallard, and P.D. Dolwick, 2018: The potential effects of climate change on air quality across the conterminous US at 2030 under three Representative Concentration Pathways. *Atmospheric Chemistry and Physics*, **18(20)**, 15471–15489, doi:10.5194/acp-18-15471-2018.

ACCEPTED VERSION SUBJECT TO FINAL EDITING

Nowack, P.J. et al., 2015: A large ozone-circulation feedback and its implications for global warming assessments. *Nature Climate Change*, **5(1)**, 41–45, doi:10.1038/nclimate2451.
NRC, 2015: *Climate Intervention: Reflecting Sunlight to Cool Earth*. National Research Council (NRC). The National Academies Press, Washington, DC, USA, 260 pp., doi:10.17226/18988.
O'Connor, F.M. et al., 2021: Assessment of pre-industrial to present-day anthropogenic effective radiative forcing in UKESM1. *Atmospheric Chemistry and Physics*, **21**, 1211–1243, doi:10.5194/acp-21-1211-2021.
O'Neill, B.C. et al., 2016: The Scenario Model Intercomparison Project (ScenarioMIP) for CMIP6. *Geosci. Model Dev.*, **9(9)**, 3461–3482, doi:10.5194/gmd-9-3461-2016.
Oberländer-Hayn, S., S. Meul, U. Langematz, J. Abalichin, and F. Haenel, 2015: A chemistry-climate model study of past changes in the Brewer-Dobson circulation. *Journal of Geophysical Research*, **120(14)**, 6742–6757, doi:10.1002/2014jd022843.
Ohata, S., N. Moteki, T. Mori, M. Koike, and Y. Kondo, 2016: A key process controlling the wet removal of aerosols: New observational evidence. *Scientific Reports*, **6(1)**, 1–9, doi:10.1038/srep34113.
Oliveira, P.H.F. et al., 2007: The effects of biomass burning aerosols and clouds on the CO2 flux in Amazonia. *Tellus B: Chemical and Physical Meteorology*, **59(3)**, 338–349, doi:10.1111/j.1600-0889.2007.00270.x.
Oliver, R.J. et al., 2018: Large but decreasing effect of ozone on the European carbon sink. *Biogeosciences*, **15(13)**, 4245–4269, doi:10.5194/bg-15-4245-2018.
Olivié, D.J.L. and G.P. Peters, 2013: Variation in emission metrics due to variation in CO2 and temperature impulse response functions. *Earth System Dynamics*, **4(2)**, 267–286, doi:10.5194/esd-4-267-2013.
Oram, D.E. et al., 2017: A growing threat to the ozone layer from short-lived anthropogenic chlorocarbons. *Atmospheric Chemistry and Physics*, **17(19)**, 11929–11941, doi:10.5194/acp-17-11929-2017.
Orbe, C. et al., 2018: Large-scale tropospheric transport in the Chemistry–Climate Model Initiative (CCMI) simulations. *Atmospheric Chemistry and Physics*, **18(10)**, 7217–7235, doi:10.5194/acp-18-7217-2018.
Oswald, E.M., L.A. Dupigny-Giroux, E.M. Leibensperger, R. Poirot, and J. Merrell, 2015: Climate controls on air quality in the Northeastern U.S.: An examination of summertime ozone statistics during 1993-2012. *Atmospheric Environment*, **112**, 278–288, doi:10.1016/j.atmosenv.2015.04.019.
Ovadnevaite, J. et al., 2014: A sea spray aerosol flux parameterization encapsulating wave state. *Atmospheric Chemistry and Physics*, **14(4)**, 1837–1852, doi:10.5194/acp-14-1837-2014.
Paasonen, P. et al., 2013: Warming-induced increase in aerosol number concentration likely to moderate climate change. *Nature Geoscience*, **6(6)**, 438–442, doi:10.1038/ngeo1800.
Pacifico, F., G.A. Folberth, C.D. Jones, S.P. Harrison, and W.J. Collins, 2012: Sensitivity of biogenic isoprene emissions to past, present, and future environmental conditions and implications for atmospheric chemistry. *JOURNAL OF GEOPHYSICAL RESEARCH-ATMOSPHERES*, **117**, doi:10.1029/2012jd018276.
Palmer, P.I. et al., 2006: Quantifying the seasonal and interannual variability of North American isoprene emissions using satellite observations of the formaldehyde column. *Journal of Geophysical Research Atmospheres*, **111(12)**, –, doi:10.1029/2005jd006689.
Pant, P. et al., 2015: Characterization of ambient PM2.5 at a pollution hotspot in New Delhi, India and inference of sources. *Atmospheric Environment*, **109**, 178–189, doi:10.1016/j.atmosenv.2015.02.074.
Papanastasiou, D.K., A. Beltrone, P. Marshall, and J.B. Burkholder, 2018: Global warming potential estimates for the C1-C3 hydrochlorofluorocarbons (HCFCs) included in the Kigali Amendment to the Montreal Protocol. *Atmospheric Chemistry and Physics*, **18(9)**, 6317–6330, doi:10.5194/acp-18-6317-2018.
Parrish, D.D., H.B. Singh, L. Molina, and S. Madronich, 2011: Air quality progress in North American megacities: A review. *Atmospheric Environment*, **45(39)**, 7015–7025, doi:10.1016/j.atmosenv.2011.09.039.
Partanen, A.I. et al., 2012: Direct and indirect effects of sea spray geoengineering and the role of injected particle size. *Journal of Geophysical Research Atmospheres*, doi:10.1029/2011jd016428.
Partanen, A.I. et al., 2013: Climate and air quality trade-offs in altering ship fuel sulfur content. *Atmospheric Chemistry and Physics*, **13(23)**, 12059–12071, doi:10.5194/acp-13-12059-2013.
Pathak, R.K., T. Wang, K.F. Ho, and S.C. Lee, 2011: Characteristics of summertime PM2.5 organic and elemental carbon in four major Chinese cities: Implications of high acidity for water-soluble organic carbon (WSOC). *Atmospheric Environment*, **45(2)**, 318–325, doi:10.1016/j.atmosenv.2010.10.021.
Patra, P.K. et al., 2021: Methyl Chloroform Continues to Constrain the Hydroxyl (OH) Variability in the Troposphere. *Journal of Geophysical Research: Atmospheres*, **126(4)**, e2020JD033862, doi:10.1029/2020jd033862.
Patris, N. et al., 2002: First sulfur isotope measurements in central Greenland ice cores along the preindustrial and industrial periods. *Journal of Geophysical Research D: Atmospheres*, **107(11)**, ACH 6–1–ACH 6–11, doi:10.1029/2001jd000672.
Paulot, F., S. Fan, and L.W. Horowitz, 2017: Contrasting seasonal responses of sulfate aerosols to declining SO₂ emissions in the Eastern U.S.: Implications for the efficacy of SO₂ emission controls. *Geophysical Research Letters*, **44(1)**, 455–464, doi:10.1002/2016gl070695.
Paulot, F. et al., 2009: Unexpected epoxide formation in the gas-phase photooxidation of isoprene. *Science*, **325(5941)**, 730–733, doi:10.1126/science.1172910.
Paulot, F. et al., 2014: Ammonia emissions in the United States, European Union, and China derived by high-resolution

ACCEPTED VERSION SUBJECT TO FINAL EDITING

inversion of ammonium wet deposition data: Interpretation with a new agricultural emissions inventory (MASAGE_NH3). *Journal of Geophysical Research: Atmospheres*, **119(7)**, 4343–4364, doi:10.1002/2013jd021130.

Paulot, F. et al., 2016: Sensitivity of nitrate aerosols to ammonia emissions and to nitrate chemistry: Implications for present and future nitrate optical depth. *Atmospheric Chemistry and Physics*, **16(3)**, 1459–1477, doi:10.5194/acp-16-1459-2016.

Paulot, F. et al., 2018: Representing sub-grid scale variations in nitrogen deposition associated with land use in a global Earth system model: Implications for present and future nitrogen deposition fluxes over North America. *Atmospheric Chemistry and Physics*, **18(24)**, 17963–17978, doi:10.5194/acp-18-17963-2018.

Paulot, F. et al., 2020: Revisiting the Impact of Sea Salt on Climate Sensitivity. *Geophysical Research Letters*, **47(3)**, e2019GL085601, doi:10.1029/2019gl085601.

Peeters, J., T.L. Nguyen, and L. Vereecken, 2009: HOx radical regeneration in the oxidation of isoprene. *Physical Chemistry Chemical Physics*, **11(28)**, 5935–5939, doi:10.1039/b908511d.

Peeters, J., J.F. Müller, T. Stavrakou, and V.S. Nguyen, 2014: Hydroxyl radical recycling in isoprene oxidation driven by hydrogen bonding and hydrogen tunneling: The upgraded LIM1 mechanism. *Journal of Physical Chemistry A*, **118(38)**, 8625–8643, doi:10.1021/jp5033146.

Peng, S. et al., 2016: Inventory of anthropogenic methane emissions in mainland China from 1980 to 2010. *Atmospheric Chemistry and Physics*, **16(22)**, 14545–14562, doi:10.5194/acp-16-14545-2016.

Peng, W., J. Yang, F. Wagner, and D.L. Mauzerall, 2017: Substantial air quality and climate co-benefits achievable now with sectoral mitigation strategies in China. *Science of the Total Environment*, **598**, 1076–1084, doi:10.1016/j.scitotenv.2017.03.287.

Penner, J.E., C. Zhou, and X. Liu, 2015: Can cirrus cloud seeding be used for geoengineering? *Geophysical Research Letters*, doi:10.1002/2015gl065992.

Penrod, A., Y. Zhang, K. Wang, S.Y. Wu, and L.R. Leung, 2014: Impacts of future climate and emission changes on U.S. air quality. *Atmospheric Environment*, **89**, 533–547, doi:10.1016/j.atmosenv.2014.01.001.

Peñuelas, J. and M. Staudt, 2010: BVOCs and global change. *Trends in Plant Science*, **15(3)**, 133–144, doi:10.1016/j.tplants.2009.12.005.

Persad, G.G. and K. Caldeira, 2018: Divergent global-scale temperature effects from identical aerosols emitted in different regions. *Nature Communications*, **9(1)**, 3289, doi:10.1038/s41467-018-05838-6.

Petetin, H. et al., 2018: Representativeness of the IAGOS airborne measurements in the lower troposphere. *Elem Sci Anth*, doi:10.1525/elementa.280.

Petit, J.-E. et al., 2015: Two years of near real-time chemical composition of submicron aerosols in the region of Paris using an Aerosol Chemical Speciation Monitor (ACSM) and a multi-wavelength Aethalometer. *Atmospheric Chemistry and Physics*, **15(6)**, 2985–3005, doi:10.5194/acp-15-2985-2015.

Petrenko, V. et al., 2013: A 60 yr record of atmospheric carbon monoxide reconstructed from Greenland firn air. *Atmospheric Chemistry and Physics*, **13(15)**, 7567–7585, doi:10.5194/acp-13-7567-2013.

Petron, G., A.M. Crotwell, E. Dlugokencky, and J.W. Mund, 2019: Atmospheric carbon monoxide dry air mole fractions from the NOAA ESRL carbon cycle cooperative global air sampling network, 1988–2017, Version: 2019-08. Retrieved from: ftp://aftp.cmdl.noaa.gov/data/trace_gases/co/flask/surface.

Pétron, G. et al., 2014: A new look at methane and nonmethane hydrocarbon emissions from oil and natural gas operations in the Colorado Denver-Julesburg Basin. *Journal of Geophysical Research*, **119(11)**, 6836–6852, doi:10.1002/2013jd021272.

Petzold, A. et al., 2013: Recommendations for reporting black carbon measurements. *Atmospheric Chemistry and Physics*, **13(16)**, 8365–8379, doi:10.5194/acp-13-8365-2013.

Pierce, J.R., D.K. Weisenstein, P. Heckendorn, T. Peter, and D.W. Keith, 2010: Efficient formation of stratospheric aerosol for climate engineering by emission of condensible vapor from aircraft. *Geophysical Research Letters*, doi:10.1029/2010gl043975.

Pierrehumbert, R.T., 2014: Short-Lived Climate Pollution. *Annual Review of Earth and Planetary Sciences*, **42(1)**, 341–379, doi:10.1146/annurev-earth-060313-054843.

Pinder, R.W., P.J. Adams, and S.N. Pandis, 2006: Ammonia Emission Controls as a Cost-Effective Strategy for Reducing Atmospheric Particulate Matter in the Eastern United States. *Environ. Sci. Technol.*, **41(2)**, 380–386, doi:10.1021/es060379a.

Pommier, M. et al., 2018: Impact of regional climate change and future emission scenarios on surface O₃ and PM_{2.5} over India. *Atmospheric Chemistry and Physics*, **18(1)**, 103–127, doi:10.5194/acp-18-103-2018.

Ponater, M., S. Marquart, R. Sausen, and U. Schumann, 2005: On contrail climate sensitivity. *Geophysical Research Letters*, **32(10)**, doi:10.1029/2005gl022580.

Porter, W.C., C.L. Heald, D. Cooley, and B. Russell, 2015: Investigating the observed sensitivities of air-quality extremes to meteorological drivers via quantile regression. *Atmospheric Chemistry and Physics*, **15(18)**, 10349–10366, doi:10.5194/acp-15-10349-2015.

Possell, M., C. Nicholas Hewitt, and D.J. Beerling, 2005: The effects of glacial atmospheric CO2 concentrations and

ACCEPTED VERSION SUBJECT TO FINAL EDITING

climate on isoprene emissions by vascular plants. *Global Change Biology*, **11(1)**, 60–69, doi:10.1111/j.1365-2486.2004.00889.x.

Potosnak, M.J. et al., 2014: Observed and modeled ecosystem isoprene fluxes from an oak-dominated temperate forest and the influence of drought stress. *Atmospheric Environment*, **84**, 314–322, doi:10.1016/j.atmosenv.2013.11.055.

Prather, M.J., 1994: Lifetimes and eigenstates in atmospheric chemistry. *Geophysical Research Letters*, **21(9)**, 801–804, doi:10.1029/94gl00840.

Prather, M.J. and C.D. Holmes, 2017: Overexplaining or underexplaining methane's role in climate change. *Proceedings of the National Academy of Sciences*, **114(21)**, 5324 LP – 5326, doi:10.1073/pnas.1704884114.

Prather, M.J., C.D. Holmes, and J. Hsu, 2012: Reactive greenhouse gas scenarios: Systematic exploration of uncertainties and the role of atmospheric chemistry. *Geophys. Res. Lett.*, **39(9)**, L09803.

Prather, M.J. et al., 2001: Atmospheric Chemistry and Greenhouse Gases. In: *Climate Change 2001: The Physical Science Basis. Contribution of Working Group I to the Third Assessment Report of the Intergovernmental Panel on Climate Change* [Y. Ding, D.J. Griggs, M. Noguer, P.J. van der Linden, X. Dai, K. Maskell, and C.A. Johnson (eds.)]. Cambridge University Press, Cambridge, United Kingdom and New York, NY, USA, pp. 239–287.

Price, C. and D. Rind, 1992: A simple lightning parameterization for calculating global lightning distributions. *Journal of Geophysical Research*, **97(D9)**, 9919–9933, doi:10.1029/92jd00719.

Pringle, K.J. et al., 2012: A multi-model assessment of the impact of sea spray geoengineering on cloud droplet number. *Atmospheric Chemistry and Physics*, doi:10.5194/acp-12-11647-2012.

Prinn, R.G. et al., 2018: History of chemically and radiatively important atmospheric gases from the Advanced Global Atmospheric Gases Experiment (AGAGE). *Earth System Science Data*, **10(2)**, 985–1018, doi:10.5194/essd-10-985-2018.

Purohit, P. and L. Höglund-Isaksson, 2017: Global emissions of fluorinated greenhouse gases 2005-2050 with abatement potentials and costs. *Atmospheric Chemistry and Physics*, **17(4)**, 2795–2816, doi:10.5194/acp-17-2795-2017.

Purohit, P. et al., 2020: Electricity savings and greenhouse gas emission reductions from global phase-down of hydrofluorocarbons. *Atmospheric Chemistry and Physics*, **20(19)**, 11305–11327, doi:10.5194/acp-20-11305-2020.

Pusede, S.E. et al., 2016: On the effectiveness of nitrogen oxide reductions as a control over ammonium nitrate aerosol. *Atmospheric Chemistry and Physics*, **16(4)**, 2575–2596, doi:10.5194/acp-16-2575-2016.

Putaud, J.-P. et al., 2010: A European aerosol phenomenology – 3: Physical and chemical characteristics of particulate matter from 60 rural, urban, and kerbside sites across Europe. *Atmospheric Environment*, **44(10)**, 1308–1320, doi:10.1016/j.atmosenv.2009.12.011.

Qiao, X. et al., 2018: Source apportionment of PM2.5 for 25 Chinese provincial capitals and municipalities using a source-oriented Community Multiscale Air Quality model. *Science of The Total Environment*, **612**, 462–471, doi:10.1016/j.scitotenv.2017.08.272.

Querol, X. et al., 2013: Variability of carbonaceous aerosols in remote, rural, urban and industrial environments in Spain: Implications for air quality policy. *Atmospheric Chemistry and Physics*, **13(13)**, 6185–6206, doi:10.5194/acp-13-6185-2013.

Radhi, M. et al., 2010: Optical, physical and chemical characteristics of Australian continental aerosols: results from a field experiment. *Atmospheric Chemistry and Physics*, **10(13)**, 5925–5942, doi:10.5194/acp-10-5925-2010.

Rafaj, P. and M. Amann, 2018: Decomposing air pollutant emissions in Asia: Determinants and projections. *Energies*, **11(5)**, 1299, doi:10.3390/en11051299.

Rafaj, P., M. Amann, J. Siri, and H. Wuester, 2014: Changes in European greenhouse gas and air pollutant emissions 1960–2010: decomposition of determining factors. *Climatic Change*, **124(3)**, 477–504, doi:10.1007/s10584-013-0826-0.

Rafaj, P. et al., 2018: Outlook for clean air in the context of sustainable development goals. *Global Environmental Change*, **53**, 1–11, doi:10.1016/j.gloenvcha.2018.08.008.

Randerson, J.T., Y. Chen, G.R. van der Werf, B.M. Rogers, and D.C. Morton, 2012: Global burned area and biomass burning emissions from small fires. *Journal of Geophysical Research: Biogeosciences*, **117(G4)**, n/a–n/a, doi:10.1029/2012jg002128.

Randles, C.A. et al., 2017: The MERRA-2 aerosol reanalysis, 1980 onward. Part I: System description and data assimilation evaluation. *Journal of Climate*, **30(17)**, 6823–6850, doi:10.1175/jcli-d-16-0609.1.

Rao, S. et al., 2013: Better air for better health: Forging synergies in policies for energy access, climate change and air pollution. *Global Environmental Change*, **23(5)**, 1122–1130, doi:10.1016/j.gloenvcha.2013.05.003.

Rao, S. et al., 2016: A multi-model assessment of the co-bene fi ts of climate mitigation for global air quality. *Environmental Research Letters*, **11(12)**, 124013.

Rao, S. et al., 2017: Future air pollution in the Shared Socio-economic Pathways. *Global Environmental Change*, **42**, 346–358, doi:10.1016/j.gloenvcha.2016.05.012.

Rap, A., P.M. Forster, J.M. Haywood, A. Jones, and O. Boucher, 2010: Estimating the climate impact of linear contrails

ACCEPTED VERSION SUBJECT TO FINAL EDITING

using the UK Met Office climate model. *Geophysical Research Letters*, **37(20)**, doi:10.1029/2010gl045161.
Rap, A. et al., 2015: Fires increase Amazon forest productivity through increases in diffuse radiation. *Geophysical Research Letters*, **42(11)**, 4654–4662, doi:10.1002/2015gl063719.
Rasch, P.J., P.J. Crutzen, and D.B. Coleman, 2008: Exploring the geoengineering of climate using stratospheric sulfate aerosols: The role of particle size. *Geophysical Research Letters*, doi:10.1029/2007gl032179.
Rasch, P.J., J. Latham, and C.C. Chen, 2009: Geoengineering by cloud seeding: Influence on sea ice and climate system. *Environmental Research Letters*, doi:10.1088/1748-9326/4/4/045112.
Reddington, C.L. et al., 2017: The global aerosol synthesis and science project (GASSP): Measurements and modeling to reduce uncertainty. *Bulletin of the American Meteorological Society*, **98(9)**, 1857–1877, doi:10.1175/bams-d-15-00317.1.
Reddington, C.L. et al., 2019: Exploring the impacts of anthropogenic emission sectors on PM_{2.5} and human health in South and East Asia. *Atmospheric Chemistry and Physics*, **19(18)**, 11887–11910, doi:10.5194/acp-19-11887-2019.
Reis, S. et al., 2012: From acid rain to climate change. *Science*, **338(6111)**, 1153–1154, doi:10.1126/science.1226514.
Ren, L. et al., 2020a: Source attribution of Arctic black carbon and sulfate aerosols and associated Arctic surface warming during 1980–2018. *Atmos. Chem. Phys.*, **20(14)**, 9067–9085, doi:10.5194/acp-20-9067-2020.
Ren, L. et al., 2020b: Source attribution of Arctic black carbon and sulfate aerosols and associated Arctic surface warming during 1980–2018. *Atmos. Chem. Phys.*, **20(14)**, 9067–9085, doi:10.5194/acp-20-9067-2020.
Riahi, K. et al., 2017: The Shared Socioeconomic Pathways and their energy, land use, and greenhouse gas emissions implications: An overview. *Global Environmental Change*, **42**, 153–168, doi:10.1016/j.gloenvcha.2016.05.009.
Ricciardelli, I. et al., 2017: A three-year investigation of daily PM_{2.5} main chemical components in four sites: the routine measurement program of the Supersito Project (Po Valley, Italy). *Atmospheric Environment*, **152**, 418–430, doi:10.1016/j.atmosenv.2016.12.052.
Riddick, S. et al., 2016: Estimate of changes in agricultural terrestrial nitrogen pathways and ammonia emissions from 1850 to present in the\\hack{\\newline} Community Earth System Model. *Biogeosciences*, **13(11)**, 3397–3426, doi:10.5194/bg-13-3397-2016.
Rieder, H.E. et al., 2018: Combining model projections with site-level observations to estimate changes in distributions and seasonality of ozone in surface air over the U.S.A.. *Atmospheric Environment*, **193**, 302–315, doi:10.1016/j.atmosenv.2018.07.042.
Rigby, M. et al., 2017: Role of atmospheric oxidation in recent methane growth. *Proceedings of the National Academy of Sciences*.
Robinson, M.A., M.R. Olson, Z.G. Liu, and J.J. Schauer, 2015: The effects of emission control strategies on light-absorbing carbon emissions from a modern heavy-duty diesel engine. *Journal of the Air & Waste Management Association*, **65(6)**, 759–766, doi:10.1080/10962247.2015.1005850.
Robock, A., L. Oman, and G.L. Stenchikov, 2008: Regional climate responses to geoengineering with tropical and Arctic SO2 injections. *Journal of Geophysical Research Atmospheres*, **113(16)**, 1–15, doi:10.1029/2008jd010050.
Rogelj, J. et al., 2014a: Air-pollution emission ranges consistent with the representative concentration pathways. *Nature Climate Change*, **4(6)**, 446–450, doi:10.1038/nclimate2178.
Rogelj, J. et al., 2014b: Disentangling the effects of CO ₂ and short-lived climate forcer mitigation. *Proceedings of the National Academy of Sciences*, **111(46)**, 16325–16330, doi:10.1073/pnas.1415631111.
Rogelj, J. et al., 2017: Understanding the origin of Paris Agreement emission uncertainties. *Nature Communications*, **8(1)**, 1–12, doi:10.1038/ncomms15748.
Rogelj, J. et al., 2018a: Scenarios towards limiting global mean temperature increase below 1.5°C. *Nature Climate Change*, **8(4)**, 325–332, doi:10.1038/s41558-018-0091-3.
Rogelj, J. et al., 2018b: Mitigation Pathways Compatible With 1.5°C in the Context of Sustainable Development. In: *Global Warming of 1.5°C. An IPCC Special Report on the impacts of global warming of 1.5°C above pre-industrial levels and related global greenhouse gas emission pathways, in the context of strengthening the global response to the threat of climate change* [Masson-Delmotte, V., P. Zhai, H.O. Pörtner, D. Roberts, J. Skea, P.R. Shukla, A. Pirani, W. Moufouma-Okia, C. Péan, R. Pidcock, S. Connors, J.B.R. Matthews, Y. Chen, X. Zhou, M.I. Gomis, E. Lonnoy, T. Maycock, M. Tignor, and T. Waterfield (eds.)]. In Press, pp. 93–174.
Romer, P.S. et al., 2018: Effects of temperature-dependent NO_x emissions on continental ozone production. *Atmospheric Chemistry and Physics*, **18(4)**, 2601–2614, doi:10.5194/acp-18-2601-2018.
Rooney, B. et al., 2020: Air quality impact of the Northern California Camp Fire of November 2018. *Atmospheric Chemistry and Physics*, **20(23)**, 14597–14616, doi:10.5194/acp-20-14597-2020.
Rosenstiel, T.N., M.J. Potosnak, K.L. Griffin, R. Fall, and R.K. Monson, 2003: Increased CO2 uncouples growth from isoprene emission in an agriforest ecosystem. *Nature*, **421(6920)**, 256–259, doi:10.1038/nature01312.
Rossabi, S. and D. Helmig, 2018: Changes in Atmospheric Butanes and Pentanes and Their Isomeric Ratios in the Continental United States. *Journal of Geophysical Research: Atmospheres*, **123(7)**, 3772–3790,

ACCEPTED VERSION SUBJECT TO FINAL EDITING

doi:10.1002/2017jd027709.
Rowlinson, M.J. et al., 2019: Impact of El Niño-Southern Oscillation on the interannual variability of methane and tropospheric ozone. *Atmospheric Chemistry and Physics*, **19(13)**, 8669–8686, doi:10.5194/acp-19-8669-2019.
Ru, M., D.T. Shindell, K.M. Seltzer, S. Tao, and Q. Zhong, 2018: The long-term relationship between emissions and economic growth for SO 2 , CO 2 , and BC. *Environmental Research Letters*, **13(12)**, 124021, doi:10.1088/1748-9326/aaece2.
Ryder, C.L. et al., 2018: Coarse-mode mineral dust size distributions, composition and optical properties from AER-D aircraft measurements over the tropical eastern Atlantic. *Atmos. Chem. Phys.*, **18(23)**, 17225–17257, doi:10.5194/acp-18-17225-2018.
Saari, R.K., N.E. Selin, S. Rausch, and T.M. Thompson, 2015: A self-consistent method to assess air quality co-benefits from U.S. climate policies. *Journal of the Air & Waste Management Association*, **65(1)**, 74–89, doi:10.1080/10962247.2014.959139.
Sadiq, M., A.P.K. Tai, D. Lombardozzi, and M. Val Martin, 2017: Effects of ozone–vegetation coupling on surface ozone air quality via biogeochemical and meteorological feedbacks. *Atmospheric Chemistry and Physics*, **17(4)**, 3055–3066, doi:10.5194/acp-17-3055-2017.
Saiz-Lopez, A. et al., 2012: Estimating the climate significance of halogen-driven ozone loss in the tropical marine troposphere. *Atmospheric Chemistry and Physics*, **12(9)**, 3939–3949, doi:10.5194/acp-12-3939-2012.
Sajeev, E.P.M., B. Amon, C. Ammon, W. Zollitsch, and W. Winiwarter, 2018: Evaluating the potential of dietary crude protein manipulation in reducing ammonia emissions from cattle and pig manure: A meta-analysis. *Nutrient Cycling in Agroecosystems*, **110(1)**, 161–175, doi:10.1007/s10705-017-9893-3.
Saliba, G. et al., 2019: Factors driving the seasonal and hourly variability of sea-spray aerosol number in the North Atlantic. *Proceedings of the National Academy of Sciences of the United States of America*, **116(41)**, 20309–20314, doi:10.1073/pnas.1907574116.
Salter, M.E., E.D. Nilsson, A. Butcher, and M. Bilde, 2014: On the seawater temperature dependence of the sea spray aerosol generated by a continuous plunging jet. *Journal of Geophysical Research*, **119(14)**, 9052–9072, doi:10.1002/2013jd021376.
Samset, B.H., J.S. Fuglestvedt, and M.T. Lund, 2020: Delayed emergence of a global temperature response after emission mitigation. *Nature Communications*, **11(1)**, doi:10.1038/s41467-020-17001-1.
Samset, B.H. et al., 2013: Black carbon vertical profiles strongly affect its radiative forcing uncertainty. *Atmospheric Chemistry and Physics*, **13(5)**, 2423–2434, doi:10.5194/acp-13-2423-2013.
Samset, B.H. et al., 2016: Fast and slow precipitation responses to individual climate forcers: A PDRMIP multimodel study. *Geophysical Research Letters*, **43(6)**, 2782–2791, doi:10.1002/2016gl068064.
Samset, B.H. et al., 2018: Climate Impacts From a Removal of Anthropogenic Aerosol Emissions. *Geophysical Research Letters*, **45(2)**, 1020–1029, doi:10.1002/2017gl076079.
Samyn, D., C. Vega, H. Motoyama, and V. Pohjola, 2012: Nitrate and sulfate anthropogenic trends in the 20th century from five svalbard ice cores. *Arctic, Antarctic, and Alpine Research*, **44(4)**, 490–499, doi:10.1657/1938-4246-44.4.490.
Sand, M., T.K. Berntsen, Seland, and J.E. Kristjánsson, 2013a: Arctic surface temperature change to emissions of black carbon within Arctic or midlatitudes. *Journal of Geophysical Research: Atmospheres*, **118(14)**, 7788–7798, doi:10.1002/jgrd.50613.
Sand, M., T.K. Berntsen, A.M.L. Ekman, H.-C. Hansson, and A. Lewinschal, 2020: Surface temperature response to regional black carbon emissions: do location and magnitude matter? *Atmos. Chem. Phys.*, **20(5)**, 3079–3089, doi:10.5194/acp-20-3079-2020.
Sand, M. et al., 2013b: The arctic response to remote and local forcing of black carbon. *Atmospheric Chemistry and Physics*, **13(1)**, 211–224, doi:10.5194/acp-13-211-2013.
Sand, M. et al., 2016: Response of Arctic temperature to changes in emissions of short-lived climate forcers. *Nature Climate Change*, **6(3)**, 286–289, doi:10.1038/nclimate2880.
Sandrini, S. et al., 2016: Size-resolved aerosol composition at an urban and a rural site in the Po Valley in summertime: implications for secondary aerosol formation. *Atmospheric Chemistry and Physics*, **16(17)**, 10879–10897, doi:10.5194/acp-16-10879-2016.
Sarkar, C., A. Roy, A. Chatterjee, S.K. Ghosh, and S. Raha, 2019: Factors controlling the long-term (2009–2015) trend of PM 2.5 and black carbon aerosols at eastern Himalaya, India. *Science of the Total Environment*, **656**, 280–296, doi:10.1016/j.scitotenv.2018.11.367.
Sarwar, G. et al., 2015: Impact of Enhanced Ozone Deposition and Halogen Chemistry on Tropospheric Ozone over the Northern Hemisphere. *Environmental Science & Technology*, **49(15)**, 9203–9211, doi:10.1021/acs.est.5b01657.
Saunois, M. et al., 2016: The global methane budget 2000-2012. *Earth System Science Data*, **8(2)**, 697–751, doi:10.5194/essd-8-697-2016.
Saunois, M. et al., 2020: The Global Methane Budget 2000–2017. *Earth Syst. Sci. Data*, **12(3)**, 1561–1623, doi:10.5194/essd-12-1561-2020.
Schiferl, L.D. et al., 2016: Interannual variability of ammonia concentrations over the United States: Sources and

ACCEPTED VERSION SUBJECT TO FINAL EDITING

implications. *Atmospheric Chemistry and Physics*, **16(18)**, 12305–12328, doi:10.5194/acp-16-12305-2016.
Schmale, J., J. van Aardenne, and E. Von Schneidemesser, 2014a: New Directions: Support for integrated decision-making in air and climate policies – Development of a metrics-based information portal. *Atmospheric Environment*, **90**, 146–148, doi:10.1016/j.atmosenv.2014.03.016.
Schmale, J., D. Shindell, E. Von Schneidemesser, I. Chabay, and M. Lawrence, 2014b: Air pollution: Clean up our skies. *Nature*, **515(7527)**, 335–337, doi:10.1038/515335a.
Schneider, P., W.A. Lahoz, and R. Van Der A, 2015: Recent satellite-based trends of tropospheric nitrogen dioxide over large urban agglomerations worldwide. *Atmospheric Chemistry and Physics*, **15(3)**, 1205–1220, doi:10.5194/acp-15-1205-2015.
Schnell, J.L. and M.J. Prather, 2017: Co-occurrence of extremes in surface ozone, particulate matter, and temperature over eastern North America. *Proceedings of the National Academy of Sciences*, **114(11)**, 2854–2859, doi:10.1073/pnas.1614453114.
Schnell, J.L. et al., 2016: Effect of climate change on surface ozone over North America, Europe, and East Asia. *Geophysical Research Letters*, **43(7)**, 3509–3518, doi:10.1002/2016gl068060.
Schnell, J.L. et al., 2018: Exploring the relationship between surface PM2.5 and meteorology in Northern India. *Atmospheric Chemistry and Physics*, **18(14)**, 10157–10175, doi:10.5194/acp-18-10157-2018.
Schroder, J.C. et al., 2015: Size-resolved observations of refractory black carbon particles in cloud droplets at a marine boundary layer site. *Atmospheric Chemistry and Physics*, doi:10.5194/acp-15-1367-2015.
Schultz, M.G. et al., 2015: The Global Atmosphere Watch reactive gases measurement network. *Elem Sci Anth*, **3(0)**, doi:10.12952/journal.elementa.000067.
Schulz, H. et al., 2019: High Arctic aircraft measurements characterising black carbon vertical variability in spring and summer. *Atmospheric Chemistry and Physics*, **19(4)**, 2361–2384, doi:10.5194/acp-19-2361-2019.
Schwarber, A.K., S.J. Smith, C.A. Hartin, B.A. Vega-Westhoff, and R. Sriver, 2019: Evaluating climate emulation: fundamental impulse testing of simple climate models. *Earth System Dynamics*, **10(4)**, 729–739, doi:10.5194/esd-10-729-2019.
Schwarz, J.P. et al., 2013: Global-scale seasonally resolved black carbon vertical profiles over the Pacific. *Geophysical Research Letters*, **40(20)**, 5542–5547, doi:10.1002/2013gl057775.
Schwinger, J. et al., 2017: Amplification of global warming through pH dependence of DMS production simulated with a fully coupled Earth system model. *Biogeosciences*, **14(15)**, 3633–3648, doi:10.5194/bg-14-3633-2017.
Scott, C.E. et al., 2017: Impact on short-lived climate forcers (SLCFs) from a realistic land-use change scenario: Via changes in biogenic emissions. *Faraday Discussions*, **200**, 101–120, doi:10.1039/c7fd00028f.
Scott, C.E. et al., 2018: Substantial large-scale feedbacks between natural aerosols and climate. *Nature Geoscience*, **11(1)**, 44–48, doi:10.1038/s41561-017-0020-5.
Sekiya, T. and K. Sudo, 2014: Roles of transport and chemistry processes in global ozone change on interannual and multidecadal time scales. *Journal of Geophysical Research*, **119(8)**, 4903–4921, doi:10.1002/2013jd020838.
Serrano, H.C. et al., 2019: Measuring and mapping the effectiveness of the European Air Quality Directive in reducing N and S deposition at the ecosystem level. *Science of the Total Environment*, **647**, 1531–1538, doi:10.1016/j.scitotenv.2018.08.059.
Serrano-Cinca, C., Y. Fuertes-Callén, and C. Mar-Molinero, 2005: Measuring DEA efficiency in Internet companies. *Decision Support Systems*, **38(4)**, 557–573, doi:10.1016/j.dss.2003.08.004.
Sharma, S. et al., 2013a: 16-year simulation of arctic black carbon: Transport, source contribution, and sensitivity analysis on deposition. *Journal of Geophysical Research Atmospheres*, doi:10.1029/2012jd017774.
Sharma, S. et al., 2013b: 16-year simulation of arctic black carbon: Transport, source contribution, and sensitivity analysis on deposition. *Journal of Geophysical Research Atmospheres*, doi:10.1029/2012jd017774.
Sharma, S. et al., 2017: An evaluation of three methods for measuring black carbon in Alert, Canada. *Atmospheric Chemistry and Physics*, **17(24)**, 15225–15243, doi:10.5194/acp-17-15225-2017.
Shen, L., L.J. Mickley, and L.T. Murray, 2017: Influence of 2000-2050 climate change on particulate matter in the United States: Results from a new statistical model. *Atmospheric Chemistry and Physics*, **17(6)**, 4355–4367, doi:10.5194/acp-17-4355-2017.
Shen, L. et al., 2019: The 2005–2016 Trends of Formaldehyde Columns Over China Observed by Satellites: Increasing Anthropogenic Emissions of Volatile Organic Compounds and Decreasing Agricultural Fire Emissions. *Geophysical Research Letters*, **46(8)**, 4468–4475, doi:10.1029/2019gl082172.
Shephard, M.W. and K.E. Cady-Pereira, 2015: Cross-track Infrared Sounder (CrIS) satellite observations of tropospheric ammonia. *Atmospheric Measurement Techniques*, **8(3)**, 1323–1336, doi:10.5194/amt-8-1323-2015.
Shephard, M.W. et al., 2011: TES ammonia retrieval strategy and global observations of the spatial and seasonal variability of ammonia. *Atmospheric Chemistry and Physics*, **11(20)**, 10743–10763, doi:10.5194/acp-11-10743-2011.
Sheppard, L.J. et al., 2011: Dry deposition of ammonia gas drives species change faster than wet deposition of ammonium ions: evidence from a long-term field manipulation. *Glob. Chang. Biol.*, **17(12)**, 3589–3607, doi:10.1111/j.1365-2486.2011.02478.x.

ACCEPTED VERSION SUBJECT TO FINAL EDITING

Sherwen, T. et al., 2016: Global impacts of tropospheric halogens (Cl, Br, I) on oxidants and composition in GEOS-Chem. *Atmospheric Chemistry and Physics*, **16(18)**, 12239–12271, doi:10.5194/acp-16-12239-2016.
Sherwood, S.C. et al., 2020: An Assessment of Earth's Climate Sensitivity Using Multiple Lines of Evidence. *Reviews of Geophysics*, **58(4)**, e2019RG000678, doi:10.1029/2019rg000678.
Shi, G. et al., 2017: PH of Aerosols in a Polluted Atmosphere: Source Contributions to Highly Acidic Aerosol. *Environmental Science and Technology*, **51(8)**, 4289–4296, doi:10.1021/acs.est.6b05736.
Shi, Z. et al., 2021: Abrupt but smaller than expected changes in surface air quality attributable to COVID-19 lockdowns. *Science Advances*, doi:10.1126/sciadv.abd6696.
Shindell, D. and G. Faluvegi, 2009: Climate response to regional radiative forcing during the twentieth century. *Nature Geoscience*, **2(4)**, 294–300, doi:10.1038/ngeo473.
Shindell, D. and C.J. Smith, 2019: Climate and air-quality benefits of a realistic phase-out of fossil fuels. *Nature*, **573(7774)**, 408–411, doi:10.1038/s41586-019-1554-z.
Shindell, D., G. Faluvegi, K. Seltzer, and C. Shindell, 2018: Quantified, localized health benefits of accelerated carbon dioxide emissions reductions. *Nature Climate Change*, **8(4)**, 1–5, doi:10.1038/s41558-018-0108-y.
Shindell, D. et al., 2012a: Simultaneously mitigating near-term climate change and improving human health and food security. *Science*, **335(6065)**, 183–189, doi:10.1126/science.1210026.
Shindell, D. et al., 2012b: Simultaneously mitigating near-term climate change and improving human health and food security. *Science*, **335(6065)**, 183–189, doi:10.1126/science.1210026.
Shindell, D. et al., 2017: A climate policy pathway for near- and long-term benefits. *Science*, **356(6337)**, 493–494, doi:10.1126/science.aak9521.
Shindell, D.T., Y. Lee, and G. Faluvegi, 2016: Climate and health impacts of US emissions reductions consistent with 2 °C. *Nature Climate Change*, **6**, 503.
Shindell, D.T., J.S. Fuglestvedt, and W.J. Collins, 2017: The social cost of methane: theory and applications. *Faraday Discussions*, **200(0)**, 429–451, doi:10.1039/c7fd00009j.
Shindell, D.T., G. Faluvegi, L. Rotstayn, and G. Milly, 2015: Spatial patterns of radiative forcing and surface temperature response. *Journal of Geophysical Research: Atmospheres*, **120(11)**, 5385–5403, doi:10.1002/2014jd022752.
Shindell, D.T. et al., 2006: Multimodel simulations of carbon monoxide: Comparison with observations and projected near-future changes. *Journal of Geophysical Research Atmospheres*, doi:10.1029/2006jd007100.
Shindell, D.T. et al., 2009: Improved Attribution of Climate Forcing to Emissions. *SCIENCE*, **326(5953)**, 716–718, doi:10.1126/science.1174760.
Shindell, D.T. et al., 2013: Radiative forcing in the ACCMIP historical and future climate simulations. *Atmospheric Chemistry and Physics*, **13(6)**, 2939–2974, doi:10.5194/acp-13-2939-2013.
Shoemaker, J.K., D.P. Schrag, M.J. Molina, and V. Ramanathan, 2013: What role for short-lived climate pollutants in mitigation policy? *Science*, **342(6164)**, 1323–1324, doi:10.1126/science.1240162.
Shrivastava, M. et al., 2017: Recent advances in understanding secondary organic aerosol: Implications for global climate forcing. *Reviews of Geophysics*, **55(2)**, 509–559, doi:10.1002/2016rg000540.
Sicard, P. et al., 2020: Amplified ozone pollution in cities during the COVID-19 lockdown. *Science of the Total Environment*, **735**, doi:10.1016/j.scitotenv.2020.139542.
Sickles, J.E. and D.S. Shadwick, 2015: Air quality and atmospheric deposition in the eastern US: 20 years of change. *Atmospheric Chemistry and Physics*, **15(1)**, 173–197, doi:10.5194/acp-15-173-2015.
Silva, R.A., Z. Adelman, M.M. Fry, and J.J. West, 2016a: The impact of individual anthropogenic emissions sectors on the global burden of human mortality due to ambient air pollution. *Environmental Health Perspectives*, **124(11)**, 1776–1784, doi:10.1289/ehp177.
Silva, R.A., Z. Adelman, M.M. Fry, and J.J. West, 2016b: The Impact of Individual Anthropogenic Emissions Sectors on the Global Burden of Human Mortality due to Ambient Air Pollution. *Environmental Health Perspectives*, **124(11)**, 1776–1784, doi:10.1289/ehp177.
Silver, B., C.L. Reddington, S.R. Arnold, and D. Spracklen, 2018: Substantial changes in air pollution across China during 2015–2017. *Environmental Research Letters*, **13(11)**, 114012, doi:10.1088/1748-9326/aae718.
Silvern, R.F. et al., 2018: Observed NO/NO₂ Ratios in the Upper Troposphere Imply Errors in NO-NO₂-O₃ Cycling Kinetics or an Unaccounted NO_x Reservoir. *Geophysical Research Letters*, **45(9)**, 4466–4474, doi:10.1029/2018gl077728.
Simpson, I.J. et al., 2012: Long-term decline of global atmospheric ethane concentrations and implications for methane. *Nature*, **488(7412)**, 490–494, doi:10.1038/nature11342.
Singh, V., K. Ravindra, L. Sahu, and R. Sokhi, 2018: Trends of atmospheric black carbon concentration over United Kingdom. *Atmospheric Environment*, **178**, 148–157, doi:10.1016/j.atmosenv.2018.01.030.
Six, K.D. et al., 2013: Global warming amplified by reduced sulphur fluxes as a result of ocean acidification. *Nature Climate Change*, **3(11)**, 975–978, doi:10.1038/nclimate1981.
Skowron, A., D.S. Lee, R.R. De León, L.L. Lim, and B. Owen, 2021: Greater fuel efficiency is potentially preferable to reducing NOx emissions for aviation's climate impacts. *Nature Communications*, **12(1)**, 564, doi:10.1038/s41467-020-20771-3.

ACCEPTED VERSION SUBJECT TO FINAL EDITING

Smith, C.J. et al., 2018: FAIR v1.3: a simple emissions-based impulse response and carbon cycle model. *Geoscientific Model Development*, **11(6)**, 2273–2297, doi:10.5194/gmd-11-2273-2018.
Smith, C.J. et al., 2019: Current fossil fuel infrastructure does not yet commit us to 1.5°C warming. *Nature Communications*, **10(1)**, 101, doi:10.1038/s41467-018-07999-w.
Smith, S.J. and A. Mizrahi, 2013: Near-term climate mitigation by short-lived forcers. *Proceedings of the National Academy of Sciences*, **110(35)**, 14202–14206, doi:10.1073/pnas.1308470110.
Smith, S.J. et al., 2020: Impact of methane and black carbon mitigation on forcing and temperature: a multi-model scenario analysis. *Climatic Change*, doi:10.1007/s10584-020-02794-3.
Snider, G. et al., 2015: SPARTAN: a global network to evaluate and enhance satellite-based estimates of ground-level particulate matter for global health applications. *Atmospheric Measurement Techniques*, **8(1)**, 505–521, doi:10.5194/amt-8-505-2015.
Snider, G. et al., 2016: Variation in global chemical composition of PM2.5: emerging results from SPARTAN. *Atmospheric Chemistry and Physics*, **16(15)**, 9629–9653, doi:10.5194/acp-16-9629-2016.
Soares, J. et al., 2016: Impact of Climate Change on the Production and Transport of Sea Salt Aerosol on European Seas. In: *Air Pollution Modeling and its Application XXIV* [Steyn, D. and N. Chaumerliac (eds.)]. Springer Proceedings in Complexity, Springer, Cham, Switzerland, pp. 207–212, doi:10.1007/978-3-319-24478-5_34.
Sofiev, M. et al., 2018: Cleaner fuels for ships provide public health benefits with climate tradeoffs. *Nature Communications*, **9(1)**, doi:10.1038/s41467-017-02774-9.
Solomon, P.A. et al., 2014: U.S. National PM2.5 Chemical Speciation Monitoring Networks – CSN and IMPROVE: Description of networks. *Journal of the Air & Waste Management Association*, **64(12)**, 1410–1438, doi:10.1080/10962247.2014.956904.
Spracklen, D., S.R. Arnold, L. Conibear, E.W. Butt, and C. Knote, 2018: Residential energy use emissions dominate health impacts from exposure to ambient particulate matter in India. *Nature Communications*, **9(1)**, doi:10.1038/s41467-018-02986-7.
Squire, O.J. et al., 2015: Influence of isoprene chemical mechanism on modelled changes in tropospheric ozone due to climate and land use over the 21st century. *Atmospheric Chemistry and Physics*, **15(9)**, 5123–5143, doi:10.5194/acp-15-5123-2015.
Stanelle, T., I. Bey, T. Raddatz, C. Reick, and I. Tegen, 2014: Anthropogenically induced changes in twentieth century mineral dust burden and the associated impact on radiative forcing. *JOURNAL OF GEOPHYSICAL RESEARCH-ATMOSPHERES*, **119(23)**, 13526–13546, doi:10.1002/2014jd022062.
Stavrakou, T. et al., 2014: Isoprene emissions over Asia 1979–2012: impact of climate and land-use changes. *Atmospheric Chemistry and Physics*, **14(9)**, 4587–4605, doi:10.5194/acp-14-4587-2014.
Stechow, C. et al., 2016: 2°C and SDGs: United they stand, divided they fall? *Environmental Research Letters*, **11**, 34022, doi:10.1088/1748-9326/11/3/034022.
Stein, O. et al., 2014: On the wintertime low bias of Northern Hemisphere carbon monoxide found in global model simulations. *Atmospheric Chemistry and Physics*, doi:10.5194/acp-14-9295-2014.
Stevens, B. et al., 2017: {MACv}2-{SP}: a parameterization of anthropogenic aerosol optical properties and an associated {Twomey} effect for use in {CMIP}6. *Geosci. Model Dev.*, **10(1)**, 433–452, doi:10.5194/gmd-10-433-2017.
Stevenson, D.S. et al., 2006: Multimodel ensemble simulations of present-day and near-future tropospheric ozone. *Journal of Geophysical Research: Atmospheres*, **111(D8)**, doi:10.1029/2005jd006338.
Stevenson, D.S. et al., 2013: Tropospheric ozone changes, radiative forcing and attribution to emissions in the Atmospheric Chemistry and Climate Model Intercomparison Project (ACCMIP). *Atmospheric Chemistry and Physics*, **13(6)**, 3063–3085, doi:10.5194/acp-13-3063-2013.
Stevenson, D.S. et al., 2020: Trends in global tropospheric hydroxyl radical and methane lifetime since 1850 from AerChemMIP. *Atmospheric Chemistry and Physics*, **20(21)**, 12905–12920, doi:10.5194/acp-20-12905-2020.
Stjern, C.W. et al., 2017: Rapid Adjustments Cause Weak Surface Temperature Response to Increased Black Carbon Concentrations. *Journal of Geophysical Research: Atmospheres*, **122(21)**, 11,462–11,481, doi:10.1002/2017jd027326.
Stockwell, W.R., E. Saunders, W.S. Goliff, and R.M. Fitzgerald, 2020: A perspective on the development of gas-phase chemical mechanisms for Eulerian air quality models. *Journal of the Air & Waste Management Association*, **70(1)**, 44–70, doi:10.1080/10962247.2019.1694605.
Stohl, A. et al., 2013: Black carbon in the Arctic: The underestimated role of gas flaring and residential combustion emissions. *Atmospheric Chemistry and Physics*, **13(17)**, doi:10.5194/acp-13-8833-2013.
Stohl, A. et al., 2015: Evaluating the climate and air quality impacts of short-lived pollutants. *Atmospheric Chemistry and Physics*, **15(18)**, 10529–10566, doi:10.5194/acp-15-10529-2015.
Storelvmo, T. et al., 2013: Cirrus cloud seeding has potential to cool climate. *Geophysical Research Letters*, doi:10.1029/2012gl054201.
Strada, S. and N. Unger, 2016: Potential sensitivity of photosynthesis and isoprene emission to direct radiative effects of atmospheric aerosol pollution. *Atmospheric Chemistry and Physics*, **16(7)**, 4213–4234, doi:10.5194/acp-16-4213-2016.

ACCEPTED VERSION SUBJECT TO FINAL EDITING

Strefler, J., G. Luderer, E. Kriegler, and M. Meinshausen, 2014: Can air pollutant controls change global warming? *Environmental Science and Policy*, **41**, 33–43, doi:10.1016/j.envsci.2014.04.009.
Strode, S.A. et al., 2015: Implications of carbon monoxide bias for methane lifetime and atmospheric composition in chemistry climate models. *Atmospheric Chemistry and Physics*, doi:10.5194/acp-15-11789-2015.
Strode, S.A. et al., 2016: Interpreting space-based trends in carbon monoxide with multiple models. *Atmospheric Chemistry and Physics*, **16(11)**, 7285–7294, doi:10.5194/acp-16-7285-2016.
Struthers, H. et al., 2013: Climate-induced changes in sea salt aerosol number emissions: 1870 to 2100. *Journal of Geophysical Research: Atmospheres*, **118(2)**, 670–682, doi:10.1002/jgrd.50129.
Stuber, N., M. Ponater, and R. Sausen, 2001: Is the climate sensitivity to ozone perturbations enhanced by stratospheric water vapor feedback? *Geophysical Research Letters*, **28(15)**, 2887–2890, doi:10.1029/2001gl013000.
Sun, G.E. et al., 2012: Interactive influences of ozone and climate on streamflow of forested watersheds. *Global Change Biology*, **18(11)**, 3395–3409, doi:10.1111/j.1365-2486.2012.02787.x.
Sun, W., P. Hess, and C. Liu, 2017: The impact of meteorological persistence on the distribution and extremes of ozone. *Geophysical Research Letters*, **44(3)**, 1545–1553, doi:10.1002/2016gl071731.
Sun, W. et al., 2018: Long-Term Trends of Anthropogenic SO₂, NO_x, CO, and NMVOCs Emissions in China. *Earth's Future*, **6(8)**, 1112–1133, doi:10.1029/2018ef000822.
Sutton, M.A. et al., 2013: Towards a climate-dependent paradigm of ammonia emission and deposition. *Philos. Trans. R. Soc. London, Ser. B*, **368(1621)**.
Szogs, S. et al., 2017: Impact of LULCC on the emission of BVOCs during the 21st century. *Atmospheric Environment*, **165**, 73–87, doi:10.1016/j.atmosenv.2017.06.025.
Tan, J. et al., 2018: Multi-model study of HTAP II on sulfur and nitrogen deposition. *Atmospheric Chemistry and Physics*, **18(9)**, 6847–6866, doi:10.5194/acp-18-6847-2018.
Tanaka, K., M.T. Lund, B. Aamaas, and T. Berntsen, 2018: Climate effects of non-compliant Volkswagen diesel cars. *Environmental Research Letters*, **13(4)**, 44020, doi:10.1088/1748-9326/aab18c.
Tang, Y.S. et al., 2018: Drivers for spatial, temporal and long-term trends in atmospheric ammonia and ammonium in the UK. *Atmospheric Chemistry and Physics*, **18(2)**, 705–733, doi:10.5194/acp-18-705-2018.
Tanimoto, H., K. Ikeda, K.F. Boersma, R.J. A, and S. Garivait, 2015: Interannual variability of nitrogen oxides emissions from boreal fires in Siberia and Alaska during 1996–2011 as observed from space. *Environmental Research Letters*, **10(6)**, 65004.
Taylor, J.W. et al., 2014: Size-dependent wet removal of black carbon in Canadian biomass burning plumes. *Atmospheric Chemistry and Physics*, doi:10.5194/acp-14-13755-2014.
Té, Y. et al., 2016: Seasonal variability of surface and column carbon monoxide over the megacity Paris, high-altitude Jungfraujoch and Southern Hemispheric Wollongong stations. *Atmospheric Chemistry and Physics*, **16(17)**, 10911–10925, doi:10.5194/acp-16-10911-2016.
Theobald, M.R. et al., 2019: An evaluation of European nitrogen and sulfur wet deposition and their trends estimated by six chemistry transport models for the period 1990-2010. *Atmospheric Chemistry and Physics*, **19(1)**, 379–405, doi:10.5194/acp-19-379-2019.
Thompson, T.M., S. Rausch, R.K. Saari, and N.E. Selin, 2016: Air quality co-benefits of subnational carbon policies. *Journal of the Air & Waste Management Association*, **66(10)**, 988–1002, doi:10.1080/10962247.2016.1192071.
Thornhill, G. et al., 2021: Climate-driven chemistry and aerosol feedbacks in CMIP6 Earth system models. *Atmospheric Chemistry and Physics*, **21(2)**, 1105–1126, doi:10.5194/acp-21-1105-2021.
Thornhill, G.D. et al., 2021: Effective radiative forcing from emissions of reactive gases and aerosols – a multi-model comparison. *Atmos. Chem. Phys.*, **21(2)**, 853–874, doi:10.5194/acp-21-853-2021.
Tilmes, S. et al., 2019: Climate Forcing and Trends of Organic Aerosols in the Community Earth System Model (CESM2). *Journal of Advances in Modeling Earth Systems*, **11(12)**, 4323–4351, doi:10.1029/2019ms001827.
Tohjima, Y. et al., 2020: Detection of fossil-fuel CO2 plummet in China due to COVID-19 by observation at Hateruma. *Scientific Reports*, **10(1)**, 18688, doi:10.1038/s41598-020-75763-6.
Tong, D. et al., 2020: Dynamic projection of anthropogenic emissions in China: methodology and 2015--2050 emission pathways under a range of socioeconomic, climate policy, and pollution control scenarios. *Atmospheric Chemistry and Physics*, **20(9)**, 5729–5757, doi:10.5194/acp-20-5729-2020.
Tørseth, K. et al., 2012: Introduction to the European Monitoring and Evaluation Programme (EMEP) and observed atmospheric composition change during 1972-2009. *Atmospheric Chemistry and Physics*, **12(12)**, 5447–5481, doi:10.5194/acp-12-5447-2012.
Tronstad Lund, M. et al., 2012: Global-mean temperature change from shipping toward 2050: Improved representation of the indirect aerosol effect in simple climate models. *Environmental Science and Technology*, doi:10.1021/es301166e.
Tsigaridis, K. et al., 2014: The AeroCom evaluation and intercomparison of organic aerosol in global models. *Atmospheric Chemistry and Physics*, **14(19)**, 10845–10895, doi:10.5194/acp-14-10845-2014.
Turner, A.J., C. Frankenberg, P.O. Wennberg, and D.J. Jacob, 2017: Ambiguity in the causes for decadal trends in atmospheric methane and hydroxyl. *Proceedings of the National Academy of Sciences*.

ACCEPTED VERSION SUBJECT TO FINAL EDITING

Turnock, S.T. et al., 2016: The impact of European legislative and technology measures to reduce air pollutants on air quality, human health and climate. *Environmental Research Letters*, **11(2)**, doi:10.1088/1748-9326/11/2/024010.
Turnock, S.T. et al., 2019: The Impact of Changes in Cloud Water pH on Aerosol Radiative Forcing. *Geophysical Research Letters*, **46(7)**, 4039–4048, doi:10.1029/2019gl082067.
Turnock, S.T. et al., 2020: Historical and future changes in air pollutants from CMIP6 models. *Atmospheric Chemistry and Physics*, **20**, 14547–14579, doi:10.5194/acp-20-14547-2020.
Twomey, S., 1977: The Influence of Pollution on the Shortwave Albedo of Clouds. *Journal of the Atmospheric Sciences*, doi:10.1175/1520-0469(1977)034<1149:tiopot>2.0.co;2.
Tzompa-Sosa, Z.A. et al., 2019: Atmospheric Implications of Large C 2 -C 5 Alkane Emissions From the U.S. Oil and Gas Industry. *Journal of Geophysical Research: Atmospheres*, **124(2)**, 1148–1169, doi:10.1029/2018jd028955.
Uherek, E. et al., 2010: Transport impacts on atmosphere and climate: Land transport. *Atmospheric Environment*, **44(37)**, 4772–4816, doi:10.1016/j.atmosenv.2010.01.002.
UN, 1987: Montreal Protocol on Substances that Deplete the Ozone Layer. In: Final Act of the Conference on Plenipotentiaries on the Protocol on Chlorofluorocarbons to the Vienna Convention for the Protection of the Ozone Layer. , 99-115.
Dentener, F.J., T.J. Keating, and H. Akimoto (eds.), 2010: *Hemispheric Transport of Air Pollution; Part A: Ozone and Particulate Matter*. Air Pollution Studies No. 17, United Nations Economic Commission for Europe (UNECE). United Nations (UN), New York, NY, USA and Geneva, Switzerland, 278 pp.
UNEP, 2016: Amendment to the Montreal Protocol on Substances that Deplete the Ozone Layer. In: Report of the Twenty-Eighth Meeting of the Parties to the Montreal Protocol on Substances that Deplete the Ozone Layer. UNEP/OzL.Pro.28/12. , 46-53.
UNEP, 2019: *Air Pollution in Asia and the Pacific: Science-Based Solutions*. United Nations Environment Program (UNEP), Nairobi, Kenya, 232 pp.
UNEP and WMO, 2011: *Integrated Assessment of Black Carbon and Tropospheric Ozone. Summary for Decision Makers*. UNEP/GC/26/INF/20, United Nations Environment Programme (UNEP) and World Meteorological Organization (WMO). UNEP, Nairobi, Kenya, 30 pp.
UNEP and CCAC, 2018: *Integrated Assessment of Short-lived Climate Pollutants in Latin America and the Caribbean: improving air quality while mitigating climate change*. United Nations Environment Programme (UNEP) and Climate and Clean Air Coalition (CCAC). UNEP, Nairobi, Kenya, 101 pp.
Unger, N., 2013: Isoprene emission variability through the twentieth century. *Journal of Geophysical Research Atmospheres*, **118(24)**, 13606–13613.
Unger, N., 2014: Human land-use-driven reduction of forest volatiles cools global climate. *Nature Climate Change*, **4(8)**, 907–910.
Unger, N., X. Yue, and K.L. Harper, 2017: Aerosol climate change effects on land ecosystem services. *Faraday Discussions*, **200**, doi:10.1039/c7fd00033b.
Unger, N., Y. Zheng, X. Yue, and K.L. Harper, 2020: Mitigation of ozone damage to the world's land ecosystems by source sector. *Nature Climate Change*, **10(2)**, 134–137, doi:10.1038/s41558-019-0678-3.
Unger, N. et al., 2010: Attribution of climate forcing to economic sectors. *Proceedings of the National Academy of Sciences of the United States of America*, **107(8)**, 3382–3387, doi:10.1073/pnas.0906548107.
Unger, N. et al., 2013: Photosynthesis-dependent isoprene emission from leaf to planet in a global carbon-chemistry-climate model. *Atmospheric Chemistry and Physics*, **13(20)**, 10243–10269, doi:10.5194/acp-13-10243-2013.
Val Martin, M. et al., 2015: How emissions, climate, and land use change will impact mid-century air quality over the United States: a focus on effects at national parks. *Atmospheric Chemistry and Physics*, **15(5)**, 2805–2823, doi:10.5194/acp-15-2805-2015.
Van Damme, M. et al., 2015: Worldwide spatiotemporal atmospheric ammonia (NH₃) columns variability revealed by satellite. *Geophysical Research Letters*, **42(20)**, 8660–8668, doi:10.1002/2015gl065496.
Van Dingenen, R. et al., 2009: The global impact of ozone on agricultural crop yields under current and future air quality legislation. *Atmospheric Environment*, **43(3)**, 604–618, doi:10.1016/j.atmosenv.2008.10.033.
Van Dingenen, R. et al., 2018: TM5-FASST: a global atmospheric source-receptor model for rapid impact analysis of emission changes on air quality and short-lived climate pollutants. *Atmospheric Chemistry and Physics*, **18(21)**, 16173–16211, doi:10.5194/acp-18-16173-2018.
van Heerwaarden, C.C. et al., 2021: Record high solar irradiance in Western Europe during first COVID-19 lockdown largely due to unusual weather. *Communications Earth & Environment*, **2(1)**, 37, doi:10.1038/s43247-021-00110-0.
van Marle, M.J.E. et al., 2017: Historic global biomass burning emissions for CMIP6 (BB4CMIP) based on merging satellite observations with proxies and fire models (1750–2015). *Geoscientific Model Development*, **10(9)**, 3329–3357, doi:10.5194/gmd-10-3329-2017.
van Vuuren, D.P. et al., 2011: The representative concentration pathways: an overview. *Climatic Change*, **109(1)**, 5, doi:10.1007/s10584-011-0148-z.
van Zanten, M.C., R.J. Wichink Kruit, R. Hoogerbrugge, E. Van der Swaluw, and W.A.J. van Pul, 2017: Trends in

ACCEPTED VERSION SUBJECT TO FINAL EDITING

ammonia measurements in the Netherlands over the period 1993–2014. *Atmospheric Environment*, **148**, 352–360, doi:10.1016/j.atmosenv.2016.11.007.
Vandyck, T. et al., 2018: Air quality co-benefits for human health and agriculture counterbalance costs to meet Paris Agreement pledges. *Nature Communications*, **9(1)**, 4939, doi:10.1038/s41467-018-06885-9.
VanLoocke, A., A.M. Betzelberger, E.A. Ainsworth, and C.J. Bernacchi, 2012: Rising ozone concentrations decrease soybean evapotranspiration and water use efficiency whilst increasing canopy temperature. *New Phytologist*, **195(1)**, 164–171, doi:10.1111/j.1469-8137.2012.04152.x.
Vattioni, S. et al., 2019: Exploring accumulation-mode H2SO4 versus SO2 stratospheric sulfate geoengineering in a sectional aerosol-chemistry-climate model. *Atmospheric Chemistry and Physics*, **19(7)**, 4877–4897, doi:10.5194/acp-19-4877-2019.
Veira, A., G. Lasslop, and S. Kloster, 2016: Wildfires in a warmer climate: Emission fluxes, emission heights, and black carbon concentrations in 2090–2099. *Journal of Geophysical Research: Atmospheres*, **121(7)**, 3195–3223, doi:10.1002/2015jd024142.
Velders, G.J.M., D.W. Fahey, J.S. Daniel, M. McFarland, and S.O. Andersen, 2009: The large contribution of projected HFC emissions to future climate forcing. *Proceedings of the National Academy of Sciences of the United States of America*, **106(27)**, 10949–10954, doi:10.1073/pnas.0902817106.
Velders, G.J.M., D.W. Fahey, J.S. Daniel, S.O. Andersen, and M. McFarland, 2015: Future atmospheric abundances and climate forcings from scenarios of global and regional hydrofluorocarbon (HFC) emissions. *Atmospheric Environment*, **123**, 200–209, doi:10.1016/j.atmosenv.2015.10.071.
Venkataraman, C. et al., 2018: Source influence on emission pathways and ambient PM<inf>2.5</inf>pollution over India (2015-2050). *Atmospheric Chemistry and Physics*, **18(11)**, doi:10.5194/acp-18-8017-2018.
Venter, Z.S., K. Aunan, S. Chowdhury, and J. Lelieveld, 2020: COVID-19 lockdowns cause global air pollution declines. *Proceedings of the National Academy of Sciences*, **117(32)**, 18984–18990, doi:10.1073/pnas.2006853117.
Vernier, J.-P. et al., 2018: BATAL: The Balloon Measurement Campaigns of the Asian Tropopause Aerosol Layer. *Bulletin of the American Meteorological Society*, **99(5)**, 955–973, doi:10.1175/bams-d-17-0014.1.
Vet, R. et al., 2014: A global assessment of precipitation chemistry and deposition of sulfur, nitrogen, sea salt, base cations, organic acids, acidity and pH, and phosphorus. *Atmospheric Environment*, **93**, 3–100, doi:10.1016/j.atmosenv.2013.10.060.
Victor, D.G., D. Zaelke, and V. Ramanathan, 2015: Soot and short-lived pollutants provide political opportunity. *Nature Climate Change*, **5(9)**, 796–798, doi:10.1038/nclimate2703.
Vignesh, P.P. et al., 2020: Assessment of CMIP6 Cloud Fraction and Comparison with Satellite Observations. *Earth and Space Science*, **7(2)**, e2019EA000975, doi:10.1029/2019ea000975.
Vira, J., P. Hess, J. Melkonian, and W.R. Wieder, 2020: An improved mechanistic model for ammonia volatilization in Earth system models: Flow of Agricultural Nitrogen version 2 (FANv2). *Geoscientific Model Development*, **13(9)**, 4459–4490, doi:10.5194/gmd-13-4459-2020.
Visioni, D. et al., 2019: Seasonal Injection Strategies for Stratospheric Aerosol Geoengineering. *Geophysical Research Letters*, doi:10.1029/2019gl083680.
Von Schneidemesser, E. et al., 2015: Chemistry and the Linkages between Air Quality and Climate Change. *Chemical Reviews*, **115(10)**, 3856–3897, doi:10.1021/acs.chemrev.5b00089.
Voulgarakis, A. et al., 2013: Analysis of present day and future OH and methane lifetime in the ACCMIP simulations. *Atmospheric Chemistry and Physics*, **13(5)**, 2563–2587, doi:10.5194/acp-13-2563-2013.
Wang, B., J. Shuman, H.H. Shugart, and M.T. Lerdau, 2018: Biodiversity matters in feedbacks between climate change and air quality: a study using an individual-based model. *Ecological Applications*, **28(5)**, 1223–1231, doi:10.1002/eap.1721.
Wang, H., P.J. Rasch, and G. Feingold, 2011: Manipulating marine stratocumulus cloud amount and albedo: A process-modelling study of aerosol-cloud-precipitation interactions in response to injection of cloud condensation nuclei. *Atmospheric Chemistry and Physics*, doi:10.5194/acp-11-4237-2011.
Wang, M. et al., 2015: Trends of non-methane hydrocarbons (NMHC) emissions in Beijing during 2002-2013. *Atmospheric Chemistry and Physics*, **15(3)**, 1489–1502, doi:10.5194/acp-15-1489-2015.
Wang, P., K. Chen, S. Zhu, P. Wang, and H. Zhang, 2020: Severe air pollution events not avoided by reduced anthropogenic activities during COVID-19 outbreak. *Resources, Conservation and Recycling*, **158**, doi:10.1016/j.resconrec.2020.104814.
Wang, Q. et al., 2014: Global budget and radiative forcing of black carbon aerosol: Constraints from pole-to-pole (HIPPO) observations across the Pacific. *Journal of Geophysical Research*, **119(1)**, 195–206, doi:10.1002/2013jd020824.
Wang, R. et al., 2014: Trend in global black carbon emissions from 1960 to 2007. *Environmental Science and Technology*, **48(12)**, 6780–6787, doi:10.1021/es5021422.
Wang, S., M.E. Maltrud, S.M. Burrows, S.M. Elliott, and P. Cameron-Smith, 2018: Impacts of Shifts in Phytoplankton Community on Clouds and Climate via the Sulfur Cycle. *Global Biogeochemical Cycles*, **32(6)**, 1005–1026, doi:10.1029/2017gb005862.

ACCEPTED VERSION SUBJECT TO FINAL EDITING

Wang, S.X. et al., 2014: Emission trends and mitigation options for air pollutants in East Asia. *Atmospheric Chemistry and Physics*, **14(13)**, 6571–6603, doi:10.5194/acp-14-6571-2014.
Wang, X. et al., 2018: Field evidences for the positive effects of aerosols on tree growth. *Global Change Biology*, **24(10)**, 4983–4992, doi:10.1111/gcb.14339.
Wang, Y. et al., 2019: Trends in particulate matter and its chemical compositions in China from 2013--2017. *Science China Earth Sciences*, **62(12)**, 1857–1871, doi:10.1007/s11430-018-9373-1.
Wang, Z. et al., 2021: Incorrect Asian aerosols affecting the attribution and projection of regional climate change in CMIP6 models. *npj Climate and Atmospheric Science*, **4(1)**, 2, doi:10.1038/s41612-020-00159-2.
Warner, J.X., Z. Wei, L.L. Strow, R.R. Dickerson, and J.B. Nowak, 2016: The global tropospheric ammonia distribution as seen in the 13-year {AIRS} measurement record. *Atmospheric Chemistry and Physics*, **16(8)**, 5467–5479, doi:10.5194/acp-16-5467-2016.
Warner, J.X. et al., 2014: Global carbon monoxide products from combined AIRS, TES and MLS measurements on A-train satellites. *Atmospheric Chemistry and Physics*, **14(1)**, 103–114, doi:10.5194/acp-14-103-2014.
Warner, J.X. et al., 2017: Increased atmospheric ammonia over the world's major agricultural areas detected from space. *Geophysical Research Letters*, **44(6)**, 2875–2884, doi:10.1002/2016gl072305.
Weber, J. et al., 2020: Minimal Climate Impacts From Short-Lived Climate Forcers Following Emission Reductions Related to the COVID-19 Pandemic. *Geophysical Research Letters*, **47(20)**, doi:10.1029/2020gl090326.
Weber, R.J., H. Guo, A.G. Russell, and A. Nenes, 2016: High aerosol acidity despite declining atmospheric sulfate concentrations over the past 15 years. *Nature Geoscience*, **9(4)**, 282–285, doi:10.1038/ngeo2665.
Weinstein, J.P., S.R. Hedges, and S. Kimbrough, 2010: Characterization and aerosol mass balance of PM_{2.5} and PM₁₀ collected in Conakry, Guinea during the 2004 Harmattan period. *Chemosphere*, **78(8)**, 980–988, doi:10.1016/j.chemosphere.2009.12.022.
Weisenstein, D.K., D.W. Keith, and J.A. Dykema, 2015: Solar geoengineering using solid aerosol in the stratosphere. *Atmospheric Chemistry and Physics*, doi:10.5194/acp-15-11835-2015.
Wells, K.C. et al., 2020: Satellite isoprene retrievals constrain emissions and atmospheric oxidation. *Nature*, **585(7824)**, 225–233, doi:10.1038/s41586-020-2664-3.
Wen, L. et al., 2018: Summertime fine particulate nitrate pollution in the North China Plain: increasing trends, formation mechanisms and implications for control policy. *Atmospheric Chemistry and Physics*, **18(15)**, 11261–11275, doi:10.5194/acp-18-11261-2018.
Wennberg, P.O. et al., 2018: Gas-Phase Reactions of Isoprene and Its Major Oxidation Products. *Chemical Reviews*, **118(7)**, 3337–3390, doi:10.1021/acs.chemrev.7b00439.
West, J.J. et al., 2013: Co-benefits of mitigating global greenhouse gas emissions for future air quality and human health. *Nature Climate Change*, **3**, 885.
Westervelt, D.M. et al., 2016: Quantifying PM2.5-meteorology sensitivities in a global climate model. *Atmospheric Environment*, **142**, 43–56, doi:10.1016/j.atmosenv.2016.07.040.
Westervelt, D.M. et al., 2018: Connecting regional aerosol emissions reductions to local and remote precipitation responses. *Atmospheric Chemistry and Physics*, **18(16)**, 12461–12475, doi:10.5194/acp-18-12461-2018.
WHO, 2017: *Evolution of WHO air quality guidelines: past, present and future*. World Health Organization (WHO) Regional Office for Europe, Copenhagen, Denmark, 32 pp.
Wilcox, L.J. et al., 2019: Mechanisms for a remote response to Asian anthropogenic aerosol in boreal winter. *Atmos. Chem. Phys.*, **19(14)**, 9081–9095, doi:10.5194/acp-19-9081-2019.
Wilcox, L.J. et al., 2020: Accelerated increases in global and Asian summer monsoon precipitation from future aerosol reductions. *Atmospheric Chemistry and Physics*, **20(20)**, 11955–11977, doi:10.5194/acp-20-11955-2020.
Wild, O. et al., 2020: Global sensitivity analysis of chemistry–climate model budgets of tropospheric ozone and OH: exploring model diversity. *Atmos. Chem. Phys.*, **20(7)**, 4047–4058, doi:10.5194/acp-20-4047-2020.
Wilkinson, M.J. et al., 2009: Leaf isoprene emission rate as a function of atmospheric CO₂ concentration. *Global Change Biology*, **15(5)**, 1189–1200, doi:10.1111/j.1365-2486.2008.01803.x.
Williams, M.L. et al., 2018: The Lancet Countdown on health benefits from the UK Climate Change Act: a modelling study for Great Britain. *The Lancet Planetary Health*, **2(5)**, e202 – e213, doi:10.1016/s2542-5196(18)30067-6.
Wittig, V.E., E.A. Ainsworth, and S.P. Long, 2007: To what extent do current and projected increases in surface ozone affect photosynthesis and stomatal conductance of trees? A meta-analytic review of the last 3 decades of experiments. *Plant, Cell and Environment*, **30(9)**, 1150–1162, doi:10.1111/j.1365-3040.2007.01717.x.
WMO, 2018: *Scientific Assessment of Ozone Depletion: 2018*. Global Ozone Research and Monitoring Project – Report No. 58, World Meteorological Organization (WMO), Geneva, Switzerland, 588 pp.
Woodward, S., D.L. Roberts, and R.A. Betts, 2005: A simulation of the effect of climate change–induced desertification on mineral dust aerosol. *Geophysical Research Letters*, **32(18)**, doi:10.1029/2005gl023482.
Worden, H.M. et al., 2013: Decadal record of satellite carbon monoxide observations. *Atmospheric Chemistry and Physics*, doi:10.5194/acp-13-837-2013.
Wu, S., L.J. Mickley, D.J. Jacob, D. Rind, and D.G. Streets, 2008: Effects of 2000–2050 changes in climate and emissions on global tropospheric ozone and the policy-relevant background surface ozone in the United States. *Journal of Geophysical Research: Atmospheres*, **113(D18)**, doi:10.1029/2007jd009639.

ACCEPTED VERSION SUBJECT TO FINAL EDITING

Wu, X. et al., 2018: Characterization and source apportionment of carbonaceous PM2.5 particles in China - A review. *Atmospheric Environment*, **189**, 187–212, doi:10.1016/j.atmosenv.2018.06.025.

Xi, X. and I.N. Sokolik, 2016: Quantifying the anthropogenic dust emission from agricultural land use and desiccation of the aral sea in central Asia. *Journal of Geophysical Research*, **121(20)**, 12,270–12,281, doi:10.1002/2016jd025556.

Xia, A.G., D. Michelangeli, and P.A. Makar, 2009: Mechanism reduction for the formation of secondary organic aerosol for integration into a 3-dimensional regional air quality model: α-Pinene oxidation system. *Atmospheric Chemistry and Physics*, **9(13)**, 4341–4362, doi:10.5194/acp-9-4341-2009.

Xie, Y., M. Lin, and L.W. Horowitz, 2020: Summer PM2.5 Pollution Extremes Caused by Wildfires Over the Western United States During 2017–2018. *Geophysical Research Letters*, **47(16)**, e2020GL089429, doi:10.1029/2020gl089429.

Xie, Y. et al., 2018: Co-benefits of climate mitigation on air quality and human health in Asian countries. *Environment International*, **119**, 309–318, doi:10.1016/j.envint.2018.07.008.

Xu, L. and J.E. Penner, 2012: Global simulations of nitrate and ammonium aerosols and their radiative effects. *Atmospheric Chemistry and Physics*, **12(20)**, 9479–9504, doi:10.5194/acp-12-9479-2012.

Xu, Y. and J.F. Lamarque, 2018: Isolating the Meteorological Impact of 21st Century GHG Warming on the Removal and Atmospheric Loading of Anthropogenic Fine Particulate Matter Pollution at Global Scale. *Earth's Future*, **6(3)**, 428–440, doi:10.1002/2017ef000684.

Xu, Y., D. Zaelke, G.J.M. Velders, and V. Ramanathan, 2013: The role of HFCs in mitigating 21st century climate change. *Atmospheric Chemistry and Physics*, **13(12)**, 6083–6089, doi:10.5194/acp-13-6083-2013.

Yang, Y., S.J. Smith, H. Wang, S. Lou, and P.J. Rasch, 2019a: Impact of Anthropogenic Emission Injection Height Uncertainty on Global Sulfur Dioxide and Aerosol Distribution. *Journal of Geophysical Research: Atmospheres*, **124(8)**, 4812–4826, doi:10.1029/2018jd030001.

Yang, Y., S.J. Smith, H. Wang, C.M. Mills, and P.J. Rasch, 2019b: Variability, timescales, and nonlinearity in climate responses to black carbon emissions. *Atmospheric Chemistry and Physics*, **19(4)**, 2405–2420, doi:10.5194/acp-19-2405-2019.

Yang, Y. et al., 2016: Towards a quantitative understanding of total OH reactivity: A review. *Atmospheric Environment*, **134**, 147–161, doi:10.1016/j.atmosenv.2016.03.010.

Yang, Y. et al., 2020: Fast Climate Responses to Aerosol Emission Reductions During the COVID-19 Pandemic. *Geophysical Research Letters*, **47(19)**, doi:10.1029/2020gl089788.

Yao, X. and L. Zhang, 2019: Causes of Large Increases in Atmospheric Ammonia in the Last Decade across North America. *ACS Omega*, **4(26)**, 22133–22142, doi:10.1021/acsomega.9b03284.

Yarragunta, Y., S. Srivastava, and D. Mitra, 2017: Validation of lower tropospheric carbon monoxide inferred from MOZART model simulation over India. *Atmospheric Research*, doi:10.1016/j.atmosres.2016.09.010.

Yienger, J.J. and H. Levy, 1995: Empirical model of global soil-biogenic NOx emissions. *Journal of Geophysical Research*, **100(D6)**, 11447, doi:10.1029/95jd00370.

Young, P.J. et al., 2013: Pre-industrial to end 21st century projections of tropospheric ozone from the Atmospheric Chemistry and Climate Model Intercomparison Project (ACCMIP). *Atmospheric Chemistry and Physics*, **13(4)**, 2063–2090, doi:10.5194/acp-13-2063-2013.

Young, P.J. et al., 2018: Tropospheric Ozone Assessment Report: Assessment of global-scale model performance for global and regional ozone distributions, variability, and trends. *Elem Sci Anth*, **6(1)**, 10, doi:10.1525/elementa.265.

Yu, F., A.A. Nair, and G. Luo, 2018: Long-Term Trend of Gaseous Ammonia Over the United States: Modeling and Comparison With Observations. *Journal of Geophysical Research: Atmospheres*, **123(15)**, 8315–8325, doi:10.1029/2018jd028412.

Yu, M. et al., 2019: Effects of air pollution control measures on air quality improvement in Guangzhou, China. *Journal of Environmental Management*, doi:10.1016/j.jenvman.2019.05.046.

Yu, P., R. Xu, M.J. Abramson, S. Li, and Y. Guo, 2020: Bushfires in Australia: a serious health emergency under climate change. *The Lancet Planetary Health*, **4(1)**, e7–e8, doi:10.1016/s2542-5196(19)30267-0.

Yu, P. et al., 2016: Radiative forcing from anthropogenic sulfur and organic emissions reaching the stratosphere. *Geophysical Research Letters*, **43(17)**, 9361–9367, doi:10.1002/2016gl070153.

Yue, X. and N. Unger, 2014: Ozone vegetation damage effects on gross primary productivity in the United States. *Atmospheric Chemistry and Physics*, **14(17)**, 9137–9153, doi:10.5194/acp-14-9137-2014.

Yue, X. et al., 2017: Ozone and haze pollution weakens net primary productivity in China. *Atmospheric Chemistry and Physics*, **17(9)**, 6073–6089, doi:10.5194/acp-17-6073-2017.

Zakoura, M. and S.N. Pandis, 2018: Overprediction of aerosol nitrate by chemical transport models: The role of grid resolution. *Atmospheric Environment*, **187**, 390–400, doi:10.1016/j.atmosenv.2018.05.066.

Zanatta, M. et al., 2017: Source attribution of Arctic black carbon constrained by aircraft and surface measurements. *Atmospheric Chemistry and Physics*, **17(19)**, 11971–11989, doi:10.5194/acp-17-11971-2017.

Zanis, P. et al., 2020: Fast responses on pre-industrial climate from present-day aerosols in a CMIP6 multi-model study. *Atmospheric Chemistry and Physics*, **20(14)**, 8381–8404, doi:10.5194/acp-20-8381-2020.

ACCEPTED VERSION SUBJECT TO FINAL EDITING

Zare, A. et al., 2014: Quantifying the contributions of natural emissions to ozone and total fine PM concentrations in the Northern Hemisphere. *Atmospheric Chemistry and Physics*, **14(6)**, 2735–2756, doi:10.5194/acp-14-2735-2014.
Zeng, G. et al., 2012: Trends and variations in CO, C2H6, and HCN in the Southern Hemisphere point to the declining anthropogenic emissions of CO and C2H6. *Atmospheric Chemistry and Physics*, doi:10.5194/acp-12-7543-2012.
Zeng, G. et al., 2015: Multi-model simulation of CO and HCHO in the Southern Hemisphere: comparison with observations and impact of biogenic emissions. *Atmospheric Chemistry and Physics*, **15(13)**, 7217–7245, doi:10.5194/acp-15-7217-2015.
Zhang, A. et al., 2020: Modeling the global radiative effect of brown carbon: A potentially larger heating source in the tropical free troposphere than black carbon. *Atmospheric Chemistry and Physics*, **20**, 1901–1920, doi:10.5194/acp-20-1901-2020.
Zhang, F. et al., 2012: Chemical compositions and extinction coefficients of PM2.5 in peri-urban of Xiamen, China, during June 2009–May 2010. *Atmospheric Research*, **106**, 150–158, doi:10.1016/j.atmosres.2011.12.005.
Zhang, G. et al., 2017: The single-particle mixing state and cloud scavenging of black carbon: A case study at a high-altitude mountain site in southern China. *Atmospheric Chemistry and Physics*, doi:10.5194/acp-17-14975-2017.
Zhang, H., Y. Wang, T.-W. Park, and Y. Deng, 2017: Quantifying the relationship between extreme air pollution events and extreme weather events. *Atmospheric Research*, **188**, 64–79, doi:10.1016/j.atmosres.2016.11.010.
Zhang, H. et al., 2012: Source apportionment of PM2.5 nitrate and sulfate in China using a source-oriented chemical transport model. *Atmospheric Environment*, **62**, 228–242, doi:10.1016/j.atmosenv.2012.08.014.
Zhang, Q. et al., 2007: Ubiquity and dominance of oxygenated species in organic aerosols in anthropogenically-influenced Northern Hemisphere midlatitudes. *Geophysical Research Letters*, doi:10.1029/2007gl029979.
Zhang, Y. et al., 2016: Co-benefits of global and regional greenhouse gas mitigation for US air quality in 2050. *Atmospheric Chemistry and Physics*, **16(15)**, 9533–9548, doi:10.5194/acp-16-9533-2016.
Zhang, Y. et al., 2019: Six-year source apportionment of submicron organic aerosols from near-continuous highly time-resolved measurements at SIRTA (Paris area, France). *Atmospheric Chemistry and Physics*, **19(23)**, 14755–14776, doi:10.5194/acp-19-14755-2019.
Zhao, D. et al., 2019: Vertical characteristics of black carbon physical properties over Beijing region in warm and cold seasons. *Atmospheric Environment*, doi:10.1016/j.atmosenv.2019.06.007.
Zhao, P.S. et al., 2013: Characteristics of concentrations and chemical compositions for PM2.5 in the region of Beijing, Tianjin, and Hebei, China. *Atmospheric Chemistry and Physics*, **13(9)**, 4631–4644, doi:10.5194/acp-13-4631-2013.
Zhao, Y. et al., 2019: Inter-model comparison of global hydroxyl radical (OH) distributions and their impact on atmospheric methane over the 2000–2016 period. *Atmos. Chem. Phys*, **19**, 13701–13723, doi:10.5194/acp-2019-281.
Zhao, Y. et al., 2020a: Influences of hydroxyl radicals (OH) on top-down estimates of the global and regional methane budgets. *Atmos. Chem. Phys.*, **20(15)**, 9525–9546, doi:10.5194/acp-20-9525-2020.
Zhao, Y. et al., 2020b: Substantial Changes in Nitrogen Dioxide and Ozone after Excluding Meteorological Impacts during the COVID-19 Outbreak in Mainland China. *Environmental Science and Technology Letters*, **7(6)**, 402–408, doi:10.1021/acs.estlett.0c00304.
Zhao, Z. et al., 2019: Drought Impacts on Secondary Organic Aerosol: A Case Study in the Southeast United States. *Environmental Science & Technology*, **53(1)**, 242–250, doi:10.1021/acs.est.8b04842.
Zheng, B. et al., 2018a: Rapid decline in carbon monoxide emissions and export from East Asia between years 2005 and 2016. *Environmental Research Letters*, **13(4)**, 44007, doi:10.1088/1748-9326/aab2b3.
Zheng, B. et al., 2018b: Trends in China's anthropogenic emissions since 2010 as the consequence of clean air actions. *Atmospheric Chemistry and Physics*, **18**, 14095–14111, doi:10.5194/acp-2018-374.
Zheng, B. et al., 2019: Global atmospheric carbon monoxide budget 2000-2017 inferred from multi-species atmospheric inversions. *Earth System Science Data*, **11(3)**, 1411–1436, doi:10.5194/essd-11-1411-2019.
Zhou, Y., H. Mao, K. Demerjian, C. Hogrefe, and J. Liu, 2017: Regional and hemispheric influences on temporal variability in baseline carbon monoxide and ozone over the Northeast US. *Atmospheric Environment*, doi:10.1016/j.atmosenv.2017.06.017.
Zhu, L. et al., 2015: Global evaluation of ammonia bidirectional exchange and livestock diurnal variation schemes. *Atmospheric Chemistry and Physics*, **15(22)**, 12823–12843, doi:10.5194/acp-15-12823-2015.
Zhu, L. et al., 2017: Long-term (2005–2014) trends in formaldehyde (HCHO) columns across North America as seen by the OMI satellite instrument: Evidence of changing emissions of volatile organic compounds. *Geophysical Research Letters*, **44(13)**, 7079–7086, doi:10.1002/2017gl073859.
Zou, Y., Y. Wang, Y. Zhang, and J.H. Koo, 2017: Arctic sea ice, Eurasia snow, and extreme winter haze in China. *Science Advances*, **3(3)**, doi:10.1126/sciadv.1602751.
Zusman, E. et al., 2013: Co-benefits: Taking a multidisciplinary approach. *Carbon Management*, **4(2)**, 135–137, doi:10.4155/cmt.13.12.

ACCEPTED VERSION SUBJECT TO FINAL EDITING

Figures

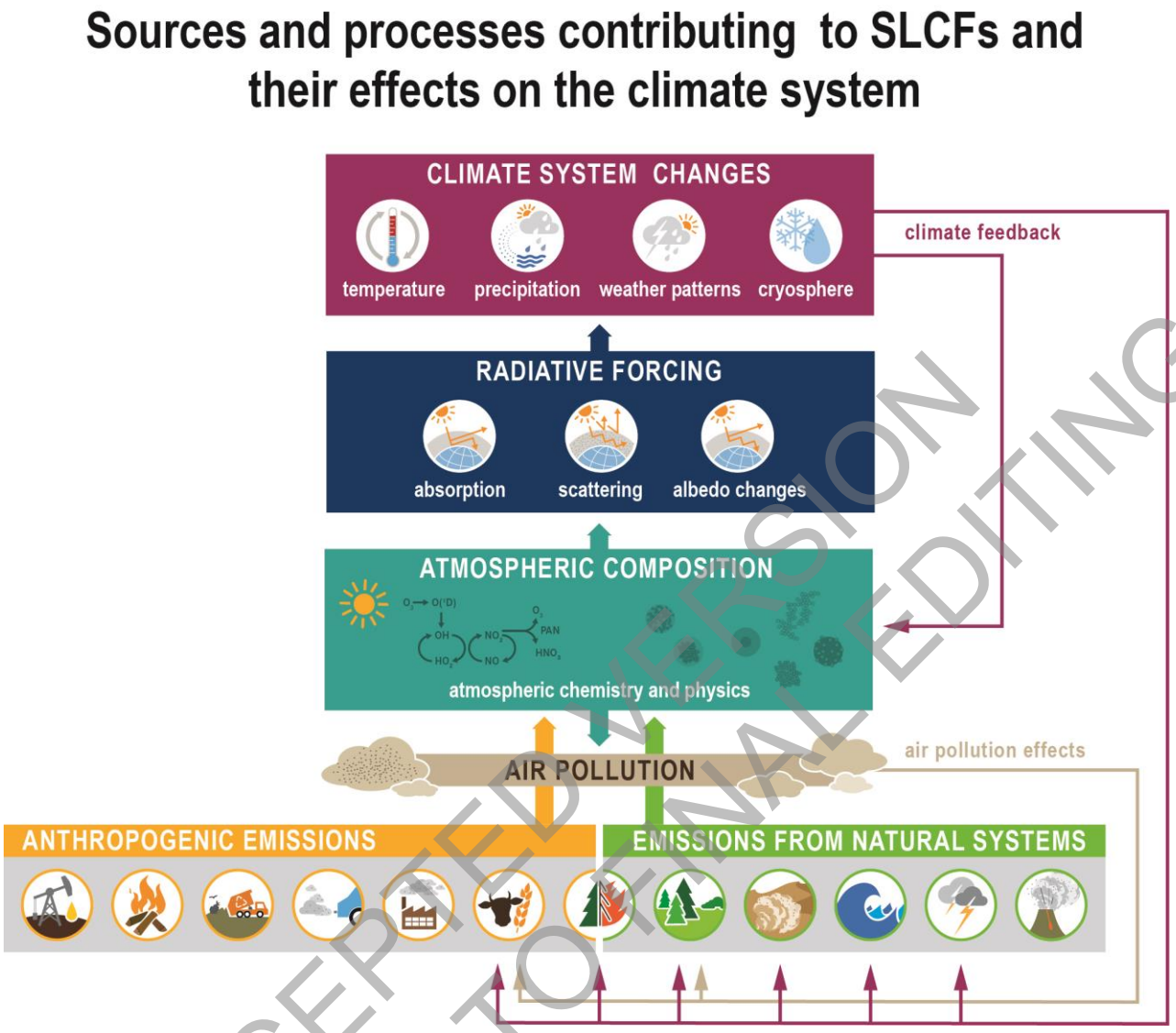


Figure 6.1: **Sources and processes leading to atmospheric short-lived climate forcer (SLCF) burden and their interactions with the climate system**. Both direct and indirect SLCFs and the role of atmospheric processes for the lifetime of SLCFs are depicted. Anthropogenic emission sectors illustrated are fossil fuel exploration, distribution and use, biofuel production and use, waste, transport, industry, agricultural sources, and open biomass burning. Emissions from natural systems include those from open biomass burning, vegetation, soil, oceans, lightning, and volcanoes. SLCFs interact with solar or terrestrial radiation, surface albedo, and cloud or precipitation system. The radiative forcing due to individual SLCF can be either positive or negative. Climate change induces changes in emissions from most natural systems as well as from some anthropogenic emission sectors (e.g. agriculture) leading to a climate feedback (purple arrows). Climate change also influences atmospheric chemistry processes, such as chemical reaction rates or via circulation changes, thus affecting atmospheric composition leading to a climate feedback. Air pollutants influence emissions from terrestrial vegetation, including agriculture (the grey arrow).

ACCEPTED VERSION SUBJECT TO FINAL EDITING

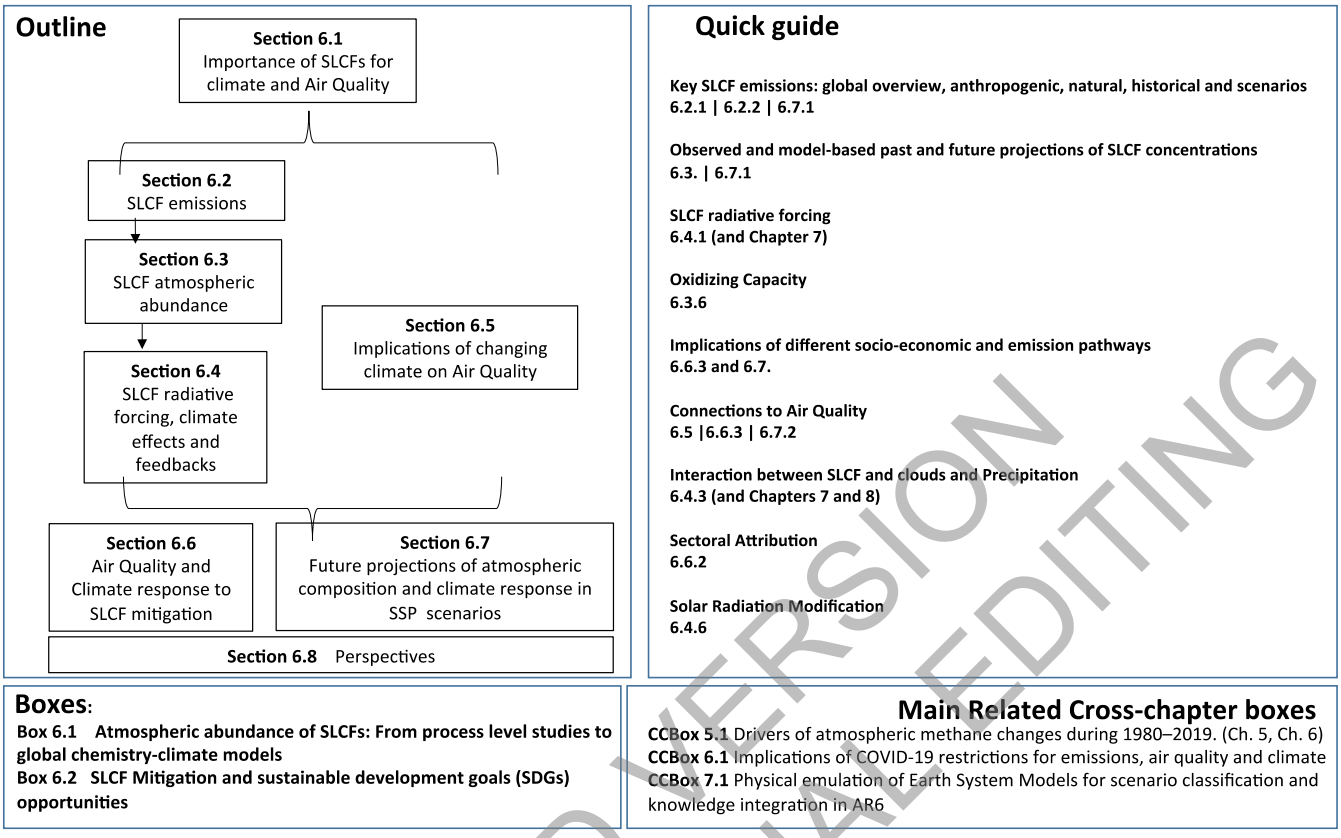
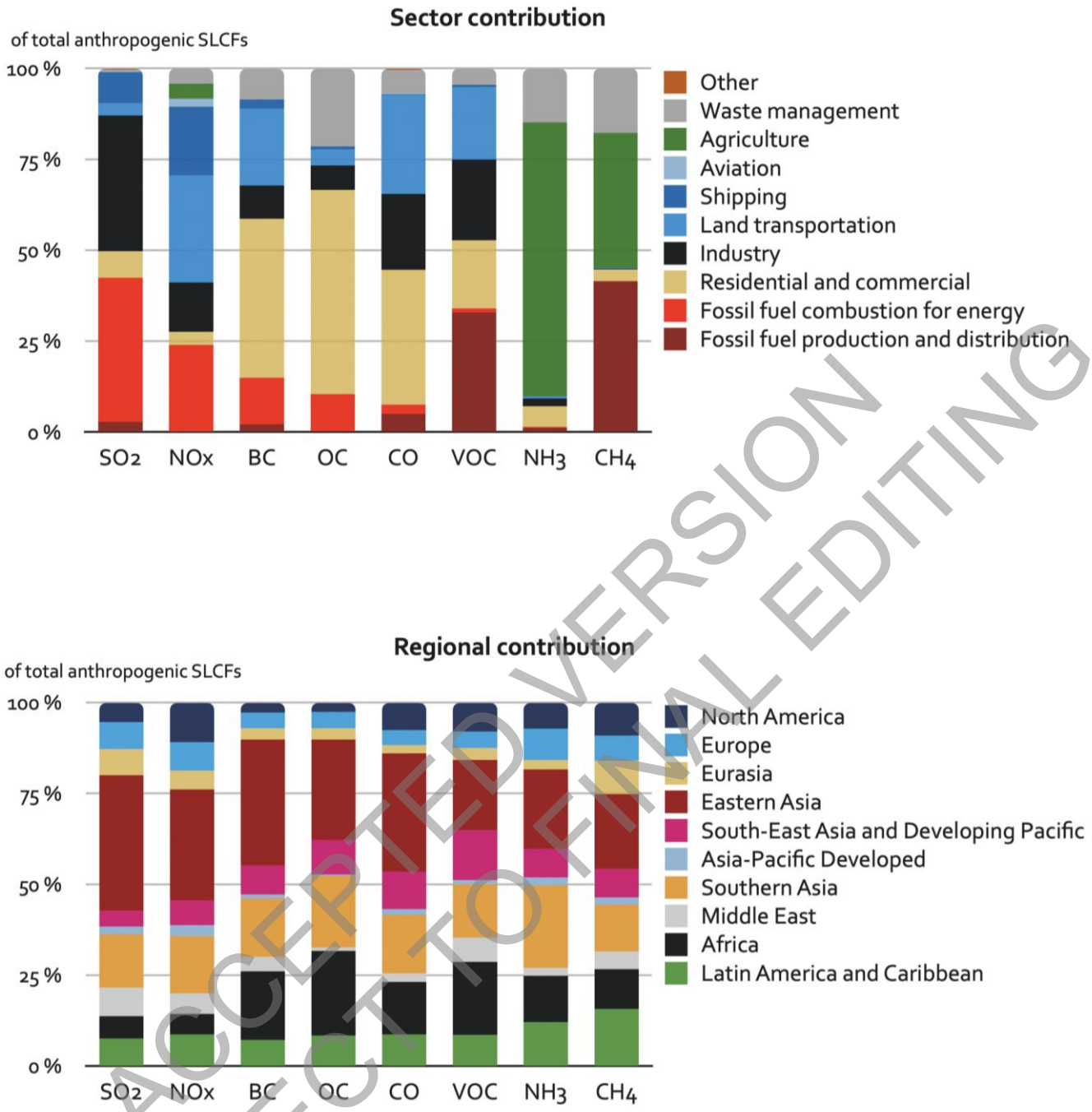


Figure 6.2: Chapter roadmap. See Section 6.1.3 for additional description of the chapter.

ACCEPTED VERSION SUBJECT TO FINAL EDITING



ACCEPTED VERSION
SUBJECT TO FINAL EDITING

Figure 6.3: Relative regional and sectoral contributions to the present day (year 2014) anthropogenic emissions of Short Lived Climate Forcers (SLCFs). Emission data are from the Community Emissions Data System (CEDS) (Hoesly et al., 2018). Emissions are aggregated into the following sectors: fossil fuel production and distribution (coal mining, oil and gas production, upstream gas flaring, gas distribution networks), fossil fuel combustion for energy (power plants), residential and commercial (fossil and biofuel use for cooking and heating), industry (combustion and production processes, solvent use losses from production and end use), transport (road and off-road vehicles), shipping (including international shipping), aviation (including international aviation), agriculture (livestock and crop production), waste management (solid waste, including landfills and open trash burning, residential and industrial waste water), and other. Further details on data sources and processing are available in the chapter data table (Table 6.SM.1).

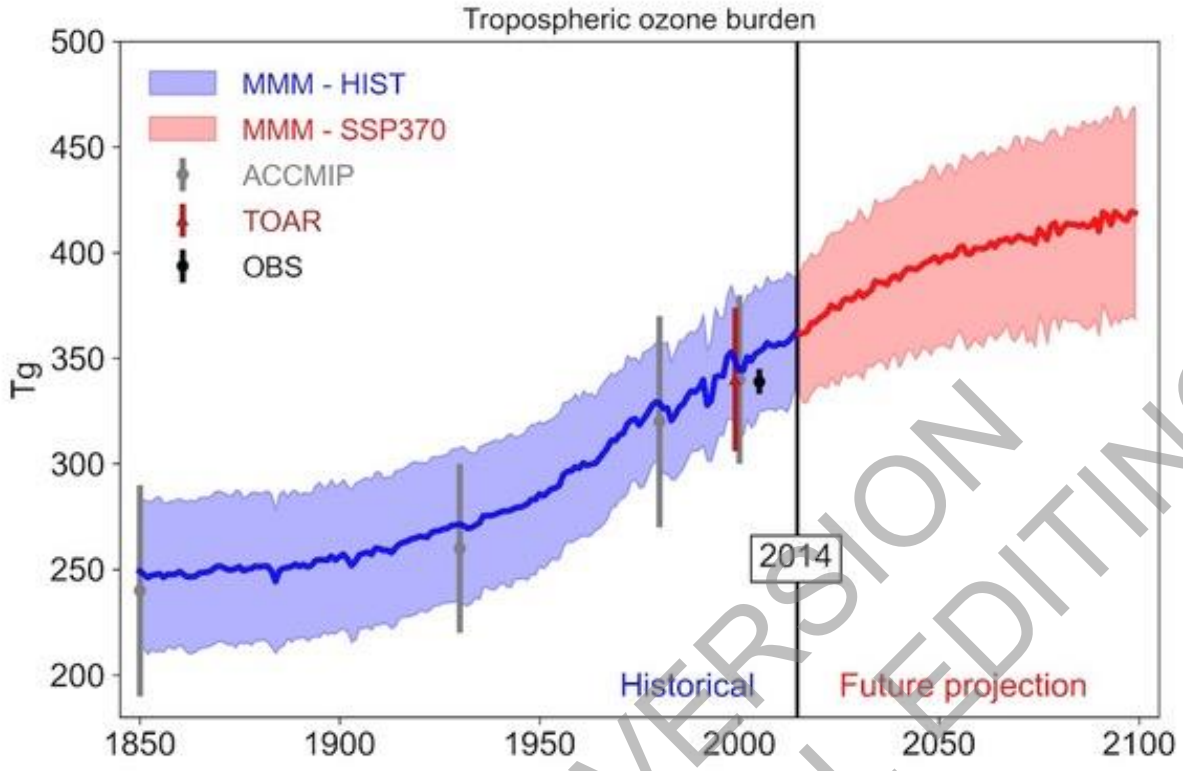


Figure 6.4: **Time evolution of global annual mean tropospheric ozone burden (in Tg) from 1850 to 2100**. Multi-model means for CMIP6 historical experiment (1850-2014) from UKESM1-LL-0, CESM2-WACCM, MRI-ESM2-0, GISS-E2.1-G and GFDL-ESM4 and for ScenarioMIP SSP3-7.0 experiment (2015-2100) are represented with their intermodel standard deviation (±1 σ , shaded areas). Observation based global tropospheric ozone burden estimate (from Table 6.3) is for 2010-2014. Tropospheric Ozone Assessment Report (TOAR) multi-model mean value (from Table 6.3) is for 2000 with a ±1 σ error-bar. Atmospheric Chemistry and Climate Model Intercomparison Project (ACCMIP) multi-model means are for 1850, 1930, 1980 and 2000 time-slices with ±1 σ error-bars. The troposphere is masked by the tropopause pressure calculated in each model using the WMO thermal tropopause definition. Further details on data sources and processing are available in the chapter data table (Table 6.SM.1).

ACCEPTED VERSION SUBJECT TO FINAL EDITING

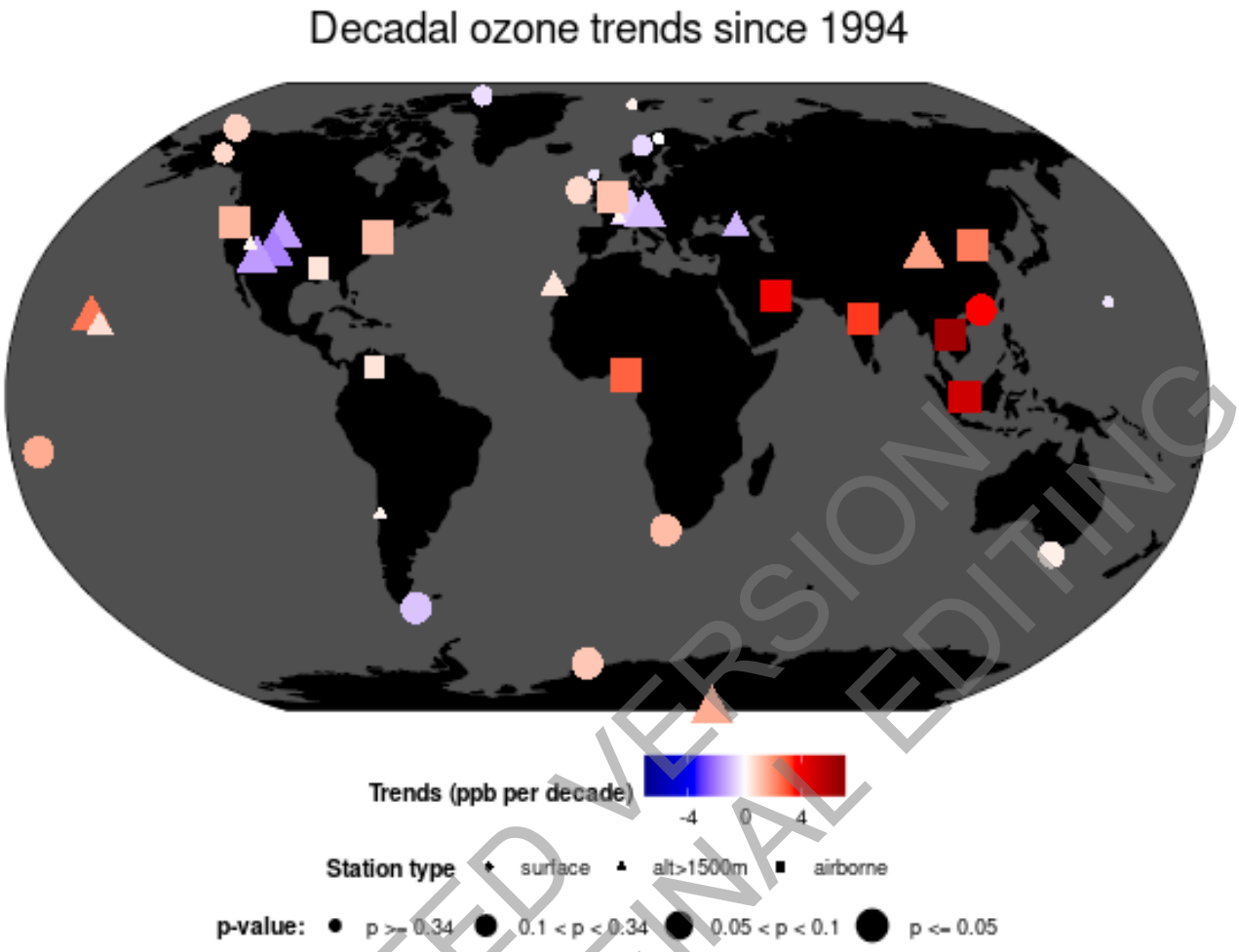
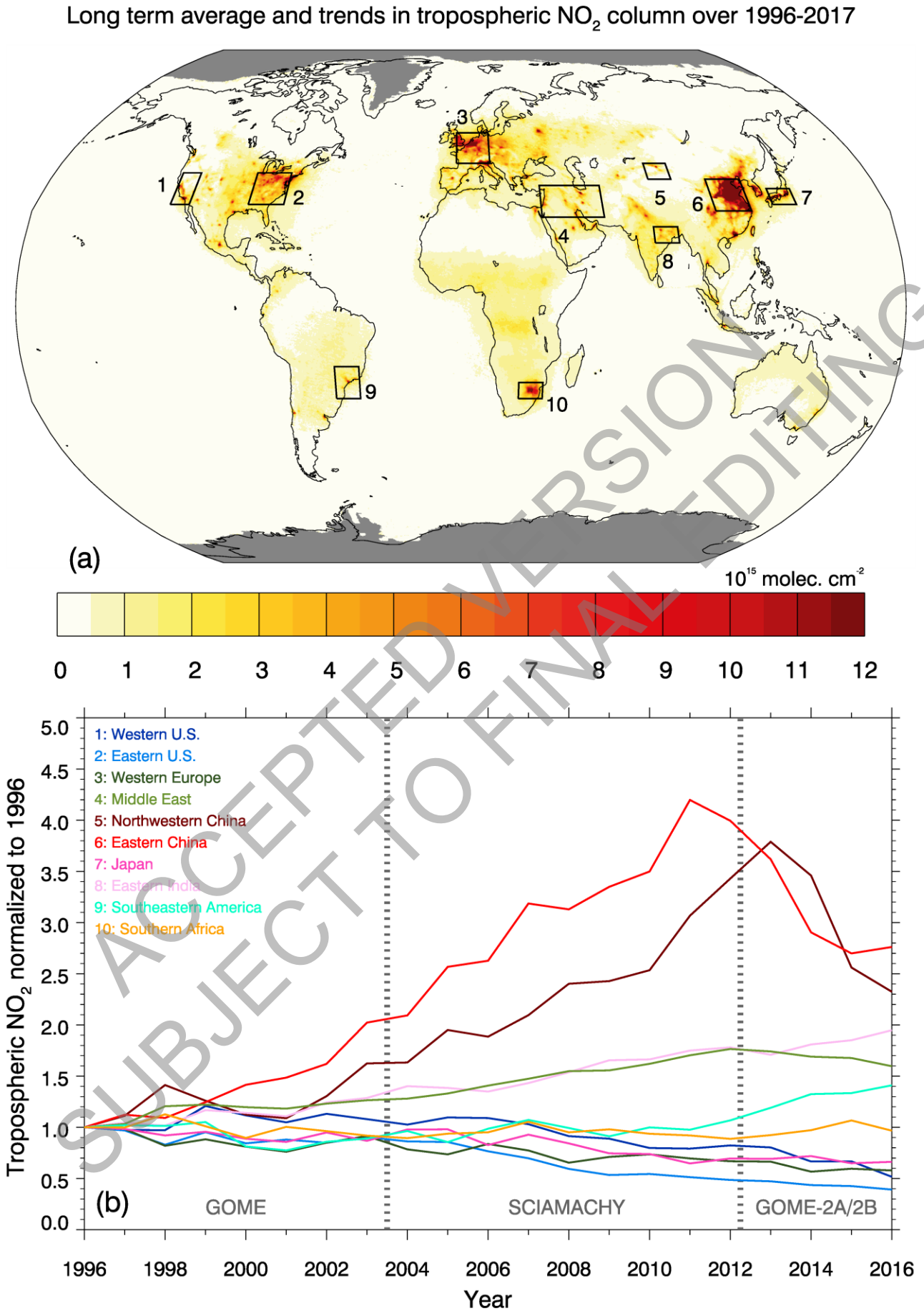


Figure 6.5: Decadal tropospheric ozone trends since 1994. Trends are shown at 28 remote and regionally representative surface sites (Cooper et al., 2020) and in 11 regions of the lower free troposphere (650 hPa, ca. 3.5 km) as measured by In-Service Aircraft for a Global Observing System (IAGOS) above Europe, northeastern USA, southeastern USA, western North America, northeast China, South East Asia, southern India, Persian Gulf, Malaysia/Indonesia, Gulf of Guinea and northern South America (Gaudel et al., 2020). High elevation surface sites are >1500 m above sea level. All trends end with the most recently available year but begin in 1995 or 1994. The sites and datasets are the same as those used in Figure 2.8, further details on data sources and processing are available in the Chapter 2 data table (Table 2.SM.1).

ACCEPTED VERSION SUBJECT TO FINAL EDITING



ACCEPTED VERSION
SUBJECT TO FINAL EDITING

1

Figure 6.6: Long term climatological mean (a) and time evolution (b) of tropospheric NO_2 vertical column density from the merged GOME/SCIAMACHY/GOME-2 (TM4NO2A version 2.3) dataset for the period 1996-2016 (Georgoulias et al., 2019). Time evolution of NO_2 column shown in panel (b) is normalized to the fitted 1996 levels for the 10 regions shown as boxes in panel (a). Further details on data sources and processing are available in the chapter data table (Table 6.SM.1).

ACCEPTED VERSION
SUBJECT TO FINAL EDITING

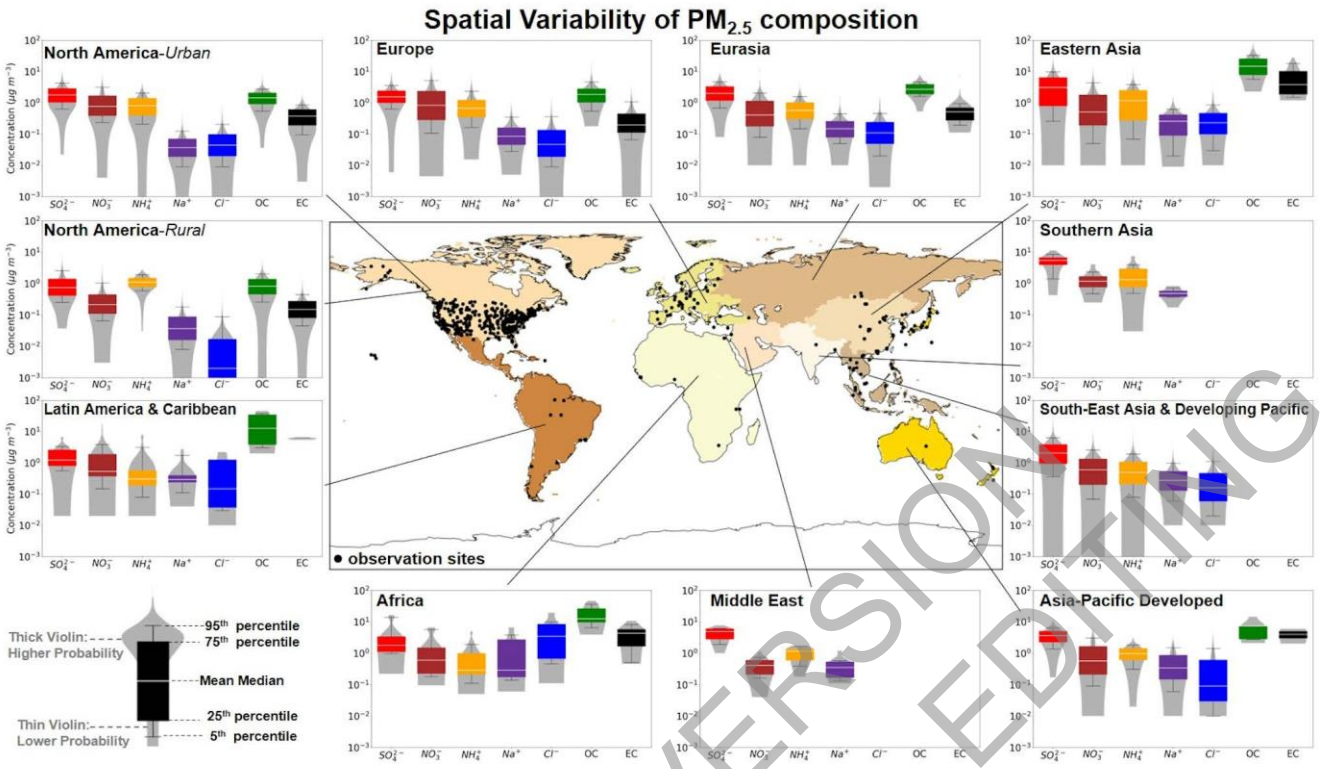


Figure 6.7: Distribution of $PM_{2.5}$ composition mass concentration (in μg m^{-3}) for the major $PM_{2.5}$ aerosol components. Those aerosol components are sulfate, nitrate, ammonium, sodium, chloride, organic carbon, and elemental carbon. The central world map depicts the intermediate level regional breakdown of observations (10 regions) following the IPCC Sixth Assessment Report Working Group III (AR6 WGIII). Monthly averaged $PM_{2.5}$ aerosol component measurements are from: (i) the Environmental Protection Agency (EPA) network which include 211 monitor sites primarily in urban areas of North America during 2000-2018 (Solomon et al., 2014) (ii) the Interagency Monitoring of Protected Visual Environments (IMPROVE) network during 2000-2018 over 198 monitoring sites representative of the regional haze conditions over North America, (iii) the European Monitoring and Evaluation Programme (EMEP) network over 70 monitoring in Europe and (eastern) Eurasia during 2000-2018, (iv) the Acid Deposition Monitoring Network in East Asia (EANET) network with 39 (18 remote, 10 rural, 11 urban) sites in Eurasia, Eastern Asia, South-East Asia and Developing Pacific, and Asia-Pacific Developed during 2001-2017, (v) the global Surface Particulate Matter Network (SPARTAN) during 2013-2019 with sites primarily in highly populated regions around the world (i.e, North America, Latin America and Caribbean, Africa, Middle East, Southern Asia, Eastern Asia, South-Eastern Asia and Developing Pacific) (Snider et al., 2015, 2016), and (vii) individual observational field campaign averages over Latin America and Caribbean, Africa, Europe, Eastern Asia, and Asia-Pacific Developed (Celis et al., 2004; Feng et al., 2006; Bourotte et al., 2007; Fuzzi et al., 2007; Mariani and de Mello, 2007; Molina et al., 2007; Favez et al., 2008; Mkoma, 2008; Aggarwal and Kawamura, 2009; Mkoma et al., 2009; de Souza et al., 2010; Li et al., 2010; Martin et al., 2010; Molina et al., 2010; Radhi et al., 2010; Weinstein et al., 2010; Batmunkh et al., 2011; Gioda et al., 2011; Pathak et al., 2011; Zhang et al., 2012; Cho and Park, 2013; Zhao et al., 2013; Wang et al., 2019; Kuzu et al., 2020). Further details on data sources and processing are available in the chapter data table (Table 6.SM.1).

ACCEPTED VERSION SUBJECT TO FINAL EDITING

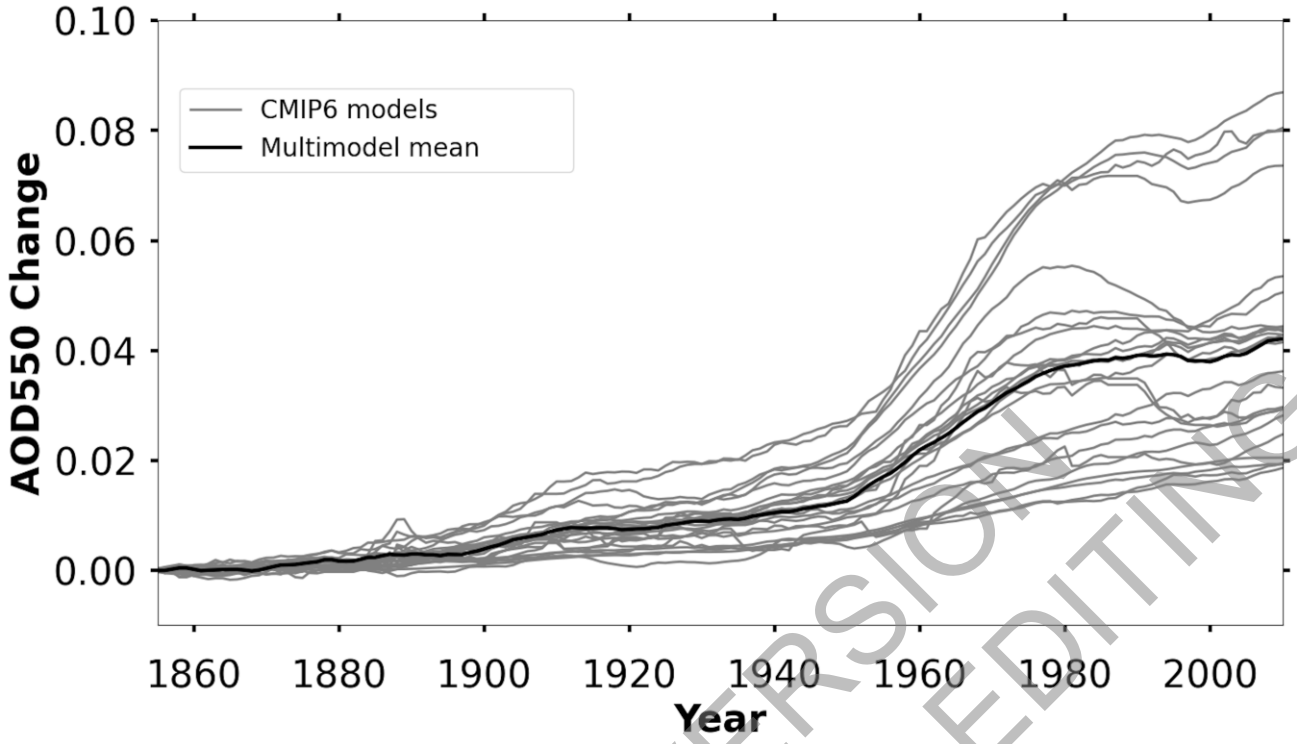


Figure 6.8: **Time evolution of changes in global mean aerosol optical depth (AOD) at 550 nm.** Year of reference is 1850. Data shown from individual Coupled Model Intercomparison Project Phase 6 (CMIP6) historical simulations. Each time series corresponds to the ensemble mean of realizations done by each model. Simulation results from years including major volcanic eruptions, e.g. Novarupta (1912) and Pinatubo (1991), are excluded from the analysis for models encompassing the contribution of stratospheric volcanic aerosols to total AOD. Further details on data sources and processing are available in the chapter data table (Table 6.SM.1).

ACCEPTED VERSION
SUBJECT TO FINAL EDITING

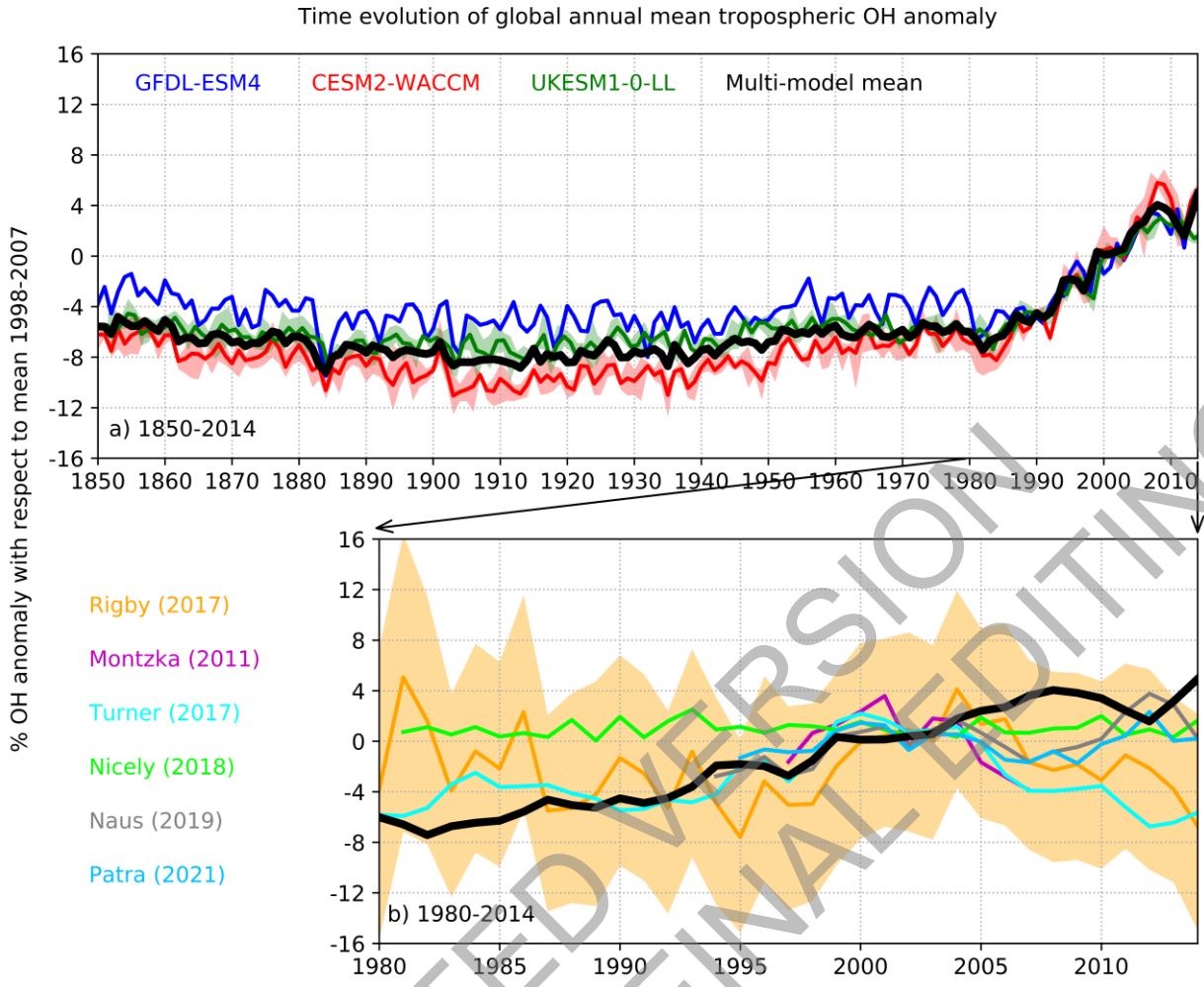
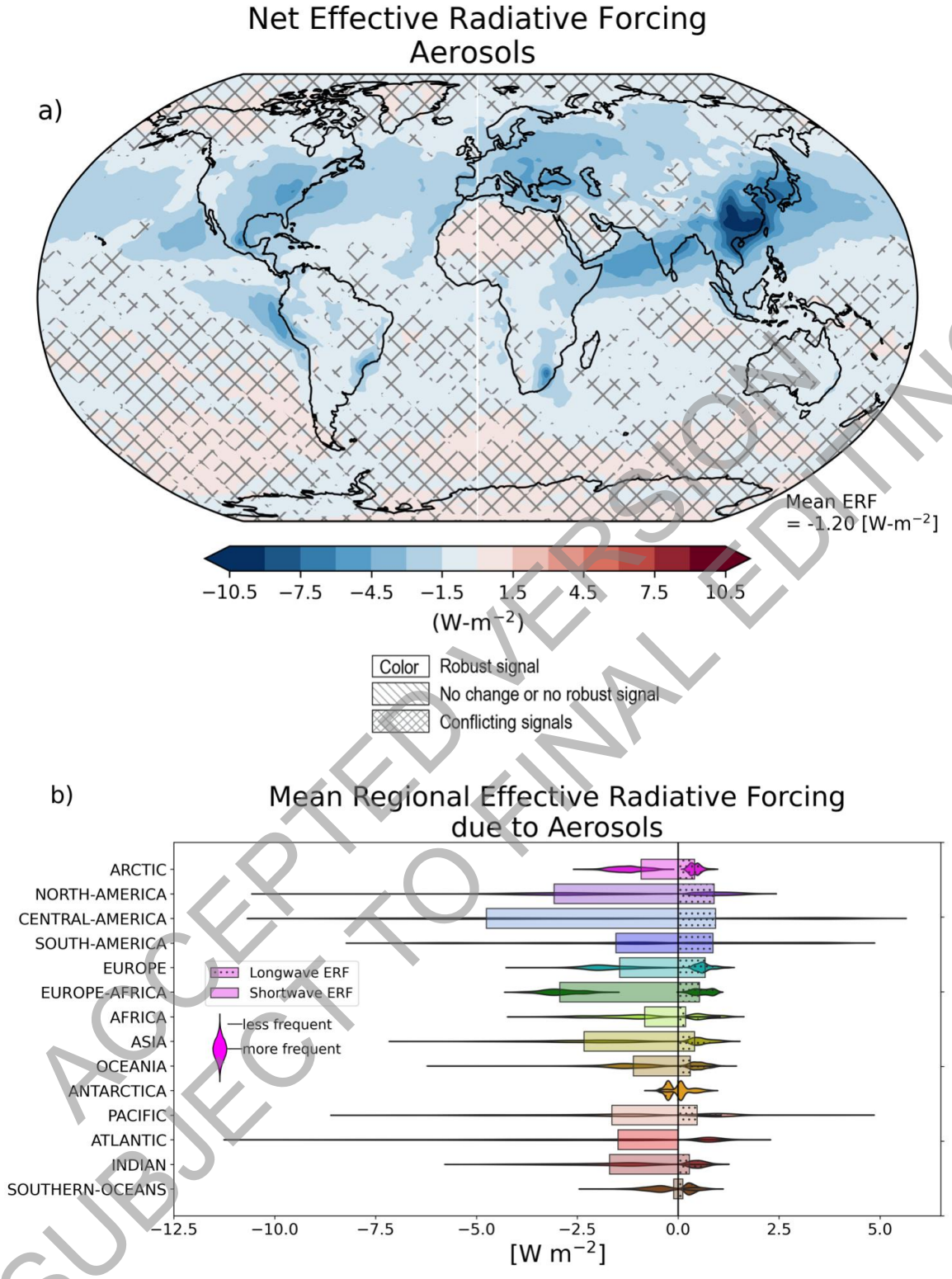


Figure 6.9: Time evolution of global annual mean tropospheric hydroxyl (OH) over the historical period, expressed as a percentage anomaly relative to the mean over 1998-2007. a) Results from three CMIP6 models, including UKESM1-0LL (green), GFDL-ESM4 (blue), and CESM2-WACCM (red), are shown; the shaded light green and light red bands show mean over multiple ensemble members for UKESM1-0LL (3) and CESM2-WACCM (3) models, respectively with the multi-model mean anomalies shown in thick black line. b) multimodel mean OH anomalies for 1980-2015 period compared with those derived from observational-based inversions from (Montzka et al., 2011; Rigby et al., 2017; Turner et al., 2017; Nicely et al., 2018; Naus et al., 2019; Patra et al., 2021) in the zoomed box. Further details on data sources and processing are available in the chapter data table (Table 6.SM.1).

ACCEPTED VERSION SUBJECT TO FINAL EDITING



ACCEPTED VERSION SUBJECT TO FINAL EDITING

Figure 6.10: Multi-model mean Effective radiative forcings (ERFs) due to aerosol changes between 1850 and recent-past (1995-2014). Panel (a) shows the spatial distribution of the net ERF with area-weighted global mean ERF shown at the lower right corner. Uncertainty is represented using the advanced approach: No overlay indicates regions with robust signal, where ≥66% of models show change greater than variability threshold and ≥80% of all models agree on sign of change; diagonal lines indicate regions with no change or no robust signal, where <66% of models show a change greater than the variability threshold; crossed lines indicate regions with conflicting signal, where ≥66% of models show change

greater than variability threshold and <80% of all models agree on sign of change. For more information on the advanced approach, please refer to the Cross-Chapter Box Atlas.1. Panel (b) shows the mean shortwave and longwave ERF for each of the 14 regions defined in the Atlas. Violins in panel (b) show the distribution of values over regions where ERFs are significant. ERFs are derived from the difference between top of the atmosphere (TOA) radiative fluxes for Aerosol Chemistry Model Intercomparison Project (AerChemMIP) experiments *histSST* and *histSST-piAer* (Collins et al., 2017) averaged over 1995-2014 (Box 1.4, Chapter 1). The results come from 7 Earth System Models: MIROC6, MPI-I-ESM-1-2-HAM, MRI-ESM2-0, GFDL-ESM4, GISS-E2-1-G, NorESM2-LM, and UKESM-0-LL. These data can be seen in the Interactive Atlas. Further details on data sources and processing are available in the chapter data table (Table 6.SM.1).

ACCEPTED VERSION
SUBJECT TO FINAL EDITING

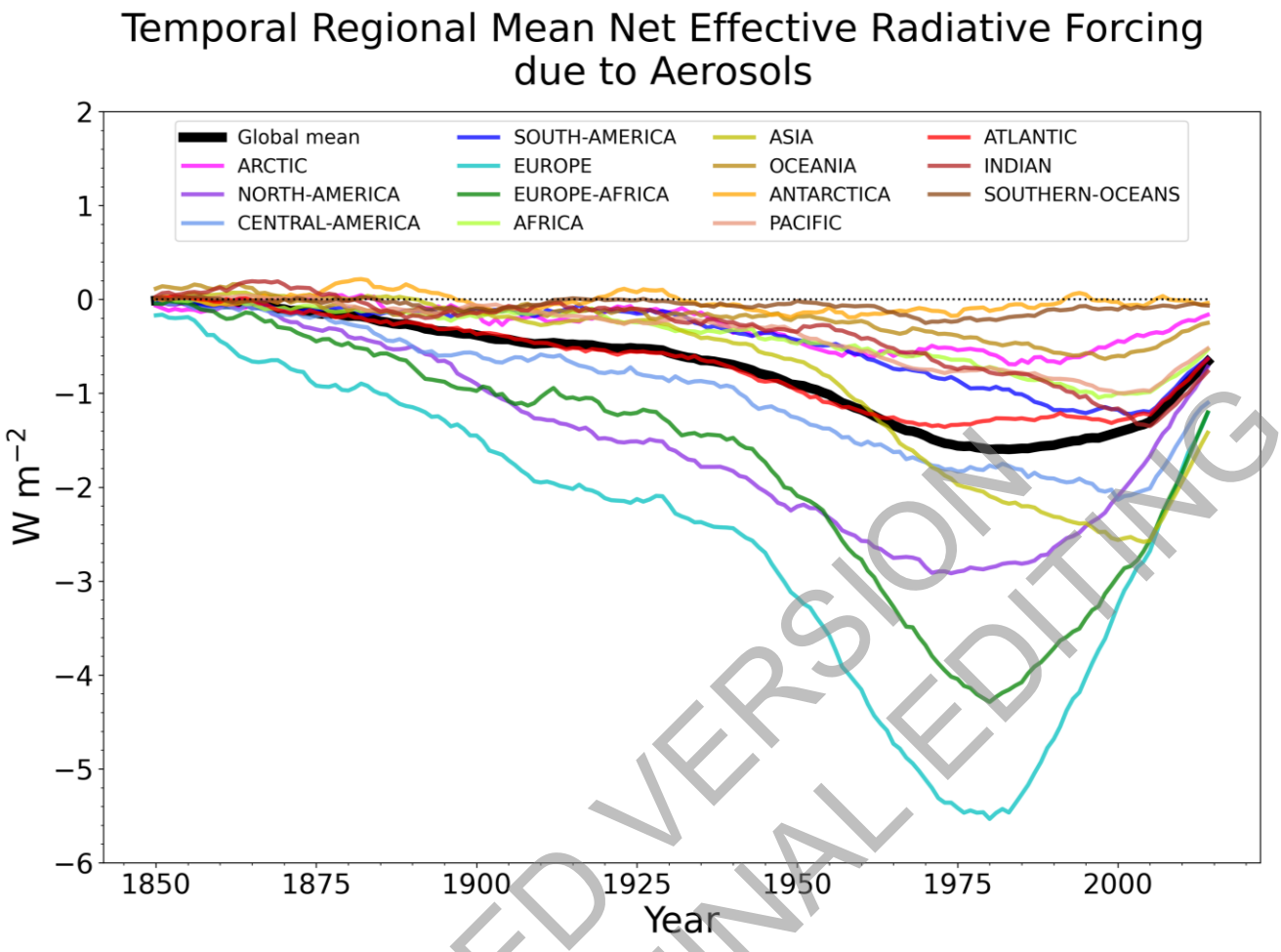


Figure 6.11: Time evolution of 20-year multi-model mean averages of the annual area-weighted mean regional net Effective Radiative Forcings (ERFs) due to aerosols for each of the 14 major regions in the Atlas, and global mean, using the models and model experiments as in Figure 6.10. Further details on data sources and processing are available in the chapter data table (Table 6.SM.1).

ACCEPTED VERSION SUBJECT TO FINAL EDITING

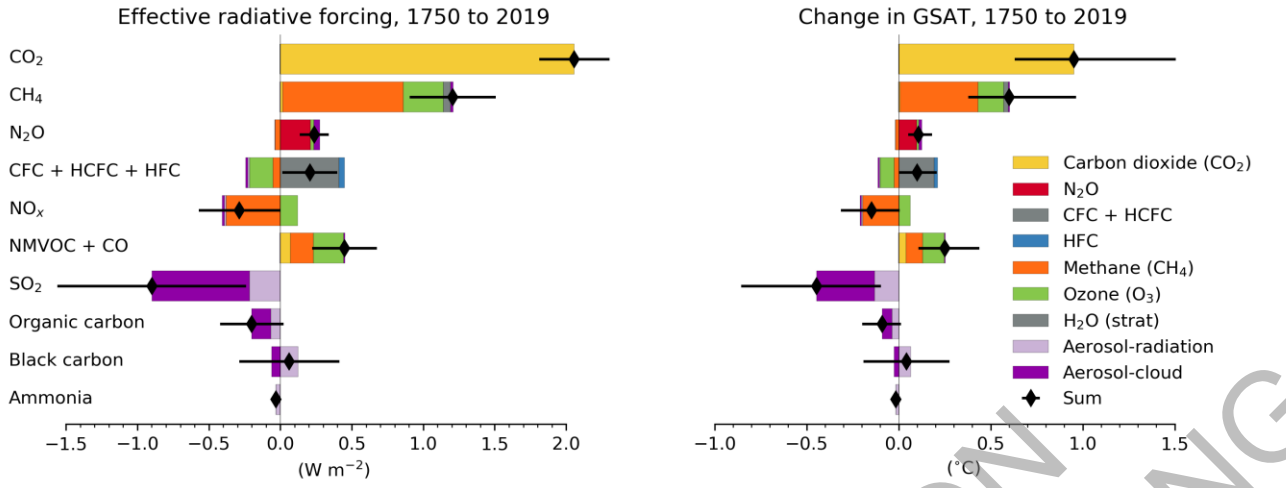


Figure 6.12: Contribution to effective radiative forcing (ERF) (left) and global mean surface air temperature (GSAT) change (right) from component emissions between 1750 to 2019 based on CMIP6 models (Thornhill et al., 2021). ERFs for the direct effect of well-mixed greenhouse gases (WMGHGs) are from the analytical formulae in section 7.3.2, H_2O (strat) is from Table 7.8. ERF for other components are multi-model means from Thornhill et al. (2021) and are based on ESM simulations in which emissions of one species at a time are increased from 1850 to 2014 levels. The derived emission-based ERFs are rescaled to match the concentration-based ERFs in Figure 7.6. Error bars are 5-95% and for the ERF account for uncertainty in radiative efficiencies and multi-model error in the means. ERF due to aerosol-radiation (ERFari) and cloud effects are calculated from separate radiation calls for clear-sky and aerosol free conditions (Ghan, 2013; Thornhill et al., 2021). "Cloud" includes cloud adjustments (semi-direct effect) and ERF from indirect aerosol-cloud to -0.22 W m^{-2} for ERFari and -0.84 W m^{-2} interactions (ERFaci). The aerosol components (SO_2, organic carbon, black carbon) are scaled to sum to -0.22 W m^{-2} for ERFari and -0.84 W m^{-2} for "cloud" (section 7.3.3). For GSAT estimates, time series (1750-2019) for the ERFs have been estimated by scaling with concentrations for WMGHGs and with historical emissions for SLCFs. The time variation of ERFaci for aerosols is from Chapter 7. The global mean temperature response is calculated from the ERF time series using an impulse response function (see Cross-Chapter Box 7.1) with a climate feedback parameter of -1.31 W m^{-2} °C^{-1}. Further details on data sources and processing are available in the chapter data table (Table 6.SM.1).

ACCEPTED VERSION SUBJECT TO FINAL EDITING

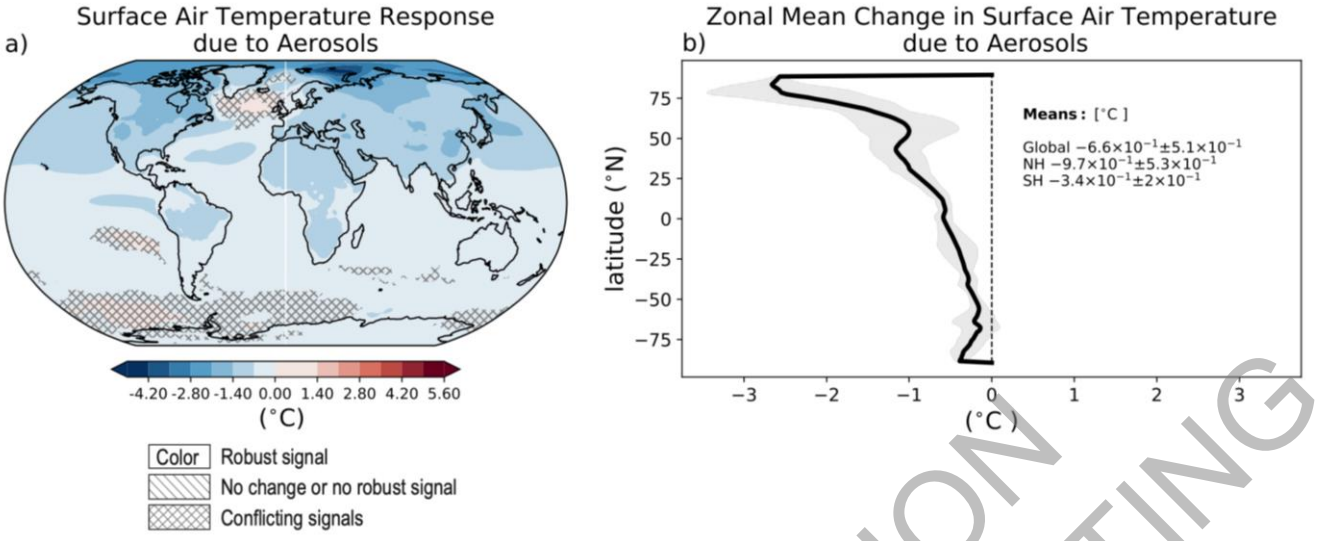


Figure 6.13: Multi-model mean surface air temperature response due to aerosol changes between 1850 and recent-past (1995-2014) calculated as the difference between CMIP6 'historical' and AerChemMIP 'hist-piAer' experiments, where a) is the spatial pattern of the annual mean surface air temperature response, and b) is the mean zonally averaged response. Model means are derived from years 1995-2014. Uncertainty is represented using the advanced approach: No overlay indicates regions with robust signal, where ≥66% of models show change greater than variability threshold and ≥80% of all models agree on sign of change; diagonal lines indicate regions with no change or no robust signal, where <66% of models show a change greater than the variability threshold; crossed lines indicate regions with conflicting signal, where ≥66% of models show change greater than variability threshold and <80% of all models agree on sign of change. For more information on the advanced approach, please refer to the Cross-Chapter Box Atlas.1. AerChemMIP models MIROC6, MRI-ESM2-0, NorESM2-LM, GFDL-ESM4, GISS-E2-1-G, UKESM1-0-LL are used in the analysis. Further details on data sources and processing are available in the chapter data table (Table 6.SM.1).

ACCEPTED VERSION SUBJECT TO FINAL EDITING

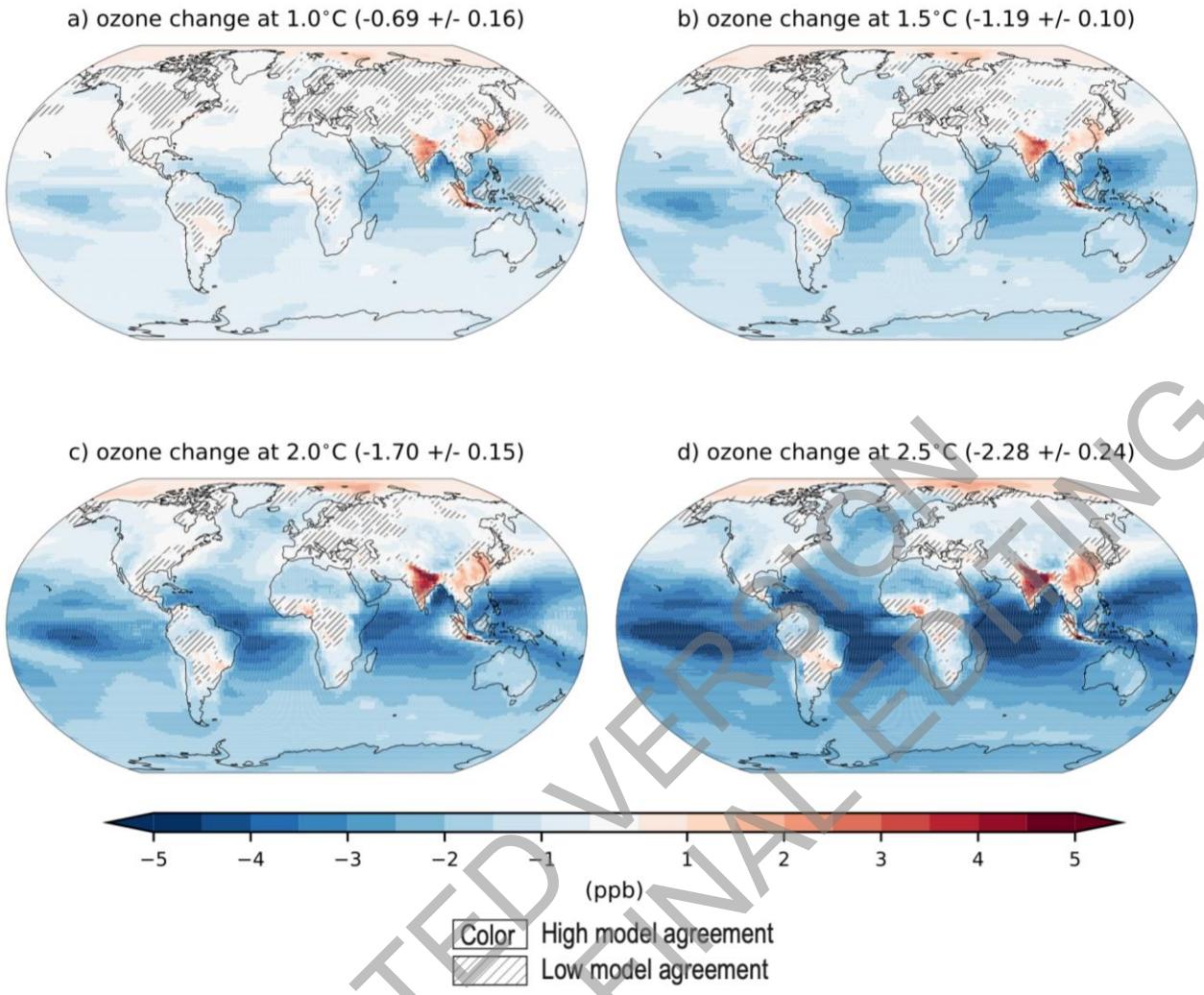


Figure 6.14: Multi-model annual mean change in surface O_3 (ppb) concentrations at different warming levels. Changes are shown for a) 1.0°C, b) 1.5°C, c) 2.0°C and d) 2.5°C increase in global mean surface air temperature. CMIP6 models include GFDL-ESM4, GISS-E2-1-G, MRI-ESM2-0 and UKESM1-0-LL. For each model the change in surface O_3 is calculated as difference between the ssp370SST and ssp370pdSST experiments in the year when the difference in the global mean surface air temperature between the experiments exceeds the temperature threshold. The difference is calculated as a 20-year mean in surface O_3 around the year when the temperature threshold in each model is exceeded. The multi-model change in global annual mean surface O_3 concentrations with ± 1 σ are shown within parenthesis. Uncertainty is represented using the simple approach: No overlay indicates regions with high model agreement, 3 out of 4 models agree on sign of change; diagonal lines indicate regions with low model agreement, where 3 out of 4 models agree on sign of change. For more information on the simple approach, please refer to the Cross-Chapter Box Atlas.1. Further details on data sources and processing are available in the chapter data table (Table 6.SM.1).

ACCEPTED VERSION SUBJECT TO FINAL EDITING

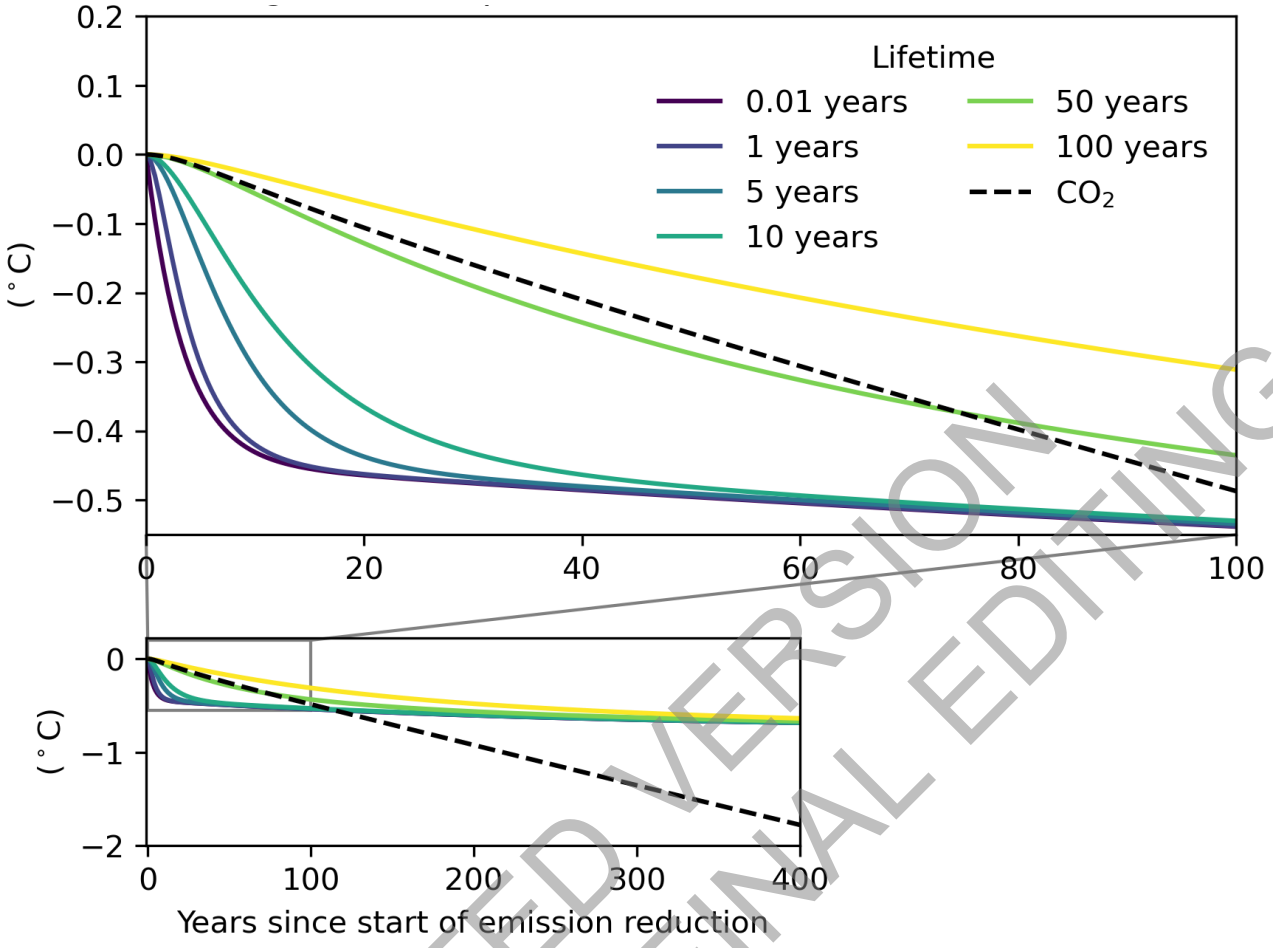


Figure 6.15: Global mean surface air temperature (GSAT) response to an abrupt reduction in emissions (at time t=0) of idealized climate forcing agents with different lifetimes. All emissions are cut to give a radiative forcing of -1 W m^{-2} at steady state (except for CO_2). In other words, if the yearly emissions are E_0 before the reduction, they will have a fixed lower value $E_{year>0} = (E_0 - \Delta E)$ for all succeeding years. For comparison, the GSAT response to a sustained reduction in CO_2 emissions resulting in an RF of -1 W m^{-2} in year 100 is included (dashed line). The temperature response is calculated using an impulse response function (see Cross-Chapter Box 7.1) with a climate feedback parameter of -1.31 W m^{-2} $°C^{-1}$. Further details on data sources and processing are available in the chapter data table (Table 6.SM.1).

ACCEPTED VERSION SUBJECT TO FINAL EDITING

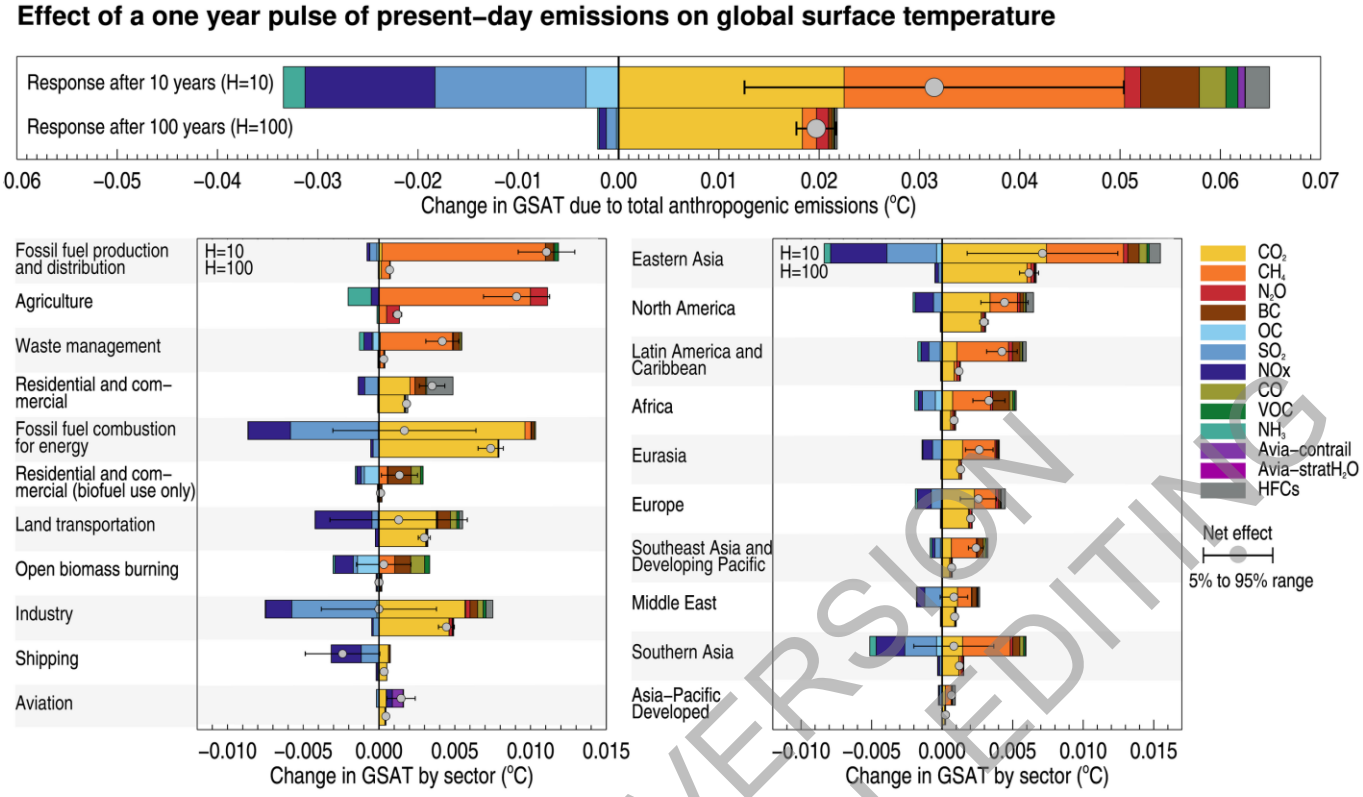


Figure 6.16: Global-mean temperature response 10 and 100 years following one year of present-day (year 2014) emissions. The temperature response is broken down by individual species and shown for total anthropogenic emissions (top), sectoral emissions (left) and regional emissions (right). Sectors and regions are sorted by (high-to-low) net temperature effect on the 10-year time scale. Error bars in the top panel show uncertainty (5-95% interval) in net temperature effect due to uncertainty in radiative forcing *only* (calculated using a Monte Carlo approach and best estimate uncertainties from the literature - see Lund et al. (Lund et al., 2020) for details). CO_2 emissions are excluded from open biomass burning and residential biofuel use due to their unavailability in CEDS and uncertainties around non-sustainable emission fraction. Emissions for 2014 originate from the Community Emissions Data System (CEDS) (Hoesly et al., 2018), except for HFCs which are from Purohit et al. (2020), open biomass burning from van Marle et al. (2017), and aviation H_2O which is from Lee et al.(2020). The split of fossil fuel production and distribution and combustion for energy and residential and commercial fuel use into fossil fuel and biofuel components obtained from the GAINS model (ECLIPSE version 6b dataset). Open biomass burning emissions are not included for the regions. Emission are aggregated into fossil fuel production and distribution (coal mining, oil and gas production, upstream gas flaring, gas distribution networks), agriculture (livestock and crop production), fossil fuel combustion for energy (power plants), industry (combustion and production processes, solvent use losses from production and end use), residential and commercial (fossil fuel use for cooking and heating as well is HFCs leakage from A/C and refrigeration), waste management (solid waste, incl. landfills and open trash burning, residential and industrial waste water), transport (road and off-road vehicles, and HFC leakage from A/C and refrigeration equipment), residential and commercial (biofuels use for cooking and heating), open biomass burning (forest, grassland, savannah fires, and agricultural waste burning), shipping (incl. international shipping), and aviation (incl. international aviation). Further details on data sources and processing are available in the chapter data table (Table 6.SM.1).

ACCEPTED VERSION SUBJECT TO FINAL EDITING

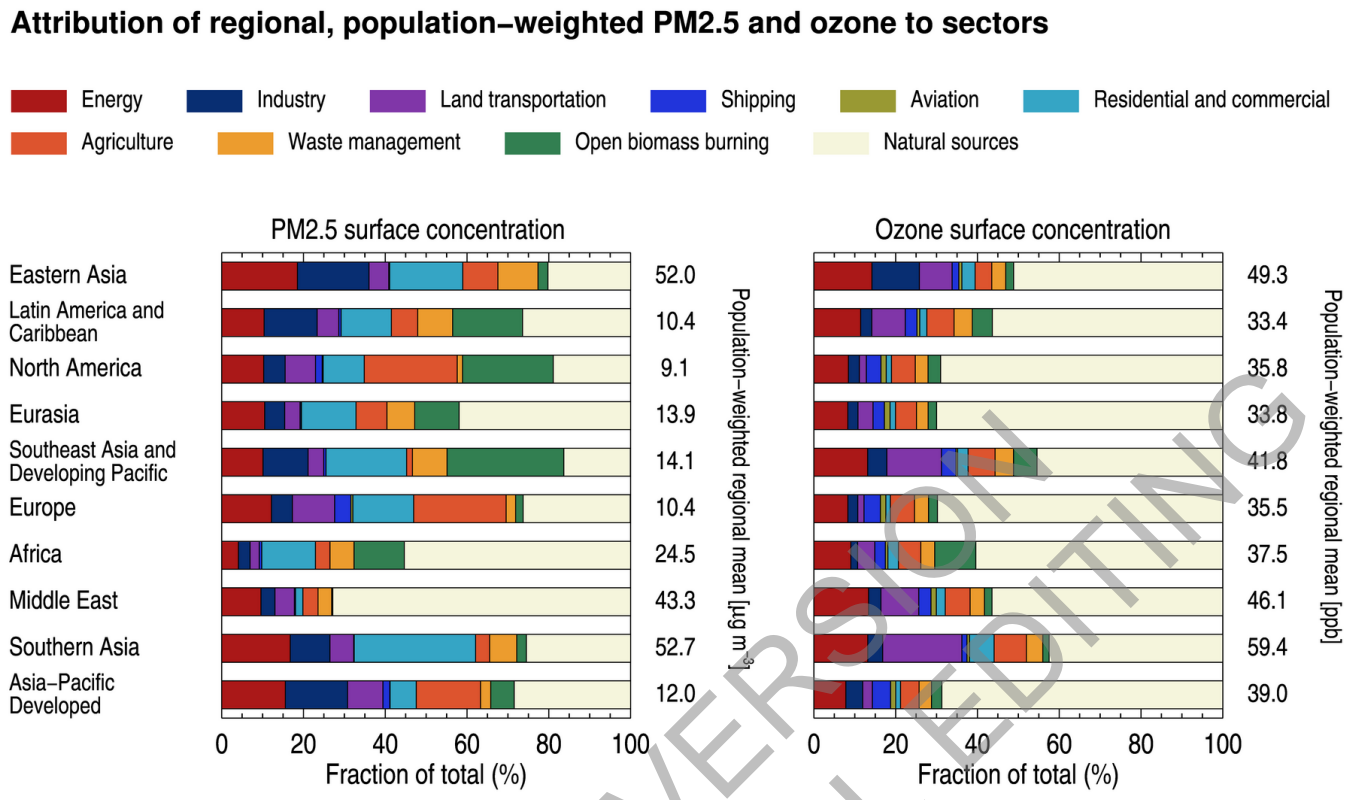


Figure 6.17: Emission source-sector attribution of regional population weighted mean concentrations of $PM_{2.5}$ and ozone for present day emissions (year 2014). Regional concentrations and source apportionment calculated with the TM5-FASST model (Van Dingenen et al., 2018) for the 2014 emission data from the Community Emissions Data System (CEDS) (Hoesly et al., 2018) and van Marle et al.(2017) for open biomass burning. $PM_{2.5}$ dust and seasalt are monthly mean climatological average over 2010-2018 from CAMS global reanalysis (EAC4) (Inness et al., 2019), generated using Copernicus Climate Change Service information [January 2020]. Anthropogenic sectors are similar to those in Figures 6.2 and 6.16 except grouping of fossil fuel production, distribution and combustion for energy under "Energy" and grouping of use of fossil fuel and biofuel use for cooking and heating under "Residential and Commercial". Further details on data sources and processing are available in the chapter data table (Table 6.SM.1).

ACCEPTED VERSION SUBJECT TO FINAL EDITING

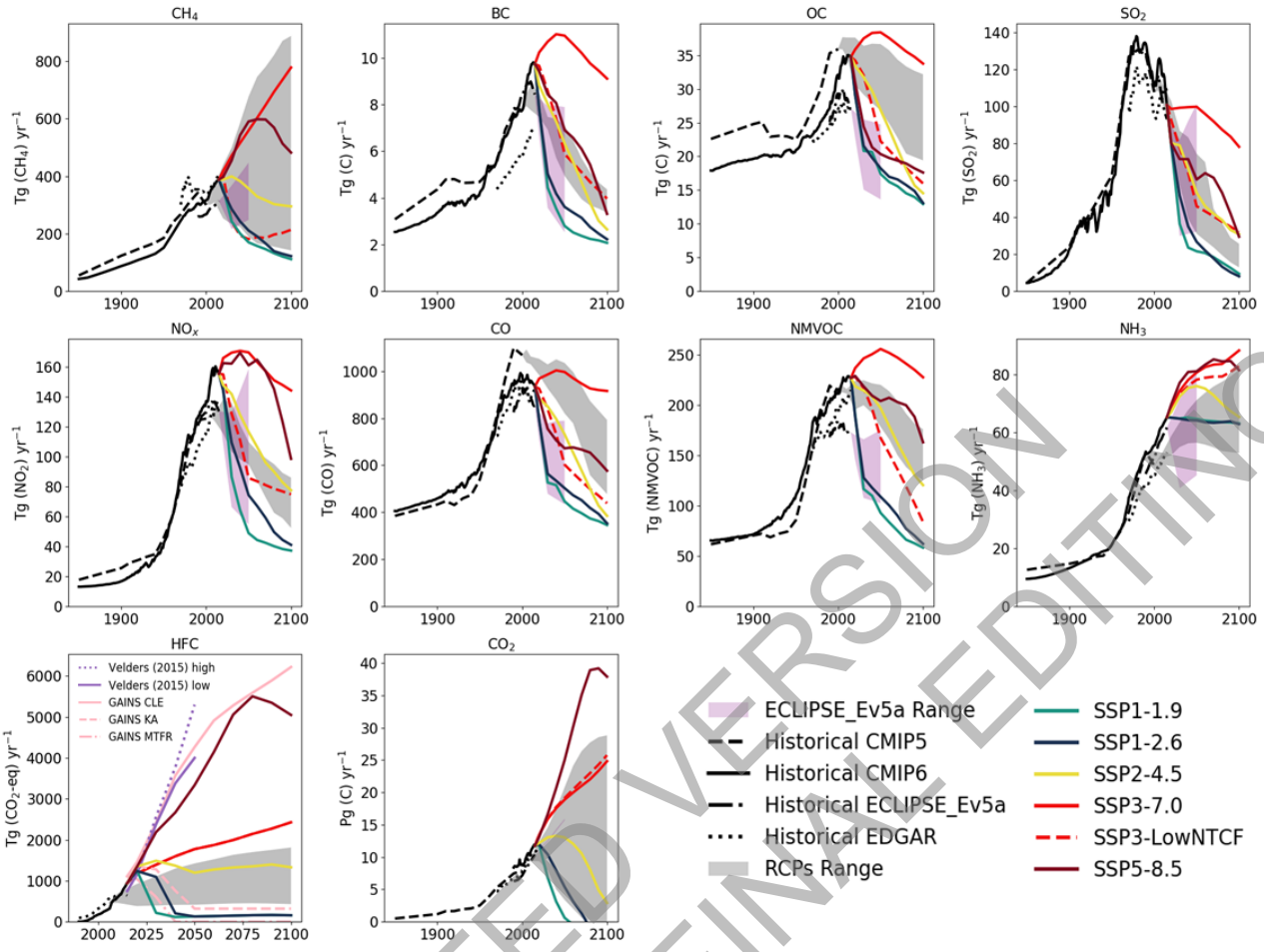
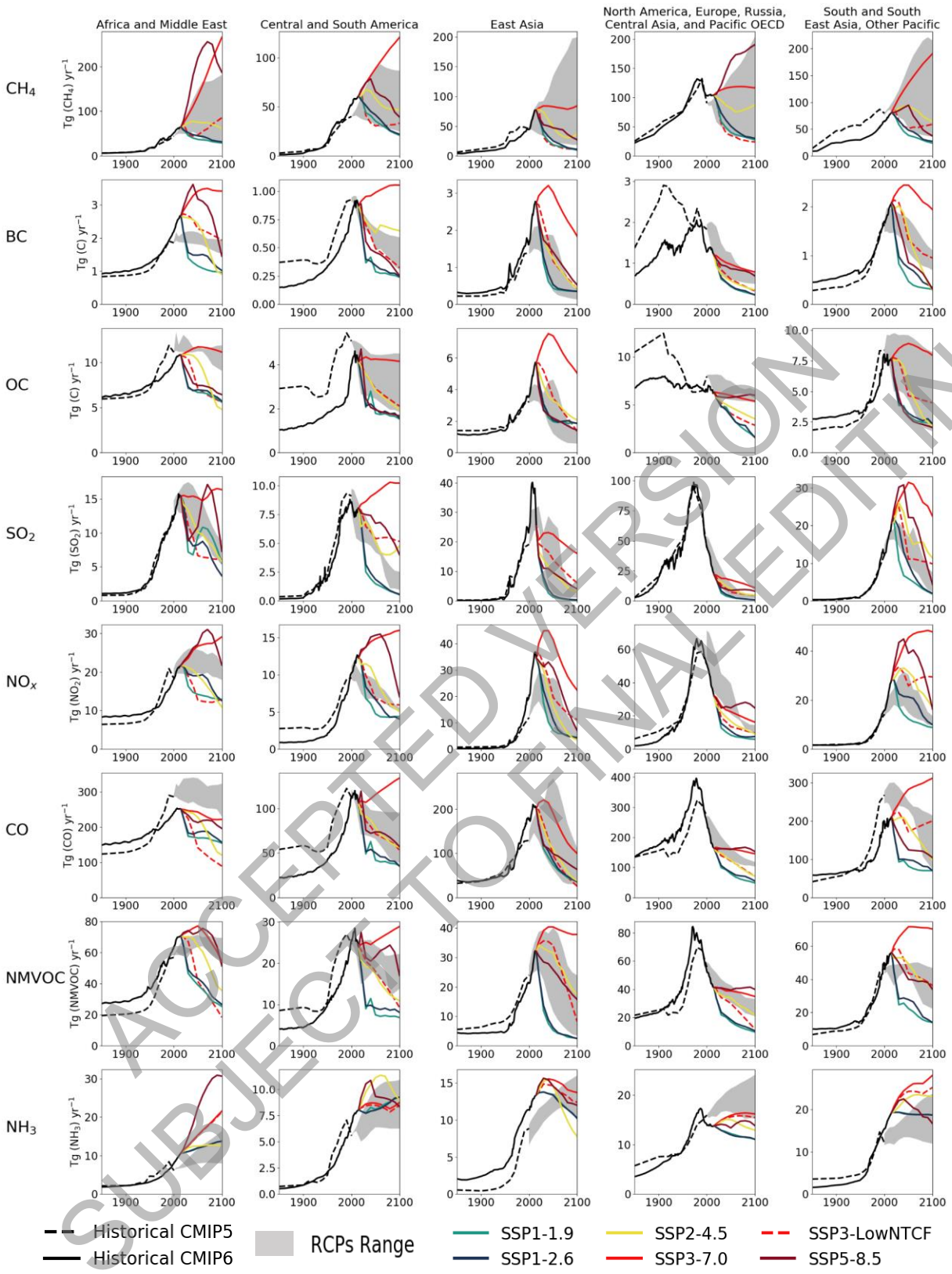


Figure 6.18: Global anthropogenic and biomass burning short-lived climate forcer (SLCF) and CO_2 emissions from 1850 to 2100 and HFC emissions from 1990 to 2100. Emissions for the Coupled Model Intercomparison Project Phase 6 (CMIP6) for the period 1850-2014 are based on Hoesly et al. (2018) and van Marle et al. (2017), emissions for CMIP5 for the period 1850-2005 are from Lamarque et al. (2010), CO_2 emissions are from EDGAR database (Crippa et al., 2020); CH_4 and HFCs are from (Crippa et al., 2019); and air pollutants are from (EC-JRC / PBL, 2020), Höglund-Isaksson (2012) and Klimont et al. (2017) for ECLIPSE. Projections originate from the Shared Socio-Economic Pathway (SSP) database (Riahi et al., 2017; Rogelj et al., 2018; Gidden et al., 2019), Representative Concentration Pathway (RCP) database (van Vuuren et al., 2011), GAINS (CLE – current legislation baseline without Kigali Amendment, KA – Kigali Amendment, MTFR – maximum technical mitigation potential) for HFCs (Purohit et al., 2020), Velders et al. (2015), ECLIPSE (Stohl et al., 2015). Further details on data sources and processing are available in the chapter data table (Table 6.SM.1).

ACCEPTED VERSION SUBJECT TO FINAL EDITING



ACCEPTED VERSION SUBJECT TO FINAL EDITING

Figure 6.19: Regional anthropogenic and biomass burning short-lived climate forcer (SLCF) emissions from 1850 to 2100. Emissions for the Coupled Model Intercomparison Project Phase 6 (CMIP6) for the period 1850-2014 are based on Hoesly et al. (2018) and van Marle et al. (2017) and emissions for CMIP5 for the period 1850-2005 are from Lamarque et al. (2010). Projections originate from the Shared Socio-

Economic Pathway (SSP) database (Riahi et al., 2017; Rogelj et al., 2018; Gidden et al., 2019) and Representative Concentration Pathway (RCP) database (van Vuuren et al., 2011). Further details on data sources and processing are available in the chapter data table (Table 6.SM.1).

ACCEPTED VERSION
SUBJECT TO FINAL EDITING

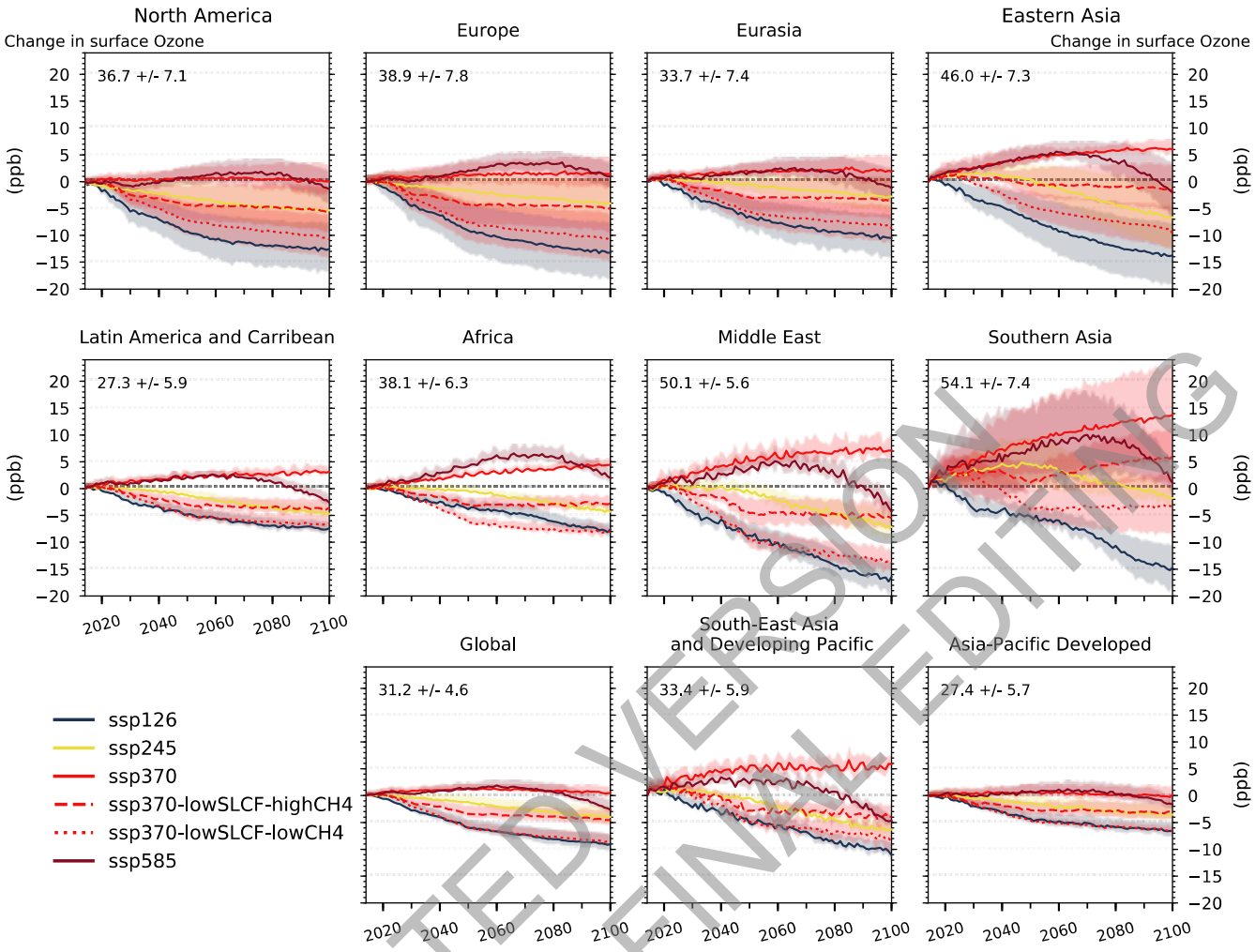


Figure 6.20: Projected changes in regional annual mean surface ozone (O_3) (ppb) from 2015 to 2100 in different shared socio-economic pathways (SSPs). Each panel represents values averaged over the corresponding land area (except for Global) shown on the map in Figure 6.7. Solid colored lines and shading indicate the multi-model mean and ±1 σ across the available CMIP6 models (Turnock et al. 2020; Allen et al. 2021) for each scenario. Changes are relative to annual mean values calculated over the period 2005-2014 from the historical experiment as indicated in the top left of each regional panel along with ±1 σ. For each model all available ensemble members are averaged before being used to calculate the multi-model mean. Ozone changes are also displayed in the Interactive Atlas. Further details on data sources and processing are available in the chapter data table (Table 6.SM.1).

ACCEPTED VERSION SUBJECT TO FINAL EDITING

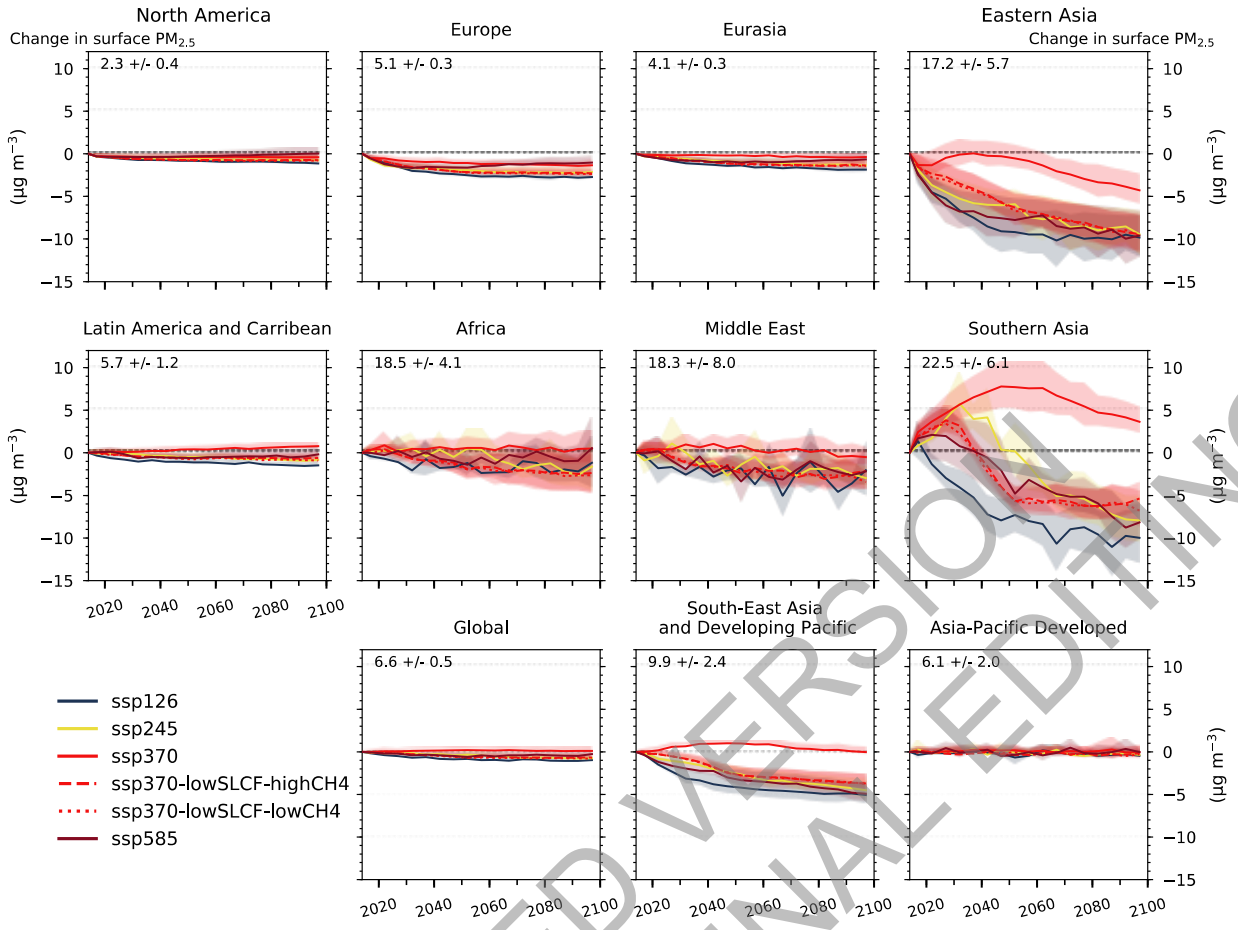
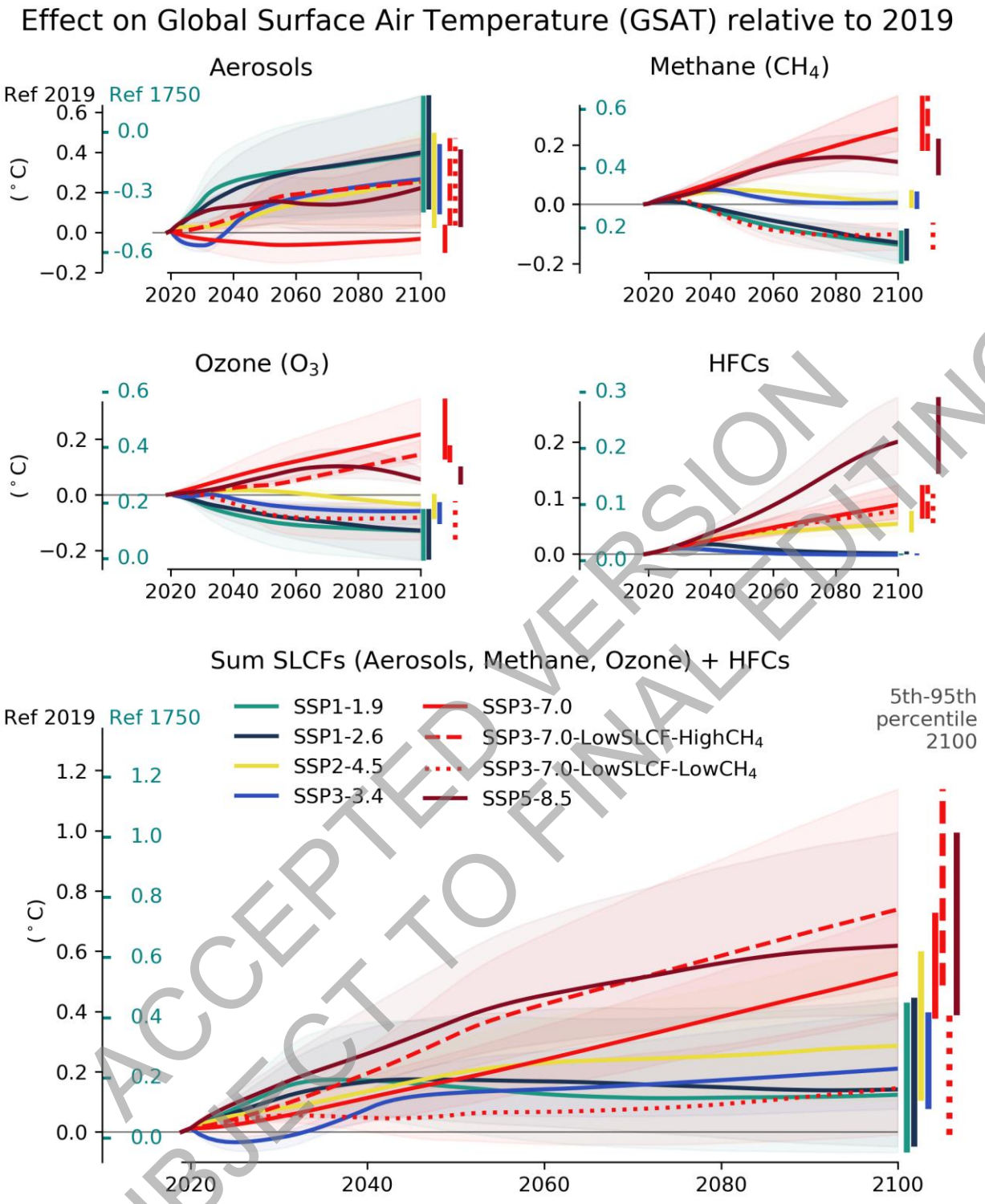


Figure 6.21: Future changes in regional 5-year mean surface $PM_{2.5}$ from 2015 to 2100 in different shared socio-economic pathways (SSPs). $PM_{2.5}$ stands for micrograms per cubic meter of aerosols with diameter less than 2.5 μm and is calculated by summing up individual aerosol mass components from each model as: black carbon + particulate organic matter + sulphate + 0.25 * sea salt + 0.1 * dust. Since not all CMIP6 models reported nitrate aerosol, it is not included here. See Figure 6.20 for further details. $PM_{2.5}$ changes are also displayed in the Interactive Atlas. Further details on data sources and processing are available in the chapter data table (Table 6.SM.1).

ACCEPTED VERSION SUBJECT TO FINAL EDITING



ACCEPTED VERSION SUBJECT TO FINAL EDITING

Figure 6.22: Time evolution of the effects of short-lived climate forcers (SLCFs) and hydrofluorocarbons (HFCs) on global surface air temperature (GSAT) across the WGI core set of Shared Socio-Economic Pathways (SSPs). Effects of net aerosols, methane, tropospheric ozone and hydrofluorocarbons (HFCs) (with lifetimes <50years), and the sum of these, relative to year 2019 and to year 1750. The GSAT changes are based on the assessed historic and future evolution of Effective Radiative Forcing (Section 7.3.5). The temperature responses to the ERFs are calculated with an impulse response function with an equilibrium climate sensitivity of 3.0°C for a doubling of atmospheric CO_2 (feedback parameter of -1.31 W m^{-2} $°C^{-1}$, see CC-Box 7.1). The vertical bars to the right in each panel show the uncertainties (5-95% ranges) for the GSAT change between 2019 and 2100. Further details on data sources and processing are available in the chapter data table (Table 6.SM.1).

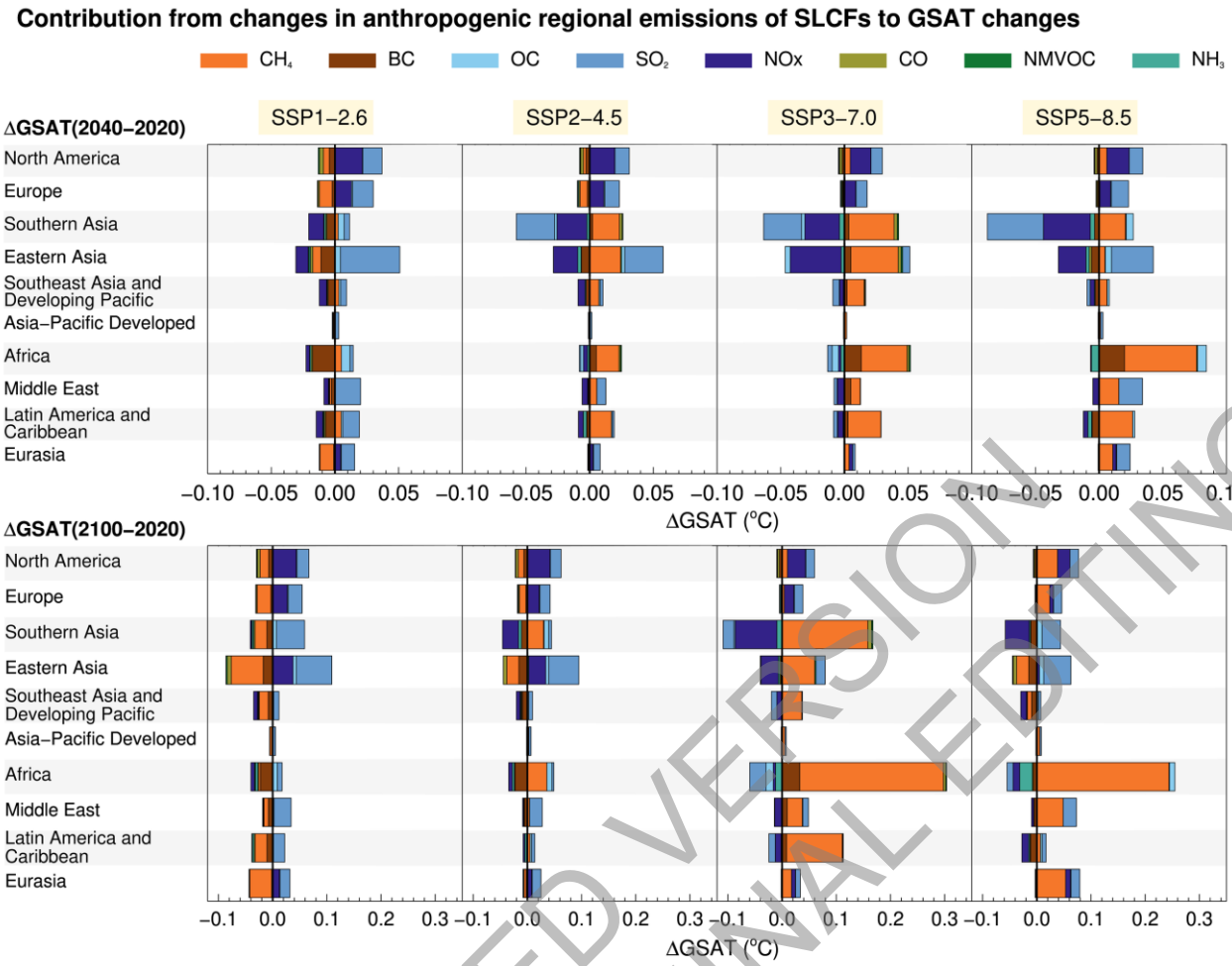


Figure 6.23: Contribution from regional emissions of short-lived climate forcers (SLCFs) to changes in global surface air temperature (GSAT) in 2040 (upper row) and 2100 (lower row), relative to 2020 for four Shared Socio-economic Pathways (SSP). Adapted from (Lund et al., 2020). NO_x, CO, and VOC account for the impact through changes in ozone and methane, NO_x additionally includes the impact through formation of nitrate aerosols. BC, SO_2 and OC accounts for the direct aerosol effect (aerosol-radiation interactions), as well as an estimate of the semi-direct effect for BC due to rapid adjustments and indirect effect (aerosol-cloud interactions) of sulfate aerosols. Regions are the same as shown in the map in Figure 6.7. Further details on data sources and processing are available in the chapter data table (Table 6.SM.1).

ACCEPTED VERSION SUBJECT TO FINAL EDITING

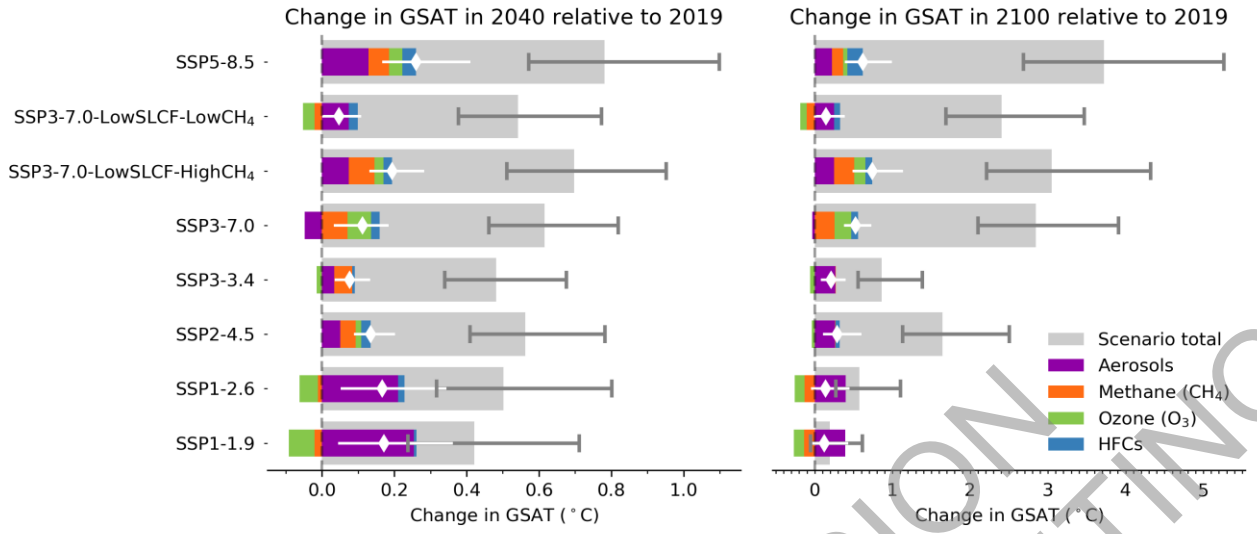
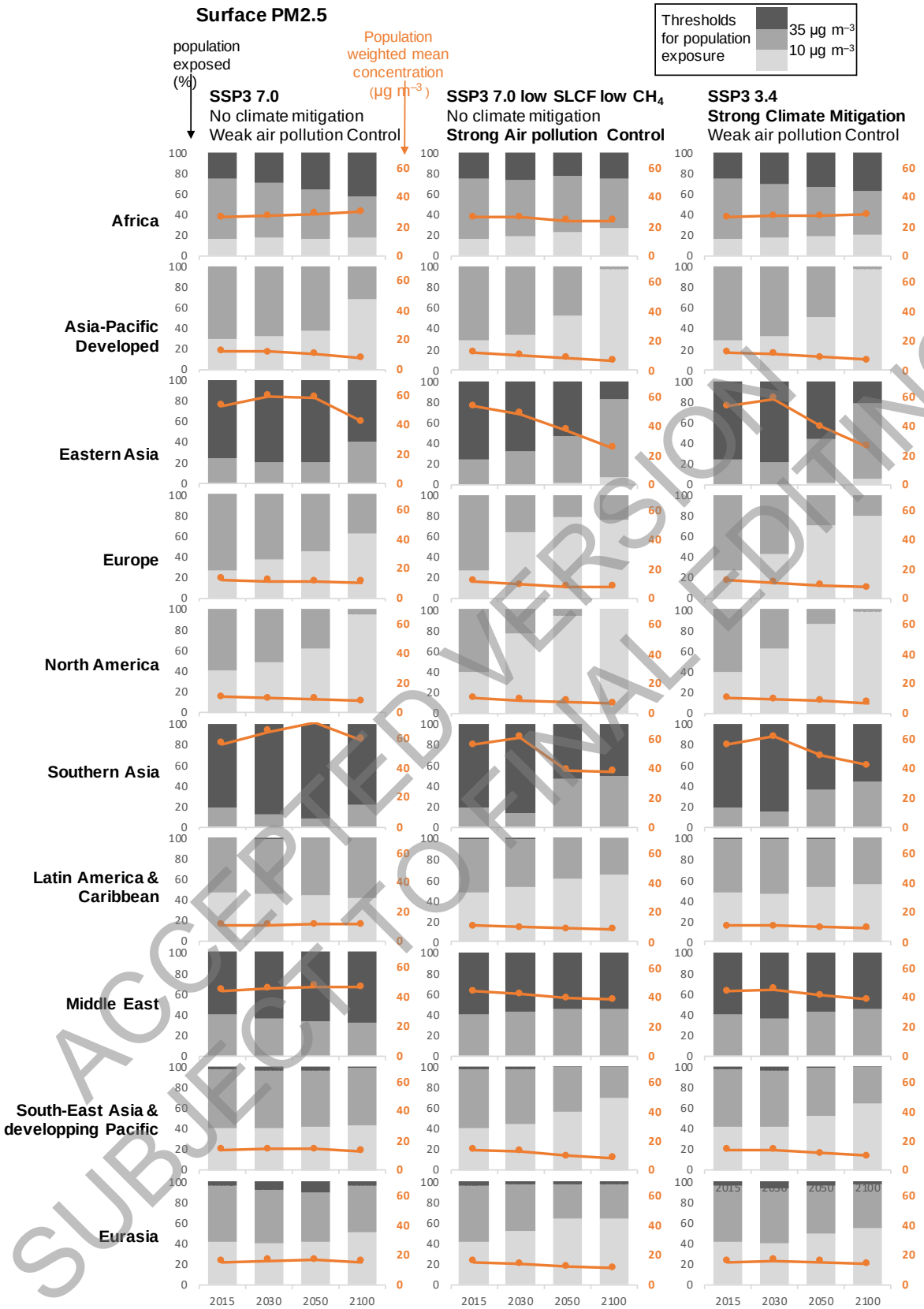


Figure 6.24: Effects of short-lived climate forcers (SLCFs) and hydrofluorocarbons (HFCs) on global surface air temperature (GSAT) across the WGI core set of Shared Socio-Economic Pathways (SSPs). Effects of net aerosols, methane, tropospheric ozone, and hydrofluorocarbons (HFCs; with lifetimes <50years), are compared with those of total anthropogenic forcing for 2040 and 2100 relative to year 2019. The GSAT changes are based on the assessed historic and future evolution of Effective Radiative Forcing (Section 7.3.5). The temperature responses to the ERFs are calculated with an impulse response function with an equilibrium climate sensitivity of 3.0°C for a doubling of atmospheric CO_2 (feedback parameter of -1.31 W m^{-2} $°C^{-1}$, see Cross-Chapter Box 7.1). Uncertainties are 5-95% ranges. The scenario total (grey bar) includes all anthropogenic forcings (long- and short-lived climate forcers, and land use changes) whereas the white points and bars show the net effects of SLCFs and HFCs and their uncertainties. Further details on data sources and processing are available in the chapter data table (Table 6.SM.1).

ACCEPTED VERSION SUBJECT TO FINAL EDITING

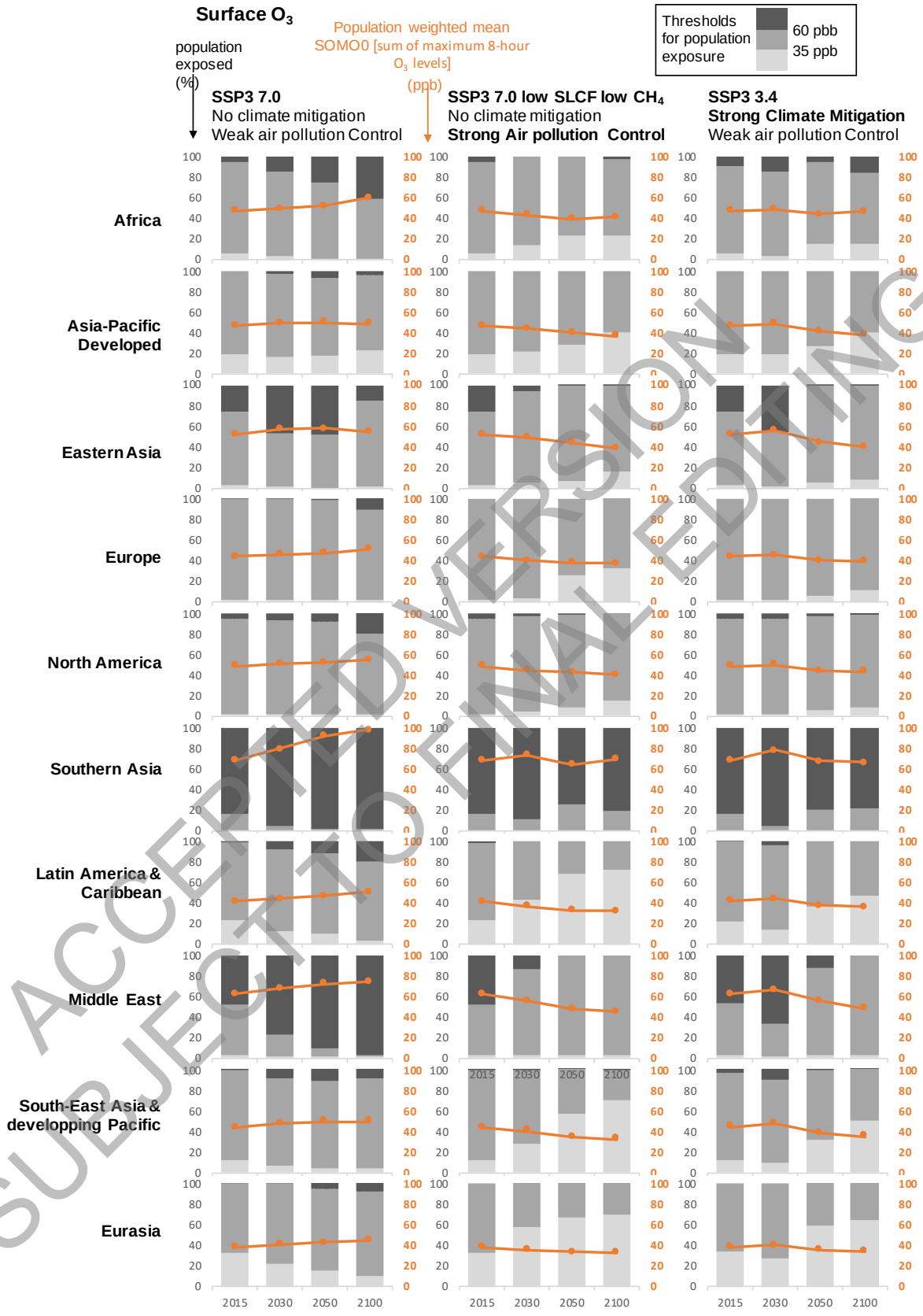


ACCEPTED VERSION SUBJECT TO FINAL EDITING

Figure 6.25: Effect of dedicated air pollution or climate policy on population-weighted $PM_{2.5}$ concentrations (µg m^{-3}) and share of population (%) exposed to different $PM_{2.5}$ levels across selected world regions. Thresholds of 10 µg m^{-3} and 35 µg m^{-3} represent the WHO air quality guideline and the WHO interim target 1, respectively; WHO (2017). Results are compared for SSP3-7.0 (no major improvement of current legislation is assumed), SSP3-LowSLCF (strong air pollution controls are assumed), and a climate

mitigation scenario SSP3-3.4; details of scenario assumptions are discussed in Riahi et al. (2017) and Rao et al. (2017). Analysis performed with the TM5-FASST model (Van Dingenen et al., 2018) using emission projections from the Shared Socio-Economic Pathway (SSP) database (Riahi et al., 2017; Rogelj et al., 2018; Gidden et al., 2019). Further details on data sources and processing are available in the chapter data table (Table 6.SM.1).

ACCEPTED VERSION
SUBJECT TO FINAL EDITING

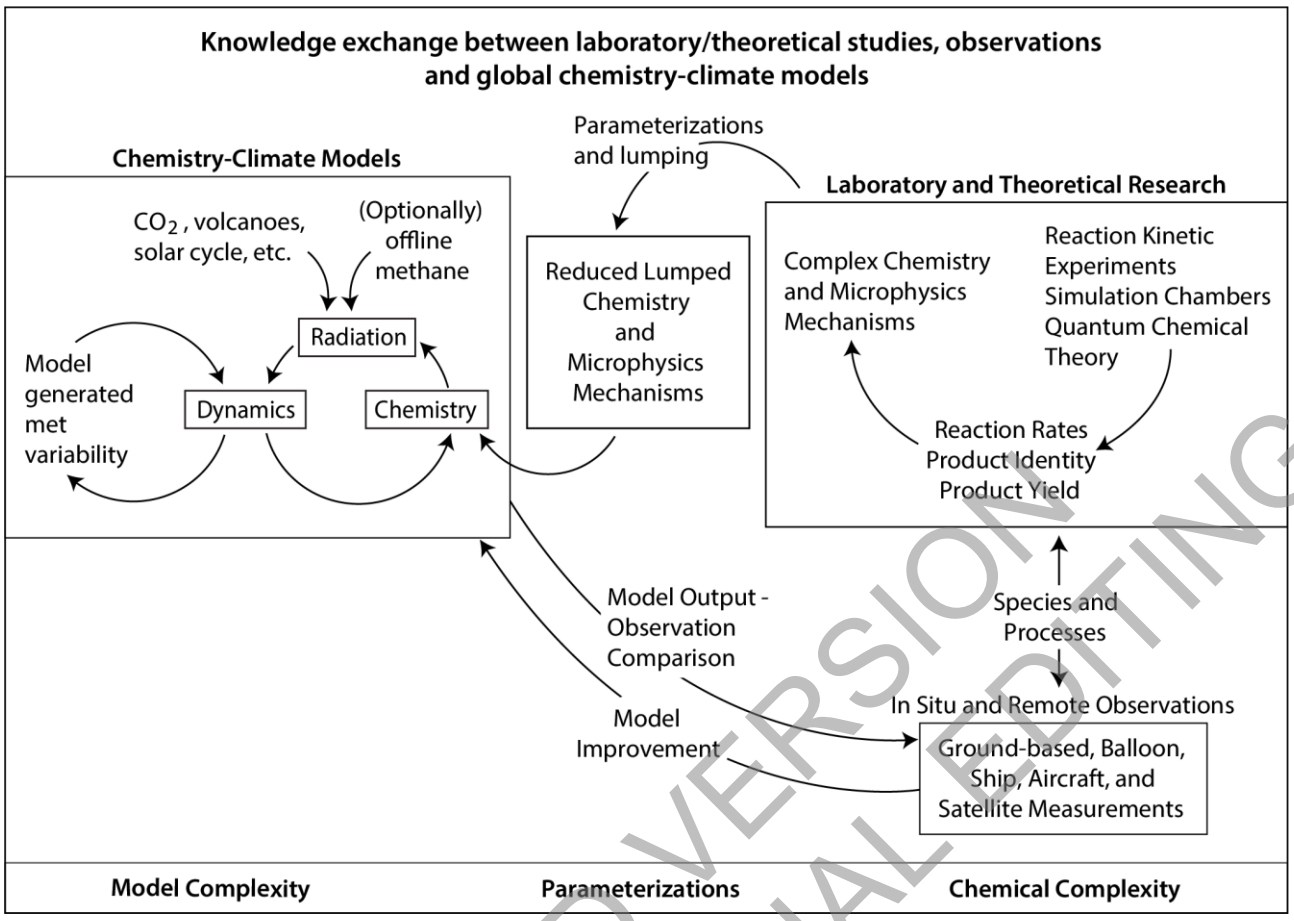


ACCEPTED VERSION SUBJECT TO FINAL EDITING

Figure 6.26: Effect of dedicated air pollution or climate policy on population-weighted ozone concentrations (SOMO0; ppb) and share of population (%) exposed to chosen ozone levels across ten world regions. Results are compared for SSP3-7.0 (no major improvement of current legislation is assumed),

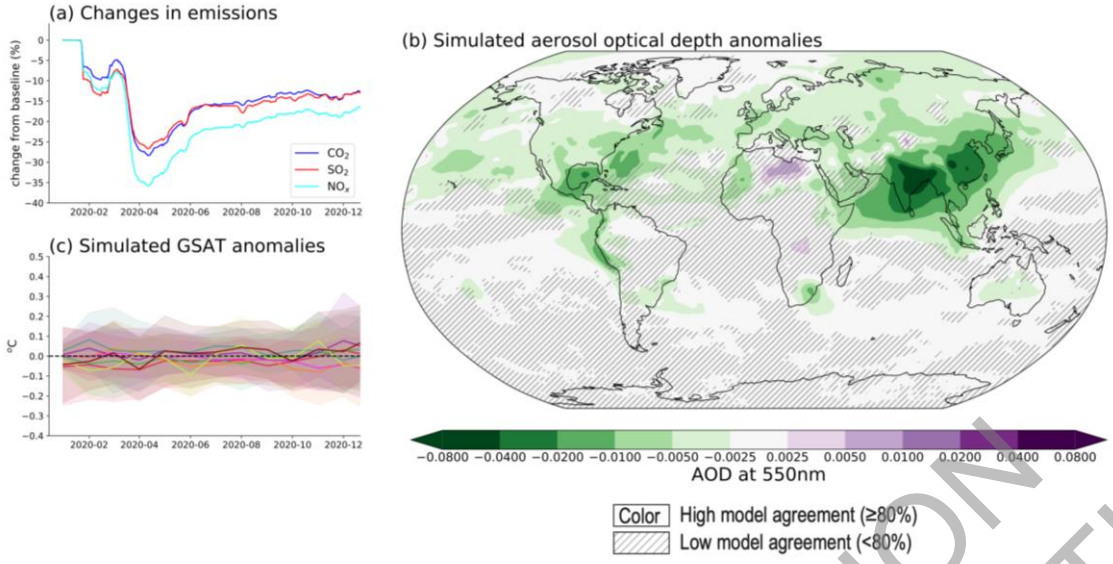
SSP3-LowSLCF (strong air pollution controls are assumed), and a climate mitigation scenario (SSP3-3.4); details of scenario assumptions are discussed in Riahi et al. (2017) and Rao et al. (2017). Analysis performed with the TM5-FASST model (Van Dingenen et al., 2018) using emission projections from the Shared Socio-Economic Pathway (SSP) database [https://tntcat.iiasa.ac.at/SspDb/dsd] (Riahi et al., 2017; Rogelj et al., 2018; Gidden et al., 2019). Further details on data sources and processing are available in the chapter data table (Table 6.SM.1).

ACCEPTED VERSION
SUBJECT TO FINAL EDITING



Box 6.1, Figure 1: Knowledge exchange between laboratory/theoretical studies, observations and global chemistry-climate models to inform our understanding of short-lived climate forcers (SLCFs).

ACCEPTED VERSION SUBJECT TO FINAL EDITING



Cross-Chapter Box 6.1, Figure 1: **Emission reductions and their effect on aerosols and climate in response to COVID-19.** Estimated reductions in emissions of CO_2, SO_2 and NO_x are shown in panel (a) based on reconstructions using activity data (updated from Forster et al., 2020). Eight Earth System Models (ESMs) performed multiple ensemble simulations of the response to COVID-19 emissions reductions forced with these assumed emission reductions up till August 2020 followed by a constant continuation near the August value to the end of 2020. Emission reductions were applied relative to the SSP2-4.5 scenario. Panel (b) shows ESM simulated AOD at 550nm (only seven models reported this variable). Panel (c) shows ESM simulated GSAT anomalies during 2020; curves denote the ensemble mean result for each model with shading used for ±1 standard deviation for each model. ESM data from these simulations ("ssp245-covid") is archived on the Earth System Grid CMIP6 database. Uncertainty is represented using the simple approach: No overlay indicates regions with high model agreement, where ≥80% of models agree on sign of change; diagonal lines indicate regions with low model agreement, where <80% of models agree on sign of change. For more information on the simple approach, please refer to the Cross-Chapter Box Atlas.1.

ACCEPTED VERSION SUBJECT TO FINAL EDITING

FAQ 6.1: **What are short-lived climate forcers and how do they affect the climate?**

Short lived climate forcers do not remain for very long in the atmosphere, thus an increase or decrease in their emissions rapidly affects the climate system.

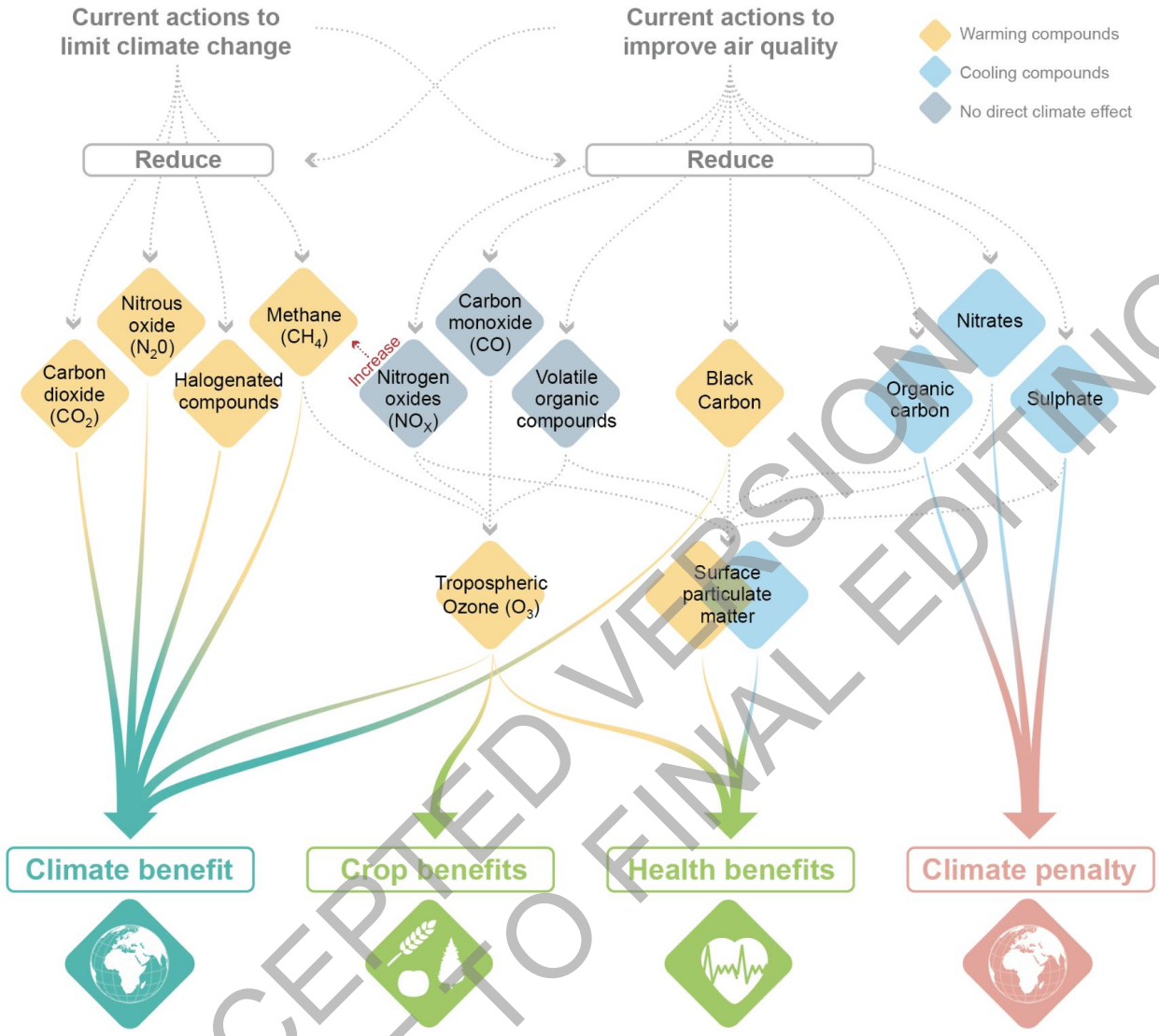


FAQ 6.1, Figure 1: Main short-lived climate forcers, their sources, how long they exist in the atmosphere, and their relative contribution to global surface temperature changes between 1750 and 2019 (area of the globe). By definition, this contribution depends on the lifetime, the warming/cooling potential (radiative efficiency), and the emissions of each compound in the atmosphere. Blue indicates cooling and orange warming. Note that, between 1750 and 2019, the cooling contribution from aerosols (blue diamonds and globe) was approximately half the warming contribution from carbon dioxide.

ACCEPTED VERSION SUBJECT TO FINAL EDITING

FAQ 6.2: **Limiting climate change and improving air quality?**

Climate change and air quality are so intimately linked that addressing one issue can affect the other one.



FAQ6.2, Figure 1: Links between actions aiming to limit climate change and actions to improve air quality. Greenhouse gases and aerosols (orange and blue) can affect directly climate. Air pollutants (bottom) can affect the human health, ecosystems and climate. All these compounds have common sources and sometimes interact with each other in the atmosphere which makes impossible to consider them separately (dotted grey arrows).

ACCEPTED VERSION SUBJECT TO FINAL EDITING

Chapter 6: Short-lived Climate Forces
Supplementary Material

Coordinating Lead Authors:
Vaishali Naik (United States of America), Sophie Szopa (France)

Lead Authors:
Bhupesh Adhikary (Nepal), Paulo Artaxo (Brazil), Terje Berntsen (Norway), William D. Collins (United States of America), Sandro Fuzzi (Italy), Laura Gallardo (Chile), Astrid Kiendler-Scharr (Germany/Austria), Zbigniew Klimont (Austria/Poland), Hong Liao (China), Nadine Unger (United Kingdom/United States of America), Prodromos Zanis (Greece)

Contributing Authors:
Wenche Aas (Norway), Dimitris Akritidis (Greece), Robert J. Allen (United States of America), Nicolas Bellouin (United Kingdom/France), Sophie Berger (France/Belgium), Sara M. Blichner (Norway), Josep G. Canadell (Australia), William Collins (United Kingdom), Owen R. Cooper (United States of America), Frank J. Dentener (EU/The Netherlands), Sarah Doherty (United States of America), Jean-Louis Dufresne (France), Sergio Henrique Faria (Spain/Brazil), Piers Forster (United Kingdom), Tzung-May Fu (China), Jan S. Fuglestvedt (Norway), John C. Fyfe (Canada), Aristeidis K. Georgoulias (Greece), Matthew J. Gidden (Austria/ United States of America), Nathan P. Gillett (Canada), Paul Ginoux (United States of America), Paul T. Griffiths (United Kingdom), Jian He (United States of America/China), Christopher Jones (United Kingdom), Svitlana Krakovska (Ukraine), Chaincy Kuo (United States of America), David S. Lee (United Kingdom), Maurice Levasseur (Canada), Martine Lizotte (Canada), Thomas K. Maycock (United States of America), Jean-François Müller (Belgium), Helène Muri (Norway), Lee T. Murray (United States of America), Zebedee R. J. Nicholls (Australia), Jurgita Ovadnevaite (Ireland/Lithuania), Prabir K. Patra (Japan/India), Fabien Paulot (United States of America/France, United States of America), Pallav Purohit (Austria/India), Johannes Quaas (Germany), Joeri Rogelj (United Kingdom /Belgium), Bjørn H. Samset (Norway), Chris Smith (United Kingdom), Izuru Takayabu (Japan), Marianne Tronstad Lund (Norway),Alexandra P. Tsimpidi (Germany/Greece), Steven Turnock United Kingdom), Rita Van Dingenen (Italy/Belgium), Hua Zhang (China), Alcide Zhao (United Kingdom/China)

Review Editors:
Yugo Kanaya (Japan), Michael J. Prather (United States of America), Noureddine Yassaa (Algeria)

Chapter Scientist:
Chaincy Kuo (United States of America)

This Supplementary Material should be cited as:
Naik, V., S. Szopa, B. Adhikary, P. Artaxo, T. Berntsen, W. D. Collins, S. Fuzzi, L. Gallardo, A. Kiendler Scharr, Z. Klimont, H. Liao, N. Unger, P. Zanis, 2021, Short-Lived Climate Forcers Supplementary Material. In: *Climate Change 2021: The Physical Science Basis. Contribution of Working Group I to the Sixth Assessment Report of the Intergovernmental Panel on Climate Change* [Masson-Delmotte, V., P. Zhai, A. Pirani, S. L. Connors, C. Péan, S. Berger, N. Caud, Y. Chen, L. Goldfarb, M. I. Gomis, M. Huang, K. Leitzell, E. Lonnoy, J. B. R. Matthews, T. K. Maycock, T. Waterfield, O. Yelekçi, R. Yu and B. Zhou (eds.)]. Available from https://ipcc.ch/static/ar6/wg1.

Date: August 2021

This document is subject to copy-editing, corrigenda and trickle backs.

ACCEPTED VERSION SUBJECT TO FINAL EDITING

Table of Contents

6.SM.1 Methodology for Emission based ERF 3
6.SM.2 ERF and GSAT timeseries from emulators for individual compounds over the historical period 3
6.SM.3 Regression coefficient of annual mean surface ozone and $PM_{2.5}$ against annual surface temperature change. 5
6.SM.4 Effect on GSAT of a one year pulse of present-day emissions after 20 and 100 years. 7
6.SM.5 Methodology to compute source sector apportionment for surface air pollutants using TM5-FASST 8
6.SM.6 Data Table 11
References 26

ACCEPTED VERSION
SUBJECT TO FINAL EDITING

6.SM.1 Methodology for Emission based ERF

Emission-based ERFs are assessed (Figure 6.12) based on multi-model attribution experiments performed under AerChemMIP (Collins et al., 2017) and analyzed by (Thornhill et al., 2021). The attribution experiments are done with the precursors emissions individually perturbed (except CO and NMVOCs that were done together). Due to the non-linear chemistry and microphysics of the atmosphere, the sum of the emission-based contributions to ERF will not be equal to the concentration-based estimates (Figure 7.6)

The simulations in (Thornhill et al., 2021) are for the 1850-2014, and estimates for the emission-based ERFs have been extrapolated to the full 1750-2019 period based on the updated emission estimates from the 11 September 2020 version of the Community Emissions Data System (CEDS) is used (Hoesly et al., 2018), obtained from https://doi.org/10.5281/zenodo.4025316 (cf 7.SM.1.4)

For the ozone ERF, in the AerChemMIP experiments the methane concentrations have been kept fixed when the individual precursors are perturbed (e.g. NO_x). This means that methane is not governed by its emissions and the atmospheric chemistry. Thus, adjustments have been done to consider the differences between CH_4 concentrations that would have been reached in a free to adjust simulation and a CH_4-fixed simulation. As a consequence of this CH_4 adjustment, a correction has to be applied to all the chemical species which are affected by CH_4 modification, either through chemistry itself (e.g. lifetime) or through stratospheric H_2O changes and cloud changes. Despite these corrections, some non-linear effects in the chemistry can not be fully captured and result in differences between the emission-based radiative forcing and the concentration-based radiative forcing (Figure 7.6 and 7.SM.1.4). So finally, only the proportion of the individual effect is kept from this methodology and applied to the concentration-based ERF which has been determined in a way that allow to consider all the non-linearities.

The emission based ERF estimates for aerosols and aerosol precursors are based on the AerChemMIP simulations (Thornhill et al., 2021). The contribution from aerosol radiation interaction (ari) is calculated as the difference between the total ERF and ERFaci. Thus, the non-cloud adjustments are included as aerosol radiation interaction. For NH_3 emissions ERFaci was not available, the ERF is contributed only to aerosol radiation interaction. As for the ozone precursors, only the proportion of the individual effect is kept from this methodology and applied to the concentration-based ERF .

For CO_2 the fraction of CO_2 in the atmosphere originating from anthropogenic emissions of non-CO_2 emissions must be subtracted from the concentration based estimate. The sum of Carbon emissions over the historical period of CH_4, halocarbons, NMVOC + CO is estimated to be 6.6, 0.02, 26 Gt(C) respectively. This includes a rough assumption that 25%, 0%, 50%, 0% (CH_4, halocarbons, NMVOC, CO) of reactive intermediates such as formaldehyde are lost to deposition. Also assumes that 12% of methane C is still in the atmosphere as methane (Stevenson et al., 2013). Using the (Joos et al., 2013) CO_2 response function to convolve the time profile of emissions gives a rise in CO_2 of 110 ppb that is proportionally subtracted from the CO_2 total.
For the halogenated species, the ERFs for CFCs and HCFCs are taken from Thornhill et al. (2021), and adjusted to include emissions up to 2019. The ERF from HFCs, taken from the concentration-based estimates (7.SM.1.4) are added, neglecting small effects through changes in OH concentrations affecting HFC lifetime.

6.SM.2 ERF and GSAT timeseries from emulators for individual compounds over the historical period

GSAT change in response to ERF from SLCFs has been estimated using an emulator (see cross chapter box 7.1 and 7.SM.2) and presented in Figures 6.12, 6.15, 6.22 and 6.24. The emulator used is an impulse response function (IRF) based on the two-layer energy balance model.
When the ERF time series is known, the response in GSAT at time *t* is given by:

$$GSAT(t) = \int_{t'=0}^{t} ERF(t') \cdot IRF(t - t')dt'$$

Where t'=0 denotes the time when the emission perturbation started, e.g. anthropogenic emissions since 1750.

ACCEPTED VERSION SUBJECT TO FINAL EDITING

The IRF used here has been calibrated according to the procedure given in 7.SM.2, and is given by:

$$IRF(t) = \sum_{j=1}^{J} \frac{c_j}{d_j} \exp\left(-\frac{t}{d_j}\right)$$

where the parameters c_j determine the equilibrium climate response and d_j are timescales of the fast and slow modes of the climate system response, and J=2 here. The parameter values are: d_1 = 3.4 years and d_2 = 285 years, c_1 = 0.44 K/(W m^{-2}) and c_2 = 0.32 K/(W m^{-2}), corresponding to an ECS of 3.0K.

Figure 6.12 shows the historical emission based contributions to GSAT (1750-2019). For this analysis the emission based ERF time series are based on the AerChemMIP simulations (Thornhill et al., 2021), and described in 6.SM.1 and 7.SM.1.4. The emission-based assessment of ERF (6.SM.1) provides ERFs for 2019 relative to 1750, and to establish the ERF time series over the whole historical period, these were scaled back according the historic emissions, i.e. assuming a liner relation between emissions and ERF historically.

Figure 6.15 shows the GSAT response to step emission reductions of idealized climate forcers with different lifetimes. All forcers are assumed to give an ERF of -1.0 Wm^{-2} when a new equilibrium concentration is reached. With this assumption the ERF(t) is given by:

$$ERF(t) = -1.0\, Wm^{-2} \cdot (1 - e^{-\frac{t}{\tau}})$$

Where τ is the atmospheric lifetime of the climate forcer.

Figure 6.22 and 6.24 show the contributions to GSAT from individual SLCFs, or groups of SLCFs, with an abundance-based perspective. The ERF time series are from the assessment of chapter 7 of this report and details are given in 7.SM.1.4.

ACCEPTED VERSION
SUBJECT TO FINAL EDITING

6.SM.3 Regression coefficient of annual mean surface ozone and $PM_{2.5}$ against annual surface temperature change.

[START FIGURE 6.SM.1 HERE]

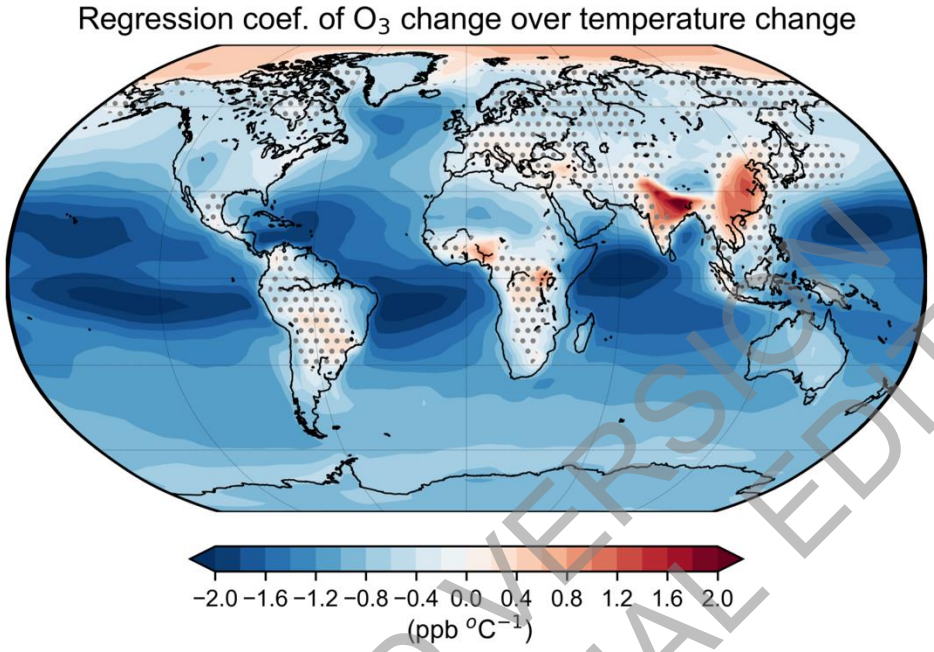


Figure 6.SM.1: Spatial pattern of the regression coefficient of annual surface ozone change (ssp370SST-ssp370pdSST) over annual surface temperature change (ssp370SST-ssp370pdSST) (ppb $^{o}C^{-1}$) during the time period from 2015 to 2100, for the CMIP6 ensemble average (GFDL-ESM4, GISS-E2-1-G, MRI-ESM2-0, UKESM1-0-LL). Regions without dots indicate that modelled regression coefficients are statistically significant (at the 95% significance level) and agree on the sign for at least three out of four models.

[END FIGURE 6.SM.1 HERE]

ACCEPTED VERSION SUBJECT TO FINAL EDITING

[START FIGURE 6.SM.2 HERE]

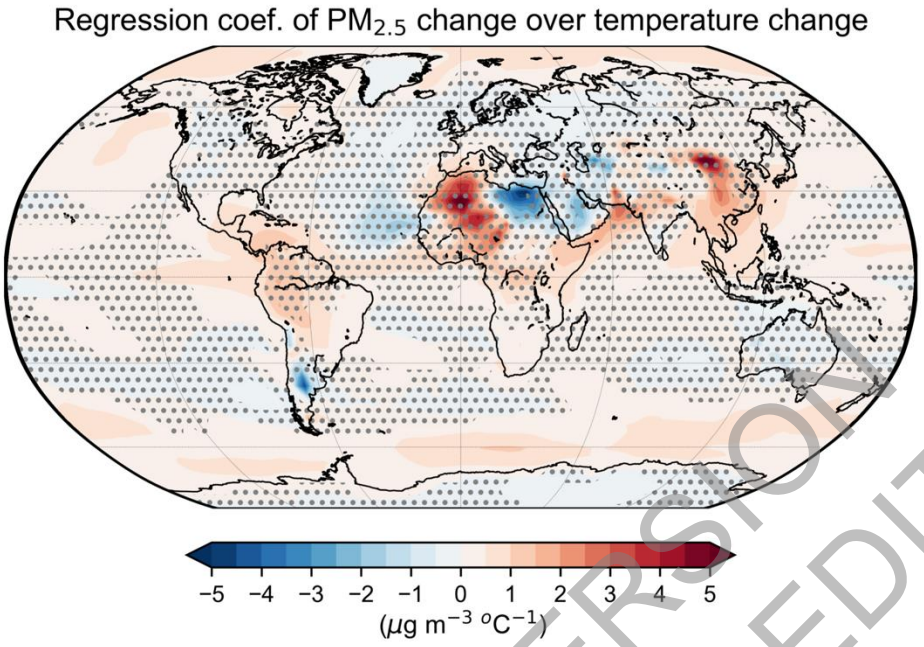


Figure 6.SM.2: Spatial pattern of the regression coefficient of annual surface $PM_{2.5}$ concentrations change (ssp370SST-ssp370pdSST) over annual surface temperature change (ssp370SST-ssp370pdSST) (μg m^{-3} $^{o}C^{-1}$) during the time period from 2015 to 2100, for the CMIP6 ensemble average (GFDL-ESM4, GISS-E2-1-G, MRI-ESM2-0). Regions without dots indicate that modelled regression coefficients are statistically significant (at the 95% significance level) and agree on the sign for at least two out of three models.

[END FIGURE 6.SM.2 HERE]

ACCEPTED VERSION SUBJECT TO FINAL EDITING

6.SM.4 Effect on GSAT of a one year pulse of present-day emissions after 20 and 100 years.

[START FIGURE 6.SM.3 HERE]

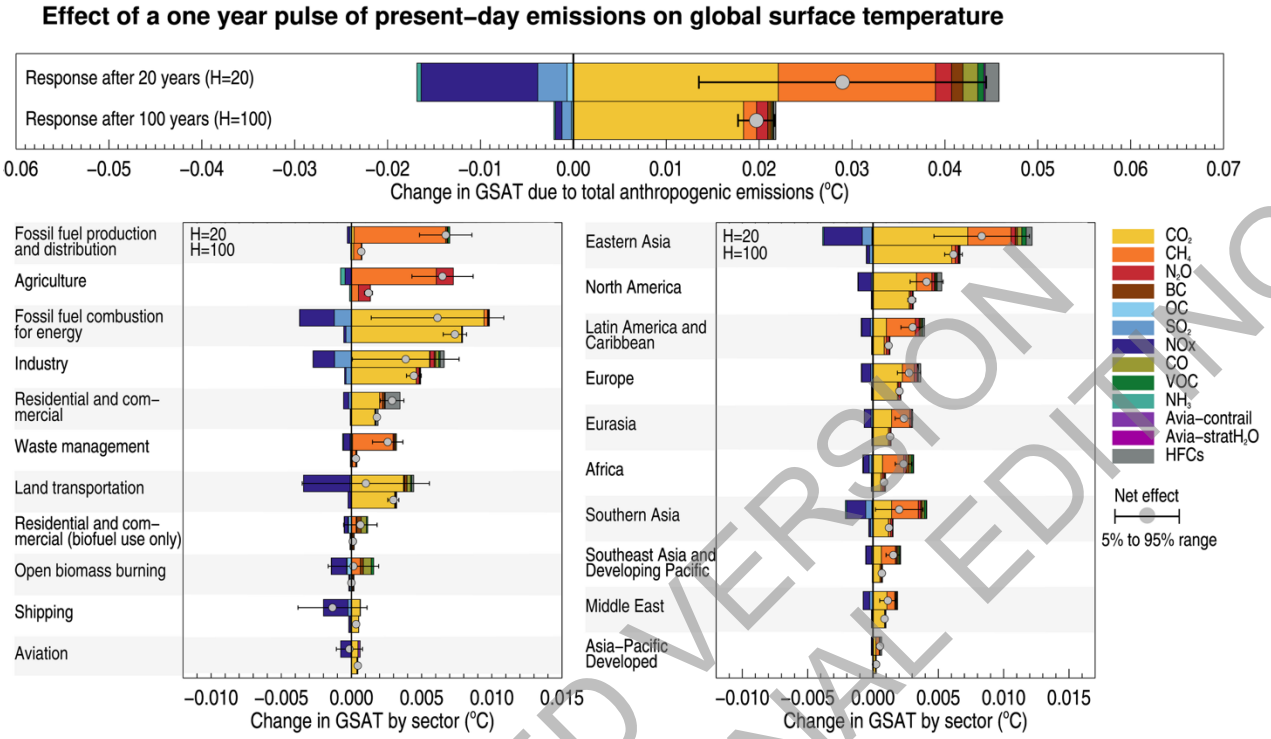


Figure 6.SM.3: Global-mean temperature response 20 and 100 years following one year of present-day (year 2014) emissions.

[END FIGURE 6.SM.3 HERE]

The temperature responses in Figure 6.16 and 6.SM.3 were calculated using the concept of absolute global temperature change potential (AGTP) (Shine et al., 2005), i.e., an emission-metric-based emulator of the climate response to individual emitted species. The approach and further details are documented in Lund et al. (2020). The emissions were taken from the Community Emissions Data System (CEDS) for year 2014 (Hoesly et al., 2018), with the exceptions of HFCs, which originate from Purohit et al. (2020) and consider HFCs with a lifetime shorter than 50 years, open biomass burning from van Marle et al. (2017), and aviation water vapour from Lee et al. (2020). The split between fossil fuel and biofuel emissions in the residential sector, and between the fossil fuel production and distribution and combustion in the energy sector, is based on the GAINS model (ECLIPSE version 6b dataset: https://iiasa.ac.at/web/home/research/researchPrograms/air/Global_emissions.html). CO_2 emissions are excluded from open biomass burning and residential biofuel use due to their unavailability in CEDS and uncertainties around non-sustainable emission fraction.

Aviation specific AGTPs have been calculated for Figure 6.SM.3 using the method described in Lund et al. (2020) and the best estimate radiative forcing values from Lee et al. (2020). For the HFCs , the AGTPs were derived from Hodnebrog et al. (2020). The AGTPs of BC, SO_2 and OC account for the direct aerosol effect due to aerosol-radiation interactions and are scaled to account for the semi-direct of BC due to rapid adjustments and indirect radiative forcing through aerosol-cloud interactions of sulfate aerosols, respectively. All AGTPs used in the temperature response calculations now include a carbon-climate feedback term based on the framework by Gasser et al. (2017), except those for HFCs. Avia-contrail refers to the impact from linear contrail formation and subsequent spreading to cirrus clouds and Avia-stratH_2O to the direct impact of aircraft water vapour emissions.

ACCEPTED VERSION SUBJECT TO FINAL EDITING

The error bars show the range (5-95% interval) in net temperature impact due to uncertainty in radiative forcing *only*. This uncertainty range is calculated using a Monte Carlo approach and estimates of uncertainties in global-mean RF of individual species from the literature - see Lund et al. (2020) for details. The uncertainty in the RF of individual halocarbons was not included due to lack of available data.

The AGTP applies an impulse response function (IRF) to calculate the temperature response as a function of time to a given forcing. The IRF is given by:

$$IRF(t) = \sum_{j=1}^{J} \frac{c_j}{d_j} \exp\left(-\frac{t}{d_j}\right)$$

where c_j and d_j are constants and timescales of the fast and slow model of the climate system response, respectively, and j=2 here. The IRF used in Lund et al. (2020) is based on Geoffroy et al. (2013), which yields d_1 = 4.1 years and d_2 = 249 years, c_1 = 0.519 K/(Wm^{-2}) and c_2 = 0.365 K/(Wm^{-2}), corresponding to an ECS of 3.5K. Note that the IRF used for calculations of GSAT for figures 6.12, 6.15, 6.22 and 6.24 use an IRF calibrated to the assessment of ECS and TCR as given in Chapter 7 of this report, and thus use slightly different values for the c_j and d_j constants (see 6.SM.2).

6.SM.5 Methodology to compute source sector apportionment for surface air pollutants using TM5-FASST

Here we provide description of the methodology used to calculate the source sector apportionment for $PM_{2.5}$ and ozone (Figure 6.17). Furthermore, Figures 6.SM4 and 6.SM.5 show a comparison of TM5-FASST and ESM models responses to changes in emissions of $PM_{2.5}$ precursors and ozone.

TM5-FASST is a reduced-form source-receptor model, describing the surface level spatial response of a pollutant metric (concentration, exposure, deposition) to changes in precursor emissions. The model is constructed from pre-computed emission-concentration transfer matrices between pollutant source regions and receptor regions. These matrices reflect underlying meteorological and chemical atmospheric processes for a predefined set of meteorological and emission data and have the advantage that concentration responses to emission changes are obtained by a simple matrix multiplication, avoiding expensive numerical computations.

TM5-FASST's source-receptor matrices have been derived with the chemistry-transport model TM5, by applying 20% emission perturbations on a reference emission set (RCP year 2000, year 2001 meteorology) for individual precursors and 56 source regions. The total concentration of component (or metric) *j* in receptor region *y*, resulting from given emissions *E* of *all* n_i precursors *i* at *all* n_x source regions *x*, is obtained as a perturbation on the base-simulation concentration, by summing up all the respective source-receptor coefficients A, scaled with the actual emission perturbation:

$$C_j(y) = C_{j,\mathrm{ref}}(y) + \sum_{k=1}^{n_x} \sum_{i=1}^{n_i} A_{ij}[x_k, y] \cdot \left[E_i(x_k) - E_{i,\mathrm{ref}}(x_k)\right] \quad (1)$$

where $A_{ij}[x_k, y] = \frac{\Delta C_{j,ref}(y)}{0.2 E_{i,\mathrm{ref}}(x_k)}$, the pre-computed source-receptor coefficient for source region x_k to receptor region *y*, for precursor i contributing to metric/pollutant j. The computational efficiency from the linearized emission-concentration sensitivities comes at some cost of accuracy, in particular because the model bypasses underlying mechanisms describing chemical and meteorological feedback processes that could lead to non-linear responses.

TM5-FASST computes $PM_{2.5}$ concentrations from precursor emissions of SO_2, NO_x, NH_3, elemental carbon and particulate organic matter. Secondary organic matter from anthropogenic emissions is not included. Ozone concentrations and long-term exposure metrics are computed from NO_x, non-methane volatile organic compounds (NMVOC) and methane precursor emissions. CO as ozone precursor is not included. The methane-ozone response is assumed to be instantaneous, neglecting the 11 year response time (Fiore et al.,

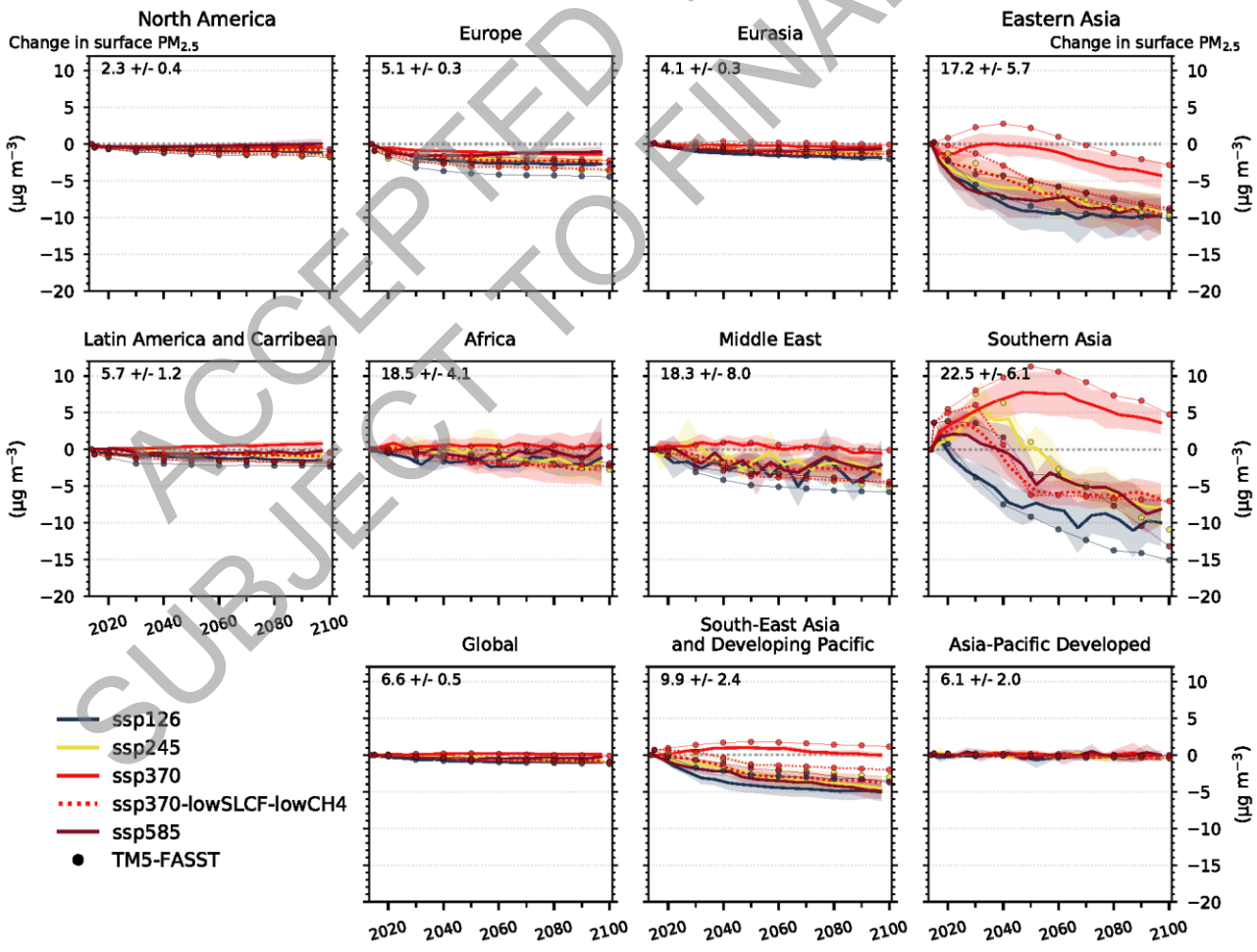
ACCEPTED VERSION SUBJECT TO FINAL EDITING

2008)

The computational efficiency of TM5-FASST allows for multiple runs exploring source attribution by region or emission source. We estimate the relative contribution of individual emission sectors shown in Figure 6.17 by subtracting their emissions one by one from the total emissions in Eq. (1) and computing the resulting concentration. Subtracting this result from the total concentration (Eq. 1) yields each sector's contribution (Karagulian et al., 2016).

TM5-FASST has been extensively documented and evaluated by (Van Dingenen et al., 2018). The model has been applied in a variety of assessment studies (e.g., Aakre et al., 2018; Brauer et al., 2016; Crippa et al., 2019; Harmsen et al., 2020; Kühn et al., 2020; Markandya et al., 2018; Rao et al., 2017; Rauner et al., 2020; Vandyck et al., 2020). Validation studies in Van Dingenen et al. (2018) show that, despite inherent simplifications and caveats, large scale $PM_{2.5}$ and O_3 responses to emission changes in TM5-FASST compare well with the chemical transport model TM5. Figure 6.SM.4 and 6.SM.5 compare TM5-FASST regional $PM_{2.5}$ and O_3 responses to emission changes with the ensemble of ESM models for selected SSP scenarios. In nearly all cases TM5-FASST results fall within ±1 standard deviation of the CMIP6 ESM ensemble. Notable differences are observed for the SSP scenarios and regions representing more extreme emission changes (in particular for the low emission scenarios in Southern Asia). As documented by Van Dingenen et al. (2018), both for $PM_{2.5}$ and O_3 the differences with full process models can be attributed to non-linear responses to NO_x emission reductions that are not captured by the linearized source-receptor model.

[START FIGURE 6.SM.4 HERE]



ACCEPTED VERSION SUBJECT TO FINAL EDITING

Figure 6.SM.4: Future global and regional changes in annual mean surface $PM_{2.5}$, relative to 2005-2014 mean, for the different SSPs used in CMIP6. Each line represents a multi-model mean across the region with shading representing the ± 1 standard deviation in the mean. Dots represent TM5-FASST results. The multi-model regional mean value (± 1 standard deviation) for the year 2005-2014 is shown in the top left corner of each panel.

[END FIGURE 6.SM.4 HERE]

[START FIGURE 6.SM.5 HERE]

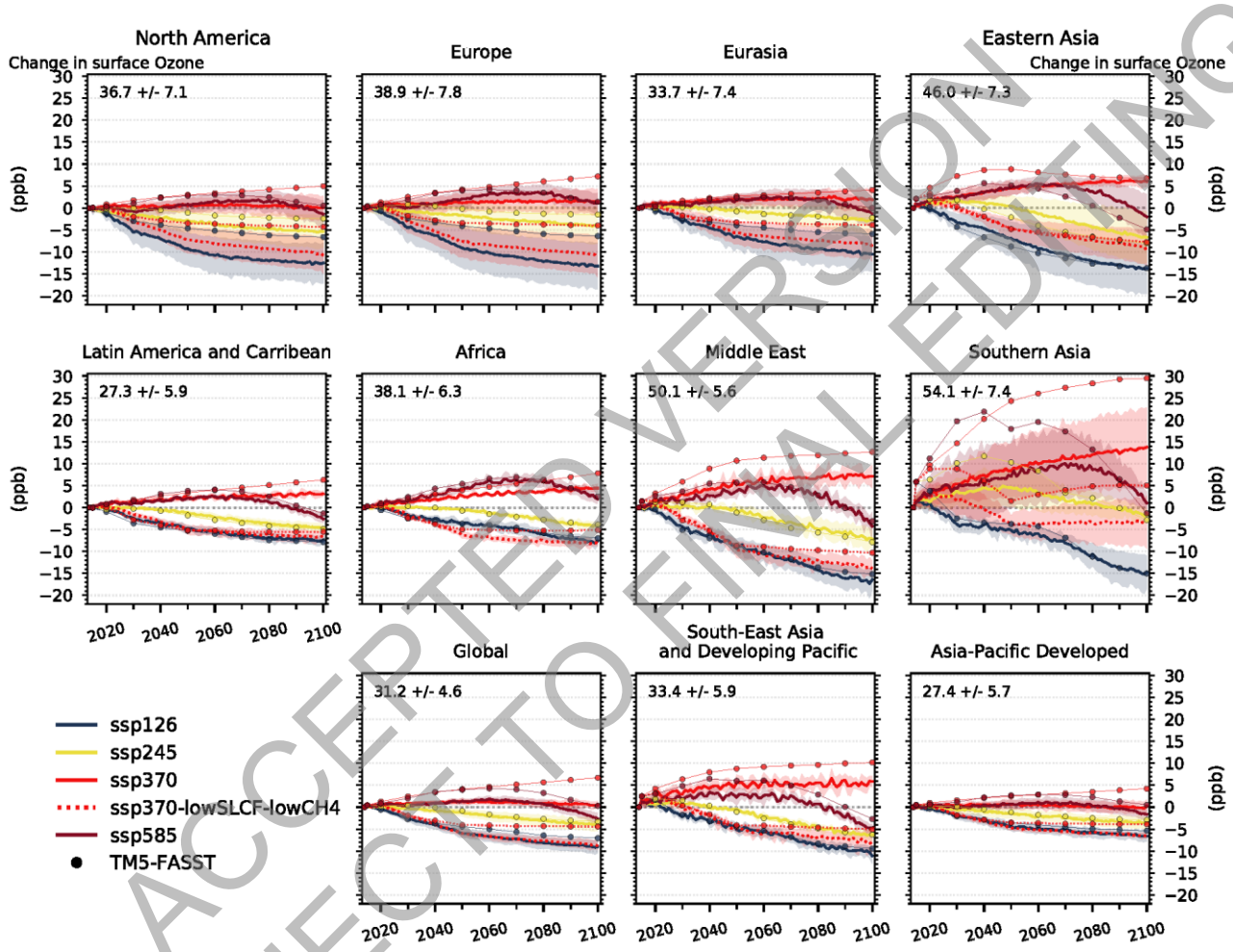


Figure 6.SM.5: Future global and regional changes in annual mean surface O3, relative to 2005-2014 mean, for the different SSPs used in CMIP6. Each line represents a multi-model mean across the region with shading representing the ± standard deviation in the mean. Dots represent TM5-FASST results. The multi-model regional mean value (± 1 standard deviation) for the year 2005-2014 is shown in the top left corner of each panel.

[END FIGURE 6.SM.5 HERE]

ACCEPTED VERSION SUBJECT TO FINAL EDITING

6.SM.6 Data Table

[START TABLE 6.SM.1 HERE]

Table 6.SM.1: Input Data Table. Input datasets and code used to create chapter figures.

Figure number/Table number/Chapter section (for calcuations)	Dataset name	Type of dataset	Filename	License type	Dataset citation	Dataset DOI/URL	Citation for relevant papers
Figure 6.3	Community Emissions Data System (CEDS)	Input dataset		Public	(Hoesly et al., 2018)	http://www.globalchange.umd.edu/ceds/	
Figure 6.4	CMIP6, ScenarioMIP, Tropospheric Ozone Assessment Report (TOAR), Atmospheric Chemistry and Climate Model Intercomparison Project (ACCMIP)	Input dataset	CMIP6 Models UKESM1-LL-0, CESM2-WACCM, GFDL-ESM4, MRI-ESM2-0,GISS-E2.1-G. Experiments : Historical experiment, ssp370	public	(Eyring et al., 2016; O'Neill et al., 2016)	https://esgf-node.llnl.gov/search/cmip6/	(Young et al., 2013, 2018; DuplicateGriffiths et al., 2020)
	Observational datasets TOST, IASI-FORLI, IASI-OFRID,OMI/MLS, OMI-SAI, OMI-RAL:	Input dataset		public		https://doi.org/10.1525/elementa.291.t1	(Gaudel et al., 2018)

ACCEPTED VERSION SUBJECT TO FINAL EDITING

	CMIP6 model data						
	CESM2-WACCM: historical, ssp370	Input dataset			(Danabasoglu, 2019b, 2019c)		
	GFDL-ESM4: esm-hist, historical, ssp370	Input dataset			(John et al., 2018c; Krasting et al., 2018b, 2018a)		
	GISS-E2-1-G: historical, ssp370	Input dataset			(NASA Goddard Institute for Space Studies (NASA/GISS), 2018, 2020h)		
	MRI-ESM2-0: historical, ssp370	Input dataset			(Yukimoto et al., 2019g, 2019c)		
	UKESM1-0-LL: historical, ssp370	Input dataset			(Good et al., 2019c; Tang et al., 2019)		
Figure 6.5	IAGOS-CORE	Input dataset	decadal	public	(Gaudel et al., 2020)	http://www.iagos-data.fr/portal.html#TimeseriesPlace:	(Cooper et al., 2020)
Figure 6.6	Merged GOME/SCIAMACHY/GOME-2 (TM4NO2A	Input dataset	GOME_SCIAMACHY_GOME2ab_TroposNO2_v2.3_041996-092017_temis.nc	public		http://www.temis.nl/airpollution/no2.html	(Georgoulias et al., 2019)

ACCEPTED VERSION SUBJECT TO FINAL EDITING

	version 2.3)						
Figure 6.7	EPA $PM_{2.5}$ aerosol component	Input dataset	Monthly-average 2000-2018	public		https://aqs.epa.gov/aqsweb/airdata/download_files.html.	(Solomon et al., 2014)
	IMPROVE aerosol	Input dataset	Monthly-average daily 2000-2018	public		http://views.cira.colostate.edu/fed/QueryWizard/Default.aspx	
	EMEP $PM_{2.5}$ aerosol component	Input dataset	Monthly-average 2000-2018	public		https://www.emep.int/	
	Network Center for EANET, EANET Data on the Acid Deposition in the East Asian Region, $PM_{2.5}$ aerosol component	Input dataset	Monthly-average 2001-2017	public		https://www.eanet.asia/document/public/index	
	SPARTAN $PM_{2.5}$ aerosol component	Input dataset	Monthly-average 2013-2019	public		https://www.spartan-network.org/	(Snider et al., 2015)
	observational field campaigns $PM_{2.5}$ aerosol component over Latin America and Caribbean, Africa, Europe, Eastern Asia, and Asia-Pacific Developed	Input dataset		public			(Celis et al., 2004; Feng et al., 2006; Mariani and de Mello, 2007; Molina et al., 2007, 2010; Bourotte et al., 2007; Fuzzi et al., 2007; Mkoma, 2008; Favez et al., 2008; Aggarwal and Kawamura, 2009; Mkoma et al., 2009; Li et al., 2010; Martin et al., 2010; Radhi et al., 2010; Weinstein et

ACCEPTED VERSION SUBJECT TO FINAL EDITING

							al., 2010; de Souza et al., 2010; Batmunkh et al., 2011; Pathak et al., 2011; Gioda et al., 2011; Zhang et al., 2012; Zhao et al., 2013; Cho and Park, 2013; Wang et al., 2019; Kuzu et al., 2020)
		Intermediate dataset				Code to be placed in https://github.com/IPCC-WG1	
Figure 6.8	CMIP6 Ambient Aerosol Optical Thickness at 550nm	Input dataset Annual average	historical experiment, Models ACCESS-CM2, BCC-ESM1, CESM2-FV2,CESM2-WACCM,CESM2,CNRM-CM6-1,CNRM-EMS2-1,CanESM5,E3SM-1-0,GFDL-CM4,GFDL-ESM4,GISS-E2-1-G,HadGEM3-GC31-LL,INM-CM4-8,IPSL-CM6A-LR,KACE-1-0-G,MIROC-ES2L,MPI-ESM-1-2,MPI-ESM1-2-HR,MPI-ESM1-2-LR,MRI-ESM2-0,NorESM2-LM,UKESM1-0-LL		(Eyring et al., 2016; O'Neill et al., 2016)		
Figure 6.9	CMIP6, mole fraction hydroxyl in air	Input dataset Decadal average	Models UKESM1-0LL, GFDL-ESM4, CESM2-WACCM	public	(Eyring et al., 2016)	https://esgf-node.llnl.gov/search/cmip6/	(Montzka et al., 2011; Rigby et al., 2017; Turner et al., 2017;

ACCEPTED VERSION SUBJECT TO FINAL EDITING

							Nicely et al., 2018; Naus et al., 2019; Patra et al., 2021)
	CMIP6 model data						
	CESM2-WACCM: historical	Input dataset			(Danabasoglu, 2019b)		
	GFDL-ESM4: historical	Input dataset			(Krasting et al., 2018b)		
	UKESM1-0-LL: historical	Input dataset			(Tang et al., 2019)		
Figure 6.10	CMIP6: AerChemMIP experiments histSST and histSST-piAer. Output variable rsut and rlut	Input dataset Averaged from monthly output	Models, MIROC6, MPI-I-ESM-1-2-HAM,GISS-E2-1-G, NorESM2-LM, MRI-ESM2-0, GFDL-ESM4, UKESM-0-LL	public	(Eyring et al., 2016; Collins et al., 2017)	https://esgf-node.llnl.gov/search/cmip6/	(Myhre et al., 2013)
		Intermediate dataset				Code to be placed in https://github.com/IPCC-WG1 TBD	
	CMIP6 model data						
	GFDL-ESM4: histSST, histSST-piAer	Input dataset			(Horowitz et al., 2018b, 2018a)		
	GISS-E2-1-G: histSST, histSST-piAer	Input dataset			(NASA Goddard Institute for Space Studies (NASA/GISS), 2019a, 2019b)		

ACCEPTED VERSION SUBJECT TO FINAL EDITING

	MIROC6: histSST, histSST-piAer	Input dataset			(Takemura, 2019a, 2019b)		
	MPI-ESM-1-2-HAM: histSST, histSST-piAer	Input dataset			(Neubauer et al., 2019b, 2019a)		
	MRI-ESM2-0: histSST, histSST-piAer	Input dataset			(Yukimoto et al., 2019a, 2020a)		
	NorESM2-LM: histSST, histSST-piAer	Input dataset			(Oliviè et al., 2019b, 2019a)		
	UKESM1-0-LL: histSST, histSST-piAer	Input dataset			(O'Connor, 2019b, 2019a)		
Figure 6.11	CMIP6: AerChemMIP experiments histSST and histSST-piAer. Output variable rsut and rlut	Input dataset Averaged from monthly output	Models, MIROC6, MPI-I-ESM-1-2-HAM,GISS-E2-1-G, NorESM2-LM, MRI-ESM2-0, GFDL-ESM4, UKESM-0-LL	public	(Eyring et al., 2016; Collins et al., 2017)	https://esgf-node.llnl.gov/search/cmip6/ Code to be placed in https://github.com/IPCC-WG1 TBD	(Myhre et al., 2013)
	Data citations						
	GFDL-ESM4: histSST, histSST-piAer	Input dataset			(Horowitz et al., 2018b, 2018a)		
	GISS-E2-1-G: histSST, histSST-piAer	Input dataset			(NASA Goddard Institute for Space Studies (NASA/GISS), 2019a,		

ACCEPTED VERSION SUBJECT TO FINAL EDITING

					2019b)		
	MIROC6: histSST, histSST-piAer	Input dataset			(Takemura, 2019a, 2019b)		
	MPI-ESM-1-2-HAM: histSST, histSST-piAer	Input dataset			(Neubauer et al., 2019b, 2019a)		
	MRI-ESM2-0: histSST, histSST-piAer	Input dataset			(Yukimoto et al., 2019a, 2020a)		
	NorESM2-LM: histSST, histSST-piAer	Input dataset			(Oliviè et al., 2019b, 2019a)		
	UKESM1-0-LL: histSST, histSST-piAer	Input dataset			(O'Connor, 2019b, 2019a)		
Figure 6.12	CMIP6,	Input dataset			(Eyring et al., 2016)	https://esgf-node.llnl.gov/search/cmip6/ Code to be placed in https://github.com/IPCC-WG1 TBD	(Ghan, 2013; DuplicateThornhill et al., 2021)
Figure 6.13	CMIP6: AerChemMIP experiments historical and hist-piAer. Output variable tas	Intermediate dataset	Models MIROC6, MRI-ESM2-0, NorESM2-LM, GFDL-ESM4, GISS-E2-1-G, UKESM1-0-LL.		(Eyring et al., 2016; Collins et al., 2017)	Code to be placed in https://github.com/IPCC-WG1 TBD	
Figure 6.14	CMIP6 historical experiment, AerChemMIP experiments ssp370 ssp370SST, ssp370pdSST experiments.	Input dataset Monthly mean	Models GFDL-ESM4, GISS-E2-1-G,MRI-ESM2-0,UKESM1-0-LL	public	(Eyring et al., 2016; Collins et al., 2017)	https://esgf-node.llnl.gov/search/cmip6/ Code to be placed in https://github.com/IPCC-WG1 TBD	

ACCEPTED VERSION SUBJECT TO FINAL EDITING

	Output variables o3, tas						
	Data citations						
	GFDL-ESM4: ssp370SST, ssp370pdSST	Input dataset			(Horowitz et al., 2018c, 2018d)		
	GISS-E2-1-G: ssp370SST, ssp370pdSST	Input dataset			(NASA Goddard Institute for Space Studies (NASA/GISS), 2020b, 2020a)		
	MRI-ESM2-0: ssp370SST, ssp370pdSST	Input dataset			(Yukimoto et al., 2019b, 2020b)		
	UKESM1-0-LL: ssp370pdSST, ssp370SST	Input dataset			(O'Connor , 2020b, 2020a)		
Figure 6.15	CMIP6, ScenarioMIP experiments ssp370SST, ssp370pdSST Mole fraction of ozone	Input dataset OUTPUT DATA FREQUENCY	Models GFDL-ESM4, GISS-E2-1-G, MRI-ESM2-0, UKESM1-0-LL	public	(Eyring et al., 2016; O'Neill et al., 2016)	https://esgf-node.llnl.gov/search/cmip6/	
Figure 6.16	CMIP6, ScenarioMIP experiments ssp370SST, ssp370pdSST	Input dataset OUTPUT DATA FREQUENCY	CMIP6 models GFDL-ESM4, GISS-E2-1-G, MRI-ESM2-0 and UKESM1-0-LL	public	(Eyring et al., 2016; O'Neill et al., 2016)	https://esgf-node.llnl.gov/search/cmip6/	

ACCEPTED VERSION SUBJECT TO FINAL EDITING

Figure 6.17	CMIP6, ScenarioMIP Mole fraction of ozone	Input dataset Intermediate data	GFDL-ESM4, BCC-ESM1, CESM2-WACCM and UKESM1-0-LL for ssp370, GFDL-ESM4, BCC-ESM1, and CESM2-WACCM for ssp370-lowNTCF, GFDL-ESM4 and UKESM1-0-LL for SSP1-2.6, SSP2-4.5 and SSP5-8.5	public	(Eyring et al., 2016; O'Neill et al., 2016)	https://esgf-node.llnl.gov/search/cmip6/	
Figure 6.20 **Figure 6.21**	GEIA/ACCENT gridded emissions	Input dataset		public		http:// geiacenter.org	(Lamarque et al., 2010)
	Community Emissions Data System (CEDS) for Historical Emissions	Input dataset		public	(van Marle et al., 2017; Hoesly et al., 2018)	http://www.globalchange.umd.edu/ceds/ http://esgf-node.llnl.gov/search/input4mips/	
	SSP Database (Shared Socioeconomic Pathways) - Version 2.0,	Input dataset		public	(Riahi et al., 2017; Rogelj et al., 2018; Gidden et al., 2019)	https://tntcat.iiasa.ac.at/SspDb/dsd	
	Representative Concentration Pathway (RCP) database	Input dataset		public	(van Vuuren et al., 2011)	ttps://tntcat.iiasa.ac.at/RcpDb/dsd	
		Intermediate dataset				https://github.com/gidden/ar6-wg1-ch6-emissions Code to be placed in https://github.com/IPCC-WG1	
	CMIP6 model data in Figure 6.20						
	BCC-ESM1: ssp370, ssp370-lowNTCF, historical	Input dataset			(Zhang et al., 2018, 2019b, 2019a)		
	CESM2-WACCM: ssp370-lowNTCF, historical, ssp370	Input dataset			(Danabasoglu, 2019a, 2019b,		

ACCEPTED VERSION SUBJECT TO FINAL EDITING

					2019c)		
	GFDL-ESM4: ssp370-lowNTCF, historical, ssp126, ssp245, ssp370, ssp585	Input dataset			(Horowitz et al., 2018a; John et al., 2018c, 2018d, 2018a, 2018b; Krasting et al., 2018b)		
	GISS-E2-1-G: historical, ssp126, ssp245, ssp370, ssp370-lowNTCF, ssp585	Input dataset			(NASA Goddard Institute for Space Studies (NASA/GISS), 2018, 2020i, 2020g, 2020e, 2020f, 2020h)		
	MRI-ESM2-0: historical, ssp126, ssp245, ssp370, ssp370-lowNTCF, ssp585	Input dataset			(Yukimoto et al., 2019d, 2019h, 2019f, 2019e, 2019g, 2019c)		
	UKESM1-0-LL: ssp370-lowNTCF, historical, ssp126, ssp245, ssp370, ssp585	Input dataset			(Good et al., 2019a, 2019d, 2019c, 2019b; Tang et al., 2019; Byun,		

ACCEPTED VERSION SUBJECT TO FINAL EDITING

					2020)		
	CMIP6 model data in Figure 6.21						
	BCC-ESM1: ssp370, ssp370-lowNTCF, historical	Input dataset			(Zhang et al., 2018, 2019b, 2019a)		
	CESM2-WACCM: ssp370-lowNTCF, historical, ssp370	Input dataset			(Danabasoglu, 2019a, 2019b, 2019c)		
	CNRM-ESM2-1: ssp370-lowNTCF, historical, ssp370	Input dataset			(Seferian, 2018, 2019; Voldoire, 2019)		
	GFDL-ESM4: ssp370-lowNTCF, historical, ssp126, ssp245, ssp370, ssp585	Input dataset			(Horowitz et al., 2018a; John et al., 2018c, 2018d, 2018a, 2018b; Krasting et al., 2018b)		
	GISS-E2-1-G: ssp370-lowNTCF, historical, ssp126, ssp245, ssp370, ssp585	Input dataset			(NASA Goddard Institute for Space Studies (NASA/GISS), 2018, 2020i, 2020g, 2020f, 2020a, 2020h)		
	HadGEM3-GC31-	Input			(Good,		

ACCEPTED VERSION SUBJECT TO FINAL EDITING

	LL: historical, ssp126, ssp245, ssp585	dataset			2019, 2020b, 2020a; Ridley et al., 2019)		
	MIROC-ES2L: historical, ssp126, ssp245, ssp370, ssp585	Input dataset			(Hajima et al., 2019; Tachiiri et al., 2019a, 2019b, 2019d, 2019c)		
	MPI-ESM-1-2-HAM: ssp370-lowNTCF, historical, ssp370	Input dataset			(Neubauer et al., 2019b, 2019a)		
	MRI-ESM2-0: ssp370-lowNTCF, historical, ssp126, ssp245, ssp370, ssp585	Input dataset			(Yukimoto et al., 2019h, 2019f, 2019e, 2019g, 2019c, 2019a)		
Figure 6.22	NorESM2-LM: ssp370-lowNTCF, historical, ssp126, ssp245, ssp370, ssp585	Input dataset			(Oliviè et al., 2019; Seland et al., 2019e, 2019d, 2019c, 2019b, 2019a)	https://esgf-node.llnl.gov/search/cmip6/	
Figure 6.23	UKESM1-0-LL: ssp370-lowNTCF, historical, ssp126, ssp245, ssp370, ssp585	Input dataset			(Good et al., 2019a, 2019d, 2019c, 2019b; Tang et al., 2019;	https://esgf-node.llnl.gov/search/cmip6/	

ACCEPTED VERSION
SUBJECT TO FINAL EDITING

					Byun, 2020)		
Figure 6.24	CMIP6, AerChemMIP Output variable rsut and rlut, monthly output ssp370SST and ssp370SST-lowNTCF	Input dataset	BCC-ESM1, CNRM-ESM2-1, CESM2-WACCM, and GFDL-ESM4.	public	(Eyring et al., 2016; Collins et al., 2017)	https://esgf-node.llnl.gov/search/cmip6/	
Figure 6.25	ScenarioMIP, RCMIP Emulator output	Input dataset		public	(Eyring et al., 2016; O'Neill et al., 2016; Nicholls et al., 2020)	https://esgf-node.llnl.gov/search/cmip6/	(Geoffroy et al., 2013)
Figure 6.26	ScenarioMIP Emulator output	Input dataset		public	(O'Neill et al., 2016)	https://esgf-node.llnl.gov/search/cmip6/	(DuplicateLund et al., 2020)
Figure 6.27	ScenarioMIP Emulator output	Input dataset		public	(O'Neill et al., 2016)	https://esgf-node.llnl.gov/search/cmip6/	
Figure 6.25 FGD						https://tntcat.iiasa.ac.at/SspDb/dsd	
Figure	**CMIP6 model data**						

ACCEPTED VERSION SUBJECT TO FINAL EDITING

6.SM.1	GFDL-ESM4: ssp370SST, ssp370pdSST	Input dataset			(Horowitz et al., 2018c, 2018d)		
	GISS-E2-1-G: ssp370SST, ssp370pdSST	Input dataset			(NASA Goddard Institute for Space Studies (NASA/GISS), 2020d, 2020c)		
	MRI-ESM2-0: ssp370SST, ssp370pdSST	Input dataset			(Yukimoto et al., 2019b, 2020b)		
	UKESM1-0-LL: ssp370pdSST, ssp370SST	Input dataset			(O'Connor, 2020c, 2020b)		
Figure 6.SM.2	CMIP6 model data						
	GFDL-ESM4: ssp370SST, ssp370pdSST	Input dataset			(Horowitz et al., 2018c, 2018d)		
	GISS-E2-1-G: ssp370SST, ssp370pdSST	Input dataset			(NASA Goddard Institute for Space Studies (NASA/GISS), 2020d, 2020c)		
	MRI-ESM2-0: ssp370SST, ssp370pdSST	Input dataset			(Yukimoto et al., 2019b, 2020b)		

ACCEPTED VERSION
SUBJECT TO FINAL EDITING

	UKESM1-0-LL: ssp370pdSST, ssp370SST	Input dataset			(O'Connor, 2020c, 2020b)		
Figure 6.SM.4	CMIP6 model data						
	GFDL-ESM4: ssp370-lowNTCFCH4	Input dataset			(Horowitz et al., 2018b)		
	GISS-E2-1-G: ssp370-lowNTCFCH4	Input dataset			(NASA Goddard Institute for Space Studies (NASA/GISS), 2020b)		
	MRI-ESM2-0: ssp370-lowNTCFCH4	Input dataset			(Yukimoto et al., 2020a)		
	UKESM1-0-LL: ssp370-lowNTCFCH4	Input dataset			(O'Connor, 2020a)		

[END TABLE 6.SM.6 HERE]

ACCEPTED VERSION
SUBJECT TO FINAL EDITING

References

Aakre, S., Kallbekken, S., Van Dingenen, R., and Victor, D. G. (2018). Incentives for small clubs of Arctic countries to limit black carbon and methane emissions. *Nat. Clim. Chang.* doi:10.1038/s41558-017-0030-8.

Brauer, M., Freedman, G., Frostad, J., van Donkelaar, A., Martin, R. V, Dentener, F., et al. (2016). Ambient Air Pollution Exposure Estimation for the Global Burden of Disease 2013. *Environ. Sci. Technol.* 50, 79–88. doi:10.1021/acs.est.5b03709.

Collins, W. J., Lamarque, J. F., Schulz, M., Boucher, O., Eyring, V., Hegglin, I. M., et al. (2017). AerChemMIP: Quantifying the effects of chemistry and aerosols in CMIP6. *Geosci. Model Dev.* 10, 585–607. doi:10.5194/gmd-10-585-2017.

Crippa, M., Janssens-Maenhout, G., Guizzardi, D., Van Dingenen, R., and Dentener, F. (2019). Contribution and uncertainty of sectorial and regional emissions to regional and global PM$_{2.5}$ health impacts. *Atmos. Chem. Phys.* 19, 5165–5186. doi:10.5194/acp-19-5165-2019.

Fiore, A. M., West, J. J., Horowitz, L. W., Naik, V., and Schwarzkopf, M. D. (2008). Characterizing the tropospheric ozone response to methane emission controls and the benefits to climate and air quality. *J. Geophys. Res. Atmos.* doi:10.1029/2007JD009162.

Fuglestvedt, J. S., Shine, K. P., Berntsen, T., Cook, J., Lee, D. S., Stenke, A., et al. (2010). Transport impacts on atmosphere and climate: Metrics. *Atmos. Environ.* 44, 4648–4677. doi:10.1016/j.atmosenv.2009.04.044.

Gasser, T., Peters, G. P., Fuglestvedt, J. S., Collins, W. J., Shindell, D. T., and Ciais, P. (2017). Accounting for the climate–carbon feedback in emission metrics. *Earth Syst. Dyn.* 8, 235–253. doi:10.5194/esd-8-235-2017.

Geoffroy, O., Saint-Martin, D., Olivié, D. J. L., Voldoire, A., Bellon, G., and Tytéca, S. (2013). Transient Climate Response in a Two-Layer Energy-Balance Model. Part I: Analytical Solution and Parameter Calibration Using CMIP5 AOGCM Experiments. *J. Clim.* 26, 1841–1857. doi:10.1175/JCLI-D-12-00195.1.

Harmsen, M. J. H. M., van Dorst, P., van Vuuren, D. P., van den Berg, M., Van Dingenen, R., and Klimont, Z. (2020). Co-benefits of black carbon mitigation for climate and air quality. *Clim. Change*. doi:10.1007/s10584-020-02800-8.

Hodnebrog, Ø., Aamaas, B., Fuglestvedt, J. S., Marston, G., Myhre, G., Nielsen, C. J., et al. (2020). Updated Global Warming Potentials and Radiative Efficiencies of Halocarbons and Other Weak Atmospheric Absorbers. *Rev. Geophys.* 58, e2019RG000691. doi:https://doi.org/10.1029/2019RG000691.

Hoesly, R. M., Smith, S. J., Feng, L., Klimont, Z., Janssens-Maenhout, G., Pitkanen, T., et al. (2018). Historical (1750-2014) anthropogenic emissions of reactive gases and aerosols from the Community Emissions Data System (CEDS). *Geosci. Model Dev.* 11, 369–408. doi:10.5194/gmd-11-369-2018.

Joos, F., Roth, R., Fuglestvedt, J. S., Peters, G. P., Enting, I. G., von Bloh, W., et al. (2013). Carbon dioxide and climate impulse response functions for the computation of greenhouse gas metrics: a multi-model analysis. *Atmos. Chem. Phys.* 13, 2793–2825. doi:10.5194/acp-13-2793-2013.

Karagulian, F., Van Dingenen, R., Belis, C. A., Janssens-Maenhout, G., Crippa, M., Guizzardi, D., et al. (2016). Attribution of anthropogenic PM2. 5 to emission sources: : A global analysis of source-receptor model results and measured source-apportionment data (No. EUR 28510 EN), JRC Technical Reports. Ispra.

Kühn, T., Kupiainen, K., Miinalainen, T., Kokkola, H., Paunu, V.-V., Laakso, A., et al. (2020). Effects of black carbon mitigation on Arctic climate. *Atmos. Chem. Phys.* 20, 5527–5546. doi:10.5194/acp-20-5527-2020.

Lee, D. S., Fahey, D. W., Skowron, A., Allen, M. R., Burkhardt, U., Chen, Q., et al. (2020). The contribution of global aviation to anthropogenic climate forcing for 2000 to 2018. *Atmos. Environ.*, 117834. doi:10.1016/j.atmosenv.2020.117834.

Lund, M. T., Aamaas, B., Stjern, C. W., Klimont, Z., Berntsen, T. K., and Samset, B. H. (2020). A continued role of Short-Lived Climate Forcers under the Shared Socioeconomic Pathways. *Earth Syst. Dyn.* 11, 977–993. doi:10.5194/esd-11-977-2020.

Markandya, A., Sampedro, J., Smith, S. J., Van Dingenen, R., Pizarro-Irizar, C., Arto, I., et al. (2018). Health co-benefits from air pollution and mitigation costs of the Paris Agreement: a modelling study. *Lancet Planet. Heal.* 2, e126–e133. doi:10.1016/S2542-5196(18)30029-9.

Purohit, P., Höglund-Isaksson, L., Dulac, J., Shah, N., Wei, M., Rafaj, P., et al. (2020). Electricity savings and greenhouse gas emission reductions from global phase-down of hydrofluorocarbons. *Atmos. Chem. Phys.* 20, 11305–11327. doi:10.5194/acp-20-11305-2020.

Rao, S., Klimont, Z., Smith, S. J., Van Dingenen, R., Dentener, F., Bouwman, L., et al. (2017). Future air pollution in the Shared Socio-economic Pathways. *Glob. Environ. Chang.* 42, 346–358. doi:10.1016/j.gloenvcha.2016.05.012.

Rauner, S., Bauer, N., Dirnaichner, A., Dingenen, R. Van, Mutel, C., and Luderer, G. (2020). Coal-exit health and environmental damage reductions outweigh economic impacts. *Nat. Clim. Chang.* 10, 308–312. doi:10.1038/s41558-020-0728-x.

Shine, K. P., Fuglestvedt, J. S., Hailemariam, K., and Stuber, N. (2005). Alternatives to the Global Warming Potential for Comparing Climate Impacts of Emissions of Greenhouse Gases. *Clim. Change* 68, 281–302. doi:10.1007/s10584-005-1146-9.

SUBJECT TO FINAL EDITING ACCEPTED VERSION

Stevenson, D. S., Young, P. J., Naik, V., Lamarque, J.-F., Shindell, D. T., Voulgarakis, A., et al. (2013). Tropospheric ozone changes, radiative forcing and attribution to emissions in the Atmospheric Chemistry and Climate Model Intercomparison Project (ACCMIP). *Atmos. Chem. Phys.* 13, 3063–3085. doi:10.5194/acp-13-3063-2013.

Thornhill, G. D., Collins, W. J., Kramer, R. J., Olivié, D., Skeie, R. B., O'Connor, F. M., et al. (2021). Effective radiative forcing from emissions of reactive gases and aerosols – a multi-model comparison. *Atmos. Chem. Phys.* 21, 853–874. doi:10.5194/acp-21-853-2021.

Van Dingenen, R., Dentener, F., Crippa, M., Leitao, J., Marmer, E., Rao, S., et al. (2018). TM5-FASST: a global atmospheric source--receptor model for rapid impact analysis of emission changes on air quality and short-lived climate pollutants. *Atmos. Chem. Phys.* 18, 16173–16211. doi:10.5194/acp-18-16173-2018.

van Marle, M. J. E., Kloster, S., Magi, B. I., Marlon, J. R., Daniau, A.-L., Field, R. D., et al. (2017). Historic global biomass burning emissions for CMIP6 (BB4CMIP) based on merging satellite observations with proxies and fire models (1750–2015). *Geosci. Model Dev.* 10, 3329–3357. doi:10.5194/gmd-10-3329-2017.

Vandyck, T., Keramidas, K., Tchung-Ming, S., Weitzel, M., and Van Dingenen, R. (2020). Quantifying air quality co-benefits of climate policy across sectors and regions. *Clim. Change* 163, 1501–1517. doi:10.1007/s10584-020-02685-7.

ACCEPTED VERSION
SUBJECT TO FINAL EDITING

Chapter 7: The Earth's energy budget, climate feedbacks, and climate sensitivity

Coordinating Lead Authors:
Piers Forster (United Kingdom), Trude Storelvmo (Norway)

Lead Authors:
Kyle Armour (United States of America), William Collins (United Kingdom), Jean-Louis Dufresne (France), David Frame (New Zealand), Daniel J. Lunt (United Kingdom), Thorsten Mauritsen (Sweden/Denmark), Matthew D. Palmer (United Kingdom), Masahiro Watanabe (Japan), Martin Wild (Switzerland), Hua Zhang (China)

Contributing Authors:
Kari Alterskjær (Norway), Chris Smith (United Kingdom), Govindasamy Bala (India/United States of America), Nicolas Bellouin (United Kingdom/France), Terje Berntsen (Norway), Fábio Boeira Dias (Finland/Brazil), Sandrine Bony (France), Natalie J. Burls (United States of America/South Africa), Michelle Cain (United Kingdom), Catia M. Domingues (Australia, United Kingdom/Brazil), Aaron Donohoe (United States of America), Mark Flanner (United States of America), Jan S. Fuglestvedt (Norway), Lily C. Hahn (United States of America), Glen R. Harris (United Kingdom/New Zealand, United Kingdom), Christopher Jones (United Kingdom), Seiji Kato (United States of America), Jared Lewis (Australia/New Zealand), Zhanqing Li (United States of America), Mike Lockwood (United Kingdom), Norman Loeb (United States of America), Jochem Marotzke (Germany), Malte Meinshausen (Australia/Germany), Sebastian Milinski (Germany), Zebedee R. J. Nicholls (Australia), Ryan S. Padron Flasher (Switzerland/Ecuador, United States of America), Anna Possner (Germany), Cristian Proistosescu (Romania), Johannes Quaas (Germany), Joeri Rogelj (United Kingdom/Belgium), Daniel Rosenfeld (Israel), Bjørn H. Samset (Norway), Abhishek Savita (Australia/India), Jessica Vial (France), Karina von Schuckmann (France/Germany), Mark Zelinka (United States of America), Shuyun Zhao (China)

Review Editors:
Robert Colman (Australia), Damon H. Matthews (Canada), Venkatachalam Ramaswamy (United States of America)

Chapter Scientists:
Kari Alterskjær (Norway), Chris Smith (United Kingdom)

This Chapter should be cited as:
Forster, P., T. Storelvmo, K. Armour, W. Collins, J. L. Dufresne, D. Frame, D. J. Lunt, T. Mauritsen, M. D. Palmer, M. Watanabe, M. Wild, H. Zhang, 2021, The Earth's Energy Budget, Climate Feedbacks, and Climate Sensitivity. In: *Climate Change 2021: The Physical Science Basis. Contribution of Working Group I to the Sixth Assessment Report of the Intergovernmental Panel on Climate Change* [Masson-Delmotte, V., P. Zhai, A. Pirani, S. L. Connors, C. Péan, S. Berger, N. Caud, Y. Chen, L. Goldfarb, M. I. Gomis, M. Huang, K. Leitzell, E. Lonnoy, J.B.R. Matthews, T. K. Maycock, T. Waterfield, O. Yelekçi, R. Yu and B. Zhou (eds.)]. Cambridge University Press. In Press.

Date: August 2021

This document is subject to copy-editing, corrigenda and trickle backs.

ACCEPTED VERSION SUBJECT TO FINAL EDITING

Table of Content

Executive Summary **6**

7.1 Introduction, conceptual framework, and advances since AR5 ..... **11**

BOX 7.1: The energy budget framework – forcing and response **12**

7.2 Earth's energy budget and its changes through time **14**

7.2.1 Present-day energy budget 15

7.2.2 Changes in Earth's energy budget 16

7.2.2.1 Changes in Earth's TOA energy budget 16

7.2.2.2 Changes in the global energy inventory 17

7.2.2.3 Changes in Earth's surface energy budget 19

BOX 7.2: The Global Energy Budget **21**

7.3 Effective radiative forcing **22**

7.3.1 Methodologies and representation in models; overview of adjustments 23

7.3.2 Greenhouse Gases 27

7.3.2.1 Carbon Dioxide 27

7.3.2.2 Methane 29

7.3.2.3 Nitrous oxide 30

7.3.2.4 Halogenated species 30

7.3.2.5 Ozone 30

7.3.2.6 Stratospheric water vapour 31

7.3.2.7 Synthesis 32

7.3.3 Aerosols 33

7.3.3.1 Aerosol-radiation interactions 34

7.3.3.1.1 Observation-based lines of evidence 34

7.3.3.1.2 Model-based lines of evidence 34

7.3.3.1.3 Overall assessment of IRFari and ERFari 35

7.3.3.2 Aerosol-cloud interactions 36

7.3.3.2.1 Observation-based evidence 37

7.3.3.2.2 Model-based evidence 40

7.3.3.2.3 Overall assessment of ERFaci 41

7.3.3.3 Energy budget constraints on the total aerosol ERF 41

7.3.3.4 Overall assessment of total aerosol ERF 42

7.3.4 Other agents 44

7.3.4.1 Land use 44

7.3.4.2 Contrails and aviation-induced cirrus 45

7.3.4.3 Light absorbing particles on snow and ice 45

ACCEPTED VERSION SUBJECT TO FINAL EDITING

7.3.4.4 Solar 46
7.3.4.5 Galactic Cosmic Rays 47
7.3.4.6 Volcanic aerosols 47
7.3.5 Synthesis of Global Mean Radiative Forcing, Past and Future 48
7.3.5.1 Major changes in forcing since IPCC AR5 48
7.3.5.2 Summary ERF assessment 49
7.3.5.3 Temperature Contribution of forcing agents 51

Cross-Chapter Box 7.1: Physical emulation of Earth System Models for scenario classification and knowledge integration in AR6 53

7.4 Climate feedbacks 59
7.4.1 Methodology of the feedback assessment 59
7.4.2 Assessing climate feedbacks 60
7.4.2.1 Planck response 61
7.4.2.2 Water vapour and temperature lapse rate feedbacks 61
7.4.2.3 Surface albedo feedback 63
7.4.2.4 Cloud feedbacks 64
7.4.2.4.1 Decomposition of clouds into regimes 64
7.4.2.4.2 Assessment for individual cloud regimes 66
7.4.2.4.3 Synthesis for the net cloud feedback 69
7.4.2.5 Biogeophysical and non-CO_2 biogeochemical feedbacks 70
7.4.2.5.1 Non-CO_2 biogeochemical feedbacks 71
7.4.2.5.2 Biogeophysical feedbacks 71
7.4.2.5.3 Synthesis of biogeophysical and non-CO_2 biogeochemical feedbacks 72
7.4.2.6 Long term radiative feedbacks associated with ice sheets 72
7.4.2.7 Synthesis 73
7.4.2.8 Climate feedbacks in ESMs 75
7.4.3 Dependence of feedbacks on climate mean state 76
7.4.3.1 State-dependence of feedbacks in models 76
7.4.3.2 State-dependence of feedbacks in the paleoclimate proxy record 77
7.4.3.3 Synthesis of state-dependence of feedbacks from modelling and paleoclimate records 78
7.4.4 Relationship between feedbacks and temperature patterns 79
7.4.4.1 Polar amplification 79
7.4.4.1.1 Critical processes driving polar amplification 80
7.4.4.1.2 Polar amplification from proxies and models during past climates associated with CO_2 change 82
7.4.4.1.3 Overall assessment of polar amplification 84
7.4.4.2 Tropical Pacific sea-surface temperature gradients 85
7.4.4.2.1 Critical processes determining changes in tropical Pacific sea-surface temperature gradients 85
7.4.4.2.2 Tropical Pacific temperature gradients in past high-CO_2 climates 86

ACCEPTED VERSION SUBJECT TO FINAL EDITING

7.4.4.2.3 Overall assessment of tropical Pacific sea-surface temperature gradients under CO_2 forcing 87
7.4.4.3 Dependence of feedbacks on temperature patterns 87

7.5 Estimates of ECS and TCR 91
7.5.1 Estimates of ECS and TCR based on process understanding 92
7.5.1.1 ECS estimated using process-based assessments of the forcing and feedbacks 92
7.5.1.2 Emulating process-based ECS to TCR 93
7.5.2 Estimates of ECS and TCR based on the instrumental record 95
7.5.2.1 Estimates of ECS and TCR based on the global energy budget 95
7.5.2.2 Estimates of ECS and TCR based on climate model emulators 98
7.5.2.3 Estimates of ECS based on variability in Earth's top-of-atmosphere radiation budget 99
7.5.2.4 Estimates of ECS based on the climate response to volcanic eruptions 100
7.5.2.5 Assessment of ECS and TCR based on the instrumental record 100
7.5.3 Estimates of ECS based on paleoclimate data 101
7.5.3.1 Estimates of ECS from the Last Glacial Maximum 101
7.5.3.2 Estimates of ECS from glacial-interglacial cycles 102
7.5.3.3 Estimates of ECS from warm periods of the pre-Quaternary 102
7.5.3.4 Synthesis of ECS based on paleo radiative forcing and temperature 103
7.5.4 Estimates of ECS and TCR based on emergent constraints 106
7.5.4.1 Emergent constraints using global or near-global surface temperature change 107
7.5.4.2 Emergent constraints focused on cloud feedbacks and present-day climate 108
7.5.4.3 Assessed ECS and TCR based on emergent constraints 109
7.5.5 Combined assessment of ECS and TCR 110
7.5.6 Considerations on the ECS and TCR in global climate models and their role in the assessment 113
7.5.7 Processes underlying uncertainty in the global temperature response to forcing 115

7.6 Metrics to evaluate emissions 118
7.6.1 Physical description of metrics 118
7.6.1.1 Radiative properties and lifetimes. 118
7.6.1.2 Physical indicators 119
7.6.1.3 Carbon cycle responses and other indirect contributions 120
7.6.1.4 Comparing long-lived with short-lived greenhouse gases 122
7.6.1.5 Emission metrics by compounds 124

BOX 7.3: Physical considerations in emission-metric choice 125

7.6.2 Applications of emission metrics 126

Frequently Asked Questions 128
FAQ 7.1: What is the Earth's energy budget, and what does it tell us about climate change? 128

ACCEPTED VERSION SUBJECT TO FINAL EDITING

FAQ 7.2: Clouds – What is the role in a warming climate? 130
FAQ 7.3: What is equilibrium climate sensitivity and how does it relate to future warming? 132

References 134

Figures 175

ACCEPTED VERSION
SUBJECT TO FINAL EDITING

Executive Summary

This chapter assesses the present state of knowledge of Earth's energy budget, that is, the main flows of energy into and out of the Earth system, and how these energy flows govern the climate response to a radiative forcing. Changes in atmospheric composition and land use, like those caused by anthropogenic greenhouse gas emissions and emissions of aerosols and their precursors, affect climate through perturbations to Earth's top-of-atmosphere energy budget. The effective radiative forcings (ERFs) quantify these perturbations, including any consequent adjustment to the climate system (but excluding surface temperature response). How the climate system responds to a given forcing is determined by climate feedbacks associated with physical, biogeophysical and biogeochemical processes. These feedback processes are assessed, as are useful measures of global climate response, namely equilibrium climate sensitivity (ECS) and the transient climate response (TCR). This chapter also assesses emission metrics, which are used to quantify how the climate response due to the emission of different greenhouse gases compares to the response to the emission of carbon dioxide (CO_2). This chapter builds on the assessment of carbon cycle and aerosol processes from Chapters 5 and 6, respectively, to quantify non-CO_2 biogeochemical feedbacks and the ERF for aerosols. Chapters 3, 4, 5, 6 and 9 use the assessment of ERF, ECS and TCR from this chapter to help understand historical and future temperature changes, the response to cumulative emissions, the remaining carbon budget and sea level rise respectively. This chapter builds on findings from the IPCC Fifth Assessment Report (AR5), the Special Report on Global Warming of 1.5°C (SR1.5), the Special Report on Ocean and Cryosphere in a Changing Climate (SROCC) and the Special Report on Climate Change and Land (SRCCL). *Very likely* ranges are presented unless otherwise indicated.

Earth's Energy Budget

Since AR5, the accumulation of energy in the Earth system, quantified by changes in the global energy inventory for all components of the climate system, has become established as a robust measure of the rate of global climate change on interannual-to-decadal timescales. Compared to changes in global surface air temperature (GSAT), the global energy inventory exhibits less variability, which can mask underlying climate trends. Compared to AR5, there is increased confidence in the quantification of changes in the global energy inventory due to improved observational records and closure of the sea level budget. Energy will continue to accumulate in the Earth system until at least the end of the 21st century, even under strong mitigation scenarios, and will primarily be manifest through ocean warming and associated with continued sea level rise through thermal expansion. (*high confidence*) {7.2.2, Box 7.2, Table 7.1, Chapter 9 Cross-Chapter Box 9.1, Table 9.5, 9.2.2, 9.6.3}

The global energy inventory increased by 435 [325 to 545] Zettajoules (ZJ) for the period 1971–2018 and 153 [101 to 206] ZJ for the period 2006–2018. This corresponds to an Earth energy imbalance of 0.57 [0.43 to 0.72] W m^{-2} for the period 1971–2018, increasing to 0.79 [0.52 to 1.06] W m^{-2} for the period 2006–2018, expressed per unit area of Earth's surface. Ocean heat uptake is by far the largest contribution and accounts for 91% of the total energy change. Compared to AR5, the contribution from land heating has been revised upwards from about 3% to about 5%. Melting of ice and warming of the atmosphere account for about 3% and 1% of the total change respectively. More comprehensive analysis of inventory components and cross-validation of satellite and in situ-based global heating rates lead to a more confident assessment relative to AR5. (*high confidence*) {Box 7.2, 7.2.2, Table 7.1, 7.5.2.3}

Improved quantification of effective radiative forcing, the climate system radiative response, and the observed energy increase in the Earth system for the period 1971–2018 demonstrate improved closure of the global energy budget compared to AR5. Combining the *likely* range of ERF with the central estimate of radiative response gives an expected energy gain of 340 [47 to 662] ZJ. Combining the *likely* range of climate response with the central estimate of ERF gives an expected energy gain of 340 [147 to 527] ZJ. Both estimates are consistent with an independent observation-based assessment of the global energy increase of 284 [96 to 471] ZJ, (*very likely range*) expressed relative to the estimated 1850-1900 Earth energy imbalance. (*high confidence*) {7.2.2, Box 7.2, 7.3.5, 7.5.2}

Since AR5, additional evidence for a widespread decline (or dimming) in solar radiation reaching the

ACCEPTED VERSION SUBJECT TO FINAL EDITING

surface is found in the observational records between the 1950s and 1980s, with a partial recovery (brightening) at many observational sites thereafter (*high confidence*). These trends are neither a local phenomenon nor a measurement artefact (*high confidence*). Multi-decadal variation in anthropogenic aerosol emissions are thought to be a major contributor (*medium confidence*), but multi-decadal variability in cloudiness may also have played a role. The downward and upward thermal radiation at the surface has increased in recent decades, in line with increased greenhouse gas concentrations and associated surface and atmospheric warming and moistening (*medium confidence*). {7.2.2}

Effective Radiative Forcing

For carbon dioxide, methane, nitrous oxide and chlorofluorocarbons, there is now evidence to quantify the effect on ERF of tropospheric adjustments (e.g., from changes in atmospheric temperatures, clouds and water vapour). The assessed ERF for a doubling of carbon dioxide compared to 1750 levels (3.93 ± 0.47 W m^{-2}) is larger than in AR5. Effective radiative forcings (ERF), introduced in AR5, have been estimated for a larger number of agents and shown to be more closely related to the temperature response than the stratospheric-temperature adjusted radiative forcing. For carbon dioxide, the adjustments include the physiological effects on vegetation. (*high confidence*) {7.3.2}

The total anthropogenic ERF over the industrial era (1750–2019) was 2.72 [1.96 to 3.48] W m^{-2}. This estimate has increased by 0.43 W m^{-2} compared to AR5 estimates for 1750–2011. This increase includes a +0.34 W m^{-2} from increases in atmospheric concentrations of well-mixed greenhouse gases (including halogenated species) since 2011, a +0.15 W m^{-2} from upwards revisions of their radiative efficiencies and a +0.10 W m^{-2} from re-evaluation of the ozone and stratospheric water vapour ERF. The 0.59 W m^{-2} increase in ERF from greenhouse gases is partly offset by a better-constrained assessment of total aerosol ERF that is more strongly negative than in AR5, based on multiple lines of evidence (*high confidence*). Changes in surface reflectance from land-use change, deposition of light-absorbing particles on ice and snow, and contrails and aviation-induced cirrus have also contributed to the total anthropogenic ERF over the industrial era, with –0.20 [–0.30 to –0.10] W m^{-2} (*medium confidence*), +0.08 [0 to 0.18] W m^{-2} (*low confidence*) and +0.06 [0.02 to 0.10] W m^{-2} (*low confidence*), respectively. {7.3.2, 7.3.4, 7.3.5}

Anthropogenic emissions of greenhouse gases (GHGs) and their precursors contribute an ERF of 3.84 [3.46 to 4.22] W m^{-2} over the industrial era (1750–2019). Most of this total ERF, 3.32 [3.03 to 3.61] W m^{-2}, comes from the well-mixed greenhouse gases, with changes in ozone and stratospheric water vapour (from methane oxidation) contributing the remainder. The ERF of GHGs is composed of 2.16 [1.90 to 2.41] W m^{-2} from carbon dioxide, 0.54 [0.43 to 0.65] W m^{-2} from methane, 0.41 [0.33 to 0.49] W m^{-2} from halogenated species, and 0.21 [0.18 to 0.24] W m^{-2} from nitrous oxide. The ERF for ozone is 0.47 [0.24 to 0.71] W m^{-2}. The estimate of ERF for ozone has increased since AR5 due to revised estimates of precursor emissions and better accounting for effects of tropospheric ozone precursors in the stratosphere. The estimated ERF for methane has slightly increased due to a combination of increases from improved spectroscopic treatments being somewhat offset by accounting for adjustments. (*high confidence*) {7.3.2, 7.3.5}

Aerosols contribute an ERF of –1.3 [–2.0 to –0.6] W m^{-2} over the industrial era (1750–2014) (*medium confidence*). The ERF due to aerosol–cloud interactions (ERFaci) contributes most to the magnitude of the total aerosol ERF (*high confidence*) and is assessed to be –1.0 [–1.7 to –0.3] W m^{-2} (*medium confidence*), with the remainder due to aerosol–radiation interactions (ERFari), assessed to be –0.3 [–0.6 to 0.0] W m^{-2} (*medium confidence*). There has been an increase in the estimated magnitude but a reduction in the uncertainty of the total aerosol ERF relative to AR5, supported by a combination of increased process-understanding and progress in modelling and observational analyses. ERF estimates from these separate lines of evidence are now consistent with each other, in contrast to AR5, and support the assessment that it is *virtually certain* that the total aerosol ERF is negative. Compared to AR5, the assessed magnitude of ERFaci has increased, while the magnitude of ERFari has decreased. The total aerosol ERF over the period 1750–2019 is less certain than the headline statement assessment. It is also assessed to be smaller in magnitude at –1.1 [–1.7 to –0.4] W m^{-2}, primarily due to recent emission changes (*medium confidence*). {7.3.3, 7.3.5, 2.2.6}

ACCEPTED VERSION SUBJECT TO FINAL EDITING

Climate Feedbacks and Sensitivity

The net effect of changes in clouds in response to global warming is to amplify human-induced warming, that is, the net cloud feedback is positive (*high confidence*). Compared to AR5, major advances in the understanding of cloud processes have increased the level of confidence and decreased the uncertainty range in the cloud feedback by about 50%. An assessment of the low-altitude cloud feedback over the subtropical oceans, which was previously the major source of uncertainty in the net cloud feedback, is improved owing to a combined use of climate model simulations, satellite observations, and explicit simulations of clouds, altogether leading to strong evidence that this type of cloud amplifies global warming. The net cloud feedback, obtained by summing the cloud feedbacks assessed for individual regimes, is 0.42 [–0.10 to 0.94] W m^{-2} $°C^{-1}$. A net negative cloud feedback is *very unlikely*. (*high confidence*) {7.4.2, Figure 7.10, Table 7.10}

The combined effect of all known radiative feedbacks (physical, biogeophysical, and non-CO_2 biogeochemical) is to amplify the base climate response, also known as the Planck temperature response (*virtually certain*). Combining these feedbacks with the base climate response, the net feedback parameter based on process understanding is assessed to be –1.16 [–1.81 to –0.51] W m^{-2} $°C^{-1}$, which is slightly less negative than that inferred from the overall ECS assessment. The combined water vapour and lapse rate feedback makes the largest single contribution to global warming, whereas the cloud feedback remains the largest contribution to overall uncertainty. Due to the state-dependence of feedbacks, as evidenced from paleoclimate observations and from models, the net feedback parameter will increase (become less negative) as global temperature increases. Furthermore, on long time scales the ice sheet feedback parameter is *very likely* positive, promoting additional warming on millennial time scales as ice sheets come into equilibrium with the forcing. (*high confidence*) {7.4.2, 7.4.3, 7.5.7}

Radiative feedbacks, particularly from clouds, are expected to become less negative (more amplifying) on multi-decadal timescales as the *spatial pattern* of surface warming evolves, leading to an ECS that is higher than was inferred in AR5 based on warming over the instrumental record. This new understanding, along with updated estimates of historical temperature change, ERF, and Earth's energy imbalance, reconciles previously disparate ECS estimates (*high confidence*). However, there is currently insufficient evidence to quantify a *likely* range of the magnitude of future changes to current climate feedbacks. Warming over the instrumental record provides robust constraints on the lower end of the ECS range (*high confidence*), but owing to the possibility of future feedback changes it does not, on its own, constrain the upper end of the range, in contrast to what was reported in AR5. {7.4.4, 7.5.2, 7.5.3}

Based on multiple lines of evidence the best estimate of ECS is 3°C, the *likely* range is 2.5°C to 4°C, and the *very likely* range is 2°C to 5°C. It is *virtually certain* that ECS is larger than 1.5°C. Substantial advances since AR5 have been made in quantifying ECS based on feedback process understanding, the instrumental record, paleoclimates and emergent constraints. There is a high level of agreement among the different lines of evidence. All lines of evidence help rule out ECS values below 1.5°C, but currently it is not possible to rule out ECS values above 5 °C. Therefore, the 5°C upper end of the *very likely* range is assessed to have *medium confidence* and the other bounds have *high confidence*. {7.5.5}

Based on process understanding, warming over the instrumental record, and emergent constraints, the best estimate of TCR is 1.8°C, the *likely* range is 1.4°C to 2.2°C and the *very likely* range is 1.2°C to 2.4°C (*high confidence*). {7.5.5}

On average, CMIP6 models have higher mean ECS and TCR values than the CMIP5 generation of models. They also have higher mean values and wider spreads than the assessed best estimates and *very likely* ranges within this Report. These higher ECS and TCR values can, in some models, be traced to changes in extra-tropical cloud feedbacks that have emerged from efforts to reduce biases in these clouds compared to satellite observations (*medium confidence*). The broader ECS and TCR ranges from CMIP6 also lead the models to project a range of future warming that is wider than the assessed warming range, which is based on multiple lines of evidence. However, some of the high-sensitivity CMIP6 models are less consistent

ACCEPTED VERSION SUBJECT TO FINAL EDITING

with observed recent changes in global warming and with paleoclimate proxy data than models with ECS within the *very likely* range. Similarly, some of the low-sensitivity models are less consistent with the paleoclimate data. The CMIP models with the highest ECS and TCR values provide insights into high-risk, low-likelihood futures, which cannot be excluded based on currently-available evidence. (*high confidence*) {4.3.1, 4.3.4, 7.4.2, 7.5.6}

Climate Response

The total human-forced GSAT change from 1750–2019 is calculated to be 1.29 [0.99 to 1.65] °C. This calculation is an emulator-based estimate, constrained by the historic GSAT and ocean heat content changes from Chapter 2 and the ERF, ECS and TCR from this chapter. The calculated GSAT change is composed of a well-mixed greenhouse gas warming of 1.58 [1.17 to 2.17] °C (*high confidence*), a warming from ozone changes of 0.23 [0.11 to 0.39] °C (*high confidence*), a cooling of –0.50 [–0.22 to –0.96] °C from aerosol effects (*medium confidence*), and a –0.06 [–0.15 to +0.01] °C contribution from surface reflectance changes from land-use change and light absorbing particles on ice and snow (*medium confidence*). Changes in solar and volcanic activity are assessed to have together contributed a small change of –0.02 [–0.06 to +0.02] °C since 1750 (*medium confidence*). {7.3.5}

Uncertainties regarding the true value of ECS and TCR are the dominant source of uncertainty in global temperature projections over the 21st century under moderate to high GHG emission scenarios. For scenarios that reach net zero carbon dioxide emissions, the uncertainty in the ERF values of aerosol and other short-lived forcings contribute substantial uncertainty in projected temperature. Global ocean heat uptake is a smaller source of uncertainty in centennial-time-scale surface warming. (*high confidence*) {7.5.7}

The assessed historical and future ranges of GSAT change in this Report are shown to be internally consistent with the Report's assessment of key physical-climate indicators: greenhouse gas ERFs, ECS and TCR. When calibrated to match the assessed ranges within the assessment, physically based emulators can reproduce the best estimate of GSAT change over 1850–1900 to 1995–2014 to within 5% and the *very likely* range of this GSAT change to within 10%. Two physically based emulators match at least two-thirds of the Chapter 4-assessed projected GSAT changes to within these levels of precision. When used for multi-scenario experiments, calibrated physically based emulators can adequately reflect assessments regarding future GSAT from Earth system models and/or other lines of evidence. (*high confidence*) {Cross-Chapter Box 7.1}

It is now well understood that the Arctic warms more quickly than the Antarctic due to differences in radiative feedbacks and ocean heat uptake between the poles, but that surface warming will eventually be amplified in both poles (*high confidence*). The causes of this polar amplification are well understood, and the evidence is stronger than at the time of AR5, supported by better agreement between modelled and observed polar amplification during warm paleo time periods (*high confidence*). The Antarctic warms more slowly than the Arctic owing primarily to upwelling in the Southern Ocean, and even at equilibrium is expected to warm less than the Arctic. The rate of Arctic surface warming will continue to exceed the global average over this century (*high confidence*). There is also *high confidence* that Antarctic amplification will emerge as the Southern Ocean surface warms on centennial time scales, although only *low confidence* regarding whether the feature will emerge during the 21st century. {7.4.4}

The assessed global warming potentials (GWP) and global temperature-change potentials (GTP) for methane and nitrous oxide are slightly lower than in AR5 due to revised estimates of their lifetimes and updated estimates of their indirect chemical effects (*medium confidence*). The assessed metrics now also include the carbon-cycle response for non-CO_2 gases. The carbon cycle estimate is lower than in AR5, but there is *high confidence* in the need for its inclusion and in the quantification methodology. Metrics for methane from fossil fuel sources account for the extra fossil CO_2 that these emissions contribute to the atmosphere and so have slightly higher emission metric values than those from biogenic sources (*high confidence*). {7.6.1}

ACCEPTED VERSION SUBJECT TO FINAL EDITING

New emission metric approaches such as GWP* and the combined-GTP (CGTP) are designed to relate emission rates of short-lived gases to cumulative emissions of CO_2. These metric approaches are well suited to estimate the GSAT response from aggregated emissions of a range of gases over time, which can be done by scaling the cumulative CO_2 equivalent emissions calculated with these metrics by the transient climate response to cumulative emissions of carbon dioxide. For a given multi-gas emission pathway, the estimated contribution of emissions to surface warming is improved by either using these new metric approaches or by treating short- and long-lived GHG emission pathways separately, as compared to approaches that aggregate emissions of GHGs using standard GWP or GTP emission metrics. By contrast, if emissions are weighted by their 100-year GWP or GTP values, different multi-gas emission pathways with the same aggregated CO_2 equivalent emissions rarely lead to the same estimated temperature outcome. (*high confidence*) {7.6.1, Box 7.3}

The choice of emission metric affects the quantification of net zero GHG emissions and therefore the resulting temperature outcome after net zero emissions are achieved. In general, achieving net zero CO_2 emissions and declining non-CO_2 radiative forcing would be sufficient to prevent additional human-caused warming. Reaching net zero GHG emissions as quantified by GWP-100 typically results in global temperatures that peak and then decline after net zero GHGs emissions are achieved, though this outcome depends on the relative sequencing of mitigation of short-lived and long-lived species. In contrast, reaching net zero GHG emissions when quantified using new emission metrics such as CGTP or GWP* would lead to approximate temperature stabilization (*high confidence*) {7.6.2}

ACCEPTED VERSION
SUBJECT TO FINAL EDITING

7.1 Introduction, conceptual framework, and advances since AR5

This chapter assesses the major physical processes that affect the evolution of Earth's energy budget and the associated changes in surface temperature and the broader climate system, integrating elements that were dealt with separately in previous reports.

The top-of-atmosphere (TOA) energy budget determines the net amount of energy entering or leaving the climate system. Its time variations can be monitored in three ways, using: (i) satellite observations of the radiative fluxes at the TOA; (ii) observations of the accumulation of energy in the climate system; and (iii) observations of surface energy fluxes. When the TOA energy budget is changed by a human or natural cause (a radiative forcing), the climate system responds by warming or cooling (i.e., the system gains or loses energy). Understanding of changes in the Earth's energy flows helps understanding of the main physical processes driving climate change. It also provides a fundamental test of climate models and their projections.

This chapter principally builds on AR5 (Boucher, 2012; Church et al., 2013; Collins et al., 2013a; Flato et al., 2013; Hartmann et al., 2013; Myhre et al., 2013b; Rhein et al., 2013). It also builds on the subsequent SR1.5 (IPCC, 2018), SROCC (IPCC, 2019a) and SRCCL (IPCC, 2019b), as well as community-led assessments (e.g., Bellouin et al. (2019) covering aerosol radiative forcing and Sherwood et al. (2020) covering equilibrium climate sensitivity).

Throughout this chapter, global surface air temperature (GSAT) is used to quantify surface temperature change (see Cross-Chapter Box 2.3, Chapter 4 Section 4.3.4). The total energy accumulation in the Earth system represents a metric of global change that is complementary to GSAT but shows considerably less variability on interannual-to-decadal timescales (Section 7.2.2). Research and new observations since AR5 have improved scientific confidence in the quantification of changes in the global energy inventory and corresponding estimates of Earth's energy imbalance (Section 7.2). Improved understanding of adjustments to radiative forcing and of aerosol-cloud interactions have led to revisions of forcing estimates (Section 7.3). New approaches to the quantification and treatment of feedbacks (Section 7.4) have improved the understanding of their nature and time-evolution, leading to a better understanding of how these feedbacks relate to Equilibrium Climate Sensitivity (ECS). This has helped to reconcile disparate estimates of ECS from different lines of evidence (Section 7.5). Innovations in the use of emission metrics have clarified the relationships between metric choice and temperature policy goals (Section 7.6), linking this chapter to WGIII which provides further information on metrics, their use, and policy goals beyond temperature. *Very likely* (5% to 95%) ranges are presented unless otherwise indicated. In particular, the addition of (one standard deviation) indicates that the range represents one standard deviation.

In Box 7.1 an energy budget framework is introduced, which forms the basis for the discussions and scientific assessment in the remainder of this chapter and across the report. The framework reflects advances in the understanding of the Earth system response to climate forcing since the publication of AR5. A schematic of this framework and the key changes relative to the science reported in AR5 are provided in Figure 7.1.

[START FIGURE 7.1 HERE]

Figure 7.1: A visual abstract of the chapter, illustrating why the Earth's energy budget matters and how it relates to the underlying chapter assessment. The methods used to assess processes and key new findings relative to AR5 are highlighted.

[END FIGURE 7.1 HERE]

A simple way to characterise the behaviour of multiple aspects of the climate system at once is to summarise them using global-scale metrics. This report distinguishes between "climate metrics" (e.g., ECS, TCR) and "emission metrics" (such as the global warming potential; GWP, or global temperature potential; GTP), but

ACCEPTED VERSION SUBJECT TO FINAL EDITING

this distinction is not definitive. Climate metrics are generally used to summarise aspects of the surface temperature response (Box 7.1). Emission metrics are generally used to summarise the relative effects of emissions of different forcing agents, usually greenhouse gases (see Section 7.6). The climate metrics used in this report typically evaluate how the Earth system response varies with atmospheric gas concentration or change in radiative forcing. Emission metrics evaluate how radiative forcing or a key climate variable (such as GSAT) is affected by the emissions of a certain amount of gas. Emission-related metrics are sometimes used in mitigation policy decisions such as trading greenhouse gas reduction measures and life cycle analysis. Climate metrics are useful to gauge the range of future climate impacts for adaptation decisions under a given emission pathway. Metrics such as the transient climate response to cumulative emissions of carbon dioxide (TCRE) are used in both adaptation and mitigation contexts: for gauging future global surface temperature change under specific emission scenarios, and to estimate remaining carbon budgets that are used to inform mitigation policies (see Chapter 5, Section 5.5).

Given that TCR and ECS are metrics of GSAT response to a theoretical doubling of atmospheric CO_2 (Box 7.1), they do not directly correspond to the warming that would occur under realistic forcing scenarios that include time-varying CO_2 concentrations and non-CO_2 forcing agents (such as aerosols and land-use changes). It has been argued that TCR, as a metric of transient warming, is more policy-relevant than ECS (Frame et al., 2006; Schwartz, 2018). However, as detailed in Chapter 4, both established and recent results (Forster et al., 2013; Gregory et al., 2015; Marotzke and Forster, 2015; Grose et al., 2018; Marotzke, 2019) indicate that TCR and ECS help explain variation across climate models both over the historical period and across a range of concentration-driven future scenarios. In emission-driven scenarios the carbon cycle response is also important (Smith et al., 2019). The proportion of variation explained by ECS and TCR varies with scenario and the time period considered, but both past and future surface warming depend on these metrics (Section 7.5.7).

Regional changes in temperature, rainfall, and climate extremes have been found to correlate well with the forced changes in GSAT within Earth System Models (ESMs) (Giorgetta et al., 2013; Tebaldi and Arblaster, 2014; Seneviratne et al., 2016; Chapter 4, Section 4.6.1). While this so-called 'pattern scaling' has important limitations arising from, for instance, localized forcings, land-use changes, or internal climate variability (Deser et al., 2012; Luyssaert et al., 2014), changes in GSAT nonetheless explain a substantial fraction of inter-model differences in projections of regional climate changes over the 21st century (Tebaldi and Knutti, 2018). This Chapter's assessments of TCR and ECS thus provide constraints on future global and regional climate change (Chapter 4 and Chapter 11).

[START BOX 7.1 HERE]

BOX 7.1: The energy budget framework – forcing and response

The forcing and response energy budget framework provides a methodology to assess the effect of individual drivers of global mean surface temperature response, and to facilitate the understanding of the key phenomena that set the magnitude of this temperature response. The framework used here is developed from that adopted in previous IPCC reports (see Ramaswamy et al., 2019 for a discussion). *Effective Radiative Forcing* (ERF), introduced in AR5 (Boucher et al., 2013; Myhre et al., 2013b) is more explicitly defined in this report and is employed as the central definition of radiative forcing (Sherwood et al. 2015, Box 7.1, Figure 1a). The framework has also been extended to allow variations in feedbacks over different timescales and with changing climate state (Section 7.4.4; Section 7.4.3).

The GSAT response to perturbations that give rise to an energy imbalance is traditionally approximated by the following linear energy budget equation, in which ΔN represents the change in the top-of-atmosphere (TOA) net energy flux, ΔF is an ***effective radiative forcing*** perturbation to the TOA net energy flux, α is the net ***feedback parameter*** and ΔT is the change in ***GSAT***:

$$\Delta N = \Delta F + \alpha \Delta T \qquad \text{Box 7.1, Equation (7.1)}$$

ERF is the TOA energy budget change resulting from the perturbation, excluding any radiative response

ACCEPTED VERSION SUBJECT TO FINAL EDITING

related to a change in GSAT (i.e., ΔT =0). Climate feedbacks (α) represent those processes that change the TOA energy budget in response to a given ΔT.

[START BOX 7.1, FIGURE 1 HERE]

Box 7.1, Figure 1: Schematics of the forcing-feedback framework adopted within the assessment, following Equation 7.1. Illustrated is how the Earth's TOA net energy flux might evolve for a hypothetical doubling of atmospheric CO_2 concentration above preindustrial levels, where an initial positive energy imbalance (energy entering the Earth system, shown on the y-axis) is gradually restored towards equilibrium as the surface temperature warms (shown on the x-axis). a) illustrates the definitions of ERF for the special case of a doubling of atmospheric CO_2 concentration, the feedback parameter and the ECS. b) illustrates how approximate estimates of these metrics are made within the chapter and how these approximations might relate to the exact definitions adopted in panel a).

[END BOX 7.1, FIGURE 1 HERE]

The ***effective radiative forcing, ERF*** (ΔF; units: W m^{-2}) quantifies the change in the net TOA energy flux of the Earth system due to an imposed perturbation (e.g., changes in greenhouse gas or aerosol concentrations, in incoming solar radiation, or land-use change). ERF is expressed as a change in net downward radiative flux at the TOA following adjustments in both tropospheric and stratospheric temperatures, water vapour, clouds, and some surface properties, such as surface albedo from vegetation changes, that are uncoupled to any GSAT change (Smith et al., 2018b). These adjustments affect the TOA energy balance and hence the ERF. They are generally assumed to be linear and additive (Section 7.3.1). Accounting for such processes gives an estimate of ERF that is more representative of the climate change response associated with forcing agents than stratospheric-temperature-adjusted radiative forcing (SARF) or the instantaneous radiative forcing (IRF) (Section 7.3.1). Adjustments are processes that are independent of GSAT change, whereas feedbacks refer to processes caused by GSAT change. Although adjustments generally occur on timescales of hours to several months, and feedbacks respond to ocean surface temperature changes on timescales of a year or more, timescale is not used to separate the definitions. ERF has often been approximated as the TOA energy balance change due to an imposed perturbation in climate model simulations with sea-surface temperature and sea-ice concentrations set to their pre-industrial climatological values (e.g., Forster et al., 2016). However, to match the adopted forcing-feedback framework, the small effects of any GSAT change from changes in land surface temperatures need to be removed from the TOA energy balance in such simulations to give an approximate measure of ERF (Box 7.1, Figure 1b and Section 7.3.1).

The ***feedback parameter,*** $\boldsymbol{\alpha}$, (units: W m^{-2} °C^{-1}) quantifies the change in net energy flux at the TOA for a given change in GSAT. Many climate variables affect the TOA energy budget, and the feedback parameter can be decomposed, to first order, into a sum of terms $\alpha = \sum_x \frac{\partial N}{\partial x}\frac{dx}{dT}$], where x represents a variable of the Earth system that has a direct effect on the energy budget at the TOA. The sum of the feedback terms (i.e., α in Equation 7.1) governs Earth's equilibrium GSAT response to an imposed ERF. In previous assessments, α and the related ECS have been associated with a distinct set of physical processes (Planck response and changes in water vapour, lapse rate, surface albedo, and clouds) (Charney et al., 1979). In this assessment, a more general definition of α and ECS is adopted such that they include additional Earth system processes that act across many timescales (e.g., changes in natural aerosol emissions or vegetation). Because, in our assessment, these additional processes sum to a near-zero value, including these additional processes does not change the assessed central value of ECS but does affect its assessed uncertainty range (Section 7.4.2). Note that there is no standardised notation or sign convention for the feedback parameter in the literature. Here the convention is used that the sum of all feedback terms (the net feedback parameter, α) is negative for a stable climate that radiates additional energy to space with a GSAT increase, with a more negative value of α corresponding to a stronger radiative response and thus a smaller GSAT change required to balance a change in ERF (Equation 7.1). A change in process x amplifies the temperature response to a forcing when the associated feedback parameter α_x is positive (positive feedback) and dampens the temperature response

ACCEPTED VERSION SUBJECT TO FINAL EDITING

when α_x is negative (negative feedback). New research since AR5 emphasises how feedbacks can vary over different timescales (Section 7.4.4) and with climate state (Section 7.4.3), giving rise to the concept of an *effective feedback parameter* that may be different from the equilibrium value of the feedback parameter governing ECS (Section 7.4.3).

The ***equilibrium climate sensitivity***, ***ECS*** (units: °C), is defined as the equilibrium value of ΔT in response to a sustained doubling of atmospheric CO_2 concentration from a pre-industrial reference state. The value of ERF for this scenario is denoted by ΔF_{2xCO2}, giving $ECS = -\Delta F_{2xCO2}/\alpha$ from Equation (7.1) applied at equilibrium (see Box 7.1, Figure 1a and Section 7.5). Equilibrium refers to a steady state where ΔN averages to zero over a multi-century period. ECS is representative of the multi-century to millennial ΔT response to ΔF_{2xCO2}, and is based on a CO_2 concentration change so any feedbacks that affect the atmospheric concentration of CO_2 do not influence its value. As employed here, ECS also excludes the long-term response of the ice sheets (Section 7.4.2.6) which may take multiple millennia to reach equilibrium, but includes all other feedbacks. Due to a number of factors, studies rarely estimate ECS or α at equilibrium or under CO_2 forcing alone. Rather, they give an *effective feedback parameter* (Section 7.4.1 and Box 7.1, Figure 1b) or an *effective ECS* (Section 7.5.1 and Box 7.1, Figure 1b), which represent approximations to the true values of α or ECS. The *effective ECS* represents the equilibrium value of ΔT in response to a sustained doubling of atmospheric CO_2 concentration that would occur assuming the *effective feedback parameter* applied at that equilibrium state. For example, a feedback parameter can be estimated from the linear slope of ΔN against ΔT over a set number of years within ESM simulations of an abrupt doubling or quadrupling of atmospheric CO_2 ($2\times CO_2$ or $4\times CO_2$, respectively), and the ECS can be estimated from the intersect of this regression line with $\Delta N = 0$ (see Box 7.1, Figure 1b). To infer ECS from a given estimate of effective ECS necessitates that assumptions are made for how ERF varies with CO_2 concentration (Section 7.3.2) and how the slope of ΔN against ΔT relates to the slope of the straight line from ERF to ECS (see Section 7.5 and Box 7.1, Figure 1b). Care has to be taken when comparing results across different lines of evidence to translate their estimates of the effective ECS into the ECS definition used here (Section 7.5.5).

The ***transient climate response, TCR*** (units: °C), is defined as the ΔT for the hypothetical scenario in which CO_2 increases at 1% yr^{-1} from a pre-industrial reference state to the time of a doubling of atmospheric CO_2 concentration (year 70) (Section 7.5). TCR is based on a CO_2 concentration change, so any feedbacks that affect the atmospheric concentration of CO_2 do not influence its value. It is a measure of transient warming accounting for the strength of climate feedbacks and ocean heat uptake. The ***transient climate response to cumulative emissions of carbon dioxide*** (***TCRE***) is defined as the transient ΔT per 1000 Gt C of cumulative CO_2 emission increase since preindustrial. TCRE combines information on the airborne fraction of cumulative CO_2 emissions (the fraction of the total CO_2 emitted that remains in the atmosphere at the time of doubling, which is determined by carbon cycle processes) with information on the TCR. TCR is assessed in this chapter, whereas TCRE is assessed in Chapter 5, Section 5.5.

[END BOX 7.1 HERE]

7.2 Earth's energy budget and its changes through time

Earth's energy budget encompasses the major energy flows of relevance for the climate system (Figure 7.2). Virtually all the energy that enters or leaves the climate system does so in the form of radiation at the TOA. The TOA energy budget is determined by the amount of incoming solar (shortwave) radiation and the outgoing radiation that is composed of reflected solar radiation and outgoing thermal (longwave) radiation emitted by the climate system. In a steady state climate, the outgoing and incoming radiative components are essentially in balance in the long-term global mean, although there are still fluctuations around this balanced state that arise through internal climate variability (Brown et al., 2014; Palmer and McNeall, 2014). However, anthropogenic forcing has given rise to a persistent imbalance in the global mean TOA radiation budget that is often referred to as Earth's energy imbalance (e.g., Trenberth et al., 2014; von Schuckmann et al., 2016) and is a key element in energy budget framework (N, Box 7.1, Equation 7.1) and an important metric of the rate of global climate change (Hansen et al., 2005a; von Schuckmann et al., 2020). In addition to the TOA energy fluxes, Earth's energy budget also includes the internal flows of energy within the climate

ACCEPTED VERSION SUBJECT TO FINAL EDITING

system, which characterize the climate state. The surface energy budget consists of the net solar and thermal radiation as well as the non-radiative components such as sensible, latent and ground heat fluxes (Figure 7.2 upper panel). It is a key driver of the global water cycle, atmosphere and ocean dynamics, as well as a variety of surface processes.

7.2.1 Present-day energy budget

Figure 7.2 (upper panel) shows a schematic representation of Earth's energy budget for the early 21st century, including globally-averaged estimates of the individual components (Wild et al., 2015). Clouds are important modulators of the global energy fluxes. Thus, any perturbations in the cloud fields, such as forced by aerosol-cloud interactions (Section 7.3) or through cloud feedbacks (Section 7.4) can have a strong influence on the energy distribution in the climate system. To illustrate the overall effects that clouds exert on the energy fluxes, Figure 7.2 (lower panel) also shows the energy budget in the absence of clouds, with otherwise identical atmospheric and surface radiative properties. It has been derived by taking into account information contained in both in-situ and satellite radiation measurements taken under cloud-free conditions (Wild et al., 2019). A comparison of the upper and lower panels in Figure 7.2 shows that without clouds, 47 W m^{-2} less solar radiation is reflected back to space globally (53 ± 2 W m^{-2} instead of 100 ± 2 W m^{-2}), while 28 W m^{-2} more thermal radiation is emitted to space (267 ± 3 W m^{-2} instead of 239± 3 W m^{-2}). As a result, there is a 20 W m^{-2} radiative imbalance at the TOA in the clear-sky energy budget (Figure 7.2 lower panel), suggesting that the Earth would warm substantially if there were no clouds.

[START FIGURE 7.2 HERE]

Figure 7.2: Schematic representation of the global mean energy budget of the Earth (upper panel), and its equivalent without considerations of cloud effects (lower panel). Numbers indicate best estimates for the magnitudes of the globally averaged energy balance components in W m^{-2} together with their uncertainty ranges in parentheses (5–95 % confidence range), representing climate conditions at the beginning of the 21st century. Note that the cloud-free energy budget shown in the lower panel is not the one that Earth would achieve in equilibrium when no clouds could form. It rather represents the global mean fluxes as determined solely by removing the clouds but otherwise retaining the entire atmospheric structure. This enables the quantification of the effects of clouds on the Earth energy budget and corresponds to the way clear-sky fluxes are calculated in climate models. Thus, the cloud-free energy budget is not closed and therefore the sensible and latent heat fluxes are not quantified in the lower panel. Adapted from Wild et al. (2015, 2019).

[END FIGURE 7.2 HERE]

AR5 (Church et al., 2013; Hartmann et al., 2013; Myhre et al., 2013b) highlighted the progress in quantifying the TOA radiation budget following new satellite observations that became available in the early 21st Century (Clouds and the Earth's Radiant Energy System, CERES; Solar Radiation and Climate Experiment, SORCE). Progress in the quantification of changes in incoming solar radiation at the TOA is discussed in Chapter 2, Section 2.2. Since AR5, the CERES Energy Balance EBAF Ed4.0 product was released, which includes algorithm improvements and consistent input datasets throughout the record (Loeb et al., 2018a). However, the overall precision of these fluxes (uncertainty in global mean TOA flux 1.7% (1.7 W m^{-2}) for reflected solar and 1.3% (3.0 W m^{-2}) for outgoing thermal radiation at the 90% confidence level) is not sufficient to quantify the Earth's energy imbalance in absolute terms. Therefore, adjustments within the uncertainty ranges of the CERES reflected solar and emitted thermal TOA fluxes were applied to the entire EBAF record to ensure that the net TOA flux for July 2005–June 2015 was consistent with the estimated Earth's energy imbalance for the same period based on ocean heat content (OHC) measurements and energy uptake estimates for the land, cryosphere and atmosphere (Johnson et al., 2016; Riser et al., 2016; Section 7.2.2.2). ESMs typically show good agreement with global mean TOA fluxes from CERES-EBAF. However, as some ESMs are known to calibrate their TOA fluxes to CERES or similar data (Hourdin et al., 2017), this is not necessarily an indication of model accuracy, especially as ESMs show significant

ACCEPTED VERSION SUBJECT TO FINAL EDITING

discrepancies on regional scales, often related to their representation of clouds (Trenberth and Fasullo, 2010; Donohoe and Battisti, 2012; Hwang and Frierson, 2013; Li et al., 2013b; Dolinar et al., 2015; Wild et al., 2015).

The radiation components of the surface energy budget are associated with substantially larger uncertainties than at the TOA, since they are less directly measured by passive satellite sensors from space and require retrieval algorithms and ancillary data for their estimation (Raschke et al., 2016; Kato et al., 2018; Huang et al., 2019). Confidence in the quantification of the global mean surface radiation components has increased recently, as independent estimates now converge to within a few W m^{-2} (Wild, 2017). Current best estimates for downward solar and thermal radiation at Earth's surface are near 185 W m^{-2} and 342 W m^{-2}, respectively (Figure 7.2). These estimates are based on complementary approaches that make use of satellite products from active and passive sensors (L'Ecuyer et al., 2015; Kato et al., 2018) and information from surface observations and Earth System Models (ESMs) (Wild et al., 2015). Inconsistencies in the quantification of the global mean energy and water budgets discussed in AR5 (Hartmann et al., 2013) have been reconciled within the (considerable) uncertainty ranges of their individual components (Wild et al., 2013, 2015; L'Ecuyer et al., 2015). However, on regional scales, the closure of the surface energy budgets remains a challenge with satellite-derived datasets (Loeb et al., 2014; L'Ecuyer et al., 2015; Kato et al., 2016). Nevertheless, attempts have been made to derive surface energy budgets over land and ocean (Wild et al., 2015), over the Arctic (Christensen et al., 2016a) and over individual continents and ocean basins (L'Ecuyer et al., 2015; Thomas et al., 2020). Since AR5, the quantification of the uncertainties in surface energy flux datasets has improved. Uncertainties in global monthly mean downward solar and thermal fluxes in the CERES-EBAF surface dataset are, respectively, 10 W m^{-2} and 8 W m^{-2} (converted to 5% to 95% ranges) (Kato et al., 2018). The uncertainty in the surface fluxes for polar regions is larger than in other regions (Kato et al., 2018) due to the limited number of surface sites and larger uncertainty in surface observations (Previdi et al., 2015). The uncertainties in ocean mean latent and sensible heat fluxes are approximately 11 W m^{-2} and 5 W m^{-2} (converted to 5% to 95% ranges), respectively (L'Ecuyer et al., 2015). A recent review of the latent and sensible heat flux accuracies over the period 2000 to 2007 highlights significant differences between several gridded products over ocean, where root mean squared differences between the multi-product ensemble and data at more than 200 moorings reached up to 25 W m^{-2} for latent heat and 5 W m^{-2} for sensible heat (Bentamy et al., 2017). This uncertainty stems from the retrieval of flux-relevant meteorological variables, as well as from differences in the flux parameterizations (Yu, 2019). Estimating the uncertainty in sensible and latent heat fluxes over land is difficult because of the large temporal and spatial variability. The flux values over land computed with three global datasets vary by 10% to 20% (L'Ecuyer et al., 2015).

ESMs also show larger discrepancies in their surface energy fluxes than at the TOA due to weaker observational constraints, with a spread of typically 10-20 W m^{-2} in the global average, and an even greater spread at regional scales (Li et al., 2013b; Wild et al., 2013; Boeke and Taylor, 2016; Wild, 2017; Zhang et al., 2018a; Wild, 2020). Differences in the land-averaged downward thermal and solar radiation in CMIP5 ESMs amount to more than 30 and 40 W m^{-2}, respectively (Wild et al., 2015). However, in the global multi-model mean, the magnitudes of the energy budget components of the CMIP6 ESMs generally show better agreement with reference estimates than previous model generations (Wild, 2020).

In summary, since AR5, the magnitudes of the global mean energy budget components have been quantified more accurately, not only at the TOA, but also at the Earth's surface, where independent estimates of the radiative components have converged (*high confidence*). Considerable uncertainties remain in regional surface energy budget estimates as well as their representation in climate models.

7.2.2 Changes in Earth's energy budget

7.2.2.1 Changes in Earth's TOA energy budget

Since 2000, changes in the TOA energy fluxes can be tracked from space using CERES satellite observations (Figure 7.3). The variations in TOA energy fluxes reflect the influence of internal climate

ACCEPTED VERSION SUBJECT TO FINAL EDITING

variability, particularly that of ENSO, in addition to radiative forcing of the climate system and climate feedbacks (Allan et al., 2014; Loeb et al., 2018a). For example, globally, the reduction in both outgoing thermal and reflected solar radiation during La Niña conditions in 2008/2009 led to an energy gain for the climate system, whereas enhanced outgoing thermal and reflected solar radiation caused an energy loss during the El Niños of 2002/2003 and 2009/2010 (Figure 7.3; Loeb et al., 2018a). An ensemble of CMIP6 models is able to track the variability in the global mean TOA fluxes observed by CERES, when driven with prescribed sea-surface temperatures (SSTs) and sea-ice concentrations (Figure 7.3; Loeb et al., 2020). Under cloud-free conditions, the CERES record shows a near zero trend in outgoing thermal radiation (Loeb et al., 2018a), which combined with an increasing surface upwelling thermal flux implies an increasing clear-sky greenhouse effect (Raghuraman et al., 2019). Conversely, clear-sky solar reflected TOA radiation in the CERES record covering March 2000 to September 2017 shows a decrease due to reductions in aerosol optical depth in the Northern Hemisphere and sea-ice fraction (Loeb et al., 2018b; Paulot et al., 2018).

An effort to reconstruct variations in the net TOA fluxes back to 1985, based on a combination of satellite data, atmospheric reanalysis and high-resolution climate model simulations (Allan et al., 2014; Liu et al., 2020), exhibits strong interannual variability associated with the volcanic eruption of Mt Pinatubo in 1991 and the ENSO events before 2000. The same reconstruction suggests that Earth's energy imbalance increased by several tenths of a W m^{-2} between the periods 1985–1999 and 2000–2016, in agreement with the assessment of changes in the global energy inventory (Section 7.2.2.2, Box 7.2, Figure 1). Comparisons of year-to-year variations in Earth's energy imbalance estimated from CERES and independent estimates based on ocean heat content change are significantly correlated with similar phase and magnitude (Johnson et al., 2016; Meyssignac et al., 2019), promoting confidence in both satellite and in situ-based estimates (Section 7.2.2.2).

In summary, variations in the energy exchange between Earth and space can be accurately tracked since the advent of improved observations since the year 2000 (*high confidence*), while reconstructions indicate that the Earth's energy imbalance was larger in the 2000s than in the 1985–1999 period (*high confidence*).

[START FIGURE 7.3 HERE]

Figure 7.3: Anomalies in global mean all-sky TOA fluxes from EBAF Ed4.0 (solid black lines) and various CMIP6 climate models (coloured lines) in terms of (a) reflected solar, (b) emitted thermal and (c) net TOA fluxes. The multi-model means are additionally depicted as dotted black lines. Model fluxes stem from simulations driven with prescribed SSTs and all known anthropogenic and natural forcings. Shown are anomalies of 12-month running means. All flux anomalies are defined as positive downwards, consistent with the sign convention used throughout this chapter. The correlations between the multi-model means (dotted black lines) and the CERES records (solid black lines) for 12-month running means are 0.85, 0.73 and 0.81 for the global mean reflected solar, outgoing thermal and net TOA radiation, respectively. Adapted from Loeb et al. (2020). Further details on data sources and processing are available in the chapter data table (Table 7.SM.14).

[END FIGURE 7.3 HERE]

7.2.2.2 Changes in the global energy inventory

The global energy inventory quantifies the integrated energy gain of the climate system associated with global ocean heat uptake, warming of the atmosphere, warming of the land, and melting of ice. Due to energy conservation, the rate of accumulation of energy in the Earth system (Section 7.1) is equivalent to the Earth energy imbalance (N in Box 7.1, Equation 7.1). On annual and longer timescales, changes in the global energy inventory are dominated by changes in global OHC (Rhein et al., 2013; Palmer and McNeall, 2014; Johnson et al., 2016). Thus, observational estimates and climate model simulations of OHC change are critical to the understanding of both past and future climate change (Chapter 2, Section 2.3.3.1, Chapter 3, Section 3.5.1.3, Chapter 4, Section 4.5.2.1, Chapter 9, Section 9.2.2.1).

ACCEPTED VERSION SUBJECT TO FINAL EDITING

Since AR5, both modelling and observational-based studies have established Earth's energy imbalance (characterised by OHC change) as a more robust metric of the rate of global climate change than GSAT on interannual-to-decadal timescales (Palmer and McNeall, 2014; von Schuckmann et al., 2016; Wijffels et al., 2016; Cheng et al., 2018; Allison et al., 2020a). This is because GSAT is influenced by large unforced variations, for example linked to ENSO and Pacific decadal variability (Roberts et al., 2015; Yan et al., 2016; Cheng et al., 2018). Measuring OHC change more comprehensively over the full ocean depth results in a higher signal-to-noise ratio and a timeseries that increases steadily over time (Box7.2, Figure 1; Allison et al., 2020). In addition, understanding of the potential effects of historical ocean sampling on estimated global ocean heating rates has improved (Durack et al., 2014; Good, 2017; Allison et al., 2019) and there are now more estimates of OHC change available that aim to mitigate the effect of limited observational sampling in the Southern Hemisphere (Lyman and Johnson, 2008; Cheng et al., 2017; Ishii et al., 2017).

The assessment of changes in the global energy inventory for the periods 1971-2018, 1993-2018 and 2006–2018 draws upon the latest observational timeseries and the assessments presented in other chapters of this report. The estimates of OHC change come directly from the assessment presented in Chapter 2, Section 2.3.3.1. The assessment of land and atmospheric heating comes from von Schuckmann et al. (2020), based on the estimates of Cuesta-Valero et al. (2021) and Steiner et al. (2020), respectively. Heating of inland waters, including lakes, reservoirs and rivers, is estimated to account for < 0.1 % of the total energy change, and is therefore neglected from this assessment (Vanderkelen et al., 2020). The cryosphere contribution from melting of grounded ice is based on the mass loss assessments presented in Chapter 9, Sections 9.4.1 (Greenland ice sheet), 9.4.2 (Antarctic ice sheet) and 9.5.1 (glaciers). Following AR5, the estimate of heating associated with loss of Arctic sea ice is based on a reanalysis (Schweiger et al., 2011), following the methods described by Slater et al. (2021). Chapter 9, Section 9.3.2 finds no significant trend in Antarctic sea ice area over the observational record, a zero contribution is assumed. Ice melt associated with the calving and thinning of floating ice shelves are based on the decadal rates presented in Slater et al. (2021). For all cryospheric components, mass loss is converted to heat input using a latent heat of fusion of 3.34×10^5 J Kg^{-1} C^{-1} with the second-order contributions from variations associated with ice type and warming of ice from sub-freezing temperatures neglected, as in AR5. The net change in energy, quantified in Zetta Joules (1 ZJ = 10^{21} Joules), is computed for each component as the difference between the first and last year of each period (Table 7.1). The uncertainties in the depth-interval contributions to OHC are summed to get the uncertainty in global OHC change. All other uncertainties are assumed to be independent and added in quadrature.

[START TABLE 7.1 HERE]

Table 7.1: Contributions of the different components of the global energy inventory for the periods 1971 to 2018, 1993 to 2018 and 2006 to 2018 (Box 7.2, Cross-chapter box 9.1). Energy changes are computed as the difference between annual mean values or year mid-points. The total heating rates correspond to Earth's energy imbalance and are expressed per unit area of Earth's surface.

Component	1971 to 2018		1993 to 2018		2006 to 2018	
	Energy Gain (ZJ)	%	Energy Gain (ZJ)	%	Energy Gain (ZJ)	%
Ocean	396.0 [285.7 to 506.2]	91.0	263.0 [194.1 to 331.9]	90.9	138.8 [86.4 to 191.3]	90.7
0-700 m	241.6 [162.7 to 320.5]	55.6	151.5 [114.1 to 188.9]	52.4	75.4 [48.7 to 102.0]	49.3
700-2000 m	123.3 [96.0 to 150.5]	28.3	82.8 [59.9 to 105.6]	28.6	49.7 [29.0 to 70.4]	32.4
> 2000 m	31.0 [15.7 to 46.4]	7.1	28.7 [14.5 to 43.0]	9.9	13.8 [7.0 to 20.6]	9.0
Land	21.8 [18.6 to 25.0]	5.0	13.7 [12.4 to 14.9]	4.7	7.2 [6.6 to 7.8]	4.7
Cryosphere	11.5 [9.0 to 14.0]	2.7	8.8 [7.0 to 10.6]	3.0	5.4 [3.9 to 6.8]	3.5
Atmosphere	5.6 [4.6 to 6.7]	1.3	3.8 [3.2 to 4.3]	1.3	1.6 [1.2 to 2.1]	1.1
TOTAL	**434.9 [324.5 to 545.5] ZJ**		**289.2 [220.3 to 358.2] ZJ**		**153.1 [100.6 to 205.5] ZJ**	

ACCEPTED VERSION SUBJECT TO FINAL EDITING

Heating Rate	**0.57 [0.43 to 0.72] W m^{-2}**	**0.72 [0.55 to 0.89] W m^{-2}**	**0.79 [0.52 to 1.06] W m^{-2}**

[END TABLE 7.1 HERE]

For the period 1971–2010, AR5 (Rhein et al., 2013) found an increase in the global energy inventory of 274 [196 to 351] ZJ with a 93% contribution from total OHC change, about 3% for both ice melt and land heating, and about 1% for warming of the atmosphere. For the same period, this Report finds an upwards revision of OHC change for the upper (< 700 m depth) and deep (> 700 m depth) ocean of about 8% and 20% compared to AR5 and a modest increase in the estimated uncertainties associated with the ensemble approach of Palmer et al. (2021). The other substantive change compared to AR5 is the updated assessment of land heating, with values approximately double those assessed previously, based on a more comprehensive analysis of the available observations (von Schuckmann et al., 2020; Cuesta-Valero et al., 2021). The result of these changes is an assessed energy gain of 329 [224 to 434] ZJ for the period 1971–2010, which is consistent with AR5 within the estimated uncertainties, despite the systematic increase.

The assessed changes in the global energy inventory (Box 7.2, Figure 1a; Table 7.1) yields an average value for Earth's energy imbalance (*N*, Box 7.1, Equation 7.1) of 0.57 [0.43 to 0.72] W m^{-2} for the period 1971 to 2018, expressed relative to Earth's surface area (*high confidence*). The estimates for the periods 1993 to 2018 and 2006 to 2018 yield substantially larger values of 0.72 [0.55 to 0.89] W m^{-2} and 0.79 ± [0.52 to 1.06] W m^{-2}, respectively, consistent with the increased radiative forcing from greenhouse gases (*high confidence*). To put these numbers in context, the 2006–2018 average Earth system heating is equivalent to approximately 20 times the rate of global energy consumption in 2018[1].

Consistent with AR5 (Rhein et al., 2013), ocean warming dominates the changes in total Earth system heating (*high confidence*), accounting for 91% of the observed change for all periods considered (Table 7.1). The contributions from the other components across all periods are approximately 5% from land heating, 3% for cryosphere heating and 1% associated with warming of the atmosphere (*high confidence*). The assessed percentage contributions are similar to the recent study by von Schuckmann et al. (2020) and the total heating rates are consistent within the assessed uncertainties. Cross-validation of heating rates based on satellite and in situ observations (Section 7.2.2.1) and closure of the global sea-level budget using consistent datasets (Cross-Chapter Box 9.1; Chapter 9, Table 9.5) strengthen scientific confidence in the assessed changes in the global energy inventory relative to AR5.

7.2.2.3 Changes in Earth's surface energy budget

AR5 (Hartmann et al., 2013) reported pronounced changes in multi-decadal records of in situ observations of surface solar radiation, including a widespread decline between the 1950s and 1980s, known as "global dimming", and a partial recovery thereafter, termed "brightening" (see also Chapter 12, Section 12.4). Over the past decades, these changes have interacted with closely-related elements of climate change, such as global and regional warming rates (Li et al., 2016b; Wild, 2016; Du et al., 2017; Zhou et al., 2018a), glacier melt (Ohmura et al., 2007; Huss et al., 2009), the intensity of the global water cycle (Wild, 2012) and terrestrial carbon uptake (Mercado et al., 2009). These observed changes have also been used as emergent constraints to quantify aerosol effective radiative forcing (see Section 7.3.3.3).

Since AR5, additional evidence for dimming and/or subsequent brightening up to several percent per decade, based on direct surface observations, has been documented in previously less studied areas of the globe, such as in Iran, Bahrain, Tenerife, Hawaii, the Taklaman desert and the Tibetan Plateau (Elagib and Alvi, 2013; You et al., 2013; Garcia et al., 2014; Longman et al., 2014; Rahimzadeh et al., 2015). Strong decadal trends in surface solar radiation remain evident after careful data quality assessment and homogenization of long-

[1] https://ourworldindata.org/energy, accessed 13 April 2021

ACCEPTED VERSION SUBJECT TO FINAL EDITING

term records (Sanchez-Lorenzo et al., 2013; Manara et al., 2015; Sanchez-Lorenzo et al., 2015; Wang et al., 2015; Li et al., 2016b; Manara et al., 2016; Wang and Wild, 2016; He et al., 2018b; Yang et al., 2018). Since AR5, new studies on the potential effects of urbanization on solar radiation trends indicate that these effects are generally small, with the exception of some specific sites in Russia and China (Wang et al., 2014; Imamovic et al., 2016; Tanaka et al., 2016). Also, surface-based solar radiation observations have been shown to be representative over large spatial domains of up to several degrees latitude/longitude on monthly and longer timescales (Hakuba et al., 2014; Schwarz et al., 2018). Thus, there is *high confidence* that the observed dimming between the 1950s and 1980s and subsequent brightening are robust and do not arise from measurement artefacts or localised phenomena.

As noted in AR5 (Hartmann et al., 2013) and supported by recent studies, the trends in surface solar radiation are less spatially coherent since the beginning of the 21st century, with evidence for continued brightening in parts of Europe and the USA, some stabilization in China and India, and dimming in other areas (Augustine and Dutton, 2013; Sanchez-Lorenzo et al., 2015; Manara et al., 2016; Soni et al., 2016; Wang and Wild, 2016; Jahani et al., 2018; Pfeifroth et al., 2018; Yang et al., 2018; Schwarz et al., 2020). The CERES-EBAF satellite-derived dataset of surface solar radiation (Kato et al., 2018) does not indicate a globally significant trend over the short period 2001–2012 (Zhang et al., 2015), whereas a statistically significant increase in surface solar radiation of +3.4 W m^{-2} per decade over the period 1996–2010 has been found in the Satellite Application Facility on Climate Monitoring (CM SAF) record of the geostationary satellite Meteosat, which views Europe, Africa and adjacent ocean (Posselt et al., 2014).

Since AR5 there is additional evidence that strong decadal changes in surface solar radiation have occurred also under cloud-free conditions, as shown for long term observational records in Europe, USA, China, India and Japan (Xu et al., 2011; Gan et al., 2014; Manara et al., 2016; Soni et al., 2016; Tanaka et al., 2016; Kazadzis et al., 2018; Li et al., 2018a; Yang et al., 2019; Wild et al., 2021). This suggests that changes in the composition of the cloud-free atmosphere, primarily in aerosols, contributed to these variations, particularly since the second half of the 20th century (Wild, 2016). Water vapour and other radiatively active gases seem to have played a minor role (Wild, 2009; Mateos et al., 2013; Posselt et al., 2014; Yang et al., 2019). For Europe and East Asia, modelling studies also point to aerosols as an important factor for dimming and brightening by comparing simulations that include/exclude variations in anthropogenic aerosol and aerosol-precursor emissions (Golaz et al., 2013; Nabat et al., 2014; Persad et al., 2014; Folini and Wild, 2015; Turnock et al., 2015; Moseid et al., 2020). Moreover, decadal changes in surface solar radiation have often occurred in line with changes in anthropogenic aerosol emissions and associated aerosol optical depth (Streets et al., 2006; Wang and Yang, 2014; Storelvmo et al., 2016; Wild, 2016; Kinne, 2019). However, further evidence for the influence of changes in cloudiness on dimming and brightening is emphasized in some studies (Augustine and Dutton, 2013; Parding et al., 2014; Stanhill et al., 2014; Pfeifroth et al., 2018; Antuña-Marrero et al., 2019). Thus, the contribution of aerosol and clouds to dimming and brightening is still debated. The relative influence of cloud-mediated aerosol effects versus direct aerosol radiative effects on dimming and brightening in a specific region may depend on the prevailing pollution levels (Wild, 2016; Section 7.3.3).

ESMs and reanalyses often do not reproduce the full extent of observed dimming and brightening (Wild and Schmucki, 2011; Allen et al., 2013; Zhou et al., 2017a; Storelvmo et al., 2018; Moseid et al., 2020; Wohland et al., 2020), potentially pointing to inadequacies in the representation of aerosol mediated effects or related emission data. The inclusion of assimilated aerosol optical depth inferred from satellite retrievals in the MERRA2 reanalysis (Buchard et al., 2017; Randles et al., 2017) helps to improve the accuracy of the simulated surface solar radiation changes in China (Feng and Wang, 2019). However, non-aerosol related deficiencies in model representations of clouds and circulation, and/or an underestimation of natural variability, could further contribute to the lack of dimming and brightening in ESMs (Wild, 2016; Storelvmo et al., 2018).

AR5 reported evidence for an increase in surface downward thermal radiation based on different studies covering in total 1964–2008, in line with expectation from an increased radiative forcing from greenhouse gases and the warming and moistening of the atmosphere. Updates of the longest observational records from the Baseline Surface Radiation Network continue to show an increase at the majority of the sites, in line with

ACCEPTED VERSION SUBJECT TO FINAL EDITING

an overall increase predicted by ESMs on the order of 2 W m^{-2} $decade^{-1}$ (Wild, 2016). Upward longwave radiation at the surface is rarely measured but expected to have increased over the same period due to rising surface temperatures.

Turbulent fluxes of latent and sensible heat are also an important part of the surface energy budget (Figure 7.2). Large uncertainties in measurements of surface turbulent fluxes continue to prevent the determination of their decadal changes. Nevertheless, over the ocean, reanalysis-based estimates of linear trends from 1948 to 2008 indicate high spatial variability and seasonality. Increases in magnitudes of 4 to 7 W m^{-2} $decade^{-1}$ for latent heat and 2 to 3 W m^{-2} $decade^{-1}$ for sensible heat in the western boundary current regions are mostly balanced by decreasing trends in other regions (Gulev and Belyaev, 2012). Over land, the terrestrial latent heat flux is estimated to have increased in magnitude by 0.09 W m^{-2} $decade^{-1}$ from 1989 to 1997, and subsequently decreased by 0.13 W m^{-2} $decade^{-1}$ from 1998 to 2005 due to soil moisture limitation mainly in the Southern Hemisphere (derived from Mueller et al. (2013)). These trends are small in comparison to the uncertainty associated with satellite-derived and in-situ observations, as well as from land surface models forced by observations and atmospheric reanalyses. Ongoing advances in remote sensing of evapotranspiration from space (Mallick et al., 2016; Fisher et al., 2017; McCabe et al., 2017b, 2017a), as well as terrestrial water storage (Rodell et al., 2018) may contribute to future constraints on changes in latent heat flux.

In summary, since AR5, multidecadal trends in surface solar radiation up to several percent per decade have been detected at many more locations also in remote areas. There is *high confidence* that these trends are widespread, and not localised phenomena or measurement artefacts. The origin of these trends is not fully understood, although there is evidence that anthropogenic aerosols have made a substantial contribution (*medium confidence*). There is *medium confidence* that downward and upward thermal radiation has increased since the 1970s, while there remains *low confidence* in the trends in surface sensible and latent heat.

[START BOX 7.2 HERE]

BOX 7.2: The Global Energy Budget

This box assesses the present knowledge of the global energy budget for the period 1971–2018, i.e. the balance between radiative forcing, the total climate feedback and observations of the changes in the global energy inventory (Box 7.2, Figure 1a, d).

The net ERF of the Earth system since 1971 has been positive (Box 7.2, Figure 1b, e; Section 7.3), mainly as a result of increases in atmospheric greenhouse gas concentrations (Chapter 2, Section 2.2.8 and Section 7.3.2). The ERF of these positive forcing agents have been partly offset by that of negative forcing agents, primarily due to anthropogenic aerosols (Section 7.3.3), which dominate the overall uncertainty. The net energy inflow to the Earth system from ERF since 1971 is estimated to be 937 ZJ (1 ZJ = 10^{21} J) with a *likely* range of 644 to 1259 ZJ (Box 7.2, Figure 1b).

The ERF-induced heating of the climate system results in increased thermal radiation to space via the Planck response, but the picture is complicated by a variety of climate feedbacks (Box 7.1; Section 7.4.2) that also influence Earth's radiative response (Box 7.2, Figure 1c). The total radiative response is estimated by multiplying the assessed net feedback parameter, α, from process-based evidence (Section 7.4.2, Table 7.10) with the observed GSAT change for the period (Chapter 2, Cross Chapter Box 2.3) and time-integrating (Box 7.2, Figure 1c). The net energy outflow from the Earth system associated with the integrated radiative response 1971 is estimated to be 621 ZJ with a *likely* range of 419 to 823 ZJ. Assuming a pattern effect (Section 7.4.4) on α of -0.5 W m^{-2} C^{-1} would lead to a systematically larger energy outflow by about 250 ZJ.

Combining the *likely* range of integrated radiative forcing (Box 7.2, Figure 1b) with the central estimate of integrated radiative response (Box 7.2, Figure 1c) gives a central estimate and *likely* range of 340 [47 to 662] ZJ (Box 7.2, Figure 1f). Combining the *likely* range of integrated radiative response with the central estimate

ACCEPTED VERSION SUBJECT TO FINAL EDITING

of integrated radiative forcing gives a *likely* range of 340 [147 to 527] ZJ (Box 7.2, Figure 1f). Both calculations yield an implied energy gain in the climate system that is consistent with an independent observation-based assessment of the increase in the global energy inventory expressed relative to the estimated 1850-1900 Earth energy imbalance (Box 7.2, Figure 1a; Section 7.5.2) with a central estimate and *very likely* range of 284 [96 to 471] ZJ (*high confidence*) (Box 7.2, Figure 1d; Table 7.1). Estimating the total uncertainty associated with radiative forcing and radiative response remains a scientific challenge and depends on the degree of correlation among the two (Box 7.2, Figure 1f). However, the central estimate of observed energy change falls well with the estimated *likely* range assuming either correlated or uncorrelated uncertainties. Furthermore, the energy budget assessment would accommodate a substantial pattern effect (Section 7.4.4.3) during 1971–2018 associated with systematically larger values of radiative response (Box 7.2, Figure 1c), and potentially improved closure of the global energy budget. For the period 1970-2011, AR5 reported that the global energy budget was closed within uncertainties (*high confidence*) and consistent with the *likely* range of assessed climate sensitivity (Church et al., 2013). This report provides a more robust quantitative assessment based on additional evidence and improved scientific understanding.

In addition to new and extended observations (Section 7.2.2), confidence in the observed accumulation of energy in the Earth system is strengthened by cross-validation of heating rates based on satellite and in situ observations (Section 7.2.2.1) and closure of the global sea-level budget using consistent datasets (Cross-Chapter Box 9.1; Chapter 9, Table 9.5). Overall, there is *high confidence* that the global energy budget is closed for 1971–2018 with improved consistency compared to AR5

[START BOX 7.2, FIGURE 1 HERE]

Box 7.2, Figure 1: Estimates of the net cumulative energy change (ZJ = 10^{21} Joules) for the period 1971–2018 associated with: (a) observations of changes in the Global Energy Inventory (b) Integrated Radiative Forcing; (c) Integrated Radiative Response. Black dotted lines indicate the central estimate with *likely* and *very likely* ranges as indicated in the legend. The grey dotted lines indicate the energy change associated with an estimated pre-industrial Earth energy imbalance of 0.2 W m^{-2} (panel a) and an illustration of an assumed pattern effect of –0.5 W m^{-2} °C^{-1} (panel c). Background grey lines indicate equivalent heating rates in W m^{-2} per unit area of Earth's surface. Panels (d) and (e) show the breakdown of components, as indicated in the legend, for the Global Energy Inventory and Integrated Radiative Forcing, respectively. Panel (f) shows the Global Energy Budget assessed for the period 1971–2018, i.e. the consistency between the change in the Global Energy Inventory relative to pre-industrial and the implied energy change from Integrated Radiative Forcing plus Integrated Radiative Response under a number of different assumptions, as indicated in the figure legend, including assumptions of correlated and uncorrelated uncertainties in Forcing plus Response. Shading represents the *very likely* range for observed energy change relative to pre-industrial and *likely* range for all other quantities. Forcing and Response timeseries are expressed relative to a baseline period of 1850–1900. Further details on data sources and processing are available in the chapter data table (Table 7.SM.14).

[END BOX 7.2, FIGURE 1 HERE]

[END BOX 7.2 HERE]

7.3 Effective radiative forcing

Effective radiative forcing (ERF) quantifies the energy gained or lost by the Earth system following an imposed perturbation (for instance in greenhouse gases, aerosols or solar irradiance). As such it is a fundamental driver of changes in the Earth's TOA energy budget. ERF is determined by the change in the net downward radiative flux at the TOA (see Box 7.1) after the system has adjusted to the perturbation but excluding the radiative response to changes in surface temperature. This section outlines the methodology for ERF calculations in Section 7.3.1 and then assesses the ERF due to greenhouse gases in Section 7.3.2, aerosols in Section 7.3.3 and other natural and anthropogenic forcing agents in Section 7.3.4. These are brought together in Section 7.3.5 for an overall assessment of the present-day ERF and its evolution over the

ACCEPTED VERSION SUBJECT TO FINAL EDITING

historical time period since 1750 until 2019. The same section also evaluates the surface temperature response to individual ERFs.

7.3.1 Methodologies and representation in models; overview of adjustments

As introduced in Box 7.1, AR5 (Boucher et al., 2013; Myhre et al., 2013b) recommended ERF as a more useful measure of the climate effects of a physical driver than the stratospheric-temperature-adjusted radiative forcing (SARF) adopted in earlier assessments. AR5 assessed that the ratios of surface temperature change to forcing resulting from perturbations of different forcing agents were more similar between species using ERF than SARF. ERF extended the SARF concept to account for not only adjustments to stratospheric temperatures, but also responses in the troposphere and effects on clouds and atmospheric circulation, referred to as "adjustments". For more details see Box 7.1. Since circulation can be affected, these responses are not confined to the locality of the initial perturbation (unlike the traditional stratospheric-temperature adjustment).

This chapter defines "adjustments" as those changes caused by the forcing agent that are independent of changes in surface temperature, rather than defining a specific timescale. AR5 used the terminology "rapid adjustment", but in this assessment the definition is based on the independence from surface temperature rather than the rapidity. The definition of ERF in Box 7.1 aims to have a clean separation between forcing (energy budget changes that are not mediated by surface temperature) and feedbacks (energy budget changes that are mediated by surface temperature). This means that changes in land or ocean surface temperature patterns (for instance as identified by Rugenstein et al. (2016b)) are not included as adjustments. As in previous assessments (Forster et al., 2007; Myhre et al., 2013b) ERFs can be attributed simply to changes in the forcing agent itself or attributed to components of emitted gases (see Chapter 6, Figure 6.12). Because ERFs can include chemical and biospheric responses to emitted gases, they can be attributed to precursor gases even if those gases do not have a direct radiative effect themselves. Similar chemical and biospheric responses to forcing agents can also be included in the ERF in addition to their direct effects.

Instantaneous Radiative Forcing (IRF) is defined here as the change in the net TOA radiative flux following a perturbation, excluding any adjustments. SARF is defined here as the change in the net radiative flux at TOA following a perturbation including the response to stratospheric temperature adjustments. These differ from AR5 where these quantities were defined at the tropopause (Myhre et al., 2013b). The net IRF values will be different using the TOA definition. The net SARF values will be the same as with the tropopause definition, but will have a different partitioning between the longwave and shortwave. Defining all quantities at the TOA enables consistency in breaking down the ERF into its component parts.

The assessment of ERFs in AR5 was preliminary because ERFs were only available for a few forcing agents, so for many forcing agents the report made the assumption that ERF and SARF were equivalent. A body of work published since AR5 is discussed in this section that has computed ERFs across many more forcing agents and models, closely examined the methods of computation, quantified the processes involved in causing adjustments and examined how well ERFs predict the ultimate temperature response. This work is assessed to have led to a much-improved understanding and increased confidence in the quantification of radiative forcing across the Report. These same techniques allow for an evaluation of radiative forcing within Earth System Models (ESMs) as a key test of their ability to represent both historical and future temperature changes (Chapter 3, Section 3.3.1 and Chapter 4, Section 4.3.4).

The ERF for a particular forcing agent is the sum of the IRF and the contribution from the adjustments, so in principle this could be constructed bottom-up by calculating the IRF and adding in the adjustment contributions one-by-one or together. However, there is no simple way to derive the global tropospheric adjustment terms or adjustments related to circulation changes without using a comprehensive climate model (e.g., CMIP5/6). There have been two main modelling approaches used to approximate the ERF definition in Box 7.1. The first approach is to use the assumed linearity (Equation 7.1) to regress the net change in the TOA radiation budget (ΔN) against change in global mean surface temperature (ΔT) following a step change in the forcing agent (Gregory et al., 2004; Box 7.1, Figure 1). The ERF (ΔF) is then derived from ΔN when

ACCEPTED VERSION SUBJECT TO FINAL EDITING

ΔT=0. Regression-based estimates of ERF depend on the temporal resolution of the data used (Modak et al., 2016, 2018). For the first few months of a simulation both surface temperature change and stratospheric temperature adjustment occur at the same time, leading to misattribution of the stratospheric temperature adjustment to the surface temperature feedback. Patterns of sea-surface temperature change also affect estimates of the forcing obtained by regression methods (Andrews et al., 2015). At multidecadal timescales the curvature of the relationship between net TOA radiation and surface temperature can also lead to biases in the ERF estimated from the regression method (Armour et al., 2013; Andrews et al., 2015; Knutti et al., 2017; Section 7.4). The second modelling approach to estimate ERF is to set the ΔT term in Box 7.1 (Equation 7.1) to zero. It is technically difficult to constrain land surface temperatures in ESMs (Shine et al., 2003; Ackerley and Dommenget, 2016; Andrews et al., 2021), so most studies reduce the ΔT term by prescribing the SSTs and sea-ice concentrations in a pair of "fixed-SST" (fSST) simulations with and without the change in forcing agent (Hansen et al., 2005b). An approximation to ERF (ΔF_{fsst}) is then given by the difference in ΔN_{fsst} between the simulations. The fSST method has less noise due to internal variability than the regression method. Nevertheless a 30-year fSST integration or 10 × 20-year regression ensemble needs to be conducted in order to reduce the 5–95% confidence range to 0.1 W m^{-2} (Forster et al., 2016), thus neither method is practical for quantifying the ERF of agents with forcing magnitudes of order 0.1 W m^{-2} or smaller. The internal variability in the fSST method can be further constrained by nudging winds towards a prescribed climatology (Kooperman et al., 2012). This allows the determination of the ERF of forcing agents with smaller magnitudes but excludes adjustments associated with circulation responses (Schmidt et al., 2018). There are insufficient studies to assess whether these circulation adjustments are significant.

Since the near-surface temperature change over land, ΔT_{land}, is not constrained in the fSST method, this response needs to be removed for consistency with the Section 7.1 definition. These changes in the near-surface temperature will also induce further responses in the tropospheric temperature and water vapour that should also be removed to conform with the physical definition of ERF. The radiative response to ΔT_{land} can be estimated through radiative transfer modelling in which a kernel, k, representing the change in net TOA radiative flux per change in unit near-surface temperature change over land (or an approximation using land surface temperature), is precomputed (Smith et al., 2018b; Richardson et al., 2019; Tang et al., 2019; Smith et al., 2020a). Thus ERF $\approx \Delta F_{\text{fsst}} - k\,\Delta T_{\text{land}}$. Since k is negative this means that ΔF_{fsst} underestimates the ERF. For 2×CO_2 this term is around 0.2 W m^{-2} (Smith et al., 2018b, 2020a). There have been estimates of the corrections due to tropospheric temperature and water vapour (Tang et al., 2019; Smith et al., 2020a) showing additional radiative responses of comparable magnitude to those directly from ΔT_{land}. An alternative to computing the response terms directly is to use the feedback parameter, α, (Hansen et al., 2005b; Sherwood et al., 2015; Tang et al., 2019). This gives approximately double the correction compared to the kernel approach (Tang et al., 2019). The response to land surface temperature change varies with location and even for GSAT change k is not expected to be the same as α (Section 7.4). One study where land-surface temperatures are constrained in a model (Andrews et al., 2021) finds this constraint adds +1.0 W m^{-2} to ΔF_{fsst} for 4×CO_2, thus confirming the need for a correction in calculations where this constraint is not applied. For this assessment the correction is conservatively based only on the direct radiative response kernel to ΔT_{land} as this has a strong theoretical basis to support it. While there is currently insufficient corroborating evidence to recommend including tropospheric temperature and water vapour corrections in this assessment, it is noted that the science is progressing rapidly on this topic.

TOA radiative flux changes due to the individual adjustments can be calculated by perturbing the meteorological fields in a climate model's radiative transfer scheme (partial radiative perturbation approach) (Colman, 2015; Mülmenstädt et al., 2019) or by using precomputed radiative kernels of sensitivities of the TOA radiation fluxes to changes in these fields (as done for near-surface temperature change above) (Vial et al., 2013; Zelinka et al., 2014; Zhang and Huang, 2014; Smith et al., 2018b, 2020a). The radiative kernel approach is easier to implement through post-processing of output from multiple ESMs, whereas it is recognized that the partial radiation perturbation approach gives a more accurate estimate of the adjustments within the setup of a single model and its own radiative transfer code. There is little difference between using a radiative kernel from the same or a different model when calculating the adjustment terms, except for stratospheric temperature adjustments where it is important to have sufficient vertical resolution in the stratosphere in the model used to derive the kernel (Smith et al., 2018b, 2020b).

ACCEPTED VERSION SUBJECT TO FINAL EDITING

For comparison with offline radiative transfer calculations the SARFs can be approximated by removing the adjustment terms (apart from stratospheric temperature) from the ERFs using radiative kernels to quantify the adjustment for each meteorological variable. Kernel analysis by Chung and Soden (2015) suggested a large spread in CO_2 SARF across climate models, but their analysis was based on regressing variables in a coupled-ocean experiment rather than using a fSST approach which leads to a large spread due to natural variability (Forster et al., 2016). Adjustments computed from radiative kernels are shown for seven different climate drivers (using a fSST approach) in Figure 7.4. Table 7.2 shows the estimates of SARF, ΔF_{fsst} and ERF (corrected for land surface temperature change) for $2\times CO_2$ from the nine climate models analysed in Smith et al. (2018b). The SARF shows a smaller spread over previous studies (Pincus et al., 2016; Soden et al., 2018) and most estimates are within 10% of the multi-model mean and the assessment of $2\times CO_2$ SARF in Section 7.3.2 (3.75 W m^{-2}). It is not possible from these studies to determine how much of this reduction in spread is due to convergence in the model radiation schemes or the meteorological conditions of the model base states; nevertheless the level of agreement in this and earlier intercomparisons gives *medium confidence* in ESM's ability to represent radiative forcing from CO_2. The $4\times CO_2$ CMIP6 fSST experiments (Smith et al., 2020a) in Table 7.2 include ESMs with varying levels of complexity in aerosols and reactive gas chemistry. The CMIP6 experimental setup allows for further climate effects of CO_2 (including on aerosols and ozone) depending on model complexity. The chemical effects are adjustments to CO_2 but are not separable from the SARF in the diagnosis in Table 7.2. In these particular models, this leads to higher SARF than when only CO_2 varies, however there are insufficient studies to make a formal assessment of composition adjustments to CO_2.

[START TABLE 7.2 HERE]

Table 7.2: SARF, ΔF_{fsst}, and ERF diagnosed from ESMs for fSST CO_2 experiments. $2\times CO_2$ data taken from fixed atmospheric composition experiments (Smith et al., 2018b). $4\times CO_2$ data taken from CMIP6 experiments with interactive aerosols (and interactive gas phase chemistry in some) (Smith et al., 2020a). The radiative forcings from the $4\times CO_2$ experiments are scaled by 0.476 for comparison with $2\times CO_2$ (Meinshausen et al., 2020). SARF is approximated by removing the (non-stratospheric temperature) adjustment terms from the ERF. In Smith et al. (2018b) separation of temperature adjustments into tropospheric and stratospheric contributions is approximate based on a fixed tropopause of 100 hPa at the equator, varying linearly in latitude to 300 hPa at the poles. In Smith et al. (2020b) this separation is based on the model-diagnosed tropopause. ERF is approximated by removing the response to land surface temperature change from ΔF_{fsst}. The confidence range is based on the inter-model standard deviation.

.

$2 \times CO_2$ (W m^{-2}) (Smith et al., 2018b)	SARF	ΔF_{fsst}	ERF
HadGEM2-ES	3.45	3.37	3.58
NorESM1	3.67	3.50	3.70
GISS-E2-R	3.98	4.06	4.27
CanESM2	3.68	3.57	3.77
MIROC-SPRINTARS	3.89	3.62	3.82
NCAR-CESM1-CAM5	3.89	4.08	4.39
HadGEM3	3.48	3.64	3.90
IPSL-CM5A	3.50	3.39	3.61
MPI-ESM	4.27	4.14	4.38
NCAR-CESM1-CAM4	3.50	3.62	3.86
Multi-model Mean and 5-95% confidence range	3.73 ± 0.44	3.70 ± 0.44	3.93 ± 0.48
$0.476 \times 4\times CO_2$ (W m^{-2}) (Smith et al., 2020a)			
ACCESS-CM2	3.56	3.78	3.98
CanESM5	3.67	3.62	3.82
CESM2	3.56	4.24	4.48

ACCEPTED VERSION SUBJECT TO FINAL EDITING

CNRM-CM6-1	3.99	3.81	4.01
CNRM-ESM2-1	3.99	3.77	3.94
EC-Earth3		3.85	4.04
GFDL-CM4	3.65	3.92	4.10
GFDL-ESM4	3.27	3.68	3.85
GISS-E2-1-G	3.78	3.50	3.69
HadGEM3-GC31-LL	3.61	3.85	4.07
IPSL-CM6A-LR	3.84	3.81	4.05
MIROC6	3.63	3.48	3.69
MPI-ESM1-2-LR	3.74	3.97	4.20
MRI-ESM2-0	3.76	3.64	3.80
NorESM2-LM	3.58	3.88	4.10
NorESM2-MM	3.62	3.99	4.22
UKESM1-0-LL	3.49	3.78	4.01
Multi-model Mean and 5-95% confidence range	3.67 ± 0.29	3.80 ± 0.30	4.00 ± 0.32

[END TABLE 7.2 HERE]

[START FIGURE 7.4 HERE]

Figure 7.4: Radiative adjustments at top of atmosphere for seven different climate drivers as a proportion of forcing. Tropospheric temperature (orange), stratospheric temperature (yellow), water vapour (blue), surface albedo (green), clouds (grey) and the total adjustment (black) is shown. For the greenhouse gases (carbon dioxide, methane, nitrous oxide, CFC-12) the adjustments are expressed as a percentage of SARF, whereas for aerosol, solar and volcanic forcing they are expressed as a percentage of IRF. Land surface temperature response (outline red bar) is shown, but included in the definition of forcing. Data from Smith et al. (2018b) for carbon dioxide and methane, Smith et al. (2018b) and Gray et al. (2009) for solar, Hodnebrog et al. (2020b) for nitrous oxide and CFC-12, Smith et al. (2020a) for aerosol, and Marshall et al. (2020) for volcanic. Further details on data sources and processing are available in the chapter data table (Table 7.SM.14).

[END FIGURE 7.4 HERE]

ERFs have been found to yield more consistent values of GSAT change per unit forcing than SARF, i.e. α shows less variation across different forcing agents (Rotstayn and Penner, 2001; Shine et al., 2003; Hansen et al., 2005b; Marvel et al., 2016; Richardson et al., 2019). Having a consistent relationship between forcing and response is advantageous when making climate projections using simple models (Cross-Chapter Box 7.1) or emission-metrics (Section 7.6). The definition of ERF used in this assessment, which excludes the radiative response to land surface temperature changes, brings the α values into closer agreement than when SARF is used (Richardson et al., 2019), although for individual models there are still variations particularly for more geographically localised forcing agents. However, even for ERF, studies find that α is not identical across all forcing agents (Shindell, 2014; Shindell et al., 2015; Modak et al., 2018; Modak and Bala, 2019; Richardson et al., 2019). Section 7.4.4 discusses the effect of different SST response patterns on α. Analysis of the climate feedbacks (Kang and Xie, 2014; Gregory et al., 2016, 2020; Marvel et al., 2016; Duan et al., 2018; Persad and Caldeira, 2018; Stuecker et al., 2018; Krishnamohan et al., 2019) suggests a weaker feedback (i.e., less-negative α) and hence larger sensitivity for forcing of the higher latitudes (particularly the Northern Hemisphere). Nonetheless, as none of these variations are robust across models, the ratio of $1/\alpha$ from non-CO_2 forcing agents (with approximately global distributions) to that from doubling CO_2 is within 10% of unity.

In summary, this Report adopts an estimate of ERF based on the change in TOA radiative fluxes in the absence of GSAT changes. This allows for a theoretically cleaner separation between forcing and feedbacks

ACCEPTED VERSION SUBJECT TO FINAL EDITING

in terms of factors respectively unrelated and related to GSAT change (Box 7.1). ERF can be computed from prescribed SST and sea-ice experiments after removing the TOA energy budget change associated with the land surface temperature response. In this assessment this is removed using a kernel accounting only for the direct radiative effect of the land surface temperature response. To compare these results with sophisticated high spectral resolution radiative transfer models the individual tropospheric adjustment terms can be removed to leave the SARF. SARFs for $2\times CO_2$ calculated by ESMs from this method agree within 10% with the more sophisticated models. The new studies highlighted above suggest that physical feedback parameters computed within this framework have less variation across forcing agents. There is *high confidence* that an α based on ERF as defined here varies by less (less than variation 10% across a range of forcing agents with global distributions), than α based on SARF. For geographically localised forcing agents there are fewer studies and less agreement between them, resulting in *low confidence* that ERF is a suitable estimator of the resulting global mean near-surface temperature response.

7.3.2 Greenhouse Gases

High spectral resolution radiative transfer models provide the most accurate calculations of radiative perturbations due to greenhouse gases (GHGs) with errors in the IRF of less than 1% (Mlynczak et al., 2016; Pincus et al., 2020). They can calculate IRFs with no adjustments, or SARFs by accounting for the adjustment of stratospheric temperatures using a fixed dynamical heating. It is not possible with offline radiation models to account for other adjustments. The high resolution model calculations of SARF for carbon dioxide, methane and nitrous oxide have been updated since AR5, which were based on Myhre et al. (1998). The new calculations include the shortwave forcing from methane and updates to the water vapour continuum (increasing the total SARF of methane by 25%) and account for the absorption band overlaps between carbon dioxide and nitrous oxide (Etminan et al., 2016). The associated simplified expressions, from a re-fitting of the Etminan et al. (2016) results by Meinshausen et al. (2020), are given in Supplementary Table 7.SM.1. The shortwave contribution to the IRF of methane has been confirmed independently (Collins et al., 2018). Since they incorporate known missing effects we assess the new calculations as being a more appropriate representation than Myhre et al. (1998).

As described in Section 7.3.1, ERFs can be estimated using ESMs, however the radiation schemes in climate models are approximations to high spectral resolution radiative transfer models with variations and biases in results between the schemes (Pincus et al., 2015). Hence ESMs alone are not sufficient to establish ERF best estimates for the well-mixed GHGs (WMGHGs). This assessment therefore estimates ERFs from a combined approach that uses the SARF from radiative transfer models and adds the tropospheric adjustments derived from EMSs.

In AR5, the main information used to assess components of ERFs beyond SARF was from Vial et al. (2013) who found a near-zero non-stratospheric adjustment (without correcting for near-surface temperature changes over land) in $4\times CO_2$ CMIP5 model experiments, with an uncertainty of ±10% of the total CO_2 ERF. No calculations were available for other WMGHGs, so ERF was therefore assessed to be approximately equal to SARF (within 10%) for all WMGHGs.

The effect of WMGHGs in ESMs can extend beyond their direct radiative effects to include effects on ozone and aerosol chemistry and natural emissions of ozone and aerosol precursors, and in the case of CO_2 to vegetation cover through physiological effects. In some cases these can have significant effects on the overall radiative budget changes from perturbing WMGHGs within ESMs (Myhre et al., 2013b; Zarakas et al., 2020; O'Connor et al., 2021; Thornhill et al., 2021a). These composition adjustments are further discussed in Chapter 6 (Section 6.4.2).

7.3.2.1 Carbon Dioxide

The SARF for CO_2 has been slightly revised due to updates to spectroscopic data and inclusion of the absorption band overlaps between N_2O and CO_2 (Etminan et al., 2016). The formulae fitting to the Etminan

ACCEPTED VERSION SUBJECT TO FINAL EDITING

et al. (2016) results in Meinshausen et al. (2020) are used. This increases the SARF due to doubling CO_2 slightly from 3.71 W m^{-2} in AR5 to 3.75 W m^{-2}. Tropospheric responses to CO_2 in fSST experiments have been found to lead to an approximate balance in their radiative effects between an increased radiative forcing due to water vapour, cloud and surface albedo adjustments and a decrease due to increased tropospheric temperature and land surface temperature response (Vial et al., 2013; Zhang and Huang, 2014; Smith et al., 2018b, 2020a; Table 7.3). The ΔF_{fsst} includes any effects represented within the ESMs on tropospheric adjustments due to changes in evapotranspiration or leaf area (mainly affecting surface and boundary layer temperature, low cloud amount and albedo) from the CO_2-physiological effects (Doutriaux-Boucher et al., 2009; Cao et al., 2010; Richardson et al., 2018b). The effect on surface temperature (negative longwave response) is consistent with the expected physiological responses and needs to be removed for consistency with the ERF definition. The split between surface and tropospheric temperature responses was not reported in Vial et al. (2013) or Zhang and Huang (2014) but the total of surface and tropospheric temperature response agrees with Smith et al. (2018b, 2020b) giving *medium confidence* in this decomposition. Doutriaux-Boucher et al. (2009) and Andrews et al. (2021) (using the same land surface model) find a 13% and 10% increase respectively in ERF due to the physiological responses to CO_2. The physiological adjustments are therefore assessed to make a substantial contribution to the overall tropospheric adjustment for CO_2 (*high confidence*), but there is insufficient evidence to provide a quantification of the split between physiological and thermodynamic adjustments. These forcing adjustments due to the effects of CO_2 on plant physiology differ from the biogeophysical feedbacks due to the effects of temperature changes on vegetation discussed in Section 7.4.2.5. The adjustment is assumed to scale with the SARF in the absence of evidence for non-linearity. The tropospheric adjustment is assessed from Table 7.3 to be +5% of the SARF with an uncertainty of 5%, which is added to the Meinshausen et al. (2020) formula for SARF. Due to the agreement between the studies and the understanding of the physical mechanisms there is *medium confidence* in the mechanisms underpinning the tropospheric adjustment, but *low confidence* in its magnitude.

[START TABLE 7.3 HERE]

Table 7.3: Adjustments to the TOA CO_2 forcing due to changes in stratospheric temperature, surface and tropospheric temperatures, water vapour, clouds and surface albedo, as a fraction of the SARF. ERF is defined in this report as excluding the surface temperature response.

Percentage of SARF	Surface temp	Trop. temp	Strat. temp	Surface albedo	Water vapour	Clouds	Troposphere (inc. surface)	Troposphere (excl. surface)
Vial et al. (2013)	–20%			2%	6%	11%	–1%	
Zhang and Huang (2014)	–23%		26%		6%	16%	–1%	
Smith et al. (2018b)	–6%	–16%	30%	3%	6%	12%	–1%	+5%
Smith et al. (2020b)	–6%	–15%	35%	3%	6%	15%	+3%	+9%

[END TABLE 7.3 HERE]

The ERF from doubling CO_2 ($2\times CO_2$) from the 1750 level (278 ppm Chapter 2, Section 2.2.3.3) is assessed to be 3.93 ± 0.47 W m^{-2} (*high confidence*). Its assessed components are given in Table 7.4. The combined spectroscopic and radiative transfer modelling uncertainties give an uncertainty in the CO_2 SARF of around 10% or less (Etminan et al., 2016; Mlynczak et al., 2016). The overall uncertainty in CO_2 ERF is assessed as ±12%, as the more uncertain adjustments only account for a small fraction of the ERF (Table 7.3). The $2\times CO_2$ ERF estimate is 0.2 W m^{-2} larger than using the AR5 formula (Myhre et al., 2013b) due to the combined effects of tropospheric adjustments which were assumed to be zero in AR5. CO_2 concentrations have increased from 278 ppm in 1750 to 410 ppm in 2019 (Chapter 2, Section 2.2.3.3). The historical ERF

ACCEPTED VERSION SUBJECT TO FINAL EDITING

estimate from CO_2 is revised upwards from the AR5 value of 1.82 ± 0.38 W m^{-2} (1750 to 2011) to 2.16 ±0.26 W m^{-2} (1750 to 2019) in this assessment, from a combination of the revisions described above (0.06 W m^{-2}) and the 19 ppm rise in atmospheric concentrations between 2011 and 2019 (0.27 W m^{-2}). The ESM estimates of 2×CO_2 ERF (Table 7.2) lie within ±12% of the assessed value (apart from CESM2). The definition of ERF can also include further physiological effects for instance on dust, natural fires and biogenic emissions from the land and ocean, but these are not typically included in the modelling set up for 2×CO_2 ERF.

[START TABLE 7.4 HERE]

Table 7.4: Assessed ERF, SARF and tropospheric adjustments to 2×CO_2 change since preindustrial times compared to the AR5 assessed range (Myhre et al., 2013b). Adjustments are due to changes in tropospheric temperatures, water vapour, clouds and surface albedo and land cover and are taken from Smith et al. (2018b) and assessed as a percentage of SARF (Table 7.3). Uncertainties are based on multi-model spread in Smith et al. (2018b). Note some of the uncertainties are anticorrelated, which means that they do not sum linearly.

2×CO_2 forcing	AR5 SARF/ ERF	SARF (W m^{-2})	Tropospheric temperature adjustment (W m^{-2})	Water vapour adjustment (W m^{-2})	Cloud adjustment (W m^{-2})	Surface albedo and land cover adjustment (W m^{-2})	Total tropospheric adjustment (W m^{-2})	ERF (W m^{-2})
2×CO_2 ERF components	3.71	3.75	–0.60	0.22	0.45	0.11	0.18	3.93
5%–95% uncertainty ranges as percentage of ERF	10% (SARF) 20% (ERF)	<10%	±6%	±4%	±7%	±2%	±7%	±12%

[END TABLE 7.4 HERE]

7.3.2.2 Methane

The SARF for methane (CH_4) has been substantially increased due to updates to spectroscopic data and inclusion of the shortwave absorption (Etminan et al., 2016). Adjustments have been calculated in nine climate models by Smith et al. (2018b). Since CH_4 is found to absorb in the shortwave near infrared, only adjustments from those models including this absorption are taken into account. For these models the adjustments act to reduce the ERF because the shortwave absorption leads to tropospheric heating and reductions in upper tropospheric cloud amounts. The adjustment is –14% ± 15% which counteracts much of the increase in SARF identified by Etminan et al. (2016). Modak et al. (2018) also found negative forcing adjustments from a methane perturbation including shortwave absorption in the NCAR CAM5 model, in agreement with the above assessment. The uncertainty in the shortwave component leads to a higher radiative modelling uncertainty (14%) than for CO_2 (Etminan et al., 2016). When combined with the uncertainty in the adjustment, this gives an overall uncertainty of ± 20%. There is *high confidence* in the spectroscopic revision but only *medium confidence* in the adjustment modification. CH_4 concentrations have increased from 729 ppb in 1750 to 1866 ppb in 2019 (Chapter 2, Section 2.2.3.3). The historical ERF estimate from AR5 of 0.48 ± 0.10 W m^{-2} (1750 to 2011) is revised to 0.54 ± 0.11 W m^{-2} (1750 to 2019) in this assessment from a combination of spectroscopic radiative efficiency revisions (+0.12 W m^{-2}), adjustments (–0.08 W m^{-2}) and the 63 ppb rise in atmospheric CH_4 concentrations between 2011 and 2019 (+0.03 W m^{-2}). As the adjustments are assessed to be small, there is *high confidence* in the overall assessment of ERF from methane. Increased methane leads to tropospheric ozone production and increased stratospheric water vapour, so that an attribution of forcing to methane emissions gives a larger effect than that directly from the methane concentration itself. This is discussed in detail in Chapter 6, Section 6.4.2 and

ACCEPTED VERSION SUBJECT TO FINAL EDITING

shown in Figure 6.12.

7.3.2.3 Nitrous oxide

The tropospheric adjustments to nitrous oxide (N_2O) have been calculated from 5 ESMs as 7% ± 13% of the SARF (Hodnebrog et al., 2020b). This value is therefore taken as the assessed adjustment, but with *low confidence*. The radiative modelling uncertainty is ± 10% (Etminan et al., 2016), giving an overall uncertainty of ± 16%. Nitrous oxide concentrations have increased from 270 ppb in 1750 to 332 ppb in 2019 (Chapter 2, Section 2.2.3.3). The historical ERF estimate from N_2O is revised upwards from 0.17 ± 0.06 W m^{-2} (1750 to 2011) in AR5 to 0.21 ± 0.03 W m^{-2} (1750 to 2019) in this assessment, of which 0.02 W m^{-2} is due to the 7 ppb increase in concentrations, and 0.02 W m^{-2} to the tropospheric adjustment. As the adjustments are assessed to be small there remains *high confidence* in the overall assessment.

Increased nitrous oxide leads to ozone depletion in the upper stratosphere which will make a positive contribution to the direct ERF here (Chapter 6, Section 6.4.2, Figure 6.12) when considering emission-based estimates of ERF.

7.3.2.4 Halogenated species

The stratospheric-temperature adjusted radiative efficiencies (SARF per ppb increase in concentration) for halogenated compounds are reviewed extensively in Hodnebrog et al. (2020a), an update to those used in AR5. Many halogenated compounds have lifetimes short enough that they can be considered short-lived climate forcers (Table 6.1). As such, they are not completely "well-mixed" and their vertical distributions are taken into account when determining their radiative efficiencies. The WMO (World Meteorological Organization, 2018) updated the lifetimes of many halogenated compounds and these were used in Hodnebrog et al. (2020a).

The tropospheric adjustments to chlorofluorocarbons (CFCs), specifically CFC-11 and CFC-12, have been quantified as 13% ± 10% and 12% ± 14% of the SARF respectively (Hodnebrog et al., 2020b). The assessed adjustment to CFCs is therefore 12 % ± 13% with *low confidence* due to the lack of corroborating studies. There have been no calculations for other halogenated species so for these the tropospheric adjustments are therefore assumed to be 0 ± 13% with *low confidence.* The radiative modelling uncertainties are 14% and 24% for compounds with lifetimes greater than and less than 5 years respectively (Hodnebrog et al., 2020a). The overall uncertainty in the ERFs of halogenated compounds is therefore assessed to be 19% and 26% depending on the lifetime. The ERF from CFCs is slowly decreasing, but this is compensated for by the increased forcing from the replacement species (HCFCs and HFCs). The ERF from HFCs has increased by 0.028 ± 0.05 W m^{-2}. Thus, the concentration changes mean that the total ERF from halogenated compounds has increased since AR5 from 0.360 ± 0.036 W m^{-2} to 0.408 ± 0.078 W m^{-2} (Table 7.5). Of this 0.034 W m^{-2} is due to increased radiative efficiencies and tropospheric adjustments, and 0.014 W m^{-2} due to increases in concentrations. As the adjustments are assessed to be small there remains *high confidence* in the overall assessment.

Halogenated compounds containing chlorine and bromine lead to ozone depletion in the stratosphere which will reduce the associated ERF (Morgenstern et al., 2020). Chapter 6, Section 6.4 and Figure 6.12 assess the ERF contributions due to the chemical effects of reactive gases.

7.3.2.5 Ozone

Estimates of the pre-industrial to present-day tropospheric ozone radiative forcing are based entirely on models. The lack of pre-industrial ozone measurements prevents an observational determination. There have been limited studies of ozone ERFs (MacIntosh et al., 2016; Xie et al., 2016; Skeie et al., 2020). Skeie et al. (2020) found little net contribution to the ERF from tropospheric adjustment terms for 1850-2000 change in

ACCEPTED VERSION SUBJECT TO FINAL EDITING

ozone (tropospheric and stratospheric ozone combined), although MacIntosh et al. (2016) suggested that increases in stratospheric or upper tropospheric ozone reduces high cloud and increases low cloud, whereas an increase in lower tropospheric ozone reduces low cloud. Further studies suggest that changes in circulation due to decreases in stratospheric ozone affect Southern Hemisphere clouds and the atmospheric levels of sea salt aerosol that would contribute additional adjustments, possibly of comparable magnitude to the SARF from stratospheric ozone depletion (Grise et al., 2013, 2014, Xia et al., 2016, 2020). ESM responses to changes in ozone depleting substances (ODS) in CMIP6 show a much more negative ERF than would be expected from offline calculations of SARF (Morgenstern et al., 2020; Thornhill et al., 2021b) again suggesting a negative contribution from adjustments. However there is insufficient evidence available to quantify this effect.

Without sufficient information to assess whether the ERFs differ from SARF, this assessment relies on offline radiative transfer calculations of SARF for both tropospheric and stratospheric ozone. Checa-Garcia et al. (2018) found SARF of 0.30 W m^{-2} for changes in ozone (1850–1860 to 2009–2014). These were based on precursor emissions and ODS concentrations from the Coupled Chemistry Model Initiative (CCMI) project (Morgenstern et al., 2017). Skeie et al. (2020) calculated an ozone SARF of 0.41 ± 0.12 W m^{-2} (1850 to 2010) (from five climate models and one chemistry transport model) using CMIP6 precursor emissions and ODS concentrations (excluding models without fully interactive ozone chemistry and one model with excessive ozone depletion). The ozone precursor emissions are higher in CMIP6 than in CCMI which explains much of the increase compared to Checa-Garcia et al. (2018).

Previous assessments have split the ozone forcing into tropospheric and stratospheric components. This does not correspond to the division between ozone production and ozone depletion and is sensitive to the choice of tropopause (Myhre et al., 2013b) (*high confidence*). The contributions to total SARF in CMIP6 (Skeie et al., 2020) are 0.39 ± 0.07 and 0.02 ± 0.07 W m^{-2} for troposphere and stratosphere respectively (using a 150 ppb ozone tropopause definition). This small positive (but with uncertainty encompassing negative values) stratospheric ozone SARF is due to contributions from ozone precursors to lower stratospheric ozone and some of the CMIP6 models showing ozone depletion in the upper stratosphere, where depletion contributes a positive radiative forcing *(medium confidence)*.

As there is insufficient evidence to quantify adjustments, for total ozone the assessed central estimate for ERF is assumed to be equal to SARF (*low confidence*) and follows Skeie et al. (2020) since that study uses the most recent emission data. The dataset is extended over the entire historical period following Skeie et al. (2020) with a SARF for 1750 to 1850 of 0.03 W m^{-2} and for 2010 to 2018 of 0.03 W m^{-2}, to give 0.47 [0.24 to 0.70] W m^{-2} for 1750 to 2019. This maintains the 50% uncertainty (5%–95% range) from AR5 which is largely due to the uncertainty in pre-industrial emissions (Rowlinson et al., 2020). There also *high confidence* that this range includes uncertainty due to the adjustments. The CMIP6 SARF is more positive than the AR5 value of 0.31 W m^{-2} for the period 1850 to 2011 (Myhre et al., 2013b) which was based on the Atmospheric Chemistry and Climate Intercomparison Project (ACCMIP) (Shindell et al., 2013). The assessment is sensitive to the assumptions on precursor emissions used to drive the models, which are larger in CMIP6 than ACCMIP.

In summary, although there is insufficient evidence to quantify adjustments, there is *high confidence* in the assessed range of ERF for ozone changes over the 1750 to 2019 period, giving an assessed ERF of 0.47 [0.24 to 0.70] W m^{-2}.

7.3.2.6 Stratospheric water vapour

This section considers direct anthropogenic effects on stratospheric water vapour by oxidation of methane. Since AR5 the SARF from methane-induced stratospheric water vapour changes has been calculated in two models (Winterstein et al., 2019; O'Connor et al., 2021), both corresponding to 0.09 W m^{-2} (1850 to 2014, by scaling the Winterstein et al., 2019 study). This is marginally larger than the AR5 assessed value of 0.07±0.05 W m^{-2} (Myhre et al., 2013b). However, O'Connor et al. (2021) found the ERF to be approximately zero due to a negative cloud adjustment. Wang and Huang (2020) quantified the adjustment

ACCEPTED VERSION SUBJECT TO FINAL EDITING

terms to a stratospheric water vapour change equivalent to that from a $2\times CO_2$ warming (which has different vertical profile, though also largest in the lower stratosphere). They found that the ERF was less than 50% of the SARF due to high cloud decrease and upper tropospheric warming. The assessed ERF is therefore 0.05±0.05 W m^{-2} with a lower limit reduced to zero and the central value and upper limit reduced to allow for adjustment terms. This still encompasses the two recent SARF studies. There is *medium confidence* in the SARF from agreement with the recent studies and AR5. There is *low confidence* in the adjustment terms.

Stratospheric water vapour may also change as an adjustment to species that warm or cool the upper troposphere-lower stratosphere region (Forster and Joshi, 2005; Stuber et al., 2005), in which case it should be included as part of the ERF for that compound. Changes in GSAT are also associated with changes in stratospheric water vapour as part of the water vapour climate feedback (Section 7.4.2.2).

7.3.2.7 Synthesis

The GHGs (excluding ozone and stratospheric water vapour) ERF over 1750 to 2019 is assessed to be 3.32 ± 0.29 W m^{-2}. It has increased by 0.49 W m^{-2} compared to AR5 (reference year 2011) *(high confidence)*. Most of this has been due to an increase in CO_2 concentration since 2011 [0.27 ± 0.03 W m^{-2}], with concentration increases in CH_4, N_2O and halogenated compounds adding 0.02, 0.02 and 0.01 W m^{-2} respectively (Table 7.5). Changes in the radiative efficiencies (including adjustments) of CO_2, CH_4, N_2O and halogenated compounds have increased the ERF by an additional 0.15 W m^{-2} compared to the AR5 values (*high confidence*). Note that the ERFs in this section do not include chemical effects of GHGs on production or destruction of ozone or aerosol formation (see Chapter 6, Section 6.2.2). The ERF for ozone is considerably increased compared to AR5 due to an increase in the assumed ozone precursor emissions in CMIP6 compared to CMIP5, and better accounting for the effects of both ozone precursors and ODSs in the stratosphere. The ERF for stratospheric water vapour is slightly reduced. The combined ERF from ozone and stratospheric water vapour has increased since AR5 by 0.10 ± 0.50 W m^{-2} (*high confidence*), although the uncertainty ranges still include the AR5 values.

[START TABLE 7.5 HERE]

Table 7.5: Present-day mole fractions in ppt (pmol mol^{-1}) (except where specified) and ERF (in W m^{-2}) for the WMGHGs. Data taken from Chapter 2, Section 2.2.3. The data for 2011 (the time of the AR5 estimates) are also shown. Some of the concentrations vary slightly from those reported in AR5 owing to averaging different data sources. Individual species are reported where 1750-2019 ERF is at least 0.001 W m^{-2}. Radiative efficiencies for the minor gases are given in Supplementary Table 7.SM.7. Uncertainties in the ERF for all gases are dominated by the uncertainties in the radiative efficiencies. Tabulated global mixing ratios of all well mixed GHGs and ERFs from 1750-2019 are provided in Annex III.

	Concentration				ERF with respect to 1850		ERF with respect to 1750	
	2019	2011	1850	1750	2019	2011	2019	2011
CO_2 (ppm)	409.9	390.5	285.5	278.3	2.012±0.241	1.738	2.156±0.259	1.882
CH_4 (ppb)	1866.3	1803.3	807.6	729.2	0.496±0.099	0.473	0.544±0.109	0.521
N_2O (ppb)	332.1	324.4	272.1	270.1	0.201±0.030	0.177	0.208±0.031	0.184
HFC-134a	107.6	62.7	0.	0.	0.018	0.010	0.018	0.010
HFC-23	32.4	24.1	0.	0.	0.006	0.005	0.006	0.005
HFC-32	20.0	4.7	0.	0.	0.002	0.001	0.002	0.001
HFC-125	29.4	10.3	0.	0.	0.007	0.002	0.007	0.002
HFC-143a	24.0	12.0	0.	0.	0.004	0.002	0.004	0.002
SF_6	10.0	7.3	0.	0.	0.006	0.004	0.006	0.004
CF_4	85.5	79.0	34.0	34.0	0.005	0.004	0.005	0.004

ACCEPTED VERSION SUBJECT TO FINAL EDITING

C_2F_6	4.8	4.2	0.	0.	0.001	0.001	0.001	0.001
CFC-11	226.2	237.3	0.	0.	0.066	0.070	0.066	0.070
CFC-12	503.1	528.6	0.	0.	0.180	0.189	0.180	0.189
CFC-113	69.8	74.6	0.	0.	0.021	0.022	0.021	0.022
CFC-114	16.0	16.3	0.	0.	0.005	0.005	0.005	0.005
CFC-115	8.7	8.4	0.	0.	0.002	0.002	0.002	0.002
HCFC-22	246.8	213.2	0.	0.	0.053	0.046	0.053	0.046
HCFC-141b	24.4	21.4	0.	0.	0.004	0.003	0.004	0.003
HCFC-142b	22.3	21.2	0.	0.	0.004	0.004	0.004	0.004
CCl_4	77.9	86.1	0.	0.	0.013	0.014	0.013	0.014
Sum of CFCs					0.276	0.289	0.276	0.289
Sum of HCFCs					0.061	0.053	0.061	0.053
Sum of HFCs					0.040	0.022	0.040	0.022
Sum of Halogenated species					0.408±0.078	0.394	0.408±0.078	0.394
Total					3.118±0.258	2.782	3.317±0.278	2.981

[END TABLE 7.5 HERE]

7.3.3 Aerosols

Anthropogenic activity, and particularly burning of biomass and fossil fuels, has led to a substantial increase in emissions of aerosols and their precursors, and thus to increased atmospheric aerosol concentrations since pre-industrial times (Chapter 2, Section 2.2.6 and Figure 2.9; Chapter 6, Section 6.3.5). This is particularly true for sulphate and carbonaceous aerosols (Chapter 6, Section 6.3.5). This has in turn led to changes in the scattering and absorption of incoming solar radiation, and also affected cloud micro- and macro-physics and thus cloud radiative properties. Aerosol changes are heterogeneous in both space and time and have impacted not just Earth's radiative energy budget but also air quality (Chapter 6, Section 6.1.1 and 6.6.2). Here, the assessment is focused exclusively on the global mean effects of aerosols on Earth's energy budget, while regional changes and changes associated with individual aerosol compounds are assessed in Chapter 6, Sections 6.4.1 and 6.4.2.

Consistent with the terminology introduced in Box 7.1, the ERF due to changes from direct aerosol-radiation interactions (ERFari) is equal to the sum of the instantaneous TOA radiation change (IRFari) and the subsequent adjustments. Likewise, the ERF following interactions between anthropogenic aerosols and clouds (ERFaci, referred to as "indirect aerosol effects" in previous assessment reports) can be divided into an instantaneous forcing component (IRFaci) due to changes in cloud droplet (and indirectly also ice crystal) number concentrations and sizes, and the subsequent adjustments of cloud water content or extent. While these changes are thought to be induced primarily by changes in the abundance of cloud condensation nuclei (CCN), a change in the number of ice nucleating particles (INPs) in the atmosphere may also have occurred, and thereby contributed to ERFaci by affecting properties of mixed-phase and cirrus (ice) clouds. In the following, an assessment of IRFari and ERFari (Section 7.3.3.1) focusing on observation-based (Section 7.3.3.1.1) as well as model-based (Section 7.3.3.1.2) evidence is presented. The same lines of evidence are presented for IRFaci and ERFaci in Section 7.3.3.2. These lines of evidence are then compared with TOA energy budget constraints on the total aerosol ERF (Section 7.3.3.3) before an overall assessment of the total aerosol ERF is given in Section 7.3.3.4. For the model-based evidence, all estimates are generally valid for 2014 relative to 1750 (the time period spanned by CMIP6 historical simulations), while for observation-based evidence the assessed studies use slightly different end points, but they all generally fall within a decade (2010-2020).

ACCEPTED VERSION SUBJECT TO FINAL EDITING

7.3.3.1 Aerosol-radiation interactions

Since AR5, deeper understanding of the processes that govern aerosol radiative properties, and thus IRFari, has emerged. Combined with new insights into adjustments to aerosol forcing, this progress has informed new observation- and model-based estimates of ERFari and associated uncertainties.

7.3.3.1.1 Observation-based lines of evidence

Estimating IRFari requires an estimate of industrial-era changes in Aerosol Optical Depth (AOD) and absorption AOD, which are often taken from global aerosol model simulations. Since AR5, updates to methods of estimating IRFari based on aerosol remote sensing or data-assimilated reanalyses of atmospheric composition have been published. Ma et al. (2014) applied the method of Quaas et al. (2008) to updated broadband radiative flux measurements from CERES, MODIS-retrieved AODs, and modelled anthropogenic aerosol fractions to find a clear-sky IRFari of −0.6 W m^{-2}. This would translate into an all-sky estimate of about −0.3 W m^{-2} based on the clear-to-all-sky ratio implied by Kinne (2019). Rémy et al. (2018) applied the methods of Bellouin et al. (2013b) to the reanalysis by the Copernicus Atmosphere Monitoring Service, which assimilates MODIS total AOD. Their estimate of IRFari varies between −0.5 W m^{-2} and −0.6 W m^{-2} over the period 2003–2018, and they attribute those relatively small variations to variability in biomass-burning activity. Kinne (2019) provided updated monthly total AOD and absorption AOD climatologies, obtained by blending multi-model averages with ground-based sun-photometer retrievals, to find a best estimate of IRFari of −0.4 W m^{-2}. The updated IRFari estimates above are all scattered around the midpoint of the IRFari range of −0.35 ± 0.5 W m^{-2} assessed by AR5 (Boucher et al., 2013).

The more negative estimate of Rémy et al. (2018) is due to neglecting a small positive contribution from absorbing aerosols above clouds and obtaining a larger anthropogenic fraction than Kinne (2019). Rémy et al. (2018) also did not update their assumptions on black carbon anthropogenic fraction and its contribution to absorption to reflect recent downward revisions (Section 7.3.3.1.2). Kinne (2019) made those revisions, so more weight is given to that study to assess the central estimate of satellite-based IRFari to be only slightly stronger than reported in AR5 at –0.4 W m^{-2}. While uncertainties in the anthropogenic fraction of total AOD remain, improved knowledge of anthropogenic absorption results in a slightly narrower *very likely* range here than in AR5. The assessed best estimate and *very likely* IRFari range from observation-based evidence is therefore –0.4 ± 0.4 W m^{-2} , but with *medium confidence* due to the limited number of studies available.

7.3.3.1.2 Model-based lines of evidence

While observation-based evidence can be used to estimate IRFari, global climate models are needed to calculate the associated adjustments and the resulting ERFari, using the methods described in Section 7.3.1. A range of developments since AR5 affect model-based estimates of IRFari. Global emissions of most major aerosol compounds and their precursors are found to be higher in the current inventories, and with increasing trends. Emissions of the sulphate precursor SO_2 are a notable exception; they are similar to those used in AR5 and approximately time-constant in recent decades (Hoesly et al., 2018). Myhre et al. (2017) showed, in a multi-model experiment, that the net result of these revised emissions is an IRFari trend that is relatively flat in recent years (post-2000), a finding confirmed by a single-model study by Paulot et al. (2018).

In AR5, the assessment of the black carbon (BC) contribution to IRFari was markedly strengthened in confidence by the review by Bond et al. (2013), where a key finding was a perceived model underestimate of atmospheric absorption when compared to Aeronet observations (Boucher et al., 2013). This assessment has since been revised considering new knowledge on the effect of the temporal resolution of emission inventories (Wang et al., 2016), the representativeness of Aeronet sites (Wang et al., 2018), issues with comparing absorption retrieval to models (Andrews et al., 2017a), and the ageing (Peng et al., 2016), lifetime (Lund et al., 2018b) and average optical parameters (Zanatta et al., 2016) of BC. Consistent with these updates, Lund et al. (2018a) estimated the net IRFari in 2014 (relative to 1750) to be –0.17 W m^{-2}, using CEDS emissions (Hoesly et al., 2018) as input to a chemical transport model. They attributed the weaker estimate relative to AR5 (–0.35 ± 0.5 W m^{-2}; Myhre et al., 2013a) to stronger absorption by organic aerosol,

ACCEPTED VERSION SUBJECT TO FINAL EDITING

updated parameterization of BC absorption, and slightly reduced sulphate cooling. Broadly consistent with Lund et al. (2018a), another single-model study by Petersik et al. (2018) estimated an IRFari of –0.19 W m^{-2}. Another single-model study by Lurton et al. (2020) reported a more negative estimate at –0.38 W m^{-2}, but is given less weight here because the model lacked interactive aerosols and instead used prescribed climatological aerosol concentrations.

The above estimates support a less negative central estimate and a slightly narrower range compared to those reported for IRFari from ESMs in AR5 of –0.35 [–0.6 to –0.13] W m^{-2}. The assessed central estimate and *very likely* IRFari range from model-based evidence alone is therefore –0.2 ± 0.2 W m^{-2} for 2014 relative to 1750, with *medium confidence* due to the limited number of studies available. Revisions due to stronger organic aerosol absorption, further developed BC parameterizations and somewhat reduced sulphate emissions in recent years.

Since AR5 considerable progress has been made in the understanding of adjustments in response to a wide range of climate forcings, as discussed in Section 7.3.1. The adjustments in ERFari are principally caused by cloud changes, but also by lapse rate and atmospheric water vapour changes, all mainly associated with absorbing aerosols like BC. Stjern et al. (2017) found that for BC, about 30% of the (positive) IRFari is offset by adjustments of clouds (specifically, an increase in low clouds and decrease in high clouds) and lapse rate, by analysing simulations by five Precipitation Driver Response Model Intercomparison Project (PDRMIP) models. Smith et al. (2018b) considered more models participating in PDRMIP and suggested that about half the IRFari was offset by adjustments for BC, a finding generally supported by single-model studies (Takemura and Suzuki, 2019; Zhao and Suzuki, 2019). Thornhill et al. (2021b) also reported a negative adjustment for BC based on AerChemMIP (Collins et al., 2017) but found it to be somewhat smaller in magnitude than those reported in Smith et al. (2018b) and Stjern et al. (2017). In contrast, Allen et al. (2019) found a positive adjustment for BC and suggested that most models simulate negative adjustment for BC because of a misrepresentation of aerosol atmospheric heating profiles.

Zelinka et al. (2014) used the Approximate Partial Radiation Perturbation technique to quantify the ERFari in 2000 relative to 1860 in nine CMIP5 models; they estimated the ERFari (accounting for a small contribution from longwave radiation) to be –0.27 ± 0.35 W m^{-2}. However, it should be noted that in Zelinka et al. (2014) adjustments of clouds caused by absorbing aerosols through changes in the thermal structure of the atmosphere (termed the semidirect effect of aerosols in AR5) are not included in ERFari but in ERFaci. The corresponding estimate emerging from the Radiative Forcing Model Intercomparison Project (RFMIP, Pincus et al., 2016) is –0.25 ± 0.40 W m^{-2} (Smith et al., 2020a), which is generally supported by single-model studies published post-AR5 (Zhang et al., 2016; Fiedler et al., 2017; Nazarenko et al., 2017; Zhou et al., 2017c; Grandey et al., 2018; Zhou et al., 2018b). A 5% inflation is applied to the CMIP5 and CMIP6 fixed-SST derived estimates of ERFari from Zelinka et al. (2014) and (Smith et al., 2020a) to account for land surface cooling (Table 7.6). Based on the above, ERFari from model-based evidence is assessed to be –0.25 ± 0.25 W m^{-2}.

7.3.3.1.3 Overall assessment of IRFari and ERFari

The observation-based assessment of IRFari of –0.4 ± 0.4 W m^{-2} and the corresponding model-based assessment of –0.2 ± 0.2 W m^{-2} can be compared to the range of –0.45 W m^{-2} to –0.05 W m^{-2} that emerged from a comprehensive review in which an observation-based estimate of anthropogenic AOD was combined with model-derived ranges for all relevant aerosol radiative properties (Bellouin et al., 2019). Based on the above, IRFari is assessed to be –0.25 ± 0.2 W m^{-2} (*medium confidence*).

ERFari from model-based evidence is –0.25 ± 0.25 W m^{-2}, which suggests a small negative adjustment relative to the model-based IRFari estimate, consistent with the literature discussed in 7.3.3.1.2. Adding this small adjustment to our assessed IRFari estimate of –0.25 W m^{-2}, and accounting for additional uncertainty in the adjustments, ERFari is assessed to –0.3 ± 0.3 (*medium confidence*). This assessment is consistent with the 5% to 95 % confidence range for ERFari in Bellouin et al. (2019) of –0.71 to –0.14 W m^{-2}, and notably implies that it is *very likely* that ERFari is negative. Differences relative to Bellouin et al. (2019) reflect the range of estimates in Table 7.6 and the fact that a more negative ERFari than -0.6 W m^{-2} would require

ACCEPTED VERSION SUBJECT TO FINAL EDITING

adjustments that considerably augment the assessed IRFari, which is not supported by the assessed literature.

[START TABLE 7.6 HERE]

Table 7.6: Present-day ERF due to changes in aerosol-radiation interactions (ERFari) and changes in aerosol-cloud interactions (ERFaci), and total aerosol ERF (ERFari+aci) from GCM CMIP6 (2014 relative to 1850) (Smith et al., 2020a and later model results) and CMIP5 (year 2000 relative to 1860) (Zelinka et al., 2014). CMIP6 results are simulated as part of RFMIP (Pincus et al., 2016). An additional 5% is applied to the CMIP5 and CMIP6 model results to account for land-surface cooling (Smith et al., 2020b; Figure 7.4).

Models	ERFari ($W\ m^{-2}$)	ERFaci ($W\ m^{-2}$)	ERFari+aci ($W\ m^{-2}$)
ACCESS-CM2	–0.24	–0.93	–1.17
ACCESS-ESM1-5	–0.07	–1.19	–1.25
BCC-ESM1	–0.79	–0.69	–1.48
CanESM5	–0.02	–1.09	–1.11
CESM2	+0.15	–1.65	–1.50
CNRM-CM6-1	–0.28	–0.86	–1.14
CNRM-ESM2-1	–0.15	–0.64	–0.79
EC-Earth3	–0.39	–0.50	–0.89
GFDL-CM4	–0.12	–0.72	–0.84
GFDL-ESM4	–0.06	–0.84	–0.90
GISS-E2-1-G (physics_version=1)	–0.55	–0.81	–1.36
GISS-E2-1-G (physics_version=3)	–0.64	–0.39	–1.02
HadGEM3-GC31-LL	–0.29	–0.87	–1.17
IPSL-CM6A-LR	–0.39	–0.29	–0.68
IPSL-CM6A-LR-INCA	–0.45	–0.35	–0.80
MIROC6	–0.22	–0.77	–0.99
MPI-ESM-1-2-HAM	+0.10	–1.40	–1.31
MRI-ESM2-0	–0.48	–0.74	–1.22
NorESM2-LM	–0.15	–1.08	–1.23
NorESM2-MM	–0.03	–1.26	–1.29
UKESM1-0-LL	–0.20	–0.99	–1.19
CMIP6 average and 5 to 95% confidence range (2014–1850)	–0.25 ± 0.40	–0.86 ± 0.57	–1.11 ± 0.38
CMIP5 average and 5 to 96% confidence range (2000–1860)	–0.27 ± 0.35	–0.96 ± 0.55	–1.23 ± 0.48

[END TABLE 7.6 HERE]

7.3.3.2 Aerosol-cloud interactions

Anthropogenic aerosol particles primarily affect water clouds by serving as additional cloud condensation nuclei (CCN) and thus increasing cloud drop number concentration (N_d) (Twomey, 1959). Increasing N_d while holding liquid water content constant reduces cloud drop effective radius (r_e), increases the cloud albedo, and induces an instantaneous negative radiative forcing (IRFaci). The clouds are thought to subsequently adjust by a slowing of the drop coalescence rate, thereby delaying or suppressing rainfall. Rain generally reduces cloud lifetime and thereby liquid water path (LWP, i.e., the vertically integrated cloud water) and/or cloud fractional coverage (Cf) (Albrecht, 1989), thus any aerosol-induced rain delay or suppression would be expected to increase LWP and/or Cf. Such adjustments could potentially lead to an ERFaci considerably larger in magnitude than the IRFaci alone. However, adding aerosols to non-

ACCEPTED VERSION SUBJECT TO FINAL EDITING

precipitating clouds has been observed to have the opposite effect (i.e., a reduction in LWP and/or Cf) (Lebsock et al., 2008; Christensen and Stephens, 2011). These findings have been explained by enhanced evaporation of the smaller droplets in the aerosol-enriched environments, and resultant enhanced mixing with ambient air, leading to cloud dispersal.

A small subset of aerosols can also serve as ice nucleating particles (INPs) that initiate the ice phase in supercooled water clouds, and thereby alter cloud radiative properties and/or lifetimes. However, the ability of anthropogenic aerosols (specifically BC) to serve as INPs in mixed-phase clouds has been found to be negligible in recent laboratory studies (e.g., Vergara-Temprado et al. (2018)). No assessment of the contribution to ERFaci from cloud phase changes induced by anthropogenic INPs will therefore be presented.

In ice (cirrus) clouds (cloud temperatures less than –40° C), INPs can initiate ice crystal formation at relative humidity much lower than that required for droplets to freeze spontaneously. Anthropogenic INPs can thereby influence ice crystal numbers and thus cirrus cloud radiative properties. At cirrus temperatures, certain types of BC have in fact been demonstrated to act as INPs in laboratory studies (Ullrich et al., 2017; Mahrt et al., 2018), suggesting a non-negligible anthropogenic contribution to INPs in cirrus clouds. Furthermore, anthropogenic changes to drop number also alter the number of droplets available for spontaneous freezing, thus representing a second pathway through which anthropogenic emissions could affect cirrus clouds.

7.3.3.2.1 Observation-based evidence

Since AR5, the analysis of observations to investigate aerosol-cloud interactions has progressed along several axes: (i) The framework of forcing and adjustments introduced rigorously in AR5 has helped better categorize studies; (ii) the literature assessing statistical relationships between aerosol- and cloud in satellite retrievals has grown, and retrieval uncertainties are better characterized; (iii) advances have been made to infer causality in aerosol-cloud relationships.

[START TABLE 7.7 HERE]

Table 7.7: Studies quantifying aspects of the global ERFaci that are mainly based on satellite retrievals and were published since AR5. All forcings/adjustments as global annual mean values in W m^{-2}. Most studies split the ERFaci into IRFaci and adjustments in LWP and cloud fraction separately. All published studies only considered liquid clouds. Some studies assessed the IRFaci and the LWP adjustment together and called this "intrinsic forcing"(Christensen et al., 2017) and the cloud fraction adjustment "extrinsic forcing". Published uncertainty ranges are converted to 5%–95 % confidence intervals, and "n/a" indicates that the study did not provide an estimate for the relevant IRF/ERF.

IRFaci	LWP adjustment	Cloud fraction adjustment	Reference
–0.6±0.6	n/a	n/a	Bellouin et al. (2013a)
–0.4 [–0.2 to –1.0]	n/a	n/a	Gryspeerdt et al. (2017)
–1.0±0.4	n/a	n/a	McCoy et al. (2017a)
n/a	n/a	–0.5 [–0.1 to –0.6]	Gryspeerdt et al. (2016)
n/a	+0.3 to 0	n/a	Gryspeerdt et al. (2019)
–0.8±0.7	n/a	n/a	Rémy et al. (2018)
–0.53	+0.15	n/a	Toll et al. (2019)
–1.14 [–1.72 to –0.84]	n/a	n/a	Hasekamp et al. (2019)
–1.2 to -0.6	n/a	n/a	McCoy et al. (2020)
–0.69 [–0.99 to –0.44]	n/a	n/a	Diamond et al. (2020)
"intrinsic forcing"			

ACCEPTED VERSION SUBJECT TO FINAL EDITING

–0.5 ± 0.5	–0.5 ± 0.5	Chen et al. (2014)
–0.4 ± 0.3	n/a	Christensen et al. (2016b)
–0.3 ± 0.4	–0.4 ± 0.5	Christensen et al. (2017)

[END TABLE 7.7 HERE]

In AR5 the statistical relationship between cloud microphysical properties and aerosol index (AI; AOD multiplied by Ångström exponent) was used to make inferences about IRFaci were assessed alongside other studies which related cloud quantities to AOD. However, it is now well-documented that the latter approach leads to low estimates of IRFaci since AOD is a poor proxy for cloud-base CCN (Penner et al., 2011; Stier, 2016). Gryspeerdt et al. (2017) demonstrated that the statistical relationship between droplet concentration and AOD leads to an inferred IRFaci that is underestimated by at least 30%, while the use of AI leads to estimates of IRFaci to within ±20%, if the anthropogenic perturbation of AI is known.

Further, studies assessed in AR5 mostly investigated linear relationships between cloud droplet concentration and aerosol (Boucher et al., 2013). Since in most cases the relationships are not linear, this leads to a bias (Gryspeerdt et al., 2016). Several studies did not relate cloud droplet concentration, but cloud droplet effective radius to the aerosol (Brenguier et al., 2000). This is problematic since then, in order to infer IRFaci, stratification by cloud LWP is required (McComiskey and Feingold, 2012). Where LWP positively co-varies with aerosol retrievals (which is often the case), IRFaci inferred from such relationships is biased towards low values. Also, it is increasingly evident that different cloud regimes show different sensitivities to aerosols (Stevens and Feingold, 2009). Averaging statistics over regimes thus bias the inferred IRFaci (Gryspeerdt et al., 2014b). AR5 concluded that IRFaci estimates tied to satellite studies generally show weak IRFaci (Boucher et al., 2013), but when correcting for the biases discussed above, this is no longer the case.

Since AR5, several studies assessed the global IRFaci from satellite observations using different methods (Table 7.7). All studies relied on statistical relationships between aerosol- and cloud quantities to infer sensitivities. Four studies inferred IRFaci by estimating the anthropogenic perturbation of N_d. For this, Bellouin et al. (2013a) and Rémy et al. (2018) made use of regional-seasonal regressions between satellite-derived N_d and AOD following Quaas et al. (2008), while Gryspeerdt et al. (2017) used AI instead of AOD in the regression to infer IRFaci. McCoy et al. (2017a) instead used the sulphate specific mass derived in the MERRA aerosol reanalysis that assimilated MODIS AOD (Rienecker et al., 2011). All approaches have in common the need to identify the anthropogenic perturbation of the aerosol to assess IRFaci. Gryspeerdt et al. (2017) and Rémy et al. (2018) used the same approach as Bellouin et al. (2013a), while McCoy et al. (2017a) used an anthropogenic fraction from the AEROCOM multi-model ensemble (Schulz et al., 2006). Chen et al. (2014), Christensen et al. (2016b) and Christensen et al. (2017) derived the combination of IRFaci and the LWP adjustment to IRFaci ("intrinsic forcing" in their terminology). They relate AI and cloud albedo statistically and use the anthropogenic aerosol fraction from Bellouin et al. (2013a). This was further refined by Hasekamp et al. (2019) who used additional polarimetric satellite information over ocean to obtain a better proxy for CCN. They derived an IRFaci of –1.14 [–1.72 to –0.84] W m^{-2}. The variant by Christensen et al. (2017) is an update compared to the Chen et al. (2014) and Christensen et al. (2016b) studies in that it better accounts for ancillary influences on the aerosol retrievals such as aerosol swelling and 3D radiative effects. McCoy et al. (2020) used the satellite-observed hemispheric difference in N_d as an emergent constraint on IRFaci as simulated by GCMs to obtain a range of –1.2 to –0.6 W m^{-2} (95% confidence interval). Diamond et al. (2020) analysed the difference in clouds affected by ship emissions with unperturbed clouds and based on this inferred a global IRFaci of –0.69 [–0.99 to –0.44] W m^{-2}.

Summarising the above findings related to statistical relationships and causal aerosol effects on cloud properties, there is *high confidence* that anthropogenic aerosols lead to an increase in cloud droplet concentrations. Taking the average across the studies providing IRFaci estimates discussed above and considering the general agreement among estimates (Table 7.7), IRFaci is assessed to be –0.7 ± 0.5 W m^{-2} (*medium confidence*).

ACCEPTED VERSION SUBJECT TO FINAL EDITING

Multiple studies have found a positive relationship between cloud fraction and/or cloud LWP and aerosols (e.g., Nakajima et al., 2001; Kaufman and Koren, 2006; Quaas et al., 2009). Since AR5, however, it has been documented that factors independent of causal aerosol-cloud interactions heavily influence such statistical relationships. These include the swelling of aerosols in the high relative humidity in the vicinity of clouds (Grandey et al., 2013) and the contamination of aerosol retrievals next to clouds by cloud remnants and cloud-side scattering (Várnai and Marshak, 2015; Christensen et al., 2017). Stratifying relationships by possible influencing factors such as relative humidity (Koren et al., 2010) does not yield satisfying results since observations of the relevant quantities are not available at the resolution and quality required. Another approach to tackle this problem was to assess the relationship of cloud fraction with droplet concentration (Gryspeerdt et al., 2016; Michibata et al., 2016; Sato et al., 2018). The relationship between satellite-retrieved cloud fraction and N_d was found to be positive (Christensen et al., 2016b, 2017; Gryspeerdt et al., 2016), implying an overall adjustment that leads to a more negative ERFaci. However, since retrieved N_d is biased low for broken clouds this result has been called into question (Grosvenor et al., 2018). Zhu et al. (2018) proposed to circumvent this problem by considering N_d of only continuous thick cloud covers, on the basis of which Rosenfeld et al. (2019) still obtained a positive cloud fraction – N_d relationship.

The relationship between LWP and cloud droplet number is debated. Most recent studies (primarily based on MODIS data) find negative statistical relationships (Michibata et al., 2016; Toll et al., 2017; Sato et al., 2018; Gryspeerdt et al., 2019), while Rosenfeld et al. (2019) obtained a modest positive relationship. To increase confidence that observed relationships between aerosol emissions and cloud adjustments are causal, known emissions of aerosols and aerosol precursor gases into otherwise pristine conditions have been exploited. Ship exhaust is one such source. Goren and Rosenfeld (2014) suggested that both LWP and Cf increase in response to ship emissions, contributing approximately 75% to the total ERF_{aci} in mid-latitude stratocumulus. Christensen and Stephens (2011) found that such strong adjustments occur for open-cell stratocumulus regimes, while adjustments are comparatively small in closed-cell regimes. Volcanic emissions have been identified as another important source of information (Gassó, 2008). From satellite observations, Yuan et al. (2011) documented substantially larger Cf, higher cloud tops, reduced precipitation likelihood, and increased albedo in cumulus clouds in the plume of the Kilauea volcano. Ebmeier et al. (2014) confirmed the increased LWP and albedo for other volcanoes. In contrast, for the large Holuhraun eruption, Malavelle et al. (2017) did not find any large-scale change in LWP in satellite observations. However, when accounting for meteorological conditions, McCoy et al. (2018) concluded that for cyclonic conditions, the extra Holuhraun aerosol did enhance LWP. Toll et al. (2017) examined a large sample of volcanoes and found a distinct albedo effect, but only modest LWP changes on average. Gryspeerdt et al. (2019) demonstrated that the negative LWP – Nd relationship becomes very small when conditioned on a volcanic eruption, and therefore concluded that LWP adjustments are small in most regions. Similarly, Toll et al. (2019) studied clouds downwind of various anthropogenic aerosol sources using satellite observations and inferred an IRFaci of –0.52 W m^{-2} that was partly offset by 29% due to aerosol-induced LWP decreases.

Apart from adjustments involving LWP and Cf, several studies have also documented a negative relationship between cloud-top temperature and AOD/AI in satellite observations (e.g., Koren et al., 2005). Wilcox et al. (2016) proposed that this could be explained by BC absorption reducing boundary layer turbulence, which in turn could lead to taller clouds. However, it has been demonstrated that the satellite-derived relationships are affected by spurious co-variation (Gryspeerdt et al., 2014a), and it therefore remains unclear whether a systematic causal effect exists.

Identifying relationships between INP concentrations and cloud properties from satellites is intractable because the INPs generally represent a very small subset of the overall aerosol population at any given time or location. For ice clouds, only few satellite studies have investigated responses to aerosol perturbations so far. Gryspeerdt et al. (2018) find a positive relationship between aerosol and ice crystal number for cold cirrus under strong dynamical forcing, which could be explained by an overall larger number of solution droplets available for homogeneous freezing in polluted regions. Zhao et al. (2018) conclude that the sign of the ice crystal size – aerosol relationship depends on humidity. While these studies support modelling results finding that ice clouds do respond to anthropogenic aerosols (Section 7.3.3.2.2), no quantitative conclusions about IRFaci or ERFaci for ice clouds can be drawn based on satellite observations.

ACCEPTED VERSION SUBJECT TO FINAL EDITING

Only a handful of studies have estimated the LWP and Cf adjustments that are needed for satellite-based estimates of ERFaci. Chen et al. (2014) and Christensen et al. (2017) used the relationship between cloud fraction and AI to infer the cloud fraction adjustment. Gryspeerdt et al. (2017) used a similar approach but tried to account for non-causal aerosol – cloud fraction correlations by using N_d as a mediating factor. These three studies together suggest a global Cf adjustment that augments ERFaci relative to IRFaci by –0.5 ± 0.4 W m^{-2} (*medium confidence*). For global estimates of the LWP adjustment, evidence is even scarcer. Gryspeerdt et al. (2019) derived an estimate of the LWP adjustment using a method similar to Gryspeerdt et al. (2016). They estimated that the LWP adjustment offsets 0 to 60% of the (negative) IRFaci (0 to +0.3 W m^{-2}). Supporting an offsetting LWP adjustment, Toll et al. (2019) estimated a moderate LWP adjustment of 29% (+0.15 W m^{-2}). The adjustment due to LWP is assessed to be small, with a central estimate and *very likely* range of 0.2 ± 0.2 W m^{-2} , but with *low confidence* due to the limited number of studies available.

Combining IRFaci and the associated adjustments in Cf and LWP (adding uncertainties in quadrature), considering only liquid-water clouds and evidence from satellite observations alone, the central estimate and *very likely* range for ERFaci is assessed to be –1.0 ± 0.7 W m^{-2} (*medium confidence*). The confidence level and wider range for ERFaci compared to IRFaci reflect the relatively large uncertainties that remain in the adjustment contribution to ERFaci.

7.3.3.2.2 Model-based evidence

As in AR5, the representation of aerosol-cloud interactions in ESMs remains a challenge, due to the limited representation of important sub-gridscale processes, from the emissions of aerosols and their precursors to precipitation formation. ESMs that simulate ERFaci typically include aerosol-cloud interactions in liquid stratiform clouds only, while very few include aerosol interactions with mixed-phase-, convective-, and ice clouds. Adding to the spread in model-derived estimates of ERFaci is the fact that model configurations and assumptions vary across studies, for example when it comes to the treatment of oxidants, which influence aerosol formation, and their changes through time (Karset et al., 2018).

In AR5, ERFaci was assessed as the residual of the total aerosol ERF and ERFari, as the total aerosol ERF was easier to calculate based on available model simulations (Boucher et al., 2013). The central estimates of total aerosol ERF and ERFari in AR5 were –0.9 W m^{-2} and –0.45 W m^{-2}, respectively, yielding an ERFaci estimate of –0.45 W m^{-2}. This value is much less negative than the bottom-up estimate of ERFaci from ESMs presented in AR5 (–1.4 W m^{-2}) and efforts have been made since to reconcile this difference. Zelinka et al. (2014) estimated ERFaci to be –0.96 ± 0.55 W m^{-2} (including semi-direct effects, and with land-surface cooling effect applied) based on nine CMIP5 models (Table 7.6). The corresponding ERFaci estimate based on 17 RFMIP models from CMIP6 is slightly less negative at –0.86 ± 0.57 W m^{-2} (Table 7.6). Other post-AR5 estimates of ERFaci based on single model studies are either in agreement with or slightly larger in magnitude than the CMIP6 estimate (Gordon et al., 2016; Fiedler et al., 2017; Neubauer et al., 2017; Karset et al., 2018; Regayre et al., 2018; Zhou et al., 2018b; Fiedler et al., 2019; Golaz et al., 2019a; Diamond et al., 2020).

The adjustment contribution to the CMIP6 ensemble mean ERFaci is –0.20 W m^{-2}, though with considerable differences between the models (Smith et al., 2020a). Generally, this adjustment in ESMs arises mainly from LWP changes (e.g., Ghan et al., 2016), while satellite observations suggest that cloud cover adjustments dominate and that aerosol effects on LWP are over-estimated in ESMs (Bender et al., 2019). Large-eddy-simulations also tend to suggest an over-estimated aerosol effect on cloud lifetime in ESMs, but some report an aerosol-induced decrease in cloud cover that is at odds with satellite observations (Seifert et al., 2015). Despite this potential disagreement when it comes to the dominant adjustment mechanism, a substantial negative contribution to ERFaci from adjustments is supported both by observational and modelling studies.

Contributions to ERFaci from anthropogenic aerosols acting as INPs are generally not included in CMIP6 models. Two global modelling studies incorporating parameterizations based on recent laboratory studies both found a negative contribution to ERFaci (Penner et al., 2018; McGraw et al., 2020), with central estimates of –0.3 and –0.13 W m^{-2}, respectively. However, previous studies have produced model estimates

ACCEPTED VERSION SUBJECT TO FINAL EDITING

of opposing signs (Storelvmo, 2017). There is thus *limited evidence* and *medium agreement* for a small negative contribution to ERFaci from anthropogenic INP-induced cirrus modifications (*low confidence*).

Similarly, aerosol effects on deep convective clouds are typically not incorporated in ESMs. However, cloud-resolving modelling studies support non-negligible aerosol effects on the radiative properties of convective clouds and associated detrained cloud anvils (Tao et al., 2012). While global ERF estimates are currently not available for these effects, the fact that they are missing in most ESMs adds to the uncertainty range for the model-based ERFaci.

From model-based evidence, ERFaci is assessed to $–1.0 \pm 0.8$ W m^{-2} (*medium confidence*). This assessment uses the mean ERFaci in Table 7.6 as a starting point, but further allows for a small negative ERF contribution from cirrus clouds. The uncertainty range is based on those reported in Table 7.6, but widened to account for uncertain but *likely* non-negligible processes currently unaccounted for in ESMs.

7.3.3.2.3 Overall assessment of ERFaci

The assessment of ERFaci based on observational evidence alone ($–1.0 \pm 0.7$ W m^{-2}) is very similar to the one based on model-evidence alone ($–1.0 \pm 0.8$ W m^{-2}), in strong contrast to what was reported in AR5. This reconciliation of observation-based and model-based estimates is the result of considerable scientific progress and reflects comparable revisions of both model-based and observation-based estimates. The strong agreement between the two largely independent lines of evidence increases confidence in the overall assessment of the central estimate and *very likely* range for ERFaci of $–1.0 \pm 0.7$ W m^{-2} (*medium confidence*). The assessed range is consistent with but narrower than that reported by the review of Bellouin et al. (2019) of –2.65 to –0.07 W m^{-2}. The difference is primarily due to a wider range in the adjustment contribution to ERFaci in Bellouin et al. (2019), however adjustments reported relative to IRFaci ranging from 40% to 150% in that study are fully consistent with the ERFaci assessment presented here.

7.3.3.3 Energy budget constraints on the total aerosol ERF

Energy balance models of reduced complexity have in recent years increasingly been combined with Monte Carlo approaches to provide valuable "top-down" (also called inverse) observational constraints on the total aerosol ERF. These top-down approaches report ranges of aerosol ERF that are found to be consistent with the global mean temperature record and, in some cases, also observed ocean heat uptake. However, the total aerosol ERF is also used together with the historical temperature record in Section 7.5 to constrain ECS and TCR. Using top-down estimates as a separate line of evidence also for the total aerosol ERF would therefore be circular. Nevertheless, it is useful to examine the development of these estimates since AR5 and the degree to which these estimates are consistent with the upper and lower bounds of the assessments of total aerosol ERF (ERFari+ERFaci).

When the first top-down estimates emerged (e.g., Knutti et al., 2002), it became clear that some of the early ("bottom-up") ESM estimates of total aerosol ERF were inconsistent with the plausible top-down range. However, as more inverse estimates have been published, it has increasingly become clear that they too are model-dependent and span a wide range of ERF estimates, with confidence intervals that in some cases do not overlap (Forest, 2018). It has also become evident that these methods are sensitive to revised estimates of other forcings and/or updates to observational data sets. A recent review of 19 such estimates reported a mean of –0.77 W m^{-2} for the total aerosol ERF, and a 95% confidence interval of –1.15 W m^{-2} to –0.31 W m^{-2} (Forest, 2018). Adding to that review, a more recent study using the same approach reported an estimate of total aerosol ERF of –0.89 [–1.82 to –0.01] W m^{-2} (Skeie et al., 2018). However, in the same study, an alternative way of incorporating ocean heat content in the analysis produced a total aerosol ERF estimate of –1.34 [–2.20 to –0.46] W m^{-2}, illustrating the sensitivity to the manner in which observations are included. A new approach to inverse estimates took advantage of independent climate radiative response estimates from eight prescribed SST and sea-ice concentration simulations over the historical period to estimate the total anthropogenic ERF. From this a total aerosol ERF of –0.8 [–1.6 to +0.1] W m^{-2} was derived (valid for near-present relative to the late 1800s). This range was found to be more invariant to

ACCEPTED VERSION SUBJECT TO FINAL EDITING

parameter choices than earlier inverse approaches (Andrews and Forster, 2020).

Beyond the inverse estimates described above, other efforts have been made since AR5 to constrain the total aerosol ERF. For example, Stevens (2015) used a simple (1-dimensional) model to simulate the historical total aerosol ERF evolution consistent with the observed temperature record. Given the lack of temporally extensive cooling trends in the 20th century record and the fact that the historical evolution of greenhouse gas forcing is relatively well constrained, the study concluded that a more negative total aerosol ERF than –1.0 W m^{-2} was incompatible with the historical temperature record. This was countered by Kretzschmar et al. (2017), who argued that the model employed in Stevens (2015) was too simplistic to account for the effect of geographical redistributions of aerosol emissions over time. Following the logic of Stevens (2015), but basing their estimates on a subset of CMIP5 models as opposed to a simplified modelling framework, they argued that a total aerosol ERF as negative as –1.6 W m^{-2} was consistent with the observed temperature record. Similar arguments were put forward by Booth et al. (2018), who emphasized that the degree of non-linearity of the total aerosol ERF with aerosol emission is a central assumption in Stevens (2015).

The historical temperature record was also the key observational constraint applied in two additional studies (Rotstayn et al., 2015; Shindell et al., 2015) based on a subset of CMIP5 models. Rotstayn et al. (2015) found a strong temporal correlation (> 0.9) between the total aerosol ERF and the global surface temperature. They used this relationship to produce a best estimate for the total aerosol ERF of –0.97 W m^{-2}, but with considerable unquantified uncertainty, in part due to uncertainties in the TCR. Shindell et al. (2015) came to a similar best estimate for the total aerosol ERF of –1.0 W m^{-2} and a 95% confidence interval of –1.4 to –0.6 W m^{-2} but based this on spatial temperature and ERF patterns in the models in comparison with observed spatial temperature patterns.

A separate observational constraint on the total ERF was proposed by Cherian et al. (2014), who compared trends in downward fluxes of solar radiation observed at surface stations across Europe (described in Section 7.2.2.3) to those simulated by a subset of CMIP5 models. Based on the relationship between solar radiation trends and the total aerosol ERF in the models, they inferred a total aerosol ERF of –1.3 W m^{-2} and a standard deviation of ± 0.4 W m^{-2}.

Based solely on energy balance considerations or other observational constraints, it is *extremely likely* that the total aerosol ERF is negative (*high confidence*), but *extremely unlikely* that the total aerosol ERF is more negative than –2.0 W m^{-2} (*high confidence*).

7.3.3.4 Overall assessment of total aerosol ERF

In AR5 (Boucher et al., 2013), the overall assessment of total aerosol ERF (ERFari+aci) used the median of all ESM estimates published prior to AR5 of –1.5 [–2.4 to –0.6] W m^{-2} as a starting point, but placed more confidence in a subset of models that were deemed more complete in their representation of aerosol-cloud interactions. These models, which included aerosol effects on mixed-phase, ice and/or convective clouds, produced a smaller estimate of –1.38 W m^{-2}. Likewise, studies that constrained models with satellite observations (five in total), which produced a median estimate of –0.85 W m^{-2}, were given extra weight. Furthermore, a longwave ERFaci of 0.2 W m^{-2} was added to studies that only reported shortwave ERFaci values. Finally, based on higher resolution models, doubt was raised regarding the ability of ESMs to represent the cloud adjustment component of ERFaci with fidelity. The expert judgement was therefore that aerosol effects on cloud lifetime were too strong in the ESMs, further reducing the overall ERF estimate. The above lines of argument resulted in a total aerosol assessment of –0.9 [–1.9 to –0.1] W m^{-2} in AR5.

Here, the best estimate and range is revised relative to AR5 (Boucher et al., 2013), partly based on updates to the above lines of argument. Firstly, the studies that included aerosol effects on mixed-phase clouds in AR5 relied on the assumption that anthropogenic black carbon (BC) could act as INPs in these clouds, which has since been challenged by laboratory experiments (Kanji et al., 2017; Vergara-Temprado et al., 2018). There is no observational evidence of appreciable ERFs associated with aerosol effects on mixed-phase and ice clouds (Section 7.3.3.2.1), and modelling studies disagree when it comes to both their magnitude and sign

ACCEPTED VERSION SUBJECT TO FINAL EDITING

(Section 7.3.3.2.2). Likewise, very few ESMs incorporate aerosol effects on deep convective clouds, and cloud-resolving modelling studies report different effects on cloud radiative properties depending on environmental conditions (Tao et al., 2012). Thus, it is not clear whether omitting such effects in ESMs would lead to any appreciable ERF biases, or if so, what the sign of such biases would be. As a result, all ESMs are given equal weight in this assessment. Furthermore, there is now a considerably expanded body of literature which suggests that early modelling studies that incorporated satellite observations may have resulted in overly conservative estimates of the magnitude of ERFaci (Section 7.3.3.2.1). Finally, based on an assessment of the longwave ERFaci in the CMIP5 models, the offset of +0.2 W m^{-2} applied in AR5 appears to be too large (Heyn et al., 2017). As in AR5, there is still reason to question the ability of ESMs to simulate adjustments in LWP and cloud cover in response to aerosol perturbation, but it is not clear that this will result in biases that exclusively increase the magnitude of the total aerosol ERF (Section 7.3.3.2.2).

The assessment of total aerosol ERF here uses the following lines of evidence: satellite-based evidence for IRFari, model-based evidence for IRFari and ERFari, satellite-based evidence of IRF/ERFaci, and finally model-based evidence for ERFaci. Based on this, ERFari and ERFaci for 2014 relative to 1750 are assessed to –0.3 ± 0.3 W m^{-2} and –1.0 ± 0.7 W m^{-2}, respectively. There is thus strong evidence for a substantive negative total aerosol ERF, which is supported by the broad agreement between observation-based and model-based lines of evidence for both ERFari and ERFaci that has emerged since AR5 (Gryspeerdt et al., 2020). However, considerable uncertainty remains, particularly with regards to the adjustment contribution to ERFaci, as well as missing processes in current ESMs, notably aerosol effects on mixed-phase, ice and convective clouds. This leads to a *medium confidence* in the estimate of ERFari+aci and a slight narrowing of the uncertainty range. Because the estimates informing the different lines of evidence are generally valid for approximately 2014 conditions, the total aerosol ERF assessment is considered valid for 2014 relative to 1750.

Combining the lines of evidence and adding uncertainties in quadrature, the ERFari+aci estimated for 2014 relative to 1750 is assessed to be –1.3 [–2.0 to –0.6] W m^{-2} *(medium confidence)*. The corresponding range from Bellouin et al. (2019) is –3.15 to –0.35 W m^{-2}, thus there is agreement for the upper bound while the lower bound assessed here is less negative. A lower bound more negative than -2.0 W m^{-2} is not supported by any of the assessed lines of evidence. There is *high confidence* that ERFaci contributes most (75–80%) to the total aerosol effect (ERFari+aci). In contrast to AR5 (Boucher et al., 2013), it is now *virtually certain* that the total aerosol ERF is negative. Figure 7.5 depicts the aerosol ERFs from the different lines of evidence along with the overall assessments.

As most modelling and observational estimates of aerosol ERF have end points in 2014 or earlier, there is limited evidence available for the assessment of how aerosol ERF has changed from 2014 to 2019. However, based on a general reduction in global mean AOD over this period (Chapter 2, Section 2.2.6, Figure 2.9), combined with a reduction in emissions of aerosols and their precursors in updated emission inventories (Hoesly et al., 2018), the aerosol ERF is assessed to have decreased in magnitude from about 2014 to 2019 *(medium confidence)*. Consistent with Chapter 2, Figure 2.10, the change in aerosol ERF from about 2014 to 2019 is assessed to be +0.2 W m^{-2}, but with *low confidence* due to limited evidence. Aerosols are therefore assessed to have contributed an ERF of –1.1 [–1.7 to –0.4] W m^{-2} over 1750–2019 (*medium confidence*).

[START FIGURE 7.5 HERE]

Figure 7.5: Net aerosol effective radiative forcing from different lines of evidence. The headline AR6 assessment of –1.3 [–2.0 to –0.6] W m^{-2} is highlighted in purple for 1750–2014 and compared to the AR5 assessment of –0.9 [–1.9 to –0.1] W m^{-2} for 1750–2011. The evidence comprising the AR6 assessment is shown below this: energy balance constraints (–2 to 0 W m^{-2} with no best estimate), observational evidence from satellite retrievals of –1.4 [–2.2 to –0.6] W m^{-2}, and climate model-based evidence of –1.25 [–2.1 to –0.4] W m^{-2}. Estimates from individual CMIP5 (Zelinka et al., 2014) and CMIP6 (Smith et al., 2020a and Table 7.6) models are depicted by blue and red crosses respectively. For each line of evidence the assessed best-estimate contributions from ERFari and ERFaci are shown with darker and paler shading respectively. The observational assessment for ERFari is taken from the IRFari. Uncertainty ranges are given in black bars for the total aerosol ERF and depict *very likely* ranges. Further details on data sources

ACCEPTED VERSION SUBJECT TO FINAL EDITING

and processing are available in the chapter data table (Table 7.SM.14).

[END FIGURE 7.5 HERE]

7.3.4 Other agents

In addition to the large anthropogenic ERFs associated with WMGHGs and atmospheric aerosols assessed in Sections 7.3.2 and 7.3.3, land use change, contrails and aviation-induced cirrus and light absorbing particles deposited on snow and ice have also contributed to the overall anthropogenic ERF and are assessed in Sections 7.3.4.1, 7.3.4.2 and 7.3.4.3. Changes in solar irradiance, galactic cosmic rays and volcanic eruptions since pre-industrial times combined represent the natural contribution to the total (anthropogenic + natural) ERF and are discussed in Sections 7.3.4.4, 7.3.4.5 and 7.3.4.6.

7.3.4.1 Land use

Land use forcing is defined as those changes in land surface properties directly caused by human activity rather than by climate processes (see also Chapter 2, Section 2.2.7). Land use change affects the surface albedo. For example, deforestation typically replaces darker forested areas with brighter cropland, and thus imposes a negative radiative forcing on climate, while afforestation and reforestation can have the opposite effect. Precise changes depend on the nature of the forest, crops and underlying soil. Land use change also affects the amount of water transpired by vegetation (Devaraju et al., 2015). Irrigation of land directly affects the evaporation (Sherwood et al., 2018) causing a global increase of 32 500 $m^3 s^{-1}$ due to human activity. Changes in evaporation and transpiration affect the latent heat budget, but do not directly affect the top-of-atmosphere radiative fluxes. The lifetime of water vapour is so short that the effect of changes in evaporation on the greenhouse contribution of water vapour are negligible (Sherwood et al., 2018). However, evaporation can affect the ERF through adjustments, particularly through changes in low cloud amounts. Land management affects the emissions or removal of greenhouse gases from the atmosphere (such as CO_2, CH_4, N_2O). These emission changes have the greatest effect on climate (Ward et al., 2014), however they are already included in greenhouse gas inventories. Land use change also affects the emissions of dust and biogenic volatile organic compounds (BVOCs), which form aerosols and affect the atmospheric concentrations of ozone and methane (Chapter 6, Section 6.2.2). The effects of land use on surface temperature and hydrology were recently assessed in SRCCL (Jia et al., 2019).

Using the definition of ERF from Section 7.1, the adjustment in land surface temperature is excluded from the definition of ERF, but changes in vegetation and snow cover (resulting from land use change) are included (Boisier et al., 2013). Land use change in the mid-latitudes induces a substantial amplifying adjustment in snow cover. Few climate model studies have attempted to quantify the ERF of land use change. Andrews et al. (2017b) calculated a very large surface albedo ERF (–0.47 W m^{-2}) from 1860 to 2005 in the HadGEM2-ES model although they did not separate out the surface albedo change from snow cover change. HadGEM2-ES is known to overestimate the amount of boreal trees and shrubs in the unperturbed state (Collins et al., 2011) so will tend to overestimate the ERF associated with land use change. The increases in dust in HadGEM2-ES contributed an extra –0.25 W m^{-2}, whereas cloud cover changes added a small positive adjustment (0.15 W m^{-2}) consistent with a reduction in transpiration. A multi-model quantification of land use forcing in CMIP6 models (excluding one outlier) (Smith et al., 2020a) found an IRF of –0.15 ± 0.12 W m^{-2} (1850 to 2014), and an ERF (correcting for land surface temperature change) of -0.11 ± 0.09 W m^{-2}. This shows a small positive adjustment term (mainly from a reduction in cloud cover. CMIP5 models show an IRF of –0.11 [–0.16 to –0.04] W m^{-2} (1850 to 2000) after excluding unrealistic models (Lejeune et al., 2020).

The contribution of land use change to albedo changes has recently been investigated using MODIS and AVHRR to attribute surface albedo to geographically-specific land cover types (Ghimire et al., 2014). When combined with a historical land use map (Hurtt et al., 2011) this gives a 1700 to 2005 SARF of –0.15 ± 0.01 W m^{-2} (of which –0.12 W m^{-2} is from 1850). This study accounted for correlations between

ACCEPTED VERSION SUBJECT TO FINAL EDITING

vegetation type and snow cover, but not the adjustment in snow cover identified in (Andrews et al., 2017b).

The indirect contributions of land use change through biogenic emissions is very uncertain. Decreases in biogenic volatile organic compounds (BVOCs) reduce ozone and methane (Unger, 2014), but also reduce the formation of organic aerosols and their effects of clouds Scott et al. (2017). Adjustments through changes in aerosols and chemistry are model dependent (Zhu et al., 2019a; Zhu and Penner, 2020), and it is not yet possible to make an assessment based on a limited number of studies.

The contribution of irrigation (mainly to low cloud amount) is assessed as –0.05 [–0.1 to 0.05] W m^{-2} for the historical period (Sherwood et al., 2018).

Since the CMIP5 and CMIP6 modelling studies are in agreement with Ghimire et al. (2014), that study is used as the assessed albedo ERF. Adding the irrigation effect to this gives an overall assessment of the ERF from land use change of –0.20 ± 0.10 W m^{-2} (*medium confidence*). Changes in ERF since 2014 are assumed to be small compared to the uncertainty, so this ERF applies to the period 1750 to 2019. The uncertainty range includes uncertainties in the adjustments.

7.3.4.2 Contrails and aviation-induced cirrus

ERF from contrails and aviation-induced cirrus is taken from the assessment of Lee et al. (2020), at 0.057 [0.019 to 0.098] W m^{-2} in 2018 (see Chapter 6, Section 6.6.2 for an assessment of the total effects of aviation). This is rounded up to address its *low confidence* and the extra year of air traffic to give an assessed ERF over 1750–2019 of 0.06 [0.02 to 0.10]. This assessment is given *low confidence* due to the potential for missing processes to affect the magnitude of contrails and aviation-induced cirrus ERF.

7.3.4.3 Light absorbing particles on snow and ice

In AR5, it was assessed that the effects of light absorbing particles (LAPs) did probably not significantly contribute to recent reductions in Arctic ice and snow (Vaughan et al., 2013). The SARF from LAPs on snow and ice was assessed to +0.04 [+0.02 to +0.09] W m^{-2} (Boucher et al., 2013), a range appreciably lower than the estimates given in AR4 (Forster et al., 2007). This effect was assessed to be *low confidence* (*medium evidence, low agreement*) (Table 8.5 in Myhre et al., 2013b).

Since AR5 there has been progress in the understanding of the physical state and processes in snow that governs the albedo reduction by black carbon (BC). The SROCC (IPCC, 2019a) assessed that there is *high confidence* that darkening of snow by deposition of BC and other light absorbing aerosol species increases the rate of snow melt (Section 2.2 in Hock et al., 2019; Section 3.4 in Meredith et al., 2019). He et al. (2018a) found that taking into account the non-spherical shape of snow grains and internal mixing of BC in snow both significantly altered the effects of BC on snow albedo. The reductions of snow albedo by dust and black carbon have been measured and characterised in the Arctic, the Tibetan Plateau, and mid latitude regions subject to seasonal snowfall including North America and Northern and Eastern Asia (Qian et al., 2015).

Since AR5, two further studies of global IRF from black carbon on snow deposition are available, with best estimates of 0.01 W m^{-2} and 0.04 W m^{-2} (Lin et al., 2014; Namazi et al., 2015). Organic carbon deposition on snow and ice has been estimated to contribute a small positive IRF of 0.001 to 0.003 W m^{-2} (Lin et al., 2014). No comprehensive global assessments of mineral dust deposition on snow are available, although the effects are potentially large in relation to the total LAPs on snow and ice forcing (Yasunari et al., 2015).

Most radiative forcing estimates have a regional emphasis. The regional focus makes estimating a global mean radiative forcing from aggregating different studies challenging, and the relative importance of each region is expected to change if the global pattern of emission sources changes (Bauer et al., 2013). The lower bound of the assessed range of black carbon on snow and ice is extended to zero to encompass Lin et al.

ACCEPTED VERSION SUBJECT TO FINAL EDITING

(2014), with the best estimate unchanged resulting in 0.04 [0.00 to 0.09] W m^{-2}. The efficacy of black carbon on snow forcing was estimated to be 2 to 4 times as large as for an equivalent CO_2 forcing as the effects are concentrated at high latitudes in the cryosphere (Bond et al., 2013). However, it is unclear how much of this effect is due to radiative adjustments leading to a higher ERF, and how much comes from a less negative feedback α due the high latitude nature of the forcing. To estimate the overall ERF, the IRF is doubled assuming that part of the increased efficacy is due to adjustments. This gives an overall assessed ERF of +0.08 [0.00 to 0.18] W m^{-2}, with *low confidence*.

7.3.4.4 Solar

Variations in the total solar irradiance (TSI) represent a natural external forcing agent. The dominant cycle is the solar 11-year activity cycle, which is superimposed on longer cycles (Chapter 2, Section 2.2). Over the last three 11-year cycles, the peak-to-trough amplitude in TSI has differed by about 1 W m^{-2} between solar maxima and minima (Chapter 2, Figure 2.2).

The fractional variability in the solar irradiance, over the solar cycle and between solar cycles, is much greater at short wavelengths in the 200–400 nm band than for the broad visible/IR band that dominates TSI (Krivova et al., 2006). The IRF can be derived simply by ΔTSI × (1 – albedo)/4 irrespective of wavelength, where the best estimate of the planetary albedo is usually taken to be 0.29 and ΔTSI represents the change in total solar irradiance (Stephens et al., 2015). (The factor 4 arises because TSI is per unit area of Earth cross section presented to the Sun and IRF is per unit area of Earth's surface). The adjustments are expected to be wavelength dependent. Gray et al. (2009) determined a stratospheric temperature adjustment of –22% to spectrally resolved changes in the solar radiance over one solar cycle. This negative adjustment is due to stratospheric heating from increased absorption by ozone at the short wavelengths, increasing the outgoing longwave radiation to space. A multi-model comparison (Smith et al., 2018b) calculated adjustments of –4% due to stratospheric temperatures and –6% due to tropospheric processes (mostly clouds), for a change in TSI across the spectrum (Figure 7.4). The smaller magnitude of the stratospheric temperature adjustment is consistent with the broad spectral change rather than the shorter wavelengths characteristic of solar variation. A single model study also found an adjustment that acts to reduce the forcing (Modak et al., 2016). While there has not yet been a calculation based on the appropriate spectral change, the –6% tropospheric adjustment from Smith et al. (2018b) is adopted along with the Gray et al. (2009) stratospheric temperature adjustment. The ERF due to solar variability over the historical period is therefore represented by 0.72 × ΔTSI × (1 – albedo)/4 using the TSI timeseries from Chapter 2, Section 2.2.1.

AR5 (Myhre et al., 2013b) assessed solar SARF from around 1750 to 2011 to be 0.05 [0.00 to 0.10] W m^{-2} which was computed from the seven-year mean around the solar minima in 1745 (being closest to 1750) and 2008 (being the most recent solar minimum). The inclusion of tropospheric adjustments that reduce ERF (compared to SARF in AR5) has a negligible effect on the overall forcing. Prior to the satellite era, proxy records are used to reconstruct historical solar activity. In AR5, historical records were constructed using observations of solar magnetic features. In this assessment historical time series are constructed from radiogenic compounds in the biosphere and in ice cores that are formed from cosmic rays (Steinhilber et al., 2012).

In this assessment the TSI from the Paleoclimate Model Intercomparison Project Phase 4 (PMIP4) reconstruction is used (Jungclaus et al., 2017; Chapter 2, Section 2.2.1). Proxies constructed from the ^{14}C and ^{10}Be radiogenic records for the SATIRE-M model (Vieira et al., 2011) and ^{14}C record for the PMOD model (Shapiro et al., 2011) for the 1745 solar minimum provide 1745 to 2008 ERFs of –0.01, –0.02 and 0.00 W m^{-2} respectively. An independent dataset from the National Oceanic and Atmospheric Administration's Climate Data Record (Coddington et al., 2016; Lean, 2018) provides a 1745 to 2008 ERF of +0.03 W m^{-2}. One substantially higher ERF estimate of +0.35 W m^{-2} derived from TSI reconstructions is provided by Egorova et al. (2018). However, the estimate from Egorova et al. (2018) hinges on assumptions about long-term changes in the quiet Sun for which there is no observed evidence. Lockwood and Ball (2020) analysed the relationship of observed changes in cosmic ray fluxes and recent, more accurate, TSI data and derived ERF between –0.01 and +0.02 W m^{-2} and Yeo et al. (2020) modelling showed the

ACCEPTED VERSION SUBJECT TO FINAL EDITING

maximum possible ERF to be 0.26 ± 0.09 W m^{-2}. Hence the Egorova et al. (2018) estimate is not explicitly taken into account in the assessment presented in this section.

In contrast to AR5, the solar ERF in this assessment uses full solar cycles rather than solar minima. The pre-industrial TSI is defined as the mean from all complete solar cycles from the start of the ^{14}C SATIRE-M proxy record in 6755 BCE to 1744 CE. The mean TSI from solar cycle 24 (2009–2019) is adopted as the assessment period for 2019. The best estimate solar ERF is assessed to be 0.01 W m^{-2}, using the ^{14}C reconstruction from SATIRE-M, with a *likely* range of –0.06 to +0.08 W m^{-2} (*medium confidence*). The uncertainty range is adopted from the evaluation of Lockwood and Ball (2020) using a Monte Carlo analysis of solar activity from the Maunder Minimum to 2019 from several datasets, leading to an ERF of –0.12 to +0.15 W m^{-2}. The Lockwood and Ball (2020) full uncertainty range is halved as the period of reduced solar activity in the Maunder Minimum had ended by 1750 *(medium confidence)*.

7.3.4.5 Galactic Cosmic Rays

Variations in the flux of galactic cosmic rays (GCR) reaching the atmosphere are modulated by solar activity and affect new particle formation in the atmosphere through their link to ionization of the troposphere (Lee et al., 2019). It has been suggested that periods of high GCR flux correlate with increased aerosol and CCN concentrations and therefore also with cloud properties (e.g., Dickinson, 1975; Kirkby, 2007).

Since AR5, the link between GCR and new particle formation has been more thoroughly studied, particularly by experiments in the CERN CLOUD chamber (Cosmics Leaving OUtdoor Droplets) (Dunne et al., 2016; Kirkby et al., 2016; Pierce, 2017). By linking the GCR-induced new particle formation from CLOUD experiments to CCN, Gordon et al. (2017) found the CCN concentration for low clouds to differ by 0.2% to 0.3% between solar maximum and solar minimum of the solar cycle. Combined with relatively small variations in the atmospheric ion concentration over centennial time scales (Usoskin et al., 2015), it is therefore unlikely that cosmic ray intensity affects present day climate via nucleation (Yu and Luo, 2014; Dunne et al., 2016; Pierce, 2017; Lee et al., 2019).

Studies continue to seek a relationship between GCR and properties of the climate system based on correlations and theory. Svensmark et al. (2017) proposed a new mechanism for ion-induced increase in aerosol growth rate and subsequent influence on the CCN concentration. The study does not include an estimate of the resulting effect on atmospheric CCN concentration and cloud radiative properties. Furthermore, Svensmark et al. (2009, 2016) find correlations between GCRs and aerosol and cloud properties in satellite and ground based data. Multiple studies investigating this link have challenged such correlations (Kristjánsson et al., 2008; Calogovic et al., 2010; Laken, 2016).

AR5 concluded that the GCR effect on CCN is too weak to have any detectable effect on climate and no robust association was found between GCR and cloudiness (Boucher et al., 2013). Published literature since then robustly support these conclusions with key laboratory, theoretical and observational evidence. There is *high confidence* that GCRs contribute a negligible ERF over the period 1750 to 2019.

7.3.4.6 Volcanic aerosols

There is large episodic negative radiative forcing associated with SO_2 being ejected into the stratosphere from explosive volcanic eruptions, accompanied by more frequent smaller eruptions (Chapter 2, Figure 2.2; Cross-Chapter Box 4.1). From SO_2 gas, reflective sulphate aerosol is formed in the stratosphere where it may persist for months, reducing the incoming solar radiation. The volcanic SARF in AR5 (Myhre et al., 2013b) was derived by scaling the stratospheric aerosol optical depth (SAOD) by a factor of –25 W m^{-2} per unit SAOD from Hansen et al. (2005b). Quantification of the adjustments to SAOD perturbations from climate model simulations have determined a significant positive adjustment driven by a reduction in cloud amount (Marshall et al., 2020; Figure 7.4). Analysis of CMIP5 models provide a mean ERF of –20 W m^{-2} per unit SAOD (Larson and Portmann, 2016). Single model studies with successive generations of Hadley Centre

ACCEPTED VERSION SUBJECT TO FINAL EDITING

climate models produce estimates between –17 and –19 W m^{-2} per unit SAOD (Gregory et al., 2016; Marshall et al., 2020), with some evidence that ERF may be non-linear with SAOD for large eruptions (Marshall et al., 2020). Analysis of the volcanically active periods of 1982-1985 and 1990-1994 using the CESM1(WACCM) aerosol-climate model provided an SAOD to ERF relationship of –21.5 (± 1.1) W m^{-2} per unit SAOD (Schmidt et al., 2018). Volcanic SO_2 emissions may contribute a positive forcing through effects on upper tropospheric ice clouds, due to additional ice nucleation on volcanic sulphate particles (Friberg et al., 2015; Schmidt et al., 2018), although one observational study found no significant effect (Meyer et al., 2015). Due to *limited agreement*, the contribution to volcanic ERF due to sulphate aerosol effects on ice clouds is not included in the overall assessment.

Non-explosive volcanic eruptions generally yield negligible global ERFs due to the short atmospheric lifetimes (a few weeks) of volcanic aerosols in the troposphere. However, as discussed in Section 7.3.3.2, the massive fissure eruption in Holuhraun, Iceland persisted for months in 2014 and 2015 and did in fact result in a marked and persistent reduction in cloud droplet radii and a corresponding increase in cloud albedo regionally (Malavelle et al., 2017). This shows that non-explosive fissure eruptions can lead to strong regional and even global ERFs, but because the Holuhraun eruption occurred in NH winter, solar insolation was weak and the observed albedo changes therefore did not result in an appreciable global ERF (Gettelman et al., 2015).

The ERF for volcanic stratospheric aerosols is assessed to be –20 ± 5 W m^{-2} per unit SAOD (*medium confidence*) based on the CMIP5 multi-model mean from the Larson and Portmann (2016) SAOD forcing efficiency calculations combined with the single-model results of Gregory et al. (2016), Schmidt et al. (2018) and Marshall et al. (2020). This is applied to the SAOD timeseries from Chapter 2, Section 2.2.2 to generate a timeseries of ERF and temperature response shown in Chapter 2, Figure 2.2 and Figure 7.8 respectively. The period from 500 BC to 1749, spanning back to the start of the record of Toohey and Sigl (2017), is defined as the pre-industrial baseline and the volcanic ERF is calculated using an SAOD anomaly from this long-term mean. As in AR5, a pre-industrial to present-day ERF assessment is not provided due to the episodic nature of volcanic eruptions.

7.3.5 Synthesis of Global Mean Radiative Forcing, Past and Future

7.3.5.1 Major changes in forcing since IPCC AR5

AR5 introduced the concept of ERF and radiative adjustments, and made a preliminary assessment that the tropospheric adjustments were zero for all species other than the effects of aerosol-cloud interaction and black carbon. Since AR5, new studies have allowed for a tentative assessment of values for tropospheric adjustments to CO_2, CH_4, N_2O, some CFCs, solar forcing, and stratospheric aerosols, and to place a tighter constraint on adjustments from aerosol-cloud interaction (Sections 7.3.2, 7.3.3, 7.3.4). In AR6, the definition of ERF explicitly removes the land-surface temperature change as part of the forcing, in contrast to AR5 where only sea-surface temperatures were fixed. The ERF is assessed to be a better predictor of modelled equilibrium temperature change (i.e. less variation in feedback parameter) than SARF (Section 7.3.1).

As discussed in Section 7.3.2, the radiative efficiencies for CO_2, CH_4 and N_2O have been updated since AR5 (Etminan et al., 2016). There has been a small (1%) increase in the stratospheric-temperature adjusted CO_2 radiative efficiency, and a +5% tropospheric adjustment has been added. The stratospheric-temperature adjusted radiative efficiency for CH_4 is increased by 25% (*high confidence*). The tropospheric adjustment is tentatively assessed to be –14% *(low confidence*). A +7% tropospheric adjustment has been added to the radiative efficiency for N_2O and +12% to CFC-11 and CFC-12 (*low confidence*).

For aerosols there has been a convergence of model and observational estimates of aerosol forcing, and the partitioning of the total aerosol ERF has changed. Compared to AR5 a greater fraction of the ERF is assessed to come from ERFaci compared to the ERFari. It is now assessed as *virtually certain* that the total aerosol ERF (ERFari+aci) is negative.

ACCEPTED VERSION SUBJECT TO FINAL EDITING

7.3.5.2 Summary ERF assessment

Figure 7.6 shows the industrial-era ERF estimates for 1750 to 2019 for the concentration change in different forcing agents. The assessed uncertainty distributions for each individual component are combined with a 100,000-member Monte Carlo simulation that samples the different distributions, assuming they are independent, to obtain the overall assessment of total present-day ERF (Supplementary Material 7.SM.1). The corresponding emissions based ERF figure is shown in Chapter 6, Figure 6.12.

[START FIGURE 7.6 HERE]

Figure 7.6: Change in effective radiative forcing from 1750 to 2019 by contributing forcing agents (carbon dioxide, other well-mixed greenhouse gases (WMGHGs), ozone, stratospheric water vapour, surface albedo, contrails and aviation-induced cirrus, aerosols, anthropogenic total, and solar). Solid bars represent best estimates, and *very likely* (5–95%) ranges are given by error bars. Non-CO_2 WMGHGs are further broken down into contributions from methane (CH_4), nitrous oxide (N_2O) and halogenated compounds. Surface albedo is broken down into land use changes and light absorbing particles on snow and ice. Aerosols are broken down into contributions from aerosol-cloud interactions (ERFaci) and aerosol-radiation interactions (ERFari). For aerosols and solar, the 2019 single-year values are given (Table 7.8) that differ from the headline assessments in both cases. Volcanic forcing is not shown due to the episodic nature of volcanic eruptions. Further details on data sources and processing are available in the chapter data table (Table 7.SM.14).

[END FIGURE 7.6 HERE]

[START TABLE 7.8 HERE]

Table 7.8: Summary table of ERF estimates for AR6 and comparison with the four previous IPCC assessment reports. Prior to AR5 values are SARF. For AR5 ari and aci are ERF, all other values assume ERF equals SARF. 5% to 95% ranges are shown. Volcanic ERF is not added to the table due to the episodic nature of volcanic eruptions which makes it difficult to compare to the other forcing mechanisms. Solar ERF is based on TSI and not spectral variation.

	Global Mean Effective Radiative Forcing (W m^{-2})					
Driver	***SAR (1750–1993)***	***TAR (1750–1998)***	***AR4 (1750–2005)***	***AR5 (1750–2011)***	***AR6* (1750–2019)**	***Comment***
CO_2	1.56 [1.33 to 1.79]	1.46 [1.31 to 1.61]	1.66 [1.49 to 1.83]	1.82 (1.63 to 2.01)	2.16 [1.90 to 2.41]	Increases in concentrations. Changes to radiative efficiencies. Inclusion of tropospheric adjustments.
CH_4	0.47 [0.40 to 0.54	0.48 [0.41 to 0.55]	0.48 [0.43 to 0.53]	0.48 [0.43 to 0.53]	0.54 [0.43 to 0.65]	
N_2O	0.14 [0.12 to 0.16]	0.15 [0.14 to 0.16]	0.16 [0.14 to 0.18]	0.17 [0.14 to 0.20]	0.21 [0.18 to 0.24]	
Halogenated species	0.26 [0.22 to 0.30]	0.36 [0.31 to 0.41]	0.33 [0.30 to 0.36]	0.36 [0.32 to 0.40]	0.41 [0.33 to 0.49]	
Tropospheric ozone	0.4 [0.2 to 0.6]	0.35 [0.20 to 0.50]	0.35 [0.25 to 0.65]	0.40 [0.20 to 0.60]	0.47 [0.24 to 0.71]	Revised precursor emissions. No tropospheric
Stratospheric	–0.1 [–0.2 to	–0.15	–0.05	–0.05 [–		

ACCEPTED VERSION SUBJECT TO FINAL EDITING

ozone	–0.05]	[–0.25 to –0.05]	[–0.15 to 0.05]	0.15 to 0.05]		adjustment assessed. No trop-strat separation.
Stratospheric water vapour	Not estimated	[0.01 to 0.03]	0.07 [0.02 to 0.1])	0.07 [0.02 to 0.12]	0.05 [0.00 to 0.10]	Downward revision due to adjustments.
Aerosol–radiation interactions	–0.5 [–0.25 to –1.0]	Not estimated	–0.50 [–0.90 to –0.10]	–0.45 [–0.95 to 0.05]	–0.22 [–0.47 to 0.04]	ERFari magnitude reduced by about 50% compared to AR5, based on agreement between observation-based and modelling-based evidence
Aerosol–cloud interactions	[–1.5 to 0.0] (sulphate only)	[–2.0 to 0.0] (all aerosols)	–0.7 [–1.8 to –0.3] (all aerosols)	–0.45 [–1.2 to 0.0]	–0.84 [–1.45 to –0.25]	ERFaci magnitude increased by about 85% compared to AR5, based on agreement between observation-based and modelling-based lines of evidence
Land use	Not estimated	–0.2 [–0.4 to 0.0]	–0.2 [–0.4 to 0.0]	–0.15 [–0.25 to –0.05]	–0.20 [–0.30 to –0.10]	Includes irrigation.
Surface albedo (black+organic carbon aerosol on snow and ice)	Not estimated	Not estimated	0.10 [0.00 to 0.20]	0.04 [0.02 to 0.09]	0.08 [0.00 to 0.18]	Increased since AR5 to better account for temperature effects
Combined contrails and aviation-induced cirrus	Not estimated	[0.00 to 0.04]	Not estimated	0.05 [0.02 to 0.15]	0.06 [0.02 to 0.10]	Narrower range since AR5
Total anthropogenic	Not estimated	Not estimated	1.6 [0.6 to 2.4]	2.3 [1.1 to 3.3]	**2.72 [1.96 to 3.48]**	Increase due to greenhouse gases, compensated slightly by aerosol ERFaci
Solar irradiance	0.3 [0.1 to 0.5]	0.3 [0.1 to 0.5]	0.12 [0.06 to 0.30]	0.05 [0.0 to 0.10]	0.01 [–0.06 to 0.08]	Revised historical TSI estimates and methodology

[END TABLE 7.8 HERE]

The total anthropogenic ERF over the industrial era (1750–2019) is estimated as 2.72 [1.96 to 3.48] W m^{-2} (Table 7.8; Annex III) (*high confidence)*. This represents a 0.43 W m^{-2} increase over the assessment made in AR5 (Myhre et al., 2013b) for the period 1750–2011. This increase is a result of compensating effects. Atmospheric concentration increases of greenhouse gases since 2011 and upwards revisions of their forcing estimates have led to a 0.59 W m^{-2} increase in their ERF. Whereas, the total aerosol ERF is assessed to be more negative compared to AR5, due to revised estimates rather than trends *(high confidence)*.

Greenhouse gases, including ozone and stratospheric water vapour from methane oxidation, are estimated to

ACCEPTED VERSION SUBJECT TO FINAL EDITING

contribute an ERF of 3.84 [3.46 to 4.22] W m^{-2} over 1750–2019. Carbon dioxide continues to contribute the largest part (56 ± 16 %) of this GHG ERF (*high confidence*).

As discussed in Section 7.3.3, aerosols have in total contributed an ERF of –1.1 [–1.7 to –0.4] W m^{-2} over 1750-2019 (*medium confidence*). Aerosol-cloud interactions contribute approximately 75–80% to this ERF with the remainder due to aerosol-radiation interactions (Table 7.8).

For the purpose of comparing forcing changes with historical temperature change (Section 7.5.2), longer averaging periods are useful. The change in ERF from the second half of the 19th century (1850–1900) compared with a recent period (2006–2019) is 2.20 [1.53 to 2.91] W m^{-2}, of which 1.71 [1.51 to 1.92] W m^{-2} is due to CO_2.

7.3.5.3 Temperature Contribution of forcing agents

The estimated contribution of forcing agents to the 2019 global surface air temperature (GSAT) change relative to 1750 is shown in Figure 7.7. These estimates were produced using concentration-derived ERF timeseries presented in Chapter 2, Figure 2.10 and described in Supplementary Material 7.SM.1.3. The resulting GSAT changes over time are shown in Figure 7.8. The historical timeseries of ERFs for the WMGHGs can be derived by applying the ERF calculations of Section 7.3.2 to the observed timeseries of WMGHG concentrations in Chapter 2, Section 2.2.

These ERF timeseries are combined with a two-layer emulator (Cross-Chapter Box 7.1, Supplementary Material 7.SM.2) using a 2,237-member constrained Monte Carlo sample of both forcing uncertainty (by sampling ERF ranges) and climate response (by sampling ECS, TCR and ocean heat capacity ranges). The net model warming over the historical period is matched to the assessment of historical GSAT warming from 1850–1900 to 1995–2014 of 0.85 [0.67 to 0.98]°C (Chapter 2, Cross-Chapter Box 2.3) and ocean heat content change from 1971 to 2018 (Section 7.2.2.2), therefore the model gives the breakdown of the GSAT trend associated with different forcing mechanisms that are consistent with the overall GSAT change. The model assumes that there is no variation in feedback parameter across forcing mechanism (see Section 7.3.1) and variations in the effective feedback parameter over the historical record (Section 7.4.4). The distribution of ECS was informed by Section 7.5.5 and chosen to approximately maintain the best estimate and *likely/very likely* ranges assessed in that section (see also Supplementary Material 7.SM.2). The TCR has an ensemble median value of 1.81°C, in good agreement with Section 7.5.5. Two error bars are shown in Figure 7.7. The dashed error bar shows the contribution of ERF uncertainty (as assessed in the Section 7.3 subsections) employing the best estimate of climate response with an ECS of 3.0 °C. The solid bar is the total response uncertainty using the Section 7.5.5 assessment of ECS. The uncertainty in the historic temperature contributions for the different forcing agents are mostly due to uncertainties in ERF, yet for the WMGHG the uncertainty is dominated by the climate response as its ERF is relatively well known (Figure 7.7). From the assessment of emulator responses in Cross-Chapter Box 7.1, there is *high confidence* that calibrated emulators such as the one employed here can represent the historical GSAT change from 1850-1900 to 1995–2014 to within 5% for the best estimate and 10% for the *very likely* range (Supplementary Table 7.SM.4). This gives *high confidence* in the overall assessment of GSAT change for the response to ERFs over 1750–2019 derived from the emulator.

The total human forced GSAT change from 1750–2019 is calculated to be 1.29 [1.00 to 1.65] °C (*high confidence*). Although the total emulated GSAT change has *high confidence*, the confidence of the individual contributions matches those given for the ERF assessment in Section 7.3 subsections. The calculated GSAT change is comprised of a well-mixed greenhouse gas warming of 1.58 [1.17 to 2.17] °C (*high confidence*), a warming from ozone changes of 0.23 [0.11 to 0.39] °C (*high confidence*), a cooling of –0.50 [–0.22 to –0.96] °C from aerosol effects (*medium confidence*). The aerosol cooling has considerable regional time dependence (Chapter 6, Section 6.4.3) but has weakened slightly over the last 20 years in the global mean (Figure 7.8 and Chapter 2, Figure 2.10). There is also a –0.06 [–0.15 to +0.01] °C contribution from surface reflectance changes which dominated by land-use change (*medium confidence*). Changes in solar and volcanic activity are assessed to have together contributed a small change of –0.02 [–0.06 to +0.02] °C since

ACCEPTED VERSION SUBJECT TO FINAL EDITING

1750 (*medium confidence*).

The total (anthropogenic plus natural) emulated GSAT between 1850–1900 and 2010–2019 is 1.14 [0.89 to 1.45]°C, compared to the assessed GSAT of 1.06 [0.88 to 1.21] °C (Section 2.3.1; Cross Chapter Box 2.3). The emulated response is slightly warmer than the observations and has a larger uncertainty range. As the emulated response attempts to constrain to multiple lines of evidence (Supplementary Material 7.SM.2), only one of which is GSAT, they should not necessarily be expected to exactly agree. The larger uncertainty range in the emulated GSAT compared to the observations is reflective of the uncertainties in ECS, TCR and ERF (particularly the aerosol ERF) which drive the emulator response.

The emulator gives a range of GSAT response for the 1750 to the 1850–1900 period of 0.09 [0.04 to 0.14] °C from a anthropogenic ERFs. These results are used as a line of evidence for the assessment of this change in Chapter 1 (Cross-Chapter Box 1.2), which gives an overall assessment of 0.1 °C [*likely* range -0.1 to 0.3] °C.

[START FIGURE 7.7 HERE]

Figure 7.7: The contribution of forcing agents to 2019 temperature change relative to 1750 produced using the two-layer emulator (Supplementary Material 7.SM.2), constrained to assessed ranges for key climate metrics described in Cross-Chapter Box 7.1. The results are from a 2,237-member ensemble. Temperature contributions are expressed for carbon dioxide, other well-mixed greenhouse gases (WMGHGs), ozone, stratospheric water vapour, surface albedo, contrails and aviation-induced cirrus, aerosols, solar, volcanic, and total. Solid bars represent best estimates, and *very likely* (5–95%) ranges are given by error bars. Dashed error bars show the contribution of forcing uncertainty alone, using best estimates of ECS (3.0°C), TCR (1.8°C) and two-layer model parameters representing the CMIP6 multi-model mean. Solid error bars show the combined effects of forcing and climate response uncertainty using the distribution of ECS and TCR from Tables 7.13 and 7.14, and the distribution of calibrated model parameters from 44 CMIP6 models. Non-CO_2 WMGHGs are further broken down into contributions from methane (CH_4), nitrous oxide (N_2O) and halogenated compounds. Surface albedo is broken down into land use changes and light absorbing particles on snow and ice. Aerosols are broken down into contributions from aerosol-cloud interactions (ERFaci) and aerosol-radiation interactions (ERFari). Further details on data sources and processing are available in the chapter data table (Table 7.SM.14).

[END FIGURE 7.7 HERE]

Figure 7.8 presents the GSAT timeseries using ERF timeseries for individual forcing agents rather than their aggregation. It shows that for most of the historical period the long timescale total GSAT trend estimate from the emulator closely follows the CO_2 contribution. The GSAT estimate from non-CO_2 greenhouse gas forcing (from other WMGHGs and ozone) has been approximately cancelled out in the global average by a cooling GSAT trend from aerosol. However, since 1980 the aerosol cooling trend has stabilised and may have started to reverse so over the last few decades the long-term warming has been occurring at a faster rate than that expected by CO_2 alone (*high confidence,* see also Chapter 2, Section 2.2.6 and 2.2.8). Throughout the record, but especially prior to 1930, periods of volcanic cooling dominate decadal variability. These estimates of the forced response are compared with model simulations and attributable warming estimates in Chapter 3, Section 3.3.1.

[START FIGURE 7.8 HERE]

Figure 7.8: Attributed global surface air temperature change (GSAT) from 1750 to 2019 produced using the two-layer emulator (Supplementary Material 7.SM.2), forced with ERF derived in this chapter (displayed in Chapter 2, Figure 2.10) and climate response constrained to assessed ranges for key climate metrics described in Cross-Chapter Box 7.1. The results shown are the medians from a 2,237-member ensemble that encompasses uncertainty in forcing and climate response (year-2019 best

ACCEPTED VERSION SUBJECT TO FINAL EDITING

estimates and uncertainties are shown in Figure 7.7 for several components). Temperature contributions are expressed for carbon dioxide, methane, nitrous oxide, other well-mixed greenhouse gases (WMGHGs), ozone, aerosols, other anthropogenic forcings, total anthropogenic, solar, volcanic, and total. Shaded uncertainty bands show *very likely* ranges. Further details on data sources and processing are available in the chapter data table (Table 7.SM.14).

[END FIGURE 7.8 HERE]

[START CROSS-CHAPTER BOX 7.1 HERE]

Cross-Chapter Box 7.1: Physical emulation of Earth System Models for scenario classification and knowledge integration in AR6

Contributors: Zebedee Nicholls (Australia), Malte Meinshausen (Australia/Germany), Piers Forster (UK), Kyle Armour (USA), Terje Berntsen (Norway), William Collins (UK), Christopher Jones (UK), Jared Lewis (Australia/New Zealand), Jochem Marotzke (Germany), Sebastian Milinski (Germany), Joeri Rogelj (Austria/Belgium), Chris Smith (UK)

Climate model emulators are simple physically-based models that are used to approximate large-scale climate responses of complex Earth System Models (ESMs). Due to their low computational cost they can populate or span wide uncertainty ranges that ESMs cannot. They need to be calibrated to do this and, once calibrated, they can aid inter-ESM comparisons and act as ESM extrapolation tools to reflect and combine knowledge from ESMs and many other lines of evidence (Geoffroy et al., 2013a; Good et al., 2013; Smith et al., 2018a). In AR6, the term 'climate model emulator' (or simply emulator) is preferred over 'simple' or 'reduced-complexity climate model' to reinforce their use as specifically calibrated tools (Cross-Chapter Box 7.1, Figure 1). Nonetheless, simple physically-based climate models have a long history of use in previous IPCC reports (Chapter 1, Section 1.5.3.4). Climate model emulators can include carbon and other gas cycles and can combine uncertainties along the cause-effect chain from emissions to temperature response. AR5(Collins et al., 2013a) used the MAGICC6 emulator (Meinshausen et al., 2011a) in a probabilistic setup (Meinshausen et al., 2009) to explore the uncertainty in future projections. A simple impulse response emulator (Good et al., 2011) was also used to ensure a consistent set of ESM projections could be shown across a range of scenarios. AR5 WGI Chapter 8 (Myhre et al., 2013b) employed a two-layer emulator for quantifying Global Temperature Potentials (GTP). In AR5 WGIII (Clarke et al., 2014), MAGICC6 was also used for the classification of scenarios, and in AR5 Synthesis Report (IPCC, 2014) this information was used to estimate carbon budgets. In SR1.5, two emulators were used to provide temperature projections of scenarios: the MAGICC6 model, which was used for the scenario classification, and the FaIR1.3 model (Millar et al., 2017; Smith et al., 2018a).

SR1.5 found that the physically-based emulators produced different projected non-CO_2 forcing and identified the largely unexplained differences between the two emulators used as a key knowledge gap (Forster et al., 2018). This led to a renewed effort to test the skill of various emulators. The Reduced Complexity Model Intercomparison Project (RCMIP; Nicholls et al. (2020)) found that the latest generation of the emulators can reproduce key characteristics of the observed changes in global surface air temperature (GSAT) together with other key responses of ESMs (Cross-Chapter Box 7.1, Figure 1a). In particular, despite their reduced structural complexity, some emulators are able to replicate the non-linear aspects of ESM GSAT response over a range of scenarios. GSAT emulation has been more thoroughly explored in the literature than other types of emulation. Structural differences between emulation approaches lead to different outcomes and there are problems with emulating particular ESMs. In conclusion, there is *medium confidence* that emulators calibrated to single ESM runs can reproduce ESM projections of the forced GSAT response to other similar emissions scenarios to within natural variability (Meinshausen et al., 2011b; Geoffroy et al., 2013a; Dorheim et al., 2020; Nicholls et al., 2020; Tsutsui, 2020), although larger differences can remain for scenarios with very different forcing characteristics. For variables other than GSAT there has not yet been a comprehensive effort to evaluate the performance of emulators.

ACCEPTED VERSION SUBJECT TO FINAL EDITING

Application of emulators in AR6 WGI

Cross-Chapter Box 7.1 Table 1 shows the use of emulators within the WGI Report. The main use of emulation in the Report is to estimate GSAT change from Effective Radiative Forcing (ERF) or concentration changes, where various versions of a two layer energy budget emulator are used. The two-layer emulator is equivalent to a two-timescale impulse response model (Geoffroy et al., 2013b, Supplementary Material 7.SM.2). Both a single configuration version and probabilistic forms are used. The emulator is an extension of the energy budget equation (Equation 7.1) and allows for heat exchange between the upper- and deeper-ocean layers, mimicking the ocean heat uptake that reduces the rate of surface warming under radiative forcing (Gregory, 2000; Held et al., 2010; Winton et al., 2010; Armour, 2017; Mauritsen and Pincus, 2017; Rohrschneider et al., 2019). Although the same energy budget emulator approach is used, different calibrations are employed in various sections, to serve different purposes and keep lines of evidence as independent as possible. Chapter 9 additionally employs projections of ocean heat content from the Chapter 7 two-layer emulator to estimate the thermostatic component to future sea-level rise (see Chapter 9, Section 9.6.3 and Supplementary Material 7.SM.2).

Emission-driven emulators, as opposed to ERF- or concentration-driven emulators are also used in the Report. In Chapter 4 (Section 4.6) MAGICC7 is used to emulate GSAT beyond 2100 since its long-term response has been assessed to be fit-for-purpose to represent the behaviour of ESMs. In Chapter 5 (Section 5.5) MAGICC7 is used to explore the non-CO_2 GSAT contribution in emissions scenarios. In Chapter 6 and Chapter 7 (Section 7.6), two-layer model configurations were tuned to match the probabilistic GSAT responses of FaIRv1.6.2 and MAGICC7 emission-driven emulators. For Chapter 6 the two median values from FaIRv1.6.2 and MAGICC7 emulators are averaged and then matched to the best-estimate ECS of 3°C and TCR of 1.8 °C (Table 7.13 and Table 7.14) under the best-estimate ERF due to a doubling of CO_2 of 3.93 W m^{-2} (Table 7.4). For Section 7.6 a distribution of responses are used from the two emulators to estimate uncertainties in Global Temperature-change Potentials.

[START CROSS-CHAPTER BOX 7.1, TABLE 1 HERE]

Cross-Chapter Box 7.1, Table 1: Use of emulation within the WGI report

Chapter (Ch) and Section	Application and emulator type	Emulated Variables
Ch1, Cross Chapter-Box 1.2	Estimate anthropogenic temperature change pre-1850, based on radiative forcing time series from Chapter 7. Uses the Chapter 7 calibrated 2-layer emulator: a two-layer energy budget emulator, probabilistically calibrated to AR6 ECS, TCR, historical warming and ocean heat uptake ranges, driven by the Chapter 7 concentration based ERFs.	GSAT
Ch 3, Section 3.3 Ch 7, Section 7.3	Investigation of the historical temperature response to individual forcing mechanisms to compliment detection and attribution results. Uses the Chapter 7 calibrated two-layer emulator.	GSAT
Ch 4, Box 4.1	Understanding the spread in global surface air temperature increase of CMIP6 models and comparison to other assessments; assessment of contributions to projected temperature uncertainty. Uses a two-layer emulator calibrated to the Chapter 7 ECS and TCR	GSAT

ACCEPTED VERSION SUBJECT TO FINAL EDITING

	assessment driven by Chapter 7 best-estimate ERFs.	
Ch 4, Section 4.6	Emulators used to assess differences in radiative forcing and GSAT response between RCP and SSP scenarios. Uses the Chapter 7 ERF timeseries and the MAGICC7 probabilistic emission-driven emulator for GSAT calibrated to the WGI assessment.	ERF, GSAT
Ch 4, Section 4.7	Emulator used for long-term GSAT projections (post-2100) to complement the small number of ESMs with data beyond 2100. Uses the MAGICC7 probabilistic emission-driven emulator calibrated to the WGI assessment.	GSAT
Ch 5, Section 5.5	Estimated non-CO_2 warming contributions of mitigation scenarios at the time of their net zero CO_2 emissions for integration in the assessment of remaining carbon budgets. Uses the MAGICC7 probabilistic emission-driven emulator calibrated to the WGI assessment.	GSAT
Ch 6, Section 6.6 Ch 6, Section 6.7	Estimated contributions to future warming from SLCFs across SSP scenarios based on ERF timeseries. Uses a single two-layer emulator configuration derived from the medians of MAGICC7 and FaIRv1.6.2 AR6 WG1 GSAT probabilistic responses and the best-estimate of ECS and TCR.	GSAT
Ch.7, Section 7.5	Estimating a process based TCR from a process based ECS. Uses a two-layer emulator in probabilistic form calibrated to process based estimates from Chapter 7; a different calibration compared to the main Chapter 7 emulator.	TCR
Ch 7, Section 7.6	Deriving emission metrics. Uses two-layer emulator configurations derived from MAGICC7 and FaIRv1.6.2 AR6 WG1 probabilistic GSAT responses.	Global Temperature-change Potentials and their uncertainty
Ch 9, Section 9.6	Deriving global mean sea level projections. Uses the Chapter 7 calibrated two-layer emulator for GSAT and ocean heat content, where GSAT drives regional statistical emulators of ice sheets and glaciers.	Sea level and ice loss
Ch 11, Section 11.2 and Cross-Chapter	Regional patterns of response are compared to global mean trends. Assessed literature includes projections with	Various regional

ACCEPTED VERSION SUBJECT TO FINAL EDITING

Box 11.1	a regional pattern scaling and variability emulator.	information

[END CROSS-CHAPTER BOX 7.1, TABLE 1 HERE]

Emission-driven emulators for scenario classification in AR6 WGIII

As in AR5 and SR1.5, emission-driven emulators are used to communicate outcomes of the physical climate science assessment and uncertainties to quantify the temperature outcome associated with different emission scenarios. In particular, the computational efficiency of these emulators allows the analysis of a large number of multi-gas emissions scenarios in terms of multiple characteristics, e.g., year of peak temperature or the 2030 emission levels in line with keeping global warming to below 1.5°C or 2.0 ºC.

Four emission-driven emulators have been considered as tools for WGIII to explore the range of GSAT response to multiple scenarios beyond those assessed in WGI. The four emulators are CICERO-SCM (Skeie et al., 2017, 2021), FaIRv1.6.2 (Millar et al., 2017; Smith et al., 2018a), MAGICC7 (Meinshausen et al., 2009) and OSCARv3.1.1 (Gasser et al., 2017a, 2020). Each emulator's probabilistic distribution has been calibrated to capture the relationship between emissions and GSAT change. The calibration is informed by the WGI assessed ranges of ECS, TCR, historical GSAT change, ERF, carbon cycle metrics and future warming projections under the (concentration-driven) SSP scenarios. The emulators are then provided as a tool for WGIII to perform a GSAT-based classification of mitigation scenarios consistent with the physical understanding assessed in WGI.. The calibration step reduced the emulator differences identified in SR1.5. Note that evaluation of both central and range estimates of each emulator's probabilistic projections is important to assess the fitness-for-purpose for the classification of scenarios in WGIII based on information beyond the central estimate of GSAT warming.

[START CROSS-CHAPTER BOX 7.1, FIGURE 1 HERE]

Cross-Chapter Box 7.1, Figure 1: A comparison between the global-mean surface air temperature response of various calibrated simple climate models, assessed ranges and Earth System Models. The top panels compare the assessed historical GSAT time series (Chapter 2, Cross Chapter Box 2.3) with four multi-gas emulators calibrated to replicate numerous assessed ranges (Cross-Chapter Box 7.1, Table 2 below) (panel a) and also compares idealized CO_2-only concentration scenario response for one ESM (IPSL CM6A-LR) and multiple emulators which participated in RCMIP Phase 1 (Nicholls et al., 2020) calibrated to that single ESM (panel b). The bottom panels compare this Report's assessed ranges for GSAT warming (Chapter 4, Box 4.1) under the multi-gas scenario SSP1-2.6 with the same calibrated emulators as in panel a (panel c and d). For context, a range of CMIP6 ESM results are also shown (thin lines in bottom-left panel c and open circles in bottom-right panel d). Panel b) adapted from Nicholls et al. (2020). Further details on data sources and processing are available in the chapter data table (Table 7.SM.14).

[END CROSS-CHAPTER BOX 7.1, FIGURE 1 HERE]

MAGICC7 and FaIRv1.6.2 emission based emulators are able to represent the WGI assessment to within small differences (defined here as within typical rounding precisions of ±5% for central estimates and ±10% for ranges) across more than 80% of metric ranges (Cross-Chapter Box 7.1, Table 2 below). Both calibrated emulators are consistent with assessed ranges of ECS, historical GSAT, historical ocean heat uptake, total greenhouse gas ERF, methane ERF and the majority of the assessed SSP warming ranges. FaIRv1.6.2 also matches the assessed central value of TCRE and airborne fraction. Whereas, MAGICC7 matches the assessed TCR ranges as well as providing a closer fit to the SSP warming ranges for the lower emission scenarios. In the evaluation framework considered here, CICERO-SCM represents historical warming to

ACCEPTED VERSION SUBJECT TO FINAL EDITING

within 2% of the assessed ranges and also represents future temperatures ranges across the majority of the assessment although it lacks the representation of the carbon cycle. In this framework, OSCARv3.1.1 is less able to represent the assessed projected GSAT ranges although it matches the range of airborne fraction estimates closely and the assessed historical GSAT *likely* range to within 0.5%. Despite these identified limitations, both CICERO-SCM and OSCARv3.1.1 provide additional information for evaluating the sensitivity of scenario classification to model choice.

How emulators match the assessed ranges used for the evaluation framework is summarised here and in Table 2. The first is too low projections in 2081–2100 under SSP1-1.9 (8% or 15% too low for the central estimate and 15% or 25% too low for the lower end in the case of MAGICC7 or FaIRv1.6.2, respectively). The second is the representation of the aerosol effective radiative forcing (both MAGICC7 and FaIRv1.6.2 are greater than 8% less negative than the central assessed range and greater than 10% less negative for the lower assessed range), as energy balance models struggle to reproduce an aerosol ERF with a magnitude as strong as the assessed best estimate and still match historical warming estimates. Both emulators have medium to large differences compared to the TCRE and airborne fraction ranges (see note of Table 2). Finally, there is also a slight overestimate of the low-end of the assessed historical GSAT range.

Overall, there is *high confidence* that emulated historical and future ranges of GSAT change can be calibrated to be internally-consistent with the assessment of key physical-climate indicators in this Report: greenhouse gas ERFs, ECS and TCR. When calibrated to match the assessed ranges of GSAT and multiple physical climate indicators, physically-based emulators can reproduce the best estimate of GSAT change over 1850–1900 to 1995–2014 to within 5% and *very likely* range of this GSAT change to within 10%. MAGICC7 and FaIRv1.6.2 match at least two-thirds of the Chapter 4 assessed projected GSAT changes to within these levels of precision.

[START CROSS-CHAPTER BOX 7.1, TABLE 2 HERE]

Cross-Chapter Box 7.1, Table 2: Percentage differences between the emulator value and the WGI assessed best estimate and range for key metrics. Values are given for four emulators in their respective AR6-calibrated probabilistic setups. Absolute values of these indicators are shown in Supplementary Table 7.SM.4.

Emulator		CICERO-SCM			FaIRv1.6.2			MAGICC7			OSCARv3.1.1		
Assessed range		**Lower**	**Central**	**Upper**	**Lower**	**Central**	**Upper**	**Lower**	**Central**	**Upper**	**Lower**	**Central**	**Upper**
Key metrics													
ECS (°C)		26%	2%	–18%	3%	–2%	1%	–3%	–1%	–3%	–8%	–15%	–22%
TCRE (°C per 1000 Gt C)**					29%	–7%	–21%	37%	5%	–5%	50%	–8%	–20%
TCR (°C)		15%	–5%	–3%	14%	0%	3%	6%	4%	9%	26%	1%	–14%
Historical warming and Effective Radiative Forcing													
GSAT warming (°C)	1995–2014 rel. 1850–1900	2%	0%	0%	7%	3%	4%	7%	1%	–1%	–0%	–8%	–0%
Ocean heat content change (ZJ)*	1971–2018	–24%	–27%	–29%	5%	–4%	–9%	–1%	–3%	–6%	–47%	–39%	10%
Total Aerosol ERF (W m^{-2})	2005–2014 rel. 1750	36%	37%	10%	16%	12%	0%	10%	8%	8%	38%	15%	–31%
GHG ERF (W m^{-2})	2019 rel. 1750	4%	–5%	–13%	1%	2%	1%	2%	1%	–0%	1%	3%	–3%
Methane ERF (W m^{-2})	2019 rel.	31%	4%	–13%	3%	3%	3%	0%	–0%	3%	8%	–1%	–5%

ACCEPTED VERSION SUBJECT TO FINAL EDITING

	1750												
Carbon Cycle metrics													
Airborne Fraction *1pctCO2* (dimensionless)*	$2\times CO_2$				8%	–3%	–11%	12%	6%	–1%	1%	–0%	8%
Airborne Fraction *1pctCO2* (dimensionless)*	$4\times CO_2$				12%	1%	–9%	15%	4%	–6%	5%	–1%	–1%
Future warming (GSAT) relative to 1995–2014													
SSP1-1.9 (°C)	2021–2040	10%	–4%	10%	3%	1%	11%	2%	–0%	4%	12%	–9%	–25%
	2041–2060	8%	–9%	7%	–11%	–8%	6%	–1%	–1%	7%	12%	–8%	–31%
	2081–2100	–12%	–25%	–2%	–25%	–15%	4%	–15%	–8%	3%	7%	–10%	–31%
SSP1-2.6 (°C)	2021–2040	7%	–5%	5%	2%	1%	8%	–1%	–2%	–0%	9%	–9%	–28%
	2041–2060	8%	–6%	2%	–2%	–2%	5%	0%	1%	2%	15%	–6%	–28%
	2081–2100	–2%	–14%	–5%	–8%	–7%	1%	–6%	–1%	1%	17%	–9%	–29%
SSP2-4.5 (°C)	2021–2040	8%	–5%	5%	7%	–1%	2%	3%	–3%	–2%	–5%	–14%	–30%
	2041–2060	4%	–4%	3%	1%	–1%	2%	1%	1%	2%	8%	–8%	–28%
	2081–2100	–1%	–10%	–3%	–2%	–3%	1%	–2%	1%	3%	8%	–4%	–25%
SSP3-7.0 (°C)	2021–2040	11%	–4%	1%	14%	1%	–1%	10%	1%	–0%	–5%	–15%	–29%
	2041–2060	4%	–5%	–0%	6%	0%	–1%	7%	4%	1%	7%	–8%	–26%
	2081–2100	–0%	–8%	–3%	3%	–1%	–1%	6%	3%	6%	5%	–6%	–25%
SSP5-8.5 (°C)	2021–2040	5%	–7%	2%	9%	2%	4%	7%	1%	2%	1%	–14%	–30%
	2041–2060	2%	–8%	–1%	4%	0%	4%	3%	2%	4%	10%	–6%	–24%
	2081–2100	4%	–7%	–3%	6%	–0%	1%	8%	4%	7%	9%	–4%	–25%

Notes. Metrics calibrated against are equilibrium climate sensitivity, ECS (Section 7.5); transient climate response to cumulative emissions of carbon dioxide, TCRE (Chapter 5, Section 5.5); transient climate response, TCR (Section 7.5), historical GSAT change (Chapter 2, Section 2.3), ocean heat uptake (Section 7.2 and Chapter 2, Section 2.3) and effective radiative forcing, ERF (Section 7.3), carbon cycle metrics, namely airborne fractions of idealized CO_2 scenarios (taking the *likely* range as twice the standard deviation across the models analysed in Arora et al. (2020), see also Chapter 5, Table 5.7, cross-AR6 lines of evidence row) and GSAT projections under the concentration-driven SSP scenarios for the near-term (2021–2040), mid-term (2041–2060) and long-term (2081–2100) relative to 1995–2014 (Chapter 4, Table 4.2). See Supplementary Table 7.SM.4 for a version of this table with the absolute values rather than percentage differences. The columns labelled "upper" and "lower" indicate 5% to 95% ranges, except for the variables demarcated with an asterisk or double asterisk (* or **), where they denote *likely* ranges from 17% to 83%. Note that the TCRE assessed range (**) is wider than the combination of the TCR and airborne fraction to account for uncertainties related to model limitations (Chapter 5, Table 5.7) hence it is expected that the emulators are too narrow on this. particular metric and/or too wide on TCR and airborne fraction. For illustrative purposes, the cells are coloured as follows: white cells indicate small differences (up to ±5% for the central value and +10% for the ranges), light blue and light teal cells indicate medium differences (up to +10% and -10% for light blue and light teal for central values, respectively; up to ±20% for the ranges) and darker cells indicate larger positive (blue) or negative (teal) differences

ACCEPTED VERSION SUBJECT TO FINAL EDITING

(note that values are rounded after the colours are applied).

[END CROSS-CHAPTER BOX 7.1, TABLE 2 HERE]

[END CROSS-CHAPTER BOX 7.1 HERE]

7.4 Climate feedbacks

The magnitude of global surface temperature change primarily depends on the strength of the radiative forcings and feedbacks, the latter defined as the changes of the net energy budget at the top of atmosphere (TOA) in response to a change in the GSAT (Box 7.1, Equation 7.1). Feedbacks in the Earth system are numerous, and it can be helpful to categorise them into three groups: (1) physical feedbacks; (2) biogeophysical and biogeochemical feedbacks; and (3) long-term feedbacks associated with ice sheets. The physical feedbacks (for example, associated with changes in lapse-rate, water vapour, surface albedo, or clouds; Sections 7.4.2.1-7.4.2.4) and biogeophysical/biogeochemical feedbacks (for example, associated with changes in methane, aerosols, ozone, or vegetation; Section 7.4.2.5) act both on time scales that are used to estimate the equilibrium climate sensitivity (ECS) in models (typically 150 years, see Box 7.1) and on longer time scales required to reach equilibrium. Long-term feedbacks associated with ice sheets (Section 7.4.2.6) are relevant primarily after several centuries or more. The feedbacks associated with biogeophysical/biogeochemical processes and ice sheets, often collectively referred to as Earth system feedbacks, had not been included in conventional estimates of the climate feedback (e.g., Hansen et al., 1984), but the former can now be quantified and included in the assessment of the total (net) climate feedback. Feedback analysis represents a formal framework for the quantification of the coupled interactions occurring within a complex Earth system in which everything influences everything else (e.g., Roe, 2009). As used here and presented in Section 7.4.1, its primary objective is to identify and understand the key processes that determine the magnitude of the surface temperature response to an external forcing. For each feedback, the basic underlying mechanisms and their assessment are presented in Section 7.4.2.

Up until AR5, process understanding and quantification of feedback mechanisms were based primarily on global climate models. Since AR5, the scientific community has undertaken a wealth of different alternative approaches, including observational and fine-scale modelling approaches. This has in some cases led to more constrained feedbacks and, on the other hand, uncovered shortcomings in global climate models, which are starting to be corrected. Consequently, AR6 achieves a more robust assessment of feedbacks in the climate system that is less reliant on global climate models than in earlier assessment reports.

It has long been recognized that the magnitude of climate feedbacks can change as the climate state evolves over time (Manabe and Bryan, 1985; Murphy, 1995), but the implications for projected future warming have been investigated only recently. Since AR5, progress has been made in understanding the key mechanisms behind this time- and state-dependence. Specifically, the state-dependence is assessed by comparing climate feedbacks between warmer and colder climate states inferred from paleoclimate proxies and model simulations (Section 7.4.3). The time-dependence of the feedbacks is evident between the historical period and future projections and is assessed to arise from the evolution of the surface warming pattern related to changes in zonal and meridional temperature gradients (Section 7.4.4).

7.4.1 Methodology of the feedback assessment

The global surface temperature changes of the climate system are generally analysed with the classical forcing-feedback framework as described in Box 7.1 (Equation 7.1). In this equation α is the net feedback parameter (W m^{-2} °C^{-1}). As surface temperature changes in response to the TOA energy imbalance, many other climate variables also change, thus affecting the radiative flux at the TOA. The aggregate feedback parameter can then be decomposed into an approximate sum of terms $\alpha = \sum_x \alpha_x$, where x is a vector representing variables that have a direct effect on the net TOA radiative flux N and $\alpha_x = \frac{\partial N}{\partial x}\frac{dx}{dT}$. Following

ACCEPTED VERSION SUBJECT TO FINAL EDITING

the conventional definition, the physical climate feedbacks are here decomposed into terms associated with a vertically uniform temperature change (Planck response, P), changes in the water vapour plus temperature lapse rate (WV+LR), surface albedo (A) and clouds (C). The water vapour plus temperature lapse rate feedback is further decomposed using two different approaches, one based on changes in specific humidity, the other on changes in relative humidity. Biogeochemical feedbacks arise due to changes in aerosols and atmospheric chemical composition in response to changes in surface temperature, and Gregory et al. (2009) and Raes et al. (2010) show that they can be analysed using the same framework as for the physical climate feedbacks (see Chapter 5, Section 5.4 and Chapter 6, Section 6.4.5 Similarly, feedbacks associated with biogeophysical and ice sheet changes can also be incorporated.

In global climate models, the feedback parameters α_x in global warming conditions are often estimated as the mean differences in the radiative fluxes between atmosphere-only simulations in which the change in SST is prescribed (Cess et al., 1990), or as the regression slope of change in radiation flux against change in global-mean surface air temperature using atmosphere-ocean coupled simulations with abrupt CO_2 changes (*abrupt4xCO2*) for 150 years (Gregory et al., 2004; Andrews et al., 2012; Caldwell et al., 2016; see Box 7.1). Neither method is perfect, but both are useful and yield consistent results (Ringer et al., 2014). In the regression method, the radiative effects of land warming are excluded from the effective radiative forcing due to doubling of CO_2 (Section 7.3.2), which may overestimate feedback values by about 10%. At the same time, the feedback calculated using the regression over years 1–150 ignores its state-dependence on multi-centennial time scales (Section 7.4.3), probably giving an underestimate of α by about 10% (Rugenstein et al., 2019a). These effects are both small and cancel each other in the ensemble mean, justifying the use of regression over 150 years as an approximation to feedbacks in ESMs.

The change of the TOA radiative flux N as a function of the change of a climate variable x (such as water vapour) is commonly computed using the 'radiative kernel' method (Soden et al., 2008). In this method, the kernel $\partial N/\partial x$ is evaluated by perturbing x within a radiation code. Then multiplying the kernel by dx/dT inferred from observations, meteorological analysis or GCMs produces a value of α_x.

Feedback parameters from lines of evidence other than global models are estimated in various ways. For example, observational data combined with GCM simulations could produce an emergent constraint on a particular feedback (Hall and Qu, 2006; Klein and Hall, 2015), or the observed interannual fluctuations in the global-mean TOA radiation and the surface air temperature, to which the linear regression analysis is applied, could generate a direct estimate of the climate feedback assuming that the feedback associated with internal climate variability at short time scales can be a surrogate of the feedback to CO_2-induced warming (Dessler, 2013; Loeb et al., 2016). The assumption is not trivial, but can be justified given that the climate feedbacks are fast enough to occur at the interannual time scale. Indeed, a broad agreement has been obtained in estimates of individual physical climate feedbacks based on interannual variability and longer climate change timescales in GCMs (Zhou et al., 2015; Colman and Hanson, 2017). This means that the climate feedbacks estimated from the observed interannual fluctuations are representative of the longer-term feedbacks (decades to centuries). Care must be taken for these observational estimates because they can be sensitive to details of the calculation such as data sets and periods used (Dessler, 2013; Proistosescu et al., 2018). In particular, there would be a dependence of physical feedbacks on the surface warming pattern at the interannual time scale due, for example, to El Niño-Southern Oscillation. However, this effect both amplifies and suppresses the feedback when data include the positive and negative phases of the interannual fluctuation, and therefore the net bias will be small.

In summary, the classical forcing-feedback framework has been extended to include biogeophysical and non-CO_2-biogeochemical feedbacks in addition to the physical feedbacks. It has also been used to analyse seasonal and interannual to decadal climate variations in observations and ESMs, in addition to long-term climate changes as seen in *abrupt4xCO2* experiments. These developments allow an assessment of the feedbacks based on a larger variety of lines of evidence compared to AR5.

7.4.2 Assessing climate feedbacks

ACCEPTED VERSION SUBJECT TO FINAL EDITING

This section provides an overall assessment of individual feedback parameters, α_x, by combining different lines of evidence from observations, theory, process models and ESMs. To achieve this, we review the understanding of the key processes governing the feedbacks, why the feedback estimates differ among models, studies or approaches, and the extent to which these approaches yield consistent results. The individual terms assessed are the Planck response (Section 7.4.2.1) and feedbacks associated with changes in water vapour and lapse rate (Section 7.4.2.2), surface albedo (Section 7.4.2.3), clouds (Section 7.4.2.4), biogeophysical and non-CO_2 biogeochemical processes (Section 7.4.2.5), and ice sheets (Section 7.4.2.6). A synthesis is provided in Section 7.4.2.7. Climate feedbacks in CMIP6 models are then evaluated in Section 7.4.2.8, with an explanation of how they have been incorporated into the assessment.

7.4.2.1 Planck response

The Planck response represents the additional thermal or longwave (LW) emission to space arising from vertically uniform warming of the surface and the atmosphere. The Planck response α_P, often called the Planck feedback, plays a fundamental stabilizing role in Earth's climate and has a value that is strongly negative: a warmer planet radiates more energy to space. A crude estimate of α_P can be made using the normalized greenhouse effect $\tilde{g}$, defined as the ratio between the greenhouse effect G and the upwelling LW flux at the surface (Raval and Ramanathan, 1989). Current estimates (Section 7.2, Figure 7.2) give G = 159 W m^{-2} and $\tilde{g} \approx 0.4$. Assuming $\tilde{g}$ is constant, one obtains for a surface temperature T_s = 288K, $\alpha_P = (\tilde{g} - 1)\, 4\, \sigma\, T_s^3 \approx -3.3$ W m^{-2} °C^{-1}, where σ is the Stefan-Boltzmann constant. This parameter α_P is estimated more accurately using kernels obtained from meteorological reanalysis or climate simulations (Soden and Held, 2006; Dessler, 2013; Vial et al., 2013; Caldwell et al., 2016; Colman and Hanson, 2017; Zelinka et al., 2020). Discrepancies among estimates primarily arise because differences in cloud distributions make the radiative kernels differ (Kramer et al., 2019). Using six different kernels, Zelinka et al. (2020) obtained a spread of ±0.1 W m^{-2} °C^{-1} (one standard deviation). Discrepancies among estimates secondarily arise from differences in the pattern of equilibrium surface temperature changes among ESMs. For the CMIP5 and CMIP6 models this introduces a spread of ±0.04 W m^{-2} °C^{-1} (one standard deviation). The multi-kernel and multi-model mean of α_P is equal to –3.20 W m^{-2} °C^{-1} for the CMIP5 and –3.22 W m^{-2} °C^{-1} for the CMIP6 models (Supplementary Table 7.SM.5). Overall, there is *high confidence* in the estimate of the Planck response, which is assessed to be α_P = –3.22 W m^{-2} °C^{-1} with a *very likely* range of –3.4 to –3.0 W m^{-2} °C^{-1} and a *likely range* of –3.3 to –3.1 W m^{-2} °C^{-1}.

The Planck temperature response ΔT_P is the equilibrium temperature change in response to a forcing ΔF when the net feedback parameter is equal to the Planck response parameter: $\Delta T_P = -\Delta F / \alpha_P$.

7.4.2.2 Water vapour and temperature lapse rate feedbacks

Two decompositions are generally used to analyse the feedbacks associated with a change in the water vapour and temperature lapse rate in the troposphere. As in any system, many feedback decompositions are possible, each of them highlighting a particular property or aspect of the system (Ingram, 2010; Held and Shell, 2012; Dufresne and Saint-Lu, 2016). The first decomposition considers separately the changes (and therefore feedbacks) in the lapse rate (LR) and specific humidity (WV). The second decomposition considers changes in the lapse rate assuming constant relative humidity (LR*) separately from changes in relative humidity (RH).

The specific humidity (WV) feedback, also known as the water vapour feedback, quantifies the change in radiative flux at the TOA due to changes in atmospheric water vapour concentration associated with a change in global mean air surface temperature. According to theory, observations and models, the water vapour increase approximately follows the Clausius-Clapeyron relationship at the global scale with regional differences dominated by dynamical processes (Chapter 8, Section 8.2.1; Sherwood et al., 2010b; Chung et al., 2014; Romps, 2014; Liu et al., 2018; Schröder et al., 2019). Greater atmospheric water vapour content, particularly in the upper troposphere, results in enhanced absorption of LW and SW radiation and reduced outgoing radiation. This is a positive feedback. Atmospheric moistening has been detected in satellite records

ACCEPTED VERSION SUBJECT TO FINAL EDITING

(Chapter 2, Section 2.3.1.3.3), is simulated by climate models (Chapter 3, Section 3.3.2.1), and the estimates agree within model and observational uncertainty (Soden et al., 2005; Dessler, 2013; Gordon et al., 2013; Chung et al., 2014). The estimate of this feedback inferred from satellite observations is $\alpha_{WV} = 1.85 \pm 0.32$ W m^{-2} °C^{-1} (Liu et al., 2018). This is consistent with the value $\alpha_{WV} = 1.77 \pm 0.20$ W m^{-2} °C^{-1} (one standard deviation) obtained with CMIP5 and CMIP6 models (Zelinka et al., 2020).

The lapse rate (LR) feedback quantifies the change in radiative flux at the TOA due to a non-uniform change in the vertical temperature profile. In the tropics, the vertical temperature profile is mainly driven by moist convection and is close to a moist adiabat. The warming is larger in the upper troposphere than in the lower troposphere (Manabe and Wetherald, 1975; Santer et al., 2005; Bony et al., 2006), leading to a larger radiative emission to space and therefore a negative feedback. This larger warming in the upper troposphere than at the surface has been observed over the last twenty years thanks to the availability of sufficiently accurate observations (Chapter 2, Section 2.3.1.2.2). In the extra-tropics, the vertical temperature profile is mainly driven by a balance between radiation, meridional heat transport and ocean heat uptake (Rose et al., 2014). Strong wintertime temperature inversions lead to warming that is larger in the lower troposphere (Payne et al., 2015; Feldl et al., 2017a) and a positive lapse rate feedback in polar regions (Manabe and Wetherald, 1975; Bintanja et al., 2012; Pithan and Mauritsen, 2014; Section 7.4.4.1). However, the tropical contribution dominates, leading to a negative global mean lapse rate feedback (Soden and Held, 2006; Dessler, 2013; Vial et al., 2013; Caldwell et al., 2016). The LR feedback has been estimated at interannual time scales using meteorological reanalysis and satellite measurements of TOA fluxes (Dessler, 2013). These estimates from climate variability are consistent between observations and ESMs (Dessler, 2013; Colman and Hanson, 2017). The mean and standard deviation of this feedback under global warming based on the cited studies are $\alpha_{LR} = -0.50 \pm 0.20$ W m^{-2} °C^{-1} (Dessler, 2013; Caldwell et al., 2016; Colman and Hanson, 2017; Zelinka et al., 2020).

The second decomposition was proposed by Held and Shell (2012) to separate the response that would occur under the assumption that relative humidity remains constant from that due to the change in relative humidity. The feedback is decomposed into three: (1) change in water vapour due to an identical temperature increase at the surface and throughout the troposphere assuming constant relative humidity, which will be called the Clausius-Clapeyron (CC) feedback here; (2) change in lapse rate assuming constant relative humidity (LR*); (3) change in relative humidity (RH). Since AR5 it has been clarified that by construction, the sum of the temperature lapse rate and specific humidity (LR+WV) feedbacks is equal to the sum of the Clausius-Clapeyron, lapse rate assuming constant relative humidity, and changes in relative humidity (CC+LR*+RH) feedbacks. Therefore, each of these two sums may simply be referred to as the "water vapour plus lapse rate" feedback.

The CC feedback has a large positive value due to well understood thermodynamic and radiative processes: $\alpha_{CC} = 1.36 \pm 0.04$ W m^{-2} °C^{-1} (one standard deviation) (Held and Shell, 2012; Zelinka et al., 2020). The lapse rate feedback assuming a constant relative humidity LR* in CMIP6 models has small absolute values ($\alpha_{LR*} = -0.10 \pm 0.07$ W m^{-2} °C^{-1} (one standard deviation)), as expected from theoretical arguments (Ingram, 2010, 2013). It includes the pattern effect of surface warming that modulates the lapse rate and associated specific humidity changes (Po-Chedley et al., 2018a). The relative humidity feedback is close to zero ($\alpha_{RH} = 0.00 \pm 0.06$ W m^{-2} °C^{-1} (one standard deviation)) and the spread among models is confined to the tropics (Sherwood et al., 2010a; Vial et al., 2013; Takahashi et al., 2016; Po-Chedley et al., 2018a). The change in upper tropospheric RH is closely related to model representation of current climate (Sherwood et al., 2010a; Po-Chedley et al., 2019), and a reduction in model RH biases is expected to reduce the uncertainty of the RH feedback. At inter-annual time scales, it has been shown that the change in RH in the tropics is related to the change of the spatial organisation of deep convection (Holloway et al., 2017; Bony et al., 2020).

Both decompositions allow estimates of the sum of the lapse rate and specific humidity feedbacks α_{LR+WV}. The multi-kernel and multi-model mean of α_{LR+WV} is equal to 1.24 and 1.26 W m^{-2} °C^{-1} respectively for CMIP5 and CMIP6 models, with a standard deviation of 0.10 W m^{-2} °C^{-1} (Zelinka et al., 2020). These values are larger than the recently assessed value of 1.15 W m^{-2} °C^{-1} by Sherwood et al. (2020) as a larger set of kernels, including those obtained from meteorological reanalysis, are used here.

ACCEPTED VERSION SUBJECT TO FINAL EDITING

Since AR5, the effect of the water vapour increase in the stratosphere with global warming has been investigated by different studies. This increase produces a positive feedback between 0.1 and 0.3 W m^{-2} °C^{-1} if the stratospheric radiative response is computed assuming temperatures that are adjusted with fixed dynamical heating (Dessler et al., 2013; Banerjee et al., 2019). However, various feedbacks reduce this temperature adjustment and the overall physical (water vapour, temperature and dynamical) stratospheric feedback becomes much smaller (0.0 to 0.1 W m^{-2} °C^{-1}) (Huang et al., 2016, 2020; Li and Newman, 2020), with uncertainty arising from limitations of current ESMs in simulating stratospheric processes. The total stratospheric feedback is assessed at 0.05 ± 0.1 W m^{-2} °C^{-1} (one standard deviation).

The combined water vapour plus lapse rate feedback is positive. The main physical processes that drive this feedback are well understood and supported by multiple lines of evidence including models, theory and observations. The combined water vapour plus lapse rate feedback parameter is assessed to be α_{LR+WV} = 1.30 W m^{-2} °C^{-1}, with a *very likely* range of 1.1 to 1.5 W m^{-2} °C^{-1} and a *likely* range of 1.2 to 1.4 W m^{-2} °C^{-1} with *high confidence.*

7.4.2.3 Surface albedo feedback

Surface albedo is determined primarily by reflectance at Earth's surface, but also by the spectral and angular distribution of incident solar radiation. Changes in surface albedo result in changes in planetary albedo that are roughly reduced by two-thirds, owing to atmospheric absorption and scattering, with variability and uncertainty arising primarily from clouds (Bender, 2011; Donohoe and Battisti, 2011; Block and Mauritsen, 2013). Temperature change induces surface albedo change through several direct and indirect means. In the present climate and at multidecadal time scales, the largest contributions by far are changes in the extent of sea ice and seasonal snow cover, as these media are highly reflective and are located in regions that are close to the melting temperature (Chapter 2, Sections 2.3.2.1 and 2.3.2.2). Reduced snow cover on sea ice may contribute as much to albedo feedback as reduced extent of sea ice (Zhang et al., 2019). Changes in the snow metamorphic rate, which generally reduces snow albedo with warmer temperature, and warming-induced consolidation of light absorbing impurities near the surface, also contribute secondarily to the albedo feedback (Flanner and Zender, 2006; Qu and Hall, 2007; Doherty et al., 2013; Tuzet et al., 2017). Other contributors to albedo change include vegetation state (assessed separately in Section 7.4.2.5), soil wetness, and ocean roughness.

Several studies have attempted to derive surface albedo feedback from observations of multidecadal changes in climate, but only over limited spatial and inconsistent temporal domains, inhibiting a purely observational synthesis of global α_A. Flanner et al. (2011) applied satellite observations to determine that the northern hemisphere (NH) cryosphere contribution to global α_A over 1979–2008 was 0.48 [*likely* range 0.29 to 0.78] W m^{-2} °C^{-1}, with roughly equal contributions from changes in land snow cover and sea ice. Since AR5, and over similar periods of observation, Crook and Forster (2014) found an estimate of 0.8 ± 0.3 W m^{-2} °C^{-1} (one standard deviation) for the total NH extratropical surface albedo feedback, when averaged over global surface area. For the Arctic sea ice alone, Pistone et al. (2014) and Cao et al. (2015) estimated the contribution to global α_A to be 0.31 ± 0.04 W m^{-2} °C^{-1} (one standard deviation) and 0.31 ± 0.08 W m^{-2} °C^{-1} (one standard deviation), respectively, whereas Donohoe et al. (2020) estimated it to be only 0.16 ± 0.04 W m^{-2} °C^{-1} (one standard deviation). Much of this discrepancy can be traced to different techniques and data used for assessing the attenuation of surface albedo change by Arctic clouds. For the NH land snow, Chen et al. (2016) estimated that observed changes during 1982–2013 contributed (after converting from NH temperature change to global mean temperature change) by 0.1 W m^{-2} °C^{-1} to global α_A, smaller than the estimate of 0.24 W m^{-2} °C^{-1} from Flanner et al. (2011). The contribution of the southern hemisphere (SH) to global α_A is expected to be small because seasonal snow cover extent in the SH is limited, and trends in SH sea ice extent are relatively flat over much of the satellite record (Chapter 2, Section 2.3.2).

CMIP5 and CMIP6 models show moderate spread in global α_A determined from century timescale changes (Qu and Hall, 2014; Schneider et al., 2018; Thackeray and Hall, 2019; Zelinka et al., 2020), owing to variations in modelled sea-ice loss and snow cover response in boreal forest regions. The multi-model mean global-scale α_A (from all contributions) over the 21st century in CMIP5 models under the RCP8.5 scenario

ACCEPTED VERSION SUBJECT TO FINAL EDITING

was derived by Schneider et al. (2018) to be 0.40 ± 0.10 W m^{-2} °C^{-1} (one standard deviation). Moreover, they found that modelled α_A does not decline over the 21st century, despite large losses of snow and sea ice, though a weakened feedback is apparent after 2100. Using the idealized *abrupt4xCO2* as for the other feedbacks, the estimate of the global-scale albedo feedback in the CMIP5 models is 0.35± 0.08 W m^{-2}°C^{-1} (one standard deviation) (Vial et al., 2013; Caldwell et al., 2016). The CMIP6 multi-model mean varies from 0.3 to 0.5 W m^{-2}°C^{-1} depending on the kernel used (Zelinka et al., 2020). Donohoe et al. (2020) derived a multi-model mean α_A and its inter-model spread of 0.37 ± 0.19 W m^{-2} °C^{-1} from the CMIP5 *abrupt4xCO2* ensemble, employing model-specific estimates of atmospheric attenuation and thereby avoiding bias associated with use of a single radiative kernel.

The surface albedo feedback estimates using centennial changes have been shown to be highly correlated to those using seasonal regional changes for NH land snow (Qu and Hall, 2014) and Arctic sea ice (Thackeray and Hall, 2019). For the NH land snow, the physics underpinning this relationship being credible, this opens the possibility to use it as an emergent constraint (Qu and Hall, 2014). Considering only the 8 models whose seasonal cycle of albedo feedback falls within the observational range does not change the multi-model mean contribution to global α_A (0.08 W m^{-2}°C^{-1}) but decreases the inter-model spread by a factor of two (from ± 0.03 to ± 0.015 W m^{-2}°C^{-1}) (Qu and Hall, 2014). For the Arctic sea-ice, Thackeray and Hall (2019) show that the seasonal cycle also provides an emergent constraint, at least until mid-century when the relationship degrades. They find that the CMIP5 multi-model mean of the Arctic sea-ice contribution to α_A is 0.13 W m^{-2} °C^{-1} and that the inter-model spread is reduced by a factor of two (from ± 0.04 to ± 0.02 W m^{-2} °C^{-1}) when the emergent constraint is used. This model estimate is smaller than observational estimates (Pistone et al., 2014; Cao et al., 2015) except those of Donohoe et al. (2020). This can be traced to CMIP5 models generally underestimating the rate of Arctic sea ice loss during recent decades (Stroeve et al., 2012; Flato et al., 2013; Chapter 9, Section 9.3.1), though this may also be an expression of internal variability, since the observed behaviour is captured within large ensemble simulations (Notz, 2015). CMIP6 models better capture the observed Arctic sea ice decline (Chapter 3, Section 3.4.1). In the SH the opposite situation is observed. Observations show relatively flat trends in SH sea ice over the satellite era (Chapter 2, Section 2.3.2.1) whereas CMIP5 models simulate a small decrease (Chapter 3, Section 3.4.1). SH α_A is presumably larger in models than observations but only contribute to about one quarter of the global α_A. Thus, we assess that α_A estimates are consistent, at global scale, in CMIP5 and CMIP6 models and satellite observations, though hemispheric differences and the role of internal variability need to be further explored.

Based on the multiple lines of evidence presented above that include observations, CMIP5 and CMIP6 models and theory, the global surface albedo feedback is assessed to be positive with *high confidence*. The basic phenomena that drive this feedback are well understood and the different studies cover a large variety of hypotheses or behaviours, including how the evolution of clouds affects this feedback. The value of the global surface albedo feedback is assessed to be α_A = 0.35 W m^{-2} °C^{-1}, with a *very likely* range from 0.10 to 0.60 W m^{-2} °C^{-1} and a *likely* range from 0.25 to 0.45 W m^{-2} °C^{-1} with *high confidence*.

7.4.2.4 Cloud feedbacks

7.4.2.4.1 Decomposition of clouds into regimes

Clouds can be formed almost anywhere in the atmosphere when moist air parcels rise and cool, enabling the water vapour to condense. The cloud droplets, ice crystals frozen from small water droplets, and their mixture may further grow into large particles of rain, snow, or drizzle. These microphysical processes interact with aerosols, radiation and atmospheric circulation, resulting in a highly complex set of processes governing cloud formation and lifecycles that operate across a wide range of spatial and temporal scales.

Clouds have various types, from optically thick convective clouds to thin stratus and cirrus clouds, depending upon thermodynamic conditions and large-scale circulation (Figure 7.9). Over the equatorial warm pool and inter-tropical convergence zone (ITCZ) regions, high SSTs stimulate the development of deep convective cloud systems, which are accompanied by anvil and cirrus clouds near the tropopause where the convective air outflows. The large-scale circulation associated with these convective clouds leads to subsidence over the subtropical cool ocean, where deep convection is suppressed by a lower tropospheric

ACCEPTED VERSION SUBJECT TO FINAL EDITING

inversion layer maintained by the subsidence and promoting the formation of shallow cumulus and stratocumulus clouds. In the extratropics, mid-latitude storm tracks control cloud formation, which occurs primarily in the frontal bands of extratropical cyclones. Since liquid droplets do not freeze spontaneously at temperatures warmer than approximately –40°C and ice nucleating particles that can aid freezing at warmer temperatures are scarce (see Section 7.3.3), extratropical clouds often consist both of super-cooled liquid and ice crystals, resulting in mixed-phase clouds.

In the global energy budget at TOA, clouds affect SW radiation by reflecting sunlight due to their high albedo (cooling the climate system) and also LW radiation by absorbing the energy from the surface and emitting at a lower temperature to space, i.e., contributing to the greenhouse effect, warming the climate system. In general, the greenhouse effect of clouds strengthens with height whereas the SW reflection depends on the cloud optical properties. The effects of clouds on Earth's energy budget are measured by the cloud radiative effect (CRE), which is the difference in the TOA radiation between clear and all skies (see Section 7.2.1). In the present climate, the SW CRE tends to be compensated by the LW CRE over the equatorial warm pool, leading to the net CRE pattern showing large negative values over the eastern part of the subtropical ocean and the extratropical ocean due to the dominant influence of highly reflective marine low clouds.

In a first attempt to systematically evaluate ECS based on fully coupled GCMs in AR4, diverging cloud feedbacks were recognized as a dominant source of uncertainty. An advance in understanding the cloud feedback was to assess feedbacks separately for different cloud regimes (Gettelman and Sherwood, 2016). A thorough assessment of cloud feedbacks in different cloud regimes was carried out in AR5 (Boucher et al., 2013), which assigned *high* or *medium confidence* for some cloud feedbacks but *low* or *no confidence* for others (Table 7.9). Many studies that estimate the net cloud feedback using CMIP5 simulations (Vial et al., 2013; Caldwell et al., 2016; Zelinka et al., 2016; Colman and Hanson, 2017) show different values depending on the methodology and the set of models used, but often report a large inter-model spread of the feedback, with the 90% confidence interval spanning both weak negative and strong positive net feedbacks. Part of this diversity arises from the dependence of the model cloud feedbacks on the parameterization of clouds and their coupling to other sub-grid scale processes (Zhao et al., 2015).

Since AR5, community efforts have been undertaken to understand and quantify the cloud feedbacks in various cloud regimes coupled with large-scale atmospheric circulation (Bony et al., 2015). For some cloud regimes, alternative tools to ESMs, such as observations, theory, high-resolution cloud resolving models (CRMs), and Large Eddy Simulations (LES), help quantify the feedbacks. Consequently, the net cloud feedback derived from ESMs has been revised by assessing the regional cloud feedbacks separately and summing them with weighting by the ratio of fractional coverage of those clouds over the globe to give the global feedback, following an approach adopted in Sherwood et al. (2020). This "bottom-up" assessment is explained below with a summary of updated confidence of individual cloud feedback components (Table 7.9). Dependence of cloud feedbacks on evolving patterns of surface warming will be discussed in Section 7.4.4 and is not explicitly taken into account in the assessment presented in this section.

[START FIGURE 7.9 HERE]

Figure 7.9: Schematic cross section of diverse cloud responses to surface warming from the tropics to polar regions. Thick solid and dashed curves indicate the tropopause and the subtropical inversion layer in the current climate, respectively. Thin grey text and arrows represent robust responses in the thermodynamic structure to greenhouse warming, of relevance to cloud changes. Text and arrows in red, orange and green show the major cloud responses assessed with *high*, *medium* and *low confidence*, respectively, and the sign of their feedbacks to the surface warming is indicated in the parenthesis. Major advances since AR5 are listed in a box.

[END FIGURE 7.9 HERE]

ACCEPTED VERSION SUBJECT TO FINAL EDITING

7.4.2.4.2 Assessment for individual cloud regimes

High-cloud altitude feedback.

It has long been argued that cloud top altitude rises under global warming, concurrent with the rising of the tropopause at all latitudes (Marvel et al., 2015; Thompson et al., 2017). This increasing altitude of high clouds was identified in early generation GCMs and the tropical high-cloud altitude feedback was assessed to be positive with *high confidence* in AR5 (Boucher et al., 2013). This assessment is supported by a theoretical argument called the fixed anvil temperature mechanism, which ensures that the temperature of the convective detrainment layer does not change when the altitude of high-cloud tops increases with the rising tropopause (Hartmann and Larson, 2002). Because the cloud top temperature does not change significantly with global warming, cloud longwave emission does not increase even though the surface warms, resulting in an enhancement of the high-cloud greenhouse effect (a positive feedback; Yoshimori et al. (2020)). The upward shift of high clouds with surface warming is detected in observed interannual variability and trends in satellite records for recent decades (Chepfer et al., 2014; Norris et al., 2016; Saint-Lu et al., 2020). The observational detection is not always successful (Davies et al., 2017), but the cloud altitude shifts similarly in many CRM experiments (Khairoutdinov and Emanuel, 2013; Tsushima et al., 2014; Narenpitak et al., 2017). The high-cloud altitude feedback was estimated to be 0.5 W m^{-2}°C^{-1} based on GCMs in AR5, but is revised, using a recent re-evaluation that excludes aliasing effects by reduced low-cloud amounts, downward to 0.22 ± 0.12 W m^{-2} °C^{-1} (one standard deviation) (Zhou et al., 2014; Zelinka et al., 2020). In conclusion, there is *high confidence* in the positive high-cloud altitude feedback simulated in ESMs as it is supported by theoretical, observational, and process modelling studies.

Tropical high-cloud amount feedback.

Updrafts in convective plumes lead to detrainment of moisture at a level where the buoyancy diminishes, and thus deep convective clouds over high SSTs in the tropics are accompanied by anvil and cirrus clouds in the upper troposphere. These clouds, rather than the convective plumes themselves, play a substantial role in the global TOA radiation budget. In the present climate, the net CRE of these clouds is small due to a cancellation between the SW and LW components (Hartmann et al., 2001). However, high clouds with different optical properties could respond to surface warming differently, potentially perturbing this radiative balance and therefore leading to a non-zero feedback.

A thermodynamic mechanism referred to as the 'stability iris effect' has been proposed to explain that the anvil cloud amount decreases with surface warming (Bony et al., 2016). In this mechanism, a temperature-mediated increase of static stability in the upper troposphere, where convective detrainment occurs, acts to balance a weakened mass outflow from convective clouds, and thereby reduce anvil cloud areal coverage (Figure 7.9). The reduction of anvil cloud amount is accompanied by enhanced convective aggregation that causes a drying of the surrounding air and thereby increases the LW emission to space that acts as a negative feedback (Bony et al., 2020). This phenomenon is found in many CRM simulations (Emanuel et al., 2014; Wing and Emanuel, 2014; Wing et al., 2020) and also identified in observed interannual variability (Stein et al., 2017; Saint-Lu et al., 2020).

Despite the reduction of anvil cloud amount supported by several lines of evidence, estimates of radiative feedback due to high-cloud amount changes is highly uncertain in models. The assessment presented here is guided by combined analyses of TOA radiation and cloud fluctuations at interannual time scale using multiple satellite data sets. The observationally based local amount feedback associated with optically thick high clouds is negative, leading to its global contribution (by multiplying the mean tropical anvil cloud fraction of about 8%) of –0.24 ± 0.05 W m^{-2} °C^{-1} (one standard deviation) for LW (Vaillant de Guélis et al., 2018). Also, there is a positive feedback due to increase of optically thin cirrus clouds in the tropopause layer, estimated to be 0.09 ± 0.09 W m^{-2} °C^{-1} (one standard deviation) (Zhou et al., 2014). The negative LW feedback due to reduced amount of thick high clouds is partly compensated by the positive SW feedback (due to less reflection of solar radiation), so that the tropical high-cloud amount feedback is assessed to be equal to or smaller than their sum. Consistently, the net high cloud feedback in the tropical convective regime, including a part of the altitude feedback, is estimated to have the global contribution of –0.13 ± 0.06 W m^{-2} °C^{-1} (one standard deviation) (Williams and Pierrehumbert, 2017). The negative cloud LW feedback is considerably biased in CMIP5 GCMs (Mauritsen and Stevens, 2015; Su et al., 2017; Li et al., 2019) and highly uncertain primarily due to differences in the convective parameterization (Webb et al., 2015).

ACCEPTED VERSION SUBJECT TO FINAL EDITING

Furthermore, high-resolution CRM simulations cannot alone be used to constrain uncertainty because the results depend on parametrized cloud microphysics and turbulence (Bretherton et al., 2014; Ohno et al., 2019). Therefore, the tropical high-cloud amount feedback is assessed as negative but with *low confidence* given the lack of modelling evidence. Taking observational estimates altogether and methodological uncertainty into account, the global contribution of the high-cloud amount feedback is assessed to –0.15 ± 0.2 W m^{-2} °C^{-1} (one standard deviation).

Subtropical marine low-cloud feedback.

It has long been argued that the response of marine boundary layer clouds over the subtropical ocean to surface warming was the largest contributor to the spread among GCMs in the net cloud feedback (Boucher et al., 2013). However, uncertainty of the marine low-cloud feedback has been reduced considerably since AR5 through combined knowledge from theoretical, modelling, and observational studies (Klein et al., 2017). Processes that control the low clouds are complex and involve coupling with atmospheric motions on multiple scales, from the boundary layer turbulence to the large-scale subsidence, which may be represented by a combination of shallow and deep convective mixing (Sherwood et al., 2014).

In order to disentangle the large-scale processes that cause the cloud amount either to increase or decrease in response to the surface warming, the cloud feedback has been expressed in terms of several 'cloud controlling factors' (Qu et al., 2014, 2015; Zhai et al., 2015; Brient and Schneider, 2016; Myers and Norris, 2016; McCoy et al., 2017b). The advantage of this approach over conventional calculation of cloud feedbacks is that the temperature-mediated cloud response can be estimated without using information of the simulated cloud responses that are less well-constrained than the changes in the environmental conditions. Two dominant factors are identified for the subtropical low clouds: a thermodynamic effect due to rising SST that acts to reduce low cloud by enhancing cloud-top entrainment of dry air, and a stability effect accompanied by an enhanced inversion strength that acts to increase low cloud (Qu et al., 2014, 2015; Kawai et al., 2017). These controlling factors compensate with a varying degree in different ESMs, but can be constrained by referring to the observed seasonal or interannual relationship between the low-cloud amount and the controlling factors in the environment as a surrogate. The analysis leads to a positive local feedback that has the global contribution of 0.14–0.36 W m^{-2} °C^{-1} (Klein et al., 2017), to which the feedback in the stratocumulus regime dominates over the feedback in the trade cumulus regime (Cesana et al., 2019; Radtke et al., 2020). The stratocumulus feedback may be underestimated because explicit simulations using LES show a larger local feedback of up to 2.5 W m^{-2} °C^{-1}, corresponding to the global contribution of 0.2 W m^{-2} °C^{-1} by multiplying the mean tropical stratocumulus fraction of about 8% (Bretherton, 2015). Supported by different lines of evidence, the subtropical marine low-cloud feedback is assessed as positive with *high confidence*. Based on the combined estimate using LESs and the cloud controlling factor analysis, the global contribution of the feedback due to marine low clouds equatorward of 30° is assessed to be 0.2 ± 0.16 W m^{-2} °C^{-1} (one standard deviation), for which the range reflects methodological uncertainties.

Land cloud feedback.

Intensification of the global hydrological cycle is a robust feature of global warming, but at the same time, many land areas in the subtropics will experience drying at the surface and in the atmosphere (Chapter 8, Section 8.2.2). This occurs due to a limited water availability in these regions, where the cloudiness is consequently expected to decrease. Reduction in clouds over land are consistently identified in the CMIP5 models and also in a GCM with explicit convection (Bretherton et al., 2014; Kamae et al., 2016). Because low clouds make up the majority of subtropical land clouds, this reduced amount of low clouds reflects less solar radiation and leads to a positive feedback similar to the marine low clouds. The mean estimate of the global land cloud feedback in CMIP5 models is smaller than the marine low cloud feedback, 0.08 ± 0.08 W m^{-2} °C^{-1} (Zelinka et al., 2016). These values are nearly unchanged in CMIP6 (Zelinka et al., 2020). However, ESMs still have considerable biases in the climatological temperature and cloud fraction over land and the magnitude of this feedback has not yet been supported by observational evidence. Therefore, the feedback due to decreasing land clouds is assessed to be 0.08 ± 0.08 W m^{-2} °C^{-1} (one standard deviation) with *low confidence*.

Mid-latitude cloud amount feedback.

Poleward shifts in the mid-latitude jets are evident since the 1980s (Chapter 2, Section 2.3.1.4.3) and are a

ACCEPTED VERSION SUBJECT TO FINAL EDITING

feature of the large-scale circulation change in future projections (Chapter 4, Section 4.5.1.6). Because mid-latitude clouds over the North Pacific, North Atlantic, and Southern Ocean are induced mainly by extratropical cyclones in the storm tracks along the jets, it has been suggested that the jet shifts should be accompanied by poleward shifts in the mid-latitude clouds, which would result in a positive feedback through the reduced reflection of insolation (Boucher et al., 2013). However, studies since AR5 have revealed that this proposed mechanism does not apply in practice (Ceppi and Hartmann, 2015). While a poleward shift of mid-latitude cloud maxima in the free troposphere has been identified in satellite and ground-based observations (Bender et al., 2012; Eastman and Warren, 2013), associated changes in net CRE are small because the responses in high and low clouds to the jet shift act to cancel each other (Grise and Medeiros, 2016; Tselioudis et al., 2016; Zelinka et al., 2018). This cancellation is not well captured in ESMs (Lipat et al., 2017), but the above findings show that the mid-latitude cloud feedback is not dynamically driven by the poleward jet shifts, which are rather suggested to occur partly in response to high cloud changes (Li et al., 2018b).

Thermodynamics play an important role in controlling extratropical cloud amount equatorward of about 50° latitude. Recent studies showed using observed cloud controlling factors that the mid-latitude low cloud fractions decrease with rising SST, which also acts to weaken stability of the atmosphere unlike the subtropics (McCoy et al., 2017b). ESMs consistently show a decrease of cloud amounts and a resultant positive shortwave feedback in the 30°–40° latitude bands, which can be constrained using observations of seasonal migration of cloud amount (Zhai et al., 2015). Based on the qualitative agreement between observations and ESMs, the mid-latitude cloud amount feedback is assessed as positive with *medium confidence.* Following these emergent constraint studies using observations and CMIP5/6 models, the global contribution of net cloud amount feedback over 30°–60° ocean areas, covering 27% of the globe, is assigned 0.09 ± 0.1 W m^{-2} °C^{-1} (one standard deviation), in which the uncertainty reflects potential errors in models' low cloud response to changes in thermodynamic conditions.

Extratropical cloud optical depth feedback.

Mixed-phase clouds that consist of both liquid and ice are dominant over the Southern Ocean (50°–80°S), which accounts for 20% of the net CRE in the present climate (Matus and L'Ecuyer, 2017). It has been argued that the cloud optical depth (opacity) will increase over the Southern Ocean as warming drives the replacement of ice-dominated clouds with liquid-dominated clouds (Tan et al., 2019). Liquid clouds generally consist of many small cloud droplets, while the crystals in ice clouds are orders of magnitudes fewer in number and much larger, causing the liquid clouds to be optically thicker and thereby resulting in a negative feedback (Boucher et al., 2013). However, this phase change feedback works effectively only below freezing temperature (Lohmann and Neubauer, 2018; Terai et al., 2019) and other processes that increase or decrease liquid water path (LWP) may also affect the optical depth feedback (McCoy et al., 2019).

Due to insufficient amounts of super-cooled liquid water in the simulated atmospheric mean state, many CMIP5 models overestimated the conversion from ice to liquid clouds with climate warming and the resultant negative phase change feedback (Kay et al., 2016a; Tan et al., 2016; Lohmann and Neubauer, 2018). This feedback can be constrained using satellite-derived LWP observations over the past 20 years that enable estimates of both long-term trends and the interannual relationship with SST variability (Gordon and Klein, 2014; Ceppi et al., 2016; Manaster et al., 2017). The observationally-constrained SW feedback ranges from –0.91 to –0.46 W m^{-2} °C^{-1} over 40°–70°S depending on the methodology (Ceppi et al., 2016; Terai et al., 2016). In some CMIP6 models, representation of super-cooled liquid water content has been improved, leading to weaker negative optical depth feedback over the Southern Ocean closer to observational estimates (Bodas-Salcedo et al., 2019; Gettelman et al., 2019). This improvement at the same time results in a positive optical depth feedback over other extratropical ocean where LWP decreased in response to reduced stability in those CMIP6 models (Zelinka et al., 2020). Given the accumulated observational estimates and an improved agreement between ESMs and observations, the extratropical optical depth feedback is assessed to be small negative with *medium confidence.* Quantitatively, the global contribution of this feedback is assessed to have a value of -0.03 ± 0.05 W m^{-2} °C^{-1} (one standard deviation) by combining estimates based on observed interannual variability and the cloud controlling factors.

Arctic cloud feedback.

ACCEPTED VERSION SUBJECT TO FINAL EDITING

Clouds in polar regions, especially over the Arctic, form at low altitude above or within a stable to neutral boundary layer and are known to co-vary with sea-ice variability beneath. Because the clouds reflect sunlight during summer but trap longwave radiation throughout the year, seasonality plays an important role for cloud effects on Arctic climate (Kay et al., 2016b). AR5 assessed that Arctic low cloud amount will increase in boreal autumn and winter in response to declining sea ice in a warming climate, due primarily to an enhanced upward moisture flux over open water. The cloudier conditions during these seasons result in more downwelling longwave radiation, acting as a positive feedback on surface warming (Kay and Gettelman, 2009). Over recent years, further evidence of the cloud contribution to the Arctic amplification has been obtained (Goosse et al., 2018; Section 7.4.4.1). Space-borne lidar observations show that the cloud response to summer sea-ice loss is small and cannot overcome the cloud effect in autumn (Taylor et al., 2015; Morrison et al., 2018). The seasonality of the cloud response to sea-ice variability is reproduced in GCM simulations (Laîné et al., 2016; Yoshimori et al., 2017). The agreement between observations and models indicates that the Arctic cloud feedback is positive at the surface. This leads to an Arctic cloud feedback at TOA that is *likely* positive, but very small in magnitude as found in some climate models (Pithan and Mauritsen, 2014; Morrison et al., 2018). The observational estimates are sensitive to the analysis period and the choice of reanalysis data, and a recent estimate of the TOA cloud feedback over 60°–90°N using atmospheric reanalysis data and CERES satellite observations suggests a regional value ranging from –0.3 to 0.5 W m^{-2} °C^{-1}, which corresponds to a global contribution of –0.02 to 0.03 W m^{-2} °C^{-1} (Zhang et al., 2018b). Based on the overall agreement between ESMs and observations, the Arctic cloud feedback is assessed small positive and has the value of 0.01 ± 0.05 W m^{-2} °C^{-1} (one standard deviation). The assessed range indicates that a negative feedback is almost as probable as a positive feedback, and the assessment that the Arctic cloud feedback is positive is therefore given *low confidence*.

7.4.2.4.3 Synthesis for the net cloud feedback

The understanding of the response of clouds to warming and associated radiative feedback has deepened since AR5 (Figure 7.9, FAQ7.2). Particular progress has been made in the assessment of the marine low-cloud feedback, which has historically been a major contributor to the cloud feedback uncertainty but is no longer the largest source of uncertainty. Multiple lines of evidence (theory, observations, emergent constraints and process modelling) are now available in addition to ESM simulations, and the positive low-cloud feedback is consequently assessed with *high confidence*.

The best estimate of net cloud feedback is obtained by summing feedbacks associated with individual cloud regimes and assessed to be α_C = 0.42 W m^{-2} °C^{-1}. By assuming that uncertainty of individual cloud feedbacks is independent of each other, their standard deviations are added in quadrature, leading to the *likely* range of 0.12 to 0.72 W m^{-2} °C^{-1} and the *very likely* range of –0.10 to 0.94 W m^{-2} °C^{-1} (Table 7.10). This approach potentially misses feedbacks from cloud regimes that are not assessed, but almost all the major cloud regimes were taken into consideration (Gettelman and Sherwood, 2016) and therefore additional uncertainty will be small. This argument is also supported by an agreement between the net cloud feedback assessed here and the net cloud feedback directly estimated using observations. The observational estimate, which is sensitive to the period considered, based on two atmospheric reanalyses (ERA-Interim and MERRA) and TOA radiation budgets derived from the CERES satellite observations for the years 2000–2010 is 0.54 ± 0.7 W m^{-2} °C^{-1} (one standard deviation) (Dessler, 2013) and overlaps with the assessed range of the net cloud feedback. The assessed *very likely* range is reduced by about 50% compared to AR5, but is still wide compared to those of other climate feedbacks (Table 7.10). The largest contribution to this uncertainty range is the estimate of tropical high-cloud amount feedback which is not yet well quantified using models.

In reality, different types of cloud feedback may occur simultaneously in one cloud regime. For example, an upward shift of high clouds associated with the altitude feedback could be coupled to an increase/decrease of cirrus/anvil cloud fractions associated with the cloud amount feedback. Alternatively, slowdown of the tropical circulation with surface warming (Chapter 4, Section 4.5.3; Figure 7.9) could affect both high and low clouds so that their feedbacks are co-dependent. Quantitative assessments of such covariances require further knowledge about cloud feedback mechanisms, which will further narrow the uncertainty range.

ACCEPTED VERSION SUBJECT TO FINAL EDITING

In summary, deepened understanding of feedback processes in individual cloud regimes since AR5 leads to an assessment of the positive net cloud feedback with *high confidence*. A small probability (less than 10%) of a net negative cloud feedback cannot be ruled out, but this would require an extremely large negative feedback due to decreases in the amount of tropical anvil clouds or increases in optical depth of extratropical clouds over the Southern Ocean; neither is supported by current evidence.

[START TABLE 7.9 HERE]

Table 7.9: Assessed sign and confidence level of cloud feedbacks in difference regimes, compared between AR5 and AR6. For some cloud regimes, the feedback was not assessed in AR5, indicated by N/A.

Feedback	AR5	AR6
High-cloud altitude feedback	Positive (*high confidence*)	Positive (*high confidence*)
Tropical high-cloud amount feedback	N/A	Negative (*low confidence*)
Subtropical marine low-cloud feedback	N/A (*low confidence*)	Positive (*high confidence*)
Land cloud feedback	N/A	Positive (*low confidence*)
Mid-latitude cloud amount feedback	Positive (*medium confidence*)	Positive (*medium confidence*)
Extratropical cloud optical depth feedback	N/A	Small negative (*medium confidence*)
Arctic cloud feedback	Small positive (*very low confidence*)	Small positive (*low confidence*)
Net cloud feedback	Positive (*medium confidence*)	Positive (*high confidence*)

[END TABLE 7.9 HERE]

7.4.2.5 Biogeophysical and non-CO_2 biogeochemical feedbacks

The feedbacks presented in the previous sections (Sections 7.4.2.1–7.4.2.4) are directly linked to physical climate variables (for example temperature, water vapour, clouds, or sea ice). The central role of climate feedbacks associated with these variables has been recognised since early studies of climate change. However, in addition to these physical climate feedbacks, the Earth system includes feedbacks for which the effect of global mean surface temperature change on the TOA energy budget is mediated through other mechanisms, such as the chemical composition of the atmosphere, or by vegetation changes. Among these additional feedbacks, the most important is the CO_2 feedback that describes how a change of the global surface temperature affects the atmospheric CO_2 concentration. In ESM simulations in which CO_2 emissions are prescribed, changes in surface carbon fluxes affect the CO_2 concentration in the atmosphere, the TOA radiative energy budget, and eventually the global mean surface temperature. In ESM simulations in which the CO_2 concentration is prescribed, changes in the carbon cycle allow compatible CO_2 emissions to be calculated, i.e., the CO_2 emissions that are compatible with both the prescribed CO_2 concentration and the representation of the carbon cycle in the ESM. The CO_2 feedback is assessed in Chapter 5, Section 5.4. The framework presented in this chapter assumes that the CO_2 concentration is prescribed, and our assessment of the net feedback parameter, α, does not include carbon-cycle feedbacks on the atmospheric CO_2 concentration (Section 7.1; Box 7.1). However, our assessment of α does include non-CO_2 biogeochemical feedbacks (Section 7.4.2.5.1; including effects due to changes in atmospheric methane concentration) and biogeophysical feedbacks (Section 7.4.2.5.2). A synthesis of the combination of biogeophysical and non-CO_2 biogeochemical feedbacks is given in Section 7.4.2.5.3.

ACCEPTED VERSION SUBJECT TO FINAL EDITING

7.4.2.5.1 Non-CO_2 biogeochemical feedbacks

The chemical composition of the atmosphere (beyond CO_2 and water vapour changes) is expected to change in response to a warming climate. These changes in greenhouse gases (CH_4, N_2O, and ozone) and aerosol amount (including dust) have the potential to alter the TOA energy budget and are collectively referred to as non-CO_2 biogeochemical feedbacks. CH_4 and N_2O feedbacks arise partly from changes in their emissions from natural sources in response to temperature change; these are assessed in Chapter 5, Section 5.4.7 (see also Figure 5.29c). Here we exclude the permafrost CH_4 feedback (Chapter 5, Section 5.4.9.1.2) because, although associated emissions are projected to increase under warming on multi-decadal to centennial timescales, on longer timescales these emissions would eventually substantially decline as the permafrost carbon pools were depleted (Schneider von Deimling et al., 2012, 2015). This leaves the wetland CH_4, land N_2O, and ocean N_2O feedbacks, the assessed mean values of which sum to a positive feedback parameter of +0.04 [0.02 to 0.06] W m^{-2} $°C^{-1}$ (Chapter 5, Section 5.4.7). Other non-CO_2 biogeochemical feedbacks that are relevant to the net feedback parameter are assessed in Chapter 6, Section 6.4.5 (Table 6.8). These feedbacks are associated with sea salt, dimethyl sulphide, dust, ozone, biogenic volatile organic compounds, lightning, and CH_4 lifetime, and sum to a negative feedback parameter of –0.20 [–0.41 to +0.01] W m^{-2} $°C^{-1}$. The overall feedback parameter for non-CO_2 biogeochemical feedbacks is obtained by summing the Chapter 5 and Chapter 6 assessments, which gives –0.16 [–0.37 to +0.05] W m^{-2} $°C^{-1}$. However, there is *low confidence* in the estimates of both the individual non-CO_2 biogeochemical feedbacks as well as their total effect, as evident from the large range in the magnitudes of α from different studies, which can be attributed to diversity in how models account for these feedbacks and limited process-level understanding.

7.4.2.5.2 Biogeophysical feedbacks

Biogeophysical feedbacks are associated with changes in the spatial distribution and/or biophysical properties of vegetation, induced by surface temperature change and attendant hydrological cycle change. These vegetation changes can alter radiative fluxes directly via albedo changes, or via surface momentum or moisture flux changes and hence changes in cloud properties. However, the direct physiological response of vegetation to changes in CO_2, including changes in stomatal conductance, is considered part of the CO_2 effective radiative forcing rather than a feedback (Section 7.3.2.1). The timescale of response of vegetation to climate change is relatively uncertain but can be from decades to hundreds of years (Willeit et al., 2014), and could occur abruptly or as a tipping point (Chapter 5, Section 5.4.9.1.1; Chapter 8, Sections 8.6.2.1 and 8.6.2.2); equilibrium only occurs when the soil system and associated nutrient and carbon pools equilibrate, which can take millennia (Brantley, 2008; Sitch et al., 2008). The overall effects of climate-induced vegetation changes may be comparable in magnitude to those from anthropogenic land-use and land cover change (Davies-Barnard et al., 2015). Climate models that include a dynamical representation of vegetation (e.g., Reick et al., 2013; Harper et al., 2018) are used to explore the importance of biogeophysical feedbacks (Notaro et al., 2007; Brovkin et al., 2009; O'ishi et al., 2009; Port et al., 2012; Willeit et al., 2014; Alo and Anagnostou, 2017; Zhang et al., 2018c; Armstrong et al., 2019). In AR5, it was discussed that such model experiments predicted that expansion of vegetation in the high latitudes of the Northern Hemisphere would enhance warming due to the associated surface albedo change, and that reduction of tropical forests in response to climate change would lead to regional surface warming, due to reduced evapotranspiration (Collins et al., 2013a), but there was no assessment of the associated feedback parameter. SRCCL stated that regional climate change can be dampened or enhanced by changes in local land cover, but that this depends on the location and the season; however, in general the focus was on anthropogenic land cover change, and no assessment of the biogeophysical feedback parameter was carried out. There are also indications of a marine biogeophysical feedback associated with surface albedo change due to changes in phytoplankton (Frouin and Iacobellis, 2002; Park et al., 2015), but there is not currently enough evidence to quantitatively assess this feedback.

Since AR5, several studies have confirmed that a shift from tundra to boreal forests and the associated albedo change leads to increased warming in Northern Hemisphere high latitudes (Willeit et al., 2014; Zhang et al., 2018c; Armstrong et al., 2019) (*high confidence*). However, regional modelling indicates that vegetation feedbacks may act to cool climate in the Mediterranean (Alo and Anagnostou, 2017), and in the tropics and subtropics the regional response is in general not consistent across models. On a global scale, several modelling studies have either carried out a feedback analysis (Stocker et al., 2013; Willeit et al.,

ACCEPTED VERSION SUBJECT TO FINAL EDITING

2014) or presented simulations that allow a feedback parameter to be estimated (O'ishi et al., 2009; Armstrong et al., 2019), in such a way that the physiological response can be accounted for as a forcing rather than a feedback. The central estimates of the biogeophysical feedback parameter from these studies range from close to zero (Willeit et al., 2014) to +0.13 W m^{-2} °C^{-1} (Stocker et al., 2013). An additional line of evidence comes from the mid-Pliocene warm period (MPWP, Chapter 2, Cross-Chapter Box 2.1), for which paleoclimate proxies provide evidence of vegetation distribution and CO_2 concentrations. Model simulations that include various combinations of modern versus MPWP vegetation and CO_2 allow an associated feedback parameter to be estimated, as long as account is also taken of the orographic forcing (Lunt et al., 2010, 2012b). This approach has the advantage over pure modelling studies in that the reconstructed vegetation is based on (paleoclimate) observations, and is in equilibrium with the CO_2 forcing. However, there are uncertainties in the vegetation reconstruction in regions with little or no proxy data, and it is uncertain how much of the vegetation change is associated with the physiological response to CO_2. This paleoclimate approach gives an estimate for the biogeophysical feedback parameter of +0.3 W m^{-2} °C^{-1}.

Given the limited number of studies, we take the full range of estimates discussed above for the biogeophysical feedback parameter, and assess the *very likely* range to be from zero to +0.3 W m^{-2} °C^{-1}, with a central estimate of +0.15 W m^{-2} °C^{-1} (*low confidence*). Although this assessment is based on evidence from both models and paleoclimate proxies, and the studies above agree on the sign of the change, there is nonetheless *limited evidence*. Higher confidence could be obtained if there were more studies that allowed calculation of a biogeophysical feedback parameter (particularly from paleoclimates), and if the partitioning between biogeophysical feedbacks and physiological forcing were clearer for all lines of evidence.

7.4.2.5.3 Synthesis of biogeophysical and non-CO_2 biogeochemical feedbacks

The non-CO_2 biogeochemical feedbacks are assessed in Section 7.4.2.5.1 to be –0.16 [–0.37 to +0.05] W m^{-2} °C^{-1} and the biogeophysical feedbacks are assessed in Section 7.4.2.5.2 to be +0.15 [0 to +0.3] W m^{-2} °C^{-1}. The sum of the biogeophysical and non-CO_2 biogeochemical feedbacks is assessed to have a central value of -0.01 W m^{-2} °C^{-1} and a *very likely* range from –0.27 to +0.25 W m^{-2} °C^{-1} (see Table 7.10). Given the relatively long timescales associated with the biological processes that mediate the biogeophysical and many of the non-CO_2 biogeochemical feedbacks, in comparison with the relatively short timescale of many of the underlying model simulations, combined with the small number of studies for some of the feedbacks, and the relatively small signals, this overall assessment has *low confidence*.

Some supporting evidence for this overall assessment can be obtained from the CMIP6 ensemble, which provides some pairs of instantaneous 4×CO_2 simulations carried out using related models with and without biogeophysical and non-CO_2 biogeochemical feedbacks. This is not a direct comparison because these pairs of simulations may differ by more than just their inclusion of these additional feedbacks; furthermore, not all biogeophysical and non-CO_2 biogeochemical feedbacks are fully represented. However, a comparison of the pairs of simulations does provide a first-order estimate of the magnitude of these additional feedbacks. Séférian et al. (2019) find a slightly more negative feedback parameter in CNRM-ESM2-1 (with additional feedbacks) then in CNRM-CM6-1 (a decrease of 0.02 W m^{-2} °C^{-1}, using the linear regression method from years 10-150). Andrews et al. (2019) also find a slightly more negative feedback parameter when these additional feedbacks are included (a decrease of 0.04 W m^{-2}°C^{-1} in UKESM1 compared with HadGEM3-GC3.1). Both of these studies suggest a small but slightly negative feedback parameter for the combination of biogeophysical and non-CO_2 biogeochemical feedbacks, but with relatively large uncertainty given (a) interannual variability and (b) that feedbacks associated with natural terrestrial emissions of CH_4 and N_2O were not represented in either pair.

7.4.2.6 Long term radiative feedbacks associated with ice sheets

Although long-term radiative feedbacks associated with ice sheets are not included in our definition of ECS (Box 7.1), the relevant feedback parameter is assessed here because the timescales on which these feedbacks act are relatively uncertain, and the long-term temperature response to CO_2 forcing of the entire Earth system may be of interest.

ACCEPTED VERSION SUBJECT TO FINAL EDITING

Earth's ice sheets (Greenland and Antarctica) are sensitive to climate change (Chapter 9, Section 9.4; Pattyn et al., 2018). Their time evolution is determined by both their surface mass balance and ice dynamic processes, with the latter being particularly important for the West Antarctic Ice Sheet. Surface mass balance depends on the net energy and hydrological fluxes at their surface, and there are mechanisms of ice sheet instability that depend on ocean temperatures and basal melt rates (Chapter 9, Section 9.4.1.1). The presence of ice sheets affects Earth's radiative budget, hydrology, and atmospheric circulation due to their characteristic high albedo, low roughness length, and high altitude, and they influence ocean circulation through freshwater input from calving and melt (e.g., Fyke et al., 2018). Ice sheet changes also modify surface albedo through the attendant change in sea level and therefore land area (Abe-Ouchi et al., 2015). The timescale for ice sheets to reach equilibrium is on the order of thousands of years (Clark et al., 2016). Due to the long timescales involved, it is a major challenge to run coupled climate-ice sheet models to equilibrium, and as a result, long-term simulations are often carried out with lower complexity models, and/or are asynchronously coupled.

In AR5, it was described that both the Greenland and Antarctic ice sheets would continue to lose mass in a warming world (Collins et al., 2013a), with a continuation in sea level rise beyond the year 2500 assessed as *virtually certain*. However, there was *low confidence* in the associated radiative feedback mechanisms, and as such, there was no assessment of the magnitude of long-term radiative feedbacks associated with ice sheets. That assessment is consistent with SROCC, wherein it was stated that 'with limited published studies to draw from and no simulations run beyond 2100, firm conclusions regarding the net importance of atmospheric versus ocean melt feedbacks on the long-term future of Antarctica cannot be made.'

The magnitude of the radiative feedback associated with changes to ice sheets can be quantified by comparing the global mean long-term equilibrium temperature response to increased CO_2 concentrations in simulations that include interactive ice sheets with that of simulations that do not include the associated ice-sheet climate interactions (Swingedouw et al., 2008; Vizcaíno et al., 2010; Goelzer et al., 2011; Bronselaer et al., 2018; Golledge et al., 2019). These simulations indicate that on multi-centennial timescales, ice sheet mass loss leads to fresh water fluxes that can modify ocean circulation (Swingedouw et al., 2008; Goelzer et al., 2011; Bronselaer et al., 2018; Golledge et al., 2019). This leads to reduced surface warming (by about 0.2°C in the global mean after 1000 years; Goelzer et al., 2011; see also Section 7.4.4.1.1), although other work suggests no net global temperature effect of ice sheet mass loss (Vizcaíno et al., 2010). However, model simulations in which the Antarctic ice sheet is removed completely in a paleoclimate context indicate a positive global mean feedback on multi-millennial timescales due primarily to the surface albedo change (Goldner et al., 2014a; Kennedy-Asser et al., 2019); in Chapter 9 (Section 9.6.3) it is assessed that such ice-free conditions could eventually occur given 7–13°C of warming. This net positive feedback due to ice sheets on long timescales is also supported by model simulations of the mid-Pliocene warm period (MPWP, Chapter 2, Cross-chapter Box 2.1) in which the volume and area of the Greenland and West Antarctic ice sheets are reduced in model simulations in agreement with geological data (Chandan and Peltier, 2018), leading to surface warming. As such, overall, on multi-centennial timescales the feedback parameter associated with ice sheets is *likely* negative (*medium confidence*), but on multi-millennial timescales by the time the ice sheets reach equilibrium, the feedback parameter is *very likely* positive (*high confidence*; see Table 7.10). However, a relative lack of models carrying out simulations with and without interactive ice sheets over centennial to millennial timescales means that there is currently not enough evidence to quantify the magnitude of these feedbacks, or the timescales on which they act.

7.4.2.7 Synthesis

Table 7.10 summarises the estimates and the assessment of the individual and the net feedbacks presented in the above sections. The uncertainty range of the net climate feedback was obtained by adding standard deviations of individual feedbacks in quadrature, assuming that they are independent and follow the Gaussian distribution. It is *virtually certain* that the net climate feedback is negative, primarily due to the Planck temperature response, indicating that climate acts to stabilise in response to radiative forcing imposed to the system. Supported by the level of confidence associated with the individual feedbacks, it is also

ACCEPTED VERSION SUBJECT TO FINAL EDITING

virtually certain that the sum of the non-Planck feedbacks is positive. Based on Table 7.10 these climate feedbacks amplify the Planck temperature response by about 2.8 [1.9 to 5.9] times. Cloud feedback remains the largest contributor to uncertainty of the net feedback, but the uncertainty is reduced compared to AR5. A secondary contribution to the net feedback uncertainty is the biogeophysical and non-CO_2 biogeochemical feedbacks, which together are assessed to have a central value near zero and thus do not affect the central estimate of ECS. The net climate feedback is assessed to be –1.16 W m^{-2} °C^{-1}, *likely* from –1.54 to –0.78 W m^{-2} °C^{-1}, and *very likely* from –1.81 to –0.51 W m^{-2}°C^{-1}.

Feedback parameters in climate models are calculated assuming that they are independent of each other, except for a well-known co-dependency between the WV and LR feedbacks. When the inter-model spread of the net climate feedback is computed by adding in quadrature the inter-model spread of individual feedbacks, it is 17% wider than the spread of the net climate feedback directly derived from the ensemble. This indicates that the feedbacks in climate models are partly co-dependent. Two possible co-dependencies have been suggested (Huybers, 2010; Caldwell et al., 2016). One is a negative covariance between the LR and longwave cloud feedbacks, which may be accompanied by a deepening of the troposphere (O'Gorman and Singh, 2013; Yoshimori et al., 2020) leading both to greater rising of high clouds and a larger upper-tropospheric warming. The other is a negative covariance between albedo and shortwave cloud feedbacks, which may originate from the Arctic regions: a reduction in sea ice enhances the shortwave cloud radiative effect because the ocean surface is darker than sea ice (Gilgen et al., 2018). This covariance is reinforced as the decrease of sea-ice leads to an increase in low-level clouds (Mauritsen et al., 2013). However, the mechanism causing these co-dependences between feedbacks is not well understood yet and a quantitative assessment based on multiple lines of evidence is difficult. Therefore, this synthesis assessment does not consider any co-dependency across individual feedbacks.

The assessment of the net climate feedback presented above is based on a single approach (i.e., process understanding) and directly results in a value for ECS given in Section 7.5.1; this is in contrast to the synthesis assessment of ECS in Section 7.5.5 which combines multiple approaches. The total (net) feedback parameter consistent with the final synthesis assessment of the ECS and Equation 7.1 is provided there.

[START TABLE 7.10 HERE]

Table 7.10: Synthesis assessment of climate feedbacks (central estimate shown by boldface). The mean values and their 90% ranges in CMIP5/6 models, derived using multiple radiative kernels (Zelinka et al., 2020), are also presented for comparison.

Feedback parameter α_x (W m^{-2} °C^{-1})	CMIP5 GCMs	CMIP6 ESMs	AR6 assessed ranges			
	Mean and the 5–95% interval	Mean and the 5–95% interval	Central estimate	*Very likely* interval	*Likely* interval	Level of confidence
Planck	–3.20 [–3.3 to –3.1]	–3.22 [–3.3 to –3.1]	**–3.22**	–3.4 to –3.0	–3.3 to –3.1	*high*
WV+LR	1.24 [1.08 to 1.35]	1.25 [1.14 to 1.45]	**1.30**	1.1 to 1.5	1.2 to 1.4	*high*
Surface albedo	0.41 [0.25 to 0.56]	0.39 [0.26 to 0.53]	**0.35**	0.10 to 0.60	0.25 to 0.45	*medium*
Clouds	0.41 [–0.09 to 1.1]	0.49 [–0.08 to 1.1]	**0.42**	–0.10 to 0.94	0.12 to 0.72	*high*
Biogeophysical and non-CO_2 biogeochemical	Not evaluated	Not evaluated	**–0.01**	–0.27 to 0.25	–0.16 to 0.14	*low*
Residual of kernel estimates	0.06 [–0.17 to 0.29]	0.05 [–0.18 to 0.28]				
Net (i.e., relevant for ECS)	–1.08 [–1.61 to –0.68]	–1.03 [–1.54 to –0.62]	**–1.16**	–1.81 to –0.51	–1.54 to –0.78	*medium*
Long-term ice				> 0.0		*high*

ACCEPTED VERSION SUBJECT TO FINAL EDITING

sheet feedbacks (millennial scale)		

[END TABLE 7.10 HERE]

7.4.2.8 Climate feedbacks in ESMs

Since AR5, many modelling groups have newly participated in CMIP experiments, leading to an increase in the number of models in CMIP6 (Chapter 1, Section 1.5.4). Other modelling groups that contributed to CMIP5 also updated their ESMs for carrying out CMIP6 experiments. While some of the CMIP6 models share components and are therefore not independent, they are analysed independently when calculating climate feedbacks. This, and more subtle forms of model inter-dependence, creates challenges when determining appropriate model weighting schemes (Chapter 1, Section 1.5.4). Additionally, it must be kept in mind that the ensemble sizes of the CMIP5 and CMIP6 models are not sufficiently large to sample the full range of model uncertainty.

The multi-model mean values of all physical climate feedbacks are calculated using the radiative kernel method (Section 7.4.1) and compared with the assessment in the previous sections (Figure 7.10). For CMIP models, there is a discrepancy between the net climate feedback calculated directly using the time evolutions of ΔT and ΔN in each model and the accumulation of individual feedbacks, but it is negligibly small (Supplementary Material 7.SM.4). Feedbacks due to biogeophysical and non-CO_2 biogeochemical processes are included in some models but neglected in the kernel analysis. In the AR6, biogeophysical and non-CO_2 biogeochemical feedbacks are explicitly assessed (Section 7.4.2.5).

All the physical climate feedbacks apart from clouds are very similar to each other in CMIP5 and CMIP6 model ensembles (see also Table 7.10). These values, where possible supported by other lines of evidence, are used for assessing feedbacks in Sections 7.4.2.1–7.4.2.3. A difference found between CMIP5 and CMIP6 models is the net cloud feedback, which is larger in CMIP6 by about 20%. This change is the major cause of less-negative values of the net climate feedback in CMIP6 than in CMIP5 and hence an increase in modelled ECS (Section 7.5.1).

A remarkable improvement of cloud representation in some CMIP6 models is the reduced error of the too weak negative SW CRE over the Southern Ocean (Bodas-Salcedo et al., 2019; Gettelman et al., 2019) due to a more realistic simulation of supercooled liquid droplets and associated cloud optical depths that were biased low commonly in CMIP5 models (McCoy et al. 2014a; 2014b). Because the negative cloud optical depth feedback occurs due to 'brightening' of clouds via phase change from ice to liquid cloud particles in response to surface warming (Cesana and Storelvmo, 2017), the extratropical cloud SW feedback tends to be less negative or even slightly positive in models with reduced errors (Bjordal et al., 2020; Zelinka et al., 2020). The assessment of cloud feedbacks in Section 7.4.2.4 incorporates estimates from these improved ESMs. Yet, there still remain other shared model errors such as in the subtropical low clouds (Calisto et al., 2014) and tropical anvil clouds (Mauritsen and Stevens, 2015), hampering an assessment of feedbacks associated with these cloud regimes based only on ESMs (Section 7.4.2.4).

[START FIGURE 7.10 HERE]

Figure 7.10: Global-mean climate feedbacks estimated in *abrupt4xCO2* simulations of 29 CMIP5 models (light blue) and 49 CMIP6 models (orange), compared with those assessed in this Report (red). Individual feedbacks for CMIP models are averaged across six radiative kernels as computed in Zelinka et al. (2020). The white line, black box and vertical line indicate the mean, 66% and 90% ranges, respectively. The shading represents the probability distribution across the full range of GCM/ESM values and for the 2.5-97.5 percentile range of the AR6 normal distribution. The unit is W m^{-2} °C^{-1}. Feedbacks associated with biogeophysical and non-CO_2 biogeochemical processes are assessed in AR6, but they are not explicitly estimated from GCMs/ESMs in CMIP5 and CMIP6. Further details on data sources and processing are available in the chapter data table (Table 7.SM.14).

ACCEPTED VERSION SUBJECT TO FINAL EDITING

[END FIGURE 7.10 HERE]

7.4.3 Dependence of feedbacks on climate mean state

In the standard framework of forcings and feedbacks (Section 7.4.1; Box 7.1), the approximation is made that the strength of climate feedbacks is independent of the background global surface mean temperature. More generally, the individual feedback parameters, α_x, are often assumed to be constant over a range of climate states, including those reconstructed from the past (encompassing a range of states warmer and colder than today, with varying continental geographies) or projected for the future. If this approximation holds, then the equilibrium global surface temperature response to a fixed radiative forcing will be constant, regardless of the climate state to which that forcing is applied.

This approximation will break down if climate feedbacks are not constant, but instead vary as a function of, e.g., background temperature (Roe and Baker, 2007; Zaliapin and Ghil, 2010; Roe and Armour, 2011; Bloch-Johnson et al., 2015), continental configuration (Farnsworth et al., 2019), or configuration of ice sheets (Yoshimori et al., 2009). If the real climate system exhibits this state dependence, then the future equilibrium temperature change in response to large forcing may be different from that inferred using the standard framework, and/or different to that inferred from paleoclimates. Such considerations are important for the assessment of ECS (Section 7.5). Climate models generally include representations of feedbacks that allow state-dependent behaviour, and so model results may also differ from the predictions from the standard framework.

In AR5 (Boucher et al., 2013), there was a recognition that climate feedbacks could be state dependent (Colman and McAvaney, 2009), but modelling studies that explored this (e.g., Manabe and Bryan, 1985; Voss and Mikolajewicz, 2001; Stouffer and Manabe, 2003; Hansen, 2005b) were not assessed in detail. Also in AR5 (Masson-Delmotte et al., 2013), it was assessed that some models exhibited weaker sensitivity to Last Glacial Maximum (LGM, Cross-Chapter Box 2.1) forcing than to $4\times CO_2$ forcing, due to state-dependence in shortwave cloud feedbacks.

Here, recent evidence for state-dependence in feedbacks from modelling studies (Section 7.4.3.1) and from the paleoclimate record (Section 7.4.3.2) are assessed, with an overall assessment in Section 7.4.3.3. The focus is on temperature-dependence of feedbacks when the system is in equilibrium with the forcing; evidence for transient changes in the net feedback parameter associated with evolving spatial patterns of warming is assessed separately in Section 7.4.4.

7.4.3.1 State-dependence of feedbacks in models

There are several modelling studies since AR5 in which ESMs of varying complexity have been used to explore temperature dependence of feedbacks, either under modern (Hansen et al., 2013; Jonko et al., 2013; Meraner et al., 2013; Good et al., 2015; Duan et al., 2019; Mauritsen et al., 2019; Rohrschneider et al., 2019; Rugenstein et al., 2019b; Stolpe et al., 2019; Bloch-Johnson et al., 2020) or paleo (Caballero and Huber, 2013; Zhu et al., 2019b) climate conditions, typically by carrying out multiple simulations across successive CO_2 doublings. A non-linear temperature response to these successive doublings may be partly due to forcing that increases more (or less) than expected from a purely logarithmic dependence (Section 7.3.2; Etminan et al., 2016), and partly due to state-dependence in feedbacks; however, not all modelling studies have partitioned the non-linearities in temperature response between these two effects. Nonetheless, there is general agreement amongst ESMs that the net feedback parameter, α, increases (i.e., becomes less negative) as temperature increases from pre-industrial levels (i.e., sensitivity to forcing increases as temperature increases; e.g., Meraner et al., 2013; see Figure 7.11). The associated increase in sensitivity to forcing is, in most models, due to the water vapour (Section 7.4.2.2) and cloud (Section 7.4.2.4) feedback parameters increasing with warming (Caballero and Huber, 2013; Meraner et al., 2013; Rugenstein et al., 2019b; Zhu et al., 2019b; Sherwood et al., 2020b). These changes are offset partially by the surface albedo feedback

ACCEPTED VERSION SUBJECT TO FINAL EDITING

parameter decreasing (Jonko et al., 2013; Meraner et al., 2013; Rugenstein et al., 2019b), as a consequence of a reduced amount of snow and sea ice cover in a much warmer climate. At the same time, there is little change in the Planck response (Section 7.4.2.1), which has been shown in one model to be due to competing effects from increasing Planck emission at warmer temperatures and decreasing planetary emissivity due to increased CO_2 and water vapour (Mauritsen et al., 2019). Analysis of the spatial patterns of the non-linearities in temperature response (Good et al., 2015) suggests that these patterns are linked to a reduced weakening of the AMOC, and changes to evapotranspiration. The temperature dependence of α is also found in model simulations of high-CO_2 paleoclimates (Caballero and Huber, 2013; Zhu et al., 2019b). The temperature dependence is not only evident at very high CO_2 concentrations in excess of $4\times CO_2$, but also apparent in the difference in temperature response to a $2\times CO_2$ forcing compared with to a $4\times CO_2$ forcing (Mauritsen et al., 2019; Rugenstein et al., 2019b), and as such is relevant for interpreting century-scale climate projections.

Despite the general agreement that α increases as temperature increases from pre-industrial levels (Figure 7.11), other modelling studies have found the opposite (Duan et al., 2019; Stolpe et al., 2019). Modelling studies exploring state dependence in climates colder than today, including in cold paleoclimates such as the LGM, provide conflicting evidence of either decreased (Yoshimori et al., 2011) or increased (Kutzbach et al., 2013; Stolpe et al., 2019) temperature response per unit forcing during cold climates compared to the modern era.

In contrast to most ESMs, the majority of Earth system models of intermediate complexity (EMICs) do not exhibit state dependence, or have a net feedback parameter that decreases with increasing temperature (Pfister and Stocker, 2017). This is unsurprising since EMICs usually do not include process-based representations of water vapour and cloud feedbacks. Although this shows that care must be taken when interpreting results from current generation EMICs, Pfister and Stocker (2017) also suggest that non-linearities in feedbacks can take a long time to emerge in model simulations due slow adjustment timescales associated with the ocean; longer simulations also allow better estimates of equilibrium warming (Bloch-Johnson et al., 2020). This implies that multi-century simulations (Rugenstein et al., 2019b) could increase confidence in ESM studies examining state dependence.

The possibility of more substantial changes in climate feedbacks, sometimes accompanied by hysteresis and/or irreversibility, has been suggested from some theoretical and modelling studies. It has been postulated that such changes could occur on a global scale and across relatively narrow temperature changes (Popp et al., 2016; von der Heydt and Ashwin, 2016; Steffen et al., 2018; Schneider et al., 2019; Ashwin and von der Heydt, 2020; Bjordal et al., 2020). However, the associated mechanisms are highly uncertain, and as such there is *low confidence* as to whether such behaviour exists at all, and in the temperature thresholds at which it might occur.

Overall, the modelling evidence indicates that there is *medium confidence* that the net feedback parameter, α, increases (i.e., becomes less negative) with increasing temperature (i.e., that sensitivity to forcing increases with increasing temperature), under global surface background temperatures at least up to 40°C (Meraner et al., 2013; Seeley and Jeevanjee, 2021), and *medium confidence* that this temperature dependence primarily derives from increases in the water vapour and shortwave cloud feedbacks. This assessment is further supported by recent analysis of CMIP6 model simulations (Bloch-Johnson et al., 2020) in the framework of nonlinMIP (Good et al., 2016), which showed that out of ten CMIP6 models, seven of them showed an increase of the net feedback parameter with temperature, primarily due to the water vapour feedback.

7.4.3.2 State-dependence of feedbacks in the paleoclimate proxy record

Several studies have estimated ECS from observations of the glacial-interglacial cycles of the last approximately 2 million years, and found a state dependence, with more-negative α (i.e., lower sensitivity to forcing) during colder periods of the cycles and less-negative α during warmer periods (von der Heydt et al., 2014; Köhler et al., 2015, 2017; Friedrich et al., 2016; Royer, 2016; Snyder, 2019); see summaries in Skinner (2012) and von der Heydt et al. (2016). However, the nature of the state dependence derived from

ACCEPTED VERSION SUBJECT TO FINAL EDITING

these observations is dependent on the assumed ice sheet forcing (Köhler et al., 2015; Stap et al., 2019), which is not well known, due to a relative lack of proxy indicators of ice sheet extent and distribution prior to the LGM (Cross-Chapter Box 2.1). Furthermore, many of these glacial-interglacial studies estimate a very strong temperature-dependence of α (Figure 7.11) that is hard to reconcile with the other lines of evidence, including proxy estimates from warmer paleoclimates. However, if the analysis excludes time periods when the temperature and CO_2 data are not well correlated, which occurs in general at times when sea level is falling and obliquity is decreasing, the state-dependence reduces (Köhler et al., 2018). Despite these uncertainties, due to the agreement in the sign of the temperature-dependence from all these studies, there is *medium confidence* from the paleoclimate proxy record that the net feedback parameter, α, was less negative in the warm periods than in the cold periods of the glacial-interglacial cycles.

Paleoclimate proxy evidence from past high-CO_2 time periods much warmer than present (the early Eocene and PETM; Cross-Chapter Box 2.1) show that the feedback parameter increases as temperature increases (Anagnostou et al., 2016, 2020; Shaffer et al., 2016). However, such temperature-dependence of feedbacks was not found in the warm Pliocene relative to the cooler Pleistocene (Martínez-Botí et al., 2015), although the temperature changes are relatively small at this time, making temperature-dependence challenging to detect given the uncertainties in reconstructing global mean temperature and forcing. Overall, the paleoclimate proxy record provides *medium confidence* that the net feedback parameter, α, was less negative in these past warm periods than in the present day.

7.4.3.3 Synthesis of state-dependence of feedbacks from modelling and paleoclimate records

Overall, independent lines of evidence from models (Section 7.4.3.1) and from the paleoclimate proxy record (Section 7.4.3.2) lead to *high confidence* that the net feedback parameter, α, increases (i.e., becomes less negative) as temperature increases; i.e., that sensitivity to forcing increases as temperature increases; see Figure 7.11. This temperature-dependence should be considered when estimating ECS from ESM simulations in which CO_2 is quadrupled (Section 7.5.5) or from paleoclimate observations from past time periods colder or warmer than today (Section 7.5.4). Although individual lines of evidence give only *medium confidence*, the overall high confidence comes from the multiple models that show the same sign of the temperature-dependence of α, the general agreement in evidence from the paleo proxy and modelling lines of evidence, and the agreement between proxy evidence from both cold and warm past climates. However, due to the large range in estimates of the magnitude of the temperature-dependence of α across studies (Figure 7.11), a quantitative assessment cannot currently be given, which provides a challenge for including this temperature-dependence in emulator-based future projections (Cross-Chapter Box 7.1). Greater confidence in the modelling lines of evidence could be obtained from simulations carried out for several hundreds of years (Rugenstein et al., 2019b), substantially longer than in many studies, and from more models carrying out simulations at multiple CO_2 concentrations. Greater confidence in the paleoclimate lines of evidence would be obtained from stronger constraints on atmospheric CO_2 concentrations, ice sheet forcing, and temperatures, during past warm climates.

[START FIGURE 7.11 HERE]

Figure 7.11: Feedback parameter, α (W m^{-2} °C^{-1}), as a function of global mean surface air temperature anomaly relative to preindustrial, for ESM simulations (red circles and lines) (Caballero and Huber, 2013; Jonko et al., 2013; Meraner et al., 2013; Good et al., 2015; Duan et al., 2019; Mauritsen et al., 2019; Stolpe et al., 2019; Zhu et al., 2019b), **and derived from paleoclimate proxies (grey squares and lines)** (von der Heydt et al., 2014; Anagnostou et al., 2016, 2020; Friedrich et al., 2016; Royer, 2016; Shaffer et al., 2016; Köhler et al., 2017; Snyder, 2019; Stap et al., 2019). For the ESM simulations, the value on the *x*-axis refers to the average of the temperature before and after the system has equilibrated to a forcing (in most cases a CO_2 doubling), and is expressed as an anomaly relative to an associated pre-industrial global mean temperature from that model. The light blue shaded square extends across the assessed range of α (Table 7.10) on the *y*-axis, and on the *x*-axis extends across the approximate temperature range over which the assessment of α is based (taken as from zero to the assessed central value of ECS (Table 7.13). Further details on data sources and processing are available in the chapter data table (Table 7.SM.14).

ACCEPTED VERSION SUBJECT TO FINAL EDITING

[END FIGURE 7.11 HERE]

7.4.4 Relationship between feedbacks and temperature patterns

The large-scale patterns of surface warming in observations since the 19th century (Chapter 2, Section 2.3.1) and climate model simulations (Chapter 4, Section 4.3.1; Figure 7.12a) share several common features. In particular, surface warming in the Arctic is greater than for the global average and greater than in the southern hemisphere (SH) high latitudes; and surface warming is generally greater over land than over the ocean. Observations and climate model simulations also show some notable differences. ESMs generally simulate a weakening of the equatorial Pacific Ocean zonal (east-west) SST gradient on multi-decadal to centennial timescales, with greater warming in the east than the west, but this trend has not been seen in observations (Chapter 2, Figure 2.11b; Chapter 9, Section 9.2.1).

Chapter 4, Section 4.5.1 discusses patterns of surface warming for 21st century climate projections under the Shared Socioeconomic Pathways (SSP) scenarios. Chapter 9, Section 9.2.1 assesses historical SST trends and the ability of coupled ESMs to replicate the observed changes. Chapter 4, Section 4.5.1 discusses the processes that cause the land to warm more than the ocean (land-ocean warming contrast). This section assesses process understanding of the large-scale patterns of surface temperature response from the perspective of a regional energy budget. It then assesses evidence from the paleoclimate proxy record for patterns of surface warming during past time periods associated with changes in atmospheric CO_2 concentrations. Finally, it assesses how radiative feedbacks depend on the spatial pattern of surface temperature, and thus how they can change in magnitude as that pattern evolves over time, with implications for the assessment of ECS based on historical warming (Sections 7.4.4.3 and 7.5.2.1).

7.4.4.1 Polar amplification

Polar amplification describes the phenomenon where surface temperature change at high latitudes exceeds the global average surface temperature change in response to radiative forcing of the climate system. Arctic amplification, often defined as the ratio of Arctic to global surface warming, is a ubiquitous emergent feature of climate model simulations (Holland and Bitz, 2003; Pithan and Mauritsen, 2014; Chapter 4, Section 4.5.1; Figure 7.12a) and is also seen in observations (Chapter 2, Section 2.3.1). However, both climate models and observations show relatively less warming of the SH high latitudes compared to the northern hemisphere (NH) high latitudes over the historical record (Chapter 2, Section 2.3.1); a characteristic that is projected to continue over the 21st century (Chapter 4, Section 4.5.1). Since AR5 there is a much-improved understanding of the processes that drive polar amplification in the NH and delay its emergence in the SH (Section 7.4.4.1.1). Furthermore, the paleoclimate record provides evidence for polar amplification from multiple time periods associated with changes in CO_2 (Hollis et al., 2019; Cleator et al., 2020; McClymont et al., 2020; Tierney et al., 2020b), and allows an evaluation of polar amplification in model simulations of these periods (Section 7.4.4.1.2). Research since AR5 identifies changes in the degree of polar amplification over time, particularly in the SH, as a key factor affecting how radiative feedbacks may evolve in the future (Section 7.4.4.3).

[START FIGURE 7.12 HERE]

Figure 7.12: Contributions of effective radiative forcing, ocean heat uptake, atmospheric heat transport, and radiative feedbacks to regional surface temperature changes at year 100 of *abrupt4xCO2* simulations of CMIP6 ESMs. (a) Pattern of near-surface air temperature change. (b-d) Contributions to net Arctic (>60°N), tropical (30°S – 30°N), and Antarctic (<60°S) warming calculated by dividing regional-average energy inputs by the magnitude of the regional-average Planck response. The contributions from radiative forcing, changes in moist, dry-static, and total atmospheric energy transport, ocean heat uptake, and radiative feedbacks (orange bars) all sum to the value of net warming (grey bar). Inset shows regional warming contributions associated with individual feedbacks, all summing to the

ACCEPTED VERSION SUBJECT TO FINAL EDITING

total feedback contribution. Uncertainties show the interquartile range (25th and 75th percentiles) across models. The warming contributions (units of °C) for each process are diagnosed by calculating the energy flux (units of W m^{-2}) that each process contributes to the atmosphere over a given region, either at the TOA or surface, then dividing that energy flux by the magnitude of the regional Planck response (around 3.2 W m^{-2} $°C^{-1}$ but varying with region). By construction, the individual warming contributions sum to the total warming in each region. Radiative kernel methods (see Section 7.4.1) are used to decompose the net energy input from radiative feedbacks into contributions from changes in atmospheric water vapour, lapse-rate, clouds, and surface albedo (Zelinka et al. (2020) using the Huang et al. (2017) radiative kernel). The CMIP6 models included are those analysed by Zelinka et al. (2020) and the warming contribution analysis is based on that of Goosse et al. (2018). Further details on data sources and processing are available in the chapter data table (Table 7.SM.14).

[END FIGURE 7.12 HERE]

7.4.4.1.1 Critical processes driving polar amplification

Several processes contribute to polar amplification under greenhouse gas forcing including the loss of sea ice and snow (an amplifying surface-albedo feedback), the confinement of warming to near the surface in the polar atmosphere (an amplifying lapse-rate feedback), and increases in poleward atmospheric and oceanic heat transport (Pithan and Mauritsen, 2014; Goosse et al., 2018; Dai et al., 2019; Feldl et al., 2020). Modelling and process studies since AR5 have led to an improved understanding of the combined effect of these different processes in driving polar amplification and how they differ between the hemispheres.

Idealized modelling studies suggest that polar amplification would occur even in the absence of any amplifying polar surface-albedo or lapse-rate feedbacks owing to changes in poleward atmospheric heat transport under global warming (Hall, 2004; Alexeev et al., 2005; Graversen and Wang, 2009; Alexeev and Jackson, 2013; Graversen et al., 2014; Roe et al., 2015; Merlis and Henry, 2018; Armour et al., 2019). Poleward heat transport changes reflect compensating changes in the transport of latent energy (moisture) and dry-static energy (sum of sensible and potential energy) by atmospheric circulations (Alexeev et al., 2005; Held and Soden, 2006; Hwang and Frierson, 2010; Hwang et al., 2011; Kay et al., 2012; Huang and Zhang, 2014; Feldl et al., 2017a; Donohoe et al., 2020). ESMs project that within the mid-latitudes, where eddies dominate the heat transport, an increase in poleward latent energy transport arises from an increase in the equator-to-pole gradient in atmospheric moisture with global warming, with moisture in the tropics increasing more than at the poles as described by the Clausius-Clapeyron relation (Chapter 8, Section 8.2). This change is partially compensated by a decrease in dry-static energy transport arising from a weakening of the equator-to-pole temperature gradient as the polar regions warm more than the tropics.

Energy balance models that approximate atmospheric heat transport in terms of a diffusive flux down the meridional gradient of near-surface moist static energy (sum of dry-static and latent energy) are able to reproduce the atmospheric heat transport changes seen within ESMs (Flannery, 1984; Hwang and Frierson, 2010; Hwang et al., 2011; Rose et al., 2014; Roe et al., 2015; Merlis and Henry, 2018), including the partitioning of latent and dry-static energy transports (Siler et al., 2018b; Armour et al., 2019). These models suggest that polar amplification is driven by enhanced poleward latent heat transport and that the magnitude of polar amplification can be enhanced or diminished by the latitudinal structure of radiative feedbacks. Amplifying polar feedbacks enhance polar warming and in turn cause a decrease in the dry-static energy transport to high latitudes (Alexeev and Jackson, 2013; Rose et al., 2014; Roe et al., 2015; Bonan et al., 2018; Merlis and Henry, 2018; Armour et al., 2019; Russotto and Biasutti, 2020). Poleward latent heat transport changes act to favour polar amplification and inhibit tropical amplification (Armour et al., 2019), resulting in a strongly polar-amplified warming response to polar forcing and a more latitudinally-uniform warming response to tropical forcing within ESMs (Alexeev et al., 2005; Rose et al., 2014; Stuecker et al., 2018). The important role for poleward latent energy transport in polar amplification is supported by studies of atmospheric reanalyses and ESMs showing that episodic increases in latent heat transport into the Arctic can enhance surface downwelling radiation and drive sea-ice loss on sub-seasonal timescales (Woods and Caballero, 2016; Gong et al., 2017; Lee et al., 2017; Luo et al., 2017a), however this may be a smaller driver of sea-ice variability than atmospheric temperature fluctuations (Olonscheck et al., 2019).

ACCEPTED VERSION SUBJECT TO FINAL EDITING

Regional energy budget analyses are commonly used to diagnose the relative contributions of radiative feedbacks and energy fluxes to polar amplification as projected by ESMs under increased CO_2 concentrations (Figure 7.12; Feldl and Roe, 2013; Pithan and Mauritsen, 2014; Goosse et al., 2018; Stuecker et al., 2018). These analyses suggest that a primary cause of amplified Arctic warming in ESMs is the latitudinal structure of radiative feedbacks, which warm the Arctic more than the tropics (Figure 7.12b), and enhanced latent energy transport into the Arctic. That net atmospheric heat transport into the Arctic does not change substantially within ESMs, on average, under CO_2 forcing (Figure 7.12b) reflects a compensating decrease in poleward dry-static energy transport as a response to polar amplified warming (Hwang et al., 2011; Armour et al., 2019; Donohoe et al., 2020). The latitudinal structure of radiative feedbacks primarily reflects that of the surface-albedo and lapse-rate feedbacks, which preferentially warm the Arctic (Graversen et al., 2014; Pithan and Mauritsen, 2014; Goosse et al., 2018). Latitudinal structure in the lapse-rate feedback reflects weak radiative damping to space with surface warming in polar regions, where atmospheric warming is constrained to the lower troposphere owing to stably stratified conditions, and strong radiative damping in the tropics, where warming is enhanced in the upper troposphere owing to moist convective processes. This is only partially compensated by latitudinal structure in the water vapour feedback (Taylor et al., 2013), which favours tropical warming (Pithan and Mauritsen, 2014). While cloud feedbacks have been found to play little role in Arctic amplification in CMIP5 models (Pithan and Mauritsen, 2014; Goosse et al., 2018; Figure 7.12b), less-negative cloud feedbacks at high latitude as seen within some CMIP6 models (Zelinka et al., 2020) tend to favour stronger polar amplification (Dong et al., 2020). A weaker Planck response at high latitudes, owing to less efficient radiative damping where surface and atmospheric temperatures are lower, also contributes to polar amplification (Pithan and Mauritsen, 2014). The effective radiative forcing of CO_2 is larger in the tropics than at high latitudes, suggesting that warming would be tropically amplified if not for radiative feedbacks and poleward latent heat transport changes (Stuecker et al., 2018; Figure 7.12b-d).

While the contributions to regional warming can be diagnosed within ESM simulations (Figure 7.12), assessment of the underlying role of individual factors is limited by interactions inherent to the coupled climate system. For example, polar feedback processes are coupled and influenced by warming at lower latitudes (Screen et al., 2012; Alexeev and Jackson, 2013; Graversen et al., 2014; Graversen and Burtu, 2016; Rose and Rencurrel, 2016; Feldl et al., 2017a; Yoshimori et al., 2017; Garuba et al., 2018; Po-Chedley et al., 2018a; Stuecker et al., 2018; Dai et al., 2019; Feldl et al., 2020), while atmospheric heat transport changes are in turn influenced by the latitudinal structure of regional feedbacks, radiative forcing, and ocean heat uptake (Hwang et al., 2011; Zelinka and Hartmann, 2012; Feldl and Roe, 2013; Huang and Zhang, 2014; Merlis, 2014; Rose et al., 2014; Roe et al., 2015; Feldl et al., 2017b; Stuecker et al., 2018; Armour et al., 2019). The use of different feedback definitions, such as a lapse-rate feedback partitioned into upper and lower tropospheric components (Feldl et al., 2020) or including the influence of water vapour at constant relative humidity (Held and Shell, 2012; Section 7.4.2), would also change the interpretation of which feedbacks contribute most to polar amplification.

The energy budget analyses (Figure 7.12) suggest that greater surface warming in the Arctic than the Antarctic under greenhouse gas forcing arises from two main processes. The first is large surface heat uptake in the Southern Ocean (Figure 7.12c) driven by the upwelling of deep waters that have not yet felt the effects of the radiative forcing; the heat taken up is predominantly transported away from Antarctica by northward-flowing surface waters (Marshall et al., 2015; Armour et al., 2016; Chapter 9, Section 9.2.1). Strong surface heat uptake also occurs in the subpolar North Atlantic Ocean under global warming (Chapter 9, Section 9.2.1). However, this heat is partially transported northward into the Arctic which leads to increased heat fluxes into the Arctic atmosphere (Rugenstein et al., 2013; Jungclaus et al., 2014; Koenigk and Brodeau, 2014; Marshall et al., 2015; Nummelin et al., 2017; Singh et al., 2017; Oldenburg et al., 2018; Figure 7.12b). The second main process contributing to differences in Arctic and Antarctic warming is the asymmetry in radiative feedbacks between the poles (Yoshimori et al., 2017; Goosse et al., 2018). This primarily reflects the weaker lapse-rate and surface-albedo feedbacks and more-negative cloud feedbacks in the SH high latitudes (Figure 7.12). However, note the SH cloud feedbacks are uncertain due to possible biases in the treatment of mixed phase clouds (Hyder et al., 2018). Idealized modelling suggests that the asymmetry in the polar lapse-rate feedback arises from the height of the Antarctic ice sheet precluding the formation of deep atmospheric inversions that are necessary to produce the stronger positive lapse-rate feedbacks seen in the Arctic (Salzmann, 2017; Hahn et al., 2020). ESM projections of the equilibrium response to CO_2 forcing

ACCEPTED VERSION SUBJECT TO FINAL EDITING

show polar amplification in both hemispheres, but generally with less warming in the Antarctic than the Arctic (Li et al., 2013a; Yoshimori et al., 2017).

Because multiple processes contribute to polar amplification, it is a robust feature of the projected long-term response to greenhouse gas forcing in both hemispheres. At the same time, contributions from multiple processes make projections of the magnitude of polar warming inherently more uncertain than global mean warming (Holland and Bitz, 2003; Roe et al., 2015; Bonan et al., 2018; Stuecker et al., 2018). The magnitude of Arctic amplification ranges from a factor of two to four in ESM projections of 21st century warming (Chapter 4, Section 4.5.1). While uncertainty in both global and tropical warming under greenhouse gas forcing is dominated by cloud feedbacks (Vial et al., 2013; Section 7.5.7), uncertainty in polar warming arises from polar surface-albedo, lapse-rate, and cloud feedbacks, changes in atmospheric and oceanic poleward heat transport, and ocean heat uptake (Hwang et al., 2011; Mahlstein and Knutti, 2011; Pithan and Mauritsen, 2014; Bonan et al., 2018).

The magnitude of polar amplification also depends on the type of radiative forcing applied (Stjern et al., 2019; Chapter 4, Section 4.5.1.1), with Chapter 6, Section 6.4.3 discussing changes in sulphate aerosol emissions and the deposition of black carbon aerosols on ice and snow as potential drivers of amplified Arctic warming. The timing of the emergence of SH polar amplification remains uncertain due to insufficient knowledge of the timescales associated with Southern Ocean warming and the response to surface wind and freshwater forcing (Bintanja et al., 2013; Kostov et al., 2017, 2018; Pauling et al., 2017; Purich et al., 2018). ESM simulations indicate that freshwater input from melting ice shelves could reduce Southern Ocean warming by up to several tenths of a °C over the 21st century by increasing stratification of the surface ocean around Antarctica (Bronselaer et al., 2018; Golledge et al., 2019; Lago and England, 2019; Section 7.4.2.6; Chapter 9, Section 9.2.1 and Box 9.3) (*low confidence* due to *medium agreement* but *limited evidence*). However, even a large reduction in the Atlantic meridional overturning circulation (AMOC) and associated northward heat transport due, for instance, to greatly increased freshwater runoff from Greenland would be insufficient to eliminate Arctic amplification (Liu et al., 2017a, 2017b; Wen et al., 2018) (*medium confidence* based on to *medium agreement* and *medium evidence*).

Arctic amplification has a distinct seasonality with a peak in early winter (Nov–Jan) owing to sea-ice loss and associated increases in heat fluxes from the ocean to the atmosphere resulting in strong near-surface warming (Pithan and Mauritsen, 2014; Dai et al., 2019). Surface warming may be further amplified by positive cloud and lapse-rate feedbacks in autumn and winter (Burt et al., 2016; Morrison et al., 2018; Hahn et al., 2020). Arctic amplification is weak in summer owing to surface temperatures remaining stable as excess energy goes into thinning the summertime sea-ice cover, which remains at the melting point, or into the ocean mixed layer. Arctic amplification can also be interpreted through changes in the surface energy budget (Burt et al., 2016; Woods and Caballero, 2016; Boeke and Taylor, 2018; Kim et al., 2019), however such analyses are complicated by the finding that a large portion of the changes in downward longwave radiation can be attributed to the lower troposphere warming along with the surface itself (Vargas Zeppetello et al., 2019).

7.4.4.1.2 Polar amplification from proxies and models during past climates associated with CO_2 change

Paleoclimate proxy data provide observational evidence of large-scale patterns of surface warming in response to past forcings, and allow an evaluation of the modelled response to these forcings (Chapter 3, Section 3.3.1.1; Section 3.8.2.1). In particular, paleoclimate data provide evidence for long-term changes in polar amplification during time periods in which the primary forcing was a change in atmospheric CO_2, although data sparsity means that for some time periods this evidence may be limited to a single hemisphere or ocean basin, or the evidence may come primarily from the mid-latitudes as opposed to the polar regions. In this context, there has been a modelling and data focus on the Last Glacial Maximum (LGM) in the context of PMIP4 (Cleator et al., 2020; Tierney et al., 2020b; Kageyama et al., 2021), the mid-Pliocene warm period (MPWP) in the context of PlioMIP2 (Chapter 2, Cross-Chapter Box 2.4; Salzmann et al., 2013; Haywood et al., 2020; McClymont et al., 2020), the early Eocene climatic optimum (EECO) in the context of DeepMIP (Hollis et al., 2019; Lunt et al., 2021), and there is growing interest in the Miocene (Goldner et al., 2014b; Steinthorsdottir et al., 2020) (for definitions of time periods see Chapter 2, Cross-Chapter Box 2.1).

ACCEPTED VERSION SUBJECT TO FINAL EDITING

For all these time periods, in addition to the CO_2 forcing there are long-term feedbacks associated with ice sheets (Section 7.4.2.6), and in particular for the early Eocene there is a forcing associated with paleogeographic change (Farnsworth et al., 2019). However, because these non-CO_2 effects can all be included as boundary conditions in model simulations, these time periods allow an assessment of the patterns of modelled response to known forcing (although uncertainty in the forcing increases further back in time). Because these changes to boundary conditions can be complex to implement in models, and because long simulations (typically >500 years) are required to approach equilibrium, these simulations have been carried out mostly by pre-CMIP6 models, with relatively few (or none for the early Eocene) fully coupled CMIP6 models in the ensembles.

At the time of AR5, polar amplification was evident in proxy reconstructions of paleoclimate SST and SAT from the LGM, MPWP and the early Eocene, but uncertainties associated with proxy calibrations (Waelbroeck et al., 2009; Dowsett et al., 2012; Lunt et al., 2012a) and the role of orbital forcing (for the MPWP; Lisiecki and Raymo, 2005) meant that the degree of polar amplification during these time periods was not accurately known. Furthermore, although some models (CCSM3; Winguth et al., 2010; Huber and Caballero, 2011) at that time were able to reproduce the strong polar amplification implied by temperature proxies of the early Eocene, this was achieved at higher CO_2 concentrations (>2000 ppm) than those indicated by CO_2 proxies (<1500 ppm; Beerling and Royer, 2011).

Since AR5 there has been progress in improving the accuracy of proxy temperature reconstructions of the LGM (Cleator et al., 2020; Tierney et al., 2020b), the MPWP (McClymont et al., 2020), and the early Eocene (Hollis et al., 2019) time periods. In addition, reconstructions of the MPWP have been focused on a short time slice with an orbit similar to modern-day (isotopic stage KM5C; Haywood et al., 2013, 2016b). Furthermore, there are more robust constraints on CO_2 concentrations from the MPWP (Martínez-Botí et al., 2015; de la Vega et al., 2020) and the early Eocene (Anagnostou et al., 2016, 2020). As such, polar amplification during the LGM, MPWP, and early Eocene time periods can now be better quantified than at the time of AR5, and the ability of climate models to reproduce this pattern can be better assessed; model-data comparisons for SAT and SST for these three time periods are shown in Figure 7.13.

[START FIGURE 7.13 HERE]

Figure 7.13: Polar amplification in paleo proxies and models of the early Eocene climatic optimum (EECO), the mid-Pliocene warm period (MPWP), and the Last Glacial Maximum (LGM). Temperature anomalies compared with pre-industrial (equivalent to CMIP6 simulation *piControl*) are shown for the high-CO_2 EECO and MPWP time periods, and for the low-CO_2 LGM (expressed as pre-industrial minus LGM). (a,b,c) Modelled near-surface air temperature anomalies for ensemble-mean simulations of the (a) EECO (Lunt et al., 2021), (b) MPWP (Haywood et al., 2020; Zhang et al., 2021), and (c) LGM (Kageyama et al., 2021; Zhu et al., 2021). Also shown are proxy near-surface air temperature anomalies (coloured circles). (d,e,f) Proxy near-surface air temperature anomalies (grey circles), including published uncertainties (grey vertical bars), model ensemble mean zonal mean anomaly (solid red line) for the same model ensembles as in (a,b,c), light red lines show the modelled temperature anomaly for the individual models that make up each ensemble (LGM, N=9; MPWP, N=17; EECO, N=5). Black dashed lines show the average of the proxy values in each latitude bands 90°S to 30°S, 30°S to 30°N, and 30°N to 90°N. Red dashed lines show the same banded average in the model ensemble mean, calculated from the same locations as the proxies. Black and red dashed lines are only shown if there are 5 or more proxy points in that band. Mean differences between the 90°S/N to 30°S/N and 30°S to 30°N bands are quantified for the models and proxies in each plot. Panels (g,h,i) are like panels (d,e,f) but for SST instead of near-surface air temperature. Panels (j,k,l) are like panels (a,b,c) but for SST instead of near-surface air temperature. For the EECO maps (a,j), the anomalies are relative to the zonal mean of the pre-industrial, due to the different continental configuration. Proxy datasets are (a,d) Hollis et al. (2019), (b,e) Salzmann et al. (2013); Vieira et al. (2018), (c,f) Cleator et al. (2020) at the sites defined in Bartlein et al. (2011), (g,j)) Hollis et al. (2019), (h,k) McClymont et al. (2020) (i,l) Tierney et al. (2020b). Where there are multiple proxy estimations at a single site, a mean is taken. Model ensembles are (a,d,g,j) DeepMIP (only model simulations carried out with a mantle-frame paleogeography, and carried out under CO_2 concentrations within the range assessed in Chapter 2, Table 2.2, are shown), (b,e,h,k) PlioMIP, and (c,f,i,l) PMIP4. Further details on data sources and processing are available in the chapter data table (Table 7.SM.14).

ACCEPTED VERSION SUBJECT TO FINAL EDITING

[END FIGURE 7.13 HERE]

Since AR5, there has been progress in the simulation of polar amplification by paleoclimate models of the early Eocene. Initial work indicated that changes to model parameters associated with aerosols and/or clouds could increase simulated polar amplification and improve agreement between models and paleoclimate data (Kiehl and Shields, 2013; Sagoo et al., 2013), but such parameter changes were not physically based. In support of these initial findings, a more recent (CMIP5) climate model, that includes a process-based representation of cloud microphysics, exhibits polar amplification in better agreement with proxies when compared to the models assessed in AR5 (Zhu et al., 2019b). Since then, some other CMIP3 and CMIP5 models in the DeepMIP multi-model ensemble (Lunt et al., 2021) have obtained polar amplification for the EECO that is consistent with proxy indications of both polar amplification and CO_2. Although there is a lack of tropical proxy SAT estimates, both proxies and DeepMIP models show greater terrestrial warming in the high latitudes than the mid-latitudes in both Hemispheres (Figure 7.13a,d). SST proxies also exhibit polar amplification in both Hemispheres, but the magnitude of this polar amplification is too low in the models, in particular in the southwest Pacific (Figure 7.13g,j).

For the MPWP, model simulations are now in better agreement with proxies than at the time of AR5 (Haywood et al., 2020; McClymont et al., 2020). In particular, in the tropics new proxy reconstructions of SSTs are warmer and in better agreement with the models, due in part to the narrower time window in the proxy reconstructions. There is also better agreement at higher latitudes (primarily in the North Atlantic), due in part to the absence of some very warm proxy SSTs due to the narrower time window (McClymont et al., 2020), and in part to a modified representation of Arctic gateways in the most recent Pliocene model simulations (Otto-Bliesner et al., 2017), which have resulted in warmer modelled SSTs in the North Atlantic (Haywood et al., 2020). Furthermore, as for the Eocene, improvements in the representation of aerosol-cloud interactions has also led to improved model-data consistency at high latitudes (Feng et al., 2019). Although all PlioMIP2 models exhibit polar amplification of SAT, due to the relatively narrow time window there are insufficient terrestrial proxies to assess this (Figure 7.13b,e). However, polar SST amplification in the PlioMIP2 ensemble mean is in reasonably good agreement with that from SST proxies in the Northern Hemisphere (Figure 7.13h,k).

The Last Glacial Maximum (LGM) also gives an opportunity to evaluate model simulation of polar amplification under CO_2 forcing, albeit under colder conditions than today (Kageyama et al., 2021). Terrestrial SAT and marine SST proxies exhibit clear polar amplification in the Northern Hemisphere, and the PMIP4 models capture this well (Figure 7.13c,f,i,l), in particular for SAT. There is less proxy data in the mid to high latitudes of the Southern Hemisphere, but here the models exhibit polar amplification of both SST and SAT. LGM regional model-data agreement is also assessed in Chapter 3, Section 3.8.2.

Overall, the proxy reconstructions give *high confidence* that there was polar amplification in the LGM, MPWP and EECO, and this is further supported by model simulations of these time periods (Zhu et al., 2019b; Haywood et al., 2020; Kageyama et al., 2021; Lunt et al., 2021; Figure 7.13). For both the MPWP and EECO, models are more consistent with the temperature and CO_2 proxies than at the time of AR5 (*high confidence*). For the LGM Northern Hemisphere, which is the region with the most data and the time period with the least uncertainty in model boundary conditions, polar amplification in the PMIP4 ensemble mean is in good agreement with the proxies, especially for SAT (*medium confidence*). Overall, the confidence in the ability of models to accurately simulate polar amplification is higher than at the time of AR5, but a more complete model evaluation could be carried out if there were more CMIP6 paleoclimate simulations included in the assessment.

7.4.4.1.3 Overall assessment of polar amplification

Based on mature process understanding of the roles of poleward latent heat transport and radiative feedbacks in polar warming, a high degree of agreement across a hierarchy of climate models, observational evidence, paleoclimate proxy records of past climates associated with CO_2 change, and ESM simulations of those past

ACCEPTED VERSION SUBJECT TO FINAL EDITING

climates, there is *high confidence* that polar amplification is a robust feature of the long-term response to greenhouse gas forcing in both hemispheres. Stronger warming in the Arctic than in the global average has already been observed (Chapter 2, Section 2.3.1) and its causes are well understood. It is *very likely* that the warming in the Arctic will be more pronounced than on global average over the 21st century (*high confidence*) (Chapter 4, Section 4.5.1.1). This is supported by models' improved ability to simulate polar amplification during past time periods, compared with at the time of AR5 (*high confidence*); although this is based on an assessment of mostly non-CMIP6 models.

Southern Ocean SSTs have been slow to warm over the instrumental period, with cooling since about 1980 owing to a combination of upper-ocean freshening from ice-shelf melt, intensification of surface westerly winds from ozone depletion, and variability in ocean convection (Chapter 9, Section 9.2.1). This stands in contrast to the equilibrium warming pattern either inferred from the proxy record or simulated by ESMs under CO_2 forcing. There is *high confidence* that the SH high latitudes will warm more than the tropics on centennial timescales as the climate equilibrates with radiative forcing and Southern Ocean heat uptake is reduced. However, there is only *low confidence* that this feature will emerge this century.

7.4.4.2 Tropical Pacific sea-surface temperature gradients

Research published since AR5 identifies changes in the tropical Pacific Ocean zonal SST gradient over time as a key factor affecting how radiative feedbacks may evolve in the future (Section 7.4.4.3). There is now a much-improved understanding of the processes that govern the tropical Pacific SST gradient (Section 7.4.4.2.1) and the paleoclimate record provides evidence for its equilibrium changes from time periods associated with changes in CO_2 (Section 7.4.4.2.2).

7.4.4.2.1 Critical processes determining changes in tropical Pacific sea-surface temperature gradients

A weakening of the equatorial Pacific Ocean east-west SST gradient, with greater warming in the East than the west, is a common feature of the climate response to greenhouse gas forcing as projected by ESMs on centennial and longer timescales (e.g., Figure 7.14b) (Chapter 4, Section 4.5.1). There are thought to be several factors contributing to this pattern. In the absence of any changes in atmospheric or oceanic circulations, the east-west surface temperature difference is theorized to decrease owing to weaker evaporative damping, and thus greater warming in response to forcing, where climatological temperatures are lower in the eastern Pacific cold tongue (Xie et al., 2010; Luo et al., 2015). Within atmospheric ESMs coupled to mixed-layer ocean, this gradient in damping has been linked to the rate of change with warming of the saturation specific humidity, which is set by the Clausius-Clapeyron relation (Merlis and Schneider, 2011). Gradients in low-cloud feedbacks may also favour eastern equatorial Pacific warming (DiNezio et al., 2009).

In the coupled climate system, changes in atmospheric and oceanic circulations will influence the east-west temperature gradient as well. It is expected that as global temperature increases and as the east-west temperature gradient weakens, east-west sea-level pressure gradients and easterly trade winds (characterizing the Walker circulation) will weaken as well (Vecchi et al., 2006, 2008; Figure 7.14b; Chapter 8, Sections 8.2.2.2 and 8.4.2.3; Chapter 4, Section 4.5.3). This would, in turn, weaken the east-west temperature gradient through a reduction of equatorial upwelling of cold water in the east Pacific and a reduction in the transport of warmer water to the western equatorial Pacific and Indian Ocean (England et al., 2014; Dong and McPhaden, 2017; Li et al., 2017; Maher et al., 2018).

Research published since AR5 (Burls and Fedorov, 2014a; Fedorov et al., 2015; Erfani and Burls, 2019) has built on an earlier theory (Liu and Huang, 1997; Barreiro and Philander, 2008) linking the east-west temperature gradient to the north-south temperature gradient. In particular, model simulations suggest that a reduction in the equator-to-pole temperature gradient (polar amplification) increases the temperature of water subducted in the extra-tropics, which in turn is upwelled in the eastern Pacific. Thus, polar amplified warming, with greater warming in the mid-latitudes and subtropics than in the deep tropics, is expected to contribute to the weakening of the east-west equatorial Pacific SST gradient on decadal to centennial

ACCEPTED VERSION SUBJECT TO FINAL EDITING

timescales.

The transient adjustment of the equatorial Pacific SST gradient is influenced by upwelling waters which delay surface warming in the east since they have not been at the surface for years-to-decades to experience the greenhouse gas forcing. This 'thermostat mechanism' (Clement et al., 1996; Cane et al., 1997) is not thought to persist to equilibrium since it does not account for the eventual increase in temperatures of upwelled waters (Liu et al., 2005; Xie et al., 2010; Luo et al., 2017b) which will occur as the subducting waters in mid-latitudes warm by more than the tropics on average as polar amplification emerges. An individual CMIP5 ESM (GFDL's ESM2M) has been found to exhibit a La Niña–like pattern of Pacific temperature change through the 21st century, similar to the SST trends seen over the historical record (Chapter 9, Section 9.2.1; Figure 7.14a), owing to a weakening asymmetry between El Niño and La Niña events (Kohyama et al., 2017), but this pattern of warming may not persist to equilibrium (Paynter et al., 2018).

Since 1870, observed SSTs in the tropical western Pacific Ocean have increased while those in the tropical eastern Pacific Ocean have changed less (Figure 7.14a; Chapter 9, Section 9.2.1). Much of the resultant strengthening of the equatorial Pacific temperature gradient has occurred since about 1980 due to strong warming in the west and cooling in the east (Chapter 2, Figure 2.11b) concurrent with an intensification of the surface equatorial easterly trade winds and Walker Circulation (England et al., 2014; Chapter 3, Section 3.3.3.1, Section 3.7.6, Figure 3.16f, Figure 3.39f; Chapter 8, Section 8.3.2.3; Chapter 9, Section 9.2). This temperature pattern is also reflected in regional ocean heat content trends and sea level changes observed from satellite altimetry since 1993 (Bilbao et al., 2015; Richter et al., 2020). The observed changes may have been influenced by one or a combination of temporary factors including sulphate aerosol forcing (Smith et al., 2016; Takahashi and Watanabe, 2016; Hua et al., 2018), internal variability within the Indo-Pacific Ocean (Luo et al., 2012; Chung et al., 2019), teleconnections from multi-decadal tropical Atlantic SST trends (Kucharski et al., 2011, 2014, 2015; McGregor et al., 2014; Chafik et al., 2016; Li et al., 2016a; Kajtar et al., 2017; Sun et al., 2017), teleconnections from multi-decadal Southern Ocean SST trends (Hwang et al., 2017), and coupled ocean–atmosphere dynamics which slow warming in the equatorial eastern Pacific (Clement et al., 1996; Cane et al., 1997; Seager et al., 2019). CMIP3 and CMIP5 ESMs have difficulties replicating the observed trends in the Walker Circulation and Pacific Ocean SSTs over the historical record (Sohn et al., 2013; Zhou et al., 2016; Coats and Karnauskas, 2017), possibly due to model deficiencies including insufficient multi-decadal Pacific Ocean SST variability (Laepple and Huybers, 2014; Bilbao et al., 2015; Chung et al., 2019), mean state biases affecting the forced response or the connection between Atlantic and Pacific basins (Kucharski et al., 2014; Kajtar et al., 2018; Luo et al., 2018; McGregor et al., 2018; Seager et al., 2019), and/or a misrepresentation of radiative forcing (Chapter 9, Section 9.2.1 and Chapter 3, Section 3.7.6). However, the observed trends in the Pacific Ocean SSTs are still within the range of internal variability as simulated by large initial condition ensembles of CMIP5 and CMIP6 models (Olonscheck et al., 2020; Watanabe et al., 2020a). Because the causes of observed equatorial Pacific temperature gradient and Walker circulation trends are not well understood (Chapter 3, Section 3.3.3.1), there is *low confidence* in their attribution to anthropogenic influences (Chapter 8, Section 8.3.2.3), while there is *medium confidence* that the observed changes have resulted from internal variability (Chapter 8, Section 8.2.2.2; Chapter 3, Section 3.7.6).

7.4.4.2.2 Tropical Pacific temperature gradients in past high-CO_2 climates

AR5 stated that paleoclimate proxies indicate a reduction in the longitudinal SST gradient across the equatorial Pacific during the mid-Pliocene warm period (MPWP; Cross-Chapter Box 2.1; Cross-Chapter Box 2.4; Masson-Delmotte et al., 2013). This assessment was based on SST reconstructions between two sites situated very close to the equator in the heart of the western Pacific warm pool and eastern Pacific cold tongue, respectively. Multiple SST reconstructions based on independent paleoclimate proxies generally agreed that during the Pliocene the SST gradient between these two sites was reduced compared with the modern long-term mean (Wara et al., 2005; Dekens et al., 2008; Fedorov et al., 2013).

Since AR5, the generation of new SST records has led to a variety of revised gradient estimates, specifically the generation of a new record for the warm pool (Zhang et al., 2014), the inclusion of SST reconstructions

ACCEPTED VERSION SUBJECT TO FINAL EDITING

from sites in the South China Sea as warm pool estimates (O'Brien et al., 2014; Zhang et al., 2014), and the inclusion of several new sites from the eastern Pacific as cold tongue estimates (Zhang et al., 2014; Fedorov et al., 2015). Published estimates of the reduction in the longitudinal SST difference for the Late Pliocene, relative to either Late Quaternary (0-0.5Ma) or pre-industrial values, include 1 to 1.5°C (Zhang et al., 2014), 0.1 to 1.9°C (Tierney et al., 2019), and about 3°C (Ravelo et al., 2014; Fedorov et al., 2015; Wycech et al., 2020). All of these studies report a further weakening of the longitudinal gradient based on records extending into the Early Pliocene. While these revised estimates differ in magnitude due to differences in the sites and SST proxies used, they all agree that the longitudinal gradient was weaker, and this is supported by the probabilistic approach of Tierney et al. (2019). However, given that there are currently relatively few western equatorial Pacific records from independent site locations, and due to uncertainties associated with the proxy calibrations (Haywood et al., 2016a), there is only *medium confidence* that the average longitudinal gradient in the tropical Pacific was weaker during the Pliocene than during the Late Quaternary.

To avoid the influence of local biases, changes in the longitudinal temperature difference within Pliocene model simulations are typically evaluated using domain-averaged SSTs within chosen east and west Pacific regions and as such there is sensitivity to methodology. Unlike the reconstructed estimates, longitudinal gradient changes simulated by the Pliocene Model Intercomparison Project Phase 1 (PlioMIP1) models do not agree on the change in sign and are reported as spanning approximately –0.5 to 0.5 °C by Brierley et al. (2015) and approximately –1 to 1 °C by Tierney et al. (2019). Initial PlioMIP Phase 2 (PlioMIP2) analysis suggests responses similar to PlioMIP1 (Feng et al., 2019; Haywood et al., 2020). Models that include hypothetical modifications to cloud albedo or ocean mixing are required to simulate the substantially weaker longitudinal differences seen in reconstructions of the early Pliocene (Fedorov et al., 2013; Burls and Fedorov, 2014b).

While more western Pacific warm pool temperature reconstructions are needed to refine estimates of the longitudinal gradient, several Pliocene SST reconstructions from the east Pacific indicate enhanced warming in the centre of the eastern equatorial cold tongue upwelling region (Liu et al., 2019). This enhanced warming in the east Pacific cold tongue appears to be dynamically consistent with reconstruction of enhanced subsurface warming (Ford et al., 2015) and enhanced warming in coastal upwelling regions, suggesting that the tropical thermocline was deeper and/or less stratified during the Pliocene. The Pliocene data therefore suggests that the observed cooling trend over the last 60 years in parts of the eastern equatorial Pacific (Seager et al., 2019; Chapter 9, Section 9.2.1.1; Figure 9.3), whether forced or due to internal variability, involves transient processes that are probably distinct from the longer-timescale process (Burls and Fedorov, 2014a, 2014b; Luo et al., 2015; Heede et al., 2020) that maintained warmer eastern Pacific SST during the Pliocene.

7.4.4.2.3 Overall assessment of tropical Pacific sea-surface temperature gradients under CO_2 forcing

The paleoclimate proxy record and ESM simulations of the MPWP, process understanding, and ESM projections of climate response to CO_2 forcing provide medium evidence and a medium degree of agreement and thus *medium confidence* that equilibrium warming in response to elevated CO_2 will be characterized by a weakening of the east-west tropical Pacific SST gradient.

Overall the observed pattern of warming over the instrumental period, with a warming minimum in the eastern tropical Pacific Ocean (Figure 7.14a), stands in contrast to the equilibrium warming pattern either inferred from the MPWP proxy record or simulated by ESMs under CO_2 forcing. There is *medium confidence* that the observed strengthening of the east-west SST gradient is temporary and will transition to a weakening of the SST gradient on centennial timescales. However, there is only *low confidence* that this transition will emerge this century owing to a low degree of agreement across studies about the factors driving the observed strengthening of the east-west SST gradient and how those factors will evolve in the future. These trends in tropical Pacific SST gradients reflect changes in the climatology, rather than changes in ENSO amplitude or variability, which are assessed in Chapter 4, Section 4.3.3.

7.4.4.3 Dependence of feedbacks on temperature patterns

ACCEPTED VERSION SUBJECT TO FINAL EDITING

The expected time-evolution of the spatial pattern of surface warming in the future has important implications for values of ECS inferred from the historical record of observed warming. In particular, changes in the global TOA radiative energy budget can be induced by changes in the regional variations of surface temperature, even without a change in the global mean temperature (Zhou et al., 2016; Ceppi and Gregory, 2019). Consequently, the global radiative feedback, characterizing the net TOA radiative response to global surface warming, depends on the *spatial pattern* of that warming. Therefore, if the equilibrium warming pattern under CO_2 forcing (similar to CMIP6 projections in Fig. 7.12a) is distinct from that observed over the historical record or indicated by paleoclimate proxies (Sections 7.4.4.1 and 7.4.4.2), then ECS will be different from the effective ECS (Box 7.1) that is inferred from those periods. Accounting for the dependence of radiative feedbacks on the spatial pattern of warming has helped to reconcile values of ECS inferred from the historical record with values of ECS based on other lines of evidence and simulated by climate models (Armour, 2017; Proistosescu and Huybers, 2017; Andrews et al., 2018; Section 7.5.2.1) but has not yet been examined in the paleoclimate context.

This temperature "pattern effect" (Stevens et al., 2016) can result from both internal variability and radiative forcing of the climate system. Importantly, it is distinct from potential radiative feedback dependencies on the global surface temperature, which are assessed in Section 7.4.3. While changes in global radiative feedbacks under transient warming have been documented in multiple generations of climate models (Williams et al., 2008; Andrews et al., 2015; Ceppi and Gregory, 2017; Dong et al., 2020), research published since AR5 has developed a much-improved understanding of the role of evolving SST patterns in driving feedback changes (Armour et al., 2013; Andrews et al., 2015, 2018, Zhou et al., 2016, 2017b; Gregory and Andrews, 2016; Proistosescu and Huybers, 2017; Ceppi and Gregory, 2017; Haugstad et al., 2017; Andrews and Webb, 2018; Silvers et al., 2018; Marvel et al., 2018; Dong et al., 2019, 2020). This section assesses process understanding of the pattern effect, which is dominated by the evolution of SSTs. Section 7.5.2.1 describes how potential feedback changes associated with the pattern effect are important to interpreting ECS estimates based on historical warming.

The radiation changes most sensitive to warming patterns are those associated with the low-cloud cover (affecting global albedo) and the tropospheric temperature profile (affecting thermal emission to space) (Ceppi and Gregory, 2017; Zhou et al., 2017b; Andrews et al., 2018; Dong et al., 2019). The mechanisms and radiative effects of these changes are illustrated in Figure 7.14a,b. SSTs in regions of deep convective ascent (e.g., in the western Pacific warm pool) govern the temperature of the tropical free troposphere and, in turn, affect low clouds through the strength of the inversion that caps the boundary layer (i.e., the lower-tropospheric stability) in subsidence regions (Wood and Bretherton, 2006; Klein et al., 2017). Surface warming within ascent regions thus warms the free troposphere and increases low-cloud cover, causing an increase in emission of thermal radiation to space and a reduction in absorbed solar radiation. In contrast, surface warming in regions of overall descent preferentially warms the boundary layer and enhances convective mixing with the dry free troposphere, decreasing low-cloud cover (Bretherton et al., 2013; Qu et al., 2014; Zhou et al., 2015). This leads to an increase in absorption of solar radiation but little change in thermal emission to space. Consequently, warming in tropical ascent regions results in negative lapse-rate and cloud feedbacks while warming in tropical descent regions results in positive lapse-rate and cloud feedbacks (Figure 7.14; Rose and Rayborn, 2016; Zhou et al., 2017b; Andrews and Webb, 2018; Dong et al., 2019). Surface warming in mid-to-high latitudes causes a weak radiative response owing to compensating changes in thermal emission (Planck and lapse-rate feedbacks) and absorbed solar radiation (shortwave cloud and surface-albedo feedbacks) (Rose and Rayborn, 2016; Dong et al., 2019), however this compensation may weaken due to less-negative shortwave cloud feedbacks at high warming (Frey and Kay, 2018; Bjordal et al., 2020; Dong et al., 2020).

[START FIGURE 7.14 HERE]

Figure 7.14: Illustration of tropospheric temperature and low-cloud response to observed and projected Pacific Ocean sea-surface temperature trends; adapted from Mauritsen (2016). (a) Atmospheric response to linear sea-surface temperature trend observed over 1870–2019 (HadISST1 dataset; Rayner et al., 2003).

ACCEPTED VERSION SUBJECT TO FINAL EDITING

(b) Atmospheric response to linear sea-surface temperature trend over 150 years following *abrupt4xCO2* forcing as projected by CMIP6 ESMs (Dong et al., 2020). Relatively large historical warming in the western tropical Pacific has been communicated aloft (a shift from grey to red atmospheric temperature profile), remotely warming the tropical free troposphere and increasing the strength of the inversion in regions of the tropics where warming has been slower, such as the eastern equatorial Pacific. In turn, an increased inversion strength has increased the low-cloud cover (Zhou et al., 2016) causing an anomalously-negative cloud and lapse-rate feedbacks over the historical record (Andrews et al., 2018; Marvel et al., 2018). Relatively large projected warming in the eastern tropical Pacific is trapped near the surface (shift from grey to red atmospheric temperature profile), decreasing the strength of the inversion locally. In turn, a decreased inversion strength combined with surface warming is projected to decrease the low-cloud cover, causing the cloud and lapse-rate feedbacks to become less negative in the future. Further details on data sources and processing are available in the chapter data table (Table 7.SM.14).

[END FIGURE 7.14 HERE]

The spatial pattern of SST changes since 1870 shows relatively little warming in key regions of less-negative radiative feedbacks, including the eastern tropical Pacific Ocean and Southern Ocean (Sections 7.4.4.1 and 7.4.4.2; Figure 7.14a; Chapter 2, Figure 2.11b). Cooling in these regions since 1980 has occurred along with an increase in the strength of the capping inversion in tropical descent regions, resulting in an observed increase in low-cloud cover over the tropical eastern Pacific (Zhou et al., 2016; Ceppi and Gregory, 2017; Fueglistaler and Silvers, 2021; Figure 7.14a). Thus, tropical low-cloud cover increased over recent decades even as global surface temperature increased, resulting in a negative low-cloud feedback which is at odds with the positive low-cloud feedback expected for the pattern of equilibrium warming under CO_2 forcing (Section 7.4.2.4; Figure 7.14b).

Andrews et al. (2018) analysed available CMIP5/6 ESM simulations (six in total) comparing effective feedback parameters diagnosed within atmosphere-only ESMs using prescribed historical SST and sea-ice concentration patterns with the equilibrium feedback parameters as estimated within coupled ESMs (using identical atmospheres) driven by abrupt 4×CO_2 forcing. The atmosphere-only ESMs show pronounced multi-decadal variations in their effective feedback parameters over the last century, with a trend toward strongly negative values since about 1980 owing primarily to negative shortwave cloud feedbacks driven by warming in the western equatorial Pacific Ocean and cooling in the eastern equatorial Pacific Ocean (Zhou et al., 2016; Andrews et al., 2018; Marvel et al., 2018; Dong et al., 2019). Yet, all six models show a less-negative net feedback parameter under *abrupt4xCO2* than for the historical period (based on regression since 1870 following Andrews et al., 2018). The average change in net feedback parameter between the historical period and the equilibrium response to CO_2 forcing, denoted here as α', for these simulations is α' = +0.6 W m^{-2} °C^{-1} (+0.3 to +1.0 W m^{-2} °C^{-1} range across models) (Figure 7.15b). These feedback parameter changes imply that the value of ECS may be substantially larger than that inferred from the historical record (Section 7.5.2.1). These findings can be understood from the fact that, due to a combination of internal variability and transient response to forcing (Section 7.4.4.2), historical sea-surface warming has been relatively large in regions of tropical ascent (Figure 7.14a), leading to an anomalously large net negative radiative feedback; however, future warming is expected to be largest in tropical descent regions, such as the eastern equatorial Pacific, and at high latitudes (Sections 7.4.4.1 and 7.4.4.2; Figure 7.14b), leading to a less-negative net radiative feedback and higher ECS.

A similar behaviour is seen within transient simulations of coupled ESMs, which project SST warming patterns that are initially characterised by relatively large warming rates in the western equatorial Pacific Ocean on decadal timescales and relatively large warming in the eastern equatorial Pacific and Southern Ocean on centennial timescales (Andrews et al., 2015; Proistosescu and Huybers, 2017; Dong et al., 2020). Recent studies based on simulations of 1% yr^{-1} CO_2 increase (*1pctCO2*) or *abrupt4xCO2* as analogues for historical warming suggest characteristic values of α' = +0.05 W m^{-2} °C^{-1} (–0.2 to +0.3 W m^{-2} °C^{-1} range across models) based on CMIP5 and CMIP6 ESMs (Armour 2017, Lewis and Curry 2018, Dong et al. 2020). Using historical simulations of one CMIP6 ESM (HadGEM3-GC3.1-LL), Andrews et al., (2019) find an average feedback parameter change of α' = +0.2 W m^{-2} °C^{-1}(–0.2 to +0.6 W m^{-2} °C^{-1} range across four ensemble members). Using historical simulations from another CMIP6 ESM (GFDL CM4.0), Winton et al.

ACCEPTED VERSION SUBJECT TO FINAL EDITING

(2020) find an average feedback parameter change of α' = +1.5 W m^{-2} °C^{-1}(+1.2 to +1.7 W m^{-2} °C^{-1} range across three ensemble members). This value is larger than the α' = +0.7 W m^{-2} °C^{-1} within GFDL CM4.0 for historical CO_2 forcing only, suggesting that the value of α' may depend on historical non-CO_2 forcings such as those associated with tropospheric and stratospheric aerosols (Marvel et al., 2016; Gregory et al., 2020; Winton et al., 2020).

The magnitude of the net feedback parameter change α' found within coupled CMIP5 and CMIP6 ESMs is generally smaller than that found when prescribing observed warming patterns within atmosphere-only ESMs (Andrews et al., 2018; Figure 7.15). This arises from the fact that the forced spatial pattern of warming within transient simulations of most coupled ESMs are distinct from observed warming patterns over the historical record in key regions such as the equatorial Pacific Ocean and Southern Ocean (Sections 7.4.4.1 and 7.4.4.2), while being more similar to the equilibrium pattern simulated under *abrupt4xCO2*. However, historical simulations with HadGEM3-GC3.1-LL (Andrews et al., 2019) and GFDL CM4.0 (Winton et al., 2020) show substantial spread in the value of α' across ensemble members, indicating a potentially important role for internal variability in setting the magnitude of the pattern effect over the historical period. Using the 100-member historical simulation ensemble of MPI- ESM1.1, Dessler et al. (2018) find that internal climate variability alone results in a 0.5 W m^{-2} °C^{-1} spread in the historical effective feedback parameter, and thus also in the value of α'. Estimates of α' using prescribed historical warming patterns provide a more realistic representation of the historical pattern effect because they account for the net effect of the transient response to historical forcing and internal variability in the observed record (Andrews et al., 2018).

The magnitude of α', as quantified by ESMs, depends on the accuracy of both the projected patterns of SST and sea-ice concentration changes in response to CO_2 forcing and the radiative response to those patterns (Andrews et al., 2018). Model biases that affect the long-term warming pattern (e.g., SST and relative humidity biases in the equatorial Pacific cold tongue as suggested by Seager et al. (2019)) will affect the value of α'. The value of α' also depends on the accuracy of the historical SST and sea-ice concentration conditions prescribed within atmosphere-only versions of ESMs to quantify the historical radiative feedback (Figure 7.15b). Historical SSTs are particularly uncertain for the early portion of the historical record (Chapter 2, Section 2.3.1), and there are few constraints on sea-ice concentration prior to the satellite era. Using alternative SST datasets, Andrews et al. (2018) found little change in the value of α' within two models (HadGEM3 and HadAM3), while Lewis and Mauritsen (2020) found a smaller value of α' within two other models (ECHAM6.3 and CAM5). The sensitivity of results to the choice of dataset represents a major source of uncertainty in the quantification of the historical pattern effect using atmosphere-only ESMs that has yet to be systematically explored, but the preliminary findings of Lewis and Mauritsen (2020) and Fueglistaler and Silvers (2021) suggest that α' could be smaller than the values reported in Andrews et al. (2018).

[START FIGURE 7.15 HERE]

Figure 7.15: Relationship between *historical* and *abrupt4xCO2* net radiative feedbacks in ESMs. (a) Radiative feedbacks in CMIP6 ESMs estimated under historical forcing (values for GFDL CM4.0 and HadGEM3-CG3.1-LL from Winton et al. (2020) and Andrews et al. (2019), respectively); horizontal lines show the range across ensemble members. The other points show effective feedback values for 29 ESMs estimated using regression over the first 50 years of *abrupt4xCO2* simulations as an analogue for historical warming (Dong et al., 2020). (b) Historical radiative feedbacks estimated from atmosphere-only ESMs with prescribed observed sea-surface temperature and sea-ice concentration changes (Andrews et al. 2018) based on a linear regression of global TOA radiation against global near-surface air temperature over the period 1870–2010 (pattern of warming similar to Figure 7.14a) and compared with equilibrium feedbacks in a *abrupt4xCO2* simulations of coupled versions of the same ESMs (pattern of warming similar to Figure 7.14b). In all cases, the equilibrium feedback magnitudes are estimated as CO_2 ERF divided by ECS where ECS is derived from regression over years 1–150 of *abrupt4xCO2* simulations (Box 7.1); similar results are found if the equilibrium feedback is estimated directly from the slope of the linear regression. Further details on data sources and processing are available in the chapter data table (Table 7.SM.14).

ACCEPTED VERSION SUBJECT TO FINAL EDITING

[END FIGURE 7.15 HERE]

While there are not yet direct observational constraints on the magnitude of the pattern effect, satellite measurements of variations in TOA radiative fluxes show strong co-variation with changing patterns of SSTs, with a strong dependence on SST changes in regions of deep convective ascent (e.g., in the western Pacific warm pool) (Loeb et al., 2018b; Fueglistaler, 2019). Cloud and TOA radiation responses to observed warming patterns in atmospheric models have been found to compare favourably with those observed by satellite (Zhou et al., 2016; Loeb et al., 2020; Section 7.2.2.1; Figure 7.3). This observational and modelling evidence indicates the potential for a strong pattern effect in nature that will only be negligible if the observed pattern of warming since pre-industrial levels persists to equilibrium – an improbable scenario given that Earth is in a relatively early phase of transient warming and that reaching equilibrium would take multiple millennia (Li et al., 2013a). Moreover, paleoclimate proxies, ESM simulations, and process understanding indicate that strong warming in the eastern equatorial Pacific Ocean (with *medium confidence*) and Southern Ocean (with *high confidence*) will emerge on centennial timescales as the response to CO_2 forcing dominates temperature changes in these regions (Sections 7.4.4.1; 7.4.4.2; Chapter 9, Section 9.2.1). However, there is *low confidence* that these features, which have been largely absent over the historical record, will emerge this century (Sections 7.4.4.1; 7.4.4.2; Chapter 9, Section 9.2.1). This leads to *high confidence* that radiative feedbacks will become less negative as the CO_2-forced pattern of surface warming emerges ($\alpha' > 0$ W m^{-2} °C^{-1}), but *low confidence* that these feedback changes will be realized this century. There is also substantial uncertainty in the magnitude of the net radiative feedback change between the present warming pattern and the projected equilibrium warming pattern in response to CO_2 forcing owing to the fact that its quantification currently relies solely on ESM results and is subject to uncertainties in historical SST patterns. Thus, based on the pattern of warming since 1870, α' is estimated to be in the range 0.0 to 1.0 W m^{-2} °C^{-1} but with a *low confidence* in the upper end of this range. A value of $\alpha' = +0.5 \pm 0.5$ W m^{-2} °C^{-1} is used to represent this range in Box 7.2 and Section 7.5.2, which respectively assess the implications of changing radiative feedbacks for Earth's energy imbalance and estimates of ECS based on the instrumental record. The value of α' is larger if quantified based on the observed pattern of warming since 1980 (Chapter 2, Figure 2.11b) which is more distinct from the equilibrium warming pattern expected under CO_2 forcing (similar to CMIP6 projections shown in Figure 7.12a) (Andrews et al., 2018) (*high confidence*).

7.5 Estimates of ECS and TCR

Equilibrium climate sensitivity (ECS) and transient climate response (TCR) are metrics of the global surface air temperature (GSAT) response to forcing, as defined in Section 7.1; Box 7.1. ECS is the magnitude of the long-term GSAT increase in response to a doubling of atmospheric CO_2 concentration after the planetary energy budget is balanced, though leaving out feedbacks associated with ice sheets; whereas the TCR is the magnitude of GSAT increase at year 70 when CO_2 concentration is doubled in a 1% yr^{-1} increase scenario. Both are idealised quantities, but can be inferred from paleoclimate or observational records or estimated directly using climate simulations, and are strongly correlated with the climate response in realistic future projections (Grose et al., 2018; Chapter 4, Section 4.3.4; Section 7.5.7).

TCR is always smaller than ECS because ocean heat uptake acts to reduce the rate of surface warming. Yet, TCR is related with ECS across CMIP5 and CMIP6 models (Grose et al., 2018; Flynn and Mauritsen, 2020) as expected since TCR and ECS are inherently measures of climate response to forcing; both depend on effective radiative forcing (ERF) and the net feedback parameter, α. The relationship between TCR and ECS is, however, non-linear and becomes more so for higher ECS values (Hansen et al., 1985; Knutti et al., 2005; Millar et al., 2015; Flynn and Mauritsen, 2020; Tsutsui, 2020) owing to ocean heat uptake processes and surface temperature pattern effects temporarily reducing the rate of surface warming. When α is small in magnitude, and correspondingly ECS is large (recall that ECS is inversely proportional to α), these temporary effects are increasingly important in reducing the ratio of TCR to ECS.

ACCEPTED VERSION SUBJECT TO FINAL EDITING

Before the AR6, the assessment of ECS relied on either CO_2-doubling experiments using global atmospheric models coupled with mixed-layer ocean or standardized CO_2-quadrupling (*abrupt4xCO2*) experiments using fully coupled ocean-atmosphere models or Earth system models (ESMs). The TCR has similarly been diagnosed from ESMs in which the CO_2 concentration is increased at 1% yr^{-1} (*1pctCO2*, an approximately linear increase in ERF over time) and is in practice estimated as the average over a 20–year period centred at the time of atmospheric CO_2 doubling, i.e., year 70. In the AR6, the assessments of ECS and TCR are made based on multiple lines of evidence, with ESMs representing only one of several sources of information. The constraints on these climate metrics are based on radiative forcing and climate feedbacks assessed from process understanding (Section 7.5.1), climate change and variability seen within the instrumental record (Section 7.5.2), paleoclimate evidence (Section 7.5.3), emergent constraints (Section 7.5.4), and a synthesis of all lines of evidence (Section 7.5.5). In AR5, these lines of evidence were not explicitly combined in the assessment of climate sensitivity, but as demonstrated by Sherwood et al.（2020) their combination narrows the uncertainty ranges of ECS compared to that assessed in AR5. ECS values found in CMIP6 models, some of which exhibit values higher than 5 °C (Meehl et al., 2020; Zelinka et al., 2020), are discussed in relation to the AR6 assessment in section 7.5.6.

7.5.1 Estimates of ECS and TCR based on process understanding

This section assesses the estimates of ECS and TCR based on process understanding of the ERF due to a doubling of CO_2 concentration and the net climate feedback (Sections 7.3.2 and 7.4.2). This process-based assessment is made in Section 7.5.1.1 and applied to TCR in Section 7.5.1.2.

7.5.1.1 ECS estimated using process-based assessments of the forcing and feedbacks

The process-based assessment is based on the global energy budget equation (Box 7.1, Equation 7.1), where the ERF (ΔF) is set equal to the effective radiative forcing due to a doubling of CO_2 concentration (denoted as $\Delta F_{2\times CO2}$) and the climate state reaches a new equilibrium, i.e., Earth's energy imbalance averages to zero ($\Delta N = 0$). ECS is calculated as the ratio between the ERF and the net feedback parameter: ECS = $-\Delta F_{2\times CO2}/\alpha$. Estimates of $\Delta F_{2\times CO2}$ and α are obtained separately based on understanding of the key processes that determine each of these quantities. Specifically, $\Delta F_{2\times CO2}$ is estimated based on instantaneous radiative forcing that can be accurately obtained using line-by-line calculations, to which uncertainty due to adjustments are added (Section 7.3.2). The range of α is derived by aggregating estimates of individual climate feedbacks based not only on ESMs but also on theory, observations, and high-resolution process modelling (Section 7.4.2).

The effective radiative forcing of CO_2 doubling is assessed to be $\Delta F_{2\times CO2} = 3.93 \pm 0.47$ W m^{-2} (Section 7.3.2.1), while the net feedback parameter is assessed to be $\alpha = -1.16 \pm 0.40$ W m^{-2} °C^{-1} (Section 7.4.2.7, Table 7.10), where the ranges indicate one standard deviation. These values are slightly different from those directly calculated from ESMs because more information is used to assess them, as explained above. Assuming $\Delta F_{2\times CO2}$ and α each follow an independent normal distribution, the uncertainty range of ECS can be obtained by substituting the respective probability density function into the expression of ECS (red curved bar in Figure 7.16). Since α is in the denominator, the normal distribution leads to a long tail in ECS toward high values, indicating the large effect of uncertainty in α in estimating the likelihood of a high ECS (Roe and Baker, 2007; Knutti and Hegerl, 2008).

The wide range of the process-based ECS estimate is not due solely to uncertainty in the estimates of $\Delta F_{2\times CO2}$ and α, but is partly explained by the assumption that $\Delta F_{2\times CO2}$ and α are independent in this approach. In CMIP5 and CMIP6 ensembles, $\Delta F_{2\times CO2}$ and α are negatively correlated when they are calculated using linear regression in *abrupt4xCO2* simulations ($r^2 = 0.34$) (Andrews et al., 2012; Webb et al., 2013; Zelinka et al., 2020). The negative correlation leads to compensation between the inter-model spreads of these quantities, thereby reducing the ECS range estimated directly from the models. If the process-based ECS distribution is reconstructed from probability distributions of $\Delta F_{2\times CO2}$ and α assuming that they are

ACCEPTED VERSION SUBJECT TO FINAL EDITING

correlated as in CMIP model ensembles, the range of ECS will be narrower by 14% (pink curved bar in Figure 7.16). If, however, the covariance between $\Delta F_{2\times CO2}$ and α is not adopted, there is no change in the mean, but the wide range still applies.

A significant correlation between $\Delta F_{2\times CO2}$ and α also occurs when the two parameters are estimated separately from AGCM fixed-SST experiments (Section 7.3.1) or fixed CO_2 concentration experiments (Ringer et al., 2014; Chung and Soden, 2018; Section 7.4.1). Hence the relationship is not expected to be an artefact of calculating them using linear regression in *abrupt4xCO2* simulations. A possible physical cause of the correlation may be a compensation between the cloud adjustment and the cloud feedback over the tropical ocean (Ringer et al., 2014; Chung and Soden, 2018). It has been shown that the change in the hydrological cycle is a controlling factor for the low-cloud adjustment (Dinh and Fueglistaler, 2019) and for the low-cloud feedback (Watanabe et al., 2018), and therefore the responses of these clouds to the direct CO_2 radiative forcing and to the surface warming may not be independent. However, robust physical mechanisms are not yet established, and furthermore, the process-based assessment of the tropical low-cloud feedback is only indirectly based on ESMs given that physical processes which control the low clouds are not sufficiently well-simulated in models (Section 7.4.2.4). For these reasons, the co-dependency between $\Delta F_{2\times CO2}$ and α is assessed to have *low confidence* and, therefore, the more conservative assumption that they are independent for the process-based assessment of ECS is retained.

In summary, the ECS based on the assessed values of $\Delta F_{2\times CO2}$ and α is assessed to have a median value of 3.4°C with a *likely* range of 2.5–5.1 °C and *very likely* range of 2.1–7.7 °C. To this assessed range of ECS, the contribution of uncertainty in α is approximately three times as large as the contribution of uncertainty in $\Delta F_{2\times CO2}$.

[START FIGURE 7.16 HERE]

Figure 7.16: Probability distributions of ERF to CO_2 doubling ($\Delta F_{2\times CO2}$, top) and the net climate feedback (α, right), derived from process-based assessments in Sections 7.3.2 and 7.4.2. Middle panel shows the joint probability density function calculated on a two-dimensional plane of $\Delta F_{2\times CO2}$ and α (red), on which the 90% range shown by an ellipse is imposed to the background theoretical values of ECS (colour shading). The white dot, thick and thin curves in the ellipse represent the mean, *likely* and *very likely* ranges of ECS. An alternative estimation of the ECS range (pink) is calculated by assuming that $\Delta F_{2\times CO2}$ and α have a covariance. The assumption about the co-dependence between $\Delta F_{2\times CO2}$ and α does not alter the mean estimate of ECS but affects its uncertainty. Further details on data sources and processing are available in the chapter data table (Table 7.SM.14).

[END FIGURE 7.16 HERE]

7.5.1.2 Emulating process-based ECS to TCR

ECS estimated using the ERF due to a doubling of CO_2 concentration and the net feedback parameter (ECS = $-\Delta F_{2\times CO2}/\alpha$) can be translated into the TCR so that both climate sensitivity metrics provide consistent information about the climate response to forcing. Here a two-layer energy budget emulator is used to transfer the process-based assessment of forcing, feedback, efficacy and heat uptake to TCR (Supplementary Material 7.SM.2.1, Cross-Chapter Box 7.1). The emulator can reproduce the transient surface temperature evolution in ESMs under *1pctCO2* simulations and other climate change scenarios, despite the very low number of degrees of freedom (Held et al., 2010; Geoffroy et al., 2012, 2013a; Palmer et al., 2018). Using this model with parameters given from assessments in the previous sections, TCR is assessed based on the process-based understanding.

In the two-layer energy balance emulator, additional parameters are introduced: heat capacities of the upper and deep ocean, heat uptake efficiency (γ), and the so-called efficacy parameter (ε) that represents the dependence of radiative feedbacks and heat uptake on the evolving SST pattern under CO_2 forcing alone (Section 7.4.4). In the real world, natural internal variability and aerosol radiative forcing also affect the

ACCEPTED VERSION SUBJECT TO FINAL EDITING

efficacy parameter, but these effects are excluded for the current discussion.

The analytical solution of the energy balance emulator reveals that the global surface temperature change to abrupt increase of the atmospheric CO_2 concentration is expressed by a combination of a fast adjustment of the surface components of the climate system and a slow response of the deep ocean, with time scales of several years and several centuries, respectively (grey curves in Figure 7.17). The equilibrium response of upper ocean temperature, approximating SST and the surface air temperature response, depends, by definition, only on the radiative forcing and the net feedback parameter. Uncertainty in α dominates (80–90%) the corresponding uncertainty range for ECS in CMIP5 models (Vial et al., 2013), and also an increase of ECS in CMIP6 models (Section 7.5.5) is attributed by about 60–80% to a change in α (Zelinka et al., 2020). For the range of TCR, the contribution from uncertainty in α is reduced to 50–60% while uncertainty in $\Delta F_{2\times CO2}$ becomes relatively more important (Geoffroy et al., 2012; Lutsko and Popp, 2019). TCR reflects the fast response occurring approximately during the first 20 years in the *abrupt4xCO2* simulation (Held et al., 2010), but the fast response is not independent of the slow response because there is a nonlinear co-dependence between them (Andrews et al., 2015). The nonlinear relationship between ECS and TCR indicates that the probability of high TCR is not very sensitive to changes in the probability of high ECS (Meehl et al., 2020).

Considering an idealized time evolution of ERF (1% increase per year until CO_2 doubling and held fixed afterwards, see Figure 7.17a), the TCR defined by the surface temperature response at year 70 is derived by substituting the process-based ECS into the analytical solution of the emulator (Figure 7.17b, see also Supplementary Material 7.SM.2.1). When additional parameters in the emulator are prescribed by using CMIP6 multi-model mean values of those estimates (Smith et al., 2020a), this calculation translates the range of ECS in Section 7.5.2.1 to the range of TCR. The transient temperature response, in reality, varies with different estimates of the ocean heat uptake efficiency (γ) and efficacy (ε). When the emulator was calibrated to the transient responses in CMIP5 models, it shows that uncertainty in heat capacities is negligible and differences in γ and ε explain 10–20% of the inter-model spread of TCR among GCMs (Geoffroy et al., 2012). Specifically, their product, $\kappa = \gamma\varepsilon$, appearing in a simplified form of the solution, i.e., $TCR \cong -\Delta F_{2\times CO2}/(\alpha - \kappa)$, gives a single parameter quantifying the damping effects of heat uptake (Jiménez-de-la-Cuesta and Mauritsen, 2019). This parameter is positive and acts to slow down the temperature response in a similar manner to the 'pattern effect' (Sections 7.4.4.3 and 7.5.2.1). The ocean heat uptake in nature is controlled by multiple processes associated with advection and mixing (Exarchou et al., 2014; Kostov et al., 2014; Kuhlbrodt et al., 2015) but is simplified to be represented by a single term of heat exchange between the upper- and deep-ocean in the emulator. Therefore, it is challenging to constrain γ and ε from process-based understanding (Section 7.5.2). Because the estimated values are only weakly correlated across models, the mean value and one standard deviation of κ are calculated as $\kappa = 0.84 \pm 0.38$ W m^{-2} °C^{-1} (one standard deviation) by ignoring their covariance (the mean value is very similar to that used for Chapter 4, Box 4.1, Figure 1) (see Supplementary Material 7.SM.2.1). By incorporating this inter-model spread in κ, the range of TCR is widened by about 10% (blue bar in Figure 7.17b). Yet, the dominant contribution to the uncertainty range of TCR arises from the net feedback parameter α, consistent with analyses of CMIP6 models (Williams et al., 2020), and this assessment remains unchanged from AR5 stating that uncertainty in ocean heat uptake is of secondary importance.

In summary, the process-based estimate of TCR is assessed to have the central value of 2.0°C with the *likely* range from 1.6 to 2.7°C and the *very likely* range from 1.3 to 3.1°C (*high confidence*). The upper bound of the assessed range was slightly reduced from AR5 but can be further constrained using multiple lines of evidence (Section 7.5.5).

[START FIGURE 7.17 HERE]

Figure 7.17: (a) Time evolution of the effective radiative forcing (ERF) to the CO_2 concentration increased by 1% per year until the year 70 (equal to the time of doubling) and kept fixed afterwards (white line). The *likely* and *very likely* ranges of ERF indicated by light and dark orange have been assessed in Section 7.3.2.1. (b) Surface temperature response to the CO_2 forcing calculated using the emulator with a given

ACCEPTED VERSION SUBJECT TO FINAL EDITING

value of ECS, considering uncertainty in $\Delta F_{2\times CO2}$, α, and κ associated with the ocean heat uptake and efficacy (white line). The *likely* and *very likely* ranges are indicated by cyan and blue. For comparison, the temperature response to abrupt doubling of the CO_2 concentration is displayed by a grey curve. The mean, *likely* and *very likely* ranges of ECS and TCR are shown at the right (the values of TCR also presented in the panel). Further details on data sources and processing are available in the chapter data table (Table 7.SM.14).

[END FIGURE 7.17 HERE]

7.5.2 Estimates of ECS and TCR based on the instrumental record

This section assesses the estimates of ECS and TCR based on the instrumental record of climate change and variability with an emphasis on new evidence since AR5. Several lines of evidence are assessed including the global energy budget (Section 7.5.2.1), the use of simple climate models evaluated against the historical temperature record (Section 7.5.2.2), and internal variability in global temperature and TOA radiation (Section 7.5.2.3). Section 7.5.2.4 provides an overall assessment of TCR and ECS based on these lines of evidence from the instrumental record.

7.5.2.1 Estimates of ECS and TCR based on the global energy budget

The GSAT change from 1850–1900 to 2006–2019 is estimated to be 1.03 [0.86 to 1.18] °C (Cross-chapter Box 2.3). Together with estimates of Earth's energy imbalance (Section 7.2.2) and the global ERF that has driven the observed warming (Section 7.3), the instrumental temperature record enables global energy budget estimates of ECS and TCR. While energy budget estimates use instrumental data, they are not based purely on observations. A conceptual model typically based on the global-mean forcing and response energy budget framework (Box 7.1) is needed to relate ECS and TCR to the estimates of global warming, ERF and Earth's energy imbalance (Forster, 2016; Knutti et al., 2017). Moreover, ESM simulations partly inform estimates of the historical ERF (Section 7.3) as well as Earth's energy imbalance in the 1850-1900 climate (the period against which changes are measured) (Forster, 2016; Lewis and Curry, 2018). ESMs are also used to estimate uncertainty due the internal climate variability that may have contributed to observed changes in temperature and energy imbalance (e.g., Palmer and McNeall, 2014; Sherwood et al., 2020). Research since AR5 has shown that global energy budget estimates of ECS may be biased low when they do not take into account how radiative feedbacks depend on the spatial pattern of surface warming (Section 7.4.4.3) or when they do not incorporate improvements in the estimation of global surface temperature trends which take better account of data-sparse regions and are more consistent in their treatment of surface temperature data (Chapter 2, Section 2.3.1). Together with updated estimates of global ERF and Earth's energy imbalance, these advances since AR5 have helped to reconcile energy budget estimates of ECS with estimates of ECS from other lines of evidence.

The traditional global-mean forcing and response energy budget framework (Gregory et al., 2002; Section 7.4.1; Box 7.1) relates the difference between the ERF (ΔF) and the radiative response to observed global warming ($\alpha\Delta T$) to the Earth's energy imbalance (ΔN): $\Delta N = \alpha\Delta T + \Delta F$. Given the relationship ECS = $-\Delta F_{2\times CO2}/\alpha$, where $\Delta F_{2\times CO2}$ is the ERF from CO_2 doubling, ECS can be estimated from historical estimates of ΔT, ΔF, ΔN and $\Delta F_{2\times CO2}$: $ECS = \Delta F_{2\times CO2}\,\Delta T/(\Delta F - \Delta N)$. Since TCR is defined as the temperature change at the time of CO_2 doubling under an idealized 1% yr^{-1} CO_2 increase, it can be inferred from the historical record as: $TCR = \Delta F_{2\times CO2}\,\Delta T/\Delta F$, under the assumption that radiative forcing increases quickly compared to the adjustment timescales of the deep ocean, but slowly enough and over a sufficiently long time that the upper ocean is adjusted, so that ΔT and ΔN increases approximately in proportion to ΔF. Because ΔN is positive, TCR is always smaller than ECS, reflecting weaker transient warming than equilibrium warming. TCR is better constrained than ECS owing to the fact that the denominator of TCR, without the quantity ΔN, is more certain and further from zero than is the denominator of ECS. The upper bounds of both TCR and ECS estimated from historical warming are inherently less certain than their lower bounds because ΔF is uncertain and in the denominator.

ACCEPTED VERSION SUBJECT TO FINAL EDITING

The traditional energy budget framework lacks a representation of how radiative feedbacks depend on the spatial pattern of warming. Thus, studies employing this framework (Otto et al., 2013; Lewis and Curry, 2015, 2018; Forster, 2016) implicitly assume that the net radiative feedback has a constant magnitude, producing an estimate of the effective ECS (defined as the value of ECS that would occur if α does not change from its current value) rather than of the true ECS. As summarized in Section 7.4.4.3, there are now multiple lines of evidence providing *high confidence* that the net radiative feedback will become less negative as the warming pattern evolves in the future (the pattern effect). This arises because historical warming has been relatively larger in key negative feedback regions (e.g., western tropical Pacific Ocean) and relatively smaller in key positive feedback regions (e.g., eastern tropical Pacific Ocean and Southern Ocean) than is projected in the near-equilibrium response to CO_2 forcing (Held et al., 2010; Proistosescu and Huybers, 2017; Dong et al., 2019; Section 7.4.4.3), implying that the true ECS will be larger than the effective ECS inferred from historical warming. This section first assesses energy budget constraints on TCR and the effective ECS based on updated estimates of historical warming, ERF, and Earth's energy imbalance. It then assesses what these energy budget constraints imply for values of ECS once the pattern effect is accounted for.

Energy budget estimates of TCR and ECS have evolved in the literature over recent decades. Prior to AR4, the global energy budget provided relatively weak constraints, primarily due to large uncertainty in the tropospheric aerosol forcing, giving ranges of the effective ECS that typically included values above 10°C (Forster, 2016; Knutti et al., 2017). Revised estimates of aerosol forcing together with a larger greenhouse-gas forcing by the time of AR5 led to an estimate of ΔF that was more positive and with reduced uncertainty relative to AR4. Using energy budget estimates and radiative forcing estimates updated to 2009, Otto et al. (2013) estimated that TCR was 1.3 [0.9 to 2.0] °C, and that the effective ECS was 2.0 [1.2 to 3.9] °C. This AR5-based energy budget estimate of ECS was lower than estimates based on other lines of evidence, leading AR5 to expand the assessed *likely* range of ECS to include lower values relative to AR4. Studies since AR5 using similar global energy budget methods have produced similar or slightly narrower ranges for TCR and effective ECS (Forster, 2016; Knutti et al., 2017).

Energy budget estimates of TCR and ECS assessed here are based on improved observations and understanding of global surface temperature trends extended to the year 2020 (Chapter 2, Section 2.3.1), revised estimates of Earth's energy imbalance (Section 7.2), and revised estimates of ERF (Section 7.3). Accurate, in situ-based estimates of Earth's energy imbalance can be made from around 2006 based on near-global ocean temperature observations from the ARGO array of autonomous profiling floats (Chapter 2 Section 2.3, Section 7.2). Over the period 2006 to 2018 the Earth's energy imbalance is estimated to be 0.79 ± 0.27 W m^{-2} (Section 7.2) and it is assumed that this value is also representative for the period 2006 to 2019. Anomalies are taken with respect to the baseline period 1850-1900, although other baselines could be chosen to avoid major volcanic activity (Otto et al., 2013; Lewis and Curry, 2018). Several lines of evidence, including ESM simulations (Lewis and Curry, 2015), energy balance modelling (Armour, 2017), inferred ocean warming given observed SSTs using ocean models (Gebbie and Huybers, 2019; Zanna et al., 2019), and ocean warming reconstructed from noble gas thermometry (Baggenstos et al., 2019) suggest a 1850-1900 Earth energy imbalance of 0.2 ± 0.2 W m^{-2}. Combined with estimates of internal variability in Earth's energy imbalance, calculated using periods of equivalent lengths of years as used in unforced ESM simulations (Palmer and McNeall, 2014; Sherwood et al., 2020b), the anomalous energy imbalance between 1850–1900 and 2006–2019 is estimated to be $\Delta N = 0.59 \pm 0.35$ W m^{-2}. GSAT change between 1850–1900 and 2006–2019 is estimated to be $\Delta T = 1.03°C \pm 0.20$ °C (Chapter 2, Cross-Chapter Box 2.3; Box 7.2) after accounting for internal temperature variability derived from unforced ESM simulations (Sherwood et al., 2020b). The ERF change between 1850–1900 and 2006–2019 is estimated to be ΔF = 2.20 [1.53 to 2.91] W m^{-2} (Section 7.3.5) and the ERF for a doubling of CO_2 is estimated to be $\Delta F_{2\times CO2} = 3.93 \pm 0.47$ W m^{-2} (Section 7.3.2). Employing these values within the traditional global energy balance framework described above (following the methods of Otto et al. (2013) and accounting for correlated uncertainties between ΔF and $\Delta F_{2\times CO2}$) produces a TCR of 1.9 [1.3 to 2.7]°C and an effective ECS of 2.5 [1.6–4.8] °C. These TCR and effective ECS values are higher than those in the recent literature (Otto et al., 2013; Lewis and Curry, 2015, 2018) but are comparable to those of Sherwood et al. (2020) who also used updated estimates of observed warming, Earth's energy imbalance, and ERF.

ACCEPTED VERSION SUBJECT TO FINAL EDITING

The trend estimation method applied to global surface temperature affects derived values of ECS and TCR from the historical record. In this Report, the effective ECS is inferred from estimates that use global coverage of GSAT to estimate the surface temperature trends. The GSAT trend is assessed to have the same best estimate as the observed global mean surface temperature (GMST), although the GSAT trend is assessed to have larger uncertainty (see Cross-Chapter Box 2.3). Many previous studies have relied on HadCRUT4 GMST estimates that used the blended observations and did not interpolate over regions of incomplete observational coverage such as the Arctic. As a result, the ECS and TCR derived from these studies has smaller ECS and TCR values than those derived from model-inferred estimates (Richardson et al., 2016, 2018a). The energy budget studies assessing ECS in AR5 employed HadCRUT4 or similar measures of GMST trends. As other lines of evidence in that report used GSAT trends, this could partly explain why AR5-based energy budget estimates of ECS were lower than those estimated from other lines of evidence, adding to the overall disparity in Collins et al. (2013a). In this report, GSAT is chosen as the standard measure of global surface temperature to aid comparison with previous model and process-based estimates of ECS, TCR and climate feedbacks (see Cross-Chapter Box 2.3).

The traditional energy budget framework has been evaluated within ESM simulations by comparing the effective ECS estimated under historical forcing with the ECS estimated using regression methods (Box 7.1) under *abrupt4xCO2* (Andrews et al., 2019; Winton et al., 2020). For one CMIP6 model (GFDL-CM4.0), the value of effective ECS derived from historical energy budget constraints is 1.8°C while ECS is estimated to be 5.0°C (Winton et al., 2020). For another model (HadGEM3-GC3.1-LL) the effective ECS derived from historical energy budget constraints is 4.1°C (average of four ensemble members) while ECS is estimated to be 5.5°C (Andrews et al., 2019). These modelling results suggest that the effective ECS under historical forcing could be lower than the true ECS owing to differences in radiative feedbacks induced by the distinct patterns of historical and equilibrium warming (Section 7.4.4.3). Using GFDL-CM4, Winton et al. (2020) also find that the value of TCR estimated from energy budget constraints within a historical simulation (1.3°C) is substantially lower than the true value of TCR (2.1°C) diagnosed within a *1pctCO₂* simulation owing to a combination of the pattern effect and differences in the efficiency of ocean heat uptake between historical and *1pctCO₂* forcing. This section next considers how the true ECS can be estimated from the historical energy budget by accounting for the pattern effect. However, owing to limited evidence this section does not attempt to account for these effects in estimates of TCR.

Research since AR5 has introduced extensions to the traditional energy budget framework that account for the feedback dependence on temperature patterns by allowing for multiple radiative feedbacks operating on different timescales (Armour et al., 2013; Geoffroy et al., 2013a; Armour, 2017; Proistosescu and Huybers, 2017; Goodwin, 2018; Rohrschneider et al., 2019), by allowing feedbacks to vary with the spatial pattern or magnitude of ocean heat uptake (Winton et al., 2010; Rose et al., 2014; Rugenstein et al., 2016a), or by allowing feedbacks to vary with the type of radiative forcing agent (Kummer and Dessler, 2014; Shindell, 2014; Marvel et al., 2016; Winton et al., 2020). A direct way to account for the pattern effect is to use the relationship $ECS = \Delta F_{2\times CO2}/(-\alpha + \alpha')$, where $\alpha = (\Delta N - \Delta F)/\Delta T$ is the effective feedback parameter (Box 7.1) estimated from historical global energy budget changes and α' represents the change in the feedback parameter between the historical period and the equilibrium response to CO_2 forcing, which can be estimated using ESMs (Armour, 2017; Andrews et al., 2018, 2019; Lewis and Curry, 2018; Dong et al., 2020; Winton et al., 2020; Section 7.4.4.3).

The net radiative feedback change between the historical warming pattern and the projected equilibrium warming pattern in response to CO_2 forcing (α') is estimated to be in the range 0.0 to 1.0 W m^{-2} °C^{-1} (Figure 7.15). Using the value $\alpha' = +0.5 \pm 0.5$ W m^{-2} °C^{-1} to represent this range illustrates the effect of changing radiative feedbacks on estimates of ECS. While the effective ECS inferred from historical warming is 2.5 [1.6–4.8] °C , $ECS = \Delta F_{2\times CO2}/(-\alpha + \alpha')$ is 3.5 [1.7–13.8] °C. For comparison, values of α' derived from the response to historical and idealized CO_2 forcing within coupled climate models (Armour, 2017; Lewis and Curry, 2018; Andrews et al., 2019; Dong et al., 2020; Winton et al., 2020) can be approximated as $\alpha' = +0.1 \pm 0.3$ W m^{-2} °C^{-1} (Section 7.4.4.3), corresponding to a value of ECS of 2.7 [1.7–5.9] °C. In both cases, the low end of the ECS range is similar to that of the effective ECS inferred using the traditional energy balance model framework that assumes $\alpha' = 0$, reflecting a weak dependence on the value of α' when ECS is small

ACCEPTED VERSION SUBJECT TO FINAL EDITING

(Armour, 2017; Andrews et al., 2018); the low end of the ECS range is robust even in the hypothetical case that α' is slightly negative. However, the high end of the ECS range is substantially larger than that of the effective ECS and strongly dependent on the value of α'.

The values of ECS obtained from the techniques outlined above are all higher than those estimated from both AR5 and recently published estimates (Collins et al., 2013a; Otto et al., 2013; Lewis and Curry, 2015; Forster, 2016; Lewis and Curry, 2018). Four revisions made in this Report are responsible for this increase: (1) An upwards revision of historic global surface temperature trends from newly published trend estimates (Chapter 2, Section 2.3.1); (2) An 8% increase in the ERF for $\Delta F_{2\times CO2}$ (Section 7.3.2); (3) A more negative central estimate of aerosol ERF, which acts to reduce estimates of historical ERF trends; and (4) Accounting for the pattern effect in ECS estimates. Values of ECS provided here are similar to those based on the historical energy budget found in Sherwood et al. (2020), with small differences owing to methodological differences and the use of different estimates of observed warming, Earth's energy imbalance, and ERF.

Overall, there is *high confidence* that the true ECS is higher than the effective ECS as inferred from the historical global energy budget, but there is substantial uncertainty in how much higher because of *limited evidence* regarding how radiative feedbacks may change in the future. While several lines of evidence indicate that $\alpha' > 0$, the quantitative accuracy of feedback changes is not known at this time (Section 7.4.4.3). Global energy budget constraints thus provide *high confidence* in the lower bound of ECS which is not sensitive to the value of α': ECS is *extremely unlikely* to be less than 1.6°C. Estimates of α' that are informed by idealized CO_2 forcing simulations of coupled ESMs (Armour, 2017; Lewis and Curry, 2018; Andrews et al., 2019; Dong et al., 2020; Winton et al., 2020) indicate a median value of ECS of around 2.7°C while estimates of α' that are informed by observed historical sea surface temperature patterns (Andrews et al., 2018) indicate a median value of ECS of around 3.5°C. Owing to large uncertainties in future feedback changes, the historical energy budget currently provides little information about the upper end of the ECS range.

7.5.2.2 Estimates of ECS and TCR based on climate model emulators

Energy budget emulators are far less complex than comprehensive ESMs (see Chapter 1, Section 1.5.3 and Cross-Chapter Box 7.1). For example, an emulator could represent the atmosphere, ocean, and land using a small number of connected boxes (e.g., Goodwin, 2016), or it could represent the global mean climate using two connected ocean layers (e.g., Cross-Chapter Box 7.1, Supplementary Material 7.SM.2). The numerical efficiency of emulators means that they can be empirically constrained by observations: a large number of possible parameter values (e.g., feedback parameter, aerosol radiative forcing, and ocean diffusivity) are randomly drawn from prior distributions; forward integrations of the model are performed with these parameters and weighted against observations of surface or ocean warming, producing posterior estimates of quantities of interest such as TCR, ECS and aerosol forcing (see Section 7.3). Owing to their reduced complexity, emulators lack full representations of the spatial patterns of sea surface temperature and radiative responses to changes in those patterns (discussed in Section 7.4.4.3) and many represent the net feedback parameter using a constant value. The ranges of ECS reported by studies using emulators are thus interpreted here as representative of the effective ECS over the historical record rather than of the true ECS.

Improved estimates of ocean heat uptake over the past two decades (Section 7.2) have diminished the role of ocean diffusivity in driving uncertainty in ECS estimates, leaving the main trade-off between posterior ranges in ECS and aerosol radiative forcing (Forest, 2002; Knutti et al., 2002; Frame et al., 2005). AR5 (Bindoff et al., 2013) assessed a variety of estimates of ECS based on emulators and found that they were sensitive to the choice of prior parameter distributions and temperature datasets used, particularly for the upper end of the ECS range, though priors can be chosen to minimize the effect on results (e.g., Lewis, 2013). Emulators generally produced estimates of effective ECS between 1°C and 5°C and ranges of TCR between 0.9°C and 2.6°C. Padilla et al. (2011) use a simple global-average emulator with two timescales (see Supplementary Material 7.SM.2 and Section 7.5.1.2) to estimate a TCR of 1.6 [1.3 to 2.6] °C. Using the same model, Schwartz (2012) finds TCR in the range 0.9–1.9°C while Schwartz (2018) finds that an effective ECS of 1.7°C provides the best fit to the historical global surface temperature record while also

ACCEPTED VERSION SUBJECT TO FINAL EDITING

finding a median aerosol forcing that is smaller than that assessed in Section 7.3. Using an eight-box representation of the atmosphere–ocean–terrestrial system constrained by historical warming, Goodwin (2016) found an effective ECS of 2.4 [1.4 to 4.4] °C while Goodwin (2018) found effective ECS to be in the range 2–4.3°C when using a prior for ECS based on paleoclimate constraints.

Using an emulator comprised of northern and southern hemispheres and an upwelling-diffusive ocean (Aldrin et al., 2012), with surface temperature and ocean heat content datasets updated to 2014, Skeie et al. (2018) estimate a TCR of 1.4 [0.9 to 2.0] °C and a median effective ECS of 1.9 [1.2 to 3.1] °C. Using a similar emulator comprised of land and ocean regions and an upwelling-diffusive ocean, with global surface temperature and ocean heat content datasets through 2011, Johansson et al. (2015) find an effective ECS of 2.5 [2.0 to 3.2] °C. The estimate is found to be sensitive to the choice of dataset endpoint and the representation of internal variability meant to capture the El Niño–Southern Oscillation and Pacific Decadal Variability. Differences between these two studies arise, in part, from their different global surface temperature and ocean heat content datasets, different radiative forcing uncertainty ranges, different priors for model parameters, and different representations of internal variability. This leads to different estimates of effective ECS, with the median estimate of Skeie et al. (2018) lying below the 5% to 95% range of effective ECS from Johansson et al. (2015). Moreover, while the Skeie et al. (2018) emulator has a constant value of the net feedback parameter, the Johansson et al. (2015) emulator allows distinct radiative feedbacks for land and ocean, contributing to the different results.

The median estimates of TCR and effective ECS inferred from emulator studies generally lie within the 5% to 95% ranges of the those inferred from historical global energy budget constraints (1.3 to 2.7°C for TCR and 1.6 to 4.8°C for effective ECS). Their estimates would be consistent with still higher values of ECS when accounting for changes in radiative feedbacks as the spatial pattern of global warming evolves in the future (Section 7.5.2.1). Cross-Chapter Box 7.1 and references therein show that four very different physically-based emulators can be calibrated to match the assessed ranges of historical GSAT change, ERF, ECS and TCR from across the report. Therefore, the fact that the emulator effective ECS values estimated from previous studies tend to lie at the lower end of the range inferred from historical global energy budget constraints may reflect that the energy budget constraints in Section 7.5.2.1 use updated estimates of Earth's energy imbalance, GSAT trends and ERF, rather than any methodological differences between the lines of evidence. The 'emergent constraints' on ECS based on observations of climate variability used in conjunction with comprehensive ESMs are assessed in Section 7.5.4.1.

7.5.2.3 Estimates of ECS based on variability in Earth's top-of-atmosphere radiation budget

While continuous satellite measurements of TOA radiative fluxes (Figure 7.3) do not have sufficient accuracy to determine the absolute magnitude of Earth's energy imbalance (Section 7.2.1), they provide accurate estimates of its variations and trends since the year 2002 that agree well with estimates based on observed changes in global ocean heat content (Loeb et al., 2012; Johnson et al., 2016; Palmer, 2017). When combined with global surface temperature observations and simple models of global energy balance, satellite measurements of TOA radiation afford estimates of the net feedback parameter associated with recent climate variability (Tsushima and Manabe, 2013; Donohoe et al., 2014; Dessler and Forster, 2018). These feedback estimates, derived from the regression of TOA radiation on surface temperature variability, imply values of ECS that are broadly consistent with those from other lines of evidence (Forster, 2016; Knutti et al., 2017). A history of regression-based feedbacks and their uncertainties is summarized in (Bindoff et al., 2013; Forster, 2016; Knutti et al., 2017).

Research since AR5 has noted that regression-based feedback estimates depend on whether annual- or monthly-mean data are used and on the choice of lag employed in the regression, complicating their interpretation (Forster, 2016). The observed lead-lag relationship between global TOA radiation and global surface temperature, and its dependence on sampling period, is well replicated within unforced simulations of ESMs (Dessler, 2011; Proistosescu et al., 2018). These features arise because the regression between global TOA radiation and global surface temperature reflects a blend of different radiative feedback processes associated with several distinct modes of variability acting on different time scales (Annex IV),

ACCEPTED VERSION SUBJECT TO FINAL EDITING

such as monthly atmospheric variability and inter-annual El Niño–Southern Oscillation (ENSO) variability (Lutsko and Takahashi, 2018; Proistosescu et al., 2018). Regression-based feedbacks thus provide estimates of the radiative feedbacks that are associated with internal climate variability (e.g., Brown et al., 2014), and do not provide a direct estimate of ECS (*high confidence*). Moreover, variations in global surface temperature that do not directly affect TOA radiation may lead to a positive bias in regression-based feedback, although this bias appears to be small, particularly when annual-mean data are used (Murphy and Forster, 2010; Spencer and Braswell, 2010, 2011; Proistosescu et al., 2018). When tested within ESMs, regression-based feedbacks have been found to be only weakly correlated with values of ECS (Chung et al., 2010), although cloudy-sky TOA radiation fluxes have been found to be moderately correlated with ECS at ENSO timescales within CMIP5 models (Lutsko and Takahashi, 2018).

Finding such correlations within models requires simulations that span multiple centuries, suggesting that the satellite record may not be of sufficient length to produce robust feedback estimates. However, correlations between regression-based feedbacks and long-term feedbacks have been found to be higher when focused on specific processes or regions, such as for cloud or the water vapour feedback (Dessler, 2013; Zhou et al., 2015; Section 7.4.2). Assessing the global radiative feedback in terms of the more stable relationship between tropospheric temperature and TOA radiation offers another potential avenue for constraining ECS. The 'emergent constraints' on ECS based on variability in the TOA energy budget are assessed in Section 7.5.4.1.

7.5.2.4 Estimates of ECS based on the climate response to volcanic eruptions

A number of studies consider the observed climate response to volcanic eruptions over the 20th century (Knutti et al., 2017; Chapter 3 Section 3.3.1, Cross-Chapter Box 4.1). However, the direct constraint on ECS is weak, particularly at the high end, because the temperature response to short-term forcing depends only weakly on radiative feedbacks and because it can take decades of a sustained forcing before the magnitude of temperature changes reflects differences in ECS across models (Geoffroy et al., 2013b; Merlis et al., 2014). It is also a challenge to separate the response to volcanic eruptions from internal climate variability in the years that follow them (Wigley et al., 2005). Based on ESM simulations, radiative feedbacks governing the global surface temperature response to volcanic eruptions can be substantially different than those governing long-term global warming (Merlis et al., 2014; Marvel et al., 2016; Ceppi and Gregory, 2019). Estimates based on the response to volcanic eruptions agree with other lines of evidence (Knutti et al., 2017), but they do not constitute a direct estimate of ECS (*high confidence*). The 'emergent constraints' on ECS based on climate variability, including volcanic eruptions, are summarized in Section 7.5.4.1.

7.5.2.5 Assessment of ECS and TCR based on the instrumental record

Evidence from the instrumental temperature record, including estimates using global energy budget changes (Section 7.5.2.1), climate emulators (Section 7.5.2.2), variability in the TOA radiation budget (Section 7.5.2.3), and the climate response to volcanic eruptions (Section 7.5.2.4) produce median ECS estimates that range between 2.5°C and 3.5°C, but a best estimate value cannot be given owing to a strong dependence on assumptions about how radiative feedbacks will change in the future. However, there is *robust evidence* and *high agreement* across the lines of evidence that ECS is *extremely likely* greater than 1.6°C (*high confidence*). There is *robust evidence* and *medium agreement* across the lines of evidence that ECS is *very likely* greater than 1.8°C and *likely* greater than 2.2°C (*high confidence)*. These ranges of ECS correspond to estimates based on historical global energy budget constraints (Section 7.5.2.1) under the assumption of no feedback dependence on evolving SST patterns (i.e., $\alpha' = 0$) and thus represent an underestimate of the true ECS ranges that can be inferred from this line of evidence (*high confidence*). Historical global energy budget changes do not provide constraints on the upper bound of ECS, while the studies assessed in Section 7.5.2.3 based on climate variability provide *low confidence* in its value owing to *limited evidence*.

Global energy budget constraints indicate a central estimate (median) TCR value of 1.9°C and that TCR is *likely* in the range 1.5°C to 2.3°C and *very likely* in the range 1.3°C to 2.7°C (*high confidence*). Studies that

ACCEPTED VERSION SUBJECT TO FINAL EDITING

constrain TCR based on the instrumental temperature record used in conjunction with ESM simulations are summarized in Section 7.5.4.3.

7.5.3 Estimates of ECS based on paleoclimate data

Estimates of ECS based on paleoclimate data are complementary to, and largely independent from, estimates based on process-based studies (Section 7.5.1) and the instrumental record (Section 7.5.2). The strengths of using paleoclimate data to estimate ECS include: (1) the estimates are based on observations of a real-world Earth system response to a forcing, in contrast to using estimates from process-based modelling studies or directly from models; (2) the forcings are often relatively large (similar in magnitude to a CO_2 doubling or more), in contrast to data from the instrumental record; (3) the forcing often changes relatively slowly so the system is close to equilibrium; as such, all individual feedback parameters, α_x, are included, and complications associated with accounting for ocean heat uptake are reduced or eliminated, in contrast to the instrumental record. However, there can be relatively large uncertainties on estimates of both the paleo forcing and paleo global surface temperature response, and care must be taken to account for long-term feedbacks associated with ice sheets (Section 7.4.2.6), which often play an important role in the paleoclimate response to forcing, but which are not included in the definition of ECS. Furthermore, the state-dependence of feedbacks (Section 7.4.3) means that climate sensitivity during Earth's past may not be the same as it is today, which should be accounted for when interpreting paleoclimate estimates of ECS.

AR5 stated that data and modelling of the Last Glacial Maximum (LGM, Cross-Chapter Box 2.1) indicated that it was *very unlikely* that ECS lay outside the range 1–6°C (Masson-Delmotte et al., 2013). Furthermore, AR5 reported that climate records of the last 65 million years indicated an ECS 95% confidence interval of 1.1–7.0°C.

Compared with AR5, there are now improved constraints on estimates of ECS from paleoclimate evidence. The strengthened understanding and improved lines of evidence come in part from the use of high-resolution paleoclimate data across multiple glacial-interglacial cycles, taking into account state-dependence (von der Heydt et al., 2014; Köhler et al., 2015, 2017, 2018; Friedrich et al., 2016; Snyder, 2019; Stap et al., 2019; Section 7.4.3) and better constrained pre-ice core estimates of atmospheric CO_2 concentrations (Martínez-Botí et al., 2015; Anagnostou et al., 2016, 2020; de la Vega et al., 2020) and surface temperature (Hollis et al., 2019; Inglis et al., 2020; McClymont et al., 2020).

Overall, the paleoclimate lines of evidence regarding climate sensitivity can be broadly categorised into two types: estimates of radiative forcing and temperature response from paleo proxy measurements, and emergent constraints on paleoclimate model simulations. This section focuses on the first type only; the second type (emergent constraints) are discussed in Section 7.5.4.

In order to provide estimates of ECS, evidence from the paleoclimate record can be used to estimate forcing (ΔF) and global surface temperature response (ΔT) in Equation 7.1, Box 7.1, under the assumption that the system is in equilibrium (i.e. ΔN=0). However, there are complicating factors when using the paleoclimate record in this way, and these challenges and uncertainties are somewhat specific to the time period being considered.

7.5.3.1 Estimates of ECS from the Last Glacial Maximum

The LGM (Cross-Chapter Box 2.1) has been used to provide estimates of ECS (Sherwood et al., 2020b; Tierney et al., 2020b) (see Table 7.11 for estimates since AR5). The major forcings and feedback processes that led to the cold climate at that time (e.g., CO_2, non-CO_2 greenhouse gases, and ice sheets) are relatively well-known (Chapter 5, Section 5.1), orbital forcing relative to pre-industrial was negligible, and there are relatively high spatial resolution and well-dated paleoclimate temperature data available for this time period (Chapter 2, Section 2.3.1). Uncertainties in deriving global surface temperature from the LGM proxy data arise partly from uncertainties in the calibration from the paleoclimate data to local annual mean surface

ACCEPTED VERSION SUBJECT TO FINAL EDITING

temperature, and partly from uncertainties in the conversion of the local temperatures to an annual mean global surface temperature. Overall, the global mean LGM cooling relative to pre-industrial is assessed to be *very likely* from 5–7°C (Chapter 2, Section 2.3.1). The LGM climate is often assumed to be in full equilibrium with the forcing, such that ΔN in Equation 7.1, Box 7.1, is zero. A calculation of sensitivity using solely CO_2 forcing, and assuming that the LGM ice sheets were in equilibrium with that forcing, would give an Earth System Sensitivity (ESS) rather than an ECS (see Box 7.1). In order to calculate an ECS, which is defined here to include all feedback processes except ice sheets, the approach of Rohling et al. (2012) can be used. This approach introduces an additional forcing term in Equation 7.1, Box 7.1, that quantifies the resulting forcing associated with the ice sheet feedback (primarily an estimate of the radiative forcing associated with the change in surface albedo). However, differences between studies as to which processes are considered as forcings (for example, some studies also include vegetation and/or aerosols, such as dust, as forcings), means that published estimates are not always directly comparable. Additional uncertainty arises from the magnitude of the ice sheet forcing itself (Stap et al., 2019; Zhu and Poulsen, 2021), which is often estimated using ESMs. Furthermore, the ECS at the LGM may differ from that of today due to state-dependence (see Section 7.4.3). Here, only studies that report values of ECS that have accounted for the long-term feedbacks associated with ice sheets, and therefore most closely estimate ECS as defined in this chapter, are assessed here (see Table 7.11).

7.5.3.2 Estimates of ECS from glacial-interglacial cycles

Since AR5, several studies have extended the Rohling et al. (2012) approach (described above for the LGM) to the glacial-interglacial cycles of the last ~1 to 2 million years (von der Heydt et al., 2014; Köhler et al., 2015; Friedrich et al., 2016; Royer, 2016; Köhler et al., 2017, 2018; Snyder, 2019; Stap et al., 2019; Friedrich and Timmermann, 2020; Table 7.11). Compared to the LGM, uncertainties in the derived ECS from these periods are in general greater, due to greater uncertainty in global surface temperature (due to fewer individual sites with proxy temperature records), ice sheet forcing (due to a lack of detailed ice sheet reconstructions), and CO_2 forcing (for those studies that include the pre-ice core period, where CO_2 reconstructions are substantially more uncertain). Furthermore, accounting for varying orbital forcing in the traditional global-mean forcing and response energy budget framework (Box 7.1) is challenging (Schmidt et al., 2017b), due to seasonal and latitudinal components of the forcing that, despite a close-to-zero orbital forcing in the global annual mean, can directly result in responses in annual mean global surface temperature (Liu et al., 2014), ice volume (Abe-Ouchi et al., 2013), and feedback processes such as those associated with methane (Singarayer et al., 2011). In addition, for time periods in which the forcing relative to the modern era is small (interglacials), the inferred ECS has relatively large uncertainties because the forcing and temperature response (ΔF and ΔT in Equation 7.1 in Box 7.1) are both close to zero.

7.5.3.3 Estimates of ECS from warm periods of the pre-Quaternary

In the pre-Quaternary (prior to about 2.5 million years ago), the forcings and response are generally of the same sign and similar magnitude as future projections of climate change (Burke et al., 2018; Tierney et al., 2020a). Similar uncertainties as for the LGM apply, but in this case a major uncertainty relates to the forcing, because prior to the ice core record there are only indirect estimates of CO_2 concentration. However, advances in pre-ice-core CO_2 reconstruction (e.g., Foster and Rae, 2016; Super et al., 2018; Witkowski et al., 2018) mean that the estimates of pre-Quaternary CO_2 have less uncertainty than at the time of AR5, and these time periods can now contribute to an assessment of climate sensitivity (see Table 7.11). The mid-Pliocene warm period (MPWP; Cross-Chapter Box 2.1; Cross-Chapter Box 2.4) has been targeted for constraints on ECS (Martínez-Botí et al., 2015; Sherwood et al., 2020b), due to the fact that CO_2 concentrations were relatively high at this time (350–425 ppm) and because the MPWP is sufficiently recent that topography and continental configuration are similar to modern-day. As such, a comparison of the MPWP with the pre-industrial climate provides probably the closest natural geological analogue for the modern day that is useful for assessing constraints on ECS, despite the effects of different geographies not being negligible (global surface temperature patterns; ocean circulation). Furthermore, the global surface temperature of the MPWP was such that non-linearities in feedbacks (Section 7.4.3) were relatively modest.

ACCEPTED VERSION SUBJECT TO FINAL EDITING

Within the MPWP, the KM5c interglacial has been identified as a particularly useful time period for assessing ECS (Haywood et al., 2013, 2016b) because Earth's orbit during that time was very similar to that of the modern-day.

Further back in time, in the early Eocene (Cross-Chapter Box 2.1), uncertainties in forcing and temperature change become larger, but the signals are generally larger too (Anagnostou et al., 2016, 2020; Shaffer et al., 2016; Inglis et al., 2020). Caution must be applied when estimating ECS from these time periods, due to differing continental position and topography/bathymetry (Farnsworth et al., 2019), and due to temperature-dependence of feedbacks (Section 7.4.3). On even longer timescales of the last 500 million years (Royer, 2016) the temperature and CO_2 measurements are generally asynchronous, presenting challenges in using this information for assessments of ECS.

7.5.3.4 Synthesis of ECS based on paleo radiative forcing and temperature

The lines of evidence directly constraining ECS from paleoclimates are summarised in Table 7.11. Although some of the estimates in Table 7.11 are not independent because they use similar proxy records to each other (e.g., von der Heydt et al., 2014; Köhler et al., 2015, 2017; Stap et al., 2019), there are still multiple independent lines of paleoclimate evidence regarding ECS, from differing past time periods (LGM (Sherwood et al., 2020b; Tierney et al., 2020b); glacial-interglacial (Royer, 2016; Köhler et al., 2017; Snyder, 2019; Friedrich and Timmermann, 2020), Pliocene (Martínez-Botí et al., 2015; Sherwood et al., 2020b) and the Eocene (Anagnostou et al., 2016, 2020; Shaffer et al., 2016; Inglis et al., 2020), with differing proxies for estimating forcing (e.g., CO_2 from ice cores or boron isotopes) and response (e.g., global surface temperature from $\delta^{18}O$, Mg/Ca or Antarctic δD). Furthermore, although different studies have uncertainty estimates that account for differing sources of uncertainty, some studies (Snyder, 2019; Inglis et al., 2020; Sherwood et al., 2020b; Tierney et al., 2020b) do consider many of the uncertainties discussed in Sections 7.5.3.1-7.5.3.3. All the studies based on glacial-interglacial cycles account for some aspects of the state-dependence of climate sensitivity (Section 7.4.3) by considering only the warm phases of the Pleistocene, although what constitutes a warm phase is defined differently across the studies.

[START TABLE 7.11 HERE]

Table 7.11: Estimates of ECS derived from paleoclimates: from AR5 (above double lines) and from post-AR5 studies (below double lines). Many studies provide an estimate of ECS that includes only CO_2 and the ice sheet feedback as forcings, providing an estimate of $S_{[CO2, LI]}$ using the notation of Rohling et al. (2012), which is equivalent to our definition of ECS (Box 7.1). However, some studies provide estimates of other types of sensitivity (column 4). Different studies (column 1) focus on different time periods (column 2) and use a variety of different paleoclimate proxies and models (column 3) to give a best estimate (column 5) and/or a range (column 5). The published ranges given account for varying sources of uncertainty (column 6). See Cross-Chapter Box 2.1 for definition of time periods. All temperature values in column (5) are shown to a precision of 1 decimal place.

(1) Study	(2) Time period	(3) Proxies/models used for CO_2, temperature (T), and global scaling (GS).	(4) Climate sensitivity classification according to Rohling et al. (2012).	(5) Published best estimate of ECS [and/or range]	(6) Range accounts for:
AR5 (Masson-Delmotte et al., 2013)	LGM	Assessment of multiple lines of evidence	S^a = ECS	[*very likely* > 1.0 ; very unlikely > 6.0 °C]	Multiple sources of uncertainty
AR5	Cenozoic (last 65	Assessment of	$S_{[CO2,LI]}$	[95% range:	Multiple

ACCEPTED VERSION SUBJECT TO FINAL EDITING

(Masson-Delmotte et al., 2013)	million years)	multiple lines of evidence		1.1 to 7.0 °C]	sources of uncertainty
Tierney et al. (2020b)	LGM	CO_2: ice core T: multiproxy	$S_{[CO2,LI,CH4, N2O]}$	3.8 °C [68% range: 3.3 to 4.3°C]	Multiple sources of uncertainty
Sherwood et al. (2020)	LGM	CO_2: ice core T: multiple lines of evidence	$S_{[CO2, LI, CH4, N2O, dust, VG]}$	maximum likelihood: 2.6 °C [*likely* range depends on chosen prior; 0.6 likelihood: 1.6 to 4.4°C]	Multiple sources of uncertainty
von der Heydt et al. (2014)	Warm states of glacial-interglacial cycles of last 800 kyrs.	CO_2: ice core T: ice core δD, benthic $\delta^{18}O$. GS: Annan and Hargreaves, Schneider von Deimling	$S_{[CO2,LI]}$	3.5°C [range: 3.1 to 5.4°C]*	Varying LGM global mean temperatures used for scaling.
Köhler et al. (2015)	Warm states of glacial-interglacial cycles of last 2 Myrs.	CO_2: ice core alkenones and boron isotopes T: benthic $\delta^{18}O$ GS: PMIP LGM and PlioMIP MPWP	$S_{[CO2,LI]}$	5.7 °C [68% range: 3.7 to 8.1 °C]*	Temporal variability in records.
Köhler et al. (2017)	Warm states of glacial-interglacial cycles of last 2 Myrs.	CO_2: boron isotopes T: benthic $\delta^{18}O$ GS: PMIP LGM and PlioMIP MPWP	$S_{[CO2,LI]}$	5.6 °C [16^{th} to 84^{th} percentile: 3.6 to 8.1 °C]*	Temporal variability in records.
Köhler et al. (2018)	Warm states of glacial-interglacial cycles of last 800 kyrs, excluding those for which CO_2 and T diverge.	CO_2: ice cores T: benthic $\delta^{18}O$, alkenone, Mg/Ca, MAT, and faunal SST GS: PMIP3 LGM	$S_{[CO2, LI]}$	[range: 3.0 to 5.9 °C]*	Varying temperature reconstructions.
(Stap et al., 2019)	States of glacial-interglacial cycles of last 800 kyrs for which forcing is zero compared with modern, excluding those for which CO_2 and T diverge.	CO_2: ice cores T: benthic $\delta^{18}O$ GS: PMIP LGM and PlioMIP MPWP	$S_{[CO2, LI]}$	[range: 6.1 to 11.0 °C]*	Varying efficacies of ice sheet forcing
Friedrich et al. (2016)	Warm states of glacial-interglacial cycles of last 780 kyrs.	CO_2: ice cores T: alkenone, Mg/Ca, MAT, and faunal SST GS: PMIP3 LGM.	$S_{[GHG,LI,AE]}$	4.9 °C [*Likely* range: 4.3 to 5.4°C]*	Varying LGM global mean temperatures, aerosol forcing.

ACCEPTED VERSION SUBJECT TO FINAL EDITING

Friedrich and Timmermann (2020)	Last glacial-interglacial cycle	CO_2: ice cores T: alkenone, Mg/Ca, MAT	$S_{[GHG,LI,AE]}$	4.2°C [range: 3.4 to 6.2°C]*	Varying aerosol forcings
Snyder (2019)	Interglacial periods and intermediate glacial climates of last 800 kyrs	CO_2: ice cores T: alkenone, Mg/Ca, species assemblages GS: PMIP models	$S_{[GHG,LI,AE,VG]}$	3.1°C [67% range : 2.6 to 3.7 °C]*	Multiple sources of uncertainty
Royer (2016)	Glacial-interglacial cycles of the Pliocene (3.4 to 2.9 Ma)	CO_2: boron isotopes T: benthic $\delta^{18}O$	$S_{[CO2,LI]}$	10.2°C [68% range: 8.1 to 12.3°C]	Temporal variability in records.
Martínez-Botí et al. (2015)	Pliocene	CO_2: boron isotopes T: benthic $\delta^{18}O$	$S_{[CO2,LI]}$	3.7 °C [68% range: 3.0 to 4.4°C]*	Pliocene sea level, temporal variability in records.
Sherwood et al. (2020)	Pliocene	CO_2: boron isotopes T: multiple lines of evidence	$S_{[CO2,LI,N2O,CH4,VG]}$	maximum likelihood: 3.2°C [*likely* range depends on chosen prior; 0.6 likelihood: 1.8 to 5.2°C]	Multiple sources of uncertainty
Anagnostou et al. (2016)	Early Eocene	CO_2: boron isotopes T: various terrestrial MAT, Mg/Ca, TEX, $\delta^{18}O$ SST.	$S_{[CO2,LI]}$	3.6 °C [66% range: 2.1 to 4.6 °C]	Varying calibrations for temperature and CO_2.
Anagnostou et al. (2020)	Late Eocene (41.2 to 33.9 Ma)	CO_2: boron isotopes T: one SST record GS: CESM1	$S_{[CO2,LI]}$	3.0 °C [68% range: 1.9 to 4.1 °C]	Temporal variability in records.
Shaffer et al. (2016)	Pre-PETM	CO_2: mineralogical, carbon cycling, and isotope constraints T: various terrestrial MAT, Mg/Ca, TEX, $\delta^{18}O$ SST.	$S_{[GHG,AE,VG,LI]}$	[range: 3.3 to 5.6 °C]	Varying calibration of temperature and CO_2.
Inglis et al. (2020)	Mean of EECO, PETM, and latest Paleocene	CO_2: boron isotopes T: multiproxy SST and SAT GS: EoMIP models	$S_{[CO2,LI, VG,AE]}$	3.7 °C [*likely* range : 2.2 to 5.3°C]	Multiple sources of uncertainty

Notes:

(Note 1) S^a in this table denotes a classification of climate sensitivity following (Rohling et al., 2012).

(Note 2) * – Although our assessed value of ERF due to CO_2 doubling is 3.93 W m^{-2} (Section 7.3.2.1), for these studies the best estimate and range of temperature is calculated from the published estimate of sensitivity in units of °C (W m^{-2})$^{-1}$ using an ERF of 3.7 W m^{-2}, for consistency with the typical value used in the studies to estimate the paleo CO_2 forcing.

[END TABLE 7.11 HERE]

ACCEPTED VERSION SUBJECT TO FINAL EDITING

None of the post-AR5 studies in Table 7.11 have an estimated lower range for ECS below 1.6 °C. As such, based solely on the paleoclimate record, it is assessed to be *very likely* that ECS is greater than 1.5°C (*high confidence*).

In general, it is the studies based on the warm periods of the glacial-interglacial cycles (Section 7.5.3.2) that give the largest values of ECS. Given the large uncertainties associated with estimating the magnitude of the ice sheet forcing during these intervals (Stap et al., 2019), and other uncertainties discussed in Section 7.5.3.2, in particular the direct effect of orbital forcing on estimates of ECS, there is only *low confidence* in estimates from the studies based on glacial-interglacial periods. This *low confidence* also results from the temperature-dependence of the net feedback parameter, α, resulting from several of these studies (Figure 7.10), that is hard to reconcile with the other lines of evidence for α, including proxy estimates from warmer paleoclimates (Section 7.4.3.2). A central estimate of ECS, derived from the LGM (Section 7.5.3.1) and warm periods of the pre-Quaternary (Section 7.5.3.3), that takes into account some of the interdependencies between the different studies, can be obtained by averaging across studies within each of these two time periods, and then averaging across the two time periods; this results in a central estimate of 3.4°C. This approach of focussing on the LGM and warm climates was also taken by Sherwood et al. (2020) in their assessment of ECS from paleoclimates. An alternative method is to average across all studies, from all periods, that have considered multiple sources of uncertainty (Table 7.11); this approach leads to a similar central estimate of 3.3°C. Overall, we assess *medium confidence* for a central estimate of 3.3–3.4°C.

There is more variation in the upper bounds of ECS than in the lower bounds. Estimates of ECS from pre-Quaternary warm periods have an average upper range of 4.9 °C, and from the LGM of 4.4°C; taking into account the independence of the estimates from these two time periods, and accounting for state-dependence (Section 7.4.3) and other uncertainties discussed in Section 7.5.3, the paleoclimate record on its own indicates that ECS is *likely* less than 4.5 °C. Given the higher values from many glacial-interglacial studies, this value has only *medium confidence*. Despite the large variation in individual studies at the extreme upper end, all except two studies (both of which are from glacial-interglacial time periods associated with *low confidence*) have central estimates that are below 6 °C; overall we assess that it is *extremely likely* that ECS is below 8 °C (*high confidence*).

7.5.4 Estimates of ECS and TCR based on emergent constraints

ESMs exhibit substantial spread in ECS and TCR (Section 7.5.7). Numerous studies have leveraged this spread in order to narrow estimates of Earth's climate sensitivity by employing methods known as “emergent constraints” (Chapter 1, Section 1.5.4). These methods establish a relationship between an observable and either ECS or TCR based on an ensemble of models, and combine this information with observations to constrain the probability distribution of ECS or TCR. Most studies of this kind have clearly benefitted from the international efforts to coordinate the CMIP and other multi-model ensembles.

A number of considerations must be taken into account when assessing the diverse literature on ECS and TCR emergent constraints. For instance, it is important to have physical and theoretical basis for the connection between the observable and modelled ECS or TCR since in model ensembles thousands of relationships that pass statistical significance can be found simply by chance (Caldwell et al., 2014). It is also important that the underlying model ensemble does not exhibit a shared bias that influences the simulation of the observable quantity on which the emergent constraint is based. Also, correctly accounting for uncertainties in both the observable (including measurement uncertainty and natural variability) and the emergent constraint statistical relationship can be challenging, in particular in cases where the latter is not expected to be linear (Annan et al., 2020a). A number of proposed emergent constraints leverage variations in modelled ECS arising from tropical low clouds, which was the dominant source of inter-model spread in the CMIP5 ensemble used in most emergent constraint studies. Since ECS is dependent on the sum of individual feedbacks (Section 7.5.1) these studies implicitly assume that all other feedback processes in models are unbiased and should therefore rather be thought of as constraints on tropical low-cloud feedback (Klein and Hall, 2015; Qu et al., 2018; Schlund et al., 2020). The following sections go through a range of

ACCEPTED VERSION SUBJECT TO FINAL EDITING

emergent constraints and assess their strengths and limitations.

7.5.4.1 Emergent constraints using global or near-global surface temperature change

Perhaps the simplest class of emergent constraints regress past equilibrium paleoclimate temperature change against modelled ECS to obtain a relationship that can be used to translate a past climate change to ECS. The advantage is that these are constraints on the sum of all feedbacks, and furthermore unlike constraints on the instrumental record they are based on climate states that are at, or close to, equilibrium. So far, these emergent constraints have been limited to the Last Glacial Maximum (LGM; Cross-Chapter Box 2.1) cooling (Hargreaves et al., 2012; Schmidt et al., 2014; Renoult et al., 2020) and warming in the mid-Pliocene Warm Period (MPWP, Hargreaves and Annan, 2016; Renoult et al., 2020; Cross-Chapter Box 2.1; Cross-Chapter Box 2.4) due to the availability of sufficiently large multi-model ensembles for these two cases. The paleoclimate emergent constraints are limited by structural uncertainties in the proxy-based global surface temperature and forcing reconstructions (Section 7.5.3), possible differences in equilibrium sea-surface temperature patterns between models and the real world, and a small number of model simulations participating, which has led to divergent results. For example, Hopcroft and Valdes (2015) repeated the study based on the LGM by Hargreaves et al. (2012) using another model ensemble and found that the emergent constraint was not robust, whereas studies using multiple available ensembles retain useful constraints (Schmidt et al., 2014; Renoult et al., 2020). Also, the results are somewhat dependent on the applied statistical methods (Hargreaves and Annan, 2016). However, Renoult et al. (2020) explored this and found 95th percentiles of ECS below 6°C for LGM and Pliocene individually, regardless of statistical approach, and by combining the two estimates the 95th percentile dropped to 4.0°C. The consistency between the cold LGM and warm MPWP emergent constraint estimates increases confidence in these estimates, and further suggests that the dependence of feedback on climate mean state (Section 7.4.3) as represented in PMIP models used in these studies is reasonable.

Various emergent constraint approaches using global warming over the instrumental record have been proposed. These benefit from more accurate data compared with paleoclimates, but suffer from the fact that the climate is not in equilibrium, thereby assuming that ESMs on average accurately depict the ratio of short term to long term global warming. Global warming in climate models over 1850 to the present day exhibits no correlation with ECS, which is partly due to a substantial number of models exhibiting compensation between a high climate sensitivity with strong historical aerosol cooling (Kiehl, 2007; Forster et al., 2013; Nijsse et al., 2020). However, the aerosol cooling increased up until the 1970s when air quality regulations reduced the emissions from Europe and North America whereas other regions saw increases resulting in a subsequently reduced pace of global mean aerosol ERF increase (Chapter 2, Section 2.2.8, Figure 2.10). Energy balance considerations over the 1970–2010 period gave a best estimate ECS of 2.0°C (Bengtsson and Schwartz, 2013), however this estimate did not account for pattern effects. To address this limitation an emergent constraint on 1970–2005 global warming was demonstrated to yield a best estimate ECS of 2.83 [1.72 to 4.12] °C (Jiménez-de-la-Cuesta and Mauritsen, 2019). The study was followed up using CMIP6 models yielding a best estimate ECS of 2.6 [1.5 to 4.0] °C based on 1975–2019 global warming (Nijsse et al., 2020), thereby confirming the emergent constraint. Internal variability and forced or unforced pattern effects may influence the results (Jiménez-de-la-Cuesta and Mauritsen, 2019; Nijsse et al., 2020). For instance the Atlantic Multidecadal Oscillation changed from negative to positive anomaly, while the Indo-Pacific Oscillation changed less over the 1970–2005 period, potentially leading to high-biased results (Jiménez-de-la-Cuesta and Mauritsen, 2019), whereas during the later period 1975–2019 these anomalies roughly cancel (Nijsse et al., 2020). Pattern effects may have been substantial over these periods (Andrews et al., 2018), however the extent to which TOA radiation anomalies influenced surface temperature may have been dampened by the deep ocean (Hedemann et al., 2017; Newsom et al., 2020). It is therefore deemed *more likely than not* that these estimates based on post-1970s global warming are biased low by internal variability.

A study that developed an emergent constraint based on the response to the Mount Pinatubo 1991 eruption yielded a best estimate of 2.4 [*likely* range 1.7–4.1] °C (Bender et al., 2010). When accounting for ENSO variations they found a somewhat higher best estimate of 2.7°C, which is in line with results of later studies

ACCEPTED VERSION SUBJECT TO FINAL EDITING

that suggest ECS inferred from periods with substantial volcanic activity are low-biased due to strong pattern effects (Gregory et al., 2020) and that the short-term nature of volcanic forcing could exacerbate possible underestimates of modelled pattern effects.

Lagged-correlations present in short term variations in the global surface temperature can be linked to ECS through the fluctuation-dissipation theorem which is derived from a single heat reservoir model (Einstein, 1905; Hasselmann, 1976; Schwartz, 2007; Cox et al., 2018a). From this it follows that the memory carried by the heat capacity of the ocean results in low-frequency global temperature variability (red noise) arising from high frequency (white noise) fluctuations in the radiation balance, e.g., caused by weather. Initial attempts to apply the theorem to observations yielded a fairly low median ECS estimate of 1.1°C (Schwartz, 2007), a result that was disputed (Foster et al., 2008; Knutti et al., 2008). Recently it was proposed by Cox et al. (2018a) to use variations in the historical experiments of the CMIP5 climate models as an emergent constraint giving a median ECS estimate of 2.8 [1.6 to 4.0] °C. A particular challenge associated with these approaches is to separate short-term from long-term variability, and slightly arbitrary choices regarding the methodology of separating these in the global surface temperature from long-term signals in the historical record, omission of the more strongly forced period after 1962, as well as input data choices, can lead to median ECS estimates ranging from 2.5–3.5°C (Brown et al., 2018; Po-Chedley et al., 2018b; Rypdal et al., 2018). Calibrating the emergent constraint using CMIP5 modelled internal variability as measured in historical control simulations (Po-Chedley et al., 2018b) will inevitably lead to an overestimated ECS due to externally forced short term variability present in the historical record (Cox et al., 2018b). Contrary to constraints based on paleoclimates or global warming since the 1970s, when based on CMIP6 models a higher, yet still well-bounded ECS estimate of 3.7 [2.6 to 4.8] °C is obtained (Schlund et al., 2020). A more problematic issue is raised by (Annan et al., 2020b) who showed that the upper bound on ECS estimated this way is less certain when considering deep ocean heat uptake. In conclusion, even if not inconsistent, these limitations prevents us from directly using this type of constraint in the assessment.

Short term variations in the TOA energy budget, observable from satellites, arising from variations in the tropical tropospheric temperature has been linked to ECS through models, either as a range of models consistent with observations (those with ECS values between 2.0°C and 3.9°C) (Dessler et al., 2018) or as a formal emergent constraint by deriving further model-based relationships to yield a median of 3.3 [2.4 to 4.5] °C (Dessler and Forster, 2018). There are major challenges associated with short term variability in the energy budget, in particular how it relates to the long-term forced response of clouds (Colman and Hanson, 2017; Lutsko and Takahashi, 2018), and variations in the surface temperature that are not directly affecting the radiation balance lead to an overestimated ECS when using linear regression techniques where it appears as noise in the independent variable (Proistosescu et al., 2018; Gregory et al., 2020). The latter issue is largely overcome when using the tropospheric mean or mid-tropospheric temperature (Trenberth et al., 2015; Dessler et al., 2018).

7.5.4.2 Emergent constraints focused on cloud feedbacks and present-day climate

A substantial number of emergent constraint studies focus on observables that are related to tropical low-cloud feedback processes (Volodin, 2008; Sherwood et al., 2014; Zhai et al., 2015; Brient and Schneider, 2016; Brient et al., 2016). These studies yield median ECS estimates of 3.5–4°C and in many cases indicate low likelihoods of values below 3°C. The approach has attracted attention since most of the spread in climate sensitivity seen in CMIP5, and earlier climate model ensembles, arises from uncertainty in low cloud feedbacks (Bony and Dufresne, 2005; Wyant et al., 2006; Randall et al., 2007; Vial et al., 2013). Nevertheless, this approach assumes that all other feedback processes are unbiased (Klein and Hall, 2015; Qu et al., 2018; Schlund et al., 2020), for instance the possibly missing negative anvil area feedback or the possibly exaggerated mixed-phase cloud feedback (Section 7.4.2.4). Thus, the subset of emergent constraints that focus on low-level tropical clouds are not necessarily inconsistent with other emergent constraints of ECS. Related emergent constraints that focus on aspects of the tropical circulation and ECS have led to conflicting results (Su et al., 2014; Tian, 2015; Lipat et al., 2017; Webb and Lock, 2020), possibly because these processes are not the dominant factors in causing the inter-model spread (Caldwell et al., 2018).

ACCEPTED VERSION SUBJECT TO FINAL EDITING

The fidelity of models in reproducing aspects of temperature variability or the radiation budget has also been proposed as emergent constraints on ECS (Covey et al., 2000; Knutti et al., 2006; Huber et al., 2010; Bender et al., 2012; Brown and Caldeira, 2017; Siler et al., 2018a). Here indices based on spatial or seasonal variability are linked to modelled ECS, and overall the group of emergent constraints yields best estimates of 3.3°C to 3.7°C. Nevertheless, the physical relevance of present-day biases to the sum of long-term climate change feedbacks is unclear and therefore these constraints on ECS are not considered reliable.

7.5.4.3 Assessed ECS and TCR based on emergent constraints

The available emergent constraint studies have been divided into two classes: (i) those that are based on global or near-global indices, such as global surface temperature and the TOA energy budget; and (ii) those that are more focussed on physical processes, such as the fidelity of phenomena related to low-level cloud feedbacks or present-day climate biases. The former class is arguably superior in representing ECS, since it is a global surface temperature or energy budget change, whereas the latter class is perhaps best thought of as providing constraints on individual climate feedbacks, e.g., the determination that low-level cloud feedbacks are positive. The latter result is consistent with and confirms process-based estimates of low cloud feedbacks (Section 7.4.2.4), but are potentially biased as a group by missing or biased feedbacks in ESMs and is accordingly not taken into account here. A limiting case here is Dessler and Forster (2018) which is focused on monthly co-variability in the global TOA energy budget with mid-tropospheric temperature, at which time scale the surface albedo feedback is unlikely to operate thus implicitly assuming it is unbiased in the model ensemble.

In the first group of emergent constraints there is broad agreement on the best estimate of ECS ranging from 2.4–3.3°C. At the lower end, nearly all studies find lower bounds (5th percentiles) around 1.5°C, whereas several studies indicate 95th percentiles as low as 4°C. Considering both classes of studies, none of them yield upper *very likely* bounds above 5°C. Since several of the emergent constraints can be considered nearly independent one could assume that emergent constraints provide very strong evidence on ECS by combining them. Nevertheless, this is not done here because there are sufficient cross-dependencies, as for instance models are re-used in many of the derived emergent constraints, and furthermore the methodology has not yet reached a sufficient level of maturity since systematic biases may not have been accounted for. Uncertainty is therefore conservatively added to reflect these potential issues. This leads to the assessment that ECS inferred from emergent constraints is *very likely* 1.5 to 5°C with *medium confidence*.

Emergent constraints on TCR with a focus on the instrumental temperature record, though less abundant, have also been proposed. These can be influenced by internal variability and pattern effects as discussed in Section 7.5.4.1, although the influence is smaller because uncertainty in forced pattern effects correlate between transient historical warming and TCR. In the simplest form Gillett et al. (2012) regressed the response of one model to individual historical forcing components to obtain a tight range of 1.3–1.8°C, but later when an ensemble of models was used the range was widened to 0.9–2.3°C (Gillett et al., 2013), and updated by Schurer et al. (2018). A related data-assimilation based approach that accounted also for uncertainty in response patterns gave 1.33–2.36°C (Ribes et al., 2021), but is dependent on the choice of prior ensemble distribution (CMIP5 or CMIP6). Another study used the response to the Pinatubo volcanic eruption to obtain a range of 0.8–2.3°C (Bender et al., 2010). A tighter range, notably at the lower end, was found in an emergent constraint focusing on the post-1970s warming exploiting the lower spread in aerosol forcing change over this period (Jiménez-de-la-Cuesta and Mauritsen, 2019). Their estimate was 1.67 [1.17 to 2.16] °C. Two studies tested this idea: Tokarska et al. (2020) estimates TCR was 1.60 [0.90 to 2.27] °C based on CMIP6 models, whereas Nijsse et al. (2020) found 1.68 [1.0 to 2.3] °C, and in both cases there was a small sensitivity to choice of ensemble with CMIP6 models yielding slightly lower values and ranges. Combining these studies gives a best estimate of 1.7°C and a *very likely* range of TCR of 1.1–2.3°C with *high confidence*.

[START TABLE 7.12 HERE]

ACCEPTED VERSION SUBJECT TO FINAL EDITING

Table 7.12: Emergent constraint studies used in the assessment of ECS. These are studies that rely on global or near-global temperature change as the observable.

Study	Emergent constraint description	Published best estimate and uncertainty (°C)	Uncertainty estimate:
(Bender et al., 2010)	Pinatubo integrated forcing normalized by CMIP3 models own forcing versus temperature change regressed against ECS	2.4 [1.7 to 4.1]	5% to 95%
(Dessler and Forster, 2018)	Emergent constraint on TOA radiation variations linked to mid-tropospheric temperature in CMIP5 models	3.3 [2.4 to 4.5]	17% to 83%
(Hargreaves et al., 2012)	Last Glacial Maximum tropical SSTs in PMIP2 models	2.5 [1.3 to 4.2]	5% to 95%
(Hargreaves and Annan, 2016)	Pliocene tropical SSTs in PlioMIP models	[1.9 to 3.7]	5% to 95%
(Jiménez-de-la-Cuesta and Mauritsen, 2019)	Post–1970s global warming, 1995–2005 relative to 1970–1989, CMIP5 models	2.83 [1.72 to 4.12]	5% to 95%
(Nijsse et al., 2020)	Post–1970s global warming, 2009–2019 relative to 1975–1985, CMIP6 models	2.6 [1.5 to 4.0]	5% to 95%
(Renoult et al., 2020)	Combined Last Glacial Maximum and Pliocene tropical SSTs in PMIP2, PMIP3, PMIP4, PlioMIP and PlioMIP2 models	2.5 [0.8 to 4.0]	5% to 95%

[END TABLE 7.12 HERE]

7.5.5 Combined assessment of ECS and TCR

Substantial quantitative progress has been made in interpreting evidence of Earth's climate sensitivity since AR5, through innovation, scrutiny, theoretical advances and a rapidly evolving data base from current, recent and paleo climates. It should be noted that, unlike AR5 and earlier reports, our assessment of ECS is not directly informed by ESM simulations (Section 7.5.6). The assessments of ECS and TCR are focussed on the following lines of evidence: process-understanding; the instrumental record of warming; paleoclimate evidence; and emergent constraints. ESMs remain essential tools throughout establishing these lines of evidence, for instance for estimating part of the feedback parameters and radiative forcings, and emergent constraints rely on substantial model spread in ECS and TCR (Section 7.5.6).

A key advance over the AR5 assessment is the broad agreement across multiple lines of evidence. These support a central estimates of ECS close to, or at least not inconsistent with, 3°C. This advance is foremost following improvements in the understanding and quantification of Earth's energy imbalance, the instrumental record of global temperature change, and the strength of anthropogenic radiative forcing. Further advances include increased understanding of how the pattern effect influences ECS inferred from historical global warming (Sections 7.4.4 and 7.5.3), improved quantification of paleo climate change from proxy evidence and a deepened understanding of how feedback mechanisms increase ECS in warmer climate states (Sections 7.4.3, 7.4.4 and 7.5.4), and also an improved quantification of individual cloud feedbacks (Sections 7.4.2 and 7.5.4.2). The assessment findings for ECS and TCR are summarized in Table 7.13 and Table 7.14, respectively, and also visualized in Figure 7.18.

[START FIGURE 7.18 HERE]

Figure 7.18: Summary of the equilibrium climate sensitivity (ECS) and transient climate response (TCR)

ACCEPTED VERSION SUBJECT TO FINAL EDITING

assessments using different lines of evidence. Assessed ranges are taken from Tables 7.13 and 7.14 for ECS and TCR respectively. Note that for the ECS assessment based on both the instrumental record and paleoclimates, limits (i.e. one-sided distributions) are given, which have twice the probability of being outside the maximum/minimum value at a given end, compared to ranges (i.e. two tailed distributions) which are given for the other lines of evidence. For example, the *extremely likely* limit of greater than 95% probability corresponds to one side of the *very likely* (5% to 95%) range. Best estimates are given as either a single number or by a range represented by grey box. CMIP6 model values are not directly used as a line of evidence but presented on the Figure for comparison. ECS values are taken from Schlund et al. (2020) and TCR values from Meehl et al. (2020), see Supplementary Material 7.SM.4. Further details on data sources and processing are available in the chapter data table (Table 7.SM.14).

[END FIGURE 7.18 HERE]

AR5 assessed ECS to have a *likely* range from 1.5 to 4.5°C (Collins et al., 2013a) based on the majority of studies and evidence available at the time. The broader evidence base presented in this Report and the general agreement among different lines of evidence means that they can be combined to yield a narrower range of ECS values. This can be done formally using Bayesian statistics, though such a process is complex and involves formulating likelihoods and priors (Annan and Hargreaves, 2006; Stevens et al., 2016; Sherwood et al., 2020b). However, it can be understood that if two lines of independent evidence each give a low probability of an outcome being true, e.g., that ECS is less than 2.0°C, then the combined probability that ECS is less than 2.0°C is lower than that of either line of evidence. On the contrary, if one line of evidence is unable to rule out an outcome, but another is able to assign a low probability, then there is a low probability that the outcome is true (Stevens et al., 2016). This general principle applies even when there is some dependency between the lines of evidence (Sherwood et al., 2020b), for instance between historical energy budget constraints (Section 7.5.2.1) and those emergent constraints that use the historically observed global warming (Section 7.5.4.1). Even in this case the combined constraint will be closer to the narrowest range associated with the individual lines of evidence.

In the process of providing a combined and self-consistent ECS assessment across all lines of evidence, the above principles were all considered. As in earlier reports, a 0.5°C precision is used. Starting with the *very likely* lower bound, there is broad support for a value of 2.0°C, including process understanding and the instrumental record (Table 7.13). For the *very likely* upper bound, emergent constraints give a value of 5.0°C whereas the three other lines of evidence are individually less tightly constrained. Nevertheless, emergent constraints are a relatively recent field of research, in part taken into account by adding uncertainty to the upper bound (Section 7.5.4.3), and the underlying studies use, to a varying extent, information that is also used in the other three lines of evidence causing statistical dependencies. However, omitting emergent constraints and statistically combining the remaining lines of evidence likewise yields 95th percentiles close to 5.0°C (Sherwood et al., 2020b). Information for the *likely* range is partly missing or one-sided, however it must necessarily reside inside the *very likely* range and is therefore supported by evidence pertaining to both the *likely* and *very likely* ranges. Hence, the upper *likely* bound is assessed to be about halfway between the best estimate and the upper *very likely* bound while the lower *likely* bound is assessed to be about halfway between the best estimate and the lower *very likely* bound. In summary, based on multiple lines of evidence the best estimate of ECS is 3°C, it is *likely* within the range 2.5 to 4°C and *very likely* within the range 2 to 5°C. It is *virtually certain* that ECS is larger than 1.5°C. Whereas there is *high confidence* based on mounting evidence that supports the best estimate, *likely* range and *very likely* lower end, a higher ECS than 5°C cannot be ruled out, hence there is *medium confidence* in the upper end of the *very likely* range. Note that the best estimate of ECS made here corresponds to a feedback parameter of –1.3 W m^{-2} $°C^{-1}$ which is slightly more negative than the feedback parameter from process based evidence alone that is assessed in Section 7.4.2.7).

There has long been a consensus (Charney et al., 1979) supporting an ECS estimates of 1.5 to 4°C. In this regard it is worth remembering the many debates challenging an ECS of this magnitude. These started as early as Ångström (1900) criticizing the results of Arrhenius (1896) arguing that the atmosphere was already saturated in infrared absorption such that adding more CO_2 would not lead to warming. The assertion of Ångström was understood half a century later to be incorrect. History has seen a multitude of studies (e.g.,

ACCEPTED VERSION SUBJECT TO FINAL EDITING

Svensmark, 1998; Lindzen et al., 2001; Schwartz, 2007) mostly implying lower ECS than the range assessed as *very likely* here. However, there are also examples of the opposite such as very large ECS estimates based on the Pleistocene records (Snyder, 2016), which has been shown to be overestimated due to a lack of accounting for orbital forcing and long term ice sheet feedbacks (Schmidt et al., 2017b), or suggestions that global climate instabilities may occur in the future (Steffen et al., 2018; Schneider et al., 2019). There is, however, no evidence for unforced instabilities of such magnitude occurring in the paleo record temperatures of the past 65 million years (Westerhold et al., 2020), possibly short of the PETM excursion (Chapter 5, Section 5.3.1.1) that occurred at more than 10°C above present (Anagnostou et al., 2020). Looking back, the resulting debates have led to a deeper understanding, strengthened the consensus, and have been scientifically valuable.

In the climate sciences, there are often good reasons to consider representing deep uncertainty, or what is sometimes referred to as unknown unknowns. This is natural in a field that considers a system that is both complex and at the same time challenging to observe. For instance, since emergent constraints represent a relatively new line of evidence, important feedback mechanisms may be biased in process-level understanding, pattern effects and aerosol cooling may be large and paleo evidence inherently builds on indirect and incomplete evidence of past climate states, there certainly can be valid reasons to add uncertainty to the ranges assessed on individual lines of evidence. This has indeed been addressed throughout Sections 7.5.1–7.5.4. Since it is neither probable that all lines of evidence assessed here are collectively biased nor is the assessment sensitive to single lines of evidence, deep uncertainty it is not considered as necessary to frame the combined assessment of ECS.

[START TABLE 7.13 HERE]

Table 7.13: Summary of ECS assessment

Equilibrium Climate Sensitivity (ECS)	Central value	*Likely*	*Very likely*	*Extremely likely*
Process understanding (7.5.1)	3.4°C	2.5 to 5.1 °C	2.1 to 7.7 °C	
Warming over instrumental record (7.5.2)	2.5 to 3.5 °C	> 2.2°C	> 1.8 °C	> 1.6 °C
Paleoclimates (7.5.3)	3.3 to 3.4°C	< 4.5 °C	> 1.5°C	< 8 °C
Emergent constraints (7.5.4)	2.4 to 3.3°C		1.5 to 5.0 °C	
Combined assessment	3°C	2.5 to 4.0 °C	2.0 to 5.0 °C	

[END TABLE 7.13 HERE]

The evidence for TCR is less abundant than for ECS, and focuses on the instrumental temperature record (Sections 7.5.2 and 7.5.6), emergent constraints (Section 7.5.4.3) and process understanding (Section 7.5.1). AR5 assessed a *likely* range of 1.0 to 2.5°C. TCR and ECS are related, though, and in any case TCR is less than ECS (see Section 7.5 introduction). Furthermore, estimates of TCR from the historical record are not as strongly influenced by externally forced surface temperature pattern effects as estimates of ECS are since both historical transient warming and TCR are affected by this phenomenon (Section 7.4.4). A slightly higher weight is given to instrumental record warming and emergent constraints since these are based on observed transient warming, whereas the process understanding estimate relies on pattern effects and ocean heat uptake efficiency from ESMs to represent the transient dampening effects of the ocean. If these effects are underestimated by ESMs then the resulting TCR would be lower. Given the interdependencies of the other two lines of evidence, a conservative approach to combining them as reflected in the assessment is adopted. Since uncertainty is substantially lower than in AR5 a 0.1°C precision is therefore used here. Otherwise the same methodology for combining the lines of evidence as applied to ECS is used for TCR. Based on process understanding, warming over the instrumental record and emergent constraints the best

ACCEPTED VERSION SUBJECT TO FINAL EDITING

estimate TCR is 1.8°C, it is *likely* 1.4 to 2.2°C and *very likely* 1.2 to 2.4°C. The assessed ranges are all assigned *high confidence* due to the high level of agreement among the lines of evidence.

[START TABLE 7.14 HERE]

Table 7.14: Summary of TCR assessment

Transient Climate Response (TCR)	Central value	*Likely* range	*Very likely* range
Process understanding (7.5.1)	2.0 °C	1.6 to 2.7 °C	1.3 to 3.1 °C
Warming over instrumental record (7.5.2)	1.9 °C	1.5 to 2.3°C	1.3 to 2.7 °C
Emergent constraints (7.5.4)	1.7 °C		1.1 to 2.3°C
Combined assessment	1.8 °C	1.4 to 2.2°C	1.2 to 2.4°C

[END TABLE 7.14 HERE]

7.5.6 Considerations on the ECS and TCR in global climate models and their role in the assessment

Coupled climate models, such as those participating in CMIP, have long played a central role in assessments of ECS and TCR. In reports up to and including TAR, climate sensitivities derived directly from ESMs were the primary line of evidence. However, since AR4, historical warming and paleoclimate information provided useful additional evidence and it was noted that assessments based on models alone were problematic (Knutti, 2010). As new lines of evidence have evolved, in AR6 various numerical models are used where they are considered accurate, or in some cases the only available source of information, and thereby support all four lines of evidence (Sections 7.5.1-7.5.4). However, AR6 differs from previous IPCC reports in excluding direct estimates of ECS and TCR from ESMs in the assessed ranges (Section 7.5.5), following several recent studies (Annan and Hargreaves, 2006; Stevens et al., 2016; Sherwood et al., 2020b). The purpose of this section is to explain why this approach has been taken and to provide a perspective on the interpretation of the climate sensitivities exhibited in CMIP6 models.

The primary consideration that led to excluding ECS and TCR directly derived from ESMs is that information from these models is incorporated in the lines of evidence used in the assessment: ESMs are partly used to estimate historical- and paleoclimate ERFs (Sections 7.5.2 and 7.5.3); to convert from local to global mean paleo temperatures (Section 7.5.3), to estimate how feedbacks change with SST patterns (Section 7.4.4.3); and to establish emergent constraints on ECS (Section 7.5.4). They are also used as important evidence in the process understanding estimates of the temperature, water vapour, albedo, biogeophysical, and non-CO_2 biogeochemical feedbacks, whereas other evidence is primarily used for cloud feedbacks where the climate model evidence is weak (Section 7.4.2). One perspective on this is that the process understanding line of evidence builds on and replaces ESM estimates.

The ECS of a model is the net result of the model's effective radiative forcing from a doubling of CO_2 and the sum of the individual feedbacks and their interactions. It is well known that most of the model spread in ECS arises from cloud feedbacks, and particularly the response of low-level clouds (Bony and Dufresne, 2005; Zelinka et al., 2020). Since these clouds are small-scale and shallow, their representation in climate models is mostly determined by sub-grid scale parameterizations. It is sometimes assumed that parameterization improvements will eventually lead to convergence in model response and therefore a decrease in the model spread of ECS. However, despite decades of model development, increases in model resolution and advances in parametrization schemes, there has been no systematic convergence in model

ACCEPTED VERSION SUBJECT TO FINAL EDITING

estimates of ECS. In fact, the overall inter model spread in ECS for CMIP6 is larger than for CMIP5; ECS and TCR values are given for CMIP6 models in Supplementary Material 7.SM.4 based on Schlund et al. (2020) for ECS and Meehl et al. (2020) for TCR, see also Figure 7.18 and FAQ 7.3. The upward shift does not apply to all models traceable to specific modelling centres, but a substantial subset of models have seen an increase in ECS between the two model generations. The increased ECS values, as discussed in Section 7.4.2.8, are partly due to shortwave cloud feedbacks (Flynn and Mauritsen, 2020) and it appears that in some models extra-tropical clouds with mixed ice and liquid phases are central to the behaviour (Zelinka et al., 2020), probably borne out of a recent focus on biases in these types of clouds (McCoy et al., 2016; Tan et al., 2016). These biases have recently been reduced in many ESMs, guided by process understanding from laboratory experiments, field measurements, and satellite observations (Lohmann and Neubauer, 2018; Bodas-Salcedo et al., 2019; Gettelman et al., 2019). However, this and other known model biases are already factored into the process-level assessment of cloud feedback (Section 7.4.2.4), and furthermore the emergent constraints used here focus on global surface temperature change, which are less susceptible to shared model biases in individual feedback parameters than emergent constraints that focus on specific physical processes (Section 7.5.4). The high values of ECS and TCR in some CMIP6 models lead to higher levels of surface warming than CMIP5 simulations and also the AR6 projections based on the assessed ranges of ECS, TCR and ERF (Chapter 4, Box 4.1; FAQ 7.3; Forster et al., 2019).

It is generally difficult to determine which information enters the formulation and development of parameterizations used in ESMs. Climate models frequently share code components and in some cases entire sub-model systems are shared and slightly modified. Therefore, models cannot be considered independent developments, but rather families of models with interdependencies (Knutti et al., 2013). It is therefore difficult to interpret the collection of models (Knutti, 2010), and it cannot be ruled out that there are common limitations and therefore systematic biases to model ensembles that are reflected in the distribution of ECS as derived from them. Although ESMs are typically well-documented, in ways that increasingly include information on critical decisions regarding tuning (Mauritsen et al., 2012; Hourdin et al., 2017; Schmidt et al., 2017a; Mauritsen and Roeckner, 2020), the full history of development decisions could involve both process-understanding and sometimes also other information such as historical warming. As outlying or poorly performing models emerge from the development process, they can become re-tuned, reconfigured or discarded and so might not see publication (Hourdin et al., 2017; Mauritsen and Roeckner, 2020). In the process of addressing such issues, modelling groups may, whether intentional or not, modify the modelled ECS.

[START FIGURE 7.19 HERE]

Figure 7.19: Global mean temperature anomaly in models and observations from 5 time periods. (a) Historical (CMIP6 models), (b) post 1975 (CMIP6 models), (c) Last Glacial Maximum (LGM; Cross-Chapter Box 2.1; PMIP4 models; (Kageyama et al., 2021; Zhu et al., 2021), (d) mid Pliocene warm period (MPWP; Cross-Chapter Box 2.4; PlioMIP models; Haywood et al., 2020; Zhang et al., 2021), (e) early Eocene climatic optimum (EECO; Cross-Chapter Box 2.1; DeepMIP models; Zhu et al., 2020; Lunt et al., 2021). Grey circles show models with ECS in the assessed *very likely* range; models in red have an ECS greater than the assessed *very likely* range (>5°C), models in blue have an ECS lower than the assessed *very likely* range (<2°C). Black ranges show the assessed temperature anomaly derived from observations (Chapter 2, Section 2.3). The Historical anomaly in models and observations is calculated as the difference between 2005–2014 and 1850–1900, and the post 1975 anomaly is calculated as the difference between 2005–2014 and 1975–1984. For the LGM, MPWP, and EECO, temperature anomalies are compared with pre-industrial (equivalent to CMIP6 simulation *piControl*). All model simulations of the MPWP and LGM were carried out with atmospheric CO_2 concentrations of 400 and 190 ppm respectively. However, CO_2 during the EECO is relatively more uncertain, and model simulations were carried out at either 1120ppm or 1680 ppm (except for the one high-ECS EECO simulation which was carried out at 560 ppm; Zhu et al., 2020). The one low-ECS EECO simulation was carried out at 1680 ppm. Further details on data sources and processing are available in the chapter data table (Table 7.SM.14).

[END FIGURE 7.19 HERE]

ACCEPTED VERSION SUBJECT TO FINAL EDITING

It is problematic and not obviously constructive to provide weights for, or rule out, individual CMIP6 model ensemble members based solely on their ECS and TCR values. Rather these models must be tested in a like-with-like way against observational evidence. Based on the currently published CMIP6 models we provide such an analysis, marking models with ECS above and below the assessed *very likely* range (Figure 7.19). In the long term historical warming (Figure 7.19a) both low and high ECS models are able to match the observed warming, presumably in part as a result of compensating aerosol cooling (Kiehl, 2007; Forster et al., 2013; Wang et al., 2021). In several cases of high ECS models that apply strong aerosol cooling it is found to result in surface warming and ocean heat uptake evolutions that are inconsistent with observations (Golaz et al., 2019b; Andrews et al., 2020; Winton et al., 2020). Modelled warming since the 1970s is less influenced by compensation between climate sensitivity and aerosol cooling (Jiménez-de-la-Cuesta and Mauritsen, 2019; Nijsse et al., 2020) resulting in the high ECS models in general warming more than observed, whereas low sensitivity models mostly perform better (Figure 7.19b); a result that may also have been influenced by temporary pattern effects (Sections 7.4.4 and 7.5.4). Paleoclimates are not influenced by such transient pattern effects, but are limited by structural uncertainties in the proxy-based temperature and forcing reconstructions as well as possible differences in equilibrium sea-surface temperature patterns between models and the real world (Section 7.5.4). Across the LGM, MPWP and EECO (Figure 7.19c-e), the few high ECS models that simulated these cases were outside the observed *very likely* ranges; see also (Feng et al., 2020; Renoult et al., 2020; Zhu et al., 2020). Also the low ECS model is either outside or on the edge of the observed *very likely* ranges.

As a result of the above considerations, in this Report projections of global surface temperature are produced using climate model emulators that are constrained by the assessments of ECS, TCR and ERF. In reports up to and including AR5, ESM values of ECS did not fully encompass the assessed *very likely* range of ECS, raising the possibility that past multi-model ensembles underestimated the uncertainty in climate change projections that existed at the times of those reports (e.g., Knutti, 2010). However, due to an increase in the modelled ECS spread and a decrease in the assessed ECS spread based on improved knowledge in multiple lines of evidence, the CMIP6 ensemble encompasses the *very likely* range of ECS (2–5°C) assessed in Section 7.5.5. Models outside of this range are useful for establishing emergent constraints on ECS and TCR and provide useful examples of "tail risk" (Sutton, 2018), producing dynamically consistent realisations of future climate change to inform impacts studies and risk assessments.

In summary, the distribution of CMIP6 models have higher average ECS and TCR values than the CMIP5 generation of models and the assessed values of ECS and TCR in Section 7.5.5. The high ECS and TCR values can in some CMIP6 models be traced to improved representation of extra-tropical cloud feedbacks (*medium confidence*). The ranges of ECS and TCR from the CMIP6 models are not considered robust samples of possible values and the models are not considered a separate line of evidence for ECS and TCR. Solely based on its ECS or TCR values an individual ESM cannot be ruled out as implausible, though some models with high (greater than 5°C) and low (less than 2°C) ECS are less consistent with past climate change (*high confidence*). High model climate sensitivity leads to generally higher projected warming in CMIP6 compared to both CMIP5 and that assessed based on multiple lines of evidence (Chapter 4, Sections 4.3.1 and 4.3.4; FAQ 7.3).

7.5.7 Processes underlying uncertainty in the global temperature response to forcing

While the magnitude of global warming by the end of the 21st century is dominated by future greenhouse gas emissions, the uncertainty in warming for a given ERF change is dominated by the uncertainty in ECS and TCR (Chapter 4, Section 4.3.4). The proportion of variation explained by ECS and TCR varies with scenario and the time period considered, but within CMIP5 models around 60% to 90% of the globally averaged projected surface warming range in 2100 can be explained by the model range of these metrics (Grose et al., 2018). Uncertainty in the long-term global surface temperature change can further be understood in terms of the processes affecting the global TOA energy budget, namely the ERF, the radiative feedbacks which govern the efficiency of radiative energy loss to space with surface warming, and the increase in the global energy inventory (dominated by ocean heat uptake) which reduces the transient surface warming. A variety

ACCEPTED VERSION SUBJECT TO FINAL EDITING

of studies evaluate the effect of each of these processes on surface changes within coupled ESM simulations by diagnosing so-called 'warming contributions' (Dufresne and Bony, 2008; Crook et al., 2011; Feldl and Roe, 2013; Vial et al., 2013; Pithan and Mauritsen, 2014; Goosse et al., 2018). By construction, the individual warming contributions sum to the total global surface warming (Figure 7.19b). For long-term warming in response to CO_2 forcing in CMIP5 models, the energy added to the climate system by radiative feedbacks is larger than the ERF of CO_2 (Figure 7.19a), implying that feedbacks more than double the magnitude of global warming (Figure 7.19b). Radiative kernel methods (see Section 7.4.1) can be used to decompose the net energy input from radiative feedbacks into its components. The water-vapour, cloud and surface-albedo feedbacks enhance global warming, while the lapse-rate feedback reduces global warming. Ocean heat uptake reduces the rate of global surface warming by sequestering heat at depth away from the ocean surface. Section 7.4.4.1 shows the warming contributions from these factors at the regional scale.

[START FIGURE 7.20 HERE]

Figure 7.20: Contributions of effective radiative forcing, ocean heat uptake and radiative feedbacks to global atmospheric energy input and near-surface air temperature change at year 100 of *abrupt4xCO2* simulations of CMIP6 models. (a) The energy flux to the global atmosphere associated with the effective CO_2 forcing, global ocean heat uptake, Planck response, and radiative feedbacks, which together sum to zero. The inset shows energy input from individual feedbacks, summing to the total feedback energy input. (b) Contributions to net global warming are calculated by dividing the energy inputs by the *magnitude* of the global Planck response (3.2 W m^{-2} $°C^{-1}$), with the contributions from radiative forcing, ocean heat uptake, and radiative feedbacks (orange bars) summing to the value of net warming (grey bar). The inset shows warming contributions associated with individual feedbacks, summing to the total feedback contribution. Uncertainties show the interquartile range (25% and 75% percentiles) across models. Radiative kernel methods (see Section 7.4.1) were used to decompose the net energy input from radiative feedbacks into contributions from changes in atmospheric water vapour, lapse-rate, clouds, and surface albedo (Zelinka et al. (2020) using the Huang et al. (2017) radiative kernel). The CMIP6 models included are those analysed by Zelinka et al. (2020) and the warming contribution analysis is based on that of Goosse et al. (2018). Further details on data sources and processing are available in the chapter data table (Table 7.SM.14).

[END FIGURE 7.20 HERE]

Differences in projected transient global warming across ESMs are dominated by differences in their radiative feedbacks, while differences in ocean heat uptake and radiative forcing play secondary roles (Figure 7.20b; Vial et al., 2013). The uncertainty in projected global surface temperature change associated with inter-model differences in cloud feedbacks is the largest source of uncertainty in CMIP5 and CMIP6 models (Figure 7.20b), just as they were for CMIP3 models (Dufresne and Bony, 2008). Extending this energy budget analysis to equilibrium surface warming suggests that about 70% of the inter-model differences in ECS arises from uncertainty in cloud feedbacks, with the largest contribution to that spread coming from shortwave low-cloud feedbacks (Vial et al., 2013; Zelinka et al., 2020).

Interactions between different feedbacks within the coupled climate system pose a challenge to our ability to understand global warming and its uncertainty based on energy budget diagnostics (Section 7.4.2). For example, water-vapour and lapse-rate feedbacks are correlated (Held and Soden, 2006) owing to their joint dependence on the spatial pattern of warming (Po-Chedley et al., 2018a). Moreover, feedbacks are not independent of ocean heat uptake because the uptake and transport of heat by the ocean influences the SST pattern on which global feedbacks depend (Section 7.4.4.3). However, alternative decompositions of warming contributions that better account for correlations between feedbacks produce similar results (Caldwell et al., 2016). The key role of radiative feedbacks in governing the magnitude of global warming is also supported by the high correlation between radiative feedbacks (or ECS) and transient 21st century warming within ESMs (Grose et al., 2018).

Another approach to evaluating the roles of forcing, feedbacks, and ocean heat uptake in projected warming

ACCEPTED VERSION SUBJECT TO FINAL EDITING

employs idealized energy balance models that emulate the response of ESMs, and which preserve the interactions between system components. One such emulator, used in Section 7.5.1.2, resolves the heat capacity of both the surface components of the climate system and the deep ocean (Held et al., 2010; Geoffroy et al., 2013a, 2013b; Kostov et al., 2014; Armour, 2017). Using this emulator, Geoffroy et al. (2012) find that: under an idealized 1% per year increase in atmospheric CO_2, radiative feedbacks constitute the greatest source of uncertainty (about 60% of variance) in transient warming beyond several decades; ERF uncertainty plays a secondary but important role in warming uncertainty (about 20% of variance) that diminishes beyond several decades; and ocean heat uptake processes play a minor role in warming uncertainty (less than 10% of variance) at all timescales.

More computationally intensive approaches evaluate how the climate response depends on perturbations to key parameter or structural choices within ESMs. Large 'perturbed parameter ensembles' wherein a range of parameter settings associated with cloud physics are explored within atmospheric ESMs produce a wide range of ECS due to changes in cloud feedbacks, but often produce unrealistic climate states (Joshi et al., 2010). Rowlands et al. (2012) generated a ESM perturbed-physics ensemble of several thousand members by perturbing model parameters associated with radiative forcing, cloud feedbacks, and ocean vertical diffusivity (an important parameter for ocean heat uptake). After constraining the ensemble to have a reasonable climatology and to match the observed historical surface warming, they found a wide range of projected warming by the year 2050 under the SRES A1B scenario (1.4–3°C relative to the 1961–1990 average) that is dominated by differences in cloud feedbacks. The finding that cloud feedbacks are the largest source of spread in the net radiative feedback has since been confirmed in perturbed parameter ensemble studies using several different ESMs (Gettelman et al., 2012; Tomassini et al., 2015; Kamae et al., 2016; Rostron et al., 2020; Tsushima et al., 2020). By swapping out different versions of the atmospheric or oceanic components in a coupled ESM, Winton et al. (2013) found that TCR and ECS depend on which atmospheric component was used (using two versions with different atmospheric physics), but that only TCR is sensitive to which oceanic component of the model was used (using two versions with different vertical coordinate systems, among other differences); TCR and ECS changed by 0.4°C and 1.4°C, respectively, when the atmospheric model component was changed, while TCR and ECS changed by 0.3°C and less than 0.05°C, respectively, when the oceanic model component was changed. By perturbing ocean vertical diffusivities over a wide range, Watanabe et al. (2020b) found that TCR changed by 0.16°C within the model MIROC5.2 while Krasting et al. (2018) found that ECS changed by about 0.6°C within the model GFDL-ESM2G, with this difference linked to different radiative feedbacks associated with different spatial patterns of sea-surface warming (see Section 7.4.4.3). By comparing simulations of CMIP6 models with and without the effects of CO_2 on vegetation, (Zarakas et al., 2020) find a physiological contribution to TCR of 0.12°C (range 0.02–0.29°C across models) owing to physiological adjustments to the CO_2 ERF (Section 7.3.2.1).

There is *robust evidence* and *high agreement* across a diverse range of modelling approaches and thus *high confidence* that radiative feedbacks are the largest source of uncertainty in projected global warming out to 2100 under increasing or stable emissions scenarios, and that cloud feedbacks in particular are the dominant source of that uncertainty. Uncertainty in radiative forcing plays an important but generally secondary role. Uncertainty in global ocean heat uptake plays a lesser role in global warming uncertainty, but ocean circulation could play an important role through its effect on sea-surface warming patterns which in turn project onto radiative feedbacks through the pattern effect (Section 7.4.4.3).

The spread in historical surface warming across CMIP5 ESMs shows a weak correlation with inter-model differences in radiative feedback or ocean heat uptake processes but a high correlation with inter-model differences in radiative forcing owing to large variations in aerosol forcing across models (Forster et al., 2013). Likewise, the spread in projected 21st century warming across ESMs depends strongly on emissions scenario (Hawkins and Sutton, 2012; Chapter 4, Section 4.3.1). Strong emissions reductions would remove aerosol forcing (Chapter 6, Section 6.7.2) and this could dominate the uncertainty in near-term warming projections (Armour and Roe, 2011; Mauritsen and Pincus, 2017; Schwartz, 2018; Smith et al., 2019). On post 2100 timescales carbon cycle uncertainty such as that related to permafrost thawing could become increasingly important, especially under high emission scenarios (Chapter 5, Figure 5.30).

In summary, there is *high confidence* that cloud feedbacks are the dominant source of uncertainty for late 21st

ACCEPTED VERSION SUBJECT TO FINAL EDITING

century projections of transient global warming under increasing or stable emissions scenarios, whereas uncertainty is dominated by aerosol ERF in strong mitigation scenarios. Global ocean heat uptake is a smaller source of uncertainty in long-term surface warming. (*high confidence*).

7.6 Metrics to evaluate emissions

Emission metrics are used to compare the relative effect of emissions of different gases over time in terms of radiative forcing, global surface temperature or other climate effects. They are introduced in Chapter 1, Box 1.3. Chapter 8 of AR5 (Myhre et al., 2013b) comprehensively discussed different emission metrics so this section focuses on updates since that report. Section 7.6.1 updates the physical assessment. Section 7.6.2 assesses developments in the comparison of emissions of short- and long-lived gases. Box 7.3 assesses physical aspects of emission metric use within climate policy.

7.6.1 Physical description of metrics

This section discusses metrics that relate emissions to physical changes in the climate system. Other metrics, for instance relating to economic costs or 'damage' are discussed in WG III Chapter 2. The same Chapter also assesses literature examining to what extent different physical metrics are linked to cost-benefit and cost-effectiveness metrics. One metric, the 100-year Global Warming Potential (GWP-100), has extensively been employed in climate policy to report emissions of different greenhouse gases on the same scale. Other physical metrics exist, which are discussed in this section.

Emission metrics can be quantified as the magnitude of the effect a unit mass of emission of a species has on a key measure of climate change. This section focuses on physical measures such as the radiative forcing, GSAT change, global average precipitation change, and global mean sea level rise (Myhre et al., 2013b; Sterner et al., 2014; Shine et al., 2015). When used to represent a climate effect, the metrics are referred to as absolute metrics and expressed in units of effect per kg (e.g., Absolute Global Warming Potential, AGWP or Absolute Global Temperature-change Potential, AGTP). More commonly, these are compared with a reference species (almost always CO_2 in kg(CO_2)), to give a dimensionless factor (written as e.g., Global Warming Potential (GWP) or Global Temperature-change Potential (GTP)). The unit mass is usually taken as a 1 kg instantaneous "pulse" (Myhre et al., 2013b), but can also refer to a "step" in emission rate of 1 kg yr^{-1}.

There is a cause-effect chain that links human activity to emissions, then from emissions to radiative forcing, climate response, and climate impacts (Fuglestvedt et al., 2003). Each step in the causal chain requires an inference or modelling framework that maps causes to effects. Emission metrics map from emissions of some compound to somewhere further down the cause and effect chain, radiative forcing (e.g., GWP) or temperature (e.g., GTP) or other effects (such as sea-level rise or socioeconomic impacts). While variables later in the chain have greater policy or societal relevance, they are also subject to greater uncertainty because each step in the chain includes more modelling systems, each of which brings its own uncertainty (Balcombe et al., 2018; Chapter 1, Figure 1.15).

Since AR5, understanding of the radiative effects of emitted compounds has continued to evolve and these changes are assessed in Section 7.6.1.1. Metrics relating to precipitation and sea level have also been quantified (Section 7.6.1.2). Understanding of how the carbon-cycle response to temperature effects emission metrics has improved. This allows the carbon cycle response to temperature to be more fully included in the emission metrics presented here (Section 7.6.1.3). There have also been developments in approaches for comparing short-lived greenhouse gases to CO_2 in the context of mitigation and global surface temperature change (Section 7.6.1.4). Emission metrics for selected key compounds are presented in Section 7.6.1.5.

7.6.1.1 Radiative properties and lifetimes.

ACCEPTED VERSION SUBJECT TO FINAL EDITING

The radiative properties and lifetimes of compounds are the fundamental component of all emission metrics. Since AR5, there have been advances in the understanding of the radiative properties of various compounds (see Sections 7.3.1, 7.3.2 and 7.3.3), and hence their effective radiative efficiencies (ERFs per unit change in concentration). For CO_2, CH_4 and N_2O, better accounting of the spectral properties of these gases has led to re-evaluation of their SARF radiative efficiencies and their dependence on the background gas concentrations (Section 7.3.2). For CO_2, CH_4, N_2O, CFC-11 and CFC-12 the tropospheric adjustments (Sections 7.3.1 and 7.3.2) are assessed to make a non-zero contribution to ERF. There is insufficient evidence to include tropospheric adjustments for other halogenated compounds. The re-evaluated effective radiative efficiency for CO_2 will affect all emission metrics relative to CO_2.

The effective radiative efficiencies (including adjustments from Section 7.3.2) for 2019 background concentrations for CO_2, CH_4 and N_2O are assessed to be 1.36×10^{-5}, 3.77×10^{-4} and 3.11×10^{-3} W m^{-2} ppb^{-1} respectively (see Table 7.15 for uncertainties), compared to AR5 assessments of 1.37×10^{-5}, 3.63×10^{-4} and 3.00×10^{-3} W m^{-2} ppb^{-1}. For CO_2, increases due to the re-evaluated radiative properties and adjustments balance the decreases due to the increasing background concentration. For CH_4, increases due to the re-evaluated radiative properties more than offset the decreases due to the increasing background concentration. For N_2O the addition of tropospheric adjustments increases the effective radiative efficiency. Radiative efficiencies of halogenated species have been revised slightly (Section 7.3.2.4) and for CFCs include tropospheric adjustments.

The perturbation lifetimes of CH_4 (Chapter 6, Section 6.3.1). and N_2O (Chapter 5, Section 5.2.3.1) have been slightly revised since AR5 to be 11.8 ± 1.8 years and 109 ± 10 years (Table 7.15). The lifetimes of halogenated compounds have also been slightly revised (Hodnebrog et al., 2020a).

Although there has been greater understanding since AR5 of the carbon cycle responses to CO_2 emissions (Chapter 5, Sections 5.4 and 5.5), there has been no new quantification of the response of the carbon-cycle to an instantaneous pulse of CO_2 emission since Joos et al. (2013).

7.6.1.2 Physical indicators

The basis of all the emission metrics is the time profile of effective radiative forcing (ERF) following the emission of a particular compound. The emission metrics are then built up by relating the forcing to the desired physical indicators. These forcing-response relationships can either be generated from emulators (Tanaka et al., 2013; Gasser et al., 2017b; Cross-Chapter Box 7.1), or from analytical expressions based on parametric equations (response functions) derived from more complex models (Myhre et al., 2013b).

To illustrate the analytical approach, the ERF time evolution following a pulse of emission can be considered an Absolute Global Forcing Potential AGFP (similar to the Instantaneous Climate Impact of Edwards and Trancik (2014)). This can be transformed into an Absolute Global Temperature Potential (AGTP) by combining the radiative forcing with a global surface temperature response function. This temperature response is typically derived from a two-layer energy balance emulator (Supplementary Material 7.SM.5; Myhre et al., 2013b). For further physical indicators further response functions are needed based on the radiative forcing or temperature, for instance. Sterner et al. (2014) used an upwelling-diffusion energy balance model to derive the thermosteric component of sea level rise (SLR) as response functions to radiative forcing or global surface temperature. A metric for precipitation combines both the radiative forcing (AGFP) and temperature (AGTP) responses to derive an Absolute Global Precipitation Potential AGPP (Shine et al., 2015). The equations relating these metrics are given in the Supplementary Material 7.SM.5.

The physical emission metrics described above are functions of time since typically the physical effects reach a peak and then decrease in the period after a pulse emission as the concentrations of the emitted compound decay. The value of the metrics can therefore be strongly dependent on the time horizon of interest. All relative metrics (GWP, GTP etc) are also affected by the time dependence of the CO_2 metrics in

ACCEPTED VERSION SUBJECT TO FINAL EDITING

the denominator. Instantaneous or endpoint metrics quantify the change (in radiative forcing, global surface temperature, global mean sea level) at a particular time after the emission. These can be appropriate when the goal is to not exceed a fixed target such as a temperature or global mean sea-level rise level at a specific time. Emission metrics can also be integrated from the time of emission. The most common of these is the Absolute Global Warming Potential (AGWP), which is the integral of the AGFP. The physical effect is then in units of forcing-years, degree-years or metre-years for forcing, temperature, or sea-level rise, respectively. These can be appropriate for trying to reduce the overall damage potential when the effect depends on how long the change occurs for, not just how large the change is. The integrated metrics still depend on the time horizon, though for the shorter-lived compounds this dependence is somewhat smoothed by the integration. The integrated version of a metric is often denoted as iAGxx, although the integral of the forcing-based metric (iAGFP) is known as the AGWP. Both the endpoint and integrated absolute metrics for non-CO_2 species can be divided by the equivalent for CO_2 to give relative emission metrics (e.g., GWP (=iGFP), GTP, iGTP).

Each step from radiative forcing to global surface temperature to SLR introduces longer timescales and therefore prolongs further the contributions to climate change of short-lived greenhouse gases (Myhre et al., 2013b). Thus, short-lived greenhouse gases become more important (relative to CO_2) for SLR than for temperature or radiative forcing (Zickfeld et al., 2017). Integrated metrics include the effects of a pulse emission from the time of emission up to the time horizon, whereas endpoint metrics only include the effects that persist out to the time horizon. Because the largest effects of short-lived greenhouse gases occur shortly after their emission and decline towards the end of the time period, short-lived greenhouse gases have relatively higher integrated metrics than their corresponding endpoint metrics (Peters et al., 2011; Levasseur et al., 2016).

For species perturbations that lead to a strong regional variation in forcing pattern, the regional temperature response can be different to that for CO_2. Regional equivalents to the global metrics can be derived by replacing the global surface temperature response function with a regional response matrix relating forcing changes in one region to temperature changes in another (Collins et al., 2013b; Aamaas et al., 2017; Lund et al., 2017).

For the research discussed above, metrics for several physical variables can be constructed that are linear functions of radiative forcing. Similar metrics could be devised for other climate variables provided they can be related by response functions to radiative forcing or global surface temperature change. The radiative forcing does not increase linearly with emissions for any species, but the non-linearities (for instance changes in CO_2 radiative efficiency) are small compared to other uncertainties.

7.6.1.3 Carbon cycle responses and other indirect contributions

The effect of a compound on climate is not limited to its direct radiative forcing. Compounds can perturb the carbon cycle affecting atmospheric CO_2 concentrations. Chemical reactions from emitted compounds can produce or destroy other greenhouse gases or aerosols.

Any agent that warms the surface perturbs the terrestrial and oceanic carbon fluxes (Chapter 5, Sections 5.4.3 and 5.4.4), typically causing a net flux of CO_2 into the atmosphere and hence further warming. This aspect is already included in the carbon cycle models that are used to generate the radiative effects of a pulse of CO_2 (Joos et al., 2013), but was neglected for non-CO_2 compounds in the conventional metrics so this introduces an inconsistency and bias in the metric values (Gillett and Matthews, 2010; MacDougall et al., 2015; Tokarska et al., 2018). A simplistic account of the carbon cycle response was tentatively included in AR5 based on a single study (Collins et al., 2013b). Since AR5 this understanding has been revised (Gasser et al., 2017b; Sterner and Johansson, 2017) using simple parameterised carbon cycle models to derive the change in CO_2 surface flux for a unit temperature pulse as an impulse response function to temperature. In Collins et al. (2013a) this response function was assumed to be simply a delta function, whereas the newer studies include a more complete functional form accounting for subsequent re-uptake of CO_2 after the removal of the temperature increase. Accounting for re-uptake has the effect of reducing the carbon-cycle

ACCEPTED VERSION SUBJECT TO FINAL EDITING

responses associated with the metrics compared to AR5, particularly at large time horizons. The increase in any metric due to the carbon cycle response can be derived from the convolution of the global surface temperature response with the CO_2 flux response to temperature and the equivalent metric for CO_2 (equation 7.SM.5.5 in the Supplementary Material). Including this response also increases the duration of the effect of short-lived greenhouse gases on climate (Fu et al., 2020). An alternative way of accounting for the carbon cycle temperature response would be to incorporate it into the temperature response function (the response functions used here and given in Supplementary Material 7.SM.5.2 do not explicitly do this). If this were done, the correction could be excluded from both the CO_2 and non-CO_2 forcing responses as in Hodnebrog et al. (2020a).

Including the carbon cycle response for non-CO_2 treats CO_2 and non-CO_2 compounds consistently and therefore we assess that its inclusion more accurately represents the climate effects of non-CO_2 species. There is *high confidence* in the methodology of using carbon cycle models for calculating the carbon cycle response. The magnitude of the carbon cycle response contributions to the emission metrics vary by a factor of two between Sterner and Johansson (2017) and Gasser et al. (2017b). The central values are taken from Gasser et al. (2017b) as the OSCAR 2.2 model used is based on parameters derived from CMIP5 models, and the climate-carbon feedback magnitude is therefore similar to the CMIP5 multi-model mean (Arora et al., 2013; Lade et al., 2018). As values have only been calculated in two simple parameterised carbon cycle models the uncertainty is assessed to be ±100%. Due to few studies and a factor of two difference between them, there is *low confidence* that the magnitude of the carbon cycle response is within the higher end of this uncertainty range, but *high confidence* that the sign is positive. Carbon cycle responses are included in all the metrics presented in Tables 7.15 and Supplementary Table 7.SM.7. The carbon cycle contribution is lower than in AR5, but there is *high confidence* in the need for its inclusion and the method by which it is quantified.

Emissions of non-CO_2 species can affect the carbon cycle in other ways: emissions of ozone precursors can reduce the carbon uptake by plants (Collins et al., 2013b); emissions of reactive nitrogen species can fertilize plants and hence increase the carbon uptake (Zaehle et al., 2015); and emissions of aerosols or their precursors can affect the utilisation of light by plants (Cohan et al., 2002; Mercado et al., 2009; Mahowald et al., 2017) (see Chapter 6, Section 6.4.4 for further discussion). There is *robust evidence* that these processes occur and are important, but *insufficient evidence* to determine the magnitude of their contributions to emission metrics. Ideally, emission metrics should include all indirect effects to be consistent, but limits to our knowledge restrict how much can be included in practice.

Indirect contributions from chemical production or destruction of other greenhouse gases are quantified in Chapter 6, Section 6.4. For methane, AR5 (Myhre et al., 2013b) assessed that the contributions from effects on ozone and stratospheric water vapour add 50% ± 30% and 15% ± 11% to the emission-based ERF, which were equivalent to $1.8 \pm 0.7 \times 10^{-4}$ and $0.5 \pm 0.4 \times 10^{-4}$ W m^{-2} ppb $(CH_4)^{-1}$. In AR6 the radiative efficiency formulation is preferred as it is independent of the assumed radiative efficiency for methane. The assessed contributions to the radiative efficiency for methane due to ozone are $1.4 \pm 0.7 \times 10^{-4}$ W m^{-2} ppb $(CH_4)^{-1}$, based on 0.14 W m^{-2} forcing from a 1023 ppb (1850 to 2014) methane change (Thornhill et al., 2021b). The contribution from stratospheric water vapour is $0.4 \pm 0.4 \times 10^{-4}$ W m^{-2} ppb $(CH_4)^{-1}$, based on 0.05 W m^{-2} forcing from a 1137 ppb (1750 to 2019) methane change (Section 7.3.2.6). N_2O depletes upper stratospheric ozone (a positive forcing) and reduces the methane lifetime. In AR5 the methane lifetime effect was assessed to reduce methane concentrations by 0.36 ppb per ppb increase in N_2O, with no assessment of the effective radiative forcing from ozone. This is now increased to –1.7 ppb methane per ppb N_2O (based on a methane lifetime decrease of 4% ± 4% for a 55 ppb increase in N_2O (Thornhill et al., 2021b) and a radiative efficiency of $5.5 \pm 0.4 \times 10^{-4}$ W m^{-2} ppb $(N_2O)^{-1}$ through ozone (Thornhill et al., 2021b). In summary, GWPs and GTPs for methane and nitrous oxide are slightly lower than in AR5 (*medium confidence*) due to revisions in their lifetimes and updates to their indirect chemical effects.

Methane can also affect the oxidation pathways of aerosol formation (Shindell et al., 2009) but the available literature is insufficient to make a robust assessment of this. Hydrocarbon and molecular hydrogen oxidation also leads to tropospheric ozone production and change in methane lifetime (Collins et al., 2002; Hodnebrog et al., 2018). For reactive species the emission metrics can depend on where the emissions occur, and the

ACCEPTED VERSION SUBJECT TO FINAL EDITING

season of emission (Aamaas et al., 2016; Lund et al., 2017; Persad and Caldeira, 2018). AR5 included a contribution to the emission metrics for ozone-depleting substances (ODSs) from the loss of stratospheric ozone. The assessment of ERFs from ODSs in Chapter 6 (Section 6.4.2) suggests the quantification of these terms may be more uncertain than the formulation in AR5 so these are not included here.

Oxidation of methane leads ultimately to the net production of atmospheric CO_2 (Boucher et al., 2009). This yield is less than 100% (on a molar basis) due to uptake by soils and some of the reaction products (mainly formaldehyde) being directly removed from the atmosphere before being completely oxidised. Estimates of the yield are 61% (Boucher et al., 2009) and 88% (Shindell et al., 2017), so the assessed range is 50-100% with a central value of 75% *(low confidence)*. For methane and hydrocarbons from fossil sources, this will lead to additional fossil CO_2 in the atmosphere whereas for biogenic sources of methane or hydrocarbons, this replaces CO_2 that has been recently removed from the atmosphere. Since the ratio of molar masses is 2.75, 1 kg of methane generates 2.1± 0.7 kg CO_2 for a 75% yield. For biogenic methane the soil uptake and removal of partially-oxidised products is equivalent to a sink of atmospheric CO_2 of 0.7 ± 0.7 kg per kg methane. The contributions of this oxidation effect to the methane metric values allow for the time delay in the oxidation of methane. Methane from fossil fuel sources has therefore slightly higher emission metric values than those from biogenic sources (*high confidence*). The CO_2 can already be included in carbon emission totals (Muñoz and Schmidt, 2016) so care needs to be taken when applying the fossil correction to avoid double counting.

7.6.1.4 Comparing long-lived with short-lived greenhouse gases

Since AR5 there have been developments in how to account for the different behaviours of short-lived and long-lived compounds. Pulse-based emission metrics for short-lived greenhouse gases with lifetimes less than twenty years are very sensitive to the choice of time horizon (e.g. Pierrehumbert, 2014). Global surface temperature changes following a pulse of CO_2 emissions are roughly constant in time (the principle behind TCRE, Figure 7.21b, Chapter 5, Section 5.5.1) whereas the temperature change following a pulse of short-lived greenhouse gas emission declines with time. In contrast to a one-off pulse, a step change in short-lived greenhouse gas emissions that is maintained indefinitely causes a concentration increase that eventually equilibrates to a steady state in a way that is more comparable to a pulse of CO_2. Similarly the resulting change in global surface temperature from a step change in short-lived greenhouse gases (Figure 7.21a) after a few decades increases only slowly (due to accumulation of heat in the deep ocean) and hence its effects are more similar to a pulse of CO_2 (Smith et al., 2012; Lauder et al., 2013; Allen et al., 2016, 2018b). The different time dependence of short-lived and long-lived compounds can be accounted for exactly with the CO_2 forcing equivalent metric (Wigley, 1998; Allen et al., 2018b; Jenkins et al., 2018) that produces a CO_2 emission time profile such that the radiative forcing matches the time evolution of that from the non-CO_2 emissions. But other metric approaches can approximate this exact approach.

The similarity in behaviour of step changes in short-lived greenhouse gas emissions and pulses of CO_2 emissions has recently been used to formulate new emissions metric concepts (Collins et al., 2020). For short-lived greenhouse gases, these new concepts use a step change in the rate of emissions, in contrast to an instantaneous pulse in a given year that is typically used (e.g. Myhre et al., 2013b). Metrics for step emission changes are denoted here by a superscript "*S*" (e.g., $AGTP_X^S$ is the absolute global surface temperature change potential from a unit step change in emissions of species "*X*"). These can be derived by integrating the more standard pulse emission changes up to the time horizon. The response to a step emission change is therefore equivalent to the integrated response to a pulse emission ($AGTP_X^S = iAGTP_X$); and the radiative forcing response to a step emission change $AGFP_X^S$ is equivalent to the integrated forcing response $iAGFP_X$which is the AGWP. The step metric for short-lived greenhouse gases can then be compared with the pulse metric for CO_2 in a ratio $AGTP_X^S/AGTP_{CO2}$ (Collins et al., 2020). This is referred to as a combined-GTP (CGTP) in Collins et al. (2020), and has units of years (the standard GTP is dimensionless). This CGTP shows less variation with time than the standard GTP (comparing Figure 7.21c with Figure 7.21d) and provides a scaling for comparing a change in emission rate (in kg yr^{-1}) of short-lived greenhouse gases with a pulse emission or change in cumulative CO_2 emissions (in kg). Cumulative CO_2 equivalent emissions are given by CGTP × emission rate of short-lived greenhouse gases. The CGTP can be

ACCEPTED VERSION SUBJECT TO FINAL EDITING

calculated for any species, but it is least dependent on the chosen time horizon for species with lifetimes less than half the time horizon of the metric (Collins et al., 2020). Pulse-step metrics can therefore be useful where time dependence of pulse metrics, like GWP or GTP, complicates their use (see Box 7.3).

For a stable global warming from non-CO_2 climate agents (gas or aerosol) their effective radiative forcing needs to gradually decrease (Tanaka and O'Neill, 2018). Cain et al. (2019) find this decrease to be around 0.3% yr^{-1} for the climate response function in AR5 (Myhre et al., 2013b). To account for this, a quantity referred to as GWP* has been defined that combines emissions (pulse) and changes in emission levels (step) approaches (Cain et al., 2019; Smith et al., 2021)[2]. The emission component accounts for the need for emissions to decrease to deliver a stable warming. The step (sometimes referred to as flow or rate) term in GWP* accounts for the change in global surface temperature that arises in from a change in short-lived greenhouse gas emission rate, as in CGTP, but here approximated by the change in emissions over the previous 20 years.

Cumulative CO_2 emissions and GWP*-based cumulative CO_2 equivalent greenhouse gas (GHG) emissions multiplied by TCRE closely approximate the global warming associated with emissions timeseries (of CO_2 and GHG, respectively) from the start of the time-series (Lynch et al., 2020). Both the CGTP and GWP* convert short-lived greenhouse gas emission rate changes into cumulative CO_2 equivalent emissions, hence scaling these by TCRE gives a direct conversion from short-lived greenhouse gas emission to global surface temperature change. By comparison expressing methane emissions as CO_2 equivalent emissions using GWP-100 overstates the effect of constant methane emissions on global surface temperature by a factor of 3-4 over a 20-year time horizon (Lynch et al., 2020, their Figure 5), while understating the effect of any new methane emission source by a factor of 4-5 over the 20 years following the introduction of the new source (Lynch et al., 2020, their Figure 4).

[START FIGURE 7.21 HERE]

Figure 7.21: Emission metrics for two short-lived greenhouse gases: HFC-32 and CH_4, (lifetimes of 5.4 and 11.8 years). The temperature response function comes from Supplementary Material 7.SM.5.2. Values for non-CO_2 species include the carbon cycle response (Section 7.6.1.3). Results for HFC-32 have been divided by 100 to show on the same scale. (a) temperature response to a step change in short-lived greenhouse gas emission. (b) temperature response to a pulse CO_2 emission. (c) conventional GTP metrics (pulse vs pulse). (d) combined-GTP metric (step versus pulse). Further details on data sources and processing are available in the chapter data table (Table 7.SM.14).

[END FIGURE 7.21 HERE]

Figure 7.22 explores how cumulative CO_2 equivalent emissions estimated for methane vary under different emission metric choices and how estimates of the global surface air temperature (GSAT) change deduced from these cumulative emissions compare to the actual temperature response computed with the two-layer emulator. Note that GWP and GTP metrics were not designed for use under a cumulative carbon dioxide equivalent emission framework (Shine et al., 1990, 2005), even if they sometimes are (e.g. Cui et al., 2017; Howard et al., 2018) and analysing them in this way can give useful insights into their physical properties. Using these standard metrics under such frameworks, the cumulative CO_2 equivalent emission associated with methane emissions would continue to rise if methane emissions were substantially reduced but remained above zero. In reality, a decline in methane emissions to a smaller but still positive value could cause a declining warming. GSAT changes estimated with cumulative CO_2 equivalent emissions computed with GWP-20 matches the warming trend for a few decades but quickly overestimates the response. Cumulative emissions using GWP-100 perform well when emissions are increasing but not when they are stable or decreasing. Cumulative emissions using GTP-100 consistently underestimate the warming. Cumulative emissions using either CGTP or GWP* approaches can more closely match the GSAT evolution (Allen et al., 2018b; Cain et al., 2019; Collins et al., 2020; Lynch et al., 2020).

[2] To calculate CO_2 equivalent emissions under GWP*, the short-lived greenhouse gas emissions are multiplied by GWP100 × 0.28 and added to the net emission increase or decrease over the previous 20 years multiplied by GWP100 x 4.24 (Smith et al., 2021).

ACCEPTED VERSION SUBJECT TO FINAL EDITING

In summary, new emission metric approaches such as GWP* and CGTP are designed to relate emission changes in short-lived greenhouse gases to emissions of CO_2 as they better account for the different physical behaviours of short and long-lived gases. Through scaling the corresponding cumulative CO_2 equivalent emissions by the TCRE, the GSAT response from emissions over time of an aggregated set of gases can be estimated. Using either these new approaches, or treating short and long-lived GHG emission pathways separately, can improve the quantification of the contribution of emissions to global warming within a cumulative emission framework, compared to approaches that aggregate emissions of GHGs using standard CO_2 equivalent emission metrics. As discussed in Box 7.3, there is *high confidence* that multi-gas emission pathways with the same time dependence of aggregated CO_2 equivalent emissions estimated from standard approaches, such as weighting emissions by their GWP-100 values, rarely lead to the same estimated temperature outcomes..

[START FIGURE 7.22 HERE]

Figure 7.22: Explores how cumulative carbon dioxide equivalent emissions estimated for methane vary under different emission metric choices and how estimates of the global surface air temperature (GSAT) change deduced from these cumulative emissions compare to the actual temperature response computed with the two-layer emulator (solid black lines). Panels a) and b) show the SSP4-6.0 and SSP1-2.6 scenarios respectively. The panels show annual methane emissions as the dotted lines (left axis) from 1750–2100. The solid lines can be read as either estimates of GSAT change or estimates of the cumulative carbon dioxide equivalent emissions. This is because they are related by a constant factor, the TCRE. Thus, values can be read using either of the right hand axes. Emission metric values are taken from Table 7.15. The GWP* calculation is given in Section 7.6.1.4. The two-layer emulator has been calibrated to the central values of the report's assessment (see Supplementary Material 7.SM.5.2). Further details on data sources and processing are available in the chapter data table (Table 7.SM.14).

[END FIGURE 7.22 HERE]

7.6.1.5 Emission metrics by compounds

Emission metrics for selected compounds are presented in Table 7.15, with further compounds presented in the Supplementary Material Table 7.SM.7. The evolution of the CO_2 concentrations in response to a pulse emission is as in AR5 (Joos et al., 2013; Myhre et al., 2013b), the perturbation lifetimes for CH_4 and N_2O are from Section 7.6.1.1. The lifetimes and radiative efficiencies for halogenated compounds are taken from Hodnebrog et al. (2020a). Combined metrics (CGTPs) are presented for compounds with lifetimes less than 20 years. Note CGTP has units of years and is applied to a change in emission rate rather than a change in emission amount. Changes since AR5 are due to changes in radiative properties and lifetimes (Section 7.6.1.1), and indirect contributions (Section 7.6.1.3). Table 7.15 also gives overall emission uncertainties in the emission metrics due to uncertainties in radiative efficiencies, lifetimes and the climate response function (Supplementary Material Tables 7.SM.8 to 7.SM.13)

Following their introduction in AR5 the assessed metrics now routinely include the carbon-cycle response for non-CO_2 gases (Section 7.6.1.3). As assessed in this earlier section, the carbon cycle contribution is lower than in AR5. Contributions to CO_2 formation are included for methane depending on whether or not the source originates from fossil carbon, thus methane from fossil fuel sources has slightly higher emission metric values than that from non-fossil sources.

[START TABLE 7.15 HERE]

Table 7.15: Emission metrics for selected species: Global Warming Potential (GWP), Global Temperature-change Potential (GTP). All values include carbon cycle responses as described in Section 7.6.1.3. Combined-GTPs (CGTPs) are shown only for species with a lifetime less than 20 years (see Section 7.6.1.4). Note CGTP has units of years and is applied to a change in emission rate rather than a change in emission

ACCEPTED VERSION SUBJECT TO FINAL EDITING

amount. The radiative efficiencies are as described in Section 7.3.2 and include tropospheric adjustments where assessed to be non-zero in Section 7.6.1.1. The climate response function is from Supplementary Material 7.SM.5.2. Uncertainty calculations are presented in Supplementary Tables 7.SM.8 to 7.SM.13. Chemical effects of CH_4 and N_2O are included (Section 7.6.1.3). Contributions from stratospheric ozone depletion to halogenated species metrics are not included. Supplementary Table 7.SM.7 presents the full table.

# Species	Lifetime (years)	Radiative efficiency (W m^{-2} ppb^{-1})	GWP-20	GWP-100	GWP-500	GTP-50	GTP-100	CGTP-50 (years)	CGTP-100 (years)
CO2	Multiple	$1.33\pm0.16 \times 10^{-5}$	1.	1.000	1.000	1.000	1.000		
CH_4-fossil	11.8 ±1.8	$5.7\pm1.4\times10^{-4}$	82.5 ±25.8	29.8 ±11	10.0 ±3.8	13.2 ±6.1	7.5 ±2.9	2823 ±1060	3531 ±1385
CH_4-non fossil	11.8 ±1.8	$5.7\pm1.4\times10^{-4}$	80.8 ±25.8	27.2 ±11	7.3 ±3.8	10.3 ±6.1	4.7 ±2.9	2701 ±1057	3254 ±1364
N_2O	109 ±10	$2.8\pm1.1 \times10^{-3}$	273 ±118	273 ±130	130 ±64	290 ±140	233 ±110		
HFC-32	5.4 ±1.1	$1.1\pm0.2 \times10^{-1}$	2693 ±842	771 ±292	220 ±87	181 ±83	142 ±51	78175 ±29402	92888 ±36534
HFC-134a	14.0 ±2.8	$1.67\pm0.32 \times10^{-1}$	4144 ±1160	1526 ±577	436 ±173	733 ±410	306 ±119	146670 ±53318	181408 ±71365
CFC-11	52.0 ±10.4	$2.91\pm0.65 \times10^{-1}$	8321 ±2419	6226 ±2297	2093 ±865	6351 ±2342	3536 ±1511		
PFC-14	50000	$9.89\pm0.19 \times10^{-2}$	5301 ±1395	7380 ±2430	10587 ±3692	7660 ±2464	9055 ±3128		

[END TABLE 7.15 HERE]

[START BOX 7.3 HERE]

BOX 7.3: Physical considerations in emission-metric choice

Following AR5, this report does not recommend an emission metric because the appropriateness of the choice depends on the purposes for which gases or forcing agents are being compared. Emission metrics can facilitate the comparison of effects of emissions in support of policy goals. They do not define policy goals or targets but can support the evaluation and implementation of choices within multi-component policies (e.g., they can help prioritise which emissions to abate). The choice of metric will depend on which aspects of climate change are most important to a particular application or stakeholder and over which time-horizons. Different international and national climate policy goals may lead to different conclusions about what is the most suitable emission metric (Myhre et al., 2013b).

GWP and GTP give the relative effect of pulse emissions, i.e. how much more energy is trapped (GWP) or how much warmer (GTP) the climate would be when unit emissions of different compounds are compared (Section 7.6.1.2). Consequently, these metrics provide information on how much energy accumulation (GWP) or how much global warming (GTP) could be avoided (over a given time period, or at a given future point in time) by avoiding the emission of a unit of a short-lived greenhouse gas compared to avoiding a unit of CO_2. By contrast, the new metric approaches of Combined-GTP and GWP* closely approximate the additional effect on climate from a time-series of short-lived greenhouse gas emissions, and can be used to

ACCEPTED VERSION SUBJECT TO FINAL EDITING

compare this to the effect on temperature from the emission or removal of a unit of CO_2 (Allen et al., 2018b; Collins et al., 2020; Section 7.6.1.4).

If global surface temperature stabilization goals are considered, cumulative CO_2 equivalent emissions computed with the GWP-100 emission metric would continue to rise when short-lived greenhouse gas emissions are reduced but remain above zero (Figure 7.22b). Such as rise would not match the expected global surface temperature stabilization or potential decline in warming that comes from a reduction in emissions of short-lived greenhouse gases (Pierrehumbert, 2014; Allen et al., 2018b; Cain et al., 2019; Collins et al., 2020; Lynch et al., 2020, 2021). This is relevant to net zero greenhouse gas emission goals (See Section 7.6.2 and Chapter 1, Box 1.4).

When individual gases are treated separately in climate model emulators (Cross-Chapter Box 7.1), or weighted and aggregated using an emission metric approach (such as CGTP or GWP*) which translate the distinct behaviour from cumulative emissions of short-lived gases, ambiguity in the future warming trajectory of a given emission scenario can be substantially reduced (Cain et al., 2019; Denison et al., 2019; Collins et al., 2020; Lynch et al., 2021). The degree of ambiguity varies with the emissions scenario. For mitigation pathways that limit warming to 2°C with an even chance, the ambiguity arising from using GWP-100 as sole constraint on emissions of a mix of greenhouse gases (without considering their economic implications or feasibility) could be as much as 0.17°C, which represents about one fifth of the remaining global warming in those pathways (Denison et al., 2019). If the evolution of the individual GHGs are not known, this can make it difficult to evaluate how a given global multi-gas emission pathway specified only in CO_2 equivalent emissions would achieve (or not) global surface temperature goals. This is potentially an issue as Nationally Determined Contributions frequently make commitments in terms of GWP-100 based CO_2- equivalent emissions at 2030 without specifying individual gases (Denison et al., 2019). Clear and transparent representation of the global warming implications of future emission pathways including Nationally Determined Contributions could be achieved either by their detailing pathways for multiple gases or by detailing a pathway of cumulative carbon dioxide equivalent emission approach aggregated across greenhouse gases evaluated by either GWP* or CGTP metric approaches (Cain et al., 2019; Collins et al., 2020; Lynch et al., 2021). Note that although the Paris Agreement Rulebook asks countries to report emissions of individual greenhouse gases separately for the global stocktake (Decision 18/CMA.1, annex, paragraph 38) which can allow the current effects of their emissions on global surface temperature to be accurately estimated, estimates of future warming are potentially ambiguous where emissions are aggregated using GWP-100 or other pulse metrics.

Although there is significant history of using single-basket approaches, supported by emission metrics such as GWP-100, in climate policies such as the Kyoto Protocol, multi-basket approaches also have many precedents in environmental management, including the Montreal Protocol (Daniel et al., 2012). Further assessment of the performance of physical and economics-based metrics in the context of climate change mitigation is provided in the contribution of Working Group III to the AR6.

[END BOX 7.3 HERE]

7.6.2 Applications of emission metrics

One prominent use of emission metrics is for comparison of efforts measured against climate change goals or targets. One of the most commonly discussed goals are in Article 2 of the Paris Agreement which aims to limit the risks and impacts of climate change by setting temperature goals. In addition, the Paris Agreement has important provisions which relate to how the goals are to be achieved, including making emissions reductions in a manner that does not threaten food production (Article 2), an early emissions peaking target, and the aim to "achieve a balance between anthropogenic emissions by sources and removals by sinks of greenhouse gases in the second half of this century" (Article 4). Article 4 also contains important context regarding international equity, sustainable development, and poverty reduction. Furthermore, the United Nations Framework Convention on Climate Change (UNFCCC) sets out as its ultimate objective, the "stabilization of greenhouse gas concentrations in the atmosphere at a level that would prevent dangerous

ACCEPTED VERSION SUBJECT TO FINAL EDITING

anthropogenic interference with the climate system."

How the interpretation of the Paris Agreement and the meaning of "net zero" emissions, reflects on the appropriate choice of metric is an active area of research (Schleussner et al., 2016, 2019; Fuglestvedt et al., 2018; Collins et al., 2020). Several possible scientific interpretations of the Article 2 and 4 goals can be devised, and these along with emission metric choice have implications both for when a balance in GHG emissions, net zero CO_2 emissions or net zero GHG emissions are achieved, and for their meaning in terms of temperature outcome (Fuglestvedt et al., 2018; Rogelj et al., 2018; Wigley, 2018). In AR6 net zero greenhouse gas emissions is defined as the condition in which metric-weighted anthropogenic GHG emissions are balanced by metric-weighted anthropogenic GHG removals over a specified period (see Chapter 1, Box 1.4, Appendix VII: Glossary). The quantification of net zero GHG emissions depends on the GHG emission metric chosen to compare emissions and removals of different gases, as well as the time horizon chosen for that metric. As the choice of emission metric affects the quantification of net zero GHG emissions, it therefore affects the resulting temperature outcome after net zero emissions are achieved (Lauder et al., 2013; Rogelj et al., 2015; Fuglestvedt et al., 2018; Schleussner et al., 2019). Schleussner et al.(2019) note that declining temperatures may be a desirable outcome of net zero. Rogelj and Schleussner (2019) also point out that the physical metrics raise questions of equity and fairness between developed and developing countries.

Based on SR1.5 (Allen et al., 2018a), there is *high confidence* that achieving net zero CO_2 emissions and declining non-CO_2 radiative forcing would halt human-induced warming. Based on (Bowerman et al., 2013; Pierrehumbert, 2014; Fuglestvedt et al., 2018; Tanaka and O'Neill, 2018; Schleussner et al., 2019) there is also *high confidence* that reaching net zero GHG emissions as quantified by GWP-100 typically leads to reductions from peak global surface temperature after net zero GHGs emissions are achieved, depending on the relative sequencing of mitigation of short-lived and long-lived species. If both short- and long-lived species are mitigated together, then temperatures peak and decline. If mitigation of short-lived species occurs much earlier than that of long-lived species, then temperatures stabilise very near peak values, rather than decline. Temperature targets can be met even with positive net GHG emissions based on GWP-100 (Tanaka and O'Neill, 2018). As demonstrated by Allen et al. (2018b), Cain et al. (2019), Schleussner et al. (2019) and Collins et al. (2020) reaching net zero GHG emissions when quantified using the new emission metric approaches such as CGTP or GWP* would lead to an approximately similar temperature evolution as achieving net zero CO_2. Hence, net zero CO_2 and net zero GHG quantified using these new approaches would both lead to approximately stable contributions to temperature change after net zero emissions are achieved (*high confidence*).

Comparisons with emission or global surface temperature stabilisation goals are not the only role for emissions metrics. Other important roles include those in pricing approaches where policymakers choose to compare short-lived and long-lived climate forcers (e.g. Manne and Richels, 2001), and in life cycle analyses (e.g. Hellweg and Milà i Canals, 2014). Several papers have reviewed the issue of metric choice for life cycle analyses, noting that analysts should be aware of the challenges and value judgements inherent in attempting to aggregate the effects of forcing agents with different timescales onto a common scale (e.g. Mallapragada and Mignone, 2017) and recommend aligning metric choice with policy goals as well as testing sensitivities of results to metric choice (Cherubini et al., 2016). Furthermore, life cycle analyses approaches which are sensitive to choice of emission metric benefit from careful communication of the reasons for the sensitivity (Levasseur et al., 2016).

ACCEPTED VERSION SUBJECT TO FINAL EDITING

Frequently Asked Questions

[START FAQ7.1 HERE]

FAQ 7.1: What is the Earth's energy budget, and what does it tell us about climate change?

The Earth's energy budget describes the flow of energy within the climate system. Since at least 1970 there has been a persistent imbalance in the energy flows that has led to excess energy being absorbed by the climate system. By measuring and understanding these energy flows and the role that human activities play in changing them, we are better able to understand the causes of climate change and project future climate change more accurately.

Our planet receives vast amounts of energy every day in the form of sunlight. Around a third of the sunlight is reflected back to space by clouds, by tiny particles called *aerosols*, and by bright surfaces such as snow and ice. The rest is absorbed by the ocean, land, ice, and atmosphere. The planet then emits energy back out to space in the form of thermal radiation. In a world that was not warming or cooling, these energy flows would balance. Human activity has caused an imbalance in these energy flows.

We measure the influence of various human and natural factors on the energy flows at the top of our atmosphere in terms of *radiative forcings*, where a positive radiative forcing has a warming effect and a negative radiative forcing has a cooling effect. In response to these forcings, the Earth system will either warm or cool, so as to restore balance through changes in the amount of outgoing thermal radiation (the warmer the Earth, the more radiations it emits). Changes in Earth's temperature in turn lead to additional changes in the climate system (known as *climate feedbacks*) that either amplify or dampen the original effect. For example, Arctic sea-ice has been melting as the Earth warms, reducing the amount of reflected sunlight and adding to the initial warming (an amplifying feedback). The most uncertain of those climate feedbacks are clouds, as they respond to warming in complex ways that affect both the emission of thermal radiation and the reflection of sunlight. However, we are now more confident that cloud changes, taken together, will amplify climate warming (see FAQ 7.2).

Human activities have unbalanced these energy flows in two main ways. First, increases in greenhouse gas levels have led to more of the emitted thermal radiation being absorbed by the atmosphere, instead of being released to space. Second, increases in pollutants have increased the amount of aerosols such as sulphates in the atmosphere (see FAQ 6.1). This has led to more incoming sunlight being reflected away, by the aerosols themselves and through the formation of more cloud drops, which increases the reflectivity of clouds (see FAQ 7.2).

Altogether, the global energy flow imbalance since the 1970s has been just over half a watt per square metre of the Earth's surface. This sounds small, but because the imbalance is persistent and because Earth's surface is large, this adds up to about 25 times the total amount of primary energy consumed by human society, compared over 1971 to 2018. Compared to the IPCC Fifth Assessment Report, we are now better able to quantify and track these energy flows from multiple lines of evidence, including satellite data, direct measurements of ocean temperatures, and a wide variety of other Earth system observations (see FAQ 1.1). We also have a better understanding of the processes contributing to this imbalance, including the complex interactions between aerosols, clouds and radiation.

Research has shown that the excess energy since the 1970s has mainly gone into warming the ocean (91%), followed by the warming of land (5%) and the melting ice sheets and glaciers (3%). The atmosphere has warmed substantially since 1970, but because it is comprised of thin gases it has absorbed only 1% of the excess energy (FAQ 7.1, Figure 1). As the ocean has absorbed the vast majority of the excess energy, especially within their top two kilometres, the deep ocean is expected to continue to warm and expand for centuries to millennia, leading to long-term sea level rise – even if atmospheric greenhouse gas levels were to decline (see FAQ 5.3). This is in addition to the sea level rise expected from melting ice sheets and glaciers.

ACCEPTED VERSION SUBJECT TO FINAL EDITING

Understanding the Earth's energy budget also helps to narrow uncertainty in future projections of climate. By testing climate models against what we know about the Earth's energy budget, we can make more confident projections of surface temperature changes we might expect this century and beyond.

[START FAQ7.1, FIGURE 1 HERE]

FAQ7.1, Figure 1: The Earth's energy budget compares the flows of incoming and outgoing of energy that are relevant for the climate system. Since the at least the 1970s, less energy is flowing out than is flowing in, which leads to excess energy being absorbed by the ocean, land, ice and atmosphere, with the ocean absorbing 91%.

[END FIGURE FAQ7.1, FIGURE 1 HERE]

[END FAQ 7.1 HERE]

ACCEPTED VERSION
SUBJECT TO FINAL EDITING

[START FAQ 7.2 HERE]

FAQ 7.2: Clouds – What is the role in a warming climate?

One of the biggest challenges in climate science has been to predict how clouds will change in a warming world and whether those changes will amplify or partially offset the warming caused by increasing concentrations of greenhouse gases and other human activities. Scientists have made significant progress over the past decade and are now more confident that changes in clouds will amplify, rather than offset, global warming in the future.

Clouds cover roughly two thirds of the Earth's surface. They consist of small droplets and/or ice crystals, which form when water vapour condenses or deposits around tiny particles called *aerosols* (such as salt, dust, or smoke). Clouds play a critical role in the Earth's *energy budget* at the top of atmosphere and therefore influence Earth's surface temperature (see FAQ 7.1) . The interactions between clouds and the climate are complex and varied. Clouds at low altitudes tend to reflect incoming solar energy back to space, preventing this energy from reaching and warming the Earth and causing a cooling effect. On the other hand, higher clouds tend to trap (i.e., absorb and then emit at a lower temperature) some of the energy leaving the Earth, leading to a warming effect. On average, clouds reflect back more incoming energy than the amount of outgoing energy they trap, resulting in an overall net cooling effect on the present climate. Human activities since the pre-industrial era have altered this climate effect of clouds in two different ways: by changing the abundance of the aerosol particles in the atmosphere and by warming the Earth's surface, primarily as a result of increases in greenhouse gas emissions.

The concentration of aerosols in the atmosphere has markedly increased since the pre-industrial era, and this has had two important effects on clouds. First, clouds now reflect more incoming energy because cloud droplets have become more numerous and smaller. Second, smaller droplets may delay rain formation, thereby making the clouds last longer, although this effect remains uncertain. Hence, aerosols released by human activities have had a cooling effect, counteracting a considerable portion of the warming caused by increases in greenhouse gases over the last century (see FAQ 3.1). Nevertheless, this cooling effect is expected to diminish in the future, as air pollution policies progress worldwide, reducing the amount of aerosols released into the atmosphere.

Since the pre-industrial period, the Earth's surface and atmosphere have warmed, altering the properties of clouds, such as their altitude, amount, and composition (water or ice), thereby affecting the Earth's energy budget and, in turn, changing temperature. This cascading effect of clouds, known as the *cloud feedback,* could either amplify or offset some of the future warming and has long been the biggest source of uncertainty in climate projections. The problem stems from the fact that clouds can change in many ways and that their processes occur on much smaller scales than what global climate models can explicitly represent. As a result, global climate models have disagreed on how clouds, particularly over the subtropical ocean, will change in the future and whether the change will amplify or suppress the global warming.

Since the last IPCC Report in 2013, understanding of cloud processes has advanced with better observations, new analysis approaches and explicit high-resolution numerical simulation of clouds. Also, current global climate models simulate cloud behaviour better than previous models, due both to advances in computational capabilities and process understanding. Altogether, this has helped to build a more complete picture of how clouds will change as the climate warms (FAQ 7.2, Figure 1). For example, the amount of low clouds will reduce over the subtropical ocean, leading to less reflection of incoming solar energy, and the altitude of high clouds will rise, making them more prone to trapping outgoing energy; both processes have a warming effect. In contrast, clouds in high latitudes will be increasingly made of water droplets rather than ice crystals. This shift from fewer, larger ice crystals to smaller but more numerous water droplets will result in more of the incoming solar energy being reflected back to space and produce a cooling effect. Better understanding of how clouds respond to warming has led to more confidence than before that future changes in clouds will, overall, cause additional warming (i.e., by weakening the current cooling effect of clouds). This is called a *positive net cloud feedback.*

ACCEPTED VERSION SUBJECT TO FINAL EDITING

In summary, clouds will amplify rather than suppress the warming of the climate system in the future, as more greenhouse gases and fewer aerosols are released to the atmosphere by human activities.

[START FAQ7.2, FIGURE 1 HERE]

FAQ7.2, Figure 1: Interactions between clouds and the climate today and in a warmer future. Global warming is expected to alter the altitude (left) and the amount (centre) of clouds, which will amplify warming. On the other hand, cloud composition will change (right), offsetting some of the warming. Overall clouds are expected to amplify future warming.

[END FAQ7.2, FIGURE 1 HERE]

[END FAQ 7.2 HERE]

ACCEPTED VERSION
SUBJECT TO FINAL EDITING

FAQ 7.3: What is equilibrium climate sensitivity and how does it relate to future warming?

For a given future scenario, climate models project a range of changes in global surface temperature. This range is closely related to equilibrium climate sensitivity, or ECS, which measures how climate models respond to a doubling of carbon dioxide in the atmosphere. Models with high climate sensitivity project stronger future warming. Some climate models of the new generation are more sensitive than the range assessed in the IPCC Sixth Assessment Report. This leads to end-of-century global warming in some simulations of up to 2°C–3°C above the current IPCC best estimate. Although these higher warming levels are not expected to occur, high-ECS models are useful for exploring high impact, low-likelihood futures.

The *equilibrium climate sensitivity* (ECS) is defined as the long-term global warming caused by a doubling of carbon dioxide above its pre-industrial concentration. For a given emission scenario, much of the uncertainty in projections of future warming can be explained by the uncertainty in ECS (FAQ 7.3, Figure 1). The significance of equilibrium climate sensitivity has long been recognised, and the first estimate was presented by Swedish scientist Svante Arrhenius in 1896.

This Sixth Assessment Report concludes that there is a 90% or more chance (*very likely*) that the ECS is between 2°C and 5°C. This represents a significant reduction in uncertainty compared to the Fifth Assessment Report, which gave a 66% chance (*likely*) of ECS being between 1.5°C and 4.5°C. This reduction in uncertainty has been possible not through a single breakthrough or discovery but instead by combining evidence from many different sources and by better understanding their strengths and weaknesses.

There are four main lines of evidence for ECS. First, the self-reinforcing processes, called *feedback loops,* that amplify or dampen the warming in response to increasing carbon dioxide are now better understood. For example, warming in the Arctic melts sea ice, resulting in more open ocean area, which is darker and therefore absorbs more sunlight, further intensifying the initial warming. It remains challenging to represent realistically all the processes involved in these feedback loops, particularly those related to clouds (see FAQ 7.2). Such identified model errors are now taken into account, and other known, but generally weak, feedback loops that are usually not included in models are now included in the assessment of ECS.

Second, historical warming since early industrialisation provides strong evidence that climate sensitivity is not small. Since 1850, the concentration of carbon dioxide and other greenhouse gases have increased, and as a result the Earth has warmed by about 1.1ºC. However, relying on this industrial-era warming to estimate ECS is challenging, partly because some of the warming from greenhouse gases was offset by cooling from aerosol particles and partly because the ocean are still responding to past increases in carbon dioxide.

Third, evidence from ancient climates that had reached equilibrium with greenhouse gas concentrations, such as the coldest period of the last ice age around 20,000 years ago, or warmer periods further back in time, provide useful data on the ECS of the climate system (see FAQ 1.3). Fourth, statistical approaches linking model ECS values with observed changes, such as global warming since the 1970s, provide complementary evidence.

All four lines of evidence rely, to some extent, on climate models, and interpreting the evidence often benefits from model diversity and spread in modelled climate sensitivity. Furthermore, high-sensitivity models can provide important insights into futures that have a low likelihood of occurring but that could result in large impacts. But, unlike in previous assessments, climate models are not considered a line of evidence in their own right in the IPCC Sixth Assessment Report.

The ECS of the latest climate models is, on average, higher than that of the previous generation of models and also higher than this report's best estimate of 3.0°C. Furthermore, the ECS values in some of the new models are both above and below the 2°C to 5°C *very likely* range, and although such models cannot be ruled out as implausible solely based on their ECS, some of them do display climate change that is inconsistent with the observed when tested with ancient climates. A slight mismatch with models is only natural because

ACCEPTED VERSION SUBJECT TO FINAL EDITING

the IPCC Sixth Assessment Report is based on observations and an improved understanding of the climate system.

[START FAQ 7.3, FIGURE 1 HERE]

FAQ7.3, Figure 1: Equilibrium climate sensitivity and future warming. (left) Equilibrium climate sensitivities for the current generation (sixth climate model intercomparison project, CMIP6) climate models, and the previous (CMIP5) generation. The assessed range in this report (AR6) is also shown. (right) Climate projections of CMIP5, CMIP6, and AR6 for the very high-emission scenarios RCP8.5, and SSP5-8.5, respectively. The thick horizontal lines represent the multi-model average and the thin horizontal lines the results of individual models. The boxes represent the model ranges for CMIP5 and CMIP6 and the range assessed in AR6.

[END FAQ 7.3, FIGURE 1 HERE]

[END FAQ 7.3 HERE]

ACCEPTED VERSION
SUBJECT TO FINAL EDITING

References

Aamaas, B., T.K. Berntsen, J.S. Fuglestvedt, K.P. Shine, and N. Bellouin, 2016: Regional emission metrics for short-lived climate forcers from multiple models. *Atmospheric Chemistry and Physics*, doi:10.5194/acp-16-7451-2016.

Aamaas, B., T.K. Berntsen, J.S. Fuglestvedt, K.P. Shine, and W.J. Collins, 2017: Regional temperature change potentials for short-lived climate forcers based on radiative forcing from multiple models. *Atmospheric Chemistry and Physics*, doi:10.5194/acp-17-10795-2017.

Abe-Ouchi, A. et al., 2013: Insolation-driven 100,000-year glacial cycles and hysteresis of ice-sheet volume. *Nature*, **500(7461)**, 190–193, doi:10.1038/nature12374.

Abe-Ouchi, A. et al., 2015: Ice-sheet configuration in the CMIP5/PMIP3 Last Glacial Maximum experiments. *Geoscientific Model Development*, **8(11)**, 3621–3637, doi:10.5194/gmd-8-3621-2015.

Ackerley, D. and D. Dommenget, 2016: Atmosphere-only GCM (ACCESS1.0) simulations with prescribed land surface temperatures. *Geoscientific Model Development*, doi:10.5194/gmd-9-2077-2016.

Albrecht, B.A., 1989: Aerosols, cloud microphysics, and fractional cloudiness.. *Science (New York, N.Y.)*, **245(4923)**, 1227–30, doi:10.1126/science.245.4923.1227.

Aldrin, M. et al., 2012: Bayesian estimation of climate sensitivity based on a simple climate model fitted to observations of hemispheric temperatures and global ocean heat content. *Environmetrics*, **23(3)**, 253–271, doi:10.1002/env.2140.

Alexeev, V.A. and C.H. Jackson, 2013: Polar amplification: is atmospheric heat transport important? *Climate Dynamics*, **41(2)**, 533–547, doi:10.1007/s00382-012-1601-z.

Alexeev, V.A., P.L. Langen, and J.R. Bates, 2005: Polar amplification of surface warming on an aquaplanet in "ghost forcing" experiments without sea ice feedbacks. *Climate Dynamics*, **24(7)**, 655–666, doi:10.1007/s00382-005-0018-3.

Allan, R.P. et al., 2014: Changes in global net radiative imbalance 1985–2012. *Geophysical Research Letters*, **41(15)**, 5588–5597, doi:10.1002/2014gl060962.

Allen, M.R. et al., 2016: New use of global warming potentials to compare cumulative and short-lived climate pollutants. *Nature Climate Change*, **6(8)**, 773–776, doi:10.1038/nclimate2998.

Allen, M.R. et al., 2018a: Framing and Context. In: *Global Warming of 1.5°C. An IPCC Special Report on the impacts of global warming of 1.5°C above pre-industrial levels and related global greenhouse gas emission pathways, in the context of strengthening the global response to the threat of climate change,* [Masson-Delmotte, V., P. Zhai, H.-O. Pörtner, D. Roberts, J. Skea, P.R. Shukla, A. Pirani, W. Moufouma-Okia, C. Péan, R. Pidcock, S. Connors, J.B.R. Matthews, Y. Chen, X. Zhou, M.I. Gomis, E. Lonnoy, T. Maycock, M. Tignor, and T. Waterfield (eds.)]. In Press, pp. 49–91.

Allen, M.R. et al., 2018b: A solution to the misrepresentations of CO2-equivalent emissions of short-lived climate pollutants under ambitious mitigation. *npj Climate and Atmospheric Science*, **1(1)**, doi:10.1038/s41612-018-0026-8.

Allen, R.J., J.R. Norris, and M. Wild, 2013: Evaluation of multidecadal variability in CMIP5 surface solar radiation and inferred underestimation of aerosol direct effects over Europe, China, Japan, and India. *Journal of Geophysical Research-Atmospheres*, **118(12)**, 6311–6336, doi:10.1002/jgrd.50426.

Allen, R.J. et al., 2019: Observationally constrained aerosol–cloud semi-direct effects. *npj Climate and Atmospheric Science*, **2(1)**, 1–12, doi:10.1038/s41612-019-0073-9.

Allison, L.C. et al., 2019: Towards quantifying uncertainty in ocean heat content changes using synthetic profiles. *Environmental Research Letters*, **14(8)**, 84037, doi:10.1088/1748-9326/ab2b0b.

Allison, L.C. et al., 2020a: Observations of planetary heating since the 1980s from multiple independent datasets. *Environmental Research Communications*, doi:10.1088/2515-7620/abbb39.

Allison, L.C. et al., 2020b: Observations of planetary heating since the 1980s from multiple independent datasets. *Environmental Research Communications*, doi:10.1088/2515-7620/abbb39.

Alo, C.A. and E.N. Anagnostou, 2017: A sensitivity study of the impact of dynamic vegetation on simulated future climate change over Southern Europe and the Mediterranean. *International Journal of Climatology*, **37(4)**, 2037–2050, doi:10.1002/joc.4833.

Anagnostou, E. et al., 2016: Changing atmospheric CO2 concentration was the primary driver of early Cenozoic climate. *Nature*, **533**, 380–384, doi:10.1038/nature17423.

Anagnostou, E. et al., 2020: Proxy evidence for state-dependence of climate sensitivity in the Eocene greenhouse. *Nature Communications*, **11(1)**, 4436, doi:10.1038/s41467-020-17887-x.

Andrews, E., J.A. Ogren, S. Kinne, and B. Samset, 2017: Comparison of AOD, AAOD and column single scattering albedo from AERONET retrievals and in situ profiling measurements. *Atmospheric Chemistry and Physics*, **17(9)**, 6041–6072, doi:10.5194/acp-17-6041-2017.

Andrews, M.B. et al., 2020: Historical Simulations With HadGEM3-GC3.1 for CMIP6. *Journal of Advances in Modeling Earth Systems*, **12(6)**, 1–34, doi:10.1029/2019ms001995.

ACCEPTED VERSION SUBJECT TO FINAL EDITING

Andrews, T. and M.J. Webb, 2018: The dependence of global cloud and lapse rate feedbacks on the spatial structure of tropical pacific warming. *Journal of Climate*, doi:10.1175/jcli-d-17-0087.1.
Andrews, T. and P.M. Forster, 2020: Energy budget constraints on historical radiative forcing. *Nature Climate Change*, **10**, 313–316, doi:10.1038/s41558-020-0696-1.
Andrews, T., J.M. Gregory, and M.J. Webb, 2015: The Dependence of Radiative Forcing and Feedback on Evolving Patterns of Surface Temperature Change in Climate Models. *Journal of Climate*, **28(4)**, 1630–1648, doi:10.1175/jcli-d-14-00545.1.
Andrews, T., J.M. Gregory, M.J. Webb, and K.E. Taylor, 2012: Forcing, feedbacks and climate sensitivity in CMIP5 coupled atmosphere-ocean climate models. *Geophysical Research Letters*, **39(9)**, L09712, doi:10.1029/2012gl051607.
Andrews, T., R.A. Betts, B.B.B. Booth, C.D. Jones, and G.S. Jones, 2017: Effective radiative forcing from historical land use change. *Climate Dynamics*, **48(11–12)**, 3489–3505, doi:10.1007/s00382-016-3280-7.
Andrews, T. et al., 2018: Accounting for Changing Temperature Patterns Increases Historical Estimates of Climate Sensitivity. *Geophysical Research Letters*, **45(16)**, 8490–8499, doi:10.1029/2018gl078887.
Andrews, T. et al., 2019: Forcings, feedbacks and climate sensitivity in HadGEM3-GC3.1 and UKESM1. *Journal of Advances in Modeling Earth Systems*, doi:10.1029/2019ms001866.
Andrews, T. et al., 2021: Effective radiative forcing in a GCM with fixed surface temperatures. *Journal of Geophysical Research: Atmospheres*, doi:10.1029/2020jd033880.
Ångström, K., 1900: Ueber die Bedeutung des Wasserdampfes und der Kohlensäure bei der Absorption der Erdatmosphäre. *Annalen der Physik*, **308(12)**, 720–732, doi:10.1002/andp.19003081208.
Annan, J.D. and J.C. Hargreaves, 2006: Using multiple observationally-based constraints to estimate climate sensitivity. *Geophysical Research Letters*, **33(6)**, doi:10.1029/2005gl025259.
Annan, J.D., J.C. Hargreaves, T. Mauritsen, and B. Stevens, 2020a: What could we learn about climate sensitivity from variability in the surface temperature record? *Earth System Dynamics*, **11**, 709–719, doi:10.5194/esd-11-709-2020.
Annan, J.D., J.C. Hargreaves, T. Mauritsen, and B. Stevens, 2020b: What could we learn about climate sensitivity from variability in the surface temperature record? *Earth System Dynamics*, **11**, 709–719, doi:10.5194/esd-11-709-2020.
Antuña-Marrero, J.C., F. García, R. Estevan, B. Barja, and A. Sánchez-Lorenzo, 2019: Simultaneous dimming and brightening under all and clear sky at Camagüey, Cuba (1981–2010). *Journal of Atmospheric and Solar-Terrestrial Physics*, **190**, 45–53, doi:10.1016/j.jastp.2019.05.004.
Armour, K.C., 2017: Energy budget constraints on climate sensitivity in light of inconstant climate feedbacks. *Nature Climate Change*, doi:10.1038/nclimate3278.
Armour, K.C. and G.H. Roe, 2011: Climate commitment in an uncertain world. *Geophysical Research Letters*, **38(1)**, doi:10.1029/2010gl045850.
Armour, K.C., C.M. Bitz, and G.H. Roe, 2013: Time-Varying Climate Sensitivity from Regional Feedbacks. *Journal of Climate*, doi:10.1175/jcli-d-12-00544.1.
Armour, K.C., N. Siler, A. Donohoe, and G.H. Roe, 2019: Meridional Atmospheric Heat Transport Constrained by Energetics and Mediated by Large-Scale Diffusion. *Journal of Climate*, **32(12)**, 3655–3680, doi:10.1175/jcli-d-18-0563.1.
Armour, K.C., J. Marshall, J.R. Scott, A. Donohoe, and E.R. Newsom, 2016: Southern Ocean warming delayed by circumpolar upwelling and equatorward transport. *Nature Geoscience*, doi:10.1038/ngeo2731.
Armstrong, E., P. Valdes, J. House, and J. Singarayer, 2019: Investigating the feedbacks between CO2, vegetation and the AMOC in a coupled climate model. *Climate Dynamics*, **53(5–6)**, 2485–2500, doi:10.1007/s00382-019-04634-2.
Arora, V.K. et al., 2013: Carbon-concentration and carbon-climate feedbacks in CMIP5 earth system models. *Journal of Climate*, **26(15)**, 5289–5314, doi:10.1175/jcli-d-12-00494.1.
Arora, V.K. et al., 2020: Carbon-concentration and carbon-climate feedbacks in CMIP6 models and their comparison to CMIP5 models. *Biogeosciences*, **17(16)**, 4173–4222, doi:10.5194/bg-17-4173-2020.
Arrhenius, S., 1896: On the Influence of Carbonic Acid in the Air upon the Temperature of the Ground. *Philosophocal Magazine and Journal of Science*, **41(page 270)**, 237–279.
Ashwin, P. and A.S. von der Heydt, 2020: Extreme Sensitivity and Climate Tipping Points. *Journal of Statistical Physics*, **179(5)**, 1531–1552, doi:10.1007/s10955-019-02425-x.
Augustine, J.A. and E.G. Dutton, 2013: Variability of the surface radiation budget over the United States from 1996 through 2011 from high-quality measurements. *Journal of Geophysical Research-Atmospheres*, **118(1)**, 43–53, doi:10.1029/2012jd018551.
Baggenstos, D. et al., 2019: Earth's radiative imbalance from the Last Glacial Maximum to the present. *Proceedings of the National Academy of Sciences of the United States of America*, **116(30)**, 14881–14886, doi:10.1073/pnas.1905447116.
Balcombe, P., J.F. Speirs, N.P. Brandon, and A.D. Hawkes, 2018: Methane emissions: choosing the right climate metric and time horizon. *Environmental Science: Processes & Impacts*, **20(10)**, 1323–1339,

ACCEPTED VERSION
SUBJECT TO FINAL EDITING

doi:10.1039/c8em00414e.
Banerjee, A. et al., 2019: Stratospheric water vapor: an important climate feedback. *Climate Dynamics*, **53(3)**, 1697–1710, doi:10.1007/s00382-019-04721-4.
Barreiro, M. and S.G. Philander, 2008: Response of the tropical Pacific to changes in extratropical clouds. *Climate Dynamics*, doi:10.1007/s00382-007-0363-5.
Bartlein, P.J. et al., 2011: Pollen-based continental climate reconstructions at 6 and 21 ka: a global synthesis. *Climate Dynamics*, **37(3)**, 775–802, doi:10.1007/s00382-010-0904-1.
Bauer, S.E. et al., 2013: Historical and future black carbon deposition on the three ice caps: Ice core measurements and model simulations from 1850 to 2100. *Journal of Geophysical Research: Atmospheres*, **118(14)**, 7948–7961, doi:10.1002/jgrd.50612.
Beerling, D.J. and D.L. Royer, 2011: Convergent Cenozoic CO2 history. *Nature Geoscience*, **4(7)**, 418–420, doi:10.1038/ngeo1186.
Bellouin, N., J. Quaas, J.-J. Morcrette, and O. Boucher, 2013a: Estimates of aerosol radiative forcing from the MACC re-analysis. *Atmospheric Chemistry and Physics*, **13(4)**, 2045–2062, doi:10.5194/acp-13-2045-2013.
Bellouin, N. et al., 2013b: Impact of the modal aerosol scheme GLOMAP-mode on aerosol forcing in the Hadley Centre Global Environmental Model. *Atmospheric Chemistry and Physics*, **13(6)**, 3027–3044, doi:10.5194/acp-13-3027-2013.
Bellouin, N. et al., 2019: Bounding global aerosol radiative forcing of climate change. *Reviews of Geophysics*, doi:10.1029/2019rg000660.
Bender, F.A.M., A.M.L. Ekman, and H. Rodhe, 2010: Response to the eruption of Mount Pinatubo in relation to climate sensitivity in the CMIP3 models. *Climate Dynamics*, **35(5)**, 875–886, doi:10.1007/s00382-010-0777-3.
Bender, F.A.M., V. Ramanathan, and G. Tselioudis, 2012: Changes in extratropical storm track cloudiness 1983-2008: Observational support for a poleward shift. *Climate Dynamics*, **38**, 2037–2053, doi:10.1007/s00382-011-1065-6.
Bender, F.A.M., L. Frey, D.T. McCoy, D.P. Grosvenor, and J.K. Mohrmann, 2019: Assessment of aerosol–cloud–radiation correlations in satellite observations, climate models and reanalysis. *Climate Dynamics*, **52(7–8)**, 4371–4392, doi:10.1007/s00382-018-4384-z.
Bender, F.A.-M., 2011: Planetary albedo in strongly forced climate, as simulated by the CMIP3 models. *Theoretical and Applied Climatology*, **105(3–4)**, 529–535, doi:10.1007/s00704-011-0411-2.
Bengtsson, L. and S.E. Schwartz, 2013: Determination of a lower bound on Earth's climate sensitivity. *Tellus B*, **1**, 1–16, doi:10.3402/tellusb.v65i0.21533.
Bentamy, A. et al., 2017: Review and assessment of latent and sensible heat flux accuracy over the global oceans. *REMOTE SENSING OF ENVIRONMENT*, **201**, 196–218, doi:10.1016/j.rse.2017.08.016.
Bilbao, R.A.F., J.M. Gregory, and N. Bouttes, 2015: Analysis of the regional pattern of sea level change due to ocean dynamics and density change for 1993–2099 in observations and CMIP5 AOGCMs. *Climate Dynamics*, **45(9–10)**, 2647–2666, doi:10.1007/s00382-015-2499-z.
Bindoff, N.L. et al., 2013: Detection and Attribution of Climate Change, from Global to Regional. In: *Climate Change 2013: The Physical Science Basis. Contribution of Working Group I to the Fifth Assessment Report of the Intergovernmental Panel on Climate Change* [Stocker, T.F., D. Qin, G.-K. Plattner, M. Tignor, S.K. Allen, J. Boschung, A. Nauels, Y. Xia, V. Bex, and P.M. Midgley (eds.)]. Cambridge University Press, Cambridge, United Kingdom and New York, NY, USA, pp. 867–952, doi:10.1017/cbo9781107415324.022.
Bintanja, R., E.C. Van Der Linden, and W. Hazeleger, 2012: Boundary layer stability and Arctic climate change: a feedback study using EC-Earth. *Climate Dynamics*, **39(11)**, 2659–2673, doi:10.1007/s00382-011-1272-1.
Bintanja, R., G.J. Van Oldenborgh, S.S. Drijfhout, B. Wouters, and C.A. Katsman, 2013: Important role for ocean warming and increased ice-shelf melt in Antarctic sea-ice expansion. *Nature Geoscience*, doi:10.1038/ngeo1767.
Bjordal, J., T. Storelvmo, K. Alterskjær, and T. Carlsen, 2020: Equilibrium climate sensitivity above 5°C plausible due to state-dependent cloud feedback. *Nature Geoscience*, **13**, 718–721, doi:10.1038/s41561-020-00649-1.
Bloch-Johnson, J., R.T. Pierrehumbert, and D.S. Abbot, 2015: Feedback temperature dependence determines the risk of high warming. *Geophysical Research Letters*, **42(12)**, 4973–4980, doi:10.1002/2015gl064240.
Bloch-Johnson, J. et al., 2020: Climate Sensitivity Increases Under Higher CO2 Levels Due to Feedback Temperature Dependence. *Geophysical Research Letters*, **48(4)**, e2020GL089074, doi:10.1029/2020gl089074.
Block, K. and T. Mauritsen, 2013: Forcing and feedback in the MPI-ESM-LR coupled model under abruptly quadrupled CO2. *Journal of Advances in Modeling Earth Systems*, **5(4)**, 676–691, doi:10.1002/jame.20041.
Bodas-Salcedo, A. et al., 2019: Strong Dependence of Atmospheric Feedbacks on Mixed-Phase Microphysics and Aerosol-Cloud Interactions in HadGEM3. *Journal of Advances in Modeling Earth Systems*, **11(6)**, 1735–1758, doi:10.1029/2019ms001688.
Boeke, R.C. and P.C. Taylor, 2016: Evaluation of the Arctic surface radiation budget in CMIP5 models. *JOURNAL OF GEOPHYSICAL RESEARCH-ATMOSPHERES*, **121(14)**, 8525–8548, doi:10.1002/2016jd025099.
Boeke, R.C. and P.C. Taylor, 2018: Seasonal energy exchange in sea ice retreat regions contributes to differences in projected Arctic warming. *Nature Communications*, **9(1)**, doi:10.1038/s41467-018-07061-9.

ACCEPTED VERSION SUBJECT TO FINAL EDITING

Boisier, J.P., N. De Noblet-Ducoudré, and P. Ciais, 2013: Inferring past land use-induced changes in surface albedo from satellite observations: A useful tool to evaluate model simulations. *Biogeosciences*, doi:10.5194/bg-10-1501-2013.

Bonan, D.B., K.C. Armour, G.H. Roe, N. Siler, and N. Feldl, 2018: Sources of Uncertainty in the Meridional Pattern of Climate Change. *Geophysical Research Letters*, **45(17)**, 9131–9140, doi:10.1029/2018gl079429.

Bond, T.C. et al., 2013: Bounding the role of black carbon in the climate system: A scientific assessment. *Journal of Geophysical Research: Atmospheres*, **118(11)**, 5380–5552, doi:10.1002/jgrd.50171.

Bony, S. and J.L. Dufresne, 2005: Marine boundary layer clouds at the heart of tropical cloud feedback uncertainties in climate models.. *Geophysical Research Letters*, **32**, L20806, doi:10.1029/2005gl023851.

Bony, S. et al., 2006: How Well do we Understand and Evaluate Climate Change Feedback Processes? *Journal of Climate*, **19(15)**, 3445–3482, doi: 10.1175/JCLI3819.1.

Bony, S. et al., 2015: Clouds, circulation and climate sensitivity. *Nature Geoscience*, **8(4)**, 261–268, doi:10.1038/ngeo2398.

Bony, S. et al., 2016: Thermodynamic control of anvil cloud amount. *Proceedings of the National Academy of Sciences of the United States of America*, **113(32)**, 8927–8932, doi:10.1073/pnas.1601472113.

Bony, S. et al., 2020: Observed Modulation of the Tropical Radiation Budget by Deep Convective Organization and Lower-Tropospheric Stability. *AGU Advances*, **1(3)**, e2019AV000155, doi:10.1029/2019av000155.

Booth, B.B.B. et al., 2018: Comments on "Rethinking the Lower Bound on Aerosol Radiative Forcing". *Journal of Climate*, **31(22)**, 9407–9412, doi:10.1175/jcli-d-17-0369.1.

Boucher, O., 2012: Comparison of physically- and economically-based CO2- equivalences for methane. *Earth System Dynamics*, doi:10.5194/esd-3-49-2012.

Boucher, O., P. Friedlingstein, B. Collins, and K.P. Shine, 2009: The indirect global warming potential and global temperature change potential due to methane oxidation. *Environmental Research Letters*, **4(4)**, doi:10.1088/1748-9326/4/4/044007.

Boucher, O. et al., 2013: Clouds and Aerosols. In: *Climate Change 2013: The Physical Science Basis. Contribution of Working Group I to the Fifth Assessment Report of the Intergovernmental Panel on Climate Change* [Stocker, T.F., D. Qin, G.-K. Plattner, M. Tignor, S.K. Allen, J. Boschung, A. Nauels, Y. Xia, V. Bex, and P.M. Midgley (eds.)]. Cambridge Univeristy Press, Cambridge, United Kingdom and New York, NY, USA, pp. 571–657, doi:10.1017/cbo9781107415324.016.

Bowerman, N.H.A. et al., 2013: The role of short-lived climate pollutants in meeting temperature goals. *Nature Climate Change*, **3(12)**, 1021–1024, doi:10.1038/nclimate2034.

Brantley, S.L., 2008: Understanding Soil Time. *Science*, **321(5895)**, 1454–1455, doi:10.1126/science.1161132.

Brenguier, J.-L. et al., 2000: Radiative Properties of Boundary Layer Clouds: Droplet Effective Radius versus Number Concentration. *Journal of the Atmospheric Sciences*, **57(6)**, 803–821, doi:10.1175/1520-0469(2000)057<0803:rpoblc>2.0.co;2.

Bretherton, C.S., 2015: Insights into low-latitude cloud feedbacks from high-resolution models. *Philosophical Transactions of the Royal Society A: Mathematical, Physical and Engineering Sciences*, **373(2054)**, doi:10.1098/rsta.2014.0415.

Bretherton, C.S., P.N. Blossey, and C.R. Jones, 2013: Mechanisms of marine low cloud sensitivity to idealized climate perturbations: A single-LES exploration extending the CGILS cases. *Journal of Advances in Modeling Earth Systems*, doi:10.1002/jame.20019.

Bretherton, C.S., P.N. Blossey, and C. Stan, 2014: Cloud feedbacks on greenhouse warming in the superparameterized climate model SP-CCSM4. *Journal of Advances in Modeling Earth Systems*, **6(4)**, 1185–1204, doi:10.1002/2014ms000355.

Brient, F. and T. Schneider, 2016: Constraints on climate sensitivity from space-based measurements of low-cloud reflection. *Journal of Climate*, **29(16)**, 5821–5835, doi:10.1175/jcli-d-15-0897.1.

Brient, F. et al., 2016: Shallowness of tropical low clouds as a predictor of climate models' response to warming. *Climate Dynamics*, **47(1–2)**, 433–449, doi:10.1007/s00382-015-2846-0.

Brierley, C., N. Burls, C. Ravelo, and A. Fedorov, 2015: Pliocene warmth and gradients. *Nature Geoscience*, **8(6)**, 419–420, doi:10.1038/ngeo2444.

Bronselaer, B. et al., 2018: Change in future climate due to Antarctic meltwater. *Nature*, **564(7734)**, 53–58, doi:10.1038/s41586-018-0712-z.

Brovkin, V., T. Raddatz, C.H. Reick, M. Claussen, and V. Gayler, 2009: Global biogeophysical interactions between forest and climate. *Geophysical Research Letters*, **36(7)**, doi:10.1029/2009gl037543.

Brown, P.T. and K. Caldeira, 2017: Greater future global warming inferred from Earth's recent energy budget. *Nature*, **552(7683)**, 45–50, doi:10.1038/nature24672.

Brown, P.T., M.B. Stolpe, and K. Caldeira, 2018: Assumptions for emergent constraints. *Nature*, **563(7729)**, E1–E3, doi:10.1038/s41586-018-0638-5.

Brown, P.T., W. Li, L. Li, and Y. Ming, 2014: Top-of-atmosphere radiative contribution to unforced decadal global temperature variability in climate models. *Geophysical Research Letters*, **41(14)**, 5175–5183, doi:10.1002/2014gl060625.

ACCEPTED VERSION SUBJECT TO FINAL EDITING

Buchard, V. et al., 2017: The MERRA-2 Aerosol Reanalysis, 1980 Onward. Part II: Evaluation and Case Studies. *JOURNAL OF CLIMATE*, **30(17)**, 6851–6872, doi:10.1175/jcli-d-16-0613.1.
Burke, K.D. et al., 2018: Pliocene and Eocene provide best analogs for near-future climates. *Proceedings of the National Academy of Sciences*, **115(52)**, 13288–13293, doi:10.1073/pnas.1809600115.
Burls, N.J. and A. Fedorov, 2014a: Simulating Pliocene warmth and a permanent El Niño-like state: The role of cloud albedo. *Paleoceanography*, **29(10)**, 893–910, doi:10.1002/2014pa002644.
Burls, N.J. and A. Fedorov, 2014b: What controls the mean east-west sea surface temperature gradient in the equatorial pacific: The role of cloud albedo. *Journal of Climate*, **27(7)**, 2757–2778, doi:10.1175/jcli-d-13-00255.1.
Burt, M.A., D.A. Randall, and M.D. Branson, 2016: Dark warming. *Journal of Climate*, doi:10.1175/jcli-d-15-0147.1.
Caballero, R. and M. Huber, 2013: State-dependent climate sensitivity in past warm climates and its implications for future climate projections. *Proceedings of the National Academy of Sciences*, **110(35)**, 14162–14167, doi:10.1073/pnas.1303365110.
Cain, M. et al., 2019: Improved calculation of warming-equivalent emissions for short-lived climate pollutants. *NPJ climate and atmospheric science*, **2(1)**, 1–7, doi:10.1038/s41612-019-0086-4.
Caldwell, P.M., M.D. Zelinka, and S.A. Klein, 2018: Evaluating Emergent Constraints on Equilibrium Climate Sensitivity. *Journal of Climate*, **31(10)**, 3921–3942, doi:10.1175/jcli-d-17-0631.1.
Caldwell, P.M., M.D. Zelinka, K.E. Taylor, and K. Marvel, 2016: Quantifying the sources of intermodel spread in equilibrium climate sensitivity. *Journal of Climate*, **29(2)**, 513–524, doi:10.1175/jcli-d-15-0352.1.
Caldwell, P.M. et al., 2014: Statistical significance of climate sensitivity predictors obtained by data mining. *Geophysical Research Letters*, **41(5)**, 1803–1808, doi:10.1002/2014gl059205.
Calisto, M., D. Folini, M. Wild, and L. Bengtsson, 2014: Cloud radiative forcing intercomparison between fully coupled CMIP5 models and CERES satellite data. *Ann. Geophys.*, **32(7)**, 793–807, doi:10.5194/angeo-32-793-2014.
Calogovic, J. et al., 2010: Sudden cosmic ray decreases: No change of global cloud cover. *Geophysical Research Letters*, **37(3)**, doi:10.1029/2009gl041327.
Cane, M.A. et al., 1997: Twentieth-Century Sea Surface Temperature Trends. *Science*, **275(5302)**, 957–960, doi:10.1126/science.275.5302.957.
Cao, L., G. Bala, K. Caldeira, R. Nemani, and G. Ban-Weiss, 2010: Importance of carbon dioxide physiological forcing to future climate change. *Proceedings of the National Academy of Sciences of the United States of America*, **107(21)**, doi:10.1073/pnas.0913000107.
Cao, Y., S. Liang, X. Chen, and T. He, 2015: Assessment of Sea Ice Albedo Radiative Forcing and Feedback over the Northern Hemisphere from 1982 to 2009 Using Satellite and Reanalysis Data. *J. Climate*, **28(3)**, 1248–1259, doi:10.1175/jcli-d-14-00389.1.
Ceppi, P. and D.L. Hartmann, 2015: Connections between clouds, radiation, and midlatitude dynamics: A review.. *Curr. Clim. Change Rep.*, **1**, 94–102, doi:10.1007/s40641-015-0010-x.
Ceppi, P. and J.M. Gregory, 2017: Relationship of tropospheric stability to climate sensitivity and Earth's observed radiation budget. *Proceedings of the National Academy of Sciences*, **114(50)**, 13126–13131, doi:10.1073/pnas.1714308114.
Ceppi, P. and J.M. Gregory, 2019: A refined model for the Earth's global energy balance. *Climate Dynamics*, **53(7–8)**, 4781–4797, doi:10.1007/s00382-019-04825-x.
Ceppi, P., D.T. McCoy, and D.L. Hartmann, 2016: Observational evidence for a negative shortwave cloud feedback in middle to high latitudes. *Geophysical Research Letters*, **43(3)**, 1331–1339, doi:10.1002/2015gl067499.
Cesana, G. and T. Storelvmo, 2017: Improving climate projections by understanding how cloud phase affects radiation. *Journal of Geophysical Research: Atmospheres*, **122(8)**, 4594–4599, doi:10.1002/2017jd026927.
Cesana, G. et al., 2019: Evaluating models' response of tropical low clouds to SST forcings using CALIPSO observations. *Atmos. Chem. Phys.*, **19(5)**, 2813–2832, doi:10.5194/acp-19-2813-2019.
Cess, R.D. et al., 1990: Intercomparison and interpretation of climate feedback processes in 19 atmospheric general circulation models. *Journal of Geophysical Research*, **95**, 16601–16615, doi:10.1029/jd095id10p16601.
Chafik, L. et al., 2016: Global linkages originating from decadal oceanic variability in the subpolar North Atlantic. *Geophysical Research Letters*, **43(20)**, 10,909–10,919, doi:10.1002/2016gl071134.
Chandan, D. and R.W. Peltier, 2018: On the mechanisms of warming the mid-Pliocene and the inference of a hierarchy of climate sensitivities with relevance to the understanding of climate futures. *Climate of the Past*, **14(6)**, 825–856, doi:10.5194/cp-14-825-2018.
Charney, J.G. et al., 1979: *Carbon Dioxide and Climate: A Scientific Assessment*. National Research Council (NRC). The National Academies Press, Washington, DC, USA, 34 pp., doi:10.17226/12181.
Checa-Garcia, R., M.I. Hegglin, D. Kinnison, D.A. Plummer, and K.P. Shine, 2018: Historical Tropospheric and Stratospheric Ozone Radiative Forcing Using the CMIP6 Database. *Geophysical Research Letters*, **45(7)**, 3264–3273, doi:10.1002/2017gl076770.
Chen, X., S. Liang, and Y. Cao, 2016: Satellite observed changes in the Northern Hemisphere snow cover phenology and the associated radiative forcing and feedback between 1982 and 2013. *Environ. Res. Lett.*, **11(8)**, 84002, doi:10.1088/1748-9326/11/8/084002.

ACCEPTED VERSION SUBJECT TO FINAL EDITING

Chen, Y.-C., M.W. Christensen, G.L. Stephens, and J.H. Seinfeld, 2014: Satellite-based estimate of global aerosol–cloud radiative forcing by marine warm clouds. *Nature Geoscience*, **7(9)**, 643–646, doi:10.1038/ngeo2214.
Cheng, L. et al., 2017: Improved estimates of ocean heat content from 1960 to 2015. *Science Advances*, **3(3)**, doi:10.1126/sciadv.1601545.
Cheng, L. et al., 2018: Taking the pulse of the planet. *Eos*, **99(1)**, 14–16, doi:10.1029/2017eo081839.
Chepfer, H., V. Noel, D. Winker, and M. Chiriaco, 2014: Where and when will we observe cloud changes due to climate warming? *Geophysical Research Letters*, **41(23)**, 8387–8395, doi:10.1002/2014gl061792.
Cherian, R., J. Quaas, M. Salzmann, and M. Wild, 2014: Pollution trends over Europe constrain global aerosol forcing as simulated by climate models. *Geophysical Research Letters*, doi:10.1002/2013gl058715.
Cherubini, F. et al., 2016: Bridging the gap between impact assessment methods and climate science. *Environmental Science & Policy*, **64(C)**, 129–140, doi:10.1016/j.envsci.2016.06.
Christensen, M.W. and G.L. Stephens, 2011: Microphysical and macrophysical responses of marine stratocumulus polluted by underlying ships: Evidence of cloud deepening. *Journal of Geophysical Research*, **116(D3)**, D03201, doi:10.1029/2010jd014638.
Christensen, M.W., Y.C. Chen, and G.L. Stephens, 2016a: Aerosol indirect effect dictated by liquid clouds. *Journal of Geophysical Research*, **121(24)**, doi:10.1002/2016jd025245.
Christensen, M.W. et al., 2016b: Arctic Observation and Reanalysis Integrated System: A New Data Product for Validation and Climate Study. *BULLETIN OF THE AMERICAN METEOROLOGICAL SOCIETY*, **97(6)**, 907–915, doi:10.1175/bams-d-14-00273.1.
Christensen, M.W. et al., 2017: Unveiling aerosol–cloud interactions – Part 1: Cloud contamination in satellite products enhances the aerosol indirect forcing estimate. *Atmospheric Chemistry and Physics*, **17(21)**, 13151–13164, doi:10.5194/acp-17-13151-2017.
Chung, E.S., B.J. Soden, and B.J. Sohn, 2010: Revisiting the determination of climate sensitivity from relationships between surface temperature and radiative fluxes. *Geophysical Research Letters*, doi:10.1029/2010gl043051.
Chung, E.S. et al., 2019: Reconciling opposing Walker circulation trends in observations and model projections. *Nature Climate Change*, **9(5)**, 405–412, doi:10.1038/s41558-019-0446-4.
Chung, E.-S. and B.J. Soden, 2015: An assessment of methods for computing radiative forcing in climate models. *Environmental Research Letters*, **10(7)**, 074004, doi:10.1088/1748-9326/10/7/074004.
Chung, E.-S. and B.J. Soden, 2018: On the compensation between cloud feedback and cloud adjustment in climate models. *Climate Dynamics*, **50(3)**, 1267–1276, doi:10.1007/s00382-017-3682-1.
Chung, E.-S., B. Soden, B.J. Sohn, and L. Shi, 2014: Upper-tropospheric moistening in response to anthropogenic warming. *Proceedings of the National Academy of Sciences*, **111(32)**, 11636–11641, doi:10.1073/pnas.1409659111.
Church, J.A. et al., 2013: Sea Level Change. In: *Climate Change 2013: The Physical Science Basis. Contribution of Working Group I to the Fifth Assessment Report of the Intergovernmental Panel on Climate Change* [Stocker, T.F., D. Qin, G.-K. Plattner, M. Tignor, S.K. Allen, J. Boschung, A. Nauels, Y. Xia, V. Bex, and P.M. Midgley (eds.)]. Cambridge University Press, Cambridge, United Kingdom and New York, NY, USA, pp. 1137–1216, doi:10.1017/cb09781107415315.026.
Clark, P.U. et al., 2016: Consequences of twenty-first-century policy for multi-millennial climate and sea-level change. *Nature Climate Change*, **6(4)**, 360–369, doi:10.1038/nclimate2923.
Clarke, L. et al., 2014: Assessing Transformation Pathways. In: *Climate Change 2014: Mitigation of Climate Change. Contribution of Working Group III to the Fifth Assessment Report of the Intergovernmental Panel on Climate Change* [Edenhofer, O., R. Pichs-Madruga, Y. Sokona, E. Farahani, S. Kadner, K. Seyboth, A. Adler, I. Baum, S. Brunner, P. Eickemeier, B. Kriemann, J. Savolainen, S. Schlömer, C. von Stechow, T. Zwickel, and J.C. Minx (eds.)]. Cambridge University Press, Cambridge, United Kingdom and New York, USA, pp. 413–510, doi:10.1017/cbo9781107415416.012.
Cleator, S.F., S.P. Harrison, N.K. Nichols, I.C. Prentice, and I. Roulstone, 2020: A new multivariable benchmark for Last Glacial Maximum climate simulations. *Climate of the Past*, **16(2)**, 699–712, doi:10.5194/cp-16-699-2020.
Clement, A.C., R. Seager, M.A. Cane, and S.E. Zebiak, 1996: An ocean dynamical thermostat. *Journal of Climate*, doi:10.1175/1520-0442(1996)009<2190:aodt>2.0.co;2.
Coats, S. and K.B. Karnauskas, 2017: Are Simulated and Observed Twentieth Century Tropical Pacific Sea Surface Temperature Trends Significant Relative to Internal Variability? *Geophysical Research Letters*, **44(19)**, 9928–9937, doi:10.1002/2017gl074622.
Coddington, O., J.L. Lean, P. Pilewskie, M. Snow, and D. Lindholm, 2016: A solar irradiance climate data record. *Bulletin of the American Meteorological Society*, **97(7)**, 1265–1282, doi:10.1175/bams-d-14-00265.1.
Cohan, D.S., J. Xu, R. Greenwald, M.H. Bergin, and W.L. Chameides, 2002: Impact of atmospheric aerosol light scattering and absorption on terrestrial net primary productivity. *Global Biogeochemical Cycles*, **16(4)**, 37–1–37–12, doi:10.1029/2001gb001441.
Collins, M. et al., 2013: Long-term Climate Change: Projections, Commitments and Irreversibility. In: *Climate Change 2013: The Physical Science Basis. Contribution of Working Group I to the Fifth Assessment Report of the Intergovernmental Panel on Climate Change* [Stocker, T.F., D. Qin, G.-K. Plattner, M. Tignor, S.K. Allen, J.

ACCEPTED VERSION SUBJECT TO FINAL EDITING

Boschung, A. Nauels, Y. Xia, V. Bex, and P.M. Midgley (eds.)]. Cambridge University Press, Cambridge, United Kingdom and New York, NY, USA, pp. 1029–1136, doi:10.1017/cbo9781107415324.024.
Collins, W.D., D.R. Feldman, C. Kuo, and N.H. Nguyen, 2018: Large regional shortwave forcing by anthropogenic methane informed by Jovian observations. *Science Advances*, **4(9)**, doi:10.1126/sciadv.aas9593.
Collins, W.J., R.G. Derwent, C.E. Johnson, and D.S. Stevenson, 2002: The oxidation of organic compounds in the troposphere and their global warming potentials. *Climatic Change*, **52**, 453–479, doi:10.1023/a:1014221225434.
Collins, W.J., D.J. Frame, J.S. Fuglestvedt, and K.P. Shine, 2020: Stable climate metrics for emissions of short and long-lived species-combining steps and pulses. *Environmental Research Letters*, **15(2)**, doi:10.1088/1748-9326/ab6039.
Collins, W.J. et al., 2011: Development and evaluation of an Earth-System model – HadGEM2. *Geoscientific Model Development*, **4**, 1051–1075, doi:10.5194/gmd-4-1051-2011.
Collins, W.J. et al., 2013: Global and regional temperature-change potentials for near-term climate forcers. *Atmospheric Chemistry and Physics*, **13**, 2471–2485, doi:10.5194/acp-13-2471-2013.
Collins, W.J. et al., 2017: AerChemMIP: Quantifying the effects of chemistry and aerosols in CMIP6. *Geoscientific Model Development*, **10(2)**, 585–607, doi:10.5194/gmd-10-585-2017.
Colman, R. and B. McAvaney, 2009: Climate feedbacks under a very broad range of forcing. *Geophysical Research Letters*, **36(1)**, 1–5, doi:10.1029/2008gl036268.
Colman, R. and L. Hanson, 2017: On the relative strength of radiative feedbacks under climate variability and change. *Climate Dynamics*, **49(5–6)**, 2115–2129, doi:10.1007/s00382-016-3441-8.
Colman, R.A., 2015: Climate radiative feedbacks and adjustments at the Earth's surface. *Journal of Geophysical Research*, **120(8)**, 3173–3182, doi:10.1002/2014jd022896.
Covey, C. et al., 2000: The seasonal cycle in coupled ocean-atmosphere general circulation models. *Climate Dynamics*, **16(10)**, 775–787, doi:10.1007/s003820000081.
Cox, P.M., C. Huntingford, and M.S. Williamson, 2018a: Emergent constraint on equilibrium climate sensitivity from global temperature variability. *Nature*, **553(7688)**, 319–322, doi:10.1038/nature25450.
Cox, P.M., M.S. Williamson, F.J.M.M. Nijsse, and C. Huntingford, 2018b: Cox et al. reply. *Nature*, **563(7729)**, E10–E15, doi:10.1038/s41586-018-0641-x.
Crook, J.A. and P.M. Forster, 2014: Comparison of surface albedo feedback in climate models and observations. *Geophysical Research Letters*, **41**, 1717–1723, doi:10.1002/2014gl059280.
Crook, J.A., P.M. Forster, and N. Stuber, 2011: Spatial patterns of modeled climate feedback and contributions to temperature response and polar amplification. *Journal of Climate*, **24(14)**, 3575–3592, doi:10.1175/2011jcli3863.1.
Cuesta-Valero, F.J., A. García-García, H. Beltrami, J.F. González-Rouco, and E. García-Bustamante, 2021: Long-term Global Ground Heat Flux and Continental Heat Storage from Geothermal Data. *Clim. Past*, **17(1)**, 451–468, doi:10.5194/cp-17-451-2021.
Cui, Y.F. et al., 2017: Effects of straw and biochar addition on soil nitrogen, carbon, and super rice yield in cold waterlogged paddy soils of North China. *Journal of Integrative Agriculture*, **16(5)**, 1064–1074, doi:10.1016/s2095-3119(16)61578-2.
Dai, A., D. Luo, M. Song, and J. Liu, 2019: Arctic amplification is caused by sea-ice loss under increasing CO2. *Nature Communications*, **10(1)**, 121, doi:10.1038/s41467-018-07954-9.
Daniel, J.S. et al., 2012: Limitations of single-basket trading: Lessons from the Montreal Protocol for climate policy. *Climatic Change*, **111(2)**, 241–248, doi:10.1007/s10584-011-0136-3.
Davies, R., V.M. Jovanovic, and C.M. Moroney, 2017: Cloud heights measured by MISR from 2000 to 2015. *Journal of Geophysical Research: Atmospheres*, **122(7)**, 3975–3986, doi:10.1002/2017jd026456.
Davies-Barnard, T., P.J. Valdes, J.S. Singarayer, A.J. Wiltshire, and C.D. Jones, 2015: Quantifying the relative importance of land cover change from climate and land use in the representative concentration pathways. *Global Biogeochemical Cycles*, **29(6)**, 842–853, doi:10.1002/2014gb004949.
de la Vega, E., T.B. Chalk, P.A. Wilson, R.P. Bysani, and G.L. Foster, 2020: Atmospheric CO2 during the Mid-Piacenzian Warm Period and the M2 glaciation. *Scientific Reports*, **10(1)**, 11002, doi:10.1038/s41598-020-67154-8.
Dekens, P.S., A.C. Ravelo, M.D. McCarthy, and C.A. Edwards, 2008: A 5 million year comparison of Mg/Ca and alkenone paleothermometers. *Geochemistry, Geophysics, Geosystems*, **9(10)**, doi:10.1029/2007gc001931.
Denison, S., P.M. Forster, and C.J. Smith, 2019: Guidance on emissions metrics for nationally determined contributions under the Paris Agreement. *Environmental Research Letters*, **14(12)**, 124002, doi:10.1088/1748-9326/ab4df4.
Deser, C., R. Knutti, S. Solomon, and A.S. Phillips, 2012: Communication of the role of natural variability in future North American climate. *Nature Clim Change*, **2**, 775–779, doi:10.1038/nclimate1562.
Dessler, A.E., 2011: Cloud variations and the Earth's energy budget. *Geophysical Research Letters*, **38(19)**, doi:10.1029/2011gl049236.
Dessler, A.E. and P.M. Forster, 2018: An estimate of equilibrium climate sensitivity from interannual variability. *Journal of Geophysical Research: Atmospheres*, **123(16)**, 8634–8645, doi:10.1029/2018jd028481.

ACCEPTED VERSION SUBJECT TO FINAL EDITING

Dessler, A.E., T. Mauritsen, and B. Stevens, 2018: The influence of internal variability on Earth's energy balance framework and implications for estimating climate sensitivity. *Atmospheric Chemistry and Physics*, **18(7)**, 5147–5155, doi:10.5194/acp-18-5147-2018.

Dessler, A.E., M.R. Schoeberl, T. Wang, S.M. Davis, and K.H. Rosenlof, 2013: Stratospheric water vapor feedback. *Proceedings of the National Academy of Sciences*, **110(45)**, 18087–18091, doi:10.1073/pnas.1310344110.

Dessler, A.E.E., 2013: Observations of climate feedbacks over 2000-10 and comparisons to climate models. *Journal of Climate*, **26(1)**, 333–342, doi:10.1175/jcli-d-11-00640.1.

Devaraju, N., G. Bala, and R. Nemani, 2015: Modelling the influence of land-use changes on biophysical and biochemical interactions at regional and global scales. *Plant, Cell and Environment*, **38(9)**, 1931–1946, doi:10.1111/pce.12488.

Diamond, M., H.M. Director, R. Eastman, A. Possner, and R. Wood, 2020: Substantial Cloud Brightening From Shipping in Subtropical Low Clouds. *AGU Advances*, **1(1)**, e2019AV000111, doi:10.1029/2019av000111.

Dickinson, R.E., 1975: Solar Variability and the Lower Atmosphere. *Bulletin of the American Meteorological Society*, **56(12)**, 1240–1248, doi:10.1175/1520-0477(1975)056<1240:svatla>2.0.co;2.

DiNezio, P.N. et al., 2009: Climate Response of the Equatorial Pacific to Global Warming. *Journal of Climate*, **22(18)**, 4873–4892, doi:10.1175/2009jcli2982.1.

Dinh, T. and S. Fueglistaler, 2019: On the Causal Relationship between the Moist Diabatic Circulation and Cloud Rapid Adjustment to Increasing CO2. *Journal of Advances in Modeling Earth Systems*, **11(11)**, 3836–3851, doi:10.1029/2019ms001853.

Doherty, S.J. et al., 2013: Observed vertical redistribution of black carbon and other insoluble light-absorbing particles in melting snow. *J. Geophys. Res. Atmos*, **118(11)**, 5553–5569, doi:10.1002/jgrd.50235.

Dolinar, E.K., X. Dong, B. Xi, J.H. Jiang, and H. Su, 2015: Evaluation of CMIP5 simulated clouds and TOA radiation budgets using NASA satellite observations. *CLIMATE DYNAMICS*, **44(7–8)**, 2229–2247, doi:10.1007/s00382-014-2158-9.

Dong, L. and M.J. McPhaden, 2017: The effects of external forcing and internal variability on the formation of interhemispheric sea surface temperature gradient trends in the Indian Ocean. *Journal of Climate*, **30(22)**, 9077–9095, doi:10.1175/jcli-d-17-0138.1.

Dong, Y., K.C. Armour, C. Proistosescu, and D.S. Battisti, 2019: Attributing Historical and Future Evolution of Radiative Feedbacks to Regional Warming. *Journal of Climate*, **32(17)**, 9, doi:10.1175/jcli-d-18-0843.1.

Dong, Y. et al., 2020: Inter-model spread in the sea-surface temperature pattern effect and its contribution to climate sensitivity in CMIP5 and CMIP6 models. *Journal of Climate*, **33**, 7755–7775, doi:10.1175/jcli-d-19-1011.1.

Donohoe, A. and D.S. Battisti, 2011: Atmospheric and Surface Contributions to Planetary Albedo. *Journal of Climate*, **24(16)**, 4402–4418, doi:10.1175/2011jcli3946.1.

Donohoe, A. and D.S. Battisti, 2012: What determines meridional heat transport in climate models? *Journal of Climate*, **25(11)**, 3832–3850, doi:10.1175/jcli-d-11-00257.1.

Donohoe, A., K.C. Armour, A.G. Pendergrass, and D.S. Battisti, 2014: Shortwave and longwave radiative contributions to global warming under increasing CO2. *Proceedings of the National Academy of Sciences*, **111(47)**, 16700–16705, doi:10.1073/pnas.1412190111.

Donohoe, A., K.C. Armour, G.H. Roe, D.S. Battisti, and L. Hahn, 2020: The partitioning of meridional heat transport from the Last Glacial Maximum to CO2 quadrupling in coupled climate models. *Journal of Climate*, **33**, 4141–4165, doi:10.1175/jcli-d-19-0797.1.

Dorheim, K., R. Link, C. Hartin, B. Kravitz, and A. Snyder, 2020: Calibrating Simple Climate Models to Individual Earth System Models: Lessons Learned From Calibrating Hector. *Earth and Space Science*, **7(11)**, e2019EA000980, doi:10.1029/2019ea000980.

Doutriaux-Boucher, M., M.J. Webb, J.M. Gregory, and O. Boucher, 2009: Carbon dioxide induced stomatal closure increases radiative forcing via a rapid reduction in low cloud. *Geophysical Research Letters*, **36(2)**, 1–5, doi:10.1029/2008gl036273.

Dowsett, H.J. et al., 2012: Assessing confidence in Pliocene sea surface temperatures to evaluate predictive models. *Nature Climate Change*, **2(5)**, 365–371, doi:10.1038/nclimate1455.

Du, J., K. Wang, J. Wang, and Q. Ma, 2017: Contributions of surface solar radiation and precipitation to the spatiotemporal patterns of surface and air warming in China from 1960 to 2003. *ATMOSPHERIC CHEMISTRY AND PHYSICS*, **17(8)**, 4931–4944, doi:10.5194/acp-17-4931-2017.

Duan, L., L. Cao, and K. Caldeira, 2019: Estimating Contributions of Sea Ice and Land Snow to Climate Feedback. *Journal of Geophysical Research: Atmospheres*, **124(1)**, 199–208, doi:10.1029/2018jd029093.

Duan, L., L. Cao, G. Bala, and K. Caldeira, 2018: Comparison of the Fast and Slow Climate Response to Three Radiation Management Geoengineering Schemes. *Journal of Geophysical Research: Atmospheres*, **123(21)**, 11,980–12,001, doi:10.1029/2018jd029034.

Dufresne, J.L. and S. Bony, 2008: An assessment of the primary sources of spread of global warming estimates from coupled atmosphere-ocean models. *Journal of Climate*, **21(19)**, 5135–5144, doi:10.1175/2008jcli2239.1.

Dufresne, J.-L. and M. Saint-Lu, 2016: Positive feedback in climate: stabilization or runaway, illustrated by a simple experiment. *Bull. Am. Meteorol. Soc.*, **97(5)**, 755–765, doi:10.1175/bams-d-14-00022.1.

ACCEPTED VERSION SUBJECT TO FINAL EDITING

Dunne, E.M. et al., 2016: Global atmospheric particle formation from CERN CLOUD measurements. *Science*, **354(6316)**, 1119–1124, doi:10.1126/science.aaf2649.
Durack, P.J., P.J. Gleckler, F.W. Landerer, and K.E. Taylor, 2014: Quantifying underestimates of long-term upper-ocean warming. *Nature Climate Change*, **4**, 999–1005, doi:10.1038/nclimate2389.
Eastman, R. and S.G. Warren, 2013: A 39-yr survey of cloud changes from land stations worldwide 1971-2009: Long-term trends, relation to aerosols, and expansion of the tropical belt. *Journal of Climate*, **26(4)**, 1286–1303, doi:10.1175/jcli-d-12-00280.1.
Ebmeier, S.K., A.M. Sayer, R.G. Grainger, T.A. Mather, and E. Carboni, 2014: Systematic satellite observations of the impact of aerosols from passive volcanic degassing on local cloud properties. *Atmospheric Chemistry and Physics*, **14(19)**, 10601–10618, doi:10.5194/acp-14-10601-2014.
Edwards, M.R. and J.E. Trancik, 2014: Climate impacts of energy technologies depend on emissions timing. *Nature Climate Change*, **4**, 347–352, doi:10.1038/nclimate2204.
Egorova, T. et al., 2018: Revised historical solar irradiance forcing. *Astronomy & Astrophysics*, **615**, A85, doi:10.1051/0004-6361/201731199.
Einstein, A., 1905: Über die von der molekularkinetischen Theorie der Wärme geforderte Bewegung von in ruhenden Flüssigkeiten suspendierten Teilchen. *Annalen der Physik*, **322(8)**, 549–560, doi:10.1002/andp.19053220806.
Elagib, N.A. and S.H. Alvi, 2013: Moderate solar dimming in an accelerating warming climate of Bahrain. *International Journal of Global Warming*, **5(1)**, 96–107, doi:10.1504/ijgw.2013.051487.
Emanuel, K., A.A. Wing, and E.M. Vincent, 2014: Radiative-convective instability. *Journal of Advances in Modeling Earth Systems*, **6(1)**, 75–90, doi:10.1002/2013ms000270.
England, M.H. et al., 2014: Recent intensification of wind-driven circulation in the Pacific and the ongoing warming hiatus. *Nature Climate Change*, **4(3)**, 222–227, doi:10.1038/nclimate2106.
Erfani, E. and N.J. Burls, 2019: The Strength of Low-Cloud Feedbacks and Tropical Climate: A CESM Sensitivity Study. *Journal of Climate*, JCLI–D–18–0551.1, doi:10.1175/jcli-d-18-0551.1.
Etminan, M., G. Myhre, E.J. Highwood, and K.P. Shine, 2016: Radiative forcing of carbon dioxide, methane, and nitrous oxide: A significant revision of the methane radiative forcing. *Geophysical Research Letters*, **43(24)**, 12,614–12,623, doi:10.1002/2016gl071930.
Exarchou, E., T. Kuhlbrodt, J.M. Gregory, and R.S. Smith, 2014: Ocean Heat Uptake Processes: A Model Intercomparison. *Journal of Climate*, **28(2)**, 887–908, doi:10.1175/jcli-d-14-00235.1.
Farnsworth, A. et al., 2019: Climate Sensitivity on Geological Timescales Controlled by Nonlinear Feedbacks and Ocean Circulation. *Geophysical Research Letters*, **46(16)**, 9880–9889, doi:10.1029/2019gl083574.
Fedorov, A., N.J. Burls, K.T. Lawrence, and L.C. Peterson, 2015: Tightly linked zonal and meridional sea surface temperature gradients over the past five million years. *Nature Geoscience*, **8**, 975–980, doi:10.1038/ngeo2577.
Fedorov, A. et al., 2013: Patterns and mechanisms of early Pliocene warmth. *Nature*, **496(7443)**, 43–49, doi:10.1038/nature12003.
Feldl, N. and G.H. Roe, 2013: The nonlinear and nonlocal nature of climate feedbacks. *Journal of Climate*, doi:10.1175/jcli-d-12-00631.1.
Feldl, N., B.T. Anderson, and S. Bordoni, 2017a: Atmospheric eddies mediate lapse rate feedback and arctic amplification. *Journal of Climate*, **30(22)**, 9213–9224, doi:10.1175/jcli-d-16-0706.1.
Feldl, N., S. Bordoni, and T.M. Merlis, 2017b: Coupled high-latitude climate feedbacks and their impact on atmospheric heat transport. *Journal of Climate*, **30(1)**, 189–201, doi:10.1175/jcli-d-16-0324.1.
Feldl, N., S. Po-Chedley, H.K.A. Singh, S. Hay, and P.J. Kushner, 2020: Sea ice and atmospheric circulation shape the high-latitude lapse rate feedback. *npj Climate and Atmospheric Science*, **3(1)**, doi:10.1038/s41612-020-00146-7.
Feng, F. and K. Wang, 2019: Does the modern-era retrospective analysis for research and applications-2 aerosol reanalysis introduce an improvement in the simulation of surface solar radiation over China? *INTERNATIONAL JOURNAL OF CLIMATOLOGY*, **39(3)**, 1305–1318, doi:10.1002/joc.5881.
Feng, R., B.L. Otto-Bliesner, E.C. Brady, and N. Rosenbloom, 2020: Increased Climate Response and Earth System Sensitivity From CCSM4 to CESM2 in Mid-Pliocene Simulations. *Journal of Advances in Modeling Earth Systems*, **12(8)**, doi:10.1029/2019ms002033.
Feng, R. et al., 2019: Contributions of aerosol-cloud interactions to mid-Piacenzian seasonally sea ice-free Arctic Ocean. *Geophysical Research Letters*, **46(16)**, 9920–9929, doi:10.1029/2019gl083960.
Fiedler, S., B. Stevens, and T. Mauritsen, 2017: On the sensitivity of anthropogenic aerosol forcing to model-internal variability and parameterizing a Twomey effect. *Journal of Advances in Modeling Earth Systems*, **9(2)**, 1325–1341, doi:10.1002/2017ms000932.
Fiedler, S. et al., 2019: Anthropogenic aerosol forcing-insights from multiple estimates from aerosol-climate models with reduced complexity. *Atmospheric Chemistry and Physics*, **19(10)**, 6821–6841, doi:10.5194/acp-19-6821-2019.
Fisher, J.B. et al., 2017: The future of evapotranspiration: Global requirements for ecosystem functioning, carbon and climate feedbacks, agricultural management, and water resources. *Water Resources Research*, **53(4)**, 2618–2626, doi:10.1002/2016wr020175.

ACCEPTED VERSION SUBJECT TO FINAL EDITING

Flanner, M.G. and C.S. Zender, 2006: Linking snowpack microphysics and albedo evolution. *J. Geophys. Res.*, **111**, doi:10.1029/2005jd006834.
Flanner, M.G., K.M. Shell, M. Barlage, D.K. Perovich, and M.A. Tschudi, 2011: Radiative forcing and albedo feedback from the Northern Hemisphere cryosphere between 1979 and 2008. *Nature Geosci.*, **4**, 151–155, doi:10.1038/ngeo1062.
Flannery, B.P., 1984: Energy Balance Models Incorporating Transport of Thermal and Latent Energy. *Journal of the Atmospheric Sciences*, **41(3)**, doi:10.1175/1520-0469(1984)041<0414:ebmito>2.0.co;2.
Flato, G. et al., 2013: Evaluation of Climate Models. In: *Climate Change 2013: The Physical Science Basis. Contribution of Working Group I to the Fifth Assessment Report of the Intergovernmental Panel on Climate Change* [Stocker, T.F., D. Qin, G.-K. Plattner, M. Tignor, S.K. Allen, J. Boschung, A. Nauels, Y. Xia, V. Bex, and P.M. Midgley (eds.)]. Cambridge University Press, Cambridge, United Kingdom and New York, NY, USA, pp. 741–866, doi:10.1017/cbo9781107415324.020.
Flynn, C.M. and T. Mauritsen, 2020: On the climate sensitivity and historical warming evolution in recent coupled model ensembles. *Atmospheric Chemistry and Physics*, **20(13)**, 7829–7842, doi:10.5194/acp-20-7829-2020.
Folini, D. and M. Wild, 2015: The effect of aerosols and sea surface temperature on China's climate in the late twentieth century from ensembles of global climate simulations. *J. Geophys. Res.*, **120** , 2261–2279, doi:10.1002/2014jd022851.
Ford, H.L., A.C. Ravelo, P.S. Dekens, J.P. LaRiviere, and M.W. Wara, 2015: The evolution of the equatorial thermocline and the early Pliocene El Padre mean state. *Geophysical Research Letters*, **42(12)**, 4878–4887, doi:10.1002/2015gl064215.
Forest, C.E., 2002: Quantifying Uncertainties in Climate System Properties with the Use of Recent Climate Observations. *Science*, **295(5552)**, 113–117, doi:10.1126/science.1064419.
Forest, C.E., 2018: Inferred Net Aerosol Forcing Based on Historical Climate Changes: a Review. *Current Climate Change Reports*, **4(1)**, 11–22, doi:10.1007/s40641-018-0085-2.
Forster, P. et al., 2007: Changes in Atmospheric Constituents and in Radiative Forcing. In: *Climate Change 2007: The Physical Science Basis. Contribution of Working Group I to the Fourth Assessment Report of the Intergovernmental Panel on Climate Change* [Solomon, S., D. Qin, M. Manning, Z. Chen, M. Marquis, K.B. Averyt, M. Tignor, and H.L. Miller (eds.)]. Cambridge University Press, Cambridge, United Kingdom and New York, NY, USA, pp. 129–234.
Forster, P. et al., 2018: Mitigation Pathways Compatible with 1.5°C in the Context of Sustainable Development Supplementary Material. In: *Global Warming of 1.5°C. An IPCC Special Report on the impacts of global warming of 1.5°C above pre-industrial levels and related global greenhouse gas emission pathways, in the context of strengthening the global response to the threat of climate change,* [Masson-Delmotte, V., P. Zhai, H.-O. Pörtner, D. Roberts, J. Skea, P.R. Shukla, A. Pirani, W. Moufouma-Okia, C. Péan, R. Pidcock, S. Connors, J.B.R. Matthews, Y. Chen, X. Zhou, M.I. Gomis, E. Lonnoy, T. Maycock, M. Tignor, and T. Waterfield (eds.)]. In Press, pp. 2SM: 1–50.
Forster, P.M., 2016: Inference of Climate Sensitivity from Analysis of Earth's Energy Budget. *Annual Review of Earth and Planetary Sciences*, **44(1)**, 85–106, doi:10.1146/annurev-earth-060614-105156.
Forster, P.M., A.C. Maycock, C.M. McKenna, and C.J. Smith, 2019: Latest climate models confirm need for urgent mitigation. *Nature Climate Change*, doi:10.1038/s41558-019-0660-0.
Forster, P.M. et al., 2013: Evaluating adjusted forcing and model spread for historical and future scenarios in the CMIP5 generation of climate models. *Journal of Geophysical Research Atmospheres*, **118(3)**, 1139–1150, doi:10.1002/jgrd.50174.
Forster, P.M. et al., 2016: Recommendations for diagnosing effective radiative forcing from climate models for CMIP6. *Journal of Geophysical Research*, doi:10.1002/2016jd025320.
Forster, P.M.D.F. and M. Joshi, 2005: The role of halocarbons in the climate change of the troposphere and stratosphere. *Climatic Change*, doi:10.1007/s10584-005-5955-7.
Foster, G., J.D. Annan, G.A. Schmidt, and M.E. Mann, 2008: Comment on "Heat capacity, time constant, and sensitivity of Earth's climate system" by S. E. Schwartz. *Journal of Geophysical Research Atmospheres*, **113(15)**, doi:10.1029/2007jd009373.
Foster, G.L. and J.W.B. Rae, 2016: Reconstructing Ocean pH with Boron Isotopes in Foraminifera. *Annual Review of Earth and Planetary Sciences*, **44(1)**, 207–237, doi:10.1146/annurev-earth-060115-012226.
Frame, D.J., D.A. Stone, P.A. Stott, and M.R. Allen, 2006: Alternatives to stabilization scenarios. *Geophysical Research Letters*, doi:10.1029/2006gl025801.
Frame, D.J. et al., 2005: Constraining climate forecasts: The role of prior assumptions. *Geophysical Research Letters*, **32(9)**, doi:10.1029/2004gl022241.
Frey, W.R. and J.E. Kay, 2018: The influence of extratropical cloud phase and amount feedbacks on climate sensitivity. *Climate Dynamics*, **50(7)**, 3097–3116, doi:10.1007/s00382-017-3796-5.
Friberg, J. et al., 2015: Influence of volcanic eruptions on midlatitude upper tropospheric aerosol and consequences for cirrus clouds. *Earth and Space Science*, **2**, 285–300, doi:10.1002/2015ea000110.
Friedrich, T. and A. Timmermann, 2020: Using Late Pleistocene sea surface temperature reconstructions to constrain

ACCEPTED VERSION SUBJECT TO FINAL EDITING

future greenhouse warming. *Earth and Planetary Science Letters*, **530**, 115911, doi:10.1016/j.epsl.2019.115911.
Friedrich, T., A. Timmermann, M. Tigchelaar, O.E. Timm, and A. Ganopolski, 2016: Nonlinear climate sensitivity and its implications for future greenhouse warming. *Science Advances*, **2(11)**, doi:10.1126/sciadv.1501923.
Frouin, R. and S.F. Iacobellis, 2002: Influence of phytoplankton on the global radiation budget. *Journal of Geophysical Research*, **107(D19)**, 4377, doi:10.1029/2001jd000562.
Fu, B. et al., 2020: Short-lived climate forcers have long-term climate impacts via the carbon–climate feedback. *Nature Climate Change*, **10(9)**, 851–855, doi:10.1038/s41558-020-0841-x.
Fueglistaler, S., 2019: Observational Evidence for Two Modes of Coupling Between Sea Surface Temperatures, Tropospheric Temperature Profile, and Shortwave Cloud Radiative Effect in the Tropics. *Geophysical Research Letters*, **46(16)**, 9890–9898, doi:10.1029/2019gl083990.
Fueglistaler, S. and L.G. Silvers, 2021: The Peculiar Trajectory of Global Warming. *Journal of Geophysical Research: Atmospheres*, **126(4)**, e2020JD033629, doi:10.1029/2020jd033629.
Fuglestvedt, J. et al., 2018: Implications of possible interpretations of 'greenhouse gas balance' in the Paris Agreement. *Philosophical Transactions of the Royal Society A: Mathematical, Physical and Engineering Sciences*, **376(2119)**, doi:10.1098/rsta.2016.0445.
Fuglestvedt, J.S. et al., 2003: Metrics of climate change: Assessing radiative forcing and emission indices. *Climatic Change*, **58(3)**, 267–331, doi:10.1023/a:1023905326842.
Fyke, J., O. Sergienko, M. Löfverström, S. Price, and J.T.M. Lenaerts, 2018: An Overview of Interactions and Feedbacks Between Ice Sheets and the Earth System. *Reviews of Geophysics*, **56(2)**, 361–408, doi:10.1029/2018rg000600.
Gan, C.M. et al., 2014: Assessment of the effect of air pollution controls on trends in shortwave radiation over the United States from 1995 through 2010 from multiple observation networks. *Atmospheric Chemistry and Physics*, **14(3)**, 1701–1715, doi:10.5194/acp-14-1701-2014.
Garcia, R.D. et al., 2014: Reconstruction of global solar radiation time series from 1933 to 2013 at the Izana Atmospheric Observatory. *Atmospheric Measurement Techniques*, **7(9)**, 3139–3150, doi:10.5194/amt-7-3139-2014.
Garuba, O.A., J. Lu, F. Liu, and H.A. Singh, 2018: The Active Role of the Ocean in the Temporal Evolution of Climate Sensitivity. *Geophysical Research Letters*, doi:10.1002/2017gl075633.
Gasser, T. et al., 2017a: The compact Earth system model OSCAR v2.2: Description and first results. *Geoscientific Model Development*, **10(1)**, 271–319, doi:10.5194/gmd-10-271-2017.
Gasser, T. et al., 2017b: Accounting for the climate–carbon feedback in emission metric. *Earth System Dynamics*, **8(2)**, 235–253, doi:10.5194/esd-8-235-2017.
Gasser, T. et al., 2020: Historical CO2 emissions from land use and land cover change and their uncertainty. *Biogeosciences*, **17(15)**, 4075–4101, doi:10.5194/bg-17-4075-2020.
Gassó, S., 2008: Satellite observations of the impact of weak volcanic activity on marine clouds. *Journal of Geophysical Research*, **113(D14)**, D14S19, doi:10.1029/2007jd009106.
Gebbie, G. and P. Huybers, 2019: The Little Ice Age and 20th Century Deep Pacific Cooling. *Science*, **363(6422)**, 70–74, doi:10.1126/science.aar8413.
Geoffroy, O., D. Saint-Martin, and A. Ribes, 2012: Quantifying the sources of spread in climate change experiments. *Geophysical Research Letters*, **39(24)**, doi:10.1029/2012gl054172.
Geoffroy, O. et al., 2013a: Transient Climate Response in a Two-Layer Energy-Balance Model. Part II: Representation of the Efficacy of Deep-Ocean Heat Uptake and Validation for CMIP5 AOGCMs. *Journal of Climate*, **26(6)**, 1859–1876, doi:10.1175/jcli-d-12-00196.1.
Geoffroy, O. et al., 2013b: Transient climate response in a two-layer energy-balance model. Part I: Analytical solution and parameter calibration using CMIP5 AOGCM experiments. *Journal of Climate*, **26(6)**, 1841–1857, doi:10.1175/jcli-d-12-00195.1.
Gettelman, A. and S.C. Sherwood, 2016: Processes Responsible for Cloud Feedback. *Current Climate Change Reports*, **2(4)**, 179–189, doi:10.1007/s40641-016-0052-8.
Gettelman, A., J.E. Kay, and K.M. Shell, 2012: The evolution of climate sensitivity and climate feedbacks in the Community Atmosphere Model.. *Journal of Climate*, **25(5)**, 1453–1469, doi:10.1175/jcli-d-11-00197.1.
Gettelman, A., A. Schmidt, and J.E. Kristjánsson, 2015: Icelandic volcanic emissions and climate. *Nature Geoscience*, **8(4)**, 243, doi:10.1038/ngeo2376.
Gettelman, A. et al., 2019: High Climate Sensitivity in the Community Earth System Model Version 2 (CESM2). *Geophysical Research Letters*, **46(14)**, 8329–8337, doi:10.1029/2019gl083978.
Ghan, S. et al., 2016: Challenges in constraining anthropogenic aerosol effects on cloud radiative forcing using present-day spatiotemporal variability.. *Proceedings of the National Academy of Sciences of the United States of America*, **113(21)**, 5804–11, doi:10.1073/pnas.1514036113.
Ghimire, B. et al., 2014: Global albedo change and radiative cooling from anthropogenic land cover change, 1700 to 2005 based on MODIS, land use harmonization, radiative kernels, and reanalysis. *Geophysical Research Letters*, doi:10.1002/2014gl061671.

ACCEPTED VERSION SUBJECT TO FINAL EDITING

Gilgen, A., W.T.K. Huang, L. Ickes, D. Neubauer, and U. Lohmann, 2018: How important are future marine and shipping aerosol emissions in a warming Arctic summer and autumn? *Atmospheric Chemistry and Physics*, **18(14)**, 10521–10555, doi:10.5194/acp-18-10521-2018.

Gillett, N.P. and H.D. Matthews, 2010: Accounting for carbon cycle feedbacks in a comparison of the global warming effects of greenhouse gases. *Environmental Research Letters*, **5(3)**, doi:10.1088/1748-9326/5/3/034011.

Gillett, N.P., V.K. Arora, D. Matthews, and M.R. Allen, 2013: Constraining the ratio of global warming to cumulative CO2 emissions using CMIP5 simulations. *Journal of Climate*, **26(18)**, 6844–6858, doi:10.1175/jcli-d-12-00476.1.

Gillett, N.P., V.K. Arora, G.M. Flato, J.F. Scinocca, and K. Von Salzen, 2012: Improved constraints on 21st-century warming derived using 160 years of temperature observations. *Geophysical Research Letters*, **39(1)**, 1–5, doi:10.1029/2011gl050226.

Giorgetta, M.A. et al., 2013: Climate and carbon cycle changes from 1850 to 2100 in MPI-ESM simulations for the Coupled Model Intercomparison Project phase 5. *Journal of Advances in Modeling Earth Systems*, **5(3)**, 572–597, doi:10.1002/jame.20038.

Goelzer, H. et al., 2011: Impact of Greenland and Antarctic ice sheet interactions on climate sensitivity. *Climate Dynamics*, **37(5)**, 1005–1018, doi:10.1007/s00382-010-0885-0.

Golaz, J.C., J.C. Golaz, and H. Levy, 2013: Cloud tuning in a coupled climate model: Impact on 20th century warming. *Geophysical Research Letters*, **40(10)**, 2246–2251, doi:10.1002/grl.50232.

Golaz, J.C. et al., 2019a: The DOE E3SM Coupled Model Version 1: Overview and Evaluation at Standard Resolution. *Journal of Advances in Modeling Earth Systems*, **11(7)**, 2089–2129, doi:10.1029/2018ms001603.

Golaz, J.C. et al., 2019b: The DOE E3SM Coupled Model Version 1: Overview and Evaluation at Standard Resolution. *Journal of Advances in Modeling Earth Systems*, **11(7)**, 2089–2129, doi:10.1029/2018ms001603.

Goldner, A., N. Herold, and M. Huber, 2014a: Antarctic glaciation caused ocean circulation changes at the Eocene-Oligocene transition. *Nature*, **511(7511)**, 574–577, doi:10.1038/nature13597.

Goldner, A., N. Herold, and M. Huber, 2014b: The challenge of simulating the warmth of the mid-Miocene climatic optimum in CESM1. *Climate of the Past*, **10(2)**, 523–536, doi:10.5194/cp-10-523-2014.

Golledge, N.R. et al., 2019: Global environmental consequences of twenty-first-century ice-sheet melt. *Nature*, **566(7742)**, 65–72, doi:10.1038/s41586-019-0889-9.

Gong, T., S. Feldstein, and S. Lee, 2017: The role of downward infrared radiation in the recent arctic winter warming trend. *Journal of Climate*, doi:10.1175/jcli-d-16-0180.1.

Good, P., J.M. Gregory, and J.A. Lowe, 2011: A step-response simple climate model to reconstruct and interpret AOGCM projections. *Geophysical Research Letters*, **38(1)**, doi:10.1029/2010gl045208.

Good, P., J.M. Gregory, J.A. Lowe, and T. Andrews, 2013: Abrupt CO2 experiments as tools for predicting and understanding CMIP5 representative concentration pathway projections. *Climate Dynamics*, **40(3)**, 1041–1053, doi:10.1007/s00382-012-1410-4.

Good, P. et al., 2015: Nonlinear regional warming with increasing CO2 concentrations. *Nature Climate Change*, **5(2)**, 138–142, doi:10.1038/nclimate2498.

Good, P. et al., 2016: NonlinMIP contribution to CMIP6: Model intercomparison project for non-linear mechanisms: Physical basis, experimental design and analysis principles (v1.0). *Geoscientific Model Development*, **9(11)**, 4019–4028, doi:10.5194/gmd-9-4019-2016.

Good, S.A., 2017: The impact of observational sampling on time series of global 0–700 m ocean average temperature: a case study. *International Journal of Climatology*, **37(5)**, 2260–2268, doi:10.1002/joc.4654.

Goodwin, P., 2016: How historic simulation–observation discrepancy affects future warming projections in a very large model ensemble. *Climate Dynamics*, **47(7–8)**, 2219–2233, doi:10.1007/s00382-015-2960-z.

Goodwin, P., 2018: On the Time Evolution of Climate Sensitivity and Future Warming. *Earth's Future*, **6(9)**, 1336–1348, doi:10.1029/2018ef000889.

Goosse, H. et al., 2018: Quantifying climate feedbacks in polar regions. *Nature Communications*, doi:10.1038/s41467-018-04173-0.

Gordon, H. et al., 2016: Reduced anthropogenic aerosol radiative forcing caused by biogenic new particle formation. *Proceedings of the National Academy of Sciences of the United States of America*, **113(43)**, 12053–12058, doi:10.1073/pnas.1602360113.

Gordon, H. et al., 2017: Causes and importance of new particle formation in the present-day and preindustrial atmospheres. *Journal of Geophysical Research: Atmospheres*, **122(16)**, 8739–8760, doi:10.1002/2017jd026844.

Gordon, N.D. and S.A. Klein, 2014: Low-cloud optical depth feedback in climate models. *Journal of Geophysical Research: Atmospheres*, **119(10)**, 6052–6065, doi:10.1002/2013jd021052.

Gordon, N.D., A.K. Jonko, P.M. Forster, and K.M. Shell, 2013: An observationally based constraint on the water-vapor feedback. *Journal of Geophysical Research Atmospheres*, **118(22)**, 12435–12443, doi:10.1002/2013jd020184.

Goren, T. and D. Rosenfeld, 2014: Decomposing aerosol cloud radiative effects into cloud cover, liquid water path and Twomey components in marine stratocumulus. *Atmospheric Research*, **138**, 378–393, doi:10.1016/j.atmosres.2013.12.008.

ACCEPTED VERSION SUBJECT TO FINAL EDITING

Grandey, B.S., P. Stier, and T.M. Wagner, 2013: Investigating relationships between aerosol optical depth and cloud fraction using satellite, aerosol reanalysis and general circulation model data. *Atmospheric Chemistry and Physics*, **13(6)**, 3177–3184, doi:10.5194/acp-13-3177-2013.

Grandey, B.S. et al., 2018: Effective radiative forcing in the aerosol-climate model CAM5.3-MARC-ARG. *Atmospheric Chemistry and Physics*, **18(21)**, 15783–15810, doi:10.5194/acp-18-15783-2018.

Graversen, R.G. and M. Wang, 2009: Polar amplification in a coupled climate model with locked albedo. *Climate Dynamics*, doi:10.1007/s00382-009-0535-6.

Graversen, R.G. and M. Burtu, 2016: Arctic amplification enhanced by latent energy transport of atmospheric planetary waves. *Quarterly Journal of the Royal Meteorological Society*, **142(698)**, 2046–2054, doi:10.1002/qj.2802.

Graversen, R.G., P.L. Langen, and T. Mauritsen, 2014: Polar Amplification in CCSM4: Contributions from the Lapse Rate and Surface Albedo Feedbacks. *Journal of Climate*, **27(12)**, 4433–4450, doi:10.1175/jcli-d-13-00551.1.

Gray, L.J., S.T. Rumbold, and K.P. Shine, 2009: Stratospheric Temperature and Radiative Forcing Response to 11-Year Solar Cycle Changes in Irradiance and Ozone. *Journal of the Atmospheric Sciences*, **66(8)**, 2402–2417, doi:10.1175/2009jas2866.1.

Gregory, J.M., 2000: Vertical heat transports in the ocean and their effect on time-dependent climate change. *Climate Dynamics*, doi:10.1007/s003820000059.

Gregory, J.M. and T. Andrews, 2016: Variation in climate sensitivity and feedback parameters during the historical period. *Geophysical Research Letters*, doi:10.1002/2016gl068406.

Gregory, J.M., T. Andrews, and P. Good, 2015: The inconstancy of the transient climate response parameter under increasing CO2. *Philosophical Transactions of the Royal Society A: Mathematical, Physical and Engineering Sciences*, **373(2054)**, doi:10.1098/rsta.2014.0417.

Gregory, J.M., C.D. Jones, P. Cadule, and P. Friedlingstein, 2009: Quantifying carbon cycle feedbacks. *Journal of Climate*, **22(19)**, 5232–5250, doi:10.1175/2009jcli2949.1.

Gregory, J.M., R.J. Stouffer, S.C.B. Raper, P.A. Stott, and N.A. Rayner, 2002: An observationally based estimate of the climate sensitivity. *Journal of Climate*, **15(22)**, 3117–3121, doi:10.1175/1520-0442(2002)015<3117:aobeot>2.0.co;2.

Gregory, J.M., T. Andrews, P. Good, T. Mauritsen, and P.M. Forster, 2016: Small global-mean cooling due to volcanic radiative forcing. *Climate Dynamics*, **47(12)**, 3979–3991, doi:10.1007/s00382-016-3055-1.

Gregory, J.M., T. Andrews, P. Ceppi, T. Mauritsen, and M.J. Webb, 2020: How accurately can the climate sensitivity to CO2 be estimated from historical climate change? *Climate Dynamics*, **54**, 129–157, doi:10.1007/s00382-019-04991-y.

Gregory, J.M. et al., 2004: A new method for diagnosing radiative forcing and climate sensitivity. *Geophysical Research Letters*, **31(3)**, L03205, doi:10.1029/2003gl018747.

Grise, K.M. and B. Medeiros, 2016: Understanding the Varied Influence of Midlatitude Jet Position on Clouds and Cloud Radiative Effects in Observations and Global Climate Models. *Journal of Climate*, **29(24)**, 9005–9025, doi:10.1175/jcli-d-16-0295.1.

Grise, K.M., S.W. Son, G.J.P. Correa, and L.M. Polvani, 2014: The response of extratropical cyclones in the Southern Hemisphere to stratospheric ozone depletion in the 20th century. *Atmospheric Science Letters*, doi:10.1002/asl2.458.

Grise, K.M., L.M. Polvani, G. Tselioudis, Y. Wu, and M.D. Zelinka, 2013: The ozone hole indirect effect: Cloud-radiative anomalies accompanying the poleward shift of the eddy-driven jet in the Southern Hemisphere. *Geophysical Research Letters*, doi:10.1002/grl.50675.

Grose, M.R., J. Gregory, R. Colman, and T. Andrews, 2018: What Climate Sensitivity Index Is Most Useful for Projections? *Geophysical Research Letters*, **45(3)**, 1559–1566, doi:10.1002/2017gl075742.

Grosvenor, D.P. et al., 2018: Remote Sensing of Droplet Number Concentration in Warm Clouds: A Review of the Current State of Knowledge and Perspectives. *Reviews of Geophysics*, **56(2)**, 409–453, doi:10.1029/2017rg000593.

Gryspeerdt, E., P. Stier, and B.S. Grandey, 2014a: Cloud fraction mediates the aerosol optical depth-cloud top height relationship. *Geophysical Research Letters*, **41(10)**, 3622–3627, doi:10.1002/2014gl059524.

Gryspeerdt, E., P. Stier, and D.G. Partridge, 2014b: Satellite observations of cloud regime development: the role of aerosol processes. *Atmospheric Chemistry and Physics*, **14(3)**, 1141–1158, doi:10.5194/acp-14-1141-2014.

Gryspeerdt, E., J. Quaas, and N. Bellouin, 2016: Constraining the aerosol influence on cloud fraction. *Journal of Geophysical Research: Atmospheres*, **121(7)**, 3566–3583, doi:10.1002/2015jd023744.

Gryspeerdt, E. et al., 2017: Constraining the instantaneous aerosol influence on cloud albedo.. *Proceedings of the National Academy of Sciences of the United States of America*, **114(19)**, 4899–4904, doi:10.1073/pnas.1617765114.

Gryspeerdt, E. et al., 2018: Ice crystal number concentration estimates from lidar–radar satellite remote sensing – Part 2: Controls on the ice crystal number concentration. *Atmospheric Chemistry and Physics*, **18(19)**, 14351–14370, doi:10.5194/acp-18-14351-2018.

Gryspeerdt, E. et al., 2019: Constraining the aerosol influence on cloud liquid water path. *Atmospheric Chemistry and Physics*, **19**, 5331–5347, doi:10.5194/acp-19-5331-2019.

ACCEPTED VERSION SUBJECT TO FINAL EDITING

Gryspeerdt, E. et al., 2020: Surprising similarities in model and observational aerosol radiative forcing estimates. *Atmospheric Chemistry and Physics*, **20(1)**, 613–623, doi:10.5194/acp-20-613-2020.
Gulev, S.K. and K. Belyaev, 2012: Probability Distribution Characteristics for Surface Air-Sea Turbulent Heat Fluxes over the Global Ocean. *JOURNAL OF CLIMATE*, **25(1)**, 184–206, doi:10.1175/2011jcli4211.1.
Hahn, L.C. et al., 2020: Antarctic Elevation Drives Hemispheric Asymmetry in Polar Lapse Rate Climatology and Feedback. *Geophysical Research Letters*, **47(16)**, doi:10.1029/2020gl088965.
Hakuba, M.Z., D. Folini, A. Sanchez-Lorenzo, and M. Wild, 2014: Spatial representativeness of ground-based solar radiation measurements-Extension to the full Meteosat disk. *JOURNAL OF GEOPHYSICAL RESEARCH-ATMOSPHERES*, **119(20)**, 11760–11771, doi:10.1002/2014jd021946.
Hall, A., 2004: The role of surface albedo feedback in climate. *Journal of Climate*, **17(7)**, 1550–1568, doi:10.1175/1520-0442(2004)017<1550:trosaf>2.0.co;2.
Hall, A. and X. Qu, 2006: Using the current seasonal cycle to constrain snow albedo feedback in future climate change. *Geophysical Research Letters*, **33(3)**, 1–4, doi:10.1029/2005gl025127.
Hansen, J., M. Sato, G. Russell, and P. Kharecha, 2013: Climate sensitivity, sea level and atmospheric carbon dioxide. *Philosophical Transactions of the Royal Society A: Mathematical, Physical and Engineering Sciences*, **371(2001)**, doi:10.1098/rsta.2012.0294.
Hansen, J. et al., 1984: Climate sensitivity: Analysis of feedback mechanisms. In: *Climate Processes and Climate Sensitivity, AGU Geophysical Monograph 29, Maurice Ewing Volume 5* [Hansen, J.E. and T. Takahashi (eds.)]. American Geophysical Union (AGU), Washington, DC, USA, pp. 130–163.
Hansen, J. et al., 1985: Climate Response Times: Dependence on Climate Sensitivity and Ocean Mixing. *Science*, **229(4716)**, 857–859, doi:10.1126/science.229.4716.857.
Hansen, J. et al., 2005a: Earth's energy imbalance: Confirmation and implications. *SCIENCE*, **308(5727)**, 1431–1435, doi:10.1126/science.1110252.
Hansen, J. et al., 2005b: Efficacy of climate forcings. *Journal of Geophysical Research*, **110(18)**, 1–45, doi:10.1029/2005jd005776.
Hargreaves, J.C. and J.D. Annan, 2016: Could the Pliocene constrain the equilibrium climate sensitivity? *Climate of the Past*, **12(8)**, 1591–1599, doi:10.5194/cp-12-1591-2016.
Hargreaves, J.C., J.D. Annan, M. Yoshimori, and A. Abe-Ouchi, 2012: Can the Last Glacial Maximum constrain climate sensitivity? *Geophysical Research Letters*, **39(24)**, 1–5, doi:10.1029/2012gl053872.
Harper, A.B. et al., 2018: Vegetation distribution and terrestrial carbon cycle in a carbon cycle configuration of JULES4.6 with new plant functional types. *Geoscientific Model Development*, **11(7)**, 2857–2873, doi:10.5194/gmd-11-2857-2018.
Hartmann, D.J. et al., 2013: Observations: Atmosphere and Surface. In: *Climate Change 2013: The Physical Science Basis. Contribution of Working Group I to the Fifth Assessment Report of the Intergovernmental Panel on Climate Change* [Stocker, T.F., D. Qin, G.-K. Plattner, M. Tignor, S.K. Allen, J. Boschung, A. Nauels, Y. Xia, V. Bex, and P.M. Midgley (eds.)]. Cambridge University Press, Cambridge, United Kingdom and New York, NY, USA, pp. 159–254, doi:10.1017/cbo9781107415324.008.
Hartmann, D.L. and K. Larson, 2002: An important constraint on tropical cloud - climate feedback. *Geophysical Research Letters*, **29**, 1951, doi:10.1029/2002gl015835.
Hartmann, D.L., L.A. Moy, and Q. Fu, 2001: Tropical Convection and the Energy Balance at the Top of the Atmosphere. *Journal of Climate*, **14(24)**, 4495–4511, doi:10.1175/1520-0442(2001)014<4495:tcateb>2.0.co;2.
Hasekamp, O.P., E. Gryspeerdt, and J. Quaas, 2019: Analysis of polarimetric satellite measurements suggests stronger cooling due to aerosol-cloud interactions. *Nature Communications*, **10(1)**, 1–7, doi:10.1038/s41467-019-13372-2.
Hasselmann, K., 1976: Stochastic climate models Part I. Theory. *Tellus*, **28(6)**, 473–485, doi:10.1111/j.2153-3490.1976.tb00696.x.
Haugstad, A.D., K.C. Armour, D.S. Battisti, and B.E.J. Rose, 2017: Relative roles of surface temperature and climate forcing patterns in the inconstancy of radiative feedbacks. *Geophysical Research Letters*, **44(14)**, 7455–7463, doi:10.1002/2017gl074372.
Hawkins, E. and R. Sutton, 2012: Time of emergence of climate signals. *Geophysical Research Letters*, **39(1)**, doi:10.1029/2011gl050087.
Haywood, A.M., H.J. Dowsett, and A.M. Dolan, 2016a: Integrating geological archives and climate models for the mid-Pliocene warm period. *Nature Communications*, **7(1)**, 10646, doi:10.1038/ncomms10646.
Haywood, A.M. et al., 2013: On the identification of a Pliocene time slice for data model comparison. *Philosophical Transactions of the Royal Society of London A: Mathematical, Physical and Engineering Sciences*, **371(2001)**, doi:10.1098/rsta.2012.0515.
Haywood, A.M. et al., 2016b: The Pliocene Model Intercomparison Project (PlioMIP) Phase 2: scientific objectives and experimental design. *Climate of the Past*, **12(3)**, 663–675, doi:10.5194/cp-12-663-2016.
Haywood, A.M. et al., 2020: The Pliocene Model Intercomparison Project Phase 2: large-scale climate features and climate sensitivity. *Climate of the Past*, **16(6)**, 2095–2123, doi:10.5194/cp-16-2095-2020.
He, C. et al., 2018: Black carbon-induced snow albedo reduction over the Tibetan Plateau: Uncertainties from snow

ACCEPTED VERSION SUBJECT TO FINAL EDITING

grain shape and aerosol-snow mixing state based on an updated SNICAR model. *Atmospheric Chemistry and Physics*, **18(15)**, 11507–11527, doi:10.5194/acp-18-11507-2018.

He, Y., K. Wang, C. Zhou, and M. Wild, 2018: A Revisit of Global Dimming and Brightening Based on the Sunshine Duration. *GEOPHYSICAL RESEARCH LETTERS*, **45(9)**, 4281–4289, doi:10.1029/2018gl077424.

Hedemann, C., T. Mauritsen, J. Jungclaus, and J. Marotzke, 2017: The subtle origins of surface-warming hiatuses. *Nature Climate Change*, **7(5)**, 336–339, doi:10.1038/nclimate3274.

Heede, U.K., A. Fedorov, and N. Burls, 2020: Time Scales and Mechanisms for the Tropical Pacific Response to Global Warming: A Tug of War between the Ocean Thermostat and Weaker Walker. *Journal of Climate*, **33(14)**, 6101–6118, doi:10.1175/jcli-d-19-0690.1.

Held, I.M. and B.J. Soden, 2006: Robust Responses of the Hydrological Cycle to Global Warming. *Journal of Climate*, **19(21)**, 5686–5699, doi:10.1175/jcli3990.1.

Held, I.M. and K.M. Shell, 2012: Using Relative Humidity as a State Variable in Climate Feedback Analysis. , **25(8)**, 2578–2582, doi:10.1175/jcli-d-11-00721.1.

Held, I.M. et al., 2010: Probing the Fast and Slow Components of Global Warming by Returning Abruptly to Preindustrial Forcing. *Journal of Climate*, **23(9)**, 2418–2427, doi:10.1175/2009jcli3466.1.

Hellweg, S. and L. Milà i Canals, 2014: Emerging approaches, challenges and opportunities in life cycle assessment. *Science*, **344(6188)**, 1109–1113, doi:10.1126/science.1248361.

Heyn, I. et al., 2017: Assessment of simulated aerosol effective radiative forcings in the terrestrial spectrum. *Geophysical Research Letters*, doi:10.1002/2016gl071975.

Hock, R. et al., 2019: High Mountain Areas. In: *IPCC Special Report on the Ocean and Cryosphere in a Changing Climate* [Pörtner, H.-O., D.C. Roberts, V. Masson-Delmotte, P. Zhai, M. Tignor, E. Poloczanska, K. Mintenbeck, A. Alegría, M. Nicolai, A. Okem, J. Petzold, B. Rama, and N.M. Weyer (eds.)]. In Press, pp. 131–202.

Hodnebrog, S.B. Dalsøren, and G. Myhre, 2018: Lifetimes, direct and indirect radiative forcing, and global warming potentials of ethane (C2H6), propane (C3H8), and butane (C4H10). *Atmospheric Science Letters*, **19(2)**, doi:10.1002/asl.804.

Hodnebrog et al., 2020a: Updated global warming potentials and radiative efficiencies of halocarbons and other weak atmospheric absorbers. *Reviews of Geophysics*, doi:10.1029/2019rg000691.

Hodnebrog et al., 2020b: The effect of rapid adjustments to halocarbons and N2O on radiative forcing. *npj Climate and Atmospheric Science*, **3(43)**, doi:10.1038/s41612-020-00150-x.

Hoesly, R.M. et al., 2018: Historical (1750–2014) anthropogenic emissions of reactive gases and aerosols from the Community Emissions Data System (CEDS). *Geoscientific Model Development*, **11(1)**, 369–408, doi:10.5194/gmd-11-369-2018.

Holland, M.M. and C.M. Bitz, 2003: Polar amplification of climate change in coupled models. *Climate Dynamics*, doi:10.1007/s00382-003-0332-6.

Hollis, C.J. et al., 2019: The DeepMIP contribution to PMIP4: methodologies for selection, compilation and analysis of latest Paleocene and early Eocene climate proxy data, incorporating version 0.1 of the DeepMIP database. *Geoscientific Model Development*, **12(7)**, 3149–3206, doi:10.5194/gmd-12-3149-2019.

Holloway, C.E. et al., 2017: Observing Convective Aggregation. *Surveys in Geophysics*, **38(6)**, 1199–1236, doi:10.1007/s10712-017-9419-1.

Hopcroft, P.O. and P.J. Valdes, 2015: How well do simulated last glacial maximum tropical temperatures constrain equilibrium climate sensitivity? *Geophysical Research Letters*, **42(13)**, 5533–5539, doi:10.1002/2015gl064903.

Hourdin, F. et al., 2017: The Art and Science of Climate Model Tuning. *Bulletin of the American Meteorological Society*, **98(3)**, 589–602, doi:10.1175/bams-d-15-00135.1.

Howard, B.S., N.E. Hamilton, M. Diesendorf, and T. Wiedmann, 2018: Modeling the carbon budget of the Australian electricity sector's transition to renewable energy. *Renewable Energy*, **125**, 712–728, doi:10.1016/j.renene.2018.02.013.

Hua, W., A. Dai, and M. Qin, 2018: Contributions of Internal Variability and External Forcing to the Recent Pacific Decadal Variations. *Geophysical Research Letters*, **45(14)**, 7084–7092, doi:10.1029/2018gl079033.

Huang, G. et al., 2019: Estimating surface solar irradiance from satellites: Past, present, and future perspectives. *Remote Sensing of Environment*, **233**, 111371, doi:10.1016/j.rse.2019.111371.

Huang, Y. and M. Zhang, 2014: The implication of radiative forcing and feedback for meridional energy transport. *Geophysical Research Letters*, doi:10.1002/2013gl059079.

Huang, Y., Y. Xia, and X. Tan, 2017: On the pattern of CO2 radiative forcing and poleward energy transport. *Journal of Geophysical Research: Atmospheres*, **122(20)**, 10,578–10,593, doi:10.1002/2017jd027221.

Huang, Y., Y. Wang, and H. Huang, 2020: Stratospheric Water Vapor Feedback Disclosed by a Locking Experiment. *Geophysical Research Letters*, **47(12)**, e2020GL087987, doi:10.1029/2020gl087987.

Huang, Y., M. Zhang, Y. Xia, Y. Hu, and S.-W. Son, 2016: Is there a stratospheric radiative feedback in global warming simulations? *Climate Dynamics*, **46(1)**, 177–186, doi:10.1007/s00382-015-2577-2.

Huber, M. and R. Caballero, 2011: The early Eocene equable climate problem revisited. *Climate of the Past*, **7(2)**, 603–

ACCEPTED VERSION SUBJECT TO FINAL EDITING

633, doi:10.5194/cp-7-603-2011.
Huber, M., I. Mahlstein, M. Wild, J. Fasullo, and R. Knutti, 2010: Constraints on Climate Sensitivity from Radiation Patterns in Climate Models. *Journal of Climate*, **24(4)**, 1034–1052, doi:10.1175/2010jcli3403.1.
Hurtt, G.C. et al., 2011: Harmonization of land-use scenarios for the period 1500-2100: 600 years of global gridded annual land-use transitions, wood harvest, and resulting secondary lands. *Climatic Change*, doi:10.1007/s10584-011-0153-2.
Huss, M., M. Funk, and A. Ohmura, 2009: Strong Alpine glacier melt in the 1940s due to enhanced solar radiation. *GEOPHYSICAL RESEARCH LETTERS*, **36**, doi:10.1029/2009gl040789.
Huybers, P., 2010: Compensation between Model Feedbacks and Curtailment of Climate Sensitivity. *Journal of Climate*, **23(11)**, 3009–3018, doi:10.1175/2010jcli3380.1.
Hwang, Y.T. and D.M.W. Frierson, 2010: Increasing atmospheric poleward energy transport with global warming. *Geophysical Research Letters*, doi:10.1029/2010gl045440.
Hwang, Y.T., D.M.W. Frierson, and J.E. Kay, 2011: Coupling between Arctic feedbacks and changes in poleward energy transport. *Geophysical Research Letters*, doi:10.1029/2011gl048546.
Hwang, Y.T., S.P. Xie, C. Deser, and S.M. Kang, 2017: Connecting tropical climate change with Southern Ocean heat uptake. *Geophysical Research Letters*, **44(18)**, 9449–9457, doi:10.1002/2017gl074972.
Hwang, Y.-T. and D.M.W. Frierson, 2013: Link between the double-Intertropical Convergence Zone problem and cloud biases over the Southern Ocean. *Proceedings of the National Academy of Sciences*, doi:10.1073/pnas.1213302110.
Hyder, P. et al., 2018: Critical Southern Ocean climate model biases traced to atmospheric model cloud errors. *Nature Communications*, **9(1)**, 1–17, doi:10.1038/s41467-018-05634-2.
Imamovic, A., K. Tanaka, D. Folini, and M. Wild, 2016: Global dimming and urbanization: did stronger negative SSR trends collocate with regions of population growth? *Atmospheric Chemistry and Physics*, **16(5)**, 2719–2725, doi:10.5194/acp-16-2719-2016.
Inglis, G.N. et al., 2020: Global mean surface temperature and climate sensitivity of the early Eocene Climatic Optimum (EECO), Paleocene--Eocene Thermal Maximum (PETM), and latest Paleocene. *Climate of the Past*, **16(5)**, 1953–1968, doi:10.5194/cp-16-1953-2020.
Ingram, W., 2010: A very simple model for the water vapour feedback on climate change. *Quarterly Journal of the Royal Meteorological Society*, **136(646)**, 30–40, doi:10.1002/qj.546.
Ingram, W., 2013: A new way of quantifying GCM water vapour feedback. *Climate Dynamics*, **40(3)**, 913–924, doi:10.1007/s00382-012-1294-3.
IPCC, 2014: Climate Change 2014: Synthesis Report. Contribution of Working Groups I, II and III to the Fifth Assessment Report of the Intergovernmental Panel on Climate Change. [Core Writing Team, R.K. Pachauri, and L.A. Meyer (eds.)]. IPCC, Geneva, Switzerland, 151 pp.
IPCC, 2018: Summary for Policymakers. In: *Global Warming of 1.5°C. An IPCC Special Report on the impacts of global warming of 1.5°C above pre-industrial levels and related global greenhouse gas emission pathways, in the context of strengthening the global response to the threat of climate change,* [Masson-Delmotte, V., P. Zhai, H.-O. Pörtner, D. Roberts, J. Skea, P.R. Shukla, A. Pirani, W. Moufouma-Okia, C. Péan, R. Pidcock, S. Connors, J.B.R. Matthews, Y. Chen, X. Zhou, M.I. Gomis, E. Lonnoy, T. Maycock, M. Tignor, and T. Waterfield (eds.)]. In Press, pp. 3–24.
IPCC, 2019a: IPCC Special Report on the Ocean and Cryosphere in a Changing Climate. [Pörtner, H.-O., D.C. Roberts, V. Masson-Delmotte, P. Zhai, M. Tignor, E. Poloczanska, K. Mintenbeck, A. Alegría, M. Nicolai, A. Okem, J. Petzold, B. Rama, and N.M. Weyer (eds.)]. In Press, 755 pp.
IPCC, 2019b: Summary for Policymakers. In: *Climate Change and Land: an IPCC special report on climate change, desertification, land degradation, sustainable land management, food security, and greenhouse gas fluxes in terrestrial ecosystems* [Shukla, P.R., J. Skea, E.C. Buendia, V. Masson-Delmotte, H.-O. Pörtner, D.C. Roberts, P. Zhai, R. Slade, S. Connors, R. Diemen, M. Ferrat, E. Haughey, S. Luz, S. Neogi, M. Pathak, J. Petzold, J.P. Pereira, P. Vyas, E. Huntley, K. Kissick, M. Belkacemi, and J. Malley (eds.)]. In Press, pp. 3–36.
Ishii, M. et al., 2017: Accuracy of Global Upper Ocean Heat Content Estimation Expected from Present Observational Data Sets. *SOLA*, **13**, 163–167, doi:10.2151/sola.2017-030.
Jahani, B., Y. Dinpashoh, and M. Wild, 2018: Dimming in Iran since the 2000s and the potential underlying causes. *INTERNATIONAL JOURNAL OF CLIMATOLOGY*, **38(3)**, 1543–1559, doi:10.1002/joc.5265.
Jenkins, S., R.J. Millar, N. Leach, and M.R. Allen, 2018: Framing Climate Goals in Terms of Cumulative CO2-Forcing-Equivalent Emissions. *Geophysical Research Letters*, doi:10.1002/2017gl076173.
Jia, G., E. Shevliakova, P. Artaxo, N. De Noblt-Ducoudre, and R. Houghton, 2019: Land–climate interactions. In: *Climate Change and Land: an IPCC special report on climate change, desertification, land degradation, sustainable land management, food security, and greenhouse gas fluxes in terrestrial ecosystems* [Shukla, P.R., J. Skea, E. Calvo Buendia, V. Masson-Delmotte, H.-O. Pörtner, D.C. Roberts, P. Zhai, R. Slade, S. Connors, R. van Diemen, M. Ferrat, E. Haughey, S. Luz, S. Neogi, M. Pathak, J. Petzold, and J.M. J. Portugal Pereira, P. Vyas, E. Huntley, K. Kissick, M, Belkacemi (eds.)]. In Press, pp. 131–247.
Jiménez-de-la-Cuesta, D. and T. Mauritsen, 2019: Emergent constraints on Earth's transient and equilibrium response

ACCEPTED VERSION SUBJECT TO FINAL EDITING

to doubled CO2 from post-1970s global warming. *Nature Geoscience*, **2015**, doi:10.1038/s41561-019-0463-y.
Johansson, D.J.A., B.C. O'Neill, C. Tebaldi, and O. Häggström, 2015: Equilibrium climate sensitivity in light of observations over the warming hiatus. *Nature Climate Change*, **5**, 449, doi:10.1038/nclimate2573.
Johnson, G.C., J.M. Lyman, and N.G. Loeb, 2016: Improving estimates of Earth's energy imbalance. *Nature Climate Change*, **6(7)**, 639–640, doi:10.1038/nclimate3043.
Jonko, A.K., K.M. Shell, B.M. Sanderson, and G. Danabasoglu, 2013: Climate Feedbacks in CCSM3 under Changing CO2 Forcing. Part II: Variation of Climate Feedbacks and Sensitivity with Forcing. *Journal of Climate*, **26(9)**, 2784–2795, doi:10.1175/jcli-d-12-00479.1.
Joos, F. et al., 2013: Carbon dioxide and climate impulse response functions for the computation of greenhouse gas metrics: A multi-model analysis. *Atmospheric Chemistry and Physics*, **13(5)**, 2793–2825, doi:10.5194/acp-13-2793-2013.
Joshi, M.M., M.J. Webb, A.C. Maycock, and M. Collins, 2010: Stratospheric water vapour and high climate sensitivity in a version of the HadSM3 climate model. *Atmospheric Chemistry and Physics*, **10(15)**, 7161–7167, doi:10.5194/acp-10-7161-2010.
Jungclaus, J.H., K. Lohmann, and D. Zanchettin, 2014: Enhanced 20th century heat transfer to the Arctic simulated in the context of climate variations over the last millennium. *Climate of the Past*, **10**, 2201–2213, doi:10.5194/cp-10-2201-2014.
Jungclaus, J.H. et al., 2017: The PMIP4 contribution to CMIP6 Part 3: The last millennium, scientific objective, and experimental design for PMIP4 simulations. *Geoscientific Model Development*, **10(11)**, 4005–4033, doi:10.5194/gmd-10-4005-2017.
Kageyama, M. et al., 2021: The PMIP4-CMIP6 Last Glacial Maximum experiments: preliminary results and comparison with the PMIP3-CMIP5 simulations. *Climate of the Past*, 1–37, doi:10.5194/cp-2019-169.
Kajtar, J.B., A. Santoso, M.H. England, and W. Cai, 2017: Tropical climate variability: interactions across the Pacific, Indian, and Atlantic Oceans. *Climate Dynamics*, **48(7–8)**, 2173–2190, doi:10.1007/s00382-016-3199-z.
Kajtar, J.B., A. Santoso, S. McGregor, M.H. England, and Z. Baillie, 2018: Model under-representation of decadal Pacific trade wind trends and its link to tropical Atlantic bias. *Climate Dynamics*, **50(3–4)**, 1471–1484, doi:10.1007/s00382-017-3699-5.
Kamae, Y., T. Ogura, M. Watanabe, S.P. Xie, and H. Ueda, 2016: Robust cloud feedback over tropical land in a warming climate. *Journal of Geophysical Research*, **121**, 2593–2609, doi:10.1002/2015jd024525.
Kang, S.M. and S.P. Xie, 2014: Dependence of climate response on meridional structure of external thermal forcing. *Journal of Climate*, **27(14)**, 5593–5600, doi:10.1175/jcli-d-13-00622.1.
Kanji, Z.A. et al., 2017: Overview of Ice Nucleating Particles. *Meteorological Monographs*, **58**, 1.1–1.33, doi:10.1175/amsmonographs-d-16-0006.1.
Karset, I.H.H. et al., 2018: Strong impacts on aerosol indirect effects from historical oxidant changes. *Atmospheric Chemistry and Physics*, **18(10)**, 7669–7690, doi:10.5194/acp-18-7669-2018.
Kato, S. et al., 2016: Investigation of the Residual in Column-Integrated Atmospheric Energy Balance Using Cloud Objects. *JOURNAL OF CLIMATE*, **29(20)**, 7435–7452, doi:10.1175/jcli-d-15-0782.1.
Kato, S. et al., 2018: Surface Irradiances of Edition 4.0 Clouds and the Earth's Radiant Energy System (CERES) Energy Balanced and Filled (EBAF) Data Product. *Journal of Climate*, **31(11)**, 4501–4527, doi:10.1175/jcli-d-17-0523.1.
Kaufman, Y.J. and I. Koren, 2006: Smoke and pollution aerosol effect on cloud cover.. *Science (New York, N.Y.)*, **313(5787)**, 655–8, doi:10.1126/science.1126232.
Kawai, H., T. Koshiro, and M.J. Webb, 2017: Interpretation of Factors Controlling Low Cloud Cover and Low Cloud Feedback Using a Unified Predictive Index. *Journal of Climate*, **30(22)**, 9119–9131, doi:10.1175/jcli-d-16-0825.1.
Kay, J.E. and A. Gettelman, 2009: Cloud influence on and response to seasonal Arctic sea ice loss. *Journal of Geophysical Research: Atmospheres*, **114(D18)**, doi:10.1029/2009jd011773.
Kay, J.E. et al., 2012: The Influence of Local Feedbacks and Northward Heat Transport on the Equilibrium Arctic Climate Response to Increased Greenhouse Gas Forcing. *Journal of Climate*, **25(16)**, 5433–5450, doi:10.1175/jcli-d-11-00622.1.
Kay, J.E. et al., 2016a: Evaluating and improving cloud phase in the Community Atmosphere Model version 5 using spaceborne lidar observations. *Journal of Geophysical Research: Atmospheres*, **121(8)**, 4162–4176, doi:10.1002/2015jd024699.
Kay, J.E. et al., 2016b: Recent Advances in Arctic Cloud and Climate Research. *Current Climate Change Reports*, **2(4)**, 159–169, doi:10.1007/s40641-016-0051-9.
Kazadzis, S. et al., 2018: Long-term series and trends in surface solar radiation in Athens, Greece. *ATMOSPHERIC CHEMISTRY AND PHYSICS*, **18(4)**, 2395–2411, doi:10.5194/acp-18-2395-2018.
Kennedy-Asser, A.T., D.J. Lunt, A. Farnsworth, and P.J. Valdes, 2019: Assessing Mechanisms and Uncertainty in Modeled Climatic Change at the Eocene-Oligocene Transition. *Paleoceanography and Paleoclimatology*, doi:10.1029/2018pa003380.
Khairoutdinov, M. and K. Emanuel, 2013: Rotating radiative-convective equilibrium simulated by a cloud-resolving

ACCEPTED VERSION SUBJECT TO FINAL EDITING

model. *Journal of Advances in Modeling Earth Systems*, **5(4)**, 816–825, doi:10.1002/2013ms000253.
Kiehl, J.T., 2007: Twentieth century climate model response and climate sensitivity. *Geophysical Research Letters*, **34(22)**, 1–4, doi:10.1029/2007gl031383.
Kiehl, J.T. and C.A. Shields, 2013: Sensitivity of the Palaeocene-Eocene Thermal Maximum climate to cloud properties. *Philosophical Transactions of the Royal Society of London A: Mathematical, Physical and Engineering Sciences*, **371(2001)**, doi:10.1098/rsta.2013.0093.
Kim, K.Y. et al., 2019: Vertical Feedback Mechanism of Winter Arctic Amplification and Sea Ice Loss. *Scientific Reports*, **9(1)**, doi:10.1038/s41598-018-38109-x.
Kinne, S., 2019: Aerosol radiative effects with MACv2. *Atmospheric Chemistry and Physics*, **19**, 10919–10959, doi:10.5194/acp-19-10919-2019.
Kirkby, J., 2007: Cosmic rays and climate. *Surveys in Geophysics*, **28(5–6)**, 333–375, doi:10.1007/s10712-008-9030-6.
Kirkby, J. et al., 2016: Ion-induced nucleation of pure biogenic particles. *Nature*, **533(7604)**, 521–526, doi:10.1038/nature17953.
Klein, S.A. and A. Hall, 2015: Emergent Constraints for Cloud Feedbacks. *Current Climate Change Reports*, **1(4)**, 276–287, doi:10.1007/s40641-015-0027-1.
Klein, S.A., A. Hall, J.R. Norris, and R. Pincus, 2017: Low-cloud feedbacks from cloud-controlling factors: A review. *Surveys in Geophysics*, **38(6)**, 1307–1329, doi:10.1007/s10712-017-9433-3.
Knutti, R., 2010: The end of model democracy? *Climatic Change*, **102(3)**, 395–404, doi:10.1007/s10584-010-9800-2.
Knutti, R. and G.C. Hegerl, 2008: The equilibrium sensitivity of the Earth's temperature to radiation changes. *Nature Geoscience*, **1**, 735, doi:10.1038/ngeo337.
Knutti, R., D. Masson, and A. Gettelman, 2013: Climate model genealogy: Generation CMIP5 and how we got there. *Geophysical Research Letters*, **40(6)**, 1194–1199, doi:10.1002/grl.50256.
Knutti, R., M.A.A. Rugenstein, and G.C. Hegerl, 2017: Beyond equilibrium climate sensitivity. *Nature Geoscience*, **10(10)**, 727–736, doi:10.1038/ngeo3017.
Knutti, R., T.F. Stocker, F. Joos, and G.-K. Plattner, 2002: Constraints on radiative forcing and future climate change from observations and climate model ensembles. *Nature*, **416(6882)**, 719–723, doi:10.1038/416719a.
Knutti, R., G.A. Meehl, M.R. Allen, and D.A. Stainforth, 2006: Constraining Climate Sensitivity from the Seasonal Cycle in Surface Temperature. *Journal of Climate*, **19(17)**, 4224–4233, doi:10.1175/jcli3865.1.
Knutti, R., S. Krähenmann, D.J. Frame, and M.R. Allen, 2008: Comment on "Heat capacity, time constant, and sensitivity of Earth's climate system" by S. E. Schwartz. *Journal of Geophysical Research Atmospheres*, **113(15)**, 1–6, doi:10.1029/2007jd009473.
Knutti, R., F. Joos, S.A. Müller, G.K. Plattner, and T.F. Stocker, 2005: Probabilistic climate change projections for CO2 stabilization profiles. *Geophysical Research Letters*, **32(20)**, 1–4, doi:10.1029/2005gl023294.
Koenigk, T. and L. Brodeau, 2014: Ocean heat transport into the Arctic in the twentieth and twenty-first century in EC-Earth. *Climate Dynamics*, doi:10.1007/s00382-013-1821-x.
Köhler, P., B. De Boer, A.S. Von Der Heydt, L.B. Stap, and R.S.W. Van De Wal, 2015: On the state dependency of the equilibrium climate sensitivity during the last 5 million years. *Climate of the Past*, **11(12)**, 1801–1823, doi:10.5194/cp-11-1801-2015.
Köhler, P. et al., 2017: A state-dependent quantification of climate sensitivity based on paleo data of the last 2.1 million years. *Paleoceanography*, 1–13, doi:10.1002/2017pa003190.
Köhler, P. et al., 2018: The Effect of Obliquity-Driven Changes on Paleoclimate Sensitivity During the Late Pleistocene. *Geophysical Research Letters*, **45**, doi:10.1029/2018gl077717.
Kohyama, T., D.L. Hartmann, and D.S. Battisti, 2017: La Niña-like mean-state response to global warming and potential oceanic roles. *Journal of Climate*, **30(11)**, 4207–4225, doi:10.1175/jcli-d-16-0441.1.
Kooperman, G.J. et al., 2012: Constraining the influence of natural variability to improve estimates of global aerosol indirect effects in a nudged version of the Community Atmosphere Model 5. *Journal of Geophysical Research Atmospheres*, doi:10.1029/2012jd018588.
Koren, I., G. Feingold, and L.A. Remer, 2010: The invigoration of deep convective clouds over the Atlantic: aerosol effect, meteorology or retrieval artifact? *Atmospheric Chemistry and Physics*, **10(18)**, 8855–8872, doi:10.5194/acp-10-8855-2010.
Koren, I., Y.J. Kaufman, D. Rosenfeld, L.A. Remer, and Y. Rudich, 2005: Aerosol invigoration and restructuring of Atlantic convective clouds. *Geophysical Research Letters*, **32(14)**, doi:10.1029/2005gl023187.
Kostov, Y., K.C. Armour, and J. Marshall, 2014: Impact of the Atlantic meridional overturning circulation on ocean heat storage and transient climate change. *Geophysical Research Letters*, doi:10.1002/2013gl058998.
Kostov, Y., D. Ferreira, K.C. Armour, and J. Marshall, 2018: Contributions of Greenhouse Gas Forcing and the Southern Annular Mode to Historical Southern Ocean Surface Temperature Trends. *Geophysical Research Letters*, doi:10.1002/2017gl074964.
Kostov, Y. et al., 2017: Fast and slow responses of Southern Ocean sea surface temperature to SAM in coupled climate models. *Climate Dynamics*, doi:10.1007/s00382-016-3162-z.
Kramer, R.J., A. Matus, B.J. Soden, and T.S. L'Ecuyer, 2019: Observation-Based Radiative Kernels From CloudSat/CALIPSO. *Journal of Geophysical Research: Atmospheres*, **124(10)**, 5431–5444,

ACCEPTED VERSION SUBJECT TO FINAL EDITING

doi:10.1029/2018jd029021.
Krasting, J.P. et al., 2018: Role of Ocean Model Formulation in Climate Response Uncertainty. *Journal of Climate*, doi:10.1175/jcli-d-18-0035.1.
Kretzschmar, J., M. Salzmann, J. Mülmenstädt, O. Boucher, and J. Quaas, 2017: Comment on "Rethinking the Lower Bound on Aerosol Radiative Forcing". *Journal of Climate*, **30(16)**, 6579–6584, doi:10.1175/jcli-d-16-0668.1.
Krishnamohan, K.S., G. Bala, L. Cao, L. Duan, and K. Caldeira, 2019: Climate System Response to Stratospheric Sulfate Aerosols: Sensitivity to Altitude of Aerosol Layer. *Earth System Dynamics*, **10(4)**, 885–900, doi:10.5194/esd-10-885-2019.
Kristjánsson, J.E. et al., 2008: Cosmic rays, cloud condensation nuclei and clouds – a reassessment using MODIS data. *Atmospheric Chemistry and Physics*, **8(24)**, 7373–7387, doi:10.5194/acp-8-7373-2008.
Krivova, N.A., S.K. Solanki, and L. Floyd, 2006: Reconstruction of solar UV irradiance in cycle 23. *Astronomy & Astrophysics*, **452(2)**, 631–639, doi:10.1051/0004-6361:20064809.
Kucharski, F., I.-S.S. Kang, R. Farneti, and L. Feudale, 2011: Tropical Pacific response to 20th century Atlantic warming. *Geophysical Research Letters*, **38(3)**, doi:10.1029/2010gl046248.
Kucharski, F., F.S. Syed, A. Burhan, I. Farah, and A. Gohar, 2014: Tropical Atlantic influence on Pacific variability and mean state in the twentieth century in observations and CMIP5. *Climate Dynamics*, **44(3–4)**, 881–896, doi:10.1007/s00382-014-2228-z.
Kucharski, F. et al., 2015: Atlantic forcing of Pacific decadal variability. *Climate Dynamics*, **46(7–8)**, 2337–2351, doi:10.1007/s00382-015-2705-z.
Kuhlbrodt, T., J.M. Gregory, and L.C. Shaffrey, 2015: A process-based analysis of ocean heat uptake in an AOGCM with an eddy-permitting ocean component. *Climate Dynamics*, **45(11)**, 3205–3226, doi:10.1007/s00382-015-2534-0.
Kummer, J.R. and A.E. Dessler, 2014: The impact of forcing efficacy on the equilibrium climate sensitivity. *Geophysical Research Letters*, **41(10)**, 3565–3568, doi:10.1002/2014gl060046.
Kutzbach, J.E., F. He, S.J. Vavrus, and W.F. Ruddiman, 2013: The dependence of equilibrium climate sensitivity on climate state: Applications to studies of climates colder than present. *Geophysical Research Letters*, **40(14)**, 3721–3726, doi:10.1002/grl.50724.
L'Ecuyer, T.S. et al., 2015: The Observed State of the Energy Budget in the Early Twenty-First Century. *Journal of Climate*, **28(21)**, 8319–8346, doi:10.1175/jcli-d-14-00556.1.
Lade, S.J. et al., 2018: Analytically tractable climate-carbon cycle feedbacks under 21st century anthropogenic forcing. *Earth System Dynamics*, doi:10.5194/esd-9-507-2018.
Laepple, T. and P. Huybers, 2014: Ocean surface temperature variability: Large model-data differences at decadal and longer periods. *Proceedings of the National Academy of Sciences of the United States of America*, **111(47)**, 16682–16687, doi:10.1073/pnas.1412077111.
Lago, V. and M.H. England, 2019: Projected slowdown of antarctic bottom water formation in response to amplified meltwater contributions. *Journal of Climate*, **32(19)**, 6319–6335, doi:10.1175/jcli-d-18-0622.1.
Laîné, A., M. Yoshimori, and A. Abe-Ouchi, 2016: Surface Arctic Amplification Factors in CMIP5 Models: Land and Oceanic Surfaces and Seasonality. *Journal of Climate*, **29(9)**, 3297–3316, doi:10.1175/jcli-d-15-0497.1.
Laken, B.A., 2016: Can Open Science save us from a solar-driven monsoon? *Journal of Space Weather and Space Climate*, **6**, A11, doi:10.1051/swsc/2016005.
Larson, E.J.L. and R.W. Portmann, 2016: A temporal kernel method to compute effective radiative forcing in CMIP5 transient simulations. *Journal of Climate*, doi:10.1175/jcli-d-15-0577.1.
Lauder, A.R. et al., 2013: Offsetting methane emissions - An alternative to emission equivalence metrics. *International Journal of Greenhouse Gas Control*, **12**, 419–429, doi:10.1016/j.ijggc.2012.11.028.
Lean, J.L., 2018: Estimating Solar Irradiance Since 850 CE. *Earth and Space Science*, **5(4)**, 133–149, doi:10.1002/2017ea000357.
Lebsock, M.D., G.L. Stephens, and C. Kummerow, 2008: Multisensor satellite observations of aerosol effects on warm clouds. *Journal of Geophysical Research*, **113(D15)**, D15205, doi:10.1029/2008jd009876.
Lee, D.S.S. et al., 2020: The contribution of global aviation to anthropogenic climate forcing for 2000 to 2018. *Atmospheric Environment*, **244(117834)**, doi:10.1016/j.atmosenv.2020.117834.
Lee, S., T. Gong, S.B. Feldstein, J.A. Screen, and I. Simmonds, 2017: Revisiting the Cause of the 1989–2009 Arctic Surface Warming Using the Surface Energy Budget: Downward Infrared Radiation Dominates the Surface Fluxes. *Geophysical Research Letters*, doi:10.1002/2017gl075375.
Lee, S.H. et al., 2019: New Particle Formation in the Atmosphere: From Molecular Clusters to Global Climate. *Journal of Geophysical Research: Atmospheres*, **124(13)**, 7098–7146, doi:10.1029/2018jd029356.
Lejeune, Q. et al., 2020: Biases in the albedo sensitivity to deforestation in CMIP5 models and their impacts on the associated historical Radiative Forcing. *Earth System Dynamics*, **11**, 1209–1232, doi:10.5194/esd-11-1209-2020.
Levasseur, A. et al., 2016: Enhancing life cycle impact assessment from climate science: Review of recent findings and recommendations for application to LCA. *Ecological Indicators*, doi:10.1016/j.ecolind.2016.06.049.
Lewis, N., 2013: An objective bayesian improved approach for applying optimal fingerprint techniques to estimate

ACCEPTED VERSION SUBJECT TO FINAL EDITING

climate sensitivity. *Journal of Climate*, **26(19)**, 7414–7429, doi:10.1175/jcli-d-12-00473.1.
Lewis, N. and J.A. Curry, 2015: The implications for climate sensitivity of AR5 forcing and heat uptake estimates. *Climate Dynamics*, **45(3–4)**, 1009–1023, doi:10.1007/s00382-014-2342-y.
Lewis, N. and J. Curry, 2018: The impact of recent forcing and ocean heat uptake data on estimates of climate sensitivity. *Journal of Climate*, JCLI–D–17–0667.1, doi:10.1175/jcli-d-17-0667.1.
Lewis, N. and T. Mauritsen, 2020: Negligible unforced historical pattern effect on climate feedback strength found in HadISST-based AMIP simulations. *Journal of Climate*, doi:10.1175/jcli-d-19-0941.1.
Li, C., J.S. von Storch, and J. Marotzke, 2013: Deep-ocean heat uptake and equilibrium climate response. *Climate Dynamics*, **40(5–6)**, 1071–1086, doi:10.1007/s00382-012-1350-z.
Li, F. and P. Newman, 2020: Stratospheric water vapor feedback and its climate impacts in the coupled atmosphere-ocean Goddard Earth Observing System Chemistry-Climate Model. *Climate Dynamics*, **55(5–6)**, 1585–1595, doi:10.1007/s00382-020-05348-6.
Li, J., Y. Jiang, X. Xia, and Y. Hu, 2018: Increase of surface solar irradiance across East China related to changes in aerosol properties during the past decade. *Environmental Research Letters*, **13(3)**, 034006, doi:10.1088/1748-9326/aaa35a.
Li, J.-L.F. et al., 2013: Characterizing and understanding radiation budget biases in CMIP3/CMIP5 GCMs, contemporary GCM, and reanalysis. *JOURNAL OF GEOPHYSICAL RESEARCH-ATMOSPHERES*, **118(15)**, 8166–8184, doi:10.1002/jgrd.50378.
Li, R.L., T. Storelvmo, A. Fedorov, and Y.-S. Choi, 2019: A Positive Iris Feedback: Insights from Climate Simulations with Temperature-Sensitive Cloud–Rain Conversion. *Journal of Climate*, **32(16)**, 5305–5324, doi:10.1175/jcli-d-18-0845.1.
Li, X., S.-P.P. Xie, S.T. Gille, and C. Yoo, 2016: Atlantic-induced pan-tropical climate change over the past three decades. *Nature Climate Change*, **6(3)**, 275–279, doi:10.1038/nclimate2840.
Li, Y., W. Han, and L. Zhang, 2017: Enhanced Decadal Warming of the Southeast Indian Ocean During the Recent Global Surface Warming Slowdown. *Geophysical Research Letters*, **44(19)**, 9876–9884, doi:10.1002/2017gl075050.
Li, Y., D.W.J. Thompson, S. Bony, and T.M. Merlis, 2018: Thermodynamic Control on the Poleward Shift of the Extratropical Jet in Climate Change Simulations: The Role of Rising High Clouds and Their Radiative Effects. *Journal of Climate*, **32(3)**, 917–934, doi:10.1175/jcli-d-18-0417.1.
Li, Z. et al., 2016: Aerosol and monsoon climate interactions over Asia. *REVIEWS OF GEOPHYSICS*, **54(4)**, 866–929, doi:10.1002/2015rg000500.
Lin, G. et al., 2014: Radiative forcing of organic aerosol in the atmosphere and on snow: Effects of SOA and brown carbon. *Journal of Geophysical Research: Atmospheres*, **119(12)**, 7453–7476, doi:10.1002/2013jd021186.
Lindzen, R.S., M.D. Chou, and A.Y. Hou, 2001: Does the Earth Have an Adaptive Infrared Iris? *Bulletin of the American Meteorological Society*, **82(3)**, 417–432, doi:10.1175/1520-0477(2001)082<0417:dtehaa>2.3.co;2.
Lipat, B.R., G. Tselioudis, K.M. Grise, and L.M. Polvani, 2017: CMIP5 models' shortwave cloud radiative response and climate sensitivity linked to the climatological Hadley cell extent. *Geophysical Research Letters*, **44(11)**, 5739–5748, doi:10.1002/2017gl073151.
Lisiecki, L.E. and M.E. Raymo, 2005: A Pliocene-Pleistocene stack of 57 globally distributed benthic δ18O records. *Paleoceanography*, **20(1)**, doi:10.1029/2004pa001071.
Liu, C. et al., 2020: Variability in the global energy budget and transports 1985-2017. *CLIMATE DYNAMICS*, **55(11–12)**, 3381–3396, doi:10.1007/s00382-020-05451-8.
Liu, J. et al., 2019: Eastern equatorial Pacific cold tongue evolution since the late Miocene linked to extratropical climate. *Science Advances*, **5(4)**, doi:10.1126/sciadv.aau6060.
Liu, R. et al., 2018: An Assessment of Tropospheric Water Vapor Feedback Using Radiative Kernels. *Journal of Geophysical Research: Atmospheres*, **123(3)**, 1499–1509, doi:10.1002/2017jd027512.
Liu, W., S.P. Xie, Z. Liu, and J. Zhu, 2017: Overlooked possibility of a collapsed atlantic meridional overturning circulation in warming climate. *Science Advances*, doi:10.1126/sciadv.1601666.
Liu, Y. et al., 2017: Climate response to the meltwater runoff from Greenland ice sheet: evolving sensitivity to discharging locations. *Climate Dynamics*, doi:10.1007/s00382-017-3980-7.
Liu, Z. and B. Huang, 1997: A coupled theory of tropical climatology: Warm pool, cold tongue, and walker circulation. *Journal of Climate*, **10(7)**, 1662–1679, doi:10.1175/1520-0442(1997)010<1662:actotc>2.0.co;2.
Liu, Z., S. Vavrus, F. He, N. Wen, and Y. Zhong, 2005: Rethinking Tropical Ocean Response to Global Warming: The Enhanced Equatorial Warming. *Journal of Climate*, **18(22)**, 4684–4700, doi:10.1175/jcli3579.1.
Liu, Z. et al., 2014: The Holocene temperature conundrum. *Proceedings of the National Academy of Sciences*, **111(34)**, E3501–E3505, doi:10.1073/pnas.1407229111.
Lockwood, M. and W.T. Ball, 2020: Placing limits on long-term variations in quiet-Sun irradiance and their contribution to total solar irradiance and solar radiative forcing of climate. *Proceedings of the Royal Society A: Mathematical, Physical and Engineering Sciences*, **476(2238)**, 20200077, doi:10.1098/rspa.2020.0077.
Loeb, N.G., D.A. Rutan, S. Kato, and W. Wang, 2014: Observing Interannual Variations in Hadley Circulation Atmospheric Diabatic Heating and Circulation Strength. *JOURNAL OF CLIMATE*, **27(11)**, 4139–4158,

ACCEPTED VERSION SUBJECT TO FINAL EDITING

doi:10.1175/jcli-d-13-00656.1.
Loeb, N.G., T.J. Thorsen, J.R. Norris, H. Wang, and W. Su, 2018a: Changes in Earth's Energy Budget during and after the "Pause" in Global Warming: An Observational Perspective. *Climate*, **6(3)**, 62, doi:10.3390/cli6030062.
Loeb, N.G. et al., 2012: Observed changes in top-of-the-atmosphere radiation and upper-ocean heating consistent within uncertainty. *Nature Geoscience*, doi:10.1038/ngeo1375.
Loeb, N.G. et al., 2016: Observational constraints on atmospheric and oceanic cross-equatorial heat transports: revisiting the precipitation asymmetry problem in climate models. *CLIMATE DYNAMICS*, **46(9–10)**, 3239–3257, doi:10.1007/s00382-015-2766-z.
Loeb, N.G. et al., 2018b: Clouds and the Earth's Radiant Energy System (CERES) Energy Balanced and Filled (EBAF) Top-of-Atmosphere (TOA) Edition-4.0 Data Product. *Journal of Climate*, **31(2)**, 895–918, doi:10.1175/jcli-d-17-0208.1.
Loeb, N.G. et al., 2020: New Generation of Climate Models Track Recent Unprecedented Changes in Earth's Radiation Budget Observed by CERES. *Geophysical Research Letters*, **47(5)**, doi:10.1029/2019gl086705.
Lohmann, U. and D. Neubauer, 2018: The importance of mixed-phase and ice clouds for climate sensitivity in the global aerosol–climate model ECHAM6-HAM2. *Atmos. Chem. Phys.*, **18(12)**, 8807–8828, doi:10.5194/acp-18-8807-2018.
Longman, R.J., T.W. Giambelluca, R.J. Alliss, and M.L. Barnes, 2014: Temporal solar radiation change at high elevations in Hawai'i. *Journal of Geophysical Research-Atmospheres*, **119(10)**, 6022–6033, doi:10.1002/2013jd021322.
Lund, M.T. et al., 2017: Emission metrics for quantifying regional climate impacts of aviation. *Earth System Dynamics*, doi:10.5194/esd-8-547-2017.
Lund, M.T. et al., 2018a: Concentrations and radiative forcing of anthropogenic aerosols from 1750 to 2014 simulated with the Oslo CTM3 and CEDS emission inventory. *Geoscientific Model Development*, **11(12)**, 4909–4931, doi:10.5194/gmd-11-4909-2018.
Lund, M.T. et al., 2018b: Short Black Carbon lifetime inferred from a global set of aircraft observations. *npj Climate and Atmospheric Science*, **1(1)**, 31, doi:10.1038/s41612-018-0040-x.
Lunt, D.J. et al., 2010: Earth system sensitivity inferred from Pliocene modelling and data. *Nature Geoscience*, **3(1)**, 60–64, doi:10.1038/ngeo706.
Lunt, D.J. et al., 2012a: A model–data comparison for a multi-model ensemble of early Eocene atmosphere–ocean simulations: EoMIP. *Climate of the Past*, **8(5)**, 1717–1736, doi:10.5194/cp-8-1717-2012.
Lunt, D.J. et al., 2012b: On the causes of mid-Pliocene warmth and polar amplification. *Earth and Planetary Science Letters*, **321–322**, 128–138, doi:10.1016/j.epsl.2011.12.042.
Lunt, D.J. et al., 2021: DeepMIP: Model intercomparison of early Eocene climatic optimum (EECO) large-scale climate features and comparison with proxy data. *Climate of the Past*, **17(1)**, 203–227, doi:10.5194/cp-17-203-2021.
Luo, B., D. Luo, L. Wu, L. Zhong, and I. Simmonds, 2017: Atmospheric circulation patterns which promote winter Arctic sea ice decline. *Environmental Research Letters*, **12(5)**, doi:10.1088/1748-9326/aa69d0.
Luo, J.J., W. Sasaki, and Y. Masumoto, 2012: Indian Ocean warming modulates Pacific climate change. *Proceedings of the National Academy of Sciences of the United States of America*, **109(46)**, 18701–18706, doi:10.1073/pnas.1210239109.
Luo, J.J., G. Wang, and D. Dommenget, 2018: May common model biases reduce CMIP5's ability to simulate the recent Pacific La Niña-like cooling? *Climate Dynamics*, **50(3–4)**, 1335–1351, doi:10.1007/s00382-017-3688-8.
Luo, Y., J. Lu, F. Liu, and W. Liu, 2015: Understanding the El Niño-like oceanic response in the tropical Pacific to global warming. *Climate Dynamics*, doi:10.1007/s00382-014-2448-2.
Luo, Y., J. Lu, F. Liu, and O. Garuba, 2017: The role of ocean dynamical thermostat in delaying the El Niño-Like response over the equatorial Pacific to climate warming. *Journal of Climate*, **30(8)**, 2811–2827, doi:10.1175/jcli-d-16-0454.1.
Lurton, T. et al., 2020: Implementation of the CMIP6 Forcing Data in the IPSL-CM6A-LR Model. *Journal of Advances in Modeling Earth Systems*, **12(4)**, 1–22, doi:10.1029/2019ms001940.
Lutsko, N.J. and K. Takahashi, 2018: What Can the Internal Variability of CMIP5 Models Tell Us about Their Climate Sensitivity? *Journal of Climate*, **31(13)**, 5051–5069, doi:10.1175/jcli-d-17-0736.1.
Lutsko, N.J. and M. Popp, 2019: Probing the Sources of Uncertainty in Transient Warming on Different Timescales. *Geophysical Research Letters*, **46(20)**, 11367–11377, doi:10.1029/2019gl084018.
Luyssaert, S. et al., 2014: Land management and land-cover change have impacts of similar magnitude on surface temperature. *Nature Climate Change*, doi:10.1038/nclimate2196.
Lyman, J.M. and G.C. Johnson, 2008: Estimating Annual Global Upper-Ocean Heat Content Anomalies despite Irregular In Situ Ocean Sampling. *Journal of Climate*, **21(21)**, 5629–5641, doi:10.1175/2008jcli2259.1.
Lynch, J., M. Cain, R. Pierrehumbert, and M. Allen, 2020: Demonstrating GWP*: A means of reporting warming-equivalent emissions that captures the contrasting impacts of short- and long-lived climate pollutants. *Environmental Research Letters*, **15(4)**, 044023, doi:10.1088/1748-9326/ab6d7e.
Lynch, J., M. Cain, D. Frame, and R. Pierrehumbert, 2021: Agriculture's Contribution to Climate Change and Role in Mitigation Is Distinct From Predominantly Fossil CO2-Emitting Sectors. *Frontiers in Sustainable Food*

ACCEPTED VERSION SUBJECT TO FINAL EDITING

Systems, **4**, 518039, doi:10.3389/fsufs.2020.518039.
Ma, X., F. Yu, and J. Quaas, 2014: Reassessment of satellite-based estimate of aerosol climate forcing. *Journal of Geophysical Research: Atmospheres*, **119(17)**, 10,310–394,409, doi:10.1002/2014jd021670.
MacDougall, A.H., K. Zickfeld, R. Knutti, and H.D. Matthews, 2015: Sensitivity of carbon budgets to permafrost carbon feedbacks and non-CO2 forcings. *Environmental Research Letters*, doi:10.1088/1748-9326/10/12/125003.
MacIntosh, C.R.R. et al., 2016: Contrasting fast precipitation responses to tropospheric and stratospheric ozone forcing. *Geophysical Research Letters*, **43(3)**, 1263–1271, doi:10.1002/2015gl067231.
Maher, N., M.H. England, A. Gupta, and P. Spence, 2018: Role of Pacific trade winds in driving ocean temperatures during the recent slowdown and projections under a wind trend reversal. *Climate Dynamics*, **51(1–2)**, 321–336, doi:10.1007/s00382-017-3923-3.
Mahlstein, I. and R. Knutti, 2011: Ocean heat transport as a cause for model uncertainty in projected arctic warming. *Journal of Climate*, doi:10.1175/2010jcli3713.1.
Mahowald, N.M. et al., 2017: Aerosol Deposition Impacts on Land and Ocean Carbon Cycles. *Current Climate Change Reports*, doi:10.1007/s40641-017-0056-z.
Mahrt, F. et al., 2018: Ice nucleation abilities of soot particles determined with the Horizontal Ice Nucleation Chamber. *Atmospheric Chemistry and Physics*, **18(18)**, 13363–13392, doi:10.5194/acp-18-13363-2018.
Malavelle, F.F. et al., 2017: Strong constraints on aerosol-cloud interactions from volcanic eruptions. *Nature*, **546(7659)**, 485–491, doi:10.1038/nature22974.
Mallapragada, D. and B.K. Mignone, 2017: A consistent conceptual framework for applying climate metrics in technology life cycle assessment. *Environmental Research Letters*, doi:10.1088/1748-9326/aa7397.
Mallick, K. et al., 2016: Canopy-scale biophysical controls of transpiration and evaporation in the Amazon Basin. *Hydrology and Earth System Sciences*, **20(10)**, 4237–4264, doi:10.5194/hess-20-4237-2016.
Manabe, S. and R.T. Wetherald, 1975: The Effects of Doubling the CO2 Concentration on the climate of a General Circulation Model. *Journal of the Atmospheric Sciences*, **32(1)**, 3–15, doi:10.1175/1520-0469(1975)032<0003:teodtc>2.0.co;2.
Manabe, S. and K. Bryan, 1985: CO2-induced change in a coupled ocean-atmosphere model and its paleoclimatic implications. *Journal of Geophysical Research*, **90(5)**, 11,611–689,707, doi:10.1029/jc090ic06p11689.
Manara, V. et al., 2015: Sunshine duration variability and trends in Italy from homogenized instrumental time series (1936-2013). *Journal of Geophysical Research-Atmospheres*, **120(9)**, 3622–3641, doi:10.1002/2014jd022560.
Manara, V. et al., 2016: Detection of dimming/brightening in Italy from homogenized all-sky and clear-sky surface solar radiation records and underlying causes (1959-2013). *Atmospheric Chemistry and Physics*, **16(17)**, 11145–11161, doi:10.5194/acp-16-11145-2016.
Manaster, A., C.W. O'Dell, and G. Elsaesser, 2017: Evaluation of Cloud Liquid Water Path Trends Using a Multidecadal Record of Passive Microwave Observations. *Journal of Climate*, **30(15)**, 5871–5884, doi:10.1175/jcli-d-16-0399.1.
Manne, A.S. and R.G. Richels, 2001: An alternative approach to establishing trade-offs among greenhouse gases. *Nature*, **410(6829)**, 675–677, doi:10.1038/35070541.
Marotzke, J., 2019: Quantifying the irreducible uncertainty in near-term climate projections. *Wiley Interdisciplinary Reviews: Climate Change*, **10(1)**, e563, doi:10.1002/wcc.563.
Marotzke, J. and P.M. Forster, 2015: Forcing, feedback and internal variability in global temperature trends. *Nature*, **517(7536)**, 565–570, doi:10.1038/nature14117.
Marshall, J. et al., 2015: The ocean's role in the transient response of climate to abrupt greenhouse gas forcing. *Climate Dynamics*, doi:10.1007/s00382-014-2308-0.
Marshall, L.R. et al., 2020: Large Variations in Volcanic Aerosol Forcing Efficiency Due to Eruption Source Parameters and Rapid Adjustments. *Geophysical Research Letters*, **47(19)**, doi:10.1029/2020gl090241.
Martínez-Botí, M.A. et al., 2015: Plio-Pleistocene climate sensitivity evaluated using high-resolution CO2 records. *Nature*, **518**, 49–54, doi:10.1038/nature14145.
Marvel, K., G.A. Schmidt, R.L. Miller, and L.S. Nazarenko, 2016: Implications for climate sensitivity from the response to individual forcings. *Nature Climate Change*, **6(4)**, 386–389, doi:10.1038/nclimate2888.
Marvel, K., R. Pincus, G.A. Schmidt, and R.L. Miller, 2018: Internal Variability and Disequilibrium Confound Estimates of Climate Sensitivity From Observations. *Geophysical Research Letters*, **45(3)**, 1595–1601, doi:10.1002/2017gl076468.
Marvel, K. et al., 2015: External influences on modeled and observed cloud trends. *Journal of Climate*, **28(12)**, 4820–4840, doi:10.1175/jcli-d-14-00734.1.
Masson-Delmotte, V. et al., 2013: Information from Paleoclimate Archives. In: *Climate Change 2013: The Physical Science Basis. Contribution of Working Group I to the Fifth Assessment Report of the Intergovernmental Panel on Climate Change* [Stocker, T.F., D. Qin, G.-K. Plattner, M. Tignor, S.K. Allen, J. Boschung, A. Nauels, Y. Xia, V. Bex, and P.M. Midgley (eds.)]. Cambridge University Press, Cambridge, United Kingdom and New York, NY, USA, pp. 383–464, doi:10.1017/cbo9781107415324.013.
Mateos, D., M. Anton, A. Sanchez-Lorenzo, J. Calbo, and M. Wild, 2013: Long-term changes in the radiative effects of

ACCEPTED VERSION SUBJECT TO FINAL EDITING

aerosols and clouds in a mid-latitude region (1985-2010). *Global and Planetary Change*, **111**, 288–295, doi:10.1016/j.gloplacha.2013.10.004.
Matus, A. and T.S. L'Ecuyer, 2017: The role of cloud phase in Earth's radiation budget. *Journal of Geophysical Research: Atmospheres*, **122(5)**, 2559–2578, doi:10.1002/2016jd025951.
Mauritsen, T., 2016: Global warming: Clouds cooled the Earth. *Nature Geoscience*, **9(12)**, 865–867, doi:10.1038/ngeo2838.
Mauritsen, T. and B. Stevens, 2015: Missing iris effect as a possible cause of muted hydrological change and high climate sensitivity in models. *Nature Geoscience*, **8(5)**, 346–351, doi:10.1038/ngeo2414.
Mauritsen, T. and R. Pincus, 2017: Committed warming inferred from observations. *Nature Climate Change*, **7(9)**, 652–655, doi:10.1038/nclimate3357.
Mauritsen, T. and E. Roeckner, 2020: Tuning the MPI-ESM1.2 Global Climate Model to Improve the Match With Instrumental Record Warming by Lowering Its Climate Sensitivity. *Journal of Advances in Modeling Earth Systems*, **12(5)**, doi:10.1029/2019ms002037.
Mauritsen, T. et al., 2012: Tuning the climate of a global model. *Journal of Advances in Modeling Earth Systems*, **4(8)**, 1–18, doi:10.1029/2012ms000154.
Mauritsen, T. et al., 2013: Climate feedback efficiency and synergy. *Climate Dynamics*, **41(9–10)**, 2539–2554, doi:10.1007/s00382-013-1808-7.
Mauritsen, T. et al., 2019: Developments in the MPI-M Earth System Model version 1.2 (MPI-ESM 1.2) and its response to increasing CO2. *Journal of Advances in Modeling Earth Systems*, doi:10.1029/2018ms001400.
McCabe, M.F., B. Aragon, R. Houborg, and J. Mascaro, 2017a: CubeSats in Hydrology: Ultrahigh-Resolution Insights Into Vegetation Dynamics and Terrestrial Evaporation. *Water Resources Research*, **53(12)**, 10017–10024, doi:10.1002/2017wr022240.
McCabe, M.F. et al., 2017b: The future of Earth observation in hydrology. *Hydrology and Earth System Sciences*, **21(7)**, 3879–3914, doi:10.5194/hess-21-3879-2017.
McClymont, E.L. et al., 2020: Lessons from a high-CO2 world: an ocean view from ~3 million years ago. *Climate of the Past*, **16(4)**, 1599–1615, doi:10.5194/cp-16-1599-2020.
McComiskey, A. and G. Feingold, 2012: The scale problem in quantifying aerosol indirect effects. *Atmospheric Chemistry and Physics*, **12(2)**, 1031–1049, doi:10.5194/acp-12-1031-2012.
McCoy, D.T., D.L. Hartmann, and D.P. Grosvenor, 2014a: Observed Southern Ocean Cloud Properties and Shortwave Reflection. Part I: Calculation of SW Flux from Observed Cloud Properties. *Journal of Climate*, **27(23)**, 8836–8857, doi:10.1175/jcli-d-14-00287.1.
McCoy, D.T., D.L. Hartmann, and D.P. Grosvenor, 2014b: Observed Southern Ocean Cloud Properties and Shortwave Reflection. Part II: Phase Changes and Low Cloud Feedback. *Journal of Climate*, **27(23)**, 8858–8868, doi:10.1175/jcli-d-14-00288.1.
McCoy, D.T., R. Eastman, D.L. Hartmann, and R. Wood, 2017a: The Change in Low Cloud Cover in a Warmed Climate Inferred from AIRS, MODIS, and ERA-Interim. *Journal of Climate*, **30(10)**, 3609–3620, doi:10.1175/jcli-d-15-0734.1.
McCoy, D.T., I. Tan, D.L. Hartmann, M.D. Zelinka, and T. Storelvmo, 2016: On the relationships among cloud cover, mixed-phase partitioning, and planetary albedo in GCMs.. *Journal of Advances in Modeling Earth Systems*, **8**, 650–668, doi:10.1002/2015ms000589.
McCoy, D.T. et al., 2017b: The global aerosol-cloud first indirect effect estimated using MODIS, MERRA, and AeroCom. *Journal of Geophysical Research: Atmospheres*, **122(3)**, 1779–1796, doi:10.1002/2016jd026141.
McCoy, D.T. et al., 2018: Aerosol midlatitude cyclone indirect effects in observations and high-resolution simulations. *Atmospheric Chemistry and Physics*, **18(8)**, 5821–5846, doi:10.5194/acp-18-5821-2018.
McCoy, D.T. et al., 2019: Cloud feedbacks in extratropical cyclones: Insight from long-term satellite data and high-resolution global simulations. *Atmospheric Chemistry and Physics*, doi:10.5194/acp-19-1147-2019.
McCoy, I.L. et al., 2020a: The hemispheric contrast in cloud microphysical properties constrains aerosol forcing. *Proceedings of the National Academy of Sciences of the United States of America*, **117(32)**, 18998–19006, doi:10.1073/pnas.1922502117.
McCoy, I.L. et al., 2020b: The hemispheric contrast in cloud microphysical properties constrains aerosol forcing. *Proceedings of the National Academy of Sciences of the United States of America*, **117(32)**, 18998–19006, doi:10.1073/pnas.1922502117.
McGraw, Z., T. Storelvmo, B.H. Samset, and C.W. Stjern, 2020: Global Radiative Impacts of Black Carbon Acting as Ice Nucleating Particles. *Geophysical Research Letters*, **47(20)**, 1–9, doi:10.1029/2020gl089056.
McGregor, S., M.F. Stuecker, J.B. Kajtar, M.H. England, and M. Collins, 2018: Model tropical Atlantic biases underpin diminished Pacific decadal variability. *Nature Climate Change*, **8(6)**, 493–498, doi:10.1038/s41558-018-0163-4.
McGregor, S. et al., 2014: Recent Walker circulation strengthening and Pacific cooling amplified by Atlantic warming. *Nature Climate Change*, **4(10)**, 888–892, doi:10.1038/nclimate2330.
Meehl, G.A. et al., 2020: Context for interpreting equilibrium climate sensitivity and transient climate response from the CMIP6 Earth system models. *Science Advances*, **6(26)**, doi:10.1126/sciadv.aba1981.

ACCEPTED VERSION SUBJECT TO FINAL EDITING

Meinshausen, M., S.C.B.B. Raper, and T.M.L.L. Wigley, 2011a: Emulating coupled atmosphere-ocean and carbon cycle models with a simpler model, MAGICC6 – Part 1: Model description and calibration. *Atmospheric Chemistry and Physics*, **11(4)**, 1417–1456, doi:10.5194/acp-11-1417-2011.

Meinshausen, M., T.M.L. Wigley, and S.C.B. Raper, 2011b: Emulating atmosphere-ocean and carbon cycle models with a simpler model, MAGICC6 - Part 2: Applications. *Atmospheric Chemistry and Physics*, **11(4)**, 1457–1471, doi:10.5194/acp-11-1457-2011.

Meinshausen, M. et al., 2009: Greenhouse-gas emission targets for limiting global warming to 2 °C. *Nature*, **458(7242)**, 1158–1162, doi:10.1038/nature08017.

Meinshausen, M. et al., 2020: The shared socio-economic pathway (SSP) greenhouse gas concentrations and their extensions to 2500. *Geoscientific Model Development*, **13(8)**, 3571–3605, doi:10.5194/gmd-13-3571-2020.

Meraner, K., T. Mauritsen, and A. Voigt, 2013: Robust increase in equilibrium climate sensitivity under global warming. *Geophysical Research Letters*, **40(22)**, 5944–5948, doi:10.1002/2013gl058118.

Mercado, L.M. et al., 2009: Impact of changes in diffuse radiation on the global land carbon sink. *Nature*, doi:10.1038/nature07949.

Meredith, M. et al., 2019: Polar Regions. In: *IPCC Special Report on the Ocean and Cryosphere in a Changing Climate* [Pörtner, H.-O., D.C. Roberts, V. Masson-Delmotte, P. Zhai, M. Tignor, E. Poloczanska, K. Mintenbeck, A. Alegría, M. Nicolai, A. Okem, J. Petzold, B. Rama, and N.M. Weyer (eds.)]. In Press, pp. 203–320.

Merlis, T.M., 2014: Interacting components of the top-of-atmosphere energy balance affect changes in regional surface temperature. *Geophysical Research Letters*, **41(20)**, 7291–7297, doi:10.1002/2014gl061700.

Merlis, T.M. and T. Schneider, 2011: Changes in zonal surface temperature gradients and Walker circulations in a wide range of climates. *Journal of Climate*, **24(17)**, 4757–4768, doi:10.1175/2011jcli4042.1.

Merlis, T.M. and M. Henry, 2018: Simple estimates of polar amplification in moist diffusive energy balance models. *Journal of Climate*, doi:10.1175/jcli-d-17-0578.1.

Merlis, T.M., I.M. Held, G.L. Stenchikov, F. Zeng, and L.W. Horowitz, 2014: Constraining transient climate sensitivity using coupled climate model simulations of volcanic eruptions. *Journal of Climate*, doi:10.1175/jcli-d-14-00214.1.

Meyer, A., J.P. Vernier, B. Luo, U. Lohmann, and T. Peter, 2015: Did the 2011 Nabro eruption affect the optical properties of ice clouds? *Journal of Geophysical Research*, **120(18)**, 9500–9513, doi:10.1002/2015jd023326.

Meyssignac, B. et al., 2019: Measuring Global Ocean Heat Content to Estimate the Earth Energy Imbalance. *Frontiers in Marine Science*, **6**, 432, doi:10.3389/fmars.2019.00432.

Michibata, T., K. Suzuki, Y. Sato, and T. Takemura, 2016: The source of discrepancies in aerosol–cloud–precipitation interactions between GCM and A-Train retrievals. *Atmospheric Chemistry and Physics*, **16(23)**, 15413–15424, doi:10.5194/acp-16-15413-2016.

Millar, J.R., Z.R. Nicholls, P. Friedlingstein, and M.R. Allen, 2017: A modified impulse-response representation of the global near-surface air temperature and atmospheric concentration response to carbon dioxide emissions. *Atmospheric Chemistry and Physics*, **17(11)**, 7213–7228, doi:10.5194/acp-17-7213-2017.

Millar, R.J. et al., 2015: Model structure in observational constraints on transient climate response. *Climatic Change*, **131(2)**, 199–211, doi:10.1007/s10584-015-1384-4.

Mlynczak, M.G. et al., 2016: The spectroscopic foundation of radiative forcing of climate by carbon dioxide. *Geophysical Research Letters*, doi:10.1002/2016gl068837.

Modak, A. and G. Bala, 2019: Efficacy of black carbon aerosols: The role of shortwave cloud feedback. *Environmental Research Letters*, doi:10.1088/1748-9326/ab21e7.

Modak, A., G. Bala, L. Cao, and K. Caldeira, 2016: Why must a solar forcing be larger than a CO2 forcing to cause the same global mean surface temperature change? *Environmental Research Letters*, **11(4)**, doi:10.1088/1748-9326/11/4/044013.

Modak, A., G. Bala, K. Caldeira, and L. Cao, 2018: Does shortwave absorption by methane influence its effectiveness? *Climate Dynamics*, 1–20, doi:10.1007/s00382-018-4102-x.

Morgenstern, O. et al., 2017: Review of the global models used within phase 1 of the Chemistry-Climate Model Initiative (CCMI). *Geoscientific Model Development*, doi:10.5194/gmd-10-639-2017.

Morgenstern, O. et al., 2020: Reappraisal of the climate impacts of ozone-depleting substances. *Earth and Space Science Open Archive*, doi:10.1002/essoar.10502742.1.

Morrison, A.L., J.E. Kay, W.R. Frey, H. Chepfer, and R. Guzman, 2018: Cloud Response to Arctic Sea Ice Loss and Implications for Future Feedbacks in the CESM1 Climate Model. *Journal of Geophysical Research: Atmospheres*, doi:10.1029/2018jd029142.

Moseid, K.O. et al., 2020: Bias in CMIP6 models compared to observed regional dimming and brightening trends (1961-2014). *Atmospheric Chemistry and Physics*, 1–20, doi:10.5194/acp-2019-1210.

Mueller, B. et al., 2013: Benchmark products for land evapotranspiration: LandFlux-EVAL multi-data set synthesis. *Hydrology and Earth System Sciences*, **17(10)**, 3707–3720, doi:10.5194/hess-17-3707-2013.

Mülmenstädt, J. et al., 2019: Separating radiative forcing by aerosol-cloud interactions and fast cloud adjustments in the ECHAM-HAMMOZ aerosol-climate model using the method of partial radiative perturbations. *Atmospheric Chemistry and Physics*, **19**, 15415–15429, doi:10.5194/acp-19-15415-2019.

ACCEPTED VERSION SUBJECT TO FINAL EDITING

Muñoz, I. and J.H. Schmidt, 2016: Methane oxidation, biogenic carbon, and the IPCC's emission metrics. Proposal for a consistent greenhouse-gas accounting. *International Journal of Life Cycle Assessment*, doi:10.1007/s11367-016-1091-z.

Murphy, D.M. and P.M. Forster, 2010: On the accuracy of deriving climate feedback parameters from correlations between surface temperature and outgoing radiation. *Journal of Climate*, doi:10.1175/2010jcli3657.1.

Murphy, J.M., 1995: Transient Response of the Hadley Centre Coupled Ocean-Atmosphere Model to Increasing Carbon Dioxide. Part III: Analysis of Global-Mean Response Using Simple Models. *Journal of Climate*, doi:10.1175/1520-0442(1995)008<0496:trothc>2.0.co;2.

Myers, T.A. and J.R. Norris, 2016: Reducing the uncertainty in subtropical cloud feedback. *Geophysical Research Letters*, **43(5)**, 2144–2148, doi:10.1002/2015gl067416.

Myhre, G., E.J. Highwood, K.P. Shine, and F. Stordal, 1998: New estimates of radiative forcing due to well mixed greenhouse gases. *Geophysical Research Letters*, **25(14)**, 2715–2718, doi:10.1029/98gl01908.

Myhre, G. et al., 2013a: Radiative forcing of the direct aerosol effect from AeroCom Phase II simulations. *Atmospheric Chemistry and Physics*, **13(4)**, 1853–1877, doi:10.5194/acp-13-1853-2013.

Myhre, G. et al., 2013b: Anthropogenic and Natural Radiative Forcing. In: *Climate Change 2013: The Physical Science Basis. Contribution of Working Group I to the Fifth Assessment Report of the Intergovernmental Panel on Climate Change* [Stocker, T.F., D. Qin, G.-K. Plattner, M. Tignor, S.K. Allen, J. Boschung, A. Nauels, Y. Xia, V. Bex, and P.M. Midgley (eds.)]. Cambridge University Press, Cambridge, United Kingdom and New York, NY, USA, pp. 659–740, doi:10.1017/ cbo9781107415324.018.

Myhre, G. et al., 2017: Multi-model simulations of aerosol and ozone radiative forcing due to anthropogenic emission changes during the period 1990-2015. *Atmospheric Chemistry and Physics*, doi:10.5194/acp-17-2709-2017.

Nabat, P., S. Somot, M. Mallet, A. Sanchez-Lorenzo, and M. Wild, 2014: Contribution of anthropogenic sulfate aerosols to the changing Euro-Mediterranean climate since 1980. *Geophysical Research Letters*, **41(15)**, 5605–5611, doi:10.1002/2014gl060798.

Nakajima, T., A. Higurashi, K. Kawamoto, and J.E. Penner, 2001: A possible correlation between satellite-derived cloud and aerosol microphysical parameters. *Geophysical Research Letters*, **28(7)**, 1171–1174, doi:10.1029/2000gl012186.

Namazi, M., K. von Salzen, and J.N.S. Cole, 2015: Simulation of black carbon in snow and its climate impact in the Canadian Global Climate Model. *Atmospheric Chemistry and Physics*, **15(18)**, 10887–10904, doi:10.5194/acp-15-10887-2015.

Narenpitak, P., C.S. Bretherton, and M.F. Khairoutdinov, 2017: Cloud and circulation feedbacks in a nearglobal aquaplanet cloudresolving model.. *Journal of Advances in Modeling Earth Systems*, **9**, 1069–1090.

Nazarenko, L. et al., 2017: Interactive nature of climate change and aerosol forcing. *Journal of Geophysical Research: Atmospheres*, **122(6)**, 3457–3480, doi:10.1002/2016jd025809.

Neubauer, D., M.W. Christensen, C.A. Poulsen, and U. Lohmann, 2017: Unveiling aerosol–cloud interactions – Part 2: Minimising the effects of aerosol swelling and wet scavenging in ECHAM6-HAM2 for comparison to satellite data. *Atmospheric Chemistry and Physics*, **17(21)**, 13165–13185, doi:10.5194/acp-17-13165-2017.

Newsom, E., L. Zanna, S. Khatiwala, and J.M. Gregory, 2020: The Influence of Warming Patterns on Passive Ocean Heat Uptake. *Geophysical Research Letters*, **47(18)**, doi:10.1029/2020gl088429.

Nicholls, Z.R.J. et al., 2020: Reduced Complexity Model Intercomparison Project Phase 1: introduction and evaluation of global-mean temperature response. *Geoscientific Model Development*, **13(11)**, 5175–5190, doi:10.5194/gmd-13-5175-2020.

Nijsse, F., P. Cox, and M. Williamson, 2020: An emergent constraint on Transient Climate Response from simulated historical warming in CMIP6 models. *Earth System Dynamics*, 1–14, doi:10.5194/esd-2019-86.

Norris, J.R. et al., 2016: Evidence for climate change in the satellite cloud record. *Nature*, **536(7614)**, 72, doi:10.1038/nature18273.

Notaro, M., S. Vavrus, and Z. Liu, 2007: Global vegetation and climate change due to future increases in CO2 as projected by a fully coupled model with dynamic vegetation. *Journal of Climate*, **20(1)**, 70–90, doi:10.1175/jcli3989.1.

Notz, D., 2015: How well must climate models agree with observations? *Philosophical Transactions of the Royal Society A: Mathematical, Physical and Engineering Sciences*, **373(2052)**, 20140164, doi:10.1098/rsta.2014.0164.

Nummelin, A., C. Li, and P.J. Hezel, 2017: Connecting ocean heat transport changes from the midlatitudes to the Arctic Ocean. *Geophysical Research Letters*, doi:10.1002/2016gl071333.

O'Brien, C.L. et al., 2014: High sea surface temperatures in tropical warm pools during the Pliocene. *Nature Geoscience*, **7(8)**, 606–611, doi:10.1038/ngeo2194.

O'Connor, F.M. et al., 2021: Assessment of pre-industrial to present-day anthropogenic climate forcing in UKESM1. *Atmospheric Chemistry and Physics*, **21(2)**, 1211–1243, doi:10.5194/acp-21-1211-2021.

O'Gorman, P.A. and M.S. Singh, 2013: Vertical structure of warming consistent with an upward shift in the middle and upper troposphere. *Geophysical Research Letters*, **40(9)**, 1838–1842, doi:10.1002/grl.50328.

O'ishi, R., A. Abe-Ouchi, I.C. Prentice, and S. Sitch, 2009: Vegetation dynamics and plant CO2 responses as positive

ACCEPTED VERSION SUBJECT TO FINAL EDITING

feedbacks in a greenhouse world. *Geophysical Research Letters*, **36(11)**, 1–5, doi:10.1029/2009gl038217.
Ohmura, A., A. Bauder, H. Mueller, and G. Kappenberger, 2007: Long-term change of mass balance and the role of radiation. *Annals of Glaciology*, **46**, 367–374, doi:10.3189/172756407782871297.
Ohno, T., M. Satoh, and A. Noda, 2019: Fine Vertical Resolution Radiative-Convective Equilibrium Experiments: Roles of Turbulent Mixing on the High-Cloud Response to Sea Surface Temperatures. *Journal of Advances in Modeling Earth Systems*, **11(6)**, 1637–1654, doi:10.1029/2019ms001704.
Oldenburg, D., K.C. Armour, L.A. Thompson, and C.M. Bitz, 2018: Distinct mechanisms of ocean heat transport into the Arctic under internal variability and climate change. *Geophysical Research Letters*, doi:10.1029/2018gl078719.
Olonscheck, D., T. Mauritsen, and D. Notz, 2019: Arctic sea-ice variability is primarily driven by atmospheric temperature fluctuations. *Nature Geoscience*, **12(6)**, 430–434, doi:10.1038/s41561-019-0363-1.
Olonscheck, D., M. Rugenstein, and J. Marotzke, 2020: Broad Consistency Between Observed and Simulated Trends in Sea Surface Temperature Patterns. *Geophysical Research Letters*, **47(10)**, doi:10.1029/2019gl086773.
Otto, A. et al., 2013: Energy budget constraints on climate response. *Nature Geoscience*, **6(6)**, 415–416, doi:10.1038/ngeo1836.
Otto-Bliesner, B.L. et al., 2017: Amplified North Atlantic warming in the late Pliocene by changes in Arctic gateways. *Geophysical Research Letters*, **44(2)**, 957–964, doi:10.1002/2016gl071805.
Padilla, L.E., G.K. Vallis, and C.W. Rowley, 2011: Probabilistic estimates of transient climate sensitivity subject to uncertainty in forcing and natural variability. *Journal of Climate*, doi:10.1175/2011jcli3989.1.
Palmer, M.D., 2017: Reconciling Estimates of Ocean Heating and Earth's Radiation Budget. *Current Climate Change Reports*, **3(1)**, 78–86, doi:10.1007/s40641-016-0053-7.
Palmer, M.D. and D.J. McNeall, 2014: Internal variability of Earth's energy budget simulated by CMIP5 climate models. *Environmental Research Letters*, **9(3)**, 34016, doi:10.1088/1748-9326/9/3/034016.
Palmer, M.D., G.R. Harris, and J.M. Gregory, 2018: Extending CMIP5 projections of global mean temperature change and sea level rise due to thermal expansion using a physically-based emulator. *Environmental Research Letters*, **13(8)**, 84003, doi:10.1088/1748-9326/aad2e4.
Palmer, M.D., C.M. Domingues, A.B.A. Slangen, and F. Boeira Dias, 2021: An ensemble approach to quantify global mean sea-level rise over the 20th century from tide gauge reconstructions. *Environ. Res. Lett*, doi:10.1088/1748-9326/abdaec.
Parding, K., J.A. Olseth, K.F. Dagestad, and B.G. Liepert, 2014: Decadal variability of clouds, solar radiation and temperature at a high-latitude coastal site in Norway. *Tellus Series B-Chemical and Physical Meteorology*, **66**, doi:10.3402/tellusb.v66.25897.
Park, J.-Y., J.-S. Kug, J. Bader, R. Rolph, and M. Kwon, 2015: Amplified Arctic warming by phytoplankton under greenhouse warming. *Proceedings of the National Academy of Sciences*, **112(19)**, 5921–5926, doi:10.1073/pnas.1416884112.
Pattyn, F. et al., 2018: The Greenland and Antarctic ice sheets under 1.5°C global warming. *Nature Climate Change*, **8(12)**, 1053–1061, doi:10.1038/s41558-018-0305-8.
Pauling, A.G., I.J. Smith, P.J. Langhorne, and C.M. Bitz, 2017: Time-Dependent Freshwater Input From Ice Shelves: Impacts on Antarctic Sea Ice and the Southern Ocean in an Earth System Model. *Geophysical Research Letters*, doi:10.1002/2017gl075017.
Paulot, F., D. Paynter, P. Ginoux, V. Naik, and L.W. Horowitz, 2018: Changes in the aerosol direct radiative forcing from 2001 to 2015: Observational constraints and regional mechanisms. *Atmospheric Chemistry and Physics*, **18(17)**, 13265–13281, doi:10.5194/acp-18-13265-2018.
Payne, A.E., M.F. Jansen, and T.W. Cronin, 2015: Conceptual model analysis of the influence of temperature feedbacks on polar amplification. *Geophysical Research Letters*, **42(21)**, 9561–9570, doi:10.1002/2015gl065889.
Paynter, D., T.L. Frölicher, L.W. Horowitz, and L.G. Silvers, 2018: Equilibrium Climate Sensitivity Obtained From Multimillennial Runs of Two GFDL Climate Models. *Journal of Geophysical Research: Atmospheres*, **123(4)**, 1921–1941, doi:10.1002/2017jd027885.
Peng, J. et al., 2016: Markedly enhanced absorption and direct radiative forcing of black carbon under polluted urban environments.. *Proceedings of the National Academy of Sciences of the United States of America*, **113(16)**, 4266–71, doi:10.1073/pnas.1602310113.
Penner, J.E., L. Xu, and M. Wang, 2011: Satellite methods underestimate indirect climate forcing by aerosols.. *Proceedings of the National Academy of Sciences of the United States of America*, **108(33)**, 13404–8, doi:10.1073/pnas.1018526108.
Penner, J.E., C. Zhou, A. Garnier, and D.L. Mitchell, 2018: Anthropogenic Aerosol Indirect Effects in Cirrus Clouds. *Journal of Geophysical Research: Atmospheres*, **123(20)**, 11,652–11,677, doi:10.1029/2018jd029204.
Persad, G.G. and K. Caldeira, 2018: Divergent global-scale temperature effects from identical aerosols emitted in different regions. *Nature Communications*, doi:10.1038/s41467-018-05838-6.
Persad, G.G., Y. Ming, and V. Ramaswamy, 2014: The role of aerosol absorption in driving clear-sky solar dimming over East Asia. *Journal of Geophysical Research-Atmospheres*, **119(17)**, 10,410–10,424, doi:10.1002/2014jd021577.

ACCEPTED VERSION SUBJECT TO FINAL EDITING

Peters, G.P., B. Aamaas, T. Berntsen, and J.S. Fuglestvedt, 2011: The integrated global temperature change potential (iGTP) and relationships between emission metrics. *Environmental Research Letters*, doi:10.1088/1748-9326/6/4/044021.
Petersik, P. et al., 2018: Subgrid-scale variability in clear-sky relative humidity and forcing by aerosol–radiation interactions in an atmosphere model. *Atmospheric Chemistry and Physics*, **18(12)**, 8589–8599, doi:10.5194/acp-18-8589-2018.
Pfeifroth, U., A. Sanchez-Lorenzo, V. Manara, J. Trentmann, and R. Hollmann, 2018: Trends and Variability of Surface Solar Radiation in Europe Based On Surface- and Satellite-Based Data Records. *JOURNAL OF GEOPHYSICAL RESEARCH-ATMOSPHERES*, **123(3)**, 1735–1754, doi:10.1002/2017jd027418.
Pfister, P.L. and T.F. Stocker, 2017: State-Dependence of the Climate Sensitivity in Earth System Models of Intermediate Complexity. *Geophysical Research Letters*, **44(20)**, 10,643–10,653, doi:10.1002/2017gl075457.
Pierce, J.R., 2017: Cosmic rays, aerosols, clouds, and climate: Recent findings from the CLOUD experiment. *Journal of Geophysical Research: Atmospheres*, **122(15)**, 8051–8055, doi:10.1002/2017jd027475.
Pierrehumbert, R.T., 2014: Short-Lived Climate Pollution. *Annual Review of Earth and Planetary Sciences*, **42(1)**, 341–379, doi:10.1146/annurev-earth-060313-054843.
Pincus, R., P.M. Forster, and B. Stevens, 2016: The Radiative Forcing Model Intercomparison Project (RFMIP): Experimental protocol for CMIP6. *Geoscientific Model Development*, **9(9)**, 3447–3460, doi:10.5194/gmd-9-3447-2016.
Pincus, R. et al., 2015: Radiative flux and forcing parameterization error in aerosol-free clear skies. *Geophysical Research Letters*, **42(13)**, 5485–5492, doi:10.1002/2015gl064291.
Pincus, R. et al., 2020: Benchmark Calculations of Radiative Forcing by Greenhouse Gases. *Journal of Geophysical Research: Atmospheres*, **125(23)**, 1–15, doi:10.1029/2020jd033483.
Pistone, K., I. Eisenman, and V. Ramanathan, 2014: Observational determination of albedo decrease caused by vanishing Arctic sea ice. *Proc. Natl. Acad. Sci.*, **111(9)**, 3322–3326, doi:10.1073/pnas.1318201111.
Pithan, F. and T. Mauritsen, 2014: Arctic amplification dominated by temperature feedbacks in contemporary climate models. *Nature Geoscience*, **7(3)**, 181–184, doi:10.1038/ngeo2071.
Po-Chedley, S., C. Proistosescu, K.C. Armour, and B.D. Santer, 2018a: Climate constraint reflects forced signal. *Nature*, **563(7729)**, E6–E9, doi:10.1038/s41586-018-0640-y.
Po-Chedley, S., K.C. Armour, C.M. Bitz, M.D. Zelinka, and B.D. Santer, 2018b: Sources of intermodel spread in the lapse rate and water vapor feedbacks. *Journal of Climate*, doi:10.1175/jcli-d-17-0674.1.
Po-Chedley, S., M.D. Zelinka, N. Jeevanjee, T.J. Thorsen, and B.D. Santer, 2019: Climatology explains intermodel spread in tropical upper tropospheric cloud and relative humidity response to greenhouse warming. *Geophysical Research Letters*, doi:10.1029/2019gl084786.
Popp, M., H. Schmidt, and J. Marotzke, 2016: Transition to a Moist Greenhouse with CO2 and solar forcing. *Nature Communications*, **7**, 10627, doi:10.1038/ncomms10627.
Port, U., V. Brovkin, and M. Claussen, 2012: The influence of vegetation dynamics on anthropogenic climate change. *Earth System Dynamics*, **3(2)**, 233–243, doi:10.5194/esd-3-233-2012.
Posselt, R., R. Mueller, J. Trentmann, R. Stockli, and M.A. Liniger, 2014: A surface radiation climatology across two Meteosat satellite generations. *Remote Sensing of Environment*, **142**, 103–110, doi:10.1016/j.rse.2013.11.007.
Previdi, M., K.L. Smith, and L.M. Polvani, 2015: How Well Do the CMIP5 Models Simulate the Antarctic Atmospheric Energy Budget? *JOURNAL OF CLIMATE*, **28(20)**, 7933–7942, doi:10.1175/jcli-d-15-0027.1.
Proistosescu, C. and P.J. Huybers, 2017: Slow climate mode reconciles historical and model-based estimates of climate sensitivity. *Science Advances*, **3(7)**, 1–7, doi:10.1126/sciadv.1602821.
Proistosescu, C. et al., 2018: Radiative Feedbacks From Stochastic Variability in Surface Temperature and Radiative Imbalance. *Geophysical Research Letters*, doi:10.1029/2018gl077678.
Purich, A., M.H. England, W. Cai, A. Sullivan, and P.J. Durack, 2018: Impacts of broad-scale surface freshening of the Southern Ocean in a coupled climate model. *Journal of Climate*, doi:10.1175/jcli-d-17-0092.1.
Qian, Y. et al., 2015: Light-absorbing particles in snow and ice: Measurement and modeling of climatic and hydrological impact. *Advances in Atmospheric Sciences*, **32(1)**, 64–91, doi:10.1007/s00376-014-0010-0.
Qu, X. and A. Hall, 2007: What controls the strength of snow-albedo feedback? *J. Climate*, **20(15)**, 3971–3981, doi:10.1175/jcli4186.1.
Qu, X. and A. Hall, 2014: On the persistent spread in snow-albedo feedback. *Clim. Dyn.*, **42**, 69–81, doi:10.1007/s00382-013-1774-0.
Qu, X., A. Hall, S.A. Klein, and P.M. Caldwell, 2014: On the spread of changes in marine low cloud cover in climate model simulations of the 21st century. *Climate Dynamics*, doi:10.1007/s00382-013-1945-z.
Qu, X., A. Hall, S.A. Klein, and A.M. DeAngelis, 2015: Positive tropical marine low-cloud cover feedback inferred from cloud-controlling factors.. *Geophysical Research Letters*, **42**, 7767–7775, doi:10.1002/2015gl065627.
Qu, X. et al., 2018: On the emergent constraints of climate sensitivity. *Journal of Climate*, **31(2)**, 863–875, doi:10.1175/jcli-d-17-0482.1.
Quaas, J., O. Boucher, N. Bellouin, and S. Kinne, 2008: Satellite-based estimate of the direct and indirect aerosol climate forcing. *Journal of Geophysical Research: Atmospheres*, **113(D5)**, doi:10.1029/2007jd008962.

ACCEPTED VERSION SUBJECT TO FINAL EDITING

Quaas, J. et al., 2009: Aerosol indirect effects – general circulation model intercomparison and evaluation with satellite data. *Atmospheric Chemistry and Physics*, **9(22)**, 8697–8717, doi:10.5194/acp-9-8697-2009.
Radtke, J., T. Mauritsen, and C. Hohenegger, 2020: Shallow cumulus cloud feedback in large eddy simulations - Bridging the gap to storm resolving models. *Atmospheric Chemistry and Physics*, 1–19, doi:10.5194/acp-2020-1160.
Raes, F., H. Liao, W.-T. Chen, and J.H. Seinfeld, 2010: Atmospheric chemistry-climate feedbacks. *Journal of Geophysical Research (Atmospheres)*, **115(D12)**, D12121, doi:10.1029/2009jd013300.
Raghuraman, S.P., D. Paynter, and V. Ramaswamy, 2019: Quantifying the Drivers of the Clear Sky Greenhouse Effect, 2000-2016. *JOURNAL OF GEOPHYSICAL RESEARCH-ATMOSPHERES*, **124(21)**, 11354–11371, doi:10.1029/2019jd031017.
Rahimzadeh, F., A. Sanchez-Lorenzo, M. Hamedi, M.C. Kruk, and M. Wild, 2015: New evidence on the dimming/brightening phenomenon and decreasing diurnal temperature range in Iran (1961-2009). *Int. J. Climatol.*, **35**, 2065–2079, doi:10.1002/joc.4107.
Ramaswamy, V. et al., 2019: Radiative Forcing of Climate: The Historical Evolution of the Radiative Forcing Concept, the Forcing Agents and their Quantification, and Applications. *Meteorological Monographs*, **59**, 14.1–14.101, doi:10.1175/amsmonographs-d-19-0001.1.
Randall, D.A. et al., 2007: Climate Models and Their Evaluation. In: *Climate Change 2007: The Scientific Basis. Contribution of Working Group I to the Fourth Assessment Report of the Intergovernmental Panel on Climate Change* [Solomon, S., D. Qin, M. Manning, Z. Chen, M. Marquis, K.B. Averyt, M. Tignor, and H.L. Miller (eds.)]. Cambridge University Press, Cambridge, United Kingdom and New York, USA, pp. 589–662.
Randles, C.A. et al., 2017: The MERRA-2 Aerosol Reanalysis, 1980 Onward. Part I: System Description and Data Assimilation Evaluation. *Journal of Climate*, **30(17)**, 6823–6850, doi:10.1175/jcli-d-16-0609.1.
Raschke, E., S. Kinne, W.B. Rossow, P.W. Stackhouse, and M. Wild, 2016: Comparison of Radiative Energy Flows in Observational Datasets and Climate Modeling. *Journal of Applied Meteorology and Climatology*, **55(1)**, 93–117, doi:10.1175/jamc-d-14-0281.1.
Raval, A. and V. Ramanathan, 1989: Observational determination of the greenhouse effect. *Nature*, **342**, 758–761, doi:10.1038/342758a0.
Ravelo, A.C., K.T. Lawrence, A. Fedorov, and H.L. Ford, 2014: Comment on "A 12-million-year temperature history of the tropical Pacific Ocean". *Science*, **346(6216)**, 1467, doi:10.1126/science.1257618.
Rayner, N.A. et al., 2003: Global analyses of sea surface temperature, sea ice, and night marine air temperature since the late nineteenth century. *Journal of Geophysical Research*, **108(D14)**, 4407, doi:10.1029/2002jd002670.
Regayre, L.A. et al., 2018: Aerosol and physical atmosphere model parameters are both important sources of uncertainty in aerosol ERF. *Atmospheric Chemistry and Physics*, **18(13)**, 9975–10006, doi:10.5194/acp-18-9975-2018.
Reick, C.H., T. Raddatz, V. Brovkin, and V. Gayler, 2013: Representation of natural and anthropogenic land cover change in MPI-ESM. *Journal of Advances in Modeling Earth Systems*, **5(3)**, 459–482, doi:10.1002/jame.20022.
Rémy, S., N. Bellouin, A. Benedetti, and O. Boucher, 2018: Aerosols [in "State of the Climate in 2017"].. *Bull. Amer. Meteor. Soc.,*, **99(8)**, S49–S51, doi:10.1175/2018bamsstateoftheclimate.1.
Renoult, M. et al., 2020: A Bayesian framework for emergent constraints: case studies of climate sensitivity with PMIP. *Climate of The Past*, **16**, 1715–1735, doi:10.5194/cp-16-1715-2020.
Rhein, M. et al., 2013: Observations: Ocean. In: *Climate Change 2013: The Physical Science Basis. Contribution of Working Group I to the Fifth Assessment Report of the Intergovernmental Panel on Climate Change* [Stocker, T.F., D. Qin, G.-K. Plattner, M. Tignor, S.K. Allen, J. Boschung, A. Nauels, Y. Xia, V. Bex, and P.M. Midgley (eds.)]. Cambridge University Press, Cambridge, United Kingdom and New York, NY, USA, pp. 255–316, doi:10.1017/cbo9781107415324.010.
Ribes, A., S. Qasmi, and N. Gillett, 2021: Making climate projections conditional on historical observations. *Science Advances*, **7(4)**, eabc0671, doi:10.1126/sciadv.abc0671.
Richardson, M., K. Cowtan, and R.J. Millar, 2018: Global temperature definition affects achievement of long-term climate goals. *Environmental Research Letters*, **13(5)**, 054004, doi:10.1088/1748-9326/aab305.
Richardson, M., K. Cowtan, E. Hawkins, and M.B. Stolpe, 2016: Reconciled climate response estimates from climate models and the energy budget of Earth. *Nature Climate Change*, **6(10)**, 931–935, doi:10.1038/nclimate3066.
Richardson, T.B. et al., 2018: Carbon Dioxide Physiological Forcing Dominates Projected Eastern Amazonian Drying. *Geophysical Research Letters*, doi:10.1002/2017gl076520.
Richardson, T.B. et al., 2019: Efficacy of climate forcings in PDRMIP models. *Journal of Geophysical Research: Atmospheres*, **124**, 12,824–12,844, doi:10.1029/2019jd030581.
Richter, K. et al., 2020: Detecting a forced signal in satellite-era sea-level change. *Environmental Research Letters*, **15(9)**, doi:10.1088/1748-9326/ab986e.
Rienecker, M.M. et al., 2011: MERRA: NASA's Modern-Era Retrospective Analysis for Research and Applications. *Journal of Climate*, **24(14)**, 3624–3648, doi:10.1175/jcli-d-11-00015.1.
Ringer, M.A., T. Andrews, and M.J. Webb, 2014: Global-mean radiative feedbacks and forcing in atmosphere-only and

ACCEPTED VERSION SUBJECT TO FINAL EDITING

coupled atmosphere-ocean climate change experiments. *Geophysical Research Letters*, **41**, 4035–4042, doi:10.1002/ 2014gl060347.
Riser, S.C. et al., 2016: Fifteen years of ocean observations with the global Argo array. *Nature Climate Change*, **6(2)**, 145–153, doi:10.1038/nclimate2872.
Roberts, C.D., M.D. Palmer, D. McNeall, and M. Collins, 2015: Quantifying the likelihood of a continued hiatus in global warming. *Nature Climate Change*, **5(4)**, 337–342, doi:10.1038/nclimate2531.
Rodell, M. et al., 2018: Emerging trends in global freshwater availability. *Nature*, **557(7707)**, 651–659, doi:10.1038/s41586-018-0123-1.
Roe, G., 2009: Feedbacks, Timescales, and Seeing Red. *Annual Review of Earth and Planetary Sciences*, **37(1)**, 93–115, doi:10.1146/annurev.earth.061008.134734.
Roe, G.H. and M.B. Baker, 2007: Why Is Climate Sensitivity So Unpredictable? *Science*, **318(5850)**, 629–632, doi:10.1126/science.1144735.
Roe, G.H. and K.C. Armour, 2011: How sensitive is climate sensitivity? *Geophysical Research Letters*, **38(14)**, n/a–n/a, doi:10.1029/2011gl047913.
Roe, G.H., N. Feldl, K.C. Armour, Y.T. Hwang, and D.M.W. Frierson, 2015: The remote impacts of climate feedbacks on regional climate predictability. *Nature Geoscience*, doi:10.1038/ngeo2346.
Rogelj, J. and C.F. Schleussner, 2019: Unintentional unfairness when applying new greenhouse gas emissions metrics at country level. *Environmental Research Letters*, **14(11)**, 114039, doi:10.1088/1748-9326/ab4928.
Rogelj, J. et al., 2015: Zero emission targets as long-term global goals for climate protection. *Environmental Research Letters*, **10(10)**, 105007, doi:10.1088/1748-9326/10/10/105007.
Rogelj, J. et al., 2018: Mitigation Pathways Compatible with 1.5°C in the Context of Sustainable Development. In: *Global Warming of 1.5°C. An IPCC Special Report on the impacts of global warming of 1.5°C above pre-industrial levels and related global greenhouse gas emission pathways, in the context of strengthening the global response to the threat of climate change,* [Masson-Delmotte, V., P. Zhai, H.-O. Pörtner, D. Roberts, J. Skea, P.R. Shukla, A. Pirani, W. Moufouma-Okia, C. Péan, R. Pidcock, S. Connors, J.B.R. Matthews, Y. Chen, X. Zhou, M.I. Gomis, E. Lonnoy, T. Maycock, M. Tignor, and T. Waterfield (eds.)]. In Press, pp. 93–174.
Rohling, E.J. et al., 2012: Making sense of palaeoclimate sensitivity. *Nature*, **491(7426)**, 683–691, doi:10.1038/nature11574.
Rohrschneider, T., B. Stevens, and T. Mauritsen, 2019: On simple representations of the climate response to external radiative forcing. *Climate Dynamics*, doi:10.1007/s00382-019-04686-4.
Romps, D.M., 2014: An Analytical Model for Tropical Relative Humidity. *Journal of Climate*, **27(19)**, 7432–7449, doi:10.1175/jcli-d-14-00255.1.
Rose, B.E.J. and L. Rayborn, 2016: The Effects of Ocean Heat Uptake on Transient Climate Sensitivity. *Current Climate Change Reports*, doi:10.1007/s40641-016-0048-4.
Rose, B.E.J. and M.C. Rencurrel, 2016: The Vertical Structure of Tropospheric Water Vapor: Comparing Radiative and Ocean-Driven Climate Changes. *Journal of Climate*, **29(11)**, 4251–4268, doi:10.1175/jcli-d-15-0482.1.
Rose, B.E.J., K.C. Armour, D.S. Battisti, N. Feldl, and D.D.B. Koll, 2014: The dependence of transient climate sensitivity and radiative feedbacks on the spatial pattern of ocean heat uptake. *Geophysical Research Letters*, doi:10.1002/2013gl058955.
Rosenfeld, D. et al., 2019: Aerosol-driven droplet concentrations dominate coverage and water of oceanic low level clouds.. *Science (New York, N.Y.)*, doi:10.1126/science.aav0566.
Rostron, J.W. et al., 2020: The impact of performance filtering on climate feedbacks in a perturbed parameter ensemble. *Climate Dynamics*, **55(3–4)**, 521–551, doi:10.1007/s00382-020-05281-8.
Rotstayn, L.D. and J.E. Penner, 2001: Indirect aerosol forcing, quasi forcing, and climate response. *Journal of Climate*, doi:10.1175/1520-0442(2001)014<2960:iafqfa>2.0.co;2.
Rotstayn, L.D., M.A. Collier, D.T. Shindell, and O. Boucher, 2015: Why does aerosol forcing control historical global-mean surface temperature change in CMIP5 models? *Journal of Climate*, **28(17)**, 6608–6625, doi:10.1175/jcli-d-14-00712.1.
Rowlands, D.J. et al., 2012: Broad range of 2050 warming from an observationally constrained large climate model ensemble. *Nature Geoscience*, doi:10.1038/ngeo1430.
Rowlinson, M. et al., 2020: Tropospheric ozone radiative forcing uncertainty due to pre-industrial fire and biogenic emissions. *Atmospheric Chemistry and Physics*, doi:10.5194/acp-2019-1065.
Royer, D.L., 2016: Climate Sensitivity in the Geologic Past. *Annual Review of Earth and Planetary Sciences*, **44(1)**, 277–293, doi:10.1146/annurev-earth-100815-024150.
Rugenstein, M. et al., 2019a: LongRunMIP – motivation and design for a large collection of millennial-length AO-GCM simulations. *Bulletin of the American Meteorological Society*, doi:10.1175/bams-d-19-0068.1.
Rugenstein, M. et al., 2019b: Equilibrium climate sensitivity estimated by equilibrating climate models. *Geophysical Research Letters*, 2019GL083898, doi:10.1029/2019gl083898.
Rugenstein, M.A.A., K. Caldeira, and R. Knutti, 2016a: Dependence of global radiative feedbacks on evolving patterns of surface heat fluxes. *Geophysical Research Letters*, doi:10.1002/2016gl070907.

ACCEPTED VERSION SUBJECT TO FINAL EDITING

Rugenstein, M.A.A., M. Winton, R.J. Stouffer, S.M. Griffies, and R. Hallberg, 2013: Northern High-Latitude Heat Budget Decomposition and Transient Warming. *Journal of Climate*, **26(2)**, 609–621, doi:10.1175/jcli-d-11-00695.1.

Rugenstein, M.A.A., J.M. Gregory, N. Schaller, J. Sedlácek, and R. Knutti, 2016b: Multiannual ocean-atmosphere adjustments to radiative forcing. *Journal of Climate*, **29(15)**, 5643–5659, doi:10.1175/jcli-d-16-0312.1.

Russotto, R.D. and M. Biasutti, 2020: Polar Amplification as an Inherent Response of a Circulating Atmosphere: Results From the TRACMIP Aquaplanets. *Geophysical Research Letters*, **47(6)**, doi:10.1029/2019gl086771.

Rypdal, M., H.-B. Fredriksen, K. Rypdal, and R.J. Steene, 2018: Emergent constraints on climate sensitivity. *Nature*, **563(7729)**, E4–E5, doi:10.1038/s41586-018-0639-4.

Sagoo, N., P. Valdes, R. Flecker, L.J. Gregoire, and P.T.R.S. A, 2013: The Early Eocene equable climate problem: can perturbations of climate model parameters identify possible solutions? *Philosophical Transactions of the Royal Society of London A: Mathematical, Physical and Engineering Sciences*, **371(2001)**, doi:10.1098/rsta.2013.0123.

Saint-Lu, M., S. Bony, and J.-L. Dufresne, 2020: Observational Evidence for a Stability Iris Effect in the Tropics. *Geophysical Research Letters*, **47(14)**, e2020GL089059, doi:10.1029/2020gl089059.

Salzmann, M., 2017: The polar amplification asymmetry: role of Antarctic surface height. *Earth System Dynamics*, **8(2)**, 323–336, doi:10.5194/esd-8-323-2017.

Salzmann, U. et al., 2013: Challenges in quantifying Pliocene terrestrial warming revealed by data-model discord. *Nature Climate Change*, **3(11)**, 969–974, doi:10.1038/nclimate2008.

Sanchez-Lorenzo, A., J. Calbo, and M. Wild, 2013: Global and diffuse solar radiation in Spain: Building a homogeneous dataset and assessing their trends. *Global and Planetary Change*, **100**, 343–352, doi:10.1016/j.gloplacha.2012.11.010.

Sanchez-Lorenzo, A. et al., 2015: Reassessment and update of long-term trends in downward surface shortwave radiation over Europe (1939-2012). *Journal of Geophysical Research-Atmospheres*, **120(18)**, 9555–9569, doi:10.1002/2015jd023321.

Santer, B.D. et al., 2005: Amplification of Surface Temperature Trends and Variability in the Tropical Atmosphere. *Science*, **309(5740)**, 1551–1556, doi:10.1126/science.1114867.

Sato, Y. et al., 2018: Aerosol effects on cloud water amounts were successfully simulated by a global cloud-system resolving model. *Nature Communications*, **9(1)**, 985, doi:10.1038/s41467-018-03379-6.

Schleussner, C.F. et al., 2016: Science and policy characteristics of the Paris Agreement temperature goal. *Nature Climate Change*, **6(9)**, 827–835, doi:10.1038/nclimate3096.

Schleussner, C.-F., A. Nauels, M. Schaeffer, W. Hare, and J. Rogelj, 2019: Inconsistencies when applying novel metrics for emissions accounting to the Paris Agreement. *Environmental Research Letters*, doi:10.1088/1748-9326/ab56e7.

Schlund, M., A. Lauer, P. Gentine, S. Sherwood, and V. Eyring, 2020: Emergent constraints on Equilibrium Climate Sensitivity in CMIP5: do they hold for CMIP6? *Earth System Dynamics*, **11**, 1233–1258, doi:10.5194/esd-11-1233-2020.

Schmidt, A. et al., 2018: Volcanic Radiative Forcing From 1979 to 2015. *Journal of Geophysical Research: Atmospheres*, doi:10.1029/2018jd028776.

Schmidt, G.A. et al., 2014: Using palaeo-climate comparisons to constrain future projections in CMIP5. *Climate of the Past*, **10(1)**, 221–250, doi:10.5194/cp-10-221-2014.

Schmidt, G.A. et al., 2017a: Practice and philosophy of climate model tuning across six US modeling centers. *Geoscientific Model Development*, **10(9)**, 3207–3223, doi:10.5194/gmd-10-3207-2017.

Schmidt, G.A. et al., 2017b: Overestimate of committed warming. *Nature*, **547(7662)**, E16–E17, doi:10.1038/nature22803.

Schneider, A., M. Flanner, and J. Perket, 2018: Multidecadal Variability in Surface Albedo Feedback Across CMIP5 Models. *Geophysical Research Letters*, **45(4)**, 1972–1980, doi:10.1002/2017gl076293.

Schneider, T., C.M. Kaul, and K.G. Pressel, 2019: Possible climate transitions from breakup of stratocumulus decks under greenhouse warming. *Nature Geoscience*, **12(3)**, 163–167, doi:10.1038/s41561-019-0310-1.

Schneider von Deimling, T. et al., 2012: Estimating the near-surface permafrost-carbon feedback on global warming. *Biogeosciences*, **9(2)**, 649–665, doi:10.5194/bg-9-649-2012.

Schneider von Deimling, T. et al., 2015: Observation-based modelling of permafrost carbon fluxes with accounting for deep carbon deposits and thermokarst activity. *Biogeosciences*, **12**, 3469–3488, doi:10.5194/bg-12-3469-2015.

Schröder, M. et al., 2019: The GEWEX Water Vapor Assessment: Overview and Introduction to Results and Recommendations. *Remote Sensing*, **11(3)**, 251, doi:10.3390/rs11030251.

Schulz, M. et al., 2006: Radiative forcing by aerosols as derived from the AeroCom present-day and pre-industrial simulations. *Atmospheric Chemistry and Physics*, **6(12)**, 5225–5246, doi:10.5194/acp-6-5225-2006.

Schurer, A. et al., 2018: Estimating the Transient Climate Response from Observed Warming. *Journal of Climate*, **31(20)**, 8645–8663, doi:10.1175/jcli-d-17-0717.1.

Schwartz, S.E., 2007: Heat capacity, time constant, and sensitivity of Earth's climate system. *Journal of Geophysical Research Atmospheres*, **112(24)**, 1–12, doi:10.1029/2007jd008746.

ACCEPTED VERSION SUBJECT TO FINAL EDITING

Schwartz, S.E., 2012: Determination of Earth's Transient and Equilibrium Climate Sensitivities from Observations Over the Twentieth Century: Strong Dependence on Assumed Forcing. *Surveys in Geophysics*, **33(3–4)**, 745–777, doi:10.1007/s10712-012-9180-4.
Schwartz, S.E., 2018: Unrealized Global Temperature Increase: Implications of Current Uncertainties. *Journal of Geophysical Research: Atmospheres*, **123(7)**, 3462–3482, doi:10.1002/2017jd028121.
Schwarz, M., D. Folini, M.Z. Hakuba, and M. Wild, 2018: From Point to Area: Worldwide Assessment of the Representativeness of Monthly Surface Solar Radiation Records. *JOURNAL OF GEOPHYSICAL RESEARCH-ATMOSPHERES*, **123(24)**, 13857–13874, doi:10.1029/2018jd029169.
Schwarz, M., D. Folini, S. Yang, R.P. Allan, and M. Wild, 2020: Changes in atmospheric shortwave absorption as important driver of dimming and brightening. *Nature Geoscience*, **13(2)**, 110–115, doi:10.1038/s41561-019-0528-y.
Schweiger, A. et al., 2011: Uncertainty in modeled Arctic sea ice volume. *Journal of Geophysical Research: Oceans*, **116(C8)**, doi:10.1029/2011jc007084.
Scott, C.E. et al., 2017: Impact on short-lived climate forcers (SLCFs) from a realistic land-use change scenario via changes in biogenic emissions. *Faraday Discussions*, doi:10.1039/c7fd00028f.
Screen, J.A., C. Deser, and I. Simmonds, 2012: Local and remote controls on observed Arctic warming. *Geophysical Research Letters*, **39(10)**, doi:10.1029/2012gl051598.
Seager, R. et al., 2019: Strengthening tropical Pacific zonal sea surface temperature gradient consistent with rising greenhouse gases. *Nature Climate Change*, **9(7)**, 517–522, doi:10.1038/s41558-019-0505-x.
Seeley, J.T. and N. Jeevanjee, 2021: H2O Windows and CO2 Radiator Fins: A Clear-Sky Explanation for the Peak in Equilibrium Climate Sensitivity. *Geophysical Research Letters*, **48(4)**, e2020GL089609, doi:10.1029/2020gl089609.
Séférian, R. et al., 2019: Evaluation of CNRM Earth-System model, CNRM-ESM2-1: role of Earth system processes in present-day and future climate. *Journal of Advances in Modeling Earth Systems*, **11**, 2019MS001791, doi:10.1029/2019ms001791.
Seifert, A., T. Heus, R. Pincus, and B. Stevens, 2015: Large-eddy simulation of the transient and near-equilibrium behavior of precipitating shallow convection. *Journal of Advances in Modeling Earth Systems*, **7(4)**, 1918–1937, doi:10.1002/2015ms000489.
Seneviratne, S.I., M.G. Donat, A.J. Pitman, R. Knutti, and R.L. Wilby, 2016: Allowable CO2 emissions based on regional and impact-related climate targets. *Nature*, **529**, 477–483, doi:10.1038/nature16542.
Shaffer, G., M. Huber, R. Rondanelli, and J.O. Pepke Pedersen, 2016: Deep time evidence for climate sensitivity increase with warming. *Geophysical Research Letters*, **43(12)**, 6538–6545, doi:10.1002/2016gl069243.
Shapiro, A.V.A.I. et al., 2011: A new approach to the long-term reconstruction of the solar irradiance leads to large historical solar forcing. *Astronomy & Astrophysics*, **529**, A67, doi:10.1051/0004-6361/201016173.
Sherwood, S. et al., 2020a: An assessment of Earth's climate sensitivity using multiple lines of evidence. *Reviews of Geophysics*, **58(4)**, doi:10.1029/2019rg000678.
Sherwood, S. et al., 2020b: An assessment of Earth's climate sensitivity using multiple lines of evidence. *Reviews of Geophysics*, **58(4)**, doi:10.1029/2019rg000678.
Sherwood, S.C., S. Bony, and J.-L. Dufresne, 2014: Spread in model climate sensitivity traced to atmospheric convective mixing. *Nature*, **505(7481)**, 37–42, doi:10.1038/nature12829.
Sherwood, S.C., V. Dixit, and C. Salomez, 2018: The global warming potential of near-surface emitted water vapour. *Environmental Research Letters*, doi:10.1088/1748-9326/aae018.
Sherwood, S.C., R. Roca, T.M. Weckwerth, and N.G. Andronova, 2010a: Tropospheric water vapor, convection, and climate. *Reviews of Geophysics*, **48(2)**, doi:10.1029/2009rg000301.
Sherwood, S.C. et al., 2010b: Relative humidity changes in a warmer climate. *Journal of Geophysical Research: Atmospheres*, **115(D9)**, doi:10.1029/2009jd012585.
Sherwood, S.C. et al., 2015: Adjustments in the forcing-feedback framework for understanding climate change. *Bulletin of the American Meteorological Society*, **96(2)**, 217–228, doi:10.1175/bams-d-13-00167.1.
Shindell, D.T., 2014: Inhomogeneous forcing and transient climate sensitivity. *Nature Climate Change*, **4**, 274–277, doi:10.1038/nclimate2136.
Shindell, D.T., J.S. Fuglestvedt, and W.J. Collins, 2017: The social cost of methane: Theory and applications. *Faraday Discussions*, doi:10.1039/c7fd00009j.
Shindell, D.T. et al., 2009: Improved attribution of climate forcing to emissions. *Science*, doi:10.1126/science.1174760.
Shindell, D.T. et al., 2013: Radiative forcing in the ACCMIP historical and future climate simulations. *Atmospheric Chemistry and Physics*, **13(6)**, 2939–2974, doi:10.5194/acp-13-2939-2013.
Shindell, D.T.D.T., G. Faluvegi, L. Rotstayn, and G. Milly, 2015: Spatial patterns of radiative forcing and surface temperature response. *Journal of Geophysical Research: Atmospheres*, **120**, 1–19, doi:10.1002/2014jd022752.
Shine, K.P., R.G. Derwent, D.J. Wuebbles, and J.-J. Morcrette, 1990: Radiative Forcing of Climate. In: *Climate Change: The IPCC Scientific Assessment* [Houghton, J.T., J.G. Jenkins, and J.J. Ephraums (eds.)]. Cambridge University Press, Cambridge, United Kingdom and New York, NY, USA, pp. 41–68.
Shine, K.P., J. Cook, E.J. Highwood, and M.M. Joshi, 2003: An alternative to radiative forcing for estimating the

ACCEPTED VERSION SUBJECT TO FINAL EDITING

relative importance of climate change mechanisms. *Geophysical Research Letters*, doi:10.1029/2003gl018141.
Shine, K.P., J.S. Fuglestvedt, K. Hailemariam, and N. Stuber, 2005: Alternatives to the Global Warming Potential for comparing climate impacts of emissions of greenhouse gases. *Climatic Change*, **68(3)**, 281–302, doi:10.1007/s10584-005-1146-9.
Shine, K.P.P., R.P.P. Allan, W.J.J. Collins, and J.S.S. Fuglestvedt, 2015: Metrics for linking emissions of gases and aerosols to global precipitation changes. *Earth System Dynamics*, **6(2)**, 525–540, doi:10.5194/esd-6-525-2015.
Siler, N., S. Po-Chedley, and C.S. Bretherton, 2018a: Variability in modeled cloud feedback tied to differences in the climatological spatial pattern of clouds. *Climate Dynamics*, **50(3)**, 1209–1220, doi:10.1007/s00382-017-3673-2.
Siler, N., G.H. Roe, and K.C. Armour, 2018b: Insights into the zonal-mean response of the hydrologic cycle to global warming from a diffusive energy balance model. *Journal of Climate*, doi:10.1175/jcli-d-18-0081.1.
Silvers, L.G., D. Paynter, and M. Zhao, 2018: The Diversity of Cloud Responses to Twentieth Century Sea Surface Temperatures. *Geophysical Research Letters*, **45(1)**, 391–400, doi:10.1002/2017gl075583.
Singarayer, J.S., P.J. Valdes, P. Friedlingstein, S. Nelson, and D.J. Beerling, 2011: Late Holocene methane rise caused by orbitally controlled increase in tropical sources. *Nature*, **470(7332)**, 82–85, doi:10.1038/nature09739.
Singh, H.A., P.J. Rasch, and B.E.J. Rose, 2017: Increased Ocean Heat Convergence Into the High Latitudes With CO2 Doubling Enhances Polar-Amplified Warming. *Geophysical Research Letters*, doi:10.1002/2017gl074561.
Sitch, S. et al., 2008: Evaluation of the terrestrial carbon cycle, future plant geography and climate-carbon cycle feedbacks using five Dynamic Global Vegetation Models (DGVMs). *Global Change Biology*, **14(9)**, 2015–2039, doi:10.1111/j.1365-2486.2008.01626.x.
Skeie, R.B., G.P. Peters, J. Fuglestvedt, and R. Andrew, 2021: A future perspective of historical contributions to climate change. *Climatic Change*, **164(1–2)**, 1–13, doi:10.1007/s10584-021-02982-9.
Skeie, R.B., T. Berntsen, M. Aldrin, M. Holden, and G. Myhre, 2018: Climate sensitivity estimates - Sensitivity to radiative forcing time series and observational data. *Earth System Dynamics*, **9(2)**, 879–894, doi:10.5194/esd-9-879-2018.
Skeie, R.B. et al., 2017: Perspective has a strong effect on the calculation of historical contributions to global warming. *Environmental Research Letters*, **12(2)**, 024022, doi:10.1088/1748-9326/aa5b0a.
Skeie, R.B. et al., 2020: Historical total ozone radiative forcing derived from CMIP6 simulations. *npj Climate and Atmospheric Science*, doi:10.1038/s41612-020-00131-0.
Skinner, L., 2012: A Long View on Climate Sensitivity. *Science*, **337(6097)**, 917–919, doi:10.1126/science.1224011.
Slater, T. et al., 2021: Review article: Earth's ice imbalance. *The Cryosphere*, **15(1)**, 233–246, doi:10.5194/tc-15-233-2021.
Smith, C.J., R.J. Kramer, and A. Sima, 2020a: The HadGEM3-GA7.1 radiative kernel: The importance of a well-resolved stratosphere. *Earth System Science Data*, **12(3)**, 2157–2168, doi:10.5194/essd-12-2157-2020.
Smith, C.J. et al., 2018a: FAIR v1.3: A simple emissions-based impulse response and carbon cycle model. *Geoscientific Model Development*, doi:10.5194/gmd-11-2273-2018.
Smith, C.J. et al., 2018b: Understanding Rapid Adjustments to Diverse Forcing Agents. *Geophysical Research Letters*, **45(21)**, doi:10.1029/2018gl079826.
Smith, C.J. et al., 2019: Current fossil fuel infrastructure does not yet commit us to 1.5°C warming. *Nature Communications*, doi:10.1038/s41467-018-07999-w.
Smith, C.J. et al., 2020b: Effective radiative forcing and adjustments in CMIP6 models. *Atmospheric Chemistry and Physics*, **20(16)**, 9591–9618, doi:10.5194/acp-20-9591-2020.
Smith, D.M. et al., 2016: Role of volcanic and anthropogenic aerosols in the recent global surface warming slowdown. *Nature Climate Change*, **6(10)**, 936–940, doi:10.1038/nclimate3058.
Smith, M.A., M. Cain, and M.R. Allen, 2021: Further improvement of warming-equivalent emissions calculation. *npj Climate and Atmospheric Science*, **accepted**, doi:10.1038/s41612-021-00169-8.
Smith, S.M. et al., 2012: Equivalence of greenhouse-gas emissions for peak temperature limits. *Nature Climate Change*, **2(7)**, 535–538, doi:10.1038/nclimate1496.
Snyder, C.W., 2016: Evolution of global temperature over the past two million years. *Nature*, **538(7624)**, 226–228, doi:10.1038/nature19798.
Snyder, C.W., 2019: Revised estimates of paleoclimate sensitivity over the past 800,000 years. *Climatic Change*, **156(1)**, 121–138, doi:10.1007/s10584-019-02536-0.
Soden, B.J. and I.M. Held, 2006: An Assessment of Climate Feedbacks in Coupled Ocean–Atmosphere Models. *Journal of Climate*, **19(14)**, 3354–3360, doi:10.1175/jcli3799.1.
Soden, B.J., D.L. Jackson, V. Ramaswamy, M.D. Schwarzkopf, and X. Huang, 2005: The Radiative Signature of Upper Tropospheric Moistening. *Science*, **310(5749)**, 841–844, doi:10.1126/science.1115602.
Soden, B.J. et al., 2008: Quantifying climate feedbacks using radiative kernels. *Journal of Climate*, **21(14)**, 3504–3520, doi:10.1175/2007jcli2110.1.
Soden, B.J.J., W.D.D. Collins, and D.R.R. Feldman, 2018: Reducing uncertainties in climate models. *Science*, **361(6400)**, 326–327, doi:10.1126/science.aau1864.
Sohn, B.J., S.W. Yeh, J. Schmetz, and H.J. Song, 2013: Observational evidences of Walker circulation change over the

ACCEPTED VERSION SUBJECT TO FINAL EDITING

last 30 years contrasting with GCM results. *Climate Dynamics*, **40(7–8)**, 1721–1732, doi:10.1007/s00382-012-1484-z.
Soni, V.K., G. Pandithurai, and D.S. Pai, 2016: Is there a transition of solar radiation from dimming to brightening over India? *ATMOSPHERIC RESEARCH*, **169(A)**, 209–224, doi:10.1016/j.atmosres.2015.10.010.
Spencer, R.W. and W.D. Braswell, 2010: On the diagnosis of radiative feedback in the presence of unknown radiative forcing. *Journal of Geophysical Research Atmospheres*, doi:10.1029/2009jd013371.
Spencer, R.W. and W.D. Braswell, 2011: On the misdiagnosis of surface temperature feedbacks from variations in Earth's radiant energy balance. *Remote Sensing*, doi:10.3390/rs3081603.
Stanhill, G., O. Achiman, R. Rosa, and S. Cohen, 2014: The cause of solar dimming and brightening at the Earth's surface during the last half century: Evidence from measurements of sunshine duration. *JOURNAL OF GEOPHYSICAL RESEARCH-ATMOSPHERES*, **119(18)**, 10902–10911, doi:10.1002/2013jd021308.
Stap, L.B., P. Köhler, and G. Lohmann, 2019: Including the efficacy of land ice changes in deriving climate sensitivity from paleodata. *Earth System Dynamics*, **10(2)**, 333–345, doi:10.5194/esd-10-333-2019.
Steffen, W. et al., 2018: Trajectories of the Earth System in the Anthropocene. *Proceedings of the National Academy of Sciences*, **115(33)**, 8252–8259, doi:10.1073/pnas.1810141115.
Stein, T.H.M., C.E. Holloway, I. Tobin, and S. Bony, 2017: Observed Relationships between Cloud Vertical Structure and Convective Aggregation over Tropical Ocean. *Journal of Climate*, **30(6)**, 2187–2207, doi:10.1175/jcli-d-16-0125.1.
Steiner, A.K. et al., 2020: Observed temperature changes in the troposphere and stratosphere from 1979 to 2018. *Journal of Climate*, doi:10.1175/jcli-d-19-0998.1.
Steinhilber, F. et al., 2012: 9,400 years of cosmic radiation and solar activity from ice cores and tree rings. *Proceedings of the National Academy of Sciences*, **109(16)**, 5967–5971, doi:10.1073/pnas.1118965109.
Steinthorsdottir, M. et al., 2020: The Miocene: the Future of the Past. *Paleoceanography and Paleoclimatology*, e2020PA004037, doi:10.1029/2020pa004037.
Stephens, G.L. et al., 2015: The albedo of Earth. *Reviews of Geophysics*, **53(1)**, 141–163, doi:10.1002/2014rg000449.
Sterner, E., D.J.A. Johansson, and C. Azar, 2014: Emission metrics and sea level rise. *Climatic Change*, **127(2)**, 335–351, doi:10.1007/s10584-014-1258-1.
Sterner, E.O. and D.J.A. Johansson, 2017: The effect of climate-carbon cycle feedbacks on emission metrics. *Environmental Research Letters*, doi:10.1088/1748-9326/aa61dc.
Stevens, B., 2015: Rethinking the lower bound on aerosol radiative forcing. *Journal of Climate*, **28(12)**, 4794–4819, doi:10.1175/jcli-d-14-00656.1.
Stevens, B. and G. Feingold, 2009: Untangling aerosol effects on clouds and precipitation in a buffered system. *Nature*, **461(7264)**, 607–613, doi:10.1038/nature08281.
Stevens, B., S.C. Sherwood, S. Bony, and M.J. Webb, 2016: Prospects for narrowing bounds on Earth's equilibrium climate sensitivity. *Earth's Future*, **4(11)**, 512–522, doi:10.1002/2016ef000376.
Stier, P., 2016: Limitations of passive remote sensing to constrain global cloud condensation nuclei. *Atmospheric Chemistry and Physics*, **16(10)**, 6595–6607, doi:10.5194/acp-16-6595-2016.
Stjern, C.W. et al., 2017: Rapid Adjustments Cause Weak Surface Temperature Response to Increased Black Carbon Concentrations. *Journal of Geophysical Research: Atmospheres*, doi:10.1002/2017jd027326.
Stjern, C.W. et al., 2019: Arctic Amplification Response to Individual Climate Drivers. *Journal of Geophysical Research: Atmospheres*, **124(13)**, 6698–6717, doi:10.1029/2018jd029726.
Stocker, B.D. et al., 2013: Multiple greenhouse-gas feedbacks from the land biosphere under future climate change scenarios. *Nature Climate Change*, **3(7)**, 666–672, doi:10.1038/nclimate1864.
Stolpe, M.B., I. Medhaug, U. Beyerle, and R. Knutti, 2019: Weak dependence of future global mean warming on the background climate state. *Climate Dynamics*, **53(7)**, 5079–5099, doi:10.1007/s00382-019-04849-3.
Storelvmo, T., 2017: Aerosol Effects on Climate via Mixed-Phase and Ice Clouds. *Annual Review of Earth and Planetary Sciences*, doi:10.1146/annurev-earth-060115-012240.
Storelvmo, T., T. Leirvik, U. Lohmann, P.C.B. Phillips, and M. Wild, 2016: Disentangling greenhouse warming and aerosol cooling to reveal Earth's climate sensitivity. *Nature Geoscience*, **9(4)**, 286–289, doi:10.1038/ngeo2670.
Storelvmo, T. et al., 2018: Lethargic response to aerosol emissions in current climate models. *Geophysical Research Letters*, **45(18)**, 9, doi:10.1029/2018gl078298.
Stouffer, R.J. and S. Manabe, 2003: Equilibrium response of thermohaline circulation to large changes in atmospheric CO2 concentration. *Climate Dynamics*, **20(7–8)**, 759–773, doi:10.1007/s00382-002-0302-4.
Streets, D.G., Y. Wu, and M. Chin, 2006: Two-decadal aerosol trends as a likely explanation of the global dimming/brightening transition. *GEOPHYSICAL RESEARCH LETTERS*, **33(15)**, doi:10.1029/2006gl026471.
Stroeve, J.C. et al., 2012: Trends in Arctic sea ice extent from CMIP5, CMIP3 and observations. *Geophys. Res. Lett.*, **39(16)**, doi:10.1029/2012gl052676.
Stuber, N., M. Ponater, and R. Sausen, 2005: Why radiative forcing might fail as a predictor of climate change. *Climate Dynamics*, doi:10.1007/s00382-004-0497-7.
Stuecker, M.F. et al., 2018: Polar amplification dominated by local forcing and feedbacks. *Nature Climate Change*,

ACCEPTED VERSION SUBJECT TO FINAL EDITING

8(12), 1076–1081, doi:10.1038/s41558-018-0339-y.
Su, H. et al., 2014: Weakening and strengthening structures in the Hadley Circulation change under global warming and implications for cloud response and climate sensitivity. *Journal of Geophysical Research: Atmospheres*, **119(10)**, 5787–5805, doi:10.1002/2014jd021642.
Su, H. et al., 2017: Tightening of tropical ascent and high clouds key to precipitation change in a warmer climate. *Nature Communications*, **8(1)**, 15771, doi:10.1038/ncomms15771.
Sun, C. et al., 2017: Western tropical Pacific multidecadal variability forced by the Atlantic multidecadal oscillation. *Nature Communications*, **8**, doi:10.1038/ncomms15998.
Super, J.R. et al., 2018: North Atlantic temperature and pCO2 coupling in the early-middle Miocene. *Geology*, **46(6)**, 519–522, doi:10.1130/g40228.1.
Sutton, R.T., 2018: ESD Ideas: A simple proposal to improve the contribution of IPCC WGI to the assessment and communication of climate change risks. *Earth System Dynamics*, **9(4)**, 1155–1158, doi:10.5194/esd-9-1155-2018.
Svensmark, H., 1998: Influence of Cosmic Rays on Earth's Climate. *Phys. Rev. Lett.*, **81(22)**, 5027–5030, doi:10.1103/physrevlett.81.5027.
Svensmark, H., T. Bondo, and J. Svensmark, 2009: Cosmic ray decreases affect atmospheric aerosols and clouds. *Geophysical Research Letters*, **36(15)**, doi:10.1029/2009gl038429.
Svensmark, H., M.B. Enghoff, N.J. Shaviv, and J. Svensmark, 2017: Increased ionization supports growth of aerosols into cloud condensation nuclei. *Nature Communications*, **8(1)**, 1–9, doi:10.1038/s41467-017-02082-2.
Svensmark, J., M.B. Enghoff, N.J. Shaviv, and H. Svensmark, 2016: The response of clouds and aerosols to cosmic ray decreases. *Journal of Geophysical Research: Space Physics*, **121(9)**, 8152–8181, doi:10.1002/2016ja022689.
Swingedouw, D. et al., 2008: Antarctic ice-sheet melting provides negative feedbacks on future climate warming. *Geophysical Research Letters*, **35(17)**, doi:10.1029/2008gl034410.
Takahashi, C. and M. Watanabe, 2016: Pacific trade winds accelerated by aerosol forcing over the past two decades. *Nature Climate Change*, **6(8)**, 768–772, doi:10.1038/nclimate2996.
Takahashi, H., H. Su, and J.H. Jiang, 2016: Water vapor changes under global warming and the linkage to present-day interannual variabilities in CMIP5 models. *Climate Dynamics*, **47(12)**, 3673–3691, doi:10.1007/s00382-016-3035-5.
Takemura, T. and K. Suzuki, 2019: Weak global warming mitigation by reducing black carbon emissions. *Scientific Reports*, **9(1)**, doi:10.1038/s41598-019-41181-6.
Tan, I., T. Storelvmo, and M.D. Zelinka, 2016: Observational constraints on mixed-phase clouds imply higher climate sensitivity. *Science*, **352(6282)**, 224–227, doi:10.1126/science.aad5300.
Tan, I., L. Oreopoulos, and N. Cho, 2019: The Role of Thermodynamic Phase Shifts in Cloud Optical Depth Variations With Temperature. *Geophysical Research Letters*, **46(8)**, 4502–4511, doi:10.1029/2018gl081590.
Tanaka, K. and B.C. O'Neill, 2018: The Paris Agreement zero-emissions goal is not always consistent with the 1.5°C and 2°C temperature targets. *Nature Climate Change*, doi:10.1038/s41558-018-0097-x.
Tanaka, K., D.J.A. Johansson, B.C. O'Neill, and J.S. Fuglestvedt, 2013: Emission metrics under the 2°C climate stabilization target. *Climatic Change*, doi:10.1007/s10584-013-0693-8.
Tanaka, K., A. Ohmura, D. Folini, M. Wild, and N. Ohkawara, 2016: Is global dimming and brightening in Japan limited to urban areas? *ATMOSPHERIC CHEMISTRY AND PHYSICS*, **16(21)**, 13969–14001, doi:10.5194/acp-16-13969-2016.
Tang, T. et al., 2019: Comparison of Effective Radiative Forcing Calculations Using Multiple Methods, Drivers, and Models. *Journal of Geophysical Research: Atmospheres*, **124(8)**, 4382–4394, doi:10.1029/2018jd030188.
Tao, W.K., J.P. Chen, Z. Li, C. Wang, and C. Zhang, 2012: Impact of aerosols on convective clouds and precipitation. *Reviews of Geophysics*, doi:10.1029/2011rg000369.
Taylor, P.C., S. Kato, K.-M. Xu, and M. Cai, 2015: Covariance between Arctic sea ice and clouds within atmospheric state regimes at the satellite footprint level. *Journal of Geophysical Research: Atmospheres*, **120(24)**, 12656–12678, doi:10.1002/2015jd023520.
Taylor, P.C. et al., 2013: A Decomposition of Feedback Contributions to Polar Warming Amplification. *Journal of Climate*, **26(18)**, 7023–7043, doi:10.1175/jcli-d-12-00696.1.
Tebaldi, C. and J.M. Arblaster, 2014: Pattern scaling: Its strengths and limitations, and an update on the latest model simulations. *Climatic Change*, doi:10.1007/s10584-013-1032-9.
Tebaldi, C. and R. Knutti, 2018: Evaluating the accuracy of climate change pattern emulation for low warming targets. *Environmental Research Letters*, **13(5)**, 55006, doi:10.1088/1748-9326/aabef2.
Terai, C.R., S.A. Klein, and M.D. Zelinka, 2016: Constraining the lowcloud optical depth feedback at middle and high latitudes using satellite observations.. *Journal of Geophysical Research*, **121**, 9696–9716, doi:10.1002/2016jd025233.
Terai, C.R. et al., 2019: Mechanisms Behind the Extratropical Stratiform Low-Cloud Optical Depth Response to Temperature in ARM Site Observations. *Journal of Geophysical Research: Atmospheres*, **124(4)**, 2127–2147, doi:10.1029/2018jd029359.
Thackeray, C.W. and A. Hall, 2019: An emergent constraint on future Arctic sea-ice albedo feedback. *Nature Climate*

ACCEPTED VERSION SUBJECT TO FINAL EDITING

Change, doi:10.1038/s41558-019-0619-1.
Thomas, C.M., B. Dong, and K. Haines, 2020: Inverse modeling of global and regional energy and water cycle fluxes using earth observation data. *Journal of Climate*, **33(5)**, 1707–1723, doi:10.1175/jcli-d-19-0343.1.
Thompson, D.W.J., S. Bony, and Y. Li, 2017: Thermodynamic constraint on the depth of the global tropospheric circulation. *Proceedings of the National Academy of Sciences*, **114(31)**, 8181 LP – 8186, doi:10.1073/pnas.1620493114.
Thornhill, G. et al., 2021: Climate-driven chemistry and aerosol feedbacks in CMIP6 Earth system models. *Atmospheric Chemistry and Physics*, **21(2)**, 1105–1126, doi:10.5194/acp-21-1105-2021.
Thornhill, G.D. et al., 2021: Effective radiative forcing from emissions of reactive gases and aerosols-A multi-model comparison. *Atmospheric Chemistry and Physics*, **21(2)**, 853–874, doi:10.5194/acp-21-853-2021.
Tian, B., 2015: Spread of model climate sensitivity linked to double-Intertropical Convergence Zone bias. *Geophysical Research Letters*, **42(10)**, 4133–4141, doi:10.1002/2015gl064119.
Tierney, J.E., A.M. Haywood, R. Feng, T. Bhattacharya, and B.L. Otto-Bliesner, 2019: Pliocene Warmth Consistent With Greenhouse Gas Forcing. *Geophysical Research Letters*, **46(15)**, 9136–9144, doi:10.1029/2019gl083802.
Tierney, J.E. et al., 2020a: Past climates inform our future. *Science*, **370(6517)**, doi:10.1126/science.aay3701.
Tierney, J.E. et al., 2020b: Glacial cooling and climate sensitivity revisited. *Nature*, **584(7822)**, 569–573, doi:10.1038/s41586-020-2617-x.
Tokarska, K.B., N.P. Gillett, V.K. Arora, W.G. Lee, and K. Zickfeld, 2018: The influence of non-CO2 forcings on cumulative carbon emissions budgets. *Environmental Research Letters*, **13**, 034039, doi:10.1088/1748-9326/aaafdd.
Tokarska, K.B. et al., 2020: Past warming trend constrains future warming in CMIP6 models. *Science Advances*, **6(12)**, 1–14, doi:10.1126/sciadv.aaz9549.
Toll, V., M. Christensen, S. Gassó, and N. Bellouin, 2017: Volcano and Ship Tracks Indicate Excessive Aerosol-Induced Cloud Water Increases in a Climate Model. *Geophysical Research Letters*, **44(24)**, 12,492–12,500, doi:10.1002/2017gl075280.
Toll, V., M. Christensen, J. Quaas, and N. Bellouin, 2019: Weak average liquid-cloud-water response to anthropogenic aerosols. *Nature*, **572(7767)**, 51–55, doi:10.1038/s41586-019-1423-9.
Tomassini, L., A. Voigt, and B. Stevens, 2015: On the connection between tropical circulation, convective mixing, and climate sensitivity. *Quarterly Journal of the Royal Meteorological Society*, **141(689)**, 1404–1416, doi:10.1002/qj.2450.
Toohey, M. and M. Sigl, 2017: Volcanic stratospheric sulfur injections and aerosol optical depth from 500 BCE to 1900 CE. *Earth System Science Data*, **9(2)**, 809–831, doi:10.5194/essd-9-809-2017.
Trenberth, K.E. and J.T. Fasullo, 2010: Simulation of Present-Day and Twenty-First-Century Energy Budgets of the Southern Oceans. *JOURNAL OF CLIMATE*, **23(2)**, 440–454, doi:10.1175/2009jcli3152.1.
Trenberth, K.E., J.T. Fasullo, and M.A. Balmaseda, 2014: Earth's Energy Imbalance. *JOURNAL OF CLIMATE*, **27(9)**, 3129–3144, doi:10.1175/jcli-d-13-00294.1.
Trenberth, K.E., Y. Zhang, J.T. Fasullo, and S. Taguchi, 2015: Climate variability and relationships between top-of-atmosphere radiation and temperatures on Earth. *Journal of Geophysical Research: Atmospheres*, **120(9)**, 3642–3659, doi:10.1002/2014jd022887.
Tselioudis, G., B.R. Lipat, D. Konsta, K.M. Grise, and L.M. Polvani, 2016: Midlatitude cloud shifts, their primary link to the Hadley cell, and their diverse radiative effects. *Geophys. Res. Lett.*, **43**, 4594–4601, doi:10.1002/2016gl068242.
Tsushima, Y. and S. Manabe, 2013: Assessment of radiative feedback in climate models using satellite observations of annual flux variation. *Proceedings of the National Academy of Sciences*, doi:10.1073/pnas.1216174110.
Tsushima, Y., M.A. Ringer, G.M. Martin, J.W. Rostron, and D.M.H. Sexton, 2020: Investigating physical constraints on climate feedbacks using a perturbed parameter ensemble. *Climate Dynamics*, **55(5–6)**, 1159–1185, doi:10.1007/s00382-020-05318-y.
Tsushima, Y. et al., 2014: High cloud increase in a perturbed SST experiment with a global nonhydrostatic model including explicit convective processes.. *Journal of Advances in Modeling Earth Systems*, **6**, 571–585, doi:10.1002/2013ms000301.
Tsutsui, J., 2020: Diagnosing Transient Response to CO2 Forcing in Coupled Atmosphere-Ocean Model Experiments Using a Climate Model Emulator. *Geophysical Research Letters*, **47(7)**, 1–12, doi:10.1029/2019gl085844.
Turnock, S.T. et al., 2015: Modelled and observed changes in aerosols and surface solar radiation over Europe between 1960 and 2009. *ATMOSPHERIC CHEMISTRY AND PHYSICS*, **15(16)**, 9477–9500, doi:10.5194/acp-15-9477-2015.
Tuzet, F. et al., 2017: A multilayer physically based snowpack model simulating direct and indirect radiative impacts of light-absorbing impurities in snow. *The Cryosphere*, **11(6)**, 2633–2653, doi:10.5194/tc-11-2633-2017.
Twomey, S., 1959: The nuclei of natural cloud formation part II: The supersaturation in natural clouds and the variation of cloud droplet concentration. *Geofisica Pura e Applicata*, **43(1)**, 243–249, doi:10.1007/bf01993560.
Ullrich, R. et al., 2017: A New Ice Nucleation Active Site Parameterization for Desert Dust and Soot. *Journal of the Atmospheric Sciences*, **74(3)**, 699–717, doi:10.1175/jas-d-16-0074.1.

ACCEPTED VERSION SUBJECT TO FINAL EDITING

Unger, N., 2014: Human land-use-driven reduction of forest volatiles cools global climate. *Nature Climate Change*, doi:10.1038/nclimate2347.
Usoskin, I.G. et al., 2015: The Maunder minimum (1645–1715) was indeed a grand minimum: A reassessment of multiple datasets. *Astronomy & Astrophysics*, **581**, A95, doi:10.1051/0004-6361/201526652.
Vaillant de Guélis, T. et al., 2018: Space lidar observations constrain longwave cloud feedback. *Scientific Reports*, **8(1)**, 16570, doi:10.1038/s41598-018-34943-1.
Vanderkelen, I. et al., 2020: Global Heat Uptake by Inland Waters. *Geophysical Research Letters*, **47(12)**, e2020GL087867, doi:10.1029/2020gl087867.
Vargas Zeppetello, L.R., A. Donohoe, and D.S. Battisti, 2019: Does Surface Temperature Respond to or Determine Downwelling Longwave Radiation? *Geophysical Research Letters*, **46(5)**, 2781–2789, doi:10.1029/2019gl082220.
Várnai, T. and A. Marshak, 2015: Effect of Cloud Fraction on Near-Cloud Aerosol Behavior in the MODIS Atmospheric Correction Ocean Color Product. *Remote Sensing*, **7(5)**, 5283–5299, doi:10.3390/rs70505283.
Vaughan, D.G. et al., 2013: Observations: Cryosphere. In: *Climate Change 2013: The Physical Science Basis. Contribution of Working Group I to the Fifth Assessment Report of the Intergovernmental Panel on Climate Change* [Stocker, T.F., D. Qin, G.K. Plattner, M. Tignor, S.K. Allen, J. Boschung, A. Nauels, Y. Xia, V. Bex, and P.M. Midgley (eds.)]. Cambridge University Press, Cambridge, United Kingdom and New York, NY, USA, pp. 317–382, doi:10.1017/cbo9781107415324.012.
Vecchi, G.A., A. Clement, and B.J. Soden, 2008: Examining the tropical Pacific's response to global warming. *Eos*, **89(9)**, 81–83, doi:10.1029/2008eo090002.
Vecchi, G.A. et al., 2006: Weakening of tropical Pacific atmospheric circulation due to anthropogenic forcing. *Nature*, **441(1)**, 73–76, doi:10.1038/nature04744.
Vergara-Temprado, J. et al., 2018: Is Black Carbon an Unimportant Ice-Nucleating Particle in Mixed-Phase Clouds? *Journal of Geophysical Research: Atmospheres*, doi:10.1002/2017jd027831.
Vial, J., J.-L.L. Dufresne, and S. Bony, 2013: On the interpretation of inter-model spread in CMIP5 climate sensitivity estimates. *Climate Dynamics*, **41(11–12)**, 3339–3362, doi:10.1007/s00382-013-1725-9.
Vieira, L.E.A., S.K. Solanki, N.A. Krivova, and I. Usoskin, 2011: Evolution of the solar irradiance during the Holocene. *Astronomy & Astrophysics*, **531**, A6, doi:10.1051/0004-6361/201015843.
Vieira, M., M.J. Pound, and D.I. Pereira, 2018: The late Pliocene palaeoenvironments and palaeoclimates of the western Iberian Atlantic margin from the Rio Maior flora. *Palaeogeography, Palaeoclimatology, Palaeoecology*, **495**, 245–258, doi:10.1016/j.palaeo.2018.01.018.
Vizcaíno, M., U. Mikolajewicz, J. Jungclaus, and G. Schurgers, 2010: Climate modification by future ice sheet changes and consequences for ice sheet mass balance. *Climate Dynamics*, **34(2)**, 301–324, doi:10.1007/s00382-009-0591-y.
Volodin, E.M., 2008: Relation between temperature sensitivity to doubled carbon dioxide and the distribution of clouds in current climate models. *Izvestiya, Atmospheric and Oceanic Physics*, **44(3)**, 288–299, doi:10.1134/s0001433808030043.
von der Heydt, A.S. and P. Ashwin, 2016: State dependence of climate sensitivity: attractor constraints and palaeoclimate regimes. *Dynamics and Statistics of the Climate System*, **1(1)**, 1–21, doi:10.1093/climsys/dzx001.
von der Heydt, A.S., H.A. Dijkstra, P. Köhler, and R. Wal, 2014: On the background state dependency of (palaeo) climate sensitivity. *Geophysical Research Letters*, **41(2)**, 6484–6492, doi:10.1002/2014gl061121.
von der Heydt, A.S. et al., 2016: Lessons on Climate Sensitivity From Past Climate Changes. *Current Climate Change Reports*, **2(4)**, 148–158, doi:10.1007/s40641-016-0049-3.
von Schuckmann, K. et al., 2016: An imperative to monitor Earth's energy imbalance. *Nature Climate Change*, **6(2)**, 138–144, doi:10.1038/nclimate2876.
von Schuckmann, K. et al., 2020: Heat stored in the Earth system: where does the energy go? *Earth System Science Data*, **12(3)**, 2013–2041, doi:10.5194/essd-12-2013-2020.
Voss, R. and U. Mikolajewicz, 2001: Long-term climate changes due to increased CO2 concentration in the coupled atmosphere-ocean general circulation model ECHAM3/LSG. *Climate Dynamics*, **17(1)**, 45–60, doi:10.1007/pl00007925.
Waelbroeck, C. et al., 2009: Constraints on the magnitude and patterns of ocean cooling at the Last Glacial Maximum. *Nature Geoscience*, **2(2)**, 127–132, doi:10.1038/ngeo411.
Wang, C., B.J.J. Soden, W. Yang, and G.A. Vecchi, 2021: Compensation between cloud feedback and aerosol-cloud interaction in CMIP6 models. *Geophysical Research Letters*, doi:10.1029/2020gl091024.
Wang, K., Q. Ma, Z. Li, and J. Wang, 2015: Decadal variability of surface incident solar radiation over China: Observations, satellite retrievals, and reanalyses. *JOURNAL OF GEOPHYSICAL RESEARCH-ATMOSPHERES*, **120(13)**, 6500–6514, doi:10.1002/2015jd023420.
Wang, K.C., Q. Ma, X.Y. Wang, and M. Wild, 2014: Urban impacts on mean and trend of surface incident solar radiation. *Geophysical Research Letters*, **41(13)**, 4664–4668, doi:10.1002/2014gl060201.
Wang, R. et al., 2016: Estimation of global black carbon direct radiative forcing and its uncertainty constrained by

ACCEPTED VERSION SUBJECT TO FINAL EDITING

observations. *Journal of Geophysical Research: Atmospheres*, **121(10)**, 5948–5971, doi:10.1002/2015jd024326.
Wang, R. et al., 2018: Spatial Representativeness Error in the Ground-Level Observation Networks for Black Carbon Radiation Absorption. *Geophysical Research Letters*, **45(4)**, 2106–2114, doi:10.1002/2017gl076817.
Wang, Y. and M. Wild, 2016: A new look at solar dimming and brightening in China. *GEOPHYSICAL RESEARCH LETTERS*, **43(22)**, 11777–11785, doi:10.1002/2016gl071009.
Wang, Y. and Y. Huang, 2020: The Surface Warming Attributable to Stratospheric Water Vapor in CO2-Caused Global Warming. *Journal of Geophysical Research: Atmospheres*, doi:10.1029/2020jd032752.
Wang, Y.W. and Y.H. Yang, 2014: China's dimming and brightening: evidence, causes and hydrological implications. *ANNALES GEOPHYSICAE*, **32(1)**, 41–55, doi:10.5194/angeo-32-41-2014.
Wara, M.W., A.C. Ravelo, and M.L. Delaney, 2005: Climate change: Permanent El Niño-like conditions during the Pliocene warm period. *Science*, **309(5735)**, 758–761, doi:10.1126/science.1112596.
Ward, D.S., N.M. Mahowald, and S. Kloster, 2014: Potential climate forcing of land use and land cover change. *Atmospheric Chemistry and Physics*, doi:10.5194/acp-14-12701-2014.
Watanabe, M., H. Tatebe, T. Suzuki, and K. Tachiiri, 2020a: Control of transient climate response and associated sea level rise by deep-ocean mixing. *Environmental Research Letters*, **15(9)**, 094001, doi:10.1088/1748-9326/ab8ca7.
Watanabe, M., Y. Kamae, H. Shiogama, A.M. DeAngelis, and K. Suzuki, 2018: Low clouds link equilibrium climate sensitivity to hydrological sensitivity. *Nature Climate Change*, **8(10)**, 901–906, doi:10.1038/s41558-018-0272-0.
Watanabe, M., J.-L. Dufresne, Y. Kosaka, T. Mauritsen, and H. Tatebe, 2020b: Enhanced warming constrained by past trends in equatorial Pacific sea surface temperature gradient. *Nature Climate Change*, doi:10.1038/s41558-020-00933-3.
Webb, M.J. and A.P. Lock, 2020: Testing a physical hypothesis for the relationship between climate sensitivity and double-ITCZ bias in climate models. *Journal of Advances in Modeling Earth Systems*, doi:10.1029/2019ms001999.
Webb, M.J., F.H. Lambert, and J.M. Gregory, 2013: Origins of differences in climate sensitivity, forcing and feedback in climate models. *Climate Dynamics*, **40(3)**, 677–707, doi:10.1007/s00382-012-1336-x.
Webb, M.J. et al., 2015: The impact of parametrized convection on cloud feedback. *Philosophical Transactions of the Royal Society A: Mathematical, Physical and Engineering Sciences*, **373(2054)**, doi:10.1098/rsta.2014.0414.
Wen, Q., J. Yao, K. Döös, and H. Yang, 2018: Decoding hosing and heating effects on global temperature and meridional circulations in a warming climate. *Journal of Climate*, doi:10.1175/jcli-d-18-0297.1.
Westerhold, T. et al., 2020: An astronomically dated record of Earth's climate and its predictability over the last 66 million years. *Science*, **369(6509)**, 1383–1388, doi:10.1126/science.aba6853.
Wigley, T.M.L., 1998: The Kyoto Protocol: CO2, CH4 and climate implications. *Geophysical Research Letters*, doi:10.1029/98gl01855.
Wigley, T.M.L., 2018: The Paris warming targets: emissions requirements and sea level consequences. *Climatic Change*, **147(1–2)**, 31–45, doi:10.1007/s10584-017-2119-5.
Wigley, T.M.L., C.M. Ammann, B.D. Santer, and S.C.B. Raper, 2005: Effect of climate sensitivity on the response to volcanic forcing. *Journal of Geophysical Research D: Atmospheres*, doi:10.1029/2004jd005557.
Wijffels, S., D. Roemmich, D. Monselesan, J. Church, and J. Gilson, 2016: Ocean temperatures chronicle the ongoing warming of Earth. *Nature Climate Change*, **6(2)**, 116–118, doi:10.1038/nclimate2924.
Wilcox, E.M. et al., 2016: Black carbon solar absorption suppresses turbulence in the atmospheric boundary layer. *Proceedings of the National Academy of Sciences of the United States of America*, **113(42)**, 11794–11799, doi:10.1073/pnas.1525746113.
Wild, M., 2009: Global dimming and brightening: A review. *JOURNAL OF GEOPHYSICAL RESEARCH-ATMOSPHERES*, **114**, doi:10.1029/2008jd011470.
Wild, M., 2012: Enlightening global dimming and brightening. *BULLETIN OF THE AMERICAN METEOROLOGICAL SOCIETY*, **93(1)**, 27–37, doi:10.1175/bams-d-11-00074.1.
Wild, M., 2016: Decadal changes in radiative fluxes at land and ocean surfaces and their relevance for global warming. *Wiley Interdisciplinary Reviews-Climate Change*, **7(1)**, 91–107, doi:10.1002/wcc.372.
Wild, M., 2017: Towards Global Estimates of the Surface Energy Budget. *Current Climate Change Reports*, **3(1)**, 87–97, doi:10.1007/s40641-017-0058-x.
Wild, M., 2020: The global energy balance as represented in CMIP6 climate models. *Climate Dynamics*, **55(3)**, 553–577, doi:10.3929/ethz-b-000418579.
Wild, M. and E. Schmucki, 2011: Assessment of global dimming and brightening in IPCC-AR4/CMIP3 models and ERA40. *Climate Dynamics*, **37(7–8)**, 1671–1688, doi:10.1007/s00382-010-0939-3.
Wild, M., S. Wacker, S. Yang, and A. Sanchez-Lorenzo, 2021: Evidence for Clear-Sky Dimming and Brightening in Central Europe. *Geophysical Research Letters*, **48(6)**, e2020GL092216, doi:10.1029/2020gl092216.
Wild, M. et al., 2013: The global energy balance from a surface perspective. *Climate Dynamics*, **40(11–12)**, 3107–3134, doi:10.1007/s00382-012-1569-8.

ACCEPTED VERSION SUBJECT TO FINAL EDITING

Wild, M. et al., 2015: The energy balance over land and oceans: an assessment based on direct observations and CMIP5 climate models. *Climate Dynamics*, **44(11–12)**, 3393–3429, doi:10.1007/s00382-014-2430-z.
Wild, M. et al., 2019: The cloud-free global energy balance and inferred cloud radiative effects: an assessment based on direct observations and climate models. *CLIMATE DYNAMICS*, doi:10.1007/s00382-018-4413-y.
Willeit, M., A. Ganopolski, and G. Feulner, 2014: Asymmetry and uncertainties in biogeophysical climate-vegetation feedback over a range of CO2 forcings. *Biogeosciences*, **11(1)**, 17–32, doi:10.5194/bg-11-17-2014.
Williams, I.N. and R.T. Pierrehumbert, 2017: Observational evidence against strongly stabilizing tropical cloud feedbacks. *Geophysical Research Letters*, **44(3)**, 1503–1510, doi:10.1002/2016gl072202.
Williams, K.D., W.J. Ingram, and J.M. Gregory, 2008: Time variation of effective climate sensitivity in GCMs. *Journal of Climate*, doi:10.1175/2008jcli2371.1.
Williams, R.G., P. Ceppi, and A. Katavouta, 2020: Controls of the transient climate response to emissions by physical feedbacks, heat uptake and carbon cycling. *Environmental Research Letters*, **15(9)**, 0940c1, doi:10.1088/1748-9326/ab97c9.
Wing, A.A. and K.A. Emanuel, 2014: Physical mechanisms controlling self-aggregation of convection in idealized numerical modeling simulations. *Journal of Advances in Modeling Earth Systems*, **6(1)**, 59–74, doi:10.1002/2013ms000269.
Wing, A.A. et al., 2020: Clouds and Convective Self-Aggregation in a Multimodel Ensemble of Radiative-Convective Equilibrium Simulations. *Journal of Advances in Modeling Earth Systems*, **12(9)**, e2020MS002138, doi:10.1029/2020ms002138.
Winguth, A., C. Shellito, C. Shields, and C. Winguth, 2010: Climate Response at the Paleocene-Eocene Thermal Maximum to Greenhouse Gas Forcing – A Model Study with CCSM3. *Journal of Climate*, **23(10)**, 2562–2584, doi:10.1175/2009jcli3113.1.
Winterstein, F., F. Tanalski, P. Jöckel, M. Dameris, and M. Ponater, 2019: Implication of strongly increased atmospheric methane concentrations for chemistry-climate connections. *Atmospheric Chemistry and Physics*, doi:10.5194/acp-19-7151-2019.
Winton, M., K. Takahashi, and I.M. Held, 2010: Importance of Ocean Heat Uptake Efficacy to Transient Climate Change. *Journal of Climate*, **23(9)**, 2333–2344, doi:10.1175/2009jcli3139.1.
Winton, M. et al., 2013: Influence of ocean and atmosphere components on simulated climate sensitivities. *Journal of Climate*, doi:10.1175/jcli-d-12-00121.1.
Winton, M. et al., 2020: Climate Sensitivity of GFDL's CM4.0. *Journal of Advances in Modeling Earth Systems*, **12(1)**, 1–17, doi:10.1029/2019ms001838.
Witkowski, C.R., J.W.H. Weijers, B. Blais, S. Schouten, and J.S. Sinninghe Damsté, 2018: Molecular fossils from phytoplankton reveal secular PCO2 trend over the Phanerozoic. *Science Advances*, **4(11)**, doi:10.1126/sciadv.aat4556.
WMO, 2018: *Scientific Assessment of Ozone Depletion: 2018*. Global Ozone Research and Monitoring Project – Report No. 58, World Meteorological Organization (WMO), Geneva, Switzerland, 588 pp.
Wohland, J., D. Brayshaw, H. Bloomfield, and M. Wild, 2020: European multidecadal solar variability badly captured in all centennial reanalyses except CERA20C. *Environmental Research Letters*, **15(10)**, 104021, doi:10.1088/1748-9326/aba7e6.
Wood, R. and C.S. Bretherton, 2006: On the relationship between stratiform low cloud cover and lower-tropospheric stability. *Journal of Climate*, doi:10.1175/jcli3988.1.
Woods, C. and R. Caballero, 2016: The role of moist intrusions in winter arctic warming and sea ice decline. *Journal of Climate*, doi:10.1175/jcli-d-15-0773.1.
Wyant, M.C. et al., 2006: A comparison of low-latitude cloud properties and their response to climate change in three AGCMs sorted into regimes using mid-tropospheric vertical velocity. *Clim Dyn*, **27(2–3)**, 261–279, doi:10.1007/s00382-006-0138-4.
Wycech, J.B., E. Gill, B. Rajagopalan, T.M. Marchitto Jr, and P.H. Molnar, 2020: Multiproxy Reduced-Dimension Reconstruction of Pliocene Equatorial Pacific Sea Surface Temperatures. *Paleoceanography and Paleoclimatology*, **35(1)**, e2019PA003685, doi:10.1029/2019pa003685.
Xia, Y., Y. Hu, and Y. Huang, 2016: Strong modification of stratospheric ozone forcing by cloud and sea-ice adjustments. *Atmospheric Chemistry and Physics*, doi:10.5194/acp-16-7559-2016.
Xia, Y. et al., 2020: Stratospheric Ozone-induced Cloud Radiative Effects on Antarctic Sea Ice. *Advances in Atmospheric Sciences*, doi:10.1007/s00376-019-8251-6.
Xie, B., H. Zhang, Z. Wang, S. Zhao, and Q. Fu, 2016: A Modeling Study of Effective Radiative Forcing and Climate Response Due to Tropospheric Ozone. , **33**, 819–828, doi:10.1007/s00376-016-5193-0.
Xie, S.P. et al., 2010: Global warming pattern formation: Sea surface temperature and rainfall. *Journal of Climate*, doi:10.1175/2009jcli3329.1.
Xu, J., C. Li, H. Shi, Q. He, and L. Pan, 2011: Analysis on the impact of aerosol optical depth on surface solar radiation in the Shanghai megacity, China. *ATMOSPHERIC CHEMISTRY AND PHYSICS*, **11(7)**, 3281–3289, doi:10.5194/acp-11-3281-2011.
Yan, X.-H. et al., 2016: The global warming hiatus: Slowdown or redistribution? *Earth's Future*, **4(11)**, 472–482,

SUBJECT TO FINAL EDITING ACCEPTED VERSION

doi:10.1002/2016ef000417.
Yang, S., X.L. Wang, and M. Wild, 2018: Homogenization and Trend Analysis of the 1958-2016 In Situ Surface Solar Radiation Records in China. *JOURNAL OF CLIMATE*, **31(11)**, 4529–4541, doi:10.1175/jcli-d-17-0891.1.
Yang, S., X.L. Wang, and M. Wild, 2019: Causes of Dimming and Brightening in China Inferred from Homogenized Daily Clear-Sky and All-Sky in situ Surface Solar Radiation Records (1958-2016). *JOURNAL OF CLIMATE*, **32(18)**, 5901–5913, doi:10.1175/jcli-d-18-0666.1.
Yasunari, T.J., R.D. Koster, W.K.M. Lau, and K.-M. Kim, 2015: Impact of snow darkening via dust, black carbon, and organic carbon on boreal spring climate in the Earth system. *Journal of Geophysical Research: Atmospheres*, **120(11)**, 5485–5503, doi:10.1002/2014jd022977.
Yeo, K.L. et al., 2020: The Dimmest State of the Sun. *Geophysical Research Letters*, **47(19)**, doi:10.1029/2020gl090243.
Yoshimori, M., T. Yokohata, and A. Abe-Ouchi, 2009: A Comparison of Climate Feedback Strength between CO2 Doubling and LGM Experiments. *Journal of Climate*, **22(12)**, 3374–3395, doi:10.1175/2009jcli2801.1.
Yoshimori, M., A. Abe-Ouchi, and A. Laîné, 2017: The role of atmospheric heat transport and regional feedbacks in the Arctic warming at equilibrium. *Climate Dynamics*, doi:10.1007/s00382-017-3523-2.
Yoshimori, M., F.H. Lambert, M.J. Webb, and T. Andrews, 2020: Fixed Anvil Temperature Feedback: Positive, Zero, or Negative? *Journal of Climate*, **33(7)**, 2719–2739, doi:10.1175/jcli-d-19-0108.1.
Yoshimori, M., J.C. Hargreaves, J.D. Annan, T. Yokohata, and A. Abe-Ouchi, 2011: Dependency of feedbacks on forcing and climate state in physics parameter ensembles. *Journal of Climate*, **24(24)**, 6440–6455, doi:10.1175/2011jcli3954.1.
You, Q.L. et al., 2013: Decadal variation of surface solar radiation in the Tibetan Plateau from observations, reanalysis and model simulations. *Climate Dynamics*, **40(7–8)**, 2073–2086, doi:10.1007/s00382-012-1383-3.
Yu, F. and G. Luo, 2014: Effect of solar variations on particle formation and cloud condensation nuclei. *Environmental Research Letters*, **9(4)**, doi:10.1088/1748-9326/9/4/045004.
Yu, L., 2019: Global Air-Sea Fluxes of Heat, Fresh Water, and Momentum: Energy Budget Closure and Unanswered Questions. *Annual Review of Marine Science*, **11**, 227–248, doi:10.1146/annurev-marine-010816-060704.
Yuan, T., L.A. Remer, and H. Yu, 2011: Microphysical, macrophysical and radiative signatures of volcanic aerosols in trade wind cumulus observed by the A-Train. *Atmospheric Chemistry and Physics*, **11(14)**, 7119–7132, doi:10.5194/acp-11-7119-2011.
Zaehle, S., C.D. Jones, B. Houlton, J.F. Lamarque, and E. Robertson, 2015: Nitrogen availability reduces CMIP5 projections of twenty-first-century land carbon uptake. *Journal of Climate*, doi:10.1175/jcli-d-13-00776.1.
Zaliapin, I. and M. Ghil, 2010: Nonlinear Processes in Geophysics Another look at climate sensitivity. *Nonlin. Processes Geophys*, **17**, 113–122, doi:10.5194/npg-17-113-2010.
Zanatta, M. et al., 2016: A European aerosol phenomenology-5: Climatology of black carbon optical properties at 9 regional background sites across Europe. *Atmospheric Environment*, **145**, 346–364, doi:10.1016/j.atmosenv.2016.09.035.
Zanna, L., S. Khatiwala, J.M. Gregory, J. Ison, and P. Heimbach, 2019: Global reconstruction of historical ocean heat storage and transport. *Proceedings of the National Academy of Sciences*, **116(4)**, 1126–1131, doi:10.1073/pnas.1808838115.
Zarakas, C.M., A.L.S. Swann, M.M. Laguë, K.C. Armour, and J.T. Randerson, 2020: Plant Physiology Increases the Magnitude and Spread of the Transient Climate Response to CO2 in CMIP6 Earth System Models. *Journal of Climate*, doi:10.1175/jcli-d-20-0078.1.
Zelinka, M.D. and D.L. Hartmann, 2012: Climate feedbacks and their implications for poleward energy flux changes in a warming climate. *Journal of Climate*, doi:10.1175/jcli-d-11-00096.1.
Zelinka, M.D., C. Zhou, and S.A. Klein, 2016: Insights from a refined decomposition of cloud feedbacks. *Geophysical Research Letters*, **43**, 9259–9269, doi:10.1002/2016gl069917.
Zelinka, M.D., T. Andrews, P.M. Forster, and K.E. Taylor, 2014: Quantifying components of aerosol-cloud-radiation interactions in climate models. *Journal of Geophysical Research: Atmospheres*, **119(12)**, 7599–7615, doi:10.1002/2014jd021710.
Zelinka, M.D. et al., 2018: Drivers of the Low-Cloud Response to Poleward Jet Shifts in the North Pacific in Observations and Models. *Journal of Climate*, **31(19)**, 7925–7947, doi:10.1175/jcli-d-18-0114.1.
Zelinka, M.D. et al., 2020: Causes of higher climate sensitivity in CMIP6 models. *Geophysical Research Letters*, **46**, 2019GL085782, doi:10.1029/2019gl085782.
Zhai, C., J.H. Jiang, and H. Su, 2015: Long-term cloud change imprinted in seasonal cloud variation: More evidence of high climate sensitivity. *Geophysical Research Letters*, **42(20)**, 8729–8737, doi:10.1002/2015gl065911.
Zhang, C. et al., 2018: CAUSES: Diagnosis of the Summertime Warm Bias in CMIP5 Climate Models at the ARM Southern Great Plains Site. *JOURNAL OF GEOPHYSICAL RESEARCH-ATMOSPHERES*, **123(6)**, 2968–2992, doi:10.1002/2017jd027200.
Zhang, H., S. Zhao, Z. Wang, X. Zhang, and L. Song, 2016: The updated effective radiative forcing of major anthropogenic aerosols and their effects on global climate at present and in the future. *International Journal of Climatology*, **36(12)**, 4029–4044, doi:10.1002/joc.4613.

ACCEPTED VERSION SUBJECT TO FINAL EDITING

Zhang, M. and Y. Huang, 2014: Radiative Forcing of Quadrupling CO2. *Journal of Climate*, **27(7)**, 2496–2508, doi:10.1175/jcli-d-13-00535.1.
Zhang, R., H. Wang, Q. Fu, P.J. Rasch, and X. Wang, 2019: Unraveling driving forces explaining significant reduction in satellite-inferred Arctic surface albedo since the 1980s. *Proceedings of the National Academy of Sciences*, doi:10.1073/pnas.1915258116.
Zhang, R. et al., 2018: Local Radiative Feedbacks Over the Arctic Based on Observed Short-Term Climate Variations. *Geophysical Research Letters*, **45(11)**, 5761–5770, doi:10.1029/2018gl077852.
Zhang, W. et al., 2018: Self-Amplifying Feedbacks Accelerate Greening and Warming of the Arctic. *Geophysical Research Letters*, **45(14)**, 7102–7111, doi:10.1029/2018gl077830.
Zhang, X.T., S.L. Liang, M. Wild, and B. Jiang, 2015: Analysis of surface incident shortwave radiation from four satellite products. *Remote Sensing of Environment*, **165**, 186–202, doi:10.1016/j.rse2015.05.015.
Zhang, Y.G., M. Pagani, and Z. Liu, 2014: A 12-Million-Year Temperature History of the Tropical Pacific Ocean. *Science*, **344(6179)**, 84 LP – 87, doi:10.1126/science.1246172.
Zhang, Z. et al., 2021: Mid-Pliocene Atlantic Meridional Overturning Circulation simulated in PlioMIP2. *Climate of the Past*, **17(1)**, 529–543, doi:10.5194/cp-17-529-2021.
Zhao, B. et al., 2018: Impact of aerosols on ice crystal size. *Atmospheric Chemistry and Physics*, **18(2)**, 1065–1078, doi:10.5194/acp-18-1065-2018.
Zhao, M. et al., 2015: Uncertainty in Model Climate Sensitivity Traced to Representations of Cumulus Precipitation Microphysics. *Journal of Climate*, **29(2)**, 543–560, doi:10.1175/jcli-d-15-0191.1.
Zhao, S. and K. Suzuki, 2019: Differing Impacts of Black Carbon and Sulfate Aerosols on Global Precipitation and the ITCZ Location via Atmosphere and Ocean Energy Perturbations. *Journal of Climate*, **32(17)**, 5567–5582, doi:10.1175/jcli-d-18-0616.1.
Zhou, C., M.D. Zelinka, and S.A. Klein, 2016: Impact of decadal cloud variations on the Earth's energy budget. *Nature Geoscience*, **9(12)**, 871–874, doi:10.1038/ngeo2828.
Zhou, C., K. Wang, and Q. Ma, 2017a: Evaluation of Eight Current Reanalyses in Simulating Land Surface Temperature from 1979 to 2003 in China. *Journal of Climate*, **30(18)**, 7379–7398, doi:10.1175/jcli-d-16-0903.1.
Zhou, C., M.D. Zelinka, and S.A. Klein, 2017b: Analyzing the dependence of global cloud feedback on the spatial pattern of sea surface temperature change with a Green's function approach. *Journal of Advances in Modeling Earth Systems*, **9(5)**, 2174–2189, doi:10.1002/2017ms001096.
Zhou, C., Y. He, and K. Wang, 2018a: On the suitability of current atmospheric reanalyses for regional warming studies over China. *ATMOSPHERIC CHEMISTRY AND PHYSICS*, **18(11)**, 8113–8136, doi:10.5194/acp-18-8113-2018.
Zhou, C., M.D. Zelinka, A.E. Dessler, and S.A. Klein, 2015: The relationship between interannual and long-term cloud feedbacks. *Geophysical Research Letters*, doi:10.1002/2015gl066698.
Zhou, C., H. Zhang, S. Zhao, and J. Li, 2017c: Simulated effects of internal mixing of anthropogenic aerosols on the aerosol–radiation interaction and global temperature. *International Journal of Climatology*, **37**, 972–986, doi:10.1002/joc.5050.
Zhou, C., H. Zhang, S. Zhao, and J. Li, 2018b: On Effective Radiative Forcing of Partial Internally and Externally Mixed Aerosols and Their Effects on Global Climate. *Journal of Geophysical Research: Atmospheres*, **123(1)**, 401–423, doi:10.1002/2017jd027603.
Zhou, C., A.E. Dessler, M.D. Zelinka, P. Yang, and T. Wang, 2014: Cirrus feedback on interannual climate fluctuations. *Geophysical Research Letters*, **41(24)**, 9166–9173, doi:10.1002/2014gl062095.
Zhu, J. and J.E. Penner, 2020: Indirect Effects of Secondary Organic Aerosol on Cirrus Clouds. *Journal of Geophysical Research: Atmospheres*, doi:10.1029/2019jd032233.
Zhu, J. and C.J. Poulsen, 2021: Last Glacial Maximum (LGM) climate forcing and ocean dynamical feedback and their implications for estimating climate sensitivity. *Climate of the Past*, **17(1)**, 253–267, doi:10.5194/cp-17-253-2021.
Zhu, J., C.J. Poulsen, and J.E. Tierney, 2019a: Simulation of Eocene extreme warmth and high climate sensitivity through cloud feedbacks. *Science Advances*, **5(9)**, doi:10.1126/sciadv.aax1874.
Zhu, J., C.J. Poulsen, and B.L. Otto-Bliesner, 2020: High climate sensitivity in CMIP6 model not supported by paleoclimate. *Nature Climate Change*, **10(5)**, 378–379, doi:10.1038/s41558-020-0764-6.
Zhu, J. et al., 2019b: Decrease in radiative forcing by organic aerosol nucleation, climate, and land use change. *Nature Communications*, doi:10.1038/s41467-019-08407-7.
Zhu, J. et al., 2021: Assessment of Equilibrium Climate Sensitivity of the Community Earth System Model Version 2 Through Simulation of the Last Glacial Maximum. *Geophysical Research Letters*, **48(3)**, e2020GL091220, doi:10.1029/2020gl091220.
Zhu, Y., D. Rosenfeld, and Z. Li, 2018: Under What Conditions Can We Trust Retrieved Cloud Drop Concentrations in Broken Marine Stratocumulus? *Journal of Geophysical Research: Atmospheres*, **123(16)**, 8754–8767, doi:10.1029/2017jd028083.
Zickfeld, K., S. Solomon, and D.M. Gilford, 2017: Centuries of thermal sea-level rise due to anthropogenic emissions

ACCEPTED VERSION SUBJECT TO FINAL EDITING

of short-lived greenhouse gases.. *Proceedings of the National Academy of Sciences of the United States of America*, **114(4)**, 657–662, doi:10.1073/pnas.1612066114.

ACCEPTED VERSION
SUBJECT TO FINAL EDITING

Figures

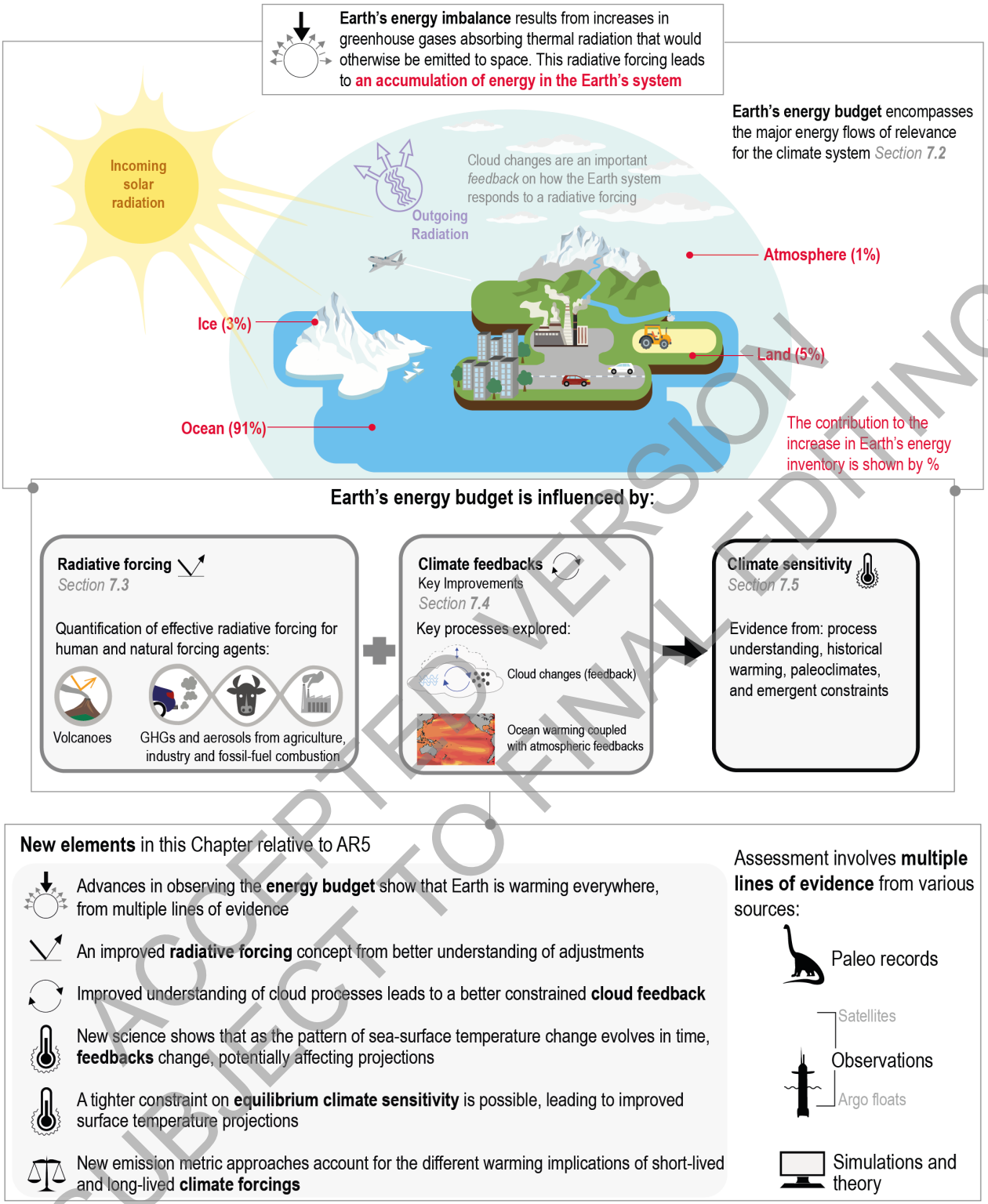
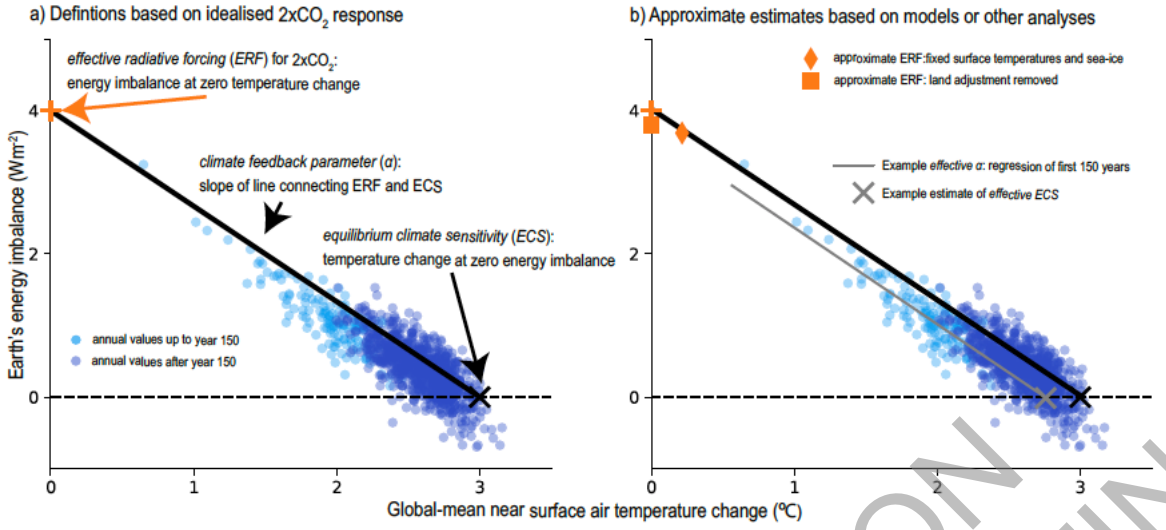


Figure 7.1: A visual abstract of the chapter, illustrating why the Earth's energy budget matters and how it relates to the underlying chapter assessment. The methods used to assess processes and key new findings relative to AR5 are highlighted.

ACCEPTED VERSION SUBJECT TO FINAL EDITING



Box 7.1, Figure 1: Schematics of the forcing-feedback framework adopted within the assessment, following Equation 7.1. Illustrated is how the Earth's TOA net energy flux might evolve for a hypothetical doubling of atmospheric CO_2 concentration above preindustrial levels, where an initial positive energy imbalance (energy entering the Earth system, shown on the y-axis) is gradually restored towards equilibrium as the surface temperature warms (shown on the x-axis). a) illustrates the definitions of ERF for the special case of a doubling of atmospheric CO_2 concentration, the feedback parameter and the ECS. b) illustrates how approximate estimates of these metrics are made within the chapter and how these approximations might relate to the exact definitions adopted in panel a).

ACCEPTED VERSION SUBJECT TO FINAL EDITING

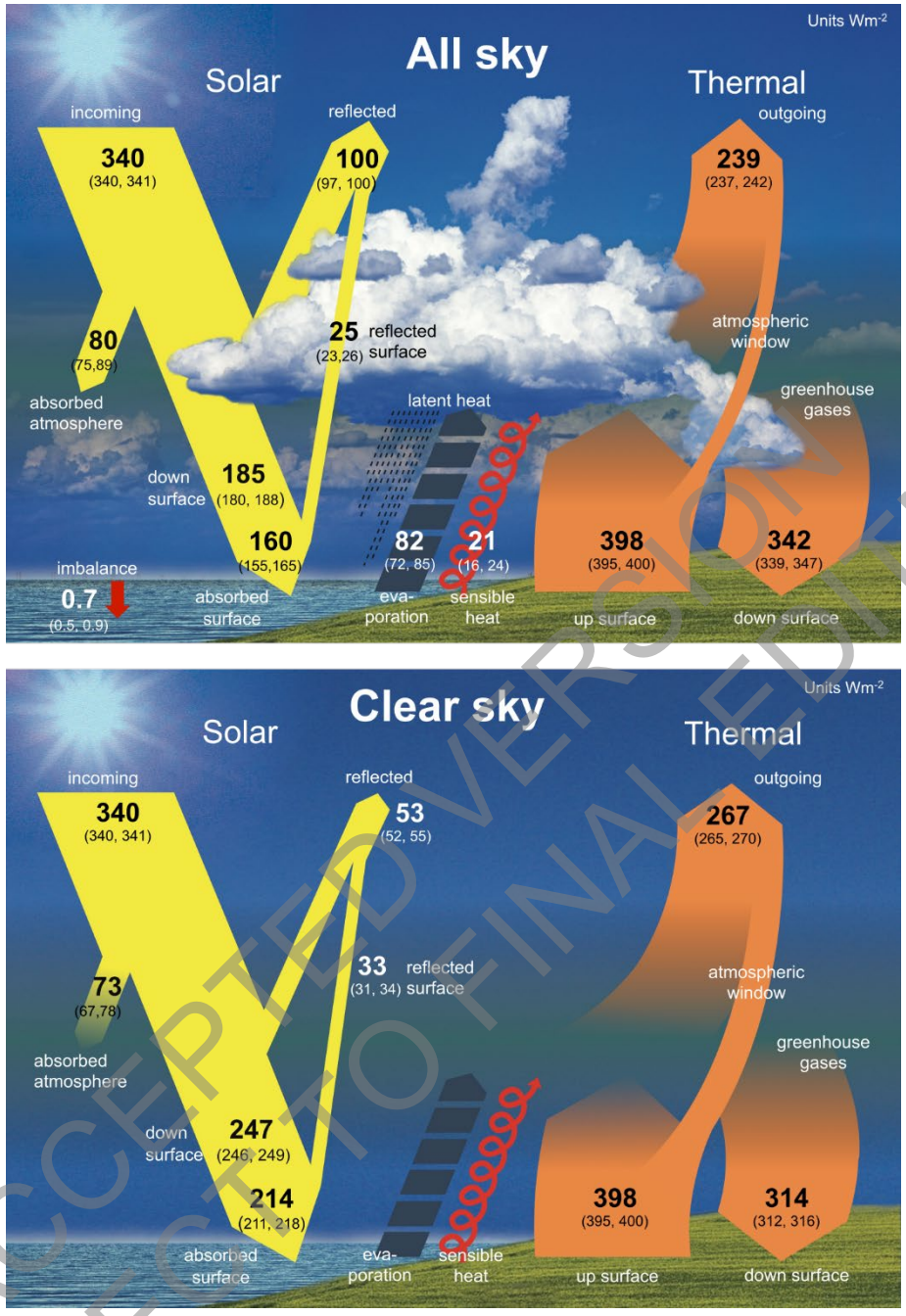
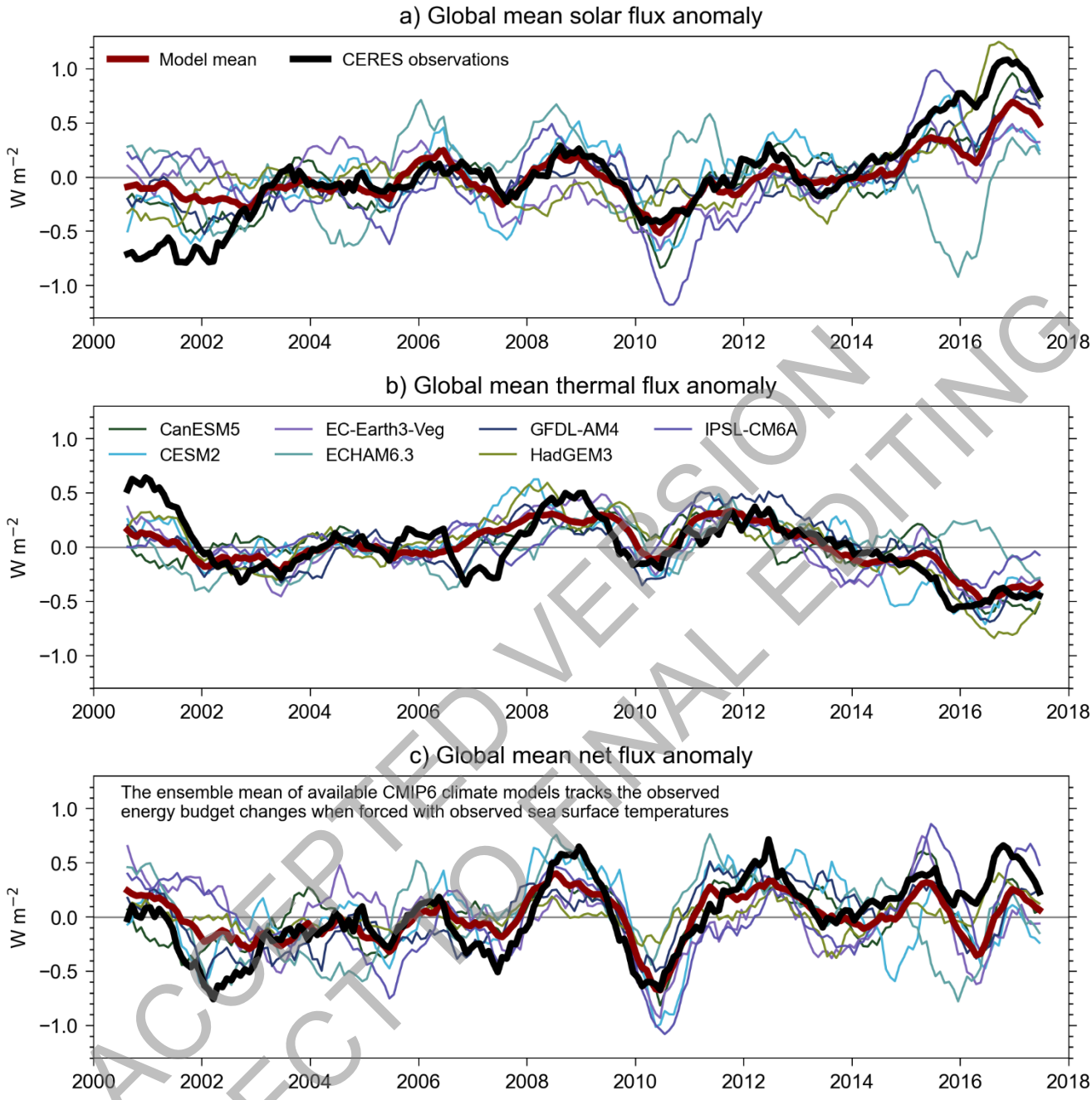


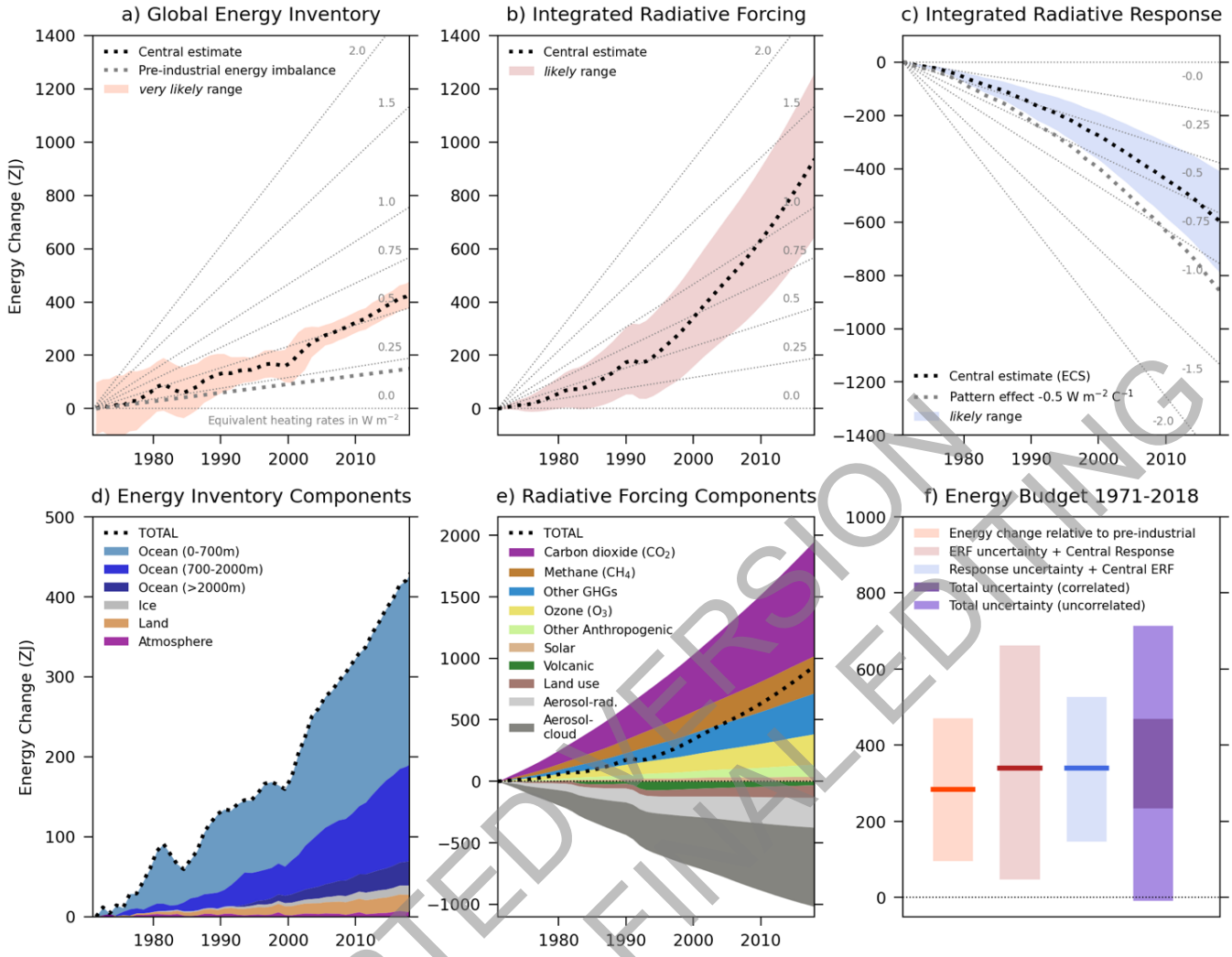
Figure 7.2: Schematic representation of the global mean energy budget of the Earth (upper panel), and its equivalent without considerations of cloud effects (lower panel). Numbers indicate best estimates for the magnitudes of the globally averaged energy balance components in W m^{-2} together with their uncertainty ranges in parentheses (5–95 % confidence range), representing climate conditions at the beginning of the 21st century. Note that the cloud-free energy budget shown in the lower panel is not the one that Earth would achieve in equilibrium when no clouds could form. It rather represents the global mean fluxes as determined solely by removing the clouds but otherwise retaining the entire atmospheric structure. This enables the quantification of the effects of clouds on the Earth energy budget and corresponds to the way clear-sky fluxes are calculated in climate models. Thus, the cloud-free energy budget is not closed and therefore the sensible and latent heat fluxes are not quantified in the lower panel. Adapted from Wild et al. (2015, 2019).

ACCEPTED VERSION SUBJECT TO FINAL EDITING



ACCEPTED VERSION SUBJECT TO FINAL EDITING

Figure 7.3: Anomalies in global mean all-sky TOA fluxes from EBAF Ed4.0 (solid black lines) and various CMIP6 climate models (coloured lines) in terms of (a) reflected solar, (b) emitted thermal and (c) net TOA fluxes. The multi-model means are additionally depicted as dotted black lines. Model fluxes stem from simulations driven with prescribed SSTs and all known anthropogenic and natural forcings. Shown are anomalies of 12-month running means. All flux anomalies are defined as positive downwards, consistent with the sign convention used throughout this chapter. The correlations between the multi-model means (dotted black lines) and the CERES records (solid black lines) for 12-month running means are 0.85, 0.73 and 0.81 for the global mean reflected solar, outgoing thermal and net TOA radiation, respectively. Adapted from Loeb et al. (2020). Further details on data sources and processing are available in the chapter data table (Table 7.SM.14).



Box 7.2, Figure 1: Estimates of the net cumulative energy change (ZJ = 10^{21} Joules) for the period 1971–2018 associated with: (a) observations of changes in the Global Energy Inventory (b) Integrated Radiative Forcing; (c) Integrated Radiative Response. Black dotted lines indicate the central estimate with *likely* and *very likely* ranges as indicated in the legend. The grey dotted lines indicate the energy change associated with an estimated pre-industrial Earth energy imbalance of 0.2 W m^{-2} (panel a) and an illustration of an assumed pattern effect of –0.5 W m^{-2} $°C^{-1}$ (panel c). Background grey lines indicate equivalent heating rates in W m^{-2} per unit area of Earth's surface. Panels (d) and (e) show the breakdown of components, as indicated in the legend, for the Global Energy Inventory and Integrated Radiative Forcing, respectively. Panel (f) shows the Global Energy Budget assessed for the period 1971–2018, i.e. the consistency between the change in the Global Energy Inventory relative to pre-industrial and the implied energy change from Integrated Radiative Forcing plus Integrated Radiative Response under a number of different assumptions, as indicated in the figure legend, including assumptions of correlated and uncorrelated uncertainties in Forcing plus Response. Shading represents the *very likely* range for observed energy change relative to pre-industrial and *likely* range for all other quantities. Forcing and Response timeseries are expressed relative to a baseline period of 1850–1900. Further details on data sources and processing are available in the chapter data table (Table 7.SM.14).

ACCEPTED VERSION SUBJECT TO FINAL EDITING

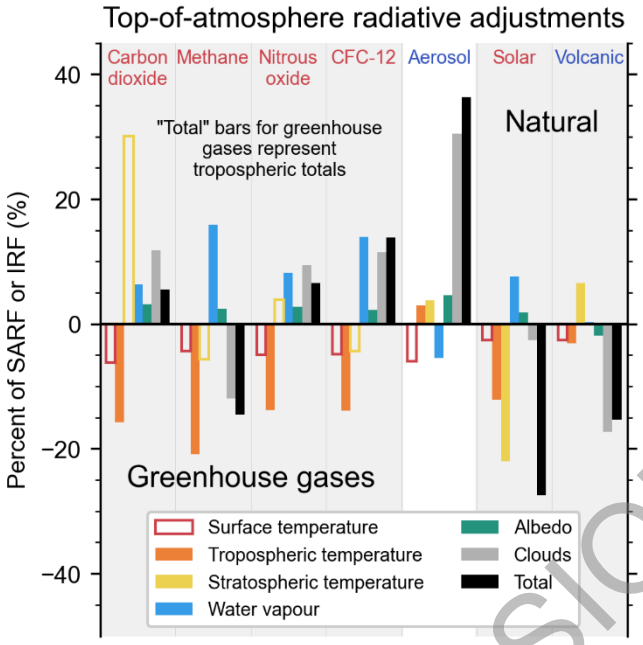


Figure 7.4: Radiative adjustments at top of atmosphere for seven different climate drivers as a proportion of forcing. Tropospheric temperature (orange), stratospheric temperature (yellow), water vapour (blue), surface albedo (green), clouds (grey) and the total adjustment (black) is shown. For the greenhouse gases (carbon dioxide, methane, nitrous oxide, CFC-12) the adjustments are expressed as a percentage of SARF, whereas for aerosol, solar and volcanic forcing they are expressed as a percentage of IRF. Land surface temperature response (outline red bar) is shown, but included in the definition of forcing. Data from Smith et al. (2018b) for carbon dioxide and methane, Smith et al. (2018b) and Gray et al. (2009) for solar, Hodnebrog et al. (2020b) for nitrous oxide and CFC-12, Smith et al. (2020a) for aerosol, and Marshall et al. (2020) for volcanic. Further details on data sources and processing are available in the chapter data table (Table 7.SM.14).

ACCEPTED VERSION SUBJECT TO FINAL EDITING

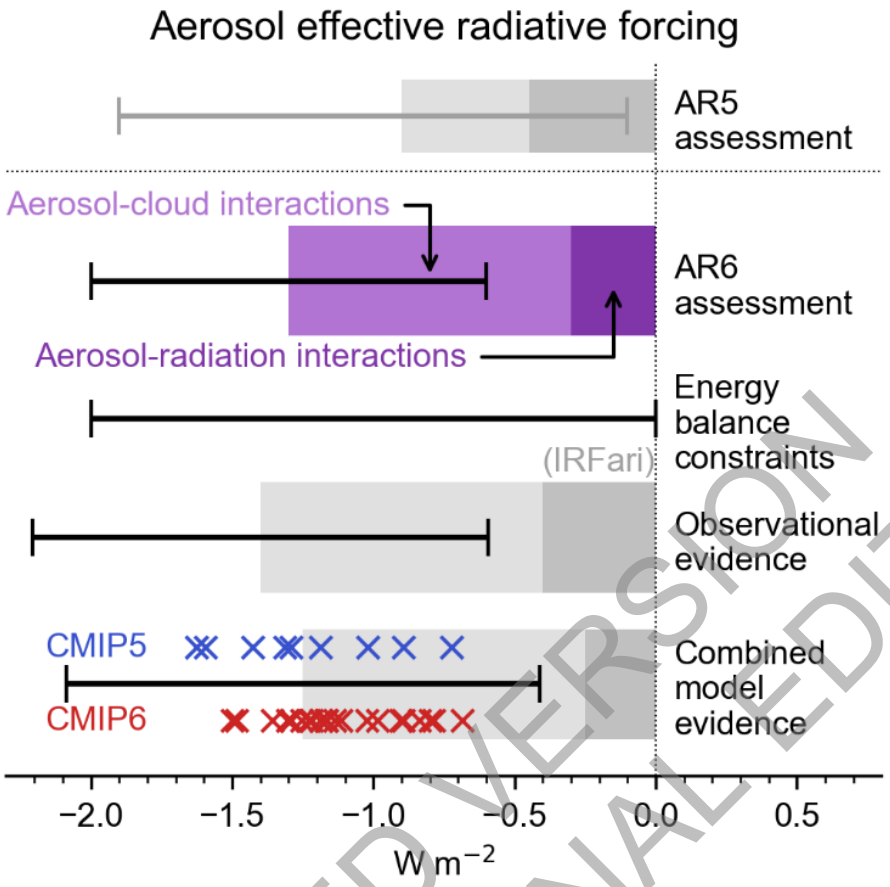


Figure 7.5: **Net aerosol effective radiative forcing from different lines of evidence.** The headline AR6 assessment of –1.3 [–2.0 to –0.6] W m^{-2} is highlighted in purple for 1750–2014 and compared to the AR5 assessment of –0.9 [–1.9 to –0.1] W m^{-2} for 1750–2011. The evidence comprising the AR6 assessment is shown below this: energy balance constraints [–2 to 0 W m^{-2} with no best estimate], observational evidence from satellite retrievals of –1.4 [–2.2 to –0.6] W m^{-2}, and climate model-based evidence of –1.25 [–2.1 to –0.4] W m^{-2}. Estimates from individual CMIP5 (Zelinka et al., 2014) and CMIP6 (Smith et al., 2020a and Table 7.6) models are depicted by blue and red crosses respectively. For each line of evidence the assessed best-estimate contributions from ERFari and ERFaci are shown with darker and paler shading respectively. The observational assessment for ERFari is taken from the IRFari. Uncertainty ranges are given in black bars for the total aerosol ERF and depict *very likely* ranges. Further details on data sources and processing are available in the chapter data table (Table 7.SM.14).

ACCEPTED VERSION SUBJECT TO FINAL EDITING

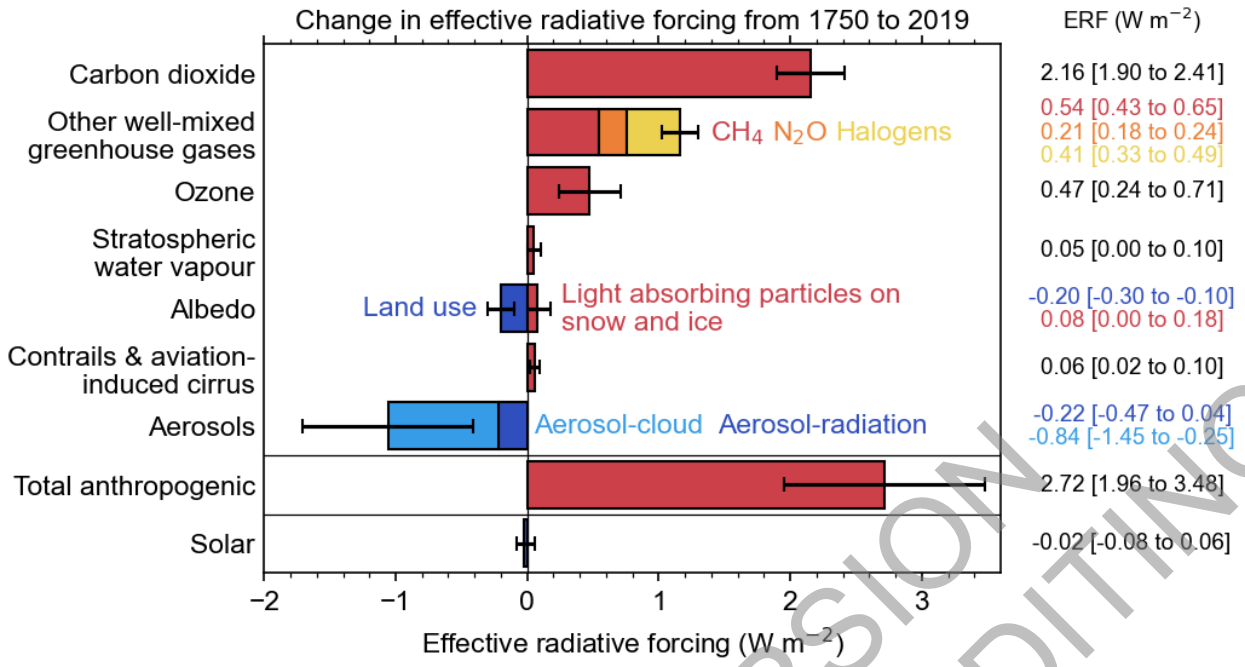


Figure 7.6: Change in effective radiative forcing from 1750 to 2019 by contributing forcing agents (carbon dioxide, other well-mixed greenhouse gases (WMGHGs), ozone, stratospheric water vapour, surface albedo, contrails and aviation-induced cirrus, aerosols, anthropogenic total, and solar). Solid bars represent best estimates, and *very likely* (5–95%) ranges are given by error bars. Non-CO_2 WMGHGs are further broken down into contributions from methane (CH_4), nitrous oxide (N_2O) and halogenated compounds. Surface albedo is broken down into land use changes and light absorbing particles on snow and ice. Aerosols are broken down into contributions from aerosol-cloud interactions (ERFaci) and aerosol-radiation interactions (ERFari). For aerosols and solar, the 2019 single-year values are given (Table 7.8) that differ from the headline assessments in both cases. Volcanic forcing is not shown due to the episodic nature of volcanic eruptions. Further details on data sources and processing are available in the chapter data table (Table 7.SM.14).

ACCEPTED VERSION SUBJECT TO FINAL EDITING

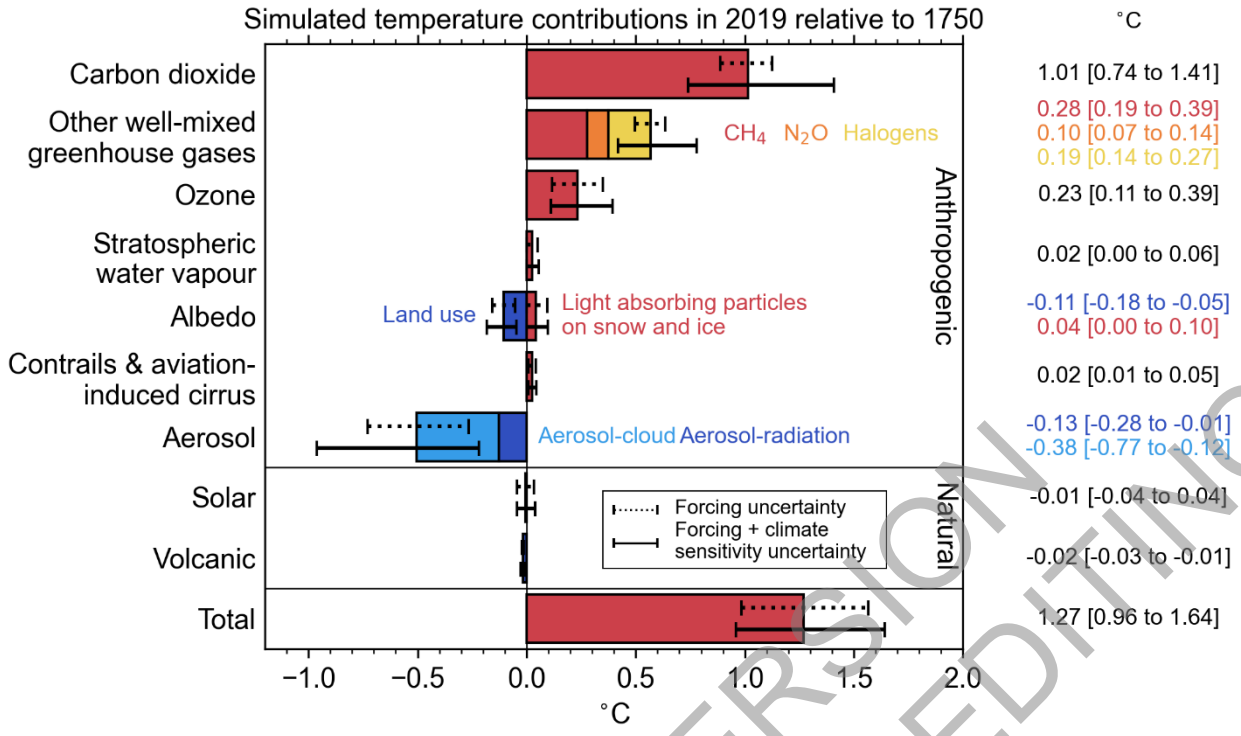


Figure 7.7: The contribution of forcing agents to 2019 temperature change relative to 1750 produced using the two-layer emulator (Supplementary Material 7.SM.2), constrained to assessed ranges for key climate metrics described in Cross-Chapter Box 7.1. The results are from a 2,237-member ensemble. Temperature contributions are expressed for carbon dioxide, other well-mixed greenhouse gases (WMGHGs), ozone, stratospheric water vapour, surface albedo, contrails and aviation-induced cirrus, aerosols, solar, volcanic, and total. Solid bars represent best estimates, and *very likely* (5–95%) ranges are given by error bars. Dashed error bars show the contribution of forcing uncertainty alone, using best estimates of ECS (3.0°C), TCR (1.8°C) and two-layer model parameters representing the CMIP6 multi-model mean. Solid error bars show the combined effects of forcing and climate response uncertainty using the distribution of ECS and TCR from Tables 7.13 and 7.14, and the distribution of calibrated model parameters from 44 CMIP6 models. Non-CO_2 WMGHGs are further broken down into contributions from methane (CH_4), nitrous oxide (N_2O) and halogenated compounds. Surface albedo is broken down into land use changes and light absorbing particles on snow and ice. Aerosols are broken down into contributions from aerosol-cloud interactions (ERFaci) and aerosol-radiation interactions (ERFari). Further details on data sources and processing are available in the chapter data table (Table 7.SM.14).

ACCEPTED VERSION SUBJECT TO FINAL EDITING

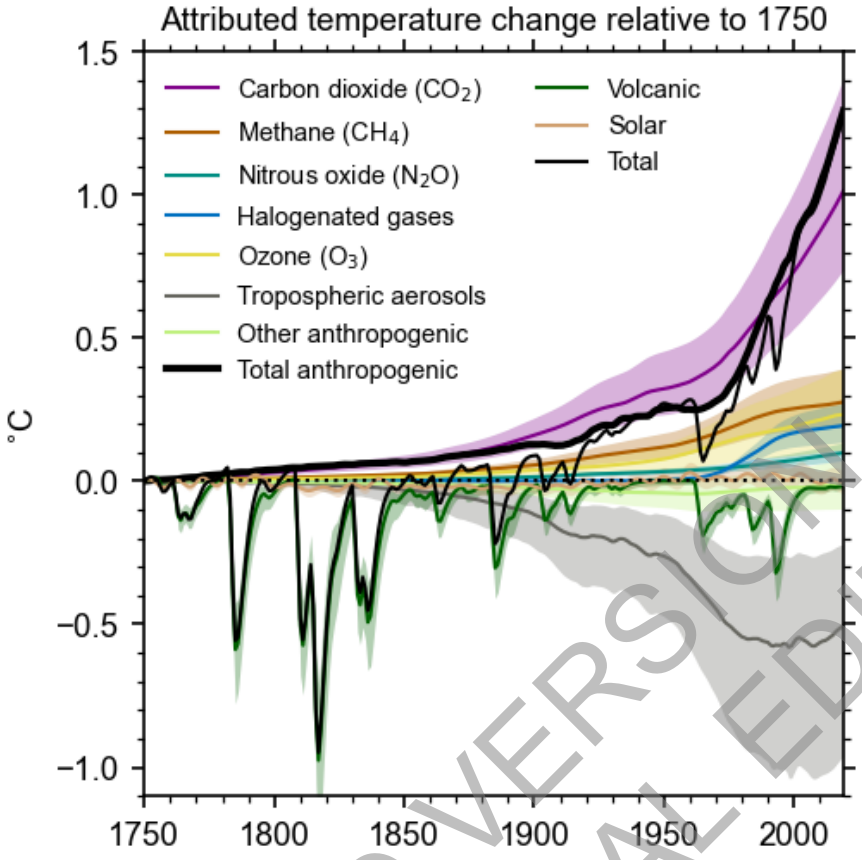
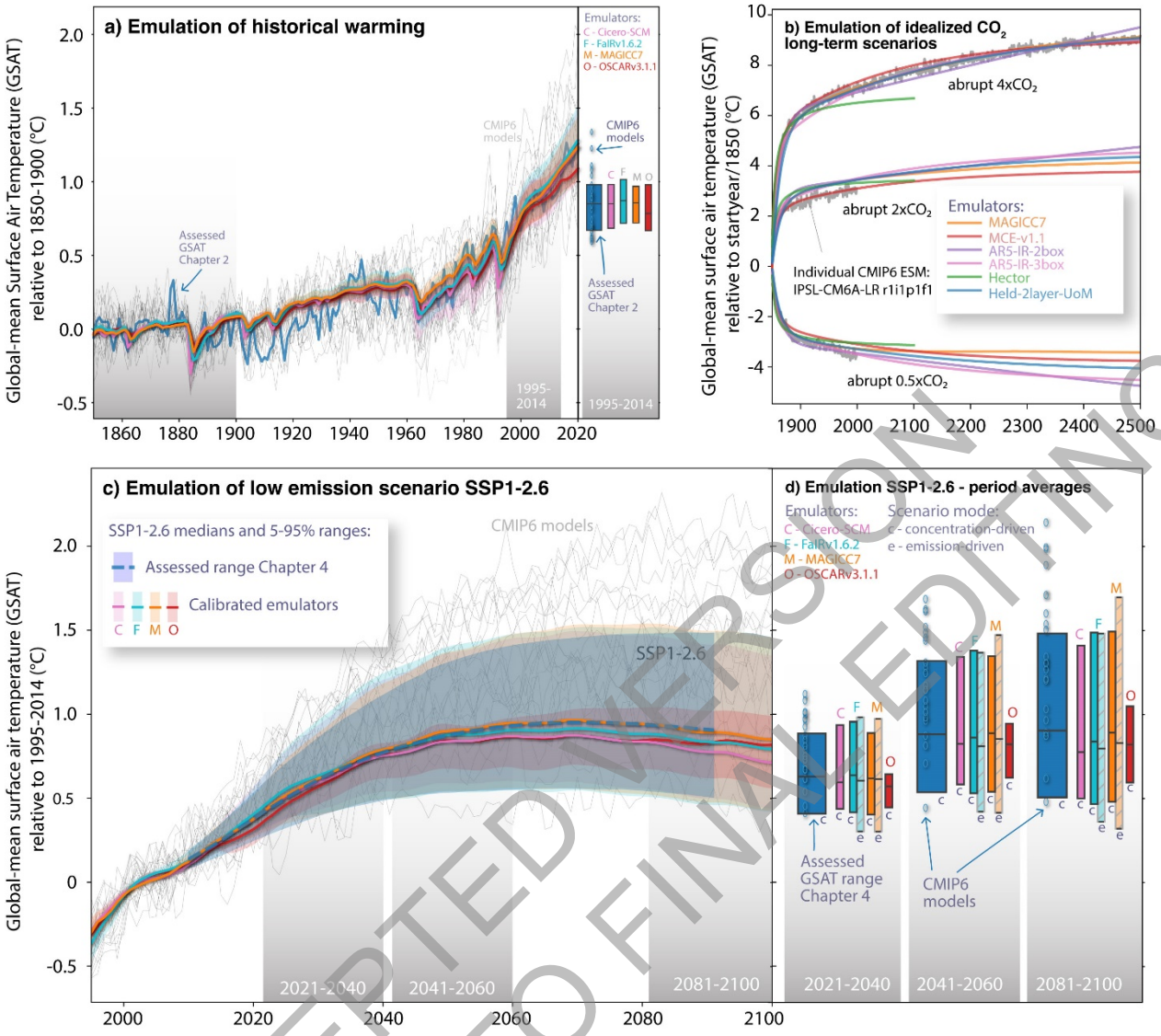


Figure 7.8: Attributed global near-surface air temperature change (GSAT) from 1750 to 2019 produced using the two-layer emulator (Supplementary Material 7.SM.2), forced with ERF derived in this chapter (displayed in Chapter 2, Figure 2.10) and climate response constrained to assessed ranges for key climate metrics described in Cross-Chapter Box 7.1. The results shown are the medians from a 2,237-member ensemble that encompasses uncertainty in forcing and climate response (year-2019 best estimates and uncertainties are shown in Figure 7.7 for several components). Temperature contributions are expressed for carbon dioxide, methane, nitrous oxide, other well-mixed greenhouse gases (WMGHGs), ozone, aerosols, other anthropogenic forcings, total anthropogenic, solar, volcanic, and total. Shaded uncertainty bands show *very likely* ranges. Further details on data sources and processing are available in the chapter data table (Table 7.SM.14).

ACCEPTED VERSION SUBJECT TO FINAL EDITING



Cross-Chapter Box 7.1, Figure 1: A comparison between the global-mean surface air temperature response of various calibrated simple climate models, assessed ranges and Earth System Models. The top panels compare the assessed historical GSAT time series (Chapter 2, Section 2.3.1) with four multi-gas emulators calibrated to replicate numerous assessed ranges (Cross-Chapter Box 7.1, Table 2 below) (panel a) and also compares idealized CO_2-only concentration scenario response for one ESM (IPSL CM6A-LR) and multiple emulators which participated in RCMIP Phase 1 (Nicholls et al., 2020) calibrated to that single ESM (panel b). The bottom panels compare this report's assessed ranges for GSAT warming (Chapter 4, Box 4.1) under the multi-gas scenario SSP1-2.6 with the same calibrated emulators as in panel a (panel c and d). For context, a range of CMIP6 ESM results are also shown (thin lines in bottom-left panel c and open circles in bottom-right panel d). Panel b) adapted from Nicholls et al. (2020). Further details on data sources and processing are available in the chapter data table (Table 7.SM.14).

ACCEPTED VERSION SUBJECT TO FINAL EDITING

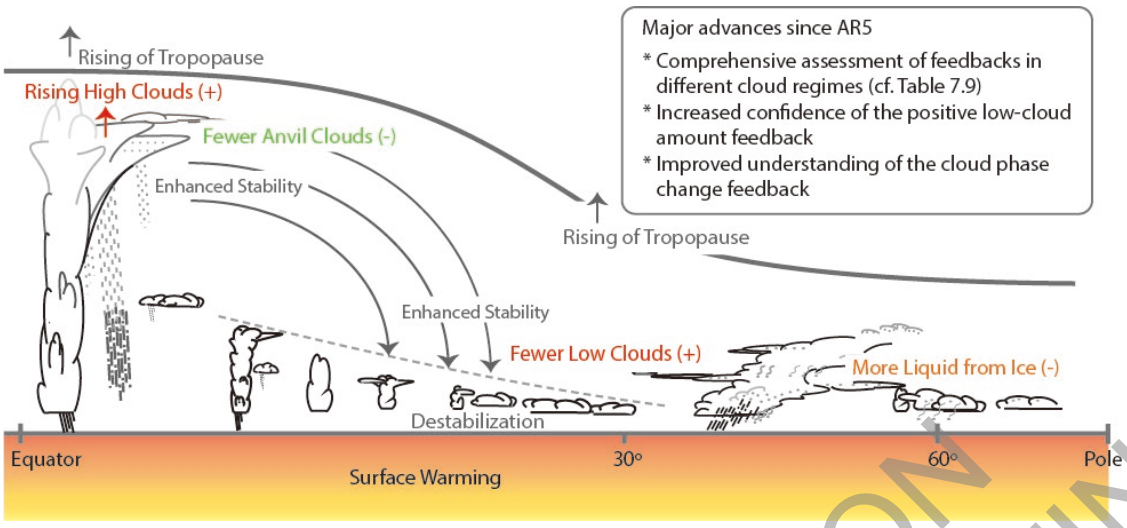


Figure 7.9: Schematic cross section of diverse cloud responses to surface warming from the tropics to polar regions. Thick solid and dashed curves indicate the tropopause and the subtropical inversion layer in the current climate, respectively. Thin grey text and arrows represent robust responses in the thermodynamic structure to greenhouse warming, of relevance to cloud changes. Text and arrows in red, orange and green show the major cloud responses assessed with *high*, *medium* and *low confidence*, respectively, and the sign of their feedbacks to the surface warming is indicated in the parenthesis. Major advances since AR5 are listed in a box.

ACCEPTED VERSION
SUBJECT TO FINAL EDITING

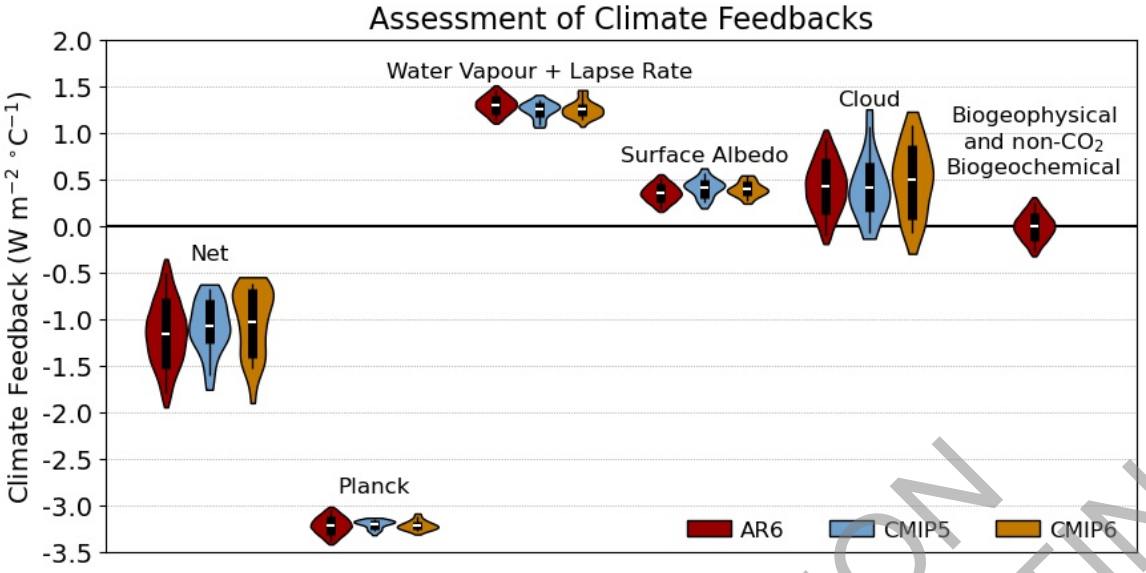


Figure 7.10: Global-mean climate feedbacks estimated in *abrupt4xCO2* simulations of 29 CMIP5 models (light blue) and 49 CMIP6 models (orange), compared with those assessed in this Report (red). Individual feedbacks for CMIP models are averaged across six radiative kernels as computed in Zelinka et al. (2020). The white line, black box and vertical line indicate the mean, 66% and 90% ranges, respectively. The shading represents the probability distribution across the full range of GCM/ESM values and for the 2.5–97.5 percentile range of the AR6 normal distribution. The unit is W m^{-2} °C^{-1}. Feedbacks associated with biogeophysical and non-CO_2 biogeochemical processes are assessed in AR6, but they are not explicitly estimated from GCMs/ESMs in CMIP5 and CMIP6. Further details on data sources and processing are available in the chapter data table (Table 7.SM.14).

ACCEPTED VERSION SUBJECT TO FINAL EDITING

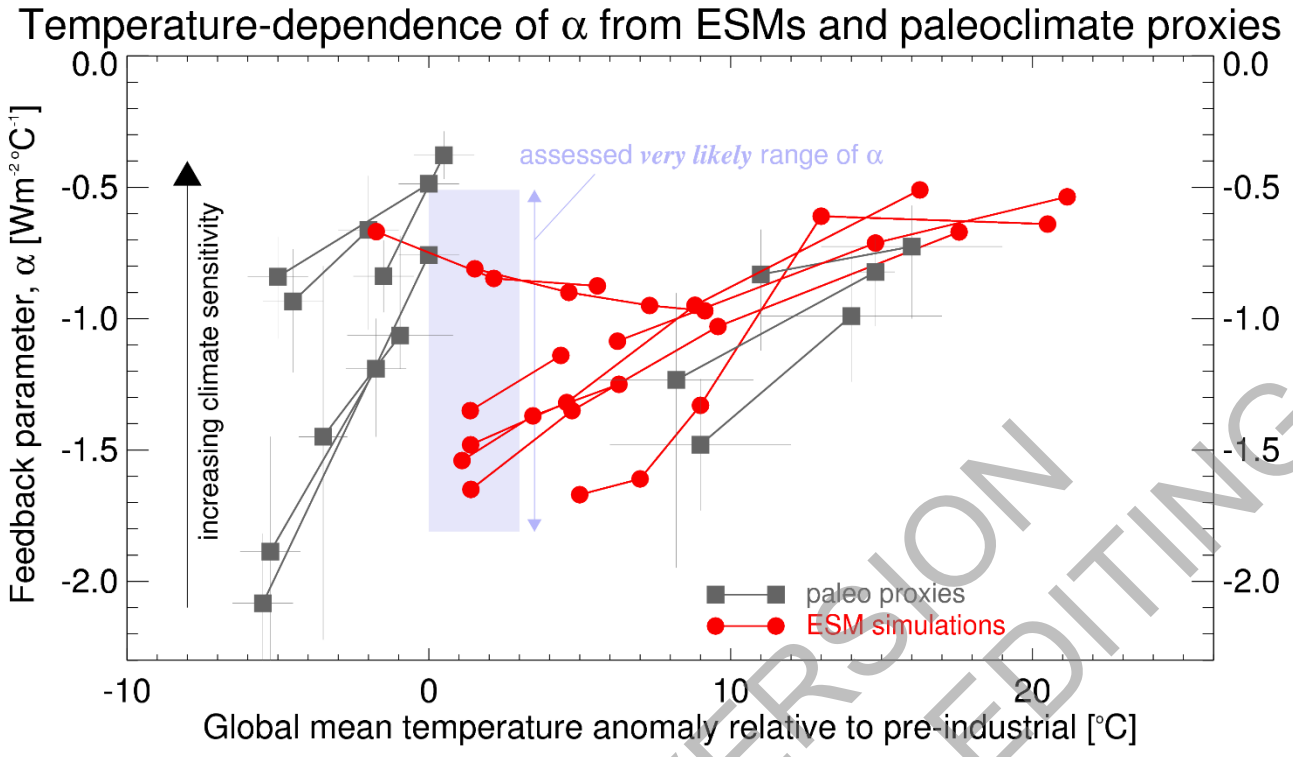


Figure 7.11: Feedback parameter, α (W m^{-2} °C^{-1}), as a function of global mean surface air temperature anomaly relative to preindustrial, for ESM simulations (red circles and lines) (Caballero and Huber, 2013; Jonko et al., 2013; Meraner et al., 2013; Good et al., 2015; Duan et al., 2019; Mauritsen et al., 2019; Stolpe et al., 2019; Zhu et al., 2019), **and derived from paleoclimate proxies (grey squares and lines)** (von der Heydt et al., 2014; Anagnostou et al., 2016, 2020; Friedrich et al., 2016; Royer, 2016; Shaffer et al., 2016; Köhler et al., 2017; Snyder, 2019; Stap et al., 2019). For the ESM simulations, the value on the *x*-axis refers to the average of the temperature before and after the system has equilibrated to a forcing (in most cases a CO_2 doubling), and is expressed as an anomaly relative to an associated pre-industrial global mean temperature from that model. The light blue shaded square extends across the assessed range of α (Table 7.10) on the *y*-axis, and on the *x*-axis extends across the approximate temperature range over which the assessment of α is based (taken as from zero to the assessed central value of ECS (Table 7.13). Further details on data sources and processing are available in the chapter data table (Table 7.SM.14).

ACCEPTED VERSION SUBJECT TO FINAL EDITING

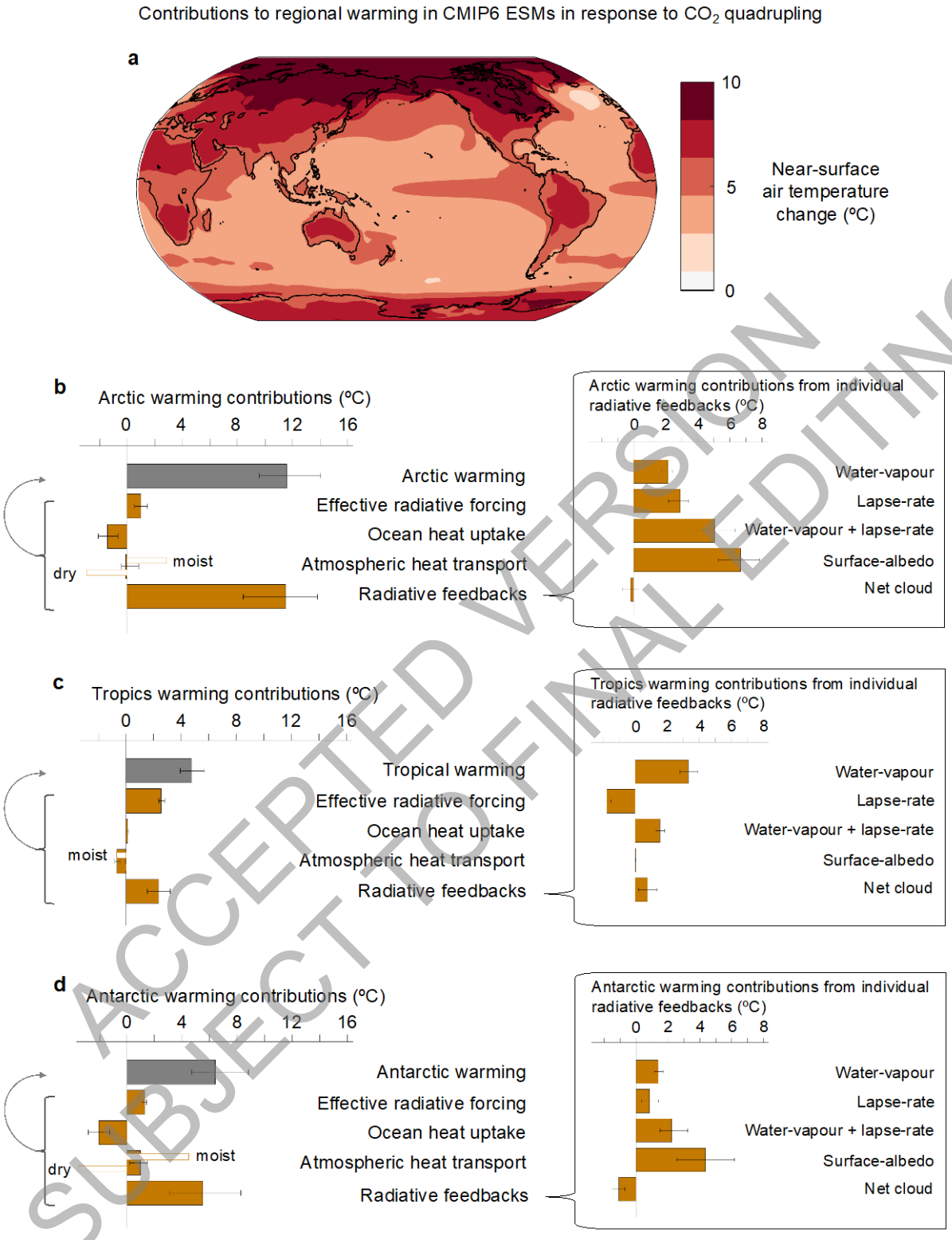
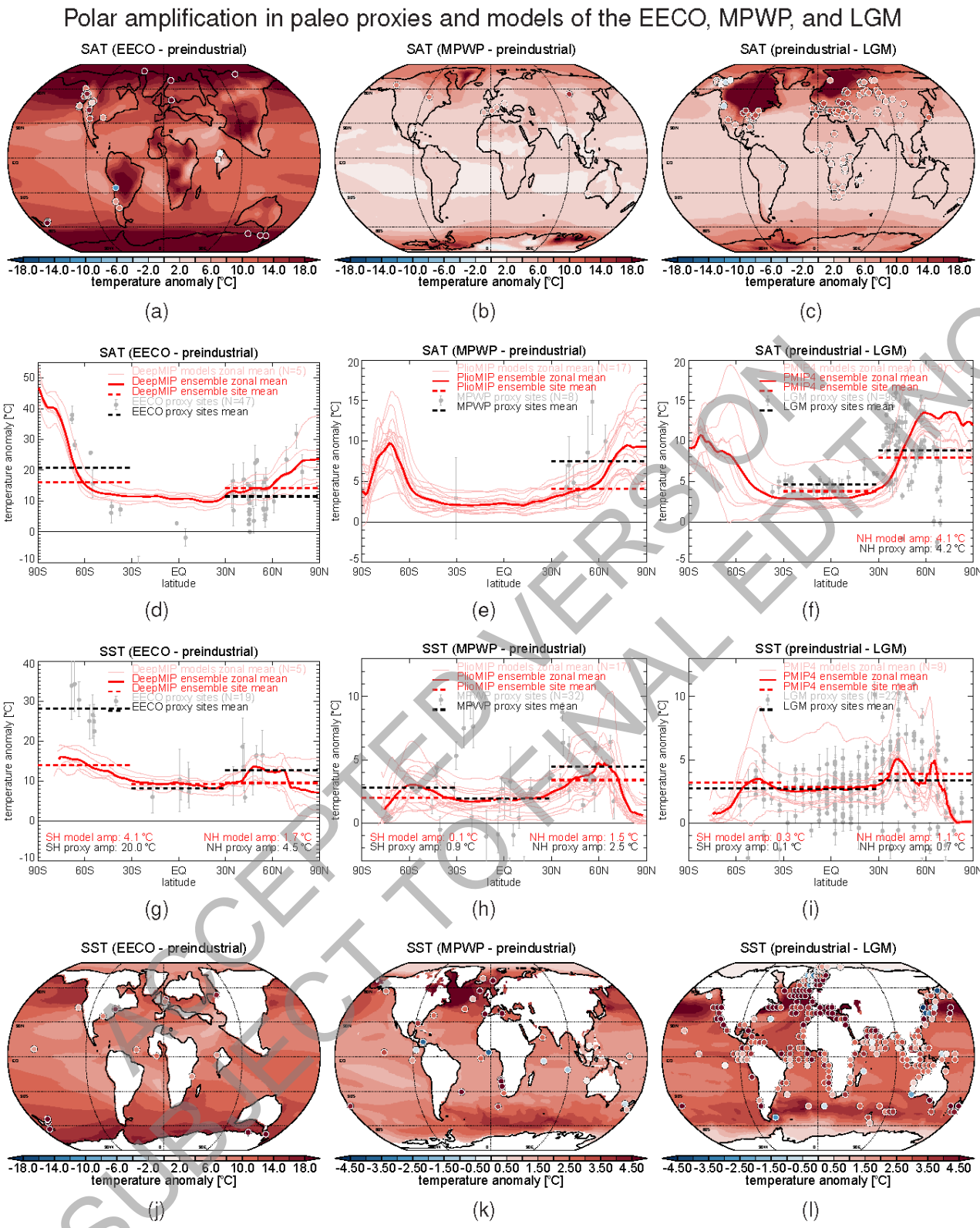


Figure 7.12: Contributions of effective radiative forcing, ocean heat uptake, atmospheric heat transport, and radiative feedbacks to regional surface temperature changes at year 100 of *abrupt4xCO2* simulations of CMIP6 ESMs. (a) Pattern of near-surface air temperature change. (b-d) Contributions to net Arctic (>60°N), tropical (30°S – 30°N), and Antarctic (<60°S) warming calculated by dividing regional-average energy inputs by the magnitude of the regional-average Planck response. The contributions from radiative forcing, changes in moist, dry-static, and total atmospheric energy transport, ocean heat uptake, and radiative feedbacks (orange bars) all sum to the value of net warming (grey bar).

ACCEPTED VERSION SUBJECT TO FINAL EDITING

Inset shows regional warming contributions associated with individual feedbacks, all summing to the total feedback contribution. Uncertainties show the interquartile range (25th and 75th percentiles) across models. The warming contributions (units of °C) for each process are diagnosed by calculating the energy flux (units of W m^{-2}) that each process contributes to the atmosphere over a given region, either at the TOA or surface, then dividing that energy flux by the magnitude of the regional Planck response (around 3.2 W m^{-2} $°C^{-1}$ but varying with region). By construction, the individual warming contributions sum to the total warming in each region. Radiative kernel methods (see Section 7.4.1) are used to decompose the net energy input from radiative feedbacks into contributions from changes in atmospheric water vapour, lapse-rate, clouds, and surface albedo (Zelinka et al. (2020) using the Huang et al. (2017) radiative kernel). The CMIP6 models included are those analysed by Zelinka et al. (2020) and the warming contribution analysis is based on that of Goosse et al. (2018). Further details on data sources and processing are available in the chapter data table (Table 7.SM.14).

ACCEPTED VERSION
SUBJECT TO FINAL EDITING



ACCEPTED VERSION SUBJECT TO FINAL EDITING

Figure 7.13: Polar amplification in paleo proxies and models of the early Eocene climatic optimum (EECO), the mid-Pliocene warm period (MPWP), and the Last Glacial Maximum (LGM). Temperature anomalies compared with pre-industrial (equivalent to CMIP6 simulation *piControl*) are shown for the high-CO_2 EECO and MPWP time periods, and for the low-CO_2 LGM (expressed as pre-industrial minus LGM). (a,b,c) Modelled near-surface air temperature anomalies for ensemble-mean simulations of the (a) EECO (Lunt et al., 2021), (b) MPWP (Haywood et al., 2020; Zhang et al., 2021), and (c) LGM (Kageyama et al., 2021; Zhu et al., 2021). Also shown are proxy near-surface air temperature anomalies (coloured circles). (d,e,f) Proxy near-surface air temperature anomalies (grey circles), including published

uncertainties (grey vertical bars), model ensemble mean zonal mean anomaly (solid red line) for the same model ensembles as in (a,b,c), light red lines show the modelled temperature anomaly for the individual models that make up each ensemble (LGM, N=9; MPWP, N=17; EECO, N=5). Black dashed lines show the average of the proxy values in each latitude bands 90°S to 30°S, 30°S to 30°N, and 30°N to 90°N. Red dashed lines show the same banded average in the model ensemble mean, calculated from the same locations as the proxies. Black and red dashed lines are only shown if there are 5 or more proxy points in that band. Mean differences between the 90°S/N to 30°S/N and 30°S to 30°N bands are quantified for the models and proxies in each plot. Panels (g,h,i) are like panels (d,e,f) but for SST instead of near-surface air temperature. Panels (j,k,l) are like panels (a,b,c) but for SST instead of near-surface air temperature. For the EECO maps (a,j), the anomalies are relative to the zonal mean of the pre-industrial, due to the different continental configuration. Proxy datasets are (a,d) Hollis et al. (2019), (b,e) Salzmann et al. (2013); Vieira et al. (2018), (c,f) Cleator et al. (2020) at the sites defined in Bartlein et al. (2011), (g,j)) Hollis et al. (2019), (h,k) McClymont et al. (2020) (i,l) Tierney et al. (2020b). Where there are multiple proxy estimations at a single site, a mean is taken. Model ensembles are (a,d,g,j) DeepMIP (only model simulations carried out with a mantle-frame paleogeography, and carried out under CO_2 concentrations within the range assessed in Chapter 2, Table 2.2, are shown), (b,e,h,k) PlioMIP, and (c,f,i,l) PMIP4. Further details on data sources and processing are available in the chapter data table (Table 7.SM.14).

ACCEPTED VERSION
SUBJECT TO FINAL EDITING

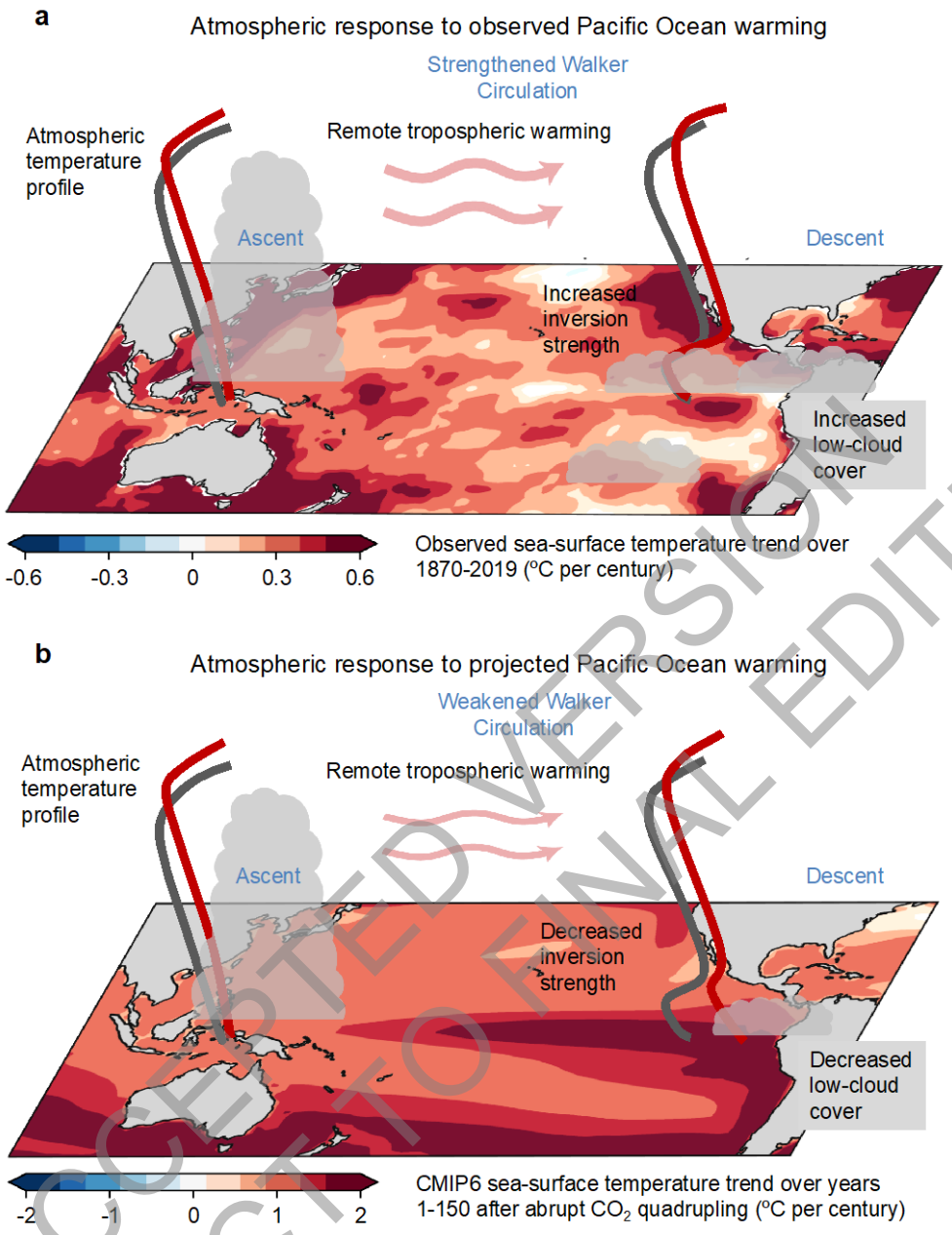


Figure 7.14: Illustration of tropospheric temperature and low-cloud response to observed and projected Pacific Ocean sea-surface temperature trends; adapted from Mauritsen (2016). (a) Atmospheric response to linear sea-surface temperature trend observed over 1870–2019 (HadISST1 dataset; Rayner et al., 2003). (b) Atmospheric response to linear sea-surface temperature trend over 150 years following *abrupt4xCO2* forcing as projected by CMIP6 ESMs (Dong et al., 2020). Relatively large historical warming in the western tropical Pacific has been communicated aloft (a shift from grey to red atmospheric temperature profile), remotely warming the tropical free troposphere and increasing the strength of the inversion in regions of the tropics where warming has been slower, such as the eastern equatorial Pacific. In turn, an increased inversion strength has increased the low-cloud cover (Zhou et al., 2016) causing an anomalously-negative cloud and lapse-rate feedbacks over the historical record (Andrews et al., 2018; Marvel et al., 2018). Relatively large projected warming in the eastern tropical Pacific is trapped near the surface (shift from grey to red atmospheric temperature profile), decreasing the strength of the inversion locally. In turn, a decreased inversion strength combined with surface warming is projected to decrease the low-cloud cover, causing the cloud and lapse-rate feedbacks to become less negative in the future. Further details on data sources and processing are available in the chapter data table (Table 7.SM.14).

ACCEPTED VERSION SUBJECT TO FINAL EDITING

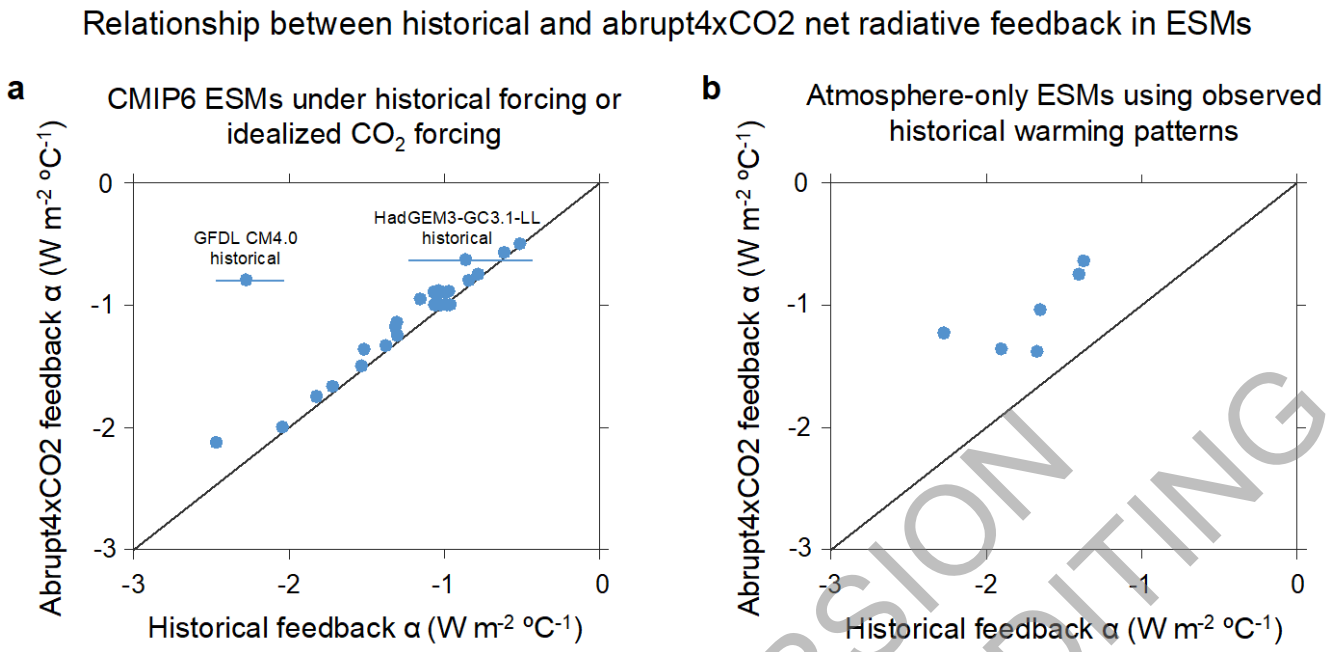


Figure 7.15: Relationship between *historical* and *abrupt4xCO2* net radiative feedbacks in ESMs. (a) Radiative feedbacks in CMIP6 ESMs estimated under historical forcing (values for GFDL CM4.0 and HadGEM3-CG3.1-LL from Winton et al. (2020) and Andrews et al. (2019), respectively); horizontal lines show the range across ensemble members. The other points show effective feedback values for 29 ESMs estimated using regression over the first 50 years of *abrupt4xCO2* simulations as an analogue for historical warming (Dong et al., 2020). (b) Historical radiative feedbacks estimated from atmosphere-only ESMs with prescribed observed sea-surface temperature and sea-ice concentration changes (Andrews et al. 2018) based on a linear regression of global TOA radiation against global near-surface air temperature over the period 1870–2010 (pattern of warming similar to Figure 7.14a) and compared with equilibrium feedbacks in a *abrupt4xCO2* simulations of coupled versions of the same ESMs (pattern of warming similar to Figure 7.14b). In all cases, the equilibrium feedback magnitudes are estimated as CO_2 ERF divided by ECS where ECS is derived from regression over years 1–150 of *abrupt4xCO2* simulations (Box 7.1); similar results are found if the equilibrium feedback is estimated directly from the slope of the linear regression. Further details on data sources and processing are available in the chapter data table (Table 7.SM.14).

ACCEPTED VERSION SUBJECT TO FINAL EDITING

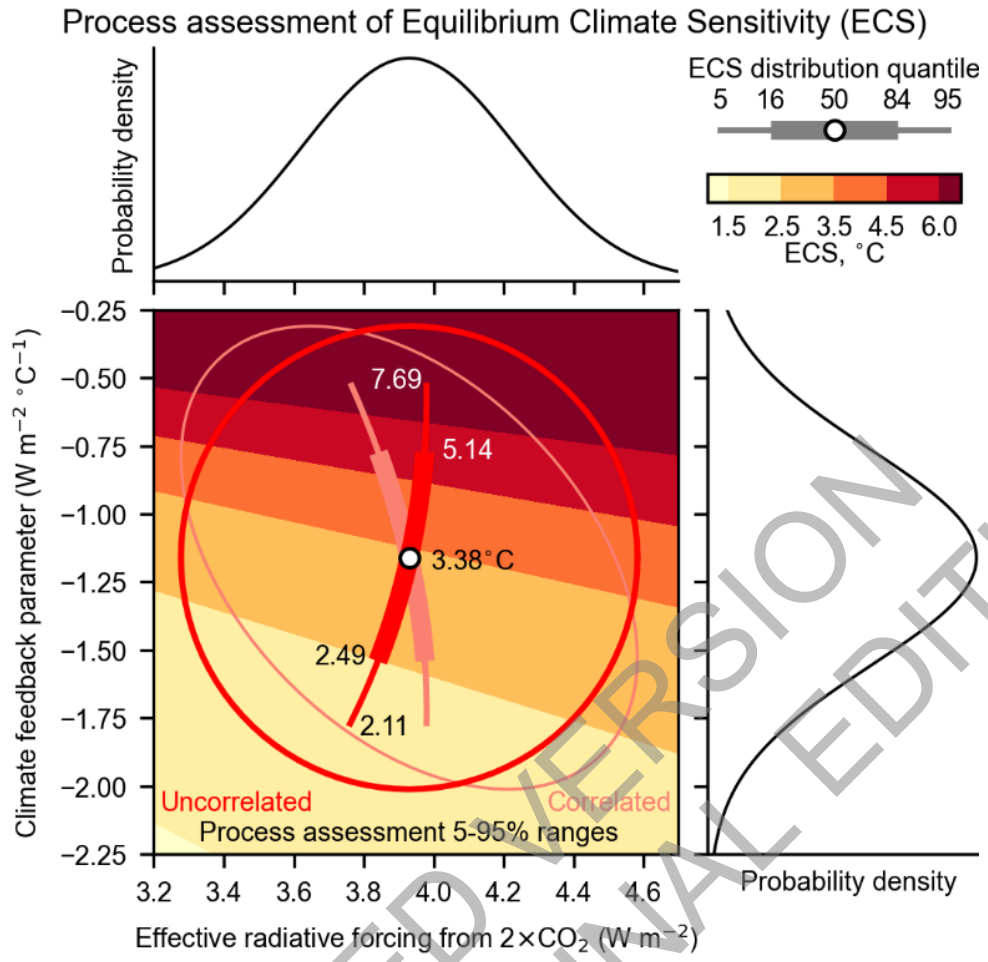


Figure 7.16: Probability distributions of ERF to CO_2 doubling ($\Delta F_{2\times CO2}$, top) and the net climate feedback (α, right), derived from process-based assessments in Sections 7.3.2 and 7.4.2. Middle panel shows the joint probability density function calculated on a two-dimensional plane of $\Delta F_{2\times CO2}$ and α (red), on which the 90% range shown by an ellipse is imposed to the background theoretical values of ECS (colour shading). The white dot, thick and thin curves in the ellipse represent the mean, *likely* and *very likely* ranges of ECS. An alternative estimation of the ECS range (pink) is calculated by assuming that $\Delta F_{2\times CO2}$ and α have a covariance. The assumption about the co-dependence between $\Delta F_{2\times CO2}$ and α does not alter the mean estimate of ECS but affects its uncertainty. Further details on data sources and processing are available in the chapter data table (Table 7.SM.14).

ACCEPTED VERSION SUBJECT TO FINAL EDITING

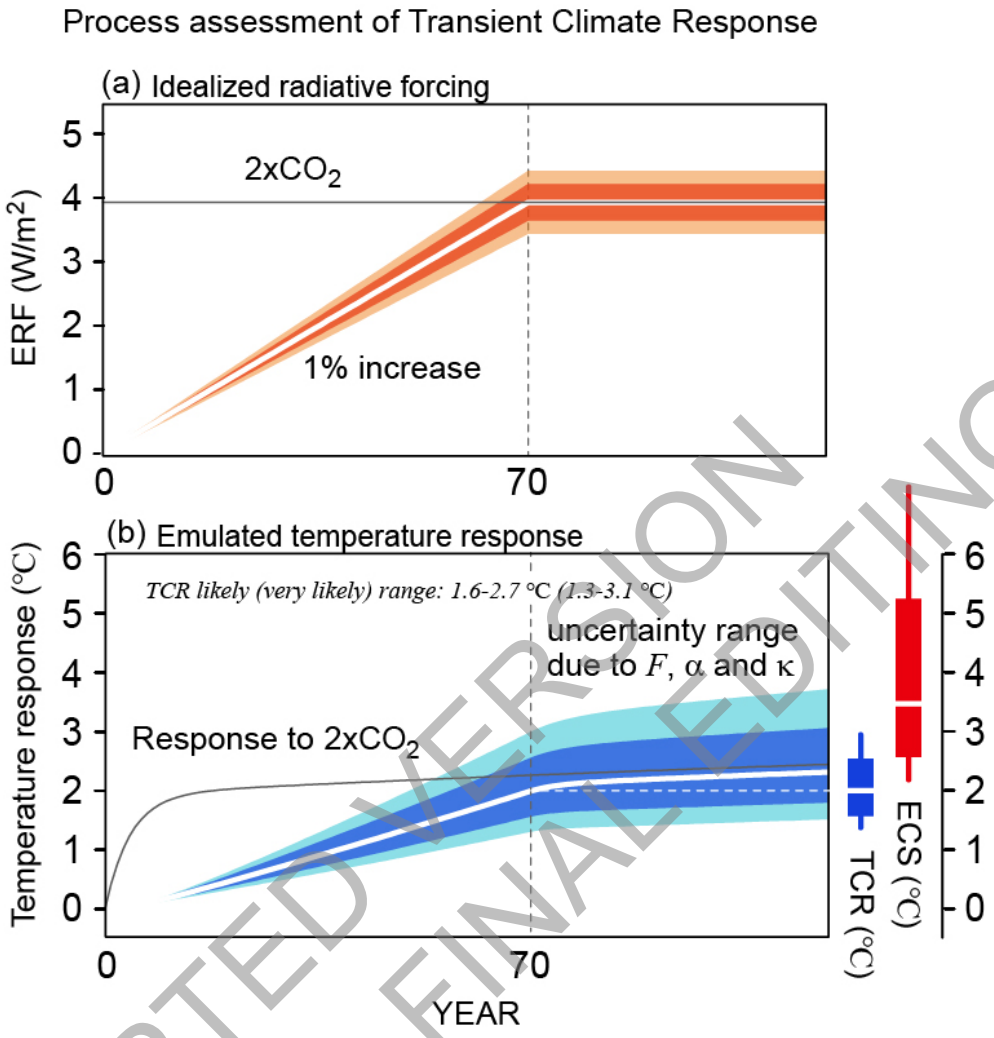


Figure 7.17: (a) Time evolution of the effective radiative forcing (ERF) to the CO_2 concentration increased by 1% per year until the year 70 (equal to the time of doubling) and kept fixed afterwards (white line). The *likely* and *very likely* ranges of ERF indicated by light and dark orange have been assessed in Section 7.3.2.1. (b) Surface temperature response to the CO_2 forcing calculated using the emulator with a given value of ECS, considering uncertainty in $\Delta F_{2\times CO2}$, α, and κ associated with the ocean heat uptake and efficacy (white line). The *likely* and *very likely* ranges are indicated by cyan and blue. For comparison, the temperature response to abrupt doubling of the CO_2 concentration is displayed by a grey curve. The mean, *likely* and *very likely* ranges of ECS and TCR are shown at the right (the values of TCR also presented in the panel). Further details on data sources and processing are available in the chapter data table (Table 7.SM.14).

ACCEPTED VERSION SUBJECT TO FINAL EDITING

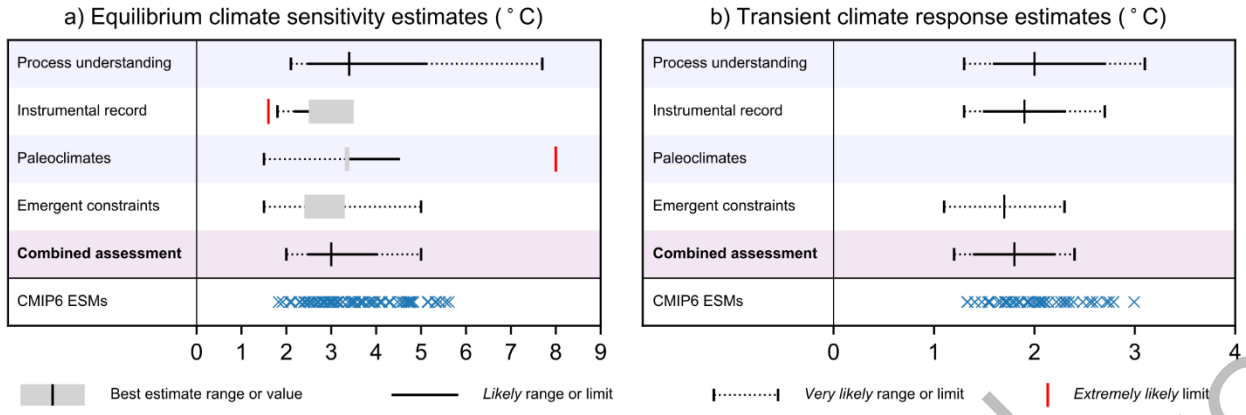


Figure 7.18: Summary of the equilibrium climate sensitivity (ECS) and transient climate response (TCR) assessments using different lines of evidence. Assessed ranges are taken from Tables 7.13 and 7.14 for ECS and TCR respectively. Note that for the ECS assessment based on both the instrumental record and paleoclimates, limits (i.e. one-sided distributions) are given, which have twice the probability of being outside the maximum/minimum value at a given end, compared to ranges (i.e. two tailed distributions) which are given for the other lines of evidence. For example, the *extremely likely* limit of greater than 95% probability corresponds to one side of the *very likely* (5% to 95%) range. Best estimates are given as either a single number or by a range represented by grey box. CMIP6 model values are not directly used as a line of evidence but presented on the Figure for comparison. ECS values are taken from Schlund et al. (2020) and TCR values from Meehl et al. (2020), see Supplementary Material 7.SM.4. Further details on data sources and processing are available in the chapter data table (Table 7.SM.14).

ACCEPTED VERSION SUBJECT TO FINAL EDITING

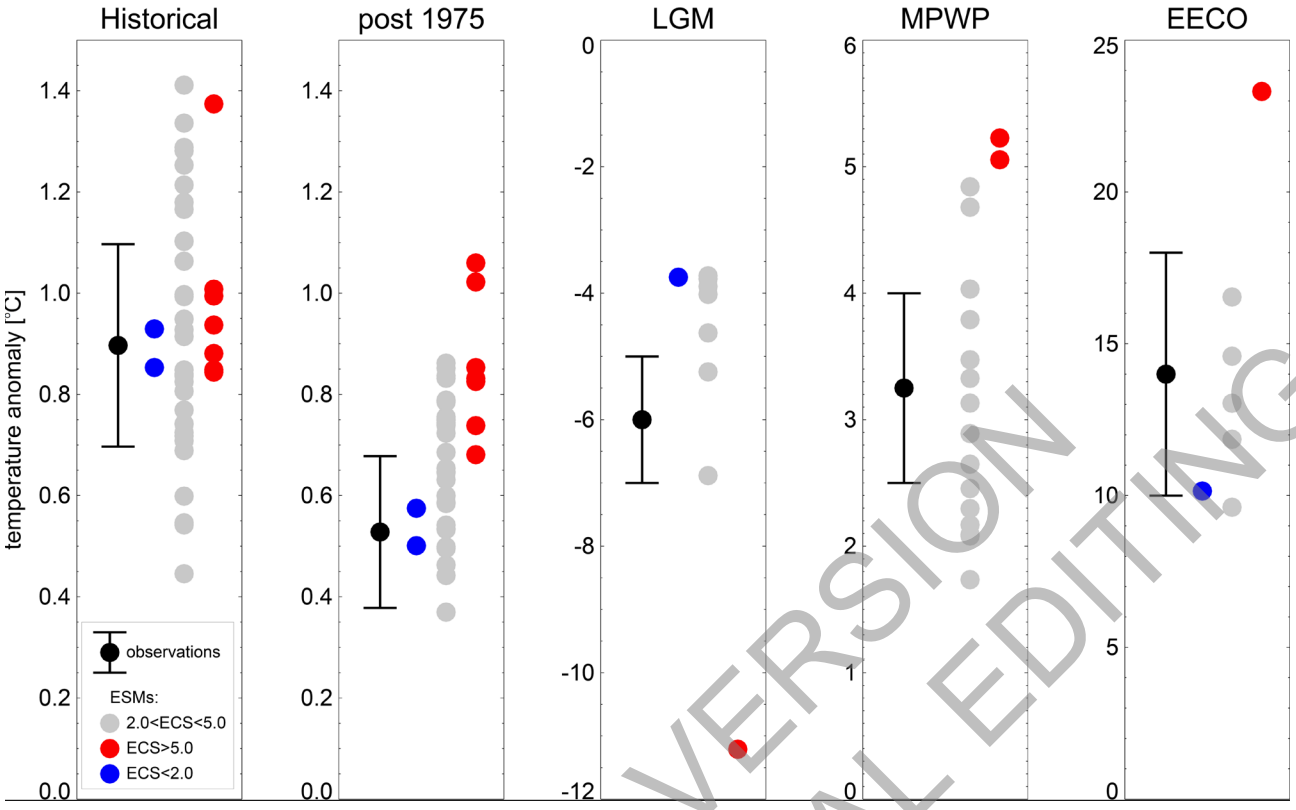


Figure 7.19: Global mean temperature anomaly in models and observations from 5 time periods. (a) Historical (CMIP6 models), (b) post 1975 (CMIP6 models), (c) Last Glacial Maximum (LGM; Cross-Chapter Box 2.1; PMIP4 models; (Kageyama et al., 2021; Zhu et al., 2021), (d) mid Pliocene warm period (MPWP; Cross-Chapter Box 2.4; PlioMIP models; Haywood et al., 2020; Zhang et al., 2021), (e) early Eocene climatic optimum (EECO; Cross-Chapter Box 2.1; DeepMIP models; Zhu et al., 2020; Lunt et al., 2021). Grey circles show models with ECS in the assessed *very likely* range; models in red have an ECS greater than the assessed *very likely* range (>5°C), models in blue have an ECS lower than the assessed *very likely* range (<2°C). Black ranges show the assessed temperature anomaly derived from observations (Chapter 2, Section 2.3). The Historical anomaly in models and observations is calculated as the difference between 2005–2014 and 1850–1900, and the post 1975 anomaly is calculated as the difference between 2005–2014 and 1975–1984. For the LGM, MPWP, and EECO, temperature anomalies are compared with pre-industrial (equivalent to CMIP6 simulation *piControl*). All model simulations of the MPWP and LGM were carried out with atmospheric CO_2 concentrations of 400 and 190 ppm respectively. However, CO_2 during the EECO is relatively more uncertain, and model simulations were carried out at either 1120ppm or 1680 ppm (except for the one high-ECS EECO simulation which was carried out at 560 ppm; Zhu et al., 2020). The one low-ECS EECO simulation was carried out at 1680 ppm. Further details on data sources and processing are available in the chapter data table (Table 7.SM.14).

ACCEPTED VERSION SUBJECT TO FINAL EDITING

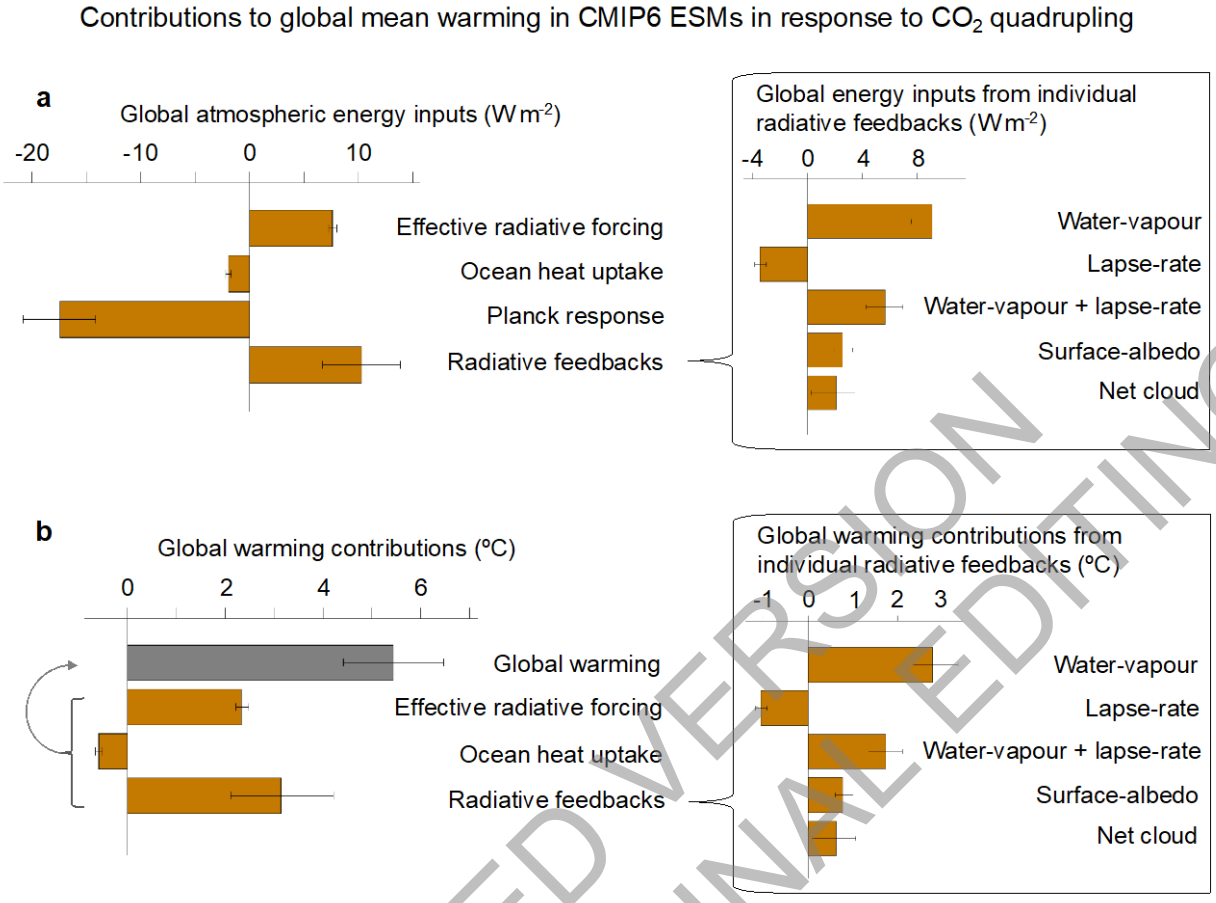


Figure 7.20: Contributions of effective radiative forcing, ocean heat uptake and radiative feedbacks to global atmospheric energy input and near-surface air temperature change at year 100 of *abrupt4xCO2* simulations of CMIP6 models. (a) The energy flux to the global atmosphere associated with the effective CO_2 forcing, global ocean heat uptake, Planck response, and radiative feedbacks, which together sum to zero. The inset shows energy input from individual feedbacks, summing to the total feedback energy input. (b) Contributions to net global warming are calculated by dividing the energy inputs by the *magnitude* of the global Planck response (3.2 W m^{-2} $°C^{-1}$), with the contributions from radiative forcing, ocean heat uptake, and radiative feedbacks (orange bars) summing to the value of net warming (grey bar). The inset shows warming contributions associated with individual feedbacks, summing to the total feedback contribution. Uncertainties show the interquartile range (25% and 75% percentiles) across models. Radiative kernel methods (see Section 7.4.1) were used to decompose the net energy input from radiative feedbacks into contributions from changes in atmospheric water vapour, lapse-rate, clouds, and surface albedo (Zelinka et al. (2020) using the Huang et al. (2017) radiative kernel). The CMIP6 models included are those analysed by Zelinka et al. (2020) and the warming contribution analysis is based on that of Goosse et al. (2018). Further details on data sources and processing are available in the chapter data table (Table 7.SM.14).

ACCEPTED VERSION SUBJECT TO FINAL EDITING

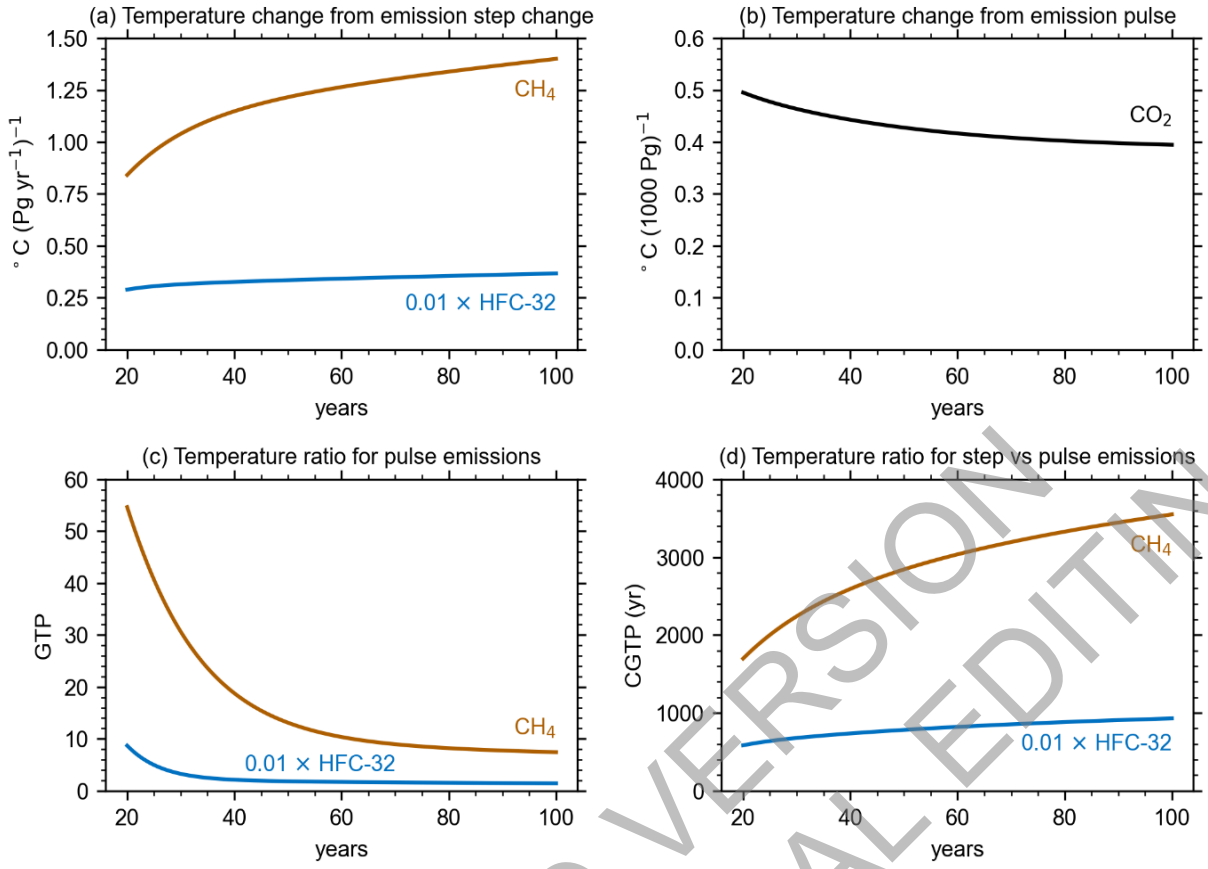


Figure 7.21: Emission metrics for two short-lived greenhouse gases: HFC-32 and CH_4, (lifetimes of 5.4 and 11.8 years). The temperature response function comes from Supplementary Material 7.SM.5.2. Values for non-CO_2 species include the carbon cycle response (Section 7.6.1.3). Results for HFC-32 have been divided by 100 to show on the same scale. (a) temperature response to a step change in short-lived greenhouse gas emission. (b) temperature response to a pulse CO_2 emission. (c) conventional GTP metrics (pulse vs pulse). (d) combined-GTP metric (step versus pulse). Further details on data sources and processing are available in the chapter data table (Table 7.SM.14).

ACCEPTED VERSION SUBJECT TO FINAL EDITING

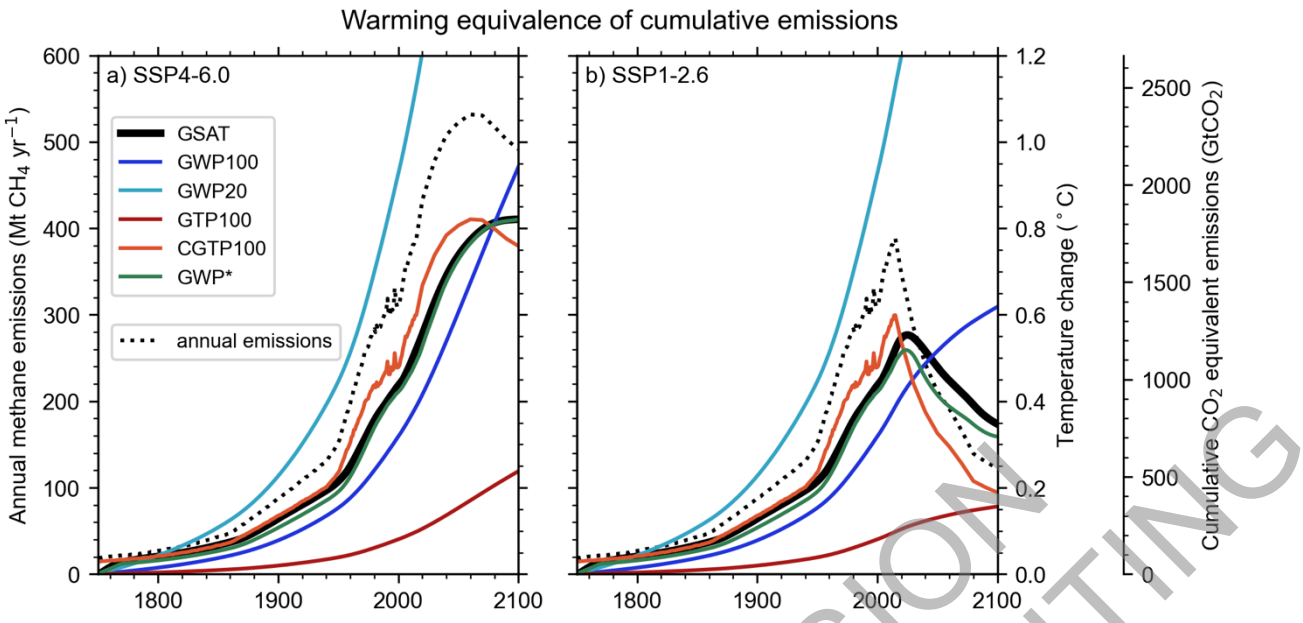
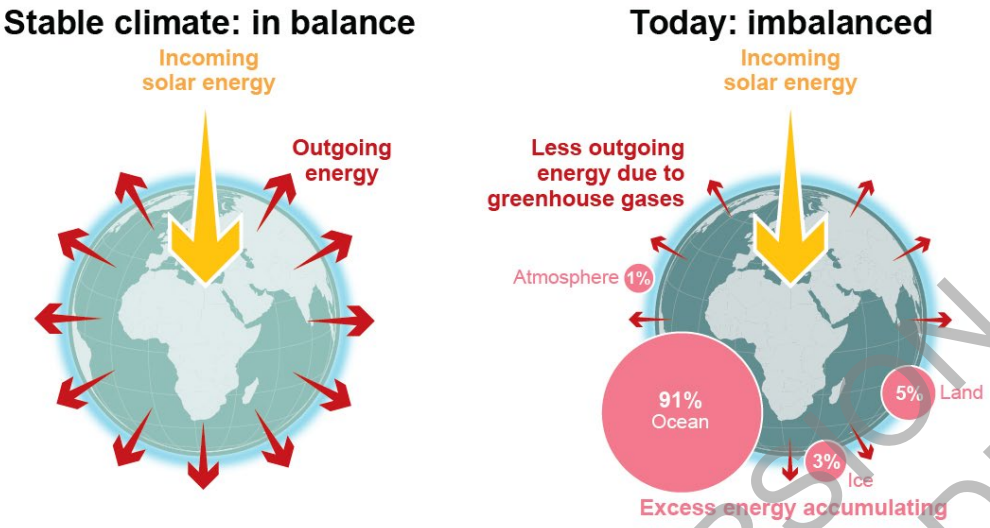


Figure 7.22: Explores how cumulative carbon dioxide equivalent emissions estimated for methane vary under different emission metric choices and how estimates of the surface temperature (GSAT) change deduced from these cumulative emissions compare to the actual temperature response computed with the two-layer emulator (solid black lines). Panels a) and b) show the SSP4-6.0 and SSP1-2.6 scenarios respectively. The panels show annual methane emissions as the dotted lines (left axis) from 1750–2100. The solid lines can be read as either estimates of GSAT change or estimates of the cumulative carbon dioxide equivalent emissions. This is because they are related by a constant factor, the TCRE. Thus, values can be read using either of the right hand axes. Emission metric values are taken from Table 7.15. The GWP* calculation is given in Section 7.6.1.4. The two-layer emulator has been calibrated to the central values of the report's assessment (see Supplementary Material 7.SM.5.2). Further details on data sources and processing are available in the chapter data table (Table 7.SM.14).

ACCEPTED VERSION SUBJECT TO FINAL EDITING

FAQ 7.1: The Earth's energy budget and climate change

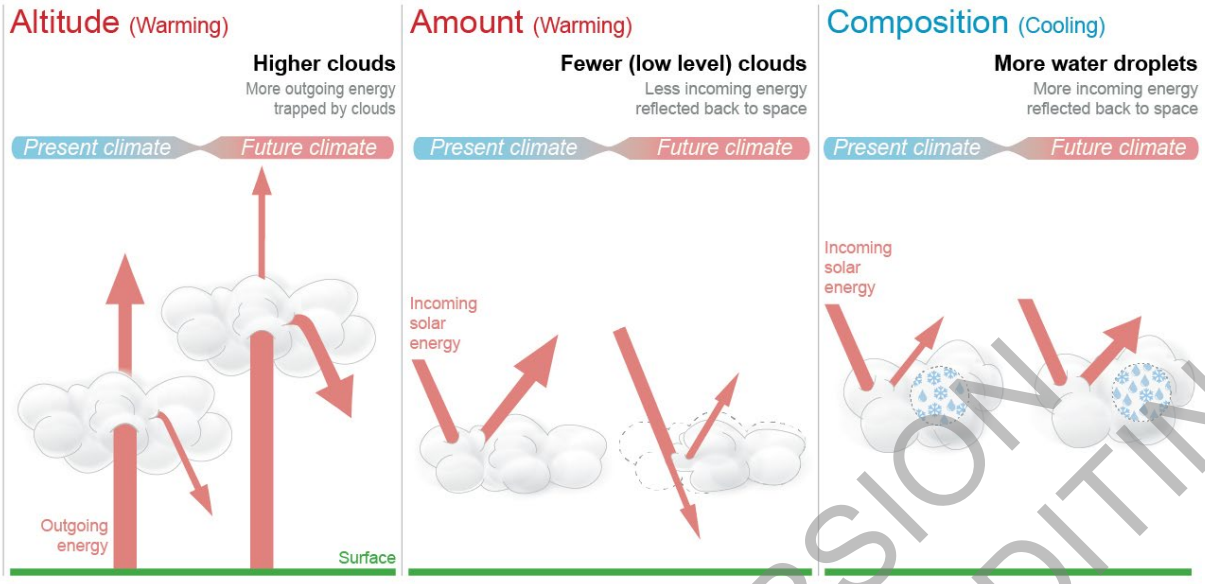
Since at least 1970, there has been a persistent imbalance in the energy flows that has led to excess energy being absorbed by different components of the climate system.



FAQ 7.1, Figure 1: **The Earth's energy budget compares the flows of incoming and outgoing of energy that are relevant for the climate system.** Since the at least the 1970s, less energy is flowing out than is flowing in, which leads to excess energy being absorbed by the ocean, land, ice and atmosphere, with the ocean absorbing 91%.

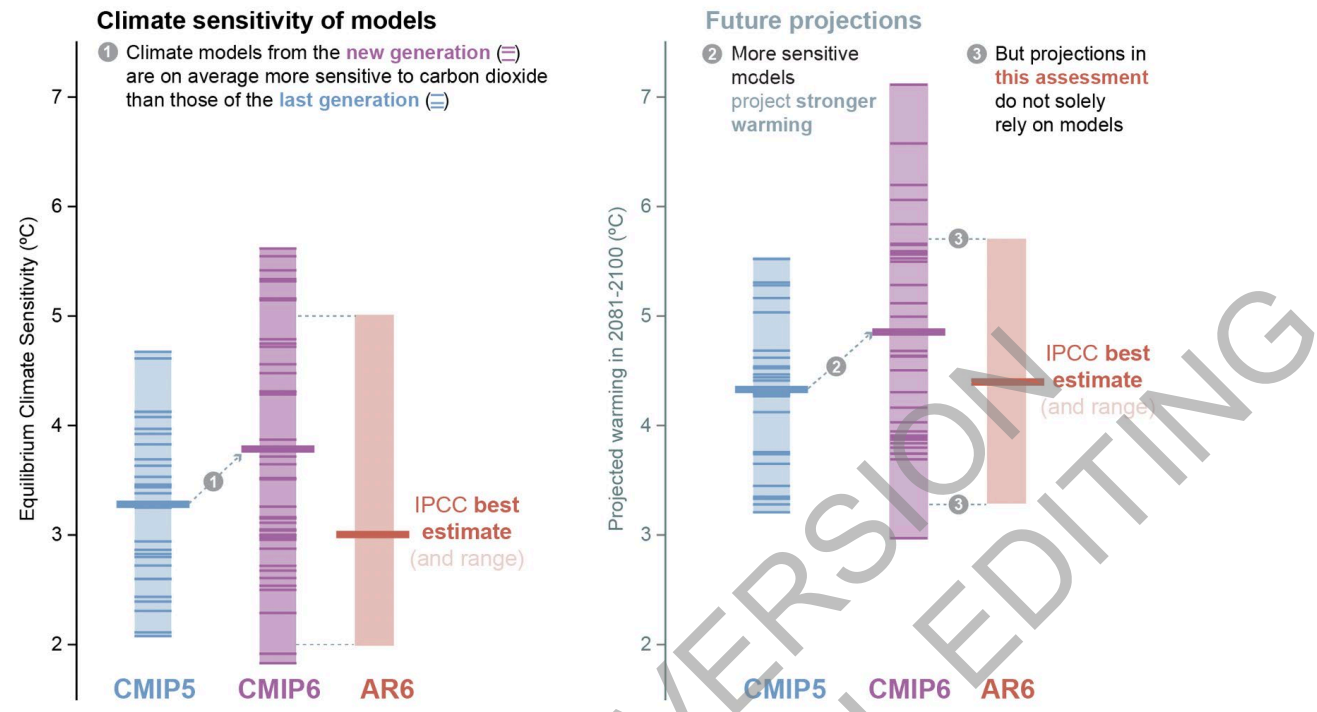
ACCEPTED VERSION SUBJECT TO FINAL EDITING

FAQ 7.2: **What is the role of clouds in a warming climate?**
Clouds affect and are affected by climate change. Overall, scientists expect clouds to **amplify future warming**.



FAQ 7.2, Figure 1: **Interactions between clouds and the climate today and in a warmer future**. Global warming is expected to alter the altitude (left) and the amount (centre) of clouds, which will amplify warming. On the other hand, cloud composition will change (right), offsetting some of the warming. Overall clouds are expected to amplify future warming.

ACCEPTED VERSION SUBJECT TO FINAL EDITING



FAQ7.3, Figure 1: Equilibrium climate sensitivity and future warming. (left) Equilibrium climate sensitivities for the current generation (sixth climate model intercomparison project, CMIP6) climate models, and the previous (CMIP5) generation. The assessed range in this report (AR6) is also shown. (right) Climate projections of CMIP5, CMIP6, and AR6 for the very high-emission scenarios RCP8.5, and SSP5-8.5, respectively. The thick horizontal lines represent the multi-model average and the thin horizontal lines the results of individual models. The boxes represent the model ranges for CMIP5 and CMIP6 and the range assessed in AR6.

ACCEPTED VERSION SUBJECT TO FINAL EDITING

7.SM Chapter 7: The Earth's energy budget, climate feedbacks, and climate sensitivity - Supplementary Material

Lead Authors:
Chris Smith (United Kingdom), Zebedee R. J. Nicholls (Australia), Kyle Armour (United States of America), William Collins (United Kingdom), Piers Forster (United Kingdom), Malte Meinshausen (Australia/Germany), Matthew D. Palmer (United Kingdom), Masahiro Watanabe (Japan)

Contributing Authors:
Thomas Gasser (Austria/France), Nicholas Leach (United Kingdom), Yann Quilcaille (Switzerland/France), Marit Sandstad (Norway), Mark Zelinka (United States of America)

This Supplementary Material should be cited as:
Smith, C., Z. R. J. Nicholls, K. Armour, W. Collins, P. Forster, M. Meinshausen, M. D. Palmer, M. Watanabe, 2021, The Earth's Energy Budget, Climate Feedbacks, and Climate Sensitivity Supplementary Material. In: *Climate Change 2021: The Physical Science Basis. Contribution of Working Group I to the Sixth Assessment Report of the Intergovernmental Panel on Climate Change* [Masson-Delmotte, V., P. Zhai, A. Pirani, S. L. Connors, C. Péan, S. Berger, N. Caud, Y. Chen, L. Goldfarb, M. I. Gomis, M. Huang, K. Leitzell, E. Lonnoy, J.B.R. Matthews, T. K. Maycock, T. Waterfield, O. Yelekçi, R. Yu and B. Zhou (eds.)]. Available from https://ipcc.ch/static/ar6/wg1.

Date: August 2021

This document is subject to copy-editing, corrigenda and trickle backs.

ACCEPTED VERSION
SUBJECT TO FINAL EDITING

Table of Contents

7.SM.1 Effective Radiative Forcing 3
7.SM.1.1 Simplified expressions for greenhouse gases 3
7.SM.1.2 Effective radiative forcing from a doubling of CO_2 4
7.SM.1.3 Historical (1750-2019) effective radiative forcing time series 5
7.SM.1.3.1 Best estimate historical time series 5
7.SM.1.3.2 Uncertainties in the historical best estimate time series 7
7.SM.1.4 SSP and RCP effective radiative forcing time series 8
7.SM.2 Two-layer energy balance model for climate emulation 11
7.SM.2.1 Emulator definition 11
7.SM.2.2 Constrained emulator ensemble 11
7.SM.2.3 Supporting information for Figures 7.7 and 7.8 12
7.SM.3 Performance of emulators compared to key physical climate assessments 13
7.SM.4 Equilibrium Climate Sensitivity and Transient Climate Response from CMIP6 models 18
7.SM.5 Climate metrics 21
7.SM.5.1 Definitions of climate metrics 21
7.SM.5.2 Impulse response functions for GTP and Chapter 6 calculations 22
7.SM.6 Tables of greenhouse gas lifetimes, radiative efficiencies and metrics 24
7.SM.7 Data Table 39
References 49

ACCEPTED VERSION
SUBJECT TO FINAL EDITING

7.SM.1 Effective Radiative Forcing

7.SM.1.1 Simplified expressions for greenhouse gases

In Section 7.3.2 and Table 7.5, simplified expressions for the stratospheric-temperature-adjusted radiative forcing (SARF) are used to convert greenhouse gas (GHG) concentrations to radiative forcing. AR5 (Myhre et al., 2013b) used relationships first introduced in Myhre et al. (1998), providing a logarithmic dependence of carbon dioxide (CO_2) SARF on CO_2 concentrations, and square root dependencies of methane (CH_4) and nitrous dioxide (N_2O) SARF on CH_4 and N_2O concentrations. The CH_4 and N_2O relationships accounted for band overlaps between these gases. These simplified expressions for SARF were revised in Etminan et al. (2016) using updated spectroscopic data. The most notable changes were a substantial revision in the methane RF of about +25% to account for previously neglected shortwave effects (Section 7.3.2.2) and inclusion of the mutual band overlap between carbon dioxide and nitrous oxide (Section 7.3.2.1). In Etminan et al. (2016), calculations from the Oslo line-by-line (LBL) radiative transfer model were conducted for 48 cases that co-varied concentrations of carbon dioxide, methane and nitrous oxide that spanned values from 180–2000 ppm CO_2, 340–3500 ppb CH_4 and 200–525 ppb N_2O. These ranges were selected to cover the minimum observed from ice core records during the Last Glacial Maximum to the maximum projected in the RCP8.5 scenario in the future (Meinshausen et al., 2011b; Riahi et al., 2011). Simplified relationships linking concentrations of CO_2, CH_4 and N_2O to the SARF from each gas, including overlaps, were provided from these 48 different cases that fit the original line-by-line results within a few percent.

A more accurate but complex functional fit was provided in Meinshausen et al. (2020) to the 48 Oslo LBL cases in Etminan et al. (2016). Two main advantages to the Meinshausen et al. (2020) fit are (i) the reduced error in the new fits to the original Oslo LBL results (maximum 0.11% for the CO_2 cases compared to 3.6% in Etminan et al. (2016)) and (ii) the extension of the valid range of the fits to CO_2 concentrations above 2000 ppm, which occurs in SSP5-8.5 in the future (though not RCP8.5). One drawback to the Meinshausen et al. (2020) fit compared to the original Etminan et al. (2016) fit is that the former is defined with respect to 1750 greenhouse gas concentrations, and requires a re-calculation of the coefficients to use baseline concentrations that are different from this, whereas the Etminan et al. (2016) fit is valid for any baseline concentration within their stated validity range (180–2000 ppm CO_2, 340–3500 ppb CH_4, 200–525 ppb N_2O). In general, AR6 and Chapter 7 in particular reports SARF and effective radiative forcing (ERF) relative to a 1750 baseline, negating this possible drawback, and so the Meinshausen et al. (2020) relationships are used for computing SARF and ERF throughout Chapter 7 and in Annex III. The relationships converting concentrations to SARF are shown in Table 7.SM.1. For halogenated greenhouse gases with concentrations in the ppt range, SARF remains a linear function of concentrations, as in AR5.

[START TABLE 7.SM.1 HERE]

Table 7.SM.1: Simplified expressions to compute radiative forcing (RF) from concentrations of greenhouse gases (Myhre et al., 1998; Meinshausen et al., 2020). C, N and M refer to concentrations of CO_2 in ppm, N_2O in ppb and CH_4 in ppb, respectively.

Gas	Radiative forcing (SARF) simplified expression	Coefficients
CO_2	$C_{\alpha_{\max}} = C_0 - \frac{b_1}{2a_1}$ $\alpha' = \begin{cases} d_1 - \frac{b_1^2}{4a_1}, & C > C_{\alpha_{\max}} \\ d_1 + a_1(C - C_0)^2 + b_1(C - C_0), & C_0 < C < C_{\alpha_{\max}} \\ d_1, & C < C_0 \end{cases}$ $\alpha_{N_2O} = c_1\sqrt{N}$ $\mathrm{SARF}_{CO_2} = (\alpha' + \alpha_{N_2O}) \cdot \ln\left(\frac{C}{C_0}\right)$	$a_1 = -2.4785 \times 10^{-7}$ W m^{-2} ppm^{-2} $b_1 = 7.5906 \times 10^{-4}$ W m^{-2} ppm^{-1} $c_1 = -2.1492 \times 10^{-3}$ W m^{-2} ppb$^{-1/2}$ $d_1 = 5.2488$ W m^{-2} $C_0 = 277.15$ ppm
N_2O	$\mathrm{SARF}_{N_2O} = (a_2\sqrt{C} + b_2\sqrt{N} + c_2\sqrt{M} + d_2) \cdot (\sqrt{N} - \sqrt{N_0})$	$a_2 = -3.4197 \times 10^{-4}$ W m^{-2} ppm^{-1} $b_2 = 2.5455 \times 10^{-4}$ W m^{-2} ppb^{-1}

ACCEPTED VERSION SUBJECT TO FINAL EDITING

		$c_2 = -2.4357 \times 10^{-4}$ W m^{-2} ppb^{-1} $d_2 = 0.12173$ W m^{-2} ppb$^{-1/2}$ $N_0 = 273.87$ ppb
CH_4	$\mathrm{SARF}_{CH_4} = \left(a_3\sqrt{M} + b_3\sqrt{N} + d_3\right) \cdot \left(\sqrt{M} - \sqrt{M_0}\right)$	$a_3 = -8.9603 \times 10^{-5}$ W m^{-2} ppb^{-1} $b_3 = -1.2462 \times 10^{-4}$ W m^{-2} ppb^{-1} $d_3 = 0.045194$ W m^{-2} ppb$^{-1/2}$ $M_0 = 731.41$ ppb
Halogenated compounds and other minor GHGs	$\mathrm{SARF}_X = e_X(X - X_0)$	X and X_0 in ppb e_X is radiative efficiency (W m^{-2} ppb^{-1}) (Table 7.SM.7)

[END TABLE 7.SM.1 HERE]

7.SM.1.2 Effective radiative forcing from a doubling of CO_2

In Section 7.3.2.1, the ERF from a doubling of CO_2 ($\Delta F_{2\times CO2}$ = 3.93 W m^{-2}) is defined relative to 1750 CE concentrations of CO_2 assessed in Chapter 2 (C_0 = 278.3 ppm) and N_2O (N_0 = 270.1 ppb) using the Meinshausen et al. (2020) fits (Table 7.SM.1) to calculate SARF of 3.75 W m^{-2} and then adding an additional 5% for tropospheric adjustments (Section 7.3.2.1; Table 7.3). Using the Etminan et al. (2016) fits with the same baseline concentrations (C_0 = 278.3 ppm, N_0 = 270.1 ppb) results in a SARF of 3.80 W m^{-2} and an ERF of 3.99 W m^{-2} (Table 7.SM.2). The simplified expressions are used as no specific line-by-line experiment was performed for a doubling of CO_2 from about 1750 concentrations in Etminan et al. (2016).

Alongside the choice of simplified expression, the baseline CO_2 and N_2O concentrations also has an impact on the SARF and ERF from a doubling of CO_2 (Table 7.SM.2). Using 1850 CE baselines results in ERF values that are close, but not exactly the same, as using 1750 CE baselines (Table 7.SM.2). Using a present-day baseline results in estimates of SARF and ERF from a doubling of CO_2 that are about 1% greater than the 1750 or 1850 values (Table 7.SM.2). The 1850 baseline is significant as it the reference pre-industrial state for CMIP6 experiments, including the *abrupt4xCO2* and *1pctCO2* experiments used to estimate ECS and TCR from climate models. It should be noted that the *1pctCO2* experiment design relies on a logarithmic increase in CO_2 SARF with concentration to estimate TCR (Gregory et al., 2015), and both the Etminan et al. (2016) and Meinshausen et al. (2020) SARF formulas are super-logarithmic with increasing CO_2 concentrations.

[START TABLE 7.SM.2 HERE]

Table 7.SM.2: Computed values of the SARF of a doubling of CO_2 using the relationships in Etminan et al. (2016) and Meinshausen et al. (2020), and the ERF from a doubling of CO_2 (assessed to be SARF + 5% in Section 7.3.2.1), from different baseline concentrations of CO_2 and N_2O, and compared to SARF in AR5.

CO_2 concentration (ppm)	**N_2O concentration (ppb)**	**SARF 2×CO_2 AR5** (Myhre et al., 2013b)	**SARF 2×CO_2 (Etminan et al., 2016)**	**ERF 2×CO_2 (Etminan et al., 2016)**	**SARF 2×CO_2 (Meinshausen et al., 2020)**	**ERF 2×CO_2 (Meinshausen et al., 2020)**	**Baseline year for GHG concentrations**
278.3	270.1	3.71	3.802	3.992	3.747	**3.934**	1750 (Chapter 2 assessment)
277.15	273.87		3.801	3.991	3.746	3.933	1750 (Meinshausen et al., 2020)
284.32	273.02		3.804	3.994	3.749	3.937	1850 used in CMIP6 model integrations (Meinshausen

ACCEPTED VERSION SUBJECT TO FINAL EDITING

							et al., 2017)
389	323		3.837	4.029	3.790	3.980	2011 (Etminan et al., 2016)
409.85	332.09		3.844	4.036	3.798	3.988	2019 (Chapter 2 assessment)

[END TABLE 7.SM.2 HERE]

7.SM.1.3 Historical (1750-2019) effective radiative forcing time series

7.SM.1.3.1 Best estimate historical time series

The historical ERF time series describes how the best estimates of changes in climate drivers translates to ERF for 1750 to 2019. The time-evolution of ERF is reported separately for CO_2, CH_4, N_2O, other well-mixed greenhouse gases (WMGHGs), ozone, stratospheric water vapour from methane oxidation, contrails and aviation-induced cirrus, aerosol-radiation interactions, aerosol-cloud interactions, light-absorbing particles on snow and ice, land-use change, volcanic, and solar. The contributions from 49 halogenated GHGs comprising the "other well-mixed greenhouse gases" category are further reported individually. Data is published in Annex III.

For CO_2, CH_4 and N_2O, the SARFs are calculated using time-dependent best-estimate concentrations of these gases from Chapter 2 using the formulae in Table 7.SM.1 and using concentrations from Chapter 2 in 1750 CE as baselines (C_0 = 278.3 ppm, N_0 = 270.1 ppb, M_0 = 729.2 ppb). Tropospheric adjustments of +5% for CO_2, –14% for CH_4 and +7 % are then added to these SARF values to produce ERF (Section 7.3.2). For 49 halogenated greenhouse gases, concentration changes since 1750 are used combined with radiative efficiencies detailed in Table 7.SM.7 to derive SARF (Table 7.SM.1). Accounting for tropospheric adjustments adds +13% and +12% to CFC-11 and CFC-12 respectively when moving from SARF to ERF. No tropospheric adjustments are assumed for other halogenated species (Section 7.3.2.4).

For historical ozone forcing, the time series from 1750 to 2020 from Skeie et al. (2020) is adopted, using the multi-model mean ERF from six independent Earth System and chemistry-climate models (BCC-ESM1, CESM2-WACCM6, GFDL-ESM4, GISS-E2-1-H, MRI-ESM2-0 and Oslo-CTM3) that used CMIP6 precursor emissions and interactively calculated ozone burdens using full stratospheric and tropospheric chemistry schemes. From the original 12 models reporting results in Skeie et al. (2020), CNRM-CM6, CNRM-ESM2-1 and E3SM1-0 were excluded as they do not include full stratospheric and tropospheric chemistry, only the first out of the similar models CESM2-WACCM6 and CESM2-CAM6 were used, the input4MIPs forcing estimate (Checa-Garcia et al., 2018) was excluded as it did not use CMIP6 precursor emissions, and UKESM-1-0-LL was excluded for having implausible time evolutions of stratospheric ozone that resulted in negative total ozone ERF estimates for 2010 relative to 1850. The extrapolations for the 1750–1850 and 2010–2020 periods (run beyond 2014 using SSP2-4.5) came from a single model (Oslo-CTM3) and results were used up to and including 2019. Stratospheric water vapour from methane oxidation is treated a linear scaling of the methane ERF and scaled to the 1750–2019 assessment of 0.05 W m^{-2} (Section 7.3.2.6).

Several forcing categories (contrails, aviation-induced cirrus aerosols, and black carbon on snow) are derived from global annual emissions totals of short-lived climate forcers. For the best estimate of historical emissions from 1750 to 2019, the 11 September 2020 version of the Community Emissions Data System (CEDS) is used (Hoesly et al., 2018), obtained from https://doi.org/10.5281/zenodo.4025316. CEDS provides emissions of black carbon (BC), organic carbon (OC), sulphur dioxide (SO_2), ammonia (NH_3), nitrogen oxides (NOx), carbon monoxide (CO) and non-methane volatile organic compounds (NMVOC) from the fossil fuel, industrial and agricultural sectors. Biomass burning emissions are used from the BB4CMIP dataset (also used for CMIP6 model integrations, from Van Marle et al. (2017)), aggregated into global annual totals. The SSP2-4.5 scenario projection from BB4CMIP is used for 2015-2019.

ERF from contrails and aviation-induced cirrus uses global aviation NOx emissions as a predictor of aviation

ACCEPTED VERSION SUBJECT TO FINAL EDITING

activity following Smith et al. (2018a), and scaled to the 2018 ERF best estimate of 0.0574 W m^{-2} from Lee et al. (2020).

ERF from aerosol-radiation interactions (ERFari) was calculated by converting emissions of BC, OC, SO_2 (representing sulphate aerosol) and NH_3 (representing nitrate aerosol) to forcing using CMIP5-era ACCMIP multi-model mean contributions for each species from Myhre et al. (2013a) and scaled to obtain the assessment of –0.3 W m^{-2} for ERFari which is applied to the 2005–2014 decade. ERFari was calculated using a simple linear relationship to emissions of BC, OC, SO_2 and NH_3 (E_{BC}, E_{OC}, E_{SO2}, E_{NH3}):

$$\mathrm{ERFari} = \beta_{\mathrm{BC}}E_{\mathrm{BC}} + \beta_{\mathrm{OC}}E_{\mathrm{OC}} + \beta_{\mathrm{SO2}}E_{\mathrm{SO2}} + \beta_{\mathrm{NH3}}E_{\mathrm{NH3}} \qquad \textit{Equation 7.SM.1.1}$$

The β coefficients are selected to represent ERFari contributions of +0.3 W m^{-2} from black carbon, –0.4 W m^{-2} from sulphate, –0.09 W m^{-2} from organic carbon and –0.11 W m^{-2} from nitrate over the 2005–2014 decade, which translates to radiative efficiencies of β_{BC} = 50.8 mW yr m^{-2} MtC^{-1}, β_{OC} = –6.21 mW yr m^{-2} MtC^{-1}, β_{SO2} = –3.62 mW yr m^{-2} $MtSO_2^{-1}$, and β_{NH3} = –2.08 mW yr m^{-2} $MtNH_3^{-1}$. Newer CMIP6 model results were not used as fewer model results are available and the complexity of aerosol schemes and internal mixing in these models makes attribution of aerosol forcing to precursors more difficult than in CMIP5-era models.

ERF from aerosol-cloud interactions (ERFaci) is modelled as a logarithmic function of emissions of SO_2, BC and OC following Smith et al. (2018a):

$$\mathrm{ERFaci} = -\beta \ln(1 + E_{\mathrm{SO2}}/s_{\mathrm{SO2}} + (E_{\mathrm{BC+OC}}/s_{\mathrm{BC+OC}})) \qquad \textit{Equation 7.SM.1.2}$$

Eq. (7.SM.1.2) is based on the offline model of Ghan et al. (2013) using a functional form developed by Stevens (2015) with the inclusion of a carbonaceous aerosol term than can influence ERFaci. Eq. (7.SM.1.2) was tuned to 11 CMIP6 models that provided historical time-varying (1850-2014) ERFaci estimates and a parameter set of β, s_{SO2} and s_{BC} was obtained for each CMIP6 model. The parameter tunings from these 11 models were used to generate distributions using kernel density estimates from which 100,000 sample members were drawn and 100,000 candidate ERFaci time series were produced. The best estimate ERFaci time series is taken from the median of this 100,000-member ensemble, and then scaled to the assessed ERFaci of –1.0 W m^{-2} for 1750 to 2005–2014.

ERF from light-absorbing particles on snow is linear with BC emissions and scaled to the 1750-2019 ERF assessment of 0.08 W m^{-2}.

ERF from land-use change is broken down into an albedo component and an irrigation component. The albedo component follows the historical ERF time series from Ghimire et al. (2014) from 1700 to 2005, and is extended forward to 2019 using cumulative land-use related CO_2 emissions from the SSP Historical and SSP2-4.5 scenarios. This follows the treatment in Smith et al. (2018a) and assumes that land-use related CO_2 is closely related to deforestation and albedo change. The 1750-2019 assessment of –0.15 W m^{-2} is then applied to the time series. The ERF from irrigation, assessed to be –0.05 W m^{-2} for 1750–2019 (Sherwood et al., 2018), scales with the albedo component.

All anthropogenic components of the ERF described above are expressed relative to a 1750 baseline.

Natural forcings comprise solar changes and volcanic eruptions (forcing from galactic cosmic rays is assessed to be negligible, Section 7.3.4.5). Volcanic ERF is derived from stratospheric aerosol optical depth (SAOD) using a conversion of –20 × ΔSAOD (Section 7.3.4.6), or ERF = –20 × SAOD + 0.2582 W m^{-2} using absolute SAOD where SAOD is nominally taken at 550 nm wavelength. The SAOD conversion to ERF is expressed as an anomaly in SAOD relative to the 500 BCE to 1749 CE mean, so that the mean volcanic ERF for 500 BCE to 1749 CE is zero. This is in order that the long-term mean GSAT change from pre-industrial volcanic forcing alone is zero, avoiding a spurious cooling effect when applying the volcanic

ACCEPTED VERSION SUBJECT TO FINAL EDITING

time series from 1750 onwards to projections in a climate emulator (e.g. Section 7.SM.2). This convention means that volcanically quiescent years experience a volcanic ERF of up to +0.2 W m^{-2} (even volcanically quiescent years have some level of background stratospheric aerosol, so volcanic ERFs approaching the offset value of +0.2582 W m^{-2} are not seen). CMIP6 uses a similar prescription for volcanic forcing in ESMs, by applying a constant background climatology of SOAD for *piControl* and *ScenarioMIP* runs that is based on the historical (1850–2014) mean SAOD (Eyring et al., 2016).

The SAOD time series is derived from a composite of three datasets: eVolv v3 (Toohey and Sigl, 2017) for 500 BCE to 1900 CE, CMIP6 for 1850 to 1989, and GloSSAC v2 (Kovilakam et al., 2020) from 1979 to 2018. SAOD from GloSSAC v2 is reported at a wavelength of 525 nm and has been converted to 550 nm using an Ångström exponent of –2.33 (Kovilakam et al., 2020). The 2018 volcanic ERF is repeated for 2019. The 1850 to 1900 overlap is performed by linearly ramping down the eVolv v3 dataset and linearly ramping up the CMIP6 dataset. The CMIP6 and GloSSAC v2 data are ramped over the 1979 to 1989 period. In both cases the correspondences between overlapping periods is good.

Solar ERF is calculated using the change in total solar irradiance (TSI) where TSI is taken from the ^{14}C SATIRE-M reconstruction from PMIP4 (Jungclaus et al., 2017) and converted to ERF using ¼ × 0.71 × 0.72 × ΔTSI (Section 7.3.4.4). The baseline for TSI is the mean TSI from 6754 BCE to 1744 CE, which encompasses complete solar cycles in the proxy reconstructions before 1750.

Aerosols and solar ERFs in 2019 both differ from the headline assessments given in Sections 7.3.3 and 7.3.4.4 respectively. For aerosols, the assessment in Section 7.3.3 of –1.3 ± 0.7 W m^{-2} is valid for 1750 to about 2014, as less evidence is available for trends in how aerosol forcing has evolved in more recent years. The emissions-based time series provides a best-estimate aerosol ERF for 1750–2019 of –1.06 W m^{-2}, less negative than the 1750–2014 assessment, owing to a recent decline in precursor emissions since around 2005 from the CEDS dataset and supported by other studies (Paulot et al., 2018; Kanaya et al., 2020). For solar ERF, the Chapter 7 assessment of +0.01 ± 0.07 W m^{-2} is for the 6754 BCE to 1744 CE pre-industrial period to the 2009–2019 solar cycle. The single year 2019, corresponding to a solar minimum, has a solar ERF of –0.02 W m^{-2} relative to this pre-industrial baseline.

7.SM.1.3.2 Uncertainties in the historical best estimate time series

The uncertainty in the historical ERF time series was generated with a 100,000-member Monte Carlo ensemble. The forcing components where uncertainty ranges are assumed to be symmetric and Gaussian in their assessments in Section 7.3 have a scale factor drawn from a Gaussian distribution with mean of unity and 5–95% uncertainty range determined as a fraction of the best estimate ERF. The forcing components with symmetric uncertainty ranges are CO_2 (fractional 5–95% uncertainty 0.12 of the best estimate), CH_4 (0.20), N_2O (0.16), halogenated gases (0.19 on the basis that the majority are "long-lived"), ozone (0.50), stratospheric water vapour (1.00), land use change (0.50) and volcanic (0.25). Contrails (and aviation-induced cirrus) and light-absorbing particles on snow and ice have asymmetric uncertainty ranges and the fractional uncertainty was determined by considering ranges below and above the best estimate separately, by dividing the 5th percentile by the best estimate to derive the lower uncertainty range and the 95th percentile by the best estimate to determine the upper range, treating them as two halves of a Gaussian distribution. In each ensemble member the sampled uncertainty scale factor for each component of the forcing is applied to the whole time series.

For aerosols, the ERFari and ERFaci are treated independently. ERFari uncertainty is developed by sampling the radiative efficiency coefficients β_{BC}, β_{OC}, β_{SO2} and β_{NH3} in Eq. (7.SM.1.1) as Gaussian distributions with 5–95% ranges uncertainties of 0.67, 0.78, 0.50 and 0.44, yielding contributions to ERFari of +0.3 ± 0.2 W m^{-2} for BC, –0.4 ± 0.2 W m^{-2} for sulphate, –0.09 ± 0.07 W m^{-2} for OC and –0.11 ± 0.05 W m^{-2} for nitrate for the 2005–2014 mean with respect to 1750. Each precursor species is sampled independently and the historical emissions from the CEDS database are used to generate the time series of ERFari. For ERFaci, the 100,000 generated time series described in Section 7.SM.1.3 are used with one additional step to scale each ERFaci candidate time series to a 2005–2014 mean ERFaci of –1.0 ± 0.7 W m^{-2} with respect to 1750. This

ACCEPTED VERSION SUBJECT TO FINAL EDITING

effectively rescales the β coefficients in each ensemble member in Eq. (7.SM.1.2) .

The 5–95% range of anthropogenic ERF of 1.96–3.48 W m^{-2} (Table 7.8) for 1750–2019 is determined from the 5th and 95th percentiles of the year 2019 anthropogenic ERF in this 100,000 member ensemble.

For solar forcing, a 0.50 fractional uncertainty was applied to the amplitude of the solar cycle, and a linear 1750 to 2019 trend of ±0.07 W m^{-2} (5–95%) range was added to this to represent the uncertainty in the change in the underlying solar forcing (Section 7.3.4.4).

7.SM.1.4 SSP and RCP effective radiative forcing time series

A similar method to the process described in Section 7.SM.1.3 is used to derive the ERF time series in RCP and SSP scenarios to 2500 (Annex III; Figure 4.36; Chapter 6; Chapter 9). From 1750 to 2014 the best estimate and uncertainty SSP projections ERF time series and the historical ERF time series described are identical. The SSPs diverge from each other, and from the historical best estimate, in 2015. For SSPs, the set of eight Tier 1 and Tier 2 scenarios defined by *ScenarioMIP* are assessed (SSP1-1.9, SSP1-2.6, SSP4-3.4, SSP5-3.4-over, SSP2-4.5, SSP4-6.0, SSP3-7.0 and SSP5-8.5). In addition two variants of SSP3-7.0 used primarily by AerChemMIP are presented: one where short-lived climate forcers are set to emissions factors consistent with strong air-quality controls that are broadly consistent with SSP1-levels of mitigation, SSP3-7.0-lowNTCF (Collins et al., 2017), plus a further variant of SSP3-7.0-lowNTCF that also takes into account methane mitigation alongside other short-lived forcers, SSP3-7.0-lowNTCFCH4 (Allen et al., 2021).

For 2015 to 2020, a linear transition between the concentrations of well-mixed greenhouse gases provided by Chapter 2 and the SSP greenhouse gas concentrations from Meinshausen et al. (2020) is performed. From 2020 onwards concentration projections from Meinshausen et al. (2020) are used. The correspondence between the Chapter 2 assessed time series and Meinshausen et al. (2017) dataset used for the CMIP6 *historical* experiment is good, with a maximum difference of 0.6% from 1850-2014 for the main three greenhouse gases and 1.4% for N_2O in 1750 (the slight 1750 concentration differences affects the $2\times CO_2$ forcing in the third decimal place; see Table 7.SM.2).

For purely emissions-based forcing estimates (aerosols, contrails and aviation-induced cirrus, and black carbon on snow), a similar 5-year transition between 2015 and 2020 is performed for fossil fuel, industrial and agricultural emissions. The best-estimate historical emissions to 2019 are provided in the 11 September 2020 version of the CEDS database (https://doi.org/10.5281/zenodo.4025316) and the SSP scenario projections used v5.1 of the RCMIP dataset (obtained from https://doi.org/10.5281/zenodo.4589756; Nicholls et al., (2020)) that provides consolidated regional and sectoral annual emissions totals from the CMIP6 SSP emissions datasets (Velders et al., 2015; Gidden et al., 2019; Meinshausen et al., 2020). Biomass burning emissions are used from the SSP emissions projections from Van Marle et al. (2017). The same parameter sets from the historical ERF estimate and 100,000 member Monte Carlo ensemble are used to derive the future ERFs from aerosols, contrails (and aviation-induced cirrus) and black carbon on snow, using the SSP emissions projections.

Future ozone forcing for SSP projections differs from the historical treatment and is based on emissions of short-lived forcers and concentrations of ozone-depleting greenhouse gases (Section 6.4). To generate the best-estimate projection, the historical time series in Skeie et al. (2020) is matched to emissions-driven estimates of ozone ERF from AerChemMIP models (Thornhill et al., 2021b), displayed in Table 7.SM.3 that sums to +0.37 W m^{-2} for 1850 to 2014. There is a temperature-dependent feedback on ozone ERF of –0.037 W m^{-2} °C^{-1} for CMIP historical runs (this differs from the assessment in Section 6.4 of –0.064 W m^{-2} °C^{-1} which is based on *abrupt4xCO2* experiments, as it includes the effects of the lightning NOx and BVOC feedbacks that act to reduce the magnitude of the temperature-ozone feedback (Thornhill et al., 2021a)). As five of the six Earth System Models run in Skeie et al. (2020) considered in the ERF ozone assessment were CMIP historical runs (all except Oslo-CTM3) and simulated the increase in historical GSAT over time, they implicitly included this feedback and as such the –0.037 W m^{-2} °C^{-1} feedback it is subtracted from the transient ozone ERF in these five models, using GSAT time series assessed in Chapter 2, to produce a "zero-

ACCEPTED VERSION SUBJECT TO FINAL EDITING

feedback" estimate of ozone forcing from 1850 to 2014 of +0.47 W m^{-2}. To apply the emissions precursors to the overall time series, they are scaled by a factor of 1.27, derived from a ratio of the zero feedback estimate from Skeie et al. (2020) to the best estimate from the sum of precursors from Thornhill et al. (2021b) (0.47/0.37) to produce radiative efficiencies for each species (Table 7.SM.3).

[START TABLE 7.SM.3 HERE]

Table 7.SM.3: ERF from ozone precursors in AerChemMIP experiments (Thornhill et al., 2021b), and radiative efficiencies derived for emissions-based SSP pathways. The contributions for CO + NMVOC are not separated in Thornhill et al. (2021b) so the ratio of CO : NMVOC from CMIP5 ACCMIP experiments is used (Stevenson et al., 2013). "Concentrations" of ozone-depleting halocarbons (ODHs) are expressed in equivalent effective stratospheric chlorine in ppt.

species	Contribution to ozone ERF 1850-2014, W m^{-2} (Stevenson et al., 2013; Thornhill et al., 2021b)	Scale factor to reproduce 1850-2014 ozone ERF in Skeie et al. (2020), after subtracting temperature feedback	Radiative efficiency for ozone ERF
CH_4	+0.14 ± 0.05	1.27	β_{CH4} = 0.175 ± 0.062 mW m^{-2} ppb^{-1}
N_2O	+0.03 ± 0.02		β_{N2O} = 0.710 ± 0.062 mW m^{-2} ppb^{-1}
Ozone-depleting halocarbons (ODH)	–0.11 ± 0.10		β_{ODH} = –0.125 ± 0.113 mW m^{-2} ppt^{-1}
CO	+0.07 ± 0.06		β_{CO} = 0.155 ± 0.131 mW m^{-2} $MtCO^{-1}$ yr
NMVOC	+0.04 ± 0.04		β_{NMVOC} = 0.329 ± 0.328 mW m^{-2} $MtNMVOC^{-1}$ yr
NOx	+0.20 ± 0.11		β_{NOx} = 1.797 ± 0.983 mW m^{-2} $MtNO_2$ yr^{-1}
Sum	+0.37 ± 0.18	+0.47 ± 0.24 W m^{-2} (total ozone ERF)	

[END TABLE 7.SM.3 HERE]

The future ozone ERF is then derived as

$$ERF_{O3} = \beta_{CH4}\Delta C_{CH4} + \beta_{N2O}\Delta C_{N2O} + \beta_{ODH}\Delta C_{ODH} + \beta_{CO}\Delta E_{CO} + \beta_{NMVOC}\Delta E_{NMVOC} + \beta_{NOx}\Delta E_{NOx} - f \cdot \Delta T \quad \textit{Equation 7.SM.1.3}$$

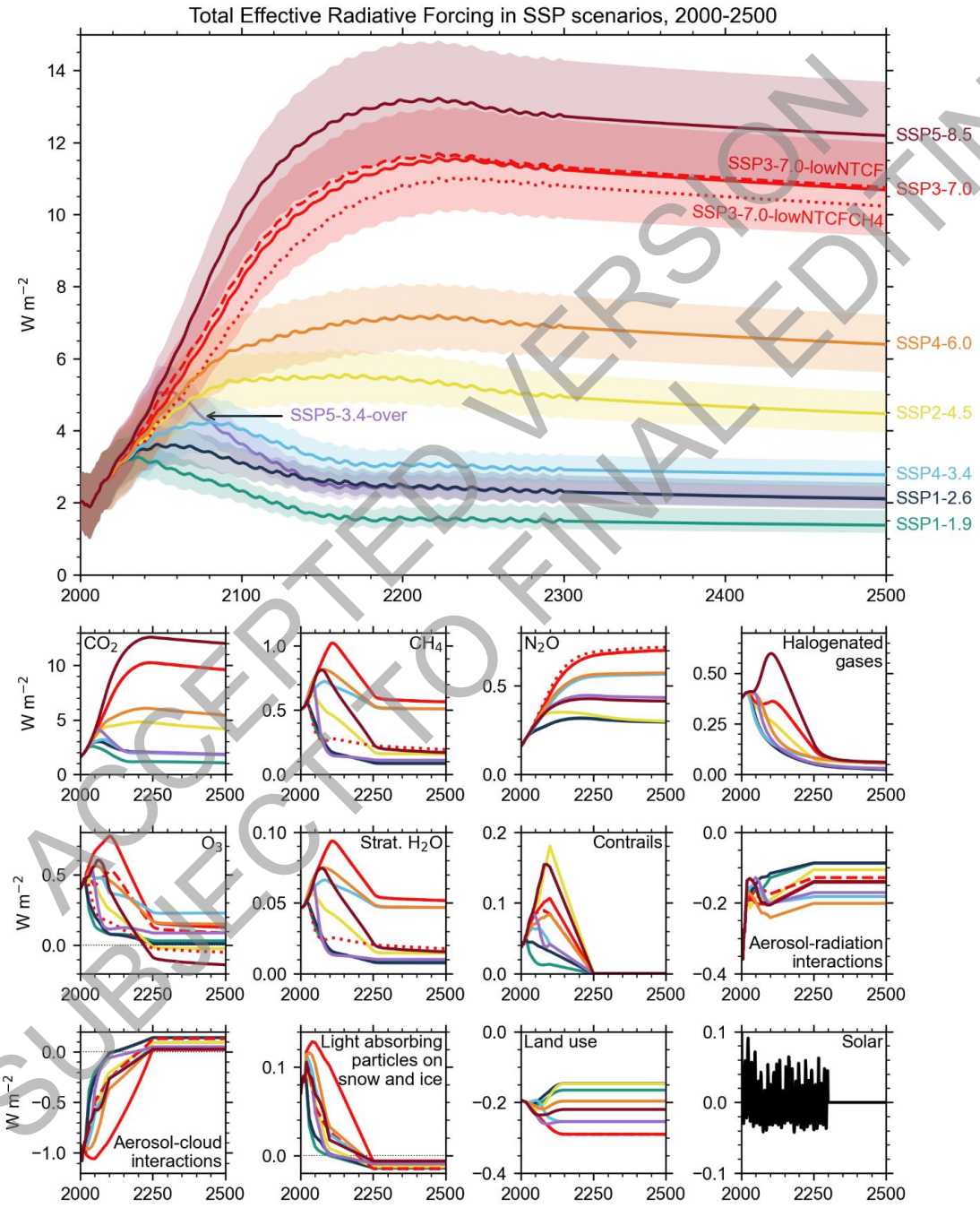
where C_{CH4} and C_{N2O} are concentrations of CH_4 and N_2O in ppb, C_{ODH} is the equivalent effective stratospheric chlorine from halogenated compounds expressed in ppt (Newman et al., 2007), and E_{CO}, E_{NMVOC} and E_{NOx} are annual emissions in Mt yr^{-1} (NOx expressed in units of $MtNO_2$), f = –0.037 W m^{-2} $°C^{-1}$ and ΔT represents GSAT anomaly. This configuration is run iteratively, with other best-estimate forcings, in the two-layer emulator (Section 7.SM.2) with the Section 7.5.5 best-estimate assessments of equilibrium climate sensitivity (ECS, 3.0°C) and transient climate response (TCR, 1.8°C) until convergence is achieved.

ERF from land use change scales with cumulative emissions of land-use-related CO_2 emissions following the end of the historical period.

ACCEPTED VERSION SUBJECT TO FINAL EDITING

Volcanic forcing is set to a ten-year linear ramp down to zero from 2014 to 2024, following the CMIP6 ScenarioMIP protocol (Eyring et al., 2016). Solar forcing uses the CMIP6 future TSI variation (Matthes et al., 2017) which provides projections to 2299, and is set to zero from 2300. For Figure 4.36 and Annex III, ERF time series for the RCP scenarios are produced using emissions and concentrations from Meinshausen et al. (2011b) using the same methods, present-day forcing best estimates, and uncertainty ranges described above, with the difference that scenarios start to diverge in 2005 and a 15-year ramp from 2005 to 2020 from historical emissions or concentrations to the future RCP projections is performed.

[START FIGURE 7.SM.1 HERE]



ACCEPTED VERSION SUBJECT TO FINAL EDITING

Figure 7.SM.1: Total effective radiative forcing from SSP scenarios with respect to 1750 for 2000-2500 (top panel), showing best estimate and 5–95% uncertainty range (shaded regions). Uncertainty ranges are not shown for SSP3-7.0-lowNTCF and SSP3-7.0-NTCFCH4 for visual clarity. Bottom matrix shows the

best estimate ERF for each anthropogenic component, and solar (volcanic ERF is zero beyond 2024).
[END FIGURE 7.SM.1 HERE]

7.SM.2 Two-layer energy balance model for climate emulation

7.SM.2.1 Emulator definition

The two-layer emulator is based on the following global mean equations:

$$C\frac{\mathrm{d}}{\mathrm{d}t}\Delta T = \Delta F(t) + \alpha\Delta T - \varepsilon\gamma(\Delta T - \Delta T_d)$$
$$C_\mathrm{d}\frac{\mathrm{d}}{\mathrm{d}t}\Delta T_\mathrm{d} = \gamma(\Delta T - \Delta T_d) \qquad \textit{Equation 7.SM.2.1}$$

where ΔT (°C) is the temperature of the surface layer (representing the surface components of the climate system), ΔT_d (°C) is the temperature change in the deep ocean layer, C and C_d are the effective heat capacities for the surface and deep layers in W yr m^{-2} °C^{-1}, ε is the efficacy of the deep ocean heat uptake and γ is the heat transfer coefficient between the surface and deep layer (W m^{-2} °C^{-1}).

The analytical solution of Eq. (7.SM.2.1) is expressed by a combination of fast and slow modes with the decay time scales of τ_f and τ_s. For a given value of ECS, TCR is obtained as

$$\mathrm{TCR} = \mathrm{ECS}\left\{1 - \frac{1}{t}\left[\tau_f a_f\left(1 - e^{-\frac{t_0}{\tau_f}}\right) - \tau_s a_s\left(1 - e^{-\frac{t_0}{\tau_s}}\right)\right]\right\}. \qquad \textit{Equation 7.SM.2.2}$$

The TCR is equal to ΔT at year $t = t_0 = 70$ in response to the forcing ΔF increasing at a rate of 1% per year, and all parameters (τ_f, τ_s, a_f, and a_s) can be calculated using C, C_d, γ, ε and the net feedback parameter α (the formulae are presented in Geoffroy et al. (2013a)). As discussed in Jiménez-de-la-Cuesta and Mauritsen (2019), TCR can also be estimated directly from the two-layer model parameters as $\mathrm{TCR} = \Delta F_{2\times\mathrm{CO2}}/(-\alpha + \kappa)$, where $\kappa = \varepsilon\gamma$.

The two-layer model can be calibrated to emulate the climate response of individual CMIP models (Geoffroy et al., 2013b, 2013a) using *abrupt4xCO2* experiments. Calibrations are performed for 44 CMIP6 models resulting in parameter estimates (mean and standard deviation) of C = 8.1 ± 1.0 W yr m^{-2} °C^{-1}, C_d = 110 ± 63 W yr m^{-2} °C^{-1}, γ = 0.62 ± 0.13 W m^{-2} °C^{-1}, ε = 1.34 ± 0.41, κ = 0.84 ± 0.38 W m^{-2} °C^{-1}. Representative values from CMIP6 models in Eq. (7.SM.2.2) are τ_f = 4.6 yr, τ_s = 333 yr, a_f = 0.541, a_s = 0.459.

7.SM.2.2 Constrained emulator ensemble

In several places in Working Group I (Chapter 1, Figure 7.7, Figure 7.8, Chapter 9), a constrained ensemble of two-layer model projections is used. The starting point for this ensemble is a 1 million-member ensemble of emissions-driven historical runs using v1.6.2 of the FaIR emulator (Millar et al., 2017; Smith et al., 2018a). The temperature module of FaIR is mathematically equivalent to the two-layer emulator in Eq. (7.SM.2.1), and the emissions- or concentrations-to-ERF relationships in FaIR are equivalent or very similar to those described in generating the ERF time series in Section 7.SM.1. The similarity of the two-layer model to FaIR is demonstrated in Figure 7.SM.2.

The 1 million ensemble members sample the uncertainty in the ERF, the climate response, and the carbon cycle. ERF uncertainties are generated using the same method described in Section 7.SM.1.3. For the climate response, the C, C_d, γ and ε components of the two-layer model in Eq. 7.SM.2.1 are generated from kernel-

ACCEPTED VERSION SUBJECT TO FINAL EDITING

density estimates that are calibrated to 44 CMIP6 models (Section 7.SM.2.1). The climate feedback parameter α is sampled from a truncated Gaussian distribution (truncated at ±2 standard deviations) with mean –1.33 W m^{-2} °C^{-1} and standard deviation 0.5 W m^{-2} °C^{-1}. The carbon cycle in FaIR is parameterised by the pre-industrial time-integrated airborne fraction of CO_2, and the change in airborne fraction with accumulated carbon emissions and GSAT change (Millar et al., 2017). These parameters are sampled as uniform distributions using the lowest and highest values based on calibrations to 11 CMIP6 models (Arora et al., 2020) as the bounds of the distributions. The 1 million-member ensemble was run in the FaIR model using emissions-driven runs from 1750 to 2019. The resulting ensemble was constrained based on agreement to:

(1) the time series of historical GSAT to the Chapter 2 (Cross Chapter Box 2.3) assessment from 1850–2020 with a root-mean-square error of 0.135°C or less, approximately recreating the headline 1850–1900 to 1995–2014 assessment of 0.67–0.98°C (Cross Chapter Box 2.3, *very likely* range);
(2) the assessment of ocean heat uptake from Section 7.2.2.2 from 1971–2018 within the *likely* range of 329–463 ZJ;
(3) CO_2 concentrations to the 2014 *very likely* range of 397.1 ± 0.4 ppm (Table 2.1);
(4) the airborne fraction from a 1% per year CO_2 increase simulation to the range assessed in Section 5.5.1 of 53 ± 6% (1 standard deviation).

From the original 1 million-member ensemble, 2,237 ensemble members passed all four constraints and are used for reporting results. This constrained ensemble set from FaIRv1.6.2 has a good correspondence to assessed ranges of key climate metrics across the Working Group I report (Cross Chapter Box 7.1 Table 1; Table 7.SM.4). While not used as formal constraints, the assessed distributions of ECS and TCR (Section 7.5.2) and projected future warming from the five major SSP scenarios (Section 4.3.4) were used as guidelines to ensure simultaneous adherence to several assessed ranges. As a comparison, the ECS from this constrained set has a median and 5–95% ranges of ECS and TCR of 2.95 [2.05 – 5.07]°C and 1.81 [1.36–2.46]°C respectively, compared to the Chapter 7 best estimates and *very likely* ranges of 3.0 [2.0–5.0]°C for ECS and 1.8 [1.2 – 2.4]°C for TCR. While constraints (3) and (4) are not required when running FaIR or the two-layer model using prescribed historical greenhouse gas concentrations, this 2,237 member ensemble set is intended to be used to evaluate future warming pathways to integrated assessment model scenario projections in Chapter 3 of Working Group III, so the same ensemble set is used here for overall consistency.

7.SM.2.3 Supporting information for Figures 7.7 and 7.8

The data contributing to Figures 7.7 and 7.8 is from the 2,237-member constrained ensemble described in Section 7.SM.2.2. To provide the contributions to historical temperature in Figures 7.7 and 7.8, one of the 13 components of the historical forcing at a time is removed from the total forcing, and the two-layer model run using the forcing and climate configuration from each of the 2,237 ensemble members. The difference between the all-forcing and leave-one-out model run provides the temperature contribution from each forcing agent. This exercise was repeated using a best-estimate climate response (hence, only assessing the impact of uncertainty in the ERF) by setting ECS = 3.0°C, TCR 1.8°C and the other two-layer model parameters set to their CMIP6 model means (C = 8.1 W yr m^{-2} °C^{-1}, C_d = 110 W yr m^{-2} °C^{-1}, γ = 0.64 W m^{-2} °C^{-1} and ε = 1.36; Section 7.SM.2.1). These simulations are shown as dashed error bars in Figure 7.7, with the full ERF and climate response uncertainty as solid error bars.

Each ensemble member uses a long (approximately 9,000-year) pre-industrial spin-up comprising only transient solar and volcanic forcing starting in 6755 BCE (Section 7.SM.1.3), and temperature changes are reported with respect to 1750 as a single baseline year. The same 2,237 ensemble member set was extended forward in time to 2500 under forcing from the SSP scenarios (Section 7.SM.1.4) and used to inform global-mean sea level projections in Chapter 9.

ACCEPTED VERSION SUBJECT TO FINAL EDITING

7.SM.3 Performance of emulators compared to key physical climate assessments

Table 7.SM.4 details the performance of the four emulators (CICERO-SCM, FaIRv1.6.2, MAGICC7.5.1 and OSCARv3.1.1) described in Cross Chapter Box 7.1 for a number of climate assessments in absolute terms, and can be compared to Cross Chapter Box 7.1 Table 2 which details the relative difference between each emulator and the AR6 assessed range.

ACCEPTED VERSION
SUBJECT TO FINAL EDITING

[START TABLE 7.SM.4 HERE]

Table 7.SM.4: Absolute differences between the emulator value and the Working Group I assessed best estimate and range for key climate assessments. Values are given for four emulators in their respective AR6-calibrated probabilistic setups. Relative values of these indicators are shown in Cross Chapter Box 7.1, Table 2. Emulator values within 5% of the assessed central value and 10% of the lower and upper ranges are unshaded, showing good correspondence between the emulator and the assessment. The columns labelled "upper" and "lower" indicate *very likely* (5% to 95%) ranges, except for the variables demarcated with an asterisk or double asterisk (* or **), where they denote *likely* ranges from 17% to 83%. Note that the TCRE assessed range (**) is wider than the combination of the TCR and airborne fraction to account for uncertainties related to model limitations.

Emulator		Assessed ranges			CICERO-SCM			FaIRv1.6.2			MAGICC7			OSCARv3.1.1		
Assessed range		**Lower**	**Central**	**Upper**	**Lower**	**Central**	**Upper**	**Lower**	**Central**	**Upper**	**Lower**	**Central**	**Upper**	**Lower**	**Central**	**Upper**
Key metrics																
ECS (°C)		2.00	3.00			3.05	4.09	2.05	2.95	5.07	1.93	2.97	4.83	1.84	2.54	3.90
TCRE (°C per 1000 GtC)**		1.00	1.65	2.30				1.29	1.53	1.82	1.37	1.73	2.19	1.50	1.52	1.83
TCR (°C)		1.20	1.80	2.40	1.38	1.71	2.32	1.36	1.81	2.46	1.27	1.88	2.61	1.51	1.82	2.05
Historical warming and Effective Radiative Forcing																
GSAT warming (°C)	1995-2014 relative to 1850-1900	0.67	0.85	0.98	0.68	0.85	0.98	0.72	0.87	1.02	0.72	0.86	0.97	0.67	0.78	0.98
Ocean heat content change (ZJ)*	1971-2018	329	396	463	250	288	329	346	381	423	325	382	436	174	243	508

ACCEPTED VERSION SUBJECT TO FINAL EDITING

Total Aerosol ERF (W m^{-2})	2005-2014 relative to 1750	-2.00	-1.30	-0.60	-1.27	-0.82	-0.54	-1.68	-1.15	-0.60	-1.79	-1.20	-0.55	-1.24	-1.11	-0.79
WMGHG ERF (W m^{-2})	2019 relative to 1750	3.03	3.32	3.61	3.14	3.14	3.14	3.07	3.38	3.66	3.10	3.35	3.60	3.06	3.42	3.49
Methane ERF (W m^{-2})	2019 rel. 1750	0.43	0.54	0.65	0.56	0.56	0.56	0.44	0.56	0.67	0.43	0.54	0.67	0.47	0.54	0.62
Carbon Cycle metrics																
Airborne Fraction 1pctCO2 (dimensionless)*	2×CO_2	0.47	0.53	0.59				0.50	0.52	0.53	0.52	0.56	0.59	0.47	0.53	0.64
Airborne Fraction 1pctCO2 (dimensionless)*	4×CO_2	0.50	0.60	0.70				0.56	0.60	0.63	0.57	0.62	0.66	0.53	0.59	0.69
Future warming (GSAT) relative to 1995-2014																
SSP1-1.9 (°C)	2021-2040	0.38	0.61	0.85	0.42	0.58	0.94	0.39	0.61	0.94	0.39	0.61	0.88	0.43	0.55	0.64
	2041-2060	0.40	0.71	1.07	0.43	0.65	1.15	0.36	0.66	1.14	0.39	0.71	1.15	0.45	0.65	0.74
	2081-2100	0.24	0.56	0.96	0.21	0.42	0.94	0.18	0.48	1.00	0.20	0.52	0.99	0.26	0.51	0.66
SSP1-2.6 (°C)	2021-2040	0.41	0.63	0.89	0.44	0.60	0.94	0.42	0.64	0.96	0.40	0.62	0.89	0.45	0.57	0.64
	2041-2060	0.54	0.88	1.32	0.58	0.83	1.34	0.53	0.86	1.38	0.54	0.89	1.35	0.62	0.82	0.95
	2081-2100	0.51	0.90	1.48	0.50	0.78	1.41	0.47	0.84	1.49	0.48	0.89	1.49	0.59	0.82	1.05

ACCEPTED VERSION SUBJECT TO FINAL EDITING

SSP2-4.5 (°C)	2021-2040	0.44	0.66	0.90	0.48	0.63	0.94	0.47	0.65	0.92	0.45	0.64	0.89	0.42	0.57	0.63
	2041-2060	0.78	1.12	1.57	0.81	1.08	1.62	0.79	1.11	1.59	0.79	1.13	1.60	0.84	1.03	1.12
	2081-2100	1.24	1.81	2.59	1.22	1.63	2.51	1.21	1.75	2.63	1.21	1.82	2.67	1.34	1.74	1.96
SSP3-7.0 (°C)	2021-2040	0.45	0.67	0.92	0.50	0.64	0.93	0.51	0.68	0.91	0.49	0.68	0.92	0.43	0.57	0.65
	2041-2060	0.92	1.28	1.75	0.96	1.22	1.74	0.98	1.28	1.72	0.98	1.33	1.77	0.99	1.17	1.29
	2081-2100	2.00	2.76	3.75	1.99	2.55	3.64	2.07	2.72	3.72	2.13	2.86	3.97	2.09	2.59	2.81
SSP5-8.5 (°C)	2021-2040	0.51	0.76	1.04	0.54	0.71	1.06	0.56	0.77	1.08	0.55	0.77	1.06	0.51	0.66	0.73
	2041-2060	1.08	1.54	2.08	1.11	1.42	2.07	1.12	1.55	2.17	1.11	1.57	2.16	1.19	1.44	1.58
	2081-2100	2.44	3.50	4.82	2.54	3.24	4.68	2.58	3.50	4.89	2.63	3.65	5.16	2.65	3.35	3.62

[START TABLE 7.SM.4 HERE]

ACCEPTED VERSION SUBJECT TO FINAL EDITING

The comparison of the constrained two-layer emulator to FaIRv1.6.2 and MAGICC7.5.1 is shown in Figure 7.SM.3 for the SSP1-2.6 and SSP5-8.5 scenarios, demonstrating the similarity between the FaIR and two-layer projections as well as the similarity between FaIR and MAGICC in their AR6 setups.

[START FIGURE 7.SM.2 HERE]

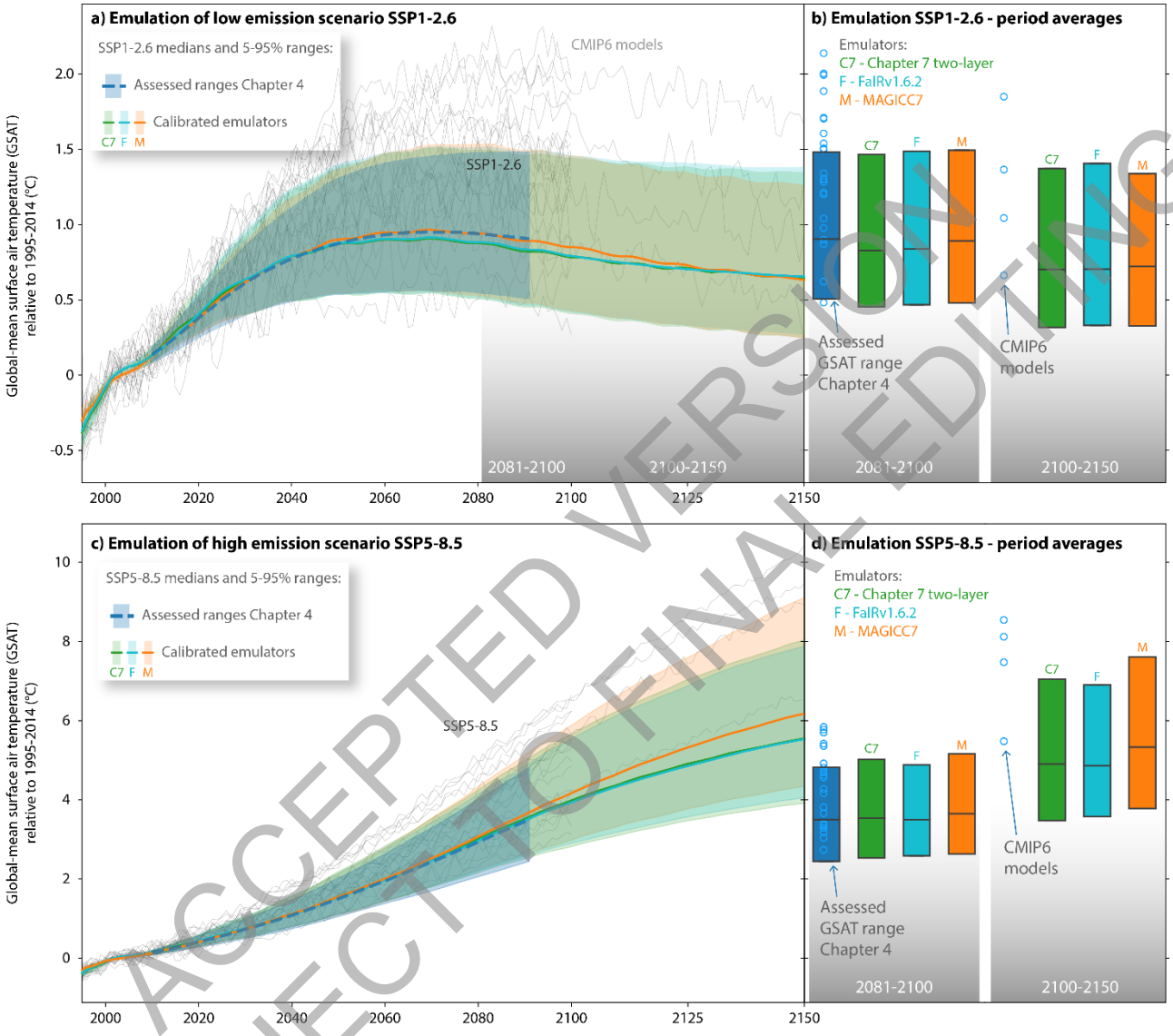


Figure 7.SM.2: (a) Time series and (b) 2100-2150 means of emulated GSAT projections from the Chapter 7 two-layer model (green), FAIRv1.6.2 (light blue), and MAGICC7.5.1 (orange) from 1995 to 2150, following the SSP1-2.6 scenario ((a) and (b)) and the SSP5-8.5 scenario ((c) and (d)). In (a) and (c) the ensemble median estimates are solid lines and the 5–95% ranges are shaded; in (b) and (d) the bar range shows 5–95% ranges with the median in black. Overlaid CMIP6 model results are shown as lines in (a) and (c), and dots in (b) and (d) (fewer dots are shown for the 2100–2150 period because only a limited number of CMIP6 models have performed runs beyond 2100). In (a) and (c), Chapter 4 assessed GSAT projections (20-year running means) are shown with a dark blue dashed line and 5-95% range in dark blue shading.

[END FIGURE 7.SM.2 HERE]

ACCEPTED VERSION SUBJECT TO FINAL EDITING

7.SM.4 Equilibrium Climate Sensitivity and Transient Climate Response from CMIP6 models

Table 7.SM.5 details the equilibrium climate sensitivity and transient climate response estimated from CMIP6 and CMIP5 models using the ESMValTool (Eyring et al., 2020; Lauer et al., 2020; Righi et al., 2020) and presented in Schlund et al. (2020) for ECS and Meehl et al. (2020) for TCR (CMIP6 only), used in Section 7.5.6, Figure 7.18 and FAQ 7.3. Climate feedback parameters, including the decomposition into Planck, water vapour plus lapse rate, surface albedo and cloud components, plus the residual, are given for CMIP6 and CMIP5 models from Zelinka et al. (2020). ECS is estimated from a 150-year integration of an *abrupt4xCO2* experiment, subtracting the parallel *piControl* integration from the same period, regressing the modelled top-of-atmosphere energy imbalance ΔN against the modelled GSAT change ΔT, and taking $\Delta T/2$ at the point where the regression slope crosses $\Delta N = 0$ (Gregory et al., 2004). TCR is estimated from the mean ΔT change from a *1pctCO2* run compared to the parallel *piControl* integration in years 60 to 79. Feedback contributions are estimated from a mean of six radiative kernels presented in Zelinka et al. (2020).

[START TABLE 7.SM.5 HERE]

Table 7.SM.5: Equilibrium climate sensitivity (ECS) and climate feedbacks estimated from CMIP5 and CMIP6 models. Transient climate response (TCR) from CMIP6 models is also provided. Data from Schlund et al. (2020), Meehl et al. (2020) and Zelinka et al. (2020).

MIP Era	Model	ECS °C	Net feedback α, W m^{-2} °C^{-1}	Components of the net feedback, W m^{-2} °C^{-1}					TCR °C
				Planck	Water vapour + lapse rate	Surface albedo	Cloud	Residual	
CMIP6	ACCESS-CM2	4.72	–0.74	–3.22	1.18	0.37	0.80	0.14	2.10
	ACCESS-ESM1-5	3.87	–0.73	–3.21	1.33	0.42	0.62	0.11	1.95
	AWI-CM-1-1-MR	3.16	–1.15	–3.16	1.27	0.42	0.29	0.04	2.06
	BCC-CSM2-MR	3.04	–1.03	–3.25	1.23	0.38	0.57	0.04	1.72
	BCC-ESM1	3.26	–0.92	–3.23	1.24	0.42	0.58	0.06	1.77
	CAMS-CSM1-0	2.29	–1.82	–3.25	1.30	0.24	-0.30	0.20	1.73
	CAS-ESM2-0	3.51							2.04
	CESM2	5.16	–0.63	–3.28	1.26	0.38	1.01	-0.01	2.06
	CESM2-FV2	5.14	–0.55	–3.23	1.17	0.40	1.10	0.01	2.05
	CESM2-WACCM	4.75	–0.71	–3.27	1.25	0.37	1.22	-0.28	1.98
	CESM2-WACCM-FV2	4.79	–0.61	–3.24	1.16	0.37	1.17	-0.07	2.01
	CIESM		–0.69	–3.19	1.19	0.27	0.84	0.20	2.39
	CMCC-CM2-SR5	3.52	–1.07	–3.26	1.27	0.31	0.58	0.04	2.09
	CMCC-ESM2		–1.05	–3.25	1.29	0.33	0.56	0.02	
	CNRM-CM6-1	4.83	–0.74	–3.22	1.24	0.49	0.61	0.14	2.14
	CNRM-CM6-1-HR	4.28	–0.92	–3.27	1.27	0.37	0.59	0.13	2.48
	CNRM-ESM2-1	4.76	–0.62	–3.23	1.27	0.47	0.63	0.25	1.86
	CanESM5	5.62	–0.65	–3.26	1.29	0.42	0.88	0.03	2.74
	E3SM-1-0	5.32	–0.63	–3.27	1.25	0.32	0.97	0.11	2.99

ACCEPTED VERSION SUBJECT TO FINAL EDITING

	EC-Earth3		–0.76	–3.18	1.45	0.53	0.39	0.05	2.30
	EC-Earth3-AerChem		–0.94	–3.18	1.39	0.54	0.27	0.05	
	EC-Earth3-Veg	4.31	–0.78	–3.21	1.45	0.53	0.37	0.07	2.62
	FGOALS-f3-L	3.00	–1.40	–3.14	1.21	0.36	0.04	0.13	1.94
	FGOALS-g3	2.88	–1.25	–3.23	1.45	0.49	0.10	-0.06	1.54
	FIO-ESM-2-0								2.22
	GFDL-CM4		–0.82	–3.18	1.23	0.50	0.64	-0.01	
	GFDL-ESM4		–1.42	–3.25	1.18	0.34	0.50	-0.19	
	GISS-E2-1-G	2.72	–1.46	–3.20	1.06	0.24	0.07	0.38	1.80
	GISS-E2-1-H	3.11	–1.13	–3.16	1.27	0.42	0.06	0.28	1.93
	GISS-E2-2-G		–1.51	–3.19	1.18	0.32	0.01	0.18	1.71
	HadGEM3-GC31-LL	5.55	–0.63	–3.21	1.19	0.38	0.84	0.17	2.55
	HadGEM3-GC31-MM	5.42	–0.66	–3.23	1.18	0.32	0.91	0.16	2.58
	IITM-ESM		–1.91	–3.22	1.16	0.26	-0.02	-0.08	1.71
	INM-CM4-8	1.83	–1.48	–3.23	1.45	0.36	-0.09	0.02	1.33
	INM-CM5-0	1.92	–1.52	–3.23	1.40	0.40	-0.06	-0.03	
	IPSL-CM5A2-INCA		–0.81	–3.25	1.23	0.33	1.05	-0.16	
	IPSL-CM6A-LR	4.56	–0.76	–3.22	1.35	0.44	0.45	0.22	2.32
	KACE-1-0-G	4.48	–0.72	–3.24	1.17	0.33	0.84	0.18	1.41
	MCM-UA-1-0	3.65							1.94
	MIROC-ES2L	2.68	–1.54	–3.26	1.19	0.40	0.04	0.08	1.55
	MIROC6	2.61	–1.40	–3.29	1.30	0.47	0.22	-0.10	1.55
	MPI-ESM-1-2-HAM	2.96	–1.41	–3.10	1.18	0.36	-0.16	0.32	1.80
	MPI-ESM1-2-HR	2.98	–1.22	–3.14	1.21	0.38	0.27	0.05	1.66
	MPI-ESM1-2-LR	3.00	–1.39	–3.11	1.12	0.37	0.18	0.05	1.84
	MRI-ESM2-0	3.15	–1.10	–3.20	1.16	0.54	0.46	-0.06	1.64
	NESM3	4.72	–0.78	–3.09	1.19	0.50	0.45	0.17	2.72
	NorCPM1	3.05	–1.10	–3.17	1.31	0.44	0.30	0.01	1.56
	NorESM2-LM	2.54	–1.34	–3.30	1.28	0.35	0.44	-0.11	1.48
	NorESM2-MM	2.50	–1.50	–3.32	1.29	0.30	0.51	-0.28	1.33
	SAM0-UNICON	3.72	–1.04	–3.27	1.13	0.38	0.75	-0.03	2.27
	TaiESM1	4.31	–0.88	–3.25	1.26	0.40	0.70	0.00	2.34
	UKESM1-0-LL	5.34	–0.67	–3.19	1.19	0.48	0.87	-0.01	2.79
CMIP6 mean		3.78	–1.03	–3.22	1.25	0.39	0.49	0.05	2.01
CMIP6 standard deviation		1.08	0.36	0.05	0.09	0.08	0.38	0.14	0.41
CMIP5	ACCESS1-0	3.83	–0.76	–3.18	1.26	0.43	0.47	0.25	

ACCEPTED VERSION SUBJECT TO FINAL EDITING

	ACCESS1-3	3.53	–0.81	–3.21	1.25	0.41	0.65	0.08	
	BNU-ESM	3.92	–0.92	–3.14	1.35	0.61	0.20	0.05	
	CCSM4	2.94	–1.18	–3.19	1.28	0.48	0.27	-0.02	
	CNRM-CM5	3.25	–1.13	–3.20	1.24	0.46	0.15	0.21	
	CNRM-CM5-2	3.44							
	CSIRO-Mk3-6-0	4.08	–0.64	–3.26	1.25	0.38	0.67	0.32	
	CanESM2	3.69	–1.03	–3.28	1.35	0.39	0.52	-0.02	
	FGOALS-g2	3.38	–0.84	–3.18	1.40	0.59	0.38	-0.03	
	FGOALS-s2		–0.91	–3.19	1.32	0.52	0.03	0.42	
	GFDL-CM3	3.97	–0.76	–3.18	1.08	0.43	0.88	0.02	
	GFDL-ESM2G	2.39	–1.23	–3.20	1.17	0.30	0.22	0.27	
	GFDL-ESM2M	2.44	–1.37	–3.20	1.13	0.29	0.11	0.30	
	GISS-E2-H	2.31	–1.66	–3.16	1.27	0.32	-0.12	0.03	
	GISS-E2-R	2.11	–1.76	–3.17	1.30	0.24	-0.14	0.01	
	HadGEM2-ES	4.61	–0.63	–3.17	1.30	0.40	0.70	0.14	
	IPSL-CM5A-LR	4.13	–0.75	–3.26	1.20	0.27	1.18	-0.14	
	IPSL-CM5A-MR	4.12	–0.80	–3.28	1.18	0.19	1.25	-0.14	
	IPSL-CM5B-LR	2.60	–1.02	–3.17	1.32	0.28	0.62	-0.06	
	MIROC-ESM	4.67	–0.92	–3.32	1.23	0.50	0.68	-0.02	
	MIROC5	2.72	–1.53	–3.24	1.29	0.48	-0.04	-0.02	
	MPI-ESM-LR	3.63	–1.13	–3.16	1.09	0.44	0.44	0.06	
	MPI-ESM-MR	3.46	–1.19	–3.17	1.05	0.39	0.47	0.06	
	MPI-ESM-P	3.45	–1.23	–3.18	1.08	0.40	0.39	0.08	
	MRI-CGCM3	2.60	–1.23	–3.24	1.25	0.51	0.28	-0.03	
	NorESM1-M	2.80	–1.10	–3.17	1.32	0.45	0.29	0.01	
	NorESM1-ME		–1.10	–3.16	1.30	0.45	0.33	-0.01	
	bcc-csm1-1-m	2.86	–1.19	–3.27	1.29	0.40	0.40	0.00	
	bcc-csm1-1	2.83	–1.15	–3.21	1.27	0.45	0.28	0.05	
	inmcm4	2.08	–1.43	–3.18	1.23	0.43	0.24	-0.15	
CMIP5 mean		3.28	–1.08	–3.20	1.24	0.41	0.41	0.06	
CMIP5 standard deviation		0.74	0.29	0.05	0.09	0.10	0.33	0.14	

[END TABLE 7.SM.5 HERE]

ACCEPTED VERSION SUBJECT TO FINAL EDITING

7.SM.5 Climate metrics

7.SM.5.1 Definitions of climate metrics

Absolute Global Forcing Potential:

$$A\mathrm{GFP}_X(H) = \Delta F_X(H) \qquad \textit{Equation 7.SM.5.1}$$

Absolute Global Warming Potential

$$A\mathrm{GWP}_X(H) = \int_0^H \Delta F_X(t)dt \qquad \textit{Equation 7.SM.5.2}$$

Absolute Global Temperature-change Potential:

$$A\mathrm{GTP}^X(H) = \Delta T^X(H) = \int_0^H A\mathrm{GFP}^X(t)R_\mathrm{T}(H-t)dt \qquad \textit{Equation 7.SM.5.3}$$

Absolute Global Sea-level Rise:

$$A\mathrm{GSR}^X(H) = \Delta\mathrm{SLR}^X(H) = \int_0^H A\mathrm{GTP}^X(t)R_\mathrm{SLR}(H-t)dt$$
$$= \int_0^H \int_0^t \mathrm{AGFP}^X(t')R_\mathrm{T}(t-t')R_\mathrm{SLR}(H-t)dt'dt$$

Equation 7.SM.5.4

where R_SLR is the sea-level rise resulting from a pulse temperature increase (Sterner et al., 2014).

Increase in absolute metric ($\Delta\mathrm{AGxx}^X$) due to the carbon cycle response:

$$\Delta\mathrm{AGxx}^X = \int_0^H \int_0^t AGTP^X(t')\gamma r_F(t-t')\mathrm{AGxx}^{\mathrm{CO2}}(H-t)dt'dt \qquad \textit{Equation 7.SM.5.5}$$

where $\gamma r_F(t)$ is the CO_2 flux perturbation following a unit temperature pulse in $kgCO_2\ yr^{-1}\ K^{-1}$ using the

ACCEPTED VERSION SUBJECT TO FINAL EDITING

parameterisation of Gasser et al. (2017b), and

$$r_F = \delta(t) - \frac{\alpha_1}{\tau_1} e^{-\frac{t}{\tau_1}} - \frac{\alpha_2}{\tau_2} e^{-\frac{t}{\tau_2}} - \frac{\alpha_3}{\tau_3} e^{-\frac{t}{\tau_3}} \qquad \textit{Equation 7.SM.5.6}$$

and the parameters used in Eqs. (7.SM.4.5) and (7.SM.4.6) are given in Table 7.SM.6.

[START TABLE 7.SM.6 HERE]

Table 7.SM.6: Parameters for the carbon cycle response function (from table 1 of (Gasser et al., 2017b)).

γ ($kgCO_2\ yr^{-1}\ °C^{-1}$)	α_1	α_2	α_3	τ_1 (yr)	τ_2 (yr)	τ_3 (yr)
11.06×10^{12}	0.6368	0.3322	0.00310	2.376	30.14	490.1

[END TABLE 7.SM.6 HERE]

Metrics for step emission changes can be derived by integrating the more standard pulse emission changes up to the time horizon:

$$\mathrm{AGTP}_X^S = \int_0^H \mathrm{AGTP}_X(H-t)dt \qquad \textit{Equation 7.SM.5.7}$$

The contribution to methane emission metrics from CO_2 from methane oxidation is given by

$$\Delta\mathrm{AGxx}^X = \int_0^H Y \frac{m_{\mathrm{CO_2}}}{m_{\mathrm{CH_4}}} \frac{1}{\tau_{\mathrm{OH}}} e^{-\frac{(H-t)}{\tau_{\mathrm{OH}}}} \mathrm{AGxx}^{\mathrm{CO2}}(H-t)dt \qquad \textit{Equation 7.SM.5.8}$$

where Y is the fractional molar yield of CO_2 from CH_4 oxidation (see Section 7.6.1.3), $m_{\mathrm{CO_2}}$ and $m_{\mathrm{CH_4}}$ are the molar masses of CO_2 and CH_4, and τ_{OH} is the methane oxidation lifetime time to OH (9.7 yr; Section 6.3.1).

7.SM.5.2 Impulse response functions for GTP and Chapter 6 calculations

To generate a suite of two-layer configurations for uncertainty estimates in GTP calculations (Tables 7.SM.8–7.SM.13), information from the FaIRv1.6.2 and MAGICC7.5.1 AR6 calibration setups (Cross Chapter Box 7.1) are used. FaIRv1.6.2 uses the two-layer model in Eq. (7.SM.2.1) as its core so converting its parameters to two-layer configurations is trivial (discussed in Section 7.SM.2.2). To convert MAGICC7.5.1's configuration to two-layer configurations, the two-layer model parameters are fitted to MAGICC7.5.1's output from an abrupt $2\times CO_2$ experiment. However, such a fitting procedure produces only an approximate translation because MAGICC7.5.1 is not well-represented by a two-timescale model. After these two conversions are done an ensemble of two-layer configurations is generated which is used for uncertainty analysis in GTP calculations.

To generate the Chapter 6 two-layer configuration, the timescales and efficacy parameters are calculated as the average of FaIRv1.6.2's median and a fit to MAGICC7.5.1's median response (both in their AR6 calibrations). Response magnitudes that describe the contributions to the fast and slow response timescales are calculated such that the Chapter 6 configuration matches the best-estimate ECS of 3.0°C and TCR of 1.8°C (Table 7.13) under the best-estimate ERF due to a doubling of CO_2 of 3.93 W m^{-2}. This results in parameter values for C = 7.7 W yr m^{-2} $°C^{-1}$, C_d = 147 W yr m^{-2} $°C^{-1}$, α = –1.31 W m^{-2} $°C^{-1}$, ε = 1.03, κ =

ACCEPTED VERSION SUBJECT TO FINAL EDITING

0.88 W m^{-2} °C^{-1}. Note these parameters differ from CMIP6 two-layer model calibrations in Section 7.SM.2.1, as the set described here is derived from a constrained ensemble from two emulators.

ACCEPTED VERSION
SUBJECT TO FINAL EDITING

7.SM.6 Tables of greenhouse gas lifetimes, radiative efficiencies and metrics

[START TABLE 7.SM.7 HERE]

Table 7.SM.7: Greenhouse gas lifetimes, radiative efficiencies, Global Warming Potentials (GWPs), Global Temperature Potentials (GTPs) and Cumulative Global Temperature Potentials (CGTPs). GWPs given for 20-year, 100-year and 500-year time horizons. GTPs and CGTPs given for 50-year and 100-year time horizons. Note CGTP has units of years and is applied to a change in emission rate rather than a change in emission amount. Also shown are absolute values of GWPs and GTPs (AGWPs and AGTPs), in units of picowatt years per square metre per kilogram (1 pW = 10^{-12} W). Radiative efficiencies for CH_4 and N_2O given in this table do not include chemical adjustments (values including chemical adjustments are given in Table 7.15).

Name	Formula	Lifetime (yr)	Radiative efficiency (W m^{-2} ppb^{-1})	AGWP 20 (pW m^{-2} yr kg^{-1})	GWP 20	AGWP 100 (pW m^{-2} yr kg^{-1})	GWP 100	AGWP 500 (pW m^{-2} yr kg^{-1})	GWP 500	AGTP 50 (pW m^{-2} yr kg^{-1})	GTP 50	AGTP 100 (pW m^{-2} yr kg^{-1})	GTP 100	CGTP 50 (yr)	CGTP 100 (yr)
Major Greenhouse Gases															
Carbon dioxide	CO_2		1.33×10^{-5}	0.0243	1	0.0895	1	0.314	1	0.000428	1	0.000395	1		
Methane	CH_4	11.8	0.000388	1.98	81.2	2.49	27.9	2.5	7.95	0.00473	11	0.00212	5.38	2730	3320
Nitrous oxide	N_2O	109	0.0032	6.65	273	24.5	273	40.7	130	0.124	290	0.0919	233		
Chlorofluorocarbons															
CFC-11	CCl_3F	52	0.259	181	7430	497	5560	586	1870	2.43	5670	1.25	3160		
CFC-12	CCl_2F_2	102	0.32	277	11400	998	11200	1600	5100	5.06	11800	3.66	9270		
CFC-13	$CClF_3$	640	0.278	301	12400	1450	16200	5500	17500	7.26	17000	7.4	18800		
CFC-112	CCl_2FCCl_2F	63.6	0.282	137	5620	413	4620	525	1670	2.06	4810	1.19	3020		
CFC-112a	CCl_3CClF_2	52	0.246	115	4740	317	3550	374	1190	1.55	3620	0.795	2010		
CFC-113	CCl_2FCClF_2	93	0.301	167	6860	583	6520	890	2830	2.96	6910	2.06	5210		
CFC-113a	CCl_3CF_3	55	0.241	124	5110	351	3930	422	1350	1.73	4030	0.917	2320		
CFC-114	$CClF_2CClF_2$	189	0.314	201	8260	844	9430	1930	6150	4.28	9990	3.71	9410		
CFC-114a	CCl_2FCF_3	105	0.297	183	7510	664	7420	1080	3450	3.37	7880	2.46	6240		

ACCEPTED VERSION SUBJECT TO FINAL EDITING

CFC-115	$CClF_2CF_3$	540	0.246	180	7410	859	9600	3100	9880	4.3	10100	4.33	11000		
E-R316c	trans cyc (-$CClFCF_2CF_2CClF$-)	75	0.27	117	4810	379	4230	518	1650	1.91	4450	1.2	3040		
Z-R316c	cis cyc (-$CClFCF_2CF_2CClF$-)	114	0.3	136	5590	507	5660	865	2760	2.57	6020	1.94	4910		
CFC 1112	$CClF=CClF$	0.019	0.013	0.0111	0.454	0.0113	0.126	0.0113	0.036	1.18×10^{-5}	0.028	8.96×10^{-6}	0.023	12.3	14.5
CFC 1112a	$CCl_2=CF_2$	0.006	0.007	0.00184	0.076	0.00188	0.021	0.00188	0.006	1.97×10^{-6}	0.005	1.49×10^{-6}	0.004	2.06	2.42
Hydrofluorochlorocarbons															
HCFC-21	$CHCl_2F$	1.7	0.145	14	575	14.3	160	14.3	45.6	0.0152	35.5	0.0114	29	15600	18300
HCFC-22	$CHClF_2$	11.9	0.214	139	5690	175	1960	176	560	0.336	785	0.15	379	184000	222000
HCFC-31	CH_2ClF	1.2	0.068	6.96	286	7.11	79.4	7.11	22.6	0.00752	17.6	0.00567	14.4	7750	9130
HCFC-121	$CHCl_2CCl_2F$	1.11	0.146	5.11	210	5.22	58.3	5.22	16.6	0.00552	12.9	0.00416	10.5	5690	6700
HCFC-122	$CHCl_2CClF_2$	0.9	0.159	4.94	203	5.05	56.4	5.05	16.1	0.00533	12.5	0.00403	10.2	5510	6490
HCFC-122a	$CHClFCCl_2F$	3.1	0.201	21.4	879	21.9	245	21.9	69.9	0.0236	55.3	0.0177	44.7	23800	28100
HCFC-123	$CHCl_2CF_3$	1.3	0.16	7.92	325	8.09	90.4	8.09	25.8	0.00857	20	0.00646	16.4	8830	10400
HCFC-123a	$CHClFCClF_2$	4	0.227	34.3	1410	35.3	395	35.3	113	0.0385	90	0.0285	72.3	38400	45200
HCFC-124	$CHClFCF_3$	5.9	0.207	50.3	2070	53.4	597	53.4	170	0.0612	143	0.0435	110	57700	68100
HCFC-124a	CHF_2CClF_2	17	0.25	124	5110	185	2070	186	592	0.521	1220	0.177	448	185000	232000
HCFC-132	CHClFCHClF	1.73	0.143	10.7	440	11	122	11	34.9	0.0116	27.2	0.00876	22.2	11900	14000
HCFC-132a	$CHCl_2CHF_2$	1.12	0.127	6.17	253	6.3	70.4	6.3	20.1	0.00666	15.6	0.00503	12.7	6870	8090
HCFC-132c	CH_2FCCl_2F	4.1	0.169	29.6	1220	30.6	342	30.6	97.6	0.0334	78.1	0.0247	62.7	33200	39100
HCFC-133a	CH_2ClCF_3	4.6	0.15	33.4	1370	34.7	388	34.7	111	0.0382	89.3	0.0281	71.3	37600	44400
HCFC-141	$CH_2ClCHClF$	1.14	0.072	4.08	168	4.17	46.6	4.17	13.3	0.00441	10.3	0.00333	8.43	4550	5350
HCFC-141b	CH_3CCl_2F	9.4	0.161	65.9	2710	77	860	77	246	0.115	269	0.064	162	82100	97700
HCFC-142b	CH_3CClF_2	18	0.193	134	5510	205	2300	207	658	0.611	1430	0.203	514	203000	257000
HCFC-225ca	$CHCl_2CF_2CF_3$	1.9	0.219	12	491	12.2	137	12.2	39	0.013	30.4	0.00979	24.8	13300	15700

ACCEPTED VERSION SUBJECT TO FINAL EDITING

HCFC-225cb	$CHClFCF_2CClF_2$	5.9	0.293	47.8	1960	50.8	568	50.8	162	0.0582	136	0.0414	105	54900	64800
HCFO-1233zd(E)	(E)-CF_3CH=CHCl	0.116	0.065	0.34	14	0.347	3.88	0.347	1.11	0.000364	0.851	0.000276	0.7	380	447
HCFO-1233zd(Z)	(Z)-CF_3CH=CHCl	0.036	0.025	0.0398	1.64	0.0406	0.454	0.0406	0.129	4.25×10^{-5}	0.099	3.23×10^{-5}	0.082	44.4	52.3
(e)-1-chloro-2-fluoroethene	(E/Z)-CHCl=CHF	0.005	0.001	0.00032	0.013	0.000327	0.004	0.000327	0.001	3.42×10^{-7}	0.001	2.6×10^{-6}	0.001	0.357	0.42
Hydrofluorocarbons															
HFC-23	CHF_3	228	0.191	301	12400	1310	14600	3300	10500	6.6	15400	5.95	15100		
HFC-32	CH_2F_2	5.4	0.111	65.5	2690	69	771	69	220	0.0775	181	0.0561	142	74600	88000
HFC-41	CH_3F	2.8	0.025	11.8	485	12.1	135	12.1	38.6	0.013	30.4	0.00972	24.6	13200	15500
HFC-125	CHF_2CF_3	30	0.234	164	6740	335	3740	349	1110	1.41	3300	0.512	1300		
HFC-134	CHF_2CHF_2	10	0.194	95	3900	113	1260	113	361	0.18	420	0.0944	239	120000	143000
HFC-134a	CH_2FCF_3	14	0.167	101	4140	137	1530	137	436	0.314	733	0.121	306	141000	172000
HFC-143	CH_2FCHF_2	3.6	0.128	31.7	1300	32.6	364	32.6	104	0.0353	82.6	0.0263	66.6	35400	41700
HFC-143a	CH_3CF_3	51	0.168	191	7840	520	5810	609	1940	2.53	5910	1.28	3250		
HFC-152	CH_2FCH_2F	0.471	0.045	1.89	77.6	1.93	21.5	1.93	6.14	0.00203	4.74	0.00153	3.89	2110	2480
HFC-152a	CH_3CHF_2	1.6	0.102	14.4	591	14.7	164	14.7	46.8	0.0156	36.5	0.0118	29.8	16000	18900
HFC-161	CH_3CH_2F	0.219	0.016	0.424	17.4	0.433	4.84	0.433	1.38	0.000454	1.06	0.000344	0.872	473	557
HFC-227ca	$CF_3CF_2CHF_2$	30	0.264	131	5370	267	2980	278	885	1.12	2620	0.407	1030		
HFC-227ea	CF_3CHFCF_3	36	0.273	142	5850	322	3600	345	1100	1.45	3400	0.588	1490		
HFC-236cb	$CH_2FCF_2CF_3$	13.4	0.231	91.2	3750	121	1350	121	387	0.265	620	0.106	268	125000	153000
HFC-236ea	CHF_2CHFCF_3	11.4	0.3	108	4420	134	1500	134	428	0.245	572	0.114	288	141000	170000
HFC-236fa	$CF_3CH_2CF_3$	213	0.251	181	7450	777	8690	1900	6040	3.93	9200	3.5	8870		
HFC-245ca	$CH_2FCF_2CHF_2$	6.6	0.24	65.3	2680	70.5	787	70.5	225	0.0836	196	0.0576	146	76000	89800
HFC-245cb	$CF_3CF_2CH_3$	39.9	0.251	170	6970	407	4550	445	1420	1.89	4410	0.817	2070		
HFC-245ea	$CHF_2CHFCHF_2$	3.2	0.16	22.2	912	22.8	255	22.8	72.6	0.0246	57.4	0.0183	46.5	24800	29200

ACCEPTED VERSION SUBJECT TO FINAL EDITING

HFC-245eb	CH2FCHFCF3	3.2	0.204	28.3	1160	29	325	29.1	92.6	0.0313	73.2	0.0234	59.2	31600	37200
HFC-245fa	$CHF_2CH_2CF_3$	7.9	0.245	77.1	3170	86.1	962	86.1	274	0.112	262	0.0708	180	92500	109000
HFC-263fb	$CH_3CH_2CF_3$	1.1	0.1	6.55	269	6.69	74.8	6.69	21.3	0.00707	16.5	0.00534	13.5	7300	8590
HFC-272ca	$CH_3CF_2CH_3$	9	0.08	46.4	1910	53.6	599	53.6	171	0.0771	180	0.0444	113	57300	68100
HFC-329p	$CHF_2CF_2CF_2CF_3$	32	0.313	122	5010	259	2890	272	866	1.12	2610	0.421	1070		
HFC-365mfc	$CH_3CF_2CH_2CF_3$	8.9	0.228	71.1	2920	81.7	914	81.8	261	0.117	272	0.0677	172	87400	104000
HFC-43-10mee	$CF_3CHFCHFCF_2CF_3$	17	0.357	96.3	3960	143	1600	144	458	0.403	943	0.137	347	143000	180000
HFO-1123	$CHF=CF_2$	0.004	0.002	0.000414	0.017	0.000423	0.005	0.000423	0.001	4.42×10^{-7}	0.001	3.36×10^{-7}	0.001	0.462	0.544
HFO-1132a	$CH_2=CF_2$	0.013	0.004	0.0046	0.189	0.00469	0.052	0.00469	0.015	4.91×10^{-6}	0.011	3.73×10^{-6}	0.009	5.13	6.04
HFO-1141	$CH_2=CHF$	0.007	0.002	0.00213	0.088	0.00217	0.024	0.00218	0.007	2.28×10^{-6}	0.005	1.73×10^{-6}	0.004	2.38	2.8
HFO-1225ye(Z)	(Z)-$CF_3CF=CHF$	0.027	0.025	0.0302	1.24	0.0308	0.344	0.0308	0.098	3.23×10^{-5}	0.075	2.45×10^{-5}	0.062	33.7	39.6
HFO-1225ye(E)	(E)-$CF_3CF=CHF$	0.016	0.015	0.0104	0.426	0.0106	0.118	0.0106	0.034	1.11×10^{-5}	0.026	8.41×10^{-6}	0.021	11.6	13.6
HFO-1234ze(Z)	(Z)-$CF_3CH=CHF$	0.027	0.02	0.0276	1.13	0.0282	0.315	0.0282	0.09	2.95×10^{-5}	0.069	2.24×10^{-5}	0.057	30.8	36.2
HFO-1234ze(E)	(E)-$CF_3CH=CHF$	0.052	0.045	0.12	4.94	0.123	1.37	0.123	0.391	0.000129	0.3	9.75×10^{-5}	0.247	134	158
HFO-1234yf	$CF_3CF=CH_2$	0.033	0.026	0.044	1.81	0.0449	0.501	0.0449	0.143	4.7×10^{-5}	0.11	3.57×10^{-5}	0.09	49.1	57.7
HFO-1336mzz(E)	(E)-$CF_3CH=CHCF_3$	0.334	0.132	1.57	64.3	1.6	17.9	1.6	5.09	0.00168	3.92	0.00127	3.22	1750	2050
HFO-1336mzz(Z)	(Z)-$CF_3CH=CHCF_3$	0.074	0.069	0.182	7.48	0.186	2.08	0.186	0.592	0.000195	0.455	0.000148	0.374	203	239
HFO-1243zf	$CF_3CH=CH_2$	0.025	0.015	0.0229	0.94	0.0234	0.261	0.0234	0.074	2.45×10^{-5}	0.057	1.86×10^{-5}	0.047	25.5	30
HFO-1345zfc	$CF_3CF_2CH=CH_2$	0.025	0.016	0.016	0.656	0.0163	0.182	0.0163	0.052	1.71×10^{-5}	0.04	1.29×10^{-5}	0.033	17.8	21
3,3,4,4,5,5,6,6,6-nonafluorohex-1-ene	n-$C_4F_9CH=CH_2$	0.025	0.03	0.0179	0.734	0.0182	0.204	0.0182	0.058	1.91×10^{-5}	0.045	1.45×10^{-5}	0.037	19.9	23.4
3,3,4,4,5,5,6,6,7,7,8,8,8-tridecafluorooct-1-ene	n-$C_6F_{13}CH=CH_2$	0.025	0.034	0.0142	0.584	0.0145	0.162	0.0145	0.046	1.52×10^{-5}	0.036	1.15×10^{-5}	0.029	15.9	18.7
3,3,4,4,5,5,6,6,7,7,8,8,9,9,10,10,10-heptadecafluorodec-1-ene	n-$C_8F_{17}CH=CH_2$	0.025	0.038	0.0124	0.508	0.0126	0.141	0.0126	0.04	1.32×10^{-5}	0.031	0.00001	0.025	13.8	16.2

ACCEPTED VERSION SUBJECT TO FINAL EDITING

3,3,3-trifluoro-2-(trifluoromethyl)prop-1-ene	$(CF_3)_2C=CH_2$	0.028	0.033	0.0331	1.36	0.0337	0.377	0.0337	0.107	3.53×10^{-5}	0.083	2.68×10^{-5}	0.068	36.9	43.4
1,1,2,2,3,3-hexafluorocyclopentane	cyc (-$CF_2CF_2CF_2CH_2CH_2$-)	1.6	0.2	10.5	431	10.7	120	10.7	34.2	0.0114	26.6	0.00857	21.7	11700	13800
1,1,2,2,3,3,4-heptafluorocyclopentane	cyc (-$CF_2CF_2CF_2CHFCH_2$-)	2.8	0.243	20.2	830	20.7	231	20.7	66	0.0222	52	0.0166	42.1	22500	26500
1,3,3,4,4,5,5-heptafluorocyclopentene	cyc (-$CF_2CF_2CF_2CF$=CH-)	0.61	0.215	3.95	162	4.03	45.1	4.03	12.8	0.00424	9.92	0.00321	8.14	4400	5180
(4s,5s)-1,1,2,2,3,3,4,5-octafluorocyclopentane	trans-cyc (-$CF_2CF_2CF_2CHFCHF$-)	3.2	0.259	22.5	925	23.1	258	23.1	73.6	0.0249	58.2	0.0186	47.1	25100	29600
HFO-1438ezy(E)	(E)-$(CF_3)_2CFCH=CHF$	0.334	0.079	0.721	29.6	0.736	8.22	0.736	2.34	0.000773	1.81	0.000585	1.48	804	946
HFO-1447fz	$CF_3(CF_2)_2CH=CH_2$	0.025	0.028	0.0206	0.847	0.021	0.235	0.021	0.067	2.2×10^{-5}	0.051	1.67×10^{-5}	0.042	23	27.1
1,3,3,4,4-pentafluorocyclobutene	cyc (-$CH=CFCF_2CF_2$-)	0.74	0.27	8.1	333	8.27	92.4	8.27	26.4	0.00872	20.4	0.00659	16.7	9030	10600
3,3,4,4-tetrafluorocyclobutene	cyc (-$CH=CHCF_2CF_2$-)	0.23	0.21	2.24	92.1	2.29	25.6	2.29	7.29	0.0024	5.61	0.00182	4.61	2500	2940
Chlorocarbons and Hydrochlorocarbons															
Methyl chloroform	CH_3CCl_3	5	0.065	13.8	567	14.4	161	14.4	46	0.016	37.5	0.0117	29.7	15600	18400
Carbon tetrachloride	CCl_4	32	0.166	92.7	3810	196	2200	206	658	0.849	1990	0.32	810		
Methyl chloride	CH_3Cl	0.9	0.005	0.485	19.9	0.495	5.54	0.496	1.58	0.000523	1.22	0.000395	1	541	637
Methylene chloride	CH_2Cl_2	0.493	0.029	0.978	40.2	0.998	11.2	0.998	3.18	0.00105	2.46	0.000795	2.01	1090	1280
Chloroform	$CHCl_3$	0.501	0.074	1.81	74.2	1.84	20.6	1.84	5.87	0.00194	4.53	0.00147	3.72	2010	2370
Chloroethane	CH_3CH_2Cl	0.132	0.004	0.0422	1.73	0.043	0.481	0.043	0.137	4.51×10^{-5}	0.105	3.42×10^{-5}	0.087	47	55.4
1,2-dichloroethane	CH_2ClCH_2Cl	0.225	0.009	0.114	4.68	0.116	1.3	0.116	0.371	0.000122	0.285	9.25×10^{-5}	0.234	127	150
1,1,2-trichloroethene	$CHCl=CCl_2$	0.015	0.006	0.00385	0.158	0.00393	0.044	0.00393	0.013	4.11×10^{-6}	0.01	3.12×10^{-5}	0.008	4.3	5.06
1,1,2,2-tetrachloroethene	$CCl_2=CCl_2$	0.301	0.052	0.556	22.8	0.567	6.34	0.567	1.81	0.000596	1.39	0.000451	1.14	620	730
2-chloropropane	$CH_3CHClCH_3$	0.06	0.004	0.0158	0.651	0.0162	0.181	0.0162	0.052	1.69×10^{-5}	0.04	1.28×10^{-6}	0.033	17.7	20.8
1-chlorobutane	$CH_3(CH_2)_2CH_2Cl$	0.012	0.001	0.000595	0.024	0.000607	0.007	0.000607	0.002	6.35×10^{-7}	0.001	4.82×10^{-7}	0.001	0.664	0.781
Bromocarbons, hydrobromocarbons and halons															

ACCEPTED VERSION SUBJECT TO FINAL EDITING

Methyl bromide	CH_3Br	0.8	0.004	0.213	8.74	0.217	2.43	0.217	0.692	0.000229	0.535	0.000173	0.438	237	279
Methylene bromide	CH_2Br_2	0.411	0.01	0.133	5.45	0.135	1.51	0.135	0.431	0.000142	0.333	0.000108	0.273	148	174
Halon-1201	$CHBrF_2$	4.9	0.152	32.5	1340	34	380	34	108	0.0376	88	0.0275	69.8	36800	43400
Halon-1202	CBr_2F_2	2.5	0.272	18.9	775	19.3	216	19.3	61.5	0.0207	48.4	0.0155	39.3	21000	24800
Halon-1211	$CBrClF_2$	16	0.3	120	4920	173	1930	173	552	0.458	1070	0.16	406	174000	217000
Halon-1301	$CBrF_3$	72	0.299	202	8320	644	7200	864	2750	3.23	7560	2	5060		
Halon-2301	CH_2BrCF_3	3.2	0.135	15.5	635	15.9	177	15.9	50.6	0.0171	40	0.0128	32.4	17200	20300
Halon-2311	$CHBrClCF_3$	1	0.133	3.94	162	4.03	45	4.03	12.8	0.00425	9.95	0.00321	8.14	4400	5170
Halon-2401	$CHBrFCF_3$	2.9	0.189	17.6	723	18	201	18	57.5	0.0194	45.3	0.0145	36.7	19600	23100
Halon-2402	$CBrF_2CBrF_2$	28	0.312	99	4070	194	2170	201	639	0.791	1850	0.277	702		
Tribromomethane	$CHBr_3$	0.156	0.006	0.0219	0.901	0.0224	0.25	0.0224	0.071	2.35×10^{-5}	0.055	0.0000178	0.045	24.5	28.8
Halon-1011	CH_2BrCl	0.452	0.02	0.415	17.1	0.424	4.74	0.424	1.35	0.000446	1.04	0.000337	0.855	463	545
Bromoethane	CH_3CH_2Br	0.137	0.006	0.0427	1.75	0.0436	0.487	0.0436	0.139	4.57×10^{-5}	0.107	3.46×10^{-5}	0.088	47.6	56
1,2-dibromoethane	CH_2BrCH_2Br	0.244	0.012	0.0894	3.67	0.0913	1.02	0.0913	0.291	9.58×10^{-5}	0.224	7.26×10^{-5}	0.184	99.7	117
1-bromopropane	$CH_3CH_2CH_2Br$	0.041	0.002	0.00457	0.188	0.00466	0.052	0.00466	0.015	4.88×10^{-6}	0.011	3.71×10^{-6}	0.009	5.1	6
2-bromopropane	$CH_3CHBrCH_3$	0.055	0.004	0.011	0.453	0.0112	0.126	0.0112	0.036	1.18×10^{-5}	0.028	8.93×10^{-6}	0.023	12.3	14.5
Fully fluorinated species															
Nitrogen trifluoride	NF_3	569	0.204	326	13400	1560	17400	5720	18200	7.81	18200	7.89	20000		
Pentadecafluorotriethylamine	$N(C_2F_5)_3$	1000	0.61	188	7700	923	10300	3860	12300	4.61	10800	4.81	12200		
Perfluorotripropylamine	$N(CF_2CF_2CF_3)_3$	1000	0.75	164	6750	808	9030	3380	10800	4.03	9430	4.21	10700		
Heptacosafluorotributylamine	$N(CF_2CF_2CF_2CF_3)_3$	1000	0.907	154	6340	759	8490	3170	10100	3.79	8860	3.96	10000		
Perfluorotripentylamine	$N(CF_2CF_2CF_2CF_2CF_3)_3$	1000	0.95	132	5420	650	7260	2720	8650	3.24	7580	3.39	8580		
Heptafluoroisobutyronitrile	$(CF_3)_2CFCN$	34.5	0.248	111	4580	246	2750	262	835	1.09	2560	0.431	1090		
Sulfur hexafluoride	SF_6	3200	0.567	445	18300	2250	25200	10700	34100	11.2	26200	12.1	30600		

ACCEPTED VERSION SUBJECT TO FINAL EDITING

Trifluromethylsulfur pentafluoride	SF_5CF_3	800	0.585	339	13900	1660	18500	6610	21100	8.27	19300	8.54	21600		
Sulfuryl fluoride	SO_2F_2	36	0.211	183	7510	414	4630	444	1410	1.87	4360	0.756	1920		
PFC-14	CF_4	50000	0.099	129	5300	660	7380	3320	10600	3.28	7660	3.57	9050		
PFC-116	C_2F_6	10000	0.261	218	8940	1110	12400	5500	17500	5.51	12900	5.99	15200		
PFC-218	C_3F_8	2600	0.27	165	6770	831	9290	3890	12400	4.13	9660	4.44	11200		
Hexafluorocyclobutene	cyc (-CF=CFCF$_2$CF$_2$-)	1.02	0.3	11	453	11.3	126	11.3	35.9	0.0119	27.8	0.00898	22.8	12300	14500
PFC-C-318	cyc (-CF$_2$CF$_2$CF$_2$CF$_2$-)	3200	0.314	180	7400	912	10200	4330	13800	4.53	10600	4.88	12400		
PFC-31-10	n-C_4F_{10}	2600	0.369	178	7300	897	10000	4200	13400	4.46	10400	4.79	12100		
Octafluorocyclopentene	cyc (-CF=CFCF$_2$CF$_2$CF$_2$-)	1.1	0.246	6.84	281	6.99	78.1	6.99	22.3	0.00739	17.3	0.00557	14.1	7620	8970
PFC-41-12	n-C_5F_{12}	4100	0.408	163	6680	825	9220	3970	12700	4.1	9580	4.43	11200		
PFC-51-14	n-C_6F_{14}	3100	0.449	153	6260	771	8620	3660	11600	3.83	8960	4.12	10500		
PFC-61-16	n-C_7F_{16}	3000	0.503	149	6120	752	8410	3560	11300	3.74	8740	4.02	10200		
PFC-71-18	n-C_8F_{18}	3000	0.558	146	6010	739	8260	3500	11100	3.67	8590	3.95	10000		
PFC-91-18	$C_{10}F_{18}$	2000	0.537	133	5480	669	7480	3070	9780	3.33	7790	3.56	9010		
1,1,2,2,3,3,4,4,4a,5,5,6,6,7,7,8,8, 8a-octadecafluoronaphthalene	Z-$C_{10}F_{18}$	2000	0.56	139	5710	698	7800	3200	10200	3.47	8120	3.71	9400		
1,1,2,2,3,3,4,4,4a,5,5,6,6,7,7,8,8, 8a-octadecafluoronaphthalene	E-$C_{10}F_{18}$	2000	0.512	127	5220	637	7120	2920	9310	3.17	7420	3.39	8580		
PFC-1114	$CF_2=CF_2$	0.003	0.002	0.000347	0.014	0.000354	0.004	0.000354	0.001	3.71×10^{-7}	0.001	2.81×10^{-7}	0.001	0.387	0.456
PFC-1216	$CF_3CF=CF_2$	0.015	0.013	0.00788	0.324	0.00804	0.09	0.00804	0.026	8.42×10^{-6}	0.02	6.39×10^{-6}	0.016	8.8	10.3
1,1,2,3,4,4-hexafluorobuta-1,3-diene	$CF_2=CFCF=CF_2$	0.003	0.003	0.000347	0.014	0.000354	0.004	0.000354	0.001	3.71×10^{-7}	0.001	2.82×10^{-7}	0.001	0.388	0.456
Octafluoro-1-butene	$CF_3CF_2CF=CF_2$	0.016	0.019	0.00891	0.366	0.00909	0.102	0.00909	0.029	9.52×10^{-6}	0.022	7.22×10^{-5}	0.018	9.94	11.7
Octafluoro-2-buene	$CF_3CF=CFCF_3$	0.085	0.07	0.173	7.1	0.176	1.97	0.176	0.562	0.000185	0.432	0.00014	0.355	193	227
Halogenated alcohols, ethers, furans, aldehydes and ketones															

ACCEPTED VERSION SUBJECT TO FINAL EDITING

HFE-125	CHF_2OCF_3	135	0.417	328	13500	1280	14300	2410	7680	6.5	15200	5.17	13100		
HFE-134	CHF_2OCHF_2	26.9	0.449	310	12700	593	6630	610	1940	2.37	5530	0.814	2060		
HFE-143a	CH_3OCF_3	4.9	0.189	52.8	2170	55.1	616	55.1	176	0.0611	143	0.0447	113	59700	70400
HFE-227ea	$CF_3CHFOCF_3$	54.8	0.459	238	9800	673	7520	808	2570	3.3	7720	1.75	4440		
HCFE-235ca2	CHF_2OCF_2CHFCl	4.42	0.409	56.4	2320	58.5	654	58.5	186	0.0642	150	0.0473	120	63400	74800
HCFE-235da2	$CHF_2OCHClCF_3$	3.5	0.426	46.9	1930	48.2	539	48.2	154	0.0522	122	0.0388	98.4	52400	61700
HCFE-236ea2	$CHF_2OCHFCF_3$	14.1	0.464	171	7020	232	2590	233	741	0.537	1260	0.206	521	239000	292000
HFE-236fa	$CF_3CH_2OCF_3$	7.5	0.371	89.4	3670	98.7	1100	98.8	315	0.125	291	0.0811	205	106000	126000
HFE-245cb2	$CF_3CF_2OCH_3$	5	0.336	64	2630	66.9	747	66.9	213	0.0743	174	0.0542	137	72400	85400
HFE-245fa1	$CHF_2CH_2OCF_3$	6.7	0.314	77.2	3170	83.6	934	83.6	266	0.0998	233	0.0683	173	90100	106000
HFE-245fa2	$CHF_2OCH_2CF_3$	5.5	0.36	74.5	3060	78.6	878	78.6	251	0.0886	207	0.0639	162	85000	100000
2,2,3,3,3-pentafluoropropan-1-ol	$CF_3CF_2CH_2OH$	0.471	0.164	3.01	123	3.07	34.3	3.07	9.78	0.00323	7.54	0.00244	6.19	3350	3940
HFE-254cb1	$CH_3OCF_2CHF_2$	2.5	0.26	28.7	1180	29.3	328	29.3	93.5	0.0314	73.4	0.0235	59.6	31900	37600
HFE-263mf	$CF_3CH_2OCH_3$	0.077	0.046	0.181	7.43	0.184	2.06	0.185	0.588	0.000193	0.452	0.000147	0.371	202	237
HFE-263m1	$CF_3OCH_2CH_3$	0.397	0.126	2.56	105	2.61	29.2	2.61	8.32	0.00274	6.42	0.00208	5.27	2850	3360
3,3,3-trifluoropropan-1-ol	$CF_3CH_2CH_2OH$	0.041	0.026	0.0544	2.23	0.0555	0.62	0.0555	0.177	5.81×10^{-5}	0.136	4.41×10^{-5}	0.112	60.7	71.4
HFE-329mcc2	$CHF_2CF_2OCF_2CF_3$	25	0.545	184	7550	337	3770	345	1100	1.29	3020	0.432	1090		
HFE-338mmz1	$(CF_3)_2CHOCHF_2$	22.3	0.452	158	6500	272	3040	276	880	0.967	2260	0.314	797		
HFE-338mcf2	$CF_3CH_2OCF_2CF_3$	7.5	0.454	84.2	3460	93	1040	93.1	297	0.117	274	0.0764	194	100000	118000
HFE-347mmz1	$(CF_3)_2CHOCH_2F$	1.9	0.308	17.1	702	17.5	195	17.5	55.7	0.0186	43.5	0.014	35.4	19000	22400
HFE-347mcc3	$CH_3OCF_2CF_2CF_3$	5.1	0.339	49.2	2020	51.5	576	51.6	164	0.0574	134	0.0418	106	55800	65800
HFE-347mcf2	$CHF_2CH_2OCF_2CF_3$	6.7	0.431	79.6	3270	86.2	963	86.2	275	0.103	241	0.0705	179	92900	110000
HFE-347pcf2	$CHF_2CF_2OCH_2CF_3$	6.1	0.482	82.1	3370	87.6	980	87.7	279	0.101	237	0.0715	181	94700	112000
HFE-347mmy1	$(CF_3)_2CFOCH_3$	3.7	0.318	34.1	1400	35.1	392	35.1	112	0.0381	89	0.0283	71.8	38100	44900

ACCEPTED VERSION SUBJECT TO FINAL EDITING

HFE-356mec3	$CH_3OCF_2CHFCF_3$	2.5	0.288	23.1	949	23.6	264	23.6	75.3	0.0253	59.2	0.019	48	25700	30300
HFE-356mff2	$CF_3CH_2OCH_2CF_3$	0.351	0.19	2.14	88	2.19	24.4	2.19	6.97	0.0023	5.37	0.00174	4.41	2390	2810
HFE-356pcf2	$CHF_2CH_2OCF_2CHF_2$	6	0.378	69.8	2870	74.4	831	74.4	237	0.0856	200	0.0606	154	80400	94800
HFE-356pcf3	$CHF_2OCH_2CF_2CHF_2$	3.5	0.378	42.1	1730	43.3	484	43.3	138	0.0469	110	0.0349	88.4	47000	55400
HFE-356pcc3	$CH_3OCF_2CF_2CHF_2$	2.5	0.303	24.2	995	24.8	277	24.8	79	0.0266	62.1	0.0199	50.4	27000	31800
HFE-356mmz1	$(CF_3)_2CHOCH_3$	0.178	0.125	0.713	29.3	0.728	8.13	0.728	2.32	0.000763	1.78	0.000579	1.47	795	936
HFE-365mcf3	$CF_3CF_2CH_2OCH_3$	0.069	0.058	0.141	5.77	0.143	1.6	0.143	0.457	0.00015	0.351	0.000114	0.289	157	184
HFE-374pc2	$CHF_2CF_2OCH_2CH_3$	0.208	0.132	1.1	45	1.12	12.5	1.12	3.56	0.00117	2.74	0.000889	2.25	1220	1440
4,4,4-trifluorobutan-1-ol	$CF_3(CH_2)_2CH_2OH$	0.015	0.006	0.00433	0.178	0.00442	0.049	0.00442	0.014	4.63×10^{-5}	0.011	3.51×10^{-5}	0.009	4.84	5.69
2,2,3,3,4,4,5,5-octafluorocyclopentan-1-ol	cyc (-$(CF_2)_4CH(OH)$-)	0.301	0.156	1.2	49.1	1.22	13.6	1.22	3.89	0.00128	3	0.000971	2.46	1330	1570
HFE-43-10pccc124	$CHF_2OCF_2OCF_2CF_2OCHF_2$	14.1	1.03	212	8720	288	3220	289	920	0.667	1560	0.255	647	297000	363000
HFE-449s1	$C_4F_9OCH_3$	4.8	0.36	39.5	1620	41.2	460	41.2	131	0.0455	106	0.0334	84.6	44600	52600
n-HFE-7100	$CF_3CF_2CF_2CF_2OCH_3$	4.8	0.425	46.7	1920	48.6	544	48.7	155	0.0538	126	0.0394	99.9	52700	62200
i-HFE-7100	$(CF_3)_2CFCF_2OCH_3$	4.8	0.341	37.5	1540	39.1	437	39.1	124	0.0432	101	0.0317	80.2	42300	49900
HFE-569sf2	$C_4F_9OC_2H_5$	0.8	0.301	5.32	219	5.43	60.7	5.43	17.3	0.00573	13.4	0.00433	11	5930	6980
i-HFE-7200	$(CF_3)_2CFCF_2OCH_2CH_3$	0.63	0.216	3.01	124	3.07	34.3	3.07	9.78	0.00323	7.56	0.00245	6.2	3350	3950
HFE-7300	$(CF_3)_2CFCFOC_2H_5CF_2CF_2CF_3$	5.24	0.48	34.5	1420	36.2	405	36.2	115	0.0405	94.7	0.0294	74.6	39200	46200
HFE-7500	n-$C_3F_7CFOC_2H_5CF(CF_3)_2$	0.3	0.27	1.14	47	1.17	13	1.17	3.72	0.00123	2.86	0.000928	2.35	1270	1500
HFE-236ca12	$CHF_2OCF_2OCHF_2$	26.5	0.648	285	11700	542	6060	557	1770	2.15	5020	0.733	1860		
HFE-338pcc13	$CHF_2OCF_2CF_2OCHF_2$	13.4	0.87	223	9180	297	3320	297	948	0.649	1520	0.259	657	307000	374000
1,1,1,3,3,3-hexafluoropropan-2-ol	$(CF_3)_2CHOH$	1.9	0.274	18.1	742	18.5	206	18.5	58.8	0.0197	46	0.0148	37.4	20100	23700
HG-02	$CHF_2(OCF_2CF_2)_2OCHF_2$	26.9	1.15	268	11000	513	5730	528	1680	2.05	4780	0.704	1780		
HG-03	$CHF_2(OCF_2CF_2)_3OCHF_2$	26.9	1.43	250	10300	479	5350	492	1570	1.91	4470	0.657	1660		

ACCEPTED VERSION SUBJECT TO FINAL EDITING

Fluroxene	$CF_3CH_2OCH=CH_2$	0.01	0.011	0.00505	0.207	0.00515	0.058	0.00515	0.016	5.39×10^{-5}	0.013	4.09×10^{-6}	0.01	5.63	6.63
2-ethoxy-3,3,4,4,5-pentafluorotetrahydro-2,5-bis[1,2,2,2-tetrafluoro-1-(trifluoromethyl)ethyl]-furan	$C_{12}H_5F_{19}O_2$	0.81	0.489	4.27	175	4.36	48.7	4.36	13.9	0.0046	10.7	0.00347	8.8	4760	5600
Difluoro(methoxy)methane	CH_3OCHF_2	1.1	0.153	11.9	491	12.2	136	12.2	38.9	0.0129	30.1	0.00973	24.7	13300	15700
HG'-01	$CH_3OCF_2CF_2OCH_3$	1.7	0.289	17.7	727	18.1	202	18.1	57.7	0.0192	45	0.0145	36.7	19700	23200
HG'-02	$CH_3O(CF_2CF_2O)_2CH_3$	1.7	0.562	20	823	20.5	229	20.5	65.3	0.0218	50.9	0.0164	41.5	22300	26300
HG'-03	$CH_3O(CF_2CF_2O)_3CH_3$	1.7	0.762	19.2	789	19.6	219	19.6	62.5	0.0209	48.8	0.0157	39.8	21400	25200
HFE-329me3	$CF_3CFHCF_2OCF_3$	33.6	0.489	180	7410	393	4390	416	1330	1.73	4040	0.671	1700		
3,3,4,4,5,5,6,6,7,7,7-undecafluoroheptan-1-ol	$CF_3(CF_2)_4CH_2CH_2OH$	0.047	0.054	0.0468	1.92	0.0477	0.533	0.0477	0.152	5×10^{-5}	0.117	3.79×10^{-5}	0.096	52.2	61.4
3,3,4,4,5,5,6,6,7,7,8,8,9,9,9-pentadecafluorononan-1-ol	$CF_3(CF_2)_6CH_2CH_2OH$	0.047	0.06	0.0394	1.62	0.0401	0.449	0.0402	0.128	4.21×10^{-5}	0.098	3.19×10^{-5}	0.081	43.9	51.7
3,3,4,4,5,5,6,6,7,7,8,8,9,9,10,10,11,11,11-nonadecafluoroundecan-1-ol	$CF_3(CF_2)_8CH_2CH_2OH$	0.047	0.045	0.024	0.985	0.0245	0.273	0.0245	0.078	2.56×10^{-5}	0.06	1.94×10^{-5}	0.049	26.8	31.5
2-chloro-1,1,2-trifluoro-1-methoxyethane	CH_3OCF_2CHClF	1.43	0.211	11.9	488	12.1	136	12.1	38.7	0.0129	30.1	0.0097	24.6	13200	15600
PFPMIE	$CF_3OCFCF_3CF_2OCF_2OCF_3$	800	0.64	189	7750	920	10300	3680	11700	4.59	10700	4.75	12000		
HFE-216	$CF_3OCF=CF_2$	0.004	0.006	0.000909	0.037	0.000927	0.01	0.000928	0.003	9.71×10^{-7}	0.002	7.37×10^{-7}	0.002	1.01	1.19
Perfluoroethyl formate	CF_3CF_2OCHO	3.6	0.408	51.9	2130	53.4	597	53.4	170	0.0579	135	0.0431	109	58000	68400
2,2,2-trifluoroethyl formate	CF_3CH_2OCHO	0.548	0.192	4.8	197	4.9	54.8	4.9	15.6	0.00516	12.1	0.0039	9.89	5350	6300
Formic acid;1,1,1,3,3,3-hexafluoropropan-2-ol	$(CF_3)_2CHOCHO$	3.1	0.255	23.5	964	24.1	269	24.1	76.7	0.0259	60.6	0.0194	49	26100	30800
Ethenyl 2,2,2-trifluoroacetate	$CF_3COOCH=CH_2$	0.004	0.004	0.000705	0.029	0.000719	0.008	0.000719	0.002	7.52×10^{-7}	0.002	5.71×10^{-7}	0.001	0.786	0.925
Ethyl 2,2,2-trifluoroacetate	$CF_3COOCH_2CH_3$	0.06	0.056	0.139	5.7	0.142	1.58	0.142	0.451	0.000148	0.347	0.000112	0.285	155	182
Prop-2-enyl 2,2,2-trifluoroacetate	$CF_3COOCH_2CH=CH_2$	0.003	0.005	0.000636	0.026	0.000648	0.007	0.000649	0.002	6.79×10^{-7}	0.002	5.15×10^{-7}	0.001	0.71	0.835

ACCEPTED VERSION SUBJECT TO FINAL EDITING

Methyl 2,2,2-trifluoroacetate	CF_3COOCH_3	1	0.158	7.21	296	7.36	82.3	7.36	23.5	0.00778	18.2	0.00587	14.9	8030	9460
2,2,3,3,4,4,4-heptafluorobutan-1-ol	$CF_3CF_2CF_2CH_2OH$	0.55	0.199	3.2	131	3.26	36.5	3.26	10.4	0.00343	8.03	0.0026	6.58	3560	4190
1,1,2-trifluoro-2-(trifluoromethoxy)ethane	$CHF_2CHFOCF_3$	9	0.353	97.6	4010	113	1260	113	359	0.162	379	0.0933	236	120000	143000
1-ethoxy-1,1,2,3,3,3-hexafluoropropane	$CF_3CHFCF_2OCH_2CH_3$	0.403	0.193	2.32	95.2	2.37	26.4	2.37	7.54	0.00249	5.81	0.00188	4.77	2580	3040
1,1,1,2,2,3,3-heptafluoro-3-(1,2,2,2-tetrafluoroethoxy)propane	$CF_3CF_2CF_2OCHFCF_3$	59.4	0.591	202	8320	593	6630	733	2340	2.94	6860	1.63	4140		
2,2,3,3-tetrafluoropropan-1-ol	$CHF_2CF_2CH_2OH$	0.255	0.112	1.27	52	1.29	14.4	1.29	4.12	0.00136	3.17	0.00103	2.6	1410	1660
2,2,3,4,4,4-hexafluorobutan-1-ol	$CF_3CHFCF_2CH_2OH$	0.367	0.227	2.67	110	2.73	30.5	2.73	8.69	0.00287	6.7	0.00217	5.5	2980	3510
1,1,2,2-tetrafluoro-3-methoxypropane	$CHF_2CF_2CH_2OCH_3$	0.071	0.052	0.147	6.03	0.15	1.68	0.15	0.478	0.000157	0.367	0.000119	0.302	164	193
1,1,1,2,2,4,5,5,5-nonafluoro-4-(trifluoromethyl)pentan-3-one	$CF_3CF_2COCF(CF_3)_2$	0.019	0.028	0.01	0.411	0.0102	0.114	0.0102	0.033	1.07×10^{-5}	0.025	8.12×10^{-5}	0.021	11.2	13.1
3,3,3-trifluoropropanal	CF_3CH_2CHO	0.008	0.005	0.00221	0.091	0.00225	0.025	0.00225	0.007	2.36×10^{-5}	0.006	1.79×10^{-5}	0.005	2.46	2.9
2-fluoroethanol	CH_2FCH_2OH	0.044	0.012	0.0465	1.91	0.0474	0.53	0.0474	0.151	4.97×10^{-5}	0.116	3.77×10^{-5}	0.095	51.9	61
2,2-difluoroethanol	CHF_2CH_2OH	0.167	0.046	0.542	22.3	0.553	6.18	0.553	1.76	0.00058	1.36	0.00044	1.11	605	711
2,2,2-trifluoroethanol	CF_3CH_2OH	0.458	0.117	3.13	129	3.2	35.7	3.2	10.2	0.00336	7.86	0.00254	6.44	3490	4110
HG-04	$CHF_2O(CF_2CF_2O)_4CHF_2$	26.9	1.46	204	8400	392	4380	403	1280	1.56	3660	0.538	1360		
Methyl-perfluoroheptene-ethers	$CH_3OC_7F_{13}$	0.304	0.27	1.32	54.4	1.35	15.1	1.35	4.3	0.00142	3.31	0.00107	2.72	1480	1740
1,1,1-trifluoropropan-2-one	CF_3COCH_3	0.014	0.011	0.00788	0.324	0.00804	0.09	0.00804	0.026	8.42×10^{-5}	0.02	6.39×10^{-5}	0.016	8.79	10.3
1,1,1-trifluorobutan-2-one	$CF_3COCH_2CH_3$	0.018	0.01	0.00834	0.343	0.00851	0.095	0.00851	0.027	8.91×10^{-5}	0.021	6.76×10^{-5}	0.017	9.31	11
1-chloro-2-ethenoxyethane	$ClCH_2CH_2OCH=CH_2$	0	0.001	1.65×10^{-5}	0.001	1.68×10^{-5}	0	1.68×10^{-5}	0	1.76×10^{-8}	0	1.33×10^{-8}	0	0.018	0.022
2-methylpentan-3-one	$CH_3CH_2COCH(CH_3)_2$	0.015	0.02	0.0175	0.719	0.0179	0.2	0.0179	0.057	1.87×10^{-5}	0.044	1.42×10^{-5}	0.036	19.5	23
Ethyl methyl ether	$CH_3CH_2OCH_3$	0.005	0.002	0.000856	0.035	0.000873	0.01	0.000873	0.003	9.14×10^{-7}	0.002	6.94×10^{-7}	0.002	0.955	1.12
Octafluorooxolane	$c\text{-}C_4F_8O$	3000	0.463	246	10100	1240	13900	5890	18800	6.18	14500	6.65	16900		

ACCEPTED VERSION SUBJECT TO FINAL EDITING

Crotonaldehyde	$CH_3CH=CHCHO$	0.001	0	0	0	0	0	0	0	0	0	0	0	0	0
Methyl vinyl ketone	$CH_3COCH=CH_2$	0.001	0	2.48×10^{-5}	0.001	2.53×10^{-5}	0	2.53×10^{-5}	0	2.64×10^{-8}	0	2.01×10^{-8}	0	0.028	0.033
Allyl ether	$(CH_2=CHCH_2)_2O$	0	0.001	1.19×10^{-5}	0	1.22×10^{-5}	0	1.22×10^{-5}	0	1.27×10^{-8}	0	9.65×10^{-9}	0	0.013	0.016
Allyl ethyl ether	$CH_3CH_2OCH_2CH=CH_2$	0.001	0.001	3.39×10^{-5}	0.001	3.46×10^{-5}	0	3.46×10^{-5}	0	3.62×10^{-8}	0	2.75×10^{-8}	0	0.038	0.045
(z)-hex-2-en-1-ol	$CH_3CH_2CH_2CH=CHCH_2OH$	0	0.038	0.000223	0.009	0.000228	0.003	0.000228	0.001	2.38×10^{-7}	0.001	1.81×10^{-7}	0	0.249	0.293
(e)-hex-2-en-1-ol	$CH_3CH_2CH_2CH=CHCH_2OH$	0	0.036	0.000208	0.009	0.000212	0.002	0.000212	0.001	2.22×10^{-7}	0.001	1.68×10^{-7}	0	0.232	0.273
Miscellaneous compounds															
Allyl cyanide	$CH_2=CHCH_2CN$	0.002	0	4.08×10^{-5}	0.002	4.16×10^{-5}	0	4.16×10^{-5}	0	4.35×10^{-8}	0	3.3×10^{-8}	0	0.045	0.054
Hexamethyldisiloxane	$C_6H_{18}OSi_2$	0.025	0.047	0.0418	1.72	0.0426	0.476	0.0426	0.136	4.46×10^{-5}	0.104	3.39×10^{-5}	0.086	46.6	54.8
Octamethyltrisiloxane	$C_8H_{24}O_2Si_3$	0.019	0.06	0.0285	1.17	0.029	0.325	0.029	0.093	3.04×10^{-5}	0.071	2.31×10^{-5}	0.058	31.8	37.4
Decamethyltetrasiloxane	$C_{10}H_{30}O_3Si_4$	0.014	0.06	0.0155	0.635	0.0158	0.176	0.0158	0.05	1.65×10^{-5}	0.039	1.25×10^{-5}	0.032	17.3	20.3
Dodecamethylpentasiloxane	$C_{12}H_{36}O_4Si_5$	0.011	0.064	0.0107	0.439	0.0109	0.122	0.0109	0.035	1.14×10^{-5}	0.027	8.67×10^{-6}	0.022	11.9	14
Hexamethylcyclotrisiloxane	$C_6H_{18}O_3Si_3$	0.038	0.1	0.101	4.14	0.103	1.15	0.103	0.328	0.000108	0.252	8.18×10^{-5}	0.207	113	132
Octamethylcyclotetrasiloxane	$C_8H_{24}O_4Si_4$	0.027	0.12	0.0648	2.66	0.0661	0.739	0.0661	0.211	6.92×10^{-5}	0.162	5.25×10^{-5}	0.133	72.3	85.1
Decamethylcyclopentasiloxane	$C_{10}H_{30}O_5Si_5$	0.016	0.098	0.0253	1.04	0.0258	0.289	0.0259	0.082	2.71×10^{-5}	0.063	2.05×10^{-5}	0.052	28.3	33.3
Dodecamethylcyclohexasiloxane	$C_{12}H_{36}O_6Si_6$	0.011	0.086	0.0124	0.51	0.0127	0.142	0.0127	0.04	1.33×10^{-5}	0.031	1.01×10^{-5}	0.026	13.9	16.3
Ethane	C_2H_6	0.159	0.001	0.0383	1.57	0.0391	0.437	0.0391	0.125	4.1×10^{-5}	0.096	3.11×10^{-5}	0.079	42.7	50.3
Propane	C_3H_8	0.036	0	0.00175	0.072	0.00178	0.02	0.00178	0.006	1.87×10^{-6}	0.004	1.42×10^{-6}	0.004	1.95	2.29
Butane	$n\text{-}C_4H_{10}$	0.019	0	0.000542	0.022	0.000553	0.006	0.000553	0.002	5.79×10^{-7}	0.001	4.4×10^{-7}	0.001	0.605	0.712

[END TABLE 7.SM.7 HERE]

ACCEPTED VERSION SUBJECT TO FINAL EDITING

[START TABLE 7.SM.8 HERE]

Table 7.SM.8: Estimated uncertainty in the GWP and GTP for CH_4 showing the total uncertainty as a percentage of the best estimate (expressed as 5-95% confidence interval), and the uncertainty by component of the total emission metric calculation (radiative efficiency, chemistry feedbacks, atmospheric lifetime, CO_2 (combined uncertainty in radiative efficiency and CO_2 impulse response), carbon cycle response, fate of oxidized fossil methane, and impulse-response function. Uncertainties in individual terms are taken from Section 7.6, except for the CO_2 impulse response which comes from (Joos et al., 2013). The impulse-response uncertainties are calculated by taking 1.645×standard deviation of the GTPs generated from 600 ensemble members of the impulse response derived from FaIRv1.6.2 and MAGICC7.5.1 (Section 7.SM.4.2)

Metric	Percentage uncertainty in the metric best estimate due to							Total uncertainty (%)
	Radiative efficiency (%)	Chemical response (%)	Lifetime (%)	CO_2 (%)	Carbon cycle (%)	Fossil fuel oxidation (%)	Impulse Response function (%)	
GWP20	20	14	9	18	3	2	0	32
GWP100	20	14	14	26	5	7	0	40
GWP500	20	14	14	29	5	26	0	48
GTP50	20	14	37	22	17	22	31	64
GTP100	20	14	18	28	8	60	38	83

[END TABLE 7.SM.8 HERE]

[START TABLE 7.SM.9 HERE]

Table 7.SM.9: As Table 7.SM.8, for N_2O

Metric	Percentage uncertainty in the metric best estimate due to						Total uncertainty (%)
	Radiative efficiency (%)	Chemical response (%)	Lifetime (%)	CO_2 (%)	Carbon cycle (%)	Impulse Response function (%)	
GWP20	16	36	1	18	2	0	43
GWP100	16	36	3	26	5	0	47
GWP500	16	36	8	29	5	0	49
GTP50	16	36	3	25	6	1	46
GTP100	16	36	7	29	6	2	49

[END TABLE 7.SM.9 HERE]

ACCEPTED VERSION SUBJECT TO FINAL EDITING

[START TABLE 7.SM.10 HERE]

Table 7.SM.10: As Table 7.SM.8, for CFC-11

Metric	Percentage uncertainty in the metric best estimate due to					Total uncertainty (%)
	Radiative efficiency (%)	Lifetime (%)	CO_2 (%)	Carbon cycle (%)	Impulse Response function (%)	
GWP20	22	3	18	2	0	29
GWP100	22	12	26	5	0	37
GWP500	22	19	29	5	0	42
GTP50	22	14	24	6	4	37
GTP100	22	28	28	7	7	47

[ENDTABLE 7.SM.10 HERE]

[START TABLE 7.SM.11 HERE]

Table 7.SM.11: As Table 7.SM.8, for PFC-14 (CF_4)

Metric	Percentage uncertainty in the metric best estimate due to					Total uncertainty (%)
	Radiative efficiency (%)	Lifetime (%)	CO_2 (%)	Carbon cycle (%)	Impulse Response function (%)	
GWP20	19	0	18	2	0	26
GWP100	19	0	26	4	0	33
GWP500	19	0	29	5	0	35
GTP50	19	0	25	5	2	32
GTP100	19	0	29	5	1	35

[END TABLE 7.SM.11 HERE]

[START TABLE 7.SM.12 HERE]

Table 7.SM.12: As Table 7.SM.8, for HFC-134a

Metric	Percentage uncertainty in the metric best estimate due to					Total uncertainty (%)
	Radiative efficiency (%)	Lifetime (%)	CO_2 (%)	Carbon cycle (%)	Impulse Response function (%)	
GWP20	19	10	18	3	0	28
GWP100	19	19	26	5	0	38

ACCEPTED VERSION SUBJECT TO FINAL EDITING

GWP500	19	19	29	5	0	40
GTP50	19	47	22	14	25	62
GTP100	19	30	28	9	37	59

[END TABLE 7.SM.12 HERE]

[START TABLE 7.SM.13 HERE]

Table 7.SM.13: As Table 7.SM.8, for HFC-32

Metric	Percentage uncertainty in the metric best estimate due to					Total uncertainty (%)
	Radiative efficiency (%)	Lifetime (%)	CO_2 (%)	Carbon cycle (%)	Impulse Response function (%)	
GWP20	19	17	18	3	0	31
GWP100	19	19	26	5	0	38
GWP500	19	19	29	5	0	40
GTP50	19	22	19	26	48	65
GTP100	19	19	29	7	39	56

[END TABLE 7.SM.13 HERE]

ACCEPTED VERSION
SUBJECT TO FINAL EDITING

7.SM.7 Data Table

[START TABLE 7.SM.14 HERE]

Table 7.SM.14: Input Data Table. Input datasets and code used to create chapter figures.

Figure number / Table number / Chapter section (for calculations)	Dataset / Code name	Type	Filename / Specificities	License type	Dataset / Code citation	Dataset / Code URL	Related publications
Box 7.2, Figure 1		Code	notebooks/350_chapter7_box7.2_fig1.ipynb	MIT	(Smith et al., 2021) [original author Matthew Palmer]	https://github.com/chrisroadmap/ar6	
Box 7.2, Figure 1		Data	data_input/fig7.1_box7.2/			https://github.com/chrisroadmap/ar6	
Figure 7.3		Code	notebooks/300_chapter7_fig7.3.ipynb	MIT	(Smith et al., 2021) [original author Matthew Palmer]	https://github.com/chrisroadmap/ar6	
Figure 7.3		Data	data_input/Loeb_et_al_2020			https://github.com/chrisroadmap/ar6	(Loeb et al., 2020)
Figure 7.4		Code	notebooks/270_chapter7_fig7.4.ipynb	MIT	(Smith et al., 2021)	https://github.com/chrisroadmap/ar6	

ACCEPTED VERSION SUBJECT TO FINAL EDITING

Figure 7.4		Data	data_input/Marshall_et_al_2020_GRL data_input/Smith_et_al_ACP_2020 data_input/Smith_et_al_GRL_2018 data_input/Hodnebrog_et_al_2020_npj			https://github.com/chrisroadmap/ar6	(Smith et al., 2018b, 2020; Hodnebrog et al., 2020; Marshall et al., 2020)
Figure 7.5		Code	notebooks/060_chapter7_fig7.5_SPM_fig15.ipynb	MIT	(Smith et al., 2021)	https://github.com/chrisroadmap/ar6	
Figure 7.5		Data	data_input/Smith_et_al_ACP_2020			https://github.com/chrisroadmap/ar6	(Zelinka et al., 2014; Smith et al., 2020)
Figure 7.6		Code	notebooks/100_chapter7_fig7.6.ipynb	MIT	(Smith et al., 2021)	https://github.com/chrisroadmap/ar6	
Figure 7.7		Code	notebooks/220_chapter7_fig7.7.ipynb	MIT	(Smith et al., 2021)	https://github.com/chrisroadmap/ar6	
Figure 7.8		Code	notebooks/230_chapter7_fig7.8.ipynb	MIT	(Smith et al., 2021)	https://github.com/chrisroadmap/ar6	

ACCEPTED VERSION
SUBJECT TO FINAL EDITING

Cross Chapter Box 7.1 Figure 7.1		Code	notebooks/box-7-1-figure-1/110_plot_box_7-1_emulator_overview_figure_projections_panels.ipynb		(Nicholls et al., 2021)	https://gitlab.com/magicc/ar6-wg1	
Cross Chapter Box 7.1 Figure 7.1	Model datasets	Data	All below models use historical and ssp126 ACCESS-CM2 r1i1p1f1 ACCESS-ESM1-5 r1i1p1f1 BCC-CSM2-MR r1i1p1f1 CESM2 r4i1p1f1 CESM2-WACCM r1i1p1f1 CMCC-CM2-SR5			https://esgf-node.llnl.gov/search/cmip6/	

ACCEPTED VERSION SUBJECT TO FINAL EDITING

			r1i1p1f1 CNRM-CM6-1 r1i1p1f2 CNRM-CM6-1-HR r1i1p1f2 CNRM-ESM2-1 r1i1p1f2 CanESM5 r1i1p1f1 CanESM5-CanOE r1i1p2f1 FGOALS-g3 r1i1p1f1 GISS-E2-1-G r1i1p1f2 IPSL-CM6A-LR				

ACCEPTED VERSION SUBJECT TO FINAL EDITING

			r1i1p1f2 MIROC-ES2L r1i1p1f2 MIROC6 r1i1p1f1 MPI-ESM1-2-LR r1i1p1f1 MRI-ESM2-0 r1i1p1f1 UKESM1-0-LL r4i1p1f2				
Cross Chapter Box 7.1 Figure 7.1		Data	data/raw/fair/v20210211/scmdatabase/FaIRv1.6.2 data/raw/cicero/2.0.1/scmdatabase/Cicero-SCM data/raw/magicc/v			https://gitlab.com/magicc/ar6-wg1	(Meinshausen et al., 2011a; Gasser et al., 2017a; Smith et al., 2018a; Nicholls et al., 2020)

ACCEPTED VERSION SUBJECT TO FINAL EDITING

			20210217/output_210_idealised_experiments_2021_02_17_230201/MAGICCv7.5.1 data/raw/oscar/v20210217/scmdatabase/OSCARv3.1.1				
Figure 7.10		Code	AR6_fbk_violin_plot.py	MIT	(Zelinka, 2021)	https://github.com/mzelinka/AR6_figure	
Figure 7.10		Data	cmip56_feedbacks_AR6.json			https://github.com/mzelinka/AR6_figure	(Zelinka et al., 2020)
Figure 7.11	non-linearity in alpha	Code	nonlin/nonlin_fgd.pro		(Lunt, 2021)	https://github.com/danlunt1976/	
Figure 7.11		Data					Models: (Caballero and Huber, 2013; Jonko et al., 2013; Meraner et al., 2013; Good et al., 2015; Duan et al., 2019; Mauritsen et al., 2019; Stolpe et al., 2019; Zhu et

ACCEPTED VERSION
SUBJECT TO FINAL EDITING

							al., 2019) Proxies: (von der Heydt et al., 2014; Anagnostou et al., 2016, 2020; Friedrich et al., 2016; Royer, 2016; Shaffer et al., 2016; Köhler et al., 2017; Snyder, 2019; Stap et al., 2019)
Figure 7.13	paleo polar amplification	Code	patterns/fgd/plot_all_fgd.pro		(Lunt, 2021)	https://github.com/danlunt1976/ipcc_ar6	
Figure 7.13		Data					Paleo models: (Haywood et al., 2020; Zhu et al., 2020, 2021; Kageyama et al., 2021; Lunt et al., 2021; Zhang et al., 2021) Proxies: (Bartlein et al., 2011; Salzmann et

ACCEPTED VERSION
SUBJECT TO FINAL EDITING

							al., 2013; Vieira et al., 2018; Hollis et al., 2019; Cleator et al., 2020; McClymont et al., 2020; Tierney et al., 2020)
Figure 7.16		Code	notebooks/020_chapter7_fig7.16.ipynb	MIT	(Smith et al., 2021)	https://github.com/chrisroadmap/ar6	
Figure 7.17		Code	contributed/fig7.17/tcr_fgd.f	MIT	(Smith et al., 2021) [original author Masahiro Watanabe]	https://github.com/chrisroadmap/ar6	
Figure 7.17		Data					(Geoffroy et al., 2013a; Smith et al., 2020)
Figure 7.18		Code	notebooks/330_chapter7_fig7.18.ipynb	MIT	(Smith et al., 2021) [original author Piers Forster]	https://github.com/chrisroadmap/ar6	
Figure 7.18		Data	data_input/Schlund_et_al_2020				(Schlund et al., 2020)
Figure 7.19		Code	patterns/fgd/plot_all_fgd.pro		(Lunt, 2021)	https://github.com/danlunt1976/ipcc	

ACCEPTED VERSION SUBJECT TO FINAL EDITING

						_ar6	
Figure 7.19		Data					(Haywood et al., 2020; Zhu et al., 2020, 2021; Kageyama et al., 2021; Lunt et al., 2021; Zhang et al., 2021)
Figure 7.21		Code	notebooks/320_chapter7_fig7.21.ipynb	MIT	(Smith et al., 2021) [original author William Collins]	https://github.com/chrisroadmap/ar6	
Figure 7.21		Data	data_input/fig7.20				
Figure 7.22		Code	notebooks/310_chapter7_fig7.22.ipynb	MIT	(Smith et al., 2021) [original authors Piers Forster and Michelle Cain]	https://github.com/chrisroadmap/ar6	
Figure 7.22		Data			(Nicholls and Lewis, 2021)	https://doi.org/10.5281/zenodo.4589756	
FAQ 7.3 Figure 1	CDO commands and Python to plot the data points	Code	contributed/faq7.3_fig1	MIT	(Smith et al., 2021) [original author Sophie Berger]	https://github.com/chrisroadmap/ar6	

ACCEPTED VERSION SUBJECT TO FINAL EDITING

FAQ 7.3 Figure 1	Input is ECS for each model and projected 2081-2100 global warming in RCP8.5 and SSP5-8.5 respectively: 69 CMIP5 and CMIP6 model outputs	Data	contributed/faq7.3_fig1			https://esgf-data.dkrz.de/ [original data from] https://github.com/chrisroadmap/ar6 [processed data stored at]	(Schlund et al., 2020)

[END TABLE 7.SM.14 HERE]

ACCEPTED VERSION SUBJECT TO FINAL EDITING

References

Allen, R. J., Horowitz, L. W., Naik, V., Oshima, N., O'Connor, F. M., Turnock, S., et al. (2021). Significant climate benefits from near-term climate forcer mitigation in spite of aerosol reductions. *Environ. Res. Lett.* doi:10.1088/1748-9326/abe06b.

Anagnostou, E., John, E. H., Babila, T. L., Sexton, P. F., Ridgwell, A., Lunt, D. J., et al. (2020). Proxy evidence for state-dependence of climate sensitivity in the Eocene greenhouse. *Nat. Commun.* 11, 4436. doi:10.1038/s41467-020-17887-x.

Anagnostou, E., John, E. H., Edgar, K. M., Foster, G. L., Ridgwell, A., Inglis, G. N., et al. (2016). Changing atmospheric CO2 concentration was the primary driver of early Cenozoic climate. *Nature* 533, 380–384. doi:10.1038/nature17423.

Arora, V. K., Katavouta, A., Williams, R. G., Jones, C. D., Brovkin, V., Friedlingstein, P., et al. (2020). Carbon-concentration and carbon-climate feedbacks in CMIP6 models and their comparison to CMIP5 models. *Biogeosciences* 17, 4173–4222. doi:10.5194/bg-17-4173-2020.

Bartlein, P. J., Harrison, S. P., Brewer, S., Connor, S., Davis, B. A. S., Gajewski, K., et al. (2011). Pollen-based continental climate reconstructions at 6 and 21 ka: a global synthesis. *Clim. Dyn.* 37, 775–802. doi:10.1007/s00382-010-0904-1.

Caballero, R., and Huber, M. (2013). State-dependent climate sensitivity in past warm climates and its implications for future climate projections. *Proc. Natl. Acad. Sci.* 110, 14162–14167. doi:10.1073/pnas.1303365110.

Checa-Garcia, R., Hegglin, M. I., Kinnison, D., Plummer, D. A., and Shine, K. P. (2018). Historical Tropospheric and Stratospheric Ozone Radiative Forcing Using the CMIP6 Database. *Geophys. Res. Lett.* 45, 3264–3273. doi:10.1002/2017GL076770.

Cleator, S. F., Harrison, S. P., Nichols, N. K., Prentice, I. C., and Roulstone, I. (2020). A new multivariable benchmark for Last Glacial Maximum climate simulations. *Clim. Past* 16, 699–712. doi:10.5194/cp-16-699-2020.

Collins, W. J., Lamarque, J. F., Schulz, M., Boucher, O., Eyring, V., Hegglin, I. M., et al. (2017). AerChemMIP: Quantifying the effects of chemistry and aerosols in CMIP6. *Geosci. Model Dev.* 10, 585–607. doi:10.5194/gmd-10-585-2017.

Duan, L., Cao, L., and Caldeira, K. (2019). Estimating Contributions of Sea Ice and Land Snow to Climate Feedback. *J. Geophys. Res. Atmos.* 124, 199–208. doi:10.1029/2018JD029093.

Etminan, M., Myhre, G., Highwood, E. J., and Shine, K. P. (2016). Radiative forcing of carbon dioxide, methane, and nitrous oxide: A significant revision of the methane radiative forcing. *Geophys. Res. Lett.* 43, 12,614-12,623. doi:10.1002/2016GL071930.

Eyring, V., Bock, L., Lauer, A., Righi, M., Schlund, M., Andela, B., et al. (2020). Earth System Model Evaluation Tool (ESMValTool) v2.0 - An extended set of large-scale diagnostics for quasi-operational and comprehensive evaluation of Earth system models in CMIP. *Geosci. Model Dev.* 13, 3383–3438. doi:10.5194/gmd-13-3383-2020.

Eyring, V., Bony, S., Meehl, G. A., Senior, C. A., Stevens, B., Stouffer, R. J., et al. (2016). Overview of the Coupled Model Intercomparison Project Phase 6 (CMIP6) experimental design and organization. *Geosci. Model Dev.* 9, 1937–1958. doi:10.5194/gmd-9-1937-2016.

Friedrich, T., Timmermann, A., Tigchelaar, M., Timm, O. E., and Ganopolski, A. (2016). Nonlinear climate sensitivity and its implications for future greenhouse warming. *Sci. Adv.* 2. doi:10.1126/sciadv.1501923.

Gasser, T., Ciais, P., Boucher, O., Quilcaille, Y., Tortora, M., Bopp, L., et al. (2017a). The compact Earth system model OSCAR v2.2: Description and first results. *Geosci. Model Dev.* 10, 271–319. doi:10.5194/gmd-10-271-2017.

Gasser, T., Peters, G. P., Fuglestvedt, J. S., Collins, W. J., Shindell, D. T., and Ciais, P. (2017b). Accounting for the climate–carbon feedback in emission metric. *Earth Syst. Dyn.* 8, 235–253. doi:10.5194/esd-8-235-2017.

Geoffroy, O., Saint-Martin, D., Bellon, G., Voldoire, A., Olivié, D. J. L. L., and Tytéca, S. (2013a). Transient Climate Response in a Two-Layer Energy-Balance Model. Part II: Representation of the Efficacy of Deep-Ocean Heat Uptake and Validation for CMIP5 AOGCMs. *J. Clim.* 26, 1859–1876. doi:10.1175/JCLI-D-12-00196.1.

Geoffroy, O., Saint-martin, D., Olivié, D. J. L., Voldoire, A., Bellon, G., and Tytéca, S. (2013b). Transient climate response in a two-layer energy-balance model. Part I: Analytical solution and parameter calibration using CMIP5 AOGCM experiments. *J. Clim.* 26, 1841–1857. doi:10.1175/JCLI-D-12-00195.1.

Ghan, S. J., Smith, S. J., Wang, M., Zhang, K., Pringle, K., Carslaw, K., et al. (2013). A simple model of global aerosol indirect effects. *J. Geophys. Res. Atmos.* 118, 6688–6707. doi:10.1002/jgrd.50567.

Ghimire, B., Williams, C. A., Masek, J., Gao, F., Wang, Z., Schaaf, C., et al. (2014). Global albedo change and radiative cooling from anthropogenic land cover change, 1700 to 2005 based on MODIS, land use harmonization, radiative kernels, and reanalysis. *Geophys. Res. Lett.* doi:10.1002/2014GL061671.

Gidden, M. J., Riahi, K., Smith, S. J., Fujimori, S., Luderer, G., Kriegler, E., et al. (2019). Global emissions pathways under different socioeconomic scenarios for use in CMIP6: a dataset of harmonized emissions trajectories through the end of the century. *Geosci. Model Dev.* 12, 1443–1475. doi:10.5194/gmd-12-1443-2019.

Good, P., Lowe, J. A., Andrews, T., Wiltshire, A., Chadwick, R., Ridley, J. K., et al. (2015). Nonlinear regional

ACCEPTED VERSION SUBJECT TO FINAL EDITING

warming with increasing CO2 concentrations. *Nat. Clim. Chang.* 5, 138–142. doi:10.1038/nclimate2498.
Gregory, J. M., Andrews, T., and Good, P. (2015). The inconstancy of the transient climate response parameter under increasing CO2. *Philos. Trans. R. Soc. A Math. Phys. Eng. Sci.* 373. doi:10.1098/rsta.2014.0417.
Gregory, J. M., Ingram, W. J., Palmer, M. A., Jones, G. S., Stott, P. A., Thorpe, R. B., et al. (2004). A new method for diagnosing radiative forcing and climate sensitivity. *Geophys. Res. Lett.* 31, L03205. doi:10.1029/2003GL018747.
Haywood, A. M., Tindall, J. C., Dowsett, H. J., Dolan, A. M., Foley, K. M., Hunter, S. J., et al. (2020). The Pliocene Model Intercomparison Project Phase 2: large-scale climate features and climate sensitivity. *Clim. Past* 16, 2095–2123. doi:10.5194/cp-16-2095-2020.
Hodnebrog, Ø., Myhre, G., Kramer, R. J., Shine, K. P., Andrews, T., Faluvegi, G., et al. (2020). The effect of rapid adjustments to halocarbons and N2O on radiative forcing. *npj Clim. Atmos. Sci.* 3. doi:https://doi.org/10.1038/s41612-020-00150-x.
Hoesly, R. M., Smith, S. J., Feng, L., Klimont, Z., Janssens-Maenhout, G., Pitkanen, T., et al. (2018). Historical (1750–2014) anthropogenic emissions of reactive gases and aerosols from the Community Emissions Data System (CEDS). *Geosci. Model Dev.* 11, 369–408. doi:10.5194/gmd-11-369-2018.
Hollis, C. J., Dunkley Jones, T., Anagnostou, E., Bijl, P. K., Cramwinckel, M. J., Cui, Y., et al. (2019). The DeepMIP contribution to PMIP4: methodologies for selection, compilation and analysis of latest Paleocene and early Eocene climate proxy data, incorporating version 0.1 of the DeepMIP database. *Geosci. Model Dev.* 12, 3149–3206. doi:10.5194/gmd-12-3149-2019.
Jiménez-de-la-Cuesta, D., and Mauritsen, T. (2019). Emergent constraints on Earth's transient and equilibrium response to doubled CO2 from post-1970s global warming. *Nat. Geosci.* 2015. doi:10.1038/s41561-019-0463-y.
Jonko, A. K., Shell, K. M., Sanderson, B. M., and Danabasoglu, G. (2013). Climate Feedbacks in CCSM3 under Changing CO2 Forcing. Part II: Variation of Climate Feedbacks and Sensitivity with Forcing. *J. Clim.* 26, 2784–2795. doi:10.1175/JCLI-D-12-00479.1.
Joos, F., Roth, R., Fuglestvedt, J. S., Peters, G. P., Enting, I. G., Von Bloh, W., et al. (2013). Carbon dioxide and climate impulse response functions for the computation of greenhouse gas metrics: A multi-model analysis. *Atmos. Chem. Phys.* 13, 2793–2825. doi:10.5194/acp-13-2793-2013.
Jungclaus, J. H., Bard, E., Baroni, M., Braconnot, P., Cao, J., Chini, L. P., et al. (2017). The PMIP4 contribution to CMIP6 Part 3: The last millennium, scientific objective, and experimental design for PMIP4 simulations. *Geosci. Model Dev.* 10, 4005–4033. doi:10.5194/gmd-10-4005-2017.
Kageyama, M., Harrison, S. P., Kapsch, M. M.-L., Löfverström, M., Lora, J. M., Mikolajewicz, U., et al. (2021). The PMIP4-CMIP6 Last Glacial Maximum experiments: preliminary results and comparison with the PMIP3-CMIP5 simulations. *Clim. Past*, 1–37. doi:10.5194/cp-2019-169.
Kanaya, Y., Yamaji, K., Miyakawa, T., Taketani, F., Zhu, C., Choi, Y., et al. (2020). Rapid reduction in black carbon emissions from China: Evidence from 2009-2019 observations on Fukue Island, Japan. *Atmos. Chem. Phys.* 20, 6339–6356. doi:10.5194/acp-20-6339-2020.
Köhler, P., Stap, L. B., von der Heydt, A. S., de Boer, B., Van De Wal, R. S. W., and Bloch-Johnson, J. (2017). A state-dependent quantification of climate sensitivity based on paleo data of the last 2.1 million years. *Paleoceanography*, 1–13. doi:10.1002/2017PA003190.
Kovilakam, M., Thomason, L. W., Ernest, N., Rieger, L., Bourassa, A., and Millán, L. (2020). The Global Space-based Stratospheric Aerosol Climatology (version 2.0): 1979–2018. *Earth Syst. Sci. Data* 12, 2607–2634. doi:10.5194/essd-12-2607-2020.
Lauer, A., Eyring, V., Bellprat, O., Bock, L., Gier, B. K., Hunter, A., et al. (2020). Earth System Model Evaluation Tool (ESMValTool) v2.0 - Diagnostics for emergent constraints and future projections from Earth system models in CMIP. *Geosci. Model Dev.* 13, 4205–4228. doi:10.5194/gmd-13-4205-2020.
Lee, D. S. S., Fahey, D. W. W., Skowron, A., Allen, M. R. R., Burkhardt, U., Chen, Q., et al. (2020). The contribution of global aviation to anthropogenic climate forcing for 2000 to 2018. *Atmos. Environ.* 244. doi:10.1016/j.atmosenv.2020.117834.
Loeb, N. G., Wang, H., Allan, R., Andrews, T., Armour, K., Cole, J. N. S., et al. (2020). New Generation of Climate Models Track Recent Unprecedented Changes in Earth's Radiation Budget Observed by CERES. *Geophys. Res. Lett.* 47. doi:10.1029/2019GL086705.
Lunt, D. J. (2021). Code and data for Chapter 7.
Lunt, D. J., Bragg, F., Chan, W. L. W.-L., Hutchinson, D. K., Ladant, J. J.-B. B. J.-B., Niezgodzki, I., et al. (2021). DeepMIP: Model intercomparison of early Eocene climatic optimum (EECO) large-scale climate features and comparison with proxy data. *Clim. Past* 17, 203–227. doi:10.5194/cp-17-203-2021.
Marshall, L. R., Smith, C. J., Forster, P. M., Schmidt, A., Aubry, T. J., Andrews, T., et al. (2020). Large Variations in Volcanic Aerosol Forcing Efficiency Due to Eruption Source Parameters and Rapid Adjustments. *Geophys. Res. Lett.* 47. doi:10.1029/2020GL090241.
Matthes, K., Funke, B., Andersson, M. E., Barnard, L., Beer, J., Charbonneau, P., et al. (2017). Solar forcing for CMIP6 (v3.2). *Geosci. Model Dev.* 10, 2247–2302. doi:10.5194/gmd-10-2247-2017.
Mauritsen, T., Bader, J., Becker, T., Behrens, J., Bittner, M., Brokopf, R., et al. (2019). Developments in the MPI-M

ACCEPTED VERSION SUBJECT TO FINAL EDITING

Earth System Model version 1.2 (MPI-ESM 1.2) and its response to increasing CO2. *J. Adv. Model. Earth Syst.* 0. doi:10.1029/2018MS001400.

McClymont, E. L., Ford, H. L., Ho, S. L., Tindall, J. C., Haywood, A. M., Alonso-Garcia, M., et al. (2020). Lessons from a high-CO2 world: an ocean view from ~3 million years ago. *Clim. Past* 16, 1599–1615. doi:10.5194/cp-16-1599-2020.

Meehl, G. A., Senior, C. A., Eyring, V., Flato, G., Lamarque, J.-F., Stouffer, R. J., et al. (2020). Context for interpreting equilibrium climate sensitivity and transient climate response from the CMIP6 Earth system models. *Sci. Adv.* 6. doi:10.1126/sciadv.aba1981.

Meinshausen, M., Nicholls, Z. R. J., Lewis, J., Gidden, M. J., Vogel, E., Freund, M., et al. (2020). The shared socio-economic pathway (SSP) greenhouse gas concentrations and their extensions to 2500. *Geosci. Model Dev.* 13, 3571–3605. doi:10.5194/gmd-13-3571-2020.

Meinshausen, M., Raper, S. C. B. B., and Wigley, T. M. L. L. (2011a). Emulating coupled atmosphere-ocean and carbon cycle models with a simpler model, MAGICC6 – Part 1: Model description and calibration. *Atmos. Chem. Phys.* 11, 1417–1456. doi:10.5194/acp-11-1417-2011.

Meinshausen, M., Smith, S. J., Calvin, K., Daniel, J. S., Kainuma, M. L. T., Lamarque, J., et al. (2011b). The RCP greenhouse gas concentrations and their extensions from 1765 to 2300. *Clim. Change* 109, 213–241. doi:10.1007/s10584-011-0156-z.

Meinshausen, M., Vogel, E., Nauels, A., Lorbacher, K., Meinshausen, N., Etheridge, D. M., et al. (2017). Historical greenhouse gas concentrations for climate modelling (CMIP6). *Geosci. Model Dev.* 10, 2057–2116. doi:10.5194/gmd-10-2057-2017.

Meraner, K., Mauritsen, T., and Voigt, A. (2013). Robust increase in equilibrium climate sensitivity under global warming. *Geophys. Res. Lett.* 40, 5944–5948. doi:10.1002/2013GL058118.

Millar, J. R., Nicholls, Z. R., Friedlingstein, P., and Allen, M. R. (2017). A modified impulse-response representation of the global near-surface air temperature and atmospheric concentration response to carbon dioxide emissions. *Atmos. Chem. Phys.* 17, 7213–7228. doi:10.5194/acp-17-7213-2017.

Myhre, G., Highwood, E. J., Shine, K. P., and Stordal, F. (1998). New estimates of radiative forcing due to well mixed greenhouse gases. *Geophys. Res. Lett.* 25, 2715–2718. doi:10.1029/98GL01908.

Myhre, G., Samset, B. H., Schulz, M., Balkanski, Y., Bauer, S., Berntsen, T. K., et al. (2013a). Radiative forcing of the direct aerosol effect from AeroCom Phase II simulations. *Atmos. Chem. Phys.* 13, 1853–1877. doi:10.5194/acp-13-1853-2013.

Myhre, G., Shindell, D., Bréon, F.-M., Collins, W., Fuglestvedt, J., Huang, J., et al. (2013b). "Anthropogenic and Natural Radiative Forcing," in *Climate Change 2013: The Physical Science Basis. Contribution of Working Group I to the Fifth Assessment Report of the Intergovernmental Panel on Climate Change*, eds. T. F. Stocker, D. Qin, G.-K. Plattner, M. Tignor, S. K. Allen, J. Boschung, et al. (Cambridge, United Kingdom and New York, NY, USA: Cambridge University Press), 659–740. doi:10.1017/ CBO9781107415324.018.

Newman, P. A., Daniel, J. S., Waugh, D. W., and Nash, E. R. (2007). A new formulation of equivalent effective stratospheric chlorine (EESC). *Atmos. Chem. Phys.* 7, 4537–4552. doi:10.5194/acp-7-4537-2007.

Nicholls, Z., and Lewis, J. (2021). Reduced Complexity Model Intercomparison Project (RCMIP) protocol. doi:10.5281/ZENODO.4589756.

Nicholls, Z., Lewis, J., and Meinshausen, M. (2021). Code and data for Cross Chapter Box 7.1.

Nicholls, Z. R. J., Meinshausen, M., Lewis, J. J., Gieseke, R., Dommenget, D., Dorheim, K., et al. (2020). Reduced Complexity Model Intercomparison Project Phase 1: introduction and evaluation of global-mean temperature response. *Geosci. Model Dev.* 13, 5175–5190. doi:10.5194/gmd-13-5175-2020.

Paulot, F., Paynter, D., Ginoux, P., Naik, V., and Horowitz, L. W. (2018). Changes in the aerosol direct radiative forcing from 2001 to 2015: Observational constraints and regional mechanisms. *Atmos. Chem. Phys.* 18, 13265–13281. doi:10.5194/acp-18-13265-2018.

Riahi, K., Rao, S., Krey, V., Cho, C., Chirkov, V., Fischer, G., et al. (2011). RCP 8.5-A scenario of comparatively high greenhouse gas emissions. *Clim. Change* 109, 33–57. doi:10.1007/s10584-011-0149-y.

Righi, M., Andela, B., Eyring, V., Lauer, A., Predoi, V., Schlund, M., et al. (2020). Earth System Model Evaluation Tool (ESMValTool) v2.0-technical overview. *Geosci. Model Dev.* 13, 1179–1199. doi:10.5194/gmd-13-1179-2020.

Royer, D. L. (2016). Climate Sensitivity in the Geologic Past. *Annu. Rev. Earth Planet. Sci.* 44, 277–293. doi:10.1146/annurev-earth-100815-024150.

Salzmann, U., Dolan, A. M., Haywood, A. M., Chan, W. Le, Voss, J., Hill, D. J., et al. (2013). Challenges in quantifying Pliocene terrestrial warming revealed by data-model discord. *Nat. Clim. Chang.* 3, 969–974. doi:10.1038/nclimate2008.

Schlund, M., Lauer, A., Gentine, P., Sherwood, S., and Eyring, V. (2020). Emergent constraints on Equilibrium Climate Sensitivity in CMIP5: do they hold for CMIP6? *Earth Syst. Dyn.* 11, 1233–1258. doi:https://doi.org/10.5194/esd-11-1233-2020.

Shaffer, G., Huber, M., Rondanelli, R., and Pepke Pedersen, J. O. (2016). Deep time evidence for climate sensitivity increase with warming. *Geophys. Res. Lett.* 43, 6538–6545. doi:10.1002/2016GL069243.

ACCEPTED VERSION SUBJECT TO FINAL EDITING

Sherwood, S. C., Dixit, V., and Salomez, C. (2018). The global warming potential of near-surface emitted water vapour. *Environ. Res. Lett.* doi:10.1088/1748-9326/aae018.
Skeie, R. B., Myhre, G., Hodnebrog, Ø., Cameron-Smith, P. J., Deushi, M., Hegglin, M. I., et al. (2020). Historical total ozone radiative forcing derived from CMIP6 simulations. *npj Clim. Atmos. Sci.* doi:10.1038/s41612-020-00131-0.
Smith, C. J., Berger, S., Cain, M., Collins, W. J., Forster, P. M., Harris, G. R., et al. (2021). Code and data for Chapter 7.
Smith, C. J., Forster, P. M., Allen, M., Leach, N., Millar, R. J., Passerello, G. A., et al. (2018a). FAIR v1.3: A simple emissions-based impulse response and carbon cycle model. *Geosci. Model Dev.* doi:10.5194/gmd-11-2273-2018.
Smith, C. J., Kramer, R. J., Myhre, G., Alterskjær, K., Collins, W., Sima, A., et al. (2020). Effective radiative forcing and adjustments in CMIP6 models. *Atmos. Chem. Phys.* 20, 9591–9618. doi:10.5194/acp-20-9591-2020.
Smith, C. J., Kramer, R. J., Myhre, G., Forster, P. M., Soden, B. J., Andrews, T., et al. (2018b). Understanding Rapid Adjustments to Diverse Forcing Agents. *Geophys. Res. Lett.* 45. doi:10.1029/2018GL079826.
Snyder, C. W. (2019). Revised estimates of paleoclimate sensitivity over the past 800,000 years. *Clim. Change* 156, 121–138. doi:10.1007/s10584-019-02536-0.
Stap, L. B., Köhler, P., and Lohmann, G. (2019). Including the efficacy of land ice changes in deriving climate sensitivity from paleodata. *Earth Syst. Dyn.* 10, 333–345. doi:10.5194/esd-10-333-2019.
Sterner, E., Johansson, D. J. A., and Azar, C. (2014). Emission metrics and sea level rise. *Clim. Change* 127, 335–351. doi:10.1007/s10584-014-1258-1.
Stevens, B. (2015). Rethinking the lower bound on aerosol radiative forcing. *J. Clim.* 28, 4794–4819. doi:10.1175/JCLI-D-14-00656.1.
Stevenson, D. S., Young, P. J., Naik, V., Lamarque, J.-F., Shindell, D. T., Voulgarakis, A., et al. (2013). Tropospheric ozone changes, radiative forcing and attribution to emissions in the Atmospheric Chemistry and Climate Model Intercomparison Project (ACCMIP). *Atmos. Chem. Phys.* 13, 3063–3085. doi:10.5194/acp-13-3063-2013.
Stolpe, M. B., Medhaug, I., Beyerle, U., and Knutti, R. (2019). Weak dependence of future global mean warming on the background climate state. *Clim. Dyn.* 53, 5079–5099. doi:10.1007/s00382-019-04849-3.
Thornhill, G., Collins, W., Olivié, D., Skeie, R. B., Archibald, A., Bauer, S., et al. (2021a). Climate-driven chemistry and aerosol feedbacks in CMIP6 Earth system models. *Atmos. Chem. Phys.* 21, 1105–1126. doi:10.5194/acp-21-1105-2021.
Thornhill, G. D., Collins, W. J., Kramer, R. J., Olivie, D., Skeie, R. B., O'Connor, F. M., et al. (2021b). Effective radiative forcing from emissions of reactive gases and aerosols-A multi-model comparison. *Atmos. Chem. Phys.* 21, 853–874. doi:10.5194/acp-21-853-2021.
Tierney, J. E., Poulsen, C. J., Montañez, I. P., Bhattacharya, T., Feng, R., Ford, H. L., et al. (2020). Past climates inform our future. *Science (80-.).* 370. doi:10.1126/science.aay3701.
Toohey, M., and Sigl, M. (2017). Volcanic stratospheric sulfur injections and aerosol optical depth from 500 BCE to 1900 CE. *Earth Syst. Sci. Data* 9, 809–831. doi:10.5194/essd-9-809-2017.
Van Marle, M. J. E., Kloster, S., Magi, B. I., Marlon, J. R., Daniau, A. L., Field, R. D., et al. (2017). Historic global biomass burning emissions for CMIP6 (BB4CMIP) based on merging satellite observations with proxies and fire models (1750-2015). *Geosci. Model Dev.* 10, 3329–3357. doi:10.5194/gmd-10-3329-2017.
Velders, G. J. M., Fahey, D. W., Daniel, J. S., Andersen, S. O., and McFarland, M. (2015). Future atmospheric abundances and climate forcings from scenarios of global and regional hydrofluorocarbon (HFC) emissions. *Atmos. Environ.* 123, 200–209. doi:https://doi.org/10.1016/j.atmosenv.2015.10.071.
Vieira, M., Pound, M. J., and Pereira, D. I. (2018). The late Pliocene palaeoenvironments and palaeoclimates of the western Iberian Atlantic margin from the Rio Maior flora. *Palaeogeogr. Palaeoclimatol. Palaeoecol.* 495, 245–258. doi:10.1016/j.palaeo.2018.01.018.
von der Heydt, A. S., Dijkstra, H. A., Köhler, P., and Wal, R. Van De (2014). On the background state dependency of (palaeo) climate sensitivity. *Geophys. Res. Lett.* 41, 6484–6492. doi:10.1002/2014GL061121.
Zelinka, M. D. (2021). IPCC AR6 Figure 7.10.
Zelinka, M. D., Andrews, T., Forster, P. M., and Taylor, K. E. (2014). Quantifying components of aerosol-cloud-radiation interactions in climate models. *J. Geophys. Res. Atmos.* 119, 7599–7615. doi:10.1002/2014JD021710.
Zelinka, M. D., Myers, T. A., McCoy, D. T., Po-Chedley, S., Caldwell, P. M., Ceppi, P., et al. (2020). Causes of higher climate sensitivity in CMIP6 models. *Geophys. Res. Lett.* 46, 2019GL085782. doi:10.1029/2019GL085782.
Zhang, Z., Li, X., Guo, C., Otterå, O. H., Nisancioglu, K. H., Tan, N., et al. (2021). Mid-Pliocene Atlantic Meridional Overturning Circulation simulated in PlioMIP2. *Clim. Past* 17, 529–543. doi:10.5194/cp-17-529-2021.
Zhu, J., Otto-Bliesner, B. L., Brady, E. C., Poulsen, C. J., Tierney, J. E., Lofverstrom, M., et al. (2021). Assessment of Equilibrium Climate Sensitivity of the Community Earth System Model Version 2 Through Simulation of the Last Glacial Maximum. *Geophys. Res. Lett.* 48, e2020GL091220. doi:10.1029/2020GL091220.
Zhu, J., Poulsen, C. J., and Otto-Bliesner, B. L. (2020). High climate sensitivity in CMIP6 model not supported by paleoclimate. *Nat. Clim. Chang.* 10, 378–379. doi:10.1038/s41558-020-0764-6.
Zhu, J., Poulsen, C. J., and Tierney, J. E. (2019). Simulation of Eocene extreme warmth and high climate sensitivity through cloud feedbacks. *Sci. Adv.* 5. doi:10.1126/sciadv.aax1874.

ACCEPTED VERSION SUBJECT TO FINAL EDITING

Chapter 8: Water cycle changes

Coordinating Lead Authors:
Hervé Douville (France), Krishnan Raghavan (India), James Renwick (New Zealand)

Lead Authors:
Richard P. Allan (United Kingdom), Paola A. Arias (Colombia), Mathew Barlow (United States of America), Ruth Cerezo-Mota (Mexico), Annalisa Cherchi (Italy), ThianY. Gan (Canada/Malaysia), Joëlle Gergis (Australia), Dabang Jiang (China), Asif Khan (Pakistan), Wilfried Pokam Mba (Cameroon), Daniel Rosenfeld (Israel), Jessica Tierney (United States of America), Olga Zolina (Russian Federation/France, Russian Federation)

Review Editors:
Pascale Braconnot (France), Arona Diedhiou (Ivory Coast/Senegal)

Contributing Authors:
Gabriel Abramowitz (Australia), Guðfinna Adalgeirsdottir (Iceland), Andrea Alessandri (Italy), Robert J. Allen (United States of America), Kevin Anchukaitis (United States of America), Richard A. Betts (United Kingdom), Céline J. W. Bonfils (United States of America/France), Michael Bosilovich (United States of America), Olivier Boucher (France), Josephine Brown (Australia), Michael P. Byrne (United Kingdom/Ireland), Robin Chadwick (United Kingdom), Sarah Connors (France/United Kingdom), Benjamin Cook (United States of America), Erika Coppola (Italy), Alejandro Di Luca (Australia, Canada/Argentina), Aïda Diongue Niang (Senegal), Petra Döll (Germany), Ellen Douglas (United States of America), Paul J. Durack (United States of America/Australia), Hayley J. Fowler (United Kingdom), Alexander Gershunov (United States of America), Nicholas R. Golledge (New Zealand/United Kingdom), James Kossin (United States of America), Won-Tae Kwon (Republic of Korea), Flavio Lehner (United States of America/Switzerland), Eric Maloney (United States of America), Vimal Mishra (India), Angeline Pendergrass (United States of America), Stefan Pfahl (Germany), Catherine Prigent (France), Catherine Rio (France), Alex C. Ruane (United States of America), Benjamin Sanderson (United Kingdom), Sonia I. Seneviratne (Switzerland), Shoichi Shige (Japan), Vijay Singh (United States of America), Abigail Swann (United States of America), Richard G. Taylor (United Kingdom/Canada, United Kingdom), Laurent Terray (France), Natalia Tilinina (Russian Federation), Bart van den Hurk (The Netherlands), Sergio M. Vicente-Serrano (Spain), Michael Wehner (United States of America), Laura J. Wilcox (United Kingdom), Cunde Xiao (China), Prodromos Zanis (Greece), Xuebin Zhang (Canada)

Chapter Scientist(s):
Stéphane Sénési (France), Sabin Thazhe Purayil (India)

This Chapter should be cited as:
Douville, H., K. Raghavan, J. Renwick, R. P. Allan, P. A. Arias, M. Barlow, R. Cerezo-Mota, A. Cherchi, T. Y. Gan, J. Gergis, D. Jiang, A. Khan, W. Pokam Mba, D. Rosenfeld, J. Tierney, O. Zolina, 2021, Water Cycle Changes. In: *Climate Change 2021: The Physical Science Basis. Contribution of Working Group I to the Sixth Assessment Report of the Intergovernmental Panel on Climate Change* [Masson-Delmotte, V., P. Zhai, A. Pirani, S. L. Connors, C. Péan, S. Berger, N. Caud, Y. Chen, L. Goldfarb, M. I. Gomis, M. Huang, K. Leitzell, E. Lonnoy, J.B.R. Matthews, T. K. Maycock, T. Waterfield, O. Yelekçi, R. Yu and B. Zhou (eds.)]. Cambridge University Press. In Press.

Date: August 2021

This document is subject to copy-editing, corrigenda and trickle backs.

ACCEPTED VERSION SUBJECT TO FINAL EDITING

Table Of Contents

Executive Summary **6**

8.1 Introduction **10**

8.1.1 Scope and overview 10
8.1.1.1 Importance of water for human societies and ecosystems 10
8.1.1.2 Overview of the global water cycle in the climate system 11
8.1.2 Summary of water cycle changes from AR5 and special reports 12
8.1.2.1 Summary of observed and projected water cycle changes from AR5 12
8.1.2.2 Key findings of AR6 special reports 13
8.1.3 Chapter motivations, framing and preview 14

8.2 Why should we expect water cycle changes? **15**

8.2.1 Global water cycle constraints 15
8.2.2 Constraints on the regional water cycle 18
8.2.2.1 Thermodynamic constraints on atmospheric moisture fluxes 18
8.2.2.2 Large-scale responses in atmospheric circulation patterns 20
8.2.3 Local-scale physical processes affecting the water cycle 23
8.2.3.1 Hydrological processes related to ice and snow 23
8.2.3.2 Processes determining heavy precipitation and flooding 24
8.2.3.3 Drivers of aridity and drought 26
8.2.3.4 Direct anthropogenic influence on the regional water cycle 28

BOX 8.1: Role of anthropogenic aerosols in water cycle changes **30**

8.3 How is the water cycle changing and why? **32**

8.3.1 Observed water cycle changes based on multiple datasets 32
8.3.1.1 Global water cycle intensity and P-E over land and oceans 32
8.3.1.2 Water vapour and its transport 33
8.3.1.3 Precipitation amount, frequency and intensity 34
8.3.1.4 Evapotranspiration 37
8.3.1.5 Runoff, streamflow and flooding 38
8.3.1.6 Aridity and drought 40
8.3.1.7 Freshwater reservoirs 43
8.3.1.7.1 Glaciers 43
8.3.1.7.2 Seasonal snow cover 43
8.3.1.7.3 Wetlands and lakes 44

ACCEPTED VERSION
SUBJECT TO FINAL EDITING

8.3.1.7.4 Groundwater 45
8.3.2 Observed variations in large-scale phenomena and regional variability 46
8.3.2.1 Intertropical Convergence Zone (ITCZ) and tropical rain belts 47
8.3.2.2 Hadley circulation and subtropical belt 48
8.3.2.3 Walker circulation 49
8.3.2.4 Monsoons 49
8.3.2.4.1 South and Southeast Asian Monsoon 50
8.3.2.4.2 East Asian Monsoon 51
8.3.2.4.3 West African Monsoon 52
8.3.2.4.4 North American Monsoon 53
8.3.2.4.5 South American Monsoon 54
8.3.2.4.6 Australian and Maritime Continent Monsoon 55
8.3.2.5 Tropical cyclones 56
8.3.2.6 Stationary waves 57
8.3.2.7 Atmospheric blocking 58
8.3.2.8 Extratropical cyclones, storm tracks and atmospheric rivers 58
8.3.2.8.1 Extratropical cyclones and storm tracks 58
8.3.2.8.2 Atmospheric rivers 60
8.3.2.9 Modes of climate variability and regional teleconnections 60
8.3.2.9.1 Tropical modes 61
8.3.2.9.2 Extra-tropical modes 62

8.4 What are the projected water cycle changes? 63

8.4.1 Projected water cycle changes 63
8.4.1.1 Global water cycle intensity and P-E over land and oceans 64
8.4.1.2 Water vapour and its transport 67
8.4.1.3 Precipitation amount, frequency and intensity 68

BOX 8.2: Changes in water cycle seasonality 70

8.4.1.4 Evapotranspiration 73
8.4.1.5 Runoff, streamflow and flooding 74
8.4.1.6 Aridity and drought 76
8.4.1.7 Freshwater reservoirs 79
8.4.1.7.1 Glaciers 79
8.4.1.7.2 Seasonal snow cover 80
8.4.1.7.3 Wetlands and lakes 80

ACCEPTED VERSION
SUBJECT TO FINAL EDITING

8.4.1.7.4 Groundwater 81
8.4.2 Projected changes in large scale phenomena and regional variability 81
8.4.2.1 ITCZ and tropical rain belts 82
8.4.2.2 Hadley Circulation and subtropical belt 82
8.4.2.3 Walker circulation 83
8.4.2.4 Monsoons 84
8.4.2.4.1 South and Southeast Asian Monsoon 87
8.4.2.4.2 East Asian Monsoon 87
8.4.2.4.3 West African Monsoon 88
8.4.2.4.4 North American Monsoon 89
8.4.2.4.5 South American Monsoon 89
8.4.2.4.6 Australian and Maritime Continent Monsoon 90
8.4.2.5 Tropical cyclones 91
8.4.2.6 Stationary waves 91
8.4.2.7 Atmospheric blocking 92
8.4.2.8 Extratropical cyclones, storm tracks and atmospheric rivers 92
8.4.2.8.1 Extratropical cyclones and storm tracks 93
8.4.2.8.2 Atmospheric Rivers 94
8.4.2.9 Modes of climate variability and regional teleconnections 95
8.4.2.9.1 Tropical modes 95
8.4.2.9.2 Extra-tropical modes 96

8.5 What are the limits for projecting water cycle changes? 96

8.5.1 Model uncertainties of relevance for the water cycle 97
8.5.1.1 Fitness-for-purpose and poorly constrained key processes 97
8.5.1.1.1 Atmospheric convection 98
8.5.1.1.2 Aerosol microphysical effects on clouds and precipitation 99
8.5.1.1.3 Land surface processes 100
8.5.1.2 Added value of increased horizontal model resolution 101
8.5.1.2.1 High-resolution global climate models 102
8.5.1.2.2 Regional Climate Models and Convective Permitting Models 103
8.5.2 Role of internal variability and volcanic forcing 103
8.5.2.1 Quantification of water cycle internal variability 104
8.5.2.2 Implications for near-term water cycle projections 106
8.5.2.3 Volcanic forcing 107
8.5.3 Non-linearities across global warming levels 107

ACCEPTED VERSION
SUBJECT TO FINAL EDITING

8.5.3.1 Non-linearities in large-scale atmospheric circulation and precipitation 108
8.5.3.2 Non-linearities in land surface processes and feedbacks 109

8.6 What is the potential for abrupt change? 111

8.6.1 Abrupt water cycle responses to a collapse of Atlantic Meridional Overturning Circulation 111
8.6.2 Abrupt water cycle responses to changes in the land surface 112
8.6.2.1 Amazon deforestation and drying 112
8.6.2.2 Greening of the Sahara and the Sahel 113
8.6.2.3 Amplification of drought by dust 114
8.6.3 Abrupt water cycle responses to initiation or termination of solar radiation modification 115

8.7 Final remarks 115

Frequently Asked Questions 117

FAQ 8.1: How does land use change alter the water cycle? 117
FAQ 8.2: Will floods become more severe or more frequent as a result of climate change? 119
FAQ 8.3: What causes droughts, and will climate change make them worse? 121

Acknowledgements 122

References 123

Figures 197

ACCEPTED VERSION
SUBJECT TO FINAL EDITING

Executive Summary

This chapter assesses multiple lines of evidence to evaluate past, present and future changes in the global water cycle. It complements material in Chapters 2, 3, and 4 on observed and projected changes in the water cycle, and Chapters 10 and 11 on regional climate change and extreme events. The assessment includes the physical basis for water cycle changes, observed changes in the water cycle and attribution of their causes, future projections and related key uncertainties, and the potential for abrupt change. Paleoclimate evidence, observations, reanalyses and global and regional model simulations are considered. The assessment shows widespread, non-uniform human-caused alterations of the water cycle, which have been obscured by a competition between different drivers across the 20th century that will be increasingly dominated by greenhouse gas (GHG) forcing at the global scale.

Physical Basis for Water Cycle Changes

Modifications of Earth's energy budget by anthropogenic radiative forcings drive substantial and widespread changes in the global water cycle. There is *high confidence* that global mean precipitation and evaporation increase with global warming, but the estimated rate is model-dependent (*very likely* range of 1–3% per 1°C). The global increase in precipitation is determined by a robust response to global mean surface air temperature (*very likely* 2–3% per 1°C) that is partly offset by fast atmospheric adjustments to atmospheric heating by GHGs and aerosols. The overall effect of anthropogenic aerosols is to reduce global precipitation and alter large-scale atmospheric circulation patterns through their well-understood surface radiative cooling effect (*high confidence*). Land-use and land-cover changes also drive regional water cycle changes through their influence on surface water and energy budgets (*high confidence*). {8.2.1, 8.2.3.4, 8.2.2.2, Box 8.1}

A warmer climate increases moisture transport into weather systems, which, on average, makes wet seasons and events wetter (*high confidence*). An increase in near-surface atmospheric water holding capacity of about 7% per 1°C of warming explains a similar magnitude of intensification of heavy precipitation events (from sub-daily up to seasonal time scales) that increases the severity of flood hazards when these extremes occur (*high confidence*). The severity of very wet and very dry events increases in a warming climate (*high confidence*), but changes in atmospheric circulation patterns alter where and how often these extremes occur with substantial regional differences and seasonal contrasts. The slowdown of tropical circulation with global warming partly offsets the warming-induced strengthening of precipitation in monsoon regions (*high confidence*). {8.2.2, 8.2.3, 8.3.1.7, 8.4.1, 8.5.1}

Warming over land drives an increase in atmospheric evaporative demand and the severity of droughts (*high confidence*). Greater warming over land than over the ocean alters atmospheric circulation patterns and, on average, reduces continental near-surface relative humidity, which contributes to regional drying (*high confidence*). Increasing atmospheric CO_2 concentrations increase plant growth and water-use efficiency, but there is *low confidence* in how these factors drive regional water cycle changes. {8.2.2, 8.2.3}

Causes of Observed Changes

Human-caused climate change has driven detectable changes in the global water cycle since the mid-20th century (*high confidence*). Global warming has contributed to an overall increase in atmospheric moisture and precipitation intensity (*high confidence*), increased terrestrial evapotranspiration (*medium confidence*), influenced global patterns in aridity (*very likely*), and enhanced contrasts in surface salinity and precipitation minus evaporation patterns over the oceans (*high confidence*). {3.4.2, 3.4.3, 3.5.2, 8.3.1, 9.2.2}

Greenhouse gas forcing has driven increased contrasts in precipitation amounts between wet and dry seasons and weather regimes over tropical land areas (*medium confidence*), with a detectable precipitation increase in the northern high latitudes (*high confidence*). GHG forcing has also contributed to drying in dry summer climates, including the Mediterranean, southwestern Australia, southwestern South America, South Africa, and western North America (*medium to high confidence*). Earlier onset of spring snowmelt and increased melting of glaciers have already contributed to seasonal changes in streamflow in

ACCEPTED VERSION SUBJECT TO FINAL EDITING

high-latitude and low-elevation mountain catchments (*high confidence*). {Box 8.2, 8.2.2.1, 8.3.1, 3.3.2, 3.3.3, 3.5.2}

Anthropogenic aerosols have driven detectable large-scale water cycle changes since at least the mid-20th century (*high confidence*). Shifts in the tropical rain belt are associated with the inter-hemispheric temperature response to the time-evolving radiative influence of anthropogenic aerosols and the ongoing warming influence of GHGs (*high confidence*). Cooling in the Northern Hemisphere by sulphate aerosols explained a southward shift in the tropical rain belt and contributed to the Sahel drought from the 1970s to the 1980s (*high confidence*), subsequent recovery from which has been linked with GHG warming (*medium confidence*). Observed changes in regional monsoon precipitation, especially over South Asia, East Asia and West Africa, have been limited over much of the 20th century due to increases driven by warming from GHGs being counteracted by decreases due to cooling from anthropogenic aerosols (*high confidence*). {8.3.1.3, 8.3.2.4, Box 8.1}

Land-use change and water extraction for irrigation have influenced local and regional responses in the water cycle (*high confidence*). Large-scale deforestation has likely decreased evapotranspiration and precipitation and increased runoff over the deforested regions. Urbanization has increased local precipitation (*medium confidence*) and runoff intensity (*high confidence*). Increased precipitation intensities have enhanced groundwater recharge, most notably in tropical regions (*medium confidence*). There is *high confidence* that groundwater depletion has occurred since at least the start of the 21st century as a consequence of groundwater withdrawals for irrigation in agricultural areas in drylands (e.g., the United States southern High Plains, California Central Valley, North China Plain, and northwest India). {8.2.3.4, 8.3.1.7, Box 10.3, FAQ8.1}

Southern Hemisphere storm tracks and associated precipitation have shifted polewards since the 1970s, especially in the austral summer and autumn (*high confidence*). It is *very likely* that these changes are associated with a positive trend in the Southern Annular Mode, related to both stratospheric ozone depletion and GHG increases. There is *medium confidence* that the recent observed expansion of the Hadley Circulation was caused by GHG forcing, especially in the Southern Hemisphere, but there is only *low confidence* in how it influences the drying of subtropical land areas. {8.2.2, 8.3.2, 3.3.3}

Future Water Cycle Changes

Without large-scale reduction in greenhouse gas emissions, global warming is projected to cause substantial changes in the water cycle at both global and regional scales (*high confidence*). Global annual precipitation over land is projected to increase on average by 2.4 [–0.2 to 4.7] % (*very likely* range) in the SSP1-1.9 low-emission scenario and by 8.3 [0.9 to 12.9] % in the SSP5-8.5 high-emission scenario by 2081–2100, relative to 1995–2014. It is *virtually certain* that evaporation will increase over the oceans and *very likely* that evapotranspiration will increase over land with regional exceptions in drying areas. There is *low confidence* in the sign and magnitude of projected changes in global land runoff in all Shared-socioeconomic Pathway scenarios. Projected increases in precipitation amount and intensity will be associated with increased runoff in the northern high latitudes (*high confidence*). There is *high confidence* that mountain glaciers will diminish in all regions and that seasonal snow cover duration will generally decrease. Runoff from small glaciers will typically decrease through loss of ice mass, while runoff from large glaciers is *likely* to increase with increasing global warming until glacier mass becomes depleted (*high confidence*). {4.5.1, 8.4.1}

Increased evapotranspiration due to growing atmospheric water demand will decrease soil moisture over the Mediterranean, southwestern North America, south Africa, southwestern South America, and southwestern Australia (*high confidence*). The total land area subject to increasing drought frequency and severity will expand (*high confidence*), and in the Mediterranean, southwestern South America, and western North America, future aridification will far exceed the magnitude of change seen in the last millennium (*high confidence*). Some tropical regions are also projected to experience increased aridity, including the Amazon basin and Central America (*high confidence*). {8.4.1}

ACCEPTED VERSION SUBJECT TO FINAL EDITING

Water cycle variability and extremes are projected to increase faster than average changes in most regions of the world and under all emission scenarios (*high confidence*). In the tropics and in the extratropics of both hemispheres during summer/warm season, interannual variability of precipitation and runoff over land is projected to increase at a faster rate than changes in seasonal mean precipitation amount (*medium confidence*). It is *very likely* that rainfall variability related to the El Niño–Southern Oscillation will be amplified by the end of the 21st century. Sub-seasonal precipitation variability is also projected to increase, with fewer rainy days but increased daily mean precipitation intensity over many land regions (*high confidence*). Precipitation extremes will increase in almost all regions (*high confidence*), even where seasonal mean precipitation is projected to decrease (*medium confidence*). There is *high confidence* that heavy precipitation events associated with both tropical and extratropical cyclones will intensify. {4.5.1.4, 4.5.3.2, 8.2.3.2, 8.4.1, 8.4.2, 8.5.2, 11.7.1.5}

There are contrasting projections in monsoon precipitation, with increases in more regions than decreases (*medium confidence*). Summer monsoon precipitation is projected to increase for the South, Southeast and East Asian monsoon domains, while North American monsoon precipitation is projected to decrease (*medium confidence*). West African monsoon precipitation is projected to increase over the Central Sahel and decrease over the far western Sahel (*medium confidence*). There is *low confidence* in projected precipitation changes in the South American and Australian monsoons (for both magnitude and sign). There is *high confidence* that the monsoon season will be delayed in North and South America and *medium confidence* that it will be delayed in the Sahel. {8.2.2, 8.4.2.4}

Precipitation associated with extratropical storms and atmospheric rivers will increase in the future in most regions (*high confidence*). A continued poleward shift of storm tracks in the Southern Hemisphere (*likely*) and the North Pacific (*medium confidence*) will lead to similar shifts in annual or seasonal precipitation. There is *low confidence* in projections of blocking and stationary waves and therefore their influence on precipitation for almost all regions. {8.4.2}

The seasonality of precipitation, water availability and streamflow will increase with global warming over the Amazon (*medium confidence*) and in the subtropics, especially in the Mediterranean and southern Africa (*high confidence*). The annual contrast between the wettest and driest month of the year is *likely* to increase by 3–5% per 1°C in most monsoon regions in terms of precipitation, precipitation minus evaporation, and runoff (*medium confidence*). There is *high confidence* in an earlier onset in spring snowmelt, with higher peak flows at the expense of summer flows in snow-dominated regions globally, but *medium confidence* that reduced snow volume in lower-latitude regions will reduce runoff from snowmelt. {8.2.2, Box 8.2, 8.4.1.7, 8.4.2.4}

Confidence in Projections, Non-Linear Responses and the Potential for Abrupt Changes

Representation of key physical processes has improved in global climate models (GCMs), but they are still limited in their ability to simulate all aspects of the present-day water cycle and to agree on future changes (*high confidence*). Climate change studies benefit from sampling the full distribution of model outputs when considering future projections at regional scales. Increasing horizontal resolution in GCMs improves the representation of small-scale features and the statistics of daily precipitation (*high confidence*). High-resolution climate and hydrological models provide a better representation of land surfaces, including topography, vegetation and land-use change, which improve the accuracy of simulations of regional changes in the water cycle (*high confidence*). There is *high confidence* in the potential added value of regional climate models but only *medium confidence* that this potential is currently realized. {8.5.1}

Natural climate variability will continue to be a major source of uncertainty in near-term (2021–2040) water cycle projections (*high confidence*). Decadal predictions of water cycle changes should be considered with *low confidence* in most land areas because the internal variability of precipitation is difficult to predict and can offset or amplify the forced water cycle response. Water cycle changes that have already emerged from natural variability will become more pronounced in the near term, but the occurrence of volcanic eruptions (either single large events or clustered smaller ones) can alter the water cycle for several years, decreasing global mean land precipitation and altering monsoon circulation (*high confidence*). {8.5.2,

ACCEPTED VERSION SUBJECT TO FINAL EDITING

CCB4.1}

Continued global warming will further amplify GHG-induced changes in large-scale atmospheric circulation and precipitation patterns (*high confidence*), but in some cases regional water cycle changes are not linearly related to global warming. Non-linear water cycle responses are explained by the interaction of multiple drivers, feedbacks and time scales (*high confidence*). Nonlinear responses of regional runoff, groundwater recharge and water scarcity highlight the limitations of simple pattern-scaling techniques (*medium confidence*). Water resources fed by melting glaciers are particularly exposed to nonlinear responses (*high confidence*). {8.5.3}

Abrupt human-caused changes to the water cycle cannot be excluded. There is evidence of abrupt change in some high-emission scenarios, but there is no overall consistency regarding the magnitude and timing of such changes. Positive land-surface feedbacks, including vegetation and dust, can contribute to abrupt changes in aridity, but there is only *low confidence* that such changes will occur during the 21st century. Continued Amazon deforestation, combined with a warming climate, raises the probability that this ecosystem will cross a tipping point into a dry state during the 21st century (*low confidence*). The paleoclimate record shows that a collapse in the Atlantic Meridional Overturning Circulation (AMOC) causes abrupt shifts in the water cycle (*high confidence*), such as a southward shift in the tropical rain belt, weakening of the African and Asian monsoons and strengthening of Southern Hemisphere monsoons. There is *medium confidence* that AMOC will not collapse before 2100, but should it collapse, it is *very likely* that there would be abrupt changes in the water cycle. {8.6.1, 8.6.2}

Solar radiation modification (SRM) could drive abrupt changes in the water cycle (*high confidence*). It is *very likely* that abrupt water cycle changes will occur if SRM techniques are implemented rapidly or terminated abruptly. The impact of SRM is spatially heterogeneous (*high confidence*), will not fully mitigate the GHG-forced water cycle changes (*medium confidence*), and can affect different regions in potentially disruptive ways (*low confidence*). {8.6.3}

ACCEPTED VERSION SUBJECT TO FINAL EDITING

8.1 Introduction

8.1.1 Scope and overview

8.1.1.1 Importance of water for human societies and ecosystems

Water is vital to all life on Earth. 71% of the Earth is covered by water, with saline ocean water accounting for around 96.6% of total water availability (Figure 8.1). Terrestrial freshwater only represents about 1.8% of all water on Earth and the remainder (1.6%) is primarily made up of saline groundwater and saline lakes (Durack, 2015; Abbott et al., 2019). Ice sheets, glaciers and snow pack account for approximately 97% of freshwater resources, with less than 3% of freshwater considered easily accessible and available for essential ecosystem functioning and human society's water resource needs (Durack, 2015; Abbott et al., 2019). This very small fraction of freshwater represents a total volume of about 835 thousand km^3, mostly contained in groundwater (630 thousand km^3), the remaining 205 thousand km^3 being stored in lakes, rivers, wetlands and soils (Abbott et al., 2019). Although the natural cycling rate of this amount is theoretically enough to meet global human and ecosystem needs, there are large geographical and seasonal differences that influence the availability of freshwater to meet regional demands.

Freshwater is the most essential natural resource on the planet (Mekonnen and Hoekstra, 2016; Djehdian et al., 2019) and underpins almost all Sustainable Development Goals (SDGs), which require access to adequate and safe resources for drinking and sanitation (SDG 6) and many other purposes. Freshwater supports a range of human activities from irrigation to industrial processes including the generation of hydroelectricity and the cooling of thermoelectric power plants (Bates et al., 2008; Schewe et al., 2014). These activities require sufficient quantities of freshwater that can be drawn from rivers, lakes, groundwater stores, and in some cases, desalinated sea water (Schewe et al., 2014). Recent estimates of global water pools and fluxes suggest that half of global river discharge is redistributed each year by human water use (Abbott et al., 2019). This emphasises the need to consider both anthropogenic climate change and direct human influences, such as population increase or migration, economic development, urbanization, and land use change, when planning water-related mitigation or adaptation strategies (Jiménez Cisneros et al., 2014).

Water scarcity occurs when there are insufficient freshwater resources to meet water demands, although water problems may also arise from water quality issues or from economic and institutional barriers (WGII Chapter 4). This affects the preservation of environmental flows that ultimately influence ecosystem functioning and services (Schewe et al., 2014; Mekonnen and Hoekstra, 2016; Djehdian et al., 2019). As such, water availability is a major constraint on human society's ability to meet the future food and energy needs of a growing population (D'Odorico et al., 2018). Water plays a key role in the production of energy, including hydroelectricity, bioenergy, and the extraction of unconventional fossil fuels (Schewe et al., 2014; D'Odorico et al., 2018; Djehdian et al., 2019). These dependencies have resulted in increasing competition for water between the food and energy sectors. Pressures on this 'food-energy-water nexus' are further compounded by increasing globalization, which can transfer large-scale water demands to other regions of the world, raising serious concerns about local food and water security in regions that are highly dependent on agricultural exports or imports (D'Odorico et al., 2018).

The consequences of climate change on terrestrial ecosystems and human societies are primarily experienced through changes to the global water cycle (Jiménez Cisneros et al., 2014). Changes in the quantity and seasonality of water due to climate change have long been recognized by IPCC and global development agencies as heavily influencing the food security and economic prosperity of many countries, particularly in the arid and semi-arid areas of the world including Asia, Africa, Australia, Latin America, the Mediterranean, and small island developing states (Bates et al., 2008; Schewe et al., 2014; Mekonnen and Hoekstra, 2016). Having too much or too little water increases the likelihood of flooding and drought, as precipitation variability increases in a warming climate (Stocker et al., 2013; Hoegh-Guldberg et al., 2019). Climate change poses a threat to both regional water availability and global water security. Changes in precipitation and glacier runoff and snowmelt influence other hydroclimate variables like surface and subsurface runoff, and groundwater recharge, which are critical to the water, food and energy security of many regions (Oki and Kanae, 2006; Jiménez Cisneros et al., 2014; Schewe et al., 2014; Mekonnen and

ACCEPTED VERSION SUBJECT TO FINAL EDITING

Hoekstra, 2016).

Currently, around four billion people live under conditions of severe freshwater scarcity for at least one month of the year, with half a billion people in the world facing severe water scarcity all year round (Mekonnen and Hoekstra, 2016). AR5 WGII reported that approximately 80% of the world's population already suffers from high levels of threat to water security (Jiménez Cisneros et al., 2014). Given the vulnerability of the planet's freshwater resources and the role of climate change in intensifying adverse impacts on human societies and ecosystems (IPCC, 2018; Hoegh-Guldberg et al., 2019), this chapter evaluates advances in the theoretical, observational and model based understanding of the global water cycle made since AR5 (IPCC, 2013) and AR6 Special Reports.

8.1.1.2 Overview of the global water cycle in the climate system

As shown in Figure 8.1, the global water cycle is the continuous, naturally occurring movement of water through the climate system from its liquid, solid and gaseous forms among reservoirs of the ocean, atmosphere, cryosphere and land (Stocker et al., 2013). In the atmosphere, water primarily occurs as a gas (water vapour), but it is also present as ice and liquid water within clouds where it substantially affects Earth's energy balance (Section 7.4.2.2 and 7.4.2.4). The water cycle primarily involves the evaporation[1] and precipitation of moisture at the Earth's surface including transpiration associated with biological processes. Water that falls on land as precipitation, supplying soil moisture, groundwater recharge, and river flows, was once evaporated from the ocean or sublimated from ice-covered regions before being transported through the atmosphere as water vapour, or in some areas was generated over land through evapotranspiration (Gimeno et al., 2010; van der Ent and Savenije, 2013). In addition, the net flux of atmospheric and continental freshwater is a key driver of sea surface salinity, which in turn influences the density and circulation of the ocean (Chapter 9).

Understanding the interactions between the water and energy cycles is one of the four core projects of the World Climate Research Programme (WCRP). Latent heat fluxes, released by condensation of atmospheric water vapour and absorbed by evaporative processes, are critical to driving the circulation of the atmosphere on scales ranging from individual thunderstorm cells to the global circulation of the atmosphere (Stocker et al., 2013; Miralles et al., 2019). Water vapour is the most important gaseous absorber in the Earth's atmosphere, playing a key role in the Earth's radiative budget (Schneider et al., 2010). As atmospheric water vapour content increases with temperature, it has a considerable influence on climate change (Section 7.4.2.2). Additionally, a small fraction of the atmospheric water content is liquid or solid and has a major effect on both solar and longwave radiative fluxes, from the Earth's surface to the top of the atmosphere. The cloud response to anthropogenic radiative forcings, both in the tropics and in the extratropics (Zelinka et al., 2020), is therefore also crucial for understanding climate change (Section 7.4.2.4).

The terrestrial water and carbon cycles are also strongly coupled (Cross-Chapter Box5.1). As atmospheric carbon dioxide (CO_2) concentration increases, the physical environment in which plants grow is altered, including the availability of soil moisture necessary for plants' CO_2 uptake and, potentially, the effectiveness of carbon dioxide removal techniques to mitigate climate change (Section 5.6.2.1.2). Rising surface CO_2 concentrations also modify stomatal (small pores at the leaf surface) regulation as well as the plants' biomass, thus affecting ecosystem photosynthesis and transpiration rates and leading generally to a net increase in water use efficiency (Lemordant et al., 2018). These coupled changes have profound implications for the simulation of the carbon and water cycles (Gentine et al., 2019; see also Section 5.4.1), which can be better assessed with the new generation Earth system models, although both the carbon concentration and carbon-climate feedbacks remain highly uncertain over land (Arora et al., 2020) {5.4.5}. The water constraints on the terrestrial carbon sinks are a matter of debate regarding the feasibility or efficiency of

[1] In this chapter, we use evaporation to include all evaporative processes that include transpiration over land while the term evapotranspiration (ET) is also used interchangeably when the focus is only on land.

ACCEPTED VERSION SUBJECT TO FINAL EDITING

some land-based carbon dioxide removal and sequestration techniques requested to comply with the Paris Agreement (Fuss et al., 2018; Belyazid and Giuliana, 2019) {5.6.2.2.1}.

[START FIGURE 8.1 HERE]

Figure 8.1: Depiction of the water cycle based on previous assessments (Trenberth et al., 2011; Rodell et al., 2015; Abbott et al., 2019) with minor adjustments for groundwater flows (Kwon et al., 2014; Zhou et al., 2019c; Luijendijk et al., 2020), seasonal snow (Pulliainen et al., 2020) and ocean precipitation and evaporation (Stephens et al., 2012; Allan et al., 2020; Gutenstein et al., 2020). In the atmosphere, which accounts for only 0.001% of all water on Earth, water primarily occurs as a gas (water vapour), but it is also present as ice and liquid water within clouds. The ocean is the primary water reservoir on Earth, which is comprised mostly of liquid water across much of the globe, but also includes areas covered by ice in polar regions. Liquid freshwater on land forms surface water (lakes, rivers), soil moisture and groundwater stores, together accounting for 1.8% of global water (Stocker et al., 2013). Solid terrestrial water that occurs as ice sheets, glaciers, snow and ice on the surface and permafrost currently represents 2.2% of the planet's water (Stocker et al., 2013). Water that falls as snow in winter provides soil moisture and streamflow after melting, which are essential for human activities and ecosystem functioning.

[END FIGURE 8.1 HERE]

8.1.2 Summary of water cycle changes from AR5 and special reports

This Report is the first IPCC assessment to include a chapter specifically dedicated to providing an integrated assessment of the global water cycle changes, by building on many chapters from previous reports. This section summarises observed and projected water cycle changes reported in the AR5 (IPCC, 2013) and in the recent IPCC special reports on global warming of 1.5ºC (SR1.5), ocean and cryosphere in a changing climate (SROCC), and climate change and land (SRCCL).

8.1.2.1 Summary of observed and projected water cycle changes from AR5

Based on long-term observational evidence (Hartmann et al., 2013), AR5 concluded it was *likely* that anthropogenic influence has affected the water cycle since the 1960s (IPCC, 2018). Detectable human influence on changes to the water cycle were found in atmospheric moisture content (*medium confidence*), global-scale changes of precipitation over land (*medium confidence*), intensification of heavy precipitation events over land regions where sufficient data networks exist (*medium confidence*), and *very likely* changes to ocean salinity through its connection with evaporation minus precipitation change patterns (Stocker et al., 2013) {2.5, 2.6, 3.3, 7.6, 10.3, 10.4}. AR5 also reported that it is *very likely* that global surface air specific humidity increased since the 1970s. There was *low confidence* in the observations of global-scale cloud variability and trends, *medium confidence* in reductions of pan-evaporation, and *medium confidence* in the non-monotonic changes of global evapotranspiration since the 1980s. In terms of streamflow and runoff, the AR5 identified that there is *low confidence* in the observed increasing trends of global river discharge during the 20th century. Similarly, AR5 concluded that there is *low confidence* in any global-scale observed trend in drought or dryness (lack of rainfall) since the mid-20th century. Yet, the frequency and intensity of drought *likely* increased in the Mediterranean and West Africa, while they *likely* decreased in central North America and north-western Australia since 1950.

Water cycle projections in AR5 (Collins et al., 2013) were considered primarily in terms of water vapour, precipitation, surface evaporation, runoff, and snowpack. Globally-averaged precipitation was projected to increase with global warming with *virtual certainty* (12ES, 12.4.1.1). Regionally, precipitation in some areas of the tropics and polar regions could increase by more than 50% by the end of the 21st century under the RCP8.5 emissions scenario, while precipitation in large areas of the subtropics could decrease by 30% or more (AR5 FAQ 12.2, Figure 12.22). Overall, the contrast of annual mean precipitation between dry and wet regions and between dry and wet seasons ("wet-get-wetter and dry-get-drier") was projected to increase over

ACCEPTED VERSION SUBJECT TO FINAL EDITING

most of the globe with *high confidence* (12ES, 12.4.5.2). Globally, the frequency of intense precipitation events was projected to increase while the frequency of all precipitation events was projected to decrease, leading to the contradictory-seeming projection of a simultaneous increase in both droughts and floods (AR5 FAQ 12.2, 12.4.5.5). Surface evaporation change was projected to be positive over most of the ocean and to generally follow the pattern of precipitation change over land (12ES, 12.4.5.4). Near-surface relative humidity reductions over many land areas were projected to be *likely*, with *medium confidence* (12.4.5.1). General decreases in soil moisture in present-day dry regions were considered *likely,* and projected with *medium confidence* under the RCP8.5 scenario (12.4.5.3). Soil moisture drying in the Mediterranean, southwest USA and southern African regions was considered *likely*, with *high confidence* by the end of this century under the RCP8.5 scenario (12.4.5.3). Projections for annual runoff included both decreases and increases. Decreases in Northern Hemisphere snow cover were assessed as *very likely* with continued global warming (12.4.6.2). As temperatures increase, snow accumulation was projected to begin later in the year and melting to start earlier, with related changes in snowmelt-driven river flows (AR5 FAQ 12.2, 12.4.6.2). In terms of the potential for abrupt change in components of the water cycle, long-term droughts and monsoonal circulation were identified as potentially undergoing rapid changes, but the assessment was reported with *low confidence* (Table 12.4, 12.5.5.8.1, 12.5.5.8.2).

8.1.2.2 Key findings of AR6 special reports

The SR1.5 assessed the impacts of global warming of 1.5°C above pre-industrial levels. The dominant human influence on observed global warming and related water cycle changes was confirmed. Further evidence that anthropogenic global warming has caused an increase in the frequency, intensity and/or amount of heavy precipitation events at the global scale (*medium confidence*), as well as in drought occurrence in the Mediterranean region (*medium confidence*) was also reported. Chapter 3 of SR1.5 (Hoegh-Guldberg et al., 2019) highlights that each half degree of additional global warming influences the climate response. Heavy precipitation shows a global tendency to increase more at 2°C compared to 1.5°C, though there is *low confidence* in projected regional differences in heavy precipitation at 1.5°C compared to 2°C global warming, except at high latitudes or at high altitude where there is *medium confidence*. A key finding is that "limiting global warming to 1.5°C compared to 2°C would approximately halve the proportion of the world population expected to suffer water scarcity, although there is considerable variability between regions (*medium confidence*)" (SR1.5). This is consistent with greater adverse impacts found at 2°C compared to 1.5°C for a number of dryness or drought indices (Schleussner et al., 2016; Lehner et al., 2017; Greve et al., 2018). There is also *medium confidence* that land areas with increased runoff and exposure to flood hazards will increase more at 2°C compared to 1.5°C of global warming.

The Special Report on the Ocean and Cryosphere in a changing Climate (SROCC) provides a comprehensive assessment of recent and projected changes, specifically in snow and ice-covered areas that form a key component of the water cycle in high-elevation and high-latitudes areas. High mountain regions have experienced significant warming since the early 20th century, resulting in reduced snowpack on average (Marty et al., 2017), with glaciers retreating globally since the mid-20th century (Marzeion 2018; Zemp et al., 2019). Glacier shrinkage and snow cover changes have led to changes (both increases and decreases) in streamflow in many mountain regions in recent decades (Milner et al., 2017). Permafrost regions have undergone degradation and ground-ice loss due to recent warming (Lu et al., 2017). Glacier mass loss is projected to continue through the 21st century under all scenarios. In high mountain areas, low-elevation snow cover is also projected to decrease, regardless of emissions scenario. Widespread permafrost thaw is projected to continue through this century and beyond. River runoff in snow- or glacier-fed basins is projected to increase in winter and to decrease in summer (and in the annual mean) by 2100. In the oceans, the Atlantic Meridional Overturning Circulation (AMOC) will *very likely* weaken over the 21st century under all emissions scenarios (SROCC), with potential effects on atmospheric circulation and the water cycle at the regional scale (cf. Section 8.6).

The Special Report on climate change, desertification, land degradation, sustainable management, food security, and greenhouse gas fluxes in terrestrial ecosystems (SRCCL) has clear connections with the water cycle. This report indicates that since 1850-1900, land surface temperature has risen nearly twice as much as

ACCEPTED VERSION SUBJECT TO FINAL EDITING

global surface temperature (*high confidence*), with an increase in dry climates (*high confidence*). Land surface processes modulate the likelihood, intensity and duration of many extreme events including droughts (*medium confidence*) and heavy precipitation (*medium confidence*). The direction and magnitude of hydrological changes induced by land use change and land surface feedbacks vary with location and season (*high confidence*). Desertification exacerbates climate change through feedbacks involving vegetation cover, greenhouse gases and mineral dust aerosol (*high confidence*). Urbanisation increases extreme rainfall events over or downwind of cities (*medium confidence*). Intensification of rainy events increase their consequences on land degradation.

8.1.3 Chapter motivations, framing and preview

AR5 report was a major step forward in the assessment of the human influence on the Earth's water cycle, yet regional projections of precipitation and water resources often remained very uncertain for a range of reasons including modelling uncertainty and the large influence of internal variability (Deser et al., 2012; Hawkins and Sutton, 2011; see also Section 1.4.3 and 8.5.2). Since AR5, longer and more homogeneous observational and reanalysis datasets have been produced along with new ensembles of historical simulations driven by all or individual anthropogenic forcings. These factors, together with improved detection-attribution tools, has enabled a more comprehensive assessment and a better understanding of recent observed water cycle changes, including the competing effects of greenhouse gases and aerosol emissions. New paleoclimate reconstructions have been also developed, particularly from the Southern Hemisphere (SH), that were not available at the time of AR5. There have also been advances in modelling clouds, precipitation, surface fluxes, vegetation, snow, floodplains, ground water and other processes relevant to the water cycle. Convection permitting and cloud resolving models have been implemented over increasingly large domains and can be used as benchmarks for the evaluation of the current-generation climate models. The added value of increased resolution in global or regional climate models can be also assessed more thoroughly based on dedicated model intercomparison projects (see Section 10.3.3 and Section 8.5.1). Ongoing research activities on decadal predictions and observational constraints are aimed at narrowing the plausible range of near-term (2021-2040) to long-term (2081-2100) water cycle changes.

This chapter assesses water cycle changes and considers climate change from the perspective of its effects on water availability (including streamflow and soil moisture, snow mass and glaciers, groundwater, wetlands and lakes) rather than only precipitation. The chapter highlights the sensitivity of the water cycle to multiple drivers and the complexity of its responses, depending on regions, seasons and timescales. Anthropogenic drivers include not only emissions of greenhouse gases but also different species of aerosols, land and water management practices. Emphasis is placed on assessing the full range of projections, including 'low likelihood, high impact' climate trajectories such as the potential for abrupt changes in the water cycle.

The chapter starts with theoretical evidence that link small-scale processes and drivers, as well as global energy budget and large-scale circulation constraints to physically-understood changes in the global water cycle (Section 8.2). Observed and projected water cycle changes (Section 8.3 and 8.4, respectively) are assessed in separate sections, but with a parallel structure to facilitate comparison of a specific topic across sections. Projections are primarily assessed on the basis of contrasted emission scenarios to emphasize the water cycle response to mitigation. Unless otherwise specified, projected anomalies are estimated relative to the 1995-2014 baseline climatology and are assessed over 20-year timeslices, 2021-2040, 2041-2060 and 2081-2100 for near-, mid- and long-term changes respectively. Beyond multi-model ensemble means, model response uncertainty, the influence of natural climate variability, and the potential non-linearities in the regional water cycle response are also considered (Section 8.5). Low likelihood but physically plausible high-impact scenarios are also assessed, especially the potential for abrupt climate change (Section 8.6). Final remarks about future studies on water cycle changes (Section 8.7) are also provided, and the chapter addresses three frequently asked questions (FAQs) on the water cycle's sensitivity to land use change (FAQ 8.1), the projected occurrence and severity of floods (FAQ 8.2) and droughts (FAQ 8.3) at the global scale. This chapter outline is summarized with a schematic (Figure 8.2) which also provides a quick guide to the main topics addressed across the different sections.

ACCEPTED VERSION SUBJECT TO FINAL EDITING

[START FIGURE 8.2 HERE]

Figure 8.2: Schematic of the chapter structure and quick guide to the chapter content.

[END FIGURE 8.2 HERE]

Chapter 8 has multiple links across all AR6 WGI chapters, so necessarily includes references to other chapter subsections and figures. Model evaluation of large-scale circulation, precipitation, and hydrological extremes is mostly covered by Chapter 3 and 11, respectively, while Chapter 8 focuses on key processes relevant to the water cycle and their resolution-dependent representation in models. Observed and projected changes in large-scale circulation and precipitation are primarily assessed in Chapters 2, 3 and 4. Beyond global and regional mean precipitation amounts, Chapter 8 also focuses on other precipitation properties (e.g., frequency, intensity and seasonality) and other water cycle variables (evapotranspiration, runoff, soil moisture and aridity, solid and liquid freshwater reservoirs). Key regional phenomena (e.g., tropical overturning circulations, monsoons, extratropical stationary waves and stormtracks, modes of variability and related teleconnections) are also assessed given their major dynamical contribution to regional water cycle changes. Although the biosphere and the cryosphere are key components of the water cycle, a more comprehensive assessment of their responses can be found in Chapters 5 and 9, respectively. Further assessment on regional water cycle changes can be found in Chapters 10 to 12 and in the Atlas. The reader is also referred to the interactive Atlas for a more detailed assessment of the range of model biases and responses at the regional scale. Beyond WGI, water is also a major topic for both adaptation and mitigation policies so has strong connections with both WGII and WGIII. Assessment of hydrological impacts at basin and catchment scales, including a broader discussion on adaptation and vulnerability, potential threats to water security, societal responses, improving resilience in water systems and related case studies is provided in WGII (Chapter 4).

8.2 Why should we expect water cycle changes?

It is well understood that global precipitation and evaporation changes are determined by Earth's energy balance (Section 8.2.1). At regional scales smaller than ~4000 km, water cycle changes become dominated by the transport of moisture (Dagan et al., 2019a; Jakob et al., 2019; Dagan and Stier, 2020), which depend on both thermodynamic and dynamical processes (Section 8.2.2). The constraints of energy budgets at global scales and moisture budgets at regional scales cause key water cycle characteristics such as precipitation intensity, duration and intermittence to alter as the climate warms (Pendergrass and Hartmann, 2014b; Döll et al., 2018a). Future water availability is also determined by changes in evaporation, which is driven by a general increase in the atmospheric evaporative demand (Scheff and Frierson, 2014) and modulated by vegetation controls on evaporative losses (Milly and Dunne, 2016; Lemordant et al., 2018; Vicente-Serrano et al., 2020b). At regional scales, water cycle changes result from the interplay between multiple potential drivers (CO_2, aerosols, land use change and human water use; Section 8.2.3). This section assesses advances in physical understanding of global to regional drivers of water cycle changes.

8.2.1 Global water cycle constraints

The Clausius-Clapeyron equation determines that low-altitude specific humidity increases by about 7% per ^{o}C of warming, assuming that relative humidity remains constant, which is approximately true at a global scale but not necessarily valid regionally. It is *very likely* that near surface specific humidity has increased since the 1970s (Section 2.3.1) and total atmospheric water vapour content (precipitable water) is *very likely* to increase at close to a thermodynamic rate on average globally with continued warming. Different radiative forcing mechanisms lead to some variation in the global mean thermodynamic response by altering the relative humidity distribution: the rate of global precipitable water increase with global surface temperature

ACCEPTED VERSION SUBJECT TO FINAL EDITING

ranges[2] from 6.4±1.5% per ºC for sulphate aerosol-induced changes to 9.8±3.3% per ºC for black carbon-induced changes based on idealised modelling (Hodnebrog et al., 2019b). Specific humidity increases at a lower rate over land due to decreasing relative humidity (Collins et al., 2013) as corroborated by observations and simple models (Byrne and O'Gorman, 2018). Prevalent increases in atmospheric water vapour drive powerful amplifying feedbacks (Section 7.4.2.2), intensify atmospheric moisture transport and heavy precipitation events (Section 8.2.3.2), and alter the surface and atmospheric energy balance, thereby influencing global evaporation and precipitation changes (Figure 8.3).

While thermodynamics exert a strong control on water vapour changes, global mean precipitation and evaporation are constrained by the balance of energy fluxes in the atmosphere and at the surface (Figure 8.3). Global mean precipitation increases of 1-3% per ºC of warming, as estimated in AR5 (Collins et al., 2013), are explained as a combination of rapid (or fast) atmospheric adjustments and slow temperature-driven responses (Figure 8.3, panels 1-4) to radiative forcings (Andrews et al., 2010; Bala et al., 2010; Cao et al., 2012). Fast atmospheric adjustments are caused by near-instantaneous (hours to days) changes in the atmospheric energy budget (Figure 8.3, panels 1-3) and atmospheric properties (e.g. temperature, clouds and water vapour) in direct response to the radiative effects of a forcing agent (Sherwood et al., 2015). A further relatively fast (days to months) adjustment of the climate system involves interactions with vegetation and land surface temperature (Figure 8.3, panel 3), which respond more rapidly than ocean temperature to a radiative forcing (Cao et al., 2012; Dong et al., 2014). The slower temperature-dependent precipitation response is driven by the increased atmospheric radiative cooling rate of a warming atmosphere. Warming drives increases in precipitation intensity while frequency is dominated by rapid atmospheric adjustments to the radiative forcing based on 4xCO_2 CMIP6 simulations (Douville and John, 2020). Since AR5, many new studies applying the dual rapid adjustment and slow response framework show that global precipitation responses to different forcing agents are physically well understood (Fläschner et al., 2016; MacIntosh et al., 2016; Samset et al., 2016; Myhre et al., 2018a). Further confidence in the coupled processes involved are provided by simple models representing the energy budget and thermodynamic constraints that limit global mean evaporation to around 1.5% per °C (Siler et al., 2018b). This strengthens the physical link between energy budget and thermodynamic drivers of the global water cycle (Section 8.2.2.1).

[START FIGURE 8.3 HERE]

Figure 8.3: Schematic representation of fast and slow responses of the atmospheric energy balance and global precipitation to radiative forcing. The atmospheric energy budget ('baseline' panel) responds instantaneously to radiative forcings (1), leading to rapid atmospheric adjustments (2) and slower semi-rapid adjustments involving the land surface and vegetation that further modify atmospheric circulation patterns (3). This slow precipitation response to global mean surface air temperature (4) is quantified as the hydrological sensitivity, η, and the total precipitation response, including initial rapid adjustments, is termed the apparent hydrological sensitivity, η_a (a). The slow precipitation response over land and ocean develops over time (b–d). Large, filled arrows ('baseline'-4) depict fluxes or circulation change while small arrows (1-4) denote increases (↑) or decreases (↓) in variables (P is precipitation; L is atmospheric longwave radiative cooling, S is solar radiation absorption by the atmosphere; H is sensible heat flux; E is surface evaporative heat flux and T is temperature). (Adapted from Allan et al., 2020, Chapter 7 Figure 7.2 and Figure 8.1)

[END FIGURE 8.3 HERE]

Hydrological sensitivity (η) is defined as the linear change in global mean precipitation with global surface air temperature (GSAT) once rapid adjustments of the hydrological cycle to radiative forcings have occurred (Figure 8.3a). There is robust understanding and high agreement across idealised CO_2 forcing CMIP5 and CMIP6 experiments (Fläschner et al., 2016; Samset et al., 2018b; Pendergrass, 2020b) that η = 2.1-3.1 % per ºC (Figure 8.4). The magnitude of η depends primarily on atmospheric net radiative cooling which is controlled by thermal deepening of the troposphere (Jeevanjee and Romps, 2018) and limited by surface

[2] 5-95% confidence range estimates are quoted unless otherwise stated

ACCEPTED VERSION SUBJECT TO FINAL EDITING

evaporation and consequent atmospheric latent heat release and warming (Webb et al., 2018). Climate feedbacks (e.g. temperature lapse rate and clouds) that vary across models (Section 7.4; Section 3.8.2) also modulate the magnitude of η (O'Gorman et al., 2012; Fläschner et al., 2016; Richardson et al., 2018c). Uncertainty in η across CMIP5 models relating to deficiencies in representing low-altitude cloud feedbacks (Watanabe et al., 2018) and absorption of shortwave radiation by atmospheric water vapour (DeAngelis et al., 2015) do not apply well to CMIP6 simulations, the latter improvement explained by more accurate radiative transfer modelling (Pendergrass, 2020b).

Observed estimates of hydrological sensitivity (η = 3.2 ± 0.8 % per ºC) based on interannual variability (Allan et al., 2020) or responses to El Niño-Southern Oscillation (ENSO) of 9 % per ºC (Adler et al., 2017) are not suitable to assess the magnitude of η (Figure 8.4). This is because these relationships depend on amplifying feedbacks associated with ENSO-related cloud changes (Stephens et al., 2018b) that may not be relevant for longer term climate change. However, there is robust evidence and high agreement across observations, modelling and supporting physics that precipitation increases at a lower % per ºC rate than water vapour content in the global mean (Held and Soden, 2006b; Collins et al., 2013; Allan et al., 2020), implying an increased residence time of atmospheric water vapour (Hodnebrog et al., 2019b; Dijk et al., 2020). Increasing global precipitation, evaporation and moisture fluxes with warming thereby drive an intensification but not acceleration of the global water cycle (Sections 8.3.1.1 and 8.4.1.1).

The overall global mean rate of precipitation change per ºC of GSAT increase, **apparent hydrological sensitivity (η_a)**, is reduced compared to hydrological sensitivity by the direct influence of radiative forcing agents on the atmospheric energy balance. Rapid atmospheric adjustments that alter precipitation are primarily caused by GHGs and absorbing aerosols, with high agreement and medium evidence across idealised simulations (Fläschner et al., 2016; Samset et al., 2016). A range of rapid precipitation adjustments to CO_2 between models are also attributed to vegetation responses leading to a repartitioning of surface latent and sensible heat fluxes (DeAngelis et al., 2016). Values obtained from six CMIP5 models simulating the Last Glacial Maximum and pre-industrial period (η_a=1.6-3.0 % per ºC) are larger than for each corresponding 4xCO_2 experiment (η_a=1.3–2.6 % per ºC) due to differences in the mix of forcings, vegetation and land surface changes and a higher thermodynamic % per ºC evaporation scaling in the colder state (Li et al., 2013b). Updated estimates across comparable experiments from 22 CMIP5/CMIP6 models (Rehfeld et al., 2020) display a consistent range (η_a=1.7±0.6 % per ºC; Figure 8.4; Section 8.4.1.1). Confirming η_a in observations (Figure 8.4) is difficult due to measurement uncertainty, varying rapid adjustments to radiative forcing and unforced variability (Dai and Bloecker, 2019; Allan et al., 2020).

Climate drivers that instantaneously affect the surface much more than the atmospheric energy budget (such as solar forcing and sulphate aerosol) produce only a small rapid adjustment of the global water cycle and therefore larger η_a than drivers that immediately modulate the atmospheric energy budget such as GHGs and absorbing aerosol (Salzmann, 2016; Samset et al., 2016; Lin et al., 2018; Liu et al., 2018a). Thus, global precipitation appears more sensitive to radiative forcing from sulphate aerosols (2.8±0.7 % per ºC; $\eta_a \approx \eta$) than GHGs (1.4±0.5 % per ºC; $\eta_a < \eta$) while the response to black carbon aerosol can be negative (-3.5±5.0 % per ºC; $\eta_a << \eta$) due to strong atmospheric solar absorption (Samset et al., 2016). Therefore, artificially reducing surface absorbed sunlight through solar radiation modification strategies to mitigate GHG warming will not mitigate precipitation changes (see Sections 4.6.3.3; 6.4.7; 8.6.3). Aerosol-induced precipitation changes depend upon the type of aerosol species and their spatial distribution. Global mean precipitation increases after complete removal of present day anthropogenic aerosol emissions (see also Section 4.4.4) in four different climate models (η_a = 1.6-5.5% per ºC) are mainly attributed to sulphate aerosol as opposed to other aerosol species (Samset et al., 2018b). Idealised modelling studies show that sulphate aerosol increases over Europe produce a larger global precipitation response than an equivalent increase in aerosol burden or radiative forcing over Asia, explained by differences in cloud climatology and cloud-aerosol interaction (Kasoar et al., 2018; Liu et al., 2018c). The vertical profiles of black carbon and ozone further influence the magnitude of the rapid global precipitation response, yet are difficult to observe and simulate (Allen and Landuyt, 2014; MacIntosh et al., 2016; Stjern et al., 2017; Sand et al., 2020).

Hydrological sensitivity is generally lower over land but with a large uncertainty range (η = -0.1 to 3.0 % per ºC GSAT) relative to the oceans (η = 2.3 to 3.3 % per ºC) based on multi-model 4xCO_2 CMIP6 simulations

ACCEPTED VERSION SUBJECT TO FINAL EDITING

(Pendergrass, 2020b), broadly consistent with comparable CMIP5 experiments (Richardson et al., 2018c; Samset et al., 2018a). Suppressed hydrological sensitivity over land (Figure 8.3d; Figure 8.4) is associated with greater warming compared with the oceans, which alters atmospheric circulation and precipitation patterns (Saint-Lu et al., 2020). Also, since oceans supply much of the moisture to fuel precipitation over land, the slower ocean warming rate means there is insufficient moisture supplied to maintain continental relative humidity levels (Byrne and O'Gorman, 2018), which can inhibit convection (Chen et al., 2020b). Land surface feedbacks involving soil-vegetation-atmosphere coupling further drive continental drying (Berg et al., 2016; Kumar et al., 2016; Chandan and Peltier, 2020). The suppressed hydrological sensitivity is counteracted by rapid precipitation responses in most GHG-forced simulations, explained by greater surface downward longwave radiation due to CO_2 increases that rapidly warm the land, destabilize the troposphere and strengthen vertical motion in the short term (Chadwick et al., 2014; Richardson et al., 2016, 2018c). There is medium understanding of how land-sea warming contrast governs rapid precipitation responses based on idealised modelling that shows similar spatial patterns of precipitation response to radiative forcing from GHGs, solar forcing and absorbing aerosols (Xie et al., 2013; Samset et al., 2016; Kasoar et al., 2018). Rapid precipitation adjustments to CO_2 have been counteracted by cooling from anthropogenic aerosol increases over land (Box 8.1) but this compensation is expected to diminish as aerosol forcing declines (Richardson et al., 2018c). The fast and slow precipitation responses over global land globally combine during transient climate change (Figure 8.3d). This explains a consistent land and ocean mean precipitation increase in projections (Chapter 4, Table 4.3) but this is determined by a complex and model-dependent evolution of continental water cycle changes over space and time.

Increases in global precipitation over time, as the climate warms, are partly offset by the overall cooling effects of anthropogenic aerosol and by rapid atmospheric adjustments to increases in GHGs and absorbing aerosol. This explains why multi-decadal trends in global precipitation responses in the satellite era (Adler et al., 2017; Allan et al., 2020) are small and difficult to interpret given observational uncertainty, internal variability and volcanic forcings. The delayed warming effect of rising CO_2 concentration, combined with declining aerosol cooling, are expected to increase the importance of the slow temperature-related effects on the energy budget relative to the more rapid direct radiative forcing effects as transient climate change progresses (Shine et al., 2015; Salzmann, 2016; Myhre et al., 2018b).

In summary, there is *high confidence* that global mean evaporation and precipitation increase with global warming, but the estimated rate is model-dependent (*very likely* range of 2-3 % per ^{o}C) The global increase in precipitation is determined by a robust response to global surface temperature only (*very likely* 2–3% per 1°C) that is partly offset by fast atmospheric adjustments to the vertical profile of atmospheric heating by GHGs and aerosols. Global precipitation increases due to GHGs are offset by the well-understood overall surface radiative cooling effect by aerosols (*high confidence*). Over land, the average warming-related increase in precipitation is expected to be smaller than over the ocean due to increasing land-ocean thermal contrast and surface feedbacks, but the overall precipitation increase over land is generally reinforced by fast atmospheric responses to GHGs that strengthens convergence of winds (*medium confidence*). Global mean precipitation and evaporation increase at a lower rate than atmospheric moisture per ^{o}C of global warming (*high confidence*) leading to longer water vapour lifetime in the atmosphere and driving changes in precipitation intensity, duration and frequency and an overall intensification but not acceleration of the global water cycle.

8.2.2 Constraints on the regional water cycle

8.2.2.1 Thermodynamic constraints on atmospheric moisture fluxes

A warming climate drives increases in atmospheric moisture and horizontal moisture transport from the divergent to the convergent portions of the atmospheric circulation (including storm systems, the tropical rain belt and monsoons) that on average amplifies existing precipitation minus evaporation (P-E) patterns (Held and Soden, 2006a). Increased latent heat transports in high latitudes also contribute to polar amplification of warming (Section 7.4.4.1). Although convergent parts of the atmospheric circulation are expected to become wetter (in terms of increasing P-E) and net evaporative regions drier (increasing E-P)

ACCEPTED VERSION SUBJECT TO FINAL EDITING

these regions are not geographically and seasonally fixed and their location and timing are expected to alter (Section 8.2.2.2). Atmospheric and ocean circulation changes overall decrease the amplification of P-E and salinity patterns. Paleoclimate evidence confirms that during the Last Glacial Maximum (21–19 thousand years ago), zonal mean changes were roughly in agreement with thermodynamic expectations (Li et al., 2013b). However regional changes can be dominated by dynamics, including responses to the large Northern Hemisphere ice sheets (DiNezio and Tierney, 2013; Bhattacharya et al., 2017b; Scheff et al., 2017; D'Agostino et al., 2019; Lowry and Morrill, 2019) such that altered P-E patterns are not well described by thermodynamic drivers (Oster et al., 2015; Lora, 2018; Morrill et al., 2018).

There is robust evidence and high agreement across thermodynamics, detailed modelling and observations that amplification of P-E patterns occurs over the oceans (Figure 8.5a) with an associated "fresh gets fresher, salty gets saltier" signature in ocean salinity (Sections 2.3.3.2 and 3.5.2). This amplification is moderated by proportionally larger increases in sub-tropical ocean evaporation and weakening of the tropical circulation (Section 8.2.2.2), an expectation supported by observations (Skliris et al., 2016) and process understanding (Yang and Roderick, 2019). Thermodynamics explain a smaller low latitude evaporation increase (1% per ^{o}C) than in high latitudes (5% per ^{o}C) with changes in surface radiation, boundary layer adjustments and ocean heat uptake playing a secondary role, based on idealised modelling (Siler et al., 2018b). Increased evaporation from warmer oceans and lakes is exacerbated by the loss of surface ice in some regions (Bintanja and Selten, 2014; Laîné et al., 2014; Wang et al., 2018d; Sharma et al., 2019; Woolway et al., 2020). This can generate a more local moisture source for precipitation, for example in northwest Greenland during non-summer months since the 1980s (Nusbaumer et al., 2019), though moisture transport changes can counteract this effect (Nygård et al., 2020). Ocean stratification due to heating of the upper layers through radiative forcing has been identified as a mechanism that further amplifies surface salinity patterns beyond the responses driven by water cycle changes alone (Zika et al., 2018).

[START FIGURE 8.4 HERE]

Figure 8.4: Estimate (5-95% range) of the increase in precipitation and its extremes with global mean surface warming. Global time averaged precipitation changes (left) are based on responses to increasing CO_2 (apparent hydrological sensitivity, η_a) and the temperature-dependent component (hydrological sensitivity, η) based on GCM experiments and including the land (L) and ocean (O) components (Fläschner et al., 2016; Richardson et al., 2018c; Samset et al., 2018a; Pendergrass, 2020b; Rehfeld et al., 2020) and observational estimates (GPCP/HadCRUTv4.6) using trends (1988-2014) as a proxy for η_a and interannual variability as a proxy for η with 90% confidence range accounting for statistical uncertainty only (Adler et al., 2017; Allan et al., 2020). For extreme precipitation, assessment is for 24 hour 99.9th percentile or annual maximum extremes from GCMs (Fischer and Knutti, 2015; Pendergrass et al., 2015; Borodina et al., 2017; Pfahl et al., 2017; Sillmann et al., 2017), regional climate models (RCMs) (Bao et al., 2017), an observationally constrained tropical estimate (O'Gorman, 2012) and estimates from observed changes (Westra et al., 2013; Donat et al., 2016; Borodina et al., 2017; Sun et al., 2020; Zeder and Fischer, 2020). For hourly and sub-hourly extremes observed changes (Barbero et al., 2017; Guerreiro et al., 2018) and high resolution models including RCM and cloud resolving models (CRMs) are assessed (Ban et al., 2015; Prein et al., 2017; Haerter and Schlemmer, 2018; Hodnebrog et al., 2019a; Lenderink et al., 2019). Further details on data sources and processing are available in the chapter data table (Table 8.SM.1).

[END FIGURE 8.4 HERE]

Since AR5, numerous studies have confirmed that changes in P-E with warming over land cannot be interpreted simply as a "wet regions get wetter, dry regions gets drier" response (Chadwick et al., 2013; Greve et al., 2014; Roderick et al., 2014; Byrne and O'Gorman, 2015; Scheff and Frierson, 2015). Firstly, P-E is a simplistic diagnostic of the water cycle that inadequately describes "dryness" or aridity (Fu and Feng, 2014; Roderick et al., 2014; Greve and Seneviratne, 2015; Scheff and Frierson, 2015; Greve et al., 2019; Vicente-Serrano et al., 2020b). Secondly, terrestrial P-E is generally positive and balanced by surface runoff and percolation into subsurface soils and aquifers (Figure 8.1). As a result, the simple thermodynamic

ACCEPTED VERSION SUBJECT TO FINAL EDITING

scaling (Figure 8.5b) predicts that P-E over land will become more positive (wetter) with warming (Greve et al., 2014; Roderick et al., 2014; Byrne and O'Gorman, 2015). This is not necessarily true, however, in the dry seasons and regions where terrestrial water is lost to the atmosphere and exported (Sheffield et al., 2013; Kumar et al., 2015; Keune and Miralles, 2019). Thirdly, regional P-E patterns over land are affected by changes in atmospheric circulation, oceanic moisture supply and land surface feedbacks. As the land warms more than oceans, spatial gradients in temperature and relative humidity influence moisture supply and reduce P-E over some land regions, such as southern Chile and Argentina around 30-50°S as captured by an extended thermodynamic scaling (Figure 8.5b). Drying of soils can be amplified by vegetation responses (Berg et al., 2016; Byrne and O'Gorman, 2016; Lambert et al., 2017) but limited by atmospheric circulation feedbacks (Zhou et al., 2021). Changes in soil moisture and rainfall intensity (Sections 8.2.3.2-8.2.3.3) can alter the partitioning of precipitation between evaporation and runoff, further complicating terrestrial P-E responses (Short Gianotti et al., 2020).

The strong physical basis for regionally and seasonally dependent responses of P-E and the expectation for an increasing contrast between wet and dry seasons and weather regimes is supported by high agreement across multiple observational and CMIP5/CMIP6 modelling studies (Liu and Allan, 2013; Kumar et al., 2015; Polson and Hegerl, 2017; Ficklin et al., 2019; Deng et al., 2020; Schurer et al., 2020). Increased moisture transports into storm systems, monsoons and high latitudes increase the intensity of wet events (Section 8.2.3.2), while stronger atmospheric evaporative demand with warming (Scheff and Frierson, 2014; Vicente-Serrano et al., 2018; Cook et al., 2019) is an important mechanism for intensifying dry events (Section 8.2.3.3) and decreasing soil moisture over many subtropical land regions. However, aridification is modulated regionally by poleward migration of the sub-tropical dry zones and an increasing land-ocean temperature contrast that drives declining relative humidity (Section 8.2.2.2).

To summarise, increased moisture transport from evaporative oceans to high precipitation regions of the atmospheric circulation will drive amplified P-E and salinity patterns over the ocean (*high confidence*) while more complex regional changes are expected over land. Greater warming over land than ocean alters atmospheric circulation patterns and on average reduces continental near-surface relative humidity which along with vegetation feedbacks can contribute to regional decreases in precipitation (*high confidence*). Based on an improved understanding of thermodynamic drivers since AR5 and multiple lines of evidence, there is *high confidence* that very wet or dry seasons and weather patterns will intensify in a warming climate such that wet spells become wetter and dry spells drier.

8.2.2.2 Large-scale responses in atmospheric circulation patterns

Responses of the large-scale atmospheric circulation to a warming climate are not as well understood as thermodynamic drivers (Shepherd, 2014). AR5 identified robust features including a weakening and broadening of tropical circulation with poleward movement of tropical dry zones and mid-latitude jets (Collins et al., 2013). These can dominate regional water cycle changes, affecting the availability of fresh water and the occurrence of climate extremes. Atmospheric circulation changes generally dominate the spatial pattern of rapid precipitation adjustments (Section 8.2.1) to different forcing agents in the tropics (Bony et al., 2013; He and Soden, 2015; Richardson et al., 2016, 2018c; Tian et al., 2017; Li et al., 2018b). Radiative forcing with heterogeneous spatial patterns such as ozone and aerosols (including cloud interactions; Box 8.1; Section 6.4.1) drive substantial responses in regional atmospheric circulation through uneven heating and cooling effects (Liu et al., 2018c; Wilcox et al., 2018b; Dagan et al., 2019b). Changes in atmospheric circulation are also driven by slower, evolving patterns of warming and associated changes in temperature and moisture gradients (Bony et al., 2013; Samset et al., 2016, 2018a; Ceppi et al., 2018; Ma et al., 2018). There is strong evidence that large regional water cycle changes arise from the atmospheric circulation response to radiative forcings and associated SST pattern evolution but low agreement in the sign and magnitude (Chadwick et al., 2016a). The role of prolonged weather regimes in determining wet and dry extremes is also better understood since AR5 (Kingston and McMecking, 2015; Schubert et al., 2016; Richardson et al., 2018a; Barlow et al., 2019). Advances in knowledge of expected large-scale dynamical responses of the water cycle are further assessed in this section (see also Figure 8.21).

ACCEPTED VERSION SUBJECT TO FINAL EDITING

Long-term weakening of the tropical atmospheric overturning circulation is expected as climate warms in response to elevated CO_2 (Collins et al., 2013). A weaker circulation is required to reconcile global mean low-level water vapour increases (around 7% per ºC) with the smaller global precipitation responses of about 1-3% per ºC (Section 8.2.1). The slowdown can occur in both the Hadley and Walker circulations, but occurs preferentially in the Walker circulation in most climate models (Vecchi and Soden, 2007) but this response has been questioned on the basis of model bias in east Pacific SST (Seager et al., 2019a). Weakening is expected to drive P-E decreases over the western Pacific and increases over the eastern Pacific. However, the driving mechanisms for Walker circulation weakening differ to those involved in determining ENSO variability, so it is too simplistic to interpret changes as an El Niño pattern of regional hydrological cycle extremes (Sohn et al., 2019). Internal variability is also capable of temporarily strengthening the Walker circulation (Section 2.3.1.4.1)(L'Heureux et al., 2013; Chung et al., 2019) while regional responses depend on the pattern of warming (Sandeep et al., 2014).

Model simulations show a stronger Pacific Walker circulation during the Last Glacial Maximum in response to a cooler climate (consistent with an expected weakening in a warmer climate), but a weaker Indian Ocean east-west circulation in response to the exposure of the Sunda and Sahul shelves due to lowered sea level (DiNezio et al., 2011). The latter effect is detectable in proxies for hydroclimate, as well as salinity and sea-surface temperature (DiNezio and Tierney, 2013; DiNezio et al., 2018). More relevant to future warming is the mid-Pliocene period (3 million years ago), the last time the Earth experienced CO_2 levels comparable to present (see Cross-Chapter Box 2.4). Sea surface temperature (SST) reconstructions show a weakening of the Pacific zonal gradient and a pattern of warmth consistent with a weaker Walker cycle response (Corvec and Fletcher, 2017; Tierney et al., 2019; McClymont et al., 2020). Although the Pliocene SST pattern and wet subtropics contrast with present conditions (Burls and Fedorov, 2017), the paleoclimate record strengthens evidence that a warmer climate is associated with a weaker Walker circulation (Cross-Chapter Box 2.4; Section 3.3.3).

Since AR5, weakening of the tropical circulation has been explained as a rapid response to increasing CO_2 concentrations and slower response to warming and evolving SST patterns (He and Soden, 2017; Xia and Huang, 2017; Shaw and Tan, 2018; Chemke and Polvani, 2020). Large-scale tropical circulation weakens by 3-4% in a rapid response to a quadrupling of CO_2 concentrations (Plesca et al., 2018), which suppresses tropospheric radiative cooling, particularly in sub-tropical ocean subsidence regions (Bony et al., 2013; Merlis, 2015; Richardson et al., 2016). The resulting increased atmospheric stability explains the rapid weakening of the Walker circulation (Wills et al., 2017) and Northern Hemisphere Hadley Cell (Chemke and Polvani, 2020). Subsequent surface warming contributes up to a 12% slowing of circulation for a uniform 4ºC SST increase, driven by thermodynamic decreases in temperature lapse rate (Plesca et al., 2018).

The regional Intertropical Convergence Zone (ITCZ) position, width and strength determine the location and seasonality of the tropical rain belt. Since AR5, multiple studies have linked cross-equatorial energy transport to the mean ITCZ position (Donohoe et al., 2013; Frierson et al., 2013; Bischoff and Schneider, 2014; Boos and Korty, 2016; Loeb et al., 2016; Adam et al., 2018; Biasutti and Voigt, 2019). Multi-model studies agree that aerosol cooling in the Northern Hemisphere led to a southward shift in the ITCZ and tropical precipitation after the 1950s up to the 1980s that is linked with the 1980s Sahel drought (Box 8.1; Section 8.3.2.4; Section 10.4.2.1). In particular, aerosol-cloud interaction was identified as a potentially important driver of this shift (Chung and Soden, 2017) but this is uncertain since observations suggest that models may overestimate (Malavelle et al., 2017; Toll et al., 2017) or underestimate (Rosenfeld et al., 2019) the aerosol cloud-mediated cooling effects. In addition, greenhouse gas forcing has been invoked in explaining much of the increase in Sahel precipitation since the 1980s through enhanced meridional temperature gradient, with only a secondary role for aerosol (Dong and Sutton, 2015).

Understanding of how ITCZ width and strength respond to a warming climate has improved since AR5 (Byrne and Schneider, 2016; Harrop and Hartmann, 2016; Popp and Silvers, 2017; Dixit et al., 2018; Zhou et al., 2020). Studies suggest that convection gets stronger and more focused within the core of the ITCZ (Lau and Kim, 2015; Byrne et al., 2018). This leads to drying on the equatorward edges of the ITCZ and a moistening tendency in the ITCZ core (Byrne and Schneider, 2016). Feedbacks involving clouds have been identified as an important mechanism leading to tightening and strengthening of the ITCZ (Popp and Silvers,

ACCEPTED VERSION SUBJECT TO FINAL EDITING

2017; Su et al., 2017, 2019, 2020; Talib et al., 2018). Stronger ascent in the core amplifies the "wet get wetter" response while reduced moisture inflow near the ITCZ edges reduces this response below the 7% per ^{o}C thermodynamic increase in moisture transport. Thus, there is a range of evidence and medium agreement for strengthening and contraction of the ITCZ with warming that sharpens contrasts between wet and dry regimes. However, understanding of how the regional ITCZ location responds in a warming climate is not robust (Section 8.4.2.1) with *limited evidence* of distinct regional responses to GHG forcing including a northward shift over eastern Africa and the Indian Ocean and a southward shift in the eastern Pacific and Atlantic oceans (Mamalakis et al., 2021). Paleoclimate evidence highlights the distinct regional ITCZ responses to hemispheric asymmetry in volcanic and orbital forcing (McGee et al., 2014; Boos and Korty, 2016; Colose et al., 2016; Denniston et al., 2016; PAGES Hydro2K Consortium, 2017; Singarayer et al., 2017; Atwood et al., 2020) and rapid (>1^{o} latitude over decades) shifts in the ITCZ and regional monsoons in response to AMOC collapse cannot be ruled out (Sections 8.6.1.1 and 5.1.3).

Monsoons are key components of the tropical overturning circulation that can be understood as a balance between net energy input (e.g. radiative and turbulent fluxes) and the export of moist static energy. This is determined by contrasting surface heat capacity between ocean and land and modified through changes in atmospheric dynamics, tropical tropospheric stability and land surface properties (Jalihal et al., 2019). Thermodynamic increases in moisture transport are expected to increase monsoon strength and area (Christensen et al., 2013). Since AR5, evidence continues to demonstrate that monsoon circulation is sensitive to spatially varying radiative forcing by anthropogenic aerosols (Hwang et al., 2013; Allen et al., 2015b; Li et al., 2016c) and GHGs (Dong and Sutton, 2015). Changes in SST patterns also play a role (Guo et al., 2016; Zhou et al., 2019b; Cao et al., 2020) by altering cross-equatorial energy transports and land-ocean temperature contrasts. This evidence continues to support a thermodynamic strengthening of monsoon precipitation that is partly offset by slowing of the tropical circulation but with *weak evidence* and *low agreement* for regional aspects of circulation changes. Disagreement between paleo-climate and modern observations, physical theory and numerical simulations of global monsoons have been partly reconciled (Section 3.3.3.2) through improved understanding of regional processes (Harrison et al., 2015; Bhattacharya et al., 2017a, 2018; Biasutti et al., 2018; D'Agostino et al., 2019; Jalihal et al., 2019; Seth et al., 2019), although interpreting past changes in the context of future projections requires careful account of differing forcings and feedbacks (D'Agostino et al., 2019). Assessment of past changes and future projections in regional monsoons are provided in Sections 2.3.1.4.2, 8.3.2.4 and 8.4.2.4.

Since AR5, understanding of poleward expansion of the Hadley Cells has improved (Section 2.3.1.4.1) but its role in subtropical drying is limited to the zonal mean and dominated by ocean regions (Byrne and O'Gorman, 2015; Grise and Polvani, 2016; He and Soden, 2017; Schmidt and Grise, 2017; Siler et al., 2018a; Chemke and Polvani, 2019; Grise and Davis, 2020). Over subtropical land, evolving SST patterns and land-ocean warming contrasts, that are partly explained by rapid responses to CO_2 increases, can dominate aspects of the atmospheric circulation response (Byrne and O'Gorman, 2015; He and Soden, 2015; Chadwick et al., 2017; Yang et al., 2020a) and resultant regional water cycle changes, particularly for projected drying in semi-arid, winter-rainfall dominated sub-tropical climates (Deitch et al., 2017; Brogli et al., 2019; Seager et al., 2019b; Zappa et al., 2020). Poleward expansion of the tropical belt is expected to drive a corresponding shift in mid-latitude storm tracks, but the controlling mechanisms differ between hemispheres. Southern Hemisphere expansion is driven by GHG forcing and amplified by stratospheric ozone depletion, while weaker Northern Hemisphere expansion in response to GHG forcing is modulated by tropospheric ozone and aerosol forcing, particularly black carbon (Davis et al., 2016; Grise et al., 2019; Watt-Meyer et al., 2019; Zhao et al., 2020). However, internal variability is found to dominate observed responses in the Northern Hemisphere, precluding attribution to radiative forcing (D'Agostino et al., 2020b). Paleoclimate evidence of poleward expansion and weakening of westerly winds in both hemispheres in the warmer Pliocene is linked to reduced equator to pole thermal gradients and ice volume (Abell et al., 2021).

The influence of amplified Arctic warming on mid-latitude regional water cycles is not well understood based on simple physical grounds due to the large number of competing physical processes (Cross Chapter Box 10.1). The thermal gradient between polar and lower latitude regions decreases at low levels due to Arctic warming amplification. However, at higher altitudes, the corresponding thermal gradient increases with warming due to cooling of the Arctic stratosphere and this is consistent with a strengthening of the

ACCEPTED VERSION SUBJECT TO FINAL EDITING

winter jet stream in both hemispheres, yet there is *low agreement* on the precise mechanisms (Vallis et al., 2015; Vihma et al., 2016). Changes in the strength of the polar stratospheric vortex can also alter the mid-latitude circulation in winter, but responses are not consistent across models (Oudar et al., 2020a). Nevertheless, thermodynamic strengthening of moisture convergence into weather systems and polar regions is robust (Section 8.2.2.1) and remains valid despite weak understanding of atmospheric circulation change.

In summary, there is *high confidence* that altered atmospheric wind patterns in response to radiative forcing and evolving surface temperature patterns will affect the regional water cycle in most regions. Mean tropical circulation is expected to slow with global warming (*high confidence*) but temporary multi-decadal strengthening is possible due to internal variability (*medium confidence*). Slowing of the tropical circulation reduces the meridional P-E gradient over the Pacific and can partly offset thermodynamic amplification of P-E patterns and strengthening of monsoons (*high confidence*) but regional characteristics of tropical rain belt changes are not well understood. There is *medium confidence* in processes driving strengthening and tightening of the ITCZ that increase the contrasts between wet and dry tropical weather regimes and seasons. There is *high confidence* in understanding of how radiative forcing and global warming drive a poleward expansion of the subtropics and mid-latitude stormtracks but only *low confidence* in how poleward expansion influences drying of sub-tropical and mid-latitude climates. There is *low confidence* in understanding how Arctic warming amplification affects mid-latitude regional water cycles but *high confidence* that thermodynamic strengthening of precipitation within weather systems and in monsoons and polar regions is robust to large-scale circulation changes.

8.2.3 Local-scale physical processes affecting the water cycle

Processes operating at local scales are capable of substantially modifying the regional water cycle. This section assesses the development in understanding of processes affecting the atmosphere, surface and subsurface, including cryosphere and biosphere interactions and the direct impacts of human activities.

8.2.3.1 Hydrological processes related to ice and snow

Declining ice sheet mass, glacier extent and Northern Hemisphere sea ice, snow cover and permafrost (Collins et al., 2013; Vaughan et al., 2013) is an expected consequence of a warming climate (Sections 2.3.2; 3.4; 4.3.2.1; 9.3-9.5). A decline in mountain snow cover and increased snow and glacier melt will alter the amount and timing of seasonal runoff in mountain regions (Sections 3.4.2; 3.4.3; 9.5). Earlier and more extensive winter and spring snowmelt (Zeng et al., 2018a) can reduce summer and autumn runoff in snow dominated river basins of mid-high latitudes of the Northern Hemisphere (Rhoades et al., 2018; Blöschl et al., 2019). Since AR5, an earlier but less rapid snowmelt has been explained by reduced winter snowfall and less intense solar radiation earlier in the season (Musselman et al., 2017; Wu et al., 2018b; Grogan et al., 2020). Reduced snow cover also increases energy available for evaporation, which can dominate declining river discharge based on modelling of the Colorado River (Milly and Dunne, 2020). An increase in the fraction of precipitation falling as rain versus snow can lead to declines in both streamflow and groundwater storage in regions where snow melt is the primary source of recharge (Earman and Dettinger, 2011; Berghuijs et al., 2014). Such regions include western South America and western North America, semi-arid regions which rely on snowmelt from high mountain chains (Ragettli et al., 2016; Milly and Dunne, 2020). Rain-on snow melt events reduce at lower altitudes due to declining snow cover but increased at higher altitudes where snow tends to be replaced by rain based on observations and modelling (Musselman et al., 2018; Pall et al., 2019), thereby altering seasonal and regional characteristics of flooding (Section 11.5).

Seasonal meltwater from high mountain glaciers in Asia (see Cross-Chapter Box 10.4) supply the basic needs of 221±97 million people (Pritchard, 2019; Immerzeel et al., 2020). Glacier-melt in response to warming can initially lead to increased runoff volumes, especially in peak summer flows, but they will eventually decline as most glaciers continue to shrink. SROCC concluded there is *high confidence* that the peak runoff has already been passed for some smaller glaciers (Hock et al., 2019b). Increased precipitation and glacier melt can also contribute to rising lake levels and flood hazards in regions such as the inner

ACCEPTED VERSION SUBJECT TO FINAL EDITING

Tibetan Plateau, Patagonia, Peru, Alaska and Greenland (Lei et al., 2017; Shugar et al., 2020; Stuart-Smith et al., 2020). Since AR5, evidence from multiple locations (New Zealand, Greenland, Antarctica) shows that intrusions of warm, moist air are important in controlling glacier mass balance, the likelihood of extreme ablation or snowfall events depending on air temperature (Gorodetskaya et al., 2014; Mackintosh et al., 2017; Mattingly et al., 2018; Oltmanns et al., 2018; Little et al., 2019; Wille et al., 2019; Adusumilli et al., 2021). Sensible heating from warm air and increased longwave radiation from atmospheric moisture and low clouds drive melt events (Stuecker et al., 2018).

Reductions in snow, freshwater ice and permafrost affect terrestrial hydrology. Permafrost degradation reduces soil ice and alters the extent of thermokarst lake coverage (Section 9.5.2; SROCC (Meredith et al., 2019b)). A lag between current climate change and permafrost degradation is expected, given the slow response rates in frozen ground and the fact that snow cover insulates soil from sensible heat exchanges with the air above (Hoegh-Guldberg et al., 2018; García-García et al., 2019; Soong et al., 2020). Post-wildfire areas are also linked with permafrost degradation in the Arctic based on satellite observations (Yanagiya and Furuya, 2020). An increase in spring rainfall can increase heat advection by infiltration, exacerbating permafrost thaw and leading to increased methane emissions (Neumann et al., 2019) (Section 5.4.7). Increased heat transport by Arctic rivers can also contribute to earlier sea ice melt (Park et al., 2020).

In summary, it is *virtually certain* that warming will cause a loss of frozen water stores, except in areas where temperatures remain below 0ºC for most of the year. There is *high confidence* that warming and reduced snow volume drives an earlier snowmelt, leading to seasonally dependent changes in streamflow. There is *medium confidence* that weaker sunlight earlier in the season can reduce the rate of snowmelt. Melting of snowpack or glaciers can increase stream flow in high latitude and high-altitude catchments until frozen water reserves are depleted (*high confidence*). There is *high confidence* that warm, moist airflows and associated precipitation dominate glacier mass balance in some regions (New Zealand, Greenland, Antarctica).

8.2.3.2 Processes determining heavy precipitation and flooding

Evidence that heavy precipitation events (from sub-daily up to seasonal timescales) intensify as the planet warms has strengthened since AR5 (Box 11.1; Section 11.4; Cross Chapter Box 3.2) based on improved physical understanding, extensive modelling and increasing observational corroboration (O'Gorman, 2015; Fischer and Knutti, 2016; Neelin et al., 2017). There is *robust evidence*, with *medium agreement* across a range of modelling and observational studies, of thermodynamic intensification of wet seasons (Chou et al., 2013; Liu and Allan, 2013; Dunning et al., 2018; Lan et al., 2019; Zhang and Fueglistaler, 2019). Extreme daily precipitation is expected to increase at close to the 7%/ºC increase in the near-surface atmospheric moisture holding capacity determined by the Clausius-Clapeyron equation (Section 11.4, Figure 8.4), with *limited evidence* that higher rates apply for shorter duration precipitation events (Formayer and Fritz, 2017; Lenderink et al., 2017; Ali et al., 2018; Guerreiro et al., 2018; Burdanowitz et al., 2019; Zhang et al., 2019b). However, observed estimates sample multiple synoptic weather states, mixing thermodynamic and dynamic factors, so are not directly relatable to climate change responses (Bao et al., 2017; Drobinski et al., 2018). The contrasting spatial scales sampled by the observations and models (from global to cloud resolving) explain the large range of daily and sub-daily precipitation scaling with temperature assessed in Figure 8.4.

[START FIGURE 8.5 HERE]

Figure 8.5: Zonally-averaged annual mean changes in precipitation minus evaporation (P-E) over (a) ocean and (b) land between the historical (1995–2014) and SSP2-4.5 (2081–2100) CMIP6 simulations (blue lines, an average of the CanESM5 and MRI-ESM2-0 models). Dashed lines show estimated P-E changes using a simple thermodynamic scaling (Held and Soden, 2006b); dotted lines show estimates using an extended scaling (Byrne and O'Gorman, 2016). All curves have been smoothed in latitude using a three grid-point moving-average filter. Further details on data sources and processing are available in the chapter data table (Table 8.SM.1).

ACCEPTED VERSION SUBJECT TO FINAL EDITING

[END FIGURE 8.5 HERE]

Since AR5, advances in understanding the expected changes in intense rainfall at the sub-daily time-scale (Section 11.4, Figure 8.4) are provided by idealised or high resolution model experiments and observations (Westra et al., 2014; Fowler et al., 2021). There is *robust evidence* from simplified calculations, convection resolving models and observations that thermodynamics drives an increase in convective available potential energy (CAPE) with warming and therefore the intensity of convective storms (Singh and O'Gorman, 2013; Romps, 2016; Barbero et al., 2019). Also, declining relative humidity over land (Sections 2.3.1.3.2; 8.2.2.1) increases lifting condensation level, thereby delaying but intensifying convective systems (Louf et al., 2019; Chen et al., 2020b). Larger systems are linked with increasing tropopause height (Lenderink et al., 2017) that can also amplify storm precipitation (Prein et al., 2017). However, the heaviest rainfall is not necessarily associated with the most intense (deepest) storms based on satellite data (Hamada et al., 2015; Hamada and Takayabu, 2018). Precipitation intensification can exceed thermodynamic expectations where and when additional latent heating invigorates individual storms (Section 11.4.1) as implied by *medium agreement* across modelling and observational studies (Berg et al., 2013; Molnar et al., 2015; Scoccimarro et al., 2015; Prein et al., 2017; Zhou and Wang, 2017; Nie et al., 2018; Zhang et al., 2018f; Kendon et al., 2019). This intensification depends on time of day, based on convection-permitting simulations (Meredith et al., 2019a).

Intensification of sub-daily rainfall is inhibited in regions and seasons where available moisture is limited (Prein et al., 2017). However, a fixed threshold temperature above which precipitation is limited by moisture availability is not supported by modelling evidence (Neelin et al., 2017; Prein et al., 2017). Enhanced latent heating within storms can also suppress convection at larger-scales due to atmospheric stabilization as demonstrated with high resolution, idealised and large ensemble modelling studies (Loriaux et al., 2017; Chan et al., 2018; Nie et al., 2018; Tandon et al., 2018; Kendon et al., 2019). Stability is also increased by the direct radiative heating effect of higher CO_2 concentrations (Baker et al., 2018) and influenced by aerosol effects on the atmospheric energy budget and cloud development (Box 8.1). Since AR5, modelling evidence shows increases in convective precipitation extremes are limited by droplet/ice fall speeds (Singh and O'Gorman, 2014; Sandvik et al., 2018) but these processes are only crudely represented (Tapiador et al., 2019b). Idealised regional and coupled global models combined with *limited* observational *evidence* shows that instantaneous precipitation extremes are sensitive to microphysical processes while daily extremes are determined more by the degree of convective aggregation (Bao and Sherwood, 2019; Pendergrass, 2020a).

Dynamical changes modify and can dominate thermodynamic drivers of local rainfall and flood hazard change (Box 11.1). For example, increased land-ocean temperature gradients (Section 8.2.2.2) explain more intense rain from convective systems over the Sahel based on satellite data since the 1980s (Taylor et al., 2017) and dynamical feedbacks can invigorate active to break phase transition over India (Karmakar et al., 2017; Roxy et al., 2017). Satellite data shows long-lived, organised mesoscale convective systems contribute disproportionally to extreme tropical precipitation (Roca and Fiolleau, 2020). Since AR5, the spatial variability in soil moisture has been linked with the timing and location of convective rainfall by altering the partitioning between latent and sensible heating. This was demonstrated for the Sahel, Europe and India in observations (Taylor et al., 2013a; Taylor, 2015; Petrova et al., 2018; Barton et al., 2019; Klein and Taylor, 2020) but depends on the moisture convergence regime (Welty et al., 2020). Only high resolution convection permitting models can capture the sub-grid scale mechanisms for convective initiation (Taylor et al., 2013a; Moon et al., 2019a). There is *medium evidence* that greater tropical cyclone rainfall totals can be caused by dynamical feedbacks (Chauvin et al., 2017) and slower propagation speed as tropical circulation weakens (Kossin, 2018). These processes amplify the thermodynamic intensification of rainfall (Section 11.7.1.2), yet observational support is weak (Chan, 2019; Lanzante, 2019; Moon et al., 2019b; Knutson et al., 2020). Slower decay following landfall, explained by larger stores of heat and moisture at higher SSTs, can also amplify rainfall amount based on observations and modelling (Li and Chakraborty, 2020). Rainfall intensity from the outer rain bands of tropical cyclones is also increased by aerosol-cloud interactions (Box 8.1).

The amount and intensity of rainfall within extratropical storms is expected to increase with atmospheric moisture. This is particularly evident for atmospheric rivers (see glossary) and research since AR5 has confirmed their link with flooding and terrestrial water storage (Froidevaux and Martius, 2016; Paltan et al.,

ACCEPTED VERSION SUBJECT TO FINAL EDITING

2017; Waliser and Guan, 2017; Adusumilli et al., 2019; Ionita et al., 2020; Payne et al., 2020). There is *robust evidence* based on simple physics and detailed modelling that extra-tropical cyclone rainfall, including atmospheric river events, will intensify through increased atmospheric moisture flux (Lavers et al., 2013; Ramos et al., 2016; Yettella and Kay, 2017; Espinoza et al., 2018b; Algarra et al., 2020; Xu et al., 2020; Zavadoff and Kirtman, 2020; Zhao, 2020), although changes in dynamical aspects will modify responses regionally (section 8.4.2.8). For example, stronger latitudinal temperature gradients in the high latitude upper troposphere drive increased extra-tropical storm speed around 30-70°N based on CMIP5 simulations (Dwyer and O'Gorman, 2017), causing reduced precipitation accumulation.

The response of flood hazard to changing rainfall characteristics depends on time and space scale and the nature of the land surface (Section 11.5.1; FAQ 8.2). Sustained and heavy rainfall can lead to widespread flooding and landslides while intensification of short-duration intense rainfall can increase the severity and frequency of flash flooding (Marengo et al., 2013; Chan et al., 2016; Gariano and Guzzetti, 2016; Sandvik et al., 2018). Flooding events in many tropical regions (e.g. north west South America, southern Africa and Australasia) are associated with ENSO variability (Emerton et al., 2017; Takahashi and Martínez, 2019; Pabón-Caicedo et al., 2020) and amplified by thermodynamic increases in water vapour. Flood hazard from heavy rainfall is modulated by snowmelt (Section 8.2.3.1), vegetation characteristics (Murphy et al., 2020; Page et al., 2020) and direct human intervention (Section 8.2.3.4; FAQ 8.2) but also can be compounded by sea level rise (Sections 4.3.2.2; 9.6.4) in coastal and delta regions (Bevacqua et al., 2019; Ganguli and Merz, 2019; Eilander et al., 2020). Antecedent soil moisture conditions are an important modulator of flooding (Section 11.5.1) but become less important for smaller catchments and for more severe floods (Wasko and Nathan, 2019). Depleted soil moisture after more intense dry seasons (Section 8.2.2.1) can allow greater uptake of wet season rainfall before soils saturate. Since AR5, evidence confirms that more intense rainfall increases the proportion of runoff and reservoir recharge relative to infiltration into the soil (Eekhout et al., 2018; Yin et al., 2018). More intense but less frequent storms (Kendon et al., 2019) favour focused groundwater recharge through leakage from surface waters (Taylor et al., 2013b; Cuthbert et al., 2019a) and runoff and flash flooding where the percolation capacity of the soil is exceeded (Yin et al., 2018).

Increased severity of flooding on larger, more slowly-responding rivers is expected as precipitation accumulations increase during persistent wet events over a season. This can occur where atmospheric blocking patterns repeatedly steer extra tropical cyclones across large river catchments, as identified for Northern Hemisphere mid-latitudes and Asia (Takahashi et al., 2015; Lenggenhager et al., 2018; Pfleiderer et al., 2018; Zhou et al., 2018; Blöschl et al., 2019; Nikumbh et al., 2019; Zanardo et al., 2019), although groundwater flooding and antecedent conditions including soil moisture and snow melt also play a role (Muchan et al., 2015; Berghuijs et al., 2019). Increased atmospheric moisture amplifies the severity of these events when they occur in a warmer climate, yet drivers of change in the occurrence of blocking patterns, stationary waves and jet stream position are not well understood (Section 8.2.2.2, Cross Chapter Box 10.1).

In summary, there is *very high confidence* that heavy precipitation events will become more intense in a warming climate. There is *high confidence* that increased moisture and its convergence within extra-tropical and tropical cyclones and storms will increase rainfall totals during wet events at close to the 7% per °C thermodynamic response, with *low confidence* of higher rates for sub-daily intensities. There is *medium confidence* that more intense but less frequent rainfall increases the proportion of rainfall leading to surface runoff and focused groundwater recharge from temporary water bodies. There is *low confidence* in how the frequency of flooding will change regionally as it is strongly dependent on catchment characteristics, antecedent conditions and how atmospheric circulation systems respond to climate change, which is less certain than thermodynamic drivers (Section 11.5). However, there is *high confidence* that increases in precipitation intensity and amount during very wet events (from sub-daily up to seasonal time-scales) will intensify severe flooding when these extremes occur.

8.2.3.3 Drivers of aridity and drought

Regional changes in aridity – broadly defined as a deficit of moisture – are expected to occur in response to anthropogenic forcings as a consequence of shifting precipitation patterns, warmer temperatures, changes in

ACCEPTED VERSION SUBJECT TO FINAL EDITING

cloudiness (affecting solar radiation), declining snowpack, changes in winds and humidity, and vegetation cover (Figure 8.6). Evapotranspiration (see Annex VII: Glossary) is a key component of aridity, and is composed of two main processes: evaporation from soil, water and vegetation surfaces; and transpiration, the exchange of moisture between plants and atmosphere through plant stomata. On a global level, warmer temperatures increase evaporative demand in the atmosphere, and thus (assuming sufficient soil moisture is available) increase moisture loss from evapotranspiration (*high confidence*) (Dai et al., 2018; Vicente-Serrano et al., 2020b). On a regional level, aridity is further modulated by seasonal rainfall patterns, runoff, water storage, and interactions with vegetation.

Vegetation is a crucial interface between subsurface water storage (in soil moisture and groundwater) and the atmosphere. Plants alter evapotranspiration and the surface energy balance, and thus can have a large influence on regional aridity (Lemordant et al., 2018). SRCCL concluded there is *high confidence* that higher atmospheric CO_2 increases the ratio of plant CO_2 uptake to water loss (water-use efficiency; WUE) through the combined enhancement of photosynthesis and stomatal regulation (De Kauwe et al., 2013; Jones et al., 2013b; Deryng et al., 2016; Swann et al., 2016; Cheng et al., 2017; Knauer et al., 2017; Peters et al., 2018; Guerrieri et al., 2019) (see also Section 5.4.1). Modelling studies suggest that increasing WUE can partly counteract water losses from increased evaporative demand in a warmer atmosphere, potentially mitigating aridification (Milly and Dunne, 2016; Bonfils et al., 2017; Cook et al., 2018; Yang et al., 2018d). However, observational studies suggest that this effect may be counter-balanced by the increase in plant growth in response to elevated CO_2, which results in increased water consumption (De Kauwe et al., 2013; Donohue et al., 2013; Ukkola et al., 2016b; Yang et al., 2016; Guerrieri et al., 2019; Mankin et al., 2019; Singh et al., 2020a). In semi-arid regions, increased plant water consumption can reduce streamflow and exacerbate aridification (Ukkola et al., 2016b; Mankin et al., 2019; Singh et al., 2020a). Thus, there is *low confidence* that increased WUE in plants can counterbalance increased evaporative demand (Cross Chapter Box 5.1).

A drought is a period of abnormally dry weather that persists for long enough to cause a serious hydrological imbalance (Wilhite and Glantz, 1985; Wilhite, 2000; Cook et al., 2018) (see Annex VII: Glossary). Most droughts begin as persistent precipitation deficits (*meteorological drought*) that propagate over time into deficits in soil moisture, streamflow, and water storage (Figure 8.6), leading to a reduction in water supply (*hydrological drought*). Increased atmospheric evaporative demand increases plant water stress, leading to *agricultural and ecological drought* (Williams et al., 2013; Allen et al., 2015a; Anderegg et al., 2016; McDowell et al., 2016; Grossiord et al., 2020). Evaporative demand affects plants in two ways. It increases evapotranspiration, depleting soil moisture and stressing plants through lack of water (Teuling et al., 2013; Sperry et al., 2016), and also directly affects plant physiology, causing a decline in hydraulic conductance and carbon metabolism, leading to mortality (Breshears et al., 2013; Hartmann, 2015; McDowell and Allen, 2015; Fontes et al., 2018) (Figure 8.6). While droughts are traditionally viewed as “slow moving" disasters that typically take months or years to develop, rapidly evolving and often unpredictable *flash droughts* can also occur (Otkin et al., 2016, 2018). *Flash droughts* can develop within a few weeks, causing substantial disruption to agriculture and water resources (Pendergrass et al., 2020). Conversely, droughts that persist for a long time (usually a decade or more) are called *megadroughts*. Droughts span a large range of spatial and temporal scales, arise through a variety of climate system dynamics (e.g., internal atmospheric variability, ocean teleconnections), and can be amplified or alleviated by a variety of physical and biological processes. As such, droughts occupy a unique space within the framework of extreme climate and weather events, possessing no singular definition.

While the role of precipitation in droughts is obvious, other climatic drivers are also important, such as temperature, radiation, wind, and humidity (Figure 8.6). These factors have a strong influence on atmospheric evaporative demand, which affects evapotranspiration and soil moisture (Figure 8.6). In snow-dominated regions, high temperatures increase the fraction of precipitation falling as rain instead of snow and advance the timing of spring snowmelt (*high confidence*) (Vincent et al., 2015; Mote et al., 2016, 2018; Berg and Hall, 2017; Solander et al., 2018). This can result in lower than normal snowpack levels (*a snow drought*), and thus reduced streamflow, even if total precipitation is at or above normal for the cold season (Harpold et al., 2017). Plants also affect the severity of droughts by modulating evapotranspiration (Figure 8.6). As discussed above, the effect of elevated CO_2 on plants has the potential to both increase and reduce water loss through evapotranspiration via enhanced WUE and plant growth, respectively (Figure 8.6), but

ACCEPTED VERSION SUBJECT TO FINAL EDITING

there is *low confidence* in whether one process dominates over another at the global scale.

Drought severity also depends on human activities and decision-making (AghaKouchak et al., 2015; Van Loon et al., 2016; Pendergrass et al., 2020). Societies have developed a variety of strategies to manipulate the water cycle to increase resiliency in the face of water scarcity, including irrigation, creation of artificial reservoirs, and groundwater pumping. While potentially buffering water resource capacity, in some cases these interventions may unexpectedly increase vulnerability (*medium confidence*). For example, while increased irrigation efficiency may ensure more water is available to crops, the corresponding reduction in runoff and subsurface recharge may exacerbate hydrologic drought (Grafton et al., 2018). Furthermore, while building dams and increasing surface reservoir capacity can boost water resources, they may actually increase drought vulnerability if demands rise to take advantage of the increased supply or if over-reliance on these surface reservoirs is encouraged (Di Baldassarre et al., 2018). Interactions between adaptation, vulnerability, and drought impacts are discussed further in WGII (Chapters 2 and 4).

In summary, there is *high confidence* that a warming climate drives an increase in atmospheric evaporative demand, decreasing available soil moisture. There is *high confidence* that higher atmospheric CO_2 increases plant water-use efficiency, but *low confidence* that this physiological effect can counterbalance water losses. Since drought can be defined in a number of ways, there are potentially different responses under a warming climate depending on drought type. Beyond a lack of precipitation, changes in evapotranspiration are critical components of drought, because these can lead to soil moisture declines (*high confidence*). Under very dry soil conditions, evapotranspiration becomes restricted and plants experience water stress in response to increased atmospheric demand (*medium confidence*). Human activities and decision-making have a critical impact on drought severity (*high confidence*).

[START FIGURE 8.6 HERE]

Figure 8.6: Climatic drivers of drought, effects on water availability, and impacts. Plus and minus signs denote the direction of change that drivers have on factors such as snowpack, evapotranspiration, soil moisture, and water storage. The three main types of drought are listed, along with some possible environmental and socioeconomic impacts of drought (bottom).

[END FIGURE 8.6 HERE]

8.2.3.4 Direct anthropogenic influence on the regional water cycle

Human activities influence the regional water cycle directly through modifying and exploiting stores and flows from rivers, lakes and ground water and by altering land cover characteristics. These actions alter surface energy and water balances through changes in permeability, surface albedo, evapotranspiration, surface roughness and leaf area. Direct redistribution of water by human activities for domestic, agricultural and industrial use of ~24,000 km^3 per year (Figure 8.1) is equivalent to half the global river discharge or double the global groundwater recharge each year (Abbott et al., 2019). Since the AR5, both modelling studies and observations have demonstrated that land use change can drive local and remote responses in precipitation and river flow by altering the surface energy balance, moisture advection and recycling, land-sea thermal contrast and associated wind patterns (Alter et al., 2015; Wey et al., 2015; De Vrese et al., 2016; Pei et al., 2016; Wang-Erlandsson et al., 2018; Vicente-Serrano et al., 2019). There is robust evidence that a warming climate combined with direct human demand for ground water will deplete ground water resources in already dry regions (Wada and Bierkens, 2014; D'Odorico et al., 2018; Jia et al., 2020).

SRCCL presented evidence that extraction of water from the ground or river systems and intensive irrigation increases evaporation and atmospheric water vapour locally (Jia et al., 2020; Mishra et al., 2020). Irrigation can explain declining groundwater storage in some regions, including north-western India and North America (Asoka et al., 2017; Ferguson et al., 2018b). Simulations spanning 1960-2010 indicate that ~30% of the present human water consumption is supplied from non-sustainable water resources (Wada and Bierkens,

ACCEPTED VERSION SUBJECT TO FINAL EDITING

2014). However, there is only limited evidence that groundwater extraction is lowering streamflow (Mukherjee et al., 2018; de Graaf et al., 2019). Model experiments show that irrigation can either aggravate or alleviate climate-induced changes of surface or sub-surface water (Leng et al., 2015). Widespread extraction of water from rivers can reduce flows and decrease the level and area of inland seas and lakes (Wurtsbaugh et al., 2017; Torres-Batlló et al., 2020; Wang et al., 2020d). Between 1985 and 2015, ~139,000 km^2 of inland water areas have become land, while creation of dams has converted about 95,000 km^2 of land to water, particularly in the Amazon and Tibetan Plateau (Donchyts et al., 2016). Direct management of river flow is comparable in magnitude to climate change effects for snow-fed rivers at a continental scale based on a global analysis and a study of 96 Canadian catchments (Tan and Gan, 2015; Arheimer et al., 2017).

SRCCL assessed with *medium confidence* that mean and extreme precipitation is increased over and downwind of urban areas (Jia et al., 2020). There is *medium confidence* that altered thermodynamic and aerodynamic properties of the land surface from urbanisation affects evaporation and increases precipitation over or downwind of cities (Box 10.3) due to altered stability and turbulence (Han et al., 2014; Pathirana et al., 2014; Jiang et al., 2016; D'Odorico et al., 2018; Sarangi et al., 2018; Boyaj et al., 2020), while reduced biogenic aerosol but increased anthropogenic aerosol emissions modify cloud microphysics and precipitation processes (Schmid and Niyogi, 2017; D'Odorico et al., 2018; Fan et al., 2020; Zheng et al., 2020)(Box 8.1). Urbanisation also decreases permeability of the surface, leading to increased surface runoff (Chen et al., 2017; Jia et al., 2020). Large-scale infrastructure, such as the construction and operation of dikes, weirs, and hydropower plants, also alters surface energy and moisture fluxes, potentially influencing the regional water cycle. *Limited* modelling *evidence* suggests that large-scale solar and wind farms can increase precipitation locally (over the Sahel and North America) when dynamic vegetation responses are represented (Li et al., 2018c; Pryor et al., 2020) with remote effects also possible (Lu et al., 2021).

Changes in land use from forest to agriculture can exert profound regional effects on the water cycle (FAQ 8.1) by modifying the surface energy balance and moisture recycling (Krishnan et al., 2016; Paul et al., 2016; Llopart et al., 2018; Singh et al., 2019). There is *medium evidence* from modelling and observations over the Amazon and East Africa that deforestation drives increased streamflow (Dos Santos et al., 2018; Guzha et al., 2018; Levy et al., 2018) but *limited evidence* that increases in global runoff due to deforestation are counterbalanced by decreases resulting from irrigation (Hoegh-Guldberg et al., 2019). Total Amazon deforestation drives large reductions in precipitation but with a 90% confidence range (-38 to +5%) based on 44 primarily pre-AR5 climate model simulations (Spracklen and Garcia-Carreras, 2015) with smaller reductions (-2.3 to -1.3%) attributed to observed Amazon deforestation up to 2010. Climate model development has reduced this uncertainty range but has not altered the median change (Lejeune et al., 2015). Large-scale global deforestation (20 million km^2) simulated by 9 CMIP6 models confirms a large range in precipitation amount reduction of -37±54 mm/yr over the deforested regions (Boysen et al., 2020). However, small-scale deforestation can increase precipitation locally (Lawrence and Vandecar, 2015). A 50–60% deforestation rate corresponded to a wet season delay of about one week and greater chance of dry spells of eight days or longer based on correlation analysis of rain gauge and land use data for South America (Leite-Filho et al., 2019). Forest and grassland fires can also modify hydrological response at the watershed scale (Havel et al., 2018). Afforestation or reforestation aimed at removing CO_2 from the atmosphere can also alter the water cycle at the regional scale (Section 8.4.3 and Cross-Chapter Box 5.1).

In summary, there is *high confidence* that land use change and water extraction for irrigation drive local, regional and remote responses in the water cycle. Large-scale deforestation is *likely* to decrease precipitation over the deforested regions but there is *low confidence* in the effects of limited deforestation. There is *medium confidence* that deforestation drives increased streamflow relative to the responses caused by climate change. There is *medium confidence* that urbanisation can increase local precipitation and runoff intensity. A warming climate combined with direct human demand for water is expected to deplete ground water resources in dry regions (*high confidence*).

[START BOX 8.1 HERE]

ACCEPTED VERSION SUBJECT TO FINAL EDITING

BOX 8.1: Role of anthropogenic aerosols in water cycle changes

Aerosols affect precipitation in two major pathways, by altering the shortwave and longwave radiation and influencing cloud microphysical properties.

Aerosol radiative effects on precipitation

Aerosols scatter and absorb solar radiation which reduces the energy available for surface evaporation and subsequent precipitation. In addition, cooling is incurred by the radiation that is reflected back to space directly by the aerosols and indirectly by the aerosol effect on cloud brightening. Northern Hemisphere (NH) station data indicate decreasing precipitation trends during 1950s-1980s, which have since partially recovered (Wild, 2012; Bonfils et al., 2020). These changes are attributable with *high confidence* to anthropogenic aerosol emissions from North America and Europe causing dimming through reduced surface solar radiation, which peaked during the late-1970s and partially recovered thereafter following improved air quality regulations (Section 6.2.1; Box 8.1, Figure 1).

[START BOX 8.1, FIGURE 1 HERE]

Box 8.1, Figure 1: Northern hemisphere surface downward radiation anomalies (Wm^{-2} ; a) and precipitation anomalies (mm/day ; b) for 1951–2014 for summer season (May–September) monsoon region (Polson et al. et al., 2014a) **from CMIP6 DAMIP experiments**. Observed solar radiation anomalies are from GEBA global data from 1961-2014 (Wild et al., 2017) and observed precipitation anomalies are from GPCC and CRU. CMIP6 multi-model mean anomalies are from all-forcings (ALL), greenhouse gas forcing (GHG) and anthropogenic aerosol forcing (AER) experiments. Anomalies are with respect to 1961–1990 and smoothed with a 11-year running mean. Red shading shows the ensemble spread of ALL forcing experiment (5%–95% range). Models are masked to the GPCC data set. Further details on data sources and processing are available in the chapter data table (Table 8.SM.1).

[END BOX 8.1, FIGURE 1 HERE]

Dimming over the NH causes a relative cooling, compared to the SH, which induces a southward shift of the northern edge of the tropical rain belt (Allen et al., 2014; Brönnimann et al., 2015) (Section 3.3.2.2). CMIP5 simulations show that most of the cooling is caused by the aerosol cloud-mediated effect (Chung and Soden, 2017). Dimming also weakens monsoon flow and precipitation, offsetting or even overcoming the expected precipitation increase due to increased GHGs (Ayantika et al et al., 2021). The oceanic response to a weakened monsoon cross-equatorial flow can further weaken the South Asian monsoon through an amplifying feedback loop (Swapna et al., 2012; Krishnan et al., 2016; Patil et al., 2019) These processes partially explain (*medium confidence*) the southward shift of the NH tropical edge of the tropical rain belt from the 1950s to the 1980s (Allen et al., 2014; Brönnimann et al., 2015) and the severe drought in the Sahel that peaked in the mid-1980s (Rotstayn et al., 2002; Undorf et al., 2018). These processes also explain (*high confidence*) the observed decrease of southeast Asian Monsoon precipitation during the second half of the 20th century (Bollasina et al. et al., 2011; Sanap et al., 2015; Krishnan et al., 2016; Lau and Kim, 2017; Lin et al., 2018; Undorf et al., 2018) (Figure 8.7).

Absorption of solar radiation by anthropogenic aerosols such as black carbon warms the lower troposphere and increases moist static energy but also results in larger convection inhibition that suppresses light rainfall (Wang et al., 2013c) (Box 8.1, Figure 2). Release of aerosol-induced instability, often triggered by topographical barriers, produces intense rainfall, flooding (Fan et al., 2015; Lee et al., 2016) and severe convective storms (Saide et al., 2015) (*medium confidence*). In particular, aerosols induce intense convection at the Himalaya foothills during the pre-monsoon season, which generates a regional convergence there (*medium confidence).* This mechanism is termed the "elevated heat pump hypothesis" (Lau and Kim, 2006; D'Errico et al., 2015).

ACCEPTED VERSION SUBJECT TO FINAL EDITING

[START BOX 8.1, FIGURE 2 HERE]

Box 8.1, Figure 2: Schematic depiction of the atmospheric effects of light absorbing aerosols on convection and cloud formation: (A) without and (B) with the presence of absorbing aerosols in the planetary boundary layer. The dashed and solid blue lines correspond to the vertical temperature profiles in the absence and presence of the absorbing aerosol layer, respectively, and the solid and dashed red lines denote the dry and moist adiabats, respectively. Absorbing aerosols result in an increasing temperature in the atmosphere but a reduced temperature at the surface. The reduced surface temperature and the increased temperature aloft lead to a larger negative energy associated with convective inhibition (-) and a higher convection condensation level (CCL) under the polluted conditions. On the other hand, the absorbing aerosol layer induces a larger convective available potential energy (+) above CCL, facilitating more intensive vertical development of clouds, if lifting is sufficient to overcome the larger convective inhibition. From (Wang et al., 2013).

[END BOX 8.1, FIGURE 2 HERE]

Aerosol cloud microphysical effects

Cloud droplets nucleate on pre-existing aerosol particles which act as cloud condensation nuclei (CCN). Anthropogenic aerosols add CCN, compared to a pristine background, and produce clouds with more numerous and smaller droplets, slower to coalesce into raindrops and to freeze into ice hydrometeors at temperatures below 0°C. Adding CCN suppresses light rainfall from shallow and short-lived clouds, but it is compensated by heavier rainfall from deep clouds. Adding aerosols to clouds in extremely clean air invigorates them by more efficient vapour condensation on the added drop surfaces (Koren et al., 2014; Fan et al., 2018). Clouds forming in more polluted air masses (hence with more numerous and smaller drops) need to grow deeper to initiate rain (Freud and Rosenfeld, 2012; Konwar et al., 2012; Campos Braga et al., 2017). This leads to larger amount of cloud water evaporating aloft while cooling and moistening the air there at the expense of the lower levels, which leads to convective invigoration (Dagan et al., 2017; Chua and Ming, 2020), followed by convergence, air mass destabilization and added rainfall in an amplifying feedback loop (Abbott and Cronin, 2021). In addition, delaying rain initiation until greater altitudes are reached transports more cloud water above the 0°C altitude and leads to additional release of latent heat of freezing and/or vapour deposition, which in combination with the added latent heat of condensation enhances the cloud updrafts (Fan et al., 2018). The stronger updrafts invigorate mixed phase precipitation and the resultant hail and cloud electrification (Rosenfeld et al., 2008a; Thornton et al., 2017). This includes the outer convective rainbands of tropical cyclones and there is *medium confidence* that air pollution enhances flood hazard associated with the outer rain bands at the expense of the inner rain bands (Wang et al., 2014; Zhao et al., 2018a; Souri et al., 2020).

The aerosol effect on invigoration and rainfall from deep convective clouds peaks at moderate levels (aerosol optical depth of 0.2 to 0.3), but reverses into suppression with more aerosols (Liu et al., 2019a). More generally, the microphysical aerosol-related processes often compensate or buffer each other (Stevens and Feingold, 2009). For example, suppressed rain by slowing drop coalescence enhances mixed phase precipitation. Therefore, despite the potentially large aerosol influence on the precipitation forming processes, the net outcome of aerosol microphysical effects on precipitation amount has generally *low confidence*, especially when evaluated with respect to the background of high natural variability in precipitation (Tao et al., 2012).

Ice nucleating particles (INP) aerosols initiate ice precipitation from persistent supercooled water clouds that have cloud droplets too small for efficient warm rain, or expedite mixed phase precipitation in short lived supercooled rain clouds (Creamean et al., 2013). Most INP are desert and soil dust particles, rather than air pollution aerosols (DeMott et al., 2010). Biogenic particles from terrestrial and marine origin are more rare, but important at temperatures above about -15°C (Murray et al., 2012; DeMott et al., 2016). Dust particles from long-range transport across the Pacific were found to enhance snow forming processes over the Sierra Nevada in California (Creamean et al., 2013; Fan et al., 2014). The impact of INP was demonstrated by

ACCEPTED VERSION SUBJECT TO FINAL EDITING

glaciogenic cloud seeding experiments, which enhanced orographic supercooled clouds with *medium confidence* of success (French et al., 2018; Rauber et al., 2019; Friedrich et al., 2020). There are still major gaps in understanding the effects of INP mainly on deep convective clouds (Kanji et al., 2017; Stanford et al., 2017; Korolev et al., 2020)

[END BOX 8.1 HERE]

8.3 How is the water cycle changing and why?

This section focuses on the evaluation and attribution of past and recent water cycle changes using observational datasets, theoretical understanding and model simulations. Paleoclimate records and historical observations provide evidence for past water cycle changes caused both by natural variability and human activities (Haug et al., 2003; Buckley et al., 2010; Pederson et al., 2014). Key elements of the observed water cycle changes are assessed in this section, including flux and storage variations across the atmosphere, the continents and to a lesser extent the ocean and cryosphere, as well as related changes in large-scale atmospheric circulation and modes of variability. Particular emphasis is placed on assessing changes across regions and seasons (Box 8.2). Detailed regional assessments are presented in Chapters 10, 11, 12 and Atlas. Further information concerning large-scale observed water cycle changes and their attribution is available in Sections 2.3.1.3 and 3.3.2.

8.3.1 Observed water cycle changes based on multiple datasets

This section provides a process-based evaluation and a comprehensive assessment of observed water cycle changes by integrating multiple lines of evidence including paleoclimate data, historical datasets, theoretical understanding (Section 8.2) and model simulations.

8.3.1.1 Global water cycle intensity and P-E over land and oceans

The human influence on the global water cycle is often summarized as an intensification (Huntington, 2006; DeAngelis et al., 2015; Zhang et al., 2019c) or an overall strengthening which has been observed since at least 1980 (*high confidence*, see Chapter 2). There is however no unique definition of the global water cycle intensity (Trenberth, 2011; Ficklin et al., 2019; Sprenger et al., 2019). One simple metric is the global and annual mean amount of precipitation. Although an increase in global precipitation is consistent with physical expectations (Section 8.2.1), it has not yet been detected and attributed to human activities given large observational uncertainties and low signal-to-noise ratio (Section 8.3.3.2). Other metrics are more suitable to detect and attribute changes in the global water cycle, including the *likely* increase in global land precipitation since 1950 (Section 2.3.1.4) which is *likely* due to a human influence (Section 3.3.2.2).

The flux of fresh water between the ocean and atmosphere is determined by the difference between precipitation and evaporation (P-E). Evaporation is measured in very few locations across the global ocean, so that directly assessing P-E over the ocean is very challenging and relies on indirect reanalysis estimates (Robertson et al., 2020). AR5 presented *robust evidence* of an amplified oceanic pattern in P-E since the 1960s from both regional and global surface and subsurface salinity measurements and reanalyses. This pattern is consistent with our theoretical understanding of human induced changes in the water cycle, leading to the conclusion that these changes are *very likely* the result of anthropogenic forcings (Section 9.2.2.2).

In contrast, AR5 did not provide a conclusive assessment of observed changes in P-E over land. Continental P-E estimated from reanalyses and data-driven land-surface models indicate that interannual variations are linked to ENSO (Robertson et al., 2014, 2020). Increasing trends in P-E since 1979 based on land models are not statistically significant. Observations and models show evidence that P-E increases in the wet parts and decreases in the dry parts of tropical circulation systems, which shift in location seasonally and from year to year, with increases in seasonality since 1979 (Chou et al., 2013; Liu and Allan, 2013; Fu and Feng, 2014,

ACCEPTED VERSION SUBJECT TO FINAL EDITING

see also Box 8.2).

In summary, a low signal-to-noise ratio, observational uncertainties and current data assimilation techniques limit the assessment of recent global trends in P-E over both land and ocean. It is *likely* that the global land P-E variations observed since the late 1970s were dominated by internal variability, mostly linked to ENSO teleconnections (*medium confidence*). In contrast, the attribution of changes in sea surface salinity (Section 3.5.2.2) suggests that it is *extremely likely* that human influence has contributed to the regional changes in P-E observed over the global ocean since the mid-20th century.

8.3.1.2 Water vapour and its transport

AR5 presented evidence of increases in global near-surface and tropospheric specific humidity since the 1970s but with *medium confidence* of a slowing of near-surface moistening trends over land associated with reduced relative humidity since the late 1990s. According to the AR5, radiosonde, Global Positioning System (GPS) and satellite observations of tropospheric water vapour indicate *very likely* increases at near global scales since the 1970s occurring at a rate that is generally consistent with the Clausius-Clapeyron relation (about 7% per ºC at low altitudes) and the observed atmospheric warming (Hartmann et al., 2013).

Since AR5, it is *very likely* that increases in global atmospheric water vapour are observed from in situ, satellite and reanalysis data (with *medium confidence* in the magnitude; Section 2.3.1.3). Satellite records show increases in upper tropospheric water vapour (constant relative humidity while temperatures have increased) since 1979 (Chung et al., 2014b; Blunden and Arndt, 2020), to which human influence has *likely* contributed (Section 3.3.2.1). Combined satellite and reanalysis estimates and CMIP6 atmosphere-only simulations (1988–2014) show global-mean precipitable water vapour increases of 6.7±0.3%/°C, very close to the Clausius Clapeyron rate (Allan et al., 2020). Satellite-based products show increases close to the Clausius-Clapeyron rate over the ice-free oceans (about 7 to 9 %/ºC; 1998-2008), but reanalysis estimates outside this range (Schröder et al., 2019) are an expected consequence of their changing observing systems (Allan et al., 2014; Parracho et al., 2018). Increases in precipitable water vapour are found over the central and sub-Arctic based on multiple reanalyses with some corroboration from sparse, in situ data (Vihma et al., 2016; Rinke et al., 2019; Nygård et al., 2020).

Declining near-surface relative humidity over land areas (e.g., United States, Mediterranean, south Asia, South America and southern Africa) is evident in surface observations (Willett et al., 2014, 2020; Dunn et al., 2017). This is consistent with a faster rate of warming over land than ocean (Byrne and O'Gorman, 2018) (see Sections 2.3.1.3 and 8.2.2.1). CMIP5 simulations underestimate the observed decreases in relative humidity over much of global land during 1979-2015 (Douville and Plazzotta, 2017; Dunn et al., 2017) even when observed SSTs are prescribed (-0.05 to -0.25 %/decade compared with an observed rate of -0.4 to -0.8 %/decade). It is not yet clear if this discrepancy is related to internal variability or can be explained by deficiencies in models (Vannière et al., 2019; Douville et al., 2020) or observations (Willett et al., 2014). Over the Northern Hemisphere mid-latitude continents, there is *medium confidence* that human influence has contributed to a decrease in near-surface relative humidity in summer (Sections 2.3.1.3 and 3.3.2.2).

Water vapour transport (or convergence) estimates from observations have substantial uncertainties even in regions of high quality radiosonde data. Consequently many studies use reanalyses for water transport estimates instead of instrumental observations. For example, increases in low-level (800-1000 hPa) moisture convergence into the tropical wet regime with a smaller outflow increase in the mid-troposphere (400-800 hPa) with warming was detected in one reanalysis (ERA-Interim) (Allan et al., 2014). Modelling evidence combined with statistical analysis demonstrate consistency between reanalysis moisture convergence and P-E over land (Robertson et al., 2016). Advances in reanalysis representation of atmospheric moisture and winds in addition to new observational isotope analysis have improved the ability to identify the main sources of water vapour for key continental regions and quantify the relative contributions from moisture advection and recycling (Gimeno et al., 2012; Van Der Ent et al., 2014; Joseph et al., 2016).

Observed changes in moisture transport can also arise from changes in atmospheric circulation as well as

ACCEPTED VERSION SUBJECT TO FINAL EDITING

thermodynamics. For instance, moisture transport into the Arctic region estimated from reanalyses datasets is consistent with radiosonde data (Dufour et al., 2016), with increases since 1979 linked to atmospheric circulation (Nygård et al., 2020). Moisture transport into the Eurasian Arctic was identified to increase by 2.6%/decade during 1948-2008 based on a reanalysis estimate (Zhang et al., 2013b). More intense moist intrusions associated with atmospheric rivers affecting the Arctic and Europe have been documented since 1979 but with a substantial influence from decadal internal variability (Ummenhofer et al., 2017; Mattingly et al., 2018). A recent strengthening of tropical circulation and associated moisture convergence has been idendified since around 2000 for the Amazon region (Arias et al., 2015; Barichivich et al., 2018; Espinoza et al., 2018a; Wang et al., 2018e). This was also strenghtened by increased moisture transport from the North Atlantic, driving more abundant latent heat release (Segura et al., 2020) and leading to an increased frequency of extreme floods in the northern Amazon (Barichivich et al., 2018; Heerspink et al., 2020). Overall, increased moisture transport has been linked to increased precipitation over wet tropical land areas (Gimeno et al., 2020) and to more extreme and persistent wet and dry weather events (Konapala et al., 2020) in many regions worldwide.

In summary, there is *high confidence* that human-caused global warming has led to an overall increase in water vapour and moisture transport throughout the troposphere, at least since the mid-1990s. In particular, there is *high confidence* that moisture transport into the Arctic has increased but only *medium confidence* in the attribution of such a trend to a human influence. There is *medium confidence* that human influence has contributed to a decrease in near-surface relative humidity over the Northern Hemisphere mid-latitude continents during summer (see also Sections 2.3.1.3 and 3.3.2.2).

8.3.1.3 Precipitation amount, frequency and intensity

This section assesses observed changes in precipitation at global and regional scales. Note that changes in precipitation seasonality are assessed in Box 8.2 and that changes in regional monsoons are assessed in section 8.3.2.4 where observed changes in both circulation and rainfall are considered. Further assessment of regional changes in precipitation is presented in Chapters 10, 12 and Atlas, while extreme precipitation is presented in Chapter 11.

AR5 concluded that it is *likely* there has been an overall increase in annual mean precipitation amount over mid-latitude land areas in the Northern Hemisphere, with *low confidence* since 1901, but *medium confidence* after 1951. There is further evidence of a faster increase since the 1980s (*medium confidence*) (Sections 2.3.1.3.4 and 3.3.2.1). Precipitation has increased from 1950 to 2018 over mid-high latitude Eurasia, most North America, southeastern South America, and northwestern Australia, while it has decreased over most of Africa, eastern Australia, the Mediterranean region, the Middle East, and parts of East Asia, central South America, and the Pacific coasts of Canada, as simulated by the CMIP5 multi-ensemble mean (Dai, 2021). Since AR5, there have been updates of several precipitation datasets, including satellite estimates, reanalysis and merged products (Adler et al., 2017; Roca, 2019). However, observational uncertainties remain an issue for assessing regional trends in seasonal or annual mean precipitation amount (Hegerl et al., 2015; Maidment et al., 2015; Sarojini et al., 2016), as well as the convective and stratiform types of precipitation (e.g., Ye et al., 2017). Precipitation trends at regional scales are dominated by internal variability across much of the world (Knutson and Zeng et al., 2018). Regional changes in precipitation amounts can also be obscured by contrasting responses to GHG versus aerosol forcings (Wu et al., 2013; Hegerl et al., 2015; Xie et al., 2016; Zhao and Suzuki, 2019; Zhao et al., 2020) and changes in precipitation intensity versus frequency (Shang et al., 2019).

Global and regional changes in precipitation frequency and intensity have been observed over recent decades. An analysis of 1875 rain gauge records worldwide over the period 1961–2018 indicates that there has been a general increase in the probability of precipitation exceeding 50 mm/day, mostly due to an overall boost in rain intensity (Benestad et al., 2019). Such changes in precipitation intensity and frequency have not been formally attributed to human activities, but are consistent with the heating effect of increasing CO_2 levels on the distribution of daily precipitation rates (Section 8.2.3.2) and with a distinct overall intensification of heavy precipitation events found in both observations and CMIP5 models, though with an

ACCEPTED VERSION SUBJECT TO FINAL EDITING

underestimated magnitude (Fischer and Knutti, 2014). Beyond amplified precipitation extremes (Section 11.4.2), CMIP5 models also indicate that anthropogenic forcings have increased temporal variability of annual precipitation amount over land from 1950 to 2005, which is most pronounced in annual mean daily precipitation intensity (Konapala et al., 2017).

Anthropogenic aerosols can alter precipitation intensities both through radiative and microphysical effects (Box 8.1; Section 8.5.1.1.2). Precipitation suppression through aerosol microphysical effects has been observed in shallow cloud regimes over South America and the southeastern Atlantic, associated with local biomass burning (Andreae et al., 2004; Costantino and Bréon, 2010), and in industrial regions in Australia (Rosenfeld, 2000; Hewson et al., 2013; Heinzeller et al., 2016). In contrast, precipitation intensification through aerosol microphysical effects in deep convective clouds is seen in many regions such as the Amazon, southern United States, India, and Korea associated with anthropogenic aerosols from cities (Hewson et al., 2013; Fan et al., 2018; Lee et al., 2018b; Sarangi et al., 2018).

In the tropics, increases in precipitation amount are observed in convergence zones and decreases in the descending branches of the atmospheric circulation since 1979 (Chou et al., 2013; Liu and Allan, 2013; Gu et al., 2016; Polson et al., 2016; Polson and Hegerl, 2017), consistent with increased moisture transports with warming (Gimeno et al., 2020). Over tropical land areas, there is substantial variability in the "wet convergent regimes get wetter" and "dry divergent regimes get drier" pattern of trends observed since 1950 that are modulated by decadal changes in ENSO (Liu and Allan, 2013; Gu and Adler, 2018). CMIP6 models indicate an increased contrast between wet and dry regions in the tropics and subtropics (Schurer et al., 2020) (Figure 8.7). This provides further evidence that rainfall has increased in wet regimes, and slightly decreased in dry regimes over the period 1988-2019 (Figure 3.14). This greater contrast is primarily attributable to greenhouse gas forcings, although the observed trends are statistically larger than the model responses (Section 3.3.2.2).

Over the African continent, there are distinct precipitation trends observed in multiple datasets since the 1980s (Maidment et al., 2015; Nguyen et al., 2018b) (Figure 8.7). Increases in intense convective storms affecting the Sahel have been attributed to increased land-ocean temperature gradients (Taylor et al., 2017), enhanced by intense heating of the Sahara (Dong and Sutton, 2015) rather than thermodynamics (Section 8.2.2). Changes in Sahel rainfall, with reduced precipitation amounts from the 1960s to the 1980s and a subsequent recovery, are assessed in Section 8.3.2.4.3 and Section 10.4.2.1. In eastern Africa, decreasing precipitation amount (−2 to −7% per decade for 1983-2010) was reported for the March-to-May Long Rains season (Lyon and Dewitt, 2012; Viste et al., 2013; Liebmann et al., 2014; Maidment et al., 2015; Rowell et al., 2015) and evidence of a recovery since, with internal variability playing a large role in these decadal changes (Wainwright et al., 2019). In contrast, the second "Short Rains" season in Eastern Africa (October to December) does not exhibit significant precipitation trends (Rowell et al., 2015). Increases in annual southern Africa rainfall of 6-7% per decade during 1983-2010 are linked with the Pacific Decadal Oscillation (PDO) (Maidment et al., 2015).

Section 8.3.1.6 assesses changes in precipitation over the Mediterranean region and its connection with drought and aridity.

Rainfall increases have been observed over northern Australia since the 1950s, with most of the increases occurring in the north-west (Dey et al., 2018, 2019b; Dai, 2021) and decreases observed in the north-east (Li et al., 2012a) since the 1970s. In contrast, there has been a decline in rainfall over southern Australia related to changes in the intensification and position of the subtropical ridge (CSIRO and Bureau of Meteorology, 2015) and anthropogenic effects (Knutson and Zeng et al., 2018). The drying trend over southwest Australia is most pronounced during May–July, where rainfall has declined by 20% below the 1900–1969 average since 1970 and by about 28% since 2000 (Bureau of Meteorology and CSIRO, 2020).

Over South America, there is observational and paleoclimate evidence of declining precipitation amount during the past 50 years over the Altiplano and central Chile, primarily explained by the PDO but with at least 25% of the decline attributed to anthropogenic influence (Morales et al., 2012; Neukom et al., 2015; Boisier et al., 2016; Seager et al., 2019b; Garreaud et al., 2020). In contrast, a significant rainfall increase has

ACCEPTED VERSION SUBJECT TO FINAL EDITING

been detected over the Peruvian-Bolivian Altiplano (from observational data and satellite-based estimations) since the 1980s (Imfeld et al., 2020; Segura et al., 2020) (Figure 8.7). Long-term (1902-2005) precipitation data indicate positive trends over southeastern South America and negative trends over the southern Andes, with at least a partial contribution from anthropogenic forcing (Gonzalez et al., 2014; Vera and Díaz, 2015; Díaz and Vera, 2017; Boisier et al., 2018; Knutson and Zeng et al., 2018) (see further assessment in Sections 10.4.2.2 and Atlas.7.2.2). The Peruvian Amazon has exhibited significant rainfall decreases during the dry season since 1980 (Lavado et al., 2013; Ronchail et al., 2018). Increases in wet season rainfall in the northern and central Amazon since the 1980s and decreases during the dry season in the southern Amazon (Barreiro et al., 2014; Gloor et al., 2015; Martín-Gómez and Barreiro, 2016; Espinoza et al., 2018a; Wang et al., 2018e; Haghtalab et al., 2020) are not explained by radiative forcing based on CMIP6 experiments (Figure 8.7) and trends are insignificant over longer periods since 1930 (Kumar et al., 2013) or more recently, since 1973 (Almeida et al., 2017) (see Section 8.3.2.4.5 for monsoon-related changes). For the tropical Andes region, trends in annual precipitation show heterogenous patterns, ranging between -4%/decade and +4%/decade in the north and south tropical Andes for a 30-year period at the end of the 20th century, although increases during 1965-1984 and decreases since 1984 have been registered in Bolivia (Carmona and Poveda, 2014; Pabón-Caicedo et al., 2020).

Over China, annual precipitation totals changed little from 1973 to 2016, but precipitation intensity significantly increased at a rate of 0.12 mm/day/decade, while the number of days with precipitation exceeding 0.1 mm/day significantly decreased at a rate of 0.9 days/decade (Shang et al., 2019). There is consistency in trend estimates during 1998-2015 over mainland China among satellite-based products and station data, which show increased precipitation amounts in autumn and winter and decreases in summer (Chen and Gao, 2018), consistent with a decreased intensity of East-Asian monsoon precipitation (Lin et al., 2014; Deng et al., 2018). Further assessment of precipitation changes over the South and Southeast Asian and the East Asian monsoon regions is presented in Section 8.3.2.4. An increasing trend in the frequency of heavy rainfall occurrences at the expense of low and moderate rainfall occurrences is found over central India (Krishnan et al., 2016; Roxy et al., 2017) and over eastern China with the latter due to increasing high aerosol levels (Qian et al., 2009; Guo et al., 2017a; Xu et al., 2017; Day et al., 2018), consistent with the effects of absorbing aerosol on stability and convective inhibition (Box 8.1).

Observed precipitation records since the early 1900s show increases in precipitation totals over central and northeastern North America that are attributable to anthropogenic warming but larger in magnitude than found in CMIP5 simulations (Knutson and Zeng et al., 2018; Guo et al., 2019). Decreases in precipitation amount over the central and southwestern United States and increases over the north-central United States during 1983-2015 (Cui et al., 2017; Nguyen et al., 2018b), are not clearly associated with forced responses in CMIP6 simulations (Figure 8.7; see also Section 10.4.2.3). Over Europe, precipitation trends since 1979 do not show coherence across datasets (Zolina et al., 2014; Nguyen et al., 2018b). Longer records since 1910 show increases for much of Scandinavia, northwestern Russia, and parts of northwestern Europe/UK and Iceland (Knutson and Zeng et al., 2018). Records since 1930 show increases of annual preciptation amount over western Russia (see also Section Atlas.8.2). Widespread increases in daily precipitation intensity appear clearly over regions with a high density of rain gauges, such as Europe and North America over the 1951-2014 period (Alexander, 2016). Observations during 1966-2016 over northern Eurasia show increases in the contribution of heavy convective showers to total precipitation by 1-2% on average (with local trends of up to 5%) for all seasons except for winter (Chernokulsky et al., 2019). Increases in convective precipitation intensity have been identified, particularly on sub-daily time-scales, using a range of modelling and observational data (Berg et al., 2013; Kanemaru et al., 2017; Pfahl et al., 2017).

Snowfall is an important component of precipitation in high-latitude and mountain watersheds. Reanalysis data indicate significant reductions in annual mean potential snowfall areas over the Northern Hemisphere land by 0.52 million km^2 per decade, with the largest decline over the Alps, with snow water equivalent reductions of about 20 mm per decade (Tamang et al., 2020). In the Tibetan Plateau, region-wide wintertime snowfall has increased but summer snowfall has decreased during the 1960-2014 period (Deng et al., 2017). State-of-the-art model simulations indicate reduced mean annual snowfall in the Arctic, despite the strong precipitation increase, mainly in summer and autum, when temperatures are close to the melting point (Bintanja and Andry, 2017).

ACCEPTED VERSION SUBJECT TO FINAL EDITING

[START FIGURE 8.7 HERE]

Figure 8.7: Linear trends in annual mean precipitation (mm/day per decade) for 1901-1984 (left) and 1985-2014 (right): (a & e) observational dataset, and the CMIP6 multi model ensemble mean historical simulations driven by, (b & f) all radiative forcings, (c & g) GHG only radiative forcings, (d & h) aerosol only radiative forcings experiment. Shade without grey cross correspond to the regions exceeding 10 % significant level. Grey crosses correspond to the regions not reaching the 10% statistical significant level. Nine CMIP6-DAMIP models have been used having at least 3 members. The ensemble mean is weighted per each model on the available and used members. Further details on data sources and processing are available in the chapter data table (Table 8.SM.1).

[END FIGURE 8.7 HERE]

In summary, regional changes in precipitation amounts can be obscured by the contrasting responses to GHG and aerosol forcings across much of the 20th century and can be thus dominated by internal variability at decadal to multi-decadal timescales (*high confidence*). There is however a detectable increase in northern high-latitude annual precipitation over land which has been primarily driven by human-induced global warming (*high confidence*, see also Section 3.3.2). Human influence has strengthened the zonal mean precipitation contrast between the wet tropics and dry subtropics since the 1980s (*medium confidence*), although regional studies suggest a more complex precipitation response to evolving anthropogenic forcings. There is *high confidence* that daily mean precipitation intensities have increased since the mid-20th century in a majority of land regions with available observations and it is *likely* that such an increase is mainly due to GHG forcing (see Section 11.4). Section 8.3.2.4 assesses monsoon precipitation changes in detail.

8.3.1.4 Evapotranspiration

AR5 assessed that there was *medium confidence* that pan evaporation declined in most regions over the last 50 years, yet *medium confidence* that evapotranspiration increased from the early 1980s to the late 1990s. Since AR5, these conflicting observations have been attributed to internal variability and by the fact that evapotranspiration is less sensitive to trends in wind speed and is partly controlled by vegetation greening (Zhang et al., 2015a, 2016d; Zeng et al., 2018c). Observation-based estimates show a robust positive trend in global terrestrial evapotranspiration between the early 1980s and the early 2010s (Miralles et al., 2014b; Zeng et al., 2014, 2018c, Zhang et al., 2015a, 2016d). The rate of increase varies among datasets, with an ensemble mean terrestrial average rate of 7.6 ± 1.3 mm $year^{-1}$ $decade^{-1}$ for 1882–2011 (Zeng et al., 2018b). In addition, a decreasing trend in pan evaporation plateaued or reversed after the mid-1990s (Stephens et al., 2018a) has been reported as due to a shift from a dominant influence of wind speed to a dominant effect of water vapour pressure deficit, which has increased sharply since the 1990s (Yuan et al., 2019). The absence of a trend in evapotranspiration in the decade following 1998 was shown to be at least partly an episodic phenomenon associated with ENSO variability (Miralles et al., 2014b; Zhang et al., 2015a; Martens et al., 2018). Thus, there is *medium confidence* that the apparent pause in the increase in global evapotranspiration from 1998 to 2008 is mostly due to internal variability. In contrast to the AR5, there are now consistent trends in pan evaporation and evapotranspiration at the global scale, given the recent increase in both variables since the mid 1990s (*medium confidence*). Given the growing number of quantitative studies, there is *high confidence* that global terrestrial annual evapotranspiration has increased since the early 1980s.

Since AR5, the predominant contribution of transpiration to the observed trends in terrestrial evapotranspiration has been revisited and confirmed (Good et al., 2015; Wei et al., 2017). Using satellite and ecosystem models, Zhu et al., (2016) found a positive trend in leaf area index during 1982-2009, indicating that greening could contribute to the observed positive trend of evapotranspiration, in line with similar studies that focused on the 1981–2012 (Zhang et al., 2016d) and 1982–2013 (Zhang et al., 2015a) periods. Zeng et al. (2018) determined that the 8% global increase in satellite-observed leaf area index between the 1980s and the 2010s may explain an increase in evapotranspiration of 12.0+/-2.4mm/yr (about 55+/-25% of

ACCEPTED VERSION SUBJECT TO FINAL EDITING

the total observed increase). Forzieri et al. (2020) estimated that the recent increase in leaf area index led to 3.66 ± 0.45 W/m^2 in latent heat flux (about 51 ± 6 mm/yr) and that the sensitivity of energy fluxes to leaf area index increased by about 20% over the 1982–2016 period. Overall, there is *medium confidence* that greening has contributed to the global increase in evapotranspiration since the 1980s.

Plant water use efficiency is expected to rise with CO_2 levels (*high confidence*, see Section 8.2.3.3 and Box 5.2), and can in theory counteract rising evapotranspiration in a warmer atmosphere (Section 8.2.3.3). However, observational studies suggest that this may not be the case in some ecosystems. For example, Frank et al. (2015) found that while the Water Use Efficency (WUE) increased in European forests across the 20th century, transpiration also increased due to more plant growth, a lengthened growing season, and increased evaporative demand. Likewise Guerrieri et al. (2019) observed that while WUE and photosynthesis increased in North American forests, stomatal conductance experienced only modest declines that were restricted to moisture-limited forests. Other studies further suggest that in many ecosystems increased WUE will not compensate for increased plant growth, amplifying declines in surface water availability (De Kauwe et al., 2013; Ukkola et al., 2016b; Singh et al., 2020a), while drought conditions can also offset the CO_2 fertilization effect and lead to a decline in WUE (Liu et al., 2020a). There is *low confidence* regarding the impact of plant physiological effects on observed trends in evapotranspiration.

An increasing number of studies have identified signals of attribution in the recent observed trends in evapotranspiration. Douville et al. (2013) found that the post-1960 rise in evapotranspiration in both the mid-latitudes and northern high latitudes was related to anthropogenic radiative forcing. An analysis of CMIP5 simulations suggests that anthropogenic forcing accounts for a large fraction of the global-mean evapotranspiration trend from 1982 to 2010 (Dong and Dai, 2017). Padrón et al., (2020) determined that increases in evapotranspiration were responsible for the majority of the anthropogenic pattern in dry-season water availability that dominates global trends since 1984. These findings are further supported by CMIP6 model results (Fig. 8.8) that show that the recent summertime increase in evapotranspiration in the northern mid-and-high latitudes is due to greenhouse gas forcing and decreasing anthropogenic aerosol emissions over Europe.

In summary, there is *high confidence* that terrestrial evapotranspiration has increased since the 1980s. There is *medium confidence* that this trend is driven by both increasing atmospheric water demand and vegetation greening, and *high confidence* that it can be partly attributed to anthropogenic forcing. There is *low confidence* about the extent to which increases in plant water use efficiency have influenced observed changes in evapotranspiration.

[START FIGURE 8.8 HERE]

Figure 8.8: Linear trends in annual mean evapotranspiration (mm/day per decade) for 1901-1984 (left) and 1985-2014 (right): (a & e) LMIP and observational dataset, and the CMIP6 multi model ensemble mean historical simulations driven by, (b & f) all radiative forcings, (c & g) GHG only radiative forcings, (d & h) aerosol only radiative forcings experiment. Shade without grey cross correspond to the regions exceeding 10 % significant level. Grey crosses correspond to the regions not reaching the 10% statistically significant level. Nine CMIP6-DAMIP models have been used having at least 3 members. The ensemble mean is weighted per each model on the available and used members. GLDAS is not available over the early 20th century so was replaced by a multi-model off-line reconstruction, LMIP, which is consistent with GLDAS over the recent period but may be less reliable over the early 20th century given larger uncertainties in the atmospheric forcings. Further details on data sources and processing are available in the chapter data table (Table 8.SM.1).

[END OF FIGURE 8.8 HERE]

8.3.1.5 Runoff, streamflow and flooding

AR5 reported *low confidence* in the assessment of trends in global river discharge during the 20th century.

ACCEPTED VERSION SUBJECT TO FINAL EDITING

This is because many streamflow observations have been impacted by land use and dam construction, and the largest river basins worldwide differ in many characteristics, including geography and morphology. In regions with seasonal snow storage, AR5 WGII assessed that there is *robust evidence* and *high agreement* that warming has led to earlier spring discharge maxima and *robust evidence* of earlier breakup of Arctic river ice, as well as indications that warming has led to increased winter flows and decreased summer flows where streamflows are lower and that the observed increases in extreme precipitation led to greater probability of flooding at regional scales with *medium confidence*. SROCC found *robust evidence* and *high agreement* that discharge due to melting glaciers has already reached its maximum point and has begun declining with smaller glaciers, but only *low confidence* that anthropogenic climate change has already affected the frequency and magnitude of floods at the global scale.

Significant trends in streamflow and continental runoff were observed in 55 out of 200 large river basins during 1948-2012, with an even distribution of increasing and decreasing trends (Dai, 2016) (see also Section 2.3.1.3.6). A global detection and attribution study shows that the simulation of spatially heterogeneous historical trends in streamflow is consistent with observed trends only if anthropogenic forcings are considered (Gudmundsson et al., 2019). Section 3.3.2.3 assesses with *medium confidence* that anthropogenic climate change has altered regional and local streamflows, although a significant trend has not been observed in the global average (Sections 2.3.1.3.6 and 3.3.2.3). Multiple human-induced and natural drivers have been shown to play an important but variable role in observed regional trends of streamflow for several different areas (Fenta et al., 2017; Ficklin et al., 2018; Glas et al., 2019; Vicente-Serrano et al., 2019). For instance, decreasing runoff during the dry season have been observed over the Peruvian Amazon since the 1980s (Lavado et al., 2013; Ronchail et al., 2018). Up to 30–50% of the recent multi-decadal decline in streamflow across the Colorado River Basin can be attributed to anthropogenic warming and its impacts on snow and evapotranspiration (Woodhouse et al., 2016; McCabe et al., 2017; Udall and Overpeck, 2017; Xiao et al., 2018; Milly and Dunne, 2020). In the Upper Missouri River basin, Martin et al. (2020) found that warming temperatures have contributed to streamflow reductions since at least the late 20th century. Cold regions in the Northern Hemisphere have experienced an earlier occurrence of snowmelt floods, an overall increase in water availability and streamflow during winter, and a decrease in water availability and streamflow during the warm season (Aygün et al., 2019).

Some studies have suggested that dam construction and water withdrawals can be the dominant drivers in observed trends in streamflow amount (Wada et al., 2013). Regionally, land use and land cover changes have been identified as important factors for streamflow (Chen et al., 2020a). The impact of surface dimming from aerosol emissions on evaporation was identified as a discernible influence in Northern Hemisphere streamflows (Gedney et al., 2014). While changes in annual mean streamflow present a complicated picture, recent studies of changes in the timing of streamflow in snow-influenced basins continue to support a prominent influence from warming (Kang et al., 2016; Dudley et al., 2017; Kam et al., 2018). Global land runoff variations correlate significantly with ENSO variability (Miralles et al., 2014b; Schubert et al., 2016).

Observed changes in flooding are assessed in detail in Chapter 11 and are summarized as follows. For changes in the magnitude of peak flow, recent studies show strong spatial heterogeneity in the sign, size and significance of trends (Section 11.5.2.1). For changes in the frequency and magnitude of high flows, the conclusions remain limited by the large influence of water management (Section 11.5.2.2). For changes in timing of peak flows, recent studies further support observed changes in snowmelt-driven rivers (Section 11.5.2.3). Observed changes in runoff and flood magnitude cannot be explained by precipitation changes alone given the possible season- and region-dependent decreases in antecedent soil moisture and snowmelt which can partly offset the increase in precipitation intensity (Sharma et al., 2018), or the expected effect of urbanization and deforestation which can on the contrary amplify the runoff response (Chen et al., 2017; Abbott et al., 2019; Cavalcante et al., 2019). Simulations of mean and extreme river flows are consistent with the observations only when anthropogenic radiative forcing is considered (Gudmundsson and et al., 2021).

In summary, the assessment of observed trends in the magnitude of runoff, streamflow, and flooding remains challenging, due to the spatial heterogeneity of the signal and to multiple drivers. There is however *high confidence* that the amount and seasonality of peak flows have changed in snowmelt-driven rivers due to warming. There is also *high confidence* that land use change, water management and water withdrawals have

ACCEPTED VERSION SUBJECT TO FINAL EDITING

altered the amount, seasonality, and variability of river discharge, especially in small and human-dominated catchments.

8.3.1.6 Aridity and drought

AR5 reported *low confidence* that changes in drought since the mid-20th century could be attributed to human influence, owing to observational uncertainties and difficulties in distinguishing decadal-scale variability from long-term trends. Changes in soil moisture, a metric of aridity, were not assessed thoroughly in AR5. Since AR5, new satellite products, land-surface reanalyses, and land-surface models have been used to document recent changes in soil moisture at the global scale. The science of detection and attribution has also progressed considerably (Trenberth et al., 2015; Easterling et al., 2016; Stott et al., 2016). Attribution efforts have further benefited from the increased use of paleoclimate information, which provides an important constraint on natural variability that is insufficiently sampled by short observational record (Cook et al., 2018; Kageyama et al., 2018).

Several studies have identified a persistent "fingerprint" of anthropogenic forcing in global trends in aridity spanning the last 120 years. Using a combination of tree ring data, CMIP5 model simulations, and reanalysis products, Marvel et al. (2019) determined that the dominant trend in aridity since 1900, characterized by drying in North and Central America and the Mediterranean, is detectable and attributable to external forcing from 1900–1949. This trend weakens from 1950–1975, possibly due to aerosol forcing (Marvel et al., 2019), but then emerges again from 1981 to present, although it is not detectable in the GLEAM nor MERRA-2 soil moisture reanalysis products. Likewise, Bonfils et al., (2020) investigated changes in precipitation, temperature and continental aridity in CMIP5 historical simulations and found that the dominant multivariate fingerprint, an amplification of wet-dry latitudinal patterns and progressive continental aridification, was associated with greenhouse gas emissions (Figure 8.9 a-d), and the second leading fingerprint was associated with anthropogenic aerosols (Figure 8.9 e-h). This study found that the anthropogenic greenhouse gas signal is statistically detectable in reanalyses over the 1950–2014 period (signal-to-noise ratio above 1.96). Gu et al. (2019) found that a global trend in declining soil moisture is detectable in the GLDAS-2 reanalysis product and is attributable to greenhouse gas forcing. Padrón et al. (2020) reconstructed the global patterns of dry season water availability from 1902–2014, and found it *extremely likely* (99% range) that trends in the last three decades of the analysis period could be attributed to anthropogenic forcing, mainly due to increases in evapotranspiration. It is *very likely* (>90% range) that anthropogenic forcing has affected global patterns of soil moisture over the 20th century.

On a regional scale, the robustness of trend attribution for drought and aridity varies widely. Key trends and their attributions are summarized here, while a complete regional assessment of observed trends in drought and aridity is in Chapter 11 (Sections 11.6.2, 12.3.2 and 12.4).

Several studies have analyzed CMIP5 and land surface models and detected a significant summertime drying trend in the Northern Hemisphere across the late 20th century that is attributable to anthropogenic forcings (Mueller and Zhang, 2016; Douville and Plazzotta, 2017). This trend is mainly driven by dryland areas such as the western United States and west-central Asia, where both reanalysis products and satellite data confirm there has been a persistent decline in soil moisture since 1990 (Liu et al., 2019d). In the western United States, snow deficits have *very likely* contributed to recent drying (Mote et al., 2018). Spring snow water equivalent across the Sierra Nevada Mountains reached a record low in 2015 (Margulis et al., 2016; Mote et al., 2016), possibly the lowest of the last five hundred years (Belmecheri et al., 2016). Over the longer California drought (2011–2015) anthropogenic warming alone reduced snowpack levels in the Sierras by 25% (Berg and Hall, 2017). The northwestern United States also experienced snow drought in 2015, despite near-normal levels of total cold season precipitation (Mote et al., 2016; Marlier et al., 2017). There is *high confidence* that anthropogenic warming contributed to these recent snow droughts (Belmecheri et al., 2016; Mote et al., 2016).

In the western United States, anthropogenic warming is amplifying drought and aridity by increasing evaporative demand and water loss to the atmosphere (Weiss et al., 2009; Overpeck, 2013; Cook et al., 2014;

ACCEPTED VERSION SUBJECT TO FINAL EDITING

Griffin and Anchukaitis, 2014; Williams et al., 2020). For the California drought between 2012–2014, Griffin and Anchukaitis (2014) used paleoclimate reconstructions to determine that while rainfall deficits were not unprecedented, record-high temperatures drove an exceptional decline in soil moisture relative to the last millennium. Williams et al. (2015) concluded that anthropogenic warming accounted for 8–27% of the these soil moisture deficits. Robeson (2015) estimated that the California drought was a 1-in-10,000 year event. Tree ring reconstructions indicate that prolonged megadroughts have occurred in the western United States throughout the last 1200 years (Cook et al., 2004, 2010, 2015a) forced by internal variability (Coats et al., 2016; Cook et al., 2016b). However, Williams et al. (2020) determined that 2000–2018 drought across the southwestern United States was the second driest 19-year period since 800 CE, and attributed nearly half the magnitude of this event to anthropogenic forcing (see also Section 10.4.2.3). Evidence for human signals in drought can also be found in western North American streamflow records, as noted above in Section 8.3.1.5. There is *high confidence* that anthropogenic forcing has contributed to recent droughts and drying trends in western North America.

Large areas of east-central Asia experienced drying in the early 2000s as a result of warmer temperatures, lower humidity, and declining soil moisture (Wei and Wang, 2013; Li et al., 2017d; Hessl et al., 2018). Paleoclimate data from the Mongolian plateau suggest that this recent central Asian drought exceeds the 900-year return interval, but is not unprecedented in the last 2060 years (Hessl et al., 2018). There is *low confidence* due to *limited evidence* that recent droughts in central Asia can be attributed to anthropogenic forcing.

The Mediterranean region has experienced notable changes in drought and aridity. A number of studies have identified a decline in precipitation since 1960 and attributed this to anthropogenic forcing (Hoerling et al., 2012; Gudmundsson and Seneviratne, 2016; Knutson and Zeng et al., 2018; Seager et al., 2019b). Kelley et al. (2015) showed that climate change caused a three-fold increase in the likelihood of the 2007–2010 meteorological drought in the eastern Mediterranean. However, historical trends in precipitation across the Mediterranean are spatially variable and contain substantial decadal variability, such that an anthropogenic influence may not be detectable in all areas (Zittis, 2018; Vicente-Serrano et al., 2020a). Records of soil moisture provide a clearer signal, indicating that higher temperatures and increased atmospheric demand have played a strong role in driving Mediterranean aridity (Vicente-Serrano et al., 2014). Hydrological modeling suggests that the recent decline in soil moisture in the Mediterranean is unprecedented in the last 250 years (Hanel et al., 2018). Paleoclimate evidence extends this view, additionally indicating that dryness in the Mediterranean is approaching an extreme condition compared to the last millennium (Markonis et al., 2018) and that the 15 year drought in the Levant (1998–2012) has an 89% likelihood of being the driest of the last 900 years (Cook et al., 2016a). Marvel et al. (2019) found that the Mediterranean region contributes strongly to the anthropogenic warming component of the global trend in aridity. There is *high confidence* that anthropogenic forcings are causing increased aridity and drought severity in the Mediterranean region.

Both central and northeastern Africa have experienced a decline in rainfall since about 1980 (Lyon and Dewitt, 2012; Lyon, 2014; Hua et al., 2016; Nicholson, 2017) (*high confidence*). In central Africa, the decline has been attributed to atmospheric responses to Indo-Pacific sea-surface temperature variability (Hua et al., 2018). In northeastern Africa, droughts have become longer and more intense in recent decades, continuing across rainy seasons (Hoell et al., 2017b; Nicholson, 2017), and this trend appears to be unusual in the context of the last 1500 years (Tierney et al., 2015). Knutson and Zeng (2018) attribute decreased annual precipitation over the Sudan to anthropogenic forcing, but other studies argue that the recent trend cannot yet be distinguished from natural variability, at least over parts of this region (Hoell et al., 2017b; Philip et al., 2018). There remains *low confidence* due to *limited evidence* that drying the northeastern Africa is attributable to human influence. In the West Cape region of South Africa, human influences increased the likelihood of the severe 2015–2017 drought by a factor of 3–6, depending on the analysis (Otto et al., 2018; Pascale et al., 2020). Anthropogenic forcing also contributed to the 2018 drought, mainly by increasing evapotranspiration (Nangombe et al., 2020). While some analysis of instrumental precipitation data in this region detect a slight long-term drying trend consistent with the simulated anthropogenic response (Seager et al., 2019b), there is strong multidecadal variability in the data (Wolski et al., 2020). However, an study of streamflow in southern Africa detected a significant decline (Gudmundsson et al., 2019) (see also Section 10.6.2). There is *medium confidence* in the long-term drying trend in this region and its attribution to

ACCEPTED VERSION SUBJECT TO FINAL EDITING

anthropogenic forcing, and *medium confidence* that anthropogenic warming has contributed to recent severe drought events.

Several subtropical, semi-arid regions in the Southern Hemisphere have experienced long-term drying trends in the late 20th century. Southwestern South America (central Chile) experienced a multi-decadal decline in precipitation and streamflow culminating in a post-2010 megadrought that has been partly attributed to anthropogenic greenhouse gas emissions and ozone depletion (Boisier et al., 2016, 2018; Saurral et al., 2017; Knutson and Zeng et al., 2018; Seager et al., 2019b; Garreaud et al., 2020). There is *medium confidence* that drying in central Chile can be attributed to human influence. The tree-ring paleoclimate record demonstrates that the mid-century increase in exteme drought events in southern South America is unusual in the context of the last 600 years, suggesting an emerging influence of anthropogenic forcing (Morales et al., 2020).

There has been a 20% decrease in winter (May–July) rainfall in southwestern Australia since 1970, with the decline increasing to around 28% since 2000 (Delworth and Zeng, 2014; Bureau of Meteorology and CSIRO, 2020). There has also been a significant increase in the average intensity of seasonal droughts in the region since 1911in response to both lower precipitation and increased atmospheric evaporative demand (Gallant et al., 2013). Several studies attribute the precipitation declines in southwestern Australia to anthropogenic changes in GHG and ozone (Delworth and Zeng, 2014; Knutson and Zeng et al., 2018; Seager et al., 2019b). There is *high confidence* that the observed drying in southwestern Australia can be attributed to anthropogenic forcing.

In southeastern Australia, the average length of droughts have increased significantly, lasting between 10 and 69% longer than droughts during the first half of the 20th Century (Gallant et al., 2013). Paleoclimate reconstructions indicate a 97.1% probability that the decadal rainfall anomaly recorded during the 1997–2009 Millennium Drought in southeastern Australia was the worst experienced since 1783 (Gergis et al., 2012), and that the spatial extent and duration of cool season (April–September) rainfall anomalies were either very much below average or unprecedented over at least the last 400 years (Freund et al., 2017). Other paleoclimate studies suggest that the Millennium Drought in eastern Australia was not unusual in the context of natural variability reconstructed over the past millennium (Palmer et al., 2015; Cook et al., 2016c; Kiem et al., 2020). While there is currently *low confidence* that recent droughts in eastern Australia can be clearly attributed to human influences (Cai et al., 2014; Delworth and Zeng, 2014; Rauniyar and Power, 2020), there is emerging evidence that declines in April–October rainfall in southeastern Australia since the 1990s would not have been as large without the influence of increasing levels of atmospheric greenhouse gases (Rauniyar and Power, 2020).

In summary, it is *very likely* that anthropogenic factors have influenced global trends in aridity, mainly through competing changes in evapotranspiration and/or atmospheric evaporative demand due to anthropogenic emissions of GHG and aerosols. There is *high confidence* that the frequency and the severity of droughts has increased over the last decades in the Mediterranean, western North America, and southwestern Australia and that this can be attributed to anthropogenic warming. There is *medium confidence* that recent drying and severe droughts in southern Africa and southwestern South America can be attributed to human influence. In some regions of western North America and the Mediterranean, paleoclimate evidence suggests that recent warming has resulted in droughts that are of similar or greater intensity than those reconstructed over the last millennium (*medium confidence*).

[START FIGURE 8.9 HERE]

Figure 8.9: Spatial expressions (a-c; e-g) of the leading multivariate fingerprints of temperature (˚C), precipitation (mm/day), and aridity (CMI; the Climate Moisture Index) in CMIP5 historical simulations and the corresponding temporal evolution in both CMIP5 and reanalysis products (d, h). The first leading fingerprint is associated with greenhouse gas forcing (a-d) and the second leading fingerprint is associated with aerosol forcing (e-h). CMI is a dimensionless aridity indicator that combines precipitation and atmospheric evaporative demand. Figure after (Bonfils et al., 2020). Further details on data sources and processing are available in the chapter data table (Table 8.SM.1).

ACCEPTED VERSION SUBJECT TO FINAL EDITING

[END FIGURE 8.9 HERE]

8.3.1.7 Freshwater reservoirs

8.3.1.7.1 Glaciers

AR5 and SROCC found, with *very high confidence,* a general decline in glaciers due to climate change in recent decades. There is *very high confidence* that during the decade 2010 to 2019 glaciers lost more mass than in any other decade since the beginning of the observational record (Chapter 2 section 2.3.2.3, Chapter 9 section 9.5.1. Human influence is *very likely* the main driver of the global, near-universal retreat of glaciers since the 1990s (Chapter 3, section 3.4.3.1). In Table 9.5, the contribution of glaciers to sea level rise for different periods is presented; in 1971-2018 glacier mass loss contributed 20.9 [10.0 to 31.7] mm or 22.1% of the sea level rise during that period. The highest mass loss rates are observed in the southern Andes, New Zealand, Alaska, Central Europe and Iceland while the largest mass loss are observed in Alaska, the periphery of Greenland and Arctic Canada (see section 9.5.1 and Figure 9.20). Predominantly, runoff from small glaciers such as in Canada has decreased because of glacier mass loss, while runoff from larger glaciers such as Alaska has typically increased (Bolch et al., 2010; Thomson et al., 2011; Tennant et al., 2012; WGMS, 2017; Huss and Hock, 2018). Asia contains the largest concentration of glaciers outside the polar regions where the total glacier mass change is −16.3 ± 3.5 Gt/yr over 2000-2016 with considerable intra-regional variability (Brun et al., 2017). Mass losses of glaciers in Asia between 2000 and 2018 are -19.0 +/-2.5 Gt/yr (Shean et al., 2020). The most negative changes were found in Nyainqentanglha with −4.0 ± 1.5 Gt/yr, while glaciers in Kunlun, northern Tibetan Plateau, slightly gained mass at 1.4 ± 0.8 Gt/yr.

There is some evidence that an increase of precipitation over high mountains can offset glacier ablation (melt) (Farinotti et al., 2020). However, this process has only been described from the Karakoram region in the northwestern Himalaya, where it is thought to be partly responsible to the advances of glacier changes in the last two decades, referred to as the 'Karakoram Anomaly' (Farinotti et al., 2020). In the Himalaya, Maurer et al. (2019) observed faster ice loss during 2000–2016 (–7.5 ± 2.3 Gt/yr) compared to 1975–2000 (–3.9 ± 2.2 Gt/yr). In the Southern Hemisphere, the rate of glacier mass lost in South America is estimated at 19.4 ± 0.6 Gt/yr based on surface elevation changes over 2000-2011, which include the North and South Patagonian Icefields of South America (Braun et al., 2019), and at −22.9 ± 5.9 Gt yr^{-1} over 2000-2018 (Dussaillant et al. 2019).

In summary, human-induced global warming has been the primary driver of a global glacier recession since the early 20th century (*high confidence*). Most glaciers have lost mass more rapidly since the 1960s and in an unprecedented way over the last decade, thereby contributing to increased glacier runoff, especially from larger glaciers until a maximum is reached, which tends to occur later in basins with larger glaciers and higher ice-cover fractions (*high confidence*).

8.3.1.7.2 Seasonal snow cover

AR5 assessed that Northern Hemisphere snow cover extent (SCE) has decreased since the late 1960s, especially in spring (*very high confidence*). This is confirmed by recent studies (Kunkel et al., 2016), (see also Chapter 2, Section 2.3.2.2). AR6 assesses that Northern Hemisphere spring snow cover has been decreasing since 1978 (*very high confidence*) and that this trend extends back to 1950 (*high confidence*) (see Section 9.5.3). Human-caused global warming is the dominant driver of this observed decline (Estilow et al., 2015) (see Section 3.4.2). Model simulations suggest that surface temperature responses at hemispheric/regional scales explain between 40% and 85% of the SCE trend variability (Mudryk, 2017). A decreasing trend in snowfall has also been detected in the Northern Hemisphere (Rupp et al., 2013) (Figure 8.1). Snowfall as a proportion of precipitation has decreased significantly in recent years (Berghuijs et al., 2014). However, a late 20th century increase in snowfall in West Antarctica observed in ice cores has been linked to a combination of factors including the anthropogenically forced deepening of the Amundsen Sea Low (Thomas et al., 2015, 2017).

Observations show a rapid recent decrease of spring SCE in Northern Hemisphere, mostly in Eurasia and

ACCEPTED VERSION SUBJECT TO FINAL EDITING

North America, closely linked to temperature change, e.g., March–April SCE is decreasing at 3.4%±1.1% decade^{-1} (1979–2005) (Brown and Robinson, 2010; Hernández-Henríquez et al., 2015). An overall increasing annual trend of the Northern Hemisphere SCE since the late 1980s has been observed, in contrast to decreasing trends over 1960s-1980s that are dominated by the autumn and winter seasons (Barry and Gan, 2020). Such recent positive trends in snow cover extent are however at odds with other surface and satellite datasets and with the negative trends simulated by most CMIP5 and CMIP6 models (Mudryk et al., 2017, 2020). Hernández-Henríquez et al., (2015) also detected positive trends in October-November SCE in NOAA-CDR which are not replicated in other datasets (Section 9.5.3). Wu et al. (2018) found slower snowmelt rates over the Northern Hemisphere in 1980–2017, with higher ablation rates in locations with deep snow water equivalent (SWE), but due to the reduction of SWE in deep snowpacks, moderate/high ablation rates showed decreasing trends. Santolaria-Otín and Zolina, (2020) reported weak but significant decline in SCE in autumn over northern Eurasia and North America during 1979-2005, and similarly for spring, except for northern Siberia which showed higher spring SCE. Kapnick and Hall (2012) detected significant loss of spring mountain snowpack in western United States in 1950-2008. For Canada, extensive decreasing snow depths, SCE and duration were detected since mid-1970s, especially in western Canada during winter and spring (DeBeer et al., 2016). Berghuijs et al. (2014) show that across the continental United States, catchments with more snowfall than rainfall generally have higher mean streamflow, which will probably decrease with smaller fractions of precipitation falling as snow because of climate warming.

In summary, a decline in the springtime Northern Hemisphere snow cover extent, snow depth and duration has been observed since the late 1960s and has been attributed to human influence (*high confidence*). Depending on the region and season, there is *low-to-medium confidence* in the main drivers of snow cover changes, although various regions exhibit a shortening of the snow cover season which is consistent with global warming. A more detailed assessment of observed changes in seasonal snow cover is provided in Section 9.5.3.

8.3.1.7.3 Wetlands and lakes

Wetlands and lakes affect the climate through their impact on carbon and methane budgets (e.g. Saunois et al., 2016, Zhang et al., 2017) (Section 5.2.2) and on surface heat fluxes, with coupled weather and climate effects (e.g., Zhan et al., 2019). Although these features are also affected by human activities and by climate change, AR5 did not specifically report on wetlands and lakes.

Inventories of surface water bodies are not systematically produced at national or regional levels. However, assessments are undertaken at the global scale (Ramsar Convention on Wetlands, 2018). Merging observations from multiple satellite sensors makes it possible to detect surface water even under vegetation and clouds, over about 25 years but with low spatial resolution (Prigent et al., 2016). Most recent multi-satellite products from visible, infrared, and microwave measurements, estimate a surface water area of ~12-14 million km^2 (including permanent and transitory surfaces, e.g., Aires et al., 2018; Davidson et al., 2018), which is much higher than those provided by optical imagery (~3 million km^2). Inventories show a strong decrease in natural surface water of ~0.8% per year in total from 1970 to the present (Ramsar Convention on Wetlands, 2018) but the sites are not evenly distributed. Multi-satellite estimates show a strong inter-annual variability in surface water extent over the period 1992-2015 with no clear long-term trend (Prigent et al., 2020).

Human-made water bodies represent ~10% of the total continental water surfaces (Figure 8.1) (Ramsar Convention on Wetlands, 2018) and consist mainly of reservoirs and rice paddies. High resolution optical imagery over the period 1984-2015 (Donchyts et al., 2016; Pekel et al., 2016) shows that a net increase of ~ 0.1 million km^2 in artifical water surfaces, mainly due to the construction of reservoirs. Surfaces of rice paddies are also increasing, especially in South East Asia (Davidson et al., 2018).

In summary, there is *high confidence* that the extent of human-made surface water has increased over the 20th and early 21st century. In contrast, due to *limited agreement* in the observational records at the global scale, there is only *low confidence* in the observed decline of the natural surface water extent in recent years (see also SRCCL).

ACCEPTED VERSION SUBJECT TO FINAL EDITING

8.3.1.7.4 Groundwater

As the world's most widespread store of freshwater (Taylor et al., 2013b), groundwater is estimated to supply between a quarter and a third of the world's annual freshwater withdrawals to meet agricultural, industrial and domestic demands (Döll et al., 2012; Wada et al., 2014; Hanasaki et al., 2018). Attribution of changes in groundwater storage, observed locally through piezometry (Taylor et al., 2013b) or estimated from GRACE satellite measurements (Rodell et al., 2018) at regional scales (> 100.000 km^2) (Figure 8.10), is often complicated by non-climate influences that include land-use change (Favreau et al., 2009) and human withdrawals (Bierkens and Wada, 2019).

Following a global review of groundwater and climate change (Taylor et al., 2013b) and AR5 WGII, evidence of an association between heavy or extreme precipitation and groundwater recharge has continued to grow, especially in tropical (Asoka et al., 2018; Cuthbert et al., 2019a; Kotchoni et al., 2019) and sub-tropical regions (Meixner et al., 2016). Stable-isotope ratios of O and H at 14 of 15 sites across the tropics trace groundwater recharge to intensive monthly rainfall, commonly exceeding the ~70th intensity percentile (Jasechko and Taylor, 2015). Further, heavy rainfall recharging groundwater resources is often influenced by climate variability such as ENSO and PDO (Taylor et al., 2013c; Kuss and Gurdak, 2014; Asoka et al., 2017; Cuthbert et al., 2019b; Kolusu et al., 2019; Shamsudduha and Taylor, 2020). Additionally, increases in groundwater storage estimated from GRACE for 37 of the world's large-scale aquifer systems from 2002 to 2016 are generally found to result from episodic recharge associated with extreme (>90th percentile) annual precipitation.

The overall underestimation of precipitation intensities in global climate models (Wehner et al., 2010, 2020; Goswami and Goswami, 2017) and of their sensitivity to warming temperatures (Borodina et al., 2017) may lead to underestimates of their recharging effect on groundwater (Mileham et al., 2009; Cuthbert et al., 2019b). The limited ability of global climate models to represent key controls on regional rainfall variability like ENSO (Chen et al., 2020d) (Technical Annex VI, Section 3.7.3) may also underestimate observed recharge from such events that are of particular importance in drylands (Taylor et al., 2013c; Cuthbert et al., 2019b). Numerical representations of the impact of precipitation intensification on groundwater recharge in large-scale models remain constrained by the challenges of including key recharge pathways that consider preferential flowpaths in soils (Beven, 2018) and focused recharge through leakage from surface waters (Döll et al., 2014).

Increasing global freshwater withdrawals, primarily associated with the expansion of irrigated agriculture in drylands, have led to global groundwater depletion that has an estimated range of ~100 and ~300 km^3 yr^{-1} from hydrological models and volumetric-based calculations (Bierkens and Wada, 2019). The magnitude of this change is such that its estimated contribution to global sea-level rise is in the order of 0.3 to 0.9 mm yr^{-1} (Wada et al., 2010; Konikow, 2011; Döll et al., 2014; Pokhrel et al., 2015; de Graaf et al., 2017; Hanasaki et al., 2018). Groundwater depletion has been observed regionally in the United States High Plains, California's Central Valley (Scanlon et al., 2012), northwest India (Rodell et al., 2009; Asoka et al., 2017), Upper Ganges in India (MacDonald et al., 2016), North China Plain (Feng et al., 2013), north-central Middle East region of Tigris-Euphrates-Western Iran (Voss et al., 2013), Central Asia (Hu et al., 2019), and North Africa (Bouchaou et al., 2013). The regional contribution of agricultural irrigation to groundwater depletion was previously highlighted by SRCCL but no formal assessment of observed changes in global or regional groundwater featured in AR5.

Quantification of changes in groundwater storage from GRACE is currently constrained by uncertainty in the estimation of changes in other terrestrial water stores using uncalibrated, global-scale Land Surface Models (Döll et al., 2014; Scanlon et al., 2018) and the limited duration of the period of GRACE observations (2002 to 2016). Centennial-scale piezometry in northwest India reveals that recent groundwater depletion traced by GRACE (Rodell et al., 2009; Chen et al., 2014), follows more than a century of groundwater accumulation through canal leakage (MacDonald et al., 2016). Further, groundwater depletion is often localised occurring below the footprint (200.000 km^2) of GRACE, as has been well demonstrated by detailed modelling studies in the California Central Valley (Scanlon et al., 2012) and North China Plain (Cao et al., 2016).

ACCEPTED VERSION SUBJECT TO FINAL EDITING

Climate variability and drought affect groundwater depletion mainly due to amplified groundwater withdrawals. For instance, the depletion rate in Central Valley aquifer in the USA from 2006 to 2010 is estimated to range from 6 to 8 km^3 yr^{-1} using GRACE data (Scanlon et al., 2012). In India, Asoka et al. (2017) show contrasting trends in groundwater storage in the north (declining at 2 cm yr^{-1}) and south (increasing at 1-2 cm yr^{-1}) that is explained by variations in human withdrawals and precipitation linked to Indian Ocean sea surface temperature variability.

Changes in meltwater regimes from glaciers and seasonal snow packs tend to reduce the seasonal duration and magnitude of recharge (Tague and Grant, 2009). Aquifers in mountain valleys show shifts in the timing and magnitude of: (1) peak groundwater levels due to an earlier spring melt; and (2) low groundwater levels associated with lower baseflow periods (Allen et al., 2010; Dierauer et al., 2018; Hayashi, 2020). The effects of receding alpine glaciers on groundwater systems are not well understood but long-term loss of glacier storage is estimated to reduce summer baseflow (Gremaud et al., 2009). In permafrost regions, coupling between surface-water and groundwater systems may be particularly enhanced by warming (Lamontagne-Hallé et al., 2018; Lemieux et al., 2020). In areas of seasonal or perennial ground frost, increased recharge is expected despite a decrease in absolute snow volume (Okkonen & Kløve, 2011; Walvoord & Kurylyk, 2016).

Coastal aquifers are the interface between the oceanic and terrestrial hydrological systems. Global sea level rise (SLR) causes fresh–saline-water interfaces to move inland. The extent of seawater intrusion into coastal aquifers depends on a variety of factors including coastal topography, recharge, and groundwater abstraction from coastal aquifers (Comte et al., 2016). Modelling results suggest that the impact of SLR on seawater intrusion is negligible compared to that of groundwater abstraction (Ferguson & Gleeson, 2012; Yu & Michael, 2019). Coastal aquifers under very low hydraulic gradients, such as the Asian mega-deltas, are theoretically sensitive to SLR but, according to evidence from Akter et al. (2019) in the Ganges-Brahmaputra-Megna Basin, may be more severely and widely affected by changes in upstream river discharge. They argue further that saltwater inundation from storm surges will have the greatest localised effects.

In summary, there is *medium confidence* that increased precipitation intensities, partly due to human influence, have enhanced groundwater recharge, most notably in the tropics. There is *high confidence* that groundwater depletion has occurred since at least the start of the 21st century as a consequence of groundwater withdrawals for irrigation in some of the world's most productive agricultural areas in drylands (e.g. southern High Plains and California Central Valley in the USA, the North China Plain, northwest India).

[START FIGURE 8.10 HERE]

Figure 8.10: Trends in Terrestrial Water Storage (TWS) (in centimetres per year) obtained on the basis of GRACE observations from April 2002 to March 2016. The cause of the trend in each outlined study region is briefly explained and colour-coded by category. The trend map was smoothed with a 150-km-radius Gaussian filter for the purpose of visualization; however, all calculations were performed at the native 3° resolution of the data product. Figure from Rodell et al. (2018). Further details on data sources and processing are available in the chapter data table (Table 8.SM.1).

[END OF FIGURE 8.10 HERE]

8.3.2 Observed variations in large-scale phenomena and regional variability

Observed changes in large-scale circulation indicators (Cross-Chapter Box 2.2) are assessed in Chapters 2 and 3 (see Sections 2.3.1.4 and 3.3.3). In this chaper we focus on the influence of regional scale teleconnection variabililty on the water cycle and the attribution of these circulation changes. While

ACCEPTED VERSION SUBJECT TO FINAL EDITING

observed changes in modes of variability are assessed in Chapters 2 and 4 (see Sections 2.4 and 4.3.3), here focus on hydrological teleconnections of relevance to the water cycle.

8.3.2.1 Intertropical Convergence Zone (ITCZ) and tropical rain belts

AR5 concluded it is *likely* that the tropical belt, as delimited by the Hadley circulation, has widened since the 1970s. Observations in the satellite era indicate precipitation increases in the core of the Pacific ITCZ and decreases on the ITCZ margins (Gu et al., 2016; Su et al., 2017). As the satellite period has lengthened, observations have increasingly been used to assess trends in the ITCZ and tropical rain belt. Since AR5, significant narrowing and strengthening of the Pacific ITCZ after 1979 have been identified in atmospheric reanalyses (Wodzicki and Rapp, 2016), but no change in the ITCZ location (Byrne et al., 2018). Atmospheric model simulations suggest that with a narrower ITCZ, the subtropical jet becomes baroclinically unstable at a lower latitude and allows midlatitude eddies to propagate farther equatorward (Watt-Meyer and Frierson, 2019). Observational analyses also show that the ITCZ narrowing (Zhou et al., 2020) is associated with increased precipitation in the ITCZ core region that is strongly coupled to increasing Outgoing Longwave Radtion (OLR) in the expanding dry zones, particularly over land regions in the subtropics and midlatitudes (Lau and Tao, 2020). In addition, an eastward movement of the South Pacific Convergence Zone (SPCZ) between 1977 and 1999 has been reported, with associated significant precipitation trends in the South Pacific regions (Salinger et al., 2014).

ITCZ trends seen in satellites, precipitation measurements and reanalysis data are further supported by ocean surface-salinity observations. Long-term salinity observations show a freshening in the cores of the Atlantic and Pacific ITCZs and increased salinity on the ITCZ margins (Durack et al., 2010, 2012; Terray et al., 2012; Skliris et al., 2014). By investigating simultaneous changes in precipitation, temperature and continental aridity in CMIP5 historical simulations, Bonfils et al. (2020a) found a secondary signal (Figure 8.9, right column) characterized by a robust interhemispheric temperature contrast (Section 3.3.1.1), a latitudinal shift in the ITCZ (in accordance with the theory of cross-equatorial energy transport; Section 8.2.2.2), and changes in aridity in the Sahel (section 8.3.1.6). These forced changes are statistically detectable in reanalyses datasets over the 1950-2014 period at the 95% confidence level.

Reconstructions in the Sahel (Carré et al., 2019) and Belize (Ridley et al., 2015) support the southward displacement of the tropical rain belt since 1850 and the narrowing trend of the tropical rainbelt detected in observations (Rotstayn et al., 2002; Hwang et al., 2013). Decreasing precipitation trends in the Northern Hemisphere during the 1950s-1980s have been attributed to anthropogenic aerosol emissions from North America and Europe, which peaked during the late1970s and declined thereafter following improved air quality regulations, causing dimming (brightening) through reduced (increased) surface solar radiation (Box 8.1 Figure 1), in agreement with model simulations (Chiang et al., 2013; Hwang et al., 2013). This is consistent with energetic constraints where tropical precipitation shifts are anti-correlated with cross-equatorial energy transport (Section 6.3.3, Box 8.1). It also provides a physical mechanism for the severe drought in the Sahel that peaked in the mid-1980s (Sections 8.3.2.4.3 and 10.4.2.1) and the southward shift of the Northern Hemisphere tropical edge from the 1950s to the 1980s (Allen et al., 2014; Brönnimann et al., 2015). However, CMIP5 and CMIP6 models still exhibit strong biases in the representation the ITCZ, such as the simulation of a double ITCZ (Oueslati and Bellon, 2015; Adam et al., 2018; Tian and Dong, 2020). The impacts of aerosols and volcanic activity on the position of the ITCZ have been investigated but changes are difficult to characterize from observations (Friedman et al., 2013; Haywood et al., 2013b; Iles et al., 2014; Colose et al., 2016; Chung and Soden, 2017) (see Section 6.3.3.2). Such systematic shifts of the ITCZ can have important regional impacts like changes in precipitation (Figure 8.9).

In summary, there is *medium confidence* that the tropical rain belts over the oceans have been narrowing and strengthening in recent decades, leading to increased precipitation in the ITCZ core region (see also Section 8.2.2.2). Decreasing precipitation trends in the Northern Hemisphere during the 1950s-1980s have been attributed to anthropogenic aerosol emissions from North America and Europe (*high confidence)*.

ACCEPTED VERSION SUBJECT TO FINAL EDITING

8.3.2.2 Hadley circulation and subtropical belt

AR5 reported *low confidence* in trends in the strength of the Hadley Circulation (HC) due to uncertainties in reanalyses but *high confidence* on the widening of the tropical belt since 1979. In AR6, Chapter 2 (see section 2.3.1.4.1) states that the HC has *very likely* widened and strengthened since at least the 1980s, mostly in the Northern Hemisphere (*medium confidence*).

The poleward shift of the HC is closely related to migration of the location of tropical cyclone trajectories in both hemispheres (Studholme and Gulev, 2018; Sharmila and Walsh, 2018), with a *very likely* poleward shift over the western North Pacific Oceans since the 1940s (Section 11.7.1.2). Moreover, the Western North Pacific Subtropical High has extended westward since the 1970s, resulting in a monsoon rain band shift over China, with excessive rainfall along the middle and lower reaches of the Yangtze River valley along ~ 30°N over eastern China. At the same time, the effect of anthropogenic aerosols dominated the response to GHG increases over East Asia, resulting in a weakening of the East Asian summer monsoon and causing a drying trend in northeastern China (Hu, 2003; Yu and Zhou, 2007; Wang et al., 2013b; Li et al., 2016c; Lau and Kim, 2017) and northern parts of South Asia (Preethi et al., 2017) (see also Section 8.3.2.4.2). During 1977-2007, the precipitation variability over the eastern United States increased due to changes in the intensity and position of the western ridge of the North Atlantic Subtropical High (Li et al., 2011; Diem, 2013).

In the Southern Hemisphere, the HC expansion has been associated with both the intensification and poleward shift of the subtropical high pressure belt (Nguyen et al., 2015), with consequences for precipitation amount over Africa, Australia, South America, and subtropical Pacific islands (Cai et al., 2012; Grose et al., 2015; Nguyen et al., 2015; Sharmila and Walsh, 2018; McGree et al., 2019). The subtropical ridge in Australia has intensified significantly since 1970, with marked declines observed in April to October rainfall across southeastern and southwestern Australia (Timbal and Drosdowsky, 2013).

The local tropical edges of the meridional overturning cells (as diagnosed from the horizontally divergent wind) are more closely associated with hydroclimate variations than the subtropical ridge (Staten et al., 2019). Poleward expansion of the tropical belt strongly contributes to precipitation decline in the poleward edge of the subtropics (Cai et al., 2012; Scheff and Frierson, 2012; Timbal and Drosdowsky, 2013; He and Soden, 2017; Nguyen et al., 2018a; Tang et al., 2018), although recent modelling evidence suggests that subtropical precipitation declines are a response to direct CO_2 radiative forcing mainly over ocean, irrespective of the HC expansion (He and Soden, 2017). Both reanalyses datasets and climate model simulations suggest that the HC expansion is not associated with widespread, zonally symmetric subtropical drying over land (Schmidt and Grise, 2017).

Since AR5, an improved understanding of the key drivers of the recent HC expansion has been achieved, identifying the role of both internal variability and anthropogenic climate change. Part of the recent expansion (1979-2005) of the HC has been driven by a swing from warm to cold phase of the Pacific Decadal Variability (PDV) (Meehl et al., 2016; Grise et al., 2019). The presence of large multidecadal variability in 20th century reanalyses means there is *limited evidence* on the human influence on the recent HC strengthening, yet the southward shift of the southern edge and widening of the Southern Hemisphere HC appeared as robust features in all reanalysis datasets, and their trends have accelerated during 1979-2010 (D'Agostino and Lionello, 2017). As assessed in Section 3.3.3.1, GHG increases and stratospheric ozone depletion have contributed to the expansion of the zonal mean HC in the Southern Hemisphere since around 1980, and the expansion of the Northern Hemisphere HC has not exceeded the range of internal variability (*medium confidence*). Moreover, Antarctic ozone depletion can cause a poleward shift in the Southern Hemisphere midlatitude jet and HC (Sections 3.3.3 and 6.3.3.2). Further assessment of the attribution of recently observed changes in the HC extent and intensity is found in Section 3.3.3.1.

In summary, it is *very likely* that the recent Hadley Circulation (HC) expansion was associated with poleward shifts of tropical cyclone tracks over the western North Pacific Ocean since the 1940s, and of extratropical storm tracks in the Southern Hemisphere since the 1970s. Changes to the HC in the Northern Hemisphere may have contributed to subtropical drying and a poleward expansion of aridity during the boreal summer, but there is *low confidence* due to *limited evidence*. GHG increases and stratospheric ozone depletion have

ACCEPTED VERSION SUBJECT TO FINAL EDITING

contributed to expansion of the zonal mean HC in the Southern Hemisphere since around 1970, while the expansion of the Northern Hemisphere HC has not exceeded the range of internal variability (*medium confidence*).

8.3.2.3 Walker circulation

AR5 concluded that the long-term weakening of the Pacific Walker Circulation (WC) from the late 19th century to the 1990s has been largely offset by a recent strengthening (*high confidence*), though with *low confidence* in trends of the WC strength due to reanalysis uncertainties and large natural variability. The observed trends in the WC since 1980 are consistent with a *very likely* WC strengthening in the Pacific, similar to a La Niña pattern, with *medium confidence* in the magnitude of these changes due to differences between satellite observations and reanalyses.

The causes of the observed strengthening of the Pacific WC during 1980-2014 are not well understood due to competing influences from individual external forcings and since this strengthening is outside the range of variability simulated in coupled models (*medium confidence*), as assessed in Chapter 3 (see Section 3.3.3.1). Recent strengthening in the WC has been linked with internal variability (Chung et al., 2019), although one study argues that it could be a response forced by GHG that models do not capture because of common SST biases in the equatorial Pacific (Seager et al., 2019a). It could be also related to an interbasin thermostat mechanism whereby the human-induced Indian Ocean warming emerged earlier than in the tropical Pacific (Zhang et al., 2018b) and induced a transient strengthening of the zonal sea level pressure gradient and easterly trades in the tropical Pacific (Zhang et al., 2019a).

The weakening of the WC observed during most of the 20th century is associated with reductions in land rainfall over the Maritime Continent during 1950-1999 (Tokinaga et al., 2012; Yoden et al., 2017). In contrast, the recent strengthening of the WC has been associated with an intensification of extreme flooding (Barichivich et al., 2018) and an increased frequency of wet days (Espinoza et al., 2016, 2018a) over the northwestern Amazon, increased precipitation in South America (Yim et al., 2017), reduced precipitation over eastern Africa (Williams and Funk, 2011; Lyon and Dewitt, 2012), and increased rainfall in southern Africa (Maidment et al., 2015). Internal variability has been shown to have a dominant role in the recent strengthening of the WC (Chung et al., 2019).

In summary, there is *high confidence* that changes in the Pacific Walker Circulation (WC) are associated with changes in the water cycle over regions like the Maritime Continent, South America and Africa. It is *very likely* that the WC has strengthened in the Pacific since the 1980s, with *medium confidence* that this strengthening is within the range of internal variability.

8.3.2.4 Monsoons

AR5 reported *low confidence* in the attribution of changes in monsoons to human influences, although a detailed attribution assessment of the observed changes in the regional monsoons was not presented.

Large human populations in the monsoon regions of the world heavily depend on freshwater supply for agriculture, water resources, industry, transport and various socio-economic activities. The effects of GHG forcing combined with water vapour feedback (Allen et al., 2015b; Dong and Sutton, 2015; Evan et al., 2015; Dunning et al., 2018) and cloud feedbacks (Stephens et al., 2015; Potter et al., 2017) are fundamental to monsoon precipitation changes in a warming world. Since AR5 there has been improved understanding of precipitation changes associated with regional monsoons. Sections 2.3.1.4.2 and 3.3.3.2 provide an assessment of observed changes and attribution for the global monsoon. Here we provide an assessment of the observed changes in regional monsoons (see Annex V and Figure 8.11) and underlying causes. In AR6, the definition of regional monsoons slightly differs from AR5 and the rationale for it is provided in Annex V (see also Annex VII: Glossary). Specific examples of regional monsoons are discussed further in section 10.4.2, from the perspective of climate change attribution and in section 10.6.3, from the viewpoint of

ACCEPTED VERSION SUBJECT TO FINAL EDITING

constructing regional climate messages.

[START FIGURE 8.11 HERE]

Figure 8.11: Regional monsoon precipitation changes from observations and model attribution. Precipitation changes during 1951-2014 are shown as least-square linear trends in box-whisker plots (first and fourth rows) over the six regional monsoons, i.e., North American monsoon (NAmerM, Jul-Aug-Sep), West African monsoon (WAfriM, Jun-Jul-Aug-Sep), South and Southeast Asian monsoon (SAsiaM, Jun-Jul-Aug-Sep), East Asian monsoon (EAsiaM, Jun-Jul-Aug), South American monsoon (SAmerM, Dec-Jan-Feb), Australian and Maritime Continent monsoon (AusMCM, Dec-Jan-Feb), and over the two land domains (i.e. equatorial America (EqAmer, Jun-Jul-Aug) and South Africa (SAfri, Dec-Jan-Feb), as identified in the map shown in the middle and as described in Annex V. Precipitation changes are computed from observations and from DAMIP CMIP6 experiments over the historical period with all-forcing (ALL), GHG-only forcing (GHG), Aerosol-only (AER) and Natural (NAT) forcings prescribed. Observations are based on the CRU (light green) and GPCC (light blue) datasets and the APHRODITE (light orange) dataset for SAsiaM and EAsiaM. CMIP6 simulations are taken from nine CMIP6 models contributing to DAMIP, with at least 3 members. Ensembles are weight-averaged for the respective model ensemble size. Observed trends are shown as coloured cirles and the simulated trends from the CMIP6 multi-model experiments are shown as box-whisker plots. Precipitation anomaly time-series are shown in the second and third row. The thick black line is the multi-model ensemble-mean precipitation anomaly time-series from the ALL experiment and the grey shading shows the spread across the multi-model ensembles. A 11-year running mean has been applied on the precipitation anomaly time-series prior to calculating the multi-model ensemble mean. Further details on data sources and processing are available in the chapter data table (Table 8.SM.1).

[END FIGURE 8.11 HERE]

8.3.2.4.1 South and Southeast Asian Monsoon

AR5 reported a decreasing trend of global land monsoon precipitation over the last half-century, with primary contributions from the weakened summer monsoon systems in the Northern Hemisphere. Since AR5, several studies have documented long-term variations and changes in the South and Southeast Asian Summer Monsoon (SAsiaM) rainfall. The SAsiaM strengthened during past periods of enhanced summer insolation in the Northern Hemisphere, such as the early-to-mid Holocene warm period around 9000 to 6000 years BP (Masson-Delmotte et al., 2013; Mohtadi et al., 2016; Braconnot et al., 2019) and weakened during cold periods (*high confidence*), such as the Last Glacial Maximum (LGM) and Younger Dryas (Shakun et al., 2007; Cheng et al., 2012; Dutt et al., 2015; Chandana et al., 2018; Hong et al., 2018; Zhang et al., 2018a). These long time-scale changes in monsoon intensity are tightly linked to orbital forcing and changes in high-latitude climate (Braconnot et al., 2008; Battisti et al., 2014; Araya-Melo et al., 2015; Rachmayani et al., 2016; Bosmans et al., 2018; Zhang et al., 2018a). A weakening trend of the SAsiaM during the last 200 years has been documented based on tree ring oxygen isotope chronology from the northern Indian subcontinent (Xu et al., 2018) and Southeast Asia (Xu et al., 2013), oxygen isotopes in speleothems from northern India (Sinha et al., 2015), and tree ring width chronologies from the Indian core monsoon region (Shi et al., 2017). Nevertheless, the detection of century-long decreases in regional monsoon rainfall is obscured by the presence of multidecadal time-scale precipitation variations (Turner and Annamalai, 2012; Knutson and Zeng et al., 2018) which are evident in long-term rain guage records extending back to the early 1800s (Sontakke et al., 2008) and emerge in long-term climate simulations (Braconnot et al., 2019).

A significant decline in summer monsoon precipitation is observed over India since the mid-20th century, which is accompanied by a weakening of the large-scale monsoon circulation (Mishra et al. et al., 2012; Abish et al., 2013; Krishnan et al., 2013, 2016; Saha et al., 2014; Roxy et al., 2015; Guhathakurta et al. et al., 2017; Samanta et al. et al., 2020). This precipitation decline is corroborated by a decreasing trend in the frequency of monsoon depressions that form over Bay of Bengal (Prajeesh et al., 2013; Vishnu et al., 2016), an increasing trend in the frequency and duration of monsoon breaks or 'dry spells' (Singh et al., 2014), significant decreases in soil moisture and increases in drought severity across different parts of India post-

ACCEPTED VERSION SUBJECT TO FINAL EDITING

1950 (Niranjan Kumar et al., 2013; Ramarao et al., 2015; Krishnan et al., 2016; Ramarao et al., 2018; Ganeshi et al., 2020; Mujumdar et al., 2020). While recent studies have reported an apparent recovery of the Indian summer monsoon over a relatively short period since 2003 (Jin and Wang, 2017; Hari et al., 2020), long-term trends for the period 1951-2015 indicate an overall decrease in the regional monsoon precipitation (Kulkarni et al., 2020; Ayantika et al et al., 2021). A case study on the Indian summer monsoon is provided in Section 10.6.3.

Evidence from several climate modelling studies indicates that the observed decrease in the regional monsoon precipitation during the second half of the 20th century is dominated by the radiative effects of Northern Hemisphere anthropogenic aerosols, with smaller contributions due to volcanic aerosols from the Mount Pinatubo (1991) and El Chichon (1982) eruptions (Bollasina et al. et al., 2011; Polson et al. et al., 2014a; Sanap et al., 2015; Krishnan et al., 2016; Liu et al., 2016; Lau and Kim, 2017; Undorf et al., 2018; Undorf et al. et al., 2018; Lin et al., 2018; Takahashi et al., 2018; Patil et al., 2019; Singh et al., 2020b) (Box 8.1 Figure 1, Figure 8.11). Land-use changes over South and Southeast Asia and the rapid warming trend of the equatorial Indian Ocean during the recent few decades also appear to have contributed to the observed decrease in monsoon precipitation (Roxy et al., 2015; Krishnan et al., 2016; Singh, 2016). Overall, the magnitude of the precipitation response to anthropogenic forcing exhibits large spread across CMIP5 models pointing to the strong internal variability of the regional monsoon (Saha et al., 2014; Salzmann et al., 2014; Sinha et al., 2015), including variations linked to phase changes of the Pacific interdecadal variability (Section AVI.2.6) (Huang et al., 2020b), uncertainties in representing aerosol-cloud interactions (Takahashi et al., 2018), and the effects of local versus remote aerosol forcing (Bollasina et al. et al., 2014; Polson et al. et al., 2014b; Undorf et al., 2018). CMIP3 and CMIP5 models do not accurately reproduce the observed seasonal cycle of precipitation over the major river basins of South and Southeast Asia, limiting the attribution of observed regional hydroclimatic changes (Hasson, 2014; Hasson et al., 2016; Biasutti, 2019). While warm rain processes and organized convection are known to dominate the heavy orographic monsoon rainfall over the Western Ghats mountains (Shige et al., 2017; Choudhury et al., 2018), in various parts of India (Konwar et al., 2012) and East Asia (Section 11.7.3.1), there are uncertainties in representing the regional physical processes of the monsoon environment, including cloud-aerosol interactions (Sarangi et al., 2017), land-atmosphere (e.g., Barton et al., 2020) and ocean-atmosphere coupling (Annamalai et al., 2017), in state-of-the-art climate models (See also Section 8.5.1).

In summary, there is *high confidence* in observational evidence for a weakening of the SAsiaM in the second half of the 20th century. Results from climate models indicate that anthropogenic aerosol forcing has dominated the recent decrease in summer monsoon precipitation, as opposed to the expected intensification due to GHG forcing (*high confidence*). On paleoclimate timescales, the SAsiaM strengthened in response to enhanced summer warming in the NH during the early-to-mid Holocene, while it weakened during cold intervals (*high confidence*). These changes are tightly linked to orbital forcing and changes in high-latitude climate (*medium confidence*).

8.3.2.4.2 East Asian Monsoon

AR5 reported *low confidence* in the observed weakening of the East Asian Monsoon (EAsiaM) since the mid-20th century. Since AR5, there has been improved understanding of changes in the EAsiaM, based on paleoclimatic evidence, instrumental observations and climate modeling simulations. Rainfall reconstructions from the Loess Plateau in China indicate that the northern extent of the monsoon rain belts migrated at least 300 km to the northwest from the LGM to the mid-Holocene (Yang et al., 2015). Similarly, Pliocene reconstructions indicate stronger intensity of the EAsiaM with a more northward penetration of the monsoon rain belt (Yang et al., 2018b). EAsiaM variability has been related to AMOC dynamics, especially during the last glacial period, but whether the relationship is negative or positive remains uncertain (Sun et al., 2012; Cheung et al., 2018; Kang et al., 2018).

Long-term precipitation observations from China indicate a trend of drying in the north and wetting in the central-eastern China along the Yangtze river valley since the 1950s (Qian and Zhou, 2014; Zhou et al., 2017a; Day et al., 2018), with a weakened EAsiaM low-level circulation that penetrates less far into northern China, increased surface pressure over northeast China and southward shift of the jet stream (Song et al.,

ACCEPTED VERSION SUBJECT TO FINAL EDITING

2014). The southward shift and enhancement of the jet stream explains the increase of rainfall especially from the Meiyu front (Day et al., 2018) at the expense of drying over northeast China.

Anthropogenic factors such as GHGs and aerosols had an influence on the EAsiaM changes (Wang et al., 2013b; Song et al., 2014; Xie et al., 2016; Chen and Sun, 2017; Ma et al., 2017; Zhang et al., 2017a; Day et al., 2018; Tian et al., 2018) (Figure 8.11). Increased precipitation in the southern region has been linked to increased moisture flux convergence driven by GHG forcing whilst changes in anthropogenic aerosols have weakened the EAsiaM and reduced precipitation in the northern regions (Tian et al., 2018). Aerosol-induced cooling, associated atmospheric circulation changes and SST feedbacks weaken the EAsiaM and favour the observed dry-north and wet-south pattern of rainfall anomalies (Wang et al., 2013b; Song et al., 2014; Zhang et al., 2017a; Chen et al., 2018a, 2018b; Undorf et al., 2018).

Internal variability and volcanic eruptions also contributed to the weakened EAsiaM (Hsu et al., 2014; Qian and Zhou, 2014; Zhou et al., 2017b; Knutson and Zeng et al., 2018). Since the late 1970s, the EAsiaM weakening has been also linked to SST changes in the Pacific Ocean with warm conditions in the central-eastern tropical part and cold ones in the north, similar to a positive phase of the Pacific Decadal Variability (PDV, Section AVI.2.6) (Li et al., 2016c; Zhou et al., 2017b). In the late 1990s the transition from a positive to a negative PDV has been associated to the recent recovery observed in the EAsiaM strength (Zhou et al., 2017b). Atlantic Multidecadal Variability (AMV) also has an influence on the EAsiaM via the global teleconnection pattern propagating from the North Atlantic through the westerly jet (Zuo et al., 2013; Wu et al., 2016a, 2016b). This North Atlantic influence has contributed to the increase of precipitation over the Huaihe-Huanghe valley since the late 1990s (Li et al., 2017c). When PDV and AMV are in opposite phase, the former has a larger influence in driving the southern flooding and northern drought pattern over the region (Yang et al., 2017b).

In summary, there is strong evidence of a stronger EAsiaM and northward migration of the rainbelt during warmer climates based on paleoclimate reconstructions. There is *high confidence* that anthropogenic forcing has been influencing historical EAsiaM changes with drying in the north and wetting in the south observed since the 1950s, but there is *low confidence* in the magnitude of the anthropogenic influence. The transition towards a positive Pacific Decadal Variability phase has been one of the main drivers of the EAsiaM weakening since the 1970s *(high confidence)*.

8.3.2.4.3 West African Monsoon

Since AR5, there has been improved understanding of the West African Monsoon (WAfriM) response to natural and anthropogenic forcing. On paleoclimate timescales, enhanced summer insolation in the Northern Hemisphere intensified the WAfriM precipitation during the early-to-mid Holocene (*high confidence*), as seen in rainfall proxy records and climate model simulations (Masson-Delmotte et al., 2013; Mohtadi et al., 2016; Braconnot et al., 2019). Despite improvements in model simulations of the present-day monsoons, CMIP5 and CMIP6 models underestimate mid-Holocene changes in the amount and spatial extent of the WAfriM precipitation (Brierley et al., 2020) (Section 3.3.3.2).

During the recent past, long-term rain gauge observations display substantial variability in the WAfriM precipitation over the 20th century (Section 10.4.2.1). The WAfriM experienced the wettest decade of the 20th century during the 1950s and early 1960s (*high confidence*), over much of the western and central Sahel region, followed abruptly by the driest years during 1970-1989 (Ali and Lebel et al., 2009; Nicholson, 2013; Descroix et al., 2015). The percentage deficit in the annual rainfall during 1970-1989, relative to the long-term mean, ranged from 60% in the north of Sahel to 25-30% in the south (Le Barbé et al., 2002; Lebel et al., 2003). The long decline in annual rainfall is related to a decrease of rain occurrence over the Sahel (Le Barbé and Lebel, 1997; Frappart et al., 2009; Bodian et al., 2016) and the Soudano-Guinean sub-region of West-Africa (Le Barbé et al., 2002), even though the interannual variability pattern is more complex (Balme et al., 2006). Decrease of rainfall occurrences resulted from decreases in large convective events in the core of the rainy season (Bell et al., 2006), that modulate interannual variability of the WAfriM (Panthou et al., 2018).

Wetter conditions of the WAfriM prevailed later from the mid-to-late 1990s, although the positive trend in

ACCEPTED VERSION SUBJECT TO FINAL EDITING

precipitation started since late 1980s (see also Section 10.4.2.1) over the Sahel (*high confidence*) and in the Guinean coastal region (*medium confidence*), indicating the geographical variation in the wetting recovery (Descroix et al., 2015; Sanogo et al., 2015; Bodian et al., 2016; Nicholson et al., 2018). While the interannual and decadal variability of annual rainfall is not homogeneous over the entire Sahel, the rainfall recovery was stronger in the east than in the west of the region (Nicholson et al., 2018) (Section 10.4.2.1). A shift in the seasonality of the Sahelian rainfall, including delayed cessation has also been reported (Nicholson, 2013; Dunning et al., 2018) (see also Section 10.4.2.1).

In the Sahel region, the emergence of this new rainfall regime is reflected in increased number of heavy and extreme events, compared to the 1970s-1980s, still not exceeding the values registered in the 1950s-1960s (Descroix et al., 2013, 2015, Panthou et al., 2014, 2018; Sanogo et al., 2015), and in higher interannual variability (Zhang et al., 2017b; Akinsanola and Zhou, 2020) associated with SST variations in the tropical Atlantic, Pacific and Mediterranean Sea (Rodríguez-Fonseca et al., 2015; Diakhate et al, 2019). Increased frequency of extreme rainfall events impacts high flow occurrences of the large Sahelian rivers as well as small to meso-scale catchments (Wilcox et al., 2018a). Overall, extreme intense precipitation events are more frequent in the Sahel since the beginning of the 21st century (Giannini et al., 2013; Panthou et al., 2014, 2018; Sanogo et al., 2015; Taylor et al., 2017). Intensification of mesoscale convective systems associated with extreme rainfall in the WAfriM is favoured by enhancement of meridional temperature gradient by the warming of the Sahara desert (Taylor et al., 2017) at a pace that is 2–4 times greater than that of the tropical-mean temperature (Cook et al., 2015c; Vizy et al., 2017). Periods of monsoon-breaks and the persistence of low rainfall events are still prominent, particularly after the onset, thus exposing West Africa simultaneously to the potential impacts of dry spells (Zhang et al., 2017b) and also extreme localized rains and floods (Engel et al., 2017; Lafore et al., 2017). Occurrence of extreme events is compounded by land use and land cover changes leading to increased runoff (Bamba et al., 2015; Descroix et al., 2018).

The Sahel drought from the 1970s until the early 1990s was related to anthropogenic emissions of sulphate aerosols in the Atlantic, which led to an inter-hemispheric pattern of SST anomalies and associated regional precipitation changes (Box 8.1; Section 6.3.3.2). Also the combined effects of anthropogenic aerosols and GHG forcing appear to have contributed to the late twentieth century drying of the Sahel through their effect on SST, by cooling the North Atlantic and warming the tropical oceans (Giannini and Kaplan, 2019; Hirasawa et al., 2020). Subsequent aerosol removal led to SST warming of the North Atlantic, shifting the ITCZ further northward and strengthening the WAfriM (Giannini and Kaplan, 2019). The recent recovery has been ascribed to prevailing positive SST anomalies in the tropical North Atlantic potentially associated with a positive phase of the Atlantic multidecadal oscillation (Diatta and Fink, 2014; Rodríguez-Fonseca et al., 2015). The Sahel rainfall recovery has also been attributed to higher levels of GHG in the atmosphere and increases in atmospheric temperature (Dong and Sutton, 2015).

In summary, most regions of West Africa experienced a wet period in the mid-20th century followed by a very dry period in the 1970s and 1980s that is attributed to aerosol cooling of the Northern Hemisphere (*high confidence*). Recent estimates provide evidence of a WAfriM recovery from the mid-to-late 1990s, with more intense extreme events partly due to the combined effects of increasing GHG and decreasing anthropogenic aerosols over Europe and North America (*high confidence*). On paleoclimate timescales, there is *high confidence* that the WAfriM strengthened during the early-to-mid Holocene in response to orbitally-forced enhancement of summer warming in the Northern Hemisphere.

8.3.2.4.4 North American Monsoon

Since AR5, there have been updates on the observed long-term variations and changes in the North American monsoon (NAmerM). During the Last Glacial Maximum (21,000-19,000 years ago), the NAmerM was substantially weaker due to cold, dry mid-latitude air associated with the Laurentide Ice Sheet (Bhattacharya et al., 2017b, 2018). The NAmerM strengthened until the mid-Holocene period, in response to ice sheet retreat and rising summer insolation, but probably did not exceed the strength of the modern system (*low confidence*), as indicated by model simulations (Metcalfe et al., 2015) and paleoclimatic reconstructions (Bhattacharya et al., 2018). Paleoclimatic evidence from proxy datasets and mid-Pliocene (PlioMIP1) simulations suggest a wetter southwestern United States during that warmer period (Haywood et al., 2013a; Pound et al., 2014; Ibarra et al., 2018) but it is not clear whether this is due to increases of precipitation

ACCEPTED VERSION SUBJECT TO FINAL EDITING

associated with the monsoon or occurring during the winter season.

During 1948-2010, trends of boreal summer precipitation amount were significantly positive over New Mexico and the core NAmerM region, but significantly negative over southwestern Mexico (Hoell et al., 2016). In addition, diverse datasets like CRU, CHIRPS and GPCP show significant decreases of precipitation in parts of the southwest United States and northwestern Mexico, including the NAmerM region (Ashfaq et al., 2020; Cavazos et al., 2020). Other studies suggest a strengthening of the NAmerM upper level anticyclone since the mid-1970s, with a more frequent northward location (Diem et al., 2013). Between 1910-2010, the number of precipitation events increased across the northern Chihuahuan desert, within the NAmerM domain, despite a decrease in their magnitude, and the length of extreme dry and wet periods also increased (Petrie et al., 2014).

An increase in intense rainfall and severe weather events has been observed in several locations, especially in southwestern Arizona since 1991, resulting from increases in atmospheric moisture content and instability; a change that has been confirmed by convective-permitting model simulations (Luong et al., 2017; Pascale et al., 2019). A dense network of 59 rain gauges located in southeastern Arizona suggests an intensification of monsoon sub-daily rainfall since the mid-1970s (Demaria et al., 2019), as expected by a stronger global warming signature for sub-daily rather than daily or monthly precipitation accumulation (Section 11.4). Section 10.4.2.3 provides further details on changes in precipitation in southwestern North America. Evidence from multiple reanalyses suggests that increases in NAmerM rainfall have contributed to the increasing trend of global monsoon precipitation (Lin et al., 2014) (see also 2.3.1.4.2). In addition, more frequent occurrence of earlier retreats of the NAmerM since 1979 is documented (Arias et al., 2012, 2015), in association with the positive phase of the Atlantic Multidecadal Variability (AMV) and a westward expansion of the North Atlantic Subtropical High (Li et al., 2011, 2012b).

Analyses from a 50-km resolution GCM indicate that the NAmerM response to CO_2 is very sensitive to SST biases, showing reductions in summer NAmerM precipitation with increased CO_2 when the SST biases are small (Pascale et al., 2017) in contrast to CMIP5 models (Cook and Seager, 2013; Maloney et al., 2014; Torres-Alavez et al., 2014; Hoell et al., 2016). The NAmerM has been shown to be also sensitive to SO_2 emissions (García-Martínez et al., 2020).

In summary, both paleoclimate evidence and observations indicate an intensification of the NAmerM in a warmer climate (*medium confidence*). The intensification recorded since about the 1970s has been partly driven by GHG emissions (*medium confidence*).

8.3.2.4.5 South American Monsoon

Since AR5, there has been improved understanding of changes in the South American monsoon (SAmerM) as evidenced from paleoclimate records, instrumental observations and climate model simulations. However, GCMs still exhibit difficulties in reproducing SAmerM precipitation amount (Rojas et al., 2016; D'Agostino et al., 2020a). Paleoclimate evidence suggests a relatively stronger SAmerM during the 1400-1600 period (Bird et al., 2011b; Vuille et al., 2012; Ledru et al., 2013; Apaéstegui et al., 2014; Novello et al., 2016; Wortham et al., 2017). Last millennium GCM simulations are able to reproduce stronger SAmerM during the 1400-1600 period in comparison with warmer epochs such as the 900-1100 period (Rojas et al., 2016) or the current warming period (Díaz and Vera, 2018). PMIP3/CMIP5 simulations indicate a consistent weaker SAmerM during the mid-Holocene (6000 years ago; see Cross-Chapter Box 2.1) in comparison to current conditions (Bird et al., 2011a; Mollier-Vogel et al., 2013; Prado et al., 2013a; D'Agostino et al., 2020a), thus favouring savannah/grassland-like vegetation (Smith and Mayle, 2018), in agreement with climate reconstructions from different proxies (Prado et al., 2013b). Signals of weak and strong SAmerM during mid-Holocene and LGM, respectively, are evident also in high-resolution long-term (> ~ 22000 years) rainfall reconstructions based on oxygen isotopes in speleothems from Brazil (Novello et al., 2017; Stríkis et al., 2018b; Campos et al., 2019).

Isotope records from caves in the central Peruvian Andes show that the late Holocene (< 3000 years b.p) was characterized by multidecadal and centennial-scale periods of significant decline in intensity of the SAmerM

ACCEPTED VERSION SUBJECT TO FINAL EDITING

(Bird et al., 2011a; Vuille et al., 2012). This could be partly due to a reduction in the zonal SST gradient of the Pacific Ocean, favouring El Niño-like conditions (Kanner et al., 2013). Other studies suggest increased SAmerM precipitation amount during the Late Holocene, in association with the expansion of the tropical forest (Smith and Mayle, 2018). Well-dated equilibrium lines of glaciers during the deglaciation suggest that the AMOC enhances Atlantic moisture sources and precipitation amount increase over the tropical and southern Andes (Beniston et al., 2018).

Observations during 1979-2014 suggest that poleward shifts in the South Atlantic Convergence Zone (SACZ) noted in recent decades (Talento and Barreiro, 2018; Zilli et al., 2019), are associated with precipitation amount decrease along the equatorward margin and increase along the poleward margin of the convergenze zone (Zilli et al., 2019). Several observational studies identified delayed onsets of the SAmerM after 1978 related to longer dry seasons in the southern Amazon (Fu et al., 2013; Yin et al., 2014; Arias et al., 2015; Debortoli et al., 2015; Arvor et al., 2017; Giráldez et al., 2020; Haghtalab et al., 2020; Correa et al., 2021). In contrast, other studies indicate a trend toward earlier onsets of the SAmerM (Jones and Carvalho, 2013). These discrepancies are explained by the methodology used and the domain considered for the SAmerM, confirming the occurrence of delayed onsets of the SAmerM since 1978 (Correa et al., 2021). CMIP5 simulations show trends toward delayed onsets of the SAmerM in association with anthropogenic forcing, although the simulated trends underestimate the observed trends (Fu et al., 2013). Total rainfall reductions are observed in the southern Amazon during September-October-November after 1978 (Fu et al., 2013; Bonini et al., 2014; Debortoli et al., 2015, 2016; Espinoza et al., 2019), consistent with reductions in river discharge in the region (Molina-Carpio et al., 2017; Espinoza et al., 2019; Heerspink et al., 2020).

Significant increases in precipitation have been observed over southeastern Brazil during 1902-2005 while non-significant decreases have been found over central Brazil (Vera and Díaz, 2015). In Bolivia, increases were observed during 1965-1984, while reductions have occurred since then (Seiler et al., 2013). However, the Peruvian Amazon does not reveal significant changes in mean rainfall during 1965–2007 (Lavado et al., 2013; Ronchail et al., 2018). Historical simulations from CMIP5 ensembles adequately capture the observed summer precipitation amount over central and southeastern Brazil, thereby providing *high confidence* in interpreting the observed variability of SAmerM for the period 1960-1999 (Gulizia and Camilloni, 2015; Pascale et al., 2019). Also, CMIP5 simulations indicate that the anthropogenic forcing associated with increased GHG emissions is necessary to explain the positive trends in upper-troposphere zonal winds observed over the South American Altiplano (Vera et al., 2019). However, the detection of anthropogenically-induced signals for precipitation is still ambiguous in monsoon regions, like the SAmerM (Hoegh-Guldberg et al., 2019).

In summary, there is *high confidence* that the SAmerM onset has been delayed since the late 1970s. This is reproduced by CMIP5 simulations that consider anthropogenic forcing. There is also *high confidence* that precipitation during the dry-to-wet transition season has been reduced over the southern Amazon. Paleoclimate reconstructions and simulations suggest a weaker SAmerM during warmer epochs such as the Mid-Holocene or the 900-1100 period, and stronger monsoon during colder epochs such as the LGM or the 1400-1600 period (*high confidence*).

8.3.2.4.6 Australian and Maritime Continent Monsoon

Since AR5, several studies have examined observed variability and changes in the Australian and Maritime Continent Monsoon (AusMCM) using paleoclimate records, instrumental observations and modeling studies (Denniston et al., 2016; Zhang and Moise, 2016). Paleoclimate reconstructions and modelling indicate that the Indo–Australian monsoon may vary in or out of phase with the EAsiaM, depending on whether there is a meridional displacement or expansion of the tropical rainfall belt (Ayliffe et al., 2013; Denniston et al., 2016). For instance, mid-Holocene simulations suggest that the AusMCM weakens and contracts due to a decreased net energy input and a weaker dynamic component (D'Agostino et al., 2020a).

Rainfall increases have been observed over northern Australia since the 1950s, with most of the increases occurring in the north-west (Dey et al., 2018, 2019b; Dai, 2021) and decreases observed in the north-east (Li et al., 2012a) since the 1970s. There is also a trend towards more intense convective rainfall from

ACCEPTED VERSION SUBJECT TO FINAL EDITING

thunderstorms over northern Australia (Dowdy, 2020). There is no consensus on the cause of the observed Australian monsoon rainfall trends, with some studies suggesting changes are due to altered circulation driving increased moisture transport or increased frequency of the wettest synoptic regimes (Catto et al., 2012; Clark et al., 2018). Other studies find that model simulations that include anthopogenic aerosols (Rotstayn et al., 2012; Dey et al., 2018) are better able to capture observed Australian monsoon rainfall trends than simulations with natural or GHG forcing only (Knutson and Zeng et al., 2018).

The Maritime Continent (MC) experiences the influence of both the Asian and the Australian monsoons, with rainfall peaking during boreal winter/austral summer (Robertson et al., 2011). Reductions in land rainfall and marine cloudiness over the MC and weakening of surface moisture flux convergence have been observed in the period 1950-1999 (Tokinaga et al., 2012; Yoden et al., 2017). These trends are indicative of a slowdown of the Walker Circulation, with positive sea level pressure trends over the MC and negative trends over the central equatorial Pacific (Tokinaga et al., 2012). More recently (1981-2014), a trend of increasing annual rainfall over large areas of the MC has been identified (Hassim and Timbal, 2019). Given the large variability in MC rainfall on interannual time scales, the choice of time period may influence the calculated rainfall trend (Hassim and Timbal, 2019).

During 1951-2007 daily rainfall extremes did not increase over the MC, in contrast to the rest of Southeast Asia (Villafuerte et al., 2015) (see Section 11.4.2). Rainfall extremes in Indonesia increased in austral summer, as evidenced from station weather observations for the period 1983-2012 (Supari et al., 2018).

In summary, notable rainfall increases have been observed in parts of northern Australia since the 1970s, although there is *low confidence* in the human contribution to these changes. Rainfall changes have been observed over the MC region but there is *low confidence* in the identification of trends because of large variability at interannual timescales.

8.3.2.5 Tropical cyclones

AR5 assessed *low confidence* in centennial changes in tropical cyclone activity globally, and in the attribution of observed changes in TCs to anthropogenic forcing. Since AR5, there has been considerable progress in understanding the observed changes of TCs and an overall improved knowledge of the sensitivity of TCs to both GHG and aerosol forcing (Knutson et al., 2019; Sobel et al., 2019).

There is *medium confidence* that anthropogenic forcing has contributed to observed heavy rainfall events over the United States associated with TCs (Kunkel et al., 2012) and other regions with sufficient data coverage (Bindoff et al., 2013) (see also Section 11.7.1.2). There has been increased frequency of TC heavy-rainfall events over several areas in the United States since the late 19th century that is greater than what would be expected solely from changes in U.S. landfall frequency, suggesting the increasing role of TCs have in causing heavy-rainfall events (Kunkel et al., 2010). For example, there is evidence for an anthropogenic contribution to the extreme rainfall of Hurricane Harvey in 2017 (Emanuel, 2017; Risser and Wehner, 2017; Van Oldenborgh et al., 2017; Trenberth et al., 2018; Wang et al., 2018c).

While TCs cause extreme local rainfall and flooding, they can be also an important contributor to annual precipitation and regional fresh water resources (Hristova-Veleva et al., 2020). Transport of moisture by TCs is an important contributor for precipitation over the coastal areas of East Asia mostly from July through October, with the TC rainfall accounting for nearly 10% to 30% of the total rainfall in the region (Guo et al., 2017b). Local TC rainfall totals depend on rain-rate and translation speed (the speed of TC movement along the storm track) with slow TCs such as Hurricane Harvey (2017), providing a clear example of the effect of slow translation speed on local rainfall accumulation, with urbanization exacerbating the storm total rainfall and flooding (Zhang et al., 2018d) (see Section 11.7.1).

In addition to evidence that rain-rates have increased, there is evidence that TC translation speed has slowed globally (Kossin, 2018) thus amplifying thermodynamic intensification of rainfall and may be linked to anthropogenic forcing (Gutmann et al., 2018). This is *limited evidence* however, so there is *medium confidence*

ACCEPTED VERSION SUBJECT TO FINAL EDITING

of a detectable change in TC translation speed over the US. Since the 1900s, and there is *low confidence* for a global signal because of *limited agreement* among models and due to data heterogeneity. However, the slowdown is consistent with theoretical and modelling studies that indicate a general weakening of the tropical circulation with warming that reduces the speed of the TC system (Chauvin et al., 2017), though there is *limited* observational *evidence* (Sections 8.2.3.5, 11.7.1). Despite growing evidence that TC rainfall measures indicating increases, in general there is *low confidence* that a global anthropogenically forced trend in TC precipitation has been detected (Knutson et al., 2019), partly due to observational data limitations (e.g., Lau and Zhou, 2012).

In summary, there is *low confidence* of an observed increase in TC precipitation intensity due to observing system limitations. However, robust physical understanding (Section 8.2.3.2) and detailed singular event attribution studies provide evidence that tropical cyclone rainfall has increased with a warming climate (*high confidence*, Section 11.7.1.4).

8.3.2.6 Stationary waves

Stationary waves are planetary-scale waves that are approximately stable (stationary) in terms of geographic position, as opposed to propogating planetary waves, and are important both as part of the climatological general circulation and seasonal and shorter-term anomalies. They are related to surface features including land-ocean contrasts and major mountain ranges, as well as atmospheric features including the jet stream, storm tracks, and blocking, which are considered separately in the following sections. While zonal mean changes in P-E are dominated by thermodynamic effects (Section 8.2.2.1), changes in stationary waves are of key importance in understanding zonal asymmetries in the water cycle response to global warming (Wills and Schneider, 2015; Wills et al., 2019). AR5 did not explicitly assess stationary waves, but noted changes in related circulation features such as a *likely* poleward shift of the Northern Hemisphere storm tracks and an increase in frequency and eastward shift in North Atlantic blocking anticyclones, although there was *low confidence* in the global assessment of blocking.

Since AR5, several studies have demonstrated a link between stationary wave amplitude and wet and dry extremes in several different regions of the Northern Hemisphere (Liu et al., 2012; Coumou et al., 2014; Screen and Simmonds, 2014; Yuan et al., 2015) with changes in moisture transport playing an important role (Yuan et al., 2015). A 'resonance mechanism' has been proposed for an increasing amplitude of stationary waves (Petoukhov et al., 2013, 2016; Coumou et al., 2014; Kornhuber et al., 2017) and several studies have linked increasing amplitude of stationary waves to Arctic warming (Francis and Vavrus, 2012, 2015; Liu et al., 2012; Tang et al., 2014) as well as to global warming (Mann et al., 2017). However, other studies have not identified an increase in stationary wave amplitude (Barnes, 2013; Screen and Simmonds, 2013b, 2013a)

There has been considerable work on linkages (teleconnections) between Arctic warming and the mid-latitude circulation (see also Cross-Chapter Box 10.1). The limited amount of research on Southern Hemisphere stationary waves suggests changes in high latitude, mid-tropospheric stationary waves which influence Antarctic precipitation (Turner et al., 2017) and changes in stratospheric stationary waves that are associated with ozone depletion rather than increases in GHGs (Wang et al., 2013a). The observed climatology of Northern Hemisphere winter stationary waves is well-represented in the CMIP5 multi-model mean (Wills et al., 2019) but individual models have important deficiencies in reproducing stationary wave variability (Lee and Black, 2013). In the Southern Hemipshere, the observed climatology of stationary waves in CMIP5 models has considerable bias in both phase and amplitude (Garfinkel et al., 2020). A comprehensive assessment is not yet available for CMIP6 models.

In summary, there is *low confidence* in strengthened wintertime stationary wave activity over the North Atlantic, associated with increased poleward moisture fluxes east of North America There is *medium confidence* in a recent amplification of the Northern Hemisphere stationary waves in summer, but no formal attribution to anthropogenic climate change.

ACCEPTED VERSION SUBJECT TO FINAL EDITING

8.3.2.7 *Atmospheric blocking*

Atmospheric blocking refers to persistent, semi-stationary weather patterns characterized by a high-pressure (anticyclonic) anomaly that interrupts the westerly flow in the mid-latitudes of both hemispheres. By redirecting the pathways of mid-latitude cyclones, blocking can affect the water cycle and lead to negative precipitation anomalies in the region of the blocking anticyclone and positive anomalies in the surrounding areas (Sousa et al., 2017). In this way, blocking can also be associated with extreme events such as heavy precipitation (Lenggenhager et al., 2018), drought (Schubert et al., 2014) and heatwaves (Miralles et al., 2014a). AR5 reported *low confidence* in global-scale changes in blocking, due to methodological differences between studies.

Currently no consensus exists on observed trends in blocking during 1979-2013. (Horton et al., 2015) identified increasing trends in anticyclonic circulation regimes based on geopotential height fields in the mid troposphere, which may be partly related to the tropospheric warming itself and thus not represent real changes in the statistics of weather (Horton et al., 2015; Woollings et al., 2018). Hanna et al. (2018) and (Davini and D'Andrea, 2020) reported a significant increase in the frequency of summertime blocking over Greenland. A weakening of the zonal wind, eddy kinetic energy and amplitude of Rossby waves in summer in the Northern Hemisphere (Coumou et al., 2015, Kornhuber et al., 2017, 2019) and an increased 'waviness' of the jet stream associated with Arctic warming (Francis and Vavrus, 2015; Pfahl et al., 2015; Luo et al., 2019) have also been identified, which may be linked to increased blocking.

In contrast, it has been shown that observed trends in blocking are sensitive the choice of the blocking index, and that there is a large internal variability that complicates the detection of forced trends (Barnes et al., 2014; Cattiaux et al., 2016; Woollings et al., 2018), compromising the attribution of any observed changes in blocking. Many climate models still underestimate the occurrence of blocking, at least in winter over northeastern Atlantic and Europe (Dunn-Sigouin and Son, 2013), which leads to caution in the interpretation of their results for these regions. However, over the Pacific Ocean there have been large improvements in the simulation of blocking for the last 20 years (Davini & D'Andrea, 2016; Patterson et al., 2019). In the Southern Hemisphere, increases in blocking frequency have occurred in the South Atlantic in austral summer (Dennison et al., 2016) and in the southern Indian Ocean in austral spring (Schemm, 2018). A reduced blocking frequency has been found over the southwestern Pacific in austral spring (Schemm, 2018) (see also sections 2.3.1.4.3 and 3.4.1.3.3).

In summary, no robust trend in atmospheric blocking has been detected in modern reanalyses and in CMIP6 historical simulations (*medium confidence*). The lack of trend is explained by strong internal variability and/or the competing effects of low-level Arctic amplification and upper-level tropical amplification of the equator-to-pole temperature gradient (*medium confidence*).

8.3.2.8 *Extratropical cyclones, storm tracks and atmospheric rivers*

8.3.2.8.1 *Extratropical cyclones and storm tracks*

AR5 indicated *low confidence* in long-term changes in the intensity of extratropical cyclones (ETC) over the 20th century derived from centennial reanalyses and storminess proxies based upon sea level pressure. This was confirmed by the SREX assessment that the main Northern Hemisphere and Southern Hemisphere extratropical storm-tracks *likely* experienced a poleward shift during the last 50 years (Seneviratne et al., 2012) with *low confidence*, and inconsistencies within reanalysis datasets remain.

Since AR5 there has been considerable progress in quantifying storm-track activity using multiple reanalysis products and different methodologies (Hodges et al., 2011; Neu et al., 2013; Tilinina et al., 2013; Wang et al., 2016b). Over the Northern Hemisphere increases in the total number of cyclones from 1979 show a large spread of trends across different estimates (Neu et al., 2013; Li et al., 2016b; Grieger et al., 2018) (see also Section 2.3.1.4.3) resulting in *low confidence* in any clear increase of in the total number of cyclones. However, starting from the early 1990s, most reanalyses show increases in the total cyclone number by about

ACCEPTED VERSION SUBJECT TO FINAL EDITING

2-5% per decade (Figure 8.12). Increasing trends in the total number of cyclones are dominated by the increase in the number of shallow and moderate cyclones (which are more dependent on the datasets and identification mentods used) than with decreasing number of deep cyclones since the early 1990s (Tilinina et al., 2013; Chang, 2018). In the Southern Hemisphere the variability of the total number of cyclones is characterized by strong interdecadal variability preventing a clear assessment of trends. However, in contrast to the Northern Hemisphere,there is a significant increasing trend in the number of deep cyclones (~10% over 1979-2018) in ERA5, ERA-Interim, JRA55 and MERRA, and in the CFSR dataset after 2000 (Reboita et al., 2015; Wang et al., 2016b) (Figure 8.12).

Changes in the number of deep storms, which are often associated with heavier precipitiation over the North Atlantic and North Pacific, exhibit strong seasonal differences and decadal variability (Colle et al., 2015; Chang et al., 2016; Matthews et al., 2016, Priestley et al., 2020). An increase in the number of summer cyclones over the Atlantic-European sector (Tilinina et al., 2013) is consistent with the increase in the strength of the strongest fronts over Europe (Schemm et al., 2018). (Chang et al., 2016) reported a decrease in the number of strong summer storms in the latitudinal band 40º-75ºN over the last decades, however, the assessment of seasonal trends in the Atlantic-European sector is complicated by the choice of region, attribution of tracks to the region selected, and thresholds used to identify trajectories, leading to *low confidence* on regional seasonal trends. For the Southern Hemisphere, Grieger et al. (2018) reported growing number of cyclones over sub-Antarctic region in the austral-summer during 1979-2010, while statistically significant trends were absent during the austral winter.

[START FIGURE 8.12 HERE]

Figure 8.12: Annual anomalies (with respect to the reference period 1979-2018) of the total number of extratropical cyclones (a, c) and of the number of deep cyclones (<980hPa) (b, d) over the Northern (a, b) and the Southern (c, d) Hemispheres in different reanalyses (shown in colours in the legend). Note different vertical scales for panels (a), (b) and (c), (d). Thin lines indicate annual anomalies and bold lines indicate 5-yr running averages. (e), (f) The number of reanalyses (out of five) simultaneously indicating statistically significant (90% level) linear trends of the same sign during 1979–2018 for JFM over the Northern Hemisphere (e) and over the Southern Hemisphere (f). Updated from (Tilinina et al., 2013). Further details on data sources and processing are available in the chapter data table (Table 8.SM.1).

[END FIGURE 8.12 HERE]

Analysis of storm-track activity over longer periods suffers from uncertainties associated with changing data assimilation and observations before and during the satellite era, resulting in inhomogeneities and discontinuities in centennial reanalyses (Krueger et al., 2013, Chang and Yau, 2016; Wang et al., 2013, 2016, Varino et al., 2019a). (Feser et al., 2015) reviewed multiple storm track records for the Atlantic-European sector and demonstrated growing storm activity north of 55°N from the 1970s to the mid 1990s with declining trend thereafter, sugesting strong interdecadal variability in storm track activity. This was also confirmed by (Krueger et al., 2019) from the analysis of geostrophic winds derived from sea level pressure gradients.

Poleward deflection of mostly oceanic winter storm tracks since 1979 was reported in both the North Atlantic and North Pacific (Tilinina et al., 2013; Wang et al., 2017b). This large-scale tendency has regional variations and may be seasonally dependent. Wise and Dannenberg (2017) reported a southward shift in the east Pacific storm-track from the 1950s to mid-1980s followed by northward deflection in the later decades. (King et al., 2019) resported an association of Atlantic storm track migrations with SSW events with Central and South European preciptiation anomalies. Over centennial time-scales, Gan and Wu (2014) reported an intensification of stormtracks in the poleward and downstream regions of the North Pacific and North Atlantic upper troposphere using 20CR reanalysis. Poleward migration of the Southern Hemisphere storm-tracks (Grise et al., 2014; Wang et al., 2016b; Dowdy et al., 2019) was identified during the austral summer and is closely associated with cyclone-associated frontal activity (Solman and Orlanski, 2014, 2016) and

ACCEPTED VERSION SUBJECT TO FINAL EDITING

cloud cover (Bender et al., 2012; Norris et al., 2016).

The representation of ETCs in both climate models and reanalyses is resolution-dependent, hence changes must be assessed with caution (Section 3.3.3.3). In particular, CMIP5 models show a systematic underestimation of the intensity of ETCs (Zappa et al., 2014), a feature that is partially related to their relatively coarse resolution or other possible deficiencies such as an excess of dissipation (Chang et al., 2013). The best representation of ETCs and their intensity in the North Atlantic are provided by relatively high horizontal resolution CMIP5 models (Zappa et al., 2014). Using a single high-resolution climate model, (Hawcroft et al., 2016) showed that precipitation amount associated with ETCs was generally well simulated though with too much precipitation during the strongest ECTs compared with observed estimations.

In summary, there is *low confidence* in recent changes in the total number of extra-tropical cyclones over both hemispheres. It is *as likely as not* that the number of deep cyclones over the Northern Hemisphere has decreased after 1979 and it is *likely* that the number of deep extra-tropical cyclones increased over the same period in the Southern Hemisphere. It is *likely* that extra-tropical cyclone activity in the Southern Hemisphere has intensified during austral summer with no significant changes in austral winter. There is *medium confidence* that boreal-winter storm tracks during the last decades experienced poleward shifts over the Northern and Southern Hemisphere oceans. There is *low confidence* of changes in extra-tropical cyclone activity prior 1979 due to inhomogeneities in the intrumental records and modern reanalyses.

8.3.2.8.2 Atmospheric rivers

Atmospheric rivers (ARs) are long, narrow (up to a few hundred km wide), shallow (up to few km deep) and transient corridors of strong horizontal water vapour transport that are typically associated with a low-level jet stream ahead of the cold front of an extratropical cyclone (Ralph et al., 2018). Atmospheric rviers were not assessed in AR5. ARs are associated with atmospheric moisture transport from the tropics to the mid and high latitudes (Zhu and Newell, 1998), although the drivers of moisture transport relative to the different airstreams within extratropical cyclones remains a subject of current study (Dacre et al., 2019). While much previous research has focused on the west coast of North America, ARs occur throughout extratropical and polar regions (e.g., Guan and Waliser, 2015) and are often associated with locally-heavy precipitation, including a substantial fraction of all midlatitude extreme precipitation events (e.g., Waliser and Guan, 2017). ARs also affect East Asia strongly during the period from late spring to summer (Kamae et al., 2017). ARs can be related to warming/melt events trough the intrusions of warm and moist air in Antarctica, Greenland and New Zealand (Bozkurt et al., 2018; Mattingly et al., 2018; Little et al., 2019), contributing about 45-60% of total annual precipitation in subtropical South America (Viale et al., 2018). They also transport moisture from South America to the western and central South Atlantic, feeding the ARs that reach the west coast of South Africa (Ramos et al., 2019). However, the estimation of precipitation rate from ARs can have large uncertainties, especially as ARs hit topographically complex coastal regions (Behrangi et al., 2016), which can cause complexities in quantifying AR-related precipitation.

Analysis of observed trends in the characteristics of ARs has been limited. (Gershunov et al., 2017) and (Sharma and Déry, 2019) have shown a rising trend in land-falling AR activity over the west coast of North American since 1948. (Gonzales et al., 2019) have also documented a seasonally-asymmetric warming of ARs affecting the United States West Coast since 1980, which has hydrological implications for the timing and magnitude of regional runoff. Longer-term paleoclimate analysis of ARs is even more limited, although Lora et al. (2017) reported that in the last glacial maximum, AR landfalls over the North America west coast were shifted southward compared to the present conditions.

In summary, it is *likely* that there was an increasing trend in the AR activity in the eastern North Pacific since the mid-20th century. However, there is *low confidence* in the magnitude of this trend and no formal attribution, although such an increase in activity is consistent with the expected and observed increase in precipitable water associated with human-induced global warming.

8.3.2.9 Modes of climate variability and regional teleconnections

ACCEPTED VERSION SUBJECT TO FINAL EDITING

Following on from the assessment in Chapters 2 and 3, this section considers changes in modes of variability at seasonal to interannual timescales in terms of their implications on recent water cycle changes. These modes are described in details in Technical Annex IV.

8.3.2.9.1 Tropical modes

The amplitude of the El Niño–Southern Oscillation (ENSO, Section AIV.2.3) variability has increased since 1950 (Section 2.4.2) but there is no clear evidence of human influence (Sections 2.4.2 and 3.7.3).

ENSO influences precipitation and evaporation dynamics, river flow and flooding at a global scale (see also Figure 3.37) (Ward et al., 2014, 2016; Martens et al., 2018). Reconstruction (1804-2005) of Thailand's Chao Praya River peak season streamflow displays a strong correlation with ENSO (Xu et al., 2019). Based on water storage estimates from 2002 to 2015, drought conditions over the Yangtze River basin followed La Niña events and flood conditions followed El Niño events (Zhang et al., 2015b). Strong correlation between ENSO and terrestrial water storage has been identified mostly in the subtropics but with diverse intensities and timelags depending on the region (Ni et al., 2018). The likelihood of increased/decreased flood hazard during ENSO events has a complex spatial pattern with large uncertainties (Emerton et al., 2017).

Tropical SSTs and associated global circulation may increase rainfall in West Africa, as observed in some years during 1950-2015, despite the presence of El Niño (Pomposi et al., 2020). During an El Niño summer, equatorial convective systems and the associated Walker circulation tend to shift eastward, leading to decreases in Indian summer monsoon rainfall (Li and Ting, 2015; Roy et al., 2019) (Lee and Tamas accepted). This teleconnection is modulated by Indian Ocean variability (Terray et al., 2021), as observed during the extreme positive IOD event in 2019 (Ratna et al., 2021). Since the end of the 19th century, synchronous hydroclimate changes (*medium confidence*) have been identified over south eastern Australia and South Africa (Gergis and Henley, 2017) modulated by ENSO, as well as other regional fluctuations like the Botswana High over Southern Africa (Driver and Reason, 2017). Over southern South America, the ENSO influence on precipitation (Cai et al., 2020; Poveda et al., 2020) interacts with the influence of SAM (Pedron et al., 2017), exhibiting large multi-decadal variations because of changes in the correlation between the two large-scale modes (Vera and Osman, 2018). Other processes underlying ENSO teleconnections of relevance for water cycle changes include water vapour and moisture transports, like over the Middle East (Sandeep and Ajayamohan, 2018), southeastern China (Yang et al., 2018c), or central Asia (Chen et al., 2018b), southeastern South America (Martín-Gómez and Barreiro, 2016; Martin-Gomez et al., 2016), Australia (Rathore et al., 2020) and southern United States (Okumura et al., 2017).

There is no evidence of trend in the Indian Ocean Dipole (IOD, Section AIV.2.4) mode and associated anthropogenic forcing (Sections 2.4.3 and 3.7.4). AR5 concluded that the IOD is *likely* to remain active, affecting climate extremes in Australia, Indonesia and east Africa. Since the AR5, IOD teleconnections have been identified extending further to the Middle East (Chandran et al., 2016), to the Yangtze river (Xiao et al., 2015), where in boreal summer and autumn positive IOD events tend to increase the precipitation in the southeastern and central part of the basin, and to the southern Africa extreme wet seasons (Hoell and Cheng, 2018). During the last millenium, the combined effect of a positive IOD and El Niño conditions have caused severe droughts over Australia (Abram et al., 2020). In the satellited period, it is found more effective in inducing significant decrease of rainfall over Indonesia, with the opposite occurring for negative IOD events (As-syakur et al., 2014; Nur'utami and Hidayat, 2016; Pan et al., 2018). Similarly, over the Ganges and Brahmaputra river basins major droughts have been recorded during co-occurring El Niño and positive IOD, while floods occurred during La Nina and negative IOD conditions (Pervez and Henebry, 2015). Over equatorial East Africa the IOD affects the short rain season (*medium confidence*) exacerbating flooding and inundations independently of ENSO (Behera et al., 2005; Conway et al., 2005; Ummenhofer et al., 2009; Hirons and Turner, 2018). Extreme conditions, like 2019 Australian bushfires and African flooding, have been associated with strong positive IOD conditions (Cai et al., 2021).

Intraseasonal variability, like the Madden Julian Oscillation (MJO, Section AIV.2.8) and the Boreal Summer Intraseasonal Oscillation (BSISO), are highly relevant to the water cycle (Maloney and Hartmann, 2000; Lee

ACCEPTED VERSION SUBJECT TO FINAL EDITING

et al., 2013; Yoshida et al., 2014; Nakano et al., 2015). Since AR5, studies on MJO teleconnections within the tropics and from the tropics to higher latitudes have continued (Guan et al., 2012; Mundhenk et al., 2018; Tseng et al., 2019; Aberson and Kaplan, 2020; Finney et al., 2020b; Fowler and Pritchard, 2020; Fromang and Rivière, 2020).

The strength and frequency of the MJO have increased over the past century (*medium confidence*) (Oliver and Thompson, 2012; Maloney et al., 2019; Cui et al., 2020) because of global warming (Arnold et al., 2015; Carlson and Caballero, 2016; Wolding et al., 2017; Maloney et al., 2019). A 20th century reconstruction suggests a 13% increase of the MJO amplitude (Oliver and Thompson, 2012), with differences in seasonal variability (Tao et al., 2015; Wang et al., 2020e). However, up to half of changes recorded during the second half of the 20th century could be due to internal variability (Schubert et al., 2013). Other observed changes in MJO characteristics include a decrease (by 3-4 days) in the residence time over the Indian Ocean but an increase (by 5-6 days) over the Indo-Pacific and Maritime Continent sectors (Roxy et al., 2019).

Consequences of these changes are increased rainfall over Southeast Asia, northern Australia, southwest Africa and the Amazon, and drying over the west coast of the United States and Equador (Roxy et al., 2019). During the austral summer, air-sea interactions and location of the MJO active phase are important to modulate the strength of the rainfall response in the South Atlantic Convergence Zone (Shimizu and Ambrizzi, 2016; Alvarez et al., 2017), including its southward shift (Barreiro et al., 2019). In the austral winter, the intraseasonal variability is mostly influential over regions of the Amazon Basin (Mayta et al., 2019). Some MJO phases are particularly effective in conjuction with tropical cyclones in enhancing westerly moisture fluxes toward east Africa (Finney et al., 2020b).

Simulated changes in MJO precipitation amplitude are extremely sensitive to the pattern of SST warming (Takahashi et al., 2011; Maloney and Xie, 2013; Arnold et al., 2015) and ocean-atmosphere coupling (DeMott et al., 2019; Klingaman and Demott, 2020). In agreement with results from previous model generations, most CMIP5 models still underestimate MJO amplitude, and struggle to generate a coherent eastward propagation of precipitation and wind (Hung et al., 2013; Jiang et al., 2015; Ahn et al., 2017), affecting regional surface climate in the tropics and extra-tropics. In addition, most CMIP5 models simulate an MJO that propagates faster compared with observations, with a poorly represented intra-seasonal precipitation variability (Ahn et al., 2017). Over the Indian Ocean, the propagation speed of convection in some CMIP5 models tends to be slower than observed due to a strong persistence of equatorial precipitation (Hung et al., 2013; Jiang et al., 2015). Among other processes, improving the moisture-convection coupling, the representation of moist convection, the interaction between lower tropospheric heating and boundary layer convergence, and the topography of the Maritime Continent improve simulations of the MJO (Ahn et al., 2017, 2020a; Kim and Maloney, 2017; Yang and Wang, 2019; Tan et al., 2020a; Yang et al., 2020b). In fact, CMIP6 models reproduce the amplitude and propagation of the MJO better than CMIP5 models due to increased horizontal moisture advection over the Maritime Continent (Ahn et al., 2020b). Despite the diverse theories of MJO evolution and processes that have been developed since its discovery, a better understanding of its dynamics is still needed (Jiang et al., 2020; Zhang et al., 2020). Furthermore, metrics based on dynamical processes are needed to assess model simulations of these events (Stechmann and Hottovy, 2017; Wang et al., 2018a) as well as related teleconnections (Wang et al., 2020c).

In summary, multiple water cycle changes related to ENSO and IOD teleconnections have been observed across the 20th century (*high confidence*), mostly dominated by interannual to multi-decadal variations. The MJO amplitude has increased in the second half of the 20th century partly because of anthropogenic global warming (*medium confidence*) altering regional precipitation signals.

8.3.2.9.2 Extra-tropical modes

A positive trend has been observed in the Northern Annular Mode (NAM, Section AIV.2.1) in the second half of the 20th century, which partially reversed since the 1990s (Section 2.4.5.1), but the detection and attribution of these changes remain difficult (Section 3.7.1). The linkages of the NAM with weather and climate extremes in the northern extra-tropics are still unclear in models and observations (Vihma, 2014; Overland et al., 2016; Screen et al., 2018). However, robust links are identified between precipitation trends

ACCEPTED VERSION SUBJECT TO FINAL EDITING

and variability in Europe and the phases of the Atlantic component of the NAM, i.e. the NAO (Moore et al., 2013; Comas-Bru and McDermott, 2014). Reduced winter precipitation is well correlated with the NAO over Southern Europe and Mediterranean countries (Kalimeris et al., 2017; Corona et al., 2018; Vazifehkhah and Kahya, 2018; Neves et al., 2019). NAO teleconnections in those regions include influences on groundwater and streamflow (Zamrane et al., 2016; Massei et al., 2017; Jemai et al., 2018). Remote teleconnections of the NAO have been identified over Northern China, the Yangtze River valley and India (Jin and Guan, 2017; Di Capua et al., 2020). The summer phase of the NAO is significantly correlated with variations in summer rainfall in East China, with the thermal forcing of the Tibetan Plateau providing a link to this Eurasian teleconnection (Wang et al., 2018f).

In the Southern Hemisphere, an observed positive trend is identified in the strength of the Southern Annular Mode (SAM, Section AIV.2.2) since 1950, especially in austral summer (*high confidence*, Section 2.4.1.2). While stratospheric ozone depletion and GHG increases largely contributed to this change, climate models still have trouble simulating the SAM and its response to ozone and GHGs (Section 3.7.2). Shifts in the southwesterly winds (Fletcher et al., 2018) and the expansion of the Southern Hemisphere Hadley cell (Kang and Polvani, 2011; Nguyen et al., 2018a) influence SAM-related rainfall anomalies in in southern South America and southern Australia during the austral spring–summer. Over New Zealand, large-scale SLP and zonal wind patterns associated with SAM phases modulate regional river flow (Li and McGregor, 2017). The SAM also influences precipitation and water vapour changes over Antarctica via moisture fluxes (Marshall et al., 2017; Oshima and Yamazaki, 2017; Grieger et al., 2018) but CMIP5 models are limted in their ability to simulate these regional teleconnections (Marshall and Bracegirdle, 2015; Palerme et al., 2017). SAM and its interaction with other large-scale modes of climate variability, like ENSO (Fogt et al., 2011) and the Indian Ocean Dipole (Hoell et al., 2017a), are responsible for fluctuations in Southern African rainfall (Nash, 2017) and southern South America (Gergis and Henley, 2017). In May, the SAM can trigger a southern Indian Ocean dipole SSTA favoring more or less precipitation over the Indian sub-continent and adjacent areas (Dou et al., 2017), also affecting subsequent summer monsoon in the South China Sea (Liu et al., 2018d). Over South America, a positive SAM is associated with dry conditions (Holz et al., 2017) due to reduced frontal and orographic precipitation and weakening of moisture convergence. Regions particularly affected include Chile (Boisier et al., 2018) and the rivers of central Patagonia (Rivera et al., 2018).

In summary, while the attribution of 20th century variations of the NAM/NAO is still unclear, there is a strong relationship with precipitation changes over Europe and in the Mediterranean region (*high confidence*). SAM teleconnections are associated with changes in moisture transport and extend to South America, Australia and Antarctica *(high confidence)* with documented drying occurring as a result of the *very likely* human-induced SAM trend toward its positive phase observed from the 1970s until the 1990s (Section 3.7.2).

8.4 What are the projected water cycle changes?

We consider global and regional climate projections of the water cycle, assessing projected changes in each component of the water cycle (Section 8.4.1) and the global-scale and regional phenomena that directly impact it (Section 8.4.2).

8.4.1 Projected water cycle changes

Most projected changes in the water cycle are not expected to be uniform in space or time. They are driven by both dynamical and thermodynamical processes (Section 8.2) and have not necessarily emerged yet in the recent observational record (Section 8.3) as they are superimposed on substantial natural fluctuations in weather and climate. Therefore, projecting regional water cycle changes remains challenging. However, a number of physically understood responses can be evaluated using both CMIP5 and CMIP6 models, which are important for guiding decision making that anticipates, prepares for, and responds to water cycle changes. In this section, global maps of projected changes in water cycle variables are assessed using the WGI AR6 'simple method' (see Cross-Chapter Box Atlas1), which uses hatching to highlight where less

ACCEPTED VERSION SUBJECT TO FINAL EDITING

than 80% of the models agree on the sign of projected changes. This choice differs from Section 4.2.6 for a number of reasons. These include the weak signal-to-noise ratio of projected hydrological changes in low to medium emission scenarios, the sensitivity of their statistical significance to the baseline reference period, and the non-Gaussian distribution of many water cycle variables (see CCB Atlas.1 for more details on strengths and limitations of the hatching methods implemented within AR6).

8.4.1.1 Global water cycle intensity and P-E over land and oceans

As discussed in 8.3.1.1, the definition of global water cycle intensity varies from the simple metric of increases in global mean precipitation to broader joint considerations of water vapour and its transport, precipitation minus evaporation (P-E) rates and continental runoff (see Figure 8.1). AR5 determined that globally averaged precipitation is *virtually certain* to increase with temperature and that there is *high confidence* that the contrast of annual mean precipitation between dry and wet regions and seasons will increase over most of the globe as temperatures and moisture transports increase (Collins et al., 2013). AR5 also highlighted that continued ocean warming for a few decades after GHG forcing stabilizes or begins to decrease will also lead to further increases in global mean precipitation and evaporation.

In this Report, Chapter 4 provides an updated assessment of global annual precipitation (Section 4.3.1), finding that it is *very likely* that annual precipitation averaged over all land regions continuously increases as global surface temperatures increase in the 21st century (*high confidence*). CMIP6 projections for long-term changes in P-E (Figure 8.13) show that, for all scenarios, P-E increases over the tropics and high latitudes and decreases over the subtropics, resulting from a thermodynamically driven amplification of P-E patterns (Section 8.2.2.1). Both the intensity of changes and the spread among the models is larger for the higher emission scenarios. A less coherent latitudinal pattern and smaller magnitude of P-E changes over land reflect the complex influence of land-ocean warming contrast, atmospheric circulation change and vegetation feedbacks (Section 8.2.2.1). However, stronger atmospheric moisture transport, increases in precipitation and evaporation over global land and ocean and larger continental runoff that is in part fed by melting of glaciers characterises a more intense water cycle with global warming.

Global and global land mean water cycle changes from CMIP6 projections are shown in Table 8.1. Increases in global and continental precipitation, P-E and runoff in both the mid-term and long-term illustrate the future intensification of the water cycle, with the magnitude of change increasing with emission scenario. Consistent with AR5, CMIP6 simulations of global mean precipitation show a systematic multi-model mean increase of 1.6% to 2.9 % per 1°C warming (apparent hydrological sensitivity; Section 8.2.1) by 2081-2100 relative to present day across the new SSP scenarios (using global surface air temperature change from Table 4.1). It is well understood that rising concentrations of CO_2 drive a long-term increase in global precipitation with warming, but with the increase partly offset by rapid atmospheric adjustments to the direct atmospheric heating from radiative forcing agents (Section 8.2.1). The largest apparent hydrological sensitivity is found for SSP1-1.9, where the suppressing effects on precipitation from atmospheric heating by greenhouse gases rapidly reduced as their concentration falls. Additional warming due to reduced aerosol loadings under the SSP scenarios (Lund et al., 2019) further increases global precipitation (Rotstayn et al., 2013; Wu et al., 2013; Salzmann, 2016; Richardson et al., 2018b; Samset et al., 2018b; Westervelt et al., 2018), with particularly strong contributions from increased monsoon rainfall over East and South Asia (Levy et al., 2013; Westervelt et al., 2015; Dwyer and O'Gorman, 2017).

Over global land there is a small range in global mean multi-model mean precipitation increase across scenarios in the mid-term (2.6-4.0%), which widens (to 2.6-8.8%) in the long-term (Table 8.1). The long term projections are consistent with the Chapter 4 assessment that global annual precipitation over land is projected to increase on average by 2.4 [-0.2 to 4.7] % (*very likely* range) in the SSP1-1.9 low-emission scenario and by 8.3 [0.9 to 12.9] % in the SSP5-8.5 high-emission scenario by 2081–2100 relative to 1995–2014. Small differences in assessed model mean changes in Chapter 4, Table 4.2 result from a slightly different set of models considered for Table 8.1. Over land, P-E increases by ~2-3% in the mid-term (apart from SSP5-8.5 where increases are almost 5%) and ~1-12% in the long-term, determined by increased moisture transport from the ocean to land (Section 8.4.1.2). Runoff increases are larger and less certain due

ACCEPTED VERSION SUBJECT TO FINAL EDITING

to additional inputs from glacier melt and changes in groundwater storage (Section 8.4.1.7). Overall, precipitation and runoff are *very likely* to increase over the global land in all scenarios in the mid term and long term. P-E is *likely* to increase over global land in the mid and long term and *very likely* in SSP1-1.9, SSP3-7.0 and SSP5-8.5 pathways. The mid-term consistency in projections across scenarios is not apparent for precipitable water vapour, which increases over land by around 6-15% in the mid-term and 5-36% in the long-term across all scenarios. This implies that increases in extreme precipitation (closely related to atmospheric water vapour content; Section 8.2.3.2) are dependent on mitigation pathway, even in the mid-term (Section 11.4.5). Water vapour residence time (computed as the ratio of precipitable water vapour to precipitation from values in Table 8.1) increases from 8 days in the present to 9 days in mid-term and up to about 10 days in the long-term over land in SSP3-7.0, indicating a longer time to moisten the atmosphere between precipitation events. The CMIP6 projections are therefore consistent with an intensification but not acceleration of the global water cycle.

In summary, it is *virtually certain* that global water cycle intensity, considered in terms of global and continental mean precipitation, evaporation and runoff, will increase with continued global warming. Global annual precipitation over land is projected to increase on average by 2.4 [-0.2 to 4.7] % (*very likely* range) in the SSP1-1.9 low-emission scenario and by 8.3 [0.9 to 12.9] % in the SSP5-8.5 high-emission scenario by 2081–2100 relative to 1995–2014.

ACCEPTED VERSION
SUBJECT TO FINAL EDITING

Table 8.1: Global and global land annual mean water cycle projections in the medium term (2041-2060) and long term (2081-2100) relative to present day (1995-2014), showing present day mean and 90% confidence range across CMIP6 models (historical experiment) and projected mean changes and the 90% confidence range across the same set of models and a range of shared socioeconomic scenarios. Note that the exact value of changes can vary slightly based on the number of models assessed, but not sufficiently to affect the assessment. Further details on data sources and processing are available in the chapter data table (Table 8.SM.1).

		Mid term: 2041–2060 minus reference period					*Long term: 2081–2100 minus reference period*				
	1995-2014 reference period	**SSP1-1.9**	**SSP1-2.6**	**SSP2-4.5**	**SSP3-7.0**	**SSP5-8.5**	**SSP1-1.9**	**SSP1-2.6**	**SSP2-4.5**	**SSP3-7.0**	**SSP5-8.5**
Global Annual											
Precipitation (mm/day)	2.96 [2.76-3.17]	0.06 [0.03-0.11]	0.07 [0.03-0.12]	0.07 [0.04-0.12]	0.06 [0.03-0.11]	0.08 [0.03-0.14]	0.06 [0.02-0.11]	0.09 [0.04-0.17]	0.12 [0.07-0.21]	0.15 [0.08-0.24]	0.2 [0.1-0.33]
Precipitable Water (kg/m2)	24.79 [23.06-26.82]	1.42 [0.7-2.26]	1.84 [1.03-2.62]	2.29 [1.6-3.09]	2.7 [1.92-3.92]	3.15 [2.13-4.38]	1.11 [0.28-2.13]	2.11 [0.98-3.15]	3.76 [2.41-5.08]	6.2 [4.24-8.83]	7.92 [5.21-10.69]
Global Land Annual											
Precipitation (mm/day)	2.27 [1.98-2.58]	0.07 [0.02-0.11]	0.07 [-0.0-0.13]	0.06 [0.01-0.13]	0.06 [0.02-0.12]	0.09 [0.01-0.16]	0.06 [0.01-0.1]	0.08 [0.02-0.16]	0.11 [0.02-0.19]	0.14 [0.03-0.22]	0.2 [0.07-0.32]
Precipitation - Evaporation (mm/day)	0.87 [0.49-1.26]	0.02 [0.0-0.03]	0.02 [-0.01-0.05]	0.02 [-0.02-0.06]	0.03 [-0.0-0.06]	0.04 [0.0-0.1]	0.01 [-0.0-0.03]	0.03 [-0.01-0.08]	0.04 [-0.01-0.07]	0.07 [0.0-0.12]	0.1 [0.01-0.22]
Runoff (mm/day)	0.79 [0.54-1.0]	0.02 [-0.0-0.05]	0.04 [-0.0-0.1]	0.04 [-0.0-0.11]	0.04 [0.01-0.08]	0.06 [0.01-0.14]	0.02 [-0.0-0.03]	0.04 [-0.0-0.13]	0.06 [0.0-0.17]	0.1 [0.02-0.2]	0.15 [0.04-0.27]
Precipitable Water (kg/m2)	18.86 [17.12-21.28]	1.23 [0.57-1.96]	1.58 [0.77-2.42]	1.96 [1.34-2.76]	2.33 [1.63-3.46]	2.72 [1.79-3.84]	0.95 [0.19-1.95]	1.78 [0.8-2.77]	3.18 [2.04-4.34]	5.33 [3.57-7.5]	6.81 [4.35-9.32]

ACCEPTED VERSION SUBJECT TO FINAL EDITING

[START FIGURE 8.13 HERE]

Figure 8.13: Zonal and annual mean projected long-term changes in the atmospheric water budget. Zonal and annual mean projected changes (mm/day) in P (precipitation, left column), E (evaporation, middle column), and P-E (right column) over both land and ocean areas (thick line) and over land only (dashed line) averaged across 36 to 38 CMIP6 models in the SSP1-2.6 (a,b), SSP2-4.5 (c,d) and SSP5-8.5 (e,f) scenario, respectively. Shading denotes confidence intervals estimated from the CMIP6 ensemble under a normal distribution hypothesis. Colour shading denotes changes over both land and ocean. Grey shading represents internal variability derived from the pre-industrial control simulations. All changes are estimated for 2081-2100 relative to the 1995-2014 base period. Further details on data sources and processing are available in the chapter data table (Table 8.SM.1).

[END FIGURE 8.13 HERE]

8.4.1.2 Water vapour and its transport

Globally, AR5 assessed that by the end of the 21st century, the average quantity of water vapour in the atmosphere could increase by 5 to 25%, depending on emissions. AR5 assessed that increases in near-surface specific humidity over land are *very likely*, but that it was also *likely* that near-surface relative humidity would decrease over many land areas, although with only *medium confidence*. In terms of moisture transport, AR5 assessed that it was *likely* that moisture transport into the high latitudes would increase and that there was *high confidence* that, over the ocean, atmospheric moisture transport from the evaporative regions to the wet regions would increase.

CMIP6 climate models continue to project a steady increase in global mean column-integrated water vapour by around 6-13% by 2041-2060 and 5-32% by 2081-2100, depending on scenario (Table 8.1). This is consistent with projected atmospheric warming (Section 4.5.1.2) and the Clausius-Clapeyron relationship (Section 8.2.1) where every degree Celsius of warming is associated with a ~7% increase in atmospheric moisture in the lower atmospheric layers where most of the water vapour is concentrated. This increase sustains a positive feedback on anthropogenic global warming (Section 7.4.2.2). In contrast, the response of clouds is much more spatially heterogeneous, microphysically complex, and model-dependent so that the projected cloud feedbacks remain a key uncertainty for constraining climate sensitivity (Section 7.4.2.4).

CMIP6 models project an overall decrease in near-surface relative humidity over land, although with some regional and seasonal variations in their response (Fig. 4.26). Regional changes in near-surface humidity over land are dominated by thermodynamic processes and are primarily controlled by moisture transport from the warming ocean (Chadwick et al., 2016b). Increases in specific humidity lower than the thermodynamic rate are explained by greater warming over land than ocean and modulated by land-atmosphere feedbacks such as soil moisture and plant stomatal changes (Section 8.2.2.1) (Berg et al., 2017; Douville et al., 2020). This explains why climate models continue to project a contrasting response of near-surface relative humidity, with a slight and possibly overestimated increase over the oceans and a consistent but possibly underestimated decrease over land (Byrne and O'Gorman, 2016; Douville and Plazzotta, 2017; Zhang et al., 2018c).

While projections of water vapour are well understood due to the constraints of the Clausius-Clapeyron relationship, projections of water vapour transport are complicated regionally by the role of changes in the wind field, which is influenced by a wide variety of factors. Additionally, there has been relatively little general evaluation of moisture transport in models. In CMIP5 models, both the mean and variability of the vertically-integrated moisture transport is projected to increase, largely due to increases in water vapour (Lavers et al., 2015), with substantial regional differences (Levang and Schmitt, 2015). Single model studies have illustrated projected increases in low-altitude moisture transport into convergence regions (Allan et al., 2014) and from ocean to land (Zahn and Allan, 2013) that are consistent with present day trends. Increases in

ACCEPTED VERSION SUBJECT TO FINAL EDITING

moisture transport have been linked to increases in large precipitation accumulations over land (Norris et al., 2019). Based on robust physics and supported by modelling studies, it is well understood that moisture transport increases into convergent parts of the atmospheric circulation such as storm systems, the tropical rain belt and high latitudes (Section 8.2.2.1), but changes in atmospheric circulation that are less well understood alter moisture transport regionally (Section 8.2.2.2). Therefore, given the limited examination of moisture transport in models, regional projections should be considered with caution. Changes in moisture transport specifically associated with monsoons, atmospheric rivers, and other specific circulation features are discussed further in the following sections.

In summary, there is *high confidence* in continued increases in global mean column integrated water vapour and near-surface specific humidity over land. There is *medium confidence* in region and season-dependent decreases in near-surface relative humidity over land, due to the complex physical processes involved. In general, there will be increases in moisture transport into storm systems, monsoons and high latitudes (*medium confidence*).

8.4.1.3 Precipitation amount, frequency and intensity

This section assesses projected changes in precipitation at regional scales. Note that changes in precipitation seasonality are assessed in Box 8.2 and that changes in regional monsoons are assessed in Section 8.4.2.4, where both circulation and rainfall are considered. Further assessments of regional projections of precipitation are presented in Chapters 10, 12 and the Atlas, while a comprehensive assessment of changes in precipitation extremes is provided in Chapter 11.

AR5 assessed that the contrast of mean precipitation amount between dry and wet regions and seasons is expected to increase over most of the globe as temperatures increase (*high confidence*), but with large regional variations. Precipitation over the high latitudes, equatorial Pacific Ocean, mid-latitude wet regions, and monsoon regions were assessed as *likely* to increase under the RCP8.5 scenario, and in many mid-latitude and subtropical dry regions as *likely* to decrease (AR5 Chapters 7, 12, and 14). Extreme precipitation over most mid-latitude land areas and wet tropical regions was assessed as *very likely* to become more intense and more frequent.

Geographical patterns of projected precipitation changes show substantial seasonal contrasts and regional differences, including over land (Figure 8.14; Figure 4.27). Projections for 2081-2100 under the SSP2-4.5 scenario suggest increased precipitation over the tropical oceans, northeastern Africa, the Arabian Peninsula, India, southeastern Asia and the Polar Regions while decreased precipitation is projected mainly over the subtropical regions (Section 4.5.1.4). Precipitation changes contrast regionally in the tropics with wetter wet seasons over South Asia, central Sahel and eastern Africa, but less precipitation over Amazonia and coastal West Africa (Section 8.4.2.4). These large-scale responses are associated with stronger moisture transports in a warmer climate that are modulated by the greater warming over land than ocean, atmospheric circulation responses and land surface feedbacks (Section 8.2.2). There is agreement across CMIP5 and CMIP6 modelling studies that precipitation increases in wet parts of the atmospheric circulation and decreases in dry parts (Liu and Allan, 2013; Kumar et al., 2015; Deng et al., 2020; Schurer et al., 2020) although these regions shift with atmospheric circulation changes. The overall pattern is robust across different model scenarios and time horizons (Tebaldi and Knutti, 2018), but some deviations from the mean pattern cannot be excluded due to the multiple timescales and non-linear atmospheric or land surface processes involved (Section 8.5.3). Near-term regional changes in precipitation are more uncertain because of a stronger sensitivity to natural variability (Section 8.5.2) and non-GHG anthropogenic forcings (Section 4.4.1.3 and 8.4.3.1).

Projected changes in regional precipitation also arise as a response to changes in large-scale atmospheric circulation (Section 8.2.2.2 and 8.4.2), both in the tropics (Chadwick et al., 2016a; Byrne et al., 2018) and extratropics (Shaw, 2019; Oudar et al., 2020b). Despite variability in simulated changes, CMIP5 climate models consistently project large rainfall changes (of varying sign) over considerable proportions of tropical land during the 21st century (Chadwick et al., 2016a). Since AR5, some robust responses in large-scale

ACCEPTED VERSION SUBJECT TO FINAL EDITING

circulation patterns have been identified. For example, and as further assessed in Section 8.4.2, CMIP6 models project a northward shift in the tropical rain belt over eastern Africa and the Indian Ocean and a southward shift in the eastern Pacific and Atlantic oceans (Mamalakis et al., 2021). A projected strengthening and tightening of the tropical rain belt increases the contrasts between wet and dry tropical weather regimes and seasons. It is less clear how the well understood poleward expansion of the subtropics and mid-latitude storm tracks influences precipitation over sub-tropical and mid-latitude continents (Section 8.2.2.2).

An ensemble of 31 CMIP6 models under the SSP5-8.5 scenario projects increases of precipitation by 10–30% over much of the United States and decreases by 10–40% over Central America and the Caribbean by 2080-2099 (Almazroui et al., 2021). This CMIP6 ensemble also projects an increase in annual precipitation over the southern Arabian Peninsula and a decrease over the northern Arabian Peninsula, as also projected by CMIP3 and CMIP5 models (Almazroui et al., 2020a). Annual mean precipitation is projected to increase over South Asia during the 21st century under all scenarios, although the rate of change varies within the region based on 27 CMIP6 models (Almazroui et al., 2020c). CMIP6 projections also display a reduction in annual mean precipitation over northern and southern Africa while increases are projected over central Africa, under the SSP1-2.6, SSP2-4.5 and SSP5-8.5 scenarios (Almazroui et al., 2020b). The AR6 Atlas assesses that regions where annual mean rainfall is *likely* to increase include the Ethiopian Highlands, East, South and North Asia, southeastern South America, northern Europe, northern and eastern North America, and the Polar Regions. In contrast, regions where annual mean rainfall is *likely* to decrease include southern Africa, coastal West Africa, Amazonia, southwestern Australia, Central America, southwestern South America, and the Mediterranean.

AR5 identified that high-latitude precipitation increase may lead to an increase in snowfall in the coldest regions and a decrease of snowfall in warmer regions due to a decreased number of freezing days. The fraction of precipitation falling as snow and the duration of snow cover was projected to decrease. Heavy snowfall events globally are not expected to decrease significantly with warming as they occur close to the water freezing point, which will migrate poleward and in altitude (O'Gorman, 2014; Turner et al., 2019). There are only a small number of studies evaluating the implications of this mechanism in specific regions. A study for the northeastern US indicates smaller reductions for major snowfall events against the broader decline in snowfall expected from thermodynamic effects (Bintanja and Andry, 2017). Arctic snowfall is projected to decrease as rainfall makes up more of the precipitation (Zarzycki, 2018).

Beyond annual or seasonal mean precipitation amounts, an implication of the parallel intensification of the global water cycle and of the increased residence time of atmospheric water vapour (Section 8.2.1) is that the distribution of daily and sub-daily precipitation intensities will experience significant changes (Pendergrass and Hartmann, 2014b; Pendergrass et al., 2015; Bador et al., 2018; Douville and John, 2020), with fewer but potentially stronger events (*high confidence,* Section 4.3.3). CMIP6 projections show that in the long-term more drier days but more intense single events of precipitation are expected, regardless of scenario (Figure 8.15). Over almost all land regions, it is *very likely* that extreme precipitation will intensify at a rate close to the 7% per 1°C of global warming, but with large spatial differences (Section 11.4; Section 8.2.3.2). The projected increase in precipitable water is expected to lead to an increase in the highest possible precipitation intensities and an increase in the probability of occurrence of extreme precipitation events on the global scale (Neelin et al., 2017), regardless of how annual mean precipitation changes (O'Gorman and Schneider, 2009; O'Gorman, 2015). The projected increase in heavy precipitation intensity is also found for daily mean precipitation intensity though at a lower rate (Pendergrass and Hartmann, 2014a).

An increase in the number of dry days is also projected in several regions of the world (Polade et al., 2014, (Polade et al., 2014; Berthou et al., 2019a)), which can dominate the annual precipitation change at least in the subtropics (Polade et al., 2014; Douville and John, 2020). These findings are supported by CMIP6 projections showing a widespread increase in daily mean precipitation intensity over land (Fig.8.15bdf) as well as an increase in the number of dry days in the subtropics and over Amazonia and Central America (Fig.8.15abc). Such changes in precipitation regimes, as well as the general increase in the frequency and intensity of precipitation extremes (Section 11.4.5), contribute to an overall increase in precipitation variability (Polade et al., 2014; Pendergrass et al., 2017; Douville and John, 2020). This is also found in

ACCEPTED VERSION SUBJECT TO FINAL EDITING

CMIP6 models, which show a stronger increase of interannual variability than in seasonal mean precipitation changes, apart from in the winter extratropics where both quantities increase at the same rate with increasing global warming levels (Fig.8.16).

In summary, it is *virtually certain* that global precipitation will increase with warming due to increases in GHG concentrations and decreases in air pollution. There is *high confidence* that total precipitation will increase in the high latitudes, with a shift from snowfall to rainfall except in the coldest regions and seasons. There is also *high confidence* that precipitation will decrease over the Mediterranean, southern Africa, Amazonia, Central America, southwestern South America, southwestern Australia and coastal West Africa and that monsoon precipitation will increase over South Asia, East Asia and central-eastern Sahel. See Section 8.4.2.4 for a more detailed assessment of changes in regional monsoons. Daily mean precipitation intensities, including extremes, are projected to increase over most regions (*high confidence*). The number of dry days is projected to increase over the subtropics, Amazonia, and Central America (*medium confidence*). There is *high confidence* in an overall increase in precipitation variability over most land areas.

[START FIGURE 8.14 HERE]

Figure 8.14: Projected long-term relative changes in seasonal mean precipitation. Global maps of projected relative changes (%) in seasonal mean of precipitation averaged across 29 CMIP6 models in the SSP2-4.5 scenario. All changes are estimated for 2081-2100 relative to the 1995-2014 base period. Uncertainty is represented using the simple approach: No overlay indicates regions with high model agreement, where ≥80% of models agree on sign of change; diagonal lines indicate regions with low model agreement, where <80% of models agree on sign of change. For more information on the simple approach, please refer to the Cross-Chapter Box Atlas.1. Further details on data sources and processing are available in the chapter data table (Table 8.SM.1).

[END FIGURE 8.14 HERE]

[START BOX 8.2 HERE]

BOX 8.2: Changes in water cycle seasonality

Observed changes

AR5 did not highlight observed changes in water cycle seasonality and SRCCL mostly emphasized changes in vegetation seasonality. Since AR5, a number of relevant studies have been published, but often with conflicting results. Based on three *in situ* datasets, reduced precipitation seasonality was identified over 62% of the terrestrial ecosystems analysed from 1950-2009 (Murray-Tortarolo et al. 2017). In contrast, both *in situ* and satellite data show a general increase in the annual range of precipitation from 1979 to 2010, which is dominated by wetter wet seasons (Chou et al., 2013). This paradox may be partly explained by a larger aerosol radiative forcing in the middle of the 20th century as well as by internal variability (Kumar et al., 2015; see also Box 8.1). For instance, the "long rains" over East Africa experienced declining trends in the 1980s and 1990s (Nicholson, 2017), which was linked to anthropogenic aerosols and SST patterns (Rowell et al., 2015), followed by a recent recovery that was linked to internal variability (Wainwright et al., 2019). Two satellite datasets revealed decreased rainfall seasonality in the tropics but an increased seasonality in the subtropics and mid-latitudes since 1979, without clear attribution (Marvel et al., 2017).

Large differences have been found across seven global precipitation datasets, with no region showing a consistent, statistically significant, positive or negative trend over the last three decades (Tan et al., 2020b). Regional studies suggest that observed changes in precipitation seasonality are neither uniform nor stable across the 20th century (Li et al., 2016a; Mallakpour and Villarini, 2017; Sahany et al., 2018; Deng et al., 2019). Since the 1980s, there is however growing evidence that contrasts between wet and dry regimes, including seasonality, have increased (Liu and Allan, 2013; Polson et al., 2013; Murray-Tortarolo et al., 2016; Tapiador et al., 2016; Gallego et al., 2017; Polson and Hegerl, 2017; Barkhordarian et al., 2018; Lan et

ACCEPTED VERSION SUBJECT TO FINAL EDITING

al., 2019; Liang et al., 2020; Schurer et al., 2020).

Additional changes in seasonality may manifest in the timing and duration of wet seasons. A later monsoon onset trend was reported throughout India from 1901 to 2013 (Sahany et al., 2018). Conversely, an earlier rainfall onset was implicated in increased springtime rainfall over the Tibetan Plateau in recent decades (Zhang et al., 2017c). Winter and early spring precipitation over the northwestern Himalaya for the period 1951-2007 shows an increasing trend of daily precipitation extremes in association with enhanced amplitude variations of extra-tropical synoptic-scale systems known as "Western Disturbances" (Cannon et al., 2015; Krishnan et al., 2019; Madhura et al., 2014). In China, an earlier onset was observed during 1961-2012 (Deng et al., 2019). In the African Sahel, rainfall has been most concentrated in the peak of the rainy season since the end of the 20th century (Biasutti, 2019). A shift in the seasonality of Sahelian rainfall, including delayed cessation has also been reported (Nicholson, 2013; Dunning et al., 2018) (Section 10.4.2.1). Over southern Africa, an observed earlier onset (1985-2007) is in contrast to a simulated historical and projected future delay in the wet season (Maidment et al., 2015; Dunning et al., 2018). An increasingly early onset of the North American monsoon has been observed from 1978 to 2009 (Arias et al., 2015). Seasonality changes in the South American monsoon indicate delayed onsets since 1978 (Fu et al., 2013; Yin et al., 2014; Arias et al., 2015; Debortoli et al., 2015; Arvor et al., 2017; Giráldez et al., 2020; Haghtalab et al., 2020; Correa et al., 2021).

In northern high latitudes, a shorter snow season (Zeng et al., 2018a) is mainly due to an earlier onset of spring snowmelt (Peng et al., 2013) which has been attributed to anthropogenic climate change (Najafi et al., 2016). Changes in snow seasonality affect streamflow at the regional scale, with an earlier peak in spring and a possible decrease of low-level flow in summer (Berghuijs et al., 2014; Kang et al., 2016; Dudley et al., 2017), while glacier shrinking can also alter the low-level flow in mountain catchments (Lutz et al., 2014; Milner et al., 2017; Huss and Hock, 2018). This can be partly ameliorated by water management in regulated catchments (Arheimer et al., 2017), but not in large river basins such as the Amazon which also shows an increased seasonality of discharge since 1979 (Liang et al., 2020).

Increasing aridity contrasts between wet and dry seasons over the late 20th century have been suggested (Kumar et al., 2015), with a human-induced decrease of water availability during the dry season over Europe, western North America, northern Asia, southern South America, Australia and eastern Africa (Padrón et al., 2020). Seasonal contrasts in microwave surface soil moisture measurements have also increased over 1979-2016 (Pan et al., 2019). Terrestrial water storage variations derived from gravimetric measurements since 2003 show a strong seasonality which is underestimated by global hydrological models (Scanlon et al., 2019) and whose multidecadal trends are difficult to interpret given the direct effect of enhanced water use (Rodell et al., 2018; Scanlon et al., 2018).

In summary, there is *medium confidence* that the annual range of precipitation has increased since the 1980s, at least in subtropical regions and over the Amazon. There is *low confidence* that this increase is due to human influence and that GHG forcing has already altered the timing or duration of wet seasons. There is *high confidence* that the human-induced retreat of the springtime snow cover and melting of glaciers have already contributed to changes in streamflow seasonality in high-latitude and low-elevation mountain catchments, and *medium confidence* that human activities have also contributed to an increased seasonality of water availability, including a drier dry season, in the extratropics.

Projected changes

AR5 reported with *high confidence* that the contrast between wet and dry seasons will generally increase with global warming and that monsoon onset dates will *likely* become earlier or show little change, while monsoon retreat dates will *likely* be delayed, resulting in a lengthening of the wet season in many regions.

Since AR5, several studies have further documented a projected increase in rainfall seasonality and the understanding of the underlying mechanisms has been improved (Sections 8.2.1 and 8.3.2). CMIP5 models show that the seasonal concentration of annual precipitation will increase over many regions by the end of the 21st century, with robust model agreement in most subtropical regions where an increase in the mean

ACCEPTED VERSION SUBJECT TO FINAL EDITING

number of dry days was also reported in the RCP8.5 scenario (Pascale et al., 2016). The semi-arid, winter rainfall dominated subtropical climate is projected to shift poleward and eastward, with the equatorward margins replaced by a more arid climate type. However, evolving SST patterns and land-ocean warming contrasts cause more complex responses (Alessandri et al., 2015; Polade et al., 2017; Brogli et al., 2019; Zappa et al., 2020). Projections over California show a stronger and shorter wet season (Polade et al., 2017; Dong et al., 2019). Decreases in future winter and spring rainfall are projected over southwestern Australia (Hope et al., 2015). Central Asia is projected to experience wetter winters, associated with an increase in snow depth in the northeastern regions (Li et al., 2019b). Even in a +2°C climate, both extreme precipitation and dryness will increase significantly in the extratropics, amplifying the seasonal precipitation range (Fujita et al., 2018). A single-model study shows that the annual range of precipitation increases globally by 2.6% per °C of global warming in stabilized low-warming scenarios (Chen et al., 2020f).

In the tropics, an amplified annual cycle (by ~3–5%/°C) of global land monsoon hydroclimates (P, $P - E$, and runoff) is projected by CMIP5 models under the RCP8.5 scenario, mostly due to a more intense wet season (Zhang et al., 2019c). A longer rainy season is projected by CMIP6 models over most regional monsoon areas except in the Americas (Moon and Ha, 2020). A delayed onset and cessation of the wet season over West Africa and the Sahel (Dunning et al., 2018) and a slightly delayed onset of South Asian monsoon rainfall (Hasson et al., 2016) are projected by CMIP5 models. CMIP5 projections suggest a strengthening of the annual cycle and a lengthening of the dry season in Southern Amazonia (Fu et al., 2013; Reboita et al., 2014; Boisier et al., 2015; Pascale et al., 2016; Sena and Magnusdottir, 2020). This is further verified by the projections from 6 CMIP6 models (Moon and Ha, 2020). A wet season shorter by 5-10 days by the end to the 21st century is projected for southern Africa (Dunning et al., 2018).

An increase in streamflow seasonality is projected over several large rivers in the low-mitigation RCP8.5 scenario, but with only small changes in the seasonality timing, except in northern high latitudes due to the earlier but potentially slower snowmelt in a warmer world (Eisner et al., 2017; Musselman et al., 2017). At the end of the century in a high-emission scenario, peak snowmelt timing is projected to occur one month earlier and peak water volume is 79% lower in the eastern USA (Rhoades et al., 2018). Earlier snow melt is projected e.g. by 30 days at the end of the 21st century in RCP4.5 for the Sierra Nevada in the western USA (Sun et al., 2018b). Sub-seasonal changes in water availability were found in many regions in the RCP8.5 scenario. However these should be considered with caution given the magnitude of model errors (Ferguson et al., 2018a). Increases in the seasonality of water availability has been found to be more pronounced in areas with high atmospheric evaporative demand, giving rise to a pattern of seasonally variable regimes becoming even more variable (Konapala et al., 2020). RCP4.5 and RCP8.5 projections show a pronounced soil drying in summer and autumn over western Europe, and a springtime drying over northern Europe due to an earlier snowmelt (Ruosteenoja et al., 2018).

A simple relative seasonality metric (Walsh and Lawler, 1981) applied to global projections based on CMIP6 models and SSP scenarios supports previous CMIP5 findings, especially the amplified seasonality of precipitation around the Mediterranean, and across southern Africa, California, southern Australia and the Amazon (Box 8.2, Figure 1). While such changes are not significant in the low-emission SSP1-2.6 scenario, they are consistent with the increased frequency of dry days projected over the same regions (Figure 8.16). In monsoon regions outside the Americas, rainfall seasonality does not show a significant increase even in high-emission scenarios. This challenges previous CMIP5 findings based on the difference between maximum and minimum monthly precipitation in a year (Zhang et al., 2019c) and higher sensitivity to the projected increase in precipitation extremes (Section 11.4.5). In the northern high-latitudes, milder winters are associated with wetter conditions and a decrease in precipitation seasonality.

In summary, the annual range of precipitation, water availability and streamflow will increase with global warming over subtropical regions and the Amazon (*medium confidence*), especially around the Mediterranean and across southern Africa (*high confidence*). The contrast between the wettest and driest month of the year is *likely* to increase by 3 to 5%/°C with global warming in most monsoon regions, in terms of precipitation, water availability (P-E) and runoff (*medium confidence*). There is *medium confidence* that the monsoon season could be delayed in a warmer climate in the Sahel. There is *high confidence* of earlier snowmelt.

ACCEPTED VERSION SUBJECT TO FINAL EDITING

[START BOX 8.2, FIGURE 1 HERE]

Box 8.2, Figure 1: Projected long-term changes in precipitation seasonality. Global maps of projected changes in precipitation seasonality (simply defined as the sum of the absolute deviations of mean monthly rainfalls from the overall monthly mean, divided by the mean annual rainfall as in Walsh and Lawler, 1981) averaged across 31 to 33 CMIP6 models in the SSP1-2.6 (b), SSP2-4.5 (c) and SSP5-8.5 (d) scenario respectively. The simulated 1995-2014 climatology is shown in panel (a). All changes are estimated in 2081-2100 relative to 1995-2014. Uncertainty is represented using the simple approach: No overlay indicates regions with high model agreement, where ≥80% of models agree on sign of change; diagonal lines indicate regions with low model agreement, where <80% of models agree on sign of change. For more information on the simple approach, please refer to the Cross-Chapter Box Atlas.1. Further details on data sources and processing are available in the chapter data table (Table 8.SM.1).

[END BOX 8.2, FIGURE 1 HERE]

[END BOX 8.2 HERE]

[START FIGURE 8.15 HERE]

Figure 8.15: Projected long-term relative changes in daily precipitation statistics. Global maps of projected seasonal mean relative changes (%) in the number of dry days (i.e. days with less than 1 mm of rain) and daily precipitation intensity (in mm/day, estimated as the mean daily precipitation amount at wet days - i.e., days with intensity above 1 mm/day) averaged across CMIP6 models in the SSP1-2.6 (a,b), SSP2-4.5 (c,d) and SSP5-8.5 (e,f) scenario respectively. Uncertainty is represented using the simple approach: No overlay indicates regions with high model agreement, where ≥80% of models agree on sign of change; diagonal lines indicate regions with low model agreement, where <80% of models agree on sign of change. For more information on the simple approach, please refer to the Cross-Chapter Box Atlas.1. Further details on data sources and processing are available in the chapter data table (Table 8.SM.1).

[END FIGURE 8.15 HERE]

[START FIGURE 8.16 HERE]

Figure 8.16: Rate of change in mean and variability across increasing global warming levels. Relative change (%) in seasonal mean total precipitable water (green dashed line), precipitation (red dashed lines), runoff (blue dashed lines), as well as in standard deviation of precipitation (red solid lines) and runoff (blue solid lines) averaged over extra-tropical land in (a) summer and (b) winter, and tropical land in (c) JJA and (d) DJF as a function of global-mean surface temperature for the CMIP6 multi-model mean across the SSP5-8.5 scenario. Extra-tropical winter refers to DJF for Northern Hemisphere and JJA for Southern Hemisphere (and the reverse for extra-tropical summer). Each marker indicates a 21-year period centered on consecutive decades between 2015 and 2085 relative to the 1995–2014 base period. Precipitation and runoff variability are estimated by their standard deviation after removing linear trends from each time series. Error bars show the 5-95% confidence interval for the warmest 5°C global warming level. Figure adapted from (Pendergrass et al., 2017) and updated with CMIP6 models. Further details on data sources and processing are available in the chapter data table (Table 8.SM.1).

[END FIGURE 8.16 HERE]

8.4.1.4 Evapotranspiration

Since AR5, there is a growing body of evidence suggesting that future projections in evapotranspiration are

ACCEPTED VERSION SUBJECT TO FINAL EDITING

driven by changes in temperature and relative humidity (Laîné et al., 2014; Pan et al., 2015; Ukkola et al., 2016a), as well as precipitation patterns, as found in AR5.

Analysis of CMIP5 models suggests that atmospheric evaporative demand will increase over most areas of the world in high-emission scenarios (*virtually certain*), mostly as a consequence of an increase in vapour pressure deficit (Scheff and Frierson, 2014, 2015; Vicente-Serrano et al., 2020b). CMIP5 models also project an increase in evapotranspiration over most land areas (*medium confidence*) (Laîné et al., 2014). However, regional changes in evapotranspiration can also be influenced by changes in soil moisture and vegetation, which modulate the moisture flux from the land to the atmosphere. Several studies of CMIP5 projections suggest that increases in plant water use efficiency will limit or counteract rising evapotranspiration (Milly and Dunne, 2016; Swann et al., 2016; Lemordant et al., 2018; Yang et al., 2018d). However, other studies have found that transpiration increases due to the impact of climate change on growing season length, leaf area, and evaporative demand (Frank et al., 2015; Mankin et al., 2017, 2018, 2019; Guerrieri et al., 2019; Zhou et al., 2019a; Vicente-Serrano et al., 2020b) (Section 8.2.3.3). The parameterizations accounting for these complex physiological processes in global climate models may also be insufficient (Franks et al., 2017; Peters et al., 2018; Peano et al., 2019). Thus, there is currently *low confidence* in the role of vegetation physiology in modulating future projections of evapotranspiration.

CMIP6 models project a geographical pattern of changes in evapotranspiration similar to previous generation models (Figure 8.17), although the magnitude is generally larger than found for CMIP5 projections (Liu et al., 2020b). There is however a strong seasonality in many regions, with a larger relative increase in the winter season of the Northern Hemisphere and smaller relative changes in the summer (Figure 8.17). Evapotranspiration increases in most land regions, except in areas that are projected to become moisture-limited (due to reduced precipitation and increased evaporative demand), such as the Mediterranean, South Africa, and the Amazon basin (*medium confidence*). The patterns of change increase in magnitude from low to high-emission SSP scenarios (*medium confidence*).

In summary, future projections indicate that anthropogenic forcings will drive an increase in global mean evaporation over most oceanic areas (*high confidence*) (Figure 8.17), an increase in global atmospheric demand (*virtually certain*) and an increase in evapotranspiration over most land areas, with the exception of moisture-limited regions (*medium confidence*). However, substantial uncertainties in projections of evapotranspiration, especially at seasonal and regional scales, remain (see also Section 8.2.3.3, Cross-Chapter Box 5.1).

[START FIGURE 8.17 HERE]

Figure 8.17: Projected long-term relative changes in seasonal mean evapotranspiration. Global maps of projected relative changes (%) in seasonal mean of surface evapotranspiration for DJF (left panels) and JJA (right panels) averaged across 29 or 30 CMIP6 models for SSP1.2-6 (a,b), SSP2-4.5 (c,d) and SSP5-8.5 (e,f) scenario respectively. All changes are estimated in 2081-2100 relative to 1995-2014. Uncertainty is represented using the simple approach: No overlay indicates regions with high model agreement, where ≥80% of models agree on sign of change; diagonal lines indicate regions with low model agreement, where <80% of models agree on sign of change. For more information on the simple approach, please refer to the Cross-Chapter Box Atlas.1. Further details on data sources and processing are available in the chapter data table (Table 8.SM.1).

[END FIGURE 8.17 HERE]

8.4.1.5 Runoff, streamflow and flooding

AR5 assessed that projected changes in runoff had *low confidence* over the period 2016-2035; however, under the RCP8.5 scenario, runoff increases by 2100 are *likely* in high northern latitudes. This is consistent with projected regional precipitation increases, and that runoff decreases that are *likely* in southern Europe, the Middle East and southern Africa, based on consistency of changes across different generations of models

ACCEPTED VERSION SUBJECT TO FINAL EDITING

and different forcing scenarios. There was considerable uncertainty in the magnitude and direction of change for some regions, largely driven by the uncertainty in projected precipitation changes, particularly across south Asia. For flooding, AR5 assessed with *medium confidence* that flooding would increase over parts of South and Southeast Asia, tropical Africa, northeast Eurasia, and South America, and decrease for parts of northern and Eastern Europe, Anatolia, central Asia, central North America, and southern South America. SR1.5 assessed with *medium confidence* that warming of 2˚C would increase the fraction of global area affected by flood hazard relative to warming of 1.5˚C. Projected climate-driven changes to runoff, streamflow, and flooding will occur in the context of potential human-caused land-use and land-cover changes, which can have a large influence on surface water (Sterling et al., 2013) but which have considerable uncertainty in projections (Prestele et al., 2016).

Since AR5, studies confirm that global mean annual runoff increases with global surface temperature increase (Zhang and Tang, 2014; Zhang et al., 2018e; Lehner et al., 2019), but varies regionally (Chen et al., 2017; Yang et al., 2017; Cook et al., 2020). CMIP5 models display a large spread in the ratio of runoff to precipitation for the present-day climate, which applies also to future runoff changes under global warming (Lehner et al., 2019). In studies of CMIP6 projections, runoff increases in most parts of the northern high latitudes and Asia and north and eastern Africa, and decreases in the Mediterranean region, southern Africa, southern Australia and in parts of western Africa, as well as in Central and South America (Greve et al., 2018; Cook et al., 2020). Projected changes in runoff also vary seasonally. In the Northern Hemisphere, runoff increases during winter since more precipitation falls as rain than snow and decreases in the summer as less snow is available to contribute to runoff during the warm season (Cook et al., 2020). Global maps of projected changes for DJF and JJA are shown in in Figure 8.18, showing projected changes becoming larger and more consistent in the higher emissions scenarios. Runoff projections for CMIP6 are also shown in Figure 8.16 for tropical and extratropical averages at a range of global mean warming levels and in Table 8.1 for global land in different future scenarios. In the tropics, both the mean and interannual variability of runoff increase with warming. The increase in variability is roughly twice as large as the increase in the mean, and has a large spread across models. In the extratropics, changes are small in the summer but there are large increases in the winter, with the mean increasing much more than the variability, in contrast to the tropics.

Changes in streamflow vary regionally and increase in magnitude with emissions scenario, as with runoff (although the two are not equivalent, as runoff includes both surface runoff and streamflow). Streamflow projections additionally require the use of hydrologic models forced by the output from climate models and have not been as widely explored as they are not variables directly included in climate models. On an annual basis, streamflows have been projected to increase in the Northern high latitudes and tropical Asia and Africa, and to decrease in the Mediterranean, tropical South America, and South Africa (Döll et al., 2018b). For a 4°C global warming, half of the global land area is projected to be exposed to increased high flows (average increase 25%), while about 60% may be exposed to decreased low flows (average decrease 50%) (Asadieh and Krakauer, 2017).

Changes in the seasonality of runoff and streamflow are assessed in Box 8.2. The seasonality of runoff and streamflow (calculated as the annual difference between the wettest and driest months of the year), is expected to increase with global warming in the subtropics, especially in the Mediterranean and southern Africa with *high confidence*, and in the Amazon with *medium confidence*. For regions where snowmelt is an important contributor to streamflow, there is *high confidence* that snowmelt occurring earlier in the year will result in peak flows also occurring earlier in the year, and *medium confidence* that reduced snow volume and the weaker solar radiation earlier in the year will reduce the most intense flows. In roughly half of 56 large-scale glacierized drainage basins, projected runoff changes show an increase until a maximum is reached, beyond which runoff steadily declines because of limited ice volumes (Huss and Hock, 2018).

As future changes in flood events are assessed in Chapters 9 and 11, only a summary is presented here. There are a number of complicating factors for projecting both pluvial (overland) and fluvial (river) flooding that limit confidence in their assessment. In addition to precipitation, flooding also depends on basin and river characteristics such as permeability, antecedent soil moisture, and antecedent flow levels for river flooding, so projections of extreme precipitation and flooding are not always closely linked (Section 8.2.3.2).

ACCEPTED VERSION SUBJECT TO FINAL EDITING

Possible changes in water resources management and land use add another layer of complexity to future changes. There is *medium confidence* in a general increase in pluvial and fluvial flooding, although there are large geographical variations in magnitude. There are increases in flooding in the West Amazon, the Andes, and northern Eurasia (Chapter 11, Section 11.5.5). There is *medium confidence* in future increases in urban and coastal floods (Chapter 11, Section 11.5.5), and *high confidence* that some coastal regions will experience large increases in surge flooding (Chapter 9, Section 9.6.4.2). There is *medium confidence* in an increase in compound flood events (Chapter 11, Section 11.8.1). Although there is currently insufficient evidence for a confident projection, flooding due to rain-on-snow events can be expected to decrease where snow decreases (Chapter 11, Section 11.8.3), and the seasonality of snowmelt-related flooding can be expected to shift in regions with temperature-driven shifts in the snowmelt season (e.g., Vormoor et al., 2015). Glacier lake outburst floods (GLOFs) are expected to increase substantially, in delayed response to glacier recession but with *low confidence*, due to the small number of studies and the complexity of the processes involved (Chapter 9, Section 9.5.3.3).

In summary, there is *medium confidence* that global runoff will increase with global warming, but with large regional and seasonal variations. There is *high confidence* that runoff will increase in the northern high latitudes and decrease in the Mediterranean region and southern Africa. There is *medium confidence* that runoff will increase in regions of central and eastern Africa, and decrease in Central America and parts of southern South America, with the magnitude of the change increasing with emissions. There is *medium confidence* that the seasonality of runoff and streamflow will increase with global warming in the subtropics. In snow-dominated regions, there is *high confidence* that peak flows associated with spring snowmelt will occur earlier in the year and *medium confidence* that snowmelt-induced runoff will decrease with reduced snow, except in glacier-fed basins where runoff may increase in the near term. There is *medium confidence* that flooding in general will increase, although with considerable variation based on geographic region and flood type. These projected climate-related changes will occur in the context of human-caused land-use and land-cover changes, which may also have a large influence.

[START FIGURE 8.18 HERE]

Figure 8.18: Projected long-term relative changes in seasonal mean runoff. Global maps of projected relative change (%) in runoff seasonal mean for DJF (left panels) and JJA (right panels) averaged across CMIP6 models SSP1.2-6 (a,b), SSP2-4.5 (c,d) and SSP5-8.5 (e,f) scenario respectively. All changes are estimated in 2081-2100 relative to 1995-2014. Uncertainty is represented using the simple approach: No overlay indicates regions with high model agreement, where ≥80% of models agree on sign of change; diagonal lines indicate regions with low model agreement, where <80% of models agree on sign of change. For more information on the simple approach, please refer to the Cross-Chapter Box Atlas.1. Further details on data sources and processing are available in the chapter data table (Table 8.SM.1).

[END FIGURE 8.18 HERE]

8.4.1.6 Aridity and drought

AR5 concluded that regional to global-scale projections of aridity and drought remained relatively uncertain compared to other aspects of the water cycle. It reported that there is a *likely* increase in drought occurrence (*medium confidence*) by 2100 in regions that are currently drought-prone under the RCP8.5 scenario due to projected decreases in soil moisture. It stated that it is *likely* that the most prominent projected decreases in soil moisture would occur in the Mediterranean, southwest USA, and southern Africa, consistent with projected changes in the Hadley Circulation and increased surface temperatures. These AR5 conclusions are generally supported by more recent analyses of CMIP5 models (Feng and Fu, 2013; Berg et al., 2017; Cook et al., 2018).

Results from the latest generation of models in CMIP6 are largely congruent with CMIP5. Consistent with the coherent nature of warming in future projections, increases in vapour pressure deficit and evaporative demand are widespread and consistent across regions, seasons, and models, increasing in magnitude in

ACCEPTED VERSION SUBJECT TO FINAL EDITING

accordance with the emissions scenario (Figure 8.19) (*high confidence*) (Scheff and Frierson, 2014, 2015; Vicente-Serrano et al., 2020b). Even under a low-emissions scenario (SSP1-2.6), projections of soil moisture show significant decreases in the Mediterranean, southern Africa, and the Amazon basin (*high confidence*) (Figure 8.19). Under mid- and high-emissions scenarios (SSP2-4.5 and SSP5-8.5), coherent declines emerge across Europe, westernmost North Africa, southwestern Australia, Central America, southwestern North America, and southwestern South America (*high confidence*) (Figure 8.19) (Cook et al., 2020). Compared to CMIP5 results, CMIP6 models exhibit more consistent drying in the Amazon basin (Parsons, 2020), more extensive declines in total soil moisture in Siberia (Cook et al., 2020), and stronger declines in westernmost North Africa and southwestern Australia (Figure 8.19).

Soil moisture in the top soil layer (10 cm) shows more widespread drying than total soil moisture, reflecting a greater sensitivity of the upper soil layer to increasing evaporative demand (Berg et al., 2017) (Figure 8.19). Conversely, total column soil moisture represents the carry-over of moisture from previous seasons deeper in the soil column, and potentially higher sensitivity to vegetation processes (Berg et al., 2017; Kumar et al., 2019). Central America, the Amazon basin, the Mediterranean region, southern Africa, and southwestern Australia are projected to experience significant declines in total soil moisture, whereas declines in Europe (north of the Mediterranean), western Siberia, and northeastern North America are limited to the surface (Figure 8.19). It should be noted that because models differ in their number of hydrologically active layers, there is less confidence in total soil moisture projections than surface soil moisture projections. Based on surface soil moisture projections, more than 40% of global land areas (excluding Antarctica and Greenland) are expected to experience robust year-round drying, even under lower emissions scenarios (Cook et al., 2020). The percentage of land area experiencing drying is slightly lower when runoff is used as an aridity metric instead (20–30%); taking this into consideration, it is estimated that about a third of global land areas will experience at least moderate drying in response to anthropogenic emissions, even under SSP1-2.6 (*medium confidence*) (Cook et al., 2020).

Although there are regions where multiple models predict consistent and significant changes in soil moisture, as with evapotranspiration (Section 8.4.1.4), there is still uncertainty in these projections related to the response of plants to elevated CO_2. Most models project increases in two variables that have opposite effects on surface water availability: plant water use efficiency (WUE) and leaf area index (LAI) (see Section 8.4.1.4). As discussed in Section 8.2.3.3, 8.3.1.4, and 8.4.1.4, there is *low confidence* in how these changes in plant physiology will affect future projections of evapotranspiration, and likewise, drought and aridity.

[START FIGURE 8.19 HERE]

Figure 8.19: Projected long-term relative changes in annual mean soil moisture and vapour pressure deficit. Global maps of projected relative changes (%) in annual mean vapour pressure deficit (left), surface soil moisture (top 10cm, middle) and total column soil moisture (right) from available CMIP6 models for the SSP1.2-6 (a,b,c), SSP2-4.5 (d,e,f) and SSP5-8.5 (g,h,i) scenarios respectively. All changes are estimated for 2081-2100 relative to a 1995-2014 base period. Uncertainty is represented using the simple approach: No overlay indicates regions with high model agreement ("Robust change"), where ≥80% of models agree on sign of change; diagonal lines indicate regions with low model agreement, where <80% of models agree on sign of change. For more information on the simple approach, please refer to the Cross-Chapter Box Atlas.1. Further details on data sources and processing are available in the chapter data table (Table 8.SM.1).

[END FIGURE 8.19 HERE]

Changes in meteorological (precipitation-based) drought duration and intensity in CMIP6 models are more robust than projected changes in mean precipitation, more than found in CMIP5 projections (Ukkola et al., 2020). Significant increases in drought duration are expected in Central America, the Amazon basin, southwestern South America, the Mediterranean, westernmost North Africa, southern Africa, and southwestern Australia, on the order of 0.5–1 month for a moderate emissions scenario (SSP2-4.5) and 2 months for a high emissions scenario (SSP5-8.5) (Ukkola et al., 2020). Drought intensity is projected to

ACCEPTED VERSION SUBJECT TO FINAL EDITING

increase in the tropics, mainly in the Amazon basin, central Africa, and southern Asia, as well as in Central America and southwestern South America (Ukkola et al., 2020). The CORDEX South Asia multi-model ensemble projections indicate an increase in the frequency and severity of droughts over central and northern India during the 21st century, under the RCP4.5 and RCP8.5 scenarios *(medium confidence)* (Mujumdar et al., 2020). Under middle or high emissions scenarios, the likelihood of extreme droughts (events that have magnitudes equal to or less than the 10th percentile of the 1851–1880 baseline period) increases by 200–300% in the Amazon basin, southwestern North America, Central America, the Mediterranean, southern Africa, and southwestern South America (Cook et al., 2020). Even under a low emissions scenario (SSP1-2.6), the likelihood of extreme droughts increases by 100% in southwestern North America, southwestern South America, the Amazon, the Mediterranean, and southern Africa (Cook et al., 2020). Thus, there is *high confidence* that drought severity and intensity will increase in the Mediterranean, southern Africa, southwestern South America, southwestern North America, southwestern Australia, Central America and the Amazon basin.

Paleoclimate records provide context for these future expected changes in drought and aridity. In the Mediterranean, western North America, and central Chile, there is *high confidence* that climate change will shift soil moisture (as represented by the Palmer Drought Severity Index) outside the range of observed and reconstructed values spanning the last millennium (Cook et al., 2014; Otto-Bliesner et al., 2016) (Figure 8.20). Warmer temperatures, leading to increased evaporative losses, are clearly implicated in the projected future drying in these semi-arid regions (Dai et al., 2018), emphasizing the central role that warming plays in driving increased evaporative demand (Vicente-Serrano et al., 2020b). In contrast, future trajectories are more uncertain in regions like central Asia and eastern Australia–New Zealand where projected changes in precipitation and soil moisture are less coherent (Hessl et al., 2018) (Figure 8.19, 8.20). More information on projected changes in drought, including specific categories or drought, can be found in Section 11.6.5 and Section 12.4.

In summary, there is *high confidence* that soil moisture will decline in semi-arid, winter-rainfall dominated areas including the Mediterranean, southern Africa, southwestern North America, southwestern South America, and southwestern Australia, as well as in Central America and the Amazon basin. In general, these regions are expected to become drier both due to reduced precipitation (*medium confidence*) and increases in evaporative demand (*high confidence*). These same regions are *likely* to experience increases in drought duration and/or severity (*high confidence*). The magnitude of expected change scales with emissions scenarios (*high confidence*) but even under low-emissions trajectories, large changes in drought and aridity are expected to occur (*high confidence*) with consequences for regional water availability. In the Mediterranean, central Chile, and western North America, future aridification will far exceed the magnitude of change seen over the last millennium (*high confidence*).

[START FIGURE 8.20 HERE]

Figure 8.20: Past-to-future drought variability in paleoclimate reconstructions and models for select regions. On the left (a,c,e,g,i), tree-ring reconstructed Palmer Drought Severity Index (PDSI) series (black line) for the Mediterranean (10˚W–45˚E, 30˚–47˚N; Cook et al., 2015, 2016), central Chile (70˚–74˚W, 32˚–37˚S; Morales et al., 2020), western North America (117˚–124˚W, 32˚–38˚N; Cook et al., 2010; Griffin and Anchukaitis, 2014), Eastern Australia and New Zealand (136˚–178˚E, 46˚–11˚S; Palmer et al., 2015), and Central Asia (99˚–107˚E, 47˚–49˚N; Pederson et al., 2014; Hessl et al., 2018) plotted in comparison to the past-to-future fully-forced simulations from four ensemble members (thin blue lines) from the NCAR CESM Last Millennium Ensemble (thick blue line = ensemble mean) (Otto-Bliesner et al., 2016) for the same regions. The shaded area represents the range (10th to 90th percentile) of historical and future (RCP8.5) PDSI (Penman-Monteith) simulations from 15 CMIP5 models and 34 ensemble members for the same regions (1900–2100; Cook et al., 2014). On the right (b,d,f,h,i), the distribution of annual PDSI values from the past and present (850 to 2005 CE) (black) is compared to the future distribution (2006 to 2100 CE) (blue). The distributions show each of the four ensemble members from the CESM LME simulations. The future component of the CESM LME follows the RCP8.5 scenario. Further details on data sources and processing are available in the chapter data table (Table 8.SM.1).

ACCEPTED VERSION SUBJECT TO FINAL EDITING

[END FIGURE 8.20 HERE]

8.4.1.7 Freshwater reservoirs

8.4.1.7.1 Glaciers

Previous assessments have concluded that recent warming has led to a reduction in low-elevation snow cover (SROCC, *high confidence*), permafrost (SROCC, *high confidence*), and glacier mass (AR5, *high confidence*; SROCC, *very high confidence*). SROCC noted that these declines are projected to continue almost everywhere over the 21st century (*high confidence*), with complete glacier loss expected in regions with only small glaciers (*very high confidence*). SROCC supported the AR5 finding that glacier recession would continue even without further changes in climate. SROCC concluded that cryosphere changes had already altered the seasonal timing and volume of runoff (*very high confidence*), which in turn had affected water resources and agriculture (*medium confidence*), and projected peak water runoff had already been reached before 2019 in some of the glacier regions considered.

Chapter 9 provides detailed assessment of glacier observations and projections (Figure 9.20 and 9.21, see Section 9.5.1). Here, a summary of their key findings is presented. Since SROCC, the coordinated glacier model intercomparison project (GlacierMIP (Marzeion et al., 2020), see also Box 9.3) has advanced modelling efforts. Global glacier volumes will substantially decline in coming decades regardless of emissions scenario; under a high emission scenario some areas will lose nearly all of their glacier mass (Section 9.5.1.3). The projected global glacier mass loss over 2015-2100 is 29 000 ± 20 000 Gt for SSP1-2.6 to 58 000 ± 30 000 Gt for SSP5-8.5 (Section 9.5.1). Because of their lagged response to warming, glaciers will continue to lose mass for decades even if global temperature is stabilized (*very high confidence*) (Section 9.5.1).

Global glacier mass loss projections show a scenario-dependent geographic partitioning of when peak in runoff occurs (Marzeion et al., 2020), consistent with previous studies (Radić et al., 2014; Huss and Hock, 2018; Hock et al., 2019a). Under a low emission scenario (Marzeion et al., 2020) all regions exhibit runoff in the decades prior to 2050. Under a high emission scenario however, low and mid-latitude regions show peak runoff before approximately 2060, whereas Arctic regions peak in later decades around 2070-2090. Antarctic glacier losses will not have peaked by the end of the century in the high emission scenario. Globally, peak runoff of 2.5 to 3 mm / year sea level equivalent occurs around 2090 (Marzeion et al., 2020). Regional projections are presented in detail in Section 9.5.1 and Figure 9.21, and briefly summarized below.

Himalaya and Central Asia: Glaciers in the Himalayas feed ten of the world's most important river systems and are critical water sources for nearly two billion people (Wester et al., 2019) However they are some of the most vulnerable 'water towers' (Immerzeel et al., 2020) that are projected to experience volume losses of approximately 30 to 100% by 2100 depending on global emissions scenarios (Marzeion et al., 2020). Under mid-range emissions scenarios glaciers in this region are projected to reach peak runoff during the period 2020 to 2040 (Marzeion et al., 2020).

Alaska, Yukon, British Columbia: Post-AR5 but pre-SROCC projections indicated a potential 70 ± 10% reduced volume of glacier ice in western Canada relative to 2005 (Clark et al., 2015), with few glaciers remaining in the Interior and Rockies regions and maritime glaciers in northwestern British Columbia surviving only in a diminished state. Recent global projections support these earlier findings, showing that glacier mass in Western Canada and the United States may reduce by 50% under low emissions scenarios and be completely lost under the highest emissions and most sensitive glacier model combinations (Marzeion et al., 2020) (Figure 9.21). Arctic Canada and Alaskan glaciers are projected to experience more modest mass loss (0 to 60% depending on region, scenario, and model; Marzeion et al., 2020).

Andes: Huss and Hock (2018) concluded that peak glacier mass was reached prior to 2019 for 82–95% of the glacier area in the tropical Andes. This is consistent with more recent global model simulations that show mass loss rates from low latitude glaciers that universally decline from the start of simulations in 2015, regardless of emissions scenario (Marzeion et al., 2020). Peak runoff in low-latitude Andean glacier-fed

ACCEPTED VERSION SUBJECT TO FINAL EDITING

rivers has therefore already passed (Frans et al., 2015; Polk et al., 2017) but in the Southern Andes may occur in the latter half of the century under high emission scenarios (Marzeion et al., 2020).

In summary, glaciers are projected to continue to lose mass under all emissions scenarios *(very high confidence*). Runoff from glaciers is projected to peak at different times in different places, with maximum rates of glacier mass loss in low latitude regions taking place in the next few decades in all scenarios (*high confidence*). While runoff from small glaciers will typically decrease because of glacier mass depletion, runoff from larger glaciers will increase with increasing global warming until glacier mass is similarly depleted, after which runoff peaks and then declines and which tends to occurs later in basins with larger glaciers and higher ice-cover fractions (*high confidence*). Glaciers in the Arctic and Antarctic will continue to lose mass through the latter half of the century and beyond (*high confidence*).

8.4.1.7.2 Seasonal snow cover

AR5 assessed as *very likely* that the amount and seasonal duration of Northern Hemisphere snow cover will reduce under global warming (AR5 Section 11.3.4.2, Section 12.4.6.2). Changes in the total amount of water in the snow cover (snow water equivalent) are less certain because of the competing influences of temperature and precipitation.

As snow cover is assessed in Chapter 9 (Section 9.5.3.3), only an overview of that assessment is provided here. Changes in seasonality of snow cover are assessed in Box 8.2. The continued consistency of reported results across all generations of model projections, along with improvements in process understanding, has increased confidence in snow cover projections since AR5.

In summary, based on the results of Chapter 9, it is now *virtually certain* that future Northern Hemisphere snow cover extent and duration will continue to decrease with global warming. While most studies have focused on the Northern Hemisphere, process understanding suggests with *high confidence* that these results apply to the Southern Hemisphere as well. There is *high confidence* in snowmelt occurring earlier in the year. Changes to the timing and amount of snowmelt will have a strong influence on all the other aspects of the water cycle in regions with seasonal snow, including run-off, soil moisture, and evapotranspiration.

8.4.1.7.3 Wetlands and lakes

AR5 did not include specific projections for wetlands and lakes. SRCCL and SROCC provided some discussion of wetlands projections. For coastal wetlands, SRCCL noted the importance of sea level rise for increased saltwater intrusion, although projections of coastal wetland area with sea level rise are inconclusive. Some studies project substantial decreases (Spencer et al., 2016) while others indicate possible increases (Schuerch et al., 2018). SRCCL also noted the general expectation for decreases in water resources, including wetlands, in areas of decreased rainfall due to increased evaporation.

Local studies of inland wetlands project decreases in a range of environments including mountain (Lee et al., 2015), mid-to-high latitude (Zhao et al., 2018b), and prairie (Sofaer et al., 2016) regions. In addition to affecting wetland extent and density, changes in flooding can also affect the connectivity between wetlands and rivers (Karim et al., 2016). Despite a number of uncertainties underlying the general response of wetlands to climate change, there are multiple ways climate change may cause considerable stress on both inland and coastal wetlands (Junk et al., 2013; Moomaw et al., 2018).

Widespread changes are also projected for lakes (Woolway et al., 2020), including changes in lake temperature (Fang and Stefan, 1999; Sahoo et al., 2016), ice (Sharma et al., 2019), evaporation (Wang et al., 2018d), and stability and mixing (Woolway and Merchant, 2019). Note that lake ice is also considered in Chapter 12 of this Report. To date, carbon dioxide-induced lake acidification, analogous to ocean acidification, has not been the focus of many studies but may occur with continued emissions (Phillips et al., 2015). While glacier lakes in general increase with melting glaciers (Linsbauer et al., 2016; Colonia et al., 2017; Magnin et al., 2020) no clear projections are currently available (see discussion in Chapter 9). Projections of lake level means and variability show substantial changes for individual lakes (Bucak et al.,

ACCEPTED VERSION SUBJECT TO FINAL EDITING

2017; Li et al., 2021) but can be sensitive to methodology, due to the competing processes involved (Notaro et al., 2015). Projected changes to wetlands and lakes due to climate change will occur in the context of widespread and continuing human-caused conversion and degradation of wetlands (e.g, Davidson, 2014), and where water withdrawals have a large impact on lake levels (e.g., (Micklin, 2016)).

In summary, there is *medium confidence* that inland wetland extent will decrease in regions of projected precipitation decrease and evaporation increase, and *high confidence* that sea level rise will increase saltwater intrusion into coastal wetlands. However, there is *low agreement* on the influence of sea level rise on the extent of coastal wetlands. Regarding lakes, there is *high confidence* for temperature increases and ice decreases, based on both projections and physical expectations, and *low confidence* for non-homogeneous decreases in mixing, given there is currently *limited evidence*.

8.4.1.7.4 Groundwater

Groundwater projections were not assessed in AR5. Groundwater processes are not explicitly included in most current CMIP6 models and so must be calculated separately with hydrologic models (e.g., Taylor et al., 2013; Cuthbert et al., 2019a). A range of factors are important in assessing groundwater projections, including the mean difference between precipitation and evaporation, the intensity of precipitation (Taylor et al., 2013b), and in changes in snow (Tague and Grant, 2009), glaciers (Gremaud et al., 2009), and permafrost (Okkonen and Kløve, 2011). Climate impacts on groundwater are occurring in the context of severe and growing human-caused groundwater depletion (Konikow and Kendy, 2005), Rodell et al. 2018; (Bierkens and Wada, 2019), also see WGII), and water scarcity issues (Mekonnen and Hoekstra, 2016). Climate-related changes to the water cycle can influence water demand (for example, precipitation decreases in an irrigated area), and anthropogenic groundwater depletion can influence the water cycle through interactions with surface energy fluxes, surface water, and vegetation (Cuthbert et al., 2019a), although uncertainties in estimates of future groundwater depletion are large ((Smerdon, 2017), (Bierkens and Wada, 2019)). Some aspects of groundwater change will be irreversible, including the increase of saltwater intrusion into coastal aquifers with sea level rise (Werner and Simmons, 2009), and depletion of fossil aquifers and aquifers with very long recharge times ((Bierkens and Wada, 2019)).

Globally, two modelling studies have shown substantial decreases in groundwater in regions including the Mediterranean, northeastern Brazil and southwestern Africa, with less clarity for other regions (Döll, 2009), Portmann et al., 2013). Recent regional-scale analyses of the impact of water cycle changes on groundwater recharge (e.g. Meixner et al., 2016; Shrestha et al., 2018; Tillman et al., 2017) suggest changes in both seasonality and spatial distribution, which are amplified under a higher greenhouse-gas emission scenario (i.e., RCP 8.5 compared to RCP4.5). Seasonality changes are linked to increases during wet winter periods and declines during dry summer periods. Changes in spatial distribution are linked with increases in more humid regions and declines in more arid locations. Uncertainty in projections of groundwater were found to be substantially influenced by the conceptual and numerical models employed to estimate groundwater recharge (Meixner et al., 2016; Hartmann et al., 2017). Accordingly, current research on estimating water cycles change on groundwater includes a focus on improving the numerical representation of groundwater systems (Bierkens et al., 2015; Döll et al., 2016)).

In summary, based on known limitations in current modelling, no confident assessment of groundwater projections is made here, although important climate-related changes in groundwater recharge are expected. In many environments, such climate-related impacts are expected to occur in the context of substantial human groundwater withdrawals depleting groundwater storage.

8.4.2 Projected changes in large scale phenomena and regional variability

A weakening of the tropical circulation represents a balance between thermodynamic increases in low level water vapour (~7%/K) and smaller increases in global precipitation (1-3%/K) that are influenced by rapid adjustments to radiative forcings as well as slow responses to warming (Bony et al., 2013; Chadwick et al., 2013; Ma et al., 2018, Section 8.2.2.2). Since AR5, additional drivers of tropical circulation weakening have

ACCEPTED VERSION SUBJECT TO FINAL EDITING

been identified, including mean SST warming and changes in spatial patterns of SST (He and Soden, 2015), and the direct CO_2 radiative effect (Bony et al., 2013; Merlis, 2015 ; He and Soden, 2015).

8.4.2.1 ITCZ and tropical rain belts

CMIP5 projections show no consistent shift in the zonal mean position of the ITCZ (Byrne et al., 2018; Donohoe et al., 2013; Donohoe and Voigt, 2017). The ITCZ position is strongly connected to cross-equatorial energy transport (Bischoff and Schneider, 2014; Kang et al., 2008), which also shows no consistent change in future projections (Donohoe et al., 2013). Since AR5 it has been reported that most CMIP5 models project a narrowing of the ITCZ in response to surface warming together with intensified ascent in the core region and weakened ascent on the ITCZ edges (Lau and Kim, 2015; Byrne et al., 2018), implying a narrowing of precipitation regions influenced by the ITCZ. Modelled changes in the width and intensity of the zonal mean ITCZ are strongly anti-correlated, i.e. narrowing is associated with increased intensity while broadening with decreased intensity. Such changes are associated with changes in tropical high cloud fraction and outgoing longwave radiation (Su et al., 2017; Byrne et al., 2018).

Regional shifts in tropical convergence zones are much larger than their zonal mean, and associated regional changes in precipitation (Chadwick et al., 2013; Mamalakis et al., 2021) are characterized by considerable uncertainties across models (Kent et al, 2015; Oueslati et al., 2016). Over the tropical oceans, shifts in rain bands are strongly coupled with changes in SSTs (Xie et al., 2010; Huang et al., 2013). Over tropical land, factors including remote SST increases (Giannini, 2010), the direct CO_2 effect (Biasutti, 2013) and land-atmosphere interactions (Chadwick et al., 2017; Kooperman et al., 2018) influence projections. CMIP6 models project a clear northward ITCZ shift over eastern Africa and the Indian Ocean and a southward shift over the eastern Pacific and Atlantic oceans, as a result of regionally-contrasting inter-hemispheric energy flows (Mamalakis et al., 2021). The northward movement of the ITCZ over Africa has been linked to an intensification of the Saharan heat low associated with greenhouse gas warming (Dong and Sutton, 2015), causing the tropical rain belt to seasonally migrate farther northward and reside there longer (Cook and Vizy, 2012; Dunning et al., 2018). In southern Africa, the projected delay in the wet season onset (Dunning et al., 2018) is also associated with a circulation-based northward shift in the tropical rain band (Lazenby et al., 2018).

In summary, consistent with the AR5, the overall weakening of the tropical circulation is projected in CMIP5 and CMIP6 simulations with *high confidence*. It is *likely* that the zonal mean of the ITCZ will narrow and strengthen in the core region with projected surface warming (*high confidence*). Distinct regional shifts in the ITCZ will be associated with regional changes in precipitation amount and seasonality (*medium confidence*).

8.4.2.2 Hadley Circulation and subtropical belt

AR5 found that the Hadley cells are *likely* to slow down and expand in response to radiative forcing, but with considerable internal variability. Given the complexities in forcing mechanisms, AR5 assigned *low confidence* to near-term changes in the structure of the Hadley circulation. The widening Hadley cells were expected to result in a poleward expansion of subtropical dry zones.

Model simulations since AR5 project a more noticeable and consistent weakening of the Northern Hemisphere winter Hadley cell than the Southern Hemisphere winter cell (Seo et al., 2014; Zhou et al., 2016), related to changes in meridional temperature gradient, static stability, and tropopause height (Seo et al., 2014; D'Agostino et al., 2017). Changes in SST patterns reduces the magnitude of Hadley cell weakening (Gastineau et al., 2009; Ma et al., 2012). There is considerable structure in Hadley circulation strength changes with longitude, associated with cloud-circulation interactions (Su et al., 2014). Subtropical anticyclones are projected to intensify over the north Atlantic and south Pacific but to weaken elsewhere (He et al., 2017).

A consistent poleward expansion of the edges of the Hadley cells is projected (Nguyen et al., 2015; Grise

ACCEPTED VERSION SUBJECT TO FINAL EDITING

and Davis, 2020), particularly in the Southern Hemisphere, consistent with observed trends (Nguyen et al., 2015) (Fig 8.21, 8.3.2.2). The main driver of future expansion appears to be greenhouse gas forcing (Grise et al., 2019), with uncertainty in magnitude due to internal variability (Kang et al., 2013). Proposed mechanisms for poleward expansion include increased dry static stability (Lu et al., 2007 ; Frierson et al., 2007), increased tropopause height (Chen and Held, 2007; Chen et al., 2008), stratospheric influences (Kidston et al., 2015) and radiative effects of clouds and water vapour (Shaw and Voigt, 2016, see also 4.5.1.5). Hadley cell expansion is thought to be associated with the precipitation declines projected in many subtropical regions (Shaw and Voigt, 2016), but more recent work suggests that these reductions are mainly due to the direct radiative effect of CO_2 forcing (He and Soden, 2015), land-sea contrasts in the response to forcing (Shaw and Voigt, 2016; Brogli et al., 2019) and SST changes (Sniderman et al., 2019). In semi-arid, winter rainfall-dominated regions (such as the Mediterranean), thermodynamic processes associated with the land-sea thermal contrast and lapse rate changes dominate the projected precipitation decline in summer, whereas circulation changes are of greater importance in winter (Brogli et al., 2019). The hydroclimates in these regions are projected to evolve with time due to changing contributions from rapid atmospheric circulation changes and their associated SST responses, as well as slower SST responses to anthropogenic forcing (Zappa et al., 2020).

In summary, CMIP5 and CMIP6 models project a weakening of the Hadley cells, with *high confidence* for the Northern Hemisphere in boreal winter and *low confidence* for the Southern Hemisphere in austral winter. The Hadley cells are projected to expand polewards with global warming, most notably in the Southern Hemisphere (*high confidence*). There is currently *low confidence* in the impacts on regional precipitation in subtropical regions.

8.4.2.3 Walker circulation

AR5 determined that the Pacific Walker circulation was *likely* to slow down over the 21st century, which would lead to decreased precipitation over the western tropical Pacific and increases over the central and eastern Pacific. Recent studies show consistency with AR5 conclusions but also show an eastward shift over the Pacific, mostly due to a shift towards more "El Niño–like" conditions under global warming (Bayr et al., 2014). Other studies suggest that the weakening of the Walker circulation is related to the response of the western North Pacific monsoon and to changing land–sea temperature contrasts, while a positive ocean–atmosphere feedback amplifies the weakening of both east–west SST gradient and trade winds in the tropical Pacific (Zhang & Li, 2017).

Since AR5, the paradox between the projected weakening and the observed strengthening of the Walker circulation since the 1990s (Section 8.3.2.2) has triggered debate about the drivers of these changes (England et al., 2014; McGregor et al., 2014; Kociuba and Power, 2015; Vilasa et al., 2017; Chung et al., 2019). Projected changes in equatorial SST gradients are not entirely consistent with observed trends (Coats and Karnauskas, 2017; Seager et al., 2019a), and one CMIP5 model that projects a future strengthening of the Walker circulation is more consistent with observations than other models (Kohyama et al., 2017). Other studies suggest that these differences arises from the dominant influence of internal climate variability to the observed trends (Chung et al., 2019), or as a consequence of a systematic cold bias of most CMIP5 models in their Equatorial Pacific cold tongues (Seager et al., 2019a). However, the latter hypothesis is based on a simplified model of tropical Pacific dynamics and is not consistent with the current physical understanding of the tropical circulation response to increasing CO_2 levels (Section 8.2.2.2) or with independent paleoclimate evidence suggesting a weaker Walker circulation under warmer climates (Tierney et al., 2019; McClymont et al., 2020). Different time scales of the tropical Pacific responses to global warming have been highlighted by numerical experiments with both comprehensive and simplified models. Results suggest a transient strengthening of the Walker circulation related to Indian Ocean warming (Zhang et al., 2018b), followed by a slower weakening linked to a strengthened eastern Pacific cold tongue warming emerging after 50-100 years (Heede et al., 2020, Section 7.4.4.2.1).

CMIP6 projections provide further evidence of a significant long-term weakening of the Walker circulation (Fig. 8.21). For instance, a pronounced weakening of the upper-level tropical easterly jet is projected both

ACCEPTED VERSION SUBJECT TO FINAL EDITING

over the Indian Ocean and tropical eastern Pacific, where declines are projected to exceed 70% by 2100 in the high-emission SSP5-8.5 scenario (Huang et al., 2020a). CMIP6 models agree on a future decrease of the equatorial zonal temperature gradient (Fredriksen et al., 2020), which can lead to weaker trade winds over the tropical Pacific. However, CMIP6 models show a diversity of SST warming patterns in the tropical Pacific (Freund et al., 2020), which contributes to uncertainties in the response of both Walker circulation and ENSO to continued warming.

In summary, there is *high confidence* that the Pacific Walker circulation will weaken by the end of the 21st century, and will be associated with decreased precipitation over the western tropical Pacific and increases farther east. Discrepancies between observed and simulated changes in SSTs in the tropics indicate that a temporary strengthening of the Walker Circulation can arise from a transient response to GHG radiative forcing (*low confidence*) and from internal variability (*medium confidence*).

[START FIGURE 8.21 HERE]

Figure 8.21: Schematic depicting large-scale circulation changes and impacts on the regional water cycle. The central figures show precipitation minus evaporation (P-E) changes at 3°C or global warming relative to a 1850-1900 base period (mean of 23 CMIP6 SSP5-8.5 simulations). Annual mean changes (large map) include contours depicting control climate P-E=0 lines with the solid contour enclosing the tropical rain belt region and dashed lines representing the edges of subtropical regions. Confidence levels assess understanding of how large-scale circulation change affect the regional water.

[END FIGURE 8.21 HERE]

8.4.2.4 Monsoons

In AR5, monsoon precipitation over land was projected to intensify by the end of the 21st century, due to thermodynamic increases in moisture convergence despite weakening of the tropical circulation (see Section 8.2.1.3). Following the definition of regional monsoons in Annex V and Figure 8.11, and the assessment of the observed changes (Section 8.3.2.4), here we provide an assessment of projected changes in regional monsoons. Assessment is provided either in terms of SSP and RCP scenarios and global warming levels available since AR5, or from the newly available CMIP6 projections (Figure 8.22 and Table 8.2). Table 8.2 provides projected changes across the five SSPs used in this report for precipitation (mm/day), P-E (mm/day) and runoff (mm/day) over the regional monsoons for the mid (2041-2060) and long term (2081-2100).

ACCEPTED VERSION SUBJECT TO FINAL EDITING

Table 8.2: Monsoon mean water cycle projections in the medium term (2041-2060) and long term (2081-2100) relative to present day (1995-2014), showing present day mean and 90% confidence range across CMIP6 models (historical experiment) and projected mean changes and the 90% confidence range across the same set of models and a range of shared socioeconomic scenarios. All statistics are in units of mm/day. Further details on data sources and processing are available in the chapter data table (Table 8.SM.1).

		Mid term: 2041–2061 minus reference period					Long term: 2081–2100 minus reference period				
	1995-2014 reference period	SSP1-1.9	SSP1-2.6	SSP2-4.5	SSP3-7.0	SSP5-8.5	SSP1-1.9	SSP1-2.6	SSP2-4.5	SSP3-7.0	SSP5-8.5
South and Southeast Asian Monsoon (JJAS)											
Precipitation	8.42 [6.66-10.14]	0.44 [0.08-0.74]	0.47 [0.1-0.96]	0.42 [0.03-0.81]	0.32 [-0.08-0.94]	0.54 [0.11-1.18]	0.46 [0.16-0.7]	0.52 [0.13-1.09]	0.66 [0.16-1.1]	0.94 [0.3-1.78]	1.46 [0.66-2.49]
Runoff	3.75 [1.8-5.71]	0.23 [0.1-0.38]	0.29 [0.02-0.65]	0.29 [-0.0-0.66]	0.24 [-0.04-0.52]	0.38 [0.07-0.78]	0.19 [-0.02-0.35]	0.29 [-0.04-0.65]	0.42 [0.04-0.83]	0.7 [0.12-1.2]	1.14 [0.36-2.05]
P-E	5.19 [3.68-6.5]	0.28 [0.03-0.52]	0.36 [-0.0-0.76]	0.36 [0.02-0.69]	0.3 [-0.04-0.85]	0.45 [0.06-0.95]	0.27 [0.06-0.38]	0.38 [0.11-0.76]	0.51 [0.02-0.83]	0.81 [0.24-1.56]	1.15 [0.45-1.84]
East Asian Monsoon (JJA)											
Precipitation	5.59 [4.47-6.86]	0.37 [-0.09-0.93]	0.37 [-0.09-0.87]	0.34 [0.05-0.76]	0.22 [-0.16-0.88]	0.43 [0.03-1.1]	0.43 [0.07-1.02]	0.44 [-0.0-1.08]	0.51 [0.11-1.09]	0.59 [0.02-1.31]	0.84 [0.24-1.74]
Runoff	2.24 [1.28-3.41]	0.11 [-0.16-0.4]	0.13 [-0.19-0.42]	0.13 [-0.15-0.4]	0.15 [-0.29-0.76]	0.2 [-0.11-0.72]	0.16 [-0.08-0.49]	0.16 [-0.13-0.58]	0.22 [-0.13-0.64]	0.36 [-0.05-0.87]	0.51 [0.06-1.24]
P-E	2.41 [1.51-3.31]	0.1 [-0.31-0.51]	0.13 [-0.2-0.48]	0.17 [-0.04-0.53]	0.17 [-0.2-0.75]	0.23 [-0.09-0.86]	0.16 [-0.07-0.57]	0.18 [-0.18-0.65]	0.24 [-0.1-0.76]	0.4 [-0.08-0.93]	0.5 [-0.13-1.34]
North American Monsoon (JAS)											
Precipitation	3.05 [2.24-3.96]	0.13 [-0.08-0.43]	0.07 [-0.27-0.32]	0.02 [-0.32-0.41]	-0.03 [-0.37-0.38]	-0.03 [-0.43-0.52]	0.18 [-0.05-0.44]	0.04 [-0.35-0.39]	-0.1 [-0.51-0.37]	-0.19 [-0.76-0.44]	-0.15 [-0.96-0.57]
Runoff	0.46 [0.09-0.87]	0.03 [-0.04-0.12]	0.03 [-0.07-0.16]	0.02 [-0.1-0.14]	-0.0 [-0.1-0.14]	-0.0 [-0.11-0.14]	0.04 [-0.03-0.15]	-0.0 [-0.19-0.15]	-0.03 [-0.22-0.14]	-0.05 [-0.23-0.19]	-0.06 [-0.29-0.23]
P-E	0.78 [-0.1-1.45]	0.06 [-0.1-0.2]	0.02 [-0.18-0.24]	0.0 [-0.22-0.23]	-0.03 [-0.24-0.2]	-0.04 [-0.31-0.27]	0.09 [-0.06-0.31]	0.01 [-0.22-0.25]	-0.08 [-0.28-0.25]	-0.17 [-0.68-0.25]	-0.18 [-0.72-0.38]
South American Monsoon (DJF)											
Precipitation	8.44 [5.98-10.22]	0.09 [-0.2-0.3]	0.12 [-0.29-0.62]	0.09 [-0.47-0.62]	0.07 [-0.55-0.62]	0.07 [-0.5-0.71]	0.02 [-0.32-0.36]	0.09 [-0.33-0.58]	0.07 [-0.63-0.81]	0.05 [-1.17-0.82]	-0.0 [-1.22-1.19]
Runoff	2.49 [1.11-4.38]	-0.02 [-0.23-0.26]	-0.01 [-0.43-0.53]	0.01 [-0.45-0.46]	-0.03 [-0.49-0.36]	-0.03 [-0.56-0.53]	-0.04 [-0.27-0.28]	-0.01 [-0.41-0.39]	-0.01 [-0.58-0.55]	-0.06 [-0.81-0.24]	-0.04 [-0.85-0.93]
P-E	4.5 [2.83-6.01]	0.04 [-0.23-0.25]	0.08 [-0.26-0.47]	0.04 [-0.43-0.53]	0.04 [-0.5-0.61]	0.02 [-0.45-0.58]	-0.01 [-0.32-0.29]	0.03 [-0.34-0.43]	-0.02 [-0.63-0.62]	-0.02 [-1.03-0.72]	-0.09 [-1.11-0.98]
Australian and Maritime Continent Monsoon (DJF)											
Precipitation	8.63 [6.79-10.7]	0.26 [0.04-0.49]	0.22 [-0.23-0.53]	0.28 [-0.2-0.79]	0.25 [-0.14-0.73]	0.38 [0.0-0.84]	0.15 [-0.09-0.34]	0.24 [-0.36-0.74]	0.5 [-0.1-1.07]	0.65 [-0.08-1.33]	0.9 [0.09-1.76]
Runoff	3.82 [1.78-7.25]	0.2 [-0.01-0.48]	0.23 [-0.11-0.48]	0.29 [-0.11-0.7]	0.24 [-0.13-0.56]	0.35 [-0.03-0.87]	0.12 [-0.06-0.39]	0.29 [-0.08-0.88]	0.49 [0.09-1.25]	0.61 [-0.09-1.05]	0.92 [0.14-1.83]
P-E	4.8 [3.19-6.63]	0.22 [0.03-0.47]	0.13 [-0.23-0.42]	0.2 [-0.16-0.7]	0.2 [-0.14-0.62]	0.27 [-0.09-0.61]	0.12 [-0.1-0.31]	0.16 [-0.31-0.54]	0.38 [-0.05-0.75]	0.54 [-0.08-1.13]	0.69 [0.09-1.27]

ACCEPTED VERSION SUBJECT TO FINAL EDITING

West African Monsoon (JJAS)											
Precipitation	5.14 [3.62-7.18]	0.16 [-0.19-0.4]	0.14 [-0.22-0.56]	0.24 [-0.14-0.72]	0.3 [-0.1-0.85]	0.38 [-0.12-1.24]	0.06 [-0.25-0.52]	0.1 [-0.25-0.57]	0.25 [-0.32-0.91]	0.38 [-0.49-1.14]	0.49 [-0.55-1.56]
Runoff	1.43 [0.34-2.57]	0.06 [-0.07-0.22]	0.05 [-0.18-0.27]	0.14 [-0.13-0.54]	0.2 [-0.05-0.7]	0.24 [-0.1-0.8]	-0.01 [-0.2-0.21]	0.03 [-0.25-0.35]	0.1 [-0.25-0.51]	0.25 [-0.28-0.85]	0.3 [-0.33-0.93]
P-E	2.41 [1.05-4.07]	0.08 [-0.2-0.35]	0.1 [-0.2-0.4]	0.2 [-0.11-0.63]	0.23 [-0.11-0.74]	0.36 [-0.06-1.11]	-0.01 [-0.27-0.35]	0.07 [-0.2-0.44]	0.18 [-0.21-0.6]	0.28 [-0.38-0.95]	0.46 [-0.44-1.4]

1

ACCEPTED VERSION
SUBJECT TO FINAL EDITING

[START FIGURE 8.22 HERE]

Figure 8.22: Projected regional monsoons precipitation changes. Percentage change in projected seasonal mean precipitation over regional monsoon domains (as defined in Fig 8.11, Section 8.3.2.4 and Annex V) for near-term (2021-2040), mid-term (2041-2060), and long-term (2081-2100) periods based on 24 CMIP6 models and three SSP scenarios (SSP1-2.6, SSP2-4.5 and SSP5-8.5). Further details on data sources and processing are available in the chapter data table (Table 8.SM.1).

[END FIGURE 8.22 HERE]

8.4.2.4.1 South and Southeast Asian Monsoon

In AR5, South and Southeast Asian Monsoon (SAsiaM) precipitation was projected to increase by the end of the 21st century but with a weakening of the circulation, with high agreement across the CMIP5 models (Kitoh, 2017; Kitoh et al., 2013; Kulkarni et al., 2020; Menon et al., 2013; Sharmila et al., 2015; Sooraj et al., 2015). Since AR5, most studies have confirmed projected increases in South Asian monsoon precipitation (*high confidence*), while one high-resolution model (35 km in latitude/longitude) projects monsoon precipitation decreases during the 21st century following the RCP4.5 scenario (Krishnan et al., 2016).

Over South Asia, the moisture-bearing monsoon low-level jet is projected to shift northward in CMIP3 and CMIP5 models (Sandeep and Ajayamohan, 2015). Greater warming over the Asian land region compared to the ocean contributes to intensification of the monsoon low-level southwesterly winds and precipitation (Endo et al., 2018), even though the combined effect of upper and lower tropospheric warming makes the Asian monsoon circulation response rather complicated. A high resolution model projection, based on the RCP8.5 scenario, indicates that a northward shift of the low-level jet and associated weakening of the large-scale monsoon circulation can induce a large reduction in the genesis of monsoon low pressure systems by the late 21st century (Sandeep et al., 2018). Experiments with constant forcing indicate that at 1.5° and 2°C global warming levels, mean precipitation and monsoon extremes are projected to intensify in summer over India and South Asia (Chevuturi et al., 2018; Lee et al., 2018a) and that a 0.5°C difference would imply a 3% increase of precipitation (Chevuturi et al., 2018). CMIP5 models project an increase in short intense active days and decrease in long active days, with no significant change in the number of break spells for India (Sudeepkumar et al, 2018).

Future monsoon projections from CMIP6 models show an increase of SAsiaM precipitation across all the scenarios and across all the time frames (Figure 8.22) with the maximum increase at the end of the 21st century in SSP5-8.5 (Almazroui et al., 2020c; Chen et al., 2020e; Ha et al., 2020; Wang et al., 2020b). Table 8.2 confirms that changes in runoff and P-E over SAsiaM region are positive and largest in the higher emission scenarios considered, as in precipitation. On the other hand, changes in the ensemble mean for all the variables considered in the SSP1-1.9 scenario are negative for both mid and long term periods (Table 8.2). This is also consistently reflected in the spatial map of future precipitation changes (Figure 8.15). Different near-term projections of the SAsiaM may result given the diversity in the future aerosol emission pathways and policies for regulating air pollution (Wilcox et al., 2020). Additionally, near-term projections of SAsiaM precipitation are expected to be constrained by internal variability associated with the PDV (Huang et al., 2020b). CMIP6 models also indicate a lengthening of the summer monsoon over India by the end of the 21st century, at least in SSP2-4.5, with considerable inter-model spread in the projected late retreat (Ha et al. et al., 2020).

In summary, consistent with AR5, there is *high confidence* that SAsiaM precipitation is projected to increase during the 21st century in response to continued global warming across the CMIP6 higher emissions scenarios, mostly in the mid and long terms.

8.4.2.4.2 East Asian Monsoon

In AR5, the East Asian monsoon (EAsiaM) was projected to intensify in terms of precipitation, with an

ACCEPTED VERSION SUBJECT TO FINAL EDITING

earlier onset and longer duration of the summer season. Since AR5, there has been improved understanding of future projected changes in the EAsiaM.

CMIP5 projections indicated a possible intensification of the EAsiaM circulation during the 21st century, in addition to precipitation increase, although there is a lack of consensus on changes in the western North Pacific subtropical high, this is an important feature of the EAsiaM circulation (Kitoh, 2017). Furthermore, the EAsiaM precipitation enhancements in the CMIP5 projections are prominent over the southern part of the Baiu rainband by the late 21st century, with no significant changes in the Meiyu precipitation over central-eastern China (Horinouchi et al., 2019). It was also shown that the Baiu precipitation response in CMIP5 projections is accompanied by a southward retreat of the western North Pacific subtropical high and a southward shift of the East Asian subtropical jet (Horinouchi et al., 2019). According to the high-resolution MRI-AGCM global warming experiments, future summer precipitation could potentially increase on the southern side and decrease on the northern side of the present-day Baiu location in response to downward-motion tendencies which can offset the 'wet-gets-wetter' effect, but is subject to large model uncertainties (Ose, 2019). Future projections of land warming over the Eurasian continent (Endo et al., 2018) and intensified land-sea thermal contrast (Wang et al., 2016c; Tian et al., 2019) can potentially intensify the EAsiaM circulation during the 21st century. However, there are large uncertainties in projected water cycle changes over the region (Endo et al., 2018), mostly in the near-term because of uncertainties in future aerosol emission scenarios (Wilcox et al., 2020), as well as due to the interplay between internal variability and anthropogenic external forcing (Wang et al., 2021).

Interhemispheric mass exchange can act as a bridge connecting Southern Hemisphere circulation with EAsiaM rainfall, however this interhemispheric link is projected to weaken in a future warmer climate as seen from a CCSM4 projection using the RCP8.5 scenario (Yu et al., 2018). A comparison of 1.5°C and 2°C global warming levels reveals how a 0.5°C difference could result in precipitation enhancement over large areas of East Asia (Lee et al., 2018a; Liu et al., 2018b; Chen et al., 2019), with substantial increases in the frequency and intensity of extremes (Chevuturi et al., 2018; Li et al., 2019a). Future monsoon projections from the CMIP6 models show increase of EAsiaM precipitation across all the scenarios (Chen et al., 2020e), though with a large model spread mostly on the long-term and in the higher emission scenarios (Figure 8.22). Considering all the five scenarios used across the report, changes in precipitation, runoff and P-E over the EAsiaM are positive and become larger for highest emission scenarios and for the long term mean, except for the mid-term SSP1-1.9 scenario where the changes are close to zero or even negative (Table 8.2). Additionally, CMIP6 models confirm a projected increased length of the EAsiaM season due to early onset and late retreat (Ha et al., 2020).

In summary, despite the uncertainties in the monsoon circulation response in CMIP5 and CMIP6 models, there is *high confidence* that summer monsoon precipitation over East Asia will increase in the 21st century and *medium confidence* that the monsoon season will be longer.

8.4.2.4.3 West African Monsoon

AR5 concluded that projections of West African monsoon (WAfriM) rainfall are highly uncertain in CMIP3 and CMIP5 models, but still suggest a small delay and intensification in late wet season rains. Studies published since AR5 are broadly consistent with this assessment. CMIP6 models agree on statistically significant projected increases in rainfall in eastern-central Sahel and a decrease in the west for the end of the 21st century (Roehrig et al., 2013; Biasutti, 2019; Monerie et al., 2020). However, the magnitude of WAfriM projected precipitation depends on the convective parameterization used (Hill et al., 2017), and large uncertainties remain in WAfriM projections because of large inter-model spread, particularly over the western Sahel (Roehrig et al., 2013; Biasutti, 2019; Monerie et al., 2020). CMIP6 models show a general increase of WAfriM precipitation across all future scenarios but with a substantial model spread for the SSP5-8.5 scenario (Figure 8.22). This sensitivity arises from the combined and contrasting influences of anthropogenic greenhouse gas and aerosol forcing that affect WAfriM precipitation (particularly over the Sahel) directly and also indirectly through sub-tropical North Atlantic SST changes (Giannini and Kaplan, 2019). The large model spread and associated uncertainties in projected precipitation changes is reflected also in runoff and P-E changes (Table 8.2). Regional climate models (RCMs) ensembles (e.g., Klutse et al.,

ACCEPTED VERSION SUBJECT TO FINAL EDITING

2018) agree with CMIP5 projected rainfall trends but some individual models show rainfall declines (e.g., Sylla et al., 2015; Akinsanola et al., 2018), highlighting the existing large uncertainties in RCMs WAfriM rainfall projections.

Changes in seasonality (see also Box 8.2) are projected with a later monsoon onset (*high confidence*) over the Sahel and a late cessation (*medium confidence*), suggesting a delayed wet season as a regional response to global GHG forcing (Biasutti, 2013; Akinsanola and Zhou, 2018; Dunning et al., 2018). Rainfall distribution is projected to be highly variable with a decrease in the number of rainy days in the western Sahel, consistent with an increase in consecutive dry days and a reduction in the number of growing season days (Cook and Vizy, 2012; Diallo et al., 2016). A decrease in the frequency but an increase in the intensity of very wet events is projected to be more pronounced over the Sahel than over Guinean coast, and also under higher emission scenarios (i.e. RCP8.5) (e.g., Sylla et al., 2015; Akinsanola et al., 2018).

In summary, post-AR5 studies and newly available CMIP6 results indicate projected rainfall increases in the eastern-central WAfriM region but decreases in the west (*high confidence*), with a delayed wet season (*medium confidence*). Overall, WAfriM summer precipitation is projected to increase during the 21st century but with larger uncertainty noted under high emission scenarios (*medium confidence*).

8.4.2.4.4 North American Monsoon

AR5 concluded that the North American Monsoon (NAmerM) will *likely* intensify in the future, even though there is *low agreement* among models. AR5 reported *medium confidence* that precipitation associated with the NAmerM will arrive later in the annual cycle and persist longer.

Since AR5, analyses of CMIP5 projections suggest little change in the overall amount of NAmerM precipitation in response to rising global surface temperature. However, significant declines are projected in the early monsoon season and increases in the late monsoon season, suggesting a shift in seasonality toward a delayed monsoon onset and demise (Cook et al., 2013). It is recognised that CMIP5 models are generally too coarsely-resolved to simulate the Gulf of California and the moisture surges associated with the NAmerM (Pascale et al., 2017). Under different RCPs, CMIP5 models tend to project a reduction in NAmerM precipitation but an increase in extreme precipitation events (Torres-Alavez et al., 2014; Bukovsky et al., 2015; Pascale et al., 2019). The almost unchanged or slight decrease in NAmerM total precipitation amount under global warming projections is at odds with paleoclimate records that suggest increased monsoon precipitation under past warm conditions (D'Agostino et al., 2019; Seth et al., 2019). However, there is *low agreement* on how those changes and the mechanisms that drive them are affected under different RCPs since most simulations are model-dependant (Cook and Seager, 2013; Geil et al., 2013; Pascale et al., 2019). Projections from six CMIP6 models show a shortening of the NAmerM under the SSP5-8.5 scenario due to earlier demises (Moon and Ha, 2020). In addition, CMIP6 projections show a decrease in NAmerM precipitation under SSP2-4.5 and SSP5-8.5 scenarios by the end of the 21st century with large inter-model spread (Figure 8.22). This result is also supported by the analysis of 31 CMIP6 models under the SSTP5-8.5 scenario for the 2080-2099 period (Almazroui et al., 2021). Non-linearities and uncertainties in the NAmerM projected changes are valid for many water cycle variables, like precipitation, runoff and P-E (Table 8.2).

In summary, there is *low agreement* on a projected decrease of NAmerM precipitation, however there is *high confidence* in delayed onsets and demises of the summer monsoon.

8.4.2.4.5 South American Monsoon

AR5 reported *medium confidence* that the South American Monsoon (SAmerM) overall precipitation will remain unchanged, and *medium confidence* in projections of extreme precipitation. AR5 also stated *high confidence* in the spatial expansion of the SAmerM, resulting from increased temperature and humidity.

Since AR5, some studies indicate that the SAmerM would experience changes in its seasonal cycle, with delayed monsoon onsets under increasing GHG emissions associated to different RCPs (Fu et al., 2013;

ACCEPTED VERSION SUBJECT TO FINAL EDITING

Reboita et al., 2014; Boisier et al., 2015; Pascale et al., 2016; Seth et al., 2019; Sena and Magnusdottir, 2020). In contrast, other studies indicate projected earlier onsets and delayed retreats of the SAmerM under the RCP8.5 scenario based on six CMIP5 models (Jones and Carvalho, 2013). These differences have been linked to the methodology used to determine monsoon timing, and sensitivity to the monsoon domain considered (Correa et al., 2021) (Section 8.3.2.4.5). Recent studies provide further evidence for the projection of delayed SAmerM onsets by the late 21 century (Sena and Magnusdottir, 2020). An analysis of six CMIP6 models under the SSP5-8.5 scenario confirm the projections of delayed SAmerM onsets by the end of the 21st century (Moon and Ha, 2020). In addition, projected changes in the intensity and length of the SAmerM season have been found to be model-dependent (Pascale et al., 2019). The analysis of CMIP5 projections of total monsoon rainfall indicate mixed signals in the Amazon and SAmerM regions (Jones and Carvalho, 2013; Marengo et al., 2014), with some studies suggesting increased summer precipitation in the core SAmerM region (Kitoh et al. et al., 2013; Seth et al., 2013). Dynamical downscaling of CMIP5 projections under the RCP4.5 and RCP8.5 scenarios with the Eta RCM suggests reductions of austral summer precipitation over the SAmerM region throughout the 21st century (Chou et al., 2014). Further analysis using 15 different CMIP6 models for the SSP2-4.5 scenario suggest reductions in total SAmerM rainfall (Wang et al., 2020a). However, other analyses of CMIP6 projections under different SSP scenarios do not report clear changes in the SAmerM precipitation throughout the 21st century (Chen et al., 2020e; Jin et al., 2020), Figure 8.22). Similar uncertainties for all the SSP scenarios used across the report are found for other water cycle variables, including runoff and P-E (Table 8.2). Furthermore, there is disagreement in projected extreme precipitation in the region, with some CMIP5-based studies suggest reductions (Marengo et al., 2014), while others indicate increases based on CMIP5 and CMIP6 models (Kitoh et al., 2013; Sena and Magnusdottir, 2020).

In summary, there is *high confidence* that the SAmerM will experience delayed onsets in association with increases in GHG. However, there is *low agreement* on the projected changes in terms of total precipitation of the South American summer monsoon season.

8.4.2.4.6 Australian and Maritime Continent Monsoon

AR5 concluded that projected changes in Australian and Maritime Continent Monsoon (AusMCM) rainfall and seasonality are uncertain in the CMIP5 models, with some projecting increases and others projecting decreases for the range of emissions scenarios. Models that perform better at simulating present day regional climate project little change or an increase in Australian monsoon rainfall (Jourdain et al., 2013; CSIRO and Bureau of Meteorology, 2015; Brown et al., 2016b). CMIP6 models project increased AusMCM precipitation in the 21st century but with a more robust signal in SSP2-4.5 and SSP5-8.5 rather than in lower emission scenarios (Figure 8.22). A reduced range of CMIP6 rainfall projections but continued disagreement on the sign of change is reported over Australia (Narsey et al., 2020).

The northern and eastern parts of the Maritime Continent have projected increases in rainfall in CMIP5 models (Siew et al., 2014), while there are projected decreases over Java, Sulawesi and southern parts of Borneo and Sumatra. Rainfall changes are correlated with the extent of warming in the western tropical Pacific in CMIP5 models (Brown et al., 2016b) but inter-model differences are also related to modelled large-scale zonal mean precipitation response in both CMIP5 and CMIP6 model ensembles (Narsey et al., 2020). Decomposition of projected rainfall changes indicates that the largest source of model uncertainty is associated with shifts in the spatial pattern of convection (Chadwick et al., 2013; Brown et al., 2016b). Uncertainties in capturing the spatial and temporal features of the Maritime Continent monsoon depend also on the horizontal resolution of coupled climate models (e.g. Jourdain et al., 2013).

The role of anthropogenic aerosol forcing in future projections of the Australian monsoon has been investigated for CMIP5 models (Dey et al., 2019); decreases in anthropogenic aerosol concentrations over the 21st century are expected to produce relatively greater warming in the Northern Hemisphere than Southern Hemisphere, favouring a northward shift of the tropical rain belt (e.g. Rotstayn et al., 2015).

There are some clear projected changes in the rainfall variability and extremes of the Australian monsoon. Rainfall variability in the Australian monsoon domain increases on time scales from daily to decadal in

ACCEPTED VERSION SUBJECT TO FINAL EDITING

CMIP5 models (Brown et al., 2017), indicating either more intense wet days or more dry days or both. There is also a projected increase in the intensity of extreme rainfall but a reduction in the frequency of heavy rainfall days for the Australian monsoon (Dey et al., 2019). This is consistent with Moise et al. (2020), who found an increase in Australian monsoon active phase or 'burst' rainfall intensity but a reduction in the number of burst days and events.

Zhang et al. (2013) examined changes in Australian monsoon onset and duration in CMIP3 models and found model agreement on a delay in onset and shortened duration to the north of Australia, but less agreement over the interior of the continent. An updated study of CMIP5 models found similar mean changes with delayed onset and shortened duration, but substantial model disagreement (Zhang et al., 2016).

In summary, CMIP6 projections show an increase of AusMCM precipitation across all emission scenarios. There is strong model agreement on an increase in monsoon precipitation over the Maritime Continent while there is low agreement on the direction of change over northern Australia. There is a projected increase in rainfall variability over northern Australia, with increased intensity of rainfall during the active or 'burst' phase (*medium confidence*).

8.4.2.5 Tropical cyclones

Tropical cyclones (TCs) projections are primarily assessed in section 11.7.1.5. Here, we extend this analysis by assessing the implications of projected changes in tropical cyclones on the water cycle.

AR5 concluded that TC rainfall rate was *likely* to increase through the 21st century. Section 11.7.1.5 assesses that the average tropical cyclone rain-rate is projected to increase with warming (*high confidence*), and peak rain-rates are projected to increase at greater than the Clausius-Clapeyron scaling rate of 7% per 1°C of warming in some regions due to increased low-level moisture convergence (*medium confidence*). The increase in TC rainfall rate is explained by increased TC intensity resulting from increasing SSTs, and increased environmental water vapour (Chauvin et al., 2017; Liu et al., 2019b).

Consistent with the observed poleward migration of tropical cyclone activity (Kossin et al., 2014), in the Southern Hemisphere a larger proportion of storms are projected to decay south of 25°S at the end of the 21st century but with negligible changes in genesis latitude and storm duration for the Australian region (CSIRO and Bureau of Meteorology, 2015)(Sharmila and Walsh, 2018). An analysis of projections for North Pacific islands indicate that the maximum intensity of storms will increase but the number of tropical cyclones will decrease in some places, such as Guam and Kwajalein Atoll in the tropical northwestern Pacific, or remain the same in other regions like near Okinawa (Japan) or Oahu (Hawaii) (Widlansky et al., 2019). TC-induced storm tides affecting landfall in the Pearl River delta over South China are projected to increase by the end of the 21st century (Chen et al., 2020c)

In summary, there is *high confidence* that heavy precipitation associated with tropical cyclones is projected to increase, in response to well-understood processes related to increased low-level moisture convergence and environmental water vapour.

8.4.2.6 Stationary waves

AR5 did not provide an assessment of stationary wave projections as distinct from other related aspects of circulation, such as blocking, modes of variability, and storm tracks. Here we provide a brief assessment of stationary wave projections from the water cycle perspective, with the related circulation aspects considered separately in the following sections.

Several studies based on CMIP5 projections show changes in Northern Hemisphere winter stationary waves that increase precipitation over the west coast of North America and decrease it over the eastern Mediterranean and parts of southwestern North America (Neelin et al., 2013; Seager et al., 2014a, 2014b,

ACCEPTED VERSION SUBJECT TO FINAL EDITING

2019b; Simpson et al., 2016; Wills et al., 2019), although the underlying dynamics are not yet fully understood (Seager et al., 2019b; Wills et al., 2019). For the Northern Hemisphere winter global teleconnection pattern, the majority of the models analyzed in (Sandler and Harnik, 2020) project the development of a preferred longitudinal phasing for the pattern, but with strong disagreement among models over the details of the phasing and therefore the associated regional hydrologic impacts.

While the potential role of increasing hydrologic extremes with quasi-resonant stationary waves during Northern Hemisphere summer has received considerable attention (see Section 8.3.2.6), as yet there is no clear evidence in model projections that this variability will increase (Teng and Branstator, 2019). The influence of the Arctic on midlatitude circulation is assessed in Cross-Chapter Box 10.1, which reports that there is *low confidence* in the dominant contribution of Arctic warming compared to other drivers in future projections. Potential changes to the stratospheric polar vortex in CMIP5 models have a substantial influence on tropospheric stationary waves and associated hydrologic impacts in both the Northern (Zappa and Shepherd, 2017) and Southern Hemisphere (Mindlin et al., 2020). CMIP5 models have some important limitations in their representation of stationary waves (Lee and Black, 2013; Simpson et al., 2016; Garfinkel et al., 2020) and this aspect of CMIP6 models has not yet been comprehensively evaluated.

In summary, future changes in stationary waves may have an important influence on both the mean state and variability of the water cycle. Limitations in model representation, dynamical understanding, and the number of targeted studies on the topic currently constrain the assessment of future changes in stationary waves. Based on current knowledge, there is *low confidence* that projected changes in stationary wave activity will contribute to decreases of cold season precipitation over the eastern Mediterranean and increases over the west coast of North America.

8.4.2.7 Atmospheric blocking

In AR5, the increased ability of models to simulate blocking and higher agreement on projections led to an assessment with *medium confidence* that the frequency of Northern and Southern Hemisphere blocking will not increase, but future changes in blocking intensity and persistence were deemed uncertain (AR5 Chapter 14, ES and Box 14.2). Blocking influences precipitation (e.g., Trigo et al., 2004), flooding (e.g., Yamada et al., 2016), drought (e.g., Dong et al., 2018b), snow (e.g., García-Herrera and Barriopedro, 2006), and glacier melt (e.g., Hanna et al., 2013), and so is of broad importance to the water cycle in areas of blocking activity.

Blocking projections are assessed in this Report in Chapter 4 (Section 4.5.1.6), and model performance in simulating blocking is also discussed in Chapter 3 (Section 3.3.3.3). CMIP5 projections suggest a complex response in blocking frequencies with an eastward shift in Northern Hemisphere winter blocking, mid-latitude decreases in boreal summer except in eastern Europe-western Russia, and Southern Hemisphere decreases in the Pacific sector during austral spring and summer. CMIP6 projections (Figure. 4.28) show a notable decrease in blocking activity over Greenland and the North Pacific for the SSP3-7.0 and SSP5-8.5 scenarios. However, the continued large differences among current models as well as the sensitivity to blocking detection methods limits confidence in projected regional changes in blocking (see also Chapter 10, Section 10.3.3.3.1). The influence of blocking on multiple elements of the water cycle means that the uncertainty in blocking projections adds a corresponding layer of uncertainty to water cycle projections.

In summary, and despite recent improvements in the simulation of blocking, there is *limited evidence* in model projections of future changes, except for boreal winter over Greenland and the North Pacific where there is *high confidence* that blocking events are not expected to increase in the SSP3-7.0 and SSP5-8.5 scenarios. As with stationary waves, this adds uncertainty to mid-latitude water cycle projections at the regional scale.

8.4.2.8 Extratropical cyclones, storm tracks and atmospheric rivers

ACCEPTED VERSION SUBJECT TO FINAL EDITING

8.4.2.8.1 Extratropical cyclones and storm tracks

AR5 found that extratropical storms were expected to decrease in the Northern Hemisphere, but only by a few percent. Meanwhile, precipitation associated with extratropical storms was projected to increase due to thermodynamic increases in moisture but potentially also due to intensification from increased latent heat release. Latent heating is a strong influence on extratropical storms, so it is plausible that changes in precipitation and associated latent heating could affect extratropical storm intensity and thus precipitation (Zhang et al, 2019).

There is increased evidence that precipitation associated with individual extratropical storms is projected to increase, following thermodynamic drivers with negligible dynamic change (Yettella and Kay, 2017). Comparisons with reanalyses also support the projected increase in thermodynamic precipitation with little dynamic response for precipitation associated with extratropical storms (Li et al., 2014). There is *high confidence* that projected increases in precipitation associated with extratropical storms in over the Northern Hemisphere (Hawcroft et al., 2018; Kodama et al., 2019; Marciano et al., 2015; Michaelis et al., 2017; Pepler et al., 2016; Yettella and Kay, 2017; Zhang and Colle, 2017). A projected decrease in the number of extratropical cyclones over the Northern Hemisphere during the boreal summer in CMIP5 models was reported by (Chang et al., 2016) who related this decrease with a decrease in cloudiness and thus accentuating increased maximum temperatures. However, model spread was quite large, especially over North America, thus there is only *low confidence* in this seasonal signal.

In AR5, the Southern Hemisphere storm track was deemed *likely* to shift poleward, the North Pacific storm track *more likely than not* to shift poleward, while the North Atlantic storm track was *unlikely* to display any discernible changes. There was *low confidence* in regional storm track changes and the associated surface climate impacts, although a weakening of the Mediterranean storm track was a robust response of the models. Since AR5, the Southern Hemisphere mid-latitude storm track is projected to shift poleward and the westerlies are projected to strengthen over Australia (CSIRO and Bureau of Meteorology, 2015). Although thermodynamic effects were considered to be the most important factor in overall projections of increased mid-latitude precipitation, the general poleward shift in cyclogenesis and an enhanced latitudinal displacement of individual cyclones may play a role (Tamarin-Brodsky and Kaspi, 2017).

In the, several factors were identified as relevant to the uncertainties in projections of cyclone intensity, frequency, location of storm tracks and precipitation associated with ETCs. These include horizontal resolution, resolution of the stratosphere, and how changes in the Atlantic meridional overturning circulation (AMOC) were simulated. Since AR5, projections of extratropical cyclones and storm tracks have been examined further, largely confirming previous assessments. In particular, extratropical cyclone precipitation scales with the product of cyclone intensity (as measured by near-surface wind speed) and atmospheric moisture content (Pfahl and Sprenger, 2016). Booth et al. (2018) showed that the fraction of rainfall generated by the convection scheme in simulated extratropical cyclones is highly model- and resolution-dependent, which may be a source of uncertainty regarding their precipitation response to anthropogenic forcings. Also, increased moisture availability may increase the maximum intensity of individual storms while reducing the overall frequency as poleward energy transport becomes more efficient.

The role of temperature trends in influencing storm tracks has been further investigated, both in terms of upper tropospheric tropical warming (Zappa and Shepherd 2017) and lower tropospheric Arctic amplification (Wang et al., 2017), including the direct role of Arctic sea ice loss (Zappa et al., 2018), and the competition between their influences (Shaw et al, 2016). Physical linkages between Arctic amplification and changes in the mid-latitudes are uncertain, as discussed in Chapter 10 (Cross-Chapter Box 10.1). The remote and local SST influence has been further examined by Ciasto et al., (2016), who confirmed sensitivity of the storm tracks to the SST trends generated by the models and suggested that the primary greenhouse gas influence on storm track changes was indirect, acting through the greenhouse gas influence on SSTs. The importance of the stratospheric polar vortex in storm track changes has received more attention (Zappa and Shepherd 2017, Mindlin et al., 2020) and the anticipated recovery of the ozone layer further complicates the role of the stratosphere (Bracegirdle et al, 2020 ; Shaw et al., 2016).

Biases remain in cyclone locations, intensities, cloud features, and precipitation (Catto, 2016, Chang et al.,

ACCEPTED VERSION SUBJECT TO FINAL EDITING

2016). Uncertainties in projected precipitation changes in many mid-latitude regions can be explained to a large degree by uncertainties in projected storm track or ETC changes. Multiple studies (Chang et al., 2013; Zappa et al., 2015; Chang, 2018) have shown strong relationships between model projected precipitation change in many regions and model projected change in storm track activity near that regions. While front frequency is well represented, frontal precipitation frequency is too high and the intensity is too low (Catto et al., 2015). Some of the bias in storm tracks appears to be related to limitations in model realization of blocking (Zappa et al. 2014). The CMIP6 generation of models has improved representation of storm tracks in both hemispheres (Bracegirdle et al., 2020; Harvey et al., 2020). Simulation of storm tracks and their associated precipitation generally improve with increasing resolution beyond that used in most current climate models (Barcikowska et al., 2018; Jung et al., 2006; Michaelis et al., 2017). In terms of projections, the decreases in cyclone occurrence over the Mediterranean were replicated in a higher resolution model (Raible et al., 2018).

The projected changes in storm tracks and the associated mechanisms have several important implications for water cycle projections. P-E changes in the Mediterranean, California and Chile are directly linked to storm track changes (Zappa et al., 2020). Where the storm tracks are robustly projected to shift (Southern Hemisphere, North Pacific) or weaken (Mediterranean), understanding the physical causes of the related changes in precipitation helps increase confidence in the projections. Understanding the competing influences provides context for why other regions do not exhibit a consistent signal and cautions against regional projections based on individual models. However, model bias and the need for relatively high resolution to reproduce the relevant dynamics is an important overall limit on confidence in current CMIP6 projections.

In summary, there is the *high confidence* that precipitation associated with extratropical storms will increase with global warming in most regions. The Southern Hemisphere storm track will *likely* shift poleward, the North Pacific storm track *more likely than not* will shift poleward, and the North Atlantic storm track is *unlikely* to have a simple poleward shift/ display any discernible changes. There is *low confidence* in regional storm track changes, although a weakening of the Mediterranean storm track is a robust response of the models.

8.4.2.8.2 Atmospheric Rivers

Atmospheric rivers were not assessed in AR5 but are important in the water cycle as they are linked to extreme rainfall, flooding, and changes in terrestrial water storage including melt and ablation of glaciers and snowpack (Section 8.2.2; 8.2.3.2). In a warming world, there is *high confidence* that thermodynamical increases in atmospheric water vapour ensure that atmospheric rivers will become wetter, hence stronger, and longer-lasting (Payne et al., 2020). This is clearly observed in several regional (Gao et al.,, 2015; Gershunov et al., 2019; Hagos et al., 2016; Payne and Magnusdottir, 2015; Ralph and Dettinger, 2011; Warner et al., 2015, Lavers et al., 2013) and in one global study (Espinoza et al., 2018) of atmospheric river activity in CMIP5 model projections. Lavers et al. (2015) indicate that integrated vapour transport under RCP 8.5 and 4.5 could increase, and consequently this thermodynamic response (O'Gorman, 2015) could affect mid-latitudes regions where orographic precipitation is important (Gershunov et al., 2019).

Under continued global warming, more intense moisture transport within atmospheric river events is projected to increase the magnitude of heavy precipitation events on the west coast of the United States (Lavers et al., 2015; Ralph and Dettinger, 2011; Warner and Mass, 2017), in western Europe (Lavers et al., 2015; Ralph et al., 2016; Ramos et al., 2016), and in east Asia (Kamae et al., 2019) (*very likely*). All CMIP5 models analysed agreed under a range of scenarios, except over the Iberian Peninsula (Ramos et al., 2016) where there is only *low confidence* in projected changes. Kamae et al. (2019) reported a 1% increase per degree Celsius warming in the frequency of atmospheric rivers affecting East Asia, but this is strongly affected by SST changes. Emerging evidence of possible regional changes due to dynamical factors are uncertain (Lavers et al., 2013; Gao and others, 2015; Payne and Magnusdottir, 2015). The frequency, magnitude and duration of atmospheric rivers making landfall along the North American west coast are projected to increase (Gershunov et al., 2019). In contrast, Espinoza et al. (2018) suggest that the number of atmospheric river events is projected to slightly decrease globally.

ACCEPTED VERSION SUBJECT TO FINAL EDITING

In semi-arid regions where atmospheric rivers have historically been important and precipitation is mainly confined to the cold season, the contribution of atmospheric rivers to annual total precipitation may be expected to grow disproportionately. For example, in California decreases in precipitation frequency are projected as a result of fewer non-atmospheric river storms, while the projected increase in heavy and extreme precipitation events are almost entirely a result of increased atmospheric river activity (Gershunov et al., 2019). Interannual variability in precipitation amounts is projected to increase because of the overall decrease in the frequency of storms but a stronger dependence on extremes (Polade et al., 2014), particularly due to atmospheric rivers (Gershunov et al., 2019), especially where interaction with topography are important (Gershunov et al., 2019; Polade et al., 2014).

In summary, there is *high confidence* that the magnitude and duration of atmospheric rivers are projected to increase in future, leading to increased precipitation. This is projected to increase the intensity of heavy precipitation events on the west coast of the United States and in western Europe (*high confidence*).

8.4.2.9 Modes of climate variability and regional teleconnections

Following on from the assessment of projected changes in modes of climate variability (MoVs) and regional teleconnections (Section 4.5.3), here we assess their consequences for projected water cycle changes.

8.4.2.9.1 Tropical modes

CMIP6 projections indicate that the amplitude of ENSO (Annex IV.2.3) variability will not substantially change during the 21st century (*high confidence*) (Section 4.4.3.2). However, rainfall variability related to ENSO is projected to increase significantly by the second half of the 21st century, regardless of ENSO amplitude (Section 4.5.3.2). Regional precipitation variability associated with ENSO increases due to increases in atmospheric moisture, regardless of changes in ENSO variability itself (Pendergrass et al., 2017). In many regions, the magnitude of the projected changes related to ENSO is small compared with historical interannual variability (Bonfils et al., 2015; Power and Delage, 2018; Perry et al., 2019). Uncertainties in precipitation projections related to ENSO depend on internal variability associated with the mode (Section 8.5.2), hence the need to have relatively large ensembles (~15 members) to adequately estimate uncertainty (Deser et al., 2018; Maher et al., 2018a; Sun et al., 2018a; Zheng et al., 2018).

Even over regions with statistically significant simulated rainfall teleconnections during the historical period, CMIP5 models do not project clear changes (Perry et al., 2019). Nonetheless, CMIP5 models that realistically reproduce Indian summer monsoon rainfall indicate a strengthening of its relationship with ENSO in RCP8.5 projections, though the response is not consistent for different varieties of ENSO events (Roy et al., 2019). Inconsistent changes in the ENSO–Indian summer monsoon relationship in response to global warming in CMIP5 and CMIP6 models may be related to statistical issues rather than dynamical changes (Bódai et al., 2020; Haszpra et al., 2020). Over East Africa during the boreal spring and summer, ENSO teleconnections are projected to become stronger in the future (Endris et al., 2019). Meteorological drought consequences of each strong El Niño are projected to become more severe in the region (Rifai et al., 2019).

Indian Ocean Dipole (IOD, Annex IV.2.4) and Indian Ocean Basin (IOB, Annex IV.2.4) interactions with ENSO are expected to persist in the future (Section 4.5.3.3) but projected changes in the frequency and intensity of events remain uncertain (Hui and Zheng, 2018; Endris et al., 2019; McKenna et al., 2020). Climate extremes such as those associated with the extreme positive IOD event of 2019 are expected to occur more frequently under continued global warming (Cai et al., 2021). Projected changes in IOD teleconnections are linked to model performance in representing the IOD and its remote influence in the present climate, apparently dominated by a positive IOD event-like mean state (Wang et al., 2017a; Huang et al., 2019). Interactions between the IOD and the Indian Ocean mean state, via atmosphere-ocean feedbacks, can affect the behaviour of the IOD (Ng et al., 2018). In the eastern Horn of Africa, OND rainfall is projected to increase because of IOD-ENSO related SST changes in the Indo-Pacific region and associated

ACCEPTED VERSION SUBJECT TO FINAL EDITING

Walker circulation changes (Endris et al., 2019).

Sensitivity studies generally project increases in Madden Julian Oscillation (MJO, Annex IV.2.8) precipitation amplitude in a warmer climate, with increases of up to 14% per °C of warming (Arnold et al., 2013, 2015; Caballero and Huber, 2013; Liu and Allan, 2013; Maloney and Xie, 2013; Schubert et al., 2013; Subramanian et al., 2014; Carlson and Caballero, 2016; Pritchard and Yang, 2016; Adames et al., 2017a; Wolding et al., 2017; Haertel, 2018). However, in CMIP5 models with realistic historical MJO behaviour, the precipitation amplitude over the Indo-Pacific warm pool region changes from -4% to +8% per °C in the RCP8.5 scenario relative to the end of the 20th Century (Bui and Maloney, 2018; Maloney et al., 2019). When simulated MJO precipitation amplitude increases with warming, the leading factor for such change is the intensification of the lower tropospheric vertical moisture gradient, that supports stronger vertical moisture advection per unit diabatic heating (Adames et al., 2017b, 2017a; Arnold et al., 2015; Wolding et al., 2017). In idealised simulations with constant carbon dioxide forcing with El Niño-like patterns, the MJO activity penetrates farther east into the central and east Pacific with increased warming (Subramanian et al., 2014; Adames et al., 2017a). Increased MJO convective variability in a warmer climate does not reflect into increased ability of the MJO to force the extratropics (Wolding et al., 2017).

In summary, even though there is *low confidence* in how the tropical MoVs will change in the future (Sections 4.3.3.2 and 4.5.3.3), their regional hydrological consequences, in terms of precipitation, are projected to intensify (*medium confidence*). For example, the ENSO influence on precipitation over the Indo–Pacific sector is projected to strengthen and shift eastward (*medium confidence*). The MJO is projected to intensify in a warmer climate, with increased associated precipitation (*medium confidence*).

8.4.2.9.2 Extra-tropical modes

CMIP6 projections indicate that the Northern Annular Mode (NAM, Annex IV.2.1) is expected to become more positive in winter throughout the 21st century in the SSP3-7.0 and SSP5-8.5 scenarios (Section 4.5.1). In the near-term, the Southern Annular Mode (SAM, Annex IV.2.2) is projected to become less positive than observed during the end of the 20th century during the austral summer in all SSPs scenarios (Section 4.3.3.1).

In the CMIP5 RCP8.5 scenario, increased amplitude and frequency of the North Atlantic Oscillation (NAO, Annex IV.2) during boreal winter (DJF) is associated with higher precipitation in northern Europe and lower precipitation in southern Europe (Tsanis and Tapoglou, 2019). However, large-ensembles analyses show how the NAO leads to significant uncertainty in future changes of regional climate (Section 8.5.2). For example, more than a 85% increase in precipitation is projected over northern Europe, western Russia and much of eastern North America, with similar decreasing resulting in drying over northwestern Africa and regions adjacent to the Mediterranean Sea (Deser et al., 2017).

In the Southern Hemisphere, the positive trend projected for the SAM in the CMIP5 RCP8.5 scenario appears to mitigate the wetting in the mid-to-high latitudes and the drying over the subtropics, but with strong seasonal dependence (Lim et al., 2016). Regional precipitation changes in South America, South Africa, Southern Australia and New Zealand are not well explained by changes in the SAM, but are related to broad-scale changes in north-south temperature gradients associated with enhanced warming of the tropical upper troposphere and strengthening of the stratospheric polar vortex (Mindlin et al., 2020).

In summary, projected changes in the intensity, frequency and phase of extratropical MoVs (see also Section 4.3 and 4.5) may amplify regional changes in precipitation and contribute to an increase in their intra-seasonal and interannual variability (*medium confidence*). Regionally, there are potentially significant precipitation and atmospheric circulation changes associated with changes in extratropical dynamics (*low confidence*).

8.5 What are the limits for projecting water cycle changes?

Understanding the limits to projecting water cycle changes are fundamental for refining climate and

ACCEPTED VERSION SUBJECT TO FINAL EDITING

hydrological models needed to develop successful climate change adaptation strategies. Regional water cycle projections depend on a range of model-dependent responses (Section 8.5.1) and are also strongly influenced by internal variability, especially in the near term (Section 8.5.2) (Hawkins and Sutton, 2012; Rowell, 2012; Orlowsky and Seneviratne, 2013; Kent et al., 2015; Fatichi et al., 2016; Greve et al., 2018; Chegwidden et al., 2019). CMIP6 models show that different model responses to the same forcing scenario remain the main source of uncertainty for projected changes in regional precipitation (Figure 8.23) (Lehner et al., 2020). Section 8.5.3 assesses the potential for non-linear responses when shifting from low to high global warming levels (James et al., 2017; see also Section 8.4.2.4). While regional uncertainties related to downscaling methods (Section 10.3.3) and impact models (WGII Chapter 4) are not covered here, the added value of regional climate models is briefly discussed (Section 8.5.1.2.2) with a focus on water cycle changes.

[START FIGURE 8.23 HERE]

Figure 8.23: Geographical and zonal mean distribution of the percentage of variance explained by the three sources of uncertainty in CMIP6 projections of 20-year mean precipitation changes in 2021–2040 (top), 2041–2060 (middle) and 2081–2100 (bottom) relative to the 1995–2014 base period: internal climate variability (left), model response uncertainty (middle) and scenario uncertainty (right, considering four plausible concentration scenarios: SSP1-2.6, SSP2-4.5, SSP3-7.0 and SSP5-8.5). Percentage numbers give the area-weighted global average value for each map. Right panels show the zonal mean fractions over both land and sea (solid lines) and over land only (dashed line). The figure was adapted from Fig.4a in (Lehner et al., 2020). The relative contributions of internal variability, models and emission scenarios to the total uncertainty depend on both region and time horizon. The scenario uncertainty is relatively low in near and mid-term time horizons while it increases in the long-term mostly over the high-latitudes. The model response uncertainty is the most influential factor across all time horizons. Internal variability also plays a key role in the near-term, especially in the subtropics. Further details on data sources and processing are available in the chapter data table (Table 8.SM.1).

[END FIGURE 8.23 HERE]

8.5.1 Model uncertainties of relevance for the water cycle

Model response uncertainty is typically estimated as the inter-model spread (range) projected by a set of climate models for a given emission scenario. It is best estimated at the end of a high-emission scenario when internal variability has a limited contribution to total uncertainty (Figure 8.23). Even for aggregated quantities, like decadal-mean precipitation averaged over relatively large domains, model response uncertainty is substantial and can exceed scenario uncertainty (Hawkins and Sutton, 2011; Lehner et al., 2020). This can also be true for other water cycle variables such as soil moisture, runoff and streamflow at the regional scale, either derived directly from global climate models (GCMs) or produced by "offline" using global hydrological models (GHMs) driven by the same GCMs (Orlowsky and Seneviratne, 2013; Giuntoli et al., 2015, 2018; Chegwidden et al., 2019). Although some of the model response uncertainty is related to climatological biases (Grose et al., 2017; Li et al., 2017b; Lehner et al., 2019; Samanta et al., 2019), model biases are not the only way to assess the reliability of climate projections (cf. Box 4.1). Therefore, our focus here is on the representation of key processes that are not completely resolved in current-generation GCMs (Section 8.5.1.1) and on the model improvements associated with increased horizontal resolution (Section 8.5.1.2).

8.5.1.1 Fitness-for-purpose and poorly constrained key processes

AR5 Chapter 7 recognized that the simulation of clouds and precipitation remains challenging for state-of-the-art GCMs. Model development and evaluation have continued since AR5, with a particular emphasis on the representation of new model components, like interactive vegetation, aerosols and biogeochemical cycles. For example, the comparison of simulated tropical precipitation across three successive generations of CMIP models (including CMIP6) indicates overall little improvement for the summer monsoons, the

ACCEPTED VERSION SUBJECT TO FINAL EDITING

double-ITCZ bias, the diurnal cycle and the frequency of precipitation (Fiedler et al., 2020). Some of these issues are related to inherent model limitations in three specific areas: atmospheric convection, cloud-aerosol interactions and land surface processes (ocean and cryosphere-related processes are addressed in Chapter 9). These limitations do not weaken the overall progress made in the large-scale simulation of present-day climate (FAQ 3.3, Section 3.3.2.2), even though the improvement of CMIP6 compared with CMIP5 models is limited (Figure 3.12) and is generally less systematic or obvious at the regional scale (e.g., Gusain et al., 2020; Monerie et al., 2020; Oudar et al., 2020). Instead, they call for a careful interpretation of hydrological projections with the full range of plausible outcomes, rather than only considering the most likely scenarios (Sutton, 2018, 2019).

8.5.1.1.1 Atmospheric convection

Moist convection is fundamental to the water cycle through its vertical transport of momentum, heat, and moisture across the atmosphere. It is particularly active in the tropics where it contributes to more than half of annual precipitation and to the development of severe weather events. Given limitations in computing resources, the current-generation GCMs cannot yet represent small-scale cloud processes and consequently shallow and deep convection is determined by sub-grid-scale parameterizations. While such parameterizations can be evaluated against field observations (e.g., Abdel-Lathif et al., 2018), it remains challenging to estimate convective entrainment that is valid for both shallow and deep convection (Zhang et al., 2016a). Comparisons between regional projections with explicit versus parameterized convection also highlight the limitations of parameterized convection for assessing climate change (Kendon et al., 2019; Jackson et al., 2020).

Atmospheric convection is particularly important for a realistic simulation of tropical precipitation intensities (Pendergrass and Hartmann, 2014a; Kendon et al., 2019). Many CMIP5 models produce rainfall at water vapour amounts lower than in observations (Takahashi, 2018), as well as too light and too frequent precipitation events (Sun et al., 2015; Trenberth et al., 2017). Such biases can be explained by a lack of convective inhibition (Rochetin et al., 2014a, 2014b) and by too much convective and too little non-convective precipitation (Chen and Dai, 2019). Tropical convection controls the amount of precipitable water simulated over the equatorial Indian Ocean, which has been identified as a key metric for differentiating model skill in simulating South Asian monsoon precipitation (Hagos et al., 2019). Many models have difficulty in adequately simulating the diurnal cycle of precipitation over land (Couvreux et al., 2015), the rainfall intensity distribution associated with the West African monsoon (Roehrig et al., 2013), and the intensity of tropical cyclones (Sections 10.3.3.4 and 11.7.1.3), phenomena for which atmospheric convection also plays a key role.

Since AR5, there have been improvements in the representation of convective clouds and related precipitation in GCMs. For instance, the drizzle issue (too light and too frequent rainfall events) has led to modifications in the deep convection triggering scheme (Rochetin et al., 2014b; Han et al., 2017; Wu et al., 2018a; Xie et al., 2018). Although high-resolution studies have highlighted these limitations, most GCMs still rely on a convective available potential energy (CAPE) closure which has been adapted to various cloud regimes (Bechtold et al., 2014; Han et al., 2017; Walters et al., 2017) or evaluated against convection-permitting models (CPMs) (Chen et al., 2020b). To increase the sensitivity of convection to tropospheric humidity, several models now include a representation of deep convective entrainment dependent on relative humidity (Bechtold et al., 2008; Han et al., 2017; Walters et al., 2017; Zhao et al., 2018c). Other efforts have focused on the improvement of shallow convection and low-level cloudiness due to their major contribution to uncertainty in climate sensitivity (Section 7.4.2.4). A cloud regime-based study however highlights an apparent disconnection between cloud and precipitation processes in GCMs (Tan et al., 2018), suggesting that a good representation of clouds does not lead to systematic improvement in simulated precipitation. A global simulation in which the parameterized convection is switched off shows a strong influence of parameterized convection on daily precipitation extremes (Maher et al., 2018b). Regional simulations at a 25km resolution suggest that an explicit deep convection can be beneficial even at such a relatively coarse resolution (Vergara-Temprado et al., 2020). Perturbed physics ensembles (PPE, Section 1.4.4) make it possible to identify parameters in the convection scheme that are most important in determining future precipitation changes (Bernstein and Neelin, 2016).

ACCEPTED VERSION SUBJECT TO FINAL EDITING

Since AR5, spatial aggregation of tropical convection has also received growing attention in both observational (Holloway et al., 2017) and modelling studies (Muller and Bony, 2015; Wing et al., 2017; Tan et al., 2018). The changing degree of convective organization was highlighted as a key mechanism for dynamic changes in extreme precipitation (Pendergrass, 2020a). Yet, convective parameterizations do not represent all aspects of mesoscale convective systems (Hourdin et al., 2013; Park et al., 2019). This is related to the complexity of mechanisms involved from synoptic to mesoscale dynamics, which are only partially resolved by models. Cloud-resolving models (CRMs, Section 8.5.1.2.2) represent a useful benchmark for improving the parameterization of mesoscale convective systems. Machine learning can also be used to parameterize moist convection after training the model with a conventional or a super parameterization scheme (Gentine et al., 2018; O'Gorman and Dwyer, 2018), but has not yet been used in the CMIP framework.

While some global modelling centres have reported progress in their parameterization of convection and in their simulation of seasonal, daily and sub-daily precipitation (e.g., Danabasoglu et al., 2020; Roehrig et al., 2020), CMIP6 models as a whole only show limited improvements in their simulation of the tropical precipitation climatology compared to CMIP5 (Fiedler et al., 2020; see also Figure 3.10). For instance, the double-ITCZ syndrome is still prominent (Tian and Dong, 2020) despite being reduced in some models (e.g., Qin and Lin, 2018). This systematic bias was shown to arise from atmospheric processes including cloud feedbacks (Tian, 2015; Dixit et al., 2018; Talib et al., 2018) and the SST threshold at which deep convection occurs in the tropics (Oueslati and Bellon, 2015; Xiang et al., 2017; Adam et al., 2018). Such biases can also arise from a too weak sensitivity of seasonal tropical precipitation to local SSTs compared with observations (Good et al., 2020). These biases are large enough to alter forced precipitation changes, and consequently limit our confidence in projected precipitation changes (Samanta et al., 2019; Aadhar and Mishra, 2020). Observational constraints can be used to narrow model response uncertainties (DeAngelis et al., 2015; Li et al., 2017b; Ham et al., 2018; Watanabe et al., 2018), although there is still no consensus that model selection or weighting is a reliable alternative to the 'one-model-one-vote' approach used in Section 8.4 (Box 4.1). The detrimental influence of model errors can also be mitigated by focusing on phenomena or events (Polson and Hegerl, 2017; Weller et al., 2017), implementing bias adjustment techniques (Section 10.2.3.2), or adopting a non-probabilistic storyline approach (Zappa and Shepherd, 2017).

In summary, since AR5 empirical convective parameterization schemes and associated precipitation biases have improved in some but not all global climate models. There is still *low confidence* in their ability to accurately simulate the spatio-temporal features of present-day precipitation, especially in the tropics where a double-ITCZ bias is still apparent in many models. While such biases limit the reliability of precipitation projections in some cases, there is currently only *medium confidence* that model selection or weighting is a better alternative to the one-model-one-vote approach (Box 4.1). Improved water cycle projections can be achieved by focusing on phenomena or weather events, such as a thermodynamic intensification of convective events (*high confidence*, Section 8.2.2.1), however accurate quantitative estimates are currently hampered by complex, model-dependent dynamical responses (Section 8.2.2.2).

8.5.1.1.2 Aerosol microphysical effects on clouds and precipitation

In AR5 Chapter 7, there was *low confidence* in the representation of cloud–aerosol interactions in climate models. Despite progresses in this field since AR5, cloud–aerosol interactions remain a major obstacle to understanding climate and severe weather (Varble, 2018). High aerosol concentrations have been observed to suppress rain in water clouds (Campos Braga et al., 2017; Fan et al., 2020). However, such aerosol effects are muted in GCMs, which tend to produce precipitation from shallow clouds too frequently at the expense of rain intensity (Suzuki et al., 2015; Jing et al., 2017). This arises from incomplete knowledge of how clouds adjust to aerosol primary effects such as cloud condensation nuclei (CCN). The adjustment occurs mainly as a dynamic response to the impacts of CCN on cloud drop size and number concentrations on precipitation-forming processes (Rosenfeld et al., 2008; Goren and Rosenfeld, 2014; Koren et al., 2014; Camponogara et al., 2018). Uncertainties are large for deep clouds, as their processes are much more complex and include also the impacts of aerosols on ice precipitation processes. Aerosols can substantially invigorate (Rosenfeld et al., 2008; Koren et al., 2014; Fan et al., 2018) and electrify (Thornton et al., 2017;

ACCEPTED VERSION SUBJECT TO FINAL EDITING

Wang et al., 2018b) deep tropical convective clouds. High-resolution atmospheric simulations suggest that high aerosol concentrations can increase environmental humidity by producing clouds that mix more condensed water into the surrounding air, which in turn favours large-scale ascent and strong convective events (Abbott and Cronin, 2021). Further assessment of uncertainties in aerosol-cloud interactions for shallow water clouds is provided in Section 7.3.3.2.

A major challenge in representing convective clouds and related precipitation events in GCMs is a lack of sophisticated cloud microphysics in convective parameterization schemes (e.g., Fan et al., 2016). Most of these schemes only include simple microphysical treatments, such as direct partition between cloud condensation and precipitation, and do not include advanced treatment of conversion among different types of hydrometeors. As such these schemes are unable to simulate microphysical cloud and precipitation responses to aerosol-related perturbations in cloud droplet concentration and ice crystals (see Box 8.1), or perturbations in thermodynamical states from global warming. Efforts have been made to include more advanced cloud microphysical treatment in cumulus parameterizations (Song and Zhang, 2011; Grell and Freitas, 2014; Berg et al., 2015) or to use explicit cloud microphysics schemes in climate models with a 'super parameterization' (Wang et al., 2015), which have been shown to improve the performance in simulating cloud properties and precipitation. However, few of these improvements have been incorporated into CMIP6 climate models so the projected precipitation response to anthropogenic perturbation may still be hindered by the inadequate microphysical treatment in cumulus parameterization (Smith et al., 2020).

In summary, there is still *low confidence* in the simulated influence of the aerosol microphysical effects on future precipitation changes.

8.5.1.1.3 Land surface processes

Land surface processes determine the partitioning of net surface radiation into sensible, latent and ground heat fluxes, the partitioning of precipitation into evapotranspiration and runoff, and the net terrestrial carbon flux at the Earth's surface. They are relevant for simulating the terrestrial water cycle responses to climate change, as well as the response to land use change (FAQ 8.1). Even basic land surface properties such as albedo (Terray et al., 2018) or the ratio of transpiration to total evaporation (Chang et al., 2018) still need to be improved in state-of-the-art coupled GCMs. Runoff sensitivities are also not well constrained in these models, which display a large spread for the present-day climate, influencing simulated changes under global warming (Lehner et al., 2019). Earth System Models (ESMs) incorporate some combined biophysical and biogeochemical processes to a limited extent, and many relevant processes about how plants and soils interactively respond to climate changes are yet to be considered (e.g., Liu et al., 2020). Consequently, land surface processes and their atmospheric coupling contribute to the range in water cycle projections (Jia et al., 2020).

Since AR5, development of new and existing processes in land surface models (LSMs) have been evaluated. These include soil freezing and permafrost (Vergnes et al., 2014; Chadburn et al., 2015; Yang et al., 2018a; Gao et al., 2019), soil and snow hydrology (Brunke et al., 2016; Decharme et al., 2016), glaciers (Shannon et al., 2019), surface waters and rivers (Decharme et al., 2012), as well as vegetation (Bartlett and Verseghy, 2015; Betts et al., 2015; Knauer et al., 2015; Tang et al., 2015) and the representation of hydraulic gradients throughout the soil-plant-atmosphere continuum (Bonan et al., 2014). Such land surface model developments have led to significant improvements in global off-line hydrological simulations driven by observed atmospheric forcings (e.g., Li et al., 2017a; Decharme et al., 2019).

Progress in the representation of land surface heterogeneity has been made, in the form of improved mapping of root zone storage capacity (Wang-Erlandsson et al., 2016), improved vegetation stand, disturbance and fire dynamics (Li et al., 2013a; Fisher et al., 2018; Haverd et al., 2018; Yue et al., 2018; Zou et al., 2019), better representation of urban surfaces (Box 10.3), and the explicit representation of inland water bodies (Gu et al., 2015; Verseghy and MacKay, 2017). The representation of realistic snow and vegetation cover significantly affects the simulation of the land surface energy and water budgets at multiple time-scales (Loranty et al., 2014; Bartlett and Verseghy, 2015; Thackeray et al., 2015; Qiu et al., 2016; Thackeray and Fletcher, 2016; Wang et al., 2016a; Alessandri et al., 2017). Groundwater remains inadequately represented

ACCEPTED VERSION SUBJECT TO FINAL EDITING

in many models, which limits our current understanding of the two-way interactions between groundwater and the rest of the hydrologic cycle (Taylor et al., 2013b; Leng et al., 2014; Vergnes et al., 2014; Pokhrel et al., 2015; Maxwell and Condon, 2016; Collins, 2017; Scanlon et al., 2018; Condon et al., 2020). Land management exerts an increasing influence on the water cycle (Abbott et al., 2019) whose representation in the current-generation climate models is generally incomplete (Section 10.3.3.7.2).

Aside from land surface models (LSMs), global hydrological models (GHMs) have been further developed for off-line simulations of the hydrological impacts of both climate change and water management (Cisneros et al., 2014; Schewe et al., 2014; Döll et al., 2016, 2018b, Pokhrel et al., 2016, 2017; Veldkamp et al., 2018). GHMs can equal or outweigh the contribution of GCMs to uncertainties in hydrological projections at the regional scale (Giuntoli et al., 2015). Historical GHM simulations are currently not sufficient to improve regional water cycle projections, due to modelling uncertainties in both the driving GCMs and land surface hydrology (Pechlivanidis et al., 2017; Samaniego et al., 2017; Hattermann et al., 2018; Krysanova et al., 2018). Biophysical vegetation processes are still not accounted for in many GHMs, which may lead to inadequate projections of terrestrial runoff and water resources. However, hydrological models that do simulate these effects often disagree (Prudhomme et al., 2014), so do not necessarily provide the added value of a more sophisticated representation of vegetation processes and land surface conditions (Döll et al., 2016).

Since AR5, there has been increasing recognition of the need to better understand the role of land–atmosphere coupling and related feedbacks (Joetzjer et al., 2014; Berg et al., 2016; Catalano et al., 2016; Berg and Sheffield, 2018a; Santanello et al., 2018). This has led to the development of dedicated field campaigns (Song et al., 2016; Phillips et al., 2017; Dirmeyer et al., 2018), remotely sensed observations (Ferguson and Wood, 2011; Roundy and Santanello, 2017), and tailored diagnostics (Tawfik et al., 2015a, 2015b, Miralles et al., 2016, 2019; Dirmeyer and Halder, 2017). Dynamic vegetation models have been introduced in global ESMs but they need further evaluation (Medlyn et al., 2015; Prentice et al., 2015; Cantú et al., 2018; Franks et al., 2018) to provide valuable information on potential vegetation feedbacks. Plant migration and mortality, increased disturbances from wild fires, insects and extreme events, interactive nitrogen cycle, or the impact of increased levels of tropospheric ozone are often ignored or poorly represented in the current-generation of ESMs (Bonan and Doney, 2018; Fisher et al., 2018).

The physiological response of plants to increasing atmospheric CO_2 is generally accounted for, but only using empirical models of stomatal conductance that are characterized by a single critical parameter of intrinsic water-use efficiency (Franks et al., 2017, 2018). This reflects a lack of structural diversity and caution about the consensus of the photosynthesis response to increasing CO_2 (Knauer et al., 2015; Huang et al., 2016), which has implications for the ability of the current-generation models to account for uncertainty in future evapotranspiration changes. Most CMIP5 models underestimate the ratio of plant transpiration to total terrestrial evapotranspiration, which may suggest that they also underestimate the impact of plant physiology on the water cycle (Lian et al., 2018). Plant hydraulics are not explicitly considered in many land surface models, which may lead to an underestimation of the influence of the increasing atmospheric moisture stress on plant transpiration under climate change (Massmann et al., 2019; Grossiord et al., 2020; Liu et al., 2020c). Most ESMs underestimate the water use efficiency measured at many sites and, consequently overestimate the ratio of evapotranspiration to precipitation (Li et al., 2018a).

In summary, since AR5 substantial advances have been made in the representation of land surface processes in current-generation Earth System Models (ESMs). Off-line hydrological models allow the application of bias-adjusted atmospheric forcings, but there is *low confidence* of an improved response compared to coupled climate models, given their inherent limitations (Box 10.2). While improvements in the representation of complex land surface feedbacks relevant to the water cycle are needed, there is currently *low confidence* that they will substantially improve of water cycle projections.

8.5.1.2 Added value of increased horizontal model resolution

Coarse spatial resolution of climate models has often been considered a key limitation in global climate projections (Di Luca et al., 2015; Roberts et al., 2018). Proposed and tested solutions include a uniform or

ACCEPTED VERSION SUBJECT TO FINAL EDITING

regional increase in the resolution of GCMs, or the use of regional climate models (RCMs). The increase in computing resources has also led to the development of convection-permitting models (Prein et al., 2015), which have been integrated over larger domains, but are still unsuitable for CMIP simulations. Statistical downscaling tools are also widely used to generate fine-scale regional climate information necessary for climate impacts and adaptation studies. A comprehensive assessment of the added value of increased spatial resolution and of the benefits and shortcomings of statistical downscaling tools are addressed in Chapter 10 (Section 10.3.3).

8.5.1.2.1 High-resolution global climate models

Since AR5, horizontal resolution has increased in most global climate models, which has led to several improvements in the simulation of the water cycle (see also Section 10.3.1.1), not only in areas with steep or complex orography, but also over the tropical oceans and within the North Pacific and North Atlantic storm tracks (Piazza et al., 2016; Roberts et al., 2018; Bui et al., 2019; Chen and Dai, 2019; Vannière et al., 2019). Yet, the added value of higher resolution global climate models is not systematic (Johnson et al., 2016; Ogata et al., 2017; Huang et al., 2018a; Mahajan et al., 2018; Vannière et al., 2019) and needs careful assessment (Haarsma et al., 2016; Caldwell et al., 2019). Several AGCM studies suggest that increased spatial resolution leads to better simulation of the atmospheric moisture transport from ocean to land, the geographical distribution of annual mean precipitation (Demory et al., 2014), and the frequency distribution of daily precipitation intensities (Zhang et al., 2016c; Chen and Dai, 2019) including extremes in many (Jacob et al., 2014; Westra et al., 2014) but not all cases (Bador et al., 2020).

Part of the improvement in simulated precipitation accuracy is related to improved simulation of the frequency and/or mean intensity of tropical (Roberts et al., 2015; Walsh et al., 2015) and extratropical (Hawcroft et al., 2016) cyclones. Idealized regional experiments also show that the North Atlantic storm-track response to global warming can be amplified in higher resolution models (Willison et al., 2015). Increased atmospheric horizontal resolution can be also important for simulating Northern Hemisphere blockings (Davini et al., 2017; Schiemann et al., 2017) and synoptic features of the East Asian summer monsoon (Yao et al., 2017; Kusunoki, 2018). Variable resolution based on grid stretching may be a valuable alternative for simulating regional phenomena like monsoons (P Sabin et al., 2013; Krishnan et al., 2016) or tropical cyclones (Harris et al., 2016; Chauvin et al., 2017), while avoiding inconsistencies in the forcings or physics that can be found in RCMs driven by GCMs (Boé et al., 2020; Tapiador et al., 2020).

Increasing horizontal model resolution in CMIP5 and CMIP6 models leads to a systematic increase in global mean precipitation, enhanced moisture advection to land in close connection with increased orographic precipitation, and a partial reduction of the long-standing double ITCZ bias (Demory et al., 2014; Caldwell et al., 2019; Vannière et al., 2019). Recent studies based on HighResMIP simulations (Haarsma et al., 2016) confirm the added value of increased horizontal resolution (at least 50 km in the atmosphere and 25 km in the ocean) for the simulation of tropical (Roberts et al., 2020) and extratropical cyclones (Priestley et al., 2020). CMIP6 model biases in annual mean precipitation are only slightly reduced at higher resolution (Figure 3.10).

High resolution representation of the land surface is also important for simulating many features of the terrestrial water cycle, such as orographic precipitation, snow, runoff and streamflow in complex topography areas (Zhao and Li, 2015). However, the added value may be easier to assess in off-line rather than online land surface simulations (Döll et al., 2016) given the possible use of bias-corrected atmospheric forcings. Off-line high-resolution GHMs are routinely used to monitor water resources or to assess the hydrological impacts of bias-adjusted global climate projections (Davie et al., 2013; Huang et al., 2017, 2018b). Yet, the development and calibration of 'hyper-resolution' hydrological models, with grid cells of typically 100m to 1km, raises a number of issues given the lack of comprehensive surface or subsurface information (Bierkens et al., 2015) and the lack of coupling with the atmosphere (Berg and Sheffield, 2018a).

In summary, there is *high confidence* that increasing horizontal resolution in GCMs can reduce a number of systematic model errors of relevance for the water cycle, including synoptic circulation and the accuracy of daily precipitation projections. High-resolution GCMs and GHMs provide improved representation of land surfaces, including topography, vegetation and land use change, which are required to accurately simulate

ACCEPTED VERSION SUBJECT TO FINAL EDITING

changes in the terrestrial water cycle. However, there is *low confidence* that the higher horizontal resolution simulations currently available provide more accurate projections of the large-scale features of the water cycle.

8.5.1.2.2 Regional Climate Models and Convective Permitting Models

Regional Climate Models (RCMs) are used to dynamically downscale global model simulations for a particular region (usually at a spatial resolution in the order of 10 to 50 km) (see Section 10.3.3). AR5 reported that RCMs are useful for regions with variable topography and for small-scale phenomena, however inherit biases from their driving GCMs and thus may lack physical consistency with them. Since AR5, the application of RCMs has largely increased due to international model inter-comparison projects such as CLARIS-LPB (Sánchez et al., 2015). Many studies have focused on present-day climatological precipitation, showing with *high confidence* improvements in its monthly to seasonal accumulation and spatial distribution (Dosio et al., 2015; Giorgi et al., 2016; Bozkurt et al., 2019; Falco et al., 2019; Di Virgilio et al., 2020), although the modelling of precipitation remains the 'Achilles heel' of both GCMs and RCMs and should be considered cautiously when informing regional climate change adaptation strategies (Tapiador et al., 2019a).

Regional Convective Permitting Models (CPMs), typically run at a resolution less than 10 km, have been implemented over increasingly large domains. Compared to models with parameterized convection (Section 8.5.1.1.1), they generally show improved simulation of key features of the water cycle such as orographic precipitation, sea-breeze dynamics, the diurnal cycle in precipitation, soil-moisture precipitation feedbacks, daily precipitation persistence, sub-daily to daily precipitation intensities and related extremes (Birch et al., 2015; Prein et al., 2015; Willetts et al., 2017; Kendon et al., 2017; Leutwyler et al., 2017; Hohenegger and Stevens, 2018; Berthou et al., 2019b; Takahashi and Polcher, 2019; Fumière et al., 2020; Scaff et al., 2020; Caillaud et al., 2021; see also Section 8.2.3.2). A growing number of studies have also assessed the potential added value of using CPMs for regional climate projections (Ban et al., 2015; Giorgi et al., 2016; Fosser et al., 2017; Kendon et al., 2017, 2019; Liu et al., 2017; Rasmussen et al., 2017; Lenderink et al., 2019; see also Atlas 5.6.3). Although projected changes in rainfall occurrence in CPMs are broadly and qualitatively consistent with the results of GCMs and RCMs (Kendon et al., 2017), there is a tendency towards stronger changes in both wet and dry extremes (Berthou et al., 2019a; Kendon et al., 2019; Lenderink et al., 2019; Finney et al., 2020a). While both GCMs and RCMs project an overall decrease in summer precipitation over the Alps, RCMs simulate an increase over the high Alpine elevations that is not present in the global simulations (Giorgi et al., 2016).

Recent studies based on both GCMs and CPMs indicate that both CAPE and convective inhibition will increase in a warmer climate (Chen et al., 2020; see also Section 8.2.3.2), consistent with a shift from moderate to less frequent but stronger convective events (Rasmussen et al., 2017). If underestimated by models with parameterized convection, such a mechanism could explain the underestimation of both projected increase in precipitation extremes (Borodina et al., 2017; Yin et al., 2018) and land surface drying (Douville and Plazzotta, 2017) in the extratropics. CMIP5 models with a larger increase in extreme precipitation also exhibit larger declines or smaller increases in light-moderate events (Thackeray et al., 2018).

In summary, there is *high confidence* that dynamical downscaling using limited area models adds value in simulating precipitation and related water cycle processes at the regional scale, especially in complex orography areas (see also Section 10.3.3.5.1). There is *high confidence* that the explicit simulation of atmospheric convection can improve the representation of weather phenomena, including the life cycle of convective storms and related precipitation extremes. Even with an improved simulation of small-scale processes, there is only *medium confidence* that there will be an improvement in RCM-based water cycle projections as they rely on GCM boundary conditions.

8.5.2 Role of internal variability and volcanic forcing

Beyond modelling uncertainties, internal variability and unpredictable natural forcings may also lower the

ACCEPTED VERSION SUBJECT TO FINAL EDITING

degree of confidence in projected water cycle changes, especially in the near-term (2021-2040) and regional-scale projections (Hawkins and Sutton, 2011; Kent et al., 2015; Thompson et al., 2015; Fatichi et al., 2016; McKinnon and Deser, 2018; Chen and Brissette, 2019; Lehner et al., 2020). Although there is *low confidence* that the main modes of climate variability (Annex IV) are altered in a warmer climate (Sections 4.4.3 and 4.5.3), increasing contrast between wet and dry weather regimes (Section 8.2.2.1) will amplify their influence on water cycle variability (Section 8.4.2.9) and therefore contribute to uncertainties in near-term precipitation changes (Figure 8.23). The role of internal variability as source of uncertainties in regional climate projections is assessed in Section 10.3.4.3. Here we assess the role of internal variability in influencing water cycle projections using paleoclimate reconstructions, preindustrial model simulations, and large single model ensembles (Section 8.5.2.1). Implications for the predictability of near-term water cycle changes are specifically assessed, as they show significant but model-dependent regional hydrological fingerprints over land (Section 8.5.2.2). The role of volcanic eruptions is also briefly assessed in terms of consequences and uncertainties in water cycle projections (Section 8.5.2.3).

8.5.2.1 Quantification of water cycle internal variability

Estimating internal variability is an important challenge in the assessment of human-induced changes in the water cycle since its magnitude and range of variability can exceed the anthropogenic signal, at least at the regional scale and for near-term projections or low-emission scenarios (Deser et al., 2012; Shepherd, 2014; Xie et al., 2015; Sarojini et al., 2016; Dai and Bloecker, 2019; Lehner et al., 2020) (Section 4.4.1.4, 8.4.2.9). Underestimating internal variability in models may result in the overestimation of anthropogenic climate change because the 'noise' in the signal-to-noise ratio is underestimated (Knutson and Zeng et al., 2018). There is *medium confidence* that this underestimation affects global water cycle projections, for instance, in terms of drought persistence and severity in the southwestern United States, eastern Australia, southern Africa, the Mediterranean, the southern Amazon basin and China (Ault et al., 2014; Cook et al., 2018; Gu et al., 2018). In CMIP6 models, the uncertainty in future projections of 20-year mean precipitation changes attributable to internal variability ranges from 41% in the near-term (2021-2040) to 5% in the long-term (2081-2100) (Figure 8.23). For decadal-mean precipitation changes, the relative contribution of internal variability is even larger when using large ensembles (Lehner et al., 2020).

Over the 20th century, CMIP5 models show a realistic magnitude of decadal precipitation variability, if not a slight overestimation in some regions (Knutson and Zeng, 2018). However, the relatively short and human-influenced instrumental record limits our ability to quantify the magnitude of internal variability in the water cycle, particularly over long timescales (decadal and beyond). Global extended reanalyses (Section 1.5.2) have been used to derive long-term variability in the regional water cycle components (Caillouet et al., 2017), merged with historical meteorological and hydrological local observations (Bonnet et al., 2017; Devers et al., 2020). Specific assessment of these types of methodology and related uncertainties is provided in Chapter 10 (Sections 10.2 and 10.3). Paleoclimate archives (tree rings, corals, ice core, speleothems, lake and ocean sediments) provide extended reconstructions of key water cycle metrics and large-scale circulation features. Some studies have suggested that CMIP5 models underestimate internal variability at decadal and longer timescales, and therefore may be missing important processes in the climate system (Ault et al., 2012, 2013; Bunde et al., 2013; Franke et al., 2013; Cheung et al., 2017; Hope et al., 2017; Kravtsov, 2017; Cassou et al., 2018). However, recent assessments using paleoclimate records have found that CMIP5 models are able to reproduce decadal-to-centennial variability, including the severity, persistence and spatial extent of megadroughts (Coats et al., 2015; Stevenson et al., 2015; PAGES Hydro2K Consortium, 2017), once signal reddening (autocorrelation) in proxy archives is accounted for (Dee et al., 2017; PAGES Hydro2K Consortium, 2017). Implementation of proxy system models, i.e., functions that transform model variables into proxy units, has reduced model-proxy disagreement, although some differences in the magnitude of internal variability remain, particularly at centennial timescales (Dee et al., 2017; Parsons et al., 2017). It is unclear whether remaining discrepancies represent limitations of the climate models, or limitations of the proxy system models. Therefore, there is *medium to high confidence* (i.e., depending on the region) that climate models do not underestimate water cycle internal variability.

The mechanisms driving internal variability in the water cycle in climate model simulations varies. While

ACCEPTED VERSION SUBJECT TO FINAL EDITING

models indicate that cool SSTs in the eastern tropical Pacific (La Niña or the cool phase of the PDO) are associated with drought in southwestern North America, they also show that atmospheric internal variability may be a more prominent driver (Coats et al., 2015, 2016; Stevenson et al., 2015; Parsons et al., 2018). CMIP5–PMIP3 last millennium simulations reproduce the observed negative correlation between eastern Australian rainfall and the central equatorial Pacific SSTs with varying skill, and also display periods when the ENSO teleconnection weakens substantially for several decades (Brown et al., 2016a). Differences in simulated internal variability have been found to be responsible for the inter-model spread in predicted shifts in subtropical dry zones for a given shift in the Hadley cell (Seviour et al., 2018). CMIP5 models show that both internal variability and anthropogenic forcings are responsible for the drying over the South Atlantic Convergence Zone region, though with large uncertainties (Zilli and Carvalho, 2021). Moreover, the detection of the anthropogenic forcing on the South Atlantic Convergence Zone is strongly dependent on the characterization of model internal variability (Talento and Barreiro, 2012).

Beyond the tropics, North Pacific decadal variability (Annex IV.2.6, 2.4.5, 3.7.6) exerts a strong modulation of extratropical ENSO teleconnections, but also influences low-frequency variability of the Walker circulation, which is underestimated by most CMIP5 models (England et al., 2014). Atlantic Multidecadal Variability (Annex IV.2.7, 2.4.6, 3.7.7) teleconnections show a high model spread among CMIP5 models, both in terms of persistence and spatial coherence (Qasmi et al., 2017), which has potential consequences for the water cycle variability simulated over Europe. For example, internal variability will continue to play an important role in the variability of river flows over France in coming decades *(medium confidence)* (Giuntoli et al., 2013; Boé and Habets, 2014; Bonnet et al., 2017).

Ensembles of atmosphere-only simulations driven by observed or reconstructed SST are useful for evaluating the ability of models to capture the circulation and/or precipitation variability observed over the historical period (Zhou et al., 2016; Deng et al., 2018; Douville et al., 2019). However, limitations of such AGCM-based attribution methods, i.e. related to the lack of air–sea interactions in the response, may lead to erroneous attribution conclusions in some regions for local circulation and mean and extreme precipitation (Dong et al., 2017). Other methods to measure the portion of precipitation variability include the partitioning into dynamical versus thermodynamical components (Saffioti et al., 2016; Fereday et al., 2018; Lehner et al., 2018), the analysis of variance (Dong et al., 2018a) and direct characterization of stochastic weather-noise (Short Gianotti et al., 2014).

Single model initial conditions large ensembles (SMILEs) are a powerful tool for estimating the magnitude of internal variability in historical and future climates (Section 1.4.4). Using SMILEs, it has been shown, for example, that internal NAO variability imparts substantial uncertainty to future changes in European precipitation (Deser et al., 2017; Figure 8.24). For the South Asian summer monsoon, internal variability can overshadow the forced monsoon rainfall trend, thereby increasing near-term projection uncertainties (Huang et al., 2020b). Specific regional applications of the use of large ensembles are further assessed in Sections 10.3.4.3 and 10.3.4.4.

Since AR5, SMILEs have helped quantify the time of emergence of climate change signals (see Sections 1.4.2.2 and 10.4.3). Results from SMILEs indicate that by 2000–2009 (compared to 1950–1999), simulated anthropogenic shifts in mean annual precipitation already emerged over 36-41% of the globe including high latitudes (Frankcombe et al., 2018; Kumar and Ganguly, 2018), the eastern subtropical oceans, and the tropics (Zhang and Delworth, 2018). By 2050 (2100), more than 60% (85%) of the globe is projected to show detectable anthropogenic shifts in mean annual precipitation (Zhang and Delworth, 2018). Other SMILE results for the 1950-2100 period (Kay et al., 2015; Sigmond and Fyfe, 2016) indicate that internal variability can obscure the detection of the anthropogenic hydroclimatic signal until the middle to late 21st century in many parts of the world for both mean and extreme precipitation (Martel et al., 2018; Dai and Bloecker, 2019). A common finding is that changes in the characteristics of wet extreme events will emerge earlier than changes in average conditions (Gaetani et al., 2020; Hawkins et al., 2020; Kusunoki et al., 2020). An assessment of the methods used to estimate time of emergence is presented in Chapter 10 (Section 10.3.4.3). For specific regional examples of climate change attribution and emergence of anthropogenic signal, see Section 10.4.2.

ACCEPTED VERSION SUBJECT TO FINAL EDITING

[START FIGURE 8.24 HERE]

Figure 8.24: Impact of the North Atlantic Oscillation (NAO) on 2016–2045 climate trends. (a) Regressions of winter sea level pressure (SLP) and precipitation trends upon the normalized leading principal component (PC)of winter SLP trends in the CESM1 Large Ensemble, multiplied by two to correspond to a two standard deviation anomaly of the PC (as internal climate variability component); (b) CESM1 ensemble-mean winter SLP and precipitation trends (as forced climate variability component); (c) b – a (forced minus internal climate variability component); (d) b + a (forced plus internal climate variability component). Precipitation in colour shading (mm/day per 30 years) and SLP in contours (interval = 1 hPa per 30 years with negative values dashed) (Adapted from Deser et al., 2017). Further details on data sources and processing are available in the chapter data table (Table 8.SM.1).

[END FIGURE 8.24 HERE]

In summary, there is *medium confidence* that climate models reproduce the general magnitude and character of internal variability that influences water cycle variables. There is *high confidence* that internal variability will continue to be a major source of uncertainty, at least for near-term water cycle projections at the regional scale. There is *low confidence* in the region-dependent time of emergence of water cycle changes (see also Section 10.4.3), but there is *medium confidence* that changes in wet extreme events will emerge earlier than changes in average conditions.

8.5.2.2 Implications for near-term water cycle projections

Adapting water resource management in the face of climate change will greatly benefit from improved prediction of land surface hydrology at the decadal timescale. Climate predictions (Section 1.4.4) differ from climate projections by constraining the initial state of the slow components of the climate system (i.e. the ocean, the cryosphere and the terrestrial hydrology) as well as volcanic aerosols and ozone depleting substances with observations. Anthropogenic and natural radiative forcing and low-frequency modes of variability (e.g., AMV and PDV, Annex IV.2.7 and IV.2.6) suggest the possible predictability of climate in the first decade or so of the 21st century, in addition to the projected response to the anthropogenic forcing (Sections 4.2.3 and 4.4.1.3).

In AR5, decadal prediction of precipitation over some land areas showed improved skill due to specified radiative forcing, with almost no added value from ocean initialization. Since AR5, more studies have been devoted to understanding the potential or effective water cycle predictability related to ocean multi-decadal variability. Decadal hindcast experiments based on large ensembles highlight increasing skill scores in annual mean precipitation 3-7 year ahead, at least over the Sahel and Europe (Yeager et al., 2018). There is relatively high predictability of the AMV impacts over the Mediterranean basin, central Asia and the Americas (from United States to northern South America) during boreal summer, but in boreal winter the signal-to-noise ratio shows only weak predictability over land (Yamamoto and Palter, 2016; Ruprich-Robert et al., 2017). The link between South Asian summer monsoon changes and the AMOC and the decadal variability in the Pacific Ocean open the possibility of increased predictability for the near future (Kushnir et al., 2017; Huang et al., 2020c; Sandeep et al., 2020).

The additional skill associated with the initialization of the cryosphere and the land surface has received limited attention. However, there is observational evidence that oceanic decadal variations can propagate into the atmosphere and, consequently accumulate into terrestrial land surface reservoirs (e.g., Bonnet et al., 2017) and vegetation (e.g., Zeng et al., 1999). This land surface memory, like in soil moisture (Alessandri and Navarra, 2008; Catalano et al., 2016) or snow (Loranty et al., 2014), may also contribute to the decadal predictability of the terrestrial component of the water cycle, but remains difficult to assess given the limitations of observational records. Vegetation initialization seems to generate as much noise as signal and does not necessarily translate into improved skill in early decadal predictions based on ESMs (Weiss et al., 2014).

ACCEPTED VERSION SUBJECT TO FINAL EDITING

Decadal hydrological predictability in an idealized setting has been also investigated through off-line land surface hindcast experiments, driven by observed atmospheric forcing and/or initial conditions, suggesting the potential for skilful predictions for terrestrial water storage, deep soil moisture, and groundwater (Yuan and Zhu, 2018). Yet, a real-world assessment is hampered by the lack of observations and is only feasible when multi-decadal records of satellite estimates of terrestrial water storage, snow mass or soil moisture are available.

In summary, there is *high confidence* that the water cycle changes that have already emerged from internal variability will become more pronounced in near-term (2021-2040) projections. However, there is *low confidence* in decadal predictions of precipitation changes, particularly over most land areas, because internal variability remains difficult to predict and can offset or amplify the forced water cycle response.

8.5.2.3 Volcanic forcing

Volcanic eruptions can affect climate projections in the near term (2021-2040) (Section 4.4.4, CCB4.1). In this chapter, they are of interest because they can trigger a transient departure from the water cycle response to anthropogenic radiative forcing. Major volcanic eruptions temporarily reduce total global and wet tropical region precipitation (*high confidence*) (Iles et al., 2014), can weaken or shift the ITCZ (Iles et al., 2014; Colose et al., 2016; Liu et al., 2016), and reduce summer monsoon rainfall (*medium confidence*) (Pausata et al., 2015b; Zambri and Robock, 2016; Zambri et al., 2017; Zuo et al., 2019; Singh et al., 2020c). Monsoon precipitation in one hemisphere can be enhanced by the remote volcanic forcing occurring in the other hemisphere (*medium confidence*) (Pausata et al., 2015a; Liu et al., 2016; Zuo et al., 2019). Over the Sahel, the sign of hydrological changes depend on the hemisphere where the volcanic eruptions occur (Haywood et al., 2013b). Out of phase changes in the Sahel and the Amazon basin are expected from the effect of volcanic aerosols on tropical Atlantic SST and the ITCZ (Hua et al., 2019). Over the last millennium, uncertainties remain in the symmetry/asymmetry of the monsoon response because it is difficult to estimate the exact latitude and season of past volcanic eruptions further back in time (Colose et al., 2016; Fasullo et al., 2019).

Data for six major eruptions over the last century along with CMIP5 historical experiments indicate that volcanic eruptions cause a detectable decrease in streamflow in northern South America, central Africa, high-latitude Asia and in wet tropical-subtropical regions, and a detectable increase in southwestern North America and southern South America (Iles and Hegerl, 2015). Attempts to include volcanic forcing in future projections show enhanced precipitation variability on annual to decadal timescales with small reductions in Asian monsoon rainfall (Bethke et al., 2017). The occurrence of volcanic eruptions in the coming century, either as single large events or clustered smaller ones, can alter the water cycle (see also CCB4.1), and regional drought events may be enhanced by co-occurring volcanic (Liu et al., 2016; Gao and Gao, 2017; Zambri et al., 2017) and GHG (e.g., Cook et al., 2018) forcing (*low confidence*). Volcanic eruptions may also lead to widespread precipitation anomalies up to several years following an eruption through their potential influence on the El Niño Southern Oscillation (*low confidence*) (Stevenson et al., 2016; Dee et al., 2020; McGregor et al., 2020).

In summary, large volcanic eruptions reduce global mean precipitation, as well as precipitation in tropical wet regions (*high confidence*). There is *low confidence* in specific regional and seasonal responses, primarily due to the limitations of the observational record.

8.5.3 Non-linearities across global warming levels

AR5 concluded that annual and seasonal mean precipitation changes can be estimated by linear pattern scaling techniques (Santer and Wigley, 1990; Arnell and Gosling, 2016; Greve et al., 2018), which represent regional changes in precipitation as a linear function of global mean temperature change. However, there are a number of caveats when pattern scaling is applied to low emission scenarios or to scenarios where localized forcing (e.g., anthropogenic aerosols) are significant and vary in time (Collins et al., 2013). Here

ACCEPTED VERSION SUBJECT TO FINAL EDITING

the focus is in on non-linear water cycle responses to increasing global warming levels, as estimated for instance from the difference between the first 2°C of global warming, and the next 2°C of warming (Fig 8.25), and their possible underlying mechanisms.

8.5.3.1 Non-linearities in large-scale atmospheric circulation and precipitation

Since AR5, there is further evidence that the pattern scaling technique has limitations (Lopez et al., 2014; Wartenburger et al., 2017; Tachiiri et al., 2019), and that alternative approaches such as multiple regressions using the land-sea warming contrast as an additional predictor offer added value (Joshi et al., 2013). The simplest traditional pattern scaling approach approximates future changes by the product of a time-evolving global surface temperature change and a pattern that varies spatially but is constant across time, scenarios, and models. This technique was shown to be more robust across scenarios rather than across models, with better results for temperature compared with precipitation (Tebaldi and Arblaster, 2014; see also Section 4.2.4). One approach which avoids scaling is to consider a period in a different scenario with the same global surface temperature change (Herger et al., 2015). It is attractive as it provides patterns of any temporal resolution that are consistent across variables. Nonetheless, this technique is still only based on global surface temperature and is not necessarily suitable for precipitation changes projected in stabilized versus transient scenarios (at the same global warming level) given the fast-atmospheric adjustment to GHG radiative forcing (Section 8.2.1, 8.4.1.1).

Even in a theoretical climate system governed by linear processes, pattern-scaling assumptions can fail because the different forcing time response of different parts of the Earth system cause evolving spatial warming patterns (Good et al., 2016a). This occurs primarily because different feedbacks occur at different timescales (Armour et al., 2013; Andrews et al., 2015), which in turn implies that the atmospheric circulation and water cycle is dependent both on the level of warming and the rate of change (McInerney and Moyer, 2012; Ceppi et al., 2018). The usual distinction between the fast adjustment to increased GHG concentrations and the slower response to SST warming (Section 8.2.2.2) may however not be sufficient to explain the time evolution of the hydroclimatic response at the regional scale, especially in subtropical land areas where this response critically depends on shifts in atmospheric circulation associated with distinct “fast” (typically 5-10 years, that is however much slower than the atmospheric adjustment assessed in Section 8.2.1) and slow SST warming patterns (Zappa et al., 2020). The changing balance between the water cycle response to anthropogenic GHG and aerosol forcings is another source of non-linearity across time and global warming levels (Ishizaki et al., 2013; Rowell et al., 2015; Liu et al., 2019c; Wilcox et al., 2020).

Nonlinearities in the climate response are thought to arise from multiple factors. These include state-dependent ice-albedo feedback and its potential influence on Northern Hemisphere storm tracks (Peings and Magnusdottir, 2014; Semenov and Latif, 2015; see also Cross-Chapter Box 10.1 and Section 8.6.1.2); a state-dependent sensitivity of tropical precipitation to increased SST (Schewe and Levermann, 2017; He et al., 2018); a complex response of the Atlantic meridional overturning circulation (AMOC; Section 9.2.4.1 and Section 8.6.1.1) and its model- and magnitude-dependent teleconnections with regional temperature and precipitation (Kageyama et al., 2013; Jackson et al., 2015; Qasmi et al., 2017, 2020); and other atmospheric and terrestrial (Section 8.5.3.2) processes such as cloud and land surface feedbacks (Ceppi and Gregory, 2017; King, 2019). The response of convective precipitation may exhibit nonlinearities because it is itself modulated by both dynamics and atmospheric water content, each responding independently to warming (Chadwick and Good, 2013; Neupane and Cook, 2013).

Based on a simple model, it was also suggested that the Indian summer monsoon may exhibit a moisture-advection feedback which allows multiple stable states as boundary conditions change (Zickfeld et al., 2005). However, limitations of this theory and comprehensive GCMs suggest a near-linear monsoon response to a broad range of radiative forcings (Boos and Storelvmo, 2016). Non-linear precipitation responses to global warming have been reported in the Indo-Pacific, where a linear increase in SSTs can trigger nonlinear changes in precipitation and a shift in the ITCZ depending on the relative amplitudes of uniform and structured SST anomalies (Chung et al., 2014a; Toda and Watanabe, 2018).

ACCEPTED VERSION SUBJECT TO FINAL EDITING

Compared to atmospheric circulation and seasonal mean precipitation, extreme precipitation has been found to scale more accurately with local and global mean temperature (Chou et al., 2012; Pendergrass et al., 2015). The projected increase in the magnitude of extreme precipitation is generally proportional to the global warming level, with an increase of around 7% per 1°C warming (Section 11.4.5) although this rate shows seasonal and geographical variations and is slightly less for 5-day than for 1-day precipitation maxima. Projected changes in extreme precipitation are the result of both thermodynamical and more model-dependent and potentially less linear dynamical contributions (Pfahl et al., 2017). Projected changes in precipitation extremes are also potentially sensitive to a nonlinear response of spatial convective organization (Pendergrass et al., 2016), and can exhibit a quadratic rather than linear response to global warming (Pendergrass et al., 2019).

Within CMIP6, the linearity to CO_2 forcing can be assessed through the comparison of the model response to abrupt doubling versus abrupt quadrupling of atmospheric CO_2 (Webb et al., 2017). Preliminary analyses based on CMIP5 models showed that annual precipitation changes following a doubling step change in $CO_2$from pre-industrial levels are not necessarily consistent with the response to the step from doubling to quadrupling despite a similar change in radiative forcings (Good et al., 2016a; Ceppi and Shepherd, 2017). Beyond the visual comparison of the climate response at various global warming levels (e.g., Figure 4.35), the linearity across global warming levels can be assessed by using the highest emission scenario and comparing seasonal mean relative precipitation changes at +2°C versus +4°C above preindustrial (1850-1900) temperatures (Figure 8.25). The results support the previous finding (Good et al., 2016b) that a second 2°C warming does not necessarily lead to the same precipitation anomaly pattern as the first 2°C, especially in the tropics where regional differences can be large but not necessarily consistent among different models. They are also consistent with a recent analysis of CMIP5 models showing that the projected drying in the Mediterranean and in Chile is substantially faster than the increase in GSAT, and therefore does not scale linearly with global warming (Zappa et al., 2020).

In summary, there is *high confidence* that continued global warming will further amplify GHG-induced changes in large-scale atmospheric circulation and precipitation. Nonetheless, there are cases where regional water cycle changes are not linearly related to global warming due to the interaction of multiple forcings, feedbacks and timescales (*medium confidence*, see also Section 4.2.4, Section 7.4.3, Section 8.2.1). Aridity in subtropical regions is highly sensitive to fast shifts in large-scale atmospheric circulation so are particularly susceptible to such non-linearities.

[START FIGURE 8.25 HERE]

Figure 8.25: Effect of first versus second 2°C of global warming relative to the 1850-1900 base period on seasonal mean precipitation (mm/day). CMIP6 multi-model ensemble mean DJF (left panels) and JJA (right panels) precipitation difference for a,b) SSP5-8.5 at +2°C; c,d) SSP5-8.5 at +4°C minus SSP5-8.5 at +2°C (second 2°C warming); e,f) second minus first 2°C fast warming (c-a and d-b). Only models reaching the +4°C warming levels in SSP5-8.5 are considered. Differences are computed based on 21-yr time windows centered on the first year reaching or exceeding the selected global warming level using a 21-yr running mean global surface atmospheric temperature criterion. Uncertainty is represented using the simple approach: No overlay indicates regions with high model agreement, where ≥80% of models agree on sign of change; diagonal lines indicate regions with low model agreement, where <80% of models agree on sign of change. For more information on the simple approach, please refer to the Cross-Chapter Box Atlas.1. Further details on data sources and processing are available in the chapter data table (Table 8.SM.1).

[END FIGURE 8.25 HERE]

8.5.3.2 Non-linearities in land surface processes and feedbacks

Land surface responses and feedbacks represent a potential source of non-linearity for the water cycle response, at least at regional and local scales. The forced response of soil moisture and freshwater resources

ACCEPTED VERSION SUBJECT TO FINAL EDITING

not only depends on precipitation, but also on evaporation (Laîné et al., 2014), snowmelt (Thackeray et al., 2016), and runoff (Zhang et al., 2018e) which are intrinsically non-linear processes depending on soil moisture or temperature thresholds. Bare ground evaporation is, for instance, usually estimated as a non-linear function of surface soil moisture (Jefferson and Maxwell, 2015). Plant transpiration requires more complex formulations with non-linear dependencies on multiple environmental factors including root-zone soil moisture and atmospheric CO_2 concentration (Franks et al., 2017). Globally, land surface evaporation is both energy and soil-moisture limited, but one of these limitations can become dominant depending on regions and seasons. Non-linearities may be particularly strong in transitional regimes where and when soil moisture limitation plays a major role (Berg and Sheffield, 2018b).

Snowmelt is a non-linear process and projected changes in snowfall are also a non-linear combination of changes in total precipitation and in the fraction of solid precipitation. In cold regions, snowfall may first increase because of the increased water capacity of a warmer atmosphere and then decrease because snow falls as rain in an even warmer atmosphere. Such non-linearities can contribute to elevation, latitudinal and seasonal contrasts in the observed and projected retreat of the Northern Hemisphere snow cover (Shi and Wang, 2015; Thackeray et al., 2016). Mountain glaciers also represent source of nonlinear runoff responses since the annual runoff can first increase due to additional melting and then decrease as the glaciers shrink (Kraaijenbrink et al., 2017; Shannon et al., 2019). Section 9.5.1.3 concludes with *high confidence* that the average annual runoff from glaciers will generally reach a peak at the latest by the end of the 21st century, and decline thereafter. This peak may have already occurred for small catchments with little ice cover, but tends to occur later in basins with large glaciers. Permafrost thawing is another mechanism which can trigger a non-linear hydrological response in the high-latitudes of the Northern Hemisphere (Walvoord and Kurylyk, 2016), whose magnitude and potential abruptness is assessed in Section 5.4.3.3.

Land surface runoff and groundwater recharge are highly nonlinear process, depending for instance on rainfall intensity, soil infiltration capacity, vertical profile of soil moisture and water table depth. A non-linear relationship between rainfall and groundwater recharge was observed in the tropics where intense seasonal rainfalls associated with internal climate variability contribute disproportionately to recharge (Taylor et al., 2013b; Cuthbert et al., 2019a). Groundwater fluxes in arid regions are generally less responsive to climate variability than in humid regions, which can temporarily buffer climate change impacts on water resources or lead to a long, initially hidden, hydrological responses to global warming (Cuthbert et al., 2019a). Hydrological model simulations driven by individual and combined forcing show that decreased precipitation can cause larger deficits in soil moisture, streamflow and water table depth than other forcings, but also that these factors are not linearly cumulative when applied in combination (Hein et al., 2018). Surface runoff was found to scale only approximately with global warming (Tanaka and Takahashi, 2017). Significant non-linearities were found in the projected annual mean runoff response to global warming in CMIP5 projections, which could not be entirely explained by precipitation changes (Zhang et al., 2018). Similar nonlinear behaviours are found in CMIP6 models over the Amazon, Yangtze, Niger, Euphrates and Mississippi river basins (Figure 8.26), highlighting the need to reassess the assumption of linearity when estimating regional water cycle changes.

Beyond changes in land surface water fluxes, nonlinearities in the response of soil moisture and freshwater reservoirs have not been well documented in global climate projections but deserve further attention given the complex interactions between the water, energy and carbon cycles (Berg and Sheffield, 2018a), the growing direct human influence on rivers and groundwater (Abbott et al., 2019), and a possible offset between the linear components of changes in precipitation and evapotranspiration. Significant nonlinearities were found in water scarcity projections, as seen by the stronger sensitivity to the first 2°C increase in global warming (Gosling and Arnell, 2016).

In summary, there is both numerical and process-based evidence that terrestrial water cycle changes can be nonlinear at the regional scale (*high confidence*). Nonlinear regional responses of runoff, groundwater recharge and water scarcity have been documented based on both CMIP5 and CMIP6 models, and highlight the limitations of simple pattern-scaling techniques (*medium confidence*). Water resources fed by melting glaciers are particularly exposed to such nonlinearities (*high confidence*).

ACCEPTED VERSION SUBJECT TO FINAL EDITING

[START FIGURE 8.26 HERE]

Figure 8.26: Rate of change in basin-scale annual mean runoff with increasing global warming levels. Relative changes (%) in basin-averaged annual mean runoff estimated as multi-model ensemble median from a variable subset of CMIP6 models for each SSP over six major river basins: a) Mississipi, b) Danube, c) Lena, d) Amazon, e) Euphrates, f) Yangtze, g) Niger, h) Indus, i) Murray. The basin averages have been estimated after a first-order conservative remapping of the model outputs on the 0.5° by 0.5° river network of (Decharme et al., 2019). The shaded area indicates the 5-95% confidence interval of the ensemble values across all SSPs. Note that the y-axis range differs across basins and is particularly large for Niger and Murray (panels g and i). The number of models considered is specified for each scenario in the legend located inside panel b. Further details on data sources and processing are available in the chapter data table (Table 8.SM.1).

[END FIGURE 8.26 HERE]

8.6 What is the potential for abrupt change?

In this report, *abrupt change* is defined as a regional-to-global scale change in the climate system that occurs faster than the typical rate of changes in its history, implying non-linearity in the climate response (see Annex VII: Glossary). Often, abrupt change arises from positive feedbacks in the climate system that cause the current state to become unstable, and cross a 'tipping point' (Lenton et al., 2008); i.e., a rapid shift from one climate state to another. The water cycle has several attributes with potential to produce abrupt change. Non-linear interactions between the ocean, atmosphere, and land surface can result in rapid shifts between wet and dry states (Sections 8.6.1 and 8.6.2). Cessation of solar radiation modification could also result in abrupt changes in the water cycle (Section 8.6.3). This section reviews these types of abrupt shifts and assesses the likelihood that they will occur by 2100.

8.6.1 Abrupt water cycle responses to a collapse of Atlantic Meridional Overturning Circulation

Multiple lines of evidence, including both paleoclimate reconstructions and simulations, suggest that a severe weakening or collapse of Atlantic Meridional Overturning Circulation (AMOC, see Glossary) causes abrupt and profound changes in the global hydrological cycle (Chiang and Bitz, 2005; Broccoli et al., 2006; Chiang and Friedman, 2012; Jackson et al., 2015; Renssen et al., 2018). Deep water formation in the North Atlantic is dependent on a delicate balance of heat and salt fluxes (Buckley and Marshall, 2016); disruption in either of these due to melting ice sheets, a change in precipitation and evaporation, or ocean circulation can force AMOC to cross a tipping point (Drijfhout et al., 2015) (SROCC). During the last deglacial transition, one such slowdown in AMOC—during the Younger Dryas event (12,800–11,700 years ago)—caused worldwide changes in precipitation patterns. These included a southward migration of the tropical ITCZ (Peterson et al., 2000; McGee et al., 2014; Schneider et al., 2014; Mohtadi et al., 2016; Reimi and Marcantonio, 2016; Wang et al., 2017c) and systematic weakening of the African and Asian monsoons (Tierney and deMenocal, 2013; Otto-Bliesner et al., 2014; Cheng et al., 2016; Grandey et al., 2016; Wurtzel et al., 2018). Conversely, the Southern Hemisphere monsoon systems intensified (Cruz et al., 2005; Ayliffe et al., 2013; Strikis et al., 2015, 2018a; Campos et al., 2019). Drying occurred in Mesoamerica (Lachniet et al., 2013) while the North American monsoon system was largely unaffected (Bhattacharya et al., 2018). The mid-latitude region in North America was wetter (Polyak et al., 2004; Grimm et al., 2006; Wagner et al., 2010; Voelker et al., 2015), while Europe was drier (Genty et al., 2006; Rach et al., 2017; Naughton et al., 2019). A transient coupled climate model simulation was able to reproduce the large-scale precipitation response to such an event (Liu et al., 2009) (Figure 8.27a).

These patterns of past hydroclimatic change are relevant for future projections because it is *very likely* that AMOC will weaken by 2100 in response to increased greenhouse gas emissions (Weaver et al., 2012; Drijfhout et al., 2015; Bakker et al., 2016; Reintges et al., 2017) (See also Section 9.2.3.1). Furthermore, there is *medium confidence* that the decline in AMOC will not involve an abrupt collapse before 2100

ACCEPTED VERSION SUBJECT TO FINAL EDITING

(Section 9.2.3.1). The response of precipitation to hypothetical AMOC collapse under elevated greenhouse gases bears resemblance to the paleoclimate response during the Younger Dryas event, with some important differences due to effects of increased CO_2 on global precipitation patterns (Figure 8.27b). As with the paleoclimate events, AMOC collapse results in a southward shift in the ITCZ that is most pronounced in the tropical Atlantic. This could cause drying in the Sahel region (Defrance et al., 2017) as well as Mesoamerica and northern Amazonia (Parsons et al., 2014; Chen et al., 2018c). AMOC collapse also causes the Asian monsoon systems to weaken (Liu et al., 2017b) (Figure 8.27b) counteracting the strengthening expected in response to elevated greenhouse gases (see Section 8.4.2). Europe is projected to experience moderate drying in response to AMOC collapse (Jackson et al., 2015).

[START FIGURE 8.27 HERE]

Figure 8.27: (a) Model simulation of precipitation response to the Younger Dryas event relative to the preceding warm Bølling-Allerød period (base colours, calculated as the difference between 12,600–11,700 yr BP and 14,500–12,900 BP from the TraCE paleoclimate simulation of Liu et al., (2009)), with paleoclimate proxy evidence superimposed on top (dots). (b) Model simulation of precipitation response to an abrupt collapse in AMOC under a doubling of 1990 CO_2 levels (after Liu et al., (2017)). Regions with rainfall rates below 20 mm/year are masked. Further details on data sources and processing are available in the chapter data table (Table 8.SM.1).

[END FIGURE 8.27 HERE]

In summary, given that there is *medium confidence* that the decline in AMOC will not involve an abrupt collapse before 2100, there is *low confidence* that an AMOC-driven abrupt change in the water cycle will occur by 2100. However, if AMOC collapse does occur, it is *very likely* that there would be large regional impacts on the water cycle.

8.6.2 Abrupt water cycle responses to changes in the land surface

Changes in the land surface, including vegetation cover and dust emissions, can trigger abrupt changes in the water cycle. Plants regulate the exchange of water and energy between the land surface and the atmosphere (Section 8.2.3.3), such that sudden shifts in plant functions, types, or biomes can trigger feedbacks that have the potential to cause abrupt changes in the regional water cycle. Dust emissions, from either climatic or land use changes, affect the radiation budget and can regionally exacerbate dry extremes. Below, we assess the likelihood of abrupt changes in the water cycle for the well-studied regions of the Amazon and the Sahel, and the potential for dust emissions to amplify drought and aridity.

8.6.2.1 Amazon deforestation and drying

The Amazon forest plays an active role in driving atmospheric moisture transport and generating precipitation in the South American region (Drumond et al., 2014; Poveda et al., 2014; Yin et al., 2014; Staal et al., 2018, 2020; Agudelo et al., 2019; Espinoza et al., 2019) (SRCCL). This close association between the land surface and the water cycle makes the Amazon a potential hotspot for abrupt change (Torres and Marengo, 2014). Both deforestation and drying are projected to increase by 2100, resulting in a worst-case scenario of up to a 50% loss in forest cover by 2050 (Soares-Filho et al., 2006; Boisier et al., 2015; Steege et al., 2015; Gomes et al., 2019). Deforestation in the Amazon also raises the probability of catastrophic fires (Brando et al., 2014). The combination of deforestation, drier conditions, and increased fire can push the rainforest ecosystem past a tipping point, beyond which there is rapid land surface degradation, a sharp reduction in atmospheric moisture recycling, an increase in the fraction of precipitation that runs off, and a further shift towards a drier climate (Staal et al., 2015; Boers et al., 2017; Zemp et al., 2017; Ruiz-Vásquez et al., 2020). A rapid drop in precipitation has a direct impact on river flows, driving basin-scale shifts from a regulated to unregulated state (Salazar et al., 2018). Regional climate modeling experiments confirm that

ACCEPTED VERSION SUBJECT TO FINAL EDITING

increased deforestation leads to a drier climate, although not all models show a true tipping point, at least under present-day climatic conditions (Lejeune et al., 2015; Spracklen and Garcia-Carreras, 2015).

In AR5, some simulations using a coupled climate-carbon cycle model exhibited an abrupt dieback of the Amazon forest in future climate scenarios (Oyama and Nobre, 2003; Cox et al., 2004; Malhi et al., 2008). However, subsequent work demonstrated that abrupt Amazon dieback does not occur consistently across, or even within, Earth system models (Lambert et al., 2013; Boulton et al., 2017). The occurrence of dieback is highly dependent on both how dry the simulated climate is in the present day (Malhi et al., 2009) as well as the representation of forest structure and competitive dynamics (Levine et al., 2016). Models with a low diversity of plant characteristics and types have a higher tendency for abrupt change (Sakschewski et al., 2016). Abrupt shifts and ecosystem disruptions can occur on the sub-regional level (Pires and Costa, 2013), highlighting the need for higher-resolution modelling studies. Since AR5, CMIP6 projections suggest that a tipping point in the Amazon system may be crossed on a local or regional scale (Staal et al., 2020) but continue to be highly dependent on model biases in precipitation and the simulation of the land surface. Consequently, the timing, and probability, of an abrupt shift remains difficult to ascertain.

In summary, while there is a strong theoretical expectation that Amazon drying and deforestation can cause a rapid change in the regional water cycle, currently there is *limited* model *evidence* to verify this response, hence there is *low confidence* that such a change will occur by 2100.

8.6.2.2 Greening of the Sahara and the Sahel

Greening of the Sahara and Sahel regions in North Africa, in response to an increase in precipitation, has long been considered an amplifying mechanism that can lead to abrupt change. Although the high surface albedo of the desert stabilizes the energy balance of the system (Charney, 1975), greening can induce strong, positive feedbacks between the land surface and precipitation that can shift the region into a "Green Sahara" state. The fact that the transition phase between a Desert Sahara and Green Sahara is not theoretically stable (Brovkin et al., 1998) creates a tipping point and allows for the possibility of an abrupt shift between dry and wet climate regimes. Paleoclimate reconstructions provide evidence of past "Green Sahara" states (deMenocal and Tierney, 2012), under which rainfall rates increased by an order of magnitude (Tierney et al., 2017), leading to a vegetated landscape (Jolly et al., 1998) with large lake basins (Gasse, 2000; Drake and Bristow, 2006). The underlying driver of the Green Sahara is the periodic increase in summer insolation associated with the orbital precession cycle (Kutzbach, 1981). In this sense, Green Saharas are not direct analogues for a response to anthropogenic greenhouse gas emissions, as these past states were forced by natural, seasonal changes in solar radiation. However, the climate dynamics of Green Saharas (which have global impacts, Pausata et al., (2020)), and the speed of the transitions between Desert Saharas and Green Saharas, are relevant for future projections.

Since AR5, paleoclimatic studies have improved our view of the timing, spatial extent, and speed of transitions associated with the early Holocene (11,000–5,000 yr BP) Green Sahara. Observed transitions into and out of Green Sahara states are always faster than the underlying forcing, in agreement with theoretical considerations (*high confidence*) (Tierney and deMenocal, 2013; Shanahan et al., 2015; Tierney et al., 2017). However, there is *low confidence* in the duration of the transition because sedimentary records cannot typically resolve changes on decadal—multi-decadal timescales (Tierney and deMenocal, 2013). Both paleoclimate data and modelling experiments suggest that the timing and speed of the transition was spatially heterogeneous (*high confidence*), with northern Saharan locations becoming drier thousands of years before more equatorial locations (Shanahan et al., 2015; Tierney et al., 2017; Dallmeyer et al., 2020). These observations are consistent with theoretical studies suggesting that spatial heterogeneity and diversity in ecosystems can mitigate the probability of catastrophic change (Van Nes and Scheffer, 2005; Bathiany et al., 2013). Conversely, low ecosystem diversity can produce local or regional "hot spots" of abrupt change such as those seen in some paleoclimate records (Claussen et al., 2013).

CMIP5 and CMIP6 models**,** some of which include dynamic vegetation schemes, cannot simulate the magnitude, nor the spatial extent, of greening and precipitation change associated with the last Green Sahara

ACCEPTED VERSION SUBJECT TO FINAL EDITING

under standard mid-Holocene (6 ka) boundary conditions (*high confidence*) (Harrison et al., 2014; Tierney et al., 2017; Brierley et al., 2020) (Figure 3.11). This result remains unchanged since AR4 (Jansen et al., 2007). This may be due to climatological biases in the models (Harrison et al., 2015) or could imply that the strength of the feedbacks between vegetation and the water cycle in the models is too weak (Hopcroft et al., 2017). To date, climate models still only produce the amount and spatial extent of rainfall that is needed to sustain a Green Sahara if they are given prescribed changes in the land surface, such as albedo, soil moisture, vegetation cover and/or dust emissions (Pausata et al., 2016; Skinner and Poulsen, 2016; Tierney et al., 2017).

Some climate model simulations suggest that under future high-emissions scenarios, CO_2 radiative forcing causes rapid greening in the Sahel and Sahara regions via precipitation change (Claussen et al., 2003; Drijfhout et al., 2015). For example, in the BNU-ESM RCP8.5 simulation, the change is abrupt with the percentage of bare soil dropping from 45% to 15%, and percentage of tree cover rising from 50% to 75%, within 10 years (2050-2060) (Drijfhout et al., 2015). However, other modelling results suggest that this may be a short-lived response to CO_2 fertilization (Bathiany et al., 2014).

In summary, given outstanding uncertainties in how well the current generation of climate models capture land-surface feedbacks in the Sahel and Sahara, there is *low confidence* that an abrupt change to a greener state will occur in these regions before 2100 or 2300.

8.6.2.3 Amplification of drought by dust

Mineral dust aerosols in the climate system originate from both semi-permanent and transient sources (Prospero et al., 2002; Ginoux et al., 2012). The former are typically arid regions where significant alluvial sediments have accumulated over time, while the latter are often associated with natural (e.g., droughts, wildfires) and anthropogenic (e.g. land use change, desertification) disturbances. Modern-day dust emissions are dominated by natural sources (Ginoux et al., 2012), although human emissions may contribute 10–60% of the global atmospheric dust load (Webb and Pierre, 2018). Paleo-dust records suggest that human factors (land use change and landscape disturbance) may have doubled global dust emissions between1750 and the last quarter of the 20th century (Hooper and Marx, 2018) (Section 2.2.6).

Dust aerosols influence the climate system and hydrologic cycle through both direct impacts on radiation (absorbing and scattering longwave and shortwave) and via indirect effects on cloud and precipitation processes (Choobari et al., 2014; Kok et al., 2018; Schepanski, 2018) (Box 8.1). The capacity of dust aerosols to suppress precipitation by reducing humidity and energy availability, and increasing stability in the atmosphere (Cook et al., 2013; Huang et al., 2014) can drive positive feedbacks (see also Section 6.3.6). Thus there is strong potential for dust to contribute to abrupt changes in the water cycle, especially in semi-arid regions where wind erosion is highly sensitive to vegetation cover and drought variability (Yu et al., 2015). One such event occurred over the Central United States during the 1930s: the Dust Bowl drought, an iconic event characterized by widespread land degradation and historically unprecedented levels of dust storm activity (Hansen and Libecap, 2004; Lee and Gill, 2015). While initialized by warm sea-surface temperatures in the North Atlantic, modeling work indicates that land cover changes and resulting dust emissions contributed to the severity and spatial extent of the drought by further suppressing precipitation (Cook et al., 2009; Hu et al., 2018; Cowan et al., 2020). There is also increasing evidence that dust aerosol feedbacks are necessary to explain the magnitude of rainfall increase during the mid-Holocene Green Sahara (Pausata et al., 2016; Tierney et al., 2017).

The importance of dust aerosol feedbacks in future abrupt climate events, like droughts or rapid aridification, is unclear. In part, this is because the response of dust aerosol emissions and loading levels in the atmosphere to climate change is highly uncertain (Tegen and Schepanski, 2018; Webb and Pierre, 2018). This difficulty in predicting future dust responses is rooted in the fact that emissions depend on both changes to the land surface (e.g., land use/land cover change, aridification, ecological responses to climate change) and the state of the atmosphere (Tegen and Schepanski, 2018). While there is some evidence that global dust aerosol concentrations in the future will increase (Allen et al., 2016; Tegen and Schepanski, 2018), it is highly

ACCEPTED VERSION SUBJECT TO FINAL EDITING

dependent on changes in precipitation patterns and atmospheric circulation (see the SRCCL, Section 2.4.1), and it is not clear what the radiative impact will be (Allen et al., 2016; Kok et al., 2018).

In summary, due to *limited evidence*, there is *low confidence* regarding the role of dust in abrupt climate change events over the next century.

8.6.3 Abrupt water cycle responses to initiation or termination of solar radiation modification

Solar radiation modification (SRM) techniques seek to reduce the impacts of climate change by modifying the Earth's radiation budget, either by reflecting incoming solar radiation or increasing the amount of heat lost to space. Note that, following SR1.5, the definition of SRM in this report refers to changes in both solar and longwave radiation (Section 4.6.3.3 and Annex VII: Glossary). A variety of methods have been proposed, including injection of aerosols or their precursors into the stratosphere, cloud brightening, and cirrus cloud thinning (Table 4.8). Since SRM alters the planetary energy balance, changes in the hydrological cycle are theoretically expected (Section 8.2). These changes can be abrupt if the initial magnitude of SRM is large, rather than increased gradually. Since AR5, a diversity of SRM techniques have been tested using climate model simulations, with an increasing focus on consequences for regional water availability. Techniques targeting shortwave radiation (sulfate injection, surface albedo modification, cloud brightening) are *likely* to reduce global mean precipitation relative to future CO_2 emissions scenarios (Bala et al., 2008; Jones et al., 2013a; Tilmes et al., 2013; Ferraro et al., 2014; Crook et al., 2015). In contrast, cirrus cloud thinning, a longwave technique, results in increased global precipitation as it causes enhanced radiative cooling in the troposphere (*medium confidence*) (Crook et al., 2015; Kristjánsson et al., 2015; Jackson et al., 2016).

The magnitude of hydrological disruption for both the initiation and termination of SRM depends on the method used, as well as the strength and duration of its implementation (Ekholm and Korhonen, 2016; Irvine et al., 2019). Under abrupt SRM implementation, hydrological shifts are rapid, occurring within the first decade (Crook et al., 2015). Artificial enhancement of albedo in Northern Hemisphere desert regions causes a southward shift in the Hadley Cell and ITCZ, and extreme drying in the northern tropics (Crook et al., 2015). Uniform or tropical stratospheric sulfate injection weakens the African and Asian summer monsoons and causes drying in the Amazon (Robock et al., 2008; Crook et al., 2015; Dagon and Schrag, 2016). Changes in evapotranspiration can produce large deficits or surpluses in soil moisture and runoff in different regions and seasons (Dagon and Schrag, 2016).

Rapid changes (years to decades) in the hydrological cycle are also expected if SRM is terminated abruptly, either purposefully or because of technical failure or political disagreement. We reiterate the AR5 conclusion that, if SRM "were terminated for any reason, there is *high confidence* that surface temperatures would increase rapidly (within a decade or two) to values consistent with the GHG forcing." The additional global warming caused by SRM termination may result in a rapid increase in global mean precipitation (*medium confidence*) (Jones et al., 2013). Heterogenous regional and seasonal changes are also expected, but are model-dependent (Jones et al., 2013a). As with SRM initiation, the impact of SRM termination is expected to be dependent on the technique deployed.

In summary, it is *very likely* that abrupt water cycle changes will occur if SRM is abruptly initiated or halted, especially in tropical regions. Further assessment of the potential side-effects of SRM is found in Section 4.6.3.3.

8.7 Final remarks

Despite the advances presented in this chapter, there are still many opportunities to improve the understanding and quantification of human influences on past, present and future water cycle changes:

- Extension and development of pre-instrumental data and paleoclimate records, particularly from the

ACCEPTED VERSION SUBJECT TO FINAL EDITING

Southern Hemisphere, will improve estimates of the range of natural climate variability and extremes, and our knowledge of how the water cycle responded in past high CO_2 climates.

- Development of longer observational time series that will improve our understanding of physical processes and the analysis and simulation of natural modes of weather and climate variability.

- The use of large model ensembles will help better understand the interactions between climate change and internal variability and in the detection and attribution of observed water cycle changes.

- The simulation of precipitation, latent heating and radiative effects of deep convective clouds would greatly benefit from a better representation of their interactions with aerosols.

- An improvement of the GCM-simulated precipitation, latent heating and radiative effects of deep convective clouds would benefit from an improved representation of their interactions with aerosols.

- Further research on land surface processes, including groundwater recharge, the role of plant physiological changes, land use change, dams and irrigation, will improve future projections of key aspects of the terrestrial water cycle such as aridity and drought.

- Ongoing efforts to develop higher-resolution, 'convection permitting', regional or global climate models will lead to an improved simulation of clouds and precipitation, their coupling with boundary layer and surface processes, their diurnal cycle and high-frequency variability, and their response to climate change, including extreme precipitation events.

- Further analysis of past and current climate variability alongside future climate change projections will provide physically understood constraints for improving the accuracy of regional water cycle simulations, adding value to the results obtained from global climate models.

- Increased understanding of internal variability and interactions with human-induced change will improve efforts to attribute changes in the water cycle and to understand and anticipate future non-linear change.

ACCEPTED VERSION
SUBJECT TO FINAL EDITING

Frequently Asked Questions

FAQ 8.1: How does land use change alter the water cycle?

The ways in which humans use and change land cover, for example, by converting fields to urban areas or clearing forests, can affect every aspect of the water cycle. Land-use changes can alter precipitation patterns and how water is absorbed into the ground, flows into streams and rivers, or floods the land surface, as well as how moisture evaporates back into the air. Changes in any of these aspects of the interconnected water cycle can affect the entire cycle and the availability of freshwater resources.

Land use describes the combination of activities and ground cover defining each area of the Earth's continental surface. Altering land use can modify the exchange of water between the atmosphere, soil and sub-surface (FAQ 8.1, Figure 1).

For instance, changes in land cover can affect the ability of soils to soak up surface water (infiltration). When soil loses its capacity to soak up water, precipitation that would normally infiltrate and contribute to groundwater reserves will instead overflow, increasing surface water (runoff) and the likelihood of flooding. For example, changing from vegetation to urban cover can cause water to flow rapidly over buildings, roads and driveways and into drains rather than soaking into the ground. Deforestation over wide areas can also directly reduce soil moisture, evaporation and rainfall locally but can also cause regional temperature changes that affect rainfall patterns.

Extracting water from the ground and river systems for agriculture, industry and drinking water depletes ground water and can increase surface evaporation because water that was previously in the ground is now in direct contact with the atmosphere, being available for evaporation

Changing land use can also alter how wet the soil is, influencing how quickly the ground heats up and cools down and the local water cycle. Drier soils evaporate less water into the air but heat up more in the day. This can lead to warmer, more buoyant plumes of air that can promote cloud development and precipitation if there is enough moisture in the air.

Changes in land use can also modify the amount of tiny aerosol particles in the air. For instance, industrial and domestic activities can contribute to aerosol emissions, as do natural environments such as forests or salt lakes. Aerosols cool down global temperature by blocking out sunlight but can also affect the formation of clouds and therefore the occurrence of precipitation (see FAQ 7.2).

Vegetation plays an important role in soaking up soil moisture and evaporating water into the air (*transpiration*) through tiny holes (*stomata*) that allow the plants to take in carbon dioxide. Some plants are better at retaining water than others, so changes in vegetation can affect how much water infiltrates into the ground, flows into streams and rivers, or is evaporated.

More globally, land-use change is currently responsible for about 15% of the emissions of carbon dioxide from human activities, leading to global warming, which in turn affects precipitation, evaporation, and plant transpiration. In addition, higher atmospheric concentrations of carbon dioxide due to human activities can make plants more efficient at retaining water because the stomata do not need to open so widely. Improved land and water management (e.g., reforestation, sustainable irrigation) can also contribute to reducing climate change and adapting to some of its adverse consequences.

In summary, there is abundant evidence that changes in land use and land cover alter the water cycle globally, regionally and locally, by changing precipitation, evaporation, flooding, ground water, and the availability of fresh water for a variety of uses. Since all the components of the water cycle are connected (and linked to the carbon cycle), changes in land use trickle down to many other components of the water cycle and climate system.

[START FAQ 8.1, FIGURE 1 HERE]

ACCEPTED VERSION SUBJECT TO FINAL EDITING

FAQ 8.1, Figure 1: Land-use changes and their consequences on the water cycle. As all the components or the water cycle are tightly connected, changes in one aspect of the cycle affects almost all the cycle.

[END FAQ 8.1, FIGURE 1 HERE]

ACCEPTED VERSION
SUBJECT TO FINAL EDITING

FAQ 8.2: Will floods become more severe or more frequent as a result of climate change?

A warmer climate increases the amount and intensity of rainfall during wet events, and this is expected to amplify the severity of flooding. However, the link between rainfall and flooding is complex, so while the most severe flooding events are expected to worsen, floods could become rarer in some regions.

Floods are a natural and important part of the water cycle but they can also threaten lives and safety, disrupt human activities, and damage infrastructure. Most inland floods occur when rivers overtop their banks (*fluvial* flooding) or when intense rainfall causes water to build up and overflow locally (*pluvial* flooding). Flooding is also caused by coastal inundation by the sea, rapid seasonal melting of snow, and the accumulation of debris, such as vegetation or ice, that stops water from draining away.

Climate change is already altering the location, frequency and severity of flooding. Close to the coasts, rising sea levels increasingly cause more frequent and severe coastal flooding, and the severity of these floods is exacerbated when combined with heavy rainfall. The heavy and sustained rainfall events responsible for most inland flooding are becoming more intense in many areas as the climate warms because air near Earth's surface can carry around 7% more water in its gas phase (vapour) for each 1°C of warming. This extra moisture is drawn into weather systems, fueling heavier rainfall (FAQ 8.2, Figure 1).

A warming climate also affects wind patterns, how storms form and evolve, and the pathway those storms usually travel. Warming also increases condensation rates, which in turn releases extra heat that can energize storm systems and further intensify rainfall. On the other hand, this energy release can also inhibit the uplift required for cloud development, while increases in particle pollution can delay rainfall but invigorate storms. These changes mean that the character of precipitation events (how often, how long-lasting and how heavy they are) will continue to change as the climate warms.

In addition to climate change, the location, frequency and timing of the heaviest rainfall events and worst flooding depend on natural fluctuations in wind patterns that make some regions unusually wet or dry for months, years, or even decades. These natural variations make it difficult to determine whether heavy rainfall events are changing locally as a result of global warming. However, when natural weather patterns bring heavy and prolonged rainfall in a warmer climate, the intensity is increased by the larger amount of moiture in the air.

An increased intensity and frequency of record-breaking daily rainfall has been detected for much of the land surface where good observational records exist, and this can only be explained by human-caused increases in atmospheric greenhouse gas concentrations. Heavy rainfall is also projected to become more intense in the future for most places. So, where unusually wet weather events or seasons occur, the rainfall amounts are expected to be greater in the future, contributing to more severe flooding.

However, heavier rainfall does not always lead to greater flooding. This is because flooding also depends upon the type of river basin, the surface landscape, the extent and duration of the rainfall, and how wet the ground is before the rainfall event (FAQ 8.2, Figure 1) Some regions will experience a drying in the soil as the climate warms, particularly in sub-tropical climates, which could make floods from a rainfall event less probable because the ground can potentially soak up more of the rain. On the other hand, less frequent but more intense downpours can lead to dry, hard ground that is less able to soak up heavy rainfall when it does occur, resulting in more runoff into lakes, rivers and hollows. Earlier spring snowmelt combined with more precipitation falling as rain rather than snow can trigger flood events in cold regions. Reduced winter snow cover can, in contrast, decrease the chance of flooding arising from the combination of rainfall and rapid snowmelt. Rapid melting of glaciers and snow in a warming climate is already increasing river flow in some regions, but as the volumes of ice diminish, flows will peak and then decline in the future. Flooding is also affected by changes in the management of the land and river systems. For example, clearing forests for agriculture or building cities can make rain water flow more rapidly into rivers or low lying areas. On the other hand, increased extraction of water from rivers can reduce water levels and the likelihood of flooding.

ACCEPTED VERSION SUBJECT TO FINAL EDITING

A mix of both increases and decreases in flooding have been observed in some regions and these changes have been attributed to multiple causes, including changes in snowmelt, soil moisture and rainfall. Although we know that a warming climate will intensify rainfall events, local and regional trends are expected to vary in both direction and magnitude as global warming results in multiple, and sometimes counteracting, influences. However, even accounting for the many factors that generate flooding, when weather patterns cause flood events in a warmer future, these floods will be more severe.

[START FAQ 8.2, FIGURE 1 HERE]

FAQ 8.2, Figure 1: Schematic illustrating factors important in determining changes in heavy precipitation and flooding.

[END FAQ 8.2, FIGURE 1 HERE]

ACCEPTED VERSION
SUBJECT TO FINAL EDITING

FAQ 8.3: What causes droughts, and will climate change make them worse?

Droughts usually begin as a deficit of precipitation, but then propagate to other parts of the water cycle (soils, rivers, snow/ice and water reservoirs). They are also influenced by factors like temperature, vegetation and human land and water management. In a warmer world, evaporation increases, which can make even wet regions more susceptible to drought.

A drought is broadly defined as drier than normal conditions; that is, a moisture deficit relative to the average water availability at a given location and season. Since they are locally defined, a drought in a wet place will not have the same amount of water deficit as a drought in a dry region. Droughts are divided into different categories based on where in the water cycle the moisture deficit occurs: meteorological drought (precipitation), hydrological drought (runoff, streamflow, and reservoir storage), and agricultural or ecological drought (plant stress from a combination of evaporation and low soil moisture). Special categories of drought also exist. For example, a snow drought occurs when winter snowpack levels are below average, which can cause abnormally low streamflow in subsequent seasons. And while many drought events develop slowly over months or years, some events, called flash droughts, can intensify over the course of days or weeks. One such event occurred in 2012 in the midwestern region of North America and had a severe impact on agricultural production, with losses exceeding $30 billion US dollars. Droughts typically only become a concern when they adversely affect people (reducing water available for municipal, industrial, agricultural, or navigational needs) and/or ecosystems (adverse effects on natural flora and fauna). When a drought lasts for a very long time (more than two decades) it is sometimes called a megadrought.

Most droughts begin when precipitation is below normal for an extended period of time (meteorological drought). This typically occurs when high pressure in the atmosphere sets up over a region, reducing cloud formation and precipitation over that area and deflecting away storms. The lack of rainfall then propagates across the water cycle to create agricultural drought in soils and hydrological drought in waterways. Other processes act to amplify or alleviate droughts. For example, if temperatures are abnormally high, evaporation increases, drying out soils and streams and stressing plants beyond what would have occurred from the lack of precipitation alone. Vegetation can play a critical role because it modulates many important hydrologic processes (soil water, evapotranspiration, runoff). Human activities can also determine how severe a drought is. For example, irrigating croplands can reduce the socioeconomic impact of a drought; at the same time, depletion of groundwater in aquifers can make a drought worse.

The effect of climate change on drought varies across regions. In the subtropical regions like the Mediterranean, southern Africa, southwestern Australia and southwestern South America, as well as tropical central America, western Africa and the Amazon basin, precipitation is expected to decline as the world warms, increasing the possibility that drought will occur throughout the year (FAQ 8.3, Figure 1). Warming will decrease snowpack, amplifying drought in regions where snowmelt is an important water resource (such as in southwestern South America). Higher temperatures lead to increased evaporation, resulting in soil drying, increased plant stress, and impacts on agriculture, even in regions where large changes in precipitation are not expected (such as central and northern Europe). If emissions of greenhouse gases are not curtailed, about a third of global land areas are projected to suffer from at least moderate drought by 2100. On the other hand, some areas and seasons (such as high-latitude regions in North America and Asia, and the South Asian monsoon region) may experience increases in precipitation as a result of climate change, which will decrease the likelihood of droughts. FAQ 8.3, Figure 1 highlights the regions where climate change is expected to increase the severity of droughts.

[START FAQ 8.3, FIGURE HERE]

FAQ 8.3, Figure 1: Drought is expected to get worse in the regions highlighted in brown as a consequence of climate change. This pattern is similar regardless of the emissions scenario; however, the magnitude of change increases under higher emissions.

[END OF FAQ 8.3, FIGURE]

ACCEPTED VERSION SUBJECT TO FINAL EDITING

Acknowledgements

The authors are extremely grateful to the WGI Bureau and Technical Support Unit for their outstanding support throughout the writing of the chapter. Special thanks to Sarah Connors for her exceptional contribution to the development of this chapter. Her help with chapter meetings and organisational support was invaluable. Thanks to Sophie Berger, Melissa Gomis, Nigel Hawtin and Tom Maycock for their contributions to figures and tables. We must also make a special acknowledgment of our chapter scientists, Sabin Thazhe Purayil and Stéphane Sénési, without whom we could not have completed our assessment nor could we have produced the excellent figures that appear in the chapter. We would also like to thank all reviewers for their useful comments. Finally, we are infinitely indebted to our families for their extended patience and support during this demanding process.

ACCEPTED VERSION
SUBJECT TO FINAL EDITING

References

Aadhar, S. and V. Mishra, 2020: On the projected decline in droughts over South Asia in CMIP6 multimodel ensemble. *Journal of Geophysical Research: Atmospheres*, 0–3, doi:10.1029/2020jd033587.

Abbott, B.W. et al., 2019: Human domination of the global water cycle absent from depictions and perceptions. *Nature Geoscience*, **12(7)**, 533–540, doi:10.1038/s41561-019-0374-y.

Abbott, T. and T. Cronin, 2021: Aerosol invigoration of atmospheric convection through increases in humidity. *Science*, **371(6524)**, 83 LP – 85, doi:10.1126/science.abc5181.

Abdel-Lathif, A.Y., R. Roehrig, I. Beau, and H. Douville, 2018: Single-Column Modeling of Convection During the CINDY2011/DYNAMO Field Campaign With the CNRM Climate Model Version 6. *Journal of Advances in Modeling Earth Systems*, **10(3)**, 578–602, doi:10.1002/2017ms001077.

Abell, J.T., G. Winckler, R.F. Anderson, and T.D. Herbert, 2021: Poleward and weakend westerlies during Pliocene warmth. *Nature*, **589(7840)**, 70–75, doi:10.1038/s41586-020-03062-1.

Aberson, S.D. and J. Kaplan, 2020: The Relationship between the Madden–Julian Oscillation and Tropical Cyclone Rapid Intensification. *Weather and Forecasting*, **35(5)**, 1865–1870, doi:10.1175/waf-d-19-0209.1.

Abish et al., 2013: Weakening trend of the tropical easterly jet stream of the boreal summer monsoon season 1950-2009. *Journal of Climate*, **26(23)**, 9408–9414, doi:10.1175/jcli-d-13-00440.1.

Abram, N.J. et al., 2020: Coupling of Indo-Pacific climate variability over the last millennium. *Nature*, **579(7799)**, 385–392, doi:10.1038/s41586-020-2084-4.

Adam, O., T. Schneider, and F. Brient, 2018: Regional and seasonal variations of the double-ITCZ bias in CMIP5 models. *Climate Dynamics*, **51(1–2)**, 101–117, doi:10.1007/s00382-017-3909-1.

Adames, F., D. Kim, A.H. Sobel, A. Del Genio, and J. Wu, 2017a: Changes in the structure and propagation of the MJO with increasing CO 2. *Journal of Advances in Modeling Earth Systems*, **9(2)**, 1251–1268, doi:10.1002/2017ms000913.

Adames, F., D. Kim, A.H. Sobel, A. Del Genio, and J. Wu, 2017b: Characterization of Moist Processes Associated With Changes in the Propagation of the MJO With Increasing CO2. *Journal of Advances in Modeling Earth Systems*, **9(8)**, 2946–2967, doi:10.1002/2017ms001040.

Adler, R.F., G. Gu, M. Sapiano, J.-J. Wang, and G.J. Huffman, 2017: Global Precipitation: Means, Variations and Trends During the Satellite Era (1979–2014). *Surveys in Geophysics*, **38(4)**, 679–699, doi:10.1007/s10712-017-9416-4.

Adusumilli, S., M. Fish, H.A. Fricker, and B. Medley, 2021: Atmospheric River Precipitation Contributed to Rapid Increases in Surface Height of the West Antarctic Ice Sheet in 2019. *Geophysical Research Letters*, **n/a(n/a)**, e2020GL091076, doi:10.1029/2020gl091076.

Adusumilli, S., A.A. Borsa, M.A. Fish, H.K. McMillan, and F. Silverii, 2019: A decade of terrestrial water storage changes across the contiguous United States from GPS and GRACE. *Geophysical Research Letters*, doi:10.1029/2019gl085370.

AghaKouchak, A., D. Feldman, M. Hoerling, T. Huxman, and J. Lund, 2015: Water and climate: Recognize anthropogenic drought. *Nature News*, **524(7566)**, 409.

Agudelo, J., P.A.P.A. Arias, S.C.S.C.S.C. Vieira, and J.A.A. Martínez, 2019: Influence of longer dry seasons in the Southern Amazon on patterns of water vapor transport over northern South America and the Caribbean. *Climate Dynamics*, **52(5–6)**, 2647–2665, doi:10.1007/s00382-018-4285-1.

Ahn, M.-S., D. Kim, Y.-G. Ham, and S. Park, 2020a: Role of Maritime Continent Land Convection on the Mean State and MJO Propagation. *Journal of Climate*, **33(5)**, 1659–1675, doi:10.1175/jcli-d-19-0342.1.

Ahn, M.-S. et al., 2017: MJO simulation in CMIP5 climate models: MJO skill metrics and process-oriented diagnosis. *Climate Dynamics*, **49(11–12)**, 4023–4045, doi:10.1007/s00382-017-3558-4.

Ahn, M.-S. et al., 2020b: MJO Propagation Across the Maritime Continent: Are CMIP6 Models Better Than CMIP5 Models? *Geophysical Research Letters*, **47(11)**, doi:10.1029/2020gl087250.

Aires, F. et al., 2017: A global dynamic long-term inundation extent dataset at high spatial resolution derived through downscaling of satellite observations. Journal of Hydrometeorology. , **18(5)**, 1305–1325.

Aires, F. et al., 2018: Comparison of visible and multi-satellite global inundation datasets at high-spatial resolution. Remote sensing of environment. *Remote Sensing of Environment*, **216**, 427–441, doi:10.1016/j.rse.2018.06.015.

Akinsanola, A.A. and W. Zhou, 2018: Ensemble-based CMIP5 simulations of West African summer monsoon rainfall: current climate and future changes. *Theoretical and Applied Climatology*, doi:10.1007/s00704-018-2516-3.

Akinsanola, A.A. and W. Zhou, 2020: Understanding the Variability of West African Summer Monsoon Rainfall: Understanding the Variability of West African Summer Monsoon Rainfall : Contrasting Tropospheric Features and Monsoon Index. , doi:10.3390/atmos11030309.

Akinsanola, A.A. et al., 2018: Evaluation of rainfall simulations over West Africa in dynamically downscaled CMIP5 global circulation models. *Theoretical and Applied Climatology*, **132(1–2)**, 437–450, doi:10.1007/s00704-017-2087-8.

SUBJECT TO FINAL EDITING ACCEPTED VERSION

Akter, R. et al., 2019: The Dominant Climate Change Event for Salinity Intrusion in the GBM Delta. *Climate*, **7(5)**, doi:10.3390/cli7050069.
Alessandri, A. and A. Navarra, 2008: On the coupling between vegetation and rainfall inter-annual anomalies: Possible contributions to seasonal rainfall predictability over land areas. *Geophysical Research Letters*, **35(2)**, L02718, doi:10.1029/2007gl032415.
Alessandri, A. et al., 2015: Robust assessment of the expansion and retreat of Mediterranean climate in the 21stcentury. *Scientific Reports*, **4(1)**, 7211, doi:10.1038/srep07211.
Alessandri, A. et al., 2017: Multi-scale enhancement of climate prediction over land by increasing the model sensitivity to vegetation variability in EC-Earth. *Climate Dynamics*, doi:10.1007/s00382-016-3372-4.
Alexander, L., 2016: Global observed long-term changes in temperature and precipitation extremes: A review of progress and limitations in IPCC assessments and beyond. *Weather and Climate Extremes*, **11**, 4–16, doi:10.1016/j.wace.2015.10.007.
Algarra, I. et al., 2020: Significant increase of global anomalous moisture uptake feeding landfalling Atmospheric Rivers. *Nature Communications*, **11(1)**, 5082, doi:10.1038/s41467-020-18876-w.
Ali, H., H.J. Fowler, and V. Mishra, 2018: Global observational evidence of strong linkage between dew point temperature and precipitation extremes. *Geophysical Research Letters*, doi:10.1029/2018gl080557.
Ali and Lebel, A. et al., 2009: The Sahelian standardized rainfall index revisited. *International Journal of Climatology*, **29(12)**, 1705–1714, doi:10.1002/joc.1832.
Allan, R.P. et al., 2014: Physically Consistent Responses of the Global Atmospheric Hydrological Cycle in Models and Observations. *Surveys in Geophysics*, **35**, 533–552, doi:10.1007/s10712-012-9213-z.
Allan, R.P. et al., 2020: Advances in understanding large-scale responses of the water cycle to climate change. *Annals of the New York Academy of Sciences*, 1–27, doi:10.1111/nyas.14337.
Allen, C.D., D.D. Breshears, and N.G. McDowell, 2015: On underestimation of global vulnerability to tree mortality and forest die-off from hotter drought in the Anthropocene. *Ecosphere*, **6(8)**, 1–55, doi:10.1890/es15-00203.1.
Allen, D.M., P.H. Whitfield, and A. Werner, 2010: Groundwater level responses in temperate mountainous terrain: Regime classification, and linkages to climate and streamflow. *Hydrological Processes*, **24**, 3392–3412.
Allen, R.J. and W. Landuyt, 2014: The vertical distribution of black carbon in CMIP5 models: Comparison to observations and the importance of convective transport. *Journal of Geophysical Research*, **119(8)**, 4808–4835, doi:10.1002/2014jd021595.
Allen, R.J., J.R. Norris, and M. Kovilakam, 2014: Influence of anthropogenic aerosols and the Pacific Decadal Oscillation on tropical belt width. *Nature Geoscience*, **7(4)**, 270–274, doi:10.1038/ngeo2091.
Allen, R.J., A.T. Evan, and B.B.B. Booth, 2015: Interhemispheric Aerosol Radiative Forcing and Tropical Precipitation Shifts during the Late Twentieth Century. *Journal of Climate*, **28(20)**, 8219–8246, doi:10.1175/jcli-d-15-0148.1.
Allen, R.J., W. Landuyt, and S.T. Rumbold, 2016: An increase in aerosol burden and radiative effects in a warmer world. *Nature Climate Change*, doi:10.1038/nclimate2827.
Almazroui, M., M.N. Islam, S. Saeed, F. Saeed, and M. Ismail, 2020a: Future Changes in Climate over the Arabian Peninsula based on CMIP6 Multimodel Simulations. *Earth Systems and Environment*, **4(4)**, 611–630, doi:10.1007/s41748-020-00183-5.
Almazroui, M. et al., 2020b: Projected Change in Temperature and Precipitation Over Africa from CMIP6. *Earth Systems and Environment*, **4(3)**, 455–475, doi:10.1007/s41748-020-00161-x.
Almazroui, M. et al., 2020c: Projections of Precipitation and Temperature over the South Asian Countries in CMIP6. *Earth Systems and Environment*, **4(2)**, 297–320, doi:10.1007/s41748-020-00157-7.
Almazroui, M. et al., 2021: Projected Changes in Temperature and Precipitation Over the United States, Central America, and the Caribbean in CMIP6 GCMs. *Earth Systems and Environment*, **5(1)**, 1–24, doi:10.1007/s41748-021-00199-5.
Almeida, C.T., J.F. Oliveira-Júnior, R.C. Delgado, P. Cubo, and M.C. Ramos, 2017: Spatiotemporal rainfall and temperature trends throughout the Brazilian Legal Amazon, 1973-2013. *International Journal of Climatology*, **37(4)**, 2013–2026, doi:10.1002/joc.4831.
Alter, R.E., E.S. Im, and E.A.B. Eltahir, 2015: Rainfall consistently enhanced around the Gezira Scheme in East Africa due to irrigation. *Nature Geoscience*, **8(10)**, 763–767, doi:10.1038/ngeo2514.
Alvarez, M., C. Vera, and G. Kiladis, 2017: MJO Modulating the Activity of the Leading Mode of Intraseasonal Variability in South America. *Atmosphere*, **8(12)**, 232, doi:10.3390/atmos8120232.
Anderegg, W.R.L. et al., 2016: Meta-analysis reveals that hydraulic traits explain cross-species patterns of drought-induced tree mortality across the globe. *Proceedings of the National Academy of Sciences of the United States of America*, doi:10.1073/pnas.1525678113.
Andreae, M.O. et al., 2004: Smoking rain clouds over the Amazon. *science*, **303(5662)**, 1337–1342.
Andrews, T., J.M. Gregory, and M.J. Webb, 2015: The dependence of radiative forcing and feedback on evolving patterns of surface temperature change in climate models. *Journal of Climate*, **28(4)**, 1630–1648, doi:10.1175/jcli-d-14-00545.1.
Andrews, T., P.M. Forster, O. Boucher, N. Bellouin, and A. Jones, 2010: Precipitation, radiative forcing and global

ACCEPTED VERSION SUBJECT TO FINAL EDITING

temperature change. *Geophysical Research Letters*, **37(14)**, n/a—n/a, doi:10.1029/2010gl043991.
Annamalai, H., B. Taguchi, J.P. McCreary, M. Nagura, and T. Miyama, 2017: Systematic Errors in South Asian Monsoon Simulation: Importance of Equatorial Indian Ocean Processes. *Journal of Climate*, **30(20)**, 8159–8178, doi:10.1175/jcli-d-16-0573.1.
Apaéstegui, J. et al., 2014: Hydroclimate variability of the northwestern Amazon Basin near the Andean foothills of Peru related to the South American Monsoon System during the last 1600 years. *Climate of the Past*, **10(6)**, 1967–1981, doi:10.5194/cp-10-1967-2014.
Araya-Melo, P.A., M. Crucifix, and N. Bounceur, 2015: Global sensitivity analysis of the Indian monsoon during the Pleistocene. *Climate of the Past*, **11(1)**, 45–61, doi:10.5194/cp-11-45-2015.
Arheimer, B., C. Donnelly, and G. Lindström, 2017: Regulation of snow-fed rivers affects flow regimes more than climate change. *Nature Communications*, **8(1)**, 1–8, doi:10.1038/s41467-017-00092-8.
Arias, P.A., R. Fu, and K. Mo, 2012: Decadal Variation of Rainfall Seasonality in the North American Monsoon Region and Its Potential Causes. *Journal of Climate*, **25(12)**, 4258–4274, doi:10.1175/jcli-d-11-00140.1.
Arias, P.A., R. Fu, C. Vera, and M. Rojas, 2015: A correlated shortening of the North and South American monsoon seasons in the past few decades. *Climate Dynamics*, **45(11)**, 3183–3203, doi:10.1007/s00382-015-2533-1.
Armour, K.C., C.M. Bitz, and G.H. Roe, 2013: Time-Varying Climate Sensitivity from Regional Feedbacks. *Journal of Climate*, **26(13)**, 4518–4534, doi:10.1175/jcli-d-12-00544.1.
Arnell, N.W. and S.N. Gosling, 2016: The impacts of climate change on river flood risk at the global scale. *Climatic Change*, **134(3)**, 387–401, doi:10.1007/s10584-014-1084-5.
Arnold, N.P., Z. Kuang, and E. Tziperman, 2013: Enhanced MJO-like Variability at High SST. *Journal of Climate*, **26(3)**, 988–1001, doi:10.1175/jcli-d-12-00272.1.
Arnold, N.P., M. Branson, Z. Kuang, D.A. Randall, and E. Tziperman, 2015: MJO Intensification with Warming in the Superparameterized CESM. *Journal of Climate*, **28(7)**, 2706–2724, doi:10.1175/jcli-d-14-00494.1.
Arora, V.K. et al., 2020: Carbon – concentration and carbon – climate feedbacks in CMIP6 models and their comparison to CMIP5 models. , 4173–4222.
Arvor, D., B.M. Funatsu, V. Michot, and V. Dubreui, 2017: Monitoring rainfall patterns in the southern amazon with PERSIANN-CDR data: Long-term characteristics and trends. *Remote Sensing*, **9(9)**, doi:10.3390/rs9090889.
Asadieh, B. and N.Y. Krakauer, 2017: Global change in streamflow extremes under climate change over the 21st century. *Hydrology and Earth System Sciences*, doi:10.5194/hess-21-5863-2017.
Ashfaq, M. et al., 2020: Robust late twenty-first century shift in the regional monsoons in RegCM-CORDEX simulations. *Climate Dynamics*, doi:10.1007/s00382-020-05306-2.
Asoka, A., T. Gleeson, Y. Wada, and V. Mishra, 2017: Relative contribution of monsoon precipitation and pumping to changes in groundwater storage in India. *Nature Geoscience*, doi:10.1038/ngeo2869.
Asoka, A., Y. Wada, R. Fishman, and V. Mishra, 2018: Strong Linkage Between Precipitation Intensity and Monsoon Season Groundwater Recharge in India. *Geophysical Research Letters*, **45(11)**, 5536–5544, doi:10.1029/2018gl078466.
As-syakur, A.R. et al., 2014: Observation of spatial patterns on the rainfall response to ENSO and IOD over Indonesia using TRMM Multisatellite Precipitation Analysis (TMPA). *International Journal of Climatology*, **34(15)**, 3825–3839, doi:10.1002/joc.3939.
Atwood, A.R., A. Donohoe, D.S. Battisti, X. Liu, and F.S.R. Pausata, 2020: Robust longitudinally-variable responses of the ITCZ to a myriad of climate forcings. *Geophys Res Lett*, **47**, e2020GL088833, doi:10.1002/essoar.10503115.1.
Ault, T.R., J.E. Cole, and S. St. George, 2012: The amplitude of decadal to multidecadal variability in precipitation simulated by state-of-the-art climate models. *Geophysical Research Letters*, doi:10.1029/2012gl053424.
Ault, T.R., J.E. Cole, J.T. Overpeck, G.T. Pederson, and D.M. Meko, 2014: Assessing the Risk of Persistent Drought Using Climate Model Simulations and Paleoclimate Data. *Journal of Climate*, **27(20)**, 7529–7549, doi:10.1175/jcli-d-12-00282.1.
Ault, T.R. et al., 2013: The Continuum of hydroclimate variability in Western North America during the last millennium. *Journal of Climate*, doi:10.1175/jcli-d-11-00732.1.
Ayantika et al, D.C. et al., 2021: Understanding the combined effects of global warming and anthropogenic aerosol forcing on the South Asian Monsoon.. *Climate Dynamics*, **in press**, doi:10.1007/s00382-020-05551-5.
Aygün, O., C. Kinnard, and S. Campeau, 2019: Impacts of climate change on the hydrology of northern midlatitude cold regions. *Progress in Physical Geography: Earth and Environment*, **44(3)**, 338–375, doi:10.1177/0309133319878123.
Ayliffe, L.K. et al., 2013: Rapid interhemispheric climate links via the Australasian monsoon during the last deglaciation. *Nature Communications*, **4**, 2908, doi:10.1038/ncomms3908.
Bador, M., M.G. Donat, O. Geoffroy, and L. Alexander, 2018: Assessing the Robustness of Future Extreme Precipitation Intensification in the CMIP5 Ensemble. *Journal of Climate*, **31(16)**, 6505–6525, doi:10.1175/jcli-d-17-0683.1.
Bador, M. et al., 2020: Impact of higher spatial atmospheric resolution on precipitation extremes over land in global climate models. *Journal of Geophysical Research: Atmospheres*, **125(13)**, e2019JD032184,

ACCEPTED VERSION SUBJECT TO FINAL EDITING

doi:10.1029/2019jd032184.
Baker, H.S. et al., 2018: Higher CO2 concentrations increase extreme event risk in a 1.5°C world. *Nature Climate Change*, **8(7)**, 604–608, doi:10.1038/s41558-018-0190-1.
Bakker, P. et al., 2016: Fate of the Atlantic Meridional Overturning Circulation: Strong decline under continued warming and Greenland melting. *Geophysical Research Letters*, doi:10.1002/2016gl070457.
Bala, G., P.B. Duffy, and K.E. Taylor, 2008: Impact of geoengineering schemes on the global hydrological cycle. *Proceedings of the National Academy of Sciences*, doi:10.1073/pnas.0711648105.
Bala, G., K. Caldeira, and R. Nemani, 2010: Fast versus slow response in climate change: implications for the global hydrological cycle. *Climate Dynamics*, **35(2–3)**, 423–434, doi:10.1007/s00382-009-0583-y.
Balme, M. Balme et al, and Balme, 2006: Années sèches et années humides au Sahel: quo vadimus? *Hydrological Sciences Journal*, **51(2)**, 254–271, doi:10.1623/hysj.51.2.254.
Bamba, A. et al., 2015: Changes in Vegetation and Rainfall over West Africa during the Last Three Decades (1981-2010). *Atmospheric and Climate Sciences*, **05(04)**, 367–379, doi:10.4236/acs.2015.54028.
Ban, N., J. Schmidli, and C. Schär, 2015: Heavy precipitation in a changing climate: Does short-term summer precipitation increase faster? *Geophysical Research Letters*, **42(4)**, 1165–1172, doi:10.1002/2014gl062588.
Bao, J. and S.C. Sherwood, 2019: The Role of Convective Self-Aggregation in Extreme Instantaneous Versus Daily Precipitation. *Journal of Advances in Modeling Earth Systems*, doi:10.1029/2018ms001503.
Bao, J., S.C. Sherwood, L. Alexander, and J.P. Evans, 2017: Future increases in extreme precipitation exceed observed scaling rates. *Nature Climate Change*, **7(2)**, 128–132, doi:10.1038/nclimate3201.
Barbero, R., H.J. Fowler, G. Lenderink, and S. Blenkinsop, 2017: Is the intensification of precipitation extremes with global warming better detected at hourly than daily resolutions? *Geophysical Research Letters*, **44(2)**, 974–983, doi:10.1002/2016gl071917.
Barbero, R. et al., 2019: A synthesis of hourly and daily precipitation extremes in different climatic regions. *Weather and Climate Extremes*, **26**, 100219, doi:10.1016/j.wace.2019.100219.
Barcikowska, M.J. et al., 2018: Euro-Atlantic winter storminess and precipitation extremes under 1.5 °C vs. 2 °C warming scenarios. *Earth System Dynamics*, **9(2)**, 679–699, doi:10.5194/esd-9-679-2018.
Barichivich, J. et al., 2018: Recent intensification of Amazon flooding extremes driven by strengthened Walker circulation. *Science Advances*, **4(9)**, eaat8785, doi:10.1126/sciadv.aat8785.
Barkhordarian, A. et al., 2018: Simultaneous Regional Detection of Land-Use Changes and Elevated GHG Levels: The Case of Spring Precipitation in Tropical South America. *Geophysical Research Letters*, **45(12)**, 6262–6271, doi:10.1029/2018gl078041.
Barlow, M. et al., 2019: North American extreme precipitation events and related large-scale meteorological patterns: a review of statistical methods, dynamics, modeling, and trends. *Climate Dynamics*, **53(11)**, 6835–6875, doi:10.1007/s00382-019-04958-z.
Barnes, E.A., 2013: Revisiting the evidence linking Arctic amplification to extreme weather in midlatitudes. *Geophysical Research Letters*, **40(17)**, 4734–4739, doi:10.1002/grl.50880.
Barnes, E.A., E. Dunn-Sigouin, G. Masato, and T. Woollings, 2014: Exploring recent trends in Northern Hemisphere blocking. *Geophysical Research Letters*, **41(2)**, 638–644, doi:10.1002/2013gl058745.
Barreiro, M., N. Díaz, and M. Renom, 2014: Role of the global oceans and land–atmosphere interaction on summertime interdecadal variability over northern Argentina. *Climate Dynamics*, **42(7)**, 1733–1753, doi:10.1007/s00382-014-2088-6.
Barreiro, M. et al., 2019: Modelling the role of Atlantic air-sea interaction in the impact of Madden-Julian Oscillation on South American climate. *International Journal of Climatology*, **39(2)**, 1104–1116, doi:10.1002/joc.5865.
Barry, R. and T.Y. Gan, 2020: Global cruosphere. Past present and future. .
Bartlett, P.A. and D.L. Verseghy, 2015: Modified treatment of intercepted snow improves the simulated forest albedo in the Canadian Land Surface Scheme. *Hydrological Processes*, **29(14)**, 3208–3226, doi:10.1002/hyp.10431.
Barton, E.J. et al., 2019: A case-study of land–atmosphere coupling during monsoon onset in northern India. *Quarterly Journal of the Royal Meteorological Society*, **n/a(n/a)**, 2891–2905, doi:10.1002/qj.3538.
Bates, B.C., Z.W. Kundzewicz, S. Wu, and J.P. Palutikof, 2008: Climate Change and Water. Technical Paper of the Intergovernmental Panel on Climate Change. *Climate Change and Water. Technical Paper of the Intergovernmental Panel on Climate Change*, 210pp.
Bathiany, S., M. Claussen, and K. Fraedrich, 2013: Detecting hotspots of atmosphere–vegetation interaction via slowing down – Part 2: Application to a global climate model. *Earth System Dynamics*, **4**, 79–93, doi:10.5194/esd-4-79-2013.
Bathiany, S., M. Claussen, and V. Brovkin, 2014: CO2-induced sahel greening in three CMIP5 earth system models. *Journal of Climate*, doi:10.1175/jcli-d-13-00528.1.
Battisti, D.S., Q. Ding, and G.H. Roe, 2014: Coherent pan-Asian climatic and isotopic response to orbital forcing of tropical insolation. *Journal of Geophysical Research: Atmospheres*, **119(21)**, 11,997–12,020, doi:10.1002/2014jd021960.
Bayr, T., D. Dommenget, T. Martin, and S.B. Power, 2014: The eastward shift of the Walker Circulation in response to

ACCEPTED VERSION SUBJECT TO FINAL EDITING

global warming and its relationship to ENSO variability. *Climate Dynamics*, doi:10.1007/s00382-014-2091-y.
Bechtold, P. et al., 2008: Advances in simulating atmospheric variability with the ECMWF model: From synoptic to decadal time-scales. *Quarterly Journal of the Royal Meteorological Society*, **134(634)**, 1337–1351, doi:10.1002/qj.289.
Bechtold, P. et al., 2014: Representing equilibrium and nonequilibrium convection in large-scale models. *Journal of the Atmospheric Sciences*, **71(2)**, 734–753, doi:10.1175/jas-d-13-0163.1.
Behera, S.K. et al., 2005: Paramount Impact of the Indian Ocean Dipole on the East African Short Rains: A CGCM Study. *Journal of Climate*, **18(21)**, 4514–4530, doi:10.1175/jcli3541.1.
Behrangi, A., B. Guan, P.J. Neiman, M. Schreier, and B. Lambrigtsen, 2016: On the Quantification of Atmospheric Rivers Precipitation from Space: Composite Assessments and Case Studies over the Eastern North Pacific Ocean and the Western United States. *Journal of Hydrometeorology*, **17(1)**, 369–382, doi:10.1175/jhm-d-15-0061.1.
Bell, M.A., P.J. Lamb, M.A. Bell, and P.J. Lamb, 2006: Integration of Weather System Variability to Multidecadal Regional Climate Change: The West African Sudan–Sahel Zone, 1951–98. *Journal of Climate*, **19(20)**, 5343–5365, doi:10.1175/jcli4020.1.
Belmecheri, S., F. Babst, E.R. Wahl, D.W. Stahle, and V. Trouet, 2016: Multi-century evaluation of Sierra Nevada snowpack. *Nature Climate Change*, doi:10.1038/nclimate2809.
Belyazid, S. and Z. Giuliana, 2019: Water limitation can negate the effect of higher temperatures on forest carbon sequestration. *European Journal of Forest Research*, **138(2)**, 287–297, doi:10.1007/s10342-019-01168-4.
Bender, F.A.M., V. Ramanathan, and G. Tselioudis, 2012: Changes in extratropical storm track cloudiness 1983-2008: Observational support for a poleward shift. *Climate Dynamics*, **38(9–10)**, 2037–2053, doi:10.1007/s00382-011-1065-6.
Benestad, R.E., K.M. Parding, H.B. Erlandsen, and A. Mezghani, 2019: A simple equation to study changes in rainfall statistics. *Environmental Research Letters*, **14(8)**, doi:10.1088/1748-9326/ab2bb2.
Beniston, M. et al., 2018: The European mountain cryosphere: a review of its current state, trends, and future challenges. *Cryosphere*, **12(2)**, 759–794, doi:10.5194/tc-12-759-2018.
Berg, A. and J. Sheffield, 2018a: Climate Change and Drought: the Soil Moisture Perspective. *Current Climate Change Reports*, doi:10.1007/s40641-018-0095-0.
Berg, A. and J. Sheffield, 2018b: Soil moisture-evapotranspiration coupling in CMIP5 models: Relationship with simulated climate and projections. *Journal of Climate*, **31(12)**, 4865–4878, doi:10.1175/jcli-d-17-0757.1.
Berg, A., J. Sheffield, and P.C.D. Milly, 2017: Divergent surface and total soil moisture projections under global warming. *Geophysical Research Letters*, **44(1)**, 236–244, doi:10.1002/2016gl071921.
Berg, A. et al., 2016: Land-atmosphere feedbacks amplify aridity increase over land under global warming. *Nature Climate Change*, **6(9)**, 869–874, doi:10.1038/nclimate3029.
Berg, L.K. et al., 2015: A new WRF-Chem treatment for studying regional-scale impacts of cloud processes on aerosol and trace gases in parameterized cumuli. *Geoscientific Model Development*, **8(2)**, 409–429, doi:10.5194/gmd-8-409-2015.
Berg, N. and A. Hall, 2017: Anthropogenic warming impacts on California snowpack during drought. *Geophysical Research Letters*, doi:10.1002/2016gl072104.
Berg, P., C. Moseley, and J.O. Haerter, 2013: Strong increase in convective precipitation in response to higher temperatures. *Nature Geoscience*, **6(3)**, 181–185, doi:10.1038/ngeo1731.
Berghuijs, W.R., R.A. Woods, M. Hrachowitz, and R. Hrachowitz, 2014: A precipitation shift from snow towards rain leads to a decrease in streamflow. *Nature Climate Change*, **4(7)**, 583-586, 10-1038/nclimate2246.
Berghuijs, W.R., S. Harrigan, P. Molnar, L.J. Slater, and J.W. Kirchner, 2019: The Relative Importance of Different Flood-Generating Mechanisms Across Europe. *Water Resources Research*, **55(6)**, 4582–4593, doi:10.1029/2019wr024841.
Bernstein, D.N. and J.D. Neelin, 2016: Identifying sensitive ranges in global warming precipitation change dependence on convective parameters. *Geophysical Research Letters*, **43(11)**, 5841–5850, doi:10.1002/2016gl069022.
Berthou, S. et al., 2019a: Larger future intensification of rainfall in the West African Sahel in a convection-permitting model. *Geophysical Research Letters*, **n/a(n/a)**, doi:10.1029/2019gl083544.
Berthou, S. et al., 2019b: Improved climatological precipitation characteristics over West Africa at convection-permitting scales. *Climate Dynamics*, **53(3–4)**, 1991–2011, doi:10.1007/s00382-019-04759-4.
Bethke, I. et al., 2017: Potential volcanic impacts on future climate variability. *Nature Climate Change*, **7(11)**, 799–805, doi:10.1038/nclimate3394.
Betts, R.A. et al., 2015: Climate and land use change impacts on global terrestrial ecosystems and river flows in the HadGEM2-ES Earth system model using the representative concentration pathways. *Biogeosciences*, **12(5)**, 1317–1338, doi:10.5194/bg-12-1317-2015.
Bevacqua, E. et al., 2019: Higher probability of compound flooding from precipitation and storm surge in Europe under anthropogenic climate change. *Science Advances*, **5(9)**, eaaw5531, doi:10.1126/sciadv.aaw5531.
Beven, K., 2018: A Century of Denial: Preferential and Nonequilibrium Water Flow in Soils, 1864-1984. *Vadose Zone Journal*, **17(1)**, 180153, doi:10.2136/vzj2018.08.0153.

ACCEPTED VERSION SUBJECT TO FINAL EDITING

Bhattacharya, R., S. Bordoni, and J. Teixeira, 2017: Tropical precipitation extremes: Response to SST-induced warming in aquaplanet simulations. *Geophysical Research Letters*, **44(7)**, 3374–3383, doi:10.1002/2017gl073121.

Bhattacharya, T., J.E. Tierney, and P. DiNezio, 2017: Glacial reduction of the North American Monsoon via surface cooling and atmospheric ventilation. *Geophysical Research Letters*, doi:10.1002/2017gl073632.

Bhattacharya, T., J.E. Tierney, J.A. Addison, and J.W. Murray, 2018: Ice-sheet modulation of deglacial North American monsoon intensification. *Nature Geoscience*, doi:10.1038/s41561-018-0220-7.

Biasutti, M., 2013: Forced Sahel rainfall trends in the CMIP5 archive. *Journal of Geophysical Research Atmospheres*, **118(4)**, 1613–1623, doi:10.1002/jgrd.50206.

Biasutti, M., 2019: Rainfall trends in the African Sahel: Characteristics, processes, and causes. *WIREs Climate Change*, **10(4)**, 1–22, doi:10.1002/wcc.591.

Biasutti, M. and A. Voigt, 2019: Seasonal and CO2-induced shifts of the ITCZ: testing energetic controls in idealized simulations with comprehensive models. *Journal of Climate*, **33(7)**, 2853–2870, doi:10.1175/jcli-d-19-0602.1.

Biasutti, M. et al., 2018: Global energetics and local physics as drivers of past, present and future monsoons. *Nature Geoscience*, **11(6)**, 392–400, doi:10.1038/s41561-018-0137-1.

Bierkens, M.F.P. and Y. Wada, 2019: Non-renewable groundwater use and groundwater depletion: a review. *Environmental Research Letters*, **14(6)**, 63002, doi:10.1088/1748-9326/ab1a5f.

Bierkens, M.F.P. et al., 2015: Hyper-resolution global hydrological modelling: What is next?: "Everywhere and locally relevant" M. F. P. Bierkens et al. Invited Commentary. *Hydrological Processes*, **29(2)**, 310–320, doi:10.1002/hyp.10391.

Bindoff, N.L. et al., 2013: Detection and Attribution of Climate Change: from Global to Regional. In: *Climate Change 2013: The Physical Science Basis. Contribution of Working Group I to the Fifth Assessment Report of the Intergovernmental Panel on Climate Change* [Stocker, T.F., D. Qin, G.-K. Plattner, M. Tignor, S.K. Allen, J. Boschung, A. Nauels, Y. Xia, V. Bex, and P.M. Midgley (eds.)]. Cambridge University Press, Cambridge, United Kingdom and New York, NY, USA, pp. 867–952, doi:10.1017/cbo9781107415324.022.

Bintanja, R. and F.M. Selten, 2014: Future increases in Arctic precipitation linked to local evaporation and sea-ice retreat. *Nature*, **509(7501)**, 479–482, doi:10.1038/nature13259.

Bintanja, R. and O. Andry, 2017: Towards a rain-dominated Arctic. *Nature Climate Change*, doi:10.1038/nclimate3240.

Birch, C.E. et al., 2015: Sea-breeze dynamics and convection initiation: The influence of convective parameterization in weather and climate model biases. *Journal of Climate*, **28(20)**, 8093–8108, doi:10.1175/jcli-d-14-00850.1.

Bird, B.W., M.B. Abbott, D.T. Rodbell, and M. Vuille, 2011a: Holocene tropical South American hydroclimate revealed from a decadally resolved lake sediment δ18O record. *Earth and Planetary Science Letters*, **310(3–4)**, 192–202, doi:10.1016/j.epsl.2011.08.040.

Bird, B.W. et al., 2011b: A 2,300-year-long annually resolved record of the South American summer monsoon from the Peruvian Andes. *Proceedings of the National Academy of Sciences*, **108(21)**, 8583 LP – 8588, doi:10.1073/pnas.1003719108.

Bischoff, T. and T. Schneider, 2014: Energetic constraints on the position of the intertropical convergence zone. *Journal of Climate*, doi:10.1175/jcli-d-13-00650.1.

Blöschl, G. et al., 2019: Changing climate both increases and decreases European floods. *Nature*, **573(7772)**, 108–111, doi:10.1038/s41586-019-1495-6.

Blunden, J. and D.S. Arndt, 2020: State of the climate in 2019. *Bulletin of the American Meteorological Society*, **100(9)**, Si–S429, doi:10.1175/2019bamsstateoftheclimate.1.

Bódai, T., G. Drótos, M. Herein, F. Lunkeit, and V. Lucarini, 2020: The Forced Response of the El Niño–Southern Oscillation–Indian Monsoon Teleconnection in Ensembles of Earth System Models. *Journal of Climate*, **33(6)**, 2163–2182, doi:10.1175/jcli-d-19-0341.1.

Bodian, A., O. Ndiaye, and H. Dacosta, 2016: Evolution des caractéristiques des pluies journalières dans le bassin versant du fleuve Sénégal: Aavant et après rupture. *Hydrological Sciences Journal*, 1–9, doi:10.1080/02626667.2014.950584.

Boé, J. and F. Habets, 2014: Multi-decadal river flow variations in France. *Hydrology and Earth System Sciences*, **18(2)**, 691–708, doi:10.5194/hess-18-691-2014.

Boé, J., S. Somot, L. Corre, and P. Nabat, 2020: Large discrepancies in summer climate change over Europe as projected by global and regional climate models: causes and consequences. *Climate Dynamics*, **54(5–6)**, 2981–3002, doi:10.1007/s00382-020-05153-1.

Boers, N., N. Marwan, H.M.J. Barbosa, and J. Kurths, 2017: A deforestation-induced tipping point for the South American monsoon system. *Scientific Reports*, **7**, 1–9, doi:10.1038/srep41489.

Boisier, J.P., P. Ciais, A. Ducharne, and M. Guimberteau, 2015: Projected strengthening of Amazonian dry season by constrained climate model simulations. *Nature Climate Change*, **5(7)**, 656–660, doi:10.1038/nclimate2658.

Boisier, J.P., R. Rondanelli, R.D. Garreaud, and F. Muñoz, 2016: Anthropogenic and natural contributions to the Southeast Pacific precipitation decline and recent megadrought in central Chile. *Geophysical Research Letters*, **43(1)**, 413–421, doi:10.1002/2015gl067265.

ACCEPTED VERSION SUBJECT TO FINAL EDITING

Boisier, J.P. et al., 2018: Anthropogenic drying in central-southern Chile evidenced by long-term observations and climate model simulations. *Elem Sci Anth*, **6(1)**, 74, doi:10.1525/elementa.328.
Bolch, T., B. Menounos, and R. Wheate, 2010: Landsat-based inventory of glaciers in western Canada, 1985–2005. *Remote Sensing of Environment*, **114(1)**, 127–137, doi:10.1016/j.rse.2009.08.015.
Bollasina et al., M.A. Bollasina, Y. Ming, V. Ramaswamy, and Bollasina et al., 2011: Anthropogenic aerosols and the weakening of the south asian summer monsoon. *Science*, **334(6055)**, 502–505, doi:10.1126/science.1204994.
Bollasina et al., M.A. et al., 2014: Contribution of local and remote anthropogenic aerosols to the twentieth century weakening of the South Asian Monsoon. *Geophysical Research Letters*, **41(2)**, 680–687, doi:10.1002/2013gl058183.
Bonan, G.B. and S.C. Doney, 2018: Climate, ecosystems, and planetary futures: The challenge to predict life in Earth system models. *Science*, **359(6375)**, eaam8328, doi:10.1126/science.aam8328.
Bonan, G.B., M. Williams, R.A. Fisher, and K.W. Oleson, 2014: Modeling stomatal conductance in the earth system: Linking leaf water-use efficiency and water transport along the soil-plant-atmosphere continuum. *Geoscientific Model Development*, **7(5)**, 2193–2222, doi:10.5194/gmd-7-2193-2014.
Bonfils, C. et al., 2017: Competing influences of anthropogenic warming, ENSO, and plant physiology on future terrestrial aridity. *Journal of Climate*, **30(17)**, 6883–6904, doi:10.1175/jcli-d-17-0005.1.
Bonfils, C.J.W. et al., 2015: Relative Contributions of Mean-State Shifts and ENSO-Driven Variability to Precipitation Changes in a Warming Climate*. *Journal of Climate*, **28(24)**, 9997–10013, doi:10.1175/jcli-d-15-0341.1.
Bonfils, C.J.W.W. et al., 2020: Human influence on joint changes in temperature, rainfall and continental aridity. *Nature Climate Change*, **10(8)**, 1–6, doi:10.1038/s41558-020-0821-1.
Bonini, I. et al., 2014: Rainfall and deforesetation in the municipality of Colider, Southern Amazon. *Revista Brasileira de Meteorologia*, **29**, 483–493.
Bonnet, R., J. Boé, G. Dayon, and E. Martin, 2017: Twentieth-Century Hydrometeorological Reconstructions to Study the Multidecadal Variations of the Water Cycle Over France. *Water Resources Research*, **53(10)**, 8366–8382, doi:10.1002/2017wr020596.
Bony, S. et al., 2013: Robust direct effect of carbon dioxide on tropical circulation and regional precipitation. *Nature Geoscience*, **6(6)**, 447–451, doi:10.1038/ngeo1799.
Boos, W.R. and R.L. Korty, 2016: Regional energy budget control of the intertropical convergence zone and application to mid-Holocene rainfall. *Nature Geoscience*, **9(12)**, 892–897, doi:10.1038/ngeo2833.
Boos, W.R. and T. Storelvmo, 2016: Near-linear response of mean monsoon strength to a broad range of radiative forcings. *Proceedings of the National Academy of Sciences*, **113(6)**, 1510–1515, doi:10.1073/pnas.1517143113.
Borodina, A., E.M. Fischer, and R. Knutti, 2017: Models are likely to underestimate increase in heavy rainfall in the extratropical regions with high rainfall intensity. *Geophysical Research Letters*, **44(14)**, 7401–7409, doi:10.1002/2017gl074530.
Bosmans, J.H.C. et al., 2018: Response of the Asian summer monsoons to idealized precession and obliquity forcing in a set of GCMs. *Quaternary Science Reviews*, **188**, 121–135, doi:10.1016/j.quascirev.2018.03.025.
Bouchaou, L. et al., 2013: Isotopic Composition and Age of Surface Water as Indicators of Groundwater Sustainability in a Semiarid Area: Case of the Souss Basin (Morocco). In: *Isotopes in Hydrology, Marine Ecosystems and Climate Change Studies, Vol. 2. Proceedings of the International Symposium*. International Atomic Energy Agency (IAEA), Vienna, Austria, pp. 169–175.
Boulton, C.A., B.B.B. Booth, and P. Good, 2017: Exploring uncertainty of Amazon dieback in a perturbed parameter Earth system ensemble. *Global Change Biology*, **23(12)**, 5032–5044, doi:10.1111/gcb.13733.
Boyaj, A., H.P. Dasari, I. Hoteit, and K. Ashok, 2020: Increasing heavy rainfall events in South India due to changing land use land cover. *Quarterly Journal of the Royal Meteorological Society*, **n/a(n/a)**, qj.3826, doi:10.1002/qj.3826.
Boysen, L. et al., 2020: Global climate response to idealized deforestation in CMIP6 models. *Biogeosciences Discuss.*, **2020**, 1–35, doi:10.5194/bg-2020-229.
Bozkurt, D., R. Rondanelli, J.C. Marín, and R. Garreaud, 2018: Foehn Event Triggered by an Atmospheric River Underlies Record-Setting Temperature Along Continental Antarctica. *Journal of Geophysical Research: Atmospheres*, **123(8)**, 3871–3892, doi:10.1002/2017jd027796.
Bozkurt, D. et al., 2019: Dynamical downscaling over the complex terrain of southwest South America: present climate conditions and added value analysis. *Climate Dynamics*, **53(11)**, 6745–6767, doi:10.1007/s00382-019-04959-y.
Bracegirdle, T.J. et al., 2020a: Improvements in Circumpolar Southern Hemisphere Extratropical Atmospheric Circulation in CMIP6 Compared to CMIP5. *Earth and Space Science*, **7(6)**, doi:10.1029/2019ea001065.
Bracegirdle, T.J. et al., 2020b: Twenty first century changes in Antarctic and Southern Ocean surface climate in CMIP6. *Atmospheric Science Letters*, **21(9)**, doi:10.1002/asl.984.
Braconnot, P., C. Marzin, L. Grégoire, E. Mosquet, and O. Marti, 2008: Monsoon response to changes in Earth's orbital parameters: comparisons between simulations of the Eemian and of the Holocene. *Climate of the Past*, **4(4)**, 281–294, doi:10.5194/cp-4-281-2008.

ACCEPTED VERSION SUBJECT TO FINAL EDITING

Braconnot, P. et al., 2019: Impact of multiscale variability on last 6000 years Indian and West African monsoon rain. *Geophysical Research Letters*, **n/a(n/a)**, doi:10.1029/2019gl084797.
Brando, P.M. et al., 2014: Abrupt increases in Amazonian tree mortality due to drought{\\textendash}fire interactions. *Proceedings of the National Academy of Sciences*, doi:10.1073/pnas.1305499111.
Braun, M.H. et al., 2019: Constraining glacier elevation and mass changes in South America. *Nature Climate Change*, **9(2)**, 130–136, doi:10.1038/s41558-018-0375-7.
Breshears, D.D. et al., 2013: The critical amplifying role of increasing atmospheric moisture demand on tree mortality and associated regional die-off. *Frontiers in Plant Science*, doi:10.3389/fpls.2013.00266.
Brierley, C.M. et al., 2020: Large-scale features and evaluation of the PMIP4-CMIP6 midHolocene simulations. *Climate of the Past*, doi:10.5194/cp-16-1847-2020.
Broccoli, A.J., K.A. Dahl, and R.J. Stouffer, 2006: Response of the ITCZ to Northern Hemisphere cooling - Broccoli - 2006 - Geophysical Research Letters - Wiley Online Library. *Geophysical Research Letters*.
Brogli, R., S.L. Sørland, N. Kröner, and C. Schär, 2019: Causes of future mediterranean precipitation decline depend on the season. *Environmental Research Letters*, **14(11)**, 114017, doi:10.1088/1748-9326/ab4438.
Brönnimann, S. et al., 2015: Southward shift of the northern tropical belt from 1945 to 1980. *Nature Geoscience*, **8(12)**, 969–974, doi:10.1038/ngeo2568.
Brovkin, V., M. Claussen, V. Petoukhov, and A. Ganopolski, 1998: On the stability of the atmosphere-vegetation system in the Sahara/Sahel region. *Journal of Geophysical Research: Atmospheres*, **103(D24)**, 31613–31624.
Brown, J.R., A.F. Moise, and R.A. Colman, 2017: Projected increases in daily to decadal variability of Asian-Australian monsoon rainfall. *Geophysical Research Letters*, **44(11)**, 5683–5690, doi:10.1002/2017gl073217.
Brown, J.R., P. Hope, J. Gergis, and B.J. Henley, 2016a: ENSO teleconnections with Australian rainfall in coupled model simulations of the last millennium. *Climate Dynamics*, **47(1)**, 79–93, doi:10.1007/s00382-015-2824-6.
Brown, J.R., A.F. Moise, R. Colman, and H. Zhang, 2016b: Will a warmer world mean a wetter or drier Australian monsoon? *Journal of Climate*, **29**, 4577–4596, doi:10.1175/jcli-d-15-0695.1.
Brown, R.D. and D.A. Robinson, 2010: Northern Hemisphere spring snow cover variability and change over 1922-2010 including an assessment of uncertainty, Cryosphere. *Discuss.*, **4(1)**, 2483–2512, doi:10.5194/tc-5-219-2011.
Brun, F., E. Berthier, P. Wagnon, A. Kääb, and D. Treichler, 2017: Asia glacier mass balances from 2000 to 2016. , **10**, doi:10.1038/ngeo2999.
Brunke, M.A. et al., 2016: Implementing and evaluating variable soil thickness in the Community Land Model, version 4.5 (CLM4.5). *Journal of Climate*, **29(9)**, 3441–3461, doi:10.1175/jcli-d-15-0307.1.
Bucak, T. et al., 2017: Future water availability in the largest freshwater Mediterranean lake is at great risk as evidenced from simulations with the SWAT model. *Science of the Total Environment*, **581–582**, 413–425, doi:10.1016/j.scitotenv.2016.12.149.
Buckley, B.M. et al., 2010: Climate as a contributing factor in the demise of Angkor, Cambodia. *Proceedings of the National Academy of Sciences*, doi:10.1073/pnas.0910827107.
Buckley, M.W. and J. Marshall, 2016: Observations, inferences, and mechanisms of the Atlantic Meridional Overturning Circulation: A review. *Reviews of Geophysics*, doi:10.1002/2015rg000493.
Bui, H.X. and E.D. Maloney, 2018: Changes in Madden-Julian Oscillation Precipitation and Wind Variance Under Global Warming. *Geophysical Research Letters*, **45(14)**, 7148–7155, doi:10.1029/2018gl078504.
Bui, H.X., J.Y. Yu, and C. Chou, 2019: Impacts of model spatial resolution on the vertical structure of convection in the tropics. *Climate Dynamics*, **52(1–2)**, 15–27, doi:10.1007/s00382-018-4125-3.
Bukovsky, M.S. et al., 2015: Toward assessing NARCCAP regional climate model credibility for the North American monsoon: Future climate simulations. *Journal of Climate*, doi:10.1175/jcli-d-14-00695.1.
Bunde, A., U. Büntgen, J. Ludescher, J. Luterbacher, and H. von Storch, 2013: Is there memory in precipitation? *Nature Climate Change*, doi:10.1038/nclimate1830.
Burdanowitz, J., S.A. Buehler, S. Bakan, and C. Klepp, 2019: On the sensitivity of oceanic precipitation to sea surface temperature. *Atmospheric Chemistry and Physics Discussions*, 1–21, doi:10.5194/acp-2019-136.
Bureau of Meteorology and CSIRO, 2020: State of the Climate. , 24.
Burls, N.J. and A. Fedorov, 2017: Wetter subtropics in a warmer world: Contrasting past and future hydrological cycles. *Proceedings of the National Academy of Sciences of the United States of America*, **114(49)**, 12888–12893, doi:10.1073/pnas.1703421114.
Byrne, M.P. and P.A. O'Gorman, 2015: The response of precipitation minus evapotranspiration to climate warming: Why the "Wet-get-wetter, dry-get-drier" scaling does not hold over land. *Journal of Climate*, **28(20)**, 8078–8092, doi:10.1175/jcli-d-15-0369.1.
Byrne, M.P. and P.A. O'Gorman, 2016: Understanding decreases in land relative humidity with global warming: Conceptual model and GCM simulations. *Journal of Climate*, **29(24)**, 9045–9061, doi:10.1175/jcli-d-16-0351.1.
Byrne, M.P. and T. Schneider, 2016: Narrowing of the ITCZ in a warming climate: Physical mechanisms. *Geophysical Research Letters*, **43(21)**, 11,350–11,357, doi:10.1002/2016gl070396.
Byrne, M.P. and P.A. O'Gorman, 2018: Trends in continental temperature and humidity directly linked to ocean warming. *Proceedings of the National Academy of Sciences*, **115(19)**, 4863–4868,

ACCEPTED VERSION SUBJECT TO FINAL EDITING

doi:10.1073/pnas.1722312115.
Byrne, M.P., A.G. Pendergrass, A.D. Rapp, and K.R. Wodzicki, 2018: Response of the Intertropical Convergence Zone to Climate Change : Location , Width and Strength Precipitation climatology. *Current Climate Change Reports*, **4(4)**, 355–370, doi:10.1007/s40641-018-0110-5.
Caballero, R. and M. Huber, 2013: State-dependent climate sensitivity in past warm climates and its implications for future climate projections. *Proceedings of the National Academy of Sciences*, doi:10.1073/pnas.1303365110.
Cai, W., T. Cowan, and M. Thatcher, 2012: Rainfall reductions over Southern Hemisphere semi-arid regions: The role of subtropical dry zone expansion. *Scientific Reports*, **2(1)**, 702, doi:10.1038/srep00702.
Cai, W., A. Purich, T. Cowan, P. van Rensch, and E. Weller, 2014: Did Climate Change–Induced Rainfall Trends Contribute to the Australian Millennium Drought? *Journal of Climate*, **27(9)**, 3145–3168, doi:10.1175/jcli-d-13-00322.1.
Cai, W. et al., 2020: Climate impacts of the El Niño–Southern Oscillation on South America. *Nature Reviews Earth & Environment*, **1(4)**, 215–231, doi:10.1038/s43017-020-0040-3.
Cai, W. et al., 2021: Opposite response of strong and moderate positive Indian Ocean Dipole to global warming. *Nature Climate Change*, **11(1)**, 27–32, doi:10.1038/s41558-020-00943-1.
Caillaud, C. et al., 2021: Modelling Mediterranean heavy precipitation events at climate scale: an object-oriented evaluation of the CNRM-AROME convection-permitting regional climate model. *Climate Dynamics*, doi:10.1007/s00382-020-05558-y.
Caillouet, L., J.-P. Vidal, E. Sauquet, A. Devers, and B. Graff, 2017: Ensemble reconstruction of spatio-temporal extreme low-flow events in France since 1871. *Hydrology and Earth System Sciences*, **21(6)**, 2923–2951, doi:10.5194/hess-21-2923-2017.
Caldwell, P.M. et al., 2019: The DOE E3SM Coupled Model Version 1: Description and Results at High Resolution. *Journal of Advances in Modeling Earth Systems*, **11(12)**, 4095–4146, doi:10.1029/2019ms001870.
Camponogara, G., M.A. Faus da Silva Dias, and G.G. Carrió, 2018: Biomass burning CCN enhance the dynamics of a mesoscale convective system over the La Plata Basin: a numerical approach. *Atmospheric Chemistry and Physics*, **18(3)**, 2081–2096, doi:10.5194/acp-18-2081-2018.
Campos, M.C. et al., 2019: A new mechanism for millennial scale positive precipitation anomalies over tropical South America. *Quaternary Science Reviews*, **225**, 105990, doi:10.1016/j.quascirev.2019.105990.
Campos Braga, R. et al., 2017: Further evidence for CCN aerosol concentrations determining the height of warm rain and ice initiation in convective clouds over the Amazon basin. *Atmospheric Chemistry and Physics*, **17(23)**, 14433–14456, doi:10.5194/acp-17-14433-2017.
Cannon, F., L.M. Carvalho, C. Jones, and B. Bookhagen, 2015: Multi-annual variations in winter westerly disturbance activity affecting the Himalaya. *Climate Dynamics*, **44(1–2)**, 441–455, doi:10.1007/s00382-014-2248-8.
Cantú, A.G. et al., 2018: Evaluating changes of biomass in global vegetation models: the role of turnover fluctuations and ENSO events. *Environmental Research Letters*, **13(7)**, 075002, doi:10.1088/1748-9326/aac63c.
Cao, G., B.R. Scanlon, D. Han, and C. Zheng, 2016: Impacts of thickening unsaturated zone on groundwater recharge in the North China Plain. *Journal of Hydrology*, **537**, 260–270, doi:10.1016/j.jhydrol.2016.03.049.
Cao, J. et al., 2020: Sources of the inter-model spread in projected global monsoon hydrological sensitivity. *Geophysical Research Letters*, **47(18)**, e2020GL089560, doi:10.1029/2020gl089560.
Cao, L., G. Bala, and K. Caldeira, 2012: Climate response to changes in atmospheric carbon dioxide and solar irradiance on the time scale of days to weeks. *Environmental Research Letters*, **7(3)**, 34015, doi:10.1088/1748-9326/7/3/034015.
Carlson, H. and R. Caballero, 2016: Enhanced MJO and transition to superrotation in warm climates. *Journal of Advances in Modeling Earth Systems*, **8(1)**, 304–318, doi:10.1002/2015ms000615.
Carmona, A.M. and G. Poveda, 2014: Detection of long-term trends in monthly hydro-climatic series of Colombia through Empirical Mode Decomposition. *Climatic Change*, **123(2)**, 301–313, doi:10.1007/s10584-013-1046-3.
Carré, M. et al., 2019: Modern drought conditions in western Sahel unprecedented in the past 1600 years. *Climate Dynamics*, **52(3)**, 1949–1964, doi:10.1007/s00382-018-4311-3.
Cassou, C. et al., 2018: Decadal Climate Variability and Predictability: Challenges and Opportunities. *Bulletin of the American Meteorological Society*, **99(3)**, 479–490, doi:10.1175/bams-d-16-0286.1.
Catalano, F., A. Alessandri, M. De Felice, Z. Zhu, and R.B. Myneni, 2016: Observationally based analysis of land-atmosphere coupling. *Earth System Dynamics*, **7(1)**, 251–266, doi:10.5194/esd-7-251-2016.
Cattiaux, J., Y. Peings, D. Saint-Martin, N. Trou-Kechout, and S.J. Vavrus, 2016: Sinuosity of midlatitude atmospheric flow in a warming world. *Geophysical Research Letters*, **43(15)**, 8259–8268, doi:10.1002/2016gl070309.
Catto, J., C. Jakob, and N. Nicholls, 2012: The influence of changes in synoptic regimes on north Australian wet season rainfall trends. *Journal of Geophysical Research*, **117**, doi:10.1029/2012jd017472.
Catto, J.L., 2016: Extratropical cyclone classification and its use in climate studies. *Reviews of Geophysics*, **54(2)**, 486–520, doi:10.1002/2016rg000519.
Catto, J.L., C. Jakob, and N. Nicholls, 2015: Can the CMIP5 models represent winter frontal precipitation? *Geophysical Research Letters*, **42(20)**, 8596–8604, doi:10.1002/2015gl066015.
Cavalcante, R.B.L., P.R.M. Pontes, P.W.M. Souza-Filho, and E.B. de Souza, 2019: Opposite Effects of Climate and

ACCEPTED VERSION SUBJECT TO FINAL EDITING

Land Use Changes on the Annual Water Balance in the Amazon Arc of Deforestation. *Water Resources Research*, **55(4)**, 3092-3106, doi:10.1029/2019wr025083.
Cavazos, T. et al., 2020: Climatic trends and regional climate models intercomparison over the CORDEX-CAM (Central America, Caribbean, and Mexico) domain. *International Journal of Climatology*, **40(3)**, 1396–1420, doi:10.1002/joc.6276.
Ceppi, P. and J.M. Gregory, 2017: Relationship of tropospheric stability to climate sensitivity and Earth's observed radiation budget. *Proceedings of the National Academy of Sciences of the United States of America*, **114(50)**, 13126–13131, doi:10.1073/pnas.1714308114.
Ceppi, P. and T.G. Shepherd, 2017: Contributions of climate feedbacks to changes in atmospheric circulation. *Journal of Climate*, **30(22)**, 9097–9118, doi:10.1175/jcli-d-17-0189.1.
Ceppi, P., G. Zappa, T.G. Shepherd, and J.M. Gregory, 2018: Fast and slow components of the extratropical atmospheric circulation response to CO2forcing. *Journal of Climate*, **31(3)**, 1091–1105, doi:10.1175/jcli-d-17-0323.1.
Chadburn, S. et al., 2015: An improved representation of physical permafrost dynamics in the JULES land-surface model. *Geoscientific Model Development*, **8(5)**, 1493–1508, doi:10.5194/gmd-8-1493-2015.
Chadwick, R. and P. Good, 2013: Understanding nonlinear tropical precipitation responses to CO2 forcing. *Geophysical Research Letters*, doi:10.1002/grl.50932.
Chadwick, R., I. Boutle, and G. Martin, 2013: Spatial patterns of precipitation change in CMIP5: Why the rich do not get richer in the tropics. *Journal of Climate*, **26(11)**, 3803–3822, doi:10.1175/jcli-d-12-00543.1.
Chadwick, R., P. Good, and K. Willett, 2016a: A simple moisture advection model of specific humidity change over land in response to SST warming. *Journal of Climate*, **29(21)**, 7613–7632, doi:10.1175/jcli-d-16-0241.1.
Chadwick, R., H. Douville, and C.B. Skinner, 2017: Timeslice experiments for understanding regional climate projections: applications to the tropical hydrological cycle and European winter circulation. *Climate Dynamics*, **49(9–10)**, 3011–3029, doi:10.1007/s00382-016-3488-6.
Chadwick, R., P. Good, T. Andrews, and G. Martin, 2014: Surface warming patterns drive tropical rainfall pattern responses to CO ₂ forcing on all timescales. *Geophysical Research Letters*, **41(2)**, 610–615, doi:10.1002/2013gl058504.
Chadwick, R., P. Good, G. Martin, and D.P. Rowell, 2016b: Large rainfall changes consistently projected over substantial areas of tropical land. *Nature Climate Change*, **6(2)**, 177–181, doi:10.1038/nclimate2805.
Chan, K.T.F., 2019: Are global tropical cyclones moving slower in a warming climate? *Environmental Research Letters*, **14(10)**, 104015, doi:10.1088/1748-9326/ab4031.
Chan, S.C., E.J. Kendon, N.M. Roberts, H.J. Fowler, and S. Blenkinsop, 2016: The characteristics of summer sub-hourly rainfall over the southern UK in a high-resolution convective permitting model. *Environmental Research Letters*, **11(9)**, 94024, doi:10.1088/1748-9326/11/9/094024.
Chan, S.C., E.J. Kendon, N. Roberts, S. Blenkinsop, and H.J. Fowler, 2018: Large-Scale Predictors for Extreme Hourly Precipitation Events in Convection-Permitting Climate Simulations. *Journal of Climate*, **31(6)**, 2115–2131, doi:10.1175/jcli-d-17-0404.1.
Chandan, D. and W.R. Peltier, 2020: African Humid Period Precipitation Sustained by Robust Vegetation, Soil, and Lake Feedbacks. *Geophysical Research Letters*, **47(21)**, e2020GL088728, doi:10.1029/2020gl088728.
Chandana, K.R., U.S. Banerji, and R. Bhushan, 2018: Review on Indian summer monsoon (ISM) reconstructions since LGM from Northern Indian Ocean. *Earth Science India*, **11**.
Chandran, A., G. Basha, and T.B.M.J. Ouarda, 2016: Influence of climate oscillations on temperature and precipitation over the United Arab Emirates. *International Journal of Climatology*, **36(1)**, 225–235, doi:10.1002/joc.4339.
Chang, E.K.M., 2018: CMIP5 projected change in Northern Hemisphere winter cyclones with associated extreme winds. *Journal of Climate*, **31(16)**, 6527–6542, doi:10.1175/jcli-d-17-0899.1.
Chang, E.K.M. and A.M.W. Yau, 2016: Northern Hemisphere winter storm track trends since 1959 derived from multiple reanalysis datasets. *Climate Dynamics*, **47(5–6)**, 1435–1454, doi:10.1007/s00382-015-2911-8.
Chang, E.K.M., Y. Guo, X. Xia, and M. Zheng, 2013: Storm-track activity in IPCC AR4/CMIP3 model simulations. *Journal of Climate*, **26(1)**, 246–260, doi:10.1175/jcli-d-11-00707.1.
Chang, E.K.M., C.G. Ma, C. Zheng, and A.M.W. Yau, 2016: Observed and projected decrease in Northern Hemisphere extratropical cyclone activity in summer and its impacts on maximum temperature. *Geophysical Research Letters*, doi:10.1002/2016gl068172.
Chang, L.L. et al., 2018: Why Do Large-Scale Land Surface Models Produce a Low Ratio of Transpiration to Evapotranspiration? *Journal of Geophysical Research: Atmospheres*, **123(17)**, 9109–9130, doi:10.1029/2018jd029159.
Charney, J.G., 1975: Dynamics of deserts and drought in the Sahel. *Quarterly Journal of the Royal Meteorological Society*, **101(428)**, 193–202.
Chauvin, F., H. Douville, and A. Ribes, 2017: Atlantic tropical cyclones water budget in observations and CNRM-CM5 model. *Climate Dynamics*, **49(11–12)**, 4009–4021, doi:10.1007/s00382-017-3559-3.
Chegwidden, O.S. et al., 2019: How Do Modeling Decisions Affect the Spread Among Hydrologic Climate Change Projections? Exploring a Large Ensemble of Simulations Across a Diversity of Hydroclimates. *Earth's Future*,

ACCEPTED VERSION SUBJECT TO FINAL EDITING

7(6), 623–637, doi:10.1029/2018ef001047.
Chemke, R. and L.M. Polvani, 2019: Exploiting the abrupt 4 × CO2 scenario to elucidate tropical expansion mechanisms. *Journal of Climate*, **32(3)**, 859–875, doi:10.1175/jcli-d-18-0330.1.
Chemke, R. and L.M. Polvani, 2020: Elucidating the mechanisms responsible for Hadley cell weakening under 4 ×CO2 forcing. *Geophysical Research Letters*, **n/a(n/a)**, e2020GL090348, doi:10.1029/2020gl090348.
Chen, D. and A. Dai, 2019: Precipitation Characteristics in the Community Atmosphere Model and Their Dependence on Model Physics and Resolution. *Journal of Advances in Modeling Earth Systems*, **11(7)**, 2352–2374, doi:10.1029/2018ms001536.
Chen, F. and Y. Gao, 2018: Evaluation of precipitation trends from high-resolution satellite precipitation products over Mainland China. *Climate Dynamics*, doi:10.1007/s00382-018-4080-z.
Chen, G. and I.M. Held, 2007: Phase speed spectra and the recent poleward shift of Southern Hemisphere surface westerlies. *Geophysical Research Letters*, doi:10.1029/2007gl031200.
Chen, G., J. Lu, and D.M.W. Frierson, 2008: Phase speed spectra and the latitude of surface westerlies: Interannual variability and global warming trend. *Journal of Climate*, doi:10.1175/2008jcli2306.1.
Chen, G., W.C. Wang, and J.P. Chen, 2018: Circulation responses to regional aerosol climate forcing in summer over East Asia. *Climate Dynamics*, **51(11–12)**, 3973–3984, doi:10.1007/s00382-018-4267-3.
Chen, H. and J. Sun, 2017: Anthropogenic warming has caused hot droughts more frequently in China. *Journal of Hydrology*, **544**, 306–318, doi:10.1016/j.jhydrol.2016.11.044.
Chen, H. et al., 2020: Impacts of land use change and climatic effects on streamflow in the Chinese Loess Plateau: A meta-analysis. *Science of the Total Environment*, **703**, 134989, doi:10.1016/j.scitotenv.2019.134989.
Chen, J. and F.P. Brissette, 2019: Reliability of climate model multi-member ensembles in estimating internal precipitation and temperature variability at the multi-decadal scale. *International Journal of Climatology*, **39(2)**, 843–856, doi:10.1002/joc.5846.
Chen, J., J. Li, Z. Zhang, and S. Ni, 2014: Long-term groundwater variations in Northwest India from satellite gravity measurements. *Global and Planetary Change*, **116**, 130–138, doi:10.1016/j.gloplacha.2014.02.007.
Chen, J., A. Dai, Y. Zhang, and K.L. Rasmussen, 2020a: Changes in Convective Available Potential Energy and Convective Inhibition under Global Warming. *Journal of Climate*, **33(6)**, 2025–2050, doi:10.1175/jcli-d-19-0461.1.
Chen, J., L. Theller, M.W. Gitau, B.A. Engel, and J.M. Harbor, 2017: Urbanization impacts on surface runoff of the contiguous United States. *Journal of Environmental Management*, **187**, 470–481, doi:10.1016/j.jenvman.2016.11.017.
Chen, J. et al., 2020b: Impacts of climate change on tropical cyclones and induced storm surges in the Pearl River Delta region using pseudo-global-warming method. *Scientific Reports*, **10**, doi:10.1038/s41598-020-58824-8.
Chen, L., X. Qu, G. Huang, and Y. Gong, 2019: Projections of East Asian summer monsoon under 1.5°C and 2°C warming goals. *Theoretical and Applied Climatology*, **137(3–4)**, 2187–2201, doi:10.1007/s00704-018-2720-1.
Chen, R., I.R. Simpson, C. Deser, and B. Wang, 2020: Model Biases in the Simulation of the Springtime North Pacific ENSO Teleconnection. *Journal of Climate*, **33(23)**, 9985–10002, doi:10.1175/jcli-d-19-1004.1.
Chen, X., S. Wang, Z. Hu, Q. Zhou, and Q. Hu, 2018: Spatiotemporal characteristics of seasonal precipitation and their relationships with ENSO in Central Asia during 1901–2013. *Journal of Geographical Sciences*, **28(9)**, 1341–1368, doi:10.1007/s11442-018-1529-2.
Chen, Y., B. Langenbrunner, and J.T. Randerson, 2018: Future drying in Central America and northern SouthAmerica linked with Atlantic meridional overturning circulation. *Geophysical Research Letters*, doi:10.1029/2018gl077953.
Chen, Z., T. Zhou, W. Zhang, P. Li, and S. Zhao, 2020a: Projected changes in the annual range of precipitation under stabilized 1.5°C and 2.0°C warming futures. *Earth's Future*, 0-2, doi:10.1029/2019ef001435.
Chen, Z. et al., 2020b: Global land monsoon precipitation changes in CMIP6 projections. *Geophysical Research Letters*, **n/a(n/a)**, e2019GL086902, doi:10.1029/2019gl086902.
Cheng, H., A. Sinha, X. Wang, F.W. Cruz, and R.L. Edwards, 2012: The Global Paleomonsoon as seen through speleothem records from Asia and the Americas. *Climate Dynamics*, **39(5)**, 1045–1062, doi:10.1007/s00382-012-1363-7.
Cheng, H. et al., 2016: The Asian monsoon over the past 640,000 years and ice age terminations. *Nature*, doi:10.1038/nature18591.
Cheng, L. et al., 2017: Recent increases in terrestrial carbon uptake at little cost to the water cycle. *Nature Communications*, **8(1)**, doi:10.1038/s41467-017-00114-5.
Chernokulsky, A. et al., 2019: Observed changes in convective and stratiform precipitation in Northern Eurasia over the last five decades. *Environmental Research Letters*, **14(4)**, 45001, doi:10.1088/1748-9326/aafb82.
Cheung, A.H. et al., 2017: Comparison of Low-Frequency Internal Climate Variability in CMIP5 Models and Observations. *Journal of Climate*, **30(12)**, 4763–4776, doi:10.1175/jcli-d-16-0712.1.
Cheung, R.C.W. et al., 2018: Decadal- to Centennial-Scale East Asian Summer Monsoon Variability Over the Past Millennium: An Oceanic Perspective. *Geophysical Research Letters*, **45(15)**, 7711–7718, doi:10.1029/2018gl077978.

ACCEPTED VERSION SUBJECT TO FINAL EDITING

Chevuturi, A., N.P. Klingaman, A.G. Turner, and S. Hannah, 2018: Projected changes in the Asian-Australian monsoon region in 1 . 5 ◦ C and. , **20**, 2018, doi:10.1002/eft2.297.
Chiang, J., C. Chang, and M. Wehner, 2013: Long-Term Behavior of the Atlantic Interhemispheric SST Gradient in the CMIP5 Historical Simulations. *Journal of Climate*, **26(21)**, 8628–8640, doi:10.1175/jcli-d-12-00487.1.
Chiang, J.C.H. and C.M. Bitz, 2005: Influence of high latitude ice cover on the marine Intertropical Convergence Zone. *Climate Dynamics*, doi:10.1007/s00382-005-0040-5.
Chiang, J.C.H. and A.R. Friedman, 2012: Extratropical Cooling, Interhemispheric Thermal Gradients, and Tropical Climate Change. *Annual Review of Earth and Planetary Sciences*, doi:10.1146/annurev-earth-042711-105545.
Choobari, O.A., P. Zawar-Reza, and A. Sturman, 2014: The global distribution of mineral dust and its impacts on the climate system: A review. *Atmospheric Research*, doi:10.1016/j.atmosres.2013.11.007.
Chou, C., C.A. Chen, P.H. Tan, and K.T. Chen, 2012: Mechanisms for global warming impacts on precipitation frequency and intensity. *Journal of Climate*, doi:10.1175/jcli-d-11-00239.1.
Chou, C. et al., 2013: Increase in the range between wet and dry season precipitation. *Nature Geoscience*, **6(4)**, 263–267, doi:10.1038/ngeo1744.
Chou, S.C. et al., 2014: Assessment of Climate Change over South America under RCP 4.5 and 8.5 Downscaling Scenarios. *American Journal of Climate Change*, doi:10.4236/ajcc.2014.35043.
Choudhury, A.D. et al., 2018: A Phenomenological Paradigm for Midtropospheric Cyclogenesis in the Indian Summer Monsoon. *Journal of the Atmospheric Sciences*, **75(9)**, 2931–2954, doi:10.1175/jas-d-17-0356.1.
Christensen, J.H. et al., 2013: Climate Phenomena and their Relevance for Future Regional Climate Change. In: *Climate Change 2013: The Physical Science Basis. Contribution of Working Group I to the Fifth Assessment Report of the Intergovernmental Panel on Climate Change* [Stocker, T.F., D. Qin, G.-K. Plattner, M. Tignor, S.K. Allen, J. Boschung, A. Nauels, Y. Xia, V. Bex, and P.M. Midgley (eds.)]. Cambridge University Press, Cambridge, United Kingdom and New York, NY, USA, pp. 1217–1308, doi:10.1017/cbo9781107415324.028.
Chua, X.R. and Y. Ming, 2020: Convective invigoration traced to warm-rain microphysics. *Geophysical Research Letters*, **n/a(n/a)**, e2020GL089134, doi:10.1029/2020gl089134.
Chung, C.T.Y., S.B. Power, J.M. Arblaster, H.A. Rashid, and G.L. Roff, 2014: Nonlinear precipitation response to El Niño and global warming in the Indo-Pacific. *Climate Dynamics*, **42(7–8)**, 1837–1856, doi:10.1007/s00382-013-1892-8.
Chung, E.S. and B.J. Soden, 2017: Hemispheric climate shifts driven by anthropogenic aerosol-cloud interactions. *Nature Geoscience*, **10(8)**, 566–571, doi:10.1038/ngeo2988.
Chung, E.S., B. Soden, B.J. Sohn, and L. Shi, 2014: Upper-tropospheric moistening in response to anthropogenic warming. *Proceedings of the National Academy of Sciences of the United States of America*, **111(32)**, 11636–11641, doi:10.1073/pnas.1409659111.
Chung, E.-S. et al., 2019: Reconciling opposing Walker circulation trends in observations and model projections. *Nature Climate Change*, **9(5)**, 405–412, doi:10.1038/s41558-019-0446-4.
Ciasto, L.M., C. Li, J.J. Wettstein, and N.G. Kvamstø, 2016: North Atlantic Storm-Track Sensitivity to Projected Sea Surface Temperature: Local versus Remote Influences. *Journal of Climate*, **29(19)**, 6973–6991, doi:10.1175/jcli-d-15-0860.1.
Cisneros, J. et al., 2014: Freshwater Resources. In: *Climate Change 2014: Impacts, Adaptation, and Vulnerability. Part A: Global and Sectoral Aspects. Contribution of Working Group II to the Fifth Assessment Report of the Intergovernmental Panel on Climate* []. Cambridge University Press, Cambridge, United Kingdom and New York, NY, USA, pp. 229–270, doi:10.1017/cbo9781107415379.008.
Clark, P.U., J.A. Church, J.M. Gregory, and A.J. Payne, 2015: Recent Progress in Understanding and Projecting Regional and Global Mean Sea Level Change. *Current Climate Change Reports*, **1(4)**, 224–246, doi:10.1007/s40641-015-0024-4.
Clark, S., M.J. Reeder, and C. Jakob, 2018: Rainfall regimes over northwestern Australia. , doi:10.1002/qj.3217.
Claussen, M., S. Bathiany, V. Brovkin, and T. Kleinen, 2013: Simulated climate-vegetation interaction in semi-arid regions affected by plant diversity. *Nature Geoscience*, **6**, 954–958, doi:10.1038/ngeo1962.
Claussen, M., V. Brovkin, A. Ganopolski, C. Kubatzki, and V. Petoukhov, 2003: Climate change in northern Africa: The past is not the future. *Climatic Change*, **57**, 99–118, doi:10.1023/a:1022115604225.
Coats, S. and K.B. Karnauskas, 2017: Are Simulated and Observed Twentieth Century Tropical Pacific Sea Surface Temperature Trends Significant Relative to Internal Variability? *Geophysical Research Letters*, **44**, 9928–9937, doi:10.1002/2017gl074622.
Coats, S., J.E. Smerdon, B.I. Cook, and R. Seager, 2015: Are Simulated Megadroughts in the North American Southwest Forced? *Journal of Climate*, **28(1)**, 124–142, doi:10.1175/jcli-d-14-00071.1.
Coats, S. et al., 2016: Internal ocean-atmosphere variability drives megadroughts in Western North America. *Geophysical Research Letters*, **43(18)**, 9886–9894, doi:10.1002/2016gl070105.
Colle, B.A., J.F. Booth, and E.K.M. Chang, 2015: A Review of Historical and Future Changes of Extratropical Cyclones and Associated Impacts Along the US East Coast. Curr. Clim. Change Rep. , **1(125)**, 13–17.
Collins, M. et al., 2013: Long-term Climate Change: Projections, Commitments and Irreversibility. In: *Climate Change 2013: The Physical Science Basis. Contribution of Working Group I to the Fifth Assessment Report of the*

ACCEPTED VERSION SUBJECT TO FINAL EDITING

Intergovernmental Panel on Climate Change [Stocker, T.F., D. Qin, G.-K. Plattner, M. Tignor, S.K. Allen, J. Boschung, A. Nauels, Y. Xia, V. Bex, and P.M. Midgley (eds.)]. Cambridge University Press, Cambridge, United Kingdom and New York, NY, USA, pp. 1029–1136, doi:10.1017/cbo9781107415324.024.

Collins, S., 2017: Incorporating groundwater flow in land surface models: literature review and recommendations for further work. *British Geological Survey Open Report, OR/*, **68**, 23.

Colonia, D. et al., 2017: Compiling an Inventory of Glacier-Bed Overdeepenings and Potential New Lakes in De-Glaciating Areas of the Peruvian Andes: Approach, First Results, and Perspectives for Adaptation to Climate Change. *Water*, **9(5)**, 336, doi:10.3390/w9050336.

Colose, C.M., A.N. LeGrande, and M. Vuille, 2016: Hemispherically asymmetric volcanic forcing of tropical hydroclimate during the last millennium. *Earth System Dynamics*, **7(3)**, 681–696, doi:10.5194/esd-7-681-2016.

Comas-Bru, L. and F. McDermott, 2014: Impacts of the EA and SCA patterns on the European twentieth century NAO-winter climate relationship. *Quarterly Journal of the Royal Meteorological Society*, **140(679)**, 354–363, doi:10.1002/qj.2158.

Comte, J.-C. et al., 2016: Challenges in groundwater resource management in coastal aquifers of East Africa: Investigations and lessons learnt in the Comoros Islands, Kenya and Tanzania. *Journal of Hydrology: Regional Studies*, **5**, 179–199, doi:10.1016/j.ejrh.2015.12.065.

Condon, L.E., A.L. Atchley, and R.M. Maxwell, 2020: Evapotranspiration depletes groundwater under warming over the contiguous United States. *Nature Communications*, **11(1)**, doi:10.1038/s41467-020-14688-0.

Conway, D., E. Allison, R. Felstead, and M. Goulden, 2005: Rainfall variability in East Africa: implications for natural resources management and livelihoods. *Philosophical Transactions of the Royal Society A: Mathematical, Physical and Engineering Sciences*, **363(1826)**, 49–54, doi:10.1098/rsta.2004.1475.

Cook, B.I. and R. Seager, 2013: The response of the North American Monsoon to increased greenhouse gas forcing. *Journal of Geophysical Research: Atmospheres*, **118(4)**, 1690–1699, doi:10.1002/jgrd.50111.

Cook, B.I., R.L. Miller, and R. Seager, 2009: Amplification of the North American "Dust Bowl" drought through human-induced land degradation. *Proceedings of the National Academy of Sciences*, doi:10.1073/pnas.0810200106.

Cook, B.I., T.R. Ault, and J.E. Smerdon, 2015: Unprecedented 21st century drought risk in the American Southwest and Central Plains. *Science Advances*, **1(1)**, e1400082.

Cook, B.I., J.S. Mankin, and K.J. Anchukaitis, 2018: Climate Change and Drought: From Past to Future. *Current Climate Change Reports*, **4(2)**, 164–179, doi:10.1007/s40641-018-0093-2.

Cook, B.I., R. Seager, R.L. Miller, and J.A. Mason, 2013: Intensification of north american megadroughts through surface and dust aerosol forcing. *Journal of Climate*, doi:10.1175/jcli-d-12-00022.1.

Cook, B.I., J.E. Smerdon, R. Seager, and S. Coats, 2014: Global warming and 21stcentury drying. *Climate Dynamics*, **43(9–10)**, 2607–2627, doi:10.1007/s00382-014-2075-y.

Cook, B.I., K.J. Anchukaitis, R. Touchan, D.M. Meko, and E.R. Cook, 2016a: Spatiotemporal drought variability in the mediterranean over the last 900 years. *Journal of Geophysical Research*, doi:10.1002/2015jd023929.

Cook, B.I. et al., 2016b: North American megadroughts in the Common Era: reconstructions and simulations. *Wiley Interdisciplinary Reviews: Climate Change*, **7(3)**, 411–432, doi:10.1002/wcc.394.

Cook, B.I. et al., 2016c: The paleoclimate context and future trajectory of extreme summer hydroclimate in eastern Australia. *Journal of Geophysical Research: Atmospheres*, **121(21)**, 12,812–820,838, doi:10.1002/2016jd024892.

Cook, B.I. et al., 2019: Climate Change Amplification of Natural Drought Variability: The Historic Mid-Twentieth Century North American Drought In a Warmer World. *Journal of Climate*, **32(17)**, Article, doi:10.1175/jcli-d-18-0832.1.

Cook, B.I. et al., 2020: Twenty-first Century Drought Projections in the CMIP6 Forcing Scenarios. *Earth's Future*, **8**, e2019EF001461.

Cook, E.R., C.A. Woodhouse, C.M. Eakin, D.H. Meko, and D.W. Stahle, 2004: Long-term aridity changes in the western United States. *Science*, doi:10.1126/science.1102586.

Cook, E.R. et al., 2010: Megadroughts in North America: Placing IPCC projections of hydroclimatic change in a long-term palaeoclimate context. *Journal of Quaternary Science*, doi:10.1002/jqs.1303.

Cook, E.R. et al., 2015: Old World megadroughts and pluvials during the Common Era. *Science Advances*, doi:10.1126/sciadv.1500561.

Cook, K.H. and E.K. Vizy, 2012: Impact of climate change on mid-twenty-first century growing seasons in Africa. *Climate Dynamics*, **39(12)**, 2937–2955, doi:10.1007/s00382-012-1324-1.

Cook, K.H., E.K. Vizy, K.H. Cook, and E.K. Vizy, 2015: Detection and analysis of an amplified warming of the Sahara Desert. *Journal of Climate*, **28(16)**, 6560–6580, doi:10.1175/jcli-d-14-00230.1.

Corona, R., N. Montaldo, and J.D. Albertson, 2018: On the Role of NAO-Driven Interannual Variability in Rainfall Seasonality on Water Resources and Hydrologic Design in a Typical Mediterranean Basin. *Journal of Hydrometeorology*, **19(3)**, 485–498, doi:10.1175/jhm-d-17-0078.1.

Correa, I., P.A. Arias, and M. Rojas, 2021: Evaluation of multiple indices of the South American monsoon. *International Journal of Climatology*, **41**, E2801–E2819, doi: 10.1002/joc.6880.

ACCEPTED VERSION SUBJECT TO FINAL EDITING

Corvec, S. and C.G. Fletcher, 2017: Changes to the tropical circulation in the mid-Pliocene and their implications for future climate. *Climate of the Past*, doi:10.5194/cp-13-135-2017.
Costantino, L. and F.-M. Bréon, 2010: Analysis of aerosol-cloud interaction from multi-sensor satellite observations. *Geophysical Research Letters*, **37(11)**, n/a–n/a, doi:10.1029/2009gl041828.
Coumou, D., J. Lehmann, and J. Beckmann, 2015: The weakening summer circulation in the Northern Hemisphere mid-latitudes. *Science*, **348(6232)**, 324–327, doi:10.1126/science.1261768.
Coumou, D., V. Petoukhov, S. Rahmstorf, S. Petri, and H.J. Schellnhuber, 2014: Quasi-resonant circulation regimes and hemispheric synchronization of extreme weather in boreal summer. *Proceedings of the National Academy of Sciences of the United States of America*, **111(34)**, 12331–12336, doi:10.1073/pnas.1412797111.
Couvreux, F. et al., 2015: Representation of daytime moist convection over the semi-arid Tropics by parametrizations used in climate and meteorological models. *Quarterly Journal of the Royal Meteorological Society*, **141(691)**, 2220–2236, doi:10.1002/qj.2517.
Cowan, T. et al., 2020: Ocean and land forcing of the record-breaking Dust Bowl heatwaves across central United States. *Nature Communications*, doi:10.1038/s41467-020-16676-w.
Cox, P.M. et al., 2004: Amazonian forest dieback under climate-carbon cycle projections for the 21st century. *Theoretical and Applied Climatology*, doi:10.1007/s00704-004-0049-4.
Creamean, J.M. et al., 2013: Dust and biological aerosols from the Sahara and Asia influence precipitation in the Western U.S. *Science*, **340(6127)**, doi:10.1126/science.1227279.
Crook, J.A., L.S. Jackson, S.M. Osprey, and P.M. Forster, 2015: A comparison of temperature and precipitation responses to different earth radiation management geoengineering schemes. *Journal of Geophysical Research*, doi:10.1002/2015jd023269.
Cruz, F.W. et al., 2005: Insolation-driven changes in atmospheric circulation over the past 116,000 years in subtropical Brazil. *Nature*, doi:10.1038/nature03365.
CSIRO and Bureau of Meteorology, 2015: Climate Change in Australia Information for Australia's Natural Resource Management Regions: Technical Report. .
Cui, J., L. Wang, T. Li, and B. Wu, 2020: Can reanalysis products with only surface variables assimilated capture Madden–Julian oscillation characteristics? *International Journal of Climatology*, **40(2)**, 1279–1293, doi:10.1002/joc.6270.
Cui, W., X. Dong, B. Xi, and A. Kennedy, 2017: Evaluation of Reanalyzed Precipitation Variability and Trends Using the Gridded Gauge-Based Analysis over the CONUS. *Journal of Hydrometeorology*, doi:10.1175/jhm-d-17-0029.1.
Cuthbert, M.O. et al., 2019a: Global patterns and dynamics of climate–groundwater interactions. *Nature Climate Change*, doi:10.1038/s41558-018-0386-4.
Cuthbert, M.O. et al., 2019b: Observed controls on resilience of groundwater to climate variability in sub-Saharan Africa. *Nature*, **572(7768)**, 230–234, doi:10.1038/s41586-019-1441-7.
D'Agostino, R. and P. Lionello, 2017: Evidence of global warming impact on the evolution of the Hadley Circulation in ECMWF centennial reanalyses. *Climate Dynamics*, **48(9–10)**, 3047–3060, doi:10.1007/s00382-016-3250-0.
D'Agostino, R., P. Lionello, O. Adam, and T. Schneider, 2017: Factors controlling Hadley circulation changes from the Last Glacial Maximum to the end of the 21st century. *Geophysical Research Letters*, doi:10.1002/2017gl074533.
D'Agostino, R., A.L. Scambiati, J. Jungclaus, and P. Lionello, 2020a: Poleward Shift of Northern Subtropics in winter: Time of Emergence of Zonal versus Regional Signals. *Geophysical Research Letters*, **n/a(n/a)**, e2020GL089325, doi:10.1029/2020gl089325.
D'Agostino, R. et al., 2019: Northern Hemisphere monsoon response to mid-Holocene orbital forcing and greenhouse gas-induced global warming. *Geophysical Research Letters*, 1591–1601, doi:10.1029/2018gl081589.
D'Agostino, R. et al., 2020b: Contrasting Southern Hemisphere monsoon response: midHolocene orbital forcing versus future greenhouse-gas induced global warming. *Journal of Climate*, 1–56, doi:10.1175/jcli-d-19-0672.1.
D'Errico, M. et al., 2015: Indian monsoon and the elevated-heat-pump mechanism in a coupled aerosol-climate model. *Journal of Geophysical Research: Atmospheres*, **120(17)**, 8712–8723, doi:10.1002/2015jd023346.
D'Odorico, P. et al., 2018: The Global Food-Energy-Water Nexus. *Reviews of Geophysics*, **56(3)**, 1–76, doi:10.1029/2017rg000591.
Dacre, H.F., O. Martínez-Alvarado, and C.O. Mbengue, 2019: Linking atmospheric rivers and warm conveyor belt airflows. *Journal of Hydrometeorology*, JHM–D–18–0175.1, doi:10.1175/jhm-d-18-0175.1.
Dagan, G. and P. Stier, 2020: Constraint on precipitation response to climate change by combination of atmospheric energy and water budgets. *npj Climate and Atmospheric Science*, **3(1)**, 34, doi:10.1038/s41612-020-00137-8.
Dagan, G., P. Stier, and D. Watson-Parris, 2019a: Analysis of the atmospheric water budget for elucidating the spatial scale of precipitation changes under climate change. *Geophysical Research Letters*, 2019GL084173, doi:10.1029/2019gl084173.
Dagan, G., P. Stier, and D. Watson-Parris, 2019b: Contrasting response of precipitation to aerosol perturbation in the tropics and extra-tropics explained by energy budget considerations. *Geophysical Research Letters*, 2019GL083479, doi:10.1029/2019gl083479.

ACCEPTED VERSION SUBJECT TO FINAL EDITING

Dagan, G., I. Koren, O. Altaratz, and R.H. Heiblum, 2017: Time-dependent, non-monotonic response of warm convective cloud fields to changes in aerosol loading. *Atmospheric Chemistry and Physics*, **17(12)**, 7435–7444, doi:10.5194/acp-17-7435-2017.

Dagon, K. and D.P. Schrag, 2016: Exploring the effects of solar radiation management on water cycling in a coupled land-atmosphere model. *Journal of Climate*, **29(7)**, 2635–2650, doi:10.1175/jcli-d-15-0472.1.

Dai, A., 2016: Historical and Future Changes in Streamflow and Continental Runoff. In: *Terrestrial Water Cycle and Climate Change* [Tang, Q. and T. Oki (eds.)]. American Geophysical Union (AGU), pp. 17–37, doi:10.1002/9781118971772.ch2.

Dai, A., 2021: Hydroclimatic trends during 1950–2018 over global land. *Climate Dynamics*, doi:10.1007/s00382-021-05684-1.

Dai, A. and C.E. Bloecker, 2019: Impacts of internal variability on temperature and precipitation trends in large ensemble simulations by two climate models. *Climate Dynamics*, **52(1–2)**, 289–306, doi:10.1007/s00382-018-4132-4.

Dai, A., T. Zhao, and J. Chen, 2018: Climate Change and Drought: a Precipitation and Evaporation Perspective. *Current climate change reports*, **4(3)**, 301–312.

Dallmeyer, A., M. Claussen, S.J. Lorenz, and T. Shanahan, 2020: The end of the African humid period as seen by a transient comprehensive Earth system model simulation of the last 8000 years. *Climate of the Past*, **16(1)**, 117–140, doi:10.5194/cp-16-117-2020.

Danabasoglu, G. et al., 2020: The Community Earth System Model Version 2 (CESM2). *Journal of Advances in Modeling Earth Systems*, **12(2)**, 1–35, doi:10.1029/2019ms001916.

Davidson, N.C., 2014: How much wetland has the world lost? Long-term and recent trends in global wetland area. *Marine and Freshwater Research*, **65(10)**, 934, doi:10.1071/mf14173.

Davidson, N.C., E. Fluet-Chouinard, and C.M. Finlayson, 2018: Global extent and distribution of wetlands: trends and issues. Marine and Freshwater Research. *Marine and Freshwater Research*, **69(4)**, 620–627, doi:10.1071/mf17019.

Davie, J.C.S. et al., 2013: Comparing projections of future changes in runoff from hydrological and biome models in ISI-MIP. *Earth System Dynamics*, **4(2)**, 359–374, doi:10.5194/esd-4-359-2013.

Davini, P. and F. D'Andrea, 2016: Northern Hemisphere atmospheric blocking representation in global climate models: Twenty years of improvements? *Journal of Climate*, **29(24)**, 8823–8840, doi:10.1175/jcli-d-16-0242.1.

Davini, P. and F. D'Andrea, 2020: From CMIP3 to CMIP6: Northern Hemisphere Atmospheric Blocking Simulation in Present and Future Climate. *Journal of Climate*, **33(23)**, 10021–10038, doi:10.1175/jcli-d-19-0862.1.

Davini, P., S. Corti, F. D'Andrea, G. Rivière, and J. von Hardenberg, 2017: Improved Winter European Atmospheric Blocking Frequencies in High-Resolution Global Climate Simulations. *Journal of Advances in Modeling Earth Systems*, **9(7)**, 2615–2634, doi:10.1002/2017ms001082.

Davis, N.A., D.J. Seidel, T. Birner, S.M. Davis, and S. Tilmes, 2016: Changes in the width of the tropical belt due to simple radiative forcing changes in the GeoMIP simulations. *Atmospheric Chemistry and Physics*, **16(15)**, 10083–10095, doi:10.5194/acp-16-10083-2016.

Day, J.A., I. Fung, and W. Liu, 2018: Changing character of rainfall in eastern China, 1951-2007.. *Proceedings of the National Academy of Sciences of the United States of America*, **115(9)**, 2016–2021, doi:10.1073/pnas.1715386115.

de Graaf, I.E.M., T. Gleeson, L.P.H. (Rens) van Beek, E.H. Sutanudjaja, and M.F.P. Bierkens, 2019: Environmental flow limits to global groundwater pumping. *Nature*, **574(7776)**, 90–94, doi:10.1038/s41586-019-1594-4.

de Graaf, I.E.M. et al., 2017: A global-scale two-layer transient groundwater model: Development and application to groundwater depletion. *Advances in Water Resources*, **102**, 53–67, doi:10.1016/j.advwatres.2017.01.011.

De Kauwe, M.G. et al., 2013: Forest water use and water use efficiency at elevated CO2: A model-data intercomparison at two contrasting temperate forest FACE sites. *Global Change Biology*, doi:10.1111/gcb.12164.

De Vrese, P., S. Hagemann, and M. Claussen, 2016: Asian irrigation, African rain: Remote impacts of irrigation. *Geophysical Research Letters*, **43(8)**, 3737–3745, doi:10.1002/2016gl068146.

DeAngelis, A.M., X. Qu, and A. Hall, 2016: Importance of vegetation processes for model spread in the fast precipitation response to CO2forcing. *Geophysical Research Letters*, **43(24)**, 12,550–12,559, doi:10.1002/2016gl071392.

DeAngelis, A.M., X. Qu, M.D. Zelinka, and A. Hall, 2015: An observational radiative constraint on hydrologic cycle intensification. *Nature*, **528(7581)**, 249–253, doi:10.1038/nature15770.

DeBeer, C.M., H.S. Wheater, S.K. Carey, and K.P. Chun, 2016: Recent climatic, cryospheric, and hydrological changes over the interior of western Canada: a review and synthesis. *Hydrology and Earth System Sciences*, **20(4)**, 1573–1598, doi:10.5194/hess-20-1573-2016.

Debortoli, N. et al., 2015: Rainfall Patterns in the Southern Amazon: a chronological perspective (1970-2010). *Climatic Change*, **130**, 1573–1480, doi: 10.1007/s10584-015-1415-1.

Debortoli, N.S. et al., 2016: Detecting deforestation impacts in Southern Amazonia rainfall using rain gauges. *International Journal of Climatology*, **37(6)**, 2889–2900, doi:10.1002/joc.4886.

Decharme, B. et al., 2012: Global off-line evaluation of the ISBA-TRIP flood model. *Climate Dynamics*, **38(7–8)**,

ACCEPTED VERSION SUBJECT TO FINAL EDITING

1389–1412, doi:10.1007/s00382-011-1054-9.
Decharme, B. et al., 2016: Impacts of snow and organic soils parameterization on northern Eurasian soil temperature profiles simulated by the ISBA land surface model. *Cryosphere*, **10(2)**, 853–877, doi:10.5194/tc-10-853-2016.
Decharme, B. et al., 2019: Recent Changes in the ISBA-CTRIP Land Surface System for Use in the CNRM-CM6 Climate Model and in Global Off-Line Hydrological Applications. *Journal of Advances in Modeling Earth Systems*, **11(5)**, 1207–1252, doi:10.1029/2018ms001545.
Dee, S.G. et al., 2017: Improved spectral comparisons of paleoclimate models and observations via proxy system modeling: Implications for multi-decadal variability. *Earth and Planetary Science Letters*, doi:10.1016/j.epsl.2017.07.036.
Dee, S.G. et al., 2020: No consistent ENSO response to volcanic forcing over the last millennium. *Science*, doi:10.1126/science.aax2000.
Defrance, D. et al., 2017: Consequences of rapid ice sheet melting on the Sahelian population vulnerability. *Proceedings of the National Academy of Sciences*, doi:10.1073/pnas.1619358114.
Deitch, M.J., M.J. Sapundjieff, and S.T. Feirer, 2017: Characterizing precipitation variability and trends in the world's mediterranean-climate areas. *Water (Switzerland)*, **9(4)**, 1–21, doi:10.3390/w9040259.
Delworth, T.L. and F. Zeng, 2014: Regional rainfall decline in Australia attributed to anthropogenic greenhouse gases and ozone levels. *Nature Geoscience*, doi:10.1038/ngeo2201.
Demaria, E.M.C. et al., 2019: Intensification of the North American Monsoon Rainfall as Observed From a Long-Term High-Density Gauge Network. *Geophysical Research Letters*, **46(12)**, 6839–6847, doi:10.1029/2019gl082461.
deMenocal, P.B. and J.E. Tierney, 2012: Green Sahara: African humid periods paced by Earth's orbital changes. *Nature Education Knowledge*, **3(10)**, 12.
Demory, M.E. et al., 2014: The role of horizontal resolution in simulating drivers of the global hydrological cycle. *Climate Dynamics*, **42(7–8)**, 2201–2225, doi:10.1007/s00382-013-1924-4.
DeMott, C.A. et al., 2019: The Convection Connection: How Ocean Feedbacks Affect Tropical Mean Moisture and MJO Propagation. *Journal of Geophysical Research: Atmospheres*, **124(22)**, 11910–11931, doi:10.1029/2019jd031015.
DeMott, P.J. et al., 2010: Predicting global atmospheric ice nuclei distributions and their impacts on climate.. *Proceedings of the National Academy of Sciences of the United States of America*, **107(25)**, 11217–22, doi:10.1073/pnas.0910818107.
DeMott, P.J. et al., 2016: Sea spray aerosol as a unique source of ice nucleating particles. *Proceedings of the National Academy of Sciences of the United States of America*, **113(21)**, 5797–5803, doi:10.1073/pnas.1514034112.
Deng, H., N.C. Pepin, and Y. Chen, 2017: Changes of snowfall under warming in the Tibetan Plateau. *Journal of Geophysical Research: Atmospheres*, **122(14)**, 7323–7341, doi:10.1002/2017jd026524.
Deng, K., S. Yang, M. Ting, Y. Tan, and S. He, 2018: Global Monsoon Precipitation: Trends, Leading Modes, and Associated Drought and Heat Wave in the Northern Hemisphere. *Journal of Climate*, **31(17)**, 6947–6966, doi:10.1175/jcli-d-17-0569.1.
Deng, S., C. Sheng, N. Yang, L. Song, and Q. Huang, 2020: Anthropogenic forcing enhances rainfall seasonality in global land monsoon regions. *Environmental Research Letters*, **15(10)**, 104057, doi:10.1088/1748-9326/abafd3.
Deng, S. et al., 2019: Rainfall seasonality changes and its possible teleconnections with global climate events in China. *Climate Dynamics*, **53(5)**, 3529–3546, doi:10.1007/s00382-019-04722-3.
Dennison, F.W., A. McDonald, and O. Morgenstern, 2016: The influence of ozone forcing on blocking in the Southern Hemisphere. *Journal of Geophysical Research: Atmospheres*, **121(24)**, 14,314–358,371, doi:10.1002/2016jd025033.
Denniston, R.F. et al., 2016: Expansion and contraction of the indo-pacific tropical rain belt over the last three millennia. *Scientific Reports*, **6**, 34485, doi:10.1038/srep34485.
Deryng, D. et al., 2016: Regional disparities in the beneficial effects of rising CO2 concentrations on crop water productivity. *Nature Climate Change*, **6(8)**, 786–790, doi:10.1038/nclimate2995.
Descroix, L. et al., 2013: Évolution des pluies de cumul élevé et recrudescence des crues depuis 1951 dans le bassin du Niger moyen (Sahel). *Climatologie*, **10**, 37–49, doi:10.4267/climatologie.78.
Descroix, L. et al., 2015: Évolution récente de la pluviométrie en Afrique de l'ouest à travers deux régions : la Sénégambie et le bassin du Niger moyen. *Climatologie*, **12**, 25–43, doi:10.4267/climatologie.1105.
Descroix, L. et al., 2018: Evolution of Surface Hydrology in the Sahelo-Sudanian Strip: An Updated Review. *Water*, **10(6)**, 748, doi:10.3390/w10060748.
Deser, C., J.W. Hurrell, and A.S. Phillips, 2017: The role of the North Atlantic Oscillation in European climate projections. *Climate Dynamics*, **49(9–10)**, 3141–3157, doi:10.1007/s00382-016-3502-z.
Deser, C., A. Phillips, V. Bourdette, and H. Teng, 2012: Uncertainty in climate change projections: the role of internal variability. *Climate Dynamics*, **38(3–4)**, 527–546, doi:10.1007/s00382-010-0977-x.
Deser, C., I.R. Simpson, A.S. Phillips, and K.A. McKinnon, 2018: How Well Do We Know ENSO's Climate Impacts over North America, and How Do We Evaluate Models Accordingly? *Journal of Climate*, **31(13)**, 4991–5014, doi:10.1175/jcli-d-17-0783.1.

ACCEPTED VERSION SUBJECT TO FINAL EDITING

Devers, A., J.-P. Vidal, C. Lauvernet, B. Graff, and O. Vannier, 2020: A framework for high-resolution meteorological surface reanalysis through offline data assimilation in an ensemble of downscaled reconstructions. *Quarterly Journal of the Royal Meteorological Society*, **146(726)**, 153–173, doi:10.1002/qj.3663.

Dey, R., S.C. Lewis, and A. N. J., 2018: Investigating observed northwest Australian rainfall trends in Coupled Model Intercomparison Project phase 5 detection and attribution experiments. *International Journal of Climatology*, **10(1002)**, 1–16.

Dey, R., S.C. Lewis, and N.J. Abram, 2019a: Investigating observed northwest Australian rainfall trends in Coupled Model Intercomparison Project phase 5 detection and attribution experiments. *International Journal of Climatology*, **39(1)**, 112–127, doi:10.1002/joc.5788.

Dey, R., S.C. Lewis, J.M. Arblaster, and N.J. Abram, 2019b: A review of past and projected changes in Australia's rainfall. *WIREs Climate Change*, **10(3)**, e577, doi:10.1002/wcc.577.

Di Baldassarre, G. et al., 2018: Water shortages worsened by reservoir effects. *Nature Sustainability*, **1(11)**, 617–622.

Di Capua, G. et al., 2020: Tropical and mid-latitude teleconnections interacting with the Indian summer monsoon rainfall: a theory-guided causal effect network approach. *Earth System Dynamics*, **11(1)**, 17–34, doi:10.5194/esd-11-17-2020.

Di Luca, A., R. de Elía, and R. Laprise, 2015: Challenges in the Quest for Added Value of Regional Climate Dynamical Downscaling. *Current Climate Change Reports*, **1(1)**, 10–21, doi:10.1007/s40641-015-0003-9.

Di Virgilio, G. et al., 2020: Realised added value in dynamical downscaling of Australian climate change. *Climate Dynamics*, **54(11–12)**, 4675–4692, doi:10.1007/s00382-020-05250-1.

Diakhate et al, M., 2019: Oceanic Forcing on Interannual Variability of Sahel Heavy and Moderate Daily Rainfall. , 397–410, doi:10.1175/jhm-d-18-0035.1.

Diallo, I. et al., 2016: Projected changes of summer monsoon extremes and hydroclimatic regimes over West Africa for the twenty-first century. *Climate Dynamics*, **47(12)**, 3931–3954, doi:10.1007/s00382-016-3052-4.

Diatta, S. and A.H. Fink, 2014: Statistical relationship between remote climate indices and West African monsoon variability. *International Journal of Climatology*, **34(12)**, 3348–3367, doi:10.1002/joc.3912.

Díaz, L.B. and C.S. Vera, 2017: Austral summer precipitation interannual variability and trends over Southeastern South America in CMIP5 models. *Internatio*, 1–15, doi:10.1002/joc.5031.

Díaz, L.B. and C.S. Vera, 2018: South American precipitation changes simulated by PMIP3/CMIP5 models during the Little Ice Age and the recent global warming period. *International Journal of Climatology*, **38(6)**, 2638–2650, doi:10.1002/joc.5449.

Diem, J.E., 2013: Influences of the Bermuda High and atmospheric moistening on changes in summer rainfall in the Atlanta, Georgia region, USA. *International Journal of Climatology*, **33(1)**, 160–172, doi:10.1002/joc.3421.

Diem, J.E., D.P. Brown, and J. McCann, 2013: Multi-decadal changes in the North American monsoon anticyclone. *International Journal of Climatology*, **33(9)**, 2274–2279, doi:10.1002/joc.3576.

Dierauer, J.R., P.H. Whitfield, and D.M. Allen, 2018: Climate Controls on Runoff and Low Flows in Mountain Catchments of Western North America. *Water Resources Research*, **54(10)**, 7495–7510, doi:10.1029/2018wr023087.

Dijk, J. et al., 2020: Spatial pattern of super-greenhouse warmth controlled by elevated specific humidity. *Nature Geoscience*, **13(11)**, 739–744, doi:10.1038/s41561-020-00648-2.

Dimri, A.P. et al., 2015: Western Disturbances: A review. *Reviews of Geophysics*, **53(2)**, 225–246, doi:10.1002/2014rg000460.

DiNezio, P.N. and J.E. Tierney, 2013: The effect of sea level on glacial Indo-Pacific climate. *Nature Geoscience*, **6(6)**, 485–491, doi:10.1038/ngeo1823.

DiNezio, P.N. et al., 2011: The response of the Walker circulation to Last Glacial Maximum forcing: Implications for detection in proxies. *Paleoceanography*, **26(3)**, doi:10.1029/2010pa002083.

DiNezio, P.N. et al., 2018: Glacial changes in tropical climate amplified by the Indian Ocean. *Science Advances*, **4(12)**, eaat9658.

Dirmeyer, P.A. and S. Halder, 2017: Application of the Land–Atmosphere Coupling Paradigm to the Operational Coupled Forecast System, Version 2 (CFSv2). *Journal of Hydrometeorology*, **18**, 85.

Dirmeyer, P.A. et al., 2018: Verification of Land–Atmosphere Coupling in Forecast Models, Reanalyses, and Land Surface Models Using Flux Site Observations. *Journal of Hydrometeorology*, **19**, 375.

Dixit, V., O. Geoffroy, and S.C. Sherwood, 2018: Control of ITCZ Width by Low-Level Radiative Heating From Upper-Level Clouds in Aquaplanet Simulations. *Geophys Res Lett*, **10(1029)**, 5788–5797, doi:10.1029/2018gl078292.

Djehdian, L.A., C.M. Chini, L. Marston, M. Konar, and A.S. Stillwell, 2019: Exposure of urban food–energy–water (FEW) systems to water scarcity. *Sustainable Cities and Society*, **50**, 101621, doi:10.1016/j.scs.2019.101621.

Döll, P., 2009: Vulnerability to the impact of climate change on renewable groundwater resources: A global-scale assessment. *Environmental Research Letters*, **4(3)**, 035006, doi:10.1088/1748-9326/4/3/035006.

Döll, P. et al., 2012: Impact of water withdrawals from groundwater and surface water on continental water storage variations. *Journal of Geodynamics*, **59**, 143–156.

Döll, P. et al., 2014: Global-scale assessment of groundwater depletion and related groundwater abstractions:

ACCEPTED VERSION SUBJECT TO FINAL EDITING

Combining hydrological modeling with information from well observations and GRACE satellites. *Water Resources Research*, **50(7)**, 5698–5720, doi:10.1002/2014wr015595.
Döll, P. et al., 2016: Modelling Freshwater Resources at the Global Scale: Challenges and Prospects. *Surveys in Geophysics*, **37(2)**, 195–221, doi:10.1007/s10712-015-9343-1.
Döll, P. et al., 2018a: Risks for the global freshwater system at 1.5°C and 2°C global warming.. *Environmental Research Letters*, **Volume 13**, 15.
Döll, P. et al., 2018b: Risks for the global freshwater system at 1.5 °C and 2 °C global warming. *Environmental Research Letters*, **13(4)**, 044038, doi:10.1088/1748-9326/aab792.
Donat, M.G., A.L. Lowry, L. Alexander, P.A. O'Gorman, and N. Maher, 2016: More extreme precipitation in the world's dry and wet regions. *Nature Climate Change*, **6(5)**, 508–513, doi:10.1038/nclimate2941.
Donchyts, G. et al., 2016: Earth's surface water change over the past 30 years. Nature Climate Change. *Nature Climate Change*, **6(9)**, 810, doi:10.1038/nclimate3111.
Dong, B. and R. Sutton, 2015: Dominant role of greenhouse-gas forcing in the recovery of Sahel rainfall. *Nature Climate Change*, **5(8)**, 757–760, doi:10.1038/nclimate2664.
Dong, B. and A. Dai, 2017: The uncertainties and causes of the recent changes in global evapotranspiration from 1982 to 2010. *Climate Dynamics*, **49(1–2)**, 279–296, doi:10.1007/s00382-016-3342-x.
Dong, B., R.T. Sutton, E. Highwood, and L. Wilcox, 2014: The impacts of European and Asian anthropogenic sulfur dioxide emissions on Sahel rainfall. *Journal of Climate*, **27(18)**, 7000–7017, doi:10.1175/jcli-d-13-00769.1.
Dong, B., R.T. Sutton, L. Shaffrey, and N.P. Klingaman, 2017: Attribution of Forced Decadal Climate Change in Coupled and Uncoupled Ocean–Atmosphere Model Experiments. *Journal of Climate*, **30(16)**, 6203–6223, doi:10.1175/jcli-d-16-0578.1.
Dong, L., L.R. Leung, F. Song, and J. Lu, 2018a: Roles of SST versus Internal Atmospheric Variability in Winter Extreme Precipitation Variability along the U.S. West Coast. *Journal of Climate*, **31(19)**, 8039–8058, doi:10.1175/jcli-d-18-0062.1.
Dong, L., C. Mitra, S. Greer, and E. Burt, 2018b: The dynamical linkage of atmospheric blocking to drought, heatwave and urban heat island in southeastern US: A multi-scale case study. *Atmosphere*, **9(1)**, 33, doi:10.3390/atmos9010033.
Dong, L., L.R. Leung, J. Lu, and F. Song, 2019: Mechanisms for an amplified precipitation seasonal cycle in the u.s. west coast under global warming. *Journal of Climate*, **32(15)**, 4681–4698, doi:10.1175/jcli-d-19-0093.1.
Donohoe, A. and A. Voigt, 2017: Why Future Shifts in Tropical Precipitation Will Likely Be Small. , doi:10.1002/9781119068020.ch8.
Donohoe, A., J. Marshall, D. Ferreira, and D. Mcgee, 2013: The relationship between ITCZ location and cross-equatorial atmospheric heat transport: From the seasonal cycle to the last glacial maximum. *Journal of Climate*, **26(11)**, 3597–3618, doi:10.1175/jcli-d-12-00467.1.
Donohue, R.J., M.L. Roderick, T.R. McVicar, and G.D. Farquhar, 2013: Impact of CO2 fertilization on maximum foliage cover across the globe's warm, arid environments. *Geophysical Research Letters*, doi:10.1002/grl.50563.
Dos Santos, V., F. Laurent, C. Abe, and F. Messner, 2018: Hydrologic response to land use change in a large basin in eastern Amazon. *Water (Switzerland)*, **10(4)**, doi:10.3390/w10040429.
Dosio, A., H.J. Panitz, M. Schubert-Frisius, and D. Lüthi, 2015: Dynamical downscaling of CMIP5 global circulation models over CORDEX-Africa with COSMO-CLM: evaluation over the present climate and analysis of the added value. *Climate Dynamics*, doi:10.1007/s00382-014-2262-x.
Dou, J., Z. Wu, and Y. Zhou, 2017: Potential impact of the May Southern Hemisphere annular mode on the Indian summer monsoon rainfall. *Climate Dynamics*, **49(4)**, 1257–1269, doi:10.1007/s00382-016-3380-4.
Douville, H. and M. Plazzotta, 2017: Midlatitude Summer Drying: An Underestimated Threat in CMIP5 Models? *Geophysical Research Letters*, **44(19)**, 9967–9975, doi:10.1002/2017gl075353.
Douville, H. and A. John, 2020: Fast adjustment versus slow SST-mediated response of daily precipitation statistics to abrupt 4xCO2. *Climate Dynamics*, doi:10.1007/s00382-020-05522-w.
Douville, H., A. Ribes, and S. Tyteca, 2019: Breakdown of NAO reproducibility into internal versus externally-forced components: a two-tier pilot study. *Climate Dynamics*, **52(1–2)**, 29–48, doi:10.1007/s00382-018-4141-3.
Douville, H., B. Decharme, A. Ribes, R. Alkama, and J. Sheffield, 2012: Anthropogenic influence on multi-decadal changes in reconstructed global evapotranspiration. , doi:10.1038/nclimate1632.
Douville, H. et al., 2020: Drivers of the enhanced decline of land near-surface relative humidity to abrupt 4xCO2 in CNRM-CM6-1. *Climate Dynamics*, **55(0123456789)**, 1613–1629, doi:10.1007/s00382-020-05351-x.
Dowdy, A.J., 2020: Climatology of thunderstorms, convective rainfall and dry lightning environments in Australia. *Climate Dynamics*, **54(5)**, 3041–3052, doi:10.1007/s00382-020-05167-9.
Dowdy, A.J. et al., 2019: Review of Australian east coast low pressure systems and associated extremes. *Climate Dynamics*, **53(7)**, 4887–4910, doi:10.1007/s00382-019-04836-8.
Drake, N. and C. Bristow, 2006: Shorelines in the Sahara: Geomorphological evidence for an enhanced monsoon from palaeolake Megachad. *Holocene*, **16**, 901–911, doi:10.1191/0959683606hol981rr.
Drijfhout, S. et al., 2015: Catalogue of abrupt shifts in Intergovernmental Panel on Climate Change climate models.

ACCEPTED VERSION SUBJECT TO FINAL EDITING

Proceedings of the National Academy of Sciences, **112(43)**, E5777–E5786, doi:10.1073/pnas.1511451112.
Driver, P. and C.J.C. Reason, 2017: Variability in the Botswana High and its relationships with rainfall and temperature characteristics over southern Africa. *International Journal of Climatology*, **37**, 570–581, doi:10.1002/joc.5022.
Drobinski, P. et al., 2018: Scaling precipitation extremes with temperature in the Mediterranean: past climate assessment and projection in anthropogenic scenarios. *Climate Dynamics*, **51(3)**, 1237–1257, doi:10.1007/s00382-016-3083-x.
Drumond, A. et al., 2014: The role of the Amazon Basin moisture in the atmospheric branch of the hydrological cycle: a Lagrangian analysis. *Hydrology and Earth System Sciences*, **18(7)**, 2577–2598, doi:10.5194/hess-18-2577-2014.
Dudley, R.W., G.A. Hodgkins, M.R. McHale, M.J. Kolian, and B. Renard, 2017: Trends in snowmelt-related streamflow timing in the conterminous United States. *Journal of Hydrology*, **547**, 208–221, doi:10.1016/j.jhydrol.2017.01.051.
Dufour, A., O. Zolina, and S.K. Gulev, 2016: Atmospheric Moisture Transport to the Arctic: Assessment of Reanalyses and Analysis of Transport Components. *Journal of Climate*, **29(14)**, 5061–5081, doi:10.1175/jcli-d-15-0559.1.
Dunn, R.J.H.H., K.M. Willett, A. Ciavarella, and P.A. Stott, 2017: Comparison of land surface humidity between observations and CMIP5 models. *Earth System Dynamics*, **8(3)**, 719–747, doi:10.5194/esd-8-719-2017.
Dunning, C.M., E. Black, and R.P. Allan, 2018: Later wet seasons with more intense rainfall over Africa under future climate change. *Journal of Climate*, **31(23)**, JCLI–D–18–0102.1, doi:10.1175/jcli-d-18-0102.1.
Dunn-Sigouin, E. and S.W. Son, 2013: Northern Hemisphere blocking frequency and duration in the CMIP5 models. *Journal of Geophysical Research Atmospheres*, **118(3)**, 1179–1188, doi:10.1002/jgrd.50143.
Durack, P.J., 2015: Ocean salinity and the global water cycle. *Oceanography*, **28(1)**, 20–31, doi:10.5670/oceanog.2015.03.
Durack, P.J., S.E. Wijffels, and R.J. Matear, 2012: During 1950 to 2000. *Science*, **336**, 455–458, doi:10.1126/science.1212222.
Durack, P.J., S.E. Wijffels, P.J. Durack, and S.E. Wijffels, 2010: Fifty-year trends in global ocean salinities and their relationship to broad-scale warming. *J. Climate*, **23(16)**, 4342–4362, doi:10.1175/2010jcli3377.1.
Dussaillant, I. et al., 2019: Two decades of glacier mass loss along the Andes. *Nature Geoscience*, **12(10)**, 802–808, doi:10.1038/s41561-019-0432-5.
Dutt, S. et al., 2015: Abrupt changes in Indian summer monsoon strength during 33,800 to 5500 years B.P.. *Geophysical Research Letters*, **42(13)**, 5526–5532, doi:10.1002/2015gl064015.
Dwyer, J.G. and P.A. O'Gorman, 2017: Changing duration and spatial extent of midlatitude precipitation extremes across different climates. *Geophysical Research Letters*, **44(11)**, 5863–5871, doi:10.1002/2017gl072855.
Earman, S. and M. Dettinger, 2011: Potential impacts of climate change on groundwater resources - A global review. *Journal of Water and Climate Change*, doi:10.2166/wcc.2011.034.
Easterling, D.R., K.E. Kunkel, M.F. Wehner, and L. Sun, 2016: Detection and attribution of climate extremes in the observed record. *Weather and Climate Extremes*, doi:10.1016/j.wace.2016.01.001.
Eekhout, J.P.C., J.E. Hunink, W. Terink, and J. de Vente, 2018: Why increased extreme precipitation under climate change negatively affects water security. *Hydrology and Earth System Sciences*, **22(11)**, 5935–5946, doi:10.5194/hess-22-5935-2018.
Eilander, D. et al., 2020: The effect of surge on riverine flood hazard and impact in deltas globally. *Environmental Research Letters*, **15(10)**, 104007, doi:10.1088/1748-9326/ab8ca6.
Eisner, S. et al., 2017: An ensemble analysis of climate change impacts on streamflow seasonality across 11 large river basins. *Climatic Change*, **141(3)**, 401–417, doi:10.1007/s10584-016-1844-5.
Ekholm, T. and H. Korhonen, 2016: Climate change mitigation strategy under an uncertain Solar Radiation Management possibility. *Climatic Change*, **139(3–4)**, 503–515, doi:10.1007/s10584-016-1828-5.
Emanuel, K., 2017: Assessing the present and future probability of Hurricane Harvey's rainfall. *Proc. Nat*, 12681–12684.
Emerton, R. et al., 2017: Complex picture for likelihood of ENSO-driven flood hazard. *Nature Communications*, **8**, 14796, doi:10.1038/ncomms14796.
Endo, H., A. Kitoh, and H. Ueda, 2018: A Unique Feature of the Asian Summer Monsoon Response to Global Warming: The Role of Different Land–Sea Thermal Contrast Change between the Lower and Upper Troposphere. *SOLA*, **14**, 57–63, doi:10.2151/sola.2018-010.
Endris, H.S. et al., 2019: Future changes in rainfall associated with ENSO, IOD and changes in the mean state over Eastern Africa. *Climate Dynamics*, **52(3–4)**, 2029–2053, doi:10.1007/s00382-018-4239-7.
Engel, T. et al., 2017: Extreme Precipitation in the West African Cities of Dakar and Ouagadougou: Atmospheric Dynamics and Implications for Flood Risk Assessments. *Journal of Hydrometeorology*, **18(11)**, 2937–2957, doi:10.1175/jhm-d-16-0218.1.
England, M.H. et al., 2014: Recent intensification of wind-driven circulation in the Pacific and the ongoing warming hiatus. *Nature Climate Change*, **4(3)**, 222–227, doi:10.1038/nclimate2106.
Espinoza, J.C., J. Ronchail, J.A. Marengo, and H. Segura, 2018: Contrasting North–South changes in Amazon wet-day and dry-day frequency and related atmospheric features (1981–2017). *Climate Dynamics*, **52(9–10)**, 1–22,

ACCEPTED VERSION SUBJECT TO FINAL EDITING

doi:10.1007/s00382-018-4462-2.
Espinoza, J.C., H. Segura, J. Ronchail, G. Drapeau, and O. Gutierrez-Cori, 2016: Evolution of wet-day and dry-day frequency in the western Amazon basin: Relationship with atmospheric circulation and impacts on vegetation. *Water Resources Research*, **52(11)**, 8546–8560, doi:10.1002/2016wr019305.
Espinoza, J.C. et al., 2019: Regional hydro-climatic changes in the Southern Amazon Basin (Upper Madeira Basin) during the 1982–2017 period. *Journal of Hydrology: Regional Studies*, **26**, 100637, doi:10.1016/j.ejrh.2019.100637.
Espinoza, V., D.E. Waliser, B. Guan, D.A. Lavers, and F.M. Ralph, 2018: Global Analysis of Climate Change Projection Effects on Atmospheric Rivers. *Geophysical Research Letters*, **45(9)**, 4299–4308, doi:10.1029/2017gl076968.
Estilow, T.W., A.H. Young, and D.A. Robinson, 2015: A long-term Northern Hemisphere snow cover extent. , 137–142, doi:10.7289/v5n014g9.
Evan, A.T., C. Flamant, C. Lavaysse, C. Kocha, and A. Saci, 2015: Water vapor-forced greenhouse warming over the Sahara desert and the recent recovery from the Sahelian drought. *Journal of Climate*, **28(1)**, 108–123, doi:10.1175/jcli-d-14-00039.1.
Falco, M., A.F. Carril, C.G. Menéndez, P.G. Zaninelli, and Z.X.L. Laurent, 2019: Assessment of CORDEX simulations over South America: added value on seasonal climatology and resolution considerations. *Climate Dynamics*, **52(7–8)**, 4771–4786, doi:10.1007/s00382-018-4412-z.
Fan, C. et al., 2020: Strong Precipitation Suppression by Aerosols in Marine Low Clouds. *Geophysical Research Letters*, **47(7)**, doi:10.1029/2019gl086207.
Fan, J., Y. Wang, D. Rosenfeld, and X. Liu, 2016: Review of Aerosol–Cloud Interactions: Mechanisms, Significance, and Challenges. *Journal of the Atmospheric Sciences*, **73(11)**, 4221–4252, doi:10.1175/jas-d-16-0037.1.
Fan, J. et al., 2014: Aerosol impacts on California winter clouds and precipitation during calwater 2011: Local pollution versus long-range transported dust. *Atmospheric Chemistry and Physics*, **14(1)**, doi:10.5194/acp-14-81-2014.
Fan, J. et al., 2015: Substantial contribution of anthropogenic air pollution to catastrophic floods in Southwest China. *Geophysical Research Letters*, **42(14)**, 6066–6075, doi:10.1002/2015gl064479.
Fan, J. et al., 2018: Substantial convection and precipitation enhancements by ultrafine aerosol particles. *Science*, **359(6374)**, 411–418, doi:10.1126/science.aan8461.
Fang, X. and H.G. Stefan, 1999: Projections of climate change effects on water temperature characteristics of small lakes in the contiguous U.S.. *Climatic Change*, doi:10.1023/a:1005431523281.
Farinotti, D., W.W. Immerzeel, R.J. Kok, D.J. Quincey, and A. Dehecq, 2020: Manifestations and mechanisms of the Karakoram glacier Anomaly. *Nature Geoscience*, **13**, doi:10.1038/s41561-019-0513-5.
Fasullo, J.T., B.L. Otto-Bliesner, and S. Stevenson, 2019: The Influence of Volcanic Aerosol Meridional Structure on Monsoon Responses over the Last Millennium. *Geophysical Research Letters*, **46(21)**, 12350–12359, doi:10.1029/2019gl084377.
Fatichi, S. et al., 2016: Uncertainty partition challenges the predictability of vital details of climate change. *Earth's Future*, **4(5)**, 240–251, doi:10.1002/2015ef000336.
Favreau, G. et al., 2009: Land clearing, climate variability, and water resources increase in semiarid southwest Niger: A review. *Water Resources Research*, **45**.
Feng, S. and Q. Fu, 2013: Expansion of global drylands under a warming climate. *Atmospheric Chemistry and Physics*, **13(19)**, 10081–10094, doi:10.5194/acp-13-10081-2013.
Feng, W. et al., 2013: Evaluation of groundwater depletion in North China using the Gravity Recovery and Climate Experiment (GRACE) data and ground-based measurements. *Water Resources Research*, **49(4)**, 2110–2118, doi:10.1002/wrcr.20192.
Fenta, A.A., H. Yasuda, K. Shimizu, and N. Haregeweyn, 2017: Response of streamflow to climate variability and changes in human activities in the semiarid highlands of northern Ethiopia. *Regional Environmental Change*, **17(4)**, 1229–1240, doi:10.1007/s10113-017-1103-y.
Fereday, D., R. Chadwick, J. Knight, and A.A. Scaife, 2018: Atmospheric Dynamics is the Largest Source of Uncertainty in Future Winter European Rainfall. *Journal of Climate*, **31(3)**, 963–977, doi:10.1175/jcli-d-17-0048.1.
Ferguson, C.R. and E.F. Wood, 2011: Observed land-Atmosphere coupling from satellite remote sensing and reanalysis. *Journal of Hydrometeorology*, **12**, 1221, doi:10.1175/2011jhm1380.1.
Ferguson, C.R., M. Pan, and T. Oki, 2018: The effect of global warming on future water availability: CMIP5 synthesis. *Water Resources Research*, doi:10.1029/2018wr022792.
Ferguson, G. and T. Gleeson, 2012: Vulnerability of coastal aquifers to groundwater use and climate change. *Nature Climate Change*, **2**, 342–345.
Ferguson, G., J.C. McIntosh, D. Perrone, and S. Jasechko, 2018: Competition for shrinking window of low salinity groundwater. *Environmental Research Letters*, **13(11)**, 114013, doi:10.1088/1748-9326/aae6d8.
Ferraro, A.J., E.J. Highwood, and A.J. Charlton-Perez, 2014: Weakened tropical circulation and reduced precipitation in response to geoengineering. *Environmental Research Letters*, doi:10.1088/1748-9326/9/1/014001.
Feser, F. et al., 2015: Storminess over the North Atlantic and northwestern Europe-A review. *Quarterly Journal of the*

ACCEPTED VERSION SUBJECT TO FINAL EDITING

Royal Meteorological Society, **141(687)**, 350–382, doi:10.1002/qj.2364.
Ficklin, D.L., J.T. Abatzoglou, and K.A. Novick, 2019: A New Perspective on Terrestrial Hydrologic Intensity That Incorporates Atmospheric Water Demand. *Geophysical Research Letters*, **46(14)**, 8114–8124, doi:10.1029/2019gl084015.
Ficklin, D.L., J.T. Abatzoglou, S.M. Robeson, S.E. Null, and J.H. Knouft, 2018: Natural and managed watersheds show similar responses to recent climate change. *Proceedings of the National Academy of Sciences of the United States of America*, **115(34)**, 8553–8557, doi:10.1073/pnas.1801026115.
Fiedler, S. et al., 2020: Simulated tropical precipitation assessed across three major phases of the coupled model intercomparison project (CMIP). *Monthly Weather Review*, **148(9)**, 3653–3680, doi:10.1175/mwr-d-19-0404.1.
Finney, D.L. et al., 2020a: Effects of Explicit Convection on Future Projections of Mesoscale Circulations, Rainfall, and Rainfall Extremes over Eastern Africa. *Journal of Climate*, **33(7)**, 2701–2718, doi:10.1175/jcli-d-19-0328.1.
Finney, D.L. et al., 2020b: The effect of westerlies on East African rainfall and the associated role of tropical cyclones and the Madden–Julian Oscillation. *Quarterly Journal of the Royal Meteorological Society*, **146(727)**, 647–664, doi:10.1002/qj.3698.
Fischer, E.M. and R. Knutti, 2014: Detection of spatially aggregated changes in temperature and precipitation extremes. *Geophysical Research Letters*, **41(2)**, 547–554, doi:10.1002/2013gl058499.
Fischer, E.M. and R. Knutti, 2015: Anthropogenic contribution to global occurrence of heavy-precipitation and high-temperature extremes. *Nature Climate Change*, **5(6)**, 560–564, doi:10.1038/nclimate2617.
Fischer, E.M. and R. Knutti, 2016: Observed heavy precipitation increase confirms theory and early models. *Nature Climate Change*, **6(11)**, 986–991, doi:10.1038/nclimate3110.
Fisher, R.A. et al., 2018: Vegetation demographics in Earth System Models: A review of progress and priorities. *Global Change Biology*, **24(1)**, 35–54, doi:10.1111/gcb.13910.
Fläschner, D., T. Mauritsen, and B. Stevens, 2016: Understanding the intermodel spread in global-mean hydrological sensitivity. *Journal of Climate*, **29(2)**, 801–817, doi:10.1175/jcli-d-15-0351.1.
Fletcher, M.-S. et al., 2018: Centennial-scale trends in the Southern Annular Mode revealed by hemisphere-wide fire and hydroclimatic trends over the past 2400 years. *Geology*, **46(4)**, 363–366, doi:10.1130/g39661.1.
Fluet-Chouinard, E., B. Lehner, L.M. Rebelo, F. Papa, and S.K. Hamilton, 2015: Development of a global inundation map at high spatial resolution from topographic downscaling of coarse-scale remote sensing data. Remote Sensing of Environment. , **158**, 348–361.
Fogt, R.L., D.H. Bromwich, and K.M. Hines, 2011: Understanding the SAM influence on the South Pacific ENSO teleconnection. *Climate Dynamics*, **36(7–8)**, 1555–1576, doi:10.1007/s00382-010-0905-0.
Fontes, C.G. et al., 2018: Dry and hot: The hydraulic consequences of a climate change–type drought for Amazonian trees. *Philosophical Transactions of the Royal Society B: Biological Sciences*, doi:10.1098/rstb.2018.0209.
Formayer, H. and A. Fritz, 2017: Temperature dependency of hourly precipitation intensities – surface versus cloud layer temperature. *International Journal of Climatology*, **37(1)**, 1–10, doi:10.1002/joc.4678.
Forzieri, G. et al., 2020: Increased control of vegetation on global terrestrial energy fluxes. *Nature Climate Change*, **10(4)**, 356–362, doi:10.1038/s41558-020-0717-0.
Fosser, G., S. Khodayar, and P. Berg, 2017: Climate change in the next 30 years: What can a convection-permitting model tell us that we did not already know? *Climate Dynamics*, **48(5–6)**, 1987–2003, doi:10.1007/s00382-016-3186-4.
Fowler, H.J. et al., 2021: Anthropogenic intensification of short-duration rainfall extremes. *Nature Reviews Earth and Environment*, in press, doi:10.1038/s43017-020-00128-6.
Fowler, M.D. and M.S. Pritchard, 2020: Regional MJO Modulation of Northwest Pacific Tropical Cyclones Driven by Multiple Transient Controls. *Geophysical Research Letters*, **47(11)**, doi:10.1029/2020gl087148.
Francis, J.A. and S.J. Vavrus, 2012: Evidence linking Arctic amplification to extreme weather in mid-latitudes. *Geophysical Research Letters*, **39(6)**, n/a—n/a, doi:10.1029/2012gl051000.
Francis, J.A. and S.J. Vavrus, 2015: Evidence for a wavier jet stream in response to rapid Arctic warming. *Environ Research Letters*, **10(1)**, 14005, doi:10.1088/1748-9326/10/1/014005.
Frank, D.C. et al., 2015: Water-use efficiency and transpiration across European forests during the Anthropocene. *Nature Climate Change*, **5(6)**, 579–583, doi:10.1038/nclimate2614.
Frankcombe, L.M., M.H. England, J.B. Kajtar, M.E. Mann, and B.A. Steinman, 2018: On the Choice of Ensemble Mean for Estimating the Forced Signal in the Presence of Internal Variability. *Journal of Climate*, **31(14)**, 5681–5693, doi:10.1175/jcli-d-17-0662.1.
Franke, J., D. Frank, C.C. Raible, J. Esper, and S. Brönnimann, 2013: Spectral biases in tree-ring climate proxies. *Nature Climate Change*, doi:10.1038/nclimate1816.
Franks, P.J., J.A. Berry, D.L. Lombardozzi, and G.B. Bonan, 2017: Stomatal Function across Temporal and Spatial Scales: Deep-Time Trends, Land-Atmosphere Coupling and Global Models. *Plant Physiology*, **174(2)**, 583–602, doi:10.1104/pp.17.00287.
Franks, P.J. et al., 2018: Comparing optimal and empirical stomatal conductance models for application in Earth system

ACCEPTED VERSION SUBJECT TO FINAL EDITING

models. *Global Change Biology*, **24(12)**, 5708–5723, doi:10.1111/gcb.14445.
Frans, C. et al., 2015: Predicting glacio-hydrologic change in the headwaters of the Zongo River, Cordillera Real, Bolivia. *Water Resources Research*, doi:10.1002/2014wr016728.
Frappart, F. et al., 2009: Rainfall regime across the Sahel band in the Gourma region, Mali. *Journal of Hydrology*, **375(1–2)**, 128–142, doi:10.1016/j.jhydrol.2009.03.007.
Fredriksen, H.-B., J. Berner, A.C. Subramanian, and A. Capotondi, 2020: How Does El Niño–Southern Oscillation Change Under Global Warming-A First Look at CMIP6. *Geophysical Research Letters*, **47(22)**, doi:10.1029/2020gl090640.
French, J.R. et al., 2018: Precipitation formation from orographic cloud seeding.. *Proceedings of the National Academy of Sciences of the United States of America*, **115(6)**, 1168–1173, doi:10.1073/pnas.1716995115.
Freud, E. and D. Rosenfeld, 2012: Linear relation between convective cloud drop number concentration and depth for rain initiation. *Journal of Geophysical Research: Atmospheres*, **117(D2)**.
Freund, M., B.J. Henley, D.J. Karoly, K.J. Allen, and P.J. Baker, 2017: Multi-century cool- and warm-season rainfall reconstructions for Australia's major climatic regions. *Climate of the Past*, **13(12)**, 1751–1770, doi:10.5194/cp-13-1751-2017.
Freund, M.B., J.R. Brown, B.J. Henley, D.J. Karoly, and J.N. Brown, 2020: Warming Patterns Affect El Niño Diversity in CMIP5 and CMIP6 Models. *Journal of Climate*, **33(19)**, 8237–8260, doi:10.1175/jcli-d-19-0890.1.
Friedman, A.R., Y.-T. Hwang, J.C.H. Chiang, and D.M.W. Frierson, 2013: Interhemispheric temperature asymmetry over the twentieth century and in future projections. *J. Climate*, **26**, 5419–5433.
Friedrich, K. et al., 2020: Quantifying snowfall from orographic cloud seeding. *Proceedings of the National Academy of Sciences of the United States of America*, **117(10)**, 5190–5195, doi:10.1073/pnas.1917204117.
Frierson, D.M.W. et al., 2013: Contribution of ocean overturning circulation to tropical rainfall peak in the Northern Hemisphere. *Nature Geoscience*, **6(11)**, 940–944, doi:10.1038/ngeo1987.
Froidevaux, P. and O. Martius, 2016: Exceptional integrated vapour transport toward orography: an important precursor to severe floods in Switzerland. *Quarterly Journal of the Royal Meteorological Society*, **142(698)**, 1997–2012, doi:10.1002/qj.2793.
Fromang, S. and G. Rivière, 2020: The Effect of the Madden–Julian Oscillation on the North Atlantic Oscillation Using Idealized Numerical Experiments. *Journal of the Atmospheric Sciences*, **77(5)**, 1613–1635, doi:10.1175/jas-d-19-0178.1.
Fu, Q. and S. Feng, 2014: Responses of terrestrial aridity to global warming. *Journal of Geophysical Research*, **119(13)**, 7863–7875, doi:10.1002/2014jd021608.
Fu, R. et al., 2013: Increased dry season length over southern Amazonia in recent decades and its implication for future climate projection. *Proceedings of the Natural Academy of Sciences*, **110(45)**, 18110–18115, doi:10.1073/pnas.1302584110.
Fujita, M., R. Mizuta, M. Ishii, and H. Endo, 2018: Precipitation Changes in a Climate With 2-K Surface Warming From Large Ensemble Simulations Using 60-km Global and 20-km Regional Atmospheric Models. , 435–442, doi:10.1029/2018gl079885.
Fumière, Q. et al., 2020: Extreme rainfall in Mediterranean France during the fall: added value of the CNRM-AROME Convection-Permitting Regional Climate Model. *Climate Dynamics*, **55(1–2)**, 77–91, doi:10.1007/s00382-019-04898-8.
Fuss, S. et al., 2018: Negative emissions - Part 2: Costs, potentials and side effects. *Environmental Research Letters*, **13(6)**, doi:10.1088/1748-9326/aabf9f.
Gaetani, M., S. Janicot, M. Vrac, A.M. Famien, and B. Sultan, 2020: Robust assessment of the time of emergence of precipitation change in West Africa. *Scientific Reports*, **10(1)**, 7670, doi:10.1038/s41598-020-63782-2.
Gallant, A.J.E., M.J. Reeder, J.S. Risbey, and K.J. Hennessy, 2013: The characteristics of seasonal-scale droughts in Australia, 1911-2009. *International Journal of Climatology*, doi:10.1002/joc.3540.
Gallego, D., R. García-Herrera, C. Peña-Ortiz, and P. Ribera, 2017: The steady enhancement of the Australian Summer Monsoon in the last 200 years. *Scientific Reports*, **7(1)**, 1–7, doi:10.1038/s41598-017-16414-1.
Gan, B. and L. Wu, 2014: Centennial trends in Northern Hemisphere winter storm tracks over the twentieth century.. *Q. J. R Meteorol. Soc.*, **140**, 1945–1957, doi:10.1002/qj.2263.
Ganeshi et al., 2020: Understanding the linkage between soil moisture variability and temperature extremes over the Indian region. *Journal of Hydrology*, **589**, 125183, doi:10.1016/j.jhydrol.2020.125183.
Ganguli, P. and B. Merz, 2019: Trends in Compound Flooding in Northwestern Europe during 1901–2014. *Geophysical Research Letters*, doi:10.1029/2019gl084220.
Gao, J. et al., 2019: A New Frozen Soil Parameterization Including Frost and Thaw Fronts in the Community Land Model. *Journal of Advances in Modeling Earth Systems*, **11(3)**, 659–679, doi:10.1029/2018ms001399.
Gao, Y. and others, 2015: Dynamical and thermodynamical modulations on future changes of landfalling atmospheric rivers over western North America. *Geophysical Research Letters*, **42**, 7179–7186.
Gao, Y. and C. Gao, 2017: European hydroclimate response to volcanic eruptions over the past nine centuries. *International Journal of Climatology*, **37(11)**, 4146–4157, doi:10.1002/joc.5054.
García-García, A., F.J. Cuesta-Valero, H. Beltrami, and J.E. Smerdon, 2019: Characterization of Air and Ground

SUBJECT TO FINAL EDITING ACCEPTED VERSION

Temperature Relationships within the CMIP5 Historical and Future Climate Simulations. *Journal of Geophysical Research: Atmospheres*, **124(7)**, 3903–3929, doi:10.1029/2018jd030117.
García-Herrera, R. and D. Barriopedro, 2006: Northern Hemisphere snow cover and atmospheric blocking variability. *Journal of Geophysical Research*, **111(D21)**, D21104, doi:10.1029/2005jd006975.
García-Martínez, I.M., M.A. Bollasina, and S. Undorf, 2020: Strong large-scale climate response to North American sulphate aerosols in CESM. *Environmental Research Letters*, **15(11)**, doi:10.1088/1748-9326/abbe45.
Garfinkel, C.I., I. White, E.P. Gerber, and M. Jucker, 2020: The Impact of SST Biases in the Tropical East Pacific and Agulhas Current Region on Atmospheric Stationary Waves in the Southern Hemisphere. *Journal of Climate*, **33(21)**, 9351–9374, doi:10.1175/jcli-d-20-0195.1.
Gariano, S.L. and F. Guzzetti, 2016: Landslides in a changing climate. *Earth-Science Reviews*, **162**, 227–252, doi:10.1016/j.earscirev.2016.08.011.
Garreaud, R.D. et al., 2020: The Central Chile Mega Drought (2010–2018): A climate dynamics perspective. *International Journal of Climatology*, **40(1)**, 421–439, doi:10.1002/joc.6219.
Gasse, F., 2000: Hydrological changes in the African tropics since the Last Glacial Maximum. *Quaternary Science Reviews*, **19(1)**, 189–211.
Gastineau, G., L. Li, and H. Le Treut, 2009: The Hadley and Walker circulation changes in global warming conditions described by idealized atmospheric simulations. *Journal of Climate*, doi:10.1175/2009jcli2794.1.
Gedney, N. et al., 2014: Detection of solar dimming and brightening effects on Northern Hemisphere river flow. *Nature Geoscience*, **7(11)**, 796-800, doi:10.1038/ngeo2263.
Geil, K.L., Y.L. Serra, and X. Zeng, 2013: Assessment of CMIP5 model simulations of the North American monsoon system. *Journal of Climate*, doi:10.1175/jcli-d-13-00044.1.
Gentine, P., M. Pritchard, S. Rasp, G. Reinaudi, and G. Yacalis, 2018: Could Machine Learning Break the Convection Parameterization Deadlock? *Geophysical Research Letters*, **45(11)**, 5742–5751, doi:10.1029/2018gl078202.
Gentine, P. et al., 2019: Coupling between the terrestrial carbon and water cycles – A review. *Environmental Research Letters*, **14(8)**, 83003, doi:10.1088/1748-9326/ab22d6.
Genty, D. et al., 2006: Timing and dynamics of the last deglaciation from European and North African δ13C stalagmite profiles-comparison with Chinese and South Hemisphere stalagmites. *Quaternary Science Reviews*, doi:10.1016/j.quascirev.2006.01.030.
Gergis, J. and B.J. Henley, 2017: Southern Hemisphere rainfall variability over the past 200 years. *Climate Dynamics*, **48(7–8)**, 2087–2105, doi:10.1007/s00382-016-3191-7.
Gergis, J. et al., 2012: On the long-term context of the 1997--2009 `Big Dry' in South-Eastern Australia: insights from a 206-year multi-proxy rainfall reconstruction. *Climatic Change*, **111(3)**, 923–944, doi:10.1007/s10584-011-0263-x.
Gershunov, A., T. Shulgina, F.M. Ralph, D.A. Lavers, and J.J. Rutz, 2017: Assessing the climate-scale variability of atmospheric rivers affecting western North America. *Geophysical Research Letters*, **44(15)**, 7900–7908.
Gershunov, A. et al., 2019: Precipitation regime change in Western North America: The role of Atmospheric Rivers. *Scientific Reports*, **9(1)**, 9944, doi:10.1038/s41598-019-46169-w.
Giannini, A., 2010: Mechanisms of climate change in the semiarid African Sahel: The local view. *Journal of Climate*, doi:10.1175/2009jcli3123.1.
Giannini, A. and A. Kaplan, 2019: The role of aerosols and greenhouse gases in Sahel drought and recovery. *Climatic Change*, **152(3–4)**, 449–466, doi:10.1007/s10584-018-2341-9.
Giannini, A. et al., 2013: A unifying view of climate change in the Sahel linking intra-seasonal, interannual and longer time scales. *Environmental Research Letters*, **8(2)**, 024010, doi:10.1088/1748-9326/8/2/024010.
Gimeno, L., R. Nieto, and R. Sorí, 2020: The growing importance of oceanic moisture sources for continental precipitation. *npj Climate and Atmospheric Science*, **3(1)**, 27, doi:10.1038/s41612-020-00133-y.
Gimeno, L., A. Drumond, R. Nieto, R.M. Trigo, and A. Stohl, 2010: On the origin of continental precipitation. *Geophysical Research Letters*, **37(13)**, doi:10.1029/2010gl043712.
Gimeno, L. et al., 2012: Oceanic and terrestrial sources of continental precipitation. *Reviews of Geophysics*, **50(4)**, RG4003, doi:10.1029/2012rg000389.
Ginoux, P., J.M. Prospero, T.E. Gill, N.C. Hsu, and M. Zhao, 2012: Global-scale attribution of anthropogenic and natural dust sources and their emission rates based on MODIS Deep Blue aerosol products. *Reviews of Geophysics*, doi:10.1029/2012rg000388.
Giorgi, F. et al., 2016: Enhanced summer convective rainfall at Alpine high elevations in response to climate warming. *Nature Geoscience*, **9(8)**, 584–589, doi:10.1038/ngeo2761.
Giráldez, L., Y. Silva, R. Zubieta, and J. Sulca, 2020: Change of the rainfall seasonality over central peruvian andes: Onset, end, duration and its relationship with large-scale atmospheric circulation. *Climate*, **8(2)**, doi:10.3390/cli8020023.
Giuntoli, I., B. Renard, J.-P. Vidal, and A. Bard, 2013: Low flows in France and their relationship to large-scale climate indices. *Journal of Hydrology*, **482**, 105–118, doi:10.1016/j.jhydrol.2012.12.038.
Giuntoli, I., J.-P. Vidal, C. Prudhomme, and D.M. Hannah, 2015: Future hydrological extremes: the uncertainty from multiple global climate and global hydrological models. *Earth System Dynamics*, **6(1)**, 267–285,

ACCEPTED VERSION SUBJECT TO FINAL EDITING

doi:10.5194/esd-6-267-2015.
Giuntoli, I., G. Villarini, C. Prudhomme, and D.M. Hannah, 2018: Uncertainties in projected runoff over the conterminous United States. *Climatic Change*, **150(3–4)**, 149–162, doi:10.1007/s10584-018-2280-5.
Glas, R., D. Burns, and L. Lautz, 2019: Historical changes in New York State streamflow: Attribution of temporal shifts and spatial patterns from 1961 to 2016. *Journal of Hydrology*, **574**, 308–323, doi:10.1016/j.jhydrol.2019.04.060.
Gloor, M. et al., 2015: Recent Amazon climate as background for possible ongoing and future changes of Amazon humid forests. *Global Biogeochemical Cycles*, **29(9)**, 1384–1399, doi:10.1002/2014gb005080.
Gomes, V.H.F., I.C.G. Vieira, R.P. Salomão, and H. ter Steege, 2019: Amazonian tree species threatened by deforestation and climate change. *Nature Climate Change*, doi:10.1038/s41558-019-0500-2.
Gonzales, K.R., D.L. Swain, K.M. Nardi, E.A. Barnes, and N.S. Diffenbaugh, 2019: Recent warming of landfalling atmospheric rivers along the west coast of the United States. *Journal of Geophysical Research: Atmospheres*, **124(13)**, 2018JD029860, doi:10.1029/2018jd029860.
Gonzalez, P.L.M., L.M. Polvani, R. Seager, and G.J.P. Correa, 2014: Stratospheric ozone depletion: A key driver of recent precipitation trends in South Eastern South America. *Climate Dynamics*, **42(7–8)**, 1775–1792, doi:10.1007/s00382-013-1777-x.
Good, P. et al., 2015: Nonlinear regional warming with increasing CO2concentrations. *Nature Climate Change*, **5(2)**, 138–142, doi:10.1038/nclimate2498.
Good, P. et al., 2016a: NonlinMIP contribution to CMIP6: Model intercomparison project for non-linear mechanisms: Physical basis, experimental design and analysis principles (v1.0). *Geoscientific Model Development*, doi:10.5194/gmd-9-4019-2016.
Good, P. et al., 2016b: Large differences in regional precipitation change between a first and second 2 K of global warming. *Nature Communications*, **7**, doi:10.1038/ncomms13667.
Good, P. et al., 2020: High sensitivity of tropical precipitation to local sea-surface temperature. *Nature*, doi:10.1038/s41586-020-2887-3.
Goren, T. and D. Rosenfeld, 2014: Decomposing aerosol cloud radiative effects into cloud cover, liquid water path and Twomey components in marine stratocumulus. *Atmospheric Research*, **138**, 378–393, doi:10.1016/j.atmosres.2013.12.008.
Gorodetskaya, I. et al., 2014: The role of atmospheric rivers in anomalous snow accumulation in East Antarctica. *Geophysical Research Letters*, **41(17)**, 6199–6206, doi:10.1002/2014gl060881.
Gosling, S.N. and N.W. Arnell, 2016: A global assessment of the impact of climate change on water scarcity. *Climatic Change*, **134(3)**, 371–385, doi:10.1007/s10584-013-0853-x.
Goswami, B.N.B. and B.N.B. Goswami, 2017: A road map for improving dry-bias in simulating the South Asian monsoon precipitation by climate models. *Climate Dynamics*, **49(5)**, 2025–2034, doi:10.1007/s00382-016-3439-2.
Grafton, R.Q. et al., 2018: The paradox of irrigation efficiency. *Science*, **361(6404)**, 748–750.
Grandey, B.S., H. Cheng, and C. Wang, 2016: Transient Climate Impacts for Scenarios of Aerosol Emissions from Asia: A Story of Coal versus Gas. *Journal of Climate*, **29(8)**, 2849–2867, doi:10.1175/jcli-d-15-0555.1.
Grell, G.A. and S.R. Freitas, 2014: A scale and aerosol aware stochastic convective parameterization for weather and air quality modeling. *Atmospheric Chemistry and Physics*, **14(10)**, 5233–5250, doi:10.5194/acp-14-5233-2014.
Gremaud, V., N. Goldscheider, L. Savoy, G. Favre, and H. Masson, 2009: Geological structure, recharge processes and underground drainage of a glacierised karst aquifer system, Tsanfleuron-Sanetsch, Swiss Alps. *Hydrogeology Journal*, **17**, 1833–1848.
Greve, P. and S.I. Seneviratne, 2015: Assessment of future changes in water availability and aridity. *Geophysical Research Letters*, **42**, 5493–5499, doi:10.1002/2015gl064127.received.
Greve, P., L. Gudmundsson, and S.I. Seneviratne, 2018: Regional scaling of annual mean precipitation and water availability with global temperature change. *Earth System Dynamics*, **9(1)**, 227–240, doi:10.5194/esd-9-227-2018.
Greve, P., M. Roderick, A.M. Ukkola, and Y. Wada, 2019: The Aridity Index under global warming. *Environmental Research Letters*, **14(12)**, 124006, doi:10.1088/1748-9326/ab5046.
Greve, P. et al., 2014: Global assessment of trends in wetting and drying over land. *Nature Geoscience*, **7(10)**, 716–721, doi:10.1038/ngeo2247.
Grieger, J., G.C. Leckebusch, C.C. Raible, I. Rudeva, and I. Simmonds, 2018: Subantarctic cyclones identified by 14 tracking methods, and their role for moisture transports into the continent. *Tellus, Series A: Dynamic Meteorology and Oceanography*, **70(1)**, 1, doi:10.1080/16000870.2018.1454808.
Griffin, D. and K.J. Anchukaitis, 2014: How unusual is the 2012-2014 California drought? *Geophysical Research Letters*, doi:10.1002/2014gl062433.
Grimm, E.C. et al., 2006: Evidence for warm wet Heinrich events in Florida. *Quaternary Science Reviews*, doi:10.1016/j.quascirev.2006.04.008.
Grise, K.M. and L.M. Polvani, 2016: Is climate sensitivity related to dynamical sensitivity? *Journal of Geophysical Research*, **121(10)**, 5159–5176, doi:10.1002/2015jd024687.

ACCEPTED VERSION SUBJECT TO FINAL EDITING

Grise, K.M. and S.M. Davis, 2020: Hadley cell expansion in CMIP6 models. *Atmospheric Chemistry and Physics*, **20(9)**, 5249–5268, doi:10.5194/acp-20-5249-2020.
Grise, K.M., S.W. Son, G.J.P.P. Correa, and L.M. Polvani, 2014: The response of extratropical cyclones in the Southern Hemisphere to stratospheric ozone depletion in the 20th century. *Atmospheric Science Letters*, **15(1)**, 29–36, doi:10.1002/asl2.458.
Grise, K.M. et al., 2019: Recent Tropical Expansion: Natural Variability or Forced Response? *Journal of Climate*, **32(5)**, 1551–1571, doi:10.1175/jcli-d-18-0444.1.
Grogan, D.S., E.A. Burakowski, and A.R. Contosta, 2020: Snowmelt control on spring hydrology declines as the vernal window lengthens. *Environmental Research Letters*, **15(11)**, 114040, doi:10.1088/1748-9326/abbd00.
Grose, M., B. Timbal, L. Wilson, J. Bathols, and D. Kent, 2015: The subtropical ridge in CMIP5 models, and implications for projections of rainfall in southeast Australia.. *Australian Meteorological and Oceanographic Journal*, **65(1)**, 90–106.
Grose, M.R. et al., 2017: Constraints on Southern Australian rainfall change based on atmospheric circulation in CMIP5 simulations. *Journal of Climate*, **30(1)**, 225–242, doi:10.1175/jcli-d-16-0142.1.
Grossiord, C. et al., 2020: Plant responses to rising vapor pressure deficit. *New Phytologist*, **226(6)**, 1550–1566, doi:10.1111/nph.16485.
Gu, G. and R.F. Adler, 2018: Precipitation Intensity Changes in the Tropics from Observations and Models. *Journal of Climate*, **31(12)**, JCLI–D–17–0550.1, doi:10.1175/jcli-d-17-0550.1.
Gu, G., R.F. Adler, and G.J. Huffman, 2016: Long-term changes/trends in surface temperature and precipitation during the satellite era (1979–2012). *Climate Dynamics*, **46(3–4)**, 1091–1105, doi:10.1007/s00382-015-2634-x.
Gu, H., J. Jin, Y. Wu, M.B. Ek, and Z.M. Subin, 2015: Calibration and validation of lake surface temperature simulations with the coupled WRF-lake model. *Climatic Change*, **129**, 471.
Gu, L., J. Chen, C.-Y. Xu, H.-M. Wang, and L.P. Zhang, 2018: Synthetic Impacts of Internal Climate Variability and Anthropogenic Change on Future Meteorological Droughts over China. *Water*, **10(11)**, 1702, doi:10.3390/w10111702.
Gu, X. et al., 2019: Attribution of global soil moisture drying to human activities: a quantitative viewpoint. *Geophysical Research Letters*, doi:10.1029/2018gl080768.
Guan, B. and D.E. Waliser, 2015: Detection of atmospheric rivers: Evaluation and application of an algorithm for global studies. *Journal of Geophysical Research*, **120(24)**, 12,514–12,535, doi:10.1002/2015jd024257.
Guan, B., D.E. Waliser, N.P. Molotch, E.J. Fetzer, and P.J. Neiman, 2012: Does the Madden–Julian Oscillation Influence Wintertime Atmospheric Rivers and Snowpack in the Sierra Nevada? *Monthly Weather Review*, **140(2)**, 325–342, doi:10.1175/mwr-d-11-00087.1.
Gudmundsson, L. and S.I. Seneviratne, 2016: Anthropogenic climate change affects meteorological drought risk in Europe. *Environmental Research Letters*, doi:10.1088/1748-9326/11/4/044005.
Gudmundsson, L. and et al., 2021: Globally observed trends in mean and extreme river flow attributed to man-made climate change. *Science*.
Gudmundsson, L., M. Leonard, H.X. Do, S. Westra, and S.I. Seneviratne, 2019: Observed Trends in Global Indicators of Mean and Extreme Streamflow. *Geophysical Research Letters*, **46**, 756–766, doi:10.1029/2018gl079725.
Guerreiro, S.B. et al., 2018: Detection of continental-scale intensification of hourly rainfall extremes. *Nature Climate Change*, **8(9)**, 803–807, doi:10.1038/s41558-018-0245-3.
Guerrieri, R. et al., 2019: Disentangling the role of photosynthesis and stomatal conductance on rising forest water-use efficiency. *Proceedings of the National Academy of Sciences of the United States of America*, **116(34)**, 16909–16914, doi:10.1073/pnas.1905912116.
Guhathakurta et al. et al., 2017: Trends and variability of meteorological drought over the districts of India using standardized precipitation index. *Journal of Earth System Science*, **126(8)**, 1–18, doi:10.1007/s12040-017-0896-x.
Gulizia, C. and I. Camilloni, 2015: Comparative analysis of the ability of a set of CMIP3 and CMIP5 global climate models to represent precipitation in South America. *International Journal of Climatology*, **35(4)**, 583–595, doi:10.1002/joc.4005.
Guo, J. et al., 2017: Declining frequency of summertime local-scale precipitation over eastern China from 1970 to 2010 and its potential link to aerosols. *Geophysical Research Letters*, **44(11)**, 5700–5708, doi:10.1002/2017gl073533.
Guo, L., A.G. Turner, and E.J. Highwood, 2016: Local and remote impacts of aerosol species on indian summer monsoon rainfall in a GCM. *Journal of Climate*, **29(19)**, 6937–6955, doi:10.1175/jcli-d-15-0728.1.
Guo, L. et al., 2017: Contribution of Tropical Cyclones to Atmospheric Moisture Transport and Rainfall over East Asia. *Journal of Climate*, **30(10)**, 3853–3865, doi:10.1175/jcli-d-16-0308.1.
Guo, R., C. Deser, L. Terray, and F. Lehner, 2019: Human Influence on Winter Precipitation Trends (1921–2015) over North America and Eurasia Revealed by Dynamical Adjustment. *Geophysical Research Letters*, **46(6)**, 3426–3434, doi:10.1029/2018gl081316.
Gusain, A., S. Ghosh, and S. Karmakar, 2020: Added value of CMIP6 over CMIP5 models in simulating Indian summer monsoon rainfall. *Atmospheric Research*, **232**, 104680, doi:10.1016/j.atmosres.2019.104680.

ACCEPTED VERSION SUBJECT TO FINAL EDITING

Gutenstein, M. et al., 2020: Intercomparison of freshwater fluxes over ocean and investigations into water budget closure. *Hydrology and Earth System Sciences Discussions*, **2020**, 1–35, doi:10.5194/hess-2020-317.
Gutmann, E.D. et al., 2018: Changes in hurricanes from a 13-year convection-permitting pseudo-global warming simulation. *J. Climate*, **31**, 3643–3657.
Guzha, A.C., M.C. Rufino, S. Okoth, S. Jacobs, and R.L.B. Nóbrega, 2018: Impacts of land use and land cover change on surface runoff, discharge and low flows: Evidence from East Africa. *Journal of Hydrology: Regional Studies*, **15**, 49–67, doi:10.1016/j.ejrh.2017.11.005.
Ha et al. et al., 2020: Future Changes of Summer Monsoon Characteristics and Evaporative Demand Over Asia in CMIP6 Simulations. *Geophysical Research Letters*, **47(8)**, 1–10, doi:10.1029/2020gl087492.
Haarsma, R.J. et al., 2016: High Resolution Model Intercomparison Project (HighResMIP v1.0) for CMIP6. *Geoscientific Model Development*, **9(11)**, 4185–4208, doi:10.5194/gmd-9-4185-2016.
Haertel, P., 2018: Sensitivity of the Madden Julian Oscillation to Ocean Warming in a Lagrangian Atmospheric Model. *Climate*, **6(2)**, 45, doi:10.3390/cli6020045.
Haerter, J.O. and L. Schlemmer, 2018: Intensified Cold Pool Dynamics Under Stronger Surface Heating. *Geophysical Research Letters*, **45(12)**, 6299–6310, doi:10.1029/2017gl076874.
Haghtalab, N., N. Moore, B.P. Heerspink, and D.W. Hyndman, 2020: Evaluating spatial patterns in precipitation trends across the Amazon basin driven by land cover and global scale forcings. *Theoretical and Applied Climatology*, **140(1–2)**, 411–427, doi:10.1007/s00704-019-03085-3.
Hagos, S., L.R. Leung, M. Ashfaq, and K. Balaguru, 2019: South Asian monsoon precipitation in CMIP5: a link between inter-model spread and the representations of tropical convection. *Climate Dynamics*, **52(1–2)**, 1049–1061, doi:10.1007/s00382-018-4177-4.
Hagos, S.M., L.R. Leung, J.-H. Yoon, J. Lu, and Y. Gao, 2016: A projection of changes in landfalling atmospheric river frequency and extreme precipitation over western North America from the Large Ensemble CESM simulations. *Geophysical Research Letters*, **43(3)**, 1357–1363, doi:10.1002/2015gl067392.
Ham, Y.G., J.S. Kug, J.Y. Choi, F.F. Jin, and M. Watanabe, 2018: Inverse relationship between present-day tropical precipitation and its sensitivity to greenhouse warming. *Nature Climate Change*, **8(1)**, 64–69, doi:10.1038/s41558-017-0033-5.
Hamada, A. and Y.N. Takayabu, 2018: Large-scale environmental conditions related to midsummer extreme rainfall events around Japan in the TRMM region. *Journal of Climate*, **31(17)**, 6933–6945, doi:10.1175/jcli-d-17-0632.1.
Hamada, A., Y.N. Takayabu, C. Liu, and E.J. Zipser, 2015: Weak linkage between the heaviest rainfall and tallest storms. *Nature Communications*, **6(1)**, 6213, doi:10.1038/ncomms7213.
Han, J. et al., 2017: Updates in the NCEP GFS Cumulus Convection Schemes with Scale and Aerosol Awareness. *Weather and Forecasting*, **32(5)**, 2005–2017, doi:10.1175/waf-d-17-0046.1.
Han, J.Y., J.J. Baik, and H. Lee, 2014: Urban impacts on precipitation. *Asia-Pacific Journal of Atmospheric Sciences*, **50(1)**, 17–30, doi:10.1007/s13143-014-0016-7.
Hanasaki, N., S. Yoshikawa, Y. Pokhrel, and S. Kanae, 2018: A global hydrological simulation to specify the sources of water used by humans. *Hydrology and Earth System Sciences*, **22(1)**, 789–817, doi:10.5194/hess-22-789-2018.
Hanel, M. et al., 2018: Revisiting the recent European droughts from a long-term perspective. *Scientific Reports*, doi:10.1038/s41598-018-27464-4.
Hanna, E., X. Fettweis, and R.J. Hall, 2018: Brief communication: Recent changes in summer Greenland blocking captured by none of the CMIP5 models. *Cryosphere*, **12(10)**, 3287–3292, doi:10.5194/tc-12-3287-2018.
Hanna, E. et al., 2013: The influence of North Atlantic atmospheric and oceanic forcing effects on 1900-2010 Greenland summer climate and ice melt/runoff. *International Journal of Climatology*, **33(4)**, 862–880, doi:10.1002/joc.3475.
Hansen, Z.K. and G.D. Libecap, 2004: Small farms, externalities, and the Dust Bowl of the 1930s. *Journal of Political Economy*, **112(3)**, 665–694.
Hari, V., G. Villarini, S. Karmakar, L.J. Wilcox, and M. Collins, 2020: Northward Propagation of the Inter Tropical Convergence Zone and Strengthening of Indian Summer Monsoon Rainfall. *Geophysical Research Letters*, **n/a(n/a)**, e2020GL089823, doi:10.1029/2020gl089823.
Harpold, A., M. Dettinger, and S. Rajagopal, 2017: Defining snow drought and why it matters. *Eos, Earth and Space Science News*, **98**, doi:10.1029/2017eo068775.
Harris, L.M., S.-J. Lin, and C.Y. Tu, 2016: High-Resolution Climate Simulations Using GFDL HiRAM with a Stretched Global Grid. *Journal of Climate*, **29(11)**, 4293–4314, doi:10.1175/jcli-d-15-0389.1.
Harrison, S.P. et al., 2015: Evaluation of CMIP5 palaeo-simulations to improve climate projections. *Nature Climate Change*, **5(8)**, 735–743.
Harrison, S.P.P. et al., 2014: Climate model benchmarking with glacial and mid-Holocene climates. *Climate Dynamics*, **43**, 671–688, doi:10.1007/s00382-013-1922-6.
Harrop, B.E. and D.L. Hartmann, 2016: The role of cloud radiative heating in determining the location of the ITCZ in aquaplanet simulations. *Journal of Climate*, doi:10.1175/jcli-d-15-0521.1.
Hartmann, A., T. Gleeson, Y. Wada, and T. Wagener, 2017: Enhanced groundwater recharge rates and altered recharge

ACCEPTED VERSION SUBJECT TO FINAL EDITING

sensitivity to climate variability through subsurface heterogeneity. *Proceedings of the National Academy of Sciences*, doi:10.1073/pnas.1614941114.

Hartmann, D.L.J.L. et al., 2013: Observations: Atmosphere and Surface. In: *Climate Change 2013: The Physical Science Basis. Contribution of Working Group I to the Fifth Assessment Report of the Intergovernmental Panel on Climate Change* [Stocker, T.F., D. Qin, G.-K. Plattner, M. Tignor, S.K. Allen, J. Boschung, A. Nauels, Y. Xia, V. Bex, and P.M. Midgley (eds.)]. Cambridge University Press, Cambridge, United Kingdom and New York, NY, USA, pp. 159–254, doi:10.1017/cbo9781107415324.008.

Hartmann, H., 2015: Carbon starvation during drought-induced tree mortality – are we chasing a myth? *Journal of Plant Hydraulics*, doi:10.20870/jph.2015.e005.

Harvey, B., P. Cook, L.C. Shaffrey, and R. Schiemann, 2020: The response of the Northern Hemisphere storm tracks and jetstreams to climate change in the CMIP3, CMIP5, and CMIP6 climate models. *Journal of Geophysical Research (Atmospheres)*, **(submitted**.

Hassim, M.E.E. and B. Timbal, 2019: Observed Rainfall Trends over Singapore and the Maritime Continent from the Perspective of Regional-Scale Weather Regimes. *Journal of Applied Meteorology and Climatology*, **58(2)**, 365–384, doi:10.1175/jamc-d-18-0136.1.

Hasson, 2014: Seasonality of the hydrological cycle in major South and Southeast Asian river basins as simulated by PCMDI / CMIP3 experiments. , 67–87, doi:10.5194/esd-5-67-2014.

Hasson, S. et al., 2016: Seasonal cycle of Precipitation over Major River Basins in South and Southeast Asia: A Review of the CMIP5 climate models data for present climate and future climate projections. *Atmospheric Research*, **180**, 42–63, doi:10.1016/j.atmosres.2016.05.008.

Haszpra, T., M. Herein, and T. Bódai, 2020: Investigating ENSO and its teleconnections under climate change in an ensemble view – a new perspective. *Earth System Dynamics*, **11(1)**, 267–280, doi:10.5194/esd-11-267-2020.

Hattermann, F.F. et al., 2018: Sources of uncertainty in hydrological climate impact assessment: a cross-scale study. *Environmental Research Letters*, **13(1)**, 015006, doi:10.1088/1748-9326/aa9938.

Haug, G.H. et al., 2003: Climate and the collapse of Maya civilization. *Science*, doi:10.1126/science.1080444.

Havel, A., A. Tasdighi, and M. Arabi, 2018: Assessing the hydrologic response to wildfires in mountainous regions. *Hydrology and Earth System Sciences*, **22(4)**, 2527–2550, doi:10.5194/hess-22-2527-2018.

Haverd, V. et al., 2018: A new version of the CABLE land surface model (Subversion revision r4601) incorporating land use and land cover change, woody vegetation demography, and a novel optimisation-based approach to plant coordination of photosynthesis. *Geoscientific Model Development*, **11**, 2995–3026, doi:10.5194/gmd-11-2995-2018.

Hawcroft, M., E. Walsh, K. Hodges, and G. Zappa, 2018: Significantly increased extreme precipitation expected in Europe and North America from extratropical cyclones. *Environmental Research Letters*, **13(12)**, doi:10.1088/1748-9326/aaed59.

Hawcroft, M.K., L.C. Shaffrey, K.I. Hodges, and H.F. Dacre, 2016: Can climate models represent the precipitation associated with extratropical cyclones? *Climate Dynamics*, doi:10.1007/s00382-015-2863-z.

Hawkins, E. and R. Sutton, 2011: The potential to narrow uncertainty in projections of regional precipitation change. *Climate Dynamics*, **37(1)**, 407–418, doi:10.1007/s00382-010-0810-6.

Hawkins, E. and R. Sutton, 2012: Time of emergence of climate signals. *Geophysical Research Letters*, **39(1)**, doi:10.1029/2011gl050087.

Hawkins, E. et al., 2020: Observed Emergence of the Climate Change Signal: From the Familiar to the Unknown. *Geophysical Research Letters*, **47(6)**, doi:10.1029/2019gl086259.

Hayashi, M., 2020: Alpine Hydrogeology: The Critical Role of Groundwater in Sourcing the Headwaters of the World. *Groundwater*, **58(4)**, 498–510, doi:10.1111/gwat.12965.

Haywood, A.M. et al., 2013: Large-scale features of Pliocene climate: Results from the Pliocene Model Intercomparison Project. *Climate of the Past*, 191–209, doi:10.5194/cp-9-191-2013.

Haywood, J.M., A. Jones, N. Bellouin, and D. Stephenson, 2013: Asymmetric forcing from stratospheric aerosols impacts Sahelian rainfall. *Nature Climate Change*, **3(7)**, 660–665, doi:10.1038/nclimate1857.

He, C., B. Wu, L. Zou, and T. Zhou, 2017: Responses of the Summertime Subtropical Anticyclones to Global Warming. *Journal of Climate*, **30(16)**, 6465–6479, doi:10.1175/jcli-d-16-0529.1.

He, J. and B.J. Soden, 2015: Anthropogenic weakening of the tropical circulation: The relative roles of direct CO2 forcing and sea surface temperature change. *Journal of Climate*, **28(22)**, 8728–8742, doi:10.1175/jcli-d-15-0205.1.

He, J. and B.J. Soden, 2017: A re-examination of the projected subtropical precipitation decline. *Nature Climate Change*, **7(1)**, 53–57, doi:10.1038/nclimate3157.

He, J. et al., 2018: Precipitation sensitivity to local variations in tropical sea surface temperature. *Journal of Climate*, **31(22)**, 9225–9238, doi:10.1175/jcli-d-18-0262.1.

Heede, U.K., A. Fedorov, and N.J. Burls, 2020: Time Scales and Mechanisms for the Tropical Pacific Response to Global Warming: A Tug of War between the Ocean Thermostat and Weaker Walker. *Journal of Climate*, **33(14)**, 6101–6118, doi:10.1175/jcli-d-19-0690.1.

Heerspink, B.P., A.D. Kendall, M.T. Coe, and D.W. Hyndman, 2020: Trends in streamflow, evapotranspiration, and

ACCEPTED VERSION SUBJECT TO FINAL EDITING

groundwater storage across the Amazon Basin linked to changing precipitation and land cover. *Journal of Hydrology: Regional Studies*, **32**, 100755, doi:10.1016/j.ejrh.2020.100755.
Hegerl, G.C. et al., 2015: Challenges in quantifying changes in the global water cycle. *Bulletin of the American Meteorological Society*, **96(7)**, 1097–1115, doi:10.1175/bams-d-13-00212.1.
Hein, A., L. Condon, and R. Maxwell, 2018: Unravelling the impacts of precipitation, temperature and land-cover change for extreme drought over the North American High Plains. *Hydrology and Earth System Sciences Discussions*, 1–30, doi:10.5194/hess-2018-485.
Heinzeller, D., W. Junkermann, and H. Kunstmann, 2016: Anthropogenic Aerosol Emissions and Rainfall Decline in Southwestern Australia: Coincidence or Causality? *Journal of Climate*, **29(23)**, 8471–8493, doi:10.1175/jcli-d-16-0082.1.
Held, I.M. and B.J. Soden, 2006a: Robust responses of the hydrologic cycle to global warming. *J. Clim.*, **19**, 5686–5699, doi:10.1175/jcli3990.1.
Held, I.M. and B.J. Soden, 2006b: Robust responses of the hydrological cycle to global warming (vol 19, pg 5686, 2006). *Journal of Climate*, **19(5)**, 5686–5699, doi:10.1175/2010jcli4045.1.
Herger, N., B.M. Sanderson, and R. Knutti, 2015: Improved pattern scaling approaches for the use in climate impact studies Supplementary Information. *Geophysical Research Letters*, **42(9)**, n/a–n/a, doi:10.1002/2015gl063569.
Hernández-Henríquez, M.A., S.J. Déry, and C. Derksen, 2015: Polar amplification and elevation-dependence in trends of Northern Hemisphere snow cover extent, 1971–2014. *Environmental Research Letters*, **10(4)**, 044010, doi:10.1088/1748-9326/10/4/044010.
Hessl, A.E. et al., 2018: Past and future drought in Mongolia. *Science Advances*, **4(3)**, e1701832.
Hewson, M., H. McGowan, S. Phinn, S. Peckham, and G. Grell, 2013: Exploring aerosol effects on rainfall for Brisbane, Australia. *Climate*, **1(3)**, 120–147.
Hill, S.A., Y. Ming, I.M. Held, and M. Zhao, 2017: A Moist Static Energy Budget–Based Analysis of the Sahel Rainfall Response to Uniform Oceanic Warming. *Journal of Climate*, **30(15)**, 5637–5660, doi:10.1175/jcli-d-16-0785.1.
Hirasawa, H.A.R.U.K.I., P.A.U.L.J. Kushner, M.I.C.H.A.E.L. Sigmond, J.O.H.N. Fyfe, and C.L.A.R.A. Deser, 2020: Anthropogenic aerosols dominate forced multidecadal sahel precipitation change through distinct atmospheric and oceanic drivers. *Journal of Climate*, **33(23)**, 10187–10204, doi:10.1175/jcli-d-19-0829.1.
Hirons, L. and A. Turner, 2018: The Impact of Indian Ocean Mean-State Biases in Climate Models on the Representation of the East African Short Rains. *Journal of Climate*, **31(16)**, 6611–6631, doi:10.1175/jcli-d-17-0804.1.
Hock, R., G. Rasul, C. Adler, and et al, 2019a: High Mountain Areas In: IPCC Special Report on the Ocean and Cryosphere in a Changing Climate [H.-O. Pörtner, D.C. Roberts, V. Masson-Delmotte, P. Zhai, M. Tignor, E. Poloczanska, K. Mintenbeck, A. Alegría, M. Nicolai, A. Okem, J. Petzold, B. Rama, N.M.. *Special Report on the Ocean and Cryosphere in a Changing Climate*.
Hock, R. et al., 2019b: GlacierMIP - A model intercomparison of global-scale glacier mass-balance models and projections. *Journal of Glaciology*, **65(251)**, 453–467.
Hodges, K.I., R.W. Lee, and L. Bengtsson, 2011: A comparison of extratropical cyclones in recent reanalyses ERA-Interim, NASA MERRA, NCEP CFSR, and JRA-25. *Journal of Climate*, **24(18)**, 4888–4906, doi:10.1175/2011jcli4097.1.
Hodnebrog et al., 2019a: Intensification of summer precipitation with shorter time-scales in Europe. *Environmental Research Letters*, **14(12)**, 124050, doi:10.1088/1748-9326/ab549c.
Hodnebrog et al., 2019b: Water vapour adjustments and responses differ between climate drivers. *Atmos. Chem. Phys.*, **19(20)**, 12887–12899, doi:10.5194/acp-19-12887-2019.
Hoegh-Guldberg, O. et al., 2018: Impacts of 1.5°C Global Warming on Natural and Human Systems. In: *IPCC Special Report on the impacts of global warming of 1.5°C above pre-industrial levels and related global greenhouse gas emission pathways, in the context of strengthening the global response to the threat of climate change.* [Masson-Delmotte, V., P. Zhai, H.-O. Pörtner, D. Roberts, J. Skea, P.R. Shukla, A. Pirani, W. Moufouma-Okia, C. Péan, R. Pidcock, S. Connors, J.B.R. Matthews, Y. Chen, X. Zhou, M.I. Gomis, E. Lonnoy, T. Maycock, M. Tignor, and T. Waterfield (eds.)]. In Press, pp. 175–311.
Hoegh-Guldberg, O. et al., 2019: Impacts of 1.5°C global warming on natural and human systems. *IPCC Special Report on the impacts of global warming of 1.5°C above pre-industrial levels and related global greenhouse gas emission pathways, in the context of strengthening the global response to the threat of climate change.* 175–311.
Hoell, A. and L. Cheng, 2018: Austral summer Southern Africa precipitation extremes forced by the El Niño-Southern oscillation and the subtropical Indian Ocean dipole. *Climate Dynamics*, **50(9–10)**, 3219–3236, doi:10.1007/s00382-017-3801-z.
Hoell, A., C. Funk, M. Barlow, and S. Shukla, 2016: Recent and Possible Future Variations in the North American Monsoon. In: *The Monsoons and Climate Change* [de Carvalho, L.M.V. and C. Jones (eds.)]. Springer, pp. 149–162, doi:10.1007/978-3-319-21650-8_7.
Hoell, A., C. Funk, J. Zinke, and L. Harrison, 2017a: Modulation of the Southern Africa precipitation response to the El

ACCEPTED VERSION SUBJECT TO FINAL EDITING

Niño Southern Oscillation by the subtropical Indian Ocean Dipole. *Climate Dynamics*, **48(7–8)**, 2529–2540, doi:10.1007/s00382-016-3220-6.
Hoell, A., M. Hoerling, J. Eischeid, X.-W. Quan, and B. Liebmann, 2017b: Reconciling Theories for Human and Natural Attribution of Recent East Africa Drying. *Journal of Climate*, **30(6)**, 1939–1957, doi:10.1175/jcli-d-16-0558.1.
Hoerling, M. et al., 2012: On the increased frequency of mediterranean drought. *Journal of Climate*, doi:10.1175/jcli-d-11-00296.1.
Hohenegger, C. and B. Stevens, 2018: The role of the permanent wilting point in controlling the spatial distribution of precipitation. *Proceedings of the National Academy of Sciences*, **115(22)**, 5692–5697, doi:10.1073/pnas.1718842115.
Holloway, C.E. et al., 2017: Observing Convective Aggregation. *Surveys in Geophysics*, **38(6)**, 1199-1236, doi:10.1007/s10712-017-9419-1.
Holz, A. et al., 2017: Southern Annular Mode drives multicentury wildfire activity in southern South America. *Proceedings of the National Academy of Sciences*, **114(36)**, 9552–9557, doi:10.1073/pnas.1705168114.
Hong, B. et al., 2018: The respective characteristics of millennial-scale changes of the India summer monsoon in the Holocene and the Last Glacial. *Palaeogeography, Palaeoclimatology, Palaeoecology*, **496**, 155–165, doi:10.1016/j.palaeo.2018.01.033.
Hooper, J. and S. Marx, 2018: A global doubling of dust emissions during the Anthropocene? *Global and Planetary Change*, doi:10.1016/j.gloplacha.2018.07.003.
Hopcroft, P.O., P.J. Valdes, A.B. Harper, and D.J. Beerling, 2017: Multi vegetation model evaluation of the Green Sahara climate regime. *Geophysical Research Letters*, doi:10.1002/2017gl073740.
Hope, P., B.J. Henley, J. Gergis, J. Brown, and H. Ye, 2017: Time-varying spectral characteristics of ENSO over the Last Millennium. *Climate Dynamics*, **49(5)**, 1705–1727, doi:10.1007/s00382-016-3393-z.
Hope, P. et al., 2015: Seasonal and regional signature of the projected southern Australian rainfall reduction. *Australian Meteorological and Oceanographic Journal*, **65(1)**, 54–71, doi:10.22499/2.6501.005.
Horinouchi, T., S. Matsumura, T. Ose, and Y.N. Takayabu, 2019: Jet–Precipitation Relation and Future Change of the Mei-Yu–Baiu Rainband and Subtropical Jet in CMIP5 Coupled GCM Simulations. *Journal of Climate*, **32(8)**, 2247–2259, doi:10.1175/jcli-d-18-0426.1.
Horton, D.E. et al., 2015: Contribution of changes in atmospheric circulation patterns to extreme temperature trends. *Nature*, **522(7557)**, 465–469, doi:10.1038/nature14550.
Hourdin, F. et al., 2013: LMDZ5B: the atmospheric component of the IPSL climate model with revisited parameterizations for clouds and convection. *Clim Dyn*, **40(2193)**, 12–382.
Hristova-Veleva, S.M. et al., 2020: An Eye on the Storm: Integrating a Wealth of Data for Quickly Advancing the Physical Understanding and Forecasting of Tropical Cyclones. *Bulletin of the American Meteorological Society*, **101(10)**, E1718–E1742, doi:10.1175/bams-d-19-0020.1.
Hsu, H.-H., T. Zhou, and J. Matsumoto, 2014: East Asian, Indochina and Western North Pacific Summer Monsoon - An update. *Asia-Pacific Journal of Atmospheric Sciences*, **50(1)**, 45–68, doi:10.1007/s13143-014-0027-4.
Hu, Q., J.A. Torres-Alavez, and M.S. Van Den Broeke, 2018: Land-cover change and the "Dust Bowl" drought in the U.S. Great Plains. *Journal of Climate*, doi:10.1175/jcli-d-17-0515.1.
Hu, Z. et al., 2019: Groundwater Depletion Estimated from GRACE: A Challenge of Sustainable Development in an Arid Region of Central Asia. *Remote Sensing*, **11(16)**, doi:10.3390/rs11161908.
Hu, Z.-Z., 2003: Long-term climate variations in China and global warming signals. *Journal of Geophysical Research*, **108(D19)**, 4614, doi:10.1029/2003jd003651.
Hua, W., A. Dai, L. Zhou, M. Qin, and H. Chen, 2019: An Externally Forced Decadal Rainfall Seesaw Pattern Over the Sahel and Southeast Amazon. *Geophysical Research Letters*, **46(2)**, 923–932, doi:10.1029/2018gl081406.
Hua, W. et al., 2016: Possible causes of the Central Equatorial African long-term drought. *Environmental Research Letters*, doi:10.1088/1748-9326/11/12/124002.
Hua, W. et al., 2018: Understanding the Central Equatorial African long-term drought using AMIP-type simulations. *Climate Dynamics*, **50(3–4)**, 1115–1128, doi:10.1007/s00382-017-3665-2.
Huang, D. et al., 2018: Uncertainty of global summer precipitation in the CMIP5 models: a comparison between high-resolution and low-resolution models. *Theoretical and Applied Climatology*, **132(1–2)**, 55–69, doi:10.1007/s00704-017-2078-9.
Huang, J., T. Wang, W. Wang, Z. Li, and H. Yan, 2014: Climate effects of dust aerosols over east asian arid and semiarid regions. *Journal of Geophysical Research*, doi:10.1002/2014jd021796.
Huang, P., X.-T. Zheng, and J. Ying, 2019: Disentangling the Changes in the Indian Ocean Dipole–Related SST and Rainfall Variability under Global Warming in CMIP5 Models. *Journal of Climate*, **32(13)**, 3803–3818, doi:10.1175/jcli-d-18-0847.1.
Huang, S., B. Wang, and Z. Wen, 2020: Dramatic Weakening of the Tropical Easterly Jet Projected by CMIP6 Models. *Journal of Climate*, **33(19)**, 8439–8455, doi:10.1175/jcli-d-19-1002.1.
Huang, S. et al., 2017: Evaluation of an ensemble of regional hydrological models in 12 large-scale river basins worldwide. *Climatic Change*, **141(3)**, 381–397, doi:10.1007/s10584-016-1841-8.

ACCEPTED VERSION SUBJECT TO FINAL EDITING

Huang, S. et al., 2018: Multimodel assessment of flood characteristics in four large river basins at global warming of 1.5, 2.0 and 3.0 K above the pre-industrial level. *Environmental Research Letters*, **13(12)**, 124005, doi:10.1088/1748-9326/aae94b.

Huang, X. et al., 2020a: South Asian summer monsoon projections constrained by the interdecadal Pacific oscillation. *Science Advances*, **6(11)**, eaay6546, doi:10.1126/sciadv.aay6546.

Huang, X. et al., 2020b: The Recent Decline and Recovery of Indian Summer Monsoon Rainfall: Relative Roles of External Forcing and Internal Variability. *Journal of Climate*, **33(12)**, 5035–5060, doi:10.1175/jcli-d-19-0833.1.

Huang, Y., S. Gerber, T. Huang, and J.W. Lichstein, 2016: Evaluating the drought response of CMIP5 models using global gross primary productivity, leaf area, precipitation, and soil moisture data. *Global Biogeochemical Cycles*, **30(12)**, 1827–1846, doi:10.1002/2016gb005480.

Hui, C. and X.-T. Zheng, 2018: Uncertainty in Indian Ocean Dipole response to global warming: the role of internal variability. *Climate Dynamics*, doi:10.1007/s00382-018-4098-2.

Humphrey, V., L. Gudmundsson, and S.I. Seneviratne, 2017: A global reconstruction of climate-driven subdecadal water storage variability. *Geophysical Research Letters*, **44(5)**, 2300–2309, doi:10.1002/2017gl072564.

Hung, M.-P. et al., 2013: MJO and Convectively Coupled Equatorial Waves Simulated by CMIP5 Climate Models. *Journal of Climate*, **26(17)**, 6185–6214, doi:10.1175/jcli-d-12-00541.1.

Hunt, K.M.R., A.G. Turner, and L.C. Shaffrey, 2018: The evolution, seasonality and impacts of western disturbances. *Quarterly Journal of the Royal Meteorological Society*, **144(710)**, 278–290, doi:10.1002/qj.3200.

Huntington, T.G., 2006: Evidence for intensification of the global water cycle: Review and synthesis. *Journal of Hydrology*, **319(1–4)**, 83–95, doi:10.1016/j.jhydrol.2005.07.003.

Huss, M. and R. Hock, 2018: Global-scale hydrological response to future glacier mass loss. *Nature Climate Change*, **8(2)**, 135–140, doi:10.1038/s41558-017-0049-x.

Hwang, Y.-T.T., D.M.W.W. Frierson, and S.M. Kang, 2013: Anthropogenic sulfate aerosol and the southward shift of tropical precipitation in the late 20th century. *Geophysical Research Letters*, **40(11)**, 2845–2850, doi:10.1002/grl.50502.

Ibarra, D.E. et al., 2018: Warm and cold wet states in the western United States during the Pliocene-Pleistocene. *Geology*, **46(4)**, 355–358, doi:10.1130/g39962.1.

Iles, C.E. and G.C. Hegerl, 2015: Systematic change in global patterns of streamflow following volcanic eruptions. *Nature Geoscience*, **8(11)**, 838–842, doi:10.1038/ngeo2545.

Iles, C.E., G.C. Hegerl, and G. Iles, C., Heger, 2014: The global precipitation response to volcanic eruptions in the CMIP5 models. *Environmental Research Letters*, **9(10)**, 104012, doi:10.1088/1748-9326/9/10/104012.

Imfeld, N. et al., 2020: A combined view on precipitation and temperature climatology and trends in the southern Andes of Peru. *International Journal of Climatology*, **41**, 679–698, doi:10.1002/joc.6645.

Immerzeel, W.W. et al., 2020: Importance and vulnerability of the world's water towers. *Nature*, **577(7790)**, 364–369, doi:10.1038/s41586-019-1822-y.

Ionita, M., V. Nagavciuc, and B. Guan, 2020: Rivers in the sky, flooding on the ground: the role of atmospheric rivers in inland flooding in central Europe. *Hydrol. Earth Syst. Sci.*, **24(11)**, 5125–5147, doi:10.5194/hess-24-5125-2020.

IPCC, 2013: Climate Change 2013: The Physical Science Basis. Contribution of Working Group I to the Fifth Assessment Report of the Intergovernmental Panel on Climate Change. [Stocker, T.F., D. Qin, G.-K. Plattner, M. Tignor, S.K. Allen, J. Boschung, A. Nauels, Y. Xia, V. Bex, and P.M. Midgley (eds.)]. Cambridge University Press, Cambridge, United Kingdom and New York, NY, USA, 1535 pp., doi:10.1017/cbo9781107415324.

IPCC, 2018: Summary for Policymakers. In: *Global Warming of 1.5°C. An IPCC Special Report on the impacts of global warming of 1.5°C above pre-industrial levels and related global greenhouse gas emission pathways, in the context of strengthening the global response to the threat of climate change,* [Masson-Delmotte, V., P. Zhai, H.-O. Pörtner, D. Roberts, J. Skea, P.R. Shukla, A. Pirani, W. Moufouma-Okia, C. Péan, R. Pidcock, S. Connors, J.B.R. Matthews, Y. Chen, X. Zhou, M.I. Gomis, E. Lonnoy, T. Maycock, M. Tignor, and T. Waterfield (eds.)]. In Press, pp. 1–30.

Irvine, P. et al., 2019: Halving warming with idealized solar geoengineering moderates key climate hazards. *Nature Climate Change*, doi:10.1038/s41558-019-0398-8.

Ishizaki, Y. et al., 2013: Dependence of precipitation scaling patterns on emission scenarios for representative concentration pathways. *Journal of Climate*, **26(22)**, 8868–8879, doi:10.1175/jcli-d-12-00540.1.

Jackson, L.C. et al., 2015: Global and European climate impacts of a slowdown of the AMOC in a high resolution GCM. *Climate Dynamics*, doi:10.1007/s00382-015-2540-2.

Jackson, L.S., J.A. Crook, and P.M. Forster, 2016: An intensified hydrological cycle in the simulation of geoengineering by cirrus cloud thinning using ice crystal fall speed changes. *Journal of Geophysical Research: Atmospheres*, **121(12)**, 6822–6840, doi:10.1002/2015jd024304.

Jackson, L.S. et al., 2020: The Effect of Explicit Convection on Couplings between Rainfall, Humidity, and Ascent over Africa under Climate Change. *Journal of Climate*, **33(19)**, 8315–8337, doi:10.1175/jcli-d-19-0322.1.

ACCEPTED VERSION SUBJECT TO FINAL EDITING

Jacob, D. et al., 2014: EURO-CORDEX: New high-resolution climate change projections for European impact research. *Regional Environmental Change*, **14(2)**, 563–578, doi:10.1007/s10113-013-0499-2.
Jakob, C., M.S. Singh, and L. Jungandreas, 2019: Radiative Convective Equilibrium and Organized Convection: An Observational Perspective. *Journal of Geophysical Research: Atmospheres*, **124(10)**, 5418–5430, doi:10.1029/2018jd030092.
Jalihal, C., J. Srinivasan, and A. Chakraborty, 2019: Modulation of Indian monsoon by water vapor and cloud feedback over the past 22,000 years. *Nature Communications*, **10(1)**, 5701, doi:10.1038/s41467-019-13754-6.
James, R., R. Washington, C.F. Schleussner, J. Rogelj, and D. Conway, 2017: Characterizing half-a-degree difference: a review of methods for identifying regional climate responses to global warming targets. *Wiley Interdisciplinary Reviews: Climate Change*, **8(2)**, doi:10.1002/wcc.457.
Jansen, E. et al., 2007: Palaeoclimate. In: *Climate Change 2007: The Physical Science Basis. Contribution of Working Group I to the Fourth Assessment Report of the Intergovernmental Panel on Climate Change* [Solomon, S., D. Qin, M. Manning, Z. Chen, M. Marquis, K.B. Averyt, M. Tignor, and H.L. Miller (eds.)]. Cambridge Univeristy Press, Cambridge, United Kingdom and New York, NY, USA, pp. 434–497.
Jasechko, S. and R.G. Taylor, 2015: Intensive rainfall recharges tropical groundwaters. *Environmental Research Letters*, **10(12401)**, 5.
Jeevanjee, N. and D.M. Romps, 2018: Mean precipitation change from a deepening troposphere. *Proceedings of the National Academy of Sciences*, 201720683, doi:10.1073/pnas.1720683115.
Jefferson, J.L. and R.M. Maxwell, 2015: Evaluation of simple to complex parameterizations of bare ground evaporation. *Journal of Advances in Modeling Earth Systems*, **7(3)**, 1075–1092, doi:10.1002/2014ms000398.
Jemai, H., M. Ellouze, H. Abida, and B. Laignel, 2018: Spatial and temporal variability of rainfall: case of Bizerte-Ichkeul Basin (Northern Tunisia). *Arabian Journal of Geosciences*, **11(8)**, 177, doi:10.1007/s12517-018-3482-x.
Jia, G. et al., 2020: Land–Climate interactions. *Climate Change and Land: an IPCC special report on climate change, desertification, land degradation, sustainable land management, food security, and greenhouse gas fluxes in terrestrial ecosystems*, In Press.
Jiang, P., D. Wang, and Y. Cao, 2016: Spatiotemporal characteristics of precipitation concentration and their possible links to urban extent in China. *Theoretical and Applied Climatology*, **123(3–4)**, 757–768, doi:10.1007/s00704-015-1393-2.
Jiang, X. et al., 2015: Vertical structure and physical processes of the Madden-Julian oscillation: Exploring key model physics in climate simulations. *Journal of Geophysical Research: Atmospheres*, **120(10)**, 4718–4748, doi:10.1002/2014jd022375.
Jiang, X. et al., 2020: Fifty Years of Research on the Madden-Julian Oscillation: Recent Progress, Challenges, and Perspectives. *Journal of Geophysical Research: Atmospheres*, doi:10.1029/2019jd030911.
Jiménez Cisneros, B.E. et al., 2014: Freshwater resources. In: *Climate Change 2014: Impacts, Adaptation, and Vulnerability. Part A: Global and Sectoral Aspects. Contribution of Working Group II to the Fifth Assessment Report of the Intergovernmental Panel of Climate Change* [Field, C.B., V.R. Barros, D.J. Dokken, K.J. Mach, M.D. Mastrandrea, T.E. Bilir, M. Chatterjee, K.L. Ebi, Y.O. Estrada, R.C. Genova, B. Girma, E.S. Kissel, A.N. Levy, S. MacCracken, P.R. Mastrandrea, and L.L. White (eds.)]. Cambridge University Press, Cambridge, United Kingdom and New York, NY, USA, pp. 229–269, doi:10.1017/cbo9781107415379.008.
Jin, C., B. Wang, and J. Liu, 2020: Future Changes and Controlling Factors of the Eight Regional Monsoons Projected by CMIP6 Models. *Journal of Climate*, **33(21)**, 9307–9326, doi:10.1175/jcli-d-20-0236.1.
Jin, D. and Z. Guan, 2017: Summer Rainfall Seesaw between Hetao and the Middle and Lower Reaches of the Yangtze River and Its Relationship with the North Atlantic Oscillation. *Journal of Climate*, **30(17)**, 6629–6643, doi:10.1175/jcli-d-16-0760.1.
Jin, Q. and C. Wang, 2017: A revival of Indian summer monsoon rainfall since 2002. *Nature Climate Change*, **7(8)**, 587–594, doi:10.1038/nclimate3348.
Jing, X. et al., 2017: A Multimodel Study on Warm Precipitation Biases in Global Models Compared to Satellite Observations. *Journal of Geophysical Research: Atmospheres*, **122(21)**, 11,806–11,824, doi:10.1002/2017jd027310.
Joetzjer, E. et al., 2014: Predicting the response of the Amazon rainforest to persistent drought conditions under current and future climates: A major challenge for global land surface models. *Geoscientific Model Development*, **7(6)**, 2933–2950, doi:10.5194/gmd-7-2933-2014.
Johnson, S.J. et al., 2016: The resolution sensitivity of the South Asian monsoon and Indo-Pacific in a global 0.35° AGCM. *Climate Dynamics*, **46(3–4)**, 807–831, doi:10.1007/s00382-015-2614-1.
Jolly, D. et al., 1998: Biome reconstruction from pollen and plant macrofossil data for Africa and the Arabian peninsula at 0 and 6000 years. *Journal of Biogeography*, **25(6)**, 1007–1027.
Jones, A. et al., 2013: The impact of abrupt suspension of solar radiation management (termination effect) in experiment G2 of the Geoengineering Model Intercomparison Project (GeoMIP). , **118**, 9743–9752, doi:10.1002/jgrd.50762.
Jones, C. and L.M.V. Carvalho, 2013: Climate Change in the South American Monsoon System: Present Climate and

ACCEPTED VERSION SUBJECT TO FINAL EDITING

CMIP5 Projections. *Journal of Climate*, **26(17)**, 6660–6678, doi:10.1175/jcli-d-12-00412.1.
Jones, C.D. et al., 2013: Uncertainties in CMIP5 Climate Projections due to Carbon Cycle Feedbacks. *Journal of Climate*, **27(2)**, 511–526, doi:10.1175/jcli-d-12-00579.1.
Joseph, G. et al., 2016: Stable isotopes in atmospheric water vapor and applications to the hydrologic cycle. *Reviews of Geophysics*, **54(4)**, 809–865, doi:10.1002/2015rg000512.
Joshi, M.M., A.G. Turner, and C. Hope, 2013: The use of the land-sea warming contrast under climate change to improve impact metrics. , 951–960, doi:10.1007/s10584-013-0715-6.
Jourdain, N.C. et al., 2013: The Indo-Australian monsoon and its relationship to ENSO and IOD in reanalysis data and the CMIP3/CMIP5 simulations. *Climate Dynamics*, **41(11–12)**, 3073–3102, doi:10.1007/s00382-013-1676-1.
Jung, T., S.K. Gulev, I. Rudeva, and V. Soloviov, 2006: Sensitivity of extratropical cyclone characteristics to horizontal resolution in the ECMWF model. *Quarterly Journal of the Royal Meteorological Society*, **132(619)**, 1839–1857, doi:10.1256/qj.05.212.
Junk, W.J. et al., 2013: Current state of knowledge regarding the world's wetlands and their future under global climate change: A synthesis. *Aquatic Sciences*, doi:10.1007/s00027-012-0278-z.
Kageyama, M. et al., 2013: Climatic impacts of fresh water hosing under last glacial Maximum conditions: A multi-model study. *Climate of the Past*, **9(2)**, 935–953, doi:10.5194/cp-9-935-2013.
Kageyama, M. et al., 2018: The PMIP4 contribution to CMIP6 – Part 1: Overview and over-arching analysis plan. *Geoscientific Model Development*, **11(3)**, 1033–1057, doi:10.5194/gmd-11-1033-2018.
Kalimeris, A., E. Ranieri, D. Founda, and C. Norrant, 2017: Variability modes of precipitation along a Central Mediterranean area and their relations with ENSO, NAO, and other climatic patterns. *Atmospheric Research*, **198**, 56–80, doi:10.1016/j.atmosres.2017.07.031.
Kam, J., T.R. Knutson, and P.C.D. Milly, 2018: Climate model assessment of changes in winter-spring streamflow timing over North America. *Journal of Climate*, **31(14)**, 5581–5593, doi:10.1175/jcli-d-17-0813.1.
Kamae, Y., W. Mei, and S.-P. Xie, 2019: Ocean warming pattern effects on future changes in East Asian atmospheric rivers. *Environmental Research Letters*, **14(5)**, 54019, doi:10.1088/1748-9326/ab128a.
Kamae, Y., W. Mei, S.-P. Xie, M. Naoi, and H. Ueda, 2017: Atmospheric Rivers over the Northwestern Pacific: Climatology and Interannual Variability. *Journal of Climate*, **30(15)**, 5605–5619, doi:10.1175/jcli-d-16-0875.1.
Kanemaru, K. et al., 2017: Development of a Precipitation Climate Record from Spaceborne Precipitation Radar Data. Part I: Mitigation of the Effects of Switching to Redundancy Electronics in the TRMM Precipitation Radar. *Journal of Atmospheric and Oceanic Technology*, **34(9)**, 2043–2057, doi:10.1175/jtech-d-17-0026.1.
Kang, D.H., H. Gao, X. Shi, S.U. Islam, and S.J. Déry, 2016: Impacts of a Rapidly Declining Mountain Snowpack on Streamflow Timing in Canada's Fraser River Basin. *Scientific Reports*, **6(1)**, 1–8, doi:10.1038/srep19299.
Kang, S. et al., 2018: Late Holocene anti-phase change in the East Asian summer and winter monsoons. *Quaternary Science Reviews*, **188**, 28–36, doi:10.1016/j.quascirev.2018.03.028.
Kang, S.M. and L.M. Polvani, 2011: The Interannual Relationship between the Latitude of the Eddy-Driven Jet and the Edge of the Hadley Cell. *Journal of Climate*, **24(2)**, 563–568, doi:10.1175/2010jcli4077.1.
Kang, S.M., C. Deser, and L.M. Polvani, 2013: Uncertainty in climate change projections of the hadley circulation: The role of internal variability. *Journal of Climate*, doi:10.1175/jcli-d-12-00788.1.
Kang, S.M., I.M. Held, D.M.W. Frierson, and M. Zhao, 2008: The response of the ITCZ to extratropical thermal forcing: Idealized slab-ocean experiments with a GCM. *Journal of Climate*, **21(14)**, 3521–3532, doi:10.1175/2007jcli2146.1.
Kanji, Z.A. et al., 2017: Overview of Ice Nucleating Particles. *Meteorological Monographs*, **58**, 1.1–1.33, doi:10.1175/amsmonographs-d-16-0006.1.
Kanner, L.C., S.J. Burns, H. Cheng, R.L. Edwards, and M. Vuille, 2013: High-resolution variability of the South American summer monsoon over the last seven millennia: Insights from a speleothem record from the central Peruvian Andes. *Quaternary Science Reviews*, **75**, 1–10, doi:10.1016/j.quascirev.2013.05.008.
Kapnick, S. and A. Hall, 2012: Causes of recent changes in western North American snowpack. *Climate Dynamics*, **38(9–10)**, 1885–1899.
Karim, F. et al., 2016: Impact of climate change on floodplain inundation and hydrological connectivity between wetlands and rivers in a tropical river catchment. *Hydrological Processes*, doi:10.1002/hyp.10714.
Karmakar, N., A. Chakraborty, and R.S. Nanjundiah, 2017: Increased sporadic extremes decrease the intraseasonal variability in the Indian summer monsoon rainfall. *Scientific Reports*, **7(1)**, 7824, doi:10.1038/s41598-017-07529-6.
Kasoar, M., D. Shawki, and A. Voulgarakis, 2018: Similar spatial patterns of global climate response to aerosols from different regions. *npj Climate and Atmospheric Science*, **1(1)**, 12, doi:10.1038/s41612-018-0022-z.
Kay, J.E. et al., 2015: The Community Earth System Model (CESM) Large Ensemble Project: A Community Resource for Studying Climate Change in the Presence of Internal Climate Variability. *Bulletin of the American Meteorological Society*, **96(8)**, 1333–1349, doi:10.1175/bams-d-13-00255.1.
Kelley, C.P., S. Mohtadi, M.A. Cane, R. Seager, and Y. Kushnir, 2015: Climate change in the Fertile Crescent and implications of the recent Syrian drought. *Proceedings of the National Academy of Sciences*, **112(11)**, 3241–

ACCEPTED VERSION SUBJECT TO FINAL EDITING

3246.
Kendon, E.J. et al., 2017: Do Convection-Permitting Regional Climate Models Improve Projections of Future Precipitation Change? *Bulletin of the American Meteorological Society*, **98(1)**, 79–93, doi:10.1175/bams-d-15-0004.1.
Kendon, E.J. et al., 2019: Enhanced future changes in wet and dry extremes over Africa at convection-permitting scale. *Nature communications*, **10(1)**, 1794, doi:10.1038/s41467-019-09776-9.
Kent, C., R. Chadwick, and D.P. Rowell, 2015: Understanding Uncertainties in Future Projections of Seasonal Tropical Precipitation. *Journal of Climate*, **28(11)**, 4390–4413, doi:10.1175/jcli-d-14-00613.1.
Keune, J. and D.G. Miralles, 2019: A Precipitation Recycling Network to Assess Freshwater Vulnerability: Challenging the Watershed Convention. *Water Resources Research*, **55(11)**, 9947–9961, doi:10.1029/2019wr025310.
Kidston, J. et al., 2015: Stratospheric influence on tropospheric jet streams, storm tracks and surface weather. *Nature Geoscience*, doi:10.1038/ngeo2424.
Kiem, A.S. et al., 2020: Learning from the past – Using palaeoclimate data to better understand and manage drought in South East Queensland (SEQ), Australia. *Journal of Hydrology: Regional Studies*, doi:10.1016/j.ejrh.2020.100686.
Kim, D. and E.D. Maloney, 2017: Simulation of the Madden-Julian Oscillation Using General Circulation Models. In: *The Global Monsoon System: Research and Forecast (3rd Edition)* [Chang, C.-P., H.-C. Kuo, N.-C. Lau, R.H. Johnson, B. Wang, and M.C. Wheeler (eds.)]. World Scientific, Singapore, pp. 119–130, doi:10.1142/9789813200913_0009.
King, A.D., 2019: The drivers of nonlinear local temperature change under global warming. *Environmental Research Letters*, **14(6)**, 64005, doi:10.1088/1748-9326/ab1976.
King, A.D., A.H. Butler, M. Jucker, N.O. Earl, and I. Rudeva, 2019: Observed Relationships Between Sudden Stratospheric Warmings and European Climate Extremes. *Journal of Geophysical Research: Atmospheres*, **124(24)**, 13943–13961, doi:10.1029/2019jd030480.
Kingston, D.G. and J. McMecking, 2015: Precipitation delivery trajectories associated with extreme river flow for the Waitaki River, New Zealand. *IAHS-AISH Proceedings and Reports*, **369**, 19–24, doi:10.5194/piahs-369-19-2015.
Kitoh, A., 2017: The Asian Monsoon and its Future Change in Climate Models: A Review. *Journal of the Meteorological Society of Japan. Ser. II*, **95(1)**, 7–33, doi:10.2151/jmsj.2017-002.
Kitoh et al. et al., 2013: Monsoons in a changing world: A regional perspective in a global context. *Journal of Geophysical Research: Atmospheres*, **118(8)**, 3053–3065, doi:10.1002/jgrd.50258.
Klein, C. and C.M. Taylor, 2020: Dry soils can intensify mesoscale convective systems. *Proceedings of the National Academy of Sciences of the United States of America*, **117(35)**, 21132–21137, doi:10.1073/pnas.2007998117.
Klingaman, N.P. and C.A. Demott, 2020: Mean State Biases and Interannual Variability Affect Perceived Sensitivities of the Madden-Julian Oscillation to Air-Sea Coupling. *Journal of Advances in Modeling Earth Systems*, **12(2)**, doi:10.1029/2019ms001799.
Klutse, N.A.B. et al., 2018: Potential impact of 1.5°C and 2°C global warming on consecutive dry and wet days over West Africa. *Environmental Research Letters*, **13(5)**, 055013, doi:10.1088/1748-9326/aab37b.
Knauer, J., C. Werner, and S. Zachle, 2015: Evaluating stomatal models and their atmospheric drought response in a land surface scheme: A multibiome analysis. *Journal of Geophysical Research: Biogeosciences*, **120(10)**, 1894–1911, doi:10.1002/2015jg003114.
Knauer, J. et al., 2017: The response of ecosystem water-use efficiency to rising atmospheric CO2 concentrations: sensitivity and large-scale biogeochemical implications. *New Phytologist*, **213(4)**, 1654–1666, doi:10.1111/nph.14288.
Knutson, T. et al., 2019: Tropical cyclones and climate change assessment: Part I. *Bulletin of the American Meteorological Society*, **100(10)**, 1987-2007, doi:10.1175/bams-d-18-0189.1.
Knutson, T. et al., 2020: Tropical cyclones and climate change assessment part II: Projected response to anthropogenic warming. *Bulletin of the American Meteorological Society*, **101(3)**, E303–E322, doi:10.1175/bams-d-18-0194.1.
Knutson and Zeng, T.R. et al., 2018: Model assessment of observed precipitation trends over land regions: Detectable human influences and possible low bias in model trends. *Journal of Climate*, **31(12)**, 4617–4637, doi:10.1175/jcli-d-17-0672.1.
Kociuba, G. and S.B. Power, 2015: Inability of CMIP5 models to simulate recent strengthening of the Walker circulation: Implications for projections. *J. Climate*, **28**, 20–35, doi:10.1175/jcli-d-13-00752.1.
Kodama, C., B. Stevens, T. Mauritsen, T. Seiki, and M. Satoh, 2019: A New Perspective for Future Precipitation Change from Intense Extratropical Cyclones. *Geophysical Research Letters*, **n/a(n/a)**, doi:10.1029/2019gl084001.
Kohyama, T., D.L. Hartmann, and D.S. Battisti, 2017: La Niña-like mean-state response to global warming and potential oceanic roles. *Journal of Climate*, doi:10.1175/jcli-d-16-0441.1.
Kok, J.F., D.S. Ward, N.M. Mahowald, and A.T. Evan, 2018: Global and regional importance of the direct dust-climate feedback. *Nature Communications*, doi:10.1038/s41467-017-02620-y.

ACCEPTED VERSION SUBJECT TO FINAL EDITING

Kolusu, S.R. et al., 2019: The El Niño event of 2015–2016: climate anomalies and their impact on groundwater resources in East and Southern Africa. *Hydrology and Earth System Sciences*, **23(3)**, 1751–1762, doi:10.5194/hess-23-1751-2019.

Konapala, G., A. Mishra, and L.R. Leung, 2017: Changes in temporal variability of precipitation over land due to anthropogenic forcings. *Environmental Research Letters*, **12(2)**, doi:10.1088/1748-9326/aa568a.

Konapala, G., A.K. Mishra, Y. Wada, and M.E. Mann, 2020: Climate change will affect global water availability through compounding changes in seasonal precipitation and evaporation. *Nature Communications*, **11(1)**, 3044, doi:10.1038/s41467-020-16757-w.

Konikow, L.F., 2011: Contribution of global groundwater depletion since 1900 to sea-level rise. *Geophysical Research Letters*, **38(17)**, doi:10.1029/2011gl048604.

Konikow, L.F. and E. Kendy, 2005: Groundwater depletion: A global problem. *Hydrogeology Journal*, **13(1)**, 317–320, doi:10.1007/s10040-004-0411-8.

Konwar, M. et al., 2012: Aerosol control on depth of warm rain in convective clouds. *Journal of Geophysical Research: Atmospheres*, **117(D13)**.

Kooperman, G.J. et al., 2018: Forest response to rising CO2 drives zonally asymmetric rainfall change over tropical land. *Nature Climate Change*, **8(5)**, 434–440, doi:10.1038/s41558-018-0144-7.

Koren, I., G. Dagan, and O. Altaratz, 2014: From aerosol-limited to invigoration of warm convective clouds. *Science*, **344(6188)**, 1143–1146.

Kornhuber, K., V. Petoukhov, S. Petri, S. Rahmstorf, and D. Coumou, 2017: Evidence for wave resonance as a key mechanism for generating high-amplitude quasi-stationary waves in boreal summer. *Climate Dynamics*, **49(5–6)**, 1961–1979, doi:10.1007/s00382-016-3399-6.

Korolev, A. et al., 2020: A new look at the environmental conditions favorable to secondary ice production. *Atmospheric Chemistry and Physics*, **20(3)**, 1391–1429, doi:10.5194/acp-20-1391-2020.

Kossin, J.P., 2018: A global slowdown of tropical-cyclone translation speed. *Nature*, **558(7708)**, 104–107, doi:10.1038/s41586-018-0158-3.

Kossin, J.P., K.A. Emanuel, and G.A. Vecchi, 2014: The poleward migration of the location of tropical cyclone maximum intensity. *Nature*, **509(7500)**, 349–352, doi:10.1038/nature13278.

Kotchoni, V.D.O. et al., 2019: Relationships between rainfall and groundwater recharge in seasonally humid Benin: a comparative analysis of long-term hydrographs in sedimentary and crystalline rock aquifers. *Hydrogeology Journal*, **27**, 447–457.

Kraaijenbrink, P.D.A., M.F.P. Bierkens, A.F. Lutz, and W.W. Immerzeel, 2017: Impact of a global temperature rise of 1.5 degrees Celsius on Asia's glaciers. *Nature*, **549(7671)**, 257–260, doi:10.1038/nature23878.

Kravtsov, S., 2017: Pronounced differences between observed and CMIP5-simulated multidecadal climate variability in the twentieth century. *Geophysical Research Letters*, **44(11)**, 5749–5757, doi:10.1002/2017gl074016.

Krishnan, R. et al., 2013: Will the South Asian monsoon overturning circulation stabilize any further? *Climate Dynamics*, **40(1–2)**, 187–211, doi:10.1007/s00382-012-1317-0.

Krishnan, R. et al., 2016: Deciphering the desiccation trend of the South Asian monsoon hydroclimate in a warming world. *Climate Dynamics*, **47(3–4)**, 1007–1027, doi:10.1007/s00382-015-2886-5.

Krishnan, R. et al., 2018: Non-monsoonal precipitation response over the Western Himalayas to climate change. *Climate Dynamics*, 0, doi:10.1007/s00382-018-4357-2.

Kristjánsson, J.E., H. Muri, and H. Schmidt, 2015: The hydrological cycle response to cirrus cloud thinning. *Geophysical Research Letters*, **42(24)**, 10,807–10,815, doi:10.1002/2015gl066795.

Krueger, O., F. Feser, and R. Weisse, 2019: Northeast Atlantic storm activity and its uncertainty from the late nineteenth to the twenty-first century. *Journal of Climate*, **32(6)**, 1919–1931, doi:10.1175/jcli-d-18-0505.1.

Krueger, O., F. Schenk, F. Feser, and R. Weisse, 2013: Inconsistencies between long-term trends in storminess derived from the 20CR reanalysis and observations. *Journal of Climate*, **26(3)**, 868–874, doi:10.1175/jcli-d-12-00309.1.

Krysanova, V. et al., 2018: How the performance of hydrological models relates to credibility of projections under climate change. *Hydrological Sciences Journal*, **63(5)**, 696–720, doi:10.1080/02626667.2018.1446214.

Kulkarni, A. et al., 2020: Precipitation Changes in India. In: *Assessment of Climate Change over the Indian Region: A Report of the Ministry of Earth Sciences (MoES), Government of India* [Krishnan, R., J. Sanjay, C. Gnanaseelan, M. Mujumdar, A. Kulkarni, and S. Chakraborty (eds.)]. Springer Singapore, Singapore, pp. 47–72, doi:10.1007/978-981-15-4327-2_3.

Kumar, D. and A.R. Ganguly, 2018: Intercomparison of model response and internal variability across climate model ensembles. *Climate Dynamics*, **51(1–2)**, 207–219, doi:10.1007/s00382-017-3914-4.

Kumar, S., V. Merwade, J.L. Kinter, and D. Niyogi, 2013: Evaluation of temperature and precipitation trends and long-term persistence in CMIP5 twentieth-century climate simulations. *Journal of Climate*, doi:10.1175/jcli-d-12-00259.1.

Kumar, S., M. Newman, Y. Wang, and B. Livneh, 2019: Potential reemergence of seasonal soil moisture anomalies in North America. *Journal of Climate*, **32(10)**, 2707–2734, doi:10.1175/jcli-d-18-0540.1.

Kumar, S., R.P. Allan, F. Zwiers, D.M. Lawrence, and P.A. Dirmeyer, 2015: Revisiting trends in wetness and dryness

ACCEPTED VERSION SUBJECT TO FINAL EDITING

in the presence of internal climate variability and water limitations over land. *Geophysical Research Letters*, **42(24)**, 10867–10875, doi:10.1002/2015gl066858.
Kumar, S. et al., 2016: Terrestrial contribution to the heterogeneity in hydrological changes under global warming. *Water Resources Research*, **52(4)**, 3127–3142, doi:10.1002/2016wr018607.
Kunkel, K.E. et al., 2010: Recent increases in {U}.S. heavy precipitation associated with tropical cyclones. *Geophys. Res*, **37**, doi:10.1029/2010gl045164.
Kunkel, K.E. et al., 2012: Meteorological causes of the secular variations in observed extreme precipitation events for the conterminous United States. *Journal of Hydrometeorology*, **13**, 1131–1141, doi:10.1175/jhm-d-11-0108.1.
Kunkel, K.E. et al., 2016: Trends and Extremes in Northern Hemisphere Snow Characteristics. *Current Climate Change Reports*, **2(2)**, 65–73, doi:10.1007/s40641-016-0036-8.
Kushnir, Y., C. Cassou, and S. St George, 2017: Editorial: Decadal Climate Variability. *Past Global Changes Magazine*, **25(1)**, 1–1, doi:10.22498/pages.25.1.1.
Kuss, A.J.M. and J.J. Gurdak, 2014: Groundwater level response in U.S. principal aquifers to ENSO, NAO, PDO, and AMO. *Journal of Hydrology*, **519**, 1939–1952, doi:10.1016/j.jhydrol.2014.09.069.
Kusunoki, S., 2018: Is the global atmospheric model MRI-AGCM3.2 better than the CMIP5 atmospheric models in simulating precipitation over East Asia? *Climate Dynamics*, **51(11–12)**, 4489–4510, doi:10.1007/s00382-016-3335-9.
Kusunoki, S., T. Ose, and M. Hosaka, 2020: Emergence of unprecedented climate change in projected future precipitation. *Scientific Reports*, **10(1)**, 4802, doi:10.1038/s41598-020-61792-8.
Kutzbach, J.E., 1981: Monsoon climate of the early Holocene: climate experiment with the Earth's orbital parameters for 9000 years ago. *Science*, **214(4516)**, 59–61.
Kwon, E.Y. et al., 2014: Global estimate of submarine groundwater discharge based on an observationally constrained radium isotope model. *Geophysical Research Letters*, **41(23)**, 8438–8444, doi:10.1002/2014gl061574.
L'Heureux, M.L. et al., 2013: Recent multidecadal strengthening of the Walker circulation across the tropical Pacific. *Nature Climate Change*, **3(6)**, 571–576, doi:10.1038/nclimate1840.
Lachniet, M.S., Y. Asmerom, J.P. Bernal, V.J. Polyak, and L. Vazquez-Selem, 2013: Orbital pacing and ocean circulation-induced collapses of the Mesoamerican monsoon over the past 22,000 y. *Proceedings of the National Academy of Sciences*, doi:10.1073/pnas.1222804110.
Lafore, J.-P. et al., 2017: A multi-scale analysis of the extreme rain event of Ouagadougou in 2009. *Quarterly Journal of the Royal Meteorological Society*, **143(709)**, 3094–3109, doi:10.1002/qj.3165.
Laîné, A., H. Nakamura, K. Nishii, and T. Miyasaka, 2014: A diagnostic study of future evaporation changes projected in CMIP5 climate models. *Climate Dynamics*, **42(9–10)**, 2745–2761, doi:10.1007/s00382-014-2087-7.
Lambert, F.H., A.J. Ferraro, and R. Chadwick, 2017: Land-ocean shifts in tropical precipitation linked to surface temperature and humidity change. *Journal of Climate*, **30(12)**, 4527–4545, doi:10.1175/jcli-d-16-0649.1.
Lambert, F.H. et al., 2013: Interactions between perturbations to different Earth system components simulated by a fully-coupled climate model. *Climate Dynamics*, **41(11)**, 3055–3072, doi:10.1007/s00382-012-1618-3.
Lamontagne-Hallé, P., J.M. McKenzie, B.L. Kurylyk, and S.C. Zipper, 2018: Changing groundwater discharge dynamics in permafrost regions. *Environmental Research Letters*, **13(8)**, 84017, doi:10.1088/1748-9326/aad404.
Lan, C.-W.W., M.-H.H. Lo, C.-A.A. Chen, and J.-Y.Y. Yu, 2019: The mechanisms behind changes in the seasonality of global precipitation found in reanalysis products and CMIP5 simulations. *Climate Dynamics*, **53(7)**, 4173–4187, doi:10.1007/s00382-019-04781-6.
Lanzante, J.R., 2019: Uncertainties in tropical-cyclone translation speed. *Nature*, **570(7759)**, E6–E15, doi:10.1038/s41586-019-1223-2.
Lau, K.-M. and K.-M. Kim, 2006: Observational relationships between aerosol and Asian monsoon rainfall, and circulation. *Geophysical Research Letters*, **33(21)**, doi:10.1029/2006gl027546.
Lau, W.K.M. and Y.P. Zhou, 2012: Observed recent trends in tropical cyclone rainfall over the North Atlantic and North Pacific. *J. Geophys. Res*, **117**, doi:10.1029/2011jd016510.
Lau, W.K.M. and K.-M. Kim, 2015: Robust Hadley Circulation changes and increasing global dryness due to CO2warming from CMIP5 model projections. *Proc. Natl. Acad. Sci. U. S. A.*, **112**, 3630–3635, doi:10.1073/pnas.1418682112.
Lau, W.K.M. and W. Tao, 2020: Precipitation–Radiation–Circulation Feedback Processes Associated with Structural Changes of the ITCZ in a Warming Climate during 1980–2014: An Observational Portrayal. *Journal of Climate*, **33(20)**, 8737–8749, doi:10.1175/jcli-d-20-0068.1.
Lau, W.K.-M. and K.-M. Kim, 2017: Competing influences of greenhouse warming and aerosols on Asian summer monsoon circulation and rainfall. *Asia-Pacific Journal of Atmospheric Sciences*, **53(2)**, 181–194, doi:10.1007/s13143-017-0033-4.
Lavado, W.S., D. Labat, J. Ronchail, J.C. Espinoza, and J.L. Guyot, 2013: Trends in rainfall and temperature in the Peruvian Amazon-Andes basin over the last 40years (1965-2007). *Hydrological Processes*, **27(20)**, 2944–2957, doi:10.1002/hyp.9418.
Lavers, D.A., F.M. Ralph, D.E. Waliser, A. Gershunov, and M.D. Dettinger, 2015: Climate change intensification of

SUBJECT TO FINAL EDITING ACCEPTED VERSION

horizontal water vapor transport in CMIP5. *Geophysical Research Letters*, **42(13)**, 5617–5625, doi:10.1002/2015gl064672.
Lavers, D.A. et al., 2013: Future changes in atmospheric rivers and their implications for winter flooding in Britain. *Environmental Research Letters*, **8(3)**, doi:10.1088/1748-9326/8/3/034010.
Lawrence, D. and K. Vandecar, 2015: Effects of tropical deforestation on climate and agriculture. *Nature Climate Change*, **5(1)**, 27–36, doi:10.1038/nclimate2430.
Le Barbé, L., T. Lebel, and D. Tapsoba, 2002: Rainfall Variability in West Africa during the Years 1950–90. *Journal of Climate*, **15(2)**, 187–202, doi:10.1175/1520-0442(2002)015<0187:rviwad>2.0.co;2.
Le Barbé and Lebel, T., 1997: Rainfall climatology of the HAPEX-Sahel region during the years 1950–1990. *Journal of Hydrology*, **188–189**, 43–73, doi:10.1016/s0022-1694(96)03154-x.
Lebel, T., A. Diedhiou, and H. Laurent, 2003: Seasonal cycle and interannual variability of the Sahelian rainfall at hydrological scales. *Journal of Geophysical Research*, **108(D8)**, 8389, doi:10.1029/2001jd001580.
Ledru, M.-P. et al., 2013: The Medieval Climate Anomaly and the Little Ice Age in the eastern Ecuadorian Andes. *Climate of the Past*, **9(1)**, 307–321, doi:10.5194/cp-9-307-2013.
Lee, D. et al., 2018: Impacts of half a degree additional warming on the Asian summer monsoon rainfall characteristics. *Environmental Research Letters*, **13(4)**, 044033, doi:10.1088/1748-9326/aab55d.
Lee, J.A. and T.E. Gill, 2015: Multiple causes of wind erosion in the Dust Bowl. *Aeolian Research*, doi:10.1016/j.aeolia.2015.09.002.
Lee, J.-Y. et al., 2013: Real-time multivariate indices for the boreal summer intraseasonal oscillation over the Asian summer monsoon region. *Climate Dynamics*, **40(1–2)**, 493–509, doi:10.1007/s00382-012-1544-4.
Lee, S.S., J. Guo, and Z. Li, 2016: Delaying precipitation by air pollution over the Pearl River Delta: 2. Model simulations. *Journal of Geophysical Research: Atmospheres*, **121(19)**, 11,739–11,760, doi:10.1002/2015jd024362.
Lee, S.S. et al., 2018: Aerosol as a potential factor to control the increasing torrential rain events in urban areas over the last decades. *Atmospheric Chemistry and Physics*, **18(16)**, 12531–12550, doi:10.5194/acp-18-12531-2018.
Lee, S.-Y.Y. et al., 2015: Projecting the hydrologic impacts of climate change on montane wetlands. *PLoS ONE*, **10(9)**, e0136385, doi:10.1371/journal.pone.0136385.
Lee, Y.-Y. and R.X. Black, 2013: Boreal winter low-frequency variability in CMIP5 models. *Journal of Geophysical Research: Atmospheres*, **118(13)**, 6891–6904, doi:10.1002/jgrd.50493.
Lehner, F., C. Deser, I.R. Simpson, and L. Terray, 2018: Attributing the U.S. Southwest's Recent Shift Into Drier Conditions. *Geophysical Research Letters*, doi:10.1029/2018gl078312.
Lehner, F. et al., 2017: Projected drought risk in 1.5°C and 2°C warmer climates. *Geophysical Research Letters*, **44(14)**, 7419–7428, doi:10.1002/2017gl074117.
Lehner, F. et al., 2019: The potential to reduce uncertainty in regional runoff projections from climate models. *Nature Climate Change*, **9(12)**, 926–933, doi:10.1038/s41558-019-0639-x.
Lehner, F. et al., 2020: Partitioning climate projection uncertainty with multiple Large Ensembles and CMIP5/6. *Earth System Dynamics*, **11(2)**, 1–28, doi:10.5194/esd-11-491-2020.
Lei, Y. et al., 2017: Lake seasonality across the Tibetan Plateau and their varying relationship with regional mass changes and local hydrology. *Geophysical Research Letters*, **44(2)**, 892–900, doi:10.1002/2016gl072062.
Leite-Filho, A.T., V.Y.S. Pontes, and M.H. Costa, 2019: Effects of deforestation on the onset of the rainy season and the duration of dry spells in southern Amazonia. *Journal of Geophysical Research: Atmospheres*, 2018JD029537, doi:10.1029/2018jd029537.
Lejeune, Q., E.L. Davin, B.P. Guillod, and S.I. Seneviratne, 2015: Influence of Amazonian deforestation on the future evolution of regional surface fluxes, circulation, surface temperature and precipitation. *Climate Dynamics*, **44(9–10)**, 2769–2786, doi:10.1007/s00382-014-2203-8.
Lemieux, J.-M. et al., 2020: Groundwater dynamics within a watershed in the discontinuous permafrost zone near Umiujaq (Nunavik, Canada). *Hydrogeology Journal*, **28(3)**, 833–851, doi:10.1007/s10040-020-02110-4.
Lemordant, L., P. Gentine, A.S. Swann, B.I. Cook, and J. Scheff, 2018: Critical impact of vegetation physiology on the continental hydrologic cycle in response to increasing CO2. *Proceedings of the National Academy of Sciences of the United States of America*, **115(16)**, 4093–4098, doi:10.1073/pnas.1720712115.
Lenderink, G., R. Barbero, J.M. Loriaux, and H.J. Fowler, 2017: Super-Clausius-Clapeyron scaling of extreme hourly convective precipitation and its relation to large-scale atmospheric conditions. *Journal of Climate*, **30(15)**, 6037–6052, doi:10.1175/jcli-d-16-0808.1.
Lenderink, G. et al., 2019: Systematic increases in the thermodynamic response of hourly precipitation extremes in an idealized warming experiment with a convection-permitting climate model. *Environmental Research Letters*, **14(7)**, 074012, doi:10.1088/1748-9326/ab214a.
Leng, G., M. Huang, Q. Tang, and L.R. Leung, 2015: A modeling study of irrigation effects on global surface water and groundwater resources under a changing climate. *Journal of Advances in Modeling Earth Systems*, **7(3)**, 1285–1304, doi:10.1002/2015ms000437.
Leng, G., M. Huang, Q. Tang, H. Gao, and L. Leung, 2014: Modeling the Effects of Groundwater-Fed Irrigation on Terrestrial Hydrology over the Conterminous United States. *Journal of Hydrometeorology*, **15(957)**, 13–49.

SUBJECT TO FINAL EDITING
ACCEPTED VERSION

Lenggenhager, S., M. Croci-Maspoli, S. Brönnimann, and O. Martius, 2018: On the dynamical coupling between atmospheric blocks and heavy precipitation events: A discussion of the southern Alpine flood in October 2000. *Quarterly Journal of the Royal Meteorological Society*, doi:10.1002/qj.3449.

Lenton, T.M. et al., 2008: Tipping elements in the Earth's climate system. *Proceedings of the National Academy of Sciences*, **105(6)**, 1786–1793.

Leutwyler, D., D. Lüthi, N. Ban, O. Fuhrer, and C. Schär, 2017: Evaluation of the convection-resolving climate modeling approach on continental scales. *Journal of Geophysical Research*, **122(10)**, 5237–5258, doi:10.1002/2016jd026013.

Levang, S.J. and R.W. Schmitt, 2015: Centennial changes of the global water cycle in CMIP5 models. *Journal of Climate*, **28(16)**, 6489–6502, doi:10.1175/jcli-d-15-0143.1.

Levine, N.M. et al., 2016: Ecosystem heterogeneity determines the ecological resilience of the Amazon to climate change. *Proceedings of the National Academy of Sciences*, **113(3)**, 793–797, doi:10.1073/pnas.1511344112.

Levy, A.A.L. et al., 2013: Can correcting feature location in simulated mean climate improve agreement on projected changes? *Geophysical Research Letters*, **40(2)**, 354–358, doi:10.1029/2012gl053964.

Levy, M.C., A. Lopes, A. Cohn, L.G. Larsen, and S.E. Thompson, 2018: Land Use Change Increases Streamflow Across the Arc of Deforestation in Brazil. *Geophysical Research Letters*, **45(8)**, 3520–3530, doi:10.1002/2017gl076526.

Li, C. et al., 2017: Evaluation of the Common Land Model (CoLM) from the perspective of water and energy budget simulation: Towards inclusion in CMIP6. *Atmosphere*, **8(8)**, doi:10.3390/atmos8080141.

Li, D., T. Zhou, and W. Zhang, 2019: Extreme precipitation over East Asia under 1.5°C and 2°C global warming targets: a comparison of stabilized and overshoot projections. *Environmental Research Communications*, **1(8)**, 085002, doi:10.1088/2515-7620/ab3971.

Li, F., S. Levis, and D.S. Ward, 2013: Quantifying the role of fire in the Earth system – Part 1: Improved global fire modeling in the Community Earth System Model (CESM1). *Biogeosciences*, **10**, 2293–2314.

Li, G., S.P. Xie, C. He, and Z. Chen, 2017: Western Pacific emergent constraint lowers projected increase in Indian summer monsoon rainfall. *Nature Climate Change*, **7(10)**, 708–712, doi:10.1038/nclimate3387.

Li, G., S.P. Harrison, P.J. Bartlein, K. Izumi, and I. Colin Prentice, 2013: Precipitation scaling with temperature in warm and cold climates: An analysis of CMIP5 simulations. *Geophysical Research Letters*, **40(15)**, 4018–4024, doi:10.1002/grl.50730.

Li, J., J. Feng, and Y. Li, 2012: A possible cause of decreasing summer rainfall in northeast Australia. *International Journal of Climatology*, **32**, 995–1005, doi:10.1002/joc.2328.

Li, J. et al., 2018: Parameter optimization for carbon and water fluxes in two global land surface models based on surrogate modelling. *International Journal of Climatology*, **38**, e1016–e1031, doi:10.1002/joc.5428.

Li, L. and P. Chakraborty, 2020: Slower decay of landfalling hurricanes in a warming world. *Nature*, **587(7833)**, 230–234, doi:10.1038/s41586-020-2867-7.

Li, M., T. Woollings, K. Hodges, and G. Masato, 2014: Extratropical cyclones in a warmer, moister climate: A recent Atlantic analogue. *Geophysical Research Letters*, doi:10.1002/2014gl062186.

Li, N. and G.R. McGregor, 2017: Linking interannual river flow river variability across New Zealand to the Southern Annular Mode, 1979-2011. *Hydrological Processes*, **31(12)**, 2261–2276, doi:10.1002/hyp.11184.

Li, W., L. Li, M. Ting, and Y. Liu, 2012: Intensification of Northern Hemisphere subtropical highs in a warming climate. *Nature Geoscience*, **5(11)**, 830–834, doi:10.1038/ngeo1590.

Li, W., L. Li, R. Fu, Y. Deng, and H. Wang, 2011: Changes to the North Atlantic Subtropical High and Its Role in the Intensification of Summer Rainfall Variability in the Southeastern United States. *Journal of Climate*, **24(5)**, 1499–1506, doi:10.1175/2010jcli3829.1.

Li, X. and M. Ting, 2015: Recent and future changes in the Asian monsoon-ENSO relationship: Natural or forced? *Geophysical Research Letters*, **42(9)**, 3502–3512, doi:10.1002/2015gl063557.

Li, X., M. Ting, and D.E. Lee, 2018: Fast Adjustments of the Asian Summer Monsoon to Anthropogenic Aerosols. *Geophysical Research Letters*, **45(2)**, 1001–1010, doi:10.1002/2017gl076667.

Li, X. et al., 2016: Trend and seasonality of land precipitation in observations and CMIP5 model simulations. *International Journal of Climatology*, **3793**, 3781–3793, doi:10.1002/joc.4592.

Li, Y., Y. Ding, and W. Li, 2017: Interdecadal variability of the Afro-Asian summer monsoon system. *Advances in Atmospheric Sciences*, **34(7)**, 833–846, doi:10.1007/s00376-017-6247-7.

Li, Y., Q. Zhang, H. Tao, and J. Yao, 2021: Integrated model projections of climate change impacts on water-level dynamics in the large Poyang Lake (China). *Hydrology Research*, **52(1)**, 43–60, doi:10.2166/nh.2019.064.

Li, Y., H. Tao, B. Su, Z.W. Kundzewicz, and T. Jiang, 2019: Impacts of 1.5°C and 2°C global warming on winter snow depth in Central Asia. *Science of The Total Environment*, **651**, 2866–2873, doi:10.1016/j.scitotenv.2018.10.126.

Li, Y. et al., 2018: Climate Model Shows Large-Scale Wind and Solar Farms in the Sahara Increase Rain and Vegetation. *Science*, **361(6406)**, 1019–1022, doi:10.1126/science.aar5629.

Li, Z., Y.N. Chen, Y. Wang, and G.H. Fang, 2016a: Dynamic changes in terrestrial net primary production and their effects on evapotranspiration. *Hydrol. Earth Syst. Sci*, **20**, 2169–2178.

ACCEPTED VERSION SUBJECT TO FINAL EDITING

Li, Z., Y. Chen, G. Fang, and Y. Li, 2017: Multivariate assessment and attribution of droughts in Central Asia. *Scientific Reports*, doi:10.1038/s41598-017-01473-1.
Li, Z. et al., 2016b: Aerosol and monsoon climate interactions over Asia. *Reviews of Geophysics*, **54(4)**, 866–929, doi:10.1002/2015rg000500.
Lian, X. et al., 2018: Partitioning global land evapotranspiration using CMIP5 models constrained by observations. *Nature Climate Change*, **8(7)**, 640–646, doi:10.1038/s41558-018-0207-9.
Liang, Y.C. et al., 2020: Amplified seasonal cycle in hydroclimate over the Amazon river basin and its plume region. *Nature Communications*, **11(1)**, 1–11, doi:10.1038/s41467-020-18187-0.
Liebmann, B. et al., 2014: Understanding Recent Eastern Horn of Africa Rainfall Variability and Change. *Journal of Climate*, **27**, 8630–8645, doi:10.1175/jcli-d-13-00714.1.
Lim, E.-P. et al., 2016: The impact of the Southern Annular Mode on future changes in Southern Hemisphere rainfall. *Geophysical Research Letters*, **43(13)**, 7160–7167, doi:10.1002/2016gl069453.
Lin, L., Z. Wang, Y. Xu, Q. Fu, and W. Dong, 2018: Larger Sensitivity of Precipitation Extremes to Aerosol Than Greenhouse Gas Forcing in CMIP5 Models. *Journal of Geophysical Research: Atmospheres*, **123(15)**, 8062–8073, doi:10.1029/2018jd028821.
Lin, R., T. Zhou, and Y. Qian, 2014: Evaluation of global monsoon precipitation changes based on five reanalysis datasets. *Journal of Climate*, **27(3)**, 1271–1289, doi:10.1175/jcli-d-13-00215.1.
Linsbauer, A. et al., 2016: Modelling glacier-bed overdeepenings and possible future lakes for the glaciers in the Himalaya-Karakoram region. *Annals of Glaciology*, **57(71)**, 119–130, doi:10.3189/2016aog71a627.
Little, K., D.G. Kingston, N.J. Cullen, and P.B. Gibson, 2019: The Role of Atmospheric Rivers for Extreme Ablation and Snowfall Events in the Southern Alps of New Zealand. *Geophysical Research Letters*, doi:10.1029/2018gl081669.
Liu, C. and R.P. Allan, 2013: Observed and simulated precipitation responses in wet and dry regions 1850-2100. *Environmental Research Letters*, **8(3)**, doi:10.1088/1748-9326/8/3/034002.
Liu, C. et al., 2017: Continental - scale convection - permitting modeling of the current and future climate of North America. *Climate Dynamics*, **49(1)**, 71–95, doi:10.1007/s00382-016-3327-9.
Liu, F., T. Zhao, B. Wang, J. Liu, and W. Luo, 2018: Different Global Precipitation Responses to Solar, Volcanic, and Greenhouse Gas Forcings. *Journal of Geophysical Research: Atmospheres*, **123(8)**, 4060–4072, doi:10.1029/2017jd027391.
Liu, F. et al., 2016: Global monsoon precipitation responses to large volcanic eruptions. *Scientific Reports*, **6(1)**, 24331, doi:10.1038/srep24331.
Liu, H. et al., 2019: Non-Monotonic Aerosol Effect on Precipitation in Convective Clouds over Tropical Oceans. *Scientific Reports*, **9(1)**, 7809, doi:10.1038/s41598-019-44284-2.
Liu, J., H. Xu, and J. Deng, 2018: Projections of East Asian summer monsoon change at global warming of 1.5 and 2°C. *Earth System Dynamics*, **9(2)**, 427–439, doi:10.5194/esd-9-427-2018.
Liu, J., J.A. Curry, H. Wang, M. Song, and R.M. Horton, 2012: Impact of declining Arctic sea ice on winter snowfall. *Proceedings of the National Academy of Sciences of the United States of America*, **109(11)**, 4074–4079, doi:10.1073/pnas.1114910109.
Liu, L. et al., 2018: A PDRMIP Multimodel study on the impacts of regional aerosol forcings on global and regional precipitation. *Journal of Climate*, **31(11)**, 4429–4447, doi:10.1175/jcli-d-17-0439.1.
Liu, M., G.A. Vecchi, J.A. Smith, and T.R. Knutson, 2019: Causes of large projected increases in hurricane precipitation rates with global warming. *npj Climate and Atmospheric Science*, **2(1)**, 38, doi:10.1038/s41612-019-0095-3.
Liu, N. et al., 2020: Drought can offset potential water use efficiency of forest ecosystems from rising atmospheric CO2. *Journal of Environmental Sciences (China)*, doi:10.1016/j.jes.2019.11.020.
Liu, T. et al., 2018: Influence of the May Southern annular mode on the South China Sea summer monsoon. *Climate Dynamics*, **51(11–12)**, 4095–4107, doi:10.1007/s00382-017-3753-3.
Liu, W., S.P. Xie, Z. Liu, and J. Zhu, 2017: Overlooked possibility of a collapsed atlantic meridional overturning circulation in warming climate. *Science Advances*, doi:10.1126/sciadv.1601666.
Liu, X., C. Li, T. Zhao, and L. Han, 2020: Future changes of global potential evapotranspiration simulated from CMIP5 to CMIP6 models. *Atmospheric and Oceanic Science Letters*, **13(6)**, 568–575, doi:10.1080/16742834.2020.1824983.
Liu, Y., Y. Liu, and W. Wang, 2019a: Inter-comparison of satellite-retrieved and Global Land Data Assimilation System-simulated soil moisture datasets for global drought analysis. *Remote Sensing of Environment*, **220**, 1–18, doi:10.1016/j.rse.2018.10.026.
Liu, Y., M. Kumar, G.G. Katul, X. Feng, and A.G. Konings, 2020: Plant hydraulics accentuates the effect of atmospheric moisture stress on transpiration. *Nature Climate Change*, **10(7)**, 691–695, doi:10.1038/s41558-020-0781-5.
Liu, Y. et al., 2019b: Anthropogenic Aerosols Cause Recent Pronounced Weakening of Asian Summer Monsoon Relative to Last Four Centuries. *Geophysical Research Letters*, **46(10)**, 5469–5479, doi:10.1029/2019gl082497.

ACCEPTED VERSION SUBJECT TO FINAL EDITING

Liu, Z. et al., 2009: Transient simulation of last deglaciation with a new mechanism for bolling-allerod warming. *Science*, doi:10.1126/science.1171041.
Llopart, M. et al., 2018: Land use change over the Amazon forest and its impact on the local climate. *Water (Switzerland)*, **10(2)**, doi:10.3390/w10020149.
Loeb, N.G. et al., 2016: Observational constraints on atmospheric and oceanic cross-equatorial heat transports: revisiting the precipitation asymmetry problem in climate models. *Climate Dynamics*, **46(9–10)**, 3239–3257, doi:10.1007/s00382-015-2766-z.
Lopez, A., E.B. Suckling, and L.A. Smith, 2014: Robustness of pattern scaled climate change scenarios for adaptation decision support. *Climatic Change*, **122(4)**, 555–566, doi:10.1007/s10584-013-1022-y.
Lora, J.M., 2018: Components and mechanisms of hydrologic cycle changes over North America at the Last Glacial Maximum. *Journal of Climate*, **31(17)**, 7035–7051, doi:10.1175/jcli-d-17-0544.1.
Loranty, M.M., L.T. Berner, S.J. Goetz, Y. Jin, and J.T. Randerson, 2014: Vegetation controls on northern high latitude snow-albedo feedback: Observations and CMIP5 model simulations. *Global Change Biology*, **20(2)**, 594–606, doi:10.1111/gcb.12391.
Loriaux, J.M., G. Lenderink, and A. Pier Siebesma, 2017: Large-scale controls on extreme precipitation. *Journal of Climate*, **30(3)**, 955–968, doi:10.1175/jcli-d-16-0381.1.
Louf, V., C. Jakob, A. Protat, M. Bergemann, and S. Narsey, 2019: The Relationship of Cloud Number and Size With Their Large-Scale Environment in Deep Tropical Convection. *Geophysical Research Letters*, **46(15)**, 9203–9212, doi:10.1029/2019gl083964.
Lowry, D.P. and C. Morrill, 2019: Is the Last Glacial Maximum a reverse analog for future hydroclimate changes in the Americas? *Climate Dynamics*, **52(7)**, 4407–4427, doi:10.1007/s00382-018-4385-y.
Lu, J., G.A. Vecchi, and T. Reichler, 2007: Expansion of the Hadley cell under global warming. *Geophysical Research Letters*, doi:10.1029/2006gl028443.
Lu, Q., D. Zhao, and S. Wu, 2017: Simulated responses of permafrost distribution to climate change on the Qinghai–Tibet Plateau. *Scientific Reports*, **7(1)**, 3845, doi:10.1038/s41598-017-04140-7.
Lu, Z. et al., 2021: Impacts of Large-Scale Sahara Solar Farms on Global Climate and Vegetation Cover. *Geophysical Research Letters*, **48(2)**, e2020GL090789, doi:10.1029/2020gl090789.
Luijendijk, E., T. Gleeson, and N. Moosdorf, 2020: Fresh groundwater discharge insignificant for the world's oceans but important for coastal ecosystems. *Nature Communications*, **11(1)**, 1260, doi:10.1038/s41467-020-15064-8.
Lund, M.T., G. Myhre, and B.H. Samset, 2019: Anthropogenic aerosol forcing under the Shared Socioeconomic Pathways. *Atmospheric Chemistry and Physics*, **19(22)**, 13827–13839, doi:10.5194/acp-19-13827-2019.
Luo, D., W. Zhang, L. Zhong, and A. Dai, 2019: A nonlinear theory of atmospheric blocking: A potential vorticity gradient view. *Journal of the Atmospheric Sciences*, **76(8)**, 2399–2427, doi:10.1175/jas-d-18-0324.1.
Luong, T.M. et al., 2017: The More Extreme Nature of North American Monsoon Precipitation in the Southwestern United States as Revealed by a Historical Climatology of Simulated Severe Weather Events. *Journal of Applied Meteorology and Climatology*, **56(9)**, 2509–2529, doi:10.1175/jamc-d-16-0358.1.
Lutz, A.F., W.W. Immerzeel, A.B. Shrestha, and M.F.P.P. Bierkens, 2014: Consistent increase in High Asia's runoff due to increasing glacier melt and precipitation. *Nature Climate Change*, **4(7)**, 587–592, doi:10.1038/nclimate2237.
Lyon, B., 2014: Seasonal drought in the Greater Horn of Africa and its recent increase during the March-May long rains. *Journal of Climate*, doi:10.1175/jcli-d-13-00459.1.
Lyon, B. and D.G. Dewitt, 2012: A recent and abrupt decline in the East African long rains. *Geophysical Research Letters*, **39**, 1–5, doi:10.1029/2011gl050337.
Ma, J., S.P. Xie, and Y. Kosaka, 2012: Mechanisms for tropical tropospheric circulation change in response to global warming. *Journal of Climate*, doi:10.1175/jcli-d-11-00048.1.
Ma, J. et al., 2018: Responses of the Tropical Atmospheric Circulation to Climate Change and Connection to the Hydrological Cycle. *Annual Review of Earth and Planetary Sciences*, **46(1)**, 549–580, doi:10.1146/annurev-earth-082517-010102.
Ma, S. et al., 2017: Detectable Anthropogenic Shift toward Heavy Precipitation over Eastern China. *Journal of Climate*, **30(4)**, 1381–1396, doi:10.1175/jcli-d-16-0311.1.
MacDonald, A.M. et al., 2016: Groundwater quality and depletion in the Indo-Gangetic Basin mapped from in situ observations. *Nature Geoscience*, **9(10)**, 762–766, doi:10.1038/ngeo2791.
MacIntosh, C.R. et al., 2016: Contrasting fast precipitation responses to tropospheric and stratospheric ozone forcing. *Geophysical Research Letters*, **43(3)**, 1263–1271, doi:10.1002/2015gl067231.
Mackintosh, A.N. et al., 2017: Regional cooling caused recent New Zealand glacier advances in a period of global warming. *Nature Communications*, **8(1)**, 14202, doi:10.1038/ncomms14202.
Madhura, R.K., R. Krishnan, J. Revadekar, M. Mujumdar, and B.N. Goswami, 2014: Changes in western disturbances over the Western Himalayas in a warming environment. *Climate Dynamics*, **44(3–4)**, 1157–1168, doi:10.1007/s00382-014-2166-9.
Magnin, F., W. Haeberli, A. Linsbauer, P. Deline, and L. Ravanel, 2020: Estimating glacier-bed overdeepenings as possible sites of future lakes in the de-glaciating Mont Blanc massif (Western European Alps).

ACCEPTED VERSION SUBJECT TO FINAL EDITING

Geomorphology, **350**, 106913, doi:10.1016/j.geomorph.2019.106913.
Mahajan, S., K.J. Evans, M.L. Branstetter, and Q. Tang, 2018: Model Resolution Sensitivity of the Simulation of North Atlantic Oscillation Teleconnections to Precipitation Extremes. *Journal of Geophysical Research: Atmospheres*, **123(20)**, 11,392–11,409, doi:10.1029/2018jd028594.
Maher, N., D. Matei, S. Milinski, and J. Marotzke, 2018: ENSO Change in Climate Projections: Forced Response or Internal Variability? *Geophysical Research Letters*, **45(20)**, 11,390–11,398, doi:10.1029/2018gl079764.
Maher, P., G.K. Vallis, S.C. Sherwood, M.J. Webb, and P.G. Sansom, 2018: The Impact of Parameterized Convection on Climatological Precipitation in Atmospheric Global Climate Models. *Geophysical Research Letters*, **45(8)**, 3728–3736, doi:10.1002/2017gl076826.
Maidment, R.I., R.P. Allan, and E. Black, 2015: Recent observed and simulated changes in precipitation over Africa. *Geophysical Research Letters*, **42(19)**, 8155–8164, doi:10.1002/2015gl065765.
Malavelle, F.F. et al., 2017: Strong constraints on aerosol–cloud interactions from volcanic eruptions. *Nature*, **546(7659)**, 485–491, doi:10.1038/nature22974.
Malhi, Y. et al., 2008: Climate change, deforestation, and the fate of the Amazon. *Science*, doi:10.1126/science.1146961.
Malhi, Y. et al., 2009: Exploring the likelihood and mechanism of a climate-change-induced dieback of the Amazon rainforest. *Proceedings of the National Academy of Sciences*, **106(49)**, 20610.
Mallakpour, I. and G. Villarini, 2017: Analysis of changes in the magnitude , frequency , and seasonality of heavy precipitation over the contiguous USA. *Theoretical and Applied Climatology*, **130**, 345–363, doi:10.1007/s00704-016-1881-z.
Maloney, E.D. and D.L. Hartmann, 2000: Modulation of Eastern North Pacific Hurricanes by the Madden–Julian Oscillation. *Journal of Climate*, **13(9)**, 1451–1460, doi:10.1175/1520-0442(2000)013<1451:moenph>2.0.co;2.
Maloney, E.D. and S.-P. Xie, 2013: Sensitivity of tropical intraseasonal variability to the pattern of climate warming. *Journal of Advances in Modeling Earth Systems*, **5(1)**, 32–47, doi:10.1029/2012ms000171.
Maloney, E.D., F. Adames, and H.X. Bui, 2019: Madden–Julian oscillation changes under anthropogenic warming. *Nature Climate Change*, **9(1)**, 26–33, doi:10.1038/s41558-018-0331-6.
Maloney, E.D. et al., 2014: North American Climate in CMIP5 Experiments: Part III: Assessment of Twenty-First-Century Projections. *Journal of Climate*, **27(6)**, 2230–2270, doi:10.1175/jcli-d-13-00273.1.
Mamalakis, A. et al., 2021: Zonally contrasting shifts of the tropical rain belt in response to climate change. *Nature Climate Change*, doi:10.1038/s41558-020-00963-x.
Mankin, J.S., J.E. Smerdon, B.I. Cook, A.P. Williams, and R. Seager, 2017: The Curious Case of Projected Twenty-First-Century Drying but Greening in the American West. *Journal of Climate*, **30(21)**, 8689–8710, doi:10.1175/jcli-d-17-0213.1.
Mankin, J.S., R. Seager, J.E. Smerdon, B.I. Cook, and A.P. Williams, 2019: Mid-latitude freshwater availability reduced by projected vegetation responses to climate change. *Nature Geoscience*, **12(12)**, 983–988, doi:10.1038/s41561-019-0480-x.
Mankin, J.S. et al., 2018: Blue Water Trade-Offs With Vegetation in a CO2-Enriched Climate. *Geophysical Research Letters*, **45(7)**, 3115–3125, doi:10.1002/2018gl077051.
Mann, M.E. et al., 2017: Influence of Anthropogenic Climate Change on Planetary Wave Resonance and Extreme Weather Events. *Scientific Reports*, **7(1)**, 45242, doi:10.1038/srep45242.
Marciano, C.G., G.M. Lackmann, and W.A. Robinson, 2015: Changes in U.S. East Coast cyclone dynamics with climate change. *Journal of Climate*, **28(2)**, 468–484, doi:10.1175/jcli-d-14-00418.1.
Marengo, J.A., M.C. Valverde, and G.O. Obregon, 2013: Observed and projected changes in rainfall extremes in the Metropolitan Area of São Paulo. *Climate Research*, **57(1)**, 61–72, doi:10.3354/cr01160.
Marengo, J.A. et al., 2014: *Climate Change in Central and South America: Recent Trends, Future Projections, and Impacts on Regional Agriculture*. CCAFS Working Paper no. 73, CGIAR Research Program on Climate Change, Agriculture and Food Security (CCAFS), Copenhagen, Denmark, 91 pp.
Margulis, S.A., G. Cortés, M. Girotto, and M. Durand, 2016: A Landsat-era Sierra Nevada snow reanalysis (1985--2015). *Journal of Hydrometeorology*, **17(4)**, 1203–1221.
Markonis, Y., M. Hanel, P. Máca, J. Kyselý, and E.R. Cook, 2018: Persistent multi-scale fluctuations shift European hydroclimate to its millennial boundaries. *Nature Communications*, doi:10.1038/s41467-018-04207-7.
Marlier, M.E. et al., 2017: The 2015 drought in Washington State: A harbinger of things to come? *Environmental Research Letters*, doi:10.1088/1748-9326/aa8fde.
Marshall, G.J. and T.J. Bracegirdle, 2015: An examination of the relationship between the Southern Annular Mode and Antarctic surface air temperatures in the CMIP5 historical runs. *Climate Dynamics*, **45(5–6)**, 1513–1535, doi:10.1007/s00382-014-2406-z.
Marshall, G.J., D.W.J. Thompson, and M.R. van den Broeke, 2017: The Signature of Southern Hemisphere Atmospheric Circulation Patterns in Antarctic Precipitation. *Geophysical Research Letters*, **44(22)**, 11,580–11,589, doi:10.1002/2017gl075998.
Martel, J.-L., A. Mailhot, F. Brissette, and D. Caya, 2018: Role of Natural Climate Variability in the Detection of Anthropogenic Climate Change Signal for Mean and Extreme Precipitation at Local and Regional Scales.

ACCEPTED VERSION SUBJECT TO FINAL EDITING

Journal of Climate, **31(11)**, 4241–4263, doi:10.1175/jcli-d-17-0282.1.
Martens, B., W. Waegeman, W.A. Dorigo, N.E.C. Verhoest, and D.G. Miralles, 2018: Terrestrial evaporation response to modes of climate variability. *npj Climate and Atmospheric Science*, **1(1)**, 43, doi:10.1038/s41612-018-0053-5.
Martin, J.T. et al., 2020: Increased drought severity tracks warming in the United States' largest river basin. *Proceedings of the National Academy of Sciences of the United States of America*, doi:10.1073/pnas.1916208117.
Martin-Gomez, V., E. Hernandez-Garcia, M. Barreiro, and C. Lopez, 2016: Interdecadal Variability of Southeastern South America Rainfall and Moisture Sources during the Austral Summertime. *Journal of Climate*, **29**, 6751–6763, doi:10.1175/jcli-d-15-0803.1.
Martín-Gómez, V. and M. Barreiro, 2016: Analysis of oceans' influence on spring time rainfall variability over Southeastern South America during the 20th century. *International Journal of Climatology*, **36(3)**, 1344–1358, doi:10.1002/joc.4428.
Marty, C., A.- Tilg, and T. Jonas, 2017: Recent evidence of large scale receding snow water equivalents in the European Alps, J. , doi:10.1175/jhm-d-16-0188.s1.
Marvel, K. et al., 2017: Observed and projected changes to the precipitation annual cycle. *Journal of Climate*, 4983–4995, doi:10.1175/jcli-d-16-0572.1.
Marvel, K. et al., 2019: Evidence for human influence on twentieth century hydroclimate. *Nature*, **1**, 1.
Marzeion, B. et al., 2020: Partitioning the Uncertainty of Ensemble Projections of Global Glacier Mass Change. *Earth's Future*, **8(7)**, doi:10.1029/2019ef001470.
Marzeion 2018, : Limited influence of climate change mitigation on short-term glacier mass loss. , doi:10.1038/s41558-018-0093-1.
Massei, N. et al., 2017: Multi-time-scale hydroclimate dynamics of a regional watershed and links to large-scale atmospheric circulation: Application to the Seine river catchment, France. *Journal of Hydrology*, **546**, 262–275, doi:10.1016/j.jhydrol.2017.01.008.
Massmann, A., P. Gentine, and C. Lin, 2019: When Does Vapor Pressure Deficit Drive or Reduce Evapotranspiration? *Journal of Advances in Modeling Earth Systems*, **11(10)**, 3305–3320, doi:10.1029/2019ms001790.
Masson-Delmotte, V. et al., 2013: Information from Paleoclimate Archives. In: *Climate Change 2013: The Physical Science Basis. Contribution of Working Group I to the Fifth Assessment Report of the Intergovernmental Panel on Climate Change* [Stocker, T.F., D. Qin, G.-K. Plattner, M. Tignor, S.K. Allen, J. Boschung, A. Nauels, Y. Xia, V. Bex, and P.M. Midgley (eds.)]. Cambridge University Press, Cambridge, United Kingdom and New York, NY, USA, pp. 383–464, doi:10.1017/cbo9781107415324.013.
Matthews, T., C. Murphy, R.L. Wilby, and S. Harrigan, 2016: A cyclone climatology of the British-Irish Isles 1871--2012. *International Journal of Climatology*, **36(3)**, 1299–1312.
Mattingly, K.S., T.L. Mote, and X. Fettweis, 2018: Atmospheric River Impacts on Greenland Ice Sheet Surface Mass Balance. *Journal of Geophysical Research: Atmospheres*, **123(16)**, 8538–8560, doi:10.1029/2018jd028714.
Maurer, J.M., J.M. Schaefer, S. Rupper, and A. Corley, 2019: Acceleration of ice loss across the Himalayas over the past 40 years. *Science Advances*, **5(6)**, eaav7266, doi:10.1126/sciadv.aav7266.
Maxwell, R.M. and L.E. Condon, 2016: Connections between groundwater flow and transpiration partitioning. *Science*, **353(0000)**, 377–380, doi:10.1126/science.aaf7891.
Mayta, V.C., T. Ambrizzi, J.C. Espinoza, and P.L. Silva Dias, 2019: The role of the Madden-Julian oscillation on the Amazon Basin intraseasonal rainfall variability. *International Journal of Climatology*, **39(1)**, 343–360, doi:10.1002/joc.5810.
McCabe, G.J., D.M. Wolock, G.T. Pederson, C.A. Woodhouse, and S. McAfee, 2017: Evidence that recent warming is reducing upper Colorado river flows. *Earth Interactions*, doi:10.1175/ei-d-17-0007.1.
McClymont, E. et al., 2020: Lessons from a high CO2 world: an ocean view from ~ 3 million years ago. *Climate of The Past Discussions*, **2020**, 1–27, doi:10.5194/cp-2019-161.
McDowell, N.G. and C.D. Allen, 2015: Darcy's law predicts widespread forest mortality under climate warming. *Nature Climate Change*, doi:10.1038/nclimate2641.
McDowell, N.G. et al., 2016: Multi-scale predictions of massive conifer mortality due to chronic temperature rise. *Nature Climate Change*, doi:10.1038/nclimate2873.
McGee, D., A. Donohoe, J. Marshall, and D. Ferreira, 2014: Changes in ITCZ location and cross-equatorial heat transport at the Last Glacial Maximum, Heinrich Stadial 1, and the mid-Holocene. *Earth and Planetary Science Letters*, doi:10.1016/j.epsl.2013.12.043.
McGree, S. et al., 2019: Recent Changes in Mean and Extreme Temperature and Precipitation in the Western Pacific Islands. *Journal of Climate*, **32(16)**, 4919–4941, doi:10.1175/jcli-d-18-0748.1.
McGregor, S. et al., 2014: Recent Walker circulation strengthening and Pacific cooling amplified by Atlantic warming. *Nature Climate Change*, **4(10)**, 888–892, doi:10.1038/nclimate2330.
McGregor, S. et al., 2020: The Effect of Strong Volcanic Eruptions on ENSO. In: *El Niño Southern Oscillation in a Changing Climate* [McPhaden, M.J., A. Santoso, and W. Cai (eds.)]. American Geophysical Union (AGU), Washington, DC, USA, pp. 267–287, doi:10.1002/9781119548164.ch12.

ACCEPTED VERSION SUBJECT TO FINAL EDITING

McInerney, D. and E. Moyer, 2012: Direct and disequilibrium effects on precipitation in transient climates. *Atmospheric Chemistry and Physics Discussions*, **12(8)**, 19649–19681, doi:10.5194/acpd-12-19649-2012.
McKenna, S., A. Santoso, A. Gupta, A.S. Taschetto, and W. Cai, 2020: Indian Ocean Dipole in CMIP5 and CMIP6: characteristics, biases, and links to ENSO. *Scientific Reports*, **10(1)**, 11500, doi:10.1038/s41598-020-68268-9.
McKinnon, K.A. and C. Deser, 2018: Internal Variability and Regional Climate Trends in an Observational Large Ensemble. *Journal of Climate*, **31(17)**, 6783–6802, doi:10.1175/jcli-d-17-0901.1.
Medlyn, B.E. et al., 2015: Using ecosystem experiments to improve vegetation models. *Nature Climate Change*, **5(6)**, 528–534, doi:10.1038/nclimate2621.
Meehl, G.A., A. Hu, B.D. Santer, and S.-P. Xie, 2016: Contribution of the Interdecadal Pacific Oscillation to twentieth-century global surface temperature trends. *Nature Climate Change*, **6(11)**, 1005–1008, doi:10.1038/nclimate3107.
Meixner, T. et al., 2016: Implications of projected climate change for groundwater recharge in the western United States. *Journal of Hydrology*, **534**, 124–138, doi:10.1016/j.jhydrol.2015.12.027.
Mekonnen, M.M. and A.Y. Hoekstra, 2016: Four billion people facing severe water scarcity. *Science Advances*, **2(2)**, DOI: 10.1126/sciadv.1500323.
Menon et al., 2013: Consistent increase in Indian monsoon rainfall and its variability Geoscientific across CMIP-5 models. , 287–300, doi:10.5194/esd-4-287-2013.
Meredith, E.P., U. Ulbrich, and H.W. Rust, 2019: The diurnal nature of future extreme precipitation intensification. *Geophysical Research Letters*, 2019GL082385, doi:10.1029/2019gl082385.
Meredith, M. et al., 2019: Polar Regions. In: *IPCC Special Report on the Ocean and Cryosphere in a Changing Climate* [Pörtner, H.-O., D.C. Roberts, V. Masson-Delmotte, P. Zhai, M. Tignor, E. Poloczanska, K. Mintenbeck, A. Alegría, M. Nicolai, A. Okem, J. Petzold, B. Rama, and N.M. Weyer (eds.)]. In Press, pp. 203–320.
Merlis, T.M., 2015: Direct weakening of tropical circulations from masked CO 2 radiative forcing . *Proceedings of the National Academy of Sciences*, doi:10.1073/pnas.1508268112.
Metcalfe, S.E., J.A. Barron, and S.J. Davies, 2015: The Holocene history of the North American Monsoon: 'known knowns' and 'known unknowns' in understanding its spatial and temporal complexity. *Quaternary Science Reviews*, **120**, 1–27, doi:10.1016/j.quascirev.2015.04.004.
Michaelis, A.C., J. Willison, G.M. Lackmann, and W.A. Robinson, 2017: Changes in winter North Atlantic extratropical cyclones in high-resolution regional pseudo-global warming simulations. *Journal of Climate*, **30(17)**, 6905–6925, doi:10.1175/jcli-d-16-0697.1.
Micklin, P., 2016: The future Aral Sea: hope and despair. *Environmental Earth Sciences*, **75(9)**, 1–15, doi:10.1007/s12665-016-5614-5.
Mileham, L., R.G. Taylor, M. Tood, C. Tindimugaya, and J. Thompson, 2009: The impact of climate change on groundwater recharge and runoff in a humid, equatorial catchment: sensitivity of projections to rainfall intensity. *Hydrological Sciences Journal*, **54(4)**, 727–738, doi:10.1623/hysj.54.4.727.
Milly, P.C.D. and K.A. Dunne, 2016: Potential evapotranspiration and continental drying. *Nature Climate Change*, **6(10)**, 946–949, doi:10.1038/nclimate3046.
Milly, P.C.D.C.D.D. and K.A.A. Dunne, 2020: Colorado River flow dwindles as warming-driven loss of reflective snow energizes evaporation. *Science*, **367(6483)**, 1252 LP – 1255, doi:10.1126/science.aay9187.
Milner, A.M. et al., 2017: Glacier shrinkage driving global changes in downstream systems. *Proceedings of the National Academy of Sciences*, **114(37)**, 9770 LP – 9778, doi:10.1073/pnas.1619807114.
Mindlin, J. et al., 2020: Storyline description of Southern Hemisphere midlatitude circulation and precipitation response to greenhouse gas forcing. *Climate Dynamics*, **54(9–10)**, 4399–4421, doi:10.1007/s00382-020-05234-1.
Miralles, D.G., A.J. Teuling, C.C. Van Heerwaarden, and J.V.G. De Arellano, 2014a: Mega-heatwave temperatures due to combined soil desiccation and atmospheric heat accumulation. *Nature Geoscience*, **7(5)**, 345–349, doi:10.1038/ngeo2141.
Miralles, D.G., P. Gentine, S.I. Seneviratne, and A.J. Teuling, 2019: Land–atmospheric feedbacks during droughts and heatwaves: state of the science and current challenges. *Annals of the New York Academy of Sciences*, **1436(1)**, 19–35, doi:10.1111/nyas.13912.
Miralles, D.G. et al., 2014b: El Niño–La Niña cycle and recent trends in continental evaporation. *Nature Climate Change*, **4(2)**, 122–126, doi:10.1038/nclimate2068.
Miralles, D.G. et al., 2016: The WACMOS-ET project - Part 2: Evaluation of global terrestrial evaporation data sets. *Hydrology and Earth System Sciences*, **20(2)**, 823–842, doi:10.5194/hess-20-823-2016.
Mishra, V. et al., 2020: Moist heat stress extremes in India enhanced by irrigation. *Nature Geoscience*, **13(11)**, 722–728, doi:10.1038/s41561-020-00650-8.
Mishra et al., V. Mishra, B. Smoliak, D.P. Lettenmaier, and J.M. Wallace, 2012: A prominent pattern of year-to-year variability in Indian Summer Monsoon Rainfall. *Proceedings of the National Academy of Sciences*, **109(19)**, 7213–7217, doi:10.1073/pnas.1119150109.
Mohtadi, M., M. Prange, and S. Steinke, 2016: Palaeoclimatic insights into forcing and response of monsoon rainfall. *Nature*, doi:10.1038/nature17450.
Moise, A., I. Smith, J.R. Brown, R. Colman, and S. Narsey, 2020: Observed and projected intra-seasonal variability of

ACCEPTED VERSION SUBJECT TO FINAL EDITING

Australian monsoon rainfall. *International Journal of Climatology*, **40(4)**, 2310–2327, doi:10.1002/joc.6334.
Molina-Carpio, J. et al., 2017: Hydroclimatology of the Upper Madeira River basin: spatio-temporal variability and trends. *Hydrological Sciences Journal*, **62(6)**, 911–927, doi:10.1080/02626667.2016.1267861.
Mollier-Vogel, E., G. Leduc, T. Böschen, P. Martinez, and R.R. Schneider, 2013: Rainfall response to orbital and millennial forcing in northern Peru over the last 18ka. *Quaternary Science Reviews*, **76**, 29–38, doi:10.1016/j.quascirev.2013.06.021.
Molnar, P., S. Fatichi, L. Gaál, J. Szolgay, and P. Burlando, 2015: Storm type effects on super Clausius-Clapeyron scaling of intense rainstorm properties with air temperature. *Hydrology and Earth System Sciences*, **19(4)**, 1753–1766, doi:10.5194/hess-19-1753-2015.
Monerie, P.-A., C.M. Wainwright, M. Sidibe, and A.A. Akinsanola, 2020: Model uncertainties in climate change impacts on Sahel precipitation in ensembles of CMIP5 and CMIP6 simulations. *Climate Dynamics*, doi:10.1007/s00382-020-05332-0.
Moomaw, W.R. et al., 2018: Wetlands In a Changing Climate: Science, Policy and Management. *Wetlands*, doi:10.1007/s13157-018-1023-8.
Moon, H., B.P. Guillod, L. Gudmundsson, and S.I. Seneviratne, 2019: Soil moisture effects on afternoon precipitation occurrence in current climate models. *Geophysical Research Letters*, doi:10.1029/2018gl080879.
Moon, I.J., S.H. Kim, and J.C.L. Chan, 2019: Climate change and tropical cyclone trend. *Nature*, **570(7759)**, E3–E5, doi:10.1038/s41586-019-1222-3.
Moon, S. and K.-J. Ha, 2020: Future changes in monsoon duration and precipitation using CMIP6. *Climate and Atmospheric Science*, **3(45)**, 1–7, doi:10.1038/s41612-020-00151-w.
Moore, G.W.K., I.A. Renfrew, and R.S. Pickart, 2013: Multidecadal Mobility of the North Atlantic Oscillation. *Journal of Climate*, **26(8)**, 2453–2466, doi:10.1175/jcli-d-12-00023.1.
Morales, M.S. et al., 2012: Precipitation changes in the South American Altiplano since 1300 AD reconstructed by tree-rings. *Climate of the Past*, **8**, 653–666.
Morales, M.S. et al., 2020: Six hundred years of South American tree rings reveal an increase in severe hydroclimatic events since mid-20th century. *Proceedings of the National Academy of Sciences of the United States of America*, doi:10.1073/pnas.2002411117.
Morrill, C., D.P. Lowry, and A. Hoell, 2018: Thermodynamic and Dynamic Causes of Pluvial Conditions During the Last Glacial Maximum in Western North America. *Geophysical Research Letters*, **45(1)**, 335–345, doi:10.1002/2017gl075807.
Mote, P.W., S. Li, D.P. Lettenmaier, M. Xiao, and R. Engel, 2018: Dramatic declines in snowpack in the western US. *Npj Climate and Atmospheric Science*, **1(1)**, 2.
Mote, P.W. et al., 2016: Perspectives on the causes of exceptionally low 2015 snowpack in the western United States. *Geophysical Research Letters*, doi:10.1002/2016gl069965.
Muchan, K., M. Lewis, J. Hannaford, and S. Parry, 2015: The winter storms of 2013/2014 in the UK: hydrological responses and impacts. *Weather*, **70(2)**, 55–61, doi:10.1002/wea.2469.
Mudryk, 2017: Snow cover response to temperature in observational. , doi:10.1002/2016gl071789.
Mudryk, L. et al., 2020: Historical Northern Hemisphere snow cover trends and projected changes in the CMIP6 multi-model ensemble. *The Cryosphere*, **14(7)**, 2495–2514, doi:10.5194/tc-14-2495-2020.
Mudryk, L.R., P.J. Kushner, C. Derksen, and C. Thackeray, 2017: Snow cover response to temperature in observational and climate model ensembles. *Geophysical Research Letters*, **44(2)**, 919–926, doi:10.1002/2016gl071789.
Mueller, B. and X. Zhang, 2016: Causes of drying trends in northern hemispheric land areas in reconstructed soil moisture data. *Climatic Change*, **134(1–2)**, 255–267, doi:10.1007/s10584-015-1499-7.
Mujumdar, M. et al., 2020: Droughts and Floods. In: *Assessment of Climate Change over the Indian Region: A Report of the Ministry of Earth Sciences (MoES), Government of India* [Krishnan, R., J. Sanjay, C. Gnanaseelan, M. Mujumdar, A. Kulkarni, and S. Chakraborty (eds.)]. Springer, Singapore, pp. 117–141, doi:10.1007/978-981-15-4327-2_6.
Mukherjee, A., S.N. Bhanja, and Y. Wada, 2018: Groundwater depletion causing reduction of baseflow triggering Ganges river summer drying. *Scientific Reports*, **8(1)**, doi:10.1038/s41598-018-30246-7.
Muller, C. and S. Bony, 2015: What favors convective aggregation and why? *Geophysical Research Letters*, **42(13)**, 5626–5634, doi:10.1002/2015gl064260.
Mundhenk, B.D., E.A. Barnes, E.D. Maloney, and C.F. Baggett, 2018: Skillful empirical subseasonal prediction of landfalling atmospheric river activity using the Madden–Julian oscillation and quasi-biennial oscillation. *npj Climate and Atmospheric Science*, **1(1)**, 20177, doi:10.1038/s41612-017-0008-2.
Murphy, T.R., M.E. Hanley, J.S. Ellis, and P.H. Lunt, 2020: Native woodland establishment improves soil hydrological functioning in UK upland pastoral catchments. *Land Degradation & Development*, **n/a(n/a)**, doi:10.1002/ldr.3762.
Murray, B.J., D. O'sullivan, J.D. Atkinson, and M.E. Webb, 2012: Ice nucleation by particles immersed in supercooled cloud droplets. *Chemical Society Reviews*, **41(19)**, 6519–6554, doi:10.1039/c2cs35200a.
Murray-Tortarolo, G., V.J. Jaramillo, M. Maass, P. Friedlingstein, and S. Sitch, 2017: The decreasing range between dry- and wet-season precipitation over land and its effect on vegetation primary productivity. *PLoS ONE*,

ACCEPTED VERSION SUBJECT TO FINAL EDITING

12(12), e0190304, doi:10.1371/journal.pone.0190304.
Murray-Tortarolo, G. et al., 2016: The dry season intensity as a key driver of NPP trends. *Geophysical Research Letters*, **43(6)**, 2632–2639, doi:10.1002/2016gl068240.
Musselman, K.N., M.P. Clark, C. Liu, K. Ikeda, and R. Rasmussen, 2017: Slower snowmelt in a warmer world. *Nature Climate Change*, **7(3)**, 214–219, doi:10.1038/nclimate3225.
Musselman, K.N. et al., 2018: Projected increases and shifts in rain-on-snow flood risk over western North America. *Nature Climate Change*, **8(9)**, 808–812, doi:10.1038/s41558-018-0236-4.
Myhre, G. et al., 2018a: Quantifying the Importance of Rapid Adjustments for Global Precipitation Changes. *Geophysical Research Letters*, **45(20)**, 11,399–11,405, doi:10.1029/2018gl079474.
Myhre, G. et al., 2018b: Sensible heat has significantly affected the global hydrological cycle over the historical period. *Nature Communications*, **9(1)**, doi:10.1038/s41467-018-04307-4.
Najafi, M., F. Zwiers, and N. Gillett, 2016: Attribution of the spring snow cover extent decline in the Northern Hemisphere, Eurasia and North America to anthropogenic influence. *Climatic Change*, **136(3–4)**, 571–586, doi:10.1007/s10584-016-1632-2.
Nakano, M., M. Sawada, T. Nasuno, and M. Satoh, 2015: Intraseasonal variability and tropical cyclogenesis in the western North Pacific simulated by a global nonhydrostatic atmospheric model. *Geophysical Research Letters*, **42(2)**, 565–571, doi:10.1002/2014gl062479.
Nangombe, S., T. Zhou, L. Zhang, and W. Zhang, 2020: Attribution Of The 2018 October–December Drought Over South Southern Africa. *Bulletin of the American Meteorological Society*, **101(1)**, S135–S140, doi:10.1175/bams-d-19-0179.1.
Narsey, S.Y. et al., 2020: Climate Change Projections for the Australian Monsoon From CMIP6 Models. *Geophysical Research Letters*, **47(13)**, e2019GL086816, doi:10.1029/2019gl086816.
Nash, D., 2017: Changes in Precipitation Over Southern Africa During Recent Centuries. In: *Oxford Research Encyclopedia of Climate Science*. Oxford University Press, doi:10.1093/acrefore/9780190228620.013.539.
Naughton, F. et al., 2019: Coupled ocean and atmospheric changes during Greenland stadial 1 in southwestern Europe. *Quaternary Science Reviews*, doi:10.1016/j.quascirev.2019.03.033.
Neelin, J.D., S. Sahany, S.N. Stechmann, and D.N. Bernstein, 2017: Global warming precipitation accumulation increases above the current-climate cutoff scale. *Proceedings of the National Academy of Sciences*, **114(6)**, 1258–1263, doi:10.1073/pnas.1615333114.
Neelin, J.D., B. Langenbrunner, J.E. Meyerson, A. Hall, and N. Berg, 2013: California winter precipitation change under global warming in the coupled model intercomparison project phase 5 ensemble. *Journal of Climate*, **26(17)**, 6238–6256, doi:10.1175/jcli-d-12-00514.1.
Neu, U. et al., 2013: Imilast: A community effort to intercompare extratropical cyclone detection and tracking algorithms. *Bulletin of the American Meteorological Society*, **94(4)**, 529–547, doi:10.1175/bams-d-11-00154.1.
Neukom, R. et al., 2015: Facing unprecedented drying of the Central Andes? Precipitation variability over the period AD 1000–2100. *Environmental Research Letters*, **10(8)**, 84017, doi:10.1088/1748-9326/10/8/084017.
Neumann, R.B. et al., 2019: Warming Effects of Spring Rainfall Increase Methane Emissions From Thawing Permafrost. *Geophysical Research Letters*, doi:10.1029/2018gl081274.
Neupane, N. and K.H. Cook, 2013: A nonlinear response of sahel rainfall to atlantic warming. *Journal of Climate*, **26(18)**, 7080–7096, doi:10.1175/jcli-d-12-00475.1.
Neves, M.C., S. Jerez, and R.M. Trigo, 2019: The response of piezometric levels in Portugal to NAO, EA, and SCAND climate patterns. *Journal of Hydrology*, **568**, 1105–1117, doi:10.1016/j.jhydrol.2018.11.054.
Ng, B., W. Cai, T. Cowan, and D. Bi, 2018: Influence of internal climate variability on Indian Ocean Dipole properties. *Scientific Reports*, **8(1)**, 13500, doi:10.1038/s41598-018-31842-3.
Nguyen, H., C. Lucas, A. Evans, B. Timbal, and L. Hanson, 2015: Expansion of the Southern Hemisphere Hadley Cell in Response to Greenhouse Gas Forcing. *Journal of Climate*, **28(20)**, 8067–8077, doi:10.1175/jcli-d-15-0139.1.
Nguyen, H. et al., 2018: Variability of the extent of the Hadley circulation in the southern hemisphere: a regional perspective. *Climate Dynamics*, **50(1–2)**, 129–142, doi:10.1007/s00382-017-3592-2.
Nguyen, P. et al., 2018: Global precipitation trends across spatial scales using satellite observations. *Bulletin of the American Meteorological Society*, **99(4)**, 689–697, doi:10.1175/bams-d-17-0065.1.
Ni, S. et al., 2018: Global Terrestrial Water Storage Changes and Connections to ENSO Events. *Surveys in Geophysics*, **39(1)**, 1–22, doi:10.1007/s10712-017-9421-7.
Nicholson, S.E., 2013: The West African Sahel: A Review of Recent Studies on the Rainfall Regime and Its Interannual Variability. *ISRN Meteorology*, **2013**, 1–32, doi:10.1155/2013/453521.
Nicholson, S.E., 2017: Climate and climatic variability of rainfall over eastern Africa. *Reviews of Geophysics*, **55(3)**, 590–635, doi:10.1002/2016rg000544.
Nicholson, S.E., A.H. Fink, and C. Funk, 2018: Assessing recovery and change in West Africa's rainfall regime from a 161-year record. *International Journal of Climatology*, **38(10)**, 3770–3786, doi:10.1002/joc.5530.
Nie, J., A.H. Sobel, D.A. Shaevitz, and S. Wang, 2018: Dynamic amplification of extreme precipitation sensitivity. *Proceedings of the National Academy of Sciences*, **115(38)**, 201800357, doi:10.1073/pnas.1800357115.

ACCEPTED VERSION SUBJECT TO FINAL EDITING

Nikumbh, A., A. Chakraborty, and G.S. Bhat, 2019: Recent spatial aggregation tendency of rainfall extremes over India. *Scientific Reports*, **9(1)**, 1–29, doi:10.1038/s41598-019-46719-2.
Niranjan Kumar, K. et al., 2013: On the observed variability of monsoon droughts over India. *Weather and Climate Extremes*, **1**, 42–50, doi:10.1016/j.wace.2013.07.006.
Norris, J., G. Chen, and J.D. Neelin, 2019: Changes in frequency of large precipitation accumulations over land in a warming climate from the CESM Large Ensemble: the roles of moisture, circulation and duration. *Journal of Climate*, **32(17)**, JCLI–D–18–0600.1, doi:10.1175/jcli-d-18-0600.1.
Norris, J.R. et al., 2016: Evidence for climate change in the satellite cloud record. *Nature*, **536(7614)**, 72–75, doi:10.1038/nature18273.
Notaro, M., V. Bennington, and B. Lofgren, 2015: Dynamical downscaling-based projections of great lakes water levels. *Journal of Climate*, **28(24)**, 9721–9745, doi:10.1175/jcli-d-14-00847.1.
Novello, V.F. et al., 2016: Centennial-scale solar forcing of the South American Monsoon System recorded in stalagmites. *Scientific Reports*, **6(1)**, 1–8, doi:10.1038/srep24762.
Novello, V.F. et al., 2017: A high-resolution history of the South American Monsoon from Last Glacial Maximum to the Holocene. *Scientific Reports*, **7(1)**, 1–8, doi:10.1038/srep44267.
Nur'utami, M.N. and R. Hidayat, 2016: Influences of IOD and ENSO to Indonesian Rainfall Variability: Role of Atmosphere-ocean Interaction in the Indo-pacific Sector. *Procedia Environmental Sciences*, **33**, 196–203, doi:10.1016/j.proenv.2016.03.070.
Nusbaumer, J., P.M. Alexander, A.N. LeGrande, and M. Tedesco, 2019: Spatial shift of Greenland moisture sources related to enhanced Arctic warming. *Geophysical Research Letters*, **n/a(n/a)**, doi:10.1029/2019gl084633.
Nygård, T., T. Naakka, and T. Vihma, 2020: Horizontal Moisture Transport Dominates the Regional Moistening Patterns in the Arctic. *Journal of Climate*, **33(16)**, 6793–6807, doi:10.1175/jcli-d-19-0891.1.
O'Gorman, P.A., 2012: Sensitivity of tropical precipitation extremes to climate change. *Nature Geoscience*, **5(10)**, 697–700, doi:10.1038/ngeo1568.
O'Gorman, P.A., 2014: Contrasting responses of mean and extreme snowfall to climate change. *Nature*, **512(7515)**, 416–418, doi:10.1038/nature13625.
O'Gorman, P.A., 2015: Precipitation Extremes Under Climate Change. *Current Climate Change Reports*, **1(2)**, 49–59, doi:10.1007/s40641-015-0009-3.
O'Gorman, P.A. and T. Schneider, 2009: The physical basis for increases in precipitation extremes in simulations of 21st-century climate change. *Proceedings of the National Academy of Sciences*, **106(35)**, 14773–14777, doi:10.1073/pnas.0907610106.
O'Gorman, P.A. and J.G. Dwyer, 2018: Using Machine Learning to Parameterize Moist Convection: Potential for Modeling of Climate, Climate Change, and Extreme Events. *Journal of Advances in Modeling Earth Systems*, doi:10.1029/2018ms001351.
O'Gorman, P.A., R.P. Allan, M.P. Byrne, and M. Previdi, 2012: Energetic Constraints on Precipitation Under Climate Change. *Surveys in Geophysics*, **33(3–4)**, 585–608, doi:10.1007/s10712-011-9159-6.
Ogata, T. et al., 2017: The resolution sensitivity of the Asian summer monsoon and its inter-model comparison between MRI-AGCM and MetUM. *Climate Dynamics*, **49(9–10)**, 3345–3361, doi:10.1007/s00382-016-3517-5.
Oki, T. and S. Kanae, 2006: Global Hydrological Cycles and World Water Resources. *Science*, **313(5790)**, 1068 LP – 1072, doi:10.1126/science.1128845.
Okkonen, J. and B. Kløve, 2011: A sequential modelling approach to assess groundwater-surface water resources in a snow dominated region of Finland. *Journal of Hydrology*, **411**, 91–107.
Okumura, Y.M., P. DiNezio, and C. Deser, 2017: Evolving Impacts of Multiyear La Niña Events on Atmospheric Circulation and U.S. Drought. *Geophysical Research Letters*, **44(22)**, 11,614–11,623, doi:10.1002/2017gl075034.
Oliver, E.C.J. and K.R. Thompson, 2012: A Reconstruction of Madden–Julian Oscillation Variability from 1905 to 2008. *Journal of Climate*, **25(6)**, 1996–2019, doi:10.1175/jcli-d-11-00154.1.
Oltmanns, M., F. Straneo, and M. Tedesco, 2018: Increased Greenland melt triggered by large-scale, year-round precipitation events. *The Cryosphere Discussions*, **13(3)**, 1–18, doi:10.5194/tc-2018-243.
Orlowsky, B. and S.I. Seneviratne, 2013: Elusive drought: Uncertainty in observed trends and short-and long-term CMIP5 projections. *Hydrology and Earth System Sciences*, **17(5)**, 1765–1781, doi:10.5194/hess-17-1765-2013.
Ose, T., 2019: Characteristics of future changes in summertime East Asian monthly precipitation in MRI-AGCM global warming experiments. *Journal of Meteorological Society of Japan*, **97**, doi:10.2151/jmsj.2019-018.
Oshima, K. and K. Yamazaki, 2017: Atmospheric hydrological cycles in the Arctic and Antarctic during the past four decades. *Czech Polar Reports*, **7(2)**, 169–180, doi:10.5817/cpr2017-2-17.
Oster, J.L., D.E. Ibarra, M.J. Winnick, and K. Maher, 2015: Steering of westerly storms over western North America at the Last Glacial Maximum. *Nature Geoscience*, doi:10.1038/ngeo2365.
Otkin, J.A. et al., 2016: Assessing the evolution of soil moisture and vegetation conditions during the 2012 United States flash drought. *Agricultural and Forest Meteorology*, doi:10.1016/j.agrformet.2015.12.065.
Otkin, J.A. et al., 2018: Flash droughts: A review and assessment of the challenges imposed by rapid-onset droughts in

ACCEPTED VERSION SUBJECT TO FINAL EDITING

the United States. *Bulletin of the American Meteorological Society*, doi:10.1175/bams-d-17-0149.1.
Otto, F.E.L. et al., 2018: Anthropogenic influence on the drivers of the Western Cape drought 2015–2017. *Environmental Research Letters*, **13(12)**, 124010, doi:10.1088/1748-9326/aae9f9.
Otto-Bliesner, B.L. et al., 2014: Coherent changes of southeastern equatorial and northern African rainfall during the last deglaciation. *Science*, **346(6214)**, 1223–1227, doi:10.1126/science.1259531.
Otto-Bliesner, B.L. et al., 2016: Climate Variability and Change since 850 CE: An Ensemble Approach with the Community Earth System Model. *Bulletin of the American Meteorological Society*, **97(5)**, 735–754, doi:10.1175/bams-d-14-00233.1.
Oudar, T., J. Cattiaux, and H. Douville, 2020a: Drivers of the Northern Extratropical Eddy-Driven Jet Change in CMIP5 and CMIP6 Models. *Geophysical Research Letters*, **47(8)**, 1–9, doi:10.1029/2019gl086695.
Oudar, T. et al., 2020b: Robustness and drivers of the Northern Hemisphere extratropical atmospheric circulation response to a CO2-induced warming in CNRM-CM6-1. *Climate Dynamics*, **54(3–4)**, 2267–2285, doi:10.1007/s00382-019-05113-4.
Oueslati, B. and G. Bellon, 2015: The double ITCZ bias in CMIP5 models: interaction between SST, large-scale circulation and precipitation. *Climate Dynamics*, **44(3–4)**, 585–607, doi:10.1007/s00382-015-2468-6.
Oueslati, B., S. Bony, C. Risi, and J.L. Dufresne, 2016: Interpreting the inter-model spread in regional precipitation projections in the tropics: role of surface evaporation and cloud radiative effects. *Climate Dynamics*, **47(9–10)**, 2801–2815, doi:10.1007/s00382-016-2998-6.
Overland, J.E. et al., 2016: Nonlinear response of mid-latitude weather to the changing Arctic. *Nature Climate Change*, **6(11)**, 992–999, doi:10.1038/nclimate3121.
Overpeck, J.T., 2013: Climate science: The challenge of hot drought. *Nature*, **503(7476)**, 350–351.
Oyama, M.D. and C.A. Nobre, 2003: A new climate-vegetation equilibrium state for Tropical South America. *Geophysical Research Letters*, doi:10.1029/2003gl018600.
P Sabin, T. et al., 2013: High resolution simulation of the South Asian monsoon using a variable resolution global climate model. *Climate Dynamics*, **41(1)**, 173–194, doi:10.1007/s00382-012-1658-8.
Pabón-Caicedo, J.D. et al., 2020: Observed and Projected Hydroclimate Changes in the Andes. *Frontiers in Earth Science*, **8(61)**, 1–29, doi:10.3389/feart.2020.00061.
Padrón, R.S. et al., 2020: Observed changes in dry-season water availability attributed to human-induced climate change. *Nature Geoscience*, **13(7)**, 477–481, doi:10.1038/s41561-020-0594-1.
Page, T., N.A. Chappell, K.J. Beven, B. Hankin, and A. Kretzschmar, 2020: Assessing the significance of wet-canopy evaporation from forests during extreme rainfall events for flood mitigation in mountainous regions of the United Kingdom. *Hydrological Processes*, **n/a(n/a)**, doi:10.1002/hyp.13895.
PAGES Hydro2K Consortium, 2017: Comparing proxy and model estimates of hydroclimate variability and change over the Common Era. *Climate of the Past*, **13(12)**, 1851–1900, doi:10.5194/cp-13-1851-2017.
Palerme, C. et al., 2017: Evaluation of current and projected Antarctic precipitation in CMIP5 models. *Climate Dynamics*, **48(1–2)**, 225–239, doi:10.1007/s00382-016-3071-1.
Pall, P., L.M. Tallaksen, and F. Stordal, 2019: A Climatology of Rain-on-Snow Events for Norway. *Journal of Climate*, **32(20)**, 6995–7016, doi:10.1175/jcli-d-18-0529.1.
Palmer, J.G. et al., 2015: Drought variability in the eastern Australia and New Zealand summer drought atlas (ANZDA, CE 1500-2012) modulated by the Interdecadal Pacific Oscillation. *Environmental Research Letters*, doi:10.1088/1748-9326/10/12/124002.
Paltan, H. et al., 2017: Global Floods and Water Availability Driven by Atmospheric Rivers. *Geophysical Research Letters*, **44(20)**, 10,387–10,395, doi:10.1002/2017gl074882.
Pan, N., S. Wang, Y. Liu, W. Zhao, and B. Fu, 2019: Global surface soil moisture dynamics in 1979-2016 observed from ESA CCI SM dataset. *Water (Switzerland)*, **11(5)**, doi:10.3390/w11050883.
Pan, S. et al., 2015: Responses of global terrestrial evapotranspiration to climate change and increasing atmospheric CO2in the 21st century. *Earth's Future*, doi:10.1002/2014ef000263.
Pan, X., M. Chin, C.M. Ichoku, and R.D. Field, 2018: Connecting Indonesian Fires and Drought With the Type of El Niño and Phase of the Indian Ocean Dipole During 1979-2016. *Journal of Geophysical Research: Atmospheres*, doi:10.1029/2018jd028402.
Panthou, G., T. Vischel, and T. Lebel, 2014: Recent trends in the regime of extreme rainfall in the Central Sahel. *International Journal of Climatology*, **34(15)**, 3998–4006, doi:10.1002/joc.3984.
Panthou, G. et al., 2018: Rainfall intensification in tropical semi-arid regions: the Sahelian case. *Environmental Research Letters*, **13(6)**, 064013, doi:10.1088/1748-9326/aac334.
Park, H. et al., 2020: Increasing riverine heat influx triggers Arctic sea ice decline and oceanic and atmospheric warming. *Science Advances*, **6(45)**, 1–8, doi:10.1126/sciadv.abc4699.
Park, S., J. Shin, S. Kim, E. Oh, and Y. Kim, 2019: Global climate simulated by the Seoul National University Atmosphere Model version 0 with a unified convection scheme (SAM0-UNICON). *Journal of Climate*, **32(10)**, 2917–2949, doi:10.1175/jcli-d-18-0796.1.
Parracho, A.C., O. Bock, and S. Bastin, 2018: Global IWV trends and variability in atmospheric reanalyses and GPS observations. *Atmospheric Chemistry and Physics*, **18(22)**, 16213–16237, doi:10.5194/acp-18-16213-2018.

ACCEPTED VERSION SUBJECT TO FINAL EDITING

Parsons, L.A., 2020: Implications of CMIP6 projected drying trends for 21 st century Amazonian drought risk. *Earth's Future*, **8(10)**, e2020EF001608, doi:10.1029/2020ef001608.
Parsons, L.A., S. Coats, and J.T. Overpeck, 2018: The continuum of drought in southwestern North America. *Journal of Climate*, **31(20)**, 8627–8643.
Parsons, L.A., J. Yin, J.T. Overpeck, R.J. Stouffer, and S. Malyshev, 2014: Influence of the atlantic meridional overturning circulation on the monsoon rainfall and carbon balance of the American tropics. *Geophysical Research Letters*, doi:10.1002/2013gl058454.
Parsons, L.A. et al., 2017: Temperature and Precipitation Variance in CMIP5 Simulations and Paleoclimate Records of the Last Millennium. *Journal of Climate*, **30(22)**, 8885–8912, doi:10.1175/jcli-d-16-0863.1.
Pascale, S., S.B. Kapnick, T.L. Delworth, and W.F. Cooke, 2020: Increasing risk of another Cape Town "Day Zero" drought in the 21st century. *Proceedings of the National Academy of Sciences*, doi:10.1073/pnas.2009144117.
Pascale, S., V. Lucarini, X. Feng, A. Porporato, and S. ul Hasson, 2016: Projected changes of rainfall seasonality and dry spells in a high greenhouse gas emissions scenario. *Climate Dynamics*, doi:10.1007/s00382-015-2648-4.
Pascale, S., L.M.V. Carvalho, D.K. Adams, C.L. Castro, and I.F.A.A. Cavalcanti, 2019: Current and Future Variations of the Monsoons of the Americas in a Warming Climate. *Current Climate Change Reports*, **5(3)**, 125–144, doi:10.1007/s40641-019-00135-w.
Pascale, S. et al., 2017: Weakening of the North American monsoon with global warming. *Nature Climate Change*, **7(11)**, 806–812, doi:10.1038/nclimate3412.
Pathirana, A., H.B. Denekew, W. Veerbeek, C. Zevenbergen, and A.T. Banda, 2014: Impact of urban growth-driven landuse change on microclimate and extreme precipitation - A sensitivity study. *Atmospheric Research*, **138**, 59–72, doi:10.1016/j.atmosres.2013.10.005.
Patil, N., C. Venkataraman, K. Muduchuru, S. Ghosh, and A. Mondal, 2019: Disentangling sea-surface temperature and anthropogenic aerosol influences on recent trends in South Asian monsoon rainfall. *Climate Dynamics*, **52(3–4)**, 2287–2302, doi:10.1007/s00382-018-4251-y.
Patterson, M., T. Bracegirdle, and T. Woollings, 2019: Southern Hemisphere Atmospheric Blocking in CMIP5 and Future Changes in the Australia-New Zealand Sector. *Geophysical Research Letters*, **46(15)**, 9281–9290, doi:10.1029/2019gl083264.
Paul, S. et al., 2016: Weakening of Indian Summer Monsoon Rainfall due to Changes in Land Use Land Cover. *Scientific Reports*, **6(1)**, 32177, doi:10.1038/srep32177.
Pausata, F.S.R., G. Messori, and Q. Zhang, 2016: Impacts of dust reduction on the northware expansion of the African monsoon during the Green Sahara period. *Earth and Planetary Science Letters*, **434**, 298–307.
Pausata, F.S.R., L. Chafik, R. Caballero, and D.S. Battisti, 2015a: Impacts of high-latitude volcanic eruptions on ENSO and AMOC. *Proceedings of the National Academy of Sciences*, **112(45)**, 13784–13788, doi:10.1073/pnas.1509153112.
Pausata, F.S.R., A. Grini, R. Caballero, A. Hannachi, and Seland, 2015b: High-latitude volcanic eruptions in the Norwegian Earth System Model: The effect of different initial conditions and of the ensemble size. *Tellus, Series B: Chemical and Physical Meteorology*, doi:10.3402/tellusb.v67.26728.
Pausata, F.S.R. et al., 2020: The Greening of the Sahara: Past Changes and Future Implications. *One Earth*, doi:10.1016/j.oneear.2020.03.002.
Payne, A.E. and G. Magnusdottir, 2015: An evaluation of atmospheric rivers over the North Pacific in CMIP5 and their response to warming under RCP 8.5. *Journal of Geophysical Research*, **120**, 11173–11190.
Payne, A.E. et al., 2020: Responses and impacts of atmospheric rivers to climate change. *Nature Reviews Earth & Environment*, **1(3)**, 143–157, doi:10.1038/s43017-020-0030-5.
Peano, D. et al., 2019: Global Variability of Simulated and Observed Vegetation Growing Season. *Journal of Geophysical Research: Biogeosciences*, doi:10.1029/2018jg004881.
Pechlivanidis, I.G. et al., 2017: Analysis of hydrological extremes at different hydro-climatic regimes under present and future conditions. *Climatic Change*, **141(3)**, 467–481, doi:10.1007/s10584-016-1723-0.
Pederson, N., A.E. Hessl, N. Baatarbileg, K.J. Anchukaitis, and N. Di Cosmo, 2014: Pluvials, droughts, the Mongol Empire, and modern Mongolia. *Proceedings of the National Academy of Sciences*, doi:10.1073/pnas.1318677111.
Pedron, I.T., M.A.F. Silva Dias, S. de Paula Dias, L.M. Carvalho, and E.D. Freitas, 2017: Trends and variability in extremes of precipitation in Curitiba - Southern Brazil. *International Journal of Climatology*, **37(3)**, 1250–1264, doi:10.1002/joc.4773.
Pei, L. et al., 2016: Effects of irrigation on summer precipitation over the United States. *Journal of Climate*, **29(10)**, 3541–3558, doi:10.1175/jcli-d-15-0337.1.
Peings, Y. and G. Magnusdottir, 2014: Response of the wintertime northern hemisphere atmospheric circulation to current and projected arctic sea ice decline: A numerical study with CAM5. *Journal of Climate*, **27(1)**, 244–264, doi:10.1175/jcli-d-13-00272.1.
Pekel, J.-, A. Cottam, N. Gorelick, and A.S. Belward, 2016: High-resolution mapping of global surface water and its long-term changes. *Nature*, **540**, 418–422.
Pendergrass, A.G., 2020a: Changing Degree of Convective Organization as a Mechanism for Dynamic Changes in

ACCEPTED VERSION SUBJECT TO FINAL EDITING

Extreme Precipitation. *Current Climate Change Reports*, **6(2)**, 47–54, doi:10.1007/s40641-020-00157-9.
Pendergrass, A.G., 2020b: The Global-Mean Precipitation Response to CO2-Induced Warming in CMIP6 Models. *Geophysical Research Letters*, **47(17)**, e2020GL089964, doi:10.1029/2020gl089964.
Pendergrass, A.G. and D.L. Hartmann, 2014a: Changes in the distribution of rain frequency and intensity in response to global warming. *Journal of Climate*, **27(22)**, 8372–8383, doi:10.1175/jcli-d-14-00183.1.
Pendergrass, A.G. and D.L. Hartmann, 2014b: Two modes of change of the distribution of rain. *Journal of Climate*, **27(22)**, 8357–8371, doi:10.1175/jcli-d-14-00182.1.
Pendergrass, A.G., K.A. Reed, and B. Medeiros, 2016: The link between extreme precipitation and convective organization in a warming climate: Global radiative-convective equilibrium simulations. *Geophysical Research Letters*, **43(21)**, 11,445–11,452, doi:10.1002/2016gl071285.
Pendergrass, A.G., F. Lehner, B.M. Sanderson, and Y. Xu, 2015: Does extreme precipitation intensity depend on the emissions scenario? *Geophysical Research Letters*, **42(20)**, 8767–8774, doi:10.1002/2015gl065854.
Pendergrass, A.G., R. Knutti, F. Lehner, C. Deser, and B.M. Sanderson, 2017: Precipitation variability increases in a warmer climate. *Scientific Reports*, **7(1)**, 1–9, doi:10.1038/s41598-017-17966-y.
Pendergrass, A.G. et al., 2019: Nonlinear response of extreme precipitation to warming in CESM1. *Geophysical Research Letters*, 2019GL084826, doi:10.1029/2019gl084826.
Pendergrass, A.G. et al., 2020: Flash droughts present a new challenge for subseasonal-to-seasonal prediction. *Nature Climate Change*, doi:10.1038/s41558-020-0709-0.
Peng, S. et al., 2013: Change in snow phenology and its potential feedback to temperature in the Northern Hemisphere over the last three decades. *Environmental Research Letters*, **8(1)**, doi:10.1088/1748-9326/8/1/014008.
Pepler, A.S. et al., 2016: Projected changes in east Australian midlatitude cyclones during the 21st century. *Geophysical Research Letters*, **43(1)**, 334–340, doi:10.1002/2015gl067267.received.
Perry, S.J., S. McGregor, A. Sen Gupta, M.H. England, and N. Maher, 2019: Projected late 21st century changes to the regional impacts of the El Niño-Southern Oscillation. *Climate Dynamics*, doi:10.1007/s00382-019-05006-6.
Pervez, M.S. and G.M. Henebry, 2015: Spatial and seasonal responses of precipitation in the Ganges and Brahmaputra river basins to ENSO and Indian Ocean dipole modes: implications for flooding and drought. *Natural Hazards and Earth System Sciences*, **15(1)**, 147–162, doi:10.5194/nhess-15-147-2015.
Peters, W. et al., 2018: Increased water-use efficiency and reduced CO2 uptake by plants during droughts at a continental scale. *Nature Geoscience*, 11–16, doi:10.1038/s41561-018-0212-7.
Peterson, L.C., G.H. Haug, K.A. Hughen, and U. Rohl, 2000: Rapid changes in the hydrologic cycle of the tropical Atlantic during the last glacial. *Science*, doi:10.1126/science.290.5498.1947.
Petoukhov, V., S. Rahmstorf, S. Petri, and H.J. Schellnhuber, 2013: Quasiresonant amplification of planetary waves and recent Northern Hemisphere weather extremes.. *Proceedings of the National Academy of Sciences of the United States of America*, **110(14)**, 5336–41, doi:10.1073/pnas.1222000110.
Petoukhov, V. et al., 2016: Role of quasiresonant planetary wave dynamics in recent boreal spring-to-autumn extreme events.. *Proceedings of the National Academy of Sciences of the United States of America*, **113(25)**, 6862–7, doi:10.1073/pnas.1606300113.
Petrie, M.D., S.L. Collins, D.S. Gutzler, and D.M. Moore, 2014: Regional trends and local variability in monsoon precipitation in the northern Chihuahuan Desert, USA. *Journal of Arid Environments*, **103**, 63–70, doi:10.1016/j.jaridenv.2014.01.005.
Petrova, I.Y., D.G. Miralles, C.C. Van Heerwaarden, and H. Wouters, 2018: Relation between Convective Rainfall Properties and Antecedent Soil Moisture Heterogeneity Conditions in North Africa. *Remote Sensing*, **10(6)**, doi:10.3390/rs10060969.
Pfahl, S., C. Schwierz, M. Croci-Maspoli, C.M. Grams, and H. Wernli, 2015: Importance of latent heat release in ascending air streams for atmospheric blocking. *Nature Geoscience*, **8(8)**, 610–614, doi:10.1038/ngeo2487.
Pfahl, S. et al., 2017: Understanding the regional pattern of projected future changes in extreme precipitation. *Nature Climate Change*, **7(6)**, 423–427, doi:10.1038/nclimate3287.
Pfleiderer, P., C.- Schleussner, and D. Coumou, 2018: Boreal summer weather becomes more persistent in a warmer world. *Nature Climate Change*, **9(9)**, 666–671, doi:10.1038/s41558-019-0555-0.
Philip, S. et al., 2018: Attribution analysis of the Ethiopian drought of 2015. *Journal of Climate*, **31(6)**, 2465–2486, doi:10.1175/jcli-d-17-0274.1.
Phillips, J.C. et al., 2015: The potential for CO2-induced acidification in freshwater: A great lakes case study. *Oceanography*, **28(2)**, 136–145, doi:10.5670/oceanog.2015.37.
Phillips, T.J. et al., 2017: Using ARM observations to evaluate climate model simulations of land-atmosphere coupling on the U.S. *Southern Great Plains, Journal of Geophysical Research: Atmospheres*, **122**, 11.
Piazza, M., L. Terray, J. Boé, E. Maisonnave, and E. Sanchez-Gomez, 2016: Influence of small-scale North Atlantic sea surface temperature patterns on the marine boundary layer and free troposphere: a study using the atmospheric ARPEGE model. *Climate Dynamics*, **46(5–6)**, 1699–1717, doi:10.1007/s00382-015-2669-z.
Pires, G.F. and M.H. Costa, 2013: Deforestation causes different subregional effects on the Amazon bioclimatic equilibrium. *Geophysical Research Letters*, **40(14)**, 3618–3623, doi:10.1002/grl.50570.
Plesca, E., S.A. Buehler, and V. Grützun, 2018: The fast response of the tropical circulation to CO2 forcing. *Journal of*

ACCEPTED VERSION SUBJECT TO FINAL EDITING

Climate, JCLI–D–18–0086.1, doi:10.1175/jcli-d-18-0086.1.
Pokhrel, Y.N., N. Hanasaki, Y. Wada, and H. Kim, 2016: Recent progresses in incorporating human land–water management into global land surface models toward their integration into Earth system models. *WIREs Water*, **3**, 548–574, doi:10.1002/wat2.1150.
Pokhrel, Y.N., F. Felfelani, S. Shin, T. Yamada, and Y. Satoh, 2017: Modeling large-scale human alteration of land surface hydrology and climate. *Geoscience Letters*, **4**, 10.
Pokhrel, Y.N. et al., 2015: Incorporation of groundwater pumping in a global Land Surface Model with the representation of human impacts. *Water Resources Research*, **51(1)**, 78–96, doi:10.1002/2014wr015602.
Polade, S.D., D.W. Pierce, D.R. Cayan, A. Gershunov, and M.D. Dettinger, 2014: The key role of dry days in changing regional climate and precipitation regimes. *Scientific Reports*, **4**, 1–8, doi:10.1038/srep04364.
Polade, S.D., A. Gershunov, D.R. Cayan, M.D. Dettinger, and D.W. Pierce, 2017: Precipitation in a warming world: Assessing projected hydro-climate changes in California and other Mediterranean climate regions. *Scientific Reports*, **7(1)**, 10783, doi:10.1038/s41598-017-11285-y.
Polk, M.H. et al., 2017: Exploring hydrologic connections between tropical mountain wetlands and glacier recession in Peru's Cordillera Blanca. *Applied Geography*, doi:10.1016/j.apgeog.2016.11.004.
Polson, D. and G.C. Hegerl, 2017: Strengthening contrast between precipitation in tropical wet and dry regions. *Geophysical Research Letters*, **44(1)**, 365–373, doi:10.1002/2016gl071194.
Polson, D., G.C. Hegerl, and S. Solomon, 2016: Precipitation sensitivity to warming estimated from long island records. *Environmental Research Letters*, **11(7)**, 74024, doi:10.1088/1748-9326/11/7/074024.
Polson, D., G.C. Hegerl, R.P. Allan, and B.B. Sarojini, 2013: Have greenhouse gases intensified the contrast between wet and dry regions? *Geophysical Research Letters*, **40(17)**, 4783–4787, doi:10.1002/grl.50923.
Polson et al., D. et al., 2014a: Decreased monsoon precipitation in the Northern Hemisphere due to anthropogenic aerosols. *Geophysical Research Letters*, **41(16)**, 6023–6029, doi:10.1002/2014gl060811.
Polson et al., D. et al., 2014b: Geophysical Research Letters. *Geophysical Prospecting*, **41(9)**, 3307–3314, doi:10.1002/2014gl061184.received.
Polyak, V.J., J.B.T. Rasmussen, and Y. Asmerom, 2004: Prolonged wet period in the southwestern United States through the Younger Dryas. *Geology*, doi:10.1130/g19957.1.
Pomposi, C., Y. Kushnir, A. Giannini, and M. Biasutti, 2020: Toward Understanding the Occurrence of Both Wet and Dry Sahel Seasons during El Niño: The Modulating Role of the Global Ocean. *Journal of Climate*, **33(4)**, 1193–1207, doi:10.1175/jcli-d-19-0219.1.
Popp, M. and L.G. Silvers, 2017: Double and single ITCZs with and without clouds. *Journal of Climate*, doi:10.1175/jcli-d-17-0062.1.
Portmann, F.T., P. Döll, S. Eisner, and M. Flörke, 2013: Impact of climate change on renewable groundwater resources: Assessing the benefits of avoided greenhouse gas emissions using selected CMIP5 climate projections. *Environmental Research Letters*, **8(2)**, 024023, doi:10.1088/1748-9326/8/2/024023.
Potter, S.F., E.J. Dawson, and D.M.W. Frierson, 2017: Southern African orography impacts on low clouds and the Atlantic ITCZ in a coupled model. *Geophysical Research Letters*, **44(7)**, 3283–3289, doi:10.1002/2017gl073098.
Pound, M.J. et al., 2014: Late Pliocene lakes and soils : a global data set for the analysis of climate feedbacks in a warmer world. *Climate of the Past*, **10**, 167–180, doi:10.5194/cp-10-167-2014.
Poveda, G., L. Jaramillo, and L.F. Vallejo, 2014: Seasonal precipitation patterns along pathways of South American low-level jets and aerial rivers. *Water Resources Research*, **50(3)**, 98–118, doi:10.1002/2013wr014087.
Poveda, G. et al., 2020: High Impact Weather Events in the Andes. *Frontiers in Earth Science*, **8**, 1–32, doi:10.3389/feart.2020.00162.
Power, S.B. and F.P.D. Delage, 2018: El Niño–Southern Oscillation and Associated Climatic Conditions around the World during the Latter Half of the Twenty-First Century. *Journal of Climate*, **31(15)**, 6189–6207, doi:10.1175/jcli-d-18-0138.1.
Prado, L.F., I. Wainer, and C.M. Chiessi, 2013a: Mid-Holocene PMIP3/CMIP5 model results: Intercomparison for the South American Monsoon System. *Holocene*, **23(12)**, 1915–1920, doi:10.1177/0959683613505336.
Prado, L.F., I. Wainer, C.M. Chiessi, M.-P. Ledru, and B. Turcq, 2013b: A mid-Holocene climate reconstruction for eastern South America. *Climate of the Past*, **9(5)**, 2117–2133, doi:10.5194/cp-9-2117-2013.
Prajeesh, A.G., K. Ashok, and D.V.B. Rao, 2013: Falling monsoon depression frequency: A Gray-Sikka conditions perspective. *Scientific Reports*, **3(1)**, 2989, doi:10.1038/srep02989.
Preethi, B., M. Mujumdar, R.H. Kripalani, A. Prabhu, and R. Krishnan, 2017: Recent trends and tele-connections among South and East Asian summer monsoons in a warming environment. *Climate Dynamics*, **48(7–8)**, 2489–2505, doi:10.1007/s00382-016-3218-0.
Prein, A.F. et al., 2015: Reviews of Geophysics A review on regional convection-permitting climate modeling : Demonstrations , prospects , and challenges. *Reviews of Geophysics*, **53(2)**, 323–361, doi:10.1002/2014rg000475.received.
Prein, A.F. et al., 2017: The future intensification of hourly precipitation extremes. *Nature Climate Change*, **7(1)**, 48–52, doi:10.1038/nclimate3168.

ACCEPTED VERSION SUBJECT TO FINAL EDITING

Prentice, I.C., X. Liang, B.E. Medlyn, and Y.-P. Wang, 2015: Reliable, robust and realistic: the three R's of next-generation land-surface modelling. *Atmospheric Chemistry and Physics*, **15(10)**, 5987–6005, doi:10.5194/acp-15-5987-2015.

Prestele, R. et al., 2016: Hotspots of uncertainty in land-use and land-cover change projections: a global-scale model comparison. *Global Change Biology*, **22(12)**, 3967–3983, doi:10.1111/gcb.13337.

Priestley, M.D.K., H.F. Dacre, L.C. Shaffrey, S. Schemm, and J.G. Pinto, 2020a: The role of secondary cyclones and cyclone families for the North Atlantic storm track and clustering over western Europe. *Quarterly Journal of the Royal Meteorological Society*, **146(728)**, 1184–1205, doi:10.1002/qj.3733.

Priestley, M.D.K. et al., 2020b: An Overview of the Extratropical Storm Tracks in CMIP6 Historical Simulations. *Journal of Climate*, **33(15)**, 6315–6343, doi:10.1175/jcli-d-19-0928.1.

Prigent, C., C. Jimenez, and P. Bousquet, 2020: Satellite-Derived Global Surface Water Extent and Dynamics Over the Last 25 Years (GIEMS-2). *Journal of Geophysical Research: Atmospheres*, **125(3)**, e2019JD030711, doi:10.1029/2019jd030711.

Prigent, C., D.P. Lettenmaier, F. Aires, and F. Papa, 2016: Toward a High-Resolution Monitoring of Continental Surface Water Extent and Dynamics, at Global Scale: from GIEMS (Global Inundation Extent from Multi-Satellites) to SWOT (Surface Water Ocean Topography). *Surveys in Geophysics*, **37(2)**, 339–355, doi:10.1007/s10712-015-9339-x.

Pritchard, H.D., 2019: Asia's shrinking glaciers protect large populations from drought stress. *Nature*, **569(7758)**, 649–654, doi:10.1038/s41586-019-1240-1.

Pritchard, M.S. and D. Yang, 2016: Response of the Superparameterized Madden–Julian Oscillation to Extreme Climate and Basic-State Variation Challenges a Moisture Mode View. *Journal of Climate*, **29(13)**, 4995–5008, doi:10.1175/jcli-d-15-0790.1.

Prospero, J.M., P. Ginoux, O. Torres, S.E. Nicholson, and T.E. Gill, 2002: Environmental characterization of global sources of atmospheric soil dust identified with the Nimbus 7 Total Ozone Mapping Spectrometer (TOMS) absorbing aerosol product. *Reviews of Geophysics*, doi:10.1029/2000rg000095.

Prudhomme, C. et al., 2014: Hydrological droughts in the 21st century , hotspots and uncertainties from a global multimodel ensemble experiment. , **111(9)**, doi:10.1073/pnas.1222473110.

Pryor, S.C., R.J. Barthelmie, and T.J. Shepherd, 2020: 20% of US electricity from wind will have limited impacts on system efficiency and regional climate. *Scientific Reports*, **10(1)**, 541, doi:10.1038/s41598-019-57371-1.

Pulliainen, J. et al., 2020: Patterns and trends of Northern Hemisphere snow mass from 1980 to 2018. *Nature*, **581(7808)**, 294–298, doi:10.1038/s41586-020-2258-0.

Qasmi, S., C. Cassou, and J. Boé, 2017: Teleconnection Between Atlantic Multidecadal Variability and European Temperature: Diversity and Evaluation of the Coupled Model Intercomparison Project Phase 5 Models. *Geophysical Research Letters*, **44(21)**, 11,140–11,149, doi:10.1002/2017gl074886.

Qasmi, S., C. Cassou, and J. Boé, 2020: Teleconnection processes linking the intensity of the atlantic multidecadal variability to the climate impacts over Europe in boreal winter. *Journal of Climate*, **33(7)**, 2681–2700, doi:10.1175/jcli-d-19-0428.1.

Qian, C. and T. Zhou, 2014: Multidecadal Variability of North China Aridity and Its Relationship to PDO during 1900–2010. *Journal of Climate*, **27(3)**, 1210–1222, doi:10.1175/jcli-d-13-00235.1.

Qian, Y. et al., 2009: Heavy pollution suppresses light rain in China: Observations and modeling. *Journal of Geophysical Research*, **114**, D00K02, doi:10.1029/2008jd011575.

Qin, Y. and Y. Lin, 2018: Alleviated Double ITCZ Problem in the NCAR CESM1: A New Cloud Scheme and the Working Mechanisms. *Journal of Advances in Modeling Earth Systems*, **10(9)**, 2318–2332, doi:10.1029/2018ms001343.

Qiu, B., W. Guo, Y. Xue, and Q. Dai, 2016: Journal of Geophysical Research : Atmospheres. , 145–163, doi:10.1002/2016jd025328.

Rach, O., A. Kahmen, A. Brauer, and D. Sachse, 2017: A dual-biomarker approach for quantification of changes in relative humidity from sedimentary lipid D/H ratios. *Climate of the Past*, doi:10.5194/cp-13-741-2017.

Rachmayani, R., M. Prange, and M. Schulz, 2016: Intra-interglacial climate variability: model simulations of Marine Isotope Stages 1, 5, 11, 13, and 15. *Climate of the Past*, **12(3)**, 677–695, doi:10.5194/cp-12-677-2016.

Radić, V. et al., 2014: Regional and global projections of twenty-first century glacier mass changes in response to climate scenarios from global climate models. *Climate Dynamics*, doi:10.1007/s00382-013-1719-7.

Ragettli, S., W.W. Immerzeel, and F. Pellicciotti, 2016: Contrasting climate change impact on river flows from high-altitude catchments in the Himalayan and Andes Mountains. *Proceedings of the National Academy of Sciences of the United States of America*, doi:10.1073/pnas.1606526113.

Raible, C.C., M. Messmer, F. Lehner, T.F. Stocker, and R. Blender, 2018: Extratropical cyclone statistics during the last millennium and the 21st century. *Climate of the Past*, **14(10)**, 1499–1514, doi:10.5194/cp-14-1499-2018.

Ralph, F.M. and M.D. Dettinger, 2011: Storms, floods, and the science of atmospheric rivers. *Eos, Transactions American Geophysical Union*, **92(32)**, 265–266.

Ralph, F.M., M.C.L.D. Dettinger, M.M. Cairns, T.J. Galarneau, and J. Eylander, 2018: Defining "Atmospheric river" : How the glossary of meteorology helped resolve a debate. *Bulletin of the American Meteorological Society*,

SUBJECT TO FINAL EDITING ACCEPTED VERSION

99(4), 837–839, doi:10.1175/bams-d-17-0157.1.
Ralph, F.M. et al., 2016: Calwater field studies designed to quantify the roles of atmospheric rivers and aerosols in modulating U.S. West Coast Precipitation in a changing climate. *Bulletin of the American Meteorological Society*, doi:10.1175/bams-d-14-00043.1.
Ramarao et al., 2015: Understanding land surface response to changing South Asian monsoon in a warming climate. *Earth System Dynamics*, **6(2)**, doi:10.5194/esd-6-569-2015.
Ramarao et al., 2018: On observed aridity changes over the semiarid regions of India in a warming climate. *Theoretical and Applied Climatology*, doi:10.1007/s00704-018-2513-6.
Ramos, A.M., R. Tomé, R.M. Trigo, M.L.R. Liberato, and J.G. Pinto, 2016: Projected changes in atmospheric rivers affecting Europe in CMIP5 models. *Geophysical Research Letters*, **43(17)**, 9315–9323, doi:10.1002/2016gl070634.
Ramos, A.M. et al., 2019: From Amazonia to southern Africa: atmospheric moisture transport through low-level jets and atmospheric rivers. *Annals of the New York Academy of Sciences*, **1436(1)**, 217–230, doi:10.1111/nyas.13960.
Ramsar Convention on Wetlands, 2018: *Global Wetland Outlook: State of the World's Wetlands and their Services to People*. Ramsar Convention Secretariat, Gland, Switzerland, 84 pp.
Rasmussen, K.L., A.F. Prein, R.M. Rasmussen, K. Ikeda, and C. Liu, 2017: Changes in the convective population and thermodynamic environments in convection-permitting regional climate simulations over the United States. *Climate Dynamics*, 1–26, doi:10.1007/s00382-017-4000-7.
Rathore, S., N.L. Bindoff, C.C. Ummenhofer, H.E. Phillips, and M. Feng, 2020: Near-Surface Salinity Reveals the Oceanic Sources of Moisture for Australian Precipitation through Atmospheric Moisture Transport. *Journal of Climate*, **33(15)**, 6707–6730, doi:10.1175/jcli-d-19-0579.1.
Ratna, S.B., A. Cherchi, T.J. Osborn, M. Joshi, and U. Uppara, 2021: The Extreme Positive Indian Ocean Dipole of 2019 and Associated Indian Summer Monsoon Rainfall Response. *Geophysical Research Letters*, **48(2)**, doi:10.1029/2020gl091497.
Rauber, R.M. et al., 2019: Wintertime Orographic Cloud Seeding-A Review. *Journal of Applied Meteorology and Climatology*, **58(10)**, 2117–2140, doi:10.1175/jamc-d-18-0341.1.
Rauniyar, S.P. and S.B. Power, 2020: The Impact of Anthropogenic Forcing and Natural Processes on Past, Present, and Future Rainfall over Victoria, Australia. *Journal of Climate*, **33(18)**, 8087–8106, doi:10.1175/jcli-d-19-0759.1.
Reboita, M.S., R.P. Da Rocha, C.G. Dias, and R.Y. Ynoue, 2014: Climate projections for South America: RegCM3 driven by HadCM3 and ECHAM5. *Advances in Meteorology*, doi:10.1155/2014/376738.
Reboita, M.S., R.P. da Rocha, T. Ambrizzi, and C.D. Gouveia, 2015: Trend and teleconnection patterns in the climatology of extratropical cyclones over the Southern Hemisphere. *Climate Dynamics*, **45(7–8)**, 1929–1944, doi:10.1007/s00382-014-2447-3.
Rehfeld, K., R. Hébert, J. Lora, M. Lofverstrom, and C. Brierley, 2020: Variability of surface climate in simulations of past and future. *Earth System Dynamics Discussions*, **11(2)**, 1–30, doi:10.5194/esd-2019-92.
Reimi, M.A. and F. Marcantonio, 2016: Constraints on the magnitude of the deglacial migration of the ITCZ in the Central Equatorial Pacific Ocean. *Earth and Planetary Science Letters*, doi:10.1016/j.epsl.2016.07.058.
Reintges, A., T. Martin, M. Latif, and N.S. Keenlyside, 2017: Uncertainty in twenty-first century projections of the Atlantic Meridional Overturning Circulation in CMIP3 and CMIP5 models. *Climate Dynamics*, doi:10.1007/s00382-016-3180-x.
Renssen, H., H. Goosse, D.M. Roche, and H. Seppä, 2018: The global hydroclimate response during the Younger Dryas event. *Quaternary Science Reviews*, **193**, 84–97, doi:10.1016/j.quascirev.2018.05.033.
Rhoades, A.M., A.D. Jones, and P.A. Ullrich, 2018: The Changing Character of the California Sierra Nevada as a Natural Reservoir. *Geophysical Research Letters*, **45(23)**, 8–13,13,19, doi:10.1029/2018gl080308.
Richardson, D., H.J. Fowler, C.G. Kilsby, and R. Neal, 2018: A new precipitation and drought climatology based on weather patterns. *International Journal of Climatology*, **38(2)**, 630–648, doi:10.1002/joc.5199.
Richardson, T.B., P.M. Forster, T. Andrews, and D.J. Parker, 2016: Understanding the rapid precipitation response to CO 2 and aerosol forcing on a regional scale. *Journal of Climate*, **29(2)**, 583–594, doi:10.1175/jcli-d-15-0174.1.
Richardson, T.B. et al., 2018a: Carbon Dioxide Physiological Forcing Dominates Projected Eastern Amazonian Drying. *Geophysical Research Letters*, doi:10.1002/2017gl076520.
Richardson, T.B. et al., 2018b: Drivers of precipitation change: An energetic understanding. *Journal of Climate*, **31(23)**, 9641–9657, doi:10.1175/jcli-d-17-0240.1.
Ridley, H.E. et al., 2015: Aerosol forcing of the position of the intertropical convergence zone since ad 1550. *Nature Geoscience*, **8(3)**, 195–200, doi:10.1038/ngeo2353.
Rifai, S.W., S. Li, and Y. Malhi, 2019: Coupling of El Niño events and long-term warming leads to pervasive climate extremes in the terrestrial tropics. *Environmental Research Letters*, **14(10)**, 105002, doi:10.1088/1748-9326/ab402f.
Rinke, A. et al., 2019: Trends of vertically integrated water vapor over the Arctic during 1979-2016: Consistent

ACCEPTED VERSION SUBJECT TO FINAL EDITING

moistening all over? *Journal of Climate*, **32(18)**, 6097–6116, doi:10.1175/jcli-d-19-0092.1.
Risser, M.D. and M.F. Wehner, 2017: Attributable human-induced changes in the likelihood and magnitude of the observed extreme precipitation during Hurricane Harvey. *Geophys. Res*, **44(12)**, 412–457, doi:10.1002/2017gl075888.
Rivera, J.A., D.C. Araneo, O.C. Penalba, and R. Villalba, 2018: Regional aspects of streamflow droughts in the Andean rivers of Patagonia, Argentina. Links with large-scale climatic oscillations. *Hydrology Research*, **49(1)**, 134–149, doi:10.2166/nh.2017.207.
Roberts, M.J. et al., 2015: Tropical cyclones in the UPSCALE ensemble of high-resolution global climate models. *Journal of Climate*, **28(2)**, 574–596, doi:10.1175/jcli-d-14-00131.1.
Roberts, M.J. et al., 2018: The benefits of global high-resolution for climate simulation: process-understanding and the enabling of stakeholder decisions at the regional scale.. *Bulletin of the American Meteorological Society*, BAMS–D–15–00320.1, doi:10.1175/bams-d-15-00320.1.
Roberts, M.J. et al., 2020: Projected Future Changes in Tropical Cyclones Using the CMIP6 HighResMIP Multimodel Ensemble. *Geophysical Research Letters*, **47(14)**, 1–12, doi:10.1029/2020gl088662.
Robertson, A.W. et al., 2011: The Maritime Continent Monsoon. In: *The Global Monsoon System: Research and Forecast (2nd Edition)* [Chang, C.-P., Y. Ding, N.-C. Lau, R.H. Johnson, B. Wang, and T. Yasunari (eds.)]. World Scientific, Singapore, pp. 85–98, doi:10.1142/9789814343411_0006.
Robertson, F.R., M.G. Bosilovich, and J.B. Roberts, 2016: Reconciling Land-Ocean Moisture Transport Variability in Reanalyses with P - ET in Observationally Driven Land Surface Models. *Journal of Climate*, **29(23)**, 8625–8646, doi:10.1175/jcli-d-16-0379.1.
Robertson, F.R. et al., 2014: Consistency of estimated global water cycle variations over the satellite era. *Journal of Climate*, **27(16)**, 6135–6154.
Robertson, F.R. et al., 2020: Uncertainties in ocean latent heat flux variations over recent decades in satellite-based estimates and reduced observation reanalyses. *Journal of Climate*, **33(19)**, 8415–8437, doi:10.1175/jcli-d-19-0954.1.
Robeson, S.M., 2015: Revisiting the recent California drought as an extreme value. *Geophysical Research Letters*, **42(16)**, 6771–6779, doi:10.1002/2015gl064593.
Robock, A., L. Oman, and G.L. Stenchikov, 2008: Regional climate responses to geoengineering with tropical and Arctic SO<inf>2</inf> injections. *Journal of Geophysical Research Atmospheres*, doi:10.1029/2008jd010050.
Roca, R., 2019: Estimation of extreme daily precipitation thermodynamic scaling using gridded satellite precipitation products over tropical land. *Environmental Research Letters*, **14(9)**, 95009, doi:10.1088/1748-9326/ab35c6.
Roca, R. and T. Fiolleau, 2020: Extreme precipitation in the tropics is closely associated with long-lived convective systems. *Communications Earth & Environment*, **1(1)**, 18, doi:10.1038/s43247-020-00015-4.
Rochetin, N., F. Couvreux, J.Y. Grandpeix, and C. Rio, 2014a: Deep convection triggering by boundary layer thermals. Part I: LES analysis and stochastic triggering formulation. *Journal of the Atmospheric Sciences*, **71(2)**, 496–514, doi:10.1175/jas-d-12-0336.1.
Rochetin, N., J.-Y. Grandpeix, C. Rio, and F. Couvreux, 2014b: Deep convection triggering by boundary layer thermals. Part II: Stochastic triggering parameterization for the LMDZ GCM. *Journal of the Atmospheric Sciences*, **71(2)**, 515–538.
Rodell, M., I. Velicogna, and J.S. Famiglietti, 2009: Satellite-based estimates of groundwater depletion in India. *Nature*, **460(7258)**, 999–1002, doi:10.1038/nature08238.
Rodell, M. et al., 2015: The observed state of the water cycle in the early twenty-first century. *Journal of Climate*, **28(21)**, 8289–8318, doi:10.1175/jcli-d-14-00555.1.
Rodell, M. et al., 2018: Emerging trends in global freshwater availability. *Nature*, **557(7707)**, 651–659, doi:10.1038/s41586-018-0123-1.
Roderick, M.L., F. Sun, W.H. Lim, and G.D. Farquhar, 2014: A general framework for understanding the response of the water cycle to global warming over land and ocean. *Hydrology and Earth System Sciences*, **18(5)**, 1575–1589, doi:10.5194/hess-18-1575-2014.
Rodríguez-Fonseca, B. et al., 2015: Variability and predictability of west African droughts: A review on the role of sea surface temperature anomalies. *Journal of Climate*, **28(10)**, 4034–4060, doi:10.1175/jcli-d-14-00130.1.
Roehrig, R., D. Bouniol, F. Guichard, F. Hourdin, and J.-L. Redelsperger, 2013: The Present and Future of the West African Monsoon: A Process-Oriented Assessment of CMIP5 Simulations along the AMMA Transect. *Journal of Climate*, **26(17)**, 6471–6505, doi:10.1175/jcli-d-12-00505.1.
Roehrig, R. et al., 2020: The CNRM Global Atmosphere Model ARPEGE-Climat 6.3: Description and Evaluation. *Journal of Advances in Modeling Earth Systems*, **12(7)**, 1–53, doi:10.1029/2020ms002075.
Rojas, M., P.A. Arias, V. Flores-Aqueveque, A. Seth, and M. Vuille, 2016: The South American monsoon variability over the last millennium in climate models. *Climate of the Past*, **12(8)**, 1681–1691, doi:10.5194/cp-12-1681-2016.
Romps, D.M., 2016: Clausius–Clapeyron Scaling of CAPE from Analytical Solutions to RCE. *Journal of the Atmospheric Sciences*, doi:10.1175/jas-d-15-0327.1.
Ronchail, J. et al., 2018: The flood recession period in Western Amazonia and its variability during the 1985–2015

ACCEPTED VERSION SUBJECT TO FINAL EDITING

period. *Journal of Hydrology: Regional Studies*, **15**, 16–30, doi:10.1016/j.ejrh.2017.11.008.
Rosenfeld, D., 2000: Suppression of rain and snow by urban and industrial air pollution. *Science*, **287(5459)**, 1793–1796, doi:10.1126/science.287.5459.1793.
Rosenfeld, D. et al., 2008: Flood or drought: How do aerosols affect precipitation? *science*, **321(5894)**, 1309–1313.
Rosenfeld, D. et al., 2019: Aerosol-driven droplet concentrations dominate converage and water of oceanic low level clouds. *Science*, **accepted**, eaav0566, doi:10.1126/science.aav0566.
Rotstayn, L.D., M.A. Collier, and J.- Luo, 2015: Effects of declining aerosols on projections of zonally averaged tropical precipitation. *Environmental Research Letters*, **10**, doi:10.1088/1748-9326/10/4/044018.
Rotstayn, L.D., U. Lohmann, L.D. Rotstayn, and U. Lohmann, 2002: Tropical Rainfall Trends and the Indirect Aerosol Effect. *Journal of Climate*, **15(15)**, 2103–2116, doi:10.1175/1520-0442(2002)015<2103:trtati>2.0.co;2.
Rotstayn, L.D., M.A. Collier, A. Chrastansky, S.J. Jeffrey, and J.J. Luo, 2013: Projected effects of declining aerosols in RCP4.5: Unmasking global warming? *Atmospheric Chemistry and Physics*, doi:10.5194/acp-13-10883-2013.
Rotstayn, L.D. et al., 2012: Aerosol- and greenhouse gas-induced changes in summer rainfall and circulation in the Australasian region: a study using single-forcing climate simulations. *Atmospheric Chemistry and Physics*, **12(14)**, 6377–6404, doi:10.5194/acp-12-6377-2012.
Roundy, J.K. and J.A. Santanello, 2017: Utility of Satellite Remote Sensing for Land–Atmosphere Coupling and Drought Metrics. *Journal of Hydrometeorology*, **18**, 863.
Rowell, D.P., 2012: Sources of uncertainty in future changes in local precipitation. *Climate Dynamics*, **39(7–8)**, 1929–1950, doi:10.1007/s00382-011-1210-2.
Rowell, D.P., B.B.B. Booth, S.E. Nicholson, and P. Good, 2015: Reconciling past and future rainfall trends over East Africa. *Journal of Climate*, **28(24)**, 9768–9788, doi:10.1175/jcli-d-15-0140.1.
Roxy, M.K. et al., 2015: Drying of Indian subcontinent by rapid Indian ocean warming and a weakening land-sea thermal gradient. *Nature Communications*, **6**, 1–10, doi:10.1038/ncomms8423.
Roxy, M.K. et al., 2017: A threefold rise in widespread extreme rain events over central India. *Nature Communications*, **8(1)**, doi:10.1038/s41467-017-00744-9.
Roxy, M.K. et al., 2019: Twofold expansion of the Indo-Pacific warm pool warps the MJO life cycle. *Nature*, **575(7784)**, 647–651, doi:10.1038/s41586-019-1764-4.
Roy, I., R.G. Tedeschi, and M. Collins, 2019: ENSO teleconnections to the Indian summer monsoon under changing climate. *International Journal of Climatology*, doi:10.1002/joc.5999.
Ruiz-Vásquez, M., P.A. Arias, J.A. Martínez, and J.C. Espinoza, 2020: Effects of Amazon basin deforestation on regional atmospheric circulation and water vapor transport towards tropical South America. *Climate Dynamics*, doi:10.1007/s00382-020-05223-4.
Ruosteenoja, K., T. Markkanen, A. Venäläinen, P. Räisänen, and H. Peltola, 2018: Seasonal soil moisture and drought occurrence in Europe in CMIP5 projections for the 21st century. *Climate Dynamics*, **50(3–4)**, 1177–1192, doi:10.1007/s00382-017-3671-4.
Rupp, D.E., J.T. Abatzoglou, K.C. Hegewisch, and P.W. Mote, 2013: Evaluation of CMIP5 20th century climate simulations for the Pacific Northwest USA. *Journal of Geophysical Research Atmospheres*, **118(19)**, 10884–10906, doi:10.1002/jgrd.50843.
Ruprich-Robert, Y. et al., 2017: Assessing the Climate Impacts of the Observed Atlantic Multidecadal Variability Using the GFDL CM2.1 and NCAR CESM1 Global Coupled Models. *Journal of Climate*, **30(8)**, 2785–2810, doi:10.1175/jcli-d-16-0127.1.
Saffioti, C., E.M. Fischer, S.C. Scherrer, and R. Knutti, 2016: Reconciling observed and modeled temperature and precipitation trends over Europe by adjusting for circulation variability. *Geophysical Research Letters*, **43(15)**, 8189–8198, doi:10.1002/2016gl069802.
Saha et al., 2014: Failure of CMIP5 climate models in simulating post-1950 decreasing trend of Indian monsoon. *Geophysical Research Letters*, **41(20)**, 7323–7330, doi:10.1002/2014gl061573.
Sahany, S., S.K. Mishra, R. Pathak, and B. Rajagopalan, 2018: Spatiotemporal Variability of Seasonality of Rainfall Over India. *Geophysical Research Letters*, **45(14)**, 7140–7147, doi:10.1029/2018gl077932.
Sahoo, G.B. et al., 2016: Climate change impacts on lake thermal dynamics and ecosystem vulnerabilities. *Limnology and Oceanography*, doi:10.1002/lno.10228.
Saide, P.E. et al., 2015: Central American biomass burning smoke can increase tornado severity in the U.S.. *Geophysical Research Letters*, **42(3)**, 956–965, doi:10.1002/2014gl062826.
Saint-Lu, M. et al., 2020: Influences of local and remote conditions on tropical precipitation and its response to climate change. *Journal of Climate*, **33(10)**, 4045–4063, doi:10.1175/jcli-d-19-0450.1.
Sakschewski, B. et al., 2016: Resilience of Amazon forests emerges from plant trait diversity. *Nature Climate Change*, **6**, 1032 EP –.
Salazar, J.F. et al., 2018: Scaling properties reveal regulation of river flows in the Amazon through a ”forest reservoir”. *Hydrology and Earth System Sciences*, **22(3)**, 1735–1748, doi:10.5194/hess-22-1735-2018.
Salinger, M.J., S. McGree, F. Beucher, S.B. Power, and F. Delage, 2014: A new index for variations in the position of the South Pacific convergence zone 1910/11–2011/2012. *Climate Dynamics*, **43(3)**, 881–892, doi:10.1007/s00382-013-2035-y.

SUBMITTED VERSION SUBJECT TO FINAL EDITING

Salzmann, M., 2016: Global warming without global mean precipitation increase'. *Science Advances*, **2(6)**, e1501572—e1501572, doi:10.1126/sciadv.1501572.
Salzmann, M., H. Weser, and R. Cherian, 2014: Robust response of Asian summer monsoon to anthropogenic aerosols in CMIP5 models. *Journal of Geophysical Research: Atmospheres*, **119(19)**, 11,321–11,337, doi:10.1002/2014jd021783.
Samaniego, L. et al., 2017: Propagation of forcing and model uncertainties on to hydrological drought characteristics in a multi-model century-long experiment in large river basins. *Climatic Change*, **141(3)**, 435–449, doi:10.1007/s10584-016-1778-y.
Samanta, D., K.B. Karnauskas, and N.F. Goodkin, 2019: Tropical Pacific SST and ITCZ Biases in Climate Models: Double Trouble for Future Rainfall Projections? *Geophysical Research Letters*, doi:10.1029/2018gl081363.
Samanta et al. et al., 2020: La Niña's Diminishing Fingerprint on the Central Indian Summer Monsoon. *Geophysical Research Letters*, **47(2)**, e2019GL086237, doi:10.1029/2019gl086237.
Samset, B.H. et al., 2016: Fast and slow precipitation responses to individual climate forcers: A PDRMIP multimodel study. *Geophysical Research Letters*, **43(6)**, 2782–2791, doi:10.1002/2016gl068064.
Samset, B.H. et al., 2018a: Weak hydrological sensitivity to temperature change over land, independent of climate forcing. *npj Climate and Atmospheric Science*, **1(1)**, 3, doi:10.1038/s41612-017-0005-5.
Samset, B.H. et al., 2018b: Climate Impacts From a Removal of Anthropogenic Aerosol Emissions. *Geophysical Research Letters*, **45(2)**, 1020–1029, doi:10.1002/2017gl076079.
Sanap, S.D., G. Pandithurai, and M.G. Manoj, 2015: On the response of Indian summer monsoon to aerosol forcing in CMIP5 model simulations. *Climate Dynamics*, **45(9–10)**, 2949–2961, doi:10.1007/s00382-015-2516-2.
Sánchez, E. et al., 2015: Regional climate modelling in CLARIS-LPB: a concerted approach towards twentyfirst century projections of regional temperature and precipitation over South America. *Climate Dynamics*, **45(7)**, 2193–2212, doi:10.1007/s00382-014-2466-0.
Sand, M., B.H. Samset, K. Tsigaridis, S.E. Bauer, and G. Myhre, 2020: Black Carbon and Precipitation: An Energetics Perspective. *Journal of Geophysical Research: Atmospheres*, **125(13)**, e2019JD032239, doi:10.1029/2019jd032239.
Sandeep, N. et al., 2020: South Asian monsoon response to weakening of Atlantic meridional overturning circulation in a warming climate. *Climate Dynamics*, **54(7–8)**, 3507–3524, doi:10.1007/s00382-020-05180-y.
Sandeep, S. and R.S. Ajayamohan, 2015: Poleward shift in Indian summer monsoon low level jetstream under global warming. *Climate Dynamics*, **45(1–2)**, 337–351, doi:10.1007/s00382-014-2261-y.
Sandeep, S. and R.S. Ajayamohan, 2018: Modulation of Winter Precipitation Dynamics Over the Arabian Gulf by ENSO. *Journal of Geophysical Research: Atmospheres*, **123(1)**, 198–210, doi:10.1002/2017jd027263.
Sandeep, S., F. Stordal, P.D. Sardeshmukh, and G.P. Compo, 2014: Pacific Walker Circulation variability in coupled and uncoupled climate models. *Climate Dynamics*, **43(1–2)**, 103–117, doi:10.1007/s00382-014-2135-3.
Sandeep, S., R.S. Ajayamohan, W.R. Boos, T.P. Sabin, and V. Praveen, 2018: Decline and poleward shift in Indian summer monsoon synoptic activity in a warming climate. *Proceedings of the National Academy of Sciences*, **115(11)**, 2681–2686, doi:10.1073/pnas.1709031115.
Sandler, D. and N. Harnik, 2020: Future wintertime meridional wind trends through the lens of subseasonal teleconnections. *Weather and Climate Dynamics*, **1(2)**, 427–443, doi:10.5194/wcd-1-427-2020.
Sandvik, M.I., A. Sorteberg, and R. Rasmussen, 2018: Sensitivity of historical orographically enhanced extreme precipitation events to idealized temperature perturbations. *Climate Dynamics*, **50(1–2)**, 143–157, doi:10.1007/s00382-017-3593-1.
Sanogo, S. et al., 2015: Spatio-temporal characteristics of the recent rainfall recovery in West Africa. *International Journal of Climatology*, **35(15)**, 4589–4605, doi:10.1002/joc.4309.
Santanello, J.A. et al., 2018: Land–Atmosphere Interactions: The LoCo Perspective. *Bulletin of the American Meteorological Society*, **99**, 1253.
Santer, B.D. and T.M.L. Wigley, 1990: Regional validation of means, variances, and spatial patterns in general circulation model control runs. *Journal of Geophysical Research*, **95(D1)**, 829–850, doi:10.1029/jd095id01p00829.
Santolaria-Otín, M. and O. Zolina, 2020: Evaluation of snow cover and snow water equivalent in the continental Arctic in CMIP5 models. *Climate Dynamics*, **55(11)**, 2993–3016, doi:10.1007/s00382-020-05434-9.
Sarangi, C., S.N. Tripathi, V.P. Kanawade, I. Koren, and D.S. Pai, 2017: Investigation of the aerosol – cloud – rainfall association over the Indian summer monsoon region. , 5185–5204, doi:10.5194/acp-17-5185-2017.
Sarangi, C., S.N. Tripathi, Y. Qian, S. Kumar, and L. Ruby Leung, 2018: Aerosol and Urban Land Use Effect on Rainfall Around Cities in Indo-Gangetic Basin From Observations and Cloud Resolving Model Simulations. *Journal of Geophysical Research: Atmospheres*, **123(7)**, 3645–3667, doi:10.1002/2017jd028004.
Sarojini, B.B., P.A. Stott, and E. Black, 2016: Detection and attribution of human influence on regional precipitation. *Nature Climate Change*, **6(7)**, 669–675, doi:10.1038/nclimate2976.
Saunois, M. et al., : ... & Janssens-Maenhout, G. (2016). *The global methane budget*, **8(2)**, 697–751.
Saurral, R.I., I.I.A. Camilloni, and V.R. Barros, 2017: Low-frequency variability and trends in centennial precipitation stations in southern South America. *International Journal of Climatology*, **37**, 1774–1793,

ACCEPTED VERSION SUBJECT TO FINAL EDITING

doi:10.1002/joc.4810.
Scaff, L. et al., 2020: Simulating the convective precipitation diurnal cycle in North America ' s current and future climate. *Climate Dynamics*, **55(1)**, 369–382, doi:10.1007/s00382-019-04754-9.
Scanlon, B.R. et al., 2012: Groundwater depletion and sustainability of irrigation in the US High Plains and Central Valley.. *Proceedings of the National Academy of Sciences of the United States of America*, **109(24)**, 9320–5, doi:10.1073/pnas.1200311109.
Scanlon, B.R. et al., 2018: Global models underestimate large decadal declining and rising water storage trends relative to GRACE satellite data. *Proceedings of the National Academy of Sciences*, doi:10.1073/pnas.1704665115.
Scanlon, B.R.R. et al., 2019: Tracking Seasonal Fluctuations in Land Water Storage Using Global Models and GRACE Satellites. *Geophysical Research Letters*, **46(10)**, 5254–5264, doi:10.1029/2018gl081836.
Scheff, J. and D.M.W. Frierson, 2012: Robust future precipitation declines in CMIP5 largely reflect the poleward expansion of model subtropical dry zones. *Geophysical Research Letters*, **39(17)**, doi:10.1029/2012gl052910.
Scheff, J. and D.M.W. Frierson, 2014: Scaling potential evapotranspiration with greenhouse warming. *Journal of Climate*, **27(4)**, 1539–1558, doi:10.1175/jcli-d-13-00233.1.
Scheff, J. and D.M.W. Frierson, 2015: Terrestrial aridity and its response to greenhouse warming across CMIP5 climate models. *Journal of Climate*, **28(14)**, 5583–5600, doi:10.1175/jcli-d-14-00480.1.
Scheff, J., R. Seager, H. Liu, and S. Coats, 2017: Are glacials dry? Consequences for paleoclimatology and for greenhouse warming. *Journal of Climate*, **30(17)**, 6593–6609, doi:10.1175/jcli-d-16-0854.1.
Schemm, S., 2018: Regional Trends in Weather Systems Help Explain Antarctic Sea Ice Trends. *Geophysical Research Letters*, **45(14)**, 7165–7175, doi:10.1029/2018gl079109.
Schemm, S.S., M. Sprenger, and H. Wernli, 2018: When during their life cycle are extratropical cyclones attended by fronts? *Bulletin of the American Meteorological Society*, **99(1)**, 149–165, doi:10.1175/bams-d-16-0261.1.
Schepanski, K., 2018: Transport of mineral dust and its impact on climate. *Geosciences*, **8(5)**, 151.
Schewe, J. and A. Levermann, 2017: Non-linear intensification of Sahel rainfall as a possible dynamic response to future warming. *Earth System Dynamics*, **8(3)**, 495–505, doi:10.5194/esd-8-495-2017.
Schewe, J. et al., 2014: Multimodel assessment of water scarcity under climate change. *Proceedings of the National Academy of Sciences*, **111(9)**, 3245 LP – 3250, doi:10.1073/pnas.1222460110.
Schiemann, R. et al., 2017: The resolution sensitivity of Northern Hemisphere blocking in four 25-km atmospheric global circulation models. *Journal of Climate*, **30(1)**, 337–358, doi:10.1175/jcli-d-16-0100.1.
Schleussner, C.-F. et al., 2016: Differential climate impacts for policy-relevant limits to global warming: the case of 1.5°C and 2°C. *Earth System Dynamics*, **7(2)**, 327–351, doi:10.5194/esd-7-327-2016.
Schmid, P.E. and D. Niyogi, 2017: Modeling urban precipitation modification by spatially heterogeneous aerosols. *Journal of Applied Meteorology and Climatology*, **56(8)**, 2141–2153, doi:10.1175/jamc-d-16-0320.1.
Schmidt, D.F. and K.M. Grise, 2017: The Response of Local Precipitation and Sea Level Pressure to Hadley Cell Expansion. *Geophysical Research Letters*, **44(20)**, 10,573–10,582, doi:10.1002/2017gl075380.
Schneider, T., P.A. O'Gorman, and X.J. Levine, 2010: Water vapor and the dynamics of climate changes. *Reviews of Geophysics*, **48(1)**, 1–22, doi:10.1029/2009rg000302.
Schneider, T., T. Bischoff, and G.H. Haug, 2014: Migrations and dynamics of the intertropical convergence zone.. *Nature*, doi:10.1038/nature13636.
Schröder, M. et al., 2019: The GEWEX Water Vapor Assessment : Overview and Introduction to Results and Recommendations. *Remote Sensing*, **11**, 1–28, doi:10.3390/rs11030251.
Schubert, J.J., B. Stevens, and T. Crueger, 2013: Madden-Julian oscillation as simulated by the MPI Earth System Model: Over the last and into the next millennium. *Journal of Advances in Modeling Earth Systems*, **5(1)**, 71–84, doi:10.1029/2012ms000180.
Schubert, S.D., H. Wang, R.D. Koster, M.J. Suarez, and P.Y. Groisman, 2014: Northern Eurasian heat waves and droughts. *Journal of Climate*, **27**, 3169–3207, doi:10.1175/jcli-d-13-00360.1.
Schubert, S.D. et al., 2016: Global Meteorological Drought: A Synthesis of Current Understanding with a Focus on SST Drivers of Precipitation Deficits. *Journal of Climate*, **29(11)**, 3989–4019, doi:10.1175/jcli-d-15-0452.1.
Schuerch, M. et al., 2018: Future response of global coastal wetlands to sea-level rise. *Nature*, doi:10.1038/s41586-018-0476-5.
Schurer, A.P., G.C. Hegerl, A. Ballinger, and A.R. Friedman, 2020: Human influence strengthens the contrast between tropical wet and dry regions. *Environ. Res. Lett.*
Scoccimarro, E. et al., 2015: Projected changes in intense precipitation over Europe at the daily and subdaily time scales. *Journal of Climate*, **28(15)**, 6193–6203, doi:10.1175/jcli-d-14-00779.1.
Screen, J.A. and I. Simmonds, 2013a: Caution needed when linking weather extremes to amplified planetary waves. *Proceedings of the National Academy of Sciences of the United States of America*, **110(26)**, E2327–E2327, doi:10.1073/pnas.1304867110.
Screen, J.A. and I. Simmonds, 2013b: Exploring links between Arctic amplification and mid-latitude weather. *Geophysical Research Letters*, **40(5)**, 959–964, doi:10.1002/grl.50174.
Screen, J.A. and I. Simmonds, 2014: Amplified mid-latitude planetary waves favour particular regional weather extremes. *Nature Climate Change*, **4(8)**, 704–709, doi:10.1038/nclimate2271.

ACCEPTED VERSION SUBJECT TO FINAL EDITING

Screen, J.A., T.J. Bracegirdle, and I. Simmonds, 2018: Polar Climate Change as Manifest in Atmospheric Circulation. *Current Climate Change Reports*, **4(4)**, 383–395, doi:10.1007/s40641-018-0111-4.
Seager, R. et al., 2014a: Causes of increasing aridification of the mediterranean region in response to rising greenhouse gases. *Journal of Climate*, **27(12)**, 4655–4676, doi:10.1175/jcli-d-13-00446.1.
Seager, R. et al., 2014b: Dynamical and Thermodynamical Causes of Large-Scale Changes in the Hydrological Cycle over North America in Response to Global Warming*. *Journal of Climate*, **27(20)**, 7921–7948, doi:10.1175/jcli-d-14-00153.1.
Seager, R. et al., 2019a: Strengthening tropical Pacific zonal sea surface temperature gradient consistent with rising greenhouse gases. *Nature Climate Change*, **9(7)**, 517–522, doi:10.1038/s41558-019-0505-x.
Seager, R. et al., 2019b: Climate variability and change of mediterranean-type climates. *Journal of Climate*, doi:10.1175/jcli-d-18-0472.1.
Segura, H. et al., 2020: Recent changes in the precipitation-driving processes over the southern tropical Andes/western Amazon. *Climate Dynamics*, **54(5–6)**, 2613–2631, doi:10.1007/s00382-020-05132-6.
Seiler, C., R.W.A. Hutjes, and P. Kabat, 2013: Climate variability and trends in bolivia. *Journal of Applied Meteorology and Climatology*, **52(1)**, 130–146, doi:10.1175/jamc-d-12-0105.1.
Semenov, V.A. and M. Latif, 2015: Nonlinear winter atmospheric circulation response to Arctic sea ice concentration anomalies for different periods during 1966-2012. *Environmental Research Letters*, **10(5)**, doi:10.1088/1748-9326/10/5/054020.
Sena, A.C.T. and G. Magnusdottir, 2020: Projected End-of-Century Changes in the South American Monsoon in the CESM Large Ensemble. *Journal of Climate*, **33(18)**, 7859–7874, doi:10.1175/jcli-d-19-0645.1.
Seneviratne, S.I. et al., 2012: Changes in Climate Extremes and their Impacts on the Natural Physical Environment. In: *Managing the Risks of Extreme Events and Disasters to Advance Climate Change Adaptation. A Special Report of Working Groups I and II of the Intergovernmental Panel on Climate Change* [Field, C.B., V. Barros, T.F. Stocker, D. Qin, D.J. Dokken, K.L. Ebi, M.D. Mastrandrea, K.J. Mach, G.-K. Plattner, S.K. Allen, M. Tignor, and P.M. Midgley (eds.)]. Cambridge University Press, Cambridge, United Kingdom and New York, NY, USA, pp. 109–230, doi:10.1017/cbo9781139177245.006.
Seo, K.H., D.M.W. Frierson, and J.H. Son, 2014: A mechanism for future changes in Hadley circulation strength in CMIP5 climate change simulations. *Geophysical Research Letters*, doi:10.1002/2014gl060868.
Seth, A. et al., 2013: CMIP5 Projected Changes in the Annual Cycle of Precipitation in Monsoon Regions. *Journal of Climate*, **26(19)**, 7328–7351, doi:10.1175/jcli-d-12-00726.1.
Seth, A. et al., 2019: Monsoon Responses to Climate Changes-Connecting Past, Present and Future. *Current Climate Change Reports*, **5(2)**, 63–79, doi:10.1007/s40641-019-00125-y.
Seviour, W.J.M., S.M. Davis, K.M. Grise, and D.W. Waugh, 2018: Large Uncertainty in the Relative Rates of Dynamical and Hydrological Tropical Expansion. *Geophysical Research Letters*, **45(2)**, 1106–1113, doi:10.1002/2017gl076335.
Shakun, J.D. et al., 2007: A high-resolution, absolute-dated deglacial speleothem record of Indian Ocean climate from Socotra Island, Yemen. *Earth and Planetary Science Letters*, **259(3–4)**, 442–456, doi:10.1016/j.epsl.2007.05.004.
Shamsudduha, M. and R.G. Taylor, 2020: Groundwater storage dynamics in the world's large aquifer systems from GRACE: uncertainty and role of extreme precipitation. *Earth System Dynamics*, **11(3)**, 755–774, doi:10.5194/esd-11-755-2020.
Shanahan, T.M. et al., 2015: The time-transgressive termination of the African Humid Period. *Nature Geoscience*.
Shang, H.U.A., M. Xu, F.E.N. Zhao, and S.B. Tijjani, 2019: Spatial and temporal variations in precipitation amount, frequency, intensity, and persistence in china, 1973–2016. *Journal of Hydrometeorology*, **20(11)**, 2215–2227, doi:10.1175/jhm-d-19-0032.1.
Shannon, S. et al., 2019: Global glacier volume projections under high-end climate change scenarios. *Cryosphere*, **13(1)**, 325–350, doi:10.5194/tc-13-325-2019.
Sharma, A., C. Wasko, and D.P. Lettenmaier, 2018: If Precipitation Extremes Are Increasing, Why Aren't Floods? *Water Resources Research*, **54(11)**, 8545–8551, doi:10.1029/2018wr023749.
Sharma, A.R. and S.J. Déry, 2019: Variability and trends of landfalling atmospheric rivers along the Pacific Coast of northwestern North America. *International Journal of Climatology*, 544–558, doi:10.1002/joc.6227.
Sharma, S. et al., 2019: Widespread loss of lake ice around the Northern Hemisphere in a warming world. *Nature Climate Change*, **9(3)**, 227–231, doi:10.1038/s41558-018-0393-5.
Sharmila, S. and K.J.E. Walsh, 2018: Recent poleward shift of tropical cyclone formation linked to Hadley cell expansion. *Nature Climate Change*, **8(8)**, 730–736, doi:10.1038/s41558-018-0227-5.
Sharmila et al., 2015: Future projection of Indian summer monsoon variability under climate change scenario: An assessment from CMIP5 climate models. *Global and Planetary Change*, **124**, 62–78, doi:10.1016/j.gloplacha.2014.11.004.
Shaw, T.A., 2019: Mechanisms of Future Predicted Changes in the Zonal Mean Mid-Latitude Circulation. *Current Climate Change Reports*, **5(4)**, 345–357, doi:10.1007/s40641-019-00145-8.
Shaw, T.A. and A. Voigt, 2016: Land dominates the regional response to CO2 direct radiative forcing. *Geophysical*

ACCEPTED VERSION SUBJECT TO FINAL EDITING

Research Letters, **43(21)**, 11,383–11,391, doi:10.1002/2016gl071368.
Shaw, T.A. and Z. Tan, 2018: Testing latitudinally-dependent explanations of the circulation response to increased CO2 using aquaplanet models. *Geophysical Research Letters*, doi:10.1029/2018gl078974.
Shaw, T.A. et al., 2016: Storm track processes and the opposing influences of climate change. *Nature Geoscience*, **9(9)**, 656–664, doi:10.1038/ngeo2783.
Shean, D.E. et al., 2020: A Systematic, Regional Assessment of High Mountain Asia Glacier Mass Balance. *Frontiers in Earth Science*, **7**, 363, doi:10.3389/feart.2019.00363.
Sheffield, J. et al., 2013: North American Climate in CMIP5 Experiments. Part I: Evaluation of Historical Simulations of Continental and Regional Climatology. *Journal of Climate*, **26(23)**, 9209–9245, doi:10.1175/jcli-d-12-00592.1.
Shepherd, T.G., 2014: Atmospheric circulation as a source of uncertainty in climate change projections. *Nature Geoscience*, **7(10)**, 703–708, doi:10.1038/ngeo2253.
Sherwood, S.C. et al., 2015: Adjustments in the forcing-feedback framework for understanding climate change. *Bulletin of the American Meteorological Society*, **96(2)**, 217–228, doi:10.1175/bams-d-13-00167.1.
Shi, F., K. Fang, C. Xu, Z. Guo, and H.P. Borgaonkar, 2017: Interannual to centennial variability of the South Asian summer monsoon over the past millennium. *Climate Dynamics*, **49(7)**, 2803–2814, doi:10.1007/s00382-016-3493-9.
Shi, H.X. and C.H. Wang, 2015: Projected 21st century changes in snow water equivalent over Northern Hemisphere landmasses from the CMIP5 model ensemble. *The Cryosphere*, **9(5)**, 1943–1953, doi:10.5194/tc-9-1943-2015.
Shige, S. et al., 2017: Role of orography, diurnal cycle, and intraseasonal oscillation in summer monsoon rainfall over Western Ghats and Myanmar coast. *Journal of Climate*, **30(23)**, 9365–9381, doi:10.1175/jcli-d-16-0858.1.
Shimizu, M.H. and T. Ambrizzi, 2016: MJO influence on ENSO effects in precipitation and temperature over South America. *Theoretical and Applied Climatology*, **124(1–2)**, 291–301, doi:10.1007/s00704-015-1421-2.
Shine, K.P., R.P. Allan, W.J. Collins, and J.S. Fuglestvedt, 2015: Metrics for linking emissions of gases and aerosols to global precipitation changes. *Earth System Dynamics*, **6(2)**, 525–540, doi:10.5194/esd-6-525-2015.
Short Gianotti, D.J., B.T. Anderson, and G.D. Salvucci, 2014: The Potential Predictability of Precipitation Occurrence, Intensity, and Seasonal Totals over the Continental United States. *Journal of Climate*, **27(18)**, 6904–6918, doi:10.1175/jcli-d-13-00695.1.
Short Gianotti, D.J., R. Akbar, A.F. Feldman, G.D. Salvucci, and D. Entekhabi, 2020: Terrestrial Evaporation and Moisture Drainage in a Warmer Climate. *Geophysical Research Letters*, **47(5)**, e2019GL086498, doi:10.1029/2019gl086498.
Shrestha, S., N.A.T. Hoang, P.K. Shrestha, and B. Bhatta, 2018: Climate change impact on groundwater recharge and suggested adaptation strategies for selected Asian cities. *APN Science Bulletin*, doi:10.30852/sb.2018.499.
Shugar, D.H. et al., 2020: Rapid worldwide growth of glacial lakes since 1990. *Nature Climate Change*, **10(10)**, 939–945, doi:10.1038/s41558-020-0855-4.
Siew, J.H., F.T. Tangang, and L. Juneng, 2014: Evaluation of CMIP5 coupled atmosphere--ocean general circulation models and projection of the Southeast Asian winter monsoon in the 21st century, Int. *J. Climatol.*, **34**, 2872–2884, doi:10.1002/joc.3880.
Sigmond, M. and J.C. Fyfe, 2016: Tropical Pacific impacts on cooling North American winters. *Nature Climate Change*, **6(10)**, 970–974, doi:10.1038/nclimate3069.
Siler, N., G.H. Roe, and K.C. Armour, 2018a: Insights into the zonal-mean response of the hydrologic cycle to global warming from a diffusive energy balance model. *Journal of Climate*, **31(18)**, JCLI–D–18–0081.1, doi:10.1175/jcli-d-18-0081.1.
Siler, N., G.H. Roe, K.C. Armour, and N. Feldl, 2018b: Revisiting the surface-energy-flux perspective on the sensitivity of global precipitation to climate change. *Climate Dynamics*, doi:10.1007/s00382-018-4359-0.
Sillmann, J., C.W. Stjern, G. Myhre, and P.M. Forster, 2017: Slow and fast responses of mean and extreme precipitation to different forcing in CMIP5 simulations. *Geophysical Research Letters*, **44(12)**, 6383–6390, doi:10.1002/2017gl073229.
Simpson, I.R., R. Seager, M. Ting, and T.A. Shaw, 2016: Causes of change in Northern Hemisphere winter meridional winds and regional hydroclimate. *Nature Climate Change*, **6(1)**, 65–70, doi:10.1038/nclimate2783.
Singarayer, J.S., P.J. Valdes, and W.H.G. Roberts, 2017: Ocean dominated expansion and contraction of the late Quaternary tropical rainbelt. *Scientific Reports*, **7(1)**, doi:10.1038/s41598-017-09816-8.
Singh, A., S. Kumar, S. Akula, D.M. Lawrence, and D.L. Lombardozzi, 2020: Plant Growth Nullifies the Effect of Increased Water-Use Efficiency on Streamflow Under Elevated CO2 in the Southeastern United States. *Geophysical Research Letters*, **47(4)**, e2019GL086940, doi:10.1029/2019gl086940.
Singh, D., 2016: South Asian monsoon: Tug of war on rainfall changes. *Nature Climate Change*, **6(1)**, 20–22, doi:10.1038/nclimate2901.
Singh, D., S. Ghosh, M.K. Roxy, and S. McDermid, 2019: Indian summer monsoon: Extreme events, historical changes, and role of anthropogenic forcings. *Wiley Interdisciplinary Reviews: Climate Change*, **10(2)**, e571, doi:10.1002/wcc.571.
Singh, D., M. Tsiang, B. Rajaratnam, N.S. Diffenbaugh, and Singh et al., 2014: Observed changes in extreme wet and

ACCEPTED VERSION SUBJECT TO FINAL EDITING

dry spells during the south Asian summer monsoon season. *Nature Climate Change*, **4(6)**, 456–461, doi:10.1038/nclimate2208.
Singh, M. et al., 2020a: Fingerprint of volcanic forcing on the ENSO – Indian monsoon coupling. .
Singh, M. et al., 2020b: Fingerprint of volcanic forcing on the ENSO–Indian monsoon coupling. *Science Advances*, **6(38)**, eaba8164, doi:10.1126/sciadv.aba8164.
Singh, M.S. and P.A. O'Gorman, 2013: Influence of entrainment on the thermal stratification in simulations of radiative-convective equilibrium. *Geophysical Research Letters*, **40(16)**, 4398–4403, doi:10.1002/grl.50796.
Singh, M.S. and P.A. O'Gorman, 2014: Influence of microphysics on the scaling of precipitation extremes with temperature. *Geophysical Research Letters*, **41(16)**, 6037–6044, doi:10.1002/2014gl061222.
Sinha, A. et al., 2015: monsoon rainfall over the last two millennia. *Nature Communications*, **6**, 1–8, doi:10.1038/ncomms7309.
Skinner, C.B. and C.J. Poulsen, 2016: The role of fall season tropical plumes in enhancing Saharan rainfall during the African Humid Period. *Geophysical Research Letters*, doi:10.1002/2015gl066318.
Skliris, N., J.D. Zika, G. Nurser, S.A. Josey, and R. Marsh, 2016: Global water cycle amplifying at less than the Clausius-Clapeyron rate. *Scientific Reports*, **6(1)**, doi:10.1038/srep38752.
Skliris, N. et al., 2014: Salinity changes in the World Ocean since 1950 in relation to changing surface freshwater fluxes. *Climate Dyn.*, **43(3–4)**, 709–736, doi:10.1007/s00382-014-2131-7.
Smerdon, B.D., 2017: A synopsis of climate change effects on groundwater recharge. *Journal of Hydrology*, **555**, 125–128, doi:10.1016/j.jhydrol.2017.09.047.
Smith, C.J. et al., 2020: Effective radiative forcing and adjustments in CMIP6 models. *Atmospheric Chemistry and Physics*, **20(16)**, 9591–9618, doi:10.5194/acp-20-9591-2020.
Smith, R.J. and F.E. Mayle, 2018: Impact of mid- to late Holocene precipitation changes on vegetation across lowland tropical South America: a paleo-data synthesis. *Quaternary Research*, **89(1)**, 134–155, doi:10.1017/qua.2017.89.
Sniderman, J.M.K. et al., 2019: Southern Hemisphere subtropical drying as a transient response to warming. *Nature Climate Change*, doi:10.1038/s41558-019-0397-9.
Soares-Filho, B.S. et al., 2006: Modelling conservation in the Amazon basin. *Nature*, doi:10.1038/nature04389.
Sobel, A.H., S.J. Camargo, and M. Previdi, 2019: Aerosol vs. Greenhouse Gas Effects on Tropical Cyclone Potential Intensity and the Hydrologic Cycle. *Journal of Climate*, **32(17)**, 5511–5527, doi:10.1175/jcli-d-18-0357.1.
Sofaer, H.R. et al., 2016: Projected wetland densities under climate change: Habitat loss but little geographic shift in conservation strategy. *Ecological Applications*, doi:10.1890/15-0750.1.
Sohn, B.J., S.W. Yeh, A. Lee, and W.K.M. Lau, 2019: Regulation of atmospheric circulation controlling the tropical Pacific precipitation change in response to CO2 increases. *Nature Communications*, **10(1)**, 1108, doi:10.1038/s41467-019-08913-8.
Solander, K.C. et al., 2018: Interactions between climate change and complex topography drive observed streamflow changes in the Colorado River Basin. *Journal of Hydrometeorology*, doi:10.1175/jhm-d-18-0012.1.
Solman, S.A. and I. Orlanski, 2014: Poleward Shift and Change of Frontal Activity in the Southern Hemisphere over the Last 40 Years. *Journal of the Atmospheric Sciences*, **71(2)**, 539–552, doi:10.1175/jas-d-13-0105.1.
Solman, S.A. and I. Orlanski, 2016: Climate change over the extratropical Southern Hemisphere: The tale from an ensemble of reanalysis datasets. *Journal of Climate*, **29(5)**, 1673–1687, doi:10.1175/jcli-d-15-0588.1.
Song, F., T. Zhou, and Y. Qian, 2014: Responses of East Asian summer monsoon to natural and anthropogenic forcings in the 17 latest CMIP5 models. *Geophysical Research Letters*, **41(2)**, 596–603, doi:10.1002/2013gl058705.
Song, H., C.R. Ferguson, and J.K. Roundy, 2016: Land–Atmosphere Coupling at the Southern Great Plains Atmospheric Radiation Measurement (ARM) Field Site and Its Role in Anomalous Afternoon Peak Precipitation. *Journal of Hydrometeorology*, **17**, 541.
Song, X. and G.J. Zhang, 2011: Microphysics parameterization for convective clouds in a global climate model: Description and single-column model tests. *Journal of Geophysical Research Atmospheres*, **116(2)**, doi:10.1029/2010jd014833.
Sontakke, N.A., N. Singh, and H.N. Singh, 2008: Instrumental period rainfall series of the Indian region (AD 1813-2005): revised reconstruction, update and analysis. *The Holocene*, **18(7)**, 1055–1066, doi:10.1177/0959683608095576.
Soong, J.L., C.L. Phillips, C. Ledna, C.D. Koven, and M.S. Torn, 2020: CMIP5 Models Predict Rapid and Deep Soil Warming Over the 21st Century. *Journal of Geophysical Research: Biogeosciences*, **125(2)**, e2019JG005266, doi:10.1029/2019jg005266.
Sooraj et al., 2015: Global warming and the weakening of the Asian summer monsoon circulation: assessments from the CMIP5 models. *Climate Dynamics*, **45(1–2)**, 233–252, doi:10.1007/s00382-014-2257-7.
Souri, A.H. et al., 2020: Response of Hurricane Harvey's rainfall to anthropogenic aerosols: A sensitivity study based on spectral bin microphysics with simulated aerosols. *Atmospheric Research*, **242**, 104965, doi:10.1016/j.atmosres.2020.104965.
Sousa, P.M. et al., 2017: Responses of European precipitation distributions and regimes to different blocking locations. *Climate Dynamics*, **48(3–4)**, 1141–1160, doi:10.1007/s00382-016-3132-5.

ACCEPTED VERSION SUBJECT TO FINAL EDITING

Spencer, T. et al., 2016: Global coastal wetland change under sea-level rise and related stresses: The DIVA Wetland Change Model. *Global and Planetary Change*, doi:10.1016/j.gloplacha.2015.12.018.
Sperry, J.S. et al., 2016: Pragmatic hydraulic theory predicts stomatal responses to climatic water deficits. *New Phytologist*, doi:10.1111/nph.14059.
Spracklen, D. and L. Garcia-Carreras, 2015: The impact of Amazonian deforestation on Amazon basin rainfall. *Geophysical Research Letters*, **42(21)**, 9546–9552, doi:10.1002/2015gl066063.
Sprenger, M. et al., 2019: The demographics of water: A review of water ages in the critical zone. *Reviews of Geophysics*, 2018RG000633, doi:10.1029/2018rg000633.
Staal, A., S.C. Dekker, M. Hirota, and E.H. van Nes, 2015: Synergistic effects of drought and deforestation on the resilience of the south-eastern Amazon rainforest. *Ecological Complexity*, **22**, 65–75, doi:10.1016/j.ecocom.2015.01.003.
Staal, A. et al., 2018: Forest-rainfall cascades buffer against drought across the Amazon. *Nature Climate Change*, doi:10.1038/s41558-018-0177-y.
Staal, A. et al., 2020: Hysteresis of tropical forests in the 21st century. *Nature Communications*, doi:10.1038/s41467-020-18728-7.
Stanford, M.K.W. et al., 2017: A ubiquitous ice size bias in simulations of tropical deep convection. *Atmospheric Chemistry and Physics*, **17(15)**, 9599–9621, doi:10.5194/acp-17-9599-2017.
Staten, P.W., K.M. Grise, S.M. Davis, K. Karnauskas, and N. Davis, 2019: Regional Widening of Tropical Overturning: Forced Change, Natural Variability, and Recent Trends. *Journal of Geophysical Research: Atmospheres*, **124(12)**, 6104–6119, doi:10.1029/2018jd030100.
Stechmann, S.N. and S. Hottovy, 2017: Unified Spectrum of Tropical Rainfall and Waves in a Simple Stochastic Model. *Geophysical Research Letters*, **44(20)**, 10,713–10,724, doi:10.1002/2017gl075754.
Steege, H. et al., 2015: Estimating the global conservation status of more than 15,000 Amazonian tree species. *Science Advances*, doi:10.1126/sciadv.1500936.
Stephens, C.M., T.R. McVicar, F.M. Johnson, and L.A. Marshall, 2018: Revisiting Pan Evaporation Trends in Australia a Decade on. *Geophysical Research Letters*, doi:10.1029/2018gl079332.
Stephens, G.L. et al., 2012: An update on Earth's energy balance in light of the latest global observations. *Nature Geoscience*, **5(10)**, 691–696, doi:10.1038/ngeo1580.
Stephens, G.L. et al., 2015: The albedo of earth. *Reviews of Geophysics*, **53(1)**, 141–163, doi:10.1002/2014rg000449.
Stephens, G.L. et al., 2018: Regional Intensification of the Tropical Hydrological Cycle During ENSO. *Geophysical Research Letters*, **45(9)**, 4361–4370, doi:10.1029/2018gl077598.
Sterling, S.M., A. Ducharne, and J. Polcher, 2013: The impact of global land-cover change on the terrestrial water cycle. *Nature Climate Change*, **3(4)**, 385–390, doi:10.1038/nclimate1690.
Stevens, B. and G. Feingold, 2009: Untangling aerosol effects on clouds and precipitation in a buffered system. *Nature*, **461(7264)**, 607, doi:10.1038/nature08281.
Stevenson, S., B. Otto-Bliesner, J. Fasullo, and E. Brady, 2016: "El Niño Like" hydroclimate responses to last millennium volcanic eruptions. *Journal of Climate*, doi:10.1175/jcli-d-15-0239.1.
Stevenson, S., A. Timmermann, Y. Chikamoto, S. Langford, and P. DiNezio, 2015: Stochastically Generated North American Megadroughts. *Journal of Climate*, **28(5)**, 1865–1880, doi:10.1175/jcli-d-13-00689.1.
Stjern, C.W. et al., 2017: Rapid Adjustments Cause Weak Surface Temperature Response to Increased Black Carbon Concentrations. *Journal of Geophysical Research: Atmospheres*, **122(21)**, 11,462–11,481, doi:10.1002/2017jd027326.
Stocker, T.F. et al., 2013: Technical Summary. In: *Climate Change 2013: The Physical Science Basis. Contribution of Working Group I to the Fifth Assessment Report of the Intergovernmental Panel on Climate Change* [Stocker, T.F., D. Qin, G.-K. Plattner, M. Tignor, S.K. Allen, J. Boschung, A. Nauels, Y. Xia, V. Bex, and P.M. Midgley (eds.)]. Cambridge University Press, Cambridge, United Kingdom and New York, NY, USA, pp. 33–115, doi:10.1017/cbo9781107415324.005.
Stott, P.A. et al., 2016: Attribution of extreme weather and climate-related events. *Wiley Interdisciplinary Reviews: Climate Change*, **7(1)**, 23–41, doi:10.1002/wcc.380.
Stríkis, N.M. et al., 2015: Timing and structure of Mega-SACZ events during Heinrich Stadial 1. *Geophysical Research Letters*, doi:10.1002/2015gl064048.
Stríkis, N.M. et al., 2018a: South American monsoon response to iceberg discharge in the North Atlantic. *Proceedings of the National Academy of Sciences of the United States of America*, doi:10.1073/pnas.1717784115.
Stríkis, N.M. et al., 2018b: South American monsoon response to iceberg discharge in the North Atlantic. *Proceedings of the National Academy of Sciences*, **115(15)**, 3788 LP – 3793, doi:10.1073/pnas.1717784115.
Stuart-Smith, R., G.H. Roe, S. Li, and M. Allen, 2020: Increased outburst flood hazard from Lake Palcacocha due to human-induced glacier retreat. *Nature Geoscience*, **14(2)**, 85–90, doi:10.1038/s41561-021-00686-4.
Studholme, J. and S. Gulev, 2018: Concurrent changes to Hadley circulation and the meridional distribution of tropical cyclones. *Journal of Climate*, **31(11)**, 4367–4389.
Stuecker, M.F. et al., 2018: Polar amplification dominated by local forcing and feedbacks. *Nature Climate Change*, **8(12)**, 1076–1081, doi:10.1038/s41558-018-0339-y.

ACCEPTED VERSION SUBJECT TO FINAL EDITING

Su, H. et al., 2014: Weakening and strengthening structures in the Hadley Circulation change under global warming and implications for cloud response and climate sensitivity. *Journal of Geophysical Research*, doi:10.1002/2014jd021642.
Su, H. et al., 2017: Tightening of tropical ascent and high clouds key to precipitation change in a warmer climate. *Nature Communications*, **8**, 15771, doi:10.1038/ncomms15771.
Su, H. et al., 2019: A dichotomy between model responses of tropical ascent and descent to surface warming. *npj Climate and Atmospheric Science*, **2(1)**, 8, doi:10.1038/s41612-019-0066-8.
Su, H. et al., 2020: Observed Tightening of Tropical Ascent in Recent Decades and Linkage to Regional Precipitation Changes. *Geophysical Research Letters*, **n/a(n/a)**, e2019GL085809, doi:10.1029/2019gl085809.
Subramanian, A. et al., 2014: The MJO and global warming: a study in CCSM4. *Climate Dynamics*, **42(7–8)**, 2019–2031, doi:10.1007/s00382-013-1846-1.
Sudeepkumar, B.L., C.A. Babu, and H. Varikoden, 2018: Future projections of active-break spells of Indian summer monsoon in a climate change perspective. *Global and Planetary Change*, **161**, 222–230, doi:10.1016/j.gloplacha.2017.12.020.
Sun, C. et al., 2018: Uncertainties in simulated El Niño-Southern Oscillation arising from internal climate variability. *Atmospheric Science Letters*, **19(3)**, e805, doi:10.1002/asl.805.
Sun, F., N. Berg, A. Hall, M. Schwartz, and D. Walton, 2018: Understanding End-of-century Snowpack Changes Over California's Sierra Nevada. *Geophysical Research Letters*, **46(2)**, 933–943, doi:10.1029/2018gl080362.
Sun, Q., C. Miao, and Q. Duan, 2015: Comparative analysis of CMIP3 and CMIP5 global climate models for simulating the daily mean, maximum, and minimum temperatures and daily precipitation over China. *Journal of Geophysical Research: Atmospheres*, **120(10)**, 4806–4824, doi:10.1002/2014jd022994.
Sun, Q., X. Zhang, F. Zwiers, S. Westra, and L. Alexander, 2020: A global, continental and regional analysis of changes in extreme precipitation. *Journal of Climate*, 1–52, doi:10.1175/jcli-d-19-0892.1.
Sun, Y. et al., 2012: Influence of Atlantic meridional overturning circulation on the East Asian winter monsoon. *Nature Geoscience*, **5(1)**, 46–49, doi:10.1038/ngeo1326.
Supari et al., 2018: ENSO modulation of seasonal rainfall and extremes in Indonesia. *Climate Dynamics*, **51(7–8)**, 2559–2580, doi:10.1007/s00382-017-4028-8.
Sutton, R.T., 2018: ESD Ideas: A simple proposal to improve the contribution of IPCC WGI to the assessment and communication of climate change risks. *Earth System Dynamics*, **9(4)**, 1155–1158, doi:10.5194/esd-9-1155-2018.
Sutton, R.T., 2019: Climate science needs to take risk assessment much more seriously. , 1–18, doi:10.1175/bams-d-18-0280.1.
Suzuki, K. et al., 2015: Evaluation of the Warm Rain Formation Process in Global Models with Satellite Observations. *Journal of the Atmospheric Sciences*, **72(10)**, 3996–4014, doi:10.1175/jas-d-14-0265.1.
Swann, A.L.S., F.M. Hoffman, C.D. Koven, and J.T. Randerson, 2016: Plant responses to increasing CO2 reduce estimates of climate impacts on drought severity. *Proceedings of the National Academy of Sciences*, **113(36)**, 10019–10024, doi:10.1073/pnas.1604581113.
Swapna, P., R. Krishnan, and J.M. Wallace, 2012: Indian Ocean and monsoon coupled interactions in a warming environment. *Climate Dynamics*, **42(9–10)**, 2439–2454, doi:10.1007/s00382-013-1787-8.
Sylla, M.B. et al., 2015: Projected changes in the annual cycle of high-intensity precipitation events over West Africa for the late twenty-first century. *Journal of Climate*, **28(16)**, 6475–6488, doi:10.1175/jcli-d-14-00854.1.
Tachiiri, K., D. Silva Herran, X. Su, and M. Kawamiya, 2019: Effect on the Earth system of realizing a 1.5°C warming climate target after overshooting to the 2°C level. *Environmental Research Letters*, **14(12)**, 124063, doi:10.1088/1748-9326/ab5199.
Tague, C. and G.E. Grant, 2009: Groundwater dynamics mediate low-flow response to global warming in snow-dominated alpine regions. *Water Resources Research*, **45**.
Takahashi, C., N. Sato, A. Seiki, K. Yoneyama, and R. Shirooka, 2011: Projected Future Change of MJO and its Extratropical Teleconnection in East Asia during the Northern Winter Simulated in IPCC AR4 Models. *SOLA*, **7**, 201–204, doi:10.2151/sola.2011-051.
Takahashi, H.G., 2018: A systematic tropospheric dry bias in the tropics in cmip5 models: Relationship between water vapor and rainfall characteristics. *Journal of the Meteorological Society of Japan*, **96(4)**, 415–423, doi:10.2151/jmsj.2018-046.
Takahashi, H.G. and J. Polcher, 2019: Weakening of rainfall intensity on wet soils over the wet Asian monsoon region using a high-resolution regional climate model. *Progress in Earth and Planetary Science*, **6(1)**, 26, doi:10.1186/s40645-019-0272-3.
Takahashi, H.G., S. Watanabe, M. Nakata, and T. Takemura, 2018: Response of the atmospheric hydrological cycle over the tropical Asian monsoon regions to anthropogenic aerosols and its seasonality. *Progress in Earth and Planetary Science*, **5(1)**, 44, doi:10.1186/s40645-018-0197-2.
Takahashi, H.G., H. Fujinami, T. Yasunari, J. Matsumoto, and S. Baimoung, 2015: Role of tropical cyclones along the monsoon trough in the 2011 Thai flood and interannual variability. *Journal of Climate*, **28(4)**, 1465–1476, doi:10.1175/jcli-d-14-00147.1.

SUBJECT TO FINAL EDITING ACCEPTED VERSION

Takahashi, K. and A.G. Martínez, 2019: The very strong coastal El Niño in 1925 in the far-eastern Pacific. *Climate Dynamics*, **52(12)**, 7389–7415, doi:10.1007/s00382-017-3702-1.
Talento, S. and M. Barreiro, 2012: Estimation of Natural Variability and Detection of Anthropogenic Signal in Summertime Precipitation over South America. *Advances in Meteorology*, **2012**, 1–10, doi:10.1155/2012/725343.
Talento, S. and M. Barreiro, 2018: Control of the South Atlantic Convergence Zone by extratropical thermal forcing. *Climate Dynamics*, **50(3)**, 885–900, doi:10.1007/s00382-017-3647-4.
Talib, J., S.J. Woolnough, N.P. Klingaman, and C.E. Holloway, 2018: The Role of the Cloud Radiative Effect in the Sensitivity of the Intertropical Convergence Zone to Convective Mixing. *Journal of Climate*, **31(17)**, 6821–6838, doi:10.1175/jcli-d-17-0794.1.
Tamang, S.K., A.M. Ebtehaj, A.F. Prein, and A.J. Heymsfield, 2020: Linking global changes of snowfall and wet-bulb temperature. *Journal of Climate*, **33(1)**, 39–59, doi:10.1175/jcli-d-19-0254.1.
Tamarin-Brodsky, T. and Y. Kaspi, 2017: Enhanced poleward propagation of storms under climate change. *Nature Geoscience*, **10(12)**, 908–913, doi:10.1038/s41561-017-0001-8.
Tan, H., P. Ray, B.S. Barrett, M. Tewari, and M.W. Moncrieff, 2020: Role of topography on the MJO in the maritime continent: a numerical case study. *Climate Dynamics*, **55(1–2)**, 295–314, doi:10.1007/s00382-018-4275-3.
Tan, J., L. Oreopoulos, C. Jakob, and D. Jin, 2018: Evaluating rainfall errors in global climate models through cloud regimes. *Climate Dynamics*, **50(9–10)**, 3301–3314, doi:10.1007/s00382-017-3806-7.
Tan, X. and T.Y. Gan, 2015: Contribution of human and climate change impacts to changes in streamflow of Canada. *Scientific Reports*, **5(1)**, doi:10.1038/srep17767.
Tan, X., Y. Wu, B. Liu, and S. Chen, 2020: Inconsistent changes in global precipitation seasonality in seven precipitation datasets. *Climate Dynamics*, **54(5–6)**, 3091–3108, doi:10.1007/s00382-020-05158-w.
Tanaka, A. and K. Takahashi, 2017: On the scaling of climate impact indicators with global mean temperature increase : a case study of terrestrial ecosystems and water resources. , 775–782, doi:10.1007/s10584-017-1911-6.
Tandon, N.F., X. Zhang, and A.H. Sobel, 2018: Understanding the Dynamics of Future Changes in Extreme Precipitation Intensity. *Geophysical Research Letters*, **45(6)**, 2870–2878, doi:10.1002/2017gl076361.
Tang, J., W.J. Riley, and J. Niu, 2015: Incorporating root hydraulic redistribution in CLM4.5: Effects on predicted site and global evapotranspiration, soil moisture, and water storage. *Journal of Advances in Modeling Earth Systems*, **7(4)**, 1828–1848, doi:10.1002/2015ms000484.
Tang, Q., X. Zhang, and J.A. Francis, 2014: Extreme summer weather in northern mid-latitudes linked to a vanishing cryosphere. *Nature Climate Change*, **4(1)**, 45–50, doi:10.1038/nclimate2065.
Tang, T. et al., 2018: Dynamical response of Mediterranean precipitation to greenhouse gases and aerosols. *Atmospheric Chemistry and Physics*, **18(11)**, 8439–8452, doi:10.5194/acp-18-8439-2018.
Tao, L., J. Zhao, and T. Li, 2015: Trend analysis of tropical intraseasonal oscillations in the summer and winter during 1982-2009. *International Journal of Climatology*, **35(13)**, 3969–3978, doi:10.1002/joc.4258.
Tao, W.-K., J.-P. Chen, Z. Li, C. Wang, and C. Zhang, 2012: Impact of aerosols on convective clouds and precipitation. *Reviews of Geophysics*, **50(2)**, doi:10.1029/2011rg000369.
Tapiador, F.J., J.L. Sánchez, and E. García-Ortega, 2019a: Empirical values and assumptions in the microphysics of numerical models. *Atmospheric Research*, **215**, 214–238, doi:10.1016/j.atmosres.2018.09.010.
Tapiador, F.J., A. Behrangi, Z.S. Haddad, D. Katsanos, and M. de Castro, 2016: Disruptions in precipitation cycles: Attribution to anthropogenic forcing. *Journal of Geophysical Research*, doi:10.1002/2015jd023406.
Tapiador, F.J., R. Moreno, A. Navarro, J.L. Sánchez, and E. García-Ortega, 2019b: Climate classifications from regional and global climate models: Performances for present climate estimates and expected changes in the future at high spatial resolution. *Atmospheric Research*, **228**, 107–121, doi:10.1016/j.atmosres.2019.05.022.
Tapiador, F.J., A. Navarro, R. Moreno, J.L. Sánchez, and E. García-Ortega, 2020: Regional climate models: 30 years of dynamical downscaling. *Atmospheric Research*, **235**, 104785, doi:10.1016/j.atmosres.2019.104785.
Tawfik, A.B., P.A. Dirmeyer, and A. Santanello, 2015: The heated condensation framework. *Part II: Climatological behavior of convective initiation and land–atmosphere coupling over the conterminous United States, Journal of Hydrometeorology*, **16**, 1946.
Taylor, C.M., 2015: Detecting soil moisture impacts on convective initiation in Europe. *Geophysical Research Letters*, **42(11)**, 4631–4638, doi:10.1002/2015gl064030.
Taylor, C.M. et al., 2013: Modeling soil moisture-precipitation feedback in the Sahel: Importance of spatial scale versus convective parameterization. *Geophysical Research Letters*, **40(23)**, 6213–6218, doi:10.1002/2013gl058511.
Taylor, C.M. et al., 2017: Frequency of extreme Sahelian storms tripled since 1982 in satellite observations. *Nature*, **544(7651)**, 475–478, doi:10.1038/nature22069.
Taylor, R.G. et al., 2013a: Ground water and climate change. *Nature Climate Change*, **3(4)**, 322–329, doi:10.1038/nclimate1744.
Taylor, R.G. et al., 2013b: Evidence of the dependence of groundwater resources on extreme rainfall in East Africa. *Nature Climate Change*, **3**, 374–378, doi:10.1038/nclimate1731.
Tebaldi, C. and J.M. Arblaster, 2014: Pattern scaling: Its strengths and limitations, and an update on the latest model simulations. *Climatic Change*, **122(3)**, 459–471, doi:10.1007/s10584-013-1032-9.

ACCEPTED VERSION SUBJECT TO FINAL EDITING

Tebaldi, C. and R. Knutti, 2018: Evaluating the accuracy of climate change pattern emulation for low warming targets. *Environmental Research Letters*, **13(5)**, doi:10.1088/1748-9326/aabef2.
Tegen, I. and K. Schepanski, 2018: Climate feedback on aerosol emission and atmospheric concentrations. *Current Climate Change Reports*, **4(1)**, 1–10.
Teng, H. and G. Branstator, 2019: Amplification of Waveguide Teleconnections in the Boreal Summer. *Current Climate Change Reports*, **5(4)**, 421–432, doi:10.1007/s40641-019-00150-x.
Tennant, C., B. Menounos, R. Wheate, and J.J. Clague, 2012: Area change of glaciers in the Canadian Rocky Mountains, 1919 to 2006. *The Cryosphere*, **6(6)**, 1541–1552, doi:10.5194/tc-6-1541-2012.
Terray, L. et al., 2012: Near-Surface Salinity as Nature's Rain Gauge to Detect Human Influence on the Tropical Water Cycle. *Journal of Climate*, **25(3)**, 958–977, doi:10.1175/jcli-d-10-05025.1.
Terray, P., K.P. Sooraj, S. Masson, and C. Prodhomme, 2021: Anatomy of the Indian Summer Monsoon and ENSO relationships in state-of-the-art CGCMs: role of the tropical Indian Ocean. *Climate Dynamics*, **56(1–2)**, 329–356, doi:10.1007/s00382-020-05484-z.
Terray, P. et al., 2018: Towards a realistic simulation of boreal summer tropical rainfall climatology in state-of-the-art coupled models: role of the background snow-free land albedo. *Climate Dynamics*, **50(9–10)**, 3413–3439, doi:10.1007/s00382-017-3812-9.
Teuling, A.J. et al., 2013: Evapotranspiration amplifies European summer drought. *Geophysical Research Letters*, doi:10.1002/grl.50495.
Thackeray, C.W. and C.G. Fletcher, 2016: Snow albedo feedback. *Progress in Physical Geography*, **40(3)**, 392–408, doi:10.1177/0309133315620999.
Thackeray, C.W., C.G. Fletcher, and C. Derksen, 2015: Quantifying the skill of CMIP5 models in simulating seasonal albedo and snow cover evolution. *Journal of Geophysical Research: Atmospheres*, **120(12)**, 5831–5849, doi:10.1002/2015jd023325.
Thackeray, C.W., C.G. Fletcher, L.R. Mudryk, and C. Derksen, 2016: Quantifying the uncertainty in historical and future simulations of Northern Hemisphere spring snow cover. *Journal of Climate*, **29(23)**, 8647–8663, doi:10.1175/jcli-d-16-0341.1.
Thackeray, C.W. et al., 2018: On the Connection Between Global Hydrologic Sensitivity and Regional Wet Extremes. *Geophysical Research Letters*, doi:10.1029/2018gl079698.
Thomas, E.R., J.S. Hosking, R.R. Tuckwell, R.A. Warren, and E.C. Ludlow, 2015: Twentieth century increase in snowfall in coastal West Antarctica. , 9387–9393, doi:10.1002/2015gl065750.received.
Thomas, E.R.R. et al., 2017: Regional Antarctic snow accumulation over the past 1000 years. *Climate of the Past*, **13(11)**, 1491–1513, doi:10.5194/cp-13-1491-2017.
Thompson, D.W.J., E.A. Barnes, C. Deser, W.E. Foust, and A.S. Phillips, 2015: Quantifying the Role of Internal Climate Variability in Future Climate Trends. *Journal of Climate*, **28(16)**, 6443–6456, doi:10.1175/jcli-d-14-00830.1.
Thomson, L.I., G.R. Osinski, and C.S.L. Ommanney, 2011: Glacier change on Axel Heiberg Island, Nunavut, Canada. *Journal of Glaciology*, **57(206)**, 1079–1086, doi:10.3189/002214311798843287.
Thornton, J.A., K.S. Virts, R.H. Holzworth, and T.P. Mitchell, 2017: Lightning enhancement over major oceanic shipping lanes. *Geophysical Research Letters*, **44(17)**, 9102–9111, doi:10.1002/2017gl074982.
Tian, B., 2015: Spread of model climate sensitivity linked to double-Intertropical Convergence Zone bias. *Geophysical Research Letters*, **42(10)**, 4133–4141, doi:10.1002/2015gl064119.
Tian, B. and X. Dong, 2020: The Double-ITCZ Bias in CMIP3, CMIP5, and CMIP6 Models Based on Annual Mean Precipitation. *Geophysical Research Letters*, **47(8)**, 1–11, doi:10.1029/2020gl087232.
Tian, D., W. Dong, D. Gong, Y. Guo, and S. Yang, 2017: Fast responses of climate system to carbon dioxide, aerosols and sulfate aerosols without the mediation of SST in the CMIP5. *International Journal of Climatology*, **37(3)**, 1156–1166, doi:10.1002/joc.4763.
Tian, F., B. Dong, J. Robson, and R. Sutton, 2018: Forced decadal changes in the East Asian summer monsoon: the roles of greenhouse gases and anthropogenic aerosols. *Climate Dynamics*, **51(9–10)**, 3699–3715, doi:10.1007/s00382-018-4105-7.
Tian, F., B. Dong, J. Robson, R. Sutton, and S.F.B. Tett, 2019: Projected near term changes in the East Asian summer monsoon and its uncertainty. *Environmental Research Letters*, **14(8)**, 084038, doi:10.1088/1748-9326/ab28a6.
Tierney, J.E. and P.B. deMenocal, 2013: Abrupt shifts in Horn of Africa hydroclimate since the last glacial maximum. *Science*, **342(6160)**, doi:10.1126/science.1240411.
Tierney, J.E., C.C. Ummenhofer, and P.B. DeMenocal, 2015: Past and future rainfall in the Horn of Africa. *Science Advances*, **1(9)**, e1500682, doi:10.1126/sciadv.1500682.
Tierney, J.E., F.S.R. Pausata, and P.B. deMenocal, 2017: Rainfall regimes of the Green Sahara. *Science Advances*, **3(1)**, doi:10.1126/sciadv.1601503.
Tierney, J.E., A.M. Haywood, R. Feng, T. Bhattacharya, and B.L. Otto-Bliesner, 2019: Pliocene warmth consistent with greenhouse gas forcing. *Geophysical Research Letters*, **46(15)**, 9136–9144, doi:10.1029/2019gl083802.
Tilinina, N., S. Gulev, and O. Zolina, 9999: Poleward deflection of midlatitude storm tracks since 1979 from multiple reanalyses. *Current Climate Change Reports*.

ACCEPTED VERSION SUBJECT TO FINAL EDITING

Tilinina, N., S.K. Gulev, I. Rudeva, and P. Koltermann, 2013: Comparing cyclone life cycle characteristics and their interannual variability in different reanalyses. *Journal of Climate*, **26(17)**, 6419–6438, doi:10.1175/jcli-d-12-00777.1.

Tillman, F.D., S. Gangopadhyay, and T. Pruitt, 2017: Changes in Projected Spatial and Seasonal Groundwater Recharge in the Upper Colorado River Basin. *Groundwater*, doi:10.1111/gwat.12507.

Tilmes, S. et al., 2013: The hydrological impact of geoengineering in the Geoengineering Model Intercomparison Project (GeoMIP). *Journal of Geophysical Research Atmospheres*, doi:10.1002/jgrd.50868.

Timbal, B. and W. Drosdowsky, 2013: The relationship between the decline of Southeastern Australian rainfall and the strengthening of the subtropical ridge. *International Journal of Climatology*, **33(4)**, 1021–1034, doi:10.1002/joc.3492.

Toda, M. and M. Watanabe, 2018: Linear and Nonlinear Hydrological Cycle Responses to Increasing Sea Surface Temperature. *Geophysical Research Letters*, **45(3)**, 1551–1558, doi:10.1002/2017gl076745.

Tokinaga, H., S.P. Xie, C. Deser, Y. Kosaka, and Y.M. Okumura, 2012: Slowdown of the Walker circulation driven by tropical Indo-Pacific warming. *Nature*, **491**, 439–443, doi:10.1038/nature11576.

Toll, V., M. Christensen, S. Gassó, and N. Bellouin, 2017: Volcano and Ship Tracks Indicate Excessive Aerosol-Induced Cloud Water Increases in a Climate Model. *Geophysical Research Letters*, **44(24)**, 12,492–12,500, doi:10.1002/2017gl075280.

Torres, R.R. and J.A. Marengo, 2014: Climate change hotspots over South America: From CMIP3 to CMIP5 multi-model datasets. *Theoretical and Applied Climatology*, doi:10.1007/s00704-013-1030-x.

Torres-Alavez, A., T. Cavazos, and C. Turrent, 2014: Land–Sea Thermal Contrast and Intensity of the North American Monsoon under Climate Change Conditions. *Journal of Climate*, **27(12)**, 4566–4580, doi:10.1175/jcli-d-13-00557.1.

Torres-Batlló, J., B. Martí-Cardona, and R. Pillco-Zolá, 2020: Mapping evapotranspiration, vegetation and precipitation trends in the catchment of the shrinking lake poopo. *Remote Sensing*, **12(1)**, doi:10.3390/rs12010073.

Trenberth, K.E., 2011: Changes in precipitation with climate change. *Climate Research*, **47(1–2)**, 123–138, doi:10.3354/cr00953.

Trenberth, K.E., J.T. Fasullo, and J. Mackaro, 2011: Atmospheric moisture transports from ocean to land and global energy flows in reanalyses. *Journal of Climate*, **24(18)**, 4907–4924, doi:10.1175/2011jcli4171.1.

Trenberth, K.E., J.T. Fasullo, and T.G. Shepherd, 2015: Attribution of climate extreme events. *Nature Climate Change*, doi:10.1038/nclimate2657.

Trenberth, K.E., Y. Zhang, and M. Gehne, 2017: Intermittency in Precipitation: Duration, Frequency, Intensity, and Amounts Using Hourly Data. *Journal of Hydrometeorology*, **18(5)**, 1393–1412, doi:10.1175/jhm-d-16-0263.1.

Trenberth, K.E., L. Cheng, P. Jacobs, Y. Zhang, and J. Fasullo, 2018: Hurricane Harvey links to ocean heat content and climate change adaptation. *Earth's Future*, **2018**.

Trigo, R.M., I.F. Trigo, C.C. DaCamara, and T.J. Osborn, 2004: Climate impact of the European winter blocking episodes from the NCEP/NCAR reanalyses. *Climate Dynamics*, **23(1)**, 17–28, doi:10.1007/s00382-004-0410-4.

Tsanis, I. and E. Tapoglou, 2019: Winter North Atlantic Oscillation impact on European precipitation and drought under climate change. *Theoretical and Applied Climatology*, **135(1–2)**, 323–330, doi:10.1007/s00704-018-2379-7.

Tseng, K.-C., E. Maloney, and E. Barnes, 2019: The Consistency of MJO Teleconnection Patterns: An Explanation Using Linear Rossby Wave Theory. *Journal of Climate*, **32(2)**, 531–548, doi:10.1175/jcli-d-18-0211.1.

Turner, A.J., A.M. Fiore, L.W. Horowitz, and M. Bauer, 2013: Summertime cyclones over the Great Lakes Storm Track from 1860--2100: variability, trends, and association with ozone pollution. *Atmos. Chem*, **13**, 565–578, doi:10.5194/acp-13-565-2013.

Turner, J., J.S. Hosking, T.J. Bracegirdle, T. Phillips, and G.J. Marshall, 2017: Variability and trends in the Southern Hemisphere high latitude, quasi-stationary planetary waves. *International Journal of Climatology*, **37(5)**, 2325–2336, doi:10.1002/joc.4848.

Turner, J. et al., 2019: The Dominant Role of Extreme Precipitation Events in Antarctic Snowfall Variability. *Geophysical Research Letters*, doi:10.1029/2018gl081517.

Turner and Annamalai, A.G., 2012: summer monsoon. *Nature Climate Change*, doi:10.1038/nclimate1495.

Udall, B. and J. Overpeck, 2017: The twenty-first century Colorado River hot drought and implications for the future. *Water Resources Research*, doi:10.1002/2016wr019638.

Ukkola, A.M., M.G. De Kauwe, M.L. Roderick, G. Abramowitz, and A.J. Pitman, 2020: Robust Future Changes in Meteorological Drought in CMIP6 Projections Despite Uncertainty in Precipitation. *Geophysical Research Letters*, doi:10.1029/2020gl087820.

Ukkola, A.M. et al., 2016a: Modelling evapotranspiration during precipitation deficits: Identifying critical processes in a land surface model. *Hydrology and Earth System Sciences*, **20(6)**, 2403–2419, doi:10.5194/hess-20-2403-2016.

Ukkola, A.M. et al., 2016b: Reduced streamflow in water-stressed climates consistent with CO2 effects on vegetation. *Nature Climate Change*, doi:10.1038/nclimate2831.

ACCEPTED VERSION SUBJECT TO FINAL EDITING

Ummenhofer, C.C., A. Sen Gupta, M.H. England, and C.J.C. Reason, 2009: Contributions of Indian Ocean Sea Surface Temperatures to Enhanced East African Rainfall. *Journal of Climate*, **22(4)**, 993–1013, doi:10.1175/2008jcli2493.1.

Ummenhofer, C.C. et al., 2017: Emerging European winter precipitation pattern linked to atmospheric circulation changes over the North Atlantic region in recent decades. *Geophysical Research Letters*, **44(16)**, 8557–8566, doi:10.1002/2017gl074188.

Undorf, S. et al., 2018: Detectable Impact of Local and Remote Anthropogenic Aerosols on the 20th Century Changes of West African and South Asian Monsoon Precipitation. *Journal of Geophysical Research: Atmospheres*, **123(10)**, 4871–4889, doi:10.1029/2017jd027711.

Undorf et al., S., S. Undorf, M.A. Bollasina, G.C. Hegerl, and S. Undorf et al., 2018: Impacts of the 1900--74 Increase in Anthropogenic Aerosol Emissions from North America and Europe on Eurasian Summer Climate. *Journal of Climate*, **31(20)**, 8381–8399.

Vallis, G.K., P. Zurita-Gotor, C. Cairns, and J. Kidston, 2015: Response of the large-scale structure of the atmosphere to global warming. *Quarterly Journal of the Royal Meteorological Society*, doi:10.1002/qj.2456.

van der Ent, R.J. and H.H.G. Savenije, 2013: Oceanic sources of continental precipitation and the correlation with sea surface temperature. *Water Resources Research*, **49(7)**, 3993–4004, doi:10.1002/wrcr.20296.

Van Der Ent, R.J., P.W. Keys, and H.H.G. Savenije, 2014: Contrasting roles of interception and transpiration in the hydrological cycle – Part 2 : Moisture recycling. *Earth System Dynamics*, **5**, 471–489, doi:10.5194/esd-5-471-2014.

Van Loon, A.F. et al., 2016: Drought in the Anthropocene. *Nature Geoscience*, **9(2)**, 89.

Van Nes, E.H. and M. Scheffer, 2005: Implications of spatial heterogeneity for catastrophic regime shifts in ecosystems. *Ecology*, **86**, 1797–1807, doi:10.1890/04-0550.

Van Oldenborgh, G.J. et al., 2017: Attribution of extreme rainfall from Hurricane Harvey, August 2017. *Environ. Res*, **12(12)**, 12400.

Vannière, B. et al., 2019: Multi-model evaluation of the sensitivity of the global energy budget and hydrological cycle to resolution. *Climate Dynamics*, **52(11)**, 6817–6846, doi:10.1007/s00382-018-4547-y.

Varble, A., 2018: Erroneous Attribution of Deep Convective Invigoration to Aerosol Concentration. *Journal of the Atmospheric Sciences*, **75(4)**, 1351–1368, doi:10.1175/jas-d-17-0217.1.

Vaughan, D.G. et al., 2013: Observations: Cryosphere. In: *Climate Change 2013: The Physical Science Basis. Contribution of Working Group I to the Fifth Assessment Report of the Intergovernmental Panel on Climate Change* [Stocker, T.F., D. Qin, G.-K. Plattner, M. Tignor, S.K. Allen, J. Boschung, A. Nauels, Y. Xia, V. Bex, and P.M. Midgley (eds.)]. Cambridge University Press, Cambridge, United Kingdom and New York, NY, USA, pp. 317–382, doi:10.1017/cbo9781107415324.012.

Vazifehkhah, S. and E. Kahya, 2018: Hydrological drought associations with extreme phases of the North Atlantic and Arctic Oscillations over Turkey and northern Iran. *International Journal of Climatology*, **38(12)**, 4459–4475, doi:10.1002/joc.5680.

Vecchi, G.A. and B.J. Soden, 2007: Global warming and the weakening of the tropical circulation. *Journal of Climate*, **20(17)**, 4316–4340, doi:10.1175/jcli4258.1.

Veldkamp, T.I.E. et al., 2018: Human impact parameterizations in global hydrological models improve estimates of monthly discharges and hydrological extremes: a multi-model validation study. *Environmental Research Letters*, **13(5)**, 055008, doi:10.1088/1748-9326/aab96f.

Vera, C.S. and L. Díaz, 2015: Anthropogenic influence on summer precipitation trends over South America in CMIP5 models. *International Journal of Climatology*, **35(10)**, 3172–3177, doi:10.1002/joc.4153.

Vera, C.S. and M. Osman, 2018: Activity of the Southern Annular Mode during 2015-2016 El Niño event and its impact on Southern Hemisphere climate anomalies. *International Journal of Climatology*, **38**, e1288–e1295, doi:10.1002/joc.5419.

Vera, C.S., L.B. Díaz, and R.I. Saurral, 2019: Influence of Anthropogenically-Forced Global Warming and Natural Climate Variability in the Rainfall Changes Observed Over the South American Altiplano. *Frontiers in Environmental Science*, **7**, 87, doi:10.3389/fenvs.2019.00087.

Vergara-Temprado, J., N. Ban, D. Panosetti, L. Schlemmer, and C. Schär, 2020: Climate models permit convection at much coarser resolutions than previously considered. *Journal of Climate*, **33(5)**, 1915–1933, doi:10.1175/jcli-d-19-0286.1.

Vergnes, J.-P., B. Decharme, and F. Habets, 2014: Introduction of groundwater capillary rises using subgrid spatial variability of topography into the ISBA land surface model. *Journal of Geophysical Research: Atmospheres*, **119(19)**, 11,065–11,086, doi:10.1002/2014jd021573.

Verseghy, D.L. and M.D. MacKay, 2017: Offline Implementation and Evaluation of the Canadian Small Lake Model with the Canadian Land Surface Scheme over Western Canada. *Journal of Hydrometeorology*, **18**, 1563.

Viale, M., R. Valenzuela, R.D. Garreaud, and F.M. Ralph, 2018: Impacts of Atmospheric Rivers on Precipitation in Southern South America. *Journal of Hydrometeorology*, **19(10)**, 1671–1687, doi:10.1175/jhm-d-18-0006.1.

Vicente-Serrano, S.M., T.R. McVicar, D.G. Miralles, Y. Yang, and M. Tomas-Burguera, 2020a: Unraveling the influence of atmospheric evaporative demand on drought and its response to climate change. *Wiley*

ACCEPTED VERSION SUBJECT TO FINAL EDITING

Interdisciplinary Reviews: Climate Change, **11(2)**, e632, doi:10.1002/wcc.632.
Vicente-Serrano, S.M. et al., 2014: Evidence of increasing drought severity caused by temperature rise in southern Europe. *Environmental Research Letters*, doi:10.1088/1748-9326/9/4/044001.
Vicente-Serrano, S.M. et al., 2018: Global assessment of the standardized evapotranspiration deficit index (SEDI) for drought analysis and monitoring. *Journal of Climate*, **31(14)**, 5371–5393, doi:10.1175/jcli-d-17-0775.1.
Vicente-Serrano, S.M. et al., 2019: Climate, irrigation and land-cover change explain streamflow trends in Western Europe. *Under Review*, doi:10.1029/2019gl084084.
Vicente-Serrano, S.M. et al., 2020b: Long-term variability and trends in meteorological droughts in Western Europe (1851–2018). *International Journal of Climatology*, doi:10.1002/joc.6719.
Vihma, T., 2014: Effects of Arctic Sea Ice Decline on Weather and Climate: A Review. *Surveys in Geophysics*, **35(5)**, 1175–1214, doi:10.1007/s10712-014-9284-0.
Vihma, T. et al., 2016: The atmospheric role in the Arctic water cycle: A review on processes, past and future changes, and their impacts. *Journal of Geophysical Research: Biogeosciences*, **121(3)**, 586–620, doi:10.1002/2015jg003132.
Vilasa, L. et al., 2017: Recent Walker circulation strengthening and Pacific cooling amplified by Atlantic warming. *Nature*, **44(4)**, 20–35, doi:10.1175/2011jcli4101.1.
Villafuerte, M.Q., J. Matsumoto, and M. Villafuerte MQ, 2015: Significant influences of global mean temperature and ENSO on extreme rainfall in Southeast Asia. *Journal of Climate, ,*, **28(5)**, 1905–1919, doi:10.1175/jcli-d-14-00531.1.
Vincent, L.A. et al., 2015: Observed trends in Canada's climate and influence of low-frequency variability modes. *Journal of Climate*, doi:10.1175/jcli-d-14-00697.1.
Vishnu, S., P.A. Francis, S.S.C. Shenoi, and S.S.V.S. Ramakrishna, 2016: On the decreasing trend of the number of monsoon depressions in the Bay of Bengal On the decreasing trend of the number of monsoon depressions in the Bay of Bengal. .
Viste, E., D. Korecha, and A. Sorteberg, 2013: Recent drought and precipitation tendencies in Ethiopia. *Theoretical and Applied Climatology*, **112**, 535–551, doi:10.1007/s00704-012-0746-3.
Vizy, E.K., K.H. Cook, E.K. Vizy, and K.H. Cook, 2017: Seasonality of the Observed Amplified Sahara Warming Trend and Implications for Sahel Rainfall. *Journal of Climate*, **30(9)**, 3073–3094, doi:10.1175/jcli-d-16-0687.1.
Voelker, S.L. et al., 2015: Deglacial hydroclimate of midcontinental North America. *Quaternary Research (United States)*, doi:10.1016/j.yqres.2015.01.001.
Vormoor, K., D. Lawrence, M. Heistermann, and A. Bronstert, 2015: Climate change impacts on the seasonality and generation processes of floods – Projections and uncertainties for catchments with mixed snowmelt/rainfall regimes. *Hydrology and Earth System Sciences*, **19(2)**, 913–931, doi:10.5194/hess-19-913-2015.
Voss, K.A. et al., 2013: Groundwater depletion in the Middle East from GRACE with implications for transboundary water management in the Tigris-Euphrates-Western Iran region. *Water Resources Research*, **49(2)**, 904–914, doi:10.1002/wrcr.20078.
Vuille, M. et al., 2012: A review of the South American monsoon history as recorded in stable isotopic proxies over the past two millennia. *Climate of the Past*, **8(4)**, 1309–1321, doi:10.5194/cp-8-1309-2012.
Wada, Y. and M.F.P. Bierkens, 2014: Sustainability of global water use: Past reconstruction and future projections. *Environmental Research Letters*, **9(10)**, 104003, doi:10.1088/1748-9326/9/10/104003.
Wada, Y., D. Wisser, and M.F.P. Bierkens, 2014: Global modeling of withdrawal, allocation and consumptive use of surface water and groundwater resources. *Earth System Dynamics*, **5(1)**, 15–40, doi:10.5194/esd-5-15-2014.
Wada, Y. et al., 2010: Global depletion of groundwater resources. *Geophysical Research Letters*, **37(20)**, 1–5, doi:10.1029/2010gl044571.
Wada, Y. et al., 2013: Multimodel projections and uncertainties of irrigation water demand under climate change. *Geophysical Research Letters*, **40(17)**, 4626–4632, doi:10.1002/grl.50686.
Wagner, J.D.M. et al., 2010: Moisture variability in the southwestern United States linked to abrupt glacial climate change. *Nature Geoscience*, doi:10.1038/ngeo707.
Wainwright, C.M. et al., 2019: 'Eastern African Paradox' rainfall decline due to shorter not less intense Long Rains. *npj Climate and Atmospheric Science*, **2(1)**, 34, doi:10.1038/s41612-019-0091-7.
Waliser, D. and B. Guan, 2017: Extreme winds and precipitation during landfall of atmospheric rivers. *Nature Geoscience*, **10(3)**, 179–183, doi:10.1038/ngeo2894.
Walsh, K.J.E. et al., 2015: Hurricanes and climate: The U.S. Clivar working group on hurricanes. *Bulletin of the American Meteorological Society*, **96(6)**, 997–1017, doi:10.1175/bams-d-13-00242.1.
Walsh, R.P.D. and D.M. Lawler, 1981: Rainfall seasonality: description, spatial patterns and change through time (British Isles, Africa). *Weather*, **36(7)**, 201–208, doi:10.1002/j.1477-8696.1981.tb05400.x.
Walters, D. et al., 2017: The Met Office Unified Model Global Atmosphere 7.0/7.1 and JULES Global Land 7.0 configurations, Geosci. .
Walvoord, M.A. and B.L. Kurylyk, 2016: Hydrologic Impacts of Thawing Permafrost-A Review. *Vadose Zone Journal*,

ACCEPTED VERSION SUBJECT TO FINAL EDITING

15(6), 0, doi:10.2136/vzj2016.01.0010.
Wang, B., C. Jin, and J. Liu, 2020: Understanding Future Change of Global Monsoons Projected by CMIP6 Models. *Journal of Climate*, **33(15)**, 6471–6489, doi:10.1175/jcli-d-19-0993.1.
Wang, B. et al., 2018: Dynamics-oriented diagnostics for the Madden-Julian Oscillation. *Journal of Climate*, JCLI–D–17–0332.1, doi:10.1175/jcli-d-17-0332.1.
Wang, B. et al., 2021: Monsoons Climate Change Assessment. *Bull. Amer. Meteor. Soc.* 1–19, doi:10.1175/bams-d-19-0335.1.
Wang, G., W. Cai, and A. Santoso, 2017: Assessing the Impact of Model Biases on the Projected Increase in Frequency of Extreme Positive Indian Ocean Dipole Events. *Journal of Climate*, **30(8)**, 2757–2767, doi:10.1175/jcli-d-16-0509.1.
Wang, J., H.-M. Kim, and E.K.M. Chang, 2017: Changes in Northern Hemisphere Winter Storm Tracks under the Background of Arctic Amplification. *Journal of Climate*, **30(10)**, 3705–3724, doi:10.1175/jcli-d-16-0650.1.
Wang, J. et al., 2020: MJO Teleconnections over the PNA Region in Climate Models. Part I: Performance- and Process-Based Skill Metrics. *Journal of Climate*, **33(3)**, 1051–1067, doi:10.1175/jcli-d-19-0253.1.
Wang, L., P.J. Kushner, and D.W. Waugh, 2013: Southern hemisphere stationary wave response to changes of ozone and greenhouse gases. *Journal of Climate*, **26(24)**, 10205–10217, doi:10.1175/jcli-d-13-00160.1.
Wang, L. et al., 2016: Journal of Geophysical Research : Atmospheres for snow-covered forests in CMIP5 models. , 1104–1119, doi:10.1002/2015jd023824.received.
Wang, M. et al., 2015: A multiscale modeling framework model (superparameterized CAM5) with a higher-order turbulence closure: Model description and low-cloud simulations. *Journal of Advances in Modeling Earth Systems*, **7(2)**, 484–509, doi:10.1002/2014ms000375.
Wang, P.X. et al., 2017: The global monsoon across time scales: Mechanisms and outstanding issues. *Earth-Science Reviews*, doi:10.1016/j.earscirev.2017.07.006.
Wang, Q., Z. Li, J. Guo, C. Zhao, and M. Cribb, 2018: The climate impact of aerosols on the lightning flash rate: is it detectable from long-term measurements? *Atmospheric Chemistry and Physics*, **18(17)**, 12797–12816, doi:10.5194/acp-18-12797-2018.
Wang, S.S.-, L. Zhao, J.- Yoon, P. Klotzbach, and R.R. Gillies, 2018: Quantitative attribution of climate effects on Hurricane Harvey's extreme rainfall in Texas. *Environ. Res*, **13**.
Wang, T. et al., 2013: Anthropogenic agent implicated as a prime driver of shift in precipitation in eastern China in the late 1970s. *Atmospheric Chemistry and Physics*, **13(24)**, 12433–12450, doi:10.5194/acp-13-12433-2013.
Wang, W. et al., 2018: Global lake evaporation accelerated by changes in surface energy allocation in a warmer climate. *Nature Geoscience*, **11(6)**, 410–414, doi:10.1038/s41561-018-0114-8.
Wang, X. et al., 2020: The impact of climate change and human activities on the Aral Sea Basin over the past 50 years. *Atmospheric Research*, **245**, 105125, doi:10.1016/j.atmosres.2020.105125.
Wang, X.L., Y. Feng, R. Chan, and V. Isaac, 2016: Inter-comparison of extra-tropical cyclone activity in nine reanalysis datasets. *Atmospheric Research*, **181**, 133–153, doi:10.1016/j.atmosres.2016.06.010.
Wang, X.Y., X. Li, J. Zhu, and C.A.S. Tanajura, 2018: The strengthening of Amazonian precipitation during the wet season driven by tropical sea surface temperature forcing. *Environmental Research Letters*, **13(9)**, 94015, doi:10.1088/1748-9326/aadbb9.
Wang, Y., A. Khalizov, M. Levy, and R. Zhang, 2013: New Directions: Light absorbing aerosols and their atmospheric impacts. *Atmospheric Environment*, **81**, 713–715, doi:10.1016/j.atmosenv.2013.09.034.
Wang, Y., K.-H. Lee, Y. Lin, M. Levy, and R. Zhang, 2014: Distinct effects of anthropogenic aerosols on tropical cyclones. *Nature Climate Change*, **4(5)**, 368–373, doi:10.1038/nclimate2144.
Wang, Z., H. Zhang, and X. Zhang, 2016: Projected response of East Asian summer monsoon system to future reductions in emissions of anthropogenic aerosols and their precursors. *Climate Dynamics*, **47(5–6)**, 1455–1468, doi:10.1007/s00382-015-2912-7.
Wang, Z., S. Yang, N.-C. Lau, and A. Duan, 2018: Teleconnection between Summer NAO and East China Rainfall Variations: A Bridge Effect of the Tibetan Plateau. *Journal of Climate*, **31(16)**, 6433–6444, doi:10.1175/jcli-d-17-0413.1.
Wang, Z., T. Li, J. Gao, and M. Peng, 2020: Enhanced winter and summer trend difference of Madden-Julian Oscillation intensity since 1871. *International Journal of Climatology*, doi:10.1002/joc.6586.
Wang et al., 2020: Monsoons Climate Change Assessment. *Bulletin of the American Meteorological Society* ,, doi:10.1175/bams-d-19-0335.1.
Wang-Erlandsson, L. et al., 2016: Global root zone storage capacity from satellite-based evaporation. *Hydrology and Earth System Sciences*, **20(4)**, 1459–1481, doi:10.5194/hess-20-1459-2016.
Wang-Erlandsson, L. et al., 2018: Remote land use impacts on river flows through atmospheric teleconnections. *Hydrology and Earth System Sciences*, **22(8)**, 4311–4328, doi:10.5194/hess-22-4311-2018.
Ward, K., S. Lauf, B. Kleinschmit, and W. Endlicher, 2016: Heat waves and urban heat islands in Europe: A review of relevant drivers. *Science of the Total Environment*, **569–570**, 527–539, doi:10.1016/j.scitotenv.2016.06.119.
Ward, P.J., S. Eisner, M. Flörke, M.D. Dettinger, and M. Kummu, 2014: Annual flood sensitivities to El Niño–Southern Oscillation at the global scale. *Hydrology and Earth System Sciences*, **18(1)**, 47–66, doi:10.5194/hess-18-47-

ACCEPTED VERSION SUBJECT TO FINAL EDITING

2014.
Warner, M.D. and C.F. Mass, 2017: Changes in the Climatology, Structure, and Seasonality of Northeast Pacific Atmospheric Rivers in CMIP5 Climate Simulations. *Journal of Hydrometeorology*, doi:10.1175/jhm-d-16-0200.1.
Warner, M.D., C.F. Mass, and E.P. Salathé, 2015: Changes in Winter Atmospheric Rivers along the North {A}merican West Coast in CMIP5 Climate Models. *J. Hydrometeorol.*, **16**, 118–128.
Wartenburger, R. et al., 2017: Changes in regional climate extremes as a function of global mean temperature: an interactive plotting framework. *Geoscientific Model Development*, **10(9)**, 3609–3634, doi:10.5194/gmd-10-3609-2017.
Wasko, C. and R. Nathan, 2019: Influence of changes in rainfall and soil moisture on trends in flooding. *Journal of Hydrology*, **575**, 432–441, doi:10.1016/j.jhydrol.2019.05.054.
Watanabe, M., Y. Kamae, H. Shiogama, A.M. DeAngelis, and K. Suzuki, 2018: Low clouds link equilibrium climate sensitivity to hydrological sensitivity. *Nature Climate Change*, 1, doi:10.1038/s41558-018-0272-0.
Watt-Meyer, O. and D.M.W. Frierson, 2019: ITCZ width controls on Hadley cell extent and eddy-driven jet position and their response to warming. *Journal of Climate*, **32(4)**, 1151–1166, doi:10.1175/jcli-d-18-0434.1.
Watt-Meyer, O., D.M.W. Frierson, and Q. Fu, 2019: Hemispheric asymmetry of tropical expansion under CO 2 forcing. *Geophysical Research Letters*, 2019GL083695, doi:10.1029/2019gl083695.
Weaver, A.J. et al., 2012: Stability of the Atlantic meridional overturning circulation: A model intercomparison. *Geophysical Research Letters*, doi:10.1029/2012gl053763.
Webb, M.J., A.P. Lock, and F.H. Lambert, 2018: Interactions between hydrological sensitivity, radiative cooling, stability, and low-level cloud amount feedback. *Journal of Climate*, **31(5)**, 1833–1850, doi:10.1175/jcli-d-16-0895.1.
Webb, M.J. et al., 2017: The Cloud Feedback Model Intercomparison Project (CFMIP) contribution to CMIP6. *Geoscientific Model Development*, **10(1)**, 359–384, doi:10.5194/gmd-10-359-2017.
Webb, N.P. and C. Pierre, 2018: Quantifying anthropogenic dust emissions. *Earth's Future*, **6(2)**, 286–295.
Wehner, M., P. Gleckler, and J. Lee, 2020: Characterization of long period return values of extreme daily temperature and precipitation in the CMIP6 models: Part 1, model evaluation. *Weather and Climate Extremes*, **30**, 100283, doi:10.1016/j.wace.2020.100283.
Wehner, M.F., R.L. Smith, G. Bala, and P. Duffy, 2010: The effect of horizontal resolution on simulation of very extreme US precipitation events in a global atmosphere model. *Climate Dynamics*, **34(2)**, 241–247, doi:10.1007/s00382-009-0656-y.
Wei, K. and L. Wang, 2013: Reexamination of the aridity conditions in arid Northwestern China for the last decade. *Journal of Climate*, doi:10.1175/jcli-d-12-00605.1.
Wei, Z. et al., 2017: Revisiting the contribution of transpiration to global terrestrial evapotranspiration. *Geophysical Research Letters*, **44(6)**, 2792–2801, doi:10.1002/2016gl072235.
Weiss, J.L., C.L. Castro, and J.T. Overpeck, 2009: Distinguishing pronounced droughts in the southwestern United States: seasonality and effects of warmer temperatures. *Journal of Climate*, **22(22)**, 5918–5932.
Weiss, M. et al., 2014: Contribution of dynamic vegetation phenology to decadal climate predictability. *Journal of Climate*, **27(22)**, 8563–8577, doi:10.1175/jcli-d-13-00684.1.
Weller, E., C. Jakob, and M.J. Reeder, 2017: Projected Response of Low-Level Convergence and Associated Precipitation to Greenhouse Warming. *Geophysical Research Letters*, **44(20)**, 10,682–10,690, doi:10.1002/2017gl075489.
Welty, J., S. Stillman, X. Zeng, and J. Santanello, 2020: Increased likelihood of appreciable afternoon rainfall over wetter or drier soils dependent upon atmospheric dynamic influence. *Geophysical Research Letters*, **n/a(n/a)**, e2020GL087779, doi:10.1029/2020gl087779.
Werner, A.D. and C.T. Simmons, 2009: Impact of Sea-Level Rise on Sea Water Intrusion in Coastal Aquifers. *Ground Water*, **47(2)**, 197–204, doi:10.1111/j.1745-6584.2008.00535.x.
Wester, P., A. Mishra, A. Mukherji, and A.B. Shrestha (eds.), 2019: *The Hindu Kush Himalaya Assessment*. Springer, Cham, Switzerland, 627 pp., doi:10.1007/978-3-319-92288-1.
Westervelt, D.M., L.W. Horowitz, V. Naik, J.C. Golaz, and D.L. Mauzerall, 2015: Radiative forcing and climate response to projected 21st century aerosol decreases. *Atmospheric Chemistry and Physics*, doi:10.5194/acp-15-12681-2015.
Westervelt, D.M. et al., 2018: Connecting regional aerosol emissions reductions to local and remote precipitation responses. *Atmospheric Chemistry and Physics*, **18(16)**, 12461–12475.
Westra, S., L. Alexander, and F.W. Zwiers, 2013: Global increasing trends in annual maximum daily precipitation. *Journal of Climate*, doi:10.1175/jcli-d-12-00502.1.
Westra, S. et al., 2014: Future changes to the intensity and frequency of short-duration extreme rainfall. *Reviews of Geophysics*, **52(3)**, 522–555, doi:10.1002/2014rg000464.
Wey, H.W., M.H. Lo, S.Y. Lee, J.Y. Yu, and H.H. Hsu, 2015: Potential impacts of wintertime soil moisture anomalies from agricultural irrigation at low latitudes on regional and global climates. *Geophysical Research Letters*, **42(20)**, 8605–8614, doi:10.1002/2015gl065883.

ACCEPTED VERSION SUBJECT TO FINAL EDITING

WGMS, 2017: Global Glacier Change Bulletin No. 2 (2014-2015). , **1(1)**, 244.
Widlansky, M.J. et al., 2019: Tropical Cyclone Projections: Changing Climate Threats for Pacific Island Defense Installations. *Weather, Climate, and Society*, **11(1)**, 3–15, doi:10.1175/wcas-d-17-0112.1.
Wilcox, C. et al., 2018: Trends in hydrological extremes in the Senegal and Niger Rivers. *Journal of Hydrology*, **566**, 531–545, doi:10.1016/j.jhydrol.2018.07.063.
Wilcox, L. et al., 2018: Mechanisms for a remote response to Asian aerosol emissions in boreal winter. *Atmospheric Chemistry and Physics Discussions*, **19(14)**, 1–21, doi:10.5194/acp-2018-980.
Wilcox, L.J. et al., 2020: Accelerated increases in global and Asian summer monsoon precipitation from future aerosol reductions. *Atmos. Chem. Phys. Discuss.*, **2020**, 11955–11977, doi:10.5194/acp-2019-1188.
Wild, M., 2012: Enlightening Global Dimming and Brightening. *Bulletin of the American Meteorological Society*, **93(1)**, 27–37, doi:10.1175/bams-d-11-00074.1.
Wild, M. et al., 2017: The Global Energy Balance Archive (GEBA) version 2017: A database for worldwide measured surface energy fluxes. *Earth System Science Data*, **9(2)**, 601–613, doi:10.5194/essd-9-601-2017.
Wilhite, D.A., 2000: Chapter I Drought as a Natural Hazard: Concepts and Definitions. *Drought: A Global Assessment*, doi:10.1177/0956247807076912.
Wilhite, D.A. and M.H. Glantz, 1985: Understanding: The drought phenomenon: The role of definitions. *Water International*, doi:10.1080/02508068508686328.
Wille, J.D. et al., 2019: West Antarctic surface melt triggered by atmospheric rivers. *Nature Geoscience*, **12(11)**, 911–916, doi:10.1038/s41561-019-0460-1.
Willett, K., R. Dunn, J. Kennedy, and D. Berry, 2020: Development of the HadISDH marine humidity climate monitoring dataset. *Earth System Science Data*, **12**, 2853–2880, doi:10.5194/essd-12-2853-2020.
Willett, K.M. et al., 2014: HadISDH land surface multi-variable humidity and temperature record for climate monitoring. *Climate of the Past*, **10(6)**, 1983–2006, doi:10.5194/cp-10-1983-2014.
Willetts, P.D. et al., 2017: Moist convection and its upscale effects in simulations of the Indian monsoon with explicit and parametrized convection. *Quarterly Journal of the Royal Meteorological Society*, **143(703)**, 1073–1085, doi:10.1002/qj.2991.
Williams, A.P. and C. Funk, 2011: A westward extension of the warm pool leads to a westward extension of the Walker circulation, drying eastern Africa. *Climate Dynamics*, **37(11–12)**, 2417–2435, doi:10.1007/s00382-010-0984-y.
Williams, A.P. et al., 2013: Temperature as a potent driver of regional forest drought stress and tree mortality. *Nature Climate Change*, doi:10.1038/nclimate1693.
Williams, A.P. et al., 2015: Contribution of anthropogenic warming to California drought during 2012-2014. *Geophysical Research Letters*, doi:10.1002/2015gl064924.
Williams, A.P. et al., 2020: Large contribution from anthropogenic warming to an emerging North American megadrought. *Science*, doi:10.1126/science.aaz9600.
Willison, J., W.A. Robinson, and G.M. Lackmann, 2015: North Atlantic storm-track sensitivity to warming increases with model resolution. *Journal of Climate*, **28(11)**, 4513–4524, doi:10.1175/jcli-d-14-00715.1.
Wills, R.C. and T. Schneider, 2015: Stationary Eddies and the Zonal Asymmetry of Net Precipitation and Ocean Freshwater Forcing. *Journal of Climate*, **28(13)**, 5115–5133, doi:10.1175/jcli-d-14-00573.1.
Wills, R.C., X.J. Levine, and T. Schneider, 2017: Local energetic constraints on walker circulation strength. *Journal of the Atmospheric Sciences*, **74(6)**, 1907–1922, doi:10.1175/jas-d-16-0219.1.
Wills, R.C.J., R.H. White, and X.J. Levine, 2019: Northern Hemisphere Stationary Waves in a Changing Climate. *Current Climate Change Reports*, doi:10.1007/s40641-019-00147-6.
Wing, A.A., K. Emanuel, C.E. Holloway, and C. Muller, 2017: Convective Self-Aggregation in Numerical Simulations: A Review. *Surveys in Geophysics*, **38(6)**, 1173–1197, doi:10.1007/s10712-017-9408-4.
Wise, E.K. and M.P. Dannenberg, 2017: Reconstructed storm tracks reveal three centuries of changing moisture delivery to North America. *Sci. Adv*, **2017**, 3.
Wodzicki, K.R. and A.D. Rapp, 2016: Long-term characterization of the Pacific ITCZ using TRMM, GPCP, and ERA-Interim. *Journal of Geophysical Research: Atmospheres*, **121(7)**, 3153–3170, doi:10.1002/2015jd024458.
Wolding, B.O., E.D. Maloney, S. Henderson, and M. Branson, 2017: Climate change and the Madden-Julian Oscillation: A vertically resolved weak temperature gradient analysis. *Journal of Advances in Modeling Earth Systems*, **9(1)**, 307–331, doi:10.1002/2016ms000843.
Wolski, P., S. Conradie, C. Jack, and M. Tadross, 2020: Spatio-temporal patterns of rainfall trends and the 2015–2017 drought over the winter rainfall region of South Africa. *International Journal of Climatology*, **n/a(n/a)**, doi:10.1002/joc.6768.
Woodhouse, C.A., G.T. Pederson, K. Morino, S.A. McAfee, and G.J. McCabe, 2016: Increasing influence of air temperature on upper Colorado River streamflow. *Geophysical Research Letters*, doi:10.1002/2015gl067613.
Woollings, T. et al., 2018: Blocking and its Response to Climate Change. *Current Climate Change Reports*, **4(3)**, 287–300, doi:10.1007/s40641-018-0108-z.
Woolway, R.I. and C.J. Merchant, 2019: Worldwide alteration of lake mixing regimes in response to climate change. *Nature Geoscience 2019*, **12**, doi:10.1038/s41561-019-0322-x.

ACCEPTED VERSION SUBJECT TO FINAL EDITING

Woolway, R.I. et al., 2020: Global lake responses to climate change. *Nature Reviews Earth and Environment*, In press, doi:10.1038/s43017-020-0067-5.

Wortham, B.E. et al., 2017: Assessing response of local moisture conditions in central Brazil to variability in regional monsoon intensity using speleothem 87 Sr/ 86 Sr values. *Earth and Planetary Science Letters*, **463**, 310–322, doi:10.1016/j.epsl.2017.01.034.

Wu, B., J. Lin, and T. Zhou, 2016a: Interdecadal circumglobal teleconnection pattern during boreal summer. *Atmospheric Science Letters*, **17(8)**, 446–452, doi:10.1002/asl.677.

Wu, B., T. Zhou, and T. Li, 2016b: Impacts of the Pacific–Japan and Circumglobal Teleconnection Patterns on the Interdecadal Variability of the East Asian Summer Monsoon. *Journal of Climate*, **29(9)**, 3253–3271, doi:10.1175/jcli-d-15-0105.1.

Wu, P., N. Christidis, and P. Stott, 2013: Anthropogenic impact on Earth's hydrological cycle. *Nature Climate Change*, **3(9)**, 807–810, doi:10.1038/nclimate1932.

Wu, T. et al., 2018: The Beijing Climate Center Climate System Model (BCC-CSM): Main Progress from CMIP5 to CMIP6, Geosci. .

Wu, X., T. Che, X. Li, N. Wang, and X. Yang, 2018: Slower snowmelt in spring along with climate warming across the Northern Hemisphere. *Geophysical Research Letters*, **45(22)**, 12,331–12,339, doi:10.1029/2018gl079511.

Wurtsbaugh, W.A. et al., 2017: Decline of the world's saline lakes. *Nature Geoscience*, **10(11)**, 816–821, doi:10.1038/ngeo3052.

Wurtzel, J.B. et al., 2018: Tropical Indo-Pacific hydroclimate response to North Atlantic forcing during the last deglaciation as recorded by a speleothem from Sumatra, Indonesia. *Earth and Planetary Science Letters*, doi:10.1016/j.epsl.2018.04.001.

Xia, Y. and Y. Huang, 2017: Differential Radiative Heating Drives Tropical Atmospheric Circulation Weakening. *Geophysical Research Letters*, **44(20)**, 10,592–10,600, doi:10.1002/2017gl075678.

Xiang, B., M. Zhao, I.M. Held, and J.C. Golaz, 2017: Predicting the severity of spurious "double ITCZ" problem in CMIP5 coupled models from AMIP simulations. *Geophysical Research Letters*, **44(3)**, 1520–1527, doi:10.1002/2016gl071992.

Xiao, M., Q. Zhang, and V.P. Singh, 2015: Influences of ENSO, NAO, IOD and PDO on seasonal precipitation regimes in the Yangtze River basin, China. *International Journal of Climatology*, **35(12)**, 3556–3567, doi:10.1002/joc.4228.

Xiao, M., B. Udall, and D.P. Lettenmaier, 2018: On the Causes of Declining Colorado River Streamflows. *Water Resources Research*, doi:10.1029/2018wr023153.

Xie, S. et al., 2018: Understanding Cloud and Convective Characteristics in Version 1 of the E3SM Atmosphere Model. *Journal of Advances in Modeling Earth Systems*, **10(10)**, 2618–2644, doi:10.1029/2018ms001350.

Xie, S.-P., B. Lu, and B. Xiang, 2013: Similar spatial patterns of climate responses to aerosol and greenhouse gas changes. *Nature Geoscience*, **6(10)**, 828–832, doi:10.1038/ngeo1931.

Xie, S.-P. et al., 2015: Towards predictive understanding of regional climate change. *Nature Climate Change*, **5(10)**, 921–930, doi:10.1038/nclimate2689.

Xie, X. et al., 2016: Distinct effects of anthropogenic aerosols on the East Asian summermonsoon between multidecadal strong and weakmonsoon stages. *Journal of Geophysical Research*, **121(12)**, 7026–7040, doi:10.1002/2015jd024228.

Xu, C., M. Sano, and T. Nakatsuka, 2013: A 400-year record of hydroclimate variability and local ENSO history in northern Southeast Asia inferred from tree-ring δ 18 O. *Palaeogeography, Palaeoclimatology, Palaeoecology*, **386**, 588–598, doi:10.1016/j.palaeo.2013.06.025.

Xu, C. et al., 2018: Decreasing Indian summer monsoon on the northern Indian sub-continent during the last 180 years: evidence from five tree-ring cellulose oxygen isotope chronologies. *Climate of the Past*, **14(5)**, 653–664, doi:10.5194/cp-14-653-2018.

Xu, C. et al., 2019: Increased Variability of Thailand's Chao Phraya River Peak Season Flow and Its Association With ENSO Variability: Evidence From Tree Ring δ 18 O. *Geophysical Research Letters*, **46(9)**, 4863–4872, doi:10.1029/2018gl081458.

Xu, T., A.J. Valocchi, M. Ye, F. Liang, and Y.-F. Lin, 2017: Bayesian calibration of groundwater models with input data uncertainty. *Water Resources Research*, **53(4)**, 3224–3245, doi:10.1002/2016wr019512.

Xu, Y., H. Zhang, Y. Liu, Z. Han, and B. Zhou, 2020: Atmospheric rivers in the Australia–Asian region under current and future climate in CMIP5 models. *Journal of Southern Hemisphere Earth Systems Science*.

Yamada, T.J., D. Takeuchi, M.A. Farukh, and Y. Kitano, 2016: Climatological characteristics of heavy rainfall in northern Pakistan and atmospheric blocking over western Russia. *Journal of Climate*, **29(21)**, 7743–7754, doi:10.1175/jcli-d-15-0445.1.

Yamamoto, A. and J.B. Palter, 2016: The absence of an Atlantic imprint on the multidecadal variability of wintertime European temperature. *Nature Communications*, **7(1)**, 10930, doi:10.1038/ncomms10930.

Yanagiya, K. and M. Furuya, 2020: Post-Wildfire Surface Deformation Near Batagay, Eastern Siberia, Detected by L-Band and C-Band InSAR. *Journal of Geophysical Research: Earth Surface*, **125(7)**, e2019JF005473, doi:10.1029/2019jf005473.

ACCEPTED VERSION SUBJECT TO FINAL EDITING

Yang, H. et al., 2017: Regional patterns of future runoff changes from Earth system models constrained by observation. *Geophysical Research Letters*, **44(11)**, 5540–5549, doi:10.1002/2017gl073454.
Yang, H. et al., 2020: Tropical Expansion Driven by Poleward Advancing Midlatitude Meridional Temperature Gradients. *Journal of Geophysical Research: Atmospheres*, **125(16)**, e2020JD033158, doi:10.1029/2020jd033158.
Yang, K., C. Wang, and S. Li, 2018: Improved Simulation of Frozen-Thawing Process in Land Surface Model (CLM4.5). *Journal of Geophysical Research: Atmospheres*, **123(23)**, 2017JD028260, doi:10.1029/2017jd028260.
Yang, Q. et al., 2017: Decadal Modulation of Precipitation Patterns over Eastern China by Sea Surface Temperature Anomalies. *Journal of Climate*, **30(17)**, 7017–7033, doi:10.1175/jcli-d-16-0793.1.
Yang, S. et al., 2015: Warming-induced northwestward migration of the East Asian monsoon rain belt from the Last Glacial Maximum to the mid-Holocene. , **112(43)**, 13178–13183, doi:10.1073/pnas.1504688112.
Yang, S. et al., 2018a: A strengthened East Asian Summer Monsoon during Pliocene warmth: Evidence from 'red clay' sediments at Pianguan, northern China. *Journal of Asian Earth Sciences*, **155**, 124–133, doi:10.1016/j.jseaes.2017.10.020.
Yang, S. et al., 2018b: El Niño–Southern Oscillation and its impact in the changing climate. *National Science Review*, **5(6)**, 840–857, doi:10.1093/nsr/nwy046.
Yang, Y. and M.L. Roderick, 2019: Radiation, surface temperature and evaporation over wet surfaces. *Quarterly Journal of the Royal Meteorological Society*, doi:10.1002/qj.3481.
Yang, Y., R.J. Donohue, T.R. McVicar, M.L. Roderick, and H.E. Beck, 2016: Long-term CO2 fertilization increases vegetation productivity and has little effect on hydrological partitioning in tropical rainforests. *Journal of Geophysical Research: Biogeosciences*, doi:10.1002/2016jg003475.
Yang, Y., M.L. Roderick, S. Zhang, T.R. McVicar, and R.J. Donohue, 2018: Hydrologic implications of vegetation response to elevated CO2 in climate projections. *Nature Climate Change*, **9(1)**, 44–48, doi:10.1038/s41558-018-0361-0.
Yang, Y.-M. and B. Wang, 2019: Improving MJO simulation by enhancing the interaction between boundary layer convergence and lower tropospheric heating. *Climate Dynamics*, **52(7–8)**, 4671–4693, doi:10.1007/s00382-018-4407-9.
Yang, Y.-M., B. Wang, J. Cao, L. Ma, and J. Li, 2020: Improved historical simulation by enhancing moist physical parameterizations in the climate system model NESM3.0. *Climate Dynamics*, **54(7–8)**, 3819–3840, doi:10.1007/s00382-020-05209-2.
Yao, J. et al., 2017: Improved performance of high-resolution atmospheric models in simulating the East Asian summer monsoon rain belt. *Journal of Climate*, **30(21)**, 8825–8840, doi:10.1175/jcli-d-16-0372.1.
Ye, H., E.J. Fetzer, S. Wong, and B.H. Lambrigtsen, 2017: Rapid decadal convective precipitation increase over Eurasia during the last three decades of the 20th century. *Science Advances*, **3(1)**, 1–8, doi:10.1126/sciadv.1600944.
Yeager, S.G. et al., 2018: Predicting Near-Term Changes in the Earth System: A Large Ensemble of Initialized Decadal Prediction Simulations Using the Community Earth System Model. *Bulletin of the American Meteorological Society*, **99(9)**, 1867–1886, doi:10.1175/bams-d-17-0098.1.
Yettella, V. and J.E. Kay, 2017: How will precipitation change in extratropical cyclones as the planet warms? Insights from a large initial condition climate model ensemble. *Climate Dynamics*, **49(5)**, 1765–1781, doi:10.1007/s00382-016-3410-2.
Yim, B.Y., S.W. Yeh, H.J. Song, D. Dommenget, and B.J. Sohn, 2017: Land-sea thermal contrast determines the trend of Walker circulation simulated in atmospheric general circulation models. *Geophysical Research Letters*, **44(11)**, 5854–5862, doi:10.1002/2017gl073778.
Yin, J. et al., 2018: Large increase in global storm runoff extremes driven by climate and anthropogenic changes. *Nature Communications*, **9(1)**, 4389, doi:10.1038/s41467-018-06765-2.
Yin, L. et al., 2014: What controls the interannual variation of the wetseason onsets over the Amazon? *Journal of Geophysical Research : Atmospheres*, **119**, 2314–2328.
Yoden, S., S. Otsuka, N.J. Trilaksono, and T.W. Hadi, 2017: Recent progress in research on the Maritime Continent Monsoon. In: *The Global Monsoon System: Research and Forecast (3rd Edition)* [Chang, C.-P., H.-C. Kuo, N.-C. Lau, R.H. Johnson, B. Wang, and M.C. Wheeler (eds.)]. World Scientific, Singapore, pp. 63–77, doi:10.1142/9789813200913_0006.
Yoshida, R., Y. Kajikawa, and H. Ishikawa, 2014: Impact of Boreal Summer Intraseasonal Oscillation on Environment of Tropical Cyclone Genesis over the Western North Pacific. *SOLA*, **10**, 15–18, doi:10.2151/sola.2014-004.
Yu, K., P. D'Odorico, A. Bhattachan, G.S. Okin, and A.T. Evan, 2015: Dust-rainfall feedback in West African Sahel. *Geophysical Research Letters*, **42(18)**, 7563–7571, doi:10.1002/2015gl065533.
Yu, R. and T. Zhou, 2007: Seasonality and Three-Dimensional Structure of Interdecadal Change in the East Asian Monsoon. *Journal of Climate*, **20(21)**, 5344–5355, doi:10.1175/2007jcli1559.1.
Yu, T. et al., 2018: Reduced connection between the East Asian Summer Monsoon and Southern Hemisphere Circulation on interannual timescales under intense global warming. *Climate Dynamics*, doi:10.1007/s00382-

ACCEPTED VERSION SUBJECT TO FINAL EDITING

018-4121-7.
Yu, X. and H.A. Michael, 2019: Mechanisms, configuration typology, and vulnerability of pumping-induced seawater intrusion in heterogeneous aquifers. *Advances in Water Resources*, **128**, 117–128, doi:10.1016/j.advwatres.2019.04.013.
Yuan, J., W. Li, and Y. Deng, 2015: Amplified subtropical stationary waves in boreal summer and their implications for regional water extremes. *Environmental Research Letters*, **10(10)**, doi:10.1088/1748-9326/10/10/104009.
Yuan, W. et al., 2019: Increased atmospheric vapor pressure deficit reduces global vegetation growth. *Science Advances*, doi:10.1126/sciadv.aax1396.
Yuan, X. and E. Zhu, 2018: A First Look at Decadal Hydrological Predictability by Land Surface Ensemble Simulations. *Geophysical Research Letters*, **45(5)**, 2362–2369, doi:10.1002/2018gl077211.
Yue, C. et al., 2018: Representing anthropogenic gross land use change, wood harvest, and forest age dynamics in a global vegetation model ORCHIDEE-MICT v8.4.2. *Geoscientific Model Development*, **11**, 409–428.
Zahn, M. and R.P. Allan, 2013: Quantifying present and projected future atmospheric moisture transports onto land. *Water Resources Research*, **49(11)**, 7266–7277, doi:10.1002/2012wr013209.
Zambri, B. and A. Robock, 2016: Winter warming and summer monsoon reduction after volcanic eruptions in Coupled Model Intercomparison Project 5 (CMIP5) simulations. *Geophysical Research Letters*, doi:10.1002/2016gl070460.
Zambri, B., A.N. LeGrande, A. Robock, and J. Slawinska, 2017: Northern Hemisphere winter warming and summer monsoon reduction after volcanic eruptions over the last millennium. *Journal of Geophysical Research*, **122(15)**, 7971–7989, doi:10.1002/2017jd026728.
Zamrane, Z., I. Turki, B. Laignel, G. Mahé, and N.-E. Laftouhi, 2016: Characterization of the Interannual Variability of Precipitation and Streamflow in Tensift and Ksob Basins (Morocco) and Links with the NAO. *Atmosphere*, **7(6)**, 84, doi:10.3390/atmos7060084.
Zanardo, S., L. Nicotina, A.G.J. Hilberts, and S.P. Jewson, 2019: Modulation of economic losses from European floods by the North Atlantic Oscillation. *Geophysical Research Letters*, doi:10.1029/2019gl081956.
Zappa, G. and T.G. Shepherd, 2017: Storylines of atmospheric circulation change for European regional climate impact assessment. *Journal of Climate*, **30(16)**, 6561–6577, doi:10.1175/jcli-d-16-0807.1.
Zappa, G., F. Pithan, and T.G. Shepherd, 2018: Multimodel Evidence for an Atmospheric Circulation Response to Arctic Sea Ice Loss in the CMIP5 Future Projections. *Geophysical Research Letters*, **45(2)**, 1011–1019, doi:10.1002/2017gl076096.
Zappa, G., P. Ceppi, and T.G. Shepherd, 2020: Time-evolving sea-surface warming patterns modulate the climate change response of subtropical precipitation over land. *Proceedings of the National Academy of Sciences*, **117(9)**, 201911015, doi:10.1073/pnas.1911015117.
Zappa, G., L.C. Shaffrey, K.I. Hodges, P.G. Sansom, and D.B. Stephenson, 2013: A multimodel assessment of future projections of north atlantic and european extratropical cyclones in the CMIP5 climate models. *Journal of Climate*, **26(16)**, 5846–5862, doi:10.1175/jcli-d-12-00573.1.
Zappa, G., G. Masato, L. Shaffrey, T. Woollings, and K. Hodges, 2014: Linking Northern Hemisphere blocking and storm track biases in the CMIP5 climate models. *Geophysical Research Letters*, **41(1)**, 135–139, doi:10.1002/2013gl058480.
Zappa, G., M.K. Hawcroft, L. Shaffrey, E. Black, and D.J. Brayshaw, 2015: Extratropical cyclones and the projected decline of winter Mediterranean precipitation in the CMIP5 models. *Climate Dynamics*, doi:10.1007/s00382-014-2426-8.
Zarzycki, C.M., 2018: Projecting Changes in Societally Impactful Northeastern U.S. Snowstorms. *Geophysical Research Letters*, doi:10.1029/2018gl079820.
Zavadoff, B.L. and B.P. Kirtman, 2020: Dynamic and Thermodynamic Modulators of European Atmospheric Rivers. *Journal of Climate*, **33(10)**, 4167–4185, doi:10.1175/jcli-d-19-0601.1.
Zeder, J. and E.M. Fischer, 2020: Observed extreme precipitation trends and scaling in Central Europe. *Weather and Climate Extremes*, **29**, 100266, doi:10.1016/j.wace.2020.100266.
Zelinka, M.D. et al., 2020: Causes of Higher Climate Sensitivity in CMIP6 Models. *Geophysical Research Letters*, **47(1)**, doi:10.1029/2019gl085782.
Zemp, D.C. et al., 2017: Self-amplified Amazon forest loss due to vegetation-atmosphere feedbacks. *Nature Communications*, doi:10.1038/ncomms14681.
Zemp, M. et al., 2019: Global glacier mass changes and their contributions to sea-level rise from 1961 to 2016. *Nature*, **568(7752)**, 382–386, doi:10.1038/s41586-019-1071-0.
Zeng, N., J.D. Neelin, K.M. Lau, and C.J. Tucker, 1999: Enhancement of interdecadal climate variability in the Sahel by vegetation interaction. *Science*, **286(5444)**, 1537–1540, doi:10.1126/science.286.5444.1537.
Zeng, X., P. Broxton, and N. Dawson, 2018: Snowpack Change From 1982 to 2016 Over Conterminous United States. *Geophysical Research Letters*, doi:10.1029/2018gl079621.
Zeng, Z., L. Peng, and S. Piao, 2018a: Response of terrestrial evapotranspiration to Earth's greening. *Current Opinion in Environmental Sustainability*, doi:10.1016/j.cosust.2018.03.001.
Zeng, Z. et al., 2014: A worldwide analysis of spatiotemporal changes in water balance-based evapotranspiration from

ACCEPTED VERSION SUBJECT TO FINAL EDITING

1982 to 2009. *Journal of Geophysical Research: Atmospheres*, **119(3)**, 1186–1202, doi:10.1002/2013jd020941.
Zeng, Z. et al., 2018b: Impact of Earth greening on the terrestrial water cycle. *Journal of Climate*, **31(7)**, 2633–2650, doi:10.1175/jcli-d-17-0236.1.
Zhan, S., C. Song, J. Wang, Y. Sheng, and J. Quan, 2019: A Global Assessment of Terrestrial Evapotranspiration Increase Due to Surface Water Area Change. *Earth's Future*, **7(3)**, 266–282, doi:10.1029/2018ef001066.
Zhang, C., F. Adames, B. Khouider, B. Wang, and D. Yang, 2020: Four Theories of the Madden-Julian Oscillation. *Reviews of Geophysics*, **58(3)**, doi:10.1029/2019rg000685.
Zhang, E., W. Sun, J. Chang, D. Ning, and J. Shulmeister, 2018: Variations of the Indian summer monsoon over the last 30 000 years inferred from a pyrogenic carbon record from south-west China. *Journal of Quaternary Science*, **33(1)**, 131–138, doi:10.1002/jqs.3008.
Zhang, G.J., X. Wu, X. Zeng, and T. Mitovski, 2016: Estimation of convective entrainment properties from a cloud resolving model simulation during twp-ice. *Climate dynamics*, **47(7–8)**, 2177–2192.
Zhang, H. and A. Moise, 2016: The Australian summer monsoon in current and future climate. In: *The Monsoons and Climate Change* [Jones, C. and L. Carvalho (eds.)]. Springer, Cham, Switzerland, pp. 67–120, doi:10.1007/978-3-319-21650-8_5.
Zhang, H. and T.L. Delworth, 2018: Robustness of anthropogenically forced decadal precipitation changes projected for the 21st century. *Nature Communications*, **9(1)**, 1150, doi:10.1038/s41467-018-03611-3.
Zhang, H., A. Moise, P. Liang, and L. Hanson, 2013: The response of summer monsoon onset/retreat in Sumatra-Java and tropical Australia region to global warming in CMIP3 models. *Climate Dynamics*, **40(1)**, 377–399, doi:10.1007/s00382-012-1389-x.
Zhang, H. et al., 2016: Uncertainty in CMIP5 model-projected changes in the onset/retreat of the Australian summer monsoon. *Climate Dynamics*, **46**, 2371–2389, doi:10.1007/s00382-015-2107-x.
Zhang, K. et al., 2015: Vegetation Greening and Climate Change Promote Multidecadal Rises of Global Land Evapotranspiration. *Scientific Reports*, doi:10.1038/srep15956.
Zhang, L. and T. Li, 2017: Relative roles of differential SST warming, uniform SST warming and land surface warming in determining the Walker circulation changes under global warming. *Climate Dynamics*, doi:10.1007/s00382-016-3123-6.
Zhang, L., P. Wu, and T. Zhou, 2017: Aerosol forcing of extreme summer drought over North China. *Environmental Research Letters*, **12(3)**, 034020, doi:10.1088/1748-9326/aa5fb3.
Zhang, L., W. Han, and F. Sienzn, 2018: Unraveling causes for the changing behavior of the tropical Indian Ocean in the past few decades. *Journal of Climate*, **31(6)**, 2377–2388, doi:10.1175/jcli-d-17-0445.1.
Zhang, L., P. Wu, T. Zhou, M.J. Roberts, and R. Schiemann, 2016: Added value of high resolution models in simulating global precipitation characteristics. *Atmospheric Science Letters*, **17(12)**, 646–657, doi:10.1002/asl.715.
Zhang, L. et al., 2019: Indian Ocean Warming Trend Reduces Pacific Warming Response to Anthropogenic Greenhouse Gases: An Interbasin Thermostat Mechanism. *Geophysical Research Letters*, **46(19)**, 10882–10890, doi:10.1029/2019gl084088.
Zhang, R., X. Wang, and C. Wang, 2018: On the Simulations of Global Oceanic Latent Heat Flux in the CMIP5 Multimodel Ensemble. *Journal of Climate*, **31(17)**, 7111–7128, doi:10.1175/jcli-d-17-0713.1.
Zhang, W., T. Zhou, and L. Zhang, 2017a: Wetting and greening Tibetan Plateau in early summer in recent decades. *Journal of Geophysical Research: Atmospheres*, **122(11)**, 5808–5822, doi:10.1002/2017jd026468.
Zhang, W., G. Villarini, and M. Wehner, 2019a: Contrasting the responses of extreme precipitation to changes in surface air and dew point temperatures. *Climatic Change*, **154(1)**, 257–271, doi:10.1007/s10584-019-02415-8.
Zhang, W., G. Villarini, G.A. Vecchi, and J.A. Smith, 2018: Urbanization exacerbated the rainfall and flooding caused by hurricane Harvey in Houston. *Nature*, **563(7731)**, 384–388, doi:10.1038/s41586-018-0676-z.
Zhang, W., T. Zhou, L. Zhang, and L. Zou, 2019b: Future intensification of the water cycle with an enhanced annual cycle over global land monsoon regions. *Journal of Climate*, **32(17)**, JCLI–D–18–0628.1, doi:10.1175/jcli-d-18-0628.1.
Zhang, W., M. Brandt, F. Guichard, Q. Tian, and R. Fensholt, 2017b: Using long-term daily satellite based rainfall data (1983–2015) to analyze spatio-temporal changes in the sahelian rainfall regime. *Journal of Hydrology*, **550**, 427–440, doi:10.1016/j.jhydrol.2017.05.033.
Zhang, X. and Q. Tang, 2014: Runoff sensitivity to global mean temperature change in the CMIP5 Models. *Geophysical Research …*, 5492–5498, doi:10.1002/2014gl060382.received.
Zhang, X., Q. Tang, X. Liu, G. Leng, and C. Di, 2018: Nonlinearity of Runoff Response to Global Mean Temperature Change Over Major Global River Basins. *Geophysical Research Letters*, **45(12)**, 6109–6116, doi:10.1029/2018gl078646.
Zhang, X. et al., 2013: Enhanced poleward moisture transport and amplified northern high-latitude wetting trend. *Nature Climate Change*, **3(1)**, 47–51, doi:10.1038/nclimate1631.
Zhang, Y. and S. Fueglistaler, 2019: Mechanism for Increasing Tropical Rainfall Unevenness with Global Warming. *Geophysical Research Letters*, **n/a(n/a)**, doi:10.1029/2019gl086058.

ACCEPTED VERSION SUBJECT TO FINAL EDITING

Zhang, Y. et al., 2016: Multi-decadal trends in global terrestrial evapotranspiration and its components. *Scientific Reports*, **6**, 1–12, doi:10.1038/srep19124.
Zhang, Z. and B.A. Colle, 2017: Changes in Extratropical Cyclone Precipitation and Associated Processes during the Twenty-First Century over Eastern North America and the Western Atlantic Using a Cyclone-Relative Approach. *Journal of Climate*, **30(21)**, 8633–8656, doi:10.1175/jcli-d-16-0906.1.
Zhang, Z., F.M. Ralph, and M. Zheng, 2018: The Relationship between Extratropical Cyclone Strength and Atmospheric River Intensity and Position. *Geophysical Research Letters*, **46(3)**, 1814–1823, doi:10.1029/2018gl079071.
Zhang, Z., B.F. Chao, J. Chen, and C.R. Wilson, 2015: Terrestrial water storage anomalies of Yangtze River Basin droughts observed by GRACE and connections with ENSO. *Global and Planetary Change*, **126**, 35–45, doi:10.1016/j.gloplacha.2015.01.002.
Zhao, C. et al., 2018: Enlarging rainfall area of tropical cyclones by atmospheric aerosols. *Geophysical Research Letters*, doi:10.1029/2018gl079427.
Zhao, D. et al., 2018: Predictingwetland distribution changes under climate change and human activities in a midand high-latitude region. *Sustainability (Switzerland)*, doi:10.3390/su10030863.
Zhao, M., 2020: Simulations of Atmospheric Rivers, Their Variability, and Response to Global Warming Using GFDL's New High-Resolution General Circulation Model. *Journal of Climate*, **33(23)**, 10287–10303, doi:10.1175/jcli-d-20-0241.1.
Zhao, M. et al., 2018: The GFDL Global Atmosphere and Land Model AM4.0/LM4.0: 2. Model Description, Sensitivity Studies, and Tuning Strategies. *Journal of Advances in Modeling Earth Systems*, **10(3)**, 735–769, doi:10.1002/2017ms001209.
Zhao, S. and K. Suzuki, 2019: Differing impacts of black carbon and sulfate aerosols on global precipitation and the ITCZ location via atmosphere and ocean energy perturbations. *Journal of Climate*, **32(17)**, 5567–5582, doi:10.1175/jcli-d-18-0616.1.
Zhao, W. and A. Li, 2015: A Review on Land Surface Processes Modelling over Complex Terrain. *Advances in Meteorology*, **2015**, doi:10.1155/2015/607181.
Zhao, X., R.J. Allen, T. Wood, and A.C. Maycock, 2020: Tropical belt width proportionately more sensitive to aerosols than greenhouse gases. *Geophysical Research Letters*, **n/a(n/a)**, e2019GL086425, doi:10.1029/2019gl086425.
Zheng, X.-T., C. Hui, and S.-W. Yeh, 2018: Response of ENSO amplitude to global warming in CESM large ensemble: uncertainty due to internal variability. *Climate Dynamics*, **50(11–12)**, 4019–4035, doi:10.1007/s00382-017-3859-7.
Zheng, Z. et al., 2020: Diurnal variation of summer precipitation modulated by air pollution: observational evidences in the beijing metropolitan area. *Environmental Research Letters*, **15(9)**, 94053, doi:10.1088/1748-9326/ab99fc.
Zhou, C. and K. Wang, 2017: Quantifying the sensitivity of precipitation to the long-term warming trend and interannual-decadal variation of surface air temperature over China. *Journal of Climate*, **30(10)**, 3687–3703, doi:10.1175/jcli-d-16-0515.1.
Zhou, C., K. Wang, and D. Qi, 2018: 21. Attribution of the July 2016 extreme precipitation event over China's Wuhan. *Bulletin of the American Meteorological Society*, **99(1)**, S107–S112, doi:10.1175/bams-d-17-0090.1.
Zhou, S. et al., 2019: Land–atmosphere feedbacks exacerbate concurrent soil drought and atmospheric aridity. *Proceedings of the National Academy of Sciences of the United States of America*, doi:10.1073/pnas.1904955116.
Zhou, S. et al., 2021: Soil moisture–atmosphere feedbacks mitigate declining water availability in drylands. *Nature Climate Change*, **11(1)**, 38–44, doi:10.1038/s41558-020-00945-z.
Zhou, T., F. Song, K.-J. Ha, and X. Chen, 2017a: Decadal Change of East Asian Summer Monsoon: Contributions of Internal Variability and External Forcing. In: *The Global Monsoon System: Research and Forecast (3rd Edition)* [Chang, C.-P., H.-C. Kuo, N.-C. Lau, R.H. Johnson, B. Wang, and M.C. Wheeler (eds.)]. World Scientific, Singapore, pp. 327–336, doi:10.1142/9789813200913_0026.
Zhou, T. et al., 2016: Overview of the Global Monsoons Model Inter-comparison Project (GMMIP). *Geoscientific Model Development Discussions*, 1–25, doi:10.5194/gmd-2016-69.
Zhou, T. et al., 2017b: A Robustness Analysis of CMIP5 Models over the East Asia-Western North Pacific Domain. *Engineering*, **3(5)**, 773–778, doi:10.1016/j.eng.2017.05.018.
Zhou, W., S.-P. Xie, and D. Yang, 2019: Enhanced equatorial warming causes deep-tropical contraction and subtropical monsoon shift. *Nature Climate Change*, doi:10.1038/s41558-019-0603-9.
Zhou, W., L.R. Leung, J. Lu, D. Yang, and F. Song, 2020: Contrasting recent and future ITCZ changes from distinct tropical warming patterns. *Geophysical Research Letters*, **n/a(n/a)**, e2020GL089846, doi:10.1029/2020gl089846.
Zhou, Y.Q., A.H. Sawyer, C.H. David, and J.S. Famiglietti, 2019: Fresh submarine groundwater discharge to the near-global coast. *Geophysical Research Letters*, 2019GL082749, doi:10.1029/2019gl082749.
Zhu, Y. and R.E. Newell, 1998: A Proposed Algorithm for Moisture Fluxes from Atmospheric Rivers. *Monthly Weather Review*, **126(3)**, 725–735, doi:10.1175/1520-0493(1998)126<0725:apafmf>2.0.co;2.
Zhu, Z. et al., 2016: Greening of the Earth and its drivers. *Nat Clim Change*, **6**, 791–795.

ACCEPTED VERSION SUBJECT TO FINAL EDITING

Zickfeld, K., B. Knopf, V. Petoukhov, and H.J. Schellnhuber, 2005: Is the Indian summer monsoon stable against global change? *Geophys Res Lett*, **32(15)**, doi:10.1029/2005gl022771.
Zika, J.D. et al., 2018: Improved estimates of water cycle change from ocean salinity: The key role of ocean warming. *Environmental Research Letters*, **13(7)**, doi:10.1088/1748-9326/aace42.
Zilli, M.T. and L.M. Carvalho, 2021: Detection and attribution of precipitation trends associated with the poleward shift of the South Atlantic Convergence Zone using CMIP5 simulations. *International Journal of Climatology*, joc.7007, doi:10.1002/joc.7007.
Zilli, M.T., L.M. Carvalho, and B.R. Lintner, 2019: The poleward shift of South Atlantic Convergence Zone in recent decades. *Climate Dynamics*, **52(5)**, 2545–2563, doi:10.1007/s00382-018-4277-1.
Zittis, G., 2018: Observed rainfall trends and precipitation uncertainty in the vicinity of the Mediterranean, Middle East and North Africa. *Theoretical and Applied Climatology*, doi:10.1007/s00704-017-2333-0.
Zolina, O. et al., 2014: Precipitation variability and extremes in Central Europe: New View from STAMMEX Results. *Bulletin of the American Meteorological Society*, **95(7)**, 995–1002, doi:10.1175/bams-d-12-00134.1.
Zou, Y. et al., 2019: Development of a REgion-specific ecosystem feedback fire (RESFire) model in the Community Earth System Model. *Journal of Advances in Modeling Earth Systems*, **11**.
Zuo, M., T. Zhou, and W. Man, 2019: Hydroclimate responses over global monsoon regions following volcanic eruptions at different latitudes. *Journal of Climate*, **32(14)**, 4367–4385, doi:10.1175/jcli-d-18-0707.1.
Zuo, Z. et al., 2013: Long-Term Variations of Broad-Scale Asian Summer Monsoon Circulation and Possible Causes. *Journal of Climate*, **26(22)**, 8947–8961, doi:10.1175/jcli-d-12-00691.1.

ACCEPTED VERSION
SUBJECT TO FINAL EDITING

Figures

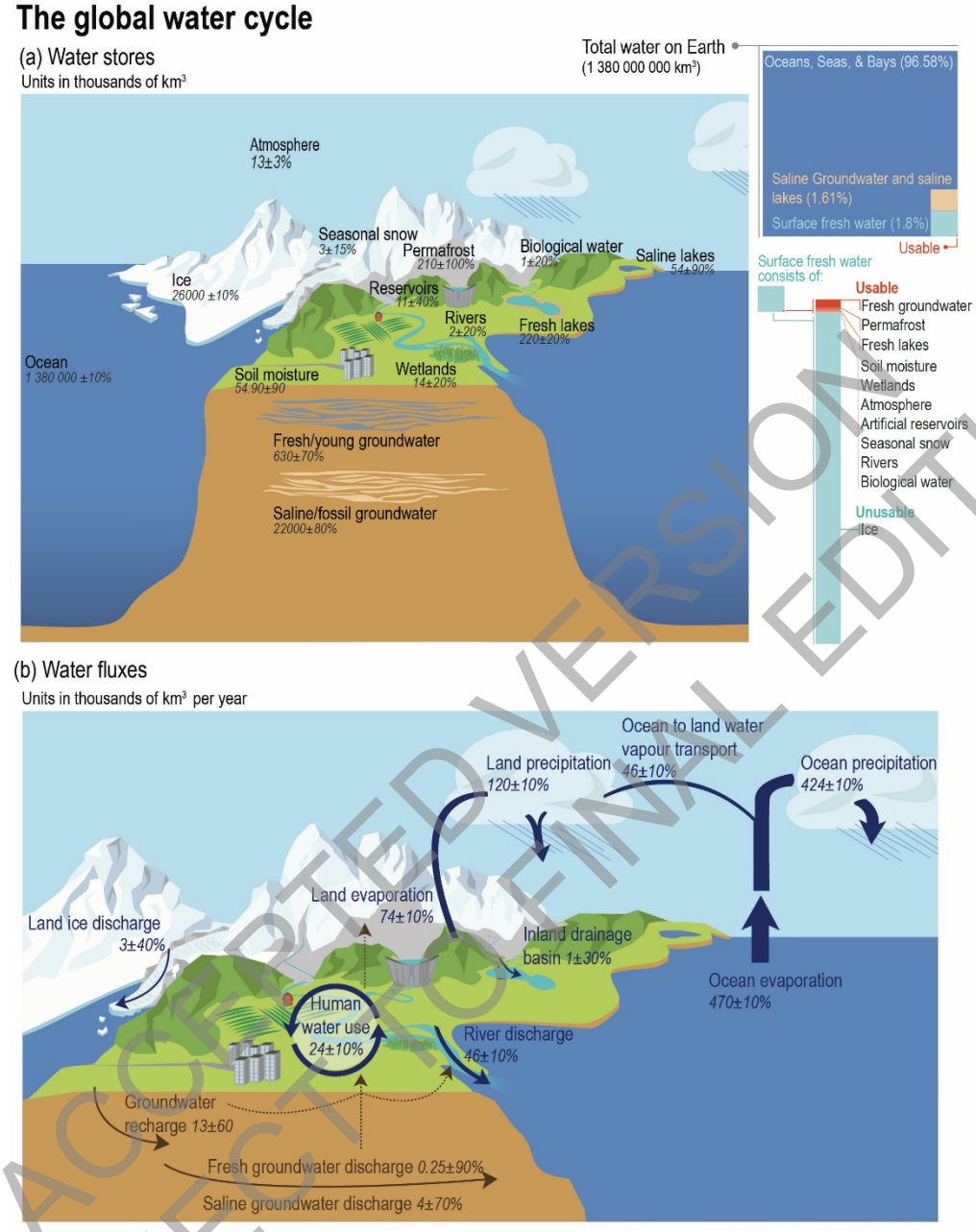


Figure 8.1: Depiction of the water cycle based on previous assessments (Trenberth et al., 2011; Rodell et al., 2015; Abbott et al., 2019) with minor adjustments for groundwater flows (Kwon et al., 2014; Zhou et al., 2019; Luijendijk et al., 2020), seasonal snow (Pulliainen et al., 2020) and ocean precipitation and evaporation (Stephens et al., 2012; Allan et al., 2020; Gutenstein et al., 2020). In the atmosphere, which accounts for only 0.001% of all water on Earth, water primarily occurs as a gas (water vapour), but it is also present as ice and liquid water within clouds. The ocean is the primary water reservoir on Earth, which is comprised mostly of liquid water across much of the globe, but also includes areas covered by ice in polar regions. Liquid freshwater on land forms surface water (lakes, rivers), soil moisture and groundwater stores, together accounting for 1.8% of global water (Stocker et al., 2013). Solid terrestrial water that occurs as ice sheets, glaciers, snow and ice on the surface and permafrost currently represents 2.2% of the planet's water (Stocker et al., 2013). Water that falls as snow in winter provides soil moisture and streamflow after melting, which are essential for human activities and ecosystem functioning.

ACCEPTED VERSION SUBJECT TO FINAL EDITING

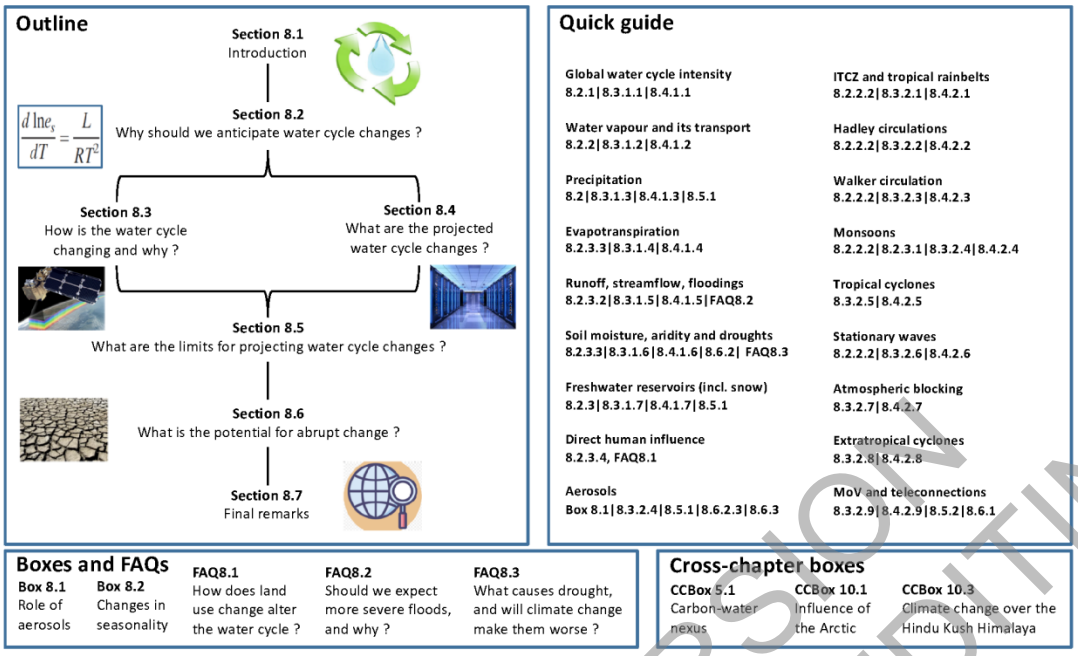


Figure 8.2: Schematic of the chapter structure and quick guide to the chapter content.

ACCEPTED VERSION
SUBJECT TO FINAL EDITING

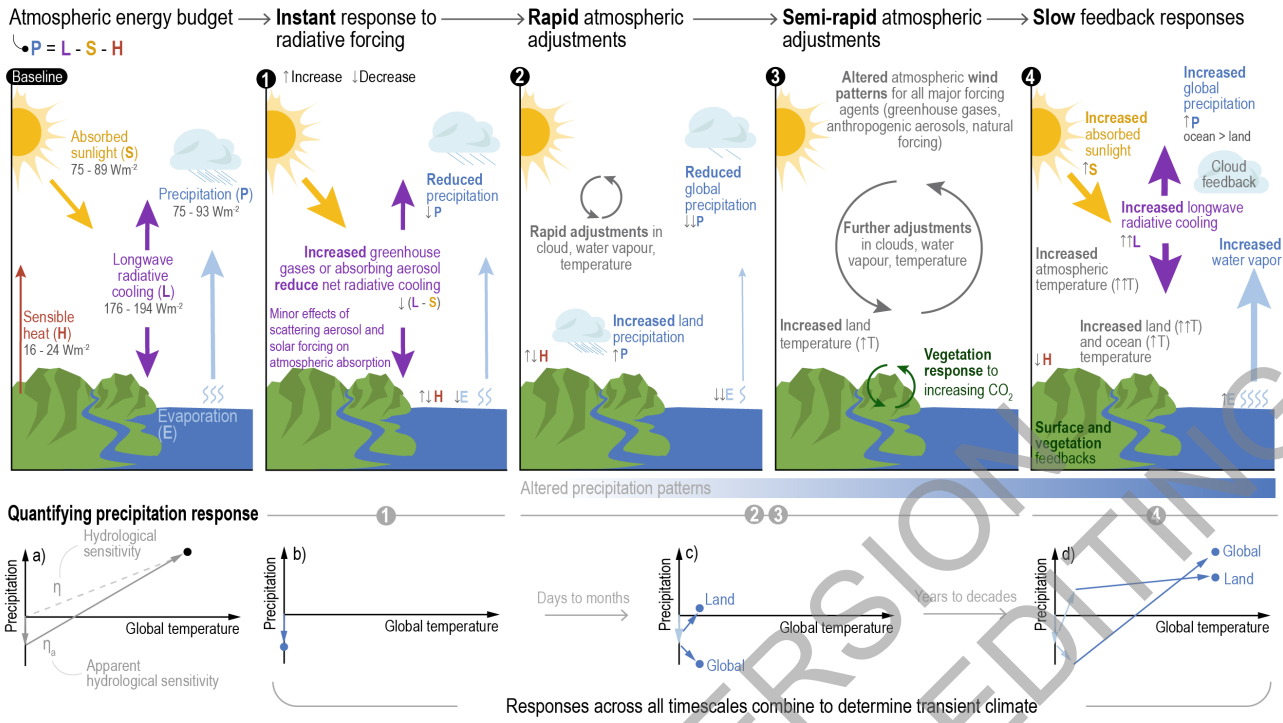


Figure 8.3: Schematic representation of fast and slow responses of the atmospheric energy balance and global precipitation to radiative forcing. The atmospheric energy budget ('baseline' panel) responds instantaneously to radiative forcings (1), leading to rapid atmospheric adjustments (2) and slower semi-rapid adjustments involving the land surface and vegetation that further modify atmospheric circulation patterns (3). This slow precipitation response to global mean surface air temperature (4) is quantified as the hydrological sensitivity, η, and the total precipitation response, including initial rapid adjustments, is termed the apparent hydrological sensitivity, η_a (a). The slow precipitation response over land and ocean develops over time (b-d). Large, filled arrows (in panels from 'baseline' to 4) depict fluxes or circulation change while small arrows (1-4) denote increases (↑) or decreases (↓) in variables (P is precipitation; L is atmospheric longwave radiative cooling, S is solar radiation absorption by the atmosphere; H is sensible heat flux; E is surface evaporative heat flux and T is temperature). (Adapted from Allan et al., 2020, Chapter 7 Figure 7.2 and Figure 8.1).

ACCEPTED VERSION SUBJECT TO FINAL EDITING

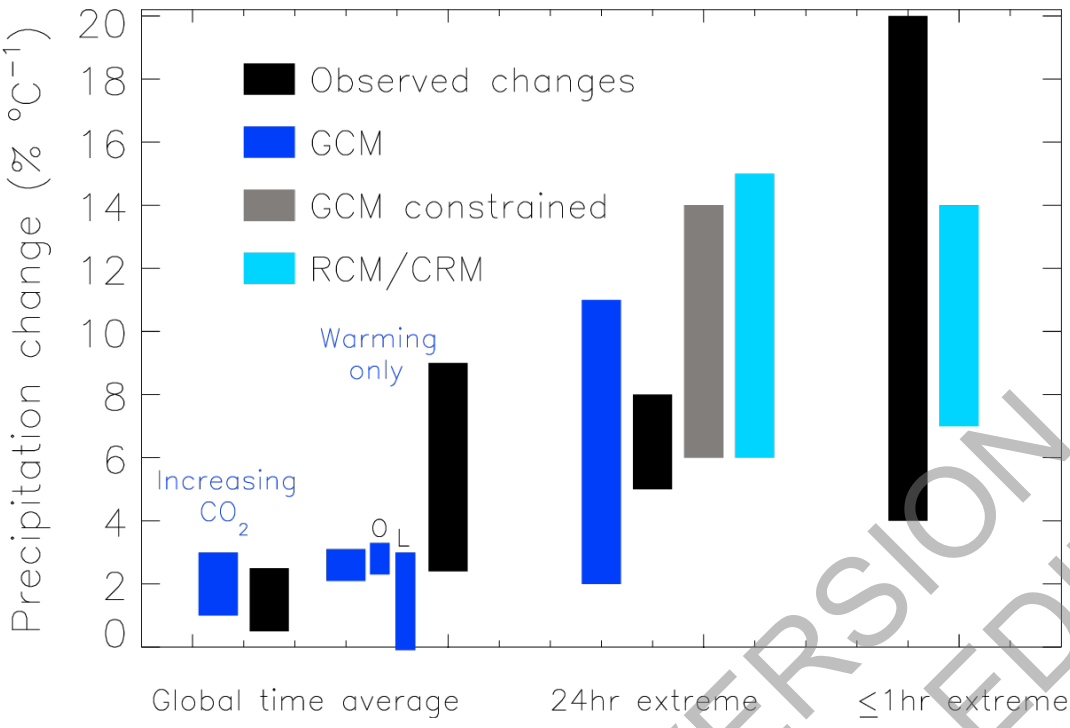


Figure 8.4: Estimate (5-95% range) of the increase in precipitation and its extremes with global mean surface warming. Global time averaged precipitation changes (left) are based on responses to increasing CO_2 (apparent hydrological sensitivity, η_a) and the temperature-dependent component (hydrological sensitivity, η) based on GCM experiments and including the land (L) and ocean (O) components (Fläschner et al., 2016; Richardson et al., 2018; Samset et al., 2018; Pendergrass, 2020; Rehfeld et al., 2020) and observational estimates (GPCP/HadCRUTv4.6) using trends (1988-2014) as a proxy for η_a and interannual variability as a proxy for η with 90% confidence range accounting for statistical uncertainty only (Adler et al., 2017; Allan et al., 2020). For extreme precipitation, assessment is for 24 hour 99.9th percentile or annual maximum extremes from GCMs (Fischer and Knutti, 2015; Pendergrass et al., 2015; Borodina et al., 2017; Pfahl et al., 2017; Sillmann et al., 2017), regional climate models (RCMs) (Bao et al., 2017), an observationally constrained tropical estimate (O'Gorman, 2012) and estimates from observed changes (Westra et al., 2013; Donat et al., 2016; Borodina et al., 2017; Sun et al., 2020; Zeder and Fischer, 2020). For hourly and sub-hourly extremes observed changes (Barbero et al., 2017; Guerreiro et al., 2018) and high resolution models including RCM and cloud resolving models (CRMs) are assessed (Ban et al., 2015; Prein et al., 2017; Haerter and Schlemmer, 2018; Hodnebrog et al., 2019; Lenderink et al., 2019). Further details on data sources and processing are available in the chapter data table (Table 8.SM.1).

ACCEPTED VERSION SUBJECT TO FINAL EDITING

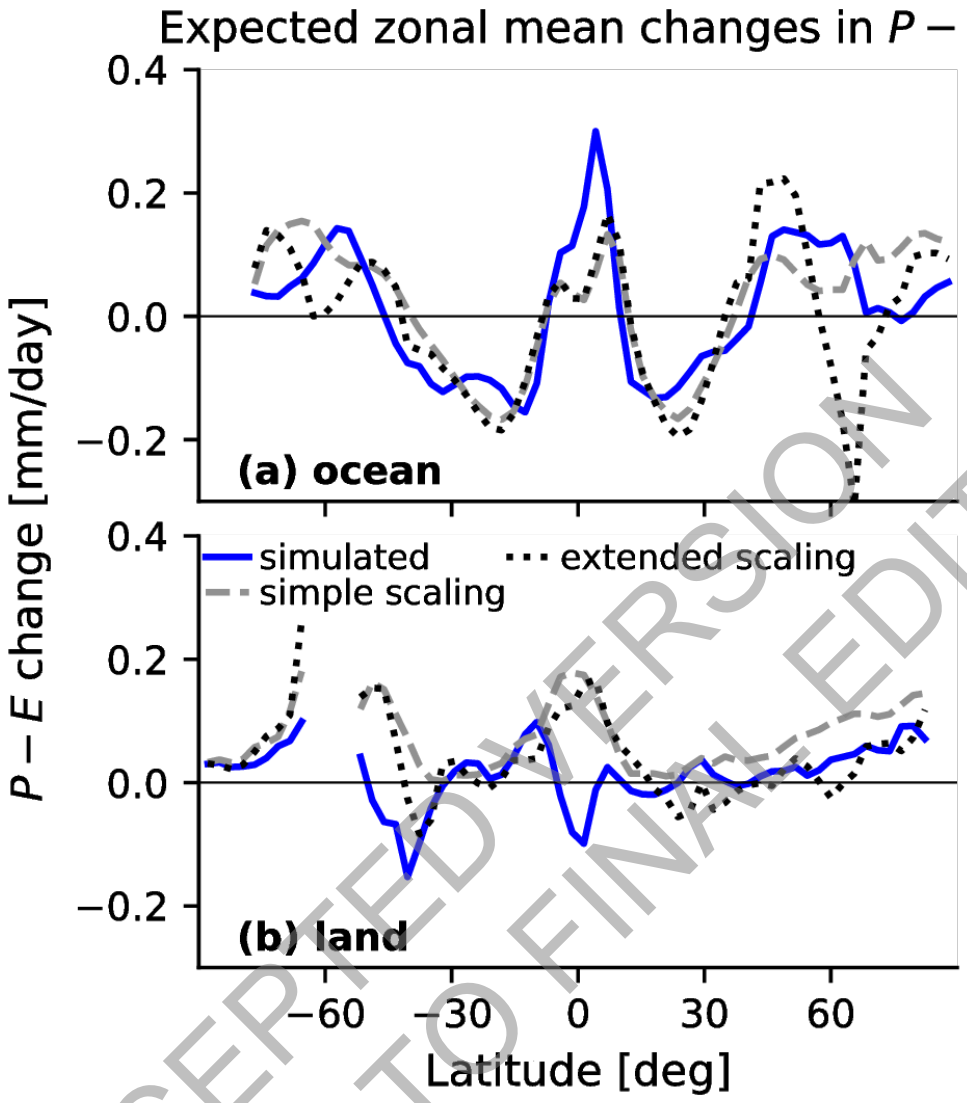


Figure 8.5: **Zonally-averaged annual mean changes in precipitation minus evaporation (P-E) over (a) ocean and (b) land between the historical (1995–2014) and SSP2-4.5 (2081–2100) CMIP6 simulations (blue lines, an average of the CanESM5 and MRI-ESM2-0 models).** Dashed lines show estimated P-E changes using a simple thermodynamic scaling (Held and Soden, 2006); dotted lines show estimates using an extended scaling (Byrne and O'Gorman, 2016). All curves have been smoothed in latitude using a three grid-point moving-average filter. Further details on data sources and processing are available in the chapter data table (Table 8.SM.1).

ACCEPTED VERSION SUBJECT TO FINAL EDITING

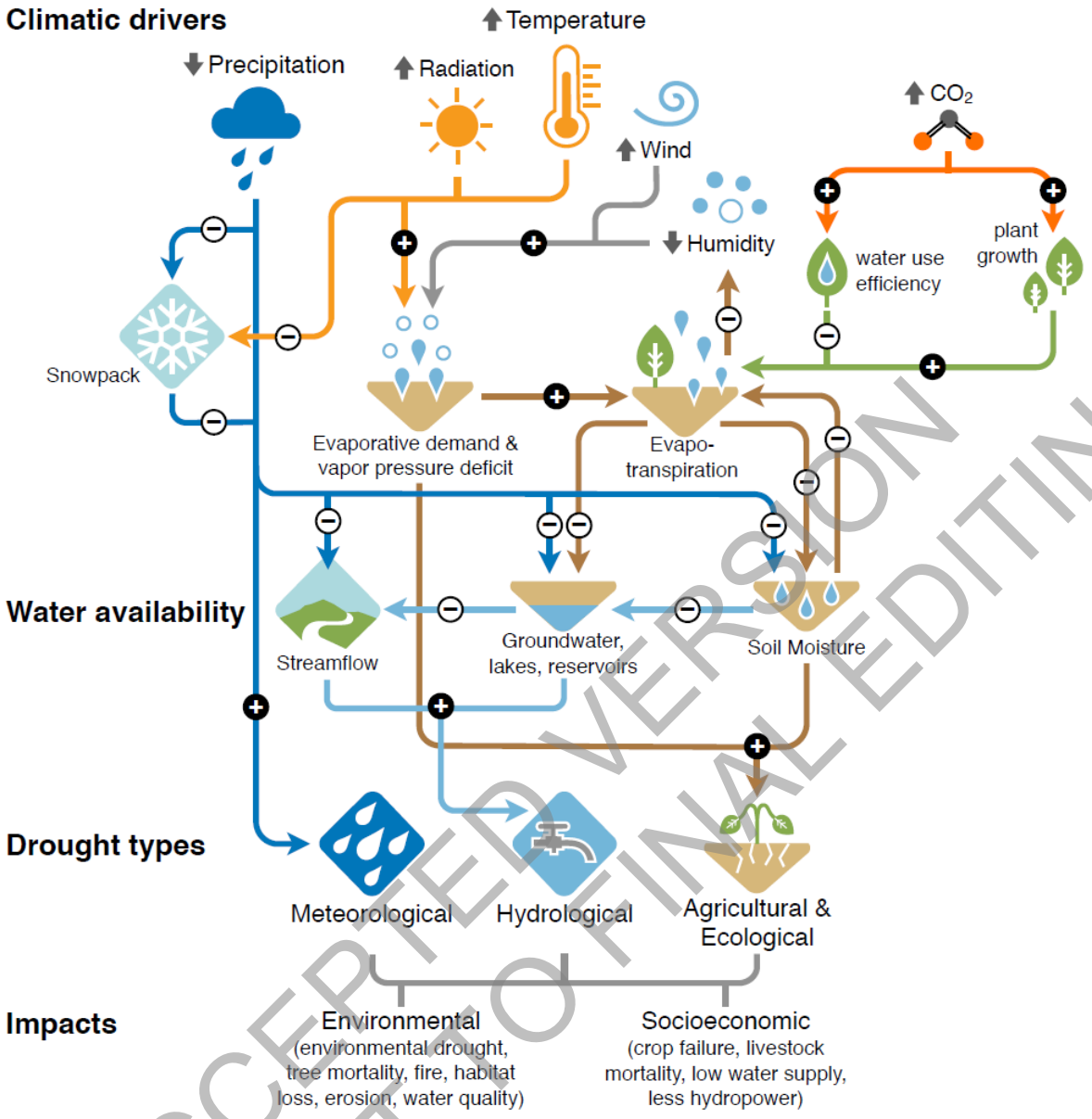
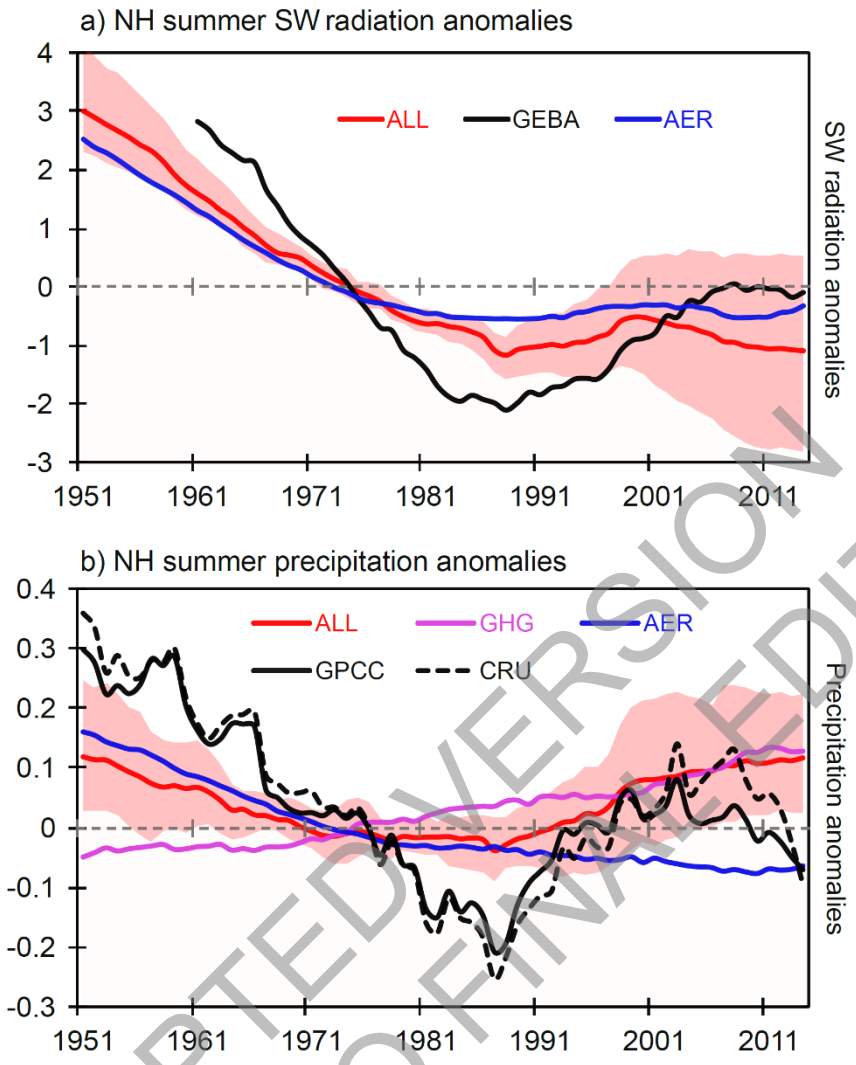


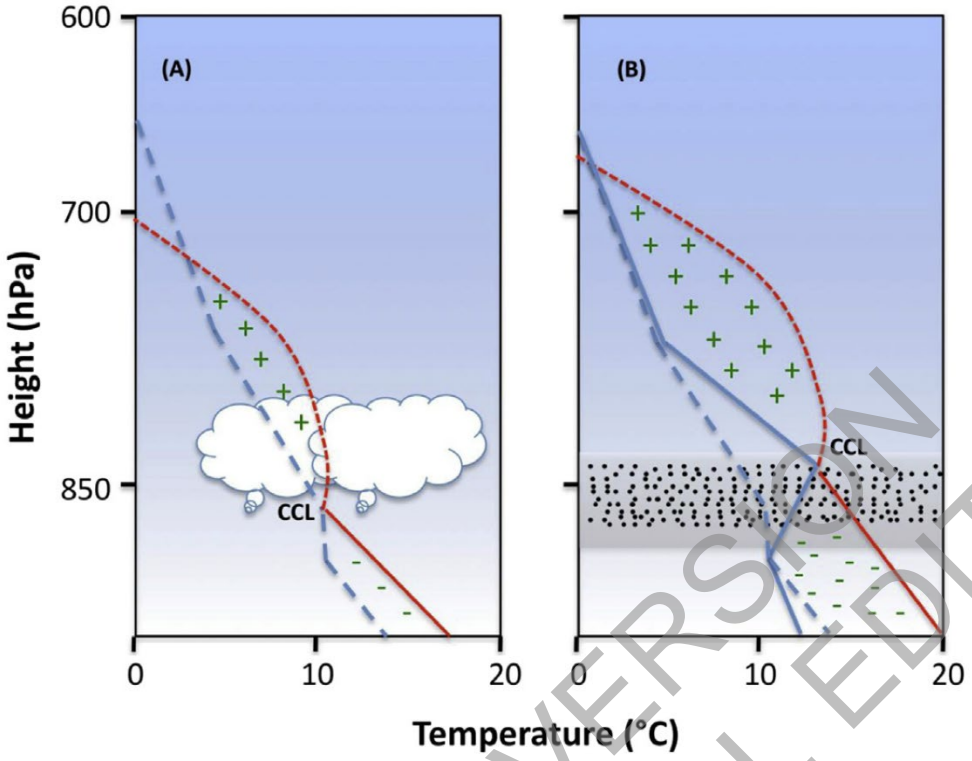
Figure 8.6: Climatic drivers of drought, effects on water availability, and impacts. Plus and minus signs denote the direction of change that drivers have on factors such as snowpack, evapotranspiration, soil moisture, and water storage. The three main types of drought are listed, along with some possible environmental and socioeconomic impacts of drought (bottom).

ACCEPTED VERSION SUBJECT TO FINAL EDITING



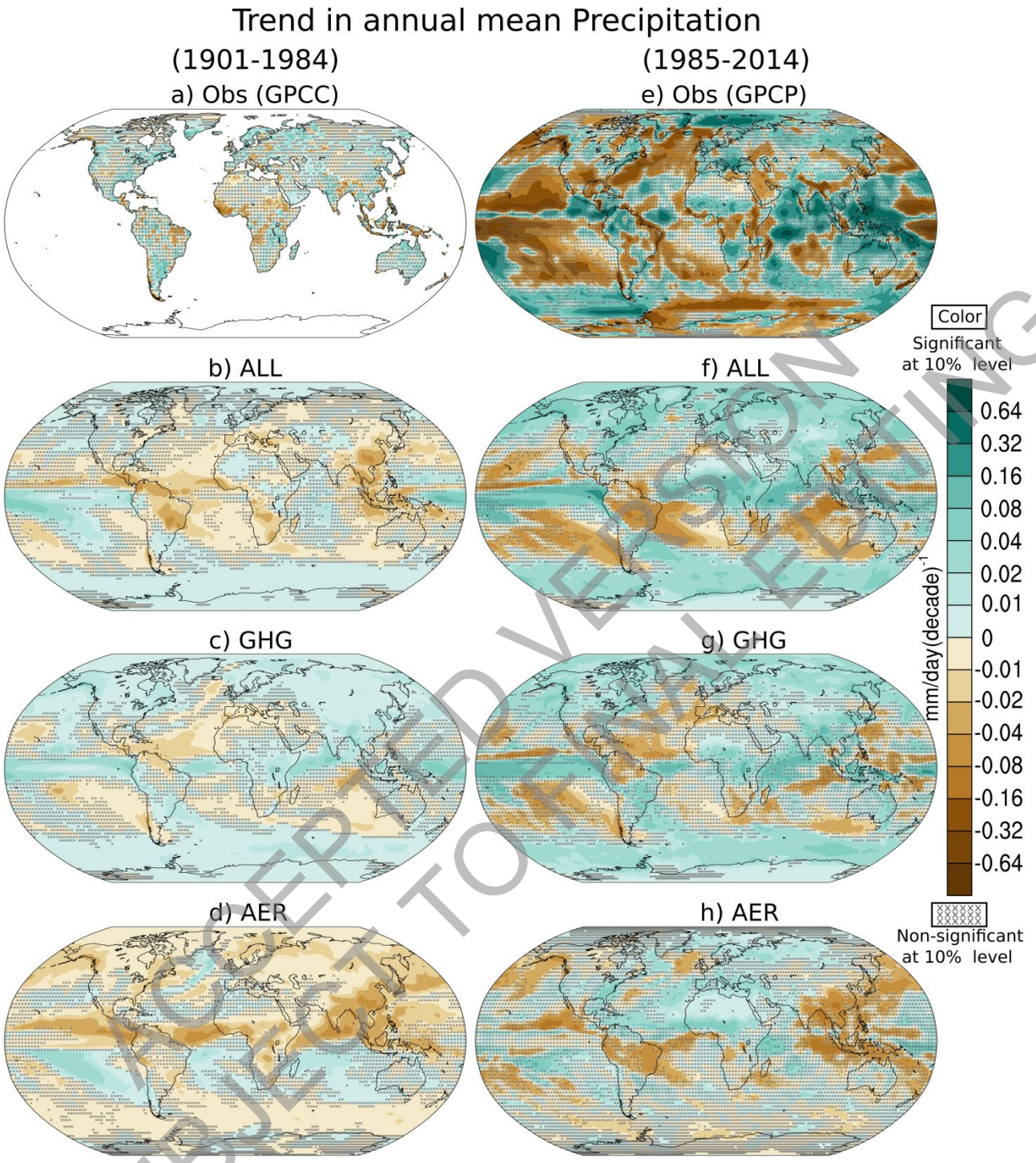
Box 8.1, Figure 1: Northern hemisphere surface downward radiation anomalies (Wm^{-2} ; a) and precipitation anomalies (mm/day ; b) for 1951–2014 for summer season (May–September) monsoon region (Polson et al. et al., 2014) from CMIP6 DAMIP experiments. Observed solar radiation anomalies are from GEBA global data from 1961-2014 (Wild et al., 2017) and observed precipitation anomalies are from GPCC and CRU. CMIP6 multi-model mean anomalies are from all-forcings (ALL), greenhouse gas forcing (GHG) and anthropogenic aerosol forcing (AER) experiments. Anomalies are with respect to 1961–1990 and smoothed with a 11-year running mean. Red shading shows the ensemble spread of ALL forcing experiment (5%–95% range). Models are masked to the GPCC data set. Further details on data sources and processing are available in the chapter data table (Table 8.SM.1).

ACCEPTED VERSION SUBJECT TO FINAL EDITING



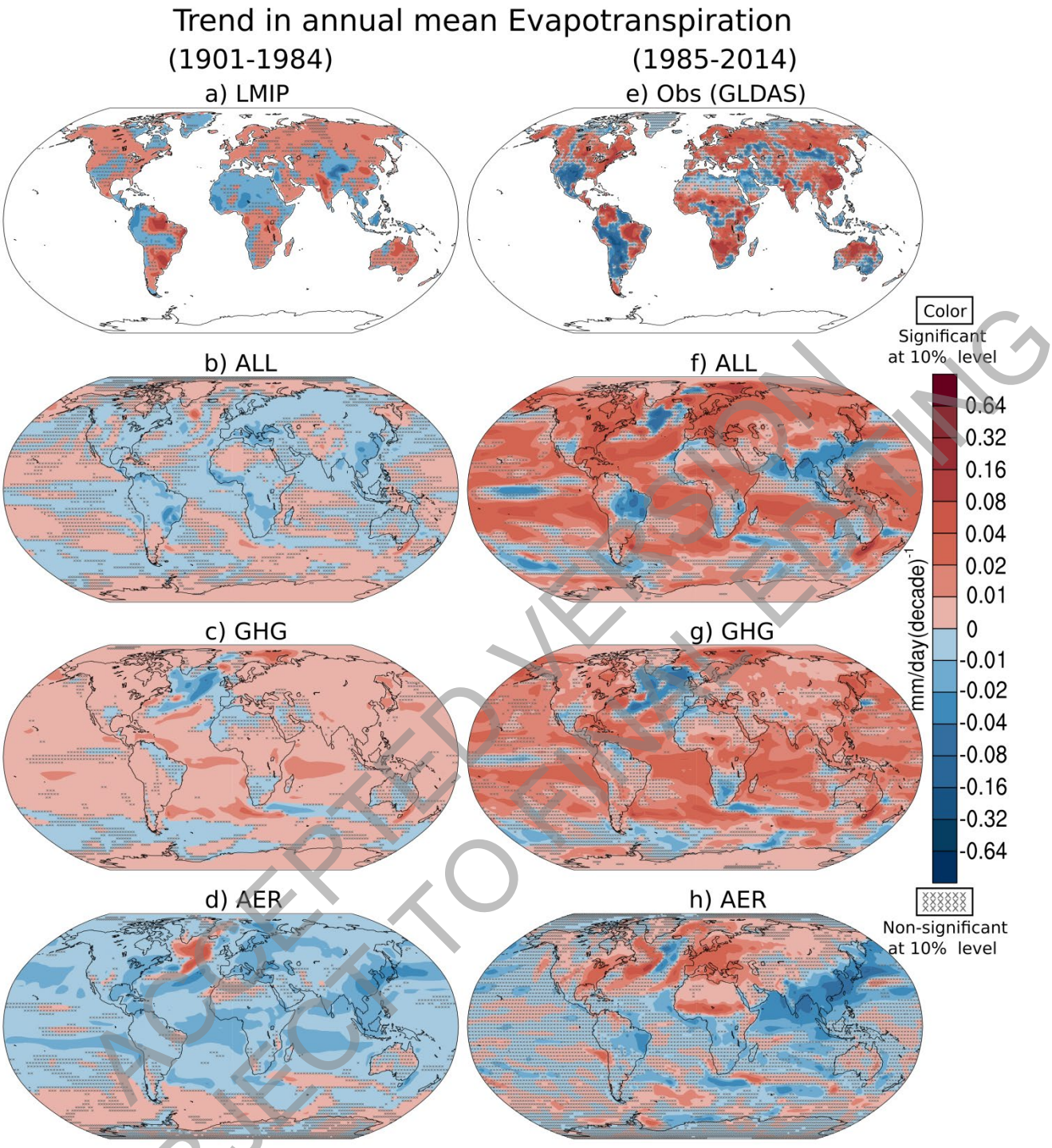
Box 8.1, Figure 2: Schematic depiction of the atmospheric effects of light absorbing aerosols on convection and cloud formation: (A) without and (B) with the presence of absorbing aerosols in the planetary boundary layer. The dashed and solid blue lines correspond to the vertical temperature profiles in the absence and presence of the absorbing aerosol layer, respectively, and the solid and dashed red lines denote the dry and moist adiabats, respectively. Absorbing aerosols result in an increasing temperature in the atmosphere but a reduced temperature at the surface. The reduced surface temperature and the increased temperature aloft lead to a larger negative energy associated with convective inhibition (-) and a higher convection condensation level (CCL) under the polluted conditions. On the other hand, the absorbing aerosol layer induces a larger convective available potential energy (+) above CCL, facilitating more intensive vertical development of clouds, if lifting is sufficient to overcome the larger convective inhibition. From (Wang et al., 2013).

ACCEPTED VERSION SUBJECT TO FINAL EDITING



ACCEPTED VERSION SUBJECT TO FINAL EDITING

Figure 8.7: Linear trends in annual mean precipitation (mm/day per decade) for 1901-1984 (left) and 1985-2014 (right): (a & e) observational dataset, and the CMIP6 multi model ensemble mean historical simulations driven by, (b & f) all radiative forcings, (c & g) GHG only radiative forcings, (d & h) aerosol only radiative forcings experiment. Colour shades without grey cross correspond to the regions exceeding 10 % significant level. Grey crosses correspond to the regions not reaching the 10% statistical significant level. Nine CMIP6-DAMIP models have been used having at least 3 members. The ensemble mean is weighted per each model on the available and used members. Further details on data sources and processing are available in the chapter data table (Table 8.SM.1).



ACCEPTED VERSION SUBJECT TO FINAL EDITING

Figure 8.8: Linear trends in annual mean evapotranspiration (mm/day per decade) for 1901-1984 (left) and 1985-2014 (right): (a & e) LMIP and observational dataset, and the CMIP6 multi model ensemble mean historical simulations driven by, (b & f) all radiative forcings, (c & g) GHG only radiative forcings, (d & h) aerosol only radiative forcings experiment. Colour shade without grey cross correspond to the regions exceeding 10 % significant level. Grey crosses correspond to the regions not reaching the 10% statistically significant level. Nine CMIP6-DAMIP models have been used having at least 3 members. The ensemble mean is weighted per each model on the available and used members. GLDAS is not available over the early 20th century so was replaced by a multi-model off-line reconstruction, LMIP, which is consistent with GLDAS over the recent period but may be less reliable over the early 20th century given larger uncertainties in the atmospheric forcings. Further details on data sources and processing are available in the chapter data table (Table 8.SM.1).

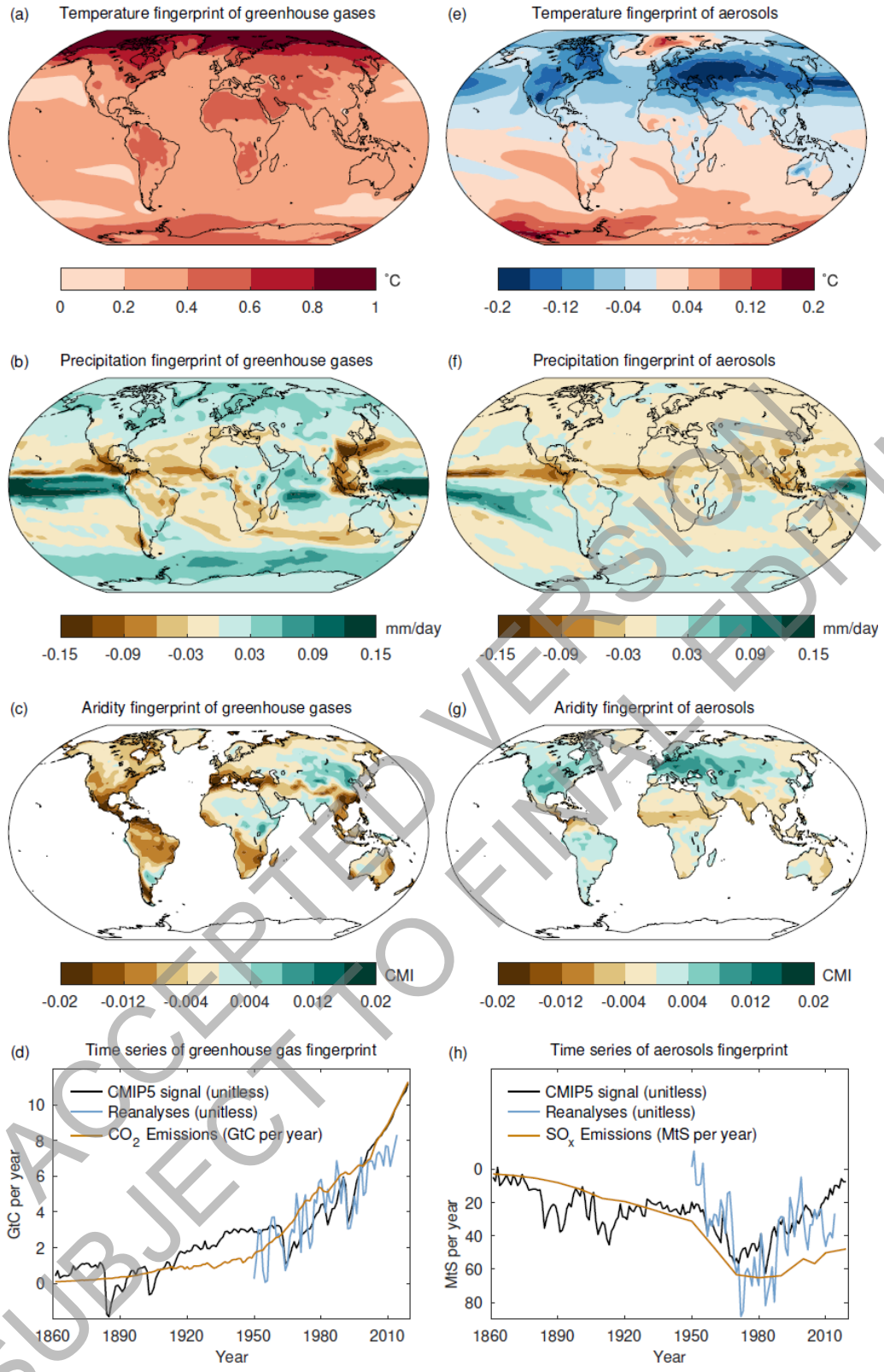


Figure 8.9: Spatial expressions (a-c; e-g) of the leading multivariate fingerprints of temperature (˚C), precipitation (mm/day), and aridity (CMI; the Climate Moisture Index) in CMIP5 historical simulations and the corresponding temporal evolution in both CMIP5 and reanalysis products (d, h). The first leading fingerprint is associated with greenhouse gas forcing (a-d) and the second leading fingerprint is associated with aerosol forcing (e-h). CMI is a dimensionless aridity indicator that combines precipitation and atmospheric evaporative demand. Figure after (Bonfils et al., 2020). Further details on data sources and processing are available in the chapter data table (Table 8.SM.1).

ACCEPTED VERSION SUBJECT TO FINAL EDITING

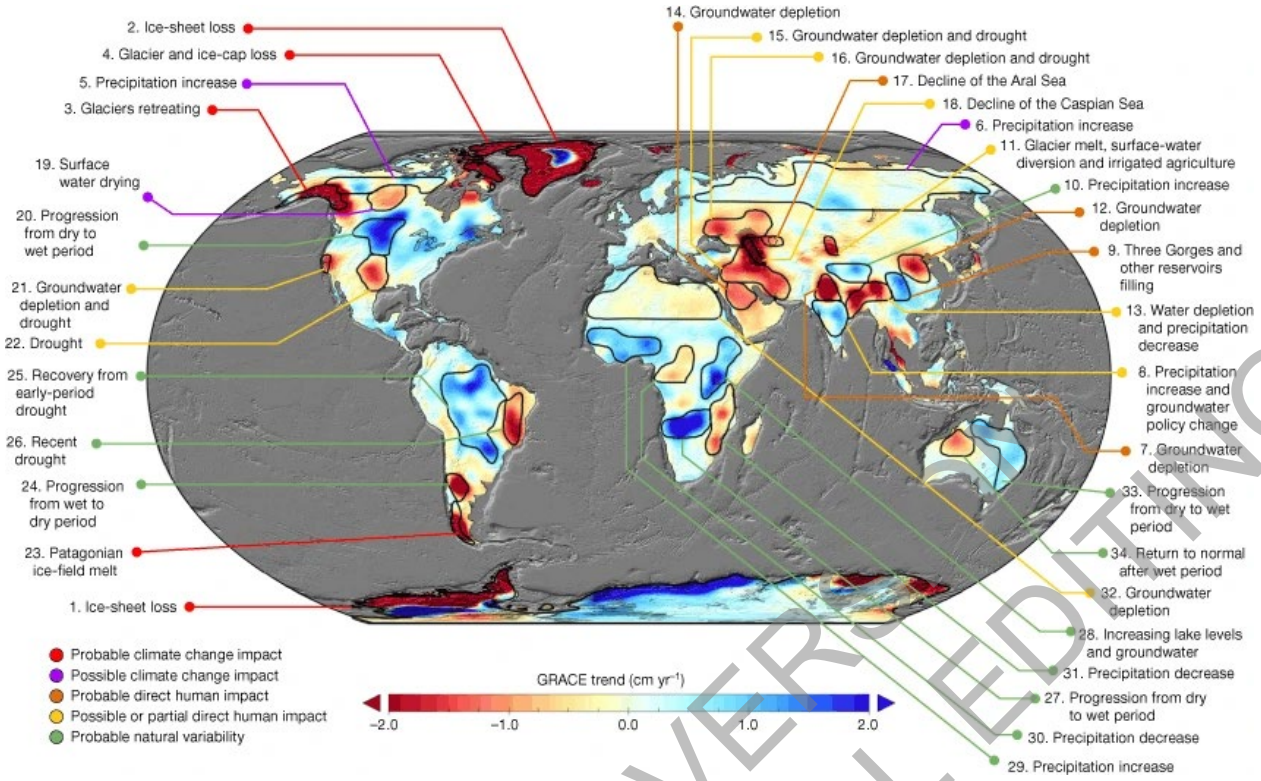


Figure 8.10: Trends in Terrestrial Water Storage (TWS) (in centimetres per year) obtained on the basis of GRACE observations from April 2002 to March 2016. The cause of the trend in each outlined study region is briefly explained and colour-coded by category. The trend map was smoothed with a 150-km-radius Gaussian filter for the purpose of visualization; however, all calculations were performed at the native 3° resolution of the data product. Figure from Rodell et al. (2018). Further details on data sources and processing are available in the chapter data table (Table 8.SM.1).

ACCEPTED VERSION SUBJECT TO FINAL EDITING

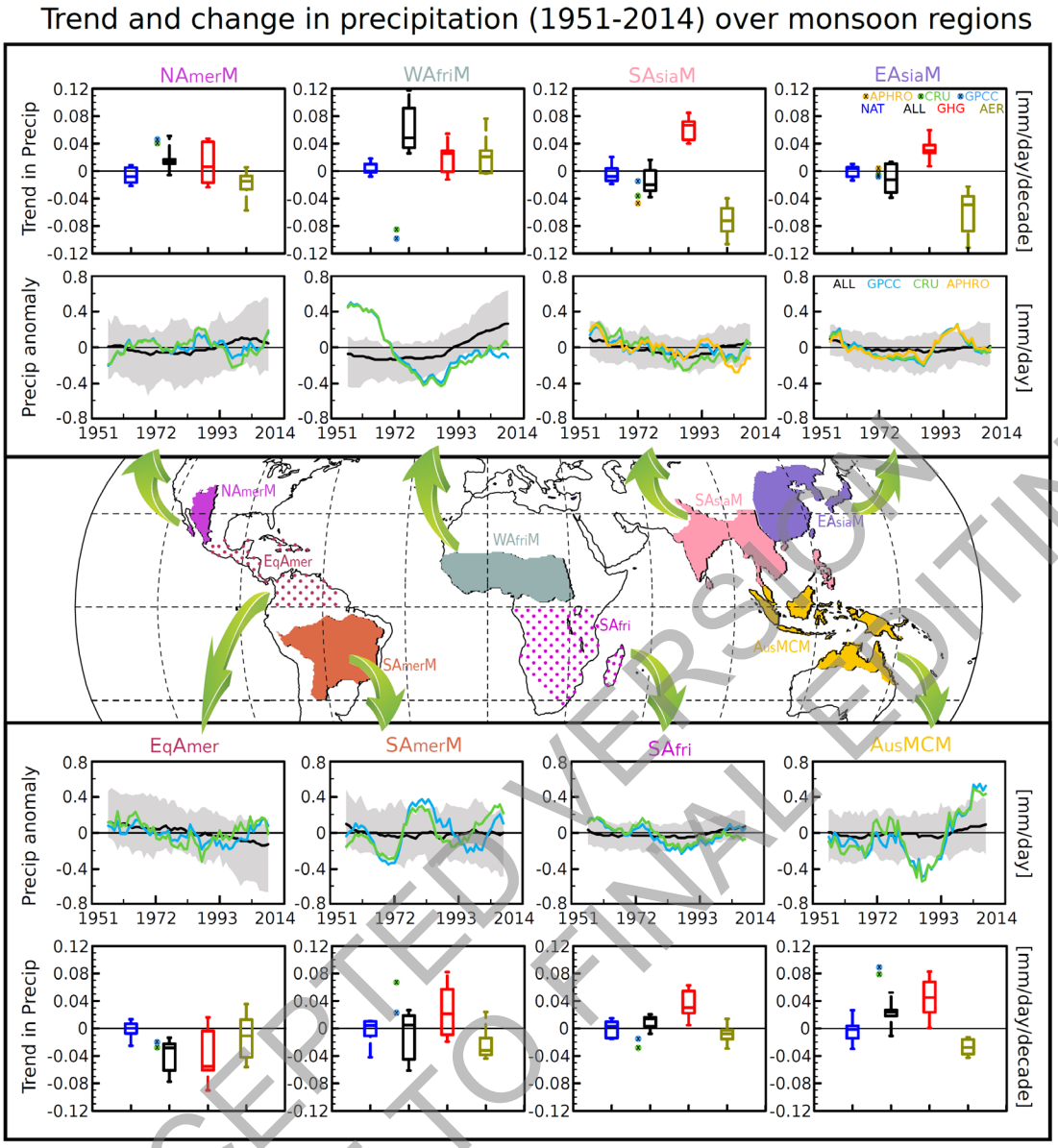
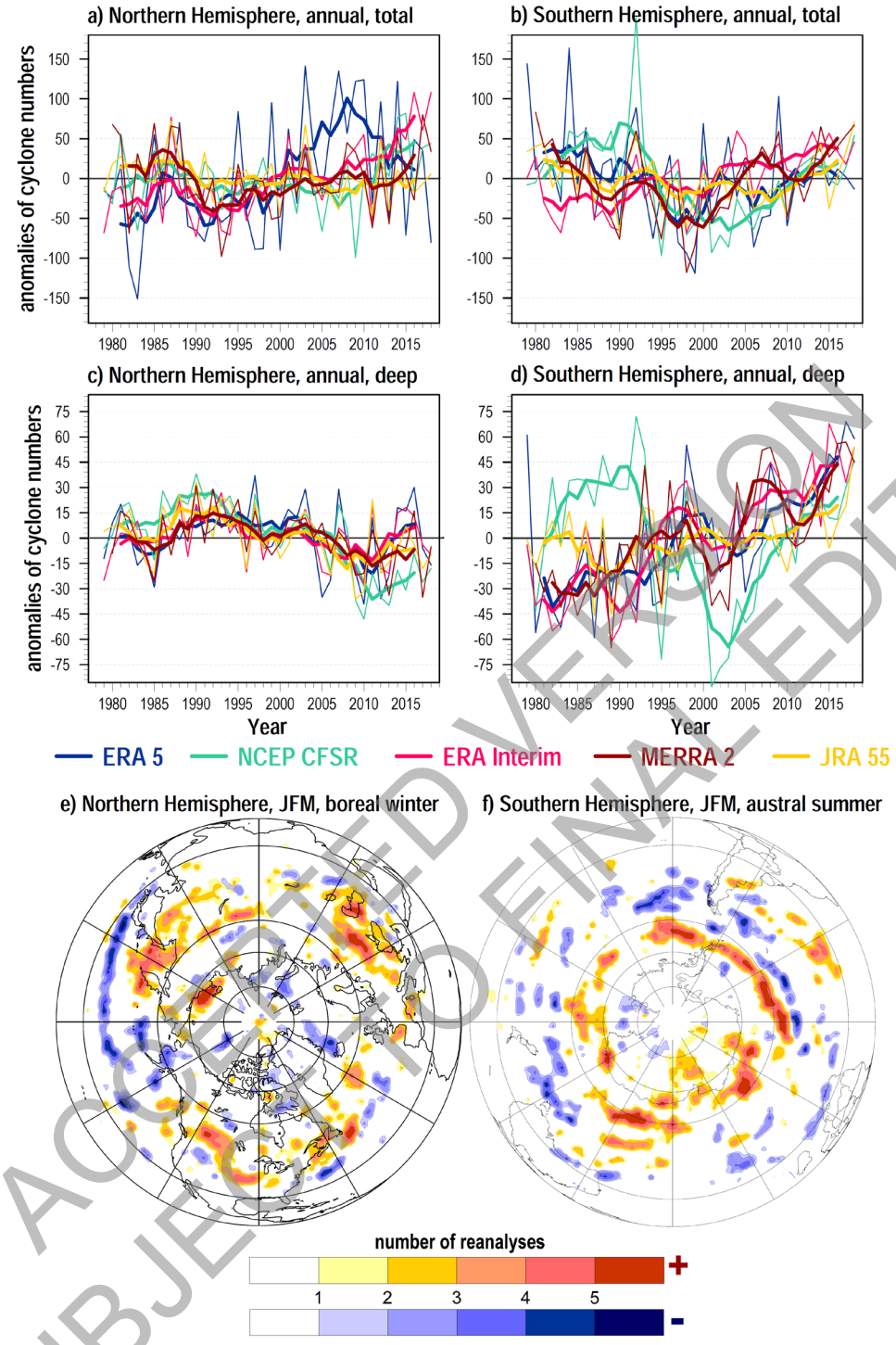


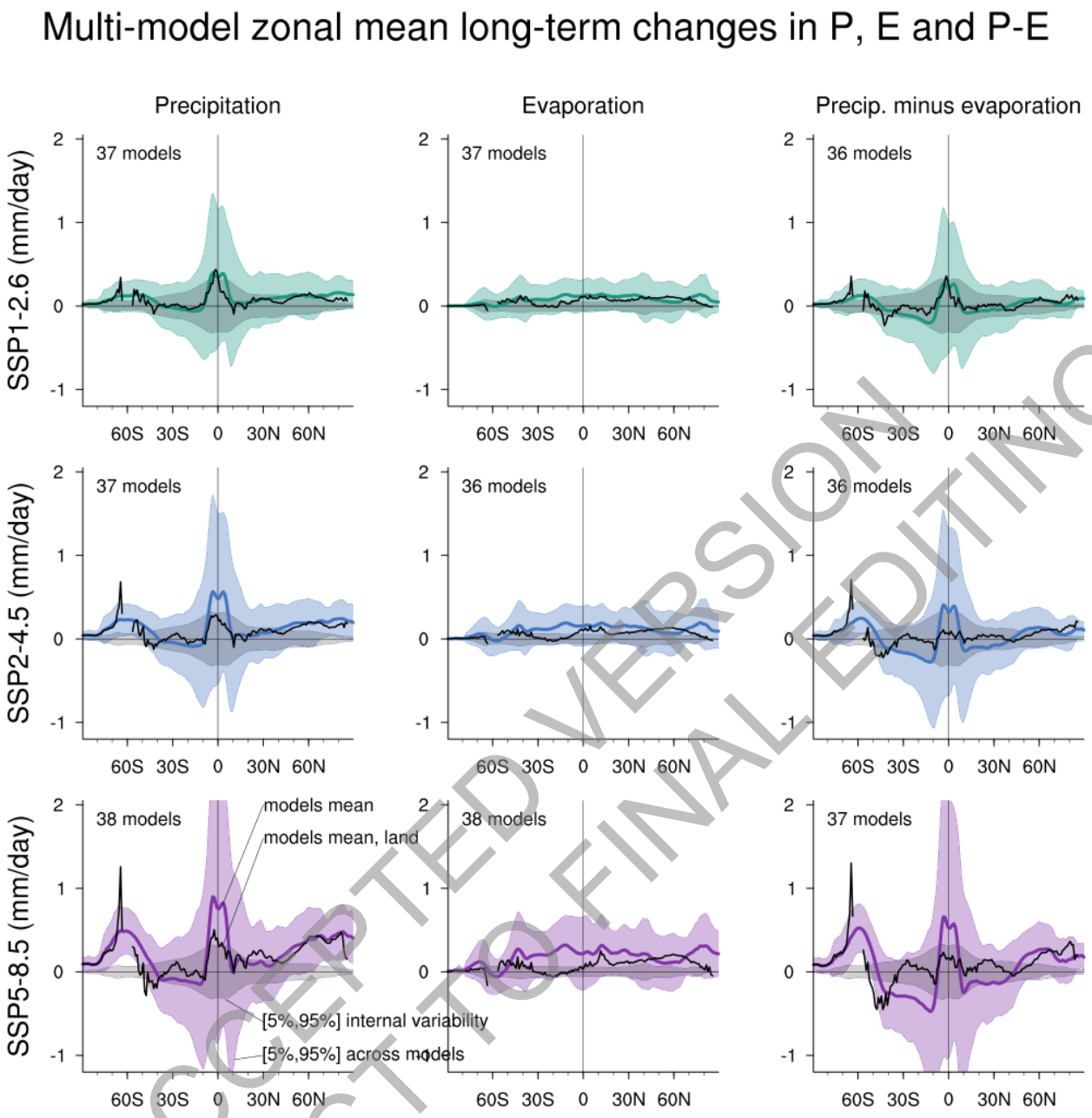
Figure 8.11: Regional monsoon precipitation changes from observations and model attribution. Precipitation changes during 1951-2014 are shown as least-square linear trends in box-whisker plots (first and fourth rows) over the six regional monsoons, i.e., North American monsoon (NAmerM, Jul-Aug-Sep), West African monsoon (WAfriM, Jun-Jul-Aug-Sep), South and Southeast Asian monsoon (SAsiaM, Jun-Jul-Aug-Sep), East Asian monsoon (EAsiaM, Jun-Jul-Aug), South American monsoon (SAmerM, Dec-Jan-Feb), Australian and Maritime Continent monsoon (AusMCM, Dec-Jan-Feb), and over the two land domains (i.e. equatorial America (EqAmer, Jun-Jul-Aug) and South Africa (SAfri, Dec-Jan-Feb), as identified in the map shown in the middle and as described in Annex V. Precipitation changes are computed from observations and from DAMIP CMIP6 experiments over the historical period with all-forcing (ALL), GHG-only forcing (GHG), Aerosol-only (AER) and Natural (NAT) forcings prescribed. Observations are based on the CRU (light green) and GPCC (light blue) datasets and the APHRODITE (light orange) dataset for SAsiaM and EAsiaM. CMIP6 simulations are taken from nine CMIP6 models contributing to DAMIP, with at least 3 members. Ensembles are weight-averaged for the respective model ensemble size. Observed trends are shown as colored cirles and the simulated trends from the CMIP6 multi-model experiments are shown as box-whisker plots. Precipitation anomaly time-series are shown in the second and third row. The thick black line is the multi-model ensemble-mean precipitation anomaly time-series from the ALL experiment and the grey shading shows the spread across the multi-model ensembles. A 11-year running mean has been applied on the precipitation anomaly time-series prior to calculating the multi-model ensemble mean. Further details on data sources and processing are available in the chapter data table (Table 8.SM.1).

ACCEPTED VERSION SUBJECT TO FINAL EDITING



ACCEPTED VERSION SUBJECT TO FINAL EDITING

Figure 8.12: Annual anomalies (with respect to the reference period 1979-2018) of the total number of extratropical cyclones (a, c) and of the number of deep cyclones (<980hPa) (b, d) over the Northern (a, b) and the Southern (c, d) Hemispheres in different reanalyses (shown in colors in the legend). Note different vertical scales for panels (a), (b) and (c), (d). Thin lines indicate annual anomalies and bold lines indicate 5-yr running averages. (e), (f) The number of reanalyses (out of five) simultaneously indicating statistically significant (90% level) linear trends of the same sign during 1979–2018 for JFM over the Northern Hemisphere (e) and over the Southern Hemisphere (f). Updated from (Tilinina et al., 2013). Further details on data sources and processing are available in the chapter data table (Table 8.SM.1).



ACCEPTED VERSION SUBJECT TO FINAL EDITING

Figure 8.13: Zonal and annual mean projected long-term changes in the atmospheric water budget. Zonal and annual mean projected changes (mm/day) in P (precipitation, left column), E (evaporation, middle column), and P-E (right column) over both land and ocean areas (thick line) and over land only (dashed line) averaged across 36 to 38 CMIP6 models in the SSP1-2.6 (a,b), SSP2-4.5 (c,d) and SSP5-8.5 (e,f) scenario, respectively. Shading denotes confidence intervals estimated from the CMIP6 ensemble under a normal distribution hypothesis. Color shading denotes changes over both land and ocean. Grey shading represents internal variability derived from the pre-industrial control simulations. All changes are estimated for 2081-2100 relative to the 1995-2014 base period. Further details on data sources and processing are available in the chapter data table (Table 8.SM.1).

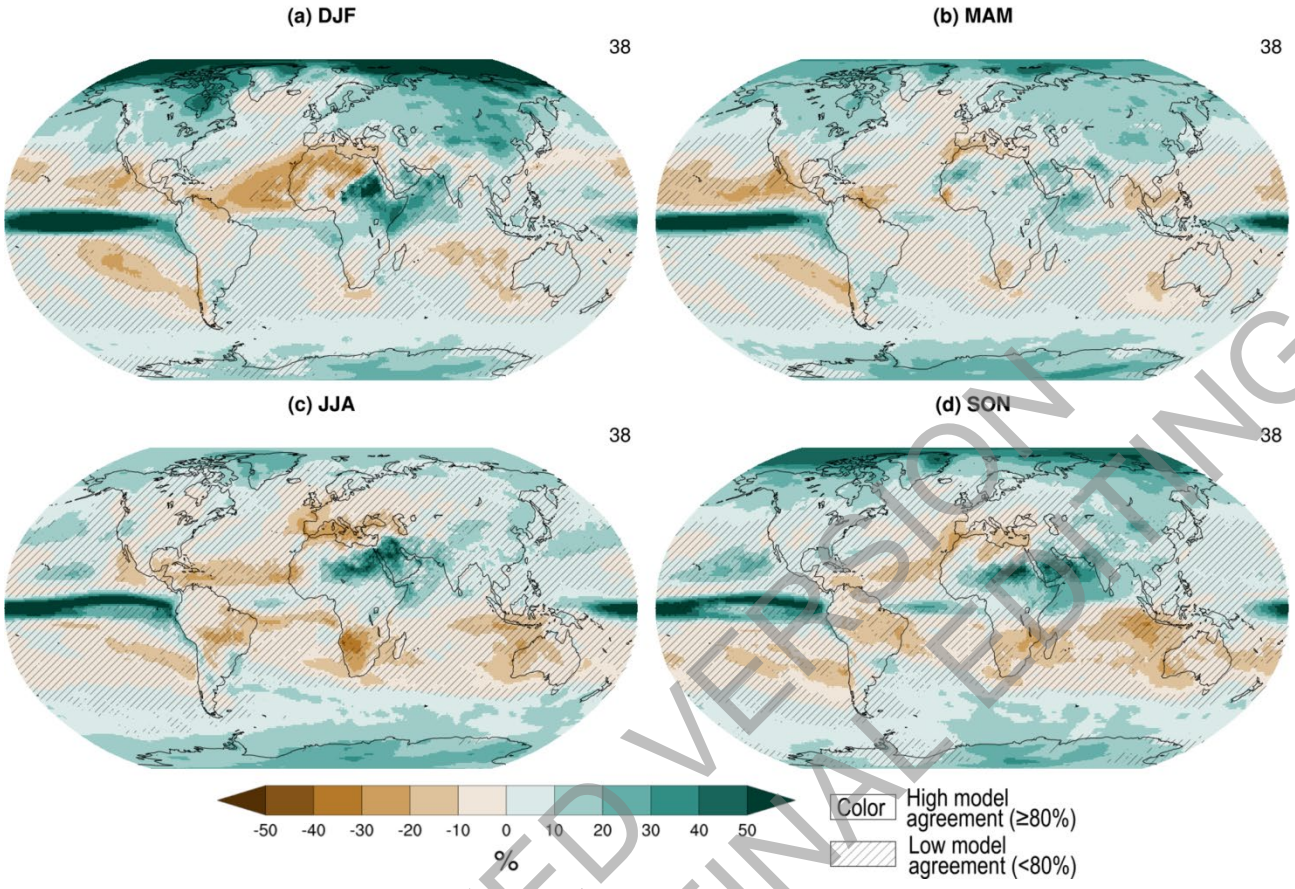
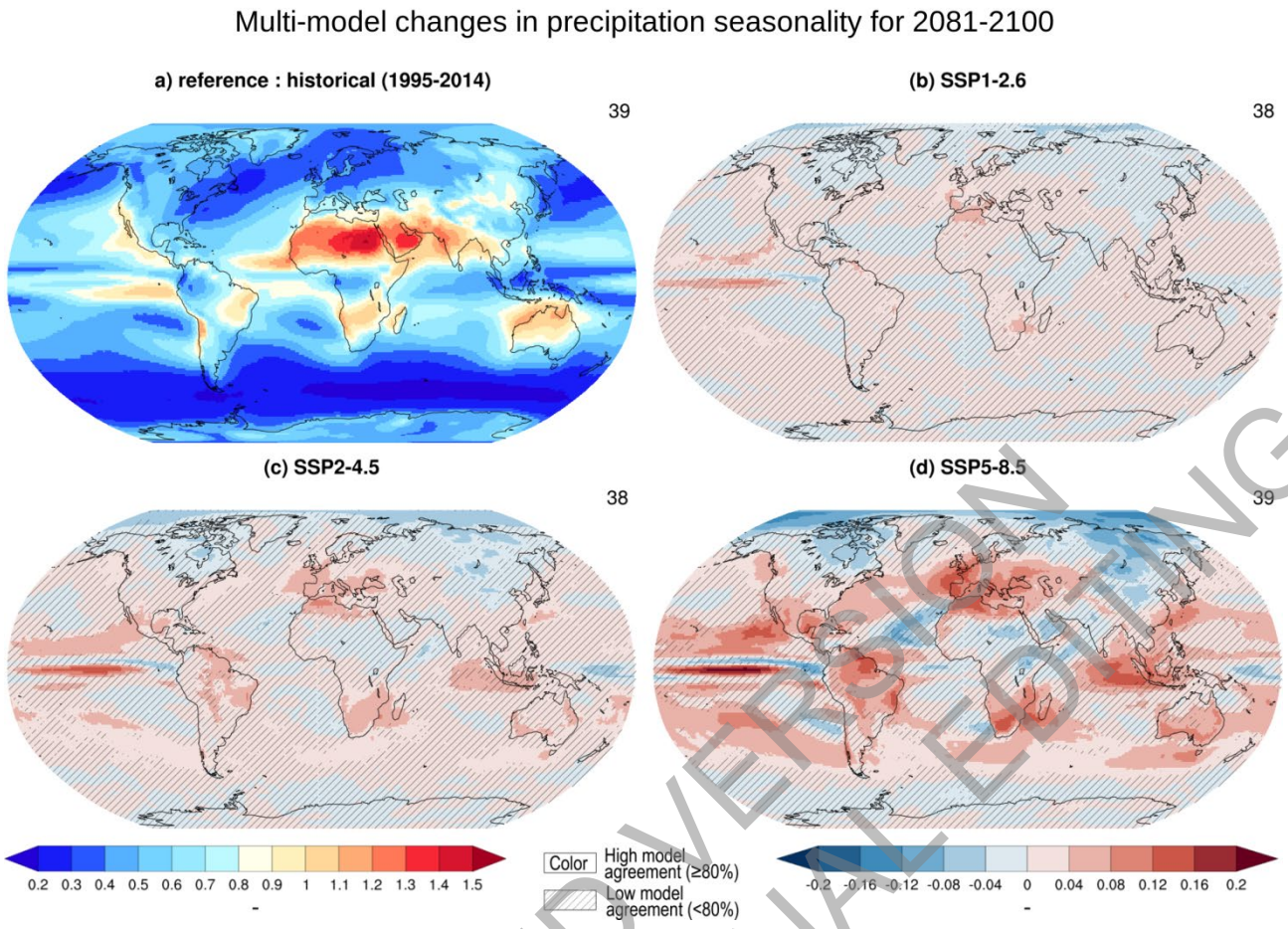


Figure 8.14: Projected long-term relative changes in seasonal mean precipitation. Global maps of projected relative changes (%) in seasonal mean of precipitation averaged across 29 CMIP6 models in the SSP2-4.5 scenario. All changes are estimated for 2081-2100 relative to the 1995-2014 base period. Uncertainty is represented using the simple approach: No overlay indicates regions with high model agreement, where ≥80% of models agree on sign of change; diagonal lines indicate regions with low model agreement, where <80% of models agree on sign of change. For more information on the simple approach, please refer to the Cross-Chapter Box Atlas.1. Further details on data sources and processing are available in the chapter data table (Table 8.SM.1).

ACCEPTED VERSION SUBJECT TO FINAL EDITING



Box 8.2, Figure 1: Projected long-term changes in precipitation seasonality. Global maps of projected changes in precipitation seasonality (simply defined as the sum of the absolute deviations of mean monthly rainfalls from the overall monthly mean, divided by the mean annual rainfall as in Walsh and Lawler, 1981) averaged across 31 to 33 CMIP6 models in the SSP1-2.6 (b), SSP2-4.5 (c) and SSP5-8.5 (d) scenario respectively. The simulated 1995-2014 climatology is shown in panel (a). All changes are estimated in 2081-2100 relative to 1995-2014. Uncertainty is represented using the simple approach: No overlay indicates regions with high model agreement, where ≥80% of models agree on sign of change; diagonal lines indicate regions with low model agreement, where <80% of models agree on sign of change. For more information on the simple approach, please refer to the Cross-Chapter Box Atlas.1. Further details on data sources and processing are available in the chapter data table (Table 8.SM.1).

ACCEPTED VERSION SUBJECT TO FINAL EDITING

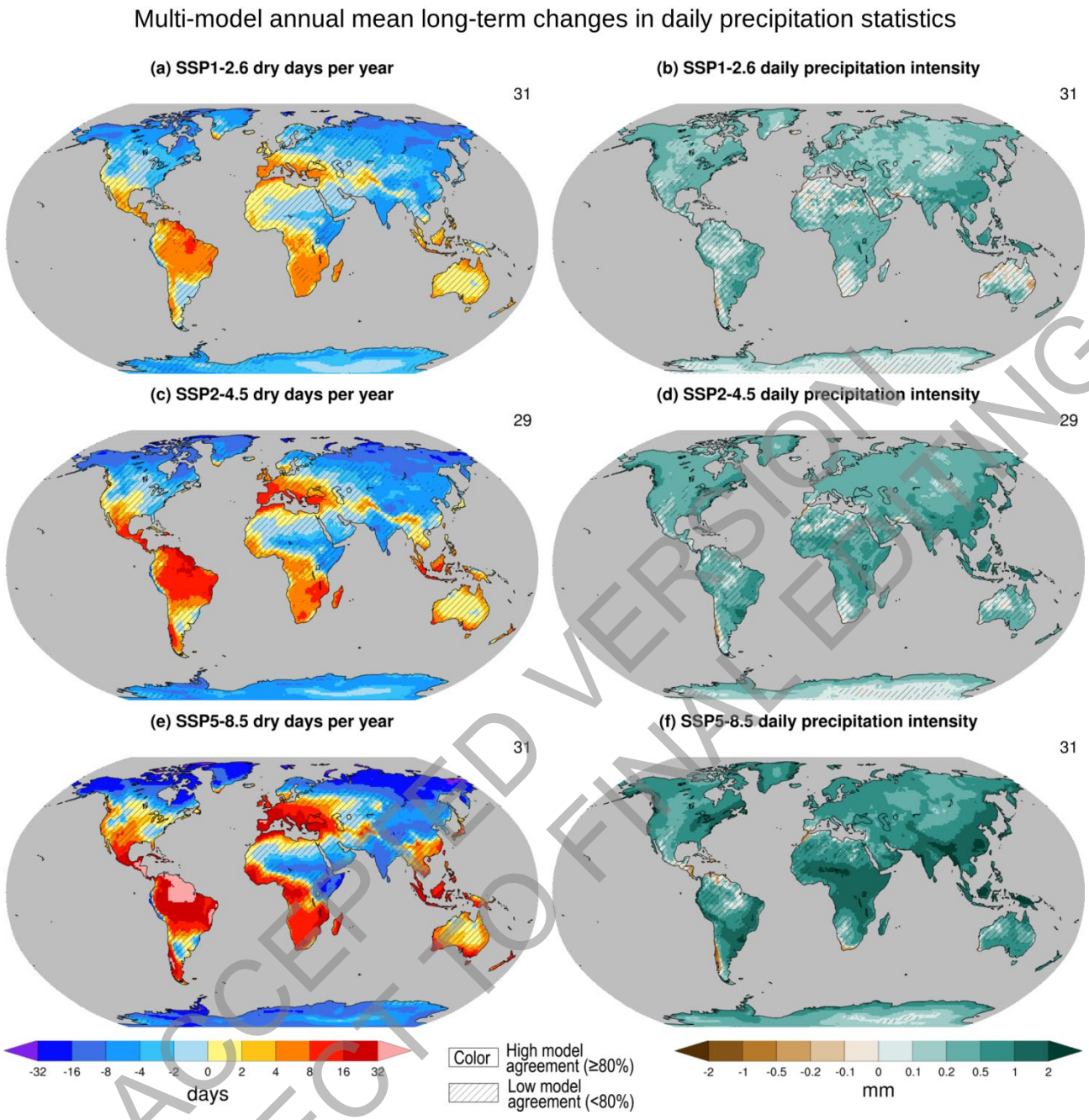
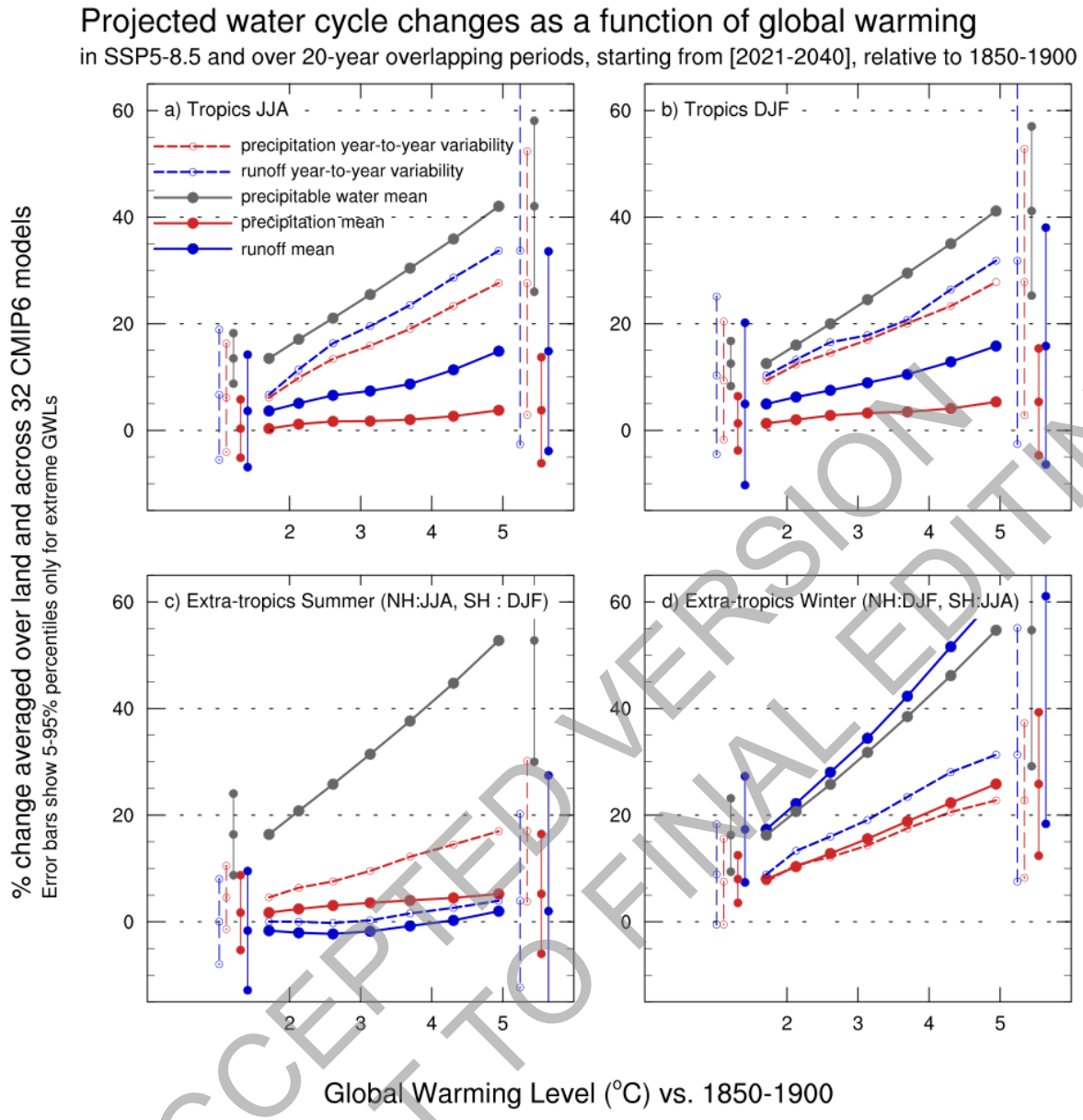


Figure 8.15: Projected long-term relative changes in daily precipitation statistics. Global maps of projected seasonal mean relative changes (%) in the number of dry days (i.e. days with less than 1 mm of rain) and daily precipitation intensity (in mm/day, estimated as the mean daily precipitation amount at wet days - i.e., days with intensity above 1 mm/day) averaged across CMIP6 models in the SSP1-2.6 (a,b), SSP2-4.5 (c,d) and SSP5-8.5 (e,f) scenario respectively. Uncertainty is represented using the simple approach: No overlay indicates regions with high model agreement, where ≥80% of models agree on sign of change; diagonal lines indicate regions with low model agreement, where <80% of models agree on sign of change. For more information on the simple approach, please refer to the Cross-Chapter Box Atlas.1. Further details on data sources and processing are available in the chapter data table (Table 8.SM.1).

ACCEPTED VERSION SUBJECT TO FINAL EDITING



ACCEPTED VERSION SUBJECT TO FINAL EDITING

Figure 8.16: Rate of change in mean and variability across increasing global warming levels. Relative change (%) in seasonal mean total precipitable water (green dashed line), precipitation (red dashed lines), runoff (blue dashed lines), as well as in standard deviation of precipitation (red solid lines) and runoff (blue solid lines) averaged over extra-tropical land in (a) summer and (b) winter, and tropical land in (c) JJA and (d) DJF as a function of global-mean surface temperature for the CMIP6 multi-model mean across the SSP5-8.5 scenario. Extra-tropical winter refers to DJF for Northern Hemisphere and JJA for Southern Hemisphere (and the reverse for extra-tropical summer). Each marker indicates a 21-year period centered on consecutive decades between 2015 and 2085 relative to the 1995–2014 base period. Precipitation and runoff variability are estimated by their standard deviation after removing linear trends from each time series. Error bars show the 5-95% confidence interval for the warmest 5°C global warming level. Figure adapted from (Pendergrass et al., 2017) and updated with CMIP6 models. Further details on data sources and processing are available in the chapter data table (Table 8.SM.1).

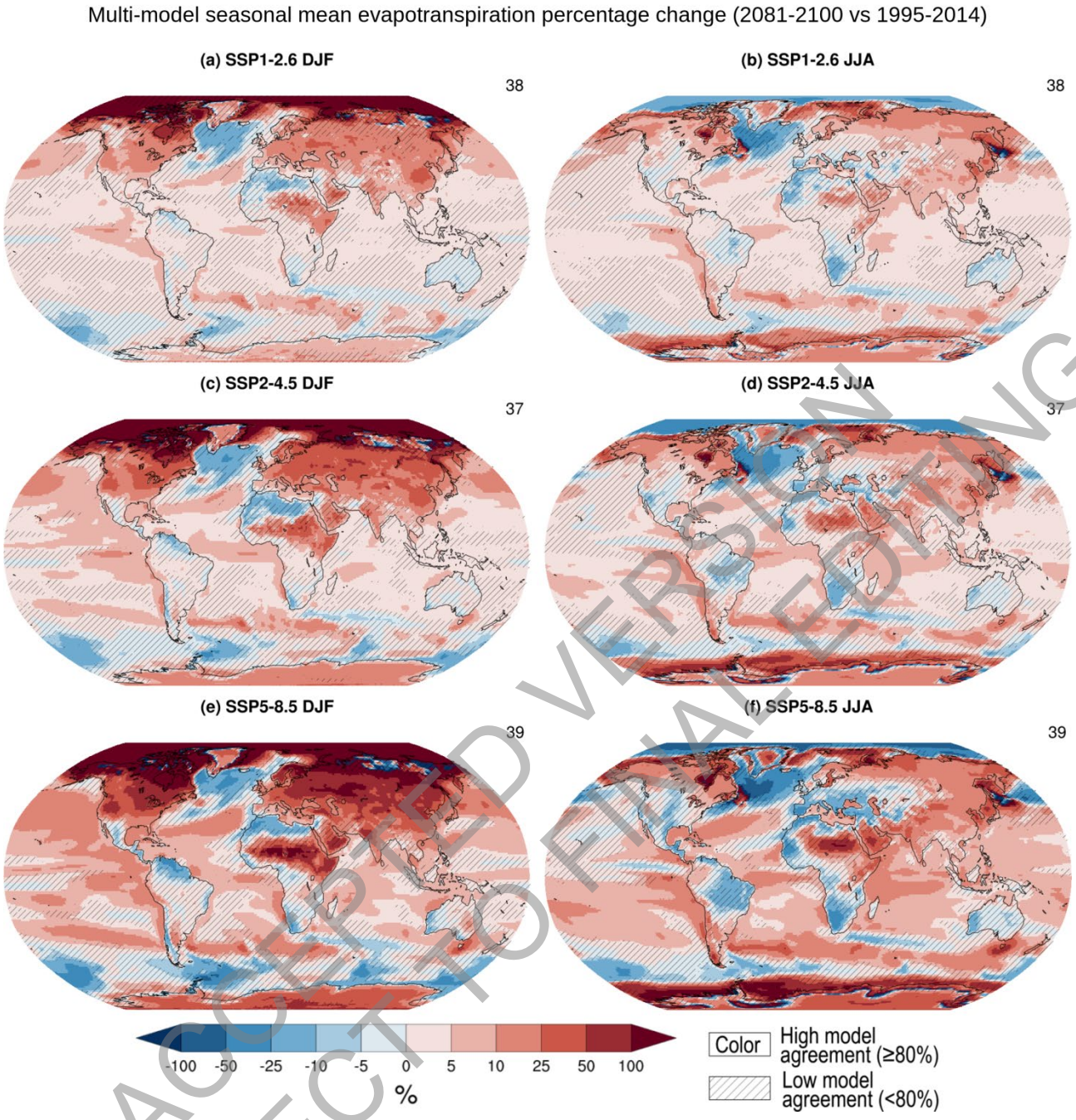


Figure 8.17: Projected long-term relative changes in seasonal mean evapotranspiration. Global maps of projected relative changes (%) in seasonal mean of surface evapotranspiration for DJF (left panels) and JJA (right panels) averaged across 29 or 30 CMIP6 models for SSP1.2-6 (a,b), SSP2-4.5 (c,d) and SSP5-8.5 (e,f) scenario respectively. All changes are estimated in 2081-2100 relative to 1995-2014. Uncertainty is represented using the simple approach: No overlay indicates regions with high model agreement, where ≥80% of models agree on sign of change; diagonal lines indicate regions with low model agreement, where <80% of models agree on sign of change. For more information on the simple approach, please refer to the Cross-Chapter Box Atlas.1. Further details on data sources and processing are available in the chapter data table (Table 8.SM.1).

ACCEPTED VERSION SUBJECT TO FINAL EDITING

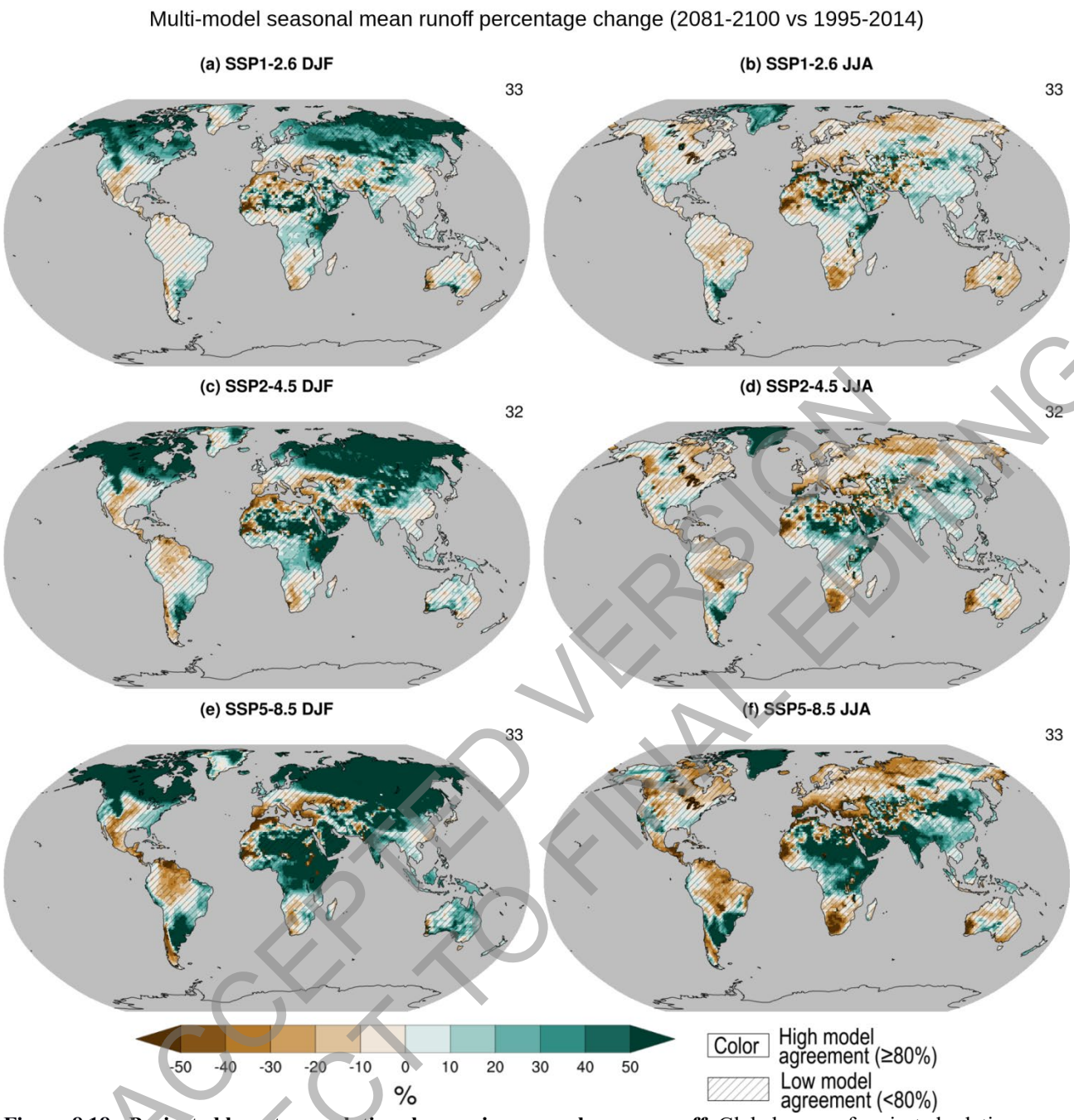


Figure 8.18: Projected long-term relative changes in seasonal mean runoff. Global maps of projected relative change (%) in runoff seasonal mean for DJF (left panels) and JJA (right panels) averaged across CMIP6 models SSP1.2-6 (a,b), SSP2-4.5 (c,d) and SSP5-8.5 (e,f) scenario respectively. All changes are estimated in 2081-2100 relative to 1995-2014. Uncertainty is represented using the simple approach: No overlay indicates regions with high model agreement, where ≥80% of models agree on sign of change; diagonal lines indicate regions with low model agreement, where <80% of models agree on sign of change. For more information on the simple approach, please refer to the Cross-Chapter Box Atlas.1. Further details on data sources and processing are available in the chapter data table (Table 8.SM.1).

ACCEPTED VERSION SUBJECT TO FINAL EDITING

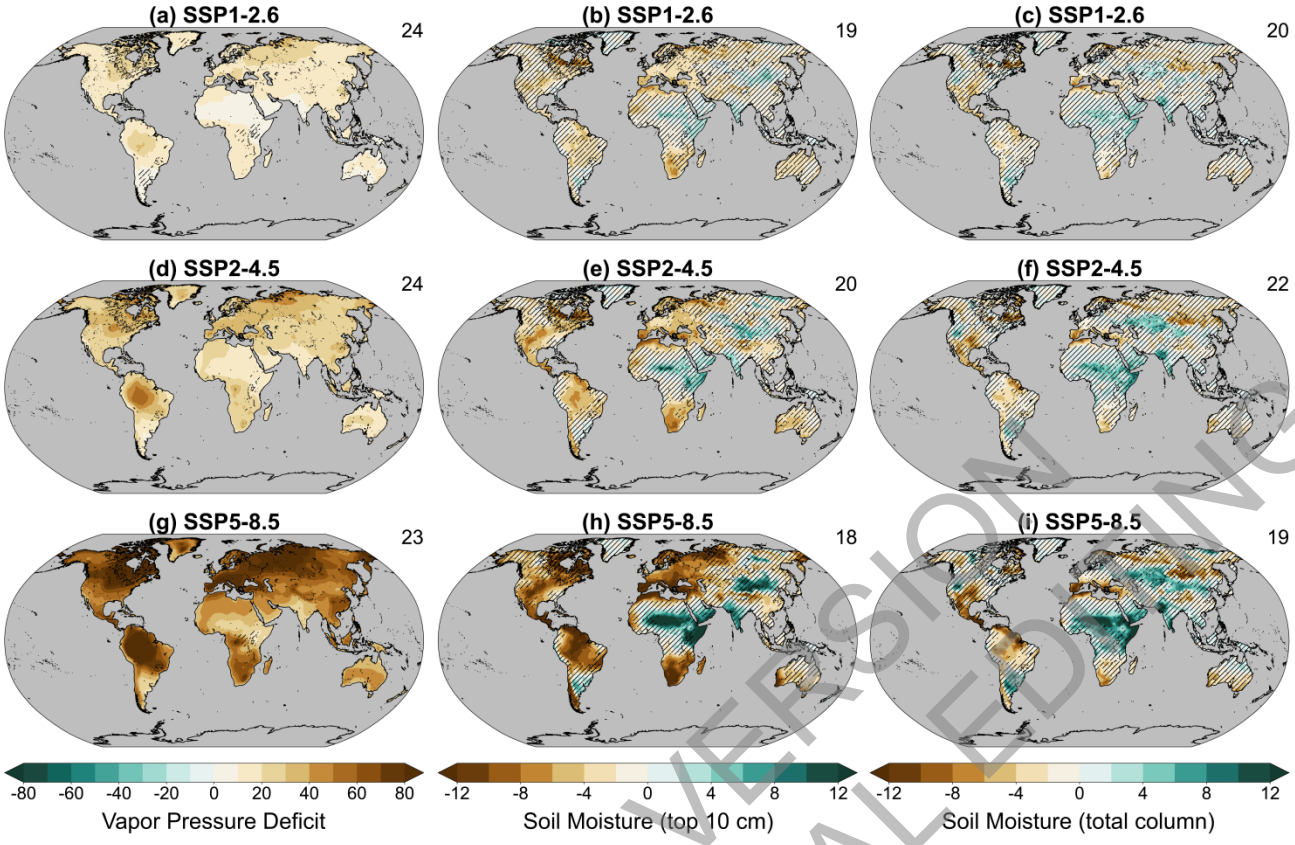
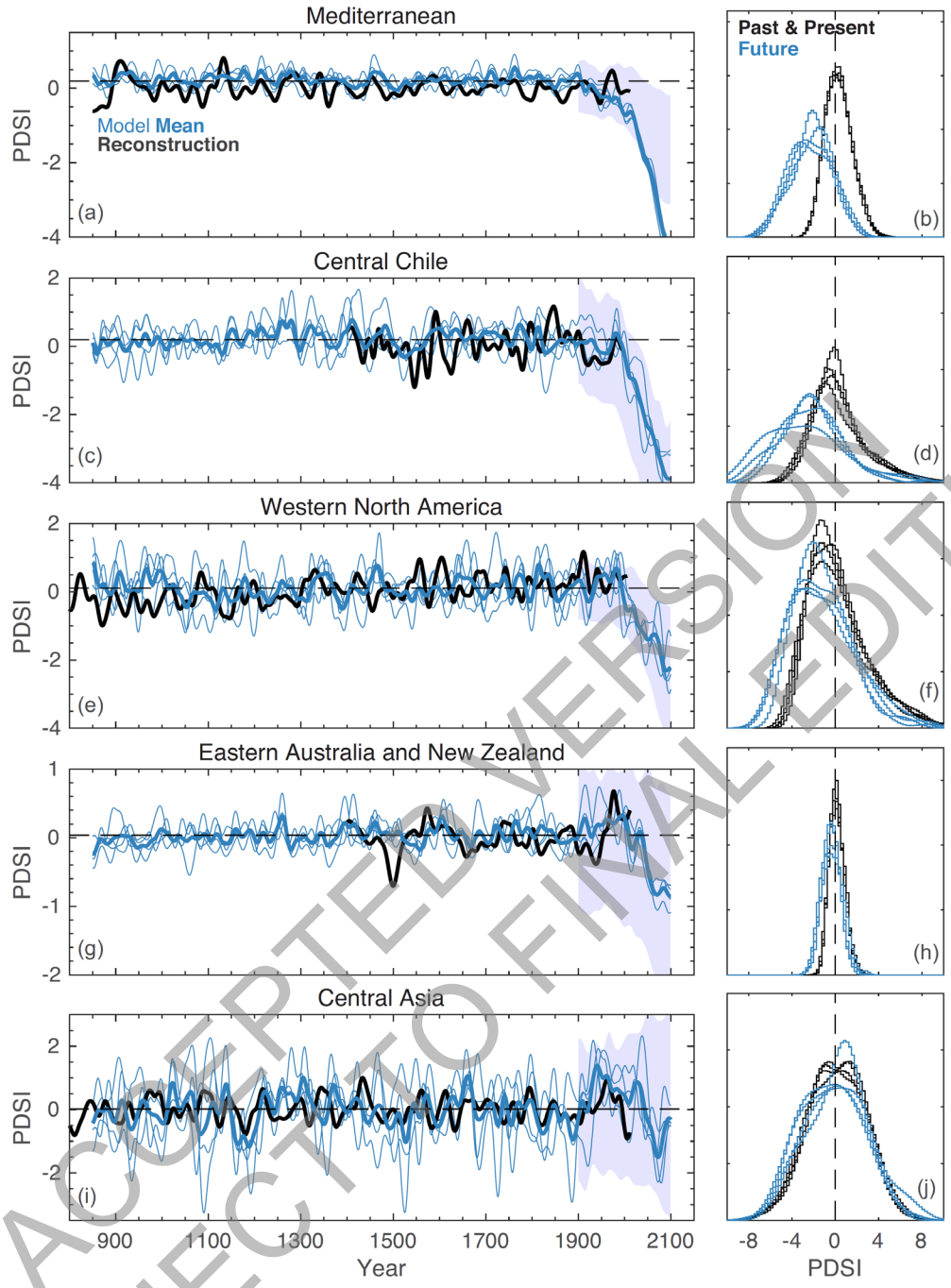


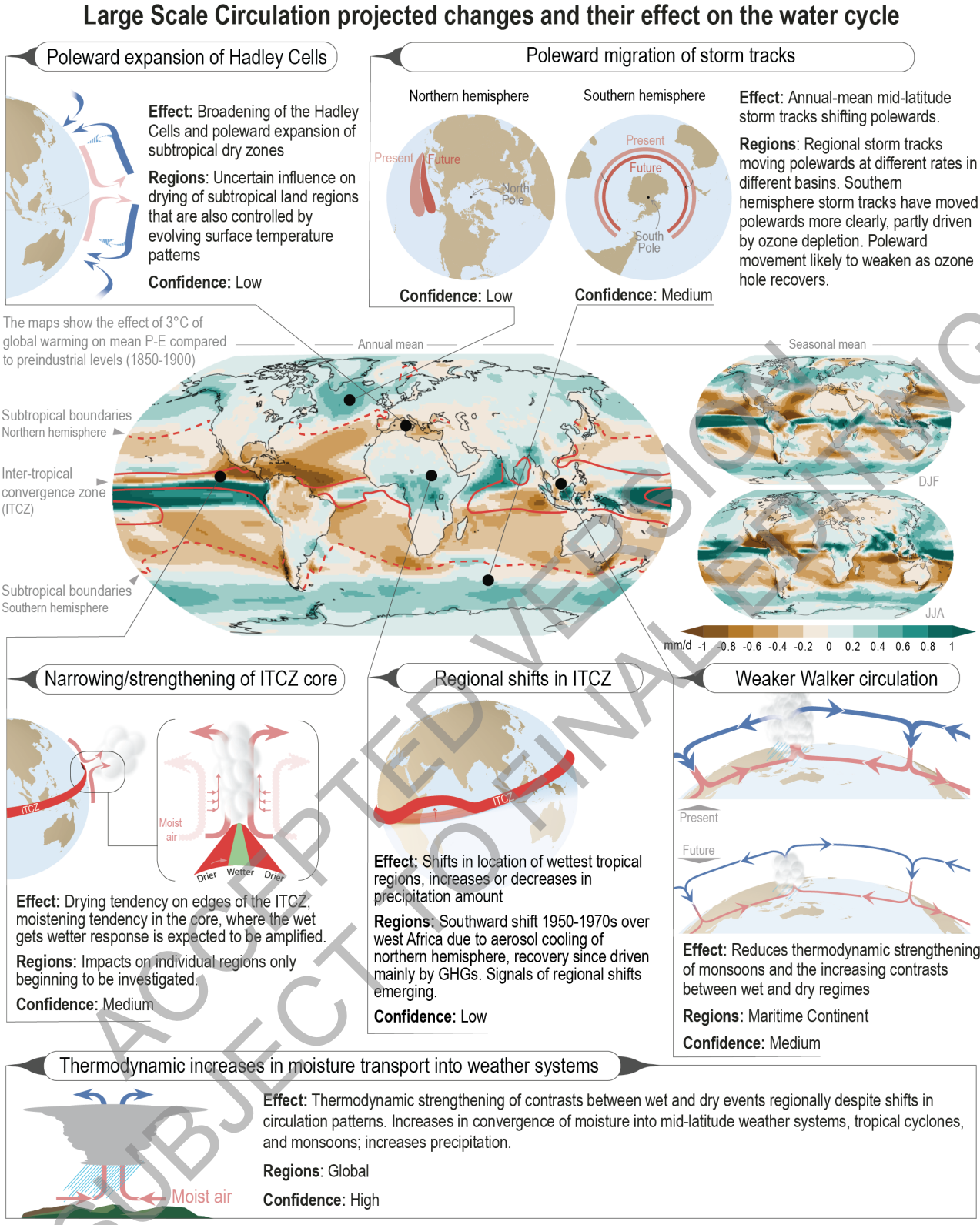
Figure 8.19: Projected long-term relative changes in annual mean soil moisture and vapor pressure deficit. Global maps of projected relative changes (%) in annual mean vapor pressure deficit (left), surface soil moisture (top 10cm, middle) and total column soil moisture (right) from available CMIP6 models for the SSP1.2-6 (a,b,c), SSP2-4.5 (d,e,f) and SSP5-8.5 (g,h,i) scenarios respectively. All changes are estimated for 2081-2100 relative to a 1995-2014 base period. Uncertainty is represented using the simple approach: No overlay indicates regions with high model agreement ("Robust change"), where ≥80% of models agree on sign of change; diagonal lines indicate regions with low model agreement, where <80% of models agree on sign of change. For more information on the simple approach, please refer to the Cross-Chapter Box Atlas.1. Further details on data sources and processing are available in the chapter data table (Table 8.SM.1).

ACCEPTED VERSION SUBJECT TO FINAL EDITING



ACCEPTED VERSION SUBJECT TO FINAL EDITING

Figure 8.20: Past-to-future drought variability in paleoclimate reconstructions and models for select regions. On the left (a,c,e,g,i), tree-ring reconstructed Palmer Drought Severity Index (PDSI) series (black line) for the Mediterranean (10°W–45°E, 30°–47°N; Cook et al., 2015, 2016), central Chile (70°–74°W, 32°–37°S; Morales et al., 2020), western North America (117°–124°W, 32°–38°N; Cook et al., 2010; Griffin and Anchukaitis, 2014), Eastern Australia and New Zealand (136°–178°E, 46°–11°S; Palmer et al., 2015), and Central Asia (99°–107°E, 47°–49°N; Pederson et al., 2014; Hessl et al., 2018) plotted in comparison to the past-to-future fully-forced simulations from four ensemble members (thin blue lines) from the NCAR CESM Last Millennium Ensemble (thick blue line = ensemble mean) (Otto-Bliesner et al., 2016) for the same regions. The shaded area represents the range (10th to 90th percentile) of historical and future (RCP8.5) PDSI (Penman-Monteith) simulations from 15 CMIP5 models and 34 ensemble members for the same regions (1900–2100; Cook et al., 2014). On the right (b,d,f,h,i), the distribution of annual PDSI values from the past and present (850 to 2005 CE) (black) is compared to the future distribution (2006 to 2100 CE) (blue). The distributions show each of the four ensemble members from the CESM LME simulations. The future component of the CESM LME follows the RCP8.5 scenario. Further details on data sources and processing are available in the chapter data table (Table 8.SM.1).



ACCEPTED VERSION SUBJECT TO FINAL EDITING

Figure 8.21: Schematic depicting large-scale circulation changes and impacts on the regional water cycle. The central figures show precipitation minus evaporation (P-E) changes at 3°C or global warming relative to a 1850-1900 base period (mean of 23 CMIP6 SSP5-8.5 simulations). Annual mean changes (large map) include contours depicting control climate P-E=0 lines with the solid contour enclosing the tropical rain belt region and dashed lines representing the edges of subtropical regions. Confidence levels assess understanding of how large-scale circulation change affect the regional water.

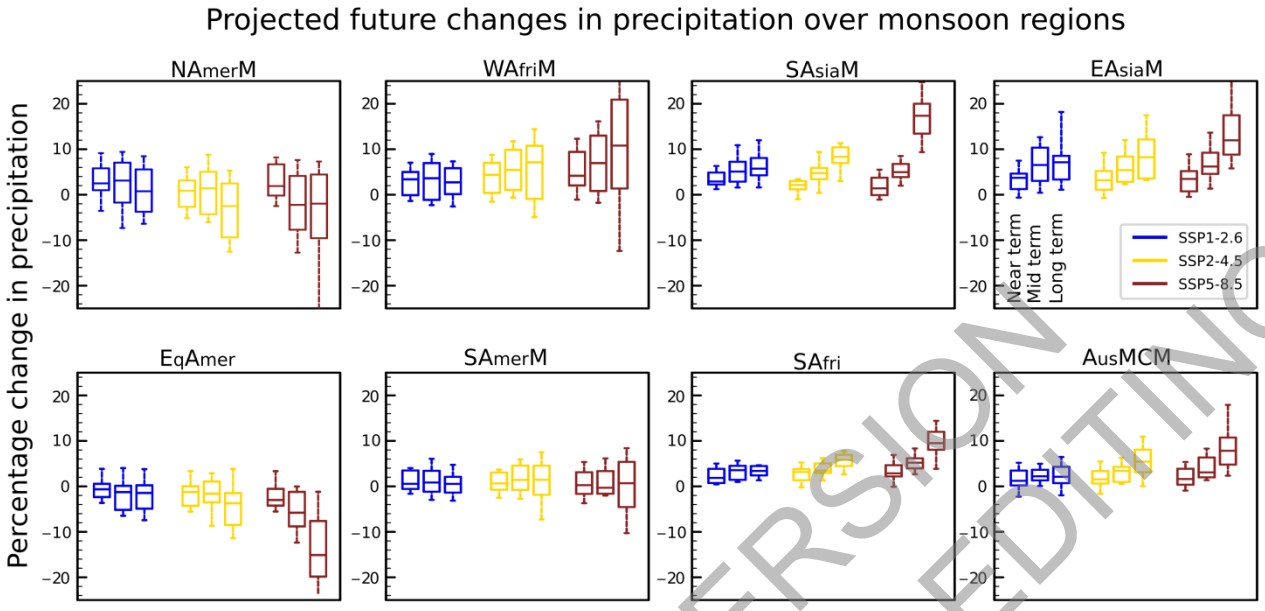


Figure 8.22: Projected regional monsoons precipitation changes. Percentage change in projected seasonal mean precipitation over regional monsoon domains (as defined in Fig 8.11, Section 8.3.2.4 and Annex V) for near-term (2021-2040), mid-term (2041-2060), and long-term (2081-2100) periods based on 24 CMIP6 models and three SSP scenarios (SSP1-2.6, SSP2-4.5 and SSP5-8.5). Further details on data sources and processing are available in the chapter data table (Table 8.SM.1).

ACCEPTED VERSION SUBJECT TO FINAL EDITING

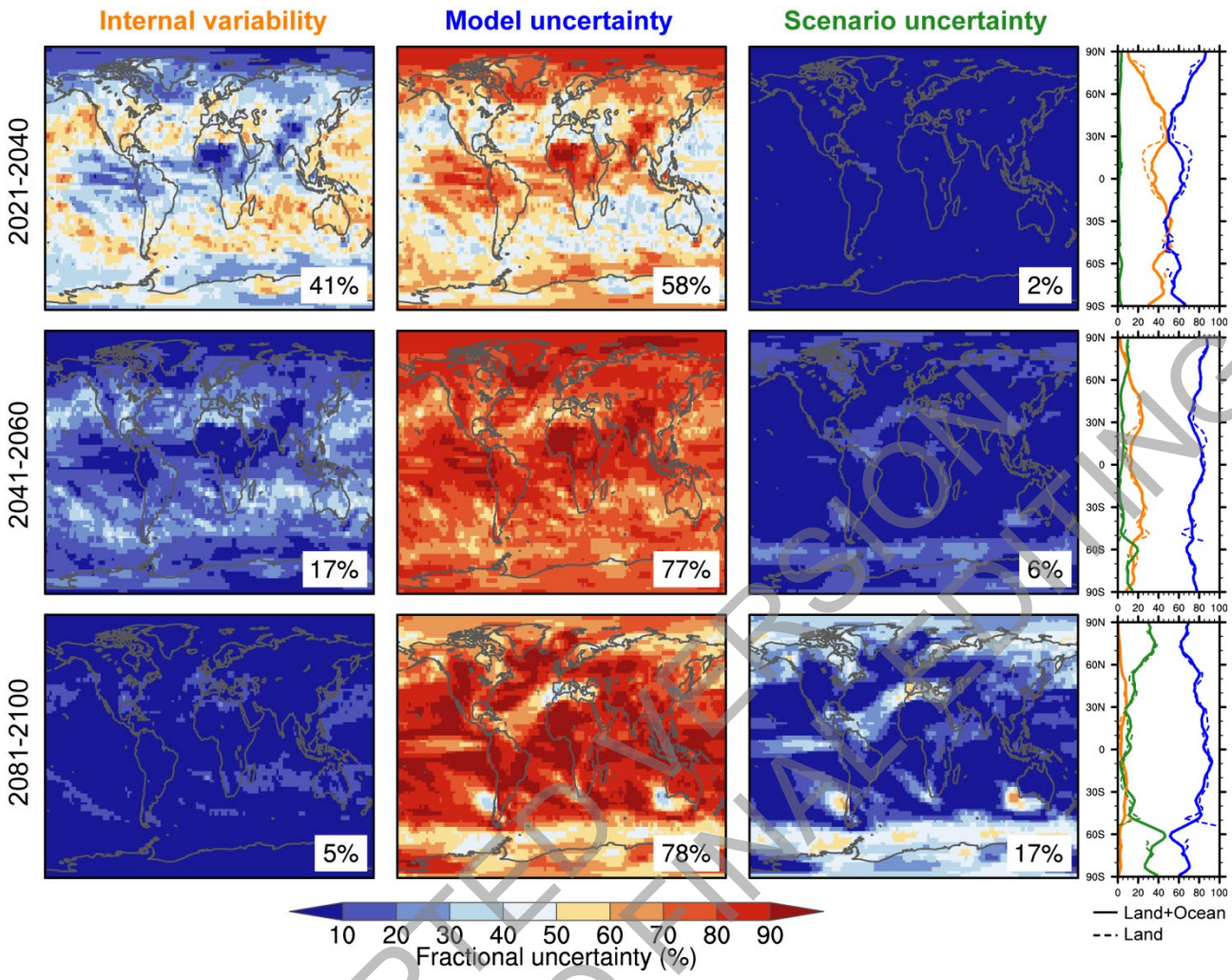


Figure 8.23: Geographical and zonal mean distribution of the percentage of variance explained by the three sources of uncertainty in CMIP6 projections of 20-year mean precipitation changes in 2021–2040 (top), 2041–2060 (middle) and 2081–2100 (bottom) relative to the 1995–2014 base period: internal climate variability (left), model response uncertainty (middle) and scenario uncertainty (right, considering four plausible concentration scenarios: SSP1-2.6, SSP2-4.5, SSP3-7.0 and SSP5-8.5). Percentage numbers give the area-weighted global average value for each map. Right panels show the zonal mean fractions over both land and sea (solid lines) and over land only (dashed line). The figure was adapted from Fig.4a in (Lehner et al., 2020). The relative contributions of internal variability, models and emission scenarios to the total uncertainty depend on both region and time horizon. The scenario uncertainty is relatively low in near and mid-term time horizons while it increases in the long-term mostly over the high-latitudes. The model response uncertainty is the most influential factor across all time horizons. Internal variability also plays a key role in the near-term, especially in the subtropics. Further details on data sources and processing are available in the chapter data table (Table 8.SM.1).

ACCEPTED VERSION SUBJECT TO FINAL EDITING

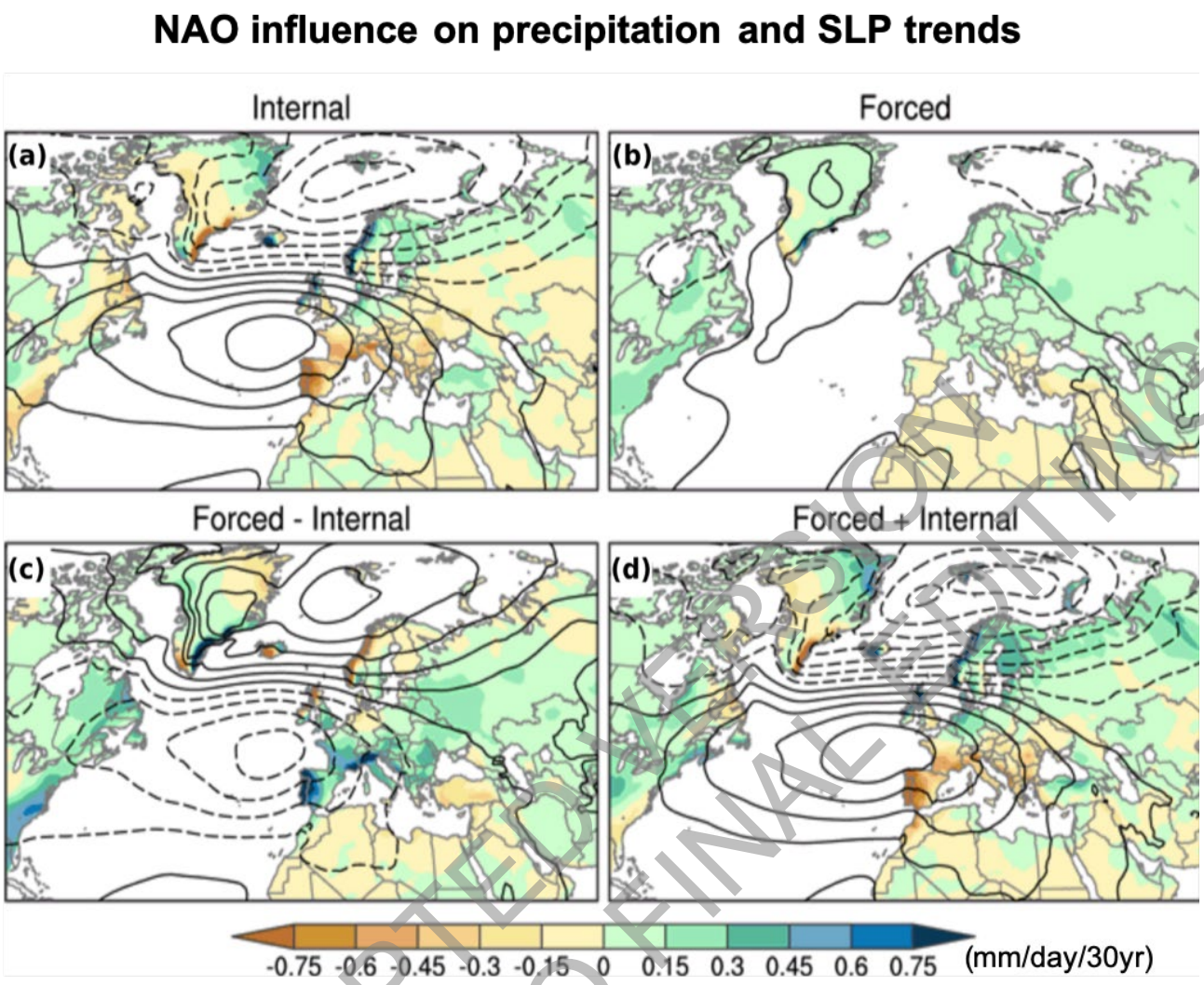
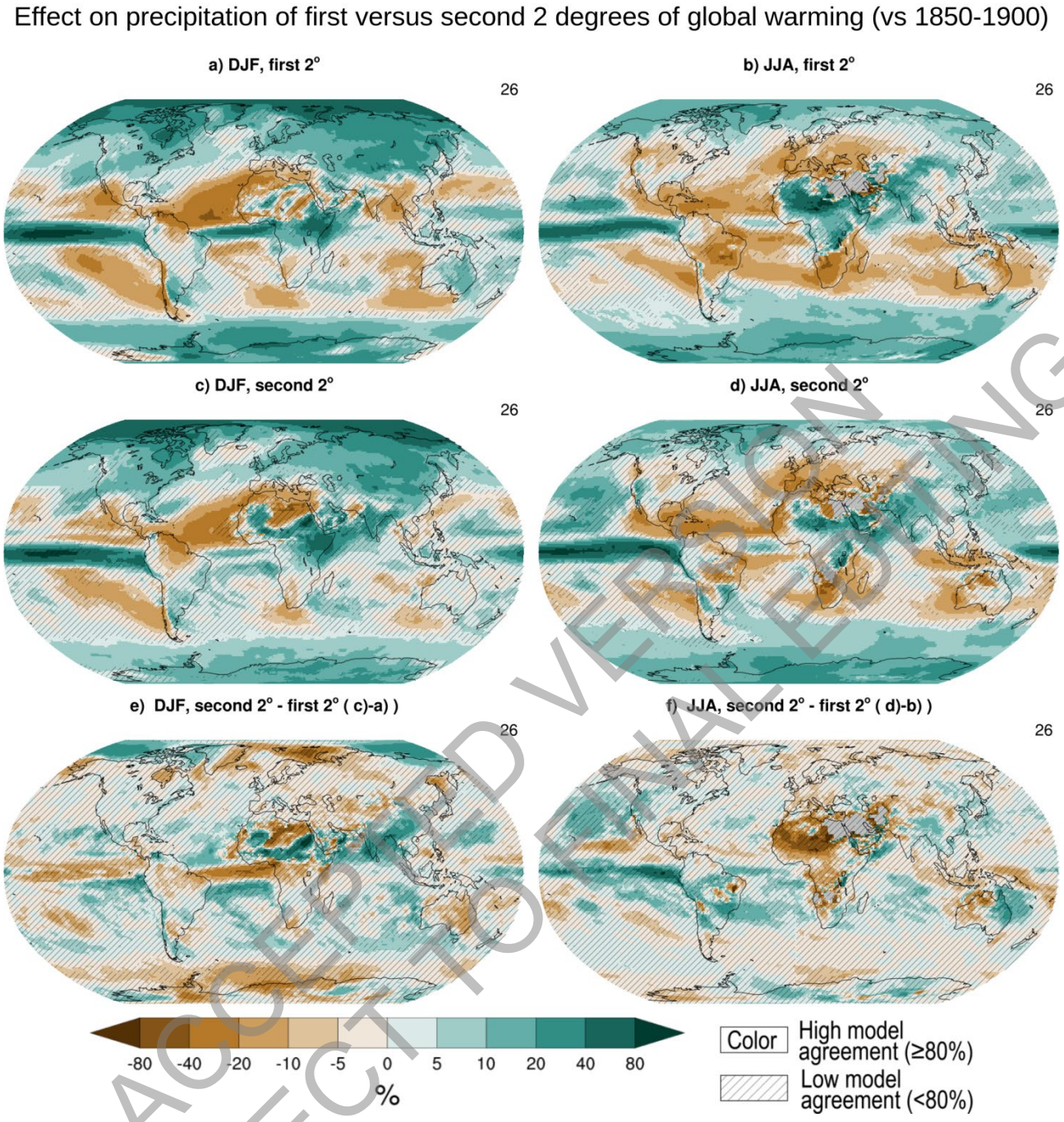


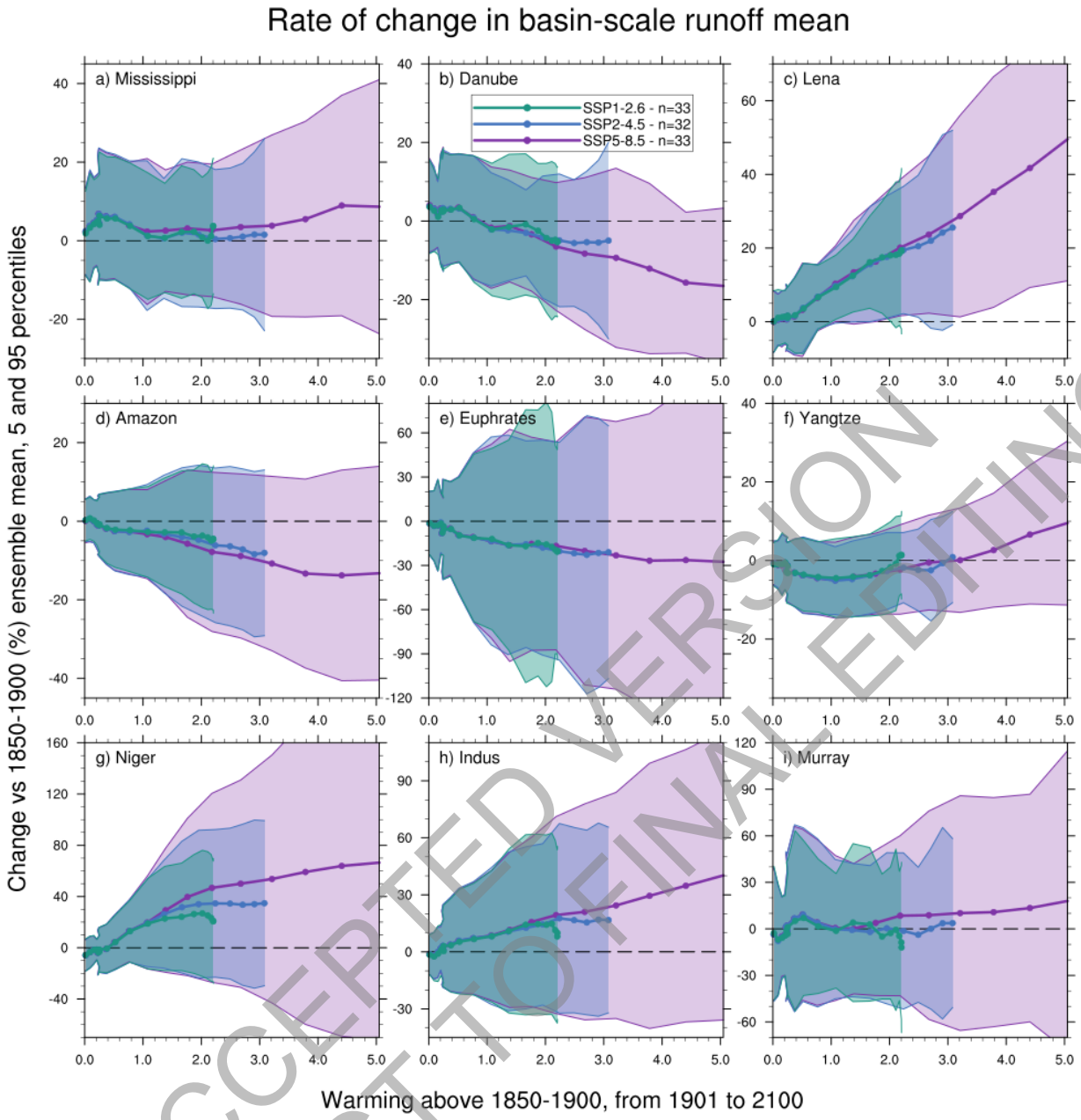
Figure 8.24: Impact of the North Atlantic Oscillation (NAO) on 2016–2045 climate trends. (a) Regressions of winter sea level pressure (SLP) and precipitation trends upon the normalized leading principal component (PC)of winter SLP trends in the CESM1 Large Ensemble, multiplied by two to correspond to a two standard deviation anomaly of the PC (as internal climate variability component); (b) CESM1 ensemble-mean winter SLP and precipitation trends (as forced climate variability component); (c) b – a (forced minus internal climate variability component); (d) b + a (forced plus internal climate variability component). Precipitation in color shading (mm/day per 30 years) and SLP in contours (interval = 1 hPa per 30 years with negative values dashed) (Adapted from Deser et al., 2017). Further details on data sources and processing are available in the chapter data table (Table 8.SM.1).

ACCEPTED VERSION SUBJECT TO FINAL EDITING



ACCEPTED VERSION SUBJECT TO FINAL EDITING

Figure 8.25: Effect of first versus second 2°C of global warming relative to the 1850-1900 base period on seasonal mean precipitation (mm/day). CMIP6 multi-model ensemble mean DJF (left panels) and JJA (right panels) precipitation difference for a,b) SSP5-8.5 at +2°C; c,d) SSP5-8.5 at +4°C minus SSP5-8.5 at +2°C (second 2°C warming); e,f) second minus first 2°C fast warming (c-a and d-b). Only models reaching the +4°C warming levels in SSP5-8.5 are considered. Differences are computed based on 21-yr time windows centered on the first year reaching or exceeding the selected global warming level using a 21-yr running mean global surface atmospheric temperature criterion. Uncertainty is represented using the simple approach: No overlay indicates regions with high model agreement, where ≥80% of models agree on sign of change; diagonal lines indicate regions with low model agreement, where <80% of models agree on sign of change. For more information on the simple approach, please refer to the Cross-Chapter Box Atlas.1. Further details on data sources and processing are available in the chapter data table (Table 8.SM.1).



ACCEPTED VERSION SUBJECT TO FINAL EDITING

Figure 8.26: Rate of change in basin-scale annual mean runoff with increasing global warming levels. Relative changes (%) in basin-averaged annual mean runoff estimated as multi-model ensemble median from a variable subset of CMIP6 models for each SSP over six major river basins: a) Mississipi, b) Danube, c) Lena, d) Amazon, e) Euphrates, f) Yangtze, g) Niger, h) Indus, i) Murray. The basin averages have been estimated after a first-order conservative remapping of the model outputs on the 0.5° by 0.5° river network of (Decharme et al., 2019). The shaded area indicates the 5-95% confidence interval of the ensemble values across all SSPs. Note that the y-axis range differs across basins and is particularly large for Niger and Murray (panels g and i). The number of models considered is specified for each scenario in the legend located inside panel b. Further details on data sources and processing are available in the chapter data table (Table 8.SM.1).

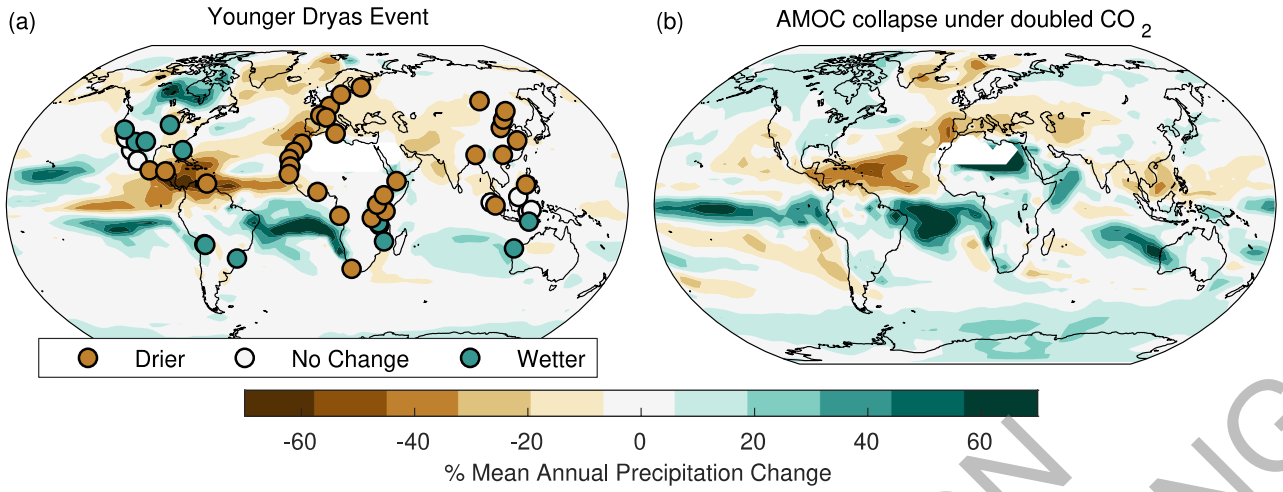


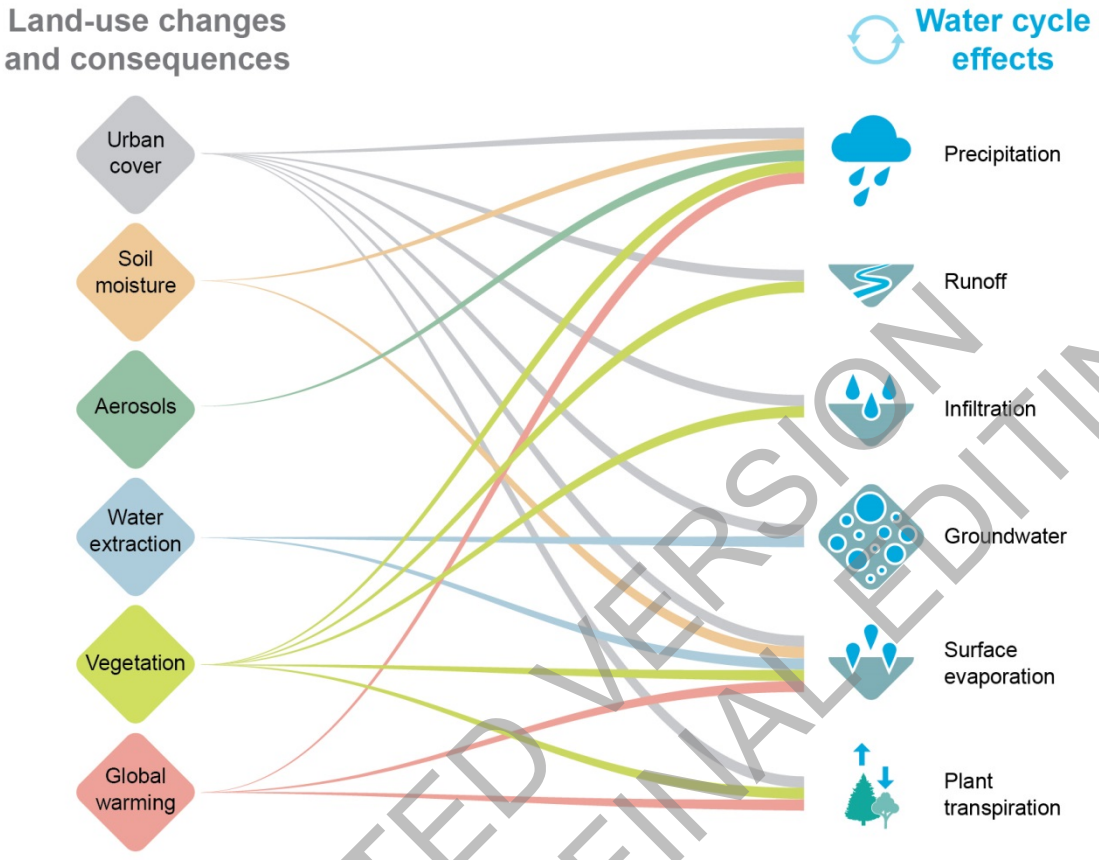
Figure 8.27: (a) Model simulation of precipitation response to the Younger Dryas event relative to the preceding warm Bølling-Allerød period (base colors, calculated as the difference between 12,600–11,700 yr BP and 14,500–12,900 BP from the TraCE paleoclimate simulation of Liu et al., (2009)), with paleoclimate proxy evidence superimposed on top (dots). (b) Model simulation of precipitation response to an abrupt collapse in AMOC under a doubling of 1990 CO_2 levels (after Liu et al., (2017)). Regions with rainfall rates below 20 mm/year are masked. Further details on data sources and processing are available in the chapter data table (Table 8.SM.1).

ACCEPTED VERSION
SUBJECT TO FINAL EDITING

1

FAQ 8.1: **How do land use changes effect the water cycle?**

Altering land use affects the water cycle in many ways, with subsequent consequences for the whole cycle.

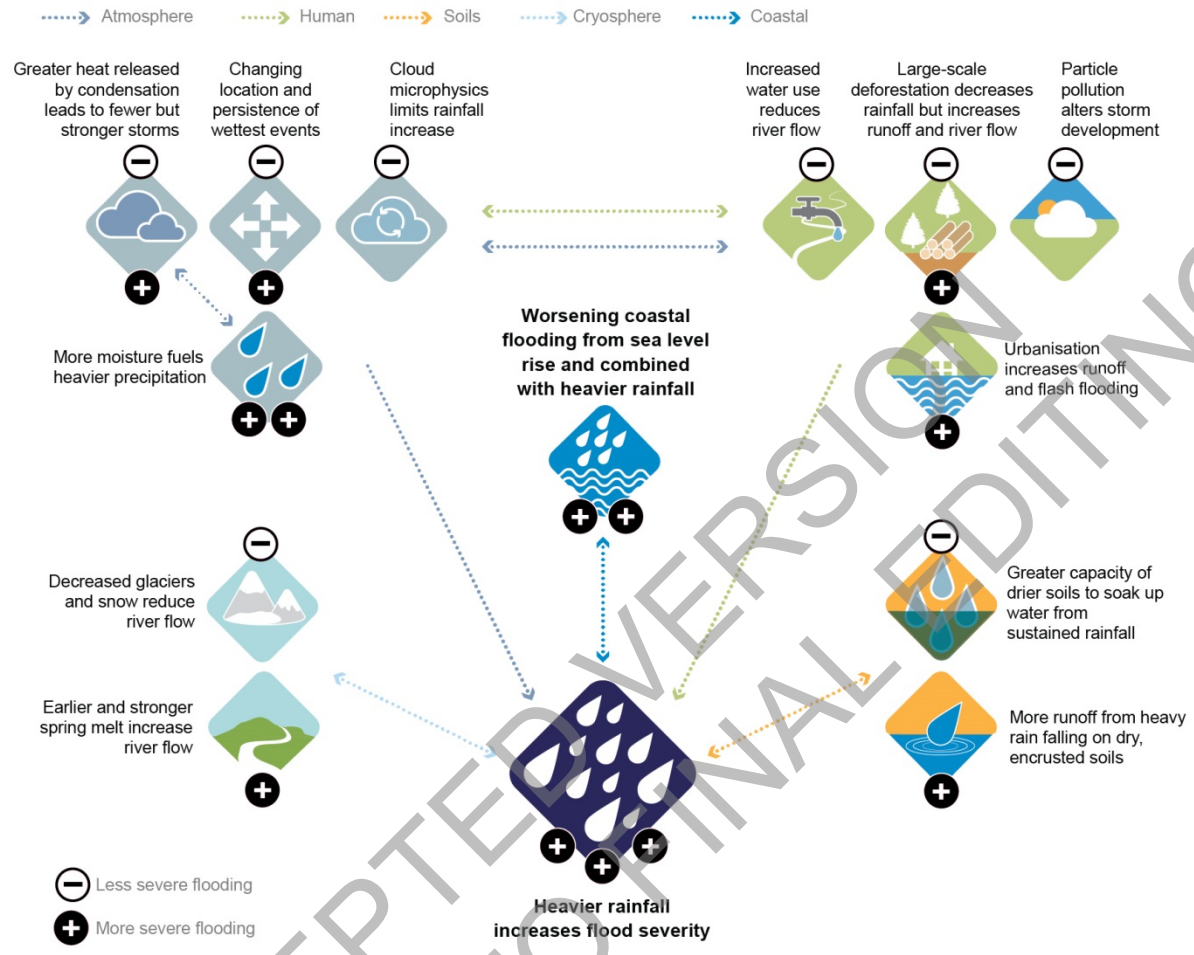


2

3 **FAQ8.1, Figure 1:** Land-use changes and their consequences on the water cycle. As all the components or the water
4 cycle are tightly connected, changes in one aspect of the cycle affects almost all the cycle.

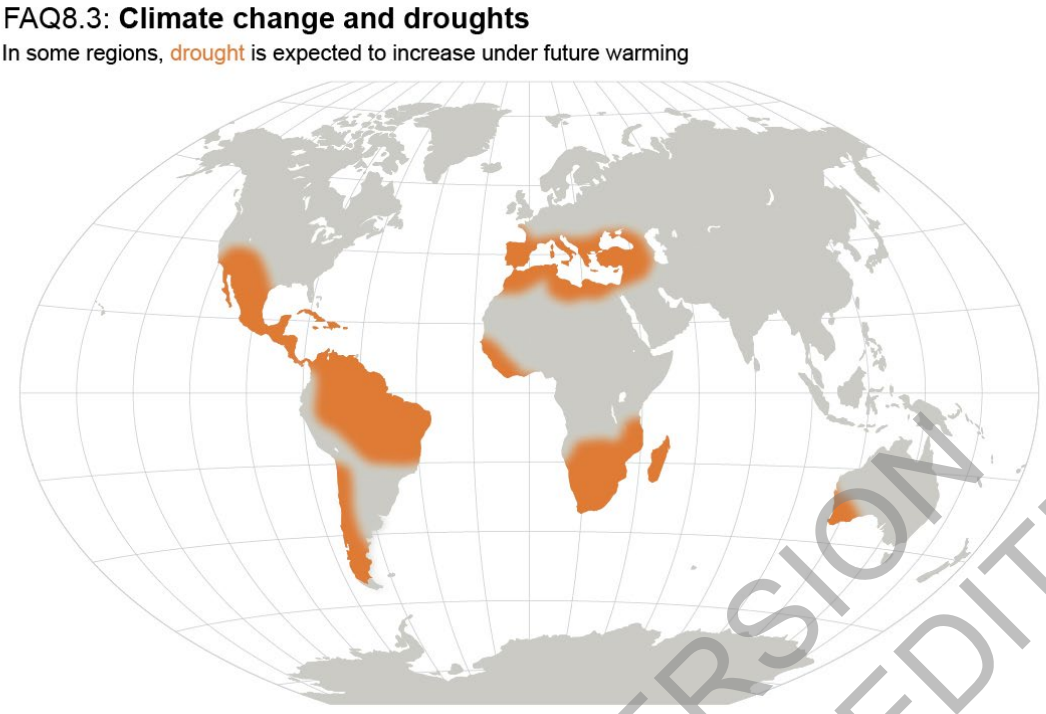
5

ACCEPTED VERSION SUBJECT TO FINAL EDITING



FAQ 8.2, Figure 1: Schematic illustrating factors important in determining changes in heavy precipitation and flooding.

ACCEPTED VERSION SUBJECT TO FINAL EDITING



FAQ 8.3, Figure 1: Schematic map highlighting in brown the regions where droughts are expected to become worse as a result of climate change. This pattern is similar regardless of the emissions scenario; however, the magnitude of change increases under higher emissions.

ACCEPTED VERSION
SUBJECT TO FINAL EDITING

Chapter 8: Water cycle changes - Supplementary Material

Coordinating Lead Authors:
Hervé Douville (France), Krishnan Raghavan (India), James Renwick (New Zealand)

Lead Authors:
Richard P. Allan (United Kingdom), Paola A. Arias (Colombia), Mathew Barlow (United States of America), Ruth Cerezo-Mota (Mexico), Annalisa Cherchi (Italy), ThianY. Gan (Canada/Malaysia), Joëlle Gergis (Australia), Dabang Jiang (China), Asif Khan (Pakistan), Wilfried Pokam Mba (Cameroon), Daniel Rosenfeld (Israel), Jessica Tierney (United States of America), Olga Zolina (Russian Federation/France, Russian Federation)

Review Editors:
Pascale Braconnot (France), Arona Diedhiou (Ivory Coast/Senegal)

Contributing Authors:
Gabriel Abramowitz (Australia), Guðfinna Adalgeirsdottir (Iceland), Andrea Alessandri (Italy), Robert J. Allen (United States of America), Kevin Anchukaitis (United States of America), Richard A. Betts (United Kingdom), Céline J. W. Bonfils (United States of America/France), Michael Bosilovich (United States of America), Olivier Boucher (France), Josephine Brown (Australia), Michael P. Byrne (United Kingdom/Ireland), Robin Chadwick (United Kingdom), Sarah Connors (France/United Kingdom), Benjamin Cook (United States of America), Erika Coppola (Italy), Alejandro Di Luca (Australia, Canada/Argentina), Aïda Diongue Niang (Senegal), Petra Döll (Germany), Ellen Douglas (United States of America), Paul J. Durack (United States of America/Australia), Hayley J. Fowler (United Kingdom), Alexander Gershunov (United States of America), Nicholas R. Golledge (New Zealand/United Kingdom), James Kossin (United States of America), Won-Tae Kwon (Republic of Korea), Flavio Lehner (United States of America/Switzerland), Eric Maloney (United States of America), Vimal Mishra (India), Angeline Pendergrass (United States of America), Stefan Pfahl (Germany), Catherine Prigent (France), Catherine Rio (France), Alex C. Ruane (United States of America), Benjamin Sanderson (United Kingdom), Sonia I. Seneviratne (Switzerland), Shoichi Shige (Japan), Vijay Singh (United States of America), Abigail Swann (United States of America), Richard G. Taylor (United Kingdom/Canada, United Kingdom), Laurent Terray (France), Natalia Tilinina (Russian Federation), Bart van den Hurk (The Netherlands), Sergio M. Vicente-Serrano (Spain), Michael Wehner (United States of America), Laura J. Wilcox (United Kingdom), Cunde Xiao (China), Prodromos Zanis (Greece), Xuebin Zhang (Canada)

Chapter Scientist(s):
Stéphane Sénési (France), Sabin Thazhe Purayil (India)

This Supplementary Material should be cited as:
Douville, H., K. Raghavan, J. Renwick, R. P. Allan, P. A. Arias, M. Barlow, R. Cerezo-Mota, A. Cherchi, T. Y. Gan, J. Gergis, D. Jiang, A. Khan, W. Pokam Mba, D. Rosenfeld, J. Tierney, O. Zolina, 2021, Water Cycle Changes Supplementary Material. In: *Climate Change 2021: The Physical Science Basis. Contribution of Working Group I to the Sixth Assessment Report of the Intergovernmental Panel on Climate Change* [Masson-Delmotte, V., P. Zhai, A. Pirani, S. L. Connors, C. Péan, S. Berger, N. Caud, Y. Chen, L. Goldfarb, M. I. Gomis, M. Huang, K. Leitzell, E. Lonnoy, J.B.R. Matthews, T. K. Maycock, T. Waterfield, O. Yelekçi, R. Yu and B. Zhou (eds.)]. Available from https://ipcc.ch/static/ar6/wg1.

Date: August 2021

This document is subject to copy-editing, corrigenda and trickle backs.

ACCEPTED VERSION SUBJECT TO FINAL EDITING

1 **Table of Contents**

2

3 **8.SM.1 Data Table 3**

4 **References 40**

5

ACCEPTED VERSION
SUBJECT TO FINAL EDITING

8.SM.1 Data Table

[START TABLE 8.SM.1 HERE]

Table 8.SM.1: Input Data Table. Input datasets and code used to create chapter figures.

Figure number / Table number / Chapter section (for calculations)	Dataset / Code name	Type	Filename / Specificities	License type	Dataset / Code citation	Dataset / Code URL	Related publications / Software used
Figure 8.1		Schematic : Depiction of the water cycle based on previous assessments					(Trenberth et al., 2011; Rodell et al., 2015; Abbott et al., 2019) with minor adjustments for groundwater flows (Kwon et al., 2014; Zhou et al., 2019; Luijendijk et al., 2020), seasonal snow (Pulliainen et al., 2020) and ocean precipitation and evaporation (Stephens et al., 2012; Allan et al., 2020; Gutenstein et al., 2020)

ACCEPTED VERSION
SUBJECT TO FINAL EDITING

Figure 8.2		Schematic of the chapter structure and quick guide to the chapter content.					
Figure 8.3		Schematic representation of fast and slow responses of the atmospheric energy balance and global precipitation to radiative forcing					adapted from (Allan et al., 2020, Chapter 7 Figure 7.2 and Figure 8.1).
Figure 8.4	Historical (1995–2014) and SSP2-4.5 (2081–2100) CMIP6 simulations.						
Figure 8.5	GPCP/HadCRUTv4.6 High resolution models including regional climate models (RCM) and cloud resolving models (CRMs)						GCM experiments (Fläschner et al., 2016; Richardson et al., 2018; Samset et al., 2018; Pendergrass, 2020; Rehfeld et al., 2020) (GPCP/HadCRUTv

ACCEPTED VERSION
SUBJECT TO FINAL EDITING

							4.6) (Adler et al., 2017; Allan et al., 2020). GCMs and a observationally constrained estimate (O'Gorman, 2012; Fischer and Knutti, 2015; Bao et al., 2017; Borodina et al., 2017) and estimates from observed changes (Westra et al., 2013; Fischer and Knutti, 2015; Donat et al., 2016; Borodina et al., 2017; Sun et al., 2020; Zeder and Fischer, 2020) and for hourly and sub-hourly extremes based on observed changes (Westra and Sisson, 2011; Westra et al., 2013; Barbero et al., 2017; Guerreiro et al., 2018) and high resolution models including regional climate models (RCM) and cloud resolving models

ACCEPTED VERSION
SUBJECT TO FINAL EDITING

							(CRMs) (Ban et al., 2015; Chan et al., 2016; Prein et al., 2017; Haerter and Schlemmer, 2018; Lenderink et al., 2019).
Figure 8.6		Schematic: Climatic drivers of drought					
Figure 8.7	GPCP GPCC CMIP6/DAMIP					https://psl.noaa.gov/data/gridded/data.gpcp.html https://psl.noaa.gov/data/gridded/data.gpcc.html https://esgf-node.llnl.gov/search/cmip6/	NCL
	CMIP6 model data						
	ACCESS-ESM1-5: historical, hist-GHG, hist-aer, hist-nat	Input dataset			(Ziehn et al., 2019a, 2020a, 2020c, 2020b)		
	BCC-CSM2-MR: historical, hist-GHG, hist-aer, hist-nat	Input dataset			(Wu et al., 2018a, 2019b, 2019a, 2019c)		
	CNRM-CM6-1: historical, hist-GHG, hist-aer, hist-nat	Input dataset			(Voldoire, 2018a, 2019f, 2019e, 2019g)		
	CanESM5: historical, hist-GHG, hist-aer, hist-nat	Input dataset			(Swart et al., 2019k, 2019j, 2019l, 2019h)		

ACCEPTED VERSION SUBJECT TO FINAL EDITING

	FGOALS-g3: hist-GHG, hist-aer, hist-nat, historical	Input dataset			(Li, 2020b, 2020d, 2020a, 2020c)		
	HadGEM3-GC31-LL: historical, hist-GHG, hist-aer, hist-nat	Input dataset			(Jones, 2019a, 2019b, 2019c; Ridley et al., 2019a)		
	IPSL-CM6A-LR: historical, hist-GHG, hist-aer, hist-nat	Input dataset			(Boucher et al., 2018f, 2018d, 2018e, 2018b)		
	MIROC6: historical, hist-GHG, hist-aer, hist-nat	Input dataset			(Tatebe and Watanabe, 2018b; Shiogama, 2019a, 2019b, 2019c)		
	MRI-ESM2-0: historical, hist-GHG, hist-aer, hist-nat	Input dataset			(Yukimoto et al., 2019b, 2019f, 2019d, 2019e)		
Figure 8.8	GLDAS CMIP6/DAMIP					https://disc.gsfc.nasa.gov/datasets?keywords=GLDAS https://esgf-node.llnl.gov/search/cmip6/	NCL
	CMIP6 model data						
	ACCESS-ESM1-5: historical, hist-GHG, hist-aer, hist-nat	Input dataset			(Ziehn et al., 2019a, 2020a, 2020c, 2020b)		
	BCC-CSM2-MR: historical, hist-GHG, hist-aer, hist-nat	Input dataset			(Wu et al., 2018a, 2019b, 2019a, 2019c)		
	CNRM-CM6-1: historical, hist-GHG, hist-aer, hist-nat	Input dataset			(Voldoire, 2018a, 2019f, 2019e, 2019g)		
	CanESM5: historical, hist-GHG, hist-aer, hist-nat	Input dataset			(Swart et al., 2019k, 2019j, 2019l, 2019h)		

ACCEPTED VERSION SUBJECT TO FINAL EDITING

	FGOALS-g3: hist-GHG, hist-aer, hist-nat, historical	Input dataset			(Li, 2020b, 2020d, 2020a, 2020c)		
	HadGEM3-GC31-LL: historical, hist-GHG, hist-aer, hist-nat	Input dataset			(Jones, 2019a, 2019b, 2019c; Ridley et al., 2019a)		
	IPSL-CM6A-LR: historical, hist-GHG, hist-aer, hist-nat	Input dataset			(Boucher et al., 2018f, 2018d, 2018e, 2018b)		
	MIROC6: historical, hist-GHG, hist-aer, hist-nat	Input dataset			(Tatebe and Watanabe, 2018b; Shiogama, 2019a, 2019b, 2019c)		
	MRI-ESM2-0: historical, hist-GHG, hist-aer, hist-nat	Input dataset			(Yukimoto et al., 2019b, 2019f, 2019d, 2019e)		
Figure 8.9	CMIP6/DAMIP						(Bonfils et al., 2020).
Figure 8.10	GRACE Satellite observations						Rodell et al. (2018).
Figure 8.11	GPCP GPCC APHRO_MA_050deg_V1101 APHRO_MA_050deg_V1901 CMIP6/DAMIP	Regional shape file				https://psl.noaa.gov/data/gridded/data.gpcp.html https://psl.noaa.gov/data/gridded/data.gpcc.html https://climatedataguide.ucar.edu/climate-data/aphrodite-asian-precipitation-highly-resolved-observational-data-integration-towards	NCL

ACCEPTED VERSION
SUBJECT TO FINAL EDITING

						https://esgf-node.llnl.gov/search/cmip6/	
	CMIP6 model data						
	ACCESS-ESM1-5: historical, hist-GHG, hist-aer, hist-nat	Input dataset			(Ziehn et al., 2019a, 2020a, 2020c, 2020b)		
	BCC-CSM2-MR: historical, hist-GHG, hist-aer, hist-nat	Input dataset			(Wu et al., 2018a, 2019b, 2019a, 2019c)		
	CNRM-CM6-1: historical, hist-GHG, hist-aer, hist-nat	Input dataset			(Voldoire, 2018a, 2019f, 2019e, 2019g)		
	CanESM5: historical, hist-GHG, hist-aer, hist-nat	Input dataset			(Swart et al., 2019k, 2019j, 2019l, 2019h)		
	FGOALS-g3: hist-GHG, hist-aer, hist-nat, historical	Input dataset			(Li, 2020b, 2020d, 2020a, 2020c)		
	HadGEM3-GC31-LL: historical, hist-GHG, hist-aer, hist-nat	Input dataset			(Jones, 2019a, 2019b, 2019c; Ridley et al., 2019a)		
	IPSL-CM6A-LR: historical, hist-GHG, hist-aer, hist-nat	Input dataset			(Boucher et al., 2018f, 2018d, 2018e, 2018b)		
	MIROC6: historical, hist-GHG, hist-aer, hist-nat	Input dataset			(Tatebe and Watanabe, 2018b; Shiogama, 2019a, 2019b, 2019c)		
	MRI-ESM2-0: historical, hist-GHG, hist-aer, hist-nat	Input dataset			(Yukimoto et al., 2019b, 2019f, 2019d, 2019e)		
Figure 8.12	CFSR, ERA5, JRA55, ERA-I, MERRA2						(Tilinina et al., submitted).

ACCEPTED VERSION SUBJECT TO FINAL EDITING

Figure 8.13	ACCESS-CM2: historical, piControl, ssp126, ssp245, ssp585	Input dataset			(Dix et al., 2019d, 2019a, 2019e, 2019b, 2019c)		
	ACCESS-ESM1-5: historical, piControl, ssp126, ssp245, ssp585	Input dataset			(Ziehn et al., 2019a, 2019e, 2019d, 2019b, 2019c)		
	AWI-CM-1-1-MR: historical, piControl, ssp126, ssp245, ssp585	Input dataset			(Semmler et al., 2018c, 2018d, 2018a, 2018b, 2019)		
	BCC-CSM2-MR: historical, piControl, ssp126, ssp245, ssp585	Input dataset			(Wu et al., 2018a, 2018b, Xin et al., 2019a, 2019c, 2019b)		
	BCC-ESM1: piControl	Input dataset			(Zhang et al., 2018)		
	CAMS-CSM1-0: historical, piControl, ssp126, ssp245, ssp585	Input dataset			(Rong, 2019d, 2019e, 2019b, 2019f, 2019c)		
	CAS-ESM2-0: piControl	Input dataset			(Chai, 2020)		
	CESM2: historical, piControl, ssp126, ssp245, ssp585	Input dataset			(Danabasoglu, 2019j, 2019m, 2019l, 2019k; Danabasoglu et al., 2019)		
	CESM2-FV2: piControl	Input dataset			(Danabasoglu, 2019a)		
	CESM2-WACCM: historical, piControl, ssp126, ssp245, ssp585	Input dataset			(Danabasoglu, 2019d, 2019e, 2019f, 2019h, 2019g)		
	CESM2-WACCM-FV2: piControl	Input dataset			(Danabasoglu, 2019b)		
	CIESM: historical, piControl, ssp126, ssp245, ssp585	Input dataset			(Huang, 2019a, 2019c, 2019b, 2020b, 2020a)		
	CMCC-CM2-SR5: historical, piControl, ssp126, ssp245, ssp585	Input dataset			(Lovato and Peano, 2020b, 2020c, 2020a, 2020d, 2020e)		

ACCEPTED VERSION SUBJECT TO FINAL EDITING

	CNRM-CM6-1: historical, piControl, ssp126, ssp245, ssp585	Input dataset			(Voldoire, 2018b, 2018a, 2019j, 2019i, 2019h)		
	CNRM-CM6-1-HR: historical, piControl, ssp126, ssp245, ssp585	Input dataset			(Voldoire, 2019a, 2019d, 2019b, 2019c, 2020)		
	CNRM-ESM2-1: historical, piControl, ssp126, ssp245, ssp585	Input dataset			(Seferian, 2018b, 2018c, Voldoire, 2019m, 2019l, 2019k)		
	CanESM5: historical, piControl, ssp126, ssp245, ssp585	Input dataset			(Swart et al., 2019n, 2019i, 2019o, 2019m, 2019h)		
	CanESM5-CanOE: historical, piControl, ssp126, ssp245, ssp585	Input dataset			(Swart et al., 2019f, 2019e, 2019d, 2019c, 2019b)		
	E3SM-1-0: piControl	Input dataset			(Bader et al., 2018)		
	EC-Earth3: historical, piControl, ssp126, ssp245, ssp585	Input dataset			(EC-Earth Consortium (EC-Earth), 2019g, 2019j, 2019h, 2019k, 2019i)		
	EC-Earth3-AerChem: piControl	Input dataset			(EC-Earth Consortium (EC-Earth), 2020a)		
	EC-Earth3-LR: piControl	Input dataset			(EC-Earth Consortium (EC-Earth), 2019a)		
	EC-Earth3-Veg: historical, piControl, ssp126, ssp245, ssp585	Input dataset			(EC-Earth Consortium (EC-Earth), 2019e, 2019c, 2019f, 2019d, 2019b)		
	EC-Earth3-Veg-LR: piControl	Input dataset			(EC-Earth Consortium (EC-Earth), 2020c)		
	FGOALS-f3-L: historical, piControl, ssp126, ssp245, ssp585	Input dataset			(Yu, 2019e, 2019c, 2019a, 2019d, 2019b)		
	FGOALS-g3: historical, piControl, ssp126, ssp245, ssp585	Input dataset			(Li, 2019f, 2019e, 2019b, 2019c, 2019d)		

ACCEPTED VERSION SUBJECT TO FINAL EDITING

	FIO-ESM-2-0: historical, piControl, ssp126, ssp245, ssp585	Input dataset			(Song et al., 2019e, 2019b, 2019d, 2019c, 2019a)		
	GFDL-CM4: historical, piControl, ssp245, ssp585	Input dataset			(Guo et al., 2018e, 2018d, 2018b, 2018c)		
	GFDL-ESM4: historical, piControl, ssp126, ssp245, ssp585	Input dataset			(John et al., 2018a, 2018b, 2018c, Krasting et al., 2018b, 2018c)		
	GISS-E2-1-G: historical, piControl, ssp126, ssp245, ssp585	Input dataset			(NASA Goddard Institute for Space Studies (NASA/GISS), 2018c, 2018b, 2020a, 2020c, 2020b)		
	GISS-E2-1-H: piControl	Input dataset			(NASA Goddard Institute for Space Studies (NASA/GISS), 2018d)		
	HadGEM3-GC31-LL: historical, piControl, ssp126, ssp245, ssp585	Input dataset			(Ridley et al., 2018, 2019a, Good, 2019, 2020a, 2020b)		
	HadGEM3-GC31-MM: historical, piControl, ssp126, ssp585	Input dataset			(Ridley et al., 2019c, 2019b, Jackson, 2020b, 2020a)		
	INM-CM4-8: historical, piControl, ssp126, ssp245, ssp585	Input dataset			(Volodin et al., 2019d, 2019b, 2019c, 2019f, 2019e)		
	INM-CM5-0: historical, piControl, ssp126, ssp245, ssp585	Input dataset			(Volodin et al., 2019j, 2019k, 2019i, 2019h, 2019l)		
	IPSL-CM5A2-INCA: historical, ssp126	Input dataset			(Boucher et al., 2020a, 2020b)		
	IPSL-CM6A-LR: historical, piControl, ssp126, ssp245, ssp585	Input dataset			(Boucher et al., 2018c, 2018b, 2019a, 2019b, 2019c)		
	KACE-1-0-G: historical, piControl, ssp126, ssp245, ssp585	Input dataset			(Byun et al., 2019b, 2019f, 2019c, 2019e, 2019a)		

ACCEPTED VERSION SUBJECT TO FINAL EDITING

	MCM-UA-1-0: historical, piControl, ssp126, ssp245, ssp585	Input dataset			(Stouffer, 2019f, 2019b, 2019c, 2019e, 2019d)		
	MIROC-ES2L: historical, piControl, ssp126, ssp245, ssp585	Input dataset			(Hajima et al., 2019b, 2019c, Tachiiri et al., 2019b, 2019c, 2019a)		
	MIROC6: historical, piControl, ssp126, ssp245, ssp585	Input dataset			(Tatebe and Watanabe, 2018b, 2018c, Shiogama et al., 2019c, 2019a, 2019b)		
	MPI-ESM-1-2-HAM: piControl	Input dataset			(Neubauer et al., 2019)		
	MPI-ESM1-2-HR: historical, piControl, ssp126, ssp245, ssp585	Input dataset			(Jungclaus et al., 2019b, 2019a, Schupfner et al., 2019a, 2019b, 2019c)		
	MPI-ESM1-2-LR: historical, piControl, ssp126, ssp245, ssp585	Input dataset			(Wieners et al., 2019b, 2019a, 2019c, 2019d, 2019e)		
	MPI-ESM2-0: historical, piControl, ssp126, ssp245, ssp585	Input dataset			(Yukimoto et al., 2019c, 2019g, 2019b, 2019h, 2019i)		
	NESM3: historical, piControl, ssp126, ssp245, ssp585	Input dataset			(Cao, 2019b, 2019c, 2019a, Cao and Wang, 2019c, 2019b)		
	NorCPM1: piControl	Input datasetInput dataset			(Bethke et al., 2019)		
	NorESM1-F: piControl	Input dataset			(Guo et al., 2019)		
	NorESM2-LM: historical, piControl, ssp126, ssp245, ssp585	Input dataset			(Seland et al., 2019d, 2019e, 2019c, 2019b, 2019a)		
	NorESM2-MM: historical, piControl, ssp126, ssp245, ssp585	Input dataset			(Bentsen et al., 2019b, 2019c, 2019a, 2019e, 2019d)		

ACCEPTED VERSION
SUBJECT TO FINAL EDITING

	SAM0-UNICON: piControl	Input dataset			(Park and Shin, 2019)		
	TaiESM1: historical, piControl, ssp585	Input dataset			(Lee and Liang, 2020b, 2020a, 2020c)		
	UKESM1-0-LL: historical, piControl, ssp126, ssp245, ssp585	Input dataset			(Good et al., 2019a, 2019c, 2019b, Tang et al., 2019b, 2019c)		
	Figure 8.13 Code	Code	Fig8-13.sh (compute and plot)			https://github.com/senesis/some_chap8_figures	CAMMAC :(Sénési, 2020) CliMAF : (Sénési et al., 2021)
Figure 8.14	**CMIP6 model data**						
	ACCESS-CM2: historical, ssp245	Input dataset			(Dix et al., 2019d, 2019a)		
	ACCESS-ESM1-5: historical, ssp245	Input dataset			(Ziehn et al., 2019a, 2019d)		
	AWI-CM-1-1-MR: historical, ssp245	Input dataset			(Semmler et al., 2018d, 2018a)		
	BCC-CSM2-MR: historical, ssp245	Input dataset			(Wu et al., 2018a; Xin et al., 2019b)		
	CAMS-CSM1-0: historical, ssp245	Input dataset			(Rong, 2019e, 2019b)		
	CESM2: historical, ssp245	Input dataset			(Danabasoglu, 2019j, 2019l)		
	CESM2-WACCM: historical, ssp245	Input dataset			(Danabasoglu, 2019d, 2019g)		
	CIESM: historical, ssp245	Input dataset			(Huang, 2019a, 2020a)		
	CMCC-CM2-SR5: historical, ssp245	Input dataset			(Lovato and Peano, 2020a, 2020d)		
	CNRM-CM6-1: historical, ssp245	Input dataset			(Voldoire, 2018a, 2019i)		
	CNRM-CM6-1-HR: historical, ssp245	Input dataset			(Voldoire, 2019a, 2019c)		

ACCEPTED VERSION SUBJECT TO FINAL EDITING

	CNRM-ESM2-1: historical, ssp245	Input dataset			(Seferian, 2018b; Voldoire, 2019l)		
	CanESM5: historical, ssp245	Input dataset			(Swart et al., 2019n, 2019h)		
	CanESM5-CanOE: historical, ssp245	Input dataset			(Swart et al., 2019e, 2019b)		
	EC-Earth3: historical, ssp245	Input dataset			(EC-Earth Consortium (EC-Earth), 2019g, 2019j)		
	EC-Earth3-Veg: historical, ssp245	Input dataset			(EC-Earth Consortium (EC-Earth), 2019e, 2019b)		
	FGOALS-f3-L: historical, ssp245	Input dataset			(Yu, 2019a, 2019d)		
	FGOALS-g3: historical, ssp245	Input dataset			(Li, 2019e, 2019b)		
	FIO-ESM-2-0: historical, ssp245	Input dataset			(Song et al., 2019d, 2019a)		
	GFDL-CM4: historical, ssp245	Input dataset			(Guo et al., 2018d, 2018b)		
	GFDL-ESM4: historical, ssp245	Input dataset			(John et al., 2018b; Krasting et al., 2018b)		
	GISS-E2-1-G: historical, ssp245	Input dataset			(NASA Goddard Institute for Space Studies (NASA/GISS), 2018b, 2020b)		
	HadGEM3-GC31-LL: historical, ssp245	Input dataset			(Good, 2019; Ridley et al., 2019a)		
	IITM-ESM: historical, ssp245	Input dataset			(Raghavan and Panickal, 2019; Panickal and Narayanasetti, 2020b)		
	INM-CM4-8: historical, ssp245	Input dataset			(Volodin et al., 2019b, 2019e)		
	INM-CM5-0: historical, ssp245	Input dataset			(Volodin et al., 2019k, 2019h)		
	IPSL-CM6A-LR: historical, ssp245	Input dataset			(Boucher et al., 2018b, 2019b)		
	KACE-1-0-G: historical, ssp245	Input dataset			(Byun et al., 2019b, 2019e)		

ACCEPTED VERSION SUBJECT TO FINAL EDITING

	MCM-UA-1-0: historical, ssp245	Input dataset			(Stouffer, 2019b, 2019e)		
	MIROC-ES2L: historical, ssp245	Input dataset			(Hajima et al., 2019b; Tachiiri et al., 2019b)		
	MIROC6: historical, ssp245	Input dataset			(Tatebe and Watanabe, 2018b; Shiogama et al., 2019b)		
	MPI-ESM1-2-HR: historical, ssp245	Input dataset			(Jungclaus et al., 2019a; Schupfner et al., 2019b)		
	MPI-ESM1-2-LR: historical, ssp245	Input dataset			(Wieners et al., 2019a, 2019d)		
	MRI-ESM2-0: historical, ssp245	Input dataset			(Yukimoto et al., 2019b, 2019h)		
	NESM3: historical, ssp245	Input dataset			(Cao, 2019b; Cao and Wang, 2019b)		
	NorESM2-LM: historical, ssp245	Input dataset			(Seland et al., 2019d, 2019a)		
	NorESM2-MM: historical, ssp245	Input dataset			(Bentsen et al., 2019a, 2019d)		
	UKESM1-0-LL: historical, ssp245	Input dataset			(Good et al., 2019b; Tang et al., 2019b)		
	Figure 8.14 Code	Code	Fig8-14.sh (compute and plot)			https://github.com/senesis/some_chap8_figures	CAMMAC :(Sénési, 2020) CliMAF : (Sénési et al., 2021)
Figure 8.15	**CMIP6 model data**						
	ACCESS-CM2: historical, ssp126, ssp245, ssp585	Input dataset			(Dix et al., 2019d, 2019a, 2019e, 2019c)		
	ACCESS-ESM1-5: historical, ssp126, ssp245, ssp585	Input dataset			(Ziehn et al., 2019a, 2019e, 2019d, 2019c)		
	BCC-CSM2-MR: historical, ssp126, ssp245, ssp585	Input dataset			(Wu et al., 2018a; Xin et al., 2019a, 2019c, 2019b)		

ACCEPTED VERSION SUBJECT TO FINAL EDITING

	CAMS-CSM1-0: historical, ssp126, ssp245, ssp585	Input dataset			(Rong, 2019d, 2019e, 2019b, 2019f)		
	CESM2-WACCM: historical, ssp126, ssp245, ssp585	Input dataset			(Danabasoglu, 2019d, 2019f, 2019h, 2019g)		
	CMCC-CM2-SR5: historical, ssp126, ssp245, ssp585	Input dataset			(Lovato and Peano, 2020c, 2020a, 2020d, 2020e)		
	CNRM-CM6-1-HR: historical, ssp126, ssp585	Input dataset			(Voldoire, 2018a, 2019j, 2019i, 2019h)		
					(Voldoire, 2019a, 2019d, 2020)		
	CNRM-ESM2-1: historical, ssp126, ssp245, ssp585	Input datasetInput dataset			(Seferian, 2018b; Voldoire, 2019m, 2019l, 2019k)		
	CanESM5: historical, ssp126, ssp245, ssp585	Input dataset			(Swart et al., 2019n, 2019o, 2019m, 2019h)		
	EC-Earth3: historical, ssp126, ssp245, ssp585	Input dataset			(EC-Earth Consortium (EC-Earth), 2019g, 2019j, 2019k, 2019i)		
	EC-Earth3-Veg: historical, ssp126, ssp245, ssp585	Input dataset			(EC-Earth Consortium (EC-Earth), 2019e, 2019f, 2019d, 2019b)		
	FGOALS-g3: historical, ssp126, ssp245, ssp585	Input dataset			(Li, 2019f, 2019e, 2019b, 2019d)		
	GFDL-CM4: historical, ssp245, ssp585	Input dataset			(Guo et al., 2018e, 2018d, 2018b)		
	GFDL-ESM4: historical, ssp126, ssp245	Input dataset			(John et al., 2018a, 2018b; Krasting et al., 2018b)		
	HadGEM3-GC31-LL: historical, ssp126, ssp245, ssp585	Input dataset			(Good, 2019, 2020a, 2020b; Ridley et al., 2019a)		
	HadGEM3-GC31-MM: historical, ssp126, ssp585	Input dataset			(Ridley et al., 2019b; Jackson, 2020b, 2020a)		

ACCEPTED VERSION SUBJECT TO FINAL EDITING

	IITM-ESM: historical, ssp126, ssp245, ssp585	Input dataset			(Raghavan and Panickal, 2019; Panickal and Narayanasetti, 2020b, 2020a, 2020c)		
	INM-CM4-8: historical, ssp126, ssp245, ssp585	Input dataset			(Volodin et al., 2019d, 2019b, 2019f, 2019e)		
	INM-CM5-0: historical, ssp126, ssp245, ssp585	Input dataset			(Volodin et al., 2019j, 2019k, 2019h, 2019l)		
	IPSL-CM5A2-INCA: historical, ssp126	Input dataset			(Boucher et al., 2020a, 2020b)		
	IPSL-CM6A-LR: historical, ssp126, ssp245, ssp585	Input dataset			(Boucher et al., 2018b, 2019a, 2019b, 2019c)		
	KACE-1-0-G: historical, ssp126, ssp245, ssp585	Input dataset			(Byun et al., 2019b, 2019c, 2019e, 2019a)		
	MIROC-ES2L: historical, ssp126, ssp245, ssp585	Input dataset			(Hajima et al., 2019b; Tachiiri et al., 2019b, 2019c, 2019a)		
	MIROC6: historical, ssp126, ssp245, ssp585	Input dataset			(Tatebe and Watanabe, 2018b; Shiogama et al., 2019c, 2019a, 2019b)		
	MPI-ESM1-2-HR: historical, ssp126, ssp245, ssp585	Input dataset			(Jungclaus et al., 2019a; Schupfner et al., 2019a, 2019b, 2019c)		
	MPI-ESM1-2-LR: historical, ssp126, ssp245, ssp585	Input dataset			(Wieners et al., 2019a, 2019c, 2019d, 2019e)		
	MRI-ESM2-0: historical, ssp126, ssp245, ssp585	Input dataset			(Yukimoto et al., 2019g, 2019b, 2019h, 2019i)		
	NESM3: historical, ssp126, ssp245, ssp585	Input dataset			(Cao, 2019b, 2019c, 2019a; Cao and Wang, 2019b)		
	NorESM2-LM: historical, ssp126, ssp245, ssp585	Input dataset			(Seland et al., 2019d, 2019e, 2019c, 2019a)		

ACCEPTED VERSION SUBJECT TO FINAL EDITING

	NorESM2-MM: historical, ssp126, ssp245, ssp585	Input dataset			(Bentsen et al., 2019c, 2019a, 2019e, 2019d)		
	TaiESM1: historical, ssp585	Input dataset			(Lee and Liang, 2020a, 2020c)		
	UKESM1-0-LL: historical, ssp126, ssp245, ssp585	Input dataset			(Good et al., 2019a, 2019c, 2019b; Tang et al., 2019b)		
	Figure 8.15 Code	Code	Fig8-15.sh (compute) Fig8-15_figure.sh (plot)			https://github.com/senesis/some_chap8_figures	CAMMAC :(Sénési, 2020) CliMAF : (Sénési et al., 2021)
Figure 8.16	**CMIP6 model data**						
	ACCESS-CM2: historical, ssp585	Input dataset			(Dix et al., 2019a, 2019e)		
	ACCESS-ESM1-5: historical, ssp585	Input dataset			(Ziehn et al., 2019a, 2019e)		
	AWI-CM-1-1-MR: historical, ssp585	Input dataset			(Semmler et al., 2018a, 2019)		
	BCC-CSM2-MR: historical, ssp585	Input dataset			(Wu et al., 2018a; Xin et al., 2019c)		
	CAMS-CSM1-0: historical, ssp585	Input dataset			(Rong, 2019b, 2019f)		
	CESM2: historical, ssp585	Input dataset			(Danabasoglu, 2019j, 2019m)		
	CESM2-WACCM: historical, ssp585	Input dataset			(Danabasoglu, 2019d, 2019h)		
	CIESM: historical, ssp585	Input dataset			(Huang, 2019a, 2020b)		
	CMCC-CM2-SR5: historical, ssp585	Input dataset			(Lovato and Peano, 2020a, 2020e)		
	CNRM-CM6-1: historical, ssp585	Input dataset			(Voldoire, 2018a, 2019j)		

ACCEPTED VERSION SUBJECT TO FINAL EDITING

	CNRM-ESM2-1: historical, ssp585	Input dataset			(Voldoire, 2019a, 2019d)		
					(Seferian, 2018b; Voldoire, 2019m)		
	CanESM5: historical, ssp585	Input datasetInput dataset			(Swart et al., 2019o, 2019h)		
	CanESM5-CanOE: historical, ssp585	Input dataset			(Swart et al., 2019f, 2019b)		
	EC-Earth3: historical, ssp585	Input dataset			(EC-Earth Consortium (EC-Earth), 2019g, 2019k)		
	EC-Earth3-Veg: historical, ssp585	Input dataset			(EC-Earth Consortium (EC-Earth), 2019f, 2019b)		
	EC-Earth3-Veg-LR: historical, ssp585	Input dataset			(EC-Earth Consortium (EC-Earth), 2020d, 2020b)		
	FGOALS-f3-L: historical, ssp585	Input dataset			(Yu, 2019e, 2019a)		
	FGOALS-g3: historical, ssp585	Input dataset			(Li, 2019f, 2019b)		
	FIO-ESM-2-0: historical, ssp585	Input dataset			(Song et al., 2019e, 2019a)		
	GFDL-CM4: historical, ssp585	Input dataset			(Guo et al., 2018e, 2018b)		
	GFDL-ESM4: historical, ssp585	Input dataset			(John et al., 2018c; Krasting et al., 2018b)		
	GISS-E2-1-G: historical, ssp585	Input dataset			(NASA Goddard Institute for Space Studies (NASA/GISS), 2018b, 2020c)		
	HadGEM3-GC31-LL: historical, ssp585	Input dataset			(Ridley et al., 2019a; Good, 2020b)		
	HadGEM3-GC31-MM: historical, ssp585	Input dataset			(Ridley et al., 2019b; Jackson, 2020b)		
	IITM-ESM: historical, ssp585	Input dataset			(Raghavan and Panickal, 2019; Panickal and Narayanasetti, 2020c)		
	INM-CM4-8: historical, ssp585	Input dataset			(Volodin et al., 2019b, 2019f)		

ACCEPTED VERSION SUBJECT TO FINAL EDITING

	INM-CM5-0: historical, ssp585	Input dataset			(Volodin et al., 2019h, 2019l)		
	IPSL-CM6A-LR: historical, ssp585	Input dataset			(Boucher et al., 2018b, 2019c)		
	KACE-1-0-G: historical, ssp585	Input dataset			(Byun et al., 2019c, 2019e)		
	MCM-UA-1-0: historical, ssp585	Input dataset			(Stouffer, 2019f, 2019b)		
	MIROC-ES2L: historical, ssp585	Input dataset			(Hajima et al., 2019b; Tachiiri et al., 2019c)		
	MIROC6: historical, ssp585	Input dataset			(Tatebe and Watanabe, 2018b; Shiogama et al., 2019c)		
	MPI-ESM1-2-HR: historical, ssp585	Input dataset			(Jungclaus et al., 2019a; Schupfner et al., 2019c)		
	MPI-ESM1-2-LR: historical, ssp585	Input dataset			(Wieners et al., 2019a, 2019e)		
	MRI-ESM2-0: historical, ssp585	Input dataset			(Yukimoto et al., 2019b, 2019i)		
	NorESM3: historical, ssp585	Input dataset			(Cao, 2019c; Cao and Wang, 2019b)		
	NorESM2-LM: historical, ssp585	Input dataset			(Seland et al., 2019e, 2019a)		
	NorESM2-MM: historical, ssp585	Input dataset			(Bentsen et al., 2019a, 2019e)		
	TaiESM1: historical, ssp585	Input dataset			(Lee and Liang, 2020a, 2020c)		
	UKESM1-0-LL: historical, ssp585	Input dataset			(Good et al., 2019c; Tang et al., 2019b)		
	Figure 8.16 Code	Code	Fig8-16.sh (compute and plot)			https://github.com/senesis/some_chap8_figures	CAMMAC :(Sénési, 2020) CliMAF : (Sénési et al., 2021)
	CMIP6 model data						

ACCEPTED VERSION SUBJECT TO FINAL EDITING

Figure 8.17	ACCESS-CM2: historical, ssp126, ssp245, ssp585	Input dataset			(Dix et al., 2019d, 2019a, 2019e, 2019c)		
	ACCESS-ESM1-5: historical, ssp126, ssp245, ssp585	Input dataset			(Ziehn et al., 2019a, 2019e, 2019d, 2019c)		
	AWI-CM-1-1-MR: historical, ssp126, ssp245, ssp585	Input dataset			(Semmler et al., 2018c, 2018d, 2018a, 2019)		
	BCC-CSM2-MR: historical, ssp126, ssp245, ssp585	Input dataset			(Wu et al., 2018a; Xin et al., 2019a, 2019c, 2019b)		
	CAMS-CSM1-0: historical, ssp126, ssp245, ssp585	Input dataset			(Rong, 2019d, 2019e, 2019b, 2019f)		
	CESM2: historical, ssp126, ssp245, ssp585	Input dataset			(Danabasoglu, 2019j, 2019m, 2019l, 2019k)		
	CESM2-WACCM: historical, ssp126, ssp245, ssp585	Input dataset			(Danabasoglu, 2019d, 2019f, 2019h, 2019g)		
	CMCC-CM2-SR5: historical, ssp126, ssp245, ssp585	Input dataset			(Lovato and Peano, 2020c, 2020a, 2020d, 2020e)		
	CNRM-CM6-1: historical, ssp126, ssp245, ssp585	Input dataset			(Voldoire, 2018a, 2019j, 2019i, 2019h)		
	CNRM-CM6-1-HR: historical, ssp126, ssp245, ssp585	Input dataset			(Voldoire, 2019a, 2019d, 2019c, 2020)		
	CNRM-ESM2-1: historical, ssp126, ssp245, ssp585	Input dataset			(Seferian, 2018b; Voldoire, 2019m, 2019l, 2019k)		
	CanESM5: historical, ssp126, ssp245, ssp585	Input dataset			(Swart et al., 2019n, 2019o, 2019m, 2019h)		

ACCEPTED VERSION SUBJECT TO FINAL EDITING

	CanESM5-CanOE: historical, ssp126, ssp245, ssp585	Input dataset			(Swart et al., 2019f, 2019e, 2019d, 2019b)		
	EC-Earth3: historical, ssp126, ssp245, ssp585	Input dataset			(EC-Earth Consortium (EC-Earth), 2019g, 2019j, 2019k, 2019i)		
	EC-Earth3-Veg: historical, ssp126, ssp245, ssp585	Input dataset			(EC-Earth Consortium (EC-Earth), 2019e, 2019f, 2019d, 2019b)		
	FGOALS-f3-L: historical, ssp126, ssp245, ssp585	Input dataset			(Yu, 2019e, 2019c, 2019a, 2019d)		
	FGOALS-g3: historical, ssp126, ssp245, ssp585	Input dataset			(Li, 2019f, 2019e, 2019b, 2019d)		
	FIO-ESM-2-0: historical, ssp126, ssp245, ssp585	Input dataset			(Song et al., 2019e, 2019d, 2019c, 2019a)		
	GFDL-CM4: historical, ssp245, ssp585	Input dataset			(Guo et al., 2018e, 2018d, 2018b)		
	GFDL-ESM4: historical, ssp126, ssp245, ssp585	Input dataset			(John et al., 2018a, 2018b, 2018c; Krasting et al., 2018b)		
	GISS-E2-1-G: historical, ssp126, ssp245, ssp585	Input dataset			(NASA Goddard Institute for Space Studies (NASA/GISS), 2018b, 2020a, 2020c, 2020b)		
	HadGEM3-GC31-LL: historical, ssp126, ssp245, ssp585	Input dataset			(Good, 2019, 2020a, 2020b; Ridley et al., 2019a)		
	HadGEM3-GC31-MM: historical, ssp126, ssp585	Input dataset			(Ridley et al., 2019b; Jackson, 2020b, 2020a)		
	IITM-ESM: historical, ssp126, ssp245, ssp585	Input dataset			(Raghavan and Panickal, 2019; Panickal and Narayanasetti, 2020b, 2020a, 2020c)		
	INM-CM4-8: historical, ssp126, ssp245, ssp585	Input dataset			(Volodin et al., 2019d, 2019b, 2019f, 2019e)		

ACCEPTED VERSION
SUBJECT TO FINAL EDITING

	INM-CM5-0: historical, ssp126, ssp245, ssp585	Input dataset			(Volodin et al., 2019j, 2019k, 2019h, 2019l)		
	IPSL-CM5A2-INCA: historical, ssp126	Input dataset			(Boucher et al., 2020a, 2020b)		
	IPSL-CM6A-LR: historical, ssp126, ssp245, ssp585	Input dataset			(Boucher et al., 2018b, 2019a, 2019b, 2019c)		
	KACE-1-0-G: historical, ssp126, ssp245, ssp585	Input dataset			(Byun et al., 2019b, 2019c, 2019e, 2019a)		
	MCM-UA-1-0: historical, ssp126, ssp245, ssp585	Input dataset			(Stouffer, 2019f, 2019b, 2019e, 2019d)		
	MIROC-ES2L: historical, ssp126, ssp245, ssp585	Input dataset			(Hajima et al., 2019b; Tachiiri et al., 2019b, 2019c, 2019a)		
	MIROC6: historical, ssp126, ssp245, ssp585	Input dataset			(Tatebe and Watanabe, 2018b; Shiogama et al., 2019c, 2019a, 2019b)		
	MPI-ESM1-2-HR: historical, ssp126, ssp245, ssp585	Input dataset			(Jungclaus et al., 2019a; Schupfner et al., 2019a, 2019b, 2019c)		
	MPI-ESM1-2-LR: historical, ssp126, ssp245, ssp585	Input dataset			(Wieners et al., 2019a, 2019c, 2019d, 2019e)		
	MRI-ESM2-0: historical, ssp126, ssp245, ssp585	Input dataset			(Yukimoto et al., 2019g, 2019b, 2019h, 2019i)		
	NESM3: historical, ssp126, ssp245, ssp585	Input dataset			(Cao, 2019b, 2019c, 2019a; Cao and Wang, 2019b)		
	NorESM2-LM: historical, ssp126, ssp245, ssp585	Input dataset			(Seland et al., 2019d, 2019e, 2019c, 2019a)		
	NorESM2-MM: historical, ssp126, ssp245, ssp585	Input dataset			(Bentsen et al., 2019c, 2019a, 2019e, 2019d)		

ACCEPTED VERSION SUBJECT TO FINAL EDITING

	TaiESM1: historical, ssp585	Input dataset			(Lee and Liang, 2020a, 2020c)		
	UKESM1-0-LL: historical, ssp126, ssp245, ssp585	Input dataset			(Good et al., 2019a, 2019c, 2019b; Tang et al., 2019b)		
	Figure 8.17 Code	Code	Fig8-17.sh (compute and plot)			https://github.com/senesis/some_chap8_figures	CAMMAC :(Sénési, 2020) CliMAF : (Sénési et al., 2021)
Figure 8.18	**CMIP6 model data**						
	ACCESS-CM2: historical, ssp126, ssp245, ssp585	Input dataset			(Dix et al., 2019d, 2019a, 2019e, 2019c)		
	ACCESS-ESM1-5: historical, ssp126, ssp245, ssp585	Input dataset			(Ziehn et al., 2019a, 2019e, 2019d, 2019c)		
	BCC-CSM2-MR: historical, ssp126, ssp245, ssp585	Input dataset			(Wu et al., 2018a; Xin et al., 2019a, 2019c, 2019b)		
	CAMS-CSM1-0: historical, ssp126, ssp245, ssp585	Input dataset			(Rong, 2019d, 2019e, 2019b, 2019f)		
	CESM2: historical, ssp126, ssp245, ssp585	Input dataset			(Danabasoglu, 2019j, 2019m, 2019l, 2019k)		
	CESM2-WACCM: historical, ssp126, ssp245, ssp585	Input dataset			(Danabasoglu, 2019d, 2019f, 2019h, 2019g)		
	CIESM: historical, ssp126, ssp245, ssp585	Input dataset			(Huang, 2019a, 2019c, 2020b, 2020a)		
	CMCC-CM2-SR5: historical, ssp126, ssp245, ssp585	Input dataset			(Lovato and Peano, 2020c, 2020a, 2020d, 2020e)		
	CNRM-CM6-1: historical, ssp126, ssp245, ssp585	Input dataset			(Voldoire, 2018a, 2019j, 2019i, 2019h)		

ACCEPTED VERSION SUBJECT TO FINAL EDITING

	CNRM-CM6-1-HR: historical, ssp126, ssp245, ssp585	Input dataset			(Voldoire, 2019a, 2019d, 2019c, 2020)		
	CNRM-ESM2-1: historical, ssp126, ssp245, ssp585	Input dataset			(Seferian, 2018b; Voldoire, 2019m, 2019l, 2019k)		
	CanESM5: historical, ssp126, ssp245, ssp585	Input dataset			(Swart et al., 2019n, 2019o, 2019m, 2019h)		
	CanESM5-CanOE: historical, ssp126, ssp245, ssp585	Input dataset			(Swart et al., 2019f, 2019e, 2019d, 2019b)		
	EC-Earth3: historical, ssp126, ssp245, ssp585	Input dataset			(EC-Earth Consortium (EC-Earth), 2019g, 2019j, 2019k, 2019i)		
	EC-Earth3-Veg: historical, ssp126, ssp245, ssp585	Input dataset			(EC-Earth Consortium (EC-Earth), 2019e, 2019f, 2019d, 2019b)		
	FGOALS-f3-L: historical, ssp126, ssp245, ssp585	Input datasetInput datasetInput dataset			(Yu, 2019e, 2019c, 2019a, 2019d)		
	FGOALS-g3: historical, ssp126, ssp245, ssp585	Input dataset			(Li, 2019f, 2019e, 2019b, 2019d)		
	FIO-ESM-2-0: historical, ssp126, ssp245, ssp585	Input dataset			(Song et al., 2019e, 2019d, 2019c, 2019a)		
	GFDL-CM4: historical, ssp245, ssp585	Input dataset			(Guo et al., 2018e, 2018d, 2018b)		
	GISS-E2-1-G: historical, ssp126, ssp245, ssp585	Input dataset			(NASA Goddard Institute for Space Studies (NASA/GISS), 2018b, 2020a, 2020c, 2020b)		
	HadGEM3-GC31-LL: historical, ssp126, ssp245, ssp585	Input dataset			(Good, 2019, 2020a, 2020b; Ridley et al., 2019a)		

ACCEPTED VERSION SUBJECT TO FINAL EDITING

	HadGEM3-GC31-MM: historical, ssp126, ssp585	Input dataset			(Ridley et al., 2019b; Jackson, 2020b, 2020a)		
	INM-CM4-8: historical, ssp126, ssp245, ssp585	Input dataset			(Volodin et al., 2019d, 2019b, 2019f, 2019e)		
	INM-CM5-0: historical, ssp126, ssp245, ssp585	Input dataset			(Volodin et al., 2019j, 2019k, 2019h, 2019l)		
	IPSL-CM6A-LR: historical, ssp126, ssp245, ssp585	Input dataset			(Boucher et al., 2020a, 2020b)		
					(Boucher et al., 2018b, 2019a, 2019b, 2019c)		
	KACE-1-0-G: historical, ssp126, ssp245, ssp585	Input datasetInput dataset			(Byun et al., 2019b, 2019c, 2019e, 2019a)		
	MCM-UA-1-0: historical, ssp126, ssp245, ssp585	Input dataset			(Stouffer, 2019f, 2019b, 2019e, 2019d)		
	MIROC-ES2L: historical, ssp126, ssp245, ssp585	Input dataset			(Hajima et al., 2019b; Tachiiri et al., 2019b, 2019c, 2019a)		
	MIROC6: historical, ssp126, ssp245, ssp585	Input dataset			(Tatebe and Watanabe, 2018b; Shiogama et al., 2019c, 2019a, 2019b)		
	MPI-ESM1-2-HR: historical, ssp126, ssp245, ssp585	Input dataset			(Jungclaus et al., 2019a; Schupfner et al., 2019a, 2019b, 2019c)		
	MPI-ESM1-2-LR: historical, ssp126, ssp245, ssp585	Input dataset			(Wieners et al., 2019a, 2019c, 2019d, 2019e)		
	MRI-ESM2-0: historical, ssp126, ssp245, ssp585	Input dataset			(Yukimoto et al., 2019g, 2019b, 2019h, 2019i)		
	UKESM1-0-LL: historical, ssp126, ssp245, ssp585	Input dataset			(Good et al., 2019a, 2019c, 2019b; Tang et al., 2019b)		

ACCEPTED VERSION SUBJECT TO FINAL EDITING

	Figure 8.18 Code	Code	Fig8-18.sh (compute and plot)			https://github.com/senesis/some_chap8_figures	CAMMAC :(Sénési, 2020) CliMAF : (Sénési et al., 2021)
Figure 8.19	CMIP6 / SSP1.2-6 SSP2-4.5 SSP5-8.5					**https://esgf-node.llnl.gov/search/cmip6/**	
Figure 8.20	Tree-ring reconstructed Palmer Drought Severity Index & NCAR CESM Last Millennium Ensemble from CMIP5						Morales et al., 2020; Palmer et al., 2015), Pederson et al., 2014; Hessl et al., 2018)
Figure 8.21	Schematic						
	CMIP6 model data						
	BCC-CSM2-MR: historical, piControl, ssp585	Input dataset			(Wu et al., 2018a, 2018b, Xin et al., 2018, 2019c)		
	CAMS-CSM1-0: historical, piControl, ssp585	Input dataset			(Rong, 2019b, 2019f, 2019a, 2019c)		
	CESM2: historical, piControl, ssp585	Input dataset			(Danabasoglu, 2019i, 2019j, 2019m; Danabasoglu et al., 2019)		
	CESM2-WACCM: historical, piControl, ssp585	Input dataset			(Danabasoglu, 2019d, 2019e, 2019h, 2019c)		
	CNRM-ESM2-1: historical, piControl, ssp585	Input dataset			(Seferian, 2018a, 2018b, 2018c; Voldoire, 2019m)		
	CanESM5: historical, piControl, ssp585	Input dataset			(Swart et al., 2019i, 2019o, 2019g, 2019h)		
	CanESM5-CanOE: historical, piControl, ssp585	Input dataset			(Swart et al., 2019f, 2019a, 2019c, 2019b)		

ACCEPTED VERSION SUBJECT TO FINAL EDITING

	FGOALS-g3: historical, piControl, ssp585	Input dataset			(Yu, 2018, 2019e, 2019a, 2019b)		
	GFDL-CM4: historical, piControl, ssp585				(Li, 2019f, 2019b, 2019a, 2019c)		
					(Guo et al., 2018e, 2018a, 2018b, 2018c)		
	GFDL-ESM4: historical, piControl, ssp585	Input datasetInput datasetInput dataset			(John et al., 2018c; Krasting et al., 2018b, 2018a, 2018c)		
	GISS-E2-1-G: historical, piControl, ssp585	Input dataset			(NASA Goddard Institute for Space Studies (NASA/GISS), 2018c, 2018a, 2018b, 2020c)		
	INM-CM4-8: historical, piControl, ssp585	Input dataset			(Volodin et al., 2019b, 2019c, 2019a, 2019f)		
	INM-CM5-0: historical, piControl, ssp585	Input dataset			(Volodin et al., 2019g, 2019i, 2019h, 2019l)		
	IPSL-CM6A-LR: historical, piControl, ssp585	Input dataset			(Boucher et al., 2018a, 2018c, 2018b, 2019c)		
	KACE-1-0-G: historical, piControl, ssp585	Input dataset			(Byun et al., 2019f, 2019c, 2019e, 2019d)		
	MCM-UA-1-0: historical, piControl, ssp585	Input dataset			(Stouffer, 2019f, 2019b, 2019a, 2019c)		
	MIROC-ES2L: historical, piControl, ssp585	Input dataset			(Hajima et al., 2019a, 2019b, 2019c; Tachiiri et al., 2019c)		
	MPI-ESM1-2-HR: historical, piControl, ssp585	Input dataset			(Tatebe and Watanabe, 2018b, 2018a, 2018c; Shiogama et al., 2019c)		
	MRI-ESM2-0: historical, piControl, ssp585				(Jungclaus et al., 2019b, 2019c, 2019a; Schupfner et al., 2019c)		

ACCEPTED VERSION SUBJECT TO FINAL EDITING

					(Yukimoto et al., 2019c, 2019a, 2019b, 2019i)		
	NESM3: historical, piControl, ssp585	Input datasetInput datasetInput dataset			(Cao, 2019c; Cao and Wang, 2019c, 2019a, 2019b)		
	UKESM1-0-LL: historical, piControl, ssp585	Input dataset			(Good et al., 2019c; Tang et al., 2019b, 2019c, 2019a)		
Figure 8.22	CMIP6 / SSP1.2-6 SSP2-4.5 SSP5-8.5					**https://esgf-node.llnl.gov/search/cmip6/**	
Figure 8.23	CMIP6 SSP1-2.6, SSP2-4.5, SSP3-7.0, SSP5-8.5					**https://esgf-node.llnl.gov/search/cmip6/**	(Lehner et al., 2020).
Figure 8.24	CESM1						(Deser et al., 2017)
Figure 8.25	ACCESS-CM2: historical, ssp585	Input dataset			(Dix et al., 2019a, 2019e)		
	ACCESS-ESM1-5: historical, ssp585	Input dataset			(Ziehn et al., 2019a, 2019e)		
	AWI-CM-1-1-MR: historical, ssp585	Input dataset			(Semmler et al., 2018a, 2019)		
	CESM2: historical, ssp585	Input dataset			(Danabasoglu, 2019j, 2019m)		
	CESM2-WACCM: historical, ssp585	Input dataset			(Danabasoglu, 2019d, 2019h)		
	CIESM: historical, ssp585	Input dataset			(Huang, 2019a, 2020b)		
	CMCC-CM2-SR5: historical, ssp585	Input dataset			(Lovato and Peano, 2020a, 2020e)		
	CNRM-CM6-1: historical, ssp585	Input dataset			(Voldoire, 2018a, 2019j)		

ACCEPTED VERSION SUBJECT TO FINAL EDITING

	CNRM-CM6-1-HR: historical, ssp585	Input dataset			(Voldoire, 2019a, 2019d)		
	CNRM-ESM2-1: historical, ssp585	Input dataset			(Seferian, 2018b; Voldoire, 2019m)		
	CanESM5: historical, ssp585	Input dataset			(Swart et al., 2019o, 2019h)		
	CanESM5-CanOE: historical, ssp585	Input dataset			(Swart et al., 2019f, 2019b)		
	EC-Earth3: historical, ssp585	Input dataset			(EC-Earth Consortium (EC-Earth), 2019g, 2019k)		
	EC-Earth3-Veg: historical, ssp585	Input dataset			(EC-Earth Consortium (EC-Earth), 2019f, 2019b)		
	FGOALS-f3-L: historical, ssp585	Input dataset			(Yu, 2019e, 2019a)		
	FIO-ESM-2-0: historical, ssp585	Input dataset			(Song et al., 2019e, 2019a)		
	GFDL-CM4: historical, ssp585	Input dataset			(Guo et al., 2018e, 2018b)		
	HadGEM3-GC31-LL: historical, ssp585	Input dataset			(Ridley et al., 2019a; Good, 2020b)		
	HadGEM3-GC31-MM: historical, ssp585	Input dataset			(Ridley et al., 2019b; Jackson, 2020b)		
	IPSL-CM6A-LR: historical, ssp585	Input dataset			(Boucher et al., 2018b, 2019c)		
	KACE-1-0-G: historical, ssp585	Input dataset			(Byun et al., 2019c, 2019e)		
	MCM-UA-1-0: historical, ssp585	Input dataset			(Stouffer, 2019f, 2019b)		
	MRI-ESM2-0: historical, ssp585	Input dataset			(Yukimoto et al., 2019b, 2019i)		
	NESM3: historical, ssp585	Input dataset			(Cao, 2019c; Cao and Wang, 2019b)		
	TaiESM1: historical, ssp585	Input dataset			(Lee and Liang, 2020a, 2020c)		

ACCEPTED VERSION SUBJECT TO FINAL EDITING

	UKESM1-0-LL: historical, ssp585	Input dataset			(Good et al., 2019c; Tang et al., 2019b)		
Figure 8.25	Figure 8.25 Code	Code	Fig8-25.sh (compute and plot)			https://github.com/senesis/some_chap8_figures	CAMMAC :(Sénési, 2020) CliMAF : (Sénési et al., 2021)
Figure 8.26	**CMIP6 model data**						
	ACCESS-CM2: historical, ssp126, ssp245, ssp585	Input dataset			(Dix et al., 2019d, 2019a, 2019e, 2019c)		
	ACCESS-ESM1-5: historical, ssp126, ssp245, ssp585	Input dataset			(Ziehn et al., 2019a, 2019e, 2019d, 2019c)		
	BCC-CSM2-MR: historical, ssp126, ssp245, ssp585	Input dataset			(Wu et al., 2018a; Xin et al., 2019a, 2019c, 2019b)		
	CAMS-CSM1-0: historical, ssp126, ssp245, ssp585	Input dataset			(Rong, 2019d, 2019e, 2019b, 2019f)		
	CESM2: historical, ssp126, ssp245, ssp585	Input dataset			(Danabasoglu, 2019j, 2019m, 2019l, 2019k)		
	CESM2-WACCM: historical, ssp126, ssp245, ssp585	Input dataset			(Danabasoglu, 2019d, 2019f, 2019h, 2019g)		
	CIESM: historical, ssp126, ssp245, ssp585	Input dataset			(Huang, 2019a, 2019c, 2020b, 2020a)		
	CMCC-CM2-SR5: historical, ssp126, ssp245, ssp585	Input dataset			(Lovato and Peano, 2020c, 2020a, 2020d, 2020e)		
	CNRM-CM6-1: historical, ssp126, ssp245, ssp585	Input dataset			(Voldoire, 2018a, 2019j, 2019i, 2019h)		
	CNRM-CM6-1-HR: historical, ssp126, ssp245, ssp585	Input dataset			(Voldoire, 2019a, 2019d, 2019c, 2020)		

ACCEPTED VERSION SUBJECT TO FINAL EDITING

	CNRM-ESM2-1: historical, ssp126, ssp245, ssp585	Input dataset			(Seferian, 2018b; Voldoire, 2019m, 2019l, 2019k)		
	CanESM5: historical, ssp126, ssp245, ssp585	Input dataset			(Swart et al., 2019n, 2019o, 2019m, 2019h)		
	CanESM5-CanOE: historical, ssp126, ssp245, ssp585	Input dataset			(Swart et al., 2019f, 2019e, 2019d, 2019b)		
	EC-Earth3: historical, ssp126, ssp245, ssp585	Input dataset			(EC-Earth Consortium (EC-Earth), 2019g, 2019j, 2019k, 2019i)		
	EC-Earth3-Veg: historical, ssp126, ssp245, ssp585	Input dataset			(EC-Earth Consortium (EC-Earth), 2019e, 2019f, 2019d, 2019b)		
	FGOALS-f3-L: historical, ssp126, ssp245, ssp585	Input dataset			(Yu, 2019e, 2019c, 2019a, 2019d)		
	FGOALS-g3: historical, ssp126, ssp245, ssp585	Input dataset			(Li, 2019f, 2019e, 2019b, 2019d)		
	FIO-ESM-2-0: historical, ssp126, ssp245, ssp585	Input dataset			(Song et al., 2019e, 2019d, 2019c, 2019a)		
	GFDL-CM4: historical, ssp245, ssp585	Input dataset			(Guo et al., 2018e, 2018d, 2018b)		
	GISS-E2-1-G: historical, ssp126, ssp245, ssp585	Input dataset			(NASA Goddard Institute for Space Studies (NASA/GISS), 2018b, 2020a, 2020c, 2020b)		
	HadGEM3-GC31-LL: historical, ssp126, ssp245, ssp585	Input dataset			(Good, 2019, 2020a, 2020b; Ridley et al., 2019a)		
	HadGEM3-GC31-MM: historical, ssp126, ssp585	Input dataset			(Ridley et al., 2019b; Jackson, 2020b, 2020a)		
	INM-CM4-8: historical, ssp126, ssp245, ssp585	Input dataset			(Volodin et al., 2019d, 2019b, 2019f, 2019e)		

ACCEPTED VERSION SUBJECT TO FINAL EDITING

	INM-CM5-0: historical, ssp126, ssp245, ssp585	Input dataset			(Volodin et al., 2019j, 2019k, 2019h, 2019l)		
	IPSL-CM5A2-INCA: historical, ssp126	Input dataset			(Boucher et al., 2020a, 2020b)		
	IPSL-CM6A-LR: historical, ssp126, ssp245, ssp585	Input dataset			(Boucher et al., 2018b, 2019a, 2019b, 2019c)		
	KACE-1-0-G: historical, ssp126, ssp245, ssp585	Input dataset			(Byun et al., 2019b, 2019c, 2019e, 2019a)		
	MCM-UA-1-0: historical, ssp126, ssp245, ssp585	Input dataset			(Stouffer, 2019f, 2019b, 2019e, 2019d)		
	MIROC-ES2L: historical, ssp126, ssp245, ssp585	Input dataset			(Hajima et al., 2019b; Tachiiri et al., 2019b, 2019c, 2019a)		
	MIROC6: historical, ssp126, ssp245, ssp585	Input dataset			(Tatebe and Watanabe, 2018b; Shiogama et al., 2019c, 2019a, 2019b)		
	MPI-ESM1-2-HR: historical, ssp126, ssp245, ssp585	Input dataset			(Jungclaus et al., 2019a; Schupfner et al., 2019a, 2019b, 2019c)		
	MPI-ESM1-2-LR: historical, ssp126, ssp245, ssp585	Input datasetInput dataset			(Wieners et al., 2019a, 2019c, 2019d, 2019e)		
	MRI-ESM2-0: historical, ssp126, ssp245, ssp585	Input dataset			(Yukimoto et al., 2019g, 2019b, 2019h, 2019i)		
	UKESM1-0-LL: historical, ssp126, ssp245, ssp585	Input dataset			(Good et al., 2019a, 2019c, 2019b; Tang et al., 2019b)		
	Figure 8.26 Code	Code	Fig8-28.sh (compute and plot)			https://github.com/senesis/some_chap8_figures	CAMMAC :(Sénési, 2020) CliMAF : (Sénési et al., 2021)
Figure 8.27	TraCE paleoclimate simulation, paleoclimate						(Liu et al., 2009)), (Liu et al., 2017b)).

ACCEPTED VERSION SUBJECT TO FINAL EDITING

	proxy &doubling of CO_2 experiment						
Figure Box8-1	CMIP6 DAMIP GPCC, CRU GEBA					https://esgf-node.llnl.gov/search/obs4mips/ **https://psl.noaa.gov/data/gridded/data.gpcp.html** **https://crudata.uea.ac.uk/cru/data/hrg/cru_ts_4.04/ge/**	(Huffman et al., 1997, 2009, Adler et al., 2003, 2016) (Harris et al., 2014) Storelvmo et al (2018)
Figure Box8-2	Schematic						(Wang et al., 2013)
Figure Box8-2-f1	**CMIP6 model data**						
	ACCESS-CM2: historical, ssp126, ssp245, ssp585	Input dataset			(Dix et al., 2019d, 2019a, 2019e, 2019c)		
	ACCESS-ESM1-5: historical, ssp126, ssp245, ssp585	Input dataset			(Ziehn et al., 2019a, 2019e, 2019d, 2019c)		
	AWI-CM-1-1-MR: historical, ssp126, ssp245, ssp585	Input dataset			(Semmler et al., 2018c, 2018d, 2018a, 2019)		
	BCC-CSM2-MR: historical, ssp126, ssp245, ssp585	Input dataset			(Wu et al., 2018a; Xin et al., 2019a, 2019c, 2019b)		
	CAMS-CSM1-0: historical, ssp126, ssp245, ssp585	Input dataset			(Rong, 2019d, 2019e, 2019b, 2019f)		
	CESM2: historical, ssp126, ssp245, ssp585	Input dataset			(Danabasoglu, 2019j, 2019m, 2019l, 2019k)		
	CESM2-WACCM: historical, ssp126, ssp245, ssp585	Input dataset			(Danabasoglu, 2019d, 2019f, 2019h, 2019g)		

ACCEPTED VERSION SUBJECT TO FINAL EDITING

	CIESM: historical, ssp126, ssp245, ssp585	Input dataset			(Huang, 2019a, 2019c, 2020b, 2020a)		
	CMCC-CM2-SR5: historical, ssp126, ssp245, ssp585	Input dataset			(Lovato and Peano, 2020c, 2020a, 2020d, 2020e)		
	CNRM-CM6-1: historical, ssp126, ssp245, ssp585	Input dataset			(Voldoire, 2018a, 2019j, 2019i, 2019h)		
	CNRM-CM6-1-HR: historical, ssp126, ssp245, ssp585	Input dataset			(Voldoire, 2019a, 2019d, 2019c, 2020)		
	CNRM-ESM2-1: historical, ssp126, ssp245, ssp585	Input dataset			(Seferian, 2018b; Voldoire, 2019m, 2019l, 2019k)		
	CanESM5: historical, ssp126, ssp245, ssp585	Input dataset			(Swart et al., 2019n, 2019o, 2019m, 2019h)		
	CanESM5-CanOE: historical, ssp126, ssp245, ssp585	Input dataset			(Swart et al., 2019f, 2019e, 2019d, 2019b)		
	EC-Earth3: historical, ssp126, ssp245, ssp585	Input dataset			(EC-Earth Consortium (EC-Earth), 2019g, 2019j, 2019k, 2019i)		
	EC-Earth3-Veg: historical, ssp126, ssp245, ssp585	Input dataset			(EC-Earth Consortium (EC-Earth), 2019e, 2019f, 2019d, 2019b)		
	FGOALS-f3-L: historical, ssp126, ssp245, ssp585	Input dataset			(Yu, 2019e, 2019c, 2019a, 2019d)		
	FGOALS-g3: historical, ssp126, ssp245, ssp585	Input dataset			(Li, 2019f, 2019e, 2019b, 2019d)		
	FIO-ESM-2-0: historical, ssp126, ssp245, ssp585	Input dataset			(Song et al., 2019e, 2019d, 2019c, 2019a)		
	GFDL-CM4: historical, ssp245, ssp585	Input dataset			(Guo et al., 2018e, 2018d, 2018b)		

ACCEPTED VERSION SUBJECT TO FINAL EDITING

	GFDL-ESM4: historical, ssp126, ssp245, ssp585	Input dataset			(John et al., 2018a, 2018b, 2018c; Krasting et al., 2018b)		
	GISS-E2-1-G: historical, ssp126, ssp245, ssp585	Input dataset			(NASA Goddard Institute for Space Studies (NASA/GISS), 2018b, 2020a, 2020c, 2020b)		
	HadGEM3-GC31-LL: historical, ssp126, ssp245, ssp585	Input dataset			(Good, 2019, 2020a, 2020b; Ridley et al., 2019a)		
	HadGEM3-GC31-MM: historical, ssp126, ssp585	Input dataset			(Ridley et al., 2019b; Jackson, 2020b, 2020a)		
	IITM-ESM: historical, ssp126, ssp245, ssp585	Input dataset			(Raghavan and Panickal, 2019; Panickal and Narayanasetti, 2020b, 2020a, 2020c)		
	INM-CM4-8: historical, ssp126, ssp245, ssp585	Input dataset			(Volodin et al., 2019d, 2019b, 2019f, 2019e)		
	INM-CM5-0: historical, ssp126, ssp245, ssp585	Input dataset			(Volodin et al., 2019j, 2019k, 2019h, 2019l)		
	IPSL-CM5A2-INCA: historical, ssp126	Input dataset			(Boucher et al., 2020a, 2020b)		
	IPSL-CM6A-LR: historical, ssp126, ssp245, ssp585	Input dataset			(Boucher et al., 2018b, 2019a, 2019b, 2019c)		
	KACE-1-0-G: historical, ssp126, ssp245, ssp585	Input dataset			(Byun et al., 2019b, 2019c, 2019e, 2019a)		
	MCM-UA-1-0: historical, ssp126, ssp245, ssp585	Input dataset			(Stouffer, 2019f, 2019b, 2019e, 2019d)		
	MIROC-ES2L: historical, ssp126, ssp245, ssp585	Input dataset			(Hajima et al., 2019b; Tachiiri et al., 2019b, 2019c, 2019a)		
	MIROC6: historical, ssp126, ssp245, ssp585	Input dataset			(Tatebe and Watanabe, 2018b; Shiogama et al., 2019c, 2019a, 2019b)		

ACCEPTED VERSION SUBJECT TO FINAL EDITING

	MPI-ESM1-2-HR: historical, ssp126, ssp245, ssp585	Input dataset			(Jungclaus et al., 2019a; Schupfner et al., 2019a, 2019b, 2019c)		
	MPI-ESM1-2-LR: historical, ssp126, ssp245, ssp585	Input dataset			(Wieners et al., 2019a, 2019c, 2019d, 2019e)		
	MRI-ESM2-0: historical, ssp126, ssp245, ssp585	Input dataset			(Yukimoto et al., 2019g, 2019b, 2019h, 2019i)		
	NESM3: historical, ssp126, ssp245, ssp585	Input dataset			(Cao, 2019b, 2019c, 2019a; Cao and Wang, 2019b)		
	NorESM2-LM: historical, ssp245	Input dataset			(Seland et al., 2019d, 2019a)		
	NorESM2-MM: historical, ssp126, ssp245, ssp585	Input dataset			(Bentsen et al., 2019c, 2019a, 2019e, 2019d)		
	TaiESM1: historical, ssp585	Input dataset			(Lee and Liang, 2020a, 2020c)		
	UKESM1-0-LL: historical, ssp126, ssp245, ssp585	Input dataset			(Good et al., 2019a, 2019c, 2019b; Tang et al., 2019b)		
	Figure Box8-2-f1 Code	Code	FigBox8-2-f1.sh (compute and plot)			https://github.com/senesis/some_chap8_figures	CAMMAC :(Sénési, 2020) CliMAF : (Sénési et al., 2021)
FAQ8.1, Figure 1:	Schematic		Schematic summarizing the influence of land cover and land use change on regional water cycle				

ACCEPTED VERSION SUBJECT TO FINAL EDITING

FAQ8.2, Figure 1:	Schematic		Schematic illustrating factors important in determining changes in heavy precipitation and flooding.				
FAQ8.3, Figure 1:	Schematic		Drought.				
Table 8.1	Table 8.1 code	Code	Table8.1.sh			**https://github.com/senesis/some_chap8_figures**	CAMMAC :(Sénési, 2020) CliMAF : (Sénési et al., 2021)
Table 8.2	Table 8.2 code	Code	Table8.2.sh			**https://github.com/senesis/some_chap8_figures**	CAMMAC :(Sénési, 2020) CliMAF : (Sénési et al., 2021)

[END TABLE 8.SM.1 HERE]

ACCEPTED VERSION
SUBJECT TO FINAL EDITING

References

Abbott, B. W., Bishop, K., Zarnetske, J. P., Minaudo, C., Chapin, F. S., Krause, S., et al. (2019). Human domination of the global water cycle absent from depictions and perceptions. *Nat. Geosci.* 12, 533–540. doi:10.1038/s41561-019-0374-y.

Adler, R. F., Gu, G., Sapiano, M., Wang, J.-J., and Huffman, G. J. (2017). Global Precipitation: Means, Variations and Trends During the Satellite Era (1979–2014). *Surv. Geophys.* 38, 679–699. doi:10.1007/s10712-017-9416-4.

Adler, R. F., Huffman, G. J., Chang, A., Ferraro, R., Xie, P.-P., Janowiak, J., et al. (2003). The Version-2 Global Precipitation Climatology Project (GPCP) Monthly Precipitation Analysis (1979–Present). *J. Hydrometeorol.* 4, 1147–1167. doi:10.1175/1525-7541(2003)004<1147:TVGPCP>2.0.CO;2.

Adler, R., Sapiano, M., Huffman, G., Bolvin, D., Gu, G., Wang, J., et al. (2016). The new version 2.3 of the Global Precipitation Climatology Project (GPCP) monthly analysis product. *Univ. Maryland, April*, 1072–1084.

Allan, R. P., Barlow, M., Byrne, M. P., Cherchi, A., Douville, H., Fowler, H. J., et al. (2020). Advances in understanding large-scale responses of the water cycle to climate change. *Ann. N. Y. Acad. Sci.*, 1–27. doi:10.1111/nyas.14337.

Bader, D. C., Leung, R., Taylor, M., and McCoy, R. B. (2018). E3SM-Project E3SM1.0 model output prepared for CMIP6 CMIP piControl. doi:10.22033/ESGF/CMIP6.4499.

Ban, N., Schmidli, J., and Schär, C. (2015). Heavy precipitation in a changing climate: Does short-term summer precipitation increase faster? *Geophys. Res. Lett.* 42, 1165–1172. doi:10.1002/2014GL062588.

Bao, J., Sherwood, S. C., Alexander, L. V., and Evans, J. P. (2017). Future increases in extreme precipitation exceed observed scaling rates. *Nat. Clim. Chang.* 7, 128–132. doi:10.1038/nclimate3201.

Barbero, R., Fowler, H. J., Lenderink, G., and Blenkinsop, S. (2017). Is the intensification of precipitation extremes with global warming better detected at hourly than daily resolutions? *Geophys. Res. Lett.* 44, 974–983. doi:10.1002/2016GL071917.

Bentsen, M., Oliviè, D. J. L., Seland, Ø., Toniazzo, T., Gjermundsen, A., Graff, L. S., et al. (2019a). NCC NorESM2-MM model output prepared for CMIP6 CMIP historical. doi:10.22033/ESGF/CMIP6.8040.

Bentsen, M., Oliviè, D. J. L., Seland, Ø., Toniazzo, T., Gjermundsen, A., Graff, L. S., et al. (2019b). NCC NorESM2-MM model output prepared for CMIP6 CMIP piControl. doi:10.22033/ESGF/CMIP6.8221.

Bentsen, M., Oliviè, D. J. L., Seland, Ø., Toniazzo, T., Gjermundsen, A., Graff, L. S., et al. (2019c). NCC NorESM2-MM model output prepared for CMIP6 ScenarioMIP ssp126. doi:10.22033/ESGF/CMIP6.8250.

Bentsen, M., Oliviè, D. J. L., Seland, Ø., Toniazzo, T., Gjermundsen, A., Graff, L. S., et al. (2019d). NCC NorESM2-MM model output prepared for CMIP6 ScenarioMIP ssp245. doi:10.22033/ESGF/CMIP6.8255.

Bentsen, M., Oliviè, D. J. L., Seland, Ø., Toniazzo, T., Gjermundsen, A., Graff, L. S., et al. (2019e). NCC NorESM2-MM model output prepared for CMIP6 ScenarioMIP ssp585. doi:10.22033/ESGF/CMIP6.8321.

Bethke, I., Wang, Y., Counillon, F., Kimmritz, M., Fransner, F., Samuelsen, A., et al. (2019). NCC NorCPM1 model output prepared for CMIP6 CMIP piControl. doi:10.22033/ESGF/CMIP6.10896.

Bonfils, C. J. W. W., Santer, B. D., Fyfe, J. C., Marvel, K., Phillips, T. J., and Zimmerman, S. R. H. H. (2020). Human influence on joint changes in temperature, rainfall and continental aridity. *Nat. Clim. Chang.* 10, 1–6. doi:10.1038/s41558-020-0821-1.

Borodina, A., Fischer, E. M., and Knutti, R. (2017). Models are likely to underestimate increase in heavy rainfall in the extratropical regions with high rainfall intensity. *Geophys. Res. Lett.* 44, 7401–7409. doi:10.1002/2017GL074530.

Boucher, O., Denvil, S., Levavasseur, G., Cozic, A., Caubel, A., Foujols, M.-A., et al. (2018a). IPSL IPSL-CM6A-LR model output prepared for CMIP6 CMIP. doi:10.22033/ESGF/CMIP6.1534.

Boucher, O., Denvil, S., Levavasseur, G., Cozic, A., Caubel, A., Foujols, M.-A., et al. (2018b). IPSL IPSL-CM6A-LR model output prepared for CMIP6 CMIP historical. doi:10.22033/ESGF/CMIP6.5195.

Boucher, O., Denvil, S., Levavasseur, G., Cozic, A., Caubel, A., Foujols, M.-A., et al. (2018c). IPSL IPSL-CM6A-LR model output prepared for CMIP6 CMIP piControl. doi:10.22033/ESGF/CMIP6.5251.

Boucher, O., Denvil, S., Levavasseur, G., Cozic, A., Caubel, A., Foujols, M.-A., et al. (2018d). IPSL IPSL-CM6A-LR model output prepared for CMIP6 DAMIP hist-aer. doi:10.22033/ESGF/CMIP6.13827.

Boucher, O., Denvil, S., Levavasseur, G., Cozic, A., Caubel, A., Foujols, M.-A., et al. (2018e). IPSL IPSL-CM6A-LR model output prepared for CMIP6 DAMIP hist-GHG. doi:10.22033/ESGF/CMIP6.13825.

Boucher, O., Denvil, S., Levavasseur, G., Cozic, A., Caubel, A., Foujols, M.-A., et al. (2018f). IPSL IPSL-CM6A-LR model output prepared for CMIP6 DAMIP hist-nat. doi:10.22033/ESGF/CMIP6.13831.

Boucher, O., Denvil, S., Levavasseur, G., Cozic, A., Caubel, A., Foujols, M.-A., et al. (2019a). IPSL IPSL-CM6A-LR model output prepared for CMIP6 ScenarioMIP ssp126. doi:10.22033/ESGF/CMIP6.5262.

Boucher, O., Denvil, S., Levavasseur, G., Cozic, A., Caubel, A., Foujols, M.-A., et al. (2019b). IPSL IPSL-CM6A-LR model output prepared for CMIP6 ScenarioMIP ssp245. doi:10.22033/ESGF/CMIP6.5264.

Boucher, O., Denvil, S., Levavasseur, G., Cozic, A., Caubel, A., Foujols, M.-A., et al. (2019c). IPSL IPSL-CM6A-LR model output prepared for CMIP6 ScenarioMIP ssp585. doi:10.22033/ESGF/CMIP6.5271.

ACCEPTED VERSION SUBJECT TO FINAL EDITING

Boucher, O., Denvil, S., Levavasseur, G., Cozic, A., Caubel, A., Foujols, M.-A., et al. (2020a). IPSL IPSL-CM5A2-INCA model output prepared for CMIP6 CMIP historical. doi:10.22033/ESGF/CMIP6.13661.
Boucher, O., Denvil, S., Levavasseur, G., Cozic, A., Caubel, A., Foujols, M.-A., et al. (2020b). IPSL IPSL-CM5A2-INCA model output prepared for CMIP6 ScenarioMIP ssp126. doi:10.22033/ESGF/CMIP6.15711.
Byun, Y.-H., Lim, Y.-J., Shim, S., Sung, H. M., Sun, M., Kim, J., et al. (2019a). NIMS-KMA KACE1.0-G model output prepared for CMIP6 ScenarioMIP ssp126. doi:10.22033/ESGF/CMIP6.8432.
Byun, Y.-H., Lim, Y.-J., Shim, S., Sung, H. M., Sun, M., Kim, J., et al. (2019b). NIMS-KMA KACE1.0-G model output prepared for CMIP6 ScenarioMIP ssp245. doi:10.22033/ESGF/CMIP6.8435.
Byun, Y.-H., Lim, Y.-J., Shim, S., Sung, H. M., Sun, M., Kim, J., et al. (2019c). NIMS-KMA KACE1.0-G model output prepared for CMIP6 ScenarioMIP ssp585. doi:10.22033/ESGF/CMIP6.8456.
Byun, Y.-H., Lim, Y.-J., Sung, H. M., Kim, J., Sun, M., and Kim, B.-H. (2019d). NIMS-KMA KACE1.0-G model output prepared for CMIP6 CMIP. doi:10.22033/ESGF/CMIP6.2241.
Byun, Y.-H., Lim, Y.-J., Sung, H. M., Kim, J., Sun, M., and Kim, B.-H. (2019e). NIMS-KMA KACE1.0-G model output prepared for CMIP6 CMIP historical. doi:10.22033/ESGF/CMIP6.8378.
Byun, Y.-H., Lim, Y.-J., Sung, H. M., Kim, J., Sun, M., and Kim, B.-H. (2019f). NIMS-KMA KACE1.0-G model output prepared for CMIP6 CMIP piControl. doi:10.22033/ESGF/CMIP6.8425.
Cao, J. (2019a). NUIST NESMv3 model output prepared for CMIP6 ScenarioMIP ssp126. doi:10.22033/ESGF/CMIP6.8780.
Cao, J. (2019b). NUIST NESMv3 model output prepared for CMIP6 ScenarioMIP ssp245. doi:10.22033/ESGF/CMIP6.8781.
Cao, J. (2019c). NUIST NESMv3 model output prepared for CMIP6 ScenarioMIP ssp585. doi:10.22033/ESGF/CMIP6.8790.
Cao, J., and Wang, B. (2019a). NUIST NESMv3 model output prepared for CMIP6 CMIP. doi:10.22033/ESGF/CMIP6.2021.
Cao, J., and Wang, B. (2019b). NUIST NESMv3 model output prepared for CMIP6 CMIP historical. doi:10.22033/ESGF/CMIP6.8769.
Cao, J., and Wang, B. (2019c). NUIST NESMv3 model output prepared for CMIP6 CMIP piControl. doi:10.22033/ESGF/CMIP6.8776.
Chai, Z. (2020). CAS CAS-ESM1.0 model output prepared for CMIP6 CMIP piControl. doi:10.22033/ESGF/CMIP6.3445.
Chan, S. C., Kendon, E. J., Roberts, N. M., Fowler, H. J., and Blenkinsop, S. (2016). Downturn in scaling of UK extreme rainfall with temperature for future hottest days. *Nat. Geosci.* 9, 24–28. doi:10.1038/ngeo2596.
Danabasoglu, G. (2019a). NCAR CESM2-FV2 model output prepared for CMIP6 CMIP piControl. doi:10.22033/ESGF/CMIP6.11301.
Danabasoglu, G. (2019b). NCAR CESM2-WACCM-FV2 model output prepared for CMIP6 CMIP piControl. doi:10.22033/ESGF/CMIP6.11302.
Danabasoglu, G. (2019c). NCAR CESM2-WACCM model output prepared for CMIP6 CMIP. doi:10.22033/ESGF/CMIP6.10024.
Danabasoglu, G. (2019d). NCAR CESM2-WACCM model output prepared for CMIP6 CMIP historical. doi:10.22033/ESGF/CMIP6.10071.
Danabasoglu, G. (2019e). NCAR CESM2-WACCM model output prepared for CMIP6 CMIP piControl. doi:10.22033/ESGF/CMIP6.10094.
Danabasoglu, G. (2019f). NCAR CESM2-WACCM model output prepared for CMIP6 ScenarioMIP ssp126. doi:10.22033/ESGF/CMIP6.10100.
Danabasoglu, G. (2019g). NCAR CESM2-WACCM model output prepared for CMIP6 ScenarioMIP ssp245. doi:10.22033/ESGF/CMIP6.10101.
Danabasoglu, G. (2019h). NCAR CESM2-WACCM model output prepared for CMIP6 ScenarioMIP ssp585. doi:10.22033/ESGF/CMIP6.10115.
Danabasoglu, G. (2019i). NCAR CESM2 model output prepared for CMIP6 CMIP. doi:10.22033/ESGF/CMIP6.2185.
Danabasoglu, G. (2019j). NCAR CESM2 model output prepared for CMIP6 CMIP historical. doi:10.22033/ESGF/CMIP6.7627.
Danabasoglu, G. (2019k). NCAR CESM2 model output prepared for CMIP6 ScenarioMIP ssp126. doi:10.22033/ESGF/CMIP6.7746.
Danabasoglu, G. (2019l). NCAR CESM2 model output prepared for CMIP6 ScenarioMIP ssp245. doi:10.22033/ESGF/CMIP6.7748.
Danabasoglu, G. (2019m). NCAR CESM2 model output prepared for CMIP6 ScenarioMIP ssp585. doi:10.22033/ESGF/CMIP6.7768.
Danabasoglu, G., Lawrence, D., Lindsay, K., Lipscomb, W., and Strand, G. (2019). NCAR CESM2 model output prepared for CMIP6 CMIP piControl. doi:10.22033/ESGF/CMIP6.7733.
Deser, C., Hurrell, J. W., and Phillips, A. S. (2017). The role of the North Atlantic Oscillation in European climate projections. *Clim. Dyn.* 49, 3141–3157. doi:10.1007/s00382-016-3502-z.

SUBMITTED VERSION
SUBJECT TO FINAL EDITING

Dix, M., Bi, D., Dobrohotoff, P., Fiedler, R., Harman, I., Law, R., et al. (2019a). CSIRO-ARCCSS ACCESS-CM2 model output prepared for CMIP6 CMIP historical. doi:10.22033/ESGF/CMIP6.4271.
Dix, M., Bi, D., Dobrohotoff, P., Fiedler, R., Harman, I., Law, R., et al. (2019b). CSIRO-ARCCSS ACCESS-CM2 model output prepared for CMIP6 CMIP piControl. doi:10.22033/ESGF/CMIP6.4311.
Dix, M., Bi, D., Dobrohotoff, P., Fiedler, R., Harman, I., Law, R., et al. (2019c). CSIRO-ARCCSS ACCESS-CM2 model output prepared for CMIP6 ScenarioMIP ssp126. doi:10.22033/ESGF/CMIP6.4319.
Dix, M., Bi, D., Dobrohotoff, P., Fiedler, R., Harman, I., Law, R., et al. (2019d). CSIRO-ARCCSS ACCESS-CM2 model output prepared for CMIP6 ScenarioMIP ssp245. doi:10.22033/ESGF/CMIP6.4321.
Dix, M., Bi, D., Dobrohotoff, P., Fiedler, R., Harman, I., Law, R., et al. (2019e). CSIRO-ARCCSS ACCESS-CM2 model output prepared for CMIP6 ScenarioMIP ssp585. doi:10.22033/ESGF/CMIP6.4332.
Donat, M. G., Lowry, A. L., Alexander, L. V., O'Gorman, P. A., and Maher, N. (2016). More extreme precipitation in the world's dry and wet regions. *Nat. Clim. Chang.* 6, 508–513. doi:10.1038/nclimate2941.
EC-Earth Consortium (EC-Earth) (2019a). EC-Earth-Consortium EC-Earth3-LR model output prepared for CMIP6 CMIP piControl. doi:10.22033/ESGF/CMIP6.4847.
EC-Earth Consortium (EC-Earth) (2019b). EC-Earth-Consortium EC-Earth3-Veg model output prepared for CMIP6 CMIP historical. doi:10.22033/ESGF/CMIP6.4706.
EC-Earth Consortium (EC-Earth) (2019c). EC-Earth-Consortium EC-Earth3-Veg model output prepared for CMIP6 CMIP piControl. doi:10.22033/ESGF/CMIP6.4848.
EC-Earth Consortium (EC-Earth) (2019d). EC-Earth-Consortium EC-Earth3-Veg model output prepared for CMIP6 ScenarioMIP ssp126. doi:10.22033/ESGF/CMIP6.4876.
EC-Earth Consortium (EC-Earth) (2019e). EC-Earth-Consortium EC-Earth3-Veg model output prepared for CMIP6 ScenarioMIP ssp245. doi:10.22033/ESGF/CMIP6.4882.
EC-Earth Consortium (EC-Earth) (2019f). EC-Earth-Consortium EC-Earth3-Veg model output prepared for CMIP6 ScenarioMIP ssp585. doi:10.22033/ESGF/CMIP6.4914.
EC-Earth Consortium (EC-Earth) (2019g). EC-Earth-Consortium EC-Earth3 model output prepared for CMIP6 CMIP historical. doi:10.22033/ESGF/CMIP6.4700.
EC-Earth Consortium (EC-Earth) (2019h). EC-Earth-Consortium EC-Earth3 model output prepared for CMIP6 CMIP piControl. doi:10.22033/ESGF/CMIP6.4842.
EC-Earth Consortium (EC-Earth) (2019i). EC-Earth-Consortium EC-Earth3 model output prepared for CMIP6 ScenarioMIP ssp126. doi:10.22033/ESGF/CMIP6.4874.
EC-Earth Consortium (EC-Earth) (2019j). EC-Earth-Consortium EC-Earth3 model output prepared for CMIP6 ScenarioMIP ssp245. doi:10.22033/ESGF/CMIP6.4880.
EC-Earth Consortium (EC-Earth) (2019k). EC-Earth-Consortium EC-Earth3 model output prepared for CMIP6 ScenarioMIP ssp585. doi:10.22033/ESGF/CMIP6.4912.
EC-Earth Consortium (EC-Earth) (2020a). EC-Earth-Consortium EC-Earth3-AerChem model output prepared for CMIP6 CMIP piControl. doi:10.22033/ESGF/CMIP6.4843.
EC-Earth Consortium (EC-Earth) (2020b). EC-Earth-Consortium EC-Earth3-Veg-LR model output prepared for CMIP6 CMIP historical. doi:10.22033/ESGF/CMIP6.4707.
EC-Earth Consortium (EC-Earth) (2020c). EC-Earth-Consortium EC-Earth3-Veg-LR model output prepared for CMIP6 CMIP piControl. doi:10.22033/ESGF/CMIP6.4849.
EC-Earth Consortium (EC-Earth) (2020d). EC-Earth-Consortium EC-Earth3-Veg-LR model output prepared for CMIP6 ScenarioMIP ssp585. doi:10.22033/ESGF/CMIP6.4915.
Fischer, E. M., and Knutti, R. (2015). Anthropogenic contribution to global occurrence of heavy-precipitation and high-temperature extremes. *Nat. Clim. Chang.* 5, 560–564. doi:10.1038/nclimate2617.
Fläschner, D., Mauritsen, T., and Stevens, B. (2016). Understanding the intermodel spread in global-mean hydrological sensitivity. *J. Clim.* 29, 801–817. doi:10.1175/JCLI-D-15-0351.1.
Good, P. (2019). MOHC HadGEM3-GC31-LL model output prepared for CMIP6 ScenarioMIP ssp245. doi:10.22033/ESGF/CMIP6.10851.
Good, P. (2020a). MOHC HadGEM3-GC31-LL model output prepared for CMIP6 ScenarioMIP ssp126. doi:10.22033/ESGF/CMIP6.10849.
Good, P. (2020b). MOHC HadGEM3-GC31-LL model output prepared for CMIP6 ScenarioMIP ssp585. doi:10.22033/ESGF/CMIP6.10901.
Good, P., Sellar, A., Tang, Y., Rumbold, S., Ellis, R., Kelley, D., et al. (2019a). MOHC UKESM1.0-LL model output prepared for CMIP6 ScenarioMIP ssp126. doi:10.22033/ESGF/CMIP6.6333.
Good, P., Sellar, A., Tang, Y., Rumbold, S., Ellis, R., Kelley, D., et al. (2019b). MOHC UKESM1.0-LL model output prepared for CMIP6 ScenarioMIP ssp245. doi:10.22033/ESGF/CMIP6.6339.
Good, P., Sellar, A., Tang, Y., Rumbold, S., Ellis, R., Kelley, D., et al. (2019c). MOHC UKESM1.0-LL model output prepared for CMIP6 ScenarioMIP ssp585. doi:10.22033/ESGF/CMIP6.6405.
Guerreiro, S. B., Fowler, H. J., Barbero, R., Westra, S., Lenderink, G., Blenkinsop, S., et al. (2018). Detection of continental-scale intensification of hourly rainfall extremes. *Nat. Clim. Chang.* 8, 803–807. doi:10.1038/s41558-018-0245-3.

SUBJECT TO FINAL EDITING ACCEPTED VERSION

Guo, C., Bentsen, M., Bethke, I., Ilicak, M., Tjiputra, J., Toniazzo, T., et al. (2019). NCC NorESM1-F model output prepared for CMIP6 CMIP piControl. doi:10.22033/ESGF/CMIP6.11595.
Guo, H., John, J. G., Blanton, C., McHugh, C., Nikonov, S., Radhakrishnan, A., et al. (2018a). NOAA-GFDL GFDL-CM4 model output. doi:10.22033/ESGF/CMIP6.1402.
Guo, H., John, J. G., Blanton, C., McHugh, C., Nikonov, S., Radhakrishnan, A., et al. (2018b). NOAA-GFDL GFDL-CM4 model output historical. doi:10.22033/ESGF/CMIP6.8594.
Guo, H., John, J. G., Blanton, C., McHugh, C., Nikonov, S., Radhakrishnan, A., et al. (2018c). NOAA-GFDL GFDL-CM4 model output piControl. doi:10.22033/ESGF/CMIP6.8666.
Guo, H., John, J. G., Blanton, C., McHugh, C., Nikonov, S., Radhakrishnan, A., et al. (2018d). NOAA-GFDL GFDL-CM4 model output prepared for CMIP6 ScenarioMIP ssp245. doi:10.22033/ESGF/CMIP6.9263.
Guo, H., John, J. G., Blanton, C., McHugh, C., Nikonov, S., Radhakrishnan, A., et al. (2018e). NOAA-GFDL GFDL-CM4 model output prepared for CMIP6 ScenarioMIP ssp585. doi:10.22033/ESGF/CMIP6.9268.
Gutenstein, M., Fennig, K., Schröder, M., Trent, T., Bakan, S., Roberts, J. B., et al. (2020). Intercomparison of freshwater fluxes over ocean and investigations into water budget closure. *Hydrol. Earth Syst. Sci. Discuss.* 2020, 1–35. doi:10.5194/hess-2020-317.
Haerter, J. O., and Schlemmer, L. (2018). Intensified Cold Pool Dynamics Under Stronger Surface Heating. *Geophys. Res. Lett.* 45, 6299–6310. doi:10.1029/2017GL076874.
Hajima, T., Abe, M., Arakawa, O., Suzuki, T., Komuro, Y., Ogura, T., et al. (2019a). MIROC MIROC-ES2L model output prepared for CMIP6 CMIP. doi:10.22033/ESGF/CMIP6.902.
Hajima, T., Abe, M., Arakawa, O., Suzuki, T., Komuro, Y., Ogura, T., et al. (2019b). MIROC MIROC-ES2L model output prepared for CMIP6 CMIP historical. doi:10.22033/ESGF/CMIP6.5602.
Hajima, T., Abe, M., Arakawa, O., Suzuki, T., Komuro, Y., Ogura, T., et al. (2019c). MIROC MIROC-ES2L model output prepared for CMIP6 CMIP piControl. doi:10.22033/ESGF/CMIP6.5710.
Harris, I., Jones, P. D., Osborn, T. J., and Lister, D. H. (2014). Updated high-resolution grids of monthly climatic observations – the CRU TS3.10 Dataset. *Int. J. Climatol.* 34, 623–642. doi:10.1002/joc.3711.
Hessl, A. E., Anchukaitis, K. J., Jelsema, C., Cook, B., Byambasuren, O., Leland, C., et al. (2018). Past and future drought in Mongolia. *Sci. Adv.* 4, e1701832.
Huang, W. (2019a). THU CIESM model output prepared for CMIP6 CMIP historical. doi:10.22033/ESGF/CMIP6.8843.
Huang, W. (2019b). THU CIESM model output prepared for CMIP6 CMIP piControl. doi:10.22033/ESGF/CMIP6.8849.
Huang, W. (2019c). THU CIESM model output prepared for CMIP6 ScenarioMIP ssp126. doi:10.22033/ESGF/CMIP6.8857.
Huang, W. (2020a). THU CIESM model output prepared for CMIP6 ScenarioMIP ssp245. doi:10.22033/ESGF/CMIP6.8858.
Huang, W. (2020b). THU CIESM model output prepared for CMIP6 ScenarioMIP ssp585. doi:10.22033/ESGF/CMIP6.8863.
Huffman, G. J., Adler, R. F., Arkin, P., Chang, A., Ferraro, R., Gruber, A., et al. (1997). The Global Precipitation Climatology Project (GPCP) Combined Precipitation Dataset. *Bull. Am. Meteorol. Soc.* doi:10.1175/1520-0477(1997)078<0005:TGPCPG>2.0.CO;2.
Huffman, G. J., Adler, R. F., Bolvin, D. T., and Gu, G. (2009). Improving the global precipitation record: GPCP Version 2.1. *Geophys. Res. Lett.* 36. doi:https://doi.org/10.1029/2009GL040000.
Jackson, L. (2020a). MOHC HadGEM3-GC31-MM model output prepared for CMIP6 ScenarioMIP ssp126. doi:10.22033/ESGF/CMIP6.10850.
Jackson, L. (2020b). MOHC HadGEM3-GC31-MM model output prepared for CMIP6 ScenarioMIP ssp585. doi:10.22033/ESGF/CMIP6.10902.
John, J. G., Blanton, C., McHugh, C., Radhakrishnan, A., Rand, K., Vahlenkamp, H., et al. (2018a). NOAA-GFDL GFDL-ESM4 model output prepared for CMIP6 ScenarioMIP ssp126. doi:10.22033/ESGF/CMIP6.8684.
John, J. G., Blanton, C., McHugh, C., Radhakrishnan, A., Rand, K., Vahlenkamp, H., et al. (2018b). NOAA-GFDL GFDL-ESM4 model output prepared for CMIP6 ScenarioMIP ssp245. doi:10.22033/ESGF/CMIP6.8686.
John, J. G., Blanton, C., McHugh, C., Radhakrishnan, A., Rand, K., Vahlenkamp, H., et al. (2018c). NOAA-GFDL GFDL-ESM4 model output prepared for CMIP6 ScenarioMIP ssp585. doi:10.22033/ESGF/CMIP6.8706.
Jones, G. (2019a). MOHC HadGEM3-GC31-LL model output prepared for CMIP6 DAMIP hist-aer. doi:10.22033/ESGF/CMIP6.6052.
Jones, G. (2019b). MOHC HadGEM3-GC31-LL model output prepared for CMIP6 DAMIP hist-GHG. doi:10.22033/ESGF/CMIP6.6051.
Jones, G. (2019c). MOHC HadGEM3-GC31-LL model output prepared for CMIP6 DAMIP hist-nat. doi:10.22033/ESGF/CMIP6.6059.
Jungclaus, J., Bittner, M., Wieners, K.-H., Wachsmann, F., Schupfner, M., Legutke, S., et al. (2019a). MPI-M MPI-ESM1.2-HR model output prepared for CMIP6 CMIP historical. doi:10.22033/ESGF/CMIP6.6594.
Jungclaus, J., Bittner, M., Wieners, K.-H., Wachsmann, F., Schupfner, M., Legutke, S., et al. (2019b). MPI-M MPI-

ACCEPTED VERSION SUBJECT TO FINAL EDITING

ESM1.2-HR model output prepared for CMIP6 CMIP piControl. doi:10.22033/ESGF/CMIP6.6674.
Jungclaus, J., Bittner, M., Wieners, K.-H., Wachsmann, F., Schupfner, M., Legutke, S., et al. (2019c). MPI-M MPIESM1.2-HR model output prepared for CMIP6 CMIP. doi:10.22033/ESGF/CMIP6.741.
Krasting, J. P., John, J. G., Blanton, C., McHugh, C., Nikonov, S., Radhakrishnan, A., et al. (2018a). NOAA-GFDL GFDL-ESM4 model output prepared for CMIP6 CMIP. doi:10.22033/ESGF/CMIP6.1407.
Krasting, J. P., John, J. G., Blanton, C., McHugh, C., Nikonov, S., Radhakrishnan, A., et al. (2018b). NOAA-GFDL GFDL-ESM4 model output prepared for CMIP6 CMIP historical. doi:10.22033/ESGF/CMIP6.8597.
Krasting, J. P., John, J. G., Blanton, C., McHugh, C., Nikonov, S., Radhakrishnan, A., et al. (2018c). NOAA-GFDL GFDL-ESM4 model output prepared for CMIP6 CMIP piControl. doi:10.22033/ESGF/CMIP6.8669.
Kwon, E. Y., Kim, G., Primeau, F., Moore, W. S., Cho, H.-M., DeVries, T., et al. (2014). Global estimate of submarine groundwater discharge based on an observationally constrained radium isotope model. *Geophys. Res. Lett.* 41, 8438–8444. doi:10.1002/2014GL061574.
Lee, W.-L., and Liang, H.-C. (2020a). AS-RCEC TaiESM1.0 model output prepared for CMIP6 CMIP historical. doi:10.22033/ESGF/CMIP6.9755.
Lee, W.-L., and Liang, H.-C. (2020b). AS-RCEC TaiESM1.0 model output prepared for CMIP6 CMIP piControl. doi:10.22033/ESGF/CMIP6.9798.
Lee, W.-L., and Liang, H.-C. (2020c). AS-RCEC TaiESM1.0 model output prepared for CMIP6 ScenarioMIP ssp585. doi:10.22033/ESGF/CMIP6.9823.
Lehner, F., Deser, C., Maher, N., Marotzke, J., Fischer, E. M., Brunner, L., et al. (2020). Partitioning climate projection uncertainty with multiple Large Ensembles and CMIP5/6. *Earth Syst. Dyn.* 11, 1–28. doi:10.5194/esd-11-491-2020.
Lenderink, G., Belušić, D., Fowler, H. J., Kjellström, E., Lind, P., van Meijgaard, E., et al. (2019). Systematic increases in the thermodynamic response of hourly precipitation extremes in an idealized warming experiment with a convection-permitting climate model. *Environ. Res. Lett.* 14, 074012. doi:10.1088/1748-9326/ab214a.
Li, L. (2019a). CAS FGOALS-g3 model output prepared for CMIP6 CMIP. doi:10.22033/ESGF/CMIP6.1783.
Li, L. (2019b). CAS FGOALS-g3 model output prepared for CMIP6 CMIP historical. doi:10.22033/ESGF/CMIP6.3356.
Li, L. (2019c). CAS FGOALS-g3 model output prepared for CMIP6 CMIP piControl. doi:10.22033/ESGF/CMIP6.3448.
Li, L. (2019d). CAS FGOALS-g3 model output prepared for CMIP6 ScenarioMIP ssp126. doi:10.22033/ESGF/CMIP6.3465.
Li, L. (2019e). CAS FGOALS-g3 model output prepared for CMIP6 ScenarioMIP ssp245. doi:10.22033/ESGF/CMIP6.3469.
Li, L. (2019f). CAS FGOALS-g3 model output prepared for CMIP6 ScenarioMIP ssp585. doi:10.22033/ESGF/CMIP6.3503.
Li, L. (2020a). CAS FGOALS-g3 model output prepared for CMIP6 DAMIP. doi:10.22033/ESGF/CMIP6.2048.
Li, L. (2020b). CAS FGOALS-g3 model output prepared for CMIP6 DAMIP hist-aer. doi:10.22033/ESGF/CMIP6.3323.
Li, L. (2020c). CAS FGOALS-g3 model output prepared for CMIP6 DAMIP hist-GHG. doi:10.22033/ESGF/CMIP6.3321.
Li, L. (2020d). CAS FGOALS-g3 model output prepared for CMIP6 DAMIP hist-nat. doi:10.22033/ESGF/CMIP6.3330.
Liu, W., Xie, S. P., Liu, Z., and Zhu, J. (2017). Overlooked possibility of a collapsed atlantic meridional overturning circulation in warming climate. *Sci. Adv.* doi:10.1126/sciadv.1601666.
Liu, Z., Otto-Bliesner, B. L., He, F., Brady, E. C., Tomas, R., Clark, P. U., et al. (2009). Transient simulation of last deglaciation with a new mechanism for bolling-allerod warming. *Science (80-.).* doi:10.1126/science.1171041.
Lovato, T., and Peano, D. (2020a). CMCC CMCC-CM2-SR5 model output prepared for CMIP6 CMIP historical. doi:10.22033/ESGF/CMIP6.3825.
Lovato, T., and Peano, D. (2020b). CMCC CMCC-CM2-SR5 model output prepared for CMIP6 CMIP piControl. doi:10.22033/ESGF/CMIP6.3874.
Lovato, T., and Peano, D. (2020c). CMCC CMCC-CM2-SR5 model output prepared for CMIP6 ScenarioMIP ssp126. doi:10.22033/ESGF/CMIP6.3887.
Lovato, T., and Peano, D. (2020d). CMCC CMCC-CM2-SR5 model output prepared for CMIP6 ScenarioMIP ssp245. doi:10.22033/ESGF/CMIP6.3889.
Lovato, T., and Peano, D. (2020e). CMCC CMCC-CM2-SR5 model output prepared for CMIP6 ScenarioMIP ssp585. doi:10.22033/ESGF/CMIP6.3896.
Luijendijk, E., Gleeson, T., and Moosdorf, N. (2020). Fresh groundwater discharge insignificant for the world's oceans but important for coastal ecosystems. *Nat. Commun.* 11, 1260. doi:10.1038/s41467-020-15064-8.
NASA Goddard Institute for Space Studies (NASA/GISS) (2018a). NASA-GISS GISS-E2.1G model output prepared for CMIP6 CMIP. doi:10.22033/ESGF/CMIP6.1400.
NASA Goddard Institute for Space Studies (NASA/GISS) (2018b). NASA-GISS GISS-E2.1G model output prepared

ACCEPTED VERSION
SUBJECT TO FINAL EDITING

for CMIP6 CMIP historical. doi:10.22033/ESGF/CMIP6.7127.
NASA Goddard Institute for Space Studies (NASA/GISS) (2018c). NASA-GISS GISS-E2.1G model output prepared for CMIP6 CMIP piControl. doi:10.22033/ESGF/CMIP6.7380.
NASA Goddard Institute for Space Studies (NASA/GISS) (2018d). NASA-GISS GISS-E2.1H model output prepared for CMIP6 CMIP piControl. doi:10.22033/ESGF/CMIP6.7381.
NASA Goddard Institute for Space Studies (NASA/GISS) (2020a). NASA-GISS GISS-E2.1G model output prepared for CMIP6 ScenarioMIP ssp126. doi:10.22033/ESGF/CMIP6.7410.
NASA Goddard Institute for Space Studies (NASA/GISS) (2020b). NASA-GISS GISS-E2.1G model output prepared for CMIP6 ScenarioMIP ssp245. doi:10.22033/ESGF/CMIP6.7415.
NASA Goddard Institute for Space Studies (NASA/GISS) (2020c). NASA-GISS GISS-E2.1G model output prepared for CMIP6 ScenarioMIP ssp585. doi:10.22033/ESGF/CMIP6.7460.
Neubauer, D., Ferrachat, S., Siegenthaler-Le Drian, C., Stoll, J., Folini, D. S., Tegen, I., et al. (2019). HAMMOZ-Consortium MPI-ESM1.2-HAM model output prepared for CMIP6 CMIP piControl. doi:10.22033/ESGF/CMIP6.5037.
O'Gorman, P. A. (2012). Sensitivity of tropical precipitation extremes to climate change. *Nat. Geosci.* 5, 697–700. doi:10.1038/ngeo1568.
Palmer, J. G., Cook, E. R., Turney, C. S. M., Allen, K., Fenwick, P., Cook, B. I., et al. (2015). Drought variability in the eastern Australia and New Zealand summer drought atlas (ANZDA, CE 1500-2012) modulated by the Interdecadal Pacific Oscillation. *Environ. Res. Lett.* doi:10.1088/1748-9326/10/12/124002.
Panickal, S., and Narayanasetti, S. (2020a). CCCR-IITM IITM-ESM model output prepared for CMIP6 ScenarioMIP ssp126. doi:10.22033/ESGF/CMIP6.14747.
Panickal, S., and Narayanasetti, S. (2020b). CCCR-IITM IITM-ESM model output prepared for CMIP6 ScenarioMIP ssp245. doi:10.22033/ESGF/CMIP6.14748.
Panickal, S., and Narayanasetti, S. (2020c). CCCR-IITM IITM-ESM model output prepared for CMIP6 ScenarioMIP ssp585. doi:10.22033/ESGF/CMIP6.14753.
Park, S., and Shin, J. (2019). SNU SAM0-UNICON model output prepared for CMIP6 CMIP piControl. doi:10.22033/ESGF/CMIP6.7791.
Pederson, N., Hessl, A. E., Baatarbileg, N., Anchukaitis, K. J., and Di Cosmo, N. (2014). Pluvials, droughts, the Mongol Empire, and modern Mongolia. *Proc. Natl. Acad. Sci.* doi:10.1073/pnas.1318677111.
Pendergrass, A. G. (2020). The global-mean precipitation response to CO2-induced warming in CMIP6 models. *Geophyisical Res. Lett.* 47, e2020GL089964. doi:10.1029/2020GL089964.
Prein, A. F., Rasmussen, R. M., Ikeda, K., Liu, C., Clark, M. P., and Holland, G. J. (2017). The future intensification of hourly precipitation extremes. *Nat. Clim. Chang.* 7, 48–52. doi:10.1038/nclimate3168.
Pulliainen, J., Luojus, K., Derksen, C., Mudryk, L., Lemmetyinen, J., Salminen, M., et al. (2020). Patterns and trends of Northern Hemisphere snow mass from 1980 to 2018. *Nature* 581, 294–298. doi:10.1038/s41586-020-2258-0.
Raghavan, K., and Panickal, S. (2019). CCCR-IITM IITM-ESM model output prepared for CMIP6 CMIP historical. doi:10.22033/ESGF/CMIP6.3708.
Rehfeld, K., Hébert, R., Lora, J., Lofverstrom, M., and Brierley, C. (2020). Variability of surface climate in simulations of past and future. *Earth Syst. Dyn. Discuss.* 11, 1–30. doi:10.5194/esd-2019-92.
Richardson, T. B., Forster, P. M. P., Andrews, T., Boucher, O., Faluvegi, G., Fläschner, D., et al. (2018). Drivers of precipitation change: An energetic understanding. *J. Clim.* 31, 9641–9657. doi:10.1175/JCLI-D-17-0240.1.
Ridley, J., Menary, M., Kuhlbrodt, T., Andrews, M., and Andrews, T. (2018). MOHC HadGEM3-GC31-LL model output prepared for CMIP6 CMIP piControl. doi:10.22033/ESGF/CMIP6.6294.
Ridley, J., Menary, M., Kuhlbrodt, T., Andrews, M., and Andrews, T. (2019a). MOHC HadGEM3-GC31-LL model output prepared for CMIP6 CMIP historical. doi:10.22033/ESGF/CMIP6.6109.
Ridley, J., Menary, M., Kuhlbrodt, T., Andrews, M., and Andrews, T. (2019b). MOHC HadGEM3-GC31-MM model output prepared for CMIP6 CMIP historical. doi:10.22033/ESGF/CMIP6.6112.
Ridley, J., Menary, M., Kuhlbrodt, T., Andrews, M., and Andrews, T. (2019c). MOHC HadGEM3-GC31-MM model output prepared for CMIP6 CMIP piControl. doi:10.22033/ESGF/CMIP6.6297.
Rodell, M., Beaudoing, H. K., L'Ecuyer, T. S., Olson, W. S., Famiglietti, J. S., Houser, P. R., et al. (2015). The observed state of the water cycle in the early twenty-first century. *J. Clim.* 28, 8289–8318. doi:10.1175/JCLI-D-14-00555.1.
Rodell, M., Famiglietti, J. S., Wiese, D. N., Reager, J. T., Beaudoing, H. K., Landerer, F. W., et al. (2018). Emerging trends in global freshwater availability. *Nature* 557, 651–659. doi:10.1038/s41586-018-0123-1.
Rong, X. (2019a). CAMS CAMS_CSM1.0 model output prepared for CMIP6 CMIP. doi:10.22033/ESGF/CMIP6.1399.
Rong, X. (2019b). CAMS CAMS_CSM1.0 model output prepared for CMIP6 CMIP historical. doi:10.22033/ESGF/CMIP6.9754.
Rong, X. (2019c). CAMS CAMS_CSM1.0 model output prepared for CMIP6 CMIP piControl. doi:10.22033/ESGF/CMIP6.9797.
Rong, X. (2019d). CAMS CAMS-CSM1.0 model output prepared for CMIP6 ScenarioMIP ssp126. doi:10.22033/ESGF/CMIP6.11046.

ACCEPTED VERSION SUBJECT TO FINAL EDITING

Rong, X. (2019e). CAMS CAMS-CSM1.0 model output prepared for CMIP6 ScenarioMIP ssp245. doi:10.22033/ESGF/CMIP6.11047.
Rong, X. (2019f). CAMS CAMS-CSM1.0 model output prepared for CMIP6 ScenarioMIP ssp585. doi:10.22033/ESGF/CMIP6.11052.
Samset, B. H., Myhre, G., Forster, P. M., Hodnebrog, Ø., Andrews, T., Boucher, O., et al. (2018). Weak hydrological sensitivity to temperature change over land, independent of climate forcing. *npj Clim. Atmos. Sci.* 1, 3. doi:10.1038/s41612-017-0005-5.
Schupfner, M., Wieners, K.-H., Wachsmann, F., Steger, C., Bittner, M., Jungclaus, J., et al. (2019a). DKRZ MPI-ESM1.2-HR model output prepared for CMIP6 ScenarioMIP ssp126. doi:10.22033/ESGF/CMIP6.4397.
Schupfner, M., Wieners, K.-H., Wachsmann, F., Steger, C., Bittner, M., Jungclaus, J., et al. (2019b). DKRZ MPI-ESM1.2-HR model output prepared for CMIP6 ScenarioMIP ssp245. doi:10.22033/ESGF/CMIP6.4398.
Schupfner, M., Wieners, K.-H., Wachsmann, F., Steger, C., Bittner, M., Jungclaus, J., et al. (2019c). DKRZ MPI-ESM1.2-HR model output prepared for CMIP6 ScenarioMIP ssp585. doi:10.22033/ESGF/CMIP6.4403.
Seferian, R. (2018a). CNRM-CERFACS CNRM-ESM2-1 model output prepared for CMIP6 CMIP. doi:10.22033/ESGF/CMIP6.1391.
Seferian, R. (2018b). CNRM-CERFACS CNRM-ESM2-1 model output prepared for CMIP6 CMIP historical. doi:10.22033/ESGF/CMIP6.4068.
Seferian, R. (2018c). CNRM-CERFACS CNRM-ESM2-1 model output prepared for CMIP6 CMIP piControl. doi:10.22033/ESGF/CMIP6.4165.
Seland, Ø., Bentsen, M., Oliviè, D. J. L., Toniazzo, T., Gjermundsen, A., Graff, L. S., et al. (2019a). NCC NorESM2-LM model output prepared for CMIP6 CMIP historical. doi:10.22033/ESGF/CMIP6.8036.
Seland, Ø., Bentsen, M., Oliviè, D. J. L., Toniazzo, T., Gjermundsen, A., Graff, L. S., et al. (2019b). NCC NorESM2-LM model output prepared for CMIP6 CMIP piControl. doi:10.22033/ESGF/CMIP6.8217.
Seland, Ø., Bentsen, M., Oliviè, D. J. L., Toniazzo, T., Gjermundsen, A., Graff, L. S., et al. (2019c). NCC NorESM2-LM model output prepared for CMIP6 ScenarioMIP ssp126. doi:10.22033/ESGF/CMIP6.8248.
Seland, Ø., Bentsen, M., Oliviè, D. J. L., Toniazzo, T., Gjermundsen, A., Graff, L. S., et al. (2019d). NCC NorESM2-LM model output prepared for CMIP6 ScenarioMIP ssp245. doi:10.22033/ESGF/CMIP6.8253.
Seland, Ø., Bentsen, M., Oliviè, D. J. L., Toniazzo, T., Gjermundsen, A., Graff, L. S., et al. (2019e). NCC NorESM2-LM model output prepared for CMIP6 ScenarioMIP ssp585. doi:10.22033/ESGF/CMIP6.8319.
Semmler, T., Danilov, S., Rackow, T., Sidorenko, D., Barbi, D., Hegewald, J., et al. (2018a). AWI AWI-CM1.1MR model output prepared for CMIP6 CMIP historical. doi:10.22033/ESGF/CMIP6.2686.
Semmler, T., Danilov, S., Rackow, T., Sidorenko, D., Barbi, D., Hegewald, J., et al. (2018b). AWI AWI-CM1.1MR model output prepared for CMIP6 CMIP piControl. doi:10.22033/ESGF/CMIP6.2777.
Semmler, T., Danilov, S., Rackow, T., Sidorenko, D., Barbi, D., Hegewald, J., et al. (2018c). AWI AWI-CM1.1MR model output prepared for CMIP6 ScenarioMIP ssp126. doi:10.22033/ESGF/CMIP6.2796.
Semmler, T., Danilov, S., Rackow, T., Sidorenko, D., Barbi, D., Hegewald, J., et al. (2018d). AWI AWI-CM1.1MR model output prepared for CMIP6 ScenarioMIP ssp245. doi:10.22033/ESGF/CMIP6.2800.
Semmler, T., Danilov, S., Rackow, T., Sidorenko, D., Barbi, D., Hegewald, J., et al. (2019). AWI AWI-CM1.1MR model output prepared for CMIP6 ScenarioMIP ssp585. doi:10.22033/ESGF/CMIP6.2817.
Sénési, S. (2020). CAMMAC - Climate Change Analysis using Multi-Model outputs and CliMAF. doi:10.5281/zenodo.4061814.
Sénési, S., Servonnat, J., Rigoudy, G., and Vignon, L. (2021). CliMAF V2.0.1 pre-release. doi:10.5281/zenodo.4681071.
Shiogama, H. (2019a). MIROC MIROC6 model output prepared for CMIP6 DAMIP hist-aer. doi:10.22033/ESGF/CMIP6.5579.
Shiogama, H. (2019b). MIROC MIROC6 model output prepared for CMIP6 DAMIP hist-GHG. doi:10.22033/ESGF/CMIP6.5578.
Shiogama, H. (2019c). MIROC MIROC6 model output prepared for CMIP6 DAMIP hist-nat. doi:10.22033/ESGF/CMIP6.5583.
Shiogama, H., Abe, M., and Tatebe, H. (2019a). MIROC MIROC6 model output prepared for CMIP6 ScenarioMIP ssp126. doi:10.22033/ESGF/CMIP6.5743.
Shiogama, H., Abe, M., and Tatebe, H. (2019b). MIROC MIROC6 model output prepared for CMIP6 ScenarioMIP ssp245. doi:10.22033/ESGF/CMIP6.5746.
Shiogama, H., Abe, M., and Tatebe, H. (2019c). MIROC MIROC6 model output prepared for CMIP6 ScenarioMIP ssp585. doi:10.22033/ESGF/CMIP6.5771.
Song, Z., Qiao, F., Bao, Y., Shu, Q., Song, Y., and Yang, X. (2019a). FIO-QLNM FIO-ESM2.0 model output prepared for CMIP6 CMIP historical. doi:10.22033/ESGF/CMIP6.9199.
Song, Z., Qiao, F., Bao, Y., Shu, Q., Song, Y., and Yang, X. (2019b). FIO-QLNM FIO-ESM2.0 model output prepared for CMIP6 CMIP piControl. doi:10.22033/ESGF/CMIP6.9205.
Song, Z., Qiao, F., Bao, Y., Shu, Q., Song, Y., and Yang, X. (2019c). FIO-QLNM FIO-ESM2.0 model output prepared for CMIP6 ScenarioMIP ssp126. doi:10.22033/ESGF/CMIP6.9208.

ACCEPTED VERSION SUBJECT TO FINAL EDITING

Song, Z., Qiao, F., Bao, Y., Shu, Q., Song, Y., and Yang, X. (2019d). FIO-QLNM FIO-ESM2.0 model output prepared for CMIP6 ScenarioMIP ssp245. doi:10.22033/ESGF/CMIP6.9209.
Song, Z., Qiao, F., Bao, Y., Shu, Q., Song, Y., and Yang, X. (2019e). FIO-QLNM FIO-ESM2.0 model output prepared for CMIP6 ScenarioMIP ssp585. doi:10.22033/ESGF/CMIP6.9214.
Stephens, G. L., Li, J., Wild, M., Clayson, C. A., Loeb, N., Kato, S., et al. (2012). An update on Earth's energy balance in light of the latest global observations. *Nat. Geosci.* 5, 691–696. doi:10.1038/ngeo1580.
Stouffer, R. (2019a). U of Arizona MCM-UA-1-0 model output prepared for CMIP6 CMIP. doi:10.22033/ESGF/CMIP6.2421.
Stouffer, R. (2019b). UA MCM-UA-1-0 model output prepared for CMIP6 CMIP historical. doi:10.22033/ESGF/CMIP6.8888.
Stouffer, R. (2019c). UA MCM-UA-1-0 model output prepared for CMIP6 CMIP piControl. doi:10.22033/ESGF/CMIP6.8890.
Stouffer, R. (2019d). UA MCM-UA-1-0 model output prepared for CMIP6 ScenarioMIP ssp126. doi:10.22033/ESGF/CMIP6.13895.
Stouffer, R. (2019e). UA MCM-UA-1-0 model output prepared for CMIP6 ScenarioMIP ssp245. doi:10.22033/ESGF/CMIP6.13896.
Stouffer, R. (2019f). UA MCM-UA-1-0 model output prepared for CMIP6 ScenarioMIP ssp585. doi:10.22033/ESGF/CMIP6.13901.
Sun, Q., Zhang, X., Zwiers, F., Westra, S., and Alexander, L. V. (2020). A global, continental and regional analysis of changes in extreme precipitation. *J. Clim.*, 1–52. doi:10.1175/jcli-d-19-0892.1.
Swart, N. C., Cole, J. N. S., Kharin, V. V, Lazare, M., Scinocca, J. F., Gillett, N. P., et al. (2019a). CCCma CanESM5-CanOE model output prepared for CMIP6 CMIP. doi:10.22033/ESGF/CMIP6.10205.
Swart, N. C., Cole, J. N. S., Kharin, V. V, Lazare, M., Scinocca, J. F., Gillett, N. P., et al. (2019b). CCCma CanESM5-CanOE model output prepared for CMIP6 CMIP historical. doi:10.22033/ESGF/CMIP6.10260.
Swart, N. C., Cole, J. N. S., Kharin, V. V, Lazare, M., Scinocca, J. F., Gillett, N. P., et al. (2019c). CCCma CanESM5-CanOE model output prepared for CMIP6 CMIP piControl. doi:10.22033/ESGF/CMIP6.10266.
Swart, N. C., Cole, J. N. S., Kharin, V. V, Lazare, M., Scinocca, J. F., Gillett, N. P., et al. (2019d). CCCma CanESM5-CanOE model output prepared for CMIP6 ScenarioMIP ssp126. doi:10.22033/ESGF/CMIP6.10269.
Swart, N. C., Cole, J. N. S., Kharin, V. V, Lazare, M., Scinocca, J. F., Gillett, N. P., et al. (2019e). CCCma CanESM5-CanOE model output prepared for CMIP6 ScenarioMIP ssp245. doi:10.22033/ESGF/CMIP6.10270.
Swart, N. C., Cole, J. N. S., Kharin, V. V, Lazare, M., Scinocca, J. F., Gillett, N. P., et al. (2019f). CCCma CanESM5-CanOE model output prepared for CMIP6 ScenarioMIP ssp585. doi:10.22033/ESGF/CMIP6.10276.
Swart, N. C., Cole, J. N. S., Kharin, V. V, Lazare, M., Scinocca, J. F., Gillett, N. P., et al. (2019g). CCCma CanESM5 model output prepared for CMIP6 CMIP. doi:10.22033/ESGF/CMIP6.1303.
Swart, N. C., Cole, J. N. S., Kharin, V. V, Lazare, M., Scinocca, J. F., Gillett, N. P., et al. (2019h). CCCma CanESM5 model output prepared for CMIP6 CMIP historical. doi:10.22033/ESGF/CMIP6.3610.
Swart, N. C., Cole, J. N. S., Kharin, V. V, Lazare, M., Scinocca, J. F., Gillett, N. P., et al. (2019i). CCCma CanESM5 model output prepared for CMIP6 CMIP piControl. doi:10.22033/ESGF/CMIP6.3673.
Swart, N. C., Cole, J. N. S., Kharin, V. V, Lazare, M., Scinocca, J. F., Gillett, N. P., et al. (2019j). CCCma CanESM5 model output prepared for CMIP6 DAMIP hist-aer. doi:10.22033/ESGF/CMIP6.3597.
Swart, N. C., Cole, J. N. S., Kharin, V. V, Lazare, M., Scinocca, J. F., Gillett, N. P., et al. (2019k). CCCma CanESM5 model output prepared for CMIP6 DAMIP hist-GHG. doi:10.22033/ESGF/CMIP6.3596.
Swart, N. C., Cole, J. N. S., Kharin, V. V, Lazare, M., Scinocca, J. F., Gillett, N. P., et al. (2019l). CCCma CanESM5 model output prepared for CMIP6 DAMIP hist-nat. doi:10.22033/ESGF/CMIP6.3601.
Swart, N. C., Cole, J. N. S., Kharin, V. V, Lazare, M., Scinocca, J. F., Gillett, N. P., et al. (2019m). CCCma CanESM5 model output prepared for CMIP6 ScenarioMIP ssp126. doi:10.22033/ESGF/CMIP6.3683.
Swart, N. C., Cole, J. N. S., Kharin, V. V, Lazare, M., Scinocca, J. F., Gillett, N. P., et al. (2019n). CCCma CanESM5 model output prepared for CMIP6 ScenarioMIP ssp245. doi:10.22033/ESGF/CMIP6.3685.
Swart, N. C., Cole, J. N. S., Kharin, V. V, Lazare, M., Scinocca, J. F., Gillett, N. P., et al. (2019o). CCCma CanESM5 model output prepared for CMIP6 ScenarioMIP ssp585. doi:10.22033/ESGF/CMIP6.3696.
Tachiiri, K., Abe, M., Hajima, T., Arakawa, O., Suzuki, T., Komuro, Y., et al. (2019a). MIROC MIROC-ES2L model output prepared for CMIP6 ScenarioMIP ssp126. doi:10.22033/ESGF/CMIP6.5742.
Tachiiri, K., Abe, M., Hajima, T., Arakawa, O., Suzuki, T., Komuro, Y., et al. (2019b). MIROC MIROC-ES2L model output prepared for CMIP6 ScenarioMIP ssp245. doi:10.22033/ESGF/CMIP6.5745.
Tachiiri, K., Abe, M., Hajima, T., Arakawa, O., Suzuki, T., Komuro, Y., et al. (2019c). MIROC MIROC-ES2L model output prepared for CMIP6 ScenarioMIP ssp585. doi:10.22033/ESGF/CMIP6.5770.
Tang, Y., Rumbold, S., Ellis, R., Kelley, D., Mulcahy, J., Sellar, A., et al. (2019a). MOHC UKESM1.0-LL model output prepared for CMIP6 CMIP. doi:10.22033/ESGF/CMIP6.1569.
Tang, Y., Rumbold, S., Ellis, R., Kelley, D., Mulcahy, J., Sellar, A., et al. (2019b). MOHC UKESM1.0-LL model output prepared for CMIP6 CMIP historical. doi:10.22033/ESGF/CMIP6.6113.
Tang, Y., Rumbold, S., Ellis, R., Kelley, D., Mulcahy, J., Sellar, A., et al. (2019c). MOHC UKESM1.0-LL model

ACCEPTED VERSION SUBJECT TO FINAL EDITING

output prepared for CMIP6 CMIP piControl. doi:10.22033/ESGF/CMIP6.6298.
Tatebe, H., and Watanabe, M. (2018a). MIROC MIROC6 model output prepared for CMIP6 CMIP. doi:10.22033/ESGF/CMIP6.881.
Tatebe, H., and Watanabe, M. (2018b). MIROC MIROC6 model output prepared for CMIP6 CMIP historical. doi:10.22033/ESGF/CMIP6.5603.
Tatebe, H., and Watanabe, M. (2018c). MIROC MIROC6 model output prepared for CMIP6 CMIP piControl. doi:10.22033/ESGF/CMIP6.5711.
Tilinina, N., Gulev, S. K., Rudeva, I., and Koltermann, P. (2013). Comparing cyclone life cycle characteristics and their interannual variability in different reanalyses. *J. Clim.* 26, 6419–6438. doi:10.1175/JCLI-D-12-00777.1.
Trenberth, K. E., Fasullo, J. T., and Mackaro, J. (2011). Atmospheric moisture transports from ocean to land and global energy flows in reanalyses. *J. Clim.* 24, 4907–4924. doi:10.1175/2011JCLI4171.1.
Voldoire, A. (2018a). CMIP6 simulations of the CNRM-CERFACS based on CNRM-CM6-1 model for CMIP experiment historical. doi:10.22033/ESGF/CMIP6.4066.
Voldoire, A. (2018b). CMIP6 simulations of the CNRM-CERFACS based on CNRM-CM6-1 model for CMIP experiment piControl. doi:10.22033/ESGF/CMIP6.4163.
Voldoire, A. (2019a). CNRM-CERFACS CNRM-CM6-1-HR model output prepared for CMIP6 CMIP historical. doi:10.22033/ESGF/CMIP6.4067.
Voldoire, A. (2019b). CNRM-CERFACS CNRM-CM6-1-HR model output prepared for CMIP6 CMIP piControl. doi:10.22033/ESGF/CMIP6.4164.
Voldoire, A. (2019c). CNRM-CERFACS CNRM-CM6-1-HR model output prepared for CMIP6 ScenarioMIP ssp245. doi:10.22033/ESGF/CMIP6.4190.
Voldoire, A. (2019d). CNRM-CERFACS CNRM-CM6-1-HR model output prepared for CMIP6 ScenarioMIP ssp585. doi:10.22033/ESGF/CMIP6.4225.
Voldoire, A. (2019e). CNRM-CERFACS CNRM-CM6-1 model output prepared for CMIP6 DAMIP hist-aer. doi:10.22033/ESGF/CMIP6.4044.
Voldoire, A. (2019f). CNRM-CERFACS CNRM-CM6-1 model output prepared for CMIP6 DAMIP hist-GHG. doi:10.22033/ESGF/CMIP6.4043.
Voldoire, A. (2019g). CNRM-CERFACS CNRM-CM6-1 model output prepared for CMIP6 DAMIP hist-nat. doi:10.22033/ESGF/CMIP6.4048.
Voldoire, A. (2019h). CNRM-CERFACS CNRM-CM6-1 model output prepared for CMIP6 ScenarioMIP ssp126. doi:10.22033/ESGF/CMIP6.4184.
Voldoire, A. (2019i). CNRM-CERFACS CNRM-CM6-1 model output prepared for CMIP6 ScenarioMIP ssp245. doi:10.22033/ESGF/CMIP6.4189.
Voldoire, A. (2019j). CNRM-CERFACS CNRM-CM6-1 model output prepared for CMIP6 ScenarioMIP ssp585. doi:10.22033/ESGF/CMIP6.4224.
Voldoire, A. (2019k). CNRM-CERFACS CNRM-ESM2-1 model output prepared for CMIP6 ScenarioMIP ssp126. doi:10.22033/ESGF/CMIP6.4186.
Voldoire, A. (2019l). CNRM-CERFACS CNRM-ESM2-1 model output prepared for CMIP6 ScenarioMIP ssp245. doi:10.22033/ESGF/CMIP6.4191.
Voldoire, A. (2019m). CNRM-CERFACS CNRM-ESM2-1 model output prepared for CMIP6 ScenarioMIP ssp585. doi:10.22033/ESGF/CMIP6.4226.
Voldoire, A. (2020). CNRM-CERFACS CNRM-CM6-1-HR model output prepared for CMIP6 ScenarioMIP ssp126. doi:10.22033/ESGF/CMIP6.4185.
Volodin, E., Mortikov, E., Gritsun, A., Lykossov, V., Galin, V., Diansky, N., et al. (2019a). INM INM-CM4-8 model output prepared for CMIP6 CMIP. doi:10.22033/ESGF/CMIP6.1422.
Volodin, E., Mortikov, E., Gritsun, A., Lykossov, V., Galin, V., Diansky, N., et al. (2019b). INM INM-CM4-8 model output prepared for CMIP6 CMIP historical. doi:10.22033/ESGF/CMIP6.5069.
Volodin, E., Mortikov, E., Gritsun, A., Lykossov, V., Galin, V., Diansky, N., et al. (2019c). INM INM-CM4-8 model output prepared for CMIP6 CMIP piControl. doi:10.22033/ESGF/CMIP6.5080.
Volodin, E., Mortikov, E., Gritsun, A., Lykossov, V., Galin, V., Diansky, N., et al. (2019d). INM INM-CM4-8 model output prepared for CMIP6 ScenarioMIP ssp126. doi:10.22033/ESGF/CMIP6.12325.
Volodin, E., Mortikov, E., Gritsun, A., Lykossov, V., Galin, V., Diansky, N., et al. (2019e). INM INM-CM4-8 model output prepared for CMIP6 ScenarioMIP ssp245. doi:10.22033/ESGF/CMIP6.12327.
Volodin, E., Mortikov, E., Gritsun, A., Lykossov, V., Galin, V., Diansky, N., et al. (2019f). INM INM-CM4-8 model output prepared for CMIP6 ScenarioMIP ssp585. doi:10.22033/ESGF/CMIP6.12337.
Volodin, E., Mortikov, E., Gritsun, A., Lykossov, V., Galin, V., Diansky, N., et al. (2019g). INM INM-CM5-0 model output prepared for CMIP6 CMIP. doi:10.22033/ESGF/CMIP6.1423.
Volodin, E., Mortikov, E., Gritsun, A., Lykossov, V., Galin, V., Diansky, N., et al. (2019h). INM INM-CM5-0 model output prepared for CMIP6 CMIP historical. doi:10.22033/ESGF/CMIP6.5070.
Volodin, E., Mortikov, E., Gritsun, A., Lykossov, V., Galin, V., Diansky, N., et al. (2019i). INM INM-CM5-0 model output prepared for CMIP6 CMIP piControl. doi:10.22033/ESGF/CMIP6.5081.

ACCEPTED VERSION
SUBJECT TO FINAL EDITING

Volodin, E., Mortikov, E., Gritsun, A., Lykossov, V., Galin, V., Diansky, N., et al. (2019j). INM INM-CM5-0 model output prepared for CMIP6 ScenarioMIP ssp126. doi:10.22033/ESGF/CMIP6.12326.
Volodin, E., Mortikov, E., Gritsun, A., Lykossov, V., Galin, V., Diansky, N., et al. (2019k). INM INM-CM5-0 model output prepared for CMIP6 ScenarioMIP ssp245. doi:10.22033/ESGF/CMIP6.12328.
Volodin, E., Mortikov, E., Gritsun, A., Lykossov, V., Galin, V., Diansky, N., et al. (2019l). INM INM-CM5-0 model output prepared for CMIP6 ScenarioMIP ssp585. doi:10.22033/ESGF/CMIP6.12338.
Wang, T., Wang, H. J., Otterå, O. H., Gao, Y. Q., Suo, L. L., Furevik, T., et al. (2013). Anthropogenic agent implicated as a prime driver of shift in precipitation in eastern China in the late 1970s. *Atmos. Chem. Phys.* 13, 12433–12450. doi:10.5194/acp-13-12433-2013.
Westra, S., Alexander, L. V., and Zwiers, F. W. (2013). Global increasing trends in annual maximum daily precipitation. *J. Clim.* doi:10.1175/JCLI-D-12-00502.1.
Westra, S., and Sisson, S. A. (2011). Detection of non-stationarity in precipitation extremes using a max-stable process model. *J. Hydrol.* 406, 119–128. doi:10.1016/j.jhydrol.2011.06.014.
Wieners, K.-H., Giorgetta, M., Jungclaus, J., Reick, C., Esch, M., Bittner, M., et al. (2019a). MPI-M MPI-ESM1.2-LR model output prepared for CMIP6 CMIP historical. doi:10.22033/ESGF/CMIP6.6595.
Wieners, K.-H., Giorgetta, M., Jungclaus, J., Reick, C., Esch, M., Bittner, M., et al. (2019b). MPI-M MPI-ESM1.2-LR model output prepared for CMIP6 CMIP piControl. doi:10.22033/ESGF/CMIP6.6675.
Wieners, K.-H., Giorgetta, M., Jungclaus, J., Reick, C., Esch, M., Bittner, M., et al. (2019c). MPI-M MPI-ESM1.2-LR model output prepared for CMIP6 ScenarioMIP ssp126. doi:10.22033/ESGF/CMIP6.6690.
Wieners, K.-H., Giorgetta, M., Jungclaus, J., Reick, C., Esch, M., Bittner, M., et al. (2019d). MPI-M MPI-ESM1.2-LR model output prepared for CMIP6 ScenarioMIP ssp245. doi:10.22033/ESGF/CMIP6.6693.
Wieners, K.-H., Giorgetta, M., Jungclaus, J., Reick, C., Esch, M., Bittner, M., et al. (2019e). MPI-M MPI-ESM1.2-LR model output prepared for CMIP6 ScenarioMIP ssp585. doi:10.22033/ESGF/CMIP6.6705.
Wu, T., Chu, M., Dong, M., Fang, Y., Jie, W., Li, J., et al. (2018a). BCC BCC-CSM2MR model output prepared for CMIP6 CMIP historical. doi:10.22033/ESGF/CMIP6.2948.
Wu, T., Chu, M., Dong, M., Fang, Y., Jie, W., Li, J., et al. (2018b). BCC BCC-CSM2MR model output prepared for CMIP6 CMIP piControl. doi:10.22033/ESGF/CMIP6.3016.
Wu, T., Chu, M., Dong, M., Fang, Y., Jie, W., Li, J., et al. (2019a). BCC BCC-CSM2MR model output prepared for CMIP6 DAMIP hist-aer. doi:10.22033/ESGF/CMIP6.2925.
Wu, T., Chu, M., Dong, M., Fang, Y., Jie, W., Li, J., et al. (2019b). BCC BCC-CSM2MR model output prepared for CMIP6 DAMIP hist-GHG. doi:10.22033/ESGF/CMIP6.2924.
Wu, T., Chu, M., Dong, M., Fang, Y., Jie, W., Li, J., et al. (2019c). BCC BCC-CSM2MR model output prepared for CMIP6 DAMIP hist-nat. doi:10.22033/ESGF/CMIP6.2929.
Xin, X., Wu, T., Shi, X., Zhang, F., Li, J., Chu, M., et al. (2019a). BCC BCC-CSM2MR model output prepared for CMIP6 ScenarioMIP ssp126. doi:10.22033/ESGF/CMIP6.3028.
Xin, X., Wu, T., Shi, X., Zhang, F., Li, J., Chu, M., et al. (2019b). BCC BCC-CSM2MR model output prepared for CMIP6 ScenarioMIP ssp245. doi:10.22033/ESGF/CMIP6.3030.
Xin, X., Wu, T., Shi, X., Zhang, F., Li, J., Chu, M., et al. (2019c). BCC BCC-CSM2MR model output prepared for CMIP6 ScenarioMIP ssp585. doi:10.22033/ESGF/CMIP6.3050.
Xin, X., Zhang, J., Zhang, F., Wu, T., Shi, X., Li, J., et al. (2018). BCC BCC-CSM2MR model output prepared for CMIP6 CMIP. doi:10.22033/ESGF/CMIP6.1725.
Yu, Y. (2018). CAS FGOALS-f3-L model output prepared for CMIP6 CMIP. doi:10.22033/ESGF/CMIP6.1782.
Yu, Y. (2019a). CAS FGOALS-f3-L model output prepared for CMIP6 CMIP historical. doi:10.22033/ESGF/CMIP6.3355.
Yu, Y. (2019b). CAS FGOALS-f3-L model output prepared for CMIP6 CMIP piControl. doi:10.22033/ESGF/CMIP6.3447.
Yu, Y. (2019c). CAS FGOALS-f3-L model output prepared for CMIP6 ScenarioMIP ssp126. doi:10.22033/ESGF/CMIP6.3464.
Yu, Y. (2019d). CAS FGOALS-f3-L model output prepared for CMIP6 ScenarioMIP ssp245. doi:10.22033/ESGF/CMIP6.3468.
Yu, Y. (2019e). CAS FGOALS-f3-L model output prepared for CMIP6 ScenarioMIP ssp585. doi:10.22033/ESGF/CMIP6.3502.
Yukimoto, S., Koshiro, T., Kawai, H., Oshima, N., Yoshida, K., Urakawa, S., et al. (2019a). MRI MRI-ESM2.0 model output prepared for CMIP6 CMIP. doi:10.22033/ESGF/CMIP6.621.
Yukimoto, S., Koshiro, T., Kawai, H., Oshima, N., Yoshida, K., Urakawa, S., et al. (2019b). MRI MRI-ESM2.0 model output prepared for CMIP6 CMIP historical. doi:10.22033/ESGF/CMIP6.6842.
Yukimoto, S., Koshiro, T., Kawai, H., Oshima, N., Yoshida, K., Urakawa, S., et al. (2019c). MRI MRI-ESM2.0 model output prepared for CMIP6 CMIP piControl. doi:10.22033/ESGF/CMIP6.6900.
Yukimoto, S., Koshiro, T., Kawai, H., Oshima, N., Yoshida, K., Urakawa, S., et al. (2019d). MRI MRI-ESM2.0 model output prepared for CMIP6 DAMIP hist-aer. doi:10.22033/ESGF/CMIP6.6821.
Yukimoto, S., Koshiro, T., Kawai, H., Oshima, N., Yoshida, K., Urakawa, S., et al. (2019e). MRI MRI-ESM2.0 model

SUBJECT TO FINAL EDITING ACCEPTED VERSION

output prepared for CMIP6 DAMIP hist-GHG. doi:10.22033/ESGF/CMIP6.6820.
Yukimoto, S., Koshiro, T., Kawai, H., Oshima, N., Yoshida, K., Urakawa, S., et al. (2019f). MRI MRI-ESM2.0 model output prepared for CMIP6 DAMIP hist-nat. doi:10.22033/ESGF/CMIP6.6825.
Yukimoto, S., Koshiro, T., Kawai, H., Oshima, N., Yoshida, K., Urakawa, S., et al. (2019g). MRI MRI-ESM2.0 model output prepared for CMIP6 ScenarioMIP ssp126. doi:10.22033/ESGF/CMIP6.6909.
Yukimoto, S., Koshiro, T., Kawai, H., Oshima, N., Yoshida, K., Urakawa, S., et al. (2019h). MRI MRI-ESM2.0 model output prepared for CMIP6 ScenarioMIP ssp245. doi:10.22033/ESGF/CMIP6.6910.
Yukimoto, S., Koshiro, T., Kawai, H., Oshima, N., Yoshida, K., Urakawa, S., et al. (2019i). MRI MRI-ESM2.0 model output prepared for CMIP6 ScenarioMIP ssp585. doi:10.22033/ESGF/CMIP6.6929.
Zeder, J., and Fischer, E. M. (2020). Observed extreme precipitation trends and scaling in Central Europe. *Weather Clim. Extrem.* 29, 100266. doi:10.1016/j.wace.2020.100266.
Zhang, J., Wu, T., Shi, X., Zhang, F., Li, J., Chu, M., et al. (2018). BCC BCC-ESM1 model output prepared for CMIP6 CMIP piControl. doi:10.22033/ESGF/CMIP6.3017.
Zhou, Y., Sawyer, A. H., David, C. H., and Famiglietti, J. S. (2019). Fresh submarine groundwater discharge to the near-global coast. *Geophys. Res. Lett.*, 2019GL082749. doi:10.1029/2019GL082749.
Ziehn, T., Chamberlain, M., Lenton, A., Law, R., Bodman, R., Dix, M., et al. (2019a). CSIRO ACCESS-ESM1.5 model output prepared for CMIP6 CMIP historical. doi:10.22033/ESGF/CMIP6.4272.
Ziehn, T., Chamberlain, M., Lenton, A., Law, R., Bodman, R., Dix, M., et al. (2019b). CSIRO ACCESS-ESM1.5 model output prepared for CMIP6 CMIP piControl. doi:10.22033/ESGF/CMIP6.4312.
Ziehn, T., Chamberlain, M., Lenton, A., Law, R., Bodman, R., Dix, M., et al. (2019c). CSIRO ACCESS-ESM1.5 model output prepared for CMIP6 ScenarioMIP ssp126. doi:10.22033/ESGF/CMIP6.4320.
Ziehn, T., Chamberlain, M., Lenton, A., Law, R., Bodman, R., Dix, M., et al. (2019d). CSIRO ACCESS-ESM1.5 model output prepared for CMIP6 ScenarioMIP ssp245. doi:10.22033/ESGF/CMIP6.4322.
Ziehn, T., Chamberlain, M., Lenton, A., Law, R., Bodman, R., Dix, M., et al. (2019e). CSIRO ACCESS-ESM1.5 model output prepared for CMIP6 ScenarioMIP ssp585. doi:10.22033/ESGF/CMIP6.4333.
Ziehn, T., Dix, M., Mackallah, C., Chamberlain, M., Lenton, A., Law, R., et al. (2020a). CSIRO ACCESS-ESM1.5 model output prepared for CMIP6 DAMIP hist-aer. doi:10.22033/ESGF/CMIP6.14370.
Ziehn, T., Dix, M., Mackallah, C., Chamberlain, M., Lenton, A., Law, R., et al. (2020b). CSIRO ACCESS-ESM1.5 model output prepared for CMIP6 DAMIP hist-GHG. doi:10.22033/ESGF/CMIP6.14366.
Ziehn, T., Dix, M., Mackallah, C., Chamberlain, M., Lenton, A., Law, R., et al. (2020c). CSIRO ACCESS-ESM1.5 model output prepared for CMIP6 DAMIP hist-nat. doi:10.22033/ESGF/CMIP6.14378.

ACCEPTED VERSION
SUBJECT TO FINAL EDITING

Chapter 9: Ocean, cryosphere and sea level change

Coordinating Lead Authors:
Baylor Fox-Kemper (United States of America), Helene T. Hewitt (United Kingdom), Cunde Xiao (China)

Lead Authors:
Guðfinna Aðalgeirsdóttir (Iceland), Sybren S. Drijfhout (The Netherlands), Tamsin L. Edwards (United Kingdom), Nicholas R. Golledge (New Zealand/United Kingdom), Mark Hemer (Australia), Robert E. Kopp (United States of America), Gerhard Krinner (France/Germany, France), Alan Mix (United States of America), Dirk Notz (Germany), Sophie Nowicki (United States of America/France, United States of America), Intan Suci Nurhati (Indonesia), Lucas Ruiz (Argentina), Jean-Baptiste Sallée (France), Aimee B. A. Slangen (The Netherlands), Yongqiang Yu (China)

Contributing Authors:
Cecile Agosta (France), Kyle Armour (United States of America), Mathias Aschwanden (Switzerland), Jonathan L. Bamber (United Kingdom), Sophie Berger (France/Belgium), Fábio Boeira Dias (Finland/Brazil), Jason E. Box (Denmark/USA), Eleanor J. Burke (United Kingdom), Kevin D. Burke (United States of America), Xavier Capet (France), John A. Church (Australia), Lee de Mora (United Kingdom), Chris Derksen (Canada), Catia M. Domingues (Australia, United Kingdom/Brazil), Jakob Dörr (Norway/Germany), Paul J. Durack (United States of America/Australia), Thomas L. Frölicher (Switzerland), Thian Y. Gan (Canada/Malaysia), Gregory G. Garner (United States of America), Sebastian Gerland (Norway/Germany), Heiko Goelzer (Norway/Germany), Natalya Gomez (Canada), Irina V. Gorodetskaya (Portugal/Belgium,Russian Federation), Jonathan M. Gregory (United Kingdom), Robert Hallberg (United States of America), F. Alexander Haumann (United States of America/Germany), Tim H. J. Hermans (The Netherlands), Emma M. Hill (Singapore/United States of America, United Kingdom), Regine Hock (United States of America, Norway/Germany), Stefan Hofer (Norway/Austria), Romain Hugonnet (France,Switzerland/France), Philippe Huybrechts (Belgium), Akm Saiful Islam (Bangladesh), Laura C. Jackson (United Kingdom), Nicolas C. Jourdain (France), Andreas Kääb (Norway/Germany), Nicole S. Khan (Hong Kong,China/USA), Shfaqat Abbas Khan (Denmark), Matthew Kirwan (United States of America), James Kossin (United States of America), Anders Levermann (Germany), Sophie Lewis (Australia), Shiyin Liu (China), Daniel Lowry (New Zealand/United States of America), Marta Marcos (Spain), Ben Marzeion (Germany), Matthew Menary (France/United Kingdom), Sebastian H. Mernild (Norway, Denmark/Norway), Philip Orton (United States of America), Matthew D. Palmer (United Kingdom), Frank Pattyn (Belgium), Brodie Pearson (United States of America/United Kingdom), Cécile Pellet (Switzerland), Chris Perry (United Kingdom), Mark D. Pickering (United Kingdom), Johannes Quaas (Germany), Roshanka Ranasinghe (The Netherlands/Sri Lanka,Australia), Roelof Rietbroek (The Netherlands), Malcom J. Roberts (United Kingdom), Alessio Rovere (Germany/Italy), Mathew Koll Roxy (India), Maria Santolaria Otin (Spain,France/Spain), Abhishek Savita (Australia/India), Alex Sen Gupta (Australia/ United Kingdom, Australia), Helene Seroussi (United States of America/France), Sharon L. Smith (Canada), Olga N. Solomina (Russian Federation), Esther Stouthamer (The Netherlands), Fiametta Straneo (United States of America/Italy, United States of America), William V. Sweet (United States of America), Thomas Wahl (United States of America/Germany), Lisan Yu (United States of America), Jiacan Yuan (United States of America/China), Jan David Zika (Australia)

Review Editors:
Unnikrishnan Alakkat (India), Benjamin P. Horton (Singapore/United Kingdom), Simon Marsland (Australia)

ACCEPTED VERSION SUBJECT TO FINAL EDITING

Chapter Scientists:
Gregory G. Garner (United States of America), Tim H. J. Hermans (The Netherlands), Lijuan Hua (China), Tamzin Palmer (United Kingdom), Brodie Pearson (United States of America/ United Kingdom)

This Chapter should be cited as:
Fox-Kemper, B., H. T. Hewitt, C. Xiao, G. Aðalgeirsdóttir, S. S. Drijfhout, T. L. Edwards, N. R. Golledge, M. Hemer, R. E. Kopp, G. Krinner, A. Mix, D. Notz, S. Nowicki, I. S. Nurhati, L. Ruiz, J-B. Sallée, A. B. A. Slangen, Y. Yu, 2021, Ocean, Cryosphere and Sea Level Change. In: *Climate Change 2021: The Physical Science Basis. Contribution of Working Group I to the Sixth Assessment Report of the Intergovernmental Panel on Climate Change* [Masson-Delmotte, V., P. Zhai, A. Pirani, S. L. Connors, C. Péan, S. Berger, N. Caud, Y. Chen, L. Goldfarb, M. I. Gomis, M. Huang, K. Leitzell, E. Lonnoy, J.B.R. Matthews, T. K. Maycock, T. Waterfield, O. Yelekçi, R. Yu and B. Zhou (eds.)]. Cambridge University Press. In Press.

Date: August 2021

This document is subject to copy-editing, corrigenda and trickle backs.

ACCEPTED VERSION
SUBJECT TO FINAL EDITING

Table of Contents

Executive Summary *5*
9.1 Introduction **11**
BOX 9.1: Key processes driving sea level change ***12***
9.2 Oceans **14**
9.2.1 Ocean surface **14**
9.2.1.1 Sea Surface Temperature (SST) **14**
9.2.1.2 Air-sea fluxes **16**
9.2.1.3 Upper Ocean Stratification and Surface Mixed Layers **18**
BOX 9.2: Marine Heatwaves ***20***
9.2.2 Changes in Heat and Salinity **21**
9.2.2.1 Ocean Heat Content and Heat Transport **21**
9.2.2.2 Ocean Salinity **26**
9.2.2.3 Water Masses **28**
9.2.3 Regional Ocean Circulation **30**
9.2.3.1 Atlantic Meridional Overturning Circulation **30**
9.2.3.2 Southern Ocean **33**
9.2.3.3 Tropical Oceans **36**
9.2.3.4 Gyres, Western Boundary Currents, and Inter-Basin Exchanges **36**
9.2.3.5 Eastern Boundary Upwelling Systems **39**
9.2.3.6 Coastal Systems and Marginal Seas **40**
9.2.4 Steric and dynamic sea-level change **41**
9.2.4.1 Global mean thermosteric sea-level change **41**
9.2.4.2 Ocean dynamic sea-level change **42**
9.3 Sea ice **44**
9.3.1 Arctic Sea Ice **44**
9.3.1.1 Arctic Sea-Ice Coverage **44**
9.3.1.2 Arctic Sea-Ice volume and thickness **48**
9.3.2 Antarctic Sea Ice **49**
9.3.2.1 Antarctic sea-ice coverage **49**
9.3.2.2 Antarctic sea-ice thickness **51**
9.4 Ice Sheets **52**

ACCEPTED VERSION SUBJECT TO FINAL EDITING

9.4.1 Greenland Ice Sheet 52
9.4.1.1 Recent observed changes 52
9.4.1.2 Model evaluation 56
9.4.1.3 Projections to 2100 57
9.4.1.4 Projections beyond 2100 61
BOX 9.3: Insights into land ice evolution from model intercomparison projects 62
9.4.2 Antarctic Ice Sheet 64
9.4.2.1 Recent observed changes 64
9.4.2.2 Model evaluation 67
9.4.2.3 Drivers of future Antarctic ice sheet change 69
9.4.2.4 Ice sheet instabilities 71
9.4.2.5 Projections to 2100 72
9.4.2.6 Projections beyond 2100 76
9.5 Glaciers, permafrost and seasonal snow cover 78
9.5.1 Glaciers 78
9.5.1.1 Observed and reconstructed glacier extent and mass changes 78
9.5.1.2 Model evaluation 82
9.5.1.3 Projections 83
9.5.2 Permafrost 85
9.5.2.1 Observed and reconstructed changes 85
9.5.2.2 Evaluation of permafrost in climate models 87
9.5.2.3 Projected permafrost changes 89
9.5.3 Seasonal snow cover 89
9.5.3.1 Observed changes of seasonal snow cover 90
9.5.3.2 Evaluation of seasonal snow in climate models 92
9.5.3.3 Projected snow cover changes 94
9.6 Sea Level Change 94
9.6.1 Global and regional sea-level change in the instrumental era 94
9.6.1.1 Global mean sea-level change budget in the pre-satellite era 94
9.6.1.2 Global mean sea-level change budget in the satellite era 96
9.6.1.3 Regional sea-level change in the satellite era 98
9.6.1.4 Attribution and time of emergence of regional sea-level change 99

ACCEPTED VERSION
SUBJECT TO FINAL EDITING

Cross-Chapter Box 9.1: Global energy inventory and sea level budget *100*

9.6.2 Paleo context of global and regional sea-level change **101**

9.6.3 Future sea-level changes **106**

9.6.3.1 Global mean sea level projections based on the Representative Concentration Pathways... ..... **106**

9.6.3.2 Drivers of projected sea-level change **108**

9.6.3.3 Sea-level projections to 2150 based on SSP scenarios **115**

9.6.3.4 Sea-level projections up to 2100 based on global warming levels **118**

9.6.3.5 Multi-century and multi-millennial sea-level rise **119**

BOX 9.4: High-end storyline of 21st century sea-level rise ***122***

9.6.4 Extreme sea levels: Tides, surges and waves **124**

9.6.4.1 Past changes **124**

9.6.4.2 Future changes **126**

9.7 Final Remarks **129**

Frequently Asked Questions ***131***

Acknowledgements ***137***

Reference ***138***

Figures ***202***

ACCEPTED VERSION
SUBJECT TO FINAL EDITING

Executive Summary

This chapter assesses past and projected changes in the ocean, cryosphere and sea level using paleo-reconstructions, instrumental observations and model simulations. In the following summary, we update and expand the related assessments from the IPCC Fifth Assessment Report (AR5), the Special Report on Global Warming of 1.5ºC (SR1.5) and the Special Report on Ocean and Cryosphere in a Changing Climate (SROCC). Major advances in this chapter since the SROCC include the synthesis of extended and new observations, which allows for improved assessment of past change, processes and budgets for the last century, and the use of a hierarchy of models and emulators, which provide improved projections and uncertainty estimates of future change. In addition, the systematic use of model emulators makes our projections of ocean heat content, land-ice loss and sea level rise fully consistent both with each other and with the assessed equilibrium climate sensitivity and projections of global surface air temperature across the entire report. In this executive summary, uncertainty ranges are reported as *very likely* ranges and expressed by square brackets, unless otherwise noted.

Ocean Heat and Salinity

At the ocean surface, temperature has on average increased by 0.88 [0.68–1.01] °C from 1850-1900 to 2011-2020, with 0.60 [0.44–0.74] °C of this warming having occurred since 1980. The ocean surface temperature is projected to increase from 1995–2014 to 2081–2100 on average by 0.86 [0.43–1.47, *likely* range] °C in SSP1-2.6 and by 2.89 [2.01–4.07, *likely* range] °C in SSP5-8.5. Since the 1950s, the fastest surface warming has occurred in the Indian Ocean and in Western Boundary Currents, while ocean circulation has caused slow warming or surface cooling in the Southern Ocean, equatorial Pacific, North Atlantic, and coastal upwelling systems (*very high confidence*). At least 83% of the ocean surface will *very likely* warm over the 21st century in all SSP scenarios. {2.3.3, 9.2.1}

The heat content of the global ocean has increased since at least 1970 and will continue to increase over the 21st century (*virtually certain*). The associated warming will *likely* continue until at least 2300 even for low-emission scenarios because of the slow circulation of the deep ocean. Ocean heat content has increased from 1971 to 2018 by [0.28–0.55] yottajoules and will *likely* increase until 2100 by 2 to 4 times that amount under SSP1-2.6 and 4 to 8 times that amount under SSP5-8.5. The long time scale also implies that the amount of deep-ocean warming will only become scenario-dependent after about 2040 and that the warming is irreversible over centuries to millennia (*medium confidence*). On annual to decadal time scales, the redistribution of heat by the ocean circulation dominates spatial patterns of temperature change (*high confidence*). At longer time scales, the spatial patterns are dominated by additional heat primarily stored in water-masses formed in the Southern Ocean, and by weaker warming in the North Atlantic where heat redistribution caused by changing circulation counteracts the additional heat input through the surface (*high confidence*). {9.2.2, 9.2.4, 9.6.1, Cross-Chapter Box 9.1}

Marine heatwaves – sustained periods of anomalously high near-surface temperatures that can lead to severe and persistent impacts on marine ecosystems – have become more frequent over the 20th century (*high confidence*). Since the 1980s, they have approximately doubled in frequency (*high confidence*) and have become more intense and longer (*medium confidence*). This trend will continue, with marine heatwaves at global scale becoming 4 [2–9, *likely* range] times more frequent in 2081–2100 compared to 1995–2014 under SSP1-2.6, and 8 [3–15, *likely* range] times more frequent under SSP5-8.5. The largest changes will occur in the tropical ocean and the Arctic (*medium confidence*). {Box 9.2}

The upper ocean has become more stably stratified since at least 1970 over the vast majority of the globe (*virtually certain*), primarily due to surface-intensified warming and high-latitude surface freshening (*very high confidence*). Changes in ocean stability affect vertical exchanges of surface waters with the deep ocean and large-scale ocean circulation. Based on recent refined analyses of the available

ACCEPTED VERSION SUBJECT TO FINAL EDITING

observations, the global 0–200 m stratification is now assessed to have increased about twice as much as reported by the SROCC, with a 4.9 ± 1.5% increase from 1970 to 2018 (*high confidence*) and even higher increases at the base of the surface mixed layer. Upper-ocean stratification will continue to increase throughout the 21st century (*virtually certain*). {9.2.1}

Ocean Circulation

The Atlantic Meridional Overturning Circulation (AMOC) will *very likely* decline over the 21st century for all SSP scenarios. There is *medium confidence* that the decline will not involve an abrupt collapse before 2100. For the 20th century, there is *low confidence* in reconstructed and modelled AMOC changes because of their *low agreement* in quantitative trends. The *low confidence* also arises from new observations that indicate missing key processes in both models and measurements used for formulating proxies and from new evaluations of modelled AMOC variability. This results in *low confidence* in quantitative projections of AMOC decline in the 21st century, despite the *high confidence* in the future decline as a qualitative feature based on process understanding. {9.2.3}

Southern Ocean circulation and associated temperature changes in Antarctic ice-shelf cavities are sensitive to changes in wind patterns and increased ice-shelf melt (*high confidence*). However, limitations in understanding feedback mechanisms involving the ocean, atmosphere and cryosphere, which are not fully represented in the current generation of climate models, generally limit our confidence in future projections of the Southern Ocean and of its forcing on Antarctic sea ice and ice shelves. {9.2.3, 9.3.2, 9.4.2}

Many ocean currents will change in the 21st century as a response to changes in wind stress associated with anthropogenic warming (*high confidence*). Western boundary currents have shifted poleward since 1993 (*medium confidence*), consistent with a poleward shift of the subtropical gyres. Of the four eastern boundary upwelling systems, only the California current system has experienced some large-scale upwelling-favourable wind intensification since the 1980s (*medium confidence*). In the 21st century, consistent with projected changes in the surface winds, the East Australian Current Extension and Agulhas Current Extension will intensify, while the Gulf Stream and Indonesian Throughflow will weaken (*medium confidence*). Eastern boundary upwelling systems will change, with a dipole spatial pattern within each system of reduction at low latitude and enhancement at high latitude (*high confidence*). {9.2.1, 9.2.3}

Sea Ice

The Arctic Ocean will *likely* become practically sea ice–free[1] during the seasonal sea ice minimum for the first time before 2050 in all considered SSP scenarios. There is no tipping point for this loss of Arctic summer sea ice (*high confidence*). The practically ice-free state is projected to occur more often with higher greenhouse gas concentrations and will become the new normal for high-emission scenarios by the end of this century (*high confidence*). Based on observational evidence, Coupled Model Intercomparison Project Phase 6 (CMIP6) models and conceptual understanding, the substantial satellite-observed decrease of Arctic sea ice area over the period 1979–2019 is well described as a linear function of global mean surface temperature, and thus of cumulative anthropogenic CO_2 emissions, with superimposed internal variability (*high confidence*). According to both process understanding and CMIP6 simulations, a practically sea ice–free state will *likely* be observed in some years before additional (post-2020) cumulative anthropogenic CO_2 emissions reach 1000 $GtCO_2$. {4.3.2, 9.3.1}

[1] sea ice area below 1 million km^2

ACCEPTED VERSION SUBJECT TO FINAL EDITING

For Antarctic sea ice, regionally opposing trends and large interannual variability result in no significant trend in satellite-observed sea ice area from 1979 to 2020 in both winter and summer (*high confidence*). The regionally opposing trends result primarily from changing regional wind forcing (*medium confidence*). There is *low confidence* in model simulations of past and future Antarctic sea ice evolution due to deficiencies of process representation, in particular at the regional level. {2.3.2, 9.2.3, 9.3.2}

Ice Sheets

The Greenland Ice Sheet has lost 4890 [4140–5640] Gt mass over the period 1992–2020, equivalent to 13.5 [11.4–15.6] mm global mean sea level rise. The mass-loss rate was on average 39 [–3 to 80] Gt yr^{-1} over the period 1992–1999, 175 [131 to 220] Gt yr^{-1} over the period 2000–2009 and 243 [197 to 290] Gt yr^{-1} over the period 2010–2019. This mass loss is driven by both discharge and surface melt, with the latter increasingly becoming the dominating component of mass loss with high interannual variability in the last decade (*high confidence*). The largest mass losses occurred in the Northwest and the Southeast of Greenland (*high confidence*). {2.3.2, 9.4.1}

The Antarctic Ice Sheet has lost 2670 [1800–3540] Gt mass over the period 1992–2020, equivalent to 7.4 [5.0–9.8] mm global mean sea level rise. The mass-loss rate was on average 49 [–2 to 100] Gt yr^{-1} over the period 1992–1999, 70 [22 to 119] Gt yr^{-1} over the period 2000–2009 and 148 [94 to 202] Gt yr^{-1} over the period 2010–2019. Mass losses from West Antarctic outlet glaciers outpaced mass gain from increased snow accumulation on the continent and dominated the ice sheet mass losses since 1992 (*very high confidence*). These mass losses from the West Antarctic outlet glaciers were mainly induced by ice shelf basal melt (*high confidence*) and locally by ice shelf disintegration preceded by strong surface melt (*high confidence*). Parts of the East Antarctic Ice Sheet have lost mass in the last two decades (*high confidence*). {2.3.2, 9.4.2, Atlas.11.1}

Both the Greenland Ice Sheet (*virtually certain*) and the Antarctic Ice Sheet (*likely*) will continue to lose mass throughout this century under all considered SSP scenarios. The related contribution to global mean sea level rise until 2100 from the Greenland Ice Sheet will *likely* be 0.01–0.10 m under SSP 1-2.6, 0.04–0.13 m under SSP2-4.5 and 0.09–0.18 m under SSP5-8.5, while the Antarctic Ice Sheet will *likely* contribute 0.03–0.27 m under SSP1-2.6, 0.03–0.29 m under SSP2-4.5 and 0.03–0.34 m under SSP5-8.5. The loss of ice from Greenland will become increasingly dominated by surface melt, as marine margins retreat and the ocean-forced dynamic response of ice-sheet margins diminishes (*high confidence*). In the Antarctic, dynamic losses driven by ocean warming and ice shelf disintegration will *likely* continue to outpace increasing snowfall this century (*medium confidence*). Beyond 2100, total mass loss from both ice sheets will be greater under high-emission scenarios than under low-emission scenarios (*high confidence*). The assessed *likely* ranges consider those ice-sheet processes in whose representation in current models we have at least *medium confidence*, including surface mass balance and grounding-line retreat in the absence of instabilities. Under high-emission scenarios, poorly understood processes related to Marine Ice Sheet Instability and Marine Ice Cliff Instability, characterized by deep uncertainty, have the potential to strongly increase Antarctic mass loss on century to multi-century time scales. {9.4.1, 9.4.2, 9.6.3, Box 9.3, Box 9.4}

Glaciers

Glaciers lost 6200 [4600–7800] Gt of mass (17.1 [12.7–21.5] mm global mean sea level equivalent) over the period 1993 to 2019 and will continue losing mass under all SSP scenarios (*very high confidence*). During the decade 2010 to 2019, glaciers lost more mass than in any other decade since the beginning of the observational record (*very high confidence*). For all regions with long-term observations, glacier mass in the decade 2010 to 2019 is the smallest since at least the beginning of the 20th century (*medium confidence*). Because of their lagged response, glaciers will continue to lose mass at least for several decades even if global temperature is stabilized (*very high confidence*). Glaciers will lose 29,000 [9,000–49,000] Gt

ACCEPTED VERSION SUBJECT TO FINAL EDITING

and 58,000 [28,000–88,000] Gt over the period 2015–2100 for RCP2.6 and RCP8.5, respectively (*medium confidence*), which represents 18 [5–31] % and 36 [16–56] % of their early-21st-century mass, respectively. {2.3.2, 9.5.1, 9.6.1, 9.6.3, 12.4}

Permafrost

Increases in permafrost temperature have been observed over the past three to four decades throughout the permafrost regions (*high confidence*), and further global warming will lead to near-surface permafrost volume loss (*high confidence*). Complete permafrost thaw in recent decades is a common phenomenon in discontinuous and sporadic permafrost regions (*medium confidence*). Permafrost warmed globally by 0.29 [0.17–0.41, *likely* range] °C between 2007 and 2016 (*medium confidence*). An increase in the active layer thickness is a pan-Arctic phenomenon (*medium confidence*), subject to strong heterogeneity in surface conditions. The volume of perennially frozen soil within the upper 3 m of the ground will decrease by about 25% per 1°C of global surface air temperature change (up to 4°C above pre-industrial temperature) (*medium confidence*). {9.5.2}

Snow

Northern Hemisphere spring snow cover extent has been decreasing since 1978 (*very high confidence*), and there is *high confidence* that this trend extends back to 1950. Further decrease of Northern Hemisphere seasonal snow cover extent is *virtually certain* under further global warming. The observed sensitivity of Northern Hemisphere snow cover extent to Northern Hemisphere land surface air temperature for 1981–2010 is –1.9 [–2.8 to –1.0, *likely* range] million km^2 per 1°C throughout the snow season. It is *virtually certain* that Northern Hemisphere snow cover extent will continue to decrease as global climate continues to warm, and process understanding strongly suggests that this also applies to Southern Hemisphere seasonal snow cover (*high confidence*). Northern Hemisphere spring snow cover extent will decrease by about 8% per 1°C of global surface air temperature change (up to 4°C above pre-industrial temperature) (*medium confidence*). {9.5.3}

Sea Level

Global mean sea level (GMSL) rose faster in the 20th century than in any prior century over the last three millennia (*high confidence*), with a 0.20 [0.15–0.25] m rise over the period 1901 to 2018 (*high confidence*). GMSL rise has accelerated since the late 1960s, with an average rate of 2.3 [1.6–3.1] mm yr^{-1} over the period 1971–2018 increasing to 3.7 [3.2–4.2] mm yr^{-1} over the period 2006–2018 (*high confidence*). New observation-based estimates published since SROCC lead to an assessed sea level rise over the period 1901 to 2018 that is consistent with the sum of individual components. While ocean thermal expansion (38%) and mass loss from glaciers (41%) dominate the total change from 1901 to 2018, ice sheet mass loss has increased and accounts for about 35% of the sea level increase during the period 2006–2018 (*high confidence*). {2.3.3, 9.6.1, 9.6.2, Cross-Chapter Box 9.1, Box 7.2}

At the basin scale, sea levels rose fastest in the Western Pacific and slowest in the Eastern Pacific over the period 1993–2018 (*medium confidence*). Regional differences in sea level arise from ocean dynamics; changes in Earth gravity, rotation and deformation due to land-ice and land-water changes; and vertical land motion. Temporal variability in ocean dynamics dominates regional patterns on annual to decadal time scales (*high confidence*). The anthropogenic signal in regional sea level change will emerge in most regions by 2100 (*medium confidence*). {9.2.4, 9.6.1}

Regional sea level change has been the main driver of changes in extreme still water levels across the quasi-global tide gauge network over the 20th century (*high confidence*) and will be the main driver of

ACCEPTED VERSION SUBJECT TO FINAL EDITING

a substantial increase in the frequency of extreme still water levels over the next century (*medium confidence*). Observations show that high tide flooding events that occurred five times per year during the period 1960–1980 occurred on average more than eight times per year during the period 1995–2014 (*high confidence*). Under the assumption that other contributors to extreme sea levels remain constant (e.g., stationary tides, storm-surge, and wave climate), extreme sea levels that occurred once per century in the recent past will occur annually or more frequently at about 19–31% of tide gauges by 2050 and at about 60% (SSP1-2.6) to 82% (SSP5-8.5) of tide gauges by 2100 (*medium confidence*). In total, such extreme sea levels will occur about 20 to 30 times more frequently by 2050 and 160 to 530 times more frequently by 2100 compared to the recent past, as inferred from the median amplification factors for SSP1-2.6, SSP2-4.5, and SSP5-8.5 (*medium confidence*). Over the 21st century, the majority of coastal locations will experience a median projected regional sea level rise within +/- 20% of the median projected GMSL change (*medium confidence*). {9.6.4}

It is *virtually certain* that global mean sea level will continue to rise through 2100, because all assessed contributors to global mean sea level are *likely* to *virtually certain* to continue contributing throughout this century. Considering only processes for which projections can be made with at least *medium confidence*, relative to the period 1995–2014 GMSL will rise by 2050 between 0.18 [0.15–0.23, *likely* range] m (SSP1-1.9) and 0.23 [0.20–0.30, *likely* range] m (SSP5-8.5), and by 2100 between 0.38 [0.28–0.55, *likely* range] m (SSP1-1.9) and 0.77 [0.63–1.02, *likely* range] m (SSP5-8.5). This GMSL rise is primarily caused by thermal expansion and mass loss from glaciers and ice sheets, with minor contributions from changes in land-water storage. These *likely* range projections do not include those ice-sheet-related processes that are characterized by deep uncertainty. {9.6.3}

Higher amounts of GMSL rise before 2100 could be caused by earlier-than-projected disintegration of marine ice shelves, the abrupt, widespread onset of Marine Ice Sheet Instability and Marine Ice Cliff Instability around Antarctica, and faster-than-projected changes in the surface mass balance and discharge from Greenland. These processes are characterised by deep uncertainty arising from limited process understanding, limited availability of evaluation data, uncertainties in their external forcing and high sensitivity to uncertain boundary conditions and parameters. In a low-likelihood, high-impact storyline, under high emissions such processes could in combination contribute more than one additional meter of sea level rise by 2100. {9.6.3, Box 9.4}

Beyond 2100, GMSL will continue to rise for centuries due to continuing deep ocean heat uptake and mass loss of the Greenland and Antarctic Ice Sheets, and will remain elevated for thousands of years (*high confidence*). Considering only processes for which projections can be made with at least *medium confidence* and assuming no increase in ice-mass flux after 2100, relative to the period 1995–2014, by 2150, GMSL will rise between 0.6 [0.4–0.9, *likely* range] m (SSP1-1.9) and 1.4 [1.0–1.9, *likely* range] m (SSP5-8.5). By 2300, GMSL will rise between 0.3 m and 3.1 m under SSP1-2.6, between 1.7 m and 6.8 m under SSP5-8.5 in the absence of Marine Ice Cliff Instability, and by up to 16 m under SSP5-8.5 considering Marine Ice Cliff Instability (*low confidence*). {9.6.3}

Cryospheric Changes and Sea Level Rise at Specific Levels of Global Warming

At sustained warming levels between 1.5°C and 2°C, the Arctic Ocean will become practically sea ice–free in September in some years (*medium confidence*); the ice sheets will continue to lose mass (*high confidence*), but will not fully disintegrate on time scales of multiple centuries (*medium confidence*); there is *limited evidence* that the Greenland and West Antarctic Ice Sheets will be lost almost completely and irreversibly over multiple millennia; about 50–60% of current glacier mass excluding the two ice sheets and the glaciers peripheral to the Antarctic Ice Sheet will remain, predominantly in the polar regions (*low confidence*); Northern hemisphere spring snow cover extent will decrease by up to 20% relative to 1995–2014 (*medium confidence*); the permafrost volume in the top 3 m will decrease by up to 50% relative to

ACCEPTED VERSION SUBJECT TO FINAL EDITING

1995–2014 (*medium confidence*). Committed GMSL rise over 2000 years will be about 2-6 m with 2°C of peak warming (*medium agreement, limited evidence*). {9.3.1, 9.4.1, 9.4.2, 9.5.1, 9.5.2, 9.5.3, 9.6.3}

At sustained warming levels between 2°C and 3°C, the Arctic Ocean will be practically sea ice–free throughout September in most years (*medium confidence*); there is *limited evidence* that the Greenland and West Antarctic Ice Sheets will be lost almost completely and irreversibly over multiple millennia; both the probability of their complete loss and the rate of mass loss will increase with higher temperatures (*high confidence*); about 50–60% of current glacier mass outside Antarctica will be lost (*low confidence*); Northern hemisphere spring snow cover extent will decrease by up to 30% relative to 1995–2014 (*medium confidence*); permafrost volume in the top 3 m will decrease by up to 75% relative to 1995–2014 (*medium confidence*). Committed GMSL rise over 2000 years will be about 4-10 m with 3°C of peak warming (*medium agreement, limited evidence*). {9.3.1, 9.4.1, 9.4.2, 9.5.1, 9.5.2, 9.5.3, 9.6.3}

At sustained warming levels between 3°C and 5°C, the Arctic Ocean will become practically sea ice–free throughout several months in most years (*high confidence*); near-complete loss of the Greenland Ice Sheet and complete loss of the West Antarctic Ice Sheet will occur irreversibly over multiple millennia (*medium confidence*); substantial parts or all of Wilkes Subglacial Basin in East Antarctica will be lost over multiple millennia (*low confidence*); 60–75% of current glacier mass outside Antarctica will disappear (*low confidence*); nearly all glacier mass in low latitudes, Central Europe, Caucasus, Western Canada and USA, North Asia, Scandinavia and New Zealand will *likely* disappear; Northern Hemisphere spring snow cover extent will decrease by up to 50% relative to 1995–2014 (*medium confidence*); permafrost volume in the top 3 m will decrease by up to 90% compared to 1995–2014 (*medium confidence*). Committed GMSL rise over 2000 years will be about 12–16 m with 4°C of peak warming and 19–22 m with 5°C of peak warming (*medium agreement, limited evidence*). {9.3.1, 9.4.1, 9.4.2, 9.5.1, 9.5.2, 9.5.3, 9.6.3}

ACCEPTED VERSION
SUBJECT TO FINAL EDITING

9.1 Introduction

This chapter provides a holistic assessment of the physical processes underlying global and regional changes in the ocean, cryosphere and sea level, as well as improved understanding of observed, attributed and projected future changes since the AR5 and the SROCC (see outline in Figure 9.1). The ocean and cryosphere (defined as the frozen components of the Earth system such as sea ice, ice sheets, glaciers, permafrost and snow) exchange heat and freshwater with the atmosphere and each other (Figure 9.2). In a warming climate, the combined effects of thermal expansion of seawater and melting of the terrestrial cryosphere result in global mean sea-level rise (Box 9.1).

[START FIGURE 9.1 HERE]

Figure 9.1: Visual guide to chapter 9 with relevant chapter numbers indicated in red.

[END FIGURE 9.1 HERE]

Ocean acidification and deoxygenation are covered in Chapter 5 and regional changes to the ocean and cryosphere are covered in Chapter 12 and the Atlas. Ecosystem range shifts and climate risk for marine biodiversity associated with ocean change are assessed in AR6 Working Group II. The notion of "climate velocity" often used in impact studies, which is defined as the speed and direction at which a climate variable moves across a corresponding spatial field is underpinned by the assessment of changes in the physical characteristics of the ocean provided in this chapter.

There are two major advances of this chapter compared with the AR5 and the SROCC facilitated by community efforts. The first is the temporal and spatial increase in observations of both the ocean and the cryosphere (Section 1.5.1.1). In particular, extended observations have allowed improved assessment of past change and closure of both the energy and sea-level budget in a consistent way (Cross-Chapter Box 9.1) and the sea level budget for the last century (Section 9.6.1.1). Higher resolution observations have revealed the details of the Atlantic meridional overturning circulation (Section 9.2.3.1) and globally resolved glacier changes for the first time (Section 9.5.1.1). Improved methodology has resulted in a doubling of the assessed level of observed increase in global ocean 0–200 m stratification compared to the SROCC assessment (Section 9.2.1.3).

The second advance is the use of a hierarchy of models and emulators to update projections of oceanic, cryospheric and sea-level change arising from CMIP6 and related projects (Section 1.5.4.3; Table 1.3, Annex II).[2] CMIP6 included an ice sheet modelling intercomparison for the first time. Particular modelling advances relevant to this chapter are the increase in ocean resolution in the HighResMIP and OMIP2 experiments (Section 1.5.3.1; Section 9.2), projections of future glacier (GlacierMIP) and ice sheet (ISMIP6 and LARMIP-2) response from multi-model studies (Sections 9.5.1, 9.4; Box 9.3), and new methods to synthesize ocean and cryosphere models into sea level projections for all SSPs (Section 1.6.1; Cross-Chapter Box 1.4; Sections 9.4.1.3, 9.4.2.5, 9.6.3) and warming levels (Sections 9.6.3; 1.6.2; Cross-Chapter Box 11.1). In particular, sea level projections and the individual contributions (Section 9.6.3.3) are consistent with equilibrium climate sensitivity and surface temperature assessments across this report (Box 4.1, Cross-Chapter Box 7.1).

There are other advances in scientific understanding. In the cryosphere, this chapter assesses how fast-responding elements (sea ice, permafrost and snow (Sections 9.3 9.5.2; 9.5.3) track warming levels across observations and projections independent of scenario, process understanding of uncertainty in Antarctic ice

[2] In particular, this range of tools leads to advance in evaluation of confidence in projections. When CMIP6 models are used without additional evidence, the 5-95% confidence range of projections is assigned to a *likely* range to acknowledge that there are uncertainty sources not reflected by model spread, consistent with Chapter 4.

ACCEPTED VERSION SUBJECT TO FINAL EDITING

sheet projections (Section 9.4.2; Box 9.4) and new insight into thresholds for Arctic sea ice (Section 9.3.1.1) and Greenland and West Antarctic ice sheets (Section 9.4.1.4; 9.4.2.6). In the ocean, process understanding of ocean heat uptake (Section 9.2.2.1; Cross-chapter Box 5.3) and observed changes in ocean stratification (Section 9.2.1.3) have implications for ocean biogeochemistry are also important.

[START FIGURE 9.2 HERE]

Figure 9.2: Components of ocean, cryosphere and sea level assessed in this chapter. (a) Schematic of processes (mCDW=modified Circumpolar Deep Water, GIA=Glacial Isostatic Adjustment). White arrows indicate ocean circulation. Pinning points indicate where the grounding line is most stable and ice sheet retreat will slow. (b) Geographic distribution of ocean and cryosphere components (numbers indicate (RGI Consortium, 2017) glacierized regions, see Figures 9.20 and 9.21 for labels). Sea ice shaded to indicate the annual mean concentration. Green ocean colours indicate larger surface current speed. Further details on data sources and processing are available in the chapter data table (Table 9.SM.9).

[END FIGURE 9.2 HERE]

[START BOX 9.1 HERE]

BOX 9.1: Key processes driving sea level change

Sea-level change arises from processes acting on a range of spatial and temporal scales, in the ocean, cryosphere, solid Earth, atmosphere and on land (Figure 9.2). ***Relative sea-level change*** is the change in local mean sea surface height relative to the sea floor, as measured by instruments that are fixed to the Earth's surface (e.g., tide gauges). This reference frame is used when considering coastal impacts, hazards and adaptation needs. In contrast, ***geocentric sea-level change*** is the change in local mean sea surface height with respect to the terrestrial reference frame and is the sea-level change observed with instruments from space. This box provides a brief summary of sea-level processes using standard terminology (Gregory et al., 2019).

Global processes

Global mean sea-level change (Sections 9.6, 2.3.3.3) is the change in volume of the ocean divided by the ocean surface area. It is the sum of changes in ocean density (*global mean thermosteric sea-level change*) and changes in the ocean mass as a result of changes in the cryosphere or land water storage (*barystatic sea-level change*).

Steric sea-level change is caused by changes in the ocean density and is composed of *thermosteric sea-level change* and *halosteric sea-level change*. ***Thermosteric sea-level change*** (also referred to as *thermal expansion*) occurs as a result of changes in ocean temperature: increasing temperature reduces ocean density and increases the volume per unit of mass. ***Halosteric sea-level change*** occurs as a result of salinity variations: higher salinity leads to higher density and decreases the volume per unit of mass. Although both processes can be relevant on regional to local scales, thermosteric changes contribute to global mean sea-level change, whereas global mean halosteric change is negligible (Gregory et al., 2019). There is *high confidence* in the understanding of processes causing thermosteric sea-level change (Section 9.2.4.1).

The Greenland and Antarctic ice sheets are the largest reservoirs of frozen freshwater and therefore potentially the largest contributors to sea-level rise. Fluctuations in ice sheet volume arise from the imbalance between accumulation (either at the ice sheet surface or on the underside of ice shelves) and loss from sublimation, surface and basal melting, and iceberg calving. Ice sheets discharge the majority of their mass through marine-terminating ice streams that are in some cases buttressed by floating ice shelves. Changes in the thickness and extent of the ice shelves due to melt from below, calving, or disintegration, as a result of surface meltwater penetrating crevasses, can affect the flow of the inland ice streams. There is *medium confidence* in ice sheet processes but *low confidence* in their forcing (ocean changes and ice shelf

ACCEPTED VERSION SUBJECT TO FINAL EDITING

collapse) and in instability processes (Sections 9.4.1, 9.4.2).[3]

Glaciers contribute to sea-level change via an imbalance between mass gain and mass loss processes, which leads to adjustments in the glacier geometry over an extended period of time, called the response time. The response time may range from a few years to a few hundred years. The glacial meltwater does not all flow immediately into the ocean: it can refreeze, feed rivers (where it may be extracted for domestic use), evaporate, or be stored in (proglacial) lakes or closed basins. There is *medium* to *high confidence* in the understanding of processes leading to sea level contributions from glaciers (Section 9.5.1).

Land water storage includes surface water, soil moisture, groundwater storage and snow, but excludes water stored in glaciers and ice sheets. Changes in land water storage can be caused either by direct human intervention in the water cycle (e.g., storage of water in reservoirs by building dams in rivers, groundwater extraction for consumption and irrigation, or deforestation) or by climate variations (e.g., changes in the amount of water in internally drained lakes and wetlands, the canopy, the soil, the permafrost and the snowpack). Land water storage changes caused by climate variations may be indirectly affected by anthropogenic influences. It is difficult to assign a single confidence level to land water storage as understanding can vary from *low confidence* in groundwater recharge processes to *high confidence* in water storage via snowpack changes (Sections 8.2.3, 8.3.1.7).

Regional and local processes

Ocean dynamic sea-level change refers to the change in mean sea level relative to the geoid and is associated with the circulation and density-driven changes in the ocean. Ocean dynamic sea-level change varies regionally but by definition has a zero global mean. It includes the depression of the sea surface by atmospheric pressure. There is *medium confidence* in the understanding of ocean processes leading to dynamic sea-level change (Section 9.2.4.2).

Changes in Earth Gravity, Earth Rotation and viscoelastic solid Earth Deformation (GRD) result from the redistribution of mass between terrestrial ice and water reservoirs and the ocean. Contemporary terrestrial mass loss leads to elastic solid Earth uplift and a nearby relative sea-level fall (for a single source of terrestrial mass loss this is within ~2000 km, for multiple sources the distance depends on the interaction of the different relative sea-level patterns). Farther away (more than ~7000 km for a single source of terrestrial mass loss), relative sea level rises more than the global average, due, to first order, to gravitational effects. Earth deformation associated with adding water to the ocean and a shift of the Earth's rotation axis towards the source of terrestrial mass loss leads to second-order effects that increase spatial variability of the pattern globally. GRD effects due to the redistribution of ocean water within the ocean itself are referred to as ***self-attraction and loading effects***. There is *high confidence* in the understanding of GRD processes.

Glacial Isostatic Adjustment is ongoing GRD in response to past changes in the distribution of ice and water on Earth's surface. On a timescale of decades to tens of millennia following mass redistribution, Earth's mantle flows viscously as it evolves toward isostatic equilibrium, causing solid Earth movement and geoid changes, which can result in regional to local sea-level variations. There is *medium confidence* in the understanding of glacial isostatic adjustment processes.

Vertical land motion is the change in height of the land surface or the sea floor and can have several causes in addition to elastic deformation associated with contemporary GRD and viscoelastic deformation associated with glacial isostatic adjustment. Subsidence (sinking of the land surface or sea floor) can occur through compaction of alluvial sediments in deltaic regions, removal of fluids such as gas, oil, and water, or drainage of peatlands. Tectonic deformation of the Earth's crust can occur as a result of earthquakes and volcanic eruptions. There is *medium confidence* in the understanding of vertical land motion processes.

[3] The conversion of land ice mass loss to global mean sea-level rise used in this report (the Sea Level Equivalent, SLE) is 362.5 gigatons (Gt) of ice loss for 1 mm of sea-level rise

ACCEPTED VERSION SUBJECT TO FINAL EDITING

Extreme sea level is an exceptionally low or high local sea-surface height arising from combined short-term phenomena (e.g. storm surges, tides and waves). Relative sea-level changes affect extreme sea levels directly by shifting the mean water levels and indirectly by modulating the depth for propagation of tides, waves and/or surges. Extreme sea levels can be influenced by changes in the frequency, tracks, or strength of weather systems, or anthropogenic changes such as dredging. ***Extreme Still Water Level*** refers to the combined contribution of relative sea-level change, tides and storm surges. Wind-waves also contribute to coastal sea level. ***Extreme Total Water Level*** is the extreme still water level plus wave setup (time-mean sea-level elevation due to wave energy dissipation). When considering coastal impacts, swash (vertical displacement up the shore-face induced by individual waves) is also important and included in ***Extreme Coastal Water Level***. There is *low* to *medium confidence* in the understanding of extreme sea level processes (Sections 9.6.4, 12.4).

[END BOX 9.1 HERE]

9.2 Oceans

9.2.1 Ocean surface

9.2.1.1 Sea Surface Temperature (SST)

The AR5 (Hartmann et al., 2013) assessed that it is certain that global sea-surface temperature (SST) has increased since the beginning of the 20th century (*very high confidence*). The SROCC did not assess past SST change. Since the AR5, improvements in the understanding of recent SST biases in the observational records, especially extending ship-based observations with buoy-based observations and improved treatment of sea ice, have had important consequences for key climate change indicators such as global mean surface temperature (GMST), global mean surface air temperature (GSAT), and SST (Cross-Chapter Box 2.3). The AR5 assessment is confirmed, and it is now *very likely* that global mean SST changed by 0.88°C [0.68-1.01°C] from 1850-1900 to 2011-2020, and 0.60°C [0.44-0.74°C] from 1980 to 2020 (Figure 9.3, Table 2.4).

Regions vary in the rate of SST warming, with slight cooling in some regions (Figure 9.3). The SROCC (Collins et al., 2019) and Section 7.4.4 assess SST changes over specific regions, which are consistent with the changes reported here. The tropical ocean has been warming faster than other regions since 1950, with the fastest warming in regions of the tropical Indian and western Pacific Oceans (Figure 9.3), due to a combination of local atmosphere-ocean coupling, the Indonesian Throughflow (Section 9.2.3.4; Figure 9.11), and trends in the Walker circulation (Section 2.3.1.4.1; Section 3.3.3.1; Figure 3.16). The Western Boundary Currents of the subtropical gyres have warmed faster than the global mean over the past century. There remains *low agreement* in the changes of both the location and the dynamical changes in western boundary current extensions (Sections 2.3.3.4.2, 9.2.3.4, Figure 9.3). In the Arctic, the mean SST increase over the last two decades is similar to or only slightly higher than the global average (Chen et al., 2019b). In contrast, the eastern Pacific Ocean, subpolar North Atlantic Ocean and Southern Ocean have warmed more slowly than the global average or cooled. (Figure 9.3). Surface warming in the subpolar Southern Ocean has been slower than the global average since the 1950s, and this pattern is consistent with the upwelling around Antarctica renewing surface water with pre-industrial, deeper water-masses (Section 9.2.3.2) (Frölicher et al., 2015; Marshall et al., 2015b; Armour et al., 2016). New evidence since the SROCC (Meredith et al., 2019) confirms slight cooling since the 1980s around the subpolar Southern Ocean, contrasting with marked warming directly northward of it (Section 9.2.3.2) (Haumann et al., 2020; Rye et al., 2020; Auger et al., 2021). In Eastern Boundary Upwelling Systems, the SROCC (Bindoff et al., 2019) reported *low agreement* between SST trends in recent decades, due to varying spatio-temporal resolution and interannual to multi-decadal variability. Satellite evidence not included in SROCC show that 92% of these regions warmed more slowly than neighbouring offshore locations between 1982-2015, so upwelling may buffer the near shore from warming (Varela et al., 2018) (Section 9.2.3.5). Coupled ocean-atmospheric modes of variability strongly affect regional SST (Cross-Chapter Box 3.1, Annex IV). In summary, a positive SST trend since 1950 is evident globally, but there is *very high confidence* that the Indian Ocean, western equatorial Pacific

ACCEPTED VERSION SUBJECT TO FINAL EDITING

Ocean, and western boundary currents have warmed faster than the global average, while the Southern Ocean, the eastern equatorial Pacific, and the North Atlantic Ocean have warmed more slowly or slightly cooled.

[START FIGURE 9.3 HERE]

Figure 9.3: Sea Surface Temperature (SST) and its changes with time. (a) Time series of global mean SST anomaly relative to 1950-1980 climatology. Shown are observational reanalyses (HadISST) and multi-model means from the CMIP historical, CMIP projections, and HighResMIP experiment. (b) Map of observed SST (1995-2014 climatology HadISST), (e) bias of CMIP and (h) bias of HighResMIP (bottom left) over 1995-2014. Also shown are 1950-2014 c) historical SST changes from observations, (f) CMIP and (i) HighResMIP, and (d) 2005-2100 SST change rate, (g) 2005-2050 change rate for SSP5-8.5 for the CMIP ensemble, and (j) 2005-2050 change rate for SSP5-8.5 for the HighResMIP ensemble. No overlay indicates regions with high model agreement, where ≥80% of models agree on sign of change; diagonal lines indicate regions with low model agreement, where <80% of models agree on sign of change (see Cross-Chapter Box Atlas.1 for more information). Further details on data sources and processing are available in the chapter data table (Table 9.SM.9).

[END FIGURE 9.3 HERE]

In the AR5 (Flato et al., 2013), a marginal improvement in CMIP5 climate model SST biases was noted compared to CMIP3 models in the AR4, with a reduction in the magnitude of biases. The AR5 noted that in several regions large SST biases are symptomatic of errors in the representation of important processes, such as dynamics in the equatorial Pacific and North Atlantic, and Southern Ocean. Common regional biases in SST or historical SST trends are not exclusively linked to the representation of the ocean (*high confidence*), but can have multiple causes, including errors in the representation of long term historical trends in equatorial winds (Section 9.2.1.2); misrepresentation of the forced equatorial ocean response (Karnauskas et al., 2012; Kohyama et al., 2017; Coats and Karnauskas, 2018); thermocline depth errors (Linz et al., 2014); errors in atmospheric model cloud-related short-wave radiation (Hyder et al., 2018); biases in ocean circulation variability (Wang et al., 2014a); and deficiencies in upper ocean (Li et al., 2019b) and atmospheric (Bates et al., 2012) boundary layer parameterizations. In CMIP6, the mid-latitude biases in the northern hemisphere are improved in the multi-model mean and the inter-model standard deviation of the zonal mean SST error is significantly decreased in the northern Hemisphere south of 50°N compared to CMIP5, though biases in equatorial regions remains essentially unchanged (Section 3.5.1.1; Figures 3.23, 3.24, 9.3). Some longstanding ocean model biases have been reduced through increases in model resolution in CMIP6 (Bock et al., 2020) and improved parameterizations (Fox-Kemper et al., 2011; Li et al., 2016a; Qiao et al., 2016; Reichl and Hallberg, 2018). The high resolution HighResMIP ensemble (Figure 9.3) has smaller cold biases in the North Atlantic and the tropical Pacific, and smaller warm biases in the upwelling regions off the western coasts of Africa, North and South America (Roberts et al., 2018, 2019; Caldwell et al., 2019; Docquier et al., 2019). In summary, CMIP6 models show persistent regional biases in representing the climatological SST state (*very high confidence*), but higher resolution reduces some biases particularly in the North Atlantic and Eastern Boundary Upwelling Systems (Figure 9.3; *high confidence*).

CMIP6 models represent the observed trends in SST patterns with greater fidelity than CMIP5, with the ocean area that is inconsistent with the observed trends decreasing by about three quarters from CMIP5 to CMIP6 (Olonscheck et al., 2020). In some regions, the direction of SST changes in observations are consistent with CMIP6 only when including internal variability (Olonscheck et al., 2020). This is notably the case in the equatorial Pacific, North Atlantic, and Southern Ocean, which are regions where SST is of known importance in controlling heat uptake (Section 9.2.2.1) and the global radiative feedback parameter (Section 7.4.4.3). Overall, despite some persistent regional biases, CMIP6 coupled climate models reproduce the observed SST trends or high internal variability over the past century over a range of different multidecadal periods (Olonscheck et al., 2020; Watanabe et al., 2021) (Figure 9.3), highlighting their skill to inform future large-scale SST changes at regional scale. Warming is projected at varying rates in all regions by 2050, except the North Atlantic Subpolar Region, the equatorial Pacific, and the Southern Ocean where models

ACCEPTED VERSION SUBJECT TO FINAL EDITING

disagree (*high confidence*).

It is *virtually certain* that SST will continue to increase in the 21st century at a rate depending on future emission scenario. The future global mean SST increase projected by CMIP6 models for the period 1995-2014 to 2081-2100 is 0.86°C (5-95% range: 0.43-1.47°C) under SSP1-2.6, 1.51 °C [1.02-2.19°C] under SSP2-4.5, 2.19°C (1.56-3.30°C) under SSP3-7.0, and 2.89°C (2.01-4.07°C) under SSP5-8.5 (Figure 9.3). While under SSP1-2.6, the CMIP6 ensemble consistently projects that it is *very likely* at least 83% of the world ocean surface will have warmed by 2100, under SSP5-8.5, at least 98% of the world ocean surface will have warmed. The spatial pattern of future change is consistent with observed SST change over the 20th century, though with notable regional differences (Figure 9.3). Long-term change in SST patterns is important for regional impacts but also affects radiative feedbacks, and therefore long-term change in climate sensitivity (Section 7.4.4.3). In the Southern Ocean, CMIP6 models project that SSTs will eventually consistently increase in the 21st century at a rate dependent on future scenario (Bracegirdle et al., 2020) (Figure 9.3, Section 9.2.3.2). Yet, there is only *low confidence* that this Southern Ocean warming will emerge by the end of the century (Section 7.4.4.1), due the inconsistent historical and near-term simulations and observations over the 20th century (Figure 9.3). Furthermore, the equilibrium SST pattern from proxy records or simulated by climate models under CO_2 forcing stand in contrast with the cooling trends in the Southern Ocean observed over the past decades (Section 7.4.4.1.2). Similarly, the SST change pattern observed in the tropical Pacific Ocean will transition on centennial timescales to a mean pattern resembling the El Niño pattern (*medium confidence*, Annex IV). However, it is difficult to delineate a climate change trend ressembling an El Niño pattern and El Niño variability (Wittenberg, 2009; Collins et al., 2010) without large ensembles (Kay et al., 2015). Several Pliocene SST reconstructions indicate enhanced warming in the centre of the eastern Pacific equatorial cold tongue upwelling region, consistent with reconstruction of enhanced subsurface warming and enhanced warming in coastal upwelling regions (Section 7.4.4.2.2). The North Atlantic subpolar gyre is projected to continue to warm more slowly than surrounding regions (Suo et al., 2017), as the Gulf Stream concurrently warms rapidly (Cheng et al., 2013) (Figure 9.3) and the Atlantic Meridional Overturning Circulation further declines under greenhouse gas forcing although models disagree about the rate of change (Figure 9.3, Section 9.2.3.1). In summary, CMIP6 models show a future pattern of SST change comparable to historical trends with intensity depending on future emission scenario, and some of the observed cooling trends over the 20th century will eventually transition to a warming SST on centennial timescales, in particular in the Southern Ocean (*high confidence)* and in the equatorial Pacific (*medium confidence*), while the North Atlantic subpolar gyre will continue to warm more slowly than the global average (*high confidence)*.

9.2.1.2 Air-sea fluxes

Air-sea fluxes of energy, freshwater, and momentum (wind stresses) are difficult to observe directly (Cronin et al., 2019), so estimates of the global mean net air-sea heat flux are inferred from observed ocean warming (Section 2.3.3.1, Box 7.2, and Cross-Chapter Box 9.1). Air-Sea heat fluxes resemble the warming patterns of CMIP3 (Domingues et al., 2008; Levitus et al., 2012) and are consistent with the ensemble mean warming rate of CMIP5 (Cheng et al., 2017, 2019) and CMIP6 models (Section 3.5.1.3). Regional air-sea fluxes in models remain a key driver of uncertainty (Huber and Zanna, 2017; Tsujino et al., 2020). A substantial part of the upper 700 m energy increase is *very likely* attributed to anthropogenic forcing via increasing radiative forcing (Sections 3.5.1.3, 7.2, 7.3).

The SROCC (Abram et al., 2019) and AR5 (Rhein et al., 2013) assessed that observations of air-sea fluxes had not yet reached the density or accuracy to directly detect trends beyond the noise. New evidence since SROCC confirms that direct heat and freshwater flux trends have not emerged yet as spatial (Figure 9.4), annual (Yu, 2019), and decadal (Zanna et al., 2019a) variability overwhelm detection. Since the AR5, comprehensive comparisons (Bentamy et al., 2017; Valdivieso et al., 2017; Yu et al., 2017) have used updated and new surface flux products to improve surface flux uncertainty estimates, and these comparisons note that implied global energy imbalances often exceed the observed ocean warming. Flux estimates using top of atmosphere observations and atmospheric fluxes from reanalysis have improved over past products (Trenberth and Fasullo, 2018) but require consistency adjustments (Trenberth et al., 2019) as the energy

ACCEPTED VERSION SUBJECT TO FINAL EDITING

budget is not closed. Adjustments are needed for all flux products, and they remain less accurate than direct ocean heat content change measurements (Cheng et al., 2017). Some regional changes are *likely* robust in both satellite observations and projections (Figure 9.4). Recent satellite-based surface flux products with improved retrieval algorithms and new satellites, e.g., J-OFURO3 (Tomita et al., 2019) and OAFlux-HR (Yu, 2019), provide a complete suite of turbulent fluxes including heat, moisture, and momentum. When combined with satellite-based surface radiation from CERES EBAF (Kato et al., 2018) and precipitation from GPCP (Adler et al., 2003), full ocean-surface forcing is available since 1987 (Figure 9.4). These products agree with sparse buoy and ship observations within 30 W m^{-2} (Bentamy et al., 2017; Cronin et al., 2019). While patterns agree between models and satellites in net fluxes (Figure 9.4), the trend magnitudes are substantially weaker in models. The fluxes tending to warm the North Atlantic and Southern Ocean are consistent with the largest changes observed in the surface properties and water-masses (Sections 9.2.1.1, 9.2.2.1, 9.2.2.3). The observed trend toward a saltier Atlantic Ocean and a fresher Indian Ocean as well as trends in evaporation minus precipitation (E-P) patterns in the equatorial Pacific (see also Section 8.3.1) enhance the present mean pattern of wetting and drying. Elsewhere patterns are less clear with only partial, large-scale agreement with the wet gets wetter simplification (Sections 3.3.2.2, 4.4.1, 4.5.1). In summary, globally-integrated and large-scale fluxes are more reliably inferred from heat content and salinity change, while regional trends are rarely robust in observations and where robust tend to be underestimated or in disagreement in models (*very high confidence*).

[START FIGURE 9.4 HERE]

Figure 9.4: Global maps of observed mean fluxes (a, d, g), the observed trends in these fluxes (b, e, h) and the projected rate of change in these fluxes from SSP5-8.5 (c, f, i). Shown are the freshwater flux (a, b, c), net heat flux (d, e, f), and momentum flux or wind stress magnitude (g, h, i), with positive numbers indicating ocean freshening, warming, and accelerating respectively. The means and observed trends are calculated between 1995-2014 (freshwater and wind stress) or 2001-2014 (heat) and the SSP5-8.5 projected rates are between 1995-2100 using 20-year averages at each end of the time period. Observations show objective interpolation from CERES EBAF v4 (Kato et al., 2018), OAFlux-HR (Yu, 2019), and GPCP (Adler et al., 2003) of fluxes and flux trends. (b, e, h) Observed trends with no overlay indicates regions where the trends are significant at $p = 0.34$ level. Crosses indicate regions where trends are not significant. For (c, f, i) projections, no overlay indicates regions with high model agreement, where ≥80% of models agree on the sign of change, diagonal lines indicate regions with low model agreement, where <80% of models agree on the sign of change (see Cross-Chapter Box Atlas.1 for more information). Further details on data sources and processing are available in the chapter data table (Table 9.SM.9).

[END FIGURE 9.4 HERE]

There is *low confidence* in long-term wind stress trends in most regions, but a few locations have *likely* trends over the scatterometer era and in projections, as shown in Figure 9.4 (Desbiolles et al., 2017; Young and Ribal, 2019; Yu, 2019). The AR5 (Rhein et al., 2013) assessed with *medium confidence* that zonal wind stress over the Southern Ocean increased from the early 1980s to the 1990s (Figure 9.4, *medium confidence*). Over 1995-2014, the zonal wind stress over the Southern Ocean continued to increase, westerly winds in the North Pacific and North Atlantic weakened while the easterly equatorial Pacific winds of the Walker circulation strengthened (Figure 9.4). In historical simulations, CMIP5 models projected annular modes (Annex IV) to move poleward and strengthen in both hemispheres (Yang et al., 2016a), while in CMIP6 models westerlies only strengthen over the Southern Ocean, with a weaker trend than recently observed (Figure 9.4, Sections 4.5.1, 4.5.3). In the tropical Pacific Ocean, a weakening trend in easterly winds and Walker circulation in the 20th century has been inferred based on observed sea level pressure data (Vecchi et al., 2006; Vecchi and Soden, 2007) and coral proxies (Carilli et al., 2014) and is projected to continue by CMIP6 models (Figure 9.4), yet over 1995-2014 observed winds have strengthened (Figure 9.4). The observed strengthening may have been influenced by a combination of factors (Section 7.4.4.2.1), but there is *low confidence* in the attribution of this signal to anthropogenic warming (Section 3.3.3.1) and *medium confidence* that it reflects internal variability (Section 8.3.2.3). Near-term projected changes over the

ACCEPTED VERSION SUBJECT TO FINAL EDITING

Southern Ocean result from ozone recovery and greenhouse gases (Sections 4.3.3, 4.4.3). Overall, there is only *low confidence* in observed and projected wind stress trends in most regions because trends in oceanic wind stresses during the satellite era have not emerged or are inconsistent with historical simulated changes.

Air-sea flux biases result from common causes in most models, many are the same as during AR5 (Rhein et al., 2013). Important currents (e.g., Gulf Stream, Kuroshio, Antarctic Circum-polar Current patterns) are often found in erroneous locations in models, affecting SST and flux signatures (Bates et al., 2012; Beadling et al., 2020; Li et al., 2020b), but their locations are improved in high-resolution ocean models (Chassignet et al., 2017, 2020; Hewitt et al., 2020), and high-resolution coupled models reduce the mean air-sea flux biases (Delworth et al., 2012; Sakamoto et al., 2012; Small et al., 2014a; Haarsma et al., 2016; Caldwell et al., 2019; Jackson et al., 2020a). Oceanic variability stems either from internal chaotic variability or atmospheric forcing (Hasselmann, 1976; Sérazin et al., 2016, 2017). Large scale variability in the ocean tends to follow atmospheric forcing in low resolution models, while in high-resolution coupled models ocean variability drives atmospheric variability on small scales (Bishop et al., 2017; Small et al., 2019), allowing these high-resolution models to mimic the coupling with clouds, precipitation, and atmospheric and oceanic boundary layers apparent in observations (Chelton and Xie, 2010; Frenger et al., 2013). Even coarse resolution models, such as the ocean and sea-ice components used in CMIP6, show significant sensitivity in the mean and variability of SST and sea ice to modest changes in flux forcing (Tsujino et al., 2020). Finally, there is still considerable disagreement between different parameterizations of air-sea fluxes used in models and strong scatter in direct observations (Renault et al., 2016; Brodeau et al., 2017). In summary, there is *very high confidence* that air-sea heat flux and stress biases are reduced in coupled models with high ocean resolution over coarse resolution models, although the effect on trends remain unclear.

9.2.1.3 Upper Ocean Stratification and Surface Mixed Layers

The density difference from surface to deep ocean is the upper-ocean stratification. The AR5 (Rhein et al., 2013) assessed that it is *very likely* that the thermal contribution to stratification over the fixed 0-200 m layer increased by about 1% per decade between 1971 and 2010 (based on linear trend consistently across reports). The SROCC (Bindoff et al., 2019) found it *very likely* that density stratification increased by 0.46-0.51% per decade between 60°S and 60°N from 1970 to 2017). New published estimates based on a variety of different interpolated observations show that the SROCC assessed rate is too low, even using the same data and methods (Li et al., 2020a). The 1960-2018 stratification increase is estimated at 1.2±0.1% per decade from the IAP product, 1.2±0.4% per decade from the Ishii product, 0.7±0.5% per decade from the EN4 product, 0.9±0.5% per decade from the ORAS4 product, and 1.2 ±0.3% per decade from the NCEI product (Li et al., 2020a). The improved methodology of computing stratification change on individual profiles before gridding yields a global annual mean increase of 0-200 m stratification change of 0.8±0.2% per decade between 1960 and 2018 (Yamaguchi and Suga, 2019) and a global summer mean increase of 0-200 m stratification change of 1.3±0.3% per decade between 1970 and 2018 (Sallée et al., 2021)is of a similar magnitude to the long term trend (Yamaguchi and Suga, 2019; Li et al., 2020a). In summary, there is *limited evidence* that focusing on changes over a fixed depth range might hide larger increases occurring at the seasonally and regionally variable pycnocline depth. There is also *limited evidence* that summer stratification change within the pycnocline has occurred at a rate of 8.9±2.7% per decade from 1970 to 2018, and *limited evidence* of a winter pycnocline stratification increase (Cummins and Ross, 2020a; Sallée et al., 2021).

[START FIGURE 9.5 HERE]

Figure 9.5: Mixed layer depth in (a-d) winter and (e-h) summer. (a, e) Observed climatological mean mixed layer depth (based on density threshold) from the Argo Mixed Layer Depth (Holte et al., 2017) observations 2000-2019. (b, f) Bias between the observation-based estimate (2000-2019) and the 1995-2014 CMIP6 climatological mean mixed layer depth. (c, d, g, h) Projected MLD change from 1995-2014 to 2081-2100 under (c, g) SSP1-2.6 and (d, h) SSP5-8.5 scenarios. The (a, b, c, d) Winter row shows DJF in the Northern Hemisphere and JJA in the Southern Hemisphere, and the (e, f, g, h) Summer row shows JJA in the Northern Hemisphere and DJF in the Southern Hemisphere. The mixed layer depth is the depth where

ACCEPTED VERSION SUBJECT TO FINAL EDITING

the potential density is 0.03 kg m^{-3} denser than at 10m. No overlay indicates regions with high model agreement, where ≥80% of models agree on the sign of change; diagonal lines indicate regions with low model agreement, where <80% of models agree on the sign of change (see Cross-Chapter Box Atlas.1 for more information). Further details on data sources and processing are available in the chapter data table (Table 9.SM.9).

[END FIGURE 9.5 HERE]

While AR5 and the SROCC did not assess change in mixed-layer depth, the reported changes in stratification can modulate the surface mixed layer depth, which is set by a balance between fluxes and dynamical mixing (winds, tides, waves, convection) acting against the background stratification and restratification processes (solar and dynamical). Despite the large stratification increase observed at a global scale, new evidence shows that summer mixed-layer depth deepened consistently over the globe at a rate of 2.9±0.5% per decade from 1970 to 2018, with the largest deepening observed in the Southern Ocean, corresponding to overall deepening from 3-15 m per decade depending on region (Somavilla et al., 2017; Sallée et al., 2021). While the shorter observational record in winter than in summer does not allow global winter mixed-layer trends to be reliably assessed (Sallée et al., 2021), winter mixed-layer depths deepening at rates of 10 m per decade have been reported at individual long-term mid-latitude monitoring sites (Somavilla et al., 2017). Projections agree that shoaling of mixed layer depth is expected in the 21st century, but only for strong emissions scenarios and only in some regions (Figure 9.5). In summary, there is *limited* observational *evidence* that the mixed layer is globally deepening, while models show no emergence of a trend until later in the 21st century under strong emissions.

The SROCC assessed that upper ocean stratification will continue to increase in the 21st century under increased radiative forcing (*high confidence*), due to increased surface temperature and high-latitude surface freshening (Bindoff et al., 2019). New climate model simulations concur with the SROCC assessment of a future increase of the 0-200 m stratification under increased radiative forcing in all regions of the world ocean (Kwiatkowski et al., 2020). In addition, CMIP6 climate models project a shallowing of the mixed-layer both in summer and winter by the end of the century under increased radiative forcing (Kwiatkowski et al., 2020) (Figure 9.5), with the exception of the Arctic showing deepening of the mixed-layer as a result of sea-ice retreat (Lique et al., 2018a) (Figure 9.5). The regions of largest shallowing are associated with the deepest climatological mixed layer both in winter and summer, particularly affecting the North Atlantic and the Southern Ocean basins (Figure 9.5). While CMIP6 models tend to project shallowing mixed-layers under a warming climate, except at high latitudes (Figure 9.5) (Lique et al., 2018b; Kwiatkowski et al., 2020), a deepening in the summer mixed-layer depth by intensification of the surface winds and storms may explain inconsistency among models in many regions (Figure 9.5) (Young and Ribal, 2019), although model mixed layer biases are large in the summertime in the Southern Ocean (Belcher et al., 2012; Sallée et al., 2013a; Li et al., 2016a; Tsujino et al., 2020). Lack of observed ocean turbulence and climate model limitations do not allow for direct assessment of ocean surface turbulence change and limit confidence in past and future mixed-layer change. Understanding of turbulent processes, its representation in ocean and climate models, and its effect on mixed layer biases have been an active and rapidly evolving topic of research since AR5 (Buckingham et al., 2019; Li et al., 2019b). Small-scale mixed layer processes are not resolved in climate models (D'Asaro, 2014; Buckingham et al., 2019; McWilliams, 2019) and despite significant improvements in their parameterisation over the last decade (Fox-Kemper et al., 2011; Jochum et al., 2013; Li et al., 2016a; Qiao et al., 2016; Li et al., 2019b) and significant improvement in some models (Li and Fox-Kemper, 2017; Dunne et al., 2020), biases in mixed-layer representation generally persist (Heuzé, 2017; Williams et al., 2018; Cherchi et al., 2019; Golaz et al., 2019; Voldoire et al., 2019; Yukimoto et al., 2019; Boucher et al., 2020; Danabasoglu et al., 2020; Dunne et al., 2020; Kelley et al., 2020). In summary, the representation of upper ocean stratification and mixed layers has improved in CMIP6 compared to CMIP5. While it is *virtually certain* that the global mean upper ocean will continue to stratify in the 21st century, there is only *low confidence* in the future evolution of mixed-layer depth, which is projected to mostly shoal under high emissions scenarios except in high latitude regions where sea-ice retreats.

ACCEPTED VERSION SUBJECT TO FINAL EDITING

[START BOX 9.2 HERE]

BOX 9.2: Marine Heatwaves

Marine heatwaves (MHW) are periods of extreme high sea temperature relative to the long-term mean seasonal cycle (Hobday et al., 2016). Studies since the SROCC (Collins et al., 2019) confirm the assessment that MHW can lead to severe and persistent impacts on marine ecosystems, from mass mortality of benthic communities including coral bleaching, changes in phytoplankton blooms, shifts in species composition and geographical distribution, toxic algal blooms to decline in fisheries catch and mariculture (Smale et al., 2019; Cheung and Frölicher, 2020; Hayashida et al., 2020a; Piatt et al., 2020). Unlike synoptic atmospheric heatwaves (Section 11.3), MHWs can extend for millions of square kilometres, persist for weeks to months, and occur at subsurface (Bond et al., 2015; Schaeffer and Roughan, 2017; Perkins-Kirkpatrick et al., 2018; Laufkötter et al., 2020).

The SROCC established that MHWs have occurred in all basins over the last decades. Additional evidence documenting widespread occurrence of marine heat waves in all basins and marginal seas continues to accumulate (Li et al., 2019c; Yao et al., 2020). The SROCC highlighted the role of large-scale climate modes of variability in amplifying or suppressing MHW occurrences, which has since been further corroborated, increasing confidence in climate modes as important drivers of MHWs (Holbrook et al., 2019; Sen Gupta et al., 2020). More generally, understanding of processes leading to MHWs has increased since the SROCC, including air-sea heat flux (Section 9.2.1.2), increased horizontal heat advection, shoaling of the mixed layer and suppressed mixing processes (Section 9.2.1.3), reduced coastal upwelling and Ekman pumping (Section 9.2.3.5), changes in eddy activities and planetary waves, and the re-emergence of warm subsurface anomalies (Holbrook et al., 2020; Sen Gupta et al., 2020).

The SROCC reported with *high confidence* that MHWs (defined as days exceeding the 99th percentile in SST from 1982 to 2016) have *very likely* doubled in frequency between 1982 and 2016. Additional observation-based evidence and acquisition of longer observation time-series since the SROCC have confirmed and expanded on this assessment: since the 1980s MHWs have also become more intense and longer (Frölicher and Laufkötter, 2018; Smale et al., 2019; Laufkötter et al. 2020). Satellite observations and reanalyses of SST show increase in intensity of 0.04°C per decade from 1982 to 2016, an increase in spatial extent of 19 % per decade from 1982 to 2016, and an increase in annual MHW days of 54 % between the 1987-2016 period compared to 1925-1954 (Frölicher et al., 2018; Oliver, 2019). The SROCC assessed that 84-90% of all MHWs that occurred between 2006 and 2015 are *very likely* caused by anthropogenic warming. There is new evidence since SROCC that the frequency of the most impactful marine heatwaves over the last few decades has increased more than 20-fold because of anthropogenic global warming (Laufkötter et al., 2020). In summary, there is *high confidence* that MHWs have increased in frequency over the 20th century, with an approximate doubling from 1982-2016, and *medium confidence* that they have become more intense and longer since the 1980s.

[START BOX 9.2, FIGURE 1 HERE]

Box 9.2, Figure 1: Observed and simulated regional probability ratio of marine heatwaves (MHWs) for the 1985-2014 period and for the end of the 21st century under two different greenhouse gas emissions scenarios. The probability ratio is the proportion by which the number of MHW days per year has increased relative to pre-industrial times. A MHW is defined as a deviation beyond the daily 99th percentile (11-day window) in the deseasonalized sea surface temperature. (a) The MHW probability ratio from satellite observations (NOAA OISST V2.1; (Huang et al., 2021) during 1985-2014. The mean warming pattern (difference in ERSST5 (Huang et al., 2017) sea surface temperature between the 1985-2014 and 1854-1900 periods) has been added to the satellite observations to calculate the probability ratio. (b-d) CMIP6 simulated multi-model mean probability ratio of the (b) 1985-2014 period, and 2081-2100 period in the (c) SSP1 2.6 and (d) SSP5 8.5 scenarios. The areas with grey diagonal lines in (d) indicate permanent MHWs (> 360 heatwave days per year). These 14 CMIP6 models are included in the analysis: ACCESS-CM2, CESM2, CESM2-WACCM, CMCCCM2-SR5, CNRM-CM6-1, CNRM-ESM2-1, CanESM5, EC-Earth3,

ACCEPTED VERSION SUBJECT TO FINAL EDITING

IPSL-CM6A-LR, MIROC6, MRI-ESM2-0, NESM3, NorESM2-LM, NorESM2-MM. Further details on data sources and processing are available in the chapter data table (Table 9.SM.9).

[END BOX 9.2, FIGURE 1 HERE]

Consistent with the SROCC, future MHWs are defined with reference to the historical climate conditions. The SROCC assessed that MHWs will *very likely* further increase in frequency, duration, spatial extent and intensity under future global warming in the 21st century. CMIP6 projections allow us to confirm this assessment and quantify future change based on global mean probability ratio change (Box 9.2, Figure 1): they project MHWs will become 4 (5-95% range: 2-9) times more frequent in 2081-2100 compared to 1995-2014 under SSP1-2.6, or 8 (3-15) times more frequent under SSP5-8.5. The SROCC highlighted that future change of MHWs will not be globally uniform, with the largest changes in the frequency of marine heatwaves being projected to occur in the western tropical Pacific and the Arctic Ocean (*medium confidence*). New evidence from the latest generation of climate models confirms and complements the SROCC assessment (Box 9.2, Figure 1). Moderate increases are projected for mid-latitudes, and only small increases are projected for the Southern Ocean (*medium confidence*) (Hayashida et al., 2020b). While under the SSP5-8.5 scenario, permanent MHWs (more than 360 days per year) are projected to occur in the 21st century in parts of the tropical ocean, the Arctic Ocean and around 45°S, the occurrence of such permanent MHWs can largely be avoided under the SSP1-2.6 scenario (Frölicher et al., 2018; Oliver et al., 2019; Plecha and Soares, 2020). The resolution of current climate models (CMIP5 and CMIP6) capture the broad features of MHWs, but they may have a bias towards weaker and longer MHWs in the historical period (*medium confidence*) (Frölicher et al., 2018; Pilo et al., 2019; Plecha and Soares, 2020) and greater intensification in western boundary current regions (Hayashida et al., 2020b).

[END BOX 9.2 HERE]

9.2.2 Changes in Heat and Salinity

9.2.2.1 Ocean Heat Content and Heat Transport

Ocean warming, i.e., changing ocean heat content, is an important aspect of energy on Earth: the SROCC (Bindoff et al., 2019) reported that there is *high confidence* that ocean warming during 1971-2010 dominated the increase in the Earth's energy inventory, which is confirmed by the Box 7.2 assessment that the ocean has stored 91% of the total energy gained from 1971 to 2018. As reported in Sections 2.3.3.1, 3.5.1.3 and 7.2.2.2, Box 7.2 and Cross-Chapter Box 9.1, confidence in the assessment of global ocean heat content (OHC) change since 1971 is strengthened compared to previous reports and extended backward to include *likely* warming since 1871. Table 7.1 updates the estimates of total ocean heat gains from 1971 to 2018, 1993 to 2018 and 2006 to 2018. Section 3.5.1.3 assesses that it is *extremely likely* that anthropogenic forcing was the main driver of the OHC increase over the historical period. Section 2.3.3.1 reports that current multidecadal to centennial rates of OHC gain are greater than at any point since the last deglaciation (*medium confidence*).

Ocean warming is not uniform with depth. The AR5 (Rhein et al., 2013) assessed that since 1971 ocean warming was *virtually certain* for the upper 700 m and *likely* for the 700-2000 m layer. Both the AR5 and the SROCC (Bindoff et al., 2019) assessed that the deep ocean below 2000 m had *likely* warmed since 1992, especially in the Southern Ocean. Section 2.3.3.1 provides an updated assessment of ocean temperature change for different depth layers, different time periods and different observation-based reconstructions (Table 2.7). Section 2.3.3.1 confirms the previous assessment that it is *virtually certain* that the upper ocean (0-700m) has warmed since 1971, that ocean warming at intermediate depths (700-2000 m) is *very likely* since 2006, and that it is *likely* that ocean warming has occurred below 2000 m since 1992. Section 3.5.1.3 assessed that it is *extremely likely* that human influence was the main driver of the ocean heat content increase observed since the 1970s, which extends into the deeper ocean (*very high confidence*), and shows

ACCEPTED VERSION SUBJECT TO FINAL EDITING

that biases in potential temperature have a complex pattern (Figure 3.25). In the present section, we assess the regional patterns of this warming and associated processes driving regional ocean warming.

The rate of ocean warming varies regionally, with some regions having experienced slight cooling (Figure 9.6). The SROCC (Bindoff et al., 2019) assessed that ocean warming in the 0-700 m is globally widespread, with slower than global average warming in the subpolar North Atlantic. The SROCC (Meredith et al., 2019) also estimated that the Southern Ocean accounted for ~75% of global ocean heat uptake during 1870–1995 and that 35-43% of the upper 2000 m global ocean warming occurred in the Southern Ocean over 1970-2017 (45-62% for 2005-2017). The SROCC noted that this interhemispheric asymmetry might at least partially be explained by high concentrations of aerosols in the northern hemisphere. Here, we confirm these assessments, bring new evidence attributing these regional trends, and discuss the role of decadal ocean circulation variability in redistributing heat, driving interhemispheric asymmetry of the recent rate of ocean warming (Rathore et al., 2020; Wang et al., 2021b). Since the SROCC, one new study shows that the subpolar North Atlantic "warming hole" observed since the 1980s has emerged from internal climate variability and can be attributed to greenhouse gas emissions (Chemke et al., 2020). A new analysis of a suite of climate models (Hobbs et al., 2020) confirms the SROCC assessment, based on one paper (Swart et al., 2018), attributing the observed Southern Ocean warming to anthropogenic forcing. Given the large fraction of global ocean warming in the Southern Ocean and the sparse observations there before 2005, there is *limited evidence* that global OHC increase since 1971 might have been underestimated (Cheng and Zhu, 2014; Durack et al., 2014). Cross-Chapter Box 9.1 accounts for an increased error before 2005 in global OHC change. In summary, in the upper 2000 m since the 1970s, the subpolar North Atlantic has been slowly warming, and the Southern Ocean has stored a disproportionally large amount of anthropogenic heat (*medium confidence*).

[START FIGURE 9.6 HERE]

Figure 9.6: Ocean heat content (OHC) and its changes with time. (a) Time series of global ocean heat content anomaly relative to a 2005-2014 climatology in the upper 2000m of the ocean. Shown are observations (Ishii et al., 2017; Baggenstos et al., 2019; Shackleton et al., 2020), model-observation hybrids (Cheng et al., 2019; Zanna et al., 2019a), and multi-model means from the CMIP6 historical (29 models) and SSP scenarios (label subscripts indicate number of models per SSP). (b-g) Maps of Ocean Heat Content across different time periods, in different layers, and from different data sets/experiments. Maps show the CMIP6 ensemble bias and observed (Ishii et al., 2017) trends of OHC for (b, c) 0-700m for the period 1971-2014, and (e, f) 0-2000m for the period 2005-2017. CMIP6 ensemble mean maps show projected rate of change 2015-2100 for (d) SSP5-8.5 and (g) SSP1-2.6 scenarios. Also shown are the projected changes in 0-700m OHC for (d) SSP1-2.6 and (g) SSP5-8.5 in the CMIP6 ensembles, for the period 2091-2100 versus 2005-2014. No overlay indicates regions with high model agreement, where ≥80% of models agree on the sign of change; diagonal lines indicate regions with low model agreement, where <80% of models agree on the sign of change (see Cross-Chapter Box Atlas.1 for more information). Further details on data sources and processing are available in the chapter data table (Table 9.SM.9).

[END FIGURE 9.6 HERE]

Below 2000 m, direct observations of full-depth ocean temperature change are limited to ship-based, high-quality deep ocean temperature measurements. Such high quality full-depth ship-based sampling has improved from 1990 to the present due to the World Ocean Circulation Experiment (WOCE) and the Global Ocean Ship-based Hydrographic Investigations Program (GO-SHIP) (Sloyan et al., 2019). The SROCC (Bindoff et al., 2019) assessed that the *likely* warming of the ocean since the 1990s below 2000 m is associated with a marked regional pattern, with larger warming in the Southern Ocean. In the deep North Atlantic, warming has reversed to cooling over the past decade, possibly due to internal variability fed by North Atlantic Deep Water (Section 9.2.2.3). Over the past decade, the warming rate of Antarctic Bottom Water (AABW, Section 9.2.2.3) has been dependent on origin: slower from the Weddell Sea and faster from the Ross Sea and Adélie Land. One new study (Purkey et al., 2019a) strengthens confidence in AABW warming: below 4000 m a monotonic, basin-wide, and multidecadal temperature change is found in the

ACCEPTED VERSION SUBJECT TO FINAL EDITING

southern Pacific basin, with larger warming rates near the bottom water formation sites than further downstream. New analysis of one model provides *limited evidence* that the sparse observational record may underestimate the rate of deep ocean warming over 1990-2010 by about 20% (Garry et al., 2019) which is included in the assessed OHC error (Cross-Chapter Box 9.1). There is still *low agreement* in deep ocean changes from ocean data-assimilation reanalyses (Palmer et al., 2017) and *low confidence* in such inferences. In summary, while observational coverage below 2000 m is sparser than in the upper 2000 m, there is *high confidence* that deep ocean warming below 2000 m has been larger in the Southern Ocean than in other ocean basins due to widespread AABW warming.

[START FIGURE 9.7 HERE]

Figure 9.7: Meridional-depth profiles of zonal-mean potential temperature in the ocean and its rate of change in the upper 2000m of the Global, Pacific, Atlantic, and Indian Oceans. Shown are (a, e, i, m) observed temperature (Argo climatology 2005-2014), (b, f, j, n) bias of the CMIP6 ensemble over this period, and future changes under (c, g, k, o) SSP1-2.6 and (d, h, l, p) SSP5-8.5. No overlay indicates regions with high model agreement, where ≥80% of models agree on the sign of change; diagonal lines indicate regions with low model agreement, where <80% of models agree on the sign of change (see Cross-Chapter Box Atlas.1 for more information). Further details on data sources and processing are available in the chapter data table (Table 9.SM.9).

[END FIGURE 9.7 HERE]

Different processes drive OHC patterns over a range of timescales. Recent literature has highlighted the role of ocean circulation variability in driving OHC patterns by decomposing the global pattern of OHC change into a combination of added heat due to climate change taken up under fixed ocean circulation ("added heat"), and redistribution of heat associated with changing ocean currents ("redistributed heat") (Gregory et al., 2016; Bronselaer and Zanna, 2020; Couldrey et al., 2020). Redistributed heat alters regional patterns of heat storage (and carbon storage; Cross-Chapter Box 5.3) (Bronselaer and Zanna, 2020; Couldrey et al., 2020; Todd et al., 2020) but does not affect the global OHC. There is *medium confidence* that decadal variability of the ocean circulation strengthened the rate of ocean warming in the Southern Hemisphere compared to the Northern Hemisphere in the decade from 2005 (Rathore et al., 2020; Wang et al., 2020; Zika et al., 2021). More generally, since 2005, the OHC pattern observed is predominantly due to heat redistribution with regions of both warming and cooling (Zika et al., 2021) (Figure 9.6) but extending analysis back to 1972 shows the importance of added heat setting a large-scale warming pattern with mid-latitude maxima consistent with subduction of water masses, particularly in Southern Hemisphere Mode Waters (Section 9.2.2.3;Figures 9.6, 9.8) (Bronselaer and Zanna, 2020). The longer the analysis window, the more added heat dominates over redistributed heat. This translates into more ocean area with statistically significant warming trends and less area with statistically significant cooling trends (Johnson and Lyman, 2020). The region where added heat is most compensated for by redistributed cooling is in the northern North Atlantic basin, where changes in the subpolar gyre circulation and AMOC result in cooling (Section 9.2.3.1) (Williams et al., 2015b; Piecuch et al., 2017; Zanna et al., 2019a; Bronselaer and Zanna, 2020). In summary, and strengthening the SROCC assessment, ocean warming is not globally uniform due to patterns of uptake predominantly along known water mass pathways, and due to changing ocean circulation redistributing heat within the ocean (*high confidence*).

[START FIGURE 9.8 HERE]

Figure 9.8: Decomposition of ocean simulated ocean heat content and northward heat transport. (a, c, e) Total ocean heat content (0-2000 m) warming rate as observed and simulated by CMIP5 models over the historical period (1951-2011) and under the RCP8.5 future (2011-2060) versus the associated decomposed (b, d, f) added heat contribution (neglecting changes in ocean circulation) to the total (Bronselaer and Zanna, 2020). (g) Relationship between northward heat transport and Atlantic Meridional Overturning Circulation in HighResMIP models (1950-2050) and observations during the RAPID period

ACCEPTED VERSION SUBJECT TO FINAL EDITING

(2004-2018). Further details on data sources and processing are available in the chapter data table (Table 9.SM.9).

[END FIGURE 9.8 HERE]

While heat redistribution reflects changes in ocean circulation and is a useful concept to understand the underlying processes driving OHC patterns, change in ocean heat transport (OHT) arises due to changes in both ocean circulation and ocean temperature and affects regional OHC change. The AR5 did not assess change in OHT and the SROCC (Meredith et al., 2019) only assessed projected OHT increases into the Nordic Seas and the Arctic Ocean. New evidence of increasing northward OHT into the Arctic has been observed in recent decades (Muilwijk et al., 2018; Wang et al., 2019b; Tsubouchi et al., 2021), similar to the SROCC assessment, and consistent with observed increase in OHC in the ice free Arctic ocean (Mayer et al., 2019). It is estimated that an increase of 0.021 PW of OHT occurred after 2001 into the Arctic, which is sufficient to account for the recent OHC change in the northern seas (Tsubouchi et al., 2021). However, these trends cannot yet be attributed to anthropogenic forcing due to potential internal variability (Muilwijk et al., 2018; Wang et al., 2019b). New evidence strengthens the case that ENSO and the Northern Annular Mode affect interannual OHT variability (Trenberth et al., 2019) and shows that a slowing AMOC reduces northward OHT in the Atlantic at 26.5°N (Bryden et al., 2020) (Section 9.2.3.1, Figure 9.8). Despite a decrease of AMOC northward heat (0.17 PW) and mass (2.5 Sv) transport, OHT has increased toward the Arctic through increased upper northern North Atlantic temperatures and stronger wind-driven gyres (*medium confidence*) (Section 9.2.3.4, Figure 9.11) (Singh et al., 2017; Oldenburg et al., 2018a). In summary, OHT has increased toward the Arctic in recent decades, which at least partially explains the recent OHC change in the Arctic (*medium confidence*).

Major volcanic eruptions have caused interannual to decadal cooling phases within the marked long-term increase in global OHC (Agung in 1963, El Chichón in 1982 and Pinatubo in 1991; Cross-Chapter Box 4.1) (Church et al., 2005; Fasullo et al., 2016; Stevenson et al., 2016; Fasullo and Nerem, 2018). In the first few years following an eruption, heat exchange with the subsurface ocean allows atmospheric cooling to be sequestered into the seasonal thermocline, therefore reducing the magnitude of the peak atmospheric temperature anomaly (Gupta and Marshall, 2018). However, while explosive volcanic eruptions only disturb the Earth's radiative budget and surface fluxes for a few years, the ocean preserves an anomaly in OHC in the upper 500m (also affecting thermosteric sea level) many years after the eruption (Gupta and Marshall, 2018; Bilbao et al., 2019). The anomaly affects the atmosphere through air-sea heat fluxes with surface conditions returning to normal only after several decades (Gupta and Marshall, 2018; Bilbao et al., 2019), or on centennial time-scales in the case of repeated eruptions (Miller et al., 2012a; Atwood et al., 2016; Gupta and Marshall, 2018). In summary, there is *medium confidence* that oceanic mechanisms buffer the atmospheric response to volcanic eruptions on annual timescales by storing volcanic cooling in the subsurface ocean, affecting ocean heat content and thermosteric sea level on decadal to centennial timescales.

CMIP5 and CMIP6 models simulate OHC changes that are consistent with the updated observational and improved estimates of OHC over the period 1960 to 2018 (Figures 9.6, 9.7, 9.8), and they replicate the vertical partitioning of OHC change for the industrial era, although with a tendency to underestimate OHC gain shallower than 2000 m and overestimate it deeper than 2000 m (Section 3.5.1.3). The AR5 (Flato et al., 2013) assessed that climate models transport heat downward more than the real ocean. Since the AR5, studies have shown that increasing the horizontal resolution of ocean models tends to increase agreement of vertical heat transport with observations as the dependency on ad-hoc choices of eddy parameterizations is relaxed (Griffies et al., 2015; Chassignet et al., 2020). The magnitude of the AMOC and Indonesian Throughflow affect future OHC change, e.g. through overestimated modelled downward heat pumping (Kostov et al., 2014), and there are indications of greater model consistency in these transports at higher resolution (Chassignet et al., 2020; Jackson et al., 2020a) (Figure 9.10). Climate models tend to reproduce the observed added heat, but redistributed heat is less well represented (Figure 9.8) (Bronselaer and Zanna, 2020; Dias et al., 2020; Couldrey et al., 2021). Since redistributed heat dominates historical OHC change, historical simulations poorly reproduce regional patterns, but as future OHC change will become dominated

ACCEPTED VERSION SUBJECT TO FINAL EDITING

by added heat, more skill in future modelled OHC patterns is expected (Bronselaer and Zanna, 2020). In summary, climate models have more skill in representing OHC change from added heat than from ocean circulation change (*high confidence*). Since added heat dominates over redistributed heat on a centennial scale (especially under high emissions scenarios) confidence in future modelled OHC patterns at the end of the 21st century is greater than at decadal scale.

The SROCC (Bindoff et al., 2019) assessed that the ocean will continue to take up heat in the coming decades for all plausible scenarios, and here this assessment is confirmed with *very high confidence*. The SROCC reported that compared with the observed changes since the 1970s, the warming of the ocean by 2100 would *very likely* double to quadruple for low emissions scenarios (RCP2.6) and increase 5 to 7 times for high emissions scenarios (RCP8.5). The SROCC also concluded with *high confidence* that the overall warming of the ocean would continue this century even after radiative forcing and mean surface temperatures stabilize, and SROCC projected that ocean heat content in the 0–2000 m layer will increase from 2017 to 2100 by 0.900±0.345 YJ under RCP2.6 and 2.150±0.540 YJ under RCP8.5. Updating the SROCC estimates with CMIP6 projections gives heat content increases and 17-83% ranges in the 0–2000 m layer from 1995-2014 to 2081-2100 of 1.06 (0.80 – 1.31) YJ, 1.35 (1.08 – 1.67) YJ, 1.62 (1.37 – 1.91) YJ, 1.89 (1.60 – 2.29) YJ under scenarios SSP1-2.6, SSP2-4.5, SSP3-7.0, and SSP5-8.5, respectively (Figure 9.6, Table 9.1). The two-layer model used here to calculate thermosteric sea level rise (9.SM.4) and tuned for AR6-assessed ECS (Section 7.SM.2), provides consistent 17-83% ranges of 1.18 (0.99 – 1.42) YJ, 1.56 (1.33 – 1.86) YJ, 1.90 (1.63 – 2.21) YJ, 2.23 (1.92 – 2.64) YJ under scenarios SSP1-2.6, SSP2-4.5, SSP3-7.0, and SSP5- 8.5, respectively (Table 9.1). Based on both CMIP6 models and the two-layer model, it is *likely* that, from 1995-2014 to 2081-2100, OHC will increase 2 to 5 times the amount of the 1971-2018 OHC increase under SSP1-2.6, and 4 to 8 times that amount under SSP5-8.5. CMIP6 models show that the dependence of OHC on scenarios begins only after about 2040 (Figure 9.6).

The patterns of OHC projected by CMIP6 models (Figures 9.6, 9.7) are similar to the CMIP5 projections assessed in the SROCC (Bindoff et al., 2019): faster warming in all water mass subduction regions (e.g., subtropical cells and Mode waters); deeper penetration in the centre of subtropical gyres; slower northern North Atlantic warming due to slowing AMOC; and slower subpolar Southern Ocean warming due upwelled pre-industrial water masses. Decreased aerosol forcing will allow Northern Hemisphere ocean warming to be faster and less dominated by Southern Hemisphere change (Shi et al., 2018; Irving et al., 2019). Since the SROCC, distinguishing between added and redistributed heat has aided in understanding projections (Bronselaer and Zanna, 2020; Couldrey et al., 2020; Dias et al., 2020). The near-term decades will feature patterns strongly influenced by heat redistribution and internal variability (Rathore et al., 2020). Strengthening Southern Hemisphere westerlies are projected except for stringent mitigation scenarios (Bracegirdle et al., 2020) and will cause a northward and downward OHT. There is *low agreement* in future Southern Ocean warming across model results due to uncertainties in the magnitude of westerly wind changes (Figure 9.4) (Liu et al., 2018; He et al., 2019; Dias et al., 2020; Lyu et al., 2020b) and the degree of eddy compensation of overturning across different parameterisations and resolutions (9.2.3.2) (Beal and Elipot, 2016; Mak et al., 2017; Roberts et al., 2020a). By 2100 however, the OHC change will be dominated by the added heat response, particularly for strong warming scenarios (Garuba and Klinger, 2018; Bronselaer and Zanna, 2020) with added heat following unperturbed water mass pathways in the North Atlantic and Southern Ocean (Couldrey et al., 2020; Dias et al., 2020) (Figure 9.8). There is *high confidence* that projected weakening of the AMOC (Section 9.2.3.1) will cause a decrease in northward OHT in the northern hemisphere mid-latitudes (Figure 9.8; Sections 9.2.3.1,4.3.2.3; Weijer et al., 2020) associated with a dipole pattern of Atlantic OHC redistributed from northern to low latitudes that may override added heating in the northern North Atlantic (Figures 9.6, 9.7, 9.8). Variations in the degree of AMOC redistributed heat (Menary and Wood, 2018) causes large intermodel spread in SST (Figure 9.3) and OHC (Figure 9.6) change (Kostov et al., 2014; Bronselaer and Zanna, 2020; Couldrey et al., 2020; Todd et al., 2020). In the 700-2000m depth range, CMIP5 and CMIP6 models project the largest warming to be in the North Atlantic Deep Water and Antarctic Intermediate Water (Figure 9.7) while below 2000 m, the North Atlantic cools in many models, and Antarctic Bottom Waters warm (Sallée et al., 2013b; Heuzé et al., 2015). In summary, on decadal timescales, redistribution will dominate regional patterns of OHC change without affecting the globally integrated OHC, but by 2100, particularly under strong warming scenarios, there is *high confidence* that regional patterns of OHC change will be dominated by added heat entering the sea surface primarily in

ACCEPTED VERSION SUBJECT TO FINAL EDITING

water-mass formation regions in the subtropics, with reduced aerosols increasing the relative rate of Northern Hemisphere heat uptake (*medium confidence*).

The SROCC assessed that the warming of the deep ocean is slow to manifest, with multi-century or longer response times, so global OHC (and global mean thermosteric sea level) will continue to rise for centuries (Figures 9.9, 9.30). New studies show that this continuation persists even after cessation of greenhouse gas emissions (Ehlert and Zickfeld, 2018a). Ocean warming will continue even after emissions reach zero because of slow ocean circulation (Larson et al., 2020). Ocean heat content will increase until at least 2300 even for low emission scenarios, but with a scenario-dependent rate (Nauels et al., 2017; Palmer et al., 2018) and depends not only on cumulative CO_2 emissions, but also on the time profile of emissions (Bouttes et al., 2013). Past long-term changes in total OHC illustrate adjustment relevant to expected future changes (Figure 9.9). Observational data (Figure 9.9) from ice core rare gas elemental and isotopic ratios document a rise in global OHC relative to the Last Glacial Maximum of >17,000 ZJ (change in mean ocean temperature >3.1ºC) (Bereiter et al., 2018; Baggenstos et al., 2019; Shackleton et al., 2019, 2020). This temperature increase is significantly larger than the modelled OHC changes associated with collapse of AMOC alone and tracks rising Southern Ocean SST (Uemura et al., 2018), strengthening of the deep abyssal overturning cell (Du et al., 2020) and increased North Atlantic water in the Southern Ocean (Wilson et al., 2020), underscoring the importance of Antarctic abyssal ventilation on long-term oceanic heat budgets (Section 9.2.3.2). An ensemble of four intermediate-complexity models project 10,000-year future responses to CO_2 emissions (Clark et al., 2016) with SST change peaking around 2300 with varying scenario-dependent magnitude approaching the scale of glacial-to-interglacial changes in paleodata (Figure 9.9). Long-term OHC commitments relative 1850-1900 conditions are 2.6, 9.7, 15.2, 21.6, and 28.0 YJ (with mean ocean temperature change as much as 5.1ºC) for emissions of 0, 1280, 2560, and 3840 and 5120 Gt after 2000 CE respectively, with OHC peaking near 4000 CE reflecting whole-ocean warming lagging SST by thousands of years. The exact timing is uncertain subject to rates of high-latitude meltwater input (Van Breedam et al., 2020) and circulation time (Gebbie and Huybers, 2019). In summary, there is *high confidence* that there is a long-term commitment to increased OHC in response to anthropogenic CO_2 emissions, which is essentially irreversible on human timescales.

[START FIGURE 9.9 HERE]

Figure 9.9: Long-term trends of ocean heat content and surface temperature. (a, b) Ice-core rare gas estimates of past mean ocean heat content OHC (ZJ), scaled to global mean ocean temperature (°C) and to steric GMSL (m) (red dashed line) are compared to surface temperatures (black solid line, gold solid line; °C rightmost axis). Southern Ocean SST from multiple proxies in 11 sediment cores and from ice core deuterium excess (Uemura et al., 2018). a) Penultimate glacial interval to last interglacial, 150,000-100,000 yr B2K (Shackleton et al., 2020). b) Last glacial interval to modern interglacial, 40,000-0 yr B2K (Baggenstos et al., 2019; Shackleton et al., 2019). Changes in OHC (dashed lines) track changes in Southern Ocean SST (solid lines). c) Long-term projected (2000 to 12000 CE) changes of OHC (dashed lines) in response to four greenhouse gas emissions scenarios (Clark et al., 2016) scale similarly to large-scale paleo changes but lag projected gobal mean SST (solid lines). d) model simulated 1500-1999 OHC (Gregory et al., 2006) and 1955-2019 observations (Levitus et al., 2012) updated by NOAA NODC. All data expressed as anomalies relative to pre-industrial time. Further details on data sources and processing are available in the chapter data table (Table 9.SM.9).

[END FIGURE 9.9 HERE]

9.2.2.2 Ocean Salinity

The AR5 (Rhein et al., 2013) assessed that it was *very likely* that subsurface salinity changes reflect surface salinity change, and that basin-scale regions of high salinity and evaporation had trended more saline, while regions of low salinity and more precipitation had trended fresher since the 1950s. The SROCC (Bindoff et al., 2019) assessment was consistent with the AR5. Section 2.3.3.2 strengthens evidence that subsurface salinity trends are connected to surface trends (*very likely*), which are in turn linked to an intensifying

ACCEPTED VERSION SUBJECT TO FINAL EDITING

hydrological cycle (*medium confidence*) and increasing evidence from updated observational records indicates it is now *virtually certain* that surface salinity contrasts are increasing. At basin scale, Section 2.3.3.2 and the AR5 concur that it is *very likely* that the Pacific and Southern Ocean have freshened, and the Atlantic has become more saline. Figures 3.25 and 3.27 compare CMIP6 models to salinity observations.

Globally the mean salinity contrast at near-surface between high- and low- salinity regions increased 0.14 [0.07 to 0.20] from 1950 to 2019 (Section 2.3.3.2). At regional scale, the SROCC (Meredith et al., 2019) assessed an Arctic liquid freshwater trend of 600 ± 300 km^3 yr^{-1} (600 ± 200 Gt yr^{-1}) between 1992 and 2012, reflecting changes associated with continental freshwater imports that affect ocean mass (land ice, rivers) as well as changes in sea ice volume. Since the AR5, regional observation-based analyses not assessed in the SROCC further confirm the long-term, large-scale and regional patterns of salinity change, both at the ocean surface and in the subsurface ocean, including almost 120 years of changes in the North Atlantic (Friedman et al., 2017) and 60 years of monitoring in the subpolar North Pacific (Cummins and Ross, 2020b). These longer time-series also provide context to detect large multi-annual change, from 2012 to 2016 in the subpolar North Atlantic, unprecedented over the centennial record (Holliday et al., 2020). In summary, there is *high confidence* that salinity trends have extended for more than 60-100 years in the regions with long historical observation records such as the North Pacific and the North Atlantic basin.

While there is *low confidence* in direct estimates of trends in surface freshwater fluxes (Sections 2.3.1.3.5, 8.3.1.1, 9.2.1.2), as discussed in the SROCC (Meredith et al., 2019), observational studies coupled with modelling studies suggest that surface flux changes drive many observed near-surface salinity changes, on top of changes specific to polar regions. Advances in salinity observations (e.g., the Argo program (Riser et al., 2016); SMOS, Aquarius and SMAP (Supply et al., 2018; Vinogradova et al., 2019)), combined with process-studies (SPURS-1/2; (Lindstrom et al., 2015; SPURS-2 Planning Group 2015)) and methodological and numerical advances, have increased understanding of how subsurface salinity anomalies link to surface fluxes, and thus increase confidence that near-surface and subsurface salinity pattern changes since the 1950s are linked to changing surface freshwater fluxes (Zika et al., 2018; Cheng et al., 2020) with an additional contribution from changes in sea-ice and land-ice discharge at high latitudes (Haumann et al., 2016; Purich et al., 2018; Dukhovskoy et al., 2019a; Rye et al., 2020). There is therefore *medium confidence* in the processes linking surface fluxes to surface and subsurface salinity change.

Ocean circulation changes also affect salinity, largely on annual to decadal timescales (Du et al., 2019; Liu et al., 2019; Holliday et al., 2020). For instance, in the subpolar North Atlantic, increasing northward transport of "Atlantic waters" entering the subpolar gyre from the South have compensated the salinity decrease expected from increased Greenland meltwater flux since the early 1990s (Dukhovskoy et al., 2016, 2019b; Stendardo et al., 2020). After the mid-2010s the trend reversed towards a broad freshening, the largest in 120 years, in the North Atlantic (Holliday et al., 2020). The long term freshening in the Pacific Ocean has also been subject to decadal variability, such as a marked salinification since 2005 associated with increased surface fluxes (Li et al., 2019a). Local salinity anomalies forced by water cycle intensification can be weakened by rapid exchange between basins with opposing trends, such as by water-mass exchange in shallow wind-driven cells between the tropics and the subtropics (Levang and Schmitt, 2020). Similarly, eddy exchanges between neighbouring gyres can partly counterbalance decadal time scale long-term subpolar freshening and affect deep convection (Levang and Schmitt, 2020). There is *high confidence* that, at annual to decadal timescales, regional salinity changes are driven by ocean circulation change superimposed on longer term trends.

CMIP5 historical simulations have patterns similar to, but greater spatial variability than, observed estimates and correspondingly smaller amplitudes in the multi-model mean (Durack, 2015; Cheng et al., 2020; Silvy et al., 2020a). Section 3.5.2.1 reports, however, that the fidelity of ocean salinity simulation has improved in CMIP6, and near-surface and subsurface biases have been reduced (*medium confidence*), though the structure of the biases strongly reflects those of CMIP5. At regional scale, salinity biases are at least partially a result of inaccurate ocean dynamics (Levang and Schmitt, 2020). Despite the regional limitations, Section 3.5.2.2 assesses that at the global scale it is *extremely likely* that human influence has contributed to observed surface and subsurface salinity changes since the mid-20th century (strengthened from the *very likely* AR5 assessment).

ACCEPTED VERSION SUBJECT TO FINAL EDITING

The SROCC (Bindoff et al., 2019) assessed that projected salinity changes in the subsurface ocean reflect changes in the rates of formation of water masses or their newly formed properties. Additional consistent newer evidence based on CMIP5 and regional climate models confirms that 21st century projections adhere to the fresh gets fresher, salty gets saltier paradigm, through subduction of freshening high latitude waters into the ventilated water-masses in both hemispheres in the Pacific, Indian and Southern Ocean, especially the Arctic and upper Southern Ocean, and saltier subtropical and Mediterranean surface waters lead to saltier pycnoclines and North Atlantic mode water (Metzner et al., 2020; Parras-Berrocal et al., 2020; Silvy et al., 2020a; Soto-Navarro et al., 2020). Overall, projections confirm the SROCC assessment that fresh ocean regions will continue to get fresher and salty ocean regions will continue to get saltier in the 21st century (*medium confidence*).

9.2.2.3 Water Masses

Water masses refer to connected bodies of ocean water, formed at the ocean surface with identifiable properties (temperature, salinity, density, chemical tracers) resulting from the unique formation conditions of the overlying atmosphere and/or ice, before being transferred (subducted) to the deeper ocean below the surface turbulent layer. As water masses subduct, they ventilate the subsurface ocean, transferring characteristics acquired at the ocean surface to the subsurface. By integrating surface flux changes, water masses provide higher signal-to-noise ratios for detecting and monitoring climate change than surface fluxes (Bindoff and McDougall, 2000; Durack and Wijffels, 2010; Silvy et al., 2020b).

SubTropical Mode Waters (STMW) ventilate the main thermocline of the ocean at mid- to low-latitudes and have circulation timescales away from the surface of the order of years to decades. The SROCC (Bindoff et al., 2019) reported that warming in the subtropical gyres penetrates deeper than in other gyres, following the density surfaces in these gyres. Consistently, we assess that STMW have deepened worldwide, with greatest deepening in the Southern Hemisphere (*high confidence*) (Häkkinen et al., 2016; Desbruyères et al., 2017). Subsurface warming in the Northern Hemisphere STMW is larger than at the surface (Sugimoto et al., 2017) because they are formed in wintertime western boundary current extensions, where surface warming is larger than the global average (Section 9.2.1.1). Variability in STMW thickness or temperature has a large imprint on ocean heat content (Section 9.2.2.1) (Kolodziejczyk et al., 2019). STMW are observed to be freshening in the North Pacific and to be associated with increased salinity in the North Atlantic (Oka et al., 2017; Silvy et al., 2020a), with large decadal variability (Oka et al., 2019; Wu et al., 2020). Anthropogenic temperature and salinity changes in the STMW layer are projected to intensify in the future, with emergence from natural variability around 2020 to 2040 (Silvy et al., 2020a).

SubAntarctic Mode Water (SAMW) and Antarctic Intermediate Waters (AAIW) form at the Southern Ocean surface directly north of the Antarctic Circumpolar Current and ventilate the upper 1000 m of the Southern Hemisphere subtropics. The SROCC (Meredith et al., 2019) reported a freshening of these water masses between 1950 and 2018, and they are projected to have the largest subsurface temperature increase of the Southern Hemisphere oceans, along with a continued freshening, in the 21st century. The SROCC connected SAMW and AAIW to Southern Ocean temperature changes as the large Southern Ocean surface heat uptake is circulated and mixed along with these water masses (*high confidence*). Close to its formation region, SAMW is predominantly affected by air-sea flux changes, while further northward it is influenced by wind-forced changes (Meredith et al., 2019). New evidence shows that a change in SAMW heat content over the last decade is primarily attributable to its thickening (Kolodziejczyk et al., 2019). Over the past decade, the SAMW and AAIW volumes have changed by thickening of the lighter and thinning of the denser parts of SAMW and AAIW, leading to lightening of these ventilated ocean layers overall (Hong et al., 2020; Portela et al., 2020). Over the last decade, there is *limited evidence* of increased subduction of SAMW due to deepening mixed layers in the SAMW formation region (9.2.1.3) (Qu et al., 2020). Climate models from CMIP3 to CMIP5 generally simulated shallower and lighter SAMW and AAIW than is observed (Flato et al., 2013). New analysis of CMIP5 models suggests that the freshening of these water masses is one of the most prominent projected salinity changes in the world ocean, and that this freshening emerged from internal variability as early as the 1980–1990s (Silvy et al., 2020b).

ACCEPTED VERSION SUBJECT TO FINAL EDITING

Trends in North Atlantic Deep Water (NADW) are obscured by decadal variability (Rhein et al., 2013; Bindoff et al., 2019). The AR5 (Rhein et al., 2013) assessed that it is *very likely* that the temperature, salinity, and formation rate of the Upper NADW (formed by deep convection in the Labrador and Irminger Seas) is dominated by strong decadal variability related to the North Atlantic Oscillation (NAO) and it is *likely* that Lower NADW (formed in the Nordic Seas and supplied to the North Atlantic by deep overflows over the sills between Scotland and Greenland) cooled from 1955 to 2005. New insights from observations have emphasized the stability of the deep overflows associated with Lower NADW (Hansen et al., 2016; Jochumsen et al., 2017; Østerhus et al., 2019) and even slight warming in the Faroe Bank Channel (Hansen et al., 2016). As a result, the AR5 assessment that Lower NADW *likely* cooled between 1955 and 2005 is revised to: it is *likely* that any observed changes in temperature, salinity, and formation rate of the Lower NADW are dominated by decadal variability. For CMIP5 models it was shown that AMOC variability is linked to variability in NADW formation (Heuzé, 2017) and projected AMOC decline to decreased NADW formation (both Lower NADW and Upper NADW) (Heuzé et al., 2015). For CMIP6 models, projected AMOC decline is also associated with a decline in NADW formation (Reintges et al., 2017; Weijer et al., 2020). The link between AMOC and NADW formation appears insensitive to the large range in model bias in NADW water mass characteristics (Heuzé, 2017). Many models may overestimate deep water formation in the Labrador Sea, but at least one new model is consistent with recent OSNAP observations showing very weak overturning in the western subpolar gyre, where Labrador Sea Water is formed (Menary et al., 2020a). CMIP6 models show a reduced bias in NADW properties compared to CMIP5 models, but still feature varying locations of deep convection in the subpolar gyre: some convect only in the Labrador Sea (6/35 models), most in both the Labrador and Irminger Seas (26/35 models; as is observed), and some only in the Irminger Sea (3/35 models), but in general the area where deep convection takes place has expanded relative to CMIP5, which appears unrealistic (Heuzé, 2021). Models with most deep convection in the subpolar gyre feature the smallest bias in NADW characteristics, partly associated with NADW formed in the Nordic Seas (as observed) being largely unable to leave the area (Heuzé, 2021) due to inaccurate overflows (Danabasoglu et al., 2010; Deshayes et al., 2014; Wang et al., 2015b). Despite the wide range in model bias, it remains *very likely* that any long-term (multi-decadal or longer) decrease in AMOC is accompanied by a decline in NADW formation, associated with lighter densities in the northern North Atlantic and Arctic basins.

The SROCC (Meredith et al., 2019) assessed that the global volume of Antarctic Bottom Water (AABW) had decreased and warmed since the 1980s, most noticeably near Antarctica. The SROCC also noted freshening in the Indian and Pacific sectors of the Southern Ocean and a higher rate of freshening in the Indian Sector from the 2000s to 2010s than from the 1990s to 2000s (*low confidence*). Since the SROCC, freshening of Indian Ocean AABW from 1974 to 2016 has been revealed (Aoki et al., 2020). Additionally, interannual to decadal variability in AABW has been quantified to be larger than previously thought in terms of temperature, salinity and thickness, and in volume transport (Abrahamsen et al., 2019; Purkey et al., 2019b; Gordon et al., 2020; Silvano et al., 2020). Multidecadal-to-centennial modes of variability could have driven the observed trends of the lower cell over the past decades via the opening of a Weddell Sea polynya (Zhang et al., 2019b), although other studies find it contributed minimally to the observed abyssal warming (Zanowski et al., 2015; Zanowski and Hallberg, 2017). Therefore, there is *limited evidence* and *low agreement* in the role of open ocean polynyas in driving past decadal observed trends of AABW. Beyond variability, all observational, theoretical, and numerical evidence supports the SROCC assessment that formation and export of AABW will continue to decrease due to warming and freshening of surface source waters near the Antarctic continent. Consistent with Section 9.2.3.2, confidence in this assessment is increased to *medium confidence* compared to the SROCC.

Circumpolar Deep Water (CDW) lies in the Southern Ocean and forms by mixing of North Atlantic Deep Water and Antarctic Bottom Water (Talley, 2013). The SROCC (Meredith et al., 2019) assessed with *low confidence* that mean southward and upward CDW transport is linked to decadal wind variability (Section 9.2.3.2), and that CDW has warmed south of the Antarctic Circumpolar Current (ACC) in the past decades. New evidence reinforces the SROCC assessment: changes in Southern Ocean wind stress have been confirmed to drive variability and increase the large-scale southward CDW transport (Waugh et al., 2019). In addition, growing evidence suggests that the upper ocean stratification increase in the subpolar Southern Ocean since the 1970s (Section 9.2.1.3) has reduced the volume of CDW that is mixed to the surface, causing subsurface CDW warming (Bronselaer et al., 2020; Haumann et al., 2020; Jeong et al., 2020;

ACCEPTED VERSION SUBJECT TO FINAL EDITING

Moorman et al., 2020). Large regions of the Antarctic shelves are currently isolated from warm CDW (Thompson et al., 2018; Jourdain et al., 2020). The SROCC (Meredith et al., 2019) assessed that subsurface warming extends close to Antarctica and has co-occurred with shoaling of the CDW since the 1980s, influencing the continental shelf most in the Amundsen-Bellingshausen Seas, Wilkes Land, and the Antarctic Peninsula. New evidence since the SROCC reinforces confidence in the importance of the role of winds in transporting heat associated with CDW to continental shelves and ice cavities in the Amundsen-Bellingshausen Seas (Dotto et al., 2019) and via variable small-scale undercurrents to the Shirase Glacier Tongue in East Antarctica (Hirano et al., 2020; Kusahara et al., 2021). There is *limited evidence* that increased greenhouse gas forcing has caused a slight mean change of the local winds from 1920-2018 facilitating CDW heat intrusion onto the Amundsen-Bellingshausen continental shelf and ice-shelf melt (Holland et al., 2019). Multiple lines of observational, numerical, theoretical, and paleo evidence provide *high confidence* that changes in wind pattern (Spence et al., 2014; Dotto et al., 2019; Holland et al., 2019), increased ice-shelf melt (Golledge et al., 2019a; Moorman et al., 2020), reduction in sea-ice production (Timmermann and Hellmer, 2013; Obase et al., 2017), and eddies (Stewart and Thompson, 2015; Thompson et al., 2018) can facilitate access of CDW to the sub-ice-shelf cavities (9.4.2.1). However, there is *low confidence* in the quantitification, importance and the ability of present models, especially at coarse resolution, to project changes in each of these processes (9.4.2.2). Some studies have projected a possible shift from cold to warm sub-ice shelf cavities causing a sudden flush of warm water underneath ice shelves, but there is *low confidence* both in the driving processes and the threshold to trigger the shift (Box 9.4) (Hellmer et al., 2012, 2017; Silvano et al., 2018; Hazel and Stewart, 2020).

9.2.3 Regional Ocean Circulation

9.2.3.1 Atlantic Meridional Overturning Circulation

The Atlantic meridional overturning circulation (AMOC) is the main overturning current system in the South and North Atlantic Oceans. It transports warm upper-ocean water northwards, and cold, deep water southwards, as part of the global ocean circulation system (Section 2.3.3.4.1). AMOC changes influence global ocean heat content and transport (Section 9.2.2.1); global ocean anthropogenic carbon uptake changes and climate sensitivity (Cross-Chapter Box 5.3); and dynamical sea level (Section 9.2.4). Since the AR5/SROCC, confidence in modelled and reconstructed AMOC has decreased due to new observations and model disagreement. Confidence in modelled AMOC evolution during the 20th century, the magnitude of 21st century AMOC decline, and the possibility of an abrupt collapse before 2100 have been revisited.

The AR5 (Flato et al., 2013) found that the mean AMOC strength in CMIP5 models ranges from 15 to 30 Sv for the historical period. The multi-model mean overturning at 26°N in CMIP5 and CMIP6 is comparable to the RAPID measurements (Reintges et al., 2017), but the inter-model spread in CMIP6 is as large (10-31 Sv) as in CMIP5 ((Weijer et al., 2020); Section 3.5.4). Biases in simulations of the present day AMOC and associated deep convection in the subpolar gyre and Nordic Seas were large in CMIP5 models with many models exhibiting ocean convection that is too deep, over too large an area, too far south and occurring too frequently (Heuzé, 2017) (Section 9.2.1.3; Figure 9.5) related to biases in sea-ice extent, overflows, and freshwater forcing (Deshayes et al., 2014; Wang, Legg and Hallberg, 2015). As a result, the AMOC in CMIP5 was nearly always too shallow, with too weak a temperature contrast between the northward and southward flowing branches. Deep convection errors are still large in CMIP6 and the shallow bias in AMOC persists (Weijer et al., 2020; Heuzé, 2021). Since the AR5, there is emerging evidence that enhancing horizontal resolution can reduce longstanding climate model biases in AMOC strength, where the magnitude and profile of northward heat transport at 26°N become more comparable to observations (Chassignet et al., 2020; Roberts et al., 2020a). The sensitivity of the AMOC to ocean resolution, however, is model-dependent and can be positive as well as negative (Roberts et al., 2020b). An increase in AMOC strength at 26°N with higher resolution in the ocean component has been associated with too strong (deep) convection in the subpolar gyre and too deep winter mixed layers (Jackson et al., 2020a), which occurs in most CMIP6 models that are unable to overflow deep water formed in the Nordic Seas across the Greenland-Iceland-Scotland Ridge. Thus models with a correct AMOC strength may do so by compensating a lack of deep water outflow from the Nordic Seas through too much deep convection and deep-water formation in the Labrador and

ACCEPTED VERSION SUBJECT TO FINAL EDITING

Irminger Seas (Heuzé, 2021).

Models and paleo-reconstructions have often assumed a close relation between the AMOC and deep convection in the Labrador Sea, and Labrador Sea convection variability has been interpreted as connecting to AMOC variability. Observational studies have been inconclusive on whether this relation exists (Buckley and Marshall, 2016). New insight from observed overturning in the eastern and western subpolar gyre in the North Atlantic in OSNAP (Lozier et al., 2019; Petit et al., 2020) reveal that 15.6±3.1Sv takes place north of the OSNAP array between Greenland and Scotland, with only 2.1±0.9 Sv of overturning occurring across the Labrador Sea as found with the OSNAP 53ºN array spanning the mouth, explicitly questioning the validity of the Labrador Sea convection-AMOC link (Lozier et al., 2019). Although their results are derived from only the first 21 months of data of monitoring since 2014, hydrographic observations during 1990-1997 previously found small overturning (1-2 Sv) in the Labrador Sea (Pickart and Spall, 2007). On the other hand, previous estimates of Labrador Sea Water formation (obtained with different techniques) suggest larger overturning (Haine et al., 2008). Part of this controversy could be explained if a large fraction of newly formed Labrador Sea Water is not exported from the Labrador Sea. The OSNAP observations are supported by previous hydrographic measurements in showing strong east-west symmetry in isopycnal slope in the Labrador Sea in periods of both strong and weak convection, implying compensating northward and southward transport above and below the potential density surface that separates the upper and lower overturning limbs (Lozier et al., 2019), despite large deep convection variability (Yashayaev, 2007; Yashayaev and Loder, 2016). New observations of deep winter mixing in the Irminger Basin (de Jong et al., 2018; Josey et al., 2019) support the assertion that the Irminger Sea, in addition to the Nordic Seas (Chafik and Rossby, 2019), are the main sources of overturning in the eastern subpolar gyre, consistent with OSNAP (Petit et al., 2020). It is unclear to what extent models are in disagreement with this view of overturning in the subpolar gyre, as a direct comparison with OSNAP in terms of partitioning the overturning in a western and eastern part is lacking for most models, with a notable exception (Menary et al., 2020a). The analysis of water mass formation in CMIP6 models (Heuzé, 2021); the analysis between Labrador Sea water formation and AMOC in a suite of ocean-only models (Danabasoglu et al., 2014); the fact that when the OSNAP observing system design was tested in an eddy-permitting ocean model, almost equal amounts of overturning in the western and eastern subpolar gyre were found (Lozier et al., 2017), give rise to considerable uncertainty over the models' veracity in simulating the overturning partitioning between east and west and the role of various drivers of AMOC variability. Disagreement between models and OSNAP observations may decrease in higher-resolution models (Menary et al., 2020a). In summary, multiple lines of evidence provide *medium agreement* between models and observations on drivers of change and variability in the AMOC and in particular the role of Labrador Sea deep convection in constituting AMOC variability.

The AMOC is a potential driver of Atlantic Multidecadal Variability (AMV), but there is new evidence that anthropogenic aerosol changes have contributed to observed AMV changes, and that underestimation of the magnitude and duration of AMV changesin CMIP5 is tempered in CMIP6 (Section 3.7.7, Annex IV.2.7). Comparison of observed AMOC variability at the RAPID section with modelled variability reveals that CMIP5 models appear to largely underestimate the interannual and decadal timescale variability (Roberts et al., 2014; Yan et al., 2018), and similar results are found when analysing CMIP6 models (Section 3.5.4.1). By underestimating the multi-decadal AMOC-AMV link and other low-frequency AMOC variability climate models also underestimate internal variability in subpolar SSTs that feedback on the North Atlantic Oscillation (NAO), causing the NAO to lack variability on multidecadal timescales (Kim et al., 2018). Despite the role of the AMOC in generating AMV through subsurface temperatures in antiphase with SST and downward heat fluxes into the ocean that anticorrelate with SSTs (Zhang et al., 2019d), it is generally accepted that AMOC forcing of SST variability exists alongside stochastic wind forcing and external forcing by aerosols (Bellomo et al., 2018; Haustein et al., 2019; O'Reilly et al., 2019; Wills et al., 2019).

The SROCC (Collins et al., 2019) assessed that in situ observations (2004–2017) and sea surface temperature reconstructions indicate that the AMOC has weakened relative to 1850–1900 (*medium confidence*). However, the SROCC also assessed that there is insufficient data to quantify the magnitude of the weakening, or to properly attribute it to anthropogenic forcing, due to the limited length of the observational record. Here, this assessment is adjusted to *low confidence*in the weakening as also discussed in Sections 2.3.3.4.1 and 3.5.4.1. The CMIP5 multi-model mean showed no 20th century trend in the AMOC

ACCEPTED VERSION SUBJECT TO FINAL EDITING

(Cheng et al., 2013). The CMIP6 multi-model mean even slightly opposes the reconstructed decline due to a strong increase in the 1940-1985 period (Menary et al., 2020c; Weijer et al., 2020), thought to be in response to aerosol forcing (Section 3.5.4.1), followed by a smaller decline since the nineties. Also, agreement between different proxy-based reconstructions is weak in many details (Moffa-Sánchez et al., 2019) and questions can be raised regarding various proxies used in reconstructions (Section 2.3.3.4.1). For instance, SST-based proxies can be influenced by atmospheric and other processes acting on different timescales (Moffa-Sánchez et al., 2019; Jackson and Wood, 2020). In addition, many proxies are indirect and based on AMOC-related processes assumed to be similar as found in models, such as the link between AMOC and Labrador Sea convection, which has been questioned recently (see above). In addition, the subpolar gyre from which many AMOC-proxies are taken may vary independently of the AMOC with rather similar patterns in SST and ocean heat content driven by wind variability (Williams et al., 2014; Piecuch et al., 2017). Finally, a new dynamic reconstruction of the Atlantic inflow to the Nordic Seas suggest no slowdown over the past 70-100 years (Rossby et al., 2020), in contrast to a new compilation of proxy reconstructions which suggests that the AMOC is presently in its weakest state in the last millennium (Caesar et al., 2021), reinforcing the evidence that motivated the previous SROCC assessment. Section 3.5.4.1 also questions the veracity of the models' forced AMOC response during the twentieth century. Given the large discrepancy between modelled and reconstructed AMOC in the twentieth century and the uncertainty over the realism of the 20th century modelled AMOC response (Section 3.5.4.1), we have *low confidence* in both.

The strength of the AMOC has been measured directly since 2004 using the RAPID Array (Smeed et al., 2018) (Section 2.3.3.4.1). RAPID-based estimates show a large amount of variability compared to CMIP models (Roberts et al., 2014). Observed changes since 2004 are too short for the evaluation of a long-term trend given the decadal scale internal variability (Section 2.3.3.4.1). Nevertheless, Smeed et al. (2018) argue that between 2007 and 2011 the AMOC shifted to a state of reduced overturning; decreasing from 18.8 Sv between 2004 and 2008 to 16.1 Sv after 2008. A shift in AMOC strength of this magnitude is not captured by CMIP5 and CMIP6 models, which generally underestimate interannual to decadal AMOC variability (Section 3.5.4.1). Additional evidence since SROCC also raises the inconsistency between the RAPID weakening in the 3000-5000 m depth range and the relative constancy of deep overflows from the Arctic (Østerhus et al., 2019), implying that the recent decrease in AMOC at 26.5ºN (Smeed et al., 2018) is not caused by overflow weakening or reduced overturning in the Nordic Seas, although the weakening occurred almost exclusively in the 3000 – 5000 m depth range associated with a reduction of Lower NADW (Section 9.2.2.3). It is unclear what causes a weakening of the deepest limb of the AMOC at 26.5ºN, if the main sources for this flow farther north remain constant. Various estimates of AMOC and associated heat transport suggest an increase since the 1940s with a subsequent decrease since the 1990s (Section 2.3.3.4.1), supported by ocean reanalysis (Jackson et al., 2019), forced ocean model simulations (Robson et al., 2012; Danabasoglu et al., 2016) and CMIP6 simulations (Menary et al., 2020b). This suggests that the observed AMOC-shift between 2007 and 2011 may be part of a longer-term decrease (*medium confidence*), which has been attributed to be part of multiannual variability (Rhein et al., 2019).

[START FIGURE 9.10 HERE]

Figure 9.10: AMOC strength in simulations and sensitivity to resolution and forcing. (Top left) AMOC magnitude in PMIP experiments. (Top right) Time series of AMOC from CMIP5 and CMIP6 based on (Menary et al., 2020c). (Bottom left) Percent change in AMOC strength per year at different resolutions over the 1950-2050 period with colours for model families (Roberts et al., 2020b). (Bottom right) A compilation (Jackson and Wood, 2018) of percentage changes in the simulated AMOC after applying an additional freshwater flux in the subpolar North Atlantic at the surface for a limited time (de Vries and Weber, 2005; Stouffer et al., 2006; Yin and Stouffer, 2007; Jackson, 2013; Liu and Liu, 2013; Jackson and Wood, 2018; Haskins et al., 2019). Symbols indicate whether the AMOC recovers within 200 years (circles), is starting to recover (upwards arrow) or does not recover within 200 years (downwards arrow). Symbol size indicates rate of freshwater input. Further details on data sources and processing are available in the chapter data table (Table 9.SM.9).

[END FIGURE 9.10 HERE]

ACCEPTED VERSION SUBJECT TO FINAL EDITING

The SROCC (Collins et al., 2019) found that the AMOC will *very likely* weaken over the 21st century. In CMIP6 projections, the modelled decline starting in the 1990s continues in all future projections, almost independent of the forcing scenario until about 2060, after which low emission scenarios show stabilization, while high-emission scenarios continue to exhibit AMOC decline (Figure 9.10) (Menary et al., 2020b, Weijer et al., 2020).Despite differences in overall AMOC strength, location and latitude of deep convection, sea-ice and SST bias and representation of deep overflows, the model projections are qualitatively similar. This agreement suggests that AMOC decline may be governed by large-scale constraints independent of the details of the models. In theoretical models of the thermohaline circulation, the circulation strength is proportional to a density or pressure difference between the subpolar North Atlantic and subtropical South Atlantic (Kuhlbrodt et al., 2007; Weijer et al., 2019). In all models, the north-south pressure gradient decreases in the 21st century, as subpolar waters warm faster than subtropical waters and an enhanced hydrological cycle drives freshening at subpolar latitudes, while subtropical latitudes feature more evaporation and salinification (Section 9.2.1). As a result, surface waters at subpolar latitudes become more buoyant and more stable, so that deep water formation driving the AMOC declines (Section 9.2.1.3). Projected AMOC decline by 2100 ranges from 24% (4-46%) in SSP1-2.6 to 39% (17-55%) in SSP5-8.5 (*medium confidence*; Section 4.3.2.3). Note that these ranges are based on ensemble means of individual models, largely smoothing out internal variability. If single realisations are considered the ranges become larger, lowering especially the low end of the range (Section 4.3.2.3). In summary, it is *very likely* that AMOC will decline in the 21st century, but there is *low confidence* in the models' projected timing and magnitude. In addition, freshwater from the melting of the Greenland ice sheet (Sections 9.4.1.3, 9.4.1.4) could further enhance the future weakening of the AMOC in the 21st century (Collins et al., 2019; Golledge et al., 2019).

Both the AR5 (Collins et al., 2013) and the SROCC (Collins et al., 2019) assessed that an abrupt collapse of the AMOC before 2100 was *very unlikely*, but the SROCC added that by 2300 an AMOC collapse was *as likely as not* for high-emission scenarios. The SROCC also assessed that model-bias may considerably affect the sensitivity of the modelled AMOC to freshwater forcing. Tuning towards stability and model biases (Valdes, 2011; Liu et al., 2017; Mecking et al., 2017; Weijer et al., 2019) provides CMIP models a tendency toward unrealistic stability (*medium confidence*). By correcting for existing salinity biases, Liu et al. (2017) demonstrated that AMOC behaviour may change dramatically on centennial to millennial timescales and that the probability of a collapsed state increases. None of the CMIP6 models features an abrupt AMOC collapse in the 21st century, but they neglect meltwater release from the Greenland ice sheet and a recent process study reveals that a collapse of the AMOC can be induced even by small-amplitude changes in freshwater forcing (Lohmann and Ditlevsen, 2021). As a result, we change the assessment of an abrupt collapse before 2100 to *medium confidence* that it will not occur.

9.2.3.2 Southern Ocean

The changing Southern Ocean circulation system exerts a strong influence on the global climate by modulating (i) global ocean heat content (Section 9.2.2.1); (ii) global ocean anthropogenic carbon uptake (Cross-chapter Box 5.3); global ocean overturning circulation (Section 9.2.3.1); climate sensitivity (Section 7.4.4 and Cross-chapter Box 5.3); (iii) sea level through basal melt of ice shelves (9.4.2); and Southern Hemisphere sea-ice cover (Section 9.3.2).

The SROCC (Meredith et al., 2019) had *low confidence* in all CMIP5-based model projections due to their inability to explicitly resolve eddy processes and their inability to properly consider future meltwater change from the Antarctic Ice Sheet. These limitations of climate models to represent the Southern Ocean persist due to most CMIP6 models still using parameterized mesoscale eddy processes that are limited in projecting the future response of the horizontal and vertical circulation under climate warming, and due to the continued absence of active ice shelf and ice sheet coupling in the CMIP6 model suite, therefore ignoring basal meltwater and calving feedback on the circulation (Meredith et al., 2019). In addition, two important limitations of CMIP6 models of the Southern Ocean involve processes that were not assessed in the SROCC. First, the poor representation of dense overflows causes most of the Antarctic Bottom Water (AABW) to be formed by spurious open ocean convection rather than by dense overflows from the Antarctic continental

ACCEPTED VERSION SUBJECT TO FINAL EDITING

shelves that feed the lower overturning cell (Snow et al., 2015; Dufour et al., 2017; Heuzé, 2021). Second, Antarctic continental shelf waters are poorly simulated because potentially important controlling mechanisms tend to be too small and transient to observe and resolve in CMIP ocean models. These small processes include the heterogeneity of observed sub-ice shelf melt with warm water driving narrow basal channels that cut underneath the ice (Drews, 2015; Alley et al., 2016; Marsh et al., 2016; Milillo et al., 2019); eddies and tides (Stewart et al., 2018; Jourdain et al., 2019; Hausmann et al., 2020), which can drive Circumpolar Deep Water (CDW) onto the continental shelves or dynamically increase melting (Section 9.2.3.6); and feedback mechanisms between ocean, atmosphere and cryosphere that can weaken or amplify initial perturbations (Donat-Magnin et al., 2017; Spence et al., 2017; Turner et al., 2017; Silvano et al., 2018; Webber et al., 2019; Hazel and Stewart, 2020). In addition, the Southern Ocean in CMIP5 and CMIP6 models exhibit surface temperature biases (Section 9.2.1.1), which have been linked in CMIP5 model to errors in atmospheric model cloud-related short-wave radiation (Hyder et al., 2018) and are somewhat improved in HighResMIP models (Figure 9.3). In summary, there is *high confidence* that future change in the subpolar Southern Ocean region including sea-ice cover and ocean temperature change on Antarctic continental shelves depends on feedback mechanisms involving the ocean, atmosphere and cryosphere that are poorly understood and not represented in the current generation of climate models. This results in large uncertainty and *low confidence* in the future sea-ice cover (Section 9.3.2) and in ocean temperature change on the Antarctic continental shelf (Section 9.4.2.3).

Despite these challenges, the CMIP6 ensemble does represent the main Southern Ocean circulation characteristics; the simulated Antarctic Circumpolar Current (ACC) transport is generally lower than observation-based values but consistent when considering ensemble spread and the inter-model spread in ACC transport has greatly reduced from previous generations of climate models from CMIP3 to CMIP6 (Beadling et al., 2019, 2020). The structure (but not the magnitude) of the two-cell zonally-averaged overturning is captured by most CMIP6 models (Russell et al., 2018; Beadling et al., 2019). In addition, while issues remain, CMIP6 climate models show clear improvements in their representation of AABW compared to CMIP5: several models correctly represent or parameterise Antarctic shelf processes, fewer models exhibit Southern Ocean deep convection, bottom density biases are reduced, and abyssal overturning is more realistic (Heuzé, 2021). In terms of atmospheric wind forcing, CMIP6 models show an improvement compared to CMIP5 models with an overall reduction in the equatorward bias of the annual mean westerly jet from 1.9° in CMIP5 to 0.4° in CMIP6, but in contrast they show no such overall improvements for their representation of the Amundsen Sea Low (Bracegirdle et al., 2020; Lyu et al., 2020a), which can be critical in driving variability of water-masses on the Antarctic continental shelf in west Antarctica, the Weddell Sea or the Ross Sea(Holland et al., 2019; Silvano et al., 2020).

The SROCC (Meredith et al., 2019) established that while trends in the atmospheric forcing of the Southern Ocean have been dominated by a strengthening of the southern hemisphere westerly winds in recent decades, there is *medium confidence* that ACC transport is weakly sensitive to changes in winds. It also reported that instead of increasing the mean ACC transport, additional energy input associated with increased wind stress cascades into the eddy field (*medium confidence*). In contrast with the AR5 assessment (Rhein et al., 2013), the SROCC evaluated that it was *unlikely* that there has been a net southward migration of the mean ACC position over the past 20 years. There is no additional evidence to revisit the SROCC assessment on wind sensitivity. However, new evidence does suggest that air-sea buoyancy forcing associated with idealised $4xCO_2$ forcing leads to an increase in ACC transport (Shi et al., 2020) (*limited evidence*). The SROCC noted that if the general strengthening in westerly winds is sustained, then it is *very likely* that the eddy field will continue to increase in intensity, and that is *likely* that the mean position and strength of the ACC will remain only weakly sensitive to winds. In the future, the strength of the Southern Hemisphere westerly wind jet results from a competition between decrease due to ozone hole recovery and increase due to increased radiative forcing (Section 4.3.3.1). This competition results in an increased atmospheric jet by 2100 compared to present day under SSP2-4.5, SSP3-7.0, and SSP5-8.5, but a decreased jet by 2100 under SSP1-2.6 (Bracegirdle et al., 2020). There is little inter-model spread in the CMIP6 future response of the atmospheric westerly jet, providing *high confidence* in this assessment (in contrast, CMIP6 models show no consistency in their future projection of easterly wind change along the Antarctic continental shelf break) (Bracegirdle et al., 2020). Paleo-oceanographic evidence suggests that ACC flow through Drake Passage was consistently stronger during warm intervals of the past (both during interstadials and interglacials), but with

ACCEPTED VERSION
SUBJECT TO FINAL EDITING

relatively little change and no consensus on the sign of change in other regions (Lamy et al., 2015; Toyos et al., 2020). In summary, additional evidence since the SROCC confirms that there is *medium confidence* that the ACC has been weakly sensitive to Southern Hemisphere atmospheric jet increase in the past decades. New evidence since the SROCC suggests that there is *high confidence* that the Southern Hemisphere atmospheric jet will increase in the 21st century for all scenarios (except for SSP1-1.9 and SSP1-2.6; Section 4.3.3.1) with a greater increase for larger radiative forcing. An increase in westerly winds will *very likely* force an increase of the eddy field in the ACC, and while there is *medium confidence* that the ACC is weakly sensitive to wind change, new advances since the SROCC provide *limited evidence* that the ACC transport will nevertheless increase in response to wind and buoyancy fluxes.

For the upper cell overturning circulation, the SROCC concluded that its transport has experienced significant inter-decadal variability in response to wind forcing since the 1990s, and that there is *low confidence* in the assessments of a long-term increase in upper ocean overturning. Consistent with the SROCC, the importance of both eddy processes and winds in driving long-term change and variability have been reinforced, with a potential fast wind response partially counteracted by a slower eddy response (Doddridge et al., 2019; Waugh et al., 2019; Stewart et al., 2020). Eddy parameterizations affect the strength of overturning, its sensitivity to winds and the ACC transport (Mak et al., 2017). Even in eddy resolving simulations sub-gridscale dissipation affects the overturning and ACC (Pearson et al., 2017). In addition, there has been progress in understanding the importance of Antarctic Ice Shelf meltwater and sea-ice, in driving the observed changes in the near surface and in the upper overturning cell over the past decades, on top of changes induced by winds and eddies (Bronselaer et al., 2020; Haumann et al., 2020; Jeong et al., 2020; Rye et al., 2020). In particular, increased stratification caused by increased freshwater flux to the surface ocean (Section 9.2.1.3) can cause a shoaling and warming of the Circumpolar Deep Water layer, and create a positive feedback enhancing basal melt of the Antarctic Ice Sheet (Section 9.4.2.1) (Bronselaer et al., 2018; Golledge et al., 2019a; Schloesser et al., 2019; Sadai et al., 2020). There is *medium confidence* in the existence of this feedback mechanism but *low agreement* on the magnitude of the feedback. The SROCC reported that CMIP5 models project that the overall transport of upper ocean overturning cell will increase by up to 20% in the 21st century, and no new studies alter that assessment.

For the lower cell overturning circulation, the SROCC assessed that a slowdown of its transport is consistent with the observed decrease in volume (*medium confidence*) of AABW in the global ocean (Section 9.2.2.3). Additional evidence since the SROCC, strengthens confidence that increased glacial meltwater flux will reduce the density of bottom waters during the 21st century, eventually reaching a point where deep convection will be curtailed and shelf water will become too buoyant to sink to the ocean interior, thereby slowing the lower cell overturning circulation (Bronselaer et al., 2018; Golledge et al., 2019a; Lago and England, 2019; Moorman et al., 2020). While such changes are consistent with the observed freshening and volume decrease of the AABW layer reported in the SROCC, as discussed in Section 9.2.2.3, new observation-based studies have highlighted how the lower cell overturning can episodically increase as a response to climate anomalies, temporally counteracting the tendency for melt to reduce AABW formation (Abrahamsen et al., 2019; Castagno et al., 2019; Gordon et al., 2020; Silvano et al., 2020). In addition, while the opening of open ocean polynyas can affect the lower cell on decadal to centennial time-scales, there is *limited evidence* and *low agreement* in the role of open ocean polynyas in driving observed trends of the lower cell in the last decade (Section 9.2.2.3). Based on CMIP5 models, the SROCC reported with *low confidence* that formation and export of AABW associated with the lower overturning cell will decrease in the 21st century, and there is no new evidence to revisit that assessment from climate models. However, additional paleo evidence from marine sediments suggest that AABW formation/ventilation was vulnerable to freshwater fluxes during past interglacials (Hayes et al., 2014; Huang et al., 2020; Turney et al., 2020) and that AABW formation was strongly reduced (Skinner et al., 2010; Gottschalk et al., 2016; Jaccard et al., 2016) or possibly totally curtailed (Huang et al., 2020) during the LGM and transient cold intervals of MIS 2 & 3. Specifically, sedimentary reconstructions show a transient reduction in AABW ventilation in the Atlantic sector of the Southern Ocean during MIS5e, which is assessed to have been warmer than modern climate (Thomas et al., 2020). However, long multi-centennial or millennial model runs under higher-than-pre-industrial CO_2 concentrations show that after 500 -1000 years, ventilation in the Southern Ocean resumes, and even possibly overshoots with enhanced convection in the Weddell and Ross seas leading to enhanced bottom water ventilation globally (Yamamoto et al., 2015; Frölicher et al., 2020). AABW

ACCEPTED VERSION SUBJECT TO FINAL EDITING

ventilation increased at the onset of the last deglacial transition, promoting the release of previously sequestered CO_2 to the atmosphere on centennial to millennial timescales (Bauska et al., 2016; Jaccard et al., 2016; Rae et al., 2018), concomitant with a southward shift of the SH westerly wind belt (Denton et al., 2010; Jaccard et al., 2016) and reduced sea-ice cover (Ferrari et al., 2014; Stein et al., 2020). In summary, the combination of observational, numerical and paleoclimate evidence provides us with *medium confidence* that the lower cell will continue decreasing in the 21st century as a result of increased basal melt from the Antarctic Ice Sheet.

9.2.3.3 Tropical Oceans

The tropics are a tightly coupled ocean-atmosphere system with tightly interconnected basins (Cai et al., 2019). The zonal atmospheric Walker Circulation and the Indonesian Throughflow (ITF, Figure 9.11) are key connections between the Pacific and Indian Oceans, and variations in the Walker and Hadley Circulations are tightly linked to the tropical Pacific SST and currents. The tropics have a profound influence on the climate system through the multiple modes of variability they host, which have widespread global influence at seasonal to annual timescale (Annex IV).

The effect of tropical modes of variability on climate and their long-term changes are reviewed in detail in Annex IV, while changes to the tropical ocean are assessed throughout the report and briefly summarized here. Section 2.4 concludes that a sustained shift beyond multi-centennial variability has not been observed for ENSO (*medium confidence*) and that there is *limited evidence* and *limited agreement* about the long-term behaviour of other tropical modes. Section 3.7 assesses with *high confidence* that human influence has not affected the principal tropical modes of interannual climate variability and their associated regional teleconnections beyond the range of internal variability. Section 4.3.3.2 assesses with *medium confidence* that there is no consensus from models for a systematic change in the amplitude of El Niño–Southern Oscillation sea surface temperature variability over the 21st century. The related change in tropical SSTs is covered in Section 9.2.1.1. The projected changes in SST have implications for marine heat wave characteristics, which are assessed in Box 9.2. SST changes in the tropics are related to changes in the atmospheric circulation, including surface equatorial easterly trade winds and Walker Circulation (Section 4.5.3.2), and the weakening Indonesian Throughflow and strengthening Agulhas Extension and leakage (Section 9.2.3.4). Weakening trade winds under climate change (Vecchi and Soden, 2007) will tend to decrease upwelling, along isopycnals in the eastern Pacific and diapycnal upwelling in the central Pacific and thus the meridional temperature gradients that drive Tropical Instability Waves (Terada et al., 2020), along with a weakening, flattening and shoaling of the tropical thermocline and equatorial undercurrent (Luo and Rothstein, 2011). A weak or absent Equatorial Undercurrent (Kuntz and Schrag, 2020) and a too diffuse and incorrectly sloped tropical thermocline (Zhu et al., 2020) remain issues in most CMIP6 models. In summary, while future changes in tropical modes of variability remain unclear, change in atmospheric and ocean circulation will drive continued change in tropical ocean temperature in the 21st century (*medium confidence*), with part of the region experiencing drastic marine heat wave conditions (*high confidence*).

9.2.3.4 Gyres, Western Boundary Currents, and Inter-Basin Exchanges

The AR5 (Rhein et al., 2013) assessed with *medium* to *high confidence* that the North Pacific subpolar gyre, the South Pacific subtropical gyre, and the subtropical cells have intensified. They also reported that the North Pacific subtropical gyre had expanded since the 1990s, and that overall the changes in gyre systems were *likely* predominantly due to interannual-to-decadal variability. The SROCC (Meredith et al., 2019) complemented the AR5 assessment by reporting that the polar Beaufort Gyre in the Arctic expanded to the northwest between 2003 and 2014, contemporaneous with changes in its freshwater accumulation and alterations in wind forcing. Consistent with the reported change over the gyres, both the AR5 and the SROCC (Bindoff et al., 2019; Collins et al., 2019) reported that Western Boundary Currents (WBCs) have intensified (Figure 9.11), and expanded poleward, except for the Gulf Stream and the Kuroshio. Section 2.3.3.4 provides an overall assessment of gyres and WBCs including an assessment of change from paleoclimate archives. Section 2.3.3.4 assesses that while WBC strength is highly variable at multidecadal

ACCEPTED VERSION SUBJECT TO FINAL EDITING

scale (*high confidence*), WBCs and subtropical gyres have shifted poleward since 1993 (*medium confidence*), at a rate on the order of 0.04-0.1 degree per decade during 1993-2018. Figure 9.11 shows that CMIP5 and CMIP6 models agree in projecting a weaker Gulf Stream and Gulf Stream Extension, while the Kuroshio changes less (Sen Gupta et al., 2016).

Although the observed wind stress curl shows systematic poleward shift in each basin as a result of anthropogenic warming (Section 2.3.1.4) (Chen and Wu, 2012; Wu et al., 2012; Zhai et al., 2014), which has caused a systematic shift of the WBCs and subtropical gyres since 1993 (Wu et al., 2012; Yang et al., 2016b, 2020), the response of current strength is more complex and inconsistent across regions (Sloyan and O'Kane, 2015; Wang et al., 2016c; Elipot and Beal, 2018; McCarthy et al., 2018; Wang and Wu, 2018; Dong et al., 2019). The strength of WBCs and gyres exhibit inconsistent responses because they are not only dependent on wind stress forcing, but multi-scale interaction and air-sea interaction have an important role in their long-term trends and variability (Zhang et al., 2020). Observed changes in gyre circulation are dominated by interannual and decadal modes of variability globally (Qiu and Chen, 2012; Melzer and Subrahmanyam, 2017; McCarthy et al., 2018; Hu et al., 2020). The North Atlantic subpolar gyre is strongly modulated by variability associated with the NAO and AMV (Robson et al., 2016) (Annex IV). Subpolar gyre systems can change abruptly due to a positive feedback between convective mixing and salinity transport (Born et al., 2013, 2016) and air-sea interaction (Moffa-Sánchez et al., 2014; Moreno-Chamarro et al., 2017) within the gyre. In the Arctic, both the Beaufort gyre and mesoscale eddies strengthened between 2003 and 2014 (Armitage et al., 2017), which might be partly due to increased wind stress (Oldenburg et al., 2018b) or reduced sea-ice thickness and changes in sea-ice pack morphology (van der Linden et al., 2019). Presently, there is *limited evidence* in attributing causality to these changes for any of the proposed mechanisms. In the North Pacific, there has been an increasing trend in the Alaska Gyre from 1993 to 2017 (Cummins and Masson, 2018), which might be attributed to PDO (Hristova et al., 2019) (*low confidence*). In the Southern Ocean, *limited evidence* indicates that the subpolar gyres respond to Southern Hemisphere atmospheric modes of variability at interannual time-scale (Armitage et al., 2018; Dotto et al., 2018).

All climate models reproduce WBCs and gyres, but eddy-present or eddy-rich models (roughly 10-25 km and ~10 km resolution, respectively) represent these currents more realistically than eddy-parameterized models (Small et al., 2014a; Griffies et al., 2015; Chassignet et al., 2017; Hewitt et al., 2017; Roberts et al., 2018; Chassignet et al., 2020; Hewitt et al., 2020) (*very high confidence*). Compared to observations or to eddy-present and eddy-rich models, the eddy-parameterized models from CMIP5 and CMIP6 simulate weaker and wider WBCs as well as less realistic locations of subtropical and subpolar gyre boundaries (Figure 9.11). Increased resolution not only admits mesoscale eddies, but also improves simulation of the strength and position of WBCs such as the Kuroshio Current, Gulf Stream, and East Australian Current (Sasaki et al., 2004; Chassignet and Marshall, 2008; Delworth et al., 2012; Yu et al., 2012; Small et al., 2014b; Haarsma et al., 2016; Chassignet et al., 2017, 2020; Hewitt et al., 2020) (*very high confidence*). Improved boundary current location relates to improved recirculation regions (Jayne et al., 2009), mean path and variability and existence of multiple stable paths (Qiu et al., 2005; Delman et al., 2015), air-sea fluxes (Small et al., 2014a), and related coastal weather patterns (Kaspi and Schneider, 2011). The wind-current feedback, implemented by considering relative velocity of currents and wind, realistically dampens mesoscale eddies and WBCs, through mesoscale air-sea interaction (Ma et al., 2016; Renault et al., 2016, 2019), even though sub-mesoscale wind-current damping feedback is missing in these models (Zhang et al., 2016c) (*medium confidence*). As eddies potentially play a role in determining the strength of gyre circulations and their low-frequency variability (Fox-Kemper and Pedlosky, 2004; Berloff et al., 2007), it is expected that eddy-present and eddy-rich models will differ in their decadal variability and sensitivity to changes in wind stress of gyres from eddy-parameterized models (*medium confidence*). Nonetheless, important aspects of gyre strength depend primarily on forcing and not resolution, allowing long term changes in gyre strength to be investigated with low resolution climate models (Hughes and de Cuevas, 2001; Yeager, 2015).

Under future scenarios RCP4.5 and RCP8.5, the AR5 (Collins et al., 2013) assessed an intensification and poleward extension of the southern Hemisphere subtropical gyres in the 21st century. New evidence since the AR5 further reinforce their conclusions which are now extended to all subtropical gyre systems, in both the northern and southern hemispheres (Yang et al., 2016a, 2020). CMIP6 models project changes in WBCs that

ACCEPTED VERSION SUBJECT TO FINAL EDITING

are consistent with projected changes in the surface winds. Under strong radiative forcing, in scenario SSP5-8.5, CMIP6 models project that the East Australian Current Extension and Agulhas Current Extension will intensify in the 21st century, while the Gulf Stream and Brazil Current will weaken (Figure 9.11). Although CMIP5/CMIP6 are limited in resolution, *medium confidence* is given to changes in western boundary currents due to consistency across generations of climate models, including CMIP6, despite changes in model structure, resolution and parameterisations.

[START FIGURE 9.11 HERE]

Figure 9.11: Simulated barotropic streamfunction, surface speed and major current transport in CMIP5 and CMIP6. (a) Mean barotropic streamfunction (Sv) 1995-2014 and projected barotropic streamfunction change (Sv, 2018-2100 vs. 1995-2014) under (b) SSP5-8.5. (d) Mean surface (0-100 m) speed (m/s) and projected surface speed change (m/s, 2081-2100) versus 1995-2014 under (e) SSP5-8.5. (c, f) Median and likely range of 1995-2014 and 2081-2100 transport of 3 currents with the largest transport change and 4 with the largest fractional change (Sen Gupta et al., 2016). (c) Deep currents: Agulhas Extension (ACx), Gulf Stream (GS), Gulf Stream Extension (GSx), Tasman Leakage (TASL), East Australia Current Extension (EACx), Indonesian Throughflow (ITF), and Brazil Current (BC). (f) Shallow currents: as for deep but with New Guinea Current (NGC), and without ACx. No overlay indicates regions with high model agreement, where ≥80% of models agree on the sign of change; diagonal lines indicate regions with low model agreement, where <80% of models agree on the sign of change (see Cross-Chapter Box Atlas.1 for more information). Further details on data sources and processing are available in the chapter data table (Table 9.SM.9).

[END FIGURE 9.11 HERE]

The SROCC (Collins et al., 2019) concluded with *high confidence* that ITF transport from the Pacific to Indian ocean has increased in the past two decades, as a result (*medium confidence*) of an unprecedented intensification of the equatorial Pacific trade wind system. Section 2.3.3.4 assesses that there is *high confidence* that the increase in the ITF over the past two decades is linked to multi-decadal scale variability rather than a longer-term trend. Consistently, in the future, as winds change under increased radiative forcing, most models project a decline of the ITF on the centennial timescale (Figure 9.11). Indeed, one of the clearest changes of ocean current transport simulated by climate models is a weakening of the Indonesian Throughflow projected in CMIP5 simulations under RCP4.5 and RCP8.5 scenarios (Sen Gupta et al., 2016; Stellema et al., 2019), as well as in CMIP6 simulations under the SSP5-8.5 scenario (*high confidence*, Figure 9.11).

The SROCC reports with *high confidence* that the Agulhas leakage from the Indian to the Atlantic ocean has increased in the past two decades (Collins et al., 2019), and there is no additional evidence since then allowing to revisit this assessment (Biastoch et al., 2015; Loveday et al., 2015; Lübbecke et al., 2015). There is *low confidence* in future projections of Agulhas leakage because most CMIP models cannot directly simulate it, due to coarse resolution. However, there is *medium evidence* that the strength of the Southern Hemisphere westerlies controls Agulhas leakage (Durgadoo et al., 2013; Biastoch et al., 2015; Loveday et al., 2015), and *high confidence* that the strength of the Southern Hemisphere westerlies will increase under increased radiative forcing except in lower warming scenarios (SSP1-1.9, SSP1.2-6; Section 4.3.3.1) (Bracegirdle et al., 2020). There is also evidence that increasing Agulhas leakage is consistent with observed change of the temperature and salinity structure in the Atlantic ocean, and with variability of the AMOC (Section 9.2.3.1) (Biastoch et al., 2015). This range of indirect evidence provides *medium confidence* that the Agulhas leakage will increase in the 21st century, except for the strongest mitigation scenario (Figure 9.11).

The SROCC assessed that the annual Bering Strait volume transport from the Pacific to the Arctic Ocean increased from 2001–2014, consistent with an estimated increased northward heat transport of about 60% from 2001–2014, and an increased freshwater transport of 30±20 $km^3\ yr^{-1}$ from 1991 to 2015 (Meredith et al., 2019). Section 2.3.3.4 assesses that volume transport from the Pacific to the Arctic has increased since the 1990s from 0.8 Sv to 1.0 Sv over 1990-2015. Realistic representation of the Bering Strait transport in the current generation of climate models is challenging because the strait is narrow compared to the resolution of climate models

ACCEPTED VERSION SUBJECT TO FINAL EDITING

(Clement Kinney et al., 2014; Aksenov et al., 2016). For the Atlantic to Arctic transport, Section 2.3.3.4 reports that the major branches of Atlantic Water inflow across the Greenland-Scotland Ridge have remained stable, with only the smaller pathway of Atlantic Water north of Iceland showing a strengthening trend during 1993-2018. Section 2.3.3.4 also assesses that the Arctic outflow remained stable from the mid 1990s to the mid 2010s. Future changes in these currents have not yet been studied in CMIP6 models.

9.2.3.5 Eastern Boundary Upwelling Systems

Eastern boundary upwelling systems (EBUS) exist where trade winds draw cold and generally low-pH/low-oxygen waters upward. Coastal upwelling plays a key role in supplying the food chain with nutrients, hence the richness and productivity of EBUS (Bindoff et al., 2019). The SROCC (Bindoff et al., 2019) assessed with *high confidence* that three out of the four major EBUS have experienced large-scale wind intensification in the past 60 years (only the trend for the Canary current is considered uncertain). However, it also emphasized that various processes can also modulate or even reverse wind trends locally (Bindoff et al., 2019). Here we revisit the SROCC (Bindoff et al., 2019) assessment based on evidence showing *low agreement* between studies that have investigated trends over past decadess of upwelling-favourable winds (Varela et al., 2015). This *low agreement* has been related to differences in wind products, season of interest, and length of the considered time series (Varela et al., 2015). Based on this, we assess that only the California current system has experienced large-scale upwelling-favorable wind intensification over the period 1982-2010 albeit with regional differences (García-Reyes and Largier, 2010; Seo et al., 2012). In the Benguela, Canary, and Humboldt systems, large-scale, upwelling-favourable wind trends are ambiguous, owing to *low confidence* in long-term in situ marine wind data (Cardone et al., 1990; Bakun et al., 2010) and *low agreement* among available studies (Narayan et al., 2010; Sydeman et al., 2014; Varela et al., 2015). Our assessment confirms the SROCC (Bindoff et al., 2019) in that high natural variability of EBUS and their inadequate representation by most climate models gives *low confidence* in attribution of observed changes, while anthropogenic changes are projected to emerge primarily in the second half of the 21st century (*limited evidence*: one model and one study) (Brady et al., 2017).

Under increased radiative forcing, the SROCC (Bindoff et al., 2019) assessed that climate models project, in the 21st century, a reduction of wind and upwelling intensity in EBUS at low latitudes and enhancement at high latitudes under scenario RCP8.5, with an overall reduction in either upwelling intensity or extension. It also highlighted that coastal warming and wind intensification may lead to variable countervailing responses to upwelling intensification at local scales. Despite differences among EBUS (Wang et al., 2015a), there is growing evidence since the SROCC in this pattern of change. While it has long been hypothesized that for upwelling winds, change is linked to air temperature contrast between ocean and land (Bakun, 1990), this hypothesis has increasingly been challenged. Changes in sea level pressure and wind fields in EBUS appear to be primarily tied to those affecting subtropical highs (García-Reyes et al., 2013). Poleward expansion of the Hadley cell (Section 2.3.1.4.1) (Staten et al., 2018) and the related poleward migration of subtropical highs (He et al., 2017; Cherchi et al., 2018), produce robust patterns of changes of reduced upwelling at low latitude and enhanced upwelling at high latitude (Echevin et al., 2012; Belmadani et al., 2014; Bettencourt et al., 2015; Rykaczewski et al., 2015; Sousa et al., 2017; Lamont et al., 2018; Sylla et al., 2019). These patterns are most apparent in summer in both hemispheres. Synoptic variability of upwelling winds, important to the functioning of upwelling ecosystems (García-Reyes et al., 2014), may also be affected by climate change (Aguirre et al., 2019). However, coarse resolution model projections of winds in upwelling regions may be more consistent than higher-resolution projections as these regions are highly sensitive to resolution (Small et al., 2015).

Projected future annual cumulative upwelling wind changes at most locations and seasons remain within ±10-20% of present-day values in the 21st century, even in the context of high-end emission scenarios (4xCO2 or RCP8.5) (*medium confidence*). Changes due to wind stress curl and alongshore pressure gradients do tend to agree with alongshore wind changes (Oerder et al., 2015a; Sylla et al., 2019). Direct estimation of oceanic upward transport (Oyarzún and Brierley, 2019; Sylla et al., 2019) and nutrient flux into the euphotic layer (Jacox et al., 2018) provide a meaningful estimator of upwelling, integrating all relevant processes, including changes in wind stress curl. However, there is *limited evidence* from vertical velocity of climate

ACCEPTED VERSION SUBJECT TO FINAL EDITING

models and missing processes in coarse-resolution climate models that presently limit this approach. Change in upper ocean stratification (Section 9.2.1.3) is projected to increase confinement of upwelling vertical velocities to near the ocean surface (Oerder et al., 2015a; Oyarzún and Brierley, 2019) (*high confidence*).

In summary, the SROCC and we conclude that the California current system has experienced some upwelling-favourable wind intensification since the 1980s (*high confidence*), while *low agreement* among reported wind changes in the Benguela, Canary, and Humboldt systems prevents a similar assessment. As in the SROCC, there is *low confidence* in attribution of observed changes to anthropogenic or natural causes. New evidence reinforces our confidence in the SROCC assessment that under increased radiative forcing, EBUS winds will change with a dipole spatial pattern within each EBUS of reduction (weaker and/or shorter) at low latitude, and enhancement (stronger and/or longer) at high latitude (*high confidence*). There is *medium confidence* that, across all scenarios, upwelling wind changes in EBUS will remain moderate in the 21st century, within ±10-20% from present-day values.

9.2.3.6 Coastal Systems and Marginal Seas

Beyond the world's coastlines lie the shoreline, shallow estuaries, continental shelves, and deeper fjords and slopes, where depths increase rapidly from the shelves to the deep ocean floor. It is more difficult to transport fluid across the shelf-break or slope than along (Brink, 2016), and estuaries and shelves have complex circulations and mixing leading to indirect connections between the inner shelves and coastlines and offshore conditions. Coastal processes link to both large-scale metrics of climate and regional effects, from changing rivers and estuaries, melt and runoff to deep water, to how changes offshore affect regional and coastal conditions.

Shelf-deep ocean exchanges involve eddying, tidal, or turbulent motions and small-scale topography such as submarine canyons; high resolution observations and models are needed to capture these effects (Greenberg et al., 2007; Capet et al., 2008; Allen and Durrieu de Madron, 2009; Colas et al., 2012; Trotta et al., 2017). Example coastal processes that introduce uncertainty into large-scale projections are exchange of CDW across the Antarctic shelf-break, which affects AABW formation and Antarctic ice shelf-ocean interaction (Sections 9.2.2.3, 9.2.3.2) (Stewart and Thompson, 2013, 2015), river and estuarine plumes and their responses to water level and hydrology change (Banas et al., 2009; Sun et al., 2017), fjord dynamics linked to glacial outflows (Straneo and Cenedese, 2015; Torsvik et al., 2019), and changing formation of water masses in marginal seas (Kim et al., 2001; Greene and Pershing, 2007; Giorgi and Lionello, 2008; Renner et al., 2009). Downscaling projections to the local level allows process detail (Foreman et al., 2013; Mathis and Pohlmann, 2014; Meier, 2015; Tinker et al., 2016). Some processes can only be simulated when coastal models are forced by larger-scale models of the atmosphere, cryosphere, or hydrosphere (Seo et al., 2007, 2008; Somot et al., 2008; Oerder et al., 2015b; Renault et al., 2016; Zhang et al., 2016a; Wåhlin et al., 2020), including the addition of tides (Janeković and Powell, 2012; Timko et al., 2013; Tinker et al., 2015; Pickering et al., 2017; Hausmann et al., 2020). Due to coastal process complexity and small scale, linking the effects of coastal ocean changes to global ocean changes requires high resolution modelling (Holt et al., 2017, 2018), two-way nesting, or local mesh refinement (Fringer et al., 2006; Zhang and Baptista, 2008; Mason et al., 2010; Dietrich et al., 2012; Hellmer et al., 2012; Ringler et al., 2013; Wang et al., 2014b; Zängl et al., 2015; Zhang et al., 2016b; Soto-Navarro et al., 2020). Coarse climate models and even HighResMIP models do not represent some coastal phenomena such as cross-shelf exchanges and sub-mesoscale eddies which require 1km or finer resolution. Thus, there is *low confidence* in projecting centennial scale coastal climate change where regional downscaling or refinement is lacking. There is *high confidence* in the ability of regional coupled models to improve coastal climate change process understanding and provide regional information (Section 12.4), but many sites globally await such projections.

ACCEPTED VERSION SUBJECT TO FINAL EDITING

9.2.4 Steric and dynamic sea-level change

9.2.4.1 Global mean thermosteric sea-level change

Changes in globally averaged ocean heat content (OHC) cause global mean thermosteric sea-level (GMTSL) change (Box 9.1). The observed increased OHC for 1971-2018 of 325 to 546 ZJ (*very likely* range, Section 7.2, Box 7.2) has led to a GMTSL rise of 0.03 to 0.06 m out of a total GMSL of 0.07 to 0.15 m (*very likely* range, Section 2.3.3.3, Table 2.7, Table 9.5, Cross-Chapter Box 9.1).

Projections of GMTSL rise in the AR5 (Church et al., 2013a) and the SROCC (Oppenheimer et al., 2019) were derived from the CMIP5 ensemble, after removing drift estimated based on pre-industrial control simulations. Differences between removing a linear and a quadratic drift are small (Hermans et al. 2021) (Hobbs et al., 2016b; Hermans et al., 2021). These prior assessments filled in projections for models that did not provide GMTSL rise for all scenarios, by calculating the heat content of the climate system from global surface air temperature and net radiative flux, then converting this to GMTSL rise using each model's diagnosed expansion efficiency coefficient. In the AR5, the associated uncertainties were derived by assuming a normal distribution, with the 5^{th}-95^{th} percentile CMIP5 ensemble range taken as the *likely* range (±1 standard deviation).

In this report, global surface air temperature projections are not derived directly from the CMIP6 ensemble (Box 4.1). Therefore, in order to produce projections of OHC and GMTSL rise that are consistent with the report's assessment of equilibrium climate sensitivity and transient climate response (Section 7.5.2.2), this chapter employs a two-layer energy budget emulator (Supplementary Materials 7.SM.2, 9.SM.4.3). Since the AR5, climate model emulators have been increasingly used to predict GMTSL (Kostov et al., 2014; Palmer et al., 2018, 2020; Nauels et al., 2019) (Cross-Chapter Box 7.1). The expansion efficiency coefficient that relates GMTSL and OHC for the two-layer emulator has a mean and standard deviation of 0.113 ± 0.013 m/YJ (Supplementary Material 9.SM.4.3). This approach yields a *likely* thermosteric contribution between 1995 to 2014 and 2100 that represents a minimal change from the AR5 and the SROCC (Table 9.8). The two-layer emulator GMTSL projected median and 17^{th}-83^{rd} percentile, or *likely*, range is 0.12 (0.09-0.15) m for SSP1-1.9, 0.14 (0.11-0.18) m for SSP1-2.6, 0.20 (0.16-0.24) m for SSP2-4.5, 0.25 (0.21-0.30) m for SSP3-7.0, and 0.30 (0.24-0.36) m for SSP5-8.5 by 2100 (Section 9.6.3.2; Tables 9.1, 9.8,9.9). The two-layer model heat content increases slightly faster than that of the total depth CMIP6 ensemble, which is related to its role in the assessed energy balance (Section 7.SM.2), but with a similar ensemble spread (Table 9.1). Projecting the *likely* factor by which 1995-2014 to 2081-2100 ocean heat content change exceeds change over 1971 to 2018 in CMIP6 yields 3 to 5 for SSP1-2.6, 4 to 6 for SSP2-4.5, 5 to 7 for SSP3-7.0, and 5 to 8 for SSP5-8.5. The two-layer model *likely* equivalents are 2 to 3 for SSP1-2.6, 3 to 4 for SSP2-4.5, 4 to 5 for SSP3-7.0, and 4 to 6 for SSP5-8.5.

For reconstructions, the expansion efficiency coefficient is required for the conversion between ocean temperature and steric sea level over a specific time scale. Combining the assessed sea level and energy data over 1995 to 2014 (drawn from the analysis in Cross-Chapter Box 9.1) results in a coefficient of 0.1210 ± 0.0014 m/YJ, or 0.6607 ± 0.0076 m/ºC in terms of mean ocean temperature. The two-layer emulator assessment used in AR6 results in 0.113 ± 0.013 m/YJ, or 0.617 ± 0.071 m/ºC (Appendices 7.SM.2, 9.SM.4). Both of these estimates are in line with an independent estimate of 0.70 m/ºC (Hieronymus, 2019) and other estimates, e.g., 0.116 ± 0.011 m/YJ (Kuhlbrodt and Gregory, 2012), but are significantly larger than the temperature to sea level conversion used in the AR5 (0.42 m/ºC based on SST and the estimated range from (Levermann et al., 2013)). The expansion coefficient is not fixed across models nor in time, as it varies depending on which water masses are storing the added heat and the commitment time scale (Hallberg et al., 2013). For paleoclimate, a scaling for sea surface temperature (0.6 m/ºC) or GSAT (see Cross-Chapter Box 2.3) can be estimated, but mean ocean temperature is in phase with steric sea-level change while sea surface temperatures are not (Shakun et al., 2012; Tierney et al., 2020) (Figure 9.9). Thus, while conversions between OHC, mean ocean temperature and GMTSL across applications are within uncertainty ranges (*medium confidence*, Table 9.1), little consistency is found when correlating these variables to SST or GSAT which may vary independently.

ACCEPTED VERSION SUBJECT TO FINAL EDITING

Short-lived climate forcers (Sections 6.3, 6.6.3) are associated with a sea-level commitment, due to an ocean heat content and mean ocean temperature response that lasts substantially longer than their atmospheric forcing and SST response, although not as long as the sea-level commitment associated with CO_2 emissions (Sections 9.2.1.1, 4.4.4). For example, Zickfeld et al., (2017) find that about 70% of the thermosteric sea-level rise associated with methane forcing would persist 100 years after the elimination of methane emissions and 40% would persist for over 500 years.

In summary, consistent relationships between OHC (Section 9.2.2.1), mean ocean temperature and GMTSL are found using two-layer emulators, CMIP6 models, and modern and paleo observations to provide *medium confidence* in the 0.113 ± 0.013 m/YJ, or 0.617 ± 0.071 m/ºC *likely* ranges of assessed conversion values. It is possible to estimate relationships between SST or GSAT change and GMTSL rise, but conversions are not generally applicable and depend on time scale and application.

[START TABLE 9.1 HERE]

Table 9.1: Projected contributions to median and 17-83% (parentheses) and 5-95% (square brackets) ranges of thermosteric sea level from AR5 (Church et al., 2013), CMIP6 (Jevrejeva et al., 2020; Hermans et al., 2021) and the two-layer energy balance model (described in Sections 7.SM.2, 9.SM.4 and Box 4.1) averaged over 2081-2100, with respect to a baseline of 1995-2014. Note that AR5 and SROCC interpret 5-95% range as the *likely* range, while in this table square brackets are used for consistency.

Study	RCP2.6/SSP1-2.6	RCP4.5/SSP2-4.5	RCP8.5/SSP5-8.5
IPCC AR5 and SROCC GMTSL (Oppenheimer et al., 2019) (Church et al., 2013a)	0.13 [0.09 – 0.17] m	0.18 [0.13 - 0.22] m	0.26 [0.20 – 0.32] m
CMIP6 5-95% GMTSL (Hermans et al. 2021)	0.14 [0.08 – 0.17] m	0.18 [0.11 – 0.23] m	0.26 [0.17 – 0.33] m
CMIP6 5-95% GMTSL (Jevrejeva et al., 2020)	–	0.19 [0.13 – 0.24] m	0.27 [0.19 – 0.35] m
Assessed GMTSL based on two-layer model 17-83% and 5-95% (Sections 7.SM.2, 9.SM.4)	0.13 (0.11 – 0.16) [0.09 – 0.19] m	0.17 (0.14 – 0.21) [0.12 – 0.25] m	0.25 (0.20 – 0.30) [0.18 – 0.35] m
Total OHC 17-83% and 5-95% from assessed two-layer model (Sections 7.SM.2, 9.SM.4)	1.18 (0.99 – 1.42) [0.86 – 1.65] YJ	1.56 (1.33 – 1.86) [1.19 – 2.12] YJ	2.23 (1.92 – 2.64) [1.71 – 3.00] YJ
0-2000m OHC 17-83% and 5-95% from CMIP6 (Figure 9.6)	1.06 (0.80 – 1.31) [0.66 – 1.64] YJ	1.35 (1.08 – 1.67) [0.90 – 1.84] YJ	1.89 (1.60 – 2.29) [1.28 – 2.58] YJ

[END TABLE 9.1]

9.2.4.2 Ocean dynamic sea-level change

Projections of ocean dynamic sea-level change (Box 9.1) on multiannual timescales resemble the patterns of steric sea-level change in the open ocean (Figures 9.11 and 9.12) (Lowe and Gregory, 2006; Pardaens et al.,

ACCEPTED VERSION SUBJECT TO FINAL EDITING

2011; Couldrey et al., 2020). On shorter timescales, especially in extratropical coastal areas, there may be an important barotropic component (also called bottom pressure change) due mostly to changes in wind-driven circulation and eddies apparent in the variance of ocean dynamic sea level (Figure 9.12, (Roberts et al., 2016; Hughes et al., 2018). This component is highly sensitive to ocean model resolution (Chassignet et al., 2020). Steric sea-level change is associated with local changes in temperature and salinity, which come about through changes in surface fluxes of heat and freshwater (Section 9.2.1.2) and through redistribution of existing water masses by changed ocean circulation and mixing processes (Figure 9.12**,** Sections 9.2.2.1, 9.2.3). Redistribution of water masses often involves anticorrelated thermosteric and halosteric changes (Figure 9.12), especially in the Atlantic (Pardaens et al., 2011; Bouttes et al., 2014; Durack et al., 2014; Griffies et al., 2014; Han et al., 2017).

[START FIGURE 9.12 HERE]

Figure 9.12: (a-f) CMIP6 multi-model mean projected change contributions to relative sea level change in (a,d) steric sea level anomaly, (b, e) thermosteric sea level anomaly, and (c, f) halosteric sea level anomaly between 1995-2014 and 2081-2100 using a method that does not require a reference level (Landerer et al., 2007). Global mean change has been removed from these figures, consistent with the methods in Sections 9.6.3 and 9.SM.4.3 and the definitions of (Gregory et al., 2019). See Figure 9.27 for GMSL. (g-i) Standard deviation of ocean dynamic sea-level change from (g) Aviso observations (10 day highpass filter), (h) 5-day mean of high-resolution OMIP-2 models forced with observed fluxes, and (i) 5-day mean of low-resolution OMIP-2 models which are comparable in resolution to the models in (a-f). No overlay indicates regions with high model agreement, where ≥80% of models agree on the sign of change; diagonal lines indicate regions with low model agreement, where <80% of models agree on the sign of change (see Cross-Chapter Box Atlas.1 for more information). Further details on data sources and processing are available in the chapter data table (Table 9.SM.9).

[END FIGURE 9.12 HERE]

Ocean dynamic sea-level change is strongly affected by internal variability (Section 9.6.1.4), partly from interannual to decadal coupled atmosphere-ocean modes of variability via wind-driven redistribution (Annex IV; Griffies et al., 2014; Han et al., 2017) and partly from intrinsic ocean variability, particularly in higher resolution simulations (such as HighResMIP), which statistically resemble observations, even on short timescales (Figure 9.12, Griffies et al., 2014; Sérazin et al., 2016; Llovel et al., 2018; Chassignet et al., 2020). High-resolution simulations are not used in relative sea level projections (Section 9.6.3) due to the limited range of forcing scenarios. The most marked feature of long-term regional sea-level change in the continuous satellite altimetry record, beginning in 1992, is the east-west dipole in the Pacific Ocean (rising more rapidly in the east, see also Section 9.6.1.3), which persisted until 2015 and can be explained by anomalously strong trade winds (Merrifield et al., 2012; England et al., 2014; Griffies et al., 2014; Takahashi and Watanabe, 2016; Han et al., 2017) together with associated changes in surface heat flux (Piecuch et al., 2019). The most notable features of sub-annual variability in altimetry are eddies and tides, which are directly simulated only in high resolution models (Haigh et al., 2019; Chassignet et al., 2020).

Projections of the pattern and amplitude of regional ocean dynamic sea-level change in CMIP6 and previous model generations show a large model spread, of a similar size to the geographical spread (Figure 9.12). The model spread derives from model dependence of changes both in surface fluxes (Section 9.2.1.2) and in the ocean response (Section 9.2.2). The spread is similar in CMIP6 and CMIP5, and is largest in regions with large projected variations in ensemble-mean ocean dynamic sea-level change (Lyu et al., 2020a), such as the Southern Ocean dipole with an ocean dynamic sea-level rise north of the ACC and a fall to the south, the Atlantic dipole with a sea-level rise north of 40ºN and a fall in 20-40ºN, the north-west Pacific dipole, and the large sea-level rise in the Arctic (Church et al., 2013a; Slangen et al., 2014b; Bilbao et al., 2015; Slangen et al., 2015; Gregory et al., 2016; Chen et al., 2019a; Couldrey et al., 2020; Lyu et al., 2020a). Patterns of change are consistent between model simulations and observations (*medium confidence*). The major model ensemble-mean features resemble thermosteric sea level change, as expected from altered input of heat to the ocean without changing circulation, while model spread results from the diversity in redistribution of the heat content of the unperturbed ocean (Section 9.2.2.1; (Bouttes and Gregory, 2014; Gregory et al., 2016;

ACCEPTED VERSION SUBJECT TO FINAL EDITING

Huber and Zanna, 2017; Couldrey et al., 2020; Lyu et al., 2020b; Todd et al., 2020)).

The Southern Ocean meridional dipole is driven by a northward advection of excess heat (from changes in surface fluxes) by the wind-driven circulation followed by subduction or diffusive uptake in mid-latitudes, northward redistribution of existing heat by the strengthening of that circulation, and the meridional contrast in thermal expansivity due to its temperature-dependence (Armour et al., 2016; Gregory et al., 2016; Couldrey et al., 2020; Lyu et al., 2020b; Todd et al., 2020).

The positive Arctic ocean dynamic sea-level change is driven by increased freshwater input (Couldrey et al., 2020). The north-west Pacific dipole is driven by the intensification of the Kuroshio current in response to reduced heat loss and in some models to wind stress change (Chen et al., 2019a; Couldrey et al., 2020).

The North Atlantic sea-level change dipole is forced by a reduction in heat loss from the ocean north of 40ºN (i.e., net heat uptake), which in all Earth system models leads to a weakening of the AMOC, although the magnitude has a large model spread (Gregory et al., 2016; Huber and Zanna, 2017, Section 9.2.3.1). The reduced northward transport of warm, salty water (Section 9.2.2) causes further ocean dynamic sea-level change, whose details are model-dependent. North of 40ºN, this redistribution leads to a sea-level rise, predominantly halosteric, reinforcing the thermosteric effect of heat uptake (Couldrey et al., 2020). Comparison of observed Atlantic ocean heat content for 1955-2017 with a reconstruction assuming no change in circulation indicates that the thermosteric sea-level change resulting from southward redistribution of heat may be detectable (Zanna et al., 2019a). This redistribution causes a tendency for SST cooling north of 40ºN and anomalous heat input from the atmosphere, and thus a positive feedback on AMOC weakening (Winton et al., 2013; Gregory et al., 2016; Couldrey et al., 2020; Todd et al., 2020). Many climate and ocean models agree that the AMOC weakening is associated with pronounced thermosteric sea-level rise along the American coast around 40ºN (Figures 9.12, 9.26), leading to a relatively large ocean dynamic sea-level rise in this region (Yin, 2012; Bouttes et al., 2014; Slangen et al., 2014a; Little et al., 2019; Lyu et al., 2020a).

In summary, ocean dynamic sea-level change involves changes to temperature and salinity and responses of currents to changing forcing, with significant variability driven by unforced oceanic variability. Projections of dynamic sea-level variability require fully three-dimensional ocean models and only high-resolution ocean models are statistically consistent on short timescales with satellite altimeter observations (*very high confidence*).

9.3 Sea ice

9.3.1 Arctic Sea Ice

9.3.1.1 Arctic Sea-Ice Coverage

The observed decrease of Arctic sea-ice area is a key indicator of large-scale climate change (Section 2.3.2.1.1, Cross-Chapter Box 2.2). The SROCC (Meredith et al., 2019) assesses that sea-ice extent, which is the total area of all grid cells with at least 15% sea-ice concentration, has declined since 1979 in each month of the year (*very high confidence*). In contrast to the SROCC, we assess changes in sea-ice area (the actual area of the ocean covered by sea ice) rather than sea-ice extent, because sea-ice area is geophysically more relevant and not grid-dependent (Notz, 2014; Ivanova et al., 2016; Notz et al., 2016; Notz and SIMIP Community, 2020). Arctic sea-ice area is calculated based on measurements by passive microwave satellite sensors that provide near-continuous measurements of gridded, pan-Arctic sea-ice concentration from 1979 onwards. Irreducible uncertainties in the conversion of thermal microwave brightness temperature to sea-ice concentration and choices in algorithm design cause uncertainties in observed Arctic sea-ice area, which are, though, far smaller than the observed sea-ice loss (e.g., Comiso et al., 2017b; Niederdrenk and Notz, 2018; Alekseeva et al., 2019; Kern et al., 2019; Meier and Stewart, 2019). Sea-ice area has decreased from 1979 to the present in every month of the year (*very high confidence*, Figure 9.13). The absolute and the relative ice losses are highest in late summer-early autumn (*high confidence*, Figure 9.13). Averaged over the decade 2010-2019, monthly-average Arctic sea-ice area in August, September and October has been around 2

ACCEPTED VERSION SUBJECT TO FINAL EDITING

million km² (or about 25%) smaller than that during 1979-1988 (*high confidence*, Figure 9.13).

[START FIGURE 9.13 HERE]

Figure 9.13: Arctic sea-ice historical records and CMIP6 projections. Left: Absolute anomaly of monthly-mean Arctic sea-ice area during the period 1979 to 2019 relative to the average monthly-mean Arctic sea-ice area during the period 1979 to 2008. Right: Sea-ice concentration in the Arctic for March and September, which usually are the months of maximum and minimum sea-ice area, respectively. First column: Satellite-retrieved mean sea-ice concentration during the decade 1979-1988. Second column: Satellite-retrieved mean sea-ice concentration during the decade 2010-2019. Third column: Absolute change in sea-ice concentration between these two decades, with grid lines indicating non-significant differences. Fourth column: number of available CMIP6 models that simulate a mean sea-ice concentration above 15 % for the decade 2045-2054. The average observational record of sea-ice area is derived from the UHH sea-ice area product (Doerr et al., 2021), based on the average sea-ice concentration of OSISAF/CCI (OSI-450 for 1979-2015, OSI-430b for 2016-2019)(Lavergne et al., 2019), NASA Team (version 1, 1979-2019)(Cavalieri et al., 1996) and Bootstrap (version 3, 1979-2019)(Comiso, 2017) that is also used for the figure panels showing observed sea-ice concentration. Further details on data sources and processing are available in the chapter data table (Table 9.SM.9).

[END FIGURE 9.13 HERE]

The SROCC discussed the regional distribution of Arctic sea-ice loss and their findings remain valid for the updated time series covering 2019 (Figure 9.13). Sea-ice loss in winter is strongest in the Barents Sea, while summer losses occur primarily at the summer sea-ice region margins, in particular in the East Siberian, Chukchi, Kara and Beaufort Seas (Frey et al., 2015; Chen et al., 2016; Onarheim et al., 2018; Peng and Meier, 2018; Maksym, 2019). In the Bering Sea, expanding winter sea-ice cover was observed until 2017 (Frey et al., 2015; Onarheim et al., 2018; Peng and Meier, 2018), but a marked reduction in sea-ice concentration has occurred since then (Stabeno and Bell, 2019)(*high confidence*).

With respect to seasonal changes in the sea-ice cover, the winter sea-ice loss causes a decrease in the average sea-ice age and fraction of multi-year ice as assessed by the SROCC (*very high confidence*), and also of the ocean area covered intermittently by sea ice (Bliss et al., 2019). In contrast, the seasonal ice zone (covered by sea ice in winter but not in summer) has expanded regionally (Bliss et al., 2019) and over the whole Arctic (Steele and Ermold, 2015), because the loss of summer sea-ice area is larger than the loss of winter sea-ice area. Arctic sea ice retreat includes an earlier onset of surface melt in spring and a later freeze up in fall, lengthening the open-water season in the seasonal sea-ice zone (Stroeve and Notz, 2018). However, there is *low agreement* in quantification of regional trends of melt and freeze onset between different observational products (Bliss et al., 2017; Smith and Jahn, 2019).

Reconstructions of Arctic sea-ice coverage put the satellite period changes into centennial context. Direct observational data coverage (Walsh et al., 2017) and model reconstructions (Brennan et al., 2020) warrant *high confidence* that the low Arctic sea-ice area of summer 2012 is unprecedented since 1850, and that the summer sea-ice loss is significant in all Arctic regions except for the Central Arctic (Cai et al., 2021). Direct wintertime observational data coverage before 1953 is too sparse to reliably assess Arctic sea-ice area. Since 1953, the years 2015 to 2018 had the four lowest values of maximum Arctic sea-ice area, which usually occurs in March (Figure 2.20) (*high confidence*). Reconstructions of Arctic sea-ice area before 1850 remain sparse, and as in the SROCC, there remains *medium confidence* that the current sea-ice levels in late summer are unique during the past 1 kyr (Kinnard et al., 2011; De Vernal et al., 2013b). (Section 2.3.2.1.1)

The observed fluctuations and trends of the Arctic sea-ice cover arise from a combination of changes in natural external forcing and anthropogenic forcing, internal variability and internal feedbacks (e.g., Notz and Stroeve, 2018; Halloran et al., 2020). New paleo-proxy techniques indicate regional sea-ice changes over epochs and millennia and allow possible drivers to be assessed. Biomarker IP25 (Belt et al., 2007) together with other sedimentary biomarkers (Belt, 2018) provides local temporal information on seasonal sea-ice

ACCEPTED VERSION SUBJECT TO FINAL EDITING

coverage, permanent sea-ice coverage and ice-free waters with occasional ambiguous contrasting results (Belt, 2019). These records and other proposed paleo proxies including bromine in ice cores (Spolaor et al., 2016), dinocyst assemblages (e.g., De Vernal et al., 2013b) and driftwood (e.g., Funder et al., 2011) provide evidence of sea-ice fluctuations that exceed internal variability (*high confidence*).

The inferred sea-ice fluctuations over millennia can be related to Northern-hemisphere temperature evolution and give rise to Arctic-wide fluctuations in sea-ice coverage in the paleo record (Section 2.3.2.1.1). On a regional scale, fluctuations include decreased sea-ice cover during the Allerød warm period (14.7-12.9 ka) in the Laptev (Hörner et al., 2016) and Bering Sea (Méheust et al., 2018); an extensive sea-ice cover during the Younger Dryas (~12 ka) in the Bering (Méheust et al., 2018), Kara (Hörner et al., 2018), Laptev (Hörner et al., 2016) and Barents (Belt et al., 2015) Seas and at the Yermak Plateau (Kremer et al., 2018); little sea ice during the early Holocene, when Northern hemisphere summer insolation was higher than today (8000 to 9000 years before present), in the North Icelandic Shelf area (Cabedo-Sanz et al., 2016; Xiao et al., 2017), Sea of Okhotsk (Lo et al., 2018), Canadian Arctic (Spolaor et al., 2016), Barents (Berben et al., 2017), Bering (Méheust et al., 2018), and Chukchi (Stein et al., 2017) Seas, at the Yermak Plateau (Kremer et al., 2018) and north of Greenland (Funder et al., 2011); increasing sea-ice cover throughout much of the middle and late Holocene around Svalbard (Knies et al., 2017), in the North Icelandic Shelf area (Cabedo-Sanz et al., 2016; Harning et al., 2019; Halloran et al., 2020), north of Greenland (Funder et al., 2011), and in the Western Greenland (Kolling et al., 2018), Barents (Belt et al., 2015; Berben et al., 2017), Chukchi (De Vernal et al., 2013a; Stein et al., 2017) and Laptev (Hörner et al., 2016) Seas. The consistent, Arctic-wide changes give *high confidence* in millennial-scale co-variability of the sea-ice cover with temperature fluctuation.

The SROCC assessed that approximately half of the satellite-observed Arctic summer sea ice loss is driven by increased concentrations of atmospheric greenhouse gases (*medium confidence*). Recent attribution studies now allow the strengthened assessment that it is *very likely* that more than half of the observed Arctic sea-ice loss in summer is anthropogenic (Section 3.4.1.1). This assessment is confirmed by process-based analyses of Arctic sea-ice loss not assessed by the SROCC. Similar to the paleo record, the satellite record of Arctic sea-ice area from 1979 onwards is strongly linearly correlated with global mean temperature on decadal and longer time scales (Figure 9.14a,e) (e.g., Gregory et al., 2002; Rosenblum and Eisenman, 2017) . The correlation holds across all months with R^2 ranging from 0.61 to 0.81 (Niederdrenk and Notz, 2018). However, in contrast to paleo-records, sea-ice fluctuations during the satellite period are only weakly correlated with Northern Hemisphere insolation (Notz and Marotzke, 2012); modern Northern Hemisphere sea-ice area is more strongly correlated with atmospheric CO_2 concentration (Johannessen, 2008; Notz and Marotzke, 2012) and cumulative anthropogenic CO_2 emissions (Figure 9.14b,f) (Zickfeld et al., 2012; Herrington and Zickfeld, 2014; Notz and Stroeve, 2016). R^2 values of the correlation between sea-ice area and cumulative CO_2 emissions range across all months from 0.76 to 0.92 (Stroeve and Notz, 2018). In summary, there is *high confidence* that satellite-observed Arctic sea-ice area is strongly correlated with global mean temperature, CO_2 concentration and cumulative anthropogenic CO_2 emissions.

In addition to changes in the external forcing, internal variability substantially affects Arctic sea ice, evidenced from both paleo records (e.g., (Chan et al., 2017; Hörner et al., 2017; Kolling et al., 2018)) and satellites after 1979 (e.g., Notz and Stroeve, 2018; Roberts et al., 2020) (*high confidence*). Most of the internal variability on annual time scales is related to atmospheric temperature fluctuations, for example linked to cyclone activities (Wernli and Papritz, 2018; Olonscheck et al., 2019), while multidecadal internal variability is primarily related to changes in oceanic heat transport (Zhang, 2015; Halloran et al., 2020). These mechanisms are represented in current climate models (Olonscheck et al., 2019; Halloran et al., 2020), but the resulting internal variability of September sea-ice area in CMIP5 and CMIP6 models, as given by the ensemble mean standard deviation $s_{SIA,Sep}$=0.5 million km² (Olonscheck and Notz, 2017; Notz and SIMIP Community, 2020), exceeds the estimated internal variability for the period 1850 to 1979 from both reanalyses ($s_{SIA,Sep}$ =0.3 million km^2) and direct observational reconstructions ($s_{SIA,Sep}$ =0.2 million km^2) (Brennan et al., 2020) (*medium confidence* because of limited reliability of longer-term sea-ice reconstructions). Internal variability has been estimated to have contributed 30 to 50% of the observed Arctic summer sea-ice loss since 1979 (Kay et al., 2011; Stroeve et al., 2012; Ding et al., 2017, 2019; England et al., 2019). However, this estimate from models might be biased towards internal over forced variability

ACCEPTED VERSION SUBJECT TO FINAL EDITING

because of the models' high internal variability and because the CMIP5 simulated September sea-ice sensitivity to forcing is lower than observed, even if internal variability is taken into account (Notz and Stroeve, 2016; Rosenblum and Eisenman, 2017). Most CMIP6 models fail to simulate the observed sensitivity of sea-ice loss to CO_2 emissions (as a proxy for time) and to temperature simultaneously. However, they better capture the observed sensitivity of sea-ice loss to CO_2 emissions than CMIP5 models (Section 3.4.1, Figure 9.14h; (Notz and SIMIP Community, 2020)).

The SROCC examined the different atmospheric and oceanic processes that caused the observed sea-ice loss, with recent studies providing new evidence for the importance of variations in air temperature (Olonscheck et al., 2019; Dahlke et al., 2020), wind patterns (Graham et al., 2019), oceanic heat flux (Docquier et al., 2021) and riverine heat influx (Park et al., 2020). As in the SROCC, the relative contribution of each physical cause to the sea-ice loss cannot be robustly quantified because of disagreement among models (Burgard and Notz, 2017), sparse observations and limited understanding of the variation of each factor with global mean temperature. This is addressed by new diagnostics available from CMIP6 simulations, which now allow for more detailed analyses of the drivers of sea-ice loss at a process level (Keen et al., 2021).

In examining temperature thresholds for the loss of Arctic summer sea ice, the SR1.5 (Hoegh-Guldberg et al., 2018) and the SROCC assess that a reduction of September-mean sea-ice area to below 1 million km^2, practically a sea-ice-free Arctic Ocean, is more probable for a global mean warming of 2°C compared to global mean warming of 1.5°C (*high confidence*). Analyses of CMIP6 simulations (Notz and SIMIP Community, 2020) confirm this result, as they show that on decadal and longer time scales, Arctic summer sea ice area will remain highly correlated with global mean temperature until the summer sea ice has vanished (Figure 9.14a,e). Quantitatively, existing studies (Screen and Williamson, 2017; Jahn, 2018; Ridley and Blockley, 2018; Sigmond et al., 2018; Notz and SIMIP Community, 2020) additionally show that for a warming between 1.5 and 2 ˚C, the Arctic will only be practically sea-ice free in September in some years, while at 3 ˚C warming the Arctic is practically sea-ice free in September in most years, with longer practically sea-ice-free periods at higher warming levels (*medium confidence*). However, because of the CMIP5 and CMIP6 models' generally too low sensitivity of sea-ice loss to global warming, there is only *low confidence* regarding the specific warming level at which the Arctic Ocean first becomes practically sea-ice free (Notz and SIMIP Community, 2020). (Section 4.3.2.1)

[START FIGURE 9.14 HERE]

Figure 9.14: Monthly mean March (a-d) and September (e-h) sea-ice area as a function of global surface air temperature (GSAT) anomaly (a,e); cumulative anthropogenic CO_2 emissions (b,f); year (c,g) in CMIP6 model simulations (shading, ensemble mean as bold line) and in observations (black dots). Panels d and h show the sensitivity of sea-ice loss to anthropogenic CO_2 emissions as a function of the modelled sensitivity of GSAT to anthropogenic CO_2 emissions. In panels d and h, the black dot denotes the observed sensitivity, while the shading around it denotes internal variability as inferred from CMIP6 simulations (after Notz and SIMIP Community, 2020). Further details on data sources and processing are available in the chapter data table (Table 9.SM.9).

[END FIGURE 9.14 HERE]

In contrast, CMIP6 models capture the observed sensitivity of Arctic sea ice area to cumulative anthropogenic CO_2 emissions well, providing *high confidence* that the Arctic Ocean will *likely* become practically sea-ice free in the September mean for the first time for future CO_2 emissions of less than 1000 Gt and before the year 2050 in all SSP scenarios (Notz and SIMIP Community, 2020). This new assessment is consistent with an observation-based projection of a practically sea-ice free Arctic Ocean in September for additional anthropogenic CO_2 emissions of 800± 330 $GtCO_2$ beyond the year 2018 (Notz and Stroeve, 2018; Stroeve and Notz, 2018). This estimate may, however, be too high due to neglecting possible future reduction in atmospheric aerosol load that would cause additional warming (Gagné et al., 2015a; Wang et al., 2018) and is subject to the same constraints as the carbon budget analysis for global mean temperature (see section 5.5 for details). Based on CMIP6 simulations, it is *very likely* that the Arctic Ocean will remain sea-

ACCEPTED VERSION SUBJECT TO FINAL EDITING

ice covered in winter in all scenarios throughout this century (Sections 4.3.2, 4.4.2).

There is indication that CMIP6 simulations of Arctic sea ice have improved relative to CMIP5 (Section 3.4.1.1), but detailed evaluation studies exist mainly for CMIP5 models. These studies found that CMIP5 model projections and reanalyses show a large spread of simulated regional Arctic sea-ice concentration (Laliberté et al., 2016; Chevallier et al., 2017), which remains true for CMIP6 models (Shu et al., 2020; Wei et al., 2020). In addition, both CMIP5 and CMIP6 models show a large spread in the simulated seasonal cycle of Arctic sea-ice area, with too high a sea-ice area in March in the ensemble mean (Notz and SIMIP Community, 2020). CMIP5 models also have been found to have difficulty simulating realistic landfast sea ice (Laliberté et al., 2018). These findings imply that both CMIP5 and CMIP6 models do not realistically capture the regional and seasonal processes governing observed Arctic sea-ice evolution, causing *low confidence* in the models' projections of future regional sea-ice evolution, including updated projections for shipping routes across the Northern Sea Route and Northwest Passage (Wei et al., 2020).

CMIP5 models also have issues with capturing the seasonal cycle of observed changes in Arctic sea-ice drift speed, which affects their simulation of regional sea-ice concentration patterns. Direct measurements of Arctic sea ice from drift buoys and satellites show that drift speed of Arctic sea ice has increased over the satellite period in all seasons (e.g., Rampal et al., 2009; Docquier et al., 2017). In summer, CMIP5 models show a slowdown of Arctic sea-ice drift rather than the observed acceleration (Tandon et al., 2018). In winter, CMIP5 models generally capture the observed acceleration of Arctic drift speed. The drift acceleration is primarily caused by the decrease in concentration and thickness, both in the observational record (Rampal et al., 2009; Spreen et al., 2011; Olason and Notz, 2014; Docquier et al., 2017) and, for winter, in CMIP5 models (Tandon et al., 2018). Changes in wind speed are less important for the observed large-scale changes (Spreen et al., 2011; Vihma et al., 2012; Olason and Notz, 2014; Docquier et al., 2017; Tandon et al., 2018). In summary, there is *high confidence* that Arctic sea-ice drift has accelerated because of the decrease in sea ice concentration and thickness.

The SR1.5 assessed with *high confidence* that there is no hysteresis in the loss of Arctic summer sea ice. In addition, there is no tipping point or critical threshold in global mean temperature beyond which the loss of summer sea ice becomes self-accelerating and irreversible (*high confidence*). This is because stabilizing feedbacks during winter related to increased heat loss through thin ice and thin snow, and increased emission of longwave radiation from open water, dominate over the amplifying ice-albedo feedback (e.g., Eisenman, 2012; Wagner and Eisenman, 2015; Notz and Stroeve, 2018) (see section 7.4.2 for details on the individual feedbacks). Observed and modelled Arctic summer sea ice and global mean temperature are linked with little temporal delay, and the summer sea-ice loss is reversible on decadal time scales (Armour et al., 2011; Ridley et al., 2012; Li et al., 2013; Jahn, 2018). The loss of winter sea ice is reversible as well, but the loss of winter sea-ice area per degree of warming in CMIP5 and CMIP6 projections increases as the ice retreats from the continental shore lines, because these limit the possible areal fluctuations (e.g., Bathiany et al., 2016, 2020; Meccia et al., 2020) (*high confidence*) (Section 4.3.2.1).

9.3.1.2 Arctic Sea-Ice volume and thickness

The SROCC assessed with *very high confidence* that Arctic sea ice has become thinner over the satellite period from 1979 onwards, and this assessment is confirmed for the updated time series (section 2.3.2.1.1). Sea-ice area has also decreased substantially over this period (section 9.3.1.1), leading to the assessment that Arctic sea-ice volume has also decreased with *very high confidence* over the satellite period since 1979. There is, however, only *low confidence* in quantitative estimates of the sea-ice volume loss over this period because of a lack of reliable, long-term, pan-Arctic observations and substantial spread in available reanalyses (Chevallier et al., 2017). Current best estimates from reanalyses suggest a reduction of September Arctic sea ice volume of 55 to 65 % over the period 1979 to 2010, and of about 72 % over the period 1979 to 2016, with the latter deemed a conservative estimate (Schweiger et al., 2019).

For the more recent past, ice-thickness can be directly estimated from satellite estimates of sea-ice freeboard (Kwok and Cunningham, 2015; Kwok, 2018). Based on these retrievals, there is *medium confidence* that

ACCEPTED VERSION SUBJECT TO FINAL EDITING

Arctic sea-ice volume has decreased since 2003. There is *low confidence* in the amount of decrease over this period and over the CryoSat-2 period from 2011 onwards primarily because of snow-induced uncertainties in the retrieval algorithms, the shortness of the record, and the small identified trend (e.g., (Bunzel et al., 2018; Petty et al., 2018, 2020)).

Observations of regional changes in sea-ice thickness vary in quality. Analysis of submarine data in the central Arctic Ocean suggests that sea ice there has thinned by about 75 cm compared to the mid-1970s (Section 2.3.2.1.1). For smaller regions, data are too sparse to allow for quantitative estimates of long-term trends (King et al., 2017; Rösel et al., 2018), but a clear thinning signal over 10 to 20 years has been found for sea ice in Fram Strait (Spreen et al., 2020), north of Canada (Haas et al., 2017) and for landfast ice in Kongsfjorden/Svalbard (Pavlova et al., 2019). CMIP5 models and reanalyses fail to capture the observed distribution (Stroeve et al., 2014; Shu et al., 2015) and evolution (Chevallier et al., 2017) of Arctic sea-ice thickness. Most CMIP6 models do not capture the observed spatial distribution of sea-ice thickness realistically (Wei et al., 2020). This leads to *low confidence* in estimates of thickness from reanalyses and from CMIP5 and CMIP6 models, and in these models' projections of sea-ice volume.

9.3.2 Antarctic Sea Ice

9.3.2.1 Antarctic sea-ice coverage

The SROCC (Meredith et al., 2019) assessed that there was no significant trend in annual mean Antarctic sea-ice area over the period of reliable satellite retrievals starting in 1979 *(high confidence)*. The updated time series is consistent with this assessment. It includes a maximum sea-ice area in 2014, a substantial decline from then until the minimum sea-ice area in 2017, and an increase in sea-ice area since then (Schlosser et al., 2018; Maksym, 2019; Parkinson, 2019) (Figure 9.15, Figure 2.20). As assessed in Section 2.3.2.1.2, the possible significance of the increase in mean Antarctic sea-ice area over the shorter period 1979 to 2014 (Figure 2.20) (Simmonds, 2015; Comiso et al., 2017a) is unclear. This is because of observational uncertainty (see section 9.3.1.1), large year-to-year fluctuations in all months (Figure 9.15), and limited understanding of the processes and reliability of year-to-year correlation of Antarctic sea-ice area (Yuan et al., 2017).

As assessed by the SROCC, the evolution of mean Antarctic sea-ice area is the result of opposing regional trends (*high confidence*), with slightly decreasing sea-ice cover during the period 1979 to 2019 in the Amundsen Sea and the Bellingshausen Sea, particularly during summer, and slightly increasing sea-ice cover in the eastern parts of the Weddell Sea and the Ross Sea (Figure 9.15). With the exception of the Ross Sea, these trends are not significant considering the large variability of the time series (Yuan et al., 2017).

The SROCC assessed that the regional trends are closely related to meridional wind trends (*high confidence*). This is the case as the regional trends in the maximum northward extent of the ice cover (Figure 9.15) are determined by the balance between the northward advection of the ice that is formed in polynyas near the continental margin, and the lateral and subsurface melting through oceanic heat fluxes. The advection of the sea ice is strongly correlated with winds and cyclones (Schemm, 2018; Vichi et al., 2019; Alberello et al., 2020). Accordingly, the increasing sea-ice area in the Ross Sea can be linked to a strengthening of the Amundsen Sea low (e.g., (Holland et al., 2017b, 2018)), while other regional sea-ice trends in the austral fall can be linked to changes in westerly winds, cyclone activity and the Southern Annular Mode (SAM) in summer and spring (Doddridge and Marshall, 2017; Holland et al., 2017a; Schemm, 2018). In addition to the wind-driven changes, increased near-surface ocean stratification (Section 9.2.1.3) has contributed to the observed increase in sea-ice coverage (e.g., (Purich et al., 2018; Zhang et al., 2019b)) as it tends to cool the surface ocean (Sections 9.2.1.1, 9.2.3.2). The changes in stratification result partly from surface freshening (De Lavergne et al., 2014) (associated with increased northward sea-ice advection (Haumann et al., 2020) and/or melting of the Antarctic ice sheet (e.g., (Haumann et al., 2020; Jeong et al., 2020; Mackie et al., 2020)) (*medium confidence*)) and are amplified by local ice-ocean feedbacks (Goosse and Zunz, 2014; Lecomte et al., 2017; Goosse et al., 2018). In the Amundsen Sea, strong ice-shelf melting can cause local sea-ice melt next to the ice-shelf front by entraining warm Circumpolar Deep Water to the ice-shelf cavity

ACCEPTED VERSION SUBJECT TO FINAL EDITING

and surface ocean (*medium confidence*) (Sections 9.2.3.2, 9.4.2.2) (Jourdain et al., 2017; Merino et al., 2018). It has also been suggested that the observed regional increase in sea ice coverage since 1979 results from a long-term Southern Ocean surface cooling trend (e.g., (Kusahara et al., 2019; Jeong et al., 2020)) but the importance of this mechanism for the observed sea-ice evolution is unclear owing to intricate feedbacks between sea-ice change and surface cooling (Haumann et al., 2020). The importance of changing wave activity (Section 9.6.4.2; Kohout et al., 2014; Bennetts et al., 2017; Roach et al., 2018b) on sea ice is unclear due to limited process understanding. In summary, there is *high confidence* that regional Antarctic trends are primarily caused by changes in sea-ice drift and decay, with *medium confidence* in a dominating role of changing wind pattern. The precise relative contribution of individual drivers remains uncertain because of limited observations, disagreement between models, unresolved processes, and temporal and spatial remote linkages caused by sea-ice drift (Section 9.2.3.2, (Pope et al., 2017)).

Recent research has confirmed the SROCC assessment of atmospheric and oceanic drivers of the sea-ice decline from 2014 to 2017, which can be linked to changes in both subsurface ocean heat flux (Meehl et al., 2019; Purich and England, 2019) and atmospheric circulation, with the latter partly related to teleconnections with the tropics (Meehl et al., 2019; Purich and England, 2019; Wang et al., 2019a). In the Weddell Sea, these changes caused in 2017 the re-emergence of the largest polynya over the Maud Rise since the 1970s (Campbell et al., 2019; Jena et al., 2019; Turner et al., 2020) (Section 9.2.3.2).

[START FIGURE 9.15 HERE]

Figure 9.15: Antarctic sea-ice historical records and CMIP6 projections. Left: Absolute anomaly of observed monthly-mean Antarctic sea-ice area during the period 1979 to 2019 relative to the average monthly-mean Antarctic sea-ice area during the period 1979 to 2008. Right: Sea-ice coverage in the Antarctic as given by the average of the three most widely used satellite-based estimates for September and February, which usually are the months of maximum and minimum sea-ice coverage, respectively. First column: Mean sea-ice coverage during the decade 1979-1988. Second column: Mean sea-ice coverage during the decade 2010-2019. Third column: Absolute change in sea-ice concentration between these two decades, with grid lines indicating non-significant differences. Fourth column: number of available CMIP6 models that simulate a mean sea-ice concentration above 15 % for the decade 2045-2054. The average observational record of sea-ice area is derived from the UHH sea-ice area product (Doerr et al., 2021), based on the average sea-ice concentration of OSISAF/CCI (OSI-450 for 1979-2015, OSI-430b for 2016-2019)(Lavergne et al., 2019), NASA Team (version 1, 1979-2019)(Cavalieri et al., 1996) and Bootstrap (version 3, 1979-2019)(Comiso, 2017) that is also used for the figure panels showing observed sea-ice concentration. Further details on data sources and processing are available in the chapter data table (Table 9.SM.9).

[END FIGURE 9.15 HERE]

The AR5 (Collins et al., 2013) and the SROCC found *low confidence* in future projections of Antarctic sea ice. This includes the projected mitigation of the sea-ice loss by stratospheric ozone recovery (Smith et al., 2012) and by an increased freshwater input from melting of the Antarctic ice sheet (Bronselaer et al., 2018). Compared to the interannual variability during the satellite record from 1979 onwards, models simulate too much variability both in CMIP5 (Zunz et al., 2013) and in CMIP6 (Roach et al., 2020). The seasonal cycle in sea-ice coverage is misrepresented in most CMIP5 (e.g., (Holmes et al., 2019)) and CMIP6 models (Roach et al., 2020), but the multi-model mean seasonal cycle in CMIP5 and CMIP6 agrees well with observations (Shu et al., 2015; Roach et al., 2020). Most CMIP5 models do not realistically simulate the evolution of Antarctic sea-ice volume (Shu et al., 2015) and consistently overestimate the amount of low concentration sea ice and underestimate the amount of high concentration sea ice (Roach et al., 2018a). CMIP6 models, in contrast, simulate a more realistic distribution of regional sea-ice coverage (Roach et al., 2020). Most CMIP5 models poorly represent Antarctic sea-ice drift (e.g., (Schroeter et al., 2018; Holmes et al., 2019)), affecting simulated historical trends, with models that simulate a strong sea-ice motion showing more variability in sea-ice coverage than models with weaker sea-ice motion (Schroeter et al., 2018). Owing to *limited agreement* between model simulations and observations, limited reliable observations on a process level and

ACCEPTED VERSION SUBJECT TO FINAL EDITING

a lack of process understanding of the substantial spread in CMIP5 and CMIP6 model simulations, there remains *low confidence* in existing future projections of Antarctic sea-ice evolution.

The discrepancy between the modelled and observed evolution of Antarctic sea ice has been related by the SROCC to deficiencies in stratification, freshening by ice shelf melt water, clouds, and other wind and ocean driven processes. Recent studies highlight the possible mis-representation of freshwater fluxes from ice shelves (Jeong et al., 2020), and the possible effect of the low resolution of most models (Sidorenko et al., 2019), even though lower-resolution models are in principle capable of a realistic simulation of the seasonal sea-ice budgets in the Southern Ocean (Holmes et al., 2019). The relative importance of these possible reasons for model-shortcomings remains unclear (see section 3.4.1.2 for details).

The analysis and understanding of the long-term evolution of the Antarctic sea-ice cover is hindered by the scarcity of observational records before the satellite period and the scarcity of paleo records (see section 2.3.2.1.2 for further details). Such long records are particularly relevant given that the Southern Ocean response to external forcing takes longer than the length of the available direct observational record (Goosse and Renssen, 2001; Armour et al., 2016). There is only *limited evidence* for large-scale decadal fluctuations in sea-ice coverage caused by large-scale temperature and wind forcing. Sparse direct pre-satellite observations suggest a decrease in sea-ice coverage from the 1950s to the 1970s (Fan et al., 2014). Paleo-proxy data indicate that, on multi-decadal to multi-centennial time scales, sea-ice coverage of the Southern Ocean follows large-scale temperature trends (e.g., (Crosta et al., 2018; Chadwick et al., 2020; Lamping et al., 2020)), for example linked to fluctuations in the El Niño Southern Oscillation and Southern Annular Mode (Crosta et al., 2021), and that during the Last Glacial Maximum Antarctic sea ice extended to about the polar front latitude in most regions during winter, whereas the extent during summer is less well understood (e.g., (Benz et al., 2016; Xiao et al., 2016; Nair et al., 2019)).

Regionally, proxy data from ice cores consistently indicate that the increase of sea-ice area in the Ross Sea and the decrease of sea-ice area in the Bellingshausen Sea are part of longer centennial trends and exceed internal variability on multi-decadal time-scales (e.g., (Thomas et al., 2019; Tesi et al., 2020)) (*medium confidence*). These centennial trends are consistent with simulations from CMIP5 models (Hobbs et al., 2016a; Jones et al., 2016b; Kimura et al., 2017).

There is *low confidence* in the attribution of the observed changes in Antarctic sea-ice area (Section 3.4.1.2). Based on the available evidence, the lack of a negative trend of Antarctic sea-ice area despite substantial global warming in recent decades has been attributed to internal variability in analyses of the observational record (Meier et al., 2013; Gallaher et al., 2014; Gagné et al., 2015b), reconstructions from early observations (Fan et al., 2014; Edinburgh and Day, 2016) and proxy data (Hobbs et al., 2016a), and model simulations (Turner et al., 2013; Zunz et al., 2013; Zhang et al., 2019c). Nonetheless, without accurate simulations of observed changes, the possible contribution of anthropogenic forcing to the regional changes in sea-ice area remains unclear (Hosking et al., 2013; Turner et al., 2013; Haumann et al., 2014; Zhang et al., 2019c)

The attribution of the observed trends in atmospheric and oceanic forcing is also uncertain because of limited observational records and discrepancies between modelled and observed evolution of the sea-ice cover. More specifically, there is contrasting evidence for a direct role of stratospheric ozone depletion on the observed changes in atmospheric circulation (Haumann et al., 2014; England et al., 2016; Landrum et al., 2017). In contrast, there is *high confidence* that multi-decadal variations in the tropical Pacific and in the Atlantic affect the Amundsen Sea low (Li et al., 2014; Kwok et al., 2016; Meehl et al., 2016; Purich et al., 2016; Simpkins et al., 2016), while other modes of climate variability (Annex IV) affect, for example, Southern Ocean cyclone activity (Simpkins et al., 2012; Cerrone et al., 2017; Schemm, 2018).

9.3.2.2 Antarctic sea-ice thickness

The SROCC assessed that observations are too sparse to reliably estimate long-term trends in Antarctic sea-ice thickness. This remains true, and only qualitative statements on prevailing thicknesses are possible. Data

ACCEPTED VERSION SUBJECT TO FINAL EDITING

from ICESat-1 laser altimetry (Kurtz and Markus, 2012), from Operation IceBridge (Kwok and Kacimi, 2018), and long-term ship-board observations collected in the ASPeCt data set (Worby et al., 2008) suggest that sea ice thicker than 1 m prevails in regions of multi-year ice along the eastern coast of the Antarctic Peninsula in the Weddell Sea, in the high-latitude embayment of the Weddell Sea, and along the coast of the Amundsen Sea, with remaining regions dominated by thinner first year sea ice (*high confidence*). Regional patterns in ice thickness are affected by large snow deposition and resulting snow-ice formation (Massom et al., 2001; Maksym and Markus, 2008), and deformation, ridging, and rafting that regionally cause formation of very thick sea ice (Massom et al., 2006; Williams et al., 2015a). In addition, near ice shelves a sub-ice platelet layer from supercooled water can significantly increase sea-ice thickness (Hoppmann et al., 2020; Haas et al., 2021). Regarding snow thickness, observations are too sparse in space and time to reliably estimate changes across Southern Ocean sea ice (Webster et al., 2018).

There is *low confidence* in the long-term trend of Antarctic sea-ice thickness. Both ASPeCt and ICESat-1 measurements are biased low in regions with thick ice (Kern and Spreen, 2015), compared to results from reanalyses (Massonnet et al., 2013; Haumann et al., 2016) and observations with autonomous vehicles under sea ice (Williams et al., 2015a). Estimates of sea-ice thickness from Cryosat-2 do not substantially reduce uncertainty, primarily because of the unknown snow thickness and radar scattering above the snow–ice interface (Bunzel et al., 2018; Kwok and Kacimi, 2018; Kacimi and Kwok, 2020). Isolated in-situ time series show no clear long-term trend in landfast ice thickness in the Weddell Sea (Arndt et al., 2020). Reanalyses suggest overall increasing sea-ice thickness and volume between 1980 and 2010 (Holland et al., 2014; Zhang, 2014; Massonnet et al., 2015), while CMIP5 (Shu et al., 2015; Schroeter et al., 2018) and CMIP6 models simulate a decrease in Antarctic sea-ice volume over the historical period. Because of this discrepancy, and the unclear reliability of the reanalyses (Uotila et al., 2019), there is *low confidence* in CMIP5 and CMIP6 simulated future Antarctic sea-ice thickness.

9.4 Ice Sheets

9.4.1 Greenland Ice Sheet

9.4.1.1 Recent observed changes

In this section we present regional mass change time series for the Greenland Ice Sheet and assess the different processes causing the increase in mass loss. The vast increase in observational products from various platforms (e.g, GRACE, PROMICE, ESA-CCI, NASA MEaSUREs) provide a consistent and clear picture of a shrinking Greenland Ice Sheet (Colgan et al., 2019; Mottram et al., 2019; Mouginot et al., 2019; King et al., 2020; Mankoff et al., 2020; Moon et al., 2020; Sasgen et al., 2020; The IMBIE Team, 2020; Velicogna et al., 2020). Section 2.3.2.4.1 provides an updated estimate of the total Greenland Ice Sheet mass change in a global context (Figure 2.24). A paleo perspective on Greenland Ice Sheet evolution is presented in Section 9.6.2 with estimated ice sheet extent at different times shown in Figure 9.17.

For the 20th century, the SROCC (Meredith et al., 2019) presented one reconstruction for 1900-1983 and estimated mass change for the Greenland Ice Sheet and its peripheral glaciers for the period 1901-1990. Since the SROCC, a comprehensive new study has extended the satellite record back to 1972 (Mouginot et al., 2019,Figure 9.16). The rate of change of ice sheet mass was positive (i.e., it gained mass) in 1972-1980 (47±21 Gt yr^{-1}) and then negative (i.e., it lost mass) (-51±17 Gt yr^{-1} and -41±17 Gt yr^{-1}) in 1980-1990 and 1990-2000, respectively. Other ice discharge time series starting in 1985 (King et al., 2018, 2020, Mankoff et al., 2019, 2020) agree with (Mouginot et al., 2019, Figure 9.16). There is *limited evidence* of temporally and spatially heterogeneous Greenland outlet glacier evolution during 20th century (Lea et al., 2014; Lüthi et al., 2016; Andresen et al., 2017; Khan et al., 2020; Vermassen et al., 2020). Historical photographs (Khan et al., 2020) show large mass losses of Jakobshavn and Kangerlussuaq glaciers in West Greenland from 1880 until the 1940s, exceeding their 21st century mass loss, whereas the Helheim Glacier in East Greenland remained stable, gained mass in the 1990s then rapidly lost mass after 2000. Together, these 3 large outlet glaciers, draining ~12% of the ice sheet surface area, have lost 22±3 Gt yr^{-1} in the period 1880-2012 (Khan et al., 2020). Overall, these studies provide a variable picture of the Greenland Ice Sheet mass change in the 20th

ACCEPTED VERSION SUBJECT TO FINAL EDITING

century. The updated mass loss of Greenland Ice Sheet including peripheral glaciers for period 1901-1990 is 120 [70–170] Gt yr^{-1} (see Table 9.5 and Figures 9.16, 9.17).

Post-1992, the SROCC stated that it is *extremely likely* that the rate of mass change of Greenland Ice Sheet was more negative during 2012-2016 than during 1992-2001, with *very high confidence* that summer melting has increased since the 1990s to a level unprecedented over at least the last 350 years. Since the SROCC, the updated synthesis of satellite observations by the Ice Sheet Mass Balance Intercomparison Exercise (The IMBIE Team, 2020) and the GRACE Follow-On (GRACE-FO) Mission (Abich et al., 2019; Kornfeld et al., 2019), have confirmed the mass change record and the record has been extended to 2020 (The IMBIE team, 2021) as presented in 2.3.2.4.. The Greenland Ice Sheet lost 4890 [4140–5640] Gt of ice between 1992 and 2020, causing sea level to rise by 13.5 [11.4–15.6] mm (The IMBIE Team, 2021) (Section 2.3.2.4.1; Figure 9.16, Table 9.5). The IMBIE Team (2020) estimates are consistent with other post-AR5 reviews (Figure 9.17, Table 9.SM.1) (Bamber et al., 2018a; Cazenave et al., 2018; Mouginot et al., 2019; Slater et al., 2021). Recent GRACE-FO data (Sasgen et al., 2020; Velicogna et al., 2020) show that after two cold summers in 2017 and 2018, with relatively moderate mass change of about -100 Gt yr^{-1}, the 2019 mass change (-532 ± 58 Gt yr^{-1}) was the largest annual mass loss in the record. The *high agreement* across a variety of methods confirms the SROCC and Chapter 2 assessments. The mass-loss rate was on average 39 [–3 to 80] Gt yr^{-1} over the period 1992–1999, 175 [131 to 220] Gt yr^{-1} over the period 2000–2009 and 243 [197 to 290] Gt yr^{-1} over the period 2010–2019 (see Table 9.SM.1).

[START FIGURE 9.16 HERE]

Figure 9.16: Mass changes and mass change rates for Greenland and Antarctic ice sheet regions. (Upper Left) Time series of mass changes in Greenland for each of the major drainage basins shown in the inset figure (Bamber et al., 2018b; Mouginot et al., 2019) for the periods 1972 – 2018 and 1992-2018. (Upper Right) Time series of mass changes for three portions of Antarctica (Bamber et al., 2018b) for the period 1992 – 2018. (Lower rows) Estimates of mass change rates of surface mass balance, discharge and mass balance in seven Greenland regions (Bamber et al., 2018b; Mankoff et al., 2019; Mouginot et al., 2019; King et al., 2020). Estimates of mass change rates of surface mass balance, discharge and mass balance for three regions of Antarctica (Bamber et al., 2018b; The IMBIE Team et al., 2018; Rignot et al., 2019). Further details on data sources and processing are available in the chapter data table (Table 9.SM.9).

[END FIGURE 9.16 HERE]

The SROCC assessed with *high confidence* that surface mass balance (SMB), rather than discharge, has started to dominate the mass loss of the Greenland Ice Sheet (due to increased surface melting and runoff), increasing from 42% of the total mass loss for 2000–2005 to 68% for 2009–2012. While these estimates have been confirmed since the SROCC (Mouginot et al., 2019), the new longer record, as well as further comprehensive studies (Khan et al., 2015; Colgan et al., 2019; Mottram et al., 2019; The IMBIE Team, 2020) and detailed discharge records (King et al., 2020; Mankoff et al., 2020) reveal a more complex picture than the continuous trajectory this statement may have implied. Discharge was relatively constant from 1972-1999, varying by around 6% for the whole ice sheet, while SMB varied by over a factor of two interannually, leading to either mass gain or loss in a given year (Figure 9.16). During 2000-2005, the rate of discharge increased by 18%, then remained fairly constant again (increasing by 6% from 2006-2018). After 2000, SMB decreased more rapidly than discharge increased. In summary, the consistent temporal pattern in these longer datasets leads to *high confidence* that the Greenland Ice Sheet mass losses are increasingly dominated by SMB, but there is *high confidence* that mass loss varies strongly, due to large interannual variability in SMB.

On a regional scale, the surface elevation is lowering in all regions, and widespread terminus and calving front retreats have been observed (with no glaciers advancing) (Mottram et al., 2019; Moon et al., 2020). The largest mass losses have occurred along the west coast and in southeast Greenland (Figure 9.16), concentrated at a few major outlet glaciers (Mouginot et al., 2019; Khan et al., 2020). This regional pattern is consistent with independent Global Navigation Satellite System (GNSS) observations from the Greenland

ACCEPTED VERSION SUBJECT TO FINAL EDITING

GPS network which show elastic bedrock uplift of tens of centimetres between 2007-2019 as a result of ongoing ice mass loss (Bevis et al., 2019). The regional time series (Figures 9.16, Atlas.30) show that SMB has been gradually decreasing in all regions while the increase in discharge in the southeast, central east, northwest and central west has been linked to retreating tidewater glaciers (Figure 9.16). In summary, the detailed regional records show an increase in mass loss in all regions after the 1980s, caused by both increases in discharge and decreases in SMB (*high confidence*), although the timing and patterns vary between regions. The largest mass loss occurred in the northwest and the southeast of Greenland (*high confidence*).

[START FIGURE 9.17 HERE]

Figure 9.17: Greenland Ice Sheet cumulative mass change and equivalent sea level contribution. (a) A p-box (Section 9.6.3.2) based estimate of the range of values of paleo Greenland ice sheet mass and sea level equivalents relative to present day and the median over all central estimates (Simpson et al., 2009; Argus and Peltier, 2010; Fyke et al., 2011; Robinson et al., 2011; Colville et al., 2011; Dolan et al., 2011; Born and Nisancioglu, 2012; Miller et al., 2012b; Helsen et al., 2013; Nick et al., 2013; Quiquet et al., 2013; Stone et al., 2013; Dahl-Jensen et al., 2013; Lecavalier et al., 2014; Robinson and Goelzer, 2014; Colleoni et al., 2014; Koenig et al., 2015; Peltier et al., 2015; Calov et al., 2015; Stuhne and Peltier, 2015; Vizcaino et al., 2015; Calov et al., 2018; Dutton et al., 2015; Goelzer et al., 2016; Khan et al., 2016; Yau et al., 2016; de Boer et al., 2017; Simms et al., 2019); and (b) cumulative mass loss (and sea level equivalent) from 1972 (Mouginot et al., 2019) and 1992 (Bamber et al., 2018b; The IMBIE Team, 2019), the estimated mass loss from 1840 (Box and Colgan, 2013; Kjeldsen et al., 2015) indicated with a shaded box and projections from ISMIP6 by 2100 under RCP8.5/SSP5-8.5 and RCP2.6/SSP1-2.6 scenarios (thin lines from (Goelzer et al., 2020; Edwards et al., 2021; Payne et al., 2021) and *likely* and *very likely* range of the ISMIP6 emulation (shades and bold line (Edwards et al., 2021)) are shown as a timeseries. Schematic interpretations of individual reconstructions (Lecavalier et al., 2014; Goelzer et al., 2016; Berends et al., 2019) of the spatial extent of the Greenland ice sheet are shown for the (c) mid-Pliocene Warm Period, (d) the Last Interglacial and (e) the Last Glacial Maximum: grey shading shows extent of grounded ice. Maps of mean elevation changes (f) 2010-2017 derived from CryoSat 2 radar altimetry (Bamber et al., 2018b) and (g) ISMIP6 model mean (2093-2100) projected changes for the MIROC5 climate model under the RCP8.5 scenario (Goelzer et al., 2020). Further details on data sources and processing are available in the chapter data table (Table 9.SM.9).

[END FIGURE 9.17 HERE]

The SROCC stated with *high confidence* that variability in large-scale atmospheric circulation is an important driver of short-term SMB changes for the Greenland Ice Sheet. This effect of atmospheric circulation variability on both precipitation and melt rates (and the SROCC assessment) is confirmed by more recent publications (Välisuo et al., 2018; Zhang et al., 2019a; Velicogna et al., 2020). The strong mass loss in 2019 (Cullather et al., 2020; Hanna et al., 2020; Tedesco and Fettweis, 2020) was driven by highly anomalous atmospheric circulation patterns, both on daily (Cullather et al., 2020) and seasonal timescales (Tedesco and Fettweis, 2020). Although surface melt is anticorrelated with the summer North Atlantic Oscillation index (Välisuo et al., 2018; Ruan et al., 2019; Sherman et al., 2020), especially in West Greenland (Bevis et al., 2019), Greenland Ice Sheet melt is more strongly correlated with the Greenland Blocking Index (Hanna et al., 2016, 2018) than with the summer North Atlantic Oscillation index (Huai et al., 2020).

The SROCC did not assess the role of cloud changes in detail. Studies since the AR5 have shown that higher incident shortwave radiation in conjunction with reduced cloud cover leads to increased melt rates, particularly over the low albedo ablation zone in the southern part of the Greenland Ice Sheet (Hofer et al., 2017; Niwano et al., 2019; Ruan et al., 2019). Conversely, an increase in cloud cover over the high-albedo central parts of the ice sheet, leading to higher downwelling longwave radiation, was shown to lead either to increased melt (Bennartz et al., 2013) or reduced refreezing of meltwater (van Tricht et al., 2016). The elevation dependence of the cloud radiative effect and its control on surface meltwater generation and refreezing (Wang et al., 2019c; Hahn et al., 2020) can induce a spatially consistent response of the integrated

ACCEPTED VERSION SUBJECT TO FINAL EDITING

Greenland Ice Sheet melt to dominant patterns of cloudand atmospheric variability. The short- and longwave radiation effects on surface melt by clouds have been shown to compensate for each other during events of strong atmospheric rivers and the increase in melt is caused by increased sensible heat fluxes during such events (Mattingly et al., 2020). In summary, there is *medium confidence* that cloud cover changes are an important driver of the increasing melt rates in the southern and western part of the Greenland Ice Sheet.

The SROCC stated with *high confidence* that positive albedo feedbacks contributed substantially to the post-1990s Greenland Ice Sheet melt increase. Several, mostly positive, feedbacks involving surface albedo operate on ice sheets (e.g., Fyke et al., 2018). Melt amplification by the observed increase of bare ice exposure through snowline migration to higher parts of the ice sheet since 2000 (Shimada et al., 2016; Ryan et al., 2019) was five times stronger than the effect of hydrological and biological processes that lead to reduced bare ice albedo (Ryan et al., 2019). Impurities, in part biologically active (Ryan et al., 2018), have been observed to lead to albedo reduction (Stibal et al., 2017) and are estimated to have increased runoff from bare ice in the south-western sector of the Greenland Ice Sheet by about 10% (Cook et al., 2020). In summary, new studies confirm that there is *high confidence* that the Greenland Ice Sheet melt increase since about 2000 has been amplified by positive albedo feedbacks, with the expansion of bare-ice extent being the dominant factor, and albedo in the bare-ice zone being primarily controlled by distributed biologically active impurities (see also Section 7.3.4.3.

The SROCC reported with *medium confidence* that around half of the 1960-2014 Greenland Ice Sheet surface meltwater ran off, while most of the remainder infiltrated firn and snow, where it either refroze or accumulated in firn aquifers. Studies since SROCC show a decrease of firn air content between 1998-2008 and 2010-2017 (Vandecrux et al., 2019) in the low-accumulation percolation area of western Greenland, reducing meltwater retention capacity. Moreover, meltwater infiltration into firn can be strongly limited by low-permeability ice slabs created by refreezing of infiltrated meltwater (Machguth et al., 2016). Recent observations and modelling efforts indicate that rapidly expanding low-permeability layers have led to an increase in runoff area since 2001 (MacFerrin et al., 2019). In summary, there is *medium confidence* that meltwater storage and refreezing can temporarily buffer a large-scale melt increase but limiting factors have been identified.

The SROCC reported that there was *medium confidence* that ocean temperatures near the grounding zone of tidewater glaciers are critically important to their calving rate, but there was *low confidence* in understanding their response to ocean forcing. The increase in ice discharge in the late 1990s and early 2000s (Mouginot et al., 2019; King et al., 2020; Mankoff et al., 2020) has been associated with a period of widespread tidewater glacier retreat (Murray et al., 2015; Wood et al., 2021) and speed up (Moon et al., 2020). Since the SROCC, new studies provide strong evidence for rapid submarine melting at tidewater glaciers (Sutherland et al., 2019; Wagner et al., 2019; Bunce et al., 2020; Jackson et al., 2020b). Changes in submarine melting and subglacial meltwater discharge can trigger increased ice discharge by reducing the buttressing to ice flow and promoting calving (Benn et al., 2017; Todd et al., 2018; Ma and Bassis, 2019; Mercenier et al., 2020); through undercutting (Rignot et al., 2015; Slater et al., 2017b; Wood et al., 2018; Fried et al., 2019) and frontal incision (Cowton et al., 2019). Warming ocean waters have been implicated in the recent thinning and breakup of floating ice tongues in northeastern and northwestern Greenland (Mouginot et al., 2015; Wilson et al., 2017; Mayer et al., 2018; Washam et al., 2018; An et al., 2021; Wood et al., 2021). On decadal timescales, tidewater glacier terminus position correlates with submarine melting (Slater et al., 2019). Over shorter timescales, individual glaciers or clusters of glaciers can behave differently and asynchronously (Bunce et al., 2018; Vijay et al., 2019; An et al., 2021), and there are not always clear associations between water temperature and glacier calving rates (Motyka et al., 2017), retreat or speedup (Joughin et al., 2020; Solgaard et al., 2020). Variations in ice mélange at the front of a glacier, associated with changes in ocean and air temperature, have also emerged as a plausible control on calving (Burton et al., 2018; Xie et al., 2019; Joughin et al., 2020). In summary, there is *high confidence* that warmer ocean waters and increased subglacial discharge of surface melt at the margins of marine-terminating glaciers increase submarine melt, which leads to increased ice discharge, and *medium confidence* that this contributed to the increased rate of mass loss from Greenland particularly in the period 2000-2010 when increased discharge was observed in the southeast and northwest.

ACCEPTED VERSION SUBJECT TO FINAL EDITING

The SROCC reported that accurate bedrock topography is required for understanding and projecting the glacier response to ocean forcing. Accurate bathymetry is essential for both establishing which water masses enter glacial fjords and for reliable estimates of the submarine melt rates experienced by tidewater glaciers (Schaffer et al., 2020; Slater et al., 2020b; Wood et al., 2021). Subglacial and lateral topography is known to strongly modulate tidewater glacier dynamics and the sensitivity of tidewater glaciers to climatic forcing (Enderlin et al., 2013; Catania et al., 2018). Bathymetric mapping around the ice sheet has greatly improved with direct and gravimetric surveys (Millan et al., 2018; An et al., 2019a, 2019b; Jakobsson et al., 2020) leading to the improvement of Greenland-wide bathymetric and topographic mapping (e.g., Morlighem et al., 2017). However, large uncertainties in ice thickness remain for around half of the outlet glaciers (Mouginot et al., 2019; Wood et al., 2021) and sea-ice covered and iceberg-packed regions remain poorly sampled near glacier termini (Morlighem et al., 2017). There is *high confidence* that bathymetry (governing the water masses that flow into fjord cavities) and fjord geometry and bedrock topography (controlling ice dynamics) modulate the response of individual glaciers to climate forcing.

The AR5 assessed that it is *likely* that anthropogenic forcing contributed to the surface melting of Greenland since 1993 (Bindoff et al., 2013). Section 3.4.3.2 assesses that it is *very likely* that human influence has contributed to the observed surface melting of the Greenland Ice Sheet over the past two decades, and there is *medium confidence* of an anthropogenic contribution to recent mass loss from Greenland.

9.4.1.2 Model evaluation

The SROCC (Oppenheimer et al., 2019) stated that substantial challenges remained for modelling of both the Greenland surface mass balance and the dynamical ice sheet. Since the SROCC, further insights into modelling of the Greenland ice sheet has come from model intercomparison studies of both the surface mass balance (Fettweis et al., 2020) and dynamical ice sheets (Goelzer et al., 2020). Further aspects relevant to the forcing of the ice sheet from large scale global climate models and regional climate models are discussed in Box 9.3 and Section Atlas.11.2.

The SROCC stated that climate model simulations of Greenland surface mass balance (SMB) had improved since the AR5 giving *medium confidence* in the ability of climate models to simulate changes in Greenland SMB. Since the SROCC, a multi-model intercomparison study (Fettweis et al., 2020) of regional and global climate models has shown that the greatest inter-model spread occurs in the ablation zone, due to deficiencies in an accurate model representation of the ablation zone extent and processes related to surface melt and runoff, confirming the SROCC statement that bare-ice model uncertainty is large (Ryan et al., 2019). This intercomparison showed that simple, well-tuned SMB models using positive degree-day melt schemes can perform as well as more complex physically-based models (Figure Atlas.30). Furthermore, the ensemble-mean of the models produced the best estimate of the present-day SMB relative to observations (particularly in the ablation zone). Further assessment of Greenland ice sheet regional SMB can be found in Section Atlas 11.2.3. Recent progress confirms the SROCC assessment that there is *medium confidence* in the ability of climate models to simulate changes in Greenland SMB.

The SROCC noted increased use of coupled climate-ice sheet models for simulating the Greenland ice sheet, but also that remaining deficiencies in coupling between models of climate and ice sheets (e.g., low spatial resolution) limited the adequate representation of the feedbacks between them. Some Earth System Models now incorporate multi-layer snow models and full energy balance models (Punge et al., 2012; Cullather et al., 2014; van Kampenhout et al., 2017; Alexander et al., 2019a; van Kampenhout et al., 2020) or use elevation classes to compensate for their coarser resolution (Lipscomb et al., 2013; Sellevold et al., 2019; Muntjewerf et al., 2020a, 2020b; Gregory et al., 2020). Resulting SMB simulations compare better with Regional Climate Models and observations (Alexander et al., 2019b; van Kampenhout et al., 2020), but remaining shortcomings lead to problems reproducing a present-day ice sheet state close to observations. In summary, there is *medium confidence* in quantitative simulations of the present-day state of the Greenland ice sheet in ESMs.

The SROCC (Meredith et al., 2019) stated that there is *low confidence* in understanding coastal glacier

ACCEPTED VERSION SUBJECT TO FINAL EDITING

response to ocean forcing because submarine melt rates, calving rates, bed and fjord geometry and the roles of ice mélange and subglacial discharge are poorly understood. Ice-ocean interactions remain poorly understood and difficult to model, with parameterizations often used for calving of marine-terminating glaciers (Mercenier et al., 2018) and submarine and plume-driven melt (Beckmann et al., 2019). Due to the difficulties of modelling the large number of marine-terminating glaciers and limited availability of high-resolution bedrock data, the majority of recent modelling work on Greenland outlet glaciers is focused on individual or a limited number of glaciers (Krug et al., 2014; Bondzio et al., 2016; Morlighem et al., 2016a; Muresan et al., 2016; Bondzio et al., 2017; Choi et al., 2017; Beckmann et al., 2019), or a specific region (Morlighem et al., 2019). Since the SROCC, using a flowline model that includes calving and submarine melting, Beckmann et al. (2019) concluded that the AR5 upscaling of contributions from four of the largest glaciers (Nick et al., 2013) overestimated the total glacier contribution from the Greenland ice sheet, due to differences in response between large and small glaciers. The regional study of Morlighem et al. (2019) confirms that ice-ocean interactions have the potential to trigger extensive glacier retreat over decadal timescales as indicated by observations (Section 9.4.1.1). A focus in continental ice sheet models has been the improved treatment of marine-terminating glaciers via inclusion of calving processes and freely moving calving fronts (Aschwanden et al., 2019; Choi et al., 2021). An improved bedrock topographic dataset (Morlighem et al., 2017) allows for ice discharge to be better captured for outlet glaciers in continental ice sheet models and simulations indicate that bedrock topography controls the magnitude and rate of retreat (Aschwanden et al., 2019; Rückamp et al., 2020). Overall, although there is *high confidence* that the dynamic response of Greenland outlet glaciers is controlled by bedrock topography, there is *low confidence* in quantification of future mass loss from Greenland triggered by warming ocean conditions due to limitations in current understanding of ice-ocean interactions, its implementation in ice sheet models, and knowledge of bedrock topography.

The SROCC (Oppenheimer et al., 2019) noted the progress made in Greenland Ice Sheet models since the AR5. New since the SROCC is a focus on improved representation of the present-day state of the ice sheet (Goelzer et al., 2018, 2020) (Box 9.3). Improvements are closely linked to the growing number and quality of observations (Section 9.4.1.1), new techniques to generate internally consistent input data sets (Morlighem et al., 2014, 2016b), wider use of data assimilation techniques (Larour et al., 2014, 2016; Perego et al., 2014; Goldberg et al., 2015; Lee et al., 2015; Schlegel et al., 2015; Mosbeux et al., 2016), increased model resolution (Aschwanden et al., 2016) and tuning of key processes such as calving (Choi et al., 2021). A remaining challenge is *low confidence* in reproducing historical mass changes of the Greenland Ice Sheet (Box 9.3). However, there is *medium confidence* in ice sheet models reproducing the present state of the Greenland Ice Sheet leading to *medium confidence* in current ability to accurately project its future evolution.

9.4.1.3 Projections to 2100

The AR5 and the SROCC projected that changes in Greenland surface mass balance (SMB) will contribute to sea level in 2100 by 0.03 (0.01 to 0.07) m SLE under RCP2.6 and 0.07 (0.03 to 0.16) m SLE under RCP8.5. New since the SROCC are projections of SMB obtained by an Earth system model, two regional climate models, and reconstructions based on temperature from the CMIP5 and CMIP6 ensembles (Hofer et al., 2020; Noël et al., 2021). The range of sea level contribution from Greenland surface mass balance in Noël et al. (2021) are comparable to the AR5 assessment when either CMIP5 or CMIP6 models are used while Hofer et al., (2020) find a greater mass loss across all CMIP6 emission scenarios when compared to CMIP5 scenarios. Using SSP5-8.5 instead of RCP8.5 increases the mean projected sea level from 2005-2100 by up to 0.06 m in the regional climate model simulations of Hofer et al., (2020) who attribute the difference mainly to a greater Arctic amplification and associated cloud and sea ice feedbacks in the CMIP6 SSP5-8.5 simulations. In summary, these new projections with fixed ice sheet topography do not provide sufficient evidence to change the AR5 and SROCC assessment.

Reviewing modelling studies since the AR5 (Church et al., 2013a), the SROCC (Oppenheimer et al., 2019) assessed Greenland's contribution to future sea level to be relatively similar to the AR5 (Table 9.2). The baseline for projections has shifted from 1986-2005, in the SROCC, to 1995-2014 in this report. Adjusted to the new 1995-2014 baseline by subtracting 0.01 m, the SROCC projected a *likely* contribution of 0.07 (0.03

ACCEPTED VERSION SUBJECT TO FINAL EDITING

– 0.11) m SLE under RCP2.6 and 0.14 (0.08 – 0.27) m SLE under RCP8.5 by 2100. Since the SROCC, new projections for the 21st century have included dynamic ice sheets coupled to Earth system models (Muntjewerf et al., 2020a; Van Breedam et al., 2020) or regional atmospheric models (Le clec'h et al., 2019) (Table 9.2). The coupled ESM-ice sheet CESM2-CISM2 model projects a sea level rise of 0.109 m in 2100 relative to 2015 under SSP5-8.5 (Muntjewerf et al., 2020a) and a similar contribution under the idealized 1% yr^{-1} increase in CO_2 scenario (Muntjewerf et al., 2020b). The CESM2-CISM2 simulations include ice sheet-atmosphere interactions and ice sheet surface meltwater is routed to the ocean. The coupled regional atmospheric model and ice sheet model (MAR-GRISLI) projects a sea level rise of 0.079 m in 2100 relative to 2000 under RCP8.5 (Le clec'h et al., 2019). An Earth System model of lower complexity coupled to an ice sheet model gives a sea level contribution of 0.025 to 0.064 m under RCP2.6 and 0.056 to 0.12 m under RCP8.5 (the range is due to four simulations with different parameter sets for the atmosphere model) (Van Breedam et al., 2020). Van Breedam et al., (2020) identify a simulation with a preferred parameter set, that projects 0.034 m for RCP2.6and 0.073 m for RCP8.5 Although the ocean does not directly force the ice sheet models in these simulations, the new coupled models allow for interactions between ice sheet dynamics, surface mass balance and local climate. The coupled projections fall within the lower bounds of the AR5 and the SROCC, and as these studies do not prescribe ocean forcing directly, it is possible that the dynamic response is underestimated.

Since the SROCC, projections of the Greenland Ice Sheet are also now available from ISMIP6 (Nowicki et al., 2016, 2020a; Box 9.3; Annex II; Figure 9.17). The ISMIP6 multi-model projections are corrected with an assessment of the historical dynamical response to pre-2015 climate forcing (Box 9.3). For the period 2015-2100, the ISMIP6 uncorrected multi-model ensemble projects a sea level contributions ranging from 0.01 to 0.05 m under RCP2.6, 0.04 to 0.14 m under RCP8.5 (Goelzer et al., 2020), 0.02 to 0.06 m under SSP1-2.6 and 0.08 to 0.25 m under SSP5-8.5 (Payne et al., 2021)(Table 9.2). The higher mass loss in the SSPs is attributed to a larger decrease in SMB due to the high climate sensitivity of the models used (Payne et al., 2021). This finding is confirmed by (Choi et al., 2021), where CMIP6 SSP5-8.5 SMB leads to larger ice loss than CMIP5 RCP8.5 while ice discharge is similar. As the ISMIP6 framework considers a subset of the RCPs/SSPs and CMIP models, SSP-based projections have been inferred from multiple approaches. First, the ISMIP6 CMIP5-forced (Goelzer et al., 2020) and CMIP6-forced (Payne et al., 2021) combined ensemble projections were corrected with the historical trend (Box 9.3) using bootstrapping. Second, an emulator of the ISMIP6 projections (Edwards et al., 9998, Box 9.3) is forced by distributions of global surface air temperature for each SSP from a two-layer energy budget emulator (Supplementary Material 7.SM.2) and then corrected with the historical trend in the same way. These two approaches result in projections that are similar in their median values to the AR5 and SROCC projections (Table 9.2), but differ in their range. Similar results are obtained when the AR5 parametric fit is applied to the ISMIP6 models (Table 9.2, Supplementary Material 9.SM.4.4), which is used to estimate rates of change and post-2100 projections (Sections 9.4.1.4, 9.6.3.2).

The SROCC noted that the study by Aschwanden et al.,(2019) projects a significantly higher Greenland contribution to sea level than the assessed *likely* range in the AR5 and the SROCC. Under RCP8.5, Aschwanden et al., (2019) found that Greenland could contribute up to 0.33 m to sea level by 2100 relative to 2000 (the ensemble member that best reproduces 2000-2015 mean surface mass balance from a regional climate model projects Greenland mass losses of 0.08 m SLE under RCP2.6 and 0.18 m SLE under RCP8.5.) The SROCC noted that the potentially high sea level in this study could be due to the assumption of spatially uniform warming which can overestimate surface melt rates. However, it also reflects the *deep uncertainty* surrounding atmospheric forcing, surface processes, submarine melt, calving and ice dynamics. Goelzer et al., (2020) ascribe 40% of the ISMIP6 multi-model ensemble spread to ice sheet model uncertainty, 40% to climate model uncertainty and 20% to ocean forcing uncertainty. We note that this finding reflects the current challenges associated with the representation of ice-ocean interactions in models, and the uncertainty in basal conditions (Section 9.4.1.2). However, this finding is consistent with the work of Aschwanden et al., (2019) and thus, there is *medium confidence* that uncertainty in mass loss from the Greenland Ice Sheet is dominated by uncertainty in climate scenario and surface processes, whereas uncertainty in calving and frontal melt play a minor role.

The SROCC stated that surface processes, rather than ice discharged into the ocean, will dominate Greenland

ACCEPTED VERSION SUBJECT TO FINAL EDITING

ice loss over the 21st century, regardless of the emissions scenario (*high confidence*). This is confirmed by the ISMIP6 projections (Goelzer et al., 2020; Payne et al., 2021). The projected mass loss of Greenland is predominantly due to increased surface meltwater and loss in refreezing capacity resulting in decreasing SMB (*high confidence*), concurrent with rising temperatures and darkening of the ice sheet surface (Fettweis et al., 2013; Vizcaino et al., 2015; Le clec'h et al., 2019; Muntjewerf et al., 2020b, 2020a; Sellevold and Vizcaíno, 2020). Mass changes due to SMB and outlet glacier dynamics are linked (Goelzer et al., 2013; Fürst et al., 2015; Rückamp et al., 2020) as mass loss by one process decreases mass loss by the other (for example, SMB removes ice before it can reach the marine glacier terminus). There is *medium confidence* that the mass loss through ice discharge will decrease in the future (Fürst et al., 2015; Aschwanden et al., 2019; Golledge et al., 2019a), because an increase in mass loss (via increased discharge or surface runoff) leads, in most areas, to a retreat of the glacier margin onto land above sea level, isolating the ice sheet from marine influence.

In summary, it is *virtually certain* that the Greenland Ice Sheet will continue to lose mass this century under all emissions scenarios and *high confidence* that total mass loss by 2100 will increase with cumulative emissions. The sea level assessment (Section 9.6.3.3) is based on the emulated ISMIP6 projections allowing a more consistent approach to a wider range of climate and ocean forcings. The Greenland ice sheet is *likely* to contribute 0.06 (0.01 to 0.10) m under SSP1-2.6 and 0.13 (0.09 to 0.18) m under SSP5-8.5 by 2100 relative to 1995-2014. These projections (as well as those of AR5 and SROCC) are lower than the study of (Aschwanden et al., 2019) (or the range of possible sea level changes resulting from structured expert judgement (Bamber et al., 2019); Section 9.6.3.2), contributing to the *deep uncertainty* in projected sea level (Box 9.4). There is however *high confidence* that the loss from Greenland will become increasingly dominated by SMB and surface melt, as the ocean-forced dynamic response of glaciers will diminish as marine margins retreat to higher grounds.

[START TABLE 9.2 HERE]

Table 9.2: Projected sea level contributions in meters from the Greenland ice sheet by 2100 relative to 1995-2014, unless otherwise stated, for selected RCP and SSP scenarios. Italics denote partial contributions. Historical dynamic response omitted from ISMIP6 simulations is estimated to be 0.19 ± 0.10 mm yr^{-1} (0.02 m ± 0.01 m in 2100 relative to 2015). The climate forcing is described in Appendix 7.SM.2.

Representative Concentration Pathways (RCPs)				
Study	**RCP2.6**	**RCP4.5**	**RCP8.5**	**Notes**
IPCC AR5 and SROCC (Oppenheimer et al., 2019)	0.07 (0.03 to 0.11)	0.08 (0.04 to 0.15)	0.14 (0.08 to 0.27)	Median and *likely* (66% range) contributions in 2100 relative to 1995-2014. Median of multiple studies.
ISMIP6 CMIP5-forced (Goelzer et al., 2020); excludes historical dynamic response	*0.01 to 0.05*	---	*0.04 to 0.14*	*Range of multi-model contributions in 2100 relative to 2015 from 1 ESM for RCP2.6 and 6 ESMs for RCP8.5. (see caption).*
Coupled regional atmosphere-ice sheet model (Le clec'h et al.,	---	---	0.079	Contribution in 2100 relative to 2000 from MAR-GRISLI model.

ACCEPTED VERSION SUBJECT TO FINAL EDITING

2019)				
Coupled Earth system model of lower complexity-ice sheet model (Van Breedam et al., 2020)	0.034 (0.025 to 0.064)		0.073 (0.056 to 0.12)	Contribution in 2100 relative to 2000 from LOVECLIM-AGISM model. Preferred parameter set and range from 4 simulations with different parameters for atmosphere model.
Shared Socioeconomic Pathways (SSPs)				
Study	**SSP1-2.6**	**SSP2-4.5**	**SSP5-8.5**	**Notes**
Coupled Earth system model-ice sheet model (Muntjewerf et al., 2020, a)	---	---	0.109	Contribution in 2100 relative to 2015 from coupled CESM2-CISM2.
ISMIP6 CMIP6-forced (Payne et al., 2021)*; excludes historical dynamic response*	*0.02 to 0.06*	---	*0.08 to 0.25*	*Range of multi-model contributions in 2100 relative to 2015 from 1 ESM for SSP1-2.6 and 4 ESMs for SSP5-8.5.*
ISMIP6 CMIP5 and CMIP6 forced ensemble including historical dynamic response	0.06 (0.05 to 0.07) [0.04 to 0.08]	---	0.11 (0.09 to 0.14) [0.07 to 0.17]	Median (66% range) [90% range] contribution from ISMIP6 CMIP5- and CMIP6-forced multi-model ensembles
ISMIP6 with AR5 parametric fit: used to estimate rates (Supplementary Material 9.SM.4.4) including historical dynamic response.	0.08 (0.06 to 0.10) [0.05 to 0.12]	0.10 (0.08 to 0.13) [0.07 to 0.15]	0.14 (0.11 to 0.18) [0.10 to 0.22]	Median (66% range) [90% range] contribution from AR5 parametric fit to ISMIP6 ensemble, relative to 1995-2014.
Emulated ISMIP6; excludes historical dynamic response (Edwards et al.,	*0.03 (-0.01 to 0.08) [-0.04 to 0.12]*	*0.06 (0.01 to 0.10) [-0.02 to 0.15]*	*0.11 (0.06 to 0.16) [0.03 to 0.21]*	*Median (66% range) [90% range] contribution in 2100 relative to 2015 from emulator of ISMIP6 used with*

ACCEPTED VERSION SUBJECT TO FINAL EDITING

2021)				*chapter 7 climate forcing.*
This assessment: emulated ISMIP6 total	**0.06 (0.01 to 0.10) [-0.02 to 0.15]**	**0.08 (0.04 to 0.13) [0.01 to 0.18]**	**0.13 (0.09 to 0.18) [0.05 to 0.23]**	**As above, but relative to 1995-2014 and including historical dynamic response.**

[END TABLE 9.2 HERE]

9.4.1.4 Projections beyond 2100

The AR5 (Church et al., 2013a) assessed the contribution from Greenland to sea level projections in 2300 as 0.15 m SLE in low emissions scenarios (~RCP2.6) and 0.31-1.19 m in high scenarios (~RCP6.0/RCP8.5). The SROCC (Oppenheimer et al., 2019) did not update the AR5 estimates given *limited evidence* and *low agreement* from three new studies (Vizcaino et al., 2015; Calov et al., 2018; Aschwanden et al., 2019). Since the SROCC, a new study gives a sea level contribution of 0.11 to 0.20 m in low- and 0.61 to 1.29 m in high-emissions scenarios (Van Breedam et al., 2020). The low emissions projections by Van Breedam et al., (2020) encompass the AR5 assessed contribution, while the high emissions are higher than that from the AR5. The 'optimal' ensemble member of Aschwanden et al., (2019) (Section 9.4.1.3) indicates that Greenland could contribute 0.25 m under RCP2.6 and 1.74 m under RCP8.5. Structured expert judgement (Bamber et al., 2019) projects Greenland losses of 0.54 (0.28-1.28) m under 2ºC warming and 0.97 (0.4-2.23) m under 5ºC warming. These studies therefore agree that the AR5 and SROCC assessments are at the low end of the range of projections. In addition, observations suggest that Greenland Ice Sheet losses are tracking the upper range of AR5 projections (Slater et al., 2020b). Therefore, we update the *likely* range for the contribution of the Greenland Ice Sheet to GMSL by 2300 to 0.11-0.25 m under RCP2.6 and 0.31-1.74 m under RCP8.5. However, given the uncertainty in climatic drivers used to project ice sheet change over the 21st century (Goelzer et al., 2020; Hofer et al., 2020; Noël et al., 2021) and the large range in simulations since AR5 extending beyond 2100, we only have *low confidence* in the contribution to GMSL by 2300 and beyond.

The role of the elevation-mass feedback for future projections of Greenland can be assessed from paleo simulations. Ice sheet model simulations of the Laurentide (Gomez et al., 2015; Gregoire et al., 2016) and Eurasian (Alvarez-Solas et al., 2019) ice sheets invoke at least some contribution to last glacial termination mass loss from SMB reduction, as a consequence of an elevation–mass balance feedback (Levermann and Winkelmann, 2016). In a model spanning Meltwater Pulse 1A this mechanism increased mass loss by approximately 66% (Gregoire et al., 2016) but in Last Interglacial simulations the effect of this feedback is shown to depend on the surface scheme of the climate model employed (Plach et al., 2019). Given the agreement between theoretical analyses and paleo-ice sheet model experiments there is *high confidence* that the elevation-mass balance feedback is most relevant at multi-centennial and millennial timescales, consistent with future-focused studies (Gregory et al., 2020, Aschwanden et al. 2019, Le clec'h et al., 2019).

The SROCC adopted the AR5 assessment that complete loss of Greenland ice, contributing about 7 m to sea level, over a millennium or more would occur for a sustained GMST between 1ºC (*low confidence*) and 4ºC (*medium confidence*) above pre-industrial levels. New studies since the SROCC (Gregory et al., 2020; Van Breedam et al., 2020) confirm this assessment (see also Figure 9.30). Clark et al., (2016) estimate a complete loss to take about 8000 years at 5.5°C and about 3000 years at 8.6°C. Based on agreement between new and previous studies there is therefore *high confidence* that the rate at which Greenland ice sheet commitment is realized depends upon the amount of warming.

Accounting for more detailed feedbacks between the atmosphere and the ice sheet (Gregory et al., 2020) found a gradual relationship between sustained global mean warming and the corresponding near-

ACCEPTED VERSION SUBJECT TO FINAL EDITING

equilibrium ice sheet volume, in contrast to a sharp threshold as found by (Robinson et al., 2012). Rather than a climatically-controlled tipping point for irreversible loss of the Greenland Ice Sheet, (Gregory et al., 2020) found a threshold of irreversibility linked to ice sheet size, similar to previous work (Ridley et al., 2010). The results of Gregory et al., (2020) show that if the ice sheet loses mass equivalent to about 3-3.5 m of sea-level rise, it would not regrow to its present state, and 2m of the sea-level rise would be irreversible. At which point in time the current ice sheet might reach this critical volume depends on oceanic and atmospheric conditions, ice dynamics, and climate-ice sheet feedbacks (Gregory et al., 2020; Van Breedam et al., 2020), so projections differ in the magnitude and rate of temperature change to cross the threshold for irreversible loss. Projections from a large ensemble indicate that the mass threshold may be reached as early as in 400 years, if warming reaches as high as >10°C above present under extended RCP8.5 (Aschwanden et al., 2019). In summary, there is *high confidence* in the existence of threshold behaviour of the Greenland Ice Sheet in a warmer climate, however there is *low agreement* on the nature of the thresholds and the associated tipping points.

[START BOX 9.3 HERE]

BOX 9.3: Insights into land ice evolution from model intercomparison projects

Projections of ice sheets and glaciers in the AR5 (Church et al., 2013a) and the SROCC (Oppenheimer et al., 2019) were assessed by collecting single model studies (with the exception of glaciers in SROCC (Hock et al., 2019b)). Community benchmark experiments (ISMIP-HOM; (Pattyn et al., 2008) or Marine Ice Sheet Model Intercomparison Projects (MISMIP, (Pattyn et al., 2012); MISMIP3d, (Pattyn and Durand, 2013); MISMIP+ (Asay-Davis et al., 2016; Cornford et al., 2020)) have substantially advanced ice sheet modelling since the AR5. Model Intercomparison Projects (MIPs) now inform projections of both ice sheets and glaciers: the Ice Sheet MIP for CMIP6 (ISMIP6) (Section 9.4.1.3; 9.4.2.5), the Linear Antarctic Response MIP (LARMIP-2; Section 9.4.2.5) and GlacierMIP (Section 9.5.1.3).

Regional forcing for land ice intercomparison projects

Simulations of ice sheets and glaciers are dependent on forcing provided by atmosphere and ocean models. Despite progress in representing processes, reducing biases and increasing resolution, regional and global models still have difficulties reproducing observed regional air temperature, surface mass balance and ocean changes (Section 9.4.1.2, 9.4.2.2, Atlas.11). Assessment of CMIP5 and CMIP6 climate models, as forcing for land ice models, has been undertaken (Walsh et al., 2018; Barthel et al., 2020a; Marzeion et al., 2020; Nowicki et al., 2020b) with the aim of selecting the best available historical forcings and sampling potential regional future climate changes. Despite improvement in simulation of atmospheric forcing, persistent biases remain in CMIP5/6, which reduces the fidelity of historical and future simulations of land ice.

ISMIP6 initial state intercomparison projects (initMIP)

The ISMIP6 initial state intercomparison projects (initMIP) for the Greenland (Goelzer et al., 2018) and Antarctic (Seroussi et al., 2019) ice sheets were designed to understand the uncertainty in sea level projections resulting from the choice of initialization procedures used for projections of sea level (Nowicki et al., 2016). Participating modelling groups (Annex II) were free to decide on the initialization method used to bring ice sheet models to a present-day state with the effect of these choices captured in a control simulation (starting from the present day state, with no further climate forcing applied), which measures intrinsic model drift. Compared to the earlier SeaRISE intercomparison project (Bindschadler et al., 2013; Nowicki et al., 2013), the modelled present day ice sheets are in closer agreement with observations and the model drift has been reduced (Goelzer et al., 2018; Seroussi et al., 2019). Nonetheless, historical simulations remain challenging for ice sheet models, due to limited ice sheet observations prior to the satellite era and biases in the historical atmospheric and oceanic forcings from climate models (Nowicki and Seroussi, 2018).ISMIP6 and LARMIP-2 therefore did not provide a protocol for the historical runs used to bring the ice sheets to present-day, nor criteria for sub-selecting models from the multi-model ensemble based on ability to reproduce historical changes (Levermann et al., 2020a; Nowicki et al., 2020a).

ACCEPTED VERSION SUBJECT TO FINAL EDITING

ISMIP6 projections for the Greenland and Antarctic ice sheets

The ISMIP6 projection protocol (Nowicki et al., 2016, 2020a) was designed to sample the uncertainty in future sea level due to climate scenarios (via the use of high and low emission scenarios and multiple climate models), ice-ocean interactions and inland response to ice shelf collapse, and ice sheet model diversity. The participanting ice sheet models are listed in Annex II. For each ice sheet, forcing was selected (Barthel et al., 2020b) from the CMIP5 (Taylor et al., 2012) and CMIP6 (Eyring et al., 2016) models. Atmospheric forcing fields consisted of anomalies in surface mass balance and surface air temperatures generated directly from the CMIP models for the Antarctic ice sheet and downscaled using the MAR regional climate model for the Greenland ice sheet (Hofer et al., 2020). To sample the uncertainty due to ocean forcings, models used either a model-specific scheme using the ISMIP6-provided oceanic dataset or a standard ISMIP6 approach. For the Greenland ice sheet, the oceanic dataset consists of thermal forcing (temperature minus freezing temperature) extrapolated into fjords and subglacial runoff. The standard approach uses timelines of tidewater glacier retreat (Slater et al., 2019, 2020a). For the Antarctic ice sheet, the oceanic dataset consists of salinity, thermal forcing and temperature added to an observationally derived climatology and extrapolated under ice shelves. The standard approach is a basal melt rate that depends quadratically on thermal forcing, adapted from Favier et al., (2019), with two different calibrations (Figure 9.19, Jourdain et al., 2020) that reproduce observed basal melt rates across Antarctica or Pine Island Glacier, respectively (Sections 9.4.2.2, 9.4.2.3). Antarctic ice shelf disintegration datasets (Nowicki et al., 2020a) assume that ice shelves disintegrate when annual surface melt reaches a threshold (Trusel et al., 2015).

The ISMIP6 projections (Goelzer et al., 2020; Seroussi et al., 2020; Payne et al., 2021) are reported as experiment minus control and represent the sea level resulting from future climate change only. The control simulation, which has constant climate conditions starting in 2015 from the historical run, captures drift associated with the choices made for the initialization method and historical run. Subtraction of this control removes any long-term dynamic response of the ice sheet to pre-2015 climate change. This response has been assessed using dynamic discharge derived from observations over the last 40 years (Mouginot et al., 2019; Rignot et al., 2019), under an assumption that it persists at the past rate until 2100 rather than diminishing. The dynamic response to historical forcing is estimated as 0.19 ± 0.10 mm yr^{-1} for the Greenland ice sheet (Section 9.4.1.3) and 0.33 ± 0.16 mm yr^{-1} for the Antarctic ice sheet (Section 9.4.2.5). Over the period 2015-2100, this leads to an additional sea level contribution of 1.7 cm for Greenland and 2.8 cm for Antarctica.

LARMIP-2 projections for the Antarctic ice sheet

LARMIP-2 is focused on the uncertainty in the ocean forcing and associated ice shelf melting (Levermann et al., 2014, 2020a) with the majority of the models also participating in ISMIP6 (Annex II). The experiments start from present day and impose an additional basal ice shelf melting of 8 m yr^{-1} at the beginning of the 100 yr simulation. A control run is used to remove drift resulting from initialization. The time derivative of the ice sheet response yields a linear response function, which is then convoluted with a forcing of basal shelf melt time series for five Antarctic regions. The forcing time series for RCP2.6, 4.5, 6.0 and 8.5 were obtained from a random combination of global mean temperature for each RCP from MAGICC-6.0 (Meinshausen et al., 2011), a scaling factor and time delay for the relationship between global surface air temperature and subsurface ocean warming in a given sector of the Southern Ocean from one of 19 CMIP5 models (Taylor et al., 2012) and a basal melting sensitivity from the interval [7,- 16] m yr^{-1} $^{o}C^{-1}$ to convert the regional subsurface warming into basal ice shelf melting. This process is repeated 20,000 times to obtain a probability distribution of the sea level contribution for five Antarctic sectors. The linear response framework captures complex temporal responses of the ice sheets resulting from an increase in basal ice shelf melting, but neglects the response to surface mass balance and any self-dampening or self-amplifying processes, such as MISI. The LARMIP-2 method is applied to temperature projections for the SSPs (Supplementary Material 7.SM.2) and an estimate of surface mass balance change from the AR5 parametric Antarctic ice sheet surface mass balance model (Church et al., 2013a) is added to the results (Sections 9.4.2.4, 9.4.2.5, 9.6.3.2). It is not necessary to add a long-term dynamic response to the LARMIP-2 projections, as this is incorporated in the basal melt time series.

GlacierMIP projections

GlacierMIP (Marzeion et al., 2020) was designed to estimate the glacier contribution to sea level rise,

ACCEPTED VERSION SUBJECT TO FINAL EDITING

including from peripheral glaciers in Greenland and Antarctica that can be considered to be dynamically decoupled, or entirely separate, from the ice sheets. Glacier models are described in Annex II. Initial conditions were based on version 6 of the Randolph Glacier Inventory (RGI Consortium, 2017) and initial ice thickness and volume were provided from an update of Huss and Farinotti, (2012) (although some glacier models used their own estimates). Forcings were taken from ten different CMIP5 GCMs, selected based on availability of multiple RCPs, the choice in a previous model intercomparison (Hock et al., 2019a), and performance in glacier-covered regions according to Walsh et al., (2018). In addition, two global glacier models performed the same experiment with thirteen CMIP6 models (Section 9.5.1.3).

Use of an emulator with ISMIP6 and GlacierMIP projections

The ISMIP6 and GlacierMIP projections are primarily based on a limited number of CMIP5 RCPs and CMIP6 SSPs, and a limited sampling of ice-ocean interaction parameters and ice shelf collapse simulations. Emulators provide a method for expanding these projections to a range of SSPs with more comprehensive sampling of climate, ice sheet and glacier modelling uncertainties. Sections 9.4.1.3, 9.4.2.5 and 9.5.1.3 show estimates from the emulator of (Edwards et al., 2021). This is a Gaussian Process (rather than physically-based: Cross-Chapter Box 7.1) model derived from the ISMIP6 and GlacierMIP simulations; projections use distributions of GSAT from the two-layer emulator (Supplementary Material 7.SM.2) and ice sheet parameters as inputs, and include estimates of the emulator uncertainty. Probability intervals are therefore not inflated by a further factor, as is often the case for multi-model ensemble projections, to account for missing uncertainties (Section 9.6.3.2). The emulator is used in Section 9.6.3 to provide projections of the land-ice contribution to sea level that are fully consistent with each other, ocean heat content, and the assessed equilibrium climate sensitivity and projections of GSAT across the entire report.

[END BOX 9.3 HERE]

9.4.2 Antarctic Ice Sheet

9.4.2.1 Recent observed changes

As stated in Section 2.3.2.4, satellite observations by IMBIE combining multi-team estimates based on altimetry, gravity anomalies (GRACE) and the input-output method, already presented in the SROCC (Meredith et al., 2019), is updated and extended to 2020 (The IMBIE team, 2021). The Antarctic ice sheet (AIS) lost 2670 [1800–3540] Gt mass over the period 1992–2020, equivalent to 7.4 [5.0–9.8] mm global mean sea level rise (see Table 9.5 for contribution to sea-level budget and Figures 9.16, 9.18). Within uncertainties, this estimate agrees with a review of post-AR5 studies up to 2016 (Bamber et al., 2018b) and is consistent with recent single studies based on satellite laser altimetry (Smith et al., 2020), the input-output method (Rignot et al., 2019) and gravimetry (Velicogna et al., 2020). The mass-loss rate was on average 49 [-2 to 100] Gt yr^{-1} over the period 1992–1999, 70 [22 to 119] Gt yr^{-1} over the period 2000–2009 and 148 [94 to 202] Gt yr^{-1} over the period 2010–2016 (see Figures 9.16, 9.18 and Table 9.SM.1). However, recent work suggests that the mass loss has not further increased since 2016 because of regional mass gains in Dronning Maud Land (Velicogna et al., 2020). Mass loss of the West Antarctic and Antarctic Peninsula Ice Sheets has increased since about 2000 (*very high confidence*), essentially due to increased ice discharge (Harig and Simons, 2015; Paolo et al., 2015; Forsberg et al., 2017; Bamber et al., 2018b; Gardner et al., 2018; The IMBIE Team et al., 2018; Rignot et al., 2019)

The SROCC reported with *very high confidence* that the acceleration, retreat and thinning of the principal West Antarctic outlet glaciers has dominated the observed Antarctic mass loss over the last decades, and stated with *high confidence* that these losses were driven by melting of ice shelves by warm ocean waters. The average West Antarctic Ice Sheet (WAIS) mass loss of 82 ± 9 Gt yr^{-1} between 1992 and 2017 (The IMBIE Team et al., 2021) leads to substantial observed surface lowering (e.g., Schröder et al., 2019; Shepherd et al., 2019), particularly in coastal regions (Figure 9.18). Recent studies using satellite altimetry (Schröder et al., 2019) and the input-output method (Rignot et al., 2019) consistently show mass loss in these coastal regions since the late 1970s (Figure 9.16). Because of consistent multiple lines of evidence, there is *high confidence* in mass loss of the Totten Glacier in East Antarctica (Miles et al., 2013; Li et al., 2016b;

ACCEPTED VERSION SUBJECT TO FINAL EDITING

Mohajerani et al., 2018; Rignot et al., 2019; Schröder et al., 2019; Shepherd et al., 2019) since about 2000, dominated by changes in coastal ice dynamics (Li et al., 2016b). It is currently unclear whether mass loss of the East Antarctic Ice Sheet (EAIS) over the last three decades has been significant (Rignot et al., 2019) or, at 5 ± 46 Gt yr^{-1} between 1992 and 2017, essentially zero within uncertainties (The IMBIE Team et al., 2018). In summary, WAIS losses, through acceleration, retreat and thinning of the principal outlet glaciers, dominated the AIS mass losses over the last decades (*very high confidence*) and there is *high confidence* that this is the case since the late 1970s. Furthermore, parts of the EAIS have lost mass in the last two decades (*high confidence*).

As stated in the SROCC, snowfall and glacier flow are the largest components determining AIS mass changes, with glacier flow acceleration (dynamic thinning) on the WAIS and the Antarctic Peninsula driving total loss trends in recent decades (*very high confidence*), and a partial offset of the dominating dynamic-thinning losses by increased snowfall (*high confidence)*. The SROCC attributed *medium confidence* to estimates of 20th-century snowfall increases equivalent to a sea level change of -7.7 ± 4.0 mm on the EAIS and -2.8 ± 1.7 mm on the WAIS, respectively (Medley and Thomas, 2019). Loss of buttressing, which can be caused by ice shelf thinning, gradual ice shelf front retreat or ice shelf disintegration, has been linked to instantaneous ice velocity increases and thus dynamic thinning since the early 1990s. This link is clearly evident in the Amundsen and, to a lesser degree, Bellingshausen sectors (Gudmundsson et al., 2019), where passive shelf ice (ice that can be removed without major effects on the ice shelf dynamics) is very limited or absent (Fürst et al., 2016). Surface mass balance (SMB) changes, dominated by snowfall, exhibit strong regional and temporal variability, for example with multidecadal increases in the Antarctic Peninsula inferred since the 1930s (Medley and Thomas, 2019), and dominate the interannual to decadal variability of the AIS mass balance (Rignot et al., 2019). However, no significant continent-wide SMB trend is inferred since 1979 (The IMBIE Team et al., 2018; Medley and Thomas, 2019) (regional changes of Antarctic SMB are assessed further in Atlas Section 11.1). In summary, there is *very high confidence* that the observed AIS mass loss since the early 1990s is primarily linked to ice shelf changes.

[START FIGURE 9.18 HERE]

Figure 9.18: (a) A p-box (Section 9.6.3.2) based estimate of the range of values of paleo Antarctic ice sheet mass and sea level equivalents relative to present day and the median over all central estimates (Bamber et al., 2009; Argus and Peltier, 2010; Dolan et al., 2011; Mackintosh et al., 2011; Golledge et al., 2012; Miller et al., 2012b; Whitehouse et al., 2012; Golledge et al., 2013; Ivins et al., 2013; Argus et al., 2014; Briggs et al., 2014; Golledge et al., 2014; Maris et al., 2014; De Boer et al., 2015; Dutton et al., 2015; Golledge et al., 2015; Pollard et al., 2015; DeConto and Pollard, 2016; Gasson et al., 2016; Goelzer et al., 2016; Yan et al., 2016; de Boer et al., 2017; Golledge et al., 2017b; Kopp et al., 2017; Simms et al., 2019) ; and cumulative mass loss (and sea level equivalent) since 2015, with satellite observations shown from 1993 (Bamber et al., 2018a; The IMBIE Team et al., 2018; WCRP Global Sea Level Budget Group, 2018a) and observations from 1979 (Rignot et al., 2019), ISMIP6 projected changes by 2100 under RCP8.5/SSP5-8.5 and RCP2.6/SSP1-2.6 scenarios (thin lines from (Seroussi et al., 2020; Edwards et al., 2021; Payne et al., 2021) and 17th to 83rd, 5th to 95th percentile ranges of the ISMIP6 emulation (shaded line, (Edwards et al., 2021)). Right, 17th to 83rd, 5th to 95th percentile ranges for ISMIP6, emulator, and LARMIP-2 including SMB at 2100. Schematic interpretations of individual reconstructions (Anderson et al., 2002; Bentley et al., 2014; De Boer et al., 2015; Goelzer et al., 2016) of the spatial extent of the Antarctic ice sheet are shown for the (b) mid-Pliocene Warm Period, (c) the Last Interglacial and (d) the Last Glacial Maximum (Fretwell et al., 2013): grey shading shows extent of grounded ice. Maps of mean elevation changes (e) 1978-2017 derived from multi-mission satellite altimetry (Schröder et al., 2019) and (f) ISMIP6 (2061-2100) projected changes for an ensemble using the NorESM1-M climate model under the RCP8.5 scenario (Seroussi et al., 2020). Further details on data sources and processing are available in the chapter data table (Table 9.SM.9).

[END FIGURE 9.18 HERE]

The SROCC stated with *high confidence* that melting of ice shelves by warm ocean waters, leading to reduction of ice shelf buttressing, has driven the observed ongoing thinning of major WAIS outlet glaciers.

ACCEPTED VERSION SUBJECT TO FINAL EDITING

Since the SROCC, digitized radar measurements have shown that the eastern ice shelf of Thwaites Glacier in the Amundsen Sea Embayment thinned between 10 and 33% during the three decades after 1978 (Schroeder et al., 2019), and the role of basal ice shelf melting has been emphasized (Smith et al., 2020). Strong surface meltwater production has been noted as a precursor of ice shelf disintegration in and since the SROCC (Bell et al., 2018), and recent work placed strong meltwater production events (Lenaerts et al., 2017; Nicolas et al., 2017; Wille et al., 2019) and seasons (Robel and Banwell, 2019) in this context. Antarctic ice shelf basal meltwater flux varied between about 1100±150 Gt yr^{-1} in the mid-1990s and about 1570±140 Gt yr^{-1} in the late 2000s before decreasing to 1160 ± 150 Gt yr^{-1} in 2018, and basal melt rates strongly vary with geographical position and depth, as a function of the surrounding water temperature (Adusumilli et al., 2020). Section 9.2.2.3 assesses that the intrusion of warm Circumpolar Deep Water, which has warmed and shoaled since the 1980s, has been at least partially controlled by forcing with significant decadal variability. *Limited evidence* suggests that beyond strong internal decadal wind variability, increased greenhouse gas forcing has slightly modified the mean local winds between 1920 and 2018, facilitating intrusion of Circumpolar Deep Water heat on the Amundsen-Bellingshausen continental shelf and increased ice-shelf melt (Section 9.2.2.3). However, theoretical understanding is still incomplete and in situ measurements within the ice-ocean boundary layer are sparse (Wåhlin et al., 2020). Moreover, modelling and therefore attribution of ice-shelf basal melt remains challenging because of insufficient process understanding, required spatial resolution, the paucity of in-situ observations (Dinniman et al., 2016; Asay-Davis et al., 2017; Turner et al., 2017), and uncertainties of bathymetric datasets under ice shelf cavities (Goldberg et al., 2019, 2020; Morlighem et al., 2020). In summary, ice shelf thinning, mainly driven by basal melt, is widespread around the Antarctic coast and particularly strong around the WAIS (*high confidence*), although basal melt rates show substantial spatio-temporal variability.

Satellite observations suggest that changes in sea ice coverage and thickness can modulate iceberg calving, ice-shelf flow and glacier terminus position around Antarctica (Miles et al., 2013, 2016, 2017; Massom et al., 2015; Greene et al., 2018; Bevan et al., 2019), either through mechanical coupling or via changes to ocean stratification, influencing basal melting. A combined observational and modelling study (Massom et al., 2018) showed that regional loss of a protective sea-ice buffer played a role in the rapid disintegration events of the Larsen A and B and Wilkins ice shelves in the Antarctic Peninsula between 1995 and 2009, by exposing damaged (rifted) outer ice-shelf margins to enhanced flexure by storm-generated ocean swells. One observational study (Sun et al., 2019) suggests that the absence of sea ice in front of ice shelves, which leads to strengthened topographic waves, favours ice shelf basal melt rates by increasing the baroclinic (depth varying) ocean heat flux which can enter the cavity (Wåhlin et al., 2020). Paleo evidence for sea ice control on ice sheets is lacking, but geologic evidence shows a concordance between periods of ice sheet growth and the expansion of sea ice (Patterson et al., 2014; Levy et al., 2019), both being favoured by reduced sea surface temperatures. Modelling confirms that sea ice controls the strength of ice mélange (Robel, 2017; Schlemm and Levermann, 2021) and thus influences ice shelf flexure and calving rates and stability of floating ice margins, but one model shows this had negligible effect on AIS retreat rates during past warm periods (Pollard et al., 2018). Loss of ice shelf-proximal sea ice is also associated with increased solar heating of surface waters and increased sub-shelf melting (Bendtsen et al., 2017; Stewart et al., 2019). In summary, although in some cases sea-ice decrease and glacier and ice shelf flow and terminus position changes can have the same common cause, there is *medium confidence* that sea ice decrease ultimately favours the mass loss of nearby ice shelves through a variety of processes.

The SROCC stated with *high confidence* that ice shelf disintegration has driven dynamic thinning in the northern Antarctic Peninsula over recent decades and expressed *high confidence* in currently ongoing mass loss from glaciers that fed now disintegrated ice shelves, although the mass loss rate has decreased in the 20 years since the immediate speed-up following ice shelf disintegration in 1995 and 2002. Observed flow speed of these tributary glaciers is still 26% higher than before the ice-shelf disintegration (Seehaus et al., 2018). Conversely, flow speed increase of the tributary glaciers of the Scar Inlet Ice Shelf has been interpreted as a sign of evolving instability of the currently intact ice shelf in one study (Qiao et al., 2020).

Ongoing grounding line retreat, indicating dynamic thinning, is observed with *high confidence* in many areas of Antarctica and particularly on the WAIS, with the highest rates being in the Amundsen and Bellingshausen Sea areas, and around Totten Glacier in East Antarctica, as stated in the SROCC. Research

ACCEPTED VERSION SUBJECT TO FINAL EDITING

published since the SROCC has evidenced grounding line retreat of the West Antarctic Berry Glacier on Getz Coast (Millan et al., 2020) and on the East Antarctic Denman Glacier (Brancato et al., 2020), both since 1996. Furthermore observed grounding line retreat in excess of 1.5 km between 2003 and 2015 has been reported for parts of Marie Byrd Land (Christie et al., 2018). In summary, there is *high confidence* that grounding lines of marine-terminating glaciers are currently retreating in many areas around Antarctica, and particularly around the WAIS, and additional areas of grounding line retreat have been evidenced since the SROCC.

The SROCC stated with *medium confidence* that sustained mass losses of several major glaciers in the Amundsen Sea Embayment (ASE) are compatible with the onset of Marine Ice Sheet Instability (MISI), but that whether unstable WAIS retreat had begun or was imminent remained a critical uncertainty. New publications since the SROCC have not substantially clarified this question. On the one hand, a study combining satellite measurements with a numerical model with prescribed ice shelf thinning (Gudmundsson et al., 2019) suggests that MISI is not required to explain the observed current mass loss rates of the WAIS, because they are consistent with external climate drivers. Furthermore, the fast grounding-line retreat of the Pine Island Glacier in the ASE, which was triggered in the 1940s (Smith et al., 2017), observed after 1992 (Rignot et al., 2014) and previously interpreted as a sign of MISI (Favier et al., 2014), seems to have stabilized recently (Milillo et al., 2017; Konrad et al., 2018), and its current flow patterns do not suggest ongoing or imminent MISI (Bamber and Dawson, 2020). On the other hand, sustained fast grounding line retreat has been observed for Smith Glacier in the ASE (Scheuchl et al., 2016), and an analysis of flow patterns and grounding line retreat of the ASE Thwaites Glacier between 1992 and 2017 (Milillo et al., 2019) showed sustained, albeit spatially heterogeneous, grounding line retreat, highlighting ice-ocean interactions that lead to increased basal melt. In addition, Denman Glacier in East Antarctica was shown to hold potential for unstable retreat (Brancato et al., 2020). In summary, the observed evolution of the ASE glaciers is compatible with, but not unequivocally indicating an ongoing MISI (*medium confidence*).

The SROCC reported *limited evidence* and *medium agreement* for anthropogenic forcing of the observed AIS mass balance changes. As stated in Section 3.4.3.2, there remains *low confidence* in attributing the causes of the observed mass of loss from the Antarctic ice sheet since 1993 in spite of some additional process-based evidence to support attribution to anthropogenic forcing.

9.4.2.2 Model evaluation

The AR5 (Church et al., 2013a; Flato et al., 2013) stated that regional climate models and global models with bias-corrected SST and sea ice concentration tended to produce more accurate simulations of Antarctic surface mass balance (SMB) than coupled climate models, and also noted strong climate model temperature biases over the Antarctic, though the latter may reflect known biases in the reanalysis used (Fréville et al., 2014). Section Atlas.11.1 assesses that there is *medium confidence* in the capacity of climate models to simulate Antarctic climatology and surface mass balance changes.

Section 9.2.3.2 assesses that there is *low confidence* in simulations of Southern Ocean temperature. Few ocean models resolve ice shelf cavities, and biases in present-day melt rates can be substantial in some sectors, including the key region of the Amundsen Sea (FESOM: Figure 9.19) (Naughten et al., 2018). An increasing number of observational studies from which basal melt rates are calculated (Huhn et al., 2018; Adusumilli et al., 2020; Das et al., 2020; Hirano et al., 2020; Stevens et al., 2020), combined with improved understanding of water-mass-specific influences and modes of melting or dissolving (Silvano et al., 2018; Adusumilli et al., 2020; Malyarenko et al., 2020; Wåhlin et al., 2020), may help to refine these models in the future. However, given the limited number of available models and their biases, there is currently *low confidence* in the sub-shelf melt rates simulated by ocean models.

Improvements in the representation of grounding line evolution in ice sheet models since the AR5 (such as sub-grid schemes for basal friction and ice shelf melt, and local grid refinement) means that most of the model simulations presented in the SROCC were dominated by physical processes. Since then, these advances have been applied in several model intercomparison projects (MISMIP+: Cornford et al., (2020);

ACCEPTED VERSION SUBJECT TO FINAL EDITING

ABUMIP: Sun et al., (2020); ISMIP6 and LARMIP-2: Box 9.3). All models participating in ISMIP6 and LARMIP-2, for example, simulate ice shelf and grounding line evolution, and include subshelf melt parameterisation, which was not the case in the SeaRISE intercomparison (Bindschadler et al., 2013; Nowicki et al., 2013). Simulations of grounding line evolution (Seroussi et al., 2017, 2020) have benefited from improved bedrock topography (Morlighem et al., 2020). Treatment of subshelf melting, however, remains one of the causes of large differences in Antarctic ice sheet models, particularly for partially floating grid cells in models with coarse resolution (Levermann et al., 2020a; Edwards et al., 2021). Due to the limitations in resolving cavities in ocean models, as described above, basal melt rates are generally parameterized at the ice-shelf base, based on ocean model simulations of temperatures and salinity instead (Nowicki et al., 2020b; Seroussi et al., 2020). While this has the advantage of connecting melt rates to emission scenarios, a large variety of melt parameterisations exist (DeConto and Pollard, 2016; Lazeroms et al., 2018; Reese et al., 2018; Hoffman et al., 2019; Pelle et al., 2019; Jourdain et al., 2020), and there is *low agreement* due to limited observational constraints (ocean temperature, salinity, velocity, and ice shelf draft)(Jourdain et al., 2020), uncertainty in the physics of parameterized processes, missing processes (e.g., tides), and uncertainty in the treatment of ice-sheet–climate feedbacks (Donat-Magnin et al., 2017; Bronselaer et al., 2018; Golledge et al., 2019a). Parameterisations are usually calibrated to present-day melt rates, but can respond differently to projected ocean warming (Favier et al., 2019; Jourdain et al., 2020). Two different calibrations were used in ISMIP6 (Jourdain et al., 2020; Nowicki et al., 2020b;Box 9.3): one reproducing melt rates averaged around the whole continent (MeanAnt: Figure 9.19), and the other reproducing melt rates near the grounding line of Pine Island Glacier (PIGL: Figure 9.19), leading to large differences in melt rates. Evaluation with observations and two cavity-resolving models suggests that the MeanAnt parameterisation better reproduces observed melt rates and projected increases in both the warm Amundsen Sea Embayment and cold Ronne-Filchner shelf cavity, as well as total Antarctic melting (Jourdain et al., 2020). The PIGL calibration represents the upper end for increased basal melt sensitivity that would be caused by continent-wide changes to ocean water properties and circulation under strong future forcing (Jourdain et al., 2020). The basal sliding law also has a strong influence on grounding line retreat and glacier acceleration in response to perturbations, and varies spatially (Sun et al., 2020). Sliding laws (Joughin et al., 2019) can only be constrained with observations in regions experiencing significant change and with sufficiently long observational records.

[START FIGURE 9.19 HERE]

Figure 9.19: Ice shelf basal melt rates for present-day (upper panels) and changes from present-day to the end of the 21st century under the RCP8.5 scenario (lower panels). Present-day melt rates were estimated through: the input-output method constrained by satellite observations and atmosphere/snow simulations (Rignot et al., 2013) and representative of 2003-2008 (upper left); the non-local-PIGL parameterization constrained by observation-based ocean properties (Jourdain et al., 2020) and representative of 1995-2014 (upper centre); the Finite Element Sea-ice/ice-shelf Ocean Model (FESOM) simulation over 2006-2015, forced by atmospheric conditions from a CMIP5 multi-model mean (MMM) under the RCP8.5 scenario ((Naughten et al., 2018) upper right). Future anomalies are calculated as 2081-2100 minus present-day using the ISMIP6 non-local-MeanAnt and non-local-PIGL parameterizations (Jourdain et al., 2020) lower left and centre respectively) based on projections from the NorESM1-M CMIP5 model, and the FESOM-MMM projection (lower right). Note the symmetric-log colour bar (linear around zero, logarithmic for stronger negative and positive values). Inset highlights the Amundsen Sea Region. Further details on data sources and processing are available in the chapter data table (Table 9.SM.9).

[END FIGURE 9.19 HERE]

The SROCC noted that Antarctic ice sheet simulations are increasingly evaluated or formally calibrated with modern observations and/or paleodata – to obtain more realistic initial conditions (ice sheet geometry, velocity and forcing) and to constrain uncertainty in probabilistic projections. This trend continues (Nias et

ACCEPTED VERSION SUBJECT TO FINAL EDITING

al., 2019; Gilford et al., 2020; Hamlington et al., 2020b; Wernecke et al., 2020). However, while the large-scale characteristics of the initial ice sheet state have improved significantly (Box 9.3), capturing the smaller-scale rates of change, including mass trends, remains challenging for many models (Goldberg et al., 2015; Reese et al., 2020; Seroussi et al., 2020; Siegert et al., 2020). This increases uncertainty in projections, especially for the 21st century (Section 9.4.2.5). Uncertainties in ice sheet model simulations have been, however, much better quantified since the AR5, through model intercomparison projects (in particular, ISMIP6 and LARMIP-2: Box 9.3), perturbed parameter ensembles, and increasing use of statistical emulation (Gilford et al., 2020; Levermann et al., 2020a; Wernecke et al., 2020; DeConto et al., 2021; Edwards et al., 2021) to better sample the parameter space. By exploring uncertainties more fully, these methods have the potential to identify better simulations of the historical period.

An important difficulty is how to evaluate simulations of processes that are not currently observed, or rare, or indirectly deduced: in particular, the ice shelf disintegrations and cliff failures that would drive the proposed Marine Ice Cliff Instability (MICI: Section 9.4.2.4 and Box 9.4)(DeConto and Pollard, 2016; DeConto et al., 2021). Models of ice cliff failure can only be indirectly and partially evaluated, using existing (i.e., static) cliffs and laboratory experiments (Clerc et al., 2019). The SROCC stated that there was *low agreement* on the exact MICI mechanism and *limited evidence* of its occurrence in the present or the past, and that the validity of MICI remains unproven. Only one ice sheet model represents MICI (Pollard et al., 2015; DeConto and Pollard, 2016; DeConto et al., 2021). The mechanism has not been found to be essential for reproducing Mid Pliocene Warm Period and Last Interglacial reconstructions or satellite observations, though Last Interglacial data slightly favours it in this model (Edwards et al., 2019a; Gilford et al., 2020; DeConto et al., 2021).

In summary, there is now *medium confidence* in many ice sheet processes in ice sheet models, including grounding line evolution. However, there remains *low confidence* in the ocean forcing affecting the basal melt rates and *low confidence* in simulating mechanisms that have the potential to cause widespread, sustained and very rapid ice loss from Antarctica through MICI.

9.4.2.3 Drivers of future Antarctic ice sheet change

Surface mass balance

The AR5 projected a negative contribution from Antarctic surface mass balance (SMB) changes to sea level over the 21st century (i.e., mitigating sea-level rise), due to increased snowfall associated with warmer air temperatures. Sensitivity of SMB to Antarctic surface air temperature change varied from 3.7 to 7 % $^{o}C^{-1}$, and the sea level projections assumed a sensitivity of 5.1 ± 1.5 % $^{o}C^{-1}$ from CMIP3 era models (Gregory and Huybrechts, 2006) to estimate SMB changes from Antarctic temperatures in the CMIP5 ensemble. Since the AR5, analyses of CMIP5 and CMIP6 models have found Antarctic temperature sensitivity for accumulation (precipitation minus sublimation) of 3.5 to 8.7 % $^{o}C^{-1}$ (Frieler et al., 2015), for SMB of 6.0 to 9.9 % $^{o}C^{-1}$ (Previdi and Polvani, 2016) and for precipitation of around 4 to 9% $^{o}C^{-1}$ (Bracegirdle et al., 2020) (± 1 s.d. ranges). An accumulation sensitivity estimate derived from ice core data lies in the middle of the range ~6% $^{o}C^{-1}$ (Frieler et al., 2015). These are consistent, within uncertainties, with each other and the AR5, under the approximation that SMB is dominated by snowfall.

The AR5 found that the median and *likely* sea level contributions due to SMB from 1986-2005 to 2100 were -0.05 (-0.09 to -0.02) under RCP8.5 and -0.02 (-0.05 to 0.00) m under RCP2.6. The SROCC did not present a separate SMB contribution, instead showing total Antarctic projections derived from ice sheet models (Section 9.4.2.5). Projections of the SMB contribution to sea level tend to be slightly more negative since the AR5, due at least in part to the higher range in equilibrium climate sensitivity values in CMIP6 (Payne et al., 2021). Mean and ± 1 s.d. ranges for grounded Antarctic ice sheet SMB changes from 2000 to 2100 computed from CMIP5 models are -0.08 (-0.13 to -0.04) m SLE for RCP8.5 and similarly for CMIP6 models are -0.07 (-0.11 to -0.03) m for SSP5-8.5 (Gorte et al., 2020). The GCMs used to drive ice sheet models in ISMIP6 (Box 9.3) project mean grounded AIS SMB changes from 2005 to 2100 of -0.06 (range -0.08 to -0.03) m SLE under RCP8.5 for the six CMIP5 models (Seroussi et al., 2020) and -0.09 (range -0.10 to -0.07) m SLE under SSP5-8.5 for the four CMIP6 models, which have climate sensitivity values of 4.8-5.3 ^{o}C (Payne et al.,

ACCEPTED VERSION SUBJECT TO FINAL EDITING

2021). We apply the AR5 parametric AIS SMB model (Section 9.6.3.2) to updated projections of global mean temperature from a two-layer energy budget emulator (Supplementary Material 7.SM.2.), which gives a median -0.05 (5-95% range -0.07 to -0.02) m SLE for SSP5-8.5 (Section 9.4.2.5, Table 9.3), i.e., similar to the AR5 assessment and slightly smaller than the CMIP6 estimate. This estimate is used to augment the LARMIP-2 dynamic projections (Box 9.3) in Sections 9.4.2.5 and 9.4.2.6. Overall, then, CMIP5 and CMIP6 GCM simulations of sea level fall by 2100 due to Antarctic SMB increases are around 2-4 cm greater than estimates derived with the statistical method used in the AR5. Further details about projections of Antarctic temperature, precipitation and SMB are provided in Section Atlas.11.1.4, which assesses that, due to the challenges of model evaluation (Section 9.4.2.2) and the possibility of increased meltwater runoff (Kittel et al., 2021), there is only *medium confidence* that the future contribution of Antarctic SMB to sea level this century will be negative under all greenhouse gas emissions scenarios. Longer timescales are discussed in 9.4.2.6.

Sub-shelf melting

The SROCC highlighted that an important ongoing deficiency in projections of Antarctic sub-shelf melting is the lack of ice-ocean coupling in most continental-scale studies. Increased basal melting is mainly caused by warmer Circumpolar Deep Water (CDW; Section 9.2.2.3) on the continental shelves and warming surface waters intruding under ice shelves (Naughten et al., 2018). Predicting whether or not open ocean water masses will freely penetrate ice-shelf cavities, or will be partially blocked by ocean density gradients, is complex (Wåhlin et al., 2020), and whilst melting related to CDW inflow is currently dominant in the Amundsen Sea Embayment, melt in other embayments is limited by deep inflows of high salinity shelf water or seasonally-warmed shallow incursions of Antarctic Surface Water (Stewart et al., 2019; Adusumilli et al., 2020). There is little consensus regarding future change in CDW (Section 9.2.2.3), and more generally *low confidence* in future change in the temperature of Antarctic ice shelf cavities (Section 9.2.3.2).

The response of sub-shelf melting to ocean warming is also poorly constrained. A key unknown is whether, and when, cold ice shelf cavities might become more similar to the Amundsen Sea Embayment, not only in ocean temperature but also ice-ocean heat exchange, which depends on the cavity geometry and ocean circulation (Little et al., 2009). Only two ocean models with ice shelf cavities have been used to make subshelf basal melting projections for SRES and RCP scenarios (Hellmer et al., 2012; Timmermann and Hellmer, 2013; Timmermann and Goeller, 2017; Naughten et al., 2018). FESOM forced by a CMIP5 multi-model mean under RCP8.5 projects a 90% increase in melting (Figure 9.19), although this could be overestimated due to an underestimation of present day melt rates (Naughten et al., 2018)(Section 9.4.2.2). The temperature-melt relationship was parameterised by ISMIP6 in terms of heat exchange velocity in m a^{-1}, and by LARMIP-2 as basal melt sensitivity in m a^{-1} $^{o}C^{-1}$ (Box 9.3; (Jourdain et al., 2020; Levermann et al., 2020a; Reese et al., 2020), and both vary widely around the continent depending on cavity type. Median values of ISMIP6 heat exchange velocity vary by a factor of 5-10 when calibrating to either mean Antarctic or high Pine Island Glacier observed melt rates (Section 9.4.2.2; Box 9.3; (Jourdain et al., 2020). Basal melt sensitivities near the grounding line estimated by Reese et al., (2020) with a box model of ocean overturning range from 3.9 m a^{-1} $^{o}C^{-1}$ for the Weddell Sea to 10.5 m a^{-1} $^{o}C^{-1}$ for the Amundsen Sea region, with a continental mean of 5.3 m a^{-1} $^{o}C^{-1}$. Similarly high Amundsen Sea sensitivities are estimated in coupled ice-ocean simulations of Thwaites Glacier (mean 9.4 m a^{-1} $^{o}C^{-1}$; range 6 to 16 m a^{-1} $^{o}C^{-1}$)(Seroussi et al., 2017). These large variations lead to large differences in basal melt rates and projected sea level contributions when applied to the whole ice sheet in ISMIP6 and LARMIP-2 (Box 9.3). Projections of melt rates from the two ISMIP6 calibrations are higher than those from FESOM driven by a CMIP5 multi-model mean (Figure 9.19; Jourdain et al., 2020). The ISMIP6 ensemble mostly uses the mean Antarctic calibration, but includes some simulations with the Pine Island Glacier calibration and the ISMIP6 emulator samples more of these higher values; LARMIP-2 use basal melt sensitivities (7 to 16 m a^{-1} $^{o}C^{-1}$) consistent with estimates for the Amundsen Sea Embayment. Due to the limited availability of cavity-resolving ocean models and the wide regional variation in estimates of basal melt sensitivity to ocean temperature, there is therefore only *low confidence* in projected future sub-ice shelf melt rates. The impact of this uncertainty on Antarctic ice sheet model projections to 2100 is discussed in Section 9.4.2.5.

Ice shelf disintegration

Antarctic ice shelves modulate grounded ice flow through buttressing, so their weakening or disintegration is

ACCEPTED VERSION SUBJECT TO FINAL EDITING

crucial for the timing and magnitude of ice loss and onset of instabilities (Section 9.4.2.4; Box 9.4). Projections of ice shelf disintegration are uncertain in terms of both atmospheric warming and the response of the shelf surface (surface melting, and whether shelves then disintegrate due to hydrofracturing and flexing, or are resilient through refreezing or drainage; (Bell et al., 2018). The SROCC stated it is not expected that widespread ice shelf loss will occur before the end of the 21st century, but this was based on only one study, using a regional climate model forced by five GCMs (Trusel et al., 2015), so there was *low confidence* in this assessment. The study of DeConto and Pollard (2016) projected the appearance of extensive surface meltwater several decades earlier than (Trusel et al., 2015) and was therefore assessed to be too uncertain to include in the SROCC projections of the Antarctic ice sheet.

Since the SROCC, further studies have highlighted the modelling uncertainties in this area. Coastal surface air temperature projections in CMIP6 models show large inter-model differences driven by sea ice retreat, and exhibit more warming relative to global mean temperature under low emissions than high, due to delayed response of the Southern Ocean to stabilised emissions and stratospheric ozone recovery (Bracegirdle et al., 2020). The updated study of DeConto et al., (9998) includes improvements to the climate simulations relative to those in DeConto and Pollard, (2016) and the resulting surface meltwater projections are now consistent with Trusel et al., (2015). However, the net effect of meltwater feedbacks on ice shelves is uncertain. Ice discharge is expected to lead to surface ocean and atmosphere cooling: this increases ocean stratification and sub-shelf melting, but also reduces ice shelf surface melting and delays hydrofracturing (Golledge et al., 2019a; Sadai et al., 2020; DeConto et al., 2021). The new studies are insufficient to change the SROCC *low confidence* assessment on ice shelf loss. The consequence of this uncertainty on projections is discussed in Section 9.4.2.5 and Box 9.4.

9.4.2.4 Ice sheet instabilities

A major uncertainty in future Antarctic mass losses is the possibility of rapid and/or irreversible ice losses through instability of marine parts of the ice sheet, proposed via the mechanisms of Marine Ice Sheet Instability (MISI) and Marine Ice Cliff Instability (MICI), and whether these processes will lead to a collapse of the West Antarctic ice sheet (WAIS).

MISI is a proposed self-reinforcing mechanism within marine ice sheets that lie on a bed that slopes down towards the interior of the ice sheet, whereby, in the absence of ice shelf buttressing, the position of the grounding line is inherently unstable until reaching an upward sloping bed. The SROCC (Meredith et al., 2019) noted advances in modelling MISI since the AR5, but that 'significant discrepancies' remained in projections due to poor understanding of mechanisms and lack of observational data to constrain the models. Since the SROCC, modelling uncertainties have been more thoroughly explored, rather than constrained. (compatibility of current observations in the Amundsen Sea Embayment with MISI is assessed in Section 9.4.2.1). Internal climate variability might either slow (Hoffman et al., 2019) or amplify (Robel et al., 2019) MISI, and stable grounding line positions can be reached on downward sloping beds if ice shelves provide buttressing (Sergienko and Wingham, 2019; Cornford et al., 2020). Ice sheet model simulations that remove all Antarctic ice shelves (and prevent them from reforming) show 2-10 m SLE Antarctic mass loss after 500 years due to MISI, of which WAIS collapse contributes 2–5 m (Sun et al., 2020), with the majority of the mass loss in the first one to two centuries. Much of the multi-model variation is due to the sliding law (Section 9.4.2.2). However, it is not expected that widespread ice shelf loss will occur before the end of the 21st century (Section 9.4.2.3; Box 9.4). A recent update of bed topography that has unveiled large and overdeepened subglacial troughs in East Antarctica potentially vulnerable to MISI (Morlighem et al., 2020) has only been used by a few models (Seroussi et al., 2020; Sun et al., 2020), so current projections could underestimate vulnerability in these regions. The sea level rise contribution of the Antarctic ice sheet therefore crucially depends on the behaviour of individual ice shelves and outlet glacier systems and whether they enter MISI for a given level of warming (Pattyn and Morlighem, 2020, Box 9.4). As for Antarctic simulations generally (Sections 9.4.2.2, 9.4.2.3), there is *medium confidence* in simulating MISI but *low confidence* in projecting the subshelf melting and ice shelf disintegration that drive it.

The SROCC noted *limited evidence* from geological records and ice sheet modelling suggesting that parts of

ACCEPTED VERSION SUBJECT TO FINAL EDITING

the AIS experienced rapid (centennial) retreat *likely* due to MISI between 20,000 and 9,000 years ago, and also described more uncertain evidence for the LIG and MPWP. Recent support for past MISI is provided by model simulations of the WAIS during the LIG (Clark et al., 2020), the British Ice Sheet during the last termination (Gandy et al., 2018) and the Laurentide Ice Sheet during the Younger Dryas (Pico et al., 2019), which show progressive retreat despite declining temperatures, indicative of a true (ice dynamic) instability. Direct observational evidence of rapid paleo-ice sheet grounding-line retreat is rare, but on the Larsen continental shelf retreat rates of >10 km yr^{-1} during the deglaciation have been estimated (Dowdeswell et al., 2020). MISI has also been inferred from sedimentological evidence of ice loss from Wilkes Subglacial Basin, East Antarctica (Bertram et al., 2018; Wilson et al., 2018; Blackburn et al., 2020) but these reconstructions cannot unambiguously identify unstable from progressive retreat. Therefore there is *limited evidence* to identify the operation of instability mechanisms such as MISI in paleo-ice sheet retreat.

The SROCC assessed that ice-sheet interactions with the solid Earth are not expected to substantially slow sea-level rise from marine-based ice in Antarctica over the 21st century (*medium confidence*), but that these processes could become important on multi-century and longer time scales. More recent modelling of deglaciation of the Ross Embayment by (Lowry et al., 2020) is consistent with this assessment. However, new projections for Pine Island Glacier (Kachuck et al., 2020) support previous work (Barletta et al., 2018) suggesting lower mantle viscosity in this region leads to a negative feedback on decadal time scales. Grounding-line stabilisation by the solid Earth response may therefore occur over the 21st century in the Amundsen Sea Embayment, where most mass loss is occurring (Section 9.4.2.1), but more generally occurs over multi-centennial to millennial timescales (*medium confidence*).

The MICI hypothesis describes rapid, unmitigated calving triggered by ice shelf collapse (Pollard et al., 2015). The SROCC noted that the MICI mechanism led one model (DeConto and Pollard, 2016) to lose mass far more rapidly, but excluded the mechanism from its projections due to uncertainty in the timing of the ice shelf disintegration (Section 9.4.2.3). They stated that MICI could lead to sea level contributions beyond 2100 considerably higher than the *likely* range projected by other models, but given the *low agreement* on the exact MICI mechanism and *limited evidence* of its occurrence in the present or the past (Section 9.4.2.2), its potential to affect future sea level rise was very uncertain. Since the SROCC, new simulations show later ice shelf disintegration, in agreement with other models (DeConto et al., 9998; Section 9.4.2.3), and therefore lower projections at 2100 (Section 9.4.2.5). New theoretical evidence suggests that ice cliff collapse may only occur after very rapid ice shelf disintegration caused by unusually high meltwater production (Clerc et al., 2019; Robel and Banwell, 2019), and that the subsequent rate of retreat depends on the terminus geometry (Bassis and Ultee, 2019). As SROCC noted, only Crane Glacier on the Peninsula has shown retreat consistent with MICI, after the Larsen B ice shelf collapsed, and MICI-style behaviour at Jakobshavn and Helheim glaciers in Greenland might not be representative of wider Antarctic glaciers. Observations from Greenland show that steep cliffs commonly evolve into short floating extensions, rather than collapsing catastrophically (Joughin et al., 2020). As assessed in Section 9.4.2.2 and 9.4.2.3, there is therefore *low confidence* in simulating mechanisms that have the potential to cause widespread, sustained and very rapid ice loss from Antarctica this century through MICI, and *low confidence* in projecting the driver of ice shelf disintegration.

In summary, poorly understood processes of instabilities, characterized by *deep uncertainty*, have the potential to strongly increase Antarctic mass loss under high greenhouse gas emissions on century to multicentury timescales (Box 9.4). These instabilities are therefore considered separately in assessments of the future contribution to GMSL (Sections 9.4.2.5, 9.4.2.6, 9.6.3.2, 9.6.3.5).

9.4.2.5 Projections to 2100

The AR5 assessed the median and *likely* (66-100% probability) sea level contributions of the Antarctic ice sheet (AIS) in 2100 relative to 1986-2005 to be 0.06 (-0.04 to 0.16) m SLE under RCP2.6 and 0.04 (-0.08 to 0.14) m SLE under RCP8.5 (Table 9.3; no change when using the AR6 baseline). The AR5 stated that only the collapse of the marine-based sectors of the AIS, if initiated, could cause global mean sea level to rise substantially above the *likely* range during the 21st century, with *medium confidence* this would not exceed

ACCEPTED VERSION SUBJECT TO FINAL EDITING

several tenths of a metre during this period. The assessment of the dynamical contribution had no dependence on emissions scenario, due to the lack of literature, so the decrease in sea level contribution in the higher emissions scenario was solely due to increased SMB (Section 9.4.2.3). The SROCC (Oppenheimer et al., 2019) assessed the total contribution based on five new ice sheet modelling studies that incorporated marine ice sheet dynamics, combining their estimates and interpreting the 5-95th percentile range of the resulting distribution as the *likely* range (17-83% probability interval, i.e., not open-ended as in the AR5). The median and *likely* range contributions by 2100 were 0.04 (0.01–0.11) m under RCP2.6 and 0.12 (0.03-0.28) m under RCP8.5 (Table 9.3). The positive scenario-dependence in the SROCC - where increases in dynamic losses driven by ocean warming and ice shelf disintegration under higher emissions (Section 9.4.2.3) dominate over increases in surface mass balance - arose from a combination of physical processes and model limitations. Modelling improvements in these studies included improved representations of grounding line response to drivers, more extensive exploration of uncertainties, and inclusion of a positive feedback of meltwater on climate (Golledge et al., 2019b). However, two of the projections did not include surface mass balance changes that would offset dynamic losses (Levermann et al., 2014; Ritz et al., 2015), and the scenario dependence may have been further amplified by highly sensitive subshelf melt parameterisations and use of simplified surface mass balance schemes (Golledge et al., 2015, 2019b; Bulthuis et al., 2019; Oppenheimer et al., 2019).

Since the SROCC, new projections have arisen from multi-model intercomparison projects ISMIP6 and LARMIP-2 (Box 9.3), with one model including MICI (Section 9.4.2.4) (DeConto et al., 2021)(Table 9.3). Corrections are added to allow comparison: all ISMIP6-derived projections have an estimate of the historical dynamical response to pre-2015 climate forcing added, which increases contributions (Box 9.3; Figure 9.18); the LARMIP-2 dynamic projections are combined with an estimate of surface mass balance, which decreases contributions (Sections 9.4.2.3, 9.6.3.2); and the ISMIP6 emulated and LARMIP-2 projections were re-estimated using the global surface air temperature distributions from the two-layer energy budget emulator described in Supplementary Material 7.SM.2. The majority of the new projections indicate that the AIS will overall lose mass and contribute to sea level rise, under all emissions scenarios. Most thinning occurs in the Amundsen Sea sector in WAIS and Totten Glacier in EAIS (Figure 9.18). The most negative contribution is -0.02 m (5th percentile of ISMIP6 combined RCP8.5 and SSP5-8.5 projections after correction) and the largest contribution is 0.57 m SLE (95th percentile; (Levermann et al., 2020b)), or 0.63 m SLE with MICI (95th percentile; (DeConto et al., 2021)). ISMIP6 ensemble ranges are wider for the high scenarios (RCP8.5/SSP5-8.5) than the low (RCP2.6/SSP1-2.6), in part because more simulations were available. The ISMIP6 simulations that apply an ice shelf collapse scenario based on exceedance of a surface meltwater threshold (Trusel et al., 2015) driven by CMIP5 models show only a small increase in mass loss (~0-0.04 m), mostly from the Peninsula, due in part to the small number of ice shelves predicted to collapse this century (Seroussi et al., 2020). Simulations driven by the CMIP5 model HadGEM2-ES, which has unusually extreme warming in the Ross Sea (Barthel et al., 2020b), show a larger mass loss (up to ~0.05 m) in East Antarctica under ice shelf collapse (Edwards et al., 2021). The ISMIP6 projections do not include the efficient meltwater drainage or atmospheric feedbacks that could reduce mass loss further (Seroussi et al., 2020).

The relationship between emissions scenario and AIS response varies across the studies, with emulated ISMIP6 projections showing a slight negative scenario-dependence in the median (-0.01 m) from SSP1-2.6 to SSP5-8.5, and LARMIP-2-based projections showing a slight positive scenario-dependence in the median (0.02 m) (Table 9.3). A lack of clear scenario-dependence in the median masks large individual variations across climate and ice sheet models, whereby the net AIS contribution response to emissions scenario depends on the relative magnitudes of the atmosphere, ocean and ice sheet responses (Barthel et al., 2020b; Seroussi et al., 2020; Edwards et al., 2021). Climate and ice sheet models do not project that the AIS response will be the same under high or low greenhouse gas emissions in 2100, but rather there is no consensus on the sign of the change. In contrast, strong scenario dependence is seen from RCP4.5 to RCP8.5 in projections that allow MICI (Section 9.4.2.4;(DeConto et al., 2021), though less so than earlier projections (DeConto and Pollard, 2016) due to later ice shelf disintegrations. A negative or positive scenario-dependence of the AIS response this century cannot be deduced from recent observations, because there is still *low confidence* in attributing the causes of observed mass loss (Section 9.4.2.1), and neither regional mass increases by surface mass balance nor regional mass losses by ice flow have a linear relationship with global mean temperature (Sections 9.4.2.1, 9.4.2.2, 9.4.2.3). There is therefore *low agreement* on the

ACCEPTED VERSION SUBJECT TO FINAL EDITING

relationship between emissions scenario and AIS response. However, in the longer-term, mass loss is expected to dominate (Section 9.4.2.6).

The LARMIP-2 median projections are higher than those of the ISMIP6 emulator (by 0.04-0.07 m), and the 95th percentiles are two to three times higher. Two possible reasons for the differences between the emulated ISMIP6 and LARMIP-2 projections are assessed: the set of ice sheet models (Annex II) and the parameter values determining subshelf melt sensitivity to ocean temperature (Section 9.4.2.3; Box 9.3). Using only the thirteen ice sheet models common to ISMIP6 and LARMIP-2 reduces the LARMIP-2 median projections by 0.02-0.03 m SLE and the 95th percentiles by 0.04-0.08m SLE (Table 9.3), approximately halving the difference in medians but having relatively small effect on the upper end. Subshelf melt sensitivity has a larger effect, due to the wide variation of estimates from different regions and methods. Using only the Pine Island Glacier subshelf melt distribution (Sections 9.4.2.2, 9.4.2.3) in the ISMIP6 emulator gives a median Antarctic projection of ~0.08 m in 2100 in all scenarios before historical correction, compared with ~0 m using only the mean Antarctic distribution; the published projections use a joint distribution (Edwards et al., 2021). Reese et al., (2020) find that using the basal melt sensitivities of LARMIP-2 yield an order of magnitude greater mass loss under RCP8.5 than with the ISMIP6 mean Antarctic values. Halving the basal melt sensitivity parameter range (i.e., in line with a continental mean estimate: Section 9.4.2.3) would lead to a halving of the LARMIP-2 dynamic contribution. This would reconcile the LARMIP-2 and ISMIP6 emulator median and 95th percentile projections using the common subset of models within ~0.02-0.05 m. There is therefore *limited evidence* that the ISMIP6 and LARMIP-2 projections could be reconciled by using common ice sheet models and basal melt sensitivity values.

It is not possible to distinguish which of ISMIP6 and LARMIP-2 is more realistic due to limitations in historical simulations (Box 9.3) and understanding of basal melting (Section 9.4.3), so the projections are combined using a 'p-box' approach (Section 9.6.3.2). The mean of the ISMIP6 emulated and LARMIP-2 medians gives the assessed median projections, and the outer edges of the 17-83% ranges give the outer edges of the assessed *likely* (17-83%) ranges, i.e., encompassing the structural and parametric uncertainties of both methods, giving *medium confidence* in their combined projections. The main difference between this assessment and the SROCC is to increase the medians of the lower scenarios by 0.05-0.07 m, so that all SSPs are similar to the SROCC assessment of RCP8.5, and to substantially increase the upper ends of the *likely* ranges: by 0.14-0.16 m for RCP2.6/SSP1-2.6 and RCP4.5/SSP2-4.5, and 0.06 m for RCP8.5/SSP5-8.5. The increase relative to the SROCC is partly due to the increase in LARMIP-2 projections relative to the original LARMIP study (Levermann et al., 2014), arising from the larger number of participating ice sheet models (Levermann et al., 2020b). The historical dynamic response to pre-2015 climate forcing applied to the ISMIP6 emulator could be overestimated, due to the assumption of a constant future rate (Box 9.3). This assessment encompasses the SROCC and all projections since, except the 83rd percentiles of projections that allow MICI under RCP8.5 (DeConto et al., 2021) and the structured expert judgement under 5°C shown in the SROCC (Bamber et al., 2019). Both are used in further p-box estimates to give the outer limits of *low confidence* assessments (Section 9.6.3.2).

In summary, it is *likely* that the Antarctic ice sheet will continue to lose mass throughout this century under all emissions scenarios, i.e., that dynamic losses driven by ocean warming and ice shelf disintegration will *likely* continue to outpace increasing snowfall (*medium confidence*). The upper end of projections is not well constrained, due to different assumptions about the future sensitivity of subshelf basal melting to ocean warming and the proposed Marine Ice Cliff Instability triggered by ice shelf disintegration (Sections 9.4.2.3 and 9.4.2.4; Box 9.4).

[START TABLE 9.3 HERE]

Table 9.3: Projected sea level contributions in meters from the Antarctic ice sheet in 2100 relative to 1995-2014, unless otherwise stated, for selected RCP and SSP scenarios. Italics denote partial contributions. The historical dynamic response omitted from ISMIP6 simulations is estimated to be 0.33 ± 0.16 mm yr^{-1} (0.03 m ± 0.01 m in 2100 relative to 2015; Box 9.3). The climate forcing is described in Supplementary Material 7.SM.2.

ACCEPTED VERSION SUBJECT TO FINAL EDITING

1

Representative Concentration Pathways (RCPs)

Study	RCP2.6	RCP4.5	RCP8.5	Notes
IPCC AR5 (Church et al., 2013a)	0.06 (-0.04 to 0.16)	0.05 (-0.05 to 0.15)	0.04 (-0.08 to 0.14)	Median and *likely* (>= 66% range) contribution.
IPCC SROCC (Oppenheimer et al., 2019)	0.04 (0.01 to 0.11)	0.06 (0.01 to 0.15)	0.12 (0.03 to 0.28)	Median and *likely* (66% range) contribution. Combination of five studies.
ISMIP6 CMIP5-forced (Seroussi et al., 2020); excludes historical dynamic response	*-0.01 to 0.16*	---	*-0.08 to 0.30*	*Range of ISMIP6 multi-model contributions in 2100 relative to 2015 from 2 ESMs for RCP2.6 and 6 ESMs for RCP8.5.*
LARMIP-2; excludes surface mass balance (Levermann et al., 2020b)	*0.13 (0.07 to 0.24) [0.04 to 0.37]*	*0.14 (0.07 to 0.28) [0.05 to 0.44]*	*0.17 (0.09 to 0.36) [0.06 to 0.58]*	*Median (67% range) [90% range] LARMIP-2 multi-model dynamic contribution in 2100 relative to 1900.*
MICI (DeConto et al., 2021)	0.08 (0.06 to 0.12) [0.06 to 0.15]	0.09 (0.07 to 0.11) [0.07 to 0.15]	0.34 (0.19 to 0.53) [0.11 to 0.63]	Median (66% range) [90% range]

Shared Socioeconomic Pathways (SSPs)

Study	SSP1-2.6	SSP2-4.5	SSP5-8.5	
Multi-model ensemble projections				
ISMIP6 CMIP6-forced (Payne et al., 2021)*; excludes historical dynamic response*	*-0.05 to 0.01*	---	*-0.09 to 0.11*	*Range of ISMIP6 multi-model contributions in 2100 relative to 2015 from 1 ESM for SSP1-2.6 and 4 ESMs for SSP5-8.5.*
ISMIP6 all (CMIP5 and CMIP6-forced) including historical dynamic response	0.05 (0.04 to 0.08) [0.03 to 0.11]	---	0.04 (0.00 to 0.12) [-0.02 to 0.23]	Median (66% range) [90% range] contribution from ISMIP6 CMIP5- and CMIP5-forced multi-model ensembles, (see caption).
Emulated ISMIP6; excludes historical dynamic response (Edwards et al., 2021)	*0.04 (-0.01 to 0.10) [-0.05 to 0.14]*	*0.04 (-0.02 to 0.10) [-0.06 to 0.14]*	*0.04 (-0.01 to 0.09) [-0.05 to 0.14]*	*Median (66% range) [90% range] contribution in 2100 relative to 2015 from emulator of ISMIP6 used with Chapter 7 climate forcing.*

ACCEPTED VERSION SUBJECT TO FINAL EDITING

Emulated ISMIP6 total	**0.09 (0.03 to 0.14) [-0.01 to 0.19]**	**0.09 (0.03 to 0.14) [-0.01 to 0.18]**	**0.08 (0.03 to 0.14) [0.00 to 0.18]**	**Emulated ISMIP6, but relative to 1995-2014 and including historical dynamic response (see caption)**
Surface mass balance	*-0.02 (-0.03 to -0.01) [-0.04 to -0.01]*	*-0.03 (-0.04 to -0.02) [-0.06 to -0.01]*	*-0.05 (-0.07 to -0.03) [-0.09 to -0.02]*	*Median (66% range) [90% range] surface mass balance estimated for the AR5, used to correct LARMIP-2 below.*
LARMIP-2; excludes surface mass balance	*0.15 (0.08 to 0.29) [0.05 to 0.44]*	*0.17 (0.09 to 0.33) [0.06 to 0.49]*	*0.20 (0.10 to 0.39) [0.07 to 0.61]*	*Median (66% range) [90% range] dynamic contribution from LARMIP-2 multi-model method used with Chapter 7 climate forcing.*
LARMIP-2 subset of models; excludes surface mass balance	*0.14 (0.08 to 0.26) [0.05 to 0.39]*	*0.15 (0.08 to 0.29) [0.05 to 0.45]*	*0.17 (0.10 to 0.35) [0.06 to 0.54]*	*As above, but using only the 13 of 16 ice sheet models common to both ISMIP6 and LARMIP-2.*
LARMIP-2 subset of models; includes surface mass balance	*0.11 (0.05 to 0.24) [0.03 to 0.37]*	*0.12 (0.05 to 0.26) [0.02 to 0.42]*	*0.12 (0.05 to 0.30) [0.01 to 0.49]*	*As above, but including the surface mass balance estimate.*
LARMIP-2 total	**0.13 (0.06 to 0.27) [0.03 to 0.41]**	**0.14 (0.06 to 0.29) [0.02 to 0.46]**	**0.15 (0.05 to 0.34) [0.01 to 0.57]**	*Median (66% range) [90% range] dynamic contribution from LARMIP-2 multi-model method used with Chapter 7 climate forcing, including the surface mass balance estimate.*
This assessment: combination of emulated ISMIP6 and LARMIP-2	**0.11 (0.03 to 0.27) [-0.01 to 0.41]**	**0.11 (0.03 to 0.29) [-0.01 to 0.46]**	**0.12 (0.03 to 0.34) [0.00 to 0.57]**	**Median (66% range) [90% range] assessment combining emulated ISMIP6 and LARMIP-2.**

[END TABLE 9.3 HERE]

9.4.2.6 Projections beyond 2100

The SROCC assessed the median and *likely* range of Antarctic sea level equivalent contributions at 2300 as 0.16 (0.07 – 0.37) m under RCP2.6 and 1.46 (0.60 – 2.89) m under RCP8.5, based on three studies. It was noted that *deep uncertainty* remained beyond 2100: whilst solid Earth feedbacks could reduce ice loss over

ACCEPTED VERSION SUBJECT TO FINAL EDITING

multi-century timescales, Marine Ice Cliff Instability (MICI; Section 9.4.2.4) might give contributions higher than the *likely* ranges. The SROCC also presented structured expert judgement (SEJ) projections for comparison (Bamber et al., 2019), which give higher values. Since the SROCC, three studies have made projections to 2300. Rodehacke et al., (2020) assessed two methods for implementing precipitation changes (based on repeating 2071-2100 forcings beyond 2100), which both gave negative projections at 2300 because the dynamic response was very small (-0.11 to -0.01 m SLE for RCP2.6; -0.25 to -0.07 m for RCP8.5 forcing). In contrast, simulations forced by 2081-2100 ocean-only projections under RCP8.5/SSP5-8.5 beyond 2100, using two implementations of the ISMIP6 'non-local' basal melt parameterisations (Box 9.3; Section 9.4.2.2) and two sliding laws, are all positive (0.08 m to 0.96 m SLE by 2300), though these do not include the negative contribution from surface mass balance changes (Lipscomb et al., 2021). Finally, DeConto et al., (9998) update projections for the MICI hypothesis (Section 9.4.2.4) using the extensions of the RCPs to 2300, and obtain far higher contributions: median (17-83%) ranges of 1.09 (0.71 to 1.35) m SLE under RCP2.6 and 9.60 (6.87 to 13.54) m SLE under RCP8.5. These are larger than previous estimates (DeConto and Pollard, 2016), particularly at the upper end: 0.68 (0.29 to 1.13) m SLE for RCP2.6 and 8.40 (7.47 to 9.76) m for RCP8.5 (Edwards et al., 2019b), which can largely be explained by the higher maximum ice-cliff calving rate. LARMIP-2 dynamic projections (Box 9.3) are also estimated under the extended SSPs and corrected with surface mass balance (as in Section 9.4.2.5), giving median (17-83%) ranges of 0.40 (0.18–0.78) m SLE at 2300 under SSP1-2.6 and 1.57 (0.68–3.14) m under SSP5-8.5. The longer timescale may invalidate the linear response assumption of LARMIP-2, which neglects any self-dampening or self-amplifying processes. The ranges of projections for 2300 without MICI (Golledge et al., 2015; Bulthuis et al., 2019; Levermann et al., 2020a; Rodehacke et al., 2020; Lipscomb et al., 2021); 'assessed ice-sheet contributions' in Section 9.6.3.5) are -0.14 to 0.78 m SLE under RCP2.6/SSP1-2.6, and -0.27 to 3.14 m SLE under RCP8.5/SSP5-8.5. The lower bounds are the 5th percentile of (Bulthuis et al., 2019) and the lowest mean/median from (Rodehacke et al., 2020), respectively; the upper bounds are the 83% percentiles of the LARMIP-2 estimates. These ranges are wider than the SROCC *likely* ranges, and more consistent with the SEJ (Bamber et al., 2019). However, projections in which Antarctica contributes much more than the assessed ranges under sustained very high greenhouse gas emissions, i.e., around 7–14 m to GMSL by 2300 (DeConto et al., 2021), cannot be ruled out and are taken as a sensitivity case (Section 9.6.3.5; Table 9.11). In summary, there is *high confidence* that Antarctic mass loss will be greater beyond 2100 under high greenhouse gas emissions than low, but the large range of projections mean we have only *low confidence* in the likely AIS contribution to GMSL by 2300 for a given scenario. *Deep uncertainty* remains in the role of Antarctic ice sheet instabilities under very high emissions.

The West and East Antarctic ice sheets are considered to be tipping elements, i.e., susceptible to critical thresholds. The SR1.5 (Hoegh-Guldberg et al., 2018) assessed that a threshold for WAIS instability may be close to 1.5–2°C (*medium confidence*), as only RCP2.6 led to long-term projections of less than 1 m (Golledge et al., 2015; DeConto and Pollard, 2016). Based on the agreement of a further study (Bulthuis et al., 2019), the SROCC confirmed that low emissions would limit Antarctic ice loss over multi-century timescales (*high confidence*), but it was not possible to determine whether this was sufficient to prevent substantial ice loss (*medium confidence*). Since the SROCC, new studies have revisited this topic (Garbe et al., 2020; Rodehacke et al., 2020; Van Breedam et al., 2020; DeConto et al., 2021; Lipscomb et al., 2021), allowing a more complete assessment along with other studies (Feldmann and Levermann, 2015; Clark et al., 2016; Golledge et al., 2017a; Edwards et al., 2019b) and the extension to LARMIP-2 above. The majority project 0–1.3 m SLE on multi-century timescales under scenarios of 1–2°C warming. Projections can increase up to 2 m SLE under high basal melt sensitivity to ocean warming (Section 9.4.2.3)(Lipscomb et al., 2021) or MICI (Section 9.4.2.4). On multi-millennial timescales (≥ 2,000 years), many projections remain below 1.6 m SLE under 1–2°C warming, i.e. less than about half of the West Antarctic ice sheet in sea level equivalent (see also Section 9.6.3.5 and Figure 9.30). Other studies project majority or total loss of WAIS under 1–2°C warming, exceeding 2 m SLE, under the higher end of the warming range (≥ 1.5°C), or high ocean warming (≥ 0.5°C) and/or high basal melting around WAIS, or MICI. All but two of these multi-millennial studies use variants of the same ice sheet model, though different modelling choices mean they can be considered quasi-independent. Simulations of previous interglacial periods often show near or total WAIS disintegration, with mass loss exceeding 3 m SLE (e.g. Figure 9.18), although limitations of these studies or inferences that can be drawn under different forcings limit confidence in the robustness of these as quantitative analogues (Sections 9.4.2.4, 9.6.2). Overall, increased evidence and agreement on the timescales

ACCEPTED VERSION SUBJECT TO FINAL EDITING

and drivers of mass loss confirm the SR1.5 assessment that a threshold for WAIS instability may be close to 1.5–2°C (*medium confidence*), and that the probability of passing a threshold is larger for 2°C warming than for 1.5°C (*medium confidence*), particularly under strong ocean warming. New projections agree with previous studies that only part of WAIS would be lost on multi-century timescales if warming remains less than 2°C (*medium confidence*). There is *limited agreement* about whether complete disintegration would eventually occur at this level of warming, but *medium confidence* this would take millennia.

Under ~2–3°C peak warming, complete or near-complete loss of the West Antarctic ice sheet is projected in most studies after multiple millennia (*low confidence*), with continent-wide mass losses of ~2–5 m SLE or more; this could occur on multi-century timescales under very high basal melting (Lipscomb et al., 2021) or widespread ice shelf loss and/or MICI (Sun et al., 2020; DeConto et al., 2021) (*low confidence*). Mass losses under ~2–3°C warming could be less than 2 m SLE, particularly for multi-century timescales, low basal melting, or less responsive sliding laws. If warming exceeds ~3°C above pre-industrial, part of the East Antarctic ice sheet (typically the Wilkes Subglacial Basin) is projected to be lost on multi-millennial timescales (*low confidence*), with total AIS mass loss equivalent to around 6–12 m or more sea level rise; mass loss could be much smaller if the dynamic response is small (Bulthuis et al., 2019; Rodehacke et al., 2020), or much faster under widespread ice shelf loss and/or MICI (Sun et al., 2020; DeConto et al., 2021). A new study by Garbe et al., (2020) suggests that 6°C sustained warming and associated mass loss of ~12 m SLE may be a critical threshold beyond which the ice sheet re-organises to a new state, leading to large losses from East Antarctica (including the Aurora Subglacial Basin) and leading to a further 10 m sea level contribution per degree of warming; other studies also show much higher mass loss per °C at higher levels of warming (Van Breedam et al., 2020; DeConto et al., 2021) (Section 9.6.3.5; Figure 9.30).

The SROCC (Meredith et al., 2019; Oppenheimer et al., 2019) assessed that Antarctic mass losses could be irreversible over decades to millennia (*low confidence*). Garbe et al., (2020) show that the Antarctic ice sheet is always volumetrically smaller when regrowing under a given warming level than when it retreats under the same forcing, and that even if retreat followed by regrowth results in a net zero change in volume, the spatial distribution of mass may be altered, especially in parts of West Antarctica vulnerable to MISI. Projections that start reducing CO_2 concentrations from 2030 onwards, reaching pre-industrial levels around 2300, show sea level contributions exceeding 1 m by 2500 when including MICI (DeConto et al., 2021). New research therefore confirms the SROCC assessment that mass loss from the AIS is irreversible on decadal to millennial timescales (*low confidence*) (FAQ 9.1), and suggests that reducing atmospheric CO_2 concentrations or temperatures to pre-industrial levels may not be sufficient to prevent or reverse substantial Antarctic mass losses (*low confidence*).

9.5 Glaciers, permafrost and seasonal snow cover

9.5.1 Glaciers

9.5.1.1 Observed and reconstructed glacier extent and mass changes

Global glacier contribution

The AR5 (Vaughan et al., 2013) assessed glacier changes from studies based on the regions defined in the Randolph Glacier Inventory (RGI; version 2.0): a satellite observation-based, global inventory of glacier outlines for the year 2000. Following the SROCC (Hock et al., 2019b; Meredith et al., 2019), we report studies based on RGI version 6.0 (RGI Consortium, 2017). Increased volume of satellite observations and the inclusion of detailed regional glacier inventories has resulted in an improved inventory (RGI Consortium, 2017). A new consensus estimate for the ice thickness distribution of all glaciers in RGI 6.0 was obtained from an ensemble of five numerical models (although only one out of five models covered all regions (Farinotti et al., 2019)) calibrated and validated with the worldwide Glacier Thickness Database (GlaThiDa 3.0; (GlaThiDa Consortium, 2019; Welty et al., 2020)) where possible. The updated inventory shows decreases in estimated glacier volume in the Arctic, High Mountain Asia and Southern Andes, partially compensated by increases in Antarctica. 15% of the total glacier volume is estimated to be below sea level and would not contribute to sea-level rise if melted (Farinotti et al., 2019). Supplementary Material Table

ACCEPTED VERSION SUBJECT TO FINAL EDITING

9.SM.2 shows the inventory glacier area and mass for each region in the year 2000.

The SROCC found a globally coherent trend of glacier decline in the last decades despite large annual variability and regional differences (*very high confidence)*. Section 2.3.2.3 assesses the global glacier mass changes for the whole 20th century (see Table 9.5 for contribution to the sea-level budget, note that the peripheral glaciers in Greenland and Antarctica are added to the ice sheets for the budget). The AR6 assessment is based on Marzeion et al., (2015), using glacier-length reconstructions (Leclercq et al., 2011) and a glacier model forced by gridded climate observations (Marzeion et al., 2012), and not considering the estimated mass loss of uncharted glaciers (100± 50 Gt yr^{-1}) (Parkes and Marzeion, 2018). The time series are assumed independent resulting in larger uncertainty than presented in the SROCC (see also Section 9.6.1). The rate of global glacier mass loss (excluding the periphery of ice sheets) for the period 1901-1990 is estimated to be *very likely* 210 ± 90 Gt yr^{-1}, representing 16 [28 to 7]% of the glacier mass in 1901, in agreement with the SROCC within uncertainty estimates.

Since the SROCC, new regional estimates for the Andes (Dussaillant et al., 2019), High Mountain Asia (Shean et al., 2020), Iceland (Aðalgeirsdóttir et al., 2020), the European Alps (Davaze et al., 2020; Sommer et al., 2020) and Svalbard (Schuler et al., 2020), two new global (Ciracì et al., 2020; Hugonnet et al., 2021) and an ad-hoc estimate for the latest glaciological observations (Zemp et al., 2020) have extended the glacier mass change time series up to 2018/2019 (Figure 9.21 and Supplementary Material Table 9.SM.3). A reconciled global estimate for the period 1962 to 2019 has been compiled by Slater et al., (2021). However, in contrast to Slater et al., (2021), after 2000 this assessment is based on the first globally complete and consistent estimate of 21st-century glacier mass change from differencing of digital elevation models (Hugonnet et al., 2021) covering 94.7% of glacier area with glacier mass change for each glacier in the inventory produced with unprecedented accuracy. The estimates from (Hugonnet et al., 2021) agree within uncertainties with new and previous estimates at global (Hock et al., 2019b; Wouters et al., 2019; Zemp et al., 2019; Ciracì et al., 2020; Slater et al., 2021) and regional scale (Dussaillant et al., 2019; Aðalgeirsdóttir et al., 2020; Schuler et al., 2020; Shean et al., 2020). Excluding peripheral glaciers of ice sheets (RGI regions 5 and 19), glacier mass loss rate was *very likely* 170 ± 80 Gt yr^{-1} for the period 1971 to 2019 (8 [14 - 4]% of 1971 glacier mass), 210 ± 50 Gt yr^{-1} over the period 1993 to 2019 (6 [8 - 4]% of 1993 glacier mass) and 240 ± 40 Gt yr^{-1} over the period 2006-2019 (3 [4 - 2]% of 2006 glacier mass) (Sections 2.3.2.3, 9.6.1; Table 9.5[4]; Cross-Chapter Box 9.1). Including the peripheral glaciers of the ice sheets, the global glacier mass loss rate in the period 2000-2019 is *very likely* 266 ± 16 Gt yr^{-1} (4 [6 -3]% of glacier mass in 2000) with an increase in the mass loss rate from 240 ± 9 Gt yr^{-1} in 2000-2009 to 290 ± 10 Gt yr^{-1} in 2010-2019 (*high confidence*). These estimates are in agreement with the SROCC estimate and extend the period to 2018/19. In summary, new evidence published since the SROCC shows that during the decade 2010 to 2019 glaciers lost more mass than in any other decade since the beginning of the observational record (*very high confidence*; Figure 9.20; Section 8.3.1.7.1).

[START FIGURE 9.20 HERE]

Figure 9.20: Global and regional glacier mass change rate between 1960 and 2019. The time series of annual and decadal mean mass change are based on glaciological and geodetic balances (Zemp et al. (2019) and Zemp et al. (2020)). Superimposed are the 2002-2019 average rates by (Ciracì et al., 2020) based on the Gravity Recovery and Climate Experiment (GRACE), 2006-2015 estimated rates as assessed in SROCC and the new decadal averages (2000-2009 and 2010-2019) by Hugonnet et al. (2021). (*) New regional estimates for the Andes (Dussaillant et al., 2019), High Mountain Asia (Shean et al., 2020), Iceland (Aðalgeirsdóttir et al., 2020), Central Europe (Sommer et al., 2020) and Svalbard (Schuler et al., 2020) are also shown. The uncertainty reported in each study is shown. See Figure 9.2 for the location of each region. Further details on data sources and processing are available in the chapter data table (Table 9.SM.9).

[END FIGURE 9.20 HERE]

[4] The periods in Table 9.5 end in 2018 leading to a slight difference in the values

ACCEPTED VERSION SUBJECT TO FINAL EDITING

Regional glacier changes

A major advance since the SROCC is the availability of high accuracy mass loss estimates for individual glaciers (Hugonnet et al., 2021). These results show that during the last 20 years, the highest regional mass loss rates (>720 kg m^{-2} yr^{-1}) were observed in the Southern Andes, New Zealand, Alaska, Central Europe, and Iceland. Meanwhile, the lowest regional mass loss rates (<250 kg m^{-2} yr^{-1}) were observed in High Mountain Asia, the Russian Arctic, and the periphery of Antarctica. Glacier mass loss in Alaska (25% of 2000-2019 total mass loss), the periphery of Greenland (13%), Arctic Canada North (11%), Arctic Canada South (10%), the periphery of Antarctica (8%), the Southern Andes (8%) and High Mountain Asia (8%), represent the majority (83%) of the total glacier mass loss during the last 20 years (2000-2019).

The glacier mass loss rate from geodetic mass balance assessments in the Southern Andes during 2006-2015 was smaller (720 ± 70 kg m^{-2} yr^{-1}) (Braun et al., 2019; Dussaillant et al., 2019; Hugonnet et al., 2021) than previously assessed in the SROCC (860 ± 160 kg m^{-2} yr^{-1}), though within uncertainties. In the Central and Desert regions of the Southern Andes, an increase in mass loss from 2000-2009 to 2010-2018, and a high loss rate in Patagonia for the whole period, are observed (Dussaillant et al., 2019). Records of glacier mass loss in Peru (Seehaus et al., 2019a) and Bolivia (Seehaus et al., 2019b) in the period 2000-2016 show an increase in mass loss towards the end of the observation period. In Western North America, outside of Alaska and western Yukon, there was a fourfold increase in mass loss for 2009-2018 (860 ± 320 kg m^{-2} yr^{-1}) compared to 2000-2009 (203 ± 214 kg m^{-2} yr^{-1}) (Menounos et al., 2019), and in the Canadian Arctic there was a doubling of mass loss in the last two decades compared with pre-1996 (Noël et al., 2018; Cook et al., 2019). The peripheral glaciers in NE Greenland experienced a 23% increase in mass loss in 1980-2014 compared to the period 1910-1978/87 (Carrivick et al., 2019). In Iceland, 16 ± 4 % of the ~1890 glacier mass has been lost; about half of that loss occurred in the period 1994-2019 (Aðalgeirsdóttir et al., 2020). Glacier records starting in 1960 in Norway show that half of the observed glaciers advanced in the 1990s but all have retreated since 2000 (Andreassen et al., 2020). In Svalbard, glaciers have been losing mass since the 1960s with a tendency towards more negative mass balance since 2000 (Deschamps-Berger et al., 2019; Van Pelt et al., 2019; Morris et al., 2020; Noël et al., 2020; Schuler et al., 2020). A similar increase in mass loss has been observed for Franz Josef Land in the Russian Arctic (Zheng et al., 2018). Rapid retreat and downwasting throughout the European Alps in the early 21st century is reported (Sommer et al., 2020) and long term records, although limited, indicate sustained glacier mass loss in High Mountain Asia since ~1850, with increased mass loss in recent decades (Shean et al., 2020). In summary, although interannual variability is high in many regions, glacier mass records throughout the world show with *very high confidence* that the loss rate has been increasing in the last two decades (see also Section 8.3.1.7.1 and 12.4 for regional glacier assessment).

Section 2.3.2.3 assesses that the rate and global character of glacier retreat in the latter part of 20th century and finds the first decades of the 21st century appear to be unusual in the context of the Holocene (*medium confidence*) and the global glacier recession in the beginning of the 21st century to be unprecedented in the last 2000 years (*medium confidence)*. These assessments are supported by regional evidence. New reconstructions of the Patagonian Ice Sheet suggest that 20th-century glacial recession occurred faster than at any time during the Holocene (Davies et al., 2020). The reconstructions of glacier variations show that the glaciers in some regions are now smaller than previously recorded: since the mid-16th century in the Mont Blanc and Grindelwald regions of the European Alps (Nussbaumer and Zumbühl, 2012), since the 9th century in Norway (Nesje et al., 2012), and for the past 1800 years in NW Iceland (Harning et al., 2016, 2018). In Arctic Canada and Svalbard, many glaciers are now smaller than they have been in at least 4000 years (Lowell et al., 2013; Miller et al., 2013, 2017, Schweinsberg et al., 2017, 2018) and more than 40,000 years in Baffin Island (Pendleton et al., 2019). Although the millennial glacier length variation records are incomplete and discontinuous, and glacier fluctuations depend on multiple factors (e.g. temperature, precipitation, topography, internal glacial dynamics), there is a coherent relationship between rising temperatures, negative mass balance and glacier retreat on centennial timescales across most of the world. Glaciological and geodetic observations show that the rates of early 21st-century mass loss are the highest since 1850 (Zemp et al., 2015). For all regions with long-term observations, glacier mass in the decade 2010 to 2019 was the smallest since at least the beginning of the 20th century (*medium confidence*).

In contrast to the global glacier mass decline (Figure 9.21, Supplementary Material 9.SM.2, Table 9.5), a few

ACCEPTED VERSION SUBJECT TO FINAL EDITING

glaciers have gained mass or advanced due to internal glacier dynamics or locally restricted climatic causes. The SROCC discusses the "Karakoram anomaly" (centred on the western Kunlun range (at about 80°E/35°N), but also covering part of the Pamir and Karakoram ranges), where glaciers have been close to balance since at least the 1970s and had a slightly positive mass balance since the 2000s. Since the SROCC, new evidence suggests that this anomaly is related to a combination of low-temperature sensitivity of debris-covered glaciers, a decrease of summer air temperatures (Cross-Chapter Box 10.3), and an increase in snowfall possibly caused by increases in evapotranspiration from irrigated agriculture (Bonekamp et al., 2019; de Kok et al., 2020; Farinotti et al., 2020; Shean et al., 2020). However, a recent geodetic mass balance estimate suggests substantially increased thinning rates of High Mountain Asian glaciers after about 2010 (Hugonnet et al.,2021). There is *limited evidence* to assess whether the "Karakoram Anomaly" will persist in coming decades, but due to the projected increase in air temperature throughout the region its long-term persistence is *unlikely* (*high confidence*) (Kraaijenbrink et al., 2017; de Kok et al., 2020; Farinotti et al., 2020; Cross-Chapter Box 10.3).

Drivers of glacier change

The AR5 (Masson-Delmotte et al., 2013) noted that early-to-mid-Holocene glacier minima could be attributed to high summer insolation (*high confidence*), unlike the current situation. Since the AR5, new and improved chronologies of glacier size variations from the end of the last glacial period and the Holocene (e.g., Solomina et al., 2015, 2016; Eaves et al., 2019; Hall et al., 2019; Marcott et al., 2019; Bohleber et al., 2020; Davies et al., 2020; Palacios et al., 2020) confirm the dominant role of orbital forcing for millennial-scale glacier fluctuations but emphasize the role of other forcings – solar and volcanic activity, ocean circulation, sea ice and internal climate variability – in explaining the regional variability of glacier fluctuations at shorter time scales. Shakun et al., (2015) demonstrated that during the last deglacial transition (18-11 ka), the mid-to-low-latitude glacier retreat was driven by an increase in atmospheric CO_2 and global temperature.

In the Northern Hemisphere, where summer insolation decreased during the Holocene (Section 2.2.1), glaciers generally waxed (Briner et al., 2016; Kaufman et al., 2016; Lecavalier et al., 2017; Zhang et al., 2017; Axford et al., 2019; Geirsdóttir et al., 2019; Larsen et al., 2019; Luckman et al., 2020). Conversely, in the Southern Hemisphere, where summer insolation increased during the Holocene, glaciers generally waned (Solomina et al., 2015; Kaplan et al., 2016; Reynhout et al., 2019). However, these general global trends were modulated by regional climate variations in temperature and precipitation (Murari et al., 2014; Kaplan et al., 2016; Batbaatar et al., 2018; Saha et al., 2018) and there are a number of examples of this. A precipitation increase led to a local early Holocene (7-8 ka) glacier maximum in arid Mongolia (Gichginii Range). Glacier advances at ~9 ka in Southwest Greenland have been suggested to be a consequence of the freshwater pulse from the Laurentide Ice Sheet, which led to cooling in the Baffin Bay area (Schweinsberg et al., 2018). Lake sediments indicate that the glaciers in the region were smaller than today or absent between 8.6 and 1.4 ka BP (Larocca et al., 2020). Glaciers on the Antarctic Peninsula and in Patagonia during the Holocene were strongly affected by the Southern Westerly Winds, sea ice extent, and ocean circulation (García et al., 2020). Recent studies indicate that explosive volcanism can drive glacier advances (Solomina et al., 2015, 2016; Schweinsberg et al., 2018; Brönnimann et al., 2019). In summary, on millennial time scales over the Holocene, there is *high confidence* orbital forcing drove hemispheric-scale glacier variations, but new studies provide a nuanced picture of responses to a variety of regional-scale forcings.

Section 3.4.3.1 assesses new attribution studies for glaciers and finds that human influence is *very likely* the main driver of the global, near-universal retreat of glaciers since the 1990s. The SROCC assessed that it is *very likely* that atmospheric warming is the primary driver for the global glacier recession. Since the SROCC, a study of glaciers in New Zealand used event attribution to confirm a connection between extreme glacier mass loss years and anthropogenic warming (Vargo et al., 2020).

The SROCC stated with *high confidence* that besides temperature, other factors, such as precipitation changes or internal glacier dynamics, have modified the temperature-induced glacier response in some regions. Deposition of a thin layer (<2 cm) of light-absorbing particles (e.g., black carbon, brown carbon, algae, mineral dust or volcanic ash) can exert an important control on glacier mass balance, by decreasing

ACCEPTED VERSION SUBJECT TO FINAL EDITING

surface albedo and thus increasing absorbed shortwave radiation and melt (see also section 7.3.4.3. The SROCC found *limited evidence* and *low agreement* that this process has had a significant effect on observed long-term glacier changes. Several studies have shown melt increases due to the deposition of light-absorbing particles (Schmale et al., 2017; Wittmann et al., 2017; Sigl et al., 2018; Di Mauro et al., 2019, 2020; Magalhães et al., 2019; Constantin et al., 2020). Conversely, increasingly thick debris cover (>2-5 cm) on retreating glaciers can slow down glacier melt (Pratap et al., 2015; Brun et al., 2016). Although debris covers only about 4-7% of the total glacier area globally (Scherler et al., 2018; Herreid and Pellicciotti, 2020), many glaciers are heavily debris-covered in their lower reaches, especially in High Mountain Asia, the Caucasus, the European Alps, Southern Andes and Alaska, resulting in different responses to warming than similar clean-ice glaciers. A shift in regional meteorological conditions driven by the location and strength of the upper level zonal wind has been found to have forced recent high mass loss rates in Western North America (Menounos et al., 2019). High geothermal heat flux areas underneath glaciers and high energy dissipation in the flow of water and ice causes additional mass loss of the glaciers in Iceland (Jóhannesson et al., 2020), accounting for 20% of the mass loss since 1994 (Aðalgeirsdóttir et al, 2020). Glacier lake volume, in front of retreating glaciers, has increased globally by around 48% between 1990 and 2018 (Shugar et al., 2020), which can increase both subaqueous melt and calving. In summary, there is *high confidence* that non-climatic drivers have and will continue to modulate the first-order temperature response of glaciers in some regions.

[START FIGURE 9.21 HERE]

Figure 9.21: Global and regional glacier mass evolution between 1901 and 2100 relative to glacier mass in 2015. Reconstructed glacier mass change through the 20th century (Marzeion et al., 2015) and observed during 1961-2016 (Zemp et al., 2019). Projected (2015-2100) glacier mass evolution is based on the median of three Representative Concentration Pathways (RCPs) emission scenarios (Marzeion et al., 2020). Uncertainties are in all cases the 90% confidence interval. For a better comparison between regions, the maximum relative mass change was set to 200%, although for three regions, the volume changes between 1901 and 2015 exceeded that value. For the Low Latitude, New Zealand, and High Mountain Asia glaciers, the changes were larger than 1000%, 350%, and 250%, respectively. See Figure 9.2 for the location of each region. Further details on data sources and processing are available in the chapter data table (Table 9.SM.9).

[END FIGURE 9.21 HERE]

9.5.1.2 Model evaluation

Since the AR5, glacier mass projections have been coordinated by the Glacier Model Intercomparison Project (GlacierMIP) (Hock et al., 2019a; Marzeion et al., 2020). The SROCC (Hock et al., 2019b) relied on six global-scale glacier models based on previously published glacier model projections (Hock et al., 2019a), and found with *high confidence* that glaciers will lose substantial mass by the end of the century but assigned *medium confidence* to the magnitude and timing of the projected glacier mass loss, because of the simplicity of the models, the limited observations in some regions to calibrate them and the diverging initial glacier volumes.

Since the SROCC, (Marzeion et al., 2020) projected 21st century global-scale glacier mass changes based on seven global-scale and four regional-scale glacier models (Annex II). All models used the same initial and boundary conditions, forming a more coherent ensemble of projections compared to the SROCC. Nevertheless, challenges remain because of scarcity of glacier thickness, surface mass balance and frontal ablation data for model calibration, but also due to uncertainties in glacier outlines, surface elevations and ice velocities. The global surface mass balance models are of varying complexity, including mass balance sensitivity approaches (van de Wal and Wild, 2001), temperature-index methods (Anderson and Mackintosh, 2012; Marzeion et al., 2012; Radić et al., 2014; Huss and Hock, 2015; Kraaijenbrink et al., 2017; Maussion et al., 2019a; Zekollari et al., 2019; Rounce et al., 2020) and simplified energy balance calculations (Sakai and Fujita, 2017; Shannon et al., 2019). Compared to simpler, empirical parameterizations, full energy-

ACCEPTED VERSION SUBJECT TO FINAL EDITING

balance models are not necessarily the most appropriate choice for simulating future glacier response to climate change, even at the local scale (Réveillet et al., 2017, 2018), because of parameter and forcing uncertainties. All models account for glacier retreat and advance but only two models (Anderson and Mackintosh, 2012; Huss and Hock, 2015) include frontal ablation.

Secondary processes such as debris-cover thickening (e.g., Herreid and Pellicciotti, 2020), albedo changes due to light-absorbing particles (e.g., Magalhães et al., 2019; Williamson et al., 2019), trends of refreezing and water storage in firn (e.g., Ochwat et al., 2021), dynamic instabilities such as surges (e.g., Thøgersen et al., 2019) or glacier collapse (e.g., Kääb et al., 2018), are not represented in global glacier models, resulting in both underestimated and overestimated sensitivity to warming that is currently not possible to quantify. Furthermore, challenges for future projections are caused by the low resolution and high spatial variability at subgrid scale of the precipitation amount provided by GCMs, which requires downscaling to the spatial scale of a glacier (Maussion et al., 2019a; Zekollari et al., 2019; Marzeion et al., 2020). In summary, in agreement with the SROCC, progress in global scale glacier modelling efforts allows *medium confidence* in the capabilityof current-generation glacier models to simulate the magnitude and timing of glacier mass changes as a response to the climatic forcing.

9.5.1.3 Projections

The AR5 (Vaughan et al., 2013) and the SROCC (Hock et al., 2019b) stated with *high confidence* that the world's glaciers are presently in imbalance due to the warming of recent decades. The observed retreat of glaciers is only a partial response to the already realized warming (Christian et al., 2018), and they are committed to losing considerable mass in the future, even without further change in air temperature (Mernild et al., 2013; Trüssel et al., 2013; Zekollari and Huybrechts, 2015; Huss and Fischer, 2016; Marzeion et al., 2018; Jouvet and Huss, 2019). One model estimates that 36 ± 8 % of global glacier mass is already committed to be lost due to past greenhouse gas emissions (Marzeion et al., 2018). Although accumulation and ablation instantly determine the surface mass balance, the glacier geometries adjust to changed atmospheric conditions over a longer time (Zekollari et al., 2020). The adjustment time, often referred to as the response time, is variable from one glacier to another, depending on the glacier geometry (thickness and steepness), surface mass balance and gradient (e.g., Jóhannesson et al., 1989; Harrison et al., 2001; Lüthi, 2009; Zekollari et al., 2020). Response time is variable: years for smaller and steeper glaciers (Beedle et al., 2009; Lüthi and Bauder, 2010; Rabatel et al., 2013), up to tens or hundreds of years for larger and gentle-sloped glaciers (e.g., Burgess and Sharp, 2004; Lüthi et al., 2010; Zekollari et al., 2020). The models indicate that the disequilibrium between the glaciers and present atmospheric conditions (1995 to 2014) reduces and then disappears at around year 2070 (Marzeion et al., 2020). There is therefore *very high confidence* that the disequilibrium of glaciers will persist as warming continues and that glaciers will continue to lose mass for at least several decades because of their lagged response even if global temperature is stabilized.

The SROCC assessed that global glacier mass loss by 2100, relative to 2015 will be 18% [*likely* range 11 to 25%] for scenario RCP2.6 and 36% [*likely* range 26 to 47%] for RCP8.5, and that many glaciers will disappear regardless of the emission scenario (*very high confidence*). Since the SROCC, new results from (Marzeion et al., 2020) have been published (Box 9.3; Figure 9.21, Table 9.4, including peripheral glaciers in Greenland and Antarctica). Glaciers will lose 29,000 [9,000 to 49,000] Gt and 58,000 [28,000 to 88,000] Gt over the period 2015-2100 for RCP2.6 and RCP8.5, respectively (*medium confidence*), which represents 18 [5 to 31] % and 36 [16 to 56] % of their early 21st century mass, respectively (Table 9.4). Within uncertainties, these agree with the SROCC estimates, although with a slightly smaller mass loss due to the inclusion of models with lower sensitivity to changing climate conditions (Marzeion et al., 2020). The greatest source of uncertainty in glacier mass loss until the middle of the 21st century is the disagreement between glacier models, with emissions scenario becoming the dominant cause of uncertainty by the end of the 21st century (Marzeion et al., 2020).

Although the GlacierMIP projections (Hock et al., 2019a; Marzeion et al., 2020) were forced by RCP scenarios, two global glacier models (Huss and Hock, 2015; Maussion et al., 2019b) were also run with 13

ACCEPTED VERSION SUBJECT TO FINAL EDITING

GCMs and SSP scenarios (Table 9.4). These results show increased mass loss compared to the RCP forced simulations, although with fewer global glacier models. To enable the glacier contribution to future sea level rise to be estimated under the full range of SSP scenarios (Section 9.6.3.3), the GlacierMIP results are emulated using a Gaussian Process model (Edwards et al., 2021) (Box 9.3, Table 9.4). The emulated projections show a narrower range than the roughly equivalent RCP projections, which may be explained by not accounting for covariance in the regional uncertainties (Marzeion et al., 2020) and by the fact that the emulator caps sea level contribution for each region at the volume above floatation estimated by (Farinotti et al., 2019) (Table 9.SM.2). Comparison of simulated and emulated regional sea level contributions support this explanation. Rates of change and post-2100 projections for the sea level projections are estimated with the AR5 parametric fit (Supplementary Material 9.SM.4.5;(Church et al., 2013a)) applied to the GlacierMIP results (Marzeion et al., 2020), and these are also shown in Table 9.4 for comparison.

[START TABLE 9.4]

Table 9.4: Projected sea level contributions in meters from global glaciers (including peripheral glaciers in Greenland and Antarctica) by 2100 relative to 2015, for selected RCP and SSP scenarios.

Representative Concentration Pathways (RCPs)				
Study	RCP2.6	RCP4.5	RCP8.5	Notes
IPCC AR5 and SROCC (Church et al., 2013a; Oppenheimer et al., 2019)	0.10 (0.04 – 0.16)	0.12 (0.06 – 0.19)	0.17 (0.09 – 0.25)	Median and *likely* (66% range) contributions in 2100 relative to 1995-2014
GlacierMIP Hock et al. (2019a)	0.094 (0.069 – 0.119)	0.142 (107 – 177)	0.200 (0.156 – 0.240)	Mean (± 1 s.d. range) contributions
GlacierMIP Marzeion et al., (2020)	0.079 [0.023 – 0.135]	0.119 [0.053 – 0.185]	0.159 [0.073 – 0.245]	Median [90% range]
Shared Socioeconomic Pathways (SSPs)				
Study	SSP1-2.6	SSP2-4.5	SSP5-8.5	Notes
GlacierMIP experimental protocol (Marzeion et al., 2020) with CMIP6 forcing	0.111 (0.077 to 0.145) [0.05 to 0.167]	0.136 (0.096 to 0.176) [0.07 to 0.201]	0.190 (0.133 to 0.247) [0.09 to 0.283]	Mean (66% range) [90% range] using 13 GCMs and 2 glacier models[1]
GlacierMIP (Marzeion et al., 2020) with AR5 parametric fit: used for rates and post-2100 projections (Supplementary Material 9.SM.4.5)	0.102 (0.076 to 0.134) [0.059 to 0.154]	0.128 (0.095 to 0.167) [0.076 to 0.192]	0.171 (0.124 to 0.224) [0.098 to 0.259]	Median (66% range) [90% range] contribution from AR5 parametric fit to GlacierMIP ensemble, relative to 1995-2014
Emulated (Marzeion et al., 2020); (Edwards et al., 2021)	0.080 (0.059 to 0.101) [0.046 to 0.116]	0.115 (0.093 to 0.137) [0.077 to 0.155]	0.170 (0.144 to 0.196) [0.124 to 0.218]	Median (66% range) [90% range] contribution in 2100 relative to

ACCEPTED VERSION SUBJECT TO FINAL EDITING

			2015 from emulator of GlacierMIP6 used with Chapter 7 climate forcing

[1] OGGM (Maussion et al., 2019a) and GloGEM (Huss and Hock, 2015)

[END TABLE 9.4]

The mass loss rates vary between regions and there are distinctively different patterns between scenarios (Marzeion et al., 2020). The global models agree that regions characterized by relatively little glacier-covered area (Low Latitude, Central Europe, Caucasus, Western Canada and US, North Asia, Scandinavia and New Zealand) will lose nearly all (>80%) glacier mass by 2100 in the RCP 8.5 scenario, but their corresponding contribution to sea-level rise will be small. A study using detailed ice dynamics for the largest glacier of the European Alps, Great Aletsch Glacier, projects 60% of present ice volume will be lost by 2100 in RCP2.6 and an almost complete wastage of the ice in RCP8.5 (Jouvet and Huss, 2019). Due to their larger mass, the largest contribution to sea level rise comes from glaciers in the Arctic and Antarctic regions (Antarctic, Arctic Canada, Alaska, Greenland, Svalbard and Russian Arctic), in spite of having the smallest relative mass loss, and it is expected that they will continue to contribute to sea level rise beyond 2100. The regions with intermediate glacier mass (Southern Andes, High Mountain Asia and Iceland) show decreasing mass loss rates for RCP2.6 throughout the 21st century, and increasing rates for RCP8.5 that peak in the mid to late 21st century (Figure 9.21). The peak in mass loss rate followed by reduction is due to both decreasing glacier volume and stabilizing mass balance (Marzeion et al., 2020). Vatnajökull, the largest glacierin Iceland, is projected to lose about 50% of its mass by 2300 in extended RCP4.5 and 80-100% in extended RCP8.5 scenarios (Schmidt et al., 2019). In summary, both global and regional studies agree that glacier mass loss will continue in all regions, with larger mass loss for high emission scenarios (*high confidence*) (see also Section 8.4.1.7.1).

In the AR5 and the SROCC, glacier mass loss beyond 2100 was calculated employing a parametric fit to available model simulations. In section 9.6.3.5, that same parametric fit is applied to (Marzeion et al., 2020) projections resulting in complete glacier mass loss at year 2300 under SSP5-8.5 and 40-100% mass loss under SSP1-2.6. (Clark et al., 2016) simulate glacier mass evolution, not including glaciers peripheral to the Antarctic ice sheet, for different warming levels for the next ten thousand years. There is *limited evidence* and *low confidence* that at sustained warming levels between 1.5 and 2°C, about 50-60% of glacier mass will remain, predominantly in the polar regions. At sustained warming levels between 2 and 3°C, about 50-60% of glacier mass outside Antarctica will be lost and at sustained warming levels between 3 and 5 °C, 60-75% of glacier mass outside Antarctica will disappear. Based on (Marzeion et al., 2020), there is *medium confidence* that nearly all glacier mass in low latitudes, Central Europe, the Caucasus, Western Canada and the US, North Asia, Scandinavia and New Zealand will disappear at this high warming level.

9.5.2 Permafrost

This section focuses on the physical aspects of permafrost (perennially frozen ground) as an element of the climate system, drawing on the assessment of observed global permafrost changes provided in Section 2.3.2.5, and treating more specifically model evaluation and projections. The permafrost carbon feedback is assessed in Box 5.1. Section 12.4 of this report provides permafrost information relevant to impacts and risk on regional scales.

9.5.2.1 Observed and reconstructed changes

The current extent of the global permafrost region is about $22 \pm 3 \times 10^6$ km^2 (Gruber, 2012). Permafrost underlies about 15% of Northern Hemisphere land and more than 50% of the unglacierized land north of

ACCEPTED VERSION SUBJECT TO FINAL EDITING

60°N (Zhang et al., 1999; Gruber, 2012; Obu et al., 2019). It is also found in high-altitude areas of mountain ranges in both hemispheres (estimated in the SROCC (Hock et al., 2019b) as representing about 27-29% of the global permafrost area (*medium confidence*) and most unglacierized areas in Antarctica (Vieira et al., 2010; Obu et al., 2020)). Ground ice volume in permafrost is variable, reaching up to 90% in syngenetic permafrost deposits (Kanevskiy et al., 2013; Gilbert et al., 2016). The SROCC (Meredith et al., 2019) reported *medium confidence* in the estimation that Earth's total perennial ground ice volume is equivalent to 2-10 cm of global sea level (Zhang et al., 2000). There is no evidence suggesting that a large part of this volume, if melted, would run off and contribute to global sea level. Therefore, and because of the modest total volume of mobilizable water, the contribution of permafrost thaw to past and future sea-level budgets is usually neglected (see section 9.6.3.2).

Permafrost changes mostly refer to changes in extent, temperature and active layer thickness. The SROCC (Hock et al., 2019b; Meredith et al., 2019) reported with *very high confidence* that record high permafrost temperatures at the depth of the zero annual amplitude (the depth about 10 to 20 m below the surface where the seasonal soil temperature cycle vanishes) were attained in recent decades in the Northern circumpolar permafrost region, *high confidence* that permafrost has warmed over recent decades in many mountain ranges, and overall *very high confidence* that global warming over the last decades has led to widespread permafrost warming. As reported in the SROCC, the global (polar and mountain) permafrost temperature has increased at 0.29 ± 0.12°C near the depth of zero annual amplitude between 2007 and 2016 (Biskaborn et al., 2019). Stronger warming has been observed in the continuous permafrost zone (0.39 ± 0.15°C) compared to the discontinuous zone (0.20 ± 0.10°C), consistent with the fact that near the melting point, a large amount of energy is required for melting the ice (Figure 9.22), and because of the reduced effect of Arctic amplification in more southerly locations (Romanovsky et al., 2017). This is consistent with longer-term Arctic trends from deep boreholes shown in Figure 2.22. Mountain permafrost temperature trends are heterogeneous, reflecting variations in local conditions such as topography, surface type, soil texture and snow cover, but again, generally weaker warming rates are observed in warmer permafrost at temperatures close to 0°C, particularly when ice content is high (e.g., Mollaret et al., 2019; Noetzli et al., 2019; PERMOS, 2019). In summary, strong variability in recent permafrost temperature trends is linked to local conditions, regionally varying temperature trends and the thermal state of permafrost itself, but as discussed in Section 2.3.2.5, there is overall *high confidence* in the observed increases in permafrost temperature over the past 3 to 4 decades throughout the permafrost regions.

Closer to the surface, the active layer undergoes annual cycles of freeze and thaw. The SROCC reported *medium confidence* in active layer thickness (ALT) increase as a pan-Arctic phenomenon. Recent evidence presented in Section 2.3.2.5 shows pervasive ALT increase in the European and Russian Arctic in the 21st century and in high elevation areas in Europe and Asia since the mid-1990s. Emergence of a clearer global picture is hampered by (1) uneven distribution of observing sites, (2) substantial variability among the existing sites, strongly influenced by local conditions (soil constituents and moisture, snow cover, vegetation); (3) interannual variability , and (4) thaw settlement in ice-rich terrain (Streletskiy et al., 2017; O'Neill et al., 2019). In summary, in agreement with the SROCC and recent evidence presented in Section 2.3.2.5, there is *medium confidence* that ALT increase is a pan-Arctic phenomenon.

There is *medium confidence* that the observed acceleration and destabilization of rock glaciers is related to warming temperatures and increase in water content at the permafrost table in recent decades (Deline et al., 2015; Cicoira et al., 2019; Marcer et al., 2019; PERMOS, 2019; Kenner et al., 2020). There is also *medium confidence* that observed increases in size and frequency of rock avalanches are linked to permafrost degradation in rock walls (Ravanel et al., 2017; Patton et al., 2019; Tapia Baldis and Trombotto Liaudat, 2019). In summary, there is *medium confidence* that mountain permafrost degradation at high altitude has increased the instability of mountain slopes in the past decade.

The SROCC assessed with *high confidence* that the extent of subsea permafrost, formed before submersion on Arctic continental shelves during the last deglaciation, is much reduced compared to older studies that had estimated the entire formerly exposed Arctic shelf area to be underlain by permafrost. This is supported by observations (Shakhova et al., 2017) that show rapid thaw of recently submerged permafrost on the East Siberian Shelf . A modelling study (Overduin et al., 2019) estimates that 97% of permafrost under Arctic

ACCEPTED VERSION SUBJECT TO FINAL EDITING

shelves is currently thinning.

Based on multiple studies, there is *medium confidence* that widespread retreat of coastal permafrost is accelerating in the Arctic (Günther et al., 2015; Cunliffe et al., 2019; Isaev et al., 2019). There is also consistent evidence of complete permafrost thaw in areas of discontinuous and sporadic permafrost since about 1980 (Camill, 2005; Kirpotin et al., 2011; James et al., 2013; Jones et al., 2016a; Borge et al., 2017; Chasmer and Hopkinson, 2017; Gibson et al., 2018a), but this evidence is geographically scattered. In spite of increasing evidence of landscape changes from site studies and remote sensing, quantifying permafrost extent change remains challenging because it is a subsurface phenomenon that cannot be observed directly (Jorgenson and Grosse, 2016; Trofaier et al., 2017). A modelling study for the Qinghai-Tibet Plateau between the 1960s and the 2000s (Ran et al., 2018) suggests transition from permafrost to seasonally frozen ground over an area of more than 400,000 km^2. In summary, there is *medium confidence* that complete permafrost thaw in recent decades is a common phenomenon in discontinuous and sporadic permafrost regions. In addition, paleoclimatic evidence presented in Section 2.3.2.5 confirms a long-term sensitivity of permafrost extent to climatic variations, although an analysis of North American speleothem records over the last two glacial cycles indicates that this apparent high sensitivity could be a consequence of regional-scale variability (Batchelor et al., 2019).

There is a lack of formal studies attributing observed permafrost changes (thaw depth, thermal state) or associated landscape changes to anthropogenic forcing. However, the observed Arctic warming has been attributed to anthropogenic forcing (e.g., Najafi et al., 2015) and an obvious physical link exists between ground temperatures (and thus permafrost) and surface air temperatures. Therefore physically consistent and convergent lines of evidence lead to *medium confidence* in anthropogenic forcing being the dominant cause of the observed pan-Arctic permafrost changes. Added to this, local permafrost change by soil and ecosystem disturbance is induced by increasing human industrial activities in the Arctic (e.g., Raynolds et al., 2014).

9.5.2.2 Evaluation of permafrost in climate models

As stated in AR5 (Flato et al., 2013), coupled models contributing to CMIP5 showed large inter-model variability of permafrost extent due to deficiencies in reproducing surface characteristics and processes (Koven et al., 2013), particularly thermal properties of the ground and snow. These deficiencies led the SROCC (Meredith et al., 2019) to express only *medium confidence* in the models' capacity to correctly project the magnitude of future permafrost changes, in spite of *high confidence* in the models' projection of a general thaw depth increase and a substantial loss of shallow permafrost. The SROCC further noted that several types of physical "pulse" disturbances, in particular fire and thermokarst formation, are usually not represented in coupled climate models. This has been discussed in detail in the SROCC, which assessed that there is *high confidence* that permafrost degradation through fire (Jones et al., 2015; Gibson et al., 2018b) is currently occurring faster in some well-studied regions than during the first half of the 20th century, and *medium confidence* that thermokarst formation, to which about 20% of the northern permafrost region is vulnerable (Olefeldt et al., 2016), can lead to faster large-scale permafrost degradation in response to climate change.

Since the SROCC, dedicated modelling of the evolution of ice- and organic-rich permafrost in the northeast Siberian lowlands (Nitzbon et al., 2020) has shown that not representing thermokarst-inducing processes in ice-rich terrain leads to a systematic underestimation of the rapidity and magnitude of permafrost thaw. Simplified inventory-based modelling (Turetsky et al., 2020) points towards similar conclusions. Although these pulse disturbances still need to be represented in CMIP-type models, there have been many new developments to that type of model since CMIP5 and the AR5. Soil freezing and its thermal and hydrological effects are now included in a large number of land-surface modules that are part of the CMIP6 ensemble (Chadburn et al., 2015a; Hagemann et al., 2016; Cuntz and Haverd, 2018; Guimberteau et al., 2018; Yokohata et al., 2020), sometimes allowing for the effects of excess ice (Lee et al., 2014). Improved representation of snow insulation in models has led to more realistic simulated permafrost extents (e.g., Paquin and Sushama, 2015). In a post-CMIP5 ensemble of land-surface models driven by observed

ACCEPTED VERSION SUBJECT TO FINAL EDITING

meteorological conditions (McGuire et al., 2016), inter-model spread was substantially reduced when the ensemble was restricted to models that appropriately represented the effect of snow insulation on the underlying soil (Wang et al., 2016b). More detailed descriptions of high-latitude vegetation characteristics, vegetation dynamics, and snow-vegetation interactions have been included in several models (Chadburn et al., 2015b; Porada et al., 2016; Druel et al., 2017) since the AR5.

A total soil column depth of at least about 10 m is required to adequately represent the dampening effect of seasonal-scale heat exchanges between shallow and deeper ground, and thus to correctly simulate active layer thickness (Lawrence et al., 2008; Ekici et al., 2015). However, many CMIP6 models still have shallower total soil columns (Burke et al., 2020) and the proportion of models with deeper total soil columns has not increased since CMIP5 (Koven et al., 2013). Another recently identified process, usually not represented in the current (CMIP6) generation of climate models (Zhu et al., 2019), is warming-driven decomposition and burning of organic material that provides strong thermal insulation of underlying ground. Decay of the insulating organic material can lead to increased permafrost thaw, creating a positive feedback loop.

In spite of the aforementioned structural improvements to many models, the simulated current permafrost extent from available CMIP6 models shows no substantial improvement with respect to CMIP5 (see Figure 9.22a). The extent of the region where permafrost is simulated within the top 15 m in the Northern Hemisphere for the 1979-1998 period is characterized by very large scatter in the coupled CMIP5 and CMIP6 historical simulations compared to estimates of the present permafrost extent based on multiple observational lines of evidence (Zhang et al., 1999) and models based on satellite observations and reanalyses (Gruber, 2012; Obu et al., 2019). Outliers with very low simulated permafrost extent are models that have only a very shallow soil column (leading to an underestimate of thermal inertia at depth) and do not take into account soil water phase changes. These inadequacies lead to an overestimate of seasonal thaw depth, exceeding the total thickness of the models' soil columns (Burke et al., 2020). Excessive simulated permafrost extent can in several cases be traced to insufficient thermal insulation by the winter snow cover (Burke et al., 2020).

Figure 9.22a also shows that the corresponding land-atmosphere simulations with prescribed observed sea-surface temperatures and sea-ice concentrations, and the land-only simulations with prescribed reanalysis-based meteorological forcing, do not provide an improved simulation of the current permafrost extent, although, by construction, they can be expected to exhibit lower land surface climate biases. This further points to deficiencies in the land modules as the main reason for biases, consistent with conclusions drawn from the analysis of CMIP5 output (Koven et al., 2013), as reported in the SROCC and the AR5.

In spite of more realistic description of permafrost-related processes in many coupled climate models, the CMIP6 models thus still produce a very scattered ensemble of estimates of current permafrost extent, and there is *high confidence* that this is strongly linked to deficiencies of the representation of soil processes. Furthermore, current-generation climate models tend to neglect several physical disturbances that can lead to faster permafrost thaw. Because of large uncertainties in the future evolution of these drivers (see SROCC), there is *limited evidence* that these shortcomings lead to an underestimate of permafrost degradation rates in response to climate change in the CMIP6 ensemble. In summary, there is *high confidence* that coupled models correctly simulate the sign of future permafrost changes linked to surface climate changes, but only *medium confidence* in the amplitude and timing of the transient response.

[START FIGURE 9.22 HERE]

Figure 9.22: Simulated versus observed permafrost extent and permafrost volume change by warming level. a) Diagnosed Northern Hemisphere permafrost extent (area with perennially frozen ground at 15 m depth, or at the deepest model soil level if this is above 15 m) for 1979-1998, for available CMIP5 and CMIP6 models, from the first ensemble member of the historical coupled run, and for CMIP6 AMIP (atmosphere+land surface, prescribed ocean) and land-hist (land only, prescribed atmospheric forcing) runs. Estimates of current permafrost extents based on physical evidence and reanalyses are indicated as black symbols (triangle: Obu et al. (2018); star: Zhang et al. (1999); circle: central value and associated

ACCEPTED VERSION SUBJECT TO FINAL EDITING

range from Gruber (2012)). b) Simulated global permafrost volume change between the surface and 3 m depth as a function of the simulated GSAT change, from the first ensemble members of a selection of scenarios, for available CMIP6 models. Further details on data sources and processing are available in the chapter data table (Table 9.SM.9).

[END FIGURE 9.22 HERE]

9.5.2.3 Projected permafrost changes

The AR5 (Collins et al., 2013) and the SROCC (Meredith et al., 2019) (based on available CMIP5 output) both expressed *high confidence* that future pan-Arctic thaw depth will increase and near-surface permafrost extent will decrease under future global warming, and *medium confidence* in the magnitude of the simulated changes because of model deficiencies and large spread of the results.

The equilibrium sensitivity of permafrost extent to stabilized global mean warming has been inferred (by constraining CMIP5 output with diagnosed relationships between the observed present-day spatial distribution of permafrost and air temperature) to be about 4.0×10^6 km^2 °C^{-1} (Chadburn et al., 2017) for GSAT changes with respect to the present below about +3°C. This equilibrium permafrost sensitivity, relevant for assessing long-term permafrost changes at a stabilized warming level, is about 20% higher than the transient centennial-scale near-surface permafrost extent sensitivity (diagnosed from seasonal thaw down to 3 m depth) suggested by direct analysis of CMIP5 output (Slater and Lawrence, 2013). Compared to these and other studies reported in the AR5 and the SROCC (Koven et al., 2013), the recently suggested equilibrium extent sensitivity to GSAT changes of about 1.5×10^6 km^2 °C^{-1} based on idealized ground temperature modelling (Liu et al., 2021) appears unrealistically low.

A strong transient temperature sensitivity of the volume of perennially frozen soil in the top 3 m below the surface is consistently suggested by the available CMIP6 models (Figure 9.22b). Relative to the current volume, the transient sensitivity of the modelled permafrost volume in the top 3 m to GSAT changes (with respect to the 1995-2014 average and up to +3°C change, that is, about up to +4°C with respect to pre-industrial levels) is about 25 ± 5 % °C^{-1} (Burke et al., 2020), but there is only *medium confidence* in this value and 1s.d. uncertainty range because of the model deficiencies discussed in 9.5.2.2. It is important to note that permafrost loss will not be limited to the top 3 m, with delayed response of deeper permafrost. The simulated transient temperature sensitivity of permafrost volume is slightly stronger in the SSP1-2.6 scenario than in other SSPs because subsurface temperature lag increases with higher atmospheric warming rates, particularly when ground ice melting induces additional delays.

Due to the role of air temperature as a major driver of permafrost change, the SROCC (Hock et al., 2019b) expressed *very high confidence* that permafrost in high-mountain regions is expected to undergo increasing thaw and degradation during the 21st century, with stronger consequences expected for higher greenhouse gas emission scenarios. Recently published studies (e.g., Zhao et al., 2019) support this SROCC assessment.

In summary, based on *high agreement* across CMIP6 and older model projections, fundamental process understanding, and paleoclimate evidence, it is *virtually certain* that permafrost extent and volume will shrink as global climate warms.

9.5.3 Seasonal snow cover

Mean snow cover extent in January and February, the usual months of maximum extent, covers about 45% of the Northern Hemisphere (NH) land surface (more than 45 million km^2 over the 1967-2014 period (Estilow et al., 2015)). In contrast, maximum seasonal snow cover in South America, the dominant ice-free land mass in the Southern Hemisphere in terms of seasonal snow cover extent, remains well below 1 million km^2 (Foster et al., 2009) or less than 2% of the Southern Hemisphere land surface.

ACCEPTED VERSION SUBJECT TO FINAL EDITING

Terrestrial snow cover is characterized via three variables: (1) areal snow cover extent (SCE), (2) the time period of continuous snow cover (snow cover duration (SCD) which reflects snow-on and snow-off dates) and (3) snow accumulation expressed either as snow depth (SD) or snow water equivalent (SWE; the depth of water stored by the snowpack).

Observed large-scale snow cover changes, their attribution to human activity and their effects on the hydrological cycle are also discussed in Chapter 2 (Section 2.3.2.2), Chapter 3 (Section 3.4.2) and Chapter 8 (Section 8.2.3.1) of this report. The role of snow in the global surface albedo feedback is assessed in Section 7.4.2.3. The effect of aerosol deposition on snow albedo and associated climate forcing is assessed in Section 7.3.4.3.

9.5.3.1 Observed changes of seasonal snow cover

The AR5 (Vaughan et al., 2013) reported that NH SCE in June *very likely* decreased by 11.7% [8.8 to 14.6 %] per decade over the 1967-2012 period, exceeding the absolute and relative reductions observed in March and April. The AR5 further reported *very high confidence* that NH March and April SCE decreased over the 90 years after 1922. The SROCC only assessed snow cover changes for the Arctic and mountain areas. For the Arctic (north of 60°N), the SROCC (Meredith et al., 2019) expressed *high confidence* in SCE decreases of -3.5 ± 1.9% per decade in May and -13.4± 5.4% per decade in June, based on a combination of multiple datasets (Mudryk et al., 2017). Concerning mountain snow cover, the SROCC (Hock et al., 2019b) reported with *high confidence* that mountain snow cover (both in terms of SCE and maximum SWE) has generally declined since the middle of the 20th century at lower elevations. At higher elevations, the SROCC reported *medium confidence* in generally insignificant snow cover trends where these were available. The large-scale assessment provided in Section 2.3.2.2 of this report reports *very high confidence* in substantial reductions of NH snow cover extent (particularly in spring) since 1978, and states that there is *limited evidence* that this decline extends back to the early 20th century.

Since the SROCC, progress in characterizing seasonal NH snow cover changes has been made through the combined analysis of datasets from multiple sources (surface observations, remote sensing, land surface models and reanalysis products). A recent combined dataset (Mudryk et al., 2020) identified negative NH SCE trends in all months between 1981 and 2018, exceeding -50×10^3 km^{2}yr^{-1} in November, December, March and May (Figure 9.23a,b). The loss of spring SCE is also reflected in earlier spring snow melt, derived from surface observations (Bulygina et al., 2011; Brown et al., 2017), satellite observations (Wang et al., 2013; Estilow et al., 2015; Anttila et al., 2018), and model-based analyses (Liston and Hiemstra, 2011). There is considerable inter-dataset and regional variability, but the continental-scale trends of spring snow-off dates from these datasets are consistently negative (Brown et al., 2017; Kouki et al., 2019).

Satellite-derived estimates of NH SCE compiled within the NOAA snow chart Climate Data Record (NOAA CDR) extend back to 1967, providing one of the longest environmental data records from spaceborne measurements (Estilow et al., 2015). Continental trends from these coarse resolution estimates (~200 km) show declining snow cover during the spring period, consistent with surface warming (Hernández-Henríquez et al., 2015; Mudryk et al., 2017). As assessed in Section 2.3.2.2, there is therefore *very high confidence* that the NH spring SCE has been decreasing since 1978.

Hemispheric reconstructions with simple snow models and in-situ observations have extended the satellite record to 1922 (Brown and Robinson, 2011), putting the satellite era in historical context. This study, also assessed in the AR5, suggests an increase in North American spring (March-April) SCE from 1915 to about 1950, followed by a decrease of the same total magnitude afterwards. In Eurasia, a negative trend in April is visible over the entire 1922-2010 period of record, while in March, a step decrease at about 1985 separates two periods with insignificant trends. Overall, combining March and April, consistency between the continental trends since 1950 and agreement in sign with the NOAA satellite record since 1967 provides *high confidence* in Northern Hemisphere spring snow cover decrease since about 1950. Analysis of paleoclimate records (Pederson et al., 2011; Belmecheri et al., 2016) suggests that recent snowpack reductions in western North America are exceptional on a millennial timescale (*medium confidence*).

ACCEPTED VERSION SUBJECT TO FINAL EDITING

Recent remote sensing global-scale studies (Hammond et al., 2018; Notarnicola, 2020) report that since 2000, snow cover area and/or duration decreased in 78% of global mountain areas (Notarnicola, 2020). Due to the shortness of these records and high spatial variability, they only provide *limited evidence* in *medium agreement* that snow cover area and duration changes over that recent period are more consistently negative at higher (>4000 m) than at lower elevations, and do not alter the *high confidence* in longer-term mountain snow cover decrease at lower elevations since the middle of the 20th century that was already reported in the SROCC.

As assessed in detail in Chapter 3 (Section 3.4.2), it is *very likely* that anthropogenic influence contributed to the observed reductions in Northern Hemisphere springtime snow cover since the mid-20th century. The reasons for this assessment are: (1) physical consistency of the observed spring snowpack and surface temperature changes both in observations and models, (2) the strong observed hemispheric and regional spring SCE and SWE trends, and (3) the general attribution of hemispheric temperature changes to human influence. Consistent between multiple observational products and historical climate model simulations, the observed NH SCE sensitivity to NH land (>30°N) warming (Mudryk et al., 2017) is approximately -1.9×10^6 km^2°C^{-1} (95% confidence range of $\pm 0.9 \times 10^6$ km^2 °C^{-1} throughout the snow season.

Compared to numerous studies on spring SCE changes, less attention has been paid to changes in NH snow cover during the onset period in the autumn, a challenging period to retrieve snow information from optical satellite imagery due to persistent clouds and decreased solar illumination at higher latitudes. Positive trends in October and November SCE in the NOAA-CDR (Hernández-Henríquez et al., 2015) are not replicated in other surface, satellite, and model datasets (Brown and Derksen, 2013; Peng et al., 2013; Hori et al., 2017; Mudryk et al., 2017). The positive trends from the NOAA-CDR are also inconsistent with later autumn snow-on dates since 1980 (-0.6 to -1.4 days per decade), based on historical surface observations, model-derived analyses and independent satellite datasets (updated from Derksen et al., 2017). Furthermore, the SCE trend sensitivity to surface temperature forcing in the NOAA-CDR is anomalous compared to other datasets during October and November (Mudryk et al., 2017). There is therefore *medium confidence* that the NH SCE trend for the 1981-2016 period was also negative during these two months (Mudryk et al., 2020).

In the low-to-mid latitude (18°S-40°S) South American Andes, a dry-season snow cover decrease of about 12% per decade has been reported for the period 1986-2018 (Cordero et al., 2019), linked to ENSO changes dominant in the northern part and an additional influence of poleward migration of the westerly wind zone in the southern part of the study area. Further South, long-term warming has been identified as the dominant cause of observed winter snow cover reduction over the 1972-2016 period at about 53°S in Brunswick Peninsula (Aguirre et al., 2018).

The AR5 (Hock et al., 2019b) reported on snow water equivalent (SWE) and snow depth (SD) in situ observations mostly from mountain areas, the majority of which showed negative trends over their respective observational periods. However, the AR5 did not provide an assessment of large-scale snow mass changes across the Northern Hemisphere. The SROCC attributed *medium confidence* to reports of negative SWE trends in the Russian Arctic between 1966 and 2014, and stated that seasonal maximum snow depth trends in the North American Arctic were mostly insignificant and of inconsistent sign. It further attributed *medium confidence* to gridded products that suggest negative pan-Arctic SWE trends between 1981 and 2016, and *high confidence* in a general decline of mountain snow mass at lower elevations, albeit with regional variations.

Since the AR5, the number of global or hemispheric-scale gridded SWE products has substantially increased. A validation and intercomparison (Mortimer et al., 2020) of datasets derived from (1) reanalysis-based products, (2) a combined surface observation – passive microwave remote sensing product and (3) stand-alone passive microwave products has led to better understanding of the strengths and limitations of each. These gridded products consistently identify negative trends in maximum pre-melt SWE over the 1981 – 2016 period over both Eurasia and North America (Mudryk et al., 2020); (Figure 9.23c and d). To further constrain SWE uncertainty, Pulliainen et al. (2020) implemented a bias correction based on snow course observations which yielded a current best estimate for the average 1980-2018 March SWE over NH non-

ACCEPTED VERSION SUBJECT TO FINAL EDITING

alpine land north of 40°N of 2938 Gt [*likely* range 2846-3062 Gt]. Using this method, the bias-corrected GlobSnow3.0 dataset suggests a 4.6 Gt yr^{-1} decrease of March SWE over this 39-year period across North America, and a negligible trend across Eurasia. These SWE trends are consistent with the continental SCE trends over this period as assessed above, but strong regional and temporal variability only allows *medium confidence* in the signs and magnitudes of these trends. However, there is *high confidence* in a general decline of NH spring SWE since 1981 (Section 2.3.2.2). In the longer term (see also Section 2.3.2.2), annual maximum snow depth trends from site measurements confirm mostly negative trends in North America (Kunkel et al., 2016) between 1960/61 and 2014/15 and strong spatial variability in Eurasia (Zhong et al., 2018) between 1966 and 2012, with spatial patterns bearing some resemblance to the shorter satellite-based trends reported by Pulliainen et al. (2020). However, over this longer period, the Eurasian measurements (Zhong et al., 2018) exhibit, on average, a positive trend. On the Qinghai–Tibetan Plateau, site measurements between 1961 and 2010 (Xu et al., 2017) suggest a shift from an initial increase of spring snow depth until about 1980 to a decreasing trend afterwards.

[START FIGURE 9.23 HERE]

Figure 9.23: Observed monthly Northern Hemisphere (a) snow cover trends and (b) anomalies, and (c) snow mass trends and (d) anomalies. From the observation-based ensemble discussed in the text (Mudryk et al., 2020). Trends and anomalies are calculated over the 1981-2018 period. Further details on data sources and processing are available in the chapter data table (Table 9.SM.9).

[END FIGURE 9.23 HERE]

Concerning the assessment of SWE trends in mountainous regions, the SROCC noted a need for observations spanning several decades because of very strong temporal variability. Moreover, determining SWE trends in mountain regions is challenging because the coarse resolution (typically 25 to 50 km) of gridded SWE products is inadequate in areas of mountainous terrain (Snauffer et al., 2016). Based on a compilation of a large number of studies of SWE trends in mountain regions, the SROCC noted strong regional variations, but a general consistency in greater reductions in SWE at lower elevations associated with shifts from solid to liquid precipitation. A recent synthesis of snow observations in the European Alps (Matiu et al., 2021) shows a 1971-2019 seasonal (November to May) snow depth trend of -8.4% per decade, along with negative maximum snow depth and seasonal snow cover duration trends. The trends are stronger and more significant during transitional seasons and at transitional (from no snow to snow) altitudes, and exhibit strong regional variations, consistent with earlier reports for the Swiss and Austrian Alps (Schöner et al., 2019) and the Pyrenees (López-Moreno et al., 2020).

In summary, since the AR5, intercomparison, dataset blending of gridded products, and bias correction using snow course measurements contributed to an improved estimate of the average 1980-2018 March SWE over NH non-alpine land north of 40°N of 2938 Gt [*likely* range 2846-3062 Gt], with *medium confidence* in the magnitudes of continental-scale trends over that period. However, there is *high confidence* in a general decline of NH spring SWE since 1981 (Section 2.3.2.2). In mountain areas, in situ observations tend to suggest that annual maximum SWE reductions are generally stronger at elevation bands where shifts from solid to liquid precipitation affected the snow mass.

9.5.3.2 Evaluation of seasonal snow in climate models

Building on the AR5 (Flato et al., 2013) and subsequent published work, the SROCC (Meredith et al., 2019) stated that CMIP5 models tended to underestimate the observed decrease of Northern Hemisphere spring snow cover extent due to inappropriate parameterisation of snow processes, misrepresentation of the snow-albedo feedback, underestimated temperature sensitivity, and biased climatological spring snow cover. Since the AR5, progress in the observation, description and understanding of snow microstructure (Kinar and Pomeroy, 2015; Calonne et al., 2017) and its links to physical (thermal and radiative) properties (Löwe et al.,

ACCEPTED VERSION SUBJECT TO FINAL EDITING

2013; Calonne et al., 2014) has prompted efforts to represent physical properties as a function of the evolving snow microstructure in models (Carmagnola et al., 2014; Calonne et al., 2015). However, even state-of-the-art snow models intended for meteorological and climate applications still struggle to correctly represent the time evolution of the snow thermal properties, particularly of cold and dry tundra snow (Domine et al., 2016). Moreover, most, if not all, CMIP6 climate models do not explicitly represent the darkening of snow by deposition of BC and other light-absorbing aerosol species that is known to influence snow melt rates (Section 7.3.4.3). Regardless of these shortcomings, snow modules of climate models continue to be improved. Recent progress includes the incorporation of multiple energy balances within the canopy and between subgrid-tiles with different snow heights (Aas et al., 2017; Boone et al., 2017) and inclusion of advanced specific snow models in coupled climate models (Niwano et al., 2018; Voldoire et al., 2019), opening the prospect of future progress in quantifying snow-related feedbacks in a changing climate. Recently developed multi-physics snow models (Essery, 2015; Lafaysse et al., 2017), which are able to emulate the behaviour of a large number of models in a broad range of climates, allow model shortcomings and key parameter uncertainties, for example, concerning snow masking by vegetation or snow thermal conductivity, to be identified. Guidance for future model improvement can be provided by improved diagnostics, such as a concise metric of snow insulation (Slater et al., 2017a), which builds on an observed relation between effective seasonal mean snow depth and the dampening of winter season temperature decrease within the soil, and allows an efficient quantification of inaccuracies in the simulated snow insulation effect.

There is *high confidence* that large inter-model variations in the snow-cover sensitivity to temperature can largely be explained by inaccuracies in the simulated snow albedo feedback (Qu and Hall, 2014); a multi-model sub-ensemble of CMIP5 models that simulate a correct magnitude of this feedback presents a 40% reduced spread in the projected 21st century Northern Hemisphere land warming trend (Thackeray and Fletcher, 2016). Errors of the simulated feedback strength were linked to 1) systematic positive albedo biases over the boreal forest belt, mostly due to unrealistic treatment of vegetation masking (Thackeray and Fletcher, 2016), 2) inaccurate prescribed tree cover fraction and inappropriate parameterization of leaf area index in some models (Loranty et al., 2014; Wang et al., 2016a) and 3) low spatial resolution leading to inaccuracies in the strength of the simulated SAF in mountainous regions (Letcher and Minder, 2015). Although the representation of snow albedo feedback improved in many CMIP5 models over CMIP3, some models deteriorated (Thackeray et al., 2018).

Analysis of the available CMIP6 historical simulations for the 1981-2014 shows that on average, CMIP6 models simulate well the observed SCE (Mudryk et al., 2020), except for outliers and a median low bias during the winter months (Figure 9.24a). This is an improvement over CMIP5 (Mudryk et al., 2020), in which many snow-related biases were linked to inadequacies of the vegetation masking of snow cover over the boreal forests (Thackeray et al., 2015). A comparison between CMIP5 and CMIP6 results (Mudryk et al., 2020) shows that there is no notable progress in the quality of the representation of the observed 1981-2014 monthly snow cover trends.

[START FIGURE 9.24 HERE]

Figure 9.24: Simulated CMIP6 and observed snow cover extent (SCE). a) Simulated CMIP6 and observed (Mudryk et al., 2020) SCE (in millions of km^2) for 1981-2014. Boxes and whiskers with outliers represent monthly mean values for the individual CMIP6 models averaged over 1981-2014, with the red bar indicating the median of the CMIP6 multi-model ensemble for that period. The observed interannual distribution over the period is represented in green, with the yellow bar indicating the median. b) Spring (March to May) Northern Hemisphere snow cover extent against GSAT (relative to the 1995-2014 average) for the CMIP6 Tier 1 scenarios (SSP1-2.6, SSP2-4.5, SSP3-7.0 and SSP5-8.5), with linear regressions. Each data point is the mean for one CMIP6 simulation (first ensemble member for each available model) in the corresponding temperature bin. Further details on data sources and processing are available in the chapter data table (Table 9.SM.9).

[END FIGURE 9.24 HERE]

ACCEPTED VERSION SUBJECT TO FINAL EDITING

9.5.3.3 Projected snow cover changes

The AR5 (Collins et al., 2013) stated that substantial NH spring snow cover reductions at the end of the 21st century were *very likely* under strong emission scenarios, and expressed *medium confidence* in the projected geographic patterns of annual maximum SWE changes. Based on studies using downscaled CMIP5 or RCM output, either directly or via snowpack models driven by such output, the SROCC (Hock et al., 2019b) reported *likely* snow depth or mass decreases at lower elevations in many mountain ranges over the 21st century and *high confidence* in smaller future changes at higher elevations.

Since the AR5, one study (Brown et al., 2017), applying a method developed by de Elía et al. (2013) to a CMIP5 sub-ensemble, suggested that over most of the Northern Hemisphere, the projected decrease of SCD will exceed natural variability before this will be the case for annual maximum SWE. The same study reports that over large parts of Eastern and Western North America and Europe, forced SCD changes are projected to exceed natural variability in the 2020s both in spring and autumn, while the signals tend to emerge later in the Arctic regions and particularly late, after 2060, in Eastern Siberia under the RCP8.5 scenario. Thackeray and Fletcher (2016) have shown that inter-model spread in projected spring SCE trends could be reduced through improved simulation of spring season warming because of the tight coupling between temperature and SCE linked to the snow albedo feedback (Qu and Hall, 2014; Thackeray and Fletcher, 2015).

Across all emission scenarios and with negligible scenario dependence (Figure 9.24b), CMIP6 models consistently (all models and all months) simulate Northern Hemisphere snow cover decrease in response to future GSAT change over the 21st century (Mudryk et al., 2020). The simulated SCE decrease is close to a linear function of global temperature change for all months (shown in Figure 9.24b for spring, with *medium confidence* in an average sensitivity of about -8% per °C of GSAT increase), except when snow cover vanishes. This occurs at about +2°C of GSAT change above the 1995-2014 level (that is, about +3°C above the pre-industrial level) for the months of July and August, and at about +3°C above the 1995-2014 level for June and September. Possible effects of such changes on the hydrological cycle are assessed in Chapter 8 (Section 8.2.3.1).

In summary, consistent projections from all generations of global climate models, elementary process understanding and strong covariance between snow cover and temperature on several time scales make it *virtually certain* that future Northern Hemisphere snow cover extent and duration will continue to decrease as global climate continues to warm, and process understanding strongly suggests that this also applies to Southern Hemisphere seasonal snow cover (*high confidence*).

Seasonal snow cover, by definition, has a clear annual cycle with usually complete disappearance in spring and summer and re-formation in autumn or winter. Therefore, there is *very high confidence* that the current and projected changes to seasonal snow cover are reversible (Verfaillie et al., 2018). In the case of global or regional cooling, abrupt large-scale snow-cover changes with a transition from seasonal to persistent snow cover due to a strong snow albedo feedback are a typical feature of glacial inceptions (e.g., Baum and Crowley, 2003; Calov et al., 2005), and these can be irreversible on centennial or longer timescales because of this feedback. In summary, based on physical understanding and the absence of occurrence of such events in climate model projections, abrupt future changes of seasonal snow cover on large scales in the absence of concomitant abrupt atmospheric change as a driver appear *very unlikely* in the context of current and projected warming.

9.6 Sea Level Change

9.6.1 Global and regional sea-level change in the instrumental era

9.6.1.1 Global mean sea-level change budget in the pre-satellite era

The SROCC (Oppenheimer et al., 2019) discussed the development and application of new statistical methodologies for reconstructing global mean sea level (GMSL; Box 9.1) from tide-gauge data over the 20th

ACCEPTED VERSION SUBJECT TO FINAL EDITING

century. Based on an ensemble of tide gauge reconstructions, the SROCC assessed an average rate of GMSL rise of 1.38 mm yr^{-1} [0.81 to 1.95 *very likely* range] for the period 1901 to 1990. Since the SROCC, two new GMSL reconstructions have been published (Dangendorf et al., 2019; Frederikse et al., 2020b) and are included in an updated ensemble estimate of GMSL change (Palmer et al., 2021, Section 2.3.3.3). Based on these updated data and methods, the GMSL change over the (pre-satellite) period 1901 to 1990 is assessed to be 0.12 m [0.07 to 0.17 *very likely* range] with an average rate of 1.35 mm yr^{-1} [0.78 to 1.92 *very likely* range] (*high confidence*) (Table 9.5; section 2.3.3.3) in agreement with the SROCC assessment. Both this assessment and SROCC have substantially larger uncertainties than the AR5 assessment, which was based upon a single tide gauge reconstruction and did not account for structural uncertainty (see Palmer et al., (2021) for a discussion).

The SROCC found that four of the five available tide gauge reconstructions that extend back to at least 1902 showed a robust acceleration (*high confidence*) of GMSL rise over the 20th century, with estimates for the period 1902-2010 (-0.002 to 0.019 mm yr^{-2}) that were consistent with the AR5. New tide gauge reconstructions published since the SROCC (Dangendorf et al., 2019; Frederikse et al., 2020b) support this assessment and suggest that increased ocean heat uptake related to changes in Southern Hemisphere winds and increased mass loss from Greenland are the primary physical mechanisms for the acceleration (section 2.3.3.3). Therefore, the SROCC assessment on the acceleration of GMSL rise over the 20th century is maintained.

The evaluation of the sea-level budget presented here, and in section 9.6.1.2, draws on assessments of the individual components (Section 2.3.3.1 and 9.2.4.1 for global-mean thermosteric and sections 9.5.1.1, 9.4.1.1 and 9.4.2.1 for ice mass loss contributions to GMSL change from glaciers and ice sheets). Following the approach of the SROCC, the mass loss from ice sheet peripheral glaciers is included in the ice sheet contributions to GMSL change (glacier mass loss from regions 5 and 19 of the Randolph Glacier Inventory 6.0 (RGI Consortium, 2017) are added to ice sheet mass loss where applicable, with uncertainties added in quadrature). The total change in GMSL for each component, and their sum, is summarised in Table 9.5 (uncertainties added in quadrature). For consistency across the report and to simplify the treatment of uncertainties, all budget calculations are based on the difference between the first and last year in each period (Palmer et al., 2021), rather than a linear fit to the underlying time series as used in SROCC and AR5.

The sea-level budget in the SROCC included the anthropogenic contribution of land water storage (LWS; Box 9.1) change from a single estimate (Wada, 2016). Since the SROCC, two studies have combined estimates of natural LWS change with anthropogenic LWS changes from reservoir impoundment and groundwater depletion (Cáceres et al., 2020; Frederikse et al., 2020b). For (Cáceres et al., 2020), zero change is assumed for the period 1901-1948, since their LWS change estimates are not available before 1948. Given the large year-to-year changes associated with hydrological variability, the assessed changes in LWS (Table 9.5) are based on linear trends for each period, following (Palmer et al., 2021). Structural uncertainty is estimated from the standard deviation of the trends across the two studies and parametric uncertainty is estimated based on the Monte Carlo simulations of (Frederikse et al., 2020b). These two sources of uncertainty are combined in quadrature and the assessed central estimate is taken as the average of the ensemble mean trends. Compared to the SROCC assessed LWS trend of -0.12 mm yr^{-1} for the period 1901-1990, the updated assessment leads to a more negative trend of -0.16 [-0.35 to 0.04] mm yr^{-1}, although the two are consistent within the estimated uncertainties. Previous studies and the SROCC have highlighted the large uncertainty in estimates of LWS change over the 20th century (Gregory et al., 2013), and therefore the SROCC assessment of *low confidence* in the estimated LWS contribution to GMSL change is maintained.

Since the SROCC, a new ocean heat content reconstruction (Zanna et al., 2019b) (Section 2.3.3.1) has allowed global thermosteric sea-level change to be estimated over the 20th century. As a result, the sea-level budget for the 20th century can now be assessed for the first time. For the periods 1901 to 1990 and 1901 to 2018 the assessed *very likely* range for the sum of components is found to be consistent with the assessed *very likely* range of observed GMSL change (*medium confidence*), in agreement with (Frederikse et al., 2020b) (Table 9.5). This represents a major step forward in the understanding of observed GMSL change over the 20th century, which is dominated by glacier (52%) and Greenland ice sheet mass loss (29%) and the effect of ocean thermal expansion (32%), with a negative contribution from the land water storage change (-

ACCEPTED VERSION SUBJECT TO FINAL EDITING

14%). While the combined mass loss for Greenland and glaciers is consistent with the SROCC, updates in the underlying datasets lead to differences in partitioning of the mass loss.

9.6.1.2 Global mean sea-level change budget in the satellite era

The SROCC (Oppenheimer et al., 2019) concluded that GMSL increased at a rate of 3.16 [2.79 to 3.53 *very likely* range] mm yr^{-1} in the period 1993 to 2015 (the satellite altimetry era) and a rate of 3.58 [3.10 to 4.06 *very likely* range] mm yr^{-1} in the period 2006 to 2015 (the GRACE/Argo era) (*high confidence*). An updated assessment for the periods 1993 to 2018 and 2006 to 2018 yields values of 3.25 [2.88 to 3.61] and 3.69 [3.21 to 4.17] mm yr^{-1} (*high confidence*) (Table 9.5), with the slightly larger central estimates consistent with the observed acceleration in GMSL rise since the late 1960s (Dangendorf et al., 2019), given the longer assessment periods. Based on the GMSL assessed time series presented in section 2.3.3.3, GMSL acceleration is estimated as 0.075 [0.066 to 0.080] mm yr^{-2} for 1971 to 2018 and 0.094 [0.082–0.115] mm yr^{-2} for 1993–2018 (*high confidence*). For the common period of 1993-2010, the assessed rate of GMSL rise based on tide gauge reconstructions (3.19 [1.18 to 5.20] mm yr^{-1}) is consistent with the assessment based on satellite altimetry (2.77 [2.26 to 3.28] mm yr^{-1}), within the estimated uncertainties.

Since the SROCC, two new estimates of the LWS contribution have been published (Cáceres et al., 2020; Frederikse et al., 2020b) (see Section 9.6.1.1). For the early 21st century (the periods 1993 to 2018 and 2006 to 2018) both publications find a positive LWS contribution (Table 9.5), based on the most recent GRACE-derived estimates. This contrasts with the negative LWS contribution presented for the same periods in the SROCC based on (WCRP Global Sea Level Budget Group, 2018b) and reinforces the *low confidence* assessment of the LWS contribution.

For both periods in the satellite era, i.e., 1993 to 2018 and 2006 to 2018, the sum of contributions is consistent with the total observed GMSL change (*high confidence*) (Table 9.5). However, the latter period, which is characterised by improved data quality and coverage associated with satellite and Argo observations, shows much closer agreement in the central estimates. The marginal sea-level budget closure for the period 1993 to 2018 may indicate underestimated uncertainty, which may be structural as well as parametric. The sea-level budget assessments across the various periods in Table 9.5 demonstrate that the acceleration in GMSL rise (Section 2.3.3.3) since the late 1960s is mostly the result of increased ice sheet mass loss. However, all contributions to GMSL rise show their largest rate during 2006 to 2018, with the ice sheets accounting for about 35% of the total change during this period.

[START TABLE 9.5 HERE]

Table 9.5: Observed contributions to global mean sea level (GMSL) change for five different periods. Values are expressed as the total change (Δ) in the annual mean or year mid-point value over each period (mm) along with the equivalent rate (mm yr^{-1}). The *very likely* ranges appear in brackets based on the various section assessments as indicated. Uncertainties for the sum of contributions are added in quadrature, assuming independence. Percentages are based on central estimate contributions compared to the central estimate of the sum of contributions.

Observed contribution to GMSL change		**1901-1990** {9.6.1.1}	**1971-2018** {CCBox 9.1}	**1993-2018** {9.6.1.2}	**2006-2018** {9.6.1.2}	**1901-2018** {9.6.1.1}
Thermal expansion (Section 2.3.3.1, Table 2.7)	Δ (mm)	31.6 [14.7 to 48.5] (31.9%)	47.5 [34.3 to 60.7] (50.3%)	32.7 [23.8 to 41.6] (45.7%)	16.7 [8.9 to 24.6] (34.4%)	63.2 [47.0 to 79.4] (38.4%)

ACCEPTED VERSION SUBJECT TO FINAL EDITING

	mm yr^{-1}	0.36 [0.17 to 0.54]	1.01 [0.73 to 1.29]	1.31 [0.95 to 1.66]	1.39 [0.74 to 2.05]	0.54 [0.40 to 0.68]
Glaciers (Excl. peripheral glaciers) (Sections 2.3.2.3, 9.5.1.1)	Δ (mm)	51.8 [30.4 to 73.2] (52.3%)	20.9 [10.0 to 31.7] (22.1%)	13.8 [10.0 to 17.6] (19.3%)	7.5 [6.8 to 8.2] (15.4%)	67.2 [41.8 to 92.6] (40.8%)
	mm yr^{-1}	0.58 [0.34 to 0.82]	0.44 [0.21 to 0.67]	0.55 [0.40 to 0.70]	0.62 [0.57 to 0.68]	0.57 [0.36 to 0.79]
Greenland ice sheet (Incl. peripheral glaciers) (Sections 2.3.2.4.1, 9.4.1.1)	Δ (mm)	29.0 [16.3 to 41.7] (29.3%)	11.9 [7.7 to 16.1] (12.6%)	10.9 [9.0 to 12.8] (15.2%)	10.9 [9.5 to 12.2] (22.3%)	40.4 [27.2 to 53.5] (24.5%)
	mm yr^{-1}	0.33 [0.18 to 0.47]	0.25 [0.16 to 0.34]	0.44 [0.36 to 0.51]	0.91 [0.79 to 1.02]	0.35 [0.23 to 0.46]
Antarctic ice sheet (Incl. peripheral glaciers) (Sections 2.3.2.4.2, 9.4.2.1)	Δ (mm)	0.4 [-8.8 to 9.6] (0.4%)	6.8 [-3.9 to 17.5 (7.2%)]	6.4 [4.3 to 8.5] (9.0%)	6.4 [4.8 to 8.0] (13.1%)	6.9 [-3.8 to 17.5] (4.2%)
	mm yr^{-1}	0.00 [-0.10 to 0.11]	0.14 [-0.08 to 0.37]	0.26 [0.17 to 0.34]	0.53 [0.40 to 0.66]	0.06 [-0.03 to 0.15]
Land water storage* (Section 9.6.1.1)	Δ (mm)	-13.8 [-31.4 to 3.8] (-13.9%)	7.3 [-2.4 to 16.9] (7.7%)	7.8 [3.3 to 12.2] (10.8%)	7.2 [3.8 to 10.6] (14.8%)	-12.9 [-45.8 to 20.0] (-7.8%)
	mm yr^{-1}	-0.15 [-0.35 to 0.04]	0.15 [-0.05 to 0.36]	0.31 [0.13 to 0.49]	0.60 [0.32 to 0.88]	-0.11 [-0.39 to 0.17]

ACCEPTED VERSION SUBJECT TO FINAL EDITING

Sum of observed contributions	Δ (mm)	**99.0** [63.0 to 135.1]	**94.4** [71.7 to 117.1]	**71.6** [60.5 to 82.6]	**48.7** [39.9 to 57.5]	**164.8** [117.0 to 212.5]
	mm yr^{-1}	**1.11** [0.71 to 1.52]	**2.01** [1.52 to 2.49]	**2.86** [2.42 to 3.30]	**4.06** [3.32 to 4.79]	**1.41** [1.00 to 1.82]
Observed GMSL change (Section 2.3.3.3)	Δ (mm)	**120.1^{T}** [69.3 to 170.8]	**109.6$^{T\&A}$** [72.8 to 146.4]	**81.2^{A}** [72.1 to 90.2]	**44.3^{A}** [38.6 to 50.0]	**201.9$^{T\&A}$** [150.3 to 253.5]
	mm yr^{-1}	**1.35^{T}** [0.78 to 1.92]	**2.33$^{T\&A}$** [1.55 to 3.12]	**3.25^{A}** [2.88 to 3.61]	**3.69^{A}** [3.21 to 4.17]	**1.73$^{T\&A}$** [1.28 to 2.17]

$^{T, A}$ and $^{T\&A}$ indicate assessments based on tide gauge reconstructions (T), satellite altimetry (A), or a combination of both (T&A). The assessment uses tide gauge reconstructions before 1993 and satellite altimetry after 1993.
*For the periods 1971-2018, 1993-2018, 2006-2018 and 1901-2018 the Caceres et al. (2020) linear trends are based on the period up to 2016.

[END TABLE 9.5 HERE]

9.6.1.3 Regional sea-level change in the satellite era

Regional sea-level changes are resolved by both tide gauge and satellite altimetry observations (Hamlington et al., 2020a). Altimeters have the advantage of quasi-global coverage but are limited to a period (1993-present) in which the forced trend response is just emerging on regional scales (Section 9.6.1.4). An analysis of the local altimetry error budget to estimate 90% confidence intervals on regional sea-level trends and accelerations reports that 98% of the ocean surface has experienced significant sea-level rise over the satellite era (Prandi et al., 2021). The same study finds that sea-level accelerations display a less uniform pattern, with an east/west dipole in the Pacific, a north/south dipole in the Southern Ocean and in the North Atlantic, and 85% of the ocean surface experiencing significant sea-level acceleration or deceleration, above instrumental and post processing noise. Longer records are available from tide gauges, albeit with variable coverage by basin. Regional departures from GMSL rise are primarily driven by ocean transport divergences that result from wind stress anomalies and spatial variability in atmospheric heat and freshwater fluxes (Section 9.2.4).

The SROCC (Oppenheimer et al., 2019) noted the occurrence of large multiannual sea-level variations in the Pacific, associated with the Pacific Decadal Oscillation (PDO) in particular, and involving the El Niño Southern Oscillation (ENSO), North Pacific Gyre Oscillation (NPGO) and Indian Ocean Dipole (IOD) (Annex IV) (Royston et al., 2018; Hamlington et al., 2020b). There was intensified sea-level rise during the 1990s and 2000s, with 10-year trends exceeding 20 mm yr^{-1} in the western tropical Pacific Ocean, while sea-level trends were negative on the North American west coast. During the 2010s, the situation reversed, with western Pacific sea level falling at more than 10 mm yr^{-1} (Hamlington et al., 2020b). For the Atlantic Ocean,

ACCEPTED VERSION SUBJECT TO FINAL EDITING

the SROCC described regional sea-level variability as being driven primarily by wind and heat flux variations associated with the North Atlantic Oscillation (NAO) and heat transport changes associated with AMOC variability. During periods of subpolar North Atlantic warming, winds along the European coast are predominantly from the south and may communicate steric anomalies onto the continental shelf, driving regional sea-level rise, with the reverse during periods of cooling (Chafik et al., 2019). High rates of sea-level rise in the North Indian Ocean are accompanied by a weakening summer South Asian monsoon circulation (Swapna et al., 2017).

The Arctic ocean is typically excluded from global sea-level studies, owing to the uncertainties associated with resolving sea-level in ice-covered regions, strong variations in GRD effects, and uncertain GIA estimates (Box 9.1). Spanning 1991-2018, a *very likely* sea-level riseof 1.16-1.81 mm yr^{-1} is observed (Rose et al., 2019). Since the SROCC, the forced response in regional sea level varies in time with the relative influence of different forcing agents (Fasullo et al., 2020).

The SROCC estimated regional sea-level changes from combinations of the various contributions to sea-level change from CMIP5 climate model outputs, allowing comparison with satellite altimeter and tide-gauge observations. Closure of the regional sea-level budget is complicated by the fact that regional sea-level variability is larger than GMSL variability and there are more processes that need to be considered, such as vertical land movement and ocean dynamical changes (Box 9.1). A number of observation-based studies have focussed on specific areas, such as the Mediterranean (García et al., 2006), the South China Sea (Feng et al., 2012), the US east coast (Frederikse et al., 2017; Piecuch et al., 2018), the North Atlantic basin (Kleinherenbrink et al., 2016) and the Northwestern European continental shelf seas (Frederikse et al., 2016). Studies using tide gauge data and observation-based estimates of the contributions find that, while local agreement is not yet possible, the observational sea-level budget can be closed on a basin scale (Slangen et al., 2014a; Frederikse et al., 2016, 2018, 2020b). A budget analysis for the GRACE era found that the budget closes in some but not all coastal regions: substantial parts of the sea-level change signal in the North Atlantic could not be explained by steric or barystatic changes (Rietbroek et al., 2016). This is in agreement with other work comparing climate model estimates to 20th century tide gauge observations (Meyssignac et al., 2017), where the majority of local spatial variability is determined by the ocean dynamic component. Vertical land movement is another major cause of local spatial variability in sea-level change, and for instance relevant for oceanic islands (Forbes et al., 2013; Martínez-Asensio et al., 2019). In summary, the regional sea-level budget, using either observations or models, can currently only be closed on basin scales (*medium confidence*), with large uncertainties remaining on smaller scales.

9.6.1.4 Attribution and time of emergence of regional sea-level change

The SROCC (Oppenheimer et al., 2019) attributed anthropogenic forcing to be the dominant cause of GMSL rise since 1970 (see also Section 3.5.3.2), but detection and attribution (Cross-Working Group Box: Attribution in Chapter 1) of 20th century externally forced regional sea-level changes is more challenging, as regional variability is larger (Section 9.6.1.3), and therefore the signal-to-noise ratio is smaller (Richter and Marzeion, 2014; Monselesan et al., 2015; Palanisamy et al., 2015). Whereas SROCC assessed with *high confidence* that GMSL rise is attributable to anthropogenic greenhouse gas emissions, they assessed with *medium confidence* that the regional anomalies in ocean basins are a combination of the response to anthropogenic GHG emissions and internal variability.

The simulated ocean dynamic and thermosteric response to external forcings during 1861-2005 is larger than simulated internal variability only in the Southern Ocean and North Pacific on a 1° grid (Slangen et al., 2015), but on spatial scales exceeding 2000 km a detectable signal is revealed in the last 45 years in 63% of the global ocean area (Richter et al., 2017). The thermosteric change in the upper 700 m in the period 1970-2005 shows similar observed and simulated forced geographical patterns, and anthropogenic forcing accounts for part (North Atlantic, 65%) or all (tropical Pacific, Southern Ocean) of the observed regional-mean (Marcos and Amores, 2014). The influences of greenhouse gases and anthropogenic aerosols can be partially distinguished by considering geographical or vertical ocean temperature variations (Slangen et al., 2015; Bilbao et al., 2019; Fasullo et al., 2020). Zonal-mean forced ocean dynamic sea-level change alone is

ACCEPTED VERSION SUBJECT TO FINAL EDITING

not detectable but, using spatial correlation, the global geographical pattern during the altimeter period is detectable in sea-level trends (Fasullo and Nerem, 2018). This pattern may already or will soon be detectable in individual years, based on an analysis of CMIP5 climate model simulations (Bilbao et al., 2015). Anthropogenic forcing, dominated by greenhouse gases, has strengthened the meridional sea-level gradient in the Southern Ocean since the 1960s (Slangen et al., 2015; Bilbao et al., 2019; Fasullo et al., 2020). New evidence finds that observed zonal-mean total sea-level trends during 1993 to 2018 in all basins are inconsistent with unforced variability alone and consistent with the modelled response to external forcing (Richter et al., 2020).

A region that has been studied intensely in the context of sea-level detection and attribution is the tropical Pacific. Observed sea-level trends in the tropical Pacific show a PDO-like (Annex IV) East-West dipole (with a greater rate of rise in the west, see section 9.6.1.3). This dipole does not occur in CMIP5 simulations with the magnitude and duration that was observed in the 1990s and 2000s, neither in response to historical forcing, nor as internal variability after removing the variability associated with the PDO (Bilbao et al., 2015). (Hamlington et al., 2014) did obtain a residual trend pattern for 1993-2010 in the tropical Pacific that may link to anthropogenic warming of the tropical Indian Ocean. Allowing for PDO and ENSO variations, (Royston et al., 2018) describe patches of the Pacific Ocean where the sea-level trend for 1993-2015 is distinguishable from temporally correlated noise. The acceleration in eastern Pacific sea-level rise is largely accounted for by variations resembling PDO and ENSO (Hamlington et al., 2020a).

In the future, the anthropogenic signal in regional sea-level change from ocean density and dynamics is projected to emerge first in regions with relatively small internal variability, such as the tropical Atlantic Ocean and the tropical Indian Ocean (Jordà, 2014; Lyu et al., 2014; Richter and Marzeion, 2014; Bilbao et al., 2015). The signal is projected to emerge over 50% of the ocean area by the 2040s (Lyu et al., 2014), but in regions where variability is large and projected changes are small, such as the Southern Ocean, the signal will not emerge before late in the century. Adding the projected sea-level change from land ice mass loss and groundwater extraction strengthens and modifies the forced signal, leading to times of emergence 10-20 years earlier in most parts of the ocean, except in regions close to sources of mass loss, with emergence over 50% of the ocean area by 2020 and nearly everywhere by 2100 (Lyu et al., 2014; Richter et al., 2017) (*medium confidence*).

In summary, detection of forced regional changes for some ocean areas in recent decades is possible *(medium confidence)*, but attribution of regional sea-level change to forcings over longer periods (20th century) and for all ocean basins isnot yet possible.

[START CROSS-CHAPTER BOX 9.1 HERE]

Cross-Chapter Box 9.1: Global energy inventory and sea level budget

Coordinators: Matthew D. Palmer (UK), Aimée B.A. Slangen (The Netherlands),

Contributors: Guðfinna Aðalgeirsdóttir (Iceland), Fábio Boeira Dias (Finland/Brazil), Catia M. Domingues (Australia/Brazil), Gerhard Krinner (France), Johannes Quaas (Germany), Lucas Ruiz (Argentina)

Increased atmospheric greenhouse gas emissions since the 19th century have led to a net positive radiative forcing of Earth's climate (Sections 2.2, 7.3) and a corresponding accumulation of energy in the Earth System. Quantification of this energy gain is essential to our understanding of observed climate change and for estimates of climate sensitivity (Section 7.5). The global energy inventory is closely linked to our understanding of observed global sea-level change, through the energy associated with loss of land-based ice and the effect of thermal expansion associated with ocean warming (Box 9.1, Sections 2.3.3.1, 9.6.1; Table 9.5).

The Earth System gained substantial energy over the period 1971-2018 (*high confidence*), with an assessed *very likely* range of 325 to 546 ZJ or 0.43 to 0.72 W m^{-2} expressed per unit area of the Earth's surface

ACCEPTED VERSION SUBJECT TO FINAL EDITING

(Cross-Chapter Box 9.1, Figure 1a; Section 7.2, Box 7.2). Ocean warming dominates the energy inventory change (*high confidence*), accounting for 91% of the observed energy increase for the period 1971-2018, with upper ocean warming (0-700 m) accounting for 56% (Section 7.2). Much smaller amounts went into melting of ice (3%) and heating of the land (5%) and atmosphere (1%). Overall, the percentage contributions are similar to those reported in IPCC AR5 for the period 1971-2010 (Rhein et al., 2013).

The observed global mean sea-level (GMSL) budget is assessed through comparison of the sum of individual components of GMSL change with independent observations of total GMSL change from tide gauge and satellite altimeter observations (Cross-Chapter Box 9.1, Figure 1b; Sections 2.3.3, 9.6.1; Table 9.5). The assessed sum of the observed components indicates that GMSL *very likely* increased by 72 to 117 mm over the period 1971-2018 (Table 9.5), with the largest contributions from ocean thermal expansion (50%) and melting of ice sheets and glaciers (42%). The assessed total GMSL change (Section 2.3.3) for the period 1971-2018 has a *very likely* range of 73-146 mm and as a result the sea-level budget is closed for this period (Cross-Chapter Box 9.1, Figure 1b, Section 9.6.1, Table 9.5).

The sea-level budget closure demonstrates improved quantification of the processes of observed GMSL change for this period relative to previous IPCC assessments (Church et al., 2013a; Oppenheimer et al., 2019). A related assessment presented in Chapter 7 demonstrates closure of the global energy budget (*high confidence*) (Box 7.2) and strengthens the confidence in scientific understanding of both of these key aspects of climate change.

[START CROSS-CHAPTER BOX 9.1, FIGURE 1 HERE]

Cross-Chapter 9.1, Figure 1: Global Energy Inventory and Sea Level Budget. a) Observed changes in the global energy inventory for 1971-2018 (shaded time series) with component contributions as indicated in the figure legend. Earth System Heating for the whole period and associated uncertainty is indicated to the right of the plot (red bar = central estimate; shading = *very likely* range); b) Observed changes in components of global mean sea-level for 1971-2018 (shaded time series) as indicated in the figure legend. Observed global mean sea-level change from tide gauge reconstructions (1971-1993) and satellite altimeter measurements (1993-2018) is shown for comparison (dashed line) as a 3-year running mean to reduce sampling noise. Closure of the global sea-level budget for the whole period is indicated to the right of the plot (red bar = component sum central estimate; red shading = *very likely* range; black bar = total sea level central estimate; grey sharing = *very likely* range). Full details of the datasets and methods used are available in Annex I. Further details on energy and sea-level components are reported in Table 7.1 and Table 9.5.

[END CROSS-CHAPTER BOX 9.1, FIGURE 1 HERE]

[END CROSS-CHAPTER BOX 9.1 HERE]

9.6.2 Paleo context of global and regional sea-level change

As the SROCC (Oppenheimer et al., 2019) noted, paleo-sea level records provide information on past ice-sheet changes, and process-based ice sheet models of past warm periods inform equilibrium responses. However, given uncertainties in paleo-sea level and polar paleoclimate and limited temporal resolution of paleo-sea level records, there is *low confidence* in the utility of paleo-sea level records for quantitatively informing near-term GMSL change. Nonetheless the paleo record does contextualise sea level and can test projection models (see also FAQ 1.3). Proxy constraints on GMSL and global ice volume are assessed in Sections 2.3.2.4. and 2.3.3.3 (see also FAQ 9.1). This section updates prior assessments of drivers of past GMSL changes and climatically coherent areas of relative sea-level variability. GMSL changes are framed in terms of GMST but noting that amplified high latitude warming is a robust equilibrium response to elevated CO_2 (Masson-Delmotte et al., 2013): polar air temperatures during past warm periods were up to twice the

ACCEPTED VERSION SUBJECT TO FINAL EDITING

GMST changes shown in Table 9.6. The SROCC assessment that past multi-metre sea-level changes have resulted from significant ice sheet changes beyond those presently observed is confirmed (*very high confidence*).

[START TABLE 9.6 HERE]

Table 9.6: Reference ranges of age, global mean surface temperature, atmospheric carbon dioxide concentration, and global mean sea level for the paleo periods discussed in this chapter.

Paleo period	**Years** **CCB 2.1**	**GMST relative to 1850-1900** **Section 2.3.1.1**	**CO_2** **Sections 2.2.3.1, 2.2.3.2**	**GMSL** **Section 2.3.3.3**
Early Eocene Climatic Optimum EECO	53 – 49 Ma	+10 to +18°C	1150 – 2500 ppm	+70 to +76m
Mid-Pliocene Warm Period (MPWP)	3.3 – 3.0 Ma	+2.5 to +4°C	360 – 420 ppm	+5 to +25 m
Marine Isotope Stage (MIS) 11	~424 – 395 ka	0.5 ± 1.6 ºC[a]	265 – 286 ppm	+6 to +13 m
Last Interglacial (LIG)	~129 – 116 ka	+0.5 to +1.5°C	266 – 282 ppm	+5 to +10 m
Last Glacial Maximum (LGM)	21- 19 ka	-5 to -7°C	188 – 194 ppm	-125 to -134 m
Last Deglacial Transition	18 – 11 ka	–	193 –> 271 ppm	-120 –> -50 m
Early Holocene	11.65 – 6.5 ka	–	250 – 268 ppm	-50 –> -3.5 m
Mid Holocene	6.5 – 5.5 ka	+0.2 to +1.0°C	260 - 268 ppm	-3.5 to +0.5 m
Last Millennium	850 to 1850 CE	-0.14 to +0.24 ºC	278 - 285 ppm	-0.05 to +0.03 m

[a]Based on one study (Irvalı et al., 2020) relative to ~year 2000 SST values

[END TABLE 9.6]

Mid-Pliocene Warm Period (MPWP)

During the MPWP, GMST was 2.5-4°C warmer than 1850-1900 (*medium confidence*) and GMSL was between 5 and 25 m higher than today (Table 9.6) (*medium confidence*) (Section 2.3.3.3). The AR5 (Masson-Delmotte et al., 2013) concluded that ice-sheet models consistently produce near-complete deglaciation of the Greenland and West Antarctic Ice Sheets, and multi-meter loss of the East Antarctic Ice Sheet in response to MPWP climate conditions. Studies since the AR5 have yielded a consistent but broader range, due in part to larger ensembles exploring more parameters (DeConto and Pollard, 2016; Yan et al., 2016; DeConto et al., 2021). Partly on the basis of these studies the SROCC proposed a 'plausible' upper bound on GMSL of 25 m (*low confidence*) with evidence suggesting an Antarctic contribution of anywhere between 5.4 – 17.8 m.

The MPWP climate had substantial polar amplification (up to 8 ºC above pre-industrial levels in Arctic Russia, (Fischer et al., 2018); Section 7.4.4.1). Ice sheet model simulations indicate that Northern Hemisphere glaciation was limited to high-elevation regions in eastern and southern Greenland (Figure 9.17) (*medium confidence*)(De Schepper et al., 2014; Yan et al., 2014; Koenig et al., 2015; Dowsett et al., 2016;

ACCEPTED VERSION SUBJECT TO FINAL EDITING

Berends et al., 2019) with Northern Hemisphere glaciation only becoming more widespread from the (cooler) late Pliocene (Bachem et al., 2017; Blake-Mizen et al., 2019; Knutz et al., 2019; Sánchez-Montes et al., 2020). Southern Hemisphere glaciation was characterised by an Antarctic ice sheet reduced in volume from present (Figure 9.18) (Dowsett et al., 2016; Berends et al., 2019; Grant et al., 2019; Miller et al., 2020) (*medium confidence*) with mountain ice fields in the Andes of South America (De Schepper et al., 2014). Ice sheet models are inconsistent in the magnitude of the sea level contribution from Antarctica (DeConto and Pollard, 2016; Yan et al., 2016; Golledge et al., 2017b; Berends et al., 2019; DeConto et al., 2021) but near-field sedimentological reconstructions support precessionally-modulated and eccentricity-paced multi-metre sea level contributions from the Wilkes Subglacial Basin over 3 – 5 kyr (Patterson et al., 2014; Bertram et al., 2018). In summary, under a past warming level of around 2.5 – 4 ºC, ice sheets in both hemispheres were reduced in extent compared to present (*high confidence*). Proxy-based evidence (Section 2.3.3.3) combined with numerical modelling indicates that, on millennial timescales, the GMSL contribution arising from ice sheets was >5 m (*high confidence*) or >10 m (*medium confidence*) (Moucha and Ruetenik, 2017; Berends et al., 2019; Dumitru et al., 2019) (Figures 9.17, 9.18).

Marine Isotope Stage 11 (MIS 11)

The SROCC (Meredith et al., 2019) noted that Greenland may have been ice-free for extensive periods during Pleistocene interglaciations, implying a high sensitivity of the Greenland ice sheet to warming levels close to present day. The AR5 (Church et al., 2013a) assigned *medium confidence* to a MIS 11 GMSL of 6–15 m above present, requiring a loss of much of the Greenland and West Antarctic ice sheets, and a possible contribution from East Antarctica. High-resolution multi-proxy sea surface temperature reconstructions and climate model simulations concur that MIS 11 was an extremely long interglacial that exhibited positive annual (0.5 ± 1.6 ºC, (Irvalı et al., 2020)) and summer (2.1–3.4 ºC, (Robinson et al., 2017)) temperature anomalies (de Wet et al., 2016). GMSL was 6-13 m above present (*medium confidence*, Section 2.3.3.3). The Greenland Ice Sheet lost 4.5–6 m (Reyes et al., 2014)) or ca. 6.1 m (3.9–7 m, 95% confidence) sea-level equivalent by ca. 7 kyr after peak summer warmth (Robinson et al., 2017), with marine-based ice from AIS (Blackburn et al., 2020) contributing 6.4–8.8 m sea-level equivalent at this time (Mas e Braga et al., 2021). Agreement between GMSL and ice-sheet reconstructions gives *high confidence* in identifying a high sensitivity of both ice sheets to the protracted duration of thermal forcing even at low warming levels (Reyes et al., 2014; Robinson et al., 2017; Irvalı et al., 2020; Mas e Braga et al., 2021). Modelled mean mass loss rates for the Greenland Ice Sheet of 0.4 m kyr^{-1} during MIS 11 (Robinson et al., 2017) are indistinguishable from recent mass loss rates averaged over 1992–2018 (Section 9.4.1.1). In summary, geological reconstructions and numerical simulations consistently show that past warming levels of <2 ºC (GMST) are sufficient to trigger multi-metre mass loss from both the Greenland and Antarctic ice sheets if maintained for millennia (*high confidence*), in agreement with the SROCC findings for comparable warming levels during MIS 5e, the Last Interglacial.

Last Interglacial (LIG)

The AR5 found the LIG GMSL was >5 m (*very high confidence*) but <10 m (*high confidence*). Their best estimate of 6 m was based on two studies (Kopp et al., 2009; Dutton and Lambeck, 2012). The SROCC concluded that during the Last Interglacial the Greenland contribution to the GMSL highstand of 6–9 m increased gradually whereas the Antarctic contribution occurred early, from ca. 129 ka. Due to widely varying reconstructions from model studies (Greenland) and the paucity of direct evidence of ice sheet change (Antarctic), the magnitude of sea-level contributions from both ice sheets was assigned *low confidence.*

Since the AR5, information about the LIG, when GMST was about 0.5-1.5°C above 1850-1900 *(medium confidence)* (Section 2.3.1.1), has improved. The LIG had higher summer insolation than present and polar amplified sea surface and surface air temperatures that reached >1–4 ºC and >3–11 ºC in the Arctic respectively (Landais et al., 2016; Capron et al., 2017; Fischer et al., 2018). Mean annual and maximum summer ocean temperatures peaked early (129 –125 ka) in the interglacial period, reaching 1.1 ± 0.3 ºC above the modern global mean (Shackleton et al., 2020) with summer anomalies of 2.5–3.5 ºC in the Southern Ocean (Bianchi and Gersonde, 2002) and spatially variable timing (Chadwick et al., 2020). It is *virtually certain* GMSL was higher than today, *likely* by 5–10 m (*medium confidence*) (Section 2.3.3.3). Global mean thermal expansion peaked at about 0.9 ± 0.3 m early in the LIG (~129 ka), declining to modern

ACCEPTED VERSION SUBJECT TO FINAL EDITING

levels by about 127 ka (Shackleton et al., 2020). With no more than 0.3 ± 0.1 m of GMSL rise from glaciers (Section 9.5.1), at most 1.0 ± 0.3 m of the GMSL rise originated from sources other than the polar ice sheets.

Recent LIG ice sheet simulations agree that peak loss from the Greenland Ice sheet occurred late (125–120 ka) (Goelzer et al., 2016; Tabone et al., 2018; Plach et al., 2019) when Northern Hemisphere insolation was greater than at present (Capron et al., 2017) (*medium confidence*), consistent with inferences from marine sediment records (Hatfield et al., 2016; Irvalı et al., 2020) and far-field GMSL indicators (Rohling et al., 2019). Best estimates of the GMSL contribution from Greenland (Figure 9.17) differ between models: <=1 m (Albrecht et al., 2020; Clark et al., 2020), 1–2 m (Calov et al., 2015; Goelzer et al., 2016; Bradley et al., 2018), up to 3 m (Tabone et al., 2018; Plach et al., 2019), >5 m (Yau et al., 2016). There is *high confidence* that the response time of the Greenland Ice Sheet to LIG warming was multi-millennial and *high confidence* that it contributed to LIG GMSL change, but *low agreement* in the contribution magnitude.

Far-field GMSL records suggest that the Antarctic Ice Sheet contributed to LIG sea level from 129.5–125 ka (Figure 9.18) but direct evidence is sparse. Thinning of part of the West Antarctic Ice Sheet is interpreted from a 130 ka–80 ka hiatus in the Patriot Hills horizontal ice core record (Turney et al., 2020). Marine sediment records suggest a dynamic response of the Wilkes Subglacial Basin (WSB) of the East Antarctic Ice Sheet during this period indicating a response timescale of 1000–2500 yr (Wilson et al., 2018), consistent with modelling studies (Mengel and Levermann, 2014; Golledge et al., 2017b; Sutter et al., 2020). Isotopic changes in the Talos Dome ice core are inconsistent with local surface lowering, limiting retreat to 0.4–0.8 m SLE from this sector (Sutter et al., 2020). Ice sheet models forced with unmodified atmosphere–ocean models (Goelzer et al., 2016; Clark et al., 2020) simulate 3–4.4 m sea-level equivalent mass loss, primarily from the West Antarctic Ice Sheet, with no retreat in WSB (e.g., Figure 9.18). Models forced with proxy-based or ad hoc LIG ocean temperature anomalies (DeConto and Pollard, 2016; Sutter et al., 2016) indicate collapse of West Antarctica under 2–3 ºC ocean forcing yielding 3–7.5 m sea-level contribution, but modest or no retreat in the WSB. Based on *limited evidence* and *limited agreement* between models, there is *low confidence* in both the magnitude and timing of LIG mass loss from the Antarctic Ice Sheet.

In summary, paleo-environmental and modelling studies both indicate that under past warming of the level achieved during the LIG (ca. 0.5–1.5 ºC) it is *likely* that both the Greenland and Antarctic ice sheets responded dynamically over multiple millennia (*high confidence*)

Last Glacial Maximum (LGM)

At the LGM geological proxies and GIA models indicate that GMSL was 125-134 m below present (Section 2.3.3.3; Figures 9.17, 9.18). New studies have not changed the conclusions of the AR5 regarding the size or timing of the LGM and last glacial termination but have further examined the LGM sea-level budget. Based on a synthesis of multiple prior studies, (Simms et al., 2019) estimated central 67% probability contributions to the LGM lowstand of 76 ± 7 m from the North American Laurentide ice sheet, 18 ± 5 m from the Eurasian ice sheet, 10 ± 2 m from Antarctica, 4 ± 1 m from Greenland, 5.5 ± 0.5 m from glaciers, and 2.4 ± 0.3 m due to an increase in ocean density. Of the residual, up to about 1.4 m may be ascribed to groundwater, leaving a shortfall of 16 ± 10 m yet to be allocated among land ice reservoirs or lakes.

Last Deglacial Transition: Meltwater pulse 1A (MWP-1A)

During MWP-1A, GMSL *very likely* (*medium confidence*) rose by 8–15 m (Liu et al., 2016). Consistent with the AR5, the drivers of this rapid rise remain ambiguous. The spatial patterns of relative sea-level change over this interval are inadequately observed to constrain the relative contributions of the North American and Antarctic ice sheets (Liu et al., 2016). Modelling studies of the North American ice sheet permit a 3-6 m (Gregoire et al., 2016) or 6-9 m contribution over the duration of MWP-1A (Tarasov et al., 2012). Sedimentological evidence (Weber et al., 2014; Bart et al., 2018) provides near-field evidence for an Antarctic contribution, consistent with modelling studies (Golledge et al., 2014; Stuhne and Peltier, 2015), but does not constrain the magnitude of the contribution. A recent statistical analysis of Norwegian Sea and Arctic Ocean sediments suggests a 3-7 m contribution from the Eurasian Ice Sheet (Brendryen et al., 2020), a possibility not considered in the AR5 or the meta-analysis of (Liu et al., 2016). In summary, MWP-1A appears to have been driven by a combination of melt in North America (*high confidence*), Eurasia (*low confidence*), and Antarctica (*low confidence*), but the budget is not closed.

ACCEPTED VERSION SUBJECT TO FINAL EDITING

Holocene

Around half (~50–60 m) of the GMSL rise since the LGM occurred during the early Holocene at a sustained rate of ~15 m kyr^{-1} from ~11.4–8.2 ka (Lambeck et al., 2014), possibly punctuated by abrupt meltwater pulses (Smith et al., 2011; Carlson and Clark, 2012; Törnqvist and Hijma, 2012; Harrison et al., 2019). An abrupt ~1.1 m sea-level rise at ~8.2 ka was associated with drainage of the pro-glacial lakes Agassiz and Ojibway, attributed to accelerated melt from collapsing Laurentide Ice Sheet ice saddles (Matero et al., 2017). The Laurentide Ice Sheet provided the greatest contribution (27 m) to early Holocene GMSL (Peltier et al., 2015; Roy and Peltier, 2017), the Scandinavian ice sheet contributed ~2 m from the beginning of the Holocene until its demise by ~10.5 ka, (Cuzzone et al., 2016), whilst the Barents Sea ice sheet contributed a small but unknown amount (Patton et al., 2015, 2017; Auriac et al., 2016). The Greenland Ice Sheet contributed ~4 m, consistent with ice thinning rates inferred from the Camp Century ice core (Lecavalier et al., 2017; McFarlin et al., 2018). Recent estimates of Antarctic contributions during the early Holocene vary considerably from ~1.2 m to ~8.5 m (Whitehouse et al., 2012; Ivins et al., 2013; Argus et al., 2014; Briggs et al., 2014; Golledge et al., 2014; Pollard et al., 2016; Roy and Peltier, 2017; Albrecht et al., 2020). In summary, the early Holocene was characterised by steadily rising GMSL as global ice sheets continued to retreat from their LGM extents. This steady rise was punctuated by abrupt pulses during episodes of rapid meltwater discharge.

In the middle Holocene, GMST peaked at 0.2-1.0°C higher than 1850-1900 temperature between 7 and 6 ka (Section 2.3.1.1.2). GMSL rise slowed coincidently with final melting of the Laurentide ice sheet by 6.7 ± 0.4 ka (Ullman et al., 2016), after which only Greenland and Antarctic ice sheets could have contributed significantly. At 6 ka, GMSL was -3.5 to +0.5 m (*medium confidence*) (Section 2.3.3.3). Simulations of the Holocene Thermal Maximum (HTM) give a Greenland ice sheet broadly consistent with geological reconstructions so, despite uncertainties regarding the timing of minimum ice sheet volume and extent, there is *medium confidence* that minima were reached at different times in different areas during the period 8-3 ka BP (Larsen et al., 2015; Young and Briner, 2015; Briner et al., 2016). Geochronological and numerical modelling studies indicate that it is *likely* (*medium confidence*) that the period of smaller-than-present ice extent in all sectors of Greenland persisted for at least 2000 to 3000 years (Larsen et al., 2015; Young and Briner, 2015; Briner et al., 2016; Nielsen et al., 2018). Based on ice sheet modelling and ^{14}C dating (Kingslake et al., 2018) suggested that West Antarctic grounding lines retreated prior to ~10 ka BP, followed by a readvance. Other studies from the same region conclude that retreat was fastest from 9 to 8 ka BP (Spector et al., 2017), or from 7.5 to 4.8 ka BP (Venturelli et al., 2020). Marine geological evidence indicates open marine conditions east of Ross Island by 8.6 ± 0.2 ka BP (McKay et al., 2016). In the western Weddell Sea, (Johnson et al., 2019) reported rapid glacier thinning from 7.5 to 6 ka BP. (Hein et al., 2016) concluded that the fastest thinning further south took place from 6.5 to 3.5 ka BP, potentially contributing 1.4-2 m to GMSL. Geophysical data indicate stabilisation or readvance in this area around 6 ± 2 ka BP (Wearing and Kingslake, 2019). In coastal Dronning Maud Land (East Antarctica) rapid thinning occurred 9 to 5 ka BP (Kawamata et al., 2020), whereas glaciers in the Northern Antarctic Peninsula receded during the period 11 to 8 ka BP and readvanced to their maximal extents by 7 to 4 ka BP (Kaplan et al., 2020). In summary, higher-than-pre-industrial GMST during the mid Holocene coincided with recession of the Greenland Ice Sheet to a smaller-than-present extent (*high confidence*). Multiple lines of evidence give *high confidence* that thinning or retreat in parts of Antarctica during the Holocene took place at different times in different places, but limited data means there is only *low confidence* in whether or not the ice sheet as a whole was smaller than present during the mid Holocene.

In summary, both proxies and model simulations indicate that GMSL changes during the early to mid Holocene were the result of episodic pulses, due to drainage of meltwater lakes, superimposed on a trend of steady rise due to continued ice sheet retreat (*high confidence*).

The combination of tide gauge observations and geological reconstructions indicates that a sustained increase of GMSL began between 1820 and 1860 and led to a 20th century GMSL rise that was *very likely* (*high confidence*) faster than in any preceding century in the last 3000 yr (Section 2.3.3.3). At a regional level, tide gauge and geological data from the North Atlantic and Australasia show inflections in relative sea-level trends between 1895-1935, with an increase of 0.8 to 2.5 mm yr^{-1} across the inflection (Gehrels and Woodworth, 2013). A statistical meta-analysis of globally distributed geological and tide gauge data (Kopp

ACCEPTED VERSION SUBJECT TO FINAL EDITING

et al., 2016) found that, in all twenty examined regions with geological records stretching back at least 2000 years, the rate of RSL rise in the 20th century was greater than the local average over 0-1700 CE. In four of the twenty regions, all in the North Atlantic (Connecticut, New Jersey, North Carolina, and Iceland), the 19th century rate was also greater than the 0-1700 CE average (90% confidence interval). In summary, rates of RSL rise exceeding the pre-industrial background rate of rise are apparent in parts of the North Atlantic in the nineteenth century (*medium confidence*) and in most of the world in the twentieth century (*high confidence*).

9.6.3 Future sea-level changes

This section first assesses sea-level projections since the AR5 (Church et al., 2013a) (and including the SROCC (Oppenheimer et al., 2019)) based on Representative Concentration Pathways (Section 9.6.3.1). Process-level assessments in sections 9.2.4, 9.4.1.3, 9.4.1.4, 9.4.2.5, 9.4.2.6 and 9.5.1.3 are synthesised (Section 9.6.3.2) to produce new global-mean and regional sea-level projections based on the Shared Socioeconomic Pathways up to 2150 (Section 9.6.3.3) and on global warming levels up to 2100 (Section 9.6.3.4). Long-term global mean sea-level projections, both at 2300 and on multimillennial timescales, are also assessed (Section 9.6.3.5).

In sections 9.6.3.3 and 9.6.3.4, *likely* ranges of the new global-mean sea-level projections are presented, incorporating only processes in whose projections there is at least *medium confidence*, consistent with headline projections in the AR5 and the SROCC. As emphasized by the SROCC, there is a substantial likelihood that sea level rise will be outside the *likely* range. As described in Box 1.1, since the definition of '*likely'* refers to at least 66% probability, there may be as much as a 34% probability that the processes in which there is at least *medium confidence* will generate outcomes outside the *likely* range. Furthermore, additional processes in which there is *low confidence* (Section 9.4.2.4; Box 9.4) may also contribute to sea-level change. The presentation of *likely* sea-level change (Tables 9.8-9.9 and in Figures 9.27, 9.29) is therefore accompanied by a *low confidence* range intended to reflect potential contributions from additional processes under high-emissions scenarios. The *low confidence* range incorporates ice-sheet projections based on both structured expert judgement (i.e., a formal, calibrated method of combining quantified expert assessments that incorporate all potential processes) and projections from an Antarctic ice sheet model that includes the Marine Ice Cliff Instability (a specific uncertain process not generally included in ice sheet models; Section 9.4.2.4).

9.6.3.1 Global mean sea level projections based on the Representative Concentration Pathways

The AR5 (Church et al., 2013a) generated global mean sea level (GMSL) projections for the Representative Concentration Pathways (RCPs) by combining information from CMIP5 climate models with glacier and ice-sheet surface mass balance models and assessments of projected ice-sheet dynamic and land-water storage contributions (Section 9.6.3.2). The SROCC (Oppenheimer et al., 2019) updated the AR5 projections based upon a revised assessment of the Antarctic ice sheet contribution to GMSL rise. The AR5 and the SROCC employ a baseline period of 1986 to 2005, which is updated in this report to a baseline period of 1995 to 2014 (Section 1.4.1). Between these two periods, GMSL rose by 3 cm and this correction is applied to projections from previous reports to allow comparison (Table 9.8). Accounting for this shift, the conclusion of the SROCC is that, with *medium confidence*, GMSL will rise between 0.40 m (0.26–0.56 m, *likely* range) (RCP 2.6) and 0.81 m (0.58–1.07 m, *likely* range) (RCP 8.5) by 2100 relative to 1995-2014. The AR5 and the SROCC projections of GMSL for the 2007-2018 period have been shown to be consistent with observed trends in GMSL and regional weighted mean tide gauges (Wang et al., 2021a).

Since the AR5, , a number of projections of GMSL rise have been published based on the RCPs (Slangen et al., 2014a; Kopp et al., 2014, 2017; Grinsted et al., 2015; Jackson et al., 2016; Mengel et al., 2016; Bakker et al., 2017; Bittermann et al., 2017; Nauels et al., 2017; Wong et al., 2017; Le Bars et al., 2017; Nicholls et al., 2018; Goodwin et al., 2018; Le Cozannet et al., 2019; Palmer et al., 2020)(see (Garner et al., 2018) for a database; Tables 9.SM.5, 9.SM.6). Some studies also produced associated global sets of regional projections

ACCEPTED VERSION SUBJECT TO FINAL EDITING

(Kopp et al., 2014, 2017; Slangen et al., 2014a; Le Cozannet et al., 2019; Palmer et al., 2020). Since the SROCC, (Le Cozannet et al., 2019) focussed on the low end of the probability distribution of GMSL rise, (Palmer et al., 2020) extended projections beyond 2100 using a climate model emulator (Cross-Chapter Box 7.1) and (Horton et al., 2020) conducted a survey of 106 sea-level experts, providing additional context for interpreting sea-level rise projections for 2100 and 2300.

As noted by the SROCC, the largest differences between projections of GMSL in 2100 are due to the ice sheet projection method, which generally fall into one of three categories: (1) projections from ice sheet models that represent processes in which there is at least *medium confidence* (Sections 9.4.1.2, 9.4.2.2), (2) projections from an Antarctic ice-sheet model that incorporates the Marine Ice Cliff Instability (MICI) (Section 9.4.2.4) (DeConto and Pollard, 2016), or (3) projections based on structured expert judgement (SEJ) (Sections 9.4.1.3; 9.4.1.4; 9.4.2.5; 9.4.2.6) (Bamber and Aspinall, 2013; Bamber et al., 2019). *Low confidence* is ascribed to projections incorporating MICI because there is *low confidence* in the current ability to quantify MICI (Section 9.4.2.4). *Low confidence* is also ascribed to projections based on SEJ, because individual experts participating in the SEJ study may have incorporated processes in whose quantification there is *low confidence*, and the experts' reasoning has not been examined in detail. In general, the range of GMSL projections based upon ice-sheet models not incorporating MICI overlaps with but is lower than projections incorporating MICI or employing SEJ (Figure 9.25).

There is *high agreement* across published GMSL projections for 2050 and there is little sensitivity to emissions scenario (Figure 9.25, left panel). Up to 2050, projections are broadly consistent with extrapolation of the observed acceleration of GMSL rise (Sections 2.3.3.3, 9.6.1.1, 9.6.1.2). Considering only projections incorporating ice-sheet processes in whose quantification there is at least *medium confidence*, the GMSL projections for 2050, across all emissions scenarios, fall between 0.1 and 0.4 m (5^{th}—95^{th} percentile range). Projections incorporating MICI or SEJ do not extend this range under RCP 2.6 or RCP 4.5 and extend the upper part of the range to 0.6 m under RCP 8.5. On the basis of these studies, we therefore have *high confidence* that GMSL in 2050 will be between 0.1 and 0.4 m higher than in 1995 to 2014 under low and moderate emissions scenarios and between 0.1 and 0.6 m under high emissions scenarios.

Conversely, there is *low agreement* across published GMSL projections for 2100, particularly for higher emissions scenarios, as well as a higher degree of sensitivity to the choice of emissions scenario (Figure 9.25, right panel). Considering only projections representing processes in whose quantification there is at least *medium confidence*, the GMSL projections for 2100 fall between 0.2 and 1.0 m (5^{th}—95^{th} percentile range) under RCP 2.6 and RCP 4.5, and between 0.3 and 1.6 m under RCP 8.5. Considering also projections incorporating MICI or SEJ (*low confidence*), the projections for 2100 fall between 0.2 and 1.0 m (5^{th}—95^{th} percentile range) under RCP 2.6, 0.2 and 1.6 m under RCP 4.5, and 0.4 and 2.4 m under RCP 8.5. In summary, RCP-based projections published since the AR5 show *high agreement* for 2050, but exhibit broad ranges and *low agreement* for 2100, particularly under RCP 8.5.

[START FIGURE 9.25 HERE]

Figure 9.25: Literature global mean sea level (GMSL) projections (m) for 2050 (left) and 2100 (right) since 1995-2014, for RCP 8.5/SSP5-8.5 (top set), RCP 4.5/SSP2-4.5 (middle set), and RCP 2.6/ SSP1-2.6 (bottom set). Projections are standardised to account for minor differences in time periods. Thick bars span from the 17^{th}-83^{rd} percentile projections, and thin bars span the 5^{th}-95^{th} percentile projections. The different assessments of ice sheet contributions are indicated by 'MED' (ice sheet projections including only processes in whose quantification there is *medium confidence*), 'MICI' (ice sheet projections which incorporate Marine Ice Cliff Instability), and 'SEJ' (structured expert judgement (SEJ) to assess the central range of the ice-sheet projection distributions). 'Survey' indicates the results of a 2020 survey of sea-level experts on GMSL rise from all sources (Horton et al., 2020). Projection categories incorporating processes in which there is *low confidence* ('MICI' and 'SEJ') are lightly shaded. Dispersion among the different projections represents *deep uncertainty*, which arises as a result of *low agreement* regarding appropriate conceptual models describing ice sheet behaviour and *low agreement* regarding probability distributions used to represent key uncertainties. Individual studies are shown in Tables 9.SM.5, 9.SM.6.

ACCEPTED VERSION SUBJECT TO FINAL EDITING

Further details on data sources and processing are available in the chapter data table (Table 9.SM.9).

[END FIGURE 9.25 HERE]

9.6.3.2 Drivers of projected sea-level change

This section describes the choices made for the contributions to the updated global mean and regional sea-level projections (Section 9.6.3.3) based on assessments in this report and compares the updated projections to the AR5 (Church et al., 2013a) and the SROCC (Oppenheimer et al., 2019) (Tables 9.7, 9.8). Since there is no single model that can directly compute all of the contributions to sea-level change (Box 9.1), the contributions to sea level are computed separately and then combined (Tables 9.8, 9.9). For consistency with global surface air temperature (GSAT) projections (Section 4.3.1.1) and assessment of equilibrium climate sensitivity (ECS) and transient climate response (TCR) (Section 7.5), temperature-dependent projections (thermal expansion, ice sheets, glaciers) are forced by GSAT projections from a two-layer energy budget emulator (Smith et al., 2018) that is calibrated to be consistent with the assessment of ECS and TCR (Box 7.1, Supplementary Material 7.SM.2). Throughout, *likely* ranges are assessed based upon the combination of uncertainty in the GSAT distribution and uncertainty in the relationships between GSAT and changes to individual components. In general, 17th-83rd percentile results, incorporating both GSAT and sea-level process uncertainty, are interpreted as *likely* ranges. This is distinct from the approach used by the AR5, which interpreted the 5th-95th percentile range of CMIP5 projections and therefore of GMSL projections driven by them as *likely* ranges. The shift in interpretation here is consistent with the use of the emulator for GSAT (Box 4.1, Cross-Chapter Box 7.1). *Very likely* ranges are not assessed because of the potential for processes in whose projections there is currently *low confidence* to substantially augment total projected GMSL change.

[START TABLE 9.7 HERE]

Table 9.7: Methods used to project the drivers of GMSL and RSL change in the SSP- and warming-level-based projections of GMSL, RSL and ESL change. Section numbers indicate location of primary assessment text.

Driver of Global-Mean or Regional Sea-Level change	**SROCC Projection Method**	**AR6 Projection method**
Thermal expansion (Section 9.2.4.1)	CMIP5 ensemble drift-corrected *zostoga*, with surrogates derived from climate system heat content where not available	Two-layer emulator with climate sensitivity calibrated to the AR6 assessment (Supplementary Material 7.SM.2) and expansion coefficients calibrated to emulate CMIP6 models (Supplementary Material 9.SM.4.2, 9.SM.4.3)
Greenland ice sheet (excluding peripheral glaciers) (Section 9.4.1.3; 9.4.1.4)	Surface mass balance: scaled cubic polynomial fit to GMST Dynamics: Quadratic function of time, calibrated based on multimodel assessment	*Medium confidence* processes up to 2100: Emulated ISMIP6 simulations (Box 9.3) (Edwards et al., 2021) *Medium confidence* processes after 2100: Parametric model fit to ISMIP6 simulations up to 2100, extrapolated based on either constant post-2100 rates or a quadratic interpolation to the multimodel assessed 2300 range (Supplementary Material 9.SM.4.4) *Low confidence* processes:

ACCEPTED VERSION SUBJECT TO FINAL EDITING

		Structured expert judgement (Bamber et al., 2019)
Antarctic ice sheet (excluding peripheral glaciers[a]) (Section 9.4.2.5; 9.4.2.6)	Multimodel assessment	*Medium confidence* processes up to 2100: p-box including (1) Emulated ISMIP6 simulations (Edwards et al., 2021) and (2) LARMIP-2 simulations (Levermann et al., 2020a) augmented by AR5 surface mass balance model (Box 9.3) *Medium confidence* processes after 2100: p-box including (1) AR5 parametric AIS model and (2) LARMIP-2 simulations augmented by AR5 surface mass balance model, with both methods extrapolated based on either constant post-2100 rates or a quadratic interpolation to the multimodel assessed 2300 range (Section 9.6.3.2) *Low confidence* processes: (1) Single ice-sheet-model ensemble simulations incorporating Marine Ice Cliff Instability (DeConto et al., 2021) and (2) structured expert judgement (Bamber et al., 2019)
Glaciers (including peripheral glaciers) (Section 9.5.1.3)	Power law function of integrated GMST fit to glacier models	Up to 2100: Emulated GlacierMIP (Marzeion et al., 2020; Edwards et al., 2021) simulations (Box 9.3) Beyond 2100: AR5 parametric model re-fit to GlacierMIP (Marzeion et al., 2020) (Supplementary Material 9.SM.4.5)
Land water storage (Section 9.6.3.2)	Groundwater depletion: combination of (1) continuation of early 21st century trends and (2) land-surface hydrology models (Wada et al., 2012) Water impoundment: combination of (1) continuation of historical rate and (2) assumption of no net impoundment after 2010	Groundwater depletion: Population/groundwater depletion relationship calibrated based on (Konikow, 2011; Wada et al., 2012, 2016) Water impoundment: Population/dam impoundment relationship calibrated based on (Chao et al., 2008), adjusted for new construction following (Hawley et al., 2020) for 2020 to 2040
Ocean dynamic sea level (Section 9.2.4.2)	CMIP5 ensemble *zos* field after polynomial drift removal	Distribution derived from CMIP6 ensemble *zos* field after linear drift removal (Supplementary Material 9.SM.4.2, 9.SM.4.3)
Gravitational, rotational, and deformational effects (Section 9.6.3.2)	Sea-level equation solver (Slangen et al., 2014a) driven by projections of ice sheet, glacier, and land water storage changes	

ACCEPTED VERSION SUBJECT TO FINAL EDITING

Glacial isostatic adjustment and other drivers of vertical land motion (Section 9.6.3.2)	GIA model, with ice history from mean of ANU and ICE-5G	Spatiotemporal statistical model of tide-gauge data (updated from (Kopp et al., 2014)) (Supplementary Material 9.SM.4.6)

[a] Ice sheet models include some of the larger islands in the Antarctic periphery, so there is some overlap in the projected glacier contribution and the projected Antarctic contribution, but the effect of this is estimated to be of order 0.5-1 cm or less (Edwards et al., 2021).

[END TABLE 9.7 HERE]

Global Mean Thermosteric Sea-Level Rise

In the AR5 and the SROCC, global mean thermosteric sea-level rise was derived from the 21 members of the CMIP5 ensemble that provided the required variables (Section 9.2.4.1). The AR5 and the SROCC removed drift estimated based on a pointwise polynomial fit to pre-industrial control simulations. They extended projections to scenarios not provided by the models by calculating the heat content of the climate system from global mean surface temperature and net radiative flux, and converting this to global mean thermosteric sea-level rise using each model's diagnosed expansion efficiency coefficient. The AR5 and the SROCC derived the associated uncertainties by assuming a normal distribution, with the 5th-95th percentile CMIP5 ensemble interpreted as the *likely* range. In this report, global mean thermosteric sea-level rise is derived from a two-layer energy budget emulator consistent with the assessment of ECS and TCR (Section 9.2.4.1; Supplementary Material 9.SM.4.2, 9.SM.4.3). Despite the change in methodology, this leads to a *likely* global mean thermosteric contribution (17th-83rd percentile) between 1995 to 2014 and 2100 that represents a minimal change from the AR5 and the SROCC (Table 9.8).

Greenland ice sheet

The AR5 and the SROCC projected the Greenland surface-mass balance using a cubic polynomial fit to a regional climate model as a function of global mean surface temperature (with a log-normal scaling factor reflecting uncertainty in surface-mass balance models, and another scaling factor reflecting the positive feedback of ice-sheet elevation changes on mass loss), and the dynamic contribution was estimated based on a multi-model assessment interpolated as a quadratic function of time.

For processes in whose projections we have at least *medium confidence*, the updated projections use emulated ISMIP6 projections of the Greenland ice sheet (Section 9.4.1.3; Box 9.3; Tables 9.2, 9.7; Figure 9.17). Since the ISMIP6 emulator does not account for temporal correlation, a parametric fit to the ISMIP6 results is employed to calculate rates of change (Supplementary Material 9.SM.4.4). For projections beyond 2100 (when the ISMIP6 simulations end), the polynomial fit is extrapolated based on two alternate approaches: (1) an assumption of constant rates of mass change after 2100, and (2) for SSP1-2.6 and SSP5-8.5, a quadratic function of time extending to 2300 based on the multimodel assessment of contributions under RCP 2.6 and RCP 8.5 at 2300 (Section 9.4.1.4). Differences between the two approaches are small up to 2150, and since the latter approach is not available for all scenarios, only the former (constant rates) is used for time-series projections up to 2150. Both approaches are used for examining uncertainty in the timing of different levels of GMSL rise and to inform projections for the year 2300 (Section 9.4.1.4). For 2100, the ISMIP6 emulator yields the *likely* contribution from the Greenland ice sheet shown in Table 9.2 and Figure 9.17, representing a slight narrowing from the AR5 projections.

Antarctic ice sheet

For the Antarctic ice sheet, the AR5 applied a temperature-based scaling approach for surface mass balance and a quadratic function of time, calibrated to a multimodel assessment, for dynamic contributions. The

ACCEPTED VERSION SUBJECT TO FINAL EDITING

SROCC used a new assessment based on the results of five process-based studies (Section 9.4.2.5). For processes in whose projections we have at least *medium confidence*, the *likely range* projections for the Antarctic ice sheet are based upon 1) the emulated ISMIP6 ensemble and 2) the LARMIP-2 ensemble, augmented with the AR5 parametric Antarctic surface mass balance model. GMSL projections are produced with both distributions and combined in a 'p-box' (Kriegler and Held, 2005; Le Cozannet et al., 2017), which represents the upper and lower bounds of the distribution (Section 9.4.2.5, Box 9.3, Table 9.3). A *likely* range is then identified, spanning the lower of the two 17th percentile projections and the higher of the two 83rd percentile projections[5], with the median taken as the mean of the medians of the two projections. Since the ISMIP6 emulator does not account for temporal correlation, the AR5 parametric AIS model is substituted for the emulator in the p-box for rates of change. As the AR5 projections are modestly lower than those from the ISMIP6 emulator, this substitution modestly broadens the *likely* range at the low end for projections of rate and changes beyond 2100. For projections beyond 2100 (when the ISMIP6 and LARMIP-2 simulations end), the AIS simulations are extrapolated using the same two approaches as the GrIS projections (Section 9.2.4.6). The *likely* ranges to 2100 are consistent with the SROCC (Table 9.8).

Low confidence ice sheet projections

To test the possible effect of additional ice-sheet processes for which there is *low confidence* (Sections 9.4.1.3, 9.4.1.4, 9.4.2.5, 9.4.2.6, 9.6.3.1; Box 9.4), two additional approaches are considered. For both the Greenland and Antarctic ice sheets, we produce sensitivity cases employing the SEJ projections of (Bamber et al., 2019), mapping 2°C and 5°C stabilization scenarios to SSP1-2.6 and SSP5-8.5, respectively. For the Antarctic ice sheet, we produce an additional sensitivity case using projections, which incorporate the Marine Ice Cliff Instability (DeConto et al., 2021), mapping projections for RCP 2.6 and RCP 8.5 to SSP1-2.6 and SSP5-8.5. For the Greenland ice sheet, the SEJ projections indicate the potential for outcomes outside the corresponding *likely* ranges (Table 9.8). For the Antarctic ice sheet, there is no evidence from these studies to suggest an important role under lower emissions scenarios for processes in whose projections we have *low confidence*. By contrast, for SSP5-8.5, the SEJ and MICI projections exhibit 17th-83rd percentile ranges of 0.02-0.56 m and 0.19-0.53 m by 2100, consistent with one another but considerably broader than the *likely* contribution for *medium confidence* processes of 0.03 to 0.34 m. This lower level of agreement for higher emissions scenarios reflects the *deep uncertainty* in the AIS contribution to GMSL change under higher emissions scenarios (Box 9.4). This *deep uncertainty* grows after 2100: by 2150, under SSP 5-8.5, *medium confidence* processes *likely* lead to a -0.1 to 0.7 m AIS contribution, while SEJ and MICI-based projections indicate 0.0-1.1 m and 1.4-3.7 m, respectively.

Glaciers

In the AR5 and the SROCC, global glacier mass changes were derived from a power law of integrated global-mean surface temperature change fit to results from four different glacier models. The updated projections use emulated GlacierMIP projections (Section 9.5.1.3, Box 9.3). Since the GlacierMIP emulator does not account for temporal correlation and terminates, along with the GlacierMIP simulations, in 2100, we employ a parametric fit to the GlacierMIP simulations, with a functional form similar to that employed by the AR5, to calculate rates of change and extrapolate changes beyond 2100 (up to a maximum potential contribution of 0.32 m) (see Supplementary Material 9.SM.4.5). This approach leads to a median glacier contribution that is a minimal change (Table 9.8) from the AR5 and the SROCC and a modest narrowing of *likely* ranges (Section 9.5.1.3). For RCP 2.6, the AR5 projected 0.10 (0.04-0.16, *likely* range) m, compared to 0.09 (0.07-0.11) m projected here for SSP1-2.6. For RCP 8.5, the AR5 projected a *likely* contribution of 0.17 (0.09-0.25) m, compared to 0.18 (0.15-0.21) m projected here.

Land water storage

In the AR5 and the SROCC, the groundwater depletion contribution to GMSL rise was based on combining results from two approaches, one assuming a continuation of early 21st century trends (Konikow, 2011) and the other using land-surface hydrology models (Wada et al., 2012). Together, these yielded a range of about 0.02-0.09 m of GMSL rise by 2080-2099. The rate of water impoundment in reservoirs was likewise based

[5] Note that the use of this approach implies that the *likely* ranges are *likely* in the use of the term to mean 66–100% probable; this is distinct from the usage in the SROCC, where *likely* range was defined to have a precise 66% probability.

ACCEPTED VERSION SUBJECT TO FINAL EDITING

on two approaches, one assuming the continuation of the average rate over 1971-2010 (and thus -0.01 to -0.03 m by 2080-2099) (Chao et al., 2008), and the other assuming no net impoundment after 2010 (Lettenmaier and Milly, 2009). Together, these yield a GMSL contribution from groundwater impoundment of -0.03 to 0 m. Combining groundwater depletion and water impoundment led the AR5 and the SROCC to infer a projected range of -0.01 to +0.11 m by 2100.

In the updated projections, a statistical relationship is applied linking historical and future SSP global population to dam impoundment and groundwater extraction (Rahmstorf et al., 2012; Kopp et al., 2014). The population/groundwater depletion relationship is calibrated based on the same studies used in the AR5 (Konikow, 2011; Wada et al., 2012), reduced by ~20% to account for water retained on land (Wada et al., 2016). The population/dam impoundment relationship is calibrated based upon (Chao et al., 2008). However, while historically dam impoundment has been declining with population, recent literature shows that planned dam construction considerably exceeds the historical trend (Zarfl et al., 2015; Hawley et al., 2020). Over 2020-2040, the impoundment contribution to GMSL rise based upon past trends would be about -0.1 mm yr^{-1}, compared to about -0.5 mm yr^{-1}if all currently planned dams are built (Hawley et al., 2020) and the statistical projection is therefore augmented by an additional -0.4 to 0.0 mm yr^{-1}over 2020-2040 to account for the possible effects of planned dam construction. As in the AR5 and the SROCC, climatically driven changes to LWS have not been included in published sea-level projections, as they are not well quantified (e.g., (Jensen et al., 2019)) or are considered negligible (e.g., permafrost, Section 9.5.2). This approach yields a *likely* global-mean land water storage contribution (Figure 9.27, Table 9.8) that is slightly lower and narrower than the AR5 and the SROCC *likely* ranges. Since the projections are explicitly population driven, these projections also exhibit a weak scenario dependence, with a ~0.01 m higher contribution under SSP3 than under other scenarios.

[START TABLE 9.8 HERE]

Table 9.8: Global mean sea-level projections between 1995-2014 and 2100 for total change and individual contributions, median values, (*likely*) ranges of the process-based model ensemble, for RCP 2.6 (from the AR5 (Church et al., 2013b) and the SROCC (Oppenheimer et al., 2019)) and SSP1-2.6 (this report), and for RCP 8.5 (from the AR5 (Church et al., 2013b) and the SROCC (Oppenheimer et al., 2019)) and SSP5-8.5 (this report). Values for the AR5 (Church et al., 2013b) and the SROCC (Oppenheimer et al., 2019) are adjusted from the 1986-2005 baseline used in past reports. Only the Antarctic contribution changed between the AR5 (Church et al., 2013b) and the SROCC (Oppenheimer et al., 2019). Unshaded cells represent processes in which there is *medium confidence*; shading indicates the inclusion of processes in which there is *low confidence*. For the MICI and SEJ-based projections, parenthetical numbers represent the 17-83rd percentile of the associated probability distributions, not assessed *likely* ranges.

	RCP 2.6		**SSP1-2.6**		
m rel. to 1995-2014	**AR5**	**SROCC**	***Medium confidence* processes**	**MICI**	**SEJ**
Thermal expansion (9.2.4.1)	0.14 (0.10-0.19)		0.14 (0.11-0.18)		
Greenland (9.4.1.3)	0.07 (0.03-0.11)		0.06 (0.01-0.10)		0.13 (0.07-0.30)
Antarctica (9.4.2.5)	0.06 (-0.04-0.16)	0.04 (0.01-0.11)	0.11 (0.03-0.27)	0.08 (0.06-0.12)	0.09 (-0.01-0.25)
Glaciers (9.5.1.3)	0.10 (0.04-0.16)		0.09 (0.07-0.11)		
Land water storage (9.6.3.2)	0.05 (-0.01-0.11)		0.03 (0.02-0.04)		

ACCEPTED VERSION SUBJECT TO FINAL EDITING

Total (2100)	0.41 (0.25-0.58)	0.40 (0.26-0.56)	0.44 (0.33-0.61)	0.41 (0.35-0.48)	0.53 (0.38-0.80)
Total (2150)	0.29-0.63	0.56 (0.40-0.73)	0.69 (0.46-1.00)	0.74 (0.63-0.91)	0.84 (0.56-1.34)
GMSL rate, 2080-2100 (mm yr^{-1})	4.4 (2.0-6.8)	4 (2-6)	5.3 (3.3-8.1)	5.2 (4.4-6.2)	6.0 (2.9-1.1)

	RCP 8.5		**SSP5-8.5**		
m rel. to 1995-2014	**AR5**	**SROCC**	***Medium confidence* processes**	**MICI**	**SEJ**
Thermal expansion (9.2.4.1)	0.31 (0.24-0.38)		0.30 (0.24-0.36)		
Greenland (9.4.1.3)	0.14 (0.08-0.27)		0.13 (0.09-0.18)		0.23 (0.10-0.59)
Antarctica (9.4.2.5)	0.04 (-0.08-0.14)	0.12 (0.03-0.28)	0.12 (0.03-0.34)	0.34 (0.19-0.53)	0.21 (0.02-0.56)
Glaciers (9.5.1.3)	0.17 (0.09-0.25)		0.18 (0.15-0.21)		
Land water storage (9.6.3.2)	0.05 (-0.01-0.11)		0.03 (0.02-0.04)		
Total (2100)	0.71 (0.49-0.95)	0.81 (0.58-1.07)	0.77 (0.63-1.02)	0.99 (0.82-1.19)	1.01 (0.70-1.61)
Total (2150)	0.34-1.35	1.27 (0.80-1.79)	1.35 (1.02-1.89)	3.48 (2.58-4.83)	1.80 (1.23-2.93)
GMSL rate, 2080-2100 (mm yr^{-1})	11.2 (7.5-15.7)	15 (10-20)	12.2 (8.8-17.7)	23.2 (17.7-30.2)	16.1 (9.8-29.1)

[END TABLE 9.8 HERE]

Ocean dynamic sea level

In the AR5 and the SROCC, the ocean dynamic sea-level contribution to relative sea-level (RSL) projections was derived from the CMIP5 ensemble, after removing drift estimated based on pre-industrial control simulations. This report uses updated simulations from the CMIP6 ensemble (Section 9.2.4.2; Supplementary Material 9.SM.4.2) to project the ocean dynamic sea-level contribution to relative sea-level change (Figure 9.26; Section 9.2.4.2). To produce ocean dynamic sea-level projections consistent with the global mean thermosteric projections from the two-layer energy budget emulator, we follow the approach of (Kopp et al., 2014), employing a correlation between global-mean thermosteric sea-level change and ocean dynamic sea level derived from the CMIP6 ensemble (Supplementary Material 9.SM.4.3). Since CMIP6 models are of fairly coarse (typically ~100km) resolution, and even the models participating in HighResMIP (near 10km resolution) do not capture all the phenomena that contribute to coastal ocean dynamic sea-level change, there is *low confidence* in the details of ocean dynamic sea-level change along the coast (Section 9.2.3.6) and in semi-enclosed basins, like the Mediterranean, where coarse models can misrepresent key dynamic processes. Regional high-resolution models can improve projections of coastal ocean dynamic sea-level change (Section 12.4) (Hermans et al., 2020), but have not been implemented at a global scale.

Gravitational, rotational, and deformational (GRD) effects

ACCEPTED VERSION SUBJECT TO FINAL EDITING

GRD effects (Box 9.1) lead to distinct variations in the RSL change pattern, which are similar across a range of benchmarked GRD solvers (Martinec et al., 2018; Palmer et al., 2020). There is *high confidence* in the understanding of GRD processes. RSL rise associated with GRD is *very likely* to be largest in the Pacific, due to the combined effects of projected GrIS, AIS and glacier mass loss (*high confidence*) (e.g., Kopp et al., 2014; Slangen et al., 2014a; Larour et al., 2017; Mitrovica et al., 2018). The GRD effect associated with mass loss from an ice sheet is sensitive to the spatial distribution of that mass loss. For example, the GRD contribution to RSL rise in Australia will be larger for Antarctic mass loss sourced fromthe Antarctic Peninsula than for Antarctic mass loss sourced fromThwaites Glacier. In parts of northeastern North America and northwestern Europe, GRD effects associated with mass loss from southern Greenland will lead to a RSL fall, whereas mass loss from northern Greenland will lead to a RSL rise (*high confidence*) (Larour et al., 2017; Mitrovica et al., 2018) (Figure 9.26). The AR5 and the SROCC computed RSL patterns using a gravitationally self-consistent GRD solver given the amounts, locations and timing of the projected barystatic sea-level changes driven by glaciers, ice sheets and LWS (Church et al., 2013a). A similar GRD solver is used in the updated projections (following (Slangen et al., 2014a)). The Earth model used is based on PREM (Dziewonski and Anderson, 1981), and is elastic, compressible and radially stratified.

Glacial isostatic adjustment and other drivers of vertical land motion

Glacial Isostatic Adjustment (GIA; Box 9.1) leads to vertical land motion (VLM; Box 9.1) and changes in sea-surface height, both of which contribute to RSL change. GIA uncertainty is caused by uncertainty in the rheological structure of the solid Earth, which drives the longer-term viscous Earth deformation, as well as in the modelled global ice history (e.g., Whitehouse, 2018). In the AR5 and the SROCC, GIA contributions to relative sea-level change were calculated using a sea-level equation solver with an ice-sheet history taken as the mean of the ICE5G (Peltier et al., 2015) and ANU (Lambeck et al., 2014) ice sheet models. Since the AR5, new global models are emerging that more rigorously treat ice and Earth structure uncertainty (Caron et al., 2018). However, there is also a growing recognition that lateral variations in Earth structure limit the utilityof global models that treat the solid Earth as though it were laterally uniform (Love et al., 2016; Huang et al., 2019; Li et al., 2020c).

As noted by the SROCC, VLM from sources other than GIA – including tectonics and mantle dynamic topography, volcanism, compaction, and anthropogenic subsidence – can be locally important, producing VLM rates comparable to or greater than rates of GMSL change. Complete global projections of these processes are not available because of the small spatial scales, the sensitivity of subsidence to local human activities, and the stochasticity of tectonics (Wöppelmann and Marcos, 2016; Oppenheimer et al., 2019). Integrated RSL projections to date have therefore either included only the component of VLM associated with GIA, as in the AR5 and SROCC, or used a constant long-term background rate of change (including both GIA and other long-term drivers of VLM) estimated from historical tide gauge trends (e.g., (Kopp et al., 2014)). The updated projections use the second approach and extrapolate the field of long-term background rates of RSL change, including long-term VLM derived from tide gauges, to global coverage using a spatiotemporal statistical approach (Kopp et al., 2014) (Supplementary Material 9.SM.4.6). The combined GIA and long-term VLM is assumed to be constant over the projected period and scenario independent. In areas (e.g., the western Gulf of Mexico) where rapid subsidence occurs in a cluster of tide-gauges, the associated rates are interpolated between the tide gauges. In areas where the available tide-gauges exhibit large, tectonically driven VLM that changes considerably in rate over short distances (e.g., Alaska and the Bering Strait) a sizable uncertainty propagates into the RSL projections (Figure 9.26). Rates of RSL rise are likely to be underestimated due to subsidence in shallow strata that are not recorded by tide gauges (Keogh and Törnqvist, 2019) and in some locations may therefore be minimum values, especially if anomalously high subsidence rates associated with fluid extraction (e.g., (Minderhoud et al., 2017)) are also considered. There is therefore, depending on location, *low* to *medium confidence* in the GIA and VLM projections employed in this report. In many regions, higher fidelity projections would require more detailed regional analysis.

ACCEPTED VERSION SUBJECT TO FINAL EDITING

[START FIGURE 9.26 HERE]

Figure 9.26: Median global mean and regional relative sea-level projections (m) by contribution for the SSP1-2.6 and SSP5-8.5 scenarios. (upper time series) Global mean contributions to sea-level change as a function of time, relative to 1995-2014. (lower maps) Regional projections of the sea-level contributions in 2100 relative to 1995-2014 for SSP5-8.5 and SSP1-2.6. Vertical land motion is common to both SSPs. Further details on data sources and processing are available in the chapter data table (Table 9.SM.9).

[END FIGURE 9.26 HERE]

9.6.3.3 Sea-level projections to 2150 based on SSP scenarios

Up to 2050, consistent with the AR5 and the SROCC, GMSL projections exhibit little scenario dependence (Figure 9.27, Table 9.9) (*high confidence*), with *likely* (*medium confidence*) sea-level rise between the baseline period (1995 to 2014) and 2050 of 0.19 (0.16-0.25) m under SSP1-2.6 and 0.23 (0.20-0.30) m under SSP5-8.5. These projections fall centrally within the range of published projections for RCP 2.6 and RCP 8.5 (Section 9.6.3.1).

Beyond 2050, the scenarios increasingly diverge. Between the baseline period (1995 to 2014) and 2100, processes in whose projection there is *medium confidence* drive *likely* GMSL rise of 0.44 m (0.33-0.61) m and 0.77 (0.63-1.02) m under SSP1-2.6 and SSP5-8.5, respectively (Tables 9.8, 9.9). While derived using substantially updated methods, these projections are broadly consistent with the SROCC, which over this period projected *likely* GMSL rise of 0.41 (0.26-0.56) m and 0.81 (0.58-1.07) m under RCP 2.6 and RCP 8.5, respectively. They are modestly higher than those of the AR5, which projected *likely* GMSL rise of 0.41 (0.25-0.58) m under RCP 2.6 and 0.71 (0.49-0.95) m under RCP 8.5 (Figure 9.25, Table 9.8). They are also broadly consistent with projections produced by driving the AR5 methods with CMIP6 temperature and thermal expansion projections, which leads to 0.44 (0.27-0.61) m under SSP1-2.6 and 0.73 (0.49-1.02) m under SSP5-8.5 (Hermans et al., 2021). The SSP1-2.6 and SSP5-8.5 projections are consistent with the ranges of published projections for RCP 2.6 and RCP 8.5 that do not incorporate MICI or SEJ (Section 9.6.3.1).

The *likely* GMSL projections for SSP3-7.0 and SSP5-8.5 are consistent with a continuation of the GMSL satellite-observed rate (*very likely* 3.25 [2.88-3.61] mm yr^{-1}) and acceleration (*very likely* 0.094 [0.082-0.115] mm yr^{-2}) of GMSL rise over 1993-2018 (Table 9.5 and Section 2.3.3.3), which would imply a *likely* GMSL rise of 0.24 m (0.23-0.25 m) by 2050 and 0.73 m (0.69-0.77 m) by 2100. This extrapolation would also imply a *likely* rate of GMSL rise of 7.5 (7.4-7.6) mm yr^{-1}over 2040-2060 and 11.2 (10.6-11.8) mm yr^{-1}over 2080-2100. Over the satellite period, the observed acceleration has been driven primarily by ice-sheet contributions (Section 9.6.1.2; Table 9.5); in the median projections for SSP3-7.0 and SSP5-8.5, these accelerations are projected to continue at a slightly lower level, while the GMSL acceleration is augmented by an acceleration of thermal expansion and glacier loss associated with rising global temperature. Overall, these extrapolations imply that, under SSP1-1.9, SSP1-2.6, and SSP2-4.5, the GMSL acceleration is projected to decrease from its current level.

[START TABLE 9.9 HERE]

Table 9.9: Global mean sea-level projections for 5 SSP scenarios, relative to a baseline of 1995-2014, in meters. Individual contributions are shown for the year 2100. Median values (*likely* ranges) are shown. Average rates for total sea-level change are shown in mm yr^{-1}. Unshaded cells represent processes in whose projections there is *medium confidence*. Shaded cells incorporate a representation of processes in which there is *low confidence*; in particular, the SSP5-8.5 *low confidence* column shows the 17th-83rd percentile range from a p-box including SEJ- and MICI-based projections rather than an assessed *likely* range. Methods are described in 9.6.3.2.

ACCEPTED VERSION SUBJECT TO FINAL EDITING

	SSP1-1.9	SSP1-2.6	SSP2-4.5	SSP3-7.0	SSP5-8.5	SSP5-8.5 *Low Confidence*
Thermal expansion	0.12 (0.09-0.15)	0.14 (0.11-0.18)	0.20 (0.16-0.24)	0.25 (0.21-0.30)	0.30 (0.24-0.36)	0.30 (0.24-0.36)
Greenland	0.05 (0.00-0.09)	0.06 (0.01-0.10)	0.08 (0.04-0.13)	0.11 (0.07-0.16)	0.13 (0.09-0.18)	0.15 (0.09-0.59)
Antarctica	0.10 (0.03-0.25)	0.11 (0.03-0.27)	0.11 (0.03-0.29)	0.11 (0.03-0.32)	0.12 (0.03-0.34)	0.19 (0.02-0.56)
Glaciers	0.08 (0.06-0.10)	0.09 (0.07-0.11)	0.12 (0.10-0.15)	0.16 (0.13-0.18)	0.18 (0.15-0.21)	0.17 (0.12-0.22)
Land Water Storage	0.03 (0.02-0.04)	0.03 (0.02-0.04)	0.03 (0.02-0.04)	0.04 (0.02-0.05)	0.03 (0.02-0.04)	0.03 (0.02-0.04)
Total (2030)	0.09 (0.08-0.12)	0.09 (0.08-0.12)	0.09 (0.08-0.12)	0.10 (0.08-0.12)	0.10 (0.09-0.12)	0.10 (0.09-0.15)
Total (2050)	0.18 (0.15-0.23)	0.19 (0.16-0.25)	0.21 (0.18-0.26)	0.22 (0.19-0.28)	0.23 (0.20-0.30)	0.24 (0.20-0.40)
Total (2090)	0.35 (0.26-0.49)	0.39 (0.30-0.54)	0.48 (0.38-0.65)	0.56 (0.46-0.74)	0.64 (0.52-0.83)	0.71 (0.52-1.31)
Total (2100)	0.38 (0.28-0.55)	0.44 (0.33-0.61)	0.56 (0.44-0.76)	0.68 (0.55-0.90)	0.77 (0.63-1.02)	0.88 (0.63-1.61)
Total (2150)	0.57 (0.37-0.85)	0.69 (0.46-1.00)	0.93 (0.67-1.33)	1.21 (0.92-1.67)	1.35 (1.02-1.89)	1.99 (1.02-4.83)
Rate (2040-2060)	4.2 (2.9-6.1)	4.9 (3.6-6.9)	5.9 (4.5-8.0)	6.5 (5.1-8.7)	7.3 (5.7-9.8)	7.9 (5.7-16.2)
Rate (2080-2100)	4.3 (2.5-6.6)	5.3 (3.3-8.1)	7.8 (5.3-11.5)	10.4 (7.5-14.9)	12.2 (8.8-17.7)	15.9 (8.8-30.2)

[END TABLE 9.9 HERE]

While ice-sheet processes in whose projection there is *low confidence* have little influence up to 2100 on projections under SSP1-1.9 and SSP1-2.6 (Table 9.9), this is not the case under higher emissions scenarios, where they could lead to GMSL rise well above the *likely* range. In particular, under SSP5-8.5, *low-confidence* processes could lead to a total GMSL rise of 0.6-1.6 m over this time period (17^{th}-83^{rd} percentile range of p-box including SEJ- and MICI-based projections), with 5^{th}-95^{th} percentile projections extending to 0.5-2.3 m (*low confidence*). The assessed *low confidence* range is slightly narrower than but broadly consistent with the full 0.4-2.4 m range of published 5^{th}-95^{th} percentile projections for RCP 8.5 since the AR5 (Section 9.6.3.1), including those based on SEJ or incorporating MICI, and highlights the *deep uncertainty* in GMSL rise under the highest emissions scenarios (Box 9.4). The assessment of the potential contribution of processes in which there is *low confidence* to GMSL rise by 2100 is broadly consistent with the assessment of the AR5 (Church et al., 2013a) , which concluded that collapse of marine-based sectors of the Antarctic ice sheet could cause several tenths of a meter of global mean sea-level rise above the *likely* range.

While prior assessment reports, starting with the First Assessment Report (Warrick et al., 1990), have focused on projecting GMSL up to the year 2100, time has progressed, and the year 2100 is now within the timeframe of some long-term infrastructure decisions. For this reason, projections up to the year 2150 are also highlighted (Table 9.9). Over this time period, assuming no acceleration in ice-sheet mass fluxes after 2100, processes in which there is *medium confidence* lead to GMSL rise of 0.5-1.0 m under SSP1-2.6 and 1.0-1.9 m under SSP5-8.5. Processes in which there is *low confidence* could drive GMSL rise under SSP5-8.5 to 1.0-4.8 m (17^{th}-83^{rd} percentile) or even 0.9-5.4 m (5^{th}-95^{th} percentile).

ACCEPTED VERSION SUBJECT TO FINAL EDITING

[START FIGURE 9.27 HERE]

Figure 9.27: Projected global mean sea level rise under different SSP scenarios. *Likely* global mean sea-level change for SSP scenarios resulting from processes in whose projection there is *medium confidence*. Projections and *likely* ranges at 2150 are shown on right. Lightly shaded ranges and thinner lightly shaded ranges on the right show the 17th-83rd and 5th-95th percentile ranges for projections including *low confidence* processes for SSP1-2.6 and SSP5-8.5 only, derived from a p-box including Structured Expert Judgement and Marine Ice Cliff Instability projections. Black lines show historical GMSL change, and thick solid and dash-dotted black lines show the mean and *likely* range extrapolating the 1993-2018 satellite altimeter trend and acceleration. Further details on data sources and processing are available in the chapter data table (Table 9.SM.9).

[END FIGURE 9.27 HERE]

Median projected relative sea-level changes are shown in Figure 9.28, with driving factors highlighted in Figure 9.26. Over the 21st century, the majority of coastal locations have a median projected regional sea-level rise within +/- 20% of the median projected GMSL change (*medium confidence*). Consistent with the AR5, loss of land-ice mass will be an important contributor to spatial patterns in relative sea-level change *(high confidence*), with ocean dynamic sea-level being particularly important as a dipolar contributor in the Northwest Atlantic, a positive contributor in the Arctic Ocean, and a negative contributor in the Southern Ocean south of the ACC (*medium confidence*) (Section 9.2.4.2). As today, vertical land motion will remain a major driver of relative sea-level change (*high confidence*). Uncertainty in relative sea-level projections is greatest in tectonically active areas in which vertical land motion varies over short distances (e.g., Alaska) and in areas potentially subject to large ocean dynamic sea-level change (e.g., the northwestern Atlantic) (*high confidence*).

[START FIGURE 9.28 HERE]

Figure 9.28: Regional sea level change at 2100 for different scenarios (with respect to 1995-2014). Median regional relative sea-level change from 1995 to 2014 up to 2100 for (a) SSP1-1.9, (b) SSP1-2.6, (c) SSP2-4.5, (d) SSP3-7.0, (e) SSP5-8.5, and (f) width of the *likely* range for SSP3-7.0. The high uncertainty in projections around Alaska and the Aleutian Islands arises from the tectonic contribution to vertical land motion, which varies greatly over short distances in this region. Further details on data sources and processing are available in the chapter data table (Table 9.SM.9).

[END FIGURE 9.28 HERE]

An alternative perspective on uncertainty in future sea-level rise is provided by looking at uncertainty in time rather than elevation; that is, looking at the range of dates when specific thresholds of sea-level rise are projected to be crossed (Figure 9.29). Considering only *medium confidence* processes, GMSL rise is *likely* to exceed 0.5 m between about 2080 and 2170 under SSP1-2.6 and between about 2070 and 2090 under SSP5-8.5. It is *likely* to exceed 1.0 m between about 2150 and some point after 2300 under SSP1-2.6, and between about 2100 and 2150 under SSP5-8.5. It is *unlikely* to exceed 2.0 m until after 2300 under SSP1-2.6, while it is *likely* to do so between about 2160 and 2300 under SSP5-8.5. However, processes in whose projections there is *low confidence* could lead to substantially earlier exceedances under higher emissions scenarios: under SSP5-8.5, 1.0 m could be exceeded by about 2080 and 2.0 m could be exceeded by about 2110 (17th percentile of p-box incorporating projections based on SEJ and MICI), with 5th percentile projections as early as about 2070 for 1.0 m and 2090 for 2.0 m.

[START FIGURE 9.29 HERE]

Figure 9.29: Timing of when GMSL thresholds of 0.5, 1.0, 1.5 and 2.0 m are exceeded, based upon four different ice-sheet projection methods informing post-2100 projections. Methods are labelled based on their

ACCEPTED VERSION SUBJECT TO FINAL EDITING

treatment of ice sheets. "No acceleration" assumes constant rates of mass change after 2100. "Assessed ice sheet" models post-2100 ice sheet losses using a parametric fit (Supplementary Material 9.SM.4) extending to 2300 based on a multimodel assessment of contributions under RCP2.6 and RCP8.5 at 2300. Structured Expert Judgement (SEJ) employs ice-sheet projections from Bamber et al. (2019) Marine Ice Cliff Instability (MICI) combines the parametric fit (Supplementary Material 9.SM.4) for Greenland with Antarctic projections based on (DeConto et al., 2021). Circles/thick bars/thin bars represent the 50th, 17th-83rd, and 5th-95th percentiles of the exceedance timing for the indicated projection method. Further details on data sources and processing are available in the chapter data table (Table 9.SM.9).

[END FIGURE 9.29 HERE]

9.6.3.4 Sea-level projections up to 2100 based on global warming levels

Global warming levels represent a new dimension of integration in the AR6 cycle (Section 1.6.2, Cross-Chapter Box 11.1). The SR1.5 (Hoegh-Guldberg et al., 2018) concluded that, based upon an assessment of GMSL projections published for 1.5°C and 2.0°C scenarios, there is *medium agreement* that GMSL in 2100 would be 0.04 –0.16 m higher in a 2°C warmer world compared to a 1.5°C warmer world based on the 17–83% confidence interval (0.00 – 0.24 m based on the 5–95% confidence interval) with a value of around 0.1 m. The SR1.5 did not attempt to standardize the definition of warming-level scenarios, or to examine additional warming levels. No new integrated GMSL projections for 1.5°C or 2.0°C scenarios have been published since the SR1.5.

Most of the contributors to GMSL are more closely tied to time-integrated GSAT than instantaneous GSAT (Hermans et al., 2021), which means that sea level projections by warming level can only be interpreted if the warming levels are linked to a specific timeframe. Here, the warming level projections are defined based on the 2081-2100 GSAT anomaly (Supplementary Material 9.SM.4.7). Different pathways in GSAT can be followed to reach a certain temperature level, which affects the temporal evolution of the different contributors to sea-level change. For instance, there will be different ice sheet and glacier responses to a fast increase to a peak warming of 2°C in 2050 followed by a plateau or a decrease, compared to a gradual increase to the same level of warming in 2100. The sea-level projections presented might include different pathways to the same warming level in 2100, which is reflected in the uncertainty ranges, and should therefore be interpreted as an illustration of sea-level scenarios under a certain warming level.

Projections of *likely* 21st century GMSL rise along climate trajectories leading to different increases in GSAT between 1850-1900 and 2081-2100 are shown in Table 9.10, along with the SSPs for which the temperature-level projections are most closely aligned. For example, considering only processes in which there is *medium confidence*, from the baseline period (1995 to 2014) up to 2100, GMSL in a 2°C scenario is *likely* to rise by 0.40-0.69, which is intermediate between the projections for SSP1-2.6 and SSP2-4.5. GMSL in a 4°C scenario is *likely* to rise by 0.58-0.91 m, similar to the projection for SSP3-7.0. Consistent with the discussion in Section 9.6.3.3, there is *deep uncertainty* in the projections for temperature levels above 3°C, and alternative approaches to projecting ice sheet changes may yield substantially different projections in 4°C and 5°C futures. For example, employing SEJ (Bamber et al., 2019) ice-sheet projections instead of the projections for *medium confidence* processes only leads to a 17th-83rd percentile rise between the baseline period (1995-2014) and 2100 of 0.7-1.6 m rather than 0.7-1.1 m in a 5°C scenario.

[START TABLE 9.10 HERE]

Table 9.10: Global mean sea-level projections and commitments for exceedance of 5 global warming levels, defined by sorting GSAT change in 2081-2100 w.r.t. 1850-1900. Median values and (*likely*) ranges are in meters relative to a 1995-2014 baseline. Rates are in mm yr^{-1}. Unshaded cells represent processes in whose projections there is *medium confidence*. Shaded cells incorporate a representation of processes in which there is *low confidence*; in particular, the SSP5-8.5 *low confidence* column shows the 17th-83rd percentile range from a p-box including SEJ- and MICI-based projections rather than an assessed *likely* range. Methods are described in 9.6.3.2.

ACCEPTED VERSION SUBJECT TO FINAL EDITING

	1.5°C	2.0°C	3.0°C	4.0°C	5.0°C	SSP5-8.5 *Low Confidence*
Closest SSPs	SSP1-2.6	SSP1-2.6/SSP2-4.5	SSP2-4.5/SSP3-7.0	SSP3-7.0	SSP5-8.5	
Total (2050)	0.19 (0.16--0.24)	0.20 (0.17--0.26)	0.21 (0.18--0.27)	0.22 (0.19--0.28)	0.25 (0.22--0.31)	0.24 (0.20--0.40)
Total (2100)	0.44 (0.34--0.59)	0.51 (0.40--0.69)	0.62 (0.50--0.81)	0.70 (0.58--0.91)	0.81 (0.68--1.05)	0.88 (0.63--1.61)
Rate (2040-2060)	4.1 (3.0--5.8)	5.1 (3.8--7.1)	6.0 (4.7--8.2)	6.5 (5.1--8.6)	7.3 (5.8--9.8)	7.9 (5.7--16.2)
Rate (2080-2100)	4.3 (2.6--6.5)	5.5 (3.5--8.3)	7.9 (5.4--11.6)	9.9 (7.2--14.2)	11.8 (8.6--17.0)	15.9 (8.8--30.2)
2000-yr commitment	2-3	2-6	4-10	12-16	19-22	
10000-yr commitment	6-7	8-13	10-24	19-33	28-37	

[END TABLE 9.10 HERE]

9.6.3.5 Multi-century and multi-millennial sea-level rise

Neither the AR5 nor the SROCC discussed the sea-level commitment associated with historical emissions. Since the AR5, new evidence has suggested that historical emissions up to 2016 will lead to a *likely* committed sea-level rise (i.e., the rise that would occur in the absence of additional emissions) of 0.7—1.1 m up to 2300, while pledged emissions through 2030 increase the committed rise to 0.8—1.4 m (Nauels et al., 2019).

Between the baseline period (1995 to 2014) and 2300, the AR5 projected a GMSL rise of 0.38-0.82 m under a non-specific low emissions scenario and 0.9-3.6 m under a non-specific high emissions scenario (Table 9.11). The SROCC projected 0.6-1.0 m under RCP 2.6 and 2.3-5.3 m under RCP 8.5 (*low confidence*). RCP-based projections for 2300 published since the AR5 span a broader range, even excluding studies employing SEJ or MICI, with 17-83rd percentile projections ranging from 0.3-2.9 m for RCP 2.6 and 1.7-6.8 m for RCP 8.5 (Kopp et al., 2014, 2017, Nauels et al., 2017, 2019; Bamber et al., 2019; Palmer et al., 2020) (Table 9.SM.8). Conservatively extending the ISMIP6- and LARMIP-2-based projections beyond 2100 by assuming no subsequent change in ice-sheet mass flux rates (an approach similar to that adopted by (Palmer et al., 2020) for the Greenland Ice Sheet and for the Antarctic Ice Sheet dynamics) leads to a GMSL change up to 2300 of 0.8-2.0 m under SSP1-2.6 and 1.9-4.1 m under SSP5-8.5 (17th-83rd percentile), while incorporating the ice-sheet contributions for 2300 assessed in Section 9.4.1.4 and Section 9.4.2.6 leads to 0.6-1.5 m and 2.2-5.9 m, respectively. Incorporating Antarctic results from a model with Marine Ice Cliff Instability (Section 9.4.2.4), using RCP forcing to inform SSP-based projections, leads to 1.4-2.1 m for SSP1-2.6 and 9.5-16.2 m for SSP5-8.5 (DeConto et al., 2021). Incorporating the SEJ-based ice-sheet projections of (Bamber et al., 2019) for 2°C and 5°C stabilization scenarios yields 1.0-3.1 m for SSP1-2.6 and 2.4-6.3 m for SSP5-8.5, though because of the differences in scenarios, the SSP1-2.6 estimates may be overestimated and the SSP5-8.5 may be underestimated. The eight-fold uncertainty range across projection methods under SSP5-8.5 reflects *deep uncertainty* in the multi-century response of ice sheets to strong climate forcing.

ACCEPTED VERSION SUBJECT TO FINAL EDITING

Taking into account all these approaches, including published projections for RCP 2.6, under SSP1-2.6 GMSL will rise between 0.3 and 3.1 m by 2300 (*low confidence*). This projection range indicates that, while the SROCC projections under low emissions to 2300 are consistent with no ice sheet acceleration after 2100, there is the possibility of a much broader range of outcomes at the high end, reflected in the range of published GMSL projections. Under SSP5-8.5, GMSL will rise between 1.7 and 6.8 m by 2300 in the absence of MICI and by up to 16 m considering MICI, a wider range than the AR5 or the SROCC assessments but consistent with published projections (*low confidence*).

[START TABLE 9.11 HERE]

Table 9.11: Global mean sea-level projections between 1995-2014 and 2300 for total change and individual contributions, for low emissions (from the AR5 (Church et al., 2013b)), RCP 2.6 (from the SROCC (Oppenheimer et al., 2019), and published projections (Table 9.SM.8)) and SSP1-2.6 (this report), and for high emissions (from the AR5(Church et al., 2013b)), RCP 8.5 (from the SROCC (Oppenheimer et al., 2019), and published projections (Table 9.SM.8)), and SSP5-8.5 (this report). Values for the AR5 (Church et al., 2013b) and the SROCC (Oppenheimer et al., 2019) are adjusted from the 1986-2005 baseline used in past reports. Only total values are shown for published ranges. Only the Antarctic contribution changed between the AR5 (Church et al., 2013b) and the SROCC (Oppenheimer et al., 2019). If a range is given it is the 17th—83rd percentile range.

	Low	**RCP 2.6**		**SSP1-2.6**			
m rel. to 1995-2014	**AR5**	**SROCC**	**Post-AR5 Published range**	**No ice-sheet acceleration after 2100**	**Assessed ice-sheet contribution**	**MICI**	**SEJ**
Thermal expansion	0.07-0.46			0.19--0.35			
Greenland	0.14			0.22--0.39	0.11--0.25		0.28--1.28
Antarctica	0.21-0.25			-0.07--1.13	-0.14--0.78	0.71--1.35	-0.11--1.56
Glaciers	–			0.13--0.30			
Land water storage	-0.03	0.07-0.37		0.05--0.10			
Total (2300)	0.38-0.82	0.57-1.04	0.3--2.9	0.8--2.0	0.6--1.5	1.4--2.1	1.0-3.1

	High	**RCP 8.5**		**SSP5-8.5**			
m rel. to 1995-2014	**AR5**	**SROCC**	**Post-AR5 Published range without (with) MICI**	**No ice-sheet acceleration after 2100**	**Assessed ice-sheet contribution**	**MICI**	**SEJ**
Thermal expansion	0.28-1.80			0.91--1.50			
Greenland	0.30-1.18			0.53--0.89	0.32--1.74		0.40--2.23
Antarctica	0.02-0.19	0.60-2.89		-0.24--1.68	-0.27--3.17	6.87--13.54	0.03--3.05

ACCEPTED VERSION SUBJECT TO FINAL EDITING

Glaciers	0.29-0.39			0.32			
Land water storage	–			0.05--0.10			
Total (2300)	0.89-3.56	2.25-5.34	1.7--6.8 (up to 14.1)	1.9--4.1	2.2--5.9	9.5--16.2	2.4--6.3

[END TABLE 9.11 HERE]

On still longer timescales, the AR5 concluded with *low confidence* that the multi-millennial GMSL commitment sensitivity to warming was about 1 to 3 m°C^{-1} GSAT increase. Two process-model-based studies since the AR5 (Clark et al., 2016; Van Breedam et al., 2020) indicate higher commitments (Figure 9.30). Ice sheets dominate the multi-millennial sea-level commitment (Sections 9.4.1.4, 9.4.2.6), but the two studies disagree on the relative contribution of the Greenland and Antarctic ice sheets. Notably, processes such as Marine Ice Cliff Instability (Section 9.4.2.4) that are a major factor behind the *deep uncertainty* in century-scale Antarctic ice sheet response do not appear to have a substantial effect on the multimillennial magnitude (DeConto and Pollard, 2016). Only one of the studies of multimillennial GMSL commitments includes scenarios consistent with 1.5°C of peak warming (Clark et al., 2016); this study suggests a 2000-year commitment at 1.5°C of about 2.3-3.1 m, with approximately an additional 1.4-2.3 m commitment between 1.5°C and 2.0°C (i.e., about 3 to 5 m °C^{-1}). Taken together, both studies show a 2000-year GMSL commitment of about 2-6 m for peak warming of about 2°C, 4-10 m for 3°C, 12-16 m for 4°C, and 19-22 m for 5°C (*medium agreement, limited evidence*, Table 9.10). GMSL rise continues after 2000 years, leading to a 10,000-year commitment of about 6-7 m for 1.5°C of peak warming (based on (Clark et al., 2016)), and of about 8-13 m for 2.0°C, 10-24 m for 3.0°C, 19-33 m for 4.0°C, and 28-37 m for 5°C (based on both studies) (*medium agreement, limited evidence*, Table 9.10).

[START FIGURE 9.30 HERE]

Figure 9.30: Global mean sea-level commitment as a function of peak global surface air temperature. From models (Clark et al., 2016; DeConto and Pollard, 2016; Garbe et al., 2020; Van Breedam et al., 2020) and paleo data on 2000-year (lower row) and 10,000 year (upper row) timescales. Columns indicate different contributors to GMSL rise (from left to right: total GMSL change, Antarctic Ice Sheet, Greenland Ice Sheet, global mean thermosteric sea-level rise, and glaciers). Further details on data sources and processing are available in the chapter data table (Table 9.SM.9).

[END FIGURE 9.30 HERE]

An indicative metric for the equilibrium sea-level response can be provided by comparing paleo global surface air temperature and GMSL during past multimillennial warm periods (Sections 2.3.1.1, 2.3.3.3 9.6.2, Figure 9.9). However, caution is needed as the present and past warm periods differ in astronomical and other forcings (Cross-chapter Box 2.1) and in terms of polar amplification. The Last Interglacial (*likely* 5-10 m higher GMSL than today and 0.5-1.5°C warmer than 1850-1900; Section 9.6.2; Table 9.6) is consistent with the (Clark et al., 2016) projections for the 10,000-year commitment associated with 1.5°C of warming. Similarly, the Mid-Pliocene Warm Period (*very likely* 5-25 m higher GMSL than today and *very likely* 2.5-4°C warmer; Section 9.6.2; Table 9.6) is consistent with the range of 10,000 year commitments associated with 2.5-4°C of warming, but GMSL reconstructions provide only a weak, broad constraint on model-based projections. An additional paleo constraint comes from the Early Eocene Climatic Optimum, which indicates that 10-18°C of warming is associated with ice-free conditions and a *likely* GMSL rise of 70-76 m (Section 2.3.3, Section 9.6.2). Together with model-based projections (Clark et al., 2016; Van Breedam et al., 2020), this period suggests that commitment to ice-free conditions would occur for peak warming of about 7 - 13°C (*medium agreement, limited evidence*).

ACCEPTED VERSION SUBJECT TO FINAL EDITING

On the basis of modeling studies, paleo constraints, single-ice sheet studies finding multimillennial nonlinear responses from both the Greenland and Antarctic ice sheets (Sections 9.4.1.4, 9.4.2.6), and the underlying physics, we conclude that GMSL commitment is nonlinear in peak warming on timescales of both 2,000 and 10,000 years (*medium confidence)* and exceeds the AR5 assessment of 1 to 3 m $°C^{-1}$ (*medium agreement, limited evidence*) (Table 9.9). Although thermosteric sea level will start to decline slowly about 2,000 years after emissions cease, the slower responses from the Greenland and Antarctic ice sheets mean that GMSL will continue to rise for 10,000 years under most scenarios (*medium confidence*).

Since the AR5, a small number of modelling studies have examined the reversibility of the multimillennial sea-level commitment under carbon dioxide removal, solar radiation modification or local ice-shelf engineering. The slow response of the deep ocean to forcing leads to global-mean thermosteric sea-level fall occurring long afterward even if CO_2 levels are restored after a transient increase: global mean thermosteric sea level takes over a millennium to reverse course (Ehlert and Zickfeld, 2018b). Rapid reversion to pre-industrial CO_2 concentrations has been found to be ineffective at fostering regrowth of the Antarctic ice sheet (DeConto et al., 2021) but may reduce the multimillennial sea-level commitment (DeConto and Pollard, 2016). Altering sub-ice shelf bathymetry (Wolovick and Moore, 2018) or triggering ice-shelf advance through massive snow deposition (Feldmann et al., 2019) might interrupt Marine Ice Sheet Instability (Section 9.4.2.4) and thus reduce sea-level commitment. A reversion to pre-industrial Greenland ice sheet temperatures with solar radiation modification is projected to stop mass loss in Greenland but leads to minimal regrowth (Applegate and Keller, 2015). Based on *limited evidence*, carbon dioxide removal, solar radiation modification, and local ice-shelf engineering may be effective at reducing the yet-to-be-realized sea-level commitment but ineffective at reversing GMSL rise (*low confidence*).

[START BOX 9.4 HERE]

BOX 9.4: High-end storyline of 21st century sea-level rise

In this box, we outline a storyline (Glossary, Box 10.2 (Shepherd et al., 2018)) for high-end sea-level projections for 2100. This storyline considers processes whose quantification is highly uncertain regarding the timing of their possible onset and/or their potential to accelerate sea-level rise. These processes are therefore not considered for the assessed upper bound of *likely* sea-level rise by 2100 in section 9.6.3.3, as the *likely* range includes only processes that can be projected skilfully with at least *medium confidence* (based on *agreement* and *evidence)*.

As noted by the SROCC, stakeholders with a low risk tolerance (e.g., those planning for coastal safety in cities and long-term investment in critical infrastructure) may wish to consider global-mean sea-level rise above the assessed *likely* range by the year 2100, because "*likely*" implies an assessed likelihood of up to 16 % that sea-level rise by 2100 will be higher (see also (Siegert et al., 2020)). Because of our limited understanding of the rate at which some of the governing processes contribute to long-term sea-level rise, we cannot currently robustly quantify the likelihood with which they can cause higher sea-level rise before 2100 (Stammer et al., 2019).

In light of such *deep uncertainty*, we employ a storyline approach in examining the potential for, and early-warning signals of a high-end sea-level scenario unfolding within this century. In doing so, we note upfront that the main uncertainty related to high-end sea-level rise is "when" rather than "if" it arises: the upper limit of 1.02 m of *likely* sea-level range by 2100 for the SSP 5-8.5 scenario will be exceeded in any future warming scenario on time scales of centuries to millennia (*high confidence*), but it is uncertain how quickly the long-term committed sea level will be reached (Section 9.6.3.5). Hence, global-mean sea level might rise well above the *likely* range before 2100, which is reflected by assessments of ice-sheet contributions based on structured expert judgment (Bamber et al., 2019) leading to a 95th percentile of projected future sea-level rise as high as 2.3 m in 2100 (Section 9.6.3.3).

A plausible storyline for such high-end sea-level rise in 2100 assumes a strong warming scenario (Section 4.8). The storyline considers faster-than-projected disintegration of marine ice shelves and the abrupt,

ACCEPTED VERSION SUBJECT TO FINAL EDITING

widespread onset of Marine Ice Cliff Instability (MICI) and Marine Ice Sheet Instability (MISI) in Antarctica (Section 9.4.2.4), and faster-than-projected changes in both the surface mass balance and dynamical ice loss in Greenland. While conceptual studies provide *medium evidence* of these processes, substantial uncertainties and *low agreement* in quantifying their future evolution arise from limited process understanding, limited availability of evaluation data, missing or crude representation in model simulations, their high sensitivity to uncertain boundary conditions and parameters, and/or uncertain atmosphere and ocean forcing (Sections 9.4.1.2; 9.4.2.2).

In Antarctica, high warming might lead to floating ice shelves starting to break up earlier than expected due to processes not yet accounted for in ice-sheet models or in current climate models used to force ice-sheet projections. Such processes include hydrofracturing driven by surface meltwater and increase in ocean thermal forcing driven by ocean circulation changes (Sections 9.2.2.3, 9.2.3.2, 9.4.2.3) (Hellmer et al., 2012, 2017; Silvano et al., 2018; Hazel and Stewart, 2020). In particular, the Thwaites and Pine Island Glacier ice shelves could potentially disintegrate this century, which might trigger MICI before 2100 (DeConto and Pollard, 2016; DeConto et al., 2021). MISI could potentially develop earlier and faster than simulated by the majority of models if fast flowing ice streams follow plastic, instead of currently assumed more viscous, sliding laws (Sun et al., 2020). Oceanic feedbacks could drive high-end sea-level rise by changes in the meltwater-driven overturning circulation in ice cavities that cause additional melting (Jeong et al., 2020); by a warming of the ocean water in contact with the ice shelves due to increased stratification and thus reduced vertical mixing (Sections 9.2.2.3, 9.2.3.2) (Golledge et al., 2019b; Moorman et al., 2020; Sadai et al., 2020); or by an increase in sea-ice cover due to increased ocean stratification (Section 9.3.2.1), which could reduce the amount of warm, moist air that reaches the continent and limit the mass gain from snowfall over the ice sheet (Sadai et al., 2020).

In Greenland, stronger mass loss than currently projected might also occur (Aschwanden et al., 2019; Khan et al., 2020; Slater et al., 2020b). For example, warming-induced dynamical changes in atmospheric circulation could enhance summer blocking and produce more frequent extreme melt events over Greenland similar to the record mass loss of more than 500 Gt in summer 2019 (Section 9.4.1.1) (Delhasse et al., 2018; Sasgen et al., 2020). Cloud processes in polar areas that are not well represented in models could further enhance surface melt (Hofer et al., 2019), as could feedbacks between surface melt and the increasing albedo from meltwater, detritus and pigmented algae (Section 9.4.1.1) (Cook et al., 2020). The same ice dynamical processes associated with basal melt and MISI discussed for Antarctica could also occur in Greenland as long as the ice sheet is in contact with the ocean.

The strength of all these processes is currently understood to depend strongly on global mean temperature and polar amplification, with additional linkages through feedback from global mean sea-level (Gomez et al., 2020). These dependencies on a joint forcing imply that processes are strongly correlated. Hence, both their uncertainties and their possible cascading contribution to high-end sea-level rise are expected to combine. High-end sea-level rise can therefore occur if one or two processes related to ice-sheet collapse in Antarctica result in an additional sea-level rise at the maximum of their plausible ranges (Sections 9.4.2.5, 9.6.3.3; Table 9.7) or if several of the processes described in this box result in individual contributions to additional sea-level rise at moderate levels. In both cases, global-mean sea-level rise by 2100 would be substantially higher than the assessed *likely* range, as indicated by the projections including *low confidence* processes reaching in 2100 as high as 1.6 m at the 83rd percentile and 2.3 m at the 95th percentile (Section 9.6.3.3).

Identifying the potential drivers of a high-end sea-level rise allows identification of sites and observables that can provide early warnings of a much faster sea-level rise than the *likely* range of this and previous reports. One potential site for such monitoring is Thwaites Glacier, which is melting faster in some places and slower in others than models simulate. At this glacier, the effect of tides and channelling of warm water flows on the melting is evident (Milillo et al., 2019), making the floating ice shelf potentially vulnerable to breakup from hydrofracturing, driven by surface meltwater, much earlier than expected. In addition, the glacier is retreating towards a zone with deeper bedrock, which at its present rate of retreat would be reached in 30 years (Yu et al., 2019). Thwaites Glacier is therefore a strong candidate to experience large-scale MISI and/or MICI (Golledge et al., 2019b; DeConto et al., 2021), making it the ideal site for monitoring early-warning signals of accelerated sea-level-rise from Antarctica. Such signals could possibly be observed within

ACCEPTED VERSION SUBJECT TO FINAL EDITING

the next few decades (Scambos et al., 2017).

[END BOX 9.4 HERE]

9.6.4 Extreme sea levels: Tides, surges and waves

An extreme sea level (ESL) refers to an occurrence of exceptionally high or low local sea surface height (Box 9.1). This section focusses on oceanographic driven changes in ESL (Box 9.1).

9.6.4.1 Past changes

The AR5 (Church et al., 2013a) concluded that changes in extreme still water levels (ESWL, combining relative sea level, tide and surge as observed by tide gauges: Box 9.1) are *very likely* to be caused by observed increases in relative sea level, but noted *low confidence* in region-specific results owing to the limited number of studies considering localised contributions from storm surge, tide or wave effects. Influences from dominant modes of climate variability, particularly ENSO and NAO (Annex IV), were also noted. Climate modes affect sea level extremes in many regions, as a result of both sea-level anomalies (Sections 9.2.4.2, 9.6.1.3) and changes in storminess (Section 11.7). The SROCC (Oppenheimer et al., 2019) concluded with *high confidence* that inclusion of local processes (wave effects, storm surges, tides plus other regional morphology changes due to erosion, sedimentation and compaction) is essential for estimation of changes in ESL events.

As in the AR5 and the SROCC, tide gauge observations show that relative sea level rise (Section 9.6.1.3) is the primary driver of changes in ESWL at most locations and, across tide gauges, has led to a median 165% increase in high-tide flooding over 1995-2014 relative to those over 1960-1980 (Figure 9.31) (*high confidence*). Some locations exhibit substantial differences between long-term relative sea level trends and ESWL (*high confidence*), particularly given decadal to multidecadal variations of other ESWL contributors (Rashid and Wahl, 2020). Since the SROCC, relative sea level rise has been shown to be the dominant contributor to ESWL rise at most gauge sites along the Chinese coast, but, at some locations, the surge contribution dominates (Feng et al., 2019). Trends in the difference between ESWL and mean relative sea level rise can result from changes (either positive or negative) in the surge or tidal components, and can include non-linear interactions between tide, surge, and relative sea level (Arns et al., 2015; Schindelegger et al., 2018). The positive phase of the 18.6 year nodal cycle of the astronomical tide is a further consideration, contributing to an increased flood hazard relative to the long term average (Talke et al., 2018; Peng et al., 2019; Baranes et al., 2020). Failing to consider the non-linear interactions between tide, surge and relative sea level may overestimate trends in ESWL (Arns et al., 2020) (*low confidence*), and, in some regions, changes in ESWL depend more on changes in surge or tide than on sea level trends.

Ongoing development of the GESLA tide gauge database (Woodworth et al., 2016) along with data archaeology (Talke and Jay, 2013) extends availability of tide gauge records back to the mid 19th Century (or earlier). Dynamical datasets used to assess trends in ESL at global or regional scales (e.g., tide and surge contributions from the Global Tide and Surge Reanalysis (GTSR) (Muis et al., 2016, 2020), or wave setup/swash contributions from available wave hindcasts/reanalyses (Melet et al., 2018)) have model biases introduced with resolution and parameterisation limitations, incomplete atmospheric data and currently span only a few decades, so they are not yet long or accurate enough to assess long-term trends in ESLs. Therefore, there is *medium confidence* in observed trends in ESWL but only *low confidence* in modelled ESL trends.

The AR5 indicated that the amplitude and phase of major tidal constituents have exhibited long-term change, but that their effects on ESL were not well understood. The SROCC (Bindoff et al., 2019) reported changes in tides (amplification and dampening) at some locations to be of comparable importance to changes in mean sea level for explaining changes in high water levels, with the sign of change being dependent on stability of shoreline position. Relative sea level rise causes water depth-based alterations to the resonant characteristics

ACCEPTED VERSION SUBJECT TO FINAL EDITING

of the basin, changes the bottom friction and increases the wave speed (Pickering et al., 2012) and remains the primary hypothesis for observed tidal changes. Other contributing processes include strong localised anthropogenic drivers (e.g., port development, dredging, flood defences, land reclamation), changes in stratification associated with ocean warming (Section 9.2.1.3), and changes in seabed roughness associated with ecological change (e.g., Haigh et al., 2019). Tide gauge data show that, although principal tidal components have varied in amplitude on the order of 2% to 10% per century (Jay, 2009; Ray, 2009), identifying direct causality remains challenging (Haigh et al., 2019). Combined, observations and models indicate relative sea level rise and direct anthropogenic factors are the primary drivers of observed tidal changes at tide gauge stations (*medium confidence*).

The SROCC (Oppenheimer et al., 2019) reported variations in storm surge not related to changes in relative sea level, and concluded with *high confidence* that consideration of localised storm surge processes was essential to monitor trends in ESL. Storm surge-driven ESL events are a response to tropical and extratropical cyclones. While historical trends in extra-tropical cyclones are less clear (Section 11.7.2.1), there is mounting evidence for an increasing proportion of stronger tropical cyclones globally, with an associated poleward migration (Section 11.7.1.2). These changes are captured in the ESL record, for example, via increasing intensity and poleward shift in the location of typhoon-driven storm surges reported across 64 years (1950-2013) in the western North Pacific (Oey and Chou, 2016). Along the US east coast, there has been an increase in frequency of ESL events due to tropical cyclone changes since 1923 that can be statistically linked to changes in global average temperature (Grinsted et al., 2013), and the signal is projected to emerge around 2030 (Lee et al., 2017). At century and longer timescales, geological proxies such as overwash deposits in coastal lagoons or sinkholes can be used to reconstruct past changes in storm activity (e.g., Brandon et al., 2013; Lin et al., 2014) and put recent events into historical perspective (e.g., Brandon et al., 2015). However, there is *low confidence* in the current ability to quantitatively compare geological proxies with gauge data. Historical storm surge activity is being increasingly assessed with use of hydrodynamic model simulations and data-driven global reconstructions to supplement tide-gauge observations to investigate historical changes at centennial to millennial time scales (e.g., (Ji et al., 2020; Muis et al., 2020; Tadesse et al., 2020). Large regional variations and limited observational data lead to *low confidence* in observed trends in the surge contribution to increasing ESL.

[START FIGURE 9.31 HERE]

Figure 9.31: Historical occurrences of minor extreme still water levels. Defined as the 99th percentile of daily observed water levels over 1995-2014. (a) Percent change in occurrences over 1995-2014 relative to those over 1960-1980. (b-g) Annual mean sea level (blue) and annual occurrences of extreme still water levels over the 1995-2014 99th percentile daily maximum (yellow) at six selected tide gauge locations. Further details on data sources and processing are available in the chapter data table (Table 9.SM.9).

[END FIGURE 9.31 HERE]

Waves contribute to ESL via wave setup, infra-gravity waves and swash processes (Dodet et al., 2019), with Extreme Total Water Level (ETWL: Box 9.1) used to represent ESWL with addition of wave setup, and Extreme Coastal Water Level (ECWL: Box 9.1) also including contributions from swash. The SROCC (Oppenheimer et al., 2019) reported the dependency of these processes on nearshore geomorphology and deep-water wave climate, and thus sensitivity to internal climate variability and climate change. Few long term deployments of in-situ measurements in the very dynamic surf zone means that long term records of ETWL or ECWL are limited to a few sites; tidal gauges are typically located in sheltered locations (e.g., harbours) where wave contributions are absent (Lambert et al., 2020). Consequently, trends in wave contributions to ESL are typically derived from trends in wave conditions observed offshore. On the basis of satellite altimeter observations, the SROCC reported increasing extreme wave heights in the Southern and North Atlantic Oceans of around 1.0 cm yr^{-1} and 0.8 cm yr^{-1} over the period 1985-2018 (*medium confidence*). The SROCC (Collins et al., 2019) also identified sea-ice loss in the Arctic as leading to increased wave heights over the period 1992 to 2014 (*medium confidence*). Since the SROCC, the satellite wave record has

ACCEPTED VERSION SUBJECT TO FINAL EDITING

been shown to be sensitive to alternate processing techniques, leading to important differences in reported trends (Timmermans et al., 2020). The most common observation platform for surface waves over the past 30 years are in-situ buoys. However, evolving biases associated with changing instrument type, configuration and sampling methodology introduce artificial trends (e.g., Gemmrich et al., 2011; Timmermans et al., 2020). Accurate metadata is required to address these issues, and, while available locally, are only beginning to be globally coordinated (Centurioni et al., 2019). Wave reanalysis and hindcast products have also been used to investigate total water level at global scale (Melet et al., 2018; Reguero et al., 2019). Their applicability for trend analysis is limited by inhomogeneous data for assimilation (Stopa et al., 2019), but they inform relationships between seasonal, inter-annual to inter-decadal variability of climate indices and wind-wave characteristics (Marshall et al., 2015a, 2018; Kumar et al., 2016; Stopa et al., 2016). To summarise, satellite era trends in wave heights of order 0.5 cm yr^{-1} have been reported, most pronounced in the Southern Ocean. However, sensitivity of processing techniques, inadequate spatial distribution of observations, and homogeneity issues in available records limit confidence in reported trends (*medium confidence*).

Only a few studies have attempted to quantify the role of anthropogenic climate change in ESL events (e.g. Mori et al., 2014, Takayabu et al., 2015, Turki et al., 2019). Detection and attribution of the human influence on climatic changes in surges, and waves remains a challenge (Ceres et al., 2017), with *limited evidence* to suggest in some instances (e.g., poleward migration of tropical cyclones in the Western North Pacific: Section 11.7.1.2), changes in surges and waves can be attributed to anthropogenic climate change (*low confidence*). With relative sea-level change being considered the primary driver of observed tidal changes, there is *medium confidence* that these changes can be attributed to human influence. The close relationship between local ESL and long-term relative sea level change, combined with the robust attribution of GMSL change (Section 9.6.1.4), implies that observed global changes in ESL can be attributed, at least in part, to human-caused climate change (*medium confidence*), but reconciling regional variation in these changes is not yet possible (Section 9.6.1.4).

9.6.4.2 Future changes

There are two distinct methods used to project future ESL changes. The static, or mean sea level offset, approach employs historical distributions of tidal, surge and wave components and adjusts future ESL distributions for mean relative sea level rise. The dynamic approach employs hydrodynamic and/or wave models forced with GCM-derived atmospheric fields to project changes in tidal, storm surge and wave distributions, which are then combined with relative sea level projections to project future ESLs. The dynamic approach is computationally expensive. Use of the dynamic approach on large spatial or global scales has only recently been successful to project 21st Century changes in ETWL (Vousdoukas et al., 2017, 2018) and ECWL (Melet et al., 2020). (Kirezci et al., 2020) assume stationarity in global wave and storm surge simulations to assess projected 21st century changes in episodic coastal ETWL driven flooding under global sea-level rise scenarios.

The SROCC (Oppenheimer et al., 2019) presents projections of ESL derived using a static approach. Such projections often quantify changes in ESL event frequency, expressed as “frequency amplification factors” (Hunter, 2010, 2012). Like relative sea level projections, frequency amplification factors increase under higher emission scenarios, and differences between scenarios increase over time. The SROCC concludes that even small to moderate changes in mean relative sea level can lead to hundred- to thousand-fold increases in the frequencies with which certain thresholds are exceeded; e.g., what is currently a 1-in-100 year ESL height (1% annual probability or 0.01 expected annual events) will be expected once or even multiple times per year in future at many locations (Figure 9.32). The SROCC showed that currently rare ESL events (e.g., with an average return period of 100 years) will occur annually or more frequently at most available locations for RCP4.5 by the end of the century (*high confidence*). Results from these assessments are sensitive to the type of ESL probability distribution assumed (Buchanan et al., 2016; Wahl et al., 2017), as well as the magnitude and uncertainty of projected relative sea level change (Slangen et al., 2017; Wahl et al., 2017; Frederikse et al., 2020a). Frequency amplification factors tend to be largest in tropical regions due in part to higher relative sea level rise projections, but primarily to the relative rarity of high ESLs in areas

ACCEPTED VERSION SUBJECT TO FINAL EDITING

with little historical exposure to tropical or extratropical cyclones. Alternative representation of changes in ESL, such as presenting changes in exceedances per year (Sweet and Park, 2014), are subject to similar sensitivities, and lead to *medium confidence* in projected changes of event frequency using these methods.

Employing a similar static approach (fitting a Gumbel distribution between Mean Higher High Water (average of higher high water height of each tidal day) and a threshold following (Buchanan et al., 2016)), this report updates the SROCC projections of ESL with the relative sea level projections from Section 9.6.3.3 (see also Supplementary Material 9.SM.4). By 2050, the median increase in frequency amplification factor at 634 tide gauge stations is 19 for SSP1-2.6, 22 for SSP2-4.5 and 30 for SSP5-8.5 (Figure 9.32). This means that by 2050 a historical (1995-2014) 1% annual probability ESL will have increased to an 19-30% annual probability. The 1% historical annual probability event is expected to become an annual event at 19-31% of the 634 stations by 2050, consistent with the SROCC. By 2100, the median frequency amplification factor is projected to be 163 for SSP1-2.6, 325 for SSP2-4.5 and 532 for SSP5-8.5, with respectively 60%, 71%, and 82% of the stations experiencing a currently 1% annual probability event at least yearly (Figure 9.32) (*medium confidence*).

In the dynamic approach, the low resolution of the forcing fields arising from GCMs limits the ability to resolve historical and future changes in tropical and extra-tropical storm frequency and intensity, and resolution of local geography and morphology limit ability to represent ECWL (Box 9.1). Not all relevant processes, e.g., river discharge, are included in the dynamic models, and ESL events are typically a combination of multiple contributing processes, which are often not independent (Jevrejeva et al., 2019). In both static and dynamical approaches, global assessment of the performance of modelled storm surge and wave contributions to ESL is limited by poor coverage of observations (limited to tide-gauges for ESWL, (Muis et al., 2020), and unavailable for the wave dependent ETWL and ECWL estimates (Vitousek et al., 2017; Vousdoukas et al., 2018; Kirezci et al., 2020; Lambert et al., 2020; Melet et al., 2020). In studies to date, individual models are used to simulate different contributions to ESL, non-linear interactions are not well captured, and uncertainties associated with downscaling methodology are poorly resolved, leading to *low confidence* in available ESL projections that include these modelled wave and surge contributions.

Assessment of dynamic ETWL changes for regions is presented in Chapter 12, following the methods of (Vousdoukas et al., 2018) and (Kirezci et al., 2020). Consistent with studies using the static approach, (Vousdoukas et al., 2018) finds that by 2050 the historical 1% average annual probability ETWL will have increased to a 2-50% average annual probability for most high latitude regions, and more often (up to multiple times a year, >100% annual probability) in the tropics, under both RCP 4.5 and RCP 8.5. For 2100, present-day 1% average annual probability extreme sea levels will be exceeded multiple times each year almost everywhere. In summary, despite waves and surges being non-negligible contributors to projected ETWL and ECWL changes (Vousdoukas et al., 2018; Melet et al., 2020), relative sea level change is expected to be the main driver in changes in future ESL return periods in most areas (*medium confidence)*.

The SROCC (Bindoff et al., 2019) concluded that the majority of coastal regions will experience statistically significant changes in tidal amplitudes through the 21st Century. Comprehensive high-resolution (of order 10km) numerical modelling studies provide evidence for spatially coherent changes in tidal amplitudes in shelf seas as a result of relative sea level rise (Haigh et al., 2019, and references therein). There is *high confidence* that GMSL rise will be the primary driver of global tidal amplitude increases and decreases over the next 100-200 years, changing the baseline tide that ESLs are imposed upon. At local and regional scales, anthropogenic factors such as major land reclamation efforts (e.g., East China Sea, Song et al., 2013) or differing national coastal management strategies (maintaining the present coastline position or managed retreat) will locally modulate the influence of GMSL rise on tidal amplitude (*medium confidence*).

The SROCC (Oppenheimer et al., 2019) concluded that the intensity of severe tropical cyclones will increase in a warmer climate (Section 11.7.1), but *low confidence* remains in the future frequency of tropical cyclones. Changes in tropical cyclone climatology will contribute to variations in frequency and magnitude of future ESL surge events, although estimates of this contribution range widely (Lin et al., 2012; McInnes et al., 2014, 2016; Little et al., 2015; Garner et al., 2017; Mori et al., 2019; Muis et al., 2020). In the Gulf of Mexico, changes in ESL due to tropical cyclone activity may be as important as SLR in enhancing future

ACCEPTED VERSION SUBJECT TO FINAL EDITING

flood hazards (Marsooli et al., 2019). For the Korean Peninsula, a maximum change in 100-year return height associated with typhoon-induced storm surges of 10% under 4°C warming is found (Yang et al., 2018). The effects of projected changes in tropical cyclone intensity may be enhanced or offset in different locations by effects of changes in tracks (Garner et al., 2017) (Section 11.7.1). There is *low confidence* in projected changes in ESL driven by changes in tropical cyclone climatology.

Changes in surface wave conditions occur in response to changes in frequency; intensity and position of forcing winds and storms (Morim et al., 2018, 2019); reduction in sea-ice and associated changes in fetch conditions (Thomson and Rogers, 2014; Casas-Prat and Wang, 2020); and changes in coastal morphology associated with relative sea level rise (Wandres et al., 2017; Storlazzi et al., 2018). A few studies considering the contribution of a non-stationary wave climate on future changes in ESL infer a small but non-negligible contribution (Vousdoukas et al., 2018; Melet et al., 2020). The SROCC presented qualitative assessments of projected changes in wave conditions. Since the SROCC, a quantitative assessment of a community ensemble of global wind-wave projections (Morim et al., 2019) found robust projected changes of ~5-10% (positive or negative, depending on region) in annual mean significant wave height, mean wave period, and/or mean wave directions along ~52% of the world's coastline that exceed internal climate variability under RCP8.5 by 2100. Continued retreat of sea-ice cover in the Arctic will lead to more energetic wind-wave conditions (Casas-Prat and Wang, 2020). Wave climate modelling methods introduce up to ~50% of the ensemble variance in mean wave climate projections (Morim et al., 2019). GCMs do not typically resolve the higher-resolution tropical and extratropical storm features required to accurately determine the contribution of extreme waves to ESLs and individual studies have sought to improve resolution to address these issues (e.g., Timmermans et al., 2017). To date, projections of wave height extremes have been constrained to single wave model configurations (e.g., Timmermans et al., 2017; Meucci et al., 2020). In summary, there is *medium confidence* in projections of changes in mean wave climate but *low confidence* in the projected changes in extreme wave conditions due to *limited evidence*.

Correlations between changes in sea level-forced (mean sea level and tidal) and atmospherically-forced drivers (ocean surface waves and surges) of ESLs have only been considered in a few studies, although high surge and high waves co-occur along a majority of the world's coastlines (Marcos et al., 2019). Along the US east coast, ocean dynamic sea level change and change in power dissipation index (a proxy for North Atlantic tropical cyclone activity) are correlated across CMIP5 GCMs, resulting in an increase in ESLs relative to analyses assuming independence of these changes (Little et al., 2015). In the Irish Sea, dynamically coupled wave-tide modelling results in high water wave heights up to 20% higher than in an uncoupled analysis (Lewis et al., 2019). In the German Bight, relative sea level rise relaxes the breaking criterion of nearshore waves (assuming no geomorphological response), allowing larger waves to propagate closer to shore, leading to increased wave runup (Arns et al., 2017). In south-western Australia, the influence of projected SLR was found to exceed the influence of projected changes in forcing winds on wave characteristics at the coast (Wandres et al., 2017). Thus, projections of ESL that do not consider correlations between and among sea level-forced and atmospherically-forced drivers can differ strongly from coupled projections (*medium confidence*).

The SROCC (Collins et al., 2019b) highlighted compound events, or coincident occurrence of multiple hazards, as an example of *deep uncertainty*, and noted that failing to account for multiple factors contributing to extreme events will lead to underestimation of the probabilities of occurrence (*high confidence*). Statistical studies have shown that high rain or streamflow often co-occurs with storm surge as examples of "compound" surge-rain or surge-discharge events (Sections 11.8.1; 12.4.5.6; Wahl and Chambers, 2015; Moftakhari et al., 2017; Ward et al., 2018; Wu et al., 2018; Couasnon et al., 2019). Dynamical modelling studies show co-occurrence of flood drivers raises ESLs at some locations in estuaries (e.g., Rhine Delta, Zhong et al., 2013; the Netherlands, van den Hurk et al., 2015; Taiwan, Chen and Liu, 2016; and the Hudson River, USA Orton et al., 2018), particularly when hydrologic catchments are steep and cause high rainfall near the coast (SW UK, Svensson and Jones, 2004). The compound effect of storm surge and rainfall contributes greater projected flood risk than climate induced amplification (Hsiao et al., 2021). However, at other locations, co-occurrence was unimportant because streamflow timing was not coincident with the coastal peak storm surge (Hudson River, Orton et al., 2012; Rhine delta, Klerk et al., 2015). The SROCC (Oppenheimer et al., 2019) detailed the complexity of interactions in deltaic environments. Direct increases

ACCEPTED VERSION SUBJECT TO FINAL EDITING

in flooding driven by increasing relative sea levels and by increased storm surge, rain, or correlations between these flood-drivers (e.g., Moftakhari et al., 2017; Orton et al., 2018) are expected to be further accompanied by increases in flooding due to subsidence (vertical land movement) and sedimentation (relative sea level driven blockage of river flows). The probability of concurrent surge, wave and precipitation events has been projected to increase by more than 25% by 2100 compared to present, with high northern latitudes displaying compound flooding becoming more than 2.5 times as frequent, and weakening in the subtropics (Bevacqua et al., 2020). However, the number of studies on compound events is still limited and therefore there is *low confidence* in understanding the extent by which compound surge-rain events will change in response to relative sea level rise and climate change.

[START FIGURE 9.32 HERE]

Figure 9.32: Projected median frequency amplification factors for the 1% average annual probability extreme still water level in 2050 (a, c, e) and 2100 (b, d, f). Based on a peak-over-threshold (99.7%) method applied to the historical extreme still water levels of GESLA2 following SROCC and additionally fitting a Gumbel distribution between MHHW and the threshold following (Buchanan et al., 2016), using the regional sea-level projections of this chapter (Section 9.6.3.3) for (a, b) SSP5-8.5, (c, d) SSP2-4.5 and (e, f) SSP1-2.6. Further details on data sources and processing are available in the chapter data table (Table 9.SM.9).

[END FIGURE 9.32 HERE]

9.7 Final Remarks

The process-based assessment of observed and projected change in the ocean, cryosphere and sea level undertaken here reveals advances and gaps in reconstructions, observations, models and process understanding. Revisiting the updated assessments since the AR5 and the SROCC helps to gauge the robustness of understanding and quantitative assessments. The CMIP6 family of models builds upon the experience of the CMIP5 models, and the projections of ISMIP6, LARMIP2 and GlacierMIP strengthen understanding. Taken together with emulators of these simulations (Box 9.3) and transparent statistical approaches (Section 9.6.3), this chapter provides projections which are consistent with the assessment of Equilibrium Climate Sensitivity in this report and that have improved estimates of uncertainty.

The largest uncertainties in future sea level and cryosphere change are related to the Greenland and Antarctic ice sheets (Sections 9.4.1.3, 9.4.1.4, 9.4.2.5, 9.4.2.6). While the ISMIP6 and LARMIP2 protocols provide simulations permitting uncertainty estimation and probabilistic inferences, remaining *deep uncertainty* relates both to ice sheet processes and the atmospheric and oceanic conditions simulated by CMIP models in polar regions (Sections 9.4.2.3, 9.4.2.4). ISMIP6 and LARMIP2 have not been simulated beyond 2100, which greatly reduces the amount and variety of state-of-the-art projections available to make ice sheet and sea level projections beyond 2150. After 2150, *limited agreement* causes us to consider all projections as *low confidence*. Critically, the uncertainty in ice sheet projections is the leading uncertainty in projections of future global sea level for the second half of this century and beyond (Section 9.6.3).

Glacier inventory and projection uncertainty has been a significant source of past sea level budget uncertainty and remains a dominant uncertainty until mid-century. Emission scenario becomes the largest source of glacier change uncertainty by 2100 just as the relative importance of glacier loss is projected to decrease (Section 9.5.1).

New high-resolution climate models show that SST, overturning circulation, ocean heat content change and sea-ice cover are considerably improved in most models when compared to the coarser resolution models. Change in the Southern Ocean and adjacent shelves (Section 9.2.3.2) is intimately linked to the future of the Antarctic ice sheet (Section 9.4.2.3), and projection of the Southern Ocean depends on both oceanic and atmospheric drivers affecting heat (and carbon) uptake and sea ice. However, resolution remains a factor, as most CMIP6 models are far from resolutions that directly represent coastal and regional shallow-water

ACCEPTED VERSION SUBJECT TO FINAL EDITING

processes such as those beneath Antarctic ice shelves, in Greenland fjords and the eddying convection found by OSNAP.

Processes that change on long timescales—particularly AMOC, ocean heat content, and ice sheets—require additional projections beyond the CMIP scenarios to explore longer term commitment, post-forcing recovery measured in centuries rather than years or decades, and potential tipping points and thresholds. There were only a few new studies focussed on longer timescales and none based on CMIP6 models.

ACCEPTED VERSION
SUBJECT TO FINAL EDITING

Frequently Asked Questions

FAQ 9.1: Can continued melting of the Greenland and Antarctic ice sheets be reversed? How long would it take for them to grow back?

Evidence from the distant past shows that some parts of the Earth system might take hundreds to thousands of years to fully adjust to changes in climate. This means that some of the consequences of human-induced climate change will continue for a very long time, even if atmospheric heat-trapping gas levels and global temperatures are stabilized or reduced in the future. This is especially true for the Greenland and Antarctic ice sheets, which grow much more slowly than they retreat. If the current melting of these ice sheets continues for long enough it becomes effectively irreversible on human timescales, as does the sea level rise caused by that melting.

Humans are changing the climate and there are mechanisms that amplify the warming in the polar regions (Arctic and Antarctic). The Arctic is already warming faster than anywhere else (see FAQ 4.3). This is significant because these colder high latitudes are home to our two remaining ice sheets: in Antarctica and Greenland. Ice sheets are huge reservoirs of frozen freshwater, built up by tens of thousands of years of snowfall. If they were to completely melt, the water released would raise global sea level by about 65 m. Understanding how these ice sheets are affected by warming of nearby ocean and atmosphere is therefore critically important. The Greenland and Antarctic ice sheets are already slowly responding to recent changes in climate, but it takes a long time for these huge masses of ice to adjust to changes in global temperature. That means that the full effects of a warming climate may take hundreds or thousands of years to play out. An important question is whether these changes can eventually be reversed, once levels of greenhouse gases in the atmosphere are stabilized or reduced by humans and natural processes. Records from the past can help us answer this question.

For at least the last 800,000 years, the Earth has followed cycles of gradual cooling followed by rapid warming caused by natural processes. During cooling phases, more and more ocean water is gradually deposited as snowfall, causing ice sheets to grow and sea level to slowly decrease. During warming phases, the ice sheets melt more quickly, resulting in more rapid rises in sea level (FAQ 9.1, Figure 1). Ice sheets build up very slowly because growth relies on the steady accumulation of falling snow that eventually compacts into ice. As the climate cools, areas that can accumulate snow expand, reflecting back more sunlight that otherwise would keep the Earth warmer. This means that once started, glacial climates develop rapidly. However, as the climate cools, the amount of moisture that the air can hold tends to decrease. As a result, even though glaciations begin quite quickly, it takes tens of thousands of years for ice sheets to grow to a point where they are in balance with the colder climate.

Ice sheets retreat more quickly than they grow because of processes that, once triggered, drive self-reinforcing ice loss. For ice sheets that are mostly resting on bedrock *above* sea level – like the Greenland ice sheet – the main self-reinforcing loop that affects them is the 'elevation–mass balance feedback' (FAQ 9.1, Figure 1, right). In this situation, the altitude of the ice sheet surface decreases as it melts, exposing the sheet to warmer air. The lowered surface then melts even more, lowering it faster still, until eventually the whole ice sheet disappears. In places where the ice sheet rests instead on bedrock that is *below* sea level and which also deepens inland, including many parts of the Antarctic ice sheet, an important process called 'marine ice-sheet instability' is thought to drive rapid retreat (FAQ 9.1, Figure 1, left). This happens when the part of the ice sheet that is surrounded by sea water melts. That leads to additional thinning, which in turn accelerates the motion of the glaciers that feed into these areas. As the ice sheet flows more quickly into the ocean, more melting takes place, leading to more thinning and even faster flow that brings ever-more glacier ice into the ocean, ultimately driving rapid deglaciation of whole ice-sheet drainage basins.

These (and other) self-reinforcing processes explain why relatively small increases in temperature in the past led to very substantial sea level rise over centuries to millennia, compared to the many tens of thousands of years it takes to grow the ice sheets that lowered the sea level in the first place. These insights from the past imply that if human-induced changes to the Greenland and Antarctic ice sheets continue for the rest of this century, it will take thousands of years to reverse that melting, even if global air temperatures decrease

ACCEPTED VERSION SUBJECT TO FINAL EDITING

within this or the next century. In this sense, these changes are therefore irreversible, since the ice sheets would take much longer to regrow than the decades or centuries for which modern society is able to plan.

[START FAQ9.1, FIGURE 1 HERE]

FAQ 9.1, Figure 1: Ice sheets growth and decay. (Top) Changes in ice-sheet volume modulate sea level variations. The grey line depicts data from a range of physical environmental sea-level recorders such as coral reefs (see Table 9.SM.5) while the blue line is a smoothed version of it. (Bottom, left) Example of destabilisation mechanism in Antarctica. (Bottom, right) Example of destabilisation mechanism in Greenland.

[END FAQ9.1, FIGURE 1 HERE]

ACCEPTED VERSION
SUBJECT TO FINAL EDITING

FAQ 9.2: How much will sea level rise in the next few decades?

As of 2018, global average sea level was about 15–25 cm higher than in 1900 and 7–15 cm higher than in 1971. Sea level will continue to rise by an additional 10–25 cm by 2050. The major reasons for this ongoing rise in sea level are the thermal expansion of seawater as its temperature increases and the melting of glaciers and ice sheets. Local sea level changes can be larger or smaller than the global average, with the smallest changes in formerly glaciated areas and the largest changes in low-lying river delta regions.

Across the globe, sea level is rising, and the rate of increase has accelerated. Sea level increased by about 4 mm per year from 2006 to 2018, which was more than double the average rate over the 20th century. Rise during the early 1900s was due to natural factors, such as glaciers catching up to warming that occurred in the Northern Hemisphere during the 1800s. However, since at least 1970, human activities have been the dominant cause of global average sea level rise, and they will continue to be for centuries into the future.

Sea level rises either through warming of ocean waters or the addition of water from melting ice and bodies of water on land. Expansion due to warming caused about 50% of the rise observed from 1971 to 2018. Melting glaciers contributed about 22% over the same period. Melting of the two large ice sheets in Greenland and Antarctica has contributed about 13% and 7%, respectively, during 1971-2018, but melting has accelerated in the recent decades, increasing their contribution to 22% and 14% since 2016. Another source is changes in land water storage: reservoirs and aquifers on land have reduced, which contributed about a 8% increase in sea level.

By 2050, sea level is expected to rise an additional 10–25 cm whether or not greenhouse gas emissions are reduced (FAQ 9.2, Figure 1). Beyond 2050, the amount by which sea level will rise is more uncertain. The accumulated total emissions of greenhouse gases over the upcoming decades will play a big role beyond 2050, especially in determining where sea level rise and ice sheet changes eventually level off.

Even if net zero emissions are reached, sea level rise will continue because the deep ocean will continue to warm and ice sheets will take time to catch up to the warming caused by past and present emissions: ocean and ice sheets are slow to respond to environmental changes (see FAQ 5.3). Some projections under low emissions show sea level rise continuing as net zero is approached at a rate comparable to today (3–8 mm per year by 2100 versus 3–4 mm per year in 2015), while others show substantial acceleration to more than five times the present rate by 2100, especially if emissions continue to be high and processes that accelerate retreat of the Antarctic Ice Sheet occur widely (FAQ 9.1).

Sea level rise will increase the frequency and severity of extreme sea level events at coasts (see FAQ 8.2),, such as storm surges, wave inundation and tidal floods: risk can be increased by even small changes in global average sea level. Scientists project that in some regions, extreme sea level events that were recently expected once in 100 years will occur annually at 20-25% of locations by 2050 regardless of emissions, but by 2100 emissions choice will matter: annually at 60% of locations for low emissions, and at 80% of locations under strong emissions.

In many places, local sea level change will be larger or smaller than the global average. From year to year and place to place, changes in ocean circulation and wind can lead to local sea level change. In regions where large ice sheets, such as the Fennoscandian in Eurasia and the Laurentide and Cordilleran in North America, covered the land during the last ice age, the land is still slowly rising up now that the extra weight of the ice sheets is gone. This local recovery is compensating for global sea level rise in these regions and can even lead to local decrease in sea level. In regions just beyond where the former ice sheets reached and the Earth bulged upwards, the land is now falling, and as a result local sea level rise is faster than the global rate. In many regions within low-lying delta regions (such as New Orleans and the Ganges–Brahmaputra delta), the land is rapidly subsiding (sinking) because of human activities such as building dams or groundwater and fossil fuel extraction. Further, when an ice sheet melts it has less gravitational pull on the ocean water nearby. This reduction in gravitational attraction causes sea level to fall close to the (now less-massive) ice sheet while causing sea level to rise farther away. Melt from a polar ice sheet therefore raises sea level most in the opposite hemisphere or in low latitudes – amounting to tens of centimetres difference in

ACCEPTED VERSION SUBJECT TO FINAL EDITING

rise between regions by 2100.

[START FAQ9.2, FIGURE 1 HERE]

FAQ 9.2, Figure 1: Observed and projected global mean sea level rise and the contributions from its major constituents.

[END FAQ9.2, FIGURE 1 HERE]

ACCEPTED VERSION
SUBJECT TO FINAL EDITING

FAQ 9.3: Will the Gulf Stream shut down?

The Gulf Stream is part of two circulation patterns in the North Atlantic: the Atlantic Meridional Overturning Circulation (AMOC) and the subtropical gyre. Based on models and theory, scientific studies indicate that, while the AMOC is expected to slow in a warming climate, the Gulf Stream will not change much and would not shut down totally, even if the AMOC did. Most climate models project that the AMOC slows in the later 21st century under most emissions scenarios, with some models showing it slowing even sooner. The Gulf Stream affects the weather and sea level, so if it slows, North America will see higher sea levels and Europe's weather and rate of relative warming will be affected.

The Gulf Stream is the biggest current in the North Atlantic Ocean. It transports about 30 billion kilograms of water per second northward past points on the east coast of North America. It is a warm current, with temperatures 5°C to 15°C warmer than surrounding waters, so it carries warmer water (thermal energy) from its southern origins and releases warmth to the atmosphere and surrounding water.

The Gulf Stream is part of two major circulation patterns, the Atlantic Meridional Overturning Circulation (AMOC) and the North Atlantic Subtropical Gyre (FAQ 9.3, Figure 1). The rotation of the Earth causes the big currents in both circulations to stay on the western side of their basin, which in the Atlantic means the circulations combine to form the Gulf Stream. Other large currents contribute to gyres, such as the Kuroshio in the North Pacific and the East Australian Current in the South Pacific, but the Gulf Stream is special in its dual role. There is no comparable deep overturning circulation in the North Pacific to the AMOC, so the Kuroshio plays only one role as part of a gyre.

The gyres circulate surface waters and result primarily from winds driving the circulation. These winds are not expected to change much and so neither will the gyres, which means the gyre portion of the Gulf Stream and the Kuroshio will continue to transport thermal energy poleward from the equator much as they do now. The gyre contribution to the Gulf Stream is 2 to 10 times larger than the AMOC contribution.

The Gulf Stream's role in the AMOC is supplying surface source water that cools, becomes denser and sinks to form cold, deep waters that travel back equatorward, spilling over features on the ocean floor and mixing with other deep Atlantic waters to form a southward current at a depth of about 1500 metres beneath the Gulf Stream. This overturning flow is the AMOC, with the Gulf Stream in the upper kilometre flowing northward and the colder deep water flowing southward.

The AMOC is expected to slow over the coming centuries. One reason why is freshening of the ocean waters: by meltwater from Greenland, changing Arctic sea ice, and increased precipitation over warmer northern seas. An array of moorings across the Atlantic has been monitoring the AMOC since 2004, with recently expanded capabilities. The monitoring of the AMOC has not been long enough for a trend to emerge from variability and detect long-term changes that may be underway (see FAQ 1.2). Other indirect signs may indicate slowing overturning – for example, slower warming where the Gulf Stream's surface waters sink. Climate models show that this 'cold spot' of slower-than-average warming occurs as the AMOC weakens, and they project that this will continue. Paleoclimate evidence indicates AMOC changed significantly in the past, especially during transitions from colder climates to warmer ones, but indicate it has been stable for 8000 years.

What happens if the AMOC slows in a warming world? The atmosphere adjusts somewhat, compensating partly for the decreases in heat carried by AMOC by carrying more heat. But the 'cold spot' makes parts of Europe warm more slowly. Models indicate that weather patterns in Greenland and around the Atlantic will be affected, with reduced precipitation in the mid-latitudes, changing strong precipitation patterns in the tropics and Europe, and stronger storms in the North Atlantic storm track. The slowing of this current combined with the rotation of the Earth means that sea level along North America rises as the AMOC contribution to the Gulf Stream slows.

The North Atlantic is not the only site of sensitive meridional overturning. Around Antarctica, the world's densest seawater is formed by freezing into sea ice, leaving behind salty, cold water that sinks to the bottom

ACCEPTED VERSION SUBJECT TO FINAL EDITING

and spreads northward. Recent studies show that melting of the Antarctic Ice Sheet and changing winds over the Southern Ocean can affect this southern meridional overturning, affecting regional weather.

[START FAQ9.3, FIGURE 1 HERE]

FAQ 9.3, Figure 1: **Horizontal (gyre) and vertical (Atlantic Meridional Overturning Circulation - AMOC) circulations in the Atlantic today (left) and in a warmer world (right).** The Gulf Stream is a warm current composed of both circulations.

[END FAQ9.3, FIGURE 1 HERE]

ACCEPTED VERSION
SUBJECT TO FINAL EDITING

Acknowledgements

We acknowledge the contribution of invited expert reviewers and the IMBIE Team. Their valuable input and advice have significantly improved the chapter. We thank colleagues, institutions and, in particular, our families for their support. Thanks to the TSU and especially Sophie Berger for support.

ACCEPTED VERSION
SUBJECT TO FINAL EDITING

Reference

Aas, K.S., K. Gisnås, S. Westermann, and T.K. Berntsen, 2017: A Tiling Approach to Represent Subgrid Snow Variability in Coupled Land Surface-Atmosphere Models. *Journal of Hydrometeorology*, **18(1)**, 49–63, doi:10.1175/jhm-d-16-0026.1.

Abich, K. et al., 2019: In-Orbit Performance of the GRACE Follow-on Laser Ranging Interferometer. *Phys. Rev. Lett.*, **123(3)**, 31101, doi:10.1103/physrevlett.123.031101.

Abrahamsen, E.P. et al., 2019: Stabilization of dense Antarctic water supply to the Atlantic Ocean overturning circulation. *Nature Climate Change*, **9(10)**, 742–746, doi:10.1038/s41558-019-0561-2.

Abram, N. et al., 2019: Framing and Context of the Report. In: *IPCC Special Report on the Ocean and Cryosphere in a Changing Climate* [Pörtner, H.-O., D.C. Roberts, V. Masson-Delmotte, P. Zhai, M. Tignor, E. Poloczanska, K. Mintenbeck, A. Alegría, M. Nicolai, A. Okem, J. Petzold, B. Rama, and N.M. Weyer (eds.)]. In Press, pp. 73–129.

Aðalgeirsdóttir, G. et al., 2020: Glacier changes in Iceland from ~1890 to 2019. *Frontiers in Earth Science*, **8**, 520, doi:10.3389/feart.2020.523646.

Adler, R.F. et al., 2003: The Version-2 Global Precipitation Climatology Project (GPCP) Monthly Precipitation Analysis (1979–Present). *Journal of Hydrometeorology*, **4(6)**, 1147–1167, doi:10.1175/1525-7541(2003)004<1147:tvgpcp>2.0.co;2.

Adusumilli, S., H.A. Fricker, B. Medley, L. Padman, and M.R. Siegfried, 2020: Interannual variations in meltwater input to the Southern Ocean from Antarctic ice shelves. *Nature Geoscience*, **13**, 616–620, doi:10.1038/s41561-020-0616-z.

Aguirre, C., M. Rojas, R.D. Garreaud, and D.A. Rahn, 2019: Role of synoptic activity on projected changes in upwelling-favourable winds at the ocean's eastern boundaries. *npj Climate and Atmospheric Science*, **2(1)**, 44, doi:10.1038/s41612-019-0101-9.

Aguirre, F. et al., 2018: Snow Cover Change as a Climate Indicator in Brunswick Peninsula, Patagonia. *Frontiers in Earth Science*, **6**, doi:10.3389/feart.2018.00130.

Aksenov, Y. et al., 2016: Arctic pathways of Pacific Water: Arctic Ocean Model Intercomparison experiments. *Journal of Geophysical Research: Oceans*, **121(1)**, 27–59, doi:10.1002/2015jc011299.

Alberello, A. et al., 2020: Drift of Pancake Ice Floes in the Winter Antarctic Marginal Ice Zone During Polar Cyclones. *Journal of Geophysical Research: Oceans*, **125(3)**, e2019JC015418, doi:10.1029/2019jc015418.

Albrecht, T., R. Winkelmann, and A. Levermann, 2020: Glacial-cycle simulations of the Antarctic Ice Sheet with the Parallel Ice Sheet Model (PISM)-Part 1: Boundary conditions and climatic forcing. *Cryosphere*, **14(2)**, 599–632, doi:10.5194/tc-14-599-2020.

Alekseeva, T. et al., 2019: Comparison of Arctic Sea Ice concentrations from the NASA team, ASI, and VASIA2 algorithms with summer and winter ship data. *Remote Sensing*, **11(21)**, doi:10.3390/rs11212481.

Alexander, P.M. et al., 2019a: Simulated Greenland Surface Mass Balance in the GISS ModelE2 GCM: Role of the Ice Sheet Surface. *Journal of Geophysical Research: Earth Surface*, **124(3)**, 750–765, doi:10.1029/2018jf004772.

Alexander, P.M. et al., 2019b: Simulated Greenland Surface Mass Balance in the GISS ModelE2 GCM: Role of the Ice Sheet Surface. *Journal of Geophysical Research: Earth Surface*, **124(3)**, 750–765, doi:10.1029/2018jf004772.

Allen, S.E. and X. Durrieu de Madron, 2009: A review of the role of submarine canyons in deep-ocean exchange with the shelf. *Ocean Science*, **5(4)**, 607–620, doi:10.5194/os-5-607-2009.

Alley, K.E., T.A. Scambos, M.R. Siegfried, and H.A. Fricker, 2016: Impacts of warm water on Antarctic ice shelf stability through basal channel formation. *Nature Geoscience*, doi:10.1038/ngeo2675.

Alvarez-Solas, J., R. Banderas, A. Robinson, and M. Montoya, 2019: Ocean-driven millennial-scale variability of the Eurasian ice sheet during the last glacial period simulated with a hybrid ice-sheet-shelf model. *Climate of the Past*, **15(3)**, 957–979, doi:10.5194/cp-15-957-2019.

An, L., E. Rignot, R. Millan, K. Tinto, and J. Willis, 2019a: Bathymetry of Northwest Greenland Using "Ocean Melting Greenland" (OMG) High-Resolution Airborne Gravity and Other Data. *Remote Sensing*, **11(2)**, 131, doi:10.3390/rs11020131.

An, L. et al., 2019b: Bathymetry of Southeast Greenland From Oceans Melting Greenland (OMG) Data. *Geophysical Research Letters*, **46(20)**, 11197–11205, doi:10.1029/2019gl083953.

An, L. et al., 2021: Ocean melting of the Zachariae Isstrøm and Nioghalvfjerdsfjorden glaciers, northeast Greenland. *Proceedings of the National Academy of Sciences*, **118(2)**, doi:10.1073/pnas.2015483118.

ACCEPTED VERSION SUBJECT TO FINAL EDITING

Anderson, B. and A. Mackintosh, 2012: Controls on mass balance sensitivity of maritime glaciers in the Southern Alps, New Zealand: The role of debris cover. *Journal of Geophysical Research: Earth Surface*, **117(F1)**, doi:10.1029/2011jf002064.

Anderson, J.B., S.S. Shipp, A.L. Lowe, J.S. Wellner, and A.B. Mosola, 2002: The Antarctic Ice Sheet during the Last Glacial Maximum and its subsequent retreat history: A review. *Quaternary Science Reviews*, **21(1–3)**, 49–70, doi:10.1016/s0277-3791(01)00083-x.

Andreassen, L.M., H. Elvehøy, B. Kjøllmoen, and J.M.C. Belart, 2020: Glacier change in Norway since the 1960s – an overview of mass balance, area, length and surface elevation changes. *Journal of Glaciology*, **66(256)**, 313–328, doi:10.1017/jog.2020.10.

Andresen, C.S. et al., 2017: Exceptional 20th century glaciological regime of a major SE Greenland outlet glacier. *Scientific Reports*, **7(1)**, 13626, doi:10.1038/s41598-017-13246-x.

Anttila, K., T. Manninen, E. Jääskeläinen, A. Riihelä, and P. Lahtinen, 2018: The role of climate and land use in the changes in surface albedo prior to snow melt and the timing of melt season of seasonal snow in northern land areas of 40°N-80°N during 1982-2015. *Remote Sensing*, **10(10)**, doi:10.3390/rs10101619.

Aoki, S. et al., 2020: Freshening of Antarctic Bottom Water off Cape Darnley, East Antarctica. *Journal of Geophysical Research: Oceans*, **125**, e2020JC016374, doi:10.1029/2020jc016374.

Applegate, P.J. and K. Keller, 2015: How effective is albedo modification (solar radiation management geoengineering) in preventing sea-level rise from the Greenland Ice Sheet? *Environmental Research Letters*, **10(8)**, 84018, doi:10.1088/1748-9326/10/8/084018.

Argus, D.F. and W.R. Peltier, 2010: Constraining models of postglacial rebound using space geodesy: a detailed assessment of model ICE-5G (VM2) and its relatives. *Geophysical Journal International*, **181(2)**, 697–723.

Argus, D.F., W.R. Peltier, R. Drummond, and A.W. Moore, 2014: The Antarctica component of postglacial rebound model ICE-6G_C (VM5a) based on GPS positioning, exposure age dating of ice thicknesses, and relative sea level histories. *Geophysical Journal International*, **198(1)**, 537–563.

Armitage, T.W.K., R. Kwok, A.F. Thompson, and G. Cunningham, 2018: Dynamic Topography and Sea Level Anomalies of the Southern Ocean: Variability and Teleconnections. *Journal of Geophysical Research: Oceans*, **123(1)**, 613–630, doi:10.1002/2017jc013534.

Armitage, T.W.K. et al., 2017: Arctic Ocean surface geostrophic circulation 2003–2014. *The Cryosphere*, **11(4)**, 1767–1780, doi:10.5194/tc-11-1767-2017.

Armour, K.C., I. Eisenman, E. Blanchard-Wrigglesworth, K.E. McCusker, and C.M. Bitz, 2011: The reversibility of sea ice loss in a state-of-the-art climate model. *Geophysical Research Letters*, **38(16)**, doi:10.1029/2011gl048739.

Armour, K.C., J. Marshall, J.R. Scott, A. Donohoe, and E.R. Newsom, 2016: Southern Ocean warming delayed by circumpolar upwelling and equatorward transport. *Nature Geoscience*, **9**, 549, doi:10.1038/ngeo2731.

Arndt, S., M. Hoppmann, H. Schmithüsen, A.D. Fraser, and M. Nicolaus, 2020: Seasonal and interannual variability of landfast sea ice in Atka Bay, Weddell Sea, Antarctica. *The Cryosphere*, **14(9)**, 2775–2793, doi:10.5194/tc-14-2775-2020.

Arns, A., T. Wahl, I.D. Haigh, and J. Jensen, 2015: Determining return water levels at ungauged coastal sites: a case study for northern Germany. *Ocean Dynamics*, doi:10.1007/s10236-015-0814-1.

Arns, A. et al., 2017: Sea-level rise induced amplification of coastal protection design heights. *Scientific reports*, **7(1)**, 40171, doi:10.1038/srep40171.

Arns, A. et al., 2020: Non-linear interaction modulates global extreme sea levels, coastal flood exposure, and impacts. *Nature Communications*, **11(1)**, 1–9, doi:10.1038/s41467-020-15752-5.

Asay-Davis, X.S., N.C. Jourdain, and Y. Nakayama, 2017: Developments in Simulating and Parameterizing Interactions Between the Southern Ocean and the Antarctic Ice Sheet. *Current Climate Change Reports*, **3(4)**, 316–329, doi:10.1007/s40641-017-0071-0.

Asay-Davis, X.S. et al., 2016: Experimental design for three interrelated marine ice sheet and ocean model intercomparison projects: MISMIP v. 3 (MISMIP +), ISOMIP v. 2 (ISOMIP +) and MISOMIP v. 1 (MISOMIP1). *Geoscientific Model Development*, **9(7)**, 2471–2497, doi:10.5194/gmd-9-2471-2016.

Aschwanden, A., M.A. Fahnestock, and M. Truffer, 2016: Complex Greenland outlet glacier flow captured. *Nature Communications*, **7**, 10524, doi:10.1038/ncomms10524.

Aschwanden, A. et al., 2019: Contribution of the Greenland Ice Sheet to sea level over the next millennium. *Science Advances*, **5(6)**, doi:10.1126/sciadv.aav9396.

Atwood, A.R., E. Wu, D.M.W. Frierson, D.S. Battisti, and J.P. Sachs, 2016: Quantifying Climate Forcings and Feedbacks over the Last Millennium in the CMIP5?PMIP3 Models. *Journal of Climate*, **29(3)**, 1161–1178, doi:10.1175/jcli-d-15-0063.1.

ACCEPTED VERSION SUBJECT TO FINAL EDITING

Auger, M., R. Morrow, E. Kestenare, J.-B. Sallée, and R. Cowley, 2021: Southern Ocean in-situ temperature trends over 25 years emerge from interannual variability. *Nature Communications*, **12(514)**, doi:10.1038/s41467-020-20781-1.

Auriac, A. et al., 2016: Glacial isostatic adjustment associated with the Barents Sea ice sheet: A modelling inter-comparison. *Quaternary Science Reviews*, **147**, 122–135, doi:10.1016/j.quascirev.2016.02.011.

Axford, Y. et al., 2019: Holocene temperature history of northwest Greenland – With new ice cap constraints and chironomid assemblages from Deltasø. *Quaternary Science Reviews*, **215**, 160–172, doi:10.1016/j.quascirev.2019.05.011.

Bachem, P.E., B. Risebrobakken, S. De Schepper, and E.L. Mcclymont, 2017: Highly variable Pliocene sea surface conditions in the Norwegian Sea. *Climate of the Past*, **13(9)**, 1153–1168, doi:10.5194/cp-13-1153-2017.

Baggenstos, D. et al., 2019: Earth's radiative imbalance from the Last Glacial Maximum to the present. *Proceedings of the National Academy of Sciences*, **116(30)**, 14881–14886, doi:10.1073/pnas.1905447116.

Bakker, A.M.R., T.E. Wong, K.L. Ruckert, and K. Keller, 2017: Sea-level projections representing the deeply uncertain contribution of the West Antarctic ice sheet. *Scientific Reports*, **7(1)**, 3880, doi:10.1038/s41598-017-04134-5.

Bakker, P. et al., 2016: Fate of the Atlantic Meridional Overturning Circulation: Strong decline under continued warming and Greenland melting. *Geophysical Research Letters*, **43(23)**, 12,252–12,260, doi:10.1002/2016gl070457.

Bakun, A., 1990: Global climate change and intensification of coastal ocean upwelling. *Science*, **247(4939)**, 198–201.

Bakun, A., D.B. Field, A. Redondo-Rodriguez, and S.J. Weeks, 2010: Greenhouse gas, upwelling-favorable winds, and the future of coastal ocean upwelling ecosystems. *Global Change Biology*, **16(4)**, 1213–1228, doi:10.1111/j.1365-2486.2009.02094.x.

Bamber, J.L. and W.P. Aspinall, 2013: An expert judgement assessment of future sea level rise from the ice sheets. *Nature Climate Change*, **3**, 424–427, doi:10.1038/nclimate1778.

Bamber, J.L. and G.J. Dawson, 2020: Complex evolving patterns of mass loss from Antarctica's largest glacier. *Nature Geoscience*, **13(2)**, 127–131, doi:10.1038/s41561-019-0527-z.

Bamber, J.L., R.E.M. Riva, B.L.A. Vermeersen, and A.M. Le Brocq, 2009: Reassessment of the Potential Sea-Level Rise from a Collapse of the West Antarctic Ice Sheet. *Science*, **324**, 901–903.

Bamber, J.L., R.M. Westaway, B. Marzeion, and B. Wouters, 2018a: A new synthesis of annual land ice mass trends 1992 to 2016. , doi:10.1594/pangaea.890030.

Bamber, J.L., R.M. Westaway, B. Marzeion, and B. Wouters, 2018b: The land ice contribution to sea level during the satellite era. *Environmental Research Letters*, **13**, 063008, doi:10.1088/1748-9326/aac2f0.

Bamber, J.L., M. Oppenheimer, R.E. Kopp, W.P. Aspinall, and R.M. Cooke, 2019: Ice sheet contributions to future sea-level rise from structured expert judgment. *Proceedings of the National Academy of Sciences*, **116(23)**, 11195–11200, doi:10.1073/pnas.1817205116.

Banas, N.S.S., P. MacCready, and B.M.M. Hickey, 2009: The Columbia River plume as cross-shelf exporter and along-coast barrier. *Continental Shelf Research*, **29(1)**, 292–301, doi:10.1016/j.csr.2008.03.011.

Baranes, H.E. et al., 2020: Tidally driven interannual variation in extreme sea level frequencies in the Gulf of Maine. *Journal of Geophysical Research: Oceans*, doi:10.1029/2020jc016291.

Barletta, V.R. et al., 2018: Observed rapid bedrock uplift in Amundsen Sea Embayment promotes ice-sheet stability. *Science*, **360(6395)**, 1335–1339.

Bart, P.J., M. DeCesare, B.E. Rosenheim, W. Majewski, and A. McGlannan, 2018: A centuries-long delay between a paleo-ice-shelf collapse and grounding-line retreat in the Whales Deep Basin, eastern Ross Sea, Antarctica. *Scientific Reports*, doi:10.1038/s41598-018-29911-8.

Barthel, A. et al., 2020a: CMIP5 model selection for ISMIP6 ice sheet model forcing: Greenland and Antarctica. *The Cryosphere*, **14**, 855–879, doi:10.5194/tc-14-855-2020.

Barthel, A. et al., 2020b: CMIP5 model selection for ISMIP6 ice sheet model forcing: Greenland and Antarctica. *The Cryosphere*, **14**, 855–879, doi:10.5194/tc-14-855-2020.

Bassis, J.N. and L. Ultee, 2019: A Thin Film Viscoplastic Theory for Calving Glaciers: Toward a Bound on the Calving Rate of Glaciers. *Journal of Geophysical Research: Earth Surface*, **124(8)**, 2036–2055, doi:10.1029/2019jf005160.

Batbaatar, J., A. Gillespie, D. Fink, A. Matmon, and T. Fujioka, 2018: Asynchronous glaciations in arid continental climate. *Quaternary Science Reviews*, **182**, 1–19, doi:10.1016/j.quascirev.2017.12.001.

Batchelor, C.J. et al., 2019: Distinct Permafrost Conditions Across the Last Two Glacial Periods in Midlatitude North America. *Geophysical Research Letters*, **46**, 13318–13326, doi:10.1029/2019gl083951.

Bates, S.C. et al., 2012: Mean biases, variability, and trends in air-sea fluxes and sea surface temperature in the CCSM4. *Journal of Climate*, **25(22)**, doi:10.1175/jcli-d-11-00442.1.

ACCEPTED VERSION SUBJECT TO FINAL EDITING

Bathiany, S., J. Hidding, and M. Scheffer, 2020: Edge Detection Reveals Abrupt and Extreme Climate Events. *Journal of Climate*, **33(15)**, 6399–6421, doi:10.1175/jcli-d-19-0449.1.

Bathiany, S., D. Notz, T. Mauritsen, G. Raedel, and V. Brovkin, 2016: On the potential for abrupt Arctic winter sea-ice loss. *Journal of Climate*, doi:10.1175/jcli-d-15-0466.1.

Baum, S.K. and T.J. Crowley, 2003: The snow/ice instability as a mechanism for rapid climate change: A Neoproterozoic Snowball Earth model example. *Geophysical Research Letters*, **30(20)**, 2030, doi:10.1029/2003gl017333.

Bauska, T.K. et al., 2016: Carbon isotopes characterize rapid changes in atmospheric carbon dioxide during the last deglaciation. *Proceedings of the National Academy of Sciences of the United States of America*, **113(13)**, 3465–3470, doi:10.1073/pnas.1513868113.

Beadling, R.L., J.L. Russell, R.J. Stouffer, P.J. Goodman, and M. Mazloff, 2019: Assessing the quality of Southern Ocean circulation in CMIP5 AOGCM and Earth System Model simulations. *Journal of Climate*, **32**, 5915–5940, doi:10.1175/jcli-d-19-0263.1.

Beadling, R.L. et al., 2020: Representation of Southern Ocean properties across Coupled Model Intercomparison Project generations: CMIP3 to CMIP6. *Journal of Climate*, **33**, 6555–6581, doi:10.1175/jcli-d-19-0970.1.

Beal, L.M. and S. Elipot, 2016: Broadening not strengthening of the Agulhas Current since the early 1990s. *Nature*, **540(7634)**, 570–573, doi:10.1038/nature19853.

Beckmann, J. et al., 2019: Modeling the response of Greenland outlet glaciers to global warming using a coupled flowline-plume model. *The Cryosphere*, **13**, 2281–2301, doi:10.5194/tc-2018-89.

Beedle, M.J., B. Menounos, B.H. Luckman, and R. Wheate, 2009: Annual push moraines as climate proxy. *Geophysical Research Letters*, **36(20)**, L20501, doi:10.1029/2009gl039533.

Belcher, S.E. et al., 2012: A global perspective on Langmuir turbulence in the ocean surface boundary layer. *Geophysical Research Letters*, **39(18)**, doi:10.1029/2012gl052932.

Bell, R.E., A.F. Banwell, L.D. Trusel, and J. Kingslake, 2018: Antarctic surface hydrology and impacts on ice-sheet mass balance. *Nature Climate Change*, **8(12)**, 1044–1052, doi:10.1038/s41558-018-0326-3.

Bellomo, K., L.N. Murphy, M.A. Cane, A.C. Clement, and L.M. Polvani, 2018: Historical forcings as main drivers of the Atlantic multidecadal variability in the CESM large ensemble. *Climate Dynamics*, **50(9–10)**, 3687–3698, doi:10.1007/s00382-017-3834-3.

Belmadani, A., V. Echevin, F. Codron, K. Takahashi, and C. Junquas, 2014: What dynamics drive future wind scenarios for coastal upwelling off Peru and Chile? *Climate dynamics*, **43(7–8)**, 1893–1914.

Belmecheri, S., F. Babst, E.R. Wahl, D.W. Stahle, and V. Trouet, 2016: Multi-century evaluation of Sierra Nevada snowpack. *Nature Climate Change*, **6**, 2–3, doi:10.1038/nclimate2809.

Belt, S.T., 2018: Source-specific biomarkers as proxies for Arctic and Antarctic sea ice. *Organic Geochemistry*, **125**, 277–298, doi:10.1016/j.orggeochem.2018.10.002.

Belt, S.T., 2019: What do IP25 and related biomarkers really reveal about sea ice change? *Quaternary Science Reviews*, **204**, 216–219, doi:10.1016/j.quascirev.2018.11.025.

Belt, S.T. et al., 2007: A novel chemical fossil of palaeo sea ice: IP25. *Organic Geochemistry*, **38(1)**, 16–27, doi:10.1016/j.orggeochem.2006.09.013.

Belt, S.T. et al., 2015: Identification of paleo Arctic winter sea ice limits and the marginal ice zone: Optimised biomarker-based reconstructions of late Quaternary Arctic sea ice. *Earth and Planetary Science Letters*, **431**, 127–139, doi:10.1016/j.epsl.2015.09.020.

Bendtsen, J. et al., 2017: Sea ice breakup and marine melt of a retreating tidewater outlet glacier in northeast Greenland (81°N). *Scientific Reports*, **7(1)**, 1–11, doi:10.1038/s41598-017-05089-3.

Benn, D.I., T. Cowton, J. Todd, and A. Luckman, 2017: Glacier Calving in Greenland. *Current Climate Change Reports*, **3(4)**, 282–290, doi:10.1007/s40641-017-0070-1.

Bennartz, R. et al., 2013: July 2012 Greenland melt extent enhanced by low-level liquid clouds. *Nature*, **496**, 83–86, doi:10.1038/nature12002.

Bennetts, L.G., S. O'Farrell, and P. Uotila, 2017: Brief communication: Impacts of ocean-wave-induced breakup of Antarctic sea ice via thermodynamics in a stand-alone version of the CICE sea-ice model. *The Cryosphere*, **11(3)**, 1035–1040, doi:10.5194/tc-11-1035-2017.

Bentamy, A. et al., 2017: Review and assessment of latent and sensible heat flux accuracy over the global oceans. *Remote Sensing of Environment*, **201**, 196–218, doi:10.1016/j.rse.2017.08.016.

Bentley, M.J. et al., 2014: A community-based geological reconstruction of Antarctic Ice Sheet deglaciation since the Last Glacial Maximum. *Quaternary Science Reviews*, **100**, 1–9, doi:10.1016/j.quascirev.2014.06.025.

ACCEPTED VERSION SUBJECT TO FINAL EDITING

Benz, V., O. Esper, R. Gersonde, F. Lamy, and R. Tiedemann, 2016: Last Glacial Maximum sea surface temperature and sea-ice extent in the Pacific sector of the Southern Ocean. *Quaternary Science Reviews*, **146**, 216–237, doi:10.1016/j.quascirev.2016.06.006.

Berben, S.M.P., K. Husum, A. Navarro-Rodriguez, S.T. Belt, and S. Aagaard-Sørensen, 2017: Semi-quantitative reconstruction of early to late Holocene spring and summer sea ice conditions in the northern Barents Sea. *Journal of Quaternary Science*, **32(5)**, 587–603, doi:10.1002/jqs.2953.

Bereiter, B., S. Shackleton, D. Baggenstos, K. Kawamura, and J. Severinghaus, 2018: Mean global ocean temperatures during the last glacial transition. *Nature*, **553(7686)**, 39–44, doi:10.1038/nature25152.

Berends, C.J., B. de Boer, A.M. Dolan, D.J. Hill, and R.S.W. van de Wal, 2019: Modelling ice sheet evolution and atmospheric CO2 during the Late Pliocene. *Climate of the Past*, **15**, 1603–1619, doi:10.5194/cp-2019-34.

Berloff, P. et al., 2007: The Turbulent Oscillator: A Mechanism of Low-Frequency Variability of the Wind-Driven Ocean Gyres. *Journal of Physical Oceanography*, **37(9)**, 2363–2386, doi:10.1175/jpo3118.1.

Bertram, R.A. et al., 2018: Pliocene deglacial event timelines and the biogeochemical response offshore Wilkes Subglacial Basin, East Antarctica. *Earth and Planetary Science Letters*, **494**, 109–116, doi:10.1016/j.epsl.2018.04.054.

Bettencourt, J.H. et al., 2015: Boundaries of the Peruvian oxygen minimum zone shaped by coherent mesoscale dynamics. *Nature Geoscience*, **8(12)**, 937.

Bevacqua, E. et al., 2020: More meteorological events that drive compound coastal flooding are projected under climate change. *Communications Earth & Environment*, **1(1)**, 1–11, doi:10.1038/s43247-020-00044-z.

Bevan, S.L., A.J. Luckman, D.I. Benn, T. Cowton, and J. Todd, 2019: Impact of warming shelf waters on ice mélange and terminus retreat at a large SE Greenland glacier. *Cryosphere*, **13(9)**, 2303–2315, doi:10.5194/tc-13-2303-2019.

Bevis, M. et al., 2019: Accelerating changes in ice mass within Greenland, and the ice sheet's sensitivity to atmospheric forcing. *Proceedings of the National Academy of Sciences of the United States of America*, **116(6)**, 1934–1939, doi:10.1073/pnas.1806562116.

Bianchi, C. and R. Gersonde, 2002: The Southern Ocean surface between Marine Isotope Stages 6 and 5d: Shape and timing of climate changes. *Palaeogeography, Palaeoclimatology, Palaeoecology*, **187(1–2)**, 151–177, doi:10.1016/s0031-0182(02)00516-3.

Biastoch, A. et al., 2015: Atlantic multi-decadal oscillation covaries with Agulhas leakage. *Nature Communications*, **6(1)**, 10082, doi:10.1038/ncomms10082.

Bilbao, R.A.F., J.M. Gregory, and N. Bouttes, 2015: Analysis of the regional pattern of sea level change due to ocean dynamics and density change for 1993-2099 in observations and CMIP5 AOGCM's. *Climate Dynamics*, doi:10.1007/s00382-015-2499-z.

Bilbao, R.A.F., J.M. Gregory, N. Bouttes, M.D. Palmer, and P. Stott, 2019: Attribution of ocean temperature change to anthropogenic and natural forcings using the temporal, vertical and geographical structure. *Climate Dynamics*, **53(9)**, 5389–5413, doi:10.1007/s00382-019-04910-1.

Bindoff, N.L. and T.J. McDougall, 2000: Decadal Changes along an Indian Ocean Section at 32°S and Their Interpretation. *Journal of Physical Oceanography*, **30(6)**, 1207–1222, doi:10.1175/1520-0485(2000)030<1207:dcaaio>2.0.co;2.

Bindoff, N.L. et al., 2013: Detection and Attribution of Climate Change: from Global to Regional. In: *Climate Change 2013: The Physical Science Basis. Contribution of Working Group I to the Fifth Assessment Report of the IPCC* [Stocker, T.F., D. Qin, G.-K. Plattner, M. Tignor, S.K. Allen, J. Boschung, A. Nauels, Y. Xia, V. Bex, and P.M. Midgley (eds.)]. Cambridge University Press, pp. 867–952, doi:10.1017/cbo9781107415324.022.

Bindoff, N.L. et al., 2019: Changing Ocean, Marine Ecosystems, and Dependent Communities. In: *IPCC Special Report on the Ocean and Cryosphere in a Changing Climate* [Pörtner, H.-O., D.C. Roberts, V. Masson-Delmotte, P. Zhai, M. Tignor, E. Poloczanska, K. Mintenbeck, M. Nicolai, A. Okem, J. Petzold, B. Rama, and N. Weyer (eds.)]. In Press, pp. 447–588.

Bindschadler, R.A. et al., 2013: Ice-sheet model sensitivities to environmental forcing and their use in projecting future sea level (the SeaRISE project). *Journal of Glaciology*, **59(214)**, 195–224, doi:10.3189/2013jog12j125.

Bishop, S.P. et al., 2017: Scale Dependence of Midlatitude Air–Sea Interaction. *Journal of Climate*, **30(20)**, 8207–8221, doi:10.1175/jcli-d-17-0159.1.

Biskaborn, B.K. et al., 2019: Permafrost is warming at a global scale. *Nature Communications*, **10(1)**, 264, doi:10.1038/s41467-018-08240-4.

Bittermann, K., S. Rahmstorf, R.E. Kopp, and A.C. Kemp, 2017: Global mean sea-level rise in a world agreed upon in Paris. *Environmental Research Letters*, **12(12)**, doi:10.1088/1748-9326/aa9def.

ACCEPTED VERSION SUBJECT TO FINAL EDITING

Blackburn, T. et al., 2020: Ice retreat in Wilkes Basin of East Antarctica during a warm interglacial. *Nature*, **583(7817)**, 554–559, doi:10.1038/s41586-020-2484-5.

Blake-Mizen, K. et al., 2019: Southern Greenland glaciation and Western Boundary Undercurrent evolution recorded on Eirik Drift during the late Pliocene intensification of Northern Hemisphere glaciation. *Quaternary Science Reviews*, **209**, 40–51, doi:10.1016/j.quascirev.2019.01.015.

Bliss, A.C., J.A. Miller, and W.N. Meier, 2017: Comparison of passive microwave-derived early melt onset records on Arctic sea ice. *Remote Sensing*, doi:10.3390/rs9030199.

Bliss, A.C., M. Steele, G. Peng, W.N. Meier, and S. Dickinson, 2019: Regional variability of Arctic sea ice seasonal change climate indicators from a passive microwave climate data record. *Environmental Research Letters*, **14(4)**, doi:10.1088/1748-9326/aafb84.

Bock, L. et al., 2020: Quantifying progress across different CMIP phases with the ESMValTool. *J. Geophys. Res.*, **submitted**.

Bohleber, P., M. Schwikowski, M. Stocker-Waldhuber, L. Fang, and A. Fischer, 2020: New glacier evidence for ice-free summits during the life of the Tyrolean Iceman. *Scientific Reports*, **10(1)**, 20513, doi:10.1038/s41598-020-77518-9.

Bond, N.A., M.F. Cronin, H. Freeland, and N. Mantua, 2015: Causes and impacts of the 2014 warm anomaly in the NE Pacific. *Geophysical Research Letters*, **42**, 3414–3420, doi:10.1002/2015gl063306.

Bondzio, J.H. et al., 2016: Modelling calving front dynamics using a level-set method: application to Jakobshavn Isbræ, West Greenland. *The Cryosphere*, **10(2)**, 497–510, doi:10.5194/tc-10-497-2016.

Bondzio, J.H. et al., 2017: The mechanisms behind Jakobshavn Isbræ's acceleration and mass loss: A 3-D thermomechanical model study. *Geophysical Research Letters*, **44(12)**, 6252–6260, doi:10.1002/2017gl073309.

Bonekamp, P.N.J., R.J. de Kok, E. Collier, and W.W. Immerzeel, 2019: Contrasting Meteorological Drivers of the Glacier Mass Balance Between the Karakoram and Central Himalaya. *Frontiers in Earth Science*, **7**, 107, doi:10.3389/feart.2019.00107.

Boone, A. et al., 2017: The interactions between soil-biosphere-atmosphere land surface model with a multi-energy balance (ISBA-MEB) option in SURFEXv8-Part 1: Model description. *Geoscientific Model Development*, doi:10.5194/gmd-10-843-2017.

Borge, A.F., S. Westermann, I. Solheim, and B. Etzelmüller, 2017: Strong degradation of palsas and peat plateaus in northern Norway during the last 60 years. *Cryosphere*, **11(1)**, 1–16, doi:10.5194/tc-11-1-2017.

Born, A. and K.H. Nisancioglu, 2012: Melting of Northern Greenland during the last interglaciation. *The Cryosphere*, **6**, 1239–1250, doi:10.5194/tc-6-1239-2012.

Born, A., T.F. Stocker, and A.B. Sandø, 2016: Transport of salt and freshwater in the Atlantic Subpolar Gyre. *Ocean Dynamics*, **66(9)**, 1051–1064, doi:10.1007/s10236-016-0970-y.

Born, A., T.F. Stocker, C.C. Raible, and A. Levermann, 2013: Is the Atlantic subpolar gyre bistable in comprehensive coupled climate models? *Climate Dynamics*, **40(11–12)**, 2993–3007, doi:10.1007/s00382-012-1525-7.

Boucher, O. et al., 2020: Presentation and Evaluation of the IPSL-CM6A-LR Climate Model. *Journal of Advances in Modeling Earth Systems*, **12(7)**, e2019MS002010, doi:10.1029/2019ms002010.

Bouttes, N. and J.M. Gregory, 2014: Attribution of the spatial pattern of CO2-forced sea level change to ocean surface flux changes. *Environmental Research Letters*, **9(3)**, 034004, doi:10.1088/1748-9326/9/3/034004.

Bouttes, N., J.M. Gregory, and J.A. Lowe, 2013: The reversibility of sea level rise. *Journal of Climate*, **26(8)**, 2502–2513, doi:10.1175/jcli-d-12-00285.1.

Bouttes, N., J.M. Gregory, T. Kuhlbrodt, and R.S. Smith, 2014: The drivers of projected North Atlantic sea level change. *Climate Dynamics*, **43(5–6)**, 1531–1544.

Box, J.E. and W. Colgan, 2013: Greenland Ice Sheet Mass Balance Reconstruction. Part III: Marine Ice Loss and Total Mass Balance (1840–2010). *Journal of Climate*, **26(18)**, 6990–7002, doi:10.1175/jcli-d-12-00546.1.

Bracegirdle, T. et al., 2020: Twenty-first century changes in Antarctic and Southern Ocean surface climate in CMIP6. *Atmospheric Science Letters*, **21(9)**, asl984, doi:10.1002/asl.984.

Bradley, S.L., T.J. Reerink, R.S.W. Van De Wal, and M.M. Helsen, 2018: Simulation of the Greenland Ice Sheet over two glacial-interglacial cycles: investigating a sub-ice-shelf melt parameterization and relative sea level forcing in an ice-sheet-ice-shelf model. *Climate of the Past*, **14(5)**, 619–635, doi:10.5194/cp-14-619-2018.

Brady, R.X., M.A. Alexander, N.S. Lovenduski, and R.R. Rykaczewski, 2017: Emergent anthropogenic trends in California Current upwelling. *Geophysical Research Letters*, **44(10)**, 5044–5052, doi:10.1002/2017gl072945.

Brancato, V. et al., 2020: Grounding Line Retreat of Denman Glacier, East Antarctica, Measured With COSMO-SkyMed Radar Interferometry Data. *Geophysical Research Letters*, **47(7)**, e2019GL086291, doi:10.1029/2019gl086291.

ACCEPTED VERSION SUBJECT TO FINAL EDITING

Brandon, C.M., J.D. Woodruff, D. Lane, and J.P. Donnelly, 2013: Tropical cyclone wind speed constraints from resultant storm surge deposition: A 2500 year reconstruction of hurricane activity from St. Marks, FL. *Geochemistry, Geophysics, Geosystems*, **14(8)**, 2993–3008, doi:10.1002/ggge.20217.

Brandon, C.M., J.D. Woodruff, J.P. Donnelly, and R.M. Sullivan, 2015: How Unique was Hurricane Sandy? Sedimentary Reconstructions of Extreme Flooding from New York Harbor. *Scientific Reports*, **4(1)**, 7366, doi:10.1038/srep07366.

Braun, M.H. et al., 2019: Constraining glacier elevation and mass changes in South America. *Nature Climate Change*, **9(2)**, 130–136, doi:10.1038/s41558-018-0375-7.

Brendryen, J., H. Haflidason, Y. Yokoyama, K.A. Haaga, and B. Hannisdal, 2020: Eurasian Ice Sheet collapse was a major source of Meltwater Pulse 1A 14,600 years ago. *Nature Geoscience*, **13(5)**, 363–368, doi:10.1038/s41561-020-0567-4.

Brennan, M.K., G.J. Hakim, and E. Blanchard-Wrigglesworth, 2020: Arctic Sea-Ice Variability During the Instrumental Era. *Geophysical Research Letters*, **47(7)**, e2019GL086843, doi:10.1029/2019gl086843.

Briggs, R.D., D. Pollard, and L. Tarasov, 2014: A data-constrained large ensemble analysis of Antarctic evolution since the Eemian. *Quaternary Science Reviews*, **103**, 91–115, doi:10.1016/j.quascirev.2014.09.003.

Briner, J.P. et al., 2016: Holocene climate change in Arctic Canada and Greenland. *Quaternary Science Reviews*, **147**, 340–364, doi:10.1016/j.quascirev.2016.02.010.

Brink, K.H., 2016: Cross-shelf exchange. *Annual review of marine science*, **8**, 59–78, doi:10.1146/annurev-marine-010814-015717.

Brodeau, L., B. Barnier, S.K. Gulev, and C. Woods, 2017: Climatologically Significant Effects of Some Approximations in the Bulk Parameterizations of Turbulent Air–Sea Fluxes. *Journal of Physical Oceanography*, **47(1)**, 5–28, doi:10.1175/jpo-d-16-0169.1.

Brönnimann, S. et al., 2019: Last phase of the Little Ice Age forced by volcanic eruptions. *Nature Geoscience*, **12(8)**, 650–656, doi:10.1038/s41561-019-0402-y.

Bronselaer, B. and L. Zanna, 2020: Heat and carbon coupling reveals ocean warming due to circulation changes. *Nature*, **584**, 227–233, doi:10.1038/s41586-020-2573-5.

Bronselaer, B. et al., 2018: Change in future climate due to Antarctic meltwater. *Nature*, **564(7734)**, 53–58, doi:10.1038/s41586-018-0712-z.

Bronselaer, B. et al., 2020: Importance of wind and meltwater for observed chemical and physical changes in the Southern Ocean. *Nature Geoscience*, **13**, 35–42.

Brown, R. et al., 2017: Arctic terrestrial snow cover. *Snow, Water, Ice and Permafrost in the Arctic (SWIPA) 2017*, 25–64.

Brown, R.D. and D.A. Robinson, 2011: Northern Hemisphere spring snow cover variability and change over 1922-2010 including an assessment of uncertainty. *The Cryosphere*, **5(1)**, 219–229, doi:10.5194/tc-5-219-2011.

Brown, R.D. and C. Derksen, 2013: Is Eurasian October snow cover extent increasing? *Environmental Research Letters*, **8(2)**, 024006, doi:10.1088/1748-9326/8/2/024006.

Brun, F. et al., 2016: Quantifying volume loss from ice cliffs on debris-covered glaciers using high-resolution terrestrial and aerial photogrammetry. *Journal of Glaciology*, **62(234)**, 684–695, doi:10.1017/jog.2016.54.

Bryden, H.L. et al., 2020: Reduction in ocean heat transport at 26°N since 2008 cools the eastern subpolar gyre of the North Atlantic Ocean. *Journal of Climate*, **33(5)**, 1677–1689, doi:10.1175/jcli-d-19-0323.1.

Buchanan, M.K., R.E. Kopp, M. Oppenheimer, and C. Tebaldi, 2016: Allowances for evolving coastal flood risk under uncertain local sea-level rise. *Climatic Change*, **137(3–4)**, doi:10.1007/s10584-016-1664-7.

Buckingham, C.E. et al., 2019: The contribution of surface and submesoscale processes to turbulence in the open ocean surface boundary layer. *Journal of Advances in Modeling Earth Systems*, **n/a(n/a)**, doi:10.1029/2019ms001801.

Buckley, M.W. and J. Marshall, 2016: Observations, inferences, and mechanisms of the Atlantic Meridional Overturning Circulation: A review. *Reviews of Geophysics*, **54(1)**, 5–63, doi:10.1002/2015rg000493.

Bulthuis, K., M. Arnst, S. Sun, and F. Pattyn, 2019: Uncertainty quantification of the multi-centennial response of the antarctic ice sheet to climate change. *Cryosphere*, **13**, 1349–1380, doi:10.5194/tc-13-1349-2019.

Bulygina, O.N., P.Y. Groisman, V.N. Razuvaev, and N.N. Korshunova, 2011: Changes in snow cover characteristics over Northern Eurasia since 1966. *Environmental Research Letters*, **6(4)**, 0452204, doi:10.1088/1748-9326/6/4/045204.

Bunce, C., J.R. Carr, P.W. Nienow, N. Ross, and R. Killick, 2018: Ice front change of marine-terminating outlet glaciers in northwest and southeast Greenland during the 21st century. *Journal of Glaciology*, **64(246)**, 523–535, doi:10.1017/jog.2018.44.

ACCEPTED VERSION SUBJECT TO FINAL EDITING

Bunce, C., P. Nienow, A. Sole, T. Cowton, and B. Davison, 2020: Influence of glacier runoff and near-terminus subglacial hydrology on frontal ablation at a large Greenlandic tidewater glacier. *Journal of Glaciology*, 1–10, doi: 10.1017/jog.2020.109.

Bunzel, F., D. Notz, and L.T. Pedersen, 2018: Retrievals of Arctic Sea-Ice Volume and Its Trend Significantly Affected by Interannual Snow Variability. *Geophysical Research Letters*, **45(21)**, 11,751–11,759, doi:10.1029/2018gl078867.

Burgard, C. and D. Notz, 2017: Drivers of Arctic Ocean warming in CMIP5 models. *Geophysical Research Letters*, **44(9)**, 4263–4271, doi:10.1002/2016gl072342.

Burgess, D.O. and M.J. Sharp, 2004: Recent Changes in Areal Extent of the Devon Ice Cap, Nunavut, Canada. *Arctic, Antarctic, and Alpine Research*, **36(2)**, 261–271, doi:10.1657/1523-0430(2004)036[0261:rciaeo]2.0.co;2.

Burke, E., Y. Zhang, and G. Krinner, 2020: Evaluating permafrost physics in the Coupled Model Intercomparison Project 6 (CMIP6) models and their sensitivity to climate change. *The Cryosphere*, **14**, 3155–3174, doi:10.5194/tc-14-3155-2020.

Burton, J.C., J.M. Amundson, R. Cassotto, C.-C. Kuo, and M. Dennin, 2018: Quantifying flow and stress in ice mélange, the world's largest granular material.. *Proceedings of the National Academy of Sciences of the United States of America*, **115(20)**, 5105–5110, doi:10.1073/pnas.1715136115.

Cabedo-Sanz, P., S.T. Belt, A.E. Jennings, J.T. Andrews, and Geirsdóttir, 2016: Variability in drift ice export from the Arctic Ocean to the North Icelandic Shelf over the last 8000 years: A multi-proxy evaluation. *Quaternary Science Reviews*, **146**, 99–115, doi:10.1016/j.quascirev.2016.06.012.

Cáceres, D. et al., 2020: Assessing global water mass transfers from continents to oceans over the period 1948–2016. *Hydrology and Earth System Sciences*, **24(10)**, 4831–4851, doi:10.5194/hess-24-4831-2020.

Caesar, L., G.D. McCarthy, D.J.R. Thornalley, N. Cahill, and S. Rahmstorf, 2021: Current Atlantic Meridional Overturning Circulation weakest in last millennium. *Nature Geoscience*, doi:10.1038/s41561-021-00699-z.

Cai, Q. et al., 2021: Accelerated decline of summer Arctic sea ice during 1850–2017 and the amplified Arctic warming during the recent decades. *Environmental Research Letters*, **16(3)**, 034015, doi:10.1088/1748-9326/abdb5f.

Cai, W. et al., 2019: Pantropical climate interactions. *Science*, **363(6430)**, doi:10.1126/science.aav4236.

Caldwell, P.M. et al., 2019: The DOE E3SM Coupled Model Version 1: Description and Results at High Resolution. *Journal of Advances in Modeling Earth Systems*, **11(12)**, 4095–4146, doi:10.1029/2019ms001870.

Calonne, N., C. Geindreau, and F. Flin, 2015: Macroscopic modeling of heat and water vapor transfer with phase change in dry snow based on an upscaling method: Influence of air convection. *Journal of Geophysical Research F: Earth Surface*, **120**, 2476–2497, doi:10.1002/2015jf003605.

Calonne, N., M. Montagnat, M. Matzl, and M. Schneebeli, 2017: The layered evolution of fabric and microstructure of snow at Point Barnola, Central East Antarctica. *Earth and Planetary Science Letters*, **460**, 293–301, doi:10.1016/j.epsl.2016.11.041.

Calonne, N., F. Flin, C. Geindreau, B. Lesaffre, and S. Rolland Du Roscoat, 2014: Study of a temperature gradient metamorphism of snow from 3-D images: Time evolution of microstructures, physical properties and their associated anisotropy. *The Cryosphere*, **8**, 2255–2274, doi:10.5194/tc-8-2255-2014.

Calov, R., A. Robinson, M. Perrette, and A. Ganopolski, 2015: Simulating the Greenland ice sheet under present-dat and palaeo constraints including a new discharge parameterization.. *The Cryosphere*, **9(1)**, 179–196.

Calov, R., A. Ganopolski, M. Claussen, V. Petoukhov, and R. Greve, 2005: Transient simulation of the last glacial inception. Part I: Glacial inception as a bifurcation in the climate system. *Climate Dynamics*, **24(6)**, 545–561, doi:10.1007/s00382-005-0007-6.

Calov, R. et al., 2018: Simulation of the future sea level contribution of Greenland with a new glacial system model. *The Cryosphere*, **12(10)**, 3097–3121, doi:10.5194/tc-12-3097-2018.

Camill, P., 2005: Permafrost thaw accelerates in boreal peatlands during late-20th century climate warming. *Climatic Change*, **68**, 135–152, doi:10.1007/s10584-005-4785-y.

Campbell, E.C. et al., 2019: Antarctic offshore polynyas linked to Southern Hemisphere climate anomalies. *Nature*, **570(7761)**, 319–325, doi:10.1038/s41586-019-1294-0.

Capet, X., E.J. Campos, and A.M. Paiva, 2008: Submesoscale activity over the Argentinian shelf. *Geophysical Research Letters*, **35(15)**, L15605, doi:10.1029/2008gl034736.

Capron, E., A. Govin, R. Feng, B.L. Otto-Bliesner, and E.W. Wolff, 2017: Critical evaluation of climate syntheses to benchmark CMIP6/PMIP4 127 ka Last Interglacial simulations in the high-latitude regions. *Quaternary Science Reviews*, doi:10.1016/j.quascirev.2017.04.019.

Cardone, V.J., J.G. Greenwood, and M.A. Cane, 1990: On Trends in Historical Marine Wind Data. *Journal of Climate*, **3(1)**, 113–127, doi:10.1175/1520-0442(1990)003<0113:otihmw>2.0.co;2.

ACCEPTED VERSION SUBJECT TO FINAL EDITING

Carilli, J.E. et al., 2014: Equatorial Pacific coral geochemical records show recent weakening of the Walker Circulation. *Paleoceanography*, **29(11)**, 1031–1045, doi:10.1002/2014pa002683.
Carlson, A.E. and P.U. Clark, 2012: Ice sheet sources of sea level rise and freshwater discharge during the last deglaciation. *Reviews of Geophysics*, doi:10.1029/2011rg000371.
Carmagnola, C.M. et al., 2014: Implementation and evaluation of prognostic representations of the optical diameter of snow in the SURFEX/ISBA-Crocus detailed snowpack model. *The Cryosphere*, **8(2)**, 417–437, doi:10.5194/tc-8-417-2014.
Caron, L. et al., 2018: GIA Model Statistics for GRACE Hydrology, Cryosphere, and Ocean Science. *Geophysical Research Letters*, doi:10.1002/2017gl076644.
Carrivick, J.L. et al., 2019: Accelerated Volume Loss in Glacier Ablation Zones of NE Greenland, Little Ice Age to Present. *Geophysical Research Letters*, **46(3)**, 1476–1484, doi:10.1029/2018gl081383.
Casas-Prat, M. and X.L. Wang, 2020: Projections of extreme ocean waves in the Arctic and potential implications for coastal inundation and erosion. *Journal of Geophysical Research: Oceans*, doi:10.1029/2019jc015745.
Castagno, P. et al., 2019: Rebound of shelf water salinity in the Ross Sea. *Nature Communications*, **10(1)**, 5441, doi:10.1038/s41467-019-13083-8.
Catania, G.A. et al., 2018: Geometric Controls on Tidewater Glacier Retreat in Central Western Greenland. *Journal of Geophysical Research: Earth Surface*, **123(8)**, 2024–2038, doi:10.1029/2017jf004499.
Cavalieri, D.J., C.L. Parkinson, P. Gloersen, and H.J. Zwally, 1996: Sea Ice Concentrations from Nimbus-7 SMMR and DMSP SSM/I-SSMIS Passive Microwave Data, Version 1. NASA National Snow and Ice Data Center Distributed Active Archive Center, Boulder, CO, USA. Retrieved from: https://nsidc.org/data/nsidc-0051.
Cazenave, A. et al., 2018: Global sea-level budget 1993-present. *Earth System Science Data*, doi:10.5194/essd-10-1551-2018.
Centurioni, L.R. et al., 2019: Global in-situ observations of essential climate and ocean variables at the air-sea interface. *Frontiers in Marine Science*, **6(JUL)**, 419, doi:10.3389/fmars.2019.00419.
Ceres, R.L., C.E. Forest, and K. Keller, 2017: Understanding the detectability of potential changes to the 100-year peak storm surge. *Climatic Change*, **145(1–2)**, 221–235, doi:10.1007/s10584-017-2075-0.
Cerrone, D., G. Fusco, I. Simmonds, G. Aulicino, and G. Budillon, 2017: Dominant covarying climate signals in the southern ocean and antarctic sea ice influence during the last three decades. *Journal of Climate*, **30(8)**, 3055–3072, doi:10.1175/jcli-d-16-0439.1.
Chadburn, S. et al., 2015: An improved representation of physical permafrost dynamics in the JULES land-surface model. *Geoscientific Model Development*, **8(5)**, 1493–1508, doi:10.5194/gmd-8-1493-2015.
Chadburn, S.E. et al., 2015: Impact of model developments on present and future simulations of permafrost in a global land-surface model. *The Cryosphere*, **9(4)**, 1505–1521, doi:10.5194/tc-9-1505-2015.
Chadburn, S.E. et al., 2017: An observation-based constraint on permafrost loss as a function of global warming. *Nature Climate Change*, **7(5)**, 340–344, doi:10.1038/nclimate3262.
Chadwick, M., C.S. Allen, L.C. Sime, and C.D. Hillenbrand, 2020: Analysing the timing of peak warming and minimum winter sea-ice extent in the Southern Ocean during MIS 5e. *Quaternary Science Reviews*, **229**, 106134, doi:10.1016/j.quascirev.2019.106134.
Chafik, L. and T. Rossby, 2019: Volume, Heat, and Freshwater Divergences in the Subpolar North Atlantic Suggest the Nordic Seas as Key to the State of the Meridional Overturning Circulation. *Geophysical Research Letters*, **46(9)**, 4799–4808, doi:10.1029/2019gl082110.
Chafik, L., J.E. Nilsen, S. Dangendorf, G. Reverdin, and T. Frederikse, 2019: North Atlantic Ocean Circulation and Decadal Sea Level Change During the Altimetry Era. *Scientific Reports*, **9(1)**, 1041, doi:10.1038/s41598-018-37603-6.
Chan, P. et al., 2017: Multicentennial record of Labrador Sea primary productivity and sea-ice variability archived in coralline algal barium. *Nature Communications*, **8**, 15543, doi:10.1038/ncomms15543.
Chao, B.F., Y.H. Wu, and Y.S. Li, 2008: Impact of artificial reservoir water impoundment on global sea level.. *Science (New York, N.Y.)*, **320(5873)**, 212–4, doi:10.1126/science.1154580.
Chasmer, L. and C. Hopkinson, 2017: Threshold loss of discontinuous permafrost and landscape evolution. *Global Change Biology*, **23**, 2672–2686, doi:10.1111/gcb.13537.
Chassignet, E.P. and D.P. Marshall, 2008: Gulf Stream separation in numerical ocean models. In: *Ocean Modeling in an Eddying Regime, Volume 177* [Hecht, M.W. and H. Hasumi (eds.)]. American Geophysical Union (AGU), Washington, DC, USA, pp. 39–61, doi:10.1029/177gm05.
Chassignet, E.P., X. Xu, E.P. Chassignet, and X. Xu, 2017: Impact of Horizontal Resolution (1/12° to 1/50°) on Gulf Stream Separation, Penetration, and Variability. *Journal of Physical Oceanography*, **47(8)**, 1999–2021, doi:10.1175/jpo-d-17-0031.1.

ACCEPTED VERSION SUBJECT TO FINAL EDITING

Chassignet, E.P. et al., 2020: Impact of horizontal resolution on global ocean–sea ice model simulations based on the experimental protocols of the Ocean Model Intercomparison Project phase 2 (OMIP-2). *Geoscientific Model Development*, **13(9)**, 4595–4637, doi:10.5194/gmd-13-4595-2020.

Chelton, D.B. and S.-P. Xie, 2010: Coupled Ocean-Atmosphere Interaction at Oceanic Mesoscales. *Oceanography*, **23**, 52–69, doi:10.2307/24860862.

Chemke, R., L. Zanna, and L.M. Polvani, 2020: Identifying a human signal in the North Atlantic warming hole. *Nature Communications*, **11(1)**, 1540, doi:10.1038/s41467-020-15285-x.

Chen, C., W. Liu, and G. Wang, 2019: Understanding the Uncertainty in the 21st Century Dynamic Sea Level Projections: The Role of the AMOC. *Geophysical Research Letters*, **46(1)**, 210–217, doi:10.1029/2018gl080676.

Chen, H.W., R.B. Alley, and F. Zhang, 2016: Interannual Arctic sea ice variability and associated winter weather patterns: A regional perspective for 1979-2014. *Journal of Geophysical Research*, **121(24)**, 14433–14455, doi:10.1002/2016jd024769.

Chen, J.-L., S.-C. Kang, X.-H. Meng, and Q.-L. You, 2019: Assessments of the Arctic amplification and the changes in the Arctic sea surface. *Advances in Climate Change Research*, **10(4)**, 193–202, doi:10.1016/j.accre.2020.03.002.

Chen, W.-B. and W.-C. Liu, 2016: Assessment of storm surge inundation and potential hazard maps for the southern coast of Taiwan. *Natural Hazards*, **82(1)**, 591–616.

Chen, Z. and L. Wu, 2012: Long-term change of the Pacific North Equatorial Current bifurcation in SODA. *Journal of Geophysical Research: Oceans*, **117(C6)**, n/a–n/a, doi:10.1029/2011jc007814.

Cheng, L. and J. Zhu, 2014: Artifacts in variations of ocean heat content induced by the observation system changes. *Geophysical Research Letters*, **41(20)**, 7276–7283, doi:10.1002/2014gl061881.

Cheng, L., J. Abraham, Z. Hausfather, and K.E. Trenberth, 2019: How fast are the oceans warming? *Science*, **363(6423)**, 128–129, doi:10.1126/science.aav7619.

Cheng, L. et al., 2017: Improved estimates of ocean heat content from 1960 to 2015. *Science Advances*, **3(3)**, e1601545, doi:10.1126/sciadv.1601545.

Cheng, L. et al., 2020: Improved Estimates of Changes in Upper Ocean Salinity and the Hydrological Cycle. *Journal of Climate*, **33(23)**, 10357–10381.

Cheng, W., J.C.H.H. Chiang, and D. Zhang, 2013: Atlantic Meridional Overturning Circulation (AMOC) in CMIP5 Models: RCP and Historical Simulations. *Journal of Climate*, **26(18)**, 7187–7197, doi:10.1175/jcli-d-12-00496.1.

Cherchi, A. et al., 2018: The response of subtropical highs to climate change. *Current Climate Change Reports*, **4(4)**, 371–382.

Cherchi, A. et al., 2019: Global Mean Climate and Main Patterns of Variability in the CMCC-CM2 Coupled Model. *Journal of Advances in Modeling Earth Systems*, **11(1)**, 185–209, doi:10.1029/2018ms001369.

Cheung, W.W.L. and T.L. Frölicher, 2020: Marine heatwaves exacerbate climate change impacts for fisheries in the northeast Pacific. *Scientific Reports*, **10(1)**, 6678, doi:10.1038/s41598-020-63650-z.

Chevallier, M. et al., 2017: Intercomparison of the Arctic sea ice cover in global ocean--sea ice reanalyses from the ORA-IP project. *Climate Dynamics*, **49(3)**, 1107–1136, doi:10.1007/s00382-016-2985-y.

Choi, Y., M. Morlighem, E. Rignot, and M. Wood, 2021: Ice dynamics will remain a primary driver of Greenland ice sheet mass loss over the next century. *Communications Earth & Environment*, **2(1)**, 26, doi:10.1038/s43247-021-00092-z.

Choi, Y., M. Morlighem, E. Rignot, J. Mouginot, and M. Wood, 2017: Modeling the Response of Nioghalvfjerdsfjorden and Zachariae Isstrøm Glaciers, Greenland, to Ocean Forcing Over the Next Century. *Geophysical Research Letters*, **44(21)**, 11,11–71,79, doi:10.1002/2017gl075174.

Christian, J.E., M. Koutnik, and G. Roe, 2018: Committed retreat: controls on glacier disequilibrium in a warming climate. *Journal of Glaciology*, **64(246)**, 675–688, doi:10.1017/jog.2018.57.

Christie, F.D.W. et al., 2018: Glacier change along West Antarctica's Marie Byrd Land Sector and links to inter-decadal atmosphere-ocean variability. *The Cryosphere*, **12**, 2461–2479, doi:10.5194/tc-12-2461-2018.

Church, J.A., N.J. White, and J.M. Arblaster, 2005: Significant decadal-scale impact of volcanic eruptions on sea level and ocean heat content. *Nature*, **438(7064)**, 74–77, doi:10.1038/nature04237.

Church, J.A., D. Monselesan, J.M. Gregory, and B. Marzeion, 2013: Evaluating the ability of process based models to project sea-level change. *Environmental Research Letters*, **8(1)**, 14051, doi:10.1088/1748-9326/8/1/014051.

Church, J.A.A. et al., 2013: Sea Level Change. In: *Climate Change 2013: The Physical Science Basis. Contribution of Working Group I to the Fifth Assessment Report of the Intergovernmental Panel on Climate Change* [Stocker, T.F., D. Qin, G.-K. Plattner, M. Tignor, S.K. Allen, J. Boschung, A. Nauels, Y. Xia, V. Bex, and P.M. Midgley

ACCEPTED VERSION SUBJECT TO FINAL EDITING

(eds.)]. Cambridge University Press, Cambridge, United Kingdom and New York, NY, USA, pp. 1137–1216, doi:10.1017/cbo9781107415324.026.
Cicoira, A., J. Beutel, J. Faillettaz, and A. Vieli, 2019: Water controls the seasonal rhythm of rock glacier flow. *Earth and Planetary Science Letters*, **528**, doi:10.1016/j.epsl.2019.115844.
Ciracì, E., I. Velicogna, and S. Swenson, 2020: Continuity of the Mass Loss of the World's Glaciers and Ice Caps From the GRACE and GRACE Follow-On Missions. *Geophysical Research Letters*, **47(9)**, e2019GL086926, doi:10.1029/2019gl086926.
Clark, P.U. et al., 2016: Consequences of twenty-first-century policy for multi-millennial climate and sea-level change. *Nature Climate Change*, **6(4)**, 360–369, doi:10.1038/nclimate2923.
Clark, P.U. et al., 2020: Oceanic forcing of penultimate deglacial and last interglacial sea-level rise. *Nature*, **577**, 660–664, doi:10.1038/s41586-020-1931-7.
Clement Kinney, J. et al., 2014: On the Flow Through Bering Strait: A Synthesis of Model Results and Observations. In: *The Pacific Arctic Region: Ecosystem Status and Trends in a Rapidly Changing Environment* [Grebmeier, J.M. and W. Maslowski (eds.)]. Springer, Dordrecht, The Netherlands, pp. 167–198, doi:10.1007/978-94-017-8863-2_7.
Clerc, F., B.M. Minchew, and M.D. Behn, 2019: Marine Ice Cliff Instability Mitigated by Slow Removal of Ice Shelves. *Geophysical Research Letters*, doi: 10.1029/2019GL084183.
Coats, S. and K.B. Karnauskas, 2018: A role for the equatorial undercurrent in the ocean dynamical thermostat. *Journal of Climate*, doi:10.1175/jcli-d-17-0513.1.
Colas, F., J.C. McWilliams, X. Capet, and J. Kurian, 2012: Heat balance and eddies in the Peru-Chile current system. *Climate Dynamics*, **39(1–2)**, 509–529, doi:10.1007/s00382-011-1170-6.
Colgan, W. et al., 2019: Programme for monitoring of the Greenland ice sheet (PROMICE): Ice sheet mass balance (1995-2015). Dataset published via Geological Survey of Denmark and Greenland.
Colleoni, F. et al., 2014: Modeling Northern Hemisphere ice-sheet distribution during MIS 5 and MIS 7 glacial inceptions. *Climate of the Past*, **10(1)**, 269–291, doi:10.5194/cp-10-269-2014.
Collins, M. et al., 2010: The impact of global warming on the tropical Pacific Ocean and El Nino. *Nature Geoscience*, doi:10.1038/ngeo868.
Collins, M. et al., 2013: Long-term Climate Change: Projections, Commitments and Irreversibility. In: *Climate Change 2013: The Physical Science Basis. Contribution of Working Group I to the Fifth Assessment Report of the Intergovernmental Panel on Climate Change* [Stocker, T.F., D. Qin, G.-K. Plattner, M. Tignor, S.K. Allen, J. Boschung, A. Nauels, Y. Xia, V. Bex, and P.M. Midgley (eds.)]. Cambridge Univeristy Press, Cambridge, United Kingdom and New York, USA, pp. 1029–1136, doi:10.1017/cbo9781107415324.024.
Collins, M. et al., 2019: Extremes, Abrupt Changes and Managing Risks. In: *IPCC Special Report on the Ocean and Cryosphere in a Changing Climate* [Pörtner, H.-O., D.C. Roberts, V. Masson-Delmotte, P. Zhai, M. Tignor, E. Poloczanska, K. Mintenbeck, M. Nicolai, A. Okem, J. Petzold, B. Rama, and N. Weyer (eds.)]. In Press, pp. 589-655.
Colville, E.J. et al., 2011: Sr-Nd-Pb isotope evidence for ice-sheet presence on southern Greenland during the Last Interglacial. *Science*, **333(6042)**, 620–623.
Comiso, J.C., 2017: Bootstrap Sea Ice Concentrations from Nimbus-7 SMMR and DMSP SSM/I-SSMIS, Version 3. NASA National Snow and Ice Data Center Distributed Active Archive Center, Boulder, CO, USA. Retrieved from: https://nsidc.org/data/nsidc-0079.
Comiso, J.C., W.N. Meier, and R. Gersten, 2017a: Variability and trends in the Arctic Sea ice cover: Results from different techniques. *Journal of Geophysical Research: Oceans*, **122(8)**, 6883–6900, doi:10.1002/2017jc012768.
Comiso, J.C. et al., 2017b: Positive Trend in the Antarctic Sea Ice Cover and Associated Changes in Surface Temperature. *Journal of Climate*, **30(6)**, 2251–2267, doi:10.1175/jcli-d-16-0408.1.
Constantin, J.G. et al., 2020: Measurements and modeling of snow albedo at Alerce Glacier, Argentina: Effects of volcanic ash, snow grain size, and cloudiness. *Cryosphere*, **14(12)**, 4581–4601, doi:10.5194/tc-14-4581-2020.
Cook, A.J. et al., 2019: Atmospheric forcing of rapid marine-terminating glacier retreat in the Canadian Arctic Archipelago. *Science Advances*, **5(3)**, eaau8507, doi:10.1126/sciadv.aau8507.
Cook, J.M. et al., 2020: Glacier algae accelerate melt rates on the south-western Greenland Ice Sheet. *The Cryosphere*, **14**, 309–330, doi:10.5194/tc-14-309-2020.
Cordero, R.R. et al., 2019: Dry-Season Snow Cover Losses in the Andes (18°–40°S) driven by Changes in Large-Scale Climate Modes. *Scientific Reports*, **9**, 16945, doi:10.1038/s41598-019-53486-7.
Cornford, S.L. et al., 2020: Results of the third Marine Ice Sheet Model Intercomparison Project (MISMIP+). *The Cryosphere*, **14(7)**, 2283–2301, doi:10.5194/tc-14-2283-2020.

ACCEPTED VERSION SUBJECT TO FINAL EDITING

Couasnon, A. et al., 2020: Measuring compound flood potential from river discharge and storm surge extremes at the global scale and its implications for flood hazard. *Natural Hazards and Earth System Sciences*, **20**, 489–504, doi:10.5194/nhess-20-489-2020.

Couldrey, M.P. et al., 2020: What causes the spread of model projections of ocean dynamic sea level change in response to greenhouse gas forcing? *Climate Dynamics*, doi:10.1007/s00382-020-05471-4.

Couldrey, M.P. et al., 2021: What causes the spread of model projections of ocean dynamic sea-level change in response to greenhouse gas forcing? *Climate Dynamics*, **56(1–2)**, 155–187, doi:10.1007/s00382-020-05471-4.

Cowton, T.R., J.A. Todd, and D.I. Benn, 2019: Sensitivity of Tidewater Glaciers to Submarine Melting Governed by Plume Locations. *Geophysical Research Letters*, **46**, 11219–11227, doi:10.1029/2019gl084215.

Cronin, M.F. et al., 2019: Air-sea fluxes with a focus on heat and momentum. *Frontiers in Marine Science*, **6(JUL)**, 430, doi:10.3389/fmars.2019.00430.

Crosta, X. et al., 2018: Ocean as the main driver of Antarctic ice sheet retreat during the Holocene. *Global and Planetary Change*, **166**, 62–74, doi:10.1016/j.gloplacha.2018.04.007.

Crosta, X. et al., 2021: Multi-decadal trends in Antarctic sea-ice extent driven by ENSO–SAM over the last 2,000 years. *Nature Geoscience*, doi:10.1038/s41561-021-00697-1.

Cullather, R.I., S.M.J. Nowicki, B. Zhao, and M.J. Suarez, 2014: Evaluation of the Surface Representation of the Greenland Ice Sheet in a General Circulation Model. *Journal of Climate*, **27(13)**, 4835–4856, doi:10.1175/jcli-d-13-00635.1.

Cullather, R.I. et al., 2020: Anomalous Circulation in July 2019 Resulting in Mass Loss on the Greenland Ice Sheet. *Geophysical Research Letters*, **47**, e2020GL087263, doi:10.1029/2020gl087263.

Cummins, P.F. and D. Masson, 2018: Low-frequency isopycnal variability in the Alaska Gyre from Argo. *Progress in Oceanography*, **168**, 310–324, doi:10.1016/j.pocean.2018.09.014.

Cummins, P.F. and T. Ross, 2020a: Secular trends in water properties at Station P in the northeast Pacific: an updated analysis. *Progress in Oceanography*, 102329, doi:10.1016/j.pocean.2020.102329.

Cummins, P.F. and T. Ross, 2020b: Secular trends in water properties at Station P in the northeast Pacific: an updated analysis. *Progress in Oceanography*, 102329, doi:10.1016/j.pocean.2020.102329.

Cunliffe, A. et al., 2019: Rapid retreat of permafrost coastline observed with aerial drone photogrammetry. *Cryosphere*, **13(5)**, 1513–1528, doi:10.5194/tc-13-1513-2019.

Cuntz, M. and V. Haverd, 2018: Physically Accurate Soil Freeze-Thaw Processes in a Global Land Surface Scheme. *Journal of Advances in Modeling Earth Systems*, **10(1)**, 54–77, doi:10.1002/2017ms001100.

Cuzzone, J.K. et al., 2016: Final deglaciation of the Scandinavian Ice Sheet and implications for the Holocene global sea-level budget. *Earth and Planetary Science Letters*, **448**, 34–41, doi:10.1016/j.epsl.2016.05.019.

D'Asaro, E.A., 2014: Turbulence in the Upper-Ocean Mixed Layer. *Annual Review of Marine Science*, **6(1)**, 101–115, doi:10.1146/annurev-marine-010213-135138.

Dahl-Jensen, D. et al., 2013: Eemian interglacial reconstructed from a Greenland folded ice core. *Nature*, **493(7433)**, 489–494, doi:10.1038/nature11789.

Dahlke, S. et al., 2020: The observed recent surface air temperature development across Svalbard and concurring footprints in local sea ice cover. *International Journal of Climatology*, **n/a(n/a)**, doi:10.1002/joc.6517.

Danabasoglu, G., W.G. Large, and B.P. Briegleb, 2010: Climate impacts of parameterized Nordic Sea overflows. *Journal of Geophysical Research*, **115(C11)**, C11005, doi:10.1029/2010jc006243.

Danabasoglu, G. et al., 2014: North Atlantic Simulations in Coordinated Ocean-ice Reference Experiments phase 2 (CORE-II). Part 1: Mean States. *Ocean Modelling*, **73**, 76–107, doi:10.1016/j.ocemod.2013.10.005.

Danabasoglu, G. et al., 2016: North Atlantic simulations in Coordinated Ocean-ice Reference Experiments phase II (CORE-II). Part II: Inter-annual to decadal variability. *Ocean Modelling*, **97**, 65–90, doi:10.1016/j.ocemod.2015.11.007.

Danabasoglu, G. et al., 2020: The Community Earth System Model Version 2 (CESM2). *Journal of Advances in Modeling Earth Systems*, **12(2)**, e2019MS001916, doi:10.1029/2019ms001916.

Dangendorf, S. et al., 2019: Persistent acceleration in global sea-level rise since the 1960s. *Nature Climate Change*, **9(9)**, 705–710, doi:10.1038/s41558-019-0531-8.

Das, I. et al., 2020: Multidecadal Basal Melt Rates and Structure of the Ross Ice Shelf, Antarctica, Using Airborne Ice Penetrating Radar. *Journal of Geophysical Research: Earth Surface*, **125(3)**, doi:10.1029/2019jf005241.

Davaze, L., A. Rabatel, A. Dufour, R. Hugonnet, and Y. Arnaud, 2020: Region-Wide Annual Glacier Surface Mass Balance for the European Alps From 2000 to 2016. *Frontiers in Earth Science*, **8**, 149, doi:10.3389/feart.2020.00149.

Davies, B.J. et al., 2020: The evolution of the Patagonian Ice Sheet from 35 ka to the present day (PATICE). *Earth-Science Reviews*, **204**, 103152, doi:10.1016/j.earscirev.2020.103152.

ACCEPTED VERSION SUBJECT TO FINAL EDITING

de Boer, B., A.M. Haywood, A.M. Dolan, S.J. Hunter, and C.L. Prescott, 2017: The transient response of ice volume to orbital forcing during the warm late Pliocene. *Geophysical Research Letters*, **44(20)**, 10–486, doi:10.1002/2017gl073535.

De Boer, B. et al., 2015: Simulating the Antarctic ice sheet in the late-Pliocene warm period: PLISMIP-ANT, an ice-sheet model intercomparison project. *Cryosphere*, **9(3)**, 881–903, doi:10.5194/tc-9-881-2015.

de Elía, R., S. Biner, and A. Frigon, 2013: Interannual variability and expected regional climate change over North America. *Climate Dynamics*, **41(5–6)**, 1245–1267, doi:10.1007/s00382-013-1717-9.

de Jong, M.F., M. Oltmanns, J. Karstensen, and L. de Steur, 2018: Deep Convection in the Irminger Sea Observed with a Dense Mooring Array. *Oceanography*, **31(1)**, 50–59, doi:10.5670/oceanog.2018.109.

de Kok, R.J., P.D.A. Kraaijenbrink, O.A. Tuinenburg, P.N.J. Bonekamp, and W.W. Immerzeel, 2020: Towards understanding the pattern of glacier mass balances in High Mountain Asia using regional climatic modelling. *The Cryosphere*, **14(9)**, 3215–3234, doi:10.5194/tc-14-3215-2020.

De Lavergne, C., J.B. Palter, E.D. Galbraith, R. Bernardello, and I. Marinov, 2014: Cessation of deep convection in the open Southern Ocean under anthropogenic climate change. *Nature Climate Change*, **4**, 278, doi:10.1038/nclimate2132.

De Schepper, S., P.L. Gibbard, U. Salzmann, and J. Ehlers, 2014: A global synthesis of the marine and terrestrial evidence for glaciation during the Pliocene Epoch. *Earth-Science Reviews*, **135**, 83–102, doi:10.1016/j.earscirev.2014.04.003.

De Vernal, A., R. Gersonde, H. Goosse, M.S. Seidenkrantz, and E.W. Wolff, 2013a: Sea ice in the paleoclimate system: The challenge of reconstructing sea ice from proxies - an introduction. *Quaternary Science Reviews*, **79**, 1–8, doi:10.1016/j.quascirev.2013.08.009.

De Vernal, A. et al., 2013b: Dinocyst-based reconstructions of sea ice cover concentration during the Holocene in the Arctic Ocean, the northern North Atlantic Ocean and its adjacent seas. *Quaternary Science Reviews*, **79**, 111–121, doi:10.1016/j.quascirev.2013.07.006.

de Vries, P. and S.L. Weber, 2005: The Atlantic freshwater budget as a diagnostic for the existence of a stable shut down of the meridional overturning circulation. *Geophysical Research Letters*, **32(9)**, doi:10.1029/2004gl021450.

de Wet, G.A., I.S. Castañeda, R.M. DeConto, and J. Brigham-Grette, 2016: A high-resolution mid-Pleistocene temperature record from Arctic Lake El'gygytgyn: A 50 kyr super interglacial from MIS 33 to MIS 31? *Earth and Planetary Science Letters*, **436**, 56–63, doi:10.1016/j.epsl.2015.12.021.

DeConto, R.M. and D. Pollard, 2016: Contribution of Antarctica to past and future sea-level rise. *Nature*, **531(7596)**, 591–597, doi:10.1038/nature17145.

DeConto, R.M. et al., 2021: The Paris Climate Agreement and future sea-level rise from Antarctica. *Nature*, **in press**.

Delhasse, A., X. Fettweis, C. Kittel, C. Amory, and C. Agosta, 2018: Brief communication: Impact of the recent atmospheric circulation change in summer on the future surface mass balance of the Greenland Ice Sheet. *The Cryosphere*, **12(11)**, 3409–3418, doi:10.5194/tc-12-3409-2018.

Deline, P. et al., 2015: Ice Loss and Slope Stability in High-Mountain Regions. In: *Snow and Ice-Related Hazards, Risks, and Disasters* [John F. Shroder, W. Haeberli, and C. Whiteman (eds.)]. Academic Press, pp. 521–561, doi:10.1016/b978-0-12-394849-6.00015-9.

Delman, A.S. et al., 2015: Effects of Eddy Vorticity Forcing on the Mean State of the Kuroshio Extension. *Journal of Physical Oceanography*, **45(5)**, 1356–1375, doi:10.1175/jpo-d-13-0259.1.

Delworth, T.L. et al., 2012: Simulated Climate and Climate Change in the GFDL CM2.5 High-Resolution Coupled Climate Model. *Journal of Climate*, **25(8)**, 2755–2781, doi:10.1175/jcli-d-11-00316.1.

Denton, G.H. et al., 2010: The Last Glacial Termination. *Science*, **328(5986)**, 1652–1656, doi:10.1126/science.1184119.

Derksen, C., R. Brown, L. Mudryk, and K. Luojus, 2017: Terrestrial snow cover. *State of the Climate in 2016. Bulletin of the American Meteorological Society. 98 (8)*, **98(8)**, S143–S145, doi:10.1175/2017bamsstateoftheclimate.1.

Desbiolles, F. et al., 2017: Two decades [1992–2012] of surface wind analyses based on satellite scatterometer observations. *Journal of Marine Systems*, **168**, 38–56, doi:10.1016/j.jmarsys.2017.01.003.

Desbruyères, D., E.L. McDonagh, B.A. King, and V. Thierry, 2017: Global and Full-Depth Ocean Temperature Trends during the Early Twenty-First Century from Argo and Repeat Hydrography. *Journal of Climate*, **30(6)**, 1985–1997, doi:10.1175/jcli-d-16-0396.1.

Deschamps-Berger, C. et al., 2019: Closing the mass budget of a tidewater glacier: The example of Kronebreen, Svalbard. *Journal of Glaciology*, **65(249)**, 136–148, doi:10.1017/jog.2018.98.

Deshayes, J. et al., 2014: CMIP5 Model Intercomparison of Freshwater Budget and Circulation in the North Atlantic. *Journal of Climate*, **27(9)**, 3298–3317, doi:10.1175/jcli-d-12-00700.1.

ACCEPTED VERSION SUBJECT TO FINAL EDITING

Di Mauro, B. et al., 2019: Saharan dust events in the European Alps: role in snowmelt and geochemical characterization. *The Cryosphere*, **13(4)**, 1147–1165, doi:10.5194/tc-13-1147-2019.
Di Mauro, B. et al., 2020: Glacier algae foster ice-albedo feedback in the European Alps. *Scientific Reports*, **10(1)**, 4739, doi:10.1038/s41598-020-61762-0.
Dias, F.B. et al., 2020: Ocean heat uptake driven by redistribution of heat in response to ocean circulation changes. *Journal of Climate*, **33(21)**, 9065–9082.
Dietrich, J.C. et al., 2012: Performance of the Unstructured-Mesh, SWAN+ADCIRC Model in Computing Hurricane Waves and Surge. *Journal of Scientific Computing*, **52(2)**, 468–497, doi:10.1007/s10915-011-9555-6.
Ding, Q. et al., 2017: Influence of high-latitude atmospheric circulation changes on summertime Arctic sea ice. *Nature Climate Change*, **7(4)**, 289–295, doi:10.1038/nclimate3241.
Ding, Q. et al., 2019: Fingerprints of internal drivers of Arctic sea ice loss in observations and model simulations. *Nature Geoscience*, **12(1)**, 28, doi:10.1038/s41561-018-0256-8.
Dinniman, M. et al., 2016: Modeling Ice Shelf/Ocean Interaction in Antarctica: A Review. *Oceanography*, **29(4)**, 144–153, doi:10.5670/oceanog.2016.106.
Docquier, D., T. Koenigk, R. Fuentes-Franco, M.P. Karami, and Y. Ruprich-Robert, 2021: Impact of ocean heat transport on the Arctic sea-ice decline: a model study with EC-Earth3. *Climate Dynamics*, doi:10.1007/s00382-020-05540-8.
Docquier, D. et al., 2017: Relationships between Arctic sea ice drift and strength modelled by NEMO-LIM3.6. *The Cryosphere*, **11(6)**, 2829–2846, doi:10.5194/tc-11-2829-2017.
Docquier, D. et al., 2019: Impact of model resolution on Arctic sea ice and North Atlantic Ocean heat transport. *Climate Dynamics*, **53(7)**, 4989–5017, doi:10.1007/s00382-019-04840-y.
Doddridge, E.W. and J. Marshall, 2017: Modulation of the Seasonal Cycle of Antarctic Sea Ice Extent Related to the Southern Annular Mode. *Geophysical Research Letters*, **44(19)**, 9761–9768, doi:10.1002/2017gl074319.
Doddridge, E.W. et al., 2019: Eddy Compensation Dampens Southern Ocean Sea Surface Temperature Response to Westerly Wind Trends. *Geophysical Research Letters*, **46(8)**, 4365–4377, doi:10.1029/2019gl082758.
Dodet, G. et al., 2019: The Contribution of Wind-Generated Waves to Coastal Sea-Level Changes. *Surveys in Geophysics*, **40(6)**, 1563–1601, doi:10.1007/s10712-019-09557-5.
Doerr, J., D. Notz, and S. Kern, 2021: UHH sea-ice area product, 1850-2019. University of Hamburg, Hamburg, Germany.
Dolan, A.M. et al., 2011: Sensitivity of Pliocene ice sheets to orbital forcing. *Palaeogeography, Palaeoclimatology, Palaeoecology*, **309(1–2)**, 98–110, doi:10.1016/j.palaeo.2011.03.030.
Domine, F., M. Barrere, and D. Sarrazin, 2016: Seasonal evolution of the effective thermal conductivity of the snow and the soil in high Arctic herb tundra at Bylot Island, Canada. *The Cryosphere*, **10(6)**, 2573–2588, doi:10.5194/tc-10-2573-2016.
Domingues, C.M. et al., 2008: Improved estimates of upper-ocean warming and multi-decadal sea-level rise. *Nature*, **453(7198)**, 1090–1093, doi:10.1038/nature07080.
Donat-Magnin, M. et al., 2017: Ice-Shelf Melt Response to Changing Winds and Glacier Dynamics in the Amundsen Sea Sector, Antarctica. *Journal of Geophysical Research: Oceans*, **122(12)**, 10206–10224, doi:10.1002/2017jc013059.
Dong, S., M.O. Baringer, and G.J. Goni, 2019: Slow Down of the Gulf Stream during 1993–2016. *Scientific Reports*, **9(1)**, 6672, doi:10.1038/s41598-019-42820-8.
Dotto, T.S. et al., 2018: Variability of the Ross Gyre, Southern Ocean: Drivers and Responses Revealed by Satellite Altimetry. *Geophysical Research Letters*, **45(12)**, 6195–6204, doi:10.1029/2018gl078607.
Dotto, T.S. et al., 2019: Wind-Driven Processes Controlling Oceanic Heat Delivery to the Amundsen Sea, Antarctica. *Journal of Physical Oceanography*, **49(11)**, 2829–2849, doi:10.1175/jpo-d-19-0064.1.
Dowdeswell, J.A. et al., 2020: Delicate seafloor landforms reveal past Antarctic grounding-line retreat of kilometers per year. *Science*, **368(6494)**, 1020–1024, doi:10.1126/science.aaz3059.
Dowsett, H. et al., 2016: The PRISM4 (mid-Piacenzian) palaeoenvironmental reconstruction. *Climate of the Past*, **12**, 1519–1538.
Drews, R., 2015: Evolution of ice-shelf channels in Antarctic ice shelves. *The Cryosphere*, **9(3)**, 1169–1181, doi:10.5194/tc-9-1169-2015.
Druel, A. et al., 2017: Towards a more detailed representation of high-latitude vegetation in the global land surface model ORCHIDEE (ORC-HL-VEGv1.0). *Geoscientific Model Development*, **10(12)**, 4693–4722, doi:10.5194/gmd-10-4693-2017.

ACCEPTED VERSION SUBJECT TO FINAL EDITING

Du, J., B.A. Haley, and A.C. Mix, 2020: Evolution of the Global Overturning Circulation since the Last Glacial Maximum based on marine authigenic neodymium isotopes. *Quaternary Science Reviews*, **241**, 106396, doi:10.1016/j.quascirev.2020.106396.

Du, Y., Y. Zhang, and J. Shi, 2019: Relationship between sea surface salinity and ocean circulation and climate change. *Science China Earth Sciences*, **62(5)**, 771–782, doi:10.1007/s11430-018-9276-6.

Dufour, C.O. et al., 2017: Preconditioning of the Weddell Sea Polynya by the Ocean Mesoscale and Dense Water Overflows. *Journal of Climate*, **30(19)**, 7719–7737, doi:10.1175/jcli-d-16-0586.1.

Dukhovskoy, D.S. et al., 2016: Greenland freshwater pathways in the sub-Arctic Seas from model experiments with passive tracers. *Journal of Geophysical Research: Oceans*, **121(1)**, 877–907, doi:10.1002/2015jc011290.

Dukhovskoy, D.S. et al., 2019a: Role of Greenland Freshwater Anomaly in the Recent Freshening of the Subpolar North Atlantic. *Journal of Geophysical Research: Oceans*, **124(5)**, 3333–3360, doi:10.1029/2018jc014686.

Dukhovskoy, D.S. et al., 2019b: Role of Greenland Freshwater Anomaly in the Recent Freshening of the Subpolar North Atlantic. *Journal of Geophysical Research: Oceans*, **124(5)**, 3333–3360, doi:10.1029/2018jc014686.

Dumitru, O.A. et al., 2019: Constraints on global mean sea level during Pliocene warmth. *Nature*, **574(7777)**, 233–236, doi:10.1038/s41586-019-1543-2.

Dunne, J.P. et al., 2020: The GFDL Earth System Model Version 4.1 (GFDL-ESM 4.1): Overall Coupled Model Description and Simulation Characteristics. *Journal of Advances in Modeling Earth Systems*, **12(11)**, e2019MS002015, doi:10.1029/2019ms002015.

Durack, P., 2015: Ocean Salinity and the Global Water Cycle. *Oceanography*, **28(1)**, 20–31, doi:10.5670/oceanog.2015.03.

Durack, P.J. and S.E. Wijffels, 2010: Fifty-Year trends in global ocean salinities and their relationship to broad-scale warming. *Journal of Climate*, doi:10.1175/2010jcli3377.1.

Durack, P.J., S.E. Wijffels, and P.J. Gleckler, 2014: Long-term sea-level change revisited: The role of salinity. *Environmental Research Letters*, **9(11)**, doi:10.1088/1748-9326/9/11/114017.

Durgadoo, J., B.R. Loveday, C.J.C. Reason, P. Penven, and A. Biastoch, 2013: Agulhas Leakage Predominantly Responds to the Southern Hemisphere Westerlies. *Journal of Physical Oceanography*, **43(10)**, 2113–2131, doi:10.1175/jpo-d-13-047.1.

Dussaillant, I. et al., 2019: Two decades of glacier mass loss along the Andes. *Nature Geoscience*, **12(10)**, 802–808, doi:10.1038/s41561-019-0432-5.

Dutton, A. and K. Lambeck, 2012: Ice Volume and Sea Level During the Last Interglacial. *Science*, **337(6091)**, 216–219, doi:10.1126/science.1205749.

Dutton, A., J.M. Webster, D. Zwartz, K. Lambeck, and B. Wohlfarth, 2015: Tropical tales of polar ice: evidence of Last Interglacial polar ice sheet retreat recorded by fossil reefs of the granitic Seychelles islands. *Quaternary Science Reviews*, **107**, 182–196.

Dziewonski, A.M. and D.L. Anderson, 1981: Preliminary reference Earth model (PREM). *Physics of the Earth and Planetary Interiors*, **25(4)**, 297–356, doi:10.1016/0031-9201(81)90046-7.

Eaves, S.R. et al., 2019: Late-glacial and Holocene glacier fluctuations in North Island, New Zealand. *Quaternary Science Reviews*, **223**, 105914, doi:10.1016/j.quascirev.2019.105914.

Echevin, V., K. Goubanova, A. Belmadani, and B. Dewitte, 2012: Sensitivity of the Humboldt Current system to global warming: a downscaling experiment of the IPSL-CM4 model. *Climate Dynamics*, **38(3–4)**, 761–774.

Edinburgh, T. and J.J. Day, 2016: Estimating the extent of Antarctic summer sea ice during the Heroic Age of Antarctic Exploration. *The Cryosphere*, **10(6)**, 2721–2730, doi:10.5194/tc-10-2721-2016.

Edwards, T.L. et al., 2019a: Revisiting Antarctic ice loss due to marine ice cliff instability. *Nature*, **566(7742)**.

Edwards, T.L. et al., 2019b: Revisiting Antarctic ice loss due to marine ice-cliff instability. *Nature*, **566(7742)**, 58–64, doi:10.1038/s41586-019-0901-4.

Edwards, T.T.L. et al., 2021: Projecting the land ice contribution to sea level rise this century. *Nature*, **in press**.

Ehlert, D. and K. Zickfeld, 2018a: Irreversible ocean thermal expansion under carbon dioxide removal. *Earth System Dynamics*, **9**, 197–210, doi:10.5194/esd-9-197-2018.

Ehlert, D. and K. Zickfeld, 2018b: Irreversible ocean thermal expansion under carbon dioxide removal. *Earth System Dynamics*, **9**, 197–210, doi:10.5194/esd-9-197-2018.

Eisenman, I., 2012: Factors controlling the bifurcation structure of sea ice retreat. *Journal of Geophysical Research Atmospheres*, **117(1)**, doi:10.1029/2011jd016164.

Ekici, A. et al., 2015: Site-level model intercomparison of high latitude and high altitude soil thermal dynamics in tundra and barren landscapes. *Cryosphere*, **9(4)**, 1343–1361, doi:10.5194/tc-9-1343-2015.

Elipot, S. and L.M. Beal, 2018: Observed Agulhas Current sensitivity to interannual and long-term trend atmospheric forcings. *Journal of Climate*, JCLI–D–17–0597.1, doi:10.1175/jcli-d-17-0597.1.

ACCEPTED VERSION SUBJECT TO FINAL EDITING

Enderlin, E.M., I.M. Howat, and A. Vieli, 2013: High sensitivity of tidewater outlet glacier dynamics to shapee. *The Cryosphere*, **7(3)**, 1007–1015.
England, M., A. Jahn, and L. Polvani, 2019: Nonuniform Contribution of Internal Variability to Recent Arctic Sea Ice Loss. *Journal of Climate*, **32(13)**, 4039–4053, doi:10.1175/jcli-d-18-0864.1.
England, M.H. et al., 2014: Recent intensification of wind-driven circulation in the Pacific and the ongoing warming hiatus. *Nature Climate Change*, doi:10.1038/nclimate2106.
England, M.R., L.M. Polvani, K.L. Smith, L. Landrum, and M.M. Holland, 2016: Robust response of the Amundsen Sea Low to stratospheric ozone depletion. *Geophysical Research Letters*, **43(15)**, 8207–8213, doi:10.1002/2016gl070055.
Essery, R., 2015: A factorial snowpack model (FSM 1.0). *Geoscientific Model Development*, **8(12)**, 3867–3876, doi:10.5194/gmd-8-3867-2015.
Estilow, T.W., A.H. Young, and D.A. Robinson, 2015: A long-term Northern Hemisphere snow cover extent data record for climate studies and monitoring. *Earth System Science Data*, **7(1)**, 137–142, doi:10.5194/essd-7-137-2015.
Eyring, V. et al., 2016: Overview of the Coupled Model Intercomparison Project Phase 6 (CMIP6) experimental design and organization. *Geoscientific Model Development*, **9(5)**, 1937–1958, doi:10.5194/gmd-9-1937-2016.
Fan, T., C. Deser, and D.P. Schneider, 2014: Recent Antarctic sea ice trends in the context of Southern Ocean surface climate variations since 1950. *Geophysical Research Letters*, **41(7)**, 2419–2426, doi:10.1002/2014gl059239.
Farinotti, D., W.W. Immerzeel, R.J. Kok, D.J. Quincey, and A. Dehecq, 2020: Manifestations and mechanisms of the Karakoram glacier Anomaly. *Nature Geoscience*, **13**, 8–16, doi:10.1038/s41561-019-0513-5.
Farinotti, D. et al., 2019: A consensus estimate for the ice thickness distribution of all glaciers on Earth. *Nature Geoscience 2019*, 1, doi:10.1038/s41561-019-0300-3.
Fasullo, J.T. and R.S. Nerem, 2018: Altimeter-era emergence of the patterns of forced sea-level rise in climate models and implications for the future. *Proceedings of the National Academy of Sciences*, **115(51)**, 12944–12949, doi:10.1073/pnas.1813233115.
Fasullo, J.T., R.S. Nerem, and B. Hamlington, 2016: Is the detection of accelerated sea level rise imminent? *Scientific Reports*, **6(1)**, 31245, doi:10.1038/srep31245.
Fasullo, J.T., P.R. Gent, and R. Steven Nerem, 2020: Sea level rise in the CESM large ensemble: The role of individual climate forcings and consequences for the coming decades. *Journal of Climate*, **33(16)**, 6911–6927, doi:10.1175/jcli-d-19-1001.1.
Favier, L. et al., 2014: Retreat of Pine Island Glacier controlled by marine ice-sheet instability. *Nature Climate Change*, **5(2)**, 117–121, doi:10.1038/nclimate2094.
Favier, L. et al., 2019: Assessment of Sub-Shelf Melting Parameterisations Using theOcean-Ice Sheet Coupled Model NEMO(v3.6)-Elmer/Ice(v8.3). *Geoscientific Model Development*, **12**, 2255–2283, doi:10.5194/gmd-2019-26.
Feldmann, J. and A. Levermann, 2015: Collapse of the West Antarctic Ice Sheet after local destabilization of the Amundsen Basin. *Proceedings of the National Academy of Sciences*, **112(46)**, 14191–14196, doi:10.1073/pnas.1512482112.
Feldmann, J., A. Levermann, and M. Mengel, 2019: Stabilizing the West Antarctic Ice Sheet by surface mass deposition. *Science advances*, **5(7)**, eaaw4132, doi:10.1126/sciadv.aaw4132.
Feng, J. et al., 2019: Acceleration of the Extreme Sea Level Rise Along the Chinese Coast. *Earth and Space Science*, **6(10)**, 1942–1956, doi:10.1029/2019ea000653.
Feng, W., M. Zhong, and H.Z. Xu, 2012: Sea level variations in the South China Sea inferred from satellite gravity, altimetry, and oceanographic data. *Science China Earth Sciences*, doi:10.1007/s11430-012-4394-3.
Ferrari, R. et al., 2014: Antarctic sea ice control on ocean circulation in present and glacial climates. *Proceedings of the National Academy of Sciences*, **111(24)**, 8753–8758, doi:10.1073/pnas.1323922111.
Fettweis, X. et al., 2013: Estimating the Greenland ice sheet surface mass balance contribution to future sea level rise using the regional atmospheric climate model MAR. *The Cryosphere*, **7(2)**, 469–489, doi:10.5194/tc-7-469-2013.
Fettweis, X. et al., 2020: GrSMBMIP: Intercomparison of the modelled 1980-2012 surface mass balance over the Greenland Ice sheet. *The Cryosphere*, **14**, 3935–3958, doi:10.5194/tc-14-3935-2020.
Fischer, H. et al., 2018: Palaeoclimate constraints on the impact of 2°C anthropogenic warming and beyond. *Nature Geoscience*, **11(7)**, 474–485, doi:10.1038/s41561-018-0146-0.
Flato, G. et al., 2013: Evaluation of Climate Models. In: *Climate Change 2013: The Physical Science Basis. Contribution of Working Group I to the Fifth Assessment Report of the IPCC* [Stocker, T.F., D. Qin, G.-K. Plattner, M. Tignor, S.K. Allen, J. Boschung, A. Nauels, Y. Xia, V. Bex, and P.M. Midgley (eds.)]. Cambridge

ACCEPTED VERSION SUBJECT TO FINAL EDITING

University Press, Cambridge, United Kingdom and New York, USA, pp. 741–866, doi:10.1017/cbo9781107415324.020.
Forbes, D.L., T.S. James, M. Sutherland, and S.E. Nichols, 2013: Physical basis of coastal adaptation on tropical small islands. *Sustainability Science*, **8(3)**, 327–344, doi:10.1007/s11625-013-0218-4.
Foreman, M.G.G., W. Callendar, D. Masson, J. Morrison, and I. Fine, 2013: A Model Simulation of Future Oceanic Conditions along the British Columbia Continental Shelf. Part II: Results and Analyses. , doi:10.1080/07055900.2013.873014.
Forsberg, R., L. Sørensen, and S. Simonsen, 2017: Greenland and Antarctica Ice Sheet Mass Changes and Effects on Global Sea Level. *Surveys in Geophysics*, **38(1)**, 89–104, doi:10.1007/s10712-016-9398-7.
Foster, J.L., D.K. Hall, R.E.J. Kelly, and L. Chiu, 2009: Seasonal snow extent and snow mass in South America using SMMR and SSM/I passive microwave data (1979-2006). *Remote Sensing of Environment*, **113**, 291–305, doi:10.1016/j.rse.2008.09.010.
Fox-Kemper, B. and J. Pedlosky, 2004: Wind-driven barotropic gyre I: Circulation control by eddy vorticity fluxes to an enhanced removal region. *Journal of Marine Research*, **62(2)**, 169–193, doi:10.1357/002224004774201681.
Fox-Kemper, B. et al., 2011: Parameterization of mixed layer eddies. III: Implementation and impact in global ocean climate simulations. *Ocean Modelling*, **39(1)**, 61–78, doi:10.1016/j.ocemod.2010.09.002.
Frederikse, T., K. Simon, C.A. Katsman, and R. Riva, 2017: The sea-level budget along the Northwest Atlantic coast: GIA , mass changes, and large-scale ocean dynamics. *Journal of Geophysical Research: Oceans*, **122(7)**, 5486–5501, doi:10.1002/2017jc012699.
Frederikse, T. et al., 2016: Closing the sea level budget on a regional scale: Trends and variability on the Northwestern European continental shelf. *Geophysical Research Letters*, **43(20)**, 10,864–10,872, doi:10.1002/2016gl070750.
Frederikse, T. et al., 2018: A Consistent Sea-Level Reconstruction and Its Budget on Basin and Global Scales over 1958–2014. *Journal of Climate*, **31(3)**, 1267–1280, doi:10.1175/jcli-d-17-0502.1.
Frederikse, T. et al., 2020a: Antarctic Ice Sheet and emission scenario controls on 21st-century extreme sea-level changes. *Nature Communications*, **11(1)**, 1–11, doi:10.1038/s41467-019-14049-6.
Frederikse, T. et al., 2020b: The causes of sea-level rise since 1900. *Nature*, **584(7821)**, 393–397, doi:10.1038/s41586-020-2591-3.
Frenger, I., N. Gruber, R. Knutti, and M. Münnich, 2013: Imprint of Southern Ocean eddies on winds, clouds and rainfall. *Nature Geoscience*, **6(8)**, 608–612, doi:10.1038/ngeo1863.
Fretwell, P. et al., 2013: Bedmap2: improved ice bed, surface and thickness datasets for Antarctica. *Cryosphere*, **7(1)**, 375–393, doi:10.5194/tc-7-375-2013.
Fréville, H. et al., 2014: Using MODIS land surface temperatures and the Crocus snow model to understand the warm bias of ERA-Interim reanalyses at the surface in Antarctica. *The Cryosphere*, **8(4)**, 1361–1373, doi:10.5194/tc-8-1361-2014.
Frey, K.E., G.W.K. Moore, L.W. Cooper, and J.M. Grebmeier, 2015: Divergent patterns of recent sea ice cover across the Bering, Chukchi, and Beaufort seas of the Pacific Arctic Region. *Progress in Oceanography*, **136**, 32–49, doi:10.1016/j.pocean.2015.05.009.
Fried, M.J. et al., 2019: Distinct Frontal Ablation Processes Drive Heterogeneous Submarine Terminus Morphology. *Geophysical Research Letters*, **46**, 12083–12091, doi:10.1029/2019gl083980.
Friedman, A.R., G. Reverdin, M. Khodri, and G. Gastineau, 2017: A new record of Atlantic sea surface salinity from 1896 to 2013 reveals the signatures of climate variability and long-term trends. *Geophysical Research Letters*, **44(4)**, 1866–1876, doi:10.1002/2017gl072582.
Frieler, K. et al., 2015: Consistent evidence of increasing Antarctic accumulation with warming. *Nature Climate Change*, **5(4)**, 348–352, doi:10.1038/nclimate2574.
Fringer, O.B., M. Gerritsen, and R.L. Street, 2006: An unstructured-grid, finite-volume, nonhydrostatic, parallel coastal ocean simulator. *Ocean Modelling*, **14(3–4)**, 139–173, doi:10.1016/j.ocemod.2006.03.006.
Frölicher, T.L. and C. Laufkötter, 2018: Emerging risks from marine heat waves. *Nature Communications*, **9(1)**, 650, doi:10.1038/s41467-018-03163-6.
Frölicher, T.L., E.M. Fischer, and N. Gruber, 2018: Marine heatwaves under global warming. *Nature*, **560(7718)**, 360–364, doi:10.1038/s41586-018-0383-9.
Frölicher, T.L. et al., 2015: Dominance of the Southern Ocean in Anthropogenic Carbon and Heat Uptake in CMIP5 Models. *Journal of Climate*, **28(2)**, 862–886, doi:10.1175/jcli-d-14-00117.1.
Frölicher, T.L. et al., 2020: Contrasting Upper and Deep Ocean Oxygen Response to Protracted Global Warming. *Global Biogeochemical Cycles*, **34(8)**, e2020GB006601, doi:10.1029/2020gb006601.

ACCEPTED VERSION SUBJECT TO FINAL EDITING

Funder, S. et al., 2011: A 10,000-year record of Arctic Ocean Sea-ice variability – View from the beach. *Science*, **333(6043)**, 747–750, doi:10.1126/science.1202760.
Fürst, J.J., H. Goelzer, and P. Huybrechts, 2015: Ice-dynamic projections of the Greenland ice sheet in response to atmospheric and oceanic warming. *The Cryosphere*, **9**, 1039–1062.
Fürst, J.J. et al., 2016: The safety band of Antarctic ice shelves. *Nature Climate Change*, **6(5)**, 479–482, doi:10.1038/nclimate2912.
Fyke, J., O. Sergienko, M. Löfverström, S. Price, and J.T.M. Lenaerts, 2018: An Overview of Interactions and Feedbacks Between Ice Sheets and the Earth System. *Reviews of Geophysics*, **56**.
Fyke, J.G. et al., 2011: A new coupled ice sheet/climate model: description and sensitivity to model physics under Eemian, Last Glacial Maximum, late Holocene and modern climate conditions. *Geoscientific Model Development*, **4(1)**, 117–136.
Gagné, M., N.P. Gillett, and J.C. Fyfe, 2015a: Impact of aerosol emission controls on future Arctic sea ice cover. *Geophysical Research Letters*, **42(20)**, 8481–8488, doi:10.1002/2015gl065504.
Gagné, M., N.P. Gillett, and J.C. Fyfe, 2015b: Observed and simulated changes in Antarctic sea ice extent over the past 50 years. *Geophysical Research Letters*, **42(1)**, 90–95, doi:10.1002/2014gl062231.
Gallaher, D.W., G.G. Campbell, and W.N. Meier, 2014: Anomalous Variability in Antarctic Sea Ice Extents During the 1960s With the Use of Nimbus Data. *IEEE Journal of Selected Topics in Applied Earth Observations and Remote Sensing*, **7(3)**, 881–887, doi:10.1109/jstars.2013.2264391.
Gandy, N. et al., 2018: Marine Ice Sheet Instability and Ice Shelf Buttressing Influenced Deglaciation of the Minch Ice Stream, Northwest Scotland. *The Cryosphere*, **12(11)**, 3635–3651, doi:10.5194//tc-12-3635-2018.
Garbe, J., T. Albrecht, A. Levermann, J.F. Donges, and R. Winkelmann, 2020: The hysteresis of the Antarctic Ice Sheet. *Nature*, **585(7826)**, 538–544, doi:10.1038/s41586-020-2727-5.
García, D., B.F. Chao, J. Del Río, I. Vigo, and J. García-Lafuente, 2006: On the steric and mass-induced contributions to the annual sea level variations in the Mediterranean Sea. *Journal of Geophysical Research*, **111(C9)**, C09030, doi:10.1029/2005jc002956.
García, J.-L. et al., 2020: 14C and 10Be dated Late Holocene fluctuations of Patagonian glaciers in Torres del Paine (Chile, 51°S) and connections to Antarctic climate change. *Quaternary Science Reviews*, **246**, 106541, doi:10.1016/j.quascirev.2020.106541.
García-Reyes, M. and J. Largier, 2010: Observations of increased wind-driven coastal upwelling off central California. *Journal of Geophysical Research: Oceans*, **115(C4)**, doi:10.1029/2009jc005576.
García-Reyes, M., J.L. Largier, and W.J. Sydeman, 2014: Synoptic-scale upwelling indices and predictions of phyto- and zooplankton populations. *Progress in Oceanography*, **120**, 177–188, doi:10.1016/j.pocean.2013.08.004.
García-Reyes, M. et al., 2013: Relative influence of oceanic and terrestrial pressure systems in driving upwelling-favorable winds. *Geophysical Research Letters*, **40(19)**, 5311–5315, doi:10.1002/2013gl057729.
Gardner, A.S. et al., 2018: Increased West Antarctic and unchanged East Antarctic ice discharge over the last 7 years. *Cryosphere*, **12**, 521–547, doi:10.5194/tc-12-521-2018.
Garner, A.J. et al., 2017: Impact of climate change on New York City's coastal flood hazard: Increasing flood heights from the preindustrial to 2300 CE. *Proceedings of the National Academy of Sciences of the United States of America*, **114(45)**, doi:10.1073/pnas.1703568114.
Garner, A.J. et al., 2018: Evolution of 21 st Century Sea-level Rise Projections. *Earth's Future*, **6(11)**, 1603–1615, doi:10.1029/2018ef000991.
Garry, F.K. et al., 2019: Model-Derived Uncertainties in Deep Ocean Temperature Trends Between 1990 and 2010. *Journal of Geophysical Research: Oceans*, **124(2)**, 1155–1169, doi:10.1029/2018jc014225.
Garuba, O.A. and B.A. Klinger, 2018: The Role of Individual Surface Flux Components in the Passive and Active Ocean Heat Uptake. *Journal of Climate*, **31(15)**, 6157–6173, doi:10.1175/jcli-d-17-0452.1.
Gasson, E., R.M.R.M. DeConto, D.P.- Geology, U. 2016, and D. Pollard, 2016: Modeling the oxygen isotope composition of the Antarctic ice sheet and its significance to Pliocene sea level. *Geology*, **44(10)**, 827–830, doi:10.1130/g38104.1.
Gebbie, G. and P. Huybers, 2019: The Little Ice Age and 20th Century Deep Pacific Cooling. *Science*, **363(6422)**, 70–74, doi:10.1126/science.aar8413.
Gehrels, W.R. and P.L. Woodworth, 2013: When did modern rates of sea-level rise start? *Global and Planetary Change*, **100**, 263–277, doi:10.1016/j.gloplacha.2012.10.020.
Geirsdóttir et al., 2019: The onset of neoglaciation in Iceland and the 4.2\\,ka event. *Climate of the Past*, **15(1)**, 25–40, doi:10.5194/cp-15-25-2019.
Gemmrich, J., B. Thomas, and R. Bouchard, 2011: Observational changes and trends in northeast Pacific wave records. *Geophysical Research Letters*, doi:10.1029/2011gl049518.

ACCEPTED VERSION SUBJECT TO FINAL EDITING

Gibson, C.M. et al., 2018a: Wildfire as a major driver of recent permafrost thaw in boreal peatlands. *Nature Communications*, **9(1)**, 3041, doi:10.1038/s41467-018-05457-1.
Gibson, C.M. et al., 2018b: Wildfire as a major driver of recent permafrost thaw in boreal peatlands. *Nature Communications*, **9(1)**, 3041, doi:10.1038/s41467-018-05457-1.
Gilbert, G.L., M. Kanevskiy, and J.B. Murton, 2016: Recent Advances (2008–2015) in the Study of Ground Ice and Cryostratigraphy. *Permafrost and Periglacial Processes*, **27(4)**, 377–389, doi:10.1002/ppp.1912.
Gilford, D.M. et al., 2020: Could the Last Interglacial Constrain Projections of Future Antarctic Ice Mass Loss and Sea-Level Rise? *Journal of Geophysical Research: Earth Surface*, **125(10)**, e2019JF005418, doi:10.1029/2019jf005418.
Giorgi, F. and P. Lionello, 2008: Climate change projections for the Mediterranean region. *Global and Planetary Change*, **63(2–3)**, 90–104, doi:10.1016/j.gloplacha.2007.09.005.
GlaThiDa Consortium, 2019: Glacier Thickness Database 3.0.1. World Glacier Monitoring Service, Zurich, Switzerland.
Goelzer, H., P. Huybrechts, M.-F.M.-F. Loutre, and T. Fichefet, 2016: Last Interglacial climate and sea-level evolution from a coupled ice sheet-climate model. *Climate of the Past*, **12(12)**, 2195–2213, doi:10.5194/cp-12-2195-2016.
Goelzer, H. et al., 2013: Sensitivity of Greenland ice sheet projections to model formulations. *Journal of Glaciology*, **59(216)**, doi:10.3189/2013jog12j182.
Goelzer, H. et al., 2018: Design and results of the ice sheet model initialisation experiments initMIP-Greenland: an ISMIP6 intercomparison. *The Cryosphere*, **12(4)**, 1433–1460, doi:10.5194/tc-12-1433-2018.
Goelzer, H. et al., 2020: The future sea-level contribution of the Greenland ice sheet: a multi-model ensemble study of ISMIP6. *The Cryosphere*, **14**, 3071–3096.
Golaz, J.-C. et al., 2019: The DOE E3SM Coupled Model Version 1: Overview and Evaluation at Standard Resolution. *Journal of Advances in Modeling Earth Systems*, **11(7)**, 2089–2129, doi:10.1029/2018ms001603.
Goldberg, D.N., P. Heimbach, I. Joughin, and B. Smith, 2015: Committed retreat of Smith, Pope, and Kohler Glaciers over the next 30 years inferred by transient model calibration. *The Cryosphere*, **9(6)**, 2429–2446, doi:10.5194/tc-9-2429-2015.
Goldberg, D.N., T.A. Smith, S.H.K. Narayanan, and P. Heimbach, 2020: Bathymetric influences on Antarctic ice-shelf melt rates. *Journal of Geophysical Research: Oceans*, 1–39, doi:10.1029/2020jc016370.
Goldberg, D.N., N. Gourmelen, S. Kimura, R. Millan, and K. Snow, 2019: How Accurately Should We Model Ice Shelf Melt Rates? *Geophysical Research Letters*, **46(1)**, 189–199, doi:10.1029/2018gl080383.
Golledge, N.R., C.J. Fogwill, A.N. Mackintosh, and K.M. Buckley, 2012: Dynamics of the last glacial maximum Antarctic ice-sheet and its response to ocean forcing. *Proceedings of the National Academy of Sciences of the United States of America*, **109(40)**, doi:10.1073/pnas.1205385109.
Golledge, N.R., R.H. Levy, R.M. McKay, and T.R. Naish, 2017a: East Antarctic ice sheet most vulnerable to Weddell Sea warming. *Geophysical Research Letters*, **44(5)**, 2343–2351, doi:10.1002/2016gl072422.
Golledge, N.R. et al., 2013: Glaciology and geological signature of the Last Glacial Maximum Antarctic ice sheet. *Quaternary Science Reviews*, **78**, doi:10.1016/j.quascirev.2013.08.011.
Golledge, N.R. et al., 2014: Antarctic contribution to meltwater pulse 1A from reduced Southern Ocean overturning. *Nature Communications*, **5**, doi:10.1038/ncomms6107.
Golledge, N.R. et al., 2015: The multi-millennial Antarctic commitment to future sea-level rise. *Nature*, **526(7573)**, doi:10.1038/nature15706.
Golledge, N.R. et al., 2017b: Antarctic climate and ice-sheet configuration during the early Pliocene interglacial at 4.23 Ma. *Climate of the Past*, **13(7)**, doi:10.5194/cp-13-959-2017.
Golledge, N.R. et al., 2019a: Global environmental consequences of twenty-first-century ice-sheet melt. *Nature*, **566(7742)**, doi:10.1038/s41586-019-0889-9.
Golledge, N.R. et al., 2019b: Global environmental consequences of twenty-first-century ice-sheet melt. *Nature*, **566(7742)**, doi:10.1038/s41586-019-0889-9.
Gomez, N., D. Pollard, and D. Holland, 2015: Sea-level feedback lowers projections of future Antarctic Ice-Sheet mass loss. *Nature Communications*, **6**, 8798.
Gomez, N., M.E. Weber, P.U. Clark, J.X. Mitrovica, and H.K. Han, 2020: Antarctic ice dynamics amplified by Northern Hemisphere sea-level forcing. *Nature*, **587(7835)**, 600–604, doi:10.1038/s41586-020-2916-2.
Goodwin, P., S. Brown, I.D. Haigh, R.J. Nicholls, and J.M. Matter, 2018: Adjusting Mitigation Pathways to Stabilize Climate at 1.5°C and 2.0°C Rise in Global Temperatures to Year 2300. *Earth's Future*, doi:10.1002/2017ef000732.

ACCEPTED VERSION SUBJECT TO FINAL EDITING

Goosse, H. and H. Renssen, 2001: A two-phase response of the Southern Ocean to an increase in greenhouse gas concentrations. *Geophysical Research Letters*, **28(18)**, 3469–3472, doi:10.1029/2001gl013525.
Goosse, H. and V. Zunz, 2014: Decadal trends in the Antarctic sea ice extent ultimately controlled by ice-ocean feedback. *The Cryosphere*, **8(2)**, 453–470, doi:10.5194/tc-8-453-2014.
Goosse, H. et al., 2018: Quantifying climate feedbacks in polar regions. *Nature Communications*, **9(1)**, 1919, doi:10.1038/s41467-018-04173-0.
Gordon, A.L., B.A. Huber, and E.P. Abrahamsen, 2020: Interannual Variability of the Outflow of Weddell Sea Bottom Water. *Geophysical Research Letters*, **47(4)**, e2020GL087014, doi:10.1029/2020gl087014.
Gorte, T., J.T.M. Lenaerts, and B. Medley, 2020: Scoring Antarctic surface mass balance in climate models to refine future projections. *The Cryosphere*, **14**, 4719–4733, doi:10.5194/tc-14-4719-202.
Gottschalk, J. et al., 2016: Biological and physical controls in the Southern Ocean on past millennial-scale atmospheric CO2 changes. *Nature Communications*, **7**, 11539, doi:10.1038/ncomms11539.
Graham, R.M. et al., 2019: Winter storms accelerate the demise of sea ice in the Atlantic sector of the Arctic Ocean. *Scientific Reports*, **9(1)**, doi:10.1038/s41598-019-45574-5.
Grant, G.R. et al., 2019: The amplitude and origin of sea-level variability during the Pliocene epoch. *Nature*, doi:10.1038/s41586-019-1619-z.
Greenberg, D.A., F. Dupont, F.H. Lyard, D.R. Lynch, and F.E. Werner, 2007: Resolution issues in numerical models of oceanic and coastal circulation. *Continental Shelf Research*, **27(9)**, 1317–1343, doi:10.1016/j.csr.2007.01.023.
Greene, C.A., D.A. Young, D.E. Gwyther, B.K. Galton-Fenzi, and D.D. Blankenship, 2018: Seasonal dynamics of Totten Ice Shelf controlled by sea ice buttressing. *The Cryosphere*, **12**, 2869–2882, doi:10.5194/tc-12-2869-2018.
Greene, C.H. and A.J. Pershing, 2007: Climate Drives Sea Change. *Science*, **315(5815)**, 1084–1085, doi:10.1126/science.1136495.
Gregoire, L.J., B. Otto-Bliesner, P.J. Valdes, and R. Ivanovic, 2016: Abrupt Bølling warming and ice saddle collapse contributions to the Meltwater Pulse 1a rapid sea level rise. *Geophysical research letters*, **43(17)**, 9130–9137.
Gregory, J., S. George, and R. Smith, 2020: Large and irreversible future decline of the Greenland ice-sheet. *The Cryosphere*, **14**, 4299–4322, doi:10.5194/tc-2020-89.
Gregory, J.M. and P. Huybrechts, 2006: Ice-sheet contributions to future sea-level change. *Philosophical Transactions of the Royal Society of London, Series A*, **364(1844)**, 1709–1731, doi:10.1098/rsta.2006.1796.
Gregory, J.M., J.A. Lowe, and S.F.B. Tett, 2006: Simulated Global-Mean Sea Level Changes over the Last Half-Millennium. *Journal of Climate*, **19(18)**, 4576–4591, doi:10.1175/jcli3881.1.
Gregory, J.M. et al., 2002: Recent and future changes in Arctic sea ice simulated by the HadCM3 AOGCM. *Geophysical Research Letters*, **29(24)**, 28–1–28–4, doi:10.1029/2001gl014575.
Gregory, J.M. et al., 2013: Twentieth-century global-mean sea level rise: Is the whole greater than the sum of the parts? *Journal of Climate*, **26(13)**, 4476–4499, doi:10.1175/jcli-d-12-00319.1.
Gregory, J.M. et al., 2016: The Flux-Anomaly-Forced Model Intercomparison Project (FAFMIP) contribution to CMIP6: investigation of sea-level and ocean climate change in response to CO forcing. *Geoscientific Model Development*, **9(11)**, 3993–4017, doi:10.5194/gmd-9-3993-2016.
Gregory, J.M. et al., 2019: Concepts and Terminology for Sea Level: Mean, Variability and Change, Both Local and Global. *Surveys in Geophysics*, **40(6)**, 1251–1289, doi:10.1007/s10712-019-09525-z.
Griffies, S.M. et al., 2014: An assessment of global and regional sea level for years 1993–2007 in a suite of interannual CORE-II simulations. *Ocean Modelling*, **78**, 35–89, doi:10.1016/j.ocemod.2014.03.004.
Griffies, S.M. et al., 2015: Impacts on ocean heat from transient mesoscale eddies in a hierarchy of climate models. *Journal of Climate*, **28(3)**, 952–977, doi:10.1175/jcli-d-14-00353.1.
Grinsted, A., J.C. Moore, and S. Jevrejeva, 2013: Projected Atlantic hurricane surge threat from rising temperatures. *Proceedings of the National Academy of Sciences*, **110(14)**, 5369–5373, doi:10.1073/pnas.1209980110.
Grinsted, A., S. Jevrejeva, R.E.M. Riva, and D. Dahl-Jensen, 2015: Sea level rise projections for Northern Europe under RCP8.5. *Climate Research, 64 (1), 2015*, doi:10.3354/cr01309.
Gruber, S., 2012: Derivation and analysis of a high-resolution estimate of global permafrost zonation. *The Cryosphere*, **6**, 221–233, doi:10.5194/tc-6-221-2012.
Gudmundsson, G.H., F.S. Paolo, S. Adusumilli, and H.A. Fricker, 2019: Instantaneous Antarctic ice sheet mass loss driven by thinning ice shelves. *Geophysical Research Letters*, **46(23)**, 13903–13909, doi:10.1029/2019gl085027.
Guimberteau, M. et al., 2018: ORCHIDEE-MICT (v8.4.1), a land surface model for the high latitudes: model description and validation. *Geoscientific Model Development*, **11**, 121–163, doi:10.5194/gmd-11-121-2018.

ACCEPTED VERSION SUBJECT TO FINAL EDITING

Günther, F. et al., 2015: Observing Muostakh disappear: Permafrost thaw subsidence and erosion of a ground-ice-rich Island in response to arctic summer warming and sea ice reduction. *Cryosphere*, **9(1)**, 151–178, doi:10.5194/tc-9-151-2015.

Gupta, M. and J. Marshall, 2018: The Climate Response to Multiple Volcanic Eruptions Mediated by Ocean Heat Uptake: Damping Processes and Accumulation Potential. *Journal of Climate*, **31(21)**, 8669–8687, doi:10.1175/jcli-d-17-0703.1.

Haarsma, R.J. et al., 2016: High Resolution Model Intercomparison Project (HighResMIP v1.0) for CMIP6. *Geoscientific Model Development*, **9(11)**, 4185–4208, doi:10.5194/gmd-9-4185-2016.

Haas, C. et al., 2017: Ice and Snow Thickness Variability and Change in the High Arctic Ocean Observed by In Situ Measurements. *Geophysical Research Letters*, doi:10.1002/2017gl075434.

Haas, C. et al., 2021: Airborne mapping of the sub-ice platelet layer under fast ice in McMurdo Sound, Antarctica. *The Cryosphere*, **15(1)**, 247–264, doi:10.5194/tc-15-247-2021.

Hagemann, S., T. Blome, A. Ekici, and C. Beer, 2016: Soil-frost-enabled soil-moisture-precipitation feedback over northern high latitudes. *Earth System Dynamics*, **7(3)**, 611–625, doi:10.5194/esd-7-611-2016.

Hahn, L.C., T. Storelvmo, S. Hofer, R. Parfitt, and C.C. Ummenhofer, 2020: Importance of orography for Greenland cloud and melt response to atmospheric blocking. *Journal of Climate*, **33(10)**, 4187–4206, doi:10.1175/jcli-d-19-0527.1.

Haigh, I.D. et al., 2019: The Tides They Are a-Changin': A comprehensive review of past and future non-astronomical changes in tides, their driving mechanisms and future implications. *Reviews of Geophysics*, 2018RG000636, doi:10.1029/2018rg000636.

Haine, T. et al., 2008: North Atlantic Deep Water Formation in the Labrador Sea, Recirculation Through the Subpolar Gyre, and Discharge to the Subtropics. In: *Arctic–Subarctic Ocean Fluxes* [Dickson, R.R., J. Meincke, and P. Rhines (eds.)]. Springer, Dordrecht, The Netherlands, pp. 653–701, doi:10.1007/978-1-4020-6774-7_28.

Häkkinen, S., P.B. Rhines, and D.L. Worthen, 2016: Warming of the Global Ocean: Spatial Structure and Water-Mass Trends. *Journal of Climate*, **29(13)**, 4949–4963, doi:10.1175/jcli-d-15-0607.1.

Hall, B.L., T. Lowell, G.R.M. Bromley, G.H. Denton, and A.E. Putnam, 2019: Holocene glacier fluctuations on the northern flank of Cordillera Darwin, southernmost South America. *Quaternary Science Reviews*, **222**, 105904, doi:10.1016/j.quascirev.2019.105904.

Hallberg, R., A. Adcroft, J.P. Dunne, J.P. Krasting, and R.J. Stouffer, 2013: Sensitivity of Twenty-First-Century Global-Mean Steric Sea Level Rise to Ocean Model Formulation. *Journal of Climate*, **26(9)**, 2947–2956, doi:10.1175/jcli-d-12-00506.1.

Halloran, P.R. et al., 2020: Natural drivers of multidecadal Arctic sea ice variability over the last millennium. *Scientific Reports*, **10(1)**, 688, doi:10.1038/s41598-020-57472-2.

Hamlington, B.D., T. Frederikse, R.S. Nerem, J.T. Fasullo, and S. Adhikari, 2020a: Investigating the Acceleration of Regional Sea Level Rise During the Satellite Altimeter Era. *Geophysical Research Letters*, **47(5)**, e2019GL086528, doi:10.1029/2019gl086528.

Hamlington, B.D. et al., 2014: Uncovering an anthropogenic sea-level rise signal in the Pacific Ocean. *Nature Clim Change*, **4(9)**, 782–785, doi:10.1038/nclimate2307.

Hamlington, B.D. et al., 2020b: Understanding of Contemporary Regional Sea-Level Change and the Implications for the Future. *Reviews of Geophysics*, **58(3)**, doi:10.1029/2019rg000672.

Hammond, J.C., F.A. Saavedra, and S.K. Kampf, 2018: Global snow zone maps and trends in snow persistence 2001–2016. *International Journal of Climatology*, **38**, 4369–4383, doi:10.1002/joc.5674.

Han, W. et al., 2017: Spatial Patterns of Sea Level Variability Associated with Natural Internal Climate Modes. *Surveys in Geophysics*, **38(1)**, 217–250, doi:10.1007/s10712-016-9386-y.

Hanna, E., X. Fettweis, and R.J. Hall, 2018: Brief communication: Recent changes in summer Greenland blocking captured by none of the CMIP5 models. *The Cryosphere*, **12(10)**, 3287–3292, doi:10.5194/tc-12-3287-2018.

Hanna, E., T.E. Cropper, R.J. Hall, and J. Cappelen, 2016: Greenland Blocking Index 1851-2015: a regional climate change signal. *International Journal of Climatology*, **36(15)**, 4847–4861, doi:10.1002/joc.4673.

Hanna, E. et al., 2020: Greenland surface air temperature changes from 1981 to 2019 and implications for ice-sheet melt and mass-balance change. *International Journal of Climatology*, 1–17, doi:10.1002/joc.6771.

Hansen, B., K.M. Húsgarð Larsen, H. Hátún, and S. Østerhus, 2016: A stable Faroe Bank Channel overflow 1995–2015. *Ocean Science*, **12(6)**, 1205–1220, doi:10.5194/os-12-1205-2016.

Harig, C. and F.J. Simons, 2015: Accelerated West Antarctic ice mass loss continues to outpace East Antarctic gains. *Earth and Planetary Science Letters*, **415**, 134–141, doi:10.1016/j.epsl.2015.01.029.

ACCEPTED VERSION SUBJECT TO FINAL EDITING

Harning, D.J., Geirsdóttir, and G.H. Miller, 2018: Punctuated Holocene climate of Vestfirðir, Iceland, linked to internal/external variables and oceanographic conditions. *Quaternary Science Reviews*, **189**, 31–42, doi:10.1016/j.quascirev.2018.04.009.

Harning, D.J., Geirsdóttir, G.H. Miller, and L. Anderson, 2016: Episodic expansion of Drangajökull, Vestfirðir, Iceland, over the last 3 ka culminating in its maximum dimension during the Little Ice Age. *Quaternary Science Reviews*, **152**, 118–131, doi:10.1016/j.quascirev.2016.10.001.

Harning, D.J. et al., 2019: Sea Ice Control on Winter Subsurface Temperatures of the North Iceland Shelf During the Little Ice Age: A TEX86 Calibration Case Study. *Paleoceanography and Paleoclimatology*, **34(6)**, 1006–1021, doi:10.1029/2018pa003523.

Harrison, S., D.E. Smith, and N.F. Glasser, 2019: Late Quaternary meltwater pulses and sea level change. *Journal of Quaternary Science*, **34(1)**, 1–15, doi:10.1002/jqs.3070.

Harrison, W.D., D.H. Elsberg, K.A. Echelmeyer, and R.M. Krimmel, 2001: On the characterization of glacier response by a single time-scale. *Journal of Glaciology*, **47(159)**, 659–664, doi:10.3189/172756501781831837.

Hartmann, D.L. et al., 2013: Observations: Atmosphere and Surface. In: *Climate Change 2013: the Physical Science Basis. Contribution of Working Group I to the Fifth Assessment Report of the Intergovernmental Panel on Climate Change* [Stocker, T.F., D. Qin, G.-K.Plattner, M. Tignor, S.K. Allen, A. J. Boschung, Nauels, Y. Xia, V. Bex, and P.M. Midgley (eds.)]. Cambridge University Press, Cambridge, United Kingdom and New York, NY, USA, pp. 159–254, doi:10.1017/cbo9781107415324.008.

Haskins, R.K., K.I.C. Oliver, L.C. Jackson, S.S. Drijfhout, and R.A. Wood, 2019: Explaining asymmetry between weakening and recovery of the AMOC in a coupled climate model. *Climate Dynamics*, **53(1)**, 67–79, doi:10.1007/s00382-018-4570-z.

Hasselmann, K., 1976: Stochastic climate models Part I. Theory. *Tellus*, **28(6)**, 473–485, doi:10.1111/j.2153-3490.1976.tb00696.x.

Hatfield, R.G. et al., 2016: Interglacial responses of the southern Greenland ice sheet over the last 430,000 years determined using particle-size specific magnetic and isotopic tracers. *Earth and Planetary Science Letters*, **454**, 225–236, doi:10.1016/j.epsl.2016.09.014.

Haumann, F.A., D. Notz, and H. Schmidt, 2014: Anthropogenic influence on recent circulation-driven Antarctic sea ice changes. *Geophysical Research Letters*, **41(23)**, 8429–8437, doi:10.1002/2014gl061659.

Haumann, F.A., N. Gruber, and M. Münnich, 2020: Sea-Ice Induced Southern Ocean Subsurface Warming and Surface Cooling in a Warming Climate. *AGU Advances*, **1(2)**, e2019AV000132, doi:10.1029/2019av000132.

Haumann, F.A., N. Gruber, M. Münnich, I. Frenger, and S. Kern, 2016: Sea-ice transport driving Southern Ocean salinity and its recent trends. *Nature*, **537(7618)**, 89–92, doi:10.1038/nature19101.

Hausmann, U. et al., 2020: The Role of Tides in Ocean-Ice Shelf Interactions in the Southwestern Weddell Sea. *Journal of Geophysical Research: Oceans*, **125(6)**, e2019JC015847, doi:10.1029/2019jc015847.

Haustein, K. et al., 2019: A Limited Role for Unforced Internal Variability in Twentieth-Century Warming. *Journal of Climate*, **32(16)**, 4893–4917, doi:10.1175/jcli-d-18-0555.1.

Hawley, W.B., C.C. Hay, J.X. Mitrovica, and R.E. Kopp, 2020: A Spatially Variable Time Series of Sea Level Change Due to Artificial Water Impoundment. *Earth's Future*, e2020EF001497.

Hayashida, H., R.J. Matear, P.G. Strutton, and X. Zhang, 2020a: Insights into projected changes in marine heatwaves from a high-resolution ocean circulation model. *Nature Communications*, **11(1)**, 4352, doi:10.1038/s41467-020-18241-x.

Hayashida, H., R.J. Matear, P.G. Strutton, and X. Zhang, 2020b: Insights into projected changes in marine heatwaves from a high-resolution ocean circulation model. *Nature Communications*, **11(1)**, 4352, doi:10.1038/s41467-020-18241-x.

Hayes, C.T. et al., 2014: A stagnation event in the deep South Atlantic during the last interglacial period. *Science*, **346(6216)**, 1514–1517, doi:10.1126/science.1256620.

Hazel, J.E. and A.L. Stewart, 2020: Bistability of the Filchner-Ronne Ice Shelf Cavity Circulation and Basal Melt. *Journal of Geophysical Research: Oceans*, **125(4)**, e2019JC015848, doi:10.1029/2019jc015848.

He, C., Z. Liu, and A. Hu, 2019: The transient response of atmospheric and oceanic heat transports to anthropogenic warming. *Nature Climate Change*, **9(3)**, 222–226, doi:10.1038/s41558-018-0387-3.

He, C., B. Wu, L. Zou, and T. Zhou, 2017: Responses of the summertime subtropical anticyclones to global warming. *Journal of Climate*, **30(16)**, 6465–6479.

Hein, A.S. et al., 2016: Mid-Holocene pulse of thinning in the Weddell Sea sector of the West Antarctic ice sheet. *Nature Communications*, **7**, 1–8, doi:10.1038/ncomms12511.

Hellmer, H.H., F. Kauker, R. Timmermann, and T. Hattermann, 2017: The fate of the Southern Weddell sea continental shelf in a warming climate. *Journal of Climate*, **30(12)**, 4337–4350, doi:10.1175/jcli-d-16-0420.1.

ACCEPTED VERSION SUBJECT TO FINAL EDITING

Hellmer, H.H., F. Kauker, R. Timmermann, J. Determann, and J. Rae, 2012: Twenty-first-century warming of a large Antarctic ice-shelf cavity by a redirected coastal current. *Nature*, **485(7397)**, 225, doi:10.1038/nature11064.

Helsen, M.M., W.J. Van De Berg, R.S.W. van de Wal, M.R. van den Broeke, and J. Oerlemans, 2013: Coupled regional climate-ice-sheet simulation shows limited Greenland ice loss during the Eemian. *Climate of the Past*, **9(4)**, 1773–1788, doi:10.5194/cp-9-1773-2013.

Hermans, T.H.J. et al., 2020: Improving sea-level projections on the Northwestern European shelf using dynamical downscaling. *Climate Dynamics*, **54(3)**, 1987–2011, doi:10.1007/s00382-019-05104-5.

Hermans, T.H.J. et al., 2021: Projecting Global Mean Sea-Level Change Using CMIP6 Models. *Geophysical Research Letters*, **48(5)**, doi:10.1029/2020gl092064.

Hernández-Henríquez, M.A., S.J. Déry, and C. Derksen, 2015: Polar amplification and elevation-dependence in trends of Northern Hemisphere snow cover extent, 1971-2014. *Environmental Research Letters*, **10(4)**, 044010, doi:10.1088/1748-9326/10/4/044010.

Herreid, S. and F. Pellicciotti, 2020: The state of rock debris covering Earth's glaciers. *Nature Geoscience*, **13(9)**, 621–627, doi:10.1038/s41561-020-0615-0.

Herrington, T. and K. Zickfeld, 2014: Path independence of climate and carbon cycle response over a broad range of cumulative carbon emissions. *Earth System Dynamics*, **5(2)**, 409–422, doi:10.5194/esd-5-409-2014.

Heuzé, C., 2017: North Atlantic deep water formation and AMOC in CMIP5 models. *Ocean Science*, **13(4)**, 609–622, doi:10.5194/os-13-609-2017.

Heuzé, C., 2021: Antarctic Bottom Water and North Atlantic Deep Water in CMIP6 models. *Ocean Science*, **17(1)**, 59–90, doi:10.5194/os-17-59-2021.

Heuzé, C., K.J. Heywood, D.P. Stevens, and J.K. Ridley, 2015: Changes in Global Ocean Bottom Properties and Volume Transports in CMIP5 Models under Climate Change Scenarios. *Journal of Climate*, **28(8)**, 2917–2944, doi:10.1175/jcli-d-14-00381.1.

Hewitt, H.T. et al., 2017: Will high-resolution global ocean models benefit coupled predictions on short-range to climate timescales? *Ocean Modelling*, **120**, doi:10.1016/j.ocemod.2017.11.002.

Hewitt, H.T. et al., 2020: Resolving and Parameterising the Ocean Mesoscale in Earth System Models. *Current Climate Change Reports*, doi:10.1007/s40641-020-00164-w.

Hieronymus, M., 2019: An update on the thermosteric sea level rise commitment to global warming. *Environmental Research Letters*, **14(5)**, 054018, doi:10.1088/1748-9326/ab1c31.

Hirano, D. et al., 2020: Strong ice-ocean interaction beneath Shirase Glacier Tongue in East Antarctica. *Nature Communications*, **11(1)**, 4221, doi:10.1038/s41467-020-17527-4.

Hobbs, W., M.D. Palmer, and D. Monselesan, 2016a: An Energy Conservation Analysis of Ocean Drift in the CMIP5 Global Coupled Models. *Journal of Climate*, **29(5)**, 1639–1653, doi:10.1175/jcli-d-15-0477.1.

Hobbs, W., M. Curran, N. Abram, and E.R. Thomas, 2016b: Century-scale perspectives on observed and simulated Southern Ocean sea ice trends from proxy reconstructions. *JOURNAL OF GEOPHYSICAL RESEARCH-OCEANS*, **121(10)**, 7804–7818, doi:10.1002/2016jc012111.

Hobbs, W.R., C. Roach, T. Roy, S. Jean-Baptiste, and N. Bindoff, 2020: Anthropogenic temperature and salinity changes in the Southern Ocean. *Journal of Climate*, 1–37, doi:10.1175/jcli-d-20-0454.1.

Hobday, A.J. et al., 2016: A hierarchical approach to defining marine heatwaves. *Progress in Oceanography*, **141**, 227–238, doi:10.1016/j.pocean.2015.12.014.

Hock, R. et al., 2019a: GlacierMIP - A model intercomparison of global-scale glacier mass-balance models and projections. *Journal of Glaciology*, **65(251)**, 453–467.

Hock, R. et al., 2019b: High Mountain Areas. In: *IPCC Special Report on the Ocean and Cryosphere in a Changing Climate* [Pörtner, H.-O., D.C. Roberts, V. Masson-Delmotte, P. Zhai, M. Tignor, E. Poloczanska, K. Mintenbeck, A. Alegría, M. Nicolai, A. Okem, J. Petzold, B. Rama, and N.M. Weyer (eds.)]. In Press, pp. 131–202.

Hoegh-Guldberg, O. et al., 2018: Impacts of 1.5°C Global Warming on Natural and Human Systems. In: *Global Warming of 1.5°C. An IPCC Special Report on the impacts of global warming of 1.5°C above pre-industrial levels and related global greenhouse gas emission pathways, in the context of strengthening the global response to the threat of climate change*, [Masson-Delmotte, V., P. Zhai, H.-O. Pörtner, D. Roberts, J. Skea, P.R. Shukla, A. Pirani, W. Moufouma-Okia, C. Péan, R. Pidcock, S. Connors, J.B.R. Matthews, Y. Chen, X. Zhou, M.I. Gomis, E. Lonnoy, T. Maycock, M. Tignor, and T. Waterfield (eds.)]. In Press, pp. 175–311.

Hofer, S., A.J. Tedstone, X. Fettweis, and J.L. Bamber, 2017: Decreasing cloud cover drives the recent mass loss on the Greenland Ice Sheet. *Science Advances*, **3(6)**, doi:10.1126/sciadv.1700584.

Hofer, S., A.J. Tedstone, X. Fettweis, and J.L. Bamber, 2019: Cloud microphysics and circulation anomalies control differences in future Greenland melt. *Nature Climate Change*, **9(7)**, 523–528, doi:10.1038/s41558-019-0507-8.

ACCEPTED VERSION SUBJECT TO FINAL EDITING

Hofer, S. et al., 2020: Greater Greenland Ice Sheet contribution to global sea level rise in CMIP6. *Nature Communications*, **11(1)**, 6289, doi:10.1038/s41467-020-20011-8.
Hoffman, M.J., X. Asay-Davis, S.F. Price, J. Fyke, and M. Perego, 2019: Effect of Subshelf Melt Variability on Sea Level Rise Contribution From Thwaites Glacier, Antarctica. *Journal of Geophysical Research: Earth Surface*, **124(12)**, 2798–2822, doi:10.1029/2019jf005155.
Holbrook, N.J. et al., 2019: A global assessment of marine heatwaves and their drivers. *Nature Communications*, **10(1)**, 2624, doi:10.1038/s41467-019-10206-z.
Holbrook, N.J. et al., 2020: Keeping pace with marine heatwaves. *Nature Reviews Earth & Environment*, **1(9)**, 482–493, doi:10.1038/s43017-020-0068-4.
Holland, M.M., L. Landrum, Y. Kostov, and J. Marshall, 2017a: Sensitivity of Antarctic sea ice to the Southern Annular Mode in coupled climate models. *CLIMATE DYNAMICS*, **49(5–6)**, 1813–1831, doi:10.1007/s00382-016-3424-9.
Holland, M.M., L. Landrum, M. Raphael, and S. Stammerjohn, 2017b: Springtime winds drive Ross Sea ice variability and change in the following autumn. *NATURE COMMUNICATIONS*, **8**, doi:10.1038/s41467-017-00820-0.
Holland, M.M., L. Landrum, M.N. Raphael, and R. Kwok, 2018: The regional, seasonal, and lagged influence of the Amundsen Sea Low on Antarctic Sea Ice. *Geophysical Research Letters*, doi:10.1029/2018gl080140.
Holland, P.R., T.J. Bracegirdle, P. Dutrieux, A. Jenkins, and E.J. Steig, 2019: West Antarctic ice loss influenced by internal climate variability and anthropogenic forcing. *Nature Geoscience*, **12(9)**, 718–724, doi:10.1038/s41561-019-0420-9.
Holland, P.R. et al., 2014: Modeled trends in Antarctic sea ice thickness. *Journal of Climate*, **27(10)**, 3784–3801, doi:10.1175/jcli-d-13-00301.1.
Holliday, N.P. et al., 2020: Ocean circulation causes the largest freshening event for 120 years in eastern subpolar North Atlantic. *Nature Communications*, **11(1)**, 585, doi:10.1038/s41467-020-14474-y.
Holmes, C.R., P.R. Holland, and T.J. Bracegirdle, 2019: Compensating biases and a noteworthy success in the CMIP5 representation of Antarctic sea ice processes. *Geophysical Research Letters*, doi:10.1029/2018gl081796.
Holt, J. et al., 2017: Prospects for improving the representation of coastal and shelf seas in global ocean models. *Geoscientific Model Development*, **10(1)**, 499–523, doi:10.5194/gmd-10-499-2017.
Holt, J. et al., 2018: Climate-Driven Change in the North Atlantic and Arctic Oceans Can Greatly Reduce the Circulation of the North Sea. *Geophysical Research Letters*, **45(21)**, 11,827–11,836, doi:10.1029/2018gl078878.
Holte, J., L.D. Talley, J. Gilson, and D. Roemmich, 2017: An Argo mixed layer climatology and database. *Geophysical Research Letters*, **44(11)**, 5618–5626, doi:10.1002/2017gl073426.
Hong, Y., Y. Du, T. Qu, Y. Zhang, and W. Cai, 2020: Variability of the Subantarctic Mode Water Volume in the South Indian Ocean During 2004–2018. *Geophysical Research Letters*, **47(10)**, e2020GL087830, doi:10.1029/2020gl087830.
Hoppmann, M. et al., 2020: Platelet ice, the Southern Ocean's hidden ice: a review. *Annals of Glaciology*, 1–28, doi:10.1017/aog.2020.54.
Hori, M. et al., 2017: A 38-year (1978–2015) Northern Hemisphere daily snow cover extent product derived using consistent objective criteria from satellite-borne optical sensors. *Remote Sensing of Environment*, **191**, 402–418, doi:10.1016/j.rse.2017.01.023.
Hörner, T., R. Stein, and K. Fahl, 2017: Evidence for Holocene centennial variability in sea ice cover based on IP25biomarker reconstruction in the southern Kara Sea (Arctic Ocean). *Geo-Marine Letters*, **37(5)**, 515–526, doi:10.1007/s00367-017-0501-y.
Hörner, T., R. Stein, and K. Fahl, 2018: Paleo-sea ice distribution and polynya variability on the Kara Sea shelf during the last 12 ka. *Arktos*, **4(1)**, 6, doi:10.1007/s41063-018-0040-4.
Hörner, T., R. Stein, K. Fahl, and D. Birgel, 2016: Post-glacial variability of sea ice cover, river run-off and biological production in the western Laptev Sea (Arctic Ocean) – A high-resolution biomarker study. *Quaternary Science Reviews*, **143**, 133–149, doi:10.1016/j.quascirev.2016.04.011.
Horton, B.P. et al., 2020: Estimating global mean sea-level rise and its uncertainties by 2100 and 2300 from an expert survey. *npj Climate and Atmospheric Science*, **3(1)**, 18, doi:10.1038/s41612-020-0121-5.
Hosking, J.S., A. Orr, G.J. Marshall, J. Turner, and T. Phillips, 2013: The influence of the Amundsen-Bellingshausen Aeas low on the climate of West Antarctica and its representation in coupled climate model simulations. *Journal of Climate*, **26(17)**, 6633–6648, doi:10.1175/jcli-d-12-00813.1.
Hristova, H.G., C. Ladd, and P.J. Stabeno, 2019: Variability and Trends of the Alaska Gyre From Argo and Satellite Altimetry. *Journal of Geophysical Research: Oceans*, **124(8)**, 5870–5887, doi:10.1029/2019jc015231.

ACCEPTED VERSION SUBJECT TO FINAL EDITING

Hsiao, S.C. et al., 2021: Flood risk influenced by the compound effect of storm surge and rainfall under climate change for low-lying coastal areas. *Science of the Total Environment*, **764**, 144439, doi:10.1016/j.scitotenv.2020.144439.

Hu, S. et al., 2020: Deep-reaching acceleration of global mean ocean circulation over the past two decades. *Science Advances*, **6(6)**, eaax7727, doi:10.1126/sciadv.aax7727.

Huai, B., M.R. van den Broeke, and C.H. Reijmer, 2020: Long-term surface energy balance of the western Greenland ice sheet and the role of large-scale circulation variability. *The Cryosphere*, **14**, 4181–4199, doi:10.5194/tc-14-4181-2020.

Huang, B. et al., 2021: Improvements of the Daily Optimum Interpolation Sea Surface Temperature (DOISST) Version 2.1. *Journal of Climate*, **34(8)**, 2923–2939, doi:10.1175/jcli-d-20-0166.1.

Huang, H., M. Gutjahr, A. Eisenhauer, and G. Kuhn, 2020: No detectable Weddell Sea Antarctic Bottom Water export during the Last and Penultimate Glacial Maximum. *Nature Communications*, **11(1)**, 424, doi:10.1038/s41467-020-14302-3.

Huang, P.P., P. Wu, and H. Steffen, 2019: In search of an ice history that is consistent with composite rheology in Glacial Isostatic Adjustment modelling. *Earth and Planetary Science Letters*, doi:10.1016/j.epsl.2019.04.011.

Huang, P.-Q., Y.-Z. Lu, and S.-Q. Zhou, 2017: An Objective Method for Determining Ocean Mixed Layer Depth with Applications to WOCE Data. *Journal of Atmospheric and Oceanic Technology*, **35(3)**, 441–458, doi:10.1175/jtech-d-17-0104.1.

Huber, M.B. and L. Zanna, 2017: Drivers of uncertainty in simulated ocean circulation and heat uptake. *Geophysical Research Letters*, **44(3)**, 1402–1413, doi:10.1002/2016gl071587.

Hughes, C.W. and B.A. de Cuevas, 2001: Why Western Boundary Currents in Realistic Oceans are Inviscid: A Link between Form Stress and Bottom Pressure Torques. *Journal of Physical Oceanography*, **31(10)**, 2871–2885, doi:10.1175/1520-0485(2001)031<2871:wwbcir>2.0.co;2.

Hughes, C.W., J. Williams, A. Blaker, A. Coward, and V. Stepanov, 2018: A window on the deep ocean: The special value of ocean bottom pressure for monitoring the large-scale, deep-ocean circulation. *Progress in Oceanography*, **161**, 19–46, doi:10.1016/j.pocean.2018.01.011.

Hugonnet, R. et al., 2021: Accelerating global glacier mass loss in the early twenty-first century. *Nature*.**592**, 726–731, doi: 10.1038/s41586-021-03436-z

Huhn, O. et al., 2018: Basal Melt and Freezing Rates From First Noble Gas Samples Beneath an Ice Shelf. *Geophysical Research Letters*, **45(16)**, doi:10.1029/2018gl079706.

Hunter, J., 2010: Estimating sea-level extremes under conditions of uncertain sea-level rise. *Climatic Change*, **99(3)**, 331–350, doi:10.1007/s10584-009-9671-6.

Hunter, J., 2012: A simple technique for estimating an allowance for uncertain sea-level rise. *Climatic Change*, **113(2)**, 239–252, doi:10.1007/s10584-011-0332-1.

Huss, M. and D. Farinotti, 2012: Distributed ice thickness and volume of all glaciers around the globe. *Journal of Geophysical Research: Earth Surface*, **117(F4)**, n/a–n/a, doi:10.1029/2012jf002523.

Huss, M. and R. Hock, 2015: A new model for global glacier change and sea-level rise. *Frontiers in Earth Science*, **3**, doi:10.3389/feart.2015.00054.

Huss, M. and M. Fischer, 2016: Sensitivity of Very Small Glaciers in the Swiss Alps to Future Climate Change. *Frontiers in Earth Science*, **4**, doi:10.3389/feart.2016.00034.

Hyder, P. et al., 2018: Critical Southern Ocean climate model biases traced to atmospheric model cloud errors. *Nature Communications*, **9(1)**, 3625, doi:10.1038/s41467-018-05634-2.

Irvalı, N. et al., 2020: A low climate threshold for south Greenland Ice Sheet demise during the Late Pleistocene. *Proceedings of the National Academy of Sciences of the United States of America*, **117(1)**, 190–195, doi:10.1073/pnas.1911902116.

Irving, D.B., S. Wijffels, and J.A. Church, 2019: Anthropogenic Aerosols, Greenhouse Gases, and the Uptake, Transport, and Storage of Excess Heat in the Climate System. *Geophysical Research Letters*, **46(9)**, 4894–4903, doi:10.1029/2019gl082015.

Isaev, V.S. et al., 2019: Cliff retreat of permafrost coast in south-west Baydaratskaya Bay, Kara Sea, during 2005–2016. *Permafrost and Periglacial Processes*, **30(1)**, 35–47, doi:10.1002/ppp.1993.

Ishii, M. et al., 2017: Accuracy of Global Upper Ocean Heat Content Estimation Expected from Present Observational Data Sets. *SOLA*, **13(0)**, 163–167, doi:10.2151/sola.2017-030.

Ivanova, D.P., P.J. Gleckler, K.E. Taylor, P.J. Durack, and K.D. Marvel, 2016: Moving beyond the total sea ice extent in gauging model biases. *Journal of Climate*, doi:10.1175/jcli-d-16-0026.1.

Ivins, E.R. et al., 2013: Antarctic contribution to sea level rise observed by GRACE with improved GIA correction. *Journal of Geophysical Research: Solid Earth*, **118(6)**, 3126–3141, doi:10.1002/jgrb.50208.

ACCEPTED VERSION
SUBJECT TO FINAL EDITING

Jaccard, S.L., E.D. Galbraith, A. Martínez-García, and R.F. Anderson, 2016: Covariation of deep Southern Ocean oxygenation and atmospheric CO2 through the last ice age. *Nature*, **530**, 207.
Jackson, L.C., 2013: Shutdown and recovery of the AMOC in a coupled global climate model: The role of the advective feedback. *Geophysical Research Letters*, **40(6)**, 1182–1188, doi:10.1002/grl.50289.
Jackson, L.C. and R.A. Wood, 2018: Timescales of AMOC decline in response to fresh water forcing. *Climate Dynamics*, doi:10.1007/s00382-017-3957-6.
Jackson, L.C. and R.A. Wood, 2020: Fingerprints for Early Detection of Changes in the AMOC. *Journal of Climate*, **33(16)**, 7027–7044, doi:10.1175/jcli-d-20-0034.1.
Jackson, L.C., K.A. Peterson, C.D. Roberts, and R.A. Wood, 2016: Recent slowing of Atlantic overturning circulation as a recovery from earlier strengthening. *Nature Geoscience*, **9(7)**, 518–522, doi:10.1038/ngeo2715.
Jackson, L.C. et al., 2019: The Mean State and Variability of the North Atlantic Circulation: A Perspective From Ocean Reanalyses. *Journal of Geophysical Research: Oceans*, **124(12)**, 9141–9170, doi:10.1029/2019jc015210.
Jackson, L.C. et al., 2020: Impact of ocean resolution and mean state on the rate of AMOC weakening. *Climate Dynamics*, doi:10.1007/s00382-020-05345-9.
Jackson, R.H. et al., 2020: Meltwater Intrusions Reveal Mechanisms for Rapid Submarine Melt at a Tidewater Glacier. *Geophysical Research Letters*, **47(2)**, doi:10.1029/2019gl085335.
Jacox, M.G., C.A. Edwards, E.L. Hazen, and S.J. Bograd, 2018: Coastal Upwelling Revisited: Ekman, Bakun, and Improved Upwelling Indices for the U.S. West Coast. *Journal of Geophysical Research: Oceans*, **123(10)**, 7332–7350, doi:10.1029/2018jc014187.
Jahn, A., 2018: Reduced probability of ice-free summers for 1.5°C compared to 2°C warming. *Nature Climate Change*, **8(5)**, 409–413, doi:10.1038/s41558-018-0127-8.
Jakobsson, M. et al., 2020: The International Bathymetric Chart of the Arctic Ocean Version 4.0. *Scientific Data*, **7(1)**, 176, doi:10.1038/s41597-020-0520-9.
James, M., A.G. Lewkowicz, S.L. Smith, and C.M. Miceli, 2013: Multi-decadal degradation and persistence of permafrost in the Alaska Highway corridor, northwest Canada. *Environmental Research Letters*, **8(4)**, 045013, doi:10.1088/1748-9326/8/4/045013.
Janeković, I. and B. Powell, 2012: Analysis of imposing tidal dynamics to nested numerical models. *Continental Shelf Research*, **34**, 30–40, doi:10.1016/j.csr.2011.11.017.
Jay, D.A., 2009: Evolution of tidal amplitudes in the eastern Pacific Ocean. *Geophysical Research Letters*, doi:10.1029/2008gl036185.
Jayne, S.R. et al., 2009: The Kuroshio Extension and its recirculation gyres. *Deep Sea Research Part I: Oceanographic Research Papers*, **56(12)**, 2088–2099, doi:10.1016/j.dsr.2009.08.006.
Jena, B., M. Ravichandran, and J. Turner, 2019: Recent Reoccurrence of Large Open-Ocean Polynya on the Maud Rise Seamount. *Geophysical Research Letters*, **46(8)**, 4320–4329, doi:10.1029/2018gl081482.
Jensen, L., A. Eicker, H. Dobslaw, T. Stacke, and V. Humphrey, 2019: Long-term wetting and drying trends in land water storage derived from GRACE and CMIP5 models. *Journal of Geophysical Research: Atmospheres*, **124(17–18)**, 9808–9823, doi:10.1029/2018jd029989.
Jeong, H. et al., 2020: Impacts of Ice-Shelf Melting on Water-Mass Transformation in the Southern Ocean from E3SM Simulations. *Journal of Climate*, **33(13)**, 5787–5807, doi:10.1175/jcli-d-19-0683.1.
Jevrejeva, S., H. Palanisamy, and L.P. Jackson, 2020: Global mean thermosteric sea level projections by 2100 in CMIP6 climate models. *Environmental Research Letters*, **16(1)**, 14028, doi:10.1088/1748-9326/abceea.
Jevrejeva, S. et al., 2019: Probabilistic Sea Level Projections at the Coast by 2100. *Surveys in Geophysics*, **40(6)**, 1673–1696, doi:10.1007/s10712-019-09550-y.
Ji, T., G. Li, and R. Liu, 2020: Historical Reconstruction of Storm Surge Activity in the Southeastern Coastal Area of China for the Past 60 Years. *Earth and Space Science*, **7(8)**, doi:10.1029/2019ea001056.
Jochum, M. et al., 2013: The Impact of Oceanic Near-Inertial Waves on Climate. *Journal of Climate*, **26(9)**, 2833–2844, doi:10.1175/jcli-d-12-00181.1.
Jochumsen, K. et al., 2017: Revised transport estimates of the Denmark Strait overflow. *Journal of Geophysical Research: Oceans*, **122(4)**, 3434–3450, doi:10.1002/2017jc012803.
Johannessen, O.M., 2008: Decreasing Arctic Sea Ice Mirrors Increasing CO2 on Decadal Time Scale. *Atmospheric and Oceanic Science Letters*, **1(1)**, 51–56, doi:10.1080/16742834.2008.11446766.
Jóhannesson, T., C. Raymond, and E. Waddington, 1989: Time-Scale for Adjustment of Glaciers to Changes in Mass Balance. *Journal of Glaciology*, **35(121)**, 355–369, doi:10.3189/s002214300000928x.
Jóhannesson, T. et al., 2020: Non-surface mass balance of glaciers in Iceland. *Journal of Glaciology*, **66(258)**, 685–697, doi:10.1017/jog.2020.37.

ACCEPTED VERSION SUBJECT TO FINAL EDITING

Johnson, G.C. and J.M. Lyman, 2020: Warming trends increasingly dominate global ocean. *Nature Climate Change*, **10(8)**, 757–761, doi:10.1038/s41558-020-0822-0.
Johnson, J.S., K.A. Nichols, B.M. Goehring, G. Balco, and J.M. Schaefer, 2019: Abrupt mid-Holocene ice loss in the western Weddell Sea Embayment of Antarctica. *Earth and Planetary Science Letters*, **518**, 127–135, doi:10.1016/j.epsl.2019.05.002.
Jones, B.M. et al., 2015: Recent Arctic tundra fire initiates widespread thermokarst development. *Scientific Reports*, doi:10.1038/srep15865.
Jones, B.M. et al., 2016: Presence of rapidly degrading permafrost plateaus in south-central Alaska. *The Cryosphere*, **10**, 2673–2692, doi:10.5194/tc-10-2673-2016.
Jones, J.M. et al., 2016: Assessing recent trends in high-latitude Southern Hemisphere surface climate. *Nature Climate Change*, **6**, 917, doi:10.1038/nclimate3103.
Jordà, G., 2014: Detection time for global and regional sea level trends and accelerations. *Journal of Geophysical Research: Oceans*, **119(10)**, 7164–7174, doi:10.1002/2014jc010005.
Jorgenson, M.T. and G. Grosse, 2016: Remote Sensing of Landscape Change in Permafrost Regions. *Permafrost and Periglacial Processes*, **27(4)**, 324–338, doi:10.1002/ppp.1914.
Josey, S.A., M.F. Jong, M. Oltmanns, G.K. Moore, and R.A. Weller, 2019: Extreme Variability in Irminger Sea Winter Heat Loss Revealed by Ocean Observatories Initiative Mooring and the ERA5 Reanalysis. *Geophysical Research Letters*, **46(1)**, 293–302, doi:10.1029/2018gl080956.
Joughin, I., B.E. Smith, and C.G. Schoof, 2019: Regularized Coulomb Friction Laws for Ice Sheet Sliding: Application to Pine Island Glacier, Antarctica. *Geophysical Research Letters*, **46(9)**, 4764–4771, doi:10.1029/2019gl082526.
Joughin, I., D. E. Shean, B. E. Smith, and D. Floricioiu, 2020: A decade of variability on Jakobshavn Isbræ: Ocean temperatures pace speed through influence on mélange rigidity. *Cryosphere*, **14(1)**, 211–227, doi:10.5194/tc-14-211-2020.
Jourdain, N.C. et al., 2017: Ocean circulation and sea-ice thinning induced by melting ice shelves in the Amundsen Sea. *JOURNAL OF GEOPHYSICAL RESEARCH-OCEANS*, **122(3)**, 2550–2573, doi:10.1002/2016jc012509.
Jourdain, N.C. et al., 2019: Simulating or prescribing the influence of tides on the Amundsen Sea ice shelves. *Ocean Modelling*, **133**, 44–55, doi:10.1016/j.ocemod.2018.11.001.
Jourdain, N.C. et al., 2020: A protocol for calculating basal melt rates in the ISMIP6 Antarctic ice sheet projections. *The Cryosphere*, **14(9)**, 3111–3134, doi:10.5194/tc-2019-277.
Jouvet, G. and M. Huss, 2019: Future retreat of Great Aletsch Glacier. *Journal of Glaciology*, **65(253)**, 869–872, doi:10.1017/jog.2019.52.
Kääb, A. et al., 2018: Massive collapse of two glaciers in western Tibet in 2016 after surge-like instability. *Nature Geoscience*, **11(2)**, 114–120, doi:10.1038/s41561-017-0039-7.
Kachuck, S.B., D.F. Martin, J.N. Bassis, and S.F. Price, 2020: Rapid Viscoelastic Deformation Slows Marine Ice Sheet Instability at Pine Island Glacier. *Geophysical Research Letters*, **47(10)**, 1–12, doi:10.1029/2019gl086446.
Kacimi, S. and R. Kwok, 2020: The Antarctic sea ice cover from ICESat-2 and CryoSat-2: freeboard, snow depth, and ice thickness. *The Cryosphere*, **14(12)**, 4453–4474, doi:10.5194/tc-14-4453-2020.
Kanevskiy, M. et al., 2013: Ground ice in the upper permafrost of the Beaufort Sea coast of Alaska. *Cold Regions Science and Technology*, **85**, 56–70, doi:10.1016/j.coldregions.2012.08.002.
Kaplan, M.R. et al., 2016: Patagonian and southern South Atlantic view of Holocene climate. *Quaternary Science Reviews*, **141**, 112–125, doi:10.1016/j.quascirev.2016.03.014.
Kaplan, M.R. et al., 2020: Holocene glacier behavior around the northern Antarctic Peninsula and possible causes. *Earth and Planetary Science Letters*, **534**, 116077, doi:10.1016/j.epsl.2020.116077.
Karnauskas, K.B., G.C. Johnson, and R. Murtugudde, 2012: An equatorial ocean bottleneck in global climate models. *Journal of Climate*, doi:10.1175/jcli-d-11-00059.1.
Kaspi, Y. and T. Schneider, 2011: Winter cold of eastern continental boundaries induced by warm ocean waters. *Nature*, **471(7340)**, 621–624, doi:10.1038/nature09924.
Kato, S. et al., 2018: Surface Irradiances of Edition 4.0 Clouds and the Earth's Radiant Energy System (CERES) Energy Balanced and Filled (EBAF) Data Product. *Journal of Climate*, **31(11)**, 4501–4527, doi:10.1175/jcli-d-17-0523.1.
Kaufman, D.S. et al., 2016: Holocene climate changes in eastern Beringia (NW North America) – A systematic review of multi-proxy evidence. *Quaternary Science Reviews*, **147**, 312–339, doi:10.1016/j.quascirev.2015.10.021.
Kawamata, M. et al., 2020: Abrupt Holocene ice-sheet thinning along the southern Soya Coast, Lützow-Holm Bay, East Antarctica, revealed by glacial geomorphology and surface exposure dating. *Quaternary Science Reviews*, **247**, 106540, doi:10.1016/j.quascirev.2020.106540.

ACCEPTED VERSION SUBJECT TO FINAL EDITING

Kay, J.E., M.M. Holland, and A. Jahn, 2011: Inter-annual to multi-decadal Arctic sea ice extent trends in a warming world. *Geophysical Research Letters*, **38(15)**, doi:10.1029/2011gl048008.
Kay, J.E. et al., 2015: The community earth system model (CESM) large ensemble project: A community resource for studying climate change in the presence of internal climate variability. *Bulletin of the American Meteorological Society*, **96(8)**, 1333–1349, doi:10.1175/bams-d-13-00255.1.
Keen, A. et al., 2021: An inter-comparison of the mass budget of the Arctic sea ice in CMIP6 models. *The Cryosphere*, **15(2)**, 951–982, doi:10.5194/tc-15-951-2021.
Kelley, M. et al., 2020: GISS-E2.1: Configurations and Climatology. *Journal of Advances in Modeling Earth Systems*, **12(8)**, e2019MS002025, doi:10.1029/2019ms002025.
Kenner, R., L. Pruessner, J. Beutel, P. Limpach, and M. Phillips, 2020: How rock glacier hydrology, deformation velocities and ground temperatures interact: Examples from the Swiss Alps. *Permafrost and Periglacial Processes*, **31(1)**, 3–14, doi:10.1002/ppp.2023.
Keogh, M.E. and T.E. Törnqvist, 2019: Measuring rates of present-day relative sea-level rise in low-elevation coastal zones: a critical evaluation. *Ocean Science*, **15(1)**, 61–73, doi:10.5194/os-15-61-2019.
Kern, S. and G. Spreen, 2015: Uncertainties in Antarctic sea-ice thickness retrieval from ICESat. *Annals of Glaciology*, **56(69)**, 107–119, doi:10.3189/2015aog69a736.
Kern, S. et al., 2019: Satellite Passive Microwave Sea-Ice Concentration Data Set Intercomparison: Closed Ice and Ship-Based Observations. *The Cryosphere*, doi:10.5194/tc-2019-120.
Khan, S.A. et al., 2015: Greenland ice sheet mass balance: a review. *Reports on Progress in Physics*, **78(4)**, 46801, doi:10.1088/0034-4885/78/4/046801.
Khan, S.A. et al., 2016: Geodetic measurements reveal similarities between post–Last Glacial Maximum and present-day mass loss from the Greenland ice sheet. *Science Advances*, **2(9)**, e1600931, doi:10.1126/sciadv.1600931.
Khan, S.A. et al., 2020: Centennial response of Greenland's three largest outlet glaciers. *Nature Communications*, **11(1)**, 5718, doi:10.1038/s41467-020-19580-5.
Kim, K. et al., 2001: Warming and structural changes in the east (Japan) Sea: A clue to future changes in global oceans? *Geophysical Research Letters*, **28(17)**, 3293–3296, doi:10.1029/2001gl013078.
Kim, W.M., S. Yeager, P. Chang, and G. Danabasoglu, 2018: Low-Frequency North Atlantic Climate Variability in the Community Earth System Model Large Ensemble. *Journal of Climate*, **31(2)**, 787–813, doi:10.1175/jcli-d-17-0193.1.
Kimura, S. et al., 2017: Oceanographic Controls on the Variability of Ice-Shelf Basal Melting and Circulation of Glacial Meltwater in the Amundsen Sea Embayment, Antarctica. *Journal of Geophysical Research: Oceans*, **122(12)**, 10131–10155, doi:10.1002/2017jc012926.
Kinar, N.J. and J.W. Pomeroy, 2015: Measurement of the physical properties of the snowpack. *Reviews of Geophysics*, **53**, 481–544, doi:10.1002/2015rg000481.
King, J. et al., 2017: Sea-ice thickness from field measurements in the northwestern Barents Sea. *Journal of Geophysical Research: Oceans*, **122(2)**, 1497–1512, doi:10.1002/2016jc012199.
King, M.D. et al., 2018: Seasonal to decadal variability in ice discharge from the Greenland Ice Sheet. *The Cryosphere*, **12(12)**, 3813–3825, doi:10.5194/tc-12-3813-2018.
King, M.D. et al., 2020: Dynamic ice loss from the Greenland Ice Sheet driven by sustained glacier retreat. *Communications Earth & Environment*, **1(1)**, 1, doi:10.1038/s43247-020-0001-2.
Kingslake, J. et al., 2018: Extensive retreat and re-advance of the West Antarctic Ice Sheet during the Holocene. *Nature*, **558(7710)**, 430–434, doi:10.1038/s41586-018-0208-x.
Kinnard, C. et al., 2011: Reconstructed changes in Arctic sea ice over the past 1,450 years. *Nature*, **479(7374)**, 509–512, doi:10.1038/nature10581.
Kirezci, E. et al., 2020: Projections of global-scale extreme sea levels and resulting episodic coastal flooding over the 21st Century. *Scientific Reports*, **10(1)**, 1–12, doi:10.1038/s41598-020-67736-6.
Kirpotin, S. et al., 2011: West Siberian palsa peatlands: Distribution, typology, cyclic development, present day climate-driven changes, seasonal hydrology and impact on CO 2 cycle. *International Journal of Environmental Studies*, **68(5)**, 603–623, doi:10.1080/00207233.2011.593901.
Kittel, C. et al., 2021: Diverging future surface mass balance between the Antarctic ice shelves and grounded ice sheet. *The Cryosphere*, **15(3)**, 1215–1236, doi:10.5194/tc-15-1215-2021.
Kjeldsen, K.K. et al., 2015: Spatial and temporal distribution of mass loss from the Greenland Ice Sheet since AD 1900. *Nature*, **528**, 396, doi:10.1038/nature16183.
Kleinherenbrink, M., R. Riva, and Y. Sun, 2016: Sub-basin-scale sea level budgets from satellite altimetry, Argo floats and satellite gravimetry: A case study in the North Atlantic Ocean. *Ocean Science*, doi:10.5194/os-12-1179-2016.

ACCEPTED VERSION SUBJECT TO FINAL EDITING

Klerk, W.-J., H.C. Winsemius, W.J. Van Verseveld, A.M.R. Bakker, and F.L.M. Diermanse, 2015: The co-incidence of storm surges and extreme discharges within the Rhine-Meuse Delta. *Environmental Research Letters*, **10(3)**, 35005.

Knies, J. et al., 2017: Sea-ice dynamics in an Arctic coastal polynya during the past 6500 years. *Arktos*, **3(1)**, 1, doi:10.1007/s41063-016-0027-y.

Knutz, P.C. et al., 2019: Eleven phases of Greenland Ice Sheet shelf-edge advance over the past 2.7 million years. *Nature Geoscience*, **12(5)**, 361–368, doi:10.1038/s41561-019-0340-8.

Koenig, S.J. et al., 2015: Ice sheet model dependency of the simulated Greenland Ice Sheet in the mid-Pliocene. *Climate of the Past*, **11**, 369–381, doi:10.5194/cp-11-369-2015.

Kohout, A.L., M.J.M. Williams, S.M. Dean, and M.H. Meylan, 2014: Storm-induced sea-ice breakup and the implications for ice extent. *Nature*, **509(7502)**, 604–607, doi:10.1038/nature13262.

Kohyama, T., D.L. Hartmann, and D.S. Battisti, 2017: La Niña-like mean-state response to global warming and potential oceanic roles. *Journal of Climate*, doi:10.1175/jcli-d-16-0441.1.

Kolling, H.M., R. Stein, K. Fahl, K. Perner, and M. Moros, 2018: New insights into sea ice changes over the past 2.2 kyr in Disko Bugt, West Greenland. *Arktos*, **4(1)**, 11, doi:10.1007/s41063-018-0045-z.

Kolodziejczyk, N., W. Llovel, and E. Portela, 2019: Interannual Variability of Upper Ocean Water Masses as Inferred From Argo Array. *Journal of Geophysical Research: Oceans*, **124(8)**, 6067–6085, doi:10.1029/2018jc014866.

Konikow, L.F., 2011: Contribution of global groundwater depletion since 1900 to sea-level rise. *Geophysical Research Letters*, **38(17)**, doi:10.1029/2011gl048604.

Konrad, H. et al., 2018: Net retreat of Antarctic glacier grounding lines. *Nature Geoscience*, **11(4)**, 258–262, doi:10.1038/s41561-018-0082-z.

Kopp, R.E., F.J. Simons, J.X. Mitrovica, A.C. Maloof, and M. Oppenheimer, 2009: Probabilistic assessment of sea level during the last interglacial stage. *Nature*, **462(7275)**, doi:10.1038/nature08686.

Kopp, R.E. et al., 2014: Probabilistic 21st and 22nd century sea-level projections at a global network of tide gauge sites. *Earth's Future*, **2**, 383–406, doi:10.1002/2014ef000239.

Kopp, R.E. et al., 2016: Temperature-driven global sea-level variability in the Common Era. *Proceedings of the National Academy of Sciences*, **113(11)**, E1434–E1441, doi:10.1073/pnas.1517056113.

Kopp, R.E. et al., 2017: Evolving Understanding of Antarctic Ice-Sheet Physics and Ambiguity in Probabilistic Sea-Level Projections. *Earth's Future*, **5(12)**, 1217–1233, doi:10.1002/2017ef000663.

Kornfeld, R.P. et al., 2019: GRACE-FO: The Gravity Recovery and Climate Experiment Follow-On Mission. *Journal of Spacecraft and Rockets*, **56(3)**, 931–951, doi:10.2514/1.a34326.

Kostov, Y., K.C. Armour, and J. Marshall, 2014: Impact of the Atlantic meridional overturning circulation on ocean heat storage and transient climate change. *Geophysical Research Letters*, **41(6)**, 2108–2116, doi:10.1002/2013gl058998.

Kouki, K. et al., 2019: Intercomparison of Snow Melt Onset Date Estimates From Optical and Microwave Satellite Instruments Over the Northern Hemisphere for the Period 1982–2015. *Journal of Geophysical Research: Atmospheres*, **124(21)**, 11205–11219, doi:10.1029/2018jd030197.

Koven, C.D., W.J. Riley, and A. Stern, 2013: Analysis of permafrost thermal dynamics and response to climate change in the CMIP5 earth system models. *Journal of Climate*, **26(6)**, 1877–1900, doi:10.1175/jcli-d-12-00228.1.

Kraaijenbrink, P.D.A., M.F.P. Bierkens, A.F. Lutz, and W.W. Immerzeel, 2017: Impact of a global temperature rise of 1.5 degrees Celsius on Asia's glaciers. *Nature*, **549(7671)**, 257–260, doi:10.1038/nature23878.

Kremer, A. et al., 2018: Changes in sea ice cover and ice sheet extent at the Yermak Plateau during the last 160 ka – Reconstructions from biomarker records. *Quaternary Science Reviews*, **182**, 93–108, doi:10.1016/j.quascirev.2017.12.016.

Kriegler, E. and H. Held, 2005: Utilizing belief functions for the estimation of future climate change. *International Journal of Approximate Reasoning*, **39(2)**, 185–209, doi:10.1016/j.ijar.2004.10.005.

Krug, J., J. Weiss, O. Gagliardini, and G. Durand, 2014: Combining damage and fracture mechanics to model calving. *The Cryosphere*, **8(6)**, 2101–2117, doi:10.5194/tc-8-2101-2014.

Kuhlbrodt, T. and J.M. Gregory, 2012: Ocean heat uptake and its consequences for the magnitude of sea level rise and climate change. *Geophysical Research Letters*, doi:10.1029/2012gl052952.

Kuhlbrodt, T. et al., 2007: On the driving processes of the Atlantic meridional overturning circulation. *Reviews of Geophysics*, **45(2)**, RG2001, doi:10.1029/2004rg000166.

Kumar, P., S.K. Min, E. Weller, H. Lee, and X.L. Wang, 2016: Influence of climate variability on extreme ocean surface wave heights assessed from ERA-interim and ERA-20C. *Journal of Climate*, doi:10.1175/jcli-d-15-0580.1.

ACCEPTED VERSION SUBJECT TO FINAL EDITING

Kunkel, K.E. et al., 2016: Trends and Extremes in Northern Hemisphere Snow Characteristics. *Current Climate Change Reports*, **2**, 65–73, doi:10.1007/s40641-016-0036-8.
Kuntz, L.B. and D.P. Schrag, 2020: Representation of the Equatorial Undercurrent in CMIP5 Models. *Journal of Physical Oceanography*, **50(10)**, 2997–3007, doi:10.1175/jpo-d-20-0007.1.
Kurtz, N.T. and T. Markus, 2012: Satellite observations of Antarctic sea ice thickness and volume. *Journal of Geophysical Research: Oceans*, **117(C8)**, C08025, doi:10.1029/2012jc008141.
Kusahara, K., G.D. Williams, R. Massom, P. Reid, and H. Hasumi, 2019: Spatiotemporal dependence of Antarctic sea ice variability to dynamic and thermodynamic forcing: a coupled ocean–sea ice model study. *Climate Dynamics*, **52(7)**, 3791–3807, doi:10.1007/s00382-018-4348-3.
Kusahara, K., D. Hirano, M. Fujii, A. Fraser, and T. Tamura, 2021: Modeling intensive ocean–cryosphere interactions in Lützow-Holm Bay, East Antarctica. *The Cryosphere*, **in press**, doi:10.5194/tc-2020-240.
Kwiatkowski, L. et al., 2020: Twenty-first century ocean warming, acidification, deoxygenation, and upper-ocean nutrient and primary production decline from CMIP6 model projections. *Biogeosciences*, **17(13)**, 3439–3470, doi:10.5194/bg-17-3439-2020.
Kwok, R., 2018: Arctic sea ice thickness, volume, and multiyear ice coverage: Losses and coupled variability (1958-2018). *Environmental Research Letters*, **13(10)**, 105005, doi:10.1088/1748-9326/aae3ec.
Kwok, R. and G.F. Cunningham, 2015: Variability of Arctic sea ice thickness and volume from CryoSat-2. *Philosophical Transactions of the Royal Society A: Mathematical, Physical and Engineering Sciences*, **373(2045)**, 20140157, doi:10.1098/rsta.2014.0157.
Kwok, R. and S. Kacimi, 2018: Three years of sea ice freeboard, snow depth, and ice thickness of the weddell sea from operation icebridge and cryosat-2. *Cryosphere*, doi:10.5194/tc-12-2789-2018.
Kwok, R., J.C. Comiso, T. Lee, and P.R. Holland, 2016: Linked trends in the South Pacific sea ice edge and Southern Oscillation Index. *Geophysical Research Letters*, **43(19)**, 10,210–295,302, doi:10.1002/2016gl070655.
Lafaysse, M. et al., 2017: A multiphysical ensemble system of numerical snow modelling. *The Cryosphere*, **11**, 1173–1198, doi:10.5194/tc-11-1173-2017.
Lago, V. and M.H. England, 2019: Projected Slowdown of Antarctic Bottom Water Formation in Response to Amplified Meltwater Contributions. *Journal of Climate*, **32(19)**, 6319–6335, doi:10.1175/jcli-d-18-0622.1.
Laliberté, F., S.E.L. Howell, and P.J. Kushner, 2016: Regional variability of a projected sea ice-free Arctic during the summer months. *Geophysical Research Letters*, **43(1)**, 256–263, doi:10.1002/2015gl066855.
Laliberté, F., S.E.L. Howell, J.-F. Lemieux, F. Dupont, and J. Lei, 2018: What historical landfast ice observations tell us about projected ice conditions in Arctic archipelagoes and marginal seas under anthropogenic forcing. *The Cryosphere*, **12(11)**, 3577–3588, doi:10.5194/tc-12-3577-2018.
Lambeck, K., H. Rouby, A. Purcell, Y. Sun, and M. Sambridge, 2014: Sea level and global ice volumes from the Last Glacial Maximum to the Holocene. *Proceedings of the National Academy of Sciences*, 201411762, doi:10.1073/pnas.1411762111.
Lambert, E., J. Rohmer, G. Le Cozannet, and R.S.W. van de Wal, 2020: Adaptation time to magnified flood hazards underestimated when derived from tide gauge records. *Environmental Research Letters*, **15(7)**, 074015, doi:10.1088/1748-9326/ab8336.
Lamont, T., M. García-Reyes, S.J. Bograd, C.D. van der Lingen, and W.J. Sydeman, 2018: Upwelling indices for comparative ecosystem studies: Variability in the Benguela Upwelling System. *Journal of Marine Systems*, **188**, 3–16, doi:10.1016/j.jmarsys.2017.05.007.
Lamping, N. et al., 2020: Highly branched isoprenoids reveal onset of deglaciation followed by dynamic sea-ice conditions in the western Amundsen Sea, Antarctica. *Quaternary Science Reviews*, **228**, 106103, doi:10.1016/j.quascirev.2019.106103.
Lamy, F. et al., 2015: Glacial reduction and millennial-scale variations in Drake Passage throughflow. *Proceedings of the National Academy of Sciences*, **112(44)**, 13496–13501, doi:10.1073/pnas.1509203112.
Landais, A. et al., 2016: How warm was Greenland during the last interglacial period? *Climate of the Past*, **12(9)**, 1933–1948, doi:10.5194/cp-12-1933-2016.
Landerer, F.W., J.H. Jungclaus, and J. Marotzke, 2007: Regional Dynamic and Steric Sea Level Change in Response to the IPCC-A1B Scenario. *Journal of Physical Oceanography*, **37(2)**, 296–312, doi:10.1175/jpo3013.1.
Landrum, L.L., M.M. Holland, M.N. Raphael, and L.M. Polvani, 2017: Stratospheric Ozone Depletion: An Unlikely Driver of the Regional Trends in Antarctic Sea Ice in Austral Fall in the Late Twentieth Century. *Geophysical Research Letters*, **44(21)**, 11,062–11,070, doi:10.1002/2017gl075618.
Larocca, L.J., Y. Axford, S.A. Woodroffe, G.E. Lasher, and B. Gawin, 2020: Holocene glacier and ice cap fluctuations in southwest Greenland inferred from two lake records. *Quaternary Science Reviews*, **246**, 106529, doi:10.1016/j.quascirev.2020.106529.

ACCEPTED VERSION SUBJECT TO FINAL EDITING

Larour, E., E.R. Ivins, and S. Adhikari, 2017: Should coastal planners have concern over where land ice is melting? *Science Advances*, **3(11)**, e1700537, doi:10.1126/sciadv.1700537.
Larour, E., J. Utke, A. Bovin, M. Morlighem, and G. Perez, 2016: An approach to computing discrete adjoints for MPI-parallelized models applied to Ice Sheet System Model 4.11. *Geoscientific Model Development*, **9(11)**, 3907–3918, doi:10.5194/gmd-9-3907-2016.
Larour, E. et al., 2014: Inferred basal friction and surface mass balance of the Northeast Greenland Ice Stream using data assimilation of ICESat (Ice Cloud and land Elevation Satellite) surface altimetry and ISSM (Ice Sheet System Model). *The Cryosphere*, **8(6)**, 2335–2351, doi:10.5194/tc-8-2335-2014.
Larsen, N.K. et al., 2015: The response of the southern Greenland ice sheet to the Holocene thermal maximum. *Geology*, **43(4)**, 291–294.
Larsen, N.K. et al., 2019: Local ice caps in Finderup Land, North Greenland, survived the Holocene Thermal Maximum. *Boreas*, **48(3)**, 551–562, doi:10.1111/bor.12384.
Larson, E.J.L., R.W. Portmann, S. Solomon, and D.M. Murphy, 2020: Decadal Attribution of Historic Temperature and Ocean Heat Content Change to Anthropogenic Emissions. *Geophysical Research Letters*, **47(3)**, e2019GL085905, doi:10.1029/2019gl085905.
Laufkötter, C., J. Zscheischler, and T.L. Frölicher, 2020: High-impact marine heatwaves attributable to human-induced global warming. *Science*, **369(6511)**, 1621–1625, doi:10.1126/science.aba0690.
Lavergne, T. et al., 2019: Version 2 of the EUMETSAT OSI SAF and ESA CCI sea-ice concentration climate data records. *The Cryosphere*, **13(1)**, 49–78, doi:10.5194/tc-13-49-2019.
Lawrence, D.M., A.G. Slater, V.E. Romanovsky, and D.J. Nicolsky, 2008: Sensitivity of a model projection of near-surface permafrost degradation to soil column depth and representation of soil organic matter. *Journal of Geophysical Research: Earth Surface*, **113(2)**, doi:10.1029/2007jf000883.
Lazeroms, W.M.J., A. Jenkins, G. Hilmar Gudmundsson, and R.S.W. Van De Wal, 2018: Modelling present-day basal melt rates for Antarctic ice shelves using a parametrization of buoyant meltwater plumes. *Cryosphere*, doi:10.5194/tc-12-49-2018.
Le Bars, D., S. Drijfhout, and H. De Vries, 2017: A high-end sea level rise probabilistic projection including rapid Antarctic ice sheet mass loss. *Environmental Research Letters*, **12(4)**, doi:10.1088/1748-9326/aa6512.
Le clec'h, S. et al., 2019: Assessment of the Greenland ice sheet–atmosphere feedbacks for the next century with a regional atmospheric model coupled to an ice sheet model. *The Cryosphere*, **13(1)**, 373–395, doi:10.5194/tc-13-373-2019.
Le Cozannet, G., J.C. Manceau, and J. Rohmer, 2017: Bounding probabilistic sea-level projections within the framework of the possibility theory. *Environmental Research Letters*, doi:10.1088/1748-9326/aa5528.
Le Cozannet, G. et al., 2019: Quantifying uncertainties of sandy shoreline change projections as sea level rises. *Scientific Reports*, **9(1)**, 42, doi:10.1038/s41598-018-37017-4.
Lea, J.M. et al., 2014: Terminus-driven retreat of a major southwest Greenland tidewater glacier during the early 19th century: insights from glacier reconstructions and numerical modelling. *Journal of Glaciology*, **60(220)**, 333–344, doi: 10.3189/2014jog13j163.
Lecavalier, B.S. et al., 2014: A model of Greenland ice sheet deglaciation constrained by observations of relative sea level and ice extent. *Quaternary Science Reviews*, **102**, 54–84, doi:10.1016/j.quascirev.2014.07.018.
Lecavalier, B.S. et al., 2017: High Arctic Holocene temperature record from the Agassiz ice cap and Greenland ice sheet evolution. *Proceedings of the National Academy of Sciences*, doi:10.1016/j.phpro.2012.10.059.
Leclercq, P.W., J. Oerlemans, and J.G. Cogley, 2011: Estimating the Glacier Contribution to Sea-Level Rise for the Period 1800–2005. *Surveys in Geophysics*, **32(4–5)**, 519–535, doi:10.1007/s10712-011-9121-7.
Lecomte, O. et al., 2017: Vertical ocean heat redistribution sustaining sea-ice concentration trends in the Ross Sea. *NATURE COMMUNICATIONS*, **8**, doi:10.1038/s41467-017-00347-4.
Lee, B.S., M. Haran, and K. Keller, 2017: Multidecadal Scale Detection Time for Potentially Increasing Atlantic Storm Surges in a Warming Climate. *Geophysical Research Letters*, **44(20)**, 10,610–617,623, doi:10.1002/2017gl074606.
Lee, H., S.C. Swenson, A.G. Slater, and D.M. Lawrence, 2014: Effects of excess ground ice on projections of permafrost in a warming climate. *Environmental Research Letters*, **9(12)**, 124006, doi:10.1088/1748-9326/9/12/124006.
Lee, V., S.L. Cornford, and A.J. Payne, 2015: Initialization of an ice-sheet model for present-day Greenland. *Annals of Glaciology*, **56(70)**, 129–140, doi:10.3189/2015aog70a121.
Lenaerts, J.T.M. et al., 2015: Representing Greenland ice sheet freshwater fluxes in climate models. *Geophysical Research Letters*, **42**, 6373–6381, doi:10.1002/2015gl064738.

ACCEPTED VERSION SUBJECT TO FINAL EDITING

Lenaerts, J.T.M. et al., 2017: Meltwater produced by wind-albedo interaction stored in an East Antarctic ice shelf. *Nature Climate Change*, **7(1)**, 58–62, doi:10.1038/nclimate3180.
Letcher, T.W. and J.R. Minder, 2015: Characterization of the simulated regional snow albedo feedback using a regional climate model over complex terrain. *Journal of Climate*, **28(19)**, 7576–7595, doi:10.1175/jcli-d-15-0166.1.
Lettenmaier, D.P. and P.C.D. Milly, 2009: Land waters and sea level. *Nature Geoscience*, doi:10.1038/ngeo567.
Levang, S.J. and R.W. Schmitt, 2020: Intergyre Salt Transport in the Climate Warming Response. *Journal of Physical Oceanography*, **50(1)**, 255–268, doi:10.1175/jpo-d-19-0166.1.
Levermann, A. and R. Winkelmann, 2016: A simple equation for the melt elevation feedback of ice sheets. *Cryosphere*, **10(4)**, 1799–1807, doi:10.5194/tc-10-1799-2016.
Levermann, A. et al., 2013: The multimillennial sea-level commitment of global warming.. *Proceedings of the National Academy of Sciences of the United States of America*, **110(34)**, 13745–50, doi:10.1073/pnas.1219414110.
Levermann, A. et al., 2014: Projecting Antarctic ice discharge using response functions from SeaRISE ice-sheet models. *Earth System Dynamics*, **5(2)**, 271–293, doi:10.5194/esd-5-271-2014.
Levermann, A. et al., 2020a: Projecting Antarctica's contribution to future sea level rise from basal ice shelf melt using linear response functions of 16 ice sheet models (LARMIP-2). *Earth System Dynamics*, **11(1)**, 35–76, doi:10.5194/esd-11-35-2020.
Levermann, A. et al., 2020b: Projecting Antarctica's contribution to future sea level rise from basal ice shelf melt using linear response functions of 16 ice sheet models (LARMIP-2). *Earth System Dynamics*, **11**, 35–76, doi:10.5194/esd-11-35-2020.
Levitus, S. et al., 2012: World ocean heat content and thermosteric sea level change (0–2000 m), 1955–2010. *Geophysical Research Letters*, **39(10)**, n/a–n/a, doi:10.1029/2012gl051106.
Levy, R.H. et al., 2019: Antarctic ice-sheet sensitivity to obliquity forcing enhanced through ocean connections. *Nature Geoscience*, **12(2)**, 132–137, doi:10.1038/s41561-018-0284-4.
Lewis, M.J. et al., 2019: Wave-tide interaction modulates nearshore wave height. *Ocean Dynamics*, doi:10.1007/s10236-018-01245-z.
Li, C., D. Notz, S. Tietsche, and J. Marotzke, 2013: The transient versus the equilibrium response of sea ice to global warming. *Journal of Climate*, **26(15)**, 5624–5636, doi:10.1175/jcli-d-12-00492.1.
Li, G. et al., 2019: Examining the salinity change in the upper Pacific Ocean during the Argo period. *Climate Dynamics*, **53(9)**, 6055–6074, doi:10.1007/s00382-019-04912-z.
Li, G. et al., 2020: Increasing ocean stratification over the past half-century. *Nature Climate Change*, doi:10.1038/s41558-020-00918-2.
Li, J.-L.F. et al., 2020: An Overview of CMIP5 and CMIP6 Simulated Cloud Ice, Radiation Fields, Surface Wind Stress, Sea Surface Temperatures, and Precipitation Over Tropical and Subtropical Oceans. *Journal of Geophysical Research: Atmospheres*, **125(15)**, e2020JD032848, doi:10.1029/2020jd032848.
Li, Q. and B. Fox-Kemper, 2017: Assessing the effects of Langmuir turbulence on the entrainment buoyancy flux in the ocean surface boundary layer. *Journal of Physical Oceanography*, **47(12)**, 2863–2886, doi:10.1175/jpo-d-17-0085.1.
Li, Q. et al., 2016: Langmuir mixing effects on global climate: WAVEWATCH III in CESM. *Ocean Modelling*, **103**, 145–160, doi:10.1016/j.ocemod.2015.07.020.
Li, Q. et al., 2019: Comparing Ocean Surface Boundary Vertical Mixing Schemes Including Langmuir Turbulence. *Journal of Advances in Modeling Earth Systems*, **11(11)**, 3545–3592, doi:10.1029/2019ms001810.
Li, T. et al., 2020: Uncertainties of Glacial Isostatic Adjustment Model Predictions in North America Associated With 3D Structure. *Geophysical Research Letters*, doi:10.1029/2020gl087944.
Li, X., D.M. Holland, E.P. Gerber, and C. Yoo, 2014: Impacts of the north and tropical Atlantic Ocean on the Antarctic Peninsula and sea ice. *Nature*, **505(7484)**, 538–542, doi:10.1038/nature12945.
Li, X., E. Rignot, J. Mouginot, and B. Scheuchl, 2016: Ice flow dynamics and mass loss of Totten Glacier, East Antarctica, from 1989 to 2015. *Geophysical Research Letters*, **43(12)**, 6366–6373, doi:10.1002/2016gl069173.
Li, Y., G. Ren, Q. Wang, and Q. You, 2019: More extreme marine heatwaves in the China Seas during the global warming hiatus. *Environmental Research Letters*, **14(10)**, 104010, doi:10.1088/1748-9326/ab28bc.
Lin, N., K. Emanuel, M. Oppenheimer, and E. Vanmarcke, 2012: Physically based assessment of hurricane surge threat under climate change. *Nature Climate Change*, **2(6)**, 462, doi:10.1038/nclimate1389.
Lin, N., P. Lane, K.A. Emanuel, R.M. Sullivan, and J.P. Donnelly, 2014: Heightened hurricane surge risk in northwest Florida revealed from climatological-hydrodynamic modeling and paleorecord reconstruction. *Journal of Geophysical Research: Atmospheres*, **119(14)**, 8606–8623, doi:10.1002/2014jd021584.
Lindstrom, E., F. Bryan, and R. Schmitt, 2015: SPURS: Salinity Processes in the Upper-ocean Regional Study – The North Atlantic Experiment. *Oceanography*, **28(1)**, 14–19, doi:10.5670/oceanog.2015.01.

ACCEPTED VERSION SUBJECT TO FINAL EDITING

Linz, M., E. Tziperman, and D.G. MacMartin, 2014: Process-based analysis of climate model ENSO simulations: Intermodel consistency and compensating errors. *Journal of Geophysical Research: Atmospheres*, **119(12)**, 7396–7409, doi:10.1002/2013jd021415.

Lipscomb, W.H. et al., 2013: Implementation and Initial Evaluation of the Glimmer Community Ice Sheet Model in the Community Earth System Model. *Journal of Climate*, **26(19)**, 7352–7371, doi:10.1175/jcli-d-12-00557.1.

Lipscomb, W.H. et al., 2021: ISMIP6-based projections of ocean-forced Antarctic Ice Sheet evolution using the Community Ice Sheet Model. *The Cryosphere*, **15**, 633–661, doi:10.5194/tc-15-633-2021.

Lique, C., H.L. Johnson, and Y. Plancherel, 2018a: Emergence of deep convection in the Arctic Ocean under a warming climate. *Climate Dynamics*, **50(9)**, 3833–3847, doi:10.1007/s00382-017-3849-9.

Lique, C., H.L. Johnson, and Y. Plancherel, 2018b: Emergence of deep convection in the Arctic Ocean under a warming climate. *Climate Dynamics*, **50(9)**, 3833–3847, doi:10.1007/s00382-017-3849-9.

Liston, G.E. and C.A. Hiemstra, 2011: The changing cryosphere: Pan-Arctic snow trends (1979-2009). *Journal of Climate*, **24(21)**, 5691–5712, doi:10.1175/jcli-d-11-00081.1.

Little, C.M., A. Gnanadesikan, and M. Oppenheimer, 2009: How ice shelf morphology controls basal melting. *Journal of Geophysical Research: Oceans*, **114(C12)**, doi:10.1029/2008jc005197.

Little, C.M. et al., 2015: Joint projections of US East Coast sea level and storm surge. *Nature Climate Change*, doi:10.1038/nclimate2801.

Little, C.M. et al., 2019: The Relationship Between U.S. East Coast Sea Level and the Atlantic Meridional Overturning Circulation: A Review. *Journal of Geophysical Research: Oceans*, **124(9)**, 6435–6458, doi:10.1029/2019jc015152.

Liu, C., X. Liang, R.M. Ponte, N. Vinogradova, and O. Wang, 2019: Vertical redistribution of salt and layered changes in global ocean salinity. *Nature Communications*, **10(1)**, 3445, doi:10.1038/s41467-019-11436-x.

Liu, J., G.A. Milne, R.E. Kopp, P.U. Clark, and I. Shennan, 2016: Sea-level constraints on the amplitude and source distribution of Meltwater Pulse 1A. *Nature Geoscience*, doi:10.1038/ngeo2616.

Liu, L. et al., 2021: Permafrost sensitivity to global warming of 1.5°C and 2°C in the Northern Hemisphere. *Environmental Research Letters*, **16(3)**, 034038, doi:10.1088/1748-9326/abd6a8.

Liu, W. and Z. Liu, 2013: A Diagnostic Indicator of the Stability of the Atlantic Meridional Overturning Circulation in CCSM3. *J. Climate*, **26**, 1926–1938, doi:10.1175/jcli-d-11-00681.1.

Liu, W., J. Lu, and S.-P. Xie, 2018: Southern Ocean Heat Uptake, Redistribution, and Storage in a Warming Climate: The Role of Meridional Overturning Circulation. *Journal of Climate*, **31**, 4727–4743, doi:10.1175/jcli-d-17.

Liu, W., S.P. Xie, Z. Liu, and J. Zhu, 2017: Overlooked possibility of a collapsed atlantic meridional overturning circulation in warming climate. *Science Advances*, **3(1)**, doi:10.1126/sciadv.1601666.

Llovel, W. et al., 2018: Contributions of Atmospheric Forcing and Chaotic Ocean Variability to Regional Sea Level Trends Over 1993–2015. *Geophysical Research Letters*, **45(24)**, 13,405–13,413, doi:10.1029/2018gl080838.

Lo, L. et al., 2018: Precession and atmospheric CO2 modulated variability of sea ice in the central Okhotsk Sea since 130,000 years ago. *Earth and Planetary Science Letters*, **488**, 36–45, doi:10.1016/j.epsl.2018.02.005.

Lohmann, J. and P.D. Ditlevsen, 2021: Risk of tipping the overturning circulation due to increasing rates of ice melt. *Proceedings of the National Academy of Sciences*, **118(9)**, e2017989118, doi:10.1073/pnas.2017989118.

López-Moreno, J.I. et al., 2020: Long-term trends (1958–2017) in snow cover duration and depth in the Pyrenees. *International Journal of Climatology*, doi:10.1002/joc.6571.

Loranty, M.M., L.T. Berner, S.J. Goetz, Y. Jin, and J.T. Randerson, 2014: Vegetation controls on northern high latitude snow-albedo feedback: Observations and CMIP5 model simulations. *Global Change Biology*, **20(2)**, 594–606, doi:10.1111/gcb.12391.

Love, R. et al., 2016: The contribution of glacial isostatic adjustment to projections of sea-level change along the Atlantic and Gulf coasts of North America. *Earth's Future*, **4(10)**, 440–464, doi:10.1002/2016ef000363.

Loveday, B.R., P. Penven, and C.J.C. Reason, 2015: Southern Annular Mode and westerly-wind-driven changes in Indian-Atlantic exchange mechanisms. *Geophysical Research Letters*, doi:10.1002/2015gl064256.

Lowe, J.A. and J.M. Gregory, 2006: Understanding projections of sea level rise in a Hadley Centre coupled climate model. *Journal of Geophysical Research*, **111(C11)**, C11014, doi:10.1029/2005jc003421.

Löwe, H., F. Riche, and M. Schneebeli, 2013: A general treatment of snow microstructure exemplified by an improved relation for thermal conductivity. *Cryosphere*, **7(5)**, 1473–1480, doi:10.5194/tc-7-1473-2013.

Lowell, T. et al., 2013: Late Holocene expansion of Istorvet ice cap, Liverpool Land, east Greenland. *Quaternary Science Reviews*, **63**, 128–140, doi:10.1016/j.quascirev.2012.11.012.

Lowry, D.P. et al., 2020: Geologic controls on ice sheet sensitivity to deglacial climate forcing in the Ross Embayment, Antarctica. *Quaternary Science Advances*, **1**, 100002, doi:10.1016/j.qsa.2020.100002.

ACCEPTED VERSION SUBJECT TO FINAL EDITING

Lozier, M.S. et al., 2019: A sea change in our view of overturning in the subpolar North Atlantic. *Science*, **363(6426)**, 516–521, doi:10.1126/science.aau6592.
Lozier, S.M. et al., 2017: Overturning in the Subpolar North Atlantic Program: a new international ocean observing system. *Bulletin of the American Meteorological Society*, **98(4)**, 737–752.
Lübbecke, J.F., J. Durgadoo, and A. Biastoch, 2015: Contribution of increased agulhas leakage to tropical Atlantic warming. *Journal of Climate*, doi:10.1175/jcli-d-15-0258.1.
Luckman, B.H., B.J.R. Sperling, and G.D. Osborn, 2020: The Holocene history of the Columbia Icefield, Canada. *Quaternary Science Reviews*, **242**, 106436, doi:10.1016/j.quascirev.2020.106436.
Luo, Y. and L.M. Rothstein, 2011: Response of the Pacific Ocean Circulation to Climate Change. *Atmosphere-Ocean*, **49(3)**, 235–244, doi:10.1080/07055900.2011.602325.
Lüthi, M.P., 2009: Transient response of idealized glaciers to climate variations. *Journal of Glaciology*, **55(193)**, 918–930, doi:10.3189/002214309790152519.
Lüthi, M.P. and A. Bauder, 2010: Analysis of Alpine glacier length change records with a macroscopic glacier model. *Geographica Helvetica*, **65(2)**, 92–102, doi:10.5194/gh-65-92-2010.
Lüthi, M.P., A. Bauder, and M. Funk, 2010: Volume change reconstruction of Swiss glaciers from length change data. *Journal of Geophysical Research*, **115(F4)**, F04022, doi:10.1029/2010jf001695.
Lüthi, M.P. et al., 2016: A century of geometry and velocity evolution at Eqip Sermia, West Greenland. *Journal of Glaciology*, **62(234)**, 640–654, doi:10.1017/jog.2016.38.
Lyu, K., X. Zhang, and J.A. Church, 2020a: Regional Dynamic Sea Level Simulated in the CMIP5 and CMIP6 Models: Mean Biases, Future Projections, and Their Linkages. *Journal of Climate*, **33(15)**, 6377–6398, doi:10.1175/jcli-d-19-1029.1.
Lyu, K., X. Zhang, J.A. Church, and Q. Wu, 2020b: Processes Responsible for the Southern Hemisphere Ocean Heat Uptake and Redistribution under Anthropogenic Warming. *Journal of Climate*, **33(9)**, 3787–3807, doi:10.1175/jcli-d-19-0478.1.
Lyu, K., X. Zhang, J.A. Church, A.B.A. Slangen, and J. Hu, 2014: Time of emergence for regional sea-level change. *Nature Climate Change*, **4**, 1006–1010, doi:10.1038/nclimate2397.
Ma, X. et al., 2016: Western boundary currents regulated by interaction between ocean eddies and the atmosphere. *Nature*, **535(7613)**, 533–537, doi:10.1038/nature18640.
Ma, Y. and J.N. Bassis, 2019: The Effect of Submarine Melting on Calving From Marine Terminating Glaciers. *Journal of Geophysical Research: Earth Surface*, **124**, 334–346, doi:10.1029/2018jf004820.
MacFerrin, M. et al., 2019: Rapid expansion of Greenland's low-permeability ice slabs. *Nature*, **573(7774)**, 403–407, doi:10.1038/s41586-019-1550-3.
Machguth, H. et al., 2016: Greenland meltwater storage in firn limited by near-surface ice formation. *Nature Climate Change*, **6**, 390, doi:10.1038/nclimate2899.
Mackie, S., I.J. Smith, J.K. Ridley, D.P. Stevens, and P.J. Langhorne, 2020: Climate response to increasing Antarctic iceberg and ice shelf melt. *Journal of Climate*, **33(20)**, 8917–8938, doi:10.1175/jcli-d-19-0881.1.
Mackintosh, A. et al., 2011: Retreat of the East Antarctic ice sheet during the last glacial termination. *Nature Geoscience*, **4(3)**, 195–202, doi:10.1038/ngeo1061.
Magalhães, N., H. Evangelista, T. Condom, A. Rabatel, and P. Ginot, 2019: Amazonian Biomass Burning Enhances Tropical Andean Glaciers Melting. *Scientific Reports*, **9(1)**, 16914, doi:10.1038/s41598-019-53284-1.
Mak, J., D.P. Marshall, J.R. Maddison, and S.D. Bachman, 2017: Emergent eddy saturation from an energy constrained eddy parameterisation. *Ocean Modelling*, **112**, 125–138, doi:10.1016/j.ocemod.2017.02.007.
Maksym, T., 2019: Arctic and Antarctic Sea Ice Change: Contrasts, Commonalities, and Causes. *Annual Review of Marine Science*, **11(1)**, 187–213, doi:10.1146/annurev-marine-010816-060610.
Maksym, T. and T. Markus, 2008: Antarctic sea ice thickness and snow-to-ice conversion from atmospheric reanalysis and passive microwave snow depth. *Journal of Geophysical Research*, **113(2)**, C02S12, doi:10.1029/2006jc004085.
Malyarenko, A. et al., 2020: A synthesis of thermodynamic ablation at ice–ocean interfaces from theory, observations and models. *Ocean Modelling*, **154**, 101692, doi:10.1016/j.ocemod.2020.101692.
Mankoff, K.D. et al., 2019: Greenland Ice Sheet discharge from 2000 to 2018. *Earth System Science Data*, **11**, 769–786, doi:10.5194/essd-11-769-2019.
Mankoff, K.D. et al., 2020: Greenland Ice Sheet solid ice discharge from 1986 through March 2020. *Earth System Science Data*, **12(2)**, 1367–1383, doi:10.5194/essd-12-1367-2020.
Marcer, M. et al., 2019: Evaluating the destabilization susceptibility of active rock glaciers in the French Alps. *The Cryosphere*, **13(1)**, 141–155, doi:10.5194/tc-13-141-2019.

ACCEPTED VERSION SUBJECT TO FINAL EDITING

Marcos, M. and A. Amores, 2014: Quantifying anthropogenic and natural contributions to thermosteric sea level rise. *Geophys Res Lett*, **41**, 2502–2507, doi:10.1002/2014gl059766.
Marcos, M. et al., 2019: Coastal Sea Level and Related Fields from Existing Observing Systems. *Surveys in Geophysics*, doi:10.1007/s10712-019-09513-3.
Marcott, S.A. et al., 2019: 10Be age constraints on latest Pleistocene and Holocene cirque glaciation across the western United States. *npj Climate and Atmospheric Science*, **2(1)**, 5, doi:10.1038/s41612-019-0062-z.
Maris, M. et al., 2014: Modelling the evolution of the Antarctic ice sheet since the last interglacial. *The Cryosphere*, **8(4)**, 1347–1360.
Marsh, O.J. et al., 2016: High basal melting forming a channel at the grounding line of Ross Ice Shelf, Antarctica. *Geophysical Research Letters*, **43(1)**, 250–255, doi:10.1002/2015gl066612.
Marshall, A.G., H.H. Hendon, T.H. Durrant, and M.A. Hemer, 2015: Madden Julian Oscillation impacts on global ocean surface waves. *Ocean Modelling*, **96**, 136–147, doi:10.1016/j.ocemod.2015.06.002.
Marshall, A.G., M.A. Hemer, H.H. Hendon, and K.L. McInnes, 2018: Southern annular mode impacts on global ocean surface waves. *Ocean Modelling*, doi:10.1016/j.ocemod.2018.07.007.
Marshall, J. et al., 2015: The ocean's role in the transient response of climate to abrupt greenhouse gas forcing. *Climate Dynamics*, **44(7–8)**, 2287–2299, doi:10.1007/s00382-014-2308-0.
Marsooli, R., N. Lin, K. Emanuel, and K. Feng, 2019: Climate change exacerbates hurricane flood hazards along US Atlantic and Gulf Coasts in spatially varying patterns. *Nature Communications*, doi:10.1038/s41467-019-11755-z.
Martinec, Z. et al., 2018: A benchmark study of numerical implementations of the sea level equation in GIA modelling. *Geophysical Journal International*, **215(1)**, 389–414, doi:10.1093/gji/ggy280.
Martínez-Asensio, A. et al., 2019: Relative sea-level rise and the influence of vertical land motion at Tropical Pacific Islands. *Global and Planetary Change*, **176**, 132–143, doi:10.1016/j.gloplacha.2019.03.008.
Marzeion, B., A.H. Jarosch, and M. Hofer, 2012: Past and future sea-level change from the surface mass balance of glaciers. *The Cryosphere*, **6(6)**, 1295–1322, doi:10.5194/tc-6-1295-2012.
Marzeion, B., P.W. Leclercq, J.G. Cogley, and A.H. Jarosch, 2015: Brief Communication: Global reconstructions of glacier mass change during the 20th century are consistent. *The Cryosphere*, **9(6)**, 2399–2404, doi:10.5194/tc-9-2399-2015.
Marzeion, B., G. Kaser, F. Maussion, and N. Champollion, 2018: Limited influence of climate change mitigation on short-term glacier mass loss. *Nature Climate Change*, **8(4)**, 305–308, doi:10.1038/s41558-018-0093-1.
Marzeion, B. et al., 2020: Partitioning the Uncertainty of Ensemble Projections of Global Glacier Mass Change. *Earth's Future*, **8(7)**, doi:10.1029/2019ef001470.
Mas e Braga, M., J. Bernales, M. Prange, A. Stroeven, and I. Rogozhina, 2021: Sensitivity of the Antarctic ice sheets to the peak warming of Marine Isotope Stage 11. *The Cryosphere*, **15**, 459–478, doi:10.5194/tc-15-459-2021.
Mason, E. et al., 2010: Procedures for offline grid nesting in regional ocean models. *Ocean Modelling*, **35(1–2)**, 1–15, doi:10.1016/j.ocemod.2010.05.007.
Massom, R.A. et al., 2001: Snow on Antarctic sea ice. *Reviews of Geophysics*, **39(3)**, 413–445, doi:10.1029/2000rg000085.
Massom, R.A. et al., 2006: Extreme Anomalous Atmospheric Circulation in the West Antarctic Peninsula Region in Austral Spring and Summer 2001/02, and Its Profound Impact on Sea Ice and Biota. *Journal of Climate*, **19(15)**, 3544–3571, doi:10.1175/jcli3805.1.
Massom, R.A. et al., 2015: External influences on the Mertz Glacier Tongue (East Antarctica) in the decade leading up to its calving in 2010. *Journal of Geophysical Research: Earth Surface*, **120(3)**, 490–506, doi:10.1002/2014jf003223.
Massom, R.A. et al., 2018: Antarctic ice shelf disintegration triggered by sea ice loss and ocean swell. *Nature*, **558(7710)**, 383–389, doi:10.1038/s41586-018-0212-1.
Masson-Delmotte, V. et al., 2013: Information from Paleoclimate Archives. In: *Climate Change 2013: The Physical Science Basis. Contribution of Working Group I to the Fifth Assessment Report of the IPCC* [Stocker, T.F., D. Qin, G.-K. Plattner, M. Tignor, S.K. Allen, J. Boschung, A. Nauels, Y. Xia, V. Bex, and P.M. Midgley (eds.)]. Cambridge University Press, Cambridge, United Kingdom and New York, USA, pp. 383–464, doi:10.1017/cbo9781107415324.013.
Massonnet, F., V. Guemas, N.S. Fučkar, and F.J. Doblas-Reyes, 2015: The 2014 High Record of Antarctic Sea Ice Extent. *Explaining Extremes of 2014 from a Climate Perspective. Bulletin of the American Meteorological Society*, **96(12)**, S163–S167, doi:10.1175/bams-d-15-00093.1.
Massonnet, F. et al., 2013: A model reconstruction of the Antarctic sea ice thickness and volume changes over 1980-2008 using data assimilation. *Ocean Modelling*, **64**, 67–75, doi:10.1016/j.ocemod.2013.01.003.

ACCEPTED VERSION SUBJECT TO FINAL EDITING

Matero, I.S.O., L.J. Gregoire, R.F. Ivanovic, J.C. Tindall, and A.M. Haywood, 2017: The 8.2 ka cooling event caused by Laurentide ice saddle collapse. *Earth and Planetary Science Letters*, **473**, 205–214, doi:10.1016/j.epsl.2017.06.011.

Mathis, M. and T. Pohlmann, 2014: Projection of physical conditions in the North Sea for the 21st century. *Climate Research*, **61(1)**, 1–17, doi:10.3354/cr01232.

Matiu, M. et al., 2021: Observed snow depth trends in the European Alps: 1971 to 2019. *The Cryosphere*, **15(3)**, 1343–1382, doi:10.5194/tc-15-1343-2021.

Mattingly, K.S. et al., 2020: Strong Summer Atmospheric Rivers Trigger Greenland Ice Sheet Melt through Spatially Varying Surface Energy Balance and Cloud Regimes. *Journal of Climate*, **33(16)**, 6809–6832, doi:10.1175/jcli-d-19-0835.1.

Maussion, F. et al., 2019a: The Open Global Glacier Model (OGGM) v1.1. *Geoscientific Model Development*, **12(3)**, 909–931, doi:10.5194/gmd-12-909-2019.

Maussion, F. et al., 2019b: The Open Global Glacier Model (OGGM) v1.1. *Geoscientific Model Development*, **12(3)**, 909–931, doi:10.5194/gmd-12-909-2019.

Mayer, C. et al., 2018: Large ice loss variability at Nioghalvfjerdsfjorden Glacier, Northeast-Greenland. *Nature Communications*, **9(1)**, 2768, doi:10.1038/s41467-018-05180-x.

Mayer, M. et al., 2019: An Improved Estimate of the Coupled Arctic Energy Budget. *Journal of Climate*, **32(22)**, 7915–7934, doi:10.1175/jcli-d-19-0233.1.

McCarthy, G.D., T.M. Joyce, and S.A. Josey, 2018: Gulf Stream Variability in the Context of Quasi-Decadal and Multidecadal Atlantic Climate Variability. *Geophysical Research Letters*, **45(20)**, doi:10.1029/2018gl079336.

McFarlin, J.M. et al., 2018: Pronounced summer warming in northwest Greenland during the Holocene and Last Interglacial. *Proceedings of the National Academy of Sciences*, **115(25)**, 6357 LP – 6362, doi:10.1073/pnas.1720420115.

McGuire, A.D. et al., 2016: Variability in the sensitivity among model simulations of permafrost and carbon dynamics in the permafrost region between 1960 and 2009. *Global Biogeochemical Cycles*, doi:10.1002/2016gb005405.

McInnes, K.L., R.K. Hoeke, K.J.E. Walsh, J.G. O'Grady, and G.D. Hubbert, 2016: Application of a synthetic cyclone method for assessment of tropical cyclone storm tides in Samoa. *Natural Hazards*, **80(1)**, 425–444, doi:10.1007/s11069-015-1975-4.

McInnes, K.L. et al., 2014: Quantifying storm tide risk in Fiji due to climate variability and change. *Global and Planetary Change*, **116**, 115–129, doi:10.1016/j.gloplacha.2014.02.004.

McKay, R. et al., 2016: Antarctic marine ice-sheet retreat in the Ross Sea during the early Holocene. *Geology*, **44(1)**, 7–10, doi:10.1130/g37315.1.

McWilliams, J.C., 2019: A survey of submesoscale currents. *Geoscience Letters*, **6(1)**, 1–15, doi:10.1186/s40562-019-0133-3.

Meccia, V.L., F. Fabiano, P. Davini, and S. Corti, 2020: Stochastic Parameterizations and the Climate Response to External Forcing: An Experiment With EC-Earth. *Geophysical Research Letters*, **47(3)**, e2019GL085951, doi:10.1029/2019gl085951.

Mecking, J.V., S.S. Drijfhout, L.C. Jackson, and M.B. Andrews, 2017: The effect of model bias on Atlantic freshwater transport and implications for AMOC bi-stability. *Tellus, Series A: Dynamic Meteorology and Oceanography*, **69(1)**, doi:10.1080/16000870.2017.1299910.

Medley, B. and E.R. Thomas, 2019: Increased snowfall over the Antarctic Ice Sheet mitigated twentieth-century sea-level rise. *Nature Climate Change*, doi:10.1038/s41558-018-0356-x.

Meehl, G.A., J.M. Arblaster, C.M. Bitz, C.T.Y. Chung, and H. Teng, 2016: Antarctic sea-ice expansion between 2000 and 2014 driven by tropical Pacific decadal climate variability. *Nature Geoscience*, **9(8)**, 590–595, doi:10.1038/ngeo2751.

Meehl, G.A. et al., 2019: Sustained ocean changes contributed to sudden Antarctic sea ice retreat in late 2016. *Nature Communications*, **10(1)**, 14, doi:10.1038/s41467-018-07865-9.

Méheust, M., R. Stein, K. Fahl, and R. Gersonde, 2018: Sea-ice variability in the subarctic North Pacific and adjacent Bering Sea during the past 25 ka: new insights from IP25 and Uk′37 proxy records. *Arktos*, **4(1)**, 8, doi:10.1007/s41063-018-0043-1.

Meier, H.E.M., 2015: Projected Change – Marine Physics. In: *Second Assessment of Climate Change for the Baltic Sea Basin* [The BACC II Author Team (ed.)]. Springer, Cham, Switzerland, pp. 243–252, doi:10.1007/978-3-319-16006-1_13.

Meier, W.N. and J.S. Stewart, 2019: Assessing uncertainties in sea ice extent climate indicators. *Environmental Research Letters*, **14(3)**, 035005, doi:10.1088/1748-9326/aaf52c.

ACCEPTED VERSION SUBJECT TO FINAL EDITING

Meier, W.N., D. Gallaher, and G.G. Campbell, 2013: New estimates of Arctic and Antarctic sea ice extent during September 1964 from recovered Nimbus I satellite imagery. *The Cryosphere*, **7(2)**, 699–705, doi:10.5194/tc-7-699-2013.

Meinshausen, M. et al., 2011: The RCP greenhouse gas concentrations and their extensions from 1765 to 2300. *Climatic change*, **109(1–2)**, 213.

Melet, A., B. Meyssignac, R. Almar, and G. Le Cozannet, 2018: Under-estimated wave contribution to coastal sea-level rise. *Nature Climate Change*, doi:10.1038/s41558-018-0088-y.

Melet, A. et al., 2020: Contribution of Wave Setup to Projected Coastal Sea Level Changes. *Journal of Geophysical Research: Oceans*, **125(8)**, doi:10.1029/2020jc016078.

Melzer, B.A. and B. Subrahmanyam, 2017: Decadal changes in salinity in the oceanic subtropical gyres. *Journal of Geophysical Research: Oceans*, **122(1)**, 336–354, doi:10.1002/2016jc012243.

Menary, M.B. and R.A. Wood, 2018: An anatomy of the projected North Atlantic warming hole in CMIP5 models. *Climate Dynamics*, doi:10.1007/s00382-017-3793-8.

Menary, M.B., L.C. Jackson, and M.S. Lozier, 2020a: Reconciling the Relationship Between the AMOC and Labrador Sea in OSNAP Observations and Climate Models. *Geophysical Research Letters*, **47(18)**, doi:10.1029/2020gl089793.

Menary, M.B., L.C. Jackson, and M.S. Lozier, 2020b: Reconciling the Relationship Between the AMOC and Labrador Sea in OSNAP Observations and Climate Models. *Geophysical Research Letters*, **47(18)**, doi:10.1029/2020gl089793.

Menary, M.B. et al., 2020c: Aerosol-Forced AMOC Changes in CMIP6 Historical Simulations. *Geophysical Research Letters*, **47(14)**, doi:10.1029/2020gl088166.

Mengel, M. and A. Levermann, 2014: Ice plug prevents irreversible discharge from East Antarctica. *Nature Climate Change*, **4**, 451–455, doi:10.1038/nclimate2226.

Mengel, M. et al., 2016: Future sea level rise constrained by observations and long-term commitment. *Proceedings of the National Academy of Sciences*, **113(10)**, 2597–2602, doi:10.1073/pnas.1500515113.

Menounos, B. et al., 2019: Heterogeneous Changes in Western North American Glaciers Linked to Decadal Variability in Zonal Wind Strength. *Geophysical Research Letters*, **46(1)**, 200–209, doi:10.1029/2018gl080942.

Mercenier, R., M.P. Lüthi, and A. Vieli, 2018: Calving relation for tidewater glaciers based on detailed stress field analysis. *The Cryosphere*, **12(2)**, 721–739, doi:10.5194/tc-12-721-2018.

Mercenier, R., M.P. Lüthi, and A. Vieli, 2020: How Oceanic Melt Controls Tidewater Glacier Evolution. *Geophysical Research Letters*, **47**, e2019GL086769, doi:10.1029/2019gl086769.

Meredith, M. et al., 2019: Polar Regions. In: *IPCC Special Report on the Ocean and Cryosphere in a Changing Climate* [Pörtner, H.-O., D.C. Roberts, V. Masson-Delmotte, P. Zhai, M. Tignor, E. Poloczanska, K. Mintenbeck, M. Nicolai, A. Okem, J. Petzold, B. Rama, and N. Weyer (eds.)]. In Press, pp. 203–320.

Merino, N. et al., 2018: Impact of increasing antarctic glacial freshwater release on regional sea-ice cover in the Southern Ocean. *OCEAN MODELLING*, **121**, 76–89, doi:10.1016/j.ocemod.2017.11.009.

Mernild, S.H., W.H. Lipscomb, D.B. Bahr, V. Radić, and M. Zemp, 2013: Global glacier changes: a revised assessment of committed mass losses and sampling uncertainties. *The Cryosphere*, **7(5)**, 1565–1577, doi:10.5194/tc-7-1565-2013.

Merrifield, M.A., P.R. Thompson, and M. Lander, 2012: Multidecadal sea level anomalies and trends in the western tropical Pacific. *Geophysical Research Letters*, **39(13)**, n/a–n/a, doi:10.1029/2012gl052032.

Metzner, E.P., M. Salzmann, and R. Gerdes, 2020: Arctic Ocean Surface Energy Flux and the Cold Halocline in Future Climate Projections. *Journal of Geophysical Research: Oceans*, **125(2)**, e2019JC015554, doi:10.1029/2019jc015554.

Meucci, A., I.R. Young, M. Hemer, E. Kirezci, and R. Ranasinghe, 2020: Projected 21st century changes in extreme wind-wave events. *Science Advances*, **6(24)**, 7295–7305, doi:10.1126/sciadv.aaz7295.

Meyssignac, B. et al., 2017: Evaluating model simulations of twentieth-century sea-level rise. Part II: Regional sea-level changes. *Journal of Climate*, **30(21)**, 8565–8593, doi:10.1175/jcli-d-17-0112.1.

Miles, B.W.J., C.R. Stokes, and S.S.R. Jamieson, 2016: Pan–ice-sheet glacier terminus change in East Antarctica reveals sensitivity of Wilkes Land to sea-ice changes. *Science Advances*, **2(5)**, e1501350, doi:10.1126/sciadv.1501350.

Miles, B.W.J., C.R. Stokes, and S.S.R. Jamieson, 2017: Simultaneous disintegration of outlet glaciers in Porpoise Bay (Wilkes Land), East Antarctica, driven by sea ice break-up. *The Cryosphere*, **11(1)**, 427–442, doi:10.5194/tc-11-427-2017.

Miles, B.W.J., C.R. Stokes, A. Vieli, and N.J. Cox, 2013: Rapid, climate-driven changes in outlet glaciers on the Pacific coast of East Antarctica. *Nature*, **500(7464)**, 563–566, doi:10.1038/nature12382.

ACCEPTED VERSION SUBJECT TO FINAL EDITING

Milillo, P. et al., 2017: On the Short-term Grounding Zone Dynamics of Pine Island Glacier, West Antarctica, Observed With COSMO-SkyMed Interferometric Data. *Geophysical Research Letters*, **44(20)**, 10,436–10,444, doi:10.1002/2017gl074320.

Milillo, P. et al., 2019: Heterogeneous retreat and ice melt of thwaites glacier, West Antarctica. *Science Advances*, **5(1)**, eaau3433, doi:10.1126/sciadv.aau3433.

Millan, R. et al., 2018: Vulnerability of Southeast Greenland Glaciers to Warm Atlantic Water From Operation IceBridge and Ocean Melting Greenland Data. *Geophysical Research Letters*, **45(6)**, 2688–2696, doi:10.1002/2017gl076561.

Millan, R. et al., 2020: Constraining an Ocean Model Under Getz Ice Shelf, Antarctica, Using A Gravity-Derived Bathymetry. *Geophysical Research Letters*, **47(13)**, e2019GL086522, doi:10.1029/2019gl086522.

Miller, G.H., J.Y. Landvik, S.J. Lehman, and J.R. Southon, 2017: Episodic Neoglacial snowline descent and glacier expansion on Svalbard reconstructed from the 14C ages of ice-entombed plants. *Quaternary Science Reviews*, **155**, 67–78, doi:10.1016/j.quascirev.2016.10.023.

Miller, G.H., S.J. Lehman, K.A. Refsnider, J.R. Southon, and Y. Zhong, 2013: Unprecedented recent summer warmth in Arctic Canada. *Geophysical Research Letters*, **40(21)**, 5745–5751, doi:10.1002/2013gl057188.

Miller, G.H. et al., 2012: Abrupt onset of the Little Ice Age triggered by volcanism and sustained by sea-ice/ocean feedbacks. *Geophysical Research Letters*, **39(2)**, doi:10.1029/2011gl050168.

Miller, K.G. et al., 2012: High tide of the warm Pliocene: Implications of global sea level for Antarctic deglaciation. *Geology*, **40(5)**, 407–410, doi:10.1130/g32869.1.

Miller, K.G. et al., 2020: Cenozoic sea-level and cryospheric evolution from deep-sea geochemical and continental margin records. *Science Advances*, **6(20)**, doi:10.1126/sciadv.aaz1346.

Minderhoud, P.S.J. et al., 2017: Impacts of 25 years of groundwater extraction on subsidence in the Mekong delta, Vietnam. *Environmental Research Letters*, **12(6)**, 64006, doi:10.1088/1748-9326/aa7146.

Mitrovica, J.X., C.C. Hay, R.E. Kopp, C. Harig, and K. Latychev, 2018: Quantifying the sensitivity of sea level change in coastal localities to the geometry of polar ice mass flux. *Journal of Climate*, **31(9)**, doi:10.1175/jcli-d-17-0465.1.

Moffa-Sánchez, P., A. Born, I.R. Hall, D.J.R. Thornalley, and S. Barker, 2014: Solar forcing of North Atlantic surface temperature and salinity over the past millennium. *Nature Geoscience*, **7(4)**, 275–278, doi:10.1038/ngeo2094.

Moffa-Sánchez, P. et al., 2019: Variability in the Northern North Atlantic and Arctic Oceans Across the Last Two Millennia: A Review. *Paleoceanography and Paleoclimatology*, **34(8)**, 1399–1436, doi:10.1029/2018pa003508.

Moftakhari, H.R., G. Salvadori, A. AghaKouchak, B.F. Sanders, and R.A. Matthew, 2017: Compounding effects of sea level rise and fluvial flooding. *Proceedings of the National Academy of Sciences*, **114(37)**, 9785–9790, doi:10.1073/pnas.1620325114.

Mohajerani, Y., I. Velicogna, and E. Rignot, 2018: Mass Loss of Totten and Moscow University Glaciers, East Antarctica, Using Regionally Optimized GRACE Mascons. *Geophysical Research Letters*, **45(14)**, 7010–7018, doi:10.1029/2018gl078173.

Mollaret, C. et al., 2019: Mountain permafrost degradation documented through a network of permanent electrical resistivity tomography sites. *The Cryosphere*, **13(10)**, 2557–2578, doi:10.5194/tc-13-2557-2019.

Monselesan, D.P., T.J. O'Kane, J.S. Risbey, and J. Church, 2015: Internal climate memory in observations and models. *Geophysical Research Letters*, doi:10.1002/2014gl062765.

Moon, T.A., A.S. Gardner, B. Csatho, I. Parmuzin, and M.A. Fahnestock, 2020: Rapid reconfiguration of the Greenland Ice Sheet coastal margin. *Journal of Geophysical Research: Earth Surface*, **125(n/a)**, e2020JF005585, doi:10.1029/2020jf005585.

Moorman, R., A.K. Morrison, and A. McC. Hogg, 2020: Thermal Responses to Antarctic Ice Shelf Melt in an Eddy-Rich Global Ocean–Sea Ice Model. *Journal of Climate*, **33(15)**, 6599–6620, doi:10.1175/jcli-d-19-0846.1.

Moreno-Chamarro, E., D. Zanchettin, K. Lohmann, and J.H. Jungclaus, 2017: An abrupt weakening of the subpolar gyre as trigger of Little Ice Age-type episodes. *Climate Dynamics*, **48(3–4)**, 727–744, doi:10.1007/s00382-016-3106-7.

Mori, N. et al., 2014: Local amplification of storm surge by Super Typhoon Haiyan in Leyte Gulf. *Geophysical Research Letters*, **41(14)**, 5106–5113, doi:10.1002/2014gl060689.

Mori, N. et al., 2019: Future changes in extreme storm surges based on mega-ensemble projection using 60-km resolution atmospheric global circulation model. *Coastal Engineering Journal*, **61(3)**, 295–307, doi:10.1080/21664250.2019.1586290.

Morim, J., M. Hemer, N. Cartwright, D. Strauss, and F. Andutta, 2018: On the concordance of 21st century wind-wave climate projections. *Global and Planetary Change*, **167**, 160–171, doi:10.1016/j.gloplacha.2018.05.005.

ACCEPTED VERSION SUBJECT TO FINAL EDITING

Morim, J. et al., 2019: Robustness and uncertainties in multivariate wind-wave climate projections. *Nature Climate Change*, **9**, 711–718, doi:10.1038/s41558-019-0542-5.
Morlighem, M., E. Rignot, and J.K. Willis, 2016a: Improving Bed Topography Mapping of Greenland Glaciers Using NASA's Oceans Melting Greenland (OMG) Data. *Oceanography*, **29(4)**, 62–71, doi:10.5670/oceanog.2016.99.
Morlighem, M., E. Rignot, J. Mouginot, H. Seroussi, and E. Larour, 2014: Deeply incised submarine glacial valleys beneath the Greenland ice sheet. *Nature Geoscience*, **7(6)**, 418–422, doi:10.1038/ngeo2167.
Morlighem, M., M. Wood, H. Seroussi, Y. Choi, and E. Rignot, 2019: Modeling the response of northwest Greenland to enhanced ocean thermal forcing and subglacial discharge. *The Cryosphere*, **13(2)**, 723–734, doi:10.5194/tc-13-723-2019.
Morlighem, M. et al., 2016b: Modeling of Store Gletscher's calving dynamics, West Greenland, in response to ocean thermal forcing. *Geophysical Research Letters*, **43(6)**, 2659–2666, doi:10.1002/2016gl067695.
Morlighem, M. et al., 2017: BedMachine v3: Complete Bed Topography and Ocean Bathymetry Mapping of Greenland From Multibeam Echo Sounding Combined With Mass Conservation. *Geophysical Research Letters*, **44(21)**, 11,051–11,061, doi:10.1002/2017gl074954.
Morlighem, M. et al., 2020: Deep glacial troughs and stabilizing ridges unveiled beneath the margins of the Antarctic ice sheet. *Nature Geoscience*, **13(2)**, 132–137, doi:10.1038/s41561-019-0510-8.
Morris, A., G. Moholdt, and L. Gray, 2020: Spread of Svalbard Glacier Mass Loss to Barents Sea Margins Revealed by CryoSat-2. *Journal of Geophysical Research: Earth Surface*, **125(8)**, doi:10.1029/2019jf005357.
Mortimer, C. et al., 2020: Evaluation of long-term Northern Hemisphere snow water equivalent products. *The Cryosphere*, **14**, 1579–1594.
Mosbeux, C., F. Gillet-Chaulet, and O. Gagliardini, 2016: Comparison of adjoint and nudging methods to initialise ice sheet model basal conditions. *Geoscientific Model Development*, **9(7)**, 2549–2562, doi:10.5194/gmd-9-2549-2016.
Mottram, R. et al., 2019: An Integrated View of Greenland Ice Sheet Mass Changes Based on Models and Satellite Observations. *Remote Sensing*, **11(12)**, doi:10.3390/rs11121407.
Motyka, R.J. et al., 2017: Asynchronous behavior of outlet glaciers feeding Godthåbsfjord (Nuup Kangerlua) and the triggering of Narsap Sermia's retreat in SW Greenland. *Journal of Glaciology*, **63(238)**, 288–308, doi:10.1017/jog.2016.138.
Moucha, R. and G.A. Ruetenik, 2017: Interplay between dynamic topography and flexure along the U.S. Atlantic passive margin: Insights from landscape evolution modeling. *Global and Planetary Change*, **149**, 72–78, doi:10.1016/j.gloplacha.2017.01.004.
Mouginot, J. et al., 2015: Fast retreat of ZachariæIsstrøm, northeast Greenland. *Science*, **350(6266)**, 1357–1361, doi:10.1126/science.aac7111.
Mouginot, J. et al., 2019: Forty-six years of Greenland Ice Sheet mass balance from 1972 to 2018. *Proceedings of the National Academy of Sciences*, **116(19)**, 9239–9244, doi:10.1073/pnas.1904242116.
Mudryk, L. et al., 2020: Historical Northern Hemisphere snow cover trends and projected changes in the CMIP6 multi-model ensemble. *The Cryosphere*, **14(7)**, 2495–2514, doi:10.5194/tc-14-2495-2020.
Mudryk, L.R., P.J. Kushner, C. Derksen, and C. Thackeray, 2017: Snow cover response to temperature in observational and climate model ensembles. *Geophysical Research Letters*, **44(2)**, 919–926, doi:10.1002/2016gl071789.
Muilwijk, M., L.H. Smedsrud, M. Ilicak, and H. Drange, 2018: Atlantic Water Heat Transport Variability in the 20th Century Arctic Ocean From a Global Ocean Model and Observations. *Journal of Geophysical Research: Oceans*, **123(11)**, 8159–8179, doi:10.1029/2018jc014327.
Muis, S., M. Verlaan, H.C. Winsemius, J.C.J.H. Aerts, and P.J. Ward, 2016: A global reanalysis of storm surges and extreme sea levels. *Nature Communications*, **7**, 11969, doi:10.1038/ncomms11969.
Muis, S. et al., 2020: A High-Resolution Global Dataset of Extreme Sea Levels, Tides, and Storm Surges, Including Future Projections. *Frontiers in Marine Science*, **7**, 263, doi:10.3389/fmars.2020.00263.
Muntjewerf, L. et al., 2020a: Greenland Ice Sheet Contribution to 21st Century Sea Level Rise as Simulated by the Coupled CESM2.1-CISM2.1. *Geophysical Research Letters*, **47(9)**, doi:10.1029/2019gl086836.
Muntjewerf, L. et al., 2020b: Accelerated Greenland Ice Sheet Mass Loss Under High Greenhouse Gas Forcing as Simulated by the Coupled CESM2.1-CISM2.1. *Journal of Advances in Modeling Earth Systems*, **12(10)**, doi:10.1029/2019ms002031.
Murari, M.K. et al., 2014: Timing and climatic drivers for glaciation across monsoon-influenced regions of the Himalayan–Tibetan orogen. *Quaternary Science Reviews*, **88**, 159–182, doi:10.1016/j.quascirev.2014.01.013.
Muresan, I.S. et al., 2016: Modelled glacier dynamics over the last quarter of a century at Jakobshavn Isbræ. *The Cryosphere*, **10(2)**, 597–611, doi:10.5194/tc-10-597-2016.

ACCEPTED VERSION SUBJECT TO FINAL EDITING

Murray, T. et al., 2015: Extensive retreat of Greenland tidewater glaciers, 2000–2010. *Arctic, Antarctic, and Alpine Research*, **47(3)**, 427–447, doi:10.1657/aaar0014-049.
Nair, A. et al., 2019: Southern Ocean sea ice and frontal changes during the Late Quaternary and their linkages to Asian summer monsoon. *Quaternary Science Reviews*, **213**, 93–104, doi:10.1016/j.quascirev.2019.04.007.
Najafi, M.R., F.W. Zwiers, and N.P. Gillett, 2015: Attribution of Arctic temperature change to greenhouse-gas and aerosol influences. *Nature Climate Change*, **5(3)**, 246–249, doi:10.1038/nclimate2524.
Narayan, N., A. Paul, S. Mulitza, and M. Schulz, 2010: Trends in coastal upwelling intensity during the late 20th century. *Ocean Science*, **6(3)**, 815–823, doi:10.5194/os-6-815-2010.
Nauels, A., M. Meinshausen, M. Mengel, K. Lorbacher, and T.M.L. Wigley, 2017: Synthesizing long-term sea level rise projections – the MAGICC sea level model v2.0. *Geoscientific Model Development*, **10(6)**, 2495–2524, doi:10.5194/gmd-10-2495-2017.
Nauels, A. et al., 2019: Attributing long-term sea-level rise to Paris Agreement emission pledges. *Proceedings of the National Academy of Sciences*, **116(47)**, 23487–23492, doi:10.1073/pnas.1907461116.
Naughten, K.A. et al., 2018: Future Projections of Antarctic Ice Shelf Melting Based on CMIP5 Scenarios. *Journal of Climate*, **31(13)**, 5243–5261, doi:10.1175/jcli-d-17-0854.1.
Nesje, A. et al., 2012: The climatic significance of artefacts related to prehistoric reindeer hunting exposed at melting ice patches in southern Norway. *The Holocene*, **22(4)**, 485–496, doi:10.1177/0959683611425552.
Nias, I.J., S.L. Cornford, T.L. Edwards, N. Gourmelen, and A.J. Payne, 2019: Assessing Uncertainty in the Dynamical Ice Response to Ocean Warming in the Amundsen Sea Embayment, West Antarctica. *Geophysical Research Letters*, **46(20)**, 11253–11260, doi:10.1029/2019gl084941.
Nicholls, R.J. et al., 2018: Stabilization of global temperature at 1.5°C and 2.0°C: Implications for coastal areas. *Philosophical Transactions of the Royal Society A: Mathematical, Physical and Engineering Sciences*, **376(2119)**, doi:10.1098/rsta.2016.0448.
Nick, F.M. et al., 2013: Future sea-level rise from Greenland's main outlet glaciers in a warming climate. *Nature*, **497(7448)**, 235–238, doi:10.1038/nature12068.
Nicolas, J.P. et al., 2017: January 2016 extensive summer melt in West Antarctica favoured by strong El Niño. *Nature Communications*, **8(1)**, 15799, doi:10.1038/ncomms15799.
Niederdrenk, A.L. and D. Notz, 2018: Arctic Sea Ice in a 1.5°C Warmer World. *Geophysical Research Letters*, **45(4)**, 1963–1971, doi:10.1002/2017gl076159.
Nielsen, L.T., G. Aðalgeirsdóttir, V. Gkinis, R. Nuterman, and C.S. Hvidberg, 2018: The effect of a Holocene climatic optimum on the evolution of the Greenland ice sheet during the last 10 kyr. *Journal of Glaciology*, **64(245)**, 477–488, doi:10.1017/jog.2018.40.
Nitzbon, J. et al., 2020: Fast response of cold ice-rich permafrost in northeast Siberia to a warming climate. *Nature Communications*, **11(1)**, 2201, doi:10.1038/s41467-020-15725-8.
Niwano, M., A. Hashimoto, and T. Aoki, 2019: Cloud-driven modulations of Greenland ice sheet surface melt. *Scientific Reports*, **9**, 10380, doi:10.1038/s41598-019-46152-5.
Niwano, M. et al., 2018: NHM-SMAP: Spatially and temporally high-resolution nonhydrostatic atmospheric model coupled with detailed snow process model for Greenland Ice Sheet. *Cryosphere*, **12(2)**, 635–655, doi:10.5194/tc-12-635-2018.
Noël, B., L. van Kampenhout, J.T.M. Lenaerts, W.J. van de Berg, and M.R. van den Broeke, 2021: A 21st Century Warming Threshold for Sustained Greenland Ice Sheet Mass Loss. *Geophysical Research Letters*, **n/a(n/a)**, e2020GL090471, doi:10.1029/2020gl090471.
Noël, B. et al., 2018: Six Decades of Glacial Mass Loss in the Canadian Arctic Archipelago. *Journal of Geophysical Research: Earth Surface*, **123(6)**, 1430–1449, doi:10.1029/2017jf004304.
Noël, B. et al., 2020: Low elevation of Svalbard glaciers drives high mass loss variability. *Nature Communications*, **11(1)**, 4597, doi:10.1038/s41467-020-18356-1.
Noetzli, J. et al., 2019: Permafrost thermal state. *State of the Climate in 2018. Bulletin of the American Meteorological Society*, **100(9)**, S21–S22, doi:10.1175/2019bamsstateoftheclimate.1.
Notarnicola, C., 2020: Hotspots of snow cover changes in global mountain regions over 2000–2018. *Remote Sensing of Environment*, **243**, 111781, doi:10.1016/j.rse.2020.111781.
Notz, D., 2014: Sea-ice extent and its trend provide limited metrics of model performance. *Cryosphere*, **8(1)**, 229–243, doi:10.5194/tc-8-229-2014.
Notz, D. and J. Marotzke, 2012: Observations reveal external driver for Arctic sea-ice retreat. *Geophysical Research Letters*, **39(8)**, doi:10.1029/2012gl051094.
Notz, D. and J. Stroeve, 2016: Observed Arctic sea-ice loss directly follows anthropogenic CO2 emission. *Science*, **354(6313)**, 747–750, doi:10.1126/science.aag2345.

ACCEPTED VERSION SUBJECT TO FINAL EDITING

Notz, D. and J. Stroeve, 2018: The Trajectory Towards a Seasonally Ice-Free Arctic Ocean. *Current Climate Change Reports*, **4(4)**, 407–416, doi:10.1007/s40641-018-0113-2.
Notz, D. and SIMIP Community, 2020: Arctic Sea Ice in CMIP6. *Geophysical Research Letters*, **47(10)**, doi:10.1029/2019gl086749.
Notz, D. et al., 2016: The CMIP6 Sea-Ice Model Intercomparison Project (SIMIP): Understanding sea ice through climate-model simulations. *Geoscientific Model Development*, **9(9)**, 3427–3446, doi:10.5194/gmd-9-3427-2016.
Nowicki, S. et al., 2013: Insights into spatial sensitivities of ice mass response to environmental change from the SeaRISE ice sheet modeling project II: Greenland. *Journal of Geophysical Research: Earth Surface*, **118(2)**, doi:10.1002/jgrf.20076.
Nowicki, S. et al., 2020a: Experimental protocol for sea level projections from ISMIP6 stand-alone ice sheet models. *Cryosphere*, **14(7)**, 2331–2368, doi:10.5194/tc-14-2331-2020.
Nowicki, S. et al., 2020b: Experimental protocol for sea level projections from ISMIP6 standalone ice sheet models. *The Cryosphere*, **14**, 2331–2368, doi:10.5194/tc-14-2331-2020.
Nowicki, S.M. and H. Seroussi, 2018: Projections of Future Sea Level Contributions from the Greenland and Antarctic Ice Sheets: Challenges Beyond Dynamical Ice Sheet Modeling. *Oceanography*, doi:10.5670/oceanog.2018.216.
Nowicki, S.M., A. Payne, E. Larour, and E. Al., 2016: Ice Sheet Model Intercomparison Project (ISMIP6) contribution to CMIP6. *Geoscientific Model Development*, **9(12)**, 4521–4545, doi:10.5194/gmd-9-4521-201.
Nussbaumer, S.U. and H.J. Zumbühl, 2012: The Little Ice Age history of the Glacier des Bossons (Mont Blanc massif, France): a new high-resolution glacier length curve based on historical documents. *Climatic Change*, **111(2)**, 301–334, doi:10.1007/s10584-011-0130-9.
O'Neill, H.B., S.L. Smith, and C. Duchesne, 2019: Long-Term Permafrost Degradation and Thermokarst Subsidence in the Mackenzie Delta Area Indicated by Thaw Tube Measurements. In: *Cold Regions Engineering 2019*. pp. 643–651, doi:10.1061/9780784482599.074.
O'Reilly, C.H., L. Zanna, and T. Woollings, 2019: Assessing External and Internal Sources of Atlantic Multidecadal Variability Using Models, Proxy Data, and Early Instrumental Indices. *Journal of Climate*, **32(22)**, 7727–7745, doi:10.1175/jcli-d-19-0177.1.
Obase, T., A. Abe-Ouchi, K. Kusahara, H. Hasumi, and R. Ohgaito, 2017: Responses of Basal Melting of Antarctic Ice Shelves to the Climatic Forcing of the Last Glacial Maximum and CO2 Doubling. *Journal of Climate*, **30(10)**, 3473–3497, doi:10.1175/jcli-d-15-0908.1.
Obu, J., S. Westermann, A. Kääb, and A. Bartsch, 2018: Ground Temperature Map, 2000-2016, Northern Hemisphere Permafrost. Alfred Wegener Institute, Helmholtz Centre for Polar and Marine Research, Bremerhaven, Germany, PANGAEA. Retrieved from: https://doi.org/10.1594/pangaea.888600.
Obu, J. et al., 2019: Northern Hemisphere permafrost map based on TTOP modelling for 2000–2016 at 1 km2 scale. *Earth-Science Reviews*, **193**, 299–316, doi:10.1016/j.earscirev.2019.04.023.
Obu, J. et al., 2020: Pan-Antarctic map of near-surface permafrost temperatures at 1 km2 scale. *The Cryosphere*, **14**, 497–519, doi:10.5194/tc-14-497-2020.
Ochwat, N.E., S.J. Marshall, B.J. Moorman, A.S. Criscitiello, and L. Copland, 2021: Meltwater Storage in the firn of Kaskawulsh Glacier, Yukon Territory, Canada. *The Cryosphere*, **in press**, doi:10.5194/tc-2020-119.
Oerder, V. et al., 2015a: Peru-Chile upwelling dynamics under climate change. *Journal of Geophysical Research: Oceans*, **120(2)**, 1152–1172, doi:10.1002/2014jc010299.
Oerder, V. et al., 2015b: Peru-Chile upwelling dynamics under climate change. *Journal of Geophysical Research: Oceans*, **120(2)**, 1152–1172, doi:10.1002/2014jc010299.
Oey, L.-Y. and S. Chou, 2016: Evidence of rising and poleward shift of storm surge in western North Pacific in recent decades. *Journal of Geophysical Research: Oceans*, **121(7)**, 5181–5192, doi:10.1002/2016jc011777.
Oka, E. et al., 2017: Long-term change and variation of salinity in the western North Pacific subtropical gyre revealed by 50-year long observations along 137°E. *Journal of Oceanography*, **73(4)**, 479–490, doi:10.1007/s10872-017-0416-2.
Oka, E. et al., 2019: Remotely Forced Decadal Physical and Biogeochemical Variability of North Pacific Subtropical Mode Water Over the Last 40 Years. *Geophysical Research Letters*, **46(3)**, 1555–1561, doi:10.1029/2018gl081330.
Olason, E. and D. Notz, 2014: Drivers of variability in Arctic sea-ice drift speed. *Journal of Geophysical Research C: Oceans*, **119(9)**, 5755–5775, doi:10.1002/2014jc009897.

ACCEPTED VERSION SUBJECT TO FINAL EDITING

Oldenburg, D., K.C. Armour, L.A. Thompson, and C.M. Bitz, 2018a: Distinct Mechanisms of Ocean Heat Transport Into the Arctic Under Internal Variability and Climate Change. *Geophysical Research Letters*, **45(15)**, 7692–7700, doi:10.1029/2018gl078719.

Oldenburg, D., K.C. Armour, L.A. Thompson, and C.M. Bitz, 2018b: Distinct Mechanisms of Ocean Heat Transport Into the Arctic Under Internal Variability and Climate Change. *Geophysical Research Letters*, **45(15)**, 7692–7700, doi:10.1029/2018gl078719.

Olefeldt, D. et al., 2016: Circumpolar distribution and carbon storage of thermokarst landscapes. *Nature Communications*, **7**, doi:10.1038/ncomms13043.

Oliver, E.C.J., 2019: Mean warming not variability drives marine heatwave trends. *Climate Dynamics*, **53(3)**, 1653–1659, doi:10.1007/s00382-019-04707-2.

Oliver, E.C.J. et al., 2019: Projected Marine Heatwaves in the 21st Century and the Potential for Ecological Impact. *Frontiers in Marine Science*, **6**, 734, doi:10.3389/fmars.2019.00734.

Olonscheck, D. and D. Notz, 2017: Consistently estimating internal climate variability from climate model simulations. *Journal of Climate*, **30(23)**, 9555–9573, doi:10.1175/jcli-d-16-0428.1.

Olonscheck, D., T. Mauritsen, and D. Notz, 2019: Arctic sea-ice variability is primarily driven by atmospheric temperature fluctuations. *Nature Geoscience*, **12(6)**, 430–434, doi:10.1038/s41561-019-0363-1.

Olonscheck, D., M. Rugenstein, and J. Marotzke, 2020: Broad Consistency Between Observed and Simulated Trends in Sea Surface Temperature Patterns. *Geophysical Research Letters*, **47(10)**, e2019GL086773, doi:10.1029/2019gl086773.

Onarheim, I.H., T. Eldevik, L.H. Smedsrud, and J.C. Stroeve, 2018: Seasonal and regional manifestation of Arctic sea ice loss. *Journal of Climate*, **31(12)**, 4917–4932, doi:10.1175/jcli-d-17-0427.1.

Oppenheimer, M. et al., 2019: Sea Level Rise and Implications for Low Lying Islands, Coasts and Communities. In: *IPCC Special Report on the Ocean and Cryosphere in a Changing Climate* [Pörtner, H.-O., D.C. Roberts, V. Masson-Delmotte, P. Zhai, M. Tignor, E. Poloczanska, K. Mintenbeck, M. Nicolai, A. Okem, J. Petzold, B. Rama, and N. Weyer (eds.)]. In Press, pp. 321–445.

Orton, P., N. Georgas, A. Blumberg, and J. Pullen, 2012: Detailed modeling of recent severe storm tides in estuaries of the New York City region. *Journal of Geophysical Research: Oceans*, **117(C9)**, n/a–n/a, doi:10.1029/2012jc008220.

Orton, P.M. et al., 2018: Flood hazard assessment from storm tides, rain and sea level rise for a tidal river estuary. *Natural Hazards*, 1–29, doi:10.1007/s11069-018-3251-x.

Østerhus, S. et al., 2019: Arctic Mediterranean exchanges: a consistent volume budget and trends in transports from two decades of observations. *Ocean Science*, **15(2)**, 379–399, doi:10.5194/os-15-379-2019.

Overduin, P.P. et al., 2019: Submarine Permafrost Map in the Arctic Modeled Using 1-D Transient Heat Flux (SuPerMAP). *Journal of Geophysical Research: Oceans*, **124(6)**, 3490–3507, doi:10.1029/2018jc014675.

Oyarzún, D. and C.M. Brierley, 2019: The future of coastal upwelling in the Humboldt current from model projections. *Climate Dynamics*, **52(1–2)**, 599–615, doi:10.1007/s00382-018-4158-7.

Palacios, D. et al., 2020: Climate sensitivity and geomorphological response of cirque glaciers from the late glacial to the Holocene, Sierra Nevada, Spain. *Quaternary Science Reviews*, **248**, 106617, doi:10.1016/j.quascirev.2020.106617.

Palanisamy, H., B. Meyssignac, A. Cazenave, and T. Delcroix, 2015: Is anthropogenic sea level fingerprint already detectable in the Pacific Ocean ? *Environmental Research Letters*, **10(8)**, 084024, doi:10.1088/1748-9326/10/8/084024.

Palmer, M.D., G.R. Harris, and J.M. Gregory, 2018: Extending CMIP5 projections of global mean temperature change and sea level rise due to thermal expansion using a physically-based emulator. *Environmental Research Letters*, **13(8)**, 84003.

Palmer, M.D., C.M. Domingues, A.B.A. Slangen, and F. Boeira Dias, 2021: An ensemble approach to quantify global mean sea-level rise over the 20th century from tide gauge reconstructions. *Environmental Research Letters*, **16(4)**, 044043, doi:10.1088/1748-9326/abdaec.

Palmer, M.D. et al., 2017: Ocean heat content variability and change in an ensemble of ocean reanalyses. *Climate Dynamics*, **49(3)**, 909–930, doi:10.1007/s00382-015-2801-0.

Palmer, M.D. et al., 2020: Exploring the Drivers of Global and Local Sea-Level Change Over the 21st Century and Beyond. *Earth's Future*, **8(9)**, e2019EF001413, doi:10.1029/2019ef001413.

Paolo, F.S., H.A. Fricker, and L. Padman, 2015: Volume loss from Antarctic ice shelves is accelerating. *Science*, **348(6232)**, 327–331, doi:10.1126/science.aaa0940.

Paquin, J.P. and L. Sushama, 2015: On the Arctic near-surface permafrost and climate sensitivities to soil and snow model formulations in climate models. *Climate Dynamics*, **44(1–2)**, 203–228, doi:10.1007/s00382-014-2185-6.

ACCEPTED VERSION SUBJECT TO FINAL EDITING

Pardaens, A.K., J.M. Gregory, and J.A. Lowe, 2011: A model study of factors influencing projected changes in regional sea level over the twenty-first century. *Climate Dynamics*, **36(9)**, 2015–2033, doi:10.1007/s00382-009-0738-x.

Park, H. et al., 2020: Increasing riverine heat influx triggers Arctic sea ice decline and oceanic and atmospheric warming. *Science Advances*, **6(45)**, eabc4699, doi:10.1126/sciadv.abc4699.

Parkes, D. and B. Marzeion, 2018: Twentieth-century contribution to sea-level rise from uncharted glaciers. *Nature*, **563(7732)**, 551–554, doi:10.1038/s41586-018-0687-9.

Parkinson, C.L., 2019: A 40-y record reveals gradual Antarctic sea ice increases followed by decreases at rates far exceeding the rates seen in the Arctic. *Proceedings of the National Academy of Sciences*, **116(29)**, 14414–14423, doi:10.1073/pnas.1906556116.

Parras-Berrocal, I.M. et al., 2020: The climate change signal in the Mediterranean Sea in a regionally coupled atmosphere-ocean model. *Ocean Science*, **16(3)**, 743–765, doi:10.5194/os-16-743-2020.

Patterson, M.O. et al., 2014: Orbital forcing of the East Antarctic ice sheet during the Pliocene and Early Pleistocene. *Nature Geoscience*, **7(11)**, 841–847, doi:10.1038/ngeo2273.

Patton, A.I., S.L. Rathburn, and D.M. Capps, 2019: Landslide response to climate change in permafrost regions. *Geomorphology*, **340**, 116–128, doi:10.1016/j.geomorph.2019.04.029.

Patton, H. et al., 2015: Geophysical constraints on the dynamics and retreat of the Barents Sea ice sheet as a paleobenchmark for models of marine ice sheet deglaciation. *Reviews of Geophysics*, **53(4)**, 1051–1098, doi:10.1002/2015rg000495.

Patton, H. et al., 2017: Deglaciation of the Eurasian ice sheet complex. *Quaternary Science Reviews*, **169**, 148–172, doi:10.1016/j.quascirev.2017.05.019.

Pattyn, F. and G. Durand, 2013: Why marine ice sheet model predictions may diverge in estimating future sea level rise. *Geophysical Research Letters*, **40(16)**, 4316–4320, doi:10.1002/grl.50824.

Pattyn, F. and M. Morlighem, 2020: The uncertain future of the Antarctic Ice Sheet. *Science*, **367(6484)**, 1331–1335, doi:10.1126/science.aaz5487.

Pattyn, F. et al., 2008: Benchmark experiments for higher-order and full-Stokes ice sheet models (ISMIP-HOM). *Cryosphere*, **2(2)**, 95–108, doi:10.5194/tc-2-95-2008.

Pattyn, F. et al., 2012: Results of the Marine Ice Sheet Model Intercomparison Project, MISMIP. *The Cryosphere*, **6(3)**, 573–588, doi:10.5194/tc-6-573-2012.

Pavlova, O., S. Gerland, and H. Hop, 2019: Changes in Sea-Ice Extent and Thickness in Kongsfjorden, Svalbard (2003–2016). In: *The Ecosystem of Kongsfjorden, Svalbard* [Hop, H. and C. Wiencke (eds.)]. Advances in Polar Ecology Vol. 2, Springer, Cham, Switzerland, pp. 105–136, doi:10.1007/978-3-319-46425-1_4.

Payne, A.J. et al., 2021: Contrasting contributions to future sea level under CMIP5 and CMIP6 scenarios from the Greenland and Antarctic ice sheets. *Geophysical Research Letters*, **in press**, 1–12.

Pearson, B., B. Fox-Kemper, S. Bachman, and F. Bryan, 2017: Evaluation of scale-aware subgrid mesoscale eddy models in a global eddy-rich model. *Ocean Modelling*, **115**, 42–58, doi:10.1016/j.ocemod.2017.05.007.

Pederson, G.T. et al., 2011: The unusual nature of recent snowpack declines in the North American Cordillera. *Science*, **333(6040)**, 332–335, doi:10.1126/science.1201570.

Pelle, T., M. Morlighem, and J. Bondzio, 2019: Brief communication: PICOP, a new ocean melt parameterization under ice shelves combining PICO and a plume model. *Cryosphere*, **13**, 1043–1049, doi:10.5194/tc-13-1043-2019.

Peltier, W.R., D.F. Argus, and R. Drummond, 2015: Space geodesy constrains ice age terminal deglaciation: The global ICE-6G_C (VM5a) model. *Journal of Geophysical Research: Solid Earth*, **120(1)**, 450–487, doi:10.1002/2014jb011176.

Pendleton, S.L. et al., 2019: Rapidly receding Arctic Canada glaciers revealing landscapes continuously ice-covered for more than 40,000 years. *Nature Communications*, **10(1)**, 445, doi:10.1038/s41467-019-08307-w.

Peng, D., E.M. Hill, A.J. Meltzner, and A.D. Switzer, 2019: Tide Gauge Records Show That the 18.61-Year Nodal Tidal Cycle Can Change High Water Levels by up to 30 cm. *Journal of Geophysical Research: Oceans*, **124(1)**, 736–749, doi:10.1029/2018jc014695.

Peng, G. and W.N. Meier, 2018: Temporal and regional variability of Arctic sea-ice coverage from satellite data. *Annals of Glaciology*, **59(76pt2)**, 191–200, doi:10.1017/aog.2017.32.

Peng, S. et al., 2013: Change in snow phenology and its potential feedback to temperature in the Northern Hemisphere over the last three decades. *Environmental Research Letters*, **8**, 014008, doi:10.1088/1748-9326/8/1/014008.

Perego, M., S. Price, and G. Stadler, 2014: Optimal initial conditions for coupling ice sheet models to Earth system models. *Journal Of Geophysical Research-Earth Surface*, **119(9)**, 1894–1917, doi:10.1002/2014jf003181.

Perkins-Kirkpatrick, S.E. et al., 2018: The role of natural variability and anthropogenic climate change in the 2017/2018 Tasman Sea marine heatwave. *Bulletin of the American Meteorological Society*, 1–4, doi:10.1175/bams-d-18-0116.1.

ACCEPTED VERSION SUBJECT TO FINAL EDITING

Noetzli, J., C. Pellet, and B. Staub (eds.), 2019: *Permafrost in Switzerland 2014/2015 to 2017/2018*. Glaciological Report (Permafrost) No. 16-19, Cryospheric Commission of the Swiss Academy of Sciences, 104 pp., doi:10.13093/permos-rep-2019-16-19.

Petit, T., M.S. Lozier, S.A. Josey, and S.A. Cunningham, 2020: Atlantic Deep Water Formation Occurs Primarily in the Iceland Basin and Irminger Sea by Local Buoyancy Forcing. *Geophysical Research Letters*, **47(22)**, doi:10.1029/2020gl091028.

Petty, A.A., M.M. Holland, D.A. Bailey, and N.T. Kurtz, 2018: Warm Arctic, Increased Winter Sea Ice Growth? *Geophysical Research Letters*, **45(23)**, 12,922–12,930, doi:10.1029/2018gl079223.

Petty, A.A., N.T. Kurtz, R. Kwok, T. Markus, and T.A. Neumann, 2020: Winter Arctic Sea Ice Thickness From ICESat-2 Freeboards. *Journal of Geophysical Research: Oceans*, **125(5)**, e2019JC015764, doi:10.1029/2019jc015764.

Piatt, J.F. et al., 2020: Extreme mortality and reproductive failure of common murres resulting from the northeast Pacific marine heatwave of 2014-2016. *PLoS ONE*, **15(1)**, doi:10.1371/journal.pone.0226087.

Pickart, R.S. and M.A. Spall, 2007: Impact of Labrador Sea convection on the North Atlantic meridional overturning circulation. *Journal of Physical Oceanography*, **37(9)**, 2207–2227, doi:10.1175/jpo3178.1.

Pickering, M.D., N.C. Wells, K.J. Horsburgh, and J.A.M. Green, 2012: The impact of future sea-level rise on the European Shelf tides. *Continental Shelf Research*, **35**, 1–15, doi:10.1016/j.csr.2011.11.011.

Pickering, M.D.D. et al., 2017: The impact of future sea-level rise on the global tides. *Continental Shelf Research*, **142**, 50–68, doi:10.1016/j.csr.2017.02.004.

Pico, T., A. Robel, E. Powell, A.C. Mix, and J.X. Mitrovica, 2019: Leveraging the Rapid Retreat of the Amundsen Gulf Ice Stream 13,000 Years Ago to Reveal Insight Into North American Deglaciation. *Geophysical Research Letters*, **46(21)**, 12101–12107, doi:10.1029/2019gl084789.

Piecuch, C.G., R.M. Ponte, C.M. Little, M.W. Buckley, and I. Fukumori, 2017: Mechanisms underlying recent decadal changes in subpolar North Atlantic Ocean heat content. *Journal of Geophysical Research: Oceans*, **122(9)**, 7181–7197, doi:10.1002/2017jc012845.

Piecuch, C.G., P.R. Thompson, R.M. Ponte, M.A. Merrifield, and B.D. Hamlington, 2019: What Caused Recent Shifts in Tropical Pacific Decadal Sea-Level Trends? *Journal of Geophysical Research: Oceans*, **124(11)**, 7575–7590, doi:10.1029/2019jc015339.

Piecuch, C.G. et al., 2018: Origin of spatial variation in US East Coast sea-level trends during 1900–2017. *Nature*, **564(7736)**, 400–404, doi:10.1038/s41586-018-0787-6.

Pilo, G.S., N.J. Holbrook, A.E. Kiss, and A.M.C. Hogg, 2019: Sensitivity of Marine Heatwave Metrics to Ocean Model Resolution. *Geophysical Research Letters*, **46**, doi:10.1029/2019gl084928.

Plach, A., K.H. Nisancioglu, P.M. Langebroek, A. Born, and S. Le Clec'h, 2019: Eemian Greenland ice sheet simulated with a higher-order model shows strong sensitivity to surface mass balance forcing. *Cryosphere*, **13(8)**, 2133–2148, doi:10.5194/tc-13-2133-2019.

Plecha, S.M. and P.M.M. Soares, 2020: Global marine heatwave events using the new CMIP6 multi-model ensemble: from shortcomings in present climate to future projections. *Environmental Research Letters*, **15(12)**, 124058, doi:10.1088/1748-9326/abc847.

Pollard, D., R.M. DeConto, and R.B. Alley, 2015: Potential Antarctic Ice Sheet retreat driven by hydrofracturing and ice cliff failure. *Earth and Planetary Science Letters*, **412**, 112–121, doi:10.1016/j.epsl.2014.12.035.

Pollard, D., N. Gomez, R.M. DeConto, and H.K. Han, 2018: Estimating Modern Elevations of Pliocene Shorelines Using a Coupled Ice Sheet-Earth-Sea Level Model. *Journal of Geophysical Research: Earth Surface*, **123(9)**, 2279–2291, doi:10.1029/2018jf004745.

Pollard, D., W. Chang, M. Haran, P. Applegate, and R. DeConto, 2016: Large ensemble modeling of the last deglacial retreat of the West Antarctic Ice Sheet: comparison of simple and advanced statistical techniques. *Geoscientific Model Development*, **9(5)**, 1697–1723, doi:10.5194/gmd-9-1697-2016.

Pope, J.O., P.R. Holland, A. Orr, G.J. Marshall, and T. Phillips, 2017: The impacts of El Niño on the observed sea ice budget of West Antarctica. *Geophysical Research Letters*, **44(12)**, 6200–6208, doi:10.1002/2017gl073414.

Porada, P., A. Ekici, and C. Beer, 2016: Effects of bryophyte and lichen cover on permafrost soil temperature at large scale. *The Cryosphere*, **10(5)**, 2291–2315, doi:10.5194/tc-10-2291-2016.

Portela, E., N. Kolodziejczyk, C. Maes, and V. Thierry, 2020: Interior water-mass variability in the Southern-Hemisphere oceans during the last decade. *Journal of Physical Oceanography*, **50(2)**, 361–381, doi:10.1175/jpo-d-19-0128.1.

Prandi, P. et al., 2021: Local sea level trends, accelerations and uncertainties over 1993–2019. *Scientific Data*, **8(1)**, 1–12, doi:10.1038/s41597-020-00786-7.

ACCEPTED VERSION SUBJECT TO FINAL EDITING

Pratap, B., D.P. Dobhal, M. Mehta, and R. Bhambri, 2015: Influence of debris cover and altitude on glacier surface melting: A case study on Dokriani Glacier, central Himalaya, India. *Annals of Glaciology*, **56(70)**, 9–16, doi:10.3189/2015aog70a971.

Previdi, M. and L.M. Polvani, 2016: Anthropogenic impact on Antarctic surface mass balance, currently masked by natural variability, to emerge by mid-century. *Environmental Research Letters*, **11(9)**, 094001, doi:10.1088/1748-9326/11/9/094001.

Pulliainen, J. et al., 2020: Patterns and trends of Northern Hemisphere snow mass from 1980 to 2018. *Nature*, **581(7808)**, 294–298, doi:10.1038/s41586-020-2258-0.

Punge, H.J., H. Gallée, M. Kageyama, and G. Krinner, 2012: Modelling snow accumulation on Greenland in Eemian, glacial inception, and modern climates in a GCM. *Climate of the Past*, **8**, 1801–1819, doi:10.5194/cp-8-1801-2012.

Purich, A. and M.H. England, 2019: Tropical Teleconnections to Antarctic Sea Ice During Austral Spring 2016 in Coupled Pacemaker Experiments. *Geophysical Research Letters*, **46(12)**, 6848–6858, doi:10.1029/2019gl082671.

Purich, A., M.H. England, W. Cai, A. Sullivan, and P.J. Durack, 2018: Impacts of broad-scale surface freshening of the Southern Ocean in a coupled climate model. *Journal of Climate*, **31(7)**, 2613–2632, doi:10.1175/jcli-d-17-0092.1.

Purich, A. et al., 2016: Tropical pacific SST drivers of recent antarctic sea ice trends. *Journal of Climate*, **29(24)**, 8931–8948, doi:10.1175/jcli-d-16-0440.1.

Purkey, S.G. et al., 2019a: Unabated Bottom Water Warming and Freshening in the South Pacific Ocean. *Journal of Geophysical Research: Oceans*, **124(3)**, 1778–1794, doi:10.1029/2018jc014775.

Purkey, S.G. et al., 2019b: Unabated Bottom Water Warming and Freshening in the South Pacific Ocean. *Journal of Geophysical Research: Oceans*, **124(3)**, 1778–1794, doi:10.1029/2018jc014775.

Qiao, F., Y. Yuan, J. Deng, D. Dai, and Z. Song, 2016: Wave–turbulence interaction-induced vertical mixing and its effects in ocean and climate models. *Philosophical Transactions of the Royal Society A: Mathematical, Physical and Engineering Sciences*, **374(2065)**, 20150201, doi:10.1098/rsta.2015.0201.

Qiao, G., Y. Li, S. Guo, and W. Ye, 2020: Evolving instability of the scar inlet ice shelf based on sequential landsat images spanning 2005-2018. *Remote Sensing*, **12(1)**, 36, doi:10.3390/rs12010036.

Qiu, B. and S. Chen, 2012: Multidecadal Sea Level and Gyre Circulation Variability in the Northwestern Tropical Pacific Ocean. *Journal of Physical Oceanography*, **42(1)**, 193–206, doi:10.1175/jpo-d-11-061.1.

Qiu, B., S. Chen, B. Qiu, and S. Chen, 2005: Variability of the Kuroshio Extension Jet, Recirculation Gyre, and Mesoscale Eddies on Decadal Time Scales. *Journal of Physical Oceanography*, **35(11)**, 2090–2103, doi:10.1175/jpo2807.1.

Qu, T., S. Gao, and R.A. Fine, 2020: Variability of the Sub-Antarctic Mode Water Subduction Rate During the Argo Period. *Geophysical Research Letters*, **47(13)**, e2020GL088248, doi:10.1029/2020gl088248.

Qu, X. and A. Hall, 2014: On the persistent spread in snow-albedo feedback. *Climate Dynamics*, **42(1–2)**, 69–81, doi:10.1007/s00382-013-1774-0.

Quiquet, A., C. Ritz, H.J. Punge, and D. y Mélia, 2013: Greenland ice sheet contribution to sea level rise during the last interglacial period: a modelling study driven and constrained by ice core data. *Climate of the Past*, **9(1)**, 353–366, doi:10.5194/cp-9-353-2013.

Rabatel, A. et al., 2013: Current state of glaciers in the tropical Andes: a multi-century perspective on glacier evolution and climate change. *The Cryosphere*, **7(1)**, 81–102, doi:10.5194/tc-7-81-2013.

Radić, V. et al., 2014: Regional and global projections of twenty-first century glacier mass changes in response to climate scenarios from global climate models. *Climate Dynamics*, **42(1–2)**, 37–58, doi:10.1007/s00382-013-1719-7.

Rae, J.W.B. et al., 2018: CO2 storage and release in the deep Southern Ocean on millennial to centennial timescales. *Nature*, **562(7728)**, 569–573, doi:10.1038/s41586-018-0614-0.

Rahmstorf, S., M. Perrette, and M. Vermeer, 2012: Testing the robustness of semi-empirical sea level projections. *Climate Dynamics*, **39(3—4)**, 861–875, doi:10.1007/s00382-011-1226-7.

Rampal, P., J. Weiss, and D. Marsan, 2009: Positive trend in the mean speed and deformation rate of Arctic sea ice, 1979-2007. *Journal of Geophysical Research: Oceans*, **114(5)**, doi:10.1029/2008jc005066.

Ran, Y., X. Li, and G. Cheng, 2018: Climate warming over the past half century has led to thermal degradation of permafrost on the Qinghai-Tibet Plateau. *Cryosphere*, **12**, 595–608, doi:10.5194/tc-12-595-2018.

Rashid, M.M. and T. Wahl, 2020: Predictability of Extreme Sea Level Variations Along the U.S. Coastline. *Journal of Geophysical Research: Oceans*, **125(9)**, doi:10.1029/2020jc016295.

ACCEPTED VERSION SUBJECT TO FINAL EDITING

Rathore, S., N.L. Bindoff, H.E. Phillips, and M. Feng, 2020: Recent hemispheric asymmetry in global ocean warming induced by climate change and internal variability. *Nature Communications*, **11(1)**, 2008, doi:10.1038/s41467-020-15754-3.

Ravanel, L., F. Magnin, and P. Deline, 2017: Impacts of the 2003 and 2015 summer heatwaves on permafrost-affected rock-walls in the Mont Blanc massif. *Science of the Total Environment*, **609**, 132–143, doi:10.1016/j.scitotenv.2017.07.055.

Ray, R.D., 2009: Secular changes in the solar semidiurnal tide of the western North Atlantic Ocean. *Geophysical Research Letters*, doi:10.1029/2009gl040217.

Raynolds, M.K. et al., 2014: Cumulative geoecological effects of 62 years of infrastructure and climate change in ice-rich permafrost landscapes, Prudhoe Bay Oilfield, Alaska. *Global Change Biology*, **20(4)**, 1211–1224, doi:10.1111/gcb.12500.

Reese, R., A. Levermann, T. Albrecht, H. Seroussi, and R. Winkelmann, 2020: The role of history and strength of the oceanic forcing in sea level projections from Antarctica with the Parallel Ice Sheet Model. *Cryosphere*, **14(9)**, 3097–3110, doi:10.5194/tc-14-3097-2020.

Reese, R. et al., 2018: The far reach of ice-shelf thinning in Antarctica. *Nature Climate Change*, **8(1)**, 53–57, doi:10.1038/s41558-017-0020-x.

Reguero, B.G., I.J. Losada, and F.J. Méndez, 2019: A recent increase in global wave power as a consequence of oceanic warming. *Nature Communications*, doi:10.1038/s41467-018-08066-0.

Reichl, B.G. and R. Hallberg, 2018: A simplified energetics based planetary boundary layer (ePBL) approach for ocean climate simulations.. *Ocean Modelling*, **132**, 112–129, doi:10.1016/j.ocemod.2018.10.004.

Reintges, A., T. Martin, M. Latif, and N.S. Keenlyside, 2017: Uncertainty in twenty-first century projections of the Atlantic Meridional Overturning Circulation in CMIP3 and CMIP5 models. *Climate Dynamics*, **49(5–6)**, 1495–1511, doi:10.1007/s00382-016-3180-x.

Renault, L., P. Marchesiello, S. Masson, and J.C. McWilliams, 2019: Remarkable Control of Western Boundary Currents by Eddy Killing , a Mechanical Air-Sea Coupling Process. *Geophysical Research Letters*, **46(5)**, 2743–2751, doi:10.1029/2018gl081211.

Renault, L. et al., 2016: Modulation of Wind Work by Oceanic Current Interaction with the Atmosphere. *Journal of Physical Oceanography*, **46(6)**, 1685–1704, doi:10.1175/jpo-d-15-0232.1.

Renner, A.H.H.H., K.J. Heywood, and S.E. Thorpe, 2009: Validation of three global ocean models in the Weddell Sea. *Ocean Modelling*, **30(1)**, 1–15, doi:10.1016/j.ocemod.2009.05.007.

Réveillet, M., C. Vincent, D. Six, and A. Rabatel, 2017: Which empirical model is best suited to simulate glacier mass balances? *Journal of Glaciology*, **63(237)**, 39–54, doi:10.1017/jog.2016.110.

Réveillet, M. et al., 2018: Relative performance of empirical and physical models in assessing the seasonal and annual glacier surface mass balance of Saint-Sorlin Glacier (French Alps). *Cryosphere*, **12(4)**, 1367–1386, doi:10.5194/tc-12-1367-2018.

Reyes, A. et al., 2014: South Greenland ice-sheet collapse during Marine Isotope Stage 11. *Nature*, **510(7506)**, 525–528, doi:10.1038/nature13456.

Reynhout, S.A. et al., 2019: Holocene glacier fluctuations in Patagonia are modulated by summer insolation intensity and paced by Southern Annular Mode-like variability. *Quaternary Science Reviews*, **220**, 178–187, doi:10.1016/j.quascirev.2019.05.029.

RGI Consortium, 2017: Randolph Glacier Inventory – A Dataset of Global Glacier Outlines: Version 6.0: Technical Report. Global Land Ice Measurements from Space, CO, USA. Retrieved from: https://doi.org/10.7265/n5-rgi-60.

Rhein, M., C. Mertens, and A. Roessler, 2019: Observed Transport Decline at 47°N, Western Atlantic. *Journal of Geophysical Research: Oceans*, **124(7)**, 4875–4890, doi:10.1029/2019jc014993.

Rhein, M. et al., 2013: Observations: Ocean. In: *Climate Change 2013 the Physical Science Basis: Working Group I Contribution to the Fifth Assessment Report of the Intergovernmental Panel on Climate Change* [Stocker, T.F., D. Qin, G.-K. Plattner, M. Tignor, S.K. Allen, J. Boschung, A. Nauels, Y. Xia, V. Bex, and P.M. Midgley (eds.)]. Cambridge University Press, Cambridge, United Kingdom and New York, NY, USA, pp. 255–316, doi:10.1017/cbo9781107415324.010.

Richter, K. and B. Marzeion, 2014: Earliest local emergence of forced dynamic and steric sea-level trends in climate models. *Environmental Research Letters*, **9(11)**, 114009, doi:10.1088/1748-9326/9/11/114009.

Richter, K., B. Marzeion, and R. Riva, 2017: The effect of spatial averaging and glacier melt on detecting a forced signal in regional sea level. *Environmental Research Letters*, doi:10.1088/1748-9326/aa5967.

Richter, K. et al., 2020: Detecting a forced signal in satellite-era sea-level change. *Environmental Research Letters*, **15(9)**, 094079, doi:10.1088/1748-9326/ab986e.

ACCEPTED VERSION SUBJECT TO FINAL EDITING

Ridley, J., J.M. Gregory, P. Huybrechts, and J. Lowe, 2010: Thresholds for irreversible decline of the Greenland ice sheet. *Climate Dynamics*, **35(6)**, 1065–1073, doi:10.1007/s00382-009-0646-0.

Ridley, J.K. and E.W. Blockley, 2018: Brief communication: Solar radiation management not as effective as CO2 mitigation for Arctic sea ice loss in hitting the 1.5 and 2°C COP climate targets. *Cryosphere*, **12(10)**, 3355–3360, doi:10.5194/tc-12-3355-2018.

Ridley, J.K., J.A. Lowe, and H.T. Hewitt, 2012: How reversible is sea ice loss? *Cryosphere*, **6(1)**, 193–198, doi:10.5194/tc-6-193-2012.

Rietbroek, R., S.-E. Brunnabend, J. Kusche, J. Schröter, and C. Dahle, 2016: Revisiting the contemporary sea-level budget on global and regional scales.. *Proceedings of the National Academy of Sciences of the United States of America*, **113(6)**, 1504–1509, doi:10.1073/pnas.1519132113.

Rignot, E., S. Jacobs, J. Mouginot, and B. Scheuchl, 2013: Ice-shelf melting around Antarctica. *Science*, **341(6143)**, 266–270, doi:10.1126/science.1235798.

Rignot, E., J. Mouginot, M. Morlighem, H. Seroussi, and B. Scheuchl, 2014: Widespread, rapid grounding line retreat of Pine Island, Thwaites, Smith, and Kohler glaciers, West Antarctica, from 1992 to 2011. *Geophysical Research Letters*, **41(10)**, 3502–3509, doi:10.1002/2014gl060140.

Rignot, E. et al., 2019: Four decades of Antarctic Ice Sheet mass balance from 1979-2017. *Proceedings of the National Academy of Sciences*, **116(4)**, 1–9, doi:10.1073/pnas.1812883116.

Rignot, E.I., C. Fenty, X. Kemp, C. Yun, and Cai, 2015: Undercutting of Greenland marine-terminating glaciers in deep glacial fjords. *Geophyiscal Research Letters*, **42(14)**, 5909–5917.

Ringler, T. et al., 2013: A multi-resolution approach to global ocean modeling. *Ocean Modelling*, **69**, 211–232, doi:10.1016/j.ocemod.2013.04.010.

Riser, S.C. et al., 2016: Fifteen years of ocean observations with the global Argo array. *Nature Climate Change*, **6**, 145.

Ritz, C. et al., 2015: Potential sea-level rise from Antarctic ice-sheet instability constrained by observations. *Nature*, **528(7580)**, 115–118, doi:10.1038/nature16147.

Roach, L.A., S.M. Dean, and J.A. Renwick, 2018a: Consistent biases in Antarctic sea ice concentration simulated by climate models. *The Cryosphere*, **12(1)**, 365–383, doi:10.5194/tc-12-365-2018.

Roach, L.A., C. Horvat, S.M. Dean, and C.M. Bitz, 2018b: An Emergent Sea Ice Floe Size Distribution in a Global Coupled Ocean-Sea Ice Model. *Journal of Geophysical Research: Oceans*, **123(6)**, 4322–4337, doi:10.1029/2017jc013692.

Roach, L.A. et al., 2020: Antarctic Sea Ice Area in CMIP6. *Geophysical Research Letters*, **47(9)**, doi:10.1029/2019gl086729.

Robel, A.A., 2017: Thinning sea ice weakens buttressing force of iceberg mélange and promotes calving. *Nature Communications*, **8**, 1–7, doi:10.1038/ncomms14596.

Robel, A.A. and A.F. Banwell, 2019: A Speed Limit on Ice Shelf Collapse Through Hydrofracture. *Geophysical Research Letters*, **46(21)**, 12092–12100, doi:10.1029/2019gl084397.

Robel, A.A., H. Seroussi, and G.H. Roe, 2019: Marine ice sheet instability amplifies and skews uncertainty in projections of future sea-level rise. *Proceedings of the National Academy of Sciences of the United States of America*, **116(30)**, 14887–14892, doi:10.1073/pnas.1904822116.

Roberts, C.D., L. Jackson, and D. McNeall, 2014: Is the 2004-2012 reduction of the Atlantic meridional overturning circulation significant? *Geophysical Research Letters*, **41(9)**, 3204–3210, doi:10.1002/2014gl059473.

Roberts, C.D. et al., 2016: On the Drivers and Predictability of Seasonal-to-Interannual Variations in Regional Sea Level. *Journal of Climate*, **29(21)**, 7565–7585, doi:10.1175/jcli-d-15-0886.1.

Roberts, M.J. et al., 2018: The Benefits of Global High Resolution for Climate Simulation: Process Understanding and the Enabling of Stakeholder Decisions at the Regional Scale. *Bulletin of the American Meteorological Society*, **99(11)**, 2341–2359, doi:10.1175/bams-d-15-00320.1.

Roberts, M.J. et al., 2019: Description of the resolution hierarchy of the global coupled HadGEM3-GC3.1 model as used in CMIP6 HighResMIP experiments. *Geoscientific Model Development*, **12(12)**, 4999–5028, doi:10.5194/gmd-12-4999-2019.

Roberts, M.J. et al., 2020a: Sensitivity of the Atlantic Meridional Overturning Circulation to Model Resolution in CMIP6 HighResMIP Simulations and Implications for Future Changes. *Journal of Advances in Modeling Earth Systems*, **12(8)**, doi:10.1029/2019ms002014.

Roberts, M.J. et al., 2020b: Sensitivity of the Atlantic Meridional Overturning Circulation to Model Resolution in CMIP6 HighResMIP Simulations and Implications for Future Changes. *Journal of Advances in Modeling Earth Systems*, **12(8)**, doi:10.1029/2019ms002014.

ACCEPTED VERSION SUBJECT TO FINAL EDITING

Roberts, M.J. et al., 2020c: Sensitivity of the Atlantic Meridional Overturning Circulation to Model Resolution in CMIP6 HighResMIP Simulations and Implications for Future Changes. *Journal of Advances in Modeling Earth Systems*, **12(8)**, doi:10.1029/2019ms002014.

Robinson, A. and H. Goelzer, 2014: The importance of insolation changes for paleo ice sheet modeling. *Cryosphere*, **8(4)**, 1419–1428, doi:10.5194/tc-8-1419-2014.

Robinson, A., R. Calov, and A. Ganopolski, 2011: Greenland ice sheet model parameters constrained using simulations of the Eemian Interglacial. *Climate of the Past*, **7(2)**, 381–396.

Robinson, A., R. Calov, and A. Ganopolski, 2012: Multistability and critical thresholds of the Greenland ice sheet. *Nature Climate Change*, **2(6)**, 429–432, doi:10.1038/nclimate1449.

Robinson, A., J. Alvarez-Solas, R. Calov, A. Ganopolski, and M. Montoya, 2017: MIS-11 duration key to disappearance of the Greenland ice sheet. *Nature Communications*, **8**, 16008.

Robson, J., P. Ortega, and R. Sutton, 2016: A reversal of climatic trends in the North Atlantic since 2005. *Nature Geoscience*, **9(7)**, 513–517, doi:10.1038/ngeo2727.

Robson, J., R. Sutton, K. Lohmann, D. Smith, and M.D. Palmer, 2012: Causes of the Rapid Warming of the North Atlantic Ocean in the Mid-1990s. *Journal of Climate*, **25(12)**, 4116–4134, doi:10.1175/jcli-d-11-00443.1.

Rodehacke, C.B., M. Pfeiffer, T. Semmler, Gurses, and T. Kleiner, 2020: Future sea level contribution from Antarctica inferred from CMIP5 model forcing and its dependence on precipitation ansatz. *Earth System Dynamics*, **11(4)**, 1153–1194, doi:10.5194/esd-11-1153-2020.

Rohling, E.J. et al., 2019: Asynchronous Antarctic and Greenland ice-volume contributions to the last interglacial sea-level highstand. *Nature Communications*, **10(1)**, 5040, doi:10.1038/s41467-019-12874-3.

Romanovsky, V. et al., 2017: Changing Permafrost and its Impacts. In: *Snow, Water, Ice and Permafrost in the Arctic (SWIPA) 2017*. Arctic Monitoring and Assessment Programme (AMAP), Oslo, Norway, pp. 65–136.

Rose, S.K., O.B. Andersen, M. Passaro, C.A. Ludwigsen, and C. Schwatke, 2019: Arctic Ocean Sea Level Record from the Complete Radar Altimetry Era: 1991–2018. *Remote Sensing*, **11(14)**, 1672, doi:10.3390/rs11141672.

Rösel, A. et al., 2018: Thin Sea Ice, Thick Snow, and Widespread Negative Freeboard Observed During N-ICE2015 North of Svalbard. *Journal of Geophysical Research: Oceans*, **123(2)**, 1156–1176, doi:10.1002/2017jc012865.

Rosenblum, E. and I. Eisenman, 2017: Sea ice trends in climate models only accurate in runs with biased global warming. *Journal of Climate*, **30(16)**, 6265–6278, doi:10.1175/jcli-d-16-0455.1.

Rossby, T., L. Chafik, and L. Houpert, 2020: What can Hydrography Tell Us About the Strength of the Nordic Seas MOC Over the Last 70 to 100 Years? *Geophysical Research Letters*, **47(12)**, doi:10.1029/2020gl087456.

Rounce, D.R., R. Hock, and D.E. Shean, 2020: Glacier Mass Change in High Mountain Asia Through 2100 Using the Open-Source Python Glacier Evolution Model (PyGEM). *Frontiers in Earth Science*, **7**, 331, doi:10.3389/feart.2019.00331.

Roy, K. and W.R. Peltier, 2017: Space-geodetic and water level gauge constraints on continental uplift and tilting over North America: regional convergence of the ICE-6G_C (VM5a/VM6) models. *Geophysical Journal International*, **210(2)**, 1115–1142, doi:10.1093/gji/ggx156.

Royston, S. et al., 2018: Sea-Level Trend Uncertainty With Pacific Climatic Variability and Temporally-Correlated Noise. *Journal of Geophysical Research: Oceans*, **123(3)**, 1978–1993, doi:10.1002/2017jc013655.

Ruan, R. et al., 2019: Decelerated Greenland Ice Sheet Melt Driven by Positive Summer North Atlantic Oscillation. *Journal of Geophysical Research: Atmospheres*, **124(14)**, 7633–7646, doi:10.1029/2019jd030689.

Rückamp, M., H. Goelzer, and A. Humbert, 2020: Sensitivity of Greenland ice sheet projections to spatial resolution in higher-order simulations: the Alfred Wegener Institute (AWI) contribution to ISMIP6 Greenland using the Ice-sheet and Sea-level System Model (ISSM). *The Cryosphere*, **14(10)**, 3309–3327, doi:10.5194/tc-14-3309-2020.

Russell, J.L. et al., 2018: Metrics for the Evaluation of the Southern Ocean in Coupled Climate Models and Earth System Models. *Journal of Geophysical Research: Oceans*, **123(5)**, 3120–3143, doi:10.1002/2017jc013461.

Ryan, J.C. et al., 2018: Dark zone of the Greenland Ice Sheet controlled by distributed biologically-active impurities. *Nature Communications*, **9(1)**, 1065, doi:10.1038/s41467-018-03353-2.

Ryan, J.C. et al., 2019: Greenland Ice Sheet surface melt amplified by snowline migration and bare ice exposure. *Science Advances*, **5(3)**, doi:10.1126/sciadv.aav3738.

Rye, C.D. et al., 2020: Antarctic Glacial Melt as a Driver of Recent Southern Ocean Climate Trends. *Geophysical Research Letters*, **47(11)**, e2019GL086892, doi:10.1029/2019gl086892.

Rykaczewski, R.R. et al., 2015: Poleward displacement of coastal upwelling-favorable winds in the ocean's eastern boundary currents through the 21st century. *Geophysical Research Letters*, **42(15)**, 6424–6431, doi:10.1002/2015gl064694.

ACCEPTED VERSION SUBJECT TO FINAL EDITING

Sadai, S., A. Condron, R. DeConto, and D. Pollard, 2020: Future climate response to Antarctic Ice Sheet melt caused by anthropogenic warming. *Science Advances*, **6(39)**, doi:10.1126/sciadv.aaz1169.

Saha, S., L. Owen, E. Orr, and M. Caffee, 2018: Timing and nature of Holocene glacier advances at the northwestern end of the Himalayan-Tibetan orogen. *Quaternary Science Reviews*, **187**, 177–202, doi:10.1016/j.quascirev.2018.03.009.

Sakai, A. and K. Fujita, 2017: Contrasting glacier responses to recent climate change in high-mountain Asia. *Scientific Reports*, **7(1)**, 13717, doi:10.1038/s41598-017-14256-5.

Sakamoto, T. et al., 2012: MIROC4h: A New High-Resolution Atmosphere-Ocean Coupled General Circulation Model. *Journal of the Meteorological Society of Japan. Ser. II*, **90(3)**, 325–359, doi:10.2151/jmsj.2012-301.

Sallée, J.-B. et al., 2013a: Assessment of Southern Ocean mixed-layer depths in CMIP5 models: Historical bias and forcing response. *Journal of Geophysical Research: Oceans*, **118(4)**, 1845–1862, doi:10.1002/jgrc.20157.

Sallée, J.-B. et al., 2013b: Assessment of Southern Ocean water mass circulation and characteristics in CMIP5 models: Historical bias and forcing response. *Journal of Geophysical Research: Oceans*, **118(4)**, 1830–1844, doi:10.1002/jgrc.20135.

Sallée, J.-B. et al., 2021: Summertime increases in upper-ocean stratification and mixed-layer depth. *Nature*, **591(7851)**, 592–598, doi:10.1038/s41586-021-03303-x.

Sánchez-Montes, M.L. et al., 2020: Late Pliocene Cordilleran Ice Sheet development with warm northeast Pacific sea surface temperatures. *Climate of the Past*, **16(1)**, 299–313, doi:10.5194/cp-16-299-2020.

Sasaki, H. et al., 2004: A series of eddy-resolving ocean simulations in the world ocean – OFES (OGCM for the Earth Simulator) project. In: *Oceans '04 MTS/IEEE Techno-Ocean '04*. IEEE, pp. 1535–1541, doi:10.1109/oceans.2004.1406350.

Sasgen, I. et al., 2020: Return to rapid ice loss in Greenland and record loss in 2019 detected by the GRACE-FO satellites. *Communications Earth & Environment*, **1(1)**, 8, doi:10.1038/s43247-020-0010-1.

Scambos, T.A. et al., 2017: How much, how fast?: A science review and outlook for research on the instability of Antarctica's Thwaites Glacier in the 21st century. *Global and Planetary Change*, **153**, 16–34, doi:10.1016/j.gloplacha.2017.04.008.

Schaeffer, A. and M. Roughan, 2017: Subsurface intensification of marine heatwaves off southeastern Australia: The role of stratification and local winds. *Geophysical Research Letters*, **44(10)**, 5025–5033, doi:10.1002/2017gl073714.

Schaffer, J. et al., 2020: Bathymetry constrains ocean heat supply to Greenland's largest glacier tongue. *Nature Geoscience*, **13(3)**, 227–231, doi:10.1038/s41561-019-0529-x.

Schemm, S., 2018: Regional Trends in Weather Systems Help Explain Antarctic Sea Ice Trends. *Geophysical Research Letters*, **45(14)**, 7165–7175, doi:10.1029/2018gl079109.

Scherler, D., H. Wulf, and N. Gorelick, 2018: Global Assessment of Supraglacial Debris-Cover Extents. *Geophysical Research Letters*, **45(21)**, 11,798–11,805, doi:10.1029/2018gl080158.

Scheuchl, B., J. Mouginot, E. Rignot, M. Morlighem, and A. Khazendar, 2016: Grounding line retreat of Pope, Smith, and Kohler Glaciers, West Antarctica, measured with Sentinel-1a radar interferometry data. *Geophysical Research Letters*, **43(16)**, 8572–8579, doi:10.1002/2016gl069287.

Schindelegger, M., J.A.M. Green, S.B. Wilmes, and I.D. Haigh, 2018: Can We Model the Effect of Observed Sea Level Rise on Tides? *Journal of Geophysical Research: Oceans*, doi:10.1029/2018jc013959.

Schlegel, N.J., E. Larour, H. Seroussi, M. Morlighem, and J.E. Box, 2015: Ice discharge uncertainties in Northeast Greenland from boundary conditions and climate forcing of an ice flow model. *Journal Of Geophysical Research-Earth Surface*, **120(1)**, 29–54, doi:10.1002/2014jf003359.

Schlemm, T. and A. Levermann, 2021: A simple model of mélange buttressing for calving glaciers. *The Cryosphere*, **15**, 531–545, doi:10.5194/tc-2020-50.

Schloesser, F., T. Friedrich, A. Timmermann, R.M. DeConto, and D. Pollard, 2019: Antarctic iceberg impacts on future Southern Hemisphere climate. *Nature Climate Change*, **9(9)**, 672–677, doi:10.1038/s41558-019-0546-1.

Schlosser, E., F.A. Haumann, and M.N. Raphael, 2018: Atmospheric influences on the anomalous 2016 Antarctic sea ice decay. *The Cryosphere*, **12(3)**, 1103–1119, doi:10.5194/tc-12-1103-2018.

Schmale, J. et al., 2017: Modulation of snow reflectance and snowmelt from Central Asian glaciers by anthropogenic black carbon. *Scientific Reports*, **7(1)**, 40501, doi:10.1038/srep40501.

Schmidt, L.S. et al., 2019: Dynamic simulations of Vatnajökull ice cap from 1980 to 2300. *Journal of Glaciology*, **66(255)**, 97–112, doi:10.1017/jog.2019.90.

Schöner, W., R. Koch, C. Matulla, C. Marty, and A.M. Tilg, 2019: Spatiotemporal patterns of snow depth within the Swiss-Austrian Alps for the past half century (1961 to 2012) and linkages to climate change. *International Journal of Climatology*, **39(3)**, 1589–1603, doi:10.1002/joc.5902.

ACCEPTED VERSION SUBJECT TO FINAL EDITING

Schröder, L. et al., 2019: Four decades of Antarctic surface elevation changes from multi-mission satellite altimetry. *The Cryosphere*, **13**, 427–449, doi:10.5194/tc-13-427-2019.
Schroeder, D.M. et al., 2019: Multidecadal observations of the Antarctic ice sheet from restored analog radar records. *ATMOSPHERIC, AND PLANETARY SCIENCES*, **116**, doi:10.25740/ykq4-9345.
Schroeter, S., W. Hobbs, N.L. Bindoff, R. Massom, and R. Matear, 2018: Drivers of Antarctic sea ice volume change in CMIP5 models. *Journal of Geophysical Research: Oceans*, **123**, 1–25, doi:10.1029/2018jc014177.
Schuler, T. et al., 2020: Reconciling Svalbard Glacier Mass Balance. *Frontiers in Earth Science*, **8**, 156, doi:10.3389/feart.2020.00156.
Schweiger, A.J., K.R. Wood, and J. Zhang, 2019: Arctic Sea Ice Volume Variability over 1901–2010: A Model-Based Reconstruction. *Journal of Climate*, **32(15)**, 4731–4752, doi:10.1175/jcli-d-19-0008.1.
Schweinsberg, A.D., J.P. Briner, G.H. Miller, O. Bennike, and E.K. Thomas, 2017: Local glaciation in West Greenland linked to North Atlantic Ocean circulation during the Holocene. *Geology*, **45(3)**, 195–198, doi:10.1130/g38114.1.
Schweinsberg, A.D. et al., 2018: Holocene mountain glacier history in the Sukkertoppen Iskappe area, southwest Greenland. *Quaternary Science Reviews*, **197**, 142–161, doi:10.1016/j.quascirev.2018.06.014.
Screen, J.A. and D. Williamson, 2017: Ice-free Arctic at 1.5°C? *Nature Climate Change*, **7(4)**, 230–231, doi:10.1038/nclimate3248.
Seehaus, T., A.J. Cook, A.B. Silva, and M. Braun, 2018: Changes in glacier dynamics in the northern Antarctic Peninsula since 1985. *Cryosphere*, **12**, 577–594, doi:10.5194/tc-12-577-2018.
Seehaus, T. et al., 2019a: Changes of the tropical glaciers throughout Peru between 2000 and 2016 – mass balance and area fluctuations. *The Cryosphere*, **13(10)**, 2537–2556, doi:10.5194/tc-13-2537-2019.
Seehaus, T. et al., 2019b: Mass balance and area changes of glaciers in the Cordillera Real and Tres Cruces, Bolivia, between 2000 and 2016. *Journal of Glaciology*, **66(255)**, 124–136, doi:10.1017/jog.2019.94.
Sellevold, R. and M. Vizcaíno, 2020: Global Warming Threshold and Mechanisms for Accelerated Greenland Ice Sheet Surface Mass Loss. *Journal of Advances in Modeling Earth Systems*, **12(9)**, e2019MS002029, doi:10.1029/2019ms002029.
Sellevold, R. et al., 2019: Surface mass balance downscaling through elevation classes in an Earth system model: application to the Greenland ice sheet. *The Cryosphere*, **13**, 3193–3208, doi:10.5194/tc-13-3193-2019.
Sen Gupta, A. et al., 2016: Future changes to the Indonesian Throughflow and Pacific circulation: The differing role of wind and deep circulation changes. *Geophysical Research Letters*, **43(4)**, 1669–1678, doi:10.1002/2016gl067757.
Sen Gupta, A. et al., 2020: Drivers and impacts of the most extreme marine heatwaves events. *Scientific Reports*, **10(1)**, 19359, doi:10.1038/s41598-020-75445-3.
Seo, H., R. Murtugudde, M. Jochum, and A.J. Miller, 2008: Modeling of mesoscale coupled ocean–atmosphere interaction and its feedback to ocean in the western Arabian Sea. *Ocean Modelling*, **25(3–4)**, 120–131, doi:10.1016/j.ocemod.2008.07.003.
Seo, H., K.H. Brink, C.E. Dorman, D. Koracin, and C.A. Edwards, 2012: What determines the spatial pattern in summer upwelling trends on the U.S. West Coast? *Journal of Geophysical Research: Oceans*, **117(C8)**, doi:10.1029/2012jc008016.
Seo, H. et al., 2007: The Scripps Coupled Ocean–Atmosphere Regional (SCOAR) Model, with Applications in the Eastern Pacific Sector. *Journal of Climate*, **20(3)**, 381–402, doi:10.1175/jcli4016.1.
Sérazin, G. et al., 2016: Quantifying uncertainties on regional sea level change induced by multidecadal intrinsic oceanic variability. *Geophysical Research Letters*, **43(15)**, 8151–8159, doi:10.1002/2016gl069273.
Sérazin, G. et al., 2017: A global probabilistic study of the ocean heat content low-frequency variability: Atmospheric forcing versus oceanic chaos. *Geophysical Research Letters*, **44(11)**, 5580–5589, doi:10.1002/2017gl073026.
Sergienko, O. and D.J. Wingham, 2019: Grounding line stability in a regime of low driving and basal stresses. *Journal of Glaciology*, **65(253)**, 833–849, doi:10.1017/jog.2019.53.
Seroussi, H. et al., 2017: Continued retreat of Thwaites Glacier, West Antarctica, controlled by bed topography and ocean circulation. *Geophysical Research Letters*, **44(12)**, 6191–6199, doi:10.1002/2017gl072910.
Seroussi, H. et al., 2019: initMIP-Antarctica: An ice sheet model initialization experiment of ISMIP6. *The Cryosphere*, **13**, 1441–1471, doi:10.5194/tc-13-1441-2019.
Seroussi, H. et al., 2020: ISMIP6 Antarctica: A multi-model ensemble of the Antarctic ice sheet evolution over the 21st century. *Cryosphere*, **14(9)**, 3033–3070, doi:10.5194/tc-14-3033-2020.
Shackleton, S. et al., 2019: Is the Noble Gas-Based Rate of Ocean Warming During the Younger Dryas Overestimated? *Geophysical Research Letters*, **46(11)**, 5928–5936, doi:10.1029/2019gl082971.

ACCEPTED VERSION SUBJECT TO FINAL EDITING

Shackleton, S. et al., 2020: Global ocean heat content in the Last Interglacial. *Nature Geoscience*, **13(1)**, 77–81, doi:10.1038/s41561-019-0498-0.
Shakhova, N. et al., 2017: Current rates and mechanisms of subsea permafrost degradation in the East Siberian Arctic Shelf. *Nature Communications*, **8**, 15872, doi:10.1038/ncomms15872.
Shakun, J.D. et al., 2012: Global warming preceded by increasing carbon dioxide concentrations during the last deglaciation. *Nature*, **484**, 49–54, doi:10.1038/nature10915.
Shakun, J.D. et al., 2015: Regional and global forcing of glacier retreat during the last deglaciation. *Nature Communications*, **6**, 8059, doi:10.1038/ncomms9059.
Shannon, S. et al., 2019: Global glacier volume projections under high-end climate change scenarios. *The Cryosphere*, **13(1)**, 325–350, doi:10.5194/tc-13-325-2019.
Shean, D.E. et al., 2020: A Systematic, Regional Assessment of High Mountain Asia Glacier Mass Balance. *Frontiers in Earth Science*, **7**, 363, doi:10.3389/feart.2019.00363.
Shepherd, A. et al., 2019: Trends in Antarctic Ice Sheet Elevation and Mass. *Geophysical Research Letters*, **46(14)**, 8174–8183, doi:10.1029/2019gl082182.
Shepherd, T.G. et al., 2018: Storylines: an alternative approach to representing uncertainty in physical aspects of climate change. *Climatic Change*, **151(3)**, 555–571, doi:10.1007/s10584-018-2317-9.
Sherman, P., E. Tziperman, C. Deser, and M. McElroy, 2020: Historical and Future Roles of Internal Atmospheric Variability in Modulating Summertime Greenland Ice Sheet Melt. *Geophysical Research Letters*, **47(6)**, e2019GL086913, doi:10.1029/2019gl086913.
Shi, J.-R., S.-P. Xie, and L.D. Talley, 2018: Evolving Relative Importance of the Southern Ocean and North Atlantic in Anthropogenic Ocean Heat Uptake. *Journal of Climate*, **31(18)**, 7459–7479, doi:10.1175/jcli-d-18-0170.1.
Shi, J.-R., L.D. Talley, S.-P. Xie, W. Liu, and S.T. Gille, 2020: Effects of Buoyancy and Wind Forcing on Southern Ocean Climate Change. *Journal of Climate*, 1–53, doi:10.1175/jcli-d-19-0877.1.
Shimada, R., N. Takeuchi, and T. Aoki, 2016: Inter-annual and geographical variations in the extent of bare ice and dark ice on the Greenland ice sheet derived from MODIS satellite images. *Frontiers in Earth Science*, **4**, 43, doi:10.3389/feart.2016.00043.
Shu, Q., Z. Song, and F. Qiao, 2015: Assessment of sea ice simulations in the CMIP5 models. *Cryosphere*, **9(1)**, 399–409, doi:10.5194/tc-9-399-2015.
Shu, Q. et al., 2020: Assessment of Sea Ice Extent in CMIP6 With Comparison to Observations and CMIP5. *Geophysical Research Letters*, **47(9)**, e2020GL087965, doi:10.1029/2020gl087965.
Shugar, D.H. et al., 2020: Rapid worldwide growth of glacial lakes since 1990. *Nature Climate Change*, **10(10)**, 939–945, doi:10.1038/s41558-020-0855-4.
Sidorenko, D. et al., 2019: Evaluation of FESOM2.0 Coupled to ECHAM6.3: Preindustrial and HighResMIP Simulations. *Journal of Advances in Modeling Earth Systems*, **11(11)**, 3794–3815, doi:10.1029/2019ms001696.
Siegert, M., R.B. Alley, E. Rignot, J. Englander, and R. Corell, 2020: Twenty-first century sea-level rise could exceed IPCC projections for strong-warming futures. *One Earth*, **3(6)**, 691–703, doi:10.1016/j.oneear.2020.11.002.
Sigl, M. et al., 2018: 19th century glacier retreat in the Alps preceded the emergence of industrial black carbon deposition on high-alpine glaciers. *The Cryosphere*, **12(10)**, 3311–3331, doi:10.5194/tc-12-3311-2018.
Sigmond, M., J.C. Fyfe, and N.C. Swart, 2018: Ice-free Arctic projections under the Paris Agreement. *Nature Climate Change*, **8(5)**, 404–408, doi:10.1038/s41558-018-0124-y.
Silvano, A. et al., 2018: Freshening by glacial meltwater enhances melting of ice shelves and reduces formation of Antarctic Bottom Water. *Science Advances*, **4(4)**, doi:10.1126/sciadv.aap9467.
Silvano, A. et al., 2020: Recent recovery of Antarctic Bottom Water formation in the Ross Sea driven by climate anomalies. *Nature Geoscience*, **13(12)**, 780–786, doi:10.1038/s41561-020-00655-3.
Silvy, Y., E. Guilyardi, J.-B. Sallée, and P.J. Durack, 2020a: Human-induced changes to the global ocean water masses and their time of emergence. *Nature Climate Change*, **10(11)**, 1030–1036, doi:10.1038/s41558-020-0878-x.
Silvy, Y., E. Guilyardi, J.-B. Sallée, and P.J. Durack, 2020b: Human-induced changes to the global ocean water masses and their time of emergence. *Nature Climate Change*, **10(11)**, 1030–1036, doi:10.1038/s41558-020-0878-x.
Simmonds, I., 2015: Comparing and contrasting the behaviour of Arctic and Antarctic sea ice over the 35 year period 1979-2013. *Annals of Glaciology*, **56(69)**, 18–28, doi:10.3189/2015aog69a909.
Simms, A.R., L. Lisiecki, G. Gebbie, P.L. Whitehouse, and J.F. Clark, 2019: Balancing the last glacial maximum (LGM) sea-level budget. *Quaternary Science Reviews*, **205**, 143–153, doi:10.1016/j.quascirev.2018.12.018.
Simpkins, G.R., Y. Peings, and G. Magnusdottir, 2016: Pacific Influences on Tropical Atlantic Teleconnections to the Southern Hemisphere High Latitudes. *Journal of Climate*, **29(18)**, 6425–6444, doi:10.1175/jcli-d-15-0645.1.

ACCEPTED VERSION SUBJECT TO FINAL EDITING

Simpkins, G.R., L.M. Ciasto, D.W.J. Thompson, and M.H. England, 2012: Seasonal relationships between large-scale climate variability and antarctic sea ice concentration. *Journal of Climate*, **25(16)**, 5451–5469, doi:10.1175/jcli-d-11-00367.1.

Simpson, M.J.R., G.A. Milne, P. Huybrechts, and A.J. Long, 2009: Calibrating a glaciological model of the Greenland ice sheet from the Last Glacial Maximum to present-day using field observations of relative sea level and ice extent. *Quaternary Science Reviews*, **28**, 1631–1657, doi:10.1016/j.quascirev.2009.03.004.

Singh, H.A., P.J. Rasch, and B.E.J. Rose, 2017: Increased Ocean Heat Convergence Into the High Latitudes With CO 2 Doubling Enhances Polar-Amplified Warming. *Geophysical Research Letters*, **44(20)**, 10,583–10,591, doi:10.1002/2017gl074561.

Skinner, L.C., S. Fallon, C. Waelbroeck, E. Michel, and S. Barker, 2010: Ventilation of the Deep Southern Ocean and Deglacial CO2 Rise. *Science*, **328(5982)**, 1147–1151, doi:10.1126/science.1183627.

Slangen, A.B.A., J.A. Church, X. Zhang, and D. Monselesan, 2014a: Detection and attribution of global mean thermosteric sea-level change. *Geophysical Research Letters*, **41(16)**, 5951–5959, doi:10.1002/2014gl061356.

Slangen, A.B.A., J.A. Church, X. Zhang, and D.P. Monselesan, 2015: The sea level response to external forcings in historical simulations of CMIP5 climate models. *Journal of Climate*, **28(21)**, 8521–8539, doi:10.1175/jcli-d-15-0376.1.

Slangen, A.B.A. et al., 2014b: Projecting twenty-first century regional sea-level changes. *Climatic Change*, **124(1–2)**, 317–332, doi:10.1007/s10584-014-1080-9.

Slangen, A.B.A. et al., 2017: Evaluating model simulations of twentieth-century sea level rise. Part I: Global mean sea level change. *Journal of Climate*, **30(21)**, 8539–8563, doi:10.1175/jcli-d-17-0110.1.

Slater, A.G. and D.M. Lawrence, 2013: Diagnosing present and future permafrost from climate models. *Journal of Climate*, **26(15)**, 5608–5623, doi:10.1175/jcli-d-12-00341.1.

Slater, A.G., D.M. Lawrence, and C.D. Koven, 2017: Process-level model evaluation: A snow and heat transfer metric. *The Cryosphere*, **11(2)**, 989–996, doi:10.5194/tc-11-989-2017.

Slater, D.A., P.W. Nienow, D.N. Goldberg, T.R. Cowton, and A.J. Sole, 2017: A model for tidewater glacier undercutting by submarine melting. *Geophysical Research Letters*, **44(5)**, 2360–2368, doi:10.1002/2016gl072374.

Slater, D.A. et al., 2019: Estimating Greenland tidewater glacier retreat driven by submarine melting. *The Cryosphere*, **13(9)**, 2489–2509, doi:10.5194/tc-13-2489-2019.

Slater, D.A. et al., 2020: Twenty-first century ocean forcing of the Greenland ice sheet for modelling of sea level contribution. *Cryosphere*, **14(3)**, 985–1008, doi:10.5194/tc-14-985-2020.

Slater, T., A.E. Hogg, and R. Mottram, 2020: Ice-sheet losses track high-end sea-level rise projections. *Nature Climate Change*, **10(10)**, 879–881, doi:10.1038/s41558-020-0893-y.

Slater, T. et al., 2021: Review article: Earth's ice imbalance. *The Cryosphere*, **15(1)**, 233–246, doi:10.5194/tc-15-233-2021.

Sloyan, B.M. and T.J. O'Kane, 2015: Drivers of decadal variability in the Tasman Sea. *Journal of Geophysical Research: Oceans*, **120(5)**, 3193–3210, doi:10.1002/2014jc010550.

Sloyan, B.M. et al., 2019: The Global Ocean Ship-Based Hydrographic Investigations Program (GO-SHIP): A Platform for Integrated Multidisciplinary Ocean Science. *Frontiers in Marine Science*, **6**, 445, doi:10.3389/fmars.2019.00445.

Smale, D.A. et al., 2019: Marine heatwaves threaten global biodiversity and the provision of ecosystem services. *Nature Climate Change*, **9(4)**, 306, doi:10.1038/s41558-019-0412-1.

Small, J. et al., 2014: A new synoptic scale resolving global climate simulation using the Community Earth System Model. *Journal of Advances in Modeling Earth Systems*, **6(4)**, 1065–1094, doi:10.1002/2014ms000363.

Small, R.J., F.O. Bryan, S.P. Bishop, and R.A. Tomas, 2019: Air-sea turbulent heat fluxes in climate models and observational analyses: What drives their variability? *Journal of Climate*, **32(8)**, 2397–2421, doi:10.1175/jcli-d-18-0576.1.

Small, R.J. et al., 2014: A new synoptic scale resolving global climate simulation using the Community Earth System Model. *Journal of Advances in Modeling Earth Systems*, **6(4)**, 1065–1094, doi:10.1002/2014ms000363.

Small, R.J. et al., 2015: The Benguela Upwelling System: Quantifying the Sensitivity to Resolution and Coastal Wind Representation in a Global Climate Model*. *Journal of Climate*, **28(23)**, 9409–9432, doi:10.1175/jcli-d-15-0192.1.

Smeed, D.A. et al., 2018: The North Atlantic Ocean Is in a State of Reduced Overturning. *Geophysical Research Letters*, **45(3)**, 1527–1533, doi:10.1002/2017gl076350.

Smith, A. and A. Jahn, 2019: Definition differences and internal variability affect the simulated Arctic sea ice melt season. *Cryosphere*, **13(1)**, 1–20, doi:10.5194/tc-13-1-2019.

ACCEPTED VERSION SUBJECT TO FINAL EDITING

Smith, B. et al., 2020: Pervasive ice sheet mass loss reflects competing ocean and atmosphere processes. *Science*, **368(6496)**, 1239–1242, doi:10.1126/science.aaz5845.
Smith, C.J. et al., 2018: FAIR v1. 3: A simple emissions-based impulse response and carbon cycle model. *Geoscientific Model Development*, **11(6)**, 2273–2297.
Smith, D.E., S. Harrison, C.R. Firth, and J.T. Jordan, 2011: The early Holocene sea level rise. *Quaternary Science Reviews*, **30(15)**, 1846–1860, doi:10.1016/j.quascirev.2011.04.019.
Smith, J.A. et al., 2017: Sub-ice-shelf sediments record history of twentieth-century retreat of Pine Island Glacier. *Nature*, **541(7635)**, 77–80, doi:10.1038/nature20136.
Smith, K.L., L.M. Polvani, and D.R. Marsh, 2012: Mitigation of 21st century Antarctic sea ice loss by stratospheric ozone recovery. *Geophysical Research Letters*, **39(20)**, 2012GL053325, doi:10.1029/2012gl053325.
Snauffer, A.M., W.W. Hsieh, and A.J. Cannon, 2016: Comparison of gridded snow water equivalent products with in situ measurements in British Columbia, Canada. *Journal of Hydrology*, **541**, 714–726, doi:10.1016/j.jhydrol.2016.07.027.
Snow, K. et al., 2015: Sensitivity of abyssal water masses to overflow parameterisations. *Ocean Modelling*, **89**, 84–103, doi:10.1016/j.ocemod.2015.03.004.
Solgaard, A.M. et al., 2020: Hagen Bræ: A Surging Glacier in North Greenland-35 Years of Observations. *Geophysical Research Letters*, **47(6)**, e2019GL085802, doi:10.1029/2019gl085802.
Solomina, O.N. et al., 2015: Holocene glacier fluctuations. *Quaternary Science Reviews*, **111**, 9–34, doi:10.1016/j.quascirev.2014.11.018.
Solomina, O.N. et al., 2016: Glacier fluctuations during the past 2000 years. *Quaternary Science Reviews*, **149**, 61–90, doi:10.1016/j.quascirev.2016.04.008.
Somavilla, R., C. González-Pola, and J. Fernández-Diaz, 2017: The warmer the ocean surface, the shallower the mixed layer. How much of this is true? *Journal of Geophysical Research: Oceans*, **122(9)**, 7698–7716, doi:10.1002/2017jc013125.
Sommer, C. et al., 2020: Rapid glacier retreat and downwasting throughout the European Alps in the early 21st century. *Nature Communications*, **11(1)**, 1–10, doi:10.1038/s41467-020-16818-0.
Somot, S., F. Sevault, M. Déqué, and M. Crépon, 2008: 21st century climate change scenario for the Mediterranean using a coupled atmosphere–ocean regional climate model. *Global and Planetary Change*, **63(2–3)**, 112–126, doi:10.1016/j.gloplacha.2007.10.003.
Song, D., X.H. Wang, X. Zhu, and X. Bao, 2013: Modeling studies of the far-field effects of tidal flat reclamation on tidal dynamics in the East China Seas. *Estuarine, Coastal and Shelf Science*, **133**, 147–160, doi:10.1016/j.ecss.2013.08.023.
Soto-Navarro, J. et al., 2020: Evolution of Mediterranean Sea water properties under climate change scenarios in the Med-CORDEX ensemble. *Climate Dynamics*, **54(3)**, 2135–2165, doi:10.1007/s00382-019-05105-4.
Sousa, M.C., M. DeCastro, I. Alvarez, M. Gomez-Gesteira, and J.M. Dias, 2017: Why coastal upwelling is expected to increase along the western Iberian Peninsula over the next century? *Science of The Total Environment*, **592**, 243–251, doi:10.1016/j.scitotenv.2017.03.046.
Spector, P. et al., 2017: Rapid early-Holocene deglaciation in the Ross Sea, Antarctica. *Geophysical Research Letters*, **44(15)**, 7817–7825, doi:10.1002/2017gl074216.
Spence, P. et al., 2014: Rapid subsurface warming and circulation changes of Antarctic coastal waters by poleward shifting winds. *Geophysical Research Letters*, **41(13)**, 4601–4610, doi:10.1002/2014gl060613.
Spence, P. et al., 2017: Localized rapid warming of West Antarctic subsurface waters by remote winds. *Nature Climate Change*, **7(8)**, 595–603, doi:10.1038/nclimate3335.
Spolaor, A. et al., 2016: Canadian arctic sea ice reconstructed from bromine in the Greenland NEEM ice core. *Scientific Reports*, **6**, 33925, doi:10.1038/srep33925.
Spreen, G., R. Kwok, and D. Menemenlis, 2011: Trends in Arctic sea ice drift and role of wind forcing: 1992–2009. *Geophysical Research Letters*, **38(19)**, doi:10.1029/2011gl048970.
Spreen, G. et al., 2020: Arctic Sea Ice Volume Export Through Fram Strait From 1992 to 2014. *Journal of Geophysical Research: Oceans*, **125(6)**, e2019JC016039, doi:10.1029/2019jc016039.
Stabeno, P.J. and S.W. Bell, 2019: Extreme Conditions in the Bering Sea (2017–2018): Record-Breaking Low Sea-Ice Extent. *Geophysical Research Letters*, **46(15)**, 8952–8959, doi:10.1029/2019gl083816.
Stammer, D. et al., 2019: Ocean Climate Observing Requirements in Support of Climate Research and Climate Information. *Frontiers in Marine Science*, **6**, 444, doi:10.3389/fmars.2019.00444.
Staten, P.W., J. Lu, K.M. Grise, S.M. Davis, and T. Birner, 2018: Re-examining tropical expansion. *Nature Climate Change*, **8(9)**, 768–775, doi:10.1038/s41558-018-0246-2.

ACCEPTED VERSION SUBJECT TO FINAL EDITING

Steele, M. and W. Ermold, 2015: Loitering of the retreating sea ice edge in the Arctic Seas. *Journal of Geophysical Research: Oceans*, **120(12)**, 7699–7721, doi:10.1002/2015jc011182.

Stein, K., A. Timmermann, E.Y. Kwon, and T. Friedrich, 2020: Timing and magnitude of Southern Ocean sea ice/carbon cycle feedbacks. *Proceedings of the National Academy of Sciences*, **117(9)**, 4498–4504, doi:10.1073/pnas.1908670117.

Stein, R. et al., 2017: Holocene variability in sea ice cover, primary production, and Pacific-Water inflow and climate change in the Chukchi and East Siberian Seas (Arctic Ocean). *Journal of Quaternary Science*, **32(3)**, 362–379, doi:10.1002/jqs.2929.

Stellema, A., A. Sen Gupta, and A.S. Taschetto, 2019: Projected slow down of South Indian Ocean circulation. *Scientific Reports*, **9(1)**, 17705, doi:10.1038/s41598-019-54092-3.

Stendardo, I., M. Rhein, and R. Steinfeldt, 2020: The North Atlantic Current and its Volume and Freshwater Transports in the Subpolar North Atlantic, Time Period 1993–2016. *Journal of Geophysical Research: Oceans*, **125(9)**, e2020JC016065, doi:10.1029/2020jc016065.

Stevens, C. et al., 2020: Ocean mixing and heat transport processes observed under the Ross Ice Shelf control its basal melting. *Proceedings of the National Academy of Sciences of the United States of America*, **117(29)**, doi:10.1073/pnas.1910760117.

Stevenson, S., B. Otto-Bliesner, J. Fasullo, and E. Brady, 2016: "El Niño Like" hydroclimate responses to last millennium volcanic eruptions. *Journal of Climate*, **29(8)**, 2907–2921, doi:10.1175/jcli-d-15-0239.1.

Stewart, A.L. and A.F. Thompson, 2013: Connecting Antarctic Cross-Slope Exchange with Southern Ocean Overturning. *Journal of Physical Oceanography*, **43(7)**, 1453–1471, doi:10.1175/jpo-d-12-0205.1.

Stewart, A.L. and A.F. Thompson, 2015: Eddy-mediated transport of warm Circumpolar Deep Water across the Antarctic Shelf Break. *Geophysical Research Letters*, **42(2)**, 432–440, doi:10.1002/2014gl062281.

Stewart, A.L., A. Klocker, and D. Menemenlis, 2018: Circum-Antarctic Shoreward Heat Transport Derived From an Eddy- and Tide-Resolving Simulation. *Geophysical Research Letters*, **45(2)**, 834–845, doi:10.1002/2017gl075677.

Stewart, C.L., P. Christoffersen, K.W. Nicholls, M.J.M. Williams, and J.A. Dowdeswell, 2019: Basal melting of Ross Ice Shelf from solar heat absorption in an ice-front polynya. *Nature Geoscience*, **12**, 435–440, doi:10.1038/s41561-019-0356-0.

Stewart, K.D., A.M.C. Hogg, M.H. England, and D.W. Waugh, 2020: Response of the Southern Ocean Overturning Circulation to Extreme Southern Annular Mode Conditions. *Geophysical Research Letters*, **47(22)**, e2020GL091103, doi:10.1029/2020gl091103.

Stibal, M. et al., 2017: Algae Drive Enhanced Darkening of Bare Ice on the Greenland Ice Sheet. *Geophysical Research Letters*, **44(22)**, 11,463–11,471, doi:10.1002/2017gl075958.

Stone, E.J., D.J. Lunt, J.D. Annan, and J.C. Hargreaves, 2013: Quantification of the Greenland ice sheet contribution to Last Interglacial sea level rise. *Climate of the Past*, **9(2)**, 621–639, doi:10.5194/cp-9-621-2013.

Stopa, J.E., F. Ardhuin, and F. Girard-Ardhuin, 2016: Wave climate in the Arctic 1992-2014: seasonality and trends. *The Cryosphere*, **10(4)**, 1605–1629, doi:10.5194/tc-10-1605-2016.

Stopa, J.E., F. Ardhuin, E. Stutzmann, and T. Lecocq, 2019: Sea State Trends and Variability: Consistency Between Models, Altimeters, Buoys, and Seismic Data (1979–2016). *Journal of Geophysical Research: Oceans*, **124(6)**, 3923–3940, doi:10.1029/2018jc014607.

Storlazzi, C.D. et al., 2018: Most atolls will be uninhabitable by the mid-21st century because of sea-level rise exacerbating wave-driven flooding. *Science Advances*, **4(4)**, doi:10.1126/sciadv.aap9741.

Stouffer, R.J. et al., 2006: Investigating the Causes of the Response of the Thermohaline Circulation to Past and Future Climate Changes. *J. Climate*, **19**, 1365–1387, doi:10.1175/jcli3689.1.

Straneo, F. and C. Cenedese, 2015: The Dynamics of Greenland's Glacial Fjords and Their Role in Climate. *Annual Review of Marine Science*, **7(1)**, 89–112, doi:10.1146/annurev-marine-010213-135133.

Streletskiy, D.A. et al., 2017: Thaw Subsidence in Undisturbed Tundra Landscapes, Barrow, Alaska, 1962–2015. *Permafrost and Periglacial Processes*, **28(3)**, 566–572, doi:10.1002/ppp.1918.

Stroeve, J. and D. Notz, 2018: Changing state of Arctic sea ice across all seasons. *Environmental Research Letters*, **13(10)**, 103001, doi:10.1088/1748-9326/aade56.

Stroeve, J., A. Barrett, M. Serreze, and A. Schweiger, 2014: Using records from submarine, aircraft and satellites to evaluate climate model simulations of Arctic sea ice thickness. *The Cryosphere*, **8(5)**, 1839–1854, doi:10.5194/tc-8-1839-2014.

Stroeve, J.C. et al., 2012: Trends in Arctic sea ice extent from CMIP5, CMIP3 and observations. *Geophysical Research Letters*, **39(16)**, doi:10.1029/2012gl052676.

ACCEPTED VERSION SUBJECT TO FINAL EDITING

Stuhne, G.R. and W.R. Peltier, 2015: Reconciling the ICE-6G_C reconstruction of glacial chronology with ice sheet dynamics: The cases of Greenland and Antarctica. *Journal of Geophysical Research*, **120(9)**, 1841–1865.
Sugimoto, S., K. Hanawa, T. Watanabe, T. Suga, and S.-P.P. Xie, 2017: Enhanced warming of the subtropical mode water in the North Pacific and North Atlantic. *Nature Climate Change*, **7**, 656, doi:10.1038/nclimate3371.
Sun, Q., M.M. Whitney, F.O. Bryan, and Y.- Tseng, 2017: A box model for representing estuarine physical processes in Earth system models. *Ocean Modelling*, **112**, 139–153, doi:10.1016/j.ocemod.2017.03.004.
Sun, S. et al., 2019: Topographic Shelf Waves Control Seasonal Melting Near Antarctic Ice Shelf Grounding Lines. *Geophysical Research Letters*, **46(16)**, 9824–9832, doi:10.1029/2019gl083881.
Sun, S. et al., 2020: Antarctic ice sheet response to sudden and sustained ice-shelf collapse (ABUMIP). *Journal of Glaciology*, 4–11, doi:10.1017/jog.2020.67.
Suo, L., Y. Gao, D. Guo, and I. Bethke, 2017: Sea-ice free Arctic contributes to the projected warming minimum in the North Atlantic. *Environmental Research Letters*, **12(7)**, 74004, doi:10.1088/1748-9326/aa6a5e.
Supply, A. et al., 2018: Precipitation Estimates from SMOS Sea-Surface Salinity. *Quarterly Journal of the Royal Meteorological Society*, **144(S1)**, 103–119, doi:10.1002/qj.3110.
Sutherland, D.A. et al., 2019: Direct observations of submarine melt and subsurface geometry at a tidewater glacier. *Science*, **365(6451)**, 369–374, doi:10.1126/science.aax3528.
Sutter, J., P. Gierz, K. Grosfeld, M. Thoma, and G. Lohmann, 2016: Ocean temperature thresholds for Last Interglacial West Antarctic Ice Sheet collapse. *Geophysical Research Letters*, **43(6)**, 2675–2682, doi:10.1002/2016gl067818.
Sutter, J. et al., 2020: Limited Retreat of the Wilkes Basin Ice Sheet During the Last Interglacial. *Geophysical Research Letters*, **47(13)**, 1–8, doi:10.1029/2020gl088131.
Svensson, C. and D.A. Jones, 2004: Dependence between sea surge, river flow and precipitation in south and west Britain. *Hydrology and Earth System Sciences*, **8(5)**, 973–992, doi:10.5194/hess-8-973-2004.
Swapna, P., J. Jyoti, R. Krishnan, N. Sandeep, and S.M. Griffies, 2017: Multidecadal Weakening of Indian Summer Monsoon Circulation Induces an Increasing Northern Indian Ocean Sea Level. *Geophysical Research Letters*, **44(20)**, 10,560–10,572, doi:10.1002/2017gl074706.
Swart, N.C., S.T. Gille, J.C. Fyfe, and N.P. Gillett, 2018: Recent Southern Ocean warming and freshening driven by greenhouse gas emissions and ozone depletion. *Nature Geoscience*, **11(11)**, 836–841, doi:10.1038/s41561-018-0226-1.
Sweet, W. and J. Park, 2014: From the extreme to the mean: Acceleration and tipping points of coastal inundation from sea level rise. *Earth's Future*, **2(12)**, 579–600, doi:10.1002/2014ef000272.
Swingedouw, D., P. Braconnot, P. Delecluse, E. Guilyardi, and O. Marti, 2006: The impact of global freshwater forcing on the thermohaline circulation: adjustment of North Atlantic convection sites in a CGCM. *Climate Dynamics*, **28(2–3)**, 291–305, doi:10.1007/s00382-006-0171-3.
Sydeman, W.J. et al., 2014: Climate change and wind intensification in coastal upwelling ecosystems. *Science*, **345(6192)**, 77–80, doi:10.1126/science.1251635.
Sylla, A., J. Mignot, X. Capet, and A.T. Gaye, 2019: Weakening of the Senegalo-Mauritania Upwelling System under climate change, Climate dynamics. *Climate dynamics*, **53**, 4447–4473.
Tabone, I., J. Blasco, A. Robinson, J. Alvarez-Solas, and M. Montoya, 2018: The sensitivity of the Greenland Ice Sheet to glacial-interglacial oceanic forcing. *Climate of the Past*, **14(4)**, 455–472, doi:10.5194/cp-14-455-2018.
Tadesse, M., T. Wahl, and A. Cid, 2020: Data-Driven Modeling of Global Storm Surges. *Frontiers in Marine Science*, **7**, 260, doi:10.3389/fmars.2020.00260.
Takahashi, C. and M. Watanabe, 2016: Pacific trade winds accelerated by aerosol forcing over the past two decades. *Nature Climate Change*, **6(8)**, 768–772, doi:10.1038/nclimate2996.
Takayabu, I. et al., 2015: Climate change effects on the worst-case storm surge: A case study of Typhoon Haiyan. *Environmental Research Letters*, doi:10.1088/1748-9326/10/6/064011.
Talke, S.A. and D.A. Jay, 2013: Nineteenth century North American and Pacific tidal data: Lost or just forgotten? *Journal of Coastal Research*, **29(6a)**, 118–127, doi:10.2112/jcoastres-d-12-00181.1.
Talke, S.A., A.C. Kemp, and J. Woodruff, 2018: Relative Sea Level, Tides, and Extreme Water Levels in Boston Harbor From 1825 to 2018. *Journal of Geophysical Research: Oceans*, **123(6)**, 3895–3914, doi:10.1029/2017jc013645.
Talley, L., 2013: Closure of the Global Overturning Circulation Through the Indian, Pacific, and Southern Oceans: Schematics and Transports. *Oceanography*, **26(1)**, 80–97, doi:10.5670/oceanog.2013.07.
Tandon, N.F., P.J. Kushner, D. Docquier, J.J. Wettstein, and C. Li, 2018: Reassessing Sea Ice Drift and Its Relationship to Long-Term Arctic Sea Ice Loss in Coupled Climate Models. *Journal of Geophysical Research: Oceans*, **123(6)**, 4338–4359, doi:10.1029/2017jc013697.

ACCEPTED VERSION SUBJECT TO FINAL EDITING

Tapia Baldis, C. and D. Trombotto Liaudat, 2019: Rockslides and rock avalanches in the Central Andes of Argentina and their possible association with permafrost degradation. *Permafrost and Periglacial Processes*, **30(4)**, 330–347, doi:10.1002/ppp.2024.

Tarasov, L., A.S. Dyke, R.M. Neal, and W.R. Peltier, 2012: A data-calibrated distribution of deglacial chronologies for the North American ice complex from glaciological modeling. *Earth and Planetary Science Letters*, **315**, 30–40, doi:10.1016/j.epsl.2011.09.010.

Taylor, K.E., R.J. Stouffer, and G.A. Meehl, 2012: An Overview of CMIP5 and the Experiment Design. *Bulletin of the American Meteorological Society*, **93(4)**, 485–498, doi:10.1175/bams-d-11-00094.1.

Tedesco, M. and X. Fettweis, 2020: Unprecedented atmospheric conditions (1948–2019) drive the 2019 exceptional melting season over the Greenland ice sheet. *The Cryosphere*, **14**, 1209–1223, doi:10.5194/tc-14-1209-2020.

Terada, M., S. Minobe, and C. Deutsch, 2020: Mechanisms of future changes in equatorial upwelling: CMIP5 intermodel analysis. *Journal of Climate*, **33(2)**, 497–510, doi:10.1175/jcli-d-19-0128.1.

Tesi, T. et al., 2020: Resolving sea ice dynamics in the north-western Ross Sea during the last 2.6 ka: From seasonal to millennial timescales. *Quaternary Science Reviews*, **237**, 106299, doi:10.1016/j.quascirev.2020.106299.

Thackeray, C.W. and C.G. Fletcher, 2016: Snow albedo feedback: Current knowledge, importance, outstanding issues and future directions. *Progress in Physical Geography*, **40(3)**, 392–408, doi:10.1177/0309133315620999.

Thackeray, C.W., C.G. Fletcher, and C. Derksen, 2015: Quantifying the skill of CMIP5 models in simulating seasonal albedo and snow cover evolution. *Journal of Geophysical Research*, **120(12)**, 5831–5849, doi:10.1002/2015jd023325.

Thackeray, C.W., X. Qu, and A. Hall, 2018: Why Do Models Produce Spread in Snow Albedo Feedback? *Geophysical Research Letters*, **45(12)**, 6223–6231, doi:10.1029/2018gl078493.

The IMBIE team, 2021: Antarctic and Greenland Ice Sheet mass balance 1992-2020 for IPCC AR6. doi:10.5285/77B64C55-7166-4A06-9DEF-2E400398E452

The IMBIE Team, 2020: Mass balance of the Greenland Ice Sheet from 1992 to 2018. *Nature*, **579**, 233–239, doi:10.1038/s41586-019-1855-2.

The IMBIE Team et al., 2018: Mass balance of the Antarctic Ice Sheet from 1992 to 2017. *Nature*, **558(7709)**, 219–222, doi:10.1038/s41586-018-0179-y.

Thøgersen, K., A. Gilbert, T.V. Schuler, and A. Malthe-Sørenssen, 2019: Rate-and-state friction explains glacier surge propagation. *Nature Communications*, **10(1)**, 2823, doi:10.1038/s41467-019-10506-4.

Thomas, E.R. et al., 2019: Antarctic Sea Ice Proxies from Marine and Ice Core Archives Suitable for Reconstructing Sea Ice over the Past 2000 Years. *Geosciences*, **9(12)**, 506, doi:10.3390/geosciences9120506.

Thomas, Z.A. et al., 2020: Tipping elements and amplified polar warming during the Last Interglacial. *Quaternary Science Reviews*, **233**, 106222, doi:10.1016/j.quascirev.2020.106222.

Thompson, A.F., A.L. Stewart, P. Spence, and K.J. Heywood, 2018: The Antarctic Slope Current in a Changing Climate. *Reviews of Geophysics*, **56(4)**, 741–770, doi:10.1029/2018rg000624.

Thomson, J. and W.E. Rogers, 2014: Swell and sea in the emerging Arctic Ocean. *Geophysical Research Letters*, **41(9)**, 3136–3140, doi:10.1002/2014gl059983.

Tierney, J.E. et al., 2020: Glacial cooling and climate sensitivity revisited. *Nature*, **584(7822)**, 569–573, doi:10.1038/s41586-020-2617-x.

Timko, P.G. et al., 2013: Skill testing a three-dimensional global tide model to historical current meter records. *Journal of Geophysical Research: Oceans*, **118(12)**, 6914–6933, doi:10.1002/2013jc009071.

Timmermann, R. and H.H. Hellmer, 2013: Southern Ocean warming and increased ice shelf basal melting in the twenty-first and twenty-second centuries based on coupled ice-ocean finite-element modelling. *Ocean Dynamics*, **63(9)**, 1011–1026, doi:10.1007/s10236-013-0642-0.

Timmermann, R. and S. Goeller, 2017: Response to Filchner-Ronne Ice Shelf cavity warming in a coupled ocean-ice sheet model – Part 1: The ocean perspective. *Ocean Science*, **13(5)**, 765–776, doi:10.5194/os-13-765-2017.

Timmermans, B., D. Stone, M. Wehner, and H. Krishnan, 2017: Impact of tropical cyclones on modeled extreme wind-wave climate. *Geophysical Research Letters*, doi:10.1002/2016gl071681.

Timmermans, B.W., C.P. Gommenginger, G. Dodet, and J.-R. Bidlot, 2020: Global Wave Height Trends and Variability from New Multimission Satellite Altimeter Products, Reanalyses, and Wave Buoys. *Geophysical Research Letters*, **47(9)**, doi:10.1029/2019gl086880.

Tinker, J., J. Lowe, J. Holt, A. Pardaens, and A. Wiltshire, 2015: Validation of an ensemble modelling system for climate projections for the northwest European shelf seas. *Progress in Oceanography*, **138**, 211–237, doi:10.1016/j.pocean.2015.07.002.

Tinker, J., J. Lowe, A. Pardaens, J. Holt, and R. Barciela, 2016: Uncertainty in climate projections for the 21st century northwest European shelf seas. *Progress in Oceanography*, **148**, 56–73, doi:10.1016/j.pocean.2016.09.003.

ACCEPTED VERSION SUBJECT TO FINAL EDITING

Todd, A. et al., 2020: Ocean-Only FAFMIP: Understanding Regional Patterns of Ocean Heat Content and Dynamic Sea Level Change. *Journal of Advances in Modeling Earth Systems*, **12**, e2019MS002027, doi:10.1029/2019ms002027.

Todd, J. et al., 2018: A Full-Stokes 3-D Calving Model Applied to a Large Greenlandic Glacier. *Journal of Geophysical Research: Earth Surface*, **123(3)**, 410–432, doi:10.1002/2017jf004349.

Tomita, H., T. Hihara, S. Kako, M. Kubota, and K. Kutsuwada, 2019: An introduction to J-OFURO3, a third-generation Japanese ocean flux data set using remote-sensing observations. *Journal of Oceanography*, **75(2)**, 171–194, doi:10.1007/s10872-018-0493-x.

Törnqvist, T.E. and M.P. Hijma, 2012: Links between early Holocene ice-sheet decay, sea-level rise and abrupt climate change. *Nature Geoscience*, **5(9)**, 601–606, doi:10.1038/ngeo1536.

Torsvik, T. et al., 2019: Impact of tidewater glacier retreat on the fjord system: Modeling present and future circulation in Kongsfjorden, Svalbard. *Estuarine, Coastal and Shelf Science*, **220**, 152–165, doi:10.1016/j.ecss.2019.02.005.

Trenberth, K.E. and J.T. Fasullo, 2018: Applications of an updated atmospheric energetics formulation. *Journal of Climate*, **31(16)**, 6263–6279, doi:10.1175/jcli-d-17-0838.1.

Trenberth, K.E., Y. Zhang, J.T. Fasullo, and L. Cheng, 2019: Observation-Based Estimates of Global and Basin Ocean Meridional Heat Transport Time Series. *Journal of Climate*, **32(14)**, 4567–4583, doi:10.1175/jcli-d-18-0872.1.

Trofaier, A.M., S. Westermann, and A. Bartsch, 2017: Progress in space-borne studies of permafrost for climate science: Towards a multi-ECV approach. *Remote Sensing of Environment*, **203**, 55–70, doi:10.1016/j.rse.2017.05.021.

Trotta, F., N. Pinardi, E. Fenu, A. Grandi, and V. Lyubartsev, 2017: Multi-nest high-resolution model of submesoscale circulation features in the Gulf of Taranto. *Ocean Dynamics*, **67(12)**, 1609–1625, doi:10.1007/s10236-017-1110-z.

Trusel, L.D. et al., 2015: Divergent trajectories of Antarctic surface melt under two twenty-first-century climate scenarios. *Nature Geoscience*, **8**, 927–932, doi:10.1038/ngeo2563.

Trüssel, B.L., R.J. Motyka, M. Truffer, and C.F. Larsen, 2013: Rapid thinning of lake-calving Yakutat Glacier and the collapse of the Yakutat Icefield, southeast Alaska, USA. *Journal of Glaciology*, **59(213)**, 149–161, doi: 10.3189/2013j0g12j081.

Tsubouchi, T. et al., 2021: Increased ocean heat transport into the Nordic Seas and Arctic Ocean over the period 1993–2016. *Nature Climate Change*, **11(1)**, 21–26, doi:10.1038/s41558-020-00941-3.

Tsujino, H. et al., 2020: Evaluation of global ocean–sea-ice model simulations based on the experimental protocols of the Ocean Model Intercomparison Project phase 2 (OMIP-2). *Geoscientific Model Development*, **13(8)**, 3643–3708, doi:10.5194/gmd-13-3643-2020.

Turetsky, M.R. et al., 2020: Carbon release through abrupt permafrost thaw. *Nature Geoscience*, **13(2)**, 138–143, doi:10.1038/s41561-019-0526-0.

Turki, I., N. Massei, and B. Laignel, 2019: Linking sea level dynamic and exceptional events to large-scale atmospheric circulation variability: A case of the Seine Bay, France. *Oceanologia*, **61(3)**, 321–330, doi:10.1016/j.oceano.2019.01.003.

Turner, J., T. Bracegirdle, T. Phillips, G. Marshall, and S. Hosking, 2013: An Initial Assessment of Antarctic Sea Ice Extent in the CMIP5 Models. *Journal of Climate*, **26**, 1473–1484.

Turner, J. et al., 2017: Atmosphere-ocean-ice interactions in the Amundsen Sea Embayment, West Antarctica. *Reviews of Geophysics*, **55**, 235–276, doi:10.1002/2016rg000532.

Turner, J. et al., 2020: Recent Decrease of Summer Sea Ice in the Weddell Sea, Antarctica. *Geophysical Research Letters*, **47(11)**, e2020GL087127, doi:10.1029/2020gl087127.

Turney, C.S.M. et al., 2020: Early Last Interglacial ocean warming drove substantial ice mass loss from Antarctica. *Proceedings of the National Academy of Sciences*, **117(8)**, 3996–4006, doi:10.1073/pnas.1902469117.

Uemura, R. et al., 2018: Asynchrony between Antarctic temperature and CO2 associated with obliquity over the past 720,000 years. *Nature communications*, **9(1)**, 1–11, doi:10.1038/s41467-018-03328-3.

Ullman, D.J. et al., 2016: Final Laurentide ice-sheet deglaciation and Holocene climate-sea level change. *Quaternary Science Reviews*, **152**, 49–59, doi:10.1016/j.quascirev.2016.09.014.

Uotila, P. et al., 2019: An assessment of ten ocean reanalyses in the polar regions. *Climate Dynamics*, **52(3)**, 1613–1650, doi:10.1007/s00382-018-4242-z.

Valdes, P., 2011: Built for stability. *Nature Geoscience*, **4(7)**, 414–416, doi:10.1038/ngeo1200.

Valdivieso, M. et al., 2017: An assessment of air–sea heat fluxes from ocean and coupled reanalyses. *Climate Dynamics*, **49(3)**, 983–1008, doi:10.1007/s00382-015-2843-3.

ACCEPTED VERSION SUBJECT TO FINAL EDITING

Välisuo, I., T. Vihma, R. Pirazzini, and M. Schäfer, 2018: Interannual Variability of Atmospheric Conditions and Surface Melt in Greenland in 2000–2014. *Journal of Geophysical Research: Atmospheres*, **123(18)**, 10,410–443,463, doi:10.1029/2018jd028445.

Van Breedam, J., H. Goelzer, and P. Huybrechts, 2020: Semi-equilibrated global sea-level change projections for the next 10 000 years. *Earth System Dynamics*, **11(4)**, 953–976, doi:10.5194/esd-11-953-2020.

Van de Wal, R.S.W. and M. Wild, 2001: Modelling the response of glaciers to climate change by applying volume-area scaling in combination with a high resolution GCM. *Climate Dynamics*, **18(3)**, 359–366, doi:10.1007/s003820100184.

van den Hurk, B., E. van Meijgaard, P. de Valk, K.-J. van Heeringen, and J. Gooijer, 2015: Analysis of a compounding surge and precipitation event in the Netherlands. *Environmental Research Letters*, **10(3)**, 35001.

van der Linden, E.C., D. Le Bars, R. Bintanja, and W. Hazeleger, 2019: Oceanic heat transport into the Arctic under high and low CO2 forcing. *Climate Dynamics*, **53(7–8)**, 4763–4780, doi:10.1007/s00382-019-04824-y.

van Kampenhout, L. et al., 2017: Improving the Representation of Polar Snow and Firn in the Community Earth System Model. *Journal of Advances in Modeling Earth Systems*, **9(7)**, 2583–2600, doi:10.1002/2017ms000988.

van Kampenhout, L. et al., 2020: Present-Day Greenland Ice Sheet Climate and Surface Mass Balance in CESM2. *Journal of Geophysical Research: Earth Surface*, **125(2)**, doi:10.1029/2019jf005318.

Van Pelt, W. et al., 2019: A long-term dataset of climatic mass balance, snow conditions, and runoff in Svalbard (1957-2018). *Cryosphere*, **13(9)**, 2259–2280, doi:10.5194/tc-13-2259-2019.

van Tricht, K. et al., 2016: Clouds enhance Greenland ice sheet meltwater runoff. *Nature Communications*, **7**, 10266, doi:10.1038/ncomms10266.

Vandecrux, B. et al., 2019: Firn data compilation reveals widespread decrease of firn air content in western Greenland. *The Cryosphere*, **13(3)**, 845–859, doi:10.5194/tc-13-845-2019.

Varela, R., I. Álvarez, F. Santos, M. Gómez-Gesteira, and others, 2015: Has upwelling strengthened along worldwide coasts over 1982-2010? *Scientific reports*, **5**, 10016, doi:10.1038/srep10016.

Varela, R., F.P. Lima, R. Seabra, C. Meneghesso, and M. Gómez-Gesteira, 2018: Coastal warming and wind-driven upwelling: A global analysis. *Science of The Total Environment*, **639**, 1501–1511, doi:10.1016/j.scitotenv.2018.05.273.

Vargo, L.J. et al., 2020: Anthropogenic warming forces extreme annual glacier mass loss. *Nature Climate Change*, **10(9)**, 856–861, doi:10.1038/s41558-020-0849-2.

Vaughan, D.G. et al., 2013: Observations: Cryosphere. In: *Climate Change 2013: The Physical Science Basis. Contribution of Working Group I to the Fifth Assessment Report of the Intergovernmental Panel on Climate Change* [Stocker, T.F., G.-K. D. Qin, M. Plattner, S.K. Tignor, J. Allen, A. Boschung, Y. Nauels, V.B. Xia, and P.M. Midgley (eds.)]. Cambridge University Press, Cambridge, United Kingdom and New York, NY, USA, pp. 317–382, doi:10.1017/cbo9781107415324.012.

Vecchi, G.A. and B.J. Soden, 2007: Global warming and the weakening of the tropical circulation. *Journal of Climate*, doi:10.1175/jcli4258.1.

Vecchi, G.A. et al., 2006: Weakening of tropical Pacific atmospheric circulation due to anthropogenic forcing. *Nature*, **441(7089)**, 73–76, doi:10.1038/nature04744.

Velicogna, I. et al., 2020: Continuity of Ice Sheet Mass Loss in Greenland and Antarctica From the GRACE and GRACE Follow-On Missions. *Geophysical Research Letters*, **47(8)**, e2020GL087291, doi:10.1029/2020gl087291.

Venturelli, R.A. et al., 2020: Mid-Holocene Grounding Line Retreat and Readvance at Whillans Ice Stream, West Antarctica. *Geophysical Research Letters*, **47(15)**, doi:10.1029/2020gl088476.

Verfaillie, D. et al., 2018: Multi-component ensembles of future meteorological and natural snow conditions for 1500 m altitude in the Chartreuse mountain range, Northern French Alps. *Cryosphere*, **12(4)**, 1249–1271, doi:10.5194/tc-12-1249-2018.

Vermassen, F. et al., 2020: A Major Collapse of Kangerlussuaq Glacier's Ice Tongue Between 1932 and 1933 in East Greenland. *Geophysical Research Letters*, **47(4)**, e2019GL085954, doi:10.1029/2019gl085954.

Vichi, M. et al., 2019: Effects of an Explosive Polar Cyclone Crossing the Antarctic Marginal Ice Zone. *Geophysical Research Letters*, **46(11)**, 5948–5958, doi:10.1029/2019gl082457.

Vieira, G. et al., 2010: Thermal state of permafrost and active-layer monitoring in the antarctic: Advances during the international polar year 2007-2009. *Permafrost and Periglacial Processes*, **21(2)**, 182–197, doi:10.1002/ppp.685.

Vihma, T., P. Tisler, and P. Uotila, 2012: Atmospheric forcing on the drift of Arctic sea ice in 1989-2009. *Geophysical Research Letters*, **39(2)**, doi:10.1029/2011gl050118.

ACCEPTED VERSION SUBJECT TO FINAL EDITING

Vijay, S. et al., 2019: Resolving Seasonal Ice Velocity of 45 Greenlandic Glaciers With Very High Temporal Details. *Geophysical Research Letters*, **46(3)**, 1485–1495, doi:10.1029/2018gl081503.
Vinogradova, N. et al., 2019: Satellite Salinity Observing System: Recent Discoveries and the Way Forward. *Frontiers in Marine Science*, **6**, 243, doi:10.3389/fmars.2019.00243.
Vitousek, S. et al., 2017: Doubling of coastal flooding frequency within decades due to sea-level rise. *Scientific Reports*, **7(1)**, 1–9, doi:10.1038/s41598-017-01362-7.
Vizcaino, M. et al., 2015: Coupled simulations of Greenland Ice Sheet and climate change up to A.D. 2300. *Geophysical Research Letters*, **42(10)**, 3927–3935, doi:10.1002/2014gl061142.
Voldoire, A. et al., 2019: Evaluation of CMIP6 DECK Experiments With CNRM-CM6-1. *Journal of Advances in Modeling Earth Systems*, **11**, 2177–2213, doi:10.1029/2019ms001683.
Vousdoukas, M.I., L. Mentaschi, E. Voukouvalas, M. Verlaan, and L. Feyen, 2017: Extreme sea levels on the rise along Europe's coasts. *Earth's Future*, **5(3)**, 304–323.
Vousdoukas, M.I. et al., 2018: Global probabilistic projections of extreme sea levels show intensification of coastal flood hazard. *Nature Communications*, **9(1)**, 2360, doi:10.1038/s41467-018-04692-w.
Wada, Y., 2016: Modeling groundwater depletion at regional and global scales: Present state and future prospects. *Surveys in Geophysics*, **37(2)**, 419–451.
Wada, Y. et al., 2012: Past and future contribution of global groundwater depletion to sea-level rise. *Geophysical Research Letters*, **39(9)**, n/a–n/a, doi:10.1029/2012gl051230.
Wada, Y. et al., 2016: Fate of water pumped from underground and contributions to sea-level rise. *Nature Climate Change*, doi:10.1038/nclimate3001.
Wagner, T.J.W. and I. Eisenman, 2015: How Climate Model Complexity Influences Sea Ice Stability. *Journal of Climate*, **28(10)**, 3998–4014, doi:10.1175/jcli-d-14-00654.1.
Wagner, T.J.W. et al., 2019: Large spatial variations in the flux balance along the front of a Greenland tidewater glacier. *Cryosphere*, **13(3)**, 911–925, doi:10.5194/tc-13-911-2019.
Wahl, T. and D.P. Chambers, 2015: Evidence for multidecadal variability in US extreme sea level records. *Journal of Geophysical Research: Oceans*, **120(3)**, 1527–1544.
Wahl, T. et al., 2017: Understanding extreme sea levels for broad-scale coastal impact and adaptation analysis. *Nature Communications*, **8**, doi:10.1038/ncomms16075.
Wåhlin, A.K. et al., 2020: Ice front blocking of ocean heat transport to an Antarctic ice shelf. *Nature*, **578**, 568–571, doi:10.1038/s41586-020-2014-5.
Walsh, J.E., F. Fetterer, J. Scott Stewart, and W.L. Chapman, 2017: A database for depicting Arctic sea ice variations back to 1850. *Geographical Review*, **107(1)**, 89–107, doi:10.1111/j.1931-0846.2016.12195.x.
Walsh, J.E. et al., 2018: Downscaling of climate model output for Alaskan stakeholders. *Environmental Modelling & Software*, **110**, 38–51, doi:10.1016/j.envsoft.2018.03.021.
Wandres, M., C. Pattiaratchi, and M.A. Hemer, 2017: Projected changes of the southwest Australian wave climate under two atmospheric greenhouse gas concentration pathways. *Ocean Modelling*, **117**, 70–87, doi:10.1016/j.ocemod.2017.08.002.
Wang, C., L. Zhang, S.-K.K. Lee, L. Wu, and C.R. Mechoso, 2014: A global perspective on CMIP5 climate model biases. *Nature Climate Change*, **4(3)**, 201–205, doi:10.1038/nclimate2118.
Wang, D., T.C. Gouhier, B.A. Menge, and A.R. Ganguly, 2015: Intensification and spatial homogenization of coastal upwelling under climate change. *Nature*, **518(7539)**, 390–394, doi:10.1038/nature14235.
Wang, G. et al., 2019: Compounding tropical and stratospheric forcing of the record low Antarctic sea-ice in 2016. *Nature Communications*, **10(1)**, 13, doi:10.1038/s41467-018-07689-7.
Wang, H., S.A. Legg, and R.W. Hallberg, 2015: Representations of the Nordic Seas overflows and their large scale climate impact in coupled models. *Ocean Modelling*, **86**, 76–92, doi:10.1016/j.ocemod.2014.12.005.
Wang, J., J.A. Church, X. Zhang, and X. Chen, 2021: Reconciling global mean and regional sea level change in projections and observations. *Nature Communications*, **12**, 990, doi:10.1038/s41467-021-21265-6.
Wang, L., C. Derksen, R. Brown, and T. Markus, 2013: Recent changes in pan-Arctic melt onset from satellite passive microwave measurements. *Geophysical Research Letters*, **40(3)**, 522–528, doi:10.1002/grl.50098.
Wang, L. et al., 2016: Investigating the spread in surface albedo for snow-covered forests in CMIP5 models. *Journal of Geophysical Research*, **121(3)**, 1104–1119, doi:10.1002/2015jd023824.
Wang, L. et al., 2020: Recent Shift in the Warming of the Southern Oceans Modulated by Decadal Climate Variability. *Geophysical Research Letters*, **n/a(n/a)**, e2020GL090889, doi:10.1029/2020gl090889.
Wang, L. et al., 2021: Recent Shift in the Warming of the Southern Oceans Modulated by Decadal Climate Variability. *Geophysical Research Letters*, **48(3)**, e2020GL090889, doi:10.1029/2020gl090889.

ACCEPTED VERSION SUBJECT TO FINAL EDITING

Wang, Q. et al., 2014: The Finite Element Sea Ice-Ocean Model (FESOM) v.1.4: formulation of an ocean general circulation model. *Geoscientific Model Development*, **7(2)**, 663–693, doi:10.5194/gmd-7-663-2014.

Wang, Q. et al., 2019: Ocean Heat Transport Into the Barents Sea: Distinct Controls on the Upward Trend and Interannual Variability. *Geophysical Research Letters*, **46(22)**, 13180–13190, doi:10.1029/2019gl083837.

Wang, W., C.S. Zender, D. van As, and N.B. Miller, 2019: Spatial Distribution of Melt Season Cloud Radiative Effects Over Greenland: Evaluating Satellite Observations, Reanalyses, and Model Simulations Against In Situ Measurements. *Journal of Geophysical Research: Atmospheres*, **124**, 57–71, doi:10.1029/2018jd028919.

Wang, W. et al., 2016: Evaluation of air-soil temperature relationships simulated by land surface models during winter across the permafrost region. *The Cryosphere*, **10(4)**, 1721–1737, doi:10.5194/tc-10-1721-2016.

Wang, Y. et al., 2018: Elucidating the Role of Anthropogenic Aerosols in Arctic Sea Ice Variations. *Journal of Climate*, **31(1)**, 99–114, doi:10.1175/jcli-d-17-0287.1.

Wang, Y.-L. and C.-R. Wu, 2018: Discordant multi-decadal trend in the intensity of the Kuroshio along its path during 1993–2013. *Scientific Reports*, **8(1)**, 14633, doi:10.1038/s41598-018-32843-y.

Wang, Y.-L., C.-R. Wu, and S.-Y. Chao, 2016: Warming and weakening trends of the Kuroshio during 1993-2013. *Geophysical Research Letters*, **43(17)**, 9200–9207, doi:10.1002/2016gl069432.

Ward, P.J. et al., 2018: Dependence between high sea-level and high river discharge increases flood hazard in global deltas and estuaries. *Environmental Research Letters*, **13(8)**, 084012, doi:10.1088/1748-9326/aad400.

Warrick, R. et al., 1990: Sea Level Rise. In: *Climate Change: The IPCC Scientific Assessment* [Houghton, J.T., G.J. Jenkins, and J.J. Ephraums (eds.)]. Cambridge University Press, Cambridge, United Kingdom and New York, NY, USA, pp. 259–281.

Washam, P., A. Münchow, and K.W. Nicholls, 2018: A Decade of Ocean changes impacting the ice shelf of Petermann Gletscher, Greenland. *Journal of Physical Oceanography*, **48(10)**, 2477–2493, doi:10.1175/jpo-d-17-0181.1.

Watanabe, M., J.L. Dufresne, Y. Kosaka, T. Mauritsen, and H. Tatebe, 2021: Enhanced warming constrained by past trends in equatorial Pacific sea surface temperature gradient. *Nature Climate Change*, **11**, 33–37, doi:10.1038/s41558-020-00933-3.

Waugh, D.W., A. McC. Hogg, P. Spence, M.H. England, and T.W.N. Haine, 2019: Response of Southern Ocean Ventilation to Changes in Midlatitude Westerly Winds. *Journal of Climate*, **32(17)**, 5345–5361, doi:10.1175/jcli-d-19-0039.1.

WCRP Global Sea Level Budget Group, 2018a: Global sea-level budget 1993–present. *Earth System Science Data*, **10(3)**, 1551–1590, doi:10.5194/essd-10-1551-2018.

WCRP Global Sea Level Budget Group, 2018b: Global sea-level budget 1993–present. *Earth System Science Data*, **10(3)**, 1551–1590, doi:10.5194/essd-10-1551-2018.

Wearing, M.G. and J. Kingslake, 2019: Holocene Formation of Henry Ice Rise, West Antarctica, Inferred From Ice-Penetrating Radar. *Journal of Geophysical Research: Earth Surface*, **124(8)**, 2224–2240, doi:10.1029/2018jf004988.

Webber, B.G.M., K.J. Heywood, D.P. Stevens, and K.M. Assmann, 2019: The Impact of Overturning and Horizontal Circulation in Pine Island Trough on Ice Shelf Melt in the Eastern Amundsen Sea. *Journal of Physical Oceanography*, **49(1)**, 63–83, doi:10.1175/jpo-d-17-0213.1.

Weber, M.E. et al., 2014: Millennial-scale variability in Antarctic ice-sheet discharge during the last deglaciation. *Nature*, **510(7503)**, 134–138, doi:10.1038/nature13397.

Webster, M. et al., 2018: Snow in the changing sea-ice systems. *Nature Climate Change*, **8(11)**, 946–953, doi:10.1038/s41558-018-0286-7.

Wei, T., Q. Yan, W. Qi, M. Ding, and C. Wang, 2020: Projections of Arctic sea ice conditions and shipping routes in the twenty-first century using CMIP6 forcing scenarios. *Environmental Research Letters*, **15(10)**, 104079, doi:10.1088/1748-9326/abb2c8.

Weijer, W., W. Cheng, O.A. Garuba, A. Hu, and B.T. Nadiga, 2020: CMIP6 Models Predict Significant 21st Century Decline of the Atlantic Meridional Overturning Circulation. *Geophysical Research Letters*, **47(12)**, doi:10.1029/2019gl086075.

Weijer, W. et al., 2019: Stability of the Atlantic Meridional Overturning Circulation: A Review and Synthesis. *Journal of Geophysical Research: Oceans*, 2019JC015083, doi:10.1029/2019jc015083.

Welty, E. et al., 2020: Worldwide version-controlled database of glacier thickness observations. *Earth System Science Data*, **12**, 3039–3055, doi:10.5194/essd-2020-87.

Wernecke, A., T.L. Edwards, I.J. Nias, P.B. Holden, and N.R. Edwards, 2020: Spatial probabilistic calibration of a high-resolution Amundsen Sea Embayment ice sheet model with satellite altimeter data. *Cryosphere*, **14(5)**, 1459–1474, doi:10.5194/tc-14-1459-2020.

ACCEPTED VERSION SUBJECT TO FINAL EDITING

Wernli, H. and L. Papritz, 2018: Role of polar anticyclones and mid-latitude cyclones for Arctic summertime sea-ice melting. *Nature Geoscience*, **11(2)**, 108–113, doi:10.1038/s41561-017-0041-0.

Whitehouse, P.L., 2018: Glacial isostatic adjustment modelling: Historical perspectives, recent advances, and future directions. *Earth Surface Dynamics*, **6(2)**, 401–429, doi:10.5194/esurf-6-401-2018.

Whitehouse, P.L., M.J. Bentley, and A.M. Le Brocq, 2012: A deglacial model for Antarctica: geological constraints and glaciological modelling as a basis for a new model of Antarctic glacial isostatic adjustment. *Quaternary Science Reviews*, **32**, 1–24, doi:10.1016/j.quascirev.2011.11.016.

Wille, J.D. et al., 2019: West Antarctic surface melt triggered by atmospheric rivers. *Nature Geoscience*, **12(11)**, 911–916, doi:10.1038/s41561-019-0460-1.

Williams, G. et al., 2015: Thick and deformed Antarctic sea ice mapped with autonomous underwater vehicles. *Nature Geoscience*, **8(1)**, 61–67, doi:10.1038/ngeo2299.

Williams, K.D. et al., 2018: The Met Office Global Coupled Model 3.0 and 3.1 (GC3.0 and GC3.1) Configurations. *Journal of Advances in Modeling Earth Systems*, **10(2)**, 357–380, doi:10.1002/2017ms001115.

Williams, R.G., V. Roussenov, D. Smith, and M.S. Lozier, 2014: Decadal Evolution of Ocean Thermal Anomalies in the North Atlantic: The Effects of Ekman, Overturning, and Horizontal Transport. *Journal of Climate*, **27(2)**, 698–719, doi:10.1175/jcli-d-12-00234.1.

Williams, R.G., V. Roussenov, M.S. Lozier, and D. Smith, 2015: Mechanisms of Heat Content and Thermocline Change in the Subtropical and Subpolar North Atlantic. *Journal of Climate*, **28(24)**, 9803–9815, doi:10.1175/jcli-d-15-0097.1.

Williamson, C.J. et al., 2019: Glacier Algae: A Dark Past and a Darker Future. *Frontiers in Microbiology*, **10**, 524, doi:10.3389/fmicb.2019.00524.

Wills, R.C.J., K.C. Armour, D.S. Battisti, and D.L. Hartmann, 2019: Ocean–Atmosphere Dynamical Coupling Fundamental to the Atlantic Multidecadal Oscillation. *Journal of Climate*, **32(1)**, 251–272, doi:10.1175/jcli-d-18-0269.1.

Wilson, D.J. et al., 2018: Ice loss from the East Antarctic Ice Sheet during late Pleistocene interglacials. *Nature*, **561(7723)**, 383–386, doi:10.1038/s41586-018-0501-8.

Wilson, D.J. et al., 2020: Sea-ice control on deglacial lower cell circulation changes recorded by Drake Passage deep-sea corals. *Earth and Planetary Science Letters*, **544**, doi:10.1016/j.epsl.2020.116405.

Wilson, N., F. Straneo, and P. Heimbach, 2017: Satellite-derived submarine melt rates and mass balance (2011-2015) for Greenland's largest remaining ice tongues. *Cryosphere*, **11(6)**, 2773–2782, doi:10.5194/tc-11-2773-2017.

Winton, M., S.M. Griffies, B.L. Samuels, J.L. Sarmiento, and T.L.F. Licher, 2013: Connecting changing ocean circulation with changing climate. *Journal of Climate*, **26(7)**, 2268–2278, doi:10.1175/jcli-d-12-00296.1.

Wittenberg, A.T., 2009: Are historical records sufficient to constrain ENSO simulations? *Geophysical Research Letters*, **36(12)**, L12702, doi:10.1029/2009gl038710.

Wittmann, M. et al., 2017: Impact of dust deposition on the albedo of Vatnajökull ice cap, Iceland. *The Cryosphere*, **11**, 741–754, doi:10.5194/tc-11-741-2017.

Wolovick, M.J. and J.C. Moore, 2018: Stopping the flood: could we use targeted geoengineering to mitigate sea level rise? *The Cryosphere*, **12(9)**, 2955–2967, doi:10.5194/tc-12-2955-2018.

Wong, T.E., A.M.R. Bakker, and K. Keller, 2017: Impacts of Antarctic fast dynamics on sea-level projections and coastal flood defense. *Climatic Change*, **144(2)**, 347–364, doi:10.1007/s10584-017-2039-4.

Wood, M. et al., 2018: Ocean-Induced Melt Triggers Glacier Retreat in Northwest Greenland. *Geophysical Research Letters*, **45(16)**, 8334–8342, doi:10.1029/2018gl078024.

Wood, M. et al., 2021: Ocean forcing drives glacier retreat in Greenland. *Science Advances*, **7(1)**, doi:10.1126/sciadv.aba7282.

Woodworth, P.L. et al., 2016: Towards a global higher-frequency sea level dataset. *Geoscience Data Journal*, **3(2)**, 50–59.

Wöppelmann, G. and M. Marcos, 2016: Vertical land motion as a key to understanding sea level change and variability. *Reviews of Geophysics*, **54(1)**, 64–92, doi:10.1002/2015rg000502.

Worby, A.P. et al., 2008: Thickness distribution of Antarctic sea ice. *Journal of Geophysical Research*, **113(C5)**, C05S92, doi:10.1029/2007jc004254.

Wouters, B., A.S. Gardner, and G. Moholdt, 2019: Global Glacier Mass Loss During the GRACE Satellite Mission (2002-2016). *Frontiers in Earth Science*, **7**, 96, doi:10.3389/feart.2019.00096.

Wu, B., X. Lin, and L. Yu, 2020: North Pacific subtropical mode water is controlled by the Atlantic Multidecadal Variability. *Nature Climate Change*, **10(3)**, 238–243, doi:10.1038/s41558-020-0692-5.

Wu, L. et al., 2012: Enhanced warming over the global subtropical western boundary currents. *Nature Climate Change*, **2(3)**, 161–166, doi:10.1038/nclimate1353.

ACCEPTED VERSION SUBJECT TO FINAL EDITING

Wu, W. et al., 2018: Mapping Dependence Between Extreme Rainfall and Storm Surge. *Journal of Geophysical Research: Oceans*, **123(4)**, 2461–2474, doi:10.1002/2017jc013472.
Xiao, W., O. Esper, and R. Gersonde, 2016: Last Glacial - Holocene climate variability in the Atlantic sector of the Southern Ocean. *Quaternary Science Reviews*, **135**, 115–137, doi:10.1016/j.quascirev.2016.01.023.
Xiao, X. et al., 2017: Deglacial and Holocene sea–ice variability north of Iceland and response to ocean circulation changes. *Earth and Planetary Science Letters*, **472**, 14–24, doi:10.1016/j.epsl.2017.05.006.
Xie, S., T.H. Dixon, D.M. Holland, D. Voytenko, and I. Vaňková, 2019: Rapid iceberg calving following removal of tightly packed pro-glacial mélange. *Nature Communications*, **10(1)**, 3250, doi:10.1038/s41467-019-10908-4.
Xu, W., L. Ma, M. Ma, H. Zhang, and W. Yuan, 2017: Spatial-temporal variability of snow cover and depth in the Qinghai-Tibetan plateau. *Journal of Climate*, **30**, 1521–1533, doi:10.1175/jcli-d-15-0732.1.
Yamaguchi, R. and T. Suga, 2019: Trend and Variability in Global Upper-Ocean Stratification Since the 1960s. *Journal of Geophysical Research: Oceans*, **n/a(n/a)**, doi:10.1029/2019jc015439.
Yamamoto, A. et al., 2015: Global deep ocean oxygenation by enhanced ventilation in the Southern Ocean under long-term global warming. *Global Biogeochemical Cycles*, **29(10)**, 1801–1815, doi:10.1002/2015gb005181.
Yan, Q., Z. Zhang, and H. Wang, 2016: Investigating uncertainty in the simulation of the Antarctic ice sheet during the mid-Piacenzian. *Journal of Geophysical Research: Atmospheres*, **121(4)**, 1559–1574, doi:10.1002/2015jd023900.
Yan, Q., Z. Zhang, H. Wang, and R. Zhang, 2014: Simulation of Greenland ice sheet during the mid-Pliocene warm period. *Chinese science bulletin*, **59(2)**, 201–211.
Yan, X., R. Zhang, and T.R. Knutson, 2018: Underestimated AMOC Variability and Implications for AMV and Predictability in CMIP Models. *Geophysical Research Letters*, **45(9)**, 4319–4328, doi:10.1029/2018gl077378.
Yang, H. et al., 2016a: Intensification and poleward shift of subtropical western boundary currents in a warming climate. *Journal of Geophysical Research: Oceans*, **121(7)**, 4928–4945, doi:10.1002/2015jc011513.
Yang, H. et al., 2016b: Intensification and poleward shift of subtropical western boundary currents in a warming climate. *Journal of Geophysical Research: Oceans*, **121(7)**, 4928–4945, doi:10.1002/2015jc011513.
Yang, H. et al., 2020: Poleward Shift of the Major Ocean Gyres Detected in a Warming Climate. *Geophysical Research Letters*, **47(5)**, doi:10.1029/2019gl085868.
Yang, J.-A., S. Kim, N. Mori, and H. Mase, 2018: Assessment of long-term impact of storm surges around the Korean Peninsula based on a large ensemble of climate projections. *Coastal Engineering*, **142**, 1–8, doi:10.1016/j.coastaleng.2018.09.008.
Yao, Y., J. Wang, J. Yin, and X. Zou, 2020: Marine Heatwaves in China's Marginal Seas and Adjacent Offshore Waters: Past, Present, and Future. *Journal of Geophysical Research: Oceans*, **125(3)**, e2019JC015801, doi:10.1029/2019jc015801.
Yashayaev, I., 2007: Hydrographic changes in the Labrador Sea, 1960–2005. *Progress in Oceanography*, **73(3–4)**, 242–276, doi:10.1016/j.pocean.2007.04.015.
Yashayaev, I. and J.W. Loder, 2016: Recurrent replenishment of Labrador Sea Water and associated decadal-scale variability. *Journal of Geophysical Research: Oceans*, **121(11)**, 8095–8114, doi:10.1002/2016jc012046.
Yau, A.M., M.L. Bender, A. Robinson, and E.J. Brook, 2016: Reconstructing the last interglacial at Summit, Greenland: Insights from GISP2. *Proceedings of the National Academy of Sciences*, **113(35)**, 9710–9715, doi:10.1073/pnas.1524766113.
Yeager, S., 2015: Topographic Coupling of the Atlantic Overturning and Gyre Circulations. *Journal of Physical Oceanography*, **45(5)**, 1258–1284, doi:10.1175/jpo-d-14-0100.1.
Yin, J., 2012: Century to multi-century sea level rise projections from CMIP5 models. *Geophysical Research Letters*, **39(17)**, n/a–n/a, doi:10.1029/2012gl052947.
Yin, J. and R.J. Stouffer, 2007: Comparison of the Stability of the Atlantic Thermohaline Circulation in Two Coupled Atmosphere–Ocean General Circulation Models. *Journal of Climate*, **20(17)**, 4293–4315, doi:10.1175/jcli4256.1.
Yokohata, T. et al., 2020: Model improvement and future projection of permafrost processes in a global land surface model. *Progress in Earth and Planetary Science*, **7(1)**, 69, doi:10.1186/s40645-020-00380-w.
Young, I.R. and A. Ribal, 2019: Multiplatform evaluation of global trends in wind speed and wave height. *Science*, **364(6440)**, 548–552, doi:10.1126/science.aav9527.
Young, N.E. and J.P. Briner, 2015: Holocene evolution of the western Greenland Ice Sheet: Assessing geophysical ice-sheet models with geological reconstructions of ice-margin change. *Quaternary Science Reviews*, **114**, 1–17, doi:10.1016/j.quascirev.2015.01.018.

ACCEPTED VERSION SUBJECT TO FINAL EDITING

Yu, H., E. Rignot, H. Seroussi, M. Morlighem, and Y. Choi, 2019: Impact of Iceberg Calving on the Retreat of Thwaites Glacier, West Antarctica Over the Next Century With Different Calving Laws and Ocean Thermal Forcing. *Geophysical Research Letters*, **46(24)**, 14539–14547, doi:10.1029/2019gl084066.

Yu, L., 2019: Global Air-Sea Fluxes of Heat, Fresh Water, and Momentum: Energy Budget Closure and Unanswered Questions. *Ann. Rev. Marine Sci.*, **11**, 227–248, doi:10.1146/annurev-marine-010816.

Yu, L. et al., 2017: The global ocean water cycle in atmospheric reanalysis, satellite, and ocean salinity. *J. Climate*, **30(10)**, 3829–3852, doi:10.1175/jcli-d-16-0479.1.

Yu, Y.Q., H.L. Liu, and P.F. Lin, 2012: A quasi-global 1/10° eddy-resolving ocean general circulation model and its preliminary results. *Chinese Science Bulletin*, **57(30)**, 3908–3916, doi:10.1007/s11434-012-5234-8.

Yuan, N. et al., 2017: Increase of the Antarctic Sea Ice Extent is highly significant only in the Ross Sea. *Scientific Reports*, **7**, 41096, doi:10.1038/srep41096.

Yukimoto, S. et al., 2019: The meteorological research institute Earth system model version 2.0, MRI-ESM2.0: Description and basic evaluation of the physical component. *Journal of the Meteorological Society of Japan*, **97(5)**, 931–965, doi:10.2151/jmsj.2019-051.

Zängl, G., D. Reinert, P. Rípodas, and M. Baldauf, 2015: The ICON (ICOsahedral Non-hydrostatic) modelling framework of DWD and MPI-M: Description of the non-hydrostatic dynamical core. *Quarterly Journal of the Royal Meteorological Society*, **141(687)**, 563–579, doi:10.1002/qj.2378.

Zanna, L., S. Khatiwala, J.M. Gregory, J. Ison, and P. Heimbach, 2019a: Global reconstruction of historical ocean heat storage and transport. *Proceedings of the National Academy of Sciences*, **116(4)**, 201808838, doi:10.1073/pnas.1808838115.

Zanna, L., S. Khatiwala, J.M. Gregory, J. Ison, and P. Heimbach, 2019b: Global reconstruction of historical ocean heat storage and transport. *Proceedings of the National Academy of Sciences*, **116(4)**, 1126–1131, doi:10.1073/pnas.1808838115.

Zanowski, H. and R. Hallberg, 2017: Weddell Polynya Transport Mechanisms in the Abyssal Ocean. *Journal of Physical Oceanography*, **47(12)**, 2907–2925, doi:10.1175/jpo-d-17-0091.1.

Zanowski, H., R. Hallberg, and J.L. Sarmiento, 2015: Abyssal Ocean Warming and Salinification after Weddell Polynyas in the GFDL CM2G Coupled Climate Model. *Journal of Physical Oceanography*, **45(11)**, 2755–2772, doi:10.1175/jpo-d-15-0109.1.

Zarfl, C., A.E. Lumsdon, J. Berlekamp, L. Tydecks, and K. Tockner, 2015: A global boom in hydropower dam construction. *Aquatic Sciences*, **77(1)**, 161–170.

Zekollari, H. and P. Huybrechts, 2015: On the climate-geometry imbalance, response time and volume-area scaling of an alpine glacier: insights from a 3-D flow model applied to Vadret da Morteratsch, Switzerland. *Annals of Glaciology*, **56(70)**, 51–62, doi:10.3189/2015aog70a921.

Zekollari, H., M. Huss, and D. Farinotti, 2019: Modelling the future evolution of glaciers in the European Alps under the EURO-CORDEX RCM ensemble. *The Cryosphere*, **13(4)**, 1125–1146, doi:10.5194/tc-13-1125-2019.

Zekollari, H., M. Huss, and D. Farinotti, 2020: On the Imbalance and Response Time of Glaciers in the European Alps. *Geophysical Research Letters*, **47(2)**, e2019GL085578, doi:10.1029/2019gl085578.

Zemp, M. et al., 2015: Historically unprecedented global glacier decline in the early 21st century. *Journal of Glaciology*, **61(228)**, 745–762, doi:10.3189/2015jog15j017.

Zemp, M. et al., 2019: Global glacier mass changes and their contributions to sea-level rise from 1961 to 2016. *Nature*, **568(7752)**, 382–386, doi:10.1038/s41586-019-1071-0.

Zemp, M. et al., 2020: Brief communication: Ad hoc estimation of glacier contributions to sea-level rise from the latest glaciological observations. *The Cryosphere*, **14(3)**, 1043–1050, doi:10.5194/tc-14-1043-2020.

Zhai, F., D. Hu, Q. Wang, and F. Wang, 2014: Long-term trend of Pacific South Equatorial Current bifurcation over 1950-2010. *Geophysical Research Letters*, **41(9)**, 3172–3180, doi:10.1002/2014gl059934.

Zhang, B. et al., 2019: Geodetic and model data reveal different spatio-temporal patterns of transient mass changes over Greenland from 2007 to 2017. *Earth and Planetary Science Letters*, **515**, 154–163, doi:10.1016/j.epsl.2019.03.028.

Zhang, J., 2014: Modeling the impact of wind intensification on Antarctic sea ice volume. *Journal of Climate*, **27(1)**, 202–214, doi:10.1175/jcli-d-12-00139.1.

Zhang, L., T.L. Delworth, W. Cooke, and X. Yang, 2019a: Natural variability of Southern Ocean convection as a driver of observed climate trends. *Nature Climate Change*, **9(1)**, 59–65, doi:10.1038/s41558-018-0350-3.

Zhang, L., T.L. Delworth, W. Cooke, and X. Yang, 2019b: Natural variability of Southern Ocean convection as a driver of observed climate trends. *Nature Climate Change*, **9(1)**, 59–65, doi:10.1038/s41558-018-0350-3.

ACCEPTED VERSION SUBJECT TO FINAL EDITING

Zhang, R., 2015: Mechanisms for low-frequency variability of summer Arctic sea ice extent. *Proceedings of the National Academy of Sciences of the United States of America*, **112(15)**, 4570–4575, doi:10.1073/pnas.1422296112.

Zhang, R. et al., 2019: A Review of the Role of the Atlantic Meridional Overturning Circulation in Atlantic Multidecadal Variability and Associated Climate Impacts. *Reviews of Geophysics*, **57(2)**, 316–375, doi:10.1029/2019rg000644.

Zhang, T., J.A. Heginbottom, R.G. Barry, and J. Brown, 2000: Further statistics on the distribution of permafrost and ground ice in the Northern Hemisphere. *Polar Geography*, **24(2)**, 126–131, doi:10.1080/10889370009377692.

Zhang, T., R.G. Barry, K. Knowles, J.A. Heginbottom, and J. Brown, 1999: Statistics and characteristics of permafrost and ground-ice distribution in the Northern Hemisphere. *Polar Geography*, **23(2)**, 132–154, doi:10.1080/10889379909377670.

Zhang, Y. and A.M. Baptista, 2008: SELFE: A semi-implicit Eulerian–Lagrangian finite-element model for cross-scale ocean circulation. *Ocean Modelling*, **21(3–4)**, 71–96, doi:10.1016/j.ocemod.2007.11.005.

Zhang, Y., H. Renssen, H. Seppä, and P.J. Valdes, 2017: Holocene temperature evolution in the Northern Hemisphere high latitudes – Model-data comparisons. *Quaternary Science Reviews*, **173**, 101–113, doi:10.1016/j.quascirev.2017.07.018.

Zhang, Y., Z. Zhang, D. Chen, B. Qiu, and W. Wang, 2020: Strengthening of the Kuroshio current by intensifying tropical cyclones. *Science*, **368(6494)**, 988–993, doi:10.1126/science.aax5758.

Zhang, Y. et al., 2016: Studies of the Canadian Arctic Archipelago water transport and its relationship to basin-local forcings: Results from AO-FVCOM. *Journal of Geophysical Research: Oceans*, **121(6)**, 4392–4415, doi:10.1002/2016jc011634.

Zhang, Y.J., F. Ye, E. Stanev, and S. Grashorn, 2016: Seamless cross-scale modeling with SCHISM. *Ocean Modelling*, **102**, 64–81, doi:10.1016/j.ocemod.2016.05.002.

Zhang, Z. et al., 2016: Observed 3D Structure, Generation, and Dissipation of Oceanic Mesoscale Eddies in the South China Sea. *Scientific Reports*, **6**, doi:10.1038/srep24349.

Zhao, S., S. Zhang, W. Cheng, and C. Zhou, 2019: Model Simulation and Prediction of Decadal Mountain Permafrost Distribution Based on Remote Sensing Data in the Qilian Mountains from the 1990s to the 2040s. *Remote Sensing*, **11(2)**, 183, doi:10.3390/rs11020183.

Zheng, W. et al., 2018: Accelerating glacier mass loss on Franz Josef Land, Russian Arctic. *Remote Sensing of Environment*, **211**, 357–375, doi:10.1016/j.rse.2018.04.004.

Zhong, H., P.-J. van Overloop, and P.H.A.J.M. van Gelder, 2013: A joint probability approach using a 1-D hydrodynamic model for estimating high water level frequencies in the Lower Rhine Delta. *Natural Hazards and Earth System Sciences*, **13(7)**, 1841–1852, doi:10.5194/nhess-13-1841-2013.

Zhong, X. et al., 2018: Spatiotemporal variability of snow depth across the Eurasian continent from 1966 to 2012. *Cryosphere*, **12**, 227–245, doi:10.5194/tc-12-227-2018.

Zhu, D. et al., 2019: Controls of soil organic matter on permafrost thermal and carbon dynamics. *Nature Communications*, **10**, 3172.

Zhu, Y., R.-H. Zhang, D. Li, and D. Chen, 2020: The thermocline biases in the tropical North Pacific and their attributions. *Journal of Climate*, **34(5)**, 1–17, doi:10.1175/jcli-d-20-0675.1.

Zickfeld, K., V.K. Arora, and N.P. Gillett, 2012: Is the climate response to CO ₂ emissions path dependent? *Geophysical Research Letters*, **39(5)**, n/a–n/a, doi:10.1029/2011gl050205.

Zickfeld, K., S. Solomon, and D.M. Gilford, 2017: Centuries of thermal sea-level rise due to anthropogenic emissions of short-lived greenhouse gases. *Proceedings of the National Academy of Sciences*, **114(4)**, 657–662, doi:10.1073/pnas.1612066114.

Zika, J.D., J.M. Gregory, E.L. McDonagh, A. Marzocchi, and L. Clement, 2021: Recent water mass changes reveal mechanisms of ocean warming. *Journal of Climate*, 1–52, doi:10.1175/jcli-d-20-0355.1.

Zika, J.D. et al., 2018: Improved estimates of water cycle change from ocean salinity: the key role of ocean warming. *Environmental Research Letters*, **13(7)**, 74036, doi:10.1088/1748-9326/aace42.

Zunz, V., H. Goosse, and F. Massonnet, 2013: How does internal variability influence the ability of CMIP5 models to reproduce the recent trend in Southern Ocean sea ice extent? *The Cryosphere*, **7(2)**, 451–468, doi:10.5194/tc-7-451-2013.

ACCEPTED VERSION SUBJECT TO FINAL EDITING

Figures

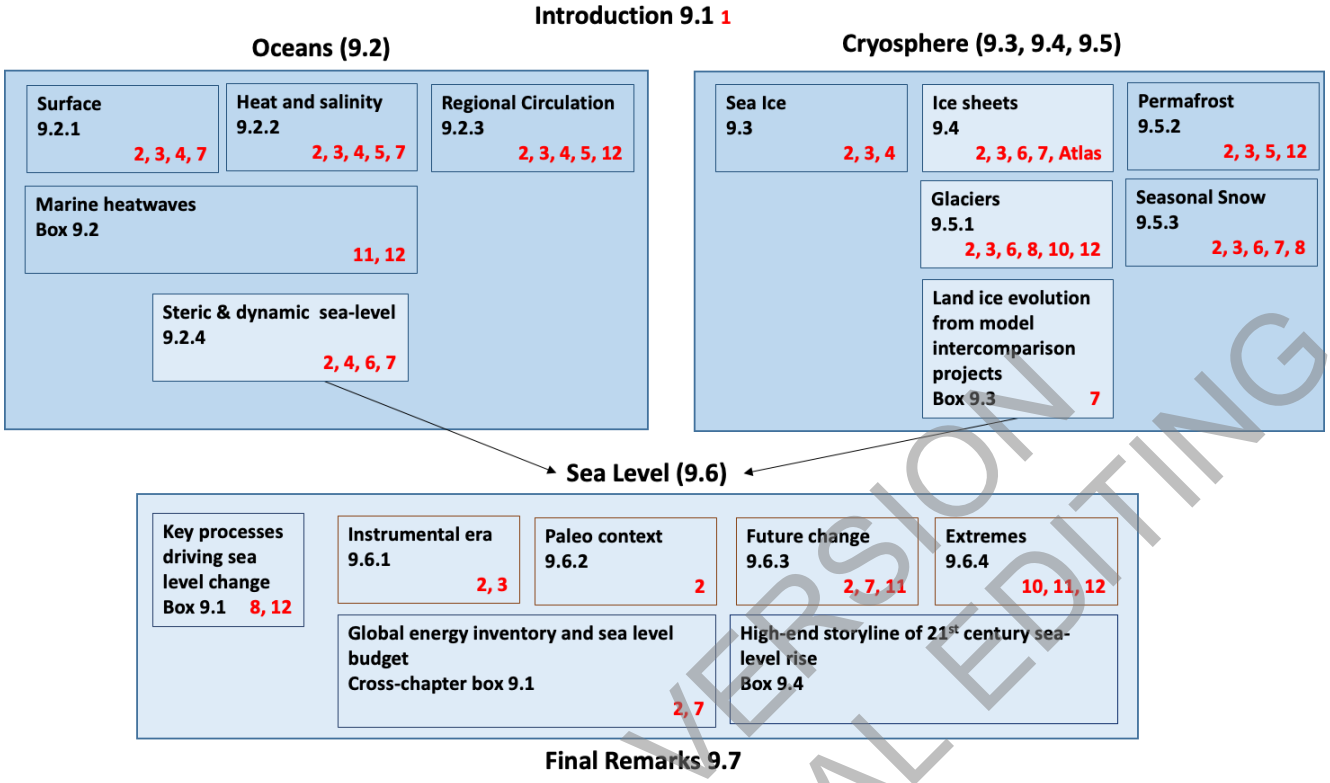
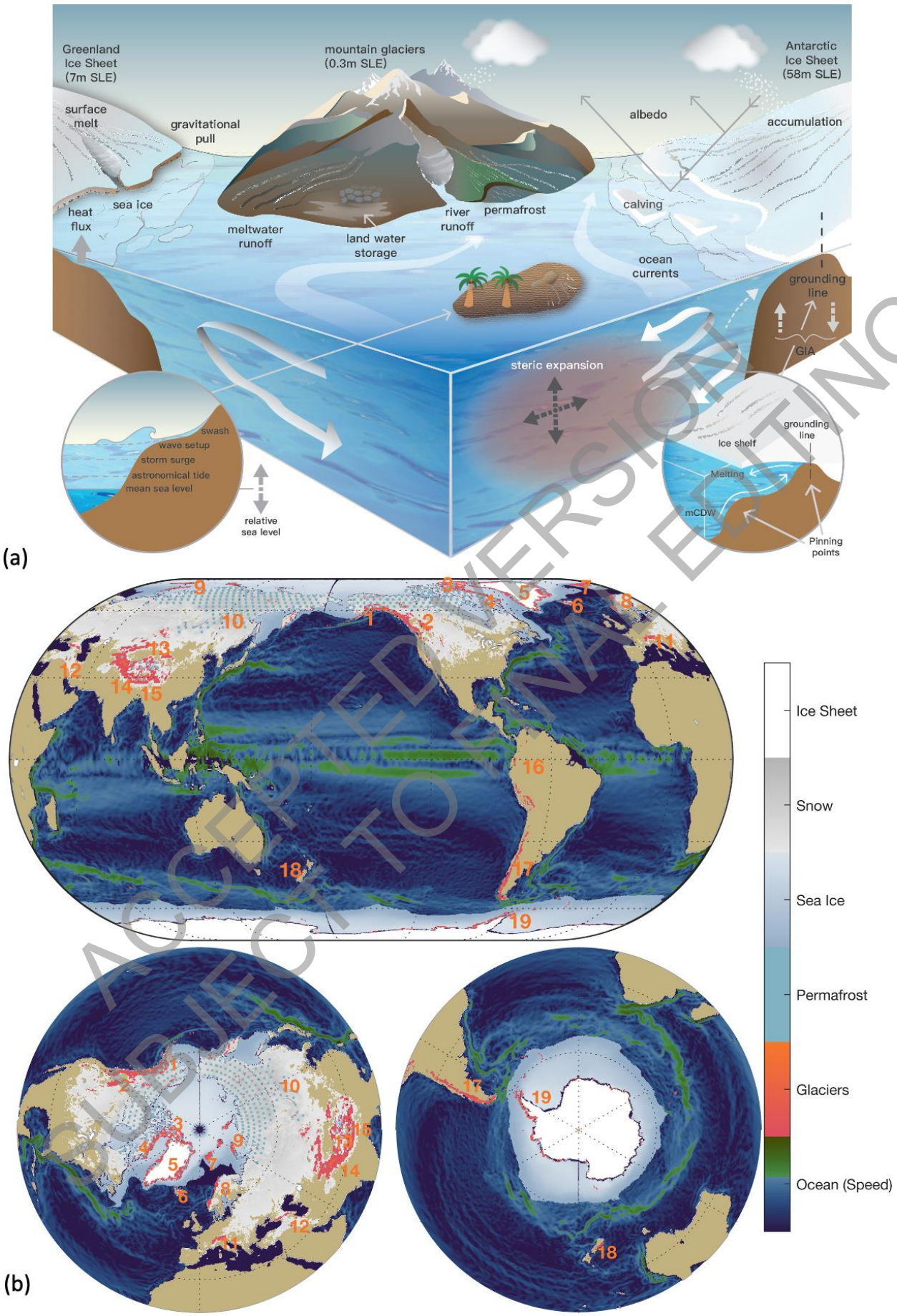


Figure 9.1: Visual guide to chapter 9 with relevant chapter numbers indicated in red.

ACCEPTED VERSION SUBJECT TO FINAL EDITING

1
2
3

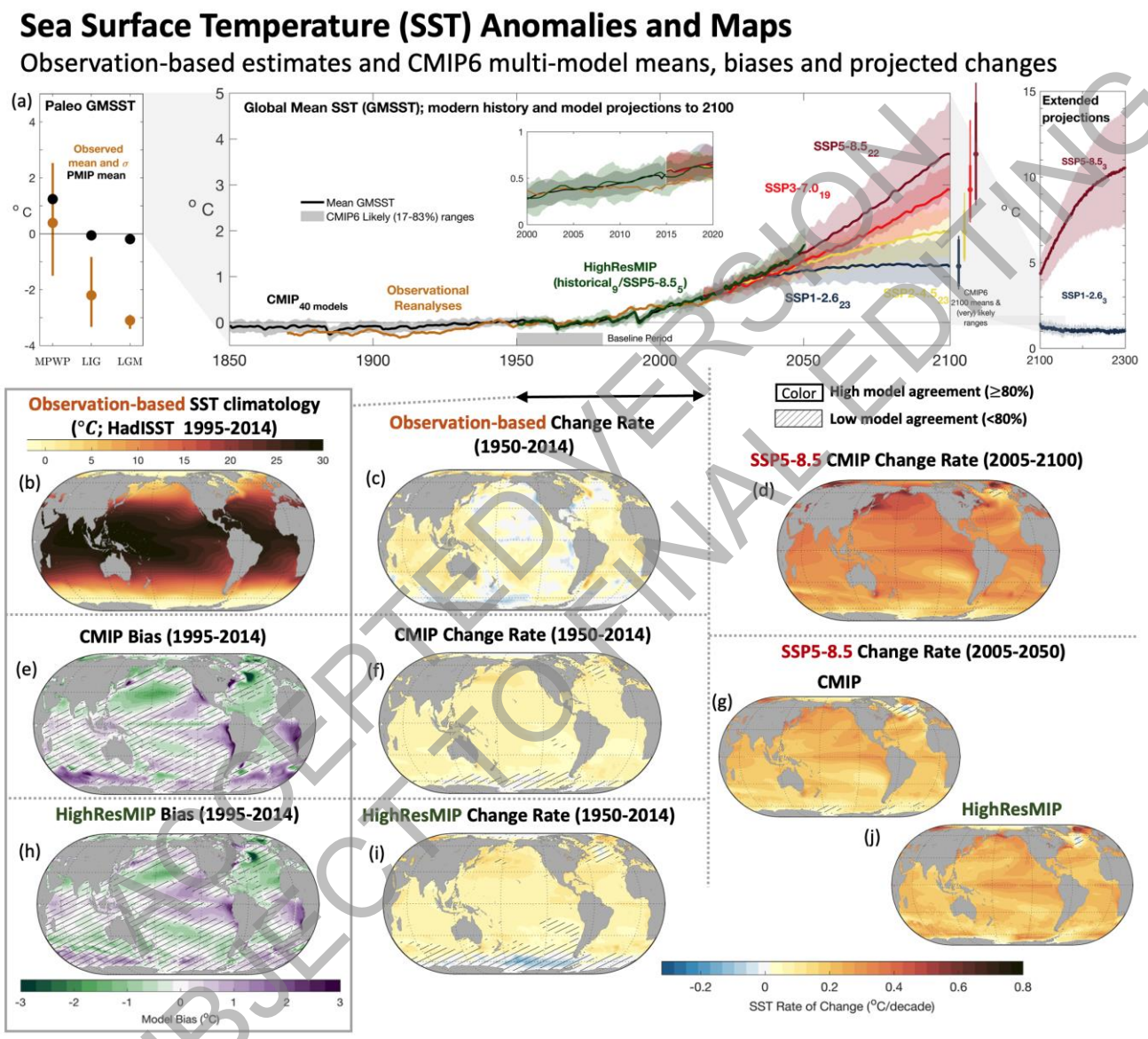
ACCEPTED VERSION
SUBJECT TO FINAL EDITING



ACCEPTED VERSION SUBJECT TO FINAL EDITING

Figure 9.2: Components of ocean, cryosphere and sea level assessed in this chapter. (a) Schematic of processes (mCDW=modified Circumpolar Deep Water, GIA=Glacial Isostatic Adjustment). White arrows indicate ocean circulation. Pinning points indicate where the grounding line is most stable and ice sheet retreat will slow. (b) Geographic distribution of ocean and cryosphere components (numbers indicate (RGI Consortium, 2017) glacierized regions, see Figures 9.20 and 9.21 for labels). Sea ice shaded to indicate the annual mean concentration. Green ocean colours indicate larger surface current speed. Further details on data sources and processing are available in the chapter data table (Table 9.SM.9).

ACCEPTED VERSION
SUBJECT TO FINAL EDITING

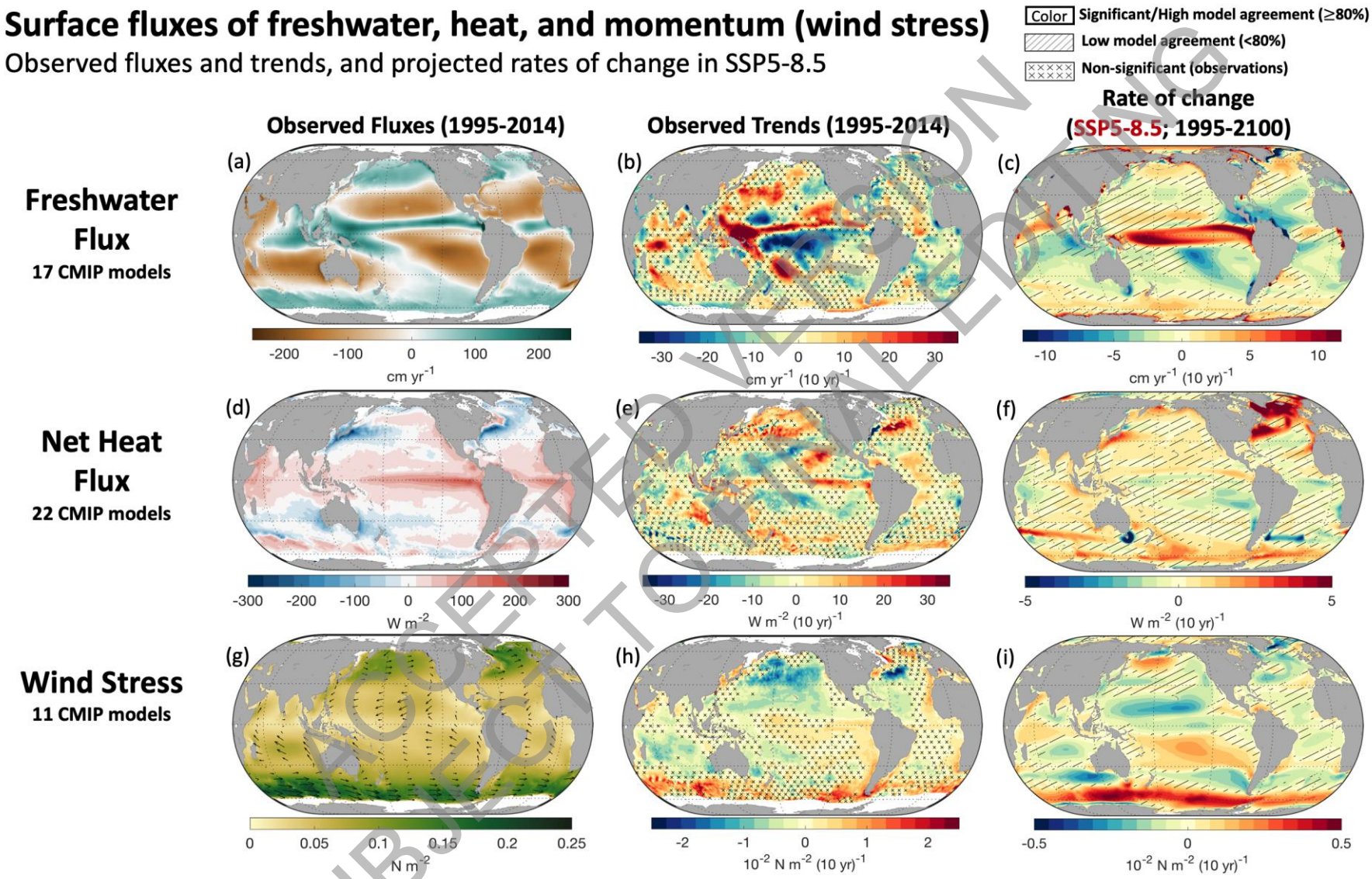


ACCEPTED VERSION SUBJECT TO FINAL EDITING

Figure 9.3: Sea Surface Temperature (SST) and its changes with time. (a) Time series of global mean SST anomaly relative to 1950-1980 climatology. Shown are observational reanalyses (HadISST) and multi-model means from the CMIP historical, CMIP projections, and HighResMIP experiment. (b) Map of observed SST (1995-2014 climatology HadISST), (e) bias of CMIP and (h) bias of HighResMIP (bottom left) over 1995-2014. Also shown are 1950-2014 c) historical SST changes from observations, (f) CMIP and (i) HighResMIP, and (d) 2005-2100 SST change rate, (g) 2005-2050 change rate for SSP5-8.5 for the CMIP ensemble, and (j) 2005-2050 change rate for SSP5-8.5 for the HighResMIP ensemble. No overlay indicates regions with high model agreement, where ≥80% of models agree on sign of change; diagonal lines indicate regions with low model agreement, where <80% of models agree on sign of change (see Cross-Chapter Box Atlas.1 for more information). Further details on data sources and processing are available in the chapter data table (Table 9.SM.9).

ACCEPTED VERSION
SUBJECT TO FINAL EDITING

1



2
3

ACCEPTED VERSION SUBJECT TO FINAL EDITING

Figure 9.4: Global maps of observed mean fluxes (a, d, g), the observed trends in these fluxes (b, e, h) and the projected rate of change in these fluxes from SSP5-8.5 (c, f, i). Shown are the freshwater flux (a, b, c), net heat flux (d, e, f), and momentum flux or wind stress magnitude (g, h, i), with positive numbers indicating ocean freshening, warming, and accelerating respectively. The means and observed trends are calculated between 1995-2014 (freshwater and wind stress) or 2001-2014 (heat) and the SSP5-8.5 projected rates are between 1995-2100 using 20-year averages at each end of the time period. Observations show objective interpolation from CERES EBAF v4 (Kato et al., 2018), OAFlux-HR (Yu, 2019), and GPCP (Adler et al., 2003) of fluxes and flux trends. (b, e, h) Observed trends with no overlay indicates regions where the trends are significant at $p = 0.34$ level. Crosses indicate regions where trends are not significant. For (c, f, i) projections, no overlay indicates regions with high model agreement, where ≥80% of models agree on the sign of change; diagonal lines indicate regions with low model agreement, where <80% of models agree on the sign of change (see Cross-Chapter Box Atlas.1 for more information). Further details on data sources and processing are available in the chapter data table (Table 9.SM.9).

ACCEPTED VERSION
SUBJECT TO FINAL EDITING

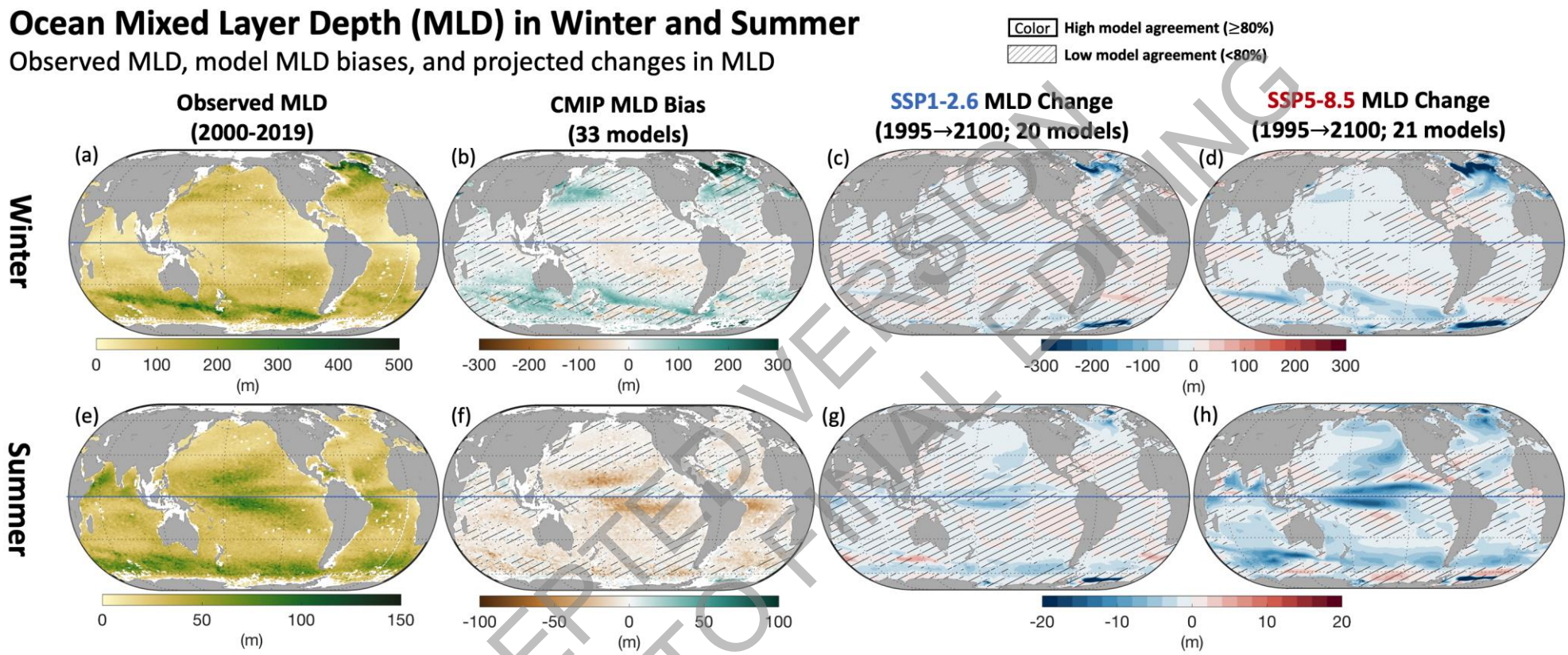
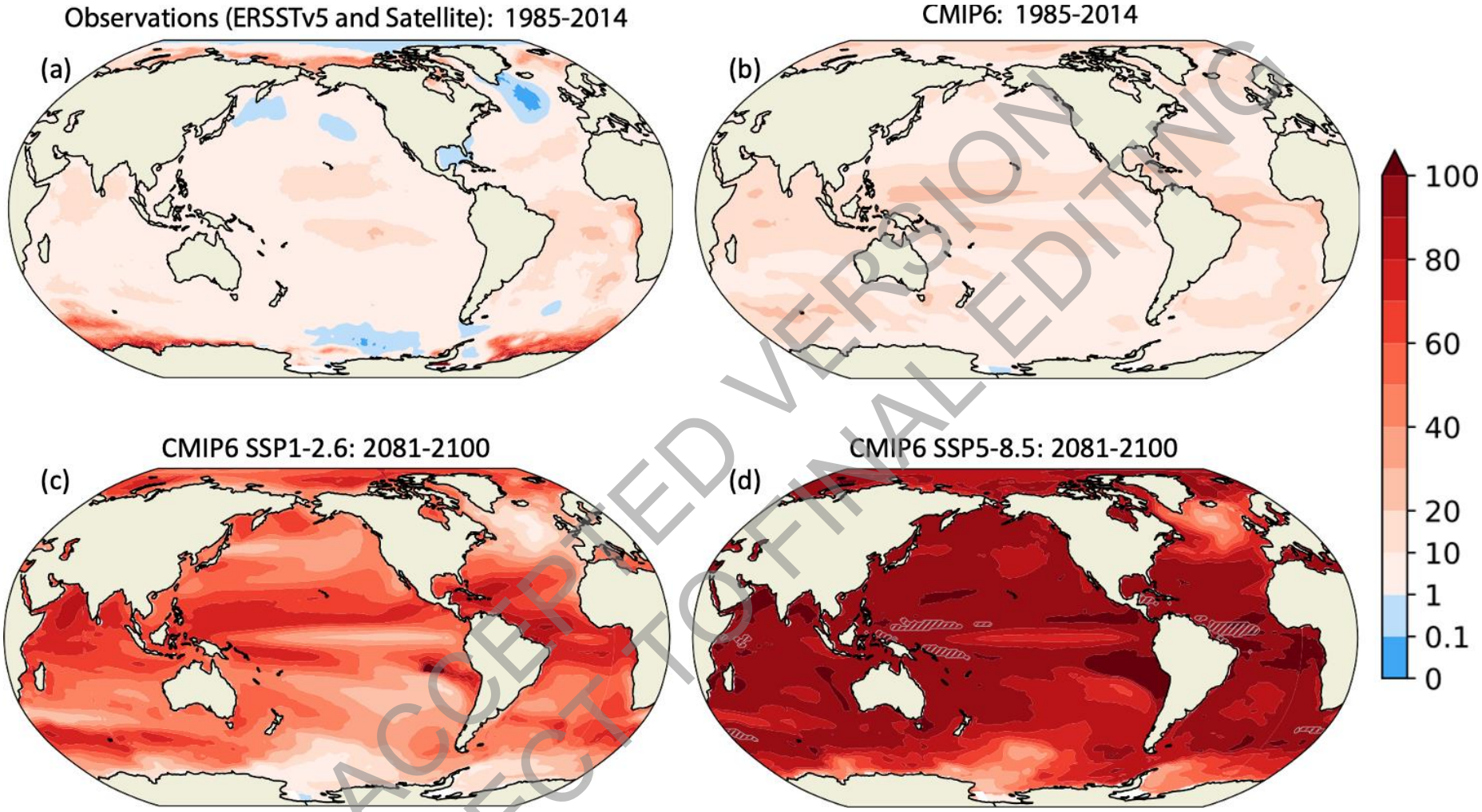


Figure 9.5: **Mixed layer depth in (a-d) winter and (e-h) summer.** (a, e) Observed climatological mean mixed layer depth (based on density threshold) from the Argo Mixed Layer Depth (Holte et al., 2017) **from** observations 2000-2019. (b, f) Bias between the observation-based estimate (2000-2019) and the 1995-2014 CMIP6 climatological mean mixed layer depth. (c, d, g, h) Projected MLD change from 1995-2014 to 2081-2100 under (c, g) SSP1-2.6 and (d, h) SSP5-8.5 scenarios. The (a, b, c, d) Winter row shows DJF in the Northern Hemisphere and JJA in the Southern Hemisphere, and the (e, f, g, h) Summer row shows JJA in the Northern Hemisphere and DJF in the Southern Hemisphere. The mixed layer depth is the depth where the potential density is 0.03 kg m^{-3} denser than at 10m. No overlay indicates regions with high model agreement, where ≥80% of models agree on the sign of change; diagonal lines indicate regions with low model agreement, where <80% of models agree on the sign of change (see Cross-Chapter Box Atlas.1 for more information). Further details on data sources and processing are available in the chapter data table (Table 9.SM.9).

ACCEPTED VERSION SUBJECT TO FINAL EDITING

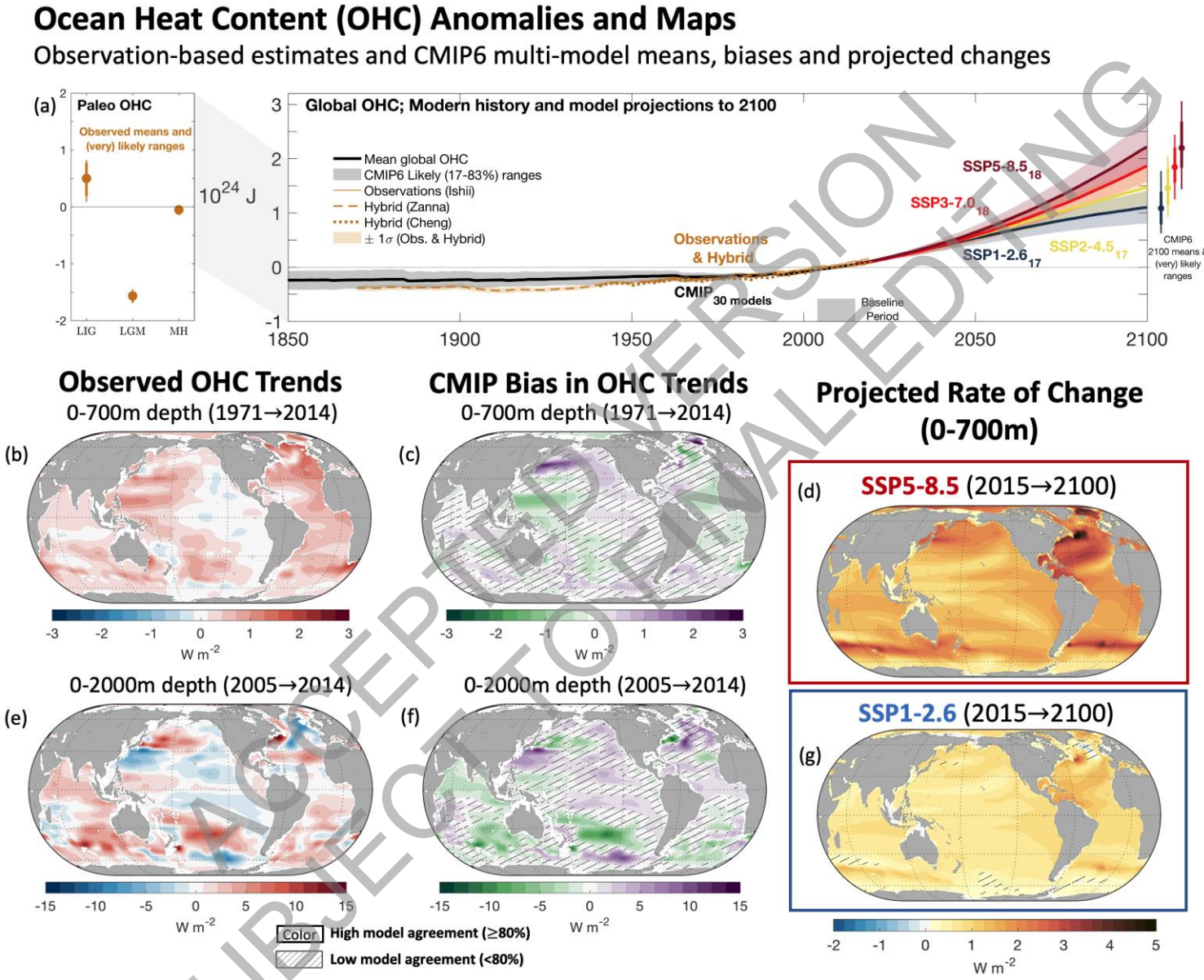


Box 9.2, Figure 1: Observed and simulated regional probability ratio of marine heatwaves (MHWs) for the 1985-2014 period and for the end of the 21st century under two different greenhouse gas emissions scenarios. The probability ratio is the proportion by which the number of MHW days per year has increased relative to preindustrial times. A MHW is defined as a deviation beyond the daily 99th percentile (11-day window) in the deseasonalized sea surface temperature. (a) The MHW probability ratio from satellite observations (NOAA OISST V2.1; Huang et al. 2020) during 1985-2014. The mean warming pattern (difference in ERSST5

ACCEPTED VERSION SUBJECT TO FINAL EDITING

(Huang et al. 2017) sea surface temperature between the 1985-2014 and 1854-1900 periods) has been added to the satellite observations to calculate the probability ratio. (b-d) CMIP6 simulated multi-model mean probability ratio of the (b) 1985-2014 period, and 2081-2100 period in the (c) SSP1 2.6 and (d) SSP5 8.5 scenarios. The areas with grey diagonal lines in (d) indicate permanent MHWs (> 360 heatwave days per year). These 14 CMIP6 models are included in the analysis: ACCESS-CM2, CESM2, CESM2-WACCM, CMCCCM2-SR5, CNRM-CM6-1, CNRM-ESM2-1, CanESM5, EC-Earth3, IPSL-CM6A-LR, MIROC6, MRI-ESM2-0, NESM3, NorESM2-LM, NorESM2-MM. Further details on data sources and processing are available in the chapter data table (Table 9.SM.9).

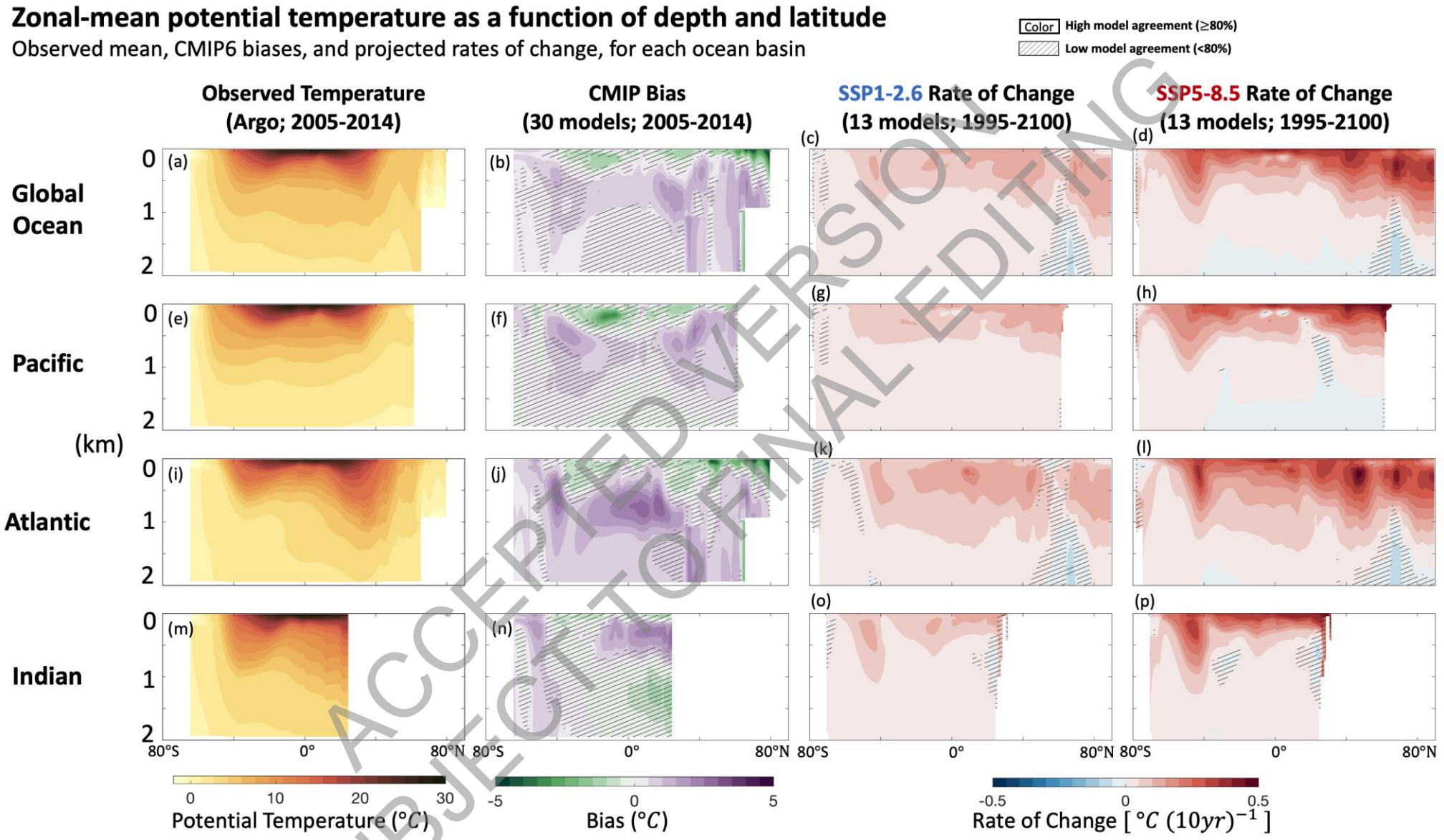
ACCEPTED VERSION
SUBJECT TO FINAL EDITING



ACCEPTED VERSION SUBJECT TO FINAL EDITING

Figure 9.6: Ocean heat content (OHC) and its changes with time. (a) Time series of global ocean heat content anomaly relative to a 2005-2014 climatology in the upper 2000m of the ocean. Shown are observations (Ishii et al., 2017; Baggenstos et al., 2019; Shackleton et al., 2020), model-observation hybrids (Cheng et al., 2019; Zanna et al., 2019), and multi-model means from the CMIP6 historical (29 models) and SSP scenarios (label subscripts indicate number of models per SSP). (b-g) Maps of Ocean Heat Content across different time periods, in different layers, and from different data sets/experiments. Maps show the CMIP6 ensemble bias and observed (Ishii et al., 2017) trends of OHC for (b, c) 0-700m for the period 1971-2014, and (e, f) 0-2000m for the period 2005-2017. CMIP6 ensemble mean maps show projected rate of change 2015-2100 for (d) SSP5-8.5 and (g) SSP1-2.6 scenarios. Also shown are the projected change in 0-700m OHC for (d) SSP1-2.6 and (g) SSP5-8.5 in the CMIP6 ensembles, for the period 2091-2100 versus 2005-2014. No overlay indicates regions with high model agreement, where ≥80% of models agree on the sign of change; diagonal lines indicate regions with low model agreement, where <80% of models agree on the sign of change (see Cross-Chapter Box Atlas.1for more information). Further details on data sources and processing are available in the chapter data table (Table 9.SM.9).

ACCEPTED VERSION
SUBJECT TO FINAL EDITING



ACCEPTED VERSION SUBJECT TO FINAL EDITING

1

Figure 9.7: Meridional-depth profiles of zonal-mean potential temperature in the ocean and its rate of change in the upper 2000m of the Global, Pacific, Atlantic, and Indian Oceans. Shown are (a, e, i, m) observed temperature (Argo climatology 2005-2014), (b, f, j, n) bias of the CMIP6 ensemble over this period, and future changes under (c, g, k, o) SSP1-2.6 and (d, h, l, p) SSP5-8.5. No overlay indicates regions with high model agreement, where ≥80% of models agree on the sign of change; diagonal lines indicate regions with low model agreement, where <80% of models agree on the sign of change (see Cross-Chapter Box Atlas.1 for more information). Further details on data sources and processing are available in the chapter data table (Table 9.SM.9).

ACCEPTED VERSION
SUBJECT TO FINAL EDITING

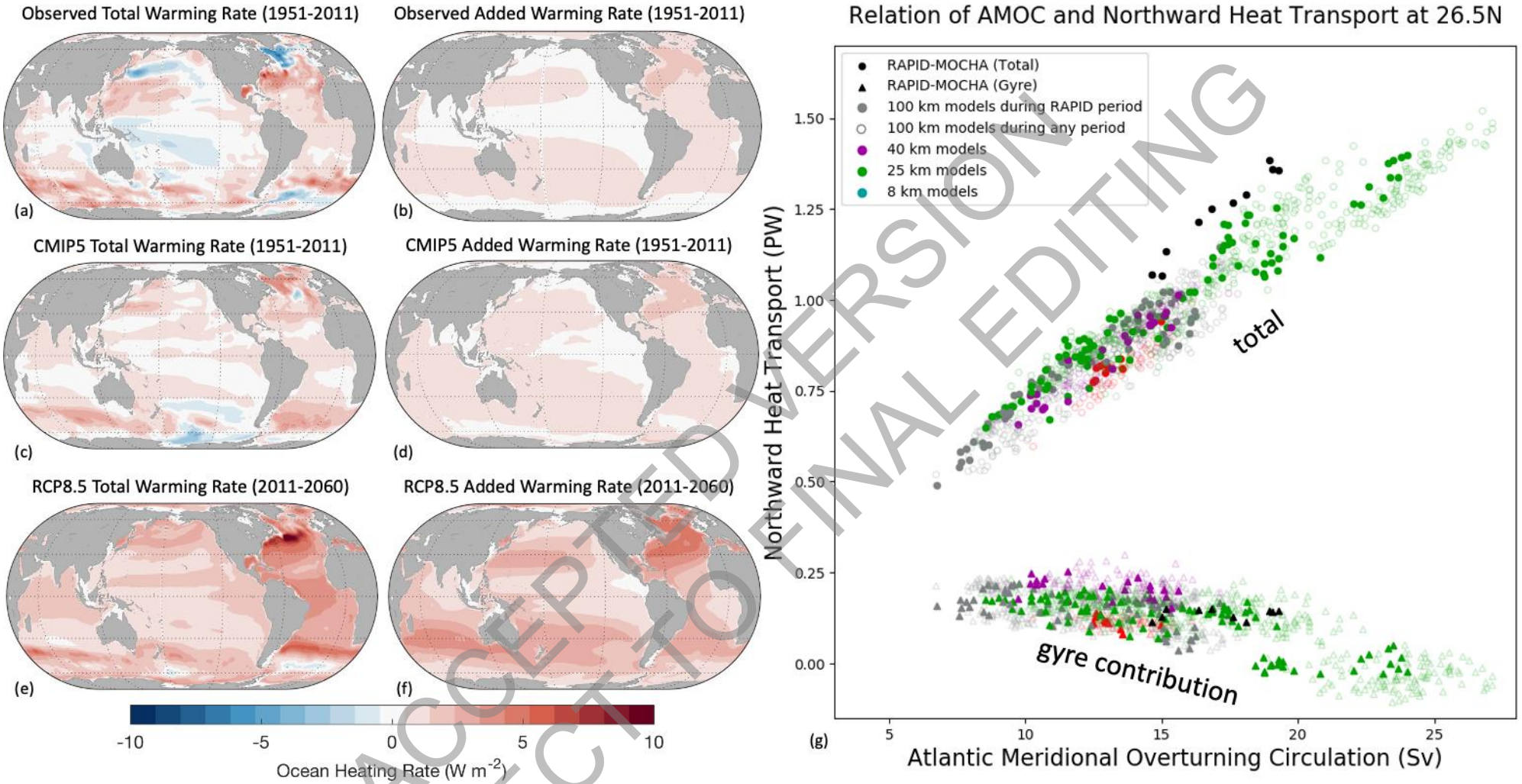


Figure 9.8: Decomposition of ocean simulated ocean heat content and northward heat transport. (a, c, e) Total ocean heat content (0-2000 m) warming rate as observed and simulated by CMIP5 models over the historical period (1951-2011) and under the RCP8.5 future (2011-2060) versus the associated decomposed (b, d, f) added heat contribution (neglecting changes in ocean circulation) to the total (Bronselaer and Zanna, 2020). (g) Relationship between northward heat transport and Atlantic Meridional Overturning Circulation in HighResMIP models (1950-2050) and observations during the RAPID period (2004-2018). Further details on data sources and processing are available in the chapter data table (Table 9.SM.9).

ACCEPTED VERSION SUBJECT TO FINAL EDITING

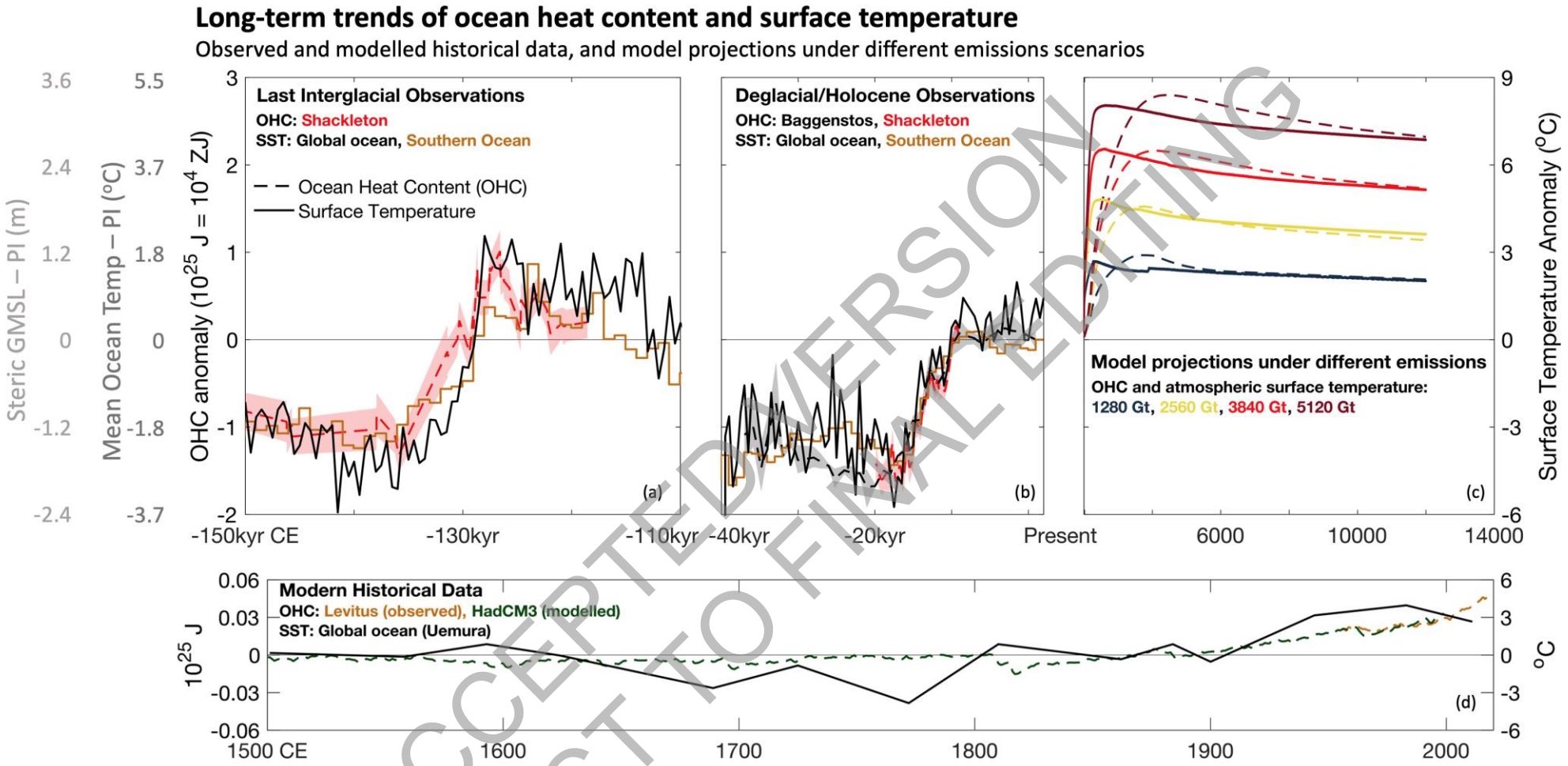
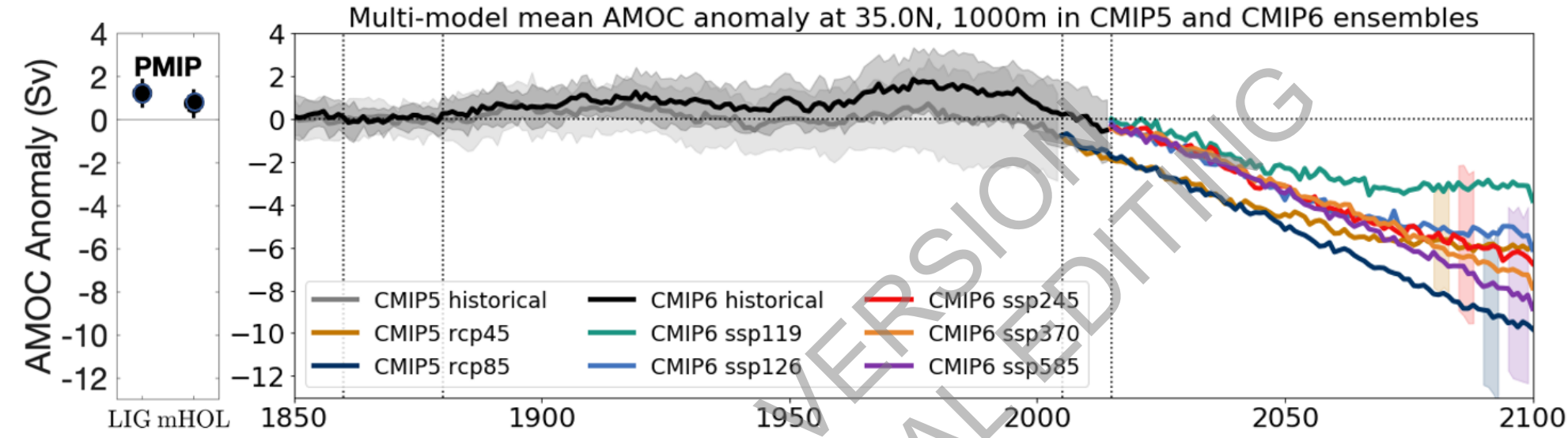


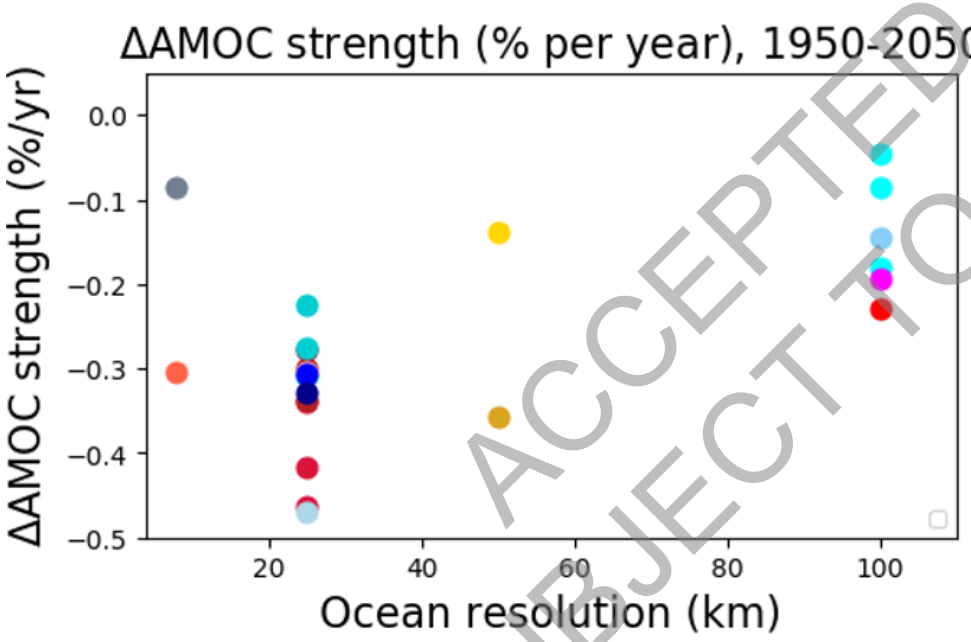
Figure 9.9: **Long-term trends of ocean heat content and surface temperature.** (a, b) Ice-core rare gas estimates of past mean ocean heat content OHC (ZJ), scaled to global mean ocean temperature (°C), and to steric GMSL (m) per CCB-2 (red dashed line), compared to surface temperatures (black solid line, gold solid line; °C rightmost axis). Southern Ocean SST from multiple proxies in 11 sediment cores and from ice core deuterium excess (Uemura et al., 2018). a) Penultimate glacial interval to last interglacial, 150,000-100,000 yr B2K (Shackleton et al., 2020). b) Last glacial interval to modern interglacial, 40,000-0 yr B2K (Baggenstos et al., 2019; Shackleton et al., 2019). Changes in OHC (dashed lines) track changes in Southern Ocean SST (solid lines). c) Long-term projected (2000 to 12000 CE) changes of OHC (dashed

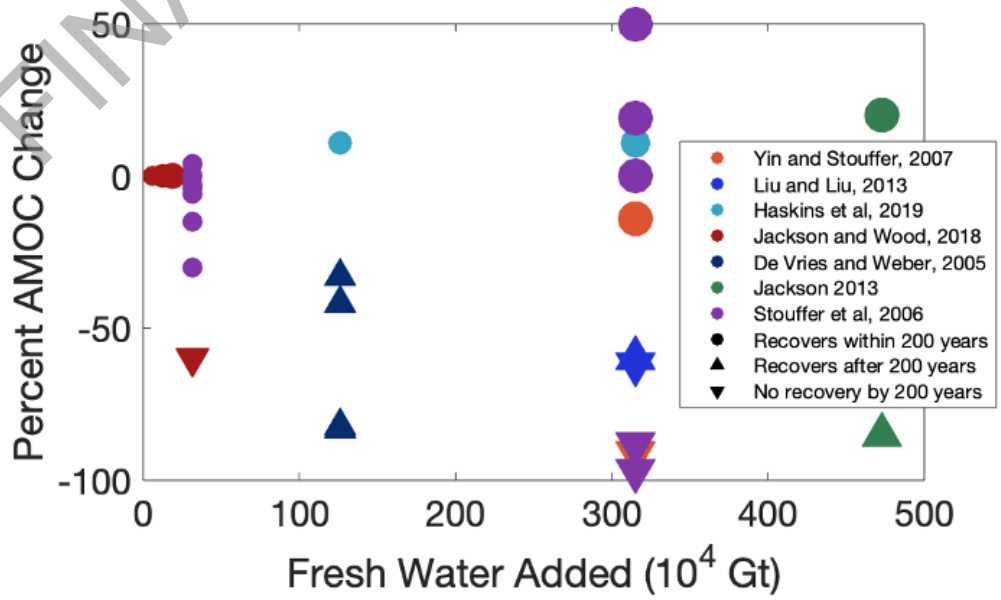
ACCEPTED VERSION SUBJECT TO FINAL EDITING

lines) in response to four greenhouse gas emissions scenarios (Clark et al., 2016) scale similarly to large-scale paleo changes but lag projected global mean SST (solid lines). d) model simulated 1500-1999 OHC (Gregory et al., 2006) and 1955-2019 observations (Levitus et al., 2012) updated by NOAA NODC. All data expressed as anomalies relative to preindustrial time. Further details on data sources and processing are available in the chapter data table (Table 9.SM.9).

ACCEPTED VERSION
SUBJECT TO FINAL EDITING







ACCEPTED VERSION SUBJECT TO FINAL EDITING

Figure 9.10: AMOC strength in simulations and sensitivity to resolution and forcing. (Top left) AMOC magnitude in PMIP experiments. (Top right) Time series of AMOC from CMIP5 and CMIP6 based on (Menary et al., 2020). (Bottom left) Percent change in AMOC strength per year at different resolutions over the 1950-2050 period with colours for model families (Roberts et al., 2020). (Bottom right) A compilation (Jackson and Wood, 2018) of percentage changes in the simulated AMOC after applying an additional freshwater flux in the subpolar North Atlantic at the surface for a limited time (de Vries and Weber, 2005; Stouffer et al., 2006; Yin and Stouffer, 2007; Jackson, 2013; Liu and Liu, 2013; Jackson and Wood, 2018; Haskins et al., 2019). Symbols indicate whether the AMOC recovers within 200 years (circles), is starting to recover (upwards arrow) or does not recover within 200 years (downwards arrow). Symbol size indicates rate of freshwater input. Further details on data sources and processing are available in the chapter data table (Table 9.SM.9).

ACCEPTED VERSION
SUBJECT TO FINAL EDITING

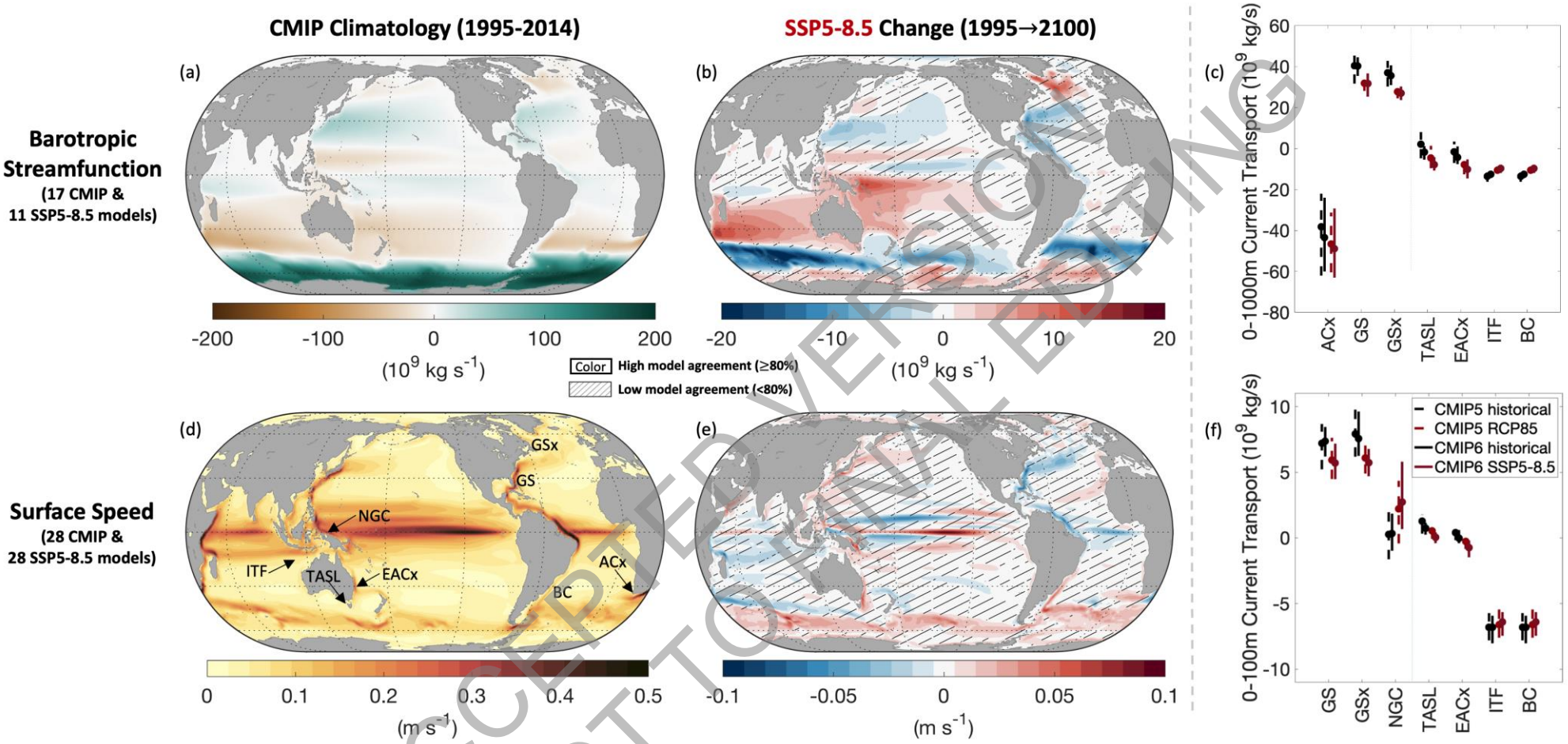
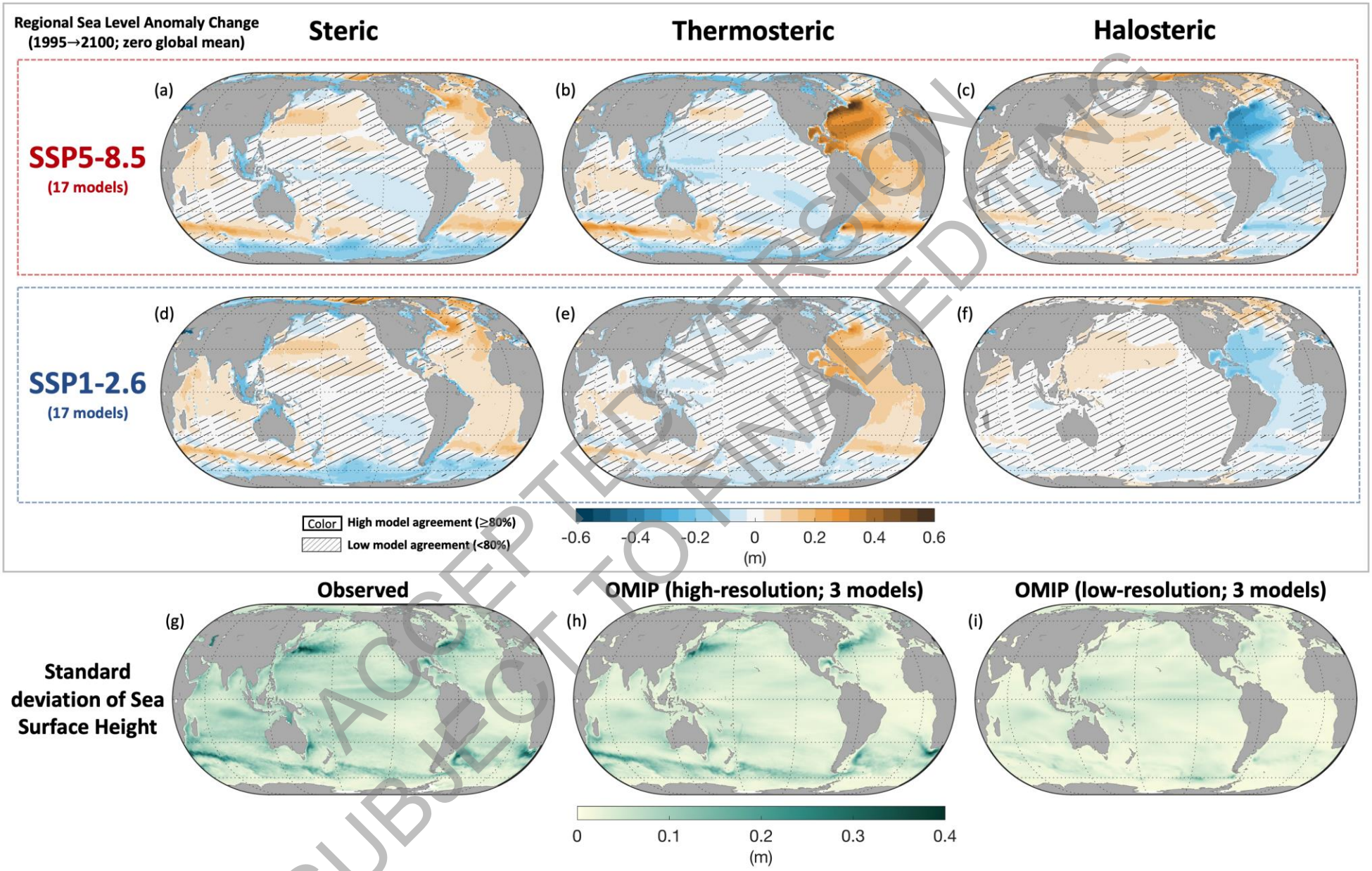


Figure 9.11: Simulated barotropic streamfunction, surface speed and major current transport in CMIP5 and CMIP6. (a) Mean barotropic streamfunction (Sv) 1995-2014 and projected barotropic streamfunction change (Sv, 2018-2100 vs. 1995-2014) under (b) SSP5-8.5. (d) Mean surface (0-100 m) speed (m/s) and projected surface speed change (m/s, 2081-2100) versus 1995-2014 under (e) SSP5-8.5. (c, f) Median and likely range of 1995-2014 and 2081-2100 transport of 3 currents with the largest transport change and 4 with the largest fractional change (Sen Gupta et al., 2016). (c) Deep currents: Agulhas Extension (ACx), Gulf Stream (GS), Gulf Stream Extension (GSx), Tasman Leakage (TASL), East Australia Current Extension (EACx), Indonesian Throughflow (ITF), and Brazil Current (BC). (f) Shallow currents: as for deep but with New Guinea Current (NGC), and without ACx. No overlay indicates regions with high model agreement, where ≥80% of models agree on the sign of change; diagonal lines indicate regions with low model agreement, where <80% of models agree on the sign of change (see Cross-Chapter Box Atlas.1 for more information). Further details on data sources and processing are available in the chapter data table (Table 9.SM.9).

ACCEPTED VERSION SUBJECT TO FINAL EDITING



ACCEPTED VERSION SUBJECT TO FINAL EDITING

1

Figure 9.12: (a-f) CMIP6 multi-model mean projected change contributions to relative sea level change in (a,d) steric sea level anomaly, (b, e) thermosteric sea level anomaly, and (c, f) halosteric sea level anomaly between 1995-2014 and 2081-2100 using a method that does not require a reference level (Landerer et al., 2007). Global mean change has been removed from these figures, consistent with the methods in Sections 9.6.3 and 9.A.4.3 and the definitions of (Gregory et al., 2019). See Figure 9.27 for GMSL. (g-i) Standard deviation of ocean dynamic sea-level change from (g) Aviso observations (10 day highpass filter), (h) 5-day mean of high-resolution OMIP-2 models forced with observed fluxes, and (i) 5-day mean of low-resolution OMIP-2 models which are comparable in resolution to the models in (a-f). No overlay indicates regions with high model agreement, where ≥80% of models agree on the sign of change; diagonal lines indicate regions with low model agreement, where <80% of models agree on the sign of change (see Cross-Chapter Box Atlas.1 for more information). Further details on data sources and processing are available in the chapter data table (Table 9.SM.9).

ACCEPTED VERSION
SUBJECT TO FINAL EDITING

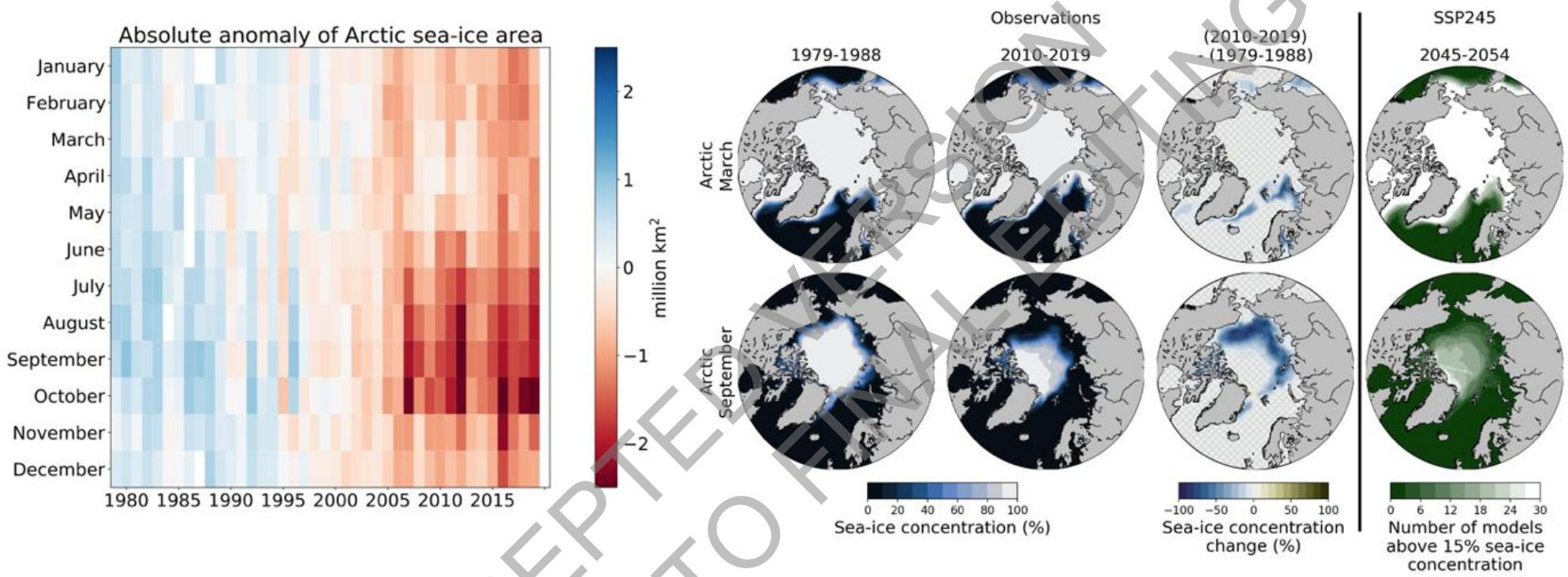
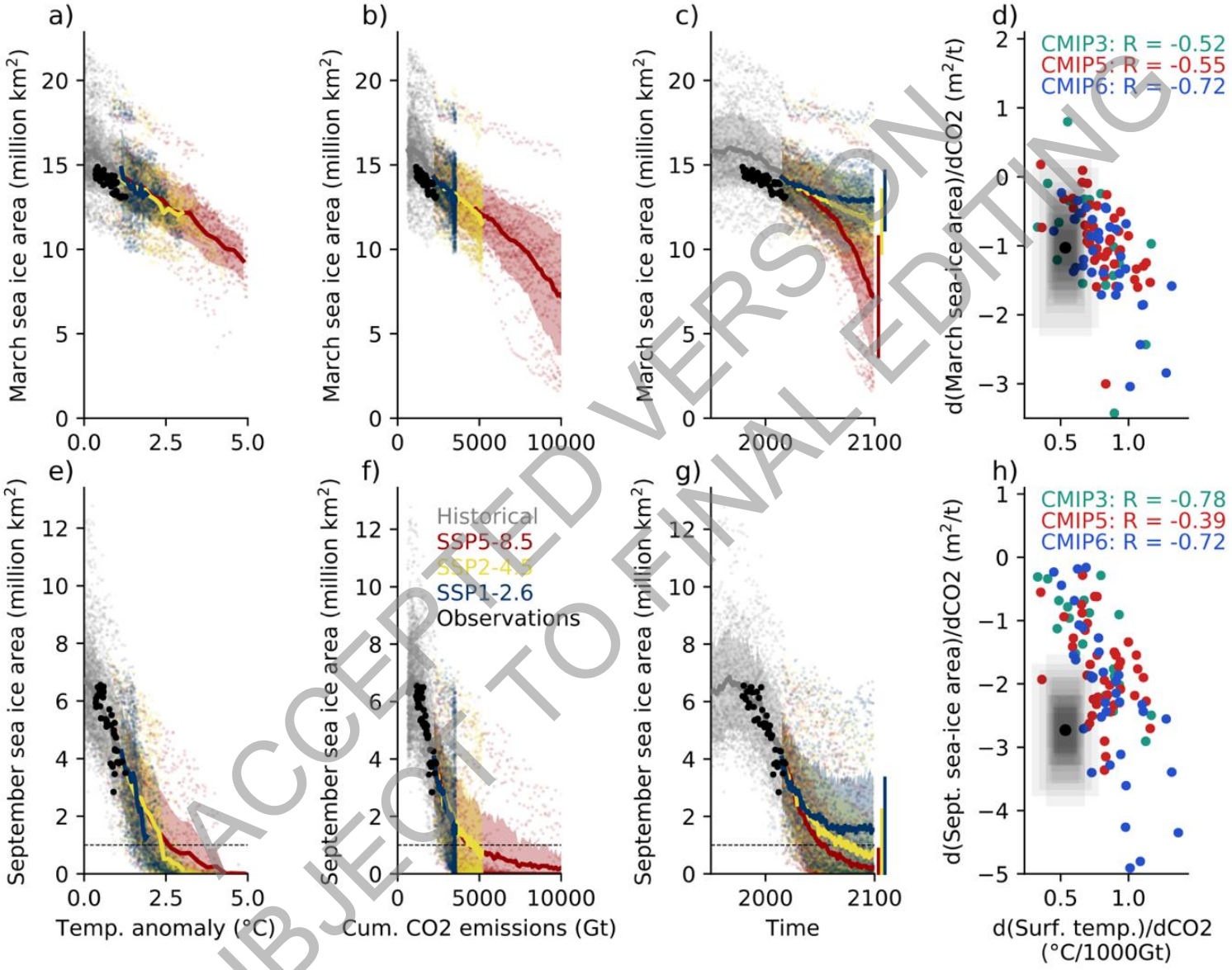


Figure 9.13: Arctic sea-ice historical records and CMIP6 projections. Left: Absolute anomaly of monthly-mean Arctic sea-ice area during the period 1979 to 2019 relative to the average monthly-mean Arctic sea-ice area during the period 1979 to 2008. Right: Sea-ice concentration in the Arctic for March and September, which usually are the months of maximum and minimum sea-ice area, respectively. First column: Satellite-retrieved mean sea-ice concentration during the decade 1979-1988. Second column: Satellite-retrieved mean sea-ice concentration during the decade 2010-2019. Third column: Absolute change in sea-ice concentration between these two decades, with grid lines indicating non-significant differences. Fourth column: number of available CMIP6 models that simulate a mean sea-ice concentration above 15 % for the decade 2045-2054. The average observational record of sea-ice area is derived from the UHH sea-ice area product (Doerr et al., 2021), based on the average sea-ice concentration of OSISAF/CCI (OSI-450 for 1979-2015, OSI-430b for 2016-2019)(Lavergne et al., 2019), NASA Team (version 1, 1979-2019)(Cavalieri et al., 1996) and Bootstrap (version 3, 1979-2019)(Comiso, 2017) that is also used for the figure panels showing observed sea-ice concentration. Further details on data sources and processing are available in the chapter data table (Table 9.SM.9).

ACCEPTED VERSION SUBJECT TO FINAL EDITING



ACCEPTED VERSION SUBJECT TO FINAL EDITING

1

Figure 9.14: Monthly mean March (a-d) and September (e-h) sea-ice area as a function of global surface air temperature (GSAT) anomaly (a,e); cumulative anthropogenic CO_2 emissions (b,f); year (c,g) in CMIP6 model simulations (shading, ensemble mean as bold line) and in observations (black dots). Panels d and h show the sensitivity of sea-ice loss to anthropogenic CO_2 emissions as a function of the modelled sensitivity of GSAT to anthropogenic CO_2 emissions. In panels d and h, the black dot denotes the observed sensitivity, while the shading around it denotes internal variability as inferred from CMIP6 simulations (after Notz and SIMIP Community, 2020). Further details on data sources and processing are available in the chapter data table (Table 9.SM.9).

ACCEPTED VERSION
SUBJECT TO FINAL EDITING

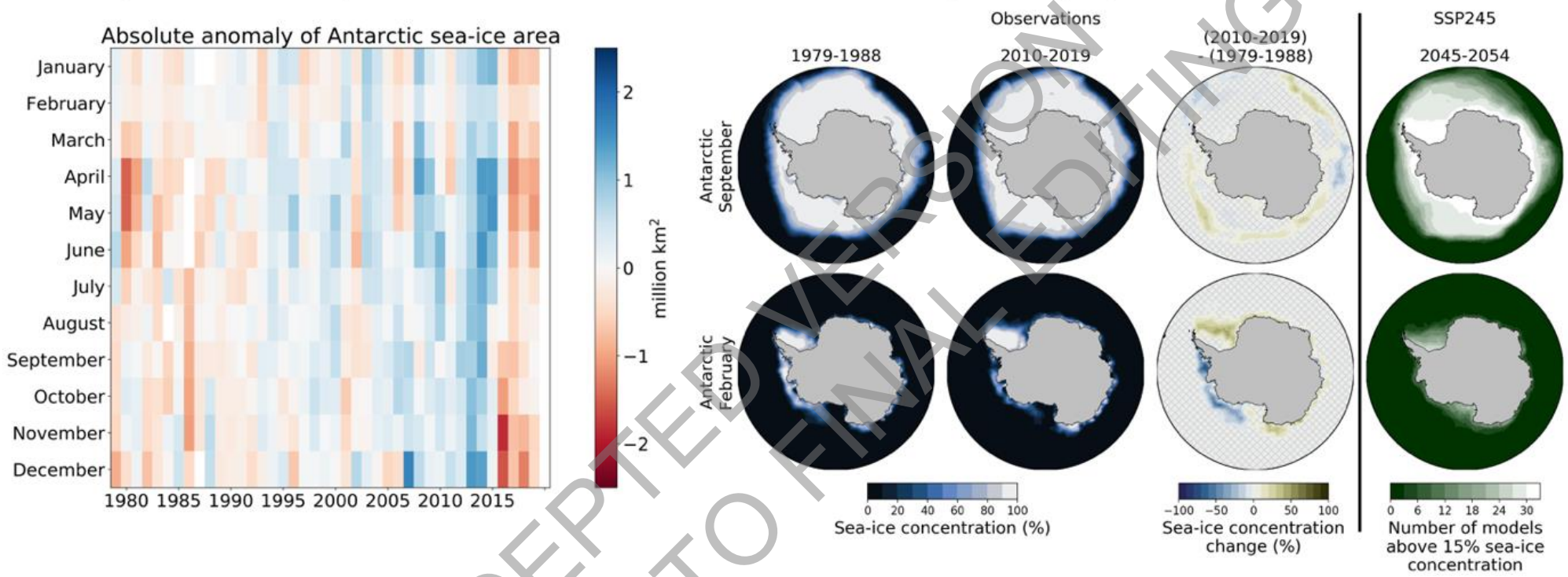
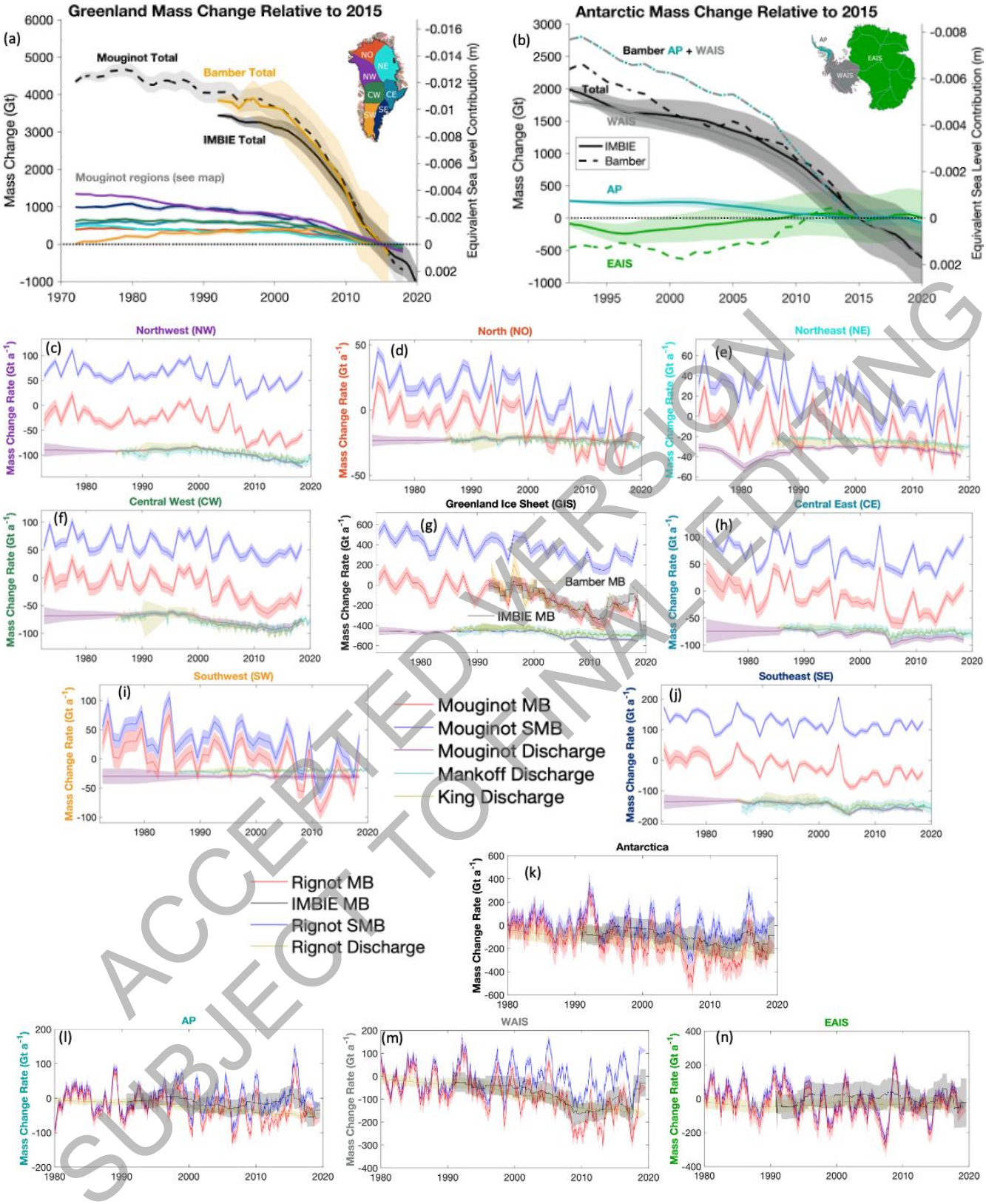


Figure 9.15: Antarctic sea-ice historical records and CMIP6 projections. Left: Absolute anomaly of observed monthly-mean Antarctic sea-ice area during the period 1979 to 2019 relative to the average monthly-mean Antarctic sea-ice area during the period 1979 to 2008. Right: Sea-ice coverage in the Antarctic as given by the average of the three most widely used satellite-based estimates for September and February, which usually are the months of maximum and minimum sea-ice coverage, respectively. First column: Mean sea-ice coverage during the decade 1979-1988. Second column: Mean sea-ice coverage during the decade 2010-2019. Third column: Absolute change in sea-ice concentration between these two decades, with grid lines indicating non-significant differences. Fourth column: number of available CMIP6 models that simulate a mean sea-ice concentration above 15 % for the decade 2045-2054. The average observational record of sea-ice area is derived from the UHH sea-ice area product (Doerr et al., 2021), based on the average sea-ice concentration of OSISAF/CCI (OSI-450 for 1979-2015, OSI-430b for 2016-2019)(Lavergne et al., 2019), NASA Team (version 1, 1979-2019)(Cavalieri et al., 1996) and Bootstrap (version 3, 1979-2019)(Comiso, 2017) that is also used for the figure panels showing observed sea-ice concentration. Further details on data sources and processing are available in the chapter data table (Table 9.SM.9).

ACCEPTED VERSION SUBJECT TO FINAL EDITING



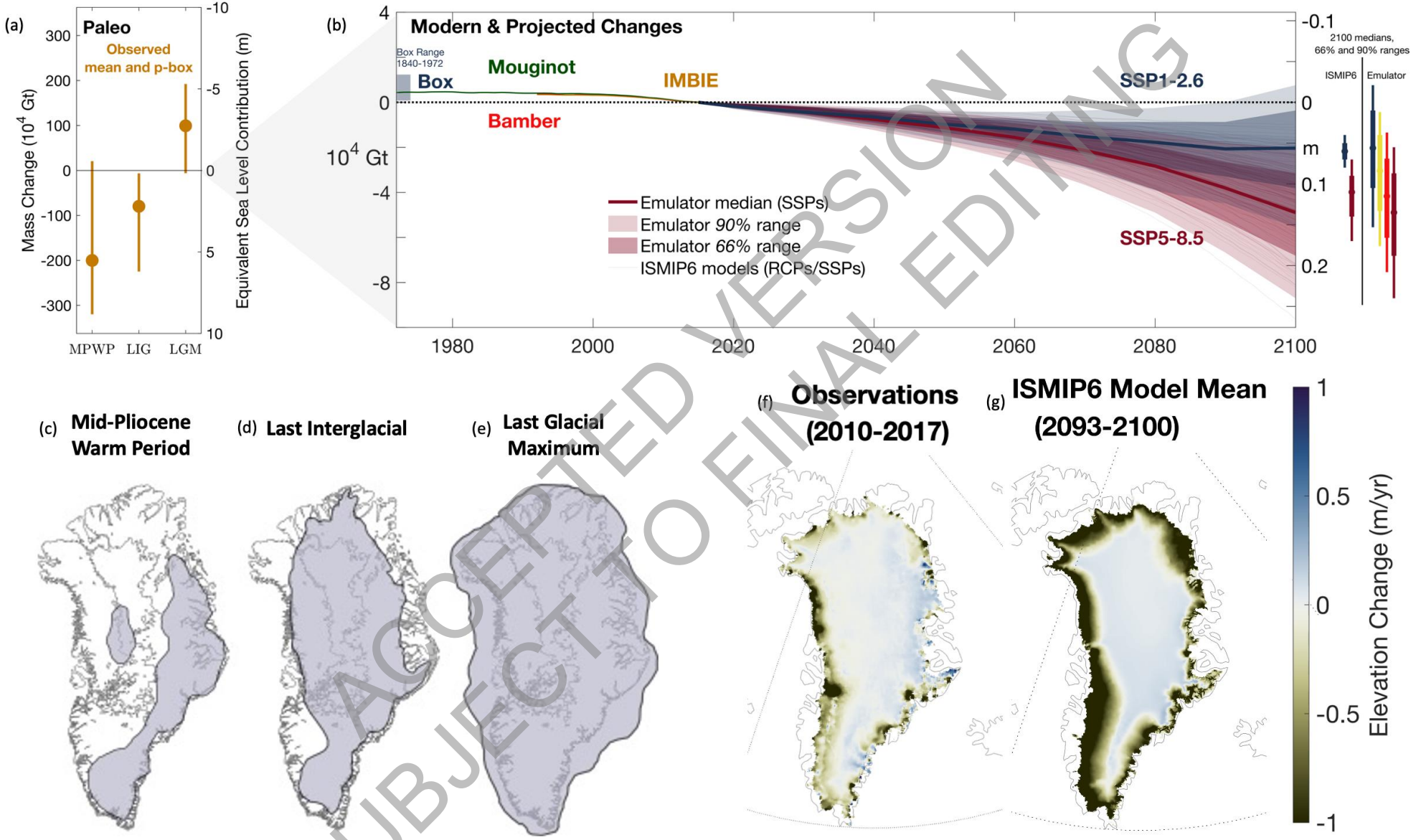
ACCEPTED VERSION SUBJECT TO FINAL EDITING

Figure 9.16: Mass changes and mass change rates for Greenland and Antarctic ice sheet regions. (Upper Left) Time series of mass changes in Greenland for each of the major drainage basins shown in the inset figure (Bamber et al., 2018b; Mouginot et al., 2019) for the periods 1972 – 2016, 1992-2018, and 1992–2020. (Upper Right) Time series of mass changes for three portions of Antarctica (Bamber et al., 2018b) for the period 1992 – 2016 and 1992–2020. (Lower rows) Estimates of mass change rates of surface mass

balance, discharge and mass balance in seven Greenland regions (Bamber et al., 2018b; Mankoff et al., 2019; Mouginot et al., 2019; King et al., 2020). (Bottom rows) Estimates of mass change rates of surface mass balance, discharge and mass balance for three regions of Antarctica (Bamber et al., 2018b; The IMBIE Team et al., 2018; Rignot et al., 2019). Further details on data sources and processing are available in the chapter data table (Table 9.SM.9).

ACCEPTED VERSION
SUBJECT TO FINAL EDITING

Greenland Ice Sheet Cumulative Mass Change & Equivalent Sea Level Contribution



ACCEPTED VERSION SUBJECT TO FINAL EDITING

Figure 9.17: Greenland Ice Sheet cumulative mass change and equivalent sea level contribution. (a) A p-box (Section 9.6.3.2) based estimate of the range of values of paleo Greenland ice sheet mass and sea level equivalents relative to present day and the median over all central estimates (Simpson et al., 2009; Argus and Peltier, 2010; Colville et al., 2011; Dolan et al., 2011; Fyke et al., 2011; Robinson et al., 2011; Born and Nisancioglu, 2012; Miller et al., 2012; Dahl-Jensen et al., 2013; Helsen et al., 2013; Nick et al., 2013; Quiquet et al., 2013; Stone et al., 2013; Colleoni et al., 2014; Lecavalier et al., 2014; Robinson and Goelzer, 2014; Calov et al., 2015; Dutton et al., 2015; Koenig et al., 2015; Peltier et al., 2015; Stuhne and Peltier, 2015; Vizcaino et al., 2015; Goelzer et al., 2016; Khan et al., 2016; Yau et al., 2016; de Boer et al., 2017; Calov et al., 2018; Simms et al., 2019); and (b) cumulative mass loss (and sea level equivalent) from 1972 (Mouginot et al., 2019) and 1992 (Bamber et al., 2018b; The IMBIE Team, 2019), the estimated mass loss from 1840 (Box and Colgan, 2013; Kjeldsen et al., 2015) indicated with a shaded box and projections from ISMIP6 by 2100 under RCP8.5/SSP5-85 and RCP2.6/SSP1-26 scenarios (thin lines from (Goelzer et al., 2020; Edwards et al., 2021; Payne et al., 2021) and likely range of the ISMIP6 emulation (shades and bold line (Edwards et al., 2021)) are shown in time. Schematic interpretations of individual reconstructions (Lecavalier et al., 2014; Goelzer et al., 2016; Berends et al., 2019) of the spatial extent of the Greenland ice sheet are shown for the (c) mid-Pliocene Warm Period, (d) the Last Interglacial and (e) the Last Glacial Maximum: grey shading shows extent of grounded ice. Maps of mean elevation changes (f) 2010-2017 derived from CryoSat 2 radar altimetry (Bamber et al., 2018b) and (g) ISMIP6 model mean (2093-2100) projected changes for the MIROC5 climate model under the RCP8.5 scenario (Goelzer et al., 2020). Further details on data sources and processing are available in the chapter data table (Table 9.SM.9).

ACCEPTED VERSION
SUBJECT TO FINAL EDITING

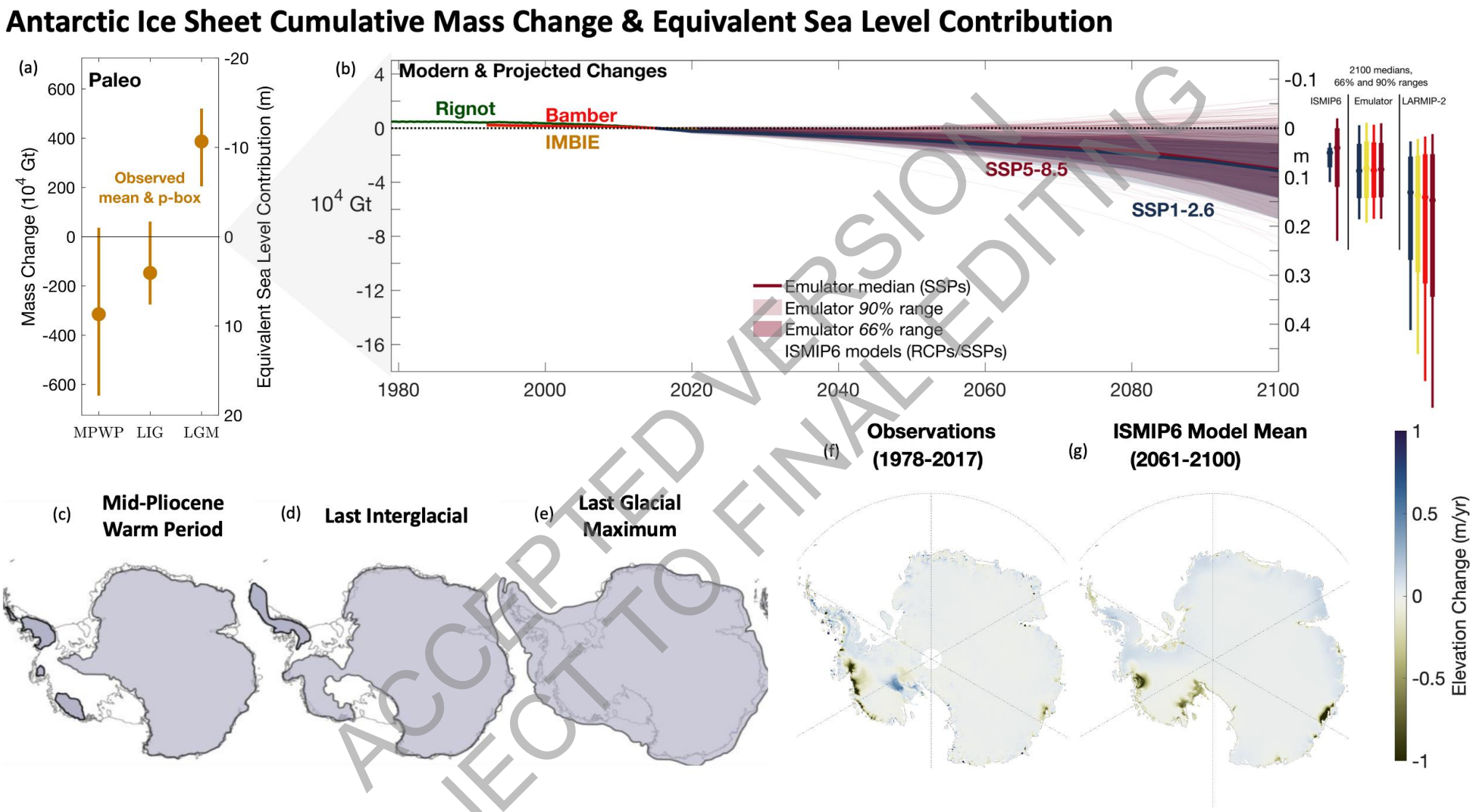
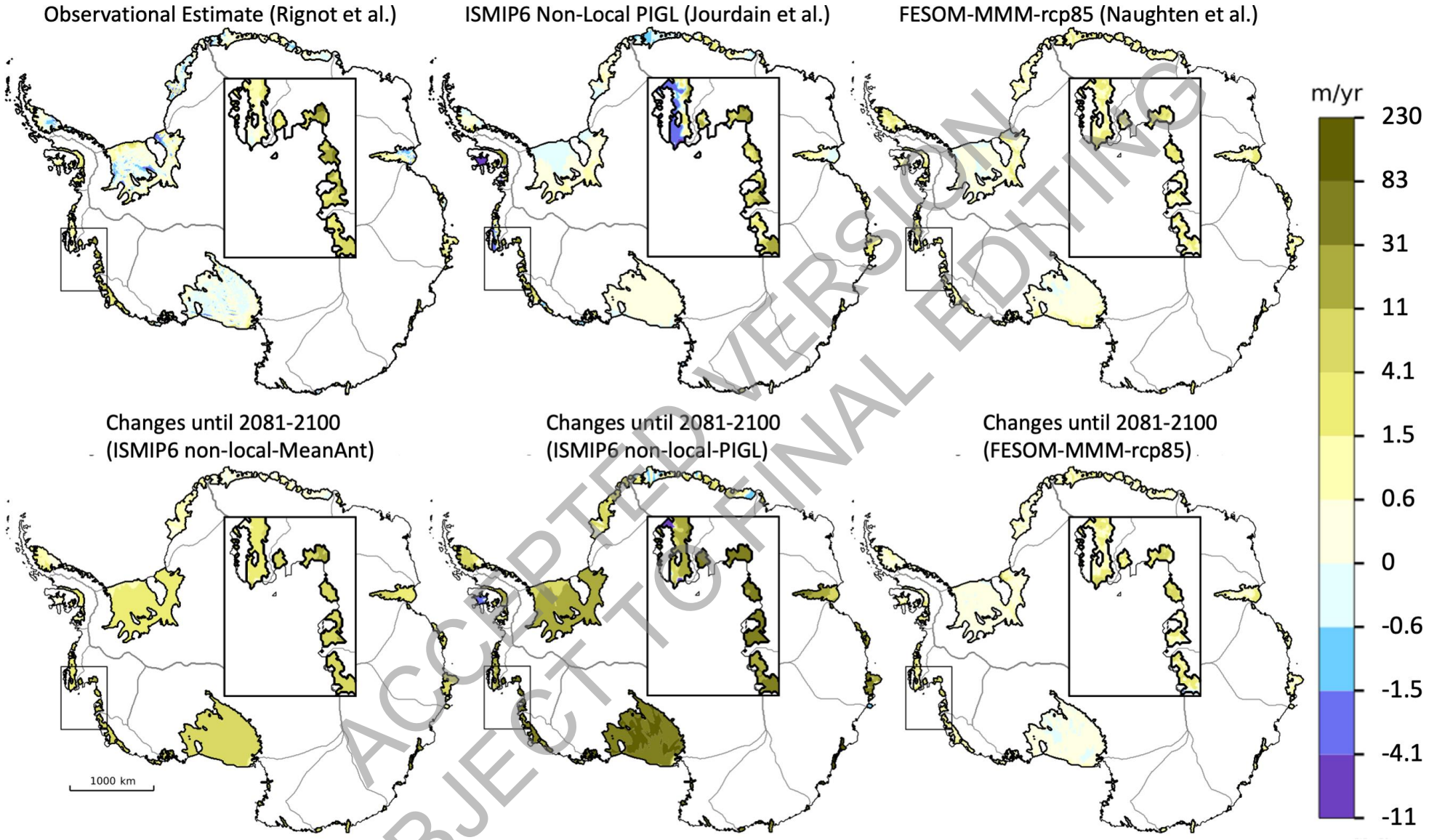


Figure 9.18: (a) A p-box (Section 9.6.3.2) based estimate of the range of values of paleo Antarctic ice sheet mass and sea level equivalents relative to present day and the median over all central estimates (Bamber et al., 2009; Argus and Peltier, 2010; Dolan et al., 2011; Mackintosh et al., 2011; Golledge et al., 2012; Miller et al., 2012; Whitehouse et al., 2012; Golledge et al., 2013; Ivins et al., 2013; Argus et al., 2014; Briggs et al., 2014; Golledge et al., 2014; Maris et al., 2014; De Boer et al., 2015;

ACCEPTED VERSION SUBJECT TO FINAL EDITING

Dutton et al., 2015; Golledge et al., 2015; Pollard et al., 2015; DeConto and Pollard, 2016; Gasson et al., 2016; Goelzer et al., 2016; Yan et al., 2016; de Boer et al., 2017; Golledge et al., 2017; Kopp et al., 2017; Simms et al., 2019) ; and cumulative mass loss (and sea level equivalent) since 2015, with satellite observations shown from 1993 (Bamber et al., 2018a; The IMBIE Team et al., 2018; WCRP Global Sea Level Budget Group, 2018) and observations from 1979 (Rignot et al., 2019), ISMIP6 projected changes by 2100 under RCP8.5/SSP5-8.5 and RCP2.6/SSP1-2.6 scenarios (thin lines from (Seroussi et al., 2020; Edwards et al., 2021; Payne et al., 2021) and 17th to 83rd, 5th to 95th percentile ranges of the ISMIP6 emulation (shaded line, (Edwards et al., 2021)). Right, 17th to 83rd, 5th to 95th percentile ranges for ISMIP6, emulator, and LARMIP-2 including SMB at 2100. Schematic interpretations of individual reconstructions (Anderson et al., 2002; Bentley et al., 2014; De Boer et al., 2015; Goelzer et al., 2016) of the spatial extent of the Antarctic ice sheet are shown for the (b) mid-Pliocene Warm Period, (c) the Last Interglacial and (d) the Last Glacial Maximum (Fretwell et al., 2013): grey shading shows extent of grounded ice. Maps of mean elevation changes (e) 1978-2017 derived from multi-mission satellite altimetry (Schröder et al., 2019) and (f) ISMIP6 (2061-2100) projected changes for an ensemble using the NorESM1-M climate model under the RCP8.5 scenario (Seroussi et al., 2020). Further details on data sources and processing are available in the chapter data table (Table 9.SM.9).

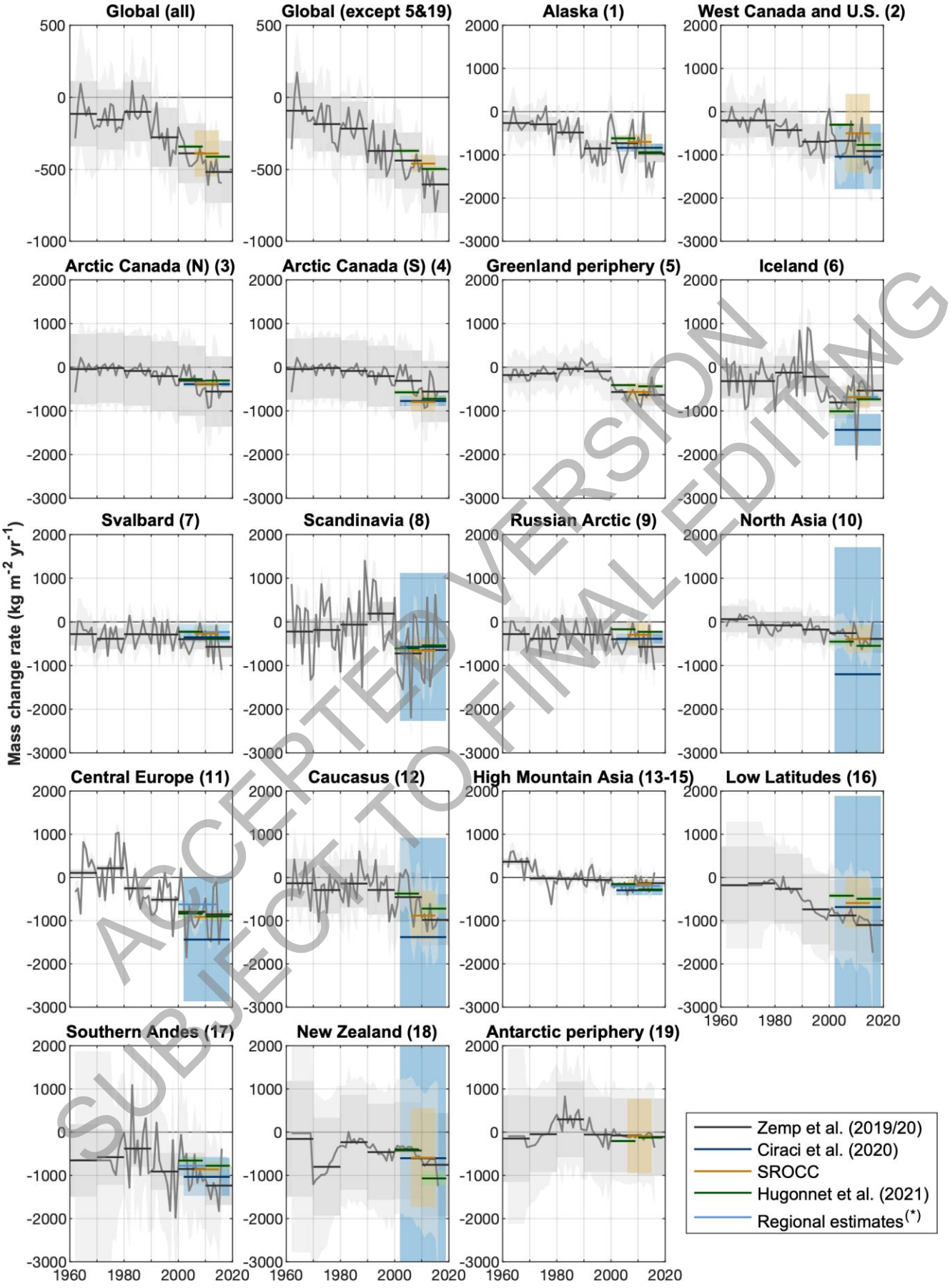
ACCEPTED VERSION
SUBJECT TO FINAL EDITING



ACCEPTED VERSION
SUBJECT TO FINAL EDITING

Figure 9.19: Ice shelf basal melt rates for present-day (upper panels) and changes from present-day to the end of the 21st century under the RCP8.5 scenario (lower panels). Present-day melt rates were estimated through: the input-output method constrained by satellite observations and atmosphere/snow simulations (Rignot et al., 2013) and representative of 2003-2008 (upper left); the non-local-PIGL parameterization constrained by observation-based ocean properties (Jourdain et al., 2020) and representative of 1995-2014 (upper centre); the Finite Element Sea-ice/ice-shelf Ocean Model (FESOM) simulation over 2006-2015, forced by atmospheric conditions from a CMIP5 multi-model mean (MMM) under the RCP8.5 scenario ((Naughten et al., 2018) upper right). Future anomalies are calculated as 2081-2100 minus present-day using the ISMIP6 non-local-MeanAnt and non-local-PIGL parameterizations (Jourdain et al., 2020) lower left and centre respectively) based on projections from the NorESM1-M CMIP5 model, and the FESOM-MMM projection (lower right). Note the symmetric-log colour bar (linear around zero, logarithmic for stronger negative and positive values). Inset highlights the Amundsen Sea Region. Further details on data sources and processing are available in the chapter data table (Table 9.SM.9).

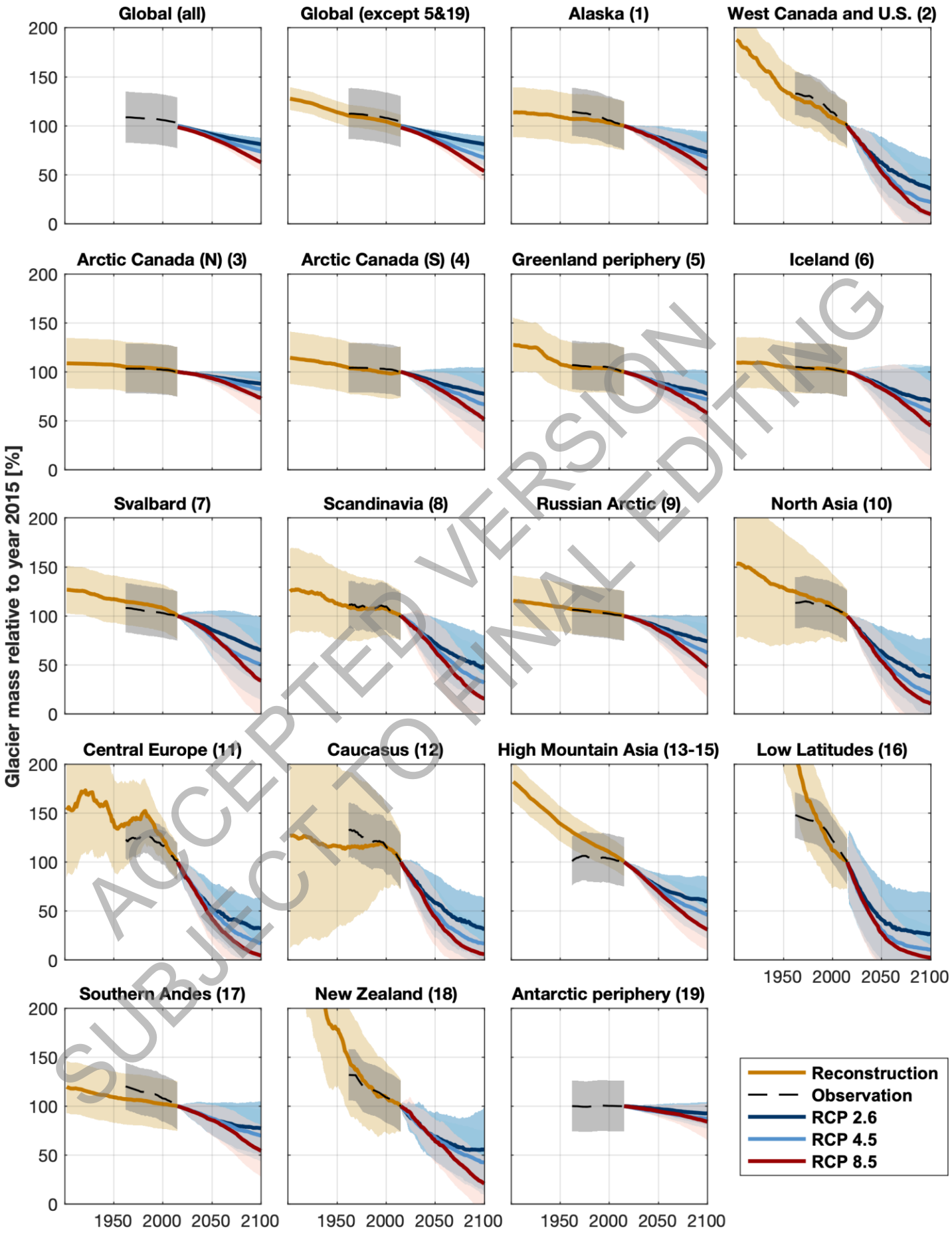
ACCEPTED VERSION
SUBJECT TO FINAL EDITING



ACCEPTED VERSION SUBJECT TO FINAL EDITING

Figure 9.20: Global and regional glacier mass change rate between 1960 and 2019. The time series of annual and decadal mean mass change are based on glaciological and geodetic balances (Zemp et al. (2019) and Zemp et al. (2020)). Superimposed are the 2002-2019 average rates by (Ciracì et al., 2020) based on the Gravity Recovery and Climate Experiment (GRACE), 2006-2015 estimated rates as assessed in SROCC and the new decadal averages (2000-2009 and 2010-2019) by Hugonnet et al. (9998). (*) New regional estimates for the Andes (Dussaillant et al., 2019), High Mountain Asia (Shean et al., 2020), Iceland (Aðalgeirsdóttir et al., 2020), Central Europe (Sommer et al., 2020) and Svalbard (Schuler et al., 2020) are also shown. The uncertainty reported in each study is shown. See Figure 9.2 for the location of each region. Further details on data sources and processing are available in the chapter data table (Table 9.SM.9).

ACCEPTED VERSION
SUBJECT TO FINAL EDITING



ACCEPTED VERSION
SUBJECT TO FINAL EDITING

Figure 9.21: Global and regional glacier mass evolution between 1901 and 2100 relative to glacier mass in 2015. Reconstructed glacier mass change through the 20th century (Marzeion et al., 2015) and observed during 1961-2016 (Zemp et al., 2019). Projected (2015-2100) glacier mass evolution is based on the median of three Representative Concentration Pathways (RCPs) emission scenarios (Marzeion et al., 2020). Uncertainties are in all cases the 90% confidence interval. For a better comparison between regions, the maximum relative mass change was set to 200%, although for three regions, the volume changes between 1901 and 2015 exceeded that value. For the Low Latitude, New Zealand, and High Mountain Asia glaciers, the changes were larger than 1000%, 350%, and 250%, respectively. See Figure 9.2 for the location of each region. Further details on data sources and processing are available in the chapter data table (Table 9.SM.9).

ACCEPTED VERSION
SUBJECT TO FINAL EDITING

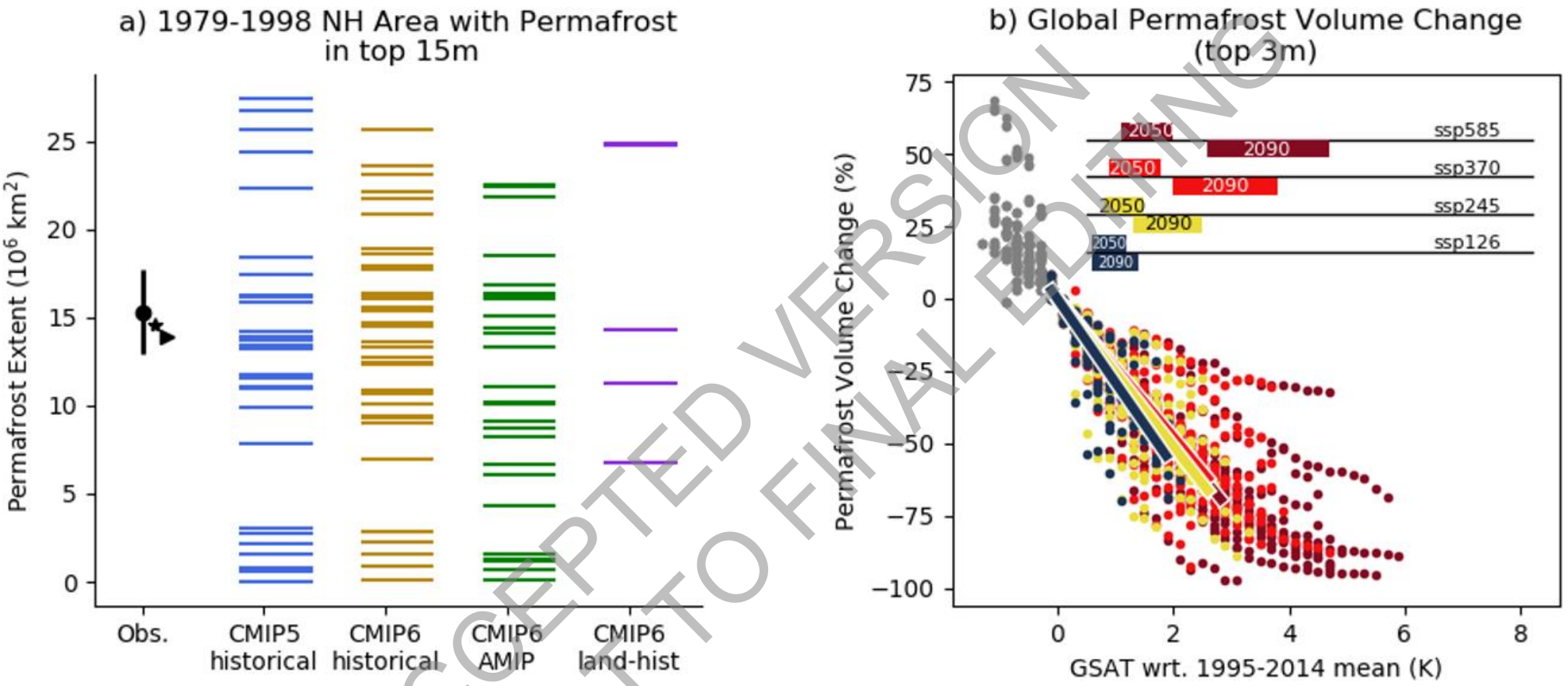


Figure 9.22: Simulated versus observed permafrost extent and permafrost volume change by warming level. a) Diagnosed Northern Hemisphere permafrost extent (area with perennially frozen ground at 15 m depth, or at the deepest model soil level if this is above 15 m) for 1979-1998, for available CMIP5 and CMIP6 models, from the first ensemble member of the historical coupled run, and for CMIP6 AMIP (atmosphere+land surface, prescribed ocean) and land-hist (land only, prescribed atmospheric forcing) runs. Estimates of current permafrost extents based on physical evidence and reanalyses are indicated as black symbols (triangle: Obu et al. (2018); star: Zhang et al. (1999); circle: central value and associated range from Gruber (2012)). b) Simulated global permafrost volume change between the surface and 3 m depth as a function of the simulated GSAT change, from the first ensemble members of a selection of scenarios, for available CMIP6 models. Further details on data sources and processing are available in the chapter data table (Table 9.SM.9).

ACCEPTED VERSION SUBJECT TO FINAL EDITING

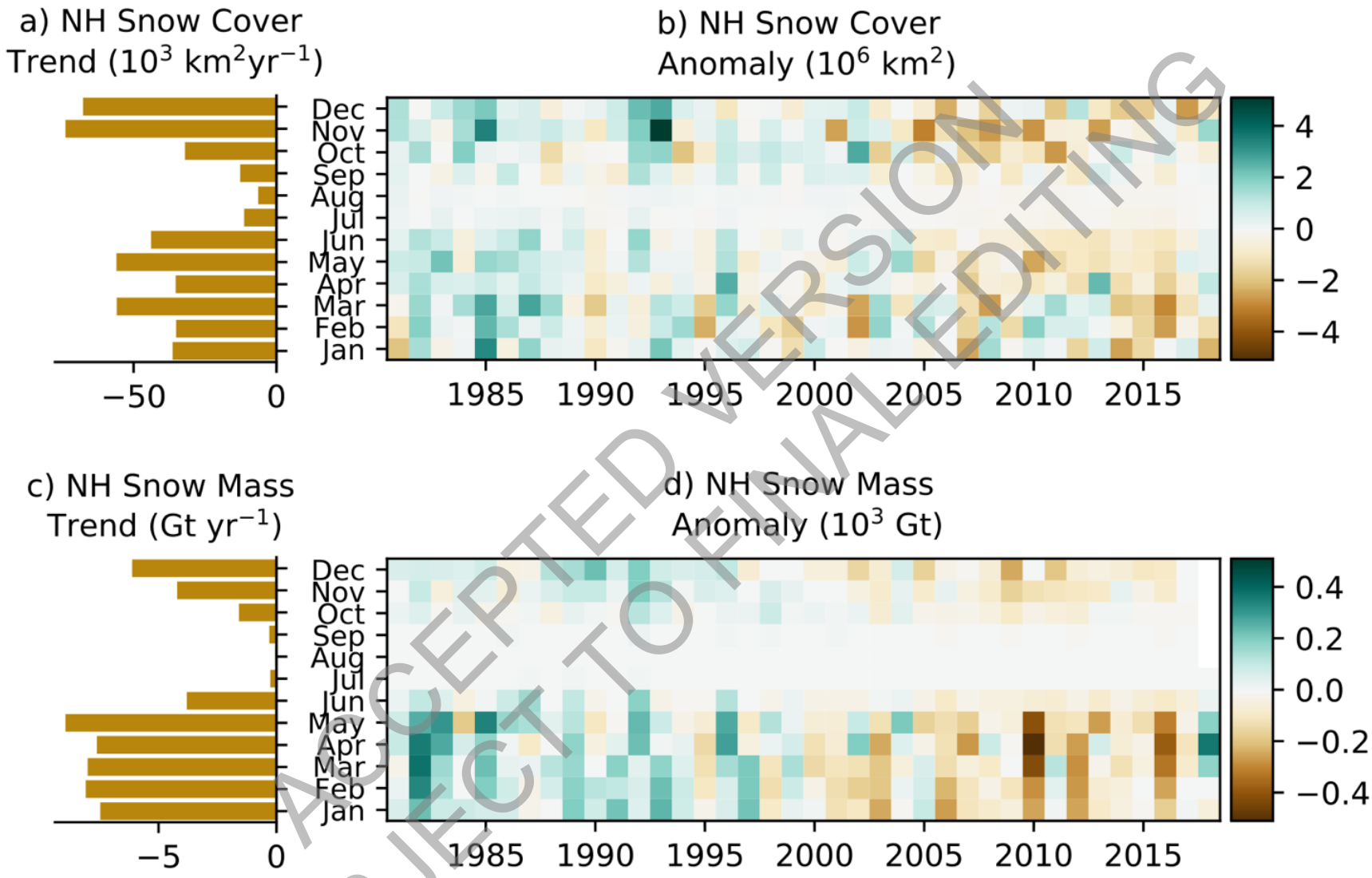


Figure 9.23: Observed monthly Northern Hemisphere (a) snow cover trends and (b) anomalies, and (c) snow mass trends and (d) anomalies. From the observation-based ensemble discussed in the text (Mudryk et al., 2020). Trends and anomalies are calculated over the 1981-2018 period. Further details on data sources and processing are available in the chapter data table (Table 9.SM.9).

ACCEPTED VERSION SUBJECT TO FINAL EDITING

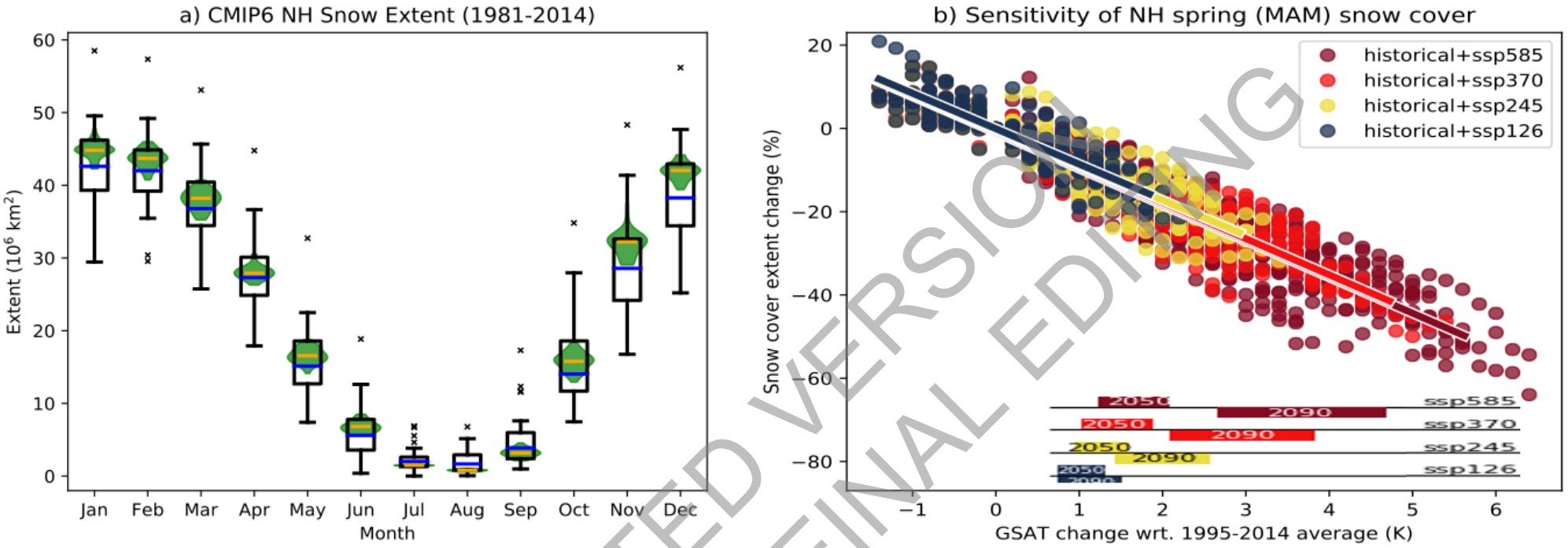
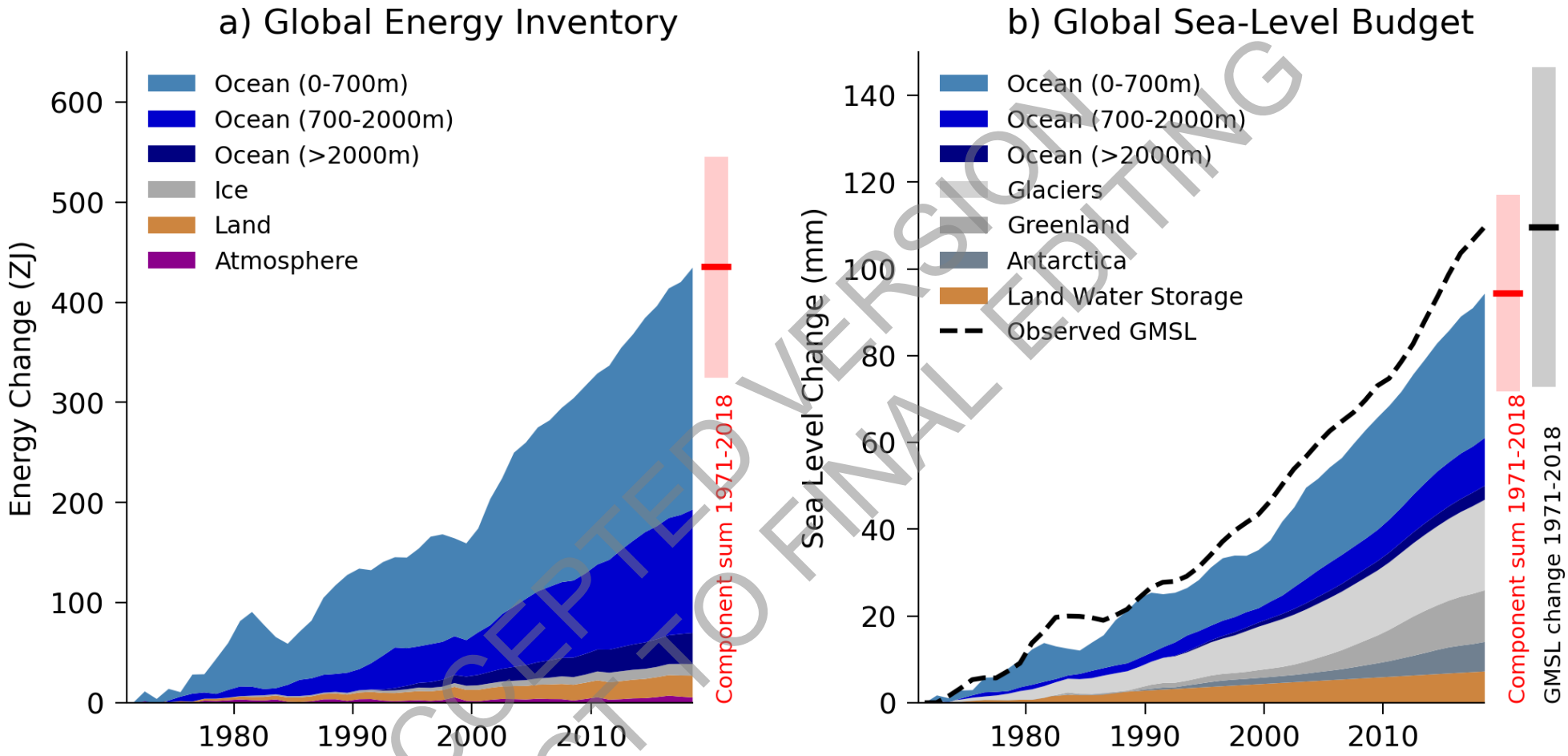


Figure 9.24: Simulated CMIP6 and observed snow cover extent (SCE). a) Simulated CMIP6 and observed (Mudryk et al., 2020) SCE (in millions of km^2) for 1981-2014. Boxes and whiskers with outliers represent monthly mean values for the individual CMIP6 models averaged over 1981-2014, with the red bar indicating the median of the CMIP6 multi-model ensemble for that period. The observed interannual distribution over the period is represented in green, with the yellow bar indicating the median. b) Spring (March to May) Northern Hemisphere snow cover extent against GSAT (relative to the 1995-2014 average) for the CMIP6 Tier 1 scenarios (SSP1-2.6, SSP2-4.5, SSP3-7.0 and SSP5-8.5), with linear regressions. Each data point is the mean for one CMIP6 simulation (first ensemble member for each available model) in the corresponding temperature bin. Further details on data sources and processing are available in the chapter data table (Table 9.SM.9).

ACCEPTED VERSION SUBJECT TO FINAL EDITING

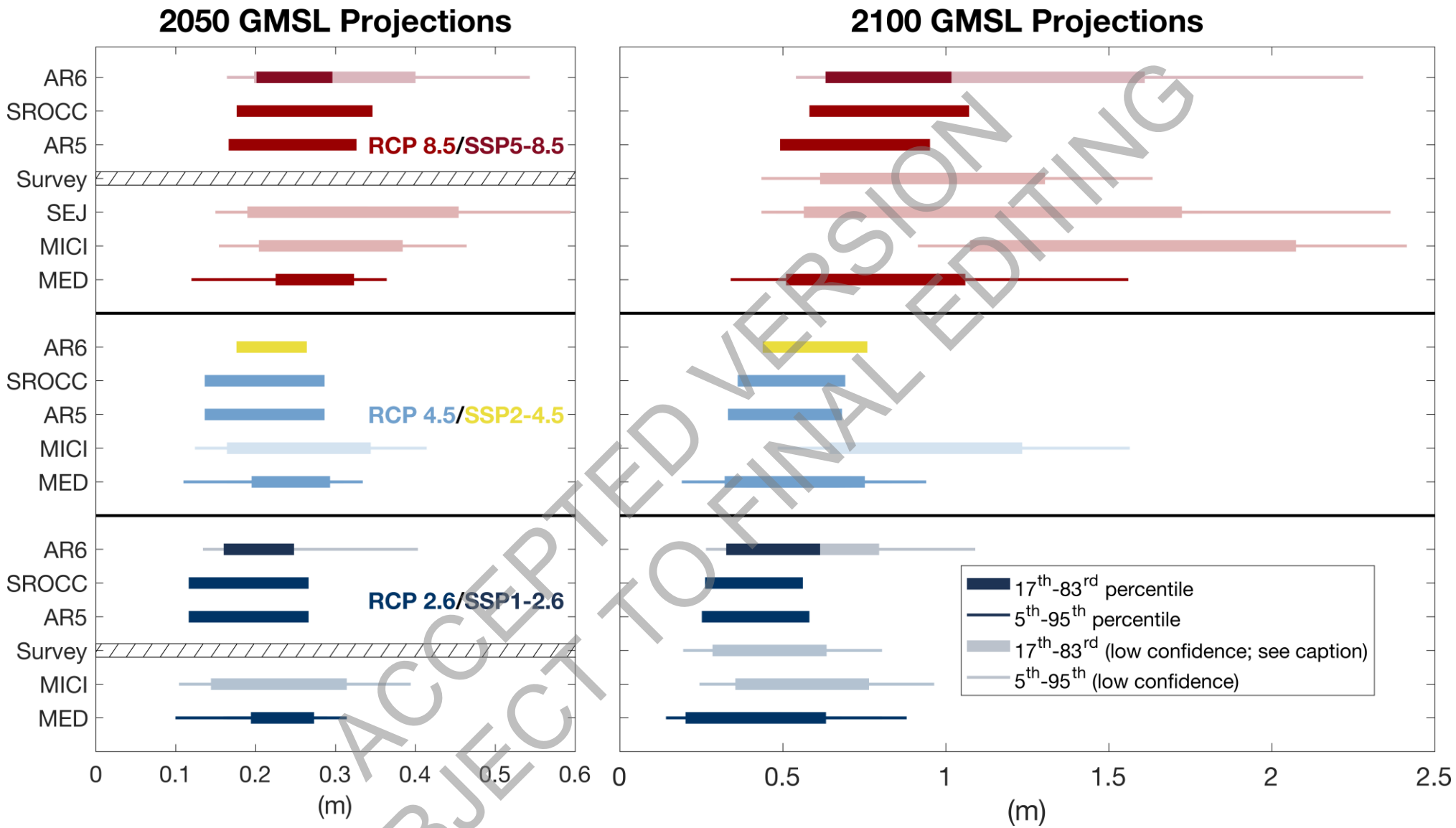


ACCEPTED VERSION SUBJECT TO FINAL EDITING

Cross-Chapter 9.1, Figure 1: Global Energy Inventory and Sea Level Budget.a) Observed changes in the global energy inventory for 1971-2018 (shaded time series) with component contributions as indicated in the figure legend. Earth System Heating for the whole period and associated uncertainty is indicated to the right of the plot (red bar = central estimate; shading = *very likely* range); b) Observed changes in components of global mean sea-level for 1971-2018 (shaded time series) as indicated in the figure legend. Observed global mean sea-level change from tide gauge reconstructions (1971-1993) and satellite altimeter measurements (1993-2018) is shown for comparison (dashed line) as a 3-year running mean to reduce sampling

noise. Closure of the global sea-level budget for the whole period is indicated to the right of the plot (red bar = component sum central estimate; red shading = *very likely* range; black bar = total sea level central estimate; grey sharing = *very likely* range). Full details of the datasets and methods used are available in Annex I. Further details on energy and sea-level components are reported in Table 7.1 and Table 9.5.

ACCEPTED VERSION
SUBJECT TO FINAL EDITING



ACCEPTED VERSION
SUBJECT TO FINAL EDITING

Figure 9.25: Literature global mean sea level (GMSL) projections (m) for 2050 (left) and 2100 (right) since 1995-2014, for RCP 8.5/SSP5-8.5 (top set), RCP 4.5/SSP2-4.5 (middle set), and RCP 2.6/ SSP1-2.6 (bottom set). Projections are standardised to account for minor differences in time periods. Thick bars span from the 17th-83rd

percentile projections, and thin bars span the 5th-95th percentile projections. The different assessments of ice sheet contributions are indicated by 'MED' (ice sheet projections including only processes in whose quantification there is *medium confidence*), 'MICI' (ice sheet projections which incorporate Marine Ice Cliff Instability), and 'SEJ' (structured expert judgement (SEJ) to assess the central range of the ice-sheet projection distributions). 'Survey' indicates the results of a 2020 survey of sea-level experts on GMSL rise from all sources (Horton et al., 2020). Projection categories incorporating processes in which there is *low confidence* ('MICI' and 'SEJ') are lightly shaded. Dispersion among the different projections represents *deep uncertainty*, which arises as a result of *low agreement* regarding appropriate conceptual models describing ice sheet behaviour and *low agreement* regarding probability distributions used to represent key uncertainties. Individual studies are shown in Tables 9.SM.5, 9.SM.6. Further details on data sources and processing are available in the chapter data table (Table 9.SM.9).

ACCEPTED VERSION
SUBJECT TO FINAL EDITING

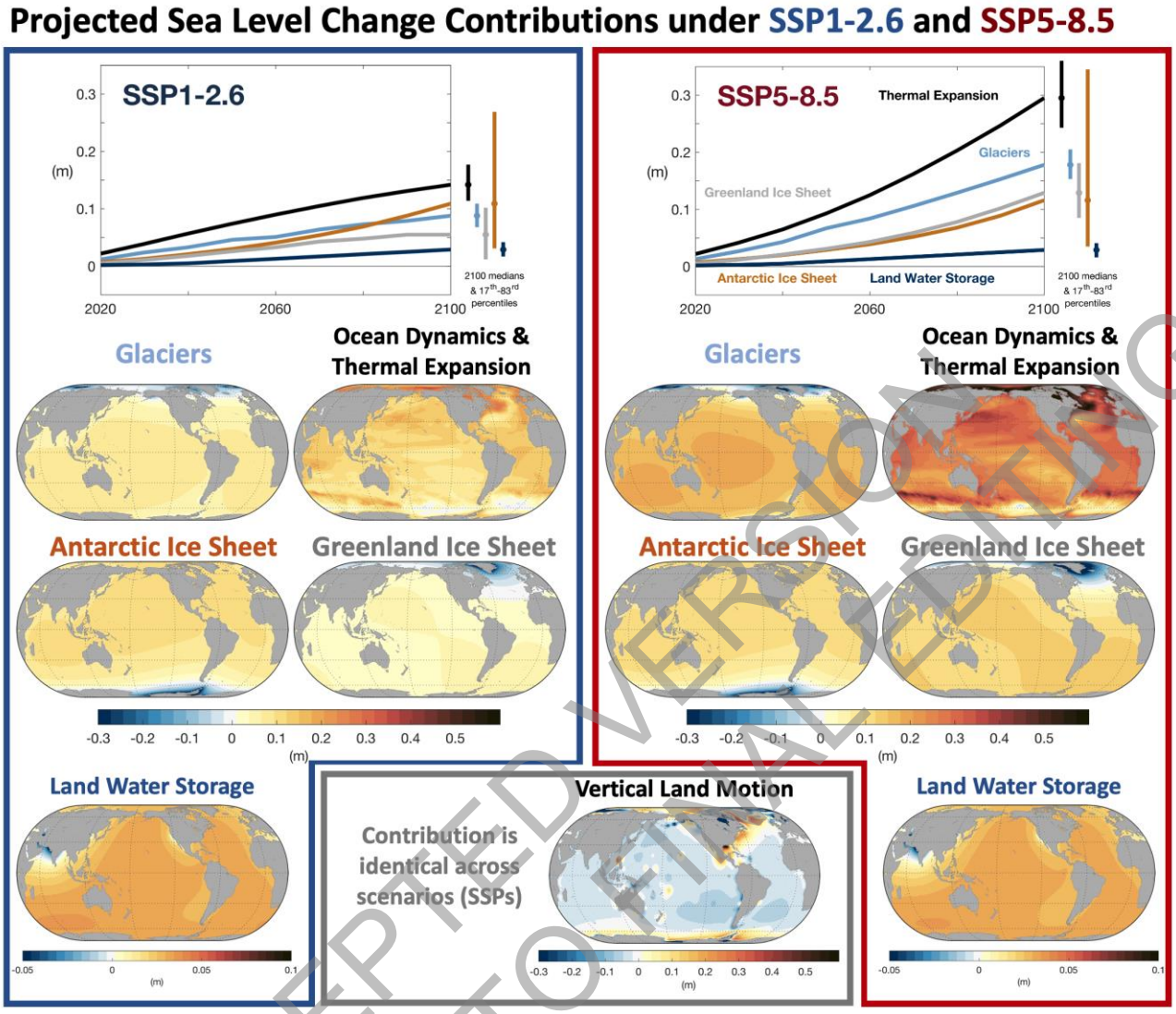


Figure 9.26: Median global mean and regional relative sea-level projections (m) by contribution for the SSP1-2.6 and SSP5-8.5 scenarios. (upper time series) Global mean contributions to sea-level change as a function of time, relative to 1995-2014. (lower maps) Regional projections of the sea-level contributions in 2100 relative to 1995-2014 for SSP5-8.5 and SSP1-2.6. Vertical land motion is common to both SSPs. Further details on data sources and processing are available in the chapter data table (Table 9.SM.9).

ACCEPTED VERSION SUBJECT TO FINAL EDITING

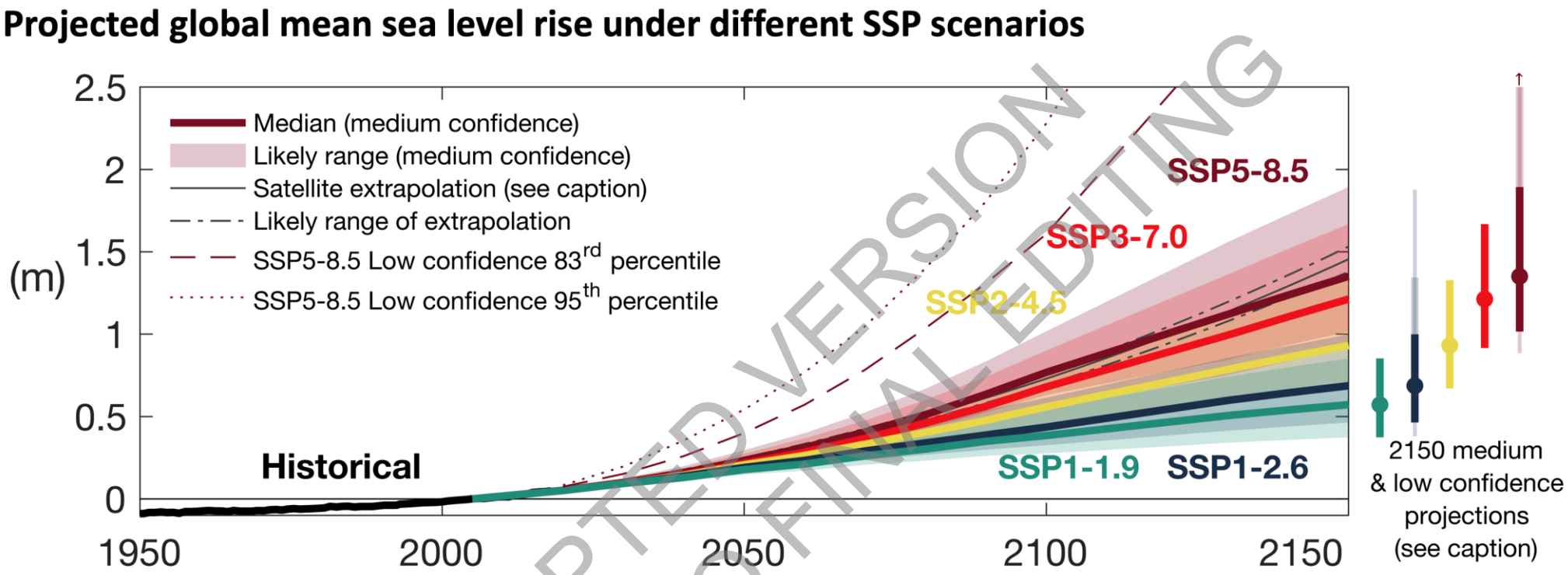


Figure 9.27: Projected global mean sea level rise under different SSP scenarios. *Likely* global mean sea-level change for SSP scenarios resulting from processes in whose projection there is *medium confidence*. Projections and *likely* ranges at 2150 are shown on right. Lightly shaded ranges and thinner lightly shaded ranges on the right show the 17th-83rd and 5th-95th percentile ranges for projections including *low confidence* processes for SSP1-2.6 and SSP5-8.5 only, derived from a p-box including Structured Expert Judgement and Marine Ice Cliff Instability projections. Black lines show historical GMSL change, and thick solid and dash-dotted black lines show the mean and *likely* range extrapolating the 1993-2018 satellite altimeter trend and acceleration. Further details on data sources and processing are available in the chapter data table (Table 9.SM.9).

ACCEPTED VERSION SUBJECT TO FINAL EDITING

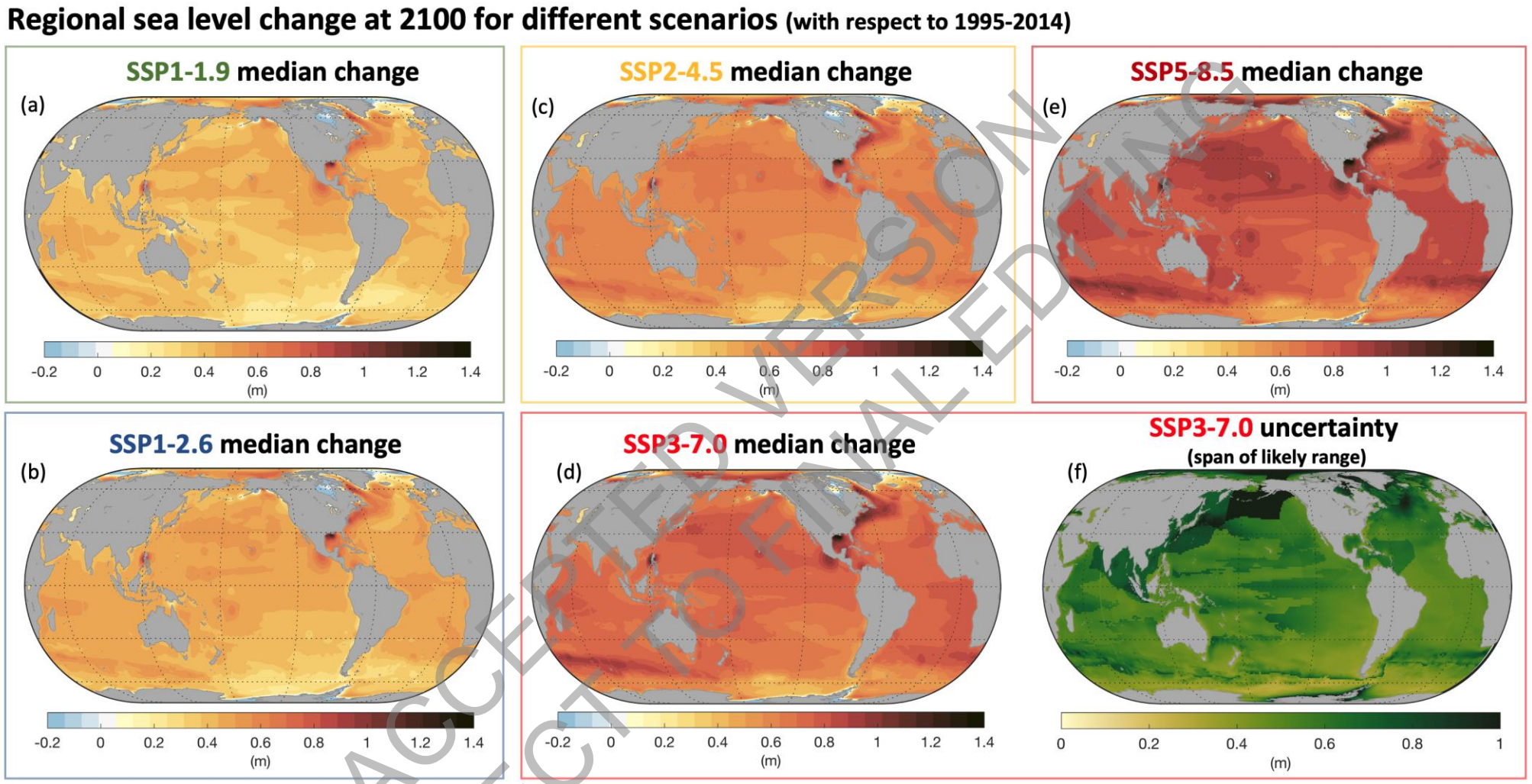


Figure 9.28: Regional sea level change at 2100 for different scenarios (with respect to 1995-2014). Median regional relative sea-level change from 1995 to 2014 up to 2100 for (a) SSP1-1.9, (b) SSP1-2.6, (c) SSP2-4.5, (d) SSP3-7.0, (e) SSP5-8.5, and (f) width of the likely range for SSP3-7.0. The high uncertainty in projections around Alaska and the Aleutian Islands arises from the tectonic contribution to vertical land motion, which varies greatly over short distances in this region. Further details on data sources and processing are available in the chapter data table (Table 9.SM.9).

ACCEPTED VERSION SUBJECT TO FINAL EDITING

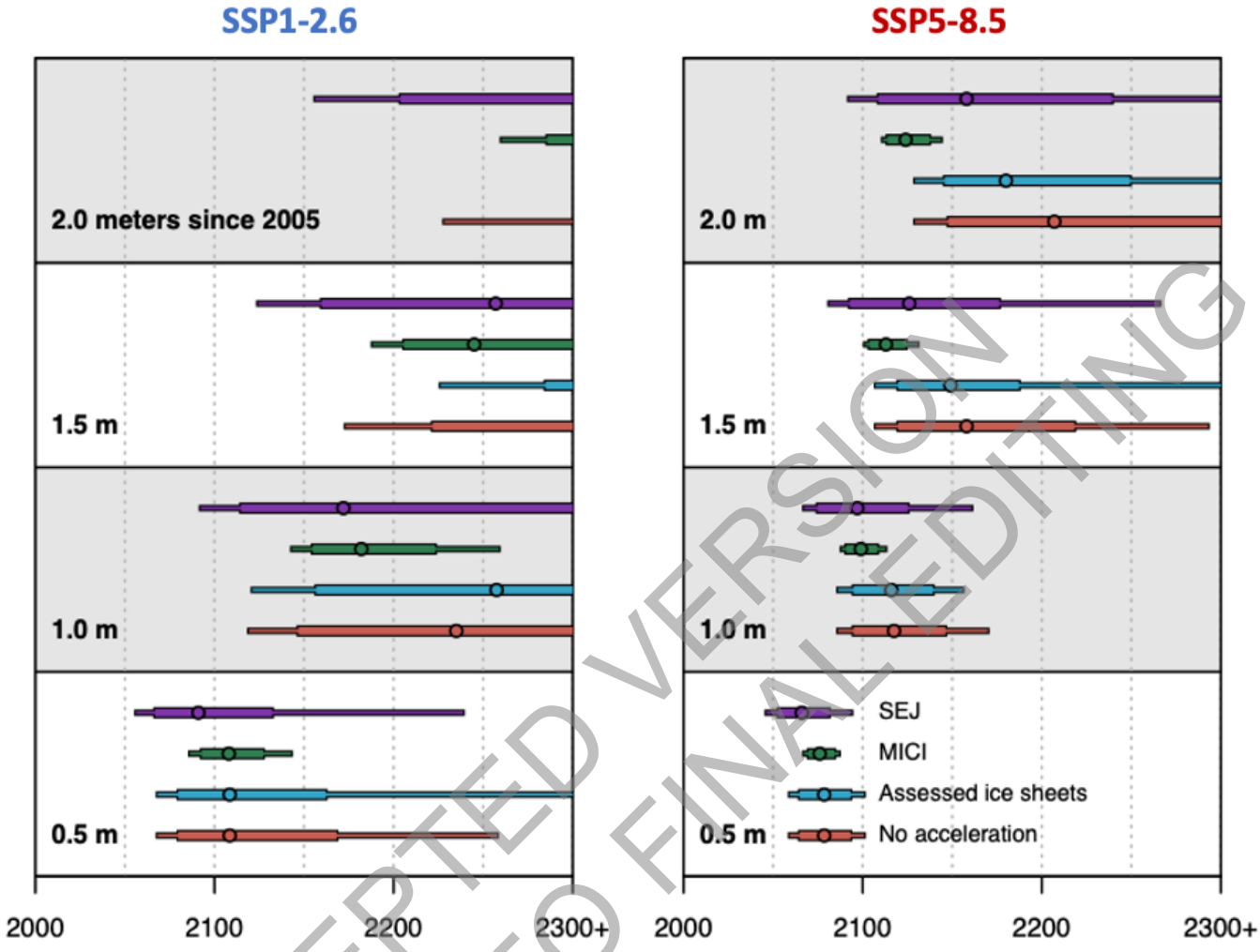


Figure 9.29: Timing of when GMSL thresholds of 0.5, 1.0, 1.5 and 2.0 m are exceeded, based upon four different ice-sheet projection methods informing post-2100 projections. Methods are labelled based on their treatment of ice sheets. "No acceleration" assumes constant rates of mass change after 2100. "Assessed ice sheet" models post-2100 ice sheet losses using a parametric fit (Supplementary Material 9.SM.4) extending to 2300 based on a multimodel assessment of contributions under RCP2.6 and RCP8.5 at 2300. Structured Expert Judgement (SEJ) employs ice-sheet projections from Bamber et al. (2019) Marine Ice Cliff Instability (MICI) combines the parametric fit (Supplementary Material 9.SM3.4) for Greenland with Antarctic projections based on DeConto et al. (2021). Circles/thick bars/thin bars represent the 50th, 17th-83rd, and 5th-95th percentiles of the exceedance timing for the indicated projection method. Further details on data sources and processing are available in the chapter data table (Table 9.SM.9).

ACCEPTED VERSION SUBJECT TO FINAL EDITING

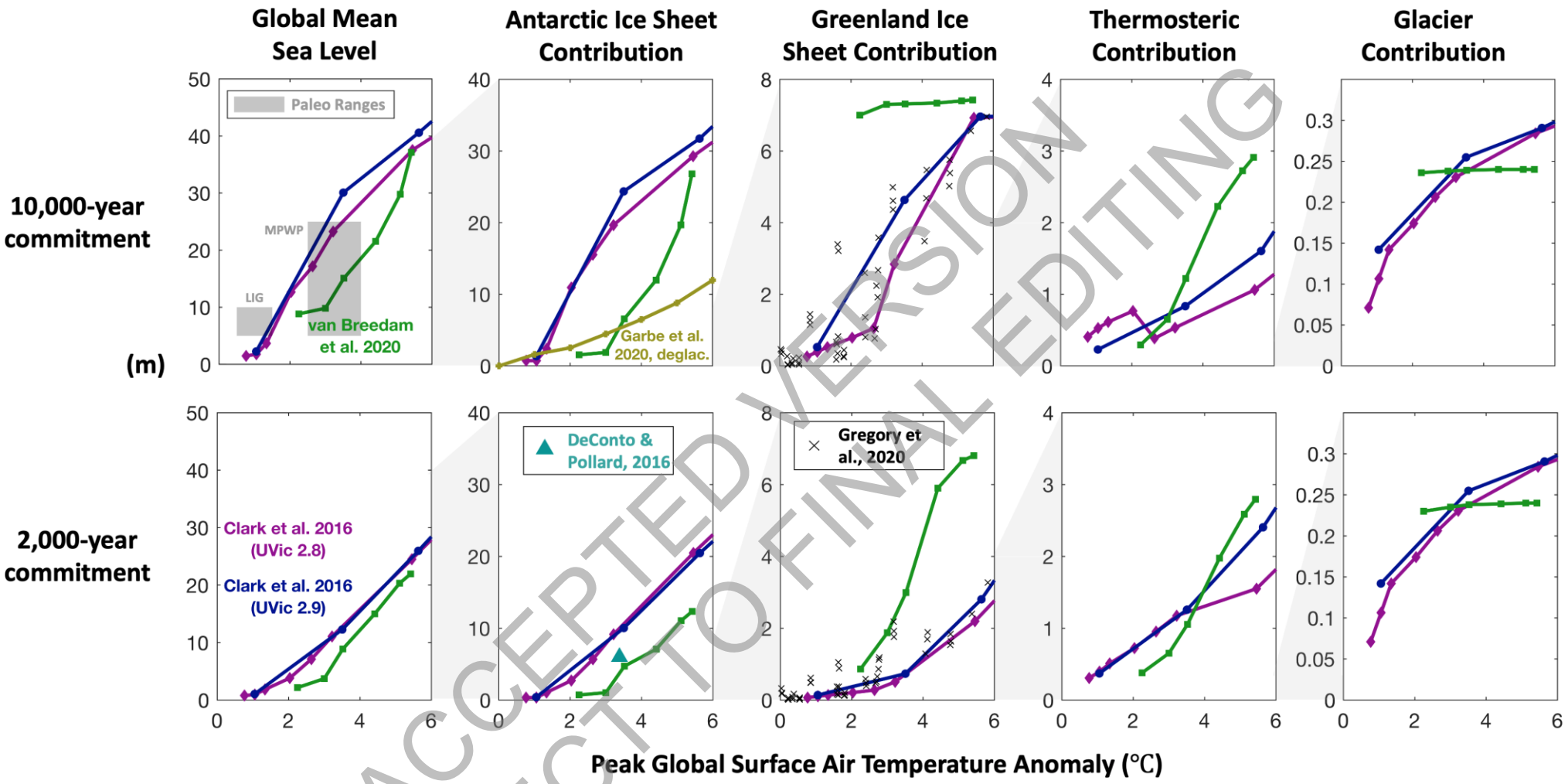


Figure 9.30: Global mean sea-level commitment as a function of peak global surface air temperature. From models (Clark et al., 2016; DeConto and Pollard, 2016; Garbe et al., 2020; Van Breedam et al., 2020) and paleo data on 2000-year (lower row) and 10,000 year (upper row) timescales. Columns indicate different contributors to GMSL rise (from left to right: total GMSL change, Antarctic Ice Sheet, Greenland Ice Sheet, global mean thermosteric sea-level rise, and glaciers). Further details on data sources and processing are available in the chapter data table (Table 9.SM.9).

ACCEPTED VERSION SUBJECT TO FINAL EDITING

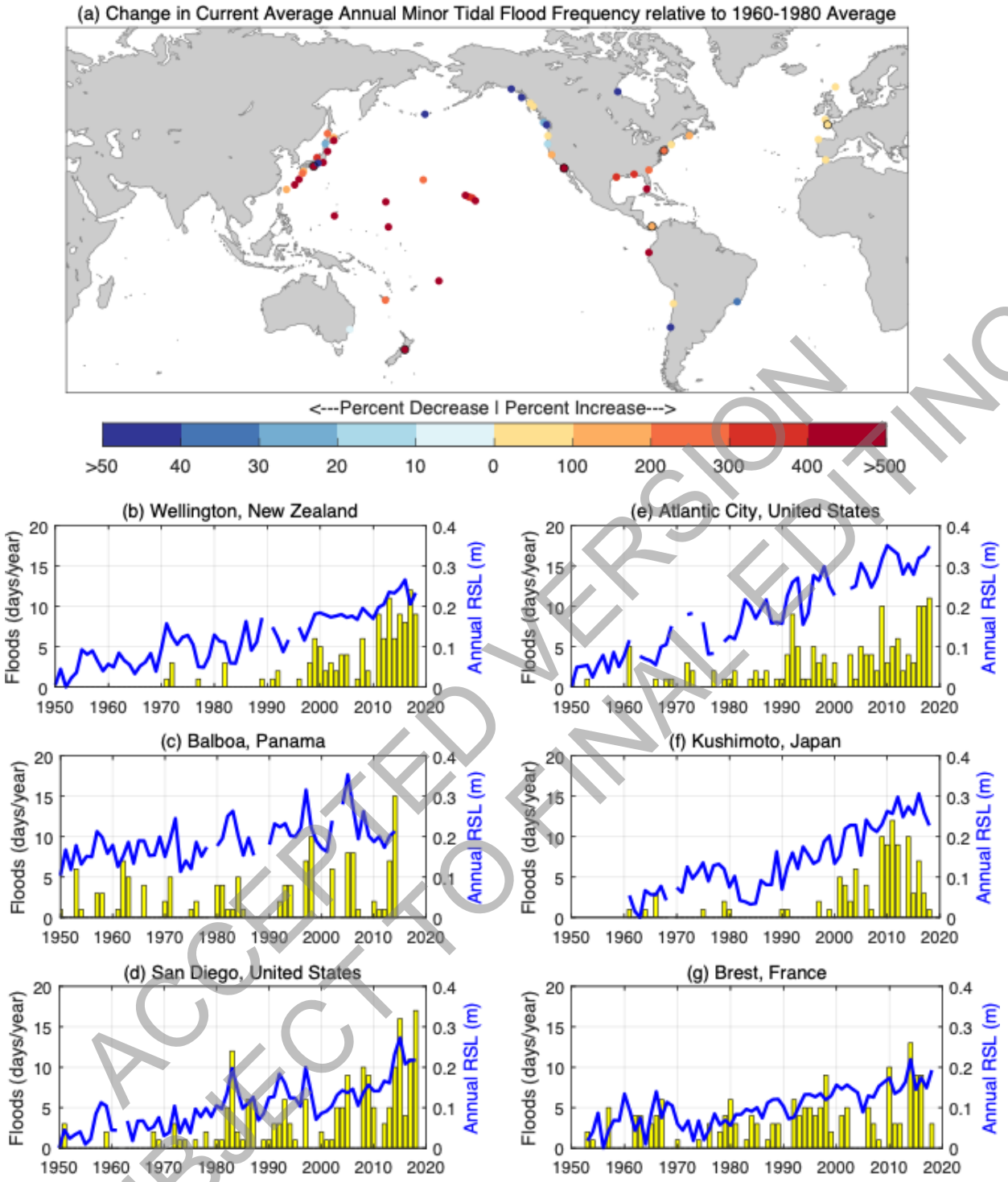


Figure 9.31: Historical occurrences of minor extreme still water levels. Defined as the 99th percentile of daily observed water levels over 1995-2014. (a) Percent change in occurrences over 1995-2014 relative to those over 1960-1980. (b-g) Annual mean sea level (blue) and annual occurrences of extreme still water levels over the 1995-2014 99th percentile daily maximum (yellow) at six selected tide gauge locations. Further details on data sources and processing are available in the chapter data table (Table 9.SM.9).

ACCEPTED VERSION SUBJECT TO FINAL EDITING

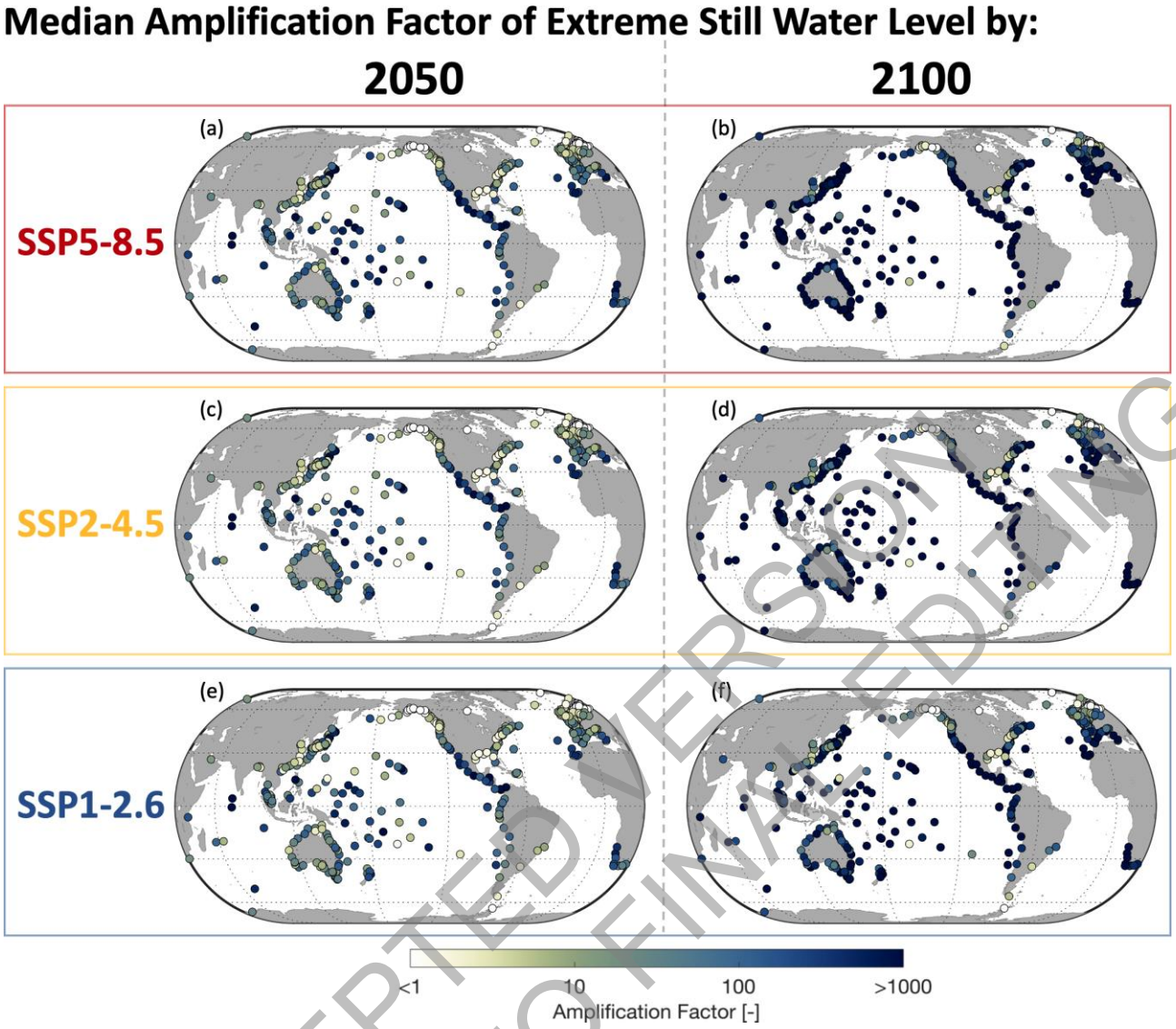
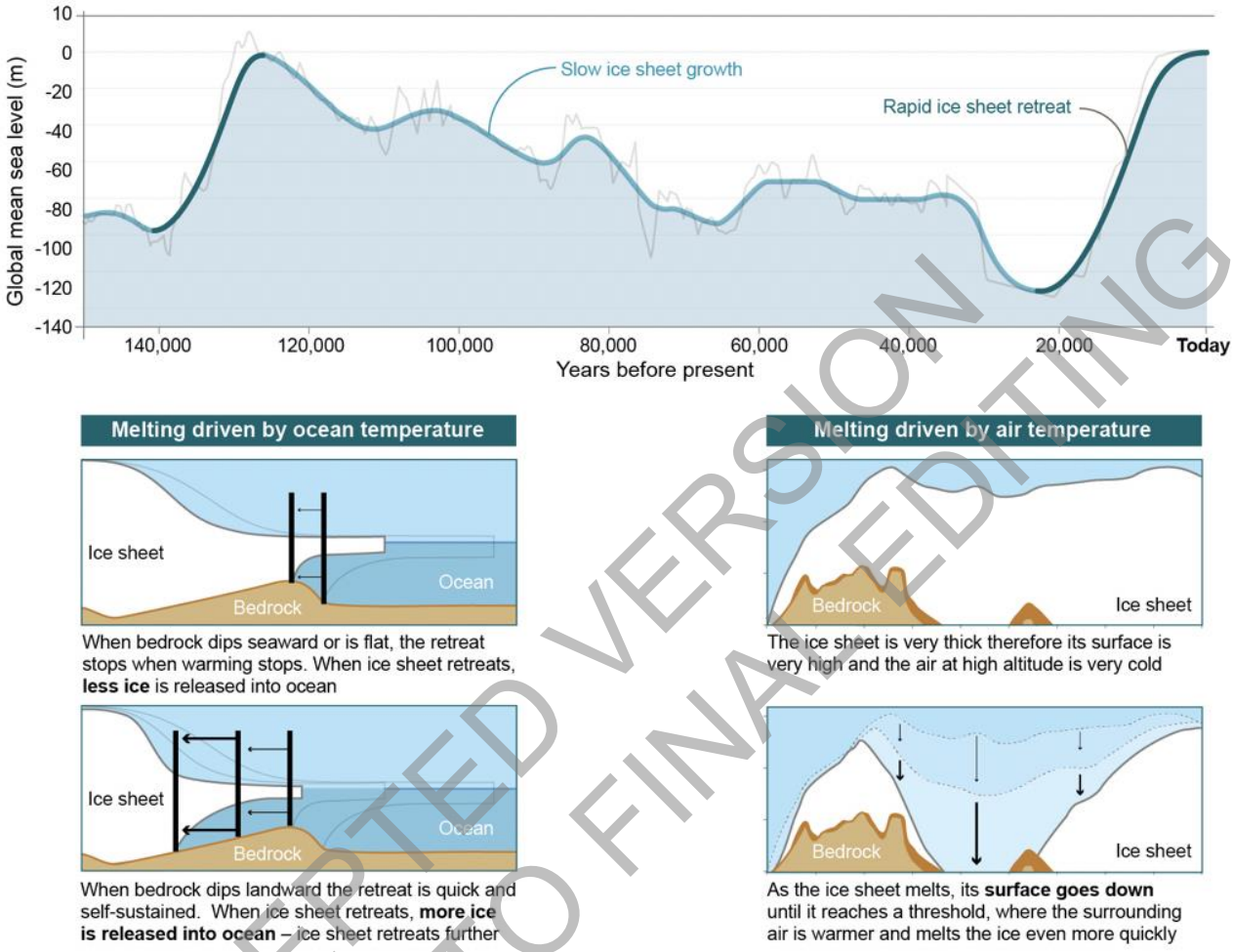


Figure 9.32: Projected median frequency amplification factors for the 1% average annual probability extreme still water level in 2050 (a, c, e) and 2100 (b, d, f). Based on a peak-over-threshold (99.7%) method applied to the historical extreme still water levels of GESLA2 following SROCC and additionally fitting a Gumbel distribution between MHHW and the threshold following (Buchanan et al., 2016), using the regional sea-level projections of this chapter (Section 9.6.3.3) for (a, b) SSP5-8.5, (c, d) SSP2-4.5 and (e, f) SSP1-2.6. Further details on data sources and processing are available in the chapter data table (Table 9.SM.9).

ACCEPTED VERSION SUBJECT TO FINAL EDITING

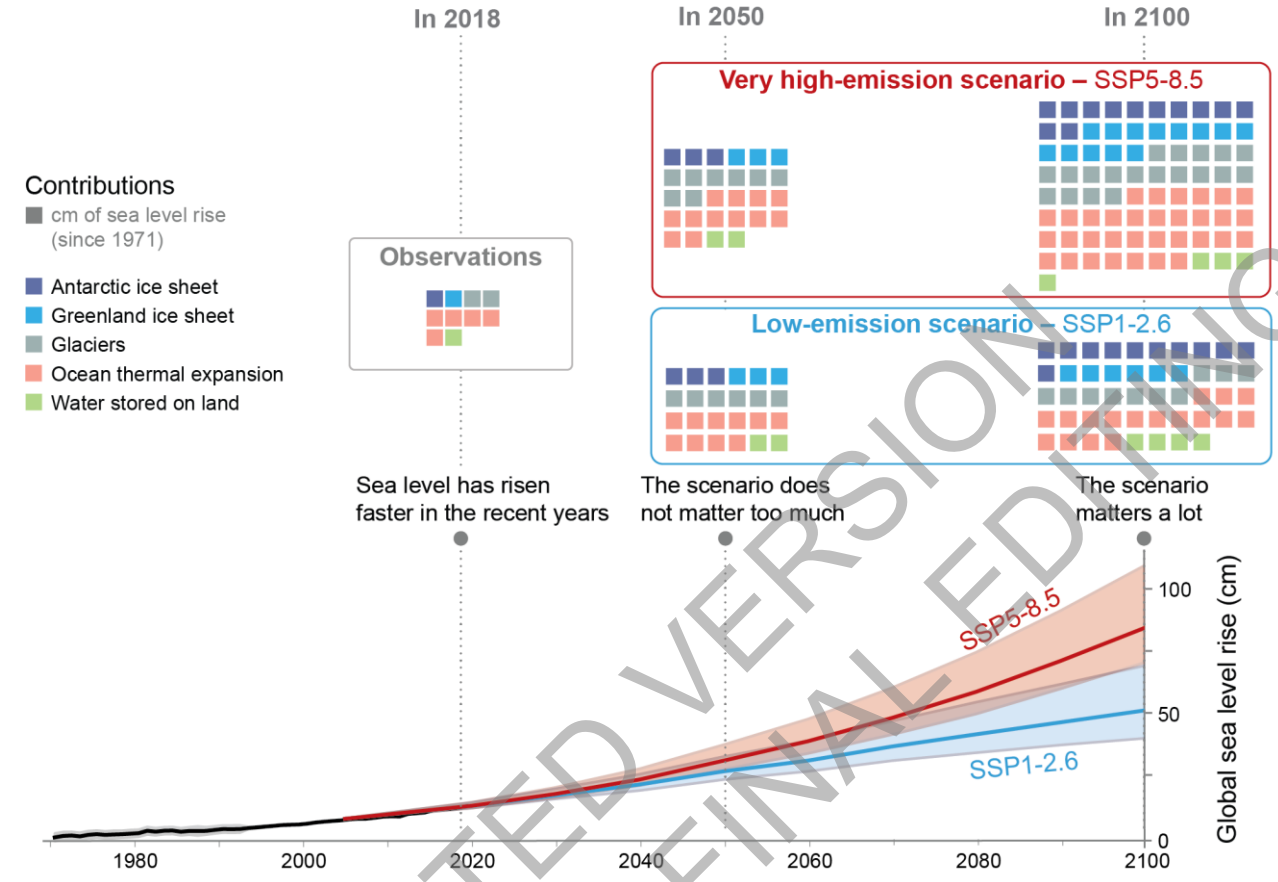
FAQ 9.1: **Can melting of the ice sheets be reversed?**

Once ice sheets are **destabilised**, it takes them tens of thousands of years to re-grow.
These changes strongly affect **sea level**.



FAQ 9.1, Figure 1: Ice sheets growth and decay (Top) Changes in ice-sheet volume modulate sea level variations. The grey line depicts data from a range of physical environmental sea-level recorders such as coral reefs (see Table 9.SM.5) while the blue line is a smoothed version of it. (Bottom, left) Example of destabilisation mechanism in Antarctica. (Bottom, right) Example of destabilisation mechanism in Greenland.

ACCEPTED VERSION SUBJECT TO FINAL EDITING

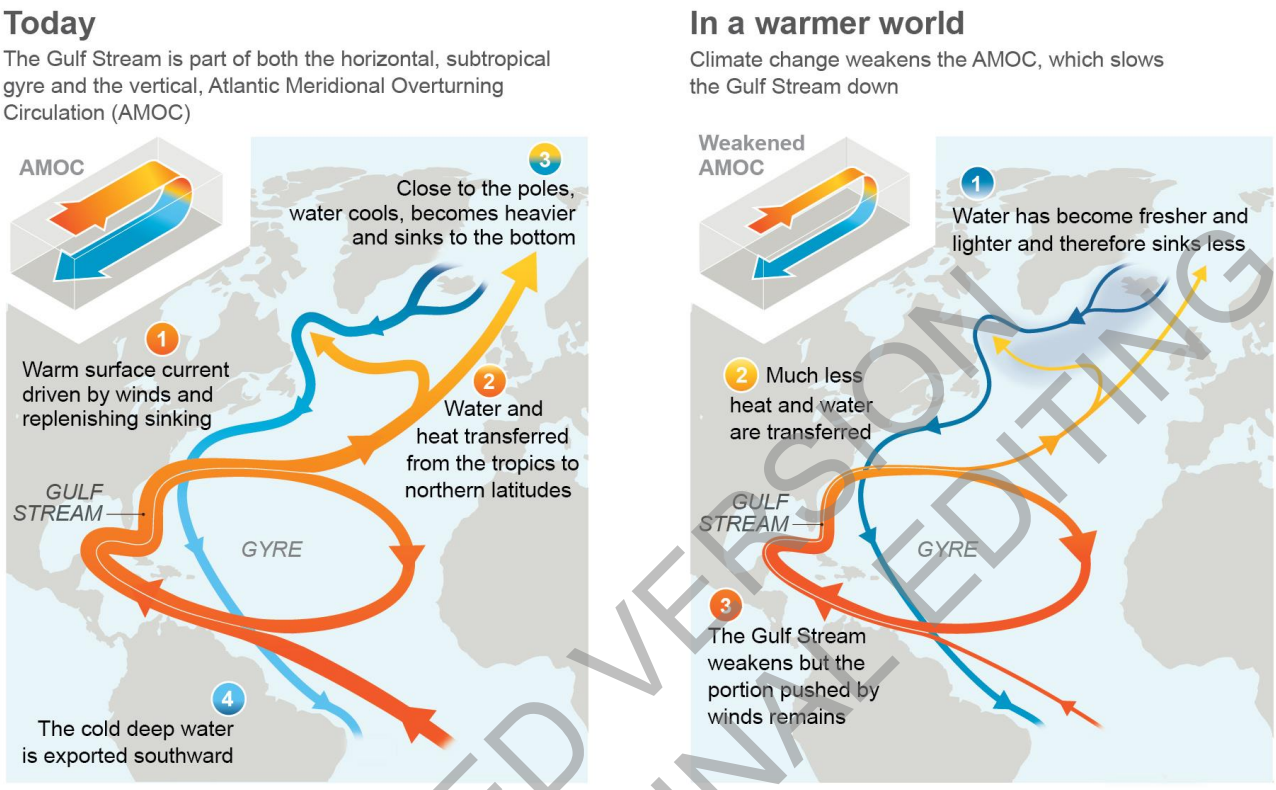


FAQ 9.2, Figure 1: Observed and projected global mean sea level rise and the contributions from its major constituents.

ACCEPTED VERSION SUBJECT TO FINAL EDITING

FAQ 9.3: **Will the Gulf Stream shut down?**

The Gulf Stream, a warm current, is expected to weaken but not cease. This slowdown will affect regional weather and sea level.



FAQ 9.3, Figure 1: **Horizontal (gyre) and vertical (Atlantic Meridional Overturning Circulation - AMOC) circulations in the Atlantic today (left) and in a warmer world (right).** The Gulf Stream is a warm current composed of both circulations.

ACCEPTED VERSION SUBJECT TO FINAL EDITING

Chapter 9: Ocean, cryosphere, and sea level change – Supplementary Material

Coordinating Lead Authors:
Baylor Fox-Kemper (United States of America), Helene T. Hewitt (United Kingdom), Cunde Xiao (China)

Lead Authors:
Guðfinna Aðalgeirsdóttir (Iceland), Sybren S. Drijfhout (The Netherlands), Tamsin L. Edwards (United Kingdom), Nicholas R. Golledge (New Zealand/United Kingdom), Mark Hemer (Australia), Robert E. Kopp (United States of America), Gerhard Krinner (France/Germany, France), Alan Mix (United States of America), Dirk Notz (Germany), Sophie Nowicki (United States of America/France, United States of America), Intan Suci Nurhati (Indonesia), Lucas Ruiz (Argentina), Jean-Baptiste Sallée (France), Aimee B. A. Slangen (The Netherlands), Yongqiang Yu (China)

Contributing Authors:
Cecile Agosta (France), Kyle Armour (United States of America), Mathias Aschwanden (Switzerland), Jonathan L. Bamber (United Kingdom), Sophie Berger (France/Belgium), Fábio Boeira Dias (Finland/Brazil), Jason E. Box (Denmark/USA), Eleanor J. Burke (United Kingdom), Kevin D. Burke (United States of America), Xavier Capet (France), John A. Church (Australia), Lee de Mora (United Kingdom), Chris Derksen (Canada), Catia M. Domingues (Australia, United Kingdom/Brazil), Jakob Dörr (Norway/Germany), Paul J. Durack (United States of America/Australia), Thomas L. Frölicher (Switzerland), Thian Y. Gan (Canada/Malaysia), Gregory G. Garner (United States of America), Sebastian Gerland (Norway/Germany), Heiko Goelzer (Norway/Germany), Natalya Gomez (Canada), Irina V. Gorodetskaya (Portugal/Belgium,Russian Federation), Jonathan M. Gregory (United Kingdom), Robert Hallberg (United States of America), F. Alexander Haumann (United States of America/Germany), Tim H. J. Hermans (The Netherlands), Emma M. Hill (Singapore/ United States of America, United Kingdom), Regine Hock (United States of America, Norway/Germany), Stefan Hofer (Norway/Austria), Romain Hugonnet (France,Switzerland/France), Philippe Huybrechts (Belgium), Akm Saiful Islam (Bangladesh), Laura C. Jackson (United Kingdom), Nicolas C. Jourdain (France), Andreas Kääb (Norway/Germany), Nicole S. Khan (China/USA), Shfaqat Abbas Khan (Denmark), Matthew Kirwan (United States of America), James Kossin (United States of America), Anders Levermann (Germany), Sophie Lewis (Australia), Shiyin Liu (China), Daniel Lowry (New Zealand/United States of America), Marta Marcos (Spain), Ben Marzeion (Germany), Matthew Menary (France/United Kingdom), Sebastian H. Mernild (Norway, Denmark/Norway), Philip Orton (United States of America), Matthew D. Palmer (United Kingdom), Frank Pattyn (Belgium), Brodie Pearson (United States of America/United Kingdom), Cécile Pellet (Switzerland), Chris Perry (United Kingdom), Mark D. Pickering (United Kingdom), Johannes Quaas (Germany), Roshanka Ranasinghe (The Netherlands/Sri Lanka,Australia), Roelof Rietbroek (The Netherlands), Malcom J. Roberts (United Kingdom), Alessio Rovere (Germany/Italy), Mathew Koll Roxy (India), Maria Santolaria Otin (Spain,France/Spain), Abhishek Savita (Australia/India), Alex Sen Gupta (Australia/ United Kingdom, Australia), Helene Seroussi (United States of America/France), Sharon L. Smith (Canada), Olga N. Solomina (Russian Federation), Esther Stouthamer (The Netherlands), Fiametta Straneo (United States of America/Italy, United States of America), William V. Sweet (United States of America), Thomas Wahl (United States of America/Germany), Lisan Yu (United States of America), Jiacan Yuan (United States of America/China), Jan David Zika (Australia)

Review Editors:
Unnikrishnan Alakkat (India), Benjamin P. Horton (Singapore/United Kingdom), Simon Marsland (Australia)

ACCEPTED VERSION SUBJECT TO FINAL EDITING

Chapter Scientists:
Gregory G. Garner (United States of America), Tim H. J. Hermans (The Netherlands), Lijuan Hua (China), Tamzin Palmer (United Kingdom), Brodie Pearson (United States of America/ United Kingdom)

This Supplementary Material should be cited as:
Fox-Kemper, B., H. T. Hewitt, C. Xiao, G. Aðalgeirsdóttir, S. S. Drijfhout, T. L. Edwards, N. R. Golledge, M. Hemer, R. E. Kopp, G. Krinner, A. Mix, D. Notz, S. Nowicki, I. S. Nurhati, L. Ruiz, J-B. Sallée, A. B. A. Slangen, Y. Yu, 2021, Ocean, Cryosphere and Sea Level Change Supplementary Material. In: *Climate Change 2021: The Physical Science Basis. Contribution of Working Group I to the Sixth Assessment Report of the Intergovernmental Panel on Climate Change* [Masson-Delmotte, V., P. Zhai, A. Pirani, S. L. Connors, C. Péan, S. Berger, N. Caud, Y. Chen, L. Goldfarb, M. I. Gomis, M. Huang, K. Leitzell, E. Lonnoy, J.B.R. Matthews, T. K. Maycock, T. Waterfield, O. Yelekçi, R. Yu and B. Zhou (eds.)]. Available from https://ipcc.ch/static/ar6/wg1.

Date: August 2021

This document is subject to copy-editing, corrigenda and trickle backs.

ACCEPTED VERSION
SUBJECT TO FINAL EDITING

Table of Content

9.SM.1 Additional ocean information *4*

9.SM.1.1 Details for Figure 9.10 ..... **4**

9.SM.2 Additional ice sheet information *4*

9.SM.3 Additional glacier information *4*

9.SM.3.1 Details for Figure 9.21 ..... **4**

9.SM.3.2 Details for Figure 9.22 ..... **4**

9.SM.4 Additional sea level information *6*

9.SM.4.1 Framework for Assessing Changes To Sea-level (FACTS) **6**

9.SM.4.2 Obtaining Global Mean Thermosteric Sea-Level Rise and Ocean Dynamic Sea-Level Change from CMIP6 ..... **7**

9.SM.4.3 Global Mean Thermosteric Sea-Level and Ocean Dynamic Sea-Level Projections based on the Two-Layer Emulator **7**

9.SM.4.4 Parametric fit to ISMIP6 Greenland Ice Sheet projections **8**

9.SM.4.5 Parametric fit to GlacierMIP2 projections **9**

9.SM.4.6 Background rates of relative sea-level change **10**

9.SM.4.7 Warming Level Scenarios **10**

9.SM.4.8 Analysis of future changes in extreme sea level return frequency **10**

9.SM.5 Data Table *14*

ACCEPTED VERSION
SUBJECT TO FINAL EDITING

9.SM.1 Additional ocean information

9.SM.1.1 Details for Figure 9.10

Lower right panel: In all experiments an additional surface freshwater flux (hosing) is applied over the subpolar North Atlantic (regions vary between studies) for a limited time. The total amount of fresh water added is then this flux multiplied by the number of years applied (in Gt). While hosing is applied the AMOC weakens. In some models the AMOC recovers quickly, in other the AMOC hasn't recovered after 200 years, and in some the AMOC is starting to recover after 200 years. These are represented by circles, downward and upward triangles respectively which show the percentage AMOC change after 200 years. Sizes of symbols represent the magnitude of the hosing (from 0.1-1Sv) and colours indicate the different studies these results were taken from (de Vries and Weber, 2005; Stouffer et al., 2006; Yin and Stouffer, 2007; Meehl et al., 2009; Jackson, 2013; Liu and Liu, 2013; Timmermans et al., 2014; Hutchings et al., 2015; Jackson and Wood, 2018; Haskins et al., 2019).

9.SM.2 Additional ice sheet information

[START TABLE 9.SM.1 HERE]

Table 9.SM.1: Observed mass loss of Greenland (The IMBIE Team, 2020, 2021) and Antarctic (The IMBIE Team et al., 2018, 2021) ice sheets for three different periods. Values are expressed as the total loss over each period (Gt) along with the equivalent rate (Gt yr^{-1}) and *very likely* ranges. Periods include both end years. The cumulative mass loss uncertainty from IMBIE is assumed to be zero at the start of each period.

Observed mass loss		**1992-1999**	**2000-2009**	**2010-2019**
Greenland (The IMBIE Team, 2019)	Δ (Gt)	309 [-24 to 642]	1753 [1308 to 2199]	2433 [1968 to 2897]
	Gt yr^{-1}	39 [-3 to 80]	175 [131 to 220]	243 [197 to 290]
Antarctica (The IMBIE Team et al., 2018)	Δ (Gt)	392 [-18 to 802]	703 [220 to 1187]	1482 [942 to 2022]
	Gt yr^{-1}	49 [-2 to 100]	70 [22 to 119]	148 [94 to 202]

[END TABLE 9.SM.1 HERE]

9.SM.3 Additional glacier information

9.SM.3.1 Details for Figure 9.21

1960-2019 time series annual and decadal values from (Zemp et al., 2019, 2020). Glacier mass change rates estimated from GRACE 2002-2016 from (Wouters et al., 2019). Glacier mass change rate between 2006-2016 and its respective uncertainty as it was assessed in SROCC (Hock et al., 2019b). Glacier mass change rates between 2000-2009 and 2010-2019 and its respective uncertainty obtained by (Hugonnet et al., 9998)

9.SM.3.2 Details for Figure 9.22

ACCEPTED VERSION SUBJECT TO FINAL EDITING

Glacier mass relative to 2015 between 1902 and 2100. Glacier change in 20th century is from (Marzeion et al., 2015). Observed mass change between 1961-2016 from (Zemp et al., 2019). Median and ± 1 standard deviation (shaded areas) projected mass change between 2015 and 2100 for RCP2.6, RCP 4.6, and RCP8.5 scenarios obtained from GlacierMIP (Marzeion et al., 2020). Data from (Bamber et al., 2018b) included in some regions

[START TABLE 9.SM.2 HERE]

Table 9.SM.2: Regional and global glacier-covered area, glacier mass (presented as potential sea level rise equivalent) in year 2000, glacier mass change rate in period 2000-2019, and projected glacier mass change between 2015 and 2100. The glacier-covered area is derived from the RGI 6.0 (RGI Consortium, 2017) and glacier-covered area uncertainties are extracted from (Pfeffer et al., 2014). Glacier mass and uncertainties are derived from Farinotti et al. (2019), based on RGI 6.0. Recent (2000-2019) mass change rate is based on (Hugonnet et al., 9998), except: [a] mean of Menounos et al. (2019) and (Hugonnet et al., 9998); [b] mean of (Aðalgeirsdóttir et al., 2020) and (Hugonnet et al., 9998); [c] mean of (Schuler et al., 2020) and (Hugonnet et al., 9998); [d] mean of (Davaze et al., 2020), (Sommer et al., 2020) and (Hugonnet et al., 9998); [e] mean of Shean et al. (2020) and (Hugonnet et al., 9998); and [f] mean of (Dussaillant et al., 2019) and (Hugonnet et al., 9998). The total projected glacier mass change between 2015-2100 is derived from (Marzeion et al., 2020). See Figure 9.22 for the time series of changes in each region.

Region	Glacier-covered area in 2000 (km^2)	Glacier mass in 2000 (mm SLE)	Glacier mass change rate 2000-2019 ($kg\ m^{-2}\ yr^{-1}$)	Projected glacier mass change between 2015-2100 (mm SLE)		
				RCP 2.6	RCP 4.5	RCP 8.5
Alaska (1)	86700 ± 4600	43 ± 11	-770 ± 60	14 ± 11	19 ± 13	25 ± 15
Western Canada and US (2)	14500 ± 1400	2.6 ± 0.7	-490 ± 170[a]	1.5 ± 0.9	2.0 ± 0.7	2.2 ± 0.7
Arctic Canada North (3)	105100 ±3400	65 ± 17	-290 ± 20	10 ± 10	16 ± 15	24 ± 20
Arctic Canada South (4)	40900 ± 2000	21 ± 5	-650 ± 50	5 ± 5	7 ± 7	11 ± 7
Greenland Periphery (5)	89700 ± 4500	34 ± 9	-430 ± 40	9 ± 10	12 ± 11	18 ± 11
Iceland (6)	11000 ± 300	9 ± 2	-860 ± 100[b]	2 ± 3	3 ± 3	5 ± 3
Svalbard (7)	34000 ± 1200	17 ± 4	-270 ± 180[c]	7 ± 7	11 ± 9	14 ± 8
Scandinavia (8)	2900 ± 300	0.7 ± 0.2	-580 ± 60	0.3 ± 0.2	0.4 ± 0.2	0.4 ± 0.2
	51600 ± 1400	32 ± 8	-200 ± 20	10 ± 8	14 ± 11	20 ± 12

ACCEPTED VERSION SUBJECT TO FINAL EDITING

Russian Arctic (9)						
North Asia (10)	2400 ± 200	0.3 ± 0.1	-500 ± 70	0.2 ± 0.2	0.3 ± 0.2	0.3 ± 0.2
Central Europe (11)	2100 ± 200	0.3 ± 0.1	-760 ± 260[d]	0.2 ± 0.1	0.3 ± 0.1	0.3 ± 0.1
Caucasus and Middle East (12)	1300 ± 100	0.2 ± 0.1	-430 ± 60	0.1 ± 0.05	0.11 ± 0.04	0.13 ± 0.04
High Mountain Asia (13 to 15)	97600 ± 7800	17 ± 3	-205 ±40[e]	8 ± 3	11 ± 4	13 ± 5
Low Latitudes (16)	2300 ± 200	0.2 ± 0.1	-450 ±60	0.13 ± 0.12	0.17 ± 0.12	0.19 ± 0.11
Southern Andes (17)	29400 ± 1700	13 ± 3	-720 ± 230[f]	3 ± 4	4 ± 3	6 ± 4
New Zealand (18)	1200 ± 100	0.2 ± 0.1	-720 ± 110	0.06 ± 0.06	0.09 ± 0.05	0.13 ± 0.04
Antarctic and Subantarctic (19)	132900 ± 2500	69 ± 18	-170 ± 20	9 ± 15	16 ± 13	20 ± 24
World	705700 ± 33200	324 ± 84	-460 ± 10	79 ± 56	119 ± 75	159 ± 86

[END TABLE 9.SM.2 HERE]

9.SM.4 Additional sea level information

9.SM.4.1 Framework for Assessing Changes To Sea-level (FACTS)

Projections of the probability distributions of global-mean and relative sea-level change are produced using the Framework for Assessing Changes to Sea-level (FACTS), a Python-based modularized framework. Contributors to sea-level change (e.g., ice sheets, ocean dynamics, etc.) are represented as individual modules which are then organized into user-defined projection workflows. The modularity of the framework enables efficient application of the different methodologies described in the chapter. The code for FACTS and its accompanying modules are open source and available through GitHub (https://github.com/radical-collaboration/facts). In the application here, the different drivers are treated as conditionally independent given GSAT.

Ideally, a FACTS module contains a sample-generation method through some sort of statistical or process-based model for the particular component. For example, the module for projecting thermal expansion and dynamic sea-level generates samples from statistical distributions calibrated within the module itself. For modules that use externally-provided ensembles for this report, which include the Emulated ISMIP6 ice sheets simulations, Emulated GlacierMIP glaciers simulations, the LARMIP-2 Antarctic ice sheet simulations, the Marine Ice Cliff Instability Antarctic ice sheet simulations, and the Structure Expert Judgement ice sheets simulations, a bootstrap sampling approach is used. This provides a consistent number

ACCEPTED VERSION SUBJECT TO FINAL EDITING

of samples across all modules within an integrated projection workflow. However, due to this sampling method, the number of samples in the provided ensemble for the module, and the seed value for the random-number generator, small differences may exist between the values of the FACTS produced projections and the values published in the paper for a particular method.

9.SM.4.2 Obtaining Global Mean Thermosteric Sea-Level Rise and Ocean Dynamic Sea-Level Change from CMIP6

We obtained monthly mean values for the CMIP6 variables 'zos' (sea-surface height above geoid), 'zostoga' (global mean thermosteric sea-level change) and 'psl' (air pressure at sea level; required to apply the inverse barometer effect). The data files were extracted from the Earth System Grid Federation (ESGF) database between 22-30 September 2020. Data were obtained for both the historical experiment (1850-2014) and the five core SSPs (2015-2100 and up to 2300 where available) with corresponding variant labels ('ripf' identifier). Additionally, models were required to provide the pre-industrial control output from which the 'zos' and 'zostoga' experiments were initialized, so that 'zos' and 'zostoga' simulations could be corrected for model ocean drift (Gupta et al., 2013; Hobbs et al., 2016b). Thus, the total number of available models used for each emissions scenario depends on the availability of these simulations (and of grid information required to carry out the preprocessing steps detailed in the next paragraph, such as ocean grid cell area 'areacello'). We obtained all available data with an experiment variant with a realization equal to one ('ripf' having 'r'=1). For each model, we use the first of the remaining experiment variants for which most SSP experiments are available, and the first alternative experiment variant for the SSPs for which that variant is not available. For UKESM1-0-LL, the air pressure sea level field yielded an anomalously large inverse barometer effect, so this was model not included.

Then, the timeseries of 'zos' and 'zostoga' were corrected for ocean model drift (Gupta et al., 2013; Hobbs et al., 2016b). This was done by fitting a linear trend to the full pre-industrial control run of each model, and subtracting the resulting linear trend from the historical and scenario runs. Since the drift in 'zostoga' is nearly linear for most CMIP6 models, quadratic or linear drift correction yields little difference compared to the magnitude of projected GTE under the emissions scenarios (Hermans et al., 2021). Additionally, the area-weighted mean of the 'zos' field was removed at each timestep for each model, since 'zos' is defined as the sea-surface height above a time-invariant geoid. Next, 'zos' and 'psl' were bilinearly interpolated to a common regular 1° by 1° grid using the ESMValTool regridding routine (Eyring et al., 2020) . Finally, the inverse barometer effect was derived from sea-level pressure anomalies with respect to the area-weighted ocean mean sea-level pressure (following Stammer and Hüttemann, 2008) and applied to 'zos' in order to obtain ocean dynamic sea-level fields (Gregory et al., 2019). Note that the inverse barometer effect due to sea-ice (e.g., Lyu et al., 2020a) was not applied here.

9.SM.4.3 Global Mean Thermosteric Sea-Level and Ocean Dynamic Sea-Level Projections based on the Two-Layer Emulator

To convert the ocean heat content projections based upon the AR6 assessment of equilibrium climate sensitivity and transient climate response (Appendix 7.A.2) to global mean thermosteric sea-level rise projections, the emulated ocean heat content projections were multiplied with expansion coefficients estimated from CMIP6. A distribution of expansion coefficients was derived by fitting drift-corrected global mean thermosteric sea-level rise (9.SM.4.2) from individual CMIP6 GCMs against total ocean heat content output of a two-layer emulator configured with CMIP6 calibration parameters (Smith et al., 2020b). Both thermosteric sea-level rise and ocean heat content were referenced to their mean values in 1995-2014. The two-layer model was forced with scenario-dependent effective radiative forcing from the RCMIP protocol (Nicholls et al., 2020) for the SSPs. Expansion coefficients were derived through linear regression with a fixed 0-intercept for the period 2015-2100 for all SSPs combined.

The resulting distribution was clipped based on the root mean square error cumulative across scenarios between the GSAT projections of individual CMIP6 models and the GSAT projection of the two-layer

ACCEPTED VERSION SUBJECT TO FINAL EDITING

model calibrated to that model. Only the expansion coefficients of models with an RMSE less than or equal to the 85th percentile of the cumulative distribution function of RMSEs were considered. Thus, the expansion coefficients for CNRM-ESM2-1 and EC-Earth3-Veg were dropped. Expansion coefficients were then randomly drawn from a normal fit to the distribution of remaining expansion coefficients, which has a mean and standard deviation of 0.113 ± 0.013 m/YJ.

To produce ocean dynamic sea-level projections consistent with the global mean thermosteric projections described in this section, we follow the approach of (Kopp et al., 2014). We fit a multivariate t-distribution to the ocean dynamic sea-level terms from CMIP6 (9.SM.4.2), and drawing from this distribution, combine the ocean dynamic sea-level terms with the emulator-based global mean thermosteric projections, accounting for the underlying correlation between global mean thermosteric sea-level rise and ocean dynamic sea-level change in CMIP6. While if the CMIP6 ensemble represented a complete representation of all relevant uncertainties, its 5th-95th percentile range would represent a *very likely* range, it is not a perfect representation, so following practice in the AR5, we treat its 5th-95th percentile range as a *likely range* (i.e., a 17th-83rd percentile range). We therefore scale the standard deviation of the t-distribution of ocean dynamic sea-level change by 1.64, so that ±1 standard deviation of the scaled fitted distribution corresponds to a central 66% *likely range*. To account for identifiable, model-specific problems in specific grid cells (e.g., in inland seas), projections for a grid cell are removed if they have an amplitude in 2099 more than ten times the median local amplitude. In cases where, after removal of extreme outliers, the standard deviation of projections in 2099 is greater than 20 cm, we also remove models that deviate from the mean by more than three standard deviations.

9.SM.4.4 Parametric fit to ISMIP6 Greenland Ice Sheet projections

Since the ISMIP6 emulator does not account for temporal correlation, a polynomial fit to the ISMIP6 results is employed to calculate rates of change. The parametric fit is a cubic fit to temperature and a quadratic fit over time:

$$\frac{\partial s}{\partial t} = \beta_0 + \beta_1 T + \beta_2 T^2 + \beta_3 T^3 + \beta_4 t + \beta_5 t^2$$

Where *s* indicates the sea-level equivalent contribution in mm, *T* is GSAT in °C, and *t* is time in years. For the purposes of fitting this function, *T* and *t* are anomalies to their respective values in year 2015. Fitting is done using maximum a posteriori estimation.

[START TABLE 9.SM.3 HERE]

Table 9.SM.3: Parameters for the fit to the ISMIP6 Greenland Ice Sheet models.

GROUP	Model	β_0	β_1	β_2	β_3	β_4	β_5
UCIJPL	ISSM1	0.11	0.68	-0.16	0.03	-0.009	1.5E-04
UAF	PISM1	0.11	2.23	-0.69	0.08	-0.046	4.7E-04
NCAR	CISM	0.31	1.60	-0.44	0.06	-0.030	2.7E-04
MUN	GSM2601	0.26	1.92	-0.64	0.07	-0.048	5.4E-04
AWI	ISSM1	0.15	0.57	-0.06	0.02	-0.002	2.6E-05
JPL	ISSMPALEO	0.08	0.67	-0.13	0.02	-0.016	1.9E-04
BGC	BISICLES	0.15	0.82	-0.24	0.04	-0.017	2.2E-04
GSFC	ISSM	0.17	1.94	-0.62	0.08	-0.035	3.8E-04
UCIJPL	ISSM2	0.22	0.34	0.05	-0.02	-0.004	8.5E-05

ACCEPTED VERSION SUBJECT TO FINAL EDITING

IMAU	IMAUICE2	0.20	2.30	-0.71	0.09	-0.044	4.5E-04
VUB	GISMHOMv1	0.39	0.85	-0.19	0.04	-0.002	-1.1E-05
IMAU	IMAUICE1	0.28	0.84	-0.13	0.03	-0.002	-7.9E-06
MUN	GSM2611	0.32	0.39	0.15	-0.04	-0.016	2.1E-04
UAF	PISM2	0.22	0.22	-0.03	0.02	0.002	-1.0E-05
VUW	PISM	0.00	1.54	-0.52	0.06	-0.037	4.6E-04
AWI	ISSM2	0.15	0.58	-0.06	0.02	-0.001	1.6E-05
ILTS_PIK	SICOPOLIS2	0.23	0.64	-0.06	0.02	-0.005	6.9E-05
ILTS_PIK	SICOPOLIS1	0.18	1.83	-0.52	0.07	-0.036	3.7E-04
AWI	ISSM3	0.09	2.12	-0.65	0.08	-0.042	4.2E-04
JPL	ISSM	0.20	0.73	-0.13	0.03	-0.004	4.9E-05
LSCE	GRISLI2	0.22	0.39	-0.04	0.02	-0.006	5.7E-05

[END TABLE 9.A.3 HERE]

9.SM.4.5 Parametric fit to GlacierMIP2 projections

Since the GlacierMIP2 emulator does not account for temporal correlation and terminates, along with the GlacierMIP2 simulations, in 2100, we employ a power law fit to the GlacierMIP2 simulations (Marzeion et al., 2020), with a functional form similar to that employed by the AR5, to calculate rates of change and extrapolate changes beyond 2100 (up to a maximum potential contribution of 0.32 m). As in the AR5 (Church et al., 2013), the glacier contribution is the integral of $fI(t)^{\rho}$, where $I(t)$ is the time integral of GSAT from 2006 to time t in degrees Celsius year, and the constants f and ρ used for each glacier model are shown in Table 9.SM.4. The spread of the results around this median projection has a coefficient of variation (standard deviation divided by the mean) σ which is determined on a per-model basis. As in the AR5, this variation is incorporated by taking for each Monte Carlo sample a normally distributed random number. This number is multiplied by the time-dependent standard deviation and added to the sample. All models are equally weighted.

[START TABLE 9.SM.4 HERE]

Table 9.SM.4: Parameters for the fit to the global glacier models.

Global Glacier Model	f (mm °C^{-1} yr^{-1})	ρ	σ
GLIMB	3.7	0.66	0.21
GloGEM	4.08	0.72	0.16
JULES	5.5	0.56	0.19
MAR2012	4.89	0.65	0.14
OGGM	4.26	0.72	0.16
RAD2014	5.18	0.71	0.14
WAL2001	2.66	0.73	0.21

[END TABLE 9.SM.4 HERE]

ACCEPTED VERSION SUBJECT TO FINAL EDITING

9.SM.4.6 Background rates of relative sea-level change

Background rates of RSL change, including glacial-isostatic adjustment as well as other factors contributing to long-term vertical land motion, are estimated from tide-gauge data following the Gaussian-process regression method of Kopp et al. (Kopp et al., 2014). The method was applied to annual-mean tide-gauge data downloaded from the Permanent Service for Mean Sea Level (Holgate et al., 2013) on 18 October 2020. As in Kopp et al. (Kopp et al., 2014), RSL is represented as the sum of three Gaussian processes: (1) a regionally varying, temporally linear process, (2) a globally-uniform process, and (3) a regionally varying, temporally autocorrelated non-linear process. The posterior estimate of the first (temporally linear) process is used as the estimate of the background rate. The analysis is conducted separately for each of 15 regions: Iceland/Svalbard, Scandinavia, Northern Europe, Russia, Mediterranean/Africa, US Pacific, US Atlantic, Gulf of Mexico, Northeastern Canada, Alaska, Latin America, Oceania, Japan, South/East Asia, and Antarctica (see Kopp et al., 2014, for details). Within each region, available tide-gauge data are used together with the GMSL curve of (Dangendorf et al., 2019) (treated as a noisy observation of the second term) to estimate the Gaussian-process model.

9.SM.4.7 Warming Level Scenarios

Because GMSL projections are more strongly related to integrated warming rather than to instantaneous warming, warming-level-based scenarios cannot be defined based on the time-slice method used for atmospheric variables (Cross-Chapter Box 11.1). Instead, consistent with the approaches of (Jackson et al., 2018; Rasmussen et al., 2018), all available SSP-based projections are pooled, then assigned to temperature levels based on the 2081-2100 GSAT anomaly projected by the two-layer energy budget emulator, using a ±0.25°C window around the targeted temperature level. For example, the 2.0°C projections are based on all realizations from all scenarios where 2081-2100 GSAT falls between 1.75°C and 2.25°C. A certain warming level may therefore include a mixture of one or more SSP scenarios.

9.SM.4.8 Analysis of future changes in extreme sea level return frequency

Frequency amplification factors for the 1% average annual-probability of extreme still-water levels are computed by combining the projected regional sea-level change (Section 9.6.3.3) with historical distributions of observed extreme events derived from the Global Extreme Sea Level Analysis 2 (GESLA2;(Woodworth et al., 2016b)) , following the approach of the SROCC and (Frederikse et al., 2020a). GESLA2 stations are included in the analysis when hourly mean data was available for at least 6,000 hours per year (250 days) for at least 20 years. For each station, the annual means were removed before fitting a General Pareto Distribution (GPD) to the hourly mean GESLA2 data using a peak-over-threshold (POT) method with a threshold of 99.7%. The extremes are de-clustered using a minimum of 72 hours between subsequent extremes. The estimated GPD location (the 99.7% threshold), scale and shape parameters are generally in agreement with (Frederikse et al., 2020a). We note that our results are sensitive to the statistical method used (Wahl et al., 2017) and may therefore differ from previous analyses.

Following the SROCC and (Frederikse et al., 2020a), we computed an ensemble of historical return curves for each station using the location parameter in combination with 50,000 random pairs of the shape and scale parameters drawn from the mean estimated shape and scale parameters and their covariance matrices. To compute the future return curves, we use the same scale and shape parameter samples but increase the location parameter at each station by the local projected mean sea-level change, effectively shifting the return curve up. The uncertainty in the local projected mean sea-level change is estimated by drawing 50,000 samples from the projected probability distribution of local mean sea-level change, clipped at its 5^{th} and 95^{th} percentiles. This differs from SROCC, where sea-level change samples were drawn from a normal distribution using the central value and a standard error.

Using the resulting 50,000 future return curves for each station, we calculated the frequency amplification factor of a 1% average annual-probability (i.e., once in 100 years) of extreme still-water level by dividing the

ACCEPTED VERSION SUBJECT TO FINAL EDITING

frequency of that water level in the future return curves by the historical frequency. This resulted in a probability distribution of frequency amplification factors that represents both the uncertainty in projected sea-level change and in the historical distribution of extremes.

Using the POT method, the frequency of extreme events is only defined for water levels above the POT threshold. If the projected sea-level change for a given location is higher than the exceedance of the historical location parameter by the historical 1% annual probability event, the historical 1% annual-probability event would have a return level below the future location parameter. Thus, for the stations where this occurs the frequency amplification factor cannot be fully determined. Therefore, we used the approach of (Buchanan et al., 2016) to describe the return frequency of return heights below the POT threshold. We fit a Gumbel distribution between Mean Higher-High Water (MHHW) and the location parameter, assuming the frequency of exceedance of the MHHW to be 182.6/year. The MHHW was estimated from the GESLA2 data as the long-term mean of 2-daily maxima for each location. Therefore, by construction, the maximum projected frequency amplification factor in our analysis is 18,262.5.

[START TABLE 9.SM.5 HERE]

Table 9.SM.5: Integrated GMSL projections for 2050, relative to 1996-2014, from the post-AR5 literature.

Study	Grouping	RCP 2.6		RCP 4.5		RCP 8.5	
		67%	90%	67%	90%	67%	90%
Bakker et al., 2017	MED		0.16--0.29		0.18--0.31		0.20--0.34
Kopp et al., 2014	MED	0.19--0.27	0.16--0.31	0.19--0.29	0.16--0.33	0.22--0.32	0.19--0.36
Mengel et al., 2016	MED		0.10--0.20		0.11--0.21		0.12--0.25
Nicholls et al., 2018	MED						0.16--0.29
Kopp et al., 2017	MICI	0.14--0.31	0.10--0.39	0.16--0.34	0.12--0.41	0.20--0.38	0.15--0.46
Wong et al., 2017	MICI		0.18--0.31		0.20--0.33		0.23--0.38
Jackson and Jevrejeva, 2016	SEJ					0.19--0.34	0.15--0.45
Bamber et al., 2019	SEJ					0.25--0.45	0.19--0.59

All projections are adjusted to a 1995-2014 baseline and 2050 end year. For projections baselined to 1986-2005 or to 2000, adjustments are made assuming a 3 mm/yr rate. For projections ending in 2046-2065, adjustments are made assuming a constant acceleration from 1996-2014 to the end year.

[END TABLE 9.SM.5 HERE]

ACCEPTED VERSION SUBJECT TO FINAL EDITING

[START TABLE 9.SM.6 HERE]

Table 9.SM.6: Integrated GMSL projections for 2100, relative to 1996-2014, from the post-AR5 literature.

Study	Grouping	RCP 2.6		RCP 4.5		RCP 8.5	
		67%	90%	67%	90%	67%	90%
Bakker et al., 2017	MED		0.37--0.68		0.51--0.94		0.82--1.56
Jackson and Jevrejeva, 2016	MED			0.33--0.69	0.19--0.82	0.51--0.95	0.34--1.15
Kopp et al., 2014	MED	0.35--0.63	0.27--0.80	0.43--0.75	0.34--0.91	0.60--0.98	0.50--1.19
Kopp et al., 2016	MED	0.26--0.49	0.22--0.59	0.37--0.67	0.31--0.83	0.57--1.03	0.50--1.29
Mengel et al., 2016	MED		0.25--0.53		0.34--0.74		0.54--1.28
Nauels et al., 2017	MED	0.34--0.56		0.45--0.71		0.65--1.06	
Slangen et al., 2014	MED			0.36--0.83		0.46--1.15	
Le Bars, 2018	MED			0.39--0.67	0.31--0.82	0.59--0.98	0.48--1.18
Le Cozannet et al., 2019	MED	0.20--0.42	0.14--0.49	0.32--0.54	0.24--0.60	0.55--0.80	0.45--0.89
Goodwin et al., 2017	MED		0.51--0.88		0.52--0.79		0.73--1.00
Nicholls et al., 2018	MED						0.51--0.88
Kopp et al., 2017	MICI	0.35--0.76	0.24--0.96	0.64--1.23	0.48--1.56	1.07--2.07	0.91--2.41
Wong et al., 2017	MICI		0.41--0.72		0.54--1.28		1.07--2.05
Grinsted et al., 2015	SEJ					0.56--1.18	0.43--1.81
Jackson and Jevrejeva, 2016	SEJ					0.60--1.18	0.48--1.64
Jevrejeva et al., 2014	SEJ						0.44--1.78
Bamber et al., 2019	SEJ					0.77--1.72	0.60--2.36
Horton et al., 2020	Survey	0.28--0.63	0.19--0.80			0.61--1.30	0.43--1.63

All projections are adjusted to a 1995-2014 baseline and 2100 end year. For projections baselined to 1986-2005 or to 2000, adjustments are made assuming a 3 mm/yr rate. For projections ending in 2081-2100, adjustments are made assuming a constant acceleration from 1996-2014 to the end year.

[END TABLE 9.SM.6 HERE]

ACCEPTED VERSION SUBJECT TO FINAL EDITING

[START TABLE 9.SM.7 HERE]

Table 9.SM.7: Global mean sea-level projections for 5 SSP scenarios, for total change and individual contributions, median values, (*likely*) ranges of the process-based model ensemble, for 1995-2014 to 2050 and 2150 in meters. Average rates for total sea-level change in mm yr^{-1}.

	SSP1-1.9	SSP1-2.6	SSP2-4.5	SSP3-7.0	SSP5-8.5	SSP5-8.5 *Low Confidence*
2050						
Thermal expansion	0.07 (0.06--0.08)	0.07 (0.06--0.09)	0.08 (0.07--0.10)	0.09 (0.07--0.10)	0.09 (0.08--0.11)	0.07 (0.06--0.09)
Greenland	0.03 (0.02--0.04)	0.03 (0.02--0.04)	0.03 (0.02--0.04)	0.03 (0.02--0.04)	0.03 (0.02--0.04)	0.03 (0.02--0.10)
Antarctica	0.03 (0.01--0.08)	0.03 (0.01--0.08)	0.03 (0.01--0.08)	0.03 (0.01--0.08)	0.03 (0.01--0.08)	0.03 (-0.00--0.08)
Glaciers	0.04 (0.03--0.05)	0.05 (0.04--0.06)	0.05 (0.05--0.06)	0.06 (0.05--0.07)	0.07 (0.06--0.08)	0.05 (0.04--0.06)
Land Water Storage	0.01 (0.00--0.02)	0.01 (0.00--0.02)	0.01 (0.00--0.02)	0.01 (0.00--0.02)	0.01 (0.00--0.02)	0.01 (0.00--0.02)
Total (2050)	0.18 (0.15--0.23)	0.19 (0.16--0.25)	0.21 (0.18--0.26)	0.22 (0.19--0.28)	0.23 (0.20--0.30)	0.20 (0.16--0.31)
2150						
Thermal expansion	0.14 (0.11--0.18)	0.18 (0.14--0.23)	0.30 (0.24--0.38)	0.46 (0.38--0.57)	0.55 (0.45--0.68)	0.55 (0.45--0.68)
Greenland	0.10 (0.08--0.13)	0.13 (0.10--0.17)	0.19 (0.15--0.24)	0.24 (0.19--0.28)	0.27 (0.22--0.35)	0.31 (0.18--0.98)
Antarctica	0.17 (-0.01--0.44)	0.18 (-0.03--0.49)	0.18 (-0.05--0.55)	0.17 (-0.07--0.61)	0.17 (-0.09--0.68)	0.77 (-0.09--3.68)
Glaciers	0.10 (0.07--0.14)	0.13 (0.09--0.18)	0.19 (0.13--0.26)	0.27 (0.18--0.32)	0.31 (0.20--0.32)	0.31 (0.20--0.32)
Land Water Storage	0.05 (0.03--0.06)	0.05 (0.03--0.06)	0.05 (0.03--0.07)	0.07 (0.04--0.09)	0.05 (0.03--0.06)	0.05 (0.03--0.06)
Total (2150)	0.57 (0.37--0.85)	0.69 (0.46--1.00)	0.93 (0.67--1.33)	1.21 (0.92--1.67)	1.35 (1.02--1.89)	1.99 (1.02--4.83)

[END TABLE 9.SM.7 HERE]

ACCEPTED VERSION SUBJECT TO FINAL EDITING

[START TABLE 9.SM.8 HERE]

Table 9.SM.8: Global mean sea-level rise projections for 2000-2300 from literature (m), for different RCP scenarios.

Study	Grouping	RCP 2.6		RCP 4.5		RCP 8.5	
		67%	90%	67%	90%	67%	90%
Kopp et al., (2014)	MED	0.3--2.9	-0.2--4.7	0.7--3.5	0.0--5.3	1.8--5.2	1.0--7.4
Nauels et al., (2017)	MED	0.8--1.4		1.8--2.3		3.4--6.8	
Palmer et al. (2020)*	MED	0.6--2.2		0.9--2.6		1.7--4.5	
Kopp et al., (2017)	MICI	0.8—2.3	0.5--3.0	2.8--6.0	2.1--7.0	9.8--14.1	9.1--15.5
Bamber et al. (2019)*	SEJ	1.2--3.6	0.5--5.3			2.6--6.5	1.8--11.8
Horton et al. (2020)	Survey	0.54-2.15	0.24-3.11			1.67-5.61	0.88-7.83

*Bamber et al. (2019) 2°C scenario is listed under the RCP 2.6 column, but GSAT does not decline in this 2°C scenario as it does in RCP 2.6. Bamber et al. (2019) "RCP 8.5" scenario assumes GSAT stabilization at 5°C above pre-industrial after 2100 and so becomes cooler than RCP 8.5 over the 22nd and 23rd century. Palmer et al. (2020) 5th-95th percentile of simulated projections are constructed to be analogous to AR5/SROCC *likely* ranges and so are presented here as 17th-83rd percentile projections.

[END TABLE 9.SM.8 HERE]

9.SM.5 Data Table

[START TABLE 9.SM.9 HERE]

Table 9.SM.9: Input datasets and code in the chapter.

Figure number	Dataset / Code name	Type	Filename / Specificities	License type	Dataset / Code citation	Dataset / Code URL	Related publications / Software used	Notes
Figure 9.2, panel b	OSCAR third degree resolution ocean surface currents. Ver. 1	Input dataset (observations)		open	10.5067/OSCAR-03D01	https://doi.org/10.5067/OSCAR-03D01	Bonjean, F., and G. S. E. Lagerloef, 2002.	time averaged over 1993-2018
	ETOPO20	Input dataset (topography)		open	doi:10.7289/V5C8276M.	http://www.ngdc.noaa.gov/mgg/global/etopo2.html	Amante, C.; Eakins, B.W. (2009). "ETOPO1 1 Arc-Minute Global Relief Model: Procedures,	

ACCEPTED VERSION SUBJECT TO FINAL EDITING

							Data Sources and Analysis". *NOAA Technical Memorandum NESDIS NGDC-24*.	
	Permafrost gridded map	input dataset		open		https://data.tpdc.ac.cn/en/data/c66bf4a7-8f20-443c-9412-53ac675bd964/	Brown, J., O. Ferrians, J. A. Heginbottom, E. Melnikov, Tingjun Zhang Tingjun Zhang Tingjun Zhang. **Circum-Arctic map of permafrost and ground ice conditions (v2) (1997)**. National Tibetan Plateau Data Center, 2011.	all permafrost types combined
	Snow water equivalent map	Input dataset		Open	https://doi.org/10.5067/KIGGFNVROX9V	https://doi.org/10.5067/KIGGFNVROX9V	Brodzik, M. J., R. Armstrong, and M. Savoie. 2007. Global EASE-Grid 8-day Blended SSM/I and MODIS Snow Cover, Version 1. [Indicate subset used]. Boulder, Colorado USA. NASA National Snow and Ice Data Center Distributed Active Archive Center. doi: https://doi.org/10.5067/KIGGFNVROX9V.	SWE converted to distribution of snowy regions and locations of ice sheets
	Northern Hemisphere sea ice data	Input dataset		Open			Meier, W. N., F. Fetterer, M. Savoie, S. Mallory, R. Duerr, and J. Stroeve. 2017. NOAA/NSIDC Climate	Annual average concentration

ACCEPTED VERSION SUBJECT TO FINAL EDITING

							Data Record of Passive Microwave Sea Ice Concentration, Version 3. [Indicate subset used]. Boulder, Colorado USA. NSIDC: National Snow and Ice Data Center. doi: https://doi.org/10.7265/N59P2ZTG.	
	Southern Hemisphere sea ice data	Input dataset		Open			Peng, et al. 2013. https://doi.org/10.5194/essd-5-311-2013	Annual average concentration
	Glacier inventory	Input dataset		Open			RGI Consortium (2017). Randolph Glacier Inventory – A Dataset of Global Glacier Outlines: Version 6.0: Technical Report, Global Land Ice Measurements from Space, Colorado, USA. Digital Media. DOI: **https://doi.org/10.7265/N5-RGI-60**	
Figure 9.3a (left: paleo panel)Figure 9.3a (left: paleo panel)	Paleo MPWP observation	Input dataset (observations)					Foley, et al. (2019) https://doi.org/10.5066/P9YP3DTV. . McClymont, et al. (2020). https://doi.org/10.5194/cp-2019-161	Anomalized relative to 1950-1980. These data used a different 'modern' period so a +0.2 correction was applied based on HadCM3.
	Paleo LIG observati	Input dataset (observ					Fischer, et al. (2018). https://doi.org/10.103	Anomalized relative to 1950-1980.

ACCEPTED VERSION SUBJECT TO FINAL EDITING

	on	ations)					8/s41561-018-0146-0; Turney, et al. (2020). https://doi.org/10.5194/essd-12-3341-2020; Hoffman et al., 2017	The references used varying 'modern' periods so the following corrections were applied; +0.2 for Fischer et al. (2018) and -0.1 for Turney et al. (2020). These corrections were based on HadCM3.
	Paleo LGM observation	Input dataset (observations)					Paul, et al. (2020). https://doi.org/10.1038/s41586-020-2617-x; MARGO (2009)	Anomalized relative to 1950-1980. The references used varying 'modern' periods so the following corrections were applied; +0.2 for Paul et al. (2021) & MARGO (2009) and +0.1 for Tierney et al., 2020. These corrections were based on HadCM3 and PAGES12K (Kaufman et al., 2020) respectively.
	Paleo MPWP Models	Model dataset					Haywood, et al. (2020).	Anomalized relative to 1950-1980. These data used a different 'modern' period so a +0.2 correction was applied based on

ACCEPTED VERSION SUBJECT TO FINAL EDITING

								HadCM3.
	Paleo LIG Models	Model dataset					Otto-Bliesner, et al. (2021).	Anomalized relative to 1950-1980. Otto-Bliesner et al. (2021) used a different 'modern' period so a +0.2 correction was applied based on HadCM3.
	Paleo LGM Models	Model dataset					Kageyama, et al. (2021). https://doi.org/10.5194/cp-2019-169	Anomalized relative to 1950-1980. Kageyama et al. (2021) used a different 'modern' reference perios so the following was applied; +0.2. This correction was based on HadCM3.
Figure 9.3a (middle and right panels)	Hadley Centre Sea Ice and Sea Surface Temperature dataset (HadISST)	Input dataset (observational reanlyses)		Crown Copyright		https://www.metoffice.gov.uk/hadobs/hadisst/	Rayner, et al., (2003), ESMValTool v2	Reformatted with ESMValTool v2.0 (March 20th 2020)
	CMIP6 (CMIP, ScenarioMIP, HighResMIP)	Model dataset						
Figure 9.3b	Hadley Centre Sea Ice and Sea Surface Temperature dataset (HadISST)	Input dataset (observational reanlyses)		Crown Copyright		https://www.metoffice.gov.uk/hadobs/hadisst/	See Figure 9.3a (middle and right panels)	Monthly data averaged between 1995 and 2014. Reformatted with ESMValTool v2.0 (March 20th

ACCEPTED VERSION SUBJECT TO FINAL EDITING

								2020)
Figure 9.3c	Hadley Centre Sea Ice and Sea Surface Temperature dataset (HadISST)	Input dataset (observational reanlyses)		Crown Copyright		https://www.metoffice.gov.uk/hadobs/hadisst/	See Figure 9.3a (middle and right panels)	Change rate calculated between the 2005-2014 mean and 1950-1959 mean.
Figure 9.3d	CMIP6 (CMIP)	Model dataset						Change rate calculated between the 2091-2100 mean and the 2005-2014 mean.
Figure 9.3e	CMIP6 (CMIP)	Model dataset						See Fig. 9.3b
Figure 9.3f	CMIP6 (CMIP)	Model dataset						See Fig. 9.3c
Figure 9.3g	CMIP6 (CMIP)	Model dataset						Change rate calculated between the 2041-2050 mean and the 2005-2014.
Figure 9.3h	CMIP6 (HighResMIP)	Model dataset						See Fig. 9.3b
Figure 9.3i	CMIP6 (HighResMIP)	Model dataset						See Fig. 9.3c
Figure 9.3j	CMIP6 (HighResMIP)	Model dataset						See Fig. 9.3g
Figure 9.4a,b,d,e,g,h	CERES EBAF v4 (Heat fluxes); OAFlux-HR (heat, freshwater and momentum fluxes); GPCP (precipitation)	Input datasets (observation-based products)				https://ceres.larc.nasa.gov/data/ ; http://oaflux.whoi.edu/ ; https://rda.ucar.edu/datasets/ds728.3/		Details of dataset merging and trend calculation to be added
Figure 9.4c,f,i	CMIP6 (CMIP, Scenario	Model datasets						Change rate calculated between

ACCEPTED VERSION SUBJECT TO FINAL EDITING

	MIP)							2081-2100 mean and 1995-2014 mean (CHECK THIS). Models include river runoff, observations do not.
Figure 9.5a,b,e,f	Argo Mixed Layers	Input datasets (observations)		Open		http://mixedlayer.ucsd.edu	Holte, et al. (2017).	Climatology of monthly mixed layer depths. Dec 2019 version. MLDs calculated using de Boyer Montégut et al.'s (2004) threshold values. DJF and JJA averages ignore missing gridpoints. Afterward, isolated missing gridpoints infilled as average of four neighbors.
Figure 9.5b,f	CMIP6 (CMIP)	Model datasets						Change rate calculated across 1995-2014 period.
Figure 9.5c,d,g,h	CMIP6 (ScenarioMIP, CMIP)	Model datasets						Change rate calculated between 2081-2100 average and 1995-2014 average.
Figure 9.6a	Observations (Ishii)	Input dataset (observations)	ishii_ohc_global_1955.txt			https://www.data.jma.go.jp/gmd/kaiyou/english/ohc/ohc_data_en.html (Downloaded 12th Jan.	Ishii et al. 2017	Anomalized relative to 2004-2015 mean.

ACCEPTED VERSION SUBJECT TO FINAL EDITING

						2021)		
	Hybrid (Zanna)	Input dataset (hybrid)	OHC_GF_1870_2018_Zanna.nc			Zanna, Laure, Khatiwala, Samar, Gregory, Jonathan, Ison, Jonathan, & Heimbach, Patrick. (2019). Global reconstruction of historical ocean heat storage and transport (Version v1) [Data set]. Zenodo. http://doi.org/10.5281/zenodo.4603700	Zanna, et al. (2019)	Anomalized relative to 2004-2015 mean.
	Hybrid (Cheng)	Input dataset (hybrid)	Cheng_2016_Global_OHC_13_Jan_2021.txt			http://159.226.119.60/cheng/images_files/OHC2000m_annual_timeseries.txt	Cheng, et al. 2019	Anomalized relative to 2004-2015 mean.
	Paleo (LIG)	Input dataset (LIG)	Stored in Excel file for Fig 9.9: 9.2.2_ACM_Fig_9.9_OHC_Paleo_Data_update_2020_12_06.xls				Shackleton, S. et al. (2020).	Last Inter-Glacial OHC anomaly relative to preindustrial. This mean is between -129 ka and -116 ka CE, and the timeseries is shown in Fig. 9.9
	Paleo (LGM)	Input dataset (LGM)	Stored in Excel file for Fig 9.9: 9.2.2_ACM_Fig_9.9				Baggenstos, D., Häberli, M., Schmitt, J., Shackleton, S. A., Birner,	Last Glacial Maximum OHC anomaly relative to

ACCEPTED VERSION SUBJECT TO FINAL EDITING

			_OHC_Paleo_Data_update_2020_12_06.xls				B., Severinghaus, J. P., Kellerhals, T & Fischer, H. (2019). Earth's radiative imbalance from the Last Glacial Maximum to the present. Proceedings of the National Academy of Sciences, 116(30), 14881-14886. DOI: 10.1073/pnas.1905447116	preindustrial. This mean is between -23 ka and -19 ka CE, and the timeseries is shown in Fig. 9.9
	Paleo (MH)	Input dataset (MH)	Stored in Excel file for Fig 9.9: 9.2.2_ACM_Fig_9.9_OHC_Paleo_Data_update_2020_12_06.xls				Baggenstos, D. et al. (2019).	Mid-holocene OHC anomaly relative to preindustrial. This mean is between -6.5 ka and -5.5 ka CE, and the timeseries is shown in Fig. 9.9
	CMIP6 (CMIP, ScenarioMIP)	Model dataset						Timeseries across 1850-2014 (CMIP) and 2015-2100 (ScenarioMIP). Anomalized relative to 2005-2014 mean
Figure 9.6b-g	Observations	Input dataset (observational reanlyses)				https://climate.mri-jma.go.jp/pub/ocean/ts/v7.3/2021-02-01/		0-700m calculated between 1971-2014 and 0-2000m calculated between 2005-2014.
	CMIP6 (CMIP)	Model dataset						0-700m Bias calculated across 1971-

ACCEPTED VERSION SUBJECT TO FINAL EDITING

								2014 mean. 0-2000m Bias calculated across 2005-2014 mean
	CMIP6 (Scenario MIP)	Model dataset						Change rate calculated between 2091-2100 mean and 2005-2014 mean.
Figure 9.7 1st and 2nd columns	Argo (observations)	Input dataset (observational reanlyses)				https://argo.ucsd.edu/		
	CMIP6 (CMIP)	Model dataset						
Figure 9.7 3rd and 4th columns	CMIP6 (CMIP, Scenario MIP)	Model dataset						Change rate calculated between 2005-2014 mean (CMIP) and 2091-2100 mean (ScenarioMIP).
Figure 9.8 Panels a-f	CMIP5 and observation based product	Model and observation analysis dataset			https://doi.org/10.1038/s41586-020-2573-5	https://doi.org/10.1038/s41586-020-2573-5	Bronselaer, B. and Zanna, L., 2020.	These data are the same as used in the paper, but projections are redrawn so as to match the chapter standards
Figure 9.8 Panel g	RAPID array	Input dataset (observations)					**Version v2015.1** Smeed D. et al. (2016).	
	CMIP6 (HighResMIP)	Model dataset					Roberts, et al. 2020.	This analysis is similar to that in the paper but combines multiple panels from the paper into one.
Figure 9.9a,b,d	Ocean heat content (OHC)	Input dataset				Inset OHC updated values	Shackleton et al, 2019; 2020; Baggenstos et	Rebased to PI: Baggenstos et al. (2019)

ACCEPTED VERSION SUBJECT TO FINAL EDITING

	estimates					from Levitus et al., 2012; https://www.nodc.noaa.gov/OC5/3M_HEAT_CONTENT/basin_tsl_data.html	al., 2019; Levitus et al. 2012 updated NOAA NODC, 2020	MOT-PI= MOT-1.51; Shackleton et al. (2019) MOT-PI = MOT+0.50 (aligned to Baggenstos et al. 2019); Shackleton et al. (2020) MOT-PI = MOT+0.25 (aligned to Baggenstos et al. 2019); assumption, Baggenstos et al. (2019) at 1000 BP =PI.
	Southern Ocean SST estimates from marine cores	Input dataset					Uemera et al., 2018	Restacked 11 records from average of three low-variability intervals, 4-8 ka, 18-22ka, and 25-29 ka, binned and averaged at 1000-year intervals.
	Southern Ocean SST estimates from ice core source	Input dataset					Uemera et al., 2018	As published, moisture source temperature based on deuterium excess
	OHC from HadCM3	Input dataset				https://crudata.uea.ac.uk/cru/projects/soap/pw/data/model/hadcm3/hadcm3_sealevel.htm	Gregory et al., 2006	Inset only, Natural + Anthropogenic forcing
Figure 9.9c	Model OHC projections	Model dataset					Clark et al., 2016	Projected OHC in response to four GHG emissions scenarios
	Model SAT	Model dataset					Clark et al., 2016	Projected SAT in

ACCEPTED VERSION SUBJECT TO FINAL EDITING

								response to four GHG emissions scenarios
Figure 9.10 Top left panel	CMIP6 (PMIP)	Model dataset						
Figure 9.10 Top right panel	CMIP6 (DAMIP, Scenario MIP), CMIP5	Model dataset					Menary, et al., 2020.	
Figure 9.10 Bottom panels	Simulated AMOC changes	Model datasets					Based on literature search from Jackson and Wood, 2018; Yin and Stouffer, 2007; Liu and Liu, 2013; Haskins et al. 2019; De Vries and Weber, 2005; Jackson 2013; Stouffer et al. 2006.	Extracted from timeseries and descriptions of models from these papers.
Figure 9.11 Maps	CMIP6 (CMIP, Scenario MIP)	Model dataset						Change rates calculated between 1995-2014 mean (CMIP) and 2081-2100 mean (ScenarioMIP).
Figure 9.11 Right column (scatter plots)	CMIP6 (CMIP, Scenario MIP)	Model dataset					Hu et al., 2015	
Figure 9.12g	AVISO Sea Surface Altimetry	Input dataset (observations)				https://www.aviso.altimetry.fr/en/home.html		Standard deviation across 2005-2014.
Figure 9.12h,i	CMIP6 (OMIP)	Model dataset				HYCOM low-res is from ftp://ftp.coaps.fsu.edu/pub/abozec/OMIP2-GLBt0.7		Standard deviation across last 10 years.

ACCEPTED VERSION SUBJECT TO FINAL EDITING

						2/. HYCOM high-res is from ftp://ftp.coaps.fsu.edu/pub/abozec/GLBb0.08/.		
Figure 9.12a-f	CMIP6 (CMIP, Scenario MIP)	Model dataset						Changes are between 1995-2014 and 2081-2100 means.
Figure 9.13 Left panel	UHH SIA	Input datasets	SeaIceArea__NorthernHemisphere__monthly__UHH__v2019_fv0.01.nc	Creative Commons Attribution 4.0 International	Doerr, Jakob, Notz, Dirk, & Kern, Stefan. (2021). UHH Sea Ice Area Product (Version 2019_fv0.01) [Data set].	http://doi.org/10.25592/uhhfdm.8559		
Figure 9.13 Left panel	Plotting code	Code	plot_9_13_and_9_15.py					
Figure 9.13 Maps (except right column)	OSISAF/ CCI 450	Input datasets			EUMETSAT Ocean and Sea Ice Satellite Application Facility. *Global sea ice concentration climate data record 1979-2015* (v2.0, 2017),	http://doi/10.15770/EUM_SAF_OSI_0008	*Lavergne et al., 2019*	
	OSISAF/ CCI 430-b	Input datasets			EUMETSAT Ocean and Sea Ice Satellite Application Facility. *Global sea ice concentration interim climate data record 2016 onwards* (v2.0, 2019), [Online]. Norwegian and Danish Meteorological Institutes.	http://osisaf.met.no/p/ice/#conc-reproc-v2 [last accessed: 2020-08-14] at time of writing available at	*Lavergne et al., 2019*	

ACCEPTED VERSION SUBJECT TO FINAL EDITING

						ftp://osisaf.met.no/reprocessed/ice/conc-cont-reproc/v2p0/		
	NASA Team and Bootstrap algorithm data as included in the NOAA/NSIDC Climate data record	Input data set			Meier, W. N., F. Fetterer, M. Savoie, S. Mallory, R. Duerr, and J. Stroeve. 2017. *NOAA/NSIDC Climate Data Record of Passive Microwave Sea Ice Concentration, Version 3*. [Indicate subset used]. Boulder, Colorado USA. NSIDC: National Snow and Ice Data Center. Cavalieri, D. J., C. L. Parkinson, P. Gloersen, and H. J. Zwally. 1996, updated yearly. *Sea Ice Concentrations from Nimbus-7 SMMR and DMSP SSM/I-SSMIS Passive Microwave Data, Version 1*. Comiso, J. C. 2017. *Bootstrap Sea Ice Concentrations from Nimbus-7 SMMR and DMSP SSM/I-SSMIS, Version 3*. Boulder, Colorado USA. NASA National Snow and Ice Data Center Distributed Active Archive Center.	https://doi.org/10.7265/N59P2ZTG	Cavalieri et al., 1996; Comiso et al., 2017	

ACCEPTED VERSION
SUBJECT TO FINAL EDITING

Figure 9.13 Right column	Plotting code	Code	plot_Fig_9_13_RIGHT_and_Fig_9_15_RIGHT.py					
Figure 9.13 Right column	CMIP6 (CMIP, Scenario MIP)	Model dataset						
Figure 9.14	Plotting code	Code	plot_Fig_9_14.py					
Figure 9.14	CMIP6 Sea-Ice Model Intercomparison Project SIMIP	Model dataset					SIMIP Community, 2020	
Figure 9.15 Left panel	UHH SIA	Input datasets	SeaIceArea__NorthernHemisphere__monthly__UHH__v2019_fv0.01.nc	Creative Commons Attribution 4.0 International	Doerr, Jakob, Notz, Dirk, & Kern, Stefan. (2021). UHH Sea Ice Area Product (Version 2019_fv0.01) [Data set].	http://doi.org/10.25592/uhhfdm.8559		
Figure 9.15 Left panel	Plotting code	Code	plot_9_13_and_9_15.py					
Figure 9.15 Maps (except right column)	OSISAF/ CCI 450	Input datasets			EUMETSAT Ocean and Sea Ice Satellite Application Facility. *Global sea ice concentration climate data record 1979-2015* (v2.0, 2017),	http://doi/10.15770/EUM_SAF_OSI_0008	*Lavergne et al., 2019*	
	OSISAF/ CCI 430-b	Input datasets			EUMETSAT Ocean and Sea Ice Satellite Application Facility. *Global sea ice concentration interim climate data record 2016 onwards* (v2.0, 2019), [Online]. Norwegian and Danish Meteorological	http://osisaf.met.no/p/ice/#conc-reproc-v2 [last accessed: 2020-08-14] at time of writing	*Lavergne et al., 2019*	

ACCEPTED VERSION SUBJECT TO FINAL EDITING

					Institutes.	available at ftp://osisaf.met.no/reprocessed/ice/conc-cont-reproc/v2p0/		
	NASA Team and Bootstrap algorithm data as included in the NOAA/NSIDC Climate data record	Input data set			Meier, W. N., F. Fetterer, M. Savoie, S. Mallory, R. Duerr, and J. Stroeve. 2017. *NOAA/NSIDC Climate Data Record of Passive Microwave Sea Ice Concentration, Version 3*. [Indicate subset used]. Boulder, Colorado USA. NSIDC: National Snow and Ice Data Center. Cavalieri, D. J., C. L. Parkinson, P. Gloersen, and H. J. Zwally. 1996, updated yearly. *Sea Ice Concentrations from Nimbus-7 SMMR and DMSP SSM/I-SSMIS Passive Microwave Data, Version 1*. Comiso, J. C. 2017. *Bootstrap Sea Ice Concentrations from Nimbus-7 SMMR and DMSP SSM/I-SSMIS, Version 3*. Boulder, Colorado USA. NASA National Snow and Ice Data Center Distributed	https://doi.org/10.7265/N59P2ZTG	Cavalieri et al., 1996; Comiso et al., 2017	

ACCEPTED VERSION SUBJECT TO FINAL EDITING

					Active Archive Center.			
Figure 9.15 Right column	CMIP6 (CMIP, Scenario MIP)	Model dataset						
Figure 9.15 Right column	Plotting code	Code	plot_Fig_9_13_RIGHT_and_Fig_9_15_RIGHT.py					
Figure 9.16 Top left panel	Regional Mass Change in Greenland	Input dataset					Colgan et al., 2019; Mouginot et al., 2019	Referenced to 2015
Figure 9.16 Top right panel	Regional Mass Change in Antarctic	Input dataset					Bamber et al., 2018a; IMBIE Team, 2018	Referenced to 2015
Figure 9.16 Lower panels	Regional Mass Change in Greenland	Input dataset					Mankoff et al., 2019; Mouginot et al., 2019; King et al., 2020	
Figure 9.17 Top-left panel	Greenland Paleo observations (MPWP)	Input dataset					Dolan et al (2011); Koenig et al. (2015); Miller et al. (2012); de Boer et al. (2017); Dolan et al. (2015); Contoux et al. (2015)	The mean of each of these studies means is plotted as a circle. The range shows the maximum and minimum of range values across all these studies.
	Greenland Paleo observations (LIG)	Input dataset					Robinson et al. (2011); Colville et al. (2011); Fyke et al. (2011); Born & Nisancioglu (2012); Quiqet et al. (2013); Dahl-Jensen et al. (2013); Helsen et al. (2013);	The mean of each of these studies means is plotted as a circle. The range shows the maximum and minimum of range values across all these studies.

ACCEPTED VERSION SUBJECT TO FINAL EDITING

							Stone et al. (2013); Colleoni et al., (2014); Robinson & Goelzer (2014); Calov et al., (2015); Dutton et al. (2015); Goezler et al (2017); Yau et al., (2016) Bradley et al. (2018); Tabone et al. (2018); Plach et al. (2019); Clark et al. (2020)	
	Greenland Paleo observations (LGM)	Input dataset					Simpson et al. (2009); Lecavalier et al. (2014); Peltier et al. (2015); Khan et al. (2016); Simms et al. (2019); Stuhne et al. (2015); Argus & Peltier (2010).; Bradley et al. (2018); Tabone et al. (2018)	The mean of each of these studies means is plotted as a circle. The range shows the maximum and minimum of range values across all these studies.
Figure 9.17 Top-right panel	Greenland mass loss historical data	Input dataset					Box and Colgan 2013; Kjeldsenet al., 2015; Mouginot et al., 2019; Bamber et al., 2018b; The UMBIE Team, 2019	
	Greenland mass loss projection (ISMIP6)	Model datasets					Goelzer et al., 2020; Payne et al., submitted	
	Greenlan	Model					Edwards et al.,	

ACCEPTED VERSION SUBJECT TO FINAL EDITING

	d mass loss projection (ISMIP6 emulation)	dataset					submitted	
Figure 9.17 Bottom panels	Paleo reconstructions (left 3 panels)	Input dataset					Lecavalier et al., 2014; Koenig et al., 2015; Goelzer et al., 2017	
	CryoSat 2 radar altimetry	Input Dataset					Bamber et al., 2018b	
	ISMIP6 projection	Input dataset					Goelzer et al., 2020	
Figure 9.18 Top-left panel	Antarctica Paleo observations (MPWP)	Input dataset					Dolan et al (2011); Miller et al. (2012); Pollard et al (2015); de Boer et al. (2015); de Boer et al. (2017); Deconto & Pollard (2016); Yan et al. (2016); Gasson et al. (2016); Golledge et al. (2017)	The mean of each of these studies means is plotted as a circle. The range shows the maximum and minimum of range values across all these studies.
	Antarctica Paleo observations (LIG)	Input dataset					Bamber et al. (2009); Dutton et al. (2015); Goezler et al (2017); Briggs et al. (2014) Clark et al. (2020) Albrecht et al. (2020)	The mean of each of these studies means is plotted as a circle. The range shows the maximum and minimum of range values across all these studies.
	Antarctica Paleo observations (LGM)	Input dataset					Whitehouse et al. (2012) Golledge et al. (2012) Golledge et al. (2013) Mackintosh et al. (2011)	The mean of each of these studies means is plotted as a circle. The range shows the

ACCEPTED VERSION SUBJECT TO FINAL EDITING

							Golledge et al. (2014) Ivins et al. (2013) Maris et al. (2014) Argus et al. (2014) Simms et al. (2019) Argus et al. (2014) Argus & Peltier (2010)	maximum and minimum of range values across all these studies.
Figure 9.18 Top-right panel	Antarctic mass loss historical data	Input dataset					WCRP Global Sea Level Budget Group, 2018	
	Antarctic mass loss projection (ISMIP6)	Model datasets					Seroussi et al., 2019; Payne et al., submitted	
	Antarctic mass loss projection (ISMIP6 emulation)	Model dataset					Edwards et al., submitted	
Figure 9.18 Bottom panels	Paleo reconstructions (left 3 panels)	Input dataset					Anderson et al., 2002; Bentley et al., 2014; De Boer et al., 2015; Goelzer et al., 2016	
	Restored analog radar records	Input Dataset					Schroeder et al., 2019	
	ISMIP6 projection	Input dataset					Seroussi et al., 2019	
Figure 9.19 Top-left panel	Present-day melt rates (input-output method)	Input dataset					Rignot et al., 2013	
Figure 9.19 Top-middle panel	Present-day melt rates (non-local PIGL)	Input dataset					Jourdain et al., 2020	
Figure 9.19	Present-day melt	Input dataset					Naughten et al., 2018	

ACCEPTED VERSION SUBJECT TO FINAL EDITING

Top-right panel	rates (FESOM simulation)							
Figure 9.19 Bottom panels	ISMIP6 projections	Input dataset						Future anomalies are calculated as 2081-2100 minus present-day using the ISMIP6 non-local-MeanAnt and non-local-PIGL parameterizations ((Jourdain et al., 2020) lower left and centre respectively) based on projections from the NorESM1-M CMIP5 model, and the FESOM-MMM projection (lower right).
Figure 9.20	Glacier change rates	Input dataset					Zemp et al., 2019; Zemp et al., 2020; Wouters et al., 2019; Hugonnet et al., submitted	
Figure 9.21	Historical glacier mass	Input dataset					Marzeion et al., 2015; Zemp et al., 2019; Bamber et al., 2018.	
	CMIP6 (Glacier MIP Phase 2)	Model dataset					Marzeion et al., 2020	
Figure 9.22	Global mean annual ground temperature data (GTN-P)	Input dataset			GTN-P, 2018			
Figure 9.22	CMIP6 (CMIP,	Model dataset	pf15m_amip_NH_19	Creative				

ACCEPTED VERSION SUBJECT TO FINAL EDITING

Left panel	AMIP, land-hist), CMIP5		79-1998.txt; pf15m_CMIP5historical_NH_1979-1998.txt; pf15m_historical_NH_1979-1998.txt; pf15m_land-hist_NH_1979-1998.txt	Commons Attribution 4.0 International				
	Observed and reanalysis-based permafrost extent	Input dataset	3 values extracted manually from the cited references	No license required	Obu et al., 2018; Zhang et al., 1999; Gruber et al., 2012	-	Obu et al., 2018; Zhang et al., 1999; Gruber et al., 2012	-
Figure 9.22 Right panel	CMIP6 (CMIP, ScenarioMIP)	Model dataset	pfvolbin-3m.tgz	Creative Commons Attribution 4.0 International			Python, Fortran	Change calculated relative to 1995-2014 over historical period and up to 2100
Figure 9.23	Observed snow trends	Input dataset	Figure directly from publication	Creative Commons Attribution 4.0 International	Mudryk et al., 2020		Mudryk et al., 2020	Trends and anomalies calculated over 1981-2018.
Figure 9.24 Left panel	Observed snow cover extent	Input dataset	Mudryk_scf_1981-2014.txt	Creative Commons Attribution 4.0 International	Mudryk et al., 2020	-	Mudryk et al., 2020	
	CMIP6 (CMIP)	Model dataset	snc_clim_CMIP6_historical_1981-2014.txt	Creative Commons Attribution 4.0 International	Mudryk et al., 2020		Mudryk et al., 2020	1981-2014
Figure 9.24 Right panel	CMIP6 (CMIP, ScenarioMIP)	Model dataset	sncbin.tgz	Creative Commons Attribution 4.0	Mudryk et al., 2020		Mudryk et al., 2020	1850-2100, relative to 1995-2014

ACCEPTED VERSION SUBJECT TO FINAL EDITING

				International				
Figure 9.25	Literature global mean sea leavel projections	Input dataset					Bakker et al. 2017 Jackson and Jevrejeva 2016 Kopp et al. 2014 Kopp et al. 2016 Mengel et al. 2016 Nauels et al. 2017a Slangen et al. 2014 LeBars et al. 2018 LeCozannet et al. 2019 Goodwin et al. 2017 Nicholls et al. 2018 Kopp et al. 2017 Wong et al. 2017 Grinsted et al. 2015 Jackson and Jevrejeva 2016 Jevrejeva et al. 2014 Bamber et al. 2019 Horton et al. 2020	See Appendix Tables 9.A.5 and 9.A.6
Figure 9.26	Sea level projections							See 9.6.3.2, Table 9.7, and Appedix 9.A.4 for methods
	Figure 9.26 Plotting code	Code	Plot_SL_Contribution_Maps.m					
	Figure 9.26 Plotting Code	Code	Plot_SL_Contribution_Timeseries.m					
Figure 9.27	GMSL projections							See 9.6.3.2, Table 9.7, and Appedix 9.A.4 for methods
	Figure 9.27	Code	Plot_GMSL_Projecte					

ACCEPTED VERSION SUBJECT TO FINAL EDITING

	Plotting Code		d_Scenarios.m					
Figure 9.28	Sea level projections							See 9.6.3.2, Table 9.7, and Appedix 9.A.4 for methods
	Figure 9.28 Plotting Code	Code	Plot_RSL_Scenario_Maps.m					
Figure 9.29	Sea level timing projections							See 9.6.3.2, Table 9.7, and Appedix 9.A.4 for methods
	Figure 9.29 Plotting Code	Code	plot_exceedance_year.r					
Figure 9.30	GMSL commitment (models)	Input dataset					Clark et al., 2016; Van Breedam et al., 2020; Garbe et al., 2020; DeConto and Pollard, 2016; Gregory et al, 2020	
	GMSL Commitment (paleo records)	Input dataset						Assessed in 2.3.3.3
	Figure 9.30 Plotting Code	Code	plot_SLR_commitments.m					
Figure 9.31A	Observed minor tidal flood frequency trend	Input dataset (observations)			Woodworth et al. (2017) ( )	Gesla.org ( )	Woodworth et al. (2017) ( )	Trends determined over 1950-2020
Figure 9.31B	Observed minor tidal flood frequency trend	Input dataset (observations)			Woodworth et al. (2017) ( )	Gesla.org ( )	Woodworth et al. (2017) ( )	Trends determined over 1950-2020
Figure 9.32	Sea level projections	Input dataset					Buchanan et al., 2016; Oppenheimer et al., 2019; Frederikse et al., 2020	See Appendix 9.A.4.8 for methods
	Global Extreme Sea Level Analysis	Input dataset	private_14032017.zip public_11092018.zip			https://www.gesla.org/	Woodworth et al, 2017	Public and private parts of dataset

ACCEPTED VERSION SUBJECT TO FINAL EDITING

	2 (GESLA 2)							
	Figure 9.32 Plotting Code	Code	Plot_fig9_32_ESL.m					

[END TABLE 9.SM.9 HERE]

ACCEPTED VERSION
SUBJECT TO FINAL EDITING

Chapter 10: Linking global to regional climate change

Coordinating Lead Authors:
Francisco J. Doblas-Reyes (Spain), Anna A. Sörensson (Argentina)

Lead Authors:
Mansour Almazroui (Saudi Arabia), Alessandro Dosio (Italy), William J. Gutowski (United States of America), Rein Haarsma (The Netherlands), Rafiq Hamdi (Belgium), Bruce Hewitson (South Africa), Won-Tae Kwon (Republic of Korea), Benjamin L. Lamptey (Niger, Ghana/Ghana), Douglas Maraun (Austria/Germany), Tannecia S. Stephenson (Jamaica), Izuru Takayabu (Japan), Laurent Terray (France), Andrew Turner (United Kingdom), Zhiyan Zuo (China)

Contributing Authors:
Martin Jury (Spain/Austria), Gudfina Aðalgeirsdóttir (Iceland), Bhupesh Adhikary (Nepal), Muhammad Adnan (Pakistan), Bodo Ahrens (Germany), Muhammad Amjad (Pakistan), Paola A. Arias (Colombia), Farooq Mohamed Azam (India), Ségolène Berthou (United Kingdom/France), Melissa S. Bukovsky (United States of America), Alex J. Cannon (Canada), Ana Casanueva (Spain), Annalisa Cherchi (Italy), Erika Coppola (Italy), Faye Abigail Cruz (Philipines), Joseph D. Daron (United Kingdom), Marie-Estelle Demory (Switzerland/France, Switzerland), Claudine Dereczynski (Brazil), Alejandro Di Luca (Australia, Canada/Argentina), Leandro B. Díaz (Argentina), Hervé Douville (France), Sergio Henrique Faria (Spain/Brazil), Baylor Fox-Kemper (United States of America), Shin Fukui (Japan) Laura Gallardo (Chile), Subimal Ghosh (India), Nathan P. Gillett (Canada), Melissa I. Gomis (France/Switzerland), Hugues Goosse (Belgium), Irina V. Gorodetskaya (Portugal/Belgium, Russian Federation), Michael Grose (Australia), José Manual Gutiérrez (Spain), Pandora Hope (Australia), Akm Saiful Islam (Bangladesh), Christopher D. Jack (South Africa), Richard G. Jones (United Kingdom), Martin W. Jury (Spain/Austria), Asif Khan (Pakistan), Akio Kitoh (Japan), Svitlana Krakovska (Ukraine), Gerhard Krinner (France/Germany, France), Hiroyuki Kusaka (Japan), Stefan Lange (Germany), Flavio Lehner (United States of America /Switzerland), Christopher Lennard (South Africa), Jian Li (China), Fei Liu (China), Martin Ménégoz (France), Thanh Ngo-Doc (Vietnam), Dirk Notz (Germany), Friederike Otto (United Kingdom /Germany), Wendy Parker (United States of America), Carlos Pérez García-Pando (Spain), Izidine Pinto (South Africa/Mozambique), Jan Polcher (France/Germany), Krishnan Raghavan (India), Roshanka Ranasinghe (The Netherlands/Sri Lanka, Australia), Ingo Richter (Japan/Germany), Alex C. Ruane (United States of America), Lucas Ruiz (Argentina), Sajjad Saeed (Belgium, Italy/Pakistan, Belgium), Ramiro I. Saurral (Argentina), Reinhard K. H. Schiemann (United Kingdom /Germany), Sonia I. Seneviratne (Switzerland), Chris Shaw (United Kingdom), Theodore G. Shepherd (United Kingdom /Canada), Jonathan K. P. Shonk (United Kingdom), Jana Sillmann (Norway/Germany), Didier Swingedouw (France), Izuru Takayabu (Japan), Bart van den Hurk (The Netherlands), Robert Vautard (France), Victor Venema (Germany/The Netherlands), Sergio M. Vicente-Serrano (Spain), Piotr Wolski (South Africa/Poland), Cunde Xiao (China), Jakob Zscheischler (Germany)

Review Editors:
Gregory M. Flato (Canada), Fredolin Tangang (Malaysia), Muhammad Irfan Tariq (Pakistan)

Chapter Scientist:
Martin W. Jury (Spain/Austria)

ACCEPTED VERSION SUBJECT TO FINAL EDITING

This Chapter should be cited as:
Doblas-Reyes, F. J,. A. A. Sörensson, M. Almazroui, A. Dosio, W. J. Gutowski, R. Haarsma, R. Hamdi, B. Hewitson, W-T. Kwon, B. L. Lamptey, D. Maraun, T. S. Stephenson, I. Takayabu, L. Terray, A. Turner, Z. Zuo, 2021, Linking Global to Regional Climate Change. In: *Climate Change 2021: The Physical Science Basis. Contribution of Working Group I to the Sixth Assessment Report of the Intergovernmental Panel on Climate Change* [Masson-Delmotte, V., P. Zhai, A. Pirani, S. L. Connors, C. Péan, S. Berger, N. Caud, Y. Chen, L. Goldfarb, M. I. Gomis, M. Huang, K. Leitzell, E. Lonnoy, J.B.R. Matthews, T. K. Maycock, T. Waterfield, O. Yelekçi, R. Yu and B. Zhou (eds.)]. Cambridge University Press. In Press.

Date: August 2021

This document is subject to copy-editing, corrigenda and trickle backs.

ACCEPTED VERSION
SUBJECT TO FINAL EDITING

Executive Summary **6**

10.1 Foundations for regional climate change information **10**
10.1.1 Introduction 10
10.1.2 Regional Climate Change and the Relevant Spatial and Temporal Scales 11
10.1.2.1 Spatial scales and definition of regions 11
10.1.2.2 Temporal scales, baselines and dimensions of integration 11
10.1.3 Sources of Regional Climate Variability and Change 13
10.1.3.1 Forcings controlling regional climate 13
10.1.3.2 Internal drivers of regional climate variability 15
10.1.3.3 Uncertainty and confidence 16
10.1.4 Distillation of Regional Climate Information 16
10.1.5 Regional Climate Information in the WGI AR6 17

BOX 10.1: Regional climate in AR5 and the Special Reports SRCCL, SROCC and SR1.5 ..... **18**

Cross-Chapter Box 10.1: Influence of the Arctic on mid-latitude climate **20**

10.2 Using Observations for Constructing Regional Climate Information **23**
10.2.1 Observation Types and Their Use at Regional Scale 23
10.2.1.1 In situ and remote-sensing data 23
10.2.1.2 Derived products 25
10.2.2 Challenges for Regional Climate Change Assessment 26
10.2.2.1 Quality control 26
10.2.2.2 Homogenization 26
10.2.2.3 Data scarcity 27
10.2.2.4 Gridding 29
10.2.2.5 Observations in mountain areas 29
10.2.2.6 Structural uncertainty 30
10.2.3 Other Uses of Observations at Regional Scale 31
10.2.3.1 Observations for calibrating statistical methods 31
10.2.3.2 Observation for paleoclimate data assimilation 31
10.2.4 Outlook for Improving Observational Data for Regional Climates 32

10.3 Using Models for Constructing Regional Climate Information **32**
10.3.1 Model Types 32
10.3.1.1 Global models, including high-resolution and variable resolution models 34
10.3.1.2 RCMs 35
10.3.1.3 Statistical approaches to generate regional climate projections 36
10.3.1.3.1 Perfect prognosis 36

ACCEPTED VERSION SUBJECT TO FINAL EDITING

10.3.1.3.2 Bias adjustment 36
10.3.1.3.3 Delta-change approaches 37
10.3.1.3.4 Weather generators 37
10.3.1.3.5 Hybrid approaches and emulators 37
10.3.2 Types of Model Experiments 37
10.3.2.1 Transient simulations and time-slice experiments 38
10.3.2.2 Pseudo-global warming experiments 38
10.3.2.3 Sensitivity studies with selected drivers 39
10.3.2.4 Control simulations 39
10.3.2.5 Simulations for evaluating downscaling methods 40
10.3.3 Model Performance and Added Value in Simulating and Projecting Regional Climate 40
10.3.3.1 Evaluation diagnostics 41
10.3.3.2 Model improvement and added value 42
10.3.3.3 Performance at simulating large-scale phenomena and teleconnections relevant for regional climate 43
10.3.3.3.1 Mid-to-high latitude atmospheric variability phenomena: blocking and extratropical cyclones 43
10.3.3.3.2 Tropical phenomena: ENSO teleconnections 44
10.3.3.4 Performance at simulating regional phenomena and processes 45
10.3.3.4.1 Convection including tropical cyclones 46
10.3.3.4.2 Mountain wind systems 47
10.3.3.4.3 Coastal winds and lake effects 47
10.3.3.4.4 Fronts 48
10.3.3.5 Performance at simulating regional feedbacks 49
10.3.3.6 Performance at simulating regional drivers of climate and climate change 50
10.3.3.7 Statistical downscaling, bias adjustment and weather generators 51
10.3.3.7.1 Performance of perfect prognosis methods 53
10.3.3.7.2 Performance of bias adjustment methods 53
10.3.3.7.3 Performance of weather generators 53
10.3.3.8 Performance at simulating historical regional climate changes 54
10.3.3.9 Fitness of climate models for projecting regional climate 55
10.3.3.10 Synthesis of model performance at simulating regional climate and climate change 57
10.3.4 Managing Uncertainties in Regional Climate Projections 59
10.3.4.1 Propagation of uncertainties 59
10.3.4.2 Representing and reducing uncertainties 59
10.3.4.3 Role of internal variability 60
10.3.4.4 Designing and using ensembles for regional climate change assessments to take uncertainty into account 62

Cross-Chapter Box 10.2: Relevance and limitations of bias adjustment 63

ACCEPTED VERSION SUBJECT TO FINAL EDITING

10.4 Interplay between Anthropogenic Change and Internal Variability at Regional Scales. 66
10.4.1 Methodologies for Regional Climate Change Attribution 66
10.4.1.1 Optimal fingerprinting methods 66
10.4.1.2 Other spatiotemporal statistical methods for isolating regional climate responses to external forcing 67
10.4.1.3 Other regional-scale attribution approaches 69
10.4.2 Regional Climate Change Attribution Examples 70
10.4.2.1 The Sahel and West African monsoon drought and recovery 70
10.4.2.2 The southeastern South America summer wetting 72
10.4.2.3 The southwestern North America drought 74
10.4.2.4 Assessment summary 76
10.4.3 Future Regional Changes: Robustness and Emergence of the Anthropogenic Signal 76
10.4.3.1 Robustness of the anthropogenic signal at regional scale 77
10.4.3.2 Emergence of the anthropogenic signal at regional scale 78

10.5 Combining Approaches to Constructing Regional Climate Information 81
10.5.1 Sources of Regional Climate Information 82
10.5.2 Framing Elements for Constructing User-Relevant Information 83
10.5.2.1 Consideration of different contexts 83
10.5.2.2 Developing climate information conditioned by values of different actors and communities . 84
10.5.2.3 The roles of spatial and temporal resolution in relation to decision scale 85
10.5.3 Distillation of Climate Information 86
10.5.3.1 Information construction 86
10.5.3.2 Translating climate information into the user context 87
10.5.3.3 Transdisciplinary approaches to stakeholder interaction 88
10.5.3.4 Barriers to the distillation of climate information 88
10.5.3.5 Synthesis assessment of climate information distillation 88
10.5.4 Climate Services and the Construction of Regional Climate Information 89

BOX 10.2: Storylines for constructing and communicating regional climate information 89

Cross-Chapter Box 10.3: Assessment of climate change information at the regional scale 91

10.6 Comprehensive Examples of Steps Toward Constructing Regional Climate Information 94
10.6.1 Introduction 94
10.6.2 Cape Town Drought 95
10.6.2.1 Motivation and regional context 95
10.6.2.2 The region's climate 96
10.6.2.3 Observational issues 97
10.6.2.4 Relevant anthropogenic and natural drivers 97

ACCEPTED VERSION SUBJECT TO FINAL EDITING

10.6.2.5 Model simulation and attribution over the historical period 99
10.6.2.6 Future climate information from global simulations 99
10.6.2.7 Future climate information from regional downscaling 99
10.6.2.8 Storyline approaches 100
10.6.2.9 Climate information distilled from multiple lines of evidence 100
10.6.3 Indian Summer Monsoon 100
10.6.3.1 Motivation and regional context 100
10.6.3.2 The regional climate of India 101
10.6.3.3 Observational issues for India 101
10.6.3.4 Relevant anthropogenic and natural drivers for long-term change 102
10.6.3.5 Model simulation and attribution of drying over the historical period 102
10.6.3.6 Future climate projections from global simulations 103
10.6.3.7 Future climate projections from regional downscaling 105
10.6.3.8 Storyline approaches for India 106
10.6.3.9 Regional climate information distilled from multiple lines of evidence 107
10.6.4 Mediterranean Summer Warming 107
10.6.4.1 Motivation and regional context 107
10.6.4.2 The region's climate 108
10.6.4.3 Observational issues 108
10.6.4.4 Relevant anthropogenic and natural drivers 108
10.6.4.5 Model simulation and attribution over the historical period 109
10.6.4.6 Future climate information from global simulations 110
10.6.4.7 Future climate information from regional downscaling 112
10.6.4.8 Storyline approaches 113
10.6.4.9 Climate information distilled from multiple lines of evidence 113

BOX 10.3: Urban Climate: Processes and Trends 113

Cross-Chapter Box 10.4: Climate Change over the Hindu Kush Himalaya 116

10.7 Final remarks 118

Frequently Asked Questions 120
FAQ 10.1: How can we provide useful climate information for regional stakeholders? 120
FAQ 10.2: Why are cities hotspots of global warming? 122

Acknowledgements 124

References 125

Figures 197

ACCEPTED VERSION SUBJECT TO FINAL EDITING

Executive Summary

Although climate change is a global phenomenon, its manifestations and consequences are different in different regions, and therefore climate information on spatial scales ranging from sub-continental to local is used for impact and risk assessments. Chapter 10 assesses the foundations of how regional climate information is distilled from multiple, sometimes contrasting, lines of evidence. Starting from the assessment of global-scale observations in Chapter 2, Chapter 10 assesses the challenges and requirements associated with observations relevant at the regional scale. Chapter 10 also assesses the fitness of modelling tools available for attributing and projecting anthropogenic climate change in a regional context starting from the methodologies assessed in Chapters 3 and 4. Regional climate change is the result of the interplay between regional responses to both natural forcings and human influence (considered in Chapters 2, 5, 6 and 7), responses to large-scale climate phenomena characterizing internal variability (considered in Chapters 1–9), and processes and feedbacks of a regional nature.

Chapter 10 is the first of four chapters that assess regional-scale information in this report. The region-by-region assessment of past and future changes in extremes (Chapter 11), climatic impact-drivers (Chapter 12) and mean climate (Atlas) relies on the sources and methodologies used for constructing regional climate change information assessed in Chapter 10. Building on the assessment of observations and modelling tools of Chapter 10, Chapter 11 assesses the observation and modelling of extremes. Chapter 10 assesses methodologies to attribute multi-decadal regional trends to the interplay between external forcing and internal variability, while Chapter 11 assesses the attribution of extreme events. The assessment of climate services in Chapter 12 builds on the assessment of distillation of regional climate information from multiple lines of evidence in Chapter 10.

Distilling regional climate information from multiple lines of evidence and taking the user context into account will increase the fitness, usefulness and relevance for decision-making and enhances the trust users will have in applying it (*high confidence*). This distillation process can draw upon multiple observational datasets, ensembles of different model types, process understanding, expert judgement and indigenous knowledge. Important elements of distillation include attribution studies, the characterization of possible outcomes associated with internal variability and a comprehensive assessment of observational, model and forcing uncertainties and possible contradictions using different analysis methods. Taking the values of the relevant actors into account when co-producing climate information, and translating this information into the broader user context, improves the usefulness and uptake of this information (*high confidence*). {10.5}

Observations and Models as Sources of Regional Information

The use of multiple sources of observations and tailored diagnostics to evaluate climate model performance increases trust in future projections of regional climate (*high confidence*). The availability of multiple observational records, including reanalyses, that are fit for evaluating the phenomena of interest and account for observational uncertainty, are fundamental for both understanding past regional climate change and assessing climate model performance at regional scales (*high confidence*). Employing tailored, process-oriented and potentially multivariate diagnostics to evaluate whether a climate model realistically simulates relevant aspects of present-day regional climate increases trust in future projections of these aspects (*high confidence*). {10.2.2, 10.3.3}

Currently, scarcity and reduced availability of adequate observations increase the uncertainty of long-term temperature and precipitation estimates (*virtually certain*). Precipitation measurements in mountainous areas, especially of solid precipitation, are strongly affected by gauge location and setup (*very high confidence*). Over data-scarce regions or over complex orography, gridded temperature and precipitation products are strongly affected by interpolation methods. Lack of access to the raw station data used to create gridded products compromises the trustworthiness of these products since the influence of the gridding process on the product cannot be assessed. The use of statistical homogenization methods reduces uncertainties related to long-term warming estimates at regional scales (*virtually certain*) {10.2.2, 10.6.2, 10.6.3, 10.6.4, Box 10.3}.

ACCEPTED VERSION SUBJECT TO FINAL EDITING

Regional reanalyses provide surrogates of observed climate variables that are highly relevant in areas with scarce surface observations. Regional reanalyses represent the distributions of precipitation, surface air temperature, and surface wind, including the frequency of extremes, better than global reanalyses (*high confidence*). However, their usefulness is limited by their short length, the typical regional model errors, and the relatively simple data assimilation algorithms. {Section 10.2.1}

Global and regional climate models are important sources of climate information at the regional scale. Global models by themselves provide a useful line of evidence for the construction of regional climate information through the attribution or projection of forced changes or the quantification of the role of the internal variability (*high confidence*). Dynamical downscaling using regional climate models adds value in representing many regional weather and climate phenomena, especially over regions of complex orography or with heterogeneous surface characteristics (*very high confidence*). Increasing climate model resolution improves some aspects of model performance (*high confidence*). Some local-scale phenomena such as land-sea breezes and mountain wind systems can only be realistically represented by simulations at a resolution of the order of 10 km or finer (*high confidence*). Simulations at kilometre-scale resolution add value in particular to the representation of convection, sub-daily precipitation extremes (*high confidence*) and soil-moisture precipitation feedbacks (*medium confidence*). Sensitivity experiments aid the understanding of regional processes and can provide additional user-relevant information. {10.3.3, 10.4, 10.5, 10.6}.

The performance of global and regional climate models and their fitness for future projections depend on their representation of relevant processes, forcings and drivers and on the specific context. Improving global model performance for regional scales is fundamental for increasing their usefulness as regional information sources. It is also key for improving the boundary conditions for dynamical downscaling and the input for statistical approaches, in particular when regional climate change is strongly influenced by large-scale circulation changes. Increasing resolution per se does not solve all performance limitations. Including the relevant forcings (e.g., aerosols, land-use change and stratospheric ozone concentrations) and representing the relevant feedbacks (e.g., snow–albedo, soil-moisture–temperature, soil-moisture–precipitation) in global and regional models is a prerequisite for reproducing historical regional trends and ensuring fitness for future projections (*high confidence*). The sign of projected regional changes of variables such as precipitation and wind speed is in some cases only simulated in a trustworthy manner if relevant regional processes are represented (*medium confidence*). {10.3.3, 10.4.1, 10.4.2, 10.6.2, Cross-Chapter Box 10.2}.

Statistical downscaling, bias adjustment and weather generators are useful approaches for improving the representation of regional climate from dynamical climate models. Statistical downscaling methods with carefully chosen predictors and an appropriate model structure for a given application realistically represent many statistical aspects of present-day daily temperature and precipitation (*high confidence*). Bias adjustment has proven beneficial as an interface between climate model projections and impact modelling in many different contexts (*high confidence*). Weather generators realistically simulate many statistical characteristics of present-day daily temperature and precipitation, such as extreme temperatures and wet- and dry-day transition probabilities (*high confidence*). {10.3.3}

The performance of statistical downscaling, bias adjustment and weather generators in climate change applications depends on the specific model and on the dynamical climate model driving it. Knowledge is still limited about suitable predictors for statistical downscaling of regional climate change, particularly for precipitation. Bias adjustment cannot overcome all consequences of unresolved or strongly misrepresented physical processes, such as large-scale circulation biases or local feedbacks, and may instead introduce other biases and implausible climate change signals (*medium confidence*). Using bias adjustment as a method for statistical downscaling, particularly for coarse-resolution global models, may lead to substantial misrepresentations of regional climate and climate change (*medium confidence*). Instead, dynamical downscaling may resolve relevant local processes prior to bias adjustment, thereby improving the representation of regional changes. The performance of statistical approaches and their fitness for future projections depends on predictors and change factors taken from the driving dynamical models (*high confidence*) {10.3.3, Cross-Chapter Box 10.2}.

ACCEPTED VERSION SUBJECT TO FINAL EDITING

Different types of climate model ensembles allow for the assessment of regional climate projection uncertainties, although ensemble spread is not a full measure of the uncertainty (*very high confidence*). Multi-model ensembles enable the assessment of regional climate response uncertainty (*very high confidence*). Discarding models that fundamentally misrepresent processes relevant for a given purpose improves the fitness of multi-model ensembles for generating regional climate information (*high confidence*). At the regional scale, multi-model mean and ensemble spread are not sufficient to characterize low-probability, high-impact changes or situations where different models simulate substantially different or even opposing changes (*high confidence*). In such cases, storylines aid the interpretation of projection uncertainties. Since AR5, the availability of multiple single-model initial-condition large ensembles (SMILEs) allows for a more robust separation of model uncertainty and internal variability in regional-scale projections and provides a more comprehensive spectrum of possible changes associated with internal variability (*high confidence*). {10.3.4}

Interplay between Human Influence and Internal Variability at Regional Scales

Human influence has been a major driver of regional mean temperature change since 1950 in many sub-continental regions of the world (*virtually certain*). Regional-scale detection and attribution studies as well as observed emergence analysis provide robust evidence supporting the dominant contribution of human influence to regional temperature changes over multidecadal periods. {10.4.1; 10.4.3}

While human influence has contributed to multi-decadal mean precipitation changes in several regions, internal variability can delay emergence of the anthropogenic signal in long-term precipitation changes in many land regions (*high confidence*). Multiple attribution approaches, including optimal fingerprinting, grid-point detection, pattern recognition and dynamical adjustment methods, as well as multi-model, single-forcing large ensembles and multi-centennial paleoclimate records, support the contribution of human influence to several regional multi-decadal mean precipitation changes (*high confidence*). At regional scale, internal variability is stronger and uncertainties in observations, models and human influence are all larger than at the global scale, precluding a robust assessment of the relative contributions of greenhouse gases, stratospheric ozone, different aerosol species and land use/land cover changes. Multiple lines of evidence, combining multi-model ensemble global projections with those coming from SMILEs, show that internal variability is largely contributing to the delayed or absent emergence of the anthropogenic signal in long-term regional mean precipitation changes (*high confidence*). {10.4.1, 10.4.2, 10.4.3, 10.6.3, 10.6.4}

Various mechanisms operating at different time scales can modify the amplitude of the regional-scale response of temperature, and both the amplitude and sign of the response of precipitation, to human influence (*high confidence*). These mechanisms include non-linear temperature, precipitation and soil moisture feedbacks, slow and fast responses of sea surface temperature patterns and atmospheric circulation changes to increasing greenhouse gases. {10.4.3}

Urban Climate

Many types of urban parameterizations simulate radiation and energy exchanges in a realistic way (*very high confidence*). For urban climate studies focusing on the interplay between the urban heat island and regional climate change, a simple single-layer parameterization is fit for purpose (*medium confidence*). New networks of monitoring stations in urban areas provide key information to enhance the understanding of urban microclimates and improve urban parameterizations. {Box 10.3}

The difference in observed warming trends between cities and their surroundings can partly be attributed to urbanization (*very high confidence*). Annual-mean daily minimum temperature is more affected by urbanization than annual-mean daily maximum temperature (*very high confidence*). The global annual-mean surface air temperature response to urbanization is, however, negligible (*very high confidence*). {Box 10.3}

ACCEPTED VERSION SUBJECT TO FINAL EDITING

Future urbanization will amplify the projected air temperature change in cities regardless of the characteristics of the background climate, resulting in a warming signal on minimum temperatures that could be as large as the global warming signal (*very high confidence*). A large effect is expected from the combination of future urban development and more frequent occurrence of extreme climatic events, such as heatwaves (*very high confidence*). {Box 10.3}

Distillation of Regional Climate Information

The process of distilling regional climate information from multiple lines of evidence can vary substantially from one case to another. Although methodologies for distillation have been established, the process is in practice conditioned by the sources available, the actors involved and the context, which depend heavily on the regions considered, and framed by the question being addressed. To make the most appropriate decisions and responses to changing climate, it is necessary to consider all physically plausible outcomes from multiple lines of evidence, especially in the case when they are contrasting. {10.5, 10.6, Cross-Chapter Box 10.1, Cross-Chapter Box 10.3}

Confidence in the distilled regional climate information is enhanced when there is agreement across multiple lines of evidence. For example, the apparent contradiction between the observed decrease in Indian monsoon rainfall over the second half of the 20th century and the projected long-term increase is explained by attribution of the trends to different forcings, with aerosols dominating recently and greenhouse gases in the future (*high confidence*). For the Mediterranean region, the agreement between different lines of evidence, such as observations, projections by regional and global models, and understanding of the underlying mechanisms, provides *high confidence* in summer warming that exceeds the global average. {10.5.3, 10.6, 10.6.3, 10.6.4, Cross-Chapter Box 10.3}

The outcome of distilling regional climate information can be limited by inconsistent or contradictory information. Initial observational analyses of the Cape Town drying showed a strong, post-1979 association between increasing greenhouse gases, changes in a key mode of variability (the Southern Annular Mode) and drought in the Cape Town region. However, not all global models show this association, and subsequent analysis extending farther back in time, when human influence was weaker, showed no strong association in observations between the Southern Annular Mode and Cape Town drought. Thus, despite the consistency among global-model future projections, there is *medium confidence* in a projected future drier climate for Cape Town. Likewise, the distillation process results in *low confidence* in the influence of Arctic warming on mid-latitude climate because of contrasting lines of evidence. {10.5.3, 10.6.2, Cross-Chapter Box 10.1, Cross-Chapter Box 10.3}

ACCEPTED VERSION SUBJECT TO FINAL EDITING

10.1 Foundations for regional climate change information

10.1.1 Introduction

This chapter assesses the foundations for the distillation of regional climate change information from multiple lines of evidence. The AR5, SR1.5 and SRCCL reports underlined the relevance of assessing regional climate information that is useful and relevant to the decision scale (Box 10.1). To respond to this need, the WGI report of AR6 includes four regional chapters of which this is the first one. Chapter 10 assesses the sources and methodologies used by the Chapters 11, 12 and Atlas to construct regional information. Chapter 10 builds on the assessment of methodologies considered to contruct global climate change information in Chapters 2–4 and on the processes assessed in Chapters 5–9. Additionally, this chapter assesses the methodologies for the co-production of regional climate information, the role of the different actors involved in the process and the relevance of the user context and values.

Regional climate change refers to a change in climate in a given region (Section 10.1.2.1) identified by changes in the mean or higher moments of the probability distribution of a climate variable and persisting for a few decades or longer. It can also refer to a change in temporal properties such as persistence and frequency of occurrence of weather and climate extreme events. Regional climate change may be caused by natural internal processes such as atmospheric internal variability and local climate response to low-frequency modes of climate variability (Technical Annex IV), as well as by changes in external forcings such as modulations of the solar cycle, orbital forcing, volcanic eruptions, and persistent anthropogenic changes in the composition of the atmosphere or in land use and land cover (Cross-Chapter Box 3.2; IPCC, 2018a), in addition to the interactions and feedbacks between them. Process interaction in space is pervasive, which means that small spatial scales have an influence on the larger scales (Palmer, 2013). Depending on the context, a region may refer to a large area such as a monsoon region, but may also be confined to smaller areas such as coastlines, mountain ranges or human settlements like cities. Users (understood as anyone incorporating climate information into their activity) often request climate information for these range of scales since their operating and adaptation decision scales range from the local to the sub-continental level.

Given the many types of regional climates, the broad range of spatial and temporal scales (Section 10.1.2), and the diversity of user needs, a variety of methodologies and approaches have been developed to construct regional climate change information. The sources include global and regional climate model simulations, statistical downscaling and bias adjustment methods. A commonly used source is long-term (end-of century) model projections of regional climate change, as well as near-term (next 10 years) climate predictions (Kushnir et al., 2019; Rössler et al., 2019a). Regional observations, with their associated challenges, are a key source for the regional climate information construction process (Li et al., 2020b). High-quality observations that enable monitoring of the regional aspects of climate are used to adjust inherent model biases and are the basis for assessing model performance. Process understanding and attribution of observed changes to large- and regional-scale anthropogenic and natural drivers and forcings are also important sources.

All these sources are used, when available, to distil regional climate information from multiple lines of evidence (Figure 10.1). The resulting climate information can then be integrated, following a co-production process involving both the user and the producer, into a user context that often is already taken into account when constructing the regional climate information. In fact, the distillation process leading to the climate information can consider the specific context of the question at stake, the values of both the user and the producer, and the challenge of communicating across different communities (Section 10.5).

The chapter (Figure 10.2) starts with an introduction of the concepts used in the distillation of regional climate information (Section 10.1). Section 10.2 addresses the aspects associated with the access to and use of observations, while different modelling approaches are introduced and assessed in Section 10.3. Section 10.3 also addresses the performance of models in simulating relevant climate characteristics as needed to estimate the credibility of future projections. Section 10.4 assesses the interplay between anthropogenic causes and internal variability at regional scales, and its relevance for the attribution of regional climate changes and the emergence of regional climate change signals. Section 10.5 tackles the issue of how regional

ACCEPTED VERSION SUBJECT TO FINAL EDITING

climate information is distilled from different sources taking into account the context and the values of both the producer and the user. Section 10.6 illustrates the distillation approach using three comprehensive examples. Finally, Section 10.7 lists some limitations to the assessment of regional climate information.

[START FIGURE 10.1 HERE]

Figure 10.1: Diagram of the processes leading to the construction of regional climate information (green) and user-relevant regional climate information (orange). The chapter sections and the other chapters of the report involved in each step are indicated in rectangles. WGII stands for Working Group II.

[END FIGURE 10.1 HERE]

[START FIGURE 10.2 HERE]

Figure 10.2: Visual abstract of the chapter, with its key elements.

[END FIGURE 10.2 HERE]

10.1.2 Regional Climate Change and the Relevant Spatial and Temporal Scales

The global coupled atmosphere-ocean-land-cryosphere system, including its feedbacks, shows variability over a wide spectrum of spatial and temporal scales (Hurrell et al., 2009). This section discusses concepts and definitions of what can be considered a region, the relevant temporal scales and region-specific aspects of the baselines used.

[START FIGURE 10.3 HERE]

Figure 10.3: Schematic diagram to display interacting spatial and temporal scales relevant to regional climate change information. Adapted from Orlanski (1975). The processes included in the different models and model components considered in Chapter 10 are indicated as a function of these scales.

[END FIGURE 10.3 HERE]

10.1.2.1 Spatial scales and definition of regions

Large-scale climate and the associated phenomena have been defined in Chapter 2 (e.g., Cross-Chapter Box 2.2) as ranging from global and hemispheric, to ocean-basin and continental scales. The definition of the regional scale is case specific in the WGI AR6 report. Section 1.4.5 provides definitions of the different regional types adopted by the different Chapters. In this chapter, regional scales are defined as ranging from the size of sub-continental areas (e.g., the Mediterranean basin) to local scales (e.g., coastlines, mountain ranges and cities) without prescribing any formal regional boundaries. These spatial length scales range from a few thousand down to a few kilometres and the relevant driving modes and processes at regional scales are summarized in Figure 10.3. In contrast to Chapters 11, 12 and Atlas, which make a region-by-region assessment of climate change, this chapter does not necessarily restrict itself to the use of the AR6 regions (Sections 1.4.5, Atlas.1.3). Different regional definitions have been used in sections 10.4 and 10.6, selected for their adequacy to illustrate methodological aspects (e.g., for the attribution of long-term regional trends, regions that display such trends have been selected). Typological regions (Sections 1.4.5, Atlas.1.3) are used in Box 10.3 and Cross-Chapter Box 10.4.

10.1.2.2 Temporal scales, baselines and dimensions of integration

ACCEPTED VERSION SUBJECT TO FINAL EDITING

The concept of a unified and seamless framework for weather and climate prediction (Brown et al., 2012a; Hoskins, 2013) provides the context for understanding and simulating regional climate across multiple spatial and temporal scales. This concept is embodied in the subseasonal-to-seasonal (Vitart et al., 2017) and the seasonal-to-multiannual (Smith et al., 2020) prediction activities that generate regional climate information across temporal scales. The seamless framework benefits from the convergence of methods traditionally used in weather forecasting and climate projections, in particular the role of the initialization in climate models and the strategies for the evaluation of physical processes relevant at different temporal scales.

The relatively short observational record (Section 10.2, Chapter 2) is a primary challenge to estimate the forced signal and to isolate low-frequency, multi-decadal and longer term internal variability (Frankcombe et al., 2015; Overland et al., 2016; Bathiany et al., 2018). Because only one realization of the actual climate exists, it is nontrivial to extract estimates of internal and forced variability from the available data (Frankcombe et al., 2015). As an alternative, approaches that use large observational ensembles can be applied (Section 10.4; McKinnon and Deser, 2018).

There is a close relationship between spatial and temporal scales (Figure 10.3). For example, an individual convective storm may exhibit scales of variability ranging from metres and seconds to kilometres and hours, while for El Niño-Southern Oscillation (ENSO) the scales of variability are regional to hemispheric in extent and multi-year in length. These scales interact and the interactions are represented in climate models, although the ability of current models to simulate regional phenomena and even large-scale climate drivers still leaves room for improvement (Section 10.3) and limits their capability to represent the interactions across spatial and temporal scales.

It is important to note that in this chapter and subsequent regional chapters, including the Interactive Atlas, the baselines and reference periods used for climate change estimates from regional models may vary from those used in Chapters 1–9. In these chapters three main time baselines are defined for the past, i.e., pre-industrial (1750), early-industrial (1850–1900) and recent (1995–2014), while the future reference periods are 2021–2040 (near term), 2041–2060 (mid-century) and 2081–2100 (long term) (Section 1.4.1, Cross-Chapter Box 1.2). Regional climate simulations used in the recent literature have been performed with different baselines. The differences are often due to the availability of the boundary conditions from global simulations, leading to periods chosen for those simulations like 1950–2005, in line with the CMIP5 historical simulations followed by projections from 2005 onwards (Vaittinada Ayar et al., 2016; Dong-feng et al., 2017; Cai et al., 2018a). For simulations that use CMIP3 boundary conditions other periods have been used. As a consequence, these regional simulations mix for the recent period historical simulations with projections. The mismatch needs to be considered when assessing results obtained from both global and regional models in the context of the climate information distillation process, or when linking the regional chapters to the assessments performed in previous chapters. The choice of baseline provides a source of uncertainty for the assessment of climate impacts (e.g., for the response of bird species in Africa; Baker et al., 2016). Besides, a range of different baselines may need to be considered to satisfy a variety of users, since this choice affects the perceived result (Dobor and Hlásny, 2018). The influence of the different baseline periods can be explored using the Interactive Atlas where different baselines are available, for example, 1986-2005 (according to AR5), 1995-2014 (AR6), and both 1961-1990 and 1981-2010 (WMO).

One way of overcoming the baseline uncertainty is to define the results for a given model based on specific global-mean temperature changes from the pre-industrial period (e.g., Sylla et al., 2018a for West Africa; Kjellström et al., 2018 for Europe; Taylor et al., 2018 for the Caribbean; Montroull et al., 2018 for South America). The specific global-mean temperature is known as global warming level (GWL; Sections 1.6.2 and 10.6.4, Cross-Chapter Box 11.1). The GWL is a useful dimension of integration because important changes in regional climate, including many types of extremes, scale quasi-linearly with the GWLs, often independently of the underlying emissions scenarios (e.g., Hoegh-Guldberg et al., 2018; Beusch et al., 2020; Seneviratne and Hauser, 2020), taking always into account caveats described in Cross-Chapter Box 11.1. In addition, GWLs allow a separated analysis of the global and regional climate responses associated with a warming level (Seneviratne and Hauser, 2020; Section 10.6.4). The choice of global temperature goal in the

ACCEPTED VERSION SUBJECT TO FINAL EDITING

context of the 2015 Paris Agreement means that there is an increasing desire for the regional climate information to be expressed as a function of GWLs.

10.1.3 Sources of Regional Climate Variability and Change

Variability in regional climate arises from natural and anthropogenic forcings, internal variability including the local expression of large-scale remote drivers (also known as teleconnections), and the feedbacks between them. Due to the many possible drivers of variability and change (Figure 10.3), quantifying the interplay between internal modes of decadal variability and any externally forced component is crucial in attempts to attribute causes of regional climate changes (e.g., Hoell et al., 2017; Nath et al., 2018). A regional climate signal could arise purely due to some anthropogenic influence or conversely, entirely due to internal variability, but it is most likely the result of a combination of both (Section 10.4). This section briefly introduces these sources of regional variability and should be read along with corresponding sections in Chapters 3, 6 and 7. Section 10.3 assesses their representation in climate models, Section 10.4 discusses their relevance for the attribution of multi-decadal trends and Section 10.6 refers to them as sources in specific examples where regional climate information is built. Section 8.2 offers a companion discussion focussing on changes in the water cycle. An example of how changes in one region could act as a source for changes in a neighbouring one is assessed in the Cross-Chapter Box 10.1 for the linkages between polar and mid-latitude regions, an interaction that has led to substantial recent research. This section also introduces the sources of uncertainty in model-derived regional climate information and how the quantification of the uncertainties influences the confidence of the regional climate information.

10.1.3.1 Forcings controlling regional climate

There are important differences in the processes affected by greenhouse gases (GHGs) over land and ocean. Over the ocean, the increased radiative forcing leads to an increase in latent heat flux and a decrease in sensible heat flux, while over land, water availability is limited and increased radiative energy is therefore converted mostly into sensible heat (Sutton et al., 2007). Notably, this leads to preferential warming of the land regions, which are themselves skewed towards the Northern Hemisphere.

Variations in solar forcing (Section 2.2.1) could influence regional climate through its modulation of circulation patterns, although this research field is still hampered by large observational and modelling uncertainties. The 11-year solar cycle has been suggested to affect the leading atmospheric circulation modes of the North Atlantic region in model based studies (Gray et al., 2013; Thiéblemont et al., 2015; Sjolte et al., 2018). In particular the solar cycle has been suggested as an important source of near-term predictability of the North Atlantic Oscillation (NAO; Kushnir et al., 2019), while other studies have not found evidence for links between the solar cycle and NAO in observational records (Ortega et al., 2015; Sjolte et al., 2018; Chiodo et al., 2019). On centennial time scales, solar fluctuations were found to be correlated with the Eastern Atlantic Pattern (Sjolte et al., 2018). Possible influences on winter circulation and temperature over Eurasia (Chen et al., 2015) and North America (Liu et al., 2014; Li and Xiao, 2018) have also been identified.

An updated assessment of past changes in stratospheric ozone can be found in Section 2.2.5.2. AR6 assesses that both GHG and stratospheric ozone depletion have contributed to the expansion of the zonal mean Hadley cell in the Southern Hemisphere for the period 1981–2000 with *medium confidence* (Section 3.3.3) (Garfinkel et al., 2015; Waugh et al., 2015; Grise et al., 2019). There is *medium confidence* that stratospheric ozone depletion contributed to the strengthening trend of the summer SAM for the period 1970-1990, but this influence has been weaker since 2000 (Section 3.7.2). The poleward shift of the Southern Hemisphere westerlies has also been explained by stratospheric ozone depletion (Solman and Orlanski, 2016). Section 10.4 assesses its role in the multi decadal increase of rainfall in Southeastern South America and Section 10.6.2 does so for the occurrence of the Cape Town drought.

Both natural and anthropogenic aerosols are often emitted at a regional scale, have a short atmospheric

ACCEPTED VERSION SUBJECT TO FINAL EDITING

lifetime (from a few hours to several days; Section 6.1), are dispersed regionally and affect climate at a regional scale through radiative cooling/heating and cloud microphysical effects (Rotstayn et al., 2015; Sherwood et al., 2015; Chapter 8). The majority of aerosols scatter solar radiation, but with strong regional variations (Shindell and Faluvegi, 2009) that lead to regional radiative effects of up to two orders of magnitude larger than the global average (Li et al., 2016c, 2016a; Mallet et al., 2016). Black carbon, instead, is known to absorb solar radiation, leading to regional atmospheric warming patterns due to its inhomogeneous spatial distribution (Gustafsson and Ramanathan, 2016). Patterns of forcing generally follow those of aerosol burden. However, temperature and precipitation responses are both local and remote (Li et al., 2016d; Kasoar et al., 2018; Liu et al., 2018c; Samset et al., 2018; Thornhill et al., 2018; Westervelt et al., 2018). For instance, changes in aerosol concentrations in the Northern Hemisphere have been reported to modulate monsoon precipitation in West Africa and the Sahel (Undorf et al., 2018; Section 10.4.2.1) and in Asia (Zhang et al., 2018; Section 10.6.3).

Natural aerosols include mineral dust, volcanic aerosol and sea salt. The feedback processes between climate and mineral dust as well as sea salt are assessed in Section 6.4, while the volcanic aerosol is dealt with in Cross-Chapter Box 4.1. Mineral dust created by wind erosion of arid and semi-arid surfaces dominates the aerosol load over some areas. The major sources of contemporary dust are located in the arid topographic basins of Northern Africa, Middle East, Central and Southwest Asia, the Indian subcontinent, and East Asia (Prospero et al., 2002; Ginoux et al., 2012) and emissions are controlled by changes in surface winds, precipitation, and vegetation (Ridley et al., 2014; Wang et al., 2015a; DeFlorio et al., 2016; Evan et al., 2016; Pu and Ginoux, 2018). Dust both scatters and absorbs radiation and serves as nuclei of warm and cold clouds (Chapter 6). The surface direct radiative effect is likely negative over land and ocean, especially when the assumed solar absorption by dust is large (Miller et al., 2014; Strong et al., 2015). Surface temperature and precipitation adjust to the direct radiative effect with both sign and magnitude depending on the dust absorptive properties. Dust often cools the surface, but in regions such as the Sahara surface air temperature increases as the shortwave absorption by dust is increased, leading to increases of surface temperature over the major reflective dust sources (Miller et al., 2014; Solmon et al., 2015; Strong et al., 2015; Jin et al., 2016; Sharma and Miller, 2017).

Volcanic eruptions load the atmosphere with large amounts of sulphur, which is transformed through chemical reactions and micro-physics processes into sulphate aerosols (Cross-Chapter Box 4.1; Stoffel et al., 2015; LeGrande et al., 2016). If the plume reaches the stratosphere, sulphate aerosols can remain there for months or years (about two to three for large eruptions) and can then be transported to other areas by the Brewer-Dobson circulation. If the eruption occurs in the tropics, its plume is dispersed across the Earth in a few years, while if the eruption occurs in the high latitudes, aerosols mainly remain in the same hemisphere (Pausata et al., 2015). The global temperature response observed after the last five major eruptions of the last two centuries is estimated to be around -0.2°C (Swingedouw et al., 2017), in association with a general decrease of precipitation (Iles and Hegerl, 2017). Nevertheless, the statistical significance of the regional response remains difficult to evaluate over the historical era (Bittner et al., 2016; Swingedouw et al., 2017) due to the small sampling of large volcanic eruptions over this period and the fact that the signal is superimposed upon relatively large internal variability (Gao and Gao, 2018; Dogar and Sato, 2019). Evidence from paleoclimate observations is therefore crucial to obtain a sufficient signal-to-noise ratio (Sigl et al., 2015). Reconstructed modes of climate variability based on proxy records allow evaluation of the influence on those modes (Zanchettin et al., 2013; Ortega et al., 2015; Michel et al., 2018; Sjolte et al., 2018).

Anthropogenic aerosols play a key role in climate change (Chapter 6). Although the global mean optical depth caused by anthropogenic aerosols did not change from 1975 to 2005 (Chapter 6), the regional pattern changed dramatically between Europe and eastern Asia (Fiedler et al., 2017, 2019; Stevens et al., 2017). Large regional differences in present-day aerosol forcing exist with consequences for regional temperature, hydrological cycle and modes of variability (Chapter 8, Section 10.6). Examples of regions with a notable role for anthropogenic aerosol forcing are the Indian monsoon region (Section 10.6.3) and the Mediterranean basin (Section 10.6.4). Anthropogenic aerosols are also very relevant in many urban areas (Box 10.3; Gao et al., 2016; Kajino et al., 2017).

ACCEPTED VERSION SUBJECT TO FINAL EDITING

SRCCL assessed that nearly three-quarters of the land surface is under some form of land use, particularly in agriculture and forest management (Jia et al., 2019). The effects of land management on climate are much less studied than land cover effects although net cropland has changed little over the past 50 years, while land management has continuously changed (Jia et al., 2019). Section 7.3.4.1 assesses the global influence of both land use and irrigation on the effective radiative forcings. Land cover changes and land management can influence climate locally, such as the urban heat island and non-locally as in the case of increased rainfall downwind of a city (Jia et al., 2019, Box 10.3) or the monsoon circulation affected by irrigation (Section 10.6.3). The influence of land cover changes and land management on regional climate extremes is assessed in Section 11.1.6.

It is *very likely* that the global land surface air temperature response to urbanization is negligible (Chapter 2, Section 2.3.1.1.3). However, there is evidence that urbanization may regionally amplify the air temperature response to climate change in different climatic zones (Mahmood et al., 2014), either under present (Doan et al., 2016; Kaplan et al., 2017; Li et al., 2018c) or future climate conditions (Argüeso et al., 2014; Kim et al., 2016; Kusaka et al., 2016; Grossman-Clarke et al., 2017; Krayenhoff et al., 2018). For instance, in northern Belgium, (Berckmans et al., 2019) found that including urbanization scenarios for the near future (up to 2035) have a comparable influence on minimum temperature (increasing it by 0.6ºC) to that of the GHG-induced warming under RCP8.5.

10.1.3.2 Internal drivers of regional climate variability

Internal climate variability on seasonal to multi-decadal temporal scales is substantial at regional scales. This variability arises from internal modes of atmospheric and oceanic variability, intrinsically coupled climate modes, and may additionally be driven by processes other than those originating the modes. It also interacts with the response of the climate system to external forcing. The teleconnections associated with the modes are useful to understand the relationship between large and regional scales (Annex IV). A description of various large-scale modes of variability can be found in Chapters 2, 3 and 8, and in Annex IV, while their future projections are assessed in Chapter 4. The specificities of their regional influence are briefly discussed here. More details of their typical temporal scales and regional influences can be found in Annex IV.

Atmospheric modes of variability may have seasonally-dependent regional effects like the North Atlantic Oscillation (NAO) in European winter (Tsanis and Tapoglou, 2019) and summer (Bladé et al., 2012; Dong et al., 2013). Even though these modes are internal to the climate system, their variability can be affected by anthropogenic forcings. For instance, the Southern Annular Mode (SAM; Hendon et al., 2014) is both internally driven (Smith and Polvani, 2017), but also affected by recent stratospheric ozone changes (Bandoro et al., 2014). The teleconnections between these modes of variability and surface weather often exhibit considerable non-stationarity (Hertig et al., 2015).

Due to the large ocean heat capacity and their long temporal scales, multiannual to multi-decadal modes of ocean variability such as the Pacific Decadal Variability (PDV; Newman et al., 2016) and the Atlantic Multidecadal Variability (AMV; Buckley and Marshall, 2016) are key drivers of regional climate change. In the case of the AMV both natural (volcanic) and anthropogenic (aerosol) external forcings are thought to be involved in its timing and intensity (Section 3.7.7). These modes not only affect nearby regions but also remote parts of the globe through atmospheric teleconnections (Meehl et al., 2013; Dong and Dai, 2015) and can act to modulate the influence of natural and anthropogenic forcings (Davini et al., 2015; Ghosh et al., 2017; Ménégoz et al., 2018b). The dynamics of the ocean modes is simultaneously affected by other modes of variability spanning the full range of spatial and temporal scales due to non-linear interactions (Kucharski et al., 2010; Dong et al., 2018) (Figure 10.3). This mutual interdependence can result in changing characteristics of the connection over time (Gallant et al., 2013; Brands, 2017; Dong and McPhaden, 2017), and of their regional climate impact (Martín-Gómez and Barreiro, 2016, 2017). As with atmospheric modes of variability, the regional influence of ocean modes of variability on regional climates can be seasonally dependent (Haarsma et al., 2015).

ACCEPTED VERSION SUBJECT TO FINAL EDITING

10.1.3.3 Uncertainty and confidence

Uncertainty and confidence are treated in the same way in regional climate change information as in larger-scale (continental and global) climate problems (Chapter 1, Section 10.3.4). The degree of confidence in climate simulations and in the resulting climate information typically depends on the identification of the role of the uncertainties (Section 10.3.4). Since the direct verification of simulations of future climate changes is not possible, model performance and reliable (i.e., trustworthy) uncertainty estimates need to be assessed indirectly through process understanding and a systematic comparison with observations of past and current climate (Section 10.3.3; Eyring et al., 2019; Knutti et al., 2010). The observational uncertainty, which is particularly large at regional scales, also has to be taken into account (Section 10.2). These uncertainty estimates are then propagated in the distillation process to generate climate information (Smith and Matthews, 2015).

Uncertainties in model-based future regional climate information arise from different sources and are introduced at various stages in the process (Lehner et al., 2020): 1) forcing uncertainties associated with the future scenario or pathway that is assumed, 2) internal variability, and 3) uncertainties related to imperfections in climate models, also referred to as structural or model uncertainty. However, the relative role of each of these sources of uncertainty differs between the global and the regional scales as well as between variables and also between different regions (Lehner et al., 2020). One way to address the internal variability and model uncertainties is to consider results from both multiple models and multiple realizations of the same model (Eyring et al., 2016a; Díaz et al., 2020; Lehner et al., 2020). These models are at times also combined with different weights that are a function of their performance and independence to increase the confidence of the multi-model ensemble (Abramowitz et al., 2019; Brunner et al., 2019).

Other elements that play a role are the inconsistency between the global and regional models in dynamical downscaling or the observational and methodological uncertainty in bias-adjustment methods (Sørland et al., 2018). These elements, in addition to those typical of the uncertainty in global and large-scale phenomena (Chapters 1–9), affect the overall confidence of regional climate information. This complex scene with different sources of uncertainty makes the collection of results available from multi-model, multi-member simulations most useful when synthesized through a distillation process (Section 10.5.3).

10.1.4 Distillation of Regional Climate Information

Regional climate information is synthesized from different lines of evidence from a number of sources (Sections 10.2–10.4) taking into account the context of a user vulnerable to climate variability and change at regional scales (Baztan et al., 2017) and the values of all relevant actors (Corner et al., 2014; Bessette et al., 2017) in a process called distillation (Section 10.5). Distillation, understood as the process of synthesizing information about climate change from different lines of evidence obtained from a variety of sources and taking into account the user context and the values of all relevant actors, allows the connection of global climate change to the local and regional scales, where adaptation responses and policy decisions take place. Climate information is translated into the user context in a co-production process that introduces further user-relevant elements leading to user-relevant climate information (Figure 10.1; Pettenger, 2016; Verrax, 2017) for a specific demand like, for instance, guiding climate-resilient development (Kruk et al., 2017; Parker and Lusk, 2019).

The approaches adopted in the distillation of regional climate information are diverse and range from the simple delivery of data as information to co-production with the user using as many lines of evidence as possible (Lourenço et al., 2016). The availability and selection of the sources and the approach followed has implications for the usefulness of the information. For instance, it is well established that it is invalid to take a time series from a grid cell of a model simulation as equivalent to an observational estimate of a point within the cell, due to the lack of representativeness (Section 10.3), and consequently the information building solely on this type of data source is of limited use. Relevant decisions are made during the distillation process such as what method is most suitable to a specific user context and the question being addressed. The information may be provided in the form of summarised raw data, a set of user-oriented

ACCEPTED VERSION SUBJECT TO FINAL EDITING

indicators, a set of figures and maps with either a brief description, in the form of a storyline, or formulated as rich and complex climate adaptation plans. The information typically includes a description of the sources and assumptions, estimates of the associated uncertainty and its sources, and guidance to prevent possible misunderstandings in its communication.

The choices made for the distillation have typically been part of a linear supply chain, starting from the access to climate data that are transformed into maps or derived climate data products, and finally formulating statements that are communicated and delivered to a broad range of users (Hewitt et al., 2012; Hewitson et al., 2017). This methodology has proven to be valuable in many cases, but it is equally fraught with dangers of not communicating important assumptions, not estimating the impact of relevant uncertainties, and possibly causing misunderstandings in the hand-over to the user community. This has led to the emergence of new pathways to generate user-oriented climate information, many in the context of emerging climate services (Buontempo et al., 2018; Hewitt et al., 2020), which are assessed in Section 10.5 and in Chapter 12.

10.1.5 Regional Climate Information in the WGI AR6

This chapter is part of a cluster devoted to regional climate (10, 11, 12 and Atlas). It introduces many of the aspects relevant to the generation of regional climate information that are dealt with in detail elsewhere. Figure 10.4 summarizes how these chapters relate to one another and to the rest of the report.

Chapter 11 assesses observed, attributed and projected changes in weather and climate extremes, provides a mechanistic understanding on how changes in extremes are related to human-induced climate change and provides regional, continental and global-scale assessments on changes in extremes, including compound events. Chapter 12 identifies elements of the climate system relevant for sectoral impacts referred to as climatic impact-drivers (CIDs), assesses past and future evolutions of sector-relevant CIDs for each AR6 region, synthesizes such evolutions for different time periods and by GWL, and assesses how CIDs are used in climate services. The Atlas assesses observed, attributed and projected changes in mean climate, performs a comparison of CMIP5, CMIP6 and CORDEX simulations, evaluates downscaling performance and assesses approaches to communicate climate information. The Interactive Atlas facilitates the exploration of datasets assessed in all chapters through a wide range of maps, graphs and tables generated in an interactive manner. This allows for the comparison of changes at warming levels and scenario/time-period combinations, display of indices for extremes and CIDs, and serves all chapters in the report to facilitate synthesis information and support the Technical Summary and the Summary for Policymakers.

Other chapters also include a strong regional component and provide context for the assessment of regional climate. Chapter 1 introduces the different types of climatic regions used in WGI AR6 and the main types of climatic models. Chapter 2 describes the recent and current state of the climate from observations, most of which are key for the production of regional information. Chapter 3 assesses human influences on the climate system and Chapter 4 assesses climate-change projections, with a global focus. These three chapters include phenomena that are important for shaping regional climate such as general circulation, jets, storm tracks, blocking and modes of variability. At the same time, the visualization of information in global maps in these chapters provides valuable information for the sub-continental scale. Chapter 5 assesses the knowledge about the carbon and biogoechemical cycles, whose fluxes and responses show variability that is strongly regional in nature. Chapter 6 assesses the regional evolution of short-lived climate forcers as well as their influence on regional climate and air quality. Chapter 8 assesses observed and projected changes in the variability of the regional water cycle, including monsoons, while changes of the regional oceans, changes in cryosphere and regional sea level change are assessed in Chapter 9.

[START FIGURE 10.4 HERE]

Figure 10.4: Schematic diagram that illustrates the treatment of regional climate change in the different parts of the WGI report and how the chapters relate to each other.

ACCEPTED VERSION SUBJECT TO FINAL EDITING

[END FIGURE 10.4 HERE]

[START BOX 10.1 HERE]

BOX 10.1: Regional climate in AR5 and the Special Reports SRCCL, SROCC and SR1.5

This box summarizes the information on linking global and regional climate change information in the Fifth Assessment Report (AR5) and the three Special Reports of the Sixth Assessment Cycle. This information frames the treatment of the production of regional climate information in previous reports and identifies some of the gaps that AR6 needs to address.

AR5

In the WGI Chapter 9 (Flato et al., 2014), regional downscaling methods were addressed as tools to provide climate information at the scales needed for many climate impact studies. The assessment found *high confidence* that downscaling adds value both in regions with highly variable topography and for various small-scale phenomena. Regional models necessarily inherit biases from the global models used to provide boundary conditions. Furthermore, the ability of AR5 to systematically evaluate RCMs, and statistical downscaling schemes, were hampered because coordinated inter-comparison studies were still emerging. However, several studies demonstrated that added value arises from higher resolution in regions where stationary small-scale features like topography and complex coastlines are present, and from improved representation of small-scale processes like convective precipitation.

WGI Chapter 14 (Christensen et al., 2013) stressed that credibility in regional climate change projections increases when key drivers of the change are known to be well-simulated and well-projected by climate models.

The Working Group II (WGII) Chapter 21 (Hewitson et al., 2014b) addressed the regional climate change context from the perspective of impacts, vulnerability and adaptation. This chapter emphasized that a good understanding of decision-making contexts is essential to define the type and scale of information required from physical climate. Further, the chapter identified that the regional climate information was limited by the paucity of comprehensive observations and their analysis along with the different levels of confidence in projections (*high confidence*). Notably, at the time of the AR5, many studies still relied on global datasets, models, and assessment methods to inform regional decisions, which were not considered as effective as tailored regional approaches. The regional scale was not defined but instead it was emphasised that climate change responses play out on a range of scales, and the relevance and limitations of information differ strongly from global to local scales, and from one region to another.

Chapter 21 noted that the production of downscaled datasets (by both dynamical and statistical methods) remains weakly coordinated, and that results indicate that high-resolution downscaled reconstructions of the current climate can have significant errors. Key in this was that the increase in downscaled data sets has not narrowed the uncertainty range, and that integrating these data with historical change and process-based understanding remains an important challenge.

The chapter identified the common perception that higher resolution (i.e., more spatial detail) equates to more usable and robust information, which is not necessarily true. Instead, it is through the integration of multiple sources of information that robust understanding of change is developed.

WGII Chapter 21 highlighted that the different contexts of an impact study are defining features for how climate risk is perceived. Perspectives were characterized as top-down (physical vulnerability) and bottom-up perspectives (social vulnerability). The top-down perspective uses climate change impacts as the starting point of how people and/or ecosystems are vulnerable to climate change, and commonly applies global-scale scenario information or refine this to the region of interest through downscaling procedures. Conversely, in the “bottom-up” approach the development context is the starting point, focusing on local scales, and layers

ACCEPTED VERSION SUBJECT TO FINAL EDITING

climate change on top of this. An impact focus tends to look to the future to see how to adjust to expected changes, whereas a vulnerability-focused approach is centred on addressing the drivers of current vulnerability.

Special Report on Climate Change and Land (SRCCL; IPCC, 2019a)

The SRCCL (Jia et al., 2019) assessed that there is *robust evidence and high agreement* that land cover and land use or management exert significant influence on atmospheric states (e.g., temperature, rainfall, wind intensity) and phenomena (e.g., monsoons), at various spatial and temporal scales, through their biophysical influences on climate. There is *robust evidence* that dry soil moisture anomalies favour summer heat waves. Part of the projected increase in heat waves and droughts can be attributed to soil moisture feedbacks in regions where evapotranspiration is limited by moisture availability (*medium confidence*). Vegetation changes can also amplify or dampen extreme events through changes in albedo and evapotranspiration, which will influence future trends in extreme events (*medium confidence*).

The influence of different changes in land use (e.g., afforestation, urbanization), on the local climate depends on the background climate (*robust evidence, high agreement*). There is *high confidence* that regional climate change can be dampened or enhanced by changes in local land cover and land use, with sign and magnitude depending on region and season.

Water management and irrigation were generally not accounted for by CMIP5 global models available at the time of the SRCCL. Additional water can modify regional energy and moisture balance particularly in areas with highly productive agricultural crops with high rate of evapotranspiration. Urbanization increases the risks associated with extreme events (*high confidence*). Urbanization suppresses evaporative cooling and amplifies heatwave intensity (*high confidence*) with a strong influence on minimum temperatures (*very likely*, *high confidence*). Urban areas enhance storm occurrence and heavy precipitation in part due to the presence of aerosols. Urbanization also increases the risk of flooding during heavy rain events.

Special Report on the Ocean and Cryosphere in a Changing Climate (SROCC; IPCC, 2019b)

The SROCC (IPCC, 2019b) stated that observations and models for assessing changes in the ocean and the cryosphere have been developed considerably during the past century but observations in some key regions remain under-sampled and were very short relative to the time scales of natural variability and anthropogenic changes. Retreat of mountain glaciers and thawing of mountain permafrost continues and will continue due to significant warming in those regions, where it is *likely* to exceed global temperature increase.

SROCC assessed that it is *virtually certain* that Antarctica and Greenland have lost mass over the past decade and observed glacier mass loss over the last decades is attributable to anthropogenic climate change (*high confidence*). It is *virtually certain* that projected warming will result in continued loss in Arctic sea ice in summer, but there is *low confidence* in climate model projections of Antarctic sea ice change because of model biases and disagreement with observed trends. Knowledge and observations of the polar regions were sparse compared to many other regions, due to remoteness and challenges of operating in them.

The sensitivity of small islands and coastal areas to increased sea level differs between emission scenarios and regionally and a consideration of local processes is critical for projections of sea level influences at local scales.

Special Report on Global Warming of 1.5°C (SR1.5; IPCC, 2018b)

The SR1.5 (Hoegh-Guldberg et al., 2018) assessed that most land regions were experiencing greater warming than the global average, with annual average warming already exceeding 1.5°C in many regions. Over one quarter of the global population live in regions that have already experienced more than 1.5°C of warming in at least one season. Land regions will warm more than ocean regions over the coming decades (transient climate conditions).

Transient climate projections reveal observable differences between 1.5°C and 2°C global warming in terms of mean temperature and extremes, both at a global scale and for most land regions. Such studies also reveal detectable differences between 1.5°C and 2°C precipitation extremes in many land regions. For mean

ACCEPTED VERSION SUBJECT TO FINAL EDITING

precipitation and various drought measures there is substantially lower risk for human systems and ecosystems in the Mediterranean region at 1.5°C compared to 2°C.

The different pathways to a 1.5ºC warmer world may involve a transition through 1.5°C, with both short and long-term stabilization (without overshoot), or a temporary rise and fall over decades and centuries (overshoot). The influence of these pathways is small for some climate variables at the regional scale (e.g., regional temperature and precipitation extremes) but can be very large for others (e.g., sea level).

[END BOX 10.1 HERE]

[START CROSS-CHAPTER BOX 10.1 HERE]

Cross-Chapter Box 10.1: Influence of the Arctic on mid-latitude climate

Coordinator: Rein Haarsma (Netherlands)
Contributors: Francisco Doblas-Reyes (Spain), Hervé Douville (France), Nathan Gillett (Canada), Gerhard Krinner (France), Dirk Notz (Germany), Krishnan Raghavan (India), Alexander C. Ruane (USA), Sonia I. Seneviratne (Switzerland), Laurent Terray (France), Cunde Xiao (China)

The Arctic has *very likely* warmed more than twice the global rate over the past 50 years with the greatest increase during the cold season (Atlas 11.2). Several mechanisms are responsible for the enhanced lower troposphere warming of the Arctic, including ice-albedo, lapse rate, Planck and cloud feedbacks (Section 7.4.4.1). The rapid Arctic warming strongly affects the ocean, atmosphere, and cryosphere in that region (Atlas 11.2, Section 2.3.2.1). Averaged over the decade 2010-2019, monthly-average sea ice area in August, September and October has been about 25% smaller than that during 1979-1988 (*high confidence*, Section 9.3.1.1). It is *very likely* that anthropogenic forcings mainly due to greenhouse gas increases have contributed substantially to Arctic sea ice loss since 1979, explaining at least half of the observed long-term decrease in summer sea-ice extent (Section 3.4.1.1).

In this box, the possible influences of the Arctic warming on the lower latitudes is assesed. This linkage was also the topic of the Box 3.2 of the Special Report on the Ocean and Cryosphere in a Changing Climate (SROCC; IPCC, 2019b). It is a topic that has been strongly debated (Ogawa et al., 2018; Wang et al., 2018a). Separate hypotheses have emerged for winter and summer that describe possible mechanisms of how the Arctic can influence the weather and climate at lower latitudes. They involve changes in the polar vortex, storm tracks, jet stream, planetary waves, stratosphere-troposphere coupling, and eddy-mean flow interactions, thereby affecting the mid-latitude atmospheric circulation, and the frequency, intensity, duration, seasonality and spatial extent of extremes and climatic impact-drivers like cold spells, heat waves, and floods (Cross-Chapter Box 10.1, Figure 1). However, we note that a decrease in the intensity of cold extremes has been observed in the Northern Hemisphere mid-latitudes in winter since 1950 (van Oldenborgh et al., 2019; Section 11.3.2). Since SROCC new literature has appeared, and the mechanisms and their criticisms are assessed here as an update and extension to the SROCC box.

[START CROSS-CHAPTER BOX 10.1, FIGURE 1 HERE]

Cross-Chapter Box 10.1, Figure 1: Mechanisms of potential influences of recent and future Arctic warming on mid-latitude climate and variability. Mechanisms are different for winter and summer with different associated influences on mid-latitudes. The mechanisms involve changes in the polar vortex, storm tracks, planetary waves and jet stream.

[END CROSS-CHAPTER BOX 10.1, FIGURE 1 HERE]

Mechanisms for a potential influence in winter

ACCEPTED VERSION SUBJECT TO FINAL EDITING

It has been proposed that Arctic amplification, by reducing the equator-pole temperature contrast, could result in a weaker and more meandering jet with Rossby waves of larger amplitude (Francis et al., 2017). This may cause weather systems to travel eastward more slowly and thus, all other things being equal, Arctic amplification could lead to more persistent weather patterns over the mid-latitudes (Francis and Vavrus, 2012). The persistent large meandering flow may increase the likelihood of connected patterns of temperature and precipitation climatic impact-drivers because they frequently occur when atmospheric circulation patterns are persistent, which tends to occur with a strong meridional wind component. Another possible consequence of Arctic warming is on the NAO/AO that shows a negative trend over the past two decades (Robson et al., 2016; Iles and Hegerl, 2017), and has been linked to the reduction of sea ice in the Barents and Kara seas, and the increase in Eurasian snow cover (Cohen et al., 2012; Nakamura et al., 2015; Yang et al., 2016). During negative NAO/AO the storm tracks shift equatorward and winters are predominantly more severe across northern Eurasia and the eastern United States, but relatively mild in the Arctic. This temperature pattern is sometimes referred to as the "warm Arctic–cold continents (WACC)" pattern (Chen et al., 2018). However, Sun et al. (2016a) noticed that the WACC is a manifestation of natural variability. Enhanced sea-ice loss in the Barents-Kara Sea has also been related to a weakening of the stratospheric polar vortex (Kretschmer et al., 2020) and its increased variability (Kretschmer et al., 2016) that would induce a negative NAO/AO (Kim et al., 2014), the WACC pattern (Kim et al., 2014), and an increase in cold-air outbreaks in mid-latitudes (Kretschmer et al., 2018). Arctic warming might also increase Eurasian snow cover in autumn caused by the moister air that is advected into Eurasia from the Arctic with reduced sea-ice cover (Cohen et al., 2014; Jaiser et al., 2016), although Peings (2019) suggests a possible influence of Ural blockings on both the autumn snow cover and the early winter polar stratosphere. The circulation changes over the Ural-Siberian region are also suggested to provide a link between Barents-Kara sea ice and the NAO (Santolaria-Otín et al., 2021).

Mechanisms for a potential influence in summer

As in winter, Arctic summer warming may result in a weakening of the westerly jet and mid-latitude storm tracks, as suggested for the recent period of Arctic warming (Coumou et al., 2015; Petrie et al., 2015; Chang et al., 2016). Additional proposed consequences are a southward shift of the jet (Butler et al., 2010) and a double jet structure associated with an increase of the land-ocean thermal gradient at the coastal boundary (Coumou et al., 2018). It is hypothesized that weaker jets, diminished meridional temperature contrast, and reduced baroclinicity might induce a larger amplitude in stationary wave response to stationary forcings (Zappa et al., 2011; Petoukhov et al., 2013; Hoskins and Woollings, 2015; Coumou et al., 2018; Mann et al., 2018; Zhang et al., 2020b), and also that a double jet structure would favour wave resonance (Kornhuber et al., 2017; Mann et al., 2017). Some studies suggest that this is corroborated by an observed increase of quasi-stationary waves (Di Capua and Coumou, 2016; Vavrus et al., 2017; Coumou et al., 2018).

Assessment

The above proposed hypotheses are based on concepts of geophysical fluid dynamics and surface coupling and can, in principle, help explain the existence of a link between the Arctic changes and the mid-latitudes with the potential to affect many impact sectors (Barnes and Screen, 2015). However, the validity of some dynamical underlying mechanisms, such as a reduced meridional temperature contrast inducing enhanced wave amplitude, has been questioned (Hassanzadeh et al., 2014; Hoskins and Woollings, 2015). On the contrary, the reduced meridional temperature contrast has been related to reduced meridional temperature advection and thereby reduced winter temperature variability (Collow et al., 2019).

Studies that support the Arctic influence are mostly based on observational relationships between the Arctic temperature or sea-ice extent and mid-latitude anomalies or extremes (Cohen et al., 2012; Francis and Vavrus, 2012, 2015; Budikova et al., 2017). They are often criticised for the lack of statistical significance and the inability to disentangle cause and effect (Barnes, 2013; Barnes and Polvani, 2013; Screen and Simmonds, 2013; Barnes et al., 2014; Hassanzadeh et al., 2014; Barnes and Screen, 2015; Sorokina et al., 2016; Douville et al., 2017; Gastineau et al., 2017; Blackport and Screen, 2020a; Oudar et al., 2020; Riboldi et al., 2020). The role of the Barents-Kara Sea ice loss is challenged by Blackport et al. (2019) who find a minimal influence of reduced sea ice on severe mid-latitude winters, and by Warner et al. (2019) who suggest that the apparent winter NAO response to the Barents-Kara sea-ice variability is mainly an artefact of the Aleutian Low internal variability and of the co-variability between sea ice and the Aleutian Low

ACCEPTED VERSION SUBJECT TO FINAL EDITING

originating from tropical-extratropical teleconnections. Also Gong et al. (2020) do not find a link between Rossby wave propagation into the midlatitudes and Arctic sea ice loss. Mori et al. (2019a) argue that models underestimate the influence of the Barents-Kara Sea ice loss on the atmosphere, which is disputed by Screen and Blackport (2019). Other studies have stressed the importance of atmospheric variability as a driver of Arctic variability (Lee, 2014; Woods and Caballero, 2016; Praetorius et al., 2018; Olonscheck et al., 2019). Analysing observed key variables of mid-latitude climate for 1980-2020, Blackport and Screen (2020b) and Riboldi et al. (2020) argue that the Arctic influence on mid-latitudes is small compared to other aspects of climate variability, and that observed periods of strong correlation are an artefact of internal variability or intermittency (Kolstad and Screen, 2019; Siew et al., 2020; Warner et al., 2020).

An additional argument in the criticism is the inability of climate models to simulate a significant response to Arctic sea-ice loss, larger than the natural variability (Screen et al., 2014; Walsh, 2014; Chen et al., 2016a; Peings et al., 2017; Dai and Song, 2020), although some studies find a significant response in summer, because then the internal variability is weaker (Petrie et al., 2015).

Finally, a warmer Arctic climate can, without any additional changes in atmospheric dynamics, reduce cold extremes in winter due to advection of increasingly warmer air from the Arctic into the mid-latitudes (Screen, 2014; Ayarzagüena and Screen, 2016; Ayarzagüena et al., 2018).

Summarizing, different hypotheses have been developed about the influence of recent Arctic warming on the mid-latitudes in both winter and summer. Although some of the proposed mechanisms seem to be supported by various studies, such as the link with Barents-Kara Sea ice loss in winter and weakened storm tracks in summer, the underlying mechanisms and relative strength compared to internal climate variability have been questioned. A recent review (Cohen et al., 2020) states that divergent conclusions between model and observational studies, and also between different model studies, continue to obfuscate a clear understanding of how Arctic warming is influencing mid-latitude weather. In this context, Shepherd (2016) stresses the need for collaboration between scientists with different viewpoints for further understanding that could be achived by carefully designed, multi-investigator, coordinated, multi-model simulations, data analyses and diagnostics (Overland et al., 2016). In agreement with Box 3.2 of SROCC, there is hence *low to medium confidence* in the exact role and quantitative effect of historical Arctic warming and sea-ice loss on mid-latitude atmospheric variability.

Regarding future climate, it is important to note that mid-latitude variability is also affected by many drivers other than the Arctic changes and that those drivers as well as the linkages to mid-latitude variability might change in a warmer world. The AMV, PDV, ENSO (see Annex IV), upper tropospheric tropical heating, polar stratospheric vortex, and land-surface processes associated with soil moisture (Miralles et al., 2014; Hauser et al., 2016) are a few examples. A considerable body of literature has shown that changes to the NAO/AO on seasonal and climate change time scales can be driven by variations in the wavelength and amplitude of Rossby waves, mainly of tropical origin (Fletcher and Kushner, 2011; Cattiaux and Cassou, 2013; Ding et al., 2014; Goss et al., 2016). The influence of future Arctic warming on mid-latitude circulation is difficult to disentangle from the effect of such a plethora of drivers (Blackport and Kushner, 2017; Li et al., 2018a). One of the consequences of climate change is a poleward shift of the jet induced by the tropical warming (Barnes and Polvani, 2013), which is less obvious in winter especially over the North Atlantic (Peings et al., 2018; Oudar et al., 2020), and the increase of the meridional temperature gradient in the upper troposphere, which increases storm track activity (Barnes and Screen, 2015). Although climate models indicate that future Arctic warming and the associated equator-pole temperature gradient could affect mid-latitude climate and variability (Haarsma et al., 2013b; McCusker et al., 2017; Zappa et al., 2018), and even the tropics and sub-tropics (Deser et al., 2015; Cvijanovic et al., 2017; Wang et al., 2018; England et al., 2020; Kennel and Yulaeva, 2020), they do not reveal a strong influence on extreme weather (Woollings et al., 2014).

In conclusion, there is *low confidence* in the relative contribution of Arctic warming to mid-latitude atmospheric changes compared to other drivers. Future climate change could affect mid-latitude variability in a number of ways that are still to be clarified, and which may also include the influence of Arctic warming. The linkages between the Arctic warming and the mid-latitude circulation is an example of

ACCEPTED VERSION SUBJECT TO FINAL EDITING

contrasting lines of evidence that cannot yet be reconciled (Section 10.5).

[END CROSS-CHAPTER BOX 10.1 HERE]

10.2 Using Observations for Constructing Regional Climate Information

Considerable challenges (and opportunities) remain in using observations for climate monitoring, for evaluating and improving climate models (Section 10.3.1), for constructing reanalyses and post-processing model outputs, and therefore, ultimately, for increasing our confidence in the attribution of past climate changes and in future climate projections at the regional scale. While an assessment of large-scale observations can be found in Chapter 2 (Cross-Chapter-Box 2.2, Section 2.3), this section discusses the specific aspects of the observations at regional scale and over the typological regions considered in the regional chapters (Section 10.1.5). This section focuses on land regions and does not consider the specific requirements of ocean observations (see Chapter 9 and the SROCC for more information on this aspect).

10.2.1 Observation Types and Their Use at Regional Scale

10.2.1.1 In situ and remote-sensing data

Surface or in situ observations can come from a variety of networks: climate reference networks, mesoscale weather and supersite observation networks, citizen science networks, among others, all with their strengths and weaknesses (McPherson, 2013; Thorne et al., 2018). Supersite observatories are surface and atmospheric boundary layer observing networks that measure a large number of atmospheric and soil variables at least hourly over a decade or more, ideally located in rural areas (Ackerman and Stokes, 2003; Haeffelin et al., 2005; Xie et al., 2010; Chiriaco et al., 2018). Adequate calibration of instruments, quality control and homogenization are essential in these sites. They produce valuable data needed to diagnose processes and changes in regional and local climate. Several climate datasets have been developed from in situ station observations, at different spatial scales and temporal frequencies (Annex I). These include sub-daily (Dumitrescu et al., 2016; Blenkinsop et al., 2017), daily (Aalto et al., 2016; Funk et al., 2015; Beck et al., 2017a, 2017b; Camera et al., 2014; Chen et al., 2008; Journée et al., 2015; Schneider et al., 2017), or monthly time scales (Aryee et al., 2018; Cuervo-Robayo et al., 2014). Sub-daily data is useful for estimating storm surge (Mori et al., 2014) or river discharge (Shrestha et al., 2015), daily data for carbon-stock dynamics (Haga et al., 2020) or tourism (Watanabe et al., 2018), and monthly data for beach morphology (Bennett et al., 2019).

Satellite products provide a valuable complement to in situ measurements, particularly over regions where in situ measurements are unavailable. They have been discussed in earlier chapters (e.g., Chapters 2 and 8) for large-scale assessment. Currently 54 essential climate variables (ECVs; Bojinski et al., 2014) are defined by the Global Climate Observing System (GCOS) program, and passed on, for example, to NASA programmes through the Decadal Survey, to the Copernicus Climate Change Service of the European Union, to the ESA Climate Change Initiative ESA-CCI, as well as to the international collaborations with geostationary Earth-orbit (GEO) satellites. Their observations are valuable (*high confidence*) for regional applications since they provide multi-channel images at very high spatiotemporal resolutions, typically 16 channels, 1–2 km, every 10 to 15 minutes. The advanced geostationary satellites are: Himawari-8 and 9 (Kurihara et al., 2016), GOES-East and GOES-17 (Goodman et al., 2018), Meteosat-10 and 11 (Schmetz et al., 2002) and FY-4 (Cao et al., 2014). Geostationary satellite networks or constellations form an essential component of the Global Observation System (https://www.wmo.int/pages/prog/www/OSY/GOS.html), providing measurements not only for various cloud properties and moisture but also for air quality, land and ocean surface conditions, and lightning.

Low Earth-orbit (LEO) satellites, with orbits typically at 400-700 km, provide advanced measurements of the Earth's surface. Sun-synchronous polar orbiters can also cover the polar regions, which cannot be observed with GEO satellites. Examples of LEO observations for land-surface monitoring are NASA's

ACCEPTED VERSION SUBJECT TO FINAL EDITING

Landsat (Wulder et al., 2016), ESA's Soil Moisture Ocean Salinity Earth Explorer (SMOS) mission (Kerr et al., 2012), the Sentinel missions of the Copernicus programme, and JAXA's ALOS-2 (Ohki et al., 2019), providing high spatial resolution land-surface images. Many kinds of data are accumulated for land use and land cover studies, targeting aspects like urban footprint (Florczyk et al., 2019), land-cover data (Global Land 30; CCI-LC: https://www.esa-landcover-cci.org; Chen and Chen,2018), land-surface temperature data (LANDSAT, Parastatidis et al., 2017), and surface albedo (Chrysoulakis et al., 2019).

Availability of active sensors on LEO satellites enables measurement of microphysical properties of aerosol, cloud and precipitation, which can advance regional climate studies and process evaluation studies to improve regional climate models (*high confidence*). An example is the polar-orbiting "afternoon-train" satellite constellation (known as the A-train), incorporating Aqua, CALIPSO, Cloudsat, PARASOL, Glory and Aura satellites. Vertical profiling observations from Cloudsat (with a W-band cloud radar) and CALIPSO (with a cloud lidar) led to considerable advances in measurements of cloud microphysics (Stephens et al., 2018). Precipitation and its extremes are essential concerns of regional climate studies. The GPM (65°N–65°S, 2014–present) and the preceding TRMM (36.5°N–36.5°S, 1997–2015) with Ku-/Ka-band precipitation radars have provided three-dimensional measurements of precipitation with ~5 km resolution and sub-daily sampling (Skofronick-Jackson et al., 2017). Their non-sun synchronous observation works to cross-calibrate the constellation satellites to produce global high-resolution mapped products of precipitation, such as Integrated Multi-satellitE Retrievals for GPM (IMERG; Huffman et al., 2007) and the Global Satellite Mapping of Precipitation (GSMaP; Kubota et al., 2007), with hourly sampling at ~11 km resolution. The CPC MORPHing technique (CMORPH) has provided 30 min interval global precipitation with ~8 km coverage since 2002 (Joyce et al., 2004). Precipitation estimations from Remotely Sensed Information using Artificial Neural Networks (PERSIANN) is a sub-daily to daily rainfall product that covers 50°S to 50°N globally with 25 km resolution from 2000 to the present (Nguyen et al., 2019), and is used for semi-global scale precipitation coverage (Benestad, 2018). TRMM/GPM observations have enabled estimates to be obtained for global four-dimensional convective heating (Shige et al., 2009; Tao et al., 2016; Takayabu and Tao, 2020).

The use of these data has enhanced our understanding of precipitation processes at regional scale (*high confidence*), such as diurnal cycles in a large river valley (Chen et al., 2012b), and in coastal (Hassim et al., 2016; Yokoi et al., 2017) and mountainous regions (Hirose et al., 2017). Three-dimensional observations revealed the contrasts in regional characteristics of rainfall extremes in monsoon regions and continental dry regions (Sohn et al., 2013; Hamada and Takayabu, 2018). Satellite measurements are also used to evaluate climate model performance, as well as to develop new parameterizations. As a demonstration of the utility of these products in studying model bias, a subtropical cumulus congestus regime has been identified that may be implicated in the unrealistic double ITCZ found in some climate models (Takayabu et al., 2010; Hirota et al., 2011, 2014). Another example is a parameterization of a land-surface model that was developed specifically for a certain soil type. By assimilating satellite brightness temperature observations with their LDAS-UT scheme, Yang et al., (2007) successfully optimized a land-surface model for the Tibetan Plateau.

For application at a regional scale, it is important to consider variations in the spatiotemporal resolution of the satellite products. A simple concatenation of data in time can show artificial jumps that are artefacts of changes in calibration and processing algorithms, or related to satellite orbital stability or changing performance of the instruments (Wielicki et al., 2013; Barrett et al., 2014). Recalibration and cross-calibration are then prerequisites for obtaining homogeneous time series of measurements across different or successive satellites that can then be used to produce long series that are valid as climate data records (Kanemaru et al., 2017; Merchant et al., 2017). Scale representativeness is also an issue in utilizing soil observations (Taylor et al., 2012, 2013). Although a variety of technologies to measure soil moisture at the point scale exist (Dobriyal et al., 2012), its spatial representativeness is less than 1 m^2 (Ochsner et al., 2013; Liu et al., 2016b). Therefore, to be able to use in situ soil moisture for validating coarser-scale data from satellites or models, networks of point-scale measurements are used (Crow et al., 2015; Polcher et al., 2016). Smaller networks are typically of the size of a single climate model grid cell or a satellite pixel and are suitable for monitoring watersheds, while small numbers of those representing larger areas (>100 km^2) are emerging (Ochsner et al., 2013).

ACCEPTED VERSION SUBJECT TO FINAL EDITING

10.2.1.2 Derived products

Derived observational products are created from raw datasets collected from surface stations, remote-sensing instruments, or research vessels, which are converted into meaningful physical quantities by applying a suitable measurement theory, using either statistical interpolation techniques (Section 10.2.2.4) or numerical atmospheric and land-surface models (Bosilovich et al., 2015).

Most global observational datasets are available at coarse temporal and spatial resolution, and do not include all available station data from a particular region, due to data availability problems. Therefore, efforts have been made to develop regional or country-scale datasets (Annex I). Radar and satellite remote sensing are resources that can provide a valuable complement to direct measurements at regional scale. Examples for precipitation have been described already, some of which have been released to the community (Bližňák et al., 2018; Dietzsch et al., 2017; Dinku et al., 2014; Krähenmann et al., 2018; Manz et al., 2016; Oyler et al., 2015; Panziera et al., 2018; Shen et al., 2018; Yang et al., 2017). However, some of these datasets are limited by their short record, varying between one (Shen et al., 2018) and 64 years (Oyler et al., 2015).

Reanalysis products are numerical climate simulations that use data assimilation to incorporate as many irregular observations as possible. These products encompass many physical and dynamical processes. They generate a coherent estimate of the state of the climate system on uniform grids either at global (Balsamo et al., 2015; Chaudhuri et al., 2013), regional (Chaney et al., 2014; Dahlgren et al., 2016; Maidment et al., 2014; Mahmood et al., 2018; Attada et al., 2018; Langodan et al., 2017) or country scales (Krähenmann et al., 2018; Mahmood et al., 2018; Rostkier-Edelstein et al., 2014).

Reanalyses incorporate an increasing volume of observations from a growing number of sources over time, which sometimes presents a difficulty for trend analysis. However, regional reanalyses are valuable for regional climate assessments, since they can employ high-resolution model simulations due to their limited spatial domain. Their accuracy is also better than global reanalyses since they are often developed over regions with a high density of observational data (sometimes not freely available for all regions) to be assimilated into the model (e.g., Yamada et al., 2012). Regional reanalyses can assimilate locally dense and high-frequency observations, such as from local observation networks (Mahmood et al., 2018; Su et al., 2019) and radar precipitation (Wahl et al., 2017) in addition to the observations assimilated by global reanalyses. In some regional reanalyses, satellite-derived high-resolution sea ice (Bromwich et al., 2016, 2018) and sea surface temperature (Su et al., 2019) are also applied as lower boundary conditions. The periods of regional reanalyses are limited by the availability of the observations for assimilation and by the global reanalyses needed as lateral boundary conditions. Most regional reanalyses cover the past 10 to 30 years. There are also regional reanalysis activities that use conventional observations only, which produce consistent datasets over 60 years to capture precipitation trends, extremes and changes (Fukui et al., 2018). Existing regional reanalyses cover North America (Mesinger et al., 2006), Europe (Dahlgren et al., 2016; Jermey and Renshaw, 2016; Kaspar et al., 2020), the Arctic (Bromwich et al., 2016, 2018), South Asia (Mahmood et al., 2018), and Australia (Su et al., 2019). A project for regional reanalysis covering Japan has also started (Fukui et al., 2018), where grid spacing is between 5 and 32 km, although cumulus parameterizations are still needed to compute sub-grid scale cumulus convection. Recently, reanalyses using convection-permitting regional models have been published (e.g., Wahl et al., 2017, for central Europe).

The data assimilation schemes used in regional reanalyses are often relatively simple methods, specifically nudging (Kaspar et al., 2020) and 3DVAR (Mesinger et al., 2006; Bromwich et al., 2016; Dahlgren et al., 2016), rather than the more complex schemes implemented in state-of-the-art global reanalysis systems. This is partly due to limitations of computational resources. Recently, a number of regional reanalyses using more sophisticated methods, such as 4DVAR and Ensemble Kalman filter, have been published (Jermey and Renshaw, 2016; Fukui et al., 2018; Mahmood et al., 2018; Su et al., 2019). The regional reanalyses also incorporate uncertainties due to deficiencies of the models, data assimilation schemes and observations. To estimate uncertainties, some regional reanalyses apply data assimilation using ensemble forecasts (Bach et al., 2016). Another approach compares multiple regional reanalyses produced with different systems covering the same domain, which represents the uncertainties better than single reanalysis systems with

ACCEPTED VERSION SUBJECT TO FINAL EDITING

ensemble data assimilation schemes (Kaiser-Weiss et al., 2019).

The regional reanalyses represent the frequencies of extremes and the distributions of precipitation, surface air temperature, and surface wind better than global reanalyses (*high confidence*). This is due to the use of high-resolution regional climate models (RCMs), as indicated by different regional climate modelling studies (Mesinger et al., 2006; Bollmeyer et al., 2015; Bromwich et al., 2016, 2018; Dahlgren et al., 2016; Jermey and Renshaw, 2016; Fukui et al., 2018; Su et al., 2019). Regional reanalyses, however, retain uncertainties due to deficiencies in the physical parametrization used in RCMs and by the use of relatively simple data assimilation algorithms (Bromwich et al., 2016; Jermey and Renshaw, 2016; Su et al., 2019). Regional reanalyses can provide estimates that are more consistent with observations than dynamical downscaling approaches, due to the assimilation of additional local observations (*high confidence*) (Bollmeyer et al., 2015; Fukui et al., 2018).

10.2.2 Challenges for Regional Climate Change Assessment

10.2.2.1 Quality control

The usefulness of any observational dataset is conditioned by the availability and outcome of a quality control (QC) process. The objective of the QC is to verify that data are representative of the measured variable and to what degree the value could be contaminated by unrelated or conflicting factors (WMO, 2017a). Data quality assessment is key for ensuring that the data are credible and to establish trusted relationships between the data provider and the users (Nightingale et al., 2019). QC is performed for all relevant global climate datasets (e.g., Menne et al., 2018). For instance, QC informs users that old reanalysis datasets can be inconsistent in the long term because they assimilated inhomogeneous observations over the reanalyses period (Kobayashi et al., 2015). As a consequence, the evaluation against independent observations suggests that reanalyses should not be automatically regarded as climate-quality products for monitoring long-term trends at the regional level (Manzanas et al., 2014; Torralba et al., 2017). QC needs to be systematically carried out by the institutions responsible for handling the data (e.g. Cao et al., 2016).

The QC procedure depends strongly on the specific nature of the dataset. It focuses on aspects such as the correct identification of sensor, time and location, detection of unfeasible or inconsistent data, error estimation, assessment of the adequacy of the uncertainty information and the adequacy of the documentation (e.g., Heaney et al., 2016). QC principles also apply to model data (Tapiador et al., 2017). An important piece of information provided is the representativeness error (Section 10.2.1.1; Gervais et al., 2014). When problems in the data representativeness are identified, observational datasets are provided with a quality mask (Contractor et al., 2020), or the problematic data are either removed or corrected (Ashcroft et al., 2018). These are factors often taken into account in constructing regional climate information (Kotlarski et al., 2019).

Quality-controlled data are now produced widely at the regional level, as in the case of sub-daily precipitation records in the United Kingdom (Blenkinsop et al., 2017) and the USA (Nelson et al., 2016). However, many more datasets and variables lack the same level of scrutiny (Alexander, 2016). Quality-controlled, high-resolution observational datasets are especially needed at regional and local scales to assess models as their resolution increases (Di Luca et al., 2016; Zittis and Hadjinicolaou, 2017), although the awareness and appropriate use of the QC information is challenging (Tapiador et al., 2017) when generating regional climate information (*high confidence*).

10.2.2.2 Homogenization

Homogenization aims to make data spatially and temporally “homogeneous”. Changes in a homogeneous time series are solely due to large-scale climatic changes (whether forced or due to internal variability). Station data are influenced by factors that act at regional scales, from the mesoscale and local scale down to the microscale (WMO, 2019). Station time series contain inhomogeneities such as artificial jumps or trends,

ACCEPTED VERSION SUBJECT TO FINAL EDITING

which hamper assessments of regional long-term trends. Typical reasons for this are the urbanization of a station's surroundings, which can lead to warming (Hamdi, 2010; Hansen et al., 2010; Adachi et al., 2012; Jones, 2016; Sun et al., 2016b), or relocations outside of the urban area, which could lead to cooling (Tuomenvirta, 2001; Yan et al., 2010; Xu et al., 2013; Dienst et al., 2017, 2019). Another potential source of inhomogeneity is a change in measurement methods that affect most instruments of an observational network over a limited time span, such as the transition to Stevenson screens (Parker, 1994; Böhm et al., 2010; Brunet et al., 2011; Auchmann and Brönnimann, 2012) or to automatic weather stations (WMO, 2017b).

The above examples have been selected as they are present in many stations and without going through homogenization they could potentially have influenced global land warming estimates (Section 1.5.1). Single-break inhomogeneities tend to have a magnitude comparable to global climate change (Tuomenvirta, 2001; Venema et al., 2012) and are thus important for analyses of small regions. Also station records in national networks often have similar changes, making them important for national climate change estimates, but many of these influences are averaged out at the global scale (Jones, 2016).

The main approach to reduce the influence of inhomogeneities in station observations is statistical homogenization by comparing the data from a candidate station with those of neighbouring reference stations in conjunction with the use of metadata (Trewin, 2010). This is a challenging task because both reference and candidate records normally have multiple inhomogeneities. Three challenges should be considered. First, most of our understanding of statistical homogenization stems from the homogenization of temperature observations from dense networks. Recent studies suggest that our ability to remove biases quickly diminishes for sparse networks (Gubler et al., 2017; Lindau and Venema, 2018a). This affects early instrumental data and observations that are not strongly correlated between stations, such as wind and humidity (Chimani et al., 2018).

Second, in addition to systematic errors, homogenized data also suffer from random errors, introduced by the homogenization process. These errors are largest at the station level but are also present in network-averaged signals (Lindau and Venema, 2018b). These errors are determined by the break time series, as well as the noise series and the performance of the homogenization method, are spatially correlated, and have an impact on activities such as interpolation and statistical post-processing of climate simulations (Section 10.2.3.1). Third, the above discussion pertains to the homogenization of monthly and annual means. Homogenization of daily variability around the mean is more difficult. For daily data, specific correction methods are used (Della-Marta and Wanner, 2006; Mestre et al., 2011; Trewin, 2013) that are able to improve the homogeneity of test cases, although recent independent validation efforts were not able to show much improvement (Chimani et al., 2018). The difference with homogenization methods of monthly and annual means may stem from assumptions on the nature of inhomogeneities for daily data, which are not yet well understood (Chimani et al., 2018).

It is *virtually certain* that statistical homogenization methods reduce the uncertainties of long-term estimates. Considering a decomposition of the long-term warming error into a bias and a noise uncertainty around the bias, the (trend) bias especially will be reduced, but also most of the noise uncertainty. This conclusion is based on our understanding of the causes of inhomogeneities and their statistical nature combined with the design principles of statistical homogenization methods, as well as on analytical (Lindau and Venema, 2018b), numerical (Venema et al., 2012; Williams et al., 2012) and empirical validation studies (Hausfather et al., 2016; Gubler et al., 2017; Killick et al., 2020).

The above section is about the homogenization of land stations. Satellite data has its own issues and methods for homogenization (Brinckmann et al., 2013; Huang et al., 2015; Brogniez et al., 2016). The homogenization of radiosonde data and land station data use similar methods (Haimberger et al., 2012; Jovanovic et al., 2017).

10.2.2.3 Data scarcity

Data scarcity arises largely due to the lack of maintenance of observing stations, inaccessibility of the data

ACCEPTED VERSION SUBJECT TO FINAL EDITING

held in national networks, and uneven spatial distribution of stations that lead to a low density in many regions. This is particularly problematic when trying to assess regional climate change, for which a high density of observational data is desirable. Although in several regions numerous stations provide (monthly) data covering more than 100 years for both temperature and precipitation (GCOS, 2015), large areas of the world remain sparsely covered. The post-1990 decline in the total number of stations contributing to the Global Precipitation Climatology Centre (GPCC) monthly product may be related to delays in data acquisition and not paucity of data (GCOS, 2015). This is because GPCC is the result of a single time scale, single Essential Climate Variable and single data collection centre. There is no similar drop-off of the rainfall reports in the Global Historical Climatology Network - Daily database (GHCND, Menne et al., 2012) or the Integrated Surface Database at the sub-daily time scale.

Kidd et al. (2017) made some assumptions about GPCC-available gauges and indicated that only 1.6% of Earth's surface lies within 10 km of a rain gauge, and many areas of the world are beyond 100 km from the nearest rain gauge. Data scarcity is especially critical over Africa (Nikulin et al. 2012, Dike et al., 2018) but the apparent data scarcity could be due to reasons other than actual paucity of data, as stated earlier. For instance, over South Africa, the number of weather stations collecting daily temperature used in the fourth version of the Climatic Research Unit Temperature dataset (CRUTEM4, Osborn and Jones, 2014) has significantly declined since 1980 (Archer et al., 2018). Although CRUTEM4 has now been replaced by CRUTEM5 (Osborn et al., 2021) it has yet to take advantage of the significant international efforts to curate and make available improved global holdings (Rennie et al., 2014) which increased the global available station count for monthly mean temperatures. This includes additional stations from many African countries. The apparent decline in stations since the 1980s could also be due to countries not contributing their data to the SYNOP/CLIMAT networks for reasons other than having non-operational stations.

Even in Europe, precipitation station density in the widely used E-OBS gridded dataset varies largely in space and time across regions (Prein and Gobiet, 2017). This variability is partly due to the reluctance of some data owners to share their data with an international effort. Regardless of the reason, low station density is a major source of uncertainty (Isotta et al., 2015). Kirchengast et al. (2014) and O and Foelsche (2018) found that at least 2 to 5 (12) stations are required for capturing the area-averaged precipitation amount of heavy summertime precipitation events on a daily (hourly) basis with a normalised root-mean-square error of less than 20%. Similar to the E-OBS dataset, gridded daily temperature and precipitation datasets are being developed for other regions of the world. Examples include Southeast Asia (SA-OBS, Van den Besselaar et al., 2017), and West Africa (WACA&D, Van Den Besselaar et al., 2015). Despite the uneven distribution of stations in space and time, the value in these initiatives is illustrated by the large number of studies in which the data product is used. This is the case, for instance, the work of Condom et al., (2020) over the Andes, a region with prominent data scarcity, and the African Monsoon Multidisciplinary Analysis Project over West Africa (e.g., Lebel and Ali, 2009). There have been efforts to reduce data scarcity through initiatives such as the International Surface Temperature Initiative (ISTI, Thorne et al., 2011), GHCND, and the Expanding Met Office Hadley Centre ISD with quality-controlled, sub-daily station data from 1931 (HadISD, Dunn et al., 2016).

Data scarcity arising from changing coverage in observation station networks results in substantial problems for climate monitoring (e.g., trend analysis of extreme events requires high temporal and spatial resolutions) or model evaluation (Section 10.3.3.1). It is *virtually certain* that the scarcity and decline of observational availability in some regions (but not necessarily globally), increase the uncertainty of the long-term global temperature and precipitation estimates. As an example, Lin and Huybers (2019) found that changes in the number of rain gauges after 1975 resulted in spurious trends in extremes of Indian rainfall in a 0.25°-gridded dataset spanning the 20th century. In fact, the number of stations used to construct the gridded dataset dropped by half after 1990, leading to inhomogeneity and spurious trends (Section 10.6.3). Over the southern part of the Mediterranean, which is an area sparsely covered by meteorological stations, data scarcity can lead to large uncertainties in the different gridded datasets and strongly affect model evaluation (Section 10.6.4). Perpetual data sparsity results in some climate characteristics not being observed (Yokoyama et al., 2019).

There are techniques for estimating and reconstructing missing data. The methods depend on the variable of

ACCEPTED VERSION
SUBJECT TO FINAL EDITING

interest, the temporal resolution (e.g., daily or monthly), and the type of climate (wet or dry), among others. There has been very little evaluation of the performance of classical and data mining methods (e.g., Sattari et al., 2017). The classical methods include the arithmetic mean, inverse-distance weighting method, multiple-regression analysis, multiple imputation, and single-best estimator, while the data-mining methods include multiple-perceptron artificial neural network, support-vector machine, adaptive neuro-fuzzy inference system, gene-expression programming method, and K-nearest neighbour. Crowd-sourced data (individuals contribute their own data points to create a dataset for others to use) could play a role in minimizing data scarcity (Section 10.2.4).

10.2.2.4 Gridding

Derived gridded datasets require merging data from different sources of observations and/or reanalysis data on a regular grid (e.g., Xie and Arkin, 1997; Section 10.2.1.2). However, in situ observations are distributed irregularly, especially over sparsely populated areas. This leads to an interpolation challenge. Gridded products of climate variables, including temperature and precipitation, are strongly affected (*high confidence*) by the interpolation method over complex orography and data scarce regions (Hofstra et al., 2008; Herrera et al., 2016).

There are two main approaches to produce gridded datasets: (1) based on in situ observations only, and (2) combining in situ observations with remote-sensing data and/or reanalysis data. The first approach has been widely employed in regions with high station density using interpolation techniques (such as inverse-distance weighting, optimal interpolation, and kriging) (Chen et al., 2008; Haylock et al., 2008; Frei, 2014; Isotta et al., 2014; Masson and Frei, 2014; Hiebl and Frei, 2016; Inoue et al., 2016). The second approach has been mainly applied in data-sparse regions with low station density, using simple bias adjustment, quantile mapping, and kriging techniques with in situ observations, remote-sensing and reanalysis data (Cheema and Bastiaanssen, 2012; Dinku et al., 2014; Abera et al., 2016; Erdin et al., 2012; Krähenmann et al., 2018).

Gridding of station data is affected by uncertainties stemming from measurement errors, inhomogeneities, the distribution of the underlying stations and the interpolation error, with station density being the dominant factor (Herrera et al., 2019). Uncertainty due to interpolation is typically small for temperature but substantial for precipitation and its derivatives, such as drought indices (Chubb et al., 2015; Hellwig et al., 2018). The largest uncertainties typically occur in sparsely sampled mountain areas (Section 10.2.2.5). Interpolation generally give rise to smoothing effects, such as low variability of the derived dataset with respect to the in situ observations (Chen et al., 2019). As a result, the effective resolution of gridded data is typically much lower than its nominal resolution. For instance, a 5 km gridded precipitation dataset for the European Alps has an effective resolution of about 10 to 25 km (Isotta et al., 2014). In an example for precipitation in Spain, the effective resolution converged to the nominal resolution only when at least 6 to 7 stations were inside the grid cell (Herrera et al., 2019). To account for the smoothing errors, new stochastic ensemble observation datasets have been introduced (Von Clarmann, 2014).

10.2.2.5 Observations in mountain areas

Spatiotemporal variability of meteorological parameters observed over mountainous areas is often large, indicating strong control exerted by local topography on meteorological parameters (Gultepe et al., 2014). Difficult access, harsh climatic conditions as well as instrumental issues make meteorological measurements extremely challenging at higher elevations (Azam et al., 2018; Beniston et al., 2018). Measurements of wind speed, temperature, relative humidity and radiative fluxes are critical for climate model evaluation, but difficult to handle due to their point-scale representativeness and small-scale spatiotemporal variability over mountainous terrain, and often need adjustment (Gultepe, 2015). High-altitude (>3000 metres) permanent meteorological stations are limited and current knowledge is mainly based on valley-bottom or low-elevation meteorological stations (Qin et al., 2009; Lawrimore et al., 2011; Gultepe, 2015; Condom et al., 2020), which, generally do not represent the higher elevation climate (Immerzeel et al., 2015; Shea et al., 2015).

ACCEPTED VERSION SUBJECT TO FINAL EDITING

Measuring precipitation amounts, especially of solid precipitation, in mountainous areas is particularly challenging due to the presence of orographic barriers, strong vertical and horizontal precipitation rate variability, and the difficulty in finding representative sites for precipitation measurements (Barry, 2012). However, the precipitation amounts can be indirectly estimated by the observed point mass balances at glacier accumulation areas representing net snow accumulation (Haimberger et al., 2012; Immerzeel et al., 2015; Sakai et al., 2015; Azam et al., 2018). There is *very high confidence* that precipitation measurements, especially solid precipitation, in mountainous areas are strongly affected by the gauge location and setup. Precipitation measurements are also affected by the type of measurement method, presence/absence of shielding, presence/absence of a heating system and operating meteorological conditions (Nitu et al., 2018). Solid precipitation measurements may have errors ranging from 20% to 50%, largely due to under-catch in windy, icing and riming conditions (Rasmussen et al., 2012), and therefore require corrections by applying transfer functions developed mainly from collected wind speed and temperature data (Kochendorfer et al., 2017). The latest Solid Precipitation Intercomparison Experiment report recommends measurements of wind speed, wind direction and temperature as the minimum standard ancillary data for solid precipitation monitoring (Nitu et al., 2018).

Recent advancements through remote-sensing methods provide an alternative, but they also have limitations over mountainous areas. Different versions of TRMM products were found to perform differently over mountainous areas (Zulkafli et al., 2014). Orographic heavy rainfall associated with Typhoon Morakot in 2009 was severely underestimated in all microwave products including TRMM 3B42 (Shige et al., 2013). The underestimation has been mitigated in the Global Satellite Mapping of Precipitation (GSMaP) product by considering the orographic effects (Shige et al., 2013). Studies have suggested a high accuracy of passive optical satellite (e.g., MODIS, Landsat) snow products under clear skies when compared with the field observations. However, cloud masking and sub-pixel cloud heterogeneity in these snow-cover products considerably restrict their applications (Kahn et al., 2011; Brun et al., 2015; Tang et al., 2017; Stillinger et al., 2019). Gridded datasets (e.g., CRU, GPCC Full Data Product, GPCC Monitoring Product, ERA-Interim, ERA5, ERA5-land, MERRA-2, MERRA-2 bias adjusted, PERSIANN-CDR) are of paramount importance, yet they often lack enough in situ observations to improve the temporal and spatial distribution of meteorological parameters over complex mountain terrain (Zandler et al., 2019).

10.2.2.6 Structural uncertainty

Beyond climate monitoring, the quality and availability of multiple observational reference datasets play a central role in model evaluation. In fact, when using observations for model evaluation, there are multiple examples where inter-observational uncertainty is as large as the inter-model variability. This has been shown for various aspects of the Indian monsoon (Section 10.6.3) (Collins et al., 2013a) and for precipitation uncertainties over Africa (Section 10.6.4) (Nikulin et al., 2012; Sylla et al., 2013; Dosio et al., 2015; Bador et al., 2020) and Europe (Prein and Gobiet, 2017). Kotlarski et al. (2019) compared three high-resolution observational temperature and precipitation datasets (E-OBS, a compilation of national/regional high-resolution gridded datasets, and the EURO4M-MESAN 0.22° reanalysis based on a high-resolution limited-area model) with five EURO-CORDEX RCMs driven by ERA-Interim. Generally, the differences between RCMs are larger than those between observation datasets, but for individual regions and performance metrics, observational uncertainty can dominate. They also showed that the choice of reference dataset can have an influence on the RCM performance score. Over the high mountain Asia region and East Asia, differences among gridded precipitation datasets can generate significant uncertainties in deriving precipitation characteristics (Kim et al., 2015b; Kim and Park, 2016; Guo et al., 2017). Over western North America, observational uncertainty induces differences in multi-decadal precipitation trends (Lehner et al., 2018). Taking a very different perspective, the agreement between model simulations may be used to estimate the uncertainty and quality of observations (Massonnet et al., 2016). There is *high confidence* that an ensemble of multiple observational references at a regional scale is fundamental for model performance assessment. The uncertainties vary according to region, season, and statistical properties (Cross-Chapter Box 10.2).

ACCEPTED VERSION SUBJECT TO FINAL EDITING

10.2.3 Other Uses of Observations at Regional Scale

10.2.3.1 Observations for calibrating statistical methods

Statistical downscaling, bias adjustment and weather generators are post-processing methods used to derive climate information from climate simulations. They all require observational data for calibration as well as evaluation (Section 10.3.3.1). Typically, the so-called perfect prognosis methods use quasi-observations for the predictors (i.e., reanalyses) and actual observations for the predictands (the surface variables of interest). By contrast, bias adjustment methods use observations only for the predictands. Weather generators typically require only observed predictands, although some are conditioned on observed predictors as well. Very often these methods are based on daily data, because of user needs, but also because of the limited availability of sub-daily observations and the limited ability of climate models to realistically simulate sub-daily weather (Iizumi et al., 2012). Some methods are calibrated on the monthly scale, but some of the generated time series are then further disaggregated to the daily scale (e.g., Thober et al., 2014). A few methods, mainly weather generators, represent sub-daily weather (Mezghani and Hingray, 2009; Kaczmarska et al., 2014). Many methods simulate temperature and precipitation only, although some also represent wind, radiation and other variables. The limited availability of high quality and long observational records typically restricts these applications to a few cases (Verfaillie et al., 2017; Pryor and Hahmann, 2019). Overall, there is *high confidence* that limited availability of station observations, including variables beyond temperature and precipitation as well as sub-daily data, limit the use of statistical modelling of regional climate.

All the limitations and challenges of observational data discussed in Section 10.2.2 also apply to its use for post-processing of climate model data. High quality and long observational data series are particularly relevant to quantify uncertainties. Different reanalyses present significant discrepancies when used as key predictor variables at the daily scale and may even affect the downscaled climate change signal (Brands et al., 2012; Dayon et al., 2015; Manzanas et al., 2015; Horton and Brönnimann, 2019). There is *high confidence* that reanalysis uncertainties limit the quality of statistical downscaling in some regions, although no assessment has been made for the most recent reanalysis products.

An important issue for bias adjustment is the correct representation of the required spatial scale. Ideally, bias adjustment is calibrated against area-averaged data of the same spatial scale as the climate model output. Hence, high-quality observed gridded datasets with an effective resolution close to the nominal model resolution are required. Driven by the need to also generate regional-scale information in station-sparse regions, researchers have considered derived datasets that blend in situ and remote sensing data to produce high-resolution observations to be used as predictands (e.g., Haiden et al., 2011; Wilby and Yu, 2013) (Sections 10.2.1.2 and 10.2.2.4).

10.2.3.2 Observation for paleoclimate data assimilation

Following some early concept studies, the first practical applications of paleoclimate data assimilation over past centuries used only selected data to reconstruct past climate changes for analysis of a specific process or case (Widmann et al., 2010). Recently, assimilation of multiple series from various data sources, including tree rings, ice cores, lake cores, corals, and bivalves, has allowed production of reconstructions that can be widely shared and applied to multiple purposes, as with modern reanalyses (Franke et al., 2017; Hakim et al., 2016; Steiger et al., 2018, Tardif et al. 2019). Most of these paleo-reanalyses are global but there are products using regional models or targeted at specific regions such as Europe, East Africa and the Indian Ocean (Fallah et al., 2018; Klein and Goosse, 2018).

Paleo-reanalyses are enabling a new range of applications and have already provided useful information on seasonal-to-multidecadal climate variability over past millennia. They are useful tools to study the covariance between variables at interannual-to-centennial time scales and at regional to global spatial scales. In particular, they have highlighted the processes that can be responsible for changes in continental hydrology at multi-decadal time scales (Franke et al., 2017; Klein and Goosse, 2018; Steiger et al., 2018).

ACCEPTED VERSION SUBJECT TO FINAL EDITING

Paleo-reanalyses have confirmed a large contribution of internal variability in past changes at regional scale during the pre-industrial period, superimposed on a weak common signal due to forcing changes (Goosse et al., 2012) and the absence of a globally coherent warm period in the common era before the recent warming (Neukom et al., 2019). Reconstructions of the atmospheric state obtained in the reanalysis also provide robust evidence of a local enhancement of warming or cooling conditions due to changes in atmospheric circulation, such as for the warm conditions in some European regions around 950–1250 CE, the cooling observed in 1809/1810, or the cold and rainy 1816 summer in Europe (Cross-Chapter Box 4.1; Goosse et al., 2012; Hakim et al., 2016; Franke et al., 2017; Schurer et al., 2019).

10.2.4 Outlook for Improving Observational Data for Regional Climates

An encouraging development for understanding climate variations over the past 250 years or so at the global and regional scale lies in the field of data rescue, in which hitherto hidden archives of meteorological data are brought to the forefront (Sections 1.5.1.1 and 2.5). Surface observations from data rescue projects may then be assimilated to derive long-term high-resolution gridded surface regional reanalysis (Devers et al., 2020). Global extended reanalyses such as 20CR (Compo et al., 2011), ERA-20C (Poli et al., 2016b, 2016a) or CERA-20C (Laloyaux et al., 2018) may be further downscaled to quantify the variability of past climate at the regional scale (Caillouet et al., 2016, 2019).

One of the main scientific challenges related to high-resolution regional climate modelling is dealing with the representation of fine-scale processes (e.g., Yano et al., 2018) in observational data sets. Additionally, reliable observation networks following WMO standards have a very sparse geographical representation. Hence, regional climate models have started to use high-resolution data combined with crowdsourced observations (Zheng et al., 2018). Recent efforts have led to the production of homogeneously processed long-term datasets for regional climate model evaluation (Goudenhoofdt and Delobbe, 2016; Humphrey et al., 2017; Yang and Ng, 2019). While they are far less reliable and accurate than professional observations, crowdsourced data are abundantly available and can give spatial representations at very high resolution. This technological trend could prove very useful (*high confidence*), and the regional climate community is making efforts to understand the extent to which these data sources can be exploited, at least as a complement to traditional datasets (Overeem et al., 2013; Meier et al., 2017; Uijlenhoet et al., 2018; de Vos et al., 2019; Langendijk et al., 2019a).

10.3 Using Models for Constructing Regional Climate Information

Much of the information available on future regional climate arises from studies based on climate model simulations (Chapters 3, 4 and 8). In this section, different types of models (Section 10.3.1) and model experiments (Section 10.3.2) for generating regional climate information are discussed, followed by an assessment of the performance, added value, and fitness-for-purpose of different model types (Section 10.3.3). The focus is on the representation of large- to local-scale phenomena and processes relevant for regional climate. Finally, uncertainties of regional climate projections and methodologies to manage these are assessed (Section 10.3.4).

10.3.1 Model Types

Regional climate change information may be derived from a hierarchy of different model types covering a wide range of spatial scales and processes (Figure 10.5). The application of any model relies on assumptions, depending on the specific model as well as the application. Table 10.1 gives an overview of the generic assumptions of the different model types discussed here for generating regional climate information. The violation of these assumptions will affect the model performance, which is discussed in Section 10.3.3.

[START FIGURE 10.5 HERE]

ACCEPTED VERSION SUBJECT TO FINAL EDITING

Figure 10.5: Typical model types and chains used in modelling regional climate. The dashed lines indicate model chains that might prove useful but have not or only rarely been used. Hybrid approaches combining the model types shown have been developed.

[END FIGURE 10.5 HERE]

[START TABLE 10.1 HERE]

Table 10.1: Assumptions underlying different model types in simulating regional climate and climate change. Violating these assumptions will affect model performance (see links to different subsections for details). All assumptions regarding future climate are in addition to those regarding present climate and predicated on the driving global model simulating a plausible global climate sensitivity (Section 1.3.5, Chapters 4 and 7). The assumptions listed for future climate applications of perfect prognosis statistical downscaling and bias adjustment are often called the "stationarity assumption". Numbers in curly brackets refer to chapters and sections assessing these assumptions.

Model type	Scale at which the assumption applies	Assumptions to realistically simulate present regional climate	Additional assumptions to be fit for simulating future regional climate
Global model (GCM or ESM; not bias adjusted) (Section 10.3.1.1)	Large (>1000km)	Global model includes all relevant large-scale forcings and realistically simulates relevant large-scale circulation {3.3.3, 8.5.1, 10.3.3.3}.	Global model realistically simulates processes controlling large-scale changes. Parameterisations are valid in future climate {Chapter 3, 4.2, 4.5, 8.5.1, 10.3.3.9}.
	Regional (<1000km)	Global model includes all relevant regional forcings and realistically simulates all relevant regional scale processes and feedbacks and their dependence on large-scale climate {8.5.1, 10.3.3.4-10.3.3.6, 10.3.3.8}.	Global model realistically simulates processes controlling regional changes. Parameterisations are valid in future climate {8.5.1, 10.3.3.9}.
Dynamical downscaling of global model with RCM (not bias adjusted) (Section 10.3.1.2)	Large	Driving global model includes all relevant large-scale forcings and realistically simulates relevant large-scale circulation, RCM does not deteriorate global simulations. Feedbacks from regional into large-scale processes are negligible {3.3.3, 8.5.1, 10.3.3.3}.	Driving global model realistically simulates processes controlling large-scale changes, RCM does not deteriorate global model changes. Parameterisations are valid in future climate {Chapter 3, 4.2, 4.5. 8.5.1, 10.3.3.9}.
	Regional	RCM includes all relevant regional forcings and realistically simulates all relevant regional scale processes and feedbacks and their dependence on large-scale climate {10.3.3.4–10.3.3.6, 10.3.3.8}.	RCM realistically simulates processes controlling regional changes. Parameterisations are valid in future climate {10.3.3.9}.
Perfect prognosis statistical	Large	Global model realistically simulates all relevant large-scale	Global model realistically simulates processes controlling

ACCEPTED VERSION SUBJECT TO FINAL EDITING

downscaling of GCM (Section 10.3.1.3)		predictors. The predictors are bias free and represent the regional variability at all desired time-scales {3.3.3, 8.5.1, 10.3.3.3}.	changes in the predictors. The predictors represent the response to external forcing {Chapter 3, 4.2, 4.5. 8.5.1, 10.3.3.9}.
	Regional	The statistical model structure is adequate to represent the predictor influence on regional-scale variability. There are no relevant feedbacks involving the predictands {10.3.3.7}.	The statistical model structure is adequate under the required extrapolation {10.3.3.9}.
Bias adjustment of dynamical model (GCM or RCM) (Section 10.3.1.3)	Large	As per driving model.	As per driving model.
	Regional	As per driving model, apart from adjustable biases. The gap between driving model resolution and target resolution is minor {10.3.3.4–10.3.3.6, 10.3.3.8, Cross-Chapter Box 10.2}.	As per driving model, apart from adjustable biases. The chosen bias adjustment is applicable in a future climate {10.3.3.9, Cross-Chapter Box 10.2}.
Delta change approach applied to dynamical model (Section 10.3.1.3)	Large	Not applicable	As per driving model. There are no changes altering the non-changed statistics (e.g., no circulation changes that alter temporal structure) {Chapter 3, 4.2, 4.5, 8.5.1, 10.3.3.9}.
	Regional	Not applicable	As per driving model. There are no changes altering the non-changed statistics. The gap between driving model resolution and target resolution is minor {10.3.3.9}.
Change factor weather generator applied to dynamical model (Section 10.3.1.3)	Large	Not applicable	As per driving model.
	Regional	The weather generator structure is adequate {10.3.3.7}.	As per driving model. The weather generator structure is adequate in a future climate. Change factors are adequately incorporated for all changing weather aspects. The gap between driving model resolution and target resolution is minor {10.3.3.9}.

[END TABLE 10.1 HERE]

10.3.1.1 Global models, including high-resolution and variable resolution models

Model-based regional climate projections are all based upon some type of global climate model, including state-of-the-art Earth system models (ESMs), coupled atmosphere-ocean general circulation models (GCMs) or atmosphere-only general circulation models (AGCMs) (see Section 1.5.3.1). They are collectively referred to as global models.

State-of-the-art global models are generally used to derive climate information at continental to global scales both for past and future climates (e.g., Chapters 3 and 4). The nominal horizontal resolution in CMIP5 global models is typically 100–200 km. The effective resolution, for which the shape of the kinetic energy spectrum is simulated correctly, is about 3 to 5 times larger (Klaver et al., 2020), and a similar relationship also applies to RCMs (Skamarock, 2004). This strongly limits their ability to resolve local details. Since AR5 the

ACCEPTED VERSION SUBJECT TO FINAL EDITING

progress in reducing biases and providing more credible regional projections by global models has been moderate in spite of the more realistic representation of a number of processes and the increase in resolution of some models. For AR6, several of the new CMIP6 (Eyring et al., 2016a) model intercomparison projects (MIPs) address some of these limitations. The list of MIPs is provided in Chapter 1 (Table 1.3). HighResMIP (High-Resolution MIP; Haarsma et al., 2016) and GMMIP (Global Monsoons MIP; Zhou et al., 2016)) specifically address the regional climate challenge using global models. HighResMIP focuses on producing global climate projections at a horizontal resolution of around 50 km grid spacing or finer while GMMIP aims at better understanding and predicting the monsoons.

An alternative to increasing resolution everywhere is offered by variable resolution global models, that is, with regionally finer resolution. They have been developed since the 1970s (Li, 1999), resulting in a first coordinated effort (SGMIP) by Fox-Rabinovitz et al., (2006, 2008). They are expected to offer the finest resolution possible in the region of interest, while still resolving the climate processes at the global scale (although at lower resolution). An overview of recent developments is in McGregor (2015). This is a rapidly developing field (Krinner et al., 2014; Ferguson et al., 2016; Huang et al., 2016) that will possibly contribute to improved future regional projections.

10.3.1.2 RCMs

RCMs are dynamical models similar to GCMs that are applied over a limited area, but with a horizontal resolution higher than that of standard GCMs. They are the basis for dynamical downscaling to produce sub-continental climate information (e.g., Chapters 11, 12 and Atlas) but are also often used for process understanding. At lateral and, if applicable, lower boundaries, RCMs take their values from a driving data set, which could be a GCM or a reanalysis. RCMs are typically one-way nested: they do not feed back into the driving model, although two-way nested GCM-RCM simulations have been performed that examine regional influence on large-scale climate, potentially improving it (Lorenz and Jacob, 2005; Harris and Lin, 2013; Junquas et al., 2016). Spectral nudging (Kida et al., 1991; Waldron et al., 1996; von Storch et al., 2000; Kanamaru and Kanamitsu, 2007) can increase consistency with the driving model, whereby selected variables, such as the wind field, are forced to closely follow a prescribed large-scale field over a specified range of spatial scales. RCMs can inherit biases from the driving GCM in addition to producing biases themselves (Dosio et al., 2015; Hall, 2014; Hong and Kanamitsu, 2014; Takayabu et al., 2016). The consistency between the circulation features simulated by the RCM and those inherited through the boundary conditions depends on 1) the relative importance of the large-scale forcing compared to local-scale phenomena, and 2) the size of the RCM domain (e.g., Diaconescu and Laprise, 2013). Large domains also allow the RCM to generate much of its own internally generated unforced variability (Nikiema et al., 2017, and references therein; Sanchez-Gomez and Somot, 2018).

The CORDEX initiative (COordinated Regional climate Downscaling EXperiment; Giorgi et al., 2009; Giorgi and Gutowski, 2015; Gutowski Jr. et al., 2016) provides ensembles of high-resolution historical (starting as early as 1950) and future climate projections for various regions. RCMs in CORDEX typically have a horizontal resolution between 10 and 50 km. But much finer spatial resolution is required to fully resolve deep convection, an important cause of precipitation in much of the world. Therefore, an emerging strand in dynamical downscaling employs simulations at convection permitting scales, at horizontal resolutions of a few kilometres, where deep-convection parameterisations can be switched off, approximately simulating deep convection (Prein et al., 2015; Stratton et al., 2018; Coppola et al., 2020). A recent study indicates that switching off the deep-convection parameterization may be beneficial also in simulations performed at coarser resolutions (Vergara-Temprado et al., 2019). Alternatively, some RCMs make use of scale-aware parameterizations that are able to adapt to increasing resolution without switching off the convection scheme (Hamdi et al., 2012; De Troch et al., 2013; Plant and Yano, 2015; Giot et al., 2016; Termonia et al., 2018; Yano et al., 2018).

RCMs have often consisted of atmospheric and land components that do not include all possible Earth-system processes and therefore neglect important processes such as air-sea coupling (in standard RCMs sea surface temperatures, SSTs, are prescribed from GCM simulations or reanalyses) or the chemistry of cloud-

ACCEPTED VERSION SUBJECT TO FINAL EDITING

aerosol interaction (aerosols prescribed with a climatology), which may influence regional climate projections. Therefore, some RCMs have been extended by coupling to additional components like interactive oceans, sometimes with sea ice (Kjellström et al., 2005; Somot et al., 2008; Van Pham et al., 2014; Sein et al., 2015; Ruti et al., 2016; Zou and Zhou, 2016a; Zou et al., 2017; Samanta et al., 2018), rivers (Sevault et al., 2014; Lee et al., 2015; Di Sante et al., 2019), glaciers (Kotlarski et al., 2010), and aerosols (Zakey et al., 2006; Zubler et al., 2011; Nabat et al., 2015). The coupling of these components allows for the investigation of additional climate processes such as regional sea-level change (Adloff et al., 2018), ocean-land interactions (Lima et al., 2019; Soares et al., 2019a), or the impact of high-frequency ocean-atmosphere coupling on the climatology of Mediterranean cyclones (Flaounas et al., 2018).

10.3.1.3 Statistical approaches to generate regional climate projections

An alternative or addition to dynamical downscaling is the use of statistical approaches to generate regional projections. In AR5 these methods were collectively referred to as statistical downscaling, but their performance assessment has received little attention. A major conclusion was that a wide range of different methods exist and a general assessment of their performance is difficult (Flato et al., 2014). Since AR5, several initiatives have been launched to improve the understanding of statistical approaches such as VALUE (now merged into EURO-CORDEX activities; Maraun et al., 2015), STARMIP (Vaittinada Ayar et al., 2016) and BADJAM (Galmarini et al., 2019). The performance of different implementations of these approaches will be assessed in Section 10.3.3.7.

10.3.1.3.1 Perfect prognosis

Perfect-prognosis models are statistical models calibrated between observation-based large-scale predictors (e.g., from reanalysis) and observed local-scale predictands (Maraun and Widmann, 2018b). Regional climate projections are then generated by replacing the quasi-observed predictors by those from climate model (typically global model) projections. Predictor patterns that are common to observations and climate model data can be defined by common empirical orthogonal functions (Benestad, 2011). The perfect prognosis approach can either be used to generate daily (or even sub-daily) time series, or local weather statistics (e.g., Benestad et al., 2018).

Regression-like models (Maraun and Widmann, 2018b) rely on a transfer function linking an observed local statistic (such as the temperature at a given day) to some set of large-scale predictors. Recent developments include stochastic regression models to explicitly simulate local variability (San-Martín et al., 2017; those explicitly modelling temporal dependence are assessed in Section 10.3.1.3.4). The use of machine learning techniques has been reinvigorated, including genetic programming to construct a data-driven model structure (Zerenner et al., 2016) and deep and convolutional neural networks (Reichstein et al., 2019; Baño-Medina et al., 2020).

Analogue methods (Martin et al., 1996; Maraun and Widmann, 2018b) compare a simulated large-scale atmospheric field with an archive of observations and select, using some distance metric, the closest observed field in the archive. The downscaled atmospheric field is then chosen as the local atmospheric field observed on the instant the analogue occurred. New analogue methods have been developed to simulate unobserved values including a rescaling of the analogue (Pierce et al., 2014) or by combining analogues and regression models (Chardon et al., 2018).

10.3.1.3.2 Bias adjustment

Bias adjustment is a statistical post-processing technique used to pragmatically reduce the mismatch between the statistics of climate model output and observations. The approach estimates the bias or relative error between a chosen simulated statistical property (such as the long-term mean or specific quantiles of the climatological distribution) and that observed over a calibration period; the simulated statistic is then adjusted taking into account the simulated deviation. Bias adjustment methods are regularly applied on a spatial scale similar to that of the simulation being adjusted, but they are often used as a simple statistical

ACCEPTED VERSION SUBJECT TO FINAL EDITING

downscaling method by calibrating them between coarse resolution (e.g., global) model output and finer observations (Maraun and Widmann, 2018b).

Typical implementations of bias adjustment are (1) additive adjustments, where the model data is adjusted by adding a constant, (2) rescaling, where the model data is adjusted by a factor, and (3) more flexible quantile mapping approaches that adjust different ranges of a distribution individually. Hempel et al. (2013), Pierce et al. (2015), Switanek et al. (2017), and (Lange, 2019) developed variants of quantile mapping that preserve trends in the mean or even further distributional statistics. Multivariate bias adjustment extends univariate methods, which adjust statistics of individual variables separately, to joint adjustment of multiple variables simultaneously. Implementations remove biases in (1) specific measures of multivariate dependence, like correlation structure, via linear transformations (Bárdossy and Pegram, 2012; Cannon, 2016), or, more flexibly, (2) the full multivariate distribution via nonlinear transformations (Vrac and Friederichs, 2015; Dekens et al., 2017; Cannon, 2018; Vrac, 2018; Robin et al., 2019). Other research strands focus on the explicit separation of bias adjustment and downscaling (Section 10.3.1.3.5), or the integration of process understanding (Maraun et al., 2017), such as by conditioning the adjustment on the occurrence of relevant phenomena (Addor et al., 2016; Verfaillie et al., 2017; Manzanas and Gutiérrez, 2019). Some authors suggest to mitigate the influence of large-scale temperature or circulation biases by performing a bias adjustment of the driving fields prior to dynamical downscaling (Colette et al., 2012; Hernández-Díaz et al., 2013, 2019). Issues that may arise when using bias adjustment are discussed in Cross-Chapter Box 10.2.

10.3.1.3.3 Delta-change approaches

In the delta change approach, selected observations are modified according to corresponding changes derived from dynamical model simulations. Traditionally, only long term means have been adjusted, but recently approaches to modify temporal dependence (Webber et al., 2018) have been developed, as well as quantile mapping approaches that individually adjust quantiles of the observed distribution (Willems and Vrac, 2011). By construction, the approach cannot modify the spatial and temporal dependence structure of the input observations (Maraun, 2016).

10.3.1.3.4 Weather generators

Weather generators are statistical models that simulate weather time series of arbitrary length. They are calibrated to represent observed weather statistics, in particular daily or even sub-daily variability. One variant of these models are advanced stochastic perfect-prognosis methods, conditioned on large-scale atmospheric predictors on a daily basis, for instance multi-site generalised linear models (Chandler, 2020). Another widely used variant is change-factor weather generators: the weather generator parameters are calibrated against present and future climate model simulations, and the climate change signals are then applied to the parameters calibrated to observations. Recent research has mainly focussed on multi-site Richardson type (Markov-chain) weather generators (Keller et al., 2015; Dubrovsky et al., 2019), some explicitly modelling extremes and their spatial dependence (Evin et al., 2018).

10.3.1.3.5 Hybrid approaches and emulators

A wide variety of approaches has been proposed to combine the advantages of different statistical approaches. For instance, to overcome the scale mismatch between climate model output and observations, bias adjustment has been combined with stochastic downscaling (Volosciuk et al., 2017; Lange, 2019) or rescaled analogues (Pierce et al., 2014). Other approaches known as emulators have been developed to emulate an RCM using a statistical model and also applied to a range of driving global models (Déqué et al., 2012; Haas and Pinto, 2012; Walton et al., 2015, 2017; Beusch et al., 2020; Erlandsen et al., 2020).

10.3.2 Types of Model Experiments

The most commonly used model experiments to generate regional climate information are transient simulations. Alternative experiment types serve specific purposes. The role of these experiment types for

ACCEPTED VERSION SUBJECT TO FINAL EDITING

generating regional climate information is assessed in this subsection.

10.3.2.1 Transient simulations and time-slice experiments

Transient simulations intend to represent the evolving climate state of the Earth system (Chapter 4). They are typically based on coupled global model simulations, such as those in the DECK and ScenarioMIP part of CMIP6 covering the period 1850–2100 (Eyring et al., 2016a), and HighResMIP (1950–2050; Haarsma et al., 2016). Global transient climate simulations may be further downscaled by either dynamical or statistical downscaling. Currently available CORDEX RCM simulations (1950–2100) are based on CMIP5 (Gutowski et al., 2016).

In contrast, time-slice experiments are designed to represent only a specific period of time (typically 30 years). They are often run using global and regional models in atmosphere-only mode, forced by SSTs derived either from observations, as AMIP experiments, or from historical simulations and future projections of coupled global models. Compared to transient simulations, they offer advantages in being computationally cheaper (due to the lack of coupled ocean and short duration), which allows for the number of ensemble members (Zhang et al., 2016c), and/or the resolution (Haarsma et al., 2013a; Davini et al., 2017) to be increased. Convection-permitting simulations, both covering the globe or particular regions, are currently conducted for short time slices only (Kendon et al., 2017; Hewitt and Lowe, 2018; Coppola et al., 2020; Pichelli et al., 2021). Another high-resolution time-slice data base is d4PDF (Mizuta et al., 2017; Ishii and Mori, 2020). Experiments covering a limited integration period have been carried out for coupled ocean-atmosphere RCMs (Sein et al., 2015; Zou and Zhou, 2016b, 2017). However, long spin-up periods are required to reach a stable stationary state in the deep ocean that otherwise might lead to invalid projections (Planton et al., 2012; Soto-Navarro et al., 2020).

10.3.2.2 Pseudo-global warming experiments

Results from downscaling experiments often suffer from large-scale circulation biases in the driving GCMs such as misplaced storm tracks (Section 10.3.3.4), while changes in atmospheric circulation are often uncertain owing to both climate response uncertainty (Section 10.3.4.2) and internal variability (Section 10.3.4.3). In a given application, if one can assume that changes in the regional climate are dominated by thermodynamic rather than by circulation changes, so-called pseudo-global warming (PGW) experiments (Schär et al., 1996) may be helpful in mitigating the effects of circulation biases, and to fix the large-scale circulation to present climate. In classical PGW experiments, boundary conditions for the downscaling are taken from reanalysis data, but modified according to the thermodynamic signals of climate change. The boundary conditions thus represent the sequence of observed weather, but with adjusted temperatures, humidity and atmospheric stability. Recent applications of PGW experiments include assessments of climate change in Japan (Adachi et al., 2012; Kawase et al., 2012, 2013), the Los Angeles area (Walton et al., 2015), Hawaii (Zhang et al., 2016a), and the Alps (Keller et al., 2018). Recently, PGW studies have been generalised to modify global model simulations with the objective of separating the drivers of regional climate change, such as the Mediterranean amplification (e.g., Brogli et al., 2019a; Section 10.3.2.3).

Equivalent simulations can be conducted for individual events, thereby allowing for very high resolution. With counterfactual past climate conditions, such simulations can be used for conditional event attribution (Trenberth et al., 2015; Chapter 11), using hypothetical future conditions to generate physical climate storylines of how specific events may manifest in a warmer climate. The approach has been employed to study extreme events that require very high resolution simulations such as tropical cyclones (Lackmann, 2015; Takayabu et al., 2015; Lau et al., 2016; Kanada et al., 2017a; Gutmann et al., 2018; Patricola and Wehner, 2018; Chen et al., 2020a) or convective precipitation events (Pall et al., 2017; Hibino et al., 2018). The range of possible events is broader and has included Korean heat waves (Kim et al., 2018) and monsoon onset in West Africa (Lawal et al., 2016). However, if only individual events are simulated, no immediate conclusions can be derived for changes to the occurrence probability of these events (Otto et al., 2016a; Shepherd, 2016a).

ACCEPTED VERSION SUBJECT TO FINAL EDITING

10.3.2.3 Sensitivity studies with selected drivers

Sensitivity studies are used to identify the impact of a specific forcing, driver or process on regional climate phenomena and changes and improve the process understanding. The influence of a single external forcing can be assessed with transient historical simulations within two different frameworks (Bindoff et al., 2013; Gillett et al., 2016). The first entails simulations taking prescribed (often observed) changes only in the external forcing of interest, the others being fixed at a constant value (often pre-industrial). The second framework is based on simulations in which all external forcings are applied other than the one of interest. Both approaches may not give the same results since the climate response to a range of forcings is not necessarily equal to the sum of climate responses to individual forcings (Ming and Ramaswamy, 2011; Jones et al., 2013; Schaller et al., 2013; Shiogama et al., 2013; Marvel et al., 2015; Deng et al., 2020).

To study the influence of internal variability, new approaches such as partial coupling simulations are now routinely used since AR5. These are coupled ocean-atmosphere simulations in which the interaction between atmosphere and ocean is only one-way over a specified ocean basin or sub-basin and two-way everywhere else. Different implementations have been used such as SST anomaly Newtonian relaxation at the air-sea interface or prescription of wind-stress anomalies from reanalysis (Kosaka and Xie, 2013, 2016; England et al., 2014; McGregor et al., 2014; Douville et al., 2015; Deser et al., 2017a). Such simulations have been applied to identify the regional impacts of the Pacific Decadal Variability (PDV) and Atlantic Multidecadal Variability (AMV) (Kosaka and Xie, 2013; Watanabe et al., 2014; Delworth et al., 2015; Boer et al., 2016; Ruprich-Robert et al., 2017, 2018).

Nudging experiments have been used to identify the relative roles of dynamic and thermodynamic processes in climate model biases and specific extreme events (Wehrli et al., 2018, 2019). Another related framework is used to evaluate the impact land conditions have on a climate phenomenon in a pair of experiments with one simulation serving as control run, and a perturbed simulation with prescribed land conditions (i.e., soil moisture, leaf area index, or surface albedo) characterizing a specific state of the land surface (i.e., afforestation or deforestation). The difference between the perturbed and control simulations enables a robust assessment of the possible impact of land conditions on events like droughts and heatwaves (Seneviratne et al., 2013; Stegehuis et al., 2015; Hauser et al., 2016, 2017; van den Hurk et al., 2016; Vogel et al., 2017; Rasmijn et al., 2018; Strandberg and Kjellström, 2019).

RCM sensitivity simulations have been used in a similar way to assess the contribution of external forcings and large-scale drivers to projected regional climate change (Nabat et al., 2014; Brogli et al., 2019b, 2019a) and the influence of selected drivers on observed extreme events (Meredith et al., 2015b; Wang et al., 2017a; Ardilouze et al., 2019).

In summary, there is *robust evidence* that sensitivity experiments are key to assessing the influence of different forcings and drivers on regional climate change.

10.3.2.4 Control simulations

In recent years, the role of internal variability in the interpretation of climate projections has become clearer, particularly at the regional scale (Section 10.3.4.3). A considerable fraction of CMIP5 and CMIP6 resources has been invested in generating an ensemble of centennial or multi-centennial control simulations with constant external forcings (Pedro et al., 2016; Rackow et al., 2018). As part of the CMIP6 DECK (Eyring et al., 2016a) pre-industrial control (piControl) simulations have been conducted (Menary et al., 2018). Similarly, control simulations with present-day conditions (pdControl) have been performed to represent internal variability under more recent forcing conditions (Pedro et al., 2016; Williams et al., 2018). Control simulations have been used to study the role of internal variability, teleconnections and many other fundamental aspects of climate models (Wang et al., 2015b; Krishnamurthy and Krishnamurthy, 2016). Control simulations are also used along with large ensembles of historical or scenario simulations to assess

ACCEPTED VERSION SUBJECT TO FINAL EDITING

the characteristics of the regional internal climate variability (Olonscheck and Notz, 2017).

10.3.2.5 Simulations for evaluating downscaling methods

Experiments driven by quasi-perfect boundary conditions or predictors (observations or reanalysis) can be useful to evaluate downscaling performance (Frei et al., 2003; Laprise et al., 2013), including the simulation of observed past trends (Lorenz and Jacob, 2010; Zubler et al., 2011; Nabat et al., 2014; Gutiérrez et al., 2018; Drugé et al., 2019; Bozkurt et al., 2020) and the added value of downscaling compared to the reanalysis fields (Section 10.3.3.2). Although the reanalysis model itself can introduce biases especially for non-assimilated variables (such as precipitation) it is assumed that in such a setting, discrepancies between the modelled and observed climate arise mostly from errors in the downscaling method (Laprise et al., 2013) or internal climate variability generated by the downscaling method (Böhnisch et al., 2020; Ehmele et al., 2020). Since AR5, reanalysis-driven RCMs have been extensively evaluated for many regions, especially in the CORDEX framework (see region specific examples in the Atlas).

Over Europe, the VALUE initiative assessed statistical downscaling for marginal, temporal, and spatial aspects of temperature and precipitation including extremes, and performed a process-based evaluation of specific climatic phenomena (Gutiérrez et al., 2018; Maraun et al., 2018). Alternatively, statistical downscaling can be evaluated in so-called perfect model or pseudo-reality simulations (Charles et al., 1999), where a high-resolution climate model simulation is used as a proxy for a hypothetical present and future realities. A statistical downscaling model is first calibrated with this pseudo present-day climate and, subsequently, assessed whether it correctly reproduces the pseudo-future conditions (Dixon et al., 2016).

10.3.3 Model Performance and Added Value in Simulating and Projecting Regional Climate

Assessing model performance is a prerequisite for building confidence in regional climate projections. This subsection assesses the performance of different model types at simulating regional climate and climate change. The subsection builds on the assessment of global model performance in Chapter 3, and complements the model assessment in Chapter 8, which focuses on the water cycle, and the Atlas.

[START FIGURE 10.6 HERE]

Figure 10.6: Illustration of some model biases in simulations performed with dynamical models. (a) Top row: Mean summer (June to August) near-surface air temperature (in °C) over the Mediterranean area in Berkeley Earth and respective mean bias for five multi-model historical experiments with GCMs (CMIP5, CMIP6 and HighResMIP) and RCMs (CORDEX EUR-44 and EUR-11) averaged between 1986–2005. Bottom row: Box-and-whisker plot shows spread of the 20 annual mean summer surface air temperature averaged over land areas in the western Mediterranean region (33°N–45°N, 10°W–10°E, black quadrilateral in the first panel of the top row) for a set of references and single model runs of the five multi-model experiments (one simulation per model) between 1986–2005. Additional observation and reanalysis data included in the bottom row are CRU TS, HadCRUT4, HadCRUT5, E-OBS, WFDE5, ERA5, ERA-Interim, CERA-20C, JRA-25, JRA-55, CFSR, MERRA2, MERRA. Berkeley Earth is shown in the first box to the left. (b) as (a) but for precipitation rate (mm day^{-1}) and showing CRU TS in the first panel of the top row. Biases of the five multi-model experiments are shown with respect to CRU TS. Additional observation and reanalysis data included in the bottom row are GPCC, REGEN, E-OBS, GHCN, WFDE5, CFSR, ERA-Interim, ERA5, JRA-55, MERRA2, MERRA. CRU TS is shown in the first box to the left. All box-and-whisker plots show the median (line), and the interquartile range (IQR = Q3–Q1, box), with top whiskers extending to the last data less than Q3+1.5×IQR and analogously for bottom whiskers. Data outside the whiskers range appear as flyers (circles). Further details on data sources and processing are available in the chapter data table (Table 10.SM.11).

[END FIGURE 10.6 HERE]

ACCEPTED VERSION SUBJECT TO FINAL EDITING

While the ability of global models to simulate large-scale indicators of climate change has improved since AR5 (Chapter 3), the simulation of regional climate and climate change poses an additional challenge. Users demand regional climate projections for decision making and have high expectations regarding accuracy and resolution (Rössler et al., 2019a), but some scientists consider such projections still a matter of basic research (Hewitson et al., 2014a). For instance, large-scale circulation biases or the misrepresentation of regional topography as well as regional phenomena and feedbacks are very relevant (Hall, 2014; Maraun and Widmann, 2018b). New global model ensembles such as CMIP6 (Eyring et al., 2016a), HighResMIP (Haarsma et al., 2016) or, at the regional scale, the convection permitting simulations from the CORDEX Flagship Pilot Study (FPS) on convective phenomena (Coppola et al., 2020) have the potential to substantially improve the basis for generating regional climate information, yet uncertainties and (often unresolved) contradictions between model projections at the regional scale can be substantial (Fernández et al., 2019).

Figure 10.6 shows the mean summer temperature and precipitation biases of several state-of-the-art climate model ensembles for the western Mediterranean. It additionally illustrates the role of observational uncertainty for model evaluation (Section 10.2), where observations display differences that can be substantial. Model performance varies strongly from model to model, but also between ensembles. These biases are an expression of model error that leads to misrepresented phenomena and processes, and thus limit the confidence in future projections of regional climate. The focus of this subsection is therefore to evaluate the representation of relevant regional scale phenomena for representing regional climate.

10.3.3.1 Evaluation diagnostics

Since AR5, model evaluation has made use of a broad combination of diagnostics (Colette et al., 2012; Kotlarski et al., 2014; Eyring et al., 2016b; Gleckler et al., 2016; Ivanov et al., 2017, 2018; Vautard et al., 2020), ranging from long-term means to indices of extreme events (Zhang et al., 2011; Sillmann et al., 2013) or a combination of these (Dittus et al., 2016). This evaluation has shown that global models have pervasive biases in some aspects of their large-scale behaviour (Section 1.5.3.1, Chapter 3). More complex diagnostics are used to characterize specific meteorological phenomena (Sprenger et al., 2017), such as feedbacks in the El Niño-Southern Oscillation (ENSO; Bellenger et al., 2014), Madden-Julian Oscillation (MJO) characteristics (Ahn et al., 2017; Benedict et al., 2014; Jiang et al., 2015; Kim et al., 2015), extra-tropical modes of variability (Lee et al., 2019), cyclone tracking (Neu et al., 2013; Flaounas et al., 2018), front detection (Hope et al., 2014; Schemm et al., 2015), thunderstorm environment parameters (Bukovsky et al., 2017), African easterly waves (McCrary et al., 2014; Martin and Thorncroft, 2015), land-atmosphere coupling (Spennemann and Saulo, 2015; Santanello et al., 2018), and sea-atmosphere coupling (Bellenger et al., 2014; Mayer et al., 2017).

New diagnostics for multivariate dependencies are needed to characterize compound events (Section 11.8; Hobaek Haff et al., 2015; Wahl et al., 2015; Sippel et al., 2016, 2017; Tencer et al., 2016; Bevacqua et al., 2017; Careto et al., 2018; Zscheischler et al., 2018b). However, their success depends on the availability of adequate observational data (Section 10.2.2). Multivariate dependencies discovered in compound events can also be used for designing and evaluating multivariate bias adjustment and statistical downscaling. Process-based diagnostics are useful for identifying the cause of model errors, although it is not always possible to associate a systematic error with a specific cause (Eyring et al., 2019). AR5 discussed two approaches of process-based evaluation: 1) the isolation of physical components or parameterizations by dedicated experiments (Section 10.3.2.4) and 2) diagnostics conditioned on relevant regimes, usually synoptic-scale weather patterns. The regime-based approach has been used with both global models (e.g., Barton et al., 2012; Catto et al., 2015; Taylor et al., 2019) and RCMs (Endris et al., 2016; Bukovsky et al., 2017; Whan and Zwiers, 2017; Pinto et al., 2018), but also with perfect prognosis and bias adjustment methods (Marteau et al., 2015; Addor et al., 2016; Beranová and Kyselý, 2016; Soares and Cardoso, 2018; Soares et al., 2019b).

Recent studies highlight the importance of user-defined or user-relevant diagnostics for model evaluation (Maraun et al., 2015; Rhoades et al., 2018; Rössler et al., 2019b; Nissan et al., 2020). Diagnostics have been

ACCEPTED VERSION SUBJECT TO FINAL EDITING

used to assess the performance of climate models to produce useful input data for impact models as in the comparison between RCMs and convection-permitting models to capture flood generating precipitation events in the Alps (Reszler et al., 2018). Alternatively, the observed impact can be compared to that simulated by an impact model that uses input from both observations and climate models. This approach has been used to evaluate the influence of statistical downscaling and bias adjustment on hydrological (Rojas et al., 2011; Chen et al., 2012b; Gutiérrez et al., 2019; Rössler et al., 2019b), agricultural (Ruiz-Ramos et al., 2016; Galmarini et al., 2019), forest and wildfire (Abatzoglou and Brown, 2012; Migliavacca et al., 2013) (Bedia et al., 2013), snow depth (Verfaillie et al., 2017), and regional ocean modelling (e.g., Macias et al., 2018).

There is *high confidence* that to assess whether a climate model realistically simulates required aspects of present-day regional climate, and to increase confidence of future projections of these aspects, evaluation needs to be based on diagnostics taking into account multiple variables and process-understanding.

10.3.3.2 Model improvement and added value

Obtaining regional information from global simulations may involve a range of different methods (Section 10.3.1). An approach with higher complexity or resolution is useful if it adds further, useful information to that of a reference model. Section 10.5 discusses the set of considerations that determine if the information is useful. This further useful information is often referred to as added value and is a function of variables, processes, and the temporal and spatial scales targeted taking into account the needs of specific users (Di Luca et al., 2012; Ekström et al., 2015; Giorgi and Gutowski, 2015; Torma et al., 2015; Rummukainen, 2016; Falco et al., 2018). There is no common definition of added value, but here it is considered a characteristic that arises when one methodology gives further value to what another methodology yields.

Downscaling is expected to improve the representation of a region's climate compared to the driving GCM (Di Luca et al., 2015). Arguably, there should be a clear physical reason for the improvement, which is applicable to the evaluation of added value in downscaled projections (Giorgi et al., 2016). The added value depends on the region, season, and governing physical processes (Lenz et al., 2017; Schaaf and Feser, 2018). Thus, added value of downscaling GCM simulations is most likely where regional- and local-scale processes play an important role in a region's climate, for example in complex or heterogeneous terrain such as mountains (Lee and Hong, 2014; Prein et al., 2016a), urban areas (Argüeso et al., 2014), along coastlines (Feser et al., 2011; Herrmann et al., 2011; Bozkurt et al., 2019), or where convective processes are important (Prein et al., 2015). Examples of model improvements and added value are given in the following subsections and the Atlas.

A first step in determining added value in downscaling is to analyse whether the downscaling procedure gives detail on spatial or temporal scales not well-resolved by a GCM, thus potentially representing climatic features missing in the GCM. This added detail, referred to as potential added value (PAV; Di Luca et al., 2012), is insufficient for demonstrating added value in downscaling (Takayabu et al., 2016), but lack of PAV indicates that the downscaling method lacks usefulness. Added value is not guaranteed simply by producing model output at finer resolution. It depends on several factors, such as the simulation setup and the specific climatic variables analysed (Di Luca et al., 2012; Hong and Kanamitsu, 2014; Xue et al., 2014). A variety of performance measures are needed to assess added value (Section 10.3.3.1; Di Luca et al., 2016; Wilks, 2016; Ivanov et al., 2017, 2018; Soares and Cardoso, 2018).

A further challenge, especially at increasingly higher resolutions, is that adequate observational data may not be available to assess added value (Section 10.2, e.g., Di Luca et al., 2016; Zittis et al., 2017; Bozkurt et al., 2019). This implies a need for additional efforts to obtain, catalogue and quality-control higher resolution observational (or observation-based) data sets (Thorne et al., 2017; Section 10.2). Univariate demonstration of added value is necessary, but may be insufficient, as better agreement with observations in the downscaled variable may be a consequence of compensating errors that are not guaranteed to compensate similarly as climate changes. Multivariate analysis of added value is better able to demonstrate physical consistency between observed and simulated behaviour (Prein et al., 2013a; Meredith et al., 2015a; Reboita et al., 2018).

ACCEPTED VERSION SUBJECT TO FINAL EDITING

10.3.3.3 Performance at simulating large-scale phenomena and teleconnections relevant for regional climate

Regional climate is often controlled by large-scale weather phenomena, modes of variability and teleconnections (e.g., Sections 2.3 and 2.4, Annex IV). In particular extreme events are often caused by specific, in some cases persistent, circulation patterns (Sections 11.3–11.7). It is therefore important for climate models to reasonably represent not only continental, but also regional climate and its variability for such extremes. As explained in Section 3.3.3, standard resolution GCMs can suffer biases in the location, occurrence frequency or intensity of large-scale phenomena, such that statements about a specific regional climate and its change can be highly uncertain (Hall, 2014). RCMs have difficulties improving especially large-scale circulation biases, although some successful examples exist. But due to their enhanced representation of complex topography and coastlines, RCMs may add value to simulating the regional expression of teleconnections. Bias adjustment cannot mitigate fundamental misrepresentations of the large-scale atmospheric circulation (Maraun et al., 2017, Cross-Chapter Box 10.2). This subsection illustrates the relevance of large-scale circulation biases for regional climate assessments with selected examples from the mid-to-high latitudes and tropics.

10.3.3.3.1 Mid-to-high latitude atmospheric variability phenomena: blocking and extratropical cyclones

Major large-scale meteorological phenomena for mid-to-high latitude mean and extreme climate include atmospheric blocking and extratropical cyclones (Section 2.3.1.4). Atmospheric blocking is characterized by a quasi-stationary long-lasting, high pressure system that blocks and diverts the movement of synoptic cyclones (Woollings et al., 2018). In regions where blocking occurs, it is known to lead to cold conditions in winter and warmth and drought during summer, defining the seasonal regional climate in certain years (Sousa et al., 2017, 2018b). Extratropical cyclones are storm systems that propagate preferentially in confined storm-track regions, characterized by large eddy-kinetic energy, heat and momentum transports that shape regional weather at mid-to-high latitudes (Shaw et al., 2016). Given their importance in shaping mean and extreme regional climate (Sections 3.3.3.3, 11.3 and 11.4), an accurate representation of blocking and extratropical cyclones in global and regional climate models is needed to better understand regional climate variability and extremes as well as to project future changes (Section 11.7.2; Grotjahn et al., 2016; Mitchell et al., 2017; Rohrer et al., 2018; Huguenin et al., 2020). An overview of CMIP5 and CMIP6 model performance in simulating blocking and extratropical cyclones is given in Section 3.3.3.3. CMIP6 models still suffer from long-standing blocking biases identified in previous generations of models. However, blocking location has improved compared to CMIP5, while comparable performance is seen for blocking frequency and persistence (Figure 10.7). Increasing horizontal model resolution to about 20 km in the HighResMIP experiments improves the representation of blocking frequency and its spatial pattern in most models, but no clear effect could be shown for blocking persistence. Biases associated with these two phenomena are highly region- and season-dependent and their amplitudes vary among CMIP models (Drouard and Woollings, 2018; Schaller et al., 2018; Woollings et al., 2018; Harvey et al., 2020; Schiemann et al., 2020).

[START FIGURE 10.7 HERE]

Figure 10.7: Northern-Hemisphere blocking performance in historical coupled simulations for different multi-model ensembles. CMIP5/6: CMIP5 and CMIP6 DECK historical simulations, 1950-2005, LC/HC: Low/High-resolution simulations from the PRIMAVERA project, 1950–2014 following the hist-1950 experiment of the CMIP6 HighResMIP Protocol, (Haarsma et al., 2016). (top) blocking frequency, i.e. fraction of blocked days; (middle) root-mean-squared error in blocking frequency; (bottom) 90th percentile of blocking persistence, aggregated over an Atlantic domain (left, ATL: 90ºW–90ºE, 50º–75ºN) and a Pacific domain (right, PAC: 90ºE–270ºE, 50º–75ºN). Results are for boreal winter (DJF) and summer (JJA). Box-and-whisker plots for CMIP5/6 follow the methodology used in Figure 10.6 and show median (line), mean (triangle), and interquartile range (box) across 29 models for each ensemble. The reference estimate (ERA, asterisk) is from a 50-year reanalysis dataset that merged ERA-40 (1962–

ACCEPTED VERSION SUBJECT TO FINAL EDITING

1978) and ERA-Interim (1979–2011) reanalyses. An estimate of internal variability for each metric (IV) is shown as a box-and-whisker plot over the asterisk and is obtained from a single-model ensemble (ECMWF-IFS high-resolution hist-1950 experiment, 6 x 65 years). For details on the methodology see (Schiemann et al., 2020). Further details on data sources and processing are available in the chapter data table (Table 10.SM.11).

[END FIGURE 10.7 HERE]

RCMs have a very limited ability to reduce large-scale circulation errors of the driving GCM (Hall, 2014). In a study of five ERA-Interim-driven RCMs, Jury et al. (2018) showed that RCMs typically simulate fewer blocking events over Europe than are present in the driving data, irrespective of the RCM horizontal resolution. Based on a simple blocking bias-decomposition method, they suggest that blocking frequency biases can contribute to the RCM mean surface biases. Over some large domains, reanalysis-driven RCMs can significantly improve the representation of storm characteristics compared to the driving reanalysis near regions with complex orography and/or large water masses (Poan et al., 2018). However, this is not necessarily true if the domain is large enough because the RCM and its biases will then control the circulation leading to a biased performance with regard to storm characteristics (Pontoppidan et al., 2019). An ensemble of 12 RCMs with and without air-sea coupling reasonably reproduced the climatology of Mediterranean cyclones, and air-sea coupling had a rather weak impact (Flaounas et al. 2018). Over the Gulf Stream, however, air-sea coupling played an important role in representing cyclone development (Vries et al., 2019). Sánchez-Gómez and Somot (2018) showed that the effect of RCM internal variability on density of cyclone tracks is very significant and larger than for other variables such as precipitation. It is larger in summer than in winter, in particular over the Iberian Peninsula, northern Africa and the eastern Mediterranean, which are regions of enhanced cyclogenesis during the warm season.

Biases in the representation of large-scale atmospheric circulation can result in biased representation of regional climate. While the connection between large-scale and regional biases is in principle obvious, given the strong control of regional climate by large-scale phenomena, research on this connection is still limited. Munday and Washington (2018) relate CMIP5 model rainfall biases over South Africa to anomalous low-level moisture transport across high-topography due to upstream wind biases and inaccurate representation of unresolved orographic drag effects. Addor et al. (2016) show that the overestimated frequency of westerly synoptic situations was a significant contributor to the wet bias in several RCMs in winter over Switzerland. Pepler et al. (2014, 2016) suggest that better capturing westerly-driven synoptic systems such as cold fronts and cut-off lows in climate models could be key in simulating the observed pattern correlation between rainfall and zonal wind in southern southeast Australia. Cannon (2020) shows global improvement in performance going from CMIP5 to CMIP6 for both frequency and persistence of circulation types.

The robust quantification of the influence of atmospheric circulation errors on regional climate remains a challenge as many parameterized processes such as cloud radiative effects and soil moisture or snow feedbacks can also contribute and interact with the circulation errors. Atmospheric nudging experiments where the simulated circulation is constrained to be close to that observed have been used to separate the circulation effect from other contributions to regional climate biases (Wehrli et al., 2018). The nudging approach requires detailed and careful implementation in order to limit detrimental effects due to the added tendency term in the model equations (Zhang et al., 2014; Lin et al., 2016). Based on single-model experiments, Wehrli et al. (2018) show that the circulation-induced biases are often not the main contributors to mean and extreme temperature and precipitation biases for many regions and seasons.

There is *high confidence* that atmospheric circulation biases can deteriorate the model representation of regional land surface climate. Assessing the relative contributions of atmospheric circulation and other sources of bias remains a challenge due to the strong coupling between the atmosphere and other components of the climate system, including the land surface.

10.3.3.3.2 Tropical phenomena: ENSO teleconnections

Model performance in simulating ENSO characteristics, including ENSO spatial pattern, frequency,

ACCEPTED VERSION SUBJECT TO FINAL EDITING

asymmetry between warm and cold events, and diversity, is assessed in Chapter 3 (Section 3.7.3). The ability of the recent generation of GCMs and RCMs to adequately simulate ENSO-related teleconnections is reviewed here along with relevant methodological issues (see also Annex IV2.3.2, Figure 3.38 and Section 3.7.3).

Langenbrunner and Neelin (2013) show that there is little improvement in CMIP5 relative to CMIP3 in amplitude and spatial patterns of the ENSO influence on boreal winter precipitation (spatial pattern correlations against observations are typically less than 0.5). However, the CMIP5 ensemble accurately represents the amplitude of the precipitation response in regions where observed teleconnections are strong. (Garcia-Villada et al., 2020) found a decline in performance of the representation of simulated ENSO teleconnection patterns for model experiments with fewer observational constraints. They also show that ENSO warm phase (El Niño) teleconnections are better represented than those for the cold phase (La Niña). Individual CMIP5 and CMIP6 models show a good ability to represent the observed teleconnections at aggregated spatial scales (Power and Delage, 2018; Section 3.7.3 and Figure 3.38). The evaluation of the atmospheric dynamical linkages is also an important part of the assessment. Hurwitz et al. (2014) showed that CMIP5 models broadly simulate the expected (as seen in the MERRA reanalysis) upper-tropospheric responses to central equatorial Pacific or eastern equatorial Pacific ENSO events in boreal autumn and winter. CMIP5 models also simulate the correct sign of the Arctic stratospheric response, consisting of polar vortex weakening during eastern and central Pacific Niño events and vortex strengthening during both types of La Niña events. In contrast, most CMIP5 models do not capture the observed weakening of the Southern Hemisphere polar vortex in response to central Pacific ENSO events (Brown et al., 2013).

In RCMs, the effects of tropical large-scale modes and teleconnections are inherited through the boundary conditions and influenced by the size of the numerical domain. Done et al. (2015) and Erfanian and Wang (2018) claim that large domains that include source oceanic regions are required to capture the remote influence of teleconnections, although, without spectral nudging, this can lead to biased synoptic-scale patterns (Prein et al., 2019). RCMs generally reproduce the regional precipitation responses to ENSO, and can sometimes even improve the representation of these teleconnections compared to the driving reanalysis (Endris et al., 2013; Fita et al., 2017), but the overall performance may depend both on the driving reanalysis or GCM (Endris et al., 2016; Chandrasa and Montenegro, 2019) and on the chosen RCMs (Whan and Zwiers, 2017).

New studies since AR5 have shown that model performance assessment regarding ENSO teleconnections remains a difficult challenge due to the different types of ENSO and model errors in ENSO spatial patterns, as well as the strong influence of atmospheric internal variability at mid-to-high latitudes (Coats et al., 2013; Polade et al., 2013; Capotondi et al., 2015; Deser et al., 2017; Tedeschi and Collins, 2017; Garcia-Villada et al., 2020). Another difficulty comes from the non-stationary aspects of teleconnections in both observations and models, raising methodological questions on how best to compare a given model with another model or observations (Herein et al., 2017; Perry et al., 2017; O'Reilly, 2018; O'Reilly et al., 2019; Abram et al., 2020).

There is *robust evidence* that an accurate representation of both atmospheric circulation and SST variability are key factors for the realistic representation of ENSO teleconnections in climate models. A robust and thorough evaluation of model performance regarding ENSO teleconnections is a challenging task with many methodological issues related to asymmetry between the warm and cold phases, non-stationarity and time-varying interaction between the Pacific and other ocean basins, signal-to-noise issues in the mid-latitudes and observational uncertainties, particularly for precipitation (Section 10.2.2.3).

10.3.3.4 Performance at simulating regional phenomena and processes

Regional climate is shaped by a wide range of weather phenomena occurring at scales from about 2,000 km to 2 km (Figure 10.3). These modulate the influence of large-scale atmospheric phenomena and create the characteristic and potentially severe weather conditions. The climate in different regions will be affected by different mesoscale phenomena, of which several may be relevant. A skilful representation of these

ACCEPTED VERSION SUBJECT TO FINAL EDITING

phenomena is a necessary condition for providing credible and relevant climate information for a given region and application. Therefore, it is important to understand the strengths and weaknesses of different model types in simulating these phenomena. The performance of different dynamical climate model types to simulate a selection of relevant mesoscale weather phenomena is assessed here.

10.3.3.4.1 Convection including tropical cyclones

Convection is the process of vertical mixing due to atmospheric instability. Deep moist convection is associated with thunderstorms and severe weather such as heavy precipitation and strong wind gusts. Convection may occur in single locations, in spatially extended severe events such as supercells, and organised into larger mesoscale convective systems such as squall lines or tropical cyclones, and embedded in fronts (see below). Shallow and deep convection are not explicitly simulated but parameterized in standard global and regional models. In consequence, these models suffer from several biases. AR5 has stated that many CMIP3 and CMIP5 models simulate the peak in the diurnal cycle of precipitation too early, but increasing resolution and better parameterisations help to mitigate this problem (Flato et al., 2014). Similar issues arise for RCMs with parameterised deep convection (Prein et al., 2015), which also tend to overestimate high cloud cover (Langhans et al., 2013; Keller et al., 2016).

Non-hydrostatic RCMs at convection-permitting resolution (4 km and finer) improve features such as the initiation and diurnal cycle of convection (Zhu et al., 2012; Prein et al., 2013a, 2013b; Fosser et al., 2015; Berthou et al., 2018a; Stratton et al., 2018; Sugimoto et al., 2018; Finney et al., 2019; Ban et al., 2021; Pichelli et al., 2021), the triggering of convection by orographic lifting (Langhans et al., 2013; Fosser et al., 2015), and maximum vertical wind speeds in convective cells (Meredith et al., 2015a). Also spatial patterns of precipitation (Prein et al., 2013a, 2013b; Stratton et al., 2018), precipitation intensities (Prein et al., 2015; Fumière et al., 2019; Ban et al., 2021; Pichelli et al., 2021), the scaling of precipitation with temperature (Ban et al., 2014), cloud cover (Böhme et al., 2011; Langhans et al., 2013) and its resultant radiative effects (Stratton et al., 2018), as well as the annual cycle of tropical convection (Hart et al., 2018) are improved. Phenomena such as supercells, mesoscale convective systems, or the local weather associated with squall lines are not captured by global models and standard RCMs. Convection-permitting RCM simulations, however, have been shown to realistically simulate supercells (Trapp et al., 2011), mesoscale convective systems, their life cycle and motion (Prein et al., 2017; Crook et al., 2019), and heavy precipitation associated with a squall line (Kendon et al., 2014). There is *high confidence* that simulations at convection permitting resolution add value to the representation of deep convection and related phenomena.

Convection is the key ingredient of tropical cyclones. An intercomparison of high-resolution AGCM simulations (Shaevitz et al., 2014) showed that tropical cyclone intensities appeared to be better represented with increasing model resolution. Takayabu et al. (2015) have compared simulations of typhoon Haiyan at different resolutions ranging from 20 km to 1 km (Figure 10.8). While the eyewall structure in the precipitation pattern was strongly smoothed in the coarse resolution simulations, it was well resolved at the highest resolution. Gentry and Lackmann (2010) found similar improvements in simulating hurricane Ivan for horizontal resolutions between 8 km and 1 km. High-resolution coupled ocean-atmosphere simulations improve the representation of the radial structure of core convection and thereby the rapid intensification of the cyclone (Kanada et al., 2017b). There is *high confidence* that convection-permitting resolution is required to realistically simulate the three-dimensional structure of tropical cyclones.

Initial studies with convection-permitting GCMs suggests that improvements in representing convection, as described for RCMs above, have a positive impact on the tropical and extra-tropical atmospheric circulation and, thus, regional climate (Satoh et al., 2019; Stevens et al., 2019; see also Section 8.5.1.2 and Chapter 7). Computational constraints currently limit these simulations to a length of few months only, such that they cannot yet be used for routine climate change studies.

[START FIGURE 10.8 HERE]

Figure 10.8: Hourly accumulated precipitation profiles (mm hour^{-1}) around the eye of Typhoon Haiyan.

ACCEPTED VERSION SUBJECT TO FINAL EDITING

Represented by (a) GSMaP (Global Satellite Mapping of Precipitation) data, (b) Guiuan radar (PAGASA), (c) Weekly Ensemble Prediction System (WEPS) data (JMA), (d) NHRCM (20 km), (e) NHRCM (5 km), and (f) WRF (1 km) models. Panels (b), (d)-(f) are adapted from Takayabu et al. (2015), CCBY3.0 https://creativecommons.org/licenses/by/3.0. Further details on data sources and processing are available in the chapter data table (Table 10.SM.11).

[END FIGURE 10.8 HERE]

10.3.3.4.2 Mountain wind systems

Mountain slope and valley winds are localised thermally generated diurnal circulations that have a strong influence on temperature and precipitation patterns in mountain regions. During the day, heating of mountain slopes induces upslope winds; during the night this circulation reverses. This phenomenon is not realistically represented by global models and coarse-resolution RCMs. RCM simulations at 4 km resolution showed good skill in simulating the diurnal cycle of temperature and wind on days of weak synoptic forcing in the Rocky Mountains (Letcher and Minder, 2017) as well as in simulating the mountain-plain wind circulation over the Tianshan mountains in Central Asia (Cai et al. 2019), while in the Alps, a 1 km resolution has been required (Zängl, 2004).

Föhn winds are synoptically-driven winds across a mountain range that are warm and dry due to adiabatic warming in the downwind side. In an RCM study for the Japanese Alps, Ishizaki and Takayabu (2009) found that at least 10 km resolution was required to realistically simulate the basic characteristics of Föhn events.

Synoptically-forced winds may be channelled and accelerated in long valleys. For instance, the Tramontana, Mistral and Bora are northerly winds blowing down-valley from central France and the Balkans into the Mediterranean (Flaounas et al., 2013). In winter, these winds may cause severe cold air outbreaks along the coast. Flaounas et al. (2013) have shown that a GCM with a horizontal resolution of roughly 3.75° longitude/1.875° latitude (roughly 400 km x 200 km depending on latitude) is unable to reproduce these winds because of the coarse representation of orography. 50-km RCM simulations did not realistically represent the Mistral (Obermann et al., 2018) and Bora winds (Belušić et al., 2018), but simulations at 12 km added substantial value. Similarly, Cholette et al. (2015) found that a 30-km RCM resolution was not sufficient to adequately simulate the channelling of winds in the St Lawrence River Valley in eastern Canada, whereas a 10 km resolution was.

There is *high confidence* that climate models with resolutions of around 10 km or finer are necessary for realistically simulating mountain wind systems such as slope and valley winds and the channelling of winds in valleys.

10.3.3.4.3 Coastal winds and lake effects

Simulating coastal climates and the influence of big lakes are a modelling challenge, due to the complex coastlines, the different heat capacities of land and water, the resulting wind system, and differential evaporation. The AR5 concluded that RCMs can add value to the simulation of coastal climates.

Summer coastal low-level jets off the mid-latitude western continental coasts are forced by the semi-permanent subtropical anticyclones, inland thermal lows, strong across-shore temperature contrasts in upwelling regions, and high coastal topography. They are important factors in shaping regional climate by, for instance, preventing onshore advection of humidity and thereby causing aridity in the Iberian Peninsula (Soares et al., 2014), or by transporting moisture towards precipitating regions as in the North American monsoon (Bukovsky et al., 2013).

Reanalyses and most global models do not well resolve the details of coastal low-level jets (Bukovsky et al., 2013; Soares et al., 2014), but they are still able to represent annual and diurnal cycles and interannual variability (Cardoso et al., 2016; Lima et al., 2019). Bukovsky et al. (2013) found RCM simulations at a 50 km resolution to improve the representation of the coastal low-level jet in the Gulf of California and the

ACCEPTED VERSION SUBJECT TO FINAL EDITING

associated precipitation pattern compared to the driving global models. Lucas-Picher et al. (2017) find indirect evidence via precipitation patterns that 12 km simulations further improve the representation. Soares et al. (2014) demonstrated that an 8-km resolution RCM simulated a realistic three-dimensional structure of the Iberian coastal low-level jet, and the surface winds compare well with observations. Lucas-Picher et al. (2017) showed that a 0.44°-resolution RCM underestimated winds along the Canadian east coast, whereas a 0.11°-resolution version simulated more realistic 10-metre wind speed. Also, the Etesian winds in the Aegean Sea were realistically simulated by 12 km-resolution RCMs (Dafka et al., 2018).

A particularly relevant coastal phenomenon is the sea breeze, which is caused by the differential heating of water and land during the diurnal cycle and typically reaches several tens of kilometres inland. Reanalyses and global models have too coarse a resolution to realistically represent this phenomenon, such that they typically underestimate precipitation over islands and misrepresent its diurnal cycle (Lucas-Picher et al., 2017). RCMs improve the representation of sea breezes and thereby precipitation in coastal areas and islands. Over Cuba and Florida only a 12 km-resolution RCM is able to realistically simulate the inland propagation of precipitation during the course of the day (Lucas-Picher et al., 2017). RCM simulations at 20 km horizontal resolution realistically represented the sea breeze circulation in the Mediterranean Gulf of Lions including the intensity, direction and inward propagation (Drobinski et al., 2018). Even though a coupled ocean-atmosphere simulation improved the representation of diurnal SST variations, the sea breeze representation itself was not improved.

Big lakes modify the downwind climate. In particular during winter they are relatively warm compared to the surrounding land, provide moisture, destabilize the passing air column and produce convective systems. The increase in friction when moving air reaches land causes convergence and uplift, and may trigger precipitation. Gula and Peltier (2012) found that a state-of-the-art GCM does not realistically simulate these effects over the North American Great Lakes, but a 10 km RCM better represents them and thereby simulates realistic downwind precipitation patterns, in particular enhanced snowfall during the winter season. Similar results were found by Wright et al. (2013), Notaro et al. (2015) and Lucas-Picher et al. (2017). In a convection permitting simulation of the Lake Victoria region, a too strong nocturnal land-breeze resulted in unrealistically high precipitation (Finney et al., 2019).

There is *high confidence* that climate models with sufficiently high resolution are necessary for realistically simulating lake and coastal weather including coastal low-level jets, lake and sea breezes, as well as lake effects on rainfall and snow.

In regions like Fenno-Scandinavia or central-eastern Canada, very large fractions of land are covered by small and medium sized lakes. Other regions have fewer but larger lakes, such as central-eastern Africa, the eastern border between the US and Canada, and central Asia. In these regions it has been considered essential to include a lake model in an RCM to realistically represent regional temperatures (Deng et al., 2013; Mallard et al., 2014; Pietikäinen et al., 2018; Samuelsson et al., 2010; Thiery et al., 2015), as well as remote effects (Spero et al., 2016). The most common approach in RCMs is the two-layer lake model, including a lake-ice model, with parameterized vertical temperature profiles (Mironov et al., 2010; Golosov et al., 2018). For the Caspian Sea, it is found that a three dimensional ocean model simulated the SST fields better than a one dimensional lake model when coupled to the same RCM (Turuncoglu et al., 2013).

There is *medium evidence* and *high agreement* that it is important to include interactive lake models in RCMs to improve the simulation of regional temperature, in particular in seasonally ice-covered areas with large fractions of lakes. There is *medium evidence* of the local influence of lakes on snow and rainfall as well as the importance of including lakes in regional climate simulations.

10.3.3.4.4 Fronts

Weather fronts are two-dimensional surfaces separating air masses of different characteristics and are a key element of mid-latitude cyclones. In particular cold fronts are regions of relatively strong uplift and hence often associated with severe weather (e.g., Schemm et al., 2016). Stationary or slowly moving fronts may cause extended heavy precipitation. The evaluation of how climate models represent fronts, however,

ACCEPTED VERSION SUBJECT TO FINAL EDITING

remains limited. Catto et al. (2014) found in both ERA-Interim and CMIP5 models that frontal frequency and strength were realistically simulated, albeit with some biases in the location. Follow-up investigations, for boreal and austral winter (Catto et al., 2015) found frontal precipitation frequency to be too high and the intensity too low, but these compensating biases resulted in only a small total precipitation bias. Blázquez and Solman (2018) found similar results for Southern Hemisphere winter, and also showed that CMIP5 models typically overestimate the fraction of frontal precipitation compared to total precipitation. As for the reference, the ERA-Interim reanalysis misrepresents conditional symmetric instability associated with fronts, and the corresponding precipitation (Glinton et al., 2017). Only a few studies evaluating fronts in RCMs have been conducted. Kawazoe and Gutowski (2013) diagnosed strong temperature gradients associated with extreme winter precipitation in the North American Regional Climate Change Assessment Program (NARCCAP) RCM ensemble (Mearns et al., 2012) and found the models agreed well with gradients in a reanalysis. De Jesus et al. (2016) diagnosed the representations of cold fronts over southern Brazil in two RCMs, finding that they were only underestimated by about 5% across the year, but in one RCM, summer cold fronts were underestimated by 17%. An RCM-based reanalysis suggests that high-resolution RCM simulations improve the representation of orographic influences on fronts (Jenkner et al., 2009).

10.3.3.5 Performance at simulating regional feedbacks

Both the SRCCL (Jia et al., 2019) and SROCC (Hock et al., 2019) highlight the weaknesses of climate models at simulating atmosphere-surface feedbacks. The performance at simulating some of these feedbacks is assessed below (climate feedbacks in urban areas are discussed in Box 10.3).

The snow-albedo feedback contributes to enhanced warming at high elevations (Pepin et al., 2015; Section 8.5). Global models often do not simulate it realistically due to their misrepresentation of orography in complex terrain (Hall, 2014; Walton et al., 2015). The elevation dependence of historical warming, which is partly caused by the snow-albedo effect, is realistically represented across Europe by the ENSEMBLES RCMs (Kotlarski et al., 2015). Some EURO-CORDEX RCMs simulate a springtime snow-albedo feedback close to that observed, whereas others considerably overestimate it (Winter et al., 2017). In a multi-physics ensemble RCM experiment, the cold bias in northeastern Europe is amplified by the albedo feedback (García-Díez et al., 2015). For the Rocky Mountains, RCM simulations generally reproduce the observed spatial and seasonal variability in snow cover, but strongly overestimate the snow albedo (Minder et al., 2016). There is *high confidence* (*medium evidence* and *high agreement*) that RCMs considerably improve the representation of the snow albedo effect in complex terrain.

Soil-moisture feedbacks influence changes in both temperature and precipitation. More than 30% of CMIP5 models overestimate the influence of preceding precipitation (a proxy for soil moisture) on temperature extremes in Europe and the USA (Donat et al., 2018), and many CMIP5 models simulate an unrealistic influence of evaporation on temperature extremes for wet regions in Europe and the US (Ukkola et al., 2018). RCMs were found to realistically simulate the correlation between latent and sensible heat fluxes and temperature (coupling strength) over Africa (Knist et al., 2017; Careto et al., 2018) and in Northern and Southern Europe, but to overestimate it in Central Europe (Knist et al., 2017). Land-surface models driven by global reanalysis agreed relatively well with observations. However, the coupling strength varied strongly across models at the regional scale, and a realistic partitioning of the incoming radiation into latent and sensible heat fluxes did not necessarily result in a realistic soil moisture-temperature coupling (Gevaert et al., 2018; Boé et al., 2020a).

Evaluating the representation of soil moisture-precipitation feedbacks in climate models is challenging as different processes may induce feedbacks including moisture recycling, boundary-layer dynamics and mesoscale circulation. Moreover, the effects of soil-moisture on precipitation may be region and scale dependent and may even change sign depending on the strength of the background flow (Taylor et al., 2013; Froidevaux et al., 2014; Guillod et al., 2015; Larsen et al., 2016; Tuttle and Salvucci, 2016). On seasonal-to-interannual time scales, CMIP5 models showed a stronger soil-moisture precipitation feedback than estimated by satellite data (Levine et al., 2016). Taylor et al. (2013) found that convection-permitting RCMs simulate well surface-induced mesoscale circulations in day-time convection and the observed negative soil

ACCEPTED VERSION SUBJECT TO FINAL EDITING

moisture feedback, whereas an RCM with parameterised convection, even when run at the same resolution, simulated an unrealistic positive feedback. There is *medium evidence* and *high agreement* that simulations at convection-permitting resolution are required to realistically represent soil-moisture precipitation feedbacks.

Ocean-atmosphere RCMs have successfully been used to understand and simulate phenomena involving strong regional feedbacks like tropical cyclones in the Indian Ocean (Samson et al., 2014), Indian summer monsoon (Samanta et al., 2018), East-Asian summer monsoon (Zou et al., 2016), near-coastline intense precipitation in the Mediterranean (Berthou et al., 2015, 2018b), air-sea fluxes influencing heat and humidity advection over land (Sevault et al., 2014; Lebeaupin Brossier et al., 2015; Akhtar et al., 2018) or snow bands in the Baltic region (Pham et al., 2017). The positive impact of ocean-coupling on the simulation of strongly convective phenomena such as Medicanes, a class of severe cyclones in the Mediterranean, can only be diagnosed when using relatively fine atmospheric resolution of about 10 km (Akhtar et al., 2014; Flaounas et al., 2018; Gaertner et al., 2018). A positive impact of ocean coupling has been quantified in marginal sea regions with reduced large-scale influence (e.g., in the Baltic Sea area during weak phases of the NAO and thus weak influence of Atlantic westerlies (Kjellström et al., 2005; Pham et al., 2018)). There is some evidence that coupled ocean-components also positively impact RCM simulations of inland climates such as precipitation extremes in Central Europe (Ho-Hagemann et al., 2017; Akhtar et al., 2019). There *is high confidence* that coupled ocean-atmosphere RCMs improve the representation of ocean-atmosphere feedbacks and related phenomena.

The influence of ice sheet mass balance on regional climate, explored with global and regional models by (Noël et al., 2018; Fettweis et al., 2020), is discussed in Section 9.4.

10.3.3.6 Performance at simulating regional drivers of climate and climate change

Dust, with its regional character in both emissions and climatic influences, has traditionally been specified in climate simulations with a climatological estimate. In CMIP5 models, the influence of vegetation changes on mineral dust is largely underestimated while the influence of surface wind and precipitation are overestimated, resulting in a low bias of dust load (Pu and Ginoux, 2018). Interactive dust emission modules that simulate the dust optical depth in most of the key emission regions have only been recently introduced (Pu and Ginoux, 2018). However, coarse dust is underestimated in global models (Adebiyi and Kok, 2020). Simulations of future changes in dust are hindered by the uncertainties in future regional wind and precipitation as the climate warms (Evan et al., 2016), in the effect of CO_2 fertilization on source extent (Huang et al., 2017), in the dust feedbacks (Evans et al., 2019), and in the effect of human activities that change land use and disturb the soil, including cropping and livestock grazing, recreation and urbanization, and water diversion for irrigation (Ginoux et al., 2012).

Volcanoes also provide forcings with a marked regional impact (Cross-Chapter Box 4.1). This implies that models are expected to capture these effects (Bethke et al., 2017). Both proxy analyses and simulations have demonstrated reduced Asian monsoon precipitation after tropical and Northern Hemisphere volcanic eruptions due to reduced humidity and divergent circulation (Man and Zhou, 2014; Zhuo et al., 2014; Liu et al., 2016a; Stevenson et al., 2016). Global model experiments (Zanchettin et al., 2013; Ortega et al., 2015; Michel et al., 2018; Sjolte et al., 2018) have suggested that tropical volcanic eruptions (larger than the one from Mount Pinatubo in 1991) may lead to a positive phase of the winter NAO in the following few years (with an uncertainty on the exact years affected), but this influence is not well reproduced in climate models (Driscoll et al., 2012; Toohey et al., 2014; Swingedouw et al., 2017; Ménégoz et al., 2018b). The ability to simulate the effect of volcanic aerosol in global models is evaluated in VolMIP (Zanchettin et al., 2016). Given the relevance of volcanic aerosol, a good knowledge of the initial conditions is important because the response has proven to be sensitive to them (Ménégoz et al., 2018a; Zanchettin et al., 2019). A few decadal prediction systems have illustrated that current systems can predict some aspects of regional climate a few years in advance (Swingedouw et al., 2017; Illing et al., 2018; Ménégoz et al., 2018a; Hermanson et al., 2020). However, a better performance requires information about volcanic location (Haywood et al., 2013; Pausata et al., 2015; Stevenson et al., 2016; Liu et al., 2018a), strength (Emile-Geay et al., 2008; Lim et al., 2016b; Liu et al., 2018b), and seasonality (Stevenson et al., 2017; Sun et al., 2019a, 2019b).

ACCEPTED VERSION SUBJECT TO FINAL EDITING

Some recent regional climate changes can only be simulated by climate models if anthropogenic aerosols are correctly included (Sections 10.4.2.1, 10.6.3 and 10.6.4; Chapters 6 and 8). Examples of the importance of correctly representing anthropogenic aerosols are the recent enhanced warming over Europe (Nabat et al., 2014; Dong et al., 2017), the cooling over the East Asian monsoon region, leading to a weakening of the monsoon (Section 8.3.2.4; Song et al., 2014; Wang et al., 2017b), as well as changes in the monsoons of West Africa (Sections 8.3.2.4 and 10.4.2.1) and South Asia (Sections 8.3.2.4 and 10.6.3; Undorf et al., 2018). The relevance of appropriately representing anthropogenic aerosols has been widely studied in regional models (Boé et al., 2020a; Gutiérrez et al., 2020), with an advantage for models with interactive aerosol schemes (Drugé et al., 2019; Nabat et al., 2020). Without a fully coupled chemistry module, radiative forcing can be simulated by including simple models of sulphate chemistry or specifying the optical properties from observations and prescribing the effect of aerosols on the cloud-droplet number (Fiedler et al., 2017, 2019; Stevens et al., 2017). In all cases, the specification of the aerosol load limits the trustworthiness of the simulations at the regional scale when enough detail is not provided (Samset et al., 2019; Shonk et al., 2020; Wang et al., 2021).

The inclusion of irrigation in global and regional models over the South Asian monsoon region (Section 10.6.3) has been found to be important to represent the monsoon circulation and rainfall correctly (Lucas-Picher et al., 2011; Guimberteau et al., 2012; Shukla et al., 2014; Tuinenburg et al., 2014; Cook et al., 2015a; Devanand et al., 2019). Similarly, the inclusion of irrigation over northern India and western Pakistan could be important for the correct simulation of precipitation over the Upper Indus Basin in northern Pakistan (Saeed et al., 2013). Irrigation in the East African Sahel inhibits rainfall over the irrigated region and enhances instead rainfall to the east, coherent with both observations and theoretical understanding of the local circulation anomalies induced by the lower surface air temperatures over the irrigated region (Alter et al., 2015). Although several studies show how modelled irrigation reduces daytime temperature extremes, few compare modelled results with observations. Global model studies have found improvements in simulated surface temperature when including irrigation (Thiery et al., 2017), in particular in areas where the model used has a strong land-atmosphere coupling (Chen and Dirmeyer, 2019). An RCM study over the North China Plain showed that the inclusion of irrigation led to a better representation of the observed night time warming (Chen and Jeong, 2018).

There is *medium confidence* that representing irrigation is important for a realistic simulation of South Asian monsoon precipitation. There is *limited evidence* that including irrigation in climate models improves the simulation of maximum and minimum daily temperatures as well as precipitation for other regions.

Regional land-radiation management, including modifying the albedo through, for instance, no-tillage practices, has been suggested as a measure to decrease regional maximum daily temperatures (see review in Seneviratne et al., 2018), but although modelled results and theoretical understanding are coherent, few studies have verified the results with observations. Hirsch et al. (2018) is an exception, showing that implementing minimal tillage, crop residue management and crop rotation in a global model over regions where it is practiced, improves the simulation of surface heat fluxes.

10.3.3.7 Statistical downscaling, bias adjustment and weather generators

The performance of statistical downscaling models, bias adjustment and weather generators is determined by the chosen model structure (e.g., to represent variability and extremes or spatial dependence) and, if applicable, the predictors selected (Maraun et al., 2019b). The VALUE initiative has assessed a range of such methods in a perfect-predictor experiment where the predictors are taken from reanalysis data (Maraun et al., 2015, 2019b; Gutiérrez et al., 2019). Table 10.2 shows an overview comprising performance results from VALUE and other studies. These results isolate the performance of the statistical method in the present climate. The overall performance in a climate change application also depends on the performance of the driving climate model (Sections 10.3.3.3–10.3.3.6) and the fitness of both the driving model and the statistical method for projecting the climatic aspects of interest (Section 10.3.3.9).

ACCEPTED VERSION SUBJECT TO FINAL EDITING

[START TABLE 10.2 HERE]

Table 10.2: Performance of different statistical method types in representing local weather at daily resolution. Individual state-of-the-art implementations may perform better. "+": should work reasonably well based on empirical evidence and/or expert judgement; “o”: problems may arise depending on the specific context; "-": weak performance either by construction or inferred from empirical evidence; "?": not studied. The categorisation assumes that predictors are provided by a well performing dynamical model. Statements about extremes refer to moderate events occurring at least once every 20 years. Adopted and extended from (Maraun and Widmann, 2018b). (1) (Casanueva et al., 2020); (2) (Dubrovsky et al., 2019); (3) (Evin et al., 2018); (4) (Frost et al., 2011); (5) (Gutiérrez et al., 2013); (6) (Gutiérrez et al., 2019); (7) (Gutmann et al., 2014); (8) (Hertig et al., 2019); (9) (Hu et al., 2013a); (10) (Huth et al., 2015) (11) (Keller et al., 2015); (12) (Maraun et al., 2019a); (13) (San-Martín et al., 2017); (14) (Widmann et al., 2019).

Aspect	Perfect Prog				Bias Adjustment				Weather generators				References
	Deterministic Regression	Inflated regression	White noise regression	Analogue method (single/multisite) SS/MS	Additive/scaling	Empirical quantile mapping	Parametric quantile mapping	Quantile mapping with model for extremes	Richardson (single/multisite)	Richardson with predictors (single/multisite)	Poisson clustering (single/multisite)	Hidden Markov (without/with predictors)	
Temperature													
Mean	+	+	+	○	+	+	+	+	+	+	+	+	6
Variance	-	○	+	○	○	+	+	+	+	+	+	+	6
Extremes	-	○	+	+	○	+	+	+	+	+	+	+	8, 10
Temperature, temporal variability													
Autocorrelation	+	+	-	-	+	+	+	+	+	+	+	+	2, 10, 12
Mean spells	○	○	-	-	+	+	+	+	+	+	+	+	2, 10, 12
Extreme spells	+	+	-	○	+	+	+	+	+	+	+	+	2, 8
Interannual variance	-	○	-	-	+	○	○	○	-	○	-	-/○	12
Climate change	+	-	+	-	+	○	○	○	+	+	+	+	1, 5, 10, 12
Temperature, spatial variability													
Means	○	○	-	-/+	+	+	+	+	-/?	-/?	-/?	?	2, 14
Extremes	-	-	-	-/+	+	+	+	+	-/?	-/?	-/?	?	8, 14
Precipitation, marginal													
Wet-day probabilities	-	-	+	+	+	+	+	+	+	+	+	+	3, 6, 7, 11
Mean intensity	-	-	+	+	+	+	+	+	+	+	+	+	3, 6, 7, 9, 11
Extremes	-	-	+	+	○	+	○	+	○	○	○	○	3, 7, 8, 9, 11
Precipitation, temporal variability													
Transition probabilities	-	-	+	+	○	+	+	+	+	+	+	+	3, 11, 12
Mean spells	-	-	+	+	○	+	+	+	○	+	○	○/+	3, 4, 7, 11, 12
Extreme spells	-	-	+	+	+	+	+	+	-	○	-	-/○	3, 4, 8, 9, 11
Interannual variance	-	○	○	○	+	○	○	○	-	○	-	-/○	4, 7, 12

ACCEPTED VERSION SUBJECT TO FINAL EDITING

Climate change	+	-	+	○	+	○	○	○	+	+	+	+	1, 12, 13
Precipitation, spatial variability													
Means	-	-	-	-/+	○	+	+	+	-/○	-/○	-/○	○	3, 4, 11, 14
Extremes	-	-	-	-/+	○	○	○	○	-/?	-/?	-/?	?	3, 14

[END TABLE 10.2 HERE]

10.3.3.7.1 Performance of perfect prognosis methods

Perfect-prognosis methods can perform well when the synoptic forcing (i.e., the explanatory power of large-scale predictors) is strong (Schoof, 2013). Using this approach, downscaling of precipitation is particularly skilful in the presence of strong orographic forcing. The representation of daily variability and extremes requires analogue methods or stochastic regression models, although the former typically do not extrapolate to unobserved values (Gutiérrez et al., 2019; Hertig et al., 2019). Temporal precipitation variability is well represented by analogue methods and stochastic regression, but analogue methods typically underestimate temporal dependence of temperature (Maraun et al., 2019a). Spatial dependence of both temperature and precipitation is only well represented by analogue methods, for which analogues are defined jointly across locations, and by stochastic regression methods explicitly representing spatial dependence (Widmann et al., 2019). Overall, there is *high confidence* that analogue methods and stochastic regression are able to represent many aspects of daily temperature and variability, but the analogue method is inherently limited in representing climate change (Gutiérrez et al., 2013).

10.3.3.7.2 Performance of bias adjustment methods

This subsection assesses the performance of bias adjustment in a perfect predictor context. In practice, climate model imperfections may cause substantial additional issues in the application of bias adjustment. These are assessed separately in Cross-Chapter Box 10.2.

Bias adjustment methods, if driven by reanalysis predictors, in principle adjust well all the aspects that they intend to address (Maraun and Widmann, 2018b). For temperature, all univariate methods are good for adjusting means, variance, and high quantiles (Gutiérrez et al., 2019; Hertig et al., 2019). For precipitation, means, intensities, wet-day frequencies, and wet-dry and dry-wet transitions are well adjusted (Gutiérrez et al., 2019; Maraun et al., 2019a). The representation of high quantiles depends on the chosen method, although flexible quantile mapping performs best (Hertig et al., 2019). Empirical (non-parametric) methods perform better than parametric methods over the observed range, but it is unclear how this translates into extrapolation to unobserved values (Hertig et al., 2018; Stocker et al., 2015). Many quantile mapping methods overestimate interannual variability (Maraun et al., 2019a). Temporal and spatial dependence are usually not adjusted and thus inherited from the driving model (Maraun et al., 2019a; Widmann et al., 2019). Spatial fields are thus typically too smooth in space, even after bias adjustment (Widmann et al., 2019).

Several studies show improved simulations of present day impacts, when the impact model is fed with bias-adjusted climate model output, including the assessment of river discharge (Rojas et al., 2011; Muerth et al., 2013; Montroull et al., 2018), forest fires (Migliavacca et al., 2013), crop production (Ruiz-Ramos et al., 2016), and regional ocean modelling (Macias et al., 2018).

There is *high confidence* that bias adjustment can improve the marginal distribution of simulated climate variables, if applied to a climate model that adequately represents the processes relevant for a given application (Cross-Chapter Box 10.2).

10.3.3.7.3 Performance of weather generators

Weather generators represent well most aspects that are explicitly calibrated. This typically includes mean, variance, high quantiles (for precipitation, if explicitly modelled), and short-term temporal variability for both temperature and precipitation, whereas interannual variability is strongly underestimated (Frost et al.,

ACCEPTED VERSION SUBJECT TO FINAL EDITING

2011; Hu et al., 2013a; Keller et al., 2015; Dubrovsky et al., 2019; Gutiérrez et al., 2019; Hertig et al., 2019; Maraun et al., 2019a; Widmann et al., 2019). There is growing evidence that some spatial weather generators fairly realistically capture the spatial dependence of temperature and precipitation (Frost et al., 2011; Hu et al., 2013a; Keller et al., 2015; Evin et al., 2018; Dubrovsky et al., 2019). There is *high confidence* that weather generators can realistically simulate a wide range of local weather characteristics at single locations, but there is *limited evidence* and *low agreement* of the ability of weather generators to realistically simulate the spatial dependence of atmospheric variables across multiple sites.

10.3.3.8 Performance at simulating historical regional climate changes

This section assesses how well climate models perform at realistically simulating historical regional climatic trends. Current global model ensembles reproduce global to continental-scale surface temperature trends at multi-decadal to centennial time scales (CMIP5, CMIP6), but underestimate precipitation trends (CMIP5) (Sections 3.3.1 and 3.3.2). For regional trends, AR5 concluded that the CMIP5 ensemble cannot be taken as a reliable representation of reality and that the true uncertainty can be larger than the simulated model spread (Kirtman et al., 2014). Case studies of regional trend simulations by global models can be found in Sections 10.4.1 and 10.6, and region-by-region assessments in the Atlas. A key limitation for assessing the representation of regional observed trends by single transient simulations of global models (or downscaled versions thereof) is the strong amplitude of internal variability compared to the forced signal at the regional scale (Section 10.3.4.3). Even on multidecadal time scales, an agreement between observed and individual simulated trends would be expected to occur only by chance (Laprise, 2014).

In the context of downscaling, the ability of downscaling methods to reproduce observed trends when driven with boundary conditions or predictors taken from reanalysis data (which reproduce the observed internal variability on long time scales) can be assessed. For temperature in the continental USA, reanalysis-driven RCMs skilfully simulated recent spring and winter trends, but did not reproduce summer and autumn trends, (Bukovsky, 2012). Over Central America, observed warming trends were reproduced (Cavazos et al., 2019). In contrast, a reanalysis-driven coupled atmosphere-ocean RCM covering the Mediterranean could not reproduce the observed SST trend (Sevault et al., 2014).

Similar studies have been carried out for statistical downscaling and bias adjustment using predictors from reanalyses (or in case of bias adjustment, dynamically downscaled reanalyses). For a range of different perfect prognosis methods, Huth et al. (2015) found that simulated temperature trends were too strong for winter and too weak for summer. The performance was similar for the different methods, indicating the importance of choosing sensible predictors. Similarly, Maraun et al. (2017) found that the performance of perfect prognosis methods depends mostly on the predictor and domain choice (for instance, temperature trends were only captured by those methods including surface temperature as predictor). Bias adjustment methods reproduced the trends of the driving reanalysis, apart from quantile mapping methods, which deteriorated these trends.

RCM experiments are often set up such that changes in forcing agents are included only via the boundary conditions, but not explicitly included inside the domain. Jerez et al. (2018) demonstrated that not including time-varying GHG concentrations within the RCM domain may misrepresent temperature trends by 1–2ºC per century. Including the past trend in anthropogenic sulphate aerosols in reanalysis-driven RCM simulations substantially improved the representation of recent brightening and warming trends in Europe (Nabat et al., 2014; Section 10.3.3.6, 10.6.4, Atlas 8.4). Similarly, Bukovsky (2012) argued that RCMs may not capture observed summer temperature trends in the USA because changes in land cover are not taken into account. Barlage et al. (2015) have revealed that including the behaviour of groundwater in land schemes increases the performance of an RCM model to represent climate variability in the central USA. Hamdi et al. (2014) found that an RCM that did not incorporate the historical urbanization in the land-use, land-cover scheme is not able to reproduce the warming trend observed in urban stations, with a larger bias for the minimum temperature trend.

Overall, there is *high confidence* that including all relevant forcings is a prerequisite for reproducing

ACCEPTED VERSION SUBJECT TO FINAL EDITING

historical trends.

10.3.3.9 Fitness of climate models for projecting regional climate

AR5 stated that confidence in climate model projections is based on the physical understanding of the climate system and its representation in climate models. A climate model's credibility for future projections may be increased if the model is able to simulate past variations in climate (Flato et al., 2014; Sections 10.3.3.8, 10.4.1 and 10.6). In particular, the credibility of downscaled information depends on the quality of both the downscaling method and of the global model providing the large-scale boundary conditions (Flato et al., 2014). Credibility is closely linked to the concept of adequacy or fitness for purpose (Parker, 2009; Section 1.5.4.1). From a regional perspective, one may ask about the fitness of a climate model for simulating future changes of specific aspects of a specific regional climate. The required level of model fitness may depend on the user context (Section 10.5). A key challenge is to link performance at representing present and past climate (Sections 10.3.3.3 to 10.3.3.8) to the confidence in future projections (Section 1.3.5; Baumberger et al., 2017) and it is addressed in this subsection.

A general idea of model fitness for a given application may be obtained by checking whether relevant large- (Section 10.3.3.4) and regional-scale (Sections 10.3.3.5 and 10.3.3.6) processes are explicitly resolved (Figure 10.3). The basis for confidence in climate projection is a solid process understanding (Flato et al., 2014; Baumberger et al., 2017). Thus, the key to assessing the fitness for purpose of a model is the evaluation of how relevant processes controlling regional climate are represented (Collins et al., 2018). A process-based evaluation may be more appropriate than an evaluation of the variables of interest (e.g., temperature, precipitation), because biases in the latter may in principle be reduced if the underlying processes are realistically simulated (Cross-Chapter Box 10.2), while individual variables may appear as well represented because of compensating errors (Flato et al., 2014; Baumberger et al., 2017). Combining a process-based evaluation with a mechanistic explanation of projected changes further increases confidence in projections (Bukovsky et al., 2017). Fitness-for-purpose can also be assessed by comparing the simulated response of a model with simulations of higher resolution models that better represent relevant processes (Baumberger et al., 2017). For instance, Giorgi et al. (2016) have corroborated their findings on precipitation changes comparing standard RCM simulations with convection-permitting simulations.

The evaluation of model performance at historical variability and long-term changes provides further relevant information (Flato et al., 2014). Trend evaluation may provide very useful insight, but has limitations in particular at the regional scale, mainly due to multi-decadal internal climate variability (Section 10.3.3.8), observational uncertainty (in both driving reanalysis and local trends; Section 10.2), and the fact that often not all regional forcings are known, and that past trends may be driven by forcings other than those driving future trends (Sections 10.4.1 and 10.6.3).

Increasing resolution (Haarsma et al., 2016) or performing downscaling may be particularly important when it modifies the climate change signal of a lower resolution model in a physically plausible way (Hall, 2014). Improvements may result from a better representation of regional processes, upscale effects, as well as the possibility of a region-specific model tuning (Sørland et al., 2018). For instance, Gula and Peltier (2012) showed that a higher resolution allows for a more realistic simulation of lake-induced precipitation, resulting in a more credible projection of changes in the snow belts of the North American Great Lakes. Similarly, Giorgi et al. (2016) demonstrated that an ensemble of RCMs better represents high-elevation surface heating and in turn increased convective instability. As a result, the summertime convective precipitation response was opposite to that simulated by the driving global models (Figure 10.9). Similarly, Walton et al. (2015) showed that a kilometre-scale RCM enables a more realistic representation of the snow-albedo feedback in mountainous terrain compared to standard resolution global models, leading to a more plausible simulation of elevation-dependent warming. Bukovsky et al. (2017) argue that strong seasonal changes in warm-season precipitation in the Southern Great Plains of the US, projected by RCMs, are more credible than the weaker global model changes because precipitation is better simulated in the RCMs.

ACCEPTED VERSION SUBJECT TO FINAL EDITING

[START FIGURE 10.9 HERE]

Figure 10.9: Projected changes in summer (June to August) precipitation (in percent with respect to the mean precipitation) over the Alps between the periods 2070–2099 and 1975–2004. (a) Mean of four GCMs regridded to a common 1.32°x1.32° grid resolution; (b) mean of six RCMs driven with these GCMs. The grey isolines show elevation at 200 m intervals of the underlying model data. Further details on data sources and processing are available in the chapter data table (Table 10.SM.11). Adapted from Giorgi et al. (2016).

[END FIGURE 10.9 HERE]

Including additional components, feedbacks and drivers can substantially modify the simulated future climate. For example, Kjellström et al. (2005) and Somot et al. (2008) have shown that a regional ESM can significantly modify the SST response to climate change of its driving global model with implications for the climate change signal over both the sea and land. In particular, coupled ocean-atmosphere RCMs may increase the credibility of projections in regions of strong air-sea coupling such as the East Asia-western North Pacific domain (Zou and Zhou, 2016b, 2017). Recent studies demonstrate the importance of including regional patterns of evolving aerosols in RCMs for simulating regional climate change (Boé et al., 2020a; Gutiérrez et al., 2020). RCMs not including the plant physiological response to increasing CO_2 concentrations have been shown to substantially underestimate projected increases in extreme temperatures across Europe compared to GCMs that explicitly model this effect (Schwingshackl et al., 2019).

A difference between the climate changes simulated by two models does not automatically imply the more complex or higher resolution model is superior (e.g., Dosio et al., 2019). Studies comparing convection-permitting RCM simulations to simulations of climate models with parameterized convection find, depending on the considered models, regions and seasons, either similar or qualitatively different projected changes in short duration extreme precipitation (Chan et al., 2014b, 2014a, 2020; Ban et al., 2015; Tabari et al., 2016; Fosser et al., 2017; Kendon et al., 2017, 2019; Vanden Broucke et al., 2018). Process studies provide evidence that convection-permitting simulations better represent crucial local and mesoscale features of convective storms and thus simulate more plausible changes (Meredith et al., 2015a; Prein et al., 2017; Fitzpatrick et al., 2020), but further research is required to confirm and reconcile the different findings.

Studies assessing the fitness of statistical approaches for regional climate projections are still very limited in number. For statistical downscaling, a key issue is to include predictors that control long-term changes in regional climate. Models differing only in the choice of predictors may perform similarly in the present climate, but may project opposite precipitation changes (Fu et al., 2018; Manzanas et al., 2020). In addition to trend-evaluation studies (Section 10.3.3.8), perfect-model experiments (Section 10.3.2.5) have been used to assess whether a given model structure with a chosen set of predictors is capable of reproducing the simulated future climates (Gutiérrez et al., 2013; Räty et al., 2014; Dayon et al., 2015; Dixon et al., 2016; San-Martín et al., 2017). Importantly, it is found that standard analogue methods inherently underestimate future warming trends because of missing analogues for a warmer climate (Gutiérrez et al., 2013).
Bias adjustment assumes that model biases are time invariant (or more precisely, independent of the climate state), such that the adjustment made to present climate simulations is still applicable to future climate simulations. Many findings challenge the validity of this assumption, as already assessed in AR5 (Flato et al., 2014). Further research has addressed this issue by means of perfect model experiments (Section 10.3.2.5) and process understanding. Perfect-model studies with GCMs found that circulation, energy, and water-cycle biases are roughly state-independent (Krinner and Flanner, 2018), whereas temperature biases depend linearly on temperature (Kerkhoff et al., 2014). Others show that regional temperature biases may depend on soil moisture and albedo, and may thus be state-dependent (Maraun, 2012; Bellprat et al., 2013; Maraun et al., 2017; see Cross-Chapter Box 10.2 for further limitations of bias adjustment). The fitness of weather generators for future projections depends on whether they account for all relevant changes in their parameters, either by predictors or change factors (Maraun and Widmann, 2018b).

ACCEPTED VERSION SUBJECT TO FINAL EDITING

In any case, the fitness of regional climate projections based on dynamical downscaling or statistical approaches depends on the fitness of the driving models in projecting boundary conditions, predictors and change factors (Hall, 2014; Maraun and Widmann, 2018b).

Overall, there is *high confidence* that an assessment of model fitness for projections applying process-based evaluation, process-based plausibility checks of projections and a comparison of different model types, increases the confidence in climate projections. There is *high confidence* that increasing model resolution, dynamical downscaling, statistical downscaling with well simulated predictors controlling regional climate change, and adding relevant model components can increase the fitness for projecting some aspects of regional climate when accompanied by a process-understanding analysis.

10.3.3.10 Synthesis of model performance at simulating regional climate and climate change

Global models reproduce many of the features of observed climate and its variability at regional scales. However, global models can show a variety of biases in, for instance, precipitation and temperature at scales ranging from continental (Prasanna, 2016) to sub-continental scales (Lovino et al., 2018), both in the mean and in higher order moments of the climatological distribution of the variable (Ren et al., 2019; Xin et al., 2020; Figure 10.6). Regional biases could occur even if all the relevant large-scale processes are correctly represented, but not their interaction with regional features such as orography or land-sea contrasts (Section 10.3.3.4). These biases have been considered an important limiting factor in model usability, especially at the regional scale (Palmer, 2016). In spite of this, global model simulations have been extensively used to create regional estimates of climate change (Chapters 11, 12 and Atlas), taking into account the result of a performance assessment (e.g., Jiang et al., 2020; Sections 10.3.3.3 to 10.3.3.8, Chapters 11 and Atlas). However, their application is limited in part by the effective resolution of these models (Klaver et al., 2020).

Global model performance at the regional scale is assessed in terms of the time or spatial averages of key variables (Brunner et al., 2019; Chapter Atlas), the ability to reproduce their seasonal cycle (Hasson et al., 2013) or a set of extreme climate indicators (Luo et al., 2020; Chapter 11) and the representation of regional processes and phenomena, feedbacks, drivers and forcing impacts (Sections 10.3.3.4–10.3.3.6). In many cases, the performance estimates have been used to select models for either an application or a more in-depth study (Lovino et al., 2018), to select the models that provide boundary conditions to perform RCM simulations (McSweeney et al., 2015) or to weight the results of the GCM simulations (Sanderson et al., 2015; Brunner et al., 2020). While some large-scale metrics are improved between the CMIP5 and CMIP6 experiments (e.g., Cannon, 2020; Chapter 3), there is not yet concluding evidence of a systematic improvement for surface variables at the regional scale.

The special class of high-resolution global models (Haarsma et al., 2016; Prodhomme et al., 2016; Sections 1.5.3.1 and 10.3.3.1, Chapter 3) is expected to improve some of the regional processes that are not appropriately represented in standard global models (Roberts et al., 2018). There is general consensus that increasing global model resolution improves some long-standing biases (Demory et al., 2014, 2020; Schiemann et al., 2014; Dawson and Palmer, 2015; van Haren et al., 2015; Feng et al., 2017; Fabiano et al., 2020; Chapter 3 and 10.3.3.3; Figures 10.6 and 10.7), although the resolution increase is not a guarantee of overall improvement (Fabiano et al., 2020; Hertwig et al., 2021; Section 8.5.1). For instance, increasing resolution in global models has been shown to improve Asian monsoon rainfall anchored to orography and the monsoon circulation (Johnson et al., 2016), but fails to solve the major dry bias. It is also difficult to disentangle the role of resolution increase and model tuning on the performance of the GCM (Anand et al., 2018). Some efforts have been undertaken to complement the performance improvements of resolution by using stochastic parameterisations (Palmer, 2019), which explicitly acknowledge the multi-scale nature of the climate system, in standard resolution global models with some success (Dawson and Palmer, 2015; MacLeod et al., 2016; Zanna et al., 2017, 2019). The expectation is to achieve a similar performance to the increase in resolution at a reduced computational cost.

Despite their known errors that affect model performance, there is *high confidence* that global models provide useful information for the production of regional climate information. There is *robust evidence* and

ACCEPTED VERSION SUBJECT TO FINAL EDITING

high agreement that the increase of global model resolution helps in reducing the biases limiting performance at the regional scale, although resolution per se does not automatically solve all performance limitations shown by global models. There is *robust evidence* that stochastic parameterisations can help to improve some aspects of the global model performance that are relevant to regional climate information.

Global models tend to have difficulties in simulating climate over regions where unresolved local scale processes, feedbacks and nonlinear scale interactions result in a degradation of the model performance compared to models with higher resolution. In this case, RCMs and variable resolution global models can resolve part of these processes in the regions of interest at an acceptable computational cost (Rummukainen, 2016; Giorgi, 2019; Gutowski et al., 2020).

The assessment of RCM performance needs to focus not only on mean climatology (Atlas), but also trends (Section 10.3.3.8) and extremes (Chapter 11), and the RCM's ability at correctly reproducing relevant processes, forcings and feedbacks (including e.g., aerosols, plant responses to increasing CO_2, etc., Schwingshackl et al., 2019; Boé et al., 2020; Sections 11.2. and 10.3.3.3 to 10.3.3.8) to be fit for future projections (Section 10.3.3.9).

When RCMs are driven by global models, part of the uncertainty in the RCM simulation is introduced by the global model biases (Kjellström et al., 2018; Sørland et al., 2018; Christensen and Kjellström, 2020). As RCMs are typically not able to mitigate global model biases in large-scale dynamical processes, if such biases are substantial, and if the corresponding large-scale processes are important drivers of regional climate, downscaling is questionable (Section 10.3.3.3). However, when global models have weak circulation biases and regional climate change is controlled mainly by regional-scale processes and feedbacks, dynamical downscaling has the potential to add substantial value to global model simulations (Hall, 2014; Rummukainen, 2016; Giorgi, 2019; Schwingshackl et al., 2019; Boé et al., 2020; Lloyd et al., 2020; Section 10.3.3.4 and Chapter Atlas).

There is *very high confidence* (*robust evidence* and *high agreement*) that RCMs add value to global simulations in representing many regional weather and climate phenomena, especially over regions of complex orography or with heterogeneous surface characteristics and for local-scale phenomena. Realistically representing local-scale phenomena such as land-sea breezes requires simulations at a resolution of the order of 10 km (*high confidence*). Simulations at kilometre-scale resolution add value in particular to the representation of convection, sub-daily summer precipitation extremes (*high confidence*) and soil moisture-precipitation feedbacks (*medium confidence*). Resolving regional processes may be required to correctly represent the sign of regional climate change (*medium confidence*). However, the performance of RCMs and their fitness for future projections depend on their representation of relevant processes, forcings and drivers in the specific context (Sections 10.3.3.4–10.3.3.8).

Statistical downscaling, bias adjustment and weather generators outperform uncorrected output of global and regional models for a range of statistical aspects at single locations due to their calibration, but RCMs are superior when spatial fields are relevant (Mehrotra et al., 2014; Vaittinada Ayar et al., 2016; Maraun et al., 2019b). Similarly, there is some evidence that bias adjustment is comparable in performance when applied to global models and dynamically downscaled global models only for single locations, but dynamical downscaling prior to bias adjustment clearly adds value once spatial dependence is relevant (Maraun et al., 2019b). These results may explain why dynamical downscaling does not add value to global model simulations for (single-site) agricultural modelling, when both global and regional model are bias adjusted (Glotter et al., 2014), but dynamical downscaling adds value compared to bias adjusted global model output for spatially distributed hydrological models (Qiao et al., 2014).

Overall, statistical downscaling methods with carefully chosen predictors and an appropriate model structure for a given application realistically represent many statistical aspects of present-day daily temperature and precipitation (*high confidence*, Section 10.3.3.7). Bias adjustment has proven beneficial as an interface between climate model projections and impact modelling in many different contexts (*high confidence*, Section 10.3.3.7). Weather generators realistically simulate many statistical aspects of present-day daily temperature and precipitation (*high confidence*, Section 10.3.3.7). The performance of these approaches and

ACCEPTED VERSION SUBJECT TO FINAL EDITING

their fitness for future projections also depends on predictors and change factors taken from the driving dynamical models (*high confidence*, Section 10.3.3.9).

10.3.4 Managing Uncertainties in Regional Climate Projections

Regional climate projections are affected by three main sources of uncertainty (Sections 10.2.2, 1.4.3 and 4.2.5): unknown future external forcings, imperfect knowledge and implementation of the response of the climate system to external forcings, and internal variability (Lehner et al., 2020). In a regional downscaling context, uncertainties arise in every step of the modelling chain. Here the propagation of uncertainties (Section 10.3.4.1), the management of uncertainties (Section 10.3.4.2), the role of the internal variability for regional projections (Section 10.3.4.3), and the design and use of ensembles to account for uncertainties (Section 10.3.4.4) will be assessed. Observational uncertainty, in particular for the calibration of statistical downscaling methods (Section 10.2.3.1), also contributes to projection uncertainty.

10.3.4.1 Propagation of uncertainties

Modelling chains for generating regional climate information range from the definition of forcing scenarios to the global modelling, and potentially to dynamical or statistical downscaling and bias adjustment (Section 10.3.1). The propagation and potential accumulation of uncertainties along the chain has been termed the cascade of uncertainty (Wilby and Dessai, 2010). Even within one model, like a global model, uncertainty propagates across scales. From a process point of view, these uncertainties are related to forcings and global climate sensitivity, and errors in the representation of the large-scale circulation (McNeall et al., 2016; Section 10.3.3.3) and regional processes (Section 10.3.3.4), feedbacks (Section 10.3.3.5) and drivers (Section 10.3.3.6). From a modelling point of view, these uncertainties are related to the choice of dynamical and statistical models (Section 10.3.1) and experimental design (Section 10.3.2). The overall uncertainty can be statistically decomposed into the individual sources (Evin et al., 2019; Christensen and Kjellström, 2020), although there might be nonlinear dependencies between them.

Uncertainty propagation often increases the spread in regional climate projections when comparing global model and downscaled results, which has been used as an argument against top-down approaches to climate information (Prudhomme et al., 2010). Increased spread in the modelling chain may also arise from a more comprehensive representation of previously unknown or underrepresented uncertainties (Maraun and Widmann, 2018b). The increased spread in this case goes together with a better representation of processes and thus an increased model fitness for purpose (Section 10.3.3.9).

10.3.4.2 Representing and reducing uncertainties

Climate response uncertainties (Chapter 1) can be represented by multi-model ensembles, although the sampled uncertainty typically underestimates the full range of uncertainty (Collins et al., 2013b; Shepherd et al., 2018; Almazroui et al., 2021). Traditionally, climate response uncertainty has been characterized by the ensemble spread around the multi-model mean change. The change has then further been qualified in terms of the agreement across models and compared to estimates of internal climate variability (Collins et al., 2013b). Since AR5, several limitations of this approach have been identified (Madsen et al., 2017) such as the failure to address physically plausible, but low probability high-impact scenarios (Chapters 1, 4, 8 and 9; Sutton, 2018) or that qualitatively different or even opposite changes may be equally plausible at the regional scale (Shepherd, 2014). In a multi-model mean these different responses would be lumped together, strongly dampened, and qualified as non-robust, whereas in fact high impacts might occur. Further, the multi-model mean itself is often implausible because it is a statistical construct (Zappa and Shepherd, 2017). Overall, there is *high confidence* that some regional future climate changes are not well characterised by multi-model mean and spread.

Since AR5, physical climate storyline approaches (see also Chapter 1, Box 10.2, Section 10.5.3, and Atlas

ACCEPTED VERSION SUBJECT TO FINAL EDITING

2.5.2) have been developed to better characterise and communicate uncertainties in regional climate projections (Shepherd, 2019). A special class of such storylines attempts to attribute regional uncertainties to uncertainties in remote drivers. For instance, the Dutch Meteorological Service has presented climate projections for the Netherlands for different plausible changes of the mid-latitude atmospheric circulation and different levels of European warming (van den Hurk et al., 2014). Manzini et al. (2014) have quantified the impact of uncertainties in tropical upper troposphere warming, polar amplification, and stratospheric wind change on Northern Hemisphere winter climate change. Based on these results, Zappa and Shepherd (2017) separated the multi-model ensemble into physically consistent sub-groups or storylines of qualitatively different projections in relevant remote drivers of the atmospheric circulation. In a similar vein, (Ose et al., 2020) trace uncertainties in projections of the East Asian summer monsoon and Mindlin et al. (2020) conditioned the response of Southern Hemisphere mid-latitude circulation and precipitation to greenhouse gas forcing on large-scale climate indicators (Section 8.4.2.9.2).

These physical climate storylines help to physically explain contradicting regional projections and thus make the conveyed information a better representation of the true uncertainty (Hewitson et al., 2014a). Additionally, the attribution of regional uncertainties to drivers may in principle help reduce uncertainty in the case where some storylines can be ruled out because the projected changes in the driving processes appear to be physically implausible (Zappa and Shepherd, 2017). There is thus *high confidence* that storylines attributing uncertainties in regional projections to uncertainties in changes of remote drivers aid the interpretation of uncertainties in climate projections.

Another approach that has continued to develop for characterising and reducing projection uncertainties is the use of emergent constraints (Hall et al., 2019; Chapters 1, 4, 5, 7). The idea is to link the spread in climate model projections via regression to the spread in present climate model biases for relevant driving processes. Models with lower biases are assigned higher weight in the projections, which in turn reduces the spread of the projections in a physical way and may additionally reduce projection uncertainty. For instance, Simpson et al. (2016) have reduced the spread in projections of North American winter hydroclimate by linking this spread to model biases in the representation of relevant stationary wave patterns. Other examples of using emergent constraints in a regional context are Brown et al. (2016), Li et al. (2017), Giannini and Kaplan (2019), Ose (2019) and Zhou et al.(2019).

10.3.4.3 Role of internal variability

A regional climate projection based on a single simulation from a single global model or driving a single RCM alone will inevitably be affected by not taking into account the internal variability (Figure 10.10). This is mainly due to the dominant influence of the chaotic atmospheric circulation on regional climate variability, in particular at mid-to-high latitudes. Internal variability is an irreducible source of uncertainty for mid-to-long-term projections with an amplitude that typically decreases with increasing spatial scale and lead time (Section 1.4.3; Section 4.2.1). However, regional-scale studies show that both large- and local-scale internal variability together can still represent a substantial fraction of the total uncertainty related to hydrological cycle variables, even at the end of the 21st century (Lafaysse et al., 2014; Vidal et al., 2016; Aalbers et al., 2018; Gu et al., 2018).

Analysis of multi-model archives such as CMIP or CORDEX simulation results cannot easily disentangle model uncertainty and uncertainty related to internal variability. Since AR5, the development of single-model (GCM and/or RCM) initial-condition large ensembles (SMILEs) has emerged as a promising way to robustly assess the regional-scale forced response to external forcings and the respective contribution of internal variability and model uncertainty to future regional climate changes (Deser et al., 2014, 2020; Kay et al., 2015; Sigmond and Fyfe, 2016; Aalbers et al., 2018; Bengtsson and Hodges, 2018; von Trentini et al., 2019b; Dai and Bloecker, 2019; Leduc et al., 2019; Maher et al., 2019; Lehner et al., 2020; Section 4.2.5). The recent development of a multi-model archive of SMILE simulations facilitates the quantification and comparison of the influence of internal variability on global model-based regional climate projections between different models (Deser et al., 2020; Lehner et al., 2020). Another related development is the more frequent use of observation-based statistical models to assess the influence of internal variability on regional-

ACCEPTED VERSION SUBJECT TO FINAL EDITING

scale global and regional model projections (Thompson et al., 2015; Salazar et al., 2016). However, these methods often implicitly assume that regional-scale internal variability does not change under anthropogenic forcing, which is a strong assumption that does not seem to hold at regional and local scales (LaJoie and DelSole, 2016; Pendergrass et al., 2017; Cai et al., 2018b; Dai and Bloecker, 2019; Mankin et al., 2020; Milinski et al., 2020).

[START FIGURE 10.10 HERE]

Figure 10.10: Observed and projected changes in austral summer (December to February) mean precipitation in GPCC, CRU TS and 100 members of the MPI-ESM. (a) 55-year trends (2015–2070) from the ensemble members with the lowest (left) and highest (right) trend (% per decade, baseline 1995–2014). (b) Time series (%, baseline 1995–2014) for different spatial scales (from top to bottom: global averages; S.E. South America; grid boxes close to São Paulo and Buenos Aires) with a five-point weighted running mean applied (a variant on the binomial filter with weights [1-3-4-3-1]). The brown (green) lines correspond to the ensemble member with weakest (strongest) 55-year trend and the grey lines to all remaining ensemble members. Box-and-whisker plots show the distribution of 55-year linear trends across all ensemble members, and follow the methodology used in Figure 10.6. Trends are estimated using ordinary least squares. Further details on data sources and processing are available in the chapter data table (Table 10.SM.11).

[END FIGURE 10.10 HERE]

The appropriate ensemble size for a robust use of SMILEs depends on the model and physical variable being investigated, the spatial and time aggregation being performed, the magnitude of the acceptable error and the type of questions one seeks to answer (Deser et al., 2012, 2017b; Kang et al., 2013; Wettstein and Deser, 2014; Dai and Bloecker, 2019; Maher et al., 2019). It is noteworthy that the recent development of ensembles with a very large ensemble size (greater than 100) have led to new insights and methodologies to robustly assess the required ensemble size for questions such as the estimation of the forced response to external forcing or a forced change in modes of internal variability, such as ENSO, and its associated teleconnections (Herein et al., 2017; Maher et al., 2018; Haszpra et al., 2020; Milinski et al., 2020).

The use of SMILEs assumes that they have a realistic representation of internal variability and its evolution under anthropogenic climate change (Eade et al., 2014; McKinnon et al., 2017; McKinnon and Deser, 2018; Chen and Brissette, 2019). Assessing the realism of simulated internal variability for past and current climates remains an active research field with a number of issues such as the shortness and uncertainties of the observed record, in particular in data-scarce regions (Section 10.2.2.3), the signal-to-noise paradox (Scaife and Smith, 2018; Section 4.4.3.1), uncertainty in past observed external forcing estimates (Chapters 2, 6 and 7) and the limitations of assumptions underlying the statistical methods used to derive observational large ensembles (McKinnon et al., 2017; McKinnon and Deser, 2018; Castruccio et al., 2019). Calibration methods inspired by weather and seasonal forecasts can be used to improve the reliability of regional-scale climate projections from large ensembles (Brunner et al., 2019; O'Reilly et al., 2020). Interestingly, reliability is improved when the calibration is performed separately for the dynamical and residual components of the ensemble resulting from dynamical adjustment (O'Reilly et al., 2020; Section 10.4.1).

Importantly, accurately partitioning uncertainty in regional climate projections can provide an incentive for immediate action, accepting a large range of possible outcomes due to internal variability, while confounding model uncertainty with internal variability may be understood as a lack of knowledge and lead to delayed action in adaptation decision-making (Maraun, 2013; Mankin et al., 2020; Section 10.5.3).

There is *high confidence* that the availability of SMILEs allows a robust assessment of the relative contributions of model uncertainty and internal variability in regional-scale projection uncertainty. There is *high confidence* that the use of SMILEs with appropriate ensemble size leads to an improved estimate of regional-scale forced response to an external forcing as well as of the full spectrum of possible changes associated with internal variability. There is *high confidence* that these improved estimates are beneficial for

ACCEPTED VERSION SUBJECT TO FINAL EDITING

characterizing the full distribution of outcomes that is a key ingredient of climate information for robust decision-making and risk-analysis frameworks.

10.3.4.4 Designing and using ensembles for regional climate change assessments to take uncertainty into account

Ensembles of climate simulations play an important role in quantifying uncertainties in the simulation output (Sections 10.3.4.2 and 10.3.4.3). In addition to providing information on internal variability, ensembles of simulations can estimate scenario uncertainty and model (structural) uncertainty. Chapter 4, especially Box 4.1, discusses issues involved with evaluating ensembles of GCM simulations and their uncertainties. In a downscaling context, further considerations are necessary, such as the selection of GCM-RCM combinations when performing dynamical downscaling. This is a relevant issue when resources are limited. The structural uncertainty of both the GCM and the downscaling method can be important (e.g., Dosio, 2017; Mearns et al., 2012), as well as further potential uncertainty created by inconsistencies between the GCM and the downscaling method (e.g., Dosio et al., 2019), which could include, for example, differences in topography or the way to model precipitation processes (Mearns et al., 2013).

An important consideration is which set of GCMs should be used for GCM-RCM combinations. If adequate resources exist, then large numbers of GCM-RCM combinations are possible (Déqué et al., 2012; Vautard et al., 2020; Coppola et al., 2021). However, coordinated downscaling programmes can be limited by the human and computational resources available, for producing ensembles of downscaled output, which limits the number of feasible GCM-RCM combinations. With this limitation in mind, a small set of GCMs may be chosen that span the range of equilibrium climate sensitivity in available GCMs (e.g., Inatsu et al., 2015; Mearns et al., 2012, 2013), though this range may be inconsistent with the likely range (Chapter 4), or some other relevant measure of sensitivity, such as the projected range of tropical SSTs (Suzuki-Parker et al., 2018). A further choice is to emphasize models that do not have the same origins or that do not use similar parameterizations and thus might be viewed as independent, a criterion that could be applied to both GCMs (Chapter 4) and RCMs (Evans et al., 2014). GCMs and RCMs could also be discarded that unrealistically represent processes controlling the regional climate of interest (McSweeney et al., 2015; Maraun et al., 2017; Bukovsky et al., 2019; Eyring et al., 2019). Box 4.1 offers a more detailed discussion of the issues surrounding these approaches. Finally, GCMs may be selected to represent different physically self-consistent changes in regional climate (Zappa and Shepherd, 2017). Statistical methods can provide estimates of outcomes from missing GCM-RCM combinations in a large matrix (Déqué et al., 2012; Heinrich et al., 2014; Evin et al., 2019).

However, even using a relatively small set of GCMs can still involve substantial computation that strains available resources, both for performing the simulations and for using all simulations in the ensemble for further impacts assessment. The NARCCAP programme (Mearns et al., 2012) used only a subset of its possible GCM-RCM combinations that balanced comprehensiveness of sampling the matrix with economy of computation demand, while still allowing discrimination, via ANOVA methods, of GCM and RCM influences on regional climate change (Mearns et al., 2013). An advantage of the sparse, but balanced matrix for those using the downscaling output for further studies, is that they have a smaller, yet comprehensive set of GCM-RCM combinations to work with. Alternatively, data-clustering methods can clump together downscaling simulations featuring similar climate-change characteristics, so that only one representative simulation from each cluster may be needed for further impacts analysis, again systematically reducing the necessary number of simulations to work with (Mendlik and Gobiet, 2016; Wilcke and Bärring, 2016).

Independently of the resources, participation of multiple models in a simulation programme such as CORDEX for RCMs or CMIP for GCMs creates ensembles of opportunity, which are ensembles populated by models that participants chose to use without there necessarily being an overarching guiding principle for an optimum choice. As discussed in Chapter 4, these ensembles are likely suboptimal for assessing sources of uncertainty. An important contributor to the suboptimal character of such an ensemble is that the models are not independent. Some may also have larger biases than others. Yet often, the output from models in these ensembles has received equal weight when viewed collectively, as was the case in much of the AR5

ACCEPTED VERSION SUBJECT TO FINAL EDITING

assessment (e.g., Collins et al., 2013; Flato et al., 2014; Kirtman et al., 2014; Knutti et al., 2013). A number of emerging methodologies aim at optimizing the ensembles available by weighting the simulation results according to a number of criteria relevant at the regional scale that aim at obtaining more realistic estimates of the uncertainty (Sanderson et al., 2015; Brunner et al., 2020)

There is *high confidence* that ensembles for regional climate projections should be selected such that models unrealistically simulating processes relevant for a given application are discarded, but at the same time, the chosen ensemble spans an appropriate range of projection uncertainties.

[START CROSS-CHAPTER BOX 10.2 HERE]

Cross-Chapter Box 10.2: Relevance and limitations of bias adjustment

Coordinators: Alessandro Dosio (Italy), Douglas Maraun (Austria/Germany)
Contributors: Ana Casanueva (Spain), José M. Gutiérrez (Spain), Stefan Lange (Germany), Jana Sillmann (Norway/Germany)

Bias adjustment is an approach to post-process climate model output and has become widely used in climate hazard and impact studies (Gangopadhyay et al., 2011; Hagemann et al., 2013; Warszawski et al., 2014) and national assessment reports (Cayan et al., 2013; Georgakakos et al., 2014). Despite its wide use, bias adjustment was not assessed in AR5 (Flato et al., 2014). Several problems have been identified that may arise from an uncritical use of bias adjustment, and that may result in misleading impact assessments. The rationale of this Cross-Chapter Box is to provide an overview of the use of bias adjustment in this report, and to assess key limitations of the approach.

Bias-adjusted climate model output is used extensively throughout this report. Several results from Chapter 8, and many of the climatic impact-drivers in Chapter 12 (Section 12.2) are based on bias adjustment. The Atlas presents many results both as raw and bias-adjusted data (Atlas.1.4.5). The application of bias adjustment in the WGI1 report was informed by the assessment in Chapter 10 and this Cross-Chapter Box. Finally, bias adjustment is crucial for many studies assessed in the WG II report. An overview of bias adjustment can be found in Section 10.3.1.3, a general performance assessment of individual method classes in Section 10.3.3.7. The fitness of bias adjustment for climate change applications is assessed in Section 10.3.3.9.

Relevance of bias adjustment
An argument made for the use of bias adjustment is the fact that impact models are commonly very sensitive, often nonlinearly, to the input climatic variables and their biases, in particular when threshold-based climate indices are required (Dosio, 2016). There are, however, cases where bias adjustment may not be necessary or useful, such as: when only qualitative statements are required; when only changes in mean climate are considered (instead of absolute values); when percentile-based indices are used.

Modification of the climate change signal
Bias adjustment methods like quantile mapping can modify simulated climate trends, with impacts on changes to climate indices, in particular, extremes (Haerter et al., 2011; Dosio et al., 2012; Ahmed et al., 2013; Hempel et al., 2013; Maurer and Pierce, 2014; Cannon et al., 2015; Dosio, 2016; Casanueva et al., 2020). Some argue that these trend modifications are implicit corrections of state-dependent biases (Boberg and Christensen, 2012; Gobiet et al., 2015). However, others argue that the modification is generally invalid because the modification is linked to the representation of day-to-day rather than long-term variability (Pierce et al., 2015; Maraun et al., 2017); a given temperature value does not necessarily belong to the same weather state in present and future climate (Maraun et al., 2017); the modification affects the models climate sensitivity (Hempel et al., 2013); and is affected by random internal climate variability (Switanek et al., 2017). Thus, trend preserving quantile mapping methods have been developed (Section 10.3.1.3.2), although some authors found no clear advantage of these methods (Maurer and Pierce, 2014). Further research is required to fully understand the validity of trend modifications by quantile-mapping.

ACCEPTED VERSION SUBJECT TO FINAL EDITING

Bias adjustment in the presence of large-scale circulation errors

The large-scale circulation has a strong impact on regional climate, thus circulation errors will cause regional climate biases (Section 10.3.3.3). As bias adjustment in general does not account for circulation errors, it is therefore important to understand the impact of these errors on the outcome of the bias adjustment (Addor et al., 2016; Photiadou et al., 2016; Maraun et al., 2017). If the frequency of precipitation-relevant weather types is biased, a standard bias adjustment (not accounting for this frequency bias) would remove the overall climatological bias, but the precipitation falling in a given weather type could still be substantially biased (Addor et al., 2016). Adjusting the number of wet days can artificially deteriorate the spell-length distribution (Maraun et al., 2017). In the presence of location biases of circulation patterns, bias adjustment may introduce physically implausible solutions (Maraun et al., 2017). Bias adjusting the location of circulation features (Levy et al., 2013) may introduce inconsistencies with the model orography, land-sea contrasts, and SSTs (Maraun et al., 2017).

There is *medium confidence* that the selection of climate models with low biases in the frequency, persistence and location of large-scale atmospheric circulation can reduce negative impacts of bias adjustment.

Using bias adjustment for statistical downscaling

Bias adjustment is often used to downscale climate model results from grid box data to finer resolution or point scale. It is sometimes even directly applied to coarse-resolution global model output to avoid an intermediate dynamical downscaling step (Johnson and Sharma, 2012; Stoner et al., 2013). But bias adjustment does not add any information about the processes acting on un-resolved scales and is therefore by construction not capable of bridging substantial scale gaps (Maraun, 2013a; Maraun et al., 2017). Using bias adjustment for downscaling has been shown to artificially modify long-term trends, misrepresent the spatial characteristics of extreme events, and misrepresent local weather phenomena such as temperature inversions (Maraun, 2013a; Gutmann et al., 2014; Maraun et al., 2017). Crucially, sub-grid influences on the local climate change signal are not represented. For instance, if a mountain chain is not resolved in the driving model, the snow-albedo feedback is not represented by the bias adjustment such that local temperature trends in high altitudes are under-represented (Maraun et al., 2017; Cross-Chapter Box 10.2, Figure 1). It has therefore been suggested to account for local random variability by combining bias adjustment with stochastic downscaling (Volosciuk et al., 2017; Lange, 2019), although this approach still does not account for local modifications of the climate change signal. Two approaches have been proposed to represent these local changes: dynamical downscaling with high-resolution RCMs (Maraun et al., 2017) or statistical emulators of such (Walton et al., 2015). Sections 10.3.3.4–10.3.3.6 and 10.3.3.9 discuss other examples where RCMs improve the representation of regional phenomena and regional climate change.

Overall, there is *high confidence* that the use of bias adjustment for statistical downscaling, in particular to downscale coarse resolution global models, has severe limitations.

[START CROSS-CHAPTER BOX 10.2, FIGURE 1 HERE]

Cross-Chapter Box 10.2, Figure 1: Boreal spring (March to May) daily mean surface air temperature in the Sierra Nevada region in California. (a) Present climate (1981–2000 average, in °C) in the GFDL-CM3 AOGCM, interpolated to 8 km (left), GCM bias adjusted (using quantile mapping) to observations at 8 km resolution (middle) and WRF RCM at 3 km horizontal resolution (right). (b) Climate change signal (2081–2100 average minus 1981–2000 average according to RCP8.5, in °C) in the AOGCM (left), the bias adjusted AOGCM (middle) and the RCM (right). Further details on data sources and processing are available in the chapter data table (Table 10.SM.11). Adapted from Maraun et al. (2017b).

[END CROSS-CHAPTER BOX 10.2, FIGURE 1 HERE]

ACCEPTED VERSION SUBJECT TO FINAL EDITING

Bias adjustment of multiple variables

Impact models, as well as indices of climatic impact-drivers, often require input of several meteorological variables (Chapter 12). In several situations, for example, if the dependence between the variables is not well simulated, univariate bias adjustment of the individual variables may increase biases in the resulting indicator (Zscheischler et al., 2019). A simple alternative would be a bias adjustment of the indicator, but such a procedure may substantially alter the climate change signal, in particular for extreme events (Casanueva et al., 2018). Multivariate bias adjustment methods are in principle good to adjust all statistical aspects of the multivariate distribution that they intend to adjust. Depending on the method, this includes the correlation structure or even broader aspects of the dependence (Cannon, 2016, 2018; Vrac, 2018; François et al., 2020). If multivariate adjustment includes a spatial dimension, then spatial dependence is adjusted well (Vrac, 2018), but care is needed when applied across large areas (François et al., 2020). Adjustment of multivariate dependence necessarily modifies the temporal sequencing of the driving model (Cannon, 2016; Maraun, 2016). The extent of the modification depends on the chosen method and the number of variables to adjust (Vrac and Friederichs, 2015; Cannon, 2016; Vrac, 2018; François et al., 2020).

Bias adjustment in the presence of observational uncertainty and internal variability

Observational uncertainties and internal variability introduce uncertainty in the estimation of biases and thus in the calibration of bias-adjustment methods. Dobor and Hlásny (2018) found a considerable influence of the choice of the observational dataset and calibration period on the adjustment for some regions. RCM biases are typically larger than observational uncertainties, but in some regions, and in particular for wet-day frequencies, spatial patterns and the intensity distribution of daily precipitation, the situation may reverse (Kotlarski et al., 2019). Switanek et al. (2017) found a strong influence of internal variability and thus of the choice of calibration period on the calibration of quantile mapping and on the modification of the climate change signal.

Bias adjustment is typically evaluated using cross-validation, i.e. by calibrating the adjustment function to one period of the observational record, and by evaluating it on a different one. Maraun et al. (2017) and Maraun and Widmann (2018) demonstrated that, in the presence of multi-decadal internal variability, cross-validation may lead to a rejection of a valid bias adjustment or even lead to a positive evaluation of an invalid adjustment. The authors therefore argued that, in the presence of substantial internal variability, the evaluation of bias adjustment requires to consider aspects that have not been adjusted, such as temporal, spatial, or multi-variable dependence.

There is *high confidence* that observational uncertainty and internal variability adversely affect bias adjustment and introduce uncertainties in bias adjusted future projections.

Overall assessment and new avenues

In the light of these issues, several authors dismiss the use of bias adjustment for climate change studies (Vannitsem, 2011; Ehret et al., 2012). Ehret et al. (2012) and Stocker et al. (2015) propose to at least provide the raw model output alongside the adjusted data. Maraun et al. (2017b) argue that the target resolution should be similar to the model resolution to avoid downscaling issues. Stocker et al. (2015) and Maraun et al. (2017) highlighted the relevance of understanding model biases and the misrepresentations of the underlying physical processes prior to any adjustment. Together with Galmarini et al. (2019) , they point out the need for collaboration between bias adjustment users, experts in climate modelling and experts in the considered regional climate. As new research avenues, development of process-oriented bias adjustment methods (Addor et al., 2016; Verfaillie et al., 2017; Manzanas and Gutiérrez, 2019) or run-time bias adjustment integrated into the climate simulation, e.g., to reduce circulation errors (Guldberg et al., 2005; Kharin et al., 2012; Krinner et al., 2019, 2020) are proposed.

[END CROSS-CHAPTER BOX 10.2 HERE]

ACCEPTED VERSION SUBJECT TO FINAL EDITING

10.4 Interplay between Anthropogenic Change and Internal Variability at Regional Scales

This section focuses on the assessment of the methodologies used to identify the physical causes of past and future regional climate change in the context of the ongoing anthropogenic influence on the global climate. The main foci are the attribution of past regional-scale changes (Sections 10.4.1–2) and the robustness and future emergence of the regional-scale response to anthropogenic forcing (Section 10.4.3).

In this chapter, regional-scale attribution is defined as the process of evaluating the relative contributions of multiple causal factors (or drivers) to regional climate change (Cross-Working Group Box: Attribution (in Chapter 1); Rosenzweig and Neofotis, 2013; Shepherd, 2019). Attribution at regional scale builds upon the usual definition of attribution used in the AR5 (Hegerl et al., 2010; Cross-Working Group Box 1.1). However, in contrast with global-scale attribution methods where internal variability might be considered as a noise problem (Section 3.2), the preliminary detection step is not always required to perform regional-scale attribution since causal factors of regional climate change may also include internal modes of variability in addition to external natural and anthropogenic forcing. Importantly, regional-scale (or process-based) attribution also seeks to determine the physical processes and uncertainties involved in the causal factor's influence (Cross-Working Group Box: Attribution).

Section 10.4.1 describes regional-scale attribution methodologies and assesses their application to regional changes of temperature and precipitation. Section 10.4.2 presents three illustrative attribution examples that illustrate a number of specific regional-scale challenges and methodological aspects. Section 10.4.3 focuses on methodologies used to assess the robustness and emergence of the regional climate response to anthropogenic forcing. A basic description of future regional climate change for all regions considered in the report (as defined in Section 1.4.5) appears in the Atlas.

10.4.1 Methodologies for Regional Climate Change Attribution

Attribution at sub-continental and regional scales is usually more complicated than at the global scale due to various factors: a larger contribution from internal variability, an increased similarity among the responses to different external forcings leading to a more difficult discrimination of their effects, the importance at regional scale of some omitted forcings in global model simulations, and model biases related to the representation of small-scale phenomena (Zhai et al., 2018). Since AR5 and in addition to standard optimal fingerprint regression-based approaches (Section 3.2.1 and Zhai et al. 2018), several emerging methodologies have been increasingly used for regional-scale climate change attribution. These include several statistical approaches that differ in their use or omission of spatiotemporal covariance information. Dynamical adjustment and pattern recognition techniques fall into the category of spatiotemporal methods while univariate detection and attribution methods rely on single grid-point analysis. Finally, the development, evaluation and use of all these methodologies rely upon the availability of multiple and high-quality observational datasets (Section 10.2) as well as multi-model simulations of the historical period constrained by different external forcing combinations, including single-forcing experiments and single-model initial-condition large ensembles (SMILEs).

10.4.1.1 Optimal fingerprinting methods

Optimal fingerprint regression-based methods have been applied to detection and attribution of mean temperature anthropogenic signal in several regions of the world such as Canada, India, Central Asia, Northern and Western China, Australia, and North Africa (Xu et al., 2015; Li et al., 2017a; Dileepkumar et al., 2018; Wang et al., 2018b; Peng et al., 2019; Wan et al., 2019). The influence of anthropogenic forcing, and in particular that of greenhouse gases (GHGs), is robustly detected in annual and seasonal mean temperatures for all considered regions. Most of the observed regional temperature changes since the mid-twentieth century can only be explained by external forcings, with anthropogenic influence being the dominant factor. GHG increase is found to be the primary factor of the anthropogenic-induced warming while the aerosol forcing leads to a cooling offsetting a fraction of the GHG change (Li et al., 2016b, 2017a).

ACCEPTED VERSION SUBJECT TO FINAL EDITING

While the influence of external natural forcing can often be detected as well, its contribution to observed changes is usually much smaller (Li et al., 2017a; Wan et al., 2019). Temperature detection results are found to be robust to the use of different observational data sets and detection methodologies (Dileepkumar et al., 2018).

Detection of mean precipitation changes caused by human influence is much more difficult, due to a larger role of internal variability at regional to local scales, as well as substantial modelling and observational uncertainty (Wan et al., 2015; Sarojini et al., 2016; Li et al., 2017a). However, multi-decadal precipitation changes due to anthropogenic forcing have been detected for several regions. Ma et al. (2017) show that anthropogenic forcing has strongly contributed to the observed shift of China daily precipitation towards heavy precipitation. The observed weakening of the East Asia summer monsoon, also known as the southern flooding and northern drought pattern has been partially linked to anthropogenic forcing (Section 8.3.2.4.2; Song et al., 2014; Tian et al., 2018; Zhou et al., 2017b). Changes in GHGs lead to increasing precipitation over southern China, whilst changes in anthropogenic aerosols over East Asia are the dominant factors determining drought conditions over northern China (Song et al., 2014; Tian et al., 2018). Based on all-forcing and single-forcing simulation ensembles with a high-resolution model, Delworth and Zeng (2014) found that the observed long-term regional austral autumn and winter rainfall decline over southern and particularly southwest Australia is partially reproduced in response to anthropogenic changes in GHGs and ozone in the atmosphere, whereas anthropogenic aerosols do not contribute to the simulated precipitation decline. In contrast, the observed increase of northwest Australian summertime rainfall since 1950 has been partially attributed to anthropogenic aerosol based on CMIP5 detection and attribution single-forcing simulations (Section 8.3.2.4.6; Dey et al., 2019b, 2019a).

It is noteworthy that these methods require a very significant reduction of spatial and temporal dimensions in order to reliably estimate the covariance matrix of internal variability (an entire region is thus often considered as being only one or a few spatial points that represent the spatial average of the whole region or a few sub-regions; time samples are often 5- or 10-year averages). Finally, model bias is rarely considered in statistical models used in detection and attribution regional studies, while it has been shown to have a strong impact on the stability of detection results and their associated confidence intervals when increasing the spatial dimension (Ribes and Terray, 2013). New statistical methods are emerging to provide some alternative to standard optimal fingerprinting but they have not yet been evaluated and applied at regional scales (Section 3.2.2).

10.4.1.2 Other spatiotemporal statistical methods for isolating regional climate responses to external forcing

The primary objective of any attribution method is to optimally separate the influences of external forcing and internal variability on a global or regional climate record. In a multi-model ensemble context, the estimation of the externally-forced climate response has been typically performed by ensemble averaging of linear trends or regional domain spatial average, thus not taking into account the available and complete space and time covariance information. Since AR5, methods using spatiotemporal information have been further developed and used to improve the separation between external and internal drivers in multiple or single historical climate realizations performed by a given global model.

The typical ensemble size of CMIP historical climate simulations for a given model traditionally ranges between one and ten members, with three often being the default choice. At the regional scale, a simple ensemble average with such sample sizes does not provide robust estimates of the response patterns to external forcing (Maher et al., 2019; Deser et al., 2020). Since AR5, pattern filtering methods such as signal-to-noise maximizing empirical orthogonal functions (Ting et al., 2009) have been shown to improve the identification of forced response patterns when only few model members are available (Wills et al., 2020). Using SMILEs as a test bed, it has been shown that pattern filtering strongly reduces the number of ensemble members needed to estimate the forced response pattern compared to simple ensemble averaging. Pattern filtering allows the identification of low signal-to-noise signals such as the El Niño-like response to volcanic eruptions (Khodri et al., 2017; Wills et al., 2020).

ACCEPTED VERSION SUBJECT TO FINAL EDITING

Methods to extract the response to external forcing in an observed or simulated single realization include dynamical adjustment (Smoliak et al., 2015; Deser et al., 2016; Sippel et al., 2019) and time-scale separation methods (DelSole et al., 2011; Wills et al., 2018, 2020). Dynamical adjustment seeks to isolate changes in surface air temperature or precipitation that are due purely to atmospheric circulation changes. The residual can then be analysed and attributed to internal changes in both land or ocean surface conditions and the thermodynamical response to external forcing. Smoliak et al. (2015) performed their dynamical adjustment using partial least squares regression of temperature to remove variations arising from sea-level pressure changes. Deser et al. (2016) used constructed atmospheric circulation analogues and resampling to estimate the dynamical contribution to changes in temperature. Sippel et al. (2019) used machine learning techniques known as regularized linear regression to provide estimates of circulation-induced components of precipitation and temperature variability from global to local scales. It is noteworthy that the dynamical adjustment method by itself cannot account for the component of the forced response associated with circulation changes that project onto atmospheric internal variability. However, this component can be estimated within a model framework by averaging the dynamical contribution across multiple members of a SMILE (Deser et al., 2016).

Dynamical adjustment methods have been used by, for instance, Deser et al. (2016), Saffioti et al. (2016), O'Reilly et al. (2017), Gong et al. (2019), and Guo et al. (2019). Deser et al. (2016) focused on the causes of observed and simulated multi-decadal trends in North American temperature. They demonstrated that the main advantage of this technique is to narrow the spread of temperature trends found by the model ensemble and to bring the dynamically-adjusted observational trend much closer to the forced response estimated by the model ensemble mean. Similar results were obtained by Saffioti et al. (2016) regarding recent observed winter temperature and precipitation trends over Europe. Similarly, O'Reilly et al. (2017) applied dynamical adjustment techniques to more carefully determine the influence of the Atlantic Multi-decadal Variability (AMV; Annex AIV.2.7) on continental climates. Over Europe, summer temperature anomalies induced thermodynamically by the warm phase of the AMV are further reinforced by circulation anomalies; meanwhile, precipitation signals are largely controlled by dynamical responses to the AMV. Based on a partial least-squares approach, Gong et al. (2019) showed that recent winter temperature 30-year trends over northern East Asia are strongly influenced by internal variability linked to decadal changes of the Arctic Oscillation. Using dynamical adjustment purely on precipitation observations, Guo et al. (2019) showed that human influence has led to increased wintertime precipitation across north-eastern North America, as well as a small region of north-western North America, and to an increase in precipitation across much of north-western and north central Eurasia. The latter results confirm previous findings obtained by standard optimal fingerprinting methods (Wan et al., 2015).

Time-scale separation methods such as the low-frequency component analysis and ensemble empirical mode decomposition methods take advantage of the longer time scale associated with anthropogenic external forcing compared to that of most internal modes of variability. The low-frequency component analysis method tries to find low-frequency variability patterns by searching for linear combinations of a moderate number of empirical orthogonal functions that maximize the ratio of low-frequency to total variance. It has first been used to separate internal modes of interannual and decadal variability from slowly varying and externally-forced variability in the Pacific and Atlantic Oceans (Wills et al., 2018, 2019). The methodology has also been applied to patterns of observed surface air temperature to isolate the slow components of observed changes that are consistent with the expected response to anthropogenic greenhouse gas and aerosol forcing (Wills et al., 2020).

The ensemble empirical mode decomposition method (Wu and Huang, 2009; Wilcox et al., 2013; Ji et al., 2014; Qian and Zhou, 2014) decomposes data, such as time series of historical temperature and precipitation, into independent oscillatory modes of decreasing frequency. The last step of the method leaves behind a smooth and low-frequency residual time series. Typically, the nonlinear anthropogenic trend (e.g., of 20th-century temperature) can be reconstructed by summing the long-term mean, the residual, and eventually the lowest-frequency mode to account for a multi-decadal forced signal, for instance associated with anthropogenic aerosol forcing. The ensemble empirical mode decomposition method is an example of a data-driven, non-parametric approach that can be used to directly provide an estimate of the forced response

ACCEPTED VERSION SUBJECT TO FINAL EDITING

without the need for model data (Qian, 2016).

10.4.1.3 Other regional-scale attribution approaches

The univariate detection method does not use spatial pattern information, but compares observed trends in gridded datasets with distributions of trends from ensembles of simulations during the historical period (Knutson et al., 2013; Knutson and Zeng, 2018). The trends arising from simulations constrained by natural forcing-only and all-forcing are compared with distributions of trends purely due to internal variability and derived from long simulations with constant pre-industrial external forcing. Consistency between observed and simulated historical trends is also assessed with statistical tests that can be applied independently over a large number of grid points. The fraction of area over a given region where the change is classified as detectable, attributable, or consistent/inconsistent, is then finally estimated. The method can be viewed as a simple consistency test for both amplitude and pattern of observed versus simulated trends. Its application to CMIP3 and CMIP5 models suggests that 80% of the Earth's surface has a detectable anthropogenic warming signal (Knutson et al., 2013). Regarding regional land precipitation changes over the 1901–2010 and 1951–2010 periods, application of the univariate detection method based on CMIP5 models suggests attributable anthropogenic changes at several locations such as increases over regions of the north-central United States, southern Canada, Europe, and southern South America and decreases over parts of the Mediterranean region, northern tropical Africa and southwestern Australia (Knutson and Zeng, 2018).

Another regional attribution technique is based on the similarity of past changes between observations and one or several simulations of a large ensemble that share the same time evolution for a suggested driver of these changes. Huang et al. (2020) used a perturbed physics ensemble to attribute the drying trend of the Indian monsoon over the latter half of the 20th century to decadal forcing from the Pacific Decadal Variability (PDV; Annex AIV.2.6). The ensemble members predicted different trends in PDV behaviour across the 20th century and the negative precipitation trend was only replicated in those members with a strong negative-to-positive PDV transition across the 1970s, consistent with the observed PDV behaviour (see also the detailed case study in Section 10.6). In a similar manner, Cvijanovic et al. (2017) addressed the possible influence of Arctic sea-ice loss on the North Pacific pressure ridge and, consequently, on south-western United States precipitation. They sampled the uncertainties in selected sea-ice physics parameters to achieve a "low Arctic sea-ice" state in their perturbed simulations. They then compared the latter with control simulations representative of sea-ice conditions at the end of the 20th century to assess changes purely due to sea-ice loss.

New methods aiming to remove underlying model biases before performing detection and attribution, for instance related to precipitation changes, are emerging based on image transformation techniques such as warping (Levy et al., 2014a). By correcting location and seasonal precipitation biases in CMIP5 models, Levy et al. (2014b) showed that the agreement between observed and fingerprint patterns can be improved, further enhancing the ability to attribute observed precipitation changes to external forcings. The improvement mainly relies on the assumption that precipitation changes are tied to the underlying climatology, which has been shown to be a reasonable assumption in regions of the world where intensification of the hydrological cycle is expected (Held and Soden, 2006).

Importantly, evidence that the models employed in regional-scale attribution are fit for purpose is essential in order to estimate the degree of confidence in the attribution results (Section 10.3.3). For example, models need to be evaluated and assessed in their ability to simulate internal variability modes that are known to be important drivers of regional climate change (Sections 3.7 and 10.3.3.3 and Annexes AIV.2 and AIV.3). Models are likely to have different performance in different regions and therefore their evaluation needs to be performed in terms of key physical processes and mechanisms relevant to the climate of the region under consideration (Section 10.3.3).

To conclude, there is *very high confidence* (*robust evidence* and *high agreement*) that the use of diverse and independent attribution methods, multiple model ensemble types and observed datasets strengthens the robustness of results of regional-scale attribution studies. Since AR5, multiple SMILEs have provided an

ACCEPTED VERSION SUBJECT TO FINAL EDITING

adequate testbed for new attribution methodologies aimed at separating forced signals from internal variability in observational records as well as small-size single-model ensembles.

10.4.2 Regional Climate Change Attribution Examples

This section focuses on three illustrative examples that span different regions, time scales, attribution methods, without aiming at being comprehensive. These examples illustrate attribution statements that are based upon multiple lines of evidence, combining multiple observational data sets, different generations and types of models, process understanding and assessment of various sources of uncertainty. Detection and attribution assessments for all AR6 regions and specific variables can be found in the Atlas.

10.4.2.1 The Sahel and West African monsoon drought and recovery

The Sahel, fed by the West African monsoon, has experienced severe decadal rainfall variations (Figure 10.11a). Abundant rainfall in the 1950s–1960s was followed by a large negative trend (Figure 10.11b) until at least the 1980s, over which annual rainfall fell by 20–30% (Hulme, 2001). The subsequent partial recovery (Wang et al., 2020) is more uncertain: rain-gauge studies suggest a return to long-term positive anomalies in the western Sahel in the early 2000s (Panthou et al., 2018), while CHIRPS merged satellite/gauge data show a wetter western Sahel since 1981 (Bichet and Diedhiou, 2018b, 2018a). The recovery has been more significant over the central rather than the western Sahel (Lebel and Ali, 2009; Sanogo et al., 2015; Maidment et al., 2015) and a multiple-gauge record supports a greater recovery to the eastern side (Nicholson et al., 2018). In this attribution example, drivers of the long-term drought and subsequent partial recovery are discussed, including anthropogenic GHG and aerosol emissions, and sea surface temperature (SST) variations that, in part, relate to internal variability. The reader is also referred to assessment in Section 8.3.2.4. We define the Sahel within 10°N–20°N across to 30°E, consistent with the eastern boundary used in Chapter 8, and the rainy season as spanning June to September.

[START FIGURE 10.11 HERE]

Figure 10.11: Attribution of historic precipitation change in the Sahelian West African monsoon during June to September. (a) Time series of CRU TS precipitation anomalies (mm day^{-1}, baseline 1955–1984) in the Sahel box (10°N–20°N, 20°W–30°E) indicated in panel (b) applying the same low-pass filter as that used in Figure 10.10. The two periods used for difference diagnostics are shown in grey columns. (b) Precipitation change (mm day^{-1}) in CRU TS data for 1980–1990 minus 1950–1960 periods. (c) Precipitation difference (mm day^{-1}) between 1.5x and 0.2x historical aerosol emissions scaling factors averaged over 1955–1984 and five ensemble members of HadGEM3 experiments after Shonk et al. (2020). (d) Sahel precipitation anomaly time series (mm day^{-1}, baseline 1955–1984) in CMIP6 for 49 historical simulations with all forcings (red), and thirteen for each of greenhouse gas-only forcing (light blue) and aerosol-only forcing (grey), with a thirteen-point weighted running mean applied (a variant on the binomial filter with weights [1-6-19-42-71-96-106-96-71-42-19-6-1]). The CMIP6 subsample of all forcings matching the individual forcing simulations is also shown (pink). (e) Precipitation linear trend (% per decade) for (left) decline (1955–1984) and (right) recovery periods (1985–2014) for ensemble means and individual CMIP6 historical experiments (including single-forcing) as in panel (d) plus 34 CMIP5 models (dark blue). Box-and-whisker plots show the trend distribution of the three coupled and the d4PDF atmosphere-only SMILEs used throughout Chapter 10 and follow the methodology used in Figure 10.6. The two black crosses represent observational estimates from GPCC and CRU TS. Trends are estimated using ordinary least-squares regression. Further details on data sources and processing are available in the chapter data table (Table 10.SM.11).

[END FIGURE 10.11 HERE]

The role of SST forcing in the rainfall decline is assessed first. Competing mechanisms from equatorial Atlantic SSTs and interhemispheric SST gradients regulate decadal variability in the Sahel (Nicholson,

ACCEPTED VERSION SUBJECT TO FINAL EDITING

2013), alternatively explained by tropical warming leading to Sahel drought, while North Atlantic warming promotes increased rainfall (Rodríguez-Fonseca et al., 2015). The SST influence has been formalised in an AMV framework (Giannini et al., 2013; Martin and Thorncroft, 2014; Martin et al., 2014; Park et al., 2015), suggesting that relative North Atlantic SST warming increases the Northern Hemisphere differential warming, enhancing Sahel rainfall. The AMV influence is supported by CMIP5 initialized decadal hindcasts (Gaetani and Mohino, 2013; Mohino et al., 2016; Sheen et al., 2017), which outperform empirical predictions based on persistence. Some caution is needed since the full magnitude of internal variability is not captured in most CMIP5 models, as poor resolution prevents reproduction of AMV teleconnection responses (Vellinga et al., 2016), and the magnitude of AMV-related SST variation may be underestimated in CMIP5 (Section 3.7.7, which also assesses that the AMV may be partially forced). The influence of PDV has been studied to a lesser extent, with the PDV positive phase having a negative impact on Sahel rainfall in combined observational/CMIP5 analysis (Villamayor and Mohino, 2015). The closer match between the observed rainfall declining trend and those in an atmosphere-only SMILE, in which SSTs are matched to observations, compared to three coupled SMILEs in which they are not, suggests that the underlying ocean surface might be essential in driving the decline (Figure 10.11e).

In terms of anthropogenic emissions, regional aerosol emissions from Europe, and to a lesser extent from Asia, have been shown in a global model to weaken Sahel precipitation either through a weakened Saharan heat low or via the Walker circulation (Dong et al., 2014). Greenhouse gases (GHGs) and anthropogenic aerosol can be considered together to control ITCZ position based on temperature asymmetry at the hemispheric scale. GHGs increase Sahel precipitation, while aerosol reduces it (in coupled slab-ocean model experiments by Ackerley et al., 2011 following Biasutti and Giannini, 2006). This effect is stronger when models account for aerosol-cloud interactions (Allen et al., 2015). Perturbed physics GCM ensembles suggests that aerosol emissions were the main driver of observed drying over 1950–1980 (Ackerley et al., 2011), supported by CMIP5 single-forcing experiments (Polson et al., 2014). A coherent drying signal in CMIP5 over the extended 1901–2010 period has also been found, although smaller than the observed trend (Knutson and Zeng, 2018). By applying aerosol scaling factors to the historical period in order to sample the uncertainty in CMIP5 aerosol radiative forcing, Shonk et al. (2020) found differences of 0.5 mm day^{-1} for Gulf of Guinea rainfall between strong and weak aerosol experiments as illustrated in Figure 10.11c, although the drying appears further south than observed due to model bias.

For the partial recovery in West African monsoon and Sahel rainfall since the late 1980s, a detection study using three reanalyses (Cook and Vizy, 2015) shows a connection to increasing Saharan temperatures at a rate 2–4 times greater than the tropical mean, also confirmed by multiple observational and satellite-based data (Zhou and Wang, 2016; Vizy and Cook, 2017) and the review of Cook and Vizy (2019). Reanalyses are also noted to significantly underestimate the Saharan warming (Zhou and Wang, 2016). Saharan warming causes a stronger thermal low and more intense monsoon flow, providing more moisture to the central and eastern Sahel, supported by CMIP5 models (Lavaysse et al., 2016), although not all models capture the observed rainfall/heat low relationship. Sahel rainfall is also incorrectly located in prototype versions of a few CMIP6 models, related to tropospheric temperature biases (Martin et al., 2017). Amplified Saharan warming has increased the wind shear, leading to a tripling of extreme storms since 1982, which may partially explain the recovery (Taylor et al., 2017). Instead, observations, multiple models and SST-sensitivity experiments with atmospheric GCMs have suggested that stronger Mediterranean Sea evaporation enhances low-level moisture convergence to the Sahel, increasing rainfall (Park et al., 2016). Meanwhile, an atmospheric GCM study suggested that GHGs alone (in the absence of SST warming) could cause Sahel rainfall recovery, with an additional role for anthropogenic aerosol (Dong and Sutton, 2015); recent changes in North Atlantic SSTs, although substantial, did not exert a significant impact on the recovery. Large spread in the recovery in a five-member atmospheric GCM ensemble suggests that atmospheric internal variability cannot be discounted (Roehrig et al., 2013).

Consistent timing of the southward ITCZ shift during the decline period in CMIP3 and CMIP5 historical simulations supports the role of external forcing, chiefly anthropogenic aerosol (Hwang et al., 2013). The evolution of the observed decline and recovery is largely followed by the CMIP5 multi-model mean, further supporting the role of external drivers (Giannini and Kaplan, 2019). Updated results from CMIP6 for historical simulations with all and single forcings are represented in Figure 10.11d,e, showing smaller trends

ACCEPTED VERSION SUBJECT TO FINAL EDITING

than those observed. Giannini and Kaplan (2019) attempted to unify the driving mechanisms for decline and recovery based on singular-value decomposition of observed and modelled SSTs. Since the 1950s, tropical warming arising from GHGs and North Atlantic cooling from aerosol led to regional stabilization, suppressing Sahel rainfall. The subsequent reduction in aerosol emissions then led to North Atlantic warming and recovery of Sahel rainfall. Such mechanisms continue into the near-term future in idealised and modified RCP experiments, with scenarios featuring more aggressive reductions in aerosol emissions, or including aerosol-cloud interactions, favouring a greater northward shift of rainfall (Allen, 2015; Westervelt et al., 2017, 2018; Scannell et al., 2019). There is paleoclimate evidence of changes to Sahel rainfall in the past, in particular with enhancement of the West African monsoon during the mid-Holocene. However, the mechanisms governing such a change have been shown to be largely dynamical in nature (D'Agostino et al., 2019), suggesting that the mid-Holocene cannot be used to inform the credibility of changes due to greenhouse warming.

There is *very high confidence* (*robust evidence* and *high agreement*) that patterns of 20th-century ocean and land surface temperature variability have caused the Sahel drought and subsequent recovery by adjusting meridional gradients. There is *high confidence* (*robust evidence* and *medium agreement*) that the changing temperature gradients that perturb the West African monsoon and Sahel rainfall are themselves driven by anthropogenic emissions: warming by GHG emissions was initially restricted to the tropics but suppressed in the North Atlantic due to nearby emissions of sulphate aerosols, leading to a reduction in rainfall. The North Atlantic subsequently warmed following the reduction of aerosol emissions, leading to rainfall recovery.

10.4.2.2 The southeastern South America summer wetting

A positive trend in summer (December to February) precipitation has been detected in multiple observational sources in southeastern South America since the beginning of the 20th century (Gonzalez et al., 2013; Vera and Díaz, 2015; Wu et al., 2016; Zhang et al., 2016; Díaz and Vera, 2017; Saurral et al., 2017). Sedimentary records from the Mar Chiquita lake indicate that the last quarter of the 20th century was wetter than any period during the last 200 years (Piovano et al., 2004). In this attribution example the drivers contributing to the positive trend for the period 1951–2014 are discussed (Figure 10.12a). Precipitation anomalies of CRU TS as well as for the two members of a SMILE with the most negative and positive trends for 1951–2014 are displayed in Figure 10.12b. The trend for 1951–2014 using CRU TS and GPCC is illustrated in Figure 10.12c, and for the region defined by the black quadrilateral, it amounts to 2.8 (CRU TS) – 3.5 (GPCC) mm per month and decade (see black crosses in Figure 10.12d) while the mean summer monthly precipitation for the same period is 104 (CRU TS) –109 (GPCC) mm. The trend is also detectable in daily and monthly extremes (Re and Barros, 2009; Marengo et al., 2010; Penalba and Robledo, 2010; Doyle et al., 2012; Donat et al., 2013; Lorenz et al., 2016).

[START FIGURE 10.12 HERE]

Figure 10.12: Southeastern South America positive mean precipitation trend and its drivers during 1951–2014. (a) Mechanisms that have been suggested to contribute to southeastern South America summer wetting. (b) Time series of austral summer (December to February) precipitation anomalies (%, baseline 1995–2014) over the south-eastern South American region (26.25°S–38.75°S, 56.25°W–66.25°W), black quadrilateral in the first map of panel (c). Black, brown and green lines show low-pass filtered time series for CRU TS, and the members with driest and wettest trends of the MPI-ESM SMILE (between 1951–2014), respectively. The filter is the same as the one used in Figure 10.10. (c) Mean austral summer precipitation spatial linear 1951–2014 trends (mm per month and decade) from CRU TS and GPCC. Trends are estimated using ordinary least squares regression. (d) Distribution of precipitation 1951–2014 trends over southeastern South America from GPCC and CRU TS (black crosses), CMIP6 all-forcing historical (red circles) and MIROC6, CSIRO-Mk3-6-0, MPI-ESM and d4PDF SMILEs (grey box-and-whisker plots). Grey squares refer to ensemble mean trends of their respective SMILE and the red circle refers to the CMIP6 multi-model mean. Box-and-whisker plots follow the methodology used in Figure 10.6. Further details on data sources and processing are available in the chapter data table (Table 10.SM.11).

ACCEPTED VERSION SUBJECT TO FINAL EDITING

[END FIGURE 10.12 HERE]

The influence of SST anomalies on southeastern South America precipitation have been studied extensively on interannual to multi-decadal time scales (Paegle and Mo, 2002). The positive phase of El Niño Southern Oscillation (ENSO; Annex AIV.2.3) is related to stronger mean and extreme rainfall over south-eastern South America (Ropelewski and Halpert, 1987; Grimm and Tedeschi, 2009; Robledo et al., 2016). The ENSO influence may be modulated by the PDV (Kayano and Andreoli, 2007; Fernandes and Rodrigues, 2018) and the AMV (Kayano and Capistrano, 2014). PDV and AMV also influence the southeastern South American climate independently of ENSO (Barreiro et al., 2014; Grimm and Saboia, 2015; Robledo et al., 2019). While Pacific SSTs dominate the overall influence of oceanic variability in the region, the Atlantic variability seems to dominate on multi-decadal time scales and has been proposed as a driver for the long-term positive trend (Seager et al., 2010; Barreiro et al., 2014). Based on experiments designed to test how southeastern South America precipitation is modulated by tropical Atlantic SSTs, Seager et al. (2010) showed that cold anomalies in the tropical Atlantic favour wetter conditions by inducing an upper-tropospheric flow towards the equator, which, via advection of vorticity, leads to ascending motion over southeastern South America (Figure 10.12a). Monerie et al. (2019) supported this argument showing a negative relationship between southeastern South America precipitation and the AMV index (Huang et al., 2015) using an atmospheric GCM coupled to an ocean mixed layer model with nudged SSTs.

The positive trend of precipitation has also been attributed to anthropogenic GHG emissions and stratospheric ozone depletion. CMIP5 models only show a positive trend when including anthropogenic forcings (Vera and Díaz, 2015). These results were supported by Knutson and Zeng (2018) based on univariate detection/attribution analysis of annual-mean trends for the 1901–2010 and 1951–2010 periods. However, the main features of summer mean precipitation and variability of South America are still not well represented in all CMIP5 and CMIP6 models (Gulizia and Camilloni, 2015; Díaz and Vera, 2017; Díaz et al., 2020). This motivates the construction of ensembles that exclude the worst performing models (Section 10.3.3.4). The construction of ensembles of CMIP5 historical simulations with realistic representation of precipitation anomalies with opposite sign over southeastern South America and eastern Brazil showed that the trend since the 1950s could be related to changes in precipitation characteristics only when simulations included anthropogenic forcings (Díaz and Vera, 2017). GHG emissions have been related to increased precipitation in southeastern South America through three different mechanisms (Figure 10.12a). First, GHG warming induces a non-zonally uniform pattern of SST warming that includes a warming pattern over the Indian and Pacific Oceans that excites wave responses over South America (Junquas et al., 2013). Zonally uniform SST patterns of warming alone lead to precipitation signals opposite to those observed in an atmospheric GCM (Junquas et al., 2013). Second, GHG radiative forcing drives an expansion of the Hadley cell so that its descending branch moves poleward from the region, generating anomalous ascending motion and precipitation (Zhang et al., 2016b; Saurral et al., 2019). The third mechanism by which increased GHG can contribute to increased precipitation in the region is through a delay of the stratospheric polar vortex breakdown. As depicted in Figure 10.12a, both stratospheric ozone depletion and increased GHGs have contributed to the later breakdown of the polar vortex in recent decades (Ceppi and Shepherd, 2019; McLandress et al., 2010; Wu and Polvani, 2017). Mindlin et al. (2020) developed future atmospheric circulation storylines (Section 10.3.4.2, Box 10.2) for Southern Hemisphere mid-latitudes with the CMIP5 models and found that for southeastern South America summer precipitation, increases are related to the late springtime breakdown of the stratospheric polar vortex. The connecting mechanism is through a lagged southward shift of the jet stream (Saggioro and Shepherd, 2019), which enhances cyclonic activity over the region (Wu and Polvani, 2017).

A common feature among the above discussed studies is that even if GCMs simulate positive trends when forced with GHG and/or stratospheric ozone, these trends are in general smaller than those observed (e.g., CMIP6 trends in red open circles in Figure 10.12d). Díaz et al. (2020) showed that to capture the observed trend a multi-model ensemble of SMILEs is needed. Out of the 12 large ensembles examined (with ensemble size varying in the 16–100 range), only seven simulated the observed trend within their range. This could partly be explained by model biases in mean precipitation and its interannual variability. In the sub-ensemble

ACCEPTED VERSION SUBJECT TO FINAL EDITING

of six models that reproduce reasonably well the observed spatial patterns of mean precipitation and interannual variability, the ensemble mean spread is lower, and the forced response, taken as the multi-model ensemble mean, is slightly more positive than that of the six poorly performing models. The signal to noise ratio, estimated as the ratio of the forced response to the spread due to internal variability, is also slightly higher for the best-performing models, suggesting that selecting the best-performing models may have an influence on both attribution of the observed trend and emergence of the forced response in future (Section 10.4.3).

There is *high confidence* that southeastern South America summer precipitation has increased since the beginning of the 20th century. Since AR5, science has advanced in the identification of the drivers of the precipitation increase in southeastern South America since 1950, including GHG through various mechanisms, stratospheric ozone depletion and Pacific and Atlantic variability. There is *high confidence* that anthropogenic forcing has contributed to the southeastern South America summer precipitation increase since 1950, but *very low confidence* on the relative contribution of each driver to the precipitation increase.

10.4.2.3 The southwestern North America drought

Persistent hydroclimatic drought in southwestern North America remains a much-studied event. Drought is a regular feature of the southwestern North America's climate regime, as can be seen in both the modern record, and through paleoclimate reconstructions (Cook et al., 2010; Woodhouse et al., 2010; Williams et al., 2020), as well as in future climate model projections (Cook et al., 2015a). Since the early 1980s, which were relatively wet in terms of precipitation and streamflow, the region has experienced major multiyear droughts such as the turn-of-the-century drought that lasted from 1999 to 2005, and the most recent and extreme 2012–2014 drought that in certain locations is perhaps unprecedented in the last millennium (Griffin and Anchukaitis, 2014; Robeson, 2015; Section 8.3.1.6). Shorter dry spells also happened between these multiyear droughts making 1980 to present a period with an exceptionally steep trend from wet to dry (Figure 10.13a), leading to strong declines in Rio Grande and Colorado river flows (Lehner et al., 2017b; Udall and Overpeck, 2017). While robust attribution of this trend is complicated by the large natural variability in this region, the 20th century warming has been suggested to increase the chances for hydrological drought periods by lowering runoff efficiency (Woodhouse et al., 2016; Lehner et al., 2017b; Woodhouse and Pederson, 2018) and affecting evapotranspiration (Williams et al., 2020). There is some evidence suggesting that the Last Glacial Maximum, a period of low atmospheric CO_2, ~21 ka ago, has a thermodynamically-driven zonal mean precipitation response similar to that of the current state with relatively high CO_2 levels when compared with the pre-industrial period. Pluvial conditions at that time and a reduction in precipitation from the Last Glacial Maximum to the pre-industrial period are consistent with drying trends for the region in models with GHG concentrations exceeding pre-industrial levels. However, the dominant large-scale drivers responsible for the precipitation changes observed during these two transitions are markedly different: mainly ice sheet retreat and increasing insolation on one hand, increasing GHGs on the other hand. This suggests that the Last Glacial Maximum correspondence is fortuitous which strongly limits its use to capture future hydrological cycle changes (Morrill et al., 2018; Lowry and Morrill, 2019; Section 8.3.2.4.4). Furthermore, the conclusion of the Last Glacial Maximum drying versus wetting seems to strongly depend on the physical property of interest, hydrologic or vegetation indicators (Scheff et al., 2017). Droughts are characterized by deficits in total soil moisture content that can be caused by a combination of decreasing precipitation and warming temperature, which promotes greater evapotranspiration. Regional-scale attribution of the prevalence of southwestern North America drought since 1980 then mostly focuses on the attribution of change in these two variables.

The observed southwestern North America drying fits the narrative of what might happen in response to increasing GHG concentrations due to a poleward expansion of the subtropics, that is conducive to drying trends over subtropical to mid-latitude regions (Hu et al., 2013b; Birner et al., 2014; Lucas et al., 2014). However, several studies based on modern reanalyses and CMIP5 models have recently shown that the current contribution of GHGs to Northern Hemisphere tropical expansion is much smaller than in the Southern Hemisphere and will remain difficult to detect due to large internal variability, even by the end of the 21st century (Section 3.3.3.1; Garfinkel et al., 2015; Allen and Kovilakam, 2017; Grise et al., 2018,

ACCEPTED VERSION SUBJECT TO FINAL EDITING

2019). In addition, the widening of the Northern Hemisphere tropical belt exhibits strong seasonality and zonal asymmetry, particularly in autumn and the North Atlantic (Amaya et al., 2018; Grise et al., 2018). Therefore, it seems that the recent Northern Hemisphere tropical expansion results from the interplay of internal and forced modes of tropical width variations and that the forced response has not robustly emerged from internal variability (Section 3.3.3.1; Section 10.4.3).

A second possible causal factor is the role for ocean-forced or internal atmospheric circulation change. Analysis of observed and CMIP5-simulated precipitation indicates that the drought prevalence since 1980 is linked to natural, internal variability in the climate system (Knutson and Zeng, 2018). Based on observations and ensembles of SST-driven atmospheric simulations, Seager and Hoerling (2014) suggested that robust tropical Pacific and tropical North Atlantic forcing drove an important fraction of annual mean precipitation and soil moisture changes and that early 21st century multiyear droughts could be attributed to natural decadal swings in tropical Pacific and North Atlantic SSTs. A cold state of the tropical Pacific would lead by well-established atmospheric teleconnections to anomalous high pressure across the North Pacific and southern North America, favouring a weaker jet stream and a diversion of the Pacific storm track away from the southwest (Delworth et al., 2015; Seager and Ting, 2017). The multiyear drought of 2012–2016 has been linked to the multiyear persistence of anomalously high atmospheric pressure over the north-eastern Pacific Ocean, which deflected the Pacific storm track northward and suppressed regional precipitation during California's rainy season (Swain et al., 2017). Going into more detail, Prein et al. (2016) used an assessment of changing occurrence of weather regimes to judge that changes in the frequency of certain regimes during 1979–2014 have led to a decline in precipitation by about 25%, chiefly related to the prevalence of anticyclonic circulation patterns in the northeast Pacific. Finally, the moderate model performance in representing Pacific SST decadal variability and its remote influence (Section 3.7.6) as well as its change under warming may affect attribution results of observed and future precipitation changes (Seager et al., 2019).

It has also been suggested that the ocean-controlled influence is limited and internal atmospheric variability has to be invoked to fully explain the observed history of drought on decadal time scales (Seager and Hoerling, 2014; Seager and Ting, 2017). From roughly 1980 to the present, the regional climate signals show an interesting mix between forced and internal variability. Lehner et al. (2018) used a dynamical adjustment method and large ensembles of coupled and SST-forced atmospheric experiments to suggest that the observed southwestern North America rainfall decline mainly results from the effects of atmospheric internal variability, which is in part driven by a PDV-related phase shift in Pacific SST around 2000 (Figure 10.13b, c). Based upon four SMILEs (three using a coupled GCM and another one an atmospheric GCM constrained by observed SSTs) and a CMIP6 multi-model suite constrained by observed external forcings, Figure 10.13 shows, in agreement with Lehner et al. (2018), that observed SSTs with their associated atmospheric response are the main drivers of the southwestern North America precipitation decrease during the 1983–2014 period. Once aspects of the internal variability are removed by dynamical adjustment, the observed precipitation-change signal and simulated anthropogenically-forced components look more similar (Lehner et al., 2018).

[START FIGURE 10.13 HERE]

Figure 10.13: Attribution of the southwestern North America precipitation decline during the 1983–2014 period. (a) Water year (October to September) precipitation spatial linear trend (in percent per decade) over North America from 1983 to 2014. Trends are estimated using ordinary least squares. Top row: Observed trends from CRU TS, REGEN, GPCC, and the Global Precipitation Climatology Project (GPCP). Middle row: Driest, mean and wettest trends (relative to the region enclosed in the black quadrilateral, bottom row) from the 100 members of the MPI-ESM coupled SMILE. Bottom row: Driest, mean and wettest trends relative to the above region from the 100 members of the d4PDF atmosphere-only SMILE. (b) Time series of water year precipitation anomalies (%, baseline 1971–2000) over the above south-western North America region for CRU TS (grey bar charts). Black, brown and green lines show low-pass filtered time series for CRU TS, driest and wettest members of the d4PDF SMILE, respectively. The filter is the same as the one used in Figure 10.10. (c) Distribution of south-western region-averaged water-year precipitation 1983–2014 trends (in percent per decade) for observations (CRU TS, REGEN, GPCC and

ACCEPTED VERSION SUBJECT TO FINAL EDITING

GPCP, black crosses), CMIP6 all-forcing historical simulations (red circles), the MIROC6, CSIRO-Mk3-6-0, MPI-ESM and d4PDF SMILEs (grey box-and-whisker plots). Grey squares refer to ensemble mean trends of their respective SMILE and the red circle refers to the CMIP6 multi-model mean. Box-and-whisker plots follow the methodology used in Figure 10.6. Further details on data sources and processing are available in the chapter data table (Table 10.SM.11).

[END FIGURE 10.13 HERE]

Importantly, as the AR6 assessment views the PDV as being mostly driven by internal variability (Section 3.7.6), the lines of evidence cited above suggest that the contribution of natural and anthropogenic forcings to the precipitation decline has a small amplitude. Unlike the precipitation deficit, the accompanying southwestern North America warming is driven primarily by anthropogenic forcing from GHGs rather than atmospheric circulation variability and may help to enhance the drought through increased evapotranspiration (Knutson et al., 2013; Diffenbaugh et al., 2015; Williams et al., 2015, 2020, Lehner et al., 2018, 2020).

To conclude, there is *high confidence* (*robust evidence* and *medium agreement*) that most (>50%) of the anomalous atmospheric circulation that caused the southwestern North America negative precipitation trend can be attributed to teleconnections arising from tropical Pacific SST variations related to PDV. There is *high confidence* (*robust evidence* and *medium agreement*) that anthropogenic forcing has made a substantial contribution (~50%) to the southwestern North America warming since 1980.

10.4.2.4 Assessment summary

The robustness of regional-scale attribution differs strongly between temperature and precipitation changes. While the influence of anthropogenic forcing on regional temperature long-term change has been detected and attributed in almost all land regions, a robust detection and attribution of human influence on regional precipitation change has not yet fully occurred for many land regions (Section 10.4.3). Although the contribution of anthropogenic forcing to long-term regional precipitation change has been detected in some regions, a robust quantification of the contributions of different drivers remains elusive. The delayed emergence of the anthropogenic precipitation fingerprint with respect to temperature is likely due to the opposing sign of the fast and slow land precipitation forced responses and time-dependent SST change patterns (Section 8.2.1, Section 10.4.3), stronger internal variability (Section 10.3.4.3) as well as larger observational uncertainty (Section 10.2) and impact of model biases. The contribution of internal variability to the observed changes can also be very sensitive to the period length and level of spatial aggregation for the region under scrutiny (Kumar et al., 2016; Cross-Chapter Box 3.1; Section 4.4.1). Finally, even in the case of temperature changes at multi-decadal time scale, internal variability can still be a substantial driver of regional changes due to cancellation between different external forcings (Nath et al., 2018).

To conclude, it is *virtually certain* (*robust evidence* and *high agreement*) that anthropogenic forcing has been a major driver of temperature change since 1950 in many sub-continental regions of the world. There is *high confidence* (*high evidence* and *medium agreement*) that anthropogenic forcing has contributed to multi-decadal mean precipitation changes in several regions such as for example West Africa, southeast South America, southwestern Australia, northern Central Eurasia, South and East Asia. However, at regional scale, the role of internal variability is stronger while uncertainties in observations, models and external forcing are all larger than at the global scale, precluding a robust assessment of the magnitude of the relative contributions of greenhouse gases, including stratospheric ozone, and different aerosol species.

10.4.3 Future Regional Changes: Robustness and Emergence of the Anthropogenic Signal

Regional climate projections are one key element of the multiple lines of evidence that are used for climate risk assessments as well as for adaptation and policy decisions at regional scales (Sections 10.3.3.9 and 10.5). Regional climate projections can be separated into two components: the regional-scale forced response

ACCEPTED VERSION SUBJECT TO FINAL EDITING

or regional-scale climate sensitivity when normalized by the global mean temperature change (Seneviratne and Hauser, 2020) and the climate internal variability characterizing the future period or global warming level under scrutiny. This section assesses a few methodological aspects related to robustness and emergence properties of the regional-scale forced response as well as the possible influence of internal variability on the emergence of the anthropogenic signal.

10.4.3.1 Robustness of the anthropogenic signal at regional scale

Standard methodologies to derive the regional forced response include pattern scaling and the time-shift or epoch approach (Tebaldi and Arblaster, 2014; Vautard et al., 2014; Herger et al., 2015; Tebaldi and Knutti, 2018; Christensen et al., 2019; Section 4.2.4). Pattern scaling assumes that the spatial patterns of regional change, often based on a time-averaged 20 or 30-year period at the end of the 21st century, are roughly constant in time, and simply scale linearly with global mean warming. The time-shift approach defines a target in terms of global warming level (GWL) and locates the time segment, usually 20 or 30 years, in historical or scenario simulations in which global mean warming matches the required GWL (Section 10.1.2; Cross-Chapter Box 11.1). Physical consistency between multiple variables and space-time covariance are fully preserved in the time-shift approach, which is not the case for pattern-scaling (Herger et al., 2015). Importantly, pattern scaling cannot account for the non-linearity arising from either interacting quasi-linear processes (Chadwick and Good, 2013) and purely nonlinear mechanisms, which have been shown to be present in CMIP5 models for high GWL (4°C) and affect precipitation more than temperature at the regional-scale (Good et al., 2015, 2016; Section 8.5.3.1). The time-shift approach can also be used to test whether regional climate change patterns depend on the rate of global mean warming and external forcing pathways, in addition to global warming magnitude. A global evaluation of both approaches in projecting the forced temperature and precipitation response for a highly mitigated scenario based on a moderately mitigated one has been performed using a perfect-model framework (Tebaldi and Knutti, 2018). The amplitude of errors for both approaches appears to be substantially smaller than model uncertainty approximated by the CMIP5 multi-model spread.

Based on large and coordinated modelling exercises such as CMIP5 and CORDEX, the time-shift approach has been largely used to assess differences in regional climate impacts for different GWLs, with a strong focus on 1.5°C versus 2°C (Karmalkar and Bradley, 2017; Dosio and Fischer, 2018; Karnauskas et al., 2018; Liu et al., 2018; Taylor et al., 2018; Weber et al., 2018; Chapter 3, SR1.5, IPCC 2018). Comparisons between pattern scaling and time-shift approaches allow assessment of the scalability of the regional climate change signal and the extent to which pattern scaling assumptions still hold at regional scale for a wide range of GWL. This was the approach followed by Matte et al. (2019) in their assessment of the scalability of European regional climate projections. Based on EURO-CORDEX projections, they performed a detailed comparison between the pattern scaling and the GWL spatial patterns (GWL range: 1°C, 2°C and 3°C) for different seasons, regional model resolutions, and both temperature and precipitation. High pattern correlation values (greater than 0.9) are found between the scaled pattern and all GWL patterns for temperature. In the case of precipitation, the correspondence is slightly lower, especially in summer, for high GWLs (2°C and 3°C) and much lower for 1°C.

Figure 10.14 illustrates a similar comparison based on the CMIP6 multi-model ensemble forced with the scenario SSP5-8.5 and applied to two large-scale continental areas. The forced response to anthropogenic forcing is simply taken as the CMIP6 multi-model mean of future regional climate change relative to the 1850–1900 reference period. Robustness of the forced response is based on both significance of the change and model agreement about the sign of change (Cross-Chapter Box Atlas.1; Figure 10.14). Caution has to be exercised against a too literal interpretation of lack of robust change given that significance and sign agreement can be sensitive to spatial and temporal aggregation (Cross-Chapter Box Atlas.1, Figure 2) and lack of a robust change does not necessarily translate to lack of regional-scale climate change impacts (McSweeney and Jones, 2013; Hibino and Takayabu, 2016).

[START FIGURE 10.14 HERE]

ACCEPTED VERSION SUBJECT TO FINAL EDITING

Figure 10.14: Robustness and scalability of anthropogenic signals at regional scale. (a) Spatial patterns of Europe and Africa summer (June to August) surface air temperature change (in °C °C^{-1}) from the CMIP6 multi-model mean (45 models, one member per model, historical simulations and scenario SSP5-8.5) at different global warming levels (GWLs) and the end-21st century scaling pattern estimated from the multi-model mean difference between 2081–2100 and the pre-industrial period (1850–1900) divided by the corresponding global mean warming. The scale of all GWL patterns has been adjusted to a global mean warming of 1°C (for example, the resulting 3°C spatial pattern has been divided by three). The scales of the GWL patterns have to be multiplied by their threshold values to obtain the actual simulated warming. The metrics shown in the bottom left corner of the GWL pattern plots indicate the spatial pattern correlation and the root-mean square difference between the GWL patterns and the scaling pattern. The number in bold just above the metrics gives the number of used CMIP6 models (out of 45) that have reached the GWL threshold. Areas with robust change (at least 66% of the models have a signal to noise ratio greater than one and 80% or more of the models agree on the sign of the change) are coloured with no pattern overlaid (Cross-Chapter Box Atlas.1). Areas with a significant change (at least 66% of the models have a signal to noise ratio greater than one) and lack of model agreement (meaning that less than 80% of the models agree on the sign of the change) are marked by cross-hatching. Areas with no change or no robust change (less than 66% of the models have a signal to noise ratio greater than one) are marked by negatively sloped hatching. (b) Same as (a) but for North, Central and South America annual mean precipitation relative change (percent °C^{-1}). The baseline for precipitation climatology is 1850–1900. Further details on data sources and processing are available in the chapter data table (Table 10.SM.11).

[END FIGURE 10.14 HERE]

If projected regional mean temperature (Figure 10.14a) and precipitation (Figure 10.14b) changes were to scale linearly with global mean warming, the adjusted spatial patterns would be congruent with each other at different GWLs. While pattern scaling seems to be a reasonable first-order approximation for both temperature and precipitation changes in tropical and high latitude regions (high pattern correlation values), there are a number of regions exhibiting substantial amplitude differences at different GWLs (Northern Africa and Middle East, southern and eastern Europe for temperature; southwestern North America, Chile and north-eastern Brazil for precipitation). These differences hint at the possible influence of nonlinear mechanisms (Good et al., 2015), including soil moisture feedbacks (Seneviratne et al., 2010; Vogel et al., 2017), a time-dependent balance between the different contributions of fast and slow response to greenhouse gas forcing as well as changing SST response patterns (Long et al., 2014; Good et al., 2016; Ceppi et al., 2018; Zappa et al., 2020). Decreasing spatial pattern amplitude with increasing GWL suggests that the initial transient regional response overshoots the long-term change in regions such as northern Africa for summer temperature and southwestern South America for precipitation (Zappa et al., 2020). In the latter region, long simulations with stabilized GHG concentrations even suggest a change of sign when near-equilibrium is reached (Sniderman et al., 2019). The reverse behaviour, increasing pattern amplitude with increasing GWL, is seen for summer temperature in southern and eastern Europe and for precipitation in southwestern North America (Sniderman et al., 2019; Zappa et al., 2020), suggesting that, in these regions, the initial transient response is lagging global mean warming and final regional climate change will be reached once GHG concentrations are stabilized.

There is *high confidence* that the time-evolving contribution of different mechanisms operating at different time scales can modify the amplitude of the regional-scale response of temperature, and both the amplitude and sign of the regional-scale response of precipitation, to anthropogenic forcing. These mechanisms include non-linear temperature, precipitation and soil moisture feedbacks, and slow and fast response of SST patterns and atmospheric circulation changes to increasing GHGs.

10.4.3.2 Emergence of the anthropogenic signal at regional scale

This section provides an assessment of the different approaches used in emergence studies as well as sensitivities to methodological choices. The section then focuses on the possible influence of internal

ACCEPTED VERSION SUBJECT TO FINAL EDITING

variability on future emergence of the simulated mean precipitation anthropogenic signal at regional scales with some illustrative examples.

In climate science, emergence or distinguishability of a signal refers to the appearance of a persistent change in the probability distribution and/or temporal properties of a climate variable compared with that of a reference period (Giorgi and Bi, 2009; Mahlstein et al., 2011, 2012; Hawkins and Sutton, 2012; Section 1.4.2). Similar to anthropogenic climate change detection (Cross-Working Group Box: Attribution (in Chapter 1)), signal emergence can be detected, at least initially, without identifying the physical causes of the emergence (Section 1.4.2). In the context of human influence on climate, the objective of emergence studies is the search for the appearance of a signal characterizing an anthropogenically-forced change relatively to the climate variability of a reference period, defined as the noise.

Precise definitions of signal and noise as well as a metric to measure the relative importance of the signal are key ingredients of the emergence framework and depend on the framing question. In particular, emergence study results can depend on the specific definitions of signal and noise such as the level of spatial and temporal aggregation (McSweeney and Jones, 2013). For instance, grid-point scale emergence will likely be delayed compared with region-average emergence (Fischer et al., 2013; Maraun, 2013; Lehner et al., 2017a; Section 11.2.4; Cross-Chapter Box Atlas.1, Figure 2). The signal is often estimated by a running mean multi-decadal average or probability distribution function of the physical variable under scrutiny in order to avoid false emergence due to manifestation of multi-decadal internal variability (King et al., 2015). In the case of extremes such as climate records, a notion of multi-year persistence or recurrence can also be used to fully characterize the anthropogenic signal and its emergence (Christiansen, 2013; Bador et al., 2016).

Emergence is also sensitive to the noise characteristics: assuming a common signal definition, larger signal-to-noise values and earlier emergence will arise if the noise is based on decadal mean variability rather than interannual variability (Kusunoki et al., 2020). Depending on the framing question, the noise can include or omit external natural forcing such as volcanic and solar forcing (Zhang and Delworth, 2018; Silvy et al., 2020). Furthermore, emergence results are very sensitive to the choice and length of the reference period (Section 1.4.1). The reference period can be the pre-industrial, the very recent past or even a time-evolving baseline, depending on both the framing and assumption that adaptation to the current climate has already occurred (King et al., 2015; Zhang and Delworth, 2018; Brouillet and Joussaume, 2020). These choices will then determine the type of simulations and periods that will be used to construct the noise distribution. Finally, the permanence of future emergence cannot be taken for granted when emergence occurs in the late-21st century based on simulations ending in 2100 (Hawkins et al., 2014; King et al., 2015; Lehner et al., 2017a).

Robust assessments and comparisons of past emergence between observations and models are strengthened by the use of consistent definitions of signal and noise (Lehner et al., 2017a; Hawkins et al., 2020). In the case of future emergence under increasing greenhouse gas emissions, two main approaches have been followed to assess emergence. The first is based on estimating the signal and noise (and sometimes the signal-to-noise ratio as well) in individual models before using the resulting distribution median or mean to construct the final emergence metric (Hawkins and Sutton, 2012; Maraun, 2013b; Sui et al., 2014; Barrow and Sauchyn, 2019). The second method first estimates the signal as a multi-model mean change and the noise variance as a combination of internal variability and model structural differences (Giorgi and Bi, 2009; Mariotti et al., 2015; Nguyen et al., 2018). The first approach allows the definition of emergence of the signal relative to internal variability only and treats model error as source of uncertainty (Maraun, 2013b; Lehner et al., 2017a). The second assumes that the multi-model mean is the optimal estimate of the signal and confounds internal variability and model structural differences in the noise estimate. It is noteworthy that most emergence studies implicitly assume model independence (Annan and Hargreaves, 2017; Boé, 2018; Box 4.1) and therefore sensitivity of emergence results to model selection or weighting is rarely performed (Akhter et al., 2018).

Metrics can vary from a simple signal-to-noise ratio to statistical distributional tests (King et al., 2015; Gaetani et al., 2020) and give median estimates and uncertainty bounds for the date (or time of emergence) corresponding to the exceedance of specific thresholds by the emergence metric. Reconciling future

ACCEPTED VERSION SUBJECT TO FINAL EDITING

emergence results among different studies is challenging due to their many methodological differences including the choice of the reference period, the selected climate models and scenario, the precise definition of signal and noise and the choice of different signal-to-noise thresholds to characterize robust emergence. Contrasting with binary yes/no statements, emergence can also be viewed as a continuous process characterized by an amplitude or level, for example the value of the signal-to-noise ratio, that is a function of time or global warming level.

Since AR5, the development and production of SMILEs (Sections 4.2.5 and 10.3.4.3) has allowed the assessment of the influence of internal variability on anthropogenic signal emergence. The influence of internal variability, and specifically of the unforced atmospheric circulation, on temperature signal emergence can delay or advance the time of emergence by a decade or two in mid-to-high latitude regions (Lehner et al., 2017a; Koenigk et al., 2020). Internal variability can also result in small or decreasing decadal to multi-decadal heatwave frequency trends under the historical anthropogenic forcing over most regions, thereby delaying emergence of unprecedented heatwave frequency trends relative to the pre-industrial trend distribution (Perkins-Kirkpatrick et al., 2017; Sections 11.2–3).

Regional precipitation future changes are much more impacted by internal variability than their temperature counterpart (Monerie et al., 2017b; Singh and AchutaRao, 2018; Dai and Bloecker, 2019; von Trentini et al., 2019; Koenigk et al., 2020). Relative to mean temperature changes, this larger influence of internal variability on mean precipitation changes contributes, among other factors (Sarojini et al., 2016), to a much delayed emergence of the forced precipitation response in observations (Hawkins et al., 2020). Based on the CMIP6 multi-model ensemble forced with the scenario SSP5-8.5, we assess the future emergence of mean precipitation forced change as a function of GWLs for all AR6 land regions (Figure 10.15a). The methodology is a straightforward adaptation of the standard approach (Hawkins and Sutton, 2012). While the standard method is only based on the signal-to-noise ratio exceedance of a specified threshold (taken as one), the approach used here assumes that grid-point emergence occurs when the forced change is considered robust following the AR6 WGI1 definition of robustness for projected changes (Cross-Chapter Box Atlas.1). At a GWL of 1°C, emergence only occurs in high-latitude regions (Wan et al., 2015; Guo et al., 2019b), albeit with only small (less than 30%) area fraction with robust change. Robust changes in tropical and subtropical regions only appear from GWLs of 1.5°C, for example in southwest South America (Boisier et al., 2016), western Africa (Hawkins et al., 2020; Section 10.4.2.1) and southern Australia (Delworth and Zeng, 2014). Substantial (taken here simply as area fraction greater than 50%) emergence only occurs in some tropical, subtropical and midlatitude regions when high GWLs (3°C–4°C) are reached. Importantly, even at these high GWL values, there are still a large number of these regions with robust changes covering less than 50% of their area. In contrast, most high-latitude regions have an area fraction with robust changes greater than 80% at GWLs of 3°C and above.

[START FIGURE 10.15 HERE]

Figure 10.15: Future emergence of anthropogenic signal at regional scale. (a) Percentage area of land regions with robust annual mean precipitation change as a function of increasing GWLs. Robustness of the precipitation change is first estimated at each grid-point followed by the estimation of the AR6 region area with robust changes. For each CMIP6 model considered (45 models, one member per model, historical simulations and scenario SSP5-8.5), the annual mean precipitation change is based on the difference between a 20-year average centred on the GWL crossing year and the mean precipitation during the pre-industrial period (1850–1900) taken as a reference. Robustness of the change is acted when at least 66% of the models (30 out of 45) have a signal to noise ratio greater than one and at least 80% of them (36 out of 45) agree on the sign of change. The signal to noise ratio is estimated for each model from the ratio between the change and the standard deviation of non-overlapping 20-year means of the corresponding pre-industrial simulation (scaled by square root of 2 times 1.645). (b) Time evolution of the percentage area of land region with robust annual mean precipitation change for five AR6 land regions. Thick solid lines represent precipitation changes based on the same CMIP6 ensemble as in (a). Thin solid, dotted and dashed lines represent changes based on the three coupled SMILEs used in Chapter 10, illustrating the influence of internal variability on the emergence of robust change. The change is estimated from the difference between all consecutive 20-year periods from 1900–1919 up to 2081–2100

ACCEPTED VERSION SUBJECT TO FINAL EDITING

and the pre-industrial period. The line colour indicates the sign of the robust change given by the multi-model mean (CMIP6) or ensemble mean (SMILE) change: brown (decreasing precipitation) and dark green (increasing precipitation). Further details on data sources and processing are available in the chapter data table (Table 10.SM.11).

[END FIGURE 10.15 HERE]

We now illustrate the potential influence of internal variability on late or lack of emergence for a few AR6 land regions (Figure 10.15b). For each of these AR6 regions, the time evolution of the percentage area with robust annual mean precipitation change is estimated for both the CMIP6 multi-model ensemble and the three coupled SMILEs used throughout Chapter 10. Similarity in percentage area time evolution between CMIP6 and the three coupled SMILEs suggests that internal variability can substantially influence the timing of emergence. For example, internal variability could explain the mid-21st century emergence (percentage area greater than 50%) of the drying and wetting signal over the Mediterranean and South Asia (see also Section 10.6.3) regions, respectively. Internal variability can also contribute to the late and moderate emergence over southeast South America (see also Section 10.4.2) and western South Africa (see also Section 10.6.2). In contrast, it cannot explain the lack of robust changes (percentage area less than 30%) over western Africa at the end of the 21st century, suggesting that model differences are also contributing to the lack of emergence (Monerie et al., 2017b, 2017a). In addition to different forced signals, the differences of time evolution between the three SMILEs, in particular for African regions, point to the issue of global model performance in accurately representing internal variability and its future changes. While overestimation and underestimation of internal variability in current models have been reported (Eade et al., 2014; Laepple and Huybers, 2014), methodological challenges to assess the magnitude and spatial pattern of model biases in simulating internal variability, still remain (Section 10.3.4.3). Therefore, the existence of model biases and the limited knowledge of their characteristics lead to limitations about a precise quantification of internal variability influence on delayed regional-scale emergence.

There is *high confidence* that consistency in definitions of signal and noise, choice of the reference period and signal-to-noise threshold, is important to robustly assess the future emergence of anthropogenic signals across different types or generations of models, as well as comparing past emergence results between observations and models. There is *high confidence* that internal variability can delay the emergence of the regional-scale mean precipitation anthropogenic signal in many regions, mainly located in the tropics, subtropics and midlatitudes. An accurate estimation of the delay in regional-scale emergence caused by internal variability remains challenging due to global model biases in their representation of internal variability as well as methodological difficulties to precisely estimate these biases (*high confidence*).

10.5 Combining Approaches to Constructing Regional Climate Information

This section assesses approaches and challenges for producing climate information for climate risk assessments as well as for adaptation and policy decisions at regional scales (Section 10.1.2.1). An overview of the different sources used for developing regional climate information is given in Section 10.5.1. The role of the user context in the construction of climate information is assessed in Section 10.5.2. The distillation to combine multiple lines of evidence is assessed in Section 10.5.3. Finally, climate services in the context of regional climate information are assessed in Section 10.5.4. The role of storylines in constructing climate information is assessed in Box 10.2. The assessment of how regional climate information is distilled in the report is treated in Cross-Chapter Box 10.3, whereas the assessment of information on regional, physical climate processes that impact society or ecosystems, termed climatic impact-drivers (Section 10.1), appears in Chapter 12, as well as more information on climate services in Cross-Chapter Box 12.2.

The rise in demand for relevant regional climate information (Hewitt et al., 2012, 2020; Lourenço et al., 2016) has resulted in diverse approaches to produce it. Historically, the construction of climate information has been embedded in a linear supply chain: extracting the source data, processing into maps or derived data products, preparing the material for communication, and delivering to users (Section 10.1.4). Typical

ACCEPTED VERSION SUBJECT TO FINAL EDITING

products are open-access, web-portal delivery services of data (Hewitson et al., 2017), which may also be implemented as commercialised climate services (Webber and Donner, 2017). Such a chain, although it is intended to meet a demand for regional climate information, contains many assumptions that are not obvious to the recipients and that may introduce possible misunderstandings in the hand-over from one community to the next (Meinke et al., 2006; Lemos et al., 2012). In recognition that data is not necessarily relevant information, a new pathway towards a tailored distillation of climate information has emerged. The construction of information assessed in this section draws on multiple sources (Figure 10.16), whereby the context framing for an application is addressed through co-design with users. The constructed information is then translated into the context of the user taking into account the values of all actors involved (Figure 10.1 and Sections 10.5.2 and 10.5.3).

10.5.1 Sources of Regional Climate Information

[START FIGURE 10.16 HERE]

Figure 10.16: Illustration of how using different sources can result in different and potentially conflicting information. Change in daily precipitation (2071–2100 RCP8.5 relative to 1981–2010) over West Africa as simulated by an ensemble of GCM-driven RCMs. (a) Change in daily precipitation (mm) for April to September, as mean of 17 CORDEX models (Dosio et al., 2020) (b-e) Time-latitude diagram of daily precipitation change for four selected RCM-GCM combinations. For each month and latitude, model results are zonally averaged between 10°W–10°E (blue box in a). Different GCM-RCM combinations can produce substantially different and contrasting results, when the same RCM is used to downscale different GCMs (b, d), or the same GCM is downscaled by different RCMs (d, e). GCM1=IPSL-IPSL-CM5A, GCM2=ICHEC-EC-EARTH, RCM1=RCA4, RCM2=REMO2009. Adapted from (Dosio et al., 2020), CCBY4.0 https://creativecommons.org/licenses/by/4.0/. Further details on data sources and processing are available in the chapter data table (Table 10.SM.11).

[END FIGURE 10.16 HERE]

Regional climate information may be constructed from a diverse range of sources, each depending on different assumptions and affected by different methodological limitations (Sections 10.2, 10.3 and 10.4). The construction of information may lead to products for direct adoption by users, or intermediate products for further analysis by users and climate services agencies in collaboration with climate scientists. Widely used sources include:

- Extrapolation of observed historical trends into the future (e.g., Livezey et al., 2007; Laaha et al., 2016). Given that internal variability can affect regional trends significantly on decadal to multidecadal time scales (Section 10.4), this approach could be potentially misleading without other supporting evidence (Westra et al., 2010), or finding congruence with other changes (e.g., Langodan et al., 2020).
- The output from global climate models (GCMs, Section 10.3.1), including high-resolution GCMs, for which performance has been assessed and documented (Section 10.3.3). Model data can be used in its raw form or may be bias adjusted (Section 10.3.1 and Cross-Chapter Box 10.2) or weighted (Section 10.3.4 and Box 4.1).
- The output from dynamically (10.3.1.2) or statistically (10.3.1.3) downscaled GCM simulations for which performance has been assessed and documented as trustworthy (Section 10.3.3). Model data can be used in its raw form or may be bias adjusted, in the case of regional climate models (RCMs, Section 10.3.1).
- Process understanding about climate and the drivers of regional climate variability and change, grounded in theory about dynamics, thermodynamics and other physics of the climate system as a basis for process-based evaluation. For instance, teleconnections are useful to understand the links between large and regional scales at both near and long-term depending on the application. (Sections 10.1.3, 10.3.3, 10.4.1, 10.4.3 and Annex IV).
- Idealized scenarios of possible future climates as narratives to explore the implications and

ACCEPTED VERSION SUBJECT TO FINAL EDITING

consequences of such scenarios in the presence of uncertainty (Jack et al., 2021). This approach has been used to explore the response to geoengineering (Cao et al., 2016), as well as alternative scenarios where model projections are highly uncertain (Brown et al., 2016; Jack et al., 2021).

- Information directly from research reported in the peer-reviewed scientific literature (e.g, Sanderson et al., 2017) or related research reports such as communications to the UN Framework on Climate Change (UNFCCC) about national adaptation.
- Engaging with climate scientists and local communities who may provide indigenous information (Makondo and Thomas, 2018; Rosenzweig and Neofotis, 2013).
- Relevant information may also be drawn from paleoclimate studies (e.g., McGregor, 2018; Armstrong et al., 2020; Kiem et al., 2020) to support and contextualize other sources about more recent and projected changes.

Different sources of information may be more appropriate for some purposes than others, as they may provide information better aligned to the spatial and temporal scales of interest, in different formats, and tailored to different types of application. In some cases, a purpose may be best served using several types of information together. For example, when model data is the primary source, it can be advantageous to employ data from multiple models or even from a range of different experiment types (Section 10.3.2) supported by assessing how the models reflect changes in driving processes. In this manner a purpose may be best served by seeking the congruence of several types of information together, though one needs to recognize how well the attributes of each source align with the specific need for information. Depending on resources, one may even design model experiments specifically for a given use, such as constructing physical climate storylines of individual events (Box 10.2 and Section 10.3.2). Such analyses may be complemented by event attribution studies (Section 11.1.4).

Users of climate information may face the so-called practitioner's dilemma: a plethora of different and potentially contrasting sources (Figure 10.16) may be available without a comprehensive and user-relevant evaluation, and these datasets may also lack a transparent and easily understandable explanation of underlying assumptions, strengths and limitations (Barsugli et al., 2013; Hewitson et al., 2017). Often, the choice of information source is therefore not determined by what is most relevant and informative for the question at hand, but rather by practical constraints such as accessibility and ease of use and may be limited to the availability of just one source in extreme cases (Rössler et al., 2019a).

10.5.2 Framing Elements for Constructing User-Relevant Information

10.5.2.1 Consideration of different contexts

Without considering the specific context, the distillation of climate information relevant to users may poorly serve the goal of informing adaptation and policy (Cash et al., 2003; Lemos et al., 2012; Baztan et al., 2017). Section 10.1.4 identifies three implicit framing issues of constructing and delivering user-relevant climate information: practical issues arising from the climate information sources, issues with including the context in constructing the information, and difficulties presented by complex networks of practitioners. The social context strongly influences decisions about constructing information and requires a nuanced and holistic approach to recognize the complexity of a coupled social and physical system (Daron et al., 2014). For example, urban water managers must recognize the dependency of the city on different water resources and the interplay of both local and national government legislation that can involve a range of different constituencies and decision makers (Scott et al., 2018; Savelli et al., 2021).

Context plays a role in determining the risks that may affect human systems and ecosystems and consequently the climate information needs. The context may also limit access to such information. Hence, the context imposes inherent constraints on how climate information can be constructed and optimally aligned with its intended application. Although contexts are unlimited in variety, some key contextual elements include:

- Whether the problem formulation needs to be constructed through consultative activities that, for instance, help identify thresholds of vulnerability in complex urban or rural systems (Baztan et al.,

ACCEPTED VERSION SUBJECT TO FINAL EDITING

2017; Willyard et al., 2018) or is more a matter of addressing a generic vulnerability already identified, such as the frequency of flood events or recurrence intervals of multi-year droughts (Hallegatte et al., 2013).

- Societal capacity, such as cultural or institutional flexibility and willingness to respond to different scientific information (e.g., Hart and Nisbet, 2012; Kahan, 2012, 2013).
- The technical capability and expertise of the different actors, including users, producers, and communicators (e.g., Sarewitz, 2004; Gorddard et al., 2016).
- Potential contrasts in value systems such as the different views of the Global North compared to those of economies in transition or under development (Henrich et al., 2010a, 2010b; Sapiains et al., 2020).
- The relative importance of climate change in relation to non-climate stressors on the temporal and spatial scales of interest to the user, which at times are not the ones initially assumed by the producers (Otto et al., 2015).
- Availability, timing and accessibility of the required climate information, including the availability of sources such as observations, model simulations, literature and experts of the relevant regional climate (Mulwa et al., 2017). In developing countries, the availability of all or some of these sources may be limited (Dinku et al., 2014).

These and other contextual elements can frame subsequent decisions about the construction of regional climate information for applications. For example, an engineer typically seeks quantitative information, while the policy community may be more responsive to storylines and how information is positioned within a causal network describing regional climate risk (Section 1.4.4 and Box 10.2). Multiple contexts can coexist and potentially result in competing approaches (for example, when urban governance contends with regional water-resource management in the same area).

10.5.2.2 Developing climate information conditioned by values of different actors and communities

Developing climate information relevant to user needs can be influenced by the explicit and implicit values of all parties: those constructing the information, those communicating the information, those receiving the information, and, critically, those who construct the problem statement being addressed. A discussion of how values in the scientific community shape climate research appears in Section 1.2.3.2. The influence of values need not be a source of bias or distortion; it is sometimes appropriate and beneficial: critical scrutiny from a diverse range of value-governing perspectives may uncover and challenge biases and omissions in the information that might otherwise go unrecognized (Longino, 2004). Dialogue among all parties in a culturally, socially, and economically heterogeneous society is therefore important for recognizing and reconciling value differences to best yield information that is salient, relevant and avoids ambiguity, most notably when informing the complexity of risks and resilience for human systems and ecosystems in developing nations (e.g., Baztan et al., 2017).

Thus, a challenge with constructing climate information for users, especially about impactful change, is that producing the information may need to involve people with a variety of backgrounds, who have different sets of experiences, capabilities, and values. The information thus would need to accommodate and be relevant to a range of different ways of viewing the problem (Sarewitz, 2004; Rosenzweig and Neofotis, 2013; Gorddard et al., 2016). Failure to recognize the variety of people using the climate information can make it ineffective, even if the source data on which it is based is of the highest quality, and may create a danger of mal-adaptation.

[START FIGURE 10.17 HERE]

Figure 10.17: **Effective regional climate information requires shared development of actionable information that engages all parties involved and the values that guide their engagement.** Participants in the development of climate information come from varying perspectives, based in part on their professions and communities. Each of the three broad categories shown in the Venn diagram (Users,

ACCEPTED VERSION SUBJECT TO FINAL EDITING

Producers, Scientists) is not a homogenous group, and often has a diversity of perspectives, values and interests among its members. The subheadings in each category are illustrative and not all-inclusive. The arrows connecting those categories represent the distillation process of providing context and sharing climate relevant information. The arrows that point toward the centre represent the distillation of climate information that involves all three categories.

[END FIGURE 10.17 HERE]

A substantial body of evidence shows that the receptivity of individuals to climate information is strongly conditioned by motivated reasoning (Hart and Nisbet, 2012; Kahan, 2012, 2013), wherein a person's reception of climate information is influenced by the values of the community with which the person identifies. Adherence to a community's values forms part of an individual's social identity (Hart and Nisbet, 2012). Individuals thus frame their analysis and understanding of climate information in the context of cultural values espoused by their community (Hart and Nisbet, 2012; Kahan, 2012, 2013; Campbell and Kay, 2014; Bessette et al., 2017; Tschakert et al., 2017; Vezér et al., 2018). Successful framing of climate information products thus seeks to identify common ground with users, taking account of their values and interests.

Given the relevance of both context and values, the effectiveness of climate information can increase if developed in partnership with the target communities (Tschakert et al., 2016; Figure 10.17). Such an approach can inspire trust among all parties and at the same time promote a co-production process (Cash et al., 2003). Recipients of information have the greatest trust when the communicator is perceived as understanding their context and sharing their values and identity (Corner et al., 2014). As a consequence, developing mental models informed by user values can help with understanding complex climate models and their outcomes (Bessette et al., 2017).

The importance of a co-production process does not preclude the climate-research community from taking steps to develop and convey relevant information on its own. Indeed, communicating expert consensus about contested scientific issues is beneficial (Goldberg et al., 2019). Climate services (Section 10.5.4), in particular, can become effective means for using sources from the climate community and crafting these to be consistent with the needs, interests and values of stakeholder communities. However, simply presenting more information without recognizing user values and the contextual elements listed in Section 10.5.2.1 may be ineffective (Kahan, 2013). An aversion to climate information discordant with one's preexisting beliefs can actually become stronger for people who are more scientifically literate: they feel more confident sifting through all sources of information to find support for their positions (Kahan, 2012). A challenge is that if climate information is not framed carefully, recognizing context and user values, it may make the sceptical person less receptive to further information about climate change (Corner et al., 2012; Hart and Nisbet, 2012; Shalev, 2015). A further complication is that audiences may view climate change as a problem distant in time and space (Spence et al., 2012), too threatening to acknowledge (Brügger et al., 2015; McDonald et al., 2015), or too economically challenging to accept (Bessette et al., 2017). Identifying positive outcomes that align with user values, instead of adaptation and mitigation efforts, appears to promote the interest in and the success of climate information (Bain et al., 2012).

10.5.2.3 The roles of spatial and temporal resolution in relation to decision scale

Climate processes occur on a range of spatial and temporal scales, from global to local, from centuries and longer to days or less (Section 10.1.2 and Figure 10.3). Similarly, decisions by stakeholders cover a range of spatial and temporal scales that can vary with the size of their region of interest and scope of activity. However, the link between decision scales and the spatial and temporal resolution of climate and related non-climatic, natural-system information is not straightforward, and failure to recognize mismatches between the two can undermine the effectiveness and relevance of the information (Cumming et al., 2006; Sayles, 2018).

Nevertheless, the scale of regional climate information does not have to be the same as the decision scale.

ACCEPTED VERSION SUBJECT TO FINAL EDITING

Physical-climate storylines (Box 10.2) valid at large scales can be used to develop understanding that is relevant to local decisions. For example, global climate change affecting Antarctic ice-mass loss is relevant to formulating Dutch responses to sea-level rise (Haasnoot et al., 2020). On the other hand, extreme precipitation processes can occur on scales of tens of kilometres and smaller and thus require high resolution climate information when projecting future changes (e.g., Xie et al., 2015). An important factor for developing effective climate information using the distillation process is aligning the vulnerabilities of the social and economic systems under consideration ranging from, for example, those important to a farmer to those important to a national agricultural ministry (Andreassen et al., 2018; O'Higgins et al., 2019). Thus, more sophisticated matching of spatial and temporal resolution of climate information with decision scales requires engagement across a hierarchy of governance structures at national, regional and local level (e.g., Lagabrielle et al., 2018).

10.5.3 Distillation of Climate Information

The preceding sections laid out the diversity of sources of climate information (Section 10.5.1) and important elements for its use in a decision context (Section 10.5.2). Here, it is assessed how context-relevant climate information can be distilled from these sources of information. Although the term distillation lacks a clear definition in the literature, it has, in principle, two aspects: the construction of (potentially user-targeted) information that is defensible and evidence-based (Giorgi, 2020), and the translation of this information into a specific context, targeting a specific purpose and set of values. The former typically involves data from multiple sources, including expert knowledge, and comprehensively considers relevant uncertainties to give physically plausible climate information. The latter translates the information explicitly into the user context, such as by linking it to experience, by formulating a narrative, by highlighting the relevance for the user context, or by putting the climate information into the context of the relevant non-climatic stressors.

Distilling climate information for a specific purpose benefits from a co-production process that includes non-climate-scientists in the research design, analysis and the exploration and interpretation of the results to best place it in context of the intended application (Collins and Ison, 2009; Berkhout et al., 2013; Wildschut, 2017; Bhave et al., 2018; Dessai et al., 2018). Consideration of the specific contexts of information requirements by the provider as well as including the user values in connecting the science with users is increasingly recognized as paramount to construct information relevant for decisions at the regional scale (Section 10.5.2; Kruk et al., 2017; Vizy and Cook, 2017; Djenontin and Meadow, 2018; Parker and Lusk, 2019; Norström et al., 2020; Turnhout et al., 2020). As a response, regional climate change information is increasingly being developed through participatory and context-specific dialogues that bring together producers and users across disciplines and define climate impacts as one of the many stressors shaping user decisions (Brown and Wilby, 2012; Lemos et al., 2012). Although there are multiple practical issues involving communication (Rössler et al., 2019a), such as providing data in a format that users can interpret, being mindful of the contextual issues raised in Section 10.5.2 allows non-scientists to be involved in decisions about approaches and assumptions for the distillation and thus to take ownership of the resultant information and to make informed decisions based on the distilled information (Pettenger, 2016; Verrax, 2017). Importantly, the application of trans-disciplinary engagement processes that emphasise the role of non-scientists in the learning and knowledge production process builds relationships and trust between information users and producers, which is arguably as important for the uptake of climate science into decision making as the nature of the climate information itself (Section 10.5.2).

10.5.3.1 Information construction

Data, either from observations or models, is in general not inherently information, but may contain relevant information if interpreted appropriately (Hewitson et al., 2017). The same applies to other sources of climate information. Relevance is controlled by the given user context (Section 10.5.2.1) and relates to the required temporal and spatial scales (Section 10.5.2.3), the characteristics of required variables (often referred to as indicators), and the meteorological and climatic phenomena driving these variables (Section 10.1.3). For

ACCEPTED VERSION SUBJECT TO FINAL EDITING

example, if climate information for driving impact models is sought (e.g., McSweeney et al., 2015), the impact modelling analysis in the target region is the specific user context.

Climate risk assessment considers all plausible outcomes (Weaver et al., 2017; Marchau et al., 2019; Sutton, 2019). Thus, a key element of information construction is the exploration and reconciliation of different sources of information (Barsugli et al., 2013; Hewitson et al., 2014b; Maraun and Widmann, 2018b) and involves mainly two issues: first, assessing the fitness of different sources in the given context and thereby potentially omitting (or down-weighting) selected sources (Sections 10.3.3), and, second, integrating different sources into a broader picture within a context (Sections 10.3.4).
A non-comprehensive selection of approaches that may contribute to the construction of information includes:

- Overall assessment and inter-comparison of different sources of information, including hierarchies of models and identification of potentially conflicting results (Figure 10.16), where observational availability plays a critical role (Section 10.2.3).
- Assessing the emergence of forced trends from internal variability (Section 10.4.3), and testing whether differences in simulations can be explained by internal variability, ideally using initial-condition large ensembles (Sections 10.3.4.3 and 10.4.3).
- Assessing the interdependence of chosen models to identify the amount of independent information (Section 10.3.4.4).
- Process-based evaluation with focus on those processes that are relevant for the specific application (Sections 10.3.3.4–10.3.3.10).
- Weighting or sub-selecting ensembles based on a priori knowledge or the outcome of a process-based evaluation, while sampling as much uncertainty as possible (Section 10.3.4.4).
- Tracing back differences in projections to the representation of fundamental processes, e.g., by using physical climate storylines (Sections 10.3.4.2 and Box 10.2) or sensitivity simulations (Section 10.3.2.3).
- Producing physical-climate storylines (Box 10.2) to explore uncertainties not sampled by available model ensembles (Shepherd et al., 2018), for example in pseudo-global warming experiments (Section 10.3.2.2), or to simulate events that have never happened before but are nevertheless plausible (Lin and Emanuel, 2016).
- Attributing observed changes to different external forcings and internal drivers (Section 10.4.1).
- Comparing observed trends with past simulated trends in order to constrain projections with, for instance, the Allen-Stott-Kettleborough method (Allen et al., 2000; Stott and Kettleborough, 2002; Stott et al., 2013) to explain drivers of past observed trends (Section 10.4.2) for understanding future trends.
- Integrating present-day performance via emergent constraints to reduce projection uncertainty (Section 10.3.2).
- Complementing the observational and model-based sources with expert judgement (e.g., integrating knowledge from theory or experience that is available from experts or the literature; Section 10.5.1).

These approaches often can be used in combination to increase confidence in conclusions drawn (Hewitson et al., 2017).

10.5.3.2 Translating climate information into the user context

Awareness and understanding of the users' decision-making context is a central and key aspect of developing tailored, context-appropriate information (Briley et al., 2015), as clearly evidenced by the climate services' experiences (e.g., Vincent et al., 2018). Understanding the context, however, is not trivial and requires understanding of both the user and provider (Guido et al., 2020) if the information is to be robust, reliable and relevant (Giorgi, 2020). Translating the information into context requires consideration of terminology and expectations (Briley et al., 2015), issues of user interpretation (Daron et al., 2015), and hence necessitating engagement in co-production with all attendant challenges (Vincent et al., 2021). The actual provision of climate information may be conducted at different levels of sophistication, ranging from

ACCEPTED VERSION SUBJECT TO FINAL EDITING

generic data provision via web portals (Hewitson et al., 2017), potentially including impact-relevant climate indicators, region-specific factsheets and stakeholder reports, social media (Pearce et al., 2019), to a close engagement with specific stakeholders in co-exploring the research (Steynor et al., 2016).

Climate information products may often lack explanations of their potential use and misuse (Street, 2016; Lamb, 2017; Chimani et al., 2020). This is particularly important if the information is provided as a generic, publicly accessible product without a specific context (Hewitson et al., 2017). Context-specific collaboration, especially if organized in workshop, enables a close transdisciplinary co-exploration of the results as in the form of climate risk narratives (Jack et al., 2020, Box 10.2). Such approaches explicitly account for the user context, values and non-climatic stressors (Steynor and Pasquini, 2019).

10.5.3.3 Transdisciplinary approaches to stakeholder interaction

The transdisciplinary interaction with stakeholders has been categorised into top-down, bottom-up and interactive approaches (Berkhout et al., 2013). Traditional top-down approaches frame the research from the perspective of global climate change as a driver of regional climate risk. Bottom-up approaches, also referred to as scenario-neutral impact studies (Prudhomme et al., 2010; Brown et al., 2012a, 2012b; Culley et al., 2016) begin with the user's articulation of vulnerability in the context of climatic and non-climatic stressors, follow with the definition of key system thresholds of climatic variables, and only incorporate climate data to assess the likelihood of threshold exceedances. Bottom-up approaches are special cases of robust decision making (Lempert et al., 2006; Lempert and Collins, 2007; Walker et al., 2013; Weaver et al., 2013), which are designed to account for uncertainties not represented by climate models as well as non-climatic stressors. Interactive approaches combine aspects of top-down and bottom-up approaches. The choice of approach depends on the context. While bottom-up approaches might be optimal in a local context, where case-specific risks are addressed, top-down approaches provide generic information that may serve a range of different purposes, e.g., at the national scale (Berkhout et al., 2013). All these approaches benefit from the integration of fully distilled climate information (Berkhout et al., 2013; Maraun and Widmann, 2018b).

10.5.3.4 Barriers to the distillation of climate information

As implied by Section 10.5.2, meeting the needs of users can be a substantial challenge for climate scientists if they misunderstand or have limited understanding of user needs and context (Porter and Dessai, 2017). Several barriers in user communities can trigger and sustain this challenge. This can include an institutional aversion to incorporating new tools into decision making (Callahan et al., 1999). Coincident with this factor, there may be limited staff capacity, lack of management support and lack of a mandate to plan for climate change (Lee and Whitely Binder, 2010).

Following from those challenges, constructing and communicating regional climate information often occurs under the overarching assumption that uncertainty is a problem and reducing uncertainty is the priority (Eisenack et al., 2014; Otto et al., 2016b). This is both a psychological (Morton et al., 2011) as well as a pragmatic barrier in cases where uncertainty appears to limit the ability to make decisions (Mukheibir and Ziervogel, 2007). However, where in-depth engagements with decision contexts are undertaken, these initial barriers are often dismantled to reveal a more complex, nuanced and potentially more productive intersection with climate information producers that can efficiently handle uncertainty (e.g., Rice et al., 2009; Lemos et al., 2012; Moss, 2016). Specifically, disclosure of all uncertainties in the climate information, transparency about the sources of these uncertainties, and tailoring the uncertainty information to specific decision frameworks have the potential for reducing problems of distilling and communicating uncertain climate information (Otto et al., 2016b).

10.5.3.5 Synthesis assessment of climate information distillation

There is *high confidence* that distilling climate information for a specific purpose benefits from a co-

ACCEPTED VERSION SUBJECT TO FINAL EDITING

production process that involves users of the information, considers the specific user context and the values of relevant actors such as users and scientists, and translates the resultant information into the broader user context. This process allows users to take ownership of the information, builds relationships and trust between information users and producers and helps to overcome barriers in the information construction. This process enhances trust in the information as well its usefulness, relevance, and uptake, especially when the communication involves complex, contextual details (*high confidence*). The optimal approach for the transdisciplinary collaboration with users depends on the specific context conditioned by the sources available and the actors involved, which together are dependent on the regions considered and the framing by the question being addressed.

Drawing upon multiple lines of evidence in the construction of climate information increases the fitness of this information and creates a stronger foundation (*high confidence*). The lines of evidence can include multiple observational datasets, ensembles of different model types, process understanding, expert judgement, and indigenous knowledge, among others. Attribution studies, the characterization of possible outcomes associated with internal variability and a comprehensive assessment of observational, model and forcing uncertainties and possible contradictions using different analysis methods are important elements of distillation. To make the most appropriate decisions and responses to changing climate it is necessary to consider all physically plausible outcomes from multiple lines of evidence, especially in the case when they are contrasting such as in the examples of Cross-Chapter Box 10.1 and Section 10.6.2.

10.5.4 Climate Services and the Construction of Regional Climate Information

Climate services have been defined as the provision of climate information to assist decision-making (Sections 1.2.3, and 12.6, and Cross-Chapter Box 12.2). Services are expected to be based on scientifically credible information and expertise, have appropriate engagement from users and providers, have an effective access mechanism and aim at meeting the users' needs (Hewitt et al., 2020). To achieve this, climate services synthesize context-relevant climate information addressing questions for a wide range of climate time scales. From this point of view, climate services are instruments for the production, translation and transfer of climate information and knowledge for their use in climate-informed decision-making and climate-smart policy and planning (Hewitt et al., 2012). The appropriate provision of climate services considers the diagnosis of climate information needs, the service itself and a number of good practices still under development (Vaughan et al., 2018).

The preceding subsections assess research on the distillation of climate information, which is directly relevant for the development of climate services. Distillation, when implemented appropriately and interpreted with all due caveats, leads to credible climate information with a broader foundation of evidence to be used in climate services practice according to the recommendations of the Global Framework for Climate Services (Hewitt et al., 2012). As stated in Chapter 12, climate services set new scientific challenges to research. Examples of some of the challenges have been given in Chapters 1 and 12, which are complemented by the barriers to the distillation assessed in Section 10.5.3.3.

[START BOX 10.2 HERE]

BOX 10.2: Storylines for constructing and communicating regional climate information

Communicating the full extent of available information on future climate for a region, including an uncertainty quantification, can act as a barrier to the uptake and use of such information (Lemos et al., 2012; Daron et al., 2018). To address the need to simplify and increase the relevance of information for specific contexts, recent studies have adopted storyline and narrative approaches (Hazeleger et al., 2015; Shepherd et al., 2018; Section 1.4.4.2). As such, these approaches are an important tool for the climate information distillation (Section 10.5.3). Here we assess these in a regional climate information context, namely for exploring uncertainties, embedding climate information into a given user context, and communicating climate change information.

ACCEPTED VERSION SUBJECT TO FINAL EDITING

Physical climate storylines are self-consistent and plausible unfoldings of a physical trajectory of the climate system, or a weather or climate event, on time scales from hours to multiple decades (Section 1.4.4.2). Storylines that condition climatic features and processes on a set of plausible but distinct large-scale climatic changes enables the exploration of uncertainties in regional climate projections (Box 10.2, Figure 1; Section 10.3.4.2). For instance, Zappa and Shepherd (2017) condition projected changes in European surface wind speeds on different plausible projections of tropical upper tropospheric warming and the polar vortex strength in the CMIP5 multi-model ensemble. Storylines of specific events are generated to explore the unfolding and impacts of comparable events in counterfactual climates (Lackmann, 2015; Meredith et al., 2015b; Takayabu et al., 2015; Hegdahl et al., 2020; Sillmann et al., 2020). Those event storylines can be based on pseudo-global warming studies (Lackmann, 2015; Meredith et al., 2015; Takayabu et al., 2015; Section 10.3.2.2), selected and possibly downscaled events from long-term climate projections (Hegdahl et al., 2020; Huang et al., 2020a), or based on expert judgment of plausible changes to observed events (Pisaric et al., 2011; Dessai et al., 2018). They can be used for attributing events to different causal factors (Lackmann, 2015; Meredith et al., 2015; Takayabu et al., 2015; Trenberth et al., 2015; Shepherd, 2016; Section 11.2.4) as well as for exploring the unfolding of events in future climates.

Physical climate storylines are complementary to probabilistic or unconditional risk-based approaches, and are particularly suitable to explore low-likelihood changes or events, which are often associated with the highest impacts (Shepherd et al., 2018; Sillmann et al., 2020; Section 4.8). They also facilitate providing local context to large-scale trends and changes, by conditioning the projections on locally relevant circumstances (Hazeleger et al., 2015). Storylines are also developed based on expert elicitation and include plausible changes beyond those simulated by existing model projections in order to explore deep uncertainties (Dessai et al., 2018).

Storylines can be combined with impact modelling (Strasser et al., 2019; Hegdahl et al., 2020) and can be embedded in a user's risk landscape (Shepherd, 2019; Box 10.2, Figure 1). This holds in particular for event storylines, where confounding factors such as regional characteristics like land-use changes and non-climatic drivers of the event are an element of the storyline (Pisaric et al., 2011; Dessai et al., 2018; Lloyd and Shepherd, 2020; Sillmann et al., 2020). In a co-production process, multi-disciplinary expert knowledge as well as the values and interests of the intended audiences and stakeholders can be explicitly considered (Kok et al., 2014; Bhave et al., 2018; Dessai et al., 2018; Scott et al., 2018; Hegdahl et al., 2020).

Storylines can also be used to communicate climate information by narrative elements describing the main climatological features and the relevant consequences in the user context (Fløttum and Gjerstad, 2017; Moezzi et al., 2017; Dessai et al., 2018; Scott et al., 2018; Jack et al., 2020). Co-produced narratives have been demonstrated to enhance knowledge integration in decision-making contexts (e.g., de Bruijn et al., 2016). Narrative elements have also been employed to convey information from climate models (Corballis, 2019). Jack et al. (2020) introduced the concept of climate risk narratives and developed a set of principles, such as using present tense in their presentation to avoid effects of future discounting, and writing individual narratives without uncertainty language to assume an imagined observer perspective. From this point of view, event storylines are particularly useful for communication purposes as they link to the experience and episodic memory of stakeholders (Schacter et al., 2007; Steynor et al., 2016; Shepherd et al., 2018).

[START BOX 10.2, FIGURE 1 HERE]

Box 10.2, Figure 1: Schematic of two types of physical climate storylines with a particular climate impact of concern (red). The storylines are defined by specified elements (dark blue). Variable elements (light blue) are simulated conditional on the specified elements. The white elements are 'blocked' since their state does not need to be known to determine the light blue elements. Other types of storylines could be defined by specifying other elements (e.g., storylines of different climate sensitivities or different representative concentration pathways). (a) Event storyline, where the particular dynamical conditions during the event as well as the regional warming are specified and control the hazard arising from the event. (b) Dynamical storyline, where the global warming level and remote drivers are specified and control the long-term changes in atmospheric dynamics and

ACCEPTED VERSION SUBJECT TO FINAL EDITING

regional warming. In both storylines, the impact is also conditioned on specified exposure and vulnerability. Adapted from Shepherd (2019).

[END BOX 10.2, FIGURE 1 HERE]

[END BOX 10.2 HERE]

[START CROSS-CHAPTER BOX 10.3 HERE]

Cross-Chapter Box 10.3: Assessment of climate change information at the regional scale

Coordinators: Erika Coppola (Italy), Alessandro Dosio (Italy), Friederike Otto (UK/Germany)
Contributors: Claudine Dereczynski (Brazil), Melissa I. Gomis (France/Switzerland), Richard G. Jones (UK), Roshanka Ranasinghe (The Netherlands, Sri Lanka, Australia), Alexander C. Ruane (USA), Sonia I. Seneviratne (Switzerland), Anna A. Sörensson (Argentina), Bart van den Hurk (The Netherlands), Robert Vautard (France), Sergio M. Vicente-Serrano (Spain)

This Cross-Chapter Box illustrates how assessments of past, present and future regional climate changes (e.g., change in an extreme event index or Climatic Impact-Driver, CID) are derived in the WGI report. Robust assessments can be derived when changes are supported by multiple lines of evidence.

Multiple, sometimes contrasting, lines of evidence are derived from the various data sources, methodologies and approaches that can be used to construct climate information (Figure 10.1, Section 10.5). Such data sources and methodologies include theoretical understanding of relevant processes, drivers and feedbacks of climate at regional scale, observed data from multiple datasets (e.g., ground station networks, satellite products, reanalysis, etc.), simulations from different model types (including GCMs, RCMs, statistical downscaling methods, etc.) and experiments (e.g., CMIP5 and 6, CORDEX, and Single-Model Initial-condition Large Ensembles), methodologies to attribute observed changes or events to large- and regional-scale anthropogenic and natural drivers and forcings as well as other relevant local knowledge (e.g., indigenous knowledge).

The assessment is derived following the IPCC uncertainty guidance through a distillation process of multiple lines of evidence on observed trends, attribution of trends or events, climate model projections and physical understanding, covered in several chapters of the WGI report.

In particular, this Cross-Chapter Box explains the methodology used to derive the regional assessments summarised in the Technical Summary (TS) table that are, in turn, used as a basis for the synthesis assessment in the Summary for Policymakers (SPM).

[START CROSS-CHAPTER BOX 10.3, FIGURE 1 HERE]

Cross-Chapter Box 10.3, Figure 1: Schematic illustration of the process to derive the assessment of regional climate change information based on a distillation process of multiple lines of evidence taken from observed trends, attribution of trends or events, climate model projections, and physical understanding.

[END CROSS-CHAPTER BOX 10.3, FIGURE 1 HERE]

The process consists of three discrete steps, listed below and schematically illustrated in Cross-Chapter Box 10.3, Figure 1:

1) Collection and assessment of the fitness for purpose of available information

ACCEPTED VERSION SUBJECT TO FINAL EDITING

Any specific climate change that is regionally relevant is assessed looking at lines of evidence, potentially across multiple indices. For example, several definitions of "drought" exist that refer to a variety of the underlying processes, temporal and spatial scales, as well as sectoral applications and associated impacts (Sections 11.6, 12.3). Such diverse definitions need to be gathered from the relevant literature, compared, and individually assessed if appropriate.

Once the indices of change are properly defined, the relevant climate information is collated from the available sources.

The information is then evaluated against its fitness for purpose, i.e., whether it is adequate to provide robust evidence to derive an assessment. In the case of observed data, issues to be considered include (but are not limited to): spatial and temporal resolution, accuracy, gaps in the recorded data, homogeneity in the station network, uncertainty treatment, etc. (Sections 10.2, 11.2, 11.9, 12.4, Atlas.1.4). In case of modeled data, an assessment of the fitness for purpose typically includes an evaluation of numerical or statistical methods adopted, adequate representation of the physical processes, forcings and feedbacks relevant for the region and the change under consideration, the availability of adequate ensembles to assess the interplay between forced response and internal variability and the uncertainty in future projections (Sections 10.3, 10.4, 11.2, 11.9, 12.4 and Chapter Atlas). Attribution assessments are usually based on models and observations for which the fitness for purpose is assessed with similar criteria as those described above (Cross-Working Group Box: Attribution (in Chapter 1)). The assessment is made either directly or indirectly by scrutinizing the data and methods of the relevant literature against the criteria listed above.

2) Assessment of confidence of the multiple lines of evidence

Once the relevant information has been collated for a given regional change, an assessment of the confidence is first made for each line of evidence separately. The assessment of confidence is the result of expert judgment drawing around a set of questions such as:

- Do we have a physical explanation of the processes responsible for past and future changes in the region?
- Do observed trends agree amongst different observational products/datasets? Are they statistically significant? Do the observations cover the same temporal period and/or spatial area? Are the observations homogeneous in time?
- Can past trends be attributed to human activities (GHGs, SLCFs or land use/management changes)? Are attributed trends and events consistent? What is the interplay between internal variability and forced response?
- Do model projections agree on the magnitude and sign of the projected signal? Are we able to understand the reasons underlying any discrepancies? Can we quantify the uncertainty in the projected signal? Are the projections based on similar SSP-RCP/time horizon or GWL (Cross-Chapter Box 11.1)? If not, are they comparable?
- Has the signal already emerged? Are there studies indicating the time of emergence of the signal?

The assessment is then tested for overall coherence across the available lines of evidence, for example:

- Are observed historical changes consistent with future projections?
- Are attributed events similar to the types of changes projected for the future?
- Is there a physical explanation for changes that are projected but have not yet been clearly observed or attributed?
- Are assessments of confidence and likelihood performed in a similar way across regions?

3) Distillation of regional information and synthesis of the independent assessments

To ensure transparency, a traceback matrix is constructed (refer to 10.SM) that, for each region and index, identifies where in the chapters the relevant information can be found, together with a summary of the relevant information in the Technical Summary.

Based on assessments mainly in Chapters 8, 9 11, 12 and Atlas, the table in Technical Summary TS.4.3.1 collates, by means of colours and symbols, the assessment of the confidence in past trend, attribution and direction of future change. This distillation process is illustrated below with two examples: (1) a relatively

ACCEPTED VERSION SUBJECT TO FINAL EDITING

simple case for the assessment of extreme heat over Southeast South America, where most of the lines of evidence agree, and (2) ecological, agricultural and hydrological drought in the Mediterranean, which is more complex due to the different definitions of 'drought' and the sometimes conflicting information arising from different lines of evidence and the example shown here is preceded by the decision to focus on these types of drought rather than, e.g., meteorological drought.

a) Extreme heat in southeastern South America (SES)

Observed past trends

Mean temperature and extreme maximum and minimum temperatures have shown an increasing trend (*high confidence*). An increase in the intensity and in the frequency of heatwave events between 1961 and 2014 is also observed. However, there is *medium confidence* that warm extremes have decreased in the last decades over the central region of SES during austral summer (Sections Atlas.7.2.2 and 11.9).

There is evidence of increasing heat stress during summertime in much of SES for the period 1973-2012 (Section 12.4.4.1).

Attribution

Based on trend detection and attribution studies of maximum and minimum temperatures and event attribution of heat waves in the region, there is *high confidence* in a human contribution to the observed increase in the intensity and frequency of hot extremes (Section 11.9).

The increasing heat stress over summertime in much of SES has been attributed to human influence on the climate system (Section 12.4.4.1).

Projections

There is *high confidence* that by the end of century most regions in South America will undergo extreme heat stress conditions much more often than in the recent past, with about 50-100 more days per year under SSP1-2.6 and more than 200 additional days per year under SSP5-8.5 (*high confidence*) (Section 12.4.4.1).

Based on different lines of evidence (GCMs, RCMs) an increase in the intensity and frequency of hot extremes is *extremely likely* for SES at all assessed warming levels (compared with pre-industrial) (Section 11.9).

Synthesized assessment in the Technical Summary from multiple lines of evidence

There is *high confidence* that extreme temperatures have increased over SES over the last decades and that human influence *likely* contributed to the observed changes in extreme temperatures. An increase in the frequency and intensity of heatwave events has been observed. Most land regions will frequently undergo extreme heat stress conditions by the end of the 21st century, with an increase in the frequency of heatwaves and heat stress conditions (Technical Summary TS.4.3.2).

b) Mediterranean ecological, agricultural and hydrological droughts

Observed past trends

Hydrological modelling suggests that the recent decline in soil moisture in the Mediterranean is unprecedented in the last 250 years. Paleoclimate evidence extends this view, additionally indicating that dryness in the Mediterranean is approaching an extreme condition compared to the last millennium (Section 8.3.1.6).

There is an increase in probability and intensity of agricultural and ecological droughts (*medium confidence*) and there is an increase in frequency and severity of hydrological droughts (*high confidence*) (Section 11.9).

Attribution

Global warming has contributed to drying in dry summer climates including the Mediterranean (*high confidence*). Records of soil moisture indicate that higher temperatures and increased atmospheric demand have played a strong role in driving Mediterranean aridity. Multiple lines of evidence suggest that anthropogenic forcings are causing increased aridity and drought severity in the Mediterranean region (*high*

ACCEPTED VERSION SUBJECT TO FINAL EDITING

confidence) (Section 8.3.1.6).

An increasing trend towards agricultural and ecological droughts has been attributed to human-induced climate change in the Mediterranean (*medium confidence*). Model-based assessment shows with *medium confidence* a human fingerprint on increased hydrological drought, related to rising temperature and atmospheric demand, and frequency and intensity of recent drought events. There is *medium confidence* that change in land use and terrestrial water management contribute to trends in hydrological drought (Section 11.9).

Projections

There is *high confidence* that drought severity and intensity will increase in the Mediterranean. Increased evapotranspiration due to growing atmospheric water demand will decrease soil moisture (*high confidence*). The seasonality of runoff and streamflow (the annual difference between the wettest and driest months of the year) is expected to increase with global warming (*high confidence*). Annual runoff is very likely to decrease. Under middle or high emissions scenarios, the likelihood of extreme droughts increases by 200–300% in the Mediterranean. The paleoclimate record provides context for these future expected changes: climate change will shift soil moisture outside the range of observed and reconstructed values spanning the last millennium (*high confidence*) (Sections 8.4.1.5 and 8.4.1.6).

There is *medium confidence* in the increase of agricultural and ecological drought at +1.5ºC, *high confidence* at +2ºC and *very likely* at +4ºC, with large decreases in soil water availability during drought events and increase in drought magnitude. There is *medium confidence* in the increase in hydrological drought at +1.5ºC, *high confidence* at +2ºC and *very likely* at +4ºC with very strong decrease (40-60%) of total runoff in the spring-summer half-year and a 50-60% increase in frequency of days under low flow (Section 11.9).

There is *high confidence* that agricultural, ecological and hydrological droughts will increase in the Mediterranean region by mid and far end of century under all RCPs (except RCP2.6/SSP1-2.6), or for GWLs equal to or higher than 2ºC (Section 12.4.5.2).

Synthesized assessment in the Technical Summary from multiple lines of evidence

There is *high confidence* that hydrological droughts have increased in the Mediterranean since the 1960s related to rising temperature and atmospheric demand, and *medium confidence* of a human fingerprint on this increase. There is *medium confidence* in the increase of ecological and agricultural droughts and in their attribution to human-induced climate change. There is *high confidence* of an increase in ecological, agricultural and hydrological droughts for warming levels exceeding 2°C, and *medium confidence* of an increase for lower warming levels (Technical Summary TS4.3.2).

[END CROSS-CHAPTER BOX 10.3 HERE]

10.6 Comprehensive Examples of Steps Toward Constructing Regional Climate Information

10.6.1 Introduction

This section presents three comprehensive examples of steps for distilling regional climate information from the multiple sources of regional climate information presented in this chapter. These examples build on the general framework presented in Section 10.5, examining in particular the strengths and challenges in linking the different sources, while also exposing the assumptions behind and consequences of decisions made in the process. The examples are framed taking into account societal perspectives that provide context for their regional climate statements. Although the nature of an IPCC Working Group I assessment precludes engaging with users of climate information (Section 10.5), we do cite relevant national and regional reports that give user perspectives to set a foundation from which one could distil climate information for users. We have chosen the recent Cape Town drought, Indian summer-monsoon trends and the Mediterranean summer warming because they provide a geographically diverse set of locations and relevant processes and because

ACCEPTED VERSION SUBJECT TO FINAL EDITING

most of the components for constructing regional climate information outlined in Chapter 10 are directly relevant to each case.

The three comprehensive examples follow a similar structure:

- Motivation and regional context
- The region's climate
- Observational issues
- Relevant anthropogenic and natural drivers
- Model simulation and attribution over the historical period
- Future climate information from global simulations
- Future climate information from regional downscaling
- Storylines
- Climate information distilled from multiple lines of evidence

Following this structure, construction of the regional climate information presented in these examples depends on an assessment of observational uncertainty relative to the magnitude of a climate-change signal (Section 10.2), the evaluations of model performance to judge the fitness for purpose of a given model (Section 10.3), and expert judgement. These factors contribute to attribution of historical climate-change signals (Section 10.4), recognizing that attribution must account for the interplay between externally forced signals and unforced internal variability. This interplay is explored using multiple model ensembles, including, when appropriate and feasible, single-model initial-condition large ensembles (SMILEs). The multiple lines of evidence for the climate information may conflict, thus requiring distillation of the evidence (Section 10.5) to arrive at climate-change statements. When moving from global climate information to climate information at the regional scale, following the structure above provides a basis for arriving at relevant and credible climate information. The comprehensive examples of distilling climate information thus show the value of working with multiple lines of evidence to develop robust climate change information for a region.

In addition to the three comprehensive examples, this section contains two additional examples analysing multiple sources of regional climate information. Box 10.3 on urban climate assesses information that provides a foundation for understanding climatic behaviour in urban areas and its projected change. Cross-Chapter Box 10.4 on climate change over the Hindu Kush Himalaya assembles information rooted in several chapters and previous assessment reports to assess understanding of several climate elements (temperature, precipitation, snow and glaciers, and extreme events) for the region and their projected changes.

As these examples will show, the distillation process of regional climate information from multiple lines of evidence can vary substantially from one case to another. Confidence in the distilled regional climate information is enhanced when there is agreement across multiple lines of evidence, but the outcome of distilling regional climate information can be limited by inconsistent or contradictory sources.

10.6.2 Cape Town Drought

10.6.2.1 Motivation and regional context

Cape Town's "Day Zero" water crisis in 2018 threatened a shut-down of water supply to 3.4 million inhabitants of the city and resulted in domestic water use restriction of 50 litres per person per day (pre-drought unconstrained water use was ~170 litres per person per day, DWA, 2013) lasting for nine months, punitive water tariffs, and temporary closure of irrigation systems. Problems with water supply in many large cities in developing countries are endemic and rarely reported internationally. The water crisis in Cape Town attracted considerable international attention to a city with functional government structures, well developed services (compared to other urban centres in Africa), a centre of international tourism, and an economic hub with GDP of USD22 billion (~USD 7,500 per capita, Gallie et al., 2018). Economic and social impacts of the crisis were significant. Loss of revenue for companies of all sizes resulted not only from the scaling down of water-dependent activities, but also from the need to invest in water-efficient technologies and processes.

ACCEPTED VERSION SUBJECT TO FINAL EDITING

Tourism was affected through reduced arrivals and bookings, although only temporarily (CTT, 2018). In the agricultural sector, 30,000 people were laid-off and production dropped by 20% (Piennaar and Boonzaaier, 2018). The crisis initially polarized society, with conflict emerging between various water users and erosion of trust in the government, but eventually social cohesion and an acute awareness of limited water resources emerged (Robins, 2019).

Cape Town's crisis resulted from a combination of a strong, rare multi-year meteorological drought (Figure 10.18), estimated at 1 in 300 years (Wolski, 2018), and factors related to the nature of the water supply system, operational water management and water resource policies. Cape Town was very successful in implementing water-saving actions after the previous drought of 2000–2003, reducing water losses from over 22% to 15% (Frame and Killick, 2007; DWA, 2013), breaking the previous coupling of growth in water demand with growth in population. As a consequence, Cape Town won a Water Smart City award from the C40 Cities program only three years prior to the crisis. However, the water-saving actions, together with changing priorities in water resource provision from infrastructure-oriented towards resource and demand management, may well have led to delays in implementation of the expansion of water supply infrastructure (Muller, 2018). The expansion plan, formulated a decade prior to the crisis, included an expectation of long-term climate-change drying in the region (DWAF, 2007). The crisis also exposed structural deficiencies of water management and inadequacy of a policy process in which decisions about local water resources are taken at a national level, particularly in a situation of political tension (Visser, 2018). The crisis was widely seen as a harbinger of future problems to be faced by the city, and a highlight of vulnerability of many cities in the world resulting from the interplay of three factors: 1) the fast urban-population growth, 2) the economic, policy, infrastructural and water resource paradigms and constraints, and 3) anthropogenic climate change.

[START FIGURE 10.18 HERE]

Figure 10.18: Historical and projected rainfall and Southern Annular Mode (SAM) over the Cape Town region. (a) Yearly accumulation of rainfall (in mm) obtained by summing monthly totals between January and December, with the drought years 2015 (orange), 2016 (red), and 2017 (purple) highlighted in colour. (b) Monthly rainfall for the drought years (in colour) compared with the 1981–2014 climatology (grey line). Rainfall in (a) and (b) is the average of 20 quality controlled and gap-filled series from stations within the Cape Town region (31°S–35°S, 18°W–20.5°W). (c) Time series of the SAM index and of historical and projected rainfall anomalies (%, baseline 1980–2010) over the Cape Town region. Observed data presented as 30-year running means of relative total annual rainfall over the Cape Town region for station-based data (black line, average of 20 stations as in (a) and (b)), and gridded data (average of all grid cells falling within 31°S–35°S, 18°W–20.5°W): GPCC (green line) and CRU TS (olive line). Model ensemble results presented as the 90th-percentile range of relative 30-year running means of rainfall and the SAM index from 35 CMIP5 (blue shading) and 35 CMIP6 (red shading) simulations, 6 CORDEX simulations driven by 1 to 10 GCMs (cyan shading), 6 CCAM (purple shading) simulations from individual ensemble members, and 50 members from the MIROC6 SMILE simulations (orange shading). The light blue, dark red and yellow lines correspond to NCEP/NCAR, ERA20C and 20CR, respectively. The SAM index is calculated from sea-level pressure reanalysis and GCM data as per Gong and Wang (1999) and averaged over the aforementioned bounding box. CMIP5, CORDEX and CCAM projections use RCP8.5, and CMIP6 and MIROC6 SMILE projections use SSP5-8.5. (d) Historical and projected trends in rainfall over the Cape Town region and in the SAM index. Observations and gridded data processed as in (c). Trends calculated as Theil-Sen trend with block-bootstrap confidence interval estimate. Markers show median trend, bars 95% confidence interval. GCMs in each CMIP group were ordered according to the magnitude of trend in rainfall, and the same order is maintained in panels showing trends in the SAM. Further details on data sources and processing are available in the chapter data table (Table 10.SM.11).

[END FIGURE 10.18 HERE]

10.6.2.2 The region's climate

ACCEPTED VERSION SUBJECT TO FINAL EDITING

An evaluation of the relative role of rainfall and temperature signal in the 2015–2017 hydrological drought gives a strong indication that lack of rainfall was the primary driver (Otto et al., 2018) leading to the 2018 water crisis. Thus, the remainder of this section focuses on rainfall. Section 11.6 offers a discussion of African drought over broader areas, including mechanisms relevant to them.

Cape Town is located at the southwestern tip of Africa, within an approximately 100 km x 300 km region that receives 80% of its rainfall during the austral winter (March to October), with the largest portion in June to August. In the vicinity of Cape Town, rainfall is strongly heterogeneous, ranging from ~300 mm/year on coastal plains to >2,000 mm/year in mountain ranges. The Cape Town water supply relies on surface water reservoirs located in a few small mountain catchments (~800 km^2 in total). The Cape Town region receives 85% of its rainfall from a series of cold fronts forming within mid-latitude cyclones. The remainder is brought in by infrequent cut-off lows that occur throughout the year (Favre et al., 2013). This creates a very strong water resource dependency on a single rainfall delivery mechanism that may be strongly affected by anthropogenic climate change (Chapter 4, Section 10.6.2.6).

The 2015–2017 drought had strong low-rainfall anomalies in shoulder seasons (March to May and September to November, though weaker in the latter), and average rainfall in June and July (Sousa et al., 2018a; Mahlalela et al., 2019). The anomaly resulted from fewer rainfall events and lower average intensity of events. The anomaly was strongest in the mountainous region where the water supply system's catchments are located (Wolski et al., 2021).

Although the 2015–2017 drought was unprecedented in the historical record, the Cape Town region has experienced other droughts of substantial magnitude, notably in the 1930s, 1970s and more recently in 2000–2003. Long term (>90 years) rainfall trends are mixed in sign, location-dependent, and weak (Kruger and Nxumalo, 2017; Wolski et al., 2021); mid-term (~50 years) trends are similarly mixed in sign (MacKellar et al., 2014). In the southwestern part of the region, rainfall is mostly decreasing in the post 1981 period, particularly in December-January-February and March-April-May, although there is no trend or a weak wetting in June-July-August (Sousa et al., 2018a; Wolski et al., 2021). Rainfall trends of similar magnitude and duration to the post-1981 trend accompanied previous strong droughts in the region (Wolski et al., 2021).

10.6.2.3 Observational issues

South Africa and the Cape Town region have good instrumental weather data. Records start in the late 1800s, with in excess of 10 gauges reporting since the 1920s, expanding to ~80 gauges in the 1980s, but the number of stations has declined since. The mountains have only a few stations, which receive more than 1,000 mm/year. In view of the strong heterogeneity of rainfall, changes in the number of stations contributing to datasets such as CRU and GPCP results in a lack of consistency between them, which limits their reliability in the region (Wolski et al., 2021; Section 10.2).

10.6.2.4 Relevant anthropogenic and natural drivers

Because the primary rainfall mechanism is frontal rain, the most relevant large-scale drivers are those that affect cyclogenesis, frontogenesis and the mid-latitude westerlies' latitudinal position and moisture supply. These drivers and, thus, the region's rainfall are linked to the Antarctic Oscillation (AAO; Reason and Rouault, 2005) or Southern Annual Mode (SAM), the dominant monthly and interannual mode of Southern Hemisphere atmospheric variability, and a measure of the pressure gradient between mid- and high-latitudes. (see Sections 3.3, 3.7, 4.3 and Annex IV.2.2 for more general discussion of the SAM.) While in the post-1930 period, the SAM displays a long-term positive trend, the Cape Town region's rainfall does not, and only the post-1979 trends of rainfall and SAM are conceptually consistent, i.e., a positive trend in the SAM is associated with a negative trend in rainfall (Section 10.6.2.5 and Figure 10.18). There is also good agreement between the seasonality of the SAM and rainfall trends in the post-1979 period: a drying trend appears strongly in December to February and March to May, but not in June to August and September to November (Wolski et al., 2021), and trends in the SAM have similar seasonal dependence (Lim et al., 2016b; Section 3.7.2).

ACCEPTED VERSION SUBJECT TO FINAL EDITING

Additionally, there is a similar seasonal pattern in the post-1979 trends in indices capturing the southern edge of the Hadley circulation (Grise et al., 2018).

In the longer-term, Cape Town regional rainfall is characterized by a multi-decadal scale quasi-periodicity (Figure 10.18; Dieppois et al., 2019; Wolski et al., 2021), with the 2015–2017 drought and previous strong droughts (1930s and 1970s) occurring during the rainfall's periodic low phases. However, the studies linking the Cape Town 2015–2017 drought to the hemispheric processes expressed by the SAM (Sousa et al., 2018a; Burls et al., 2019; Mahlalela et al., 2019) focused almost exclusively on the post-1979 period, when global reanalyses are available. Detailed understanding of the drivers of previous (1930s and 1970s) Cape Town region droughts and the role of hemispheric processes expressed by the SAM in the pre-1979 period is missing.

The Cape Town regional rainfall is also potentially linked to other hemispheric phenomena, such as the expansion of the tropics and, specifically, the South Atlantic high-pressure system and the position of the subtropical jet, which share some variability with the SAM. The relationships between these phenomena and Cape Town rainfall have not been thoroughly investigated outside of the context of the 2015–2017 drought, but the drought itself was associated with poleward expansion of the subtropical anticyclones in the South Atlantic and South Indian Oceans and (a resulting) poleward displacement of the moisture corridor across the South Atlantic (Sousa et al., 2018a), as well as a weaker subtropical jet (Mahlalela et al., 2019). Burls et al. (2019) also link the decline in the number of rainy days to the increase in sea-level pressure along the poleward flank of the South Atlantic high-pressure system and the intensity of the post-frontal ridging high. Additionally, there is a possible linkage between Cape Town rainfall and near-shore cold sea surface temperature (SST) anomalies arising from Ekman upwelling due to reduced westerly and increased south-easterly winds. These might lead to suppression of convection and reduction of rainfall over land (Rouault et al., 2010). All these phenomena are conceptually consistent with the poleward migration of the westerlies and expansion of the tropics.

Rainfall in the Cape Town region also responds to SST anomalies in the Southeast Atlantic, including the Agulhas Current retroflection region, which may drive intensification of low-pressure systems, leading to the trailing front strengthening as it makes landfall over the Cape Town region (Reason and Jagadheesha, 2005). There are also linkages at seasonal time scale between the Cape Town regional rainfall and Antarctic sea ice (Blamey and Reason, 2007).

In addition to mid-latitude controls, subtropical processes also play a role in the Cape Town region's rainfall variability. The 10˚–30˚S region of the subtropical Atlantic, parts of the South American continent and even parts of the African continent north of Cape Town are sources of moisture for atmospheric river events contributing to frontal rainfall (Blamey et al., 2018; Ramos et al., 2019), with implications for the 2015–2017 drought (Sousa et al., 2018a). Also, the second major rainfall contributing system, cut-off-lows, is conditional on moisture supply from the sub-tropics (Abba Omar and Abiodun, 2020).

Although El Niño-Southern Oscillation (ENSO) influences climate in southern Africa, any relationship between ENSO and Cape Town's rainfall is weak and inconsistent, showing the strongest impact in May to June (Philippon et al., 2012). ENSO, however, does influence large-scale processes and phenomena relevant to the drought, though the relationship between ENSO and the SAM is complex, with each ENSO event influencing the SAM differently in different seasons (Ding et al., 2012). Similarly, ENSO affects meridional circulation and thus the subtropical anticyclone as well as the polar and subtropical jets (Seager et al., 2019), but only modifying, not controlling, their role in Cape Town's rainfall.

Paleoclimate studies reveal that long-term variability in the winter rainfall region of South Africa (including Cape Town) is consistent with a general framework of warming/cooling-induced latitudinal migration of the westerlies and transformation of the subtropical high-pressure belt and associated hemispherical processes (see section 10.2.3.2 for assessment of paleoclimate analysis). The synchronicity of winter rainfall with Antarctic ice-core-derived polar temperature anomalies is consistently revealed in studies using different paleoclimate proxies and time scales of 1.4k (Stager et al., 2012), ~3k (Hahn et al., 2016) and 12k years (Weldeab et al., 2013). Changes in rainfall regimes at shorter (decadal) time scales appear to reflect influence of local processes such as the Agulhas current's interaction with the Atlantic, resulting in changes

ACCEPTED VERSION SUBJECT TO FINAL EDITING

in SST and coastal upwelling, as well as modification of the wind tracks by topography (Stager et al., 2012).

10.6.2.5 Model simulation and attribution over the historical period

Due to the small scale of the Cape Town region, robust comparison of CMIP simulations to observations is difficult. However, in general, CMIP5 models capture well the seasonality, such as the dominance of austral winter rains, although they overestimate the peak and underestimate the shoulder season rainfall (Mahlalela et al., 2019). Trends in rainfall are particularly difficult to assess as they are generally weak and depend strongly on the time period and dataset adopted for the analyses (Section 10.6.2.3). A multi-method attribution study (Otto et al., 2018) estimates the probability of the 2015–2017 drought to have increased by a factor of 3 since pre-industrial times (with a wide 95% confidence interval of 1.5 to 6). However, throughout the 20th century, a substantial portion of the global climate models (GCMs; ~36% of CMIP5 and 44% of CMIP6 models, as well as many of the MIROC SMILE members) simulate a statistically significant (95% level) decline in total annual rainfall, while there is no robust long-term trend in observations (Figure 10.18). Section 10.4 offers a more detailed assessment of attribution challenges.

GCMs capture the overall behaviour of the observed main hemispherical processes, such as the expansion of the tropics, a positive trend in SAM and the poleward shift of the westerly jet. However, they fail to capture details of their observed climatology and variability (Simpson and Polvani, 2016), and the magnitudes of simulated trends vary, though the models typically underestimate observed trends in these processes (Purich et al., 2013; Staten et al., 2018). In general, CMIP5 models do capture the SAM-regional rainfall association, although not consistently across all seasons (Purich et al., 2013; Lim et al., 2016a).

10.6.2.6 Future climate information from global simulations

GCMs show strong consistency in a drying signal for the Cape Town region, with the reduction in total annual rainfall ranging up to 20% by the end of the 21st century in CMIP5 RCP8.5 and CMIP6 SSP5-8.5 simulations (Almazroui et al., 2020a; Figure 10.18). The consistency across the models is a robust signal compared to the rest of southern Africa, where the climate change signal varies spatially: stronger drying in the west and moderate drying or weak wetting in the east (DEA, 2013, 2018; Atlas.4.4 for further discussion of southern Africa precipitation projections). Rainfall changes projected for the Cape Town region are consistent with projected changes in hemispheric-scale processes and regional-scale dynamics that point toward reduced frequency of frontal systems affecting that region. These changes include robust signals in CMIP5 models for the Southern Hemisphere for a poleward expansion of the tropics (Hu et al., 2013b), poleward displacement of mid-latitude storm tracks (Chang et al., 2012), increased strength and poleward shift of the westerly winds (Bracegirdle et al., 2018) and subtropical jet-streams (Chenoli et al., 2017), and a shift toward a more positive phase of the SAM (Lim et al., 2016a). However, despite the consistency in circulation changes, the emergence of anthropogenic rainfall change above unforced variability in southwestern Africa remains uncertain for annual rainfall throughout most of the 21st century, even under SSP5-8.5 (Section 10.4, Figure 10.15).

There is also a substantial increase in the frequency of conditions supporting atmospheric rivers and water vapour transport towards the southwest coast of southern Africa in the projected climate (Espinoza et al., 2018). This behaviour has strong implications for the region, as most topographically high locations receive rainfall from persistent atmospheric rivers (Blamey et al., 2018). A thorough understanding of the role of atmospheric rivers in the Cape Town region under a changing climate is missing.

10.6.2.7 Future climate information from regional downscaling

Dynamical downscaling studies implemented with a stretched-grid model (Engelbrecht et al., 2009) revealed a signal compatible with the driving CMIP5 ensemble, that is, consistent drying throughout the region, amplifying in time, irrespective of the considered emission scenario and the generation of GCMs (DEA,

ACCEPTED VERSION SUBJECT TO FINAL EDITING

2013, 2018). A multi-model CORDEX ensemble indicates a robust signal of reduction of total annual rainfall in the future, although there is less agreement on how changes in rainfall occurrence may evolve in the region, such as through fewer consecutive rain days or longer dry spells (Abiodun et al., 2017; Maúre et al., 2018). For the end of the century under RCP8.5, Dosio et al. (2019) also found drying. Moreover, in their analysis, the drying is associated with an increase in the number of consecutive dry days and a reduction in number of rainy days. Their results are consistent with the driving GCMs for all the precipitation indices, and they are robust independent of the choice of the regional climate model (RCM) or GCM. However, collectively, these analyses indicate that uncertainty remains in the characteristics of the precipitation decrease.

10.6.2.8 Storyline approaches

There is a consistency in rainfall projections with the projections of rainfall drivers and with the general understanding of the influence of global warming on the circulation dynamics and rainfall patterns in the region. Thus, the expansion of the South Atlantic high-pressure system, related to widespread warming of the tropics and poleward shift of the subsiding limb of the Hadley cell, is associated with the southward displacement of the subtropical jet, and southward migration of mid-latitude westerlies and storm tracks, in addition to changes in the SAM (Section 10.6.2.4). These effects are also relatively consistent with recent (post-1980s) declines in rainfall in the Cape Town region. The storyline of an extended drought is thus a set of events that can yield reduced rainfall in the Cape Town region: poleward shift of the downward branch of the Hadley cell that produces a sustained southward shift in mid-latitude westerlies and storm tracks. The behaviour is potentially reinforced by changes in the SAM.

10.6.2.9 Climate information distilled from multiple lines of evidence

There is *high agreement* among observational data and reanalyses that the recent (post-1979) downward trend in the Cape Town region's rainfall leading to the 2015–2017 drought is related to the hemispheric processes of poleward shift in the westerlies and expansion of the Hadley circulation. However, there is less support for the precipitation-circulation relationship in historical CMIP5 and CMIP6 simulations. As a consequence, there is only *medium confidence* that these process changes produced the 2015–2017 drought leading to the 2018 water crisis.

For the water-resource planner who has to deal with potential drought like the 2015-2017 event, several lines of evidence indicate future drying: the projected precipitation by GCMs and RCMs of different spatial resolutions, and the observed and projected changes of circulation patterns consistent with drier conditions, the paleoclimatic evidence confirming a millennial-scale circulation-rainfall link. However, the distillation is limited by a lack of information about whether or not a relationship between Cape Town precipitation and large-scale circulation processes adequately explains droughts in the twentieth century prior to 1979.

Thus, although a clear association appears in observations from 1979 onward between increasing GHG concentrations, drying in the Cape Town region and behaviour of a key circulation process, the SAM, further analysis suggests caution. Not all GCMs show the historical post-1979 association among these factors, and when the observational record is extended back further to times when the anthropogenic greenhouse forcing was weaker, there is no strong association between the SAM and Cape Town drought. Thus, there is only *medium confidence* in the expectation of a future drier climate for Cape Town.

10.6.3 Indian Summer Monsoon

10.6.3.1 Motivation and regional context

The Indian summer monsoon provides 80% of the country's annual rainfall from June to September, supplying the majority of water for agriculture, industry, drinking and sanitation to over a billion people.

ACCEPTED VERSION SUBJECT TO FINAL EDITING

Any variations in the monsoon on time scales from days to decades can have large impacts (Challinor et al., 2006; Gadgil and Gadgil, 2006). Evidence from paleoclimate records (Sections 8.3.2.4.1) shows *high confidence* in a weakened Indian monsoon during cold epochs of the past such as the Younger Dryas (12,800-11,600 years ago) as measured by speleothem oxygen isotopes (Kathayat et al., 2016). There is a pressing need to understand if the monsoon will change in the future under anthropogenic forcing and to quantify such changes. Multiple datasets have shown robust negative trends since the 1950s until the turn of the century (Bollasina et al., 2011) followed by a recovery (Jin and Wang, 2017), yet repeated assessments project the monsoon to increase in strength under enhanced GHG forcing (Christensen et al., 2007, 2013; Sections 8.3.2.4.1 and 8.4.2.4.1). The apparent contradiction between future projections and observed historical trends makes the region an ideal choice for an in-depth assessment. The reader is also referred to the South Asia (SAS) regional assessment of precipitation extremes (Section 11.9), which is not discussed here for brevity.

10.6.3.2 The regional climate of India

Local geography gives rise to distinct differences in societal experience of the summer monsoon. The southwesterly monsoon winds are incident upon the Western Ghats mountains on the west coast, leading to orographic enhancement and heavy rains (Shige et al., 2017), which supply rivers with water for much of the southern peninsula, often the subject of inter-regional water disputes. The northern plains contain the Ganges river and also India's most intensive agriculture, both rainfed and irrigated. Synoptic systems known as monsoon depressions cross the northern east coast, supplying much of the rain in central India (Hunt and Fletcher, 2019). Further north, the eastern Himalayas are dominated by the summer monsoon, while the western Himalayas receive most rainfall from western disturbances during winter (Palazzi et al., 2013). Meanwhile, southeastern India sits under a rain shadow (the only region to receive more rainfall during the winter monsoon).

10.6.3.3 Observational issues for India

India has one of the oldest rain-gauge networks in the world, leading to the production of numerous observational products (reviewed in Khouider et al., 2020). Gridded gauge-based products dating back to the 19th century reveal pronounced decadal variability (Sontakke et al., 2008). Trends for India over the whole 20th century are inconclusive (Knutson and Zeng, 2018), although declining over central and northern areas (Roxy et al., 2015). Assessment of multiple observational datasets covering the Indian summer monsoon reveals significant declining rainfall over the second half of the 20th century (Section 8.3.2.4.1, Figure 10.19c,d). A subsequent recovery has been noted since the early 2000s (Jin and Wang, 2017).

Observational products containing critical inhomogeneities in gauge distribution and reporting over time are acknowledged as suitable for mesoscale analysis (Rajeevan and Bhate, 2009), while use for climate trends requires consistent reporting over time from quality-controlled gauges (e.g., ~2000 gauges since the 1950s in Rajeevan et al., 2006). A newer 0.25°-gridded product covering 1901 onwards (Pai et al., 2014, 2015), based on Shepard's interpolation method for irregularly-spaced stations (Shepard, 1968), shows increased intensity of daily rainfall and extremes over some regions, especially in the late-20th century. However, changes to the inputted gauges may have introduced an artificial jump in extreme rainfall since 1975 over central India (Section 10.2.2.3; Lin and Huybers, 2019). They suggest that this method may have masked declines in mean rainfall and highlight the need for availability of raw gauge data to allow transparent assessments. Khouider et al. (2020) have successfully tested a probabilistic interpolation method for India to overcome problems inherent in algorithms based on inverse-distance weighting when applied to data-sparse regions. An example snapshot of the uneven distribution of rain gauges in a common observational product is shown in Figure 10.19a.

The uncertainty among local and international observational products for India can pose challenges when evaluating climate models (as in Section 10.2.2.6; Prakash et al., 2015). For the seasonal mean summer monsoon rainfall, Collins et al. (2013) found large biases separating many CMIP5 models from the available

ACCEPTED VERSION SUBJECT TO FINAL EDITING

observational products. However, for seasonal mean variability, the spread across observational products was larger than across the CMIP5 ensemble.

10.6.3.4 Relevant anthropogenic and natural drivers for long-term change

The relevant drivers for long-term change in the mean Indian summer monsoon are summarised briefly:

- Increased greenhouse gas (GHG) concentrations (chiefly CO_2) are a strong contributor to changes in the monsoon, with repercussions for the meridional temperature contrast driving the monsoon circulation (Ueda et al., 2006; Roxy et al., 2015), for the monsoon winds in the lower troposphere (Cherchi et al., 2011; Krishnan et al., 2013), or for the availability of moisture from the Indian Ocean (May, 2011).
- Industrial emissions of sulphate aerosol predominantly in the Northern Hemisphere could change inter-hemispheric energy transports and weaken the monsoon (Polson et al., 2014; Undorf et al., 2018). The effect of local anthropogenic emissions of black carbon (chiefly from cooking fires) is uncertain (Lau and Kim, 2006; Nigam and Bollasina, 2010).
- India's green revolution over the late-20th century led to considerable land-use change, with massive expansion of agriculture at the expense of forest and shrublands. As a result, India's northern plains feature widespread irrigation, suggested to be a cause of drying (Mathur and AchutaRao, 2020).
- Decadal modes of variability such as the Pacific Decadal Variability (PDV, Annex IV) and Atlantic Multidecadal Variability (AMV, Annex IV), which may be partly forced (Section 3.7.7), are known to cause decadal modulation of the monsoon (Krishnamurthy and Krishnamurthy, 2014; Naidu et al., 2020).

The interplay of these external and internal drivers is key to understanding past and future monsoon change.

10.6.3.5 Model simulation and attribution of drying over the historical period

The robust decline of Indian summer monsoon rainfall averaged over India in the second half of the 20th century (Section 10.6.3.3) is not in line with expectations arising from thermodynamic constraints on the water cycle in a warming world (Section 8.2.2) and has been regarded as a puzzle (Goswami et al., 2006). Assessing the attribution of 20th-century changes to Indian rainfall is the subject of coordinated modelling under the Global Monsoon MIP (GMMIP; Zhou et al., 2016), but is complicated by long-standing dry biases in coupled CMIP3, CMIP5 (Sperber et al., 2013) and CMIP6 (Figure 10.19b) GCMs. These dry biases are connected to a lower tropospheric circulation that is too weak (Sperber et al., 2013) and wet biases in the equatorial Indian Ocean (Bollasina and Ming, 2013). Section 8.3.2.4.1 finds *high confidence* that anthropogenic aerosol emissions have dominated the observed declining trends of countrywide Indian summer monsoon rainfall, consistent with findings at the global-monsoon scale (Section 3.3.3.2).

Stronger Northern Hemisphere aerosol emissions cool it relative to the Southern Hemisphere, increasing northward energy transport at the expense of moisture transport towards India (Bollasina et al., 2011). The attribution to anthropogenic aerosols is supported in CMIP5 single-forcing experiments, including some testing the sensitivity to local and remote emissions (Guo et al., 2015, 2016; Shawki et al., 2018), comparing CMIP5 GCMs forced by both aerosol and GHG to GHG only (Salzmann et al., 2014) and reducing emissions to pre-industrial levels (Takahashi et al., 2018). The large spread between individual model realisations of comparable magnitude to the aerosol-induced signal suggested to Salzmann et al. (2014) that internal variability may also play a role over regions such as northern-central India. Further uncertainty surrounds the level of radiative forcing. Dittus et al. (2020) forced a GCM with historical aerosol emissions scaled between 0.2 and 1.5 times their observed values, representing the spread in CMIP5 effective radiative forcing. The strongest forcing led to around 0.5 mm day^{-1} less late-20th century Indian monsoon rainfall than the weakest (Shonk et al., 2020). Meanwhile, the uncertainty surrounding aerosol-cloud interactions could change the sign of long-term precipitation trends (Takahashi et al., 2018).

There is some evidence that declining Indian monsoon rainfall is due to regional SST warming patterns, themselves arising due to radiative forcing from GHG (e.g., in the Indian Ocean, Guemas et al., 2013). Roxy

ACCEPTED VERSION SUBJECT TO FINAL EDITING

et al. (2015) artificially raised SST in a coupled GCM in the equatorial Indian Ocean (the region of strongest observed SST warming), leading to a weakened monsoon. Annamalai et al. (2013) used a GCM to suggest instead that preferential warming of the western North Pacific may force a Rossby-wave response to its west that weakens the monsoon through dry advection and subsidence. These hypotheses are not borne out in GHG-forced future projections (Section 10.6.3.6).

A small anthropogenic contribution may be expected from local land-use/land-cover changes and land management. India is the world's most irrigated region with around 0.5 mm/day in places, although peaking higher in summer (Cook et al., 2015b; McDermid et al., 2017). Including irrigation in GCMs and RCMs slows the monsoon circulation and diminishes rainfall (Lucas-Picher et al., 2011; Guimberteau et al., 2012; Shukla et al., 2014; Tuinenburg et al., 2014; Cook et al., 2015b) due to reduced surface temperature (Thiery et al., 2017), reducing the monsoon wind and moisture fluxes towards India (Mathur and AchutaRao, 2020). However, implementation methodologies for irrigation in climate models are simplified and often do not account for spatial heterogeneity while overestimating demand and supply (Nazemi and Wheater, 2015; Pokhrel et al., 2016; Section 10.3.3.6). Changing forest cover to agricultural land in an RCM (Paul et al, 2016) finds weakened summer monsoon rainfall especially in central and eastern India, due to decreased local evapotranspiration. Decreased evapotranspiration from a warmer surface since the 1950s in the CMIP5 ensemble may also feedback on the supply of moisture (Ramarao et al., 2015). Based on a global atmospheric GCM study and literature review, Krishnan et al. (2016) support the role of land-use/land-cover change in adding to the effects of aerosol in weakening the monsoon, in addition to dynamic effects on the circulation caused by rapid warming of the Indian Ocean.

In addition to anthropogenic forcing, there is evidence that internal variability in the Pacific is a significant driver. Huang et al. (2020b) compared a large perturbed-physics ensemble (HadCM3C) with a SMILE for the historical period. Ensemble members replicating the negative Indian rainfall trend were accompanied by a strong phase change in the PDV from negative to positive, consistent with SST observations. Jin and Wang (2017) have demonstrated increasing Indian monsoon rainfall since 2002 in a variety of observed datasets, suggesting the increase is due either to a change in dominance of a particular forcing (for example from aerosol to GHG) or to a change in phase of internal variability such as the PDV. Huang et al. (2020b) partially attribute the rainfall recovery to a phase change in the PDV, supported by a SMILE study combined with reanalyses (Ha et al., 2020).

The drying trend of Indian summer monsoon rainfall since the mid-20th century can be attributed with *high confidence* to aerosol as the dominant anthropogenic forcing with a further contribution from internal variability, supported by the review of Wang et al. (2020) including CMIP6 results. Understanding the interplay between anthropogenic and internal drivers will be important for understanding future change.

10.6.3.6 Future climate projections from global simulations

The AR5 (Christensen et al., 2013) concluded that Indian summer monsoon rainfall will strengthen under all RCP future climate scenarios, while the circulation will weaken (*medium confidence*). SR1.5 (Hoegh-Guldberg et al., 2018) found only *low confidence* in projections of monsoon change at 1.5°C and 2°C, or any difference between them. The AR6 assessment of Chapter 8 (8.4.2.4.1) finds more precipitation in future projections (also depicted in Figure 10.19c,d,e), supported by reviews of CMIP3, CMIP5 and CMIP6 models (Turner and Annamalai, 2012; Kitoh, 2017; Chen et al., 2020b; Wang et al., 2020).

Given the assessment for a future wetter monsoon dominated by GHG emissions and attribution of the late-20th century decline to aerosol (Sections 8.3.2.4.1 and 10.6.3.5), the change between dominant forcings will lead, at some point, to a positive trend. For example, RCP4.5 experiments in an atmospheric GCM forced by coupled model-derived future SSTs showed continuation of 20th-century drying, before a rainfall recovery (Krishnan et al., 2016). By holding aerosol emissions at 2005 levels, lower monsoon rainfall is found throughout the 21st century than in a standard RCP8.5 scenario (Zhao et al., 2019), suggesting that the timing of the recovery will be partially controlled by the rate at which aerosol emissions decline. The spread in spatial distribution of aerosol emissions in SSPs may also play a role in near-term projections (Samset et al.,

ACCEPTED VERSION SUBJECT TO FINAL EDITING

2019). Under divergent air-quality policies, SSP3 features a dipole of declining sulphate emissions for China but increases over India, leading to suppression of GHG-related precipitation increases there (Wilcox et al., 2020). For the near-term future around the mid-21st century, the interplay between internal variability and external forcing must be considered (Singh and AchutaRao, 2018). Huang et al. (2020a) used two SMILEs to show that internal variability related to PDV could potentially overcome the GHG-forced upward trend in Indian monsoon rainfall, consistent with assessments of the global monsoon for the near term (Section 4.4.1.4). Emergence of the anthropogenic signal for South Asian precipitation is shown from the 2050s onwards in CMIP6 (Figure 10.15b).

In long-term projections, robust signals consist of a weakened upper-tropospheric meridional temperature gradient, either due to upper-level heating over the tropical Pacific (Sooraj et al., 2015) or Indian Oceans (Sabeerali and Ajayamohan, 2018) in CMIP5, and increased seasonal mean rainfall, including in CMIP6 (Almazroui et al., 2020c; Wang et al., 2020). The weakened temperature gradient combines with increased atmospheric stability to weaken the monsoon overturning circulation, with some findings showing northward movement of the lower-tropospheric monsoon winds in response to a stronger land-sea temperature contrast in CMIP3 and CMIP5 (Sandeep and Ajayamohan, 2015; Endo et al., 2018). The northward shift was also found in the genesis of synoptic systems (monsoon depressions) in a single high-resolution atmospheric GCM forced by an ensemble of SSTs derived from four GCMs under the RCP8.5 scenario (Sandeep et al., 2018).

Projections can also be expressed in terms of global-mean warming levels (GWLs) rather than time horizons (Cross-Chapter Box 11.1). Advancing upon SR1.5, amplification of mean and extreme monsoon rainfall at 2.0°C compared to 1.5°C has been found both by an atmospheric GCM forced by future SST patterns (Chevuturi et al., 2018) and using time slices in CMIP5 GCMs (Yaduvanshi et al., 2019; Zhang et al., 2020a). These findings are consistent with the general scaling of Indian monsoon precipitation per degree of warming in CMIP5 (Zhang et al., 2019) and CMIP6 (Wang et al., 2020). Increasing GWLs also lead to emergence of the anthropogenic signal over larger proportions of the South Asian region (Figure 10.15a).

Decomposition of the increased rainfall signal showed that while the dynamic component led to a drying tendency, this was overcome by the thermodynamic contribution (Sooraj et al., 2015; Chen et al., 2020b). Alternative decomposition experiments using atmospheric GCMs and their coupled counterparts found increases in the lower-tropospheric temperature gradient and monsoon rainfall to be dominated by the fast radiative response to GHG increase rather than SST changes (Li and Ting, 2017; Endo et al., 2018). The response to SST forcing featured a large model spread, particularly arising from the dynamic component (Li and Ting, 2017). Chen and Zhou (2015) found that the Indo-Pacific SST warming pattern dominated the uncertainty in Indian monsoon rainfall change. Finally, in assessing the relative impact of CO_2 radiative forcing and plant physiological changes in quadrupled CO_2 experiments in four Earth system models, Cui et al. (2020) showed little impact of plant physiology on annual rainfall for the Indian region.

While several of the above studies selected model subsets to constrain future projections based on standard performance metrics of the historical period, such as pattern correlation and root-mean-square error, Latif et al. (2018) included a performance measure based on agreement with historical rainfall trends. This is an unproven constraint for regional projections (Section 10.3.3.9), since the 20th-century rainfall trend over India is assessed to have been driven chiefly by aerosol and other factors such as PDV (Sections 8.3.2.4.1 and 10.6.3.5), while the dominant late-21st century forcing is GHG emissions. Modern emergent-constraint techniques (Section 10.3.4.2) are being applied to the Indian monsoon such as Li et al. (2017), who found that models with excessive tropical western Pacific rainfall tend to project a greater Indian monsoon rainfall change in future, due to an exaggerated cloud-radiation feedback. Correcting for this bias reduces the future change.

[START FIGURE 10.19 HERE]

Figure 10.19: Changes in the Indian summer monsoon in the historical and future periods. (a) Observational uncertainty demonstrated by a snapshot of rain-gauge density (% of 0.05°-subgrid boxes containing at

ACCEPTED VERSION SUBJECT TO FINAL EDITING

least one gauge) in the APHRO-MA 0.5° daily precipitation dataset for June to September 1956. (b) Multi-model ensemble (MME)-mean bias of 34 CMIP6 models for June to September precipitation (mm day^{-1}) compared to CRU TS observations for the 1985–2010 period. (c) Maps of rainfall trends (mm day^{-1} per decade) in CRU TS observations (1950–2000), the CMIP6 MME-mean of SSP5-8.5 future projections for 2015–2100 (34 models), the CMIP6 hist-GHG and hist-aer runs, both measured over 1950 to 2000. (d) Low-pass filtered time series of June to September precipitation anomalies (%, relative to 1995–2014 baseline) averaged over the central India box shown in panel (b). The averaging region (20°N–28°N, 76°E–87°E) follows other works (Bollasina et al., 2011; Jin and Wang, 2017; Huang et al., 2020b). Time series are shown for CRU TS (brown), GPCC (dark blue), REGEN (green), APHRO-MA (light brown) observational estimates and the IITM all-India rainfall product (light blue) in comparison with the CMIP6 mean of 13 models for the all-forcings historical (pink), the aerosol-only (hist-aer, grey) and greenhouse gas-only (hist-GHG, blue). Dark red and blue lines show low-pass filtered MME-mean change in the CMIP6 historical/SSP5-8.5 (34 models) and CMIP5 historical/RCP8.5 (41 models) experiments for future projections to 2100. The filter is the same as that used in Figure 10.11(d). To the right, box-and-whisker plots show the 2081–2100 change averaged over the CMIP5 (blue) and CMIP6 (dark red) ensembles. Note that some models exceed the plotting range (CMIP5: GISS-E2-R-CC, GISS-E2-R & IPSL-CM5B-LRl and CMIP6: CanESM5-CanOE, CanESM5 & GISS-E2-1-G). (e) Precipitation linear trend (% per decade) over central India for historical 1950–2000 (left) and future 2015–2100 (right) periods in Indian monsoon rainfall in observed estimates (black crosses), the CMIP5 historical-RCP8.5 simulations (blue), the CMIP6 ensemble (dark red) for historical all-forcings experiment and SSP5-8.5 future projection, the CMIP6 hist-GHG (light blue triangles), hist-aer (grey triangles) and historical all-forcings (same sample as for hist-aer and hist-GHG, pink circles). Ensemble means are also shown. Box-and-whisker plots show the trend distribution of the three coupled and the d4PDF atmosphere-only (for past period only) SMILEs used throughout Chapter 10 and follow the methodology used in Figure 10.6. (f) Example spread of trends (mm day^{-1} per decade) out to the near term (2016–2045) in RCP8.5 SMILE experiments of the MPI-ESM model, showing the difference between the three driest and three wettest trends among ensemble members over central India. All trends are estimated using ordinary least-squares regression. Further details on data sources and processing are available in the chapter data table (Table 10.SM.11).

[END FIGURE 10.19 HERE]

In summary, long-term future scenarios dominated by GHG increases (such as the RCPs) suggest increases in Indian summer monsoon rainfall (*high confidence*), dominated by thermodynamic mechanisms leading to increases in the available moisture. In the near-term, there is *high confidence* (*medium agreement*, *robust evidence*) that increased rainfall trends due to GHGs could be overcome by aerosol forcing or internal variability.

10.6.3.7 Future climate projections from regional downscaling

Coordinated monsoon-relevant dynamical downscaling efforts such as CORDEX South Asia (Gutowski et al., 2016; Choudhary et al., 2018) are relevant to the Indian summer monsoon, first with assessment of their added value (Sections 10.3.3.2 and Atlas.5.3.3). Singh et al. (2017) compared nine CORDEX-South Asia RCMs against their driving CMIP5 GCMs, for present-day rainfall patterns and processes related to intraseasonal variability. They found no consistent improvement other than for spatial patterns (e.g., rainfall close to better-resolved orography); some characteristics were made worse. Both the rainfall pattern and its bias were worsened in CORDEX compared to CMIP5 in Mishra et al. (2018). In contrast, Varikoden et al. (2018) found improved representation of historical rainfall patterns, such as over the Western Ghats mountains (consistent with Singh et al., 2017), reducing the dry bias; improvements were not found over the northern plains, which are dominated by synoptic variability known as monsoon depressions. Similarly, Sabin et al. (2013) compared a uniform 1°-resolution model ensemble with another zoomed to ~35 km over South Asia. Local zooming improved simulation of orographic precipitation and the monsoon trough. For the future, a surrogate approach (like pseudo-global warming, see Section 10.3.2.2) was used in an RCM to test the impacts of warming or moistening on monsoon depressions (Sørland and Sorteberg, 2016; Sørland et al., 2016). The depressions are found to give more rainfall in future, dominated by strengthened synoptic circulation from the warming perturbation. By forcing an RCM with a perturbed parameter ensemble of a

ACCEPTED VERSION SUBJECT TO FINAL EDITING

GCM, Bal et al. (2016) made projections under SRES A1B for the 2020s, 2050s and 2080s. They noted increases in rainfall of 15–24% for India. Finally, evidence from a single CORDEX South Asia RCM showed a mixed signal for changes in peak season rainfall under RCP2.6 and RCP8.5 (Ashfaq et al., 2020).

Statistical downscaling and other post-processing require calibration in historical conditions (e.g., Akhter et al., 2019) and assessment of fitness for purpose (Section 10.3.3.9) before use for future projections. Given the noted biases in GCM monsoon simulation (Section 10.6.3.5), Vigaud et al. (2013) used a variant of quantile mapping to bias adjust (Section 10.3.1.3.2 and Cross-Chapter Box 10.2) GCM outputs. For the historical period, the pattern, mean and seasonal cycle of rainfall versus the input GCMs were improved. Increased future monsoon rain, albeit in older SRES A2 projections, was found for southern India. Salvi et al. (2013) used regression-based perfect prognosis (Section 10.3.1.3.1) for the whole country at 0.5°-resolution based on five ensemble members of a GCM in SRES scenarios. They noted increases over rainy regions of west coast and northeast India, but decreases in the north, west and southeast. Madhusoodhanan et al. (2018) statistically downscaled 20 CMIP5 models to 0.05°-resolution. While the GCMs projected increased rainfall, the downscaled ensemble depicted both increasing and decreasing trends, indicating uncertainty. However, key physical processes operating at below-GCM scale cannot be resolved nor calibrated for, such as aspects of the flow around topography. This is notably an issue given the resolution disparity between the driving GCMs and output, and the regional challenges in observational data used for calibration (Section 10.6.3.3).

There are mixed messages as to whether downscaling adds value to climate projections of the Indian summer monsoon; however, there is *high confidence* in projections of precipitation changes in orographic regions given the consistent improved representation in these regions among several dynamical downscaling studies.

10.6.3.8 Storyline approaches for India

Formal storyline approaches (see Box 10.2) have been used infrequently for the Indian summer monsoon, representing a knowledge gap. In an expert-elicitation approach (Dessai et al., 2018), physically plausible futures substantiated by climate processes were constructed, focusing on a river basin in southern India. Possible outcomes were framed based on changes in two drivers: availability of moisture from the Arabian Sea and strength of the low-level flow. The narratives identified were able to explain 70% of the variance in monsoon rainfall over 1979–2013, the implication being that climate uncertainties could be easily communicated to stakeholders in the context of present-day variability.

The storylines terminology could be used to loosely describe the interplay between internal variability and forced change (see Section 10.6.3.6), such as considering the difference between groups of wettest and driest ensemble members of a SMILE for the near-term future in Figure 10.19f. However, given the interest in low-likelihood high-impact scenarios (Sutton, 2018), we can also consider possible storylines for the Indian monsoon constructed from evidence in paleoclimate records and modelling. For example, a future AMOC collapse could cause reduced monsoon rainfall (Section 8.6.1; Liu et al., 2017), offsetting increases expected due to GHG. Large tropical volcanic eruptions are also known to weaken the Asian summer monsoon, in observations and model simulations over the last millennium (Section 8.5.2.3; Zambri et al., 2017), although a hemispheric dependence is found, with southern hemisphere eruptions even strengthening the monsoon around India (Zuo et al., 2019). Typically, future climate projections do not consider plausible eruption scenarios and their mitigating effects on greenhouse warming (see also Cross-Chapter Box 4.1). A single-model ensemble (Bethke et al., 2017) demonstrates a future drier Indian monsoon relative to conditions in which volcanic eruptions are not considered, although the effects of GHG warming dominate beyond the mid-term.

The few studies on low-likelihood high-impact scenarios, often in single models, together with findings in SR1.5 (Hoegh-Guldberg et al. 2018), noting the small radiative forcing in 1.5°C or 2°C scenarios, or the absence of large aerosol emissions at the end of the 21st century in RCPs, give us *low confidence* in abrupt changes to the monsoon on this time scale.

ACCEPTED VERSION SUBJECT TO FINAL EDITING

10.6.3.9 Regional climate information distilled from multiple lines of evidence

Above, we presented assessments from observational and model attribution studies of the historical period, followed by future climate projections in global and regional models, and storylines approaches including low-likelihood high impact events. Miscellaneous lines of evidence are considered here.

Our assessment could also be informed by attempting to constrain future projections of the Indian summer monsoon using paleoclimate evidence. In modelling work of the mid-Holocene (D'Agostino et al., 2019), the increased obliquity (axial tilt) and altered orbital precession lead to an enhanced monsoon with a stronger dynamic component (strengthening the mean monsoon overturning) controlling the increase in monsoon rainfall. In future climates however, the dynamic contribution decreases (Section 10.6.3.6), yet the increased thermodynamic component (greater moisture availability) overcomes this to cause a wetter monsoon. Monsoon changes under different epochs may not be governed by the same mechanisms (D'Agostino et al., 2019; Hill, 2019), making the mid-Holocene, in particular, unsuitable as a period to compare with.

Finally, the recent national climate-change assessment for India (Krishnan et al., 2020) has distilled multiple lines of evidence to show declining summer monsoon rainfall over the second half of the 20th century, attributable to emissions of anthropogenic aerosols, while future projections informed by CMIP5 modelling and dominated by GHG forcing show increased mean rainfall by the end of the 21st century.

There is *very high confidence* (*robust evidence, high agreement*) of a negative trend of summer monsoon rainfall over the second half of the 20th century averaged over all of India. There is *medium agreement* over trends at the regional level owing to uncertainty among observational products, which hinders model evaluation, downscaling and assessment of changes to extremes. There is *high confidence* (*robust evidence*, *medium agreement*) that anthropogenic aerosol emissions over the Northern Hemisphere and internal variability have contributed to the negative trend, while there is *high confidence* (*robust evidence*, *medium agreement*) that Indian summer monsoon rainfall will increase at the end of the 21st century in response to increased GHG forcing, due to the dominance of thermodynamic mechanisms. No contradictory evidence is found from downscaling methods. The contrast between declining rainfall in the observational record and long-term future increases can be explained using multiple lines of evidence. They are not contradictory since they are attributable to different mechanisms (primarily aerosols and greenhouse gases, respectively). The long-term future changes are generally consistent across global (including at high resolution) and regional climate models, and supported by theoretical arguments; furthermore, while there are subtle differences found in past periods with a climate similar to the future climate (the mid-Holocene), different physical mechanisms at play suggest that paleoclimate evidence does not reduce confidence in the future projections. In the near term, there is *high confidence* that internal variability will dominate.

10.6.4 Mediterranean Summer Warming

10.6.4.1 Motivation and regional context

The Mediterranean region is loosely denoted as the region that surrounds the Mediterranean Sea, and it is characterized by complex orography and strong land-sea contrasts. The region contains a dense and growing human population, with large regional differences: whereas the population of the European Mediterranean countries has been relatively stable or even declining during the past decades, the population of countries in Mediterranean areas of the Middle East and North Africa has quadrupled between 1960 and 2015, and the degree of urbanization has risen from 35 to 64% during the same period (Cramer et al., 2018) and during the more recent period 2000-2020 the urban expansion rate has exceeded 5% (Kuang et al., 2021).

The Mediterranean region has experienced significant climate variability over recent decades and has been affected in particular by severe heatwaves and droughts (Hoegh-Guldberg et al. (2018); Sections 8.3, 11.3, 11.6 and 12.4). Increasing summer temperatures will enhance the frequency and intensity of such extreme events and will cause additional environmental and socio-economic pressure on the region.

ACCEPTED VERSION SUBJECT TO FINAL EDITING

10.6.4.2 The region's climate

The Mediterranean has a heterogeneous climate that is partly semi-arid, especially along the southern coast of the Mediterranean Sea (Lionello et al., 2012). It is characterized by mild humid winters and dry warm or hot summers, which are associated with large scale subsidence that is partly related to the downward branch of the Hadley circulation. Other factors affecting the Mediterranean circulation include the monsoon heating over Asia (Rodwell and Hoskins, 1996; Cherchi et al., 2014; Ossó et al., 2019) and circulation anomalies induced by topography (Simpson et al., 2015). Seasonal and interannual variability is strongly linked to natural modes of variability (Section 10.6.4.4). The Mediterranean Sea acts as an evaporation source that dominates the regional hydrological cycle, which is characterized by local cyclogenesis and a separate branch of the mid-latitude storm track (Lionello et al., 2016). It also affects remote locations such as the Sahel (Park et al., 2016; Section 10.4.2.1). Strong storms can develop over the Mediterranean: among these, Medicanes are particularly destructive and exhibit several similarities with tropical cyclones (Cavicchia et al., 2014; Kouroutzoglou et al., 2015; Gaertner et al., 2018). The Mediterranean region is also characterized by strong land-atmosphere coupling and feedbacks (Seneviratne et al., 2006) generating prolonged droughts and intense heatwaves, which can also affect continental Europe (Zampieri et al., 2009). Other aspects of Mediterranean climate include regional winds, which can be very strong due to the channelling effect (Obermann et al., 2018) and extreme rainfall during autumn (Ducrocq et al., 2014; Ribes et al., 2019).

10.6.4.3 Observational issues

The Mediterranean region spans a wide variety of countries and economies. This has led to large differences in the existence and availability of observational records, with the southern part of the area being sparsely covered by meteorological stations (Figure 10.20b). Consequently, basin-wide, homogeneous, quality controlled observational datasets are lacking, especially before the advent of substantial satellite observations in the 1970s. Observational uncertainties exist also for those regions that are covered by high quality networks such as ECA&D (Flaounas et al., 2012).

Large differences of up to 7°C between the CRU and UDEL datasets have been found especially over mountainous areas, such as the Atlas in Morocco (Zittis and Hadjinicolaou, 2017; Strobach and Bel, 2019). Bucchignani et al., (2016b, 2016a) compared three different datasets (CRU, UDEL, and MERRA) with the available ground observations and found that although the geographical distribution of the bias is qualitatively similar for the three datasets, differences exist, with the absolute bias being generally lower in MERRA especially over North Africa during the summer and winter season. There is *high confidence* that the sparse monitoring network in parts of the Mediterranean region strongly increases the uncertainty across different gridded datasets (Section 10.2.2.3, Figure 10.20b,c).

10.6.4.4 Relevant anthropogenic and natural drivers

The Mediterranean summer climate is affected by large-scale modes of natural variability, the most dominant being the NAO (Annex IV) in winter and the summer NAO in summer (Folland et al., 2009; Bladé et al., 2012), although regional differences exist. The influence of those modes of variability over the eastern Mediterranean is recognized by some studies (Chronis et al., 2011; Kahya, 2011; Black, 2012; Bladé et al., 2012), but disputed by others (Ben-Gai et al., 2001; Ziv et al., 2006; Donat et al., 2014; Turki et al., 2016; Zamrane et al., 2016; Han et al., 2019). During positive summer NAO phase, associated with an upper-level trough over the Balkans, the Mediterranean is anomalously wet (Bladé et al., 2012). Drivers of Mediterranean climate variability include modes of variability such as the AMV (Sutton and Dong, 2012) and the Asian monsoon (Rodwell and Hoskins, 1996; Logothetis et al., 2020). In addition, the increase of GHGs (e.g., Zittis et al., 2019), the decrease of anthropogenic aerosols over Europe and the Mediterranean since the 1980's resulting from air pollution policies (Turnock et al., 2016), and anthropogenic land-use change (Millán, 2014; Cramer et al., 2020) have been shown to be linked to the regional warming. The role

ACCEPTED VERSION SUBJECT TO FINAL EDITING

of the zonal averaged circulation as a driver for the Mediterranean climate has been stressed by (Garfinkel et al., 2020).

The attribution of observed Mediterranean summer warming to above drivers and implications for future projections will be discussed in Sections 10.6.4.5 and 10.6.4.6.

10.6.4.5 Model simulation and attribution over the historical period

Observational datasets show large agreement on the historical (1960-2014) temperature evolution at basin-wide scale (Figure 10.20e), with an enhanced warming since the 1990's, and the early decades of the 21st century being on average approximately more than 1°C warmer than late 19th century levels (van der Schrier et al., 2013; Cramer et al., 2018; Lionello and Scarascia, 2018; Figure 10.20e). Over recent decades, the surface air temperature of the Mediterranean including the Mediterranean Sea has warmed by around 0.4°C per decade (Macias et al., 2013). Observed trends over land show large geographical heterogeneity (Figure 10.20d) and notable differences exist amongst different datasets at grid point scale (Figure 10.20c; Qasmi et al., 2021).

Several mechanisms have been proposed for the enhanced Mediterranean warming, although their relative importance and the possible interplay between them are not fully understood. Circulation changes might have contributed to this enhanced warming (Figure 10.20a). Sutton and Dong (2012) argued that the AMV induced a shift around the 1990s towards warmer southern European summers. This mechanism is associated with a linear baroclinic atmospheric response to the AMV-related surface heat flux. Also O'Reilly et al. (2017) related warm summer decades to the AMV, but the connection was shown to be mainly thermodynamic. Qasmi et al. (2021) estimate an increase in Mediterranean summer temperature of 0.2-0.8°C during a positive AMV.

Increased warming over land compared to the sea is expected due to the lapse-rate changes associated with tropospheric moisture contrasts (Kröner et al., 2017; Byrne and O'Gorman, 2018; Brogli et al., 2019a; Figure 10.20a). Enhanced land-sea temperature contrast leads to relative humidity and soil moisture feedbacks (Rowell and Jones, 2006), the latter also depending on weather regimes (Quesada et al., 2012). The globally enhanced land-sea contrast in near surface temperature is also a robust result in CMIP5 and CMIP6 models (section 4.5.1.1).

Due to its semi-arid climate, strong atmosphere-land coupling has contributed to the larger increase of mean summer temperature compared to the increase of annual mean temperature (Seneviratne et al., 2006). In particular, during drought spells, limits to evaporation due to low soil moisture provide a positive feedback and enhances the intensity of heat waves (Lorenz et al., 2016; Box 11.1). By comparing reanalysis-driven RCM simulations with observations, Knist et al. (2017) found that RCMs are able to reproduce soil moisture interannual variability, spatial patterns, and annual cycles of surface fluxes over the period 1990–2008, revealing a strong land-atmosphere coupling especially in southern Europe in summer. In addition cloud feedbacks can modulate the Mediterranean summer temperature (Mariotti and Dell'Aquila, 2012).

The observed trends over 1901–2010 are outside the range of internal variability shown in CMIP5 pre-industrial control experiments and consistent with, or greater than those simulated by experiments including both anthropogenic and natural forcings (Knutson et al., 2013) and therefore partly attributable to anthropogenic forcing. The decrease of anthropogenic aerosols over Europe including the Mediterranean resulting from European de-industrialisation and air pollution policies (Turnock et al., 2016) has been highlighted as an important contributor to the observed warming (Ruckstuhl et al., 2008; Philipona et al., 2009; Laat and Crok, 2013; Nabat et al., 2014; Besselaar et al., 2015; Dong et al., 2017; Boé et al., 2020a). Pfeifroth et al. (2018) argue that this brightening is mainly due to cloud changes caused by the indirect aerosol effect with a minor role for the direct aerosol effect, in contrast to Nabat et al. (2014) and Boers et al. (2017) who attribute it to the direct aerosol effect. Using model sensitivity experiments, Nabat et al., (2014) also associated the increase in Mediterranean SST since 1980-2012 with the decrease in aerosol concentrations (Atlas 8.2, 8.3, 8.5).

ACCEPTED VERSION SUBJECT TO FINAL EDITING

Over the period 1960-2014, observed trends over land are consistent with those of most of the multi-model or SMILEs ensembles (Figure 10.20f), although large differences exist for individual models and ensemble members. The modelled ensemble-mean trends show large geographical variations; generally, both global and regional models often underestimate the observed trend especially over part of North Africa, Italy, the Balkans and Turkey. The cold bias in GCMs is related to simulated SLP trends that are anti-correlated to the observed trend, which is probably due to systematic model errors (Boé et al., 2020b). Biases in the simulation of soil-moisture and cloud-cover might also have contributed to the underestimation of the warming trend in GCMs (van Oldenborgh et al., 2009). The CORDEX results (at both 0.44 and 0.11 degree resolution) show consistently smaller values than those in GCMs and the available data sets (Figure 10.20g; Vautard et al., (2020)). This is partly due to the overestimation in the temperature evolution before 1990 (Figure 10.20e), possibly because of differences in the aerosol forcing (Boé et al., 2020a), although the driving GCMs also have a cold bias (Vautard et al., 2020). Cold biases for recent decades are also found in Med-CORDEX simulations (Dell'Aquila et al., 2018) and by RCM simulations over the southern part of the Mediterranean, Middle East and North Africa region (Almazroui, 2016; Almazroui et al., 2016b, 2016a; Ozturk et al., 2018; Zittis and Hadjinicolaou, 2017), although higher resolution, new bare soil albedo and modified aerosol parameterization significantly improve the results (Bucchignani et al., 2016b, 2016a, 2018). Despite large differences in the multi-model mean trend (Figure 10.20g), in most of the land points the observed trend lies within the model range in all ensembles. For the SST bias exhibited by coupled RCMs the choice of driving GCM has the largest impact (Darmaraki et al., 2019; Soto-Navarro et al., 2020).

10.6.4.6 Future climate information from global simulations

The Mediterranean is expected to be one of the most prominent and vulnerable climate change hotspots (Diffenbaugh and Giorgi, 2012). CMIP5, CMIP6, HighResMIP and CORDEX (Section 10.6.4.7) simulations all project a future warming for the 21st century that ranges between 3.5 and 8.75 °C for RCP8.5 at the end of this century for those ending at 2100 (Figure 10.21a,b)). CMIP6 results project more pronounced warming than CMIP5 for a given emission scenario and time period (Figure 10.21c; Coppola et al., 2020b). However, when analysing the Mediterranean warming in terms of mean global warming levels, the two ensembles largely agree showing that summer warming is projected to reach values up to 40-50% larger than the global annual warming, largely independent of models and emission scenarios (Figure 10.21d). Large regional differences exist, with enhanced warming projected over Turkey, the Balkans, the Iberian Peninsula and North African regions (Almazroui et al., 2020a; Figures 10.14a, 10.21c) and reaching, locally, values of up to double the global mean (Lionello and Scarascia, 2018). The enhanced summer warming also increases the amplitude of the seasonal cycle (Yettella and England, 2018).

As noted in Section 10.6.4.4, the Mediterranean summer climate is affected by large-scale circulation patterns, of which the summer NAO is the most important (Folland et al., 2009; Bladé et al., 2012). Barcikowska et al. (2020) highlight the importance of correctly simulating the summer NAO impact on the Mediterranean climate, as it partly offsets the anthropogenic warming signal in the western and central Mediterranean.

Climate models project a reduction in precipitation in all seasons, and a northward and eastward expansion of the Mediterranean climate, with the affected areas becoming more arid with an increased summer drying (Alessandri et al., 2015; Mariotti et al., 2015; Rajczak and Schär, 2017; Waha et al., 2017; Barredo et al., 2018; Lionello and Scarascia, 2018; Spinoni et al., 2018, 2020; Atlas 8.5). The drying can contribute to the enhanced warming by land-surface feedbacks (Whan et al., 2015; Lorenz et al., 2016; Russo et al., 2019). A negative feedback to this dryness induced warming might be provided by an enhanced moisture transport into the dry area associated with the dynamical response of the atmosphere (Zhou et al., 2021). Due to the arid climate, no positive soil moisture-temperature feedback is found over the North African regions of the Mediterranean, where the surface energy budget is mostly governed by radiative cooling (Lelieveld et al., 2016), implying that soil-moisture feedbacks are not contributing to enhanced warming over those regions.

Over the Mediterranean region, daily maximum temperature is projected to increase more than the daily

ACCEPTED VERSION SUBJECT TO FINAL EDITING

minimum. Consequently, the difference between daytime maxima and night-time minima is expected to increase, particularly in summer (Lionello and Scarascia, 2018). Temperature extremes will be affected as well, with a dramatic increase in the number of warm days and reduction of cold nights (Lionello and Scarascia, 2020; Section 11.9). The Mediterranean summer warming will also increase the frequency and intensity of heatwaves (Section 11.9).

[START FIGURE 10.20 HERE]

Figure 10.20: Aspects of Mediterranean summer warming. (a) Mechanisms and feedbacks involved in enhanced Mediterranean summer warming. (b) Locations of observing stations in E-OBS and (Donat et al., 2014). (c) Differences in temperature observational data sets (NOAA Global Temp, Berkeley Earth, CRUTEM4 and GISTEMP) with respect to E-OBS for the land points between the Mediterranean Sea and 46°N and west of 30°E. (d) Observed summer (June to August) surface air temperature linear trends (°C decade^{-1}) over the 1960–2014 period from Berkeley Earth. (e) Time series of area averaged Mediterranean (25°N–50°N, 10°W–40°E) land point summer temperature anomalies (°C, baseline 1995–2014). Dark blue, brown and turquoise lines show low-pass filtered temperature of Berkeley Earth, CRU TS and HadCRUT5, respectively. Orange, light blue and green lines show low-pass filtered ensemble means of HighResMIP (4 members), CORDEX EUR-44 (20 members) and CORDEX EUR-11 (37 members). Blue and red lines and shadings show low-pass filtered ensemble means and standard deviations of CMIP5 (41 members) and CMIP6 (36 members). The filter is the same as the one used in Figure 10.10. (f) Distribution of 1960–2014 Mediterranean summer temperature linear trends (°C decade^{-1}) for observations (black crosses), CORDEX EUR-11 (green circles), CORDEX EUR-44 (light blue circles), HighResMIP (orange circles), CMIP6 (red circles), CMIP5 (blue circles) and selected SMILEs (grey box-and-whisker plots, MIROC6, CSIRO-Mk3-6-0, MPI-ESM and d4PDF). Ensemble means are also shown. CMIP6 models showing a very high ECS (Box. 4.1) have been marked with a black cross. All trends are estimated using ordinary least-squares and box-and-whisker plots follow the methodology used in Figure 10.6. (g) Ensemble mean differences with respect to the Berkeley Earth linear trend for 1960–2014 (°C decade^{-1}) of CMIP5, CMIP6, HighResMIP, CORDEX EUR-44 and CORDEX EUR-11. Further details on data sources and processing are available in the chapter data table (Table 10.SM.11).

[END FIGURE 10.20 HERE]

[START FIGURE 10.21 HERE]

Figure 10.21: Projected Mediterranean summer warming. (a) Time series of area averaged Mediterranean (25°N–50°N, 10°W–40°E) land point summer surface air temperature anomalies (°C, baseline period is 1995–2014). Orange, light blue and green lines show low-pass filtered ensemble means of HighResMIP (highres-future, 4 members), CORDEX EUR-44 (RCP8.5, 20 members) and CORDEX EUR-11 (RCP8.5, 37 members). Blue and dark red lines and shadings show low-pass filtered ensemble means and standard deviations of CMIP5 (RCP8.5, 41 members) and CMIP6 (SSP5-8.5, 36 members). The filter is the same as the one used in Figure 10.10. The box-and-whisker plots show long term (until 2081-2100) temperature changes of different CMIP6 scenarios with respect to the baseline period (SSP1-2.6 in dark blue, SSP2-4.5 in yellow, SSP3-7.0 in red, SSP5-8.5 in dark red). (b) Distribution of 2015–2050 Mediterranean summer temperature linear trends (°C decade^{-1}) for CORDEX EUR-11 (RCP8.5, green circles), CORDEX EUR-44 (RCP8.5, light blue circles), HighResMIP (highres-future, orange circles), CMIP6 (SSP5-8.5, dark red circles), CMIP5 (RCP8.5, blue circles) and selected SMILEs (grey box-and-whisker plots, MIROC6, CSIRO-Mk3-6-0 and MPI-ESM). Ensemble means are also shown. CMIP6 models showing a very high ECS (Box 4.1) have been marked with a black cross. All trends are estimated using ordinary least-squares and box-and-whisker plots follow the methodology used in Figure 10.6. (c) Projections of ensemble mean 2015–2050 linear trends (°C decade^{-1}) of CMIP5 (RCP8.5), CORDEX EUR-44 (RCP8.5), CORDEX EUR-11 (RCP8.5), CMIP6 (SSP5-8.5) and HighResMIP (highres-future). All trends are estimated using ordinary least-squares. (d) Projected Mediterranean summer warming in comparison to global annual mean warming of CMIP5 (dashed lines, RCP2.6 in dark blue, RCP4.5 in light blue, RCP6.0 in orange and RCP8.5 in red) and CMIP6 (solid lines, SSP1-2.6 in dark blue, SSP2-4.5 in yellow, SSP3-7.0 in red and SSP5-8.5 in dark red) ensemble means. Further details on data sources and processing are available in the chapter data table (Table 10.SM.11).

ACCEPTED VERSION SUBJECT TO FINAL EDITING

[END FIGURE 10.21 HERE]

10.6.4.7 Future climate information from regional downscaling

To unravel the complex interactions and feedbacks over the region on a range of spatial and temporal scales, regional downscaling projects are being developed to provide more comprehensive and detailed information on the future of the Mediterranean. The importance of regional downscaling for investigating the subregional details caused by the complex morphology of the Mediterranean region is a well-known issue in the literature (Planton et al., 2012), which has been addressed in many studies since AR5. Recent examples of dynamical downscaling are EURO-CORDEX (Jacob et al., 2014) and Med-CORDEX (Ruti et al., 2016; Somot et al., 2018), but earlier activities have included ENSEMBLES (Déqué et al., 2012; Fernández et al., 2019), PRUDENCE (Christensen et al., 2002), CIRCE (Gualdi et al., 2013) and ESCENA (Jiménez-Guerrero et al., 2013).

From an analysis of CORDEX results, studies showed that southern Europe is projected to face a robust non-linear increase in temperature larger than the global mean (Zittis et al., 2019), EURO-CORDEX projections, that are driven by CMIP5 GCMs, project a less pronounced warming thanthat of CMIP6 (Coppola et al., 2020a; Figure 10.21c). The non-linear increase is especially evident for both hot and cold extremes (Maule et al., 2017; Jacob et al., 2018; Kjellström et al., 2018; Section 11.9). In particular, Dosio and Fischer (2018) showed that in many places in southern Europe and the Mediterranean, the increase in the number of nights with temperature above 20°C is more than 60% larger under 2°C warming compared to 1.5°C. Over the region, the projected temperature increase, including a higher probability of severe heat waves (Russo et al., 2015), is accompanied by a reduction in precipitation (Jacob et al., 2014; Dosio, 2016; Rajczak and Schär, 2017), resulting in projected increases of drought frequency and severity (Spinoni et al., 2018, 2020; Raymond et al., 2019). Also, the frequency and severity of marine heat waves of the Mediterranean Sea are projected to increase (Darmaraki et al., 2019; Section 12.4, Atlas 8.4).

Only a limited number of RCM simulations for the MENA domain are currently available. For the southern and eastern Mediterranean, they project a mean warming ranging from 3°C for RCP4.5 to 9°C for RCP8.5 at the end of this century compared to its beginning (Bucchignani et al., 2018; Ozturk et al., 2018). The frequency and duration of heatwaves and annual number of extremely hot days (i.e., those with maximum temperature > 50°C) in the southern Mediterranean will increase substantially. For 2070-2099 with respect to 1971-2000 the latter might even reach 70 days for RCP8.5 (Lelieveld et al., 2016; Almazroui, 2019; Driouech et al., 2020; Varela et al., 2020).

Despite the large efforts of these regional downscaling projects, the GCM-RCM matrix is still sparse and lacking a systematic design to explore the uncertainty sources (e.g., GCM, RCM, scenario, resolution) (Section 10.3). Focusing on the Iberian peninsula, Fernández et al. (2019) argued that the driving GCM is the main contributor to uncertainty in the ensemble. Physically consistent but implausible temperature changes in RCMs can occur. An example is a strong temperature increase over the Pyrenees due to excessive snow cover in the present climate (Fernández et al., 2019). Based on an older set of RCM simulations (ENSEMBLES), Déqué et al. (2012) also argued that the largest source of uncertainty in the temperature response over Southern Europe is the choice of the driving GCM (whereas for summer precipitation the choice of the RCM dominates the uncertainty). Finally, Boé et al. (2020) found that over a large area of Europe, including parts of the Mediterranean, RCMs project a summer warming 1.5–2°C colder than in their driving GCMs for the end of the 21st century. This is caused by differences in solar radiation related to the absence of time-varying anthropogenic aerosols in RCMs (Boé et al., 2020a; Gutiérrez et al., 2020), which also affects the noted differences in cloud cover between GCMs and RCMs (Bartók et al., 2017).

Statistical downscaling studies for the Mediterranean confirm the results from GCM and RCM studies, with large agreement among future projections showing lower rates of warming in winter and spring, and, in most cases, higher ones in summer and autumn (Jacobeit et al., 2014).

ACCEPTED VERSION SUBJECT TO FINAL EDITING

10.6.4.8 Storyline approaches

The atmospheric circulation is influenced by large-scale, often slowly varying components of the climate system, such as ocean, sea ice and soil moisture. Historical and future changes of the atmospheric circulation depend, among other factors, on how these drivers have changed and will change. Zappa and Shepherd (2017) have analysed this for the Mediterranean region and developed a set of storylines based on different plausible evolutions of those drivers and their impact on the Mediterranean winter climate. Important identified drivers during winter are tropical and polar amplification of global warming and the polar stratospheric vortex (Manzini et al., 2014; Simpson et al., 2018), with implications for precipitation. Zappa (2019) discusses the relative amplitude of tropical and Arctic warming, response of the AMOC, patterns of Pacific SST change, and changes in stratospheric vortex strength as possible drivers of the Mediterranean summer climate and stresses that given the present state of knowledge, alternative storylines based on these drivers should be considered as equally plausible future manifestations of regional climate change. Brogli et al. (2019a, 2019b) and Kröner et al. (2017) have revealed thermodynamic processes, lapse rate, and circulation as important drivers for Mediterranean summer climate.

Low-likelihood high-impact events might affect future Mediterranean climate. An example of such an event is the collapse of the AMOC (Weijer et al., 2019), that would bring widespread cooling over the Northern Hemisphere. For the Mediterranean this is estimated to be a few degrees Celsius during summer in the case of a total collapse (Jackson et al., 2015).

10.6.4.9 Climate information distilled from multiple lines of evidence

There is *very high confidence (high agreement, robust evidence)* that the Mediterranean region has experienced a summer temperature increase in recent decades that is faster than the increase for the Northern Hemisphere summer mean. There is also *very high confidence* (*high agreement, robust evidence*) that the projected Mediterranean summer temperature increase will be larger than the global warming level, with an increase in the frequency and intensity of heat waves.

Traditionally, the distillation process to produce contextualised, policy relevant information has taken place at regional or national level. For example, the potential effects of climate change on public health are discussed in several national climate change and adaptation reports (Bruci et al., 2016; MoARE, 2016; MoE, 2016; MoEP, 2018; MoEU, 2018). Although these reports are extremely helpful and widely used for the development of national adaptation policies, they are often based on non-comprehensive and heterogeneous sources of climate information (e.g., MEEN, 2018; MoE/UNDP/GEF, 2019): for instance, future climate change projections are based on a limited number of socio-economic scenarios and climate model simulations, which are also often not evaluated comprehensively (e.g., Bruci ED, 2016; MoARE, 2016; MoEU, 2018). In addition, these reports are often not peer-reviewed, not available in English, and mainly limited to the country level, thus making it difficult to compare the details of the climate information across them.

[START BOX 10.3 HERE]

BOX 10.3: Urban Climate: Processes and Trends

Urban areas have special interactions with the climate system that produce heat islands. This box presents information about these processes, how they are parameterized in climate modules, and on the role of urban monitoring networks. A discussion on the observed climate trends and climate change projections for urban areas follows.

Urban Heat Island

During night-time, urban centres are often several degrees warmer than the surrounding rural area, a phenomenon known as the night-time canopy urban heat island effect (Bader et al., 2018; Kuang, 2019; Li et

ACCEPTED VERSION SUBJECT TO FINAL EDITING

al., 2019, 2020d). While green and blue infrastructures can mitigate the urban heat island effect, three main factors contribute to its development (Hamdi et al., 2020; Masson et al., 2020): 1) three-dimensional urban geometry including building density and plan area, street aspect ratio and building height, 2) thermal characteristics of impervious surfaces, and 3) anthropogenic heat release, either from building energy consumption, especially waste heat from air conditioning systems, or as direct emissions from industry, traffic, or human metabolism (Ichinose et al., 1999; Sailor, 2011; de Munck et al., 2013; Bohnenstengel et al., 2014; Chow et al., 2014; Salamanca et al., 2014; Dou and Miao, 2017; Ma et al., 2017a; Chrysoulakis et al., 2018; Takane et al., 2019). Urban heat island magnitude is also affected by aerosols due to air pollution in urban areas (Cheng et al., 2020; Han et al., 2020) and by local background climate (Zhao et al., 2014; Ward et al., 2016).

Monitoring Network

Long-term climate datasets (a year or more) at the small spatial scales required to resolve processes of interest for cities (<1 km) are scarce (Bader et al., 2018; Caluwaerts et al., 2020). Moreover, urban observation sites often represent only parts of the urban environment and are suboptimal for detecting urban effects (e.g., sites in city parks). Recently, city-scale climate monitoring networks as well as satellite and ground-based remote sensing are being used (though still missing in global south cities; Technical Annex I), enhancing our understanding of the urban microclimate and its interaction with climate change, and providing key information for users (Chen et al., 2012a; Barlow et al., 2017; Bader et al., 2018). It has been found that harmonization of collection practices, instrumentation, station locations, and quality control methodologies across urban environments needs improvement to facilitate collaborative research (Muller et al., 2013; Barlow et al., 2017). Real time crowdsourcing data is becoming available (Section 10.2.4). The urban climate community is making efforts to understand how these methods can complement traditional datasets (Meier et al., 2017; Zheng et al., 2018; Langendijk et al., 2019a; Venter et al., 2020).

Urban Modules in Climate Models

Exchanges of heat, water and momentum between the urban surface and its overlying atmosphere are calculated using specific surface-atmosphere exchange schemes. Three different schemes, here in order of increasing complexity, can be distinguished (Masson, 2006; Grimmond et al., 2010, 2011; Chen et al., 2011; Best and Grimmond, 2015): 1) In the slab or bulk approach, the three-dimensional city structure is not resolved but cities are represented by modifying soil and vegetation parameters within land surface models, increasing roughness length and displacement height (e.g., Best et al., 2006; Dandou et al., 2005; Liu et al., 2006; Seaman et al., 1989). The energy balance is often modified to account for the radiation trapped by the urban canopy, heat storage, evaporation and anthropogenic heat fluxes. 2) Single-layer urban canopy modules use a simplified geometry (urban canyon, with three surface types: roof, road and wall) that approximately capture the three-dimensional dynamical and thermal physical processes influencing radiative and energy fluxes (Masson, 2000; Kusaka et al., 2001). 3) Multi-layer urban canopy modules compute urban effects vertically, allowing a direct interaction with the planetary boundary layer (Brown, 2000; Martilli et al., 2002; Hagishima et al., 2005; Dupont and Mestayer, 2006; Hamdi and Masson, 2008; Schubert et al., 2012). Building-energy models that estimate anthropogenic heat from a building for given atmospheric conditions can be incorporated. Recent model development has focused on improving the representation of urban vegetation (Lee et al., 2016; Redon et al., 2017; Mussetti et al., 2020).

Global (McCarthy et al., 2010; Oleson et al., 2011; Zhang et al., 2013; Chen et al., 2016b; Katzfey et al., 2020; Sharma et al., 2020; Hertwig et al., 2021) and regional modelling groups (Kusaka et al., 2012b; McCarthy et al., 2012; Hamdi et al., 2014; Trusilova et al., 2016; Daniel et al., 2019; Halenka et al., 2019; Langendijk et al., 2019b) are beginning to implement these urban parameterizations within the land-surface component of their models. There is *very high confidence* (*robust evidence* and *high agreement*) that while all types of urban parameterizations generally simulate radiation exchanges in a realistic way, they have strong biases when simulating latent heat fluxes, though recent research incorporating in-canyon vegetation processes improved their performance. There is *medium confidence* (*medium evidence, high agreement*) (Kusaka et al., 2012a; McCarthy et al., 2012; Hamdi et al., 2014; Trusilova et al., 2016; Jänicke et al., 2017; Daniel et al., 2019) that a simple single-layer parameterization, is sufficient for the correct simulation of the urban heat island magnitude and its interplay with regional climate change.

ACCEPTED VERSION SUBJECT TO FINAL EDITING

Observed Trends

There is *medium evidence* but *high agreement* (Parker, 2010; Zhang et al., 2013; Chen et al., 2016b) that the global annual mean surface air temperature response to urbanization is negligible. There is very high confidence that the different observed warming trend in cities as compared to their surroundings can partly be attributed to urbanization (Box 10.3, Figure 1; Park et al., 2017).

[START BOX 10.3, FIGURE 1 HERE]

Box 10.3, Figure 1: Urban warming compared to global GHG-induced warming. (a) Change in the annual mean surface air temperature over the period 1950–2018 based on the local linear trend retrieved from CRU TS (°C per 68 years). This background warming is compared to the local warming that has been reported during 1950–2018 in the literature from historical urbanization. The relative share of the total warming as percentage between the urban warming and the surrounding warming is plotted in a circle for each city. This map has been compiled from a review study (Hamdi et al., 2020). (b) Low-pass filtered time series of the annual mean temperature (°C) observed in the urban station of Tokyo (red line) and the rural reference station in Choshi (blue line) in Japan. The filter is the same as the one used in Figure 10.10. (c) Uncertainties in the relative share of urban warming with respect to the total warming (%) related to the use of different global observational datasets: CRU TS (brown circles), Berkeley Earth (dark blue downward triangle), HadCRUT5 (cyan upward triangle), Cowtan Way (orange plus) and GISTEMP (purple squares). Further details on data sources and processing are available in the chapter data table (Table 10.SM.11).

[END BOX 10.3, FIGURE 1 HERE]

There is *very high confidence* (*robust evidence* and *high agreement*) that the annual-mean minimum temperature is more affected by urbanization than the maximum temperature (Ezber et al., 2007; Fujibe, 2009; Hamdi, 2010; Elagib, 2011; Camilloni and Barrucand, 2012; Robaa, 2013; Hausfather et al., 2013; Argüeso et al., 2014; Alghamdi and Moore, 2015; Alizadeh-Choobari et al., 2016; Sachindra et al., 2016; Liao et al., 2017; Lokoshchenko, 2017; Wang et al., 2017a; Arsiso et al., 2018). Beside temperature, urbanization can induce an urban dryness island, which refers to lower relative humidity in cities than in nearby rural locations (Lokoshchenko, 2017; Bian et al., 2020) and the urban wind island, where slower wind speeds are observed in cities (Wu et al., 2017; Bader et al., 2018; Peng et al., 2018). There is *medium confidence* (*medium evidence* and *medium agreement*) (Schlünzen et al., 2010; Ganeshan et al., 2013; Ganeshan and Murtugudde, 2015; Haberlie et al., 2015; Daniels et al., 2016; Liang and Ding, 2017; McLeod et al., 2017; Li et al., 2020c) that cities induce increases in mean and extreme precipitation over and downwind of the city especially in the afternoon and early evening.

Climate Projections

Estimates of the urban heat island under further climate change are *very uncertain* because studies using different methods report contrasting results. However, there is *very high confidence* (*robust evidence* and *high agreement*) that the projected change of the urban heat island under climate change conditions is one order of magnitude less than the projected warming in both urban and rural areas under simulation constraints of no urban growth (Adachi et al., 2012; Arsiso et al., 2018; Früh et al., 2011; Hamdi et al., 2014; Hatchett et al., 2016; Hoffmann et al., 2018; Kusaka et al., 2012; McCarthy et al., 2010, 2012; Oleson, 2012; Oleson et al., 2011; Sachindra et al., 2016).

Combining climate change conditions together with urban growth scenarios, there is *very high confidence* (*robust evidence* and *high agreement*) that future urbanization will amplify the projected air temperature warming irrespective of the background climate (Georgescu et al., 2013; Argüeso et al., 2014; Mahmood et al., 2014; Doan et al., 2016; Kim et al., 2016; Kusaka et al., 2016; Grossman-Clarke et al., 2017; Kaplan et al., 2017; Li et al., 2018c) Urbanization will have a strong influence on minimum temperatures that could be locally comparable in magnitude to the global GHG-induced warming (Berckmans et al., 2019). There is *very high confidence* (*robust evidence* and *high agreement*) for the combination of future urban development and more frequent occurrence of extreme climatic events, such as heat waves (Hamdi et al., 2016; Bader et

ACCEPTED VERSION SUBJECT TO FINAL EDITING

al., 2018; He et al., 2021).

The choice of urban planning scenarios and RCM projections shows a large sensitivity during night-time, up to 0.6°C (Kusaka et al., 2016). The sensitivity is significantly less than the uncertainties arising from global emission scenarios or GCM projections. However, there is a large difference between RCM simulations with and without urban land use, indicating that this impact is comparable to the uncertainties related to the use of different GCM projections (Hamdi et al., 2014; Kusaka et al., 2016; Daniel et al., 2019). Therefore, impact assessments and adaptation plans for urban areas require high spatial resolution climate projections along with models that represent urban processes, ensemble dynamical and statistical downscaling, and local-impact models (Masson et al., 2014; Baklanov et al., 2018, 2020; Duchêne et al., 2020; Schoetter et al., 2020; Le Roy et al., 2021; Zhao et al., 2021).

[END CHAPTER BOX 10.3 HERE]

[START CROSS-CHAPTER BOX 10.4 HERE]

Cross-Chapter Box 10.4: Climate Change over the Hindu Kush Himalaya

Coordinators: Izuru Takayabu (Japan), Andrew Turner (UK), Zhiyan Zuo (China)
Contributors: Bhupesh Adhikary (Nepal), Muhammad Adnan (Pakistan), Muhammad Amjad (Pakistan), Subimal Ghosh (India), Rafiq Hamdi (Belgium), Akm Saiful Islam (Bangladesh), Richard G. Jones (UK), Martin Jury (Austria), Asif Khan (Pakistan), Akio Kitoh (Japan), Krishnan Raghavan (India), Lucas Ruiz (Argentina), Laurent Terray (France)

The Hindu Kush Himalaya (HKH) constitutes the largest glacierized region outside the poles and provides the headwaters for several major rivers (Sharma et al., 2019). Since the 1960s, the HKH has experienced significant trends in the mean and extremes of temperature and precipitation, accompanied by glacier mass loss and retreat, snowmelt and permafrost degradation (Yao et al., 2012a, 2012b; Azam et al., 2018; Bolch et al., 2019; Krishnan et al., 2019b, 2019a; Chug et al., 2020; Sabin et al., 2020). Observational uncertainty and lack of consistent, high-quality datasets hamper reliable assessments of climate change and model evaluation over several mountain areas, including the HKH (Section 10.2.2). This box assesses observed and projected climate change in the extended HKH (outline in Cross-Chapter Box 10.4, Figure 1a), in which we include the Tibetan Plateau (TP) and Pamir mountains.

Temperature trends

Little evidence was presented in the AR5 (IPCC, 2014) other than increased minimum and maximum temperature trends in the western Himalaya (Hartmann et al., 2013). SROCC assessed that HKH (named High Mountain Asia) surface-air temperature has warmed more rapidly than the global mean over recent decades (*high confidence*). Annual mean HKH surface air temperature increased significantly (about 0.1°C per decade) over 1901–2014 (Ren et al., 2017), although Cross-Chapter Box 10.4, Figure 1d shows an observational range of 0.20–0.25°C per decade over 1961–2014. There is a rising trend of extreme warm events and fewer extreme cold events over 1961–2015 (Krishnan et al., 2019b; Wester et al., 2019). However, summer cooling over the Karakoram (western HKH) was reported for 1960–2010 (Forsythe et al., 2017). A key relevant process is elevation-dependent warming (EDW; reviewed in Pepin et al., 2015), leading to warming of 2–2.5°C at 5000m over 1961–2006, but only 0.5°C at sea level (Xu et al., 2016). However, EDW behaviour appears to depend on region, time period and elevation (Guo et al., 2019a; Li et al., 2020a) and understanding is limited by the sparse observational network (You et al., 2020). Observational and model analyses have attributed EDW to GHG and black carbon emissions, accelerating warming by snow-albedo feedback (Ming et al., 2012; Gautam et al., 2013; Xu et al., 2016; Yan et al., 2016; Lau and Kim, 2018; Zhang et al., 2018b), or the more pronounced cooling effect of scattering aerosols at low elevations and stratospheric ozone depletion (Guo and Wang, 2012; Zeng et al., 2015). There is *high confidence* that the eastern and central HKH has exhibited rising temperatures (Cross-Chapter Box 10.4, Figure 1), with warming dependent on season and elevation. There is *high confidence* that much of the warming can be attributed to GHGs, but the effect of albedo has only *medium confidence*. There is *high*

ACCEPTED VERSION SUBJECT TO FINAL EDITING

confidence in more frequent extreme warm events and fewer extreme cold events over the eastern Himalayas in the last five decades.

[START CROSS-CHAPTER BOX 10.4, FIGURE 1 HERE]

Cross-chapter Box 10.4, Figure 1: Historical annual-mean surface air temperature linear trend (°C per decade) and its attribution over the Hindu Kush Himalaya (HKH) region. (a) Observed trends from Berkeley Earth (also showing the HKH outline), CRU TS (also showing the AR6 TIB outline, for ease of comparison to the Interactive Atlas), APHRO-MA and JRA-55 datasets over 1961–2014. (b) Models showing the coldest, median and warmest HKH temperature linear trends among the CMIP6 historical ensemble over 1961–2014. (c) Lowpass-filtered time series of annual-mean surface air temperature anomalies (°C, baseline 1961–1980) over the HKH region as outlined in panel (a), showing means of CMIP6 hist all-forcings (red), and the CMIP6 hist all-forcings sample corresponding to DAMIP experiments (pink), for hist-aer (grey) and hist-GHG (pale blue). Observed datasets are Berkeley Earth (dark blue), CRU (brown), APHRO-MA (light green) and JRA-55 (dark green). The filter is the same as that used in Figure 10.10. (d) Distribution of annual mean surface air temperature trends (°C per decade) over the HKH region from 1961 to 2014 for ensemble means, the aforementioned observed and reanalysis data (black crosses), individual members of CMIP6 hist all-forcings (red circles), CMIP6 hist-GHG (blue triangles), CMIP6 hist-aer (grey triangles), and box-and-whisker plots for the SMILEs used throughout Chapter 10 (grey shading). Ensemble means are also shown. All trends are estimated using ordinary least-squares regression and box-and-whisker plots follow the methodology used in Figure 10.6. Further details on data sources and processing are available in the chapter data table (Table 10.SM.11).

[END CROSS-CHAPTER BOX 10.4, FIGURE 1 HERE]

Precipitation trends

Annual and summer precipitation over the central-eastern HKH show decreasing trends over 1979–2010 in multiple observed datasets, attributable to a weakening South Asian monsoon (Yao et al., 2012b; Palazzi et al., 2013; Roxy et al., 2015). There are contradictory trends in the western HKH (Azmat et al., 2017; Yadav et al., 2017; Li et al., 2018b; Meher et al., 2018), where most precipitation is associated with western disturbances on the subtropical westerly jet, but trends in western disturbance activity are unclear (Kumar et al., 2015; Hunt et al., 2019; Krishnan et al., 2019a). There has been an increased frequency and intensity of extreme precipitation over the central-western HKH but contrasting evidence in the east (Sheikh et al., 2015; Talchabhadel et al., 2018). The number of consecutive wet days has increased over 1961–2012, but with no uniform trend in consecutive dry days (Zhan et al., 2017). There is *medium confidence* that the eastern-central HKH has experienced decreased summer precipitation (Section 10.6.3). There is *medium confidence* in the increase of summer extreme precipitation over the western HKH.

Glacier trends

The SROCC assessed that snow cover has declined in duration, depth and accumulated mass at lower elevations in mountain regions, including the HKH (*high confidence*). Glaciers are losing mass (*very high confidence*) and permafrost is warming (*high confidence*) over high mountains in recent decades, and it is *very likely* that atmospheric warming is the main driver. A significant reduction in HKH glacier area has been observed since the 1970s, with smaller glaciers generally shrinking faster (e.g., Bolch et al., 2019). HKH glacier mass loss took place at the lowest rate among high mountain areas in the last 20 years, although with one of the largest total losses (Shean et al., 2020; Section 9.5.1.1; Figure 9.20). The highest mass-loss rates occurred in the eastern and northern HKH, while gains occurred in the west (e.g., Shean et al., 2020). Glacier mass gain has been coined as the “Karakoram anomaly” (Sections 9.5.1 and Section 8.3.1.7.1), explained by a combination of low temperature sensitivity of debris-covered glaciers, a decrease in summer air temperatures, and increased snowfall possibly linked to evapotranspiration from irrigated agriculture (You et al., 2017; Bolch et al., 2019; de Kok et al., 2020a; Farinotti et al., 2020). Meanwhile, increased air

ACCEPTED VERSION SUBJECT TO FINAL EDITING

temperature and decreased snowfall explain the glacier mass decrease elsewhere (Bonekamp et al., 2019; de Kok et al., 2020b; Farinotti et al., 2020; Shean et al., 2020). There is *high confidence* that glaciers in most HKH regions have thinned, retreated and lost mass since the 1970s.

Projections

In AR5, the HKH was projected to continue warming over the 21st century, faster than the *likely* ranges for the global mean and South Asia. New CMIP5 results show temperature increases across mountainous HKH by about 1–2°C (in some places in summer 4–5°C) during 2021–2050 compared to 1961–1990 (Shrestha et al., 2015). Projected warming differs by up to 1°C between east and west, with higher values in winter (Sanjay et al., 2017; see Interactive Atlas). Statistically significant mean warming (0.30–0.90°C per decade until the end of the 21st century) across all RCPs has been projected by CORDEX South Asia (Dimri et al., 2018). CMIP6 models report that northwestern South Asia, including the western Himalayas, are projected to experience temperature increases exceeding 6°C by the end of the 21st century under SSP5-8.5 relative to 1995–2014 (Almazroui et al., 2020c). Results from CMIP5, CMIP6 and CORDEX ensembles for different warming levels are shown in the Interactive Atlas and summarised in Figure Atlas.20. The HKH will *likely* continue warming in the coming decades.

(IPCC, 2018b) stated that heavy precipitation risk in high-elevation regions is projected to be higher at 2°C compared to 1.5°C of global warming (*medium confidence*). CMIP5 models project increased annual or summer monsoon precipitation over the HKH in the 21st century (Palazzi et al., 2015; Kitoh and Arakawa, 2016), intensifying by about 22% in the hilly south-eastern Himalaya and TP for the long term in RCP8.5, but with no trends in the western HKH (Rajbhandari et al., 2015; Krishnan et al., 2019a). CMIP6 projects an increase of winter precipitation over the western Himalayas, with a corresponding decrease in the east (Almazroui et al., 2020c). HKH projections are subject to large uncertainties in CMIP5 and CORDEX (Hasson et al., 2013, 2017; Mishra, 2015; Sanjay et al., 2017). CORDEX, in particular, has inherent limitations at reproducing the characteristics of summer monsoon rainfall variability (Singh et al., 2017). There is *medium confidence* that HKH precipitation will increase in the coming decades.

The SROCC assessed that glaciers will lose substantial mass (*high confidence*) and permafrost will undergo increasing thaw and degradation (*very high confidence*) over high mountain regions (including the HKH), with stronger changes for higher emission scenarios. Regional differences in warming and precipitation projections and glacier properties cause considerable differences in glacier response within High Mountain Asia (Kraaijenbrink et al., 2017). Glacier mass loss will accelerate through the 21st century, increasing with RCP after 2030 (Marzeion et al., 2014; Section 9.5.1.3). Loss of between 40 ± 25% to 69 ± 21 % of 2015 glacier volume is expected by 2100 in RCP 2.6 and RCP 8.5, respectively (Section 9.5.1.3; Figure 9.21). Glacier mass loss is expected due to decreased snowfall, increased snowline elevations and longer melt seasons. However, due to projection uncertainties, simplicity of the models, and limited observations, there is *medium confidence* in the magnitude and timing of glacier mass changes (Section 9.5.1.3). Glacier mass in HKH will decline through the 21st century (*high confidence*), more so under high-emissions scenarios.

[END CROSS-CHAPTER BOX 10.4 HERE]

10.7 Final remarks

The assessments in this chapter are based on a rapidly growing body of evidence from the peer-reviewed literature, most of which was not previously considered by IPCC reports. A number of challenges in the construction of regional climate change information have been identified:

- Limited climate monitoring in some regions impedes the full understanding of the relevant climate processes, an appropriate validation of model simulations, and the formulation of trustworthy regional climate information. Beyond temperature and precipitation, there is a shortage of observed variables needed for regional process understanding, attribution, and model development and validation, among others. Examples include surface evapotranspiration, soil moisture, radiation, wind and relative humidity, among many others identified by sectors sensitive to climate (Sections 10.2, 10.3 and 10.6).

ACCEPTED VERSION SUBJECT TO FINAL EDITING

- Compared to the increasing number of large-scale evaluations, there is a shortage of process-based model evaluations at regional scales to assess the fitness of the chosen models for specific purposes (Sections 10.3 and 10.4).
- There is a general lack of studies of the simulation of large-scale, downscaling-relevant processes in global models to support the design of global/regional model matrices that both span a sufficiently large range of projection uncertainty and realistically represent the regional climate of interest. The fitness of statistical methods for regional climate change studies has received limited attention by the scientific community, while as in the case of global models, process-based evaluation has proven useful (Soares et al., 2019b). Studies of past changes and pseudo-reality studies to assess the predictors and model structures required for downscaling in a future climate are promising avenues (Section 10.3).
- Internal variability is a large contributor to climate uncertainty at regional scales, especially for extreme events. Further study of the processes governing regional internal variability, such as the modes of variability and the teleconnections that connect them to the regional variability, but also of the local processes and drivers involved, will help improve its understanding. The same applies to the validation of the simulated internal variability that underpins the trustworthiness of model-based climate information (Sections 10.3, 10.4 and 10.6, Cross-Chapter Box 10.1).
- Methodologies on how to propagate climate uncertainties from global and regional scales down to the human settlement scale are still under development. In some cases, bias-adjustment methods are used with substantial neglect of the physical processes involved (Section 10.3, Cross-Chapter Box 10.2).
- The production of regional climate information relies mainly on global and regional models that often do not incorporate human-controlled surface processes (urban parametrizations is one example) in their land-surface components. This limits the representation of uncertainties for climate information at the urban scale (Box 10.2, Cross-Chapter Box 10.2, Section 10.3).
- Literature plays a central role as a source for constructing regional climate change information. The amount of climate change literature available is unevenly distributed across the world, and large bodies of literature (e.g., local and regional reports) are often overlooked in the construction of climate information. Furthermore, research tends to focus on regions that attract the attention of the Global North so that climate aspects relevant to other regions may not receive sufficient attention for generating appropriate regional climate information (Sections 10.2, 10.3, 10.5 and 10.6).
- Governmental institutions producing regional and local climate information often use diverging approaches that are not necessarily coherent with each other. Coherency could be improved by implementing a quality control system and a traceability solution for the sources of the information. Collective work with the social sciences and humanities will improve the communication, perception and response to regional climate information and help translate user requirements (Sections 10.5 and 10.6).
- There is a shortage of regional climate change studies distilling multiple lines of evidence. Most studies rely on either global models or downscaled global models, with an increasing number of studies focusing on the use of emulators and the selection and combination of models. However, there are limited studies distilling this information with a wider range of lines of evidence that includes observations, process understanding, attribution, and hierarchies of models (Sections 10.3, 10.5 and 10.6).

Addressing these challenges could facilitate the assessment of both sources and methodologies that lead to an increased fitness and usefulness of regional climate information for a wide range of purposes.

ACCEPTED VERSION SUBJECT TO FINAL EDITING

Frequently Asked Questions

[START FAQ10.1 HERE]

FAQ 10.1: How can we provide useful climate information for regional stakeholders?

The world is physically and culturally diverse, and the challenges posed by climate change vary by region and location. Because climate change affects so many aspects of people's daily work and living, climate change information can help with decision-making, but only when the information is relevant for the people involved in making those decisions. Users of climate information may be highly diverse, ranging from professionals in areas such as human health, agriculture or water management to a broader community that experiences the impacts of changing climate. Providing information that supports response actions thus requires engaging all relevant stakeholders, their knowledge and their experiences, formulating appropriate information, and developing a mutual understanding of the usefulness and limitations of the information.

The development, delivery, and use of climate change information requires engaging all parties involved: those producing the climate data and related knowledge, those communicating it, and those who combine that information with their knowledge of the community, region or activity that climate change may impact. To be successful, these parties need to work together to explore the climate data and thus co-develop the climate information needed to make decisions or solve problems, distilling output from the various sources of climate knowledge into relevant climate information. Effective partnerships recognize and respond to the diversity of all parties involved (including their values, beliefs and interests), especially when they involve culturally diverse communities their indigenous and local knowledge of weather, climate and their society. This is particularly true for climate change – a global issue posing challenges that vary by region. By recognizing this diversity, climate information can be relevant and credible, most notably when conveying the complexity of risks for human systems and ecosystems and for building resilience.

Constructing useful climate information requires considering all available sources in order to capture the fullest possible representation of projected changes and distil the information in a way that meets the needs of the stakeholders and communities impacted by the changes. For example, climate scientists can provide information on future changes by using simulations of global and/or regional climate and inferring changes in the weather behaviour influencing a region. An effective distillation process (FAQ 10.1, Figure 1) engages with the intended recipients of the information, especially stakeholders whose work involves non-climatic factors, such as human health, agriculture or water resources. The distillation evaluates the accuracy of all information sources (observations, simulations, expert judgement), weighs the credibility of possible conflicting information, and arrives at climate information that includes estimating the confidence a user should have in it. Producers of climate data should further recognize that the geographic regions and time periods governing stakeholders' interest (for example, the growing season of an agricultural zone) may not align well with the time and space resolution of available climate data; thus additional model development or data processing may be required to extract useful climate information.

One way to distil complex information for stakeholder applications is to connect this information to experiences stakeholders have already had through storylines as plausible unfoldings of weather and climate events related to stakeholders' experiences. Dialogue between stakeholders and climate scientists can determine the most relevant experiences to evaluate for possible future behaviour. The development of storylines uses the experience and expertise of stakeholders, such as water-resource managers and health professionals, who seek to develop appropriate response measures. Storylines are thus a pathway through the distillation process that can make climate information more accessible and physically comprehensible. For example, a storyline may take a common experience like an extended drought, with depleted water availability and damaged crops, and show how droughts may change in the future, perhaps with even greater precipitation deficits or longer duration. With appropriate choices, storylines can engage nuances of the climate information in a meaningful way by building on common experiences, thus enhancing the information's usefulness.

ACCEPTED VERSION SUBJECT TO FINAL EDITING

Forging partnerships among all involved with producing, exploring and distilling climate data into climate information is at the centre of creating stakeholder-relevant information. These partnerships can occur through direct interaction between climate scientists and stakeholders as well as through organizations that have emerged to facilitate this process, such as climate services, national and regional climate forums, and consulting firms providing specialized climate information. These so-called 'boundary organizations' can serve the varied needs of all who would fold climate information into their decision processes. All of these partnerships are vital for arriving at climate information that responds to physical and cultural diversity and to challenges posed by climate change that can vary region-by-region around the world.

[START FAQ 10.1, FIGURE 1 HERE]

FAQ 10.1, Figure 1: Climate information for decision makers is more useful if the physical and cultural diversity across the world is considered. The figure illustrates schematically the broad range of knowledge that must be blended with the diversity of users to distil information that will have relevance and credibility. This blending or distillation should engage the values and knowledge of both the stakeholders and the scientists. The bottom row contains examples of stakeholders' interests and is not all-inclusive. As part of the distillation, the outcomes can advance the U.N.'s Sustainable Development Goals, covered in part by these examples.

[END FAQ 10.1, FIGURE 1 HERE]

[END FAQ10.1 HERE]

ACCEPTED VERSION
SUBJECT TO FINAL EDITING

[START FAQ10.2 HERE]

FAQ 10.2: Why are cities hotspots of global warming?

Urban areas experience air temperatures that can be several degrees Celsius warmer than surrounding areas, especially during the night. This 'urban heat island' effect results from several factors, including reduced ventilation and heat trapping due to the close proximity of tall buildings, heat generated directly from human activities, the heat-absorbing properties of concrete and other urban building materials, and the limited amount of vegetation. Continuing urbanization and increasingly severe heatwaves under climate change will further amplify this effect in the future.

Today, cities are home to 55% of the world's population. This number is increasing, and every year cities welcome 67 million new residents, 90% of whom are moving to cities in developing countries. By 2030, almost 60% of the world's population is expected to live in urban areas. Cities and their inhabitants are highly vulnerable to weather and climate extremes, particularly heatwaves, because urban areas already are local hotspots. Cities are generally warmer – up to several degrees Celsius at night – than their surroundings. This warming effect, called the urban heat island, occurs because cities both receive and retain more heat than the surrounding countryside areas and because natural cooling processes are weakened in cities compared to rural areas.

Three main factors contribute to amplify the warming of urban areas (orange bars in FAQ 10.2, Figure 1). The strongest contribution comes from urban geometry, which depends on the number of buildings, their size and their proximity. Tall buildings close to each other absorb and store heat and also reduce natural ventilation. Human activities, which are very concentrated in cities, also directly warm the atmosphere locally, due to heat released from domestic and industrial heating or cooling systems, running engines, and other sources. Finally, urban warming also results directly from the heat-retaining properties of the materials that make up cities, including concrete buildings, asphalt roadways, and dark rooftops. These materials are very good at absorbing and retaining heat, and then re-emitting that heat at night.

The urban heat island effect is further amplified in cities that lack vegetation and water bodies, both of which can strongly contribute to local cooling (green bars in FAQ 10.2, Figure 1). This means that when enough vegetation and water are included in the urban fabric, they can counterbalance the urban heat island effect, to the point of even cancelling out the urban heat island effect in some neighbourhoods.

The urban heat island phenomenon is well known and understood. For instance, temperature measurements from thermometers located in cities are corrected for this effect when global warming trends are calculated. Nevertheless, observations, including long-term measurements of the urban heat island effect are currently too limited to allow a full understanding of how the urban heat island varies across the world and across different types of cities and climatic zones, or how this effect will evolve in the future.

As a result, it is hard to assess how climate change will affect the urban heat island effect, and various studies disagree. Two things are, however, very clear. First, future urbanization will expand the urban heat island areas, thereby amplifying future warming in many places all over the world. In some places, the nighttime warming from the urban heat island effect could even be on the same order of magnitude as the warming expected from human-induced climate change. Second, more intense, longer and more frequent heatwaves caused by climate change will more strongly impact cities and their inhabitants, because the extra warming from the urban heat island effect will exacerbate the impacts of climate change.

In summary, cities are currently local hotspots because their structure, material and activities trap and release heat and reduce natural cooling processes. In the future, climate change will, on average, have a limited effect on the magnitude of the urban heat island itself, but ongoing urbanization together with more frequent, longer and warmer heatwaves will make cities more exposed to global warming.

ACCEPTED VERSION!
SUBJECT TO FINAL EDITING

[START FAQ 10.2, FIGURE 1 HERE]

FAQ 10.2, Figure 1: Efficiency of the various factors at warming up or cooling down neighbourhoods of urban areas. Overall, cities tend to be warmer than their surroundings. This is called the 'urban heat island' effect. The hatched areas on the bars show how the strength of the warming or cooling effects of each factor varies depending on the local climate. For example, vegetation has a stronger cooling effect in temperate and warm climates. Further details on data sources are available in the chapter data table (Table 10.SM.11)

[START FAQ 10.2, FIGURE 1 HERE]

[END FAQ10.2 HERE]

ACCEPTED VERSION
SUBJECT TO FINAL EDITING

Acknowledgements

We acknowledge the E-OBS dataset and the data providers in the ECA&D project (https://www.ecad.eu) for their help and the Japan Aerospace Exploration Agency (JAXA) for delivering the GSMaP (Global Satellite Mapping of Precipitation) data to us. The invaluable contributions from Lisa van Aardenne (South Africa), Peng Cai (China), Joseph Ching (China), Huili He (China), Kenshi Hibino (Japan), Yukiko Imada (Japan), Nazrul Islam (Saudi Arabia), Isadora Christel Jiménez (Spain) and Misako Kachi (Japan) are also greatly acknowledged. We acknowledge the World Climate Research Programme for coordinating the modelling intercomparison projects CMIP and CORDEX and thank the climate modelling groups for producing and making available their model output.

ACCEPTED VERSION
SUBJECT TO FINAL EDITING

References

Aalbers, E.E., G. Lenderink, E. van Meijgaard, and B.J.J.M. van den Hurk, 2018: Local-scale changes in mean and heavy precipitation in Western Europe, climate change or internal variability? *Climate Dynamics*, **50(11–12)**, 4745–4766, doi:10.1007/s00382-017-3901-9.

Aalto, J., P. Pirinen, and K. Jylhä, 2016: New gridded daily climatology of Finland: Permutation-based uncertainty estimates and temporal trends in climate. *Journal of Geophysical Research: Atmospheres*, **121(8)**, 3807–3823, doi:10.1002/2015jd024651.

Abatzoglou, J.T. and T.J. Brown, 2012: A comparison of statistical downscaling methods suited for wildfire applications. *International Journal of Climatology*, **32(5)**, 772–780, doi:10.1002/joc.2312.

Abba Omar, S. and B.J. Abiodun, 2020: Characteristics of cut-off lows during the 2015–2017 drought in the Western Cape, South Africa. *Atmospheric Research*, **235**, 104772, doi:10.1016/j.atmosres.2019.104772.

Abera, W., L. Brocca, and R. Rigon, 2016: Comparative evaluation of different satellite rainfall estimation products and bias correction in the Upper Blue Nile (UBN) basin. *Atmospheric Research*, **178–179**, 471–483, doi:10.1016/j.atmosres.2016.04.017.

Abiodun, B.J. et al., 2017: Potential impacts of climate change on extreme precipitation over four African coastal cities. *Climatic Change*, **143(3–4)**, 399–413, doi:10.1007/s10584-017-2001-5.

Abram, N.J. et al., 2020: Coupling of Indo-Pacific climate variability over the last millennium. *Nature*, **579(7799)**, 385–392, doi:10.1038/s41586-020-2084-4.

Abramowitz, G. et al., 2019: ESD Reviews: Model dependence in multi-model climate ensembles: weighting, sub-selection and out-of-sample testing. *Earth System Dynamics*, **10(1)**, 91–105, doi:10.5194/esd-10-91-2019.

Ackerley, D. et al., 2011: Sensitivity of Twentieth-Century Sahel rainfall to sulfate aerosol and CO2 forcing. *Journal of Climate*, doi:10.1175/jcli-d-11-00019.1.

Ackerman, T.P. and G.M. Stokes, 2003: The Atmospheric Radiation Measurement Program. *Physics Today*, **56(1)**, 38–44, doi:10.1063/1.1554135.

Adachi, S.A., F. Kimura, H. Kusaka, T. Inoue, and H. Ueda, 2012: Comparison of the Impact of Global Climate Changes and Urbanization on Summertime Future Climate in the Tokyo Metropolitan Area. *Journal of Applied Meteorology and Climatology*, **51(8)**, 1441–1454, doi:10.1175/jamc-d-11-0137.1.

Addor, N., M. Rohrer, R. Furrer, and J. Seibert, 2016: Propagation of biases in climate models from the synoptic to the regional scale: Implications for bias adjustment. *Journal of Geophysical Research: Atmospheres*, **121(5)**, 2075–2089, doi:10.1002/2015jd024040.

Adebiyi, A.A. and J.F. Kok, 2020: Climate models miss most of the coarse dust in the atmosphere. *Science Advances*, **6(15)**, doi:10.1126/sciadv.aaz9507.

Adloff, F. et al., 2018: Improving sea level simulation in Mediterranean regional climate models. *Climate Dynamics*, **51(3)**, 1167–1178, doi:10.1007/s00382-017-3842-3.

Ahmed, K.F. et al., 2013: Statistical downscaling and bias correction of climate model outputs for climate change impact assessment in the U.S. northeast. *Global and Planetary Change*, **100**, 320–332, doi:10.1016/j.gloplacha.2012.11.003.

Ahn, M.-S. et al., 2017: MJO simulation in CMIP5 climate models: MJO skill metrics and process-oriented diagnosis. *Climate Dynamics*, **49(11–12)**, 4023–4045, doi:10.1007/s00382-017-3558-4.

Akhtar, N., J. Brauch, and B. Ahrens, 2018: Climate modeling over the Mediterranean Sea: impact of resolution and ocean coupling. *Climate Dynamics*, **51(3)**, 933–948, doi:10.1007/s00382-017-3570-8.

Akhtar, N., J. Brauch, A. Dobler, K. Béranger, and B. Ahrens, 2014: Medicanes in an ocean–atmosphere coupled regional climate model. *Natural Hazards and Earth System Sciences*, **14(8)**, 2189–2201, doi:10.5194/nhess-14-2189-2014.

Akhtar, N. et al., 2019: European marginal seas in a regional atmosphere–ocean coupled model and their impact on Vb-cyclones and associated precipitation. *Climate Dynamics*, **53(9–10)**, 5967–5984, doi:10.1007/s00382-019-04906-x.

Akhter, J., L. Das, J.K. Meher, and A. Deb, 2018: Uncertainties and time of emergence of multi-model precipitation projection over homogeneous rainfall zones of India. *Climate Dynamics*, **50(9–10)**, 3813–3831, doi:10.1007/s00382-017-3847-y.

Akhter, J., L. Das, J.K. Meher, and A. Deb, 2019: Evaluation of different large-scale predictor-based statistical downscaling models in simulating zone-wise monsoon precipitation over India. *International Journal of Climatology*, **39(1)**, 465–482, doi:10.1002/joc.5822.

Alessandri, A. et al., 2015: Robust assessment of the expansion and retreat of Mediterranean climate in the 21 st century. *Scientific Reports*, **4(1)**, 7211, doi:10.1038/srep07211.

Alexander, L., 2016: Global observed long-term changes in temperature and precipitation extremes: A review of progress and limitations in IPCC assessments and beyond. *Weather and Climate Extremes*, **11**, 4–16, doi:10.1016/j.wace.2015.10.007.

Alghamdi, A.S. and T.W. Moore, 2015: Detecting Temporal Changes in Riyadh's Urban Heat Island. *Papers in Applied Geography*, **1(4)**, 312–325, doi:10.1080/23754931.2015.1084525.

ACCEPTED VERSION SUBJECT TO FINAL EDITING

Alizadeh-Choobari, O., P. Ghafarian, and P. Adibi, 2016: Inter-annual variations and trends of the urban warming in Tehran. *Atmospheric Research*, **170**, 176–185, doi:10.1016/j.atmosres.2015.12.001.

Allen, M.R., P.A. Stott, J.F.B. Mitchell, R. Schnur, and T.L. Delworth, 2000: Quantifying the uncertainty in forecasts of anthropogenic climate change. *Nature*, **407(6804)**, 617–620, doi:10.1038/35036559.

Allen, R.J., 2015: A 21st century northward tropical precipitation shift caused by future anthropogenic aerosol reductions. *Journal of Geophysical Research: Atmospheres*, **120(18)**, 9087–9102, doi:10.1002/2015jd023623.

Allen, R.J. and M. Kovilakam, 2017: The Role of Natural Climate Variability in Recent Tropical Expansion. *Journal of Climate*, **30(16)**, 6329–6350, doi:10.1175/jcli-d-16-0735.1.

Allen, R.J., A.T. Evan, and B.B.B. Booth, 2015: Interhemispheric Aerosol Radiative Forcing and Tropical Precipitation Shifts during the Late Twentieth Century. *Journal of Climate*, **28(20)**, 8219–8246, doi:10.1175/jcli-d-15-0148.1.

Almazroui, M., 2016: RegCM4 in climate simulation over CORDEX-MENA/Arab domain: selection of suitable domain, convection and land-surface schemes. *International Journal of Climatology*, **36(1)**, 236–251, doi:10.1002/joc.4340.

Almazroui, M., 2019: Temperature Changes over the CORDEX-MENA Domain in the 21st Century Using CMIP5 Data Downscaled with RegCM4: A Focus on the Arabian Peninsula. *Advances in Meteorology*, doi:10.1155/2019/5395676.

Almazroui, M., M.N. Islam, A.K. Al-Khalaf, and F. Saeed, 2016a: Best convective parameterization scheme within RegCM4 to downscale CMIP5 multi-model data for the CORDEX-MENA/Arab domain. *Theoretical and Applied Climatology*, **124(3–4)**, 807–823, doi:10.1007/s00704-015-1463-5.

Almazroui, M., M.N.M.N. Islam, S. Saeed, M. Ismail, and E. Al., 2020a: Future changes in climate over the Arabian Peninsula based on CMIP6 multimodel simulations. *Earth Systems and Environment*, **4(3)**, 611–630.

Almazroui, M., S. Saeed, F. Saeed, M.N. Islam, and M. Ismail, 2020b: Projections of Precipitation and Temperature over the South Asian Countries in CMIP6. *Earth Systems and Environment*, **4(2)**, 297–320, doi:10.1007/s41748-020-00157-7.

Almazroui, M. et al., 2016b: Simulation of temperature and precipitation climatology for the CORDEX-MENA/Arab domain using RegCM4. *Arabian Journal of Geosciences*, **9(1)**, 13, doi:10.1007/s12517-015-2045-7.

Almazroui, M. et al., 2020c: Projected Change in Temperature and Precipitation Over Africa from CMIP6. *Earth Systems and Environment*, **4(3)**, 455–475, doi:10.1007/s41748-020-00161-x.

Almazroui, M. et al., 2021: Projected Changes in Temperature and Precipitation Over the United States, Central America, and the Caribbean in CMIP6 GCMs. *Earth Systems and Environment*, doi:10.1007/s41748-021-00199-5.

Alter, R.E., E.-S. Im, and E.A.B. Eltahir, 2015: Rainfall consistently enhanced around the Gezira Scheme in East Africa due to irrigation. *Nature Geoscience*, **8(10)**, 763–767, doi:10.1038/ngeo2514.

Amaya, D.J., N. Siler, S.-P. Xie, and A.J. Miller, 2018: The interplay of internal and forced modes of Hadley Cell expansion: lessons from the global warming hiatus. *Climate Dynamics*, **51(1–2)**, 305–319, doi:10.1007/s00382-017-3921-5.

Anand, A. et al., 2018: Indian Summer Monsoon Simulations: Usefulness of Increasing Horizontal Resolution, Manual Tuning, and Semi-Automatic Tuning in Reducing Present-Day Model Biases. *Scientific Reports*, **8(1)**, 3522, doi:10.1038/s41598-018-21865-1.

Andreassen, H.P., K.E. Gangaas, and B.P. Kaltenborn, 2018: Matching social-ecological systems by understanding the spatial scale of environmental attitudes. *Nature Conservation*, **30**, 69–81, doi:10.3897/natureconservation.30.28289.

Annamalai, H., J. Hafner, K.P. Sooraj, and P. Pillai, 2013: Global warming shifts the monsoon circulation, drying South Asia. *Journal of Climate*, **26(9)**, 2701–2718, doi:10.1175/jcli-d-12-00208.1.

Annan, J.D. and J.C. Hargreaves, 2017: On the meaning of independence in climate science. *Earth System Dynamics*, **8(1)**, 211–224, doi:10.5194/esd-8-211-2017.

Archer, E. et al., 2018: Seasonal prediction and regional climate projections for southern Africa. *Biodiversity & Ecology*, **6**, 14–21, doi:10.7809/b-e.00296.

Ardilouze, C., L. Batté, M. Déqué, E. van Meijgaard, and B. van den Hurk, 2019: Investigating the impact of soil moisture on European summer climate in ensemble numerical experiments. *Climate Dynamics*, **52(7–8)**, 4011–4026, doi:10.1007/s00382-018-4358-1.

Argüeso, D., J.P. Evans, L. Fita, and K.J. Bormann, 2014: Temperature response to future urbanization and climate change. *Climate Dynamics*, **42(7–8)**, 2183–2199, doi:10.1007/s00382-013-1789-6.

Armstrong, M.S., A.S. Kiem, and T.R. Vance, 2020: Comparing instrumental, palaeoclimate, and projected rainfall data: Implications for water resources management and hydrological modelling. *Journal of Hydrology: Regional Studies*, **31**, 100728, doi:10.1016/j.ejrh.2020.100728.

Arsiso, B.K., G. Mengistu Tsidu, G.H. Stoffberg, and T. Tadesse, 2018: Influence of urbanization-driven land use/cover change on climate: The case of Addis Ababa, Ethiopia. *Physics and Chemistry of the Earth*, doi:10.1016/j.pce.2018.02.009.

Aryee, J.N.A. et al., 2018: Development of high spatial resolution rainfall data for Ghana. *International Journal of*

ACCEPTED VERSION SUBJECT TO FINAL EDITING

Climatology, **38(3)**, 1201–1215, doi:10.1002/joc.5238.
Ashcroft, L. et al., 2018: A rescued dataset of sub-daily meteorological observations for Europe and the southern Mediterranean region, 1877–2012. *Earth System Science Data*, **10(3)**, 1613–1635, doi:10.5194/essd-10-1613-2018.
Ashfaq, M. et al., 2020: Robust late twenty-first century shift in the regional monsoons in RegCM-CORDEX simulations. *Climate Dynamics*, doi:10.1007/s00382-020-05306-2.
Ashouri, H. et al., 2015: PERSIANN-CDR: Daily Precipitation Climate Data Record from Multisatellite Observations for Hydrological and Climate Studies. *Bulletin of the American Meteorological Society*, **96(1)**, 69–83, doi:10.1175/bams-d-13-00068.1.
Attada Raju, A. and Parekh, and Chowdary J S., and and Gnanaseelan C, 2018: Reanalysis of the Indian summer monsoon: four dimensional data assimilation of AIRS retrievals in a regional data assimilation and modeling framework. *Climate Dynamics*, **50(7)**, 2905–2923, doi:10.1007/s00382-017-3781-z.
Auchmann, R. and S. Brönnimann, 2012: A physics-based correction model for homogenizing sub-daily temperature series. *Journal of Geophysical Research: Atmospheres*, **117(D17)**, doi:10.1029/2012jd018067.
Ayarzagüena, B. and J.A. Screen, 2016: Future Arctic sea ice loss reduces severity of cold air outbreaks in midlatitudes. *Geophysical Research Letters*, **43(6)**, 2801–2809, doi:10.1002/2016gl068092.
Ayarzagüena, B. et al., 2018: No robust evidence of future changes in major stratospheric sudden warmings: a multi-model assessment from CCMI. *Atmospheric Chemistry and Physics*, **18(15)**, 11277–11287, doi:10.5194/acp-18-11277-2018.
Azam, M.F. et al., 2018: Review of the status and mass changes of Himalayan-Karakoram glaciers. *Journal of Glaciology*, **64(243)**, 61–74, doi:10.1017/jog.2017.86.
Azmat, M., U.W. Liaqat, M.U. Qamar, and U.K. Awan, 2017: Impacts of changing climate and snow cover on the flow regime of Jhelum River, Western Himalayas. *Regional Environmental Change*, **17(3)**, 813–825, doi:10.1007/s10113-016-1072-6.
Bach, L., C. Schraff, J.D. Keller, and A. Hense, 2016: Towards a probabilistic regional reanalysis system for Europe: evaluation of precipitation from experiments. *Tellus A: Dynamic Meteorology and Oceanography*, **68(1)**, 32209, doi:10.3402/tellusa.v68.32209.
Bader, D.A. et al., 2018: Urban Climate Science. In: *Climate Change and Cities: Second Assessment Report of the Urban Climate Change Research Network* [Rosenzweig, C., P. Romero-Lankao, S. Mehrotra, S. Dhakal, S. Ali Ibrahim, and W.D. Solecki (eds.)]. Cambridge University Press, Cambridge, United Kingdom, pp. 27–60, doi:10.1017/9781316563878.009.
Bador, M., L. Terray, and J. Boé, 2016: Emergence of human influence on summer record-breaking temperatures over Europe. *Geophysical Research Letters*, **43(1)**, 404–412, doi:10.1002/2015gl066560.
Bador, M. et al., 2020: Impact of Higher Spatial Atmospheric Resolution on Precipitation Extremes Over Land in Global Climate Models. *Journal of Geophysical Research: Atmospheres*, **125(13)**, e2019JD032184, doi:10.1029/2019jd032184.
Bain, P.G., M.J. Hornsey, R. Bongiorno, and C. Jeffries, 2012: Promoting pro-environmental action in climate change deniers. *Nature Climate Change*, **2(8)**, 600–603, doi:10.1038/nclimate1532.
Baker, D.J., A.J. Hartley, S.H.M. Butchart, and S.G. Willis, 2016: Choice of baseline climate data impacts projected species' responses to climate change. *Global Change Biology*, **22(7)**, 2392–2404, doi:10.1111/gcb.13273.
Baklanov, A. et al., 2018: From urban meteorology, climate and environment research to integrated city services. *Urban Climate*, **23**, 330–341, doi:10.1016/j.uclim.2017.05.004.
Baklanov, A. et al., 2020: Integrated urban services: Experience from four cities on different continents. *Urban Climate*, **32**, 100610, doi:10.1016/j.uclim.2020.100610.
Bal, P.K. et al., 2016: Climate change projections over India by a downscaling approach using PRECIS. *Asia-Pacific Journal of Atmospheric Sciences*, **52(4)**, 353–369, doi:10.1007/s13143-016-0004-1.
Balsamo, G. et al., 2015: ERA-Interim/Land: a global land surface reanalysis data set. *Hydrology and Earth System Sciences*, **19(1)**, 389–407, doi:10.5194/hess-19-389-2015.
Ban, N., J. Schmidli, and C. Schär, 2014: Evaluation of the convection-resolving regional climate modeling approach in decade-long simulations. *Journal of Geophysical Research: Atmospheres*, **119(13)**, 7889–7907, doi:10.1002/2014jd021478.
Ban, N., J. Schmidli, and C. Schär, 2015: Heavy precipitation in a changing climate: Does short-term summer precipitation increase faster? *Geophysical Research Letters*, **42(4)**, 1165–1172, doi:10.1002/2014gl062588.
Ban, N. et al., 2021: The first multi-model ensemble of regional climate simulations at kilometer-scale resolution, Part I: Evaluation of precipitation. *Climate Dynamics*, doi:10.1007/s00382-021-05708-w.
Bandoro, J., S. Solomon, A. Donohoe, D.W.J. Thompson, and B.D. Santer, 2014: Influences of the Antarctic Ozone Hole on Southern Hemispheric Summer Climate Change. *Journal of Climate*, **27(16)**, 6245–6264, doi:10.1175/jcli-d-13-00698.1.
Baño-Medina, J., R. Manzanas, and J.M. Gutiérrez, 2020: Configuration and intercomparison of deep learning neural models for statistical downscaling. *Geoscientific Model Development*, **13(4)**, 2109–2124, doi:10.5194/gmd-13-2109-2020.

SUBJECT TO FINAL EDITING ACCEPTED VERSION

Barcikowska, M.J. et al., 2020: Changes in the future summer Mediterranean climate: contribution of teleconnections and local factors. *Earth System Dynamics*, **11(1)**, 161–181, doi:10.5194/esd-11-161-2020.

Bárdossy, A. and G. Pegram, 2012: Multiscale spatial recorrelation of RCM precipitation to produce unbiased climate change scenarios over large areas and small. *Water Resources Research*, **48(9)**, doi:10.1029/2011wr011524.

Barlage, M. et al., 2015: The effect of groundwater interaction in North American regional climate simulations with WRF/Noah-MP. *Climatic Change*, doi:10.1007/s10584-014-1308-8.

Barlow, J. et al., 2017: Developing a Research Strategy to Better Understand, Observe, and Simulate Urban Atmospheric Processes at Kilometer to Subkilometer Scales. *Bulletin of the American Meteorological Society*, **98(10)**, ES261–ES264, doi:10.1175/bams-d-17-0106.1.

Barnes, E.A., 2013: Revisiting the evidence linking Arctic amplification to extreme weather in midlatitudes. *Geophysical Research Letters*, **40(17)**, 4734–4739, doi:10.1002/grl.50880.

Barnes, E.A. and L. Polvani, 2013: Response of the Midlatitude Jets, and of Their Variability, to Increased Greenhouse Gases in the CMIP5 Models. *Journal of Climate*, **26(18)**, 7117–7135, doi:10.1175/jcli-d-12-00536.1.

Barnes, E.A. and J.A. Screen, 2015: The impact of Arctic warming on the midlatitude jet-stream: Can it? Has it? Will it? *Wiley Interdisciplinary Reviews: Climate Change*, **6(3)**, 277–286, doi:10.1002/wcc.337.

Barnes, E.A., E. Dunn-Sigouin, G. Masato, and T. Woollings, 2014: Exploring recent trends in Northern Hemisphere blocking. *Geophysical Research Letters*, **41(2)**, 638–644, doi:10.1002/2013gl058745.

Barredo, J.I., A. Mauri, G. Caudullo, and A. Dosio, 2018: Assessing Shifts of Mediterranean and Arid Climates Under RCP4.5 and RCP8.5 Climate Projections in Europe. *Pure and Applied Geophysics*, **175(11)**, 3955–3971, doi:10.1007/s00024-018-1853-6.

Barreiro, M., N. Díaz, and M. Renom, 2014: Role of the global oceans and land–atmosphere interaction on summertime interdecadal variability over northern Argentina. *Climate Dynamics*, **42(7–8)**, 1733–1753, doi:10.1007/s00382-014-2088-6.

Barrett, B., I. Nitze, S. Green, and F. Cawkwell, 2014: Assessment of multi-temporal, multi-sensor radar and ancillary spatial data for grasslands monitoring in Ireland using machine learning approaches. *Remote Sensing of Environment*, **152**, 109–124, doi:10.1016/j.rse.2014.05.018.

Barrow, E.M. and D.J. Sauchyn, 2019: Uncertainty in climate projections and time of emergence of climate signals in the western Canadian Prairies. *International Journal of Climatology*, **39(11)**, 4358–4371, doi:10.1002/joc.6079.

Barry, R.G., 2012: Recent advances in mountain climate research. *Theoretical and Applied Climatology*, **110(4)**, 549–553, doi:10.1007/s00704-012-0695-x.

Barsugli, J.J. et al., 2013: The Practitioner's Dilemma: How to Assess the Credibility of Downscaled Climate Projections. *Eos, Transactions American Geophysical Union*, **94(46)**, 424–425, doi:10.1002/2013eo460005.

Bartók, B. et al., 2017: Projected changes in surface solar radiation in CMIP5 global climate models and in EURO-CORDEX regional climate models for Europe. *Climate Dynamics*, **49(7–8)**, 2665–2683, doi:10.1007/s00382-016-3471-2.

Barton, N.P., S.A. Klein, J.S. Boyle, and Y.Y. Zhang, 2012: Arctic synoptic regimes: Comparing domain-wide Arctic cloud observations with CAM4 and CAM5 during similar dynamics. *Journal of Geophysical Research: Atmospheres*, **117(D15)**, n/a–n/a, doi:10.1029/2012jd017589.

Bathiany, S., V. Dakos, M. Scheffer, and T.M. Lenton, 2018: Climate models predict increasing temperature variability in poor countries. *Science Advances*, **4(5)**, 1–11, doi:10.1126/sciadv.aar5809.

Baumberger, C., R. Knutti, and G. Hirsch Hadorn, 2017: Building confidence in climate model projections: an analysis of inferences from fit. *Wiley Interdisciplinary Reviews: Climate Change*, **8(3)**, e454, doi:10.1002/wcc.454.

Baztan, J., M. Cordier, J.-M. Huctin, Z. Zhu, and J.-P. Vanderlinden, 2017: Life on thin ice: Insights from Uummannaq, Greenland for connecting climate science with Arctic communities. *Polar Science*, **13**, 100–108, doi:10.1016/j.polar.2017.05.002.

Beck, H.E. et al., 2017a: Global evaluation of runoff from 10 state-of-the-art hydrological models. *Hydrology and Earth System Sciences*, **21(6)**, 2881–2903, doi:10.5194/hess-21-2881-2017.

Beck, H.E. et al., 2017b: Global-scale evaluation of 22 precipitation datasets using gauge observations and hydrological modeling. *Hydrology and Earth System Sciences*, **21(12)**, 6201–6217, doi:10.5194/hess-21-6201-2017.

Bedia, J., S. Herrera, D.S. Martín, N. Koutsias, and J.M. Gutiérrez, 2013: Robust projections of Fire Weather Index in the Mediterranean using statistical downscaling. *Climatic Change*, **120(1–2)**, 229–247, doi:10.1007/s10584-013-0787-3.

Bellenger, H., E. Guilyardi, J. Leloup, M. Lengaigne, and J. Vialard, 2014: ENSO representation in climate models: from CMIP3 to CMIP5. *Climate Dynamics*, **42(7–8)**, 1999–2018, doi:10.1007/s00382-013-1783-z.

Bellprat, O., S. Kotlarski, D. Lüthi, and C. Schär, 2013: Physical constraints for temperature biases in climate models. *Geophysical Research Letters*, **40(15)**, 4042–4047, doi:10.1002/grl.50737.

Belušić, A. et al., 2018: Near-surface wind variability over the broader Adriatic region: insights from an ensemble of regional climate models. *Climate Dynamics*, **50(11–12)**, 4455–4480, doi:10.1007/s00382-017-3885-5.

Benedict, J.J., E.D. Maloney, A.H. Sobel, and D.M.W. Frierson, 2014: Gross Moist Stability and MJO Simulation Skill in Three Full-Physics GCMs. *Journal of the Atmospheric Sciences*, **71(9)**, 3327–3349, doi:10.1175/jas-d-13-

ACCEPTED VERSION SUBJECT TO FINAL EDITING

0240.1.
Benestad, R.E., 2011: A New Global Set of Downscaled Temperature Scenarios. *Journal of Climate*, **24(8)**, 2080–2098, doi:10.1175/2010jcli3687.1.
Benestad, R.E., 2018: Implications of a decrease in the precipitation area for the past and the future. *Environmental Research Letters*, **13(4)**, doi:10.1088/1748-9326/aab375.
Benestad, R.E. et al., 2018: Downscaling probability of long heatwaves based on seasonal mean daily maximum temperatures. *Advances in Statistical Climatology, Meteorology and Oceanography*, **4(1/2)**, 37–52, doi:10.5194/ascmo-4-37-2018.
Ben-Gai, T., A. Bitan, A. Manes, P. Alpert, and Y. Kushnir, 2001: Temperature and surface pressure anomalies in Israel and the North Atlantic Oscillation. *Theoretical and Applied Climatology*, **69(3–4)**, 171–177, doi:10.1007/s007040170023.
Bengtsson, L. and K.I. Hodges, 2018: Can an ensemble climate simulation be used to separate climate change signals from internal unforced variability? *Climate Dynamics*, doi:10.1007/s00382-018-4343-8.
Beniston, M. et al., 2018: The European mountain cryosphere: a~review of its current state, trends, and future challenges. *The Cryosphere*, **12(2)**, 759–794, doi:10.5194/tc-12-759-2018.
Bennett, W.G., H. Karunarathna, D.E. Reeve, and N. Mori, 2019: Computational modelling of morphodynamic response of a macro-tidal beach to future climate variabilities. *Marine Geology*, **415**, 105960, doi:10.1016/j.margeo.2019.105960.
Beranová, R. and J. Kyselý, 2016: Links between circulation indices and precipitation in the Mediterranean in an ensemble of regional climate models. *Theoretical and Applied Climatology*, **123(3–4)**, 693–701, doi:10.1007/s00704-015-1381-6.
Berckmans, J., R. Hamdi, and N. Dendoncker, 2019: Bridging the gap between policy-driven land use changes and regional climate projections. *journal of geophysical research*, doi:10.1029/2018jd029207.
Berkhout, F. et al., 2013: Framing climate uncertainty: socio-economic and climate scenarios in vulnerability and adaptation assessments. *Regional Environmental Change*, doi:10.1007/s10113-013-0519-2.
Berthou, S. et al., 2015: Sensitivity of an intense rain event between atmosphere-only and atmosphere-ocean regional coupled models: 19 September 1996. *Quarterly Journal of the Royal Meteorological Society*, **141(686)**, 258–271, doi:10.1002/qj.2355.
Berthou, S. et al., 2018a: Pan-European climate at convection-permitting scale: a model intercomparison study. *Climate Dynamics*, doi:10.1007/s00382-018-4114-6.
Berthou, S. et al., 2018b: Lagged effects of the Mistral wind on heavy precipitation through ocean-atmosphere coupling in the region of Valencia (Spain). *Climate Dynamics*, **51(3)**, 969–983, doi:10.1007/s00382-016-3153-0.
Besselaar, E.J.M., A. Sanchez-Lorenzo, M. Wild, A.M.G. Klein Tank, and A.T.J. Laat, 2015: Relationship between sunshine duration and temperature trends across Europe since the second half of the twentieth century. *Journal of Geophysical Research: Atmospheres*, **120(20)**, 10,810–10,836, doi:10.1002/2015jd023640.
Bessette, D.L. et al., 2017: Building a Values-Informed Mental Model for New Orleans Climate Risk Management. *Risk Analysis*, **37(10)**, 1993–2004, doi:10.1111/risa.12743.
Best, M.J. and C.S.B. Grimmond, 2015: Key Conclusions of the First International Urban Land Surface Model Comparison Project. *Bulletin of the American Meteorological Society*, **96(5)**, 805–819, doi:10.1175/bams-d-14-00122.1.
Best, M.J., C.S.B. Grimmond, and M.G. Villani, 2006: Evaluation of the urban tile in MOSES using surface energy balance observations. *Boundary-Layer Meteorology*, **118**, 503–525, doi:10.1007/s10546-005-9025-5.
Bethke, I. et al., 2017: Potential volcanic impacts on future climate variability. *Nature Climate Change*, **7(11)**, 799–805, doi:10.1038/nclimate3394.
Beusch, L., L. Gudmundsson, and S.I. Seneviratne, 2020: Emulating Earth system model temperatures with MESMER: from global mean temperature trajectories to grid-point-level realizations on land. *Earth System Dynamics*, **11(1)**, 139–159, doi:10.5194/esd-11-139-2020.
Bevacqua, E., D. Maraun, I. Hobæk Haff, M. Widmann, and M. Vrac, 2017: Multivariate statistical modelling of compound events via pair-copula constructions: analysis of floods in Ravenna (Italy). *Hydrology and Earth System Sciences*, **21(6)**, 2701–2723, doi:10.5194/hess-21-2701-2017.
Bhave, A.G., D. Conway, S. Dessai, and D.A. Stainforth, 2018: Water Resource Planning Under Future Climate and Socioeconomic Uncertainty in the Cauvery River Basin in Karnataka, India. *Water Resources Research*, **54(2)**, 708–728, doi:10.1002/2017wr020970.
Bian, T. et al., 2020: Half-century urban drying in Shijiazhuang City. *Environmental Research Communications*, **2(7)**, 75006, doi:10.1088/2515-7620/aba10f.
Biasutti, M. and A. Giannini, 2006: Robust Sahel drying in response to late 20th century forcings. *Geophysical Research Letters*, **33(11)**, L11706, doi:10.1029/2006gl026067.
Bichet, A. and A. Diedhiou, 2018a: Less frequent and more intense rainfall along the coast of the Gulf of Guinea in West and Central Africa (1981-2014). *Climate Research*, **76(3)**, 191–201, doi:10.3354/cr01537.
Bichet, A. and A. Diedhiou, 2018b: West African Sahel has become wetter during the last 30 years, but dry spells are shorter and more frequent. *Climate Research*, **75(2)**, 155–162, doi:10.3354/cr01515.

SUBJECT TO FINAL EDITING ACCEPTED VERSION

Bindoff, N.L. et al., 2013: Detection and Attribution of Climate Change: from Global to Regional. In: *Climate Change 2013: The Physical Science Basis. Contribution of Working Group I to the Fifth Assessment Report of the Intergovernmental Panel on Climate Change* []. Cambridge University Press, Cambridge, United Kingdom and New York, NY, USA, pp. 867–952, doi:10.1017/cbo9781107415324.022.

Birner, T., S.M. Davis, and D.J. Seidel, 2014: The changing width of Earth's tropical belt. *Physics Today*, **67(12)**, 38–44, doi:10.1063/pt.3.2620.

Bittner, M., H. Schmidt, C. Timmreck, and F. Sienz, 2016: Using a large ensemble of simulations to assess the Northern Hemisphere stratospheric dynamical response to tropical volcanic eruptions and its uncertainty. *Geophysical Research Letters*, **43(17)**, 9324–9332, doi:10.1002/2016gl070587.

Black, E., 2012: The influence of the North Atlantic Oscillation and European circulation regimes on the daily to interannual variability of winter precipitation in Israel. *International Journal of Climatology*, **32(11)**, 1654–1664, doi:10.1002/joc.2383.

Blackport, R. and P.J. Kushner, 2017: Isolating the Atmospheric Circulation Response to Arctic Sea Ice Loss in the Coupled Climate System. *Journal of Climate*, **30(6)**, 2163–2185, doi:10.1175/jcli-d-16-0257.1.

Blackport, R. and J.A. Screen, 2020a: Insignificant effect of Arctic amplification on the amplitude of midlatitude atmospheric waves. *Science Advances*, **6(8)**, eaay2880, doi:10.1126/sciadv.aay2880.

Blackport, R. and J.A. Screen, 2020b: Weakened evidence for mid-latitude impacts of Arctic warming. *Nature Climate Change*, doi:10.1038/s41558-020-00954-y.

Blackport, R., J.A. Screen, K. van der Wiel, and R. Bintanja, 2019: Minimal influence of reduced Arctic sea ice on coincident cold winters in mid-latitudes. *Nature Climate Change*, **9(9)**, 697–704, doi:10.1038/s41558-019-0551-4.

Bladé, I., B. Liebmann, D. Fortuny, and G.J. van Oldenborgh, 2012: Observed and simulated impacts of the summer NAO in Europe: implications for projected drying in the Mediterranean region. *Climate Dynamics*, **39(3–4)**, 709–727, doi:10.1007/s00382-011-1195-x.

Blamey, R. and C.J.C. Reason, 2007: Relationships between Antarctic sea-ice and South African winter rainfall. *Climate Research*, **33**, 183–193, doi:10.3354/cr033183.

Blamey, R.C., S.R. Kolusu, P. Mahlalela, M.C. Todd, and C.J.C. Reason, 2018: The role of regional circulation features in regulating El Niño climate impacts over southern Africa: A comparison of the 2015/2016 drought with previous events. *International Journal of Climatology*, **38(11)**, 4276–4295, doi:10.1002/joc.5668.

Blázquez, J. and S.A. Solman, 2018: Fronts and precipitation in CMIP5 models for the austral winter of the Southern Hemisphere. *Climate Dynamics*, **50(7–8)**, 2705–2717, doi:10.1007/s00382-017-3765-z.

Blenkinsop, S., E. Lewis, S.C. Chan, and H.J. Fowler, 2017: Quality-control of an hourly rainfall dataset and climatology of extremes for the UK. *International Journal of Climatology*, **37(2)**, 722–740, doi:10.1002/joc.4735.

Bližňák, V., M. Kašpar, and M. Müller, 2018: Radar-based summer precipitation climatology of the Czech Republic. *International Journal of Climatology*, **38(2)**, 677–691, doi:10.1002/joc.5202.

Boberg, F. and J.H. Christensen, 2012: Overestimation of Mediterranean summer temperature projections due to model deficiencies. *Nature Climate Change*, **2(6)**, 1–4, doi:10.1038/nclimate1454.

Boé, J., 2018: Interdependency in Multimodel Climate Projections: Component Replication and Result Similarity. *Geophysical Research Letters*, **45(6)**, 2771–2779, doi:10.1002/2017gl076829.

Boé, J., S. Somot, L. Corre, and P. Nabat, 2020a: Large discrepancies in summer climate change over Europe as projected by global and regional climate models: causes and consequences. *Climate Dynamics*, **54(5–6)**, 2981–3002, doi:10.1007/s00382-020-05153-1.

Boé, J. et al., 2020b: Past long-term summer warming over western Europe in new generation climate models: role of large-scale atmospheric circulation. *Environmental Research Letters*, **15(8)**, 084038, doi:10.1088/1748-9326/ab8a89.

Boer, G.J. et al., 2016: The Decadal Climate Prediction Project (DCPP) contribution to CMIP6. *Geoscientific Model Development*, **9(10)**, 3751–3777, doi:10.5194/gmd-9-3751-2016.

Boers, R., T. Brandsma, and A.P. Siebesma, 2017: Impact of aerosols and clouds on decadal trends in all-sky solar radiation over the Netherlands (1966–2015). *Atmospheric Chemistry and Physics*, **17(13)**, 8081–8100, doi:10.5194/acp-17-8081-2017.

Böhm, R. et al., 2010: The early instrumental warm-bias: A solution for long central European temperature series 1760-2007. *Climatic Change*, doi:10.1007/s10584-009-9649-4.

Böhme, T. et al., 2011: Long-term evaluation of COSMO forecasting using combined observational data of the GOP period. *Meteorologische Zeitschrift*, **20(2)**, 119–132, doi:10.1127/0941-2948/2011/0225.

Bohnenstengel, S.I., I. Hamilton, M. Davies, and S.E. Belcher, 2014: Impact of anthropogenic heat emissions on London's temperatures. *Quarterly Journal of the Royal Meteorological Society*, **140(679)**, 687–698, doi:10.1002/qj.2144.

Böhnisch, A., R. Ludwig, and M. Leduc, 2020: Using a nested single-model large ensemble to assess the internal variability of the North Atlantic Oscillation and its climatic implications for central Europe. *Earth System Dynamics*, **11(3)**, 617–640, doi:10.5194/esd-11-617-2020.

ACCEPTED VERSION SUBJECT TO FINAL EDITING

Boisier, J.P., R. Rondanelli, R.D. Garreaud, and F. Muñoz, 2016: Anthropogenic and natural contributions to the Southeast Pacific precipitation decline and recent megadrought in central Chile. *Geophysical Research Letters*, **43(1)**, 413–421, doi:10.1002/2015gl067265.

Bojinski, S. et al., 2014: The Concept of Essential Climate Variables in Support of Climate Research, Applications, and Policy. *Bulletin of the American Meteorological Society*, **95(9)**, 1431–1443, doi:10.1175/bams-d-13-00047.1.

Bolch, T. et al., 2019: Status and Change of the Cryosphere in the Extended Hindu Kush Himalaya Region. In: *The Hindu Kush Himalaya Assessment: Mountains, Climate Change, Sustainability and People* [Wester, P., A. Mishra, A. Mukherji, and A.B. Shrestha (eds.)]. Springer, Cham, Switzerland, pp. 209–255, doi:10.1007/978-3-319-92288-1_7.

Bollasina, M.A. and Y. Ming, 2013: The general circulation model precipitation bias over the southwestern equatorial Indian Ocean and its implications for simulating the South Asian monsoon. *Climate Dynamics*, **40(3–4)**, 823–838, doi:10.1007/s00382-012-1347-7.

Bollasina, M.A., Y. Ming, and V. Ramaswamy, 2011: Anthropogenic Aerosols and the Weakening of the South Asian Summer Monsoon. *Science*, **334(6055)**, 502–505, doi:10.1126/science.1204994.

Bollmeyer, C. et al., 2015: Towards a high-resolution regional reanalysis for the European CORDEX domain. *Quarterly Journal of the Royal Meteorological Society*, **141(686)**, 1–15, doi:10.1002/qj.2486.

Bonekamp, P.N.J., R.J. de Kok, E. Collier, and W.W. Immerzeel, 2019: Contrasting Meteorological Drivers of the Glacier Mass Balance Between the Karakoram and Central Himalaya. *Frontiers in Earth Science*, **7**, 107, doi:10.3389/feart.2019.00107.

Bosilovich, M.G., J.-D. Chern, D. Mocko, F.R. Robertson, and A.M. da Silva, 2015: Evaluating Observation Influence on Regional Water Budgets in Reanalyses. *Journal of Climate*, **28(9)**, 3631–3649, doi:10.1175/jcli-d-14-00623.1.

Bozkurt, D. et al., 2019: Dynamical downscaling over the complex terrain of southwest South America: present climate conditions and added value analysis. *Climate Dynamics*, **53(11)**, 6745–6767, doi:10.1007/s00382-019-04959-y.

Bozkurt, D. et al., 2020: Recent Near-surface Temperature Trends in the Antarctic Peninsula from Observed, Reanalysis and Regional Climate Model Data. *Advances in Atmospheric Sciences*, **37(5)**, 477–493, doi:10.1007/s00376-020-9183-x.

Bracegirdle, T.J., P. Hyder, and C.R. Holmes, 2018: CMIP5 Diversity in Southern Westerly Jet Projections Related to Historical Sea Ice Area: Strong Link to Strengthening and Weak Link to Shift. *Journal of Climate*, **31(1)**, 195–211, doi:10.1175/jcli-d-17-0320.1.

Brands, S., 2017: Which ENSO teleconnections are robust to internal atmospheric variability? *Geophysical Research Letters*, **44(3)**, 1483–1493, doi:10.1002/2016gl071529.

Brands, S., J.M. Gutiérrez, S. Herrera, and A.S. Cofiño, 2012: On the Use of Reanalysis Data for Downscaling. *Journal of Climate*, **25(7)**, 2517–2526, doi:10.1175/jcli-d-11-00251.1.

Briley, L., D. Brown, and S.E. Kalafatis, 2015: Overcoming barriers during the co-production of climate information for decision-making. *Climate Risk Management*, **9**, 41–49, doi:10.1016/j.crm.2015.04.004.

Brinckmann, S., J. Trentmann, and B. Ahrens, 2013: Homogeneity Analysis of the CM SAF Surface Solar Irradiance Dataset Derived from Geostationary Satellite Observations. *Remote Sensing*, **6(1)**, 352–378, doi:10.3390/rs6010352.

Brogli, R., S.L. Sørland, N. Kröner, and C. Schär, 2019a: Causes of future Mediterranean precipitation decline depend on the season. *Environmental Research Letters*, **14(11)**, 114017, doi:10.1088/1748-9326/ab4438.

Brogli, R., N. Kröner, S.L. Sørland, D. Lüthi, and C. Schär, 2019b: The Role of Hadley Circulation and Lapse-Rate Changes for the Future European Summer Climate. *Journal of Climate*, **32(2)**, 385–404, doi:10.1175/jcli-d-18-0431.1.

Brogniez, H. et al., 2016: A review of sources of systematic errors and uncertainties in observations and simulations at 183 GHz. *Atmospheric Measurement Techniques*, **9(5)**, 2207–2221, doi:10.5194/amt-9-2207-2016.

Bromwich, D.H., A.B. Wilson, L.-S. Bai, G.W.K. Moore, and P. Bauer, 2016: A comparison of the regional Arctic System Reanalysis and the global ERA-Interim Reanalysis for the Arctic. *Quarterly Journal of the Royal Meteorological Society*, **142(695)**, 644–658, doi:10.1002/qj.2527.

Bromwich, D.H. et al., 2018: The Arctic System Reanalysis, Version 2. *Bulletin of the American Meteorological Society*, **99(4)**, 805–828, doi:10.1175/bams-d-16-0215.1.

Brouillet, A. and S. Joussaume, 2020: More perceived but not faster evolution of heat stress than temperature extremes in the future. *Climatic Change*, **162(2)**, 527–544, doi:10.1007/s10584-020-02752-z.

Brown, A. et al., 2012: Unified Modeling and Prediction of Weather and Climate. *Bull. Amer. Meteor. Soc.*, **93**, 1865–1877, doi:10.1175/bams-d-12-00018.1.

Brown, C. and R.L.R.L. Wilby, 2012: An Alternate Approach to Assessing Climate Risks. *Eos, Transactions American Geophysical Union*, **93(41)**, 401–402, doi:10.1029/2012eo410001.

Brown, C., Y. Ghile, M. Laverty, and K. Li, 2012: Decision scaling: Linking bottom-up vulnerability analysis with climate projections in the water sector. *Water Resources Research*, **48(9)**, 1–12, doi:10.1029/2011wr011212.

Brown, J.R., A.F. Moise, and R.A. Colman, 2013: The South Pacific Convergence Zone in CMIP5 simulations of

ACCEPTED VERSION SUBJECT TO FINAL EDITING

historical and future climate. *Climate Dynamics*, **41(7–8)**, 2179–2197, doi:10.1007/s00382-012-1591-x.
Brown, J.R., A.F. Moise, R. Colman, and H. Zhang, 2016: Will a Warmer World Mean a Wetter or Drier Australian Monsoon? *Journal of Climate*, **29(12)**, 4577–4596, doi:10.1175/jcli-d-15-0695.1.
Brown, M.J., 2000: Urban parameterizations for mesoscale meteorological models. In: *Mesoscale Atmospheric Dispersion* [Boybeyi, Z. (ed.)]. Wit Press, Southampton, UK, pp. 193–255.
Bruci, E.D., B. Islami, and M. Kamberi, 2016: *Third National Communication of the Republic of Albania under the United Nations Framework Convention on Climate Change*. Ministry of Environment of the Republic of Albania, Tirana, Albania, 294 pp.
Brügger, A., S. Dessai, P. Devine-Wright, T.A. Morton, and N.F. Pidgeon, 2015: Psychological responses to the proximity of climate change. *Nature Climate Change*, **5(12)**, 1031–1037, doi:10.1038/nclimate2760.
Brun, F. et al., 2015: Seasonal changes in surface albedo of Himalayan glaciers from MODIS data and links with the annual mass balance. *The Cryosphere*, **9(1)**, 341–355, doi:10.5194/tc-9-341-2015.
Brunet, M. et al., 2011: The minimization of the screen bias from ancient Western Mediterranean air temperature records: an exploratory statistical analysis. *International Journal of Climatology*, **31(12)**, 1879–1895, doi:10.1002/joc.2192.
Brunner, L., R. Lorenz, M. Zumwald, and R. Knutti, 2019: Quantifying uncertainty in European climate projections using combined performance-independence weighting. *Environmental Research Letters*, **14(12)**, 124010, doi:10.1088/1748-9326/ab492f.
Brunner, L. et al., 2020: Comparing Methods to Constrain Future European Climate Projections Using a Consistent Framework. *Journal of Climate*, **33(20)**, 8671–8692, doi:10.1175/jcli-d-19-0953.1.
Bucchignani, E., L. Cattaneo, H.-J. Panitz, and P. Mercogliano, 2016a: Sensitivity analysis with the regional climate model COSMO-CLM over the CORDEX-MENA domain. *Meteorology and Atmospheric Physics*, **128(1)**, 73–95, doi:10.1007/s00703-015-0403-3.
Bucchignani, E., P. Mercogliano, G. Rianna, and H.J. Panitz, 2016b: Analysis of ERA-Interim-driven COSMO-CLM simulations over Middle East – North Africa domain at different spatial resolutions. *International Journal of Climatology*, **36(9)**, 3346–3369, doi:10.1002/joc.4559.
Bucchignani, E., P. Mercogliano, H.J. Panitz, and M. Montesarchio, 2018: Climate change projections for the Middle East–North Africa domain with COSMO-CLM at different spatial resolutions. *Advances in Climate Change Research*, doi:10.1016/j.accre.2018.01.004.
Buckley, M.W. and J. Marshall, 2016: Observations, inferences, and mechanisms of the Atlantic Meridional Overturning Circulation: A review. *Reviews of Geophysics*, **54(1)**, 5–63, doi:10.1002/2015rg000493.
Budikova, D., T.W. Ford, and T.J. Ballinger, 2017: Connections between north-central United States summer hydroclimatology and Arctic sea ice variability. *International Journal of Climatology*, **37(12)**, 4434–4450, doi:10.1002/joc.5097.
Bukovsky, M.S., 2012: Temperature Trends in the NARCCAP Regional Climate Models. *Journal of Climate*, **25(11)**, 3985–3991, doi:10.1175/jcli-d-11-00588.1.
Bukovsky, M.S., D.J. Gochis, and L.O. Mearns, 2013: Towards Assessing NARCCAP Regional Climate Model Credibility for the North American Monsoon: Current Climate Simulations. *Journal of Climate*, **26(22)**, 8802–8826, doi:10.1175/jcli-d-12-00538.1.
Bukovsky, M.S., J.A. Thompson, and L.O. Mearns, 2019: Weighting a regional climate model ensemble: Does it make a difference? Can it make a difference? *Climate Research*, **77(1)**, 23–43, doi:10.3354/cr01541.
Bukovsky, M.S., R.R. McCrary, A. Seth, and L.O. Mearns, 2017: A Mechanistically Credible, Poleward Shift in Warm-Season Precipitation Projected for the U.S. Southern Great Plains? *Journal of Climate*, **30(20)**, 8275–8298, doi:10.1175/jcli-d-16-0316.1.
Buontempo, C. et al., 2018: What have we learnt from EUPORIAS climate service prototypes? *Climate Services*, **9**, 21–32, doi:10.1016/j.cliser.2017.06.003.
Burls, N.J. et al., 2019: The Cape Town "Day Zero" drought and Hadley cell expansion. *npj Climate and Atmospheric Science*, **2(1)**, 27, doi:10.1038/s41612-019-0084-6.
Butler, A.H., D.W.J. Thompson, and R. Heikes, 2010: The Steady-State Atmospheric Circulation Response to Climate Change–like Thermal Forcings in a Simple General Circulation Model. *Journal of Climate*, **23(13)**, 3474–3496, doi:10.1175/2010jcli3228.1.
Byrne, M.P. and P.A. O'Gorman, 2018: Trends in continental temperature and humidity directly linked to ocean warming. *Proceedings of the National Academy of Sciences*, **115(19)**, 4863–4868, doi:10.1073/pnas.1722312115.
Cai, L. et al., 2018: The Polar WRF Downscaled Historical and Projected Twenty-First Century Climate for the Coast and Foothills of Arctic Alaska. *Frontiers in Earth Science*, **5**, 1–15, doi:10.3389/feart.2017.00111.
Cai, P. et al., 2020: Numerical Study of the Interaction between Oasis and Urban Areas within an Arid Mountains-Desert System in Xinjiang, China. *Atmosphere*, **11(1)**, 85, doi:10.3390/atmos11010085.
Cai, W. et al., 2018: Increased variability of eastern Pacific El Niño under greenhouse warming. *Nature*, **564(7735)**, 201–206, doi:10.1038/s41586-018-0776-9.
Caillouet, L., J.-P. Vidal, E. Sauquet, and B. Graff, 2016: Probabilistic precipitation and temperature downscaling of the

ACCEPTED VERSION SUBJECT TO FINAL EDITING

Twentieth Century Reanalysis over France. *Climate of the Past*, **12(3)**, 635–662, doi:10.5194/cp-12-635-2016.
Caillouet, L., J.-P. Vidal, E. Sauquet, B. Graff, and J.-M. Soubeyroux, 2019: SCOPE Climate: a 142-year daily high-resolution ensemble meteorological reconstruction dataset over France. *Earth System Science Data*, **11(1)**, 241–260, doi:10.5194/essd-11-241-2019.
Callahan, B., E. Miles, and D. Fluharty, 1999: Policy implications of climate forecasts for water resources management in the Pacific Northwest. *Policy Sciences*, **32(3)**, 269–293, doi:10.1023/1004604805647.
Caluwaerts, S. et al., 2020: The urban climate of Ghent, Belgium: A case study combining a high-accuracy monitoring network with numerical simulations. *Urban Climate*, **31**, 100565, doi:10.1016/j.uclim.2019.100565.
Camera, C., A. Bruggeman, P. Hadjinicolaou, S. Pashiardis, and M.A. Lange, 2014: Evaluation of interpolation techniques for the creation of gridded daily precipitation (1 × 1 km²); Cyprus, 1980–2010. *Journal of Geophysical Research: Atmospheres*, **119(2)**, 693–712, doi:10.1002/2013jd020611.
Camilloni, I. and M. Barrucand, 2012: Temporal variability of the Buenos Aires, Argentina, urban heat island. *Theoretical and Applied Climatology*, doi:10.1007/s00704-011-0459-z.
Campbell, T.H. and A.C. Kay, 2014: Solution aversion: On the relation between ideology and motivated disbelief. *Journal of Personality and Social Psychology*, **107(5)**, 809–824, doi:10.1037/a0037963.
Cannon, A.J., 2016: Multivariate Bias Correction of Climate Model Output: Matching Marginal Distributions and Intervariable Dependence Structure. *Journal of Climate*, **29(19)**, 7045–7064, doi:10.1175/jcli-d-15-0679.1.
Cannon, A.J., 2018: Multivariate quantile mapping bias correction: an N-dimensional probability density function transform for climate model simulations of multiple variables. *Climate Dynamics*, **50(1–2)**, 31–49, doi:10.1007/s00382-017-3580-6.
Cannon, A.J., 2020: Reductions in daily continental-scale atmospheric circulation biases between generations of global climate models: CMIP5 to CMIP6. *Environmental Research Letters*, **15(6)**, 064006, doi:10.1088/1748-9326/ab7e4f.
Cannon, A.J., S.R. Sobie, and T.Q. Murdock, 2015: Bias Correction of GCM Precipitation by Quantile Mapping: How Well Do Methods Preserve Changes in Quantiles and Extremes? *Journal of Climate*, **28(17)**, 6938–6959, doi:10.1175/jcli-d-14-00754.1.
Cao, D., F. Huang, and X. Qie, 2014: Development and Evaluation of detection algorithm for FY-4 Geostationary Lightning Imager (GLI) measurement. In: *Proceedings of XV International Conference on Atmospheric Electricity, Norman, OK, USA*. pp. 1–6.
Cao, L., L. Duan, G. Bala, and K. Caldeira, 2016a: Simulated long-term climate response to idealized solar geoengineering. *Geophysical Research Letters*, **43(5)**, 2209–2217, doi:10.1002/2016gl068079.
Cao, L., Y. Zhu, G. Tang, F. Yuan, and Z. Yan, 2016b: Climatic warming in China according to a homogenized data set from 2419 stations. *International Journal of Climatology*, **36(13)**, 4384–4392, doi:10.1002/joc.4639.
Capotondi, A. et al., 2015: Understanding ENSO Diversity. *Bulletin of the American Meteorological Society*, **96(6)**, 921–938, doi:10.1175/bams-d-13-00117.1.
Cardoso, R.M., P.M.M. Soares, D.C.A. Lima, and A. Semedo, 2016: The impact of climate change on the Iberian low-level wind jet: EURO-CORDEX regional climate simulation. *Tellus A: Dynamic Meteorology and Oceanography*, **68(1)**, 29005, doi:10.3402/tellusa.v68.29005.
Careto, J.A.M., R.M. Cardoso, P.M.M. Soares, and R.M. Trigo, 2018: Land-Atmosphere Coupling in CORDEX-Africa: Hindcast Regional Climate Simulations. *Journal of Geophysical Research: Atmospheres*, **123(19)**, 11,048–11,067, doi:10.1029/2018jd028378.
Casanueva, A., J. Bedia, S. Herrera, J. Fernández, and J.M. Gutiérrez, 2018: Direct and component-wise bias correction of multi-variate climate indices: the percentile adjustment function diagnostic tool. *Climatic Change*, **147(3–4)**, 411–425, doi:10.1007/s10584-018-2167-5.
Casanueva, A. et al., 2020: Testing bias adjustment methods for regional climate change applications under observational uncertainty and resolution mismatch. *Atmospheric Science Letters*, **21(7)**, doi:10.1002/asl.978.
Cash, D.W. et al., 2003: Knowledge Systems for Sustainable Development. *Proceedings of the national academy of sciences*, **100**, 8086–8091, doi:10.1073/pnas.1231332100.
Castruccio, S., Z. Hu, B. Sanderson, A. Karspeck, and D. Hammerling, 2019: Reproducing Internal Variability with Few Ensemble Runs. *Journal of Climate*, **32(24)**, 8511–8522, doi:10.1175/jcli-d-19-0280.1.
Cattiaux, J. and C. Cassou, 2013: Opposite CMIP3/CMIP5 trends in the wintertime Northern Annular Mode explained by combined local sea ice and remote tropical influences. *Geophysical Research Letters*, **40(14)**, 3682–3687, doi:10.1002/grl.50643.
Catto, J.L., C. Jakob, and N. Nicholls, 2015: Can the CMIP5 models represent winter frontal precipitation? *Geophysical Research Letters*, **42(20)**, 8596–8604, doi:10.1002/2015gl066015.
Catto, J.L., N. Nicholls, C. Jakob, and K.L. Shelton, 2014: Atmospheric fronts in current and future climates. *Geophysical Research Letters*, **41(21)**, 7642–7650, doi:10.1002/2014gl061943.
Cavazos, T. et al., 2019: Climatic trends and regional climate models intercomparison over the CORDEX-CAM (Central America, Caribbean, and Mexico) domain. *International Journal of Climatology*, joc.6276, doi:10.1002/joc.6276.
Cavicchia, L., H. von Storch, and S. Gualdi, 2014: A long-term climatology of medicanes. *Climate Dynamics*, **43(5–6)**,

ACCEPTED VERSION SUBJECT TO FINAL EDITING

1183–1195, doi:10.1007/s00382-013-1893-7.
Cayan, D. et al., 2013: Future climate: Projected average. In: *Assessment of Climate Change in the Southwest United States: A Report Prepared for the National Climate Assessment* [Garfin, G., A. Jardine, R. Merideth, M. Black, and S. LeRoy (eds.)]. A report by the Southwest Climate Alliance. Island Press, Washington, DC, USA, pp. 101–125, doi:10.5822/978-1-61091-484-0_6.
Ceppi, P. and T.G. Shepherd, 2019: The Role of the Stratospheric Polar Vortex for the Austral Jet Response to Greenhouse Gas Forcing. *Geophysical Research Letters*, **46(12)**, 6972–6979, doi:10.1029/2019gl082883.
Ceppi, P., G. Zappa, T.G. Shepherd, and J.M. Gregory, 2018: Fast and Slow Components of the Extratropical Atmospheric Circulation Response to CO2 Forcing. *Journal of Climate*, **31(3)**, 1091–1105, doi:10.1175/jcli-d-17-0323.1.
Chadwick, R. and P. Good, 2013: Understanding nonlinear tropical precipitation responses to CO2 forcing. *Geophysical Research Letters*, **40(18)**, 4911–4915, doi:10.1002/grl.50932.
Challinor, A., J. Slingo, A. Turner, and T. Wheeler, 2006: *Indian Monsoon: Contribution to the Stern Review*. University of Reading, Reading, UK, 3 pp.
Chan, S.C., E.J. Kendon, H.J. Fowler, S. Blenkinsop, and N.M. Roberts, 2014a: Projected increases in summer and winter UK sub-daily precipitation extremes from high-resolution regional climate models. *Environmental Research Letters*, **9(8)**, 084019, doi:10.1088/1748-9326/9/8/084019.
Chan, S.C. et al., 2014b: The value of high-resolution Met Office regional climate models in the simulation of multihourly precipitation extremes. *Journal of Climate*, **27(16)**, 6155–6174, doi:10.1175/jcli-d-13-00723.1.
Chan, S.C. et al., 2020: Europe-wide precipitation projections at convection permitting scale with the Unified Model. *Climate Dynamics*, **55(3–4)**, 409–428, doi:10.1007/s00382-020-05192-8.
Chandler, R.E., 2020: Multisite, multivariate weather generation based on generalised linear models. *Environmental Modelling & Software*, **134**, 104867, doi:10.1016/j.envsoft.2020.104867.
Chandrasa, G.T. and A. Montenegro, 2019: Evaluation of regional climate model simulated rainfall over Indonesia and its application for downscaling future climate projections. *International Journal of Climatology*, joc.6316, doi:10.1002/joc.6316.
Chaney, N.W., J. Sheffield, G. Villarini, and E.F. Wood, 2014: Development of a High-Resolution Gridded Daily Meteorological Dataset over Sub-Saharan Africa: Spatial Analysis of Trends in Climate Extremes. *Journal of Climate*, **27(15)**, 5815–5835, doi:10.1175/jcli-d-13-00423.1.
Chang, E.K.M., Y. Guo, and X. Xia, 2012: CMIP5 multimodel ensemble projection of storm track change under global warming. *Journal of Geophysical Research: Atmospheres*, **117(D23)**, n/a–n/a, doi:10.1029/2012jd018578.
Chang, E.K.M., C.-G. Ma, C. Zheng, and A.M.W. Yau, 2016: Observed and projected decrease in Northern Hemisphere extratropical cyclone activity in summer and its impacts on maximum temperature. *Geophysical Research Letters*, **43(5)**, 2200–2208, doi:10.1002/2016gl068172.
Chardon, J., B. Hingray, and A.-C. Favre, 2018: An adaptive two-stage analog/regression model for probabilistic prediction of small-scale precipitation in France. *Hydrology and Earth System Sciences*, **22(1)**, 265–286, doi:10.5194/hess-22-265-2018.
Charles, S.P., B.C. Bates, P.H. Whetton, and J.P. Hughes, 1999: Validation of downscaling models for changed climate conditions: case study of southwestern Australia. *Climate Research*, **12**, 1–14, doi:10.3354/cr012001.
Chaudhuri, A.H., R.M. Ponte, G. Forget, and P. Heimbach, 2013: A Comparison of Atmospheric Reanalysis Surface Products over the Ocean and Implications for Uncertainties in Air–Sea Boundary Forcing. *Journal of Climate*, **26(1)**, 153–170, doi:10.1175/jcli-d-12-00090.1.
Cheema, M.J.M. and W.G.M. Bastiaanssen, 2012: Local calibration of remotely sensed rainfall from the TRMM satellite for different periods and spatial scales in the Indus Basin. *International Journal of Remote Sensing*, **33(8)**, 2603–2627, doi:10.1080/01431161.2011.617397.
Chen, F. et al., 2011: The integrated WRF/urban modelling system: development, evaluation, and applications to urban environmental problems. *International Journal of Climatology*, **31(2)**, 273–288, doi:10.1002/joc.2158.
Chen, F. et al., 2012: Research Priorities in Observing and Modeling Urban Weather and Climate. *Bulletin of the American Meteorological Society*, **93(11)**, 1725–1728, doi:10.1175/bams-d-11-00217.1.
Chen, H., C.-Y. Xu, and S. Guo, 2012: Comparison and evaluation of multiple GCMs, statistical downscaling and hydrological models in the study of climate change impacts on runoff. *Journal of Hydrology*, **434–435**, 36–45, doi:10.1016/j.jhydrol.2012.02.040.
Chen, H., H. Ma, X. Li, and S. Sun, 2015: Solar influences on spatial patterns of Eurasian winter temperature and atmospheric general circulation anomalies. *Journal of Geophysical Research: Atmospheres*, **120(17)**, 8642–8657, doi:10.1002/2015jd023415.
Chen, H. et al., 2016: Large-scale urbanization effects on eastern Asian summer monsoon circulation and climate. *Climate Dynamics*, **47(1–2)**, 117–136, doi:10.1007/s00382-015-2827-3.
Chen, H.W., F. Zhang, and R.B. Alley, 2016: The Robustness of Midlatitude Weather Pattern Changes due to Arctic Sea Ice Loss. *Journal of Climate*, **29(21)**, 7831–7849, doi:10.1175/jcli-d-16-0167.1.
Chen, J. and J. Chen, 2018: GlobeLand30: Operational global land cover mapping and big-data analysis. *Science China Earth Sciences*, **61(10)**, 1533–1534, doi:10.1007/s11430-018-9255-3.

ACCEPTED VERSION SUBJECT TO FINAL EDITING

Chen, J. and F.P. Brissette, 2019: Reliability of climate model multi-member ensembles in estimating internal precipitation and temperature variability at the multi-decadal scale. *International Journal of Climatology*, **39(2)**, 843–856, doi:10.1002/joc.5846.
Chen, J. et al., 2020: Impacts of climate change on tropical cyclones and induced storm surges in the Pearl River Delta region using pseudo-global-warming method. *Scientific Reports*, **10(1)**, 1965, doi:10.1038/s41598-020-58824-8.
Chen, L. and P.A. Dirmeyer, 2019: Global observed and modelled impacts of irrigation on surface temperature. *International Journal of Climatology*, **39(5)**, 2587–2600, doi:10.1002/joc.5973.
Chen, L., J. Francis, and E. Hanna, 2018: The "Warm-Arctic/Cold-continents" pattern during 1901–2010. *International Journal of Climatology*, **38(14)**, 5245–5254, doi:10.1002/joc.5725.
Chen, M. et al., 2008: Assessing objective techniques for gauge-based analyses of global daily precipitation. *Journal of Geophysical Research*, **113(D4)**, D04110, doi:10.1029/2007jd009132.
Chen, S. et al., 2019: Added Value of a Dynamical Downscaling Approach for Simulating Precipitation and Temperature Over Tianshan Mountains Area, Central Asia. *Journal of Geophysical Research: Atmospheres*, **124(21)**, 11051–11069, doi:10.1029/2019jd031016.
Chen, X. and T. Zhou, 2015: Distinct effects of global mean warming and regional sea surface warming pattern on projected uncertainty in the South Asian summer monsoon. *Geophysical Research Letters*, **42(21)**, 9433–9439, doi:10.1002/2015gl066384.
Chen, X. and S.-J. Jeong, 2018: Irrigation enhances local warming with greater nocturnal warming effects than daytime cooling effects. *Environmental Research Letters*, **13(2)**, 024005, doi:10.1088/1748-9326/aa9dea.
Chen, Z. et al., 2020: Global Land Monsoon Precipitation Changes in CMIP6 Projections. *Geophysical Research Letters*, **47(14)**, doi:10.1029/2019gl086902.
Cheng, X. et al., 2020: Reducing air pollution increases the local diurnal temperature range: A case study of Lanzhou, China. *Meteorological Applications*, **27(4)**, e1939, doi:10.1002/met.1939.
Chenoli, S.N., M.Y. Ahmad Mazuki, J. Turner, and A.A. Samah, 2017: Historical and projected changes in the Southern Hemisphere Sub-tropical Jet during winter from the CMIP5 models. *Climate Dynamics*, **48(1–2)**, 661–681, doi:10.1007/s00382-016-3102-y.
Cherchi, A., A. Alessandri, S. Masina, and A. Navarra, 2011: Effects of increased CO2 levels on monsoons. *Climate Dynamics*, **37(1–2)**, 83–101, doi:10.1007/s00382-010-0801-7.
Cherchi, A., H. Annamalai, S. Masina, and A. Navarra, 2014: South Asian summer monsoon and the eastern Mediterranean climate: The monsoon-desert mechanism in CMIP5 simulations. *Journal of Climate*, doi:10.1175/jcli-d-13-00530.1.
Chevuturi, A., N.P. Klingaman, A.G. Turner, and S. Hannah, 2018: Projected Changes in the Asian-Australian Monsoon Region in 1.5°C and 2.0°C Global-Warming Scenarios. *Earth's Future*, **6(3)**, 339–358, doi:10.1002/2017ef000734.
Chimani, B. et al., 2018: Inter-comparison of methods to homogenize daily relative humidity. *International Journal of Climatology*, **38(7)**, 3106–3122, doi:10.1002/joc.5488.
Chimani, B. et al., 2020: Compilation of a guideline providing comprehensive information on freely available climate change data and facilitating their efficient retrieval. *Climate Services*, **19**, 100179, doi:10.1016/j.cliser.2020.100179.
Chiodo, G., J. Oehrlein, L.M. Polvani, J.C. Fyfe, and A.K. Smith, 2019: Insignificant influence of the 11-year solar cycle on the North Atlantic Oscillation. *Nature Geoscience*, **12(2)**, 94–99, doi:10.1038/s41561-018-0293-3.
Chiriaco, M. et al., 2018: ReOBS: a new approach to synthesize long-term multi-variable dataset and application to the SIRTA supersite. *Earth System Science Data*, **10(2)**, 919–940, doi:10.5194/essd-10-919-2018.
Cholette, M., R. Laprise, and J. Thériault, 2015: Perspectives for Very High-Resolution Climate Simulations with Nested Models: Illustration of Potential in Simulating St. Lawrence River Valley Channelling Winds with the Fifth-Generation Canadian Regional Climate Model. *Climate*, **3(2)**, 283–307, doi:10.3390/cli3020283.
Choudhary, A., A.P. Dimri, and P. Maharana, 2018: Assessment of CORDEX-SA experiments in representing precipitation climatology of summer monsoon over India. *Theoretical and Applied Climatology*, **134(1–2)**, 283–307, doi:10.1007/s00704-017-2274-7.
Chow, W.T.L. et al., 2014: A multi-method and multi-scale approach for estimating city-wide anthropogenic heat fluxes. *Atmospheric Environment*, **99**, 64–76, doi:10.1016/j.atmosenv.2014.09.053.
Christensen, J.H., T.R. Carter, and F. Giorgi, 2002: PRUDENCE employs new methods to assess European climate change. *Eos, Transactions American Geophysical Union*, **83(13)**, 147, doi:10.1029/2002eo000094.
Christensen, J.H., M.A.D.D. Larsen, O.B. Christensen, M. Drews, and M. Stendel, 2019: Robustness of European climate projections from dynamical downscaling. *Climate Dynamics*, **53(7–8)**, 4857–4869, doi:10.1007/s00382-019-04831-z.
Christensen, J.H. et al., 2007: Regional Climate Projections. In: *Climate Change 2007: The Physical Science Basis. Contribution of Working Group I to the Fourth Assessment Report of the Intergovernmental Panel on Climate Change* [Solomon, S., D. Qin, M. Manning, Z. Chen, M. Marquis, K.B. Averyt, M. Tignor, and H.L. Miller (eds.)]. Cambridge University Press, Cambridge, United Kingdom and New York, NY, USA, pp. 847–940.

ACCEPTED VERSION SUBJECT TO FINAL EDITING

Christensen, J.H. et al., 2013: Climate Phenomena and their Relevance for Future Regional Climate Change. In: *Climate Change 2013: The Physical Science Basis. Contribution of Working Group I to the Fifth Assessment Report of the Intergovernmental Panel on Climate Change* [Stocker, T.F., D. Qin, G.-K. Plattner, M. Tignor, S.K. Allen, J. Boschung, A. Nauels, Y. Xia, V. Bex, and P.M. Midgley (eds.)]. Cambridge University Press, Cambridge, United Kingdom and New York, NY, USA, pp. 1217–1308, doi:10.1017/cbo9781107415324.028.

Christensen, O.B. and E. Kjellström, 2020: Partitioning uncertainty components of mean climate and climate change in a large ensemble of European regional climate model projections. *Climate Dynamics*, **54(9–10)**, 4293–4308, doi:10.1007/s00382-020-05229-y.

Christiansen, B., 2013: Changes in Temperature Records and Extremes: Are They Statistically Significant? *Journal of Climate*, **26(20)**, 7863–7875, doi:10.1175/jcli-d-12-00814.1.

Chronis, T., D.E. Raitsos, D. Kassis, and A. Sarantopoulos, 2011: The Summer North Atlantic Oscillation Influence on the Eastern Mediterranean. *Journal of Climate*, **24(21)**, 5584–5596, doi:10.1175/2011jcli3839.1.

Chrysoulakis, N., Z. Mitraka, and N. Gorelick, 2019: Exploiting satellite observations for global surface albedo trends monitoring. *Theoretical and Applied Climatology*, **137(1–2)**, 1171–1179, doi:10.1007/s00704-018-2663-6.

Chrysoulakis, N. et al., 2018: Urban energy exchanges monitoring from space. *Scientific Reports*, **8(1)**, 11498, doi:10.1038/s41598-018-29873-x.

Chubb, T., M.J. Manton, A.D. Peace, and S.P. Bilish, 2015: Estimation of Wind-Induced Losses from a Precipitation Gauge Network in the Australian Snowy Mountains. *Journal of Hydrometeorology*, **16(6)**, 2619–2638, doi:10.1175/jhm-d-14-0216.1.

Chug, D. et al., 2020: Observed Evidence for Steep Rise in the Extreme Flow of Western Himalayan Rivers. *Geophysical Research Letters*, **47(15)**, doi:10.1029/2020gl087815.

Coats, S., J.E. Smerdon, B.I. Cook, and R. Seager, 2013: Stationarity of the tropical pacific teleconnection to North America in CMIP5/PMIP3 model simulations. *Geophysical Research Letters*, **40(18)**, 4927–4932, doi:10.1002/grl.50938.

Cohen, J. et al., 2014: Recent Arctic amplification and extreme mid-latitude weather. *Nature Geoscience*, **7(9)**, 627–637, doi:10.1038/ngeo2234.

Cohen, J. et al., 2020: Divergent consensuses on Arctic amplification influence on midlatitude severe winter weather. *Nature Climate Change*, **10(1)**, 20–29, doi:10.1038/s41558-019-0662-y.

Cohen, J.L., J.C. Furtado, M.A. Barlow, V.A. Alexeev, and J.E. Cherry, 2012: Arctic warming, increasing snow cover and widespread boreal winter cooling. *Environmental Research Letters*, **7(1)**, 014007, doi:10.1088/1748-9326/7/1/014007.

Colette, A., R. Vautard, and M. Vrac, 2012: Regional climate downscaling with prior statistical correction of the global climate forcing. *Geophysical Research Letters*, **39(13)**, n/a–n/a, doi:10.1029/2012gl052258.

Collins, K. and R. Ison, 2009: Jumping off Arnstein's ladder: social learning as a new policy paradigm for climate change adaptation. *Environmental Policy and Governance*, **19(6)**, 358–373, doi:10.1002/eet.523.

Collins, M. et al., 2013a: Observational challenges in evaluating climate models. *Nature Climate Change*, **3(11)**, 940–941, doi:10.1038/nclimate2012.

Collins, M. et al., 2013b: Long-term Climate Change: Projections, Commitments and Irreversibility. In: *Climate Change 2013: The Physical Science Basis. Contribution of Working Group I to the Fifth Assessment Report of the Intergovernmental Panel on Climate Change* [Stocker, T.F., D. Qin, G.-K. Plattner, M. Tignor, S.K. Allen, J. Boschung, A. Nauels, Y. Xia, V. Bex, and M. Midgley (eds.)]. Cambridge University Press, Cambridge, United Kingdom and New York, NY, USA, pp. 1029–1136, doi:10.1017/cbo9781107415324.024.

Collins, M. et al., 2018: Challenges and opportunities for improved understanding of regional climate dynamics. *Nature Climate Change*, **8(2)**, 101–108, doi:10.1038/s41558-017-0059-8.

Collow, T.W., W. Wang, and A. Kumar, 2019: Reduction in Northern Midlatitude 2-m Temperature Variability due to Arctic Sea Ice Loss. *Journal of Climate*, **32(16)**, 5021–5035, doi:10.1175/jcli-d-18-0692.1.

Compo, G.P. et al., 2011: The Twentieth Century Reanalysis Project. *Quarterly Journal of the Royal Meteorological Society*, **137(654)**, 1–28, doi:10.1002/qj.776.

Condom, T. et al., 2020: Climatological and Hydrological Observations for the South American Andes: In situ Stations, Satellite, and Reanalysis Data Sets. *Frontiers in Earth Science*, **8**, doi:10.3389/feart.2020.00092.

Contractor, S. et al., 2020: Rainfall Estimates on a Gridded Network (REGEN) – a global land-based gridded dataset of daily precipitation from 1950 to 2016. *Hydrology and Earth System Sciences*, **24(2)**, 919–943, doi:10.5194/hess-24-919-2020.

Cook, B.I., T.R. Ault, and J.E. Smerdon, 2015a: Unprecedented 21st century drought risk in the American Southwest and Central Plains. *Science Advances*, **1(1)**, e1400082, doi:10.1126/sciadv.1400082.

Cook, B.I., S.P. Shukla, M.J. Puma, and L.S. Nazarenko, 2015b: Irrigation as an historical climate forcing. *Climate Dynamics*, **44(5–6)**, 1715–1730, doi:10.1007/s00382-014-2204-7.

Cook, E.R. et al., 2010: Megadroughts in North America: placing IPCC projections of hydroclimatic change in a long-term palaeoclimate context. *Journal of Quaternary Science*, **25(1)**, 48–61, doi:10.1002/jqs.1303.

Cook, K.H. and E.K. Vizy, 2015: Detection and Analysis of an Amplified Warming of the Sahara Desert. *Journal of Climate*, **28(16)**, 6560–6580, doi:10.1175/jcli-d-14-00230.1.

ACCEPTED VERSION SUBJECT TO FINAL EDITING

Cook, K.H. and E.K. Vizy, 2019: Contemporary Climate Change of the African Monsoon Systems. *Current Climate Change Reports*, **5(3)**, 145–159, doi:10.1007/s40641-019-00130-1.
Coppola, E. et al., 2020: A first-of-its-kind multi-model convection permitting ensemble for investigating convective phenomena over Europe and the Mediterranean. *Climate Dynamics*, **55(1–2)**, 3–34, doi:10.1007/s00382-018-4521-8.
Coppola, E. et al., 2021: Assessment of the European Climate Projections as Simulated by the Large EURO-CORDEX Regional and Global Climate Model Ensemble. *Journal of Geophysical Research: Atmospheres*, **126(4)**, doi:10.1029/2019jd032356.
Corballis, T., 2019: Populating the Climate. *Environmental Philosophy*, **16(2)**, 275–289, doi:10.5840/envirophil201981284.
Corner, A., L. Whitmarsh, and D. Xenias, 2012: Uncertainty, scepticism and attitudes towards climate change: biased assimilation and attitude polarisation. *Climatic Change*, **114(3–4)**, 463–478, doi:10.1007/s10584-012-0424-6.
Corner, A., E. Markowitz, and N. Pidgeon, 2014: Public engagement with climate change: the role of human values. *Wiley Interdisciplinary Reviews: Climate Change*, **5(3)**, 411–422, doi:10.1002/wcc.269.
Coumou, D., J. Lehmann, and J. Beckmann, 2015: The weakening summer circulation in the Northern Hemisphere mid-latitudes. *Science*, **348(6232)**, 324–327, doi:10.1126/science.1261768.
Coumou, D., G. Di Capua, S. Vavrus, L. Wang, and S. Wang, 2018: The influence of Arctic amplification on mid-latitude summer circulation. *Nature Communications*, **9(1)**, 2959, doi:10.1038/s41467-018-05256-8.
Cramer, W., J. Guiot, and K. Marini, 2020: MedECCe 2020 Summary for Policymakers. In: *Climate and Environmental Change in the Mediterranean Basin – Current Situation and Risks for the Future. First Mediterranean Assessment Report* []. Union for the Mediterranean, Plan Bleu, UNEP/MAP, Marseille, France, pp. 34.
Cramer, W. et al., 2018: Climate change and interconnected risks to sustainable development in the Mediterranean. *Nature Climate Change*, **8(11)**, 972–980, doi:10.1038/s41558-018-0299-2.
Crook, J. et al., 2019: Assessment of the Representation of West African Storm Lifecycles in Convection-Permitting Simulations. *Earth and Space Science*, 2018EA000491, doi:10.1029/2018ea000491.
Crow, W.T. et al., 2015: Robust estimates of soil moisture and latent heat flux coupling strength obtained from triple collocation. *Geophysical Research Letters*, **42(20)**, 8415–8423, doi:10.1002/2015gl065929.
CTT, 2018: *Future Forward: Cape Town Tourism Annual Report 2017/2018*. 4 pp.
Cuervo-Robayo, A.P. et al., 2014: An update of high-resolution monthly climate surfaces for Mexico. *International Journal of Climatology*, **34(7)**, 2427–2437, doi:10.1002/joc.3848.
Cui, J. et al., 2020: Vegetation forcing modulates global land monsoon and water resources in a CO2-enriched climate. *Nature Communications*, **11(1)**, 5184, doi:10.1038/s41467-020-18992-7.
Culley, S. et al., 2016: A bottom-up approach to identifying the maximum operational adaptive capacity of water resource systems to a changing climate. *Water Resources Research*, **52(9)**, 6751–6768, doi:10.1002/2015wr018253.
Cumming, G.S., D.H.M. Cumming, and C.L. Redman, 2006: Scale Mismatches in Social-Ecological Systems : Causes, Consequences, and Solutions. *Ecology and Society*, **11(1)**, 14.
Cvijanovic, I. et al., 2017: Future loss of Arctic sea-ice cover could drive a substantial decrease in California's rainfall. *Nature Communications*, **8(1)**, 1947, doi:10.1038/s41467-017-01907-4.
D'Agostino, R., J. Bader, S. Bordoni, D. Ferreira, and J. Jungclaus, 2019: Northern Hemisphere Monsoon Response to Mid-Holocene Orbital Forcing and Greenhouse Gas-Induced Global Warming. *Geophysical Research Letters*, **46(3)**, 1591–1601, doi:10.1029/2018gl081589.
Dafka, S. et al., 2018: On the ability of RCMs to capture the circulation pattern of Etesians. *Climate Dynamics*, **51(5–6)**, 1687–1706, doi:10.1007/s00382-017-3977-2.
Dahlgren, P., T. Landelius, P. Kållberg, and S. Gollvik, 2016: A high-resolution regional reanalysis for Europe. Part 1: Three-dimensional reanalysis with the regional HIgh-Resolution Limited-Area Model (HIRLAM). *Quarterly Journal of the Royal Meteorological Society*, **142(698)**, 2119–2131, doi:10.1002/qj.2807.
Dai, A. and C.E. Bloecker, 2019: Impacts of internal variability on temperature and precipitation trends in large ensemble simulations by two climate models. *Climate Dynamics*, **52(1–2)**, 289–306, doi:10.1007/s00382-018-4132-4.
Dai, A. and M. Song, 2020: Little influence of Arctic amplification on mid-latitude climate. *Nature Climate Change*, **10(3)**, 231–237, doi:10.1038/s41558-020-0694-3.
Dandou, A., M. Tombrou, E. Akylas, N. Soulakellis, and E. Bossioli, 2005: Development and evaluation of an urban parameterization scheme in the Penn State/NCAR Mesoscale Model (MM5). *Journal of Geophysical Research D: Atmospheres*, **110**, doi:10.1029/2004jd005192.
Daniel, M. et al., 2019: Benefits of explicit urban parameterization in regional climate modeling to study climate and city interactions. *Climate Dynamics*, **52(5–6)**, 2745–2764, doi:10.1007/s00382-018-4289-x.
Daniels, E.E., G. Lenderink, R.W.A. Hutjes, and A.A.M. Holtslag, 2016: Observed urban effects on precipitation along the Dutch West coast. *International Journal of Climatology*, **36(4)**, 2111–2119, doi:10.1002/joc.4458.
Darmaraki, S. et al., 2019: Future evolution of Marine Heatwaves in the Mediterranean Sea. *Climate Dynamics*,

SUBJECT TO FINAL EDITING
ACCEPTED VERSION

doi:10.1007/s00382-019-04661-z.
Daron, J. et al., 2018: Providing future climate projections using multiple models and methods: insights from the Philippines. *Climatic Change*, **148(1–2)**, 187–203, doi:10.1007/s10584-018-2183-5.
Daron, J.D., K. Sutherland, C. Jack, and B.C. Hewitson, 2014: The role of regional climate projections in managing complex socio-ecological systems. *Regional Environmental Change*, **15(1)**, 1–12, doi:10.1007/s10113-014-0631-y.
Daron, J.D., S. Lorenz, P. Wolski, R.C. Blamey, and C. Jack, 2015: Interpreting climate data visualisations to inform adaptation decisions. *Climate Risk Management*, **10**, 17–26, doi:10.1016/j.crm.2015.06.007.
Davini, P., J. Hardenberg, and S. Corti, 2015: Tropical origin for the impacts of the Atlantic Multidecadal Variability on the Euro-Atlantic climate. *Environmental Research Letters*, **10(9)**, 094010, doi:10.1088/1748-9326/10/9/094010.
Davini, P. et al., 2017: Climate SPHINX: evaluating the impact of resolution and stochastic physics parameterisations in the EC-Earth global climate model. *Geoscientific Model Development*, **10(3)**, 1383–1402, doi:10.5194/gmd-10-1383-2017.
Dawson, A. and T.N. Palmer, 2015: Simulating weather regimes: impact of model resolution and stochastic parameterization. *Climate Dynamics*, **44(7)**, 2177–2193, doi:10.1007/s00382-014-2238-x.
Dayon, G., J. Boé, and E. Martin, 2015: Transferability in the future climate of a statistical downscaling method for precipitation in France. *Journal of Geophysical Research: Atmospheres*, **120(3)**, 1023–1043, doi:10.1002/2014jd022236.
de Bruijn, K.M., L. Cumiskey, R. Ní Dhubhda, M. Hounjet, and W. Hynes, 2016: Flood vulnerability of critical infrastructure in Cork, Ireland. *E3S Web of Conferences*, **7**, 07005, doi:10.1051/e3sconf/20160707005.
de Jesus, E.M. et al., 2016: Contribution of cold fronts to seasonal rainfall in simulations over the southern La Plata Basin. *Climate Research*, **68(2–3)**, 243–255.
de Kok, R.J., P.D.A. Kraaijenbrink, O.A. Tuinenburg, P.N.J. Bonekamp, and W.W. Immerzeel, 2020a: Towards understanding the pattern of glacier mass balances in High Mountain Asia using regional climatic modelling. *The Cryosphere*, **14(9)**, 3215–3234, doi:10.5194/tc-14-3215-2020.
de Kok, R.J., P.D.A. Kraaijenbrink, O.A. Tuinenburg, P.N.J. Bonekamp, and W.W. Immerzeel, 2020b: Towards understanding the pattern of glacier mass balances in High Mountain Asia using regional climatic modelling. *The Cryosphere*, **14(9)**, 3215–3234, doi:10.5194/tc-14-3215-2020.
de Munck, C. et al., 2013: How much can air conditioning increase air temperatures for a city like Paris, France? *International Journal of Climatology*, **33(1)**, 210–227, doi:10.1002/joc.3415.
De Troch, R., R. Hamdi, H. Van de Vyver, J.-F. Geleyn, and P. Termonia, 2013: Multiscale Performance of the ALARO-0 Model for Simulating Extreme Summer Precipitation Climatology in Belgium. *Journal of Climate*, **26(22)**, 8895–8915, doi:10.1175/jcli-d-12-00844.1.
de Vos, L.W., H. Leijnse, A. Overeem, and R. Uijlenhoet, 2019: Quality Control for Crowdsourced Personal Weather Stations to Enable Operational Rainfall Monitoring. *Geophysical Research Letters*, **46(15)**, 8820–8829, doi:10.1029/2019gl083731.
DEA, 2013: *Long-Term Adaptation Scenarios Flagship Research Programme (LTAS) for South Africa. Climate Trends and Scenarios for South Africa*. Department of Environmental Affairs (DEA), Pretoria, South Africa, 132 pp.
DEA, 2018: *South Africa's Third National Communication under the United Nations Framework Convention on Climate Change*. Department of Environmental Affairs (DEA), Pretoria, South Africa, 351 pp.
Dee, D.P. et al., 2011: The ERA-Interim reanalysis: Configuration and performance of the data assimilation system. *Quarterly Journal of the Royal Meteorological Society*, **137**, 553–597, doi:10.1002/qj.828.
DeFlorio, M.J. et al., 2016: Interannual modulation of subtropical Atlantic boreal summer dust variability by ENSO. *Climate Dynamics*, **46(1)**, 585–599, doi:10.1007/s00382-015-2600-7.
Dekens, L., S. Parey, M. Grandjacques, and D. Dacunha-Castelle, 2017: Multivariate distribution correction of climate model outputs: A generalization of quantile mapping approaches. *Environmetrics*, **28(6)**, e2454, doi:10.1002/env.2454.
Dell'Aquila, A. et al., 2018: Evaluation of simulated decadal variations over the Euro-Mediterranean region from ENSEMBLES to Med-CORDEX. *Climate Dynamics*, **51(3)**, 857–876, doi:10.1007/s00382-016-3143-2.
Della-Marta, P.M. and H. Wanner, 2006: A Method of Homogenizing the Extremes and Mean of Daily Temperature Measurements. *Journal of Climate*, **19(17)**, 4179–4197, doi:10.1175/jcli3855.1.
DelSole, T., M.K. Tippett, and J. Shukla, 2011: A Significant Component of Unforced Multidecadal Variability in the Recent Acceleration of Global Warming. *Journal of Climate*, **24(3)**, 909–926, doi:10.1175/2010jcli3659.1.
Delworth, T.L. and F. Zeng, 2014: Regional rainfall decline in Australia attributed to anthropogenic greenhouse gases and ozone levels. *Nature Geoscience*, **7(8)**, 583–587, doi:10.1038/ngeo2201.
Delworth, T.L., F. Zeng, A. Rosati, G.A. Vecchi, and A.T. Wittenberg, 2015: A Link between the Hiatus in Global Warming and North American Drought. *Journal of Climate*, **28(9)**, 3834–3845, doi:10.1175/jcli-d-14-00616.1.
Demory, M.-E. et al., 2014: The role of horizontal resolution in simulating drivers of the global hydrological cycle. *Climate Dynamics*, **42(7)**, 2201–2225, doi:10.1007/s00382-013-1924-4.
Demory, M.-E. et al., 2020: European daily precipitation according to EURO-CORDEX regional climate models

SUBJECT TO FINAL EDITING ACCEPTED VERSION

(RCMs) and high-resolution global climate models (GCMs) from the High-Resolution Model Intercomparison Project (HighResMIP). *Geoscientific Model Development*, **13(11)**, 5485–5506, doi:10.5194/gmd-13-5485-2020.

Deng, B. et al., 2013: Evaluation of the CLM4 Lake Model at a Large and Shallow Freshwater Lake. *Journal of Hydrometeorology*, **14(2)**, 636–649, doi:10.1175/jhm-d-12-067.1.

Deng, J., A. Dai, and H. Xu, 2020: Nonlinear Climate Responses to Increasing CO2 and Anthropogenic Aerosols Simulated by CESM1. *Journal of Climate*, **33(1)**, 281–301, doi:10.1175/jcli-d-19-0195.1.

Déqué, M. and J.P. Piedelievre, 1995: High resolution climate simulation over Europe. *Climate Dynamics*, **11(6)**, 321–339, doi:10.1007/bf00215735.

Déqué, M. et al., 2012: The spread amongst ENSEMBLES regional scenarios: regional climate models, driving general circulation models and interannual variability. *Climate Dynamics*, **38(5–6)**, 951–964, doi:10.1007/s00382-011-1053-x.

Deser, C., R.A. Tomas, and L. Sun, 2015: The Role of Ocean–Atmosphere Coupling in the Zonal-Mean Atmospheric Response to Arctic Sea Ice Loss. *Journal of Climate*, **28(6)**, 2168–2186, doi:10.1175/jcli-d-14-00325.1.

Deser, C., L. Terray, and A.S. Phillips, 2016: Forced and Internal Components of Winter Air Temperature Trends over North America during the past 50 Years: Mechanisms and Implications. *Journal of Climate*, **29(6)**, 2237–2258, doi:10.1175/jcli-d-15-0304.1.

Deser, C., R. Guo, and F. Lehner, 2017a: The relative contributions of tropical Pacific sea surface temperatures and atmospheric internal variability to the recent global warming hiatus. *Geophysical Research Letters*, **44(15)**, 7945–7954, doi:10.1002/2017gl074273.

Deser, C., J.W. Hurrell, and A.S. Phillips, 2017b: The role of the North Atlantic Oscillation in European climate projections. *Climate Dynamics*, **49(9–10)**, 3141–3157, doi:10.1007/s00382-016-3502-z.

Deser, C., A. Phillips, V. Bourdette, and H. Teng, 2012: Uncertainty in climate change projections: the role of internal variability. *Climate Dynamics*, **38(3–4)**, 527–546, doi:10.1007/s00382-010-0977-x.

Deser, C., A.S. Phillips, M.A. Alexander, and B. Smoliak, 2014: Projecting North American Climate over the Next 50 Years: Uncertainty due to Internal Variability. *Journal of Climate*, **27(6)**, 2271–2296, doi:10.1175/jcli-d-13-00451.1.

Deser, C., I.R. Simpson, K.A. McKinnon, and A.S. Phillips, 2017c: The Northern Hemisphere Extratropical Atmospheric Circulation Response to ENSO: How Well Do We Know It and How Do We Evaluate Models Accordingly? *Journal of Climate*, **30(13)**, 5059–5082, doi:10.1175/jcli-d-16-0844.1.

Deser, C. et al., 2020: Insights from Earth system model initial-condition large ensembles and future prospects. *Nature Climate Change*, **10(4)**, 277–286, doi:10.1038/s41558-020-0731-2.

Dessai, S. et al., 2018: Building narratives to characterise uncertainty in regional climate change through expert elicitation. *Environmental Research Letters*, **13(7)**, 074005, doi:10.1088/1748-9326/aabcdd.

Devanand, A., M. Huang, M. Ashfaq, B. Barik, and S. Ghosh, 2019: Choice of Irrigation Water Management Practice Affects Indian Summer Monsoon Rainfall and Its Extremes. *Geophysical Research Letters*, **46(15)**, 9126–9135, doi:10.1029/2019gl083875.

Devers, A., J.-P. Vidal, C. Lauvernet, B. Graff, and O. Vannier, 2020: A framework for high-resolution meteorological surface reanalysis through offline data assimilation in an ensemble of downscaled reconstructions. *Quarterly Journal of the Royal Meteorological Society*, **146(726)**, 153–173, doi:10.1002/qj.3663.

Dey, R., S.C. Lewis, and N.J. Abram, 2019a: Investigating observed northwest Australian rainfall trends in Coupled Model Intercomparison Project phase 5 detection and attribution experiments. *International Journal of Climatology*, **39(1)**, 112–127, doi:10.1002/joc.5788.

Dey, R., S.C. Lewis, J.M. Arblaster, and N.J. Abram, 2019b: A review of past and projected changes in Australia's rainfall. *Wiley Interdisciplinary Reviews: Climate Change*, e00577, doi:10.1002/wcc.577.

Di Capua, G. and D. Coumou, 2016: Changes in meandering of the Northern Hemisphere circulation. *Environmental Research Letters*, **11(9)**, 094028, doi:10.1088/1748-9326/11/9/094028.

Di Luca, A., R. de Elía, and R. Laprise, 2012: Potential for added value in precipitation simulated by high-resolution nested Regional Climate Models and observations. *Climate Dynamics*, **38(5–6)**, 1229–1247, doi:10.1007/s00382-011-1068-3.

Di Luca, A., R. de Elía, and R. Laprise, 2015: Challenges in the Quest for Added Value of Regional Climate Dynamical Downscaling. *Current Climate Change Reports*, 10–21, doi:10.1007/s40641-015-0003-9.

Di Luca, A., D. Argüeso, J.P. Evans, R. de Elía, and R. Laprise, 2016: Quantifying the overall added value of dynamical downscaling and the contribution from different spatial scales. *Journal of Geophysical Research: Atmospheres*, **121(4)**, 1575–1590, doi:10.1002/2015jd024009.

Di Sante, F., E. Coppola, R. Farneti, and F. Giorgi, 2019: Indian Summer Monsoon as simulated by the regional earth system model RegCM-ES: the role of local air–sea interaction. *Climate Dynamics*, doi:10.1007/s00382-019-04612-8.

Diaconescu, E.P. and R. Laprise, 2013: Can added value be expected in RCM-simulated large scales? *Climate Dynamics*, **41(7–8)**, 1769–1800, doi:10.1007/s00382-012-1649-9.

Díaz, L.B. and C.S. Vera, 2017: Austral summer precipitation interannual variability and trends over Southeastern

ACCEPTED VERSION SUBJECT TO FINAL EDITING

South America in CMIP5 models. *International Journal of Climatology*, **37(S1)**, 681–695, doi:10.1002/joc.5031.

Díaz, L.B., R.I. Saurral, and C.S. Vera, 2020: Assessment of South America summer rainfall climatology and trends in a set of global climate models large ensembles. *International Journal of Climatology*, joc.6643, doi:10.1002/joc.6643.

Dienst, M., J. Lindén, E. Engström, and J. Esper, 2017: Removing the relocation bias from the 155-year Haparanda temperature record in Northern Europe. *International Journal of Climatology*, **37(11)**, 4015–4026, doi:10.1002/joc.4981.

Dienst, M., J. Lindén, Saladié, and J. Esper, 2019: Detection and elimination of UHI effects in long temperature records from villages – A case study from Tivissa, Spain. *Urban Climate*, **27**, 372–383, doi:10.1016/j.uclim.2018.12.012.

Dieppois, B. et al., 2019: Southern African summer-rainfall variability, and its teleconnections, on interannual to interdecadal timescales in CMIP5 models. *Climate Dynamics*, **53(5–6)**, 3505–3527, doi:10.1007/s00382-019-04720-5.

Diffenbaugh, N.S. and F. Giorgi, 2012: Climate change hotspots in the CMIP5 global climate model ensemble. *Climatic Change*, **114(3–4)**, 813–822, doi:10.1007/s10584-012-0570-x.

Diffenbaugh, N.S., D.L. Swain, and D. Touma, 2015: Anthropogenic warming has increased drought risk in California. *Proceedings of the National Academy of Sciences*, **112(13)**, 3931–3936, doi:10.1073/pnas.1422385112.

Dileepkumar, R., K. AchutaRao, and T. Arulalan, 2018: Human influence on sub-regional surface air temperature change over India. *Scientific Reports*, **8(1)**, 8967, doi:10.1038/s41598-018-27185-8.

Dimri, A.P., D. Kumar, A. Choudhary, and P. Maharana, 2018: Future changes over the Himalayas: Mean temperature. *Global and Planetary Change*, **162**, 235–251, doi:10.1016/j.gloplacha.2018.01.014.

Ding, Q., E.J. Steig, D.S. Battisti, and J.M. Wallace, 2012: Influence of the Tropics on the Southern Annular Mode. *Journal of Climate*, **25(18)**, 6330–6348, doi:10.1175/jcli-d-11-00523.1.

Ding, Q. et al., 2014: Tropical forcing of the recent rapid Arctic warming in northeastern Canada and Greenland. *Nature*, **509(7499)**, 209–212, doi:10.1038/nature13260.

Dinku, T., K. Hailemariam, R. Maidment, E. Tarnavsky, and S. Connor, 2014: Combined use of satellite estimates and rain gauge observations to generate high-quality historical rainfall time series over Ethiopia. *International Journal of Climatology*, **34(7)**, 2489–2504, doi:10.1002/joc.3855.

Dittus, A.J., D.J. Karoly, S.C. Lewis, L. Alexander, and M.G. Donat, 2016: A Multiregion Model Evaluation and Attribution Study of Historical Changes in the Area Affected by Temperature and Precipitation Extremes. *Journal of Climate*, **29(23)**, 8285–8299, doi:10.1175/jcli-d-16-0164.1.

Dittus, A.J. et al., 2020: Sensitivity of Historical Climate Simulations to Uncertain Aerosol Forcing. *Geophysical Research Letters*, **47(13)**, doi:10.1029/2019gl085806.

Dixon, K.W. et al., 2016: Evaluating the stationarity assumption in statistically downscaled climate projections: is past performance an indicator of future results? *Climatic Change*, **135(3–4)**, 395–408, doi:10.1007/s10584-016-1598-0.

Djenontin, I.N.S. and A.M. Meadow, 2018: The art of co-production of knowledge in environmental sciences and management: lessons from international practice. *Environmental Management*, **61(6)**, 885–903, doi:10.1007/s00267-018-1028-3.

Doan, Q., H. Kusaka, and Q.B. Ho, 2016: Impact of future urbanization on temperature and thermal comfort index in a developing tropical city: Ho Chi Minh City. *Urban Climate*, **17**, 20–31, doi:10.1016/j.uclim.2016.04.003.

Dobor, L. and T. Hlásny, 2018: Choice of reference climate conditions matters in impact studies: Case of bias-corrected CORDEX data set. *International Journal of Climatology*, doi:10.1002/joc.5930.

Dobriyal, P., A. Qureshi, R. Badola, and S.A. Hussain, 2012: A review of the methods available for estimating soil moisture and its implications for water resource management. *Journal of Hydrology*, **458–459**, 110–117, doi:10.1016/j.jhydrol.2012.06.021.

Dogar, M.M. and T. Sato, 2019: Regional Climate Response of Middle Eastern, African, and South Asian Monsoon Regions to Explosive Volcanism and ENSO Forcing. *Journal of Geophysical Research: Atmospheres*, **124(14)**, 7580–7598, doi:10.1029/2019jd030358.

Donat, M.G., A.J. Pitman, and O. Angélil, 2018: Understanding and Reducing Future Uncertainty in Midlatitude Daily Heat Extremes Via Land Surface Feedback Constraints. *Geophysical Research Letters*, **45(19)**, 10,627–10,636, doi:10.1029/2018gl079128.

Donat, M.G. et al., 2013: Updated analyses of temperature and precipitation extreme indices since the beginning of the twentieth century: The HadEX2 dataset. *Journal of Geophysical Research: Atmospheres*, **118(5)**, 2098–2118, doi:10.1002/jgrd.50150.

Donat, M.G. et al., 2014: Changes in extreme temperature and precipitation in the Arab region: long-term trends and variability related to ENSO and NAO. *International Journal of Climatology*, **34(3)**, 581–592, doi:10.1002/joc.3707.

Done, J.M., G.J. Holland, C.L. Bruyère, L.R. Leung, and A. Suzuki-Parker, 2015: Modeling high-impact weather and climate: lessons from a tropical cyclone perspective. *Climatic Change*, **129(3–4)**, 381–395,

ACCEPTED VERSION SUBJECT TO FINAL EDITING

doi:10.1007/s10584-013-0954-6.
Dong, B. and A. Dai, 2015: The influence of the Interdecadal Pacific Oscillation on Temperature and Precipitation over the Globe. *Climate Dynamics*, **45(9)**, 2667–2681, doi:10.1007/s00382-015-2500-x.
Dong, B. and R. Sutton, 2015: Dominant role of greenhouse-gas forcing in the recovery of Sahel rainfall. *Nature Climate Change*, **5**, 757–760, doi:10.1038/nclimate2664.
Dong, B., R.T. Sutton, and L. Shaffrey, 2017: Understanding the rapid summer warming and changes in temperature extremes since the mid-1990s over Western Europe. *Climate Dynamics*, **48(5)**, 1537–1554, doi:10.1007/s00382-016-3158-8.
Dong, B., R.T. Sutton, T. Woollings, and K. Hodges, 2013: Variability of the North Atlantic summer storm track: mechanisms and impacts on European climate. *Environmental Research Letters*, **8(3)**, 034037, doi:10.1088/1748-9326/8/3/034037.
Dong, B., R.T. Sutton, E. Highwood, and L. Wilcox, 2014: The impacts of European and Asian anthropogenic sulfur dioxide emissions on Sahel rainfall. *Journal of Climate*, **27**, 7000–7017, doi:10.1175/jcli-d-13-00769.1.
Dong, B., A. Dai, M. Vuille, and O.E. Timm, 2018: Asymmetric Modulation of ENSO Teleconnections by the Interdecadal Pacific Oscillation. *Journal of Climate*, **31(18)**, 7337–7361, doi:10.1175/jcli-d-17-0663.1.
Dong, L. and M.J. McPhaden, 2017: Why Has the Relationship between Indian and Pacific Ocean Decadal Variability Changed in Recent Decades? *Journal of Climate*, **30(6)**, 1971–1983, doi:10.1175/jcli-d-16-0313.1.
Dong-feng, Z., H.A.N. Zhen-yu, and S.H.I. Ying, 2017: ScienceDirect Comparison of climate projections between driving CSIRO-Mk3 . 6 . 0 and downscaling simulation of RegCM4 . 4 over China. *Advances in Climate Change Research*, **8(4)**, 245–255, doi:10.1016/j.accre.2017.10.001.
Dosio, A., 2016: Projections of climate change indices of temperature and precipitation from an ensemble of bias-adjusted high-resolution EURO-CORDEX regional climate models. *Journal of Geophysical Research: Atmospheres*, **121(10)**, 5488–5511, doi:10.1002/2015jd024411.
Dosio, A., 2017: Projection of temperature and heat waves for Africa with an ensemble of CORDEX Regional Climate Models. *Climate Dynamics*, **49(1–2)**, 493–519, doi:10.1007/s00382-016-3355-5.
Dosio, A. and E.M. Fischer, 2018: Will Half a Degree Make a Difference? Robust Projections of Indices of Mean and Extreme Climate in Europe Under 1.5°C, 2°C, and 3°C Global Warming. *Geophysical Research Letters*, **45(2)**, 935–944, doi:10.1002/2017gl076222.
Dosio, A., P. Paruolo, and R. Rojas, 2012: Bias correction of the ENSEMBLES high resolution climate change projections for use by impact models: Analysis of the climate change signal. *Journal of Geophysical Research: Atmospheres*, **117(D17)**, n/a–n/a, doi:10.1029/2012jd017968.
Dosio, A., H.-J. Panitz, M. Schubert-Frisius, and D. Lüthi, 2015: Dynamical downscaling of CMIP5 global circulation models over CORDEX-Africa with COSMO-CLM: evaluation over the present climate and analysis of the added value. *Climate Dynamics*, **44(9–10)**, 2637–2661, doi:10.1007/s00382-014-2262-x.
Dosio, A. et al., 2019: What can we know about future precipitation in Africa? Robustness, significance and added value of projections from a large ensemble of regional climate models. *Climate Dynamics*, **53(9–10)**, 5833–5858, doi:10.1007/s00382-019-04900-3.
Dosio, A. et al., 2020: A tale of two futures: contrasting scenarios of future precipitation for West Africa from an ensemble of regional climate models. *Environmental Research Letters*, **15(6)**, 064007, doi:10.1088/1748-9326/ab7fde.
Dou, J. and S. Miao, 2017: Impact of mass human migration during Chinese New Year on Beijing urban heat island. *International Journal of Climatology*, **37(11)**, 4199–4210, doi:10.1002/joc.5061.
Douville, H., A. Voldoire, and O. Geoffroy, 2015: The recent global warming hiatus: What is the role of Pacific variability? *Geophysical Research Letters*, **42(3)**, 880–888, doi:10.1002/2014gl062775.
Douville, H., Y. Peings, and D. Saint-Martin, 2017: Snow-(N)AO relationship revisited over the whole twentieth century. *Geophysical Research Letters*, **44(1)**, 569–577, doi:10.1002/2016gl071584.
Doyle, M.E., R.I. Saurral, and V.R. Barros, 2012: Trends in the distributions of aggregated monthly precipitation over the La Plata Basin. *International Journal of Climatology*, **32(14)**, 2149–2162, doi:10.1002/joc.2429.
Driouech, F., K. ElRhaz, W. Moufouma-Okia, K. Arjdal, and S. Balhane, 2020: Assessing Future Changes of Climate Extreme Events in the CORDEX-MENA Region Using Regional Climate Model ALADIN-Climate. *Earth Systems and Environment*, doi:10.1007/s41748-020-00169-3.
Driscoll, S., A. Bozzo, L.J. Gray, A. Robock, and G. Stenchikov, 2012: Coupled Model Intercomparison Project 5 (CMIP5) simulations of climate following volcanic eruptions. *Journal of Geophysical Research: Atmospheres*, **117(D17)**, doi:10.1029/2012jd017607.
Drobinski, P. et al., 2018: North-western Mediterranean sea-breeze circulation in a regional climate system model. *Climate Dynamics*, **51(3)**, 1077–1093, doi:10.1007/s00382-017-3595-z.
Drouard, M. and T. Woollings, 2018: Contrasting Mechanisms of Summer Blocking Over Western Eurasia. *Geophysical Research Letters*, **45(21)**, 12,040–12,048, doi:10.1029/2018gl079894.
Drugé, T., P. Nabat, M. Mallet, and S. Somot, 2019: Model simulation of ammonium and nitrate aerosols distribution in the Euro-Mediterranean region and their radiative and climatic effects over 1979–2016. *Atmospheric Chemistry and Physics*, **19(6)**, 3707–3731, doi:10.5194/acp-19-3707-2019.

ACCEPTED VERSION SUBJECT TO FINAL EDITING

Dubrovsky, M., R. Huth, H. Dabhi, and M.W. Rotach, 2019: Parametric gridded weather generator for use in present and future climates: focus on spatial temperature characteristics. *Theoretical and Applied Climatology*, doi:10.1007/s00704-019-03027-z.

DuchÊne, F. et al., 2020: A Statistical-Dynamical Methodology to Downscale Regional Climate Projections to Urban Scale. *Journal of Applied Meteorology and Climatology*, **59(6)**, 1109–1123, doi:10.1175/jamc-d-19-0104.1.

Duchene et al., 9999: A statistical-dynamical methodology to downscale regional climate projections to urban scale. *Journal of Applied Meteorology and Climatology*, **(submitted**.

Ducrocq, V. et al., 2014: HyMeX-SOP1: The Field Campaign Dedicated to Heavy Precipitation and Flash Flooding in the Northwestern Mediterranean. *Bulletin of the American Meteorological Society*, **95(7)**, 1083–1100, doi:10.1175/bams-d-12-00244.1.

Dumitrescu, A., M.-V. Birsan, and A. Manea, 2016: Spatio-temporal interpolation of sub-daily (6 h) precipitation over Romania for the period 1975–2010. *International Journal of Climatology*, **36(3)**, 1331–1343, doi:10.1002/joc.4427.

Dunn, R.J.H., K.M. Willett, D.E. Parker, and L. Mitchell, 2016: Expanding HadISD: quality-controlled, sub-daily station data from 1931. *Geoscientific Instrumentation, Methods and Data Systems*, **5(2)**, 473–491, doi:10.5194/gi-5-473-2016.

Dupont, S. and P.G. Mestayer, 2006: Parameterization of the urban energy budget with the submesoscale soil model. *Journal of Applied Meteorology and Climatology*, doi:10.1175/jam2417.1.

DWA, 2013: *Metropolitan Municipality Non-Revenue / Water Loss Assessment*. Department of Water Affairs (DWA), Republic of South Africa, 82 pp.

DWAF, 2007: *Western Cape Water Supply System: Reconciliation Strategy*. P WMA 19/000/00/0507, Department of Water Affairs and Forestry (DWAF), South Africa, 160 pp.

Eade, R. et al., 2014: Do seasonal-to-decadal climate predictions underestimate the predictability of the real world? *Geophysical Research Letters*, **41(15)**, 5620–5628, doi:10.1002/2014gl061146.

Ehmele, F., L.-A. Kautz, H. Feldmann, and J.G. Pinto, 2020: Long-term variance of heavy precipitation across central Europe using a large ensemble of regional climate model simulations. *Earth System Dynamics*, **11(2)**, 469–490, doi:10.5194/esd-11-469-2020.

Ehret, U., E. Zehe, V. Wulfmeyer, K. Warrach-Sagi, and J. Liebert, 2012: HESS Opinions "Should we apply bias correction to global and regional climate model data?". *Hydrology and Earth System Sciences*, **16(9)**, 3391–3404, doi:10.5194/hess-16-3391-2012.

Eisenack, K. et al., 2014: Explaining and overcoming barriers to climate change adaptation. *Nature Climate Change*, **4(10)**, 867–872, doi:10.1038/nclimate2350.

Ekström, M., M.R. Grose, and P.H. Whetton, 2015: An appraisal of downscaling methods used in climate change research. *Wiley Interdisciplinary Reviews: Climate Change*, **6(3)**, 301–319, doi:10.1002/wcc.339.

Elagib, N.A., 2011: Evolution of urban heat island in Khartoum. *International Journal of Climatology*, **31(9)**, 1377–1388, doi:10.1002/joc.2159.

Emile-Geay, J., R. Seager, M.A. Cane, E.R. Cook, and G.H. Haug, 2008: Volcanoes and ENSO over the Past Millennium. *Journal of Climate*, **21(13)**, 3134–3148, doi:10.1175/2007jcli1884.1.

Endo, H., A. Kitoh, and H. Ueda, 2018: A Unique Feature of the Asian Summer Monsoon Response to Global Warming: The Role of Different Land–Sea Thermal Contrast Change between the Lower and Upper Troposphere. *SOLA*, **14**, 57–63, doi:10.2151/sola.2018-010.

Endris, H.S. et al., 2013: Assessment of the Performance of CORDEX Regional Climate Models in Simulating East African Rainfall. *Journal of Climate*, **26(21)**, 8453–8475, doi:10.1175/jcli-d-12-00708.1.

Endris, H.S. et al., 2016: Teleconnection responses in multi-GCM driven CORDEX RCMs over Eastern Africa. *Climate Dynamics*, **46(9–10)**, 2821–2846, doi:10.1007/s00382-015-2734-7.

Engelbrecht, F.A., J.L. McGregor, and C.J. Engelbrecht, 2009: Dynamics of the Conformal-Cubic Atmospheric Model projected climate-change signal over southern Africa. *International Journal of Climatology*, **29(7)**, 1013–1033, doi:10.1002/joc.1742.

England, M.H. et al., 2014: Recent intensification of wind-driven circulation in the Pacific and the ongoing warming hiatus. *Nature Climate Change*, **4(3)**, 222–227, doi:10.1038/nclimate2106.

England, M.R., L.M. Polvani, L. Sun, and C. Deser, 2020: Tropical climate responses to projected Arctic and Antarctic sea-ice loss. *Nature Geoscience*, **13(4)**, 275–281, doi:10.1038/s41561-020-0546-9.

Erdin, R., C. Frei, and H.R. Künsch, 2012: Data Transformation and Uncertainty in Geostatistical Combination of Radar and Rain Gauges. *Journal of Hydrometeorology*, **13(4)**, 1332–1346, doi:10.1175/jhm-d-11-096.1.

Erfanian, A. and G. Wang, 2018: Explicitly Accounting for the Role of Remote Oceans in Regional Climate Modeling of South America. *Journal of Advances in Modeling Earth Systems*, **10(10)**, 2408–2426, doi:10.1029/2018ms001444.

Erlandsen, H.B., K.M. Parding, R. Benestad, A. Mezghani, and M. Pontoppidan, 2020: A Hybrid Downscaling Approach for Future Temperature and Precipitation Change. *Journal of Applied Meteorology and Climatology*, **59(11)**, 1793–1807, doi:10.1175/jamc-d-20-0013.1.

Espinoza, V., D.E. Waliser, B. Guan, D.A. Lavers, and F.M. Ralph, 2018: Global Analysis of Climate Change

SUBJECT TO FINAL EDITING ACCEPTED VERSION

Projection Effects on Atmospheric Rivers. *Geophysical Research Letters*, **45(9)**, 4299–4308, doi:10.1029/2017gl076968.
Evan, A.T., C. Flamant, M. Gaetani, and F. Guichard, 2016: The past, present and future of African dust. *Nature*, **531(7595)**, 493–495, doi:10.1038/nature17149.
Evans, J.P. et al., 2014: Design of a regional climate modelling projection ensemble experiment – NARCliM. *Geoscientific Model Development*, **7(2)**, 621–629, doi:10.5194/gmd-7-621-2014.
Evans, S., S. Malyshev, P. Ginoux, and E. Shevliakova, 2019: The Impacts of the Dust Radiative Effect on Vegetation Growth in the Sahel. *Global Biogeochemical Cycles*, **n/a(n/a)**, doi:10.1029/2018gb006128.
Evin, G., A.-C. Favre, and B. Hingray, 2018: Stochastic generation of multi-site daily precipitation focusing on extreme events. *Hydrology and Earth System Sciences*, **22(1)**, 655–672, doi:10.5194/hess-22-655-2018.
Evin, G. et al., 2019: Partitioning Uncertainty Components of an Incomplete Ensemble of Climate Projections Using Data Augmentation. *Journal of Climate*, **32(8)**, 2423–2440, doi:10.1175/jcli-d-18-0606.1.
Eyring, V. et al., 2016a: Overview of the Coupled Model Intercomparison Project Phase 6 (CMIP6) experimental design and organization. *Geoscientific Model Development*, **9(5)**, 1937–1958, doi:10.5194/gmd-9-1937-2016.
Eyring, V. et al., 2016b: ESMValTool (v1.0) – a community diagnostic and performance metrics tool for routine evaluation of Earth system models in CMIP. *Geoscientific Model Development*, **9(5)**, 1747–1802, doi:10.5194/gmd-9-1747-2016.
Eyring, V. et al., 2019: Taking climate model evaluation to the next level. *Nature Climate Change*, **9(2)**, 102–110, doi:10.1038/s41558-018-0355-y.
Ezber, Y., O. Lutfi Sen, T. Kindap, and M. Karaca, 2007: Climatic effects of urbanization in istanbul: a statistical and modeling analysis. *International Journal of Climatology*, **27(5)**, 667–679, doi:10.1002/joc.1420.
Fabiano, F. et al., 2020: Euro-Atlantic weather Regimes in the PRIMAVERA coupled climate simulations: impact of resolution and mean state biases on model performance. *Climate Dynamics*, **54(11)**, 5031–5048, doi:10.1007/s00382-020-05271-w.
Falco, M. et al., 2018: Assessment of CORDEX simulations over South America: added value on seasonal climatology and resolution considerations. *Climate Dynamics*, doi:10.1007/s00382-018-4412-z.
Fallah, B. et al., 2018: Towards high-resolution climate reconstruction using an off-line data assimilation and COSMO-CLM 5.00 model. *Climate of the Past*, **14(9)**, 1345–1360, doi:10.5194/cp-14-1345-2018.
Farinotti, D., W.W. Immerzeel, R.J. de Kok, D.J. Quincey, and A. Dehecq, 2020: Manifestations and mechanisms of the Karakoram glacier Anomaly. *Nature Geoscience*, **13(1)**, 8–16, doi:10.1038/s41561-019-0513-5.
Favre, A., B. Hewitson, C. Lennard, R. Cerezo-Mota, and M. Tadross, 2013: Cut-off Lows in the South Africa region and their contribution to precipitation. *Climate Dynamics*, **41(9–10)**, 2331–2351, doi:10.1007/s00382-012-1579-6.
Feng, X., B. Huang, B.P. Kirtman, J.L. Kinter, and L.S. Chiu, 2017: A multi-model analysis of the resolution influence on precipitation climatology in the Gulf Stream region. *Climate Dynamics*, **48(5–6)**, 1685–1704, doi:10.1007/s00382-016-3167-7.
Ferguson, J.O. et al., 2016: Analyzing the Adaptive Mesh Refinement (AMR) Characteristics of a High-Order 2D Cubed-Sphere Shallow-Water Model. *Monthly Weather Review*, **144(12)**, 4641–4666, doi:10.1175/mwr-d-16-0197.1.
Fernandes, L.G. and R.R. Rodrigues, 2018: Changes in the patterns of extreme rainfall events in southern Brazil. *International Journal of Climatology*, **38(3)**, 1337–1352, doi:10.1002/joc.5248.
Fernández, J. et al., 2019: Consistency of climate change projections from multiple global and regional model intercomparison projects. *Climate Dynamics*, **52**, 1139–1156, doi:10.1007/s00382-018-4181-8.
Feser, F., B. Rockel, H. von Storch, J. Winterfeldt, and M. Zahn, 2011: Regional Climate Models Add Value to Global Model Data: A Review and Selected Examples. *Bulletin of the American Meteorological Society*, **92(9)**, 1181–1192, doi:10.1175/2011bams3061.1.
Fettweis, X. et al., 2020: GrSMBMIP: intercomparison of the modelled 1980–2012 surface mass balance over the Greenland Ice Sheet. *The Cryosphere*, **14(11)**, 3935–3958, doi:10.5194/tc-14-3935-2020.
Fick, S.E. and R.J. Hijmans, 2017: WorldClim 2: new 1-km spatial resolution climate surfaces for global land areas. *International Journal of Climatology*, **37(12)**, 4302–4315, doi:10.1002/joc.5086.
Fiedler, S., B. Stevens, and T. Mauritsen, 2017: On the sensitivity of anthropogenic aerosol forcing to model-internal variability and parameterizing a Twomey effect. *Journal of Advances in Modeling Earth Systems*, **9(2)**, 1325–1341, doi:10.1002/2017ms000932.
Fiedler, S. et al., 2019: Anthropogenic aerosol forcing – insights from multiple estimates from aerosol-climate models with reduced complexity. *Atmospheric Chemistry and Physics*, **19(10)**, 6821–6841, doi:10.5194/acp-19-6821-2019.
Finney, D.L. et al., 2019: Implications of Improved Representation of Convection for the East Africa Water Budget Using a Convection-Permitting Model. *Journal of Climate*, **32(7)**, 2109–2129, doi:10.1175/jcli-d-18-0387.1.
Fischer, E.M., U. Beyerle, and R. Knutti, 2013: Robust spatially aggregated projections of climate extremes. *Nature Climate Change*, **3(12)**, 1033–1038, doi:10.1038/nclimate2051.
Fita, L., J.P. Evans, D. Argüeso, A. King, and Y. Liu, 2017: Evaluation of the regional climate response in Australia to

SUBJECT TO FINAL EDITING ACCEPTED VERSION

large-scale climate modes in the historical NARCliM simulations. *Climate Dynamics*, **49(7–8)**, 2815–2829, doi:10.1007/s00382-016-3484-x.

Fitzpatrick, R.G.J. et al., 2020: What Drives the Intensification of Mesoscale Convective Systems over the West African Sahel under Climate Change? *Journal of Climate*, **33(8)**, 3151–3172, doi:10.1175/jcli-d-19-0380.1.

Flaounas, E., P. Drobinski, and S. Bastin, 2013: Dynamical downscaling of IPSL-CM5 CMIP5 historical simulations over the Mediterranean: benefits on the representation of regional surface winds and cyclogenesis. *Climate Dynamics*, **40(9–10)**, 2497–2513, doi:10.1007/s00382-012-1606-7.

Flaounas, E. et al., 2012: Assessment of gridded observations used for climate model validation in the Mediterranean region: the HyMeX and MED-CORDEX framework. *Environmental Research Letters*, **7(2)**, 024017, doi:10.1088/1748-9326/7/2/024017.

Flaounas, E. et al., 2018: Assessment of an ensemble of ocean–atmosphere coupled and uncoupled regional climate models to reproduce the climatology of Mediterranean cyclones. *Climate Dynamics*, **51(3)**, 1023–1040, doi:10.1007/s00382-016-3398-7.

Flato, G. et al., 2014: Evaluation of Climate Models. In: *Climate Change 2013: The Physical Science Basis. Contribution of Working Group I to the Fifth Assessment Report of the Intergovernmental Panel on Climate Change* []. Cambridge University Press, Cambridge, United Kingdom and New York, NY, USA, pp. 741–866, doi:10.1017/cbo9781107415324.020.

Fletcher, C.G. and P.J. Kushner, 2011: The Role of Linear Interference in the Annular Mode Response to Tropical SST Forcing. *Journal of Climate*, **24(3)**, 778–794, doi:10.1175/2010jcli3735.1.

Florczyk, A.J. et al., 2019: *GHSL Data Package 2019*. EUR 29788 EN, Publications Office of the European Union, Luxembourg, 32 pp., doi:10.2760/290498.

Fløttum, K. and Gjerstad, 2017: Narratives in climate change discourse. *Wiley Interdisciplinary Reviews: Climate Change*, **8(1)**, e429, doi:10.1002/wcc.429.

Folland, C.K. et al., 2009: The Summer North Atlantic Oscillation: Past, Present, and Future. *Journal of Climate*, **22(5)**, 1082–1103, doi:10.1175/2008jcli2459.1.

Forsythe, N., H.J. Fowler, X.F. Li, S. Blenkinsop, and D. Pritchard, 2017: Karakoram temperature and glacial melt driven by regional atmospheric circulation variability. *Nature Climate Change*, **7(9)**, 664–670, doi:10.1038/nclimate3361.

Fosser, G., S. Khodayar, and P. Berg, 2015: Benefit of convection permitting climate model simulations in the representation of convective precipitation. *Climate Dynamics*, **44(1–2)**, 45–60, doi:10.1007/s00382-014-2242-1.

Fosser, G., S. Khodayar, and P. Berg, 2017: Climate change in the next 30 years: What can a convection-permitting model tell us that we did not already know? *Climate Dynamics*, **48(5–6)**, 1987–2003, doi:10.1007/s00382-016-3186-4.

Fox-Rabinovitz, M., J. Côté, B. Dugas, M. Déqué, and J.L. McGregor, 2006: Variable resolution general circulation models: Stretched-grid model intercomparison project (SGMIP). *Journal of Geophysical Research*, **111(D16)**, D16104, doi:10.1029/2005jd006520.

Fox-Rabinovitz, M. et al., 2008: Stretched-grid Model Intercomparison Project: decadal regional climate simulations with enhanced variable and uniform-resolution GCMs. *Meteorology and Atmospheric Physics*, **100(1–4)**, 159–178, doi:10.1007/s00703-008-0301-z.

Frame, J. and M. Killick, 2007: Integrated water resource planning in the city of Cape Town. *Water SA*, **30(5)**, doi:10.4314/wsa.v30i5.5188.

Francis, J.A. and S.J. Vavrus, 2012: Evidence linking Arctic amplification to extreme weather in mid-latitudes. *Geophysical Research Letters*, **39(6)**, doi:10.1029/2012gl051000.

Francis, J.A. and S.J. Vavrus, 2015: Evidence for a wavier jet stream in response to rapid Arctic warming. *Environmental Research Letters*, **10(1)**, 014005, doi:10.1088/1748-9326/10/1/014005.

Francis, J.A., S.J. Vavrus, and J. Cohen, 2017: Amplified Arctic warming and mid-latitude weather: new perspectives on emerging connections. *Wiley Interdisciplinary Reviews: Climate Change*, **8(5)**, e474, doi:10.1002/wcc.474.

François, B., M. Vrac, A.J. Cannon, Y. Robin, and D. Allard, 2020: Multivariate bias corrections of climate simulations: which benefits for which losses? *Earth System Dynamics*, **11(2)**, 537–562, doi:10.5194/esd-11-537-2020.

Frankcombe, L.M., M.H. England, M.E. Mann, and B.A. Steinman, 2015: Separating internal variability from the externally forced climate response. *Journal of Climate*, **28(20)**, 8184–8202, doi:10.1175/jcli-d-15-0069.1.

Franke, J., S. Brönnimann, J. Bhend, and Y. Brugnara, 2017: A monthly global paleo-reanalysis of the atmosphere from 1600 to 2005 for studying past climatic variations. *Scientific data*, **4**, 170076, doi:10.1038/sdata.2017.76.

Frei, C., 2014: Interpolation of temperature in a mountainous region using nonlinear profiles and non-Euclidean distances. *International Journal of Climatology*, **1605**, 1585–1605, doi:10.1002/joc.3786.

Frei, C. et al., 2003: Daily precipitation statistics in regional climate models: Evaluation and intercomparison for the European Alps. *Journal of Geophysical Research: Atmospheres*, **108(D3)**, n/a–n/a, doi:10.1029/2002jd002287.

Froidevaux, P., L. Schlemmer, J. Schmidli, W. Langhans, and C. Schär, 2014: Influence of the Background Wind on the Local Soil Moisture–Precipitation Feedback. *Journal of the Atmospheric Sciences*, **71(2)**, 782–799,

ACCEPTED VERSION SUBJECT TO FINAL EDITING

doi:10.1175/jas-d-13-0180.1.
Frost, A.J. et al., 2011: A comparison of multi-site daily rainfall downscaling techniques under Australian conditions. *Journal of Hydrology*, **408(1–2)**, 1–18, doi:10.1016/j.jhydrol.2011.06.021.
Früh, B. et al., 2011: Estimation of Climate-Change Impacts on the Urban Heat Load Using an Urban Climate Model and Regional Climate Projections. *Journal of Applied Meteorology and Climatology*, **50(1)**, 167–184, doi:10.1175/2010jamc2377.1.
Fu, G., S.P. Charles, F.H.S. Chiew, M. Ekström, and N.J. Potter, 2018: Uncertainties of statistical downscaling from predictor selection: Equifinality and transferability. *Atmospheric Research*, **203**, 130–140, doi:10.1016/j.atmosres.2017.12.008.
Fujibe, F., 2009: Detection of urban warming in recent temperature trends in Japan. *International Journal of Climatology*, **29(12)**, 1811–1822, doi:10.1002/joc.1822.
Fukui, S., T. Iwasaki, K. Saito, H. Seko, and M. Kunii, 2018: A Feasibility Study on the High-Resolution Regional Reanalysis over Japan Assimilating Only Conventional Observations as an Alternative to the Dynamical Downscaling. *Journal of the Meteorological Society of Japan. Ser. II*, **96(6)**, 565–585, doi:10.2151/jmsj.2018-056.
Fumière, Q. et al., 2019: Extreme rainfall in Mediterranean France during the fall: added value of the CNRM-AROME Convection-Permitting Regional Climate Model. *Climate Dynamics*, doi:10.1007/s00382-019-04898-8.
Gadgil, S.S. and S.S. Gadgil, 2006: The Indian monsoon, GDP and agriculture. *Economic & Political Weekly*, doi:10.2307/4418949.
Gaertner, M. et al., 2018: Simulation of medicanes over the Mediterranean Sea in a regional climate model ensemble: impact of ocean–atmosphere coupling and increased resolution. *Climate Dynamics*, **51(3)**, 1041–1057, doi:10.1007/s00382-016-3456-1.
Gaetani, M. and E. Mohino, 2013: Decadal prediction of the sahelian precipitation in CMIP5 simulations. *Journal of Climate*, **26**, 7708–7719, doi:10.1175/jcli-d-12-00635.1.
Gaetani, M., S. Janicot, M. Vrac, A.M. Famien, and B. Sultan, 2020: Robust assessment of the time of emergence of precipitation change in West Africa. *Scientific Reports*, **10(1)**, 7670, doi:10.1038/s41598-020-63782-2.
Gallant, A.J.E., S.J. Phipps, D.J. Karoly, A.B. Mullan, and A.M. Lorrey, 2013: Nonstationary Australasian Teleconnections and Implications for Paleoclimate Reconstructions. *Journal of Climate*, **26(22)**, 8827–8849, doi:10.1175/jcli-d-12-00338.1.
Gallie, D., M. Petersen, L. Booley, and Y. Tiwe, 2018: *EPIC: Economic Performance Indicators for Cape Town – 2018: Quarter 4*. Organisational Policy and Planning Department of the City of Cape Town, Cape Town, South Africa, 20 pp.
Galmarini, S. et al., 2019: Adjusting climate model bias for agricultural impact assessment: How to cut the mustard. *Climate Services*, doi:10.1016/j.cliser.2019.01.004.
Ganeshan, M. and R. Murtugudde, 2015: Nocturnal propagating thunderstorms may favor urban ”hot-spots”: A model-based study over Minneapolis. *Urban Climate*, **14**, 606–621, doi:10.1016/j.uclim.2015.10.005.
Ganeshan, M., R. Murtugudde, and M.L. Imhoff, 2013: A multi-city analysis of the UHI-influence on warm season rainfall. *Urban Climate*, **6**, 1–23, doi:10.1016/j.uclim.2013.09.004.
Gangopadhyay, S., T. Pruitt, L. Brekke, and D. Raff, 2011: Hydrologic projections for the western United States. *Eos, Transactions American Geophysical Union*, **92(48)**, 441–442, doi:10.1029/2011eo480001.
Gao, C.C. and Y.J. Gao, 2018: Revisited Asian Monsoon Hydroclimate Response to Volcanic Eruptions. *Journal of Geophysical Research: Atmospheres*, **123(15)**, 7883–7896, doi:10.1029/2017jd027907.
Gao, M. et al., 2016: Modeling study of the 2010 regional haze event in the North China Plain. *Atmospheric Chemistry and Physics*, **16(3)**, 1673–1691, doi:10.5194/acp-16-1673-2016.
García-Díez, M., J. Fernández, and R. Vautard, 2015: An RCM multi-physics ensemble over Europe: multi-variable evaluation to avoid error compensation. *Climate Dynamics*, **45(11–12)**, 3141–3156, doi:10.1007/s00382-015-2529-x.
Garcia-Villada, L.P., M.G. Donat, O. Angélil, and A.S. Taschetto, 2020: Temperature and precipitation responses to El Niño-Southern Oscillation in a hierarchy of datasets with different levels of observational constraints. *Climate Dynamics*, **55(9–10)**, 2351–2376, doi:10.1007/s00382-020-05389-x.
Garfinkel, C.I., D.W. Waugh, and L.M. Polvani, 2015: Recent Hadley cell expansion: The role of internal atmospheric variability in reconciling modeled and observed trends. *Geophysical Research Letters*, **42(24)**, 10,824–10,831, doi:10.1002/2015gl066942.
Garfinkel, C.I. et al., 2020: The Role of Zonally Averaged Climate Change in Contributing to Intermodel Spread in CMIP5 Predicted Local Precipitation Changes. *Journal of Climate*, **33(3)**, 1141–1154, doi:10.1175/jcli-d-19-0232.1.
Gastineau, G., J. García-Serrano, and C. Frankignoul, 2017: The Influence of Autumnal Eurasian Snow Cover on Climate and Its Link with Arctic Sea Ice Cover. *Journal of Climate*, **30(19)**, 7599–7619, doi:10.1175/jcli-d-16-0623.1.
Gautam, R., N.C. Hsu, W.K.-M. Lau, and T.J. Yasunari, 2013: Satellite observations of desert dust-induced Himalayan snow darkening. *Geophysical Research Letters*, **40(5)**, 988–993, doi:10.1002/grl.50226.

ACCEPTED VERSION SUBJECT TO FINAL EDITING

GCOS, 2015: *Status of the Global Observing System for Climate*. Global Climate Observing System (GCOS) Secretariat, c/o World Meteorological Organization (WMO), Geneva, Switzerland, 353 pp.
Gentry, M.S. and G.M. Lackmann, 2010: Sensitivity of Simulated Tropical Cyclone Structure and Intensity to Horizontal Resolution. *Monthly Weather Review*, **138(3)**, 688–704, doi:10.1175/2009mwr2976.1.
Georgakakos, A. et al., 2014: Ch. 3: Water Resources. In: *Climate Change Impacts in the United States: The Third National Climate Assessment* [Melillo, J.M., T.C. Richmond, and G. Yohe (eds.)]. U.S. Global Change Research Program, pp. 69–112, doi:10.7930/j0g44n6t.
Georgescu, M., M. Moustaoui, A. Mahalov, and J. Dudhia, 2013: Summer-time climate impacts of projected megapolitan expansion in Arizona. *Nature Climate Change*, **3(1)**, 37–41, doi:10.1038/nclimate1656.
Gervais, M., L.B. Tremblay, J.R. Gyakum, and E. Atallah, 2014: Representing Extremes in a Daily Gridded Precipitation Analysis over the United States: Impacts of Station Density, Resolution, and Gridding Methods. *Journal of Climate*, **27(14)**, 5201–5218, doi:10.1175/jcli-d-13-00319.1.
Gevaert, A.I., D.G. Miralles, R.A.M. de Jeu, J. Schellekens, and A.J. Dolman, 2018: Soil Moisture-Temperature Coupling in a Set of Land Surface Models. *Journal of Geophysical Research: Atmospheres*, doi:10.1002/2017jd027346.
Ghosh, R., W.A. Müller, J. Baehr, and J. Bader, 2017: Impact of observed North Atlantic multidecadal variations to European summer climate: a linear baroclinic response to surface heating. *Climate Dynamics*, **48(11–12)**, 3547–3563, doi:10.1007/s00382-016-3283-4.
Giannini, A. and A. Kaplan, 2019: The role of aerosols and greenhouse gases in Sahel drought and recovery. *Climatic Change*, **152(3–4)**, 449–466, doi:10.1007/s10584-018-2341-9.
Giannini, A. et al., 2013: A unifying view of climate change in the Sahel linking intra-seasonal, interannual and longer time scales. *Environmental Research Letters*, **8(2)**, 024010, doi:10.1088/1748-9326/8/2/024010.
Giesen, R.H. and J. Oerlemans, 2013: Climate-model induced differences in the 21st century global and regional glacier contributions to sea-level rise. *Climate Dynamics*, **41(11–12)**, 3283–3300, doi:10.1007/s00382-013-1743-7.
Gillett, N.P. et al., 2016: The Detection and Attribution Model Intercomparison Project (DAMIP v1.0) contribution to CMIP6. *Geoscientific Model Development*, **9(10)**, 3685–3697, doi:10.5194/gmd-9-3685-2016.
Ginoux, P., J. Prospero, T. Gill, N. Hsu, and M. Zhao, 2012: Global-scale attribution of anthropogenic and natural dust sources and their emission rates based on MODIS Deep Blue aerosol products. *Reviews of Geophysics*, **50**, 3005, doi:10.1029/2012rg000388.
Giorgi, F., 2019: Thirty Years of Regional Climate Modeling: Where Are We and Where Are We Going next? *Journal of Geophysical Research: Atmospheres*, 2018JD030094, doi:10.1029/2018jd030094.
Giorgi, F., 2020: Producing actionable climate change information for regions: the distillation paradigm and the 3R framework. *The European Physical Journal Plus*, **135(5)**, 435, doi:10.1140/epjp/s13360-020-00453-1.
Giorgi, F. and X. Bi, 2009: Time of emergence (TOE) of GHG-forced precipitation change hot-spots. *Geophysical Research Letters*, **36(6)**, L06709, doi:10.1029/2009gl037593.
Giorgi, F. and W.J. Gutowski, 2015: Regional Dynamical Downscaling and the CORDEX Initiative. *Annual Review of Environment and Resources*, **40(1)**, 467–490, doi:10.1146/annurev-environ-102014-021217.
Giorgi, F., C. Jones, and G.R. Asrar, 2009: Addressing climate information needs at the regional level: the CORDEX framework. *WMO Bulletin*, **58(3)**, 175–183.
Giorgi, F. et al., 2016: Enhanced summer convective rainfall at Alpine high elevations in response to climate warming. *Nature Geoscience*, **9(8)**, 584–589, doi:10.1038/ngeo2761.
Giot, O. et al., 2016: Validation of the ALARO-0 model within the EURO-CORDEX framework. *Geoscientific Model Development*, **9(3)**, 1143–1152, doi:10.5194/gmd-9-1143-2016.
Gleckler, P. et al., 2016: A More Powerful Reality Test for Climate Models. *Eos*, **97**, doi:10.1029/2016eo051663.
Glinton, M.R., S.L. Gray, J.M. Chagnon, and C.J. Morcrette, 2017: Modulation of precipitation by conditional symmetric instability release. *Atmospheric Research*, **185**, 186–201, doi:10.1016/j.atmosres.2016.10.013.
Glotter, M. et al., 2014: Evaluating the utility of dynamical downscaling in agricultural impacts projections. *Proceedings of the National Academy of Sciences*, **111(24)**, 8776–8781, doi:10.1073/pnas.1314787111.
Gobiet, A., M. Suklitsch, and G. Heinrich, 2015: The effect of empirical-statistical correction of intensity-dependent model errors on the temperature climate change signal. *Hydrology and Earth System Sciences*, **19(10)**, 4055–4066, doi:10.5194/hess-19-4055-2015.
Goldberg, M.H., S. Linden, M.T. Ballew, S.A. Rosenthal, and A. Leiserowitz, 2019: The role of anchoring in judgments about expert consensus. *Journal of Applied Social Psychology*, **49(3)**, 192–200, doi:10.1111/jasp.12576.
Golosov, S., I. Zverev, E. Shipunova, and A. Terzhevik, 2018: Modified parameterization of the vertical water temperature profile in the FLake model. *Tellus A: Dynamic Meteorology and Oceanography*, **70(1)**, 1–7, doi:10.1080/16000870.2018.1441247.
Gong, D. and S. Wang, 1999: Definition of Antarctic Oscillation index. *Geophysical Research Letters*, **26(4)**, 459–462, doi:10.1029/1999gl900003.
Gong, H., L. Wang, W. Chen, and R. Wu, 2019: Attribution of the East Asian Winter Temperature Trends During 1979–2018: Role of External Forcing and Internal Variability. *Geophysical Research Letters*, **46(19)**, 10874–

ACCEPTED VERSION SUBJECT TO FINAL EDITING

10881, doi:10.1029/2019gl084154.
Gong, T., S.B. Feldstein, and S. Lee, 2020: Rossby Wave Propagation from the Arctic into the Midlatitudes: Does It Arise from In Situ Latent Heating or a Trans-Arctic Wave Train? *Journal of Climate*, **33(9)**, 3619–3633, doi:10.1175/jcli-d-18-0780.1.
Gonzalez, P.L.M., L. Goddard, and A.M. Greene, 2013: Twentieth-century summer precipitation in South Eastern South America: comparison of gridded and station data. *International Journal of Climatology*, **33(13)**, 2923–2928, doi:10.1002/joc.3633.
Good, P. et al., 2015: Nonlinear regional warming with increasing CO2 concentrations. *Nature Climate Change*, **5(2)**, 138–142, doi:10.1038/nclimate2498.
Good, P. et al., 2016: Large differences in regional precipitation change between a first and second 2 K of global warming. *Nature Communications*, **7(1)**, 13667, doi:10.1038/ncomms13667.
Goodman, S.J., T.J. Schmit, J. Daniels, W. Denig, and K. Metcalf, 2018: GOES: Past, Present, and Future. In: *Comprehensive Remote Sensing Vol. 1* [Liang, S. (ed.)]. Elsevier, Oxford, UK, pp. 119–149, doi:10.1016/b978-0-12-409548-9.10315-x.
Goosse, H., 2017: Reconstructed and simulated temperature asymmetry between continents in both hemispheres over the last centuries. *Climate Dynamics*, **48(5)**, 1483–1501, doi:10.1007/s00382-016-3154-z.
Goosse, H. et al., 2012: The role of forcing and internal dynamics in explaining the "Medieval Climate Anomaly". *Climate Dynamics*, **39(12)**, 2847–2866, doi:10.1007/s00382-012-1297-0.
Gorddard, R., M.J. Colloff, R.M. Wise, D. Ware, and M. Dunlop, 2016: Environmental Science & Policy Values , rules and knowledge : Adaptation as change in the decision context. *Environmental Science and Policy*, **57**, 60–69, doi:10.1016/j.envsci.2015.12.004.
Goss, M., S.B. Feldstein, and S. Lee, 2016: Stationary Wave Interference and Its Relation to Tropical Convection and Arctic Warming. *Journal of Climate*, **29(4)**, 1369–1389, doi:10.1175/jcli-d-15-0267.1.
Goswami, B.N., V. Venugopal, D. Sangupta, M.S. Madhusoodanan, and P.K. Xavier, 2006: Increasing trend of extreme rain events over India in a warming environment. *Science*, **314(5804)**, 1442–1445, doi:10.1126/science.1132027.
Goudenhoofdt, E. and L. Delobbe, 2016: Generation and Verification of Rainfall Estimates from 10-Yr Volumetric Weather Radar Measurements. *Journal of Hydrometeorology*, **17(4)**, 1223–1242, doi:10.1175/jhm-d-15-0166.1.
Gray, L.J. et al., 2013: A lagged response to the 11 year solar cycle in observed winter Atlantic/European weather patterns. *Journal of Geophysical Research: Atmospheres*, **118(24)**, 13,405–413,420, doi:10.1002/2013jd020062.
Griffin, D. and K.J. Anchukaitis, 2014: How unusual is the 2012-2014 California drought? *Geophysical Research Letters*, **41(24)**, 9017–9023, doi:10.1002/2014gl062433.
Grimm, A.M. and R.G. Tedeschi, 2009: ENSO and Extreme Rainfall Events in South America. *Journal of Climate*, **22(7)**, 1589–1609, doi:10.1175/2008jcli2429.1.
Grimm, A.M. and J.P.J. Saboia, 2015: Interdecadal Variability of the South American Precipitation in the Monsoon Season. *Journal of Climate*, **28(2)**, 755–775, doi:10.1175/jcli-d-14-00046.1.
Grimmond, C.S.B. et al., 2010: The International Urban Energy Balance Models Comparison Project: First Results from Phase 1. *Journal of Applied Meteorology and Climatology*, **49(6)**, 1268–1292, doi:10.1175/2010jamc2354.1.
Grimmond, C.S.B. et al., 2011: Initial results from Phase 2 of the international urban energy balance model comparison. *International Journal of Climatology*, **31(2)**, 244–272, doi:10.1002/joc.2227.
Grise, K.M., S.M. Davis, P.W. Staten, and O. Adam, 2018: Regional and Seasonal Characteristics of the Recent Expansion of the Tropics. *Journal of Climate*, **31(17)**, 6839–6856, doi:10.1175/jcli-d-18-0060.1.
Grise, K.M. et al., 2019: Recent Tropical Expansion: Natural Variability or Forced Response? *Journal of Climate*, **32(5)**, 1551–1571, doi:10.1175/jcli-d-18-0444.1.
Grossman-Clarke, S., S. Schubert, and D. Fenner, 2017: Urban effects on summertime air temperature in Germany under climate change. *International Journal of Climatology*, **37(2)**, 905–917, doi:10.1002/joc.4748.
Grotjahn, R. et al., 2016: North American extreme temperature events and related large scale meteorological patterns: a review of statistical methods, dynamics, modeling, and trends. *Climate Dynamics*, **46(3–4)**, 1151–1184, doi:10.1007/s00382-015-2638-6.
Gu, H. et al., 2018: High-resolution ensemble projections and uncertainty assessment of regional climate change over China in CORDEX East Asia. *Hydrology and Earth System Sciences*, **22(5)**, 3087–3103, doi:10.5194/hess-22-3087-2018.
Gualdi, S. et al., 2013: The CIRCE Simulations: Regional Climate Change Projections with Realistic Representation of the Mediterranean Sea. *Bulletin of the American Meteorological Society*, **94(1)**, 65–81, doi:10.1175/bams-d-11-00136.1.
Gubler, S. et al., 2017: The influence of station density on climate data homogenization. *International Journal of Climatology*, **37(13)**, 4670–4683, doi:10.1002/joc.5114.
Guemas, V. et al., 2013: The Indian Ocean: The Region of Highest Skill Worldwide in Decadal Climate Prediction.

ACCEPTED VERSION SUBJECT TO FINAL EDITING

Journal of Climate, **26(3)**, 726–739, doi:10.1175/jcli-d-12-00049.1.
Guido, Z., C. Knudson, D. Campbell, and J. Tomlinson, 2020: Climate information services for adaptation: what does it mean to know the context? *Climate and Development*, **12(5)**, 395–407, doi:10.1080/17565529.2019.1630352.
Guillod, B.P., B. Orlowsky, D.G. Miralles, A.J. Teuling, and S.I. Seneviratne, 2015: Reconciling spatial and temporal soil moisture effects on afternoon rainfall. *Nature Communications*, **6**, doi:10.1038/ncomms7443.
Guimberteau, M., K. Laval, A. Perrier, and J. Polcher, 2012: Global effect of irrigation and its impact on the onset of the Indian summer monsoon. *Climate Dynamics*, **39(6)**, 1329–1348, doi:10.1007/s00382-011-1252-5.
Gula, J. and W.R. Peltier, 2012: Dynamical Downscaling over the Great Lakes Basin of North America Using the WRF Regional Climate Model: The Impact of the Great Lakes System on Regional Greenhouse Warming. *Journal of Climate*, **25(21)**, 7723–7742, doi:10.1175/jcli-d-11-00388.1.
Guldberg, A., E. Kaas, M. Deque, S. Yang, and S. Thorsen, 2005: Reduction of systematic errors by empirical model correction: impact on seasonal prediction skill. *Tellus A*, **57(4)**, 575–588, doi:10.1111/j.1600-0870.2005.00120.x.
Gulizia, C. and I. Camilloni, 2015: Comparative analysis of the ability of a set of CMIP3 and CMIP5 global climate models to represent precipitation in South America. *International Journal of Climatology*, **35(4)**, 583–595, doi:10.1002/joc.4005.
Gultepe, I., 2015: Chapter Three – Mountain Weather: Observation and Modeling. In: *Advances in Geophysics Vol. 56* [Dmowska, R. (ed.)]. Elsevier, pp. 229–312, doi:10.1016/bs.agph.2015.01.001.
Gultepe, I. et al., 2014: Roundhouse (RND) Mountain Top Research Site: Measurements and Uncertainties for Winter Alpine Weather Conditions. *Pure and Applied Geophysics*, **171(1)**, 59–85, doi:10.1007/s00024-012-0582-5.
Guo, D. and H. Wang, 2012: The significant climate warming in the northern Tibetan Plateau and its possible causes. *International Journal of Climatology*, **32(12)**, 1775–1781, doi:10.1002/joc.2388.
Guo, D., J. Sun, K. Yang, N. Pepin, and Y. Xu, 2019: Revisiting Recent Elevation-Dependent Warming on the Tibetan Plateau Using Satellite-Based Data Sets. *Journal of Geophysical Research: Atmospheres*, **124(15)**, 8511–8521, doi:10.1029/2019jd030666.
Guo, H. et al., 2017: Systematical Evaluation of Satellite Precipitation Estimates Over Central Asia Using an Improved Error-Component Procedure. *Journal of Geophysical Research: Atmospheres*, **122(20)**, 10,906–910,927, doi:10.1002/2017jd026877.
Guo, L., A.G. Turner, and E.J. Highwood, 2015: Impacts of 20th century aerosol emissions on the South Asian monsoon in the CMIP5 models. *Atmospheric Chemistry and Physics*, **15(11)**, 6367–6378, doi:10.5194/acp-15-6367-2015.
Guo, L., A.G. Turner, and E.J. Highwood, 2016: Local and remote impacts of aerosol species on indian summer monsoon rainfall in a GCM. *Journal of Climate*, **29(19)**, 6937–6955, doi:10.1175/jcli-d-15-0728.1.
Guo, R., C. Deser, L. Terray, and F. Lehner, 2019: Human Influence on Winter Precipitation Trends (1921–2015) over North America and Eurasia Revealed by Dynamical Adjustment. *Geophysical Research Letters*, **46(6)**, 3426–3434, doi:10.1029/2018gl081316.
Gustafsson and V. Ramanathan, 2016: Convergence on climate warming by black carbon aerosols. *Proceedings of the National Academy of Sciences*, **113(16)**, 4243–4245, doi:10.1073/pnas.1603570113.
Gutiérrez, C. et al., 2018: Impact of aerosols on the spatiotemporal variability of photovoltaic energy production in the Euro-Mediterranean area. *Solar Energy*, **174**, 1142–1152, doi:10.1016/j.solener.2018.09.085.
Gutiérrez, C. et al., 2020: Future evolution of surface solar radiation and photovoltaic potential in Europe: investigating the role of aerosols. *Environmental Research Letters*, **15(3)**, 034035, doi:10.1088/1748-9326/ab6666.
Gutiérrez, J.M., D. San-Martín, S. Brands, R. Manzanas, and S. Herrera, 2013: Reassessing Statistical Downscaling Techniques for Their Robust Application under Climate Change Conditions. *Journal of Climate*, **26(1)**, 171–188, doi:10.1175/jcli-d-11-00687.1.
Gutiérrez, J.M. et al., 2019: An intercomparison of a large ensemble of statistical downscaling methods over Europe: Results from the VALUE perfect predictor cross-validation experiment. *International Journal of Climatology*, **39(9)**, 3750–3785, doi:10.1002/joc.5462.
Gutmann, E. et al., 2014: An intercomparison of statistical downscaling methods used for water resource assessments in the United States. *Water Resources Research*, **50(9)**, 7167–7186, doi:10.1002/2014wr015559.
Gutmann, E.D. et al., 2018: Changes in hurricanes from a 13-Yr convection-permitting pseudo- global warming simulation. *Journal of Climate*, doi:10.1175/jcli-d-17-0391.1.
Gutowski, W.J. et al., 2016: WCRP COordinated Regional Downscaling EXperiment (CORDEX): a diagnostic MIP for CMIP6. *Geoscientific Model Development*, **9(11)**, 4087–4095, doi:10.5194/gmd-9-4087-2016.
Gutowski, W.J. et al., 2020: The Ongoing Need for High-Resolution Regional Climate Models: Process Understanding and Stakeholder Information. *Bulletin of the American Meteorological Society*, **101(5)**, E664–E683, doi:10.1175/bams-d-19-0113.1.
Ha, K.-J., B.-H. Kim, E.-S. Chung, J.C.L. Chan, and C.-P. Chang, 2020: Major factors of global and regional monsoon rainfall changes: natural versus anthropogenic forcing. *Environmental Research Letters*, **15(3)**, 034055, doi:10.1088/1748-9326/ab7767.
Haarsma, R.J., F. Selten, and G.J. van Oldenborgh, 2013a: Anthropogenic changes of the thermal and zonal flow

ACCEPTED VERSION SUBJECT TO FINAL EDITING

structure over Western Europe and Eastern North Atlantic in CMIP3 and CMIP5 models. *Climate Dynamics*, **41(9–10)**, 2577–2588, doi:10.1007/s00382-013-1734-8.
Haarsma, R.J., F.M. Selten, and S.S. Drijfhout, 2015: Decelerating Atlantic meridional overturning circulation main cause of future west European summer atmospheric circulation changes. *Environmental Research Letters*, **10(9)**, 094007, doi:10.1088/1748-9326/10/9/094007.
Haarsma, R.J. et al., 2013b: More hurricanes to hit western Europe due to global warming. *Geophysical Research Letters*, **40(9)**, 1783–1788, doi:10.1002/grl.50360.
Haarsma, R.J. et al., 2016: High Resolution Model Intercomparison Project (HighResMIP v1.0) for CMIP6. *Geoscientific Model Development*, **9(11)**, 4185–4208, doi:10.5194/gmd-9-4185-2016.
Haas, R. and J.G. Pinto, 2012: A combined statistical and dynamical approach for downscaling large-scale footprints of European windstorms. *Geophysical Research Letters*, **39(23)**, n/a–n/a, doi:10.1029/2012gl054014.
Haasnoot, M. et al., 2020: Adaptation to uncertain sea-level rise; how uncertainty in Antarctic mass-loss impacts the coastal adaptation strategy of the Netherlands. *Environmental Research Letters*, **15(3)**, 034007, doi:10.1088/1748-9326/ab666c.
Haberlie, A.M., W.S. Ashley, and T.J. Pingel, 2015: The effect of urbanisation on the climatology of thunderstorm initiation. *Quarterly Journal of the Royal Meteorological Society*, **141(688)**, 663–675, doi:10.1002/qj.2499.
Haeffelin, M. et al., 2005: SIRTA, a ground-based atmospheric observatory for cloud and aerosol research. *Annales Geophysicae*, **23(2)**, 253–275, doi:10.5194/angeo-23-253-2005.
Haerter, J.O., S. Hagemann, C. Moseley, and C. Piani, 2011: Climate model bias correction and the role of timescales. *Hydrology and Earth System Sciences*, **15(3)**, 1065–1079, doi:10.5194/hess-15-1065-2011.
Haga, C. et al., 2020: Scenario Analysis of Renewable Energy–Biodiversity Nexuses Using a Forest Landscape Model. *Frontiers in Ecology and Evolution*, **8**, 1–15, doi:10.3389/fevo.2020.00155.
Hagemann, S. et al., 2013: Climate change impact on available water resources obtained using multiple global climate and hydrology models. *Earth System Dynamics*, **4(1)**, 129–144, doi:10.5194/esd-4-129-2013.
Hagishima, A., J. Tanimoto, and K.I. Narita, 2005: Intercomparisons of experimental convective heat transfer coefficients and mass transfer coefficients of urban surfaces. *Boundary-Layer Meteorology*, **117**, 551–576, doi:10.1007/s10546-005-2078-7.
Hahn, A. et al., 2016: Holocene paleo-climatic record from the South African Namaqualand mudbelt: A source to sink approach. *Quaternary International*, **404**, 121–135, doi:10.1016/j.quaint.2015.10.017.
Haiden, T. et al., 2011: The Integrated Nowcasting through Comprehensive Analysis (INCA) System and Its Validation over the Eastern Alpine Region. *Weather and Forecasting*, **26(2)**, 166–183, doi:10.1175/2010waf2222451.1.
Haimberger, L., C. Tavolato, and S. Sperka, 2012: Homogenization of the Global Radiosonde Temperature Dataset through Combined Comparison with Reanalysis Background Series and Neighboring Stations. *Journal of Climate*, **25(23)**, 8108–8131, doi:10.1175/jcli-d-11-00668.1.
Hakim, G.J. et al., 2016: The last millennium climate reanalysis project: Framework and first results. *Journal of Geophysical Research: Atmospheres*, **121(12)**, 6745–6764, doi:10.1002/2016jd024751.
Halenka, T. et al., 2019: On the comparison of urban canopy effects parameterisation. *International Journal of Environment and Pollution*, **65(1–3)**, 177–194, doi:10.1504/ijep.2019.101840.
Hall, A., 2014: Projecting regional change. *Science*, **346(6216)**, 1461–1462, doi:10.1126/science.aaa0629.
Hall, A., P. Cox, C. Huntingford, and S. Klein, 2019: Progressing emergent constraints on future climate change. *Nature Climate Change*, **9(4)**, 269–278, doi:10.1038/s41558-019-0436-6.
Hallegatte, S., C. Green, R.J. Nicholls, and J. Corfee-Morlot, 2013: Future flood losses in major coastal cities. *Nature Climate Change*, **3(9)**, 802–806, doi:10.1038/nclimate1979.
Hamada, A. and Y.N. Takayabu, 2018: Large-Scale Environmental Conditions Related to Midsummer Extreme Rainfall Events around Japan in the TRMM Region. *Journal of Climate*, **31(17)**, 6933–6945, doi:10.1175/jcli-d-17-0632.1.
Hamdi, R., 2010: Estimating Urban Heat Island Effects on the Temperature Series of Uccle (Brussels, Belgium) Using Remote Sensing Data and a Land Surface Scheme. *Remote Sensing*, **2(12)**, 2773–2784, doi:10.3390/rs2122773.
Hamdi, R. and V. Masson, 2008: Inclusion of a Drag Approach in the Town Energy Balance (TEB) Scheme: Offline 1D Evaluation in a Street Canyon. *Journal of Applied Meteorology and Climatology*, **47(10)**, 2627–2644, doi:10.1175/2008jamc1865.1.
Hamdi, R., H. Van de Vyver, and P. Termonia, 2012: New cloud and microphysics parameterisation for use in high-resolution dynamical downscaling: application for summer extreme temperature over Belgium. *International Journal of Climatology*, **32(13)**, 2051–2065, doi:10.1002/joc.2409.
Hamdi, R., H. Van de Vyver, R. De Troch, and P. Termonia, 2014: Assessment of three dynamical urban climate downscaling methods: Brussels's future urban heat island under an A1B emission scenario. *International Journal of Climatology*, **34(4)**, 978–999, doi:10.1002/joc.3734.
Hamdi, R. et al., 2016: Evolution of urban heat wave intensity for the Brussels Capital Region in the ARPEGE-Climat A1B scenario. *Urban Climate*, **17**, 176–195, doi:10.1016/j.uclim.2016.08.001.
Hamdi, R. et al., 2020: The State-of-the-Art of Urban Climate Change Modeling and Observations. *Earth Systems and*

ACCEPTED VERSION SUBJECT TO FINAL EDITING

Environment, **4(4)**, 631–646, doi:10.1007/s41748-020-00193-3.
Han, F., K.H. Cook, and E.K. Vizy, 2019: Changes in intense rainfall events and dry periods across Africa in the twenty-first century. *Climate Dynamics*, doi:10.1007/s00382-019-04653-z.
Han, W. et al., 2020: The mechanisms and seasonal differences of the impact of aerosols on daytime surface urban heat island effect. *Atmospheric Chemistry and Physics*, **20(11)**, 6479–6493, doi:10.5194/acp-20-6479-2020.
Hansen, J., R. Ruedy, M. Sato, and K. Lo, 2010: Global Surface Temperature Change. *Reviews of Geophysics*, **48(4)**, RG4004, doi:10.1029/2010rg000345.
Harris, I., P.D. Jones, T.J. Osborn, and D.H. Lister, 2014: Updated high-resolution grids of monthly climatic observations - the CRU TS3.10 Dataset. *International Journal of Climatology*, **34(3)**, 623–642, doi:10.1002/joc.3711.
Harris, L.M. and S.-J. Lin, 2013: A Two-Way Nested Global-Regional Dynamical Core on the Cubed-Sphere Grid. *Monthly Weather Review*, **141(1)**, 283–306, doi:10.1175/mwr-d-11-00201.1.
Hart, N.C.G., R. Washington, and R.A. Stratton, 2018: Stronger Local Overturning in Convective-Permitting Regional Climate Model Improves Simulation of the Subtropical Annual Cycle. *Geophysical Research Letters*, **45(20)**, doi:10.1029/2018gl079563.
Hart, P.S. and E.C. Nisbet, 2012: Boomerang Effects in Science Communication: How Motivated Reasoning and Identity Cues Amplify Opinion Polarization About Climate Mitigation Policies. *Communication Research*, **39(6)**, 701–723, doi:10.1177/0093650211416646.
Hartmann, D.L. et al., 2013: Observations: Atmosphere and surface. In: *Climate Change 2013 the Physical Science Basis: Working Group I Contribution to the Fifth Assessment Report of the Intergovernmental Panel on Climate Change* [Stocker, T.F., D. Qin, G.-K. Plattner, M. Tignor, S.K. Allen, J. Boschung, A. Nauels, Y. Xia, V. Bex, and P.M. Midgley (eds.)]. Cambridge University Press, Cambridge, United Kingdom and New York, NY, USA, pp. 159–254, doi:10.1017/cbo9781107415324.008.
Harvey, B.J., P. Cook, L.C. Shaffrey, and R. Schiemann, 2020: The Response of the Northern Hemisphere Storm Tracks and Jet Streams to Climate Change in the CMIP3, CMIP5, and CMIP6 Climate Models. *Journal of Geophysical Research: Atmospheres*, **125(23)**, doi:10.1029/2020jd032701.
Hassanzadeh, P., Z. Kuang, and B.F. Farrell, 2014: Responses of midlatitude blocks and wave amplitude to changes in the meridional temperature gradient in an idealized dry GCM. *Geophysical Research Letters*, **41(14)**, 5223–5232, doi:10.1002/2014gl060764.
Hassim, M.E.E.E., T.P. Lane, and W.W. Grabowski, 2016: The diurnal cycle of rainfall over New Guinea in convection-permitting WRF simulations. *Atmospheric Chemistry and Physics*, **16(1)**, 161–175, doi:10.5194/acp-16-161-2016.
Hasson, S., V. Lucarini, and S. Pascale, 2013: Hydrological cycle over South and Southeast Asian river basins as simulated by PCMDI/CMIP3 experiments. *Earth System Dynamics*, **4(2)**, 199–217, doi:10.5194/esd-4-199-2013.
Hasson, S., J. Böhner, and V. Lucarini, 2017: Prevailing climatic trends and runoff response from Hindukush–Karakoram–Himalaya, upper Indus Basin. *Earth System Dynamics*, **8(2)**, 337–355, doi:10.5194/esd-8-337-2017.
Haszpra, T., M. Herein, and T. Bódai, 2020: Investigating ENSO and its teleconnections under climate change in an ensemble view – a new perspective. *Earth System Dynamics*, **11(1)**, 267–280, doi:10.5194/esd-11-267-2020.
Hatchett, B.J., D. Koračin, J.F. Mejía, and D.P. Boyle, 2016: Assimilating urban heat island effects into climate projections. *Journal of Arid Environments*, **128**, 59–64, doi:10.1016/j.jaridenv.2016.01.007.
Hauser, M., R. Orth, and S.I. Seneviratne, 2016: Role of soil moisture versus recent climate change for the 2010 heat wave in western Russia. *Geophysical Research Letters*, **43(6)**, 2819–2826, doi:10.1002/2016gl068036.
Hauser, M., R. Orth, and S.I. Seneviratne, 2017: Investigating soil moisture–climate interactions with prescribed soil moisture experiments: an assessment with the Community Earth System Model (version 1.2). *Geoscientific Model Development*, **10(4)**, 1665–1677, doi:10.5194/gmd-10-1665-2017.
Hausfather, Z., K. Cowtan, M.J. Menne, and C.N. Williams Jr., 2016: Evaluating the impact of U.S. Historical Climatology Network homogenization using the U.S. Climate Reference Network. *Geophysical Research Letters*, **43(4)**, 1695–1701, doi:10.1002/2015gl067640.
Hausfather, Z. et al., 2013: Quantifying the effect of urbanization on u.s. Historical climatology network temperature records. *Journal of Geophysical Research Atmospheres*, **118(2)**, 481–494, doi:10.1029/2012jd018509.
Hawkins, E. and R. Sutton, 2012: Time of emergence of climate signals. *Geophysical Research Letters*, **39(1)**, n/a–n/a, doi:10.1029/2011gl050087.
Hawkins, E. et al., 2014: Uncertainties in the timing of unprecedented climates. *Nature*, **511(7507)**, E3–E5, doi:10.1038/nature13523.
Hawkins, E. et al., 2020: Observed Emergence of the Climate Change Signal: From the Familiar to the Unknown. *Geophysical Research Letters*, **47(6)**, doi:10.1029/2019gl086259.
Haylock, M.R. et al., 2008: A European daily high-resolution gridded data set of surface temperature and precipitation for 1950–2006. *Journal of Geophysical Research*, **113(D20)**, D20119, doi:10.1029/2008jd010201.
Haywood, J.M., A. Jones, N. Bellouin, and D. Stephenson, 2013: Asymmetric forcing from stratospheric aerosols

ACCEPTED VERSION SUBJECT TO FINAL EDITING

impacts Sahelian rainfall. *Nature Climate Change*, **3(7)**, 660–665, doi:10.1038/nclimate1857.
Hazeleger, W. et al., 2015: Tales of future weather. *Nature Climate Change*, **5(2)**, 107–113, doi:10.1038/nclimate2450.
He, B.-J., J. Wang, H. Liu, and G. Ulpiani, 2021: Localized synergies between heat waves and urban heat islands: Implications on human thermal comfort and urban heat management. *Environmental Research*, **193**, 110584, doi:10.1016/j.envres.2020.110584.
Heaney, A., E. Little, S. Ng, and J. Shaman, 2016: Meteorological variability and infectious disease in Central Africa: a review of meteorological data quality. *Annals of the New York Academy of Sciences*, **1382(1)**, 31–43, doi:10.1111/nyas.13090.
Hegdahl, T.J., K. Engeland, M. Müller, and J. Sillmann, 2020: An Event-Based Approach to Explore Selected Present and Future Atmospheric River–Induced Floods in Western Norway. *Journal of Hydrometeorology*, **21(9)**, 2003–2021, doi:10.1175/jhm-d-19-0071.1.
Hegerl, G. et al., 2010: Good Practice Guidance Paper on Detection and Attribution Related to Anthropogenic Climate Change. In: *Meeting Report of the Intergovernmental Panel on Climate Change Expert Meeting on Detection and Attribution of Anthropogenic Climate Change* [Stocker, T.F., C.B. Field, D. Qin, V. Barros, G.-K. Plattner, M. Tignor, P.M. Midgley, and K.L. Ebi (eds.)]. Working Group I Technical Support Unit, University of Bern, Bern, Switzerland, pp. 1–8.
Heinrich, G., A. Gobiet, and T. Mendlik, 2014: Extended regional climate model projections for Europe until the mid-twentyfirst century: combining ENSEMBLES and CMIP3. *Climate Dynamics*, **42(1–2)**, 521–535, doi:10.1007/s00382-013-1840-7.
Held, I.M. and B.J. Soden, 2006: Robust Responses of the Hydrological Cycle to Global Warming. *Journal of Climate*, **19(21)**, 5686–5699, doi:10.1175/jcli3990.1.
Hellwig, J., K. Stahl, M. Ziese, and A. Becker, 2018: The impact of the resolution of meteorological data sets on catchment-scale precipitation and drought studies. *International Journal of Climatology*, **38(7)**, 3069–3081, doi:10.1002/joc.5483.
Hempel, S., K. Frieler, L. Warszawski, J. Schewe, and F. Piontek, 2013: A trend-preserving bias correction – the ISI-MIP approach. *Earth System Dynamics*, **4(2)**, 219–236, doi:10.5194/esd-4-219-2013.
Hendon, H.H., E.-P. Lim, and H. Nguyen, 2014: Seasonal Variations of Subtropical Precipitation Associated with the Southern Annular Mode. *Journal of Climate*, **27(9)**, 3446–3460, doi:10.1175/jcli-d-13-00550.1.
Henrich, J., S. Heine, and A. Norenzayan, 2010a: Beyond WEIRD: Towards a broad-based behavioral science. *Behavioral and Brain Sciences*, **33(2–3)**, 111–135, doi:10.1017/s0140525x10000725.
Henrich, J., S.J. Heine, and A. Norenzayan, 2010b: The weirdest people in the world? *Behavioral and Brain Sciences*, **33(2–3)**, 61–83, doi:10.1017/s0140525x0999152x.
Herein, M., G. Drótos, T. Haszpra, J. Márfy, and T. Tél, 2017: The theory of parallel climate realizations as a new framework for teleconnection analysis. *Scientific Reports*, **7(1)**, 44529, doi:10.1038/srep44529.
Herger, N., B.M. Sanderson, and R. Knutti, 2015: Improved pattern scaling approaches for the use in climate impact studies. *Geophysical Research Letters*, **42(9)**, 3486–3494, doi:10.1002/2015gl063569.
Hermanson, L. et al., 2020: Robust Multiyear Climate Impacts of Volcanic Eruptions in Decadal Prediction Systems. *Journal of Geophysical Research: Atmospheres*, **125(9)**, e2019JD031739, doi:10.1029/2019jd031739.
Hernández-Díaz, L., O. Nikiéma, R. Laprise, K. Winger, and S. Dandoy, 2019: Effect of empirical correction of sea-surface temperature biases on the CRCM5-simulated climate and projected climate changes over North America. *Climate Dynamics*, **53(1–2)**, 453–476, doi:10.1007/s00382-018-4596-2.
Hernández-Díaz, L. et al., 2013: Climate simulation over CORDEX Africa domain using the fifth-generation Canadian Regional Climate Model (CRCM5). *Climate Dynamics*, **40(5–6)**, 1415–1433, doi:10.1007/s00382-012-1387-z.
Herrera, S., J. Fernández, and J.M. Gutiérrez, 2016: Update of the Spain02 gridded observational dataset for EURO-CORDEX evaluation: assessing the effect of the interpolation methodology. *International Journal of Climatology*, **36(2)**, 900–908, doi:10.1002/joc.4391.
Herrera, S. et al., 2019: Uncertainty in gridded precipitation products: Influence of station density, interpolation method and grid resolution. *International Journal of Climatology*, **39(9)**, 3717–3729, doi:10.1002/joc.5878.
Herrmann, M., S. Somot, S. Calmanti, C. Dubois, and F. Sevault, 2011: Representation of spatial and temporal variability of daily wind speed and of intense wind events over the Mediterranean Sea using dynamical downscaling: impact of the regional climate model configuration. *Natural Hazards and Earth System Science*, **11(7)**, 1983–2001, doi:10.5194/nhess-11-1983-2011.
Hertig, E., C. Beck, H. Wanner, and J. Jacobeit, 2015: A review of non-stationarities in climate variability of the last century with focus on the North Atlantic–European sector. *Earth-Science Reviews*, **147**, 1–17, doi:10.1016/j.earscirev.2015.04.009.
Hertig, E. et al., 2019: Comparison of statistical downscaling methods with respect to extreme events over Europe: Validation results from the perfect predictor experiment of the COST Action VALUE. *International Journal of Climatology*, **39(9)**, 3846–3867, doi:10.1002/joc.5469.
Hertwig, D., M. Ng, S. Grimmond, P.L. Vidale, and P.C. McGuire, 2021: High-resolution global climate simulations: representation of cities. *International Journal of Climatology*, **n/a(n/a)**, doi:10.1002/joc.7018.
Hewitson, B., K. Waagsaether, J. Wohland, K. Kloppers, and T. Kara, 2017: Climate information websites: an evolving

ACCEPTED VERSION SUBJECT TO FINAL EDITING

landscape. *WIREs Climate Change*, **8(5)**, e470, doi:10.1002/wcc.470.
Hewitson, B. et al., 2014: Regional context. In: *Climate Change 2014: Impacts, Adaptation, and Vulnerability. Part B: Regional Aspects. Contribution of Working Group II to the Fifth Assessment Report of the Intergovernmental Panel on Climate Change* [Barros, V.R., C.B. Field, D.J. Dokken, M.D. Mastrandrea, K.J. Mach, T.E. Bilir, M. Chatterjee, K.L. Ebi, Y.O. Estrada, R.C. Genova, B. Girma, E.S. Kissel, A.N. Levy, S. MacCracken, P.R. Mastrandrea, and L.L.White (eds.)]. Cambridge University Press, Cambridge, United Kingdom and New York, NY, USA, pp. 1133–1197, doi:10.1017/cbo9781107415386.001.
Hewitson, B.C., J. Daron, R.G. Crane, M.F. Zermoglio, and C. Jack, 2014: Interrogating empirical-statistical downscaling. *Climatic Change*, **122(4)**, 539–554, doi:10.1007/s10584-013-1021-z.
Hewitt, C., S. Mason, and D. Walland, 2012: The Global Framework for Climate Services. *Nature Climate Change*, **2**, 831.
Hewitt, C.D. and J.A. Lowe, 2018: Toward a European Climate Prediction System. *Bulletin of the American Meteorological Society*, **99(10)**, 1997–2001, doi:10.1175/bams-d-18-0022.1.
Hewitt, C.D. et al., 2020: Making Society Climate Resilient: International Progress under the Global Framework for Climate Services. *Bulletin of the American Meteorological Society*, **101(2)**, E237–E252, doi:10.1175/bams-d-18-0211.1.
Hibino, K. and I. Takayabu, 2016: A Trade-Off Relation between Temporal and Spatial Averaging Scales on Future Precipitation Assessment. *Journal of the Meteorological Society of Japan. Ser. II*, **94A**, 121–134, doi:10.2151/jmsj.2015-056.
Hibino, K., I. Takayabu, Y. Wakazuki, and T. Ogata, 2018: Physical Responses of Convective Heavy Rainfall to Future Warming Condition: Case Study of the Hiroshima Event. *Frontiers in Earth Science*, **6**, 35, doi:10.3389/feart.2018.00035.
Hiebl, J. and C. Frei, 2016: Daily temperature grids for Austria since 1961 - concept , creation and applicability. *Theor Appl Climatol*, 161–178, doi:10.1007/s00704-015-1411-4.
Hill, S.A., 2019: Theories for Past and Future Monsoon Rainfall Changes. *Current Climate Change Reports*, **5(3)**, 160–171, doi:10.1007/s40641-019-00137-8.
Hirose, M., Y.N. Takayabu, A. Hamada, S. Shige, and M.K. Yamamoto, 2017: Spatial contrast of geographically induced rainfall observed by TRMM PR. *Journal of Climate*, **30(11)**, 4165–4184, doi:10.1175/jcli-d-16-0442.1.
Hirota, N., Y.N. Takayabu, M. Watanabe, and M. Kimoto, 2011: Precipitation reproducibility over tropical oceans and its relationship to the double ITCZ problem in CMIP3 and MIROC5 climate models. *Journal of Climate*, **24(18)**, 4859–4873, doi:10.1175/2011jcli4156.1.
Hirota, N., Y.N. Takayabu, M. Watanabe, M. Kimoto, and M. Chikira, 2014: Role of convective entrainment in spatial distributions of and temporal variations in precipitation over tropical oceans. *Journal of Climate*, **27(23)**, 8707–8723, doi:10.1175/jcli-d-13-00701.1.
Hirsch, A.L. et al., 2018: Modelled biophysical impacts of conservation agriculture on local climates. *Global Change Biology*, doi:10.1111/gcb.14362.
Hobaek Haff, I., A. Frigessi, and D. Maraun, 2015: How well do regional climate models simulate the spatial dependence of precipitation? An application of pair-copula constructions. *Journal of Geophysical Research: Atmospheres*, **120(7)**, 2624–2646, doi:10.1002/2014jd022748.
Hock, R. et al., 2019: High Mountain Areas. In: *IPCC Special Report on the Ocean and Cryosphere in a Changing Climate* [Pörtner, H.-O., D.C. Roberts, V. Masson-Delmotte, P. Zhai, M. Tignor, E. Poloczanska, K. Mintenbeck, A. Alegría, M. Nicolai, A. Okem, J. Petzold, B. Rama, and N.M. Weyer (eds.)]. In Press, pp. 131–202.
Hoegh-Guldberg, O. et al., 2018: Impacts of 1.5°C of Global Warming on Natural and Human Systems. In: *Global Warming of 1.5°C. An IPCC Special Report on the impacts of global warming of 1.5°C above pre-industrial levels and related global greenhouse gas emission pathways, in the context of strengthening the global response to the threat of climate change,* [Masson-Delmotte, V., P. Zhai, H.-O. Pörtner, D. Roberts, J. Skea, P.R. Shukla, A. Pirani, W. Moufouma-Okia, C. Péan, R. Pidcock, S. Connors, J.B.R. Matthews, Y. Chen, X. Zhou, M.I. Gomis, E. Lonnoy, T. Maycock, M. Tignor, and T. Waterfield (eds.)]. In Press, pp. 175–311.
Hoell, A., M. Hoerling, J. Eischeid, X.-W. Quan, and B. Liebmann, 2017: Reconciling Theories for Human and Natural Attribution of Recent East Africa Drying. *Journal of Climate*, **30(6)**, 1939–1957, doi:10.1175/jcli-d-16-0558.1.
Hoffmann, P., R. Schoetter, and K.H. Schlünzen, 2018: Statistical-dynamical downscaling of the urban heat island in Hamburg, Germany. *Meteorologische Zeitschrift*, **27(2)**, 89–109, doi:10.1127/metz/2016/0773.
Hofstra, N., M. Haylock, M. New, P. Jones, and C. Frei, 2008: Comparison of six methods for the interpolation of daily, European climate data. *Journal of Geophysical Research*, **113(D21)**, D21110, doi:10.1029/2008jd010100.
Ho-Hagemann, H.T.M. et al., 2017: Effects of air-sea coupling over the North Sea and the Baltic Sea on simulated summer precipitation over Central Europe. *Climate Dynamics*, **49(11–12)**, 3851–3876, doi:10.1007/s00382-017-3546-8.
Hong, S.-Y. and M. Kanamitsu, 2014: Dynamical downscaling: Fundamental issues from an NWP point of view and

ACCEPTED VERSION SUBJECT TO FINAL EDITING

recommendations. *Asia-Pacific Journal of Atmospheric Sciences*, **50(1)**, 83–104, doi:10.1007/s13143-014-0029-2.
Hope, P. et al., 2014: A Comparison of Automated Methods of Front Recognition for Climate Studies: A Case Study in Southwest Western Australia. *Monthly Weather Review*, **142(1)**, 343–363, doi:10.1175/mwr-d-12-00252.1.
Horton, P. and S. Brönnimann, 2019: Impact of global atmospheric reanalyses on statistical precipitation downscaling. *Climate Dynamics*, **52(9–10)**, 5189–5211, doi:10.1007/s00382-018-4442-6.
Hoskins, B., 2013: The potential for skill across the range of the seamless weather-climate prediction problem: A stimulus for our science. *Quarterly Journal of the Royal Meteorological Society*, **139(672)**, 573–584, doi:10.1002/qj.1991.
Hoskins, B. and T. Woollings, 2015: Persistent Extratropical Regimes and Climate Extremes. *Current Climate Change Reports*, **1(3)**, 115–124, doi:10.1007/s40641-015-0020-8.
Hu, Y., S. Maskey, and S. Uhlenbrook, 2013a: Downscaling daily precipitation over the Yellow River source region in China: a comparison of three statistical downscaling methods. *Theoretical and Applied Climatology*, **112(3–4)**, 447–460, doi:10.1007/s00704-012-0745-4.
Hu, Y., L. Tao, and J. Liu, 2013b: Poleward expansion of the Hadley circulation in CMIP5 simulations. *Advances in Atmospheric Sciences*, **30(3)**, 790–795, doi:10.1007/s00376-012-2187-4.
Huang, B. et al., 2015: Extended Reconstructed Sea Surface Temperature Version 4 (ERSST.v4). Part I: Upgrades and Intercomparisons. *Journal of Climate*, **28(3)**, 911–930, doi:10.1175/jcli-d-14-00006.1.
Huang, J. et al., 2017: Dryland climate change: Recent progress and challenges. *Reviews of Geophysics*, **55(3)**, 719–778, doi:10.1002/2016rg000550.
Huang, X., A.M. Rhoades, P.A. Ullrich, and C.M. Zarzycki, 2016: An evaluation of the variable-resolution CESM for modeling California's climate. *Journal of Advances in Modeling Earth Systems*, **8(1)**, 345–369, doi:10.1002/2015ms000559.
Huang, X. et al., 2020a: South Asian summer monsoon projections constrained by the interdecadal Pacific oscillation. *Science Advances*, **6(11)**, 1–10, doi:10.1126/sciadv.aay6546.
Huang, X. et al., 2020b: The Recent Decline and Recovery of Indian Summer Monsoon Rainfall: Relative Roles of External Forcing and Internal Variability. *Journal of Climate*, JCLI–D–19–0833.1, doi:10.1175/jcli-d-19-0833.1.
Huffman, G.J. et al., 2007: The TRMM Multisatellite Precipitation Analysis (TMPA): Quasi-Global, Multiyear, Combined-Sensor Precipitation Estimates at Fine Scales. *Journal of Hydrometeorology*, **8(1)**, 38–55, doi:10.1175/jhm560.1.
Huffman, G.J. et al., 2014: Algorithm Theoretical Basis Document (ATBD) NASA Global Precipitation Measurement (GPM) Integrated Multi-satellitE Retrievals for GPM (IMERG). .
Huguenin, M.F. et al., 2020: Lack of Change in the Projected Frequency and Persistence of Atmospheric Circulation Types Over Central Europe. *Geophysical Research Letters*, **47(9)**, doi:10.1029/2019gl086132.
Hulme, M., 2001: Climatic perspectives on Sahelian desiccation: 1973–1998. *Global Environmental Change*, **11(1)**, 19–29, doi:10.1016/s0959-3780(00)00042-x.
Humphrey, V., L. Gudmundsson, and S.I. Seneviratne, 2017: A global reconstruction of climate-driven subdecadal water storage variability. *Geophysical Research Letters*, **44(5)**, 2300–2309, doi:10.1002/2017gl072564.
Hunt, K.M.R. and J.K. Fletcher, 2019: The relationship between Indian monsoon rainfall and low-pressure systems. *Climate Dynamics*, **53(3–4)**, 1859–1871, doi:10.1007/s00382-019-04744-x.
Hunt, K.M.R., A.G. Turner, and L.C. Shaffrey, 2019: Falling Trend of Western Disturbances in Future Climate Simulations. *Journal of Climate*, **32(16)**, 5037–5051, doi:10.1175/jcli-d-18-0601.1.
Hurrell, J. et al., 2009: A Unified Modeling Approach to Climate System Prediction. *Bulletin of the American Meteorological Society*, **90(12)**, 1819–1832, doi:10.1175/2009bams2752.1.
Hurwitz, M.M. et al., 2014: Extra-tropical atmospheric response to ENSO in the CMIP5 models. *Climate Dynamics*, **43(12)**, 3367–3376, doi:10.1007/s00382-014-2110-z.
Huth, R. et al., 2015: Comparative validation of statistical and dynamical downscaling models on a dense grid in central Europe: temperature. *Theoretical and Applied Climatology*, **120(3–4)**, 533–553, doi:10.1007/s00704-014-1190-3.
Hwang, Y.-T., D.M.W. Frierson, and S.M. Kang, 2013: Anthropogenic sulfate aerosol and the southward shift of tropical precipitation in the late 20th century. *Geophysical Research Letters*, **40(11)**, 2845–2850, doi:10.1002/grl.50502.
Ichinose, T., K. Shimodozono, and K. Hanaki, 1999: Impact of anthropogenic heat on urban climate in Tokyo. *Atmospheric Environment*, **33(24–25)**, 3897–3909, doi:10.1016/s1352-2310(99)00132-6.
Iizumi, T., M.A. Semenov, M. Nishimori, Y. Ishigooka, and T. Kuwagata, 2012: ELPIS-JP: a dataset of local-scale daily climate change scenarios for Japan. *Philosophical Transactions of the Royal Society A: Mathematical, Physical and Engineering Sciences*, **370(1962)**, 1121–1139, doi:10.1098/rsta.2011.0305.
Iles, C. and G. Hegerl, 2017: Role of the North Atlantic Oscillation in decadal temperature trends. *Environmental Research Letters*, **12(11)**, 114010, doi:10.1088/1748-9326/aa9152.
Illing, S., C. Kadow, H. Pohlmann, and C. Timmreck, 2018: Assessing the impact of a~future volcanic eruption on

SUBJECT TO FINAL EDITING ACCEPTED VERSION

decadal predictions. *Earth System Dynamics*, **9(2)**, 701–715, doi:10.5194/esd-9-701-2018.
Immerzeel, W.W., N. Wanders, A.F. Lutz, J.M. Shea, and M.F.P. Bierkens, 2015: Reconciling high-altitude precipitation in the upper Indus basin with glacier mass balances and runoff. *Hydrology and Earth System Sciences*, **19(11)**, 4673–4687, doi:10.5194/hess-19-4673-2015.
Inatsu, M. et al., 2015: Multi-GCM by multi-RAM experiments for dynamical downscaling on summertime climate change in Hokkaido. *Atmospheric Science Letters*, **16(3)**, 297–304, doi:10.1002/asl2.557.
Inoue, T. et al., 2016: The Vietnam Gridded Precipitation (VnGP) Dataset: Construction and Validation. *SOLA*, doi:10.2151/sola.2016-057.
IPCC, 2014: Climate Change 2014: Synthesis Report. Contribution of Working Groups I, II and III to the Fifth Assessment Report of the Intergovernmental Panel on Climate Change. [Core Writing Team, R.K. Pachauri, and L.A. Meyer (eds.)]. IPCC, Geneva, Switzerland, 151 pp.
IPCC, 2018a: Annex I: Glossary [Matthews, J.B.R. (ed.)]. In: *Global Warming of 1.5°C. An IPCC Special Report on the impacts of global warming of 1.5°C above pre-industrial levels and related global greenhouse gas emission pathways, in the context of strengthening the global response to the threat of climate change,* [Masson-Delmotte, V., P. Zhai, H.-O. Pörtner, D. Roberts, J. Skea, P.R. Shukla, A. Pirani, W. Moufouma-Okia, C. Péan, R. Pidcock, S. Connors, J.B.R. Matthews, Y. Chen, X. Zhou, M.I. Gomis, E. Lonnoy, T. Maycock, M. Tignor, and T. Waterfield (eds.)]. In Press, pp. 541–562.
IPCC, 2018b: Global Warming of 1.5°C. An IPCC Special Report on the impacts of global warming of 1.5°C above pre-industrial levels and related global greenhouse gas emission pathways, in the context of strengthening the global response to the threat of climate change. [Masson-Delmotte, V., P. Zhai, H.-O. Pörtner, D. Roberts, J. Skea, P.R. Shukla, A. Pirani, W. Moufouma-Okia, C. Péan, R. Pidcock, S. Connors, J.B.R. Matthews, Y. Chen, X. Zhou, M.I. Gomis, E. Lonnoy, T. Maycock, M. Tignor, and T. Waterfield (eds.)]. In Press, 616 pp.
IPCC, 2019a: Climate Change and Land: an IPCC special report on climate change, desertification, land degradation, sustainable land management, food security, and greenhouse gas fluxes in terrestrial ecosystems. [Shukla, P.R., J. Skea, E.C. Buendia, V. Masson-Delmotte, H.-O. Pörtner, D.C. Roberts, P. Zhai, R. Slade, S. Connors, R. Diemen, M. Ferrat, E. Haughey, S. Luz, S. Neogi, M. Pathak, J. Petzold, J.P. Pereira, P. Vyas, E. Huntley, K. Kissick, M. Belkacemi, and J. Malley (eds.)]. In Press, 896 pp.
IPCC, 2019b: IPCC Special Report on the Ocean and Cryosphere in a Changing Climate. [Pörtner, H.-O., D.C. Roberts, V. Masson-Delmotte, P. Zhai, M. Tignor, E. Poloczanska, K. Mintenbeck, A. Alegría, M. Nicolai, A. Okem, J. Petzold, B. Rama, and N.M. Weyer (eds.)]. In Press, 755 pp.
Ishii, M. and N. Mori, 2020: d4PDF: large-ensemble and high-resolution climate simulations for global warming risk assessment. *Progress in Earth and Planetary Science*, **7(1)**, 58, doi:10.1186/s40645-020-00367-7.
Ishizaki, N. and I. Takayabu, 2009: On the Warming Events over Toyama Plain by Using NHRCM. *SOLA*, **5**, 129–132, doi:10.2151/sola.2009-033.
Isotta, F.A., R. Vogel, and C. Frei, 2015: Evaluation of European regional reanalyses and downscalings for precipitation in the Alpine region. *Meteorologische Zeitschrift*, **24(1)**, 15–37, doi:10.1127/metz/2014/0584.
Isotta, F.A. et al., 2014: The climate of daily precipitation in the Alps : development and analysis of a high-resolution grid dataset from pan-Alpine rain-gauge data. *International Journal of Climatology*, **1675**, 1657–1675, doi:10.1002/joc.3794.
Ivanov, M., K. Warrach-Sagi, and V. Wulfmeyer, 2017: Field significance of performance measures in the context of regional climate model evaluation. Part 1: temperature. *Theoretical and Applied Climatology*, 1–19, doi:10.1007/s00704-017-2100-2.
Ivanov, M., K. Warrach-Sagi, and V. Wulfmeyer, 2018: Field significance of performance measures in the context of regional climate model evaluation. Part 2: precipitation. *Theoretical and Applied Climatology*, **132(1–2)**, 239–261, doi:10.1007/s00704-017-2077-x.
Jack, C.D., R. Jones, L. Burgin, and J. Daron, 2020: Climate risk narratives: An iterative reflective process for co-producing and integrating climate knowledge. *Climate Risk Management*, **29**, 100239, doi:10.1016/j.crm.2020.100239.
Jack, C.D., J. Marsham, D.P. Rowell, and R.G. Jones, 2021: Climate Information: Towards Transparent Distillation. In: *Climate Risk in Africa: Adaptation and Resilience* [Conway, D. and K. Vincent (eds.)]. Palgrave Macmillan, Cham, Switzerland, pp. 17–35, doi:10.1007/978-3-030-61160-6_2.
Jackson, L.C. et al., 2015: Global and European climate impacts of a slowdown of the AMOC in a high resolution GCM. *Climate Dynamics*, **45(11–12)**, 3299–3316, doi:10.1007/s00382-015-2540-2.
Jacob, D. et al., 2014: EURO-CORDEX: new high-resolution climate change projections for European impact research. *Regional Environmental Change*, **14(2)**, 563–578, doi:10.1007/s10113-013-0499-2.
Jacob, D. et al., 2018: Climate Impacts in Europe Under +1.5°C Global Warming. *Earth's Future*, **6(2)**, 264–285, doi:10.1002/2017ef000710.
Jacobeit, J., E. Hertig, S. Seubert, and K. Lutz, 2014: Statistical downscaling for climate change projections in the Mediterranean region: methods and results. *Regional Environmental Change*, **14(5)**, 1891–1906, doi:10.1007/s10113-014-0605-0.
Jaiser, R. et al., 2016: Atmospheric winter response to Arctic sea ice changes in reanalysis data and model simulations.

SUBJECT TO FINAL EDITING ACCEPTED VERSION

Journal of Geophysical Research: Atmospheres, **121(13)**, 7564–7577, doi:10.1002/2015jd024679.
Jänicke, B. et al., 2017: Urban-rural differences in near-surface air temperature as resolved by the Central Europe Refined analysis (CER): sensitivity to planetary boundary layer schemes and urban canopy models. *International Journal of Climatology*, **37(4)**, 2063–2079, doi:10.1002/joc.4835.
Jenkner, J. et al., 2009: Detection and climatology of fronts in a high-resolution model reanalysis over the Alps. *Meteorological Applications*, n/a–n/a, doi:10.1002/met.142.
Jerez, S. et al., 2018: Impact of evolving greenhouse gas forcing on the warming signal in regional climate model experiments. *Nature Communications*, **9(1)**, 1304, doi:10.1038/s41467-018-03527-y.
Jermey, P.M. and R.J. Renshaw, 2016: Precipitation representation over a two-year period in regional reanalysis. *Quarterly Journal of the Royal Meteorological Society*, **142(696)**, 1300–1310, doi:10.1002/qj.2733.
Ji, F., Z. Wu, J. Huang, and E.P. Chassignet, 2014: Evolution of land surface air temperature trend. *Nature Climate Change*, **4(6)**, 462–466, doi:10.1038/nclimate2223.
Jia, G. et al., 2019: Land–climate interactions. In: *Climate Change and Land: an IPCC special report on climate change, desertification, land degradation, sustainable land management, food security, and greenhouse gas fluxes in terrestrial ecosystems* [Shukla, P.R., J. Skea, E. Calvo Buendia, V. Masson-Delmotte, H.-O. Pörtner, D.C. Roberts, P. Zhai, R. Slade, S. Connors, R. van Diemen, M. Ferrat, E. Haughey, S. Luz, S. Neogi, M. Pathak, J. Petzold, J. Portugal Pereira, P. Vyas, E. Huntley, K. Kissick, M. Belkacemi, and J. Malley (eds.)]. In Press, pp. 131–248.
Jiang, J., T. Zhou, X. Chen, and L. Zhang, 2020: Future changes in precipitation over Central Asia based on CMIP6 projections. *Environmental Research Letters*, **15(5)**, 54009, doi:10.1088/1748-9326/ab7d03.
Jiang, X. et al., 2015: Vertical structure and physical processes of the Madden-Julian oscillation: Exploring key model physics in climate simulations. *Journal of Geophysical Research: Atmospheres*, **120(10)**, 4718–4748, doi:10.1002/2014jd022375.
Jiménez-Guerrero, P. et al., 2013: Mean fields and interannual variability in RCM simulations over Spain: the ESCENA project. *Climate Research*, **57(3)**, 201–220, doi:10.3354/cr01165.
Jin, Q. and C. Wang, 2017: A revival of Indian summer monsoon rainfall since 2002. *Nature Climate Change*, **7(8)**, 587–594, doi:10.1038/nclimate3348.
Jin, Q., Z.-L. Yang, and J. Wei, 2016: High sensitivity of Indian summer monsoon to Middle East dust absorptive properties. *Scientific Reports*, **6(1)**, 30690, doi:10.1038/srep30690.
Johnson, F. and A. Sharma, 2012: A nesting model for bias correction of variability at multiple time scales in general circulation model precipitation simulations. *Water Resources Research*, **48(1)**, doi:10.1029/2011wr010464.
Johnson, S.J. et al., 2016: The resolution sensitivity of the South Asian monsoon and Indo-Pacific in a global 0.35° AGCM. *Climate Dynamics*, **46(3–4)**, 807–831, doi:10.1007/s00382-015-2614-1.
Jones, A.D., W.D. Collins, and M.S. Torn, 2013: On the additivity of radiative forcing between land use change and greenhouse gases. *Geophysical Research Letters*, **40(15)**, 4036–4041, doi:10.1002/grl.50754.
Jones, P., 2016: The reliability of global and hemispheric surface temperature records. *Advances in Atmospheric Sciences*, **33(3)**, 269–282, doi:10.1007/s00376-015-5194-4.
Journée, M., C. Delvaux, and C. Bertrand, 2015: Precipitation climate maps of Belgium. *Advances in Science and Research*, **12(1)**, 73–78, doi:10.5194/asr-12-73-2015.
Jovanovic, B., R. Smalley, B. Timbal, and S. Siems, 2017: Homogenized monthly upper-air temperature data set for Australia. *International Journal of Climatology*, **37(7)**, 3209–3222, doi:10.1002/joc.4909.
Joyce, R.J., J.E. Janowiak, P.A. Arkin, and P. Xie, 2004: CMORPH: A Method that Produces Global Precipitation Estimates from Passive Microwave and Infrared Data at High Spatial and Temporal Resolution. *Journal of Hydrometeorology*, **5(3)**, 487–503, doi:10.1175/1525-7541(2004)005<0487:camtpg>2.0.co;2.
Junquas, C., C.S. Vera, L. Li, and H. Le Treut, 2013: Impact of projected SST changes on summer rainfall in southeastern South America. *Climate Dynamics*, **40(7–8)**, 1569–1589, doi:10.1007/s00382-013-1695-y.
Junquas, C., L. Li, C.S. Vera, H. Le Treut, and K. Takahashi, 2016: Influence of South America orography on summertime precipitation in Southeastern South America. *Climate Dynamics*, **46(11–12)**, 3941–3963, doi:10.1007/s00382-015-2814-8.
Jury, M.W., S. Herrera, J.M. Gutiérrez, and D. Barriopedro, 2018: Blocking representation in the ERA-Interim driven EURO-CORDEX RCMs. *Climate Dynamics*, **52**, 3291–3306, doi:10.1007/s00382-018-4335-8.
Kaczmarska, J., V. Isham, and C. Onof, 2014: Point process models for fine-resolution rainfall. *Hydrological Sciences Journal*, **59(11)**, 1972–1991, doi:10.1080/02626667.2014.925558.
Kahan, D.M., 2012: Ideology, Motivated Reasoning, and Cognitive Reflection: An Experimental Study. *SSRN Electronic Journal*, **8(4)**, 407–424, doi:10.2139/ssrn.2182588.
Kahan, D.M., 2013: Making Climate-Science Communication Evidence-Based – All the Way Down. In: *Culture, Politics and Climate Change (Culture, P edition)* [Boykoff, M. and D. Crow (eds.)]. Routledge Press, pp. 1–19, doi:10.2139/ssrn.2216469.
Kahn, B.H., S.L. Nasiri, M.M. Schreier, and B.A. Baum, 2011: Impacts of subpixel cloud heterogeneity on infrared thermodynamic phase assessment. *Journal of Geophysical Research: Atmospheres*, **116(D20)**, doi:10.1029/2011jd015774.

ACCEPTED VERSION SUBJECT TO FINAL EDITING

Kahya, E., 2011: The Impacts of NAO on the Hydrology of the Eastern Mediterranean. , 57–71, doi:10.1007/978-94-007-1372-7_5.
Kaiser-Weiss, A.K. et al., 2019: Added value of regional reanalyses for climatological applications. *Environmental Research Communications*, **1(7)**, 071004, doi:10.1088/2515-7620/ab2ec3.
Kajino, M. et al., 2017: Synergy between air pollution and urban meteorological changes through aerosol-radiation-diffusion feedback-A case study of Beijing in January 2013. *Atmospheric Environment*, **171**, 98–110, doi:10.1016/j.atmosenv.2017.10.018.
Kalnay, E. et al., 1996: The NCEP/NCAR 40-Year Reanalysis Project. *Bulletin of the American Meteorological Society*, **77(3)**, 437–471, doi:10.1175/1520-0477(1996)077<0437:tnyrp>2.0.co;2.
Kanada, S., K. Tsuboki, H. Aiki, S. Tsujino, and I. Takayabu, 2017a: Future Enhancement of Heavy Rainfall Events Associated with a Typhoon in the Midlatitude Regions. *SOLA*, **13**, 246–251, doi:10.2151/sola.2017-045.
Kanada, S. et al., 2017b: Impacts of SST Patterns on Rapid Intensification of Typhoon Megi (2010). *Journal of Geophysical Research: Atmospheres*, **122(24)**, 13,245–13,262, doi:10.1002/2017jd027252.
Kanamaru, H. and M. Kanamitsu, 2007: Scale-Selective Bias Correction in a Downscaling of Global Analysis Using a Regional Model. *Monthly Weather Review*, **135(2)**, 334–350, doi:10.1175/mwr3294.1.
Kanemaru, K., T. Kubota, T. Iguchi, Y.N. Takayabu, and R. Oki, 2017: Development of a precipitation climate record from spaceborne precipitation radar data. Part I: Mitigation of the effects of switching to redundancy electronics in the TRMM precipitation radar. *Journal of Atmospheric and Oceanic Technology*, **34(9)**, 2043–2057, doi:10.1175/jtech-d-17-0026.1.
Kang, S.M., C. Deser, and L.M. Polvani, 2013: Uncertainty in Climate Change Projections of the Hadley Circulation: The Role of Internal Variability. *Journal of Climate*, **26(19)**, 7541–7554, doi:10.1175/jcli-d-12-00788.1.
Kaplan, A. et al., 1998: Analyses of global sea surface temperature 1856-1991. *JOURNAL OF GEOPHYSICAL RESEARCH*, doi:10.1029/97jc01736.
Kaplan, S., M. Georgescu, N. Alfasi, and I. Kloog, 2017: Impact of future urbanization on a hot summer: a case study of Israel. *Theoretical and Applied Climatology*, **128(1–2)**, 325–341, doi:10.1007/s00704-015-1708-3.
Karmalkar, A. and R.S. Bradley, 2017: Consequences of Global Warming of 1.5°C and 2°C for Regional Temperature and Precipitation Changes in the Contiguous United States. *PLOS ONE*, **12(1)**, e0168697, doi:10.1371/journal.pone.0168697.
Karnauskas, K.B., C.-F. Schleussner, J.P. Donnelly, and K.J. Anchukaitis, 2018: Freshwater stress on small island developing states: population projections and aridity changes at 1.5 and 2°C. *Regional Environmental Change*, **18(8)**, 2273–2282, doi:10.1007/s10113-018-1331-9.
Kasoar, M., D. Shawki, and A. Voulgarakis, 2018: Similar spatial patterns of global climate response to aerosols from different regions. *npj Climate and Atmospheric Science*, **1(1)**, 12, doi:10.1038/s41612-018-0022-z.
Kaspar, F. et al., 2020: Regional atmospheric reanalysis activities at Deutscher Wetterdienst: review of evaluation results and application examples with a focus on renewable energy. *Advances in Science and Research*, **17**, 115–128, doi:10.5194/asr-17-115-2020.
Kathayat, G. et al., 2016: Indian monsoon variability on millennial-orbital timescales. *Scientific Reports*, **6(1)**, 24374, doi:10.1038/srep24374.
Katzfey, J., H. Schlüzen, P. Hoffmann, and M. Thatcher, 2020: How an urban parameterization affects a high-resolution global climate simulation. *Quarterly Journal of the Royal Meteorological Society*, **n/a(n/a)**, doi:10.1002/qj.3874.
Kawase, H. et al., 2012: Downscaling of Snow Cover Changes in the Late 20th Century Using a Past Climate Simulation Method over Central Japan. *SOLA*, **8**, 61–64, doi:10.2151/sola.2012-016.
Kawase, H. et al., 2013: Altitude dependency of future snow cover changes over Central Japan evaluated by a regional climate model. *Journal of Geophysical Research Atmospheres*, doi:10.1002/2013jd020429.
Kawazoe, S. and W.J. Gutowski, 2013: Regional, Very Heavy Daily Precipitation in NARCCAP Simulations. *Journal of Hydrometeorology*, **14(4)**, 1212–1227, doi:10.1175/jhm-d-12-068.1.
Kay, J.E. et al., 2015: The Community Earth System Model (CESM) Large Ensemble Project: A Community Resource for Studying Climate Change in the Presence of Internal Climate Variability. *Bulletin of the American Meteorological Society*, **96(8)**, 1333–1349, doi:10.1175/bams-d-13-00255.1.
Kayano, M.T. and R. Andreoli, 2007: Relations of South American summer rainfall interannual variations with the Pacific Decadal Oscillation. *International Journal of Climatology*, **27(4)**, 531–540, doi:10.1002/joc.1417.
Kayano, M.T. and V.B. Capistrano, 2014: How the Atlantic multidecadal oscillation (AMO) modifies the ENSO influence on the South American rainfall. *International Journal of Climatology*, **34(1)**, 162–178, doi:10.1002/joc.3674.
Keller, D.E. et al., 2015: Implementation and validation of a Wilks-type multi-site daily precipitation generator over a typical Alpine river catchment. *Hydrology and Earth System Sciences*, **19(5)**, 2163–2177, doi:10.5194/hess-19-2163-2015.
Keller, M. et al., 2016: Evaluation of convection-resolving models using satellite data: The diurnal cycle of summer convection over the Alps. *Meteorologische Zeitschrift*, **25(2)**, 165–179, doi:10.1127/metz/2015/0715.
Keller, M. et al., 2018: The sensitivity of Alpine summer convection to surrogate climate change: an intercomparison

SUBJECT TO FINAL EDITING ACCEPTED VERSION

between convection-parameterizing and convection-resolving models. *Atmospheric Chemistry and Physics*, **18(8)**, 5253–5264, doi:10.5194/acp-18-5253-2018.
Kendon, E.J. et al., 2014: Heavier summer downpours with climate change revealed by weather forecast resolution model. *Nature Climate Change*, **4**, 570, doi:10.1038/nclimate2258.
Kendon, E.J. et al., 2017: Do Convection-Permitting Regional Climate Models Improve Projections of Future Precipitation Change? *Bulletin of the American Meteorological Society*, **98(1)**, 79–93, doi:10.1175/bams-d-15-0004.1.
Kendon, E.J. et al., 2019: Enhanced future changes in wet and dry extremes over Africa at convection-permitting scale. *Nature Communications*, **10(1)**, 1794, doi:10.1038/s41467-019-09776-9.
Kennel, C.F. and E. Yulaeva, 2020: Influence of Arctic sea-ice variability on Pacific trade winds. *Proceedings of the National Academy of Sciences*, **117(6)**, 2824–2834, doi:10.1073/pnas.1717707117.
Kerkhoff, C., H.R. Künsch, and C. Schär, 2014: Assessment of Bias Assumptions for Climate Models. *Journal of Climate*, **27(17)**, 6799–6818, doi:10.1175/jcli-d-13-00716.1.
Kerr, Y.H. et al., 2012: The SMOS Soil Moisture Retrieval Algorithm. *IEEE Transactions on Geoscience and Remote Sensing*, **50(5)**, 1384–1403, doi:10.1109/tgrs.2012.2184548.
Kharin, V., G.J. Boer, W.J. Merryfield, J.F. Scinocca, and W.-S. Lee, 2012: Statistical adjustment of decadal predictions in a changing climate. *Geophysical Research Letters*, **39(19)**, n/a–n/a, doi:10.1029/2012gl052647.
Khodri, M. et al., 2017: Tropical explosive volcanic eruptions can trigger El Niño by cooling tropical Africa. *Nature Communications*, **8(1)**, 778, doi:10.1038/s41467-017-00755-6.
Khouider, B. et al., 2020: A Novel Method for Interpolating Daily Station Rainfall Data Using a Stochastic Lattice Model. *Journal of Hydrometeorology*, **21(5)**, 909–933, doi:10.1175/jhm-d-19-0143.1.
Kida, H., T. Koide, H. Sasaki, and M. Chiba, 1991: A New Approach for Coupling a Limited Area Model to a GCM for Regional Climate Simulations. *Journal of the Meteorological Society of Japan. Ser. II*, **69(6)**, 723–728, doi:10.2151/jmsj1965.69.6_723.
Kidd, C. et al., 2017: So, How Much of the Earth's Surface Is Covered by Rain Gauges? *Bulletin of the American Meteorological Society*, **98(1)**, 69–78, doi:10.1175/bams-d-14-00283.1.
Kiem, A.S. et al., 2020: Learning from the past – Using palaeoclimate data to better understand and manage drought in South East Queensland (SEQ), Australia. *Journal of Hydrology: Regional Studies*, **29**, 100686, doi:10.1016/j.ejrh.2020.100686.
Killick, R., M.I. Knight, G.P. Nason, and I.A. Eckley, 2020: The local partial autocorrelation function and some applications. *Electronic Journal of Statistics*, **14(2)**, 3268–3314, doi:10.1214/20-ejs1748.
Kim, B.-M. et al., 2014: Weakening of the stratospheric polar vortex by Arctic sea-ice loss. *Nature Communications*, **5(1)**, 4646, doi:10.1038/ncomms5646.
Kim, D., M.-S. Ahn, I.-S. Kang, and A.D. Del Genio, 2015: Role of Longwave Cloud–Radiation Feedback in the Simulation of the Madden–Julian Oscillation. *Journal of Climate*, **28(17)**, 6979–6994, doi:10.1175/jcli-d-14-00767.1.
Kim, H., Y.K. Kim, S.K. Song, and H.W. Lee, 2016: Impact of future urban growth on regional climate changes in the Seoul Metropolitan Area, Korea. *Science of the Total Environment*, **571**, 355–363, doi:10.1016/j.scitotenv.2016.05.046.
Kim, J. and S.K. Park, 2016: Uncertainties in calculating precipitation climatology in East Asia. *Hydrology and Earth System Sciences*, **20(2)**, 651–658, doi:10.5194/hess-20-651-2016.
Kim, J. et al., 2015: Uncertainties in estimating spatial and interannual variations in precipitation climatology in the India-Tibet region from multiple gridded precipitation datasets. *International Journal of Climatology*, **35(15)**, 4557–4573, doi:10.1002/joc.4306.
Kim, Y.H., S.K. Min, D.A. Stone, H. Shiogama, and P. Wolski, 2018: Multi-model event attribution of the summer 2013 heat wave in Korea. *Weather and Climate Extremes*, **20**, 33–44, doi:10.1016/j.wace.2018.03.004.
King, A.D. et al., 2015: The timing of anthropogenic emergence in simulated climate extremes. *Environmental Research Letters*, **10(9)**, 094015, doi:10.1088/1748-9326/10/9/094015.
Kirchengast, G., T. Kabas, A. Leuprecht, C. Bichler, and H. Truhetz, 2014: WegenerNet: A Pioneering High-Resolution Network for Monitoring Weather and Climate. *Bulletin of the American Meteorological Society*, **95(2)**, 227–242, doi:10.1175/bams-d-11-00161.1.
Kirtman, B.P. et al., 2014: Near-term Climate Change: Projections and Predictability. In: *Climate Change 2013: The Physical Science Basis. Contribution of Working Group I to the Fifth Assessment Report of the Intergovernmental Panel on Climate Change* [Stocker, T.F., D. Qin, G.-K. Plattner, M. Tignor, S.K. Allen, J. Boschung, A. Nauels, Y. Xia, V. Bex, and P.M. Midgley (eds.)]. Cambridge University Press, Cambridge, United Kingdom and NewYork, NY, USA, pp. 953–1028, doi:10.1017/cbo9781107415324.023.
Kitoh, A., 2017: The Asian Monsoon and its Future Change in Climate Models: A Review. *Journal of the Meteorological Society of Japan. Ser. II*, **95(1)**, 7–33, doi:10.2151/jmsj.2017-002.
Kitoh, A. and O. Arakawa, 2016: Reduction in the east–west contrast in water budget over the Tibetan Plateau under a future climate. *Hydrological Research Letters*, **10(4)**, 113–118, doi:10.3178/hrl.10.113.
Kjellström, E., R. Döscher, and H.E.M. Meier, 2005: Atmospheric response to different sea surface temperatures in the

SUBJECT TO FINAL EDITING ACCEPTED VERSION

Baltic Sea: coupled versus uncoupled regional climate model experiments. *Hydrology Research*, **36(4–5)**, 397–409, doi:10.2166/nh.2005.0030.
Kjellström, E. et al., 2013: Emerging regional climate change signals for Europe under varying large-scale circulation conditions. *Climate Research*, **56(2)**, 103–119, doi:10.3354/cr01146.
Kjellström, E. et al., 2018: European climate change at global mean temperature increases of 1.5 and 2°C above pre-industrial conditions as simulated by the EURO-CORDEX regional climate models. *Earth System Dynamics*, **9(2)**, 459–478, doi:10.5194/esd-9-459-2018.
Klaver, R., R. Haarsma, P.L. Vidale, and W. Hazeleger, 2020: Effective resolution in high resolution global atmospheric models for climate studies. *Atmospheric Science Letters*, **21(4)**, doi:10.1002/asl.952.
Klein, F. and H. Goosse, 2018: Reconstructing East African rainfall and Indian Ocean sea surface temperatures over the last centuries using data assimilation. *Climate Dynamics*, **50(11)**, 3909–3929, doi:10.1007/s00382-017-3853-0.
Knist, S. et al., 2017: Land-atmosphere coupling in EURO-CORDEX evaluation experiments. *Journal of Geophysical Research: Atmospheres*, **122(1)**, 79–103, doi:10.1002/2016jd025476.
Knutson, T.R. and F. Zeng, 2018: Model Assessment of Observed Precipitation Trends over Land Regions: Detectable Human Influences and Possible Low Bias in Model Trends. *Journal of Climate*, **31(12)**, 4617–4637, doi:10.1175/jcli-d-17-0672.1.
Knutson, T.R., F. Zeng, and A.T. Wittenberg, 2013: Multimodel Assessment of Regional Surface Temperature Trends: CMIP3 and CMIP5 Twentieth-Century Simulations. *Journal of Climate*, **26(22)**, 8709–8743, doi:10.1175/jcli-d-12-00567.1.
Knutti, R., D. Masson, and A. Gettelman, 2013: Climate model genealogy: Generation CMIP5 and how we got there. *Geophysical Research Letters*, **40(6)**, 1194–1199, doi:10.1002/grl.50256.
Knutti, R., R. Furrer, C. Tebaldi, J. Cermak, and G.A. Meehl, 2010: Challenges in combining projections from multiple climate models. *Journal of Climate*, **23(10)**, 2739–2758, doi:10.1175/2009jcli3361.1.
Kobayashi, S. et al., 2015: The JRA-55 Reanalysis: General Specifications and Basic Characteristics. *Journal of the Meteorological Society of Japan. Ser. II*, **93(1)**, 5–48, doi:10.2151/jmsj.2015-001.
Kochendorfer, J. et al., 2017: The quantification and correction of wind-induced precipitation measurement errors. *Hydrology and Earth System Sciences*, **21(4)**, 1973–1989, doi:10.5194/hess-21-1973-2017.
Koenigk, T. et al., 2020: On the contribution of internal climate variability to European future climate trends. *Tellus A: Dynamic Meteorology and Oceanography*, **72(1)**, 1–17, doi:10.1080/16000870.2020.1788901.
Kok, K. et al., 2014: European participatory scenario development: strengthening the link between stories and models. *Climatic Change*, **128(3–4)**, 187–200, doi:10.1007/s10584-014-1143-y.
Kolstad, E.W. and J.A. Screen, 2019: Nonstationary Relationship Between Autumn Arctic Sea Ice and the Winter North Atlantic Oscillation. *Geophysical Research Letters*, **46(13)**, 7583–7591, doi:10.1029/2019gl083059.
Kornhuber, K., V. Petoukhov, S. Petri, S. Rahmstorf, and D. Coumou, 2017: Evidence for wave resonance as a key mechanism for generating high-amplitude quasi-stationary waves in boreal summer. *Climate Dynamics*, **49(5–6)**, 1961–1979, doi:10.1007/s00382-016-3399-6.
Kosaka, Y. and S.P. Xie, 2013: Recent global-warming hiatus tied to equatorial Pacific surface cooling. *Nature*, doi:10.1038/nature12534.
Kosaka, Y. and S.-P. Xie, 2016: The tropical Pacific as a key pacemaker of the variable rates of global warming. *Nature Geoscience*, **9(9)**, 669–673, doi:10.1038/ngeo2770.
Kotlarski, S., D. Lüthi, and C. Schär, 2015: The elevation dependency of 21st century European climate change: an RCM ensemble perspective. *International Journal of Climatology*, **35(13)**, 3902–3920, doi:10.1002/joc.4254.
Kotlarski, S., D. Jacob, R. Podzun, and F. Paul, 2010: Representing glaciers in a regional climate model. *Climate Dynamics*, **34(1)**, 27–46, doi:10.1007/s00382-009-0685-6.
Kotlarski, S. et al., 2014: Regional climate modeling on European scales: a joint standard evaluation of the EURO-CORDEX RCM ensemble. *Geoscientific Model Development*, **7(4)**, 1297–1333, doi:10.5194/gmd-7-1297-2014.
Kotlarski, S. et al., 2019: Observational uncertainty and regional climate model evaluation: A pan-European perspective. *International Journal of Climatology*, **39(9)**, 3730–3749, doi:10.1002/joc.5249.
Kouroutzoglou, J. et al., 2015: On the dynamics of a case study of explosive cyclogenesis in the Mediterranean. *Meteorology and Atmospheric Physics*, **127(1)**, 49–73, doi:10.1007/s00703-014-0357-x.
Kraaijenbrink, P.D.A., M.F.P. Bierkens, A.F. Lutz, and W.W. Immerzeel, 2017: Impact of a global temperature rise of 1.5 degrees Celsius on Asia's glaciers. *Nature*, **549(7671)**, 257–260, doi:10.1038/nature23878.
Krähenmann S., A. and Walter, and Brienen S., and Imbery F., and and Matzarakis A, 2018: High-resolution grids of hourly meteorological variables for Germany. *Theoretical and Applied Climatology*, **131(3)**, 899–926, doi:10.1007/s00704-016-2003-7.
Krayenhoff, E.S., M. Moustaoui, A.M. Broadbent, V. Gupta, and M. Georgescu, 2018: Diurnal interaction between urban expansion, climate change and adaptation in US cities. *Nature Climate Change*, **8(12)**, 1097–1103, doi:10.1038/s41558-018-0320-9.
Kretschmer, M., G. Zappa, and T.G. Shepherd, 2020: The role of Barents–Kara sea ice loss in projected polar vortex changes. *Weather and Climate Dynamics*, **1(2)**, 715–730, doi:10.5194/wcd-1-715-2020.

ACCEPTED VERSION SUBJECT TO FINAL EDITING

Kretschmer, M., D. Coumou, J.F. Donges, and J. Runge, 2016: Using Causal Effect Networks to Analyze Different Arctic Drivers of Midlatitude Winter Circulation. *Journal of Climate*, **29(11)**, 4069–4081, doi:10.1175/jcli-d-15-0654.1.

Kretschmer, M. et al., 2018: More-Persistent Weak Stratospheric Polar Vortex States Linked to Cold Extremes. *Bulletin of the American Meteorological Society*, **99(1)**, 49–60, doi:10.1175/bams-d-16-0259.1.

Krinner, G. and C. Genthon, 1998: GCM simulations of the Last Glacial Maximum surface climate of Greenland and Antarctica. *Climate Dynamics*, **14(10)**, 741–758, doi:10.1007/s003820050252.

Krinner, G. and M.G. Flanner, 2018: Striking stationarity of large-scale climate model bias patterns under strong climate change. *Proceedings of the National Academy of Sciences*, **115(38)**, 9462–9466, doi:10.1073/pnas.1807912115.

Krinner, G., C. Largeron, M. Ménégoz, C. Agosta, and C. Brutel-Vuilmet, 2014: Oceanic Forcing of Antarctic Climate Change: A Study Using a Stretched-Grid Atmospheric General Circulation Model. *Journal of Climate*, **27(15)**, 5786–5800, doi:10.1175/jcli-d-13-00367.1.

Krinner, G., J. Beaumet, V. Favier, M. Déqué, and C. Brutel-Vuilmet, 2019: Empirical Run-Time Bias Correction for Antarctic Regional Climate Projections With a Stretched-Grid AGCM. *Journal of Advances in Modeling Earth Systems*, **11(1)**, 64–82, doi:10.1029/2018ms001438.

Krinner, G., V. Kharin, R. Roehrig, J. Scinocca, and F. Codron, 2020: Historically-based run-time bias corrections substantially improve model projections of 100 years of future climate change. *Communications Earth & Environment*, **1(1)**, 29, doi:10.1038/s43247-020-00035-0.

Krishnamurthy, L. and V. Krishnamurthy, 2014: Influence of PDO on South Asian summer monsoon and monsoon–ENSO relation. *Climate Dynamics*, **42(9–10)**, 2397–2410, doi:10.1007/s00382-013-1856-z.

Krishnamurthy, L. and V. Krishnamurthy, 2016: Teleconnections of Indian monsoon rainfall with AMO and Atlantic tripole. *Climate Dynamics*, **46(7)**, 2269–2285, doi:10.1007/s00382-015-2701-3.

Krishnan, R. et al., 2013: Will the South Asian monsoon overturning circulation stabilize any further? *Climate Dynamics*, **40(1–2)**, 187–211, doi:10.1007/s00382-012-1317-0.

Krishnan, R. et al., 2016: Deciphering the desiccation trend of the South Asian monsoon hydroclimate in a warming world. *Climate Dynamics*, **47(3–4)**, 1007–1027, doi:10.1007/s00382-015-2886-5.

Krishnan, R. et al., 2019a: Non-monsoonal precipitation response over the Western Himalayas to climate change. *Climate Dynamics*, **52(7–8)**, 4091–4109, doi:10.1007/s00382-018-4357-2.

Krishnan, R. et al., 2019b: Unravelling Climate Change in the Hindu Kush Himalaya: Rapid Warming in the Mountains and Increasing Extremes. In: *The Hindu Kush Himalaya Assessment: Mountains, Climate Change, Sustainability and People* [Wester, P., A. Mishra, A. Mukherji, and A.B. Shrestha (eds.)]. Springer, Cham, Switzerland, pp. 57–97, doi:10.1007/978-3-319-92288-1_3.

Krishnan, R., J. Sanjay, C. Gnanaseelan, M. Mujumdar, A. Kulkarni, and S. Chakraborty (eds.), 2020: *Assessment of Climate Change over the Indian Region: A Report of the Ministry of Earth Sciences (MoES), Government of India*. Springer, Singapore, 226 pp., doi:10.1007/978-981-15-4327-2.

Kröner, N. et al., 2017: Separating climate change signals into thermodynamic, lapse-rate and circulation effects: theory and application to the European summer climate. *Climate Dynamics*, **48(9–10)**, 3425–3440, doi:10.1007/s00382-016-3276-3.

Kruger, A.C. and M.P. Nxumalo, 2017: Historical rainfall trends in South Africa: 1921–2015. *Water SA*, **43(2)**, 285, doi:10.4314/wsa.v43i2.12.

Kruk, M.C. et al., 2017: Engaging with Users of Climate Information and the Coproduction of Knowledge. *Weather, Climate, and Society*, **9(4)**, 839–849, doi:10.1175/wcas-d-16-0127.1.

Kuang, W., 2019: New evidences on anomalous phenomenon of buildings in regulating urban climate from observations in Beijing , China. *Earth and space science*, **minor revi**.

Kuang, W. et al., 2021: Global observation of urban expansion and land-cover dynamics using satellite big-data. *Science Bulletin*, **66(4)**, 297–300, doi:10.1016/j.scib.2020.10.022.

Kubota, T. et al., 2007: Global Precipitation Map Using Satellite-Borne Microwave Radiometers by the GSMaP Project: Production and Validation. *IEEE Transactions on Geoscience and Remote Sensing*, doi:10.1109/tgrs.2007.895337.

Kucharski, F., I.-S. Kang, D. Straus, and M.P. King, 2010: Teleconnections in the Atmosphere and Oceans. *Bulletin of the American Meteorological Society*, **91(3)**, 381–383, doi:10.1175/2009bams2834.1.

Kumar, N., B.P. Yadav, S. Gahlot, and M. Singh, 2015: Winter frequency of western disturbances and precipitation indices over Himachal Pradesh, India: 1977-2007. *Atmósfera*, **28(1)**, 63–70, doi:10.20937/atm.2015.28.01.06.

Kumar, S., J.L. Kinter, Z. Pan, and J. Sheffield, 2016: Twentieth century temperature trends in CMIP3, CMIP5, and CESM-LE climate simulations: Spatial-temporal uncertainties, differences, and their potential sources. *Journal of Geophysical Research: Atmospheres*, **121(16)**, 9561–9575, doi:10.1002/2015jd024382.

Kurihara, Y., H. Murakami, and M. Kachi, 2016: Sea surface temperature from the new Japanese geostationary meteorological Himawari-8 satellite. *Geophysical Research Letters*, **43(3)**, 1234–1240, doi:10.1002/2015gl067159.

Kusaka, H., M. Hara, and Y. Takane, 2012a: Urban Climate Projection by the WRF Model at 3-km Horizontal Grid

ACCEPTED VERSION SUBJECT TO FINAL EDITING

Increment: Dynamical Downscaling and Predicting Heat Stress in the 2070's August for Tokyo, Osaka, and Nagoya Metropolises. *Journal of the Meteorological Society of Japan. Ser. II*, **90B(0)**, 47–63, doi:10.2151/jmsj.2012-b04.

Kusaka, H., H. Kondo, Y. Kikegawa, and F. Kimura, 2001: A simple single-layer urban canopy model for atmospheric models: Comparison with multi-layer and slab models. *Boundary-Layer Meteorology*, **101**, 329–358, doi:10.1023/a:1019207923078.

Kusaka, H., A. Suzuki-Parker, T. Aoyagi, S.A. Adachi, and Y. Yamagata, 2016: Assessment of RCM and urban scenarios uncertainties in the climate projections for August in the 2050s in Tokyo. *Climatic Change*, **137(3–4)**, 427–438, doi:10.1007/s10584-016-1693-2.

Kusaka, H. et al., 2012b: Numerical Simulation of Urban Heat Island Effect by the WRF Model with 4-km Grid Increment: An Inter-Comparison Study between the Urban Canopy Model and Slab Model. *Journal of the Meteorological Society of Japan. Ser. II*, doi:10.2151/jmsj.2012-b03.

Kushnir, Y. et al., 2019: Towards operational predictions of the near-term climate. *Nature Climate Change*, **9(2)**, 94–101, doi:10.1038/s41558-018-0359-7.

Kusunoki, S., T. Ose, and M. Hosaka, 2020: Emergence of unprecedented climate change in projected future precipitation. *Scientific Reports*, **10(1)**, 4802, doi:10.1038/s41598-020-61792-8.

Laaha, G. et al., 2016: A three-pillar approach to assessing climate impacts on low flows. *Hydrology and Earth System Sciences*, **20(9)**, 3967–3985, doi:10.5194/hess-20-3967-2016.

Laat, A.T.J. and M. Crok, 2013: A Late 20th Century European Climate Shift: Fingerprint of Regional Brightening? *Atmospheric and Climate Sciences*, **03(03)**, 291–300, doi:10.4236/acs.2013.33031.

Lackmann, G.M., 2015: Hurricane Sandy before 1900 and after 2100. *Bulletin of the American Meteorological Society*, **96(4)**, 547–560, doi:10.1175/bams-d-14-00123.1.

Laepple, T. and P. Huybers, 2014: Ocean surface temperature variability: Large model–data differences at decadal and longer periods. *Proceedings of the National Academy of Sciences*, **111(47)**, 16682–16687, doi:10.1073/pnas.1412077111.

Lafaysse, M., B. Hingray, A. Mezghani, J. Gailhard, and L. Terray, 2014: Internal variability and model uncertainty components in future hydrometeorological projections: The Alpine Durance basin. *Water Resources Research*, **50(4)**, 3317–3341, doi:10.1002/2013wr014897.

Lagabrielle, E., A.T. Lombard, J.M. Harris, and T.C. Livingstone, 2018: Multi-scale multi-level marine spatial planning: A novel methodological approach applied in south africa. *PLoS ONE*, **13(7)**, 1–29, doi:10.1371/journal.pone.0192582.

LaJoie, E. and T. DelSole, 2016: Changes in Internal Variability due to Anthropogenic Forcing: A New Field Significance Test. *Journal of Climate*, **29(15)**, 5547–5560, doi:10.1175/jcli-d-15-0718.1.

Laloyaux, P. et al., 2018: CERA-20C: A Coupled Reanalysis of the Twentieth Century. *Journal of Advances in Modeling Earth Systems*, **10(5)**, 1172–1195, doi:10.1029/2018ms001273.

Lamb, M., 2017: Ethics for Climate Change Communicators. In: *Oxford Research Encyclopedia of Climate Science*. Oxford University Press, Oxford, UK, doi:10.1093/acrefore/9780190228620.013.564.

Lange, S., 2019: Trend-preserving bias adjustment and statistical downscaling with ISIMIP3BASD (v1.0). *Geoscientific Model Development*, **12(7)**, 3055–3070, doi:10.5194/gmd-12-3055-2019.

Langenbrunner, B. and J.D. Neelin, 2013: Analyzing ENSO Teleconnections in CMIP Models as a Measure of Model Fidelity in Simulating Precipitation. *Journal of Climate*, **26(13)**, 4431–4446, doi:10.1175/jcli-d-12-00542.1.

Langendijk, G.S., D. Rechid, and D. Jacob, 2019a: Urban Areas and Urban-Rural Contrasts under Climate Change: What Does the EURO-CORDEX Ensemble Tell Us? – Investigating near Surface Humidity in Berlin and Its Surroundings. *Atmosphere*, **10(12)**, doi:10.3390/atmos10120730.

Langendijk, G.S. et al., 2019b: Three Ways Forward to Improve Regional Information for Extreme Events: An Early Career Perspective. *Frontiers in Environmental Science*, **7**, doi:10.3389/fenvs.2019.00006.

Langhans, W., J. Schmidli, O. Fuhrer, S. Bieri, and C. Schär, 2013: Long-Term Simulations of Thermally Driven Flows and Orographic Convection at Convection-Parameterizing and Cloud-Resolving Resolutions. *Journal of Applied Meteorology and Climatology*, **52(6)**, 1490–1510, doi:10.1175/jamc-d-12-0167.1.

Langodan, S., L. Cavaleri, J. Portilla, Y. Abualnaja, and I. Hoteit, 2020: Can we extrapolate climate in an inner basin? The case of the Red Sea. *Global and Planetary Change*, **188**, 103151, doi:10.1016/j.gloplacha.2020.103151.

Langodan, S. et al., 2017: The climatology of the Red Sea - part 1: the wind. *International Journal of Climatology*, **37(13)**, 4509–4517, doi:10.1002/joc.5103.

Laprise, R., 2014: Comment on "The added value to global model projections of climate change by dynamical downscaling: A case study over the continental U.S. using the GISS-ModelE2 and WRF models" by Racherla et al.. *Journal of Geophysical Research: Atmospheres*, **119(7)**, 3877–3881, doi:10.1002/2013jd019945.

Laprise, R. et al., 2013: Climate projections over CORDEX Africa domain using the fifth-generation Canadian Regional Climate Model (CRCM5). *Climate Dynamics*, **41(11–12)**, 3219–3246, doi:10.1007/s00382-012-1651-2.

Larsen, M.A.D., J.H. Christensen, M. Drews, M.B. Butts, and J.C. Refsgaard, 2016: Local control on precipitation in a fully coupled climate-hydrology model. *Scientific Reports*, **6(1)**, 22927, doi:10.1038/srep22927.

ACCEPTED VERSION SUBJECT TO FINAL EDITING

Latif, M., A. Hannachi, and F.S. Syed, 2018: Analysis of rainfall trends over Indo-Pakistan summer monsoon and related dynamics based on CMIP5 climate model simulations. *International Journal of Climatology*, **38**, e577–e595, doi:10.1002/joc.5391.

Lau, K.-M. and K.-M. Kim, 2006: Observational relationships between aerosol and Asian monsoon rainfall, and circulation. *Geophysical Research Letters*, **33(21)**, L21810, doi:10.1029/2006gl027546.

Lau, W.K.M. and K.M. Kim, 2018: Impact of snow darkening by deposition of light-absorbing aerosols on snow cover in the Himalayas-Tibetan Plateau and influence on the Asian summer monsoon: A possible mechanism for the blanford hypothesis. *Atmosphere*, **9(11)**, doi:10.3390/atmos9110438.

Lau, W.K.M., J.J. Shi, W.K. Tao, and K.M. Kim, 2016: What would happen to Superstorm Sandy under the influence of a substantially warmer Atlantic Ocean? *Geophysical Research Letters*, **43(2)**, 802–811, doi:10.1002/2015gl067050.

Lavaysse, C., C. Flamant, A. Evan, S. Janicot, and M. Gaetani, 2016: Recent climatological trend of the Saharan heat low and its impact on the West African climate. *Climate Dynamics*, **47(11)**, 3479–3498, doi:10.1007/s00382-015-2847-z.

Lawal, K.A. et al., 2016: 13. The late onset of the 2015 wet season in Nigeria. *Bulletin of the American Meteorological Society*, **97(12)**, S63–S69, doi:10.1175/bams-d-16-0131.1.

Lawrimore, J.H. et al., 2011: An overview of the Global Historical Climatology Network monthly mean temperature data set, version 3. *Journal of Geophysical Research: Atmospheres*, **116(D19)**, doi:10.1029/2011jd016187.

Le Roy, B., A. Lemonsu, and R. Schoetter, 2021: A statistical–dynamical downscaling methodology for the urban heat island applied to the EURO-CORDEX ensemble. *Climate Dynamics*, doi:10.1007/s00382-020-05600-z.

Lebeaupin Brossier, C., S. Bastin, K. Béranger, and P. Drobinski, 2015: Regional mesoscale air–sea coupling impacts and extreme meteorological events role on the Mediterranean Sea water budget. *Climate Dynamics*, **44(3–4)**, 1029–1051, doi:10.1007/s00382-014-2252-z.

Lebel, T. and A. Ali, 2009: Recent trends in the Central and Western Sahel rainfall regime (1990-2007). *Journal of Hydrology*, **375(1–2)**, 52–64, doi:10.1016/j.jhydrol.2008.11.030.

Leduc, M. et al., 2019: The ClimEx Project: A 50-Member Ensemble of Climate Change Projections at 12-km Resolution over Europe and Northeastern North America with the Canadian Regional Climate Model (CRCM5). *Journal of Applied Meteorology and Climatology*, **58(4)**, 663–693, doi:10.1175/jamc-d-18-0021.1.

Lee, C. and L. Whitely Binder, 2010: Assessing Pacific Northwest Water Resources Stakeholder Data Needs. In: *Final Report for the Columbia Basin Climate Change Scenarios Project*. Climate Impacts Group, Center for Science in the Earth System, Joint Institute for the Study of the Atmosphere and Ocean, University of Washington, Seattle, Washington, USA, pp. 12.

Lee, H.T., A. Gruber, R.G. Ellingson, and I. Laszlo, 2007: Development of the HIRS outgoing longwave radiation climate dataset. *Journal of Atmospheric and Oceanic Technology*, **24**, 2029–2047, doi:10.1175/2007jtecha989.1.

Lee, J., K.R. Sperber, P.J. Gleckler, C.J.W. Bonfils, and K.E. Taylor, 2019: Quantifying the agreement between observed and simulated extratropical modes of interannual variability. *Climate Dynamics*, **52(7–8)**, 4057–4089, doi:10.1007/s00382-018-4355-4.

Lee, J.-W. and S.-Y. Hong, 2014: Potential for added value to downscaled climate extremes over Korea by increased resolution of a regional climate model. *Theoretical and Applied Climatology*, **117(3–4)**, 667–677, doi:10.1007/s00704-013-1034-6.

Lee, J.-W. et al., 2015: Development and implementation of river-routing process module in a regional climate model and its evaluation in Korean river basins. *Journal of Geophysical Research: Atmospheres*, **120(10)**, 4613–4629, doi:10.1002/2014jd022698.

Lee, S., 2014: A theory for polar amplification from a general circulation perspective. *Asia-Pacific Journal of Atmospheric Sciences*, **50(1)**, 31–43, doi:10.1007/s13143-014-0024-7.

Lee, S.-H. et al., 2016: Impacts of in-canyon vegetation and canyon aspect ratio on the thermal environment of street canyons: numerical investigation using a coupled WRF-VUCM model. *Quarterly Journal of the Royal Meteorological Society*, **142(699)**, 2562–2578, doi:10.1002/qj.2847.

LeGrande, A.N., K. Tsigaridis, and S.E. Bauer, 2016: Role of atmospheric chemistry in the climate impacts of stratospheric volcanic injections. *Nature Geoscience*, **9(9)**, 652–655, doi:10.1038/ngeo2771.

Lehner, F., C. Deser, and L. Terray, 2017a: Toward a New Estimate of "Time of Emergence" of Anthropogenic Warming: Insights from Dynamical Adjustment and a Large Initial-Condition Model Ensemble. *Journal of Climate*, **30(19)**, 7739–7756, doi:10.1175/jcli-d-16-0792.1.

Lehner, F., C. Deser, I.R. Simpson, and L. Terray, 2018: Attributing the U.S. Southwest's Recent Shift Into Drier Conditions. *Geophysical Research Letters*, **45(12)**, 6251–6261, doi:10.1029/2018gl078312.

Lehner, F., E.R. Wahl, A.W. Wood, D.B. Blatchford, and D. Llewellyn, 2017b: Assessing recent declines in Upper Rio Grande runoff efficiency from a paleoclimate perspective. *Geophysical Research Letters*, **44(9)**, 4124–4133, doi:10.1002/2017gl073253.

Lehner, F. et al., 2020: Partitioning climate projection uncertainty with multiple large ensembles and CMIP5/6. *Earth System Dynamics*, **11(2)**, 491–508, doi:10.5194/esd-11-491-2020.

ACCEPTED VERSION SUBJECT TO FINAL EDITING

Lelieveld, J. et al., 2016: Strongly increasing heat extremes in the Middle East and North Africa (MENA) in the 21st century. *Climatic Change*, **137**, 245–260, doi:10.1007/s10584-016-1665-6.
Lemos, M.C., C.J. Kirchhoff, and V. Ramprasad, 2012: Narrowing the climate information usability gap. *Nature Climate Change*, **2(11)**, 789–794, doi:10.1038/nclimate1614.
Lempert, R.J. and M.T. Collins, 2007: Managing the Risk of Uncertain Threshold Responses: Comparison of Robust, Optimum, and Precautionary Approaches. *Risk Analysis*, **27(4)**, 1009–1026, doi:10.1111/j.1539-6924.2007.00940.x.
Lempert, R.J., D.G. Groves, S.W. Popper, and S.C. Bankes, 2006: A General, Analytic Method for Generating Robust Strategies and Narrative Scenarios. *Management Science*, **52(4)**, 514–528, doi:10.1287/mnsc.1050.0472.
Lenz, C.J., B. Früh, and F.D. Adalatpanah, 2017: Is there potential added value in COSMO–CLM forced by ERA reanalysis data? *Climate Dynamics*, **49(11–12)**, 4061–4074, doi:10.1007/s00382-017-3562-8.
Letcher, T.W. and J.R. Minder, 2017: The Simulated Response of Diurnal Mountain Winds to Regionally Enhanced Warming Caused by the Snow Albedo Feedback. *Journal of the Atmospheric Sciences*, **74(1)**, 49–67, doi:10.1175/jas-d-16-0158.1.
Levine, P.A., J.T. Randerson, S.C. Swenson, and D.M. Lawrence, 2016: Evaluating the strength of the land-atmosphere moisture feedback in Earth system models using satellite observations. *Hydrology and Earth System Sciences*, **20(12)**, 4837–4856, doi:10.5194/hess-20-4837-2016.
Levy, A.A.L., M. Jenkinson, W. Ingram, and M. Allen, 2014a: Correcting precipitation feature location in general circulation models. *Journal of Geophysical Research: Atmospheres*, **119(23)**, 13,350–13,369, doi:10.1002/2014jd022357.
Levy, A.A.L. et al., 2013: Can correcting feature location in simulated mean climate improve agreement on projected changes? *Geophysical Research Letters*, **40(2)**, 354–358, doi:10.1002/2012gl053964.
Levy, A.A.L. et al., 2014b: Increasing the detectability of external influence on precipitation by correcting feature location in GCMs. *Journal of Geophysical Research: Atmospheres*, **119(22)**, 12,466–12,478, doi:10.1002/2014jd022358.
Li, B., Y. Chen, and X. Shi, 2020: Does elevation dependent warming exist in high mountain Asia? *Environmental Research Letters*, **15(2)**, 024012, doi:10.1088/1748-9326/ab6d7f.
Li, B. et al., 2016: The contribution of China's emissions to global climate forcing. *Nature*, **531(7594)**, 357–361, doi:10.1038/nature17165.
Li, C., T. Zhao, and K. Ying, 2016: Effects of anthropogenic aerosols on temperature changes in China during the twentieth century based on CMIP5 models. *Theoretical and Applied Climatology*, doi:10.1007/s00704-015-1527-6.
Li, C., T. Zhao, and K. Ying, 2017: Quantifying the contributions of anthropogenic and natural forcings to climate changes over arid-semiarid areas during 1946–2005. *Climatic Change*, **144(3)**, 505–517, doi:10.1007/s10584-017-2028-7.
Li, D. and Z. Xiao, 2018: Can solar cycle modulate the ENSO effect on the Pacific/North American pattern? *Journal of Atmospheric and Solar-Terrestrial Physics*, **167**, 30–38, doi:10.1016/j.jastp.2017.10.007.
Li, D. et al., 2019: Urban heat island: Aerodynamics or imperviousness? *Science Advances*, **5(4)**, doi:10.1126/sciadv.aau4299.
Li, F., Y.J. Orsolini, H. Wang, Y. Gao, and S. He, 2018: Atlantic Multidecadal Oscillation Modulates the Impacts of Arctic Sea Ice Decline. *Geophysical Research Letters*, **45(5)**, 2497–2506, doi:10.1002/2017gl076210.
Li, G., S.-P. Xie, C. He, and Z. Chen, 2017: Western Pacific emergent constraint lowers projected increase in Indian summer monsoon rainfall. *Nature Climate Change*, **7(10)**, 708–712, doi:10.1038/nclimate3387.
Li, H., J.E. Haugen, and C.Y. Xu, 2018: Precipitation pattern in the Western Himalayas revealed by four datasets. *Hydrology and Earth System Sciences*, **22(10)**, 5097–5110, doi:10.5194/hess-22-5097-2018.
Li, K., H. Liao, Y. Mao, and D.A. Ridley, 2016: Source sector and region contributions to concentration and direct radiative forcing of black carbon in China. *Atmospheric Environment*, **124**, 351–366, doi:10.1016/j.atmosenv.2015.06.014.
Li, Q., W. Dong, and P. Jones, 2020: Continental scale surface air temperature variations: Experience derived from the Chinese region. *Earth-Science Reviews*, **200**, 102998, doi:10.1016/j.earscirev.2019.102998.
Li, X. and M. Ting, 2017: Understanding the Asian summer monsoon response to greenhouse warming: the relative roles of direct radiative forcing and sea surface temperature change. *Climate Dynamics*, **49(7–8)**, 2863–2880, doi:10.1007/s00382-016-3470-3.
Li, X., C. Mitra, L. Dong, and Q. Yang, 2018: Understanding land use change impacts on microclimate using Weather Research and Forecasting (WRF) model. *Physics and Chemistry of the Earth, Parts A/B/C*, **103**, 115–126, doi:10.1016/j.pce.2017.01.017.
Li, Y., S. Schubert, J.P. Kropp, and D. Rybski, 2020a: On the influence of density and morphology on the Urban Heat Island intensity. *Nature Communications*, **11(1)**, 2647, doi:10.1038/s41467-020-16461-9.
Li, Y. et al., 2020b: Strong Intensification of Hourly Rainfall Extremes by Urbanization. *Geophysical Research Letters*, **47(14)**, e2020GL088758, doi:10.1029/2020gl088758.
Li, Z. et al., 2016: Aerosol and monsoon climate interactions over Asia. *Reviews of Geophysics*, **54(4)**, 866–929,

ACCEPTED VERSION SUBJECT TO FINAL EDITING

doi:10.1002/2015rg000500.
Li, Z.-X., 1999: Ensemble Atmospheric GCM Simulation of Climate Interannual Variability from 1979 to 1994. *Journal of Climate*, **12(4)**, 986–1001, doi:10.1175/1520-0442(1999)012<0986:eagsoc>2.0.co;2.
Liang, P. and Y. Ding, 2017: The long-term variation of extreme heavy precipitation and its link to urbanization effects in Shanghai during 1916–2014. *Advances in Atmospheric Sciences*, **34(3)**, 321–334, doi:10.1007/s00376-016-6120-0.
Liao, W., D. Wang, X. Liu, G. Wang, and J. Zhang, 2017: Estimated influence of urbanization on surface warming in Eastern China using time-varying land use data. *International Journal of Climatology*, **37(7)**, 3197–3208, doi:10.1002/joc.4908.
Lim, E.-P. et al., 2016: The impact of the Southern Annular Mode on future changes in Southern Hemisphere rainfall. *Geophysical Research Letters*, **43(13)**, 7160–7167, doi:10.1002/2016gl069453.
Lim, H.-G. et al., 2016: Threshold of the volcanic forcing that leads the El Niño-like warming in the last millennium: results from the ERIK simulation. *Climate Dynamics*, **46(11)**, 3725–3736, doi:10.1007/s00382-015-2799-3.
Lima, D.C.A. et al., 2019: How Will a Warming Climate Affect the Benguela Coastal Low-Level Wind Jet? *Journal of Geophysical Research: Atmospheres*, **124(9)**, 5010–5028, doi:10.1029/2018jd029574.
Lin, G., H. Wan, K. Zhang, Y. Qian, and S.J. Ghan, 2016: Can nudging be used to quantify model sensitivities in precipitation and cloud forcing? *Journal of Advances in Modeling Earth Systems*, **8(3)**, 1073–1091, doi:10.1002/2016ms000659.
Lin, M. and P. Huybers, 2019: If Rain Falls in India and No One Reports It, Are Historical Trends in Monsoon Extremes Biased? *Geophysical Research Letters*, doi:10.1029/2018gl079709.
Lin, N. and K. Emanuel, 2016: Grey swan tropical cyclones. *Nature Climate Change*, **6(1)**, 106–111, doi:10.1038/nclimate2777.
Lindau, R. and V. Venema, 2018a: On the reduction of trend errors by the ANOVA joint correction scheme used in homogenization of climate station records. *International Journal of Climatology*, **38(14)**, 5255–5271, doi:10.1002/joc.5728.
Lindau, R. and V.K.C. Venema, 2018b: The joint influence of break and noise variance on the break detection capability in time series homogenization. *Advances in Statistical Climatology, Meteorology and Oceanography*, **4(1/2)**, 1–18, doi:10.5194/ascmo-4-1-2018.
Lionello, P. and L. Scarascia, 2018: The relation between climate change in the Mediterranean region and global warming. *Regional Environmental Change*, **18(5)**, 1481–1493, doi:10.1007/s10113-018-1290-1.
Lionello, P. and L. Scarascia, 2020: The relation of climate extremes with global warming in the Mediterranean region and its north versus south contrast. *Regional Environmental Change*, **20(1)**, 31, doi:10.1007/s10113-020-01610-z.
Lionello, P. et al., 2012: Introduction: Mediterranean Climate – Background Information. In: *The Climate of the Mediterranean Region* [Lionello, P. (ed.)]. Elsevier, Oxford, UK, pp. xxxv–xc, doi:10.1016/b978-0-12-416042-2.00012-4.
Lionello, P. et al., 2016: Objective climatology of cyclones in the Mediterranean region: a consensus view among methods with different system identification and tracking criteria. *Tellus A: Dynamic Meteorology and Oceanography*, **68(1)**, 29391, doi:10.3402/tellusa.v68.29391.
Liu, F. et al., 2016: Global monsoon precipitation responses to large volcanic eruptions. *Scientific Reports*, **6(1)**, 24331, doi:10.1038/srep24331.
Liu, F. et al., 2018a: Divergent El Niño responses to volcanic eruptions at different latitudes over the past millennium. *Climate Dynamics*, **50(9–10)**, 3799–3812, doi:10.1007/s00382-017-3846-z.
Liu, F. et al., 2018b: How Do Tropical, Northern Hemispheric, and Southern Hemispheric Volcanic Eruptions Affect ENSO Under Different Initial Ocean Conditions? *Geophysical Research Letters*, 2018GL080315, doi:10.1029/2018gl080315.
Liu, L., R. Zhang, and Z. Zuo, 2016: The Relationship between Soil Moisture and LAI in Different Types of Soil in Central Eastern China. *Journal of Hydrometeorology*, **17(11)**, 2733–2742, doi:10.1175/jhm-d-15-0240.1.
Liu, L. et al., 2018: A PDRMIP Multimodel Study on the Impacts of Regional Aerosol Forcings on Global and Regional Precipitation. *Journal of Climate*, **31(11)**, 4429–4447, doi:10.1175/jcli-d-17-0439.1.
Liu, W., S.-P. Xie, Z. Liu, and J. Zhu, 2017: Overlooked possibility of a collapsed Atlantic Meridional Overturning Circulation in warming climate. *Science Advances*, **3(1)**, e1601666, doi:10.1126/sciadv.1601666.
Liu, W. et al., 2018: Global drought and severe drought-affected populations in 1.5 and 2°C warmer worlds. *Earth System Dynamics*, **9(1)**, 267–283, doi:10.5194/esd-9-267-2018.
Liu, Y., F. Chen, T. Warner, and J. Basara, 2006: Verification of a Mesoscale Data-Assimilation and Forecasting System for the Oklahoma City Area during the Joint Urban 2003 Field Project. *Journal of Applied Meteorology and Climatology*, **45(7)**, 912–929, doi:10.1175/jam2383.1.
Liu, Z., K. Yoshimura, N.H. Buenning, and X. He, 2014: Solar cycle modulation of the Pacific–North American teleconnection influence on North American winter climate. *Environmental Research Letters*, **9(2)**, 24004, doi:10.1088/1748-9326/9/2/024004.
Livezey, R.E., K.Y. Vinnikov, M.M. Timofeyeva, R. Tinker, and H.M. van den Dool, 2007: Estimation and

ACCEPTED VERSION SUBJECT TO FINAL EDITING

Extrapolation of Climate Normals and Climatic Trends. *Journal of Applied Meteorology and Climatology*, **46(11)**, 1759–1776, doi:10.1175/2007jamc1666.1.
Lloyd, E.A. and T.G. Shepherd, 2020: Environmental catastrophes, climate change, and attribution. *Annals of the New York Academy of Sciences*, **1469(1)**, 105–124, doi:10.1111/nyas.14308.
Lloyd, E.A., M. Bukovsky, and L.O. Mearns, 2020: An analysis of the disagreement about added value by regional climate models. *Synthese*, doi:10.1007/s11229-020-02821-x.
Logothetis, I., K. Tourpali, S. Misios, and P. Zanis, 2020: Etesians and the summer circulation over East Mediterranean in Coupled Model Intercomparison Project Phase 5 simulations: Connections to the Indian summer monsoon. *International Journal of Climatology*, **40(2)**, 1118–1131, doi:10.1002/joc.6259.
Lokoshchenko, M.A., 2017: Urban Heat Island and Urban Dry Island in Moscow and Their Centennial Changes. *Journal of Applied Meteorology and Climatology*, **56(10)**, 2729–2745, doi:10.1175/jamc-d-16-0383.1.
Long, S.-M., S.-P. Xie, X.-T. Zheng, and Q. Liu, 2014: Fast and Slow Responses to Global Warming: Sea Surface Temperature and Precipitation Patterns. *Journal of Climate*, **27(1)**, 285–299, doi:10.1175/jcli-d-13-00297.1.
Longino, H.E., 2004: How Values Can Be Good for Science. In: *Science, Values, and Objectivity* [Machamer, P. and G. Wolters (eds.)]. Pittsburgh University Press, Pittsburgh, PA, USA, pp. 127–142, doi:10.2307/j.ctt5vkg7t.11.
Lorenz, P. and D. Jacob, 2005: Influence of regional scale information on the global circulation: A two-way nesting climate simulation. *Geophysical Research Letters*, **32(18)**, n/a–n/a, doi:10.1029/2005gl023351.
Lorenz, P. and D. Jacob, 2010: Validation of temperature trends in the ENSEMBLES regional climate model runs driven by ERA40. *Climate Research*, **44(2–3)**, 167–177, doi:10.3354/cr00973.
Lorenz, R. et al., 2016: Influence of land-atmosphere feedbacks on temperature and precipitation extremes in the GLACE-CMIP5 ensemble. *Journal of Geophysical Research: Atmospheres*, **121(2)**, 607–623, doi:10.1002/2015jd024053.
Lourenço, T.C., R. Swart, H. Goosen, and R. Street, 2016: The rise of demand-driven climate services. *Nature Climate Change*, **6(1)**, 13–14, doi:10.1038/nclimate2836.
Lovino, M.A., O. Müller, E.H. Berbery, and G. Müller, 2018: Evaluation of CMIP5 retrospective simulations of temperature and precipitation in northeastern Argentina. *International Journal of Climatology*, **38(S1)**, e1158–e1175, doi:10.1002/joc.5441.
Lowry, D.P. and C. Morrill, 2019: Is the Last Glacial Maximum a reverse analog for future hydroclimate changes in the Americas? *Climate Dynamics*, **52(7–8)**, 4407–4427, doi:10.1007/s00382-018-4385-y.
Lucas, C., B. Timbal, and H. Nguyen, 2014: The expanding tropics: a critical assessment of the observational and modeling studies. *Wiley Interdisciplinary Reviews: Climate Change*, **5(1)**, 89–112, doi:10.1002/wcc.251.
Lucas-Picher, P., R. Laprise, and K. Winger, 2017: Evidence of added value in North American regional climate model hindcast simulations using ever-increasing horizontal resolutions. *Climate Dynamics*, **48(7–8)**, 2611–2633, doi:10.1007/s00382-016-3227-z.
Lucas-Picher, P. et al., 2011: Can Regional Climate Models Represent the Indian Monsoon? *Journal of Hydrometeorology*, **12(5)**, 849–868, doi:10.1175/2011jhm1327.1.
Luo, N., Y. Guo, Z. Gao, K. Chen, and J. Chou, 2020: Assessment of CMIP6 and CMIP5 model performance for extreme temperature in China. *Atmospheric and Oceanic Science Letters*, **13(6)**, 589–597, doi:10.1080/16742834.2020.1808430.
Ma, S. et al., 2017a: The impact of an urban canopy and anthropogenic heat fluxes on Sydney's climate. *International Journal of Climatology*, **37**, 255–270, doi:10.1002/joc.5001.
Ma, S. et al., 2017b: Detectable Anthropogenic Shift toward Heavy Precipitation over Eastern China. *Journal of Climate*, **30(4)**, 1381–1396, doi:10.1175/jcli-d-16-0311.1.
Macias, D., E. Garcia-Gorriz, and A. Stips, 2013: Understanding the Causes of Recent Warming of Mediterranean Waters. How Much Could Be Attributed to Climate Change? *PLoS ONE*, **8(11)**, e81591, doi:10.1371/journal.pone.0081591.
Macias, D., E. Garcia-Gorriz, A. Dosio, A. Stips, and K. Keuler, 2018: Obtaining the correct sea surface temperature: bias correction of regional climate model data for the Mediterranean Sea. *Climate Dynamics*, **51(3)**, 1095–1117, doi:10.1007/s00382-016-3049-z.
MacKellar, N., M. New, and C. Jack, 2014: Observed and modelled trends in rainfall and temperature for South Africa: 1960–2010. *South African Journal of Science*, **110(7/8)**, 1–13, doi:10.1590/sajs.2014/20130353.
MacLeod, D.A., H.L. Cloke, F. Pappenberger, and A. Weisheimer, 2016: Improved seasonal prediction of the hot summer of 2003 over Europe through better representation of uncertainty in the land surface. *Quarterly Journal of the Royal Meteorological Society*, **142(694)**, 79–90, doi:10.1002/qj.2631.
Madhusoodhanan, C.G., K. Shashikanth, T.I. Eldho, and S. Ghosh, 2018: Can statistical downscaling improve consensus among CMIP5 models for Indian summer monsoon rainfall projections? *International Journal of Climatology*, **38(5)**, 2449–2461, doi:10.1002/joc.5352.
Madsen, M.S., P.L. Langen, F. Boberg, and J.H. Christensen, 2017: Inflated Uncertainty in Multimodel-Based Regional Climate Projections. *Geophysical Research Letters*, **44(22)**, 11,606–11,613, doi:10.1002/2017gl075627.
Maher, N., D. Matei, S. Milinski, and J. Marotzke, 2018: ENSO Change in Climate Projections: Forced Response or Internal Variability? *Geophysical Research Letters*, **45(20)**, doi:10.1029/2018gl079764.

SUBJECT TO FINAL EDITING ACCEPTED VERSION

Maher, N. et al., 2019: The Max Planck Institute Grand Ensemble: Enabling the Exploration of Climate System Variability. *Journal of Advances in Modeling Earth Systems*, **11(7)**, 2050–2069, doi:10.1029/2019ms001639.
Mahlalela, P.T., R.C. Blamey, and C.J.C. Reason, 2019: Mechanisms behind early winter rainfall variability in the southwestern Cape, South Africa. *Climate Dynamics*, **53**, 21–39, doi:10.1007/s00382-018-4571-y.
Mahlstein, I., G. Hegerl, and S. Solomon, 2012: Emerging local warming signals in observational data. *Geophysical Research Letters*, **39(21)**, n/a–n/a, doi:10.1029/2012gl053952.
Mahlstein, I., R. Knutti, S. Solomon, and R.W. Portmann, 2011: Early onset of significant local warming in low latitude countries. *Environmental Research Letters*, **6(3)**, 034009, doi:10.1088/1748-9326/6/3/034009.
Mahmood, R. et al., 2014: Land cover changes and their biogeophysical effects on climate. *International Journal of Climatology*, **34(4)**, 929–953, doi:10.1002/joc.3736.
Mahmood, S. et al., 2018: Indian monsoon data assimilation and analysis regional reanalysis: Configuration and performance. *Atmospheric Science Letters*, **19(3)**, e808, doi:10.1002/asl.808.
Maidment, R.I., R.P. Allan, and E. Black, 2015: Recent observed and simulated changes in precipitation over Africa. *Geophysical Research Letters*, **42(19)**, 8155–8164, doi:10.1002/2015gl065765.
Maidment, R.I. et al., 2014: The 30 year TAMSAT African Rainfall Climatology And Time series (TARCAT) data set. *Journal of Geophysical Research: Atmospheres*, **119(18)**, 10, 610–619, 644, doi:10.1002/2014jd021927.
Makondo, C.C. and D.S.G. Thomas, 2018: Climate change adaptation: Linking indigenous knowledge with western science for effective adaptation. *Environmental Science and Policy*, **88**, 83–91, doi:10.1016/j.envsci.2018.06.014.
Mallard, M.S., C.G. Nolte, O.R. Bullock, T.L. Spero, and J. Gula, 2014: Using a coupled lake model with WRF for dynamical downscaling. *Journal of Geophysical Research: Atmospheres*, **119(12)**, 7193–7208, doi:10.1002/2014jd021785.
Mallet, M. et al., 2016: Overview of the Chemistry-Aerosol Mediterranean Experiment/Aerosol Direct Radiative Forcing on the Mediterranean Climate (ChArMEx/ADRIMED) summer 2013 campaign. *Atmospheric Chemistry and Physics*, **16(2)**, 455–504, doi:10.5194/acp-16-455-2016.
Man, W. and T. Zhou, 2014: Response of the East Asian summer monsoon to large volcanic eruptions during the last millennium. *Chinese Science Bulletin*, **59(31)**, 4123–4129, doi:10.1007/s11434-014-0404-5.
Mankin, J.S., F. Lehner, S. Coats, and K.A. McKinnon, 2020: The Value of Initial Condition Large Ensembles to Robust Adaptation Decision-Making. *Earth's Future*, **8(10)**, doi:10.1029/2020ef001610.
Mann, M.E. et al., 2017: Influence of Anthropogenic Climate Change on Planetary Wave Resonance and Extreme Weather Events. *Scientific Reports*, **7(1)**, 45242, doi:10.1038/srep45242.
Mann, M.E. et al., 2018: Projected changes in persistent extreme summer weather events: The role of quasi-resonant amplification. *Science Advances*, **4(10)**, eaat3272, doi:10.1126/sciadv.aat3272.
Manz, B. et al., 2016: High-resolution satellite-gauge merged precipitation climatologies of the Tropical Andes. *Journal of Geophysical Research: Atmospheres*, **121(3)**, 1190–1207, doi:10.1002/2015jd023788.
Manzanas, R. and J.M. Gutiérrez, 2019: Process-conditioned bias correction for seasonal forecasting: a case-study with ENSO in Peru. *Climate Dynamics*, **52(3–4)**, 1673–1683, doi:10.1007/s00382-018-4226-z.
Manzanas, R., L.K. Amekudzi, K. Preko, S. Herrera, and J.M. Gutiérrez, 2014: Precipitation variability and trends in Ghana: An intercomparison of observational and reanalysis products. *Climatic Change*, **124(4)**, 805–819, doi:10.1007/s10584-014-1100-9.
Manzanas, R., L. Fiwa, C. Vanya, H. Kanamaru, and J.M. Gutiérrez, 2020: Statistical downscaling or bias adjustment? A case study involving implausible climate change projections of precipitation in Malawi. *Climatic Change*, doi:10.1007/s10584-020-02867-3.
Manzanas, R. et al., 2015: Statistical Downscaling in the Tropics Can Be Sensitive to Reanalysis Choice: A Case Study for Precipitation in the Philippines. *Journal of Climate*, **28(10)**, 4171–4184, doi:10.1175/jcli-d-14-00331.1.
Manzini, E. et al., 2014: Northern winter climate change: Assessment of uncertainty in CMIP5 projections related to stratosphere-troposphere coupling. *Journal of Geophysical Research: Atmospheres*, **119(13)**, 7979–7998, doi:10.1002/2013jd021403.
Maraun, D., 2012: Nonstationarities of regional climate model biases in European seasonal mean temperature and precipitation sums. *Geophysical Research Letters*, **39(6)**, n/a–n/a, doi:10.1029/2012gl051210.
Maraun, D., 2013a: Bias Correction, Quantile Mapping, and Downscaling: Revisiting the Inflation Issue. *Journal of Climate*, **26(6)**, 2137–2143, doi:10.1175/jcli-d-12-00821.1.
Maraun, D., 2013b: When will trends in European mean and heavy daily precipitation emerge? *Environmental Research Letters*, **8(1)**, 014004, doi:10.1088/1748-9326/8/1/014004.
Maraun, D., 2016: Bias Correcting Climate Change Simulations - a Critical Review. *Current Climate Change Reports*, **2(4)**, 211–220, doi:10.1007/s40641-016-0050-x.
Maraun, D. and M. Widmann, 2018a: Cross-validation of bias-corrected climate simulations is misleading. *Hydrology and Earth System Sciences*, **22(9)**, 4867–4873, doi:10.5194/hess-22-4867-2018.
Maraun, D. and M. Widmann, 2018b: *Statistical Downscaling and Bias Correction for Climate Research*. Cambridge University Press, Cambridge, United Kingdom and NewYork, NY, USA, 360 pp., doi:10.1017/9781107588783.

ACCEPTED VERSION SUBJECT TO FINAL EDITING

Maraun, D., M. Widmann, and J.M. Gutiérrez, 2019a: Statistical downscaling skill under present climate conditions: A synthesis of the VALUE perfect predictor experiment. *International Journal of Climatology*, **39(9)**, 3692–3703, doi:10.1002/joc.5877.
Maraun, D. et al., 2015: VALUE: A framework to validate downscaling approaches for climate change studies. *Earth's Future*, **3(1)**, 1–14, doi:10.1002/2014ef000259.
Maraun, D. et al., 2017: Towards process-informed bias correction of climate change simulations. *Nature Climate Change*, **7(11)**, 664–773, doi:10.1038/nclimate3418.
Maraun, D. et al., 2019b: The VALUE perfect predictor experiment: Evaluation of temporal variability. *International Journal of Climatology*, **39(9)**, 3786–3818, doi:10.1002/joc.5222.
Marchau, V.A.W.J., W.E. Walker, P.J.T.M. Bloemen, and S.W. Popper (eds.), 2019: *Decision Making under Deep Uncertainty: From Theory to Practice*. Springer, Cham, Switzerland, 405 pp., doi:10.1007/978-3-030-05252-2.
Marengo, J.A., M. Rusticucci, O. Penalba, and M. Renom, 2010: An intercomparison of observed and simulated extreme rainfall and temperature events during the last half of the twentieth century: part 2: historical trends. *Climatic Change*, **98(3–4)**, 509–529, doi:10.1007/s10584-009-9743-7.
Mariotti, A. and A. Dell'Aquila, 2012: Decadal climate variability in the Mediterranean region: roles of large-scale forcings and regional processes. *Climate Dynamics*, **38(5–6)**, 1129–1145, doi:10.1007/s00382-011-1056-7.
Mariotti, A., Y. Pan, N. Zeng, and A. Alessandri, 2015: Long-term climate change in the Mediterranean region in the midst of decadal variability. *Climate Dynamics*, **44(5–6)**, 1437–1456, doi:10.1007/s00382-015-2487-3.
Marteau, R., Y. Richard, B. Pohl, C.C. Smith, and T. Castel, 2015: High-resolution rainfall variability simulated by the WRF RCM: application to eastern France. *Climate Dynamics*, **44(3–4)**, 1093–1107, doi:10.1007/s00382-014-2125-5.
Martilli, A., A. Clappier, and M.W. Rotach, 2002: An urban surface exchange parameterisation for mesoscale models. *Boundary-Layer Meteorology*, **104(2)**, 261–304, doi:10.1023/a:1016099921195.
Martin, E., B. Timbal, and E. Brun, 1996: Downscaling of general circulation model outputs: simulation of the snow climatology of the French Alps and sensitivity to climate change. *Climate Dynamics*, **13(1)**, 45–56, doi:10.1007/s003820050152.
Martin, E.R. and C.D. Thorncroft, 2014: The impact of the AMO on the West African monsoon annual cycle. *Quarterly Journal of the Royal Meteorological Society*, **140**, 31–46, doi:10.1002/qj.2107.
Martin, E.R. and C. Thorncroft, 2015: Representation of African Easterly Waves in CMIP5 Models. *Journal of Climate*, **28(19)**, 7702–7715, doi:10.1175/jcli-d-15-0145.1.
Martin, E.R., C. Thorncroft, and B.B.B. Booth, 2014: The Multidecadal Atlantic SST-Sahel Rainfall Teleconnection in CMIP5 Simulations. *Journal of Climate*, **27(2)**, 784–806, doi:10.1175/jcli-d-13-00242.1.
Martin, G.M. et al., 2017: Understanding the West African Monsoon from the analysis of diabatic heating distributions as simulated by climate models. *Journal of Advances in Modeling Earth Systems*, **9(1)**, 239–270, doi:10.1002/2016ms000697.
Martín-Gómez, V. and M. Barreiro, 2016: Analysis of oceans' influence on spring time rainfall variability over Southeastern South America during the 20th century. *International Journal of Climatology*, **36(3)**, 1344–1358, doi:10.1002/joc.4428.
Martín-Gómez, V. and M. Barreiro, 2017: Effect of future climate change on the coupling between the tropical oceans and precipitation over Southeastern South America. *Climatic Change*, **141(2)**, 315–329, doi:10.1007/s10584-016-1888-6.
Martynov, A., L. Sushama, R. Laprise, K. Winger, and B. Dugas, 2012: Interactive lakes in the Canadian Regional Climate Model, version 5: the role of lakes in the regional climate of North America. *Tellus A: Dynamic Meteorology and Oceanography*, **64(1)**, 16226, doi:10.3402/tellusa.v64i0.16226.
Marvel, K. et al., 2015: Do responses to different anthropogenic forcings add linearly in climate models? *Environmental Research Letters*, **10(10)**, 104010, doi:10.1088/1748-9326/10/10/104010.
Marzeion, B., J.G. Cogley, K. Richter, and D. Parkes, 2014: Attribution of global glacier mass loss to anthropogenic and natural causes. *Science*, **345(6199)**, 919–921, doi:10.1126/science.1254702.
Masson, D. and C. Frei, 2014: Spatial analysis of precipitation in a high-mountain region : exploring methods with multi-scale topographic predictors and circulation types. *Hydrol. Earth Syst. Sci.,*, **18**, 4543–4563, doi:10.5194/hess-18-4543-2014.
Masson, V., 2000: A physically-based scheme for the urban energy budget in atmospheric models. *Boundary-Layer Meteorology*, **94(3)**, 357–397, doi:10.1023/a:1002463829265.
Masson, V., 2006: Urban surface modeling and the meso-scale impact of cities. *Theoretical and Applied Climatology*, **84**, 35–45, doi:10.1007/s00704-005-0142-3.
Masson, V., A. Lemonsu, J. Hidalgo, and J. Voogt, 2020: Urban Climates and Climate Change. *Annual Review of Environment and Resources*, **45(1)**, 411–444, doi:10.1146/annurev-environ-012320-083623.
Masson, V. et al., 2014: Adapting cities to climate change: A systemic modelling approach. *Urban Climate*, **10(P2)**, 407–429, doi:10.1016/j.uclim.2014.03.004.
Massonnet, F., O. Bellprat, V. Guemas, and F.J. Doblas-Reyes, 2016: Using climate models to estimate the quality of

ACCEPTED VERSION SUBJECT TO FINAL EDITING

global observational data sets. *Science*, **354(6311)**, 452–455, doi:10.1126/science.aaf6369.
Mathur, R. and K. AchutaRao, 2020: A modelling exploration of the sensitivity of the India's climate to irrigation. *Climate Dynamics*, **54(3–4)**, 1851–1872, doi:10.1007/s00382-019-05090-8.
Matte, D., M.A.D. Larsen, O.B. Christensen, and J.H. Christensen, 2019: Robustness and Scalability of Regional Climate Projections Over Europe. *Frontiers in Environmental Science*, **6**, 163, doi:10.3389/fenvs.2018.00163.
Maule, C.F., T. Mendlik, and O.B. Christensen, 2017: The effect of the pathway to a two degrees warmer world on the regional temperature change of Europe. *Climate Services*, **7**, 3–11, doi:10.1016/j.cliser.2016.07.002.
Maúre, G. et al., 2018: The southern African climate under 1.5°C and 2°C of global warming as simulated by CORDEX regional climate models. *Environmental Research Letters*, **13(6)**, 065002, doi:10.1088/1748-9326/aab190.
Maurer, E.P. and D.W. Pierce, 2014: Bias correction can modify climate model simulated precipitation changes without adverse effect on the ensemble mean. *Hydrology and Earth System Sciences*, **18(3)**, 915–925, doi:10.5194/hess-18-915-2014.
May, W., 2011: The sensitivity of the Indian summer monsoon to a global warming of 2°C with respect to pre-industrial times. *Climate Dynamics*, **37(9–10)**, 1843–1868, doi:10.1007/s00382-010-0942-8.
Mayer, M., L. Haimberger, J.M. Edwards, and P. Hyder, 2017: Toward Consistent Diagnostics of the Coupled Atmosphere and Ocean Energy Budgets. *Journal of Climate*, **30(22)**, 9225–9246, doi:10.1175/jcli-d-17-0137.1.
McCarthy, M.P., M.J. Best, and R.A. Betts, 2010: Climate change in cities due to global warming and urban effects. *Geophysical Research Letters*, **37(9)**, doi:10.1029/2010gl042845.
McCarthy, M.P., C. Harpham, C.M. Goodess, and P.D. Jones, 2012: Simulating climate change in UK cities using a regional climate model, HadRM3. *International Journal of Climatology*, **32(12)**, 1875–1888, doi:10.1002/joc.2402.
McCrary, R.R., D.A. Randall, and C. Stan, 2014: Simulations of the West African Monsoon with a Superparameterized Climate Model. Part II: African Easterly Waves. *Journal of Climate*, **27(22)**, 8323–8341, doi:10.1175/jcli-d-13-00677.1.
McCusker, K.E. et al., 2017: Remarkable separability of circulation response to Arctic sea ice loss and greenhouse gas forcing. *Geophysical Research Letters*, **44(15)**, 7955–7964, doi:10.1002/2017gl074327.
McDermid, S.S., L.O. Mearns, and A.C. Ruane, 2017: Representing agriculture in Earth System Models: Approaches and priorities for development. *Journal of Advances in Modeling Earth Systems*, **9(5)**, 2230–2265, doi:10.1002/2016ms000749.
McDonald, R.I., H.Y. Chai, and B.R. Newell, 2015: Personal experience and the 'psychological distance' of climate change: An integrative review. *Journal of Environmental Psychology*, **44**, 109–118, doi:10.1016/j.jenvp.2015.10.003.
McGregor, H., 2018: Regional climate goes global. *Nature Geoscience*, **11(1)**, 18–19, doi:10.1038/s41561-017-0046-8.
McGregor, J.L., 2015: Recent developments in variable-resolution global climate modelling. *Climatic Change*, **129(3–4)**, 369–380, doi:10.1007/s10584-013-0866-5.
McGregor, S. et al., 2014: Recent Walker circulation strengthening and Pacific cooling amplified by Atlantic warming. *Nature Climate Change*, **4(10)**, 888–892, doi:10.1038/nclimate2330.
McKinnon, K.A. and C. Deser, 2018: Internal Variability and Regional Climate Trends in an Observational Large Ensemble. *Journal of Climate*, **31(17)**, 6783–6802, doi:10.1175/jcli-d-17-0901.1.
McKinnon, K.A., A. Poppick, E. Dunn-Sigouin, and C. Deser, 2017: An "Observational Large Ensemble" to Compare Observed and Modeled Temperature Trend Uncertainty due to Internal Variability. *Journal of Climate*, **30(19)**, 7585–7598, doi:10.1175/jcli-d-16-0905.1.
McLandress, C. et al., 2010: Separating the Dynamical Effects of Climate Change and Ozone Depletion. Part I: Southern Hemisphere Stratosphere. *Journal of Climate*, **23(18)**, 5002–5020, doi:10.1175/2010jcli3586.1.
McLeod, J., M. Shepherd, and C.E. Konrad, 2017: Spatio-temporal rainfall patterns around Atlanta, Georgia and possible relationships to urban land cover. *Urban Climate*, **21**, 27–42, doi:10.1016/j.uclim.2017.03.004.
McNeall, D. et al., 2016: The impact of structural error on parameter constraint in a climate model. *Earth System Dynamics*, **7(4)**, 917–935, doi:10.5194/esd-7-917-2016.
McPherson, R.A., 2013: High-Resolution Surface Observations for Climate Monitoring. In: *Climate Variability – Regional and Thematic Patterns* [Tarhule, A. (ed.)]. InTechOpen, London, UK, doi:10.5772/56044.
McSweeney, C.F. and R.G. Jones, 2013: No consensus on consensus: the challenge of finding a universal approach to measuring and mapping ensemble consistency in GCM projections. *Climatic Change*, **119(3–4)**, 617–629, doi:10.1007/s10584-013-0781-9.
McSweeney, C.F., R.G. Jones, R.W. Lee, and D.P. Rowell, 2015: Selecting CMIP5 GCMs for downscaling over multiple regions. *Climate Dynamics*, **44(11–12)**, 3237–3260, doi:10.1007/s00382-014-2418-8.
Mearns, L.O. et al., 2012: The North American Regional Climate Change Assessment Program. *Bulletin of the American Meteorological Society*, **93(9)**, 1337–1362, doi:10.1175/bams-d-11-00223.1.
Mearns, L.O. et al., 2013: Climate change projections of the North American Regional Climate Change Assessment Program (NARCCAP). *Climatic Change*, **120(4)**, doi:10.1007/s10584-013-0831-3.
Meehl, G.A., A. Hu, J.M. Arblaster, J. Fasullo, and K.E. Trenberth, 2013: Externally Forced and Internally Generated

ACCEPTED VERSION SUBJECT TO FINAL EDITING

Decadal Climate Variability Associated with the Interdecadal Pacific Oscillation. *Journal of Climate*, **26(18)**, 7298–7310, doi:10.1175/jcli-d-12-00548.1.
MEEN, 2018: *7th National Communication and 3rd Biennial Report under the United Nations Framework Convention on Climate Change*. Ministry of Environment and Energy (MEEN), Greece, 461 pp.
Meher, J.K., L. Das, R.E. Benestad, and A. Mezghani, 2018: Analysis of winter rainfall change statistics over the Western Himalaya: the influence of internal variability and topography. *International Journal of Climatology*, **38**, e475–e496, doi:10.1002/joc.5385.
Mehrotra, R., J.P. Evans, A. Sharma, and B. Sivakumar, 2014: Evaluation of downscaled daily rainfall hindcasts over Sydney, Australia using statistical and dynamical downscaling approaches. *Hydrology Research*, **45(2)**, 226–249, doi:10.2166/nh.2013.094.
Meier, F., D. Fenner, T. Grassmann, M. Otto, and D. Scherer, 2017: Crowdsourcing air temperature from citizen weather stations for urban climate research. *Urban Climate*, **19**, 170–191, doi:10.1016/j.uclim.2017.01.006.
Meinke, H., R. Nelson, P. Kokic, R. Stone, and R. Selvaraju, 2006: Actionable climate knowledge: from analysis to synthesis. *Climate Research*, **33(1)**, 101–110, doi:10.3354/cr033101.
Menary, M.B. et al., 2018: Preindustrial Control Simulations With HadGEM3-GC3.1 for CMIP6. *Journal of Advances in Modeling Earth Systems*, **10(12)**, 3049–3075, doi:10.1029/2018ms001495.
Mendlik, T. and A. Gobiet, 2016: Selecting climate simulations for impact studies based on multivariate patterns of climate change. *Climatic Change*, **135(3–4)**, 381–393, doi:10.1007/s10584-015-1582-0.
Ménégoz, M., R. Bilbao, O. Bellprat, V. Guemas, and F.J. Doblas-Reyes, 2018a: Forecasting the climate response to volcanic eruptions: prediction skill related to stratospheric aerosol forcing. *Environmental Research Letters*, **13(6)**, 64022, doi:10.1088/1748-9326/aac4db.
Ménégoz, M. et al., 2018b: Role of the Atlantic Multidecadal Variability in modulating the climate response to a Pinatubo-like volcanic eruption. *Climate Dynamics*, **51(5)**, 1863–1883, doi:10.1007/s00382-017-3986-1.
Menne, M.J., I. Durre, R.S. Vose, B.E. Gleason, and T.G. Houston, 2012: An Overview of the Global Historical Climatology Network-Daily Database. *Journal of Atmospheric and Oceanic Technology*, **29(7)**, 897–910, doi:10.1175/jtech-d-11-00103.1.
Menne, M.J., C.N. Williams, B.E. Gleason, J.J. Rennie, and J.H. Lawrimore, 2018: The Global Historical Climatology Network Monthly Temperature Dataset, Version 4. *Journal of Climate*, **31(24)**, 9835–9854, doi:10.1175/jcli-d-18-0094.1.
Merchant, C.J. et al., 2017: Uncertainty information in climate data records from Earth observation. *Earth System Science Data*, **9(2)**, 511–527, doi:10.5194/essd-9-511-2017.
Meredith, E.P., D. Maraun, V.A. Semenov, and W. Park, 2015a: Evidence for added value of convection-permitting models for studying changes in extreme precipitation. *Journal of Geophysical Research: Atmospheres*, **120(24)**, 12500–12513, doi:10.1002/2015jd024238.
Meredith, E.P., V.A. Semenov, D. Maraun, W. Park, and A. Chernokulsky, 2015b: Crucial role of Black Sea warming in amplifying the 2012 Krymsk precipitation extreme. *Nature Geoscience*, **8(8)**, 615–619, doi:10.1038/ngeo2483.
Mesinger, F. et al., 2006: North American regional reanalysis. *Bulletin of the American Meteorological Society*, doi:10.1175/bams-87-3-343.
Mestre, O., C. Gruber, C. Prieur, H. Caussinus, and S. Jourdain, 2011: SPLIDHOM: A Method for Homogenization of Daily Temperature Observations. *Journal of Applied Meteorology and Climatology*, **50(11)**, 2343–2358, doi:10.1175/2011jamc2641.1.
Mezghani, A. and B. Hingray, 2009: A combined downscaling-disaggregation weather generator for stochastic generation of multisite hourly weather variables over complex terrain: Development and multi-scale validation for the Upper Rhone River basin. *Journal of Hydrology*, **377(3–4)**, 245–260, doi:10.1016/j.jhydrol.2009.08.033.
Michel, S. et al., 2018: Reconstructing climatic modes of variability from proxy records: sensitivity to the methodological approach. *Geoscientific Model Development Discussions*, **2018**, 1–48, doi:10.5194/gmd-2018-211.
Migliavacca, M. et al., 2013: Modeling biomass burning and related carbon emissions during the 21st century in Europe. *Journal of Geophysical Research: Biogeosciences*, **118(4)**, 1732–1747, doi:10.1002/2013jg002444.
Milinski, S., N. Maher, and D. Olonscheck, 2020: How large does a large ensemble need to be? *Earth System Dynamics*, **11(4)**, 885–901, doi:10.5194/esd-11-885-2020.
Millán, M.M., 2014: Extreme hydrometeorological events and climate change predictions in Europe. *Journal of Hydrology*, **518**, 206–224, doi:10.1016/j.jhydrol.2013.12.041.
Miller, R.L., P. Knippertz, C. Pérez García-Pando, J.P. Perlwitz, and I. Tegen, 2014: Impact of Dust Radiative Forcing upon Climate. In: *Mineral Dust* [Knippertz, P. and J.-B.W. Stuut (eds.)]. Springer, Dordrecht, The Netherlands, pp. 327–357, doi:10.1007/978-94-017-8978-3_13.
Minder, J.R., T.W. Letcher, and S.M.K. Skiles, 2016: An evaluation of high-resolution regional climate model simulations of snow cover and albedo over the Rocky Mountains, with implications for the simulated snow-albedo feedback. *Journal of Geophysical Research: Atmospheres*, **121(15)**, 9069–9088,

ACCEPTED VERSION SUBJECT TO FINAL EDITING

doi:10.1002/2016jd024995.
Mindlin, J. et al., 2020: Storyline description of Southern Hemisphere midlatitude circulation and precipitation response to greenhouse gas forcing. *Climate Dynamics*, **54(9–10)**, 4399–4421, doi:10.1007/s00382-020-05234-1.
Ming, J., Z. Du, C. Xiao, X. Xu, and D. Zhang, 2012: Darkening of the mid-Himalaya glaciers since 2000 and the potential causes. *Environmental Research Letters*, **7(1)**, 014021, doi:10.1088/1748-9326/7/1/014021.
Ming, Y. and V. Ramaswamy, 2011: A Model Investigation of Aerosol-Induced Changes in Tropical Circulation. *Journal of Climate*, **24(19)**, 5125–5133, doi:10.1175/2011jcli4108.1.
Miralles, D.G., A.J. Teuling, C.C. van Heerwaarden, and J. Vilà-Guerau de Arellano, 2014: Mega-heatwave temperatures due to combined soil desiccation and atmospheric heat accumulation. *Nature Geoscience*, **7**, 345, doi:10.1038/ngeo2141.
Mironov, D. et al., 2010: Implementation of the lake parameterisation scheme FLake into numerical weather prediction model COSMO. *Boreal environment research*, **15**, 218–230.
Mishra, S.K., S. Sahany, and P. Salunke, 2018: CMIP5 vs. CORDEX over the Indian region: how much do we benefit from dynamical downscaling? *Theoretical and Applied Climatology*, **133(3–4)**, 1133–1141, doi:10.1007/s00704-017-2237-z.
Mishra, V., 2015: Climatic uncertainty in Himalayan water towers. *Journal of Geophysical Research: Atmospheres*, **120(7)**, 2689–2705, doi:10.1002/2014jd022650.
Mitchell, D. et al., 2017: Assessing mid-latitude dynamics in extreme event attribution systems. *Climate Dynamics*, doi:10.1007/s00382-016-3308-z.
Mizuta, R. et al., 2017: Over 5,000 Years of Ensemble Future Climate Simulations by 60-km Global and 20-km Regional Atmospheric Models. *Bulletin of the American Meteorological Society*, **98(7)**, 1383–1398, doi:10.1175/bams-d-16-0099.1.
MJO Working Group, 2009: MJO Simulation Diagnostics. *Journal of Climate*, **22(11)**, 3006–3030, doi:10.1175/2008jcli2731.1.
MoARE, 2016: Climate Change Risk Assessment The Cyprus Climate Change Risk Assessment. , 1-165.
MoE, 2016: *Troisième Communication Nationale du Maroc à la Convention Cadre des Nations Unies sur les Changements Climatiques*. Ministère de l'Energie, des Mines, de l'Eau et de l'Environnement, Rabat, Morocco, 295 pp.
MoE/UNDP/GEF, 2019: *Lebanon's Third Biennial Update Report (BUR) to the UNFCCC*. Ministry of Environment (Lebanon), Beirut, Lebanon, 231 pp.
MoEP, 2018: *Israel's third National Communication on Climate Change*. Ministry of Environmental Protection (MoEP), Israel, 59 pp.
MoEU, 2018: *Seventh National Communication of Turkey under the United Nations Framework Convention on Climate Change*. Ministry of Environment and Urbanization (MoEU), Republic of Turkey, 265 pp.
Moezzi, M., K.B. Janda, and S. Rotmann, 2017: Using stories, narratives, and storytelling in energy and climate change research. *Energy Research & Social Science*, **31**, 1–10, doi:10.1016/j.erss.2017.06.034.
Mohino, E., N. Keenlyside, and H. Pohlmann, 2016: Decadal prediction of Sahel rainfall: where does the skill (or lack thereof) come from? *Climate Dynamics*, **47(11)**, 3593–3612, doi:10.1007/s00382-016-3416-9.
Monerie, P.-A., E. Sanchez-Gomez, and J. Boé, 2017a: On the range of future Sahel precipitation projections and the selection of a sub-sample of CMIP5 models for impact studies. *Climate Dynamics*, **48(7–8)**, 2751–2770, doi:10.1007/s00382-016-3236-y.
Monerie, P.-A., E. Sanchez-Gomez, B. Pohl, J. Robson, and B. Dong, 2017b: Impact of internal variability on projections of Sahel precipitation change. *Environmental Research Letters*, **12(11)**, 114003, doi:10.1088/1748-9326/aa8cda.
Monerie, P.-A., J. Robson, B. Dong, D.L.R. Hodson, and N.P. Klingaman, 2019: Effect of the Atlantic Multidecadal Variability on the Global Monsoon. *Geophysical Research Letters*, **46**, 1765–1775, doi:10.1029/2018gl080903.
Montroull, N.B., R.I. Saurral, and I.A. Camilloni, 2018: Hydrological impacts in La Plata basin under 1.5, 2 and 3°C global warming above the pre-industrial level. *International Journal of Climatology*, **38(8)**, 3355–3368, doi:10.1002/joc.5505.
Mori, M., Y. Kosaka, M. Watanabe, H. Nakamura, and M. Kimoto, 2019: A reconciled estimate of the influence of Arctic sea-ice loss on recent Eurasian cooling. *Nature Climate Change*, **9(2)**, 123–129, doi:10.1038/s41558-018-0379-3.
Mori, N. et al., 2014: Local amplification of storm surge by super typhoon Haiyan in Leyte Gulf. *Geophys. Res. Lett.*, **41**, 5106–5113, doi:10.1002/2014gl060689.
Morrill, C., D.P. Lowry, and A. Hoell, 2018: Thermodynamic and Dynamic Causes of Pluvial Conditions During the Last Glacial Maximum in Western North America. *Geophysical Research Letters*, **45(1)**, 335–345, doi:10.1002/2017gl075807.
Morton, T.A., A. Rabinovich, D. Marshall, and P. Bretschneider, 2011: The future that may (or may not) come: How framing changes responses to uncertainty in climate change communications. *Global Environmental Change*, **21(1)**, 103–109, doi:10.1016/j.gloenvcha.2010.09.013.

ACCEPTED VERSION SUBJECT TO FINAL EDITING

Moss, R.H., 2016: Assessing decision support systems and levels of confidence to narrow the climate information "usability gap". *Climatic Change*, **135(1)**, 143–155, doi:10.1007/s10584-015-1549-1.
Muerth, M.J. et al., 2013: On the need for bias correction in regional climate scenarios to assess climate change impacts on river runoff. *Hydrology and Earth System Sciences*, **17(3)**, 1189–1204, doi:10.5194/hess-17-1189-2013.
Mukheibir, P. and G. Ziervogel, 2007: Developing a Municipal Adaptation Plan (MAP) for climate change: the city of Cape Town. *Environment and Urbanization*, **19(1)**, 143–158, doi:10.1177/0956247807076912.
Muller, C.L., L. Chapman, C.S.B. Grimmond, D.T. Young, and X. Cai, 2013: Sensors and the city: a review of urban meteorological networks. *International Journal of Climatology*, **33(7)**, 1585–1600, doi:10.1002/joc.3678.
Muller, M., 2018: Cape Town's drought: don't blame climate change. *Nature*, **559(7713)**, 174–176, doi:10.1038/d41586-018-05649-1.
Mulwa, C., P. Marenya, D.B. Rahut, and M. Kassie, 2017: Response to climate risks among smallholder farmers in Malawi: A multivariate probit assessment of the role of information, household demographics, and farm characteristics. *Climate Risk Management*, **16**, 208–221, doi:10.1016/j.crm.2017.01.002.
Munday, C. and R. Washington, 2018: Systematic Climate Model Rainfall Biases over Southern Africa: Links to Moisture Circulation and Topography. *Journal of Climate*, **31(18)**, 7533–7548, doi:10.1175/jcli-d-18-0008.1.
Mussetti, G. et al., 2020: COSMO-BEP-Tree v1.0: a coupled urban climate model with explicit representation of street trees. *Geoscientific Model Development*, **13(3)**, 1685–1710, doi:10.5194/gmd-13-1685-2020.
Nabat, P., S. Somot, M. Mallet, A. Sanchez-Lorenzo, and M. Wild, 2014: Contribution of anthropogenic sulfate aerosols to the changing Euro-Mediterranean climate since 1980. *Geophysical Research Letters*, **41(15)**, 5605–5611, doi:10.1002/2014gl060798.
Nabat, P. et al., 2015: Dust aerosol radiative effects during summer 2012 simulated with a coupled regional aerosol–atmosphere–ocean model over the Mediterranean. *Atmospheric Chemistry and Physics*, **15(6)**, 3303–3326, doi:10.5194/acp-15-3303-2015.
Nabat, P. et al., 2020: Modulation of radiative aerosols effects by atmospheric circulation over the Euro-Mediterranean region. *Atmospheric Chemistry and Physics*, **20(14)**, 8315–8349, doi:10.5194/acp-20-8315-2020.
Naidu, P.D. et al., 2020: Coherent response of the Indian Monsoon Rainfall to Atlantic Multi-decadal Variability over the last 2000 years. *Scientific Reports*, **10(1)**, 1302, doi:10.1038/s41598-020-58265-3.
Nakamura, T. et al., 2015: A negative phase shift of the winter AO/NAO due to the recent Arctic sea-ice reduction in late autumn. *Journal of Geophysical Research: Atmospheres*, **120(8)**, 3209–3227, doi:10.1002/2014jd022848.
Nath, R., Y. Luo, W. Chen, and X. Cui, 2018: On the contribution of internal variability and external forcing factors to the Cooling trend over the Humid Subtropical Indo-Gangetic Plain in India. *Scientific Reports*, **8(1)**, 18047, doi:10.1038/s41598-018-36311-5.
Nazemi, A. and H.S. Wheater, 2015: On inclusion of water resource management in Earth system models – Part 1: Problem definition and representation of water demand. *Hydrology and Earth System Sciences*, **19(1)**, 33–61, doi:10.5194/hess-19-33-2015.
Nelson, B.R., O.P. Prat, D.-J. Seo, and E. Habib, 2016: Assessment and Implications of NCEP Stage IV Quantitative Precipitation Estimates for Product Intercomparisons. *Weather and Forecasting*, **31(2)**, 371–394, doi:10.1175/waf-d-14-00112.1.
Neu, U. et al., 2013: IMILAST: A Community Effort to Intercompare Extratropical Cyclone Detection and Tracking Algorithms. *Bulletin of the American Meteorological Society*, **94(4)**, 529–547, doi:10.1175/bams-d-11-00154.1.
Neukom, R., N. Steiger, J.J. Gómez-Navarro, J. Wang, and J.P. Werner, 2019: No evidence for globally coherent warm and cold periods over the preindustrial Common Era. *Nature*, **571(7766)**, 550–554, doi:10.1038/s41586-019-1401-2.
Newman, M. et al., 2016: The Pacific decadal oscillation, revisited. *Journal of Climate*, doi:10.1175/jcli-d-15-0508.1.
Nguyen, K.C., J.J. Katzfey, J. Riedl, and A. Troccoli, 2017: Potential impacts of solar arrays on regional climate and on array efficiency. *International Journal of Climatology*, **37(11)**, 4053–4064, doi:10.1002/joc.4995.
Nguyen, P. et al., 2019: The CHRS Data Portal, an easily accessible public repository for PERSIANN global satellite precipitation data. *Scientific Data*, **6(1)**, 180296, doi:10.1038/sdata.2018.296.
Nguyen, T.-H., S.-K. Min, S. Paik, and D. Lee, 2018: Time of emergence in regional precipitation changes: an updated assessment using the CMIP5 multi-model ensemble. *Climate Dynamics*, **51(9–10)**, 3179–3193, doi:10.1007/s00382-018-4073-y.
Nicholson, S.E., 2013: The West African Sahel: A Review of Recent Studies on the Rainfall Regime and Its Interannual Variability. *ISRN Meteorology*, **2013**, 1–32, doi:10.1155/2013/453521.
Nicholson, S.E., A.H. Fink, and C. Funk, 2018: Assessing recovery and change in West Africa's rainfall regime from a 161-year record. *International Journal of Climatology*, **38(10)**, 3770–3786, doi:10.1002/joc.5530.
Nigam, S. and M. Bollasina, 2010: "Elevated heat pump" hypothesis for the aerosol-monsoon hydroclimate link: "Grounded" in observations? *Journal of Geophysical Research*, **115(D16)**, D16201, doi:10.1029/2009jd013800.
Nightingale, J. et al., 2019: Ten Priority Science Gaps in Assessing Climate Data Record Quality. *Remote Sensing* , **11(8)**, doi:10.3390/rs11080986.

ACCEPTED VERSION SUBJECT TO FINAL EDITING

Nikiema, P.M. et al., 2017: Multi-model CMIP5 and CORDEX simulations of historical summer temperature and precipitation variabilities over West Africa. *International Journal of Climatology*, **37(5)**, 2438–2450, doi:10.1002/joc.4856.
Nikulin, G. et al., 2012: Precipitation Climatology in an Ensemble of CORDEX-Africa Regional Climate Simulations. *Journal of Climate*, **25(18)**, 6057–6078, doi:10.1175/jcli-d-11-00375.1.
Nissan, H., G. Muñoz, and S.J. Mason, 2020: Targeted model evaluations for climate services: A case study on heat waves in Bangladesh. *Climate Risk Management*, **28**, 100213, doi:10.1016/j.crm.2020.100213.
Nitu, R. et al., 2018: *WMO Solid Precipitation Intercomparison Experiment (SPICE) (2012 - 2015)*. Instruments and Observing Methods Report No. 131, World Meteorological Organization (WMO), Geneva, Switzerland, 1445 pp.
Noël, B. et al., 2018: Modelling the climate and surface mass balance of polar ice sheets using RACMO2 – Part 1: Greenland (1958–2016). *The Cryosphere*, **12(3)**, 811–831, doi:10.5194/tc-12-811-2018.
Norström, A. et al., 2020: Principles for knowledge co-production in sustainability research. *Nature Sustainability*, **3(3)**, 182–190, doi:10.1038/s41893-019-0448-2.
Notaro, M., V. Bennington, and S. Vavrus, 2015: Dynamically Downscaled Projections of Lake-Effect Snow in the Great Lakes Basin*,+. *Journal of Climate*, **28(4)**, 1661–1684, doi:10.1175/jcli-d-14-00467.1.
Notaro, M. et al., 2013: Influence of the Laurentian Great Lakes on Regional Climate*. *Journal of Climate*, **26(3)**, 789–804, doi:10.1175/jcli-d-12-00140.1.
Notz, D., 2015: How well must climate models agree with observations? *Philosophical Transactions of the Royal Society A: Mathematical, Physical and Engineering Sciences*, **373(2052)**, 20140164, doi:10.1098/rsta.2014.0164.
O, S. and U. Foelsche, 2019: Assessment of spatial uncertainty of heavy rainfall at catchment scale using a dense gauge network. *Hydrology and Earth System Sciences*, **23(7)**, 2863–2875, doi:10.5194/hess-23-2863-2019.
O'Higgins, T., A.A. Nogueira, and A.I. Lillebø, 2019: A simple spatial typology for assessment of complex coastal ecosystem services across multiple scales. *Science of the Total Environment*, **649**, 1452–1466, doi:10.1016/j.scitotenv.2018.08.420.
O'Reilly, C.H., 2018: Interdecadal variability of the ENSO teleconnection to the wintertime North Pacific. *Climate Dynamics*, **51(9–10)**, 3333–3350, doi:10.1007/s00382-018-4081-y.
O'Reilly, C.H., T. Woollings, and L. Zanna, 2017: The Dynamical Influence of the Atlantic Multidecadal Oscillation on Continental Climate. *Journal of Climate*, **30(18)**, 7213–7230, doi:10.1175/jcli-d-16-0345.1.
O'Reilly, C.H., D.J. Befort, and A. Weisheimer, 2020: Calibrating large-ensemble European climate projections using observational data. *Earth System Dynamics*, **11(4)**, 1033–1049, doi:10.5194/esd-11-1033-2020.
O'Reilly, C.H., T. Woollings, L. Zanna, and A. Weisheimer, 2019: An Interdecadal Shift of the Extratropical Teleconnection From the Tropical Pacific During Boreal Summer. *Geophysical Research Letters*, **46(22)**, 13379–13388, doi:10.1029/2019gl084079.
Obermann, A. et al., 2018: Mistral and Tramontane wind speed and wind direction patterns in regional climate simulations. *Climate Dynamics*, **51(3)**, 1059–1076, doi:10.1007/s00382-016-3053-3.
Ochsner, T.E. et al., 2013: State of the Art in Large-Scale Soil Moisture Monitoring. *Soil Science Society of America Journal*, **77(6)**, 1888, doi:10.2136/sssaj2013.03.0093.
Ogawa, F. et al., 2018: Evaluating Impacts of Recent Arctic Sea Ice Loss on the Northern Hemisphere Winter Climate Change. *Geophysical Research Letters*, **45(7)**, 3255–3263, doi:10.1002/2017gl076502.
Ohki, M. et al., 2019: Flood Area Detection Using ALOS-2 PALSAR-2 Data for the 2015 Heavy Rainfall Disaster in the Kanto and Tohoku Area, Japan. *Journal of The Remote Sensing Society of Japan*, **39**, 43–55.
Okamoto, K., T. Ushio, T. Iguchi, N. Takahashi, and K. Iwanami, 2005: The global satellite mapping of precipitation (GSMaP) project. *Proceedings. 2005 IEEE International Geoscience and Remote Sensing Symposium, 2005. IGARSS '05.*, **5**, 3414–3416, doi:10.1109/igarss.2005.1526575.
Oleson, K., 2012: Contrasts between Urban and rural climate in CCSM4 CMIP5 climate change scenarios. *Journal of Climate*, **25(5)**, 1390–1412, doi:10.1175/jcli-d-11-00098.1.
Oleson, K.W., G.B. Bonan, J. Feddema, and T. Jackson, 2011: An examination of urban heat island characteristics in a global climate model. *International Journal of Climatology*, **31(12)**, 1848–1865, doi:10.1002/joc.2201.
Olonscheck, D. and D. Notz, 2017: Consistently Estimating Internal Climate Variability from Climate Model Simulations. *Journal of Climate*, **30(23)**, 9555–9573, doi:10.1175/jcli-d-16-0428.1.
Olonscheck, D., T. Mauritsen, and D. Notz, 2019: Arctic sea-ice variability is primarily driven by atmospheric temperature fluctuations. *Nature Geoscience*, **12(6)**, 430–434, doi:10.1038/s41561-019-0363-1.
Orlanski, I., 1975: A Rational Subdivision of Scales for Atmospheric Processes. *Bulletin of the American Meteorological Society*, **56(5)**, 527–530.
Ortega, P. et al., 2015: A model-tested North Atlantic Oscillation reconstruction for the past millennium. *Nature*, **523(7558)**, 71–74, doi:10.1038/nature14518.
Osborn, T.J. and P.D. Jones, 2014: The CRUTEM4 land-surface air temperature data set: construction, previous versions and dissemination via Google Earth. *Earth System Science Data*, **6(1)**, 61–68, doi:10.5194/essd-6-61-2014.

ACCEPTED VERSION SUBJECT TO FINAL EDITING

Osborn, T.J. et al., 2021: Land Surface Air Temperature Variations Across the Globe Updated to 2019: The CRUTEM5 Data Set. *Journal of Geophysical Research: Atmospheres*, **126(2)**, e2019JD032352, doi:10.1029/2019jd032352.
Ose, T., 2019: Future Changes in Summertime East Asian Monthly Precipitation in CMIP5 and Their Dependence on Present-Day Model Climatology. *Journal of the Meteorological Society of Japan. Ser. II*, **97(5)**, 1041–1053, doi:10.2151/jmsj.2019-055.
Ose, T., Y. Takaya, S. Maeda, and T. Nakaegawa, 2020: Resolution of Summertime East Asian Pressure Pattern and Southerly Monsoon Wind in CMIP5 Multi-model Future Projections. *Journal of the Meteorological Society of Japan. Ser. II*, **98(5)**, 927–944, doi:10.2151/jmsj.2020-047.
Ossó, A., L. Shaffrey, B. Dong, and R. Sutton, 2019: Impact of air–sea coupling on Northern Hemisphere summer climate and the monsoon–desert teleconnection. *Climate Dynamics*, **53(7–8)**, 5063–5078, doi:10.1007/s00382-019-04846-6.
Otto, F.E.L. et al., 2015: Factors Other Than Climate Change, Main Drivers of 2014/15 Water Shortage in Southeast Brazil. *Bulletin of the American Meteorological Society*, **96(12)**, S35–S40, doi:10.1175/bams-d-15-00120.1.
Otto, F.E.L. et al., 2016: The attribution question. *Nature Climate Change*, **6(9)**, 813–816, doi:10.1038/nclimate3089.
Otto, F.E.L. et al., 2018: Anthropogenic influence on the drivers of the Western Cape drought 2015–2017. *Environmental Research Letters*, **13(12)**, 124010, doi:10.1088/1748-9326/aae9f9.
Otto, J. et al., 2016: Uncertainty: Lessons Learned for Climate Services. *Bulletin of the American Meteorological Society*, **97(12)**, ES265–ES269, doi:10.1175/bams-d-16-0173.1.
Oudar, T., J. Cattiaux, and H. Douville, 2020: Drivers of the Northern Extratropical Eddy-Driven Jet Change in CMIP5 and CMIP6 Models. *Geophysical Research Letters*, **47(8)**, doi:10.1029/2019gl086695.
Overeem, A. et al., 2013: Crowdsourcing urban air temperatures from smartphone battery temperatures. *Geophysical Research Letters*, **40(15)**, 4081–4085, doi:10.1002/grl.50786.
Overland, J.E. et al., 2016: Nonlinear response of mid-latitude weather to the changing Arctic. *Nature Climate Change*, **6(11)**, 992–999, doi:10.1038/nclimate3121.
Oyler, J.W., A. Ballantyne, K. Jencso, M. Sweet, and S.W. Running, 2015: Creating a topoclimatic daily air temperature dataset for the conterminous United States using homogenized station data and remotely sensed land skin temperature. *International Journal of Climatology*, **35(9)**, 2258–2279, doi:10.1002/joc.4127.
Ozturk, T., M.T. Turp, M. Türkeş, and M.L. Kurnaz, 2018: Future projections of temperature and precipitation climatology for CORDEX-MENA domain using RegCM4.4. *Atmospheric Research*, **206**, 87–107, doi:10.1016/j.atmosres.2018.02.009.
Paegle, J.N. and K.C. Mo, 2002: Linkages between Summer Rainfall Variability over South America and Sea Surface Temperature Anomalies. *Journal of Climate*, **15(12)**, 1389–1407, doi:10.1175/1520-0442(2002)015<1389:lbsrvo>2.0.co;2.
Pai, D.S., L. Sridhar, M.R. Badwaik, and M. Rajeevan, 2015: Analysis of the daily rainfall events over India using a new long period (1901–2010) high resolution (0.25° × 0.25°) gridded rainfall data set. *Climate Dynamics*, **45(3–4)**, 755–776, doi:10.1007/s00382-014-2307-1.
Pai, D.S. et al., 2014: Development of a new high spatial resolution (0.25° × 0.25°) long period (1901-2010) daily gridded rainfall data set over India and its comparison with existing data sets over the region. *Mausam*, **65(1)**, 1–18.
Palazzi, E., J. von Hardenberg, and A. Provenzale, 2013: Precipitation in the Hindu-Kush Karakoram Himalaya: Observations and future scenarios. *Journal of Geophysical Research: Atmospheres*, **118(1)**, 85–100, doi:10.1029/2012jd018697.
Palazzi, E., J. von Hardenberg, S. Terzago, and A. Provenzale, 2015: Precipitation in the Karakoram-Himalaya: a CMIP5 view. *Climate Dynamics*, **45(1–2)**, 21–45, doi:10.1007/s00382-014-2341-z.
Pall, P. et al., 2017: Diagnosing conditional anthropogenic contributions to heavy Colorado rainfall in September 2013. *Weather and Climate Extremes*, **17**, 1–6, doi:10.1016/j.wace.2017.03.004.
Palmer, T.N., 2013: Climate extremes and the role of dynamics. *Proceedings of the National Academy of Sciences*, **110(14)**, 5281–5282, doi:10.1073/pnas.1303295110.
Palmer, T.N., 2016: A personal perspective on modelling the climate system. *Proceedings of the Royal Society A: Mathematical, Physical and Engineering Sciences*, **472(2188)**, 20150772, doi:10.1098/rspa.2015.0772.
Palmer, T.N., 2019: Stochastic weather and climate models. *Nature Reviews Physics*, **1(7)**, 463–471, doi:10.1038/s42254-019-0062-2.
Panthou, G. et al., 2018: Rainfall intensification in tropical semi-arid regions: the Sahelian case. *Environmental Research Letters*, **13(6)**, 064013, doi:10.1088/1748-9326/aac334.
Panziera, L., M. Gabella, U. Germann, and O. Martius, 2018: A 12-year radar-based climatology of daily and sub-daily extreme precipitation over the Swiss Alps. *International Journal of Climatology*, **38(10)**, 3749–3769, doi:10.1002/joc.5528.
Parastatidis, D., Z. Mitraka, N. Chrysoulakis, and M. Abrams, 2017: Online Global Land Surface Temperature Estimation from Landsat. *Remote Sensing*, **9(12)**, 1208, doi:10.3390/rs9121208.
Park, B.-J. et al., 2017: Long-Term Warming Trends in Korea and Contribution of Urbanization: An Updated

ACCEPTED VERSION SUBJECT TO FINAL EDITING

Assessment. *Journal of Geophysical Research: Atmospheres*, **122(20)**, 10,610–637,654, doi:10.1002/2017jd027167.
Park, J.Y., J. Bader, and D. Matei, 2016: Anthropogenic Mediterranean warming essential driver for present and future Sahel rainfall. *Nature Climate Change*, doi:10.1038/nclimate3065.
Park, J.-Y., J. Bader, and D. Matei, 2015: Northern-hemispheric differential warming is the key to understanding the discrepancies in the projected Sahel rainfall. *Nature Communications*, **6(1)**, 5985, doi:10.1038/ncomms6985.
Parker, D.E., 1994: Effects of changing exposure of thermometers at land stations. *International Journal of Climatology*, **14(1)**, 1–31, doi:10.1002/joc.3370140102.
Parker, D.E., 2010: Urban heat island effects on estimates of observed climate change. *WIREs Climate Change*, **1(1)**, 123–133, doi:10.1002/wcc.21.
Parker, W.S., 2009: II–Confirmation and Adequacy-for-Purpose in Climate Modelling. *Aristotelian Society Supplementary Volume*, **83(1)**, 233–249, doi:10.1111/j.1467-8349.2009.00180.x.
Parker, W.S. and G. Lusk, 2019: Incorporating User Values into Climate Services. *Bulletin of the American Meteorological Society*, **100(9)**, 1643–1650, doi:10.1175/bams-d-17-0325.1.
Patricola, C.M. and M.F. Wehner, 2018: Anthropogenic influences on major tropical cyclone events. *Nature*, **563(7731)**, 339–346, doi:10.1038/s41586-018-0673-2.
Paul, S. et al., 2016: Weakening of Indian Summer Monsoon Rainfall due to Changes in Land Use Land Cover. *Scientific Reports*, **6**, doi:10.1038/srep32177.
Pausata, F.S.R., L. Chafik, R. Caballero, and D.S. Battisti, 2015: Impacts of high-latitude volcanic eruptions on ENSO and AMOC. *Proceedings of the National Academy of Sciences*, **112(45)**, 13784–13788, doi:10.1073/pnas.1509153112.
Pearce, W., S. Niederer, S.M. Özkula, and N. Sánchez Querubín, 2019: The social media life of climate change: Platforms, publics, and future imaginaries. *Wiley Interdisciplinary Reviews: Climate Change*, **10(2)**, e569, doi:10.1002/wcc.569.
Pedro, J.B. et al., 2016: Southern Ocean deep convection as a driver of Antarctic warming events. *Geophysical Research Letters*, **43(5)**, 2192–2199, doi:10.1002/2016gl067861.
Peings, Y., 2019: Ural Blocking as a Driver of Early-Winter Stratospheric Warmings. *Geophysical Research Letters*, **46(10)**, 5460–5468, doi:10.1029/2019gl082097.
Peings, Y., J. Cattiaux, S.J. Vavrus, and G. Magnusdottir, 2018: Projected squeezing of the wintertime North-Atlantic jet. *Environmental Research Letters*, **13(7)**, 074016, doi:10.1088/1748-9326/aacc79.
Peings, Y., H. Douville, J. Colin, D. Martin, and G. Magnusdottir, 2017: Snow-(N)AO Teleconnection and Its Modulation by the Quasi-Biennial Oscillation. *Journal of Climate*, **30(24)**, 10211–10235, doi:10.1175/jcli-d-17-0041.1.
Penalba, O.C. and F.A. Robledo, 2010: Spatial and temporal variability of the frequency of extreme daily rainfall regime in the La Plata Basin during the 20th century. *Climatic Change*, **98(3)**, 531–550, doi:10.1007/s10584-009-9744-6.
Pendergrass, A.G., R. Knutti, F. Lehner, C. Deser, and B.M. Sanderson, 2017: Precipitation variability increases in a warmer climate. *Scientific Reports*, **7(1)**, 17966, doi:10.1038/s41598-017-17966-y.
Peng, D., T. Zhou, L. Zhang, and L. Zou, 2019: Detecting human influence on the temperature changes in Central Asia. *Climate Dynamics*, **53(7–8)**, 4553–4568, doi:10.1007/s00382-019-04804-2.
Peng, L. et al., 2018: Wind weakening in a dense high-rise city due to over nearly five decades of urbanization. *Building and Environment*, **138**, 207–220, doi:10.1016/j.buildenv.2018.04.037.
Pepin, N. et al., 2015: Elevation-dependent warming in mountain regions of the world. *Nature Climate Change*, **5(5)**, 424–430, doi:10.1038/nclimate2563.
Pepler, A., A. Coutts-Smith, and B. Timbal, 2014: The role of East Coast Lows on rainfall patterns and inter-annual variability across the East Coast of Australia. *International Journal of Climatology*, **34(4)**, 1011–1021, doi:10.1002/joc.3741.
Pepler, A.S., L. Alexander, J.P. Evans, and S.C. Sherwood, 2016: Zonal winds and southeast Australian rainfall in global and regional climate models. *Climate Dynamics*, **46(1–2)**, 123–133, doi:10.1007/s00382-015-2573-6.
Perkins-Kirkpatrick, S.E., E.M. Fischer, O. Angélil, and P.B. Gibson, 2017: The influence of internal climate variability on heatwave frequency trends. *Environmental Research Letters*, **12(4)**, 044005, doi:10.1088/1748-9326/aa63fe.
Perry, S.J., S. McGregor, A. Gupta, and M.H. England, 2017: Future Changes to El Niño-Southern Oscillation Temperature and Precipitation Teleconnections. *Geophysical Research Letters*, **44(20)**, 10,608–10,616, doi:10.1002/2017gl074509.
Petoukhov, V., S. Rahmstorf, S. Petri, and H.J. Schellnhuber, 2013: Quasiresonant amplification of planetary waves and recent Northern Hemisphere weather extremes. *Proceedings of the National Academy of Sciences*, **110(14)**, 5336–5341, doi:10.1073/pnas.1222000110.
Petrie, R.E., L.C. Shaffrey, and R.T. Sutton, 2015: Atmospheric Impact of Arctic Sea Ice Loss in a Coupled Ocean–Atmosphere Simulation. *Journal of Climate*, **28(24)**, 9606–9622, doi:10.1175/jcli-d-15-0316.1.
Pettenger, M.E. (ed.), 2016: *The Social Construction of Climate Change*. Routledge, London, UK, 280 pp.,

ACCEPTED VERSION SUBJECT TO FINAL EDITING

doi:10.4324/9781315552842.
Pfeifroth, U. et al., 2018: Satellite-based trends of solar radiation and cloud parameters in Europe. *Advances in Science and Research*, **15**, 31–37, doi:10.5194/asr-15-31-2018.
Pham, T., J. Brauch, B. Früh, and B. Ahrens, 2017: Simulation of snowbands in the Baltic Sea area with the coupled atmosphere-ocean-ice model COSMO-CLM/NEMO. *Meteorologische Zeitschrift*, **26(1)**, 71–82, doi:10.1127/metz/2016/0775.
Pham, T., J. Brauch, B. Früh, and B. Ahrens, 2018: Added decadal prediction skill with the coupled regional climate model COSMO-CLM/NEMO. *Meteorologische Zeitschrift*, **27(5)**, 391–399, doi:10.1127/metz/2018/0872.
Philipona, R., K. Behrens, and C. Ruckstuhl, 2009: How declining aerosols and rising greenhouse gases forced rapid warming in Europe since the 1980s. *Geophysical Research Letters*, **36(2)**, L02806, doi:10.1029/2008gl036350.
Philippon, N., M. Rouault, Y. Richard, and A. Favre, 2012: The influence of ENSO on winter rainfall in South Africa. *International Journal of Climatology*, **32(15)**, 2333–2347, doi:10.1002/joc.3403.
Photiadou, C., B. van den Hurk, A. van Delden, and A. Weerts, 2016: Incorporating circulation statistics in bias correction of GCM ensembles: hydrological application for the Rhine basin. *Climate Dynamics*, **46(1–2)**, 187–203, doi:10.1007/s00382-015-2578-1.
Pichelli, E. et al., 2021: The first multi-model ensemble of regional climate simulations at kilometer-scale resolution part 2: historical and future simulations of precipitation. *Climate Dynamics*, doi:10.1007/s00382-021-05657-4.
Piennaar, L.O.U.W. and J.O.H.A.N.N. Boonzaaier, 2018: *Drought Policy Brief: Western Cape Agriculture*. Bureau for Food and Agriculture Policy, Die Wilgers, South Africa, 17 pp.
Pierce, D.W., D.R. Cayan, and B.L. Thrasher, 2014: Statistical Downscaling Using Localized Constructed Analogs (LOCA). *Journal of Hydrometeorology*, **15(6)**, 2558–2585, doi:10.1175/jhm-d-14-0082.1.
Pierce, D.W., D.R. Cayan, E.P. Maurer, J.T. Abatzoglou, and K.C. Hegewisch, 2015: Improved Bias Correction Techniques for Hydrological Simulations of Climate Change. *Journal of Hydrometeorology*, **16(6)**, 2421–2442, doi:10.1175/jhm-d-14-0236.1.
Pietikäinen, J.-P. et al., 2018: The regional climate model REMO (v2015) coupled with the 1-D freshwater lake model FLake (v1): Fenno-Scandinavian climate and lakes. *Geoscientific Model Development*, **11(4)**, 1321–1342, doi:10.5194/gmd-11-1321-2018.
Pinto, I., C. Jack, and B. Hewitson, 2018: Process-based model evaluation and projections over southern Africa from Coordinated Regional Climate Downscaling Experiment and Coupled Model Intercomparison Project Phase 5 models. *International Journal of Climatology*, **38(11)**, 4251–4261, doi:10.1002/joc.5666.
Piovano, E.L., D. Ariztegui, S.M. Bernasconi, and J.A. McKenzie, 2004: Stable isotopic record of hydrological changes in subtropical Laguna Mar Chiquita (Argentina) over the last 230 years. *The Holocene*, **14(4)**, 525–535, doi:10.1191/0959683604hl729rp.
Pisaric, M.F.J. et al., 2011: Impacts of a recent storm surge on an Arctic delta ecosystem examined in the context of the last millennium. *Proceedings of the National Academy of Sciences*, **108(22)**, 8960–8965, doi:10.1073/pnas.1018527108.
Plant, R.S. and J.-I. Yano (eds.), 2015: *Parameterization of Atmospheric Convection*. World Scientific, 1132 pp., doi:10.1142/p1005.
Planton, S. et al., 2012: The Climate of the Mediterranean Region in Future Climate Projections. In: *The Climate of the Mediterranean Region* [Lionello, P. (ed.)]. Elsevier, Oxford, UK, pp. 449–502, doi:10.1016/b978-0-12-416042-2.00008-2.
Poan, E.D., P. Gachon, R. Laprise, R. Aider, and G. Dueymes, 2018: Investigating added value of regional climate modeling in North American winter storm track simulations. *Climate Dynamics*, **50(5–6)**, 1799–1818, doi:10.1007/s00382-017-3723-9.
Pokhrel, Y.N., N. Hanasaki, Y. Wada, and H. Kim, 2016: Recent progresses in incorporating human land-water management into global land surface models toward their integration into Earth system models. *Wiley Interdisciplinary Reviews: Water*, **3(4)**, 548–574, doi:10.1002/wat2.1150.
Polade, S.D., A. Gershunov, D.R. Cayan, M.D. Dettinger, and D.W. Pierce, 2013: Natural climate variability and teleconnections to precipitation over the Pacific-North American region in CMIP3 and CMIP5 models. *Geophysical Research Letters*, **40(10)**, 2296–2301, doi:10.1002/grl.50491.
Polcher, J., M. Piles, E. Gelati, A. Barella-Ortiz, and M. Tello, 2016: Comparing surface-soil moisture from the SMOS mission and the ORCHIDEE land-surface model over the Iberian Peninsula. *Remote Sensing of Environment*, **174**, 69–81, doi:10.1016/j.rse.2015.12.004.
Poli, P. et al., 2016a: Recent Advances in Satellite Data Rescue. *Bulletin of the American Meteorological Society*, **98(7)**, 1471–1484, doi:10.1175/bams-d-15-00194.1.
Poli, P. et al., 2016b: ERA-20C: An Atmospheric Reanalysis of the Twentieth Century. *Journal of Climate*, **29(11)**, 4083–4097, doi:10.1175/jcli-d-15-0556.1.
Polson, D., M. Bollasina, G.C. Hegerl, and L.J. Wilcox, 2014: Decreased monsoon precipitation in the Northern Hemisphere due to anthropogenic aerosols. *Geophysical Research Letters*, **41(16)**, 6023–6029, doi:10.1002/2014gl060811.
Pontoppidan, M. et al., 2019: Large-scale regional model biases in the extratropical North Atlantic storm track and

ACCEPTED VERSION SUBJECT TO FINAL EDITING

impacts on downstream precipitation. *Quarterly Journal of the Royal Meteorological Society*, qj.3588, doi:10.1002/qj.3588.
Porter, J.J. and S. Dessai, 2017: Mini-me: Why do climate scientists' misunderstand users and their needs? *Environmental Science & Policy*, **77**, 9–14, doi:10.1016/j.envsci.2017.07.004.
Power, S.B. and F.P.D. Delage, 2018: El Niño–Southern Oscillation and Associated Climatic Conditions around the World during the Latter Half of the Twenty-First Century. *Journal of Climate*, **31(15)**, 6189–6207, doi:10.1175/jcli-d-18-0138.1.
Praetorius, S., M. Rugenstein, G. Persad, and K. Caldeira, 2018: Global and Arctic climate sensitivity enhanced by changes in North Pacific heat flux. *Nature Communications*, **9(1)**, 3124, doi:10.1038/s41467-018-05337-8.
Prakash, S. et al., 2015: Seasonal intercomparison of observational rainfall datasets over India during the southwest monsoon season. *International Journal of Climatology*, **35(9)**, 2326–2338, doi:10.1002/joc.4129.
Prasanna, V., 2016: Assessment of South Asian Summer Monsoon Simulation in CMIP5-Coupled Climate Models During the Historical Period (1850--2005). *Pure and Applied Geophysics*, **173(4)**, 1379–1402, doi:10.1007/s00024-015-1126-6.
Prein, A.F. and A. Gobiet, 2017: Impacts of uncertainties in European gridded precipitation observations on regional climate analysis. *International Journal of Climatology*, **37(1)**, 305–327, doi:10.1002/joc.4706.
Prein, A.F., G.J. Holland, R.M. Rasmussen, M.P. Clark, and M.R. Tye, 2016a: Running dry: The U.S. Southwest's drift into a drier climate state. *Geophysical Research Letters*, **43(3)**, 1272–1279, doi:10.1002/2015gl066727.
Prein, A.F., M.S. Bukovsky, L.O. Mearns, C.L. Bruyère, and J.M. Done, 2019: Simulating North American Weather Types With Regional Climate Models. *Frontiers in Environmental Science*, **7**, 36, doi:10.3389/fenvs.2019.00036.
Prein, A.F. et al., 2013a: Added value of convection permitting seasonal simulations. *Climate Dynamics*, **41(9–10)**, 2655–2677, doi:10.1007/s00382-013-1744-6.
Prein, A.F. et al., 2013b: Importance of Regional Climate Model Grid Spacing for the Simulation of Heavy Precipitation in the Colorado Headwaters. *Journal of Climate*, **26(13)**, 4848–4857, doi:10.1175/jcli-d-12-00727.1.
Prein, A.F. et al., 2015: A review on regional convection-permitting climate modeling: Demonstrations, prospects, and challenges. *Reviews of Geophysics*, **53(2)**, 323–361, doi:10.1002/2014rg000475.
Prein, A.F. et al., 2016b: Precipitation in the EURO-CORDEX 0.11° and 0.44° simulations: high resolution, high benefits? *Climate Dynamics*, **46(1–2)**, 383–412, doi:10.1007/s00382-015-2589-y.
Prein, A.F. et al., 2017: Increased rainfall volume from future convective storms in the US. *Nature Climate Change*, **7(12)**, 880–884, doi:10.1038/s41558-017-0007-7.
Prodhomme, C. et al., 2016: Benefits of increasing the model resolution for the seasonal forecast quality in EC-earth. *Journal of Climate*, **29(24)**, doi:10.1175/jcli-d-16-0117.1.
Prospero, J.M., P. Ginoux, O. Torres, S.E. Nicholson, and T.E. Gill, 2002: Environmental characterization of global sources of atmospheric soil dust identified with the Nimbus 7 Total Ozone Mapping Spectrometer (TOMS) absorbing aerosol product. *Reviews of Geophysics*, **40(1)**, 2–31, doi:10.1029/2000rg000095.
Prudhomme, C., R.L. Wilby, S. Crooks, A.L. Kay, and N.S. Reynard, 2010: Scenario-neutral approach to climate change impact studies: Application to flood risk. *Journal of Hydrology*, **390(3–4)**, 198–209, doi:10.1016/j.jhydrol.2010.06.043.
Pryor, S.C. and A.N. Hahmann, 2019: Downscaling Wind. In: *Oxford Research Encyclopedia of Climate Science*. Oxford University Press, Oxford, UK, doi:10.1093/acrefore/9780190228620.013.730.
Pu, B. and P. Ginoux, 2018: How reliable are CMIP5 models in simulating dust optical depth? *Atmospheric Chemistry and Physics*, **18(16)**, 12491–12510, doi:10.5194/acp-18-12491-2018.
Purich, A., T. Cowan, S.-K. Min, and W. Cai, 2013: Autumn Precipitation Trends over Southern Hemisphere Midlatitudes as Simulated by CMIP5 Models. *Journal of Climate*, **26(21)**, 8341–8356, doi:10.1175/jcli-d-13-00007.1.
Qasmi, S., E. Sanchez-Gomez, Y. Ruprich-Robert, J. Boé, and C. Cassou, 2021: Modulation of the Occurrence of Heatwaves over the Euro-Mediterranean Region by the Intensity of the Atlantic Multidecadal Variability. *Journal of Climate*, **34(3)**, 1099–1114, doi:10.1175/jcli-d-19-0982.1.
Qian, C., 2016: Disentangling the urbanization effect, multi-decadal variability, and secular trend in temperature in eastern China during 1909-2010. *Atmospheric Science Letters*, **17(2)**, 177–182, doi:10.1002/asl.640.
Qian, C. and T. Zhou, 2014: Multidecadal variability of North China aridity and its relationship to PDO during 1900-2010. *Journal of Climate*, **27(3)**, 1210–1222, doi:10.1175/jcli-d-13-00235.1.
Qiao, L. et al., 2014: Climate Change and Hydrological Response in the Trans-State Oologah Lake Watershed–Evaluating Dynamically Downscaled NARCCAP and Statistically Downscaled CMIP3 Simulations with VIC Model. *Water Resources Management*, **28(10)**, 3291–3305, doi:10.1007/s11269-014-0678-z.
Qin, J., K. Yang, S. Liang, and X. Guo, 2009: The altitudinal dependence of recent rapid warming over the Tibetan Plateau. *Climatic Change*, **97(1)**, 321, doi:10.1007/s10584-009-9733-9.
Quesada, B., R. Vautard, P. Yiou, M. Hirschi, and S.I. Seneviratne, 2012: Asymmetric European summer heat predictability from wet and dry southern winters and springs. *Nature Climate Change*, **2(10)**, 736–741,

ACCEPTED VERSION SUBJECT TO FINAL EDITING

doi:10.1038/nclimate1536.
Rackow, T. et al., 2018: Towards multi-resolution global climate modeling with ECHAM6-FESOM. Part II: climate variability. *Climate Dynamics*, **50(7)**, 2369–2394, doi:10.1007/s00382-016-3192-6.
Rajbhandari, R., A.B. Shrestha, A. Kulkarni, S.K. Patwardhan, and S.R. Bajracharya, 2015: Projected changes in climate over the Indus river basin using a high resolution regional climate model (PRECIS). *Climate Dynamics*, **44(1–2)**, 339–357, doi:10.1007/s00382-014-2183-8.
Rajczak, J. and C. Schär, 2017: Projections of Future Precipitation Extremes Over Europe: A Multimodel Assessment of Climate Simulations. *Journal of Geophysical Research: Atmospheres*, **122(20)**, 10,773–10,800, doi:10.1002/2017jd027176.
Rajeevan, M. and J. Bhate, 2009: A High Resolution Daily Gridded rainfall dataset (1971–2005) for Mesoscale Meteorological Studies. *Current Science*, **96(4)**, 558–562.
Rajeevan, M., J. Bhate, J.D. Kale, and B. Lal, 2006: High resolution daily gridded rainfall data for the Indian region: Analysis of break and active monsoon spells. *Current Science*, doi:10.1007/s12040-007-0019-1.
Ramarao, M.V.S., R. Krishnan, J. Sanjay, and T.P. Sabin, 2015: Understanding land surface response to changing South Asian monsoon in a warming climate. *Earth System Dynamics*, **6(2)**, 569–582, doi:10.5194/esd-6-569-2015.
Ramos, A.M. et al., 2019: From Amazonia to southern Africa: atmospheric moisture transport through low-level jets and atmospheric rivers. *Annals of the New York Academy of Sciences*, **1436(1)**, 217–230, doi:10.1111/nyas.13960.
Rasmijn, L.M. et al., 2018: Future equivalent of 2010 Russian heatwave intensified by weakening soil moisture constraints. *Nature Climate Change*, **8(5)**, 381–385, doi:10.1038/s41558-018-0114-0.
Rasmussen, R. et al., 2012: How Well Are We Measuring Snow: The NOAA/FAA/NCAR Winter Precipitation Test Bed. *Bulletin of the American Meteorological Society*, **93(6)**, 811–829, doi:10.1175/bams-d-11-00052.1.
Räty, O., J. Räisänen, and J.S. Ylhäisi, 2014: Evaluation of delta change and bias correction methods for future daily precipitation: intermodel cross-validation using ENSEMBLES simulations. *Climate Dynamics*, **42(9–10)**, 2287–2303, doi:10.1007/s00382-014-2130-8.
Raymond, F., A. Ullmann, Y. Tramblay, P. Drobinski, and P. Camberlin, 2019: Evolution of Mediterranean extreme dry spells during the wet season under climate change. *Regional Environmental Change*, **19(8)**, 2339–2351, doi:10.1007/s10113-019-01526-3.
Re, M. and V.R. Barros, 2009: Extreme rainfalls in SE South America. *Climatic Change*, **96(1–2)**, 119–136, doi:10.1007/s10584-009-9619-x.
Reason, C.J.C. and D. Jagadheesha, 2005: Relationships between South Atlantic SST Variability and Atmospheric Circulation over the South African Region during Austral Winter. *Journal of Climate*, **18(16)**, 3339–3355, doi:10.1175/jcli3474.1.
Reason, C.J.C. and M. Rouault, 2005: Links between the Antarctic Oscillation and winter rainfall over western South Africa. *Geophysical Research Letters*, **32(7)**, L07705, doi:10.1029/2005gl022419.
Reboita, M.S., R.P. da Rocha, M.R. de Souza, and M. Llopart, 2018: Extratropical cyclones over the southwestern South Atlantic Ocean: HadGEM2-ES and RegCM4 projections. *International Journal of Climatology*, **38(6)**, 2866–2879, doi:10.1002/joc.5468.
Redon, E.C., A. Lemonsu, V. Masson, B. Morille, and M. Musy, 2017: Implementation of street trees within the solar radiative exchange parameterization of TEB in SURFEX v8.0. *Geoscientific Model Development*, **10(1)**, 385–411, doi:10.5194/gmd-10-385-2017.
Reichstein, M. et al., 2019: Deep learning and process understanding for data-driven Earth system science. *Nature*, **566(7743)**, 195–204, doi:10.1038/s41586-019-0912-1.
Ren, Y., L. Song, Y. Xiao, and L. Du, 2019: Underestimated interannual variability of East Asian summer rainfall under climate change. *Theoretical and Applied Climatology*, **135**, 911–920, doi:10.1007/s00704-018-2398-4.
Ren, Y.-Y. et al., 2017: Observed changes in surface air temperature and precipitation in the Hindu Kush Himalayan region over the last 100-plus years. *Advances in Climate Change Research*, **8(3)**, 148–156, doi:10.1016/j.accre.2017.08.001.
Rennie, J.J. et al., 2014: The international surface temperature initiative global land surface databank: monthly temperature data release description and methods. *Geoscience Data Journal*, **1(2)**, 75–102, doi:10.1002/gdj3.8.
Reszler, C., M.B. Switanek, and H. Truhetz, 2018: Convection-permitting regional climate simulations for representing floods in small- and medium-sized catchments in the Eastern Alps. *Natural Hazards and Earth System Sciences*, **18(10)**, 2653–2674, doi:10.5194/nhess-18-2653-2018.
Rhoades, A.M., A.D. Jones, and P.A. Ullrich, 2018: Assessing Mountains as Natural Reservoirs With a Multimetric Framework. *Earth's Future*, **6(9)**, 1221–1241, doi:10.1002/2017ef000789.
Ribes, A. and L. Terray, 2013: Application of regularised optimal fingerprinting to attribution. Part II: application to global near-surface temperature. *Climate Dynamics*, **41(11–12)**, 2837–2853, doi:10.1007/s00382-013-1736-6.
Ribes, A. et al., 2019: Observed increase in extreme daily rainfall in the French Mediterranean. *Climate Dynamics*, **52(1–2)**, 1095–1114, doi:10.1007/s00382-018-4179-2.
Riboldi, J., F. Lott, F. D'Andrea, and G. Rivière, 2020: On the Linkage Between Rossby Wave Phase Speed,

SUBJECT TO FINAL EDITING ACCEPTED VERSION

Atmospheric Blocking, and Arctic Amplification. *Geophysical Research Letters*, **47(19)**, doi:10.1029/2020gl087796.
Rice, J.L., C.A. Woodhouse, and J.J. Lukas, 2009: Science and Decision Making: Water Management and Tree-Ring Data in the Western United States. *JAWRA Journal of the American Water Resources Association*, **45(5)**, 1248–1259, doi:10.1111/j.1752-1688.2009.00358.x.
Ridley, D.A., C.L. Heald, and J.M. Prospero, 2014: What controls the recent changes in African mineral dust aerosol across the Atlantic? *Atmospheric Chemistry and Physics*, **14(11)**, 5735–5747, doi:10.5194/acp-14-5735-2014.
Rienecker, M.M. et al., 2011: MERRA: NASA's Modern-Era Retrospective Analysis for Research and Applications. *Journal of Climate*, **24(14)**, 3624–3648, doi:10.1175/jcli-d-11-00015.1.
Robaa, S.M., 2013: Some aspects of the urban climates of Greater Cairo Region, Egypt. *International Journal of Climatology*, **33(15)**, 3206–3216, doi:10.1002/joc.3661.
Roberts, M.J. et al., 2018: The Benefits of Global High Resolution for Climate Simulation: Process Understanding and the Enabling of Stakeholder Decisions at the Regional Scale. *Bulletin of the American Meteorological Society*, **99(11)**, 2341–2359, doi:10.1175/bams-d-15-00320.1.
Robeson, S.M., 2015: Revisiting the recent California drought as an extreme value. *Geophysical Research Letters*, **42(16)**, 6771–6779, doi:10.1002/2015gl064593.
Robin, Y., M. Vrac, P. Naveau, and P. Yiou, 2019: Multivariate stochastic bias corrections with optimal transport. *Hydrology and Earth System Sciences*, **23(2)**, 773–786, doi:10.5194/hess-23-773-2019.
Robins, S., 2019: 'Day Zero', Hydraulic Citizenship and the Defence of the Commons in Cape Town: A Case Study of the Politics of Water and its Infrastructures (2017–2018). *Journal of Southern African Studies*, 1–25, doi:10.1080/03057070.2019.1552424.
Robledo, F., C. Vera, and O. Penalba, 2020: Multi-scale features of the co-variability between global sea surface temperature anomalies and daily extreme rainfall in Argentina. *International Journal of Climatology*, **40(9)**, 4289–4299, doi:10.1002/joc.6462.
Robledo, F.A., C. Vera, and O.C. Penalba, 2016: Influence of the large-scale climate variability on daily rainfall extremes over Argentina. *International Journal of Climatology*, **36(1)**, 412–423, doi:10.1002/joc.4359.
Robson, J., P. Ortega, and R. Sutton, 2016: A reversal of climatic trends in the North Atlantic since 2005. *Nature Geoscience*, **9(7)**, 513–517, doi:10.1038/ngeo2727.
Rodríguez-Fonseca, B. et al., 2015: Variability and Predictability of West African Droughts: A Review on the Role of Sea Surface Temperature Anomalies. *Journal of Climate*, **28(10)**, 4034–4060, doi:10.1175/jcli-d-14-00130.1.
Rodwell, M.J. and B.J. Hoskins, 1996: Monsoons and the dynamics of deserts. *Quarterly Journal of the Royal Meteorological Society*, **122(534)**, 1385–1404, doi:10.1002/qj.49712253408.
Roehrig, R., D. Bouniol, F. Guichard, F. Hourdin, and J.-L. Redelsperger, 2013: The Present and Future of the West African Monsoon: A Process-Oriented Assessment of CMIP5 Simulations along the AMMA Transect. *Journal of Climate*, **26(17)**, 6471–6505, doi:10.1175/jcli-d-12-00505.1.
Rohrer, M. et al., 2018: Representation of Extratropical Cyclones, Blocking Anticyclones, and Alpine Circulation Types in Multiple Reanalyses and Model Simulations. *Journal of Climate*, **31(8)**, 3009–3031, doi:10.1175/jcli-d-17-0350.1.
Rojas, R., L. Feyen, A. Dosio, and D. Bavera, 2011: Improving pan-European hydrological simulation of extreme events through statistical bias correction of RCM-driven climate simulations. *Hydrology and Earth System Sciences*, **15(8)**, 2599–2620, doi:10.5194/hess-15-2599-2011.
Ropelewski, C.F. and M.S. Halpert, 1987: Global and Regional Scale Precipitation Patterns Associated with the El Niño/Southern Oscillation. *Monthly Weather Review*, **115(8)**, 1606–1626, doi:10.1175/1520-0493(1987)115<1606:garspp>2.0.co;2.
Rosenzweig, C. and P. Neofotis, 2013: Detection and attribution of anthropogenic climate change impacts. *Wiley Interdisciplinary Reviews: Climate Change*, **4(2)**, 121–150, doi:10.1002/wcc.209.
Rössler, O. et al., 2019a: Challenges to link climate change data provision and user needs: Perspective from the COST-action VALUE. *International Journal of Climatology*, **39(9)**, 3704–3716, doi:10.1002/joc.5060.
Rössler, O. et al., 2019b: Evaluating the added value of the new Swiss climate scenarios for hydrology: An example from the Thur catchment. *Climate Services*, **13**, 1–13, doi:10.1016/j.cliser.2019.01.001.
Rostkier-Edelstein, D. et al., 2014: Towards a high-resolution climatography of seasonal precipitation over Israel. *International Journal of Climatology*, **34(6)**, 1964–1979, doi:10.1002/joc.3814.
Rotstayn, L.D., M.A. Collier, D.T. Shindell, and O. Boucher, 2015: Why Does Aerosol Forcing Control Historical Global-Mean Surface Temperature Change in CMIP5 Models? *Journal of Climate*, **28(17)**, 6608–6625, doi:10.1175/jcli-d-14-00712.1.
Rouault, M., B. Pohl, and P. Penven, 2010: Coastal oceanic climate change and variability from 1982 to 2009 around South Africa. *African Journal of Marine Science*, **32(2)**, 237–246, doi:10.2989/1814232x.2010.501563.
Rowell, D.P. and R.G. Jones, 2006: Causes and uncertainty of future summer drying over Europe. *Climate Dynamics*, **27(2–3)**, 281–299, doi:10.1007/s00382-006-0125-9.
Roxy, M.K. et al., 2015: Drying of Indian subcontinent by rapid Indian Ocean warming and a weakening land-sea thermal gradient. *Nature Communications*, **6(1)**, 7423, doi:10.1038/ncomms8423.

ACCEPTED VERSION SUBJECT TO FINAL EDITING

Ruckstuhl, C. et al., 2008: Aerosol and cloud effects on solar brightening and the recent rapid warming. *Geophysical Research Letters*, **35(12)**, L12708, doi:10.1029/2008gl034228.
Ruiz-Ramos, M. et al., 2016: Comparing correction methods of RCM outputs for improving crop impact projections in the Iberian Peninsula for 21st century. *Climatic Change*, **134(1–2)**, 283–297, doi:10.1007/s10584-015-1518-8.
Rummukainen, M., 2016: Added value in regional climate modeling. *Wiley Interdisciplinary Reviews: Climate Change*, **7(1)**, 145–159, doi:10.1002/wcc.378.
Ruprich-Robert, Y. et al., 2017: Assessing the Climate Impacts of the Observed Atlantic Multidecadal Variability Using the GFDL CM2.1 and NCAR CESM1 Global Coupled Models. *Journal of Climate*, **30(8)**, 2785–2810, doi:10.1175/jcli-d-16-0127.1.
Ruprich-Robert, Y. et al., 2018: Impacts of the Atlantic Multidecadal Variability on North American Summer Climate and Heat Waves. *Journal of Climate*, **31(9)**, 3679–3700, doi:10.1175/jcli-d-17-0270.1.
Russo, A., C.M. Gouveia, E. Dutra, P.M.M. Soares, and R.M. Trigo, 2019: The synergy between drought and extremely hot summers in the Mediterranean. *Environmental Research Letters*, **14(1)**, 014011, doi:10.1088/1748-9326/aaf09e.
Russo, S., J. Sillmann, and E.M. Fischer, 2015: Top ten European heatwaves since 1950 and their occurrence in the coming decades. *Environmental Research Letters*, **10(12)**, 124003, doi:10.1088/1748-9326/10/12/124003.
Ruti, P.M. et al., 2016: Med-CORDEX Initiative for Mediterranean Climate Studies. *Bulletin of the American Meteorological Society*, **97(7)**, 1187–1208, doi:10.1175/bams-d-14-00176.1.
Sabeerali, C.T. and R.S. Ajayamohan, 2018: On the shortening of Indian summer monsoon season in a warming scenario. *Climate Dynamics*, **50(5–6)**, 1609–1624, doi:10.1007/s00382-017-3709-7.
Sabin, T.P. et al., 2013: High resolution simulation of the South Asian monsoon using a variable resolution global climate model. *Climate Dynamics*, **41(1)**, 173–194, doi:10.1007/s00382-012-1658-8.
Sabin, T.P. et al., 2020: Climate Change Over the Himalayas. In: *Assessment of Climate Change over the Indian Region* [Krishnan, R., J. Sanjay, C. Gnanaseelan, M. Mujumdar, A. Kulkarni, and S. Chakraborty (eds.)]. Springer, Singapore, pp. 207–222, doi:10.1007/978-981-15-4327-2_11.
Sachindra, D.A., A.W.M. Ng, S. Muthukumaran, and B.J.C. Perera, 2016: Impact of climate change on urban heat island effect and extreme temperatures: a case-study. *Quarterly Journal of the Royal Meteorological Society*, **142(694)**, 172–186, doi:10.1002/qj.2642.
Saeed, F., S. Hagemann, S. Saeed, and D. Jacob, 2013: Influence of mid-latitude circulation on upper Indus basin precipitation: the explicit role of irrigation. *Climate Dynamics*, **40(1–2)**, 21–38, doi:10.1007/s00382-012-1480-3.
Saffioti, C., E.M. Fischer, S.C. Scherrer, and R. Knutti, 2016: Reconciling observed and modeled temperature and precipitation trends over Europe by adjusting for circulation variability. *Geophysical Research Letters*, **43(15)**, 8189–8198, doi:10.1002/2016gl069802.
Saggioro, E. and T.G. Shepherd, 2019: Quantifying the Timescale and Strength of Southern Hemisphere Intraseasonal Stratosphere-troposphere Coupling. *Geophysical Research Letters*, **46(22)**, 13479–13487, doi:10.1029/2019gl084763.
Sailor, D.J., 2011: A review of methods for estimating anthropogenic heat and moisture emissions in the urban environment. *International Journal of Climatology*, **31(2)**, 189–199, doi:10.1002/joc.2106.
Sakai, A. et al., 2015: Climate regime of Asian glaciers revealed by GAMDAM glacier inventory. *The Cryosphere*, **9(3)**, 865–880, doi:10.5194/tc-9-865-2015.
Salamanca, F., M. Georgescu, A. Mahalov, M. Moustaoui, and M. Wang, 2014: Anthropogenic heating of the urban environment due to air conditioning. *Journal of Geophysical Research: Atmospheres*, **119(10)**, 5949–5965, doi:10.1002/2013jd021225.
Salazar, E. et al., 2016: Observation-based blended projections from ensembles of regional climate models. *Climatic Change*, **138(1–2)**, 55–69, doi:10.1007/s10584-016-1722-1.
Salvi, K., S. Kannan, and S. Ghosh, 2013: High-resolution multisite daily rainfall projections in India with statistical downscaling for climate change impacts assessment. *Journal of Geophysical Research Atmospheres*, **118(9)**, 3557–3578, doi:10.1002/jgrd.502802013.
Salzmann, M., H. Weser, and R. Cherian, 2014: Robust response of Asian summer monsoon to anthropogenic aerosols in CMIP5 models. *Journal of Geophysical Research: Atmospheres*, **119(19)**, 11,321–11,337, doi:10.1002/2014jd021783.
Samanta, D. et al., 2018: Impact of a Narrow Coastal Bay of Bengal Sea Surface Temperature Front on an Indian Summer Monsoon Simulation. *Scientific Reports*, **8(1)**, 17694, doi:10.1038/s41598-018-35735-3.
Samset, B.H., M.T. Lund, M. Bollasina, G. Myhre, and L. Wilcox, 2019: Emerging Asian aerosol patterns. *Nature Geoscience*, **12(8)**, 582–584, doi:10.1038/s41561-019-0424-5.
Samset, B.H. et al., 2018: Climate Impacts From a Removal of Anthropogenic Aerosol Emissions. *Geophysical Research Letters*, **45(2)**, 1020–1029, doi:10.1002/2017gl076079.
Samson, G. et al., 2014: The NOW regional coupled model: Application to the tropical Indian Ocean climate and tropical cyclone activity. *Journal of Advances in Modeling Earth Systems*, **6(3)**, 700–722, doi:10.1002/2014ms000324.

ACCEPTED VERSION
SUBJECT TO FINAL EDITING

Samuelsson, P., E. Kourzeneva, and D. Mironov, 2010: The impact of lakes on the European climate as simulated by a regional climate model. *Boreal environment research*, **15**, 113–129.
Sanchez-Gomez, E. and S. Somot, 2018: Impact of the internal variability on the cyclone tracks simulated by a regional climate model over the Med-CORDEX domain. *Climate Dynamics*, **51(3)**, 1005–1021, doi:10.1007/s00382-016-3394-y.
Sandeep, S. and R.S. Ajayamohan, 2015: Poleward shift in Indian summer monsoon low level jetstream under global warming. *Climate Dynamics*, **45(1–2)**, 337–351, doi:10.1007/s00382-014-2261-y.
Sandeep, S., R.S. Ajayamohan, W.R. Boos, T.P. Sabin, and V. Praveen, 2018: Decline and poleward shift in Indian summer monsoon synoptic activity in a warming climate. *Proceedings of the National Academy of Sciences*, **115(11)**, 2681–2686, doi:10.1073/pnas.1709031115.
Sanderson, B.M., R. Knutti, and P. Caldwell, 2015: Addressing Interdependency in a Multimodel Ensemble by Interpolation of Model Properties. *Journal of Climate*, **28(13)**, 5150–5170, doi:10.1175/jcli-d-14-00361.1.
Sanderson, M., K. Arbuthnott, S. Kovats, S. Hajat, and P. Falloon, 2017: The use of climate information to estimate future mortality from high ambient temperature: A systematic literature review. *PLOS ONE*, **12(7)**, e0180369, doi:10.1371/journal.pone.0180369.
Sanjay, J., R. Krishnan, A.B. Shrestha, R. Rajbhandari, and G.-Y. Ren, 2017: Downscaled climate change projections for the Hindu Kush Himalayan region using CORDEX South Asia regional climate models. *Advances in Climate Change Research*, **8(3)**, 185–198, doi:10.1016/j.accre.2017.08.003.
San-Martín, D., R. Manzanas, S. Brands, S. Herrera, and J.M. Gutiérrez, 2017: Reassessing Model Uncertainty for Regional Projections of Precipitation with an Ensemble of Statistical Downscaling Methods. *Journal of Climate*, **30(1)**, 203–223, doi:10.1175/jcli-d-16-0366.1.
Sanogo, S. et al., 2015: Spatio-temporal characteristics of the recent rainfall recovery in West Africa. *International Journal of Climatology*, **35(15)**, 4589–4605, doi:10.1002/joc.4309.
Santanello, J.A. et al., 2018: Land–Atmosphere Interactions: The LoCo Perspective. *Bulletin of the American Meteorological Society*, **99(6)**, 1253–1272, doi:10.1175/bams-d-17-0001.1.
Santolaria-Otín, M., J. García-Serrano, M. Ménégoz, and J. Bech, 2021: On the observed connection between Arctic sea ice and Eurasian snow in relation to the winter North Atlantic Oscillation. *Environmental Research Letters*, **15(12)**, 124010, doi:10.1088/1748-9326/abad57.
Sapiains, R. et al., 2020: Exploring the contours of climate governance: An interdisciplinary systematic literature review from a southern perspective. *Environmental Policy and Governance*, eet.1912, doi:10.1002/eet.1912.
Sarewitz, D., 2004: How science makes environmental controversies worse. *Environmental Science and Policy*, **7(5)**, 385–403, doi:10.1016/j.envsci.2004.06.001.
Sarojini, B.B., P.A. Stott, and E. Black, 2016: Detection and attribution of human influence on regional precipitation. *Nature Climate Change*, **6(7)**, 669–675, doi:10.1038/nclimate2976.
Satoh, M. et al., 2019: Global Cloud-Resolving Models. *Current Climate Change Reports*, **5(3)**, 172–184, doi:10.1007/s40641-019-00131-0.
Sattari, M.T., A. Rezazadeh-Joudi, and A. Kusiak, 2017: Assessment of different methods for estimation of missing data in precipitation studies. *Hydrology Research*, **48(4)**, 1032–1044, doi:10.2166/nh.2016.364.
Saurral, R.I., I.A. Camilloni, and V.R. Barros, 2017: Low-frequency variability and trends in centennial precipitation stations in southern South America. *International Journal of Climatology*, **37(4)**, 1774–1793, doi:10.1002/joc.4810.
Saurral, R.I., F. Kucharski, and G.A. Raggio, 2019: Variations in ozone and greenhouse gases as drivers of Southern Hemisphere climate in a medium-complexity global climate model. *Climate Dynamics*, doi:10.1007/s00382-019-04950-7.
Savelli, E., M. Rusca, H. Cloke, and G. Di Baldassarre, 2021: Don't blame the rain: Social power and the 2015–2017 drought in Cape Town. *Journal of Hydrology*, **594**, 125953, doi:10.1016/j.jhydrol.2020.125953.
Sayles, J.S., 2018: Effects of social-ecological scale mismatches on estuary restoration at the project and landscape level in Puget Sound, USA. *Ecological Restoration*, **36(1)**, 62–75, doi:10.3368/er.36.1.62c.
Scaife, A.A. and D. Smith, 2018: A signal-to-noise paradox in climate science. *npj Climate and Atmospheric Science*, **1(1)**, 28, doi:10.1038/s41612-018-0038-4.
Scannell, C. et al., 2019: The Influence of Remote Aerosol Forcing from Industrialized Economies on the Future Evolution of East and West African Rainfall. *Journal of Climate*, **32(23)**, 8335–8354, doi:10.1175/jcli-d-18-0716.1.
Schaaf, B. and F. Feser, 2018: Is there added value of convection-permitting regional climate model simulations for storms over the German Bight and Northern Germany? *Meteorology Hydrology and Water Management*, **6(2)**, 21–37, doi:10.26491/mhwm/85507.
Schacter, D.L., D.R. Addis, and R.L. Buckner, 2007: Remembering the past to imagine the future: the prospective brain. *Nature Reviews Neuroscience*, **8(9)**, 657–661, doi:10.1038/nrn2213.
Schaller, N., J. Cermak, M. Wild, and R. Knutti, 2013: The sensitivity of the modeled energy budget and hydrological cycle to CO2 and solar forcing. *Earth System Dynamics*, **4(2)**, 253–266, doi:10.5194/esd-4-253-2013.
Schaller, N. et al., 2018: Influence of blocking on Northern European and Western Russian heatwaves in large climate

ACCEPTED VERSION SUBJECT TO FINAL EDITING

model ensembles. *Environmental Research Letters*, **13(5)**, 054015, doi:10.1088/1748-9326/aaba55.
Schär, C., C. Frei, D. Lüthi, and H.C. Davies, 1996: Surrogate climate-change scenarios for regional climate models. *Geophysical Research Letters*, **23(6)**, 669–672, doi:10.1029/96gl00265.
Scheff, J., R. Seager, H. Liu, and S. Coats, 2017: Are Glacials Dry? Consequences for Paleoclimatology and for Greenhouse Warming. *Journal of Climate*, **30(17)**, 6593–6609, doi:10.1175/jcli-d-16-0854.1.
Schemm, S., I. Rudeva, and I. Simmonds, 2015: Extratropical fronts in the lower troposphere-global perspectives obtained from two automated methods. *Quarterly Journal of the Royal Meteorological Society*, **141(690)**, 1686–1698, doi:10.1002/qj.2471.
Schemm, S., L. Nisi, A. Martinov, D. Leuenberger, and O. Martius, 2016: On the link between cold fronts and hail in Switzerland. *Atmospheric Science Letters*, **17(5)**, 315–325, doi:10.1002/asl.660.
Schiemann, R. et al., 2014: The sensitivity of the tropical circulation and Maritime Continent precipitation to climate model resolution. *Climate Dynamics*, **42(9)**, 2455–2468, doi:10.1007/s00382-013-1997-0.
Schiemann, R. et al., 2020: Northern Hemisphere blocking simulation in current climate models: evaluating progress from the Climate Model Intercomparison Project Phase 5 to 6 and sensitivity to resolution. *Weather and Climate Dynamics*, **1(1)**, 277–292, doi:10.5194/wcd-1-277-2020.
Schlünzen, K.H., P. Hoffmann, G. Rosenhagen, and W. Riecke, 2010: Long-term changes and regional differences in temperature and precipitation in the metropolitan area of Hamburg. *International Journal of Climatology*, **30(8)**, 1121–1136, doi:10.1002/joc.1968.
Schmetz, J. et al., 2002: An Introduction to Meteosat Second Generation (MSG). *Bulletin of the American Meteorological Society*, **83(7)**, 977–992, doi:10.1175/1520-0477(2002)083<0977:aitmsg>2.3.co;2.
Schneider, U. et al., 2017: Evaluating the Hydrological Cycle over Land Using the Newly-Corrected Precipitation Climatology from the Global Precipitation Climatology Centre (GPCC). *Atmosphere*, **8(12)**, 52, doi:10.3390/atmos8030052.
Schoetter, R. et al., 2020: A Statistical-Dynamical Downscaling for the Urban Heat Island and Building Energy Consumption – Analysis of Its Uncertainties. *Journal of Applied Meteorology and Climatology*, **59(5)**, 859–883, doi:10.1175/jamc-d-19-0182.1.
Schoof, J.T., 2013: Statistical Downscaling in Climatology. *Geography Compass*, **7(4)**, 249–265, doi:10.1111/gec3.12036.
Schubert, S., S. Grossman-Clarke, and A. Martilli, 2012: A Double-Canyon Radiation Scheme for Multi-Layer Urban Canopy Models. *Boundary-Layer Meteorology*, doi:10.1007/s10546-012-9728-3.
Schurer, A.P. et al., 2019: Disentangling the causes of the 1816 European year without a summer. *Environmental Research Letters*, **14(9)**, 94019, doi:10.1088/1748-9326/ab3a10.
Schwingshackl, C. et al., 2019: Regional climate model projections underestimate future warming due to missing plant physiological CO 2 response. *Environmental Research Letters*, **14(11)**, 114019, doi:10.1088/1748-9326/ab4949.
Scott, D. et al., 2018: The Story of Water in Windhoek: A Narrative Approach to Interpreting a Transdisciplinary Process. *Water*, **10(10)**, doi:10.3390/w10101366.
Screen, J.A., 2014: Arctic amplification decreases temperature variance in northern mid- to high-latitudes. *Nature Climate Change*, **4(7)**, 577–582, doi:10.1038/nclimate2268.
Screen, J.A. and I. Simmonds, 2013: Exploring links between Arctic amplification and mid-latitude weather. *Geophysical Research Letters*, **40(5)**, 959–964, doi:10.1002/grl.50174.
Screen, J.A. and R. Blackport, 2019: Is sea-ice-driven Eurasian cooling too weak in models? *Nature Climate Change*, **9(12)**, 934–936, doi:10.1038/s41558-019-0635-1.
Screen, J.A., C. Deser, I. Simmonds, and R. Tomas, 2014: Atmospheric impacts of Arctic sea-ice loss, 1979–2009: separating forced change from atmospheric internal variability. *Climate Dynamics*, **43(1–2)**, 333–344, doi:10.1007/s00382-013-1830-9.
Seager, R. and M. Hoerling, 2014: Atmosphere and Ocean Origins of North American Droughts. *Journal of Climate*, **27(12)**, 4581–4606, doi:10.1175/jcli-d-13-00329.1.
Seager, R. and M. Ting, 2017: Decadal Drought Variability Over North America: Mechanisms and Predictability. *Current Climate Change Reports*, **3(2)**, 141–149, doi:10.1007/s40641-017-0062-1.
Seager, R. et al., 2010: Tropical Oceanic Causes of Interannual to Multidecadal Precipitation Variability in Southeast South America over the Past Century. *Journal of Climate*, **23(20)**, 5517–5539, doi:10.1175/2010jcli3578.1.
Seager, R. et al., 2019: Climate Variability and Change of Mediterranean-Type Climates. *Journal of Climate*, **32(10)**, 2887–2915, doi:10.1175/jcli-d-18-0472.1.
Seaman, N.L., F.L. Ludwig, E.G. Donall, T.T. Warner, and C.M. Bhumralkar, 1989: Numerical Studies of Urban Planetary Boundary-Layer Structure under Realistic Synoptic Conditions. *Journal of Applied Meteorology*, **28(8)**, 760–781, doi:10.1175/1520-0450(1989)028<0760:nsoupb>2.0.co;2.
Sein, D. et al., 2015: Regionally coupled atmosphere-ocean-sea ice-marine biogeochemistry model ROM: 1. Description and validation. *Journal of Advances in Modeling Earth Systems*, **7(1)**, 268–304, doi:10.1002/2014ms000357.
Seneviratne, S.I. and M. Hauser, 2020: Regional Climate Sensitivity of Climate Extremes in CMIP6 Versus CMIP5

ACCEPTED VERSION
SUBJECT TO FINAL EDITING

Multimodel Ensembles. *Earth's Future*, **8(9)**, e2019EF001474, doi:10.1029/2019ef001474.
Seneviratne, S.I., D. Lüthi, M. Litschi, and C. Schär, 2006: Land-atmosphere coupling and climate change in Europe. *Nature*, **443(7108)**, 205–209, doi:10.1038/nature05095.
Seneviratne, S.I. et al., 2010: Investigating soil moisture–climate interactions in a changing climate: A review. *Earth-Science Reviews*, **99(3–4)**, 125–161, doi:10.1016/j.earscirev.2010.02.004.
Seneviratne, S.I. et al., 2013: Impact of soil moisture-climate feedbacks on CMIP5 projections: First results from the GLACE-CMIP5 experiment. *Geophysical Research Letters*, **40(19)**, 5212–5217, doi:10.1002/grl.50956.
Seneviratne, S.I. et al., 2018: Land radiative management as contributor to regional-scale climate adaptation and mitigation. *Nature Geoscience*, **11(2)**, 88–96, doi:10.1038/s41561-017-0057-5.
Sevault, F. et al., 2014: A fully coupled Mediterranean regional climate system model: design and evaluation of the ocean component for the 1980–2012 period. *Tellus A: Dynamic Meteorology and Oceanography*, **66(1)**, 23967, doi:10.3402/tellusa.v66.23967.
Shaevitz, D.A. et al., 2014: Characteristics of tropical cyclones in high-resolution models in the present climate. *Journal of Advances in Modeling Earth Systems*, **6(4)**, 1154–1172, doi:10.1002/2014ms000372.
Shalev, I., 2015: The climate change problem: promoting motivation for change when the map is not the territory. *Frontiers in Psychology*, **6**, doi:10.3389/fpsyg.2015.00131.
Sharma, A. et al., 2020: Urban-Scale Processes in High-Spatial-Resolution Earth System Models. *Bulletin of the American Meteorological Society*, **101(9)**, E1555–E1561, doi:10.1175/bams-d-20-0114.1.
Sharma, D. and R.L. Miller, 2017: Revisiting the observed correlation between weekly averaged Indian monsoon precipitation and Arabian Sea aerosol optical depth. *Geophysical Research Letters*, **44(19)**, 6–10,10,16, doi:10.1002/2017gl074373.
Sharma, E. et al., 2019: Introduction to the Hindu Kush Himalaya Assessment. In: *The Hindu Kush Himalaya Assessment: Mountains, Climate Change, Sustainability and People* [Wester, P., A. Mishra, A. Mukherji, and A.B. Shrestha (eds.)]. Springer, Cham, Switzerland, pp. 1–16, doi:10.1007/978-3-319-92288-1_1.
Shaw, T.A. et al., 2016: Storm track processes and the opposing influences of climate change. *Nature Geoscience*, **9**, 656, doi:10.1038/ngeo2783.
Shawki, D., A. Voulgarakis, A. Chakraborty, M. Kasoar, and J. Srinivasan, 2018: The South Asian Monsoon Response to Remote Aerosols: Global and Regional Mechanisms. *Journal of Geophysical Research: Atmospheres*, **123(20)**, 11,585–11,601, doi:10.1029/2018jd028623.
Shea, J.M. et al., 2015: A comparative high-altitude meteorological analysis from three catchments in the Nepalese Himalaya. *International Journal of Water Resources Development*, **31(2)**, 174–200, doi:10.1080/07900627.2015.1020417.
Shean, D.E. et al., 2020: A Systematic, Regional Assessment of High Mountain Asia Glacier Mass Balance. *Frontiers in Earth Science*, **7**, 363, doi:10.3389/feart.2019.00363.
Sheen, K.L. et al., 2017: Skilful prediction of Sahel summer rainfall on inter-annual and multi-year timescales. *Nature Communications*, **8**, 14966, doi:10.1038/ncomms14966.
Sheikh, M.M. et al., 2015: Trends in extreme daily rainfall and temperature indices over South Asia. *International Journal of Climatology*, **35**, 1625–1637, doi:10.1002/joc.4081.
Shen, Y., Z. Hong, Y. Pan, J. Yu, and L. Maguire, 2018: China's 1 km Merged Gauge, Radar and Satellite Experimental Precipitation Dataset. *Remote Sensing*, **10(2)**, doi:10.3390/rs10020264.
Shepard, D., 1968: A two-dimensional interpolation function for irregularly-spaced data. In: *Proceedings of the 1968 23rd ACM National Conference*. pp. 517–524, doi:10.1145/800186.810616.
Shepherd, T.G., 2014: Atmospheric circulation as a source of uncertainty in climate change projections. *Nature Geoscience*, **7**, 703.
Shepherd, T.G., 2016a: A Common Framework for Approaches to Extreme Event Attribution. *Current Climate Change Reports*, **2(1)**, 28–38, doi:10.1007/s40641-016-0033-y.
Shepherd, T.G., 2016b: Effects of a warming Arctic. *Science*, **353(6303)**, 989–990, doi:10.1126/science.aag2349.
Shepherd, T.G., 2019: Storyline approach to the construction of regional climate change information. *Proceedings of the Royal Society A: Mathematical, Physical and Engineering Sciences*, **475(2225)**, 20190013, doi:10.1098/rspa.2019.0013.
Shepherd, T.G. et al., 2018: Storylines: an alternative approach to representing uncertainty in physical aspects of climate change. *Climatic Change*, **151(3–4)**, 555–571, doi:10.1007/s10584-018-2317-9.
Sherwood, S.C. et al., 2015: Adjustments in the Forcing-Feedback Framework for Understanding Climate Change. *Bulletin of the American Meteorological Society*, **96(2)**, 217–228, doi:10.1175/bams-d-13-00167.1.
Shige, S., Y. Nakano, and M.K. Yamamoto, 2017: Role of Orography, Diurnal Cycle, and Intraseasonal Oscillation in Summer Monsoon Rainfall over the Western Ghats and Myanmar Coast. *Journal of Climate*, **30(23)**, 9365–9381, doi:10.1175/jcli-d-16-0858.1.
Shige, S., S. Kida, H. Ashiwake, T. Kubota, and K. Aonashi, 2013: Improvement of TMI Rain Retrievals in Mountainous Areas. *Journal of Applied Meteorology and Climatology*, **52(1)**, 242–254, doi:10.1175/jamc-d-12-074.1.
Shige, S. et al., 2009: Spectral retrieval of latent heating profiles from TRMM PR data. Part IV: comparisons of lookup

ACCEPTED VERSION SUBJECT TO FINAL EDITING

tables from two-and three-dimensional cloud-resolving model simulations. *Journal of Climate*, **22**, 5577–5594, doi:10.1175/2009jcli2919.1.
Shindell, D. and G. Faluvegi, 2009: Climate response to regional radiative forcing during the twentieth century. *Nature Geoscience*, **2(4)**, 294–300, doi:10.1038/ngeo473.
Shiogama, H., D.A. Stone, T. Nagashima, T. Nozawa, and S. Emori, 2013: On the linear additivity of climate forcing-response relationships at global and continental scales. *International Journal of Climatology*, **33(11)**, 2542–2550, doi:10.1002/joc.3607.
Shonk, J.K.P. et al., 2020: Uncertainty in aerosol radiative forcing impacts the simulated global monsoon in the 20th century. *Atmospheric Chemistry and Physics*, **20(23)**, 14903–14915, doi:10.5194/acp-20-14903-2020.
Shrestha, A.B., N.K. Agrawal, B. Alfthan, S.R. Bajracharya, J. Maréchal, and B. van Oort (eds.), 2015: *The Himalayan Climate and Water Atlas: Impact of climate change on water resources in five of Asia's major river basins*. ICIMOD,GRID-Arendal and CICERO, 1000 pp.
Shukla, S.P., M.J. Puma, and B.I. Cook, 2014: The response of the South Asian Summer Monsoon circulation to intensified irrigation in global climate model simulations. *Climate Dynamics*, **42(1–2)**, 21–36, doi:10.1007/s00382-013-1786-9.
Siew, P.Y.F., C. Li, S.P. Sobolowski, and M.P. King, 2020: Intermittency of Arctic–mid-latitude teleconnections: stratospheric pathway between autumn sea ice and the winter North Atlantic Oscillation. *Weather and Climate Dynamics*, **1(1)**, 261–275, doi:10.5194/wcd-1-261-2020.
Sigl, M. et al., 2015: Timing and climate forcing of volcanic eruptions for the past 2,500 years. *Nature*, **523(7562)**, 543–549, doi:10.1038/nature14565.
Sigmond, M. and J.C. Fyfe, 2016: Tropical Pacific impacts on cooling North American winters. *Nature Climate Change*, **6(10)**, 970–974, doi:10.1038/nclimate3069.
Sillmann, J., V. Kharin, X. Zhang, F.W. Zwiers, and D. Bronaugh, 2013: Climate extremes indices in the CMIP5 multimodel ensemble: Part 1. Model evaluation in the present climate. *Journal of Geophysical Research: Atmospheres*, **118(4)**, 1716–1733, doi:10.1002/jgrd.50203.
Sillmann, J. et al., 2020: Event-based storylines to address climate risk. *Earth's Future*, doi:10.1029/2020ef001783.
Silvy, Y., E. Guilyardi, J.-B. Sallée, and P.J. Durack, 2020: Human-induced changes to the global ocean water masses and their time of emergence. *Nature Climate Change*, **10(11)**, 1030–1036, doi:10.1038/s41558-020-0878-x.
Simpson, I.R. and L.M. Polvani, 2016: Revisiting the relationship between jet position, forced response, and annular mode variability in the southern midlatitudes. *Geophysical Research Letters*, **43(6)**, 2896–2903, doi:10.1002/2016gl067989.
Simpson, I.R., R. Seager, T.A. Shaw, and M. Ting, 2015: Mediterranean Summer Climate and the Importance of Middle East Topography. *Journal of Climate*, **28(5)**, 1977–1996, doi:10.1175/jcli-d-14-00298.1.
Simpson, I.R., R. Seager, M. Ting, and T.A. Shaw, 2016: Causes of change in Northern Hemisphere winter meridional winds and regional hydroclimate. *Nature Climate Change*, **6(1)**, 65–70, doi:10.1038/nclimate2783.
Simpson, I.R., P. Hitchcock, R. Seager, Y. Wu, and P. Callaghan, 2018: The Downward Influence of Uncertainty in the Northern Hemisphere Stratospheric Polar Vortex Response to Climate Change. *Journal of Climate*, **31(16)**, 6371–6391, doi:10.1175/jcli-d-18-0041.1.
Singh, H.K.A., G.J. Hakim, R. Tardif, J. Emile-Geay, and D.C. Noone, 2018: Insights into Atlantic multidecadal variability using the Last Millennium Reanalysis framework. *Climate of the Past*, **14(2)**, 157–174, doi:10.5194/cp-14-157-2018.
Singh, R. and K. AchutaRao, 2018: Quantifying uncertainty in twenty-first century climate change over India. *Climate Dynamics*, doi:10.1007/s00382-018-4361-6.
Singh, S., S. Ghosh, A.S. Sahana, H. Vittal, and S. Karmakar, 2017: Do dynamic regional models add value to the global model projections of Indian monsoon? *Climate Dynamics*, **48(3–4)**, 1375–1397, doi:10.1007/s00382-016-3147-y.
Sippel, S., F.E.L. Otto, M. Flach, and G.J. van Oldenborgh, 2016: The Role of Anthropogenic Warming in 2015 Central European Heat Waves. *Bulletin of the American Meteorological Society*, **97(12)**, S51–S56, doi:10.1175/bams-d-16-0150.1.
Sippel, S. et al., 2017: Refining multi-model projections of temperature extremes by evaluation against land–atmosphere coupling diagnostics. *Earth System Dynamics*, **8(2)**, 387–403, doi:10.5194/esd-8-387-2017.
Sippel, S. et al., 2019: Uncovering the Forced Climate Response from a Single Ensemble Member Using Statistical Learning. *Journal of Climate*, **32(17)**, 5677–5699, doi:10.1175/jcli-d-18-0882.1.
Sjolte, J. et al., 2018: Solar and volcanic forcing of North Atlantic climate inferred from a process-based reconstruction. *Climate of the Past*, **14(8)**, 1179–1194, doi:10.5194/cp-14-1179-2018.
Skamarock, W.C., 2004: Evaluating Mesoscale NWP Models Using Kinetic Energy Spectra. *Monthly Weather Review*, **132(12)**, 3019–3032, doi:10.1175/mwr2830.1.
Skofronick-Jackson, G. et al., 2017: The Global Precipitation Measurement (GPM) Mission for Science and Society. *Bulletin of the American Meteorological Society*, **98(8)**, 1679–1695, doi:10.1175/bams-d-15-00306.1.
Smith, A.B. and J.L. Matthews, 2015: Quantifying uncertainty and variable sensitivity within the US billion-dollar weather and climate disaster cost estimates. *Natural Hazards*, **77(3)**, 1829–1851, doi:10.1007/s11069-015-

ACCEPTED VERSION SUBJECT TO FINAL EDITING

1678-x.
Smith, D.M. et al., 2020: North Atlantic climate far more predictable than models imply. *Nature*, **583(7818)**, 796–800, doi:10.1038/s41586-020-2525-0.
Smith, K.L. and L.M. Polvani, 2017: Spatial patterns of recent Antarctic surface temperature trends and the importance of natural variability: lessons from multiple reconstructions and the CMIP5 models. *Climate Dynamics*, **48(7–8)**, 2653–2670, doi:10.1007/s00382-016-3230-4.
Smoliak, B., J.M. Wallace, P. Lin, and Q. Fu, 2015: Dynamical Adjustment of the Northern Hemisphere Surface Air Temperature Field: Methodology and Application to Observations. *Journal of Climate*, **28(4)**, 1613–1629, doi:10.1175/jcli-d-14-00111.1.
Sniderman, J.M.K. et al., 2019: Southern Hemisphere subtropical drying as a transient response to warming. *Nature Climate Change*, **9(3)**, 232–236, doi:10.1038/s41558-019-0397-9.
Soares, P.M.M. and R.M. Cardoso, 2018: A simple method to assess the added value using high-resolution climate distributions: application to the EURO-CORDEX daily precipitation. *International Journal of Climatology*, **38(3)**, 1484–1498, doi:10.1002/joc.5261.
Soares, P.M.M., R.M. Cardoso, L. Semedo, M.J. Chinita, and R. Ranjha, 2014: Climatology of the Iberia coastal low-level wind jet: weather research forecasting model high-resolution results. *Tellus A: Dynamic Meteorology and Oceanography*, **66(1)**, 22377, doi:10.3402/tellusa.v66.22377.
Soares, P.M.M. et al., 2019a: Assessing the climate change impact on the North African offshore surface wind and coastal low-level jet using coupled and uncoupled regional climate simulations. *Climate Dynamics*, **52(11)**, 7111–7132, doi:10.1007/s00382-018-4565-9.
Soares, P.M.M. et al., 2019b: Process-based evaluation of the VALUE perfect predictor experiment of statistical downscaling methods. *International Journal of Climatology*, **39(9)**, 3868–3893, doi:10.1002/joc.5911.
Sohn, B.J. et al., 2013: Characteristic Features of Warm-Type Rain Producing Heavy Rainfall over the Korean Peninsula Inferred from TRMM Measurements. *Monthly Weather Review*, **141(11)**, 3873–3888, doi:10.1175/mwr-d-13-00075.1.
Solman, S.A. and I. Orlanski, 2016: Climate Change over the Extratropical Southern Hemisphere: The Tale from an Ensemble of Reanalysis Datasets. *Journal of Climate*, **29(5)**, 1673–1687, doi:10.1175/jcli-d-15-0588.1.
Solmon, F., V.S. Nair, and M. Mallet, 2015: Increasing Arabian dust activity and the Indian summer monsoon. *Atmospheric Chemistry and Physics*, **15(14)**, 8051–8064, doi:10.5194/acp-15-8051-2015.
Somot, S., F. Sevault, M. Déqué, and M. Crépon, 2008: 21st century climate change scenario for the Mediterranean using a coupled atmosphere–ocean regional climate model. *Global and Planetary Change*, **63(2–3)**, 112–126, doi:10.1016/j.gloplacha.2007.10.003.
Somot, S. et al., 2018: Editorial for the Med-CORDEX special issue. *Climate Dynamics*, **51(3)**, 771–777, doi:10.1007/s00382-018-4325-x.
Song, F., T. Zhou, and Y. Qian, 2014: Responses of East Asian summer monsoon to natural and anthropogenic forcings in the 17 latest CMIP5 models. *Geophysical Research Letters*, **41(2)**, 596–603, doi:10.1002/2013gl058705.
Sontakke, N.A., N. Singh, and H.N. Singh, 2008: Instrumental period rainfall series of the Indian region (AD 1813-2005): revised reconstruction, update and analysis. *The Holocene*, **18(7)**, 1055–1066, doi:10.1177/0959683608095576.
Sooraj, K.P., P. Terray, and M. Mujumdar, 2015: Global warming and the weakening of the Asian summer monsoon circulation: assessments from the CMIP5 models. *Climate Dynamics*, **45(1–2)**, 233–252, doi:10.1007/s00382-014-2257-7.
Sørland, S.L. and A. Sorteberg, 2016: Low-pressure systems and extreme precipitation in central India: sensitivity to temperature changes. *Climate Dynamics*, **47(1–2)**, 465–480, doi:10.1007/s00382-015-2850-4.
Sørland, S.L., A. Sorteberg, C. Liu, and R. Rasmussen, 2016: Precipitation response of monsoon low-pressure systems to an idealized uniform temperature increase. *Journal of Geophysical Research: Atmospheres*, **121(11)**, 6258–6272, doi:10.1002/2015jd024658.
Sørland, S.L., C. Schär, D. Lüthi, and E. Kjellström, 2018: Bias patterns and climate change signals in GCM-RCM model chains. *Environmental Research Letters*, **13(7)**, 074017, doi:10.1088/1748-9326/aacc77.
Sorokina, S.A., C. Li, J.J. Wettstein, and N.G. Kvamstø, 2016: Observed Atmospheric Coupling between Barents Sea Ice and the Warm-Arctic Cold-Siberian Anomaly Pattern. *Journal of Climate*, **29(2)**, 495–511, doi:10.1175/jcli-d-15-0046.1.
Soto-Navarro, J. et al., 2020: Evolution of Mediterranean Sea water properties under climate change scenarios in the Med-CORDEX ensemble. *Climate Dynamics*, **54(3–4)**, 2135–2165, doi:10.1007/s00382-019-05105-4.
Sousa, P.M., R.C. Blamey, C.J.C. Reason, A.M. Ramos, and R.M. Trigo, 2018a: The 'Day Zero' Cape Town drought and the poleward migration of moisture corridors. *Environmental Research Letters*, **13(12)**, 124025, doi:10.1088/1748-9326/aaebc7.
Sousa, P.M., R.M. Trigo, D. Barriopedro, P.M.M. Soares, and J.A. Santos, 2018b: European temperature responses to blocking and ridge regional patterns. *Climate Dynamics*, **50(1–2)**, 457–477, doi:10.1007/s00382-017-3620-2.
Sousa, P.M. et al., 2017: Responses of European precipitation distributions and regimes to different blocking locations. *Climate Dynamics*, **48(3–4)**, 1141–1160, doi:10.1007/s00382-016-3132-5.

ACCEPTED VERSION SUBJECT TO FINAL EDITING

Spence, A., W. Poortinga, and N. Pidgeon, 2012: The Psychological Distance of Climate Change. *Risk Analysis*, **32(6)**, 957–972, doi:10.1111/j.1539-6924.2011.01695.x.
Spennemann, P.C. and A.C. Saulo, 2015: An estimation of the land-atmosphere coupling strength in South America using the Global Land Data Assimilation System. *International Journal of Climatology*, **35(14)**, 4151–4166, doi:10.1002/joc.4274.
Sperber, K.R. et al., 2013: The Asian summer monsoon: an intercomparison of CMIP5 vs. CMIP3 simulations of the late 20th century. *Climate Dynamics*, **41(9–10)**, 2711–2744, doi:10.1007/s00382-012-1607-6.
Spero, T.L., C.G. Nolte, J.H. Bowden, M.S. Mallard, and J.A. Herwehe, 2016: The Impact of Incongruous Lake Temperatures on Regional Climate Extremes Downscaled from the CMIP5 Archive Using the WRF Model. *Journal of Climate*, **29(2)**, 839–853, doi:10.1175/jcli-d-15-0233.1.
Spinoni, J., J. Vogt, G. Naumann, P. Barbosa, and A. Dosio, 2018: Will drought events become more frequent and severe in Europe? *International Journal of Climatology*, **38(4)**, 1718–1736, doi:10.1002/joc.5291.
Spinoni, J. et al., 2020: Future Global Meteorological Drought Hot Spots: A Study Based on CORDEX Data. *Journal of Climate*, **33(9)**, 3635–3661, doi:10.1175/jcli-d-19-0084.1.
Sprenger, M. et al., 2017: Global Climatologies of Eulerian and Lagrangian Flow Features based on ERA-Interim. *Bulletin of the American Meteorological Society*, **98(8)**, 1739–1748, doi:10.1175/bams-d-15-00299.1.
Stager, J.C. et al., 2012: Precipitation variability in the winter rainfall zone of South Africa during the last 1400 yr linked to the austral westerlies. *Climate of the Past*, **8(3)**, 877–887, doi:10.5194/cp-8-877-2012.
Staten, P.W., J. Lu, K.M. Grise, S.M. Davis, and T. Birner, 2018: Re-examining tropical expansion. *Nature Climate Change*, **8(9)**, 768–775, doi:10.1038/s41558-018-0246-2.
Stegehuis, A.I. et al., 2015: An observation-constrained multi-physics WRF ensemble for simulating European mega heat waves. *Geoscientific Model Development*, **8(7)**, 2285–2298, doi:10.5194/gmd-8-2285-2015.
Steiger, N.J., J.E. Smerdon, E.R. Cook, and B.I. Cook, 2018: A reconstruction of global hydroclimate and dynamical variables over the Common Era. *Scientific Data*, **5**, 180086, doi:10.1038/sdata.2018.86.
Stephens, G. et al., 2018: Cloudsat and calipso within the a-train: Ten years of actively observing the earth system. *Bulletin of the American Meteorological Society*, **99(3)**, 569–581, doi:10.1175/bams-d-16-0324.1.
Stevens, B. et al., 2017: MACv2-SP: a parameterization of anthropogenic aerosol optical properties and an associated Twomey effect for use in CMIP6. *Geoscientific Model Development*, **10(1)**, 433–452, doi:10.5194/gmd-10-433-2017.
Stevens, B. et al., 2019: DYAMOND: the DYnamics of the Atmospheric general circulation Modeled On Non-hydrostatic Domains. *Progress in Earth and Planetary Science*, **6(1)**, 61, doi:10.1186/s40645-019-0304-z.
Stevenson, S., B. Otto-Bliesner, J. Fasullo, and E. Brady, 2016: "El Niño Like" Hydroclimate Responses to Last Millennium Volcanic Eruptions. *Journal of Climate*, **29(8)**, 2907–2921, doi:10.1175/jcli-d-15-0239.1.
Stevenson, S., J.T. Fasullo, B.L. Otto-Bliesner, R.A. Tomas, and C. Gao, 2017: Role of eruption season in reconciling model and proxy responses to tropical volcanism. *Proceedings of the National Academy of Sciences*, **114(8)**, 1822 LP – 1826, doi:10.1073/pnas.1612505114.
Steynor, A. and L. Pasquini, 2019: Informing climate services in Africa through climate change risk perceptions. *Climate Services*, **15**, 100112, doi:10.1016/j.cliser.2019.100112.
Steynor, A., J. Padgham, C. Jack, B. Hewitson, and C. Lennard, 2016: Co-exploratory climate risk workshops: Experiences from urban Africa. *Climate Risk Management*, **13**, 95–102, doi:10.1016/j.crm.2016.03.001.
Stillinger, T., D.A. Roberts, N.M. Collar, and J. Dozier, 2019: Cloud Masking for Landsat 8 and MODIS Terra Over Snow-Covered Terrain: Error Analysis and Spectral Similarity Between Snow and Cloud. *Water Resources Research*, **55(7)**, 6169–6184, doi:10.1029/2019wr024932.
Stocker, T.F., Q. Dahe, G.-K. Plattner, and M. Tignor, 2015: Workshop Report of the Intergovernmental Panel on Climate Change Workshop on Regional Climate Projections and their Use in Impacts and Risk Analysis Studies. []. IPCC Working Group I Technical Support Unit, University of Bern, Bern, Switzerland, 171 pp.
Stoffel, M. et al., 2015: Estimates of volcanic-induced cooling in the Northern Hemisphere over the past 1,500 years. *Nature Geoscience*, **8(10)**, 784–788, doi:10.1038/ngeo2526.
Stoner, A.M.K., K. Hayhoe, X. Yang, and D.J. Wuebbles, 2013: An asynchronous regional regression model for statistical downscaling of daily climate variables. *International Journal of Climatology*, **33(11)**, 2473–2494, doi:10.1002/joc.3603.
Stott, P., P. Good, G. Jones, N. Gillett, and E. Hawkins, 2013: The upper end of climate model temperature projections is inconsistent with past warming. *Environmental Research Letters*, **8(1)**, 014024, doi:10.1088/1748-9326/8/1/014024.
Stott, P.A. and J.A. Kettleborough, 2002: Origins and estimates of uncertainty in predictions of twenty-first century temperature rise. *Nature*, **416(6882)**, 723–726, doi:10.1038/416723a.
Strandberg, G. and E. Kjellström, 2019: Climate Impacts from Afforestation and Deforestation in Europe. *Earth Interactions*, **23(1)**, 1–27, doi:10.1175/ei-d-17-0033.1.
Strasser, U. et al., 2019: Storylines of combined future land use and climate scenarios and their hydrological impacts in an Alpine catchment (Brixental/Austria). *Science of The Total Environment*, **657**, 746–763, doi:10.1016/j.scitotenv.2018.12.077.

ACCEPTED VERSION SUBJECT TO FINAL EDITING

Stratton, R.A. et al., 2018: A Pan-African Convection-Permitting Regional Climate Simulation with the Met Office Unified Model: CP4-Africa. *Journal of Climate*, **31(9)**, 3485–3508, doi:10.1175/jcli-d-17-0503.1.
Street, R.B., 2016: Towards a leading role on climate services in Europe: A research and innovation roadmap. *Climate Services*, **1**, 2–5, doi:10.1016/j.cliser.2015.12.001.
Strobach, E. and G. Bel, 2019: Regional decadal climate predictions using an ensemble of WRF parameterizations driven by the MIROC5 GCM. *Journal of Applied Meteorology and Climatology*, **58(3)**, 527–549, doi:10.1175/jamc-d-18-0051.1.
Strong, J.D.O., G.A. Vecchi, and P. Ginoux, 2015: The Response of the Tropical Atlantic and West African Climate to Saharan Dust in a Fully Coupled GCM. *Journal of Climate*, **28(18)**, 7071–7092, doi:10.1175/jcli-d-14-00797.1.
Su, C.-H. et al., 2019: BARRA v1.0: the Bureau of Meteorology Atmospheric high-resolution Regional Reanalysis for Australia. *Geoscientific Model Development*, **12(5)**, 2049–2068, doi:10.5194/gmd-12-2049-2019.
Sugimoto, S. et al., 2018: Impact of Spatial Resolution on Simulated Consecutive Dry Days and Near-Surface Temperature over the Central Mountains in Japan. *SOLA*, **14**, 46–51, doi:10.2151/sola.2018-008.
Sui, Y., X. Lang, and D. Jiang, 2014: Time of emergence of climate signals over China under the RCP4.5 scenario. *Climatic Change*, **125(2)**, 265–276, doi:10.1007/s10584-014-1151-y.
Sun, L., J. Perlwitz, and M. Hoerling, 2016: What caused the recent "Warm Arctic, Cold Continents" trend pattern in winter temperatures? *Geophysical Research Letters*, **43(10)**, 5345–5352, doi:10.1002/2016gl069024.
Sun, W. et al., 2019a: A "La Niña-like" state occurring in the second year after large tropical volcanic eruptions during the past 1500 years. *Climate Dynamics*, **52(12)**, 7495–7509, doi:10.1007/s00382-018-4163-x.
Sun, W. et al., 2019b: How Northern High-Latitude Volcanic Eruptions in Different Seasons Affect ENSO. *Journal of Climate*, **32(11)**, 3245–3262, doi:10.1175/jcli-d-18-0290.1.
Sun, Y., X. Zhang, G. Ren, F.W. Zwiers, and T. Hu, 2016: Contribution of urbanization to warming in China. *Nature Climate Change*, **6(7)**, 706–709, doi:10.1038/nclimate2956.
Sutton, R.T., 2018: ESD Ideas: a simple proposal to improve the contribution of IPCC WGI to the assessment and communication of climate change risks. *Earth System Dynamics*, **9(4)**, 1155–1158, doi:10.5194/esd-9-1155-2018.
Sutton, R.T., 2019: Climate Science Needs to Take Risk Assessment Much More Seriously. *Bulletin of the American Meteorological Society*, **100(9)**, 1637–1642, doi:10.1175/bams-d-18-0280.1.
Sutton, R.T. and B. Dong, 2012: Atlantic Ocean influence on a shift in European climate in the 1990s. *Nature Geoscience*, **5**, 788, doi:10.1038/ngeo1595.
Sutton, R.T., B. Dong, and J.M. Gregory, 2007: Land/sea warming ratio in response to climate change: IPCC AR4 model results and comparison with observations. *Geophysical Research Letters*, **34(2)**, L02701, doi:10.1029/2006gl028164.
Suzuki-Parker, A. et al., 2018: Contributions of GCM/RCM Uncertainty in Ensemble Dynamical Downscaling for Precipitation in East Asian Summer Monsoon Season. *SOLA*, **14**, 97–104, doi:10.2151/sola.2018-017.
Swain, D.L. et al., 2017: Remote Linkages to Anomalous Winter Atmospheric Ridging Over the Northeastern Pacific. *Journal of Geophysical Research: Atmospheres*, **122(22)**, 12,194–12,209, doi:10.1002/2017jd026575.
Swingedouw, D. et al., 2017: Impact of explosive volcanic eruptions on the main climate variability modes. *Global and Planetary Change*, **150**, 24–45, doi:10.1016/j.gloplacha.2017.01.006.
Switanek, M.B. et al., 2017: Scaled distribution mapping: a bias correction method that preserves raw climate model projected changes. *Hydrology and Earth System Sciences*, **21(6)**, 2649–2666, doi:10.5194/hess-21-2649-2017.
Sylla, M.B., F. Giorgi, E. Coppola, and L. Mariotti, 2013: Uncertainties in daily rainfall over Africa: assessment of gridded observation products and evaluation of a regional climate model simulation. *International Journal of Climatology*, **33(7)**, 1805–1817, doi:10.1002/joc.3551.
Sylla, M.B., A. Faye, F. Giorgi, A. Diedhiou, and H. Kunstmann, 2018: Projected Heat Stress Under 1.5°C and 2°C Global Warming Scenarios Creates Unprecedented Discomfort for Humans in West Africa. *Earth's Future*, **6(7)**, 1029–1044, doi:10.1029/2018ef000873.
Tabari, H. et al., 2016: Local impact analysis of climate change on precipitation extremes: are high-resolution climate models needed for realistic simulations? *Hydrology and Earth System Sciences*, **20(9)**, 3843–3857, doi:10.5194/hess-20-3843-2016.
Takahashi, H.G., S. Watanabe, M. Nakata, and T. Takemura, 2018: Response of the atmospheric hydrological cycle over the tropical Asian monsoon regions to anthropogenic aerosols and its seasonality. *Progress in Earth and Planetary Science*, **5(1)**, 44, doi:10.1186/s40645-018-0197-2.
Takane, Y., Y. Kikegawa, M. Hara, and C.S.B. Grimmond, 2019: Urban warming and future air-conditioning use in an Asian megacity: importance of positive feedback. *npj Climate and Atmospheric Science*, **2(1)**, 39, doi:10.1038/s41612-019-0096-2.
Takayabu, I. et al., 2015: Climate change effects on the worst-case storm surge: a case study of Typhoon Haiyan. *Environmental Research Letters*, **10(6)**, 064011, doi:10.1088/1748-9326/10/6/064011.
Takayabu, I. et al., 2016: Reconsidering the Quality and Utility of Downscaling. *Journal of the Meteorological Society of Japan. Ser. II*, **94A**, 31–45, doi:10.2151/jmsj.2015-042.

ACCEPTED VERSION
SUBJECT TO FINAL EDITING

Takayabu, Y.N. and W.-K. Tao, 2020: Latent heating retrievals from satellite observations. In: *Satellite Precipitation Measurement Vol. 1* [Levizzani, V., C. Kidd, D. Kirschbaum, C. Kummerow, K. Nakamura, and F.J. Turk (eds.)]. Springer, Cham, Switzerland, pp. 897–915, doi:10.1007/978-3-030-35798-6_22.

Takayabu, Y.N., S. Shige, W.K. Tao, and N. Hirota, 2010: Shallow and deep latent heating modes over tropical oceans observed with TRMM PR spectral latent heating data. *Journal of Climate*, **23**, 2030–2046, doi:10.1175/2009jcli3110.1.

Talchabhadel, R., R. Karki, B.R. Thapa, M. Maharjan, and B. Parajuli, 2018: Spatio-temporal variability of extreme precipitation in Nepal. *International Journal of Climatology*, **38(11)**, 4296–4313, doi:10.1002/joc.5669.

Tang, Z. et al., 2017: Spatiotemporal Variation of Snow Cover in Tianshan Mountains, Central Asia, Based on Cloud-Free MODIS Fractional Snow Cover Product, 2001–2015. *Remote Sensing*, **9(10)**, doi:10.3390/rs9101045.

Tao, W.-K. et al., 2016: TRMM Latent Heating Retrieval: Applications and Comparisons with Field Campaigns and Large-Scale Analyses. *Meteorological Monographs*, doi:10.1175/amsmonographs-d-15-0013.1.

Tapiador, F.J. et al., 2017: Global precipitation measurements for validating climate models. *Atmospheric Research*, **197**, 1–20, doi:10.1016/j.atmosres.2017.06.021.

Taylor, C.M., R.A.M. de Jeu, F. Guichard, P.P. Harris, and W.A. Dorigo, 2012: Afternoon rain more likely over drier soils. *Nature*, **489(7416)**, 423–426, doi:10.1038/nature11377.

Taylor, C.M. et al., 2013: Modeling soil moisture-precipitation feedback in the Sahel: Importance of spatial scale versus convective parameterization. *Geophysical Research Letters*, **40(23)**, 6213–6218, doi:10.1002/2013gl058511.

Taylor, C.M. et al., 2017: Frequency of extreme Sahelian storms tripled since 1982 in satellite observations. *Nature*, **544(7651)**, 475–478, doi:10.1038/nature22069.

Taylor, M.A. et al., 2018: Future Caribbean Climates in a World of Rising Temperatures: The 1.5 vs 2.0 Dilemma. *Journal of Climate*, **31(7)**, 2907–2926, doi:10.1175/jcli-d-17-0074.1.

Taylor, P.C., R.C. Boeke, Y. Li, and D.W.J. Thompson, 2019: Arctic cloud annual cycle biases in climate models. *Atmospheric Chemistry and Physics*, **19(13)**, 8759–8782, doi:10.5194/acp-19-8759-2019.

Tebaldi, C. and J.M. Arblaster, 2014: Pattern scaling: Its strengths and limitations, and an update on the latest model simulations. *Climatic Change*, **122(3)**, 459–471, doi:10.1007/s10584-013-1032-9.

Tebaldi, C. and R. Knutti, 2018: Evaluating the accuracy of climate change pattern emulation for low warming targets. *Environmental Research Letters*, **13(5)**, 055006, doi:10.1088/1748-9326/aabef2.

Tedeschi, R.G. and M. Collins, 2017: The influence of ENSO on South American precipitation: simulation and projection in CMIP5 models. *International Journal of Climatology*, **37(8)**, 3319–3339, doi:10.1002/joc.4919.

Tencer, B., M.L. Bettolli, and M. Rusticucci, 2016: Compound temperature and precipitation extreme events in southern South America: associated atmospheric circulation, and simulations by a multi-RCM ensemble. *Climate Research*, **68(2–3)**, 183–199, doi:10.3354/cr01396.

Termonia, P. et al., 2018: The ALADIN System and its canonical model configurations AROME CY41T1 and ALARO CY40T1. *Geoscientific Model Development*, **11(1)**, 257–281, doi:10.5194/gmd-11-257-2018.

Thiéblemont, R., K. Matthes, N.-E. Omrani, K. Kodera, and F. Hansen, 2015: Solar forcing synchronizes decadal North Atlantic climate variability. *Nature Communications*, **6(1)**, 8268, doi:10.1038/ncomms9268.

Thiery, W. et al., 2015: The Impact of the African Great Lakes on the Regional Climate. *Journal of Climate*, **28(10)**, 4061–4085, doi:10.1175/jcli-d-14-00565.1.

Thiery, W. et al., 2017: Present-day irrigation mitigates heat extremes. *Journal of Geophysical Research: Atmospheres*, **122(3)**, 1403–1422, doi:10.1002/2016jd025740.

Thober, S., J. Mai, M. Zink, and L. Samaniego, 2014: Stochastic temporal disaggregation of monthly precipitation for regional gridded data sets. *Water Resources Research*, **50(11)**, 8714–8735, doi:10.1002/2014wr015930.

Thompson, D.W.J., E.A. Barnes, C. Deser, W.E. Foust, and A.S. Phillips, 2015: Quantifying the Role of Internal Climate Variability in Future Climate Trends. *Journal of Climate*, **28(16)**, 6443–6456, doi:10.1175/jcli-d-14-00830.1.

Thorne, P.W. et al., 2011: Guiding the Creation of A Comprehensive Surface Temperature Resource for Twenty-First-Century Climate Science. *Bulletin of the American Meteorological Society*, **92(11)**, ES40–ES47, doi:10.1175/2011bams3124.1.

Thorne, P.W. et al., 2017: Toward an Integrated Set of Surface Meteorological Observations for Climate Science and Applications. *Bulletin of the American Meteorological Society*, **98(12)**, 2689–2702, doi:10.1175/bams-d-16-0165.1.

Thorne, P.W. et al., 2018: Towards a global land surface climate fiducial reference measurements network. *International Journal of Climatology*, **38(6)**, 2760–2774, doi:10.1002/joc.5458.

Thornhill, G.D., C.L. Ryder, E.J. Highwood, L.C. Shaffrey, and B.T. Johnson, 2018: The effect of South American biomass burning aerosol emissions on the regional climate. *Atmospheric Chemistry and Physics*, **18(8)**, 5321–5342, doi:10.5194/acp-18-5321-2018.

Tian, F., B. Dong, J. Robson, and R. Sutton, 2018: Forced decadal changes in the East Asian summer monsoon: the roles of greenhouse gases and anthropogenic aerosols. *Climate Dynamics*, **51(9–10)**, 3699–3715, doi:10.1007/s00382-018-4105-7.

Ting, M., Y. Kushnir, R. Seager, and C. Li, 2009: Forced and Internal Twentieth-Century SST Trends in the North

ACCEPTED VERSION SUBJECT TO FINAL EDITING

Atlantic. *Journal of Climate*, **22(6)**, 1469–1481, doi:10.1175/2008jcli2561.1.
Toohey, M., K. Krüger, M. Bittner, C. Timmreck, and H. Schmidt, 2014: The impact of volcanic aerosol on the Northern Hemisphere stratospheric polar vortex: mechanisms and sensitivity to forcing structure. *Atmospheric Chemistry and Physics*, **14(23)**, 13063–13079, doi:10.5194/acp-14-13063-2014.
Torma, C., F. Giorgi, and E. Coppola, 2015: Added value of regional climate modeling over areas characterized by complex terrain-Precipitation over the Alps. *Journal of Geophysical Research: Atmospheres*, **120(9)**, 3957–3972, doi:10.1002/2014jd022781.
Torralba, V., F.J. Doblas-Reyes, and N. Gonzalez-Reviriego, 2017: Uncertainty in recent near-surface wind speed trends: A global reanalysis intercomparison. *Environmental Research Letters*, **12**, 114019, doi:10.1088/1748-9326/aa8a58.
Trapp, R.J., E.D. Robinson, M.E. Baldwin, N.S. Diffenbaugh, and B.R.J. Schwedler, 2011: Regional climate of hazardous convective weather through high-resolution dynamical downscaling. *Climate Dynamics*, **37(3–4)**, 677–688, doi:10.1007/s00382-010-0826-y.
Trenberth, K.E., J.T. Fasullo, and T.G. Shepherd, 2015: Attribution of climate extreme events. *Nature Climate Change*, **5(8)**, 725–730, doi:10.1038/nclimate2657.
Trewin, B., 2010: Exposure, instrumentation, and observing practice effects on land temperature measurements. *Wiley Interdisciplinary Reviews: Climate Change*, **1(4)**, 490–506, doi:10.1002/wcc.46.
Trewin, B., 2013: A daily homogenized temperature data set for Australia. *International Journal of Climatology*, **33(6)**, 1510–1529, doi:10.1002/joc.3530.
Trusilova, K. et al., 2016: The urban land use in the COSMO-CLM model: a comparison of three parameterizations for Berlin. *Meteorologische Zeitschrift*, **25(2)**, 231–244, doi:10.1127/metz/2015/0587.
Tsanis, I. and E. Tapoglou, 2019: Winter North Atlantic Oscillation impact on European precipitation and drought under climate change. *Theoretical and Applied Climatology*, **135(1)**, 323–330, doi:10.1007/s00704-018-2379-7.
Tschakert, P., N. Tuana, H. Westskog, B. Koelle, and A. Afrika, 2016: TCHANGE: The role of values and visioning in transformation science. *Current Opinion in Environmental Sustainability*, **20**, 21–25, doi:10.1016/j.cosust.2016.04.003.
Tschakert, P. et al., 2017: Climate change and loss, as if people mattered: values, places, and experiences. *Wiley Interdisciplinary Reviews: Climate Change*, **8(5)**, 1–19, doi:10.1002/wcc.476.
Tuinenburg, O.A., R.W.A. Hutjes, T. Stacke, A. Wiltshire, and P. Lucas-Picher, 2014: Effects of Irrigation in India on the Atmospheric Water Budget. *Journal of Hydrometeorology*, **15(3)**, 1028–1050, doi:10.1175/jhm-d-13-078.1.
Tuomenvirta, H., 2001: Homogeneity adjustments of temperature and precipitation series – Finnish and Nordic data. *International Journal of Climatology*, **21(4)**, 495–506, doi:10.1002/joc.616.
Turki, I. et al., 2016: Hydrological variability of the Soummam watershed (Northeastern Algeria) and the possible links to climate fluctuations. *Arabian Journal of Geosciences*, **9(6)**, 477, doi:10.1007/s12517-016-2448-0.
Turner, A.G. and H. Annamalai, 2012: Climate change and the South Asian summer monsoon. *Nature Climate Change*, **2(8)**, 587–595, doi:10.1038/nclimate1495.
Turnhout, E., T. Metze, C. Wyborn, N. Klenk, and E. Louder, 2020: The politics of co-production: participation, power, and transformation. *Current Opinion in Environmental Sustainability*, **42**, 15–21, doi:10.1016/j.cosust.2019.11.009.
Turnock, S.T. et al., 2016: The impact of European legislative and technology measures to reduce air pollutants on air quality, human health and climate. *Environmental Research Letters*, **11(2)**, 24010, doi:10.1088/1748-9326/11/2/024010.
Turuncoglu, U.U., G. Giuliani, N. Elguindi, and F. Giorgi, 2013: Modelling the Caspian Sea and its catchment area using a coupled regional atmosphere-ocean model (RegCM4-ROMS): model design and preliminary results. *Geoscientific Model Development*, **6(2)**, 283–299, doi:10.5194/gmd-6-283-2013.
Tuttle, S. and G. Salvucci, 2016: Empirical evidence of contrasting soil moisture-precipitation feedbacks across the United States. *Science*, **352(6287)**, 825–828, doi:10.1126/science.aaa7185.
Udall, B. and J. Overpeck, 2017: The twenty-first century Colorado River hot drought and implications for the future. *Water Resources Research*, **53(3)**, 2404–2418, doi:10.1002/2016wr019638.
Ueda, H., A. Iwai, K. Kuwako, and M.E. Hori, 2006: Impact of anthropogenic forcing on the Asian summer monsoon as simulated by eight GCMs. *Geophysical Research Letters*, **33**, L06703, doi:10.1029/2005gl025336.
Uijlenhoet, R., A. Overeem, and H. Leijnse, 2018: Opportunistic remote sensing of rainfall using microwave links from cellular communication networks. *WIREs Water*, **5(4)**, e1289, doi:10.1002/wat2.1289.
Ukkola, A.M., A.J. Pitman, M.G. Donat, M.G. De Kauwe, and O. Angélil, 2018: Evaluating the Contribution of Land-Atmosphere Coupling to Heat Extremes in CMIP5 Models. *Geophysical Research Letters*, **45(17)**, 9003–9012, doi:10.1029/2018gl079102.
Undorf, S. et al., 2018: Detectable Impact of Local and Remote Anthropogenic Aerosols on the 20th Century Changes of West African and South Asian Monsoon Precipitation. *Journal of Geophysical Research: Atmospheres*, **123(10)**, 4871–4889, doi:10.1029/2017jd027711.

ACCEPTED VERSION
SUBJECT TO FINAL EDITING

Uppala, S.M. et al., 2006: The ERA-40 re-analysis. *Quarterly Journal of the Royal Meteorological Society*, **131(612)**, 2961–3012, doi:10.1256/qj.04.176.
Vaittinada Ayar, P. et al., 2016: Intercomparison of statistical and dynamical downscaling models under the EURO- and MED-CORDEX initiative framework: present climate evaluations. *Climate Dynamics*, **46(3–4)**, 1301–1329, doi:10.1007/s00382-015-2647-5.
Van den Besselaar, E.J.M. et al., 2015: International Climate Assessment & Dataset: Climate Services across Borders. *Bulletin of the American Meteorological Society*, **96(1)**, 16–21, doi:10.1175/bams-d-13-00249.1.
Van den Besselaar, E.J.M.M., G. van der Schrier, R.C. Cornes, A.S. Iqbal, and A.M.G. Klein Tank, 2017: SA-OBS: A Daily Gridded Surface Temperature and Precipitation Dataset for Southeast Asia. *Journal of Climate*, **30(14)**, 5151–5165, doi:10.1175/jcli-d-16-0575.1.
van den Hurk, B. et al., 2014: Drivers of mean climate change around the Netherlands derived from CMIP5. *Climate Dynamics*, **42(5–6)**, 1683–1697, doi:10.1007/s00382-013-1707-y.
van den Hurk, B. et al., 2016: LS3MIP (v1.0) contribution to CMIP6: the Land Surface, Snow and Soil moisture Model Intercomparison Project – aims, setup and expected outcome. *Geoscientific Model Development*, **9(8)**, 2809–2832, doi:10.5194/gmd-9-2809-2016.
van der Schrier, G., E.J.M. van den Besselaar, A.M.G. Klein Tank, and G. Verver, 2013: Monitoring European average temperature based on the E-OBS gridded data set. *Journal of Geophysical Research: Atmospheres*, **118(11)**, 5120–5135, doi:10.1002/jgrd.50444.
van Haren, R., R.J. Haarsma, H. de Vries, G.J. van Oldenborgh, and W. Hazeleger, 2015: Resolution dependence of circulation forced future central European summer drying. *Environmental Research Letters*, **10(5)**, 55002, doi:10.1088/1748-9326/10/5/055002.
van Oldenborgh, G.J. et al., 2009: Western Europe is warming much faster than expected. *Climate of the Past*, **5(1)**, 1–12, doi:10.5194/cp-5-1-2009.
van Oldenborgh, G.J. et al., 2019: Cold waves are getting milder in the northern midlatitudes. *Environmental Research Letters*, **14(11)**, 114004, doi:10.1088/1748-9326/ab4867.
Van Pham, T., J. Brauch, C. Dieterich, B. Frueh, and B. Ahrens, 2014: New coupled atmosphere-ocean-ice system COSMO-CLM/NEMO: assessing air temperature sensitivity over the North and Baltic Seas. *Oceanologia*, **56(2)**, 167–189, doi:10.5697/oc.56-2.167.
Vanden Broucke, S., H. Wouters, M. Demuzere, and N.P.M. van Lipzig, 2018: The influence of convection-permitting regional climate modeling on future projections of extreme precipitation: dependency on topography and timescale. *Climate Dynamics*, **52**, 1–22, doi:10.1007/s00382-018-4454-2.
Vannitsem, S., 2011: Bias correction and post-processing under climate change. *Nonlinear Processes in Geophysics*, **18(6)**, 911–924, doi:10.5194/npg-18-911-2011.
Varela, R., L. Rodríguez-Díaz, and M. DeCastro, 2020: Persistent heat waves projected for Middle East and North Africa by the end of the 21st century. *PLOS ONE*, **15(11)**, e0242477, doi:10.1371/journal.pone.0242477.
Varikoden, H. et al., 2018: Assessment of regional downscaling simulations for long term mean, excess and deficit Indian Summer Monsoons. *Global and Planetary Change*, **162**, 28–38, doi:10.1016/j.gloplacha.2017.12.002.
Vaughan, C., S. Dessai, and C. Hewitt, 2018: Surveying Climate Services: What Can We Learn from a Bird's-Eye View? *Weather, Climate, and Society*, **10(2)**, 373–395, doi:10.1175/wcas-d-17-0030.1.
Vautard, R. et al., 2014: The European climate under a 2°C global warming. *Environmental Research Letters*, **9(3)**, 034006, doi:10.1088/1748-9326/9/3/034006.
Vautard, R. et al., 2020: Evaluation of the large EURO-CORDEX regional climate model ensemble. *Journal of Geophysical Research: Atmospheres*, doi:10.1029/2019jd032344.
Vavrus, S.J. et al., 2017: Changes in North American Atmospheric Circulation and Extreme Weather: Influence of Arctic Amplification and Northern Hemisphere Snow Cover. *Journal of Climate*, **30(11)**, 4317–4333, doi:10.1175/jcli-d-16-0762.1.
Vellinga, M. et al., 2016: Sahel decadal rainfall variability and the role of model horizontal resolution. *Geophysical Research Letters*, **43(1)**, 326–333, doi:10.1002/2015gl066690.
Venema, V.K.C. et al., 2012: Benchmarking homogenization algorithms for monthly data. *Climate of the Past*, **8(1)**, 89–115, doi:10.5194/cp-8-89-2012.
Venter, Z.S., O. Brousse, I. Esau, and F. Meier, 2020: Hyperlocal mapping of urban air temperature using remote sensing and crowdsourced weather data. *Remote Sensing of Environment*, **242**, 111791, doi:10.1016/j.rse.2020.111791.
Vera, C.S. and L. Díaz, 2015: Anthropogenic influence on summer precipitation trends over South America in CMIP5 models. *International Journal of Climatology*, **35(10)**, 3172–3177, doi:10.1002/joc.4153.
Verfaillie, D., M. Déqué, S. Morin, and M. Lafaysse, 2017: The method ADAMONT v1.0 for statistical adjustment of climate projections applicable to energy balance land surface models. *Geoscientific Model Development*, **10(11)**, 4257–4283, doi:10.5194/gmd-10-4257-2017.
Vergara-Temprado, J., N. Ban, D. Panosetti, L. Schlemmer, and C. Schär, 2019: Climate models permit convection at much coarser resolutions than previously considered.. *Journal of Climate*, JCLI–D–19–0286.1, doi:10.1175/jcli-d-19-0286.1.

ACCEPTED VERSION SUBJECT TO FINAL EDITING

Verrax, F., 2017: Engineering ethics and post-normal science: A French perspective. *Futures*, **91**, 76–79, doi:10.1016/j.futures.2017.01.009.
Vezér, M., A. Bakker, K. Keller, and N. Tuana, 2018: Epistemic and ethical trade-offs in decision analytical modelling: A case study of flood risk management in New Orleans. *Climatic Change*, **147(1–2)**, 1–10, doi:10.1007/s10584-017-2123-9.
Vidal, J.-P., E. Martin, L. Franchistéguy, M. Baillon, and J.-M. Soubeyroux, 2010: A 50-year high-resolution atmospheric reanalysis over France with the Safran system. *International Journal of Climatology*, **30(11)**, 1627–1644, doi:10.1002/joc.2003.
Vidal, J.-P., B. Hingray, C. Magand, E. Sauquet, and A. Ducharne, 2016: Hierarchy of climate and hydrological uncertainties in transient low-flow projections. *Hydrology and Earth System Sciences*, **20(9)**, 3651–3672, doi:10.5194/hess-20-3651-2016.
Vigaud, N., M. Vrac, and Y. Caballero, 2013: Probabilistic downscaling of GCM scenarios over southern India. *International Journal of Climatology*, **33(5)**, 1248–1263, doi:10.1002/joc.3509.
Villamayor, J. and E. Mohino, 2015: Robust Sahel drought due to the Interdecadal Pacific Oscillation in CMIP5 simulations. *Geophysical Research Letters*, doi:10.1002/2014gl062473.
Vincent, K., M. Daly, C. Scannell, and B. Leathes, 2018: What can climate services learn from theory and practice of co-production? *Climate Services*, **12**, 48–58, doi:10.1016/j.cliser.2018.11.001.
Vincent, K. et al., 2021: Co-production: Learning from Contexts. In: *Climate Risk in Africa: Adaptation and Resilience* [Conway, D. and K. Vincent (eds.)]. Palgrave Macmillan, Cham, Switzerland, pp. 37–56, doi:10.1007/978-3-030-61160-6_3.
Visser, W.P., 2018: A perfect storm: The ramifications of Cape Town's drought crisis. *The Journal for Transdisciplinary Research in Southern Africa*, **14(1)**, 1–10, doi:10.4102/td.v14i1.567.
Vitart, F. et al., 2017: The Subseasonal to Seasonal (S2S) Prediction Project Database. *Bulletin of the American Meteorological Society*, **98(1)**, 163–173, doi:10.1175/bams-d-16-0017.1.
Vizy, E.K. and K.H. Cook, 2017: Seasonality of the Observed Amplified Sahara Warming Trend and Implications for Sahel Rainfall. *Journal of Climate*, **30(9)**, 3073–3094, doi:10.1175/jcli-d-16-0687.1.
Vogel, M.M. et al., 2017: Regional amplification of projected changes in extreme temperatures strongly controlled by soil moisture-temperature feedbacks. *Geophysical Research Letters*, **44(3)**, 1511–1519, doi:10.1002/2016gl071235.
Volosciuk, C., D. Maraun, M. Vrac, and M. Widmann, 2017: A combined statistical bias correction and stochastic downscaling method for precipitation. *Hydrology and Earth System Sciences*, **21(3)**, 1693–1719, doi:10.5194/hess-21-1693-2017.
Von Clarmann, T., 2014: Smoothing error pitfalls. *Atmospheric Measurement Techniques*, **7(9)**, 3023–3034, doi:10.5194/amt-7-3023-2014.
von Storch, H., H. Langenberg, and F. Feser, 2000: A Spectral Nudging Technique for Dynamical Downscaling Purposes. *Monthly Weather Review*, **128(10)**, 3664–3673, doi:10.1175/1520-0493(2000)128<3664:asntfd>2.0.co;2.
von Trentini, F., M. Leduc, and R. Ludwig, 2019: Assessing natural variability in RCM signals: comparison of a multi model EURO-CORDEX ensemble with a 50-member single model large ensemble. *Climate Dynamics*, **53(3–4)**, 1963–1979, doi:10.1007/s00382-019-04755-8.
Vrac, M., 2018: Multivariate bias adjustment of high-dimensional climate simulations: the Rank Resampling for Distributions and Dependences (R^2D^2) bias correction. *Hydrology and Earth System Sciences*, **22(6)**, 3175–3196, doi:10.5194/hess-22-3175-2018.
Vrac, M. and P. Friederichs, 2015: Multivariate-Intervariable, Spatial, and Temporal-Bias Correction. *Journal of Climate*, **28(1)**, 218–237, doi:10.1175/jcli-d-14-00059.1.
Vries, H., S. Scher, R. Haarsma, S. Drijfhout, and A. Delden, 2019: How Gulf-Stream SST-fronts influence Atlantic winter storms. *Climate Dynamics*, **52(9–10)**, 5899–5909, doi:10.1007/s00382-018-4486-7.
Waha, K. et al., 2017: Climate change impacts in the Middle East and Northern Africa (MENA) region and their implications for vulnerable population groups. *Regional Environmental Change*, doi:10.1007/s10113-017-1144-2.
Wahl, S. et al., 2017: A novel convective-scale regional reanalysis COSMO-REA2: Improving the representation of precipitation. *Meteorologische Zeitschrift*, **26(4)**, 345–361, doi:10.1127/metz/2017/0824.
Wahl, T., S. Jain, J. Bender, S.D. Meyers, and M.E. Luther, 2015: Increasing risk of compound flooding from storm surge and rainfall for major US cities. *Nature Climate Change*, **5(12)**, 1093–1097, doi:10.1038/nclimate2736.
Waldron, K.M., J. Paegle, and J.D. Horel, 1996: Sensitivity of a Spectrally Filtered and Nudged Limited-Area Model to Outer Model Options. *Monthly Weather Review*, **124(3)**, 529–547, doi:10.1175/1520-0493(1996)124<0529:soasfa>2.0.co;2.
Walker, W., M. Haasnoot, and J. Kwakkel, 2013: Adapt or Perish: A Review of Planning Approaches for Adaptation under Deep Uncertainty. *Sustainability*, **5(3)**, 955–979, doi:10.3390/su5030955.
Walsh, J.E., 2014: Intensified warming of the Arctic: Causes and impacts on middle latitudes. *Global and Planetary Change*, **117**, 52–63, doi:10.1016/j.gloplacha.2014.03.003.

ACCEPTED VERSION SUBJECT TO FINAL EDITING

Walton, D.B., F. Sun, A. Hall, and S. Capps, 2015: A Hybrid Dynamical–Statistical Downscaling Technique. Part I: Development and Validation of the Technique. *Journal of Climate*, **28(12)**, 4597–4617, doi:10.1175/jcli-d-14-00196.1.

Walton, D.B., A. Hall, N. Berg, M. Schwartz, and F. Sun, 2017: Incorporating Snow Albedo Feedback into Downscaled Temperature and Snow Cover Projections for California's Sierra Nevada. *Journal of Climate*, **30(4)**, 1417–1438, doi:10.1175/jcli-d-16-0168.1.

Wan, H., X. Zhang, and F. Zwiers, 2019: Human influence on Canadian temperatures. *Climate Dynamics*, **52(1–2)**, 479–494, doi:10.1007/s00382-018-4145-z.

Wan, H., X. Zhang, F. Zwiers, and S.-K. Min, 2015: Attributing northern high-latitude precipitation change over the period 1966–2005 to human influence. *Climate Dynamics*, **45(7–8)**, 1713–1726, doi:10.1007/s00382-014-2423-y.

Wang, B. et al., 2020: Monsoons Climate Change Assessment. *Bulletin of the American Meteorological Society*, **preprint(2020)**, doi:10.1175/bams-d-19-0335.1.

Wang, J., Z. Yan, X.W. Quan, and J. Feng, 2017: Urban warming in the 2013 summer heat wave in eastern China. *Climate Dynamics*, **48(9–10)**, 3015–3033, doi:10.1007/s00382-016-3248-7.

Wang, K., C. Deser, L. Sun, and R.A. Tomas, 2018: Fast Response of the Tropics to an Abrupt Loss of Arctic Sea Ice via Ocean Dynamics. *Geophysical Research Letters*, **45(9)**, 4264–4272, doi:10.1029/2018gl077325.

Wang, Q., Z. Wang, and H. Zhang, 2017: Impact of anthropogenic aerosols from global, East Asian, and non-East Asian sources on East Asian summer monsoon system. *Atmospheric Research*, **183**, 224–236, doi:10.1016/j.atmosres.2016.08.023.

Wang, W., A.T. Evan, C. Flamant, and C. Lavaysse, 2015: On the decadal scale correlation between African dust and Sahel rainfall: The role of Saharan heat low–forced winds. *Science Advances*, **1(9)**, e1500646, doi:10.1126/sciadv.1500646.

Wang, Y., Y. Sun, T. Hu, D. Qin, and L. Song, 2018: Attribution of temperature changes in Western China. *International Journal of Climatology*, **38(2)**, 742–750, doi:10.1002/joc.5206.

Wang, Z., Y. Li, B. Liu, and J. Liu, 2015: Global climate internal variability in a 2000-year control simulation with Community Earth System Model (CESM). *Chinese Geographical Science*, **25**, doi:10.1007/s11769-015-0754-1.

Wang, Z. et al., 2021: Incorrect Asian aerosols affecting the attribution and projection of regional climate change in CMIP6 models. *npj Climate and Atmospheric Science*, **4(1)**, 2, doi:10.1038/s41612-020-00159-2.

Ward, K., S. Lauf, B. Kleinschmit, and W. Endlicher, 2016: Heat waves and urban heat islands in Europe: A review of relevant drivers. *Science of the Total Environment*, **569–570**, 527–539, doi:10.1016/j.scitotenv.2016.06.119.

Warner, J.L.L., J.A.A. Screen, and A.A.A. Scaife, 2020: Links Between Barents-Kara Sea Ice and the Extratropical Atmospheric Circulation Explained by Internal Variability and Tropical Forcing. *Geophysical Research Letters*, **47(1)**, doi:10.1029/2019gl085679.

Warszawski, L. et al., 2014: The Inter-Sectoral Impact Model Intercomparison Project (ISI–MIP): Project framework. *Proceedings of the National Academy of Sciences*, **111(9)**, 3228–3232, doi:10.1073/pnas.1312330110.

Watanabe, M. et al., 2014: Contribution of natural decadal variability to global warming acceleration and hiatus. *Nature Climate Change*, **4(10)**, 893–897, doi:10.1038/nclimate2355.

Watanabe, S., N. Utsumi, and H. Kim, 2018: Projection of the Changes in Weather Potentially Affecting Tourism in the Yaeyama Islands Under Global Warming. *Journal of Japan Society of Civil Engineers, Ser. G (Environmental Research)*, **74(5)**, I_19–I_24, doi:10.2208/jscejer.74.i_19.

Waugh, D.W., C.I. Garfinkel, and L.M. Polvani, 2015: Drivers of the Recent Tropical Expansion in the Southern Hemisphere: Changing SSTs or Ozone Depletion? *Journal of Climate*, **28(16)**, 6581–6586, doi:10.1175/jcli-d-15-0138.1.

Weaver, C.P. et al., 2013: Improving the contribution of climate model information to decision making: the value and demands of robust decision frameworks. *Wiley Interdisciplinary Reviews: Climate Change*, **4(1)**, 39–60, doi:10.1002/wcc.202.

Weaver, C.P. et al., 2017: Reframing climate change assessments around risk: recommendations for the US National Climate Assessment. *Environmental Research Letters*, **12(8)**, 080201, doi:10.1088/1748-9326/aa7494.

Webber, H. et al., 2018: Diverging importance of drought stress for maize and winter wheat in Europe. *Nature Communications*, **9(1)**, 4249, doi:10.1038/s41467-018-06525-2.

Webber, S. and S.D. Donner, 2017: Climate service warnings: cautions about commercializing climate science for adaptation in the developing world. *Wiley Interdisciplinary Reviews: Climate Change*, **8(1)**, e424, doi:10.1002/wcc.424.

Weber, T. et al., 2018: Analyzing Regional Climate Change in Africa in a 1.5, 2, and 3°C Global Warming World. *Earth's Future*, **6(4)**, 643–655, doi:10.1002/2017ef000714.

Weedon, G.P. et al., 2014: The WFDEI meteorological forcing data set: WATCH Forcing data methodology applied to ERA-Interim reanalysis data. *Water Resources Research*, doi:10.1002/2014wr015638.

Wehrli, K., B.P. Guillod, M. Hauser, M. Leclair, and S.I. Seneviratne, 2018: Assessing the Dynamic Versus Thermodynamic Origin of Climate Model Biases. *Geophysical Research Letters*, **45(16)**, 8471–8479,

SUBJECT TO FINAL EDITING ACCEPTED VERSION

doi:10.1029/2018gl079220.
Wehrli, K., B.P. Guillod, M. Hauser, M. Leclair, and S.I. Seneviratne, 2019: Identifying Key Driving Processes of Major Recent Heat Waves. *Journal of Geophysical Research: Atmospheres*, **124(22)**, 11746–11765, doi:10.1029/2019jd030635.
Weijer, W. et al., 2019: Stability of the Atlantic Meridional Overturning Circulation: A Review and Synthesis. *Journal of Geophysical Research: Oceans*, **124(8)**, 5336–5375, doi:10.1029/2019jc015083.
Weldeab, S., J.-B.W. Stuut, R.R. Schneider, and W. Siebel, 2013: Holocene climate variability in the winter rainfall zone of South Africa. *Climate of the Past*, **9(5)**, 2347–2364, doi:10.5194/cp-9-2347-2013.
Wester, P., A. Mishra, A. Mukherji, and A.B. Shrestha (eds.), 2019: *The Hindu Kush Himalaya Assessment: Mountains, Climate Change, Sustainability and People*. Springer, Cham, Switzerland, 627 pp., doi:10.1007/978-3-319-92288-1.
Westervelt, D.M. et al., 2017: Multimodel precipitation responses to removal of U.S. sulfur dioxide emissions. *Journal of Geophysical Research: Atmospheres*, **122(9)**, 5024–5038, doi:10.1002/2017jd026756.
Westervelt, D.M. et al., 2018: Connecting regional aerosol emissions reductions to local and remote precipitation responses. *Atmospheric Chemistry and Physics*, **18(16)**, 12461–12475, doi:10.5194/acp-18-12461-2018.
Westra, S. et al., 2010: Addressing Climatic Non-Stationarity in the Assessment of Flood Risk. *Australasian Journal of Water Resources*, **14(1)**, 1–16, doi:10.1080/13241583.2010.11465370.
Wettstein, J.J. and C. Deser, 2014: Internal Variability in Projections of Twenty-First-Century Arctic Sea Ice Loss: Role of the Large-Scale Atmospheric Circulation. *Journal of Climate*, **27(2)**, 527–550, doi:10.1175/jcli-d-12-00839.1.
Whan, K. and F. Zwiers, 2017: The impact of ENSO and the NAO on extreme winter precipitation in North America in observations and regional climate models. *Climate Dynamics*, **48(5–6)**, 1401–1411, doi:10.1007/s00382-016-3148-x.
Whan, K. et al., 2015: Impact of soil moisture on extreme maximum temperatures in Europe. *Weather and Climate Extremes*, **9**, 57–67, doi:10.1016/j.wace.2015.05.001.
Widmann, M., H. Goosse, G. van der Schrier, R. Schnur, and J. Barkmeijer, 2010: Using data assimilation to study extratropical Northern Hemisphere climate over the last millennium. *Climate of the Past*, **6(5)**, 627–644, doi:10.5194/cp-6-627-2010.
Widmann, M. et al., 2019: Validation of spatial variability in downscaling results from the VALUE perfect predictor experiment. *International Journal of Climatology*, **39**, joc.6024, doi:10.1002/joc.6024.
Wielicki, B.A. et al., 2013: Achieving climate change absolute accuracy in orbit. *Bulletin of the American Meteorological Society*, **94(10)**, 1519–1539, doi:10.1175/bams-d-12-00149.1.
Wilby, R.L. and S. Dessai, 2010: Robust adaptation to climate change. *Weather*, **65(7)**, 180–185, doi:10.1002/wea.543.
Wilby, R.L. and D. Yu, 2013: Rainfall and temperature estimation for a data sparse region. *Hydrology and Earth System Sciences*, **17(10)**, 3937–3955, doi:10.5194/hess-17-3937-2013.
Wilcke, R.A.I. and L. Bärring, 2016: Selecting regional climate scenarios for impact modelling studies. *Environmental Modelling & Software*, **78**, 191–201, doi:10.1016/j.envsoft.2016.01.002.
Wilcox, L.J., E.J. Highwood, and N.J. Dunstone, 2013: The influence of anthropogenic aerosol on multi-decadal variations of historical global climate. *Environmental Research Letters*, **8**, 024033, doi:10.1088/1748-9326/8/2/024033.
Wilcox, L.J. et al., 2020: Accelerated increases in global and Asian summer monsoon precipitation from future aerosol reductions. *Atmospheric Chemistry and Physics*, **20(20)**, 11955–11977, doi:10.5194/acp-20-11955-2020.
Wildschut, D., 2017: The need for citizen science in the transition to a sustainable peer-to-peer-society. *Futures*, **91**, 46–52, doi:10.1016/j.futures.2016.11.010.
Wilks, D.S., 2016: "The Stippling Shows Statistically Significant Grid Points": How Research Results are Routinely Overstated and Overinterpreted, and What to Do about It. *Bulletin of the American Meteorological Society*, **97(12)**, 2263–2273, doi:10.1175/bams-d-15-00267.1.
Willems, P. and M. Vrac, 2011: Statistical precipitation downscaling for small-scale hydrological impact investigations of climate change. *Journal of Hydrology*, **402(3–4)**, 193–205, doi:10.1016/j.jhydrol.2011.02.030.
Williams, A.P. et al., 2015: Contribution of anthropogenic warming to California drought during 2012-2014. *Geophysical Research Letters*, **42(16)**, 6819–6828, doi:10.1002/2015gl064924.
Williams, A.P. et al., 2020: Large contribution from anthropogenic warming to an emerging North American megadrought. *Science*, **368(6488)**, 314–318, doi:10.1126/science.aaz9600.
Williams, C.N., M.J. Menne, and P.W. Thorne, 2012: Benchmarking the performance of pairwise homogenization of surface temperatures in the United States. *Journal of Geophysical Research: Atmospheres*, **117**, D05116, doi:10.1029/2011jd016761.
Williams, K.D. et al., 2018: The Met Office Global Coupled Model 3.0 and 3.1 (GC3.0 and GC3.1) Configurations. *Journal of Advances in Modeling Earth Systems*, **10(2)**, 357–380, doi:10.1002/2017ms001115.
Willmott, C.J. and K. Matsuura, 1995: Smart Interpolation of Annually Averaged Air Temperature in the United States. *Journal of Applied Meteorology*, **34(12)**, 2577–2586, doi:10.1175/1520-0450(1995)034<2577:sioaaa>2.0.co;2.
Wills, R.C., T. Schneider, J.M. Wallace, D.S. Battisti, and D.L. Hartmann, 2018: Disentangling Global Warming,

SUBJECT TO FINAL EDITING ACCEPTED VERSION

Multidecadal Variability, and El Niño in Pacific Temperatures. *Geophysical Research Letters*, **45(5)**, 2487–2496, doi:10.1002/2017gl076327.
Wills, R.C.J., K.C. Armour, D.S. Battisti, and D.L. Hartmann, 2019: Ocean–Atmosphere Dynamical Coupling Fundamental to the Atlantic Multidecadal Oscillation. *Journal of Climate*, **32(1)**, 251–272, doi:10.1175/jcli-d-18-0269.1.
Wills, R.C.J., D.S. Battisti, K.C. Armour, T. Schneider, and C. Deser, 2020: Pattern Recognition Methods to Separate Forced Responses from Internal Variability in Climate Model Ensembles and Observations. *Journal of Climate*, **33(20)**, 8693–8719, doi:10.1175/jcli-d-19-0855.1.
Willyard, C., M. Scudellari, and L. Nordling, 2018: How three research groups are tearing down the ivory tower. *Nature*, **562(7725)**, 24–28, doi:10.1038/d41586-018-06858-4.
Winter, K.J.-P.M., S. Kotlarski, S.C. Scherrer, and C. Schär, 2017: The Alpine snow-albedo feedback in regional climate models. *Climate Dynamics*, **48(3–4)**, 1109–1124, doi:10.1007/s00382-016-3130-7.
WMO, 2017a: *Challenges in the Transition from Conventional to Automatic Meteorological Observing Networks for Long-term Climate Records*. WMO-No. 1202, World Meteorological Organization (WMO), Geneva, Switzerland, 20 pp.
WMO, 2017b: *WMO Guidelines on Generating a Defined Set of National Climate Monitoring Products 2017*. WMO-No. 1204, World Meteorological Organization (WMO), Geneva, Switzerland, 21 pp.
WMO, 2019: *Guide to the WMO Integrated Global Observing System 2019*. WMO-No. 1165, World Meteorological Organization (WMO), Geneva, Switzerland, 81 pp.
Wolski, P., 2018: How severe is Cape Town's "Day Zero" drought? *Significance*, **15(2)**, 24–27, doi:10.1111/j.1740-9713.2018.01127.x.
Wolski, P., S. Conradie, C. Jack, and M. Tadross, 2021: Spatio-temporal patterns of rainfall trends and the 2015–2017 drought over the winter rainfall region of South Africa. *International Journal of Climatology*, **41(S1)**, doi:10.1002/joc.6768.
Woodhouse, C.A. and G.T. Pederson, 2018: Investigating Runoff Efficiency in Upper Colorado River Streamflow Over Past Centuries. *Water Resources Research*, **54(1)**, 286–300, doi:10.1002/2017wr021663.
Woodhouse, C.A., D.M. Meko, G.M. MacDonald, D.W. Stahle, and E.R. Cook, 2010: A 1,200-year perspective of 21st century drought in southwestern North America. *Proceedings of the National Academy of Sciences*, **107(50)**, 21283–21288, doi:10.1073/pnas.0911197107.
Woodhouse, C.A., G.T. Pederson, K. Morino, S.A. McAfee, and G.J. McCabe, 2016: Increasing influence of air temperature on upper Colorado River streamflow. *Geophysical Research Letters*, **43(5)**, 2174–2181, doi:10.1002/2015gl067613.
Woods, C. and R. Caballero, 2016: The Role of Moist Intrusions in Winter Arctic Warming and Sea Ice Decline. *Journal of Climate*, **29(12)**, 4473–4485, doi:10.1175/jcli-d-15-0773.1.
Woollings, T., B. Harvey, and G. Masato, 2014: Arctic warming, atmospheric blocking and cold European winters in CMIP5 models. *Environmental Research Letters*, **9(1)**, 014002, doi:10.1088/1748-9326/9/1/014002.
Woollings, T. et al., 2018: Blocking and its Response to Climate Change. *Current Climate Change Reports*, **4(3)**, 287–300, doi:10.1007/s40641-018-0108-z.
Wright, D.M., D.J. Posselt, and A.L. Steiner, 2013: Sensitivity of Lake-Effect Snowfall to Lake Ice Cover and Temperature in the Great Lakes Region. *Monthly Weather Review*, **141(2)**, 670–689, doi:10.1175/mwr-d-12-00038.1.
Wu, G.X. et al., 2016: Advances in studying interactions between aerosols and monsoon in China. *Science China Earth Sciences*, **59(1)**, 1–16, doi:10.1007/s11430-015-5198-z.
Wu, J., J. Zha, and D. Zhao, 2017: Evaluating the effects of land use and cover change on the decrease of surface wind speed over China in recent 30 years using a statistical downscaling method. *Climate Dynamics*, **48(1–2)**, 131–149, doi:10.1007/s00382-016-3065-z.
Wu, Y. and L.M. Polvani, 2017: Recent Trends in Extreme Precipitation and Temperature over Southeastern South America: The Dominant Role of Stratospheric Ozone Depletion in the CESM Large Ensemble. *Journal of Climate*, **30(16)**, 6433–6441, doi:10.1175/jcli-d-17-0124.1.
Wu, Z. and N.E. Huang, 2009: Ensemble empirical mode decomposition: a noise-assisted data analysis method. *Advances in Adaptive Data Analysis*, **01(01)**, 1–41, doi:10.1142/s1793536909000047.
Wulder, M.A. et al., 2016: The global Landsat archive: Status, consolidation, and direction. *Remote Sensing of Environment*, **185**, 271–283, doi:10.1016/j.rse.2015.11.032.
Xavier, A.C., C.W. King, and B.R. Scanlon, 2016: Daily gridded meteorological variables in Brazil (1980–2013). *International Journal of Climatology*, **36(6)**, 2644–2659, doi:10.1002/joc.4518.
Xie, P. and P.A. Arkin, 1997: Global Precipitation: A 17-Year Monthly Analysis Based on Gauge Observations, Satellite Estimates, and Numerical Model Outputs. *Bulletin of the American Meteorological Society*, **78(11)**, 2539–2558, doi:10.1175/1520-0477(1997)078<2539:gpayma>2.0.co;2.
Xie, S. et al., 2010: CLOUDS AND MORE: ARM Climate Modeling Best Estimate Data. *Bulletin of the American Meteorological Society*, **91(1)**, 13–20, doi:10.1175/2009bams2891.1.
Xie, S.-P. et al., 2015: Towards predictive understanding of regional climate change. *Nature Climate Change*, **5**, 921,

ACCEPTED VERSION SUBJECT TO FINAL EDITING

doi:10.1038/nclimate2689.
Xin, X., T. Wu, J. Zhang, J. Yao, and Y. Fang, 2020: Comparison of CMIP6 and CMIP5 simulations of precipitation in China and the East Asian summer monsoon. *International Journal of Climatology*, **40(15)**, 6423–6440, doi:10.1002/joc.6590.
Xu, W. et al., 2013: Homogenization of Chinese daily surface air temperatures and analysis of trends in the extreme temperature indices. *Journal of Geophysical Research: Atmospheres*, **118(17)**, 9708–9720, doi:10.1002/jgrd.50791.
Xu, Y., V. Ramanathan, and W.M. Washington, 2016: Observed high-altitude warming and snow cover retreat over Tibet and the Himalayas enhanced by black carbon aerosols. *Atmospheric Chemistry and Physics*, **16(3)**, 1303–1315, doi:10.5194/acp-16-1303-2016.
Xu, Y., X. Gao, Y. Shi, and Z. Botao, 2015: Detection and attribution analysis of annual mean temperature changes in China. *Climate Research*, **63(1)**, 61–71, doi:10.3354/cr01283.
Xue, Y., Z. Janjic, J. Dudhia, R. Vasic, and F. De Sales, 2014: A review on regional dynamical downscaling in intraseasonal to seasonal simulation/prediction and major factors that affect downscaling ability. *Atmospheric Research*, **147–148**, 68–85, doi:10.1016/j.atmosres.2014.05.001.
Yadav, R.R. et al., 2017: Recent Wetting and Glacier Expansion in the Northwest Himalaya and Karakoram. *Scientific Reports*, **7(1)**, 6139, doi:10.1038/s41598-017-06388-5.
Yaduvanshi, A., M. Zaroug, R. Bendapudi, and M. New, 2019: Impacts of 1.5°C and 2°C global warming on regional rainfall and temperature change across India. *Environmental Research Communications*, **1(12)**, 125002, doi:10.1088/2515-7620/ab4ee2.
Yamada, T.J., M.-I. Lee, M. Kanamitsu, and H. Kanamaru, 2012: Diurnal Characteristics of Rainfall over the Contiguous United States and Northern Mexico in the Dynamically Downscaled Reanalysis Dataset (US10). *Journal of Hydrometeorology*, **13(3)**, 1142–1148, doi:10.1175/jhm-d-11-0121.1.
Yan, L., Z. Liu, G. Chen, J.E. Kutzbach, and X. Liu, 2016: Mechanisms of elevation-dependent warming over the Tibetan plateau in quadrupled CO2 experiments. *Climatic Change*, **135(3–4)**, 509–519, doi:10.1007/s10584-016-1599-z.
Yan, Z., Z. Li, Q. li, and P. Jones, 2010: Effects of site change and urbanisation in the Beijing temperature series 1977–2006. *International Journal of Climatology*, **30(8)**, 1226–1234, doi:10.1002/joc.1971.
Yang, K. et al., 2007: Auto-calibration System Developed to Assimilate AMSR-E Data into a Land Surface Model for Estimating Soil Moisture and the Surface Energy Budget. *Journal of the Meteorological Society of Japan*, **85A**, 229–242, doi:10.2151/jmsj.85a.229.
Yang, P. and T.L. Ng, 2019: Fast Bayesian Regression Kriging Method for Real-Time Merging of Radar, Rain Gauge, and Crowdsourced Rainfall Data. *Water Resources Research*, **55(4)**, 3194–3214, doi:10.1029/2018wr023857.
Yang, X.-Y., X. Yuan, and M. Ting, 2016: Dynamical Link between the Barents–Kara Sea Ice and the Arctic Oscillation. *Journal of Climate*, **29(14)**, 5103–5122, doi:10.1175/jcli-d-15-0669.1.
Yang, Z. et al., 2017: Merging high-resolution satellite-based precipitation fields and point-scale rain gauge measurements-A case study in Chile. *Journal of Geophysical Research: Atmospheres*, **122(10)**, 5267–5284, doi:10.1002/2016jd026177.
Yano, J.-I. et al., 2018: Scientific Challenges of Convective-Scale Numerical Weather Prediction. *Bulletin of the American Meteorological Society*, **99(4)**, 699–710, doi:10.1175/bams-d-17-0125.1.
Yao, T. et al., 2012a: Different glacier status with atmospheric circulations in Tibetan Plateau and surroundings. *Nature Climate Change*, **2(9)**, 663–667, doi:10.1038/nclimate1580.
Yao, T. et al., 2012b: Third Pole Environment (TPE). *Environmental Development*, **3**, 52–64, doi:10.1016/j.envdev.2012.04.002.
Yettella, V. and M.R. England, 2018: The Role of Internal Variability in Twenty-First-Century Projections of the Seasonal Cycle of Northern Hemisphere Surface Temperature. *Journal of Geophysical Research: Atmospheres*, **123(23)**, doi:10.1029/2018jd029066.
Yokoi, S. et al., 2017: Diurnal cycle of precipitation observed in the western coastal area of Sumatra Island: Offshore preconditioning by gravity waves. *Monthly Weather Review*, **145(9)**, 3745–3761, doi:10.1175/mwr-d-16-0468.1.
Yokoyama, C., Y.N. Takayabu, O. Arakawa, and T. Ose, 2019: A Study on Future Projections of Precipitation Characteristics around Japan in Early Summer Combining GPM DPR Observation and CMIP5 Large-Scale Environments. *Journal of Climate*, **32(16)**, 5251–5274, doi:10.1175/jcli-d-18-0656.1.
You, Q. et al., 2020: Elevation dependent warming over the Tibetan Plateau: Patterns, mechanisms and perspectives. *Earth-Science Reviews*, **210(2005)**, 103349, doi:10.1016/j.earscirev.2020.103349.
You, Q.-L. et al., 2017: An overview of studies of observed climate change in the Hindu Kush Himalayan (HKH) region. *Advances in Climate Change Research*, **8(3)**, 141–147, doi:10.1016/j.accre.2017.04.001.
Zakey, A.S., F. Solmon, and F. Giorgi, 2006: Implementation and testing of a desert dust module in a regional climate model. *Atmospheric Chemistry and Physics*, **6(12)**, 4687–4704, doi:10.5194/acp-6-4687-2006.
Zambri, B., A.N. LeGrande, A. Robock, and J. Slawinska, 2017: Northern Hemisphere winter warming and summer monsoon reduction after volcanic eruptions over the last millennium. *Journal of Geophysical Research:*

ACCEPTED VERSION SUBJECT TO FINAL EDITING

Atmospheres, **122(15)**, 7971–7989, doi:10.1002/2017jd026728.
Zampieri, M. et al., 2009: Hot European Summers and the Role of Soil Moisture in the Propagation of Mediterranean Drought. *Journal of Climate*, **22(18)**, 4747–4758, doi:10.1175/2009jcli2568.1.
Zamrane, Z., I. Turki, B. Laignel, G. Mahé, and N.-E. Laftouhi, 2016: Characterization of the Interannual Variability of Precipitation and Streamflow in Tensift and Ksob Basins (Morocco) and Links with the NAO. *Atmosphere*, **7(6)**, 84, doi:10.3390/atmos7060084.
Zanchettin, D. et al., 2013: Delayed winter warming: A robust decadal response to strong tropical volcanic eruptions? *Geophysical Research Letters*, **40(1)**, 204–209, doi:10.1029/2012gl054403.
Zanchettin, D. et al., 2016: The Model Intercomparison Project on the climatic response to Volcanic forcing (VolMIP): experimental design and forcing input data for CMIP6. *Geoscientific Model Development*, **9(8)**, 2701–2719, doi:10.5194/gmd-9-2701-2016.
Zanchettin, D. et al., 2019: Clarifying the Relative Role of Forcing Uncertainties and Initial-Condition Unknowns in Spreading the Climate Response to Volcanic Eruptions. *Geophysical Research Letters*, **46(3)**, 1602–1611, doi:10.1029/2018gl081018.
Zandler, H., I. Haag, and C. Samimi, 2019: Evaluation needs and temporal performance differences of gridded precipitation products in peripheral mountain regions. *Scientific Reports*, **9(1)**, 15118, doi:10.1038/s41598-019-51666-z.
Zängl, G., 2004: A reexamination of the valley wind system in the Alpine Inn Valley with numerical simulations. *Meteorology and Atmospheric Physics*, **87(4)**, 241–256, doi:10.1007/s00703-003-0056-5.
Zanna, L., P.G.L. Porta Mana, J. Anstey, T. David, and T. Bolton, 2017: Scale-aware deterministic and stochastic parametrizations of eddy-mean flow interaction. *Ocean Modelling*, **111**, 66–80, doi:10.1016/j.ocemod.2017.01.004.
Zanna, L. et al., 2019: Uncertainty and scale interactions in ocean ensembles: From seasonal forecasts to multidecadal climate predictions. *Quarterly Journal of the Royal Meteorological Society*, **145(S1)**, 160–175, doi:10.1002/qj.3397.
Zappa, G., 2019: Regional Climate Impacts of Future Changes in the Mid–Latitude Atmospheric Circulation: a Storyline View. *Current Climate Change Reports*, **5(4)**, 358–371, doi:10.1007/s40641-019-00146-7.
Zappa, G. and T.G. Shepherd, 2017: Storylines of Atmospheric Circulation Change for European Regional Climate Impact Assessment. *Journal of Climate*, **30(16)**, 6561–6577, doi:10.1175/jcli-d-16-0807.1.
Zappa, G., V. Lucarini, and A. Navarra, 2011: Baroclinic Stationary Waves in Aquaplanet Models. *Journal of the Atmospheric Sciences*, **68(5)**, 1023–1040, doi:10.1175/2011jas3573.1.
Zappa, G., F. Pithan, and T.G. Shepherd, 2018: Multimodel Evidence for an Atmospheric Circulation Response to Arctic Sea Ice Loss in the CMIP5 Future Projections. *Geophysical Research Letters*, **45(2)**, 1011–1019, doi:10.1002/2017gl076096.
Zappa, G., P. Ceppi, and T.G. Shepherd, 2020: Time-evolving sea-surface warming patterns modulate the climate change response of subtropical precipitation over land. *Proceedings of the National Academy of Sciences*, doi:10.1073/pnas.1911015117.
Zeng, Z. et al., 2015: Regional air pollution brightening reverses the greenhouse gases induced warming-elevation relationship. *Geophysical Research Letters*, **42(11)**, 4563–4572, doi:10.1002/2015gl064410.
Zerenner, T., V. Venema, P. Friederichs, and C. Simmer, 2016: Downscaling near-surface atmospheric fields with multi-objective Genetic Programming. *Environmental Modelling & Software*, **84**, 85–98, doi:10.1016/j.envsoft.2016.06.009.
Zhai, P., B. Zhou, and Y. Chen, 2018: A Review of Climate Change Attribution Studies. *Journal of Meteorological Research*, **32(5)**, 671–692, doi:10.1007/s13351-018-8041-6.
Zhan, Y.-J. et al., 2017: Changes in extreme precipitation events over the Hindu Kush Himalayan region during 1961–2012. *Advances in Climate Change Research*, **8(3)**, 166–175, doi:10.1016/j.accre.2017.08.002.
Zhang, C., Y. Wang, K. Hamilton, and A. Lauer, 2016: Dynamical downscaling of the climate for the Hawaiian islands. Part II: Projection for the late twenty-first century. *Journal of Climate*, **29**, 8333–8354, doi:10.1175/jcli-d-16-0038.1.
Zhang, G.J., M. Cai, and A. Hu, 2013: Energy consumption and the unexplained winter warming over northern Asia and North America. *Nature Climate Change*, **3(5)**, 466–470, doi:10.1038/nclimate1803.
Zhang, H. and T.L. Delworth, 2018: Robustness of anthropogenically forced decadal precipitation changes projected for the 21st century. *Nature Communications*, **9(1)**, 1150, doi:10.1038/s41467-018-03611-3.
Zhang, H., B. Xie, and Z. Wang, 2018: Effective Radiative Forcing and Climate Response to Short-Lived Climate Pollutants Under Different Scenarios. *Earth's Future*, **6(6)**, 857–866, doi:10.1029/2018ef000832.
Zhang, H. et al., 2016: Detection, Attribution, and Projection of Regional Rainfall Changes on (Multi-) Decadal Time Scales: A Focus on Southeastern South America. *Journal of Climate*, **29(23)**, 8515–8534, doi:10.1175/jcli-d-16-0287.1.
Zhang, J., F. Wang, K.B. Tokarska, and Z. Yang, 2020: Multiple possibilities for future precipitation changes in Asia under the Paris Agreement. *International Journal of Climatology*, **40(11)**, 4888–4902, doi:10.1002/joc.6495.
Zhang, K. et al., 2014: Technical Note: On the use of nudging for aerosol–climate model intercomparison studies.

ACCEPTED VERSION SUBJECT TO FINAL EDITING

Atmospheric Chemistry and Physics, **14(16)**, 8631–8645, doi:10.5194/acp-14-8631-2014.
Zhang, R., C. Sun, J. Zhu, R. Zhang, and W. Li, 2020: Increased European heat waves in recent decades in response to shrinking Arctic sea ice and Eurasian snow cover. *npj Climate and Atmospheric Science*, **3(1)**, 7, doi:10.1038/s41612-020-0110-8.
Zhang, T., M.P. Hoerling, J. Perlwitz, and T. Xu, 2016: Forced Atmospheric Teleconnections during 1979–2014. *Journal of Climate*, **29(7)**, 2333–2357, doi:10.1175/jcli-d-15-0226.1.
Zhang, W., T. Zhou, L. Zhang, and L. Zou, 2019: Future Intensification of the Water Cycle with an Enhanced Annual Cycle over Global Land Monsoon Regions. *Journal of Climate*, **32(17)**, 5437–5452, doi:10.1175/jcli-d-18-0628.1.
Zhang, X. et al., 2011: Indices for monitoring changes in extremes based on daily temperature and precipitation data. *Wiley Interdisciplinary Reviews: Climate Change*, **2(6)**, 851–870, doi:10.1002/wcc.147.
Zhang, Y. et al., 2018: Black carbon and mineral dust in snow cover on the Tibetan Plateau. *The Cryosphere*, **12(2)**, 413–431, doi:10.5194/tc-12-413-2018.
Zhao, A.D., D.S. Stevenson, and M.A. Bollasina, 2019: The role of anthropogenic aerosols in future precipitation extremes over the Asian Monsoon Region. *Climate Dynamics*, **52(9–10)**, 6257–6278, doi:10.1007/s00382-018-4514-7.
Zhao, L., X. Lee, R.B. Smith, and K. Oleson, 2014: Strong contributions of local background climate to urban heat islands. *Nature*, **511(7508)**, 216–219, doi:10.1038/nature13462.
Zhao, L. et al., 2021: Global multi-model projections of local urban climates. *Nature Climate Change*, doi:10.1038/s41558-020-00958-8.
Zheng, F. et al., 2018: Crowdsourcing Methods for Data Collection in Geophysics: State of the Art, Issues, and Future Directions. *Reviews of Geophysics*, **56(4)**, 698–740, doi:10.1029/2018rg000616.
Zhou, C. and K. Wang, 2016: Land surface temperature over global deserts: Means, variability, and trends. *Journal of Geophysical Research: Atmospheres*, **121(24)**, 14,344–14,357, doi:10.1002/2016jd025410.
Zhou, S., P. Huang, G. Huang, and K. Hu, 2019: Leading source and constraint on the systematic spread of the changes in East Asian and western North Pacific summer monsoon. *Environmental Research Letters*, **14(12)**, 124059, doi:10.1088/1748-9326/ab547c.
Zhou, S. et al., 2021: Soil moisture–atmosphere feedbacks mitigate declining water availability in drylands. *Nature Climate Change*, **11(1)**, 38–44, doi:10.1038/s41558-020-00945-z.
Zhou, T., F. Song, K.J. Ha, and X. Chen, 2017: Decadal changes of East Asian summer monsoon: Contributions of internal variability and external forcing. In: *The Global Monsoon System: Research and Forecasting (3rd Edition)* [Chang, C.-P., H.-C. Kuo, N.-C. Lau, R.H. Johnson, B. Wang, and M.C. Wheeler (eds.)]. World Scientific, pp. 327–336, doi:10.1142/9789813200913_0026.
Zhou, T. et al., 2016: GMMIP (v1.0) contribution to CMIP6: Global Monsoons Model Inter-comparison Project. *Geoscientific Model Development*, **9(10)**, 3589–3604, doi:10.5194/gmd-9-3589-2016.
Zhu, P. et al., 2012: A limited area model (LAM) intercomparison study of a TWP-ICE active monsoon mesoscale convective event. *Journal of Geophysical Research: Atmospheres*, **117(D11)**, n/a–n/a, doi:10.1029/2011jd016447.
Zhuo, Z., C. Gao, and Y. Pan, 2014: Proxy evidence for China's monsoon precipitation response to volcanic aerosols over the past seven centuries. *Journal of Geophysical Research: Atmospheres*, **119(11)**, 6638–6652, doi:10.1002/2013jd021061.
Zittis, G. and P. Hadjinicolaou, 2017: The effect of radiation parameterization schemes on surface temperature in regional climate simulations over the MENA-CORDEX domain. *International Journal of Climatology*, **37(10)**, 3847–3862, doi:10.1002/joc.4959.
Zittis, G., A. Bruggeman, C. Camera, P. Hadjinicolaou, and J. Lelieveld, 2017: The added value of convection permitting simulations of extreme precipitation events over the eastern Mediterranean. *Atmospheric Research*, **191**, 20–33, doi:10.1016/j.atmosres.2017.03.002.
Zittis, G., P. Hadjinicolaou, M. Klangidou, Y. Proestos, and J. Lelieveld, 2019: A multi-model, multi-scenario, and multi-domain analysis of regional climate projections for the Mediterranean. *Regional Environmental Change*, **19(8)**, 2621–2635, doi:10.1007/s10113-019-01565-w.
Ziv, B., U. Dayan, Y. Kushnir, C. Roth, and Y. Enzel, 2006: Regional and global atmospheric patterns governing rainfall in the southern Levant. *International Journal of Climatology*, **26(1)**, 55–73, doi:10.1002/joc.1238.
Zou, L. and T. Zhou, 2016a: A regional ocean–atmosphere coupled model developed for CORDEX East Asia: assessment of Asian summer monsoon simulation. *Climate Dynamics*, **47(12)**, 3627–3640, doi:10.1007/s00382-016-3032-8.
Zou, L. and T. Zhou, 2016b: Future summer precipitation changes over CORDEX-East Asia domain downscaled by a regional ocean-atmosphere coupled model: A comparison to the stand-alone RCM. *Journal of Geophysical Research: Atmospheres*, **121(6)**, 2691–2704, doi:10.1002/2015jd024519.
Zou, L. and T. Zhou, 2017: Dynamical downscaling of East Asian winter monsoon changes with a regional ocean-atmosphere coupled model. *Quarterly Journal of the Royal Meteorological Society*, **143(706)**, 2245–2259, doi:10.1002/qj.3082.

ACCEPTED VERSION SUBJECT TO FINAL EDITING

Zou, L., T. Zhou, and D. Peng, 2016: Dynamical downscaling of historical climate over CORDEX East Asia domain: A comparison of regional ocean-atmosphere coupled model to stand-alone RCM simulations. *Journal of Geophysical Research: Atmospheres*, **121(4)**, 1442–1458, doi:10.1002/2015jd023912.

Zou, L., T. Zhou, F. Qiao, and W. Zhao, 2017: Development of a regional ocean–atmosphere-wave coupled model and its preliminary evaluation over the CORDEX East Asia domain. *International Journal of Climatology*, **37(12)**, 4478–4485, doi:10.1002/joc.5067.

Zscheischler, J., E.M. Fischer, and S. Lange, 2019: The effect of univariate bias adjustment on multivariate hazard estimates. *Earth System Dynamics*, **10(1)**, 31–43, doi:10.5194/esd-10-31-2019.

Zscheischler, J. et al., 2018: Future climate risk from compound events. *Nature Climate Change*, **8(6)**, 469–477, doi:10.1038/s41558-018-0156-3.

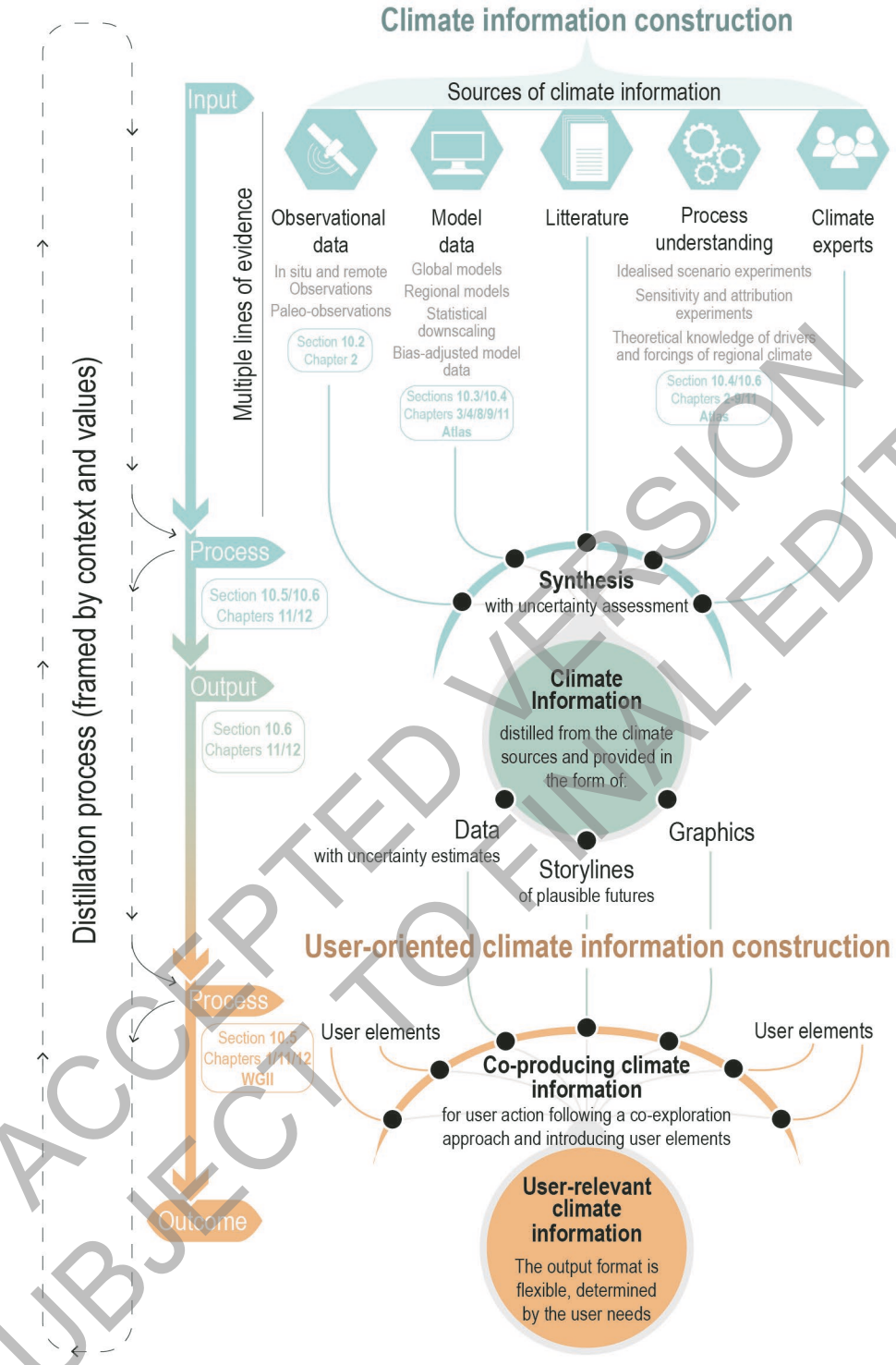
Zubler, E.M. et al., 2011: Simulation of dimming and brightening in Europe from 1958 to 2001 using a regional climate model. *Journal of Geophysical Research*, **116(D18)**, D18205, doi:10.1029/2010jd015396.

Zulkafli, Z. et al., 2014: A Comparative Performance Analysis of TRMM 3B42 (TMPA) Versions 6 and 7 for Hydrological Applications over Andean–Amazon River Basins. *Journal of Hydrometeorology*, **15(2)**, 581–592, doi:10.1175/jhm-d-13-094.1.

Zuo, M., T. Zhou, and W. Man, 2019: Hydroclimate Responses over Global Monsoon Regions Following Volcanic Eruptions at Different Latitudes. *Journal of Climate*, **32(14)**, 4367–4385, doi:10.1175/jcli-d-18-0707.1.

ACCEPTED VERSION
SUBJECT TO FINAL EDITING

Figures



ACCEPTED VERSION SUBJECT TO FINAL EDITING

Figure 10.1: Diagram of the processes leading to the construction of regional climate information (green) and user-relevant regional climate information (orange). The chapter sections and the other chapters of the report involved in each step are indicated in rectangles. WGII stands for Working Group II.

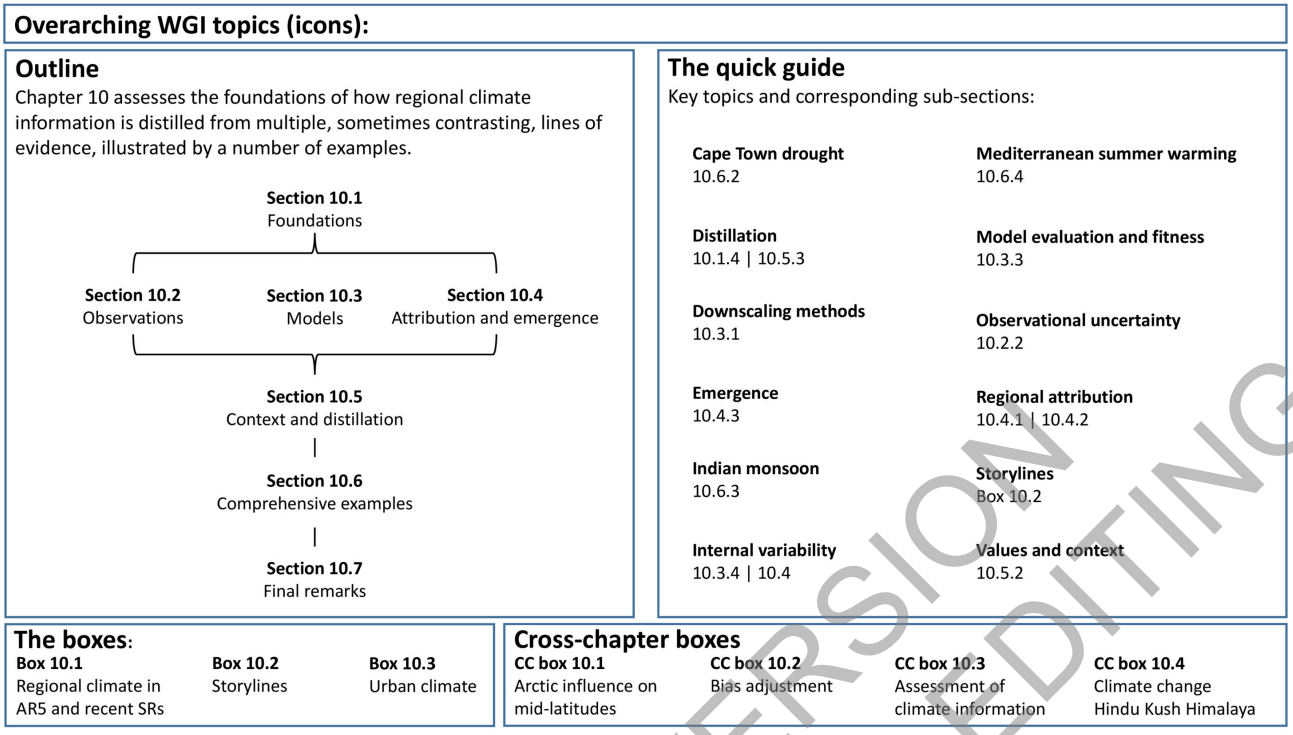


Figure 10.2: Visual abstract of the chapter, with its key elements.

ACCEPTED VERSION
SUBJECT TO FINAL EDITING

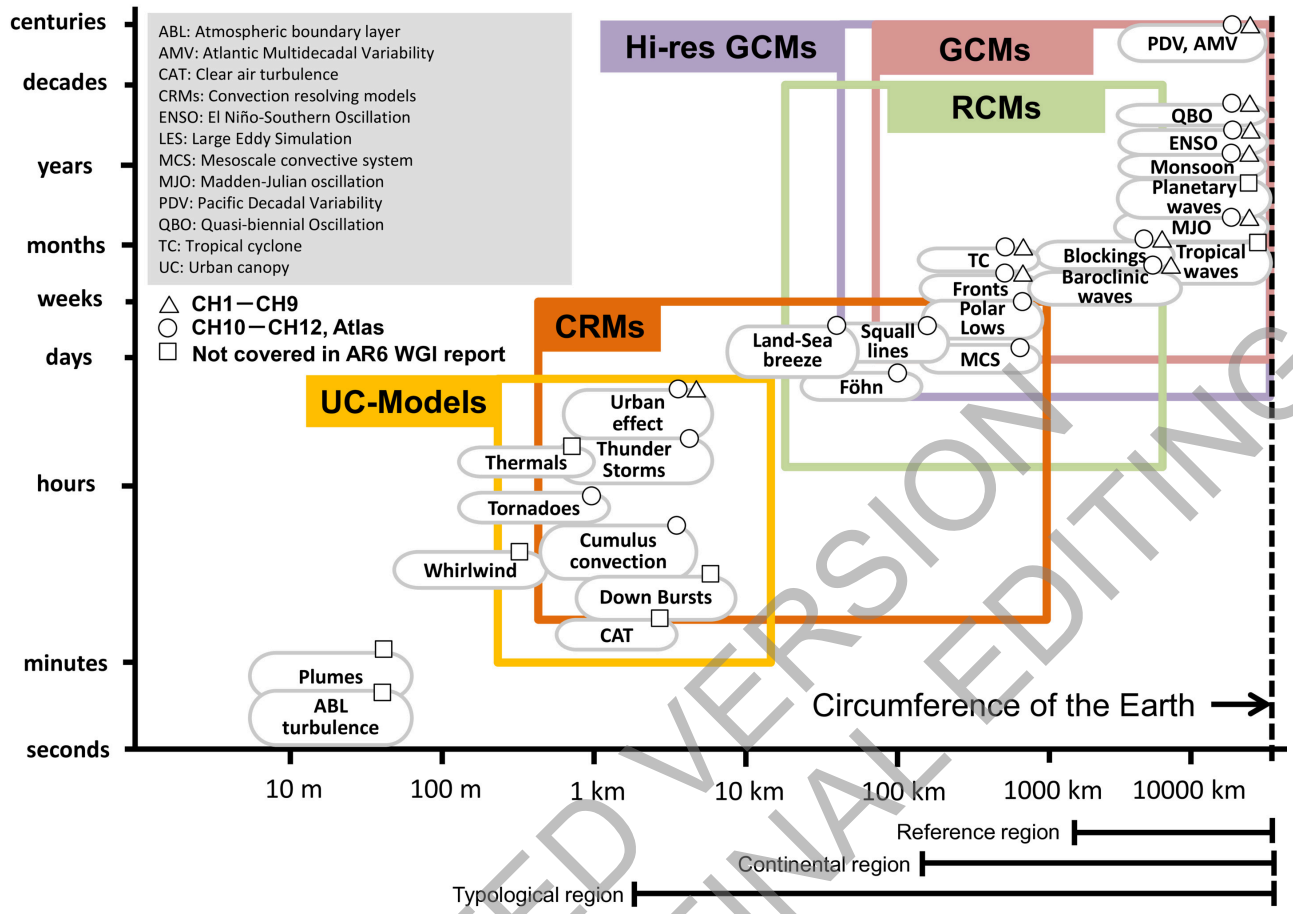
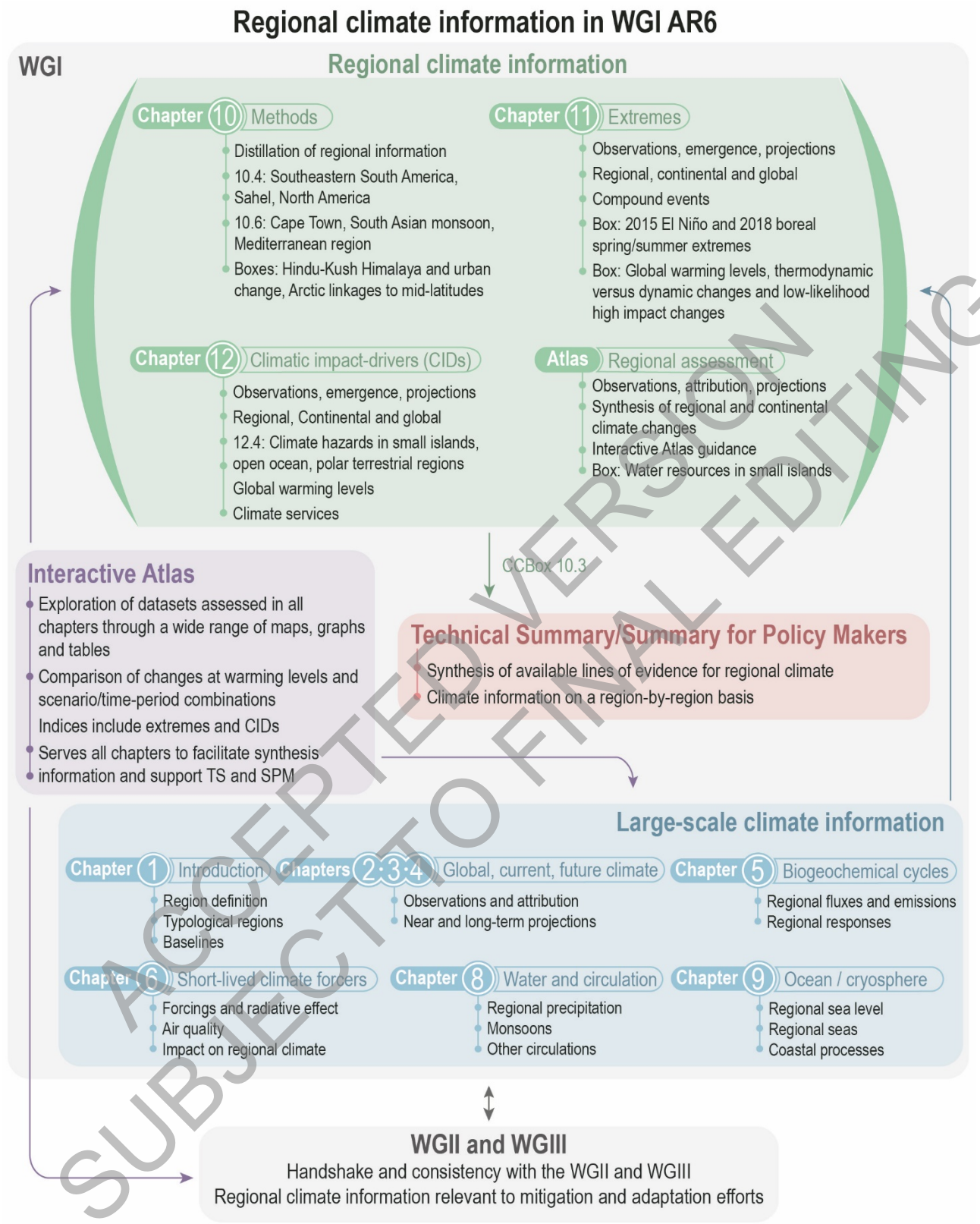


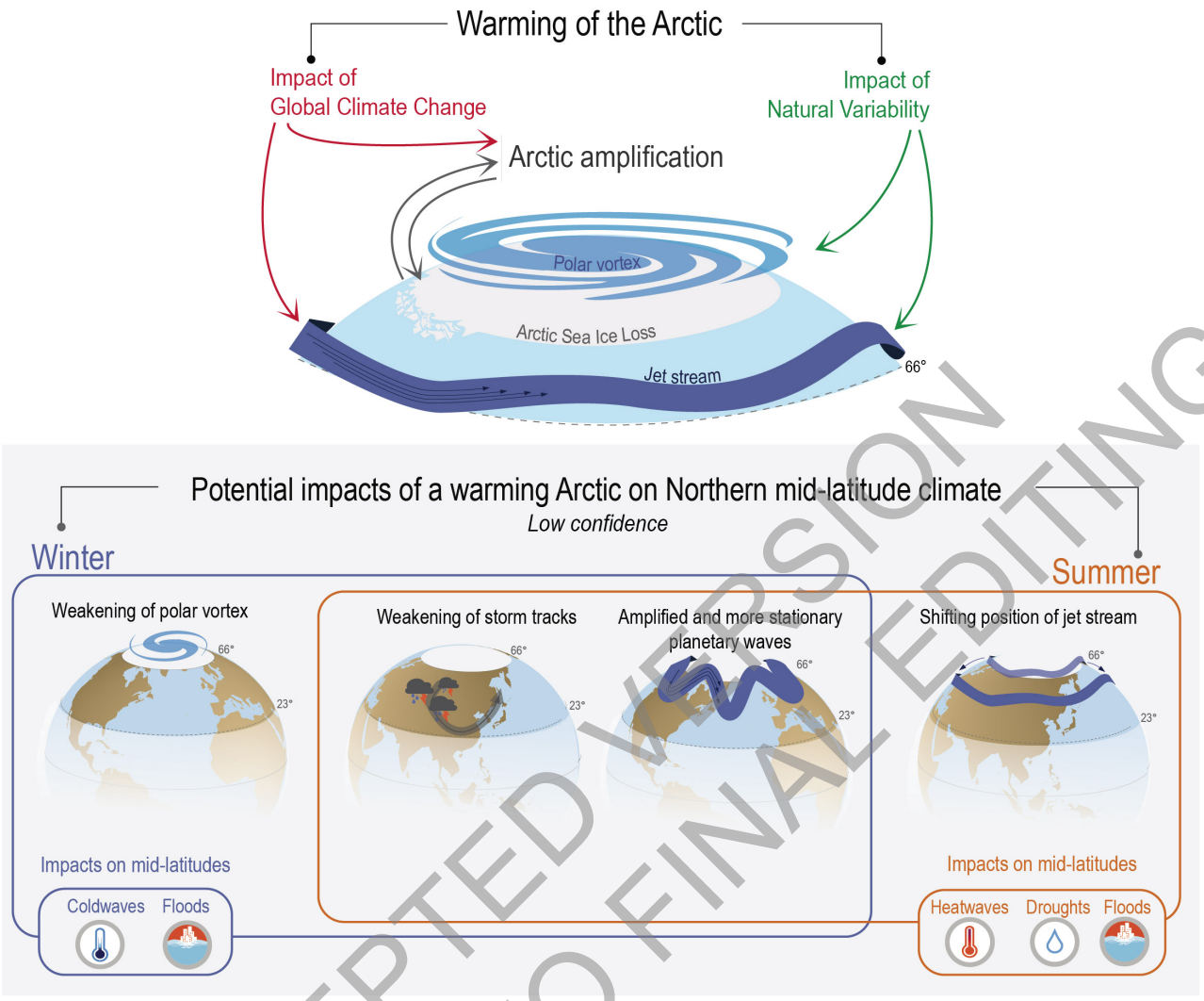
Figure 10.3: Schematic diagram to display interacting spatial and temporal scales relevant to regional climate change information. Adapted from Orlanski (1975). The processes included in the different models and model components considered in Chapter 10 are indicated as a function of these scales.

ACCEPTED VERSION SUBJECT TO FINAL EDITING



ACCEPTED VERSION SUBJECT TO FINAL EDITING

Figure 10.4: Schematic diagram that illustrates the treatment of regional climate change in the different parts of the WGI report and how the chapters relate to each other.



Cross-Chapter Box 10.1, Figure 1: Mechanisms of potential influences of recent and future Arctic warming on mid-latitude climate and variability. Mechanisms are different for winter and summer with different associated influences on mid-latitudes. The mechanisms involve changes in the polar vortex, storm tracks, planetary waves and jet stream.

ACCEPTED VERSION SUBJECT TO FINAL EDITING

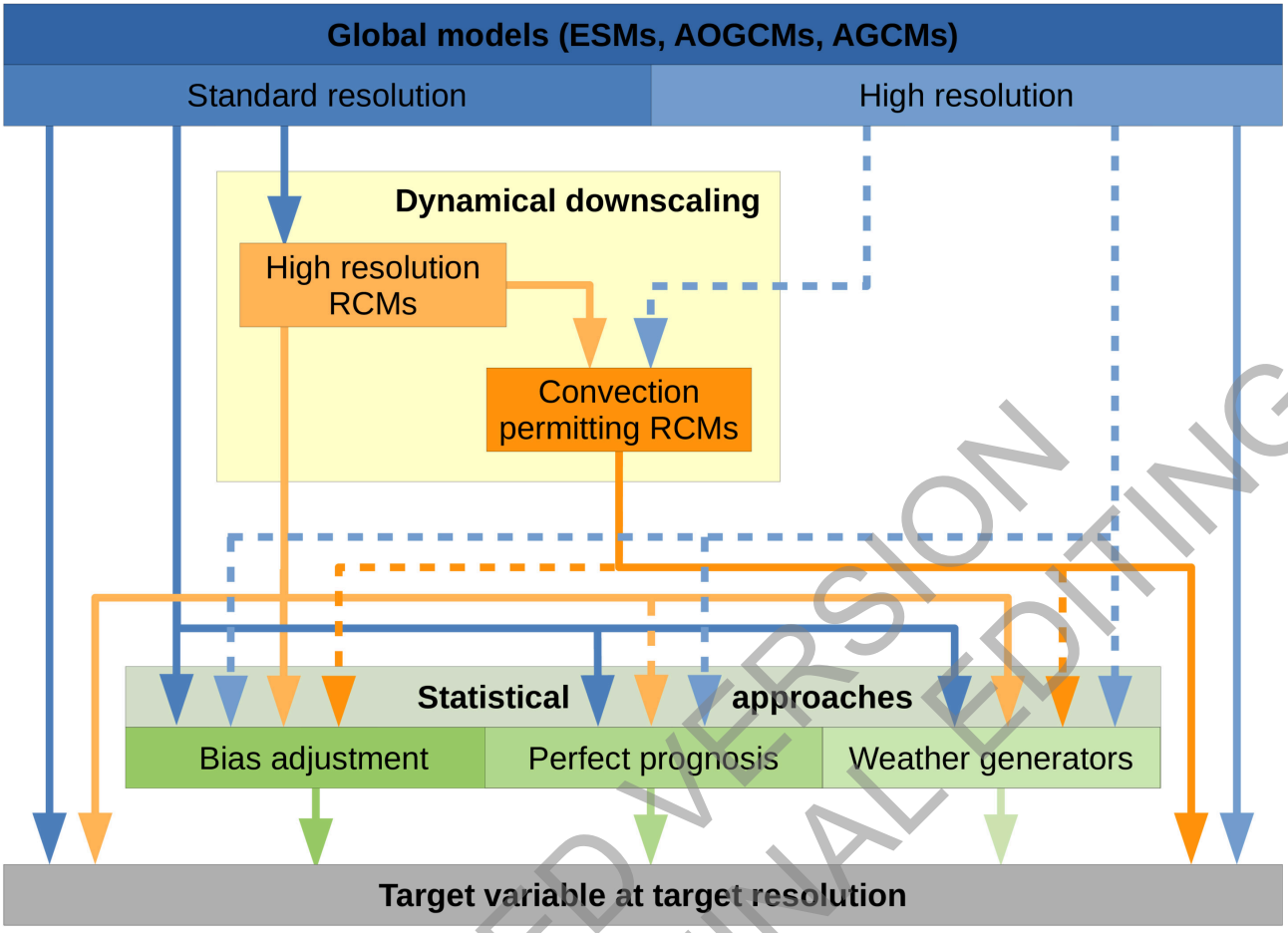
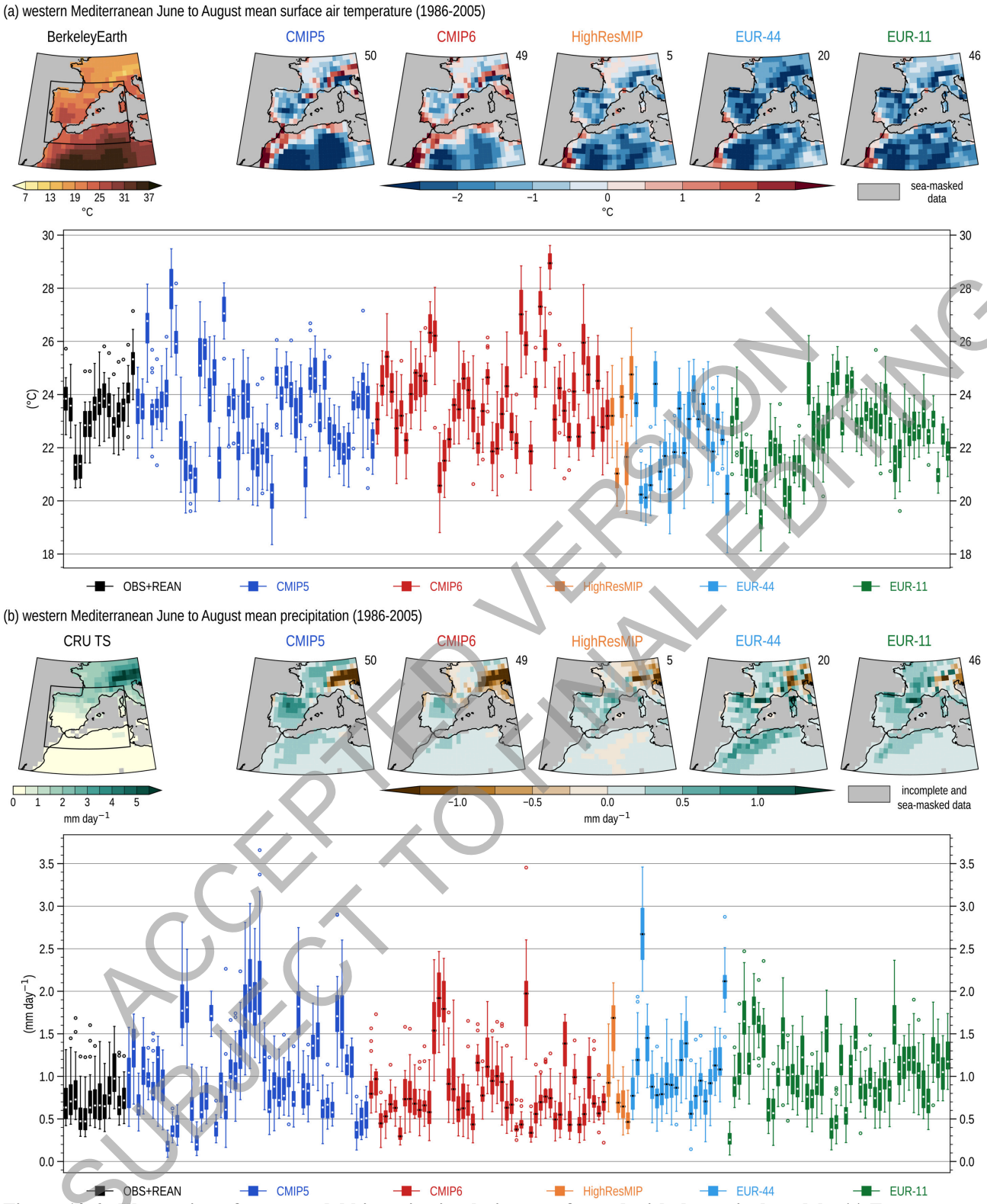


Figure 10.5: Typical model types and chains used in modelling regional climate. The dashed lines indicate model chains that might prove useful but have not or only rarely been used. Hybrid approaches combining the model types shown have been developed.

ACCEPTED VERSION SUBJECT TO FINAL EDITING

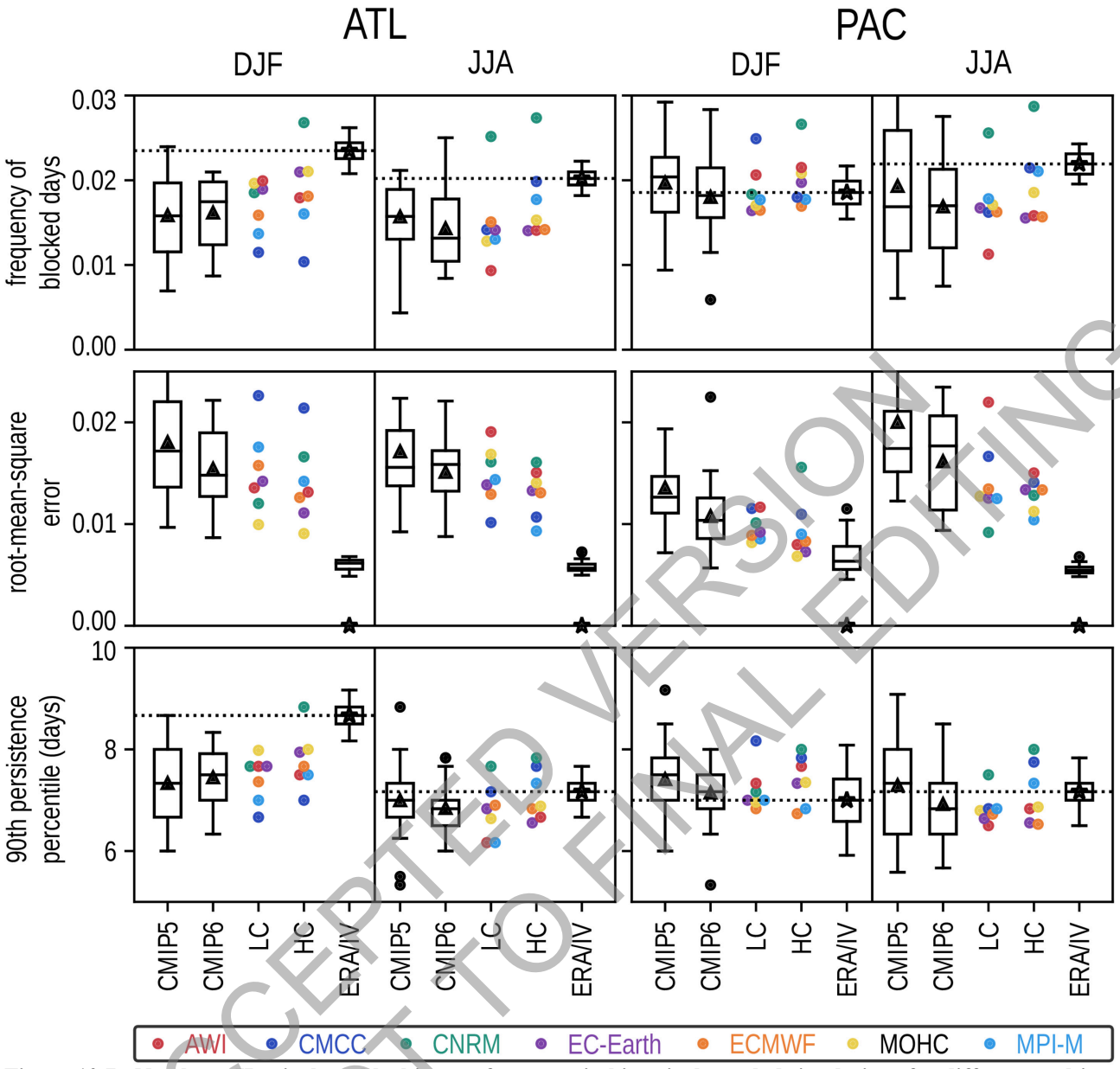


ACCEPTED VERSION SUBJECT TO FINAL EDITING

Figure 10.6: Illustration of some model biases in simulations performed with dynamical models. (a) Top row: Mean summer (June to August) near-surface air temperature (in °C) over the Mediterranean area in Berkeley Earth and respective mean bias for five multi-model historical experiments with GCMs (CMIP5, CMIP6 and HighResMIP) and RCMs (CORDEX EUR-44 and EUR-11) averaged between 1986–2005. Bottom row: Box-and-whisker plot shows spread of the 20 annual mean summer surface air temperature averaged over land areas in the western Mediterranean region (33°N–45°N, 10°W–10°E, black quadrilateral in the first panel of the top row) for a set of references and single model runs of the five multi-model experiments (one simulation per model) between 1986–2005. Additional observation and reanalysis data included in the bottom row are CRU TS, HadCRUT4, HadCRUT5, E-OBS, WFDE5, ERA5, ERA-Interim, CERA-20C, JRA-25, JRA-55, CFSR, MERRA2, MERRA. Berkeley Earth is

shown in the first box to the left. (b) as (a) but for precipitation rate (mm day^{-1}) and showing CRU TS in the first panel of the top row. Biases of the five multi-model experiments are shown with respect to CRU TS. Additional observation and reanalysis data included in the bottom row are GPCC, REGEN, E-OBS, GHCN, WFDE5, CFSR, ERA-Interim, ERA5, JRA-55, MERRA2, MERRA. CRU TS is shown in the first box to the left. All box-and-whisker plots show the median (line), and the interquartile range (IQR = Q3–Q1, box), with top whiskers extending to the last data less than Q3+1.5×IQR and analogously for bottom whiskers. Data outside the whiskers range appear as flyers (circles). Further details on data sources and processing are available in the chapter data table (Table 10.SM.11).

ACCEPTED VERSION
SUBJECT TO FINAL EDITING



ACCEPTED VERSION SUBJECT TO FINAL EDITING

Figure 10.7: Northern-Hemisphere blocking performance in historical coupled simulations for different multi-model ensembles. CMIP5/6: CMIP5 and CMIP6 DECK historical simulations, 1950-2005, LC/HC: Low/High-resolution simulations from the PRIMAVERA project, 1950–2014 following the hist-1950 experiment of the CMIP6 HighResMIP Protocol, (Haarsma et al., 2016). (top) blocking frequency, i.e. fraction of blocked days; (middle) root-mean-squared error in blocking frequency; (bottom) 90th percentile of blocking persistence, aggregated over an Atlantic domain (left, ATL: 90ºW–90ºE, 50º–75ºN) and a Pacific domain (right, PAC: 90ºE–270ºE, 50º–75ºN). Results are for boreal winter (DJF) and summer (JJA). Box-and-whisker plots for CMIP5/6 follow the methodology used in Figure 10.6 and show median (line), mean (triangle), and interquartile range (box) across 29 models for each ensemble. The reference estimate (ERA, asterisk) is from a 50-year reanalysis dataset that merged ERA-40 (1962–1978) and ERA-Interim (1979–2011) reanalyses. An estimate of internal variability for each metric (IV) is shown as a box-and-whisker plot over the asterisk and is obtained from a single-model ensemble (ECMWF-IFS high-resolution hist-1950 experiment, 6 x 65 years). For details on the methodology see (Schiemann et al., 2020). Further details on data sources and processing are available in the chapter data table (Table 10.SM.11).

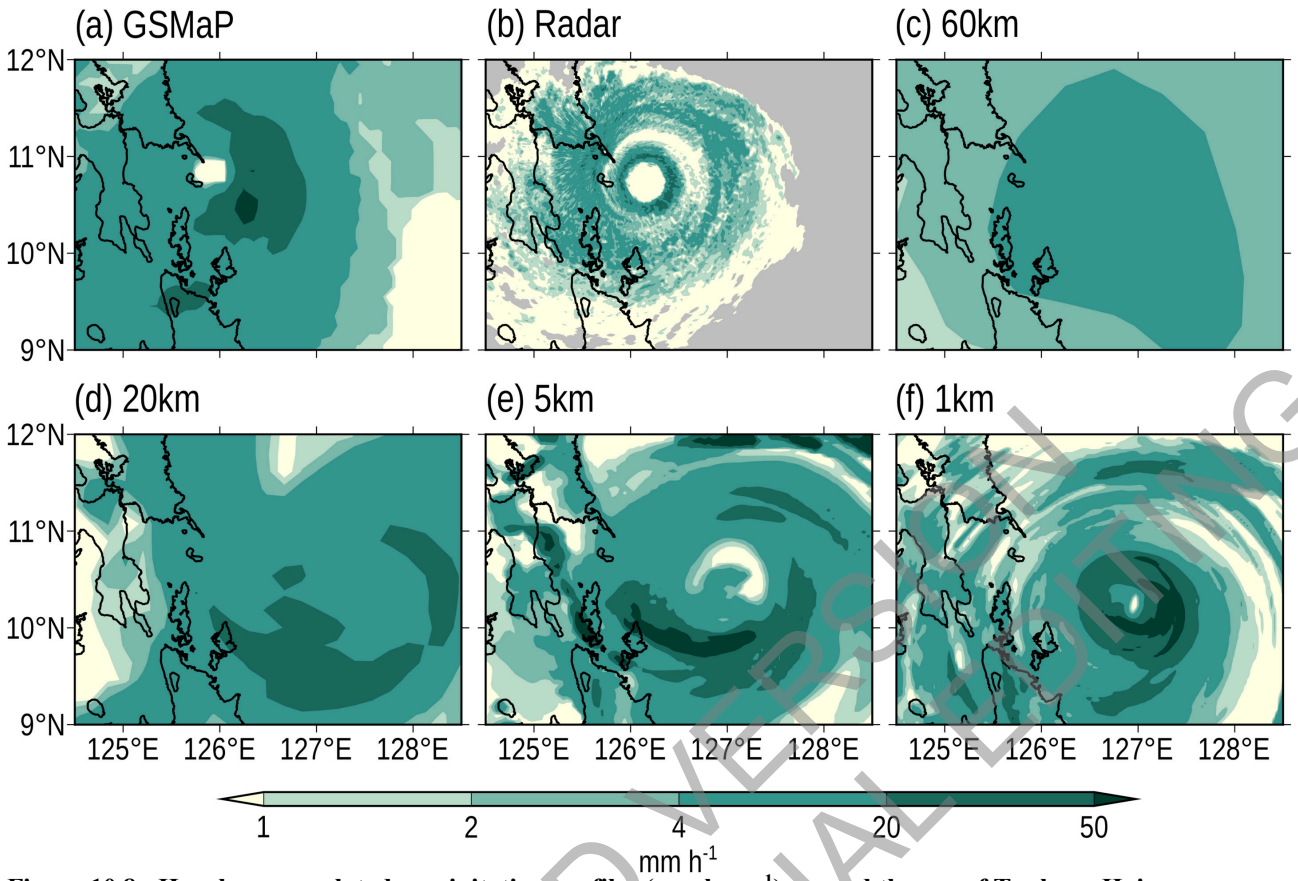


Figure 10.8: Hourly accumulated precipitation profiles (mm hour^{-1}) around the eye of Typhoon Haiyan. Represented by (a) GSMaP (Global Satellite Mapping of Precipitation) data (multi-satellite observation), (b) Guiuan radar (PAGASA), (c) Weekly Ensemble Prediction System (WEPS) data (JMA) (60 km), (d) NHRCM (20 km), (e) NHRCM (5 km), and (f) WRF (1 km) models. Panels (b), (d)-(f) are adapted from Takayabu et al. (2015). CCBY3.0 https://creativecommons.org/licenses/by/3.0. Further details on data sources and processing are available in the chapter data table (Table 10.SM.11).

ACCEPTED VERSION SUBJECT TO FINAL EDITING

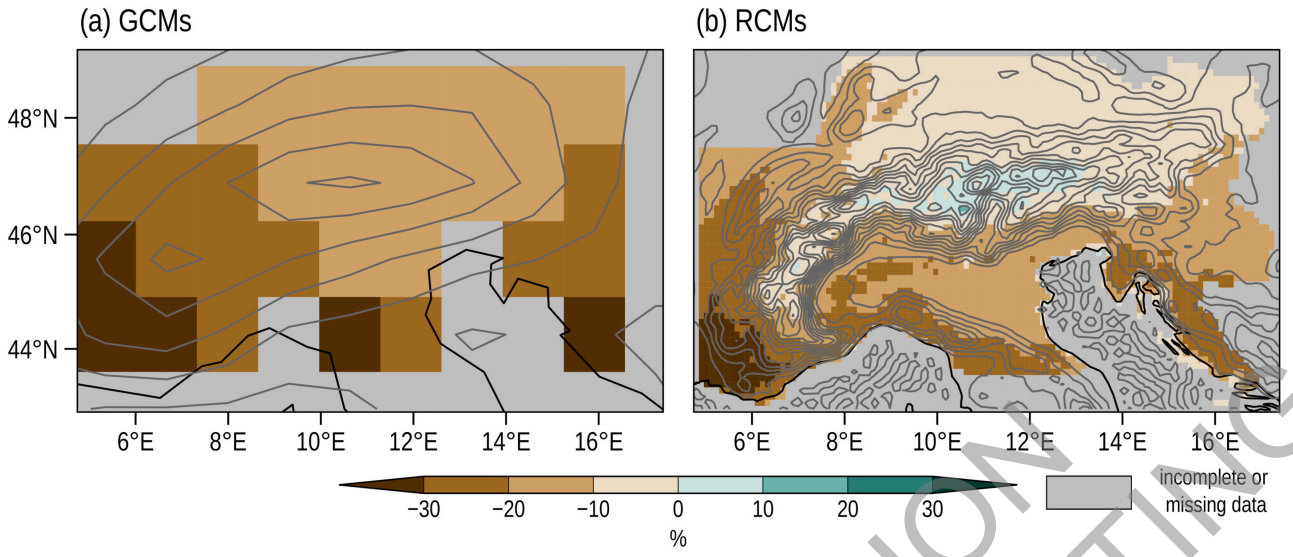


Figure 10.9: Projected changes in summer (June to August) precipitation (in percent with respect to the mean precipitation) over the Alps between the periods 2070–2099 and 1975–2004. (a) Mean of four GCMs regridded to a common 1.32°x1.32° grid resolution; (b) mean of six RCMs driven with these GCMs. The grey isolines show elevation at 200 m intervals of the underlying model data. Further details on data sources and processing are available in the chapter data table (Table 10.SM.11). Adapted from Giorgi et al. (2016).

ACCEPTED VERSION
SUBJECT TO FINAL EDITING

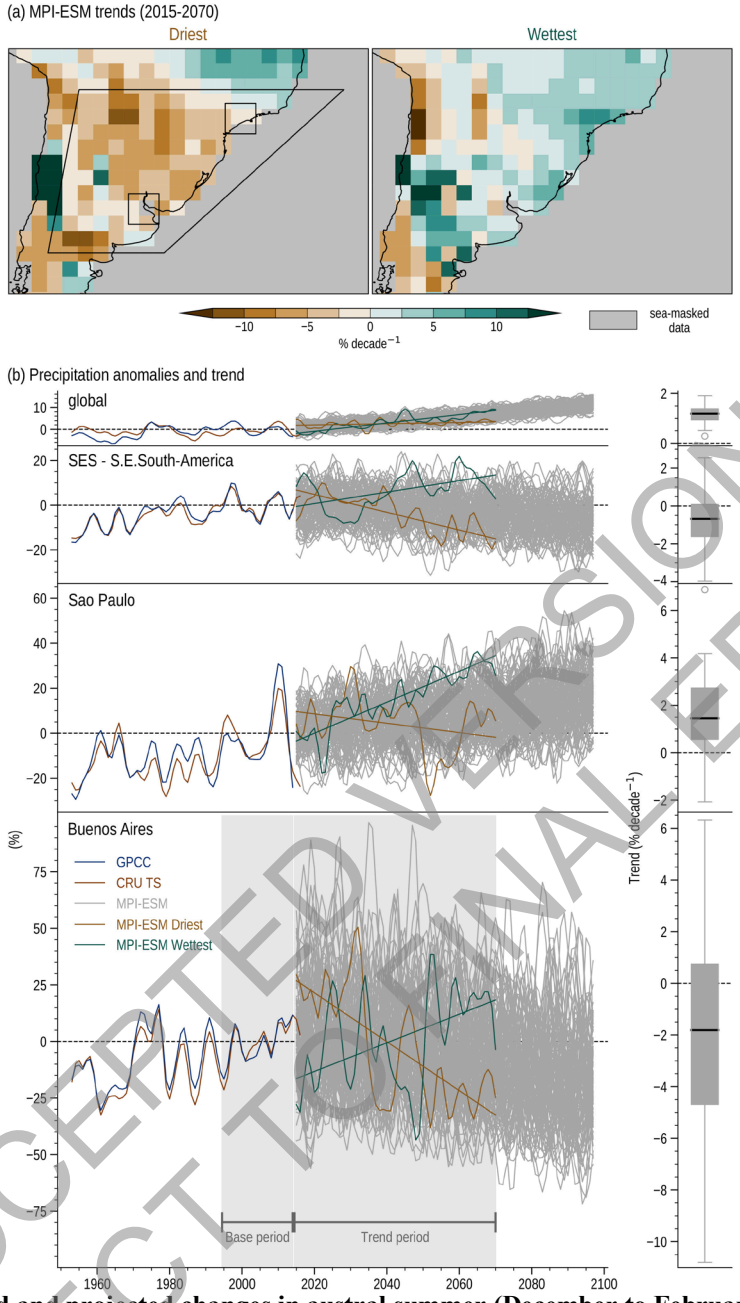
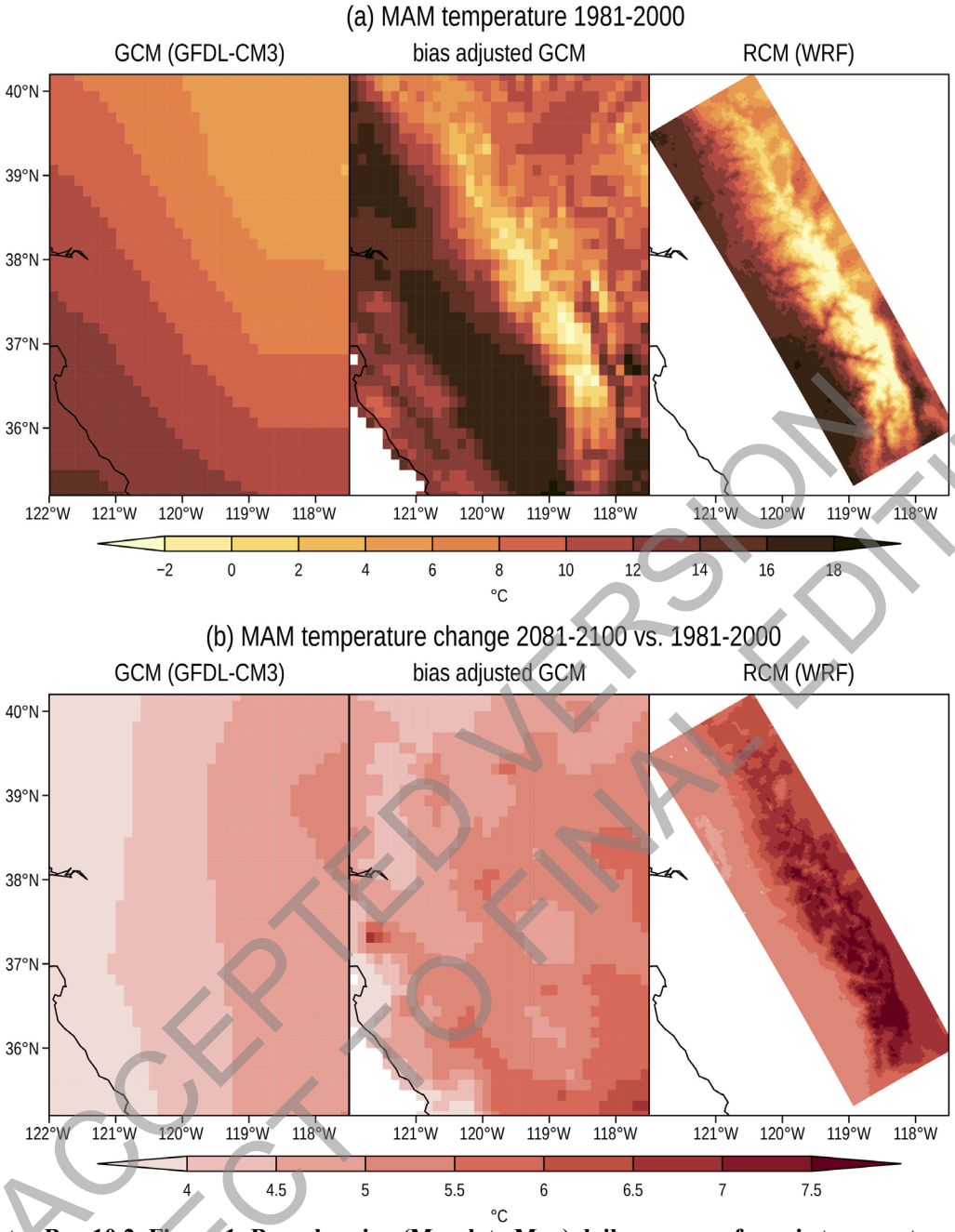


Figure 10.10: Observed and projected changes in austral summer (December to February) mean precipitation in GPCC, CRU TS and 100 members of the MPI-ESM. (a) 55-year trends (2015–2070) from the ensemble members with the lowest (left) and highest (right) trend (% per decade, baseline 1995–2014). (b) Time series (%, baseline 1995–2014) for different spatial scales (from top to bottom: global averages; S.E. South America; grid boxes close to São Paulo and Buenos Aires) with a five-point weighted running mean applied (a variant on the binomial filter with weights [1-3-4-3-1]). The brown (green) lines correspond to the ensemble member with weakest (strongest) 55-year trend and the grey lines to all remaining ensemble members. Box-and-whisker plots show the distribution of 55-year linear trends across all ensemble members, and follow the methodology used in Figure 10.6. Trends are estimated using ordinary least squares. Further details on data sources and processing are available in the chapter data table (Table 10.SM.11).

ACCEPTED VERSION SUBJECT TO FINAL EDITING



Cross-Chapter Box 10.2, Figure 1: Boreal spring (March to May) daily mean surface air temperature in the Sierra Nevada region in California. (a) Present climate (1981–2000 average, in °C) in the GFDL-CM3 AOGCM, interpolated to 8 km (left), GCM bias adjusted (using quantile mapping) to observations at 8 km resolution (middle) and WRF RCM at 3 km horizontal resolution (right). (b) Climate change signal (2081–2100 average minus 1981–2000 average according to RCP8.5, in °C) in the AOGCM (left), the bias adjusted AOGCM (middle) and the RCM (right). Further details on data sources and processing are available in the chapter data table (Table 10.SM.11). Adapted from Maraun et al. (2017b).

ACCEPTED VERSION SUBJECT TO FINAL EDITING

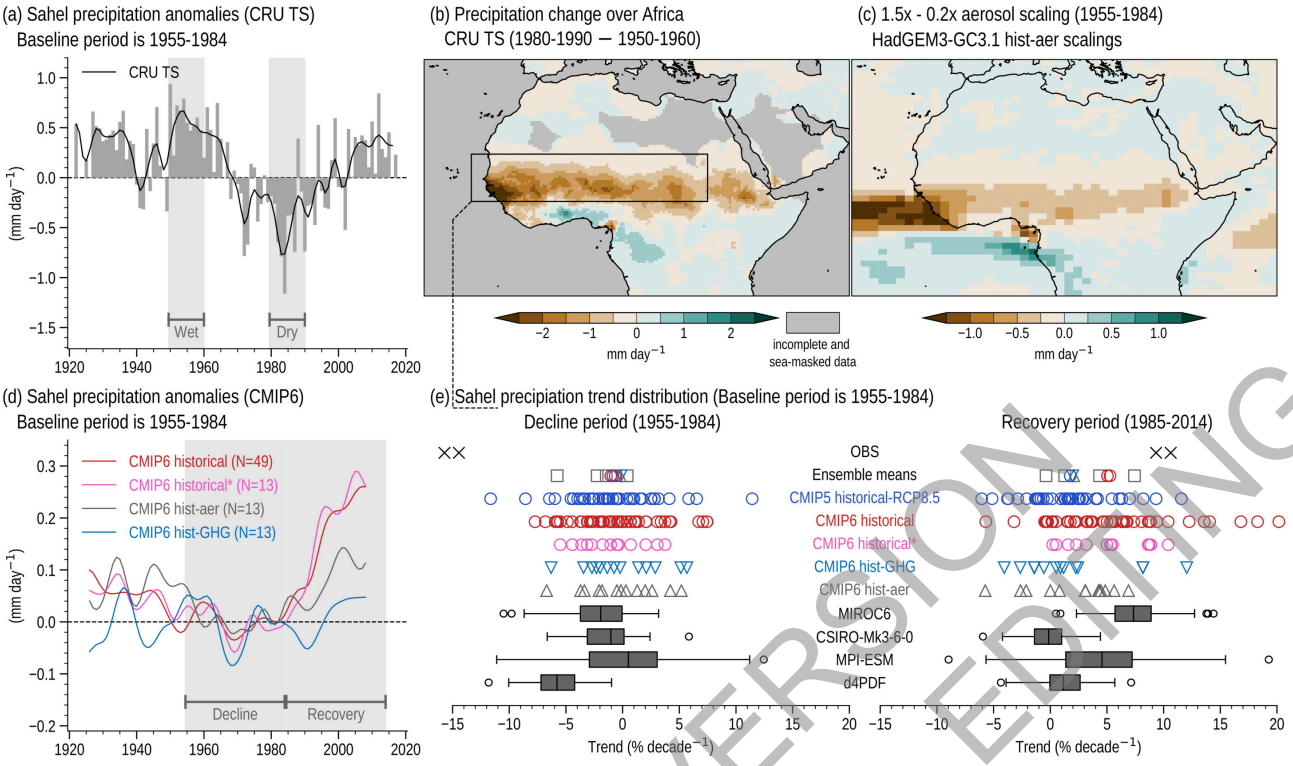


Figure 10.11: Attribution of historic precipitation change in the Sahelian West African monsoon during June to September. (a) Time series of CRU TS precipitation anomalies (mm day^{-1}, baseline 1955–1984) in the Sahel box (10°N–20°N, 20°W–30°E) indicated in panel (b) applying the same low-pass filter as that used in Figure 10.10. The two periods used for difference diagnostics are shown in grey columns. (b) Precipitation change (mm day^{-1}) in CRU TS data for 1980–1990 minus 1950–1960 periods. (c) Precipitation difference (mm day^{-1}) between 1.5x and 0.2x historical aerosol emissions scaling factors averaged over 1955–1984 and five ensemble members of HadGEM3 experiments after Shonk et al. (2020). (d) Sahel precipitation anomaly time series (mm day^{-1}, baseline 1955–1984) in CMIP6 for 49 historical simulations with all forcings (red), and thirteen for each of greenhouse gas-only forcing (light blue) and aerosol-only forcing (grey), with a thirteen-point weighted running mean applied (a variant on the binomial filter with weights [1-6-19-42-71-96-106-96-71-42-19-6-1]). The CMIP6 subsample of all forcings matching the individual forcing simulations is also shown (pink). (e) Precipitation linear trend (% per decade) for (left) decline (1955–1984) and (right) recovery periods (1985–2014) for ensemble means and individual CMIP6 historical experiments (including single-forcing) as in panel (d) plus 34 CMIP5 models (dark blue). Box-and-whisker plots show the trend distribution of the three coupled and the d4PDF atmosphere-only SMILEs used throughout Chapter 10 and follow the methodology used in Figure 10.6. The two black crosses represent observational estimates from GPCC and CRU TS. Trends are estimated using ordinary least-squares regression. Further details on data sources and processing are available in the chapter data table (Table 10.SM.11).

ACCEPTED VERSION SUBJECT TO FINAL EDITING

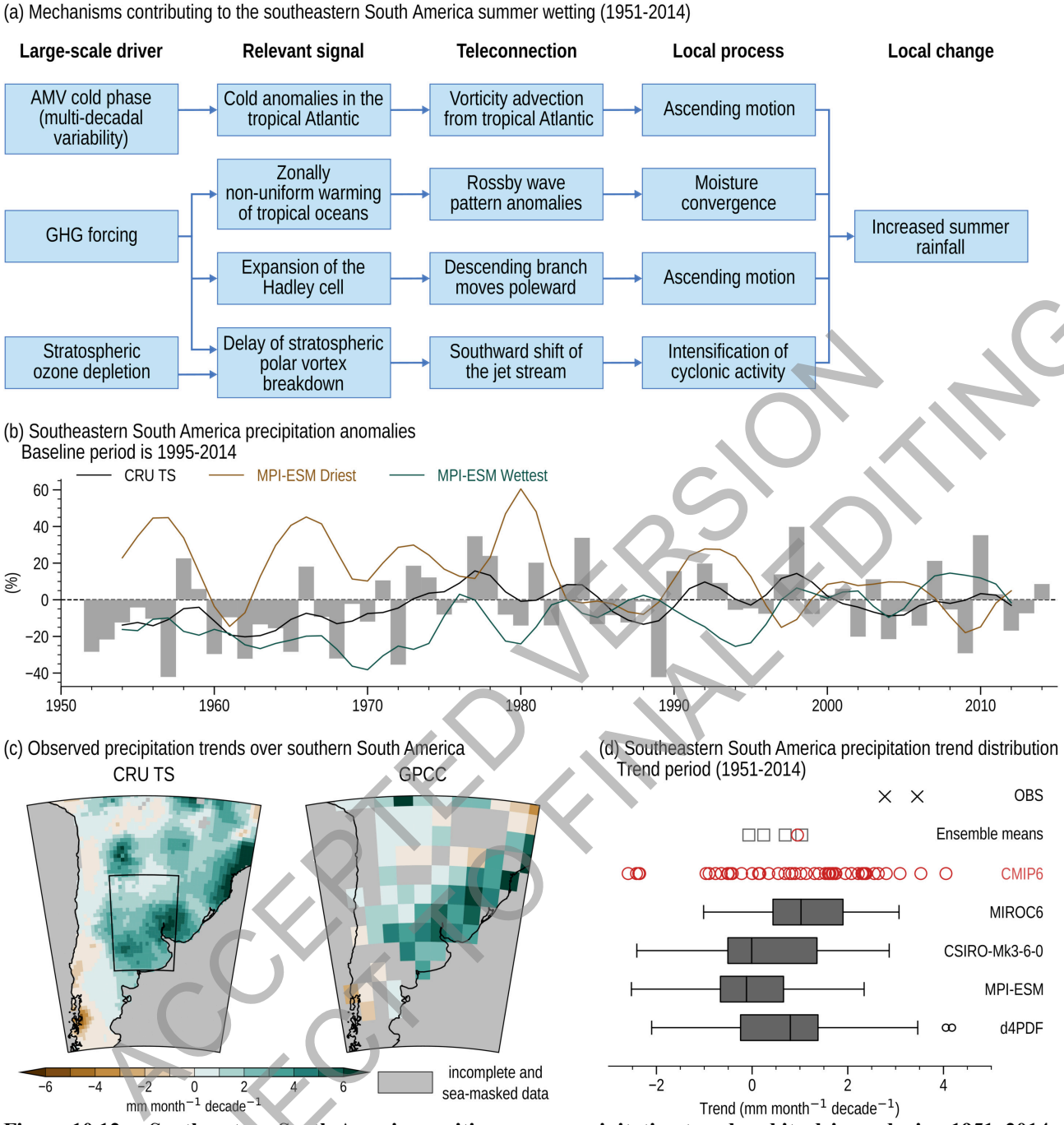


Figure 10.12: **Southeastern South America positive mean precipitation trend and its drivers during 1951–2014.** (a) Mechanisms that have been suggested to contribute to southeastern South America summer wetting. (b) Time series of austral summer (December to February) precipitation anomalies (%, baseline 1995–2014) over the south-eastern South American region (26.25°S–38.75°S, 56.25°W–66.25°W), black quadrilateral in the first map of panel (c). Black, brown and green lines show low-pass filtered time series for CRU TS, and the members with driest and wettest trends of the MPI-ESM SMILE (between 1951–2014), respectively. The filter is the same as the one used in Figure 10.10. (c) Mean austral summer precipitation spatial linear 1951–2014 trends (mm per month and decade) from CRU TS and GPCC. Trends are estimated using ordinary least squares regression. (d) Distribution of precipitation 1951–2014 trends over southeastern South America from GPCC and CRU TS (black crosses), CMIP6 all-forcing historical (red circles) and MIROC6, CSIRO-Mk3-6-0, MPI-ESM and d4PDF SMILEs (grey box-and-whisker plots). Grey squares refer to ensemble mean trends of their respective SMILE and the red circle refers to the CMIP6 multi-model mean. Box-and-whisker plots follow the methodology used in Figure 10.6. Further details on data sources and processing are available in the chapter data table (Table 10.SM.11).

ACCEPTED VERSION SUBJECT TO FINAL EDITING

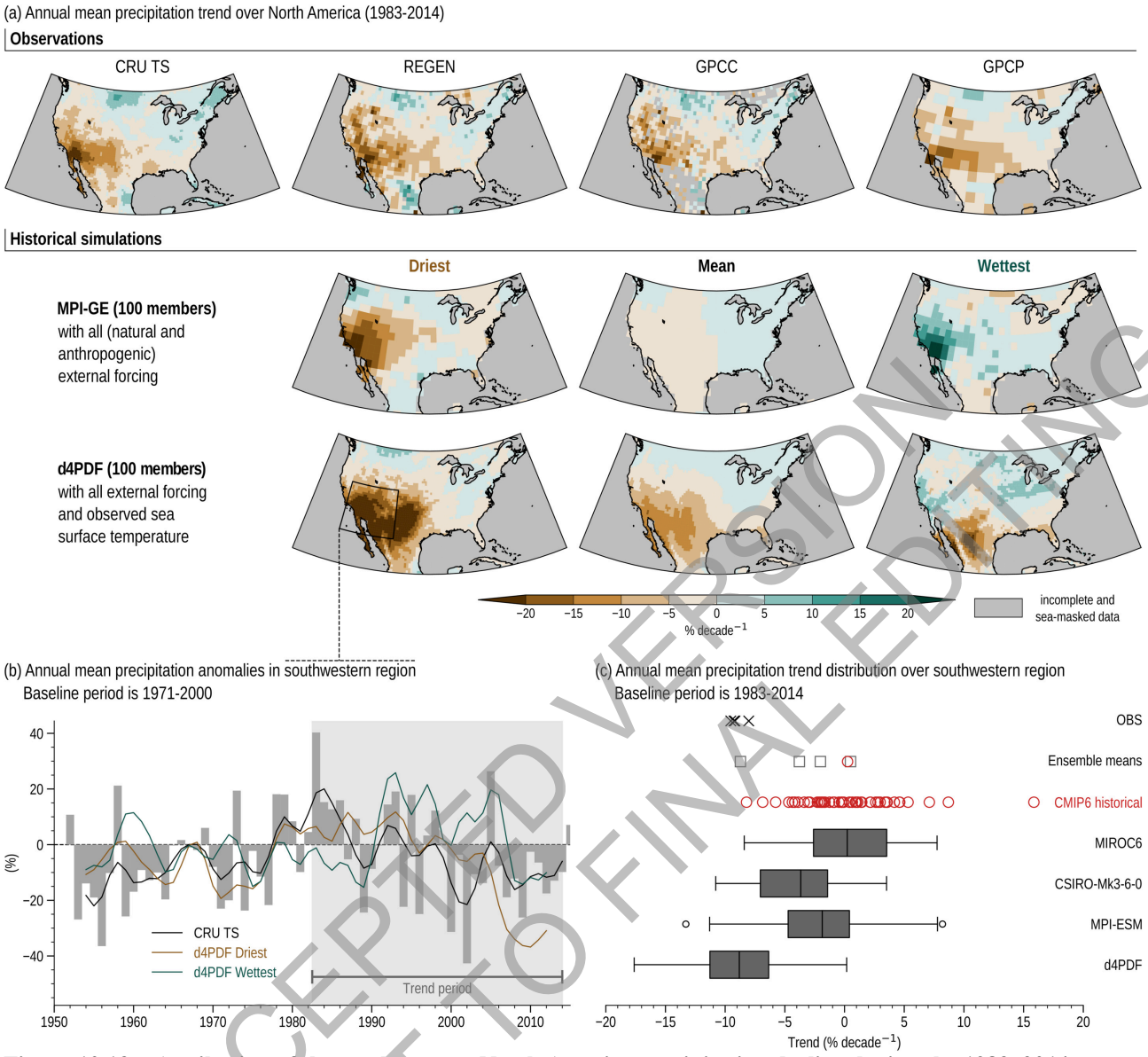


Figure 10.13: Attribution of the southwestern North America precipitation decline during the 1983–2014 period. (a) Water year (October to September) precipitation spatial linear trend (in percent per decade) over North America from 1983 to 2014. Trends are estimated using ordinary least squares. Top row: Observed trends from CRU TS, REGEN, GPCC, and the Global Precipitation Climatology Project (GPCP). Middle row: Driest, mean and wettest trends (relative to the region enclosed in the black quadrilateral, bottom row) from the 100 members of the MPI-ESM coupled SMILE. Bottom row: Driest, mean and wettest trends relative to the above region from the 100 members of the d4PDF atmosphere-only SMILE. (b) Time series of water year precipitation anomalies (%, baseline 1971–2000) over the above south-western North America region for CRU TS (grey bar charts). Black, brown and green lines show low-pass filtered time series for CRU TS, driest and wettest members of the d4PDF SMILE, respectively. The filter is the same as the one used in Figure 10.10. (c) Distribution of south-western region-averaged water-year precipitation 1983–2014 trends (in percent per decade) for observations (CRU TS, REGEN, GPCC and GPCP, black crosses), CMIP6 all-forcing historical simulations (red circles), the MIROC6, CSIRO-Mk3-6-0, MPI-ESM and d4PDF SMILEs (grey box-and-whisker plots). Grey squares refer to ensemble mean trends of their respective SMILE and the red circle refers to the CMIP6 multi-model mean. Box-and-whisker plots follow the methodology used in Figure 10.6. Further details on data sources and processing are available in the chapter data table (Table 10.SM.11).

ACCEPTED VERSION SUBJECT TO FINAL EDITING

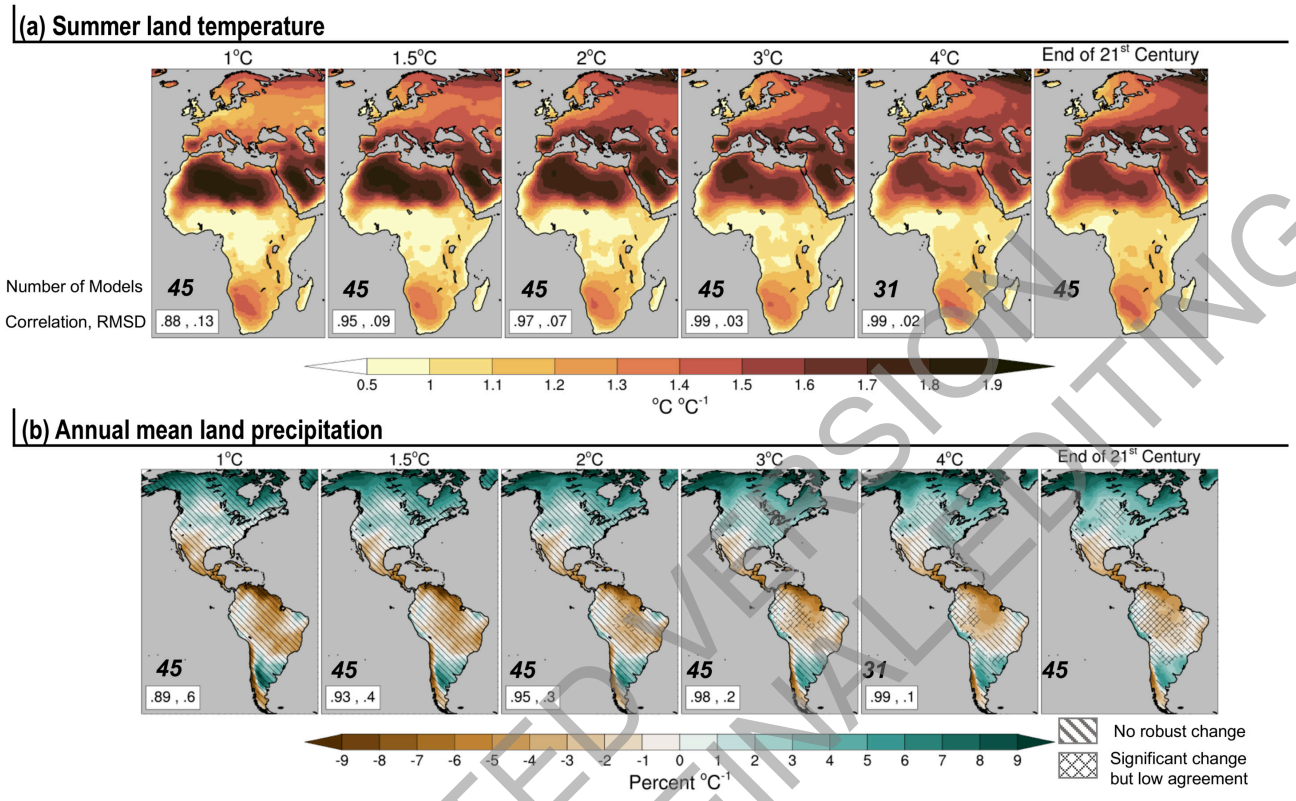


Figure 10.14: Robustness and scalability of anthropogenic signals at regional scale. (a) Spatial patterns of Europe and Africa summer (June to August) surface air temperature change (in °C °C^{-1}) from the CMIP6 multi-model mean (45 models, one member per model, historical simulations and scenario SSP5-8.5) at different global warming levels (GWLs) and the end-21st century scaling pattern estimated from the multi-model mean difference between 2081–2100 and the pre-industrial period (1850–1900) divided by the corresponding global mean warming. The scale of all GWL patterns has been adjusted to a global mean warming of 1°C (for example, the resulting 3°C spatial pattern has been divided by three). The scales of the GWL patterns have to be multiplied by their threshold values to obtain the actual simulated warming. The metrics shown in the bottom left corner of the GWL pattern plots indicate the spatial pattern correlation and the root-mean square difference between the GWL patterns and the scaling pattern. The number in bold just above the metrics gives the number of used CMIP6 models (out of 45) that have reached the GWL threshold. Areas with robust change (at least 66% of the models have a signal to noise ratio greater than one and 80% or more of the models agree on the sign of the change) are coloured with no pattern overlaid (Cross-Chapter Box Atlas.1). Areas with a significant change (at least 66% of the models have a signal to noise ratio greater than one) and lack of model agreement (meaning that less than 80% of the models agree on the sign of the change) are marked by cross-hatching. Areas with no change or no robust change (less than 66% of the models have a signal to noise ratio greater than one) are marked by negatively sloped hatching. (b) Same as (a) but for North, Central and South America annual mean precipitation relative change (percent °C^{-1}). The baseline for precipitation climatology is 1850–1900. Further details on data sources and processing are available in the chapter data table (Table 10.SM.11).

ACCEPTED VERSION SUBJECT TO FINAL EDITING

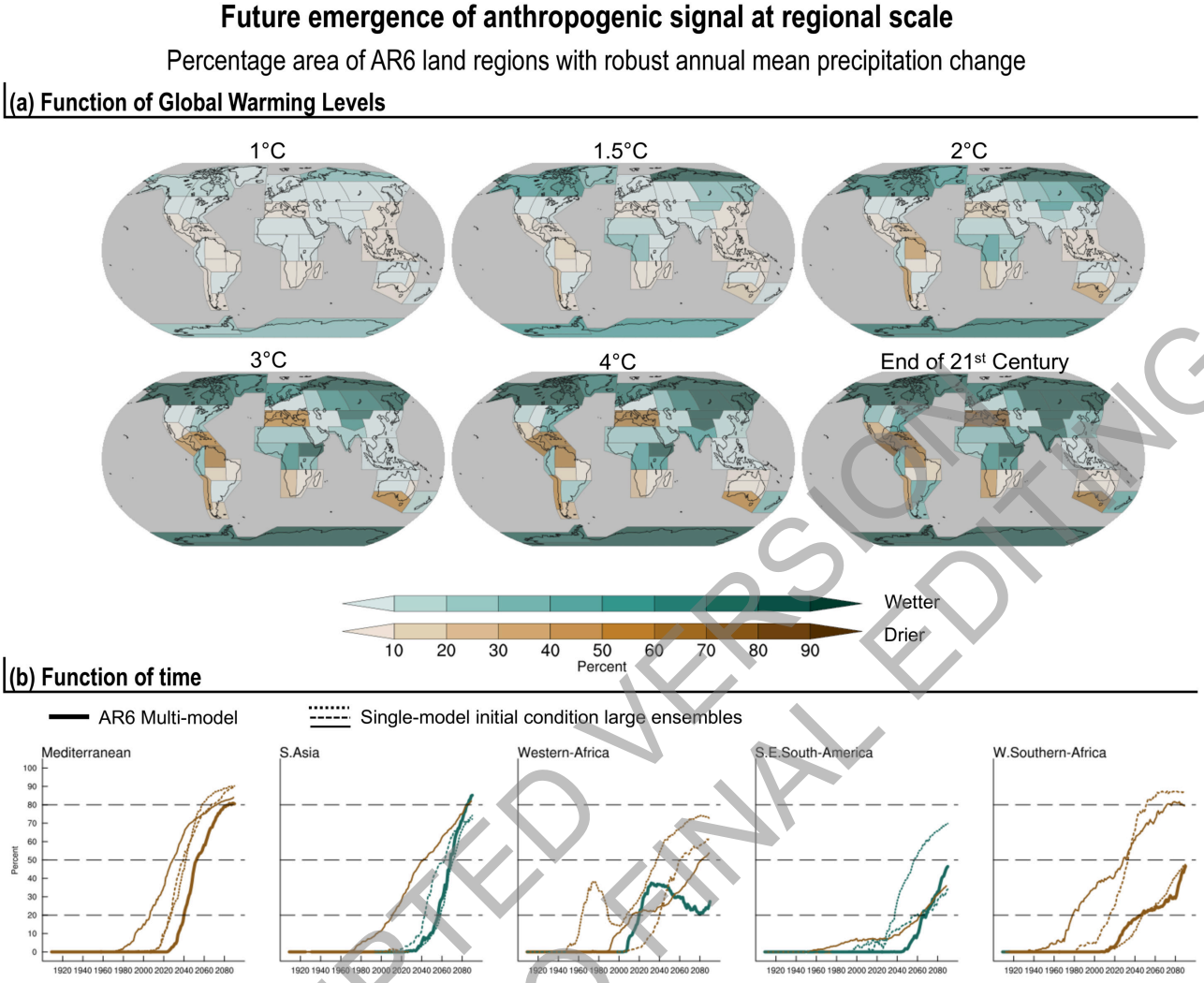


Figure 10.15: Future emergence of anthropogenic signal at regional scale. (a) Percentage area of land regions with robust annual mean precipitation change as a function of increasing GWLs. Robustness of the precipitation change is first estimated at each grid-point followed by the estimation of the AR6 region area with robust changes. For each CMIP6 model considered (45 models, one member per model, historical simulations and scenario SSP5-8.5), the annual mean precipitation change is based on the difference between a 20-year average centred on the GWL crossing year and the mean precipitation during the pre-industrial period (1850–1900) taken as a reference. Robustness of the change is acted when at least 66% of the models (30 out of 45) have a signal to noise ratio greater than one and at least 80% of them (36 out of 45) agree on the sign of change. The signal to noise ratio is estimated for each model from the ratio between the change and the standard deviation of non-overlapping 20-year means of the corresponding pre-industrial simulation (scaled by square root of 2 times 1.645). (b) Time evolution of the percentage area of land region with robust annual mean precipitation change for five AR6 land regions. Thick solid lines represent precipitation changes based on the same CMIP6 ensemble as in (a). Thin solid, dotted and dashed lines represent changes based on the three coupled SMILEs used in Chapter 10, illustrating the influence of internal variability on the emergence of robust change. The change is estimated from the difference between all consecutive 20-year periods from 1900–1919 up to 2081–2100 and the pre-industrial period. The line colour indicates the sign of the robust change given by the multi-model mean (CMIP6) or ensemble mean (SMILE) change: brown (decreasing precipitation) and dark green (increasing precipitation). Further details on data sources and processing are available in the chapter data table (Table 10.SM.11).

ACCEPTED VERSION SUBJECT TO FINAL EDITING

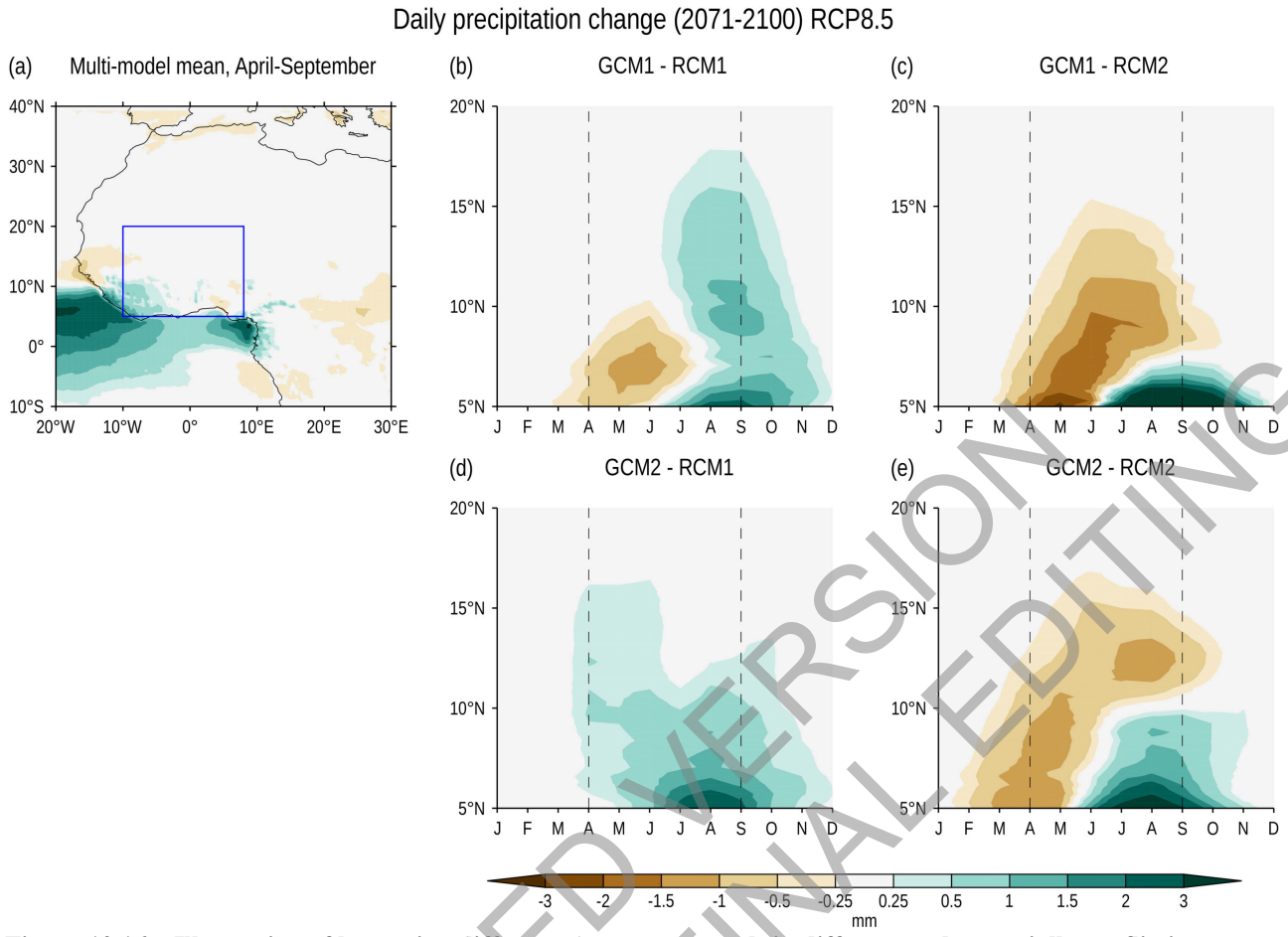


Figure 10.16: Illustration of how using different sources can result in different and potentially conflicting information. Change in daily precipitation (2071–2100 RCP8.5 relative to 1981–2010) over West Africa as simulated by an ensemble of GCM-driven RCMs. (a) Change in daily precipitation (mm) for April to September, as mean of 17 CORDEX models (Dosio et al., 2020) (b-e) Time-latitude diagram of daily precipitation change for four selected RCM-GCM combinations. For each month and latitude, model results are zonally averaged between 10°W–10°E (blue box in a). Different GCM-RCM combinations can produce substantially different and contrasting results, when the same RCM is used to downscale different GCMs (b, d), or the same GCM is downscaled by different RCMs (d, e). GCM1=IPSL-IPSL-CM5A, GCM2=ICHEC-EC-EARTH, RCM1=RCA4, RCM2=REMO2009. Adapted from (Dosio et al., 2020), CCBY4.0 https://creativecommons.org/licenses/by/4.0/. Further details on data sources and processing are available in the chapter data table (Table 10.SM.11).

ACCEPTED VERSION SUBJECT TO FINAL EDITING

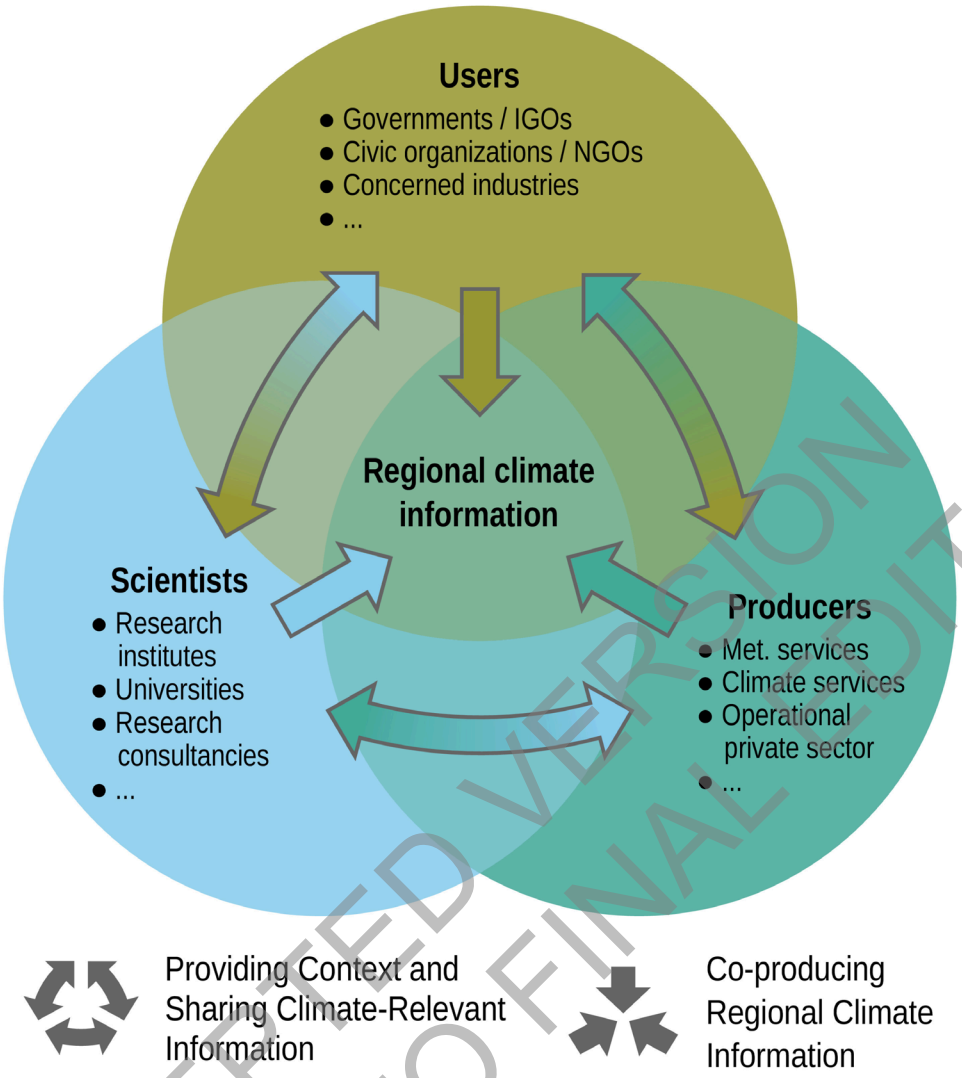
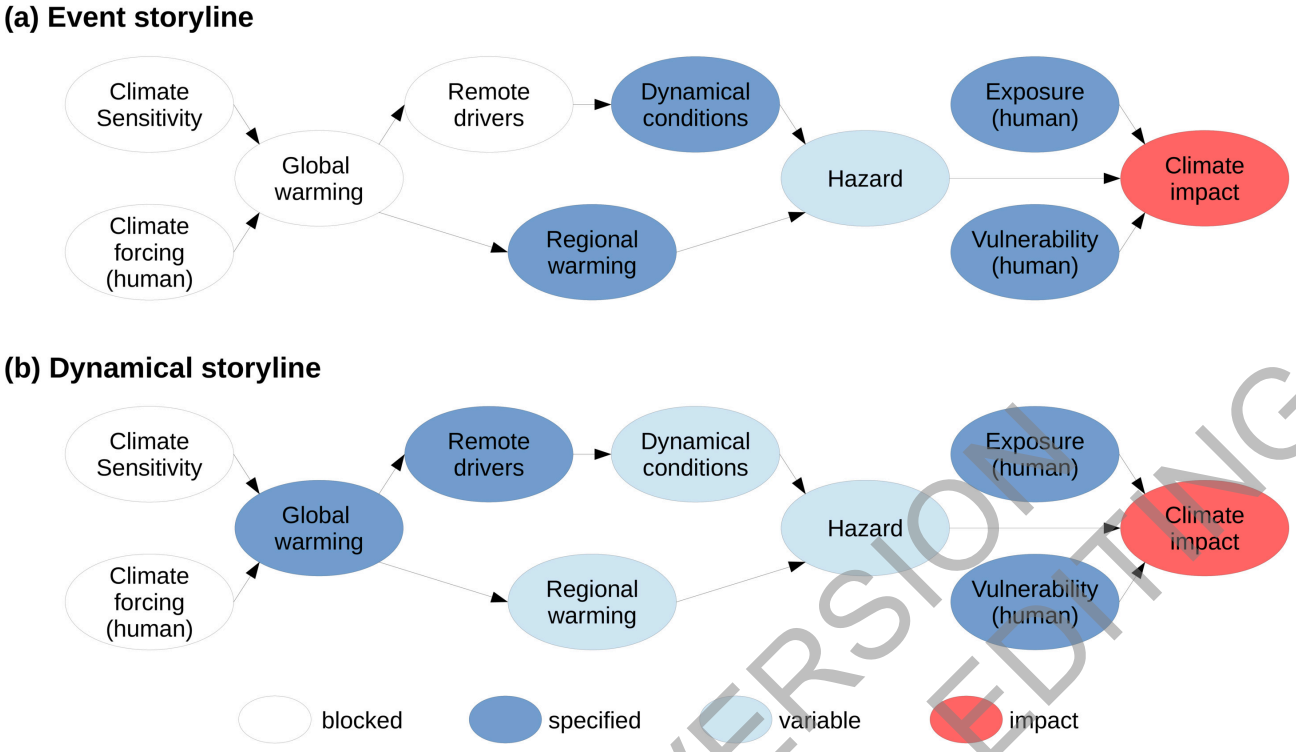


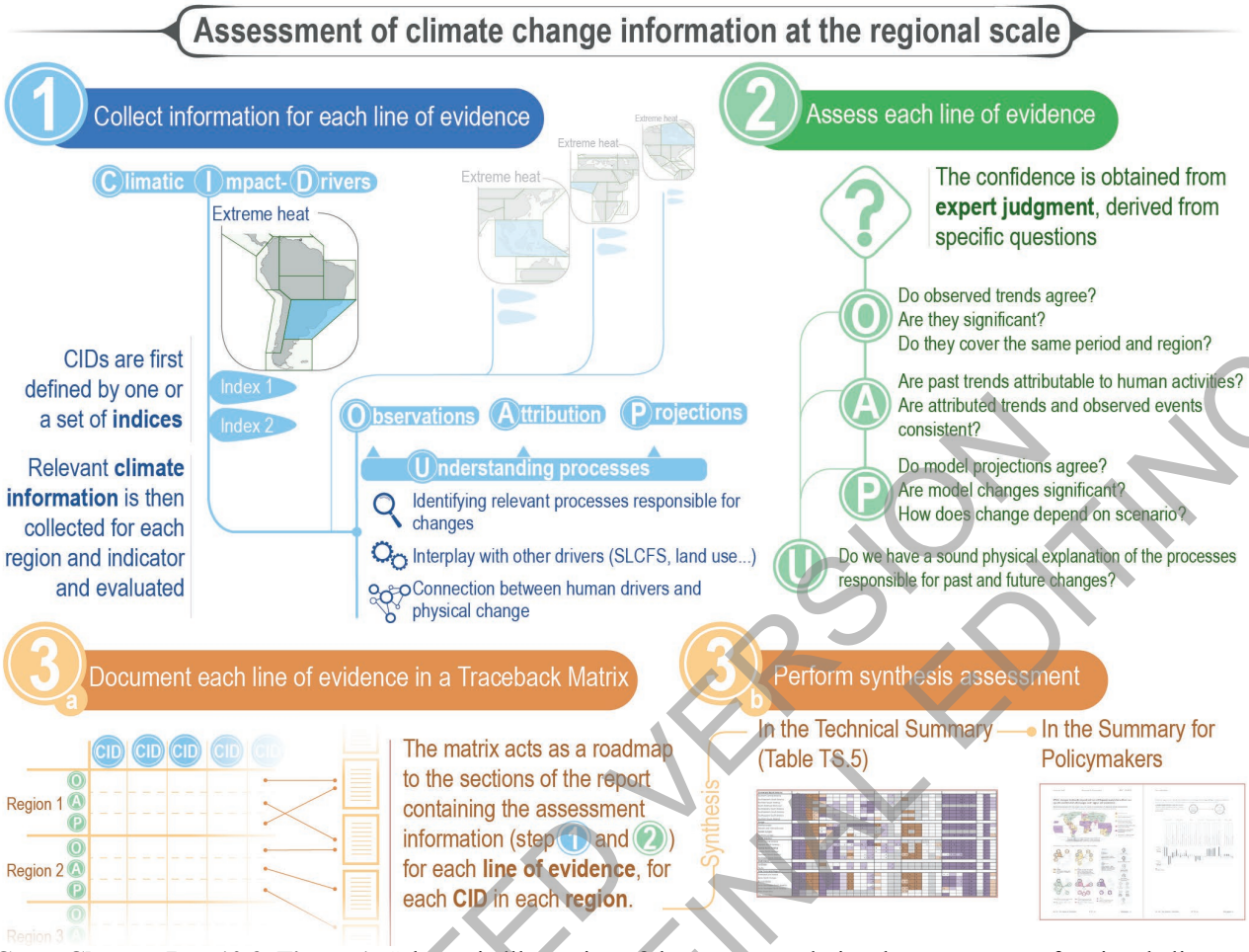
Figure 10.17: Effective regional climate information requires shared development of actionable information that engages all parties involved and the values that guide their engagement. Participants in the development of climate information come from varying perspectives, based in part on their professions and communities. Each of the three broad categories shown in the Venn diagram (Users, Producers, Scientists) is not a homogenous group, and often has a diversity of perspectives, values and interests among its members. The subheadings in each category are illustrative and not all-inclusive. The arrows connecting those categories represent the distillation process of providing context and sharing climate relevant information. The arrows that point toward the centre represent the distillation of climate information that involves all three categories.

ACCEPTED VERSION SUBJECT TO FINAL EDITING



Box 10.2, Figure 1: Schematic of two types of physical climate storylines with a particular climate impact of concern (red). The storylines are defined by specified elements (dark blue). Variable elements (light blue) are simulated conditional on the specified elements. The white elements are 'blocked' since their state does not need to be known to determine the light blue elements. Other types of storylines could be defined by specifying other elements (e.g., storylines of different climate sensitivities or different representative concentration pathways). (a) Event storyline, where the particular dynamical conditions during the event as well as the regional warming are specified and control the hazard arising from the event. (b) Dynamical storyline, where the global warming level and remote drivers are specified and control the long-term changes in atmospheric dynamics and regional warming. In both storylines, the impact is also conditioned on specified exposure and vulnerability. Adapted from Shepherd (2019).

ACCEPTED VERSION SUBJECT TO FINAL EDITING



Cross-Chapter Box 10.3, Figure 1: Schematic illustration of the process to derive the assessment of regional climate change information based on a distillation process of multiple lines of evidence taken from observed trends, attribution of trends or events, climate model projections, and physical understanding.

ACCEPTED VERSION SUBJECT TO FINAL EDITING

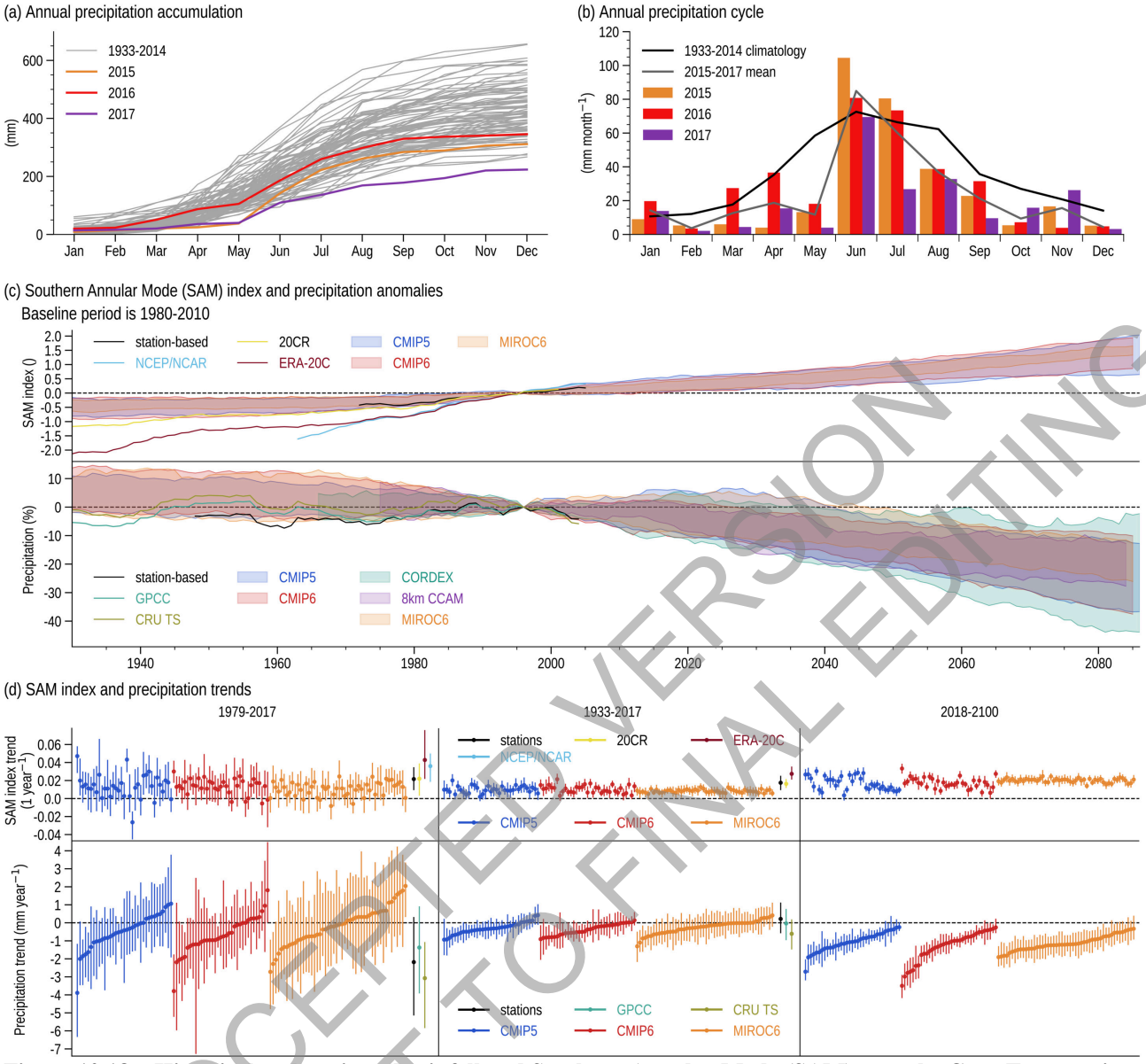
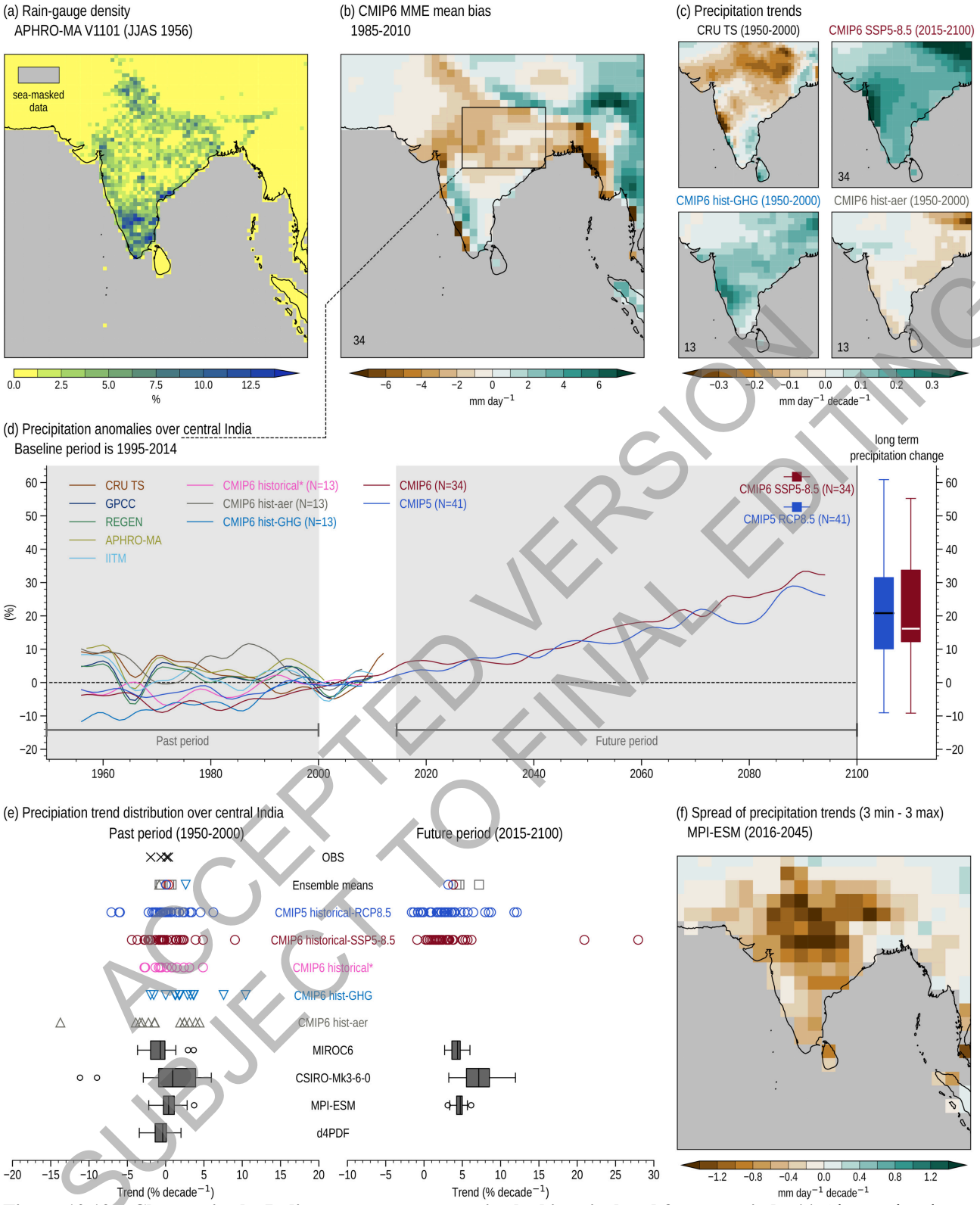


Figure 10.18: **Historical and projected rainfall and Southern Annular Mode (SAM) over the Cape Town region.** (a) Yearly accumulation of rainfall (in mm) obtained by summing monthly totals between January and December, with the drought years 2015 (orange), 2016 (red), and 2017 (purple) highlighted in colour. (b) Monthly rainfall for the drought years (in colour) compared with the 1981–2014 climatology (grey line). Rainfall in (a) and (b) is the average of 20 quality controlled and gap-filled series from stations within the Cape Town region (31ºS–35ºS, 18ºW–20.5ºW). (c) Time series of the SAM index and of historical and projected rainfall anomalies (%, baseline 1980–2010) over the Cape Town region. Observed data presented as 30-year running means of relative total annual rainfall over the Cape Town region for station-based data (black line, average of 20 stations as in (a) and (b)), and gridded data (average of all grid cells falling within 31ºS–35ºS, 18ºW–20.5ºW): GPCC (green line) and CRU TS (olive line). Model ensemble results presented as the 90th-percentile range of relative 30-year running means of rainfall and the SAM index from 35 CMIP5 (blue shading) and 35 CMIP6 (red shading) simulations, 6 CORDEX simulations driven by 1 to 10 GCMs (cyan shading), 6 CCAM (purple shading) simulations from individual ensemble members, and 50 members from the MIROC6 SMILE simulations (orange shading). The light blue, dark red and yellow lines correspond to NCEP/NCAR, ERA20C and 20CR, respectively. The SAM index is calculated from sea-level pressure reanalysis and GCM data as per Gong and Wang (1999) and averaged over the aforementioned bounding box. CMIP5, CORDEX and CCAM projections use RCP8.5, and CMIP6 and MIROC6 SMILE projections use SSP5-8.5. (d) Historical and projected trends in rainfall over the Cape Town region and in the SAM index. Observations and gridded data processed as in (c). Trends calculated as Theil-Sen trend with block-bootstrap confidence interval estimate. Markers show median trend, bars 95% confidence interval. GCMs in each CMIP group were ordered according to the magnitude of trend in rainfall, and

ACCEPTED VERSION SUBJECT TO FINAL EDITING

1 the same order is maintained in panels showing trends in the SAM. Further details on data sources and
2 processing are available in the chapter data table (Table 10.SM.11).
3

ACCEPTED VERSION
SUBJECT TO FINAL EDITING



ACCEPTED VERSION SUBJECT TO FINAL EDITING

Figure 10.19: **Changes in the Indian summer monsoon in the historical and future periods**. (a) Observational uncertainty demonstrated by a snapshot of rain-gauge density (% of 0.05°-subgrid boxes containing at least one gauge) in the APHRO-MA 0.5° daily precipitation dataset for June to September 1956. (b) Multi-model ensemble (MME)-mean bias of 34 CMIP6 models for June to September precipitation (mm day-1) compared to CRU TS observations for the 1985–2010 period. (c) Maps of rainfall trends (mm day-1 per decade) in CRU TS observations (1950–2000), the CMIP6 MME-mean of SSP5-8.5 future projections for 2015–2100 (34 models), the CMIP6 hist-GHG and hist-aer runs, both measured over 1950 to 2000. (d) Low-pass filtered time series of June to September precipitation anomalies (%, relative to 1995–2014 baseline) averaged over the central India box shown in panel (b). The averaging

region (20°N–28°N, 76°E–87°E) follows other works (Bollasina, Ming, & Ramaswamy, 2011; Huang et al., 2020; Jin & Wang, 2017). Time series are shown for CRU TS (brown), GPCC (dark blue), REGEN (green), APHRO-MA (light brown) observational estimates and the IITM all-India rainfall product (light blue) in comparison with the CMIP6 mean of 13 models for the all-forcings historical (pink) the aerosol-only (hist-aer, grey) and greenhouse gas-only (hist-GHG, blue). Dark red and blue lines show low-pass filtered MME-mean change in the CMIP6 historical/SSP5-8.5 (34 models) and CMIP5 historical/RCP8.5 (41 models) experiments for future projections to 2100. The filter is the same as that used in Figure 10.11(d). To the right, box-and-whisker plots show the 2081–2100 change averaged over the CMIP5 (blue) and CMIP6 (dark red) ensembles. Note that some models exceed the plotting range (CMIP5: GISS-E2-R-CC, GISS-E2-R & IPSL-CM5B-LRl and CMIP6: CanESM5-CanOE, CanESM5 & GISS-E2-1-G). (e) Precipitation linear trend (% per decade) over central India for historical 1950–2000 (left) and future 2015–2100 (right) periods in Indian monsoon rainfall in observed estimates (black crosses), the CMIP5 historical-RCP8.5 simulations (blue), the CMIP6 ensemble (dark red) for historical all-forcings experiment and SSP5-8.5 future projection, the CMIP6 hist-GHG (light blue triangles), hist-aer (grey triangles) and historical all-forcings (same sample as for hist-aer and hist-GHG, pink circles). Ensemble means are also shown. Box-and-whisker plots show the trend distribution of the three coupled and the d4PDF atmosphere-only (for past period only) SMILEs used throughout Chapter 10 and follow the methodology used in Figure 10.6. (f) Example spread of trends (mm day^{-1} per decade) out to the near term (2016–2045) in RCP8.5 SMILE experiments of the MPI-ESM model, showing the difference between the three driest and three wettest trends among ensemble members over central India. All trends are estimated using ordinary least-squares regression. Further details on data sources and processing are available in the chapter data table (Table 10.SM.11).

ACCEPTED VERSION
SUBJECT TO FINAL EDITING

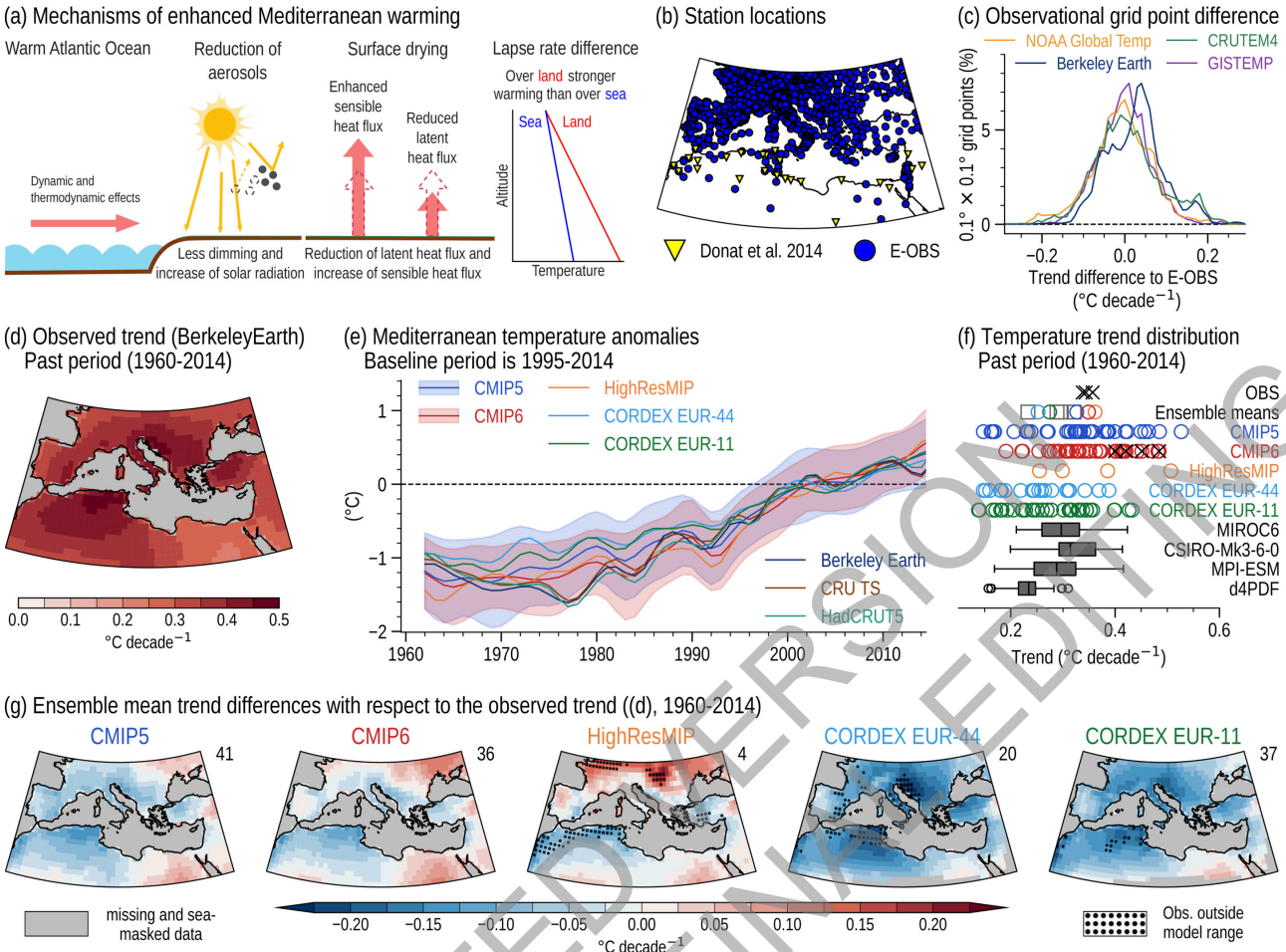


Figure 10.20: Aspects of Mediterranean summer warming. (a) Mechanisms and feedbacks involved in enhanced Mediterranean summer warming. (b) Locations of observing stations in E-OBS and (Donat et al., 2014). (c) Differences in temperature observational data sets (NOAA Global Temp, Berkeley Earth, CRUTEM4 and GISTEMP) with respect to E-OBS for the land points between the Mediterranean Sea and 46°N and west of 30°E. (d) Observed summer (June to August) surface air temperature linear trends (°C decade^{-1}) over the 1960–2014 period from Berkeley Earth. (e) Time series of area averaged Mediterranean (25°N–50°N, 10°W–40°E) land point summer temperature anomalies (°C, baseline 1995–2014). Dark blue, brown and turquoise lines show low-pass filtered temperature of Berkeley Earth, CRU TS and HadCRUT5, respectively. Orange, light blue and green lines show low-pass filtered ensemble means of HighResMIP (4 members), CORDEX EUR-44 (20 members) and CORDEX EUR-11 (37 members). Blue and red lines and shadings show low-pass filtered ensemble means and standard deviations of CMIP5 (41 members) and CMIP6 (36 members). The filter is the same as the one used in Figure 10.10. (f) Distribution of 1960–2014 Mediterranean summer temperature linear trends (°C decade^{-1}) for observations (black crosses), CORDEX EUR-11 (green circles), CORDEX EUR-44 (light blue circles), HighResMIP (orange circles), CMIP6 (red circles), CMIP5 (blue circles) and selected SMILEs (grey box-and-whisker plots, MIROC6, CSIRO-Mk3-6-0, MPI-ESM and d4PDF). Ensemble means are also shown. CMIP6 models showing a very high ECS (Box. 4.1) have been marked with a black cross. All trends are estimated using ordinary least-squares and box-and-whisker plots follow the methodology used in Figure 10.6. (g) Ensemble mean differences with respect to the Berkeley Earth linear trend for 1960–2014 (°C decade^{-1}) of CMIP5, CMIP6, HighResMIP, CORDEX EUR-44 and CORDEX EUR-11. Further details on data sources and processing are available in the chapter data table (Table 10.SM.11).

ACCEPTED VERSION SUBJECT TO FINAL EDITING

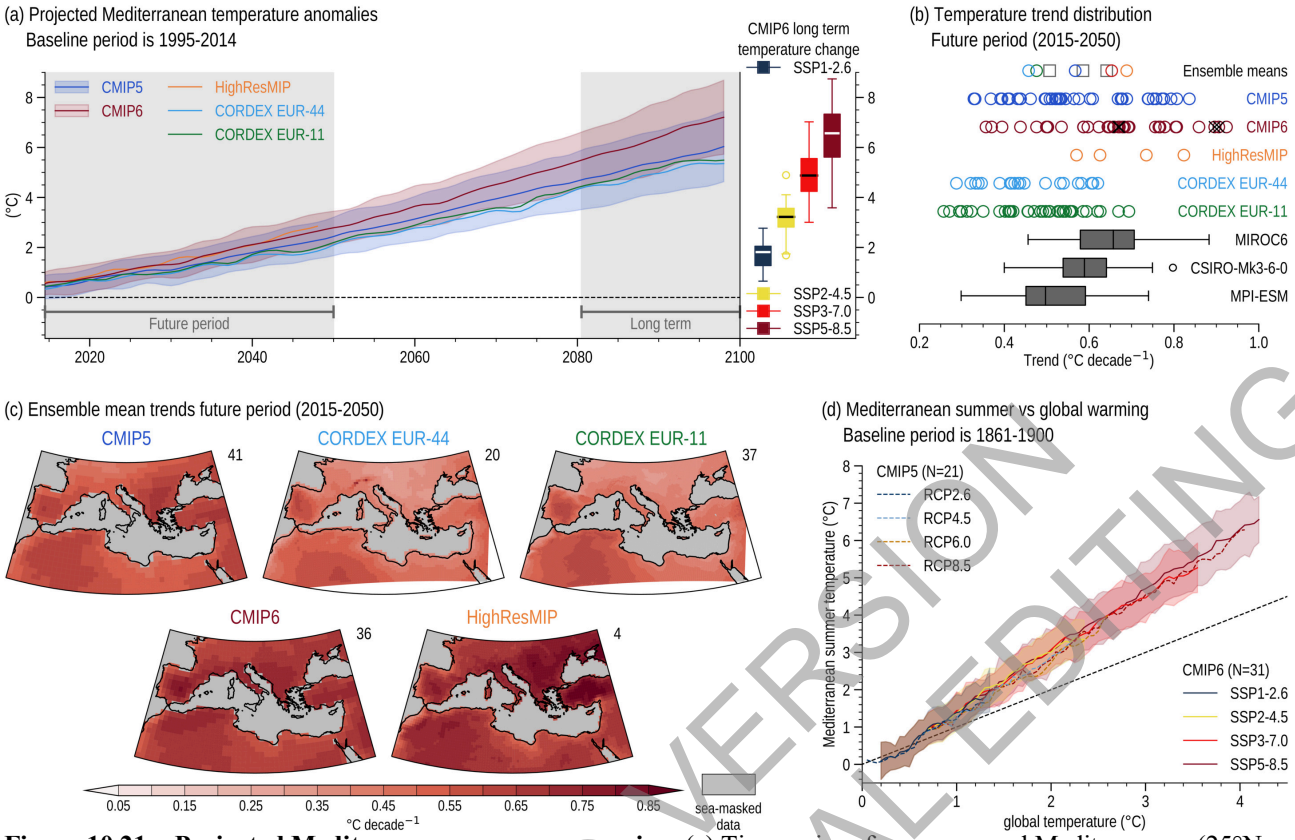
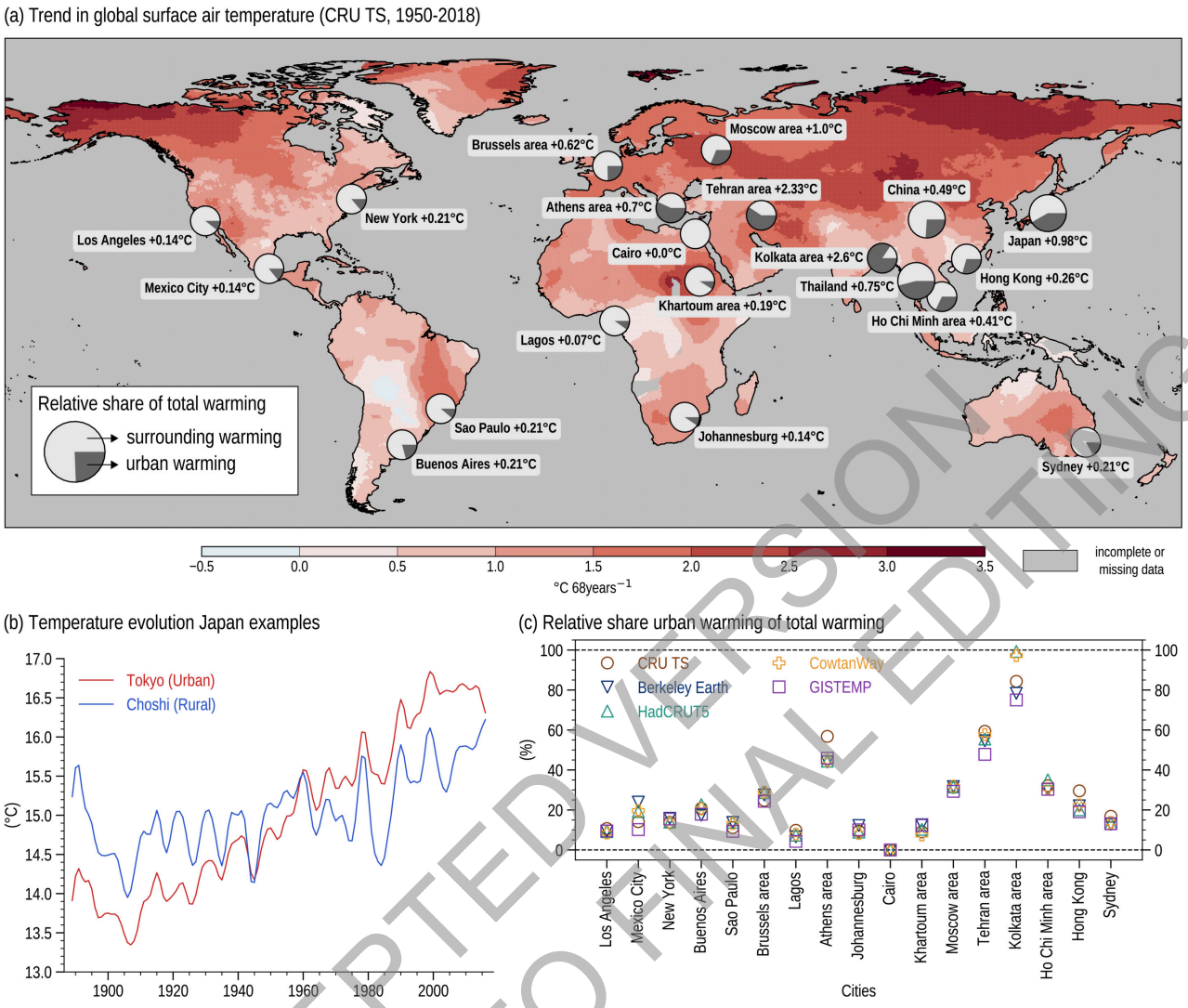


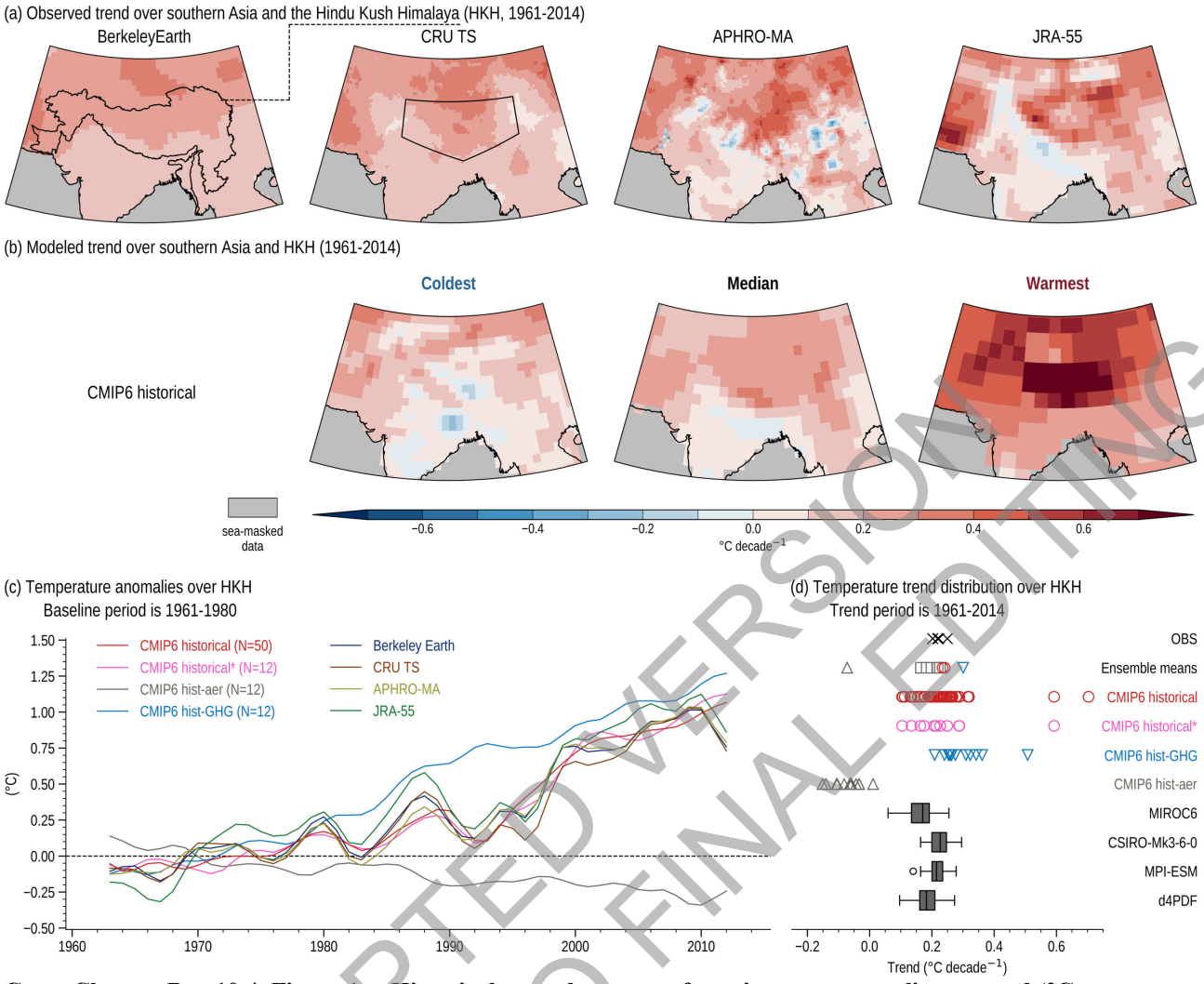
Figure 10.21: Projected Mediterranean summer warming. (a) Time series of area averaged Mediterranean (25°N–50°N, 10°W–40°E) land point summer surface air temperature anomalies (°C, baseline period is 1995–2014). Orange, light blue and green lines show low-pass filtered ensemble means of HighResMIP (highres-future, 4 members), CORDEX EUR-44 (RCP8.5, 20 members) and CORDEX EUR-11 (RCP8.5, 37 members). Blue and dark red lines and shadings show low-pass filtered ensemble means and standard deviations of CMIP5 (RCP8.5, 41 members) and CMIP6 (SSP5-8.5, 36 members). The filter is the same as the one used in Figure 10.10. The box-and-whisker plots show long term (until 2081-2100) temperature changes of different CMIP6 scenarios with respect to the baseline period (SSP1-2.6 in dark blue, SSP2-4.5 in yellow, SSP3-7.0 in red, SSP5-8.5 in dark red). (b) Distribution of 2015–2050 Mediterranean summer temperature linear trends (°C decade^{-1}) for CORDEX EUR-11 (RCP8.5, green circles), CORDEX EUR-44 (RCP8.5, light blue circles), HighResMIP (highres-future, orange circles), CMIP6 (SSP5-8.5, dark red circles), CMIP5 (RCP8.5, blue circles) and selected SMILEs (grey box-and-whisker plots, MIROC6, CSIRO-Mk3-6-0 and MPI-ESM). Ensemble means are also shown. CMIP6 models showing a very high ECS (Box 4.1) have been marked with a black cross. All trends are estimated using ordinary least-squares and box-and-whisker plots follow the methodology used in Figure 10.6. (c) Projections of ensemble mean 2015–2050 linear trends (°C decade^{-1}) of CMIP5 (RCP8.5), CORDEX EUR-44 (RCP8.5), CORDEX EUR-11 (RCP8.5), CMIP6 (SSP5-8.5) and HighResMIP (highres-future). All trends are estimated using ordinary least-squares. (d) Projected Mediterranean summer warming in comparison to global annual mean warming of CMIP5 (dashed lines, RCP2.6 in dark blue, RCP4.5 in light blue, RCP6.0 in orange and RCP8.5 in red) and CMIP6 (solid lines, SSP1-2.6 in dark blue, SSP2-4.5 in yellow, SSP3-7.0 in red and SSP5-8.5 in dark red) ensemble means. Further details on data sources and processing are available in the chapter data table (Table 10.SM.11).

SUBJECT TO FINAL EDITING ACCEPTED VERSION



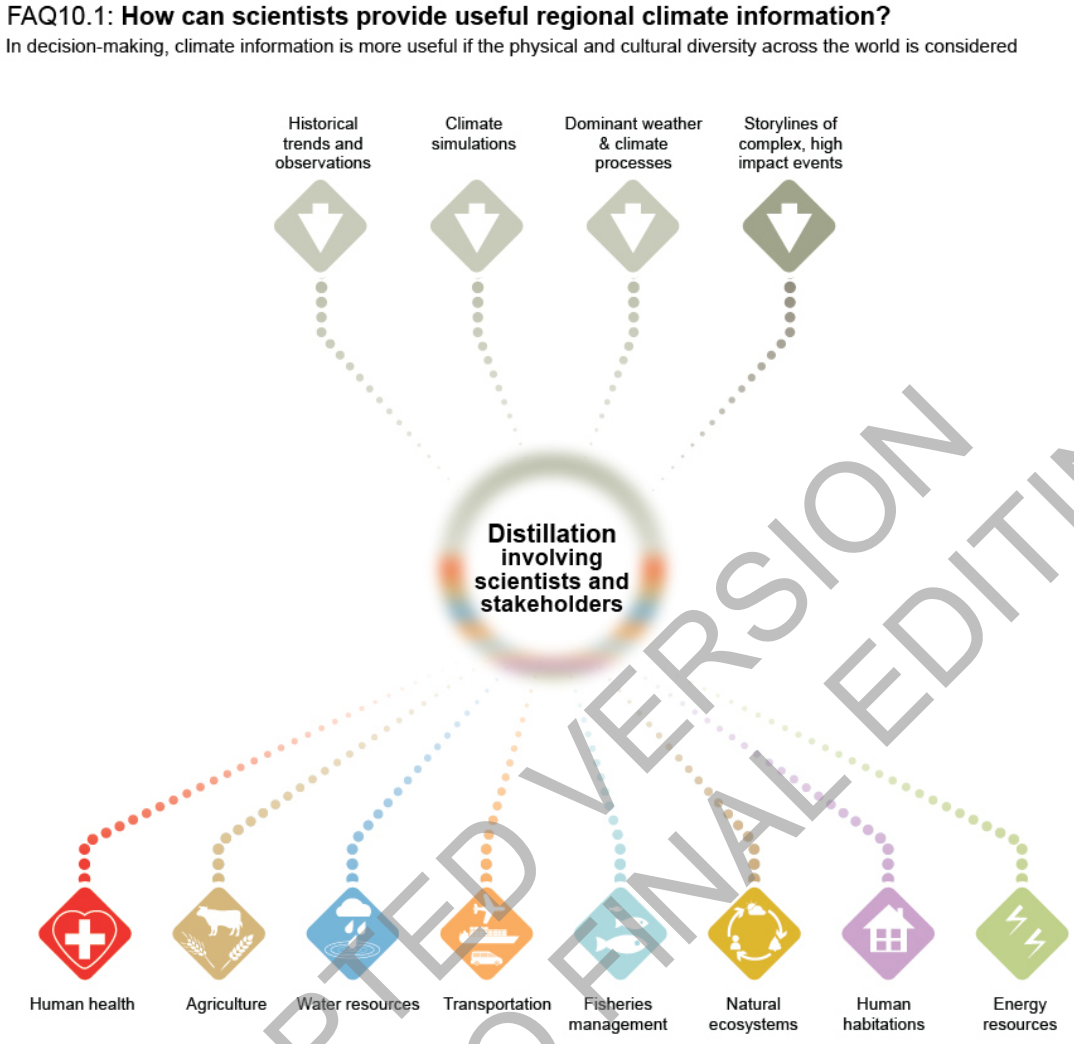
Box 10.3, Figure 1: **Urban warming compared to global GHG-induced warming.** (a) Change in the annual mean surface air temperature over the period 1950–2018 based on the local linear trend retrieved from CRU TS (°C per 68 years). This background warming is compared to the local warming that has been reported during 1950–2018 in the literature from historical urbanization. The relative share of the total warming as percentage between the urban warming and the surrounding warming is plotted in a circle for each city. This map has been compiled from a review study (Hamdi et al., 2020). (b) Low-pass filtered time series of the annual mean temperature (°C) observed in the urban station of Tokyo (red line) and the rural reference station in Choshi (blue line) in Japan. The filter is the same as the one used in Figure 10.10. (c) Uncertainties in the relative share of urban warming with respect to the total warming (%) related to the use of different global observational datasets: CRU TS (brown circles), Berkeley Earth (dark blue downward triangle), HadCRUT5 (cyan upward triangle), Cowtan Way (orange plus) and GISTEMP (purple squares). Further details on data sources and processing are available in the chapter data table (Table 10.SM.11).

ACCEPTED VERSION SUBJECT TO FINAL EDITING



Cross-Chapter Box 10.4, Figure 1: Historical annual-mean surface air temperature linear trend (°C per decade) and its attribution over the Hindu Kush Himalaya (HKH) region. (a) Observed trends from Berkeley Earth (also showing the HKH outline), CRU TS (also showing the AR6 TIB outline, for ease of comparison to the Interactive Atlas), APHRO-MA and JRA-55 datasets over 1961–2014. (b) Models showing the coldest, median and warmest HKH temperature linear trends among the CMIP6 historical ensemble over 1961–2014. (c) Lowpass-filtered time series of annual-mean surface air temperature anomalies (°C, baseline 1961–1980) over the HKH region as outlined in panel (a), showing means of CMIP6 hist all-forcings (red), and the CMIP6 hist all-forcings sample corresponding to DAMIP experiments (pink), for hist-aer (grey) and hist-GHG (pale blue). Observed datasets are Berkeley Earth (dark blue), CRU (brown), APHRO-MA (light green) and JRA-55 (dark green). The filter is the same as that used in Figure 10.10. (d) Distribution of annual mean surface air temperature trends (°C per decade) over the HKH region from 1961 to 2014 for ensemble means, the aforementioned observed and reanalysis data (black crosses), individual members of CMIP6 hist all-forcings (red circles), CMIP6 hist-GHG (blue triangles), CMIP6 hist-aer (grey triangles), and box-and-whisker plots for the SMILEs used throughout Chapter 10 (grey shading). Ensemble means are also shown. All trends are estimated using ordinary least-squares regression and box-and-whisker plots follow the methodology used in Figure 10.6. Further details on data sources and processing are available in the chapter data table (Table 10.SM.11).

ACCEPTED VERSION SUBJECT TO FINAL EDITING

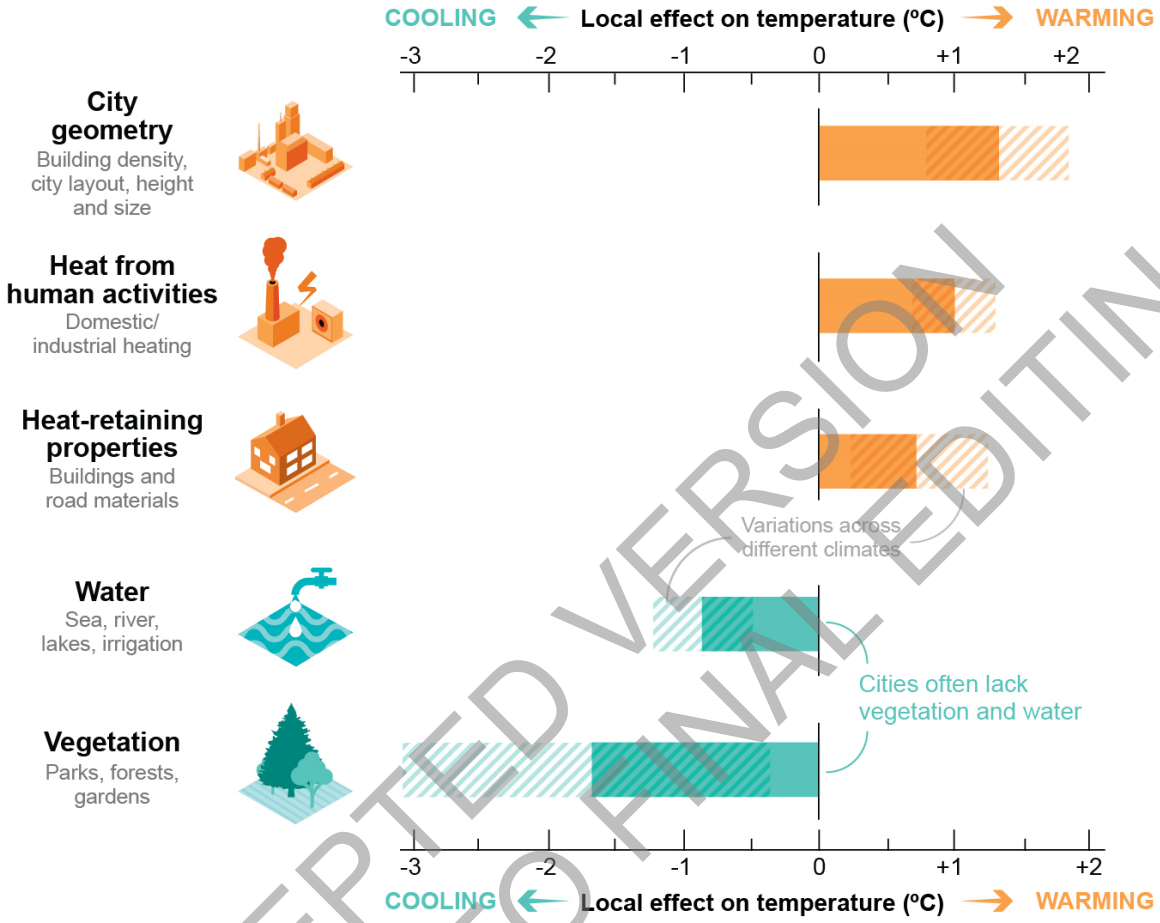


FAQ 10.1, Figure 1: **Climate information for decision makers is more useful if the physical and cultural diversity across the world is considered.** The figure illustrates schematically the broad range of knowledge that must be blended with the diversity of users to distil information that will have relevance and credibility. This blending or distillation should engage the values and knowledge of both the stakeholders and the scientists. The bottom row contains examples of stakeholders' interests and is not all-inclusive. As part of the distillation, the outcomes can advance the U.N.'s Sustainable Development Goals, covered in part by these examples.

ACCEPTED VERSION SUBJECT TO FINAL EDITING

FAQ 10.2: **Why are cities the hotspots of global warming?**

Cities are usually warmer than their surrounding areas due to factors that trap and release heat and a lack of natural cooling influences, such as water and vegetation.



FAQ 10.1, Figure 2: Efficiency of the various factors at warming up or cooling down neighbourhoods of urban areas. Overall, cities tend to be warmer than their surroundings. This is called the 'urban heat island' effect. The hatched areas on the bars show how the strength of the warming or cooling effects of each factor varies depending on the local climate. For example, vegetation has a stronger cooling effect in temperate and warm climates. Further details on data sources are available in the chapter data table (Table 10.SM.11).

ACCEPTED VERSION SUBJECT TO FINAL EDITING

Chapter 10: Linking global to regional climate change - Supplementary Material

Coordinating Lead Authors:
Francisco J. Doblas-Reyes (Spain), Anna A. Sörensson (Argentina)

Lead Authors:
Mansour Almazroui (Saudi Arabia), Alessandro Dosio (Italy), William J. Gutowski (United States of America), Rein Haarsma (The Netherlands), Rafiq Hamdi (Belgium), Bruce Hewitson (South Africa), Won-Tae Kwon (Republic of Korea), Benjamin L. Lamptey (Niger, Ghana/Ghana), Douglas Maraun (Austria/Germany), Tannecia S. Stephenson (Jamaica), Izuru Takayabu (Japan), Laurent Terray (France), Andrew Turner (United Kingdom), Zhiyan Zuo (China)

Contributing Authors:
Martin Jury (Spain/Austria), Gudfina Aðalgeirsdóttir (Iceland), Bhupesh Adhikary (Nepal), Muhammad Adnan (Pakistan), Bodo Ahrens (Germany), Muhammad Amjad (Pakistan), Paola A. Arias (Colombia), Farooq Mohamed Azam (India), Ségolène Berthou (United Kingdom/France), Melissa S. Bukovsky (United States of America), Alex J. Cannon (Canada), Ana Casanueva (Spain), Annalisa Cherchi (Italy), Erika Coppola (Italy), Faye Abigail Cruz (Philipines), Joseph D. Daron (United Kingdom), Marie-Estelle Demory (Switzerland/France, Switzerland), Claudine Dereczynski (Brazil), Alejandro Di Luca (Australia, Canada/Argentina), Leandro B. Díaz (Argentina), Hervé Douville (France), Sergio Henrique Faria (Spain/Brazil), Baylor Fox-Kemper (United States of America), Shin Fukui (Japan) Laura Gallardo (Chile), Subimal Ghosh (India), Nathan P. Gillett (Canada), Melissa I. Gomis (France/Switzerland), Hugues Goosse (Belgium), Irina V. Gorodetskaya (Portugal/Belgium, Russian Federation), Michael Grose (Australia), José Manual Gutiérrez (Spain), Pandora Hope (Australia), Akm Saiful Islam (Bangladesh), Christopher D. Jack (South Africa), Richard G. Jones (United Kingdom), Martin W. Jury (Spain/Austria), Asif Khan (Pakistan), Akio Kitoh (Japan), Svitlana Krakovska (Ukraine), Gerhard Krinner (France/Germany, France), Hiroyuki Kusaka (Japan), Stefan Lange (Germany), Flavio Lehner (United States of America /Switzerland), Christopher Lennard (South Africa), Jian Li (China), Fei Liu (China), Martin Ménégoz (France), Thanh Ngo-Doc (Vietnam), Dirk Notz (Germany), Friederike Otto (United Kingdom /Germany), Wendy Parker (United States of America), Carlos Pérez García-Pando (Spain), Izidine Pinto (South Africa/Mozambique), Jan Polcher (France/Germany), Krishnan Raghavan (India), Roshanka Ranasinghe (The Netherlands/Sri Lanka, Australia), Ingo Richter (Japan/Germany), Alex C. Ruane (United States of America), Lucas Ruiz (Argentina), Sajjad Saeed (Belgium, Italy/Pakistan, Belgium), Ramiro I. Saurral (Argentina), Reinhard K. H. Schiemann (United Kingdom /Germany), Sonia I. Seneviratne (Switzerland), Chris Shaw (United Kingdom), Theodore G. Shepherd (United Kingdom /Canada), Jonathan K. P. Shonk (United Kingdom), Jana Sillmann (Norway/Germany), Didier Swingedouw (France), Izuru Takayabu (Japan), Bart van den Hurk (The Netherlands), Robert Vautard (France), Victor Venema (Germany/The Netherlands), Sergio M. Vicente-Serrano (Spain), Piotr Wolski (South Africa/Poland), Cunde Xiao (China), Jakob Zscheischler (Germany)

Review Editors:
Gregory M. Flato (Canada), Fredolin Tangang (Malaysia), Muhammad Irfan Tariq (Pakistan)

Chapter Scientist:
Martin W. Jury (Spain/Austria)

ACCEPTED VERSION SUBJECT TO FINAL EDITING

This Supplementary Material should be cited as:
Doblas-Reyes, F. J,. A. A. Sörensson, M. Almazroui, A. Dosio, W. J. Gutowski, R. Haarsma, R. Hamdi, B. Hewitson, W-T. Kwon, B. L. Lamptey, D. Maraun, T. S. Stephenson, I. Takayabu, L. Terray, A. Turner, Z. Zuo, 2021, Linking Global to Regional Climate Change Supplementary Material. In: *Climate Change 2021: The Physical Science Basis. Contribution of Working Group I to the Sixth Assessment Report of the Intergovernmental Panel on Climate Change* [Masson-Delmotte, V., P. Zhai, A. Pirani, S. L. Connors, C. Péan, S. Berger, N. Caud, Y. Chen, L. Goldfarb, M. I. Gomis, M. Huang, K. Leitzell, E. Lonnoy, J.B.R. Matthews, T. K. Maycock, T. Waterfield, O. Yelekçi, R. Yu and B. Zhou (eds.)]. Available from https://ipcc.ch/static/ar6/wg1.

Date: August 2021

This document is subject to copy-editing, corrigenda and trickle backs.

ACCEPTED VERSION
SUBJECT TO FINAL EDITING

Table of contents

10.SM.1 Regional Traceback Matrices 3

10.SM.2 Data Table 60

References 94

ACCEPTED VERSION
SUBJECT TO FINAL EDITING

10.SM.1 Regional Traceback Matrices

[START TABLE 10.SM.1 HERE]

Table 10.SM.1: Regional Traceback Matrix for Africa. Table shows chapter traceability of the regional assessment using observed trends, attribution of trends or events, and climate model projections, as described in Cross-Chapter Box 10.3. The Table is divided into separate panels that correspond to the WGI AR6 Reference Regions. African sub-regions are: Panel A: (Mediterranean) North Africa (MED), Panel B: Sahara (SAH), Panel C: West-Africa (WAF), Panel D: Central-Africa (CAF), Panel E: N.Eastern-Africa (NEAF), Panel F: S.Eastern-Africa (SEAF), Panel G: W.Southern-Africa (WSAF), Panel H: E.Southern-Africa (ESAF), Panel I: Madagascar (MDG). Blank cells in the observations and projections columns corresponding to the "not broadly relevant" or "no evidence" category as described in the CID framework in Chapter 12. Blank cells in the detection and attribution columns correspond to no studies being available.

Panel A)

	Region	AFRICA	AFRICA	AFRICA
	Region type (Land / Ocean)	Land	Land	Land
	Sub-Region Name	(Mediterranean) North Africa	(Mediterranean) North Africa	(Mediterranean) North Africa
	Accronym	[MED]	[MED]	[MED]
	Data Type	Observational	Detection & Attribution	Projections
Heat and Cold	Mean air temperature	Table 11.1; Table 11.4;11.3.2; 12.4.1.1, Atlas 4.2	Table 11.1; Table 11.4;11.3.4, Atlas 4.2	Table 11.2; Table 11.4;11.3.5; 12.4.1.1, Table 12.3, Atlas 4.4, 4.4.1.1, 4.5.1.1, 4.6.1.1
	Extreme heat	Table 11.1; Table 11.4;11.3.2,12.4.1.1	Table 11.1; Table 11.4;11.3.4	Table 11.2; Table 11.4;11.3.5; 12.4.1.1, Table 12.3
	Cold spell	Table 11.1; Table 11.4;11.3.2,12.4.1.2	Table 11.1; Table 11.4;11.3.5	Table 11.2; Table 11.4;11.3.5; 12.4.1.1, Table 12.4
	Frost	12.4.1.1		12.4.1.1, Table 12.3
Wet and Dry	Mean precipitation	12.4.1.2, Atlas 4.2,	Atlas 4.2	12.4.1.2, Table 12.3, Atlas 4.4, 4.4.1.3, 4.5.1.4, 4.6.1.2
	River flood	11.5.2, 12.4.1.2	11.5.4	11.5.5; 12.4.1.2, Table 12.3
	Heavy precipitation and pluvial flood	11.4.2, 11.5.2,Table 11.5, 12.4.1.2	11.4.4, 11.5.4,Table 11.5,	11.4.5, 11.5.5,Table 11.5, 12.4.1.2, Table 12.3
	Landslide	12.4.1.2;		12.4.1.2, Table 12.3;
	Aridity	8.3.1.6, 12.4.1.2		12.4.1.2, Table 12.3, 8.4.1.6
	Hydrological drought	11.6.2, Table 11.6, 12.4.1.2	11.6.4, Table 11.6,	11.6.5, Table 11.6,, 12.4.1.2, Table 12.3
	Agricultural and ecological drought	11.6.2, Table 11.6, 12.4.1.2	11.6.4, Table 11.6,	11.6.5, Table 11.6,, 12.4.1.2, Table 12.4
	Fire weather	12.4.1.2		12.4.1.2, Table 12.3
Wind	Mean wind speed	12.4.1.3		12.4.1.3, Table 12.3
	Severe wind storm	12.4.1.3		12.4.1.3, Table 12.3
	Tropical cyclone			
	Sand and dust storm	12.4.1.3		12.4.1.3, Table 12.3
Snow and Ice	Snow, glacier and ice sheet	12.4.1.4		12.4.1.4, Table 12.3
	Permafrost			
	Lake, river and sea ice			
	Heavy snowfall and ice storm			
	Hail	12.4.1.4		12.4.1.4, Table 12.3
	Snow avalanche			
Coastal and Oceanic	Relative sea level	12.4.1.5		12.4.1.5, Table 12.3
	Coastal flood	12.4.1.5		12.4.1.5, Table 12.3
	Coastal erosion	12.4.1.5		12.4.1.5, Table 12.3
	Marine heatwave	12.4.1.5		12.4.1.5, Table 12.3
	Ocean acidity	12.4		12.4, Table 12.3
Other	Air pollution weather	12.4		12.4, Table 12.3
	Atmospheric CO2 at surface	12.4		12.4, Table 12.3
	Radiation at surface	12.4		12.4, Table 12.3

ACCEPTED VERSION SUBJECT TO FINAL EDITING

Panel B)

	Region	AFRICA	AFRICA	AFRICA
	Region type (Land / Ocean)	Land	Land	Land
	Sub-Region Name	Sahara	Sahara	Sahara
	Accronym	SAH	SAH	SAH
	Data Type	Observational	Detection & Attribution	Projections
Heat and Cold	Mean air temperature	Table 11.1; Table 11.4;11.3.2; 12.4.1.1, Atlas 4.2	Table 11.1; Table 11.4;11.3.4, Atlas 4.2	Table 11.2; Table 11.4;11.3.5; 12.4.1.1; Table 12.3, Atlas 4.4, 4.4.1.1, 4.5.1.1, 4.6.1.1
	Extreme heat	Table 11.1; Table 11.4;11.3.2,12.4.1.1	Table 11.1; Table 11.4;11.3.4	Table 11.2; Table 11.4;11.3.5; 12.4.1.1; Table 12.3;
	Cold spell	Table 11.1; Table 11.4;11.3.2,12.4.1.2	Table 11.1; Table 11.4;11.3.5	Table 11.2; Table 11.4;11.3.5; 12.4.1.1; Table 12.3;
	Frost	12.4.1.1;		12.4.1.1; Table 12.3;
Wet and Dry	Mean precipitation	12.4.1.2, Atlas 4.2	Atlas 4.2	12.4.1.2, Table 12.3, Atlas 4.4, 4.4.1.3, 4.5.1.4, 4.6.1.2
	River flood	11.5.2; 12.4.1.2	11.5.4	11.5.5; 12.4.1.2
	Heavy precipitation and pluvial flood	11.4.2, 11.5.2, Table 11.5, 12.4.1.2	11.4.4, 11.5.4,Table 11.5,	11.4.5, 11.5.5, Table 11.5, 12.4.1.2, Table 12.3
	Landslide	12.4.1.2;		12.4.1.2, Table 12.3;
	Aridity	12.4.1.2		12.4.1.2, Table 12.3
	Hydrological drought	11.6.2, Table 11.6,	11.6.4, Table 11.6,	11.6.5, Table 11.6, 12.4.1.2, Table 12.3
	Agricultural and ecological drought	11.6.2, Table 11.6, 12.4.1.2	11.6.4, Table 11.6,	11.6.5, Table 11.6, 12.4.1.2, Table 12.4
	Fire weather	12.4.1.2		12.4.1.2, Table 12.3
Wind	Mean wind speed	12.4.1.3		12.4.1.3, Table 12.3
	Severe wind storm	12.4.1.3		12.4.1.3, Table 12.3
	Tropical cyclone			
	Sand and dust storm	12.4.1.3		12.4.1.3, Table 12.3
Snow and Ice	Snow, glacier and ice sheet			
	Permafrost			
	Lake, river and sea ice			
	Heavy snowfall and ice storm			
	Hail	12.4.1.4		12.4.1.4, Table 12.3
	Snow avalanche			
Coastal and Oceanic	Relative sea level	12.4.1.5		12.4.1.5, Table 12.3
	Coastal flood	12.4.1.5		12.4.1.5, Table 12.3
	Coastal erosion	12.4.1.5		12.4.1.5, Table 12.3
	Marine heatwave	12.4.1.5		12.4.1.5, Table 12.3
	Ocean acidity	12.4		12.4, Table 12.3
Other	Air pollution weather	12.4		12.4, Table 12.3
	Atmospheric CO2 at surface	12.4		12.4, Table 12.3
	Radiation at surface	12.4		12.4, Table 12.3

ACCEPTED VERSION SUBJECT TO FINAL EDITING

Panel C)

	Region	AFRICA	AFRICA	AFRICA
	Region type (Land / Ocean)	Land	Land	Land
	Sub-Region Name	West-Africa	West-Africa	West-Africa
	Accronym	WAF	WAF	WAF
	Data Type	Observational	Detection & Attribution	Projections
Heat and Cold	Mean air temperature	Table 11.1; Table 11.4;11.3.2; 12.4.1.1, Atlas 4.2	Table 11.1; Table 11.4;11.3.4, Atlas 4.2	Table 11.2; Table 11.4;11.3.5; 12.4.1.1; Table 12.3; Atlas 4.4, 4.4.1.1, 4.5.1.1, 4.6.1.1
	Extreme heat	Table 11.1; Table 11.4;11.3.2,12.4.1.1	Table 11.1; Table 11.4;11.3.4	Table 11.2; Table 11.4;11.3.5; 12.4.1.1; Table 12.3;
	Cold spell	Table 11.1; Table 11.4;11.3.2,12.4.1.2	Table 11.1; Table 11.4;11.3.5	Table 11.2; Table 11.4;11.3.5; 12.4.1.1; Table 12.3;
	Frost			12.4.1.1; Table 12.3;
Wet and Dry	Mean precipitation	1.4.5.2, 12.4.1.2, Atlas 4.2, 8.3.1.3, 8.3.2.4.3, BOX 8.2	Atlas 4.2	12.4.1.2, Table 12.3, Atlas 4.4, 8.4.1.3, 8.4.2.4.3, 4.4.1.3, 4.5.1.4, 4.6.1.2
	River flood	11.5.2; 12.4.1.2	11.5.4	11.5.5; 12.4.1.2
	Heavy precipitation and pluvial flood	8.3.2.4.3, 11.4.2, 11.5.2,Table 11.5, 12.4.1.2	11.4.4, 11.5.4,Table 11.5	11.4.5, 11.5.5,Table 11.5, 12.4.1.2, Table 12.3
	Landslide	12.4.1.2;		12.4.1.2, Table 12.3;
	Aridity	12.4.1.2		12.4.1.2, Table 12.3
	Hydrological drought	11.6.2, Table 11.6, 12.4.1.2	11.6.4, Table 11.6,	11.6.5, Table 11.6, 12.4.1.2, Table 12.3
	Agricultural and ecological drought	11.6.2, Table 11.6, 12.4.1.2	11.6.4, Table 11.6,	11.6.5, Table 11.6, 12.4.1.2, Table 12.4
	Fire weather	12.4.1.2		12.4.1.2, Table 12.3
Wind	Mean wind speed	12.4.1.3		12.4.1.3, Table 12.3
	Severe wind storm	12.4.1.3		12.4.1.3, Table 12.3
	Tropical cyclone			
	Sand and dust storm	12.4.1.3		12.4.1.3, Table 12.3
Snow and Ice	Snow, glacier and ice sheet			
	Permafrost			
	Lake, river and sea ice			
	Heavy snowfall and ice storm			
	Hail	12.4.1.4		12.4.1.4, Table 12.3
	Snow avalanche			
Coastal and Oceanic	Relative sea level	12.4.1.5		12.4.1.5, Table 12.3
	Coastal flood	12.4.1.5		12.4.1.5, Table 12.3
	Coastal erosion	12.4.1.5		12.4.1.5, Table 12.3
	Marine heatwave	12.4.1.5		12.4.1.5, Table 12.3
	Ocean acidity	12.4		12.4, Table 12.3
Other	Air pollution weather	12.4		12.4, Table 12.3
	Atmospheric CO2 at surface	12.4		12.4, Table 12.3
	Radiation at surface	12.4		12.4, Table 12.3

ACCEPTED VERSION SUBJECT TO FINAL EDITING

Panel D)

	Region	AFRICA	AFRICA	AFRICA
	Region type (Land / Ocean)	Land	Land	Land
	Sub-Region Name	Central-Africa	Central-Africa	Central-Africa
	Accronym	CAF	CAF	CAF
	Data Type	Observational	Detection & Attribution	Projections
Heat and Cold	Mean air temperature	Table 11.1; Table 11.4;11.3.2; 12.4.1.1, Atlas 4.2	Table 11.1; Table 11.4;11.3.4, Atlas 4.2	Table 11.2; Table 11.4;11.3.5; 12.4.1.1; Table 12.3; Atlas 4.4, 4.4.1.1, 4.5.1.1, 4.6.1.1
	Extreme heat	Table 11.1; Table 11.4;11.3.2,12.4.1.1	Table 11.1; Table 11.4;11.3.4	Table 11.2; Table 11.4;11.3.5; 12.4.1.1; Table 12.3;
	Cold spell	Table 11.1; Table 11.4;11.3.2,12.4.1.2	Table 11.1; Table 11.4;11.3.5	Table 11.2; Table 11.4;11.3.5; 12.4.1.1; Table 12.3;
	Frost			12.4.1.1; Table 12.3;
Wet and Dry	Mean precipitation	1.4.5.2, 12.4.1.2, Atlas 4.2, 8.3.1.6	Atlas 4.2, 8.3.1.6,	12.4.1.2, Table 12.3, Atlas 4.4, 8.4.1.3, 4.4.1.3, 4.5.1.4, 4.6.1.2
	River flood	11.5.2; 12.4.1.2	11.5.4	11.5.5; 12.4.1.2
	Heavy precipitation and pluvial flood	11.4.2, 11.5.2,Table 11.5, 12.4.1.2	11.4.4, 11.5.4,Table 11.5,	11.4.5, 11.5.5, Table 11.5, 12.4.1.2, Table 12.3
	Landslide	12.4.1.2;		12.4.1.2, Table 12.3;
	Aridity	12.4.1.2		12.4.1.2, Table 12.3
	Hydrological drought	11.6.2, Table 11.6, 12.4.1.2	11.6.4, Table 11.6,	11.6.5, Table 11.6, 12.4.1.2, Table 12.3
	Agricultural and ecological drought	11.6.2, Table 11.6, 12.4.1.3	11.6.4, Table 11.6,	11.6.5, Table 11.6, 12.4.1.2, Table 12.4
	Fire weather	12.4.1.2		12.4.1.2, Table 12.3
Wind	Mean wind speed	12.4.1.3		12.4.1.3, Table 12.3
	Severe wind storm	12.4.1.3		12.4.1.3, Table 12.3
	Tropical cyclone			
	Sand and dust storm	12.4.1.3		12.4.1.3, Table 12.3
Snow and Ice	Snow, glacier and ice sheet			
	Permafrost			
	Lake, river and sea ice			
	Heavy snowfall and ice storm			
	Hail	12.4.1.4		12.4.1.4, Table 12.3
	Snow avalanche			
Coastal and Oceanic	Relative sea level	12.4.1.5		12.4.1.5, Table 12.3
	Coastal flood	12.4.1.5		12.4.1.5, Table 12.3
	Coastal erosion	12.4.1.5		12.4.1.5, Table 12.3
	Marine heatwave	12.4.1.5		12.4.1.5, Table 12.3
	Ocean acidity	12.4		12.4, Table 12.3
Other	Air pollution weather	12.4		12.4, Table 12.3
	Atmospheric CO2 at surface	12.4		12.4, Table 12.3
	Radiation at surface	12.4		12.4, Table 12.3

ACCEPTED VERSION SUBJECT TO FINAL EDITING

Panel E)

	Region	AFRICA	AFRICA	AFRICA
	Region type (Land / Ocean)	Land	Land	Land
	Sub-Region Name	N.Eastern-Africa	N.Eastern-Africa	N.Eastern-Africa
	Accronym	NEAF	NEAF	NEAF
	Data Type	Observational	Detection & Attribution	Projections
Heat and Cold	Mean air temperature	Table 11.1; Table 11.4;11.3.2; 12.4.1.1, Atlas 4.2	Table 11.1; Table 11.4;11.3.4, Atlas 4.2	Table 11.2; Table 11.4;11.3.5; 12.4.1.1; Table 12.3; Atlas 4.4, 4.4.1.1, 4.5.1.1, 4.6.1.1
	Extreme heat	Table 11.1; Table 11.4;11.3.2,12.4.1.1	Table 11.1; Table 11.4;11.3.4	Table 11.2; Table 11.4;11.3.5; 12.4.1.1; Table 12.3;
	Cold spell	Table 11.1; Table 11.4;11.3.2,12.4.1.2	Table 11.1; Table 11.4;11.3.5	Table 11.2; Table 11.4;11.3.5; 12.4.1.1; Table 12.3;
	Frost			12.4.1.1; Table 12.3;
Wet and Dry	Mean precipitation	1.4.5.2, 12.4.1.2, Atlas 4.2,8.3.1.3,8.3.1.6, BOX 8.2	Atlas 4.2, BOX 8.2	12.4.1.2, Table 12.3, Atlas 4.4, 8.4.1.3, 4.4.1.3, 4.5.1.4, 4.6.1.2
	River flood	11.5.2; 12.4.1.2	11.5.4	11.5.5; 12.4.1.2
	Heavy precipitation and pluvial flood	11.4.2, 11.5.2,Table 11.5, 12.4.1.2	11.4.4, 11.5.4,Table 11.5,	11.4.5, 11.5.5, Table 11.5, 12.4.1.2, Table 12.3
	Landslide	12.4.1.2;		12.4.1.2, Table 12.3;
	Aridity	12.4.1.2		12.4.1.2, Table 12.3
	Hydrological drought	11.6.2, Table 11.6, 12.4.1.2	11.6.4, Table 11.6,	11.6.5, Table 11.6, 12.4.1.2, Table 12.3
	Agricultural and ecological drought	11.6.2, Table 11.6, 12.4.1.3	11.6.4, Table 11.6,	11.6.5, Table 11.6, 12.4.1.2, Table 12.4
	Fire weather	12.4.1.2		12.4.1.2, Table 12.3
Wind	Mean wind speed	12.4.1.3		12.4.1.3, Table 12.3
	Severe wind storm	12.4.1.3		12.4.1.3, Table 12.3
	Tropical cyclone			
	Sand and dust storm	12.4.1.3		12.4.1.3, Table 12.3
Snow and Ice	Snow, glacier and ice sheet	12.4.1.4		12.4.1.4, Table 12.3
	Permafrost			
	Lake, river and sea ice			
	Heavy snowfall and ice storm			
	Hail	12.4.1.4		12.4.1.4, Table 12.3
	Snow avalanche			
Coastal and Oceanic	Relative sea level	12.4.1.5		12.4.1.5, Table 12.3
	Coastal flood	12.4.1.5		12.4.1.5, Table 12.3
	Coastal erosion	12.4.1.5		12.4.1.5, Table 12.3
	Marine heatwave	12.4.1.5		12.4.1.5, Table 12.3
	Ocean acidity	12.4		12.4, Table 12.3
Other	Air pollution weather	12.4		12.4, Table 12.3
	Atmospheric CO2 at surface	12.4		12.4, Table 12.3
	Radiation at surface	12.4		12.4, Table 12.3

ACCEPTED VERSION SUBJECT TO FINAL EDITING

Panel F)

	Region	AFRICA	AFRICA	AFRICA
	Region type (Land / Ocean)	Land	Land	Land
	Sub-Region Name	S.Eastern-Africa	S.Eastern-Africa	S.Eastern-Africa
	Accronym	SEAF	SEAF	SEAF
	Data Type	Observational	Detection & Attribution	Projections
Heat and Cold	Mean air temperature	Table 11.1; Table 11.4;11.3.2; 12.4.1.1, Atlas 4.2	Table 11.1; Table 11.4;11.3.4; Atlas 4.2	Table 11.2; Table 11.4;11.3.5; 12.4.1.1; Table 12.3; Atlas 4.4, 4.4.1.1, 4.5.1.1, 4.6.1.1
	Extreme heat	Table 11.1; Table 11.4;11.3.2,12.4.1.1	Table 11.1; Table 11.4;11.3.4	Table 11.2; Table 11.4;11.3.5; 12.4.1.1; Table 12.3;
	Cold spell	Table 11.1; Table 11.4;11.3.2,12.4.1.2	Table 11.1; Table 11.4;11.3.5	Table 11.2; Table 11.4;11.3.5; 12.4.1.1; Table 12.3;
	Frost			12.4.1.1; Table 12.3;
Wet and Dry	Mean precipitation	12.4.1.2, Atlas 4.2, 8.3.1.3, BOX 8.2	Atlas 4.2, BOX 8.2	12.4.1.2, Table 12.3, Atlas 4.4, 8.4.1.3, 4.4.1.3, 4.5.1.4, 4.6.1.2
	River flood	11.5.2; 12.4.1.2	11.5.4	11.5.5; 12.4.1.2
	Heavy precipitation and pluvial flood	11.4.2, 11.5.2,Table 11.5, 12.4.1.2	11.4.4, 11.5.4,Table 11.5,	11.4.5, 11.5.5, Table 11.5, 12.4.1.2, Table 12.3
	Landslide	12.4.1.2;		12.4.1.2, Table 12.3;
	Aridity	12.4.1.2		12.4.1.2, Table 12.3
	Hydrological drought	11.6.2, Table 11.6, 12.4.1.2	11.6.4, Table 11.6,	11.6.5, Table 11.6, 12.4.1.2, Table 12.3
	Agricultural and ecological drought	11.6.2, Table 11.6, 12.4.1.3	11.6.4, Table 11.6,	11.6.5, Table 11.6, 12.4.1.2, Table 12.4
	Fire weather	12.4.1.2		12.4.1.2, Table 12.3
Wind	Mean wind speed	12.4.1.3		12.4.1.3, Table 12.3
	Severe wind storm	12.4.1.3		12.4.1.3, Table 12.3
	Tropical cyclone	11.7.1.2, 12.4.1.3	11.7.1.4	11.7.1.5, 12.4.1.3, Table 12.3
	Sand and dust storm	12.4.1.3		12.4.1.3, Table 12.3
Snow and Ice	Snow, glacier and ice sheet	12.4.1.4		12.4.1.4, Table 12.3
	Permafrost			
	Lake, river and sea ice			
	Heavy snowfall and ice storm			
	Hail	12.4.1.4		12.4.1.4, Table 12.3
	Snow avalanche			
Coastal and Oceanic	Relative sea level	12.4.1.5		12.4.1.5, Table 12.3
	Coastal flood	12.4.1.5		12.4.1.5, Table 12.3
	Coastal erosion	12.4.1.5		12.4.1.5, Table 12.3
	Marine heatwave	12.4.1.5		12.4.1.5, Table 12.3
	Ocean acidity	12.4		12.4, Table 12.3
Other	Air pollution weather	12.4		12.4, Table 12.3
	Atmospheric CO2 at surface	12.4		12.4, Table 12.3
	Radiation at surface	12.4		12.4, Table 12.3

ACCEPTED VERSION SUBJECT TO FINAL EDITING

1 Panel G)

	Region	AFRICA	AFRICA	AFRICA
	Region type (Land / Ocean)	Land	Land	Land
	Sub-Region Name	W.Southern-Africa	W.Southern-Africa	W.Southern-Africa
	Accronym	WSAF	WSAF	WSAF
	Data Type	Observational	Detection & Attribution	Projections
Heat and Cold	Mean air temperature	Table 11.1; Table 11.4;11.3.2; 12.4.1.1, Atlas 4.2	Table 11.1; Table 11.4;11.3.4, Atlas 4.2	Table 11.2; Table 11.4;11.3.5; 12.4.1.1; Table 12.3; Atlas 4.4, 4.4.1.1, 4.5.1.1, 4.6.1.1
	Extreme heat	Table 11.1; Table 11.4;11.3.2,12.4.1.1	Table 11.1; Table 11.4;11.3.4	Table 11.2; Table 11.4;11.3.5; 12.4.1.1; Table 12.3;
	Cold spell	Table 11.1; Table 11.4;11.3.2,12.4.1.2	Table 11.1; Table 11.4;11.3.5	Table 11.2; Table 11.4;11.3.5; 12.4.1.1; Table 12.3;
	Frost			12.4.1.1; Table 12.3;
Wet and Dry	Mean precipitation	12.4.1.2, Atlas 4.2, 8.3.1.3	Atlas 4.2	12.4.1.2, Table 12.3, Atlas 4.4, 8.4.1.3, BOX 8.2, 4.4.1.3, 4.5.1.4, 4.6.1.2
	River flood	11.5.2; 12.4.1.2	11.5.4	11.5.5; 12.4.1.2
	Heavy precipitation and pluvial flood	11.4.2, 11.5.2, Table 11.5, 12.4.1.2	11.4.4, 11.5.4,Table 11.5,	11.4.5, 11.5.5, Table 11.5, 12.4.1.2, Table 12.3
	Landslide	12.4.1.2;		12.4.1.2, Table 12.3
	Aridity	8.3.1.6, 12.4.1.2	8.3.1.6,	12.4.1.2, Table 12.3, 8.4.1.6
	Hydrological drought	11.6.2, Table 11.6, 12.4.1.2	11.6.4, Table 11.6,	11.6.5, Table 11.6, 12.4.1.2, Table 12.3
	Agricultural and ecological drought	11.6.2, Table 11.6, 12.4.1.3	11.6.4, Table 11.6,	11.6.5, Table 11.6, 12.4.1.2, Table 12.4
	Fire weather	12.4.1.2		12.4.1.2, Table 12.3
Wind	Mean wind speed	12.4.1.3		12.4.1.3, Table 12.3
	Severe wind storm	12.4.1.3		12.4.1.3, Table 12.3
	Tropical cyclone			
	Sand and dust storm	12.4.1.3		12.4.1.3, Table 12.3
Snow and Ice	Snow, glacier and ice sheet			
	Permafrost			
	Lake, river and sea ice			
	Heavy snowfall and ice storm			
	Hail	12.4.1.4		12.4.1.4, Table 12.3
	Snow avalanche			
Coastal and Oceanic	Relative sea level	12.4.1.5		12.4.1.5, Table 12.3
	Coastal flood	12.4.1.5		12.4.1.5, Table 12.3
	Coastal erosion	12.4.1.5		12.4.1.5, Table 12.3
	Marine heatwave	12.4.1.5		12.4.1.5, Table 12.3
	Ocean acidity	12.4		12.4, Table 12.3
Other	Air pollution weather	12.4.1.6		12.4, Table 12.3
	Atmospheric CO2 at surface	12.4.1.6		12.4, Table 12.3
	Radiation at surface			12.4, Table 12.3

2
3
4

ACCEPTED VERSION SUBJECT TO FINAL EDITING

Panel H)

	Region	AFRICA	AFRICA	AFRICA
	Region type (Land / Ocean)	Land	Land	Land
	Sub-Region Name	E.Southern-Africa	E.Southern-Africa	E.Southern-Africa
	Accronym	ESAF	ESAF	ESAF
	Data Type	Observational	Detection & Attribution	Projections
Heat and Cold	Mean air temperature	Table 11.1; Table 11.4;11.3.2; 12.4.1.1, Atlas 4.2	Table 11.1; Table 11.4;11.3.4, Atlas 4.2	Table 11.2; Table 11.4;11.3.5; 12.4.1.1; Table 12.3, Atlas 4.4, 4.4.1.1, 4.5.1.1, 4.6.1.1
	Extreme heat	Table 11.1; Table 11.4;11.3.2,12.4.1.1	Table 11.1; Table 11.4;11.3.4	Table 11.2; Table 11.4;11.3.5; 12.4.1.1; Table 12.3;
	Cold spell	Table 11.1; Table 11.4;11.3.2,12.4.1.2	Table 11.1; Table 11.4;11.3.5	Table 11.2; Table 11.4;11.3.5; 12.4.1.1; Table 12.3;
	Frost			12.4.1.1; Table 12.3;
Wet and Dry	Mean precipitation	12.4.1.2, Atlas 4.2, 8.3.1.3	Atlas 4.2	12.4.1.2, Table 12.3, Atlas 4.4, 8.4.1.3, BOX 8.2, 4.4.1.3, 4.5.1.4, 4.6.1.2
	River flood	11.5.2; 12.4.1.2	11.5.4	11.5.5; 12.4.1.2
	Heavy precipitation and pluvial flood	11.4.2, 11.5.2, Table 11.5, 12.4.1.2	11.4.4, 11.5.4, Table 11.5,	11.4.5, 11.5.5,Table 11.5, 12.4.1.2, Table 12.3
	Landslide	12.4.1.2;		12.4.1.2, Table 12.3;
	Aridity	8.3.1.6, 12.4.1.2	8.3.1.6,	12.4.1.2, Table 12.3, 8.4.1.6
	Hydrological drought	11.6.2, Table 11.6, 12.4.1.2	11.6.4, Table 11.6,	11.6.5, Table 11.6, 12.4.1.2, Table 12.3
	Agricultural and ecological drought	11.6.2, Table 11.6, 12.4.1.3	11.6.4, Table 11.6,	11.6.5, Table 11.6, 12.4.1.2, Table 12.4
	Fire weather	12.4.1.2		12.4.1.2, Table 12.3
Wind	Mean wind speed	12.4.1.3		12.4.1.3, Table 12.3
	Severe wind storm	12.4.1.3		12.4.1.3, Table 12.3
	Tropical cyclone	11.7.1.2, 12.4.1.3	11.7.1.4	11.7.1.5, 12.4.1.3, Table 12.3
	Sand and dust storm	12.4.1.3		12.4.1.3, Table 12.3
Snow and Ice	Snow, glacier and ice sheet			
	Permafrost			
	Lake, river and sea ice			
	Heavy snowfall and ice storm			
	Hail	12.4.1.4		12.4.1.4, Table 12.3
	Snow avalanche			
Coastal and Oceanic	Relative sea level	12.4.1.5		12.4.1.5, Table 12.3
	Coastal flood	12.4.1.5		12.4.1.5, Table 12.3
	Coastal erosion	12.4.1.5		12.4.1.5, Table 12.3
	Marine heatwave	12.4.1.5		12.4.1.5, Table 12.3
	Ocean acidity	12.4		12.4, Table 12.3
Other	Air pollution weather	12.4.1.6		12.4, Table 12.3
	Atmospheric CO2 at surface	12.4.1.6		12.4, Table 12.3
	Radiation at surface			12.4, Table 12.3

ACCEPTED VERSION SUBJECT TO FINAL EDITING

Panel I)

	Region	AFRICA	AFRICA	AFRICA
	Region type (Land / Ocean)	Land	Land	Land
	Sub-Region Name	Madagascar	Madagascar	Madagascar
	Accronym	MDG	MDG	MDG
	Data Type	Observational	Detection & Attribution	Projections
Heat and Cold	Mean air temperature	Table 11.1; Table 11.4;11.3.2; 12.4.1.1, Atlas 4.2	Table 11.1; Table 11.4;11.3.4, Atlas 4.2	Table 11.2; Table 11.4;11.3.5; 12.4.1.1; Table 12.3, Atlas 4.4, 4.4.1.1, 4.5.1.1, 4.6.1.1
	Extreme heat	Table 11.1; Table 11.4;11.3.2,12.4.1.1	Table 11.1; Table 11.4;11.3.4	Table 11.2; Table 11.4;11.3.5; 12.4.1.1; Table 12.3;
	Cold spell	Table 11.1; Table 11.4;11.3.2,12.4.1.2	Table 11.1; Table 11.4;11.3.5	Table 11.2; Table 11.4;11.3.5; 12.4.1.1; Table 12.3;
	Frost			12.4.1.1; Table 12.3; Table 12.3;
Wet and Dry	Mean precipitation	Atlas 4.2	Atlas 4.2	12.4.1.2, Table 12.3, Atlas 4.4, 4.4.1.3, 4.5.1.4, 4.6.1.2
	River flood	11.5.2; 12.4.1.2	11.5.4	11.5.5; 12.4.1.2, Table 12.3
	Heavy precipitation and pluvial flood	11.4.2, 11.5.2, Table 11.5, 12.4.1.2	11.4.4, 11.5.4, Table 11.5,	11.4.5, 11.5.5, Table 11.5, 12.4.1.2, Table 12.3
	Landslide	12.4.1.2;		12.4.1.2, Table 12.3;
	Aridity	12.4.1.2		12.4.1.2, Table 12.3
	Hydrological drought	11.6.2, Table 11.6, 12.4.1.2	11.6.4, Table 11.6,	11.6.5, Table 11.6, 12.4.1.2, Table 12.3
	Agricultural and ecological drought	11.6.2, Table 11.6, 12.4.1.3	11.6.4, Table 11.6,	11.6.5, Table 11.6, 12.4.1.2, Table 12.4
	Fire weather	12.4.1.2		12.4.1.2, Table 12.3
Wind	Mean wind speed	12.4.1.3		12.4.1.3, Table 12.3
	Severe wind storm	12.4.1.3		12.4.1.3, Table 12.3
	Tropical cyclone	11.7.1.2, 12.4.1.3	11.7.1.4	11.7.1.5, 12.4.1.3, Table 12.3
	Sand and dust storm	12.4.1.3		12.4.1.3, Table 12.3
Snow and Ice	Snow, glacier and ice sheet			
	Permafrost			
	Lake, river and sea ice			
	Heavy snowfall and ice storm			
	Hail	12.4.1.4		12.4.1.4, Table 12.3
	Snow avalanche			
Coastal and Oceanic	Relative sea level	12.4.1.5		12.4.1.5, Table 12.3
	Coastal flood	12.4.1.5		12.4.1.5, Table 12.3
	Coastal erosion	12.4.1.5		12.4.1.5, Table 12.3
	Marine heatwave	12.4.1.5		12.4.1.5, Table 12.3
	Ocean acidity	12.4		12.4, Table 12.3
Other	Air pollution weather	12.4.1.6		12.4, Table 12.3
	Atmospheric CO2 at surface	12.4.1.6		12.4, Table 12.3
	Radiation at surface			12.4, Table 12.3

[END TABLE 10.SM.1 HERE]

ACCEPTED VERSION SUBJECT TO FINAL EDITING

[START TABLE 10.SM.2 HERE]

Table 10.SM.2: Regional Traceback Matrix for Asia. Table shows chapter traceability of the regional assessment using observed trends, attribution of trends or events, and climate model projections, as described in Cross-Chapter Box 10.3. The Table is divided into separate panels that correspond to the WGI AR6 Reference Regions. African sub-regions are: Panel A: E.Asia (EAS), Panel B: E.C.Asia (ECA), Panel C: Tibetan-Plateau (TIB), Panel D: S.Asia (SAS), Panel E: S.E.Asia (SEA), Panel F: Arabian-Peninsula (ARP), Panel G: W.C.Asia (WCA), Panel H: W.Siberia (WSB), Panel I: E.Siberia (ESB), Panel J: Russian-Far-East (RFE). Blank cells in the observations and projections columns corresponding to the "not broadly relevant" or "no evidence" category as described in the CID framework in Chapter 12. Blank cells in the detection and attribution columns correspond to no studies being available.

Panel A)

	Region	ASIA - EAST ASIA	ASIA - EAST ASIA	ASIA - EAST ASIA
	Region type (Land / Ocean)	Land	Land	Land
	Sub-Region Name	E.Asia	E.Asia	E.Asia
	Accronym	EAS	EAS	EAS
	Data Type	Observational	Detection & Attribution	Projections
Heat and Cold	Mean air temperature	Atlas 5.1.2 12.4.2.1 10.4.1.1		Atlas5.1.4 12.4.2.1, Table 12.4
	Extreme heat	12.4.2.1 11.3.2 Table 11.7	11.3.4 Table 11.7	12.4.2.1, Table 12.4, 11.3.5 Table 11.7
	Cold spell	11.3.2 12.4.2.1 Table 11.7	11.3.4 Table 11.7	11.3.5 Table 11.7 12.4.2.1, Table 12.4
	Frost	12.4.2.1		12.4.2.1, Table 12.4
Wet and Dry	Mean precipitation	8.3.2.4.2 10.4.1.1 Atlas 5.1.2 12.4.2.2	10.3.2.2	Atlas 5.1.4 8.4.2.4.2 12.4.2.2, Table 12.4
	River flood	10.4.1.1 12.4.2.2		12.4.2.2, Table 12.4
	Heavy precipitation and pluvial flood	8.3.1.3 10.4.1.1 12.4.2.2 11.4.2 Table 11.8 BOX 11.4	11.4.4 Table 11.8	12.4.2.2, Table 12.4, 11.4.5 Table 11.8
	Landslide	12.4.2.2		12.4.2.2, Table 12.4
	Aridity	12.4.2.2 Table 11.9	Table 11.9	12.4.2.2, Table 12.4, Table 11.9
	Hydrological drought	10.4.1.1 11.6.2.4 11.6.2.5 Table 11.9 12.4.2.2	Table 11.9	8.4.1.6 12.4.2.2, Table 12.4
	Agricultural and ecological drought	11.6.2.3 Table 11.9, 12.4.2.2	Table 11.9	11.6.5.3 12.4.2.2, Table 12.4, Table 11.9
	Fire weather	12.4.2.2		12.4.2.2, Table 12.4
Wind	Mean wind speed	12.4.2.3		12.4.2.3, Table 12.4
	Severe wind storm	12.4.2.3		12.4.2.3, Table 12.4
	Tropical cyclone	12.4.2.3 11.7.1.2		8.4.2.5 11.7.1.5 12.4.2.3
	Sand and dust storm	12.4.2.3		12.4.2.3, Table 12.4
Snow and Ice	Snow, glacier and ice sheet	Atlas 5.1.2 12.4.2.4		12.4.2.4, Table 12.4
	Permafrost			
	Lake, river and sea ice	12.4.2.4		12.4.2.4, Table 12.4
	Heavy snowfall and ice storm	12.4.2.4		12.4.2.4, Table 12.4
	Hail	11.7.3.2		12.4.2.4, Table 12.4
	Snow avalanche	12.4.2.4		12.4.2.4, Table 12.4
Coastal and Oceanic	Relative sea level	12.4.2.5		12.4.2.5, Table 12.4
	Coastal flood	12.4.2.5		12.4.2.5, Table 12.4
	Coastal erosion	12.4.2.5		12.4.2.5, Table 12.4
	Marine heatwave	12.4.2.5		12.4.2.5, Table 12.4
	Ocean acidity	12.4		12.4, Table 12.4
Other	Air pollution weather	12.4		12.4, Table 12.4
	Atmospheric CO2 at surface	12.4		12.4, Table 12.4
	Radiation at surface	12.4		12.4, Table 12.4

ACCEPTED VERSION SUBJECT TO FINAL EDITING

Panel B)

	Region	ASIA - EAST ASIA	ASIA - EAST ASIA	ASIA - EAST ASIA
	Region type (Land / Ocean)	Land	Land	Land
	Sub-Region Name	E.C.Asia	E.C.Asia	E.C.Asia
	Accronym	ECA	ECA	ECA
	Data Type	Observational	Detection & Attribution	Projections
Heat and Cold	Mean air temperature	12.4.2.1		12.4.2.1, Table 12.4
	Extreme heat	12.4.2.1 11.3.2		12.4.2.1, Table 12.4
	Cold spell	12.4.2.1		12.4.2.1, Table 12.4
	Frost	12.4.2.1		12.4.2.1, Table 12.4
Wet and Dry	Mean precipitation	12.4.2.2		12.4.2.2, Table 12.4
	River flood	12.4.2.2		12.4.2.2, Table 12.4
	Heavy precipitation and pluvial flood	11.4.2, 12.4.2.2		11.4.5, 12.4.2.2, Table 12.4
	Landslide	12.4.2.2		12.4.2.2, Table 12.4
	Aridity	8.3.1.6 12.4.2.2		12.4.2.2, Table 12.4
	Hydrological drought	12.4.2.2		12.4.2.2, Table 12.4
	Agricultural and ecological drought	12.4.2.2		12.4.2.2, Table 12.4
	Fire weather	12.4.2.2		12.4.2.2, Table 12.4
Wind	Mean wind speed	12.4.2.3		12.4.2.3, Table 12.4
	Severe wind storm	12.4.2.3		12.4.2.3, Table 12.4
	Tropical cyclone			
	Sand and dust storm	12.4.2.3		12.4.2.3, Table 12.4
Snow and Ice	Snow, glacier and ice sheet	12.4.2.4		12.4.2.4
	Permafrost	12.4.2.4		12.4.2.4
	Lake, river and sea ice	12.4.2.4		12.4.2.4
	Heavy snowfall and ice storm			
	Hail	12.4.2.4		12.4.2.4
	Snow avalanche			
Coastal and Oceanic	Relative sea level			
	Coastal flood			
	Coastal erosion			
	Marine heatwave			
	Ocean acidity			
Other	Air pollution weather	12.4		12.4, Table 12.4
	Atmospheric CO2 at surface	12.4		12.4, Table 12.4
	Radiation at surface	12.4		12.4, Table 12.4

ACCEPTED VERSION SUBJECT TO FINAL EDITING

Panel C)

	Region	ASIA - SOUTH ASIA	ASIA - SOUTH ASIA	ASIA - SOUTH ASIA
	Region type (Land / Ocean)	Land	Land	Land
	Sub-Region Name	Tibetan-Plateau	Tibetan-Plateau	Tibetan-Plateau
	Accronym	TIB	TIB	TIB
	Data Type	Observational	Detection & Attribution	Projections
Heat and Cold	Mean air temperature	12.4.2.1 Box 10.4	Box10.4	12.4.2.1, Table 12.4, Box 10.4
	Extreme heat	12.4.2.1 11.3.2 Box 10.4		11.3.5 12.4.2.1, Table 12.4
	Cold spell	11.3.2 12.4.2.1 Box 10.4		11.3.5 12.4.2.1, Table 12.4
	Frost	12.4.2.1		12.4.2.1, Table 12.4
Wet and Dry	Mean precipitation	12.4.2.2 Box 10.4		12.4.2.2
	River flood	12.4.2.2		
	Heavy precipitation and pluvial flood	11.4.2 Box 10.4		11.4.5 Box 10.4
	Landslide	12.4.2.2		12.4.2.2, Table 12.4
	Aridity	12.4.2.2		11.6.5.1 12.4.2.2
	Hydrological drought	12.4.2.2		12.4.2.2, Table 12.4
	Agricultural and ecological drought	12.4.2.2		12.4.2.2, Table 12.4
	Fire weather	12.4.2.2		12.4.2.2, Table 12.4
Wind	Mean wind speed	12.4.2.3		12.4.2.3, Table 12.4
	Severe wind storm	12.4.2.3		12.4.2.3, Table 12.4
	Tropical cyclone			
	Sand and dust storm	12.4.2.3		12.4.2.3, Table 12.4
Snow and Ice	Snow, glacier and ice sheet	9.5.1 9.5.3 12.4.2.4 Box 10.4 8.3.1.3 8.3.1.7 12.4.2.4		9.5.1 9.5.3 12.4.2.4 Box 10.4 8.4.1.7.1 12.4.2.4, Table 12.4.
	Permafrost	9.5.2 12.4.2.4 Box 10.4 12.4.2.4	Box10.4	9.5.2 12.4.2.4 Box 10.4 12.4.2.4, Table 12.4.
	Lake, river and sea ice			12.4.2.4, Table 12.4
	Heavy snowfall and ice storm			12.4.2.4, Table 12.4
	Hail			12.4.2.4, Table 12.4
	Snow avalanche			12.4.2.4, Table 12.4
Coastal and Oceanic	Relative sea level			
	Coastal flood			
	Coastal erosion			
	Marine heatwave			
	Ocean acidity			
Other	Air pollution weather	12.4		12.4, Table 12.4
	Atmospheric CO2 at surface	12.4		12.4, Table 12.4
	Radiation at surface	12.4		12.4, Table 12.4

ACCEPTED VERSION SUBJECT TO FINAL EDITING

Panel D)

	Region	ASIA - SOUTH ASIA	ASIA - SOUTH ASIA	ASIA - SOUTH ASIA
	Region type (Land / Ocean)	Land	Land	Land
	Sub-Region Name	S.Asia	S.Asia	S.Asia
	Accronym	SAS	SAS	SAS
	Data Type	Observational	Detection & Attribution	Projections
Heat and Cold	Mean air temperature	Atlas 1.1.2 Atlas 5.3.5.2 Atlas 5.3.5 10.6.2 10.6.3 10.6.10 12.4.2.1		Atlas 1.1.4 Atlas 5.3.5.4 10.6.3.6 10.6.3.7 10.6.3.10 12.4.2.1, Table 12.4, Table 11.7
	Extreme heat	Atlas 1.1.2 Atlas 5.3.5 Atlas 5.3.5.2 12.4.2.1 11.3.2		Table 11.5 10.6.3.9 12.4.2.1, Table 12.4, 11.3.5
	Cold spell	12.4.2.1		12.4.2.1, Table 12.4, Table 11.7
	Frost	12.4.2.1		12.4.2.1, Table 12.4, Table 11.7
Wet and Dry	Mean precipitation	Atlas 1.1.2 Atlas5.3.5.2 8.3.1.3 8.3.2.4 10.3.3.3.1 10.6.3.2 10.6.3.3 10.6.3.10 12.4.2.2	10.6.5 Atlas 1.1.2	Atlas 1.1.4 Atlas 5.3.5 Atlas 5.3.5.4 8.4.1.3.1 8.4.2.4 10.3.3.3.1 10.6.3.6 10.6.3.7 10.6.3.10 12.4.2.2, Table 12.4, 11.4.1
	River flood	8.2.3.2 12.4.2.2	11.5.4	12.4.2.2, Table 12.4, 11.5.5
	Heavy precipitation and pluvial flood	8.3.1.3 11.4.2 12.4.2.2	CH11.4.4 Box 11.4	11.4.1 11.4.5 11.5.5 12.4.2.2, Table 12.4, Table 11.8
	Landslide	12.4.2.2		12.4.2.2, Table 12.4
	Aridity	12.4.2.2		11.6.5.1 12.4.2.2, Table 12.4
	Hydrological drought	8.3.1.6 11.6.2.5 12.4.2.2	10.6.3.5	11.6.5.3 12.4.2.2, Table 12.4
	Agricultural and ecological drought	8.3.1.6 12.4.2.2		12.4.2.2, Table 12.4
	Fire weather	12.4.2.2		12.4.2.2, Table 12.4
Wind	Mean wind speed	11.7.4 12.4.2.3		12.4.2.3, Table 12.4
	Severe wind storm	11.7.3.2 12.4.2.3	11.7.3.4	12.4.2.3, Table 12.4
	Tropical cyclone			12.4.2.3, Table 12.4
	Sand and dust storm	12.4.2.3		12.4.2.3, Table 12.4
Snow and Ice	Snow, glacier and ice sheet	9.5 9.5.3 12.4.2.4		9.5.1 9.5.3 12.4.2.4, Table 12.4
	Permafrost	9.5.2, 12.4.2.4		9.5.2, 12.4.2.4, Table 12.4
	Lake, river and sea ice	12.4.2.4		12.4.2.4, Table 12.4
	Heavy snowfall and ice storm	12.4.2.4		12.4.2.4, Table 12.4
	Hail	12.4.2.4		12.4.2.4, Table 12.4
	Snow avalanche	12.4.2.4		12.4.2.4, Table 12.4
Coastal and Oceanic	Relative sea level	12.4.2.5		12.4.2.5, Table 12.4
	Coastal flood	12.4.2.5		12.4.2.5, Table 12.4
	Coastal erosion	12.4.2.5		12.4.2.5, Table 12.4
	Marine heatwave	12.4.2.5		12.4.2.5, Table 12.4
	Ocean acidity	12.4		12.4, Table 12.4
Other	Air pollution weather	12.4		10.6.3.6 12.4, Table 12.4
	Atmospheric CO2 at surface	12.4		12.4, Table 12.4
	Radiation at surface	12.4		10.6.3.6 12.4, Table 12.4

ACCEPTED VERSION SUBJECT TO FINAL EDITING

Panel E)

	Region	ASIA - SOUTH EAST ASIA	ASIA - SOUTH EAST ASIA	ASIA - SOUTH EAST ASIA
	Region type (Land / Ocean)	Land-Ocean	Land-Ocean	Land-Ocean
	Sub-Region Name	S.E.Asia	S.E.Asia	S.E.Asia
	Accronym	SEA	SEA	SEA
	Data Type	Observational	Detection & Attribution	Projections
Heat and Cold	Mean air temperature	Atlas 3.1 Atlas 5.4.1 Atlas 5.4.2 12.4.2.1		Atlas 3.1 Atlas 5.4.1 Atlas 5.4.4 12.4.2.1, Table 12.4
	Extreme heat	Atlas5.4.2 11.3.2 12.4.2.1	11.3.4	11.3.5 12.4.2.1, Table 12.4
	Cold spell	12.4.2.1		11.3.5 12.4.2.1, Table 12.4
	Frost			
Wet and Dry	Mean precipitation	Atlas 3.1 Atlas 5.4.1 Atlas5.4.2 12.4.2.2		Atlas 3.1 Atlas 5.4.1 Atlas5.4.4 12.4.2.2, Table 12.4, 11.5.5
	River flood	12.4.2.2		8.4.1.5 12.4.2.2, Table 12.4, 11.5.5
	Heavy precipitation and pluvial flood	Atlas 5.4.2 12.4.2.2 11.4.2 11.5.2		8.4.1.5 12.4.2.2, Table 12.4, 11.4.5 11.5.4
	Landslide	12.4.2.2		12.4.2.2, Table 12.4
	Aridity	12.4.2.2		12.4.2.2, Table 12.4
	Hydrological drought	12.4.2.2 11.6 11.6.2.4 11.6.2.5		12.4.2.2, Table 12.4, 11.6.5.4
	Agricultural and ecological drought	12.4.2.2		12.4.2.2, Table 12.4, BOX 11.4
	Fire weather	12.4.2.2 Box 11.4		12.4.2.2, Table 12.4, BOX 11.4
Wind	Mean wind speed	12.4.2.3		12.4.2.3, Table 12.4
	Severe wind storm	12.4.2.3		12.4.2.3, Table 12.4
	Tropical cyclone	12.4.2.3	11.7.1.4	12.4.2.3, Table 12.4
	Sand and dust storm	12.4.2.3		12.4.2.3, Table 12.4
Snow and Ice	Snow, glacier and ice sheet	9.5.1 9.5.3, 12.4.2.4		9.5.1 9.5.3, 12.4.2.4, Table 12.4
	Permafrost			
	Lake, river and sea ice			
	Heavy snowfall and ice storm			
	Hail	12.4.2.4		12.4.2.4, Table 12.4
	Snow avalanche			
Coastal and Oceanic	Relative sea level	12.4.2.5		12.4.2.5, Table 12.4
	Coastal flood	12.4.2.5		12.4.2.5, Table 12.4
	Coastal erosion	12.4.2.5		12.4.2.5, Table 12.4
	Marine heatwave	12.4.2.5		12.4.2.5, Table 12.4
	Ocean acidity	12.4		12.4, Table 12.4
Other	Air pollution weather	2.2.5.3 12.4		12.4, Table 12.4
	Atmospheric CO2 at surface	12.4		12.4, Table 12.4
	Radiation at surface	12.4		12.4, Table 12.4

ACCEPTED VERSION SUBJECT TO FINAL EDITING

Panel F)

	Region	ASIA - SOUTH WEST ASIA	ASIA - SOUTH WEST ASIA	ASIA - SOUTH WEST ASIA
	Region type (Land / Ocean)	Land	Land	Land
	Sub-Region Name	Arabian-Peninsula	Arabian-Peninsula	Arabian-Peninsula
	Accronym	ARP	ARP	ARP
	Data Type	Observational	Detection & Attribution	Projections
Heat and Cold	Mean air temperature	Atlas.5.5.2, 12.4.2.1		12.4.2.1, Table 12.4; Atlas.5.5.4
	Extreme heat	12.4.2.1, Table 11.7	Table 11.7	Table 11.7, 12.4.2.1, Table 12.4
	Cold spell	12.4.2.1, Table 11.7	Table 11.7	Table 11.7, 12.4.2.1, Table 12.4
	Frost	12.4.2.1		12.4.2.1, Table 12.4
Wet and Dry	Mean precipitation	Atlas.5.5.2, 12.4.2.2		Atlas.5.5.4 12.4.2.2, Table 12.4;
	River flood	12.4.2.2, FAQ 8.2		12.4.2.2, Table 12.4
	Heavy precipitation and pluvial flood	FAQ 8.2, Table 11.8, 12.4.2.2	Table 11.8	Table.11.8, 12.4.2.2, Table 12.4;
	Landslide	12.4.2.2		12.4.2.2, Table 12.4
	Aridity	8.2.3.3, FAQ 8.3, Table 11.9, 12.4.2.2	Table 11.9	Table 11.9, 12.4.2.2, Table 12.4
	Hydrological drought	Table 11.9, 12.4.2.2	Table 11.9	Table 11.9, 12.4.2.2, Table 12.4
	Agricultural and ecological drought	8.2.3.3, FAQ 8.3, Table 11.9, 12.4.2.2	Table 11.9	Table 11.9, 12.4.2.2, Table 12.4
	Fire weather	12.4.2.2		12.4.2.2, Table 12.4;
Wind	Mean wind speed	11.7.4, 12.4.2.3		12.4.2.3, Table 12.4
	Severe wind storm	11.7.4, 12.4.2.3		12.4.2.3, Table 12.4
	Tropical cyclone	12.4.2.3		12.4.2.3, Table 12.4
	Sand and dust storm	12.4.2.3		12.4.2.3, Table 12.4
Snow and Ice	Snow, glacier and ice sheet			
	Permafrost			
	Lake, river and sea ice			
	Heavy snowfall and ice storm			
	Hail	12.4.2.4		12.4.2.4, Table 12.4
	Snow avalanche			
Coastal and Oceanic	Relative sea level	12.4.2.5		12.4.2.5, Table 12.4;
	Coastal flood	12.4.2.5		12.4.2.5, Table 12.4;
	Coastal erosion	12.4.2.5		12.4.2.5, Table 12.4;
	Marine heatwave	12.4.2.5		12.4.2.5, Table 12.4;
	Ocean acidity	12.4		12.4, Table 12.4
Other	Air pollution weather	12.4		12.4, Table 12.4
	Atmospheric CO2 at surface	12.4		12.4, Table 12.4
	Radiation at surface	12.4		12.4, Table 12.4

ACCEPTED VERSION SUBJECT TO FINAL EDITING

Panel G)

	Region	ASIA - SOUTH WEST ASIA	ASIA - SOUTH WEST ASIA	ASIA - SOUTH WEST ASIA
	Region type (Land / Ocean)	Land	Land	Land
	Sub-Region Name	W.C.Asia	W.C.Asia	W.C.Asia
	Accronym	WCA	WCA	WCA
	Data Type	Observational	Detection & Attribution	Projections
Heat and Cold	Mean air temperature	Atlas.5.5.2 12.4.2.1		Atlas.5.5.4, 12.4.2.1, Table 12.4;
	Extreme heat	Table 11.7, 12.4.2.1	Table 11.7	Table 11.7, 11.3.5, 12.4.2.1, Table 12.4
	Cold spell	Table 11.7, 12.4.2.1	Table 11.7	Table 11.7, 12.4.2.1, Table 12.4
	Frost	12.4.2.1		12.4.2.1, Table 12.4
Wet and Dry	Mean precipitation	Atlas.5.5.2 12.4.2.2		Atlas.5.5.4 12.4.2.2, Table 12.4;
	River flood	12.4.2.2, FAQ 8.2		12.4.2.2, Table 12.4
	Heavy precipitation and pluvial flood	FAQ 8.2, Table 11.8, 12.4.2.2	Table 11.8	12.4.2.2, Table 12.4
	Landslide	12.4.2.2		12.4.2.2, Table 12.4
	Aridity	8.2.3.3, FAQ 8.3, Table 11.9, 12.4.2.2	Table 11.9	11.6.5.1, 12.4.2.2, Table 11.9, Table 12.4;
	Hydrological drought	8.3.1.6, Table 11.9, 12.4.2.2	Table 11.9	8.4.1.6, Table 11.9, 12.4.2.2, Table 12.4;
	Agricultural and ecological drought	8.2.3.3, FAQ 8.3, 8.3.1.6, Table 11.9, 12.4.2.2	Table 11.9	8.4.1.6, Table 11.9, 12.4.2.2, Table 12.4;
	Fire weather			12.4.2.2, Table 12.4
Wind	Mean wind speed	12.4.2.3		12.4.2.3, Table 12.4
	Severe wind storm	12.4.2.3		12.4.2.3, Table 12.4
	Tropical cyclone			
	Sand and dust storm	12.4.2.3		12.4.2.3, Table 12.4
Snow and Ice	Snow, glacier and ice sheet	9.5.1, 9.5.3, Atlas.5.5.2		9.5.1, 9.5.3, 12.4.2.4, Table 12.4
	Permafrost	9.5.2; 12.4.2.4		9.5.2; 12.4.2.4, Table 12.4;
	Lake, river and sea ice	12.4.2.4		12.4.2.4, Table 12.4
	Heavy snowfall and ice storm	12.4.2.4		12.4.2.4, Table 12.4
	Hail	12.4.2.4		12.4.2.4, Table 12.4
	Snow avalanche	12.4.2.4		12.4.2.4, Table 12.4
Coastal and Oceanic	Relative sea level	12.4.2.5		12.4.2.5, Table 12.4;
	Coastal flood	12.4.2.5		12.4.2.5, Table 12.4;
	Coastal erosion	12.4.2.5		12.4.2.5, Table 12.4;
	Marine heatwave	12.4.2.5		12.4.2.5, Table 12.4;
	Ocean acidity	12.4		12.4, Table 12.4
Other	Air pollution weather	12.4		12.4, Table 12.4
	Atmospheric CO2 at surface	12.4		12.4, Table 12.4
	Radiation at surface	12.4		12.4, Table 12.4

ACCEPTED VERSION SUBJECT TO FINAL EDITING

Panel H)

	Region	ASIA - NORTH ASIA	ASIA - NORTH ASIA	ASIA - NORTH ASIA
	Region type (Land / Ocean)	Land	Land	Land
	Sub-Region Name	W.Siberia	W.Siberia	W.Siberia
	Accronym	WSB	WSB	WSB
	Data Type	Observational	Detection & Attribution	Projections
Heat and Cold	Mean air temperature	Atlas.5.2.2 12.4.2.1		Atlas.5.2.4 12.4.2.1, Table 12.4
	Extreme heat	Table 11.7, 12.4.2.1	Table 11.7	11.3.5, Table 11.7, 12.4.2.1, Table 12.4
	Cold spell	Table 11.7, 12.4.2.1	Table 11.7	Table 11.7, 12.4.2.2, Table 12.4
	Frost	12.4.2.1		12.4.2.1, Table 12.4
Wet and Dry	Mean precipitation	Atlas.5.2.2, 12.4.2.2, 2.3.1.3.4, 8.3.1.3, 10.4.1.2, 10.4.2.4		Atlas.5.2.4 12.4.2.2, Table 12.4
	River flood	12.4.2.2, FAQ 8.2		11.5.5, 12.4.2.2, Table 12.4
	Heavy precipitation and pluvial flood	8.3.1.3, FAQ 8.2, 11.4.2, Table 11.8, 12.4.2.2	Table 11.8	Table 11.8, 11.4.5, 12.4.2.2, Table 12.4
	Landslide	12.4.2.2		12.4.2.2, Table 12.4
	Aridity	8.2.3.3, FAQ 8.3, Table 11.9, 12.4.2.2	Table 11.9	Table 11.9, 12.4.2.2, Table 12.4
	Hydrological drought	Table 11.9, 12.4.2.2	Table 11.9	8.4.1.6, Table 11.9, 12.4.2.2, Table 12.4
	Agricultural and ecological drought	8.2.3.3, FAQ 8.3, Table 11.9, 12.4.2.2	Table 11.9	8.4.1.6, Table 11.9, 12.4.2.2, Table 12.4
	Fire weather	12.4.2.2		12.4.2.2, Table 12.4
Wind	Mean wind speed	2.3.1.4.4, 12.4.2.3		12.4.2.3, Table 12.4
	Severe wind storm	12.4.2.3		12.4.2.3, Table 12.4
	Tropical cyclone			
	Sand and dust storm	12.4.2.3		12.4.2.3, Table 12.4
Snow and Ice	Snow, glacier and ice sheet	2.3.2.2, 8.3.1.7.2, 9.5.1, 9.5.3, Atlas.5.2.2	3.4.2	9.5.1, 9.5.3, 12.4.2.4, Table 12.4
	Permafrost	9.5.2; 12.4.2.4		9.5.2; 12.4.2.4, Table 12.4;
	Lake, river and sea ice	12.4.2.4		12.4.2.4, Table 12.4
	Heavy snowfall and ice storm	12.4.2.4		12.4.2.4, Table 12.4
	Hail	12.4.2.4		12.4.2.4, Table 12.4
	Snow avalanche	12.4.2.4		12.4.2.4, Table 12.4
Coastal and Oceanic	Relative sea level			
	Coastal flood			
	Coastal erosion			
	Marine heatwave			
	Ocean acidity			
Other	Air pollution weather	12.4		12.4, Table 12.4
	Atmospheric CO2 at surface	12.4		12.4, Table 12.4
	Radiation at surface	12.4		12.4, Table 12.4

ACCEPTED VERSION SUBJECT TO FINAL EDITING

Panel I)

	Region	ASIA - NORTH ASIA	ASIA - NORTH ASIA	ASIA - NORTH ASIA
	Region type (Land / Ocean)	Land	Land	Land
	Sub-Region Name	E.Siberia	E.Siberia	E.Siberia
	Accronym	ESB	ESB	ESB
	Data Type	Observational	Detection & Attribution	Projections
Heat and Cold	Mean air temperature	Atlas.5.2.2 12.4.2.1		Atlas.5.2.4 12.4.2.1, Table 12.4
	Extreme heat	Table 11.7, 12.4.2.1	Table 11.7	11.3.5, Table 11.7, 12.4.2.1, Table 12.4
	Cold spell	Table 11.7, 12.4.2.1	Table 11.7	Table 11.7, 12.4.2.2, Table 12.4
	Frost	12.4.2.1		12.4.2.1, Table 12.4
Wet and Dry	Mean precipitation	Atlas.5.2.2, 12.4.2.2, 2.3.1.3.4, 8.3.1.3 10.4.1.2 10.4.2.4		Atlas.5.2.4 12.4.2.2, Table 12.4
	River flood	11.5.2, 12.4.2.2, FAQ8.2		11.5.5, 12.4.2.2, Table 12.4
	Heavy precipitation and pluvial flood	8.3.1.3, 11.4.2, Table 11.8, 12.4.2.2, FAQ 8.2	Table 11.8	Table 11.8, 11.4.5, 12.4.2.2, Table 12.4
	Landslide	12.4.2.2		12.4.2.2, Table 12.4
	Aridity	8.2.3.3, FAQ 8.3, Table 11.9, 12.4.2.2	Table 11.9	Table 11.9, 12.4.2.2, Table 12.4
	Hydrological drought	Table 11.9, 12.4.2.2	Table 11.9	8.4.1.6, Table 11.9, 12.4.2.2, Table 12.4
	Agricultural and ecological drought	8.2.3.3, FAQ 8.3, Table 11.9, 12.4.2.2	Table 11.9	8.4.1.6, Table 11.9, 12.4.2.2, Table 12.4
	Fire weather	12.4.2.2		12.4.2.2, Table 12.4
Wind	Mean wind speed	2.3.1.4.4, 12.4.2.3		12.4.2.3, Table 12.4
	Severe wind storm	12.4.2.3		12.4.2.3, Table 12.4
	Tropical cyclone			
	Sand and dust storm	12.4.2.3		12.4.2.3, Table 12.4
Snow and Ice	Snow, glacier and ice sheet	2.3.2.2, 8.3.1.7.2, 9.5.1, 9.5.3, Atlas.5.2.2	3.4.2	9.5.1, 9.5.3, 12.4.2.4, Table 12.4
	Permafrost	9.5.2; 12.4.2.4		9.5.2; 12.4.2.4, Table 12.4;
	Lake, river and sea ice	12.4.2.4		12.4.2.4, Table 12.4
	Heavy snowfall and ice storm	12.4.2.4		12.4.2.4, Table 12.4
	Hail	12.4.2.4		12.4.2.4, Table 12.4
	Snow avalanche	12.4.2.4		12.4.2.4, Table 12.4
Coastal and Oceanic	Relative sea level			
	Coastal flood			
	Coastal erosion			
	Marine heatwave			
	Ocean acidity			
Other	Air pollution weather	12.4		12.4, Table 12.4
	Atmospheric CO2 at surface	12.4		12.4, Table 12.4
	Radiation at surface	12.4		12.4, Table 12.4

ACCEPTED VERSION SUBJECT TO FINAL EDITING

Panel J)

	Region	ASIA - NORTH ASIA	ASIA - NORTH ASIA	ASIA - NORTH ASIA
	Region type (Land / Ocean)	Land	Land	Land
	Sub-Region Name	Russian-Far-East	Russian-Far-East	Russian-Far-East
	Accronym	RFE	RFE	RFE
	Data Type	Observational	Detection & Attribution	Projections
Heat and Cold	Mean air temperature	Atlas.5.2.2 12.4.2.1		Atlas.5.2.4 12.4.2.1, Table 12.4
	Extreme heat	Table 11.7, 12.4.2.1	Table 11.7	11.3.5, Table 11.7, 12.4.2.1, Table 12.4
	Cold spell	Table 11.7, 12.4.2.1	Table 11.7	Table 11.7, 12.4.2.2, Table 12.4
	Frost	12.4.2.1		12.4.2.1, Table 12.4
Wet and Dry	Mean precipitation	Atlas.5.2.2, 12.4.2.2, 2.3.1.3.4, 8.3.1.3		Atlas.5.2.4 12.4.2.2, Table 12.4
	River flood	11.5.2, 12.4.2.2		11.5.5, 12.4.2.2, Table 12.4
	Heavy precipitation and pluvial flood	8.3.1.3, Table 11.8, 11.4.2, 12.4.2.2	Table 11.8	Table 11.8, 11.4.5, 12.4.2.2
	Landslide	12.4.2.2		12.4.2.2, Table 12.4
	Aridity	8.2.3.3, FAQ 8.3, Table 11.9, 11.6.5.1, 12.4.2.2	Table 11.9	11.6.5.1, Table 11.9, 12.4.2.2, Table 12.4
	Hydrological drought	Table 11.9, 12.4.2.2	Table 11.9	Table 11.9, 12.4.2.2, Table 12.4
	Agricultural and ecological drought	8.2.3.3, FAQ 8.3, Table 11.9, 12.4.2.2	Table 11.9	Table 11.9, 12.4.2.2, Table 12.4
	Fire weather	12.4.2.2		12.4.2.2, Table 12.4
Wind	Mean wind speed	12.4.2.3		12.4.2.3, Table 12.4
	Severe wind storm	12.4.2.3		12.4.2.3, Table 12.4
	Tropical cyclone			
	Sand and dust storm	12.4.2.3		12.4.2.3, Table 12.4
Snow and Ice	Snow, glacier and ice sheet	8.3.1.7.2, 9.5.1, 9.5.3, Atlas.5.2.2		9.5.1, 9.5.3, 12.4.2.4
	Permafrost	2.3.2.5; 9.5.2; 12.4.2.4		9.5.2; 12.4.2.4, Table 12.4;
	Lake, river and sea ice	12.4.2.4		12.4.2.4, Table 12.4
	Heavy snowfall and ice storm	12.4.2.4		12.4.2.4, Table 12.4
	Hail	12.4.2.4		12.4.2.4, Table 12.4
	Snow avalanche	12.4.2.4		12.4.2.4, Table 12.4
Coastal and Oceanic	Relative sea level	12.4.2.5		12.4.2.5, Table 12.4;
	Coastal flood	12.4.2.5		12.4.2.5, Table 12.4;
	Coastal erosion	12.4.2.5		12.4.2.5, Table 12.4;
	Marine heatwave	12.4.2.5		12.4.2.5, Table 12.4;
	Ocean acidity	12.4		12.4, Table 12.4
Other	Air pollution weather	12.4		12.4, Table 12.4
	Atmospheric CO2 at surface	12.4		12.4, Table 12.4
	Radiation at surface	12.4		12.4, Table 12.4

[END TABLE 10.SM.2 HERE]

ACCEPTED VERSION SUBJECT TO FINAL EDITING

[START TABLE 10.SM.3 HERE]

Table 10.SM.3: Regional Traceback Matrix for Australasia. Table shows chapter traceability of the regional assessment using observed trends, attribution of trends or events, and climate model projections, as described in Cross-Chapter Box 10.3. The Table is divided into separate panels that correspond to the WGI AR6 Reference Regions. African sub-regions are: Panel A: N.Australia (NAU), Panel B: C.Australia (CAU), Panel C: E.Australia (EAU), Panel D: S.Australia (SAU), Panel E: New-Zealand (NZ). Blank cells in the observations and projections columns corresponding to the "not broadly relevant" or "no evidence" category as described in the CID framework in Chapter 12. Blank cells in the detection and attribution columns correspond to no studies being available.

Panel A)

	Region	AUSTRALASIA	AUSTRALASIA	AUSTRALASIA
	Region type (Land / Ocean)	Land	Land	Land
	Sub-Region Name	N.Australia	N.Australia	N.Australia
	Accronym	NAU	NAU	NAU
	Data Type	Observational	Detection & Attribution	Projections
Heat and Cold	Mean air temperature	12.4.3.1; Atlas.6.2		12.4.3.1; Table 12.5; Atlas.6.4; CH1.3.6
	Extreme heat	Table 11.1; Table 11.6: 11.3.2; 12.4.3.1	Table 11.1; Table 11.6: 11.3.4	Table 11.2; Table 11.6: 11.3.5; 12.4.3.1; Table 12.5
	Cold spell	Table 11.1; Table 11.6: 11.3.2; 12.4.3.1	Table 11.1; Table 11.6: 11.3.4	Table 11.2; Table 11.6: 11.3.5; 12.4.3.1; Table 12.5
	Frost	12.4.3.1		12.4.3.1; Table 12.5
Wet and Dry	Mean precipitation	12.4.3.2; Atlas.6.2		12.4.3.2; Table 12.5; Atlas.6.4
	River flood	Table 11.1; Table 11.6: 11.5.2; 12.4.3.2	Table 11.1; Table 11.6: 11.5.4	Table 11.2; Table 11.6: 11.5.5; 12.4.3.2; Table 12.5
	Heavy precipitation and pluvial flood	Table 11.1; Table 11.6: 11.4.2; 12.4.3.2	Table 11.1; Table 11.6: 11.4.4	Table 11.2; Table 11.6: 11.4.5; 12.4.3.2; Table 12.5
	Landslide			
	Aridity	Table 11.1; Table 11.6: 11.6.2; 12.4.3.2	Table 11.1; Table 11.6: 11.6.4	Table 11.1; Table 11.6: 11.6.2; 12.4.3.2
	Hydrological drought	Table 11.1; Table 11.6: 11.6.2; 12.4.3.2	Table 11.1; Table 11.6: 11.6.4	Table 11.1; Table 11.6: 11.6.2; 12.4.3.2
	Agricultural and ecological drought	Table 11.1; Table 11.6: 11.6.2; 12.4.3.2	Table 11.1; Table 11.6: 11.6.4	Table 11.1; Table 11.6: 11.6.2; 12.4.3.2
	Fire weather	12.4.3.2		12.4.3.2; Table 12.5
Wind	Mean wind speed	12.4.3.3		12.4.3.3; Table 12.5
	Severe wind storm	12.4.3.3		12.4.3.3; Table 12.5
	Tropical cyclone	12.4.3.3		12.4.3.3; Table 12.5
	Sand and dust storm	12.4.3.3		12.4.3.3; Table 12.5
Snow and Ice	Snow, glacier and ice sheet			
	Permafrost			
	Lake, river and sea ice			
	Heavy snowfall and ice storm			
	Hail			
	Snow avalanche			
Coastal and Oceanic	Relative sea level	12.4.3.5		12.4.3.5; Table 12.5
	Coastal flood	12.4.3.5		12.4.3.5; Table 12.5
	Coastal erosion	12.4.3.5		12.4.3.5; Table 12.5
	Marine heatwave	12.4.3.5		12.4.3.5; Table 12.5
	Ocean acidity	12.4		12.4, Table 12.5
Other	Air pollution weather	12.4		12.4, Table 12.5
	Atmospheric CO2 at surface	12.4		12.4, Table 12.5
	Radiation at surface	12.4		12.4, Table 12.5

ACCEPTED VERSION SUBJECT TO FINAL EDITING

Panel B)

	Region	AUSTRALASIA	AUSTRALASIA	AUSTRALASIA
	Region type (Land / Ocean)	Land	Land	Land
	Sub-Region Name	C.Australia	C.Australia	C.Australia
	Accronym	CAU	CAU	CAU
	Data Type	Observational	Detection & Attribution	Projections
Heat and Cold	Mean air temperature	12.4.3.1; Atlas.6.2		12.4.3.1; Table 12.5; Atlas.6.4; CH1.3.6
	Extreme heat	Table 11.1; Table 11.6: 11.3.2; 12.4.3.1	Table 11.1; Table 11.6: 11.3.4	Table 11.2; Table 11.6: 11.3.5; 12.4.3.1; Table 12.5
	Cold spell	Table 11.1; Table 11.6: 11.3.2; 12.4.3.1	Table 11.1; Table 11.6: 11.3.4	Table 11.2; Table 11.6: 11.3.5; 12.4.3.1; Table 12.5
	Frost	12.4.3.1		12.4.3.1; Table 12.5
Wet and Dry	Mean precipitation	12.4.3.2; Table 12.5; Atlas.6.2		12.4.3.2; Table 12.5; Atlas.6.4
	River flood	Table 11.1; Table 11.6: 11.5.2; 12.4.3.2	Table 11.1; Table 11.6: 11.5.4	Table 11.2; Table 11.6: 11.5.5; 12.4.3.2; Table 12.5
	Heavy precipitation and pluvial flood	Table 11.1; Table 11.6: 11.4.2; 12.4.3.2	Table 11.1; Table 11.6: 11.4.4	Table 11.2; Table 11.6: 11.4.5; 12.4.3.2; Table 12.5
	Landslide			
	Aridity	Table 11.1; Table 11.6: 11.6.2; 12.4.3.2	Table 11.1; Table 11.6: 11.6.4	Table 11.1; Table 11.6: 11.6.5; 12.4.3.2; Table 12.5
	Hydrological drought	Table 11.1; Table 11.6: 11.6.2; 12.4.3.2	Table 11.1; Table 11.6: 11.6.4	Table 11.1; Table 11.6: 11.6.5; 12.4.3.2; Table 12.5
	Agricultural and ecological drought	Table 11.1; Table 11.6: 11.6.2; 12.4.3.2	Table 11.1; Table 11.6: 11.6.4	Table 11.1; Table 11.6: 11.6.5; 12.4.3.2; Table 12.5
	Fire weather	12.4.3.2		12.4.3.2; Table 12.5
Wind	Mean wind speed	12.4.3.3		12.4.3.3; Table 12.5
	Severe wind storm	12.4.3.3		12.4.3.3; Table 12.5
	Tropical cyclone	12.4.3.3		12.4.3.3; Table 12.5
	Sand and dust storm	12.4.3.3		12.4.3.3; Table 12.5
Snow and Ice	Snow, glacier and ice sheet			
	Permafrost			
	Lake, river and sea ice			
	Heavy snowfall and ice storm			
	Hail			
	Snow avalanche			
Coastal and Oceanic	Relative sea level	12.4.3.5		12.4.3.5; Table 12.5
	Coastal flood	12.4.3.5		12.4.3.5; Table 12.5
	Coastal erosion	12.4.3.5		12.4.3.5; Table 12.5
	Marine heatwave	12.4.3.5		12.4.3.5; Table 12.5
	Ocean acidity	12.4		12.4, Table 12.5
Other	Air pollution weather	12.4		12.4, Table 12.5
	Atmospheric CO2 at surface	12.4		12.4, Table 12.5
	Radiation at surface	12.4		12.4, Table 12.5

ACCEPTED VERSION SUBJECT TO FINAL EDITING

Panel C)

	Region	AUSTRALASIA	AUSTRALASIA	AUSTRALASIA
	Region type (Land / Ocean)	Land	Land	Land
	Sub-Region Name	E.Australia	E.Australia	E.Australia
	Accronym	EAU	EAU	EAU
	Data Type	Observational	Detection & Attribution	Projections
Heat and Cold	Mean air temperature	12.4.3.1; Atlas.6.2		12.4.3.1; Table 12.5; Atlas.6.4; CH1.3.6
	Extreme heat	Table 11.1; Table 11.6: 11.3.2; 12.4.3.1	Table 11.1; Table 11.6: 11.3.4	Table 11.2; Table 11.6: 11.3.5; 12.4.3.1; Table 12.5
	Cold spell	Table 11.1; Table 11.6: 11.3.2; 12.4.3.1	Table 11.1; Table 11.6: 11.3.4	Table 11.2; Table 11.6: 11.3.5; 12.4.3.1; Table 12.5
	Frost	12.4.3.1		12.4.3.1; Table 12.5
Wet and Dry	Mean precipitation	12.4.3.2; Table 12.5; Atlas.6.2		12.4.3.2; Table 12.5; Atlas.6.4
	River flood	Table 11.1; Table 11.6: 11.5.2; 12.4.3.2	Table 11.1; Table 11.6: 11.5.4	Table 11.2; Table 11.6: 11.5.5; 12.4.3.2; Table 12.5
	Heavy precipitation and pluvial flood	Table 11.1; Table 11.6: 11.4.2; 12.4.3.2	Table 11.1; Table 11.6: 11.4.4	Table 11.2; Table 11.6: 11.4.5; 12.4.3.2; Table 12.5
	Landslide			
	Aridity	Table 11.1; Table 11.6: 11.6.2; 12.4.3.2	Table 11.1; Table 11.6: 11.6.4	Table 11.1; Table 11.6: 11.6.5; 12.4.3.2; Table 12.5
	Hydrological drought	Table 11.1; Table 11.6: 11.6.2; 12.4.3.2	Table 11.1; Table 11.6: 11.6.4	Table 11.1; Table 11.6: 11.6.5; 12.4.3.2; Table 12.5
	Agricultural and ecological drought	Table 11.1; Table 11.6: 11.6.2; 12.4.3.2	Table 11.1; Table 11.6: 11.6.4	Table 11.1; Table 11.6: 11.6.5; 12.4.3.2; Table 12.5
	Fire weather	12.4.3.2		12.4.3.2; Table 12.5
Wind	Mean wind speed	12.4.3.3		12.4.3.3; Table 12.5
	Severe wind storm	12.4.3.3		12.4.3.3; Table 12.5
	Tropical cyclone	12.4.3.3		12.4.3.3; Table 12.5
	Sand and dust storm	12.4.3.3		12.4.3.3; Table 12.5
Snow and Ice	Snow, glacier and ice sheet			
	Permafrost			
	Lake, river and sea ice			
	Heavy snowfall and ice storm			
	Hail	12.4.3.4		12.4.3.4; Table 12.5
	Snow avalanche			
Coastal and Oceanic	Relative sea level	12.4.3.5		12.4.3.5; Table 12.5
	Coastal flood	12.4.3.5		12.4.3.5; Table 12.5
	Coastal erosion	12.4.3.5		12.4.3.5; Table 12.5
	Marine heatwave	12.4.3.5		12.4.3.5; Table 12.5
	Ocean acidity	12.4		12.4, Table 12.5
Other	Air pollution weather	12.4		12.4, Table 12.5
	Atmospheric CO2 at surface	12.4		12.4, Table 12.5
	Radiation at surface	12.4		12.4, Table 12.5

ACCEPTED VERSION SUBJECT TO FINAL EDITING

Panel D)

	Region	AUSTRALASIA	AUSTRALASIA	AUSTRALASIA
	Region type (Land / Ocean)	Land	Land	Land
	Sub-Region Name	S.Australia	S.Australia	S.Australia
	Accronym	SAU	SAU	SAU
	Data Type	Observational	Detection & Attribution	Projections
Heat and Cold	Mean air temperature	12.4.3.1; Atlas.6.2		12.4.3.1; Table 12.5; Atlas.6.4; CH1.3.6
	Extreme heat	Table 11.1; Table 11.6: 11.3.2; 12.4.3.1	Table 11.1; Table 11.6: 11.3.4	Table 11.2; Table 11.6: 11.3.5; 12.4.3.1; Table 12.5
	Cold spell	Table 11.1; Table 11.6: 11.3.2; 12.4.3.1	Table 11.1; Table 11.6: 11.3.4	Table 11.2; Table 11.6: 11.3.5; 12.4.3.1; Table 12.5
	Frost	12.4.3.1		12.4.3.1; Table 12.5
Wet and Dry	Mean precipitation	12.4.3.2; Table 12.5; Atlas.6.2		12.4.3.2; Table 12.5; Atlas.6.4
	River flood	Table 11.1; Table 11.6: 11.5.2; 12.4.3.2	Table 11.1; Table 11.6: 11.5.4	Table 11.2; Table 11.6: 11.5.5; 12.4.3.2; Table 12.5
	Heavy precipitation and pluvial flood	Table 11.1; Table 11.6: 11.4.2; 12.4.3.2	Table 11.1; Table 11.6: 11.4.4	Table 11.2; Table 11.6: 11.4.5; 12.4.3.2; Table 12.5
	Landslide			
	Aridity	Table 11.1; Table 11.6: 11.6.2; 12.4.3.2	Table 11.1; Table 11.6: 11.6.4	Table 11.1; Table 11.6: 11.6.5; 12.4.3.2; Table 12.5
	Hydrological drought	Table 11.1; Table 11.6: 11.6.2; 12.4.3.2	Table 11.1; Table 11.6: 11.6.4	Table 11.1; Table 11.6: 11.6.5; 12.4.3.2; Table 12.5
	Agricultural and ecological drought	Table 11.1; Table 11.6: 11.6.2; 12.4.3.2	Table 11.1; Table 11.6: 11.6.4	Table 11.1; Table 11.6: 11.6.5; 12.4.3.2; Table 12.5
	Fire weather	12.4.3.2		12.4.3.2; Table 12.5
Wind	Mean wind speed	12.4.3.3		12.4.3.3; Table 12.5
	Severe wind storm	12.4.3.3		12.4.3.3; Table 12.5
	Tropical cyclone	12.4.3.3		12.4.3.3; Table 12.5
	Sand and dust storm	12.4.3.3		12.4.3.3; Table 12.5
Snow and Ice	Snow, glacier and ice sheet	12.4.3.4		12.4.3.4; Table 12.5
	Permafrost			
	Lake, river and sea ice			
	Heavy snowfall and ice storm			
	Hail	12.4.3.4		12.4.3.4; Table 12.5
	Snow avalanche	12.4.3.4		12.4.3.4; Table 12.5
Coastal and Oceanic	Relative sea level	12.4.3.5		12.4.3.5; Table 12.5
	Coastal flood	12.4.3.5		12.4.3.5; Table 12.5
	Coastal erosion	12.4.3.5		12.4.3.5; Table 12.5
	Marine heatwave	12.4.3.5		12.4.3.5; Table 12.5
	Ocean acidity	12.4		12.4, Table 12.5
Other	Air pollution weather	12.4		12.4, Table 12.5
	Atmospheric CO2 at surface	12.4		12.4, Table 12.5
	Radiation at surface	12.4		12.4, Table 12.5

ACCEPTED VERSION SUBJECT TO FINAL EDITING

Panel E)

	Region	AUSTRALASIA	AUSTRALASIA	AUSTRALASIA
	Region type (Land / Ocean)	Land	Land	Land
	Sub-Region Name	New-Zealand	New-Zealand	New-Zealand
	Accronym	NZ	NZ	NZ
	Data Type	Observational	Detection & Attribution	Projections
Heat and Cold	Mean air temperature	12.4.3.1; Atlas.6.2		12.4.3.1; Table 12.5; Atlas.6.4
	Extreme heat	Table 11.1; Table 11.6: 11.3.2; 12.4.3.1	Table 11.1; Table 11.6: 11.3.4	Table 11.2; Table 11.6: 11.3.5; 12.4.3.1; Table 12.5
	Cold spell	Table 11.1; Table 11.6: 11.3.2; 12.4.3.1	Table 11.1; Table 11.6: 11.3.4	Table 11.2; Table 11.6: 11.3.5; 12.4.3.1; Table 12.5
	Frost	12.4.3.1		12.4.3.1; Table 12.5
Wet and Dry	Mean precipitation	12.4.3.2; Table 12.5; Atlas.6.2		12.4.3.2; Table 12.5; Atlas.6.4
	River flood	Table 11.1; Table 11.6: 11.5.2; 12.4.3.2	Table 11.1; Table 11.6: 11.5.4	Table 11.2; Table 11.6: 11.5.5; 12.4.3.2; Table 12.5
	Heavy precipitation and pluvial flood	Table 11.1; Table 11.6: 11.4.2; 12.4.3.2	Table 11.1; Table 11.6: 11.4.4	Table 11.2; Table 11.6: 11.4.5; 12.4.3.2; Table 12.5
	Landslide	12.4.3.2		12.4.3.2; Table 12.5
	Aridity	Table 11.1; Table 11.6: 11.6.2; 12.4.3.2	Table 11.1; Table 11.6: 11.6.4	Table 11.1; Table 11.6: 11.6.5; 12.4.3.2; Table 12.5
	Hydrological drought	Table 11.1; Table 11.6: 11.6.2; 12.4.3.2	Table 11.1; Table 11.6: 11.6.4	Table 11.1; Table 11.6: 11.6.5; 12.4.3.2; Table 12.5
	Agricultural and ecological drought	Table 11.1; Table 11.6: 11.6.2; 12.4.3.2	Table 11.1; Table 11.6: 11.6.4	Table 11.1; Table 11.6: 11.6.5; 12.4.3.2; Table 12.5
	Fire weather	12.4.3.2		12.4.3.2; Table 12.5
Wind	Mean wind speed	12.4.3.3		12.4.3.3; Table 12.5
	Severe wind storm	12.4.3.3		12.4.3.3; Table 12.5
	Tropical cyclone			
	Sand and dust storm			
Snow and Ice	Snow, glacier and ice sheet	12.4.3.4		12.4.3.4; Table 12.5
	Permafrost			
	Lake, river and sea ice			
	Heavy snowfall and ice storm	12.4.3.4		12.4.3.4; Table 12.5
	Hail	12.4.3.4		12.4.3.4; Table 12.5
	Snow avalanche	12.4.3.4		12.4.3.4; Table 12.5
Coastal and Oceanic	Relative sea level	12.4.3.5		12.4.3.5; Table 12.5
	Coastal flood			12.4.3.5; Table 12.5
	Coastal erosion			12.4.3.5; Table 12.5
	Marine heatwave	12.4.3.5		12.4.3.5; Table 12.5
	Ocean acidity	12.4		12.4, Table 12.5
Other	Air pollution weather	12.4		12.4, Table 12.5
	Atmospheric CO2 at surface	12.4		12.4, Table 12.5
	Radiation at surface	12.4		12.4, Table 12.5

[END TABLE 10.SM.3 HERE]

ACCEPTED VERSION SUBJECT TO FINAL EDITING

[START TABLE 10.SM.4 HERE]

Table 10.SM.4: Regional Traceback Matrix for Central America. Table shows chapter traceability of the regional assessment using observed trends, attribution of trends or events, and climate model projections, as described in Cross-Chapter Box 10.3. The Table is divided into separate panels that correspond to the WGI AR6 Reference Regions. African sub-regions are: Panel A: S.Central-America (SCA), Panel B: N.Central-America (NCA). Blank cells in the observations and projections columns corresponding to the "not broadly relevant" or "no evidence" category as described in the CID framework in Chapter 12. Blank cells in the detection and attribution columns correspond to no studies being available.

Panel A)

	Region	CENTRAL-AMERICA	CENTRAL-AMERICA	CENTRAL-AMERICA
	Region type (Land / Ocean)	Land	Land	Land
	Sub-Region Name	S.Central-America	S.Central-America	S.Central-America
	Accronym	SCA	SCA	SCA
	Data Type	Observational	Detection & Attribution	Projections
Heat and Cold	Mean air temperature	12.4.4.1		12.4.4.1, Table 12.6
	Extreme heat	Table 11.13; 11.3.2; 12.4.4.1	Table 11.13;	Table 11.13; 11.3.5; 12.4.4.1, Table 12.6
	Cold spell	Table 11.13; 11.3.2: 12.4.4.1	Table 11.13;	Table 11.13; 11.3.5; 12.4.4.1, Table 12.6
	Frost			12.4.4.1, Table 12.6
Wet and Dry	Mean precipitation	8.3.2.4.4; 12.4.4.2		8.4.1.3; 12.4.4.2, Table 12.6
	River flood	11.5.2; 12.4.4.2		11.5.5; 12.4.4.2, Table 12.6
	Heavy precipitation and pluvial flood	Table 11.14; 11.4.2; 12.4.4.2	Table 11.14	Table 11.14; 11.4.5; 12.4.4.2, Table 12.6
	Landslide	12.4.4.2		12.4.4.2, Table 12.6
	Aridity	8.3.1.6; 12.4.4.2	8.3.1.6;	8.4.1.6; 12.4.4.2, Table 12.6
	Hydrological drought	Table 11.15; 11.6.2; 12.4.4.2	Table 11.15; 11.6.4	Table 11.15; 11.6.5; 12.4.4.2; Table 12.6
	Agricultural and ecological drought	Table 11.15; 11.6.2; 12.4.4.2	Table 11.15; 11.6.4	Table 11.15; 11.6.5; 12.4.4.2; Table 12.6
	Fire weather	12.4.4.2		12.4.4.2, Table 12.6
Wind	Mean wind speed	12.4.4.3		12.4.4.3, Table 12.6
	Severe wind storm	12.4.4.3		12.4.4.3, Table 12.6
	Tropical cyclone	12.4.4.3		12.4.4.3, Table 12.6
	Sand and dust storm			
Snow and Ice	Snow, glacier and ice sheet	12.4.4.4		12.4.4.4, Table 12.6
	Permafrost	12.4.4.4		12.4.4.4, Table 12.6
	Lake, river and sea ice			
	Heavy snowfall and ice storm			
	Hail			
	Snow avalanche			
Coastal and Oceanic	Relative sea level	12.4.4.5		12.4.4.5, Table 12.6
	Coastal flood	12.4.4.5		12.4.4.5, Table 12.6
	Coastal erosion	12.4.4.5		12.4.4.5, Table 12.6
	Marine heatwave	12.4.4.5		12.4.4.5, Table 12.6
	Ocean acidity	12.4		12.4; Table 12.6
Other	Air pollution weather	12.4		12.4; Table 12.6
	Atmospheric CO2 at surface	12.4		12.4; Table 12.6
	Radiation at surface	12.4		12.4; Table 12.6

ACCEPTED VERSION SUBJECT TO FINAL EDITING

Panel B)

	Region	CENTRAL-AMERICA	CENTRAL-AMERICA	CENTRAL-AMERICA
	Region type (Land / Ocean)	Land	Land	Land
	Sub-Region Name	N.Central-America	N.Central-America	N.Central-America
	Accronym	NCA	NCA	NCA
	Data Type	Observational	Detection & Attribution	Projections
Heat and Cold	Mean air temperature	12.4.6.1, Atlas.5.7.2		12.4.6.1, Table 12.8, Atlas.5.7.4
	Extreme heat	12.4.6.1		12.4.6.1, Table 12.8
	Cold spell	12.4.6.1		12.4.6.1, Table 12.8
	Frost	12.4.6.1		12.4.6.1, Table 12.8
Wet and Dry	Mean precipitation	12.4.6.2		12.4.6.2, Table 12.8, Atlas.5.7.4
	River flood	12.4.6.2		12.4.6.2, Table 12.8
	Heavy precipitation and pluvial flood	12.4.6.2		12.4.6.2, Table 12.8
	Landslide	12.4.6.2		12.4.6.2, Table 12.8
	Aridity	12.4.6.2		12.4.6.2, Table 12.8
	Hydrological drought	12.4.6.2		12.4.6.2, Table 12.8
	Agricultural and ecological drought	12.4.6.2		12.4.6.2, Table 12.8
	Fire weather	12.4.6.2		12.4.6.2, Table 12.8
Wind	Mean wind speed	12.4.6.3		12.4.6.3, Table 12.8
	Severe wind storm	12.4.6.3		12.4.6.3, Table 12.8
	Tropical cyclone	12.4.6.3		12.4.6.3, Table 12.8
	Sand and dust storm	12.4.6.3		12.4.6.3, Table 12.8
Snow and Ice	Snow, glacier and ice sheet			
	Permafrost			
	Lake, river and sea ice			
	Heavy snowfall and ice storm			
	Hail	12.4.6.4		12.4.6.4, Table 12.8
	Snow avalanche			
Coastal and Oceanic	Relative sea level	12.4.6.5		12.4.6.5, Table 12.8
	Coastal flood	12.4.6.5		12.4.6.5, Table 12.8
	Coastal erosion	12.4.6.5		12.4.6.5, Table 12.8
	Marine heatwave	12.4.6.5		12.4.6.5, Table 12.8
	Ocean acidity	12.4		12.4, Table 12.8
Other	Air pollution weather	12.4		12.4, Table 12.8
	Atmospheric CO2 at surface	12.4		12.4, Table 12.8
	Radiation at surface	12.4		12.4, Table 12.8

[END TABLE 10.SM.4 HERE]

ACCEPTED VERSION SUBJECT TO FINAL EDITING

[START TABLE 10.SM.5 HERE]

Table 10.SM.5: Regional Traceback Matrix for South America. Table shows chapter traceability of the regional assessment using observed trends, attribution of trends or events, and climate model projections, as described in Cross-Chapter Box 10.3. The Table is divided into separate panels that correspond to the WGI AR6 Reference Regions. African sub-regions are: Panel A: N.W.South-America (NWS), Panel B: N.South-America (NSA), Panel C: N.E.South-America (NES), Panel D: South-American-Monsoon (SAM), Panel E: S.W.South-America SWS), Panel F: S.E.South-America (SES), Panel G: S.South-America (SSA). Blank cells in the observations and projections columns corresponding to the "not broadly relevant" or "no evidence" category as described in the CID framework in Chapter 12. Blank cells in the detection and attribution columns correspond to no studies being available.

Panel A)

	Region	SOUTH-AMERICA	SOUTH-AMERICA	SOUTH-AMERICA
	Region type (Land / Ocean)	Land	Land	Land
	Sub-Region Name	N.W.South-America	N.W.South-America	N.W.South-America
	Accronym	NWS	NWS	NWS
	Data Type	Observational	Detection & Attribution	Projections
Heat and Cold	Mean air temperature	12.4.4.1; Atlas7.2.2	Atlas7.2.2; CH1.4.2.2	12.4.4.1, Table 12.6; Atlas7.2.4
	Extreme heat	Table 11.13; 11.3.2; 12.4.4.1	Table 11.13;	Table 11.13; 11.3.5; 12.4.4.1, Table 12.6
	Cold spell	Table 11.13; 11.3.2: 12.4.4.1	Table 11.13;	Table 11.13; 11.3.5; 12.4.4.1, Table 12.6
	Frost	12.4.4.1		12.4.4.1, Table 12.6
Wet and Dry	Mean precipitation	8.3.1.3; 12.4.4.2; Atlas7.2.2	Atlas7.2.2	12.4.4.2, Table 12.6; Atlas7.2.4
	River flood	11.5.2; 12.4.4.2		11.5.5; 12.4.4.2, Table 12.6
	Heavy precipitation and pluvial flood	Table 11.14; 11.4.2; 12.4.4.2	Table 11.14;	Table 11.14; 11.4.5; 12.4.4.2, Table 12.6
	Landslide	12.4.4.2		12.4.4.2, Table 12.6
	Aridity	12.4.4.2		12.4.4.2, Table 12.6
	Hydrological drought	Table 11.15; 11.6.2; 12.4.4.2	Table 11.15; 11.6.4	Table 11.15; 11.6.5; 12.4.4.2; Table 12.6
	Agricultural and ecological drought	Table 11.15; 11.6.2; 12.4.4.2	Table 11.15; 11.6.4	Table 11.15; 11.6.5; 12.4.4.2; Table 12.6
	Fire weather	12.4.4.2		12.4.4.2, Table 12.6
Wind	Mean wind speed	12.4.4.3		12.4.4.3, Table 12.6
	Severe wind storm	12.4.4.3		12.4.4.3, Table 12.6
	Tropical cyclone	12.4.4.3		12.4.4.3, Table 12.6
	Sand and dust storm			
Snow and Ice	Snow, glacier and ice sheet	12.4.4.4		12.4.4.4, Table 12.6
	Permafrost	12.4.4.4		12.4.4.4, Table 12.6
	Lake, river and sea ice			
	Heavy snowfall and ice storm			
	Hail			
	Snow avalanche			
Coastal and Oceanic	Relative sea level	12.4.4.5		12.4.4.5, Table 12.6
	Coastal flood	12.4.4.5		12.4.4.5, Table 12.6
	Coastal erosion	12.4.4.5		12.4.4.5, Table 12.6
	Marine heatwave	12.4.4.5		12.4.4.5, Table 12.6
	Ocean acidity	12.4		12.4; Table 12.6
Other	Air pollution weather	12.4		12.4; Table 12.6
	Atmospheric CO2 at surface	12.4		12.4; Table 12.6
	Radiation at surface	12.4		12.4; Table 12.6

ACCEPTED VERSION SUBJECT TO FINAL EDITING

Panel B)

	Region	SOUTH-AMERICA	SOUTH-AMERICA	SOUTH-AMERICA
	Region type (Land / Ocean)	Land	Land	Land
	Sub-Region Name	N.South-America	N.South-America	N.South-America
	Accronym	NSA	NSA	NSA
	Data Type	Observational	Detection & Attribution	Projections
Heat and Cold	Mean air temperature	12.4.4.1; Atlas7.2.2; CH1FAQ1.2	Atlas7.2.2; CH1.4.2.2	12.4.4.1, Table 12.6; Atlas7.2.4; CH1.4.3.2
	Extreme heat	Table 11.13; 11.3.2; 12.4.4.1	Table 11.13;	Table 11.13; 11.3.5; 12.4.4.1, Table 12.6
	Cold spell	Table 11.13; 11.3.2: 12.4.4.1	Table 11.13;	Table 11.13; 11.3.5; 12.4.4.1, Table 12.6
	Frost			
Wet and Dry	Mean precipitation	12.4.4.2; Atlas7.2.2	Atlas7.2.2	12.4.4.2, Table 12.6; Atlas7.2.4
	River flood	11.5.2; 12.4.4.2		11.5.5; 12.4.4.2, Table 12.6
	Heavy precipitation and pluvial flood	Table 11.14; 11.4.2; 12.4.4.2	Table 11.14;	Table 11.14; 11.4.5; 12.4.4.2, Table 12.6
	Landslide	12.4.4.2		12.4.4.2, Table 12.6
	Aridity	12.4.4.2		12.4.4.2, Table 12.6
	Hydrological drought	Table 11.15; 11.6.2; 12.4.4.2	Table 11.15; 11.6.4	Table 11.15; 11.6.5; 12.4.4.2; Table 12.6
	Agricultural and ecological drought	Table 11.15; 11.6.2; 12.4.4.2	Table 11.15; 11.6.4	Table 11.15; 11.6.5; 12.4.4.2; Table 12.6
	Fire weather	12.4.4.2		12.4.4.2, Table 12.6
Wind	Mean wind speed	12.4.4.3		12.4.4.3, Table 12.6
	Severe wind storm	12.4.4.3		12.4.4.3, Table 12.6
	Tropical cyclone	12.4.4.3		12.4.4.3, Table 12.6
	Sand and dust storm			
Snow and Ice	Snow, glacier and ice sheet	12.4.4.4		8.4.1.7.1; 12.4.4.4, Table 12.6
	Permafrost	12.4.4.4		12.4.4.4, Table 12.6
	Lake, river and sea ice			
	Heavy snowfall and ice storm			
	Hail			
	Snow avalanche			
Coastal and Oceanic	Relative sea level	12.4.4.5		12.4.4.5, Table 12.6
	Coastal flood	12.4.4.5		12.4.4.5, Table 12.6
	Coastal erosion	12.4.4.5		12.4.4.5, Table 12.6
	Marine heatwave	12.4.4.5		12.4.4.5, Table 12.6
	Ocean acidity	12.4		12.4; Table 12.6
Other	Air pollution weather	12.4		12.4; Table 12.6
	Atmospheric CO2 at surface	12.4		12.4; Table 12.6
	Radiation at surface	12.4		12.4; Table 12.6

ACCEPTED VERSION SUBJECT TO FINAL EDITING

Panel C)

	Region	SOUTH-AMERICA	SOUTH-AMERICA	SOUTH-AMERICA
	Region type (Land / Ocean)	Land	Land	Land
	Sub-Region Name	N.E.South-America	N.E.South-America	N.E.South-America
	Accronym	NES	NES	NES
	Data Type	Observational	Detection & Attribution	Projections
Heat and Cold	Mean air temperature	12.4.4.1; Atlas7.2.2	Atlas7.2.2; CH1.4.2.2	12.4.4.1, Table 12.6; Atlas7.2.4
	Extreme heat	Table 11.13; 11.3.2; 12.4.4.1	Table 11.13;	Table 11.13; 11.3.5; 12.4.4.1, Table 12.6
	Cold spell	Table 11.13; 11.3.2: 12.4.4.1	Table 11.13;	Table 11.13; 11.3.5; 12.4.4.1, Table 12.6
	Frost			
Wet and Dry	Mean precipitation	8.3.2.4.5; 12.4.4.2; Atlas7.2.2	Atlas7.2.2	8.4.1.3; 12.4.4.2, Table 12.6; Atlas7.2.4
	River flood	11.5.2; 12.4.4.2		11.5.5; 12.4.4.2, Table 12.6
	Heavy precipitation and pluvial flood	Table 11.14; 11.4.2; 12.4.4.2	Table 11.14;	Table 11.14; 11.4.5; 12.4.4.2, Table 12.6
	Landslide			
	Aridity	12.4.4.2		12.4.4.2, Table 12.6
	Hydrological drought	Table 11.15; 11.6.2; 12.4.4.2	Table 11.15; 11.6.4	Table 11.15; 11.6.5; 12.4.4.2; Table 12.6
	Agricultural and ecological drought	Table 11.15; 11.6.2; 12.4.4.2	Table 11.15; 11.6.4	Table 11.15; 11.6.5; 12.4.4.2; Table 12.6
	Fire weather	12.4.4.2		12.4.4.2, Table 12.6
Wind	Mean wind speed	12.4.4.3		12.4.4.3, Table 12.6
	Severe wind storm	12.4.4.3		12.4.4.3, Table 12.6
	Tropical cyclone	12.4.4.3		12.4.4.3, Table 12.6
	Sand and dust storm			
Snow and Ice	Snow, glacier and ice sheet	12.4.4.4		12.4.4.4, Table 12.6
	Permafrost	12.4.4.4		12.4.4.4, Table 12.6
	Lake, river and sea ice			
	Heavy snowfall and ice storm			
	Hail			
	Snow avalanche			
Coastal and Oceanic	Relative sea level	12.4.4.5		12.4.4.5, Table 12.6
	Coastal flood	12.4.4.5		12.4.4.5, Table 12.6
	Coastal erosion	12.4.4.5		12.4.4.5, Table 12.6
	Marine heatwave	12.4.4.5		12.4.4.5, Table 12.6
	Ocean acidity	12.4		12.4; Table 12.6
Other	Air pollution weather	12.4		12.4; Table 12.6
	Atmospheric CO2 at surface	12.4		12.4; Table 12.6
	Radiation at surface	12.4		12.4; Table 12.6

ACCEPTED VERSION SUBJECT TO FINAL EDITING

Panel D)

	Region	SOUTH-AMERICA	SOUTH-AMERICA	SOUTH-AMERICA
	Region type (Land / Ocean)	Land	Land	Land
	Sub-Region Name	South-American-Monsoon	South-American-Monsoon	South-American-Monsoon
	Accronym	SAM	SAM	SAM
	Data Type	Observational	Detection & Attribution	Projections
Heat and Cold	Mean air temperature	12.4.4.1; Atlas7.2.2	Atlas7.2.2; CH1.4.2.2	12.4.4.1, Table 12.6; Atlas7.2.4
	Extreme heat	Table 11.13; 11.3.2; 12.4.4.1	Table 11.13;	Table 11.13; 11.3.5; 12.4.4.1, Table 12.6
	Cold spell	Table 11.13; 11.3.2: 12.4.4.1	Table 11.13;	Table 11.13; 11.3.5; 12.4.4.1, Table 12.6
	Frost	12.4.4.1		12.4.4.1, Table 12.6
Wet and Dry	Mean precipitation	8.3.1.3; 8.3.2.4.5; 12.4.4.2; Atlas7.2.2	8.3.1.3; 8.4.1.5; Atlas7.2.2	Box 8.2; 8.4.2.5; 12.4.4.2, Table 12.6; Atlas7.2.4
	River flood	11.5.2; 12.4.4.2		11.5.5; 12.4.4.2, Table 12.6
	Heavy precipitation and pluvial flood	Table 11.14; 11.4.2; 12.4.4.2	Table 11.14;	Table 11.14; 11.4.5; 12.4.4.2, Table 12.6
	Landslide			
	Aridity	12.4.4.2		8.4.1.6; 8.6.2.1; 12.4.4.2, Table 12.6
	Hydrological drought	Table 11.15; 11.6.2; 12.4.4.2	Table 11.15; 11.6.4	Table 11.15; 11.6.5; 12.4.4.2; Table 12.6
	Agricultural and ecological drought	Table 11.15; 11.6.2; 12.4.4.2	Table 11.15; 11.6.4	Table 11.15; 11.6.5; 12.4.4.2; Table 12.6
	Fire weather	12.4.4.2		12.4.4.2, Table 12.6
Wind	Mean wind speed	12.4.4.3		12.4.4.3, Table 12.6
	Severe wind storm	12.4.4.3		12.4.4.3, Table 12.6
	Tropical cyclone	12.4.4.3		12.4.4.3, Table 12.6
	Sand and dust storm			
Snow and Ice	Snow, glacier and ice sheet	12.4.4.4		12.4.4.4, Table 12.6
	Permafrost	12.4.4.4		12.4.4.4, Table 12.6
	Lake, river and sea ice			
	Heavy snowfall and ice storm			
	Hail			
	Snow avalanche			
Coastal and Oceanic	Relative sea level	12.4.4.5		12.4.4.5, Table 12.6
	Coastal flood	12.4.4.5		12.4.4.5, Table 12.6
	Coastal erosion	12.4.4.5		12.4.4.5, Table 12.6
	Marine heatwave	12.4.4.5		12.4.4.5, Table 12.6
	Ocean acidity	12.4		12.4; Table 12.6
Other	Air pollution weather	12.4		12.4; Table 12.6
	Atmospheric CO2 at surface	12.4		12.4; Table 12.6
	Radiation at surface	12.4		12.4; Table 12.6

ACCEPTED VERSION SUBJECT TO FINAL EDITING

Panel E)

	Region	SOUTH-AMERICA	SOUTH-AMERICA	SOUTH-AMERICA
	Region type (Land / Ocean)	Land	Land	Land
	Sub-Region Name	S.W.South-America	S.W.South-America	S.W.South-America
	Accronym	SWS	SWS	SWS
	Data Type	Observational	Detection & Attribution	Projections
Heat and Cold	Mean air temperature	12.4.4.1; Atlas7.2.2	Atlas7.2.2	12.4.4.1, Table 12.6; Atlas7.2.4
	Extreme heat	Table 11.13; 11.3.2; 12.4.4.1	Table 11.13;	Table 11.13; 11.3.5; 12.4.4.1, Table 12.6
	Cold spell	Table 11.13; 11.3.2: 12.4.4.1	Table 11.13;	Table 11.13; 11.3.5; 12.4.4.1, Table 12.6
	Frost	12.4.4.1		12.4.4.1, Table 12.6
Wet and Dry	Mean precipitation	8.3.1.3; 12.4.4.2; Atlas7.2.2	8.3.1.3; Atlas7.2.2	12.4.4.2, Table 12.6; Atlas7.2.4
	River flood	11.5.2; 12.4.4.2		11.5.5; 12.4.4.2, Table 12.6
	Heavy precipitation and pluvial flood	Table 11.14; 11.4.2; 12.4.4.2	Table 11.14;	Table 11.14; 11.4.5; 12.4.4.2, Table 12.6
	Landslide	12.4.4.2		12.4.4.2, Table 12.6
	Aridity	8.3.1.6; 12.4.4.2	8.3.1.6;	8.4.1.6; 12.4.4.2, Table 12.6
	Hydrological drought	Table 11.15; 11.6.2; 12.4.4.2	Table 11.15; 11.6.4	Table 11.15; 11.6.5; 12.4.4.2; Table 12.6
	Agricultural and ecological drought	Table 11.15; 11.6.2; 12.4.4.2	Table 11.15; 11.6.4	Table 11.15; 11.6.5; 12.4.4.2; Table 12.6
	Fire weather	12.4.4.2		12.4.4.2, Table 12.6
Wind	Mean wind speed	12.4.4.3		12.4.4.3, Table 12.6
	Severe wind storm	12.4.4.3		12.4.4.3, Table 12.6
	Tropical cyclone	12.4.4.3		12.4.4.3, Table 12.6
	Sand and dust storm	12.4.4.3		12.4.4.3, Table 12.6
Snow and Ice	Snow, glacier and ice sheet	12.4.4.4		12.4.4.4, Table 12.6
	Permafrost	12.4.4.4		12.4.4.4, Table 12.6
	Lake, river and sea ice			
	Heavy snowfall and ice storm			
	Hail			
	Snow avalanche			
Coastal and Oceanic	Relative sea level	12.4.4.5		12.4.4.5, Table 12.6
	Coastal flood	12.4.4.5		12.4.4.5, Table 12.6
	Coastal erosion	12.4.4.5		12.4.4.5, Table 12.6
	Marine heatwave	12.4.4.5		12.4.4.5, Table 12.6
	Ocean acidity	12.4		12.4; Table 12.6
Other	Air pollution weather	12.4		12.4; Table 12.6
	Atmospheric CO2 at surface	12.4		12.4; Table 12.6
	Radiation at surface	12.4		12.4; Table 12.6

ACCEPTED VERSION SUBJECT TO FINAL EDITING

Panel F)

	Region	SOUTH-AMERICA	SOUTH-AMERICA	SOUTH-AMERICA
	Region type (Land / Ocean)	Land	Land	Land
	Sub-Region Name	S.E.South-America	S.E.South-America	S.E.South-America
	Accronym	SES	SES	SES
	Data Type	Observational	Detection & Attribution	Projections
Heat and Cold	Mean air temperature	12.4.4.1; Atlas7.2.2	Atlas7.2.2	12.4.4.1, Table 12.6; Atlas7.2.4
	Extreme heat	CCB10.3; Table 11.13; 11.3.2; 12.4.4.1	CCB10.3; Table 11.13;	CCB10.3; Table 11.13; 11.3.5; 12.4.4.1, Table 12.6
	Cold spell	Table 11.13; 11.3.2: 12.4.4.1	Table 11.13;	Table 11.13; 11.3.5; 12.4.4.1, Table 12.6
	Frost	12.4.4.1		12.4.4.1, Table 12.6
Wet and Dry	Mean precipitation	8.3.1.3; 8.3.2.4.5; 10.4.2.2; 12.4.4.2; Atlas7.2.2	8.3.1.3; 10.4.2.2; Atlas7.2.2	8.5.2.1; 12.4.4.2, Table 12.6; Atlas7.2.4
	River flood	11.5.2; 12.4.4.2		11.5.5; 12.4.4.2, Table 12.6
	Heavy precipitation and pluvial flood	Table 11.14; 11.4.2; 12.4.4.2	Table 11.14;	Table 11.14; 11.4.5; 12.4.4.2, Table 12.6
	Landslide	12.4.4.2		12.4.4.2, Table 12.6
	Aridity	12.4.4.2; 12.4.4.2		12.4.4.2, Table 12.6
	Hydrological drought	Table 11.15; 11.6.2; 12.4.4.2	Table 11.15; 11.6.4	Table 11.15; 11.6.5; 12.4.4.2; Table 12.6
	Agricultural and ecological drought	Table 11.15; 11.6.2; 12.4.4.2	Table 11.15; 11.6.4	Table 11.15; 11.6.5; 12.4.4.2; Table 12.6
	Fire weather	12.4.4.2		12.4.4.2, Table 12.6
Wind	Mean wind speed	12.4.4.3		12.4.4.3, Table 12.6
	Severe wind storm	12.4.4.3		12.4.4.3, Table 12.6
	Tropical cyclone	12.4.4.3		12.4.4.3, Table 12.6
	Sand and dust storm	12.4.4.3		12.4.4.3, Table 12.6
Snow and Ice	Snow, glacier and ice sheet	12.4.4.4		12.4.4.4, Table 12.6
	Permafrost	12.4.4.4		12.4.4.4, Table 12.6
	Lake, river and sea ice			
	Heavy snowfall and ice storm			
	Hail			
	Snow avalanche			
Coastal and Oceanic	Relative sea level	12.4.4.5		12.4.4.5, Table 12.6
	Coastal flood	12.4.4.5		12.4.4.5, Table 12.6
	Coastal erosion	12.4.4.5		12.4.4.5, Table 12.6
	Marine heatwave	12.4.4.5		12.4.4.5, Table 12.6
	Ocean acidity	12.4		12.4; Table 12.6
Other	Air pollution weather	12.4		12.4; Table 12.6
	Atmospheric CO2 at surface	12.4		12.4; Table 12.6
	Radiation at surface	12.4		12.4; Table 12.6

ACCEPTED VERSION SUBJECT TO FINAL EDITING

Panel G)

	Region	SOUTH-AMERICA	SOUTH-AMERICA	SOUTH-AMERICA
	Region type (Land / Ocean)	Land	Land	Land
	Sub-Region Name	S.South-America	S.South-America	S.South-America
	Accronym	SSA	SSA	SSA
	Data Type	Observational	Detection & Attribution	Projections
Heat and Cold	Mean air temperature	12.4.4.1; Atlas7.2.2	Atlas7.2.2	12.4.4.1, Table 12.6; Atlas7.2.4
	Extreme heat	Table 11.13; 11.3.2; 12.4.4.1	Table 11.13;	Table 11.13; 11.3.5; 12.4.4.1, Table 12.6
	Cold spell	Table 11.13; 11.3.2: 12.4.4.1	Table 11.13;	Table 11.13; 11.3.5; 12.4.4.1, Table 12.6
	Frost	12.4.4.1		12.4.4.1, Table 12.6
Wet and Dry	Mean precipitation	12.4.4.2; Atlas7.2.2	Atlas7.2.2	12.4.4.2, Table 12.6; Atlas7.2.4
	River flood	11.5.2; 12.4.4.2		11.5.5; 12.4.4.2, Table 12.6
	Heavy precipitation and pluvial flood	Table 11.14; 11.4.2; 12.4.4.2	Table 11.14;	Table 11.14; 11.4.5; 12.4.4.2, Table 12.6
	Landslide	12.4.4.2		12.4.4.2, Table 12.6
	Aridity	12.4.4.2		12.4.4.2, Table 12.6
	Hydrological drought	Table 11.15; 11.6.2; 12.4.4.2	Table 11.15; 11.6.4	Table 11.15; 11.6.5; 12.4.4.2; Table 12.6
	Agricultural and ecological drought	Table 11.15; 11.6.2; 12.4.4.2	Table 11.15; 11.6.4	Table 11.15; 11.6.5; 12.4.4.2; Table 12.6
	Fire weather	12.4.4.2		12.4.4.2, Table 12.6
Wind	Mean wind speed	12.4.4.3		12.4.4.3, Table 12.6
	Severe wind storm	12.4.4.3		12.4.4.3, Table 12.6
	Tropical cyclone	12.4.4.3		12.4.4.3, Table 12.6
	Sand and dust storm			
Snow and Ice	Snow, glacier and ice sheet	8.3.1.7.1; 12.4.4.4		12.4.4.4, Table 12.6
	Permafrost	12.4.4.4		12.4.4.4, Table 12.6
	Lake, river and sea ice			
	Heavy snowfall and ice storm			
	Hail			
	Snow avalanche			
Coastal and Oceanic	Relative sea level	12.4.4.5		12.4.4.5, Table 12.6
	Coastal flood	12.4.4.5		12.4.4.5, Table 12.6
	Coastal erosion	12.4.4.5		12.4.4.5, Table 12.6
	Marine heatwave	12.4.4.5		12.4.4.5, Table 12.6
	Ocean acidity	12.4		12.4; Table 12.6
Other	Air pollution weather	12.4		12.4; Table 12.6
	Atmospheric CO2 at surface	12.4		12.4; Table 12.6
	Radiation at surface	12.4		12.4; Table 12.6

[END TABLE 10.SM.5 HERE]

ACCEPTED VERSION SUBJECT TO FINAL EDITING

[START TABLE 10.SM.6 HERE]

Table 10.SM.6: Regional Traceback Matrix for Europe. Table shows chapter traceability of the regional assessment using observed trends, attribution of trends or events, and climate model projections, as described in Cross-Chapter Box 10.3. The Table is divided into separate panels that correspond to the WGI AR6 Reference Regions. African sub-regions are: Panel A: N.Europe (NEU), Panel B: West&Central-Europe (WCE), Panel C: E.Europe (EEU), Panel D: Mediterranean-Europe (MED). Blank cells in the observations and projections columns corresponding to the "not broadly relevant" or "no evidence" category as described in the CID framework in Chapter 12. Blank cells in the detection and attribution columns correspond to no studies being available.

Panel A)

	Region	EUROPE	EUROPE	EUROPE
	Region type (Land / Ocean)	Land	Land	Land
	Sub-Region Name	N.Europe	N.Europe	N.Europe
	Accronym	NEU	NEU	NEU
	Data Type	Observational	Detection & Attribution	Projections
Heat and Cold	Mean air temperature	Atlas.8.2, 12.4.5.1	A.8.2; 1.4.2.2	12.4.5.1, Table 12.7; A.8.4
	Extreme heat	Table 11.8	Table 11.8	12.4.5.1, Table 12.7
	Cold spell	12.4.5.1		12.4.5.1, Table 12.7
	Frost	12.4.5.1		12.4.5.1, Table 12.7
Wet and Dry	Mean precipitation	A.8.2	A.8.2	12.4.5.2, Table 12.7, 8.4, A8.4
	River flood	12.4.5.2		12.4.5.2, Table 12.7
	Heavy precipitation and pluvial flood	Table 11.8	Table 11.8	12.4.5.2, Table 12.7
	Landslide	12.4.5.2		12.4.5.2, Table 12.7
	Aridity	12.4.5.2		12.4.5.2, Table 12.7
	Hydrological drought	Table 11.8	Table 11.8	12.4.5.2, Table 12.7
	Agricultural and ecological drought	Table 11.8	Table 11.8	12.4.5.2, Table 12.7
	Fire weather	12.4.5.2		12.4.5.2, Table 12.7
Wind	Mean wind speed	12.4.5.3		12.4.5.3, Table 12.7
	Severe wind storm	12.4.5.3		12.4.5.3, Table 12.7
	Tropical cyclone			
	Sand and dust storm			
Snow and Ice	Snow, glacier and ice sheet	12.4.5.4 9.5.1 A.8.2	A.8.2	12.4.5.4, Table 12.7; A8.4
	Permafrost	12.4.5.4		12.4.5.4, Table 12.7
	Lake, river and sea ice			12.4.5.4, Table 12.7
	Heavy snowfall and ice storm			12.4.5.4, Table 12.7
	Hail			12.4.5.4, Table 12.7
	Snow avalanche			12.4.5.4, Table 12.7
Coastal and Oceanic	Relative sea level	12.4.5.5		12.4.5.5, Table 12.7
	Coastal flood	12.4.5.5		12.4.5.5, Table 12.7
	Coastal erosion	12.4.5.5		12.4.5.5, Table 12.7
	Marine heatwave	12.4.5.5		12.4.5.5, Table 12.7
	Ocean acidity	12.4		12.4, Table 12.7
Other	Air pollution weather	12.4		12.4, Table 12.7
	Atmospheric CO2 at surface	12.4		12.4, Table 12.7
	Radiation at surface	12.4	A.8.2	12.4, Table 12.7

ACCEPTED VERSION SUBJECT TO FINAL EDITING

Panel B)

	Region	EUROPE	EUROPE	EUROPE
	Region type (Land / Ocean)	Land	Land	Land
	Sub-Region Name	West&Central-Europe	West&Central-Europe	West&Central-Europe
	Accronym	WCE	WCE	WCE
	Data Type	Observational	Detection & Attribution	Projections
Heat and Cold	Mean air temperature	12.4.5.1; A.8.2	A.8.2; 1.4.2.2	12.4.5.1, Table 12.7; A.8.4
	Extreme heat	Table 11.8	Table 11.8	12.4.5.1, Table 12.7
	Cold spell	12.4.5.1		12.4.5.1, Table 12.7
	Frost	12.4.5.1		12.4.5.1, Table 12.7
Wet and Dry	Mean precipitation	A.8.2	A.8.2	12.4.5.2,8.4.1.3,A8.4
	River flood	12.4.5.2		12.4.5.2, Table 12.7
	Heavy precipitation and pluvial flood	Table 11.8	Table 11.8	12.4.5.2, Table 12.7
	Landslide	12.4.5.2		12.4.5.2, Table 12.7
	Aridity	12.4.5.2		12.4.5.2, Table 12.7
	Hydrological drought	Table 11.8	Table 11.8	12.4.5.2, Table 12.7
	Agricultural and ecological drought	Table 11.8	Table 11.8	12.4.5.2, Table 12.7
	Fire weather	12.4.5.2		12.4.5.2, Table 12.7
Wind	Mean wind speed	12.4.5.3		12.4.5.3, Table 12.7
	Severe wind storm	12.4.5.3		12.4.5.3, Table 12.7
	Tropical cyclone			
	Sand and dust storm	12.4.5.3		12.4.5.3, Table 12.7
Snow and Ice	Snow, glacier and ice sheet	12.4.5.4 9.5.1 A.8.2	A.8.2	12.4.5.4, Table 12.7; A8.4
	Permafrost	12.4.5.4		12.4.5.4, Table 12.7
	Lake, river and sea ice			12.4.5.4, Table 12.7
	Heavy snowfall and ice storm			12.4.5.4, Table 12.7
	Hail			12.4.5.4, Table 12.7
	Snow avalanche			12.4.5.4, Table 12.7
Coastal and Oceanic	Relative sea level	12.4.5.5		12.4.5.5, Table 12.7
	Coastal flood	12.4.5.5		12.4.5.5, Table 12.7
	Coastal erosion	12.4.5.5		12.4.5.5, Table 12.7
	Marine heatwave	12.4.5.5		12.4.5.5, Table 12.7
	Ocean acidity	12.4		12.4, Table 12.7
Other	Air pollution weather	12.4		12.4, Table 12.7
	Atmospheric CO2 at surface	12.4		12.4, Table 12.7
	Radiation at surface	12.4	A.8.2	12.4, Table 12.7

ACCEPTED VERSION SUBJECT TO FINAL EDITING

Panel C)

	Region	EUROPE	EUROPE	EUROPE
	Region type (Land / Ocean)	Land	Land	Land
	Sub-Region Name	E.Europe	E.Europe	E.Europe
	Accronym	EEU	EEU	EEU
	Data Type	Observational	Detection & Attribution	Projections
Heat and Cold	Mean air temperature	A.8.2	A.8.2	12.4.5.1, Table 12.7; A.8.4
	Extreme heat	Table 11.8	Table 11.8	12.4.5.1, Table 12.7
	Cold spell	12.4.5.1		12.4.5.1, Table 12.7
	Frost	12.4.5.1		12.4.5.1, Table 12.7
Wet and Dry	Mean precipitation	A.8.2	A.8.2	12.4.5.2, Table 12.7, 8.4, A8.4
	River flood	12.4.5.2		12.4.5.2, Table 12.7
	Heavy precipitation and pluvial flood	Table 11.8	Table 11.8	12.4.5.2, Table 12.7
	Landslide	12.4.5.2		12.4.5.2, Table 12.7
	Aridity	12.4.5.2		12.4.5.2, Table 12.7
	Hydrological drought	Table 11.8	Table 11.8	12.4.5.2, Table 12.7
	Agricultural and ecological drought	Table 11.8	Table 11.8	12.4.5.2, Table 12.7
	Fire weather	12.4.5.2		12.4.5.2, Table 12.7
Wind	Mean wind speed	12.4.5.3		12.4.5.3, Table 12.7
	Severe wind storm	12.4.5.3		12.4.5.3, Table 12.7
	Tropical cyclone			
	Sand and dust storm	12.4.5.3		12.4.5.3, Table 12.7
Snow and Ice	Snow, glacier and ice sheet	12.4.5.4 9.5.1 A.8.2	A.8.2	12.4.5.4, Table 12.7; A8.4
	Permafrost			
	Lake, river and sea ice			12.4.5.4, Table 12.7
	Heavy snowfall and ice storm			12.4.5.4, Table 12.7
	Hail			12.4.5.4, Table 12.7
	Snow avalanche			12.4.5.4, Table 12.7
Coastal and Oceanic	Relative sea level			
	Coastal flood			
	Coastal erosion			
	Marine heatwave			
	Ocean acidity			
Other	Air pollution weather	12.4		12.4, Table 12.7
	Atmospheric CO2 at surface	12.4		12.4, Table 12.7
	Radiation at surface	12.4		12.4, Table 12.7

ACCEPTED VERSION SUBJECT TO FINAL EDITING

Panel D)

	Region	EUROPE	EUROPE	EUROPE
	Region type (Land / Ocean)	Land-Ocean	Land-Ocean	Land-Ocean
	Sub-Region Name	Mediterranean-Europe	Mediterranean-Europe	Mediterranean-Europe
	Accronym	[MED]	[MED]	[MED]
	Data Type	Observational	Detection & Attribution	Projections
Heat and Cold	Mean air temperature	A.8.2	A.8.2	12.4.5.1, Table 12.7; A.8.4
	Extreme heat	Table 11.8	Table 11.8	12.4.5.1, Table 12.7
	Cold spell	12.4.5.1		12.4.5.1, Table 12.7
	Frost	12.4.5.1		12.4.5.1, Table 12.7
Wet and Dry	Mean precipitation	A.8.2	A.8.2	12.4.5.2, Table 12.7, 8.4, A8.4
	River flood	12.4.5.2		12.4.5.2, Table 12.7
	Heavy precipitation and pluvial flood	Table 11.8	Table 11.8	12.4.5.2, Table 12.7
	Landslide	12.4.5.2		12.4.5.2, Table 12.7
	Aridity	12.4.5.2		12.4.5.2, Table 12.7
	Hydrological drought	Table 11.8	Table 11.8	12.4.5.2, Table 12.7
	Agricultural and ecological drought	Table 11.8	Table 11.8	12.4.5.2, Table 12.7
	Fire weather	12.4.5.2		12.4.5.2, Table 12.7
Wind	Mean wind speed	12.4.5.3		12.4.5.3, Table 12.7
	Severe wind storm	12.4.5.3		12.4.5.3, Table 12.7
	Tropical cyclone			
	Sand and dust storm	12.4.5.3		12.4.5.3, Table 12.7
Snow and Ice	Snow, glacier and ice sheet	12.4.5.4 9.5.1 A.8.2	A.8.2	12.4.5.4, Table 12.7; A8.4
	Permafrost	12.4.5.4		12.4.5.4, Table 12.7
	Lake, river and sea ice			12.4.5.4, Table 12.7
	Heavy snowfall and ice storm			12.4.5.4, Table 12.7
	Hail			12.4.5.4, Table 12.7
	Snow avalanche			12.4.5.4, Table 12.7
Coastal and Oceanic	Relative sea level	12.4.5.5		12.4.5.5, Table 12.7
	Coastal flood	12.4.5.5		12.4.5.5, Table 12.7
	Coastal erosion	12.4.5.5		12.4.5.5, Table 12.7
	Marine heatwave	12.4.5.5		12.4.5.5, Table 12.7
	Ocean acidity	12.4		12.4, Table 12.7
Other	Air pollution weather	12.4		12.4, Table 12.7
	Atmospheric CO2 at surface	12.4		12.4, Table 12.7
	Radiation at surface	12.4	A.8.2	12.4, Table 12.7

[END TABLE 10.SM.6 HERE]

ACCEPTED VERSION SUBJECT TO FINAL EDITING

[START TABLE 10.SM.7 HERE]

Table 10.SM.7: Regional Traceback Matrix for North America. Table shows chapter traceability of the regional assessment using observed trends, attribution of trends or events, and climate model projections, as described in Cross-Chapter Box 10.3. The Table is divided into separate panels that correspond to the WGI AR6 Reference Regions. African sub-regions are: Panel A: N.W.North-America (NWN), Panel B: N.E.North-America (NEN), Panel C: W.North-America (WNA), Panel D: C.North-America (CNA), Panel E: E.North-America (ENA). Blank cells in the observations and projections columns corresponding to the "not broadly relevant" or "no evidence" category as described in the CID framework in Chapter 12. Blank cells in the detection and attribution columns correspond to no studies being available.

Panel A)

	Region	NORTH-AMERICA	NORTH-AMERICA	NORTH-AMERICA
	Region type (Land / Ocean)	Land	Land	Land
	Sub-Region Name	N.W.North-America	N.W.North-America	N.W.North-America
	Accronym	NWN	NWN	NWN
	Data Type	Observational	Detection & Attribution	Projections
Heat and Cold	Mean air temperature	12.4.6.1, Atlas.5.7.2		12.4.6.1, Table 12.8, Atlas.5.7.4
	Extreme heat	12.4.6.1		12.4.6.1, Table 12.8
	Cold spell	12.4.6.1		12.4.6.1, Table 12.8
	Frost	12.4.6.1		12.4.6.1, Table 12.8
Wet and Dry	Mean precipitation	12.4.6.2		12.4.6.2, Table 12.8, Atlas.5.7.4
	River flood	12.4.6.2		12.4.6.2, Table 12.8
	Heavy precipitation and pluvial flood	12.4.6.2		12.4.6.2, Table 12.8
	Landslide	12.4.6.2		12.4.6.2, Table 12.8
	Aridity	12.4.6.2		12.4.6.2, Table 12.8
	Hydrological drought	12.4.6.2		12.4.6.2, Table 12.8
	Agricultural and ecological drought	12.4.6.2		12.4.6.2, Table 12.8
	Fire weather	12.4.6.2		12.4.6.2, Table 12.8
Wind	Mean wind speed	12.4.6.3		12.4.6.3, Table 12.8
	Severe wind storm	12.4.6.3		12.4.6.3, Table 12.8
	Tropical cyclone			
	Sand and dust storm			
Snow and Ice	Snow, glacier and ice sheet	12.4.6.4		12.4.6.4, Table 12.8, Atlas.5.7.4
	Permafrost	12.4.6.4		12.4.6.4, Table 12.8
	Lake, river and sea ice	12.4.6.4		12.4.6.4, Table 12.8
	Heavy snowfall and ice storm	12.4.6.4		12.4.6.4, Table 12.8
	Hail			
	Snow avalanche	12.4.6.4		12.4.6.4, Table 12.8
Coastal and Oceanic	Relative sea level	12.4.6.5		12.4.6.5, Table 12.8
	Coastal flood	12.4.6.5		12.4.6.5, Table 12.8
	Coastal erosion	12.4.6.5		12.4.6.5, Table 12.8
	Marine heatwave	12.4.6.5		12.4.6.5, Table 12.8
	Ocean acidity	12.4		12.4, Table 12.8
Other	Air pollution weather	12.4		12.4, Table 12.8
	Atmospheric CO2 at surface	12.4		12.4, Table 12.8
	Radiation at surface	12.4		12.4, Table 12.8

ACCEPTED VERSION SUBJECT TO FINAL EDITING

Panel B)

	Region	NORTH-AMERICA	NORTH-AMERICA	NORTH-AMERICA
	Region type (Land / Ocean)	Land	Land	Land
	Sub-Region Name	N.E.North-America	N.E.North-America	N.E.North-America
	Accronym	NEN	NEN	NEN
	Data Type	Observational	Detection & Attribution	Projections
Heat and Cold	Mean air temperature	12.4.6.1, Atlas.5.7.2		12.4.6.1, Table 12.8, Atlas.5.7.4
	Extreme heat	12.4.6.1		12.4.6.1, Table 12.8
	Cold spell	12.4.6.1		12.4.6.1, Table 12.8
	Frost	12.4.6.1		12.4.6.1, Table 12.8
Wet and Dry	Mean precipitation	12.4.6.2		12.4.6.2, Table 12.8, Atlas.5.7.4
	River flood	12.4.6.2		12.4.6.2, Table 12.8
	Heavy precipitation and pluvial flood	12.4.6.2		12.4.6.2, Table 12.8
	Landslide			
	Aridity	12.4.6.2		12.4.6.2, Table 12.8
	Hydrological drought	12.4.6.2		12.4.6.2, Table 12.8
	Agricultural and ecological drought	12.4.6.2		12.4.6.2, Table 12.8
	Fire weather	12.4.6.2		12.4.6.2, Table 12.8
Wind	Mean wind speed	12.4.6.3		12.4.6.3, Table 12.8
	Severe wind storm	12.4.6.3		12.4.6.3, Table 12.8
	Tropical cyclone			
	Sand and dust storm			
Snow and Ice	Snow, glacier and ice sheet	12.4.6.4		12.4.6.4, Table 12.8, Atlas.5.7.4
	Permafrost	12.4.6.4		12.4.6.4, Table 12.8
	Lake, river and sea ice	12.4.6.4		12.4.6.4, Table 12.8
	Heavy snowfall and ice storm	12.4.6.4		12.4.6.4, Table 12.8
	Hail			
	Snow avalanche	12.4.6.4		12.4.6.4, Table 12.8
Coastal and Oceanic	Relative sea level	12.4.6.5		12.4.6.5, Table 12.8
	Coastal flood	12.4.6.5		12.4.6.5, Table 12.8
	Coastal erosion	12.4.6.5		12.4.6.5, Table 12.8
	Marine heatwave	12.4.6.5		12.4.6.5, Table 12.8
	Ocean acidity	12.4		12.4, Table 12.8
Other	Air pollution weather	12.4		12.4, Table 12.8
	Atmospheric CO2 at surface	12.4		12.4, Table 12.8
	Radiation at surface	12.4		12.4, Table 12.8

ACCEPTED VERSION SUBJECT TO FINAL EDITING

Panel C)

	Region	NORTH-AMERICA	NORTH-AMERICA	NORTH-AMERICA
	Region type (Land / Ocean)	Land	Land	Land
	Sub-Region Name	W.North-America	W.North-America	W.North-America
	Accronym	WNA	WNA	WNA
	Data Type	Observational	Detection & Attribution	Projections
Heat and Cold	Mean air temperature	12.4.6.1, Atlas.5.7.2	10.4.2.3; 1.4.2.2	12.4.6.1, Table 12.8, Atlas.5.7.4
	Extreme heat	12.4.6.1		12.4.6.1, Table 12.8
	Cold spell	12.4.6.1		12.4.6.1, Table 12.8
	Frost	12.4.6.1		12.4.6.1, Table 12.8
Wet and Dry	Mean precipitation	12.4.6.2	10.4.2.3	12.4.6.2, Table 12.8, Atlas.5.7.4
	River flood	12.4.6.2		12.4.6.2, Table 12.8
	Heavy precipitation and pluvial flood	12.4.6.2		12.4.6.2, Table 12.8
	Landslide	12.4.6.2		12.4.6.2, Table 12.8
	Aridity	12.4.6.2		12.4.6.2, Table 12.8
	Hydrological drought	12.4.6.2		12.4.6.2, Table 12.8
	Agricultural and ecological drought	12.4.6.2		12.4.6.2, Table 12.8
	Fire weather	12.4.6.2		12.4.6.2, Table 12.8
Wind	Mean wind speed	12.4.6.3		12.4.6.3, Table 12.8
	Severe wind storm	12.4.6.3		12.4.6.3, Table 12.8
	Tropical cyclone	12.4.6.3		12.4.6.3, Table 12.8
	Sand and dust storm	12.4.6.3		12.4.6.3, Table 12.8
Snow and Ice	Snow, glacier and ice sheet	12.4.6.4		12.4.6.4, Table 12.8, Atlas.5.7.4
	Permafrost			
	Lake, river and sea ice	12.4.6.4		12.4.6.4, Table 12.8
	Heavy snowfall and ice storm	12.4.6.4		12.4.6.4, Table 12.8
	Hail	12.4.6.4		12.4.6.4, Table 12.8
	Snow avalanche	12.4.6.4		12.4.6.4, Table 12.8
Coastal and Oceanic	Relative sea level	12.4.6.5		12.4.6.5, Table 12.8
	Coastal flood	12.4.6.5		12.4.6.5, Table 12.8
	Coastal erosion	12.4.6.5		12.4.6.5, Table 12.8
	Marine heatwave	12.4.6.5		12.4.6.5, Table 12.8
	Ocean acidity	12.4		12.4, Table 12.8
Other	Air pollution weather	12.4		12.4, Table 12.8
	Atmospheric CO2 at surface	12.4		12.4, Table 12.8
	Radiation at surface	12.4		12.4, Table 12.8

ACCEPTED VERSION SUBJECT TO FINAL EDITING

Panel D)

	Region	NORTH-AMERICA	NORTH-AMERICA	NORTH-AMERICA
	Region type (Land / Ocean)	Land	Land	Land
	Sub-Region Name	C.North-America	C.North-America	C.North-America
	Accronym	CNA	CNA	CNA
	Data Type	Observational	Detection & Attribution	Projections
Heat and Cold	Mean air temperature	12.4.6.1, Atlas.5.7.2; CH1FAQ1.2	1.4.2.2	12.4.6.1, Table 12.8, Atlas.5.7.4; 1.3.6
	Extreme heat	12.4.6.1		12.4.6.1, Table 12.8
	Cold spell	12.4.6.1		12.4.6.1, Table 12.8
	Frost	12.4.6.1		12.4.6.1, Table 12.8
Wet and Dry	Mean precipitation	12.4.6.2		12.4.6.2, Table 12.8, Atlas.5.7.4
	River flood	12.4.6.2		12.4.6.2, Table 12.8
	Heavy precipitation and pluvial flood	12.4.6.2		12.4.6.2, Table 12.8
	Landslide			
	Aridity	12.4.6.2		12.4.6.2, Table 12.8
	Hydrological drought	12.4.6.2		12.4.6.2, Table 12.8
	Agricultural and ecological drought	12.4.6.2		12.4.6.2, Table 12.8
	Fire weather	12.4.6.2		12.4.6.2, Table 12.8
Wind	Mean wind speed	12.4.6.3		12.4.6.3, Table 12.8
	Severe wind storm	12.4.6.3		12.4.6.3, Table 12.8
	Tropical cyclone	12.4.6.3		12.4.6.3, Table 12.8
	Sand and dust storm	12.4.6.3		12.4.6.3, Table 12.8
Snow and Ice	Snow, glacier and ice sheet	12.4.6.4		12.4.6.4, Table 12.8, Atlas.5.7.4
	Permafrost			
	Lake, river and sea ice	12.4.6.4		12.4.6.4, Table 12.8
	Heavy snowfall and ice storm	12.4.6.4		12.4.6.4, Table 12.8
	Hail	12.4.6.4		12.4.6.4, Table 12.8
	Snow avalanche			
Coastal and Oceanic	Relative sea level	12.4.6.5		12.4.6.5, Table 12.8
	Coastal flood	12.4.6.5		12.4.6.5, Table 12.8
	Coastal erosion	12.4.6.5		12.4.6.5, Table 12.8
	Marine heatwave	12.4.6.5		12.4.6.5, Table 12.8
	Ocean acidity	12.4		12.4, Table 12.8
Other	Air pollution weather	12.4		12.4, Table 12.8
	Atmospheric CO2 at surface	12.4		12.4, Table 12.8
	Radiation at surface	12.4		12.4, Table 12.8

ACCEPTED VERSION SUBJECT TO FINAL EDITING

Panel E)

	Region	NORTH-AMERICA	NORTH-AMERICA	NORTH-AMERICA
	Region type (Land / Ocean)	Land	Land	Land
	Sub-Region Name	E.North-America	E.North-America	E.North-America
	Accronym	ENA	ENA	ENA
	Data Type	Observational	Detection & Attribution	Projections
Heat and Cold	Mean air temperature	12.4.6.1, Atlas.5.7.2		12.4.6.1, Table 12.8, Atlas.5.7.4
	Extreme heat	12.4.6.1		12.4.6.1, Table 12.8
	Cold spell	12.4.6.1		12.4.6.1, Table 12.8
	Frost	12.4.6.1		12.4.6.1, Table 12.8
Wet and Dry	Mean precipitation	12.4.6.2		12.4.6.2, Table 12.8, Atlas.5.7.4
	River flood	12.4.6.2		12.4.6.2, Table 12.8
	Heavy precipitation and pluvial flood	12.4.6.2		12.4.6.2, Table 12.8
	Landslide	12.4.6.2		12.4.6.2, Table 12.8
	Aridity	12.4.6.2		12.4.6.2, Table 12.8
	Hydrological drought	12.4.6.2		12.4.6.2, Table 12.8
	Agricultural and ecological drought	12.4.6.2		12.4.6.2, Table 12.8
	Fire weather	12.4.6.2		12.4.6.2, Table 12.8
Wind	Mean wind speed	12.4.6.3		12.4.6.3, Table 12.8
	Severe wind storm	12.4.6.3		12.4.6.3, Table 12.8
	Tropical cyclone	12.4.6.3		12.4.6.3, Table 12.8
	Sand and dust storm			
Snow and Ice	Snow, glacier and ice sheet	12.4.6.4		12.4.6.4, Table 12.8, Atlas.5.7.4
	Permafrost			
	Lake, river and sea ice	12.4.6.4		12.4.6.4, Table 12.8
	Heavy snowfall and ice storm	12.4.6.4		12.4.6.4, Table 12.8
	Hail	12.4.6.4		12.4.6.4, Table 12.8
	Snow avalanche	12.4.6.4		12.4.6.4, Table 12.8
Coastal and Oceanic	Relative sea level	12.4.6.5		12.4.6.5, Table 12.8
	Coastal flood	12.4.6.5		12.4.6.5, Table 12.8
	Coastal erosion	12.4.6.5		12.4.6.5, Table 12.8
	Marine heatwave	12.4.6.5		12.4.6.5, Table 12.8
	Ocean acidity	12.4		12.4, Table 12.8
Other	Air pollution weather	12.4		12.4, Table 12.8
	Atmospheric CO2 at surface	12.4		12.4, Table 12.8
	Radiation at surface	12.4		12.4, Table 12.8

[END TABLE 10.SM.7HERE]

ACCEPTED VERSION SUBJECT TO FINAL EDITING

[START TABLE 10.SM.8 HERE]

Table 10.SM.8: Regional Traceback Matrix for Polar. Table shows chapter traceability of the regional assessment using observed trends, attribution of trends or events, and climate model projections, as described in Cross-Chapter Box 10.3. The Table is divided into separate panels that correspond to the WGI AR6 Reference Regions. African sub-regions are: Panel A: Russian-Arctic (RAR), Panel B: Greenland/Iceland (GIC), Panel C: Arctic N.W.North-America (aNWN), Panel D: Arctic N.E.North-America (aNEN), Panel E: Arctic N.Europe (aNEU), Panel F: E.Antarctica (EAN), Panel G: W.Antarctica (WAN). Blank cells in the observations and projections columns corresponding to the "not broadly relevant" or "no evidence" category as described in the CID framework in Chapter 12. Blank cells in the detection and attribution columns correspond to no studies being available.

Panel A)

	Region	POLAR-ARCTIC	POLAR-ARCTIC	POLAR-ARCTIC
	Region type (Land / Ocean)	Land	Land	Land
	Sub-Region Name	Russian-Arctic	Russian-Arctic	Russian-Arctic
	Accronym	RAR	RAR	RAR
	Data Type	Observational	Detection & Attribution	Projections
Heat and Cold	Mean air temperature	Atlas.11.2.2; 12.4.9.1	Atlas.11.2.3	Atlas.11.2.4; 12.4.9.1; Table 12.11; Fig. 4.22; 4.3.1; 4.5.1.
	Extreme heat	12.4.9.1		12.4.9.1, Table 12.11
	Cold spell	12.4.9.1	Atlas.11.2.3	12.4.9.1, Table 12.11
	Frost	12.4.9.1		12.4.9.1, Table 12.11
Wet and Dry	Mean precipitation	Atlas.11.2.2; 12.4.9.2	Atlas.11.2.3; 8.3.2.8	Atlas.11.2.4; 12.4.9.2; Table 12.11
	River flood	12.4.9.2	8.2.3	12.4.9.2, Table 12.11
	Heavy precipitation and pluvial flood	12.4.9.2	8.3.2.8	12.4.9.2, Table 12.11
	Landslide	12.4.9.2		12.4.9.2, Table 12.11
	Aridity	12.4.9.2		12.4.9.2, Table 12.11
	Hydrological drought	12.4.9.2		12.4.9.2, Table 12.11
	Agricultural and ecological drought	12.4.9.2		12.4.9.2, Table 12.11
	Fire weather	12.4.9.2		12.4.9.2, Table 12.11
Wind	Mean wind speed	12.4.9.3		12.4.9.3, Table 12.11
	Severe wind storm	12.4.9.3		12.4.9.3, Table 12.11
	Tropical cyclone			
	Sand and dust storm			
Snow and Ice	Snow, glacier and ice sheet	Atlas.11.2.2; 12.4.9.4, 12.2.3.2.2, 12.2.3.2.3, 2.3.2.2, 2.3.2.3. 8.3.1.7.1., 8.3.1.7.2, 9.5.1.1.9.5.3.1.,Fig. 9.20	Atlas.11.2.3, 3.4.2, 3.4.3	Atlas.11.2.4; 12.4.9.4; Table 12.11, 8.4.1.7.1, 8.4.1.7.2, 9.5.1.3., 9.5.3.3., Fig 9.21, fig 9.23
	Permafrost	9.5.2.1; 12.4.9.4	9.5.2.1; 9.5.2.2	9.5.2.3; 12.4.9.4, Table 12.11
	Lake, river and sea ice	Atlas.11.2.2; 12.4.9.4; CCB1.1; CH1.3.1; CH1BOX1.2; CH1.4.2.1; CH1.5.3.1; CH1FAQ1.2, 2.3.2.1.1., 9.3.1.	Atlas.11.2.3, 3.4.1.	Atlas.11.2.4 12.4.9.4; Table 12.11 9.3.1
	Heavy snowfall and ice storm	12.4.9.4		12.4.9.4, Table 12.11
	Hail			
	Snow avalanche	12.4.9.4		12.4.9.4, Table 12.11
Coastal and Oceanic	Relative sea level	12.4.9.5		12.4.9.5, Table 12.11
	Coastal flood	12.4.9.5		12.4.9.5, Table 12.11
	Coastal erosion	12.4.9.5		12.4.9.5, Table 12.11
	Marine heatwave	12.4.9.5		12.4.9.5, Table 12.11
	Ocean acidity	12.4		12.4, Table 12.11
Other	Air pollution weather	12.4		12.4, Table 12.11
	Atmospheric CO2 at surface	12.4		12.4, Table 12.11

ACCEPTED VERSION SUBJECT TO FINAL EDITING

	Radiation at surface	12.4		12.4, Table 12.11

Panel B)

	Region	POLAR-ARCTIC	POLAR-ARCTIC	POLAR-ARCTIC
	Region type (Land / Ocean)	Land	Land	Land
	Sub-Region Name	Greenland/Iceland	Greenland/Iceland	Greenland/Iceland
	Accronym	GIC	GIC	GIC
	Data Type	Observational	Detection & Attribution	Projections
Heat and Cold	Mean air temperature	Atlas.11.2.2; 12.4.9.1; CH1.2.1.2	Atlas.11.2.3	Atlas.11.2.4; 12.4.9.1; Table 12.11; Fig. 4.22; 4.3.1; 4.5.1.
	Extreme heat	12.4.9.1		12.4.9.1, Table 12.11
	Cold spell	12.4.9.1		12.4.9.1, Table 12.11
	Frost	12.4.9.1		12.4.9.1, Table 12.11
Wet and Dry	Mean precipitation	1.1.1.2; 1.1.2; 12.4.9.2	Atlas.11.2.3; 8.3.2.8	Atlas.11.2.4; 12.4.9.2; Table 12.11
	River flood	12.4.9.2	8.2.3.1	12.4.9.2, Table 12.11
	Heavy precipitation and pluvial flood	12.4.9.2	8.2.3.1; 8.3.2.8	12.4.9.2, Table 12.11
	Landslide	12.4.9.2		12.4.9.2, Table 12.11
	Aridity	12.4.9.2		12.4.9.2, Table 12.11
	Hydrological drought	12.4.9.2		12.4.9.2, Table 12.11
	Agricultural and ecological drought	12.4.9.2		12.4.9.2, Table 12.11
	Fire weather	12.4.9.2		12.4.9.2, Table 12.11
Wind	Mean wind speed	12.4.9.3		12.4.9.3, Table 12.11
	Severe wind storm	12.4.9.3		12.4.9.3, Table 12.11
	Tropical cyclone			
	Sand and dust storm			
Snow and Ice	Snow, glacier and ice sheet	Atlas.11.2.2; 12.4.9.4, 12.2.3.2.4.1; CH1.3.1; CH1BOX1.2; CH1.5.1.1,2.3.2.2.,2.3.2.3.,2.3.2.4.1. 8.3.1.7.1, 8.3.1.7.2, 9.5.1.1, 9.5.3.1.Fig. 9.16, Fig. 9.20 Fig 9.23	Atlas.11.2.3, 3.4.2, 3.4.3; 8.2.3.1	Atlas.11.2.4; 12.4.9.4; Table 12.11; CH1BOX1.2; CH1FAQ1.1, 8.4.1.7.1, 8.4.1.7.2, 9.4.1.3, 9.4.1.4.,9.5.1.3.,9.5.3.3. Fig. 9.17, Fig 9.21
	Permafrost	12.4.9.4		12.4.9.4, Table 12.11
	Lake, river and sea ice	Atlas.11.2.2; 12.4.9.4, 2.3.2.1.1., 9.3.1.	Atlas.11.2.3,3.4.1.	12.1.1.4; 12.4.9.4; Table 12.11
	Heavy snowfall and ice storm	8.2.3; 12.4.9.4	8.2.3	12.4.9.4, Table 12.11
	Hail			
	Snow avalanche	12.4.9.4		12.4.9.4, Table 12.11
Coastal and Oceanic	Relative sea level	12.4.9.5; CH1.2.1.2; CH1.3.4		12.4.9.5; Table 12.11; CH1BOX1.2
	Coastal flood	12.4.9.5		12.4.9.5, Table 12.11
	Coastal erosion	12.4.9.5		12.4.9.5, Table 12.11
	Marine heatwave	12.4.9.5		12.4.9.5, Table 12.11
	Ocean acidity	12.4		12.4, Table 12.11
Other	Air pollution weather	12.4		12.4, Table 12.11
	Atmospheric CO2 at surface	12.4		12.4, Table 12.11
	Radiation at surface	12.4		12.4, Table 12.11

ACCEPTED VERSION SUBJECT TO FINAL EDITING

Panel C)

	Region	POLAR-ARCTIC	POLAR-ARCTIC	POLAR-ARCTIC
	Region type (Land / Ocean)	Land	Land	Land
	Sub-Region Name	Arctic N.W.North-America	Arctic N.W.North-America	Arctic N.W.North-America
	Accronym	aNWN	aNWN	aNWN
	Data Type	Observational	Detection & Attribution	Projections
Heat and Cold	Mean air temperature	12.4.9.1, Atlas.5.7.2; Atlas.9.2; Atlas.11.2.2		12.4.9.1, Table 12.11, Atlas.9.4;
	Extreme heat	12.4.9.1		12.4.9.1, Table 12.11
	Cold spell	12.4.9.1		12.4.9.1, Table 12.11
	Frost	12.4.9.1		12.4.9.1, Table 12.11
Wet and Dry	Mean precipitation	12.4.9.2; Atlas.9.2;	8.2.3.1; 8.3.2.8; 8.4	12.4.9.2, Table 12.11; Atlas.9.4; 8.4.2.8
	River flood	12.4.9.2	8.2.3.1	12.4.9.2, Table 12.11
	Heavy precipitation and pluvial flood	12.4.9.2	8.2.3.1; 8.3.2.8	12.4.9.2, Table 12.11
	Landslide	12.4.9.2		12.4.9.2, Table 12.11
	Aridity	12.4.9.2		12.4.9.2, Table 12.11
	Hydrological drought	12.4.9.2		12.4.9.2, Table 12.11
	Agricultural and ecological drought	12.4.9.2		12.4.9.2, Table 12.11
	Fire weather	12.4.9.2		12.4.9.2, Table 12.11
Wind	Mean wind speed	12.4.9.3		12.4.9.3, Table 12.11
	Severe wind storm	12.4.9.3		12.4.9.3, Table 12.11
	Tropical cyclone			
	Sand and dust storm			
Snow and Ice	Snow, glacier and ice sheet	12.4.9.4; Atlas.9.2 2.3.2.2., 2.3.2.3, 8.3.1.7.1., 8.3.1.7.2.,9.5.1.1., 9.5.3.1.,Fig. 9.20, Fig 9.23	3.4.2, 3.4.3; 8.2.3.1	12.4.9.4, Table 12.11; Atlas.9.4, 8.4.1.7.1, 8.4.1.7.1, 9.5.1.3., 9.5.3.3. Fig. 9.21
	Permafrost	9.5.2.1; 12.4.9.4	8.2.3.1; 9.5.2.1; 9.5.2.2	9.5.2.3; 12.4.9.4, Table 12.11
	Lake, river and sea ice	12.4.9.4, 2.3.2.1.1., 9.3.1.	3.4.1.	12.4.9.4, Table 12.11
	Heavy snowfall and ice storm	12.4.9.4	8.2.3.1	12.4.9.4, Table 12.11
	Hail			
	Snow avalanche	12.4.9.4		12.4.9.4, Table 12.11
Coastal and Oceanic	Relative sea level	12.4.9.5		12.4.9.5, Table 12.11
	Coastal flood	12.4.9.5		12.4.9.5, Table 12.11
	Coastal erosion	12.4.9.5		12.4.9.5, Table 12.11
	Marine heatwave	12.4.9.5		12.4.9.5, Table 12.11
	Ocean acidity	12.4		12.4, Table 12.11
Other	Air pollution weather	12.4		12.4, Table 12.11
	Atmospheric CO2 at surface	12.4		12.4, Table 12.11
	Radiation at surface	12.4		12.4, Table 12.11

ACCEPTED VERSION SUBJECT TO FINAL EDITING

Panel D)

	Region	POLAR-ARCTIC	POLAR-ARCTIC	POLAR-ARCTIC
	Region type (Land / Ocean)	Land	Land	Land
	Sub-Region Name	Arctic N.E.North-America	Arctic N.E.North-America	Arctic N.E.North-America
	Accronym	aNEN	aNEN	aNEN
	Data Type	Observational	Detection & Attribution	Projections
Heat and Cold	Mean air temperature	12.4.9.1, Atlas.9.2; Atlas.11.2.2		12.4.9.1, Table 12.11, Atlas.9.4
	Extreme heat	12.4.9.1		12.4.9.1, Table 12.11
	Cold spell	12.4.9.1		12.4.9.1, Table 12.11
	Frost	12.4.9.1		12.4.9.1, Table 12.11
Wet and Dry	Mean precipitation	12.4.9.2; Atlas.9.2;	8.2.3.1; 8.3.2.8; 8.4.2.8	12.4.9.2, Table 12.11; Atlas.9.4; 8.4
	River flood	12.4.9.2	8.2.3.1	12.4.9.2, Table 12.11
	Heavy precipitation and pluvial flood	12.4.9.2	8.2.3.1; 8.3.2.8	12.4.9.2, Table 12.11
	Landslide			
	Aridity	12.4.9.2		12.4.9.2, Table 12.11
	Hydrological drought	12.4.9.2		12.4.9.2, Table 12.11
	Agricultural and ecological drought	12.4.9.2		12.4.9.2, Table 12.11
	Fire weather	12.4.9.2		12.4.9.2, Table 12.11
Wind	Mean wind speed	12.4.9.3		12.4.9.3, Table 12.11
	Severe wind storm	12.4.9.3		12.4.9.3, Table 12.11
	Tropical cyclone			
	Sand and dust storm			
Snow and Ice	Snow, glacier and ice sheet	12.4.9.4; Atlas.9.2,2.3.2.2., 2.3.2.3, 8.3.1.7.1., 8.3.1.7.2, 9.5.1.1., 9.5.3.1., Fig. 9.20, Fig 9.23	3.4.2, 3.4.3; 8.2.3.1	12.4.9.4, Table 12.11; Atlas.9.4, 8.4.1.7.1, 8.4.1.7.1, 9.5.1.3., 9.5.3.3. Fig. 9.21
	Permafrost	9.5.2.1; 12.4.9.4	8.2.3.1; 9.5.2.1; 9.5.2.2	9.5.2.3; 12.4.9.4, Table 12.11
	Lake, river and sea ice	12.4.9.4, 2.3.2.1.1., 9.3.1.	3.4.1.	12.4.9.4, Table 12.11
	Heavy snowfall and ice storm	12.4.9.4	8.2.3.1	12.4.9.4, Table 12.11
	Hail			
	Snow avalanche	12.4.9.4		12.4.9.4, Table 12.11
Coastal and Oceanic	Relative sea level	12.4.9.5		12.4.9.5, Table 12.11
	Coastal flood	12.4.9.5		12.4.9.5, Table 12.11
	Coastal erosion	12.4.9.5		12.4.9.5, Table 12.11
	Marine heatwave	12.4.9.5		12.4.9.5, Table 12.11
	Ocean acidity	12.4		12.4, Table 12.11
Other	Air pollution weather	12.4		12.4, Table 12.11
	Atmospheric CO2 at surface	12.4		12.4, Table 12.11
	Radiation at surface	12.4		12.4, Table 12.11

ACCEPTED VERSION SUBJECT TO FINAL EDITING

Panel E)

	Region	POLAR-ARCTIC	POLAR-ARCTIC	POLAR-ARCTIC
	Region type (Land / Ocean)	Land	Land	Land
	Sub-Region Name	Arctic N.Europe	Arctic N.Europe	Arctic N.Europe
	Accronym	aNEU	aNEU	aNEU
	Data Type	Observational	Detection & Attribution	Projections
Heat and Cold	Mean air temperature	CH1.4.2.2; Atlas.8.2, 12.4.9.1	Atlas.8.2	12.4.9.1, Table 12.11; A.8.4
	Extreme heat	Table 11.8; 12.4.5.1, 12.4.9.1	Table 11.8	12.4.5.1, 12.4.9.1, Table 12.7, Table 12.11
	Cold spell	12.4.5.1, 12.4.9.1		12.4.5.1, 12.4.9.1, Table 12.7, Table 12.11
	Frost	12.4.5.1, 12.4.9.1		12.4.5.1, 12.4.9.1, Table 12.7, Table 12.11
Wet and Dry	Mean precipitation	Atlas.8.2; 12.4.5.2, 12.4.9.2	Atlas.8.2; 12.4.5.2, 12.4.9.2; 8.3.2.8; 8.4.2.8	12.4.5.2, 12.4.9.2, Table 12.7, Table 12.11; Atlas.8.4; 8.4
	River flood	12.4.5.2, 12.4.9.2		12.4.5.2, 12.4.9.2, Table 12.7, Table 12.11
	Heavy precipitation and pluvial flood	Table 11.8; 12.4.5.2, 12.4.9.2	Table 11.8; 8.3.2.8	12.4.5.2, 12.4.9.2, Table 12.7, Table 12.11
	Landslide	12.4.5.2, 12.4.9.2		12.4.5.2, 12.4.9.2
	Aridity	12.4.5.2, 12.4.9.2		12.4.5.2, 12.4.9.2
	Hydrological drought	Table 11.8; 12.4.5.2, 12.4.9.2	Table 11.8	12.4.5.2, 12.4.9.2, Table 12.7, Table 12.11
	Agricultural and ecological drought	Table 11.8; 12.4.5.2, 12.4.9.2	Table 11.8	12.4.5.2, 12.4.9.2, Table 12.7, Table 12.11
	Fire weather	12.4.5.2, 12.4.9.2		12.4.5.2, 12.4.9.2, Table 12.7, Table 12.11
Wind	Mean wind speed	12.4.9.3		12.4.9.3, Table 12.11
	Severe wind storm	12.4.9.3		12.4.9.3, Table 12.11
	Tropical cyclone			
	Sand and dust storm			
Snow and Ice	Snow, glacier and ice sheet	Atlas.8.2; 12.4.5.4, 12.4.9.4, 2.3.2.2., 2.3.2.3, 8.3.1.7.1., 8.3.1.7.2.,9.5.1.1., 9.5.3.1.,Fig. 9.20, Fig 9.23	Atlas.8.2, 3.4.2, 3.4.3	12.4.9.4, Table 12.11; Atlas.8.4, 8.4.1.7.1, 8.4.1.7.1, 9.5.1.3., 9.5.3.3. Fig. 9.21
	Permafrost	9.5.2.1; 12.4.5.4, 12.4.9.4, 2.3.2.5	9.5.2.1; 9.5.2.2	9.5.2.3; 12.4.5.4, 12.4.9.4, Table 12.7, Table 12.11
	Lake, river and sea ice	12.4.5.4, 12.4.9.4, 2.3.2.1.1., 9.3.1.	3.4.1.	12.4.5.4, 12.4.9.4, Table 12.7, Table 12.11,
	Heavy snowfall and ice storm	12.4.5.4, 12.4.9.4		12.4.5.4, 12.4.9.4
	Hail	12.4.5.4, 12.4.9.4		12.4.5.4, 12.4.9.4, Table 12.7, Table 12.11
	Snow avalanche	12.4.5.4, 12.4.9.4		12.4.5.4, 12.4.9.4, Table 12.7, Table 12.11
Coastal and Oceanic	Relative sea level	12.4.9.5		12.4.9.5, Table 12.11
	Coastal flood	12.4.9.5		12.4.9.5, Table 12.11
	Coastal erosion	12.4.9.5		12.4.9.5, Table 12.11
	Marine heatwave	12.4.9.5		12.4.9.5, Table 12.11
	Ocean acidity	12.4		12.4, Table 12.11
Other	Air pollution weather	12.4		12.4, Table 12.11
	Atmospheric CO2 at surface	12.4		12.4, Table 12.11
	Radiation at surface	Atlas..8.2; 12.4.0	Atlas.8.2	12.4, Table 12.11

ACCEPTED VERSION SUBJECT TO FINAL EDITING

Panel F)

	Region	POLAR-ANTARCTIC	POLAR-ANTARCTIC	POLAR-ANTARCTIC
	Region type (Land / Ocean)	Land	Land	Land
	Sub-Region Name	E.Antarctica	E.Antarctica	E.Antarctica
	Accronym	EAN	EAN	EAN
	Data Type	Observational	Detection & Attribution	Projections
Heat and Cold	Mean air temperature	Atlas.11.1.2; 12.4.9.1	Atlas.11.1.2	Atlas.11.1.4; 12.4.9.1; Table 12.11; Fig. 4.22; 4.3.1; 4.5.1.
	Extreme heat	12.4.9.1		12.4.9.1, Table 12.11
	Cold spell	12.4.9.1		12.4.9.1, Table 12.11
	Frost	12.4.9.1		12.4.9.1, Table 12.11
Wet and Dry	Mean precipitation	Atlas.11.1.2; 12.4.9.2	Atlas.11.1.2; 8.3.2.8	Atlas.11.1.4; 12.4.9.2; Table 12.11
	River flood	NA		NA
	Heavy precipitation and pluvial flood	12.4.9.2	8.3.2.8	12.4.9.2; Table 12.11
	Landslide	12.4.9.2		12.4.9.2; Table 12.11
	Aridity	12.4.9.2		12.4.9.2; Table 12.11
	Hydrological drought	12.4.9.2		12.4.9.2; Table 12.11
	Agricultural and ecological drought	NA		NA
	Fire weather	NA		NA
Wind	Mean wind speed	12.4.9.3		12.4.9.3, Table 12.11
	Severe wind storm	12.4.9.3		12.4.9.3, Table 12.11
	Tropical cyclone	NA		
	Sand and dust storm	NA		
Snow and Ice	Snow, glacier and ice sheet	9.4.2.1, 9.5.1.1; 2.3.2.4.2; Atlas.11.1.2; 12.4.9.4, CH1.2.1.1; CH1.3.1; CH1BOX1.2,	9.4.2.1, 9.5.1.1; Atlas.11.1.2, 3.4.3.2	9.4.2.3, Atlas.11.1.4; 12.4.9.2; Table 12.11; CH1BOX1.2 9.4.2.5, 9.4.2.6. Fig. 9.18
	Permafrost	12.4.9.4		12.4.9.4, Table 12.11
	Lake, river and sea ice	12.4.9.4; CCB1.1; CH1BOX1.2,2.3.2.1.2., 9.3.2.	3.4.1.	12.4.9.4; Table 12.11; CH1FAQ1.2
	Heavy snowfall and ice storm	12.4.9.4		12.4.9.4, Table 12.11
	Hail			
	Snow avalanche	12.4.9.4		12.4.9.4, Table 12.11
Coastal and Oceanic	Relative sea level	9.6.1; 12.4.9.5	Box 9.1, 9.6.1	9.6.3; 12.4.9.5; Table 12.11; CH1BOX1.2
	Coastal flood	12.4.9.5		12.4.9.5; Table 12.11
	Coastal erosion	12.4.9.5		12.4.9.5; Table 12.11
	Marine heatwave	9.2; 12.4.9.5		
	Ocean acidity	12.4		12.4, Table 12.11
Other	Air pollution weather			
	Atmospheric CO2 at surface	CH1.2.1.2; 12,4		12.4, Table 12.11
	Radiation at surface	12.4		12.4, Table 12.11

ACCEPTED VERSION SUBJECT TO FINAL EDITING

Panel G)

	Region	POLAR-ANTARCTIC	POLAR-ANTARCTIC	POLAR-ANTARCTIC
	Region type (Land / Ocean)	Land	Land	Land
	Sub-Region Name	W.Antarctica	W.Antarctica	W.Antarctica
	Accronym	WAN	WAN	WAN
	Data Type	Observational	Detection & Attribution	Projections
Heat and Cold	Mean air temperature	Atlas.11.1.2; 12.4.9.1	Atlas.11.1.2	Atlas.11.1.4; 12.4.9.1; Table 12.11; Fig. 4.22; 4.3.1; 4.5.1.
	Extreme heat	12.4.9.1		12.4.9.1, Table 12.11
	Cold spell	12.4.9.1		12.4.9.1, Table 12.11
	Frost	12.4.9.1		12.4.9.1, Table 12.11
Wet and Dry	Mean precipitation	Atlas.11.1.2; 12.4.9.2	Atlas.11.1.2; 8.3.2.8	Atlas.11.1.4; 12.4.9.2; Table 12.11
	River flood			
	Heavy precipitation and pluvial flood	NA	8.3.2.8	NA
	Landslide	12.4.9.2		12.4.9.2; Table 12.11
	Aridity	12.4.9.2		12.4.9.2; Table 12.11
	Hydrological drought	12.4.9.2		12.4.9.2; Table 12.11
	Agricultural and ecological drought	12.4.9.2		12.4.9.2; Table 12.11
	Fire weather			
Wind	Mean wind speed	12.4.9.3		12.4.9.3, Table 12.11
	Severe wind storm	12.4.9.3		12.4.9.3, Table 12.11
	Tropical cyclone			
	Sand and dust storm			
Snow and Ice	Snow, glacier and ice sheet	9.4.2.1, 9.5.1.1; Atlas.11.1.2; 12.4.9.4; CH1.2.1.1; CH1.3.1; CH1BOX1.2, 2.3.2.4.2;	9.4.2.1, 9.5.1.1; Atlas.11.1.2, 3.4.3.2.	9.4.2.5, 9.4.2.6, Atlas.11.1.4; 12.4.9.4; Table 12.11; CH1BOX1.2
	Permafrost	9.5.2.1; 12.4.9.4, 2.3.2.4.2	9.5.2.1; 9.5.2.2	9.5.2.3; 12.4.9.4; Table 12.11
	Lake, river and sea ice	9.5.2.3; 12.4.9.4; Table 12.11,2.3.2.1.2., 9.3.2.	3.4.1.	12.4.9.4; Table 12.11; CH1FAQ1.2
	Heavy snowfall and ice storm	12.4.9.4		12.4.9.4, Table 12.11
	Hail			
	Snow avalanche	12.4.9.4		12.4.9.4, Table 12.11
Coastal and Oceanic	Relative sea level	9.6.1; 12.4.9.5	Box 9.1, 9.6.1	9.6.3; 12.4.9.5; Table 12.11; CH1BOX1.2
	Coastal flood	12.4.9.5		12.4.9.5; Table 12.11
	Coastal erosion	12.4.9.5		12.4.9.5; Table 12.11
	Marine heatwave	9.2; 12.4.9.5		12.4.9.5; Table 12.11
	Ocean acidity	12.4		12.4, Table 12.11
Other	Air pollution weather			
	Atmospheric CO2 at surface	CH1.2.1.2; 12,4		12.4, Table 12.11
	Radiation at surface	12.4		12.4, Table 12.11

[START TABLE 10.SM.8 HERE]

ACCEPTED VERSION SUBJECT TO FINAL EDITING

[START TABLE 10.SM.9 HERE]

Table 10.SM.9: Regional Traceback Matrix for Small Islands. Table shows chapter traceability of the regional assessment using observed trends, attribution of trends or events, and climate model projections, as described in Cross-Chapter Box 10.3. The Table is divided into separate panels that correspond to the WGI AR6 Reference Regions. African sub-regions are: Panel A: Caribbean (CAR), Panel B: Pacific Islands (EPO/SPO), Panel C: Western Indian Ocean Islands (EIO/SIO). Blank cells in the observations and projections columns corresponding to the "not broadly relevant" or "no evidence" category as described in the CID framework in Chapter 12. Blank cells in the detection and attribution columns correspond to no studies being available.

Panel A)

	Region	SMALL ISLANDS	SMALL ISLANDS	SMALL ISLANDS
	Region type (Land / Ocean)	Land-Ocean	Land-Ocean	Land-Ocean
	Sub-Region Name	Caribbean	Caribbean	Caribbean
	Accronym	CAR	CAR	CAR
	Data Type	Observational	Detection & Attribution	Projections
Heat and Cold	Mean air temperature	Atlas.10.2; Cross-chapter Box Atlas.2 Table 1; 12.4.7.1		Atlas.10.4; 12.4.7.1, Table 12.9
	Extreme heat	Atlas.10.2; Cross-chapter Box Atlas.2 Table 1; Table 11.13; 11.3.2; 12.4.7.1	Table 11.13	Table 11.13; 11.3.5; 12.4.7.1, Table 12.9
	Cold spell	Atlas.10.2; Table 11.13; 11.3.2	Table 11.13	Table 11.13; 11.3.5
	Frost			
Wet and Dry	Mean precipitation	Atlas.10.2; Cross-chapter Box Atlas.2 Table 1; 12.4.7.2	Cross-chapter Box Atlas.2	Atlas.10.4; 12.4.7.2, Table 12.9
	River flood	11.5.2; 12.4.7.2		11.5.5; 12.4.7.2
	Heavy precipitation and pluvial flood	Table 11.14; 11.4.2; 12.4.7.2	Table 11.14	Table 11.14; 11.4.5; 12.4.7.2, Table 12.9
	Landslide	12.4.7.2		12.4.7.2, Table 12.9
	Aridity	Cross-chapter Box Atlas.2 Table 1; 12.4.7.2		12.4.7.2, Table 12.9
	Hydrological drought	Table 11.15; 11.6.2; 12.4.7.2	Table 11.15; 11.6.4	Table 11.15; 11.6.5; 12.4.7.2, Table 12.9
	Agricultural and ecological drought	Table 11.15; 11.6.2; 12.4.7.2	Table 11.15; 11.6.4	Table 11.15; 11.6.5; 12.4.7.2, Table 12.9
	Fire weather	12.4.7.2		12.4.7.2, Table 12.9
Wind	Mean wind speed	12.4.7.3		12.4.7.3, Table 12.9
	Severe wind storm	12.4.7.3		12.4.7.3, Table 12.9
	Tropical cyclone	12.4.7.3		12.4.7.3, Table 12.9
	Sand and dust storm			
Snow and Ice	Snow, glacier and ice sheet			
	Permafrost			
	Lake, river and sea ice			
	Heavy snowfall and ice storm			
	Hail			
	Snow avalanche			
Coastal and Oceanic	Relative sea level	Cross-chapter Box Atlas.2 Table 1; 12.4.7.5		12.4.7.5, Table 12.9
	Coastal flood	12.4.7.5		12.4.7.5, Table 12.9
	Coastal erosion	12.4.7.5		12.4.7.5, Table 12.9
	Marine heatwave	12.4.7.5		12.4.7.5, Table 12.9
	Ocean acidity	12.4		12.4; Table 12.9
Other	Air pollution weather	12.4		12.4; Table 12.9
	Atmospheric CO2 at surface	12.4		12.4; Table 12.9

ACCEPTED VERSION SUBJECT TO FINAL EDITING

	Radiation at surface	12.4		12.4; Table 12.9

Panel B)

	Region	SMALL ISLANDS	SMALL ISLANDS	SMALL ISLANDS
	Region type (Land / Ocean)	Land-Ocean	Land-Ocean	Land-Ocean
	Sub-Region Name	Pacific Islands	Pacific Islands	Pacific Islands
	Accronym	[EPO/SPO]	[EPO/SPO]	[EPO/SPO]
	Data Type	Observational	Detection & Attribution	Projections
Heat and Cold	Mean air temperature	Atlas.10.2; Cross-chapter Box Atlas.2 Table 1; 12.4.7.1		Atlas.10.4; 12.4.7.1, Table 12.9
	Extreme heat	Atlas.10.2; Cross-chapter Box Atlas.2 Table 1; 11.3.2; 12.4.7.1		12.4.7.1, Table 12.9
	Cold spell	Atlas.10.2; 11.3.2		
	Frost			
Wet and Dry	Mean precipitation	Atlas.10.2; Cross-chapter Box Atlas.2 Table 1; 12.4.7.2	Cross-chapter Box Atlas.2	Atlas.10.4; 12.4.7.2, Table 12.9
	River flood	11.5.2; 12.4.7.2		11.5.5; 12.4.7.2, Table 12.9
	Heavy precipitation and pluvial flood	11.4.2; 12.4.7.2		11.4.5; 12.4.7.2, Table 12.9
	Landslide	12.4.7.2		12.4.7.2, Table 12.9
	Aridity	Cross-chapter Box Atlas.2 Table 1; 12.4.7.2		12.4.7.2, Table 12.9
	Hydrological drought	12.4.7.2		12.4.7.2, Table 12.9
	Agricultural and ecological drought	12.4.7.2		12.4.7.2, Table 12.9
	Fire weather	12.4.7.2		12.4.7.2, Table 12.9
Wind	Mean wind speed	12.4.7.3		12.4.7.3, Table 12.9
	Severe wind storm	12.4.7.3		12.4.7.3, Table 12.9
	Tropical cyclone	Cross-chapter Box Atlas.2 Table 1; 12.4.7.3		12.4.7.3, Table 12.9
	Sand and dust storm			
Snow and Ice	Snow, glacier and ice sheet			
	Permafrost			
	Lake, river and sea ice			
	Heavy snowfall and ice storm			
	Hail			
	Snow avalanche			
Coastal and Oceanic	Relative sea level	Cross-chapter Box Atlas.2 Table 1; 12.4.7.5; 1.3.1		12.4.7.5, Table 12.9
	Coastal flood	12.4.7.5		12.4.7.5, Table 12.9
	Coastal erosion	12.4.7.5		12.4.7.5, Table 12.9
	Marine heatwave	12.4.7.5		12.4.7.5, Table 12.9
	Ocean acidity	12.4		12.4, Table 12.9
Other	Air pollution weather	12.4		12.4, Table 12.9
	Atmospheric CO2 at surface	12.4		12.4, Table 12.9
	Radiation at surface	12.4		12.4, Table 12.9

ACCEPTED VERSION SUBJECT TO FINAL EDITING

Panel C)

	Region	SMALL ISLANDS	SMALL ISLANDS	SMALL ISLANDS
	Region type (Land / Ocean)	Land-Ocean	Land-Ocean	Land-Ocean
	Sub-Region Name	Western Indian Ocean Islands	Western Indian Ocean Islands	Western Indian Ocean Islands
	Accronym	[EIO/SIO]	[EIO/SIO]	[EIO/SIO]
	Data Type	Observational	Detection & Attribution	Projections
Heat and Cold	Mean air temperature	Atlas.10.2; Cross-chapter Box Atlas.2 Table 1		Atlas.10.4
	Extreme heat			
	Cold spell			
	Frost			
Wet and Dry	Mean precipitation	Atlas.10.2; Cross-chapter Box Atlas.2 Table 1;		Atlas.10.4
	River flood			
	Heavy precipitation and pluvial flood			
	Landslide			
	Aridity			
	Hydrological drought			
	Agricultural and ecological drought			
	Fire weather			
Wind	Mean wind speed			
	Severe wind storm			
	Tropical cyclone			
	Sand and dust storm			
Snow and Ice	Snow, glacier and ice sheet			
	Permafrost			
	Lake, river and sea ice			
	Heavy snowfall and ice storm			
	Hail			
	Snow avalanche			
Coastal and Oceanic	Relative sea level	Cross-chapter Box Atlas.2 Table 1; 1.3.1		
	Coastal flood			
	Coastal erosion			
	Marine heatwave			
	Ocean acidity			
Other	Air pollution weather			
	Atmospheric CO2 at surface			
	Radiation at surface			

[END TABLE 10.SM.9 HERE]

ACCEPTED VERSION SUBJECT TO FINAL EDITING

[START TABLE 10.SM.10 HERE]

Table 10.SM.10: Regional Traceback Matrix for Open Ocean Regions. Table shows chapter traceability of the regional assessment using observed trends, attribution of trends or events, and climate model projections, as described in Cross-Chapter Box 10.3. The Table is divided into separate panels that correspond to the WGI AR6 Reference Regions. African sub-regions are: Panel A: Arctic-Ocean (ARO), Panel B: N.Pacific-Ocean (NPO), Panel C: Equatorial.Pacific-Ocean (EPO), Panel D: S.Pacific-Ocean (SPO), Panel E: N.Atlantic-Ocean (NAO), Panel F: Equatorial.Atlantic-Ocean (EAO), Panel G: S.Atlantic-Ocean (SAO), Panel H: Arabian-Sea (ARS), Panel I: Bay-of-Bengal (BOB), Panel J: Equatorial.Indic-Ocean (EIO), Panel K: S.Indic-Ocean (SIO), Panel L: Southern-Ocean (SOO). Blank cells in the observations and projections columns corresponding to the "not broadly relevant" or "no evidence" category as described in the CID framework in Chapter 12. Blank cells in the detection and attribution columns correspond to no studies being available.

Panel A)

	Region	ARCTIC	ARCTIC	ARCTIC
	Region type (Land / Ocean)	Ocean	Ocean	Ocean
	Sub-Region Name	Arctic-Ocean	Arctic-Ocean	Arctic-Ocean
	Accronym	ARO	ARO	ARO
	Data Type	Observational	Detection & Attribution	Projections
Open Oceans	Mean ocean temperature	2.3.3.1, 9.2.2.1, 12.4.8	3.5.1.1,	4.5.2.1,9.2.2.1, 12.4.8, Table 12.10
	Marine heatwave	BOX 9.2:, 12.4.8, 12.4.9		BOX 9.2:, 12.4.8, Table 12.10
	Severe storm and waves	9.6.4.1,		9.6.4.2,
	Sea ice	2.3.2.1.1, 9.3.1, 2.3.2.1.1, 9.3.1, 12.4.8, 12.4.9	3.4.1.1,	4.3.2, 9.3.1, 4.3.2, 9.3.1, 12.4.8, Table 12.4.9, Table 12.10
	Subsea permafrost	5.4.9.1.3,		5.4.9.1.3,
	Ocean acidity	2.3.3.5,5.3, 12.4.8, 12.4.9		4.5.2.2,5.3, 12.4.8, Table 12.10
	Dissolved oxygen	2.3.3.6, 12.4.8		5.3.3.2, 12.4.8, Table 12.10
	Ocean salinity	2.3.3.2,9.2.2.2, 12.4.8	3.5.2,	9.2.2.2, 12.4.8, Table 12.10

Panel B)

	Region	PACIFIC	PACIFIC	PACIFIC
	Region type (Land / Ocean)	Ocean	Ocean	Ocean
	Sub-Region Name	N.Pacific-Ocean	N.Pacific-Ocean	N.Pacific-Ocean
	Accronym	NPO	NPO	NPO
	Data Type	Observational	Detection & Attribution	Projections
Open Oceans	Mean ocean temperature	2.3.3.1, 9.2.2.1, 12.4.8	3.5.1.1,	4.5.2.1,9.2.2.1, 12.4.8, Table 12.10
	Marine heatwave	BOX 9.2:, 12.4.8		BOX 9.2:, 12.4.8, Table 12.10
	Severe storm and waves	9.6.4.1,		9.6.4.2,
	Sea ice	, 12.4.8		, 12.4.8, Table 12.10
	Subsea permafrost	5.4.9.1.3,		5.4.9.1.3,
	Ocean acidity	2.3.3.5,5.3, 12.4.8		4.5.2.2,5.3, 12.4.8, Table 12.10
	Dissolved oxygen	2.3.3.6, 12.4.8		5.3.3.2, 12.4.8, Table 12.10
	Ocean salinity	2.3.3.2,9.2.2.2, 12.4.8	3.5.2,	9.2.2.2, 12.4.8, Table 12.10

ACCEPTED VERSION SUBJECT TO FINAL EDITING

Panel C)

	Region	PACIFIC	PACIFIC	PACIFIC
	Region type (Land / Ocean)	Ocean	Ocean	Ocean
	Sub-Region Name	Equatorial.Pacific-Ocean	Equatorial.Pacific-Ocean	Equatorial.Pacific-Ocean
	Accronym	EPO	EPO	EPO
	Data Type	Observational	Detection & Attribution	Projections
Open Oceans	Mean ocean temperature	2.3.3.1, 9.2.2.1, 12.4.8	3.5.1.2,	4.5.2.1,9.2.2.1, 12.4.8, Table 12.10
	Marine heatwave	BOX 9.2:, 12.4.8		BOX 9.2:, 12.4.8, Table 12.10
	Severe storm and waves	9.6.4.1,		9.6.4.2,
	Sea ice	, 12.4.8		, 12.4.8, Table 12.10
	Subsea permafrost	5.4.9.1.3,		5.4.9.1.3,
	Ocean acidity	2.3.3.5,5.3, 12.4.8		4.5.2.2,5.3, 12.4.8, Table 12.10
	Dissolved oxygen	2.3.3.6, 12.4.8		5.3.3.2, 12.4.8, Table 12.10
	Ocean salinity	2.3.3.2,9.2.2.2, 12.4.8	3.5.2,	9.2.2.2, 12.4.8, Table 12.10

Panel D)

	Region	PACIFIC	PACIFIC	PACIFIC
	Region type (Land / Ocean)	Ocean	Ocean	Ocean
	Sub-Region Name	S.Pacific-Ocean	S.Pacific-Ocean	S.Pacific-Ocean
	Accronym	SPO	SPO	SPO
	Data Type	Observational	Detection & Attribution	Projections
Open Oceans	Mean ocean temperature	2.3.3.1, 9.2.2.1, 12.4.8	3.5.1.1,	4.5.2.1,9.2.2.1, 12.4.8, Table 12.10
	Marine heatwave	BOX 9.2:, 12.4.8		BOX 9.2:, 12.4.8, Table 12.10
	Severe storm and waves	9.6.4.1,		9.6.4.2,
	Sea ice	, 12.4.8		, 12.4.8, Table 12.10
	Subsea permafrost	5.4.9.1.3,		5.4.9.1.3,
	Ocean acidity	2.3.3.5,5.3, 12.4.8		4.5.2.2,5.3, 12.4.8, Table 12.10
	Dissolved oxygen	2.3.3.6, 12.4.8		5.3.3.2, 12.4.8, Table 12.10
	Ocean salinity	2.3.3.2,9.2.2.2, 12.4.8	3.5.2,	9.2.2.2, 12.4.8, Table 12.10

Panel E)

	Region	ATLANTIC	ATLANTIC	ATLANTIC
	Region type (Land / Ocean)	Ocean	Ocean	Ocean
	Sub-Region Name	N.Atlantic-Ocean	N.Atlantic-Ocean	N.Atlantic-Ocean
	Accronym	NAO	NAO	NAO
	Data Type	Observational	Detection & Attribution	Projections
Open Oceans	Mean ocean temperature	2.3.3.1, 9.2.2.1, 12.4.8	3.5.1.1,	4.5.2.1,9.2.2.1, 12.4.8, Table 12.10
	Marine heatwave	BOX 9.2:, 12.4.8		BOX 9.2:, 12.4.8, Table 12.10
	Severe storm and waves	9.6.4.1,		9.6.4.2,
	Sea ice	, 12.4.8		, 12.4.8, Table 12.10
	Subsea permafrost	5.4.9.1.3,		5.4.9.1.3,
	Ocean acidity	2.3.3.5,5.3, 12.4.8		4.5.2.2,5.3, 12.4.8, Table 12.10
	Dissolved oxygen	2.3.3.6, 12.4.8		5.3.3.2, 12.4.8, Table 12.10
	Ocean salinity	2.3.3.2,9.2.2.2, 12.4.8	3.5.2,	9.2.2.2, 12.4.8, Table 12.10

ACCEPTED VERSION SUBJECT TO FINAL EDITING

Panel F)

	Region	ATLANTIC	ATLANTIC	ATLANTIC
	Region type (Land / Ocean)	Ocean	Ocean	Ocean
	Sub-Region Name	Equatorial.Atlantic-Ocean	Equatorial.Atlantic-Ocean	Equatorial.Atlantic-Ocean
	Accronym	EAO	EAO	EAO
	Data Type	Observational	Detection & Attribution	Projections
Open Oceans	Mean ocean temperature	2.3.3.1, 9.2.2.1, 12.4.8	3.5.1.2,	4.5.2.1,9.2.2.1, 12.4.8, Table 12.10
	Marine heatwave	BOX 9.2:, 12.4.8		BOX 9.2:, 12.4.8, Table 12.10
	Severe storm and waves	9.6.4.1,		9.6.4.2,
	Sea ice	, 12.4.8		, 12.4.8, Table 12.10
	Subsea permafrost	5.4.9.1.3,		5.4.9.1.3,
	Ocean acidity	2.3.3.5,5.3, 12.4.8		4.5.2.2,5.3, 12.4.8, Table 12.10
	Dissolved oxygen	2.3.3.6, 12.4.8		5.3.3.2, 12.4.8, Table 12.10
	Ocean salinity	2.3.3.2,9.2.2.2, 12.4.8	3.5.2,	9.2.2.2, 12.4.8, Table 12.10

Panel G)

	Region	ATLANTIC	ATLANTIC	ATLANTIC
	Region type (Land / Ocean)	Ocean	Ocean	Ocean
	Sub-Region Name	S.Atlantic-Ocean	S.Atlantic-Ocean	S.Atlantic-Ocean
	Accronym	SAO	SAO	SAO
	Data Type	Observational	Detection & Attribution	Projections
Open Oceans	Mean ocean temperature	2.3.3.1, 9.2.2.1, 12.4.8	3.5.1.1,	4.5.2.1,9.2.2.1, 12.4.8, Table 12.10
	Marine heatwave	BOX 9.2:, 12.4.8		BOX 9.2:, 12.4.8, Table 12.10
	Severe storm and waves	9.6.4.1,		9.6.4.2,
	Sea ice	, 12.4.8		, 12.4.8, Table 12.10
	Subsea permafrost	5.4.9.1.3,		5.4.9.1.3,
	Ocean acidity	2.3.3.5,5.3, 12.4.8		4.5.2.2,5.3, 12.4.8, Table 12.10
	Dissolved oxygen	2.3.3.6, 12.4.8		5.3.3.2, 12.4.8, Table 12.10
	Ocean salinity	2.3.3.2,9.2.2.2, 12.4.8	3.5.2,	9.2.2.2, 12.4.8, Table 12.10

Panel H)

	Region	INDIAN	INDIAN	INDIAN
	Region type (Land / Ocean)	Ocean	Ocean	Ocean
	Sub-Region Name	Arabian-Sea	Arabian-Sea	Arabian-Sea
	Accronym	ARS	ARS	ARS
	Data Type	Observational	Detection & Attribution	Projections
Open Oceans	Mean ocean temperature	2.3.3.1, 9.2.2.1, 12.4.8	3.5.1.2,	4.5.2.1,9.2.2.1, 12.4.8, Table 12.10
	Marine heatwave	BOX 9.2:, 12.4.8		BOX 9.2:, 12.4.8, Table 12.10
	Severe storm and waves	9.6.4.1,		9.6.4.2,
	Sea ice	, 12.4.8		, 12.4.8, Table 12.10
	Subsea permafrost	5.4.9.1.3,		5.4.9.1.3,
	Ocean acidity	2.3.3.5,5.3, 12.4.8		4.5.2.2,5.3, 12.4.8, Table 12.10
	Dissolved oxygen	2.3.3.6, 12.4.8		5.3.3.2, 12.4.8, Table 12.10
	Ocean salinity	2.3.3.2,9.2.2.2, 12.4.8	3.5.2,	9.2.2.2, 12.4.8, Table 12.10

ACCEPTED VERSION SUBJECT TO FINAL EDITING

Panel I)

	Region	INDIAN	INDIAN	INDIAN
	Region type (Land / Ocean)	Ocean	Ocean	Ocean
	Sub-Region Name	Bay-of-Bengal	Bay-of-Bengal	Bay-of-Bengal
	Accronym	BOB	BOB	BOB
	Data Type	Observational	Detection & Attribution	Projections
Open Oceans	Mean ocean temperature	2.3.3.1, 9.2.2.1, 12.4.8	3.5.1.2,	4.5.2.1,9.2.2.1, 12.4.8, Table 12.10
	Marine heatwave	BOX 9.2:, 12.4.8		BOX 9.2:, 12.4.8, Table 12.10
	Severe storm and waves	9.6.4.1,		9.6.4.2,
	Sea ice	, 12.4.8		, 12.4.8, Table 12.10
	Subsea permafrost	5.4.9.1.3,		5.4.9.1.3,
	Ocean acidity	2.3.3.5,5.3, 12.4.8		4.5.2.2,5.3, 12.4.8, Table 12.10
	Dissolved oxygen	2.3.3.6, 12.4.8		5.3.3.2, 12.4.8, Table 12.10
	Ocean salinity	2.3.3.2,9.2.2.2, 12.4.8	3.5.2,	9.2.2.2, 12.4.8, Table 12.10

Panel J)

	Region	INDIAN	INDIAN	INDIAN
	Region type (Land / Ocean)	Ocean	Ocean	Ocean
	Sub-Region Name	Equatorial.Indic-Ocean	Equatorial.Indic-Ocean	Equatorial.Indic-Ocean
	Accronym	EIO	EIO	EIO
	Data Type	Observational	Detection & Attribution	Projections
Open Oceans	Mean ocean temperature	2.3.3.1, 9.2.2.1, 12.4.8	3.5.1.2,	4.5.2.1,9.2.2.1, 12.4.8, Table 12.10
	Marine heatwave	BOX 9.2:, 12.4.8		BOX 9.2:, 12.4.8, Table 12.10
	Severe storm and waves	9.6.4.1,		9.6.4.2,
	Sea ice	, 12.4.8		, 12.4.8, Table 12.10
	Subsea permafrost	5.4.9.1.3,		5.4.9.1.3,
	Ocean acidity	2.3.3.5,5.3, 12.4.8		4.5.2.2,5.3, 12.4.8, Table 12.10
	Dissolved oxygen	2.3.3.6, 12.4.8		5.3.3.2, 12.4.8, Table 12.10
	Ocean salinity	2.3.3.2,9.2.2.2, 12.4.8	3.5.2,	9.2.2.2, 12.4.8, Table 12.10

Panel K)

	Region	INDIAN	INDIAN	INDIAN
	Region type (Land / Ocean)	Ocean	Ocean	Ocean
	Sub-Region Name	S.Indic-Ocean	S.Indic-Ocean	S.Indic-Ocean
	Accronym	SIO	SIO	SIO
	Data Type	Observational	Detection & Attribution	Projections
Open Oceans	Mean ocean temperature	2.3.3.1, 9.2.2.1, 12.4.8	3.5.1.1,	4.5.2.1,9.2.2.1, 12.4.8, Table 12.10
	Marine heatwave	BOX 9.2:, 12.4.8		BOX 9.2:, 12.4.8, Table 12.10
	Severe storm and waves	9.6.4.1,		9.6.4.2,
	Sea ice	, 12.4.8		, 12.4.8, Table 12.10
	Subsea permafrost	5.4.9.1.3,		5.4.9.1.3,
	Ocean acidity	2.3.3.5,5.3, 12.4.8		4.5.2.2,5.3, 12.4.8, Table 12.10
	Dissolved oxygen	2.3.3.6, 12.4.8		5.3.3.2, 12.4.8, Table 12.10
	Ocean salinity	2.3.3.2,9.2.2.2, 12.4.8	3.5.2,	9.2.2.2, 12.4.8, Table 12.10

ACCEPTED VERSION SUBJECT TO FINAL EDITING

Panel L)

	Region	SOUTHERN	SOUTHERN	SOUTHERN
	Region type (Land / Ocean)	Ocean	Ocean	Ocean
	Sub-Region Name	Southern-Ocean	Southern-Ocean	Southern-Ocean
	Accronym	SOO	SOO	SOO
	Data Type	Observational	Detection & Attribution	Projections
Open Oceans	**Mean ocean temperature**	2.3.3.1, 9.2.2.1, 12.4.8	3.5.1.1,	4.5.2.1,9.2.2.1, 12.4.8, Table 12.10
	Marine heatwave	BOX 9.2:, 12.4.8		BOX 9.2:, 12.4.8, Table 12.10
	Severe storm and waves	9.6.4.1,		9.6.4.2,
	Sea ice	2.3.2.1.2, 9.3.2, 2.3.2.1.2, 9.3.2, 12.4.8, 12.4.9	3.4.1.2,	9.3.2, 9.3.2, 12.4.8, 12.4.9, Table 12.10
	Subsea permafrost	5.4.9.1.3,		5.4.9.1.3,
	Ocean acidity	2.3.3.5,5.3, 12.4.8		4.5.2.2,5.3, 12.4.8, Table 12.10
	Dissolved oxygen	2.3.3.6, 12.4.8		5.3.3.2, 12.4.8, Table 12.10
	Ocean salinity	2.3.3.2,9.2.2.2, 12.4.8	3.5.2,	9.2.2.2, 12.4.8, Table 12.10

[END TABLE 10.SM.10 HERE]

ACCEPTED VERSION
SUBJECT TO FINAL EDITING

10.SM.2 Data Table

[START TABLE 10.SM.11 HERE]

Table 10.SM.11: Input Data Table. Input datasets and code used to create chapter figures.

Figure number	Dataset / Code name	Type	Filename / Specificities	License type	Dataset / Code citation	Dataset / Code URL	Related publications / Software used	Notes
Figure 10.6	Figure 10.6 Code	Code	recipe_boxplot_Med.yml			https://github.com/ESMValGroup/ESMValTool-AR6/tree/ar6_chapter_10/esmvaltool/recipes/ar6_wgi_ch10/		Requires working_cordex_2.2 ESMValCore branch
Figure 10.6	Figure 10.6 Code	Code	diagnostic_IPCC_AR6_CH10.py , ar6_wgi_ch10.mplstyle , colormaps/ directory			https://github.com/ESMValGroup/ESMValTool-AR6/tree/ar6_chapter_10/esmvaltool/diag_scripts/ar6_wgi_ch10		Requires working_cordex_2.2 ESMValCore branch
Figure 10.6	Figure 10.6 Code	Code				https://github.com/ESMValGroup/ESMValCore/tree/working_cordex_2.2		
Figure 10.6 (a)	Berkeley Earth	Input	Land_and_Ocean_LatLong1.nc			http://berkeleyearth.lbl.gov/auto/Global/Gridded/Land_and_Ocean_LatLong1.nc	(Rohde et al., 2013)	land_source_history = "13-Jan-2020 17:22:52", ocean_source_history = "07-Jan-2020 10:46:06"
Figure 10.6 (a)	CRU TS v4.04	Input	cru_ts4.04.1901.2019.	Open Governm		https://crudata.uea.ac.uk/cru/data/hrg/cru_ts_4.04/cruts.2004151855.v4.04/	(Harris et al., 2020)	

ACCEPTED VERSION SUBJECT TO FINAL EDITING

			tmp.dat.nc	ent Licence http://www.nationalarchives.gov.uk/doc/open-government-licence/version/3/		tmp/cru_ts4.04.1901.2019.tmp.dat.nc.gz		
Figure 10.6 (a)	HadCRUT4	Input	HadCRUT.4.6.0.0.median.nc	Open Government Licence http://www.nationalarchives.gov.uk/doc/open-government-licence/version/3/		https://crudata.uea.ac.uk/cru/data/temperature/HadCRUT.4.6.0.0.median.nc	(Morice et al., 2012)	
Figure 10.6 (a)	HadCRUT5	Input	HadCRUT.5.0.0.0.anomalies.ensemble_mean.nc and absolute_v5.nc	Open Government Licence http://www.nationalarchives.gov.uk/doc/open-government-licence/v		https://crudata.uea.ac.uk/cru/data/temperature/HadCRUT.5.0.0.0.anomalies.ensemble_mean.nc	(Morice et al., 2021)	Absolute values build by adding the anomaly https://crudata.uea.ac.uk/cru/data/temperature/absolute_v5.nc

ACCEPTED VERSION SUBJECT TO FINAL EDITING

				ersion/3/				
Figure 10.6 (a)	E-OBS 0.1°	Input	tg_ens_mean_0.1deg_reg_v21.0e.nc			https://knmi-ecad-assets-prd.s3.amazonaws.com/ensembles/data/Grid_0.1deg_reg_ensemble/tg_ens_mean_0.1deg_reg_v21.0e.nc	(Cornes et al., 2018)	
Figure 10.6 (a)	E-OBS 0.25°	Input	tg_ens_mean_0.25deg_reg_v21.0e.nc			https://knmi-ecad-assets-prd.s3.amazonaws.com/ensembles/data/Grid_0.25deg_reg_ensemble/tg_ens_mean_0.25deg_reg_v21.0e.nc	(Cornes et al., 2018)	
Figure 10.6 (a)	WFDE5 v1.0	Input	Tair_WFDE5_CRU_[197901-201812]_v1.0.nc	The dataset is distributed under the Licence to Use Copernicus Products. The corrections applied are based upon CRU TS4.03, distributed under the Open Database License (OdbL)	https://doi.org/10.24381/cds.20d54e34	https://cds.climate.copernicus.eu/cdsapp#!/dataset/derived-near-surface-meteorological-variables?tab=overview	(Cucchi et al., 2020)	
Figure 10.6 (a)	ERA5	Input	tas_Amon_reanalysis_ERA5_197901-201912.nc			https://esgf.nccs.nasa.gov/thredds/fileServer/CREATE-IP/reanalysis/ECMWF/IFS-Cy41r2/ERA5/mon/atmos/tas/tas_Amon_reanalysis_ERA5_197901-201912.nc	(Hersbach et al., 2020)	tracking_id = "face81a8-3ecc-4a72-b1af-a1a430405c7b"

ACCEPTED VERSION SUBJECT TO FINAL EDITING

Figure 10.6 (a)	ERA-Interim	Input	tas_Amon_reanalysis_ERA-Interim_197901-201908.nc	CC BY-SA 4.0		https://esgf.nccs.nasa.gov/thredds/fileServer/CREATE-IP/reanalysis/ECMWF/IFS-Cy31r2/ERA-Interim/mon/atmos/tas/tas_Amon_reanalysis_ERA-Interim_197901-201908.nc	(Dee et al., 2011)	tracking_id = "0a105dae-21fd-4f6e-b8e9-0a0fada689d1"
Figure 10.6 (a)	CERA-20C	Input	tas_Amon_reanalysis_CERA-20C_190101-201012.nc			https://esgf.nccs.nasa.gov/thredds/fileServer/CREATE-IP/reanalysis/ECMWF/IFS-Cy41r2/CERA-20C/mon/atmos/tas/tas_Amon_reanalysis_CERA-20C_190101-201012.nc	(Laloyaux et al., 2018)	tracking_id = "22f6cece-ad07-4444-a07d-7a91f12b1b6e"
Figure 10.6 (a)	JRA-25	Input	tas_Amon_reanalysis_JRA-25_197901-201312.nc			https://esgf.nccs.nasa.gov/thredds/fileServer/CREATE-IP/reanalysis/JMA/JRA-25/JRA-25/mon/atmos/tas/tas_Amon_reanalysis_JRA-25_197901-201312.nc	(ONOGI et al., 2007)	tracking_id = "98441bb9-1b0f-4919-b6ee-fea8f886dd14"
Figure 10.6 (a)	JRA-55	Input	tas_Amon_reanalysis_JRA-55_195801-201912.nc	CC BY-SA 4.0		https://esgf.nccs.nasa.gov/thredds/fileServer/CREATE-IP/reanalysis/JMA/JRA-55/JRA-55/mon/atmos/tas/tas_Amon_reanalysis_JRA-55_195801-201912.nc	(Kobayashi et al., 2015)	tracking_id = "9e276e16-79d7-46e5-a3da-39ecf1c2a871"
Figure 10.6 (a)	CFSR	Input	tas_Amon_reanalysis_CFSR_197901-201912.nc			https://esgf.nccs.nasa.gov/thredds/fileServer/CREATE-IP/reanalysis/NOAA-NCEP/CFSR/CFSR/mon/atmos/tas/tas_Amon_reanalysis_CFSR_197901-201912.nc	(Saha et al., 2010)	tracking_id = "4ff071f5-37b4-4414-9ba1-d2eab7e24d0f"
Figure 10.6 (a)	MERRA	Input	tas_Amon_reanalysis_MERRA_197901-201602.nc			https://esgf.nccs.nasa.gov/thredds/fileServer/CREATE-IP/reanalysis/NASA-GMAO/GEOS-5/MERRA/mon/atmos/tas/tas_Amon_reanalysis_MERRA_197901-201602.nc	(Rienecker et al., 2011)	tracking_id = "d742c24b-6ed0-41d0-a02a-dd7039f245b2"
Figure 10.6 (a)	MERRA2	Input	tas_Amon_reanalysis_MERRA2_198001-			https://esgf.nccs.nasa.gov/thredds/fileServer/CREATE-IP/reanalysis/NASA-GMAO/GEOS-5/MERRA2/mon/atmos/tas/tas_Amo	(Gelaro et al., 2017)	tracking_id = "e77fd4de-19c2-45ad-afe2-

ACCEPTED VERSION SUBJECT TO FINAL EDITING

			201912.nc			n_reanalysis_MERRA2_198001-201912.nc		ce3f6c1eb148"
Figure 10.6 (b)	CRU TS v4.04	Input	cru_ts4.04.1901.2019.pre.dat.nc	Open Government Licence http://www.nationalarchives.gov.uk/doc/open-government-licence/version/3/		https://crudata.uea.ac.uk/cru/data/hrg/cru_ts_4.04/cruts.2004151855.v4.04/pre/cru_ts4.04.1901.2019.pre.dat.nc.gz	(Harris et al., 2020)	Precipitation is conditioned on stn (nc file variable, number of stations contributing to each datum) being at least 1. Seasonal statistics requires 2 out of 3 seasons to be valid. Climate statistics requires 80% of data to be valid.
Figure 10.6 (b)	GPCC V2018 1.0°	Input	full_data_monthly_v2018_10.nc.gz	may be used without any restrictions provided that the source is acknowledged https://www.dwd.de/EN/service/copyright/copyright_	doi: 10.5676/DWD_GPCC/FD_M_V2018_100	https://opendata.dwd.de/climate_environment/GPCC/full_data_2018/full_data_monthly_v2018_10.nc.gz	(Schneider et al., 2018)	Precipitation is conditioned on numgauge (nc file variable, gauges per gridcell) being at least 1. Seasonal statistics requires 2 out of 3 seasons to be valid.

ACCEPTED VERSION SUBJECT TO FINAL EDITING

				node.html				
Figure 10.6 (b)	REGEN	Input	REGEN_AllStns_V1-2019_[1950 … 2016].nc and REGEN_AllStns_V1-2019_1950-2016_QualityMask.nc			http://dapds00.nci.org.au/thredds/fileServer/ks32/CLEX_Data/REGEN_AllStns/v1-2019/REGEN_AllStns_V1-2019_[1950 … 2016].nc	(Contractor et al., 2020)	Precipitation data is conditioned on the Quality Mask. Seasonal statistics requires 2 out of 3 seasons to be valid.
Figure 10.6 (b)	E-OBS 0.1°	Input	rr_ens_mean_0.1deg_reg_v21.0e.nc			https://knmi-ecad-assets-prd.s3.amazonaws.com/ensembles/data/Grid_0.1deg_reg_ensemble/rr_ens_mean_0.1deg_reg_v21.0e.nc	(Cornes et al., 2018)	
Figure 10.6 (b)	E-OBS 0.25°	Input	rr_ens_mean_0.25deg_reg_v21.0e.nc			https://knmi-ecad-assets-prd.s3.amazonaws.com/ensembles/data/Grid_0.25deg_reg_ensemble/rr_ens_mean_0.25deg_reg_v21.0e.nc	(Cornes et al., 2018)	
Figure 10.6 (b)	GHCN V2	Input	precip.mon.total.nc			ftp://ftp.cdc.noaa.gov/Datasets/ghcngridded/precip.mon.total.nc	(Jones and Moberg, 2003)	
Figure 10.6 (b)	WFDE5 v1.0	Input	Rainf_WFDE5_CRU+GPCC_[197901-201612]_v1.0.nc	The dataset is distributed under the Licence to Use Copernicus Products. The corrections applied are based	https://doi.org/10.24381/cds.20d54e34	https://cds.climate.copernicus.eu/cdsapp#!/dataset/derived-near-surface-meteorological-variables?tab=overview	(Cucchi et al., 2020)	

ACCEPTED VERSION SUBJECT TO FINAL EDITING

				upon CRU TS4.03, distributed under the Open Database License (OdbL)				
Figure 10.6 (b)	CFSR	Input	pr_Amon_reanalysis_CFSR_197901-201912.nc			https://esgf.nccs.nasa.gov/thredds/fileServer/CREATE-IP/reanalysis/NOAA-NCEP/CFSR/CFSR/mon/atmos/pr/pr_Amon_reanalysis_CFSR_197901-201912.nc	(Saha et al., 2010)	tracking_id = "db487707-b207-4649-ac4b-3ed9942b869b"
Figure 10.6 (b)	ERA-Interim	Input	pr_Amon_reanalysis_ERA-Interim_197901-201908.nc	CC BY-SA 4.0		https://esgf.nccs.nasa.gov/thredds/fileServer/CREATE-IP/reanalysis/ECMWF/IFS-Cy31r2/ERA-Interim/mon/atmos/pr/pr_Amon_reanalysis_ERA-Interim_197901-201908.nc	(Dee et al., 2011)	tracking_id = "6d7345ee-46d9-460d-b367-7a91644196a9"
Figure 10.6 (b)	ERA5	Input	pr_Amon_reanalysis_ERA5_197901-201912.nc			https://esgf.nccs.nasa.gov/thredds/fileServer/CREATE-IP/reanalysis/ECMWF/IFS-Cy41r2/ERA5/mon/atmos/pr/pr_Amon_reanalysis_ERA5_197901-201912.nc	(Hersbach et al., 2020)	tracking_id = "54f6aaa0-00f1-468e-9d1d-f25b04bb9fb3"
Figure 10.6 (b)	JRA-55	Input	pr_Amon_reanalysis_JRA-55_195801-201912.nc	CC BY-SA 4.0		https://esgf.nccs.nasa.gov/thredds/fileServer/CREATE-IP/reanalysis/JMA/JRA-55/JRA-55/mon/atmos/pr/pr_Amon_reanalysis_JRA-55_195801-201912.nc	(Kobayashi et al., 2015)	tracking_id = "d5394ca7-e30d-4724-8569-e56293cebfaf"
Figure 10.6 (b)	MERRA	Input	pr_Amon_reanalysis_MERRA_197901-201602.nc			https://esgf.nccs.nasa.gov/thredds/fileServer/CREATE-IP/reanalysis/NASA-GMAO/GEOS-5/MERRA/mon/atmos/pr/pr_Amon_reanalysis_MERRA_197901-201602.nc	(Rienecker et al., 2011)	tracking_id = "eca6f8ec-36af-4a15-a5ed-606531c7c686"

ACCEPTED VERSION SUBJECT TO FINAL EDITING

Figure 10.6 (b)	MERRA2	Input	pr_Amon_reanalysis_MERRA2_198001-201912.nc			https://esgf.nccs.nasa.gov/thredds/fileServer/CREATE-IP/reanalysis/NASA-GMAO/GEOS-5/MERRA2/mon/atmos/pr/pr_Amon_reanalysis_MERRA2_198001-201912.nc	(Gelaro et al., 2017)	tracking_id = "d204afb4-0503-47ee-9935-eb0d75dc31ac"
Figure 10.7	Figure 10.7 Code	Code						
Figure 10.7	ERA-Interim	Input	Daily data, Geopotential at 500hPa			https://apps.ecmwf.int/datasets/data/interim-full-daily/levtype=pl/	(Dee et al., 2011)	concatenated with ERA-40 (ERA-40: 1962–78, ERA-Interim: 1979–2011, see Schiemann et al., (2017)
Figure 10.7	ERA-40	Input	Daily data, Geopotential at 500hPa			https://apps.ecmwf.int/datasets/data/era40-daily/levtype=pl/	(Uppala et al., 2006)	concatenated with ERA-Interim (ERA-40: 1962–78, ERA-Interim: 1979–2011, see Schiemann et al. (2017)
Figure 10.8 (a)	GSMaP	Input				ftp://mtsat.cr.chiba-u.ac.jp/MTSAT-2/gridded_V2.0/quicklooks/201311/MTSAT2-145E-201311070357UTC-VIS.jpg	(Kubota et al., 2020)	(a) MTSAT-2 Visible Data (Haiyan match-up) (gridded), Nov 07, 2013 04:30 (UTC)
Figure 10.8 (b)	PAGASA	Input						(b) Guiuan radar, addapted from Takayabu et al. (2015)
Figure 10.8 (c)	Meso-ensemble forecast (60	Input	Member of WEPS (Weekly			https://apps.ecmwf.int/datasets/data/tigge/levtype=sfc/type=cf/	(Swinbank et al., 2016)	(c) meso-ensemble forecast (60

ACCEPTED VERSION SUBJECT TO FINAL EDITING

	km)		Ensemble Prediction System) operationally driven by JMA (Japan Meteorological Agency). Data is uploaded as a member of TIGGE (THORPEX Interactive Grand Global Ensemble).					km)
Figure 10.8 (d)	NHRCM (20 km)	Input						(d) NHRCM (20 km) model, addapted from Takayabu et al. (2015)
Figure 10.8 (e)	NHRCM (5 km)	Input						(e) NHRCM (5 km) model, Addapted from Takayabu et al. (2015)
Figure 10.8 (f)	WRF (1 km)	Input						(f) WRF (1 km) model, Addapted from Takayabu et al. (2015)
Figure 10.9	Figure 10.9 Code	Code	recipe_CoppolaAlps.			https://github.com/ESMValGroup/ESMValTool-		Requires working_corde

ACCEPTED VERSION
SUBJECT TO FINAL EDITING

			yml			AR6/tree/ar6_chapter_10/esmvaltool/recipes/ar6_wgi_ch10		x_2.2 ESMValCore branch
Figure 10.9	Figure 10.9 Code	Code	diagnostic_IPCC_AR6_CH10.py , ar6_wgi_ch10.mplstyle , colormaps/ directory and CH10_additional_data/ECoppola_Alps directory			https://github.com/ESMValGroup/ESMValTool-AR6/tree/ar6_chapter_10/esmvaltool/diag_scripts/ar6_wgi_ch10		Requires working_cordex_2.2 ESMValCore branch
Figure 10.9	Figure 10.9 Code	Code				https://github.com/ESMValGroup/ESMValCore/tree/working_cordex_2.2		
Figure 10.9 (a)	4 GCM mean (CMIP5) precipitation change	Input	GCM.nc			https://github.com/ESMValGroup/ESMValTool-AR6/tree/ar6_chapter_10/esmvaltool/diag_scripts/ar6_wgi_ch10/CH10_additional_data/ECoppola_Alps/GCM.nc	GCM data from from Giorgi et al. (2016)	
Figure 10.9 (b)	6 RCM mean precipitation change	Input	RCM.nc			https://github.com/ESMValGroup/ESMValTool-AR6/tree/ar6_chapter_10/esmvaltool/diag_scripts/ar6_wgi_ch10/CH10_additional_data/ECoppola_Alps/RCM.nc	RCM data from from Giorgi et al. (2016)	
Figure 10.10	Figure 10.10 Code	Code	recipe_Douglas_SES_DJF.yml			https://github.com/ESMValGroup/ESMValTool-AR6/tree/ar6_chapter_10/esmvaltool/recipes/ar6_wgi_ch10		Requires working_cordex_2.2 ESMValCore branch
Figure 10.10	Figure 10.10 Code	Code	diagnostic_IPCC_A			https://github.com/ESMValGroup/ESMValTool-		Requires working_corde

ACCEPTED VERSION SUBJECT TO FINAL EDITING

			R6_CH10.py , ar6_wgi_ch10.mplstyle , colormaps/ directory and CH10_additional_data/Atlas_regions directory			AR6/tree/ar6_chapter_10/esmvaltool/diag_scripts/ar6_wgi_ch10		x_2.2 ESMValCore branch
Figure 10.10	Figure 10.10 Code	Code				https://github.com/ESMValGroup/ESMValCore/tree/working_cordex_2.2		
Figure 10.10 (b)	CRU TS v4.04	Input	cru_ts4.04.1901.2019.pre.dat.nc	Open Government Licence http://www.nationalarchives.gov.uk/doc/open-government-licence/version/3/		https://crudata.uea.ac.uk/cru/data/hrg/cru_ts_4.04/cruts.2004151855.v4.04/pre/cru_ts4.04.1901.2019.pre.dat.nc.gz	(Harris et al., 2020)	Precipitation is conditioned on stn (nc file variable, number of stations contributing to each datum) being at least 1. Seasonal statistics requires 2 out of 3 seasons to be valid.
Figure 10.10 (b)	GPCC V2018 2.5°	Input	full_data_monthly_v2018_25.nc.gz	may be used without any restrictions provided that the source is	doi: 10.5676/DWD_GPCC/FD_M_V2018_250	https://opendata.dwd.de/climate_environment/GPCC/full_data_2018/full_data_monthly_v2018_25.nc.gz	(Schneider et al., 2018)	Precipitation is conditioned on numgauge (nc file variable, gauges per gridcell) being at least 1. Seasonal statistics

ACCEPTED VERSION SUBJECT TO FINAL EDITING

				acknowledged https://www.dwd.de/EN/service/copyright/copyright_node.html				requires 2 out of 3 seasons to be valid.
Figure 10.10	MPI-ESM metadata	Input				DM: Home/03 - Drafts/25 - FGD/Data Tables/Chapter 10/Model metadata files/Fig10-10_md_MPI-GE.csv		
CCB 10.2 Figure 1	reprint						Addapted from Maraun et al. (2017)	
Figure 10.11	Figure 10.11 Code	Code	recipe_Sahel.yml			https://github.com/ESMValGroup/ESMValTool-AR6/tree/ar6_chapter_10/esmvaltool/recipes/ar6_wgi_ch10		Requires working_cordex_2.2 ESMValCore branch
Figure 10.11	Figure 10.11 Code	Code	diagnostic_IPCC_AR6_CH10.py , ar6_wgi_ch10.mplstyle , colormaps/ directory and CH10_additional_data/ATurner_Aerosols directory			https://github.com/ESMValGroup/ESMValTool-AR6/tree/ar6_chapter_10/esmvaltool/diag_scripts/ar6_wgi_ch10		Requires working_cordex_2.2 ESMValCore branch
Figure 10.11	Figure 10.11 Code	Code				https://github.com/ESMValGroup/ESMValCore/tree/working_cordex_2.2		
Figure	CRU TS	Input	cru_ts4.04.	Open		https://crudata.uea.ac.uk/cru/data/hrg/	(Harris et al., 2020)	Precipitation is

ACCEPTED VERSION SUBJECT TO FINAL EDITING

10.11 (a) (b) (e)	v4.04		1901.2019.pre.dat.nc	Government Licence http://www.nationalarchives.gov.uk/doc/open-government-licence/version/3/		cru_ts_4.04/cruts.2004151855.v4.04/pre/cru_ts4.04.1901.2019.pre.dat.nc.gz		conditioned on stn (nc file variable, number of stations contributing to each datum) being at least 1. Seasonal statistics requires 3 out of 4 seasons to be valid. Climate statistics requires 80% of data to be valid. Area statistics requires 80% of data to be valid. Trend calculations required at least 8 out of 10 years to be valid.
Figure 10.11 (e)	GPCC V2018 2.5°	Input	full_data_monthly_v2018_25.nc.gz	may be used without any restrictions provided that the source is acknowle	doi: 10.5676/DWD_GPCC/FD_M_V2018_250	https://opendata.dwd.de/climate_environment/GPCC/full_data_2018/full_data_monthly_v2018_25.nc.gz	(Schneider et al., 2018)	Precipitation is conditioned on numgauge (nc file variable, gauges per gridcell) being at least 1. Seasonal statistics requires 3 out

ACCEPTED VERSION SUBJECT TO FINAL EDITING

				dged https://www.dwd.de/EN/service/copyright/copyright_node.html				of 4 seasons to be valid. Climate statistics requires 80% of data to be valid. Area statistics requires 50% of data to be valid. Trend calculations required at least 7 out of 10 years to be valid.
Figure 10.11 (e)	CSIRO-Mk3-6-0	Input	pr_Amon_CSIRO-Mk3-6-0_historical_rcp85_r[1..30]i1p1_185001-210012.nc			https://www.earthsystemgrid.org/dataset/ucar.cgd.ccsm4.CLIVAR_LE.csiro_mk36_lens_new.atm.proc.monthly_ave.pr.html	(Jeffrey et al., 2013)	
Figure 10.11 (e)	d4PDF	Input	pr_1951-2014_run[001..100].grd	https://www.miroc-gcm.jp/~pub/d4PDF/img/d4PDF_Data_Policy_En_20180820.pdf		https://climate.mri-jma.go.jp/pub/d4pdf/HPB_1951-2014/pr/pr_1951-2014_run[001..100].grd	(Mizuta et al., 2017)	
Figure 10.11 (c)	HadGEM3-GC3.1 0.2x aerosol	Input				https://github.com/ESMValGroup/ESMValTool-AR6/tree/ar6_chapter_10/esmvaltool/	Model papers are: doi:10.1002/2017MS001115 and doi:10.1029/2018MS001370	

ACCEPTED VERSION SUBJECT TO FINAL EDITING

	scaling					diag_scripts/ar6_wgi_ch10/CH10_additional_data/ATurner_Aerosols/SMURPHS_r[1…5]_0p2_outJJAS.nc	The scaling experiment is described in Shonk et al. (2020)	
Figure 10.12	Figure 10.12 Code	Code	recipe_SESA.yml			https://github.com/ESMValGroup/ESMValTool-AR6/tree/ar6_chapter_10/esmvaltool/recipes/ar6_wgi_ch10		Requires working_cordex_2.2 ESMValCore branch
Figure 10.12	Figure 10.12 Code	Code	diagnostic_IPCC_AR6_CH10.py , ar6_wgi_ch10.mplstyle and colormaps/ directory			https://github.com/ESMValGroup/ESMValTool-AR6/tree/ar6_chapter_10/esmvaltool/diag_scripts/ar6_wgi_ch10		Requires working_cordex_2.2 ESMValCore branch
Figure 10.12	Figure 10.12 Code	Code				https://github.com/ESMValGroup/ESMValCore/tree/working_cordex_2.2		
Figure 10.12 (b) (c) (d)	CRU TS v4.04	Input	cru_ts4.04.1901.2019.pre.dat.nc	Open Government Licence http://www.nationalarchives.gov.uk/doc/open-government-licence/version/3/		https://crudata.uea.ac.uk/cru/data/hrg/cru_ts_4.04/cruts.2004151855.v4.04/pre/cru_ts4.04.1901.2019.pre.dat.nc.gz	(Harris et al., 2020)	Precipitation is conditioned on stn (nc file variable, number of stations contributing to each datum) being at least 1. Seasonal statistics requires 2 out of 3 seasons to be valid. Area statistics requires 70% of data to be valid. Trend

ACCEPTED VERSION SUBJECT TO FINAL EDITING

								calculations required at least 8 out of 10 years to be valid.
Figure 10.12 (c) (d)	GPCC V2018 2.5°	Input	full_data_monthly_v2018_25.nc.gz	May be used without any restrictions provided that the source is acknowledged https://www.dwd.de/EN/service/copyright/copyright_node.html	doi: 10.5676/DWD_GPCC/FD_M_V2018_250	https://opendata.dwd.de/climate_environment/GPCC/full_data_2018/full_data_monthly_v2018_25.nc.gz	(Schneider et al., 2018)	Precipitation is conditioned on numgauge (nc file variable, gauges per gridcell) being at least 1. Seasonal statistics requires 2 out of 3 seasons to be valid. Area statistics requires 70% of data to be valid. Trend calculations required at least 8 out of 10 years to be valid.
Figure 10.12 (d)	CSIRO-Mk3-6-0	Input	pr_Amon_CSIRO-Mk3-6-0_historical_rcp85_r[1..30]i1p1_185001-210012.nc			https://www.earthsystemgrid.org/dataset/ucar.cgd.ccsm4.CLIVAR_LE.csiro_mk36_lens_new.atm.proc.monthly_ave.pr.html	(Jeffrey et al., 2013)	
Figure 10.12 (d)	d4PDF	Input	pr_1951-2014_run[001..100].grd	https://www.miroc-gcm.jp/~		https://climate.mri-jma.go.jp/pub/d4pdf/HPB_1951-2014/pr/pr_1951-2014_run[001..100].grd	(Mizuta et al., 2017)	

ACCEPTED VERSION SUBJECT TO FINAL EDITING

				pub/d4PDF/img/d4PDF_Data_Policy_En_20180820.pdf				
Figure 10.13	Figure 10.13 Code	Code	recipe_NAM.yml			https://github.com/ESMValGroup/ESMValTool-AR6/tree/ar6_chapter_10/esmvaltool/recipes/ar6_wgi_ch10		Requires working_cordex_2.2 ESMValCore branch
Figure 10.13	Figure 10.13 Code	Code	diagnostic_IPCC_AR6_CH10.py , ar6_wgi_ch10.mplstyle , and colormaps/ directory			https://github.com/ESMValGroup/ESMValTool-AR6/tree/ar6_chapter_10/esmvaltool/diag_scripts/ar6_wgi_ch10		Requires working_cordex_2.2 ESMValCore branch
Figure 10.13	Figure 10.13 Code	Code				https://github.com/ESMValGroup/ESMValCore/tree/working_cordex_2.2		
Figure 10.13 (a) (b) (c)	CRU TS v4.04	Input	cru_ts4.04.1901.2019.pre.dat.nc	Open Government Licence http://www.nationalarchives.gov.uk/doc/open-government-licence/version/3/		https://crudata.uea.ac.uk/cru/data/hrg/cru_ts_4.04/cruts.2004151855.v4.04/pre/cru_ts4.04.1901.2019.pre.dat.nc.gz	(Harris et al., 2020)	Precipitation is conditioned on stn (nc file variable, number of stations contributing to each datum) being at least 1. Annual statistics requires 10 out of 12 months to be valid. Trend

ACCEPTED VERSION SUBJECT TO FINAL EDITING

								calculations required at least 8 out of 10 years to be valid.
Figure 10.13 (a) (c)	GPCC V2018 1.0°	Input	full_data_monthly_v2018_10.nc.gz	may be used without any restrictions provided that the source is acknowledged https://www.dwd.de/EN/service/copyright/copyright_node.html	doi: 10.5676/DWD_GPCC/FD_M_V2018_100	https://opendata.dwd.de/climate_environment/GPCC/full_data_2018/full_data_monthly_v2018_10.nc.gz	(Schneider et al., 2018)	Precipitation is conditioned on numgauge (nc file variable, gauges per gridcell) being at least 1. Annual statistics requires 10 out of 12 months to be valid. Trend calculations required at least 6 out of 10 years to be valid.
Figure 10.13 (a) (c)	REGEN	Input	REGEN_AllStns_V1-2019_[1950 … 2016].nc and REGEN_AllStns_V1-2019_1950-2016_QualityMask.nc			http://dapds00.nci.org.au/thredds/fileServer/ks32/CLEX_Data/REGEN_AllStns/v1-2019/REGEN_AllStns_V1-2019_[1950 … 2016].nc	(Contractor et al., 2020)	Precipitation data is conditioned on the Quality Mask. Annual statistics requires 10 out of 12 months to be valid. Trend calculations required at least 8 out of 10 years to be

ACCEPTED VERSION SUBJECT TO FINAL EDITING

								valid.
Figure 10.13 (a) (c)	GPCP v2.3	Input	precip.mon.mean.nc			https://www.esrl.noaa.gov/psd/data/gridded/data.gpcp.html	(Huffman et al., 2009)	
Figure 10.13 (c)	CSIRO-Mk3-6-0	Input	pr_Amon_CSIRO-Mk3-6-0_historical_rcp85_r[1..30]i1p1_185001-210012.nc			https://www.earthsystemgrid.org/dataset/ucar.cgd.ccsm4.CLIVAR_LE.csiro_mk36_lens_new.atm.proc.monthly_ave.pr.html	(Jeffrey et al., 2013)	
Figure 10.13 (a), (c)	d4PDF	Input	pr_1951-2014_run[001..100].grd	https://www.miroc-gcm.jp/~pub/d4PDF/img/d4PDF_Data_Policy_En_20180820.pdf		https://climate.mri-jma.go.jp/pub/d4pdf/HPB_1951-2014/pr/pr_1951-2014_run[001..100].grd	(Mizuta et al., 2017)	
Figure 10.15 (b)	CSIRO-Mk3-6-0	Input	pr_Amon_CSIRO-Mk3-6-0_historical_rcp85_r[1..30]i1p1_185001-210012.nc			https://www.earthsystemgrid.org/dataset/ucar.cgd.ccsm4.CLIVAR_LE.csiro_mk36_lens_new.atm.proc.monthly_ave.pr.html	(Jeffrey et al., 2013)	
Figure 10.18	Figure 10.18 Code	Code	Cape-Town_case_study.py, ar6_wgi_ch10.mplstyle , colormaps/ directory and			https://github.com/ESMValGroup/ESMValTool-AR6/tree/ar6_chapter_10/esmvaltool/diag_scripts/ar6_wgi_ch10		Requires working_cordex_2.2 ESMValCore branch

ACCEPTED VERSION SUBJECT TO FINAL EDITING

			CH10_additional_data/Cape_Town directory					
Figure 10.18 (c) (d)	CRU TS v4.03	Input	cru_ts4.03.1901.2018.pre.dat.nc	Open Government Licence http://www.nationalarchives.gov.uk/doc/open-government-licence/version/3/		https://dap.ceda.ac.uk/badc/cru/data/cru_ts/cru_ts_4.03/data/pre/cru_ts4.03.1901.2018.pre.dat.nc.gz	(Harris et al., 2020)	
Figure 10.18 (c) (d)	GPCC V2018 0.5°	Input	full_data_monthly_v2018_25.nc.gz	may be used without any restrictions provided that the source is acknowledged https://www.dwd.de/EN/service/copyright/copyright_node.html	doi: 10.5676/DWD_GPCC/FD_M_V2018_050	https://opendata.dwd.de/climate_environment/GPCC/full_data_2018/full_data_monthly_v2018_05.nc.gz	(Schneider et al., 2018)	
Figure	Station data	Input	[NUWEB			Station data are, obtained directly		

ACCEPTED VERSION SUBJECT TO FINAL EDITING

10.18 (a) (b) (c) (d)			ERG, RUSTFONTEIN, TUSSENBEIDE, BOSKLOOF, ROBBEN_ISLAND, VRUGBAAR, BELLEVUE, RHEBOKSKRAAL, HOPEFIELD, DARLING_-_THE_TOWERS, TOUWSRIVIER, PIKETBERG-SAPD, ELANDSFONTEIN, MERTENHOF, REENEN, PUTS, VANRHYNSDORP, CALVINIA_BO-DOWNES, DE_HOOP, NUWERU			from SAWS, available upon request from climate@csag.uct.ac.za. Some station data that were used are available from: https://www.dws.gov.za/Hydrology/		

ACCEPTED VERSION SUBJECT TO FINAL EDITING

			S] stations					
Figure 10.18 (c) (d)	NCEP-NCAR	Input	slp.mon.mean.nc	CC BY-SA 4.0		ftp://ftp.cdc.noaa.gov/Datasets/ncep.reanalysis.derived/surface/slp.mon.mean.nc	(Kalnay et al., 1996)	
Figure 10.18 (c) (d)	ERA-20C	Input	Monthly mean sea level pressure from KNMI climate explorer			https://climexp.knmi.nl/selectfield_rea.cgi?id=someone@somewhere	(Poli et al., 2016)	
Figure 10.18 (c) (d)	20CR v3	Input	Monthly mean sea level pressure from KNMI climate explorer			https://climexp.knmi.nl/selectfield_rea.cgi?id=someone@somewhere	(Slivinski et al., 2019)	
Figure 10.18	8km CCAM metadata	Input	precipitation data				(Engelbrecht et al., 2011)	CSIR (the institution that generated data) does not provide access to these data.
Figure 10.19	Figure 10.19 Code	Code	recipe_IndianMonsoon.yml			https://github.com/ESMValGroup/ESMValTool-AR6/tree/ar6_chapter_10/esmvaltool/recipes/ar6_wgi_ch10		Requires working_cordex_2.2 ESMValCore branch
Figure 10.19	Figure 10.19 Code	Code	diagnostic_IPCC_AR6_CH10.py , ar6_wgi_ch10.mplstyle , colormaps/			https://github.com/ESMValGroup/ESMValTool-AR6/tree/ar6_chapter_10/esmvaltool/diag_scripts/ar6_wgi_ch10		Requires working_cordex_2.2 ESMValCore branch

ACCEPTED VERSION SUBJECT TO FINAL EDITING

			directory , CH10_additional_data/ATurner_SouthAsia directory and CH10_additional_data/Atlas_regions directory					
Figure 10.19	Figure 10.19 Code	Code				https://github.com/ESMValGroup/ESMValCore/tree/working_cordex_2.2		
Figure 10.19 (b) (c) (d) (e)	CRU TS v4.04	Input	cru_ts4.04.1901.2019.pre.dat.nc	Open Government Licence http://www.nationalarchives.gov.uk/doc/open-government-licence/version/3/		https://crudata.uea.ac.uk/cru/data/hrg/cru_ts_4.04/cruts.2004151855.v4.04/pre/cru_ts4.04.1901.2019.pre.dat.nc.gz	(Harris et al., 2020)	Precipitation is conditioned on stn (nc file variable, number of stations contributing to each datum) being at least 1. Seasonal statistics requires 3 out of 4 seasons to be valid. Climate statistics requires 80% of data to be valid. Area statistics requires 80% of data to be valid. Trend

ACCEPTED VERSION SUBJECT TO FINAL EDITING

								calculations required at least 8 out of 10 years to be valid.
Figure 10.19 (d) (e)	GPCC V2018 2.5°	Input	full_data_monthly_v2018_25.nc.gz	may be used without any restrictions provided that the source is acknowledged https://www.dwd.de/EN/service/copyright/copyright_node.html	doi: 10.5676/DWD_GPCC/FD_M_V2018_250	https://opendata.dwd.de/climate_environment/GPCC/full_data_2018/full_data_monthly_v2018_25.nc.gz	(Schneider et al., 2018)	Precipitation is conditioned on numgauge (nc file variable, gauges per gridcell) being at least 1. Seasonal statistics requires 3 out of 4 seasons to be valid. Area statistics requires 80% of data to be valid. Trend calculations required at least 8 out of 10 years to be valid.
Figure 10.19 (d) (e)	REGEN	Input	REGEN_AllStns_V1-2019_[1950 … 2016].nc and REGEN_AllStns_V1-2019_1950-2016_QualityMask.nc			http://dapds00.nci.org.au/thredds/fileServer/ks32/CLEX_Data/REGEN_AllStns/v1-2019/REGEN_AllStns_V1-2019_[1950 … 2016].nc	(Contractor et al., 2020)	Precipitation data is conditioned on the Quality Mask. Seasonal statistics requires 3 out of 4 seasons to be valid. Area statistics requires 80%

ACCEPTED VERSION SUBJECT TO FINAL EDITING

								of data to be valid. Trend calculations required at least 8 out of 10 years to be valid.
Figure 10.19 (a) (d) (e)	APHRO-MA V1101 0.5°	Input	APHRO_MA_050deg_V1101.1951-2007.nc.gz.tar			http://aphrodite.st.hirosaki-u.ac.jp/download/	(Yatagai et al., 2012)	Variables precip ((d) and (e))and rstn (a). Seasonal statistics requires 3 out of 4 seasons to be valid. Area statistics requires 80% of data to be valid. Trend calculations required at least 8 out of 10 years to be valid.
Figure 10.19 (d)	IITM	Input	iitm-regionrf_all_india.csv			ftp://www.tropmet.res.in/pub/data/rain/iitm-regionrf.txt	(Parthasarathy et al., 1994)	ALL-INDIA RAINFALL (1871-2016), 30 SUBDIVISIONS AREA, column JJAS
Figure 10.19 (e)	CSIRO-Mk3-6-0	Input	pr_Amon_CSIRO-Mk3-6-0_historical_rcp85_r[			https://www.earthsystemgrid.org/dataset/ucar.cgd.ccsm4.CLIVAR_LE.csiro_mk36_lens_new.atm.proc.monthly_ave.pr.html	(Jeffrey et al., 2013)	

ACCEPTED VERSION SUBJECT TO FINAL EDITING

			1..30]i1p1_185001-210012.nc					
Figure 10.19 (e)	d4PDF	Input	pr_1951-2014_run[001..100].grd	https://www.miroc-gcm.jp/~pub/d4PDF/img/d4PDF_Data_Policy_En_20180820.pdf		https://climate.mri-jma.go.jp/pub/d4pdf/HPB_1951-2014/pr/pr_1951-2014_run[001..100].grd	(Mizuta et al., 2017)	
Figure 10.20	Figure 10.20 Code	Code	recipe_Mediterranean.yml			https://github.com/ESMValGroup/ESMValTool-AR6/tree/ar6_chapter_10/esmvaltool/recipes/ar6_wgi_ch10		Requires working_cordex_2.2 ESMValCore branch
Figure 10.20	Figure 10.20 Code	Code	diagnostic_IPCC_AR6_CH10.py , ar6_wgi_ch10.mplstyle , colormaps/ directory, CH10_additional_data/Mediterranean_station_info directory and CH10_additional_data/GvdSchrier_pdfs			https://github.com/ESMValGroup/ESMValTool-AR6/tree/ar6_chapter_10/esmvaltool/diag_scripts/ar6_wgi_ch10		Requires working_cordex_2.2 ESMValCore branch

ACCEPTED VERSION SUBJECT TO FINAL EDITING

			directory					
Figure 10.20	Figure 10.20 Code	Code				https://github.com/ESMValGroup/ESMValCore/tree/working_cordex_2.2		
Figure 10.20 (b)	E-OBS station information tg	Input	stations_info_tg_v21.0e.txt			https://knmi-ecad-assets-prd.s3.amazonaws.com/ensembles/data/stations_info_tg_v21.0e.txt	(Cornes et al., 2018)	
Figure 10.20 (b)	Donat et al. 2014 station information	Input	As indicated in Table 1 of Donat et al. (2014)				(Donat et al., 2014)	
Figure 10.20 (c) (d) (e) (f) (g)	Berkeley Earth	Input	Land_and_Ocean_LatLong1.nc			http://berkeleyearth.lbl.gov/auto/Global/Gridded/Land_and_Ocean_LatLong1.nc	(Rohde et al., 2013)	land_source_history = "13-Jan-2020 17:22:52", ocean_source_history = "07-Jan-2020 10:46:06"
Figure 10.20 (e) (f)	CRU TS v4.04	Input	cru_ts4.04.1901.2019.tmp.dat.nc	Open Government Licence http://www.nationalarchives.gov.uk/doc/open-government-licence/version/3/		https://crudata.uea.ac.uk/cru/data/hrg/cru_ts_4.04/cruts.2004151855.v4.04/tmp/cru_ts4.04.1901.2019.tmp.dat.nc.gz	(Harris et al., 2020)	
Figure 10.20 (e) (f)	HadCRUT5	Input	HadCRUT.5.0.0.0.anomalies.ensemble_mean.nc and	Open Government Licence http://ww		https://crudata.uea.ac.uk/cru/data/temperature/HadCRUT.5.0.0.0.anomalies.ensemble_mean.nc	(Morice et al., 2021)	Absolute values build by adding the anomaly https://crudata.

ACCEPTED VERSION SUBJECT TO FINAL EDITING

			absolute_v5.nc	w.nationalarchives.gov.uk/doc/open-government-licence/version/3/				uea.ac.uk/cru/data/temperature/absolute_v5.nc
Figure 10.20 (c)	NOAA Global Temp v5	Input	NOAAGlobalTemp_v5.0.0_gridded_s188001_e202102_c20210308T133310.nc			https://www.ncei.noaa.gov/data/noaa-global-surface-temperature/v5/access/gridded/NOAAGlobalTemp_v5.0.0_gridded_s188001_e202102_c20210308T133310.nc	(Zhang et al., 2019)	
Figure 10.20 (c)	CRUTEM4	Input	CRUTEM.4.6.0.0.anomalies.nc	Open Government Licence http://www.nationalarchives.gov.uk/doc/open-government-licence/version/3/		https://crudata.uea.ac.uk/cru/data/temperature/CRUTEM.4.6.0.0.anomalies.nc	(Jones et al., 2012)	
Figure 10.20 (c)	GISTEMP version 4	Input	gistemp250_GHCNv4.nc			https://data.giss.nasa.gov/pub/gistemp/gistemp250_GHCNv4.nc.gz	(Lenssen et al., 2019)	
Figure 10.20 (f)	CSIRO-Mk3-6-0	Input	tas_Amon_CSIRO-Mk3-6-0_historical_rcp85_r[			https://www.earthsystemgrid.org/dataset/ucar.cgd.ccsm4.CLIVAR_LE.csiro_mk36_lens_new.atm.proc.monthly_ave.tas.html	(Jeffrey et al., 2013)	

ACCEPTED VERSION SUBJECT TO FINAL EDITING

			1..30]i1p1_185001-210012.nc					
Figure 10.20 (f)	d4PDF	Input	tas_1951-2014_run[001..100].grd	https://www.miroc-gcm.jp/~pub/d4PDF/img/d4PDF_Data_Policy_En_20180820.pdf		https://climate.mri-jma.go.jp/pub/d4pdf/HPB_1951-2014/tas/tas_1951-2014_run[001..100].grd	(Mizuta et al., 2017)	
Figure 10.21	Figure 10.21 Code	Code	recipe_Mediterranean.yml			https://github.com/ESMValGroup/ESMValTool-AR6/tree/ar6_chapter_10/esmvaltool/recipes/ar6_wgi_ch10		Requires working_cordex_2.2 ESMValCore branch
Figure 10.21	Figure 10.21 Code	Code	diagnostic_IPCC_AR6_CH10.py , ar6_wgi_ch10.mplstyle and colormaps/ directory			https://github.com/ESMValGroup/ESMValTool-AR6/tree/ar6_chapter_10/esmvaltool/diag_scripts/ar6_wgi_ch10		Requires working_cordex_2.2 ESMValCore branch
Figure 10.21	Figure 10.21 Code	Code				https://github.com/ESMValGroup/ESMValCore/tree/working_cordex_2.2		
Figure 10.21 (b)	CSIRO-Mk3-6-0	Input	tas_Amon_CSIRO-Mk3-6-0_historical_rcp85_r[1..30]i1p1_185001-210012.nc			https://www.earthsystemgrid.org/dataset/ucar.cgd.ccsm4.CLIVAR_LE.csiro_mk36_lens_new.atm.proc.monthly_ave.tas.html	(Jeffrey et al., 2013)	
Box 10.3	Box 10.3	Code	recipe_Urb			https://github.com/ESMValGroup/ES		Requires

ACCEPTED VERSION SUBJECT TO FINAL EDITING

Figure 1	Figure 1 Code		anBox.yml			MValTool-AR6/tree/ar6_chapter_10/esmvaltool/recipes/ar6_wgi_ch10		working_cordex_2.2 ESMValCore branch
Box 10.3 Figure 1	Box 10.3 Figure 1 Code	Code	diagnostic_IPCC_AR6_CH10.py , ar6_wgi_ch10.mplstyle , colormaps/ directory and CH10_additional_data/Urban_Box_data directory			https://github.com/ESMValGroup/ESMValTool-AR6/tree/ar6_chapter_10/esmvaltool/diag_scripts/ar6_wgi_ch10		Requires working_cordex_2.2 ESMValCore branch
Box 10.3 Figure 1	Box 10.3 Figure 1 Code	Code				https://github.com/ESMValGroup/ESMValCore/tree/working_cordex_2.2		
Box 10.3 Figure 1 (a), (c)	Urban Warming data	Input	cities.csv			https://github.com/ESMValGroup/ESMValTool-AR6/blob/ar6_chapter_10/esmvaltool/diag_scripts/ar6_wgi_ch10/CH10_additional_data/Urban_Box_data/cities.csv	(Hamdi et al., 2020)	
Box 10.3 Figure 1 (a)	Urban Warming data	Input	countries.csv			https://github.com/ESMValGroup/ESMValTool-AR6/blob/ar6_chapter_10/esmvaltool/diag_scripts/ar6_wgi_ch10/CH10_additional_data/Urban_Box_data/countries.csv	(Hamdi et al., 2020)	
Box 10.3 Figure 1 (b)	Tokyo and Choshi (Japan) temperature evolution	Input	Tokyo_Choshi_annual.csv			https://github.com/ESMValGroup/ESMValTool-AR6/blob/ar6_chapter_10/esmvaltool/diag_scripts/ar6_wgi_ch10/CH10_additional_data/Urban_Box_data/Tokyo	Tokyo and Choshi station Japan Meteorological Agency (JMA)	

ACCEPTED VERSION
SUBJECT TO FINAL EDITING

						_Choshi_annual.csv		
Box 10.3 Figure 1 (a), (c)	CRU TS v4.04	Input	cru_ts4.04.1901.2019.tmp.dat.nc	Open Government Licence http://www.nationalarchives.gov.uk/doc/open-government-licence/version/3/		https://crudata.uea.ac.uk/cru/data/hrg/cru_ts_4.04/cruts.2004151855.v4.04/tmp/cru_ts4.04.1901.2019.tmp.dat.nc.gz	(Harris et al., 2020)	
Box 10.3 Figure 1 (c)	Berkeley Earth	Input	Land_and_Ocean_LatLong1.nc			http://berkeleyearth.lbl.gov/auto/Global/Gridded/Land_and_Ocean_LatLong1.nc	(Rohde et al., 2013)	land_source_history = "13-Jan-2020 17:22:52", ocean_source_history = "07-Jan-2020 10:46:06"
Box 10.3 Figure 1 (c)	HadCRUT5	Input	HadCRUT.5.0.0.0.anomalies.ensemble_mean.nc and absolute_v5.nc	Open Government Licence http://www.nationalarchives.gov.uk/doc/open-government-licence/version/3/		https://crudata.uea.ac.uk/cru/data/temperature/HadCRUT.5.0.0.0.anomalies.ensemble_mean.nc	(Morice et al., 2021)	Absolute values build by adding the anomaly https://crudata.uea.ac.uk/cru/data/temperature/absolute_v5.nc
Box 10.3 Figure 1 (c)	Cowtan Way	Input	had4sst4_krig_v2_0_			https://www-users.york.ac.uk/~kdc3/papers/covera	(Cowtan and Way, 2014)	

ACCEPTED VERSION SUBJECT TO FINAL EDITING

			0.nc			ge2013/had4sst4_krig_v2_0_0.nc		
Box 10.3 Figure 1 (c)	GISTEMP version 4	Input	gistemp250_GHCNv4.nc			https://data.giss.nasa.gov/pub/gistemp/gistemp250_GHCNv4.nc.gz	(Lenssen et al., 2019)	
CCB 10.4 Figure 1	CCB 10.4 Figure 1 Code	Code	recipe_HKH.yml			https://github.com/ESMValGroup/ESMValTool-AR6/tree/ar6_chapter_10/esmvaltool/recipes/ar6_wgi_ch10		Requires working_cordex_2.2 ESMValCore branch
CCB 10.4 Figure 1	CCB 10.4 Figure 1 Code	Code	diagnostic_IPCC_AR6_CH10.py , ar6_wgi_ch10.mplstyle , colormaps/ directory , CH10_additional_data/Atlas_regions directory and CH10_additional_data/HKH_shape directory			https://github.com/ESMValGroup/ESMValTool-AR6/tree/ar6_chapter_10/esmvaltool/diag_scripts/ar6_wgi_ch10		Requires working_cordex_2.2 ESMValCore branch
CCB 10.4 Figure 1	CCB 10.4 Figure 1 Code	Code				https://github.com/ESMValGroup/ESMValCore/tree/working_cordex_2.2		
CCB 10.4 Figure 1 (a) (b) (c)	Berkeley Earth	Input	Land_and_Ocean_LatLong1.nc			http://berkeleyearth.lbl.gov/auto/Global/Gridded/Land_and_Ocean_LatLong1.nc	(Rohde et al., 2013)	land_source_history = "13-Jan-2020 17:22:52", ocean_source_history = "07-Jan-2020

ACCEPTED VERSION SUBJECT TO FINAL EDITING

								10:46:06"
CCB 10.4 Figure 1 (a) (b) (c)	CRU TS v4.04	Input	cru_ts4.04.1901.2019.tmp.dat.nc	Open Government Licence http://www.nationalarchives.gov.uk/doc/open-government-licence/version/3/		https://crudata.uea.ac.uk/cru/data/hrg/cru_ts_4.04/cruts.2004151855.v4.04/tmp/cru_ts4.04.1901.2019.tmp.dat.nc.gz	(Harris et al., 2020)	
CCB 10.4 Figure 1 (a) (b) (c)	APHRO-MA V1808 0.5°	Input	APHRO_MA_TAVE_050deg_V1808.nc			http://aphrodite.st.hirosaki-u.ac.jp/download/	(Yasutomi et al., 2011)	
CCB 10.4 Figure 1 (a) (b) (c)	JRA-55	Input	tas_Amon_reanalysis_JRA-55_195801-201912.nc	CC BY-SA 4.0		https://esgf.nccs.nasa.gov/thredds/fileServer/CREATE-IP/reanalysis/JMA/JRA-55/JRA-55/mon/atmos/tas/tas_Amon_reanalysis_JRA-55_195801-201912.nc	(Kobayashi et al., 2015)	tracking_id = "9e276e16-79d7-46e5-a3da-39ecf1c2a871"
CCB 10.4 Figure 1 (d)	CSIRO-Mk3-6-0	Input	tas_Amon_CSIRO-Mk3-6-0_historical_rcp85_r[1..30]i1p1_185001-210012.nc			https://www.earthsystemgrid.org/dataset/ucar.cgd.ccsm4.CLIVAR_LE.csiro_mk36_lens_new.atm.proc.monthly_ave.tas.html	(Jeffrey et al., 2013)	
CCB 10.4 Figure 1 (d)	d4PDF	Input	tas_1951-2014_run[001..100].grd	https://www.miroc-gcm.jp/~pub/d4PDF/img/d4PDF_		https://climate.mri-jma.go.jp/pub/d4pdf/HPB_1951-2014/tas/tas_1951-2014_run[001..100].grd	(Mizuta et al., 2017)	

ACCEPTED VERSION SUBJECT TO FINAL EDITING

				Data_Policy_En_20180820.pdf				
FAQ 10.1, Figure 2	paper	Input					(Hamdi et al., 2020)	

[END TABLE 10.SM.11 HERE]

ACCEPTED VERSION
SUBJECT TO FINAL EDITING

References

Contractor, S., Donat, M. G., Alexander, L. V., Ziese, M., Meyer-Christoffer, A., Schneider, U., et al. (2020). Rainfall Estimates on a Gridded Network (REGEN) – a global land-based gridded dataset of daily precipitation from 1950 to 2016. *Hydrol. Earth Syst. Sci.* 24, 919–943. doi:10.5194/hess-24-919-2020.

Cornes, R. C., van der Schrier, G., van den Besselaar, E. J. M., and Jones, P. D. (2018). An Ensemble Version of the E-OBS Temperature and Precipitation Data Sets. *J. Geophys. Res. Atmos.* 123, 9391–9409. doi:10.1029/2017JD028200.

Cowtan, K., and Way, R. G. (2014). Coverage bias in the HadCRUT4 temperature series and its impact on recent temperature trends. *Q. J. R. Meteorol. Soc.* 140, 1935–1944. doi:10.1002/qj.2297.

Cucchi, M., Weedon, G. P., Amici, A., Bellouin, N., Lange, S., Müller Schmied, H., et al. (2020). WFDE5: bias-adjusted ERA5 reanalysis data for impact studies. *Earth Syst. Sci. Data* 12, 2097–2120. doi:10.5194/essd-12-2097-2020.

Dee, D. P., Uppala, S. M., Simmons, A. J., Berrisford, P., Poli, P., Kobayashi, S., et al. (2011). The ERA-Interim reanalysis: Configuration and performance of the data assimilation system. *Q. J. R. Meteorol. Soc.* 137, 553–597. doi:10.1002/qj.828.

Donat, M. G., Peterson, T. C., Brunet, M., King, A. D., Almazroui, M., Kolli, R. K., et al. (2014). Changes in extreme temperature and precipitation in the Arab region: long-term trends and variability related to ENSO and NAO. *Int. J. Climatol.* 34, 581–592. doi:10.1002/joc.3707.

Engelbrecht, F. A., Landman, W. A., Engelbrecht, C. J., Landman, S., Bopape, M. M., Roux, B., et al. (2011). Multi-scale climate modelling over Southern Africa using a variable-resolution global model. *Water SA* 37. doi:10.4314/wsa.v37i5.2.

Gelaro, R., McCarty, W., Suárez, M. J., Todling, R., Molod, A., Takacs, L., et al. (2017). The Modern-Era Retrospective Analysis for Research and Applications, Version 2 (MERRA-2). *J. Clim.* 30, 5419–5454. doi:10.1175/JCLI-D-16-0758.1.

Giorgi, F., Torma, C., Coppola, E., Ban, N., Schär, C., and Somot, S. (2016). Enhanced summer convective rainfall at Alpine high elevations in response to climate warming. *Nat. Geosci.* 9, 584–589. doi:10.1038/ngeo2761.

Hamdi, R., Kusaka, H., Doan, Q.-V., Cai, P., He, H., Luo, G., et al. (2020). The State-of-the-Art of Urban Climate Change Modeling and Observations. *Earth Syst. Environ.* 4, 631–646. doi:10.1007/s41748-020-00193-3.

Harris, I., Osborn, T. J., Jones, P., and Lister, D. (2020). Version 4 of the CRU TS monthly high-resolution gridded multivariate climate dataset. *Sci. Data* 7, 109. doi:10.1038/s41597-020-0453-3.

Hersbach, H., Bell, B., Berrisford, P., Hirahara, S., Horányi, A., Muñoz-Sabater, J., et al. (2020). The ERA5 global reanalysis. *Q. J. R. Meteorol. Soc.* 146, 1999–2049. doi:10.1002/qj.3803.

Huffman, G. J., Adler, R. F., Bolvin, D. T., and Gu, G. (2009). Improving the global precipitation record: GPCP Version 2.1. *Geophys. Res. Lett.* 36, L17808. doi:10.1029/2009GL040000.

Jeffrey, S., Rotstayn, L., Collier, M., Dravitzki, S., Hamalainen, C., Moeseneder, C., et al. (2013). Australia's CMIP5 submission using the CSIRO-Mk3.6 model. *Aust. Meteorol. Oceanogr. J.* 63, 1–14. doi:10.22499/2.6301.001.

Jones, P. D., Lister, D. H., Osborn, T. J., Harpham, C., Salmon, M., and Morice, C. P. (2012). Hemispheric and large-scale land-surface air temperature variations: An extensive revision and an update to 2010. *J. Geophys. Res. Atmos.* 117. doi:10.1029/2011JD017139.

Jones, P. D., and Moberg, A. (2003). Hemispheric and Large-Scale Surface Air Temperature Variations: An Extensive Revision and an Update to 2001. *J. Clim.* 16, 206–223. doi:10.1175/1520-0442(2003)016<0206:HALSSA>2.0.CO;2.

Kalnay, E., Kanamitsu, M., Kistler, R., Collins, W., Deaven, D., Gandin, L., et al. (1996). The NCEP/NCAR 40-Year Reanalysis Project. *Bull. Am. Meteorol. Soc.* 77, 437–471. doi:10.1175/1520-0477(1996)077<0437:TNYRP>2.0.CO;2.

Kobayashi, S., Ota, Y., Harada, Y., Ebita, A., Moriya, M., Onoda, H., et al. (2015). The JRA-55 Reanalysis: General Specifications and Basic Characteristics. *J. Meteorol. Soc. Japan. Ser. II* 93, 5–48. doi:10.2151/jmsj.2015-001.

Kubota, T., Aonashi, K., Ushio, T., Shige, S., Takayabu, Y. N., Kachi, M., et al. (2020). "Global Satellite Mapping of Precipitation (GSMaP) Products in the GPM Era," in, eds. V. Levizzani, C. Kidd, D. B. Kirschbaum, C. D. Kummerow, K. Nakamura, and F. J. Turk (Cham: Springer International Publishing), 355–373. doi:10.1007/978-3-030-24568-9_20.

Laloyaux, P., de Boisseson, E., Balmaseda, M., Bidlot, J.-R., Broennimann, S., Buizza, R., et al. (2018). CERA-20C: A Coupled Reanalysis of the Twentieth Century. *J. Adv. Model. Earth Syst.* 10, 1172–1195. doi:10.1029/2018MS001273.

Lenssen, N. J. L., Schmidt, G. A., Hansen, J. E., Menne, M. J., Persin, A., Ruedy, R., et al. (2019). Improvements in the GISTEMP Uncertainty Model. *J. Geophys. Res. Atmos.* doi:10.1029/2018JD029522.

Maraun, D., Shepherd, T. G., Widmann, M., Zappa, G., Walton, D., Gutiérrez, J. M., et al. (2017). Towards process-informed bias correction of climate change simulations. *Nat. Clim. Chang.* 7, 664–773. doi:10.1038/nclimate3418.

SUBJECT TO FINAL EDITING ACCEPTED VERSION

Mizuta, R., Murata, A., Ishii, M., Shiogama, H., Hibino, K., Mori, N., et al. (2017). Over 5,000 Years of Ensemble Future Climate Simulations by 60-km Global and 20-km Regional Atmospheric Models. *Bull. Am. Meteorol. Soc.* 98, 1383–1398. doi:10.1175/BAMS-D-16-0099.1.

Morice, C. P., Kennedy, J. J., Rayner, N. A., and Jones, P. D. (2012). Quantifying uncertainties in global and regional temperature change using an ensemble of observational estimates: The HadCRUT4 data set. *J. Geophys. Res. Atmos.* 117. doi:10.1029/2011JD017187.

Morice, C. P., Kennedy, J. J., Rayner, N. A., Winn, J. P., Hogan, E., Killick, R. E., et al. (2021). An Updated Assessment of Near-Surface Temperature Change From 1850: The HadCRUT5 Data Set. *J. Geophys. Res. Atmos.* 126. doi:10.1029/2019JD032361.

ONOGI, K., TSUTSUI, J., KOIDE, H., SAKAMOTO, M., KOBAYASHI, S., HATSUSHIKA, H., et al. (2007). The JRA-25 Reanalysis. *J. Meteorol. Soc. Japan. Ser. II* 85, 369–432. doi:10.2151/jmsj.85.369.

Parthasarathy, B., Munot, A. A., and Kothawale, D. R. (1994). All-India monthly and seasonal rainfall series: 1871–1993. *Theor. Appl. Climatol.* 49, 217–224. doi:10.1007/BF00867461.

Poli, P., Hersbach, H., Dee, D. P., Berrisford, P., Simmons, A. J., Vitart, F., et al. (2016). ERA-20C: An Atmospheric Reanalysis of the Twentieth Century. *J. Clim.* 29, 4083–4097. doi:10.1175/JCLI-D-15-0556.1.

Rienecker, M. M., Suarez, M. J., Gelaro, R., Todling, R., Bacmeister, J., Liu, E., et al. (2011). MERRA: NASA's Modern-Era Retrospective Analysis for Research and Applications. *J. Clim.* 24, 3624–3648. doi:10.1175/JCLI-D-11-00015.1.

Rohde, R., Muller, R., Jacobsen, R., Muller, E., Perlmutter, S., Rosenfeld, A., et al. (2013). A New Estimate of the Average Earth Surface Land Temperature Spanning 1753 to 2011. *Geoinformatics Geostatistics An Overv.* 1. doi:10.4172/2327-4581.1000101.

Saha, S., Moorthi, S., Pan, H.-L., Wu, X., Wang, J., Nadiga, S., et al. (2010). The NCEP Climate Forecast System Reanalysis. *Bull. Am. Meteorol. Soc.* 91, 1015–1058. doi:10.1175/2010BAMS3001.1.

Schiemann, R., Demory, M.-E., Shaffrey, L. C., Strachan, J., Vidale, P. L., Mizielinski, M. S., et al. (2017). The Resolution Sensitivity of Northern Hemisphere Blocking in Four 25-km Atmospheric Global Circulation Models. *J. Clim.* 30, 337–358. doi:10.1175/JCLI-D-16-0100.1.

Schneider, U., Becker, A., Finger, P., Meyer-Christoffer, A., and Ziese, M. (2018). GPCC Full Data Monthly Product Version 2018 at 1.0°: Monthly Land-Surface Precipitation from Rain-Gauges built on GTS-based and Historical Data. doi:10.5676/DWD_GPCC/FD_M_V2018_100.

Shonk, J. K. P., Turner, A. G., Chevuturi, A., Wilcox, L. J., Dittus, A. J., and Hawkins, E. (2020). Uncertainty in aerosol radiative forcing impacts the simulated global monsoon in the 20th century. *Atmos. Chem. Phys.* 20, 14903–14915. doi:10.5194/acp-20-14903-2020.

Slivinski, L. C., Compo, G. P., Whitaker, J. S., Sardeshmukh, P. D., Giese, B. S., McColl, C., et al. (2019). Towards a more reliable historical reanalysis: Improvements for version 3 of the Twentieth Century Reanalysis system. *Q. J. R. Meteorol. Soc.* 145, 2876–2908. doi:10.1002/qj.3598.

Swinbank, R., Kyouda, M., Buchanan, P., Froude, L., Hamill, T. M., Hewson, T. D., et al. (2016). The TIGGE Project and Its Achievements. *Bull. Am. Meteorol. Soc.* 97, 49–67. doi:10.1175/BAMS-D-13-00191.1.

Takayabu, I., Hibino, K., Sasaki, H., Shiogama, H., Mori, N., Shibutani, Y., et al. (2015). Climate change effects on the worst-case storm surge: a case study of Typhoon Haiyan. *Environ. Res. Lett.* 10, 064011. doi:10.1088/1748-9326/10/6/064011.

Uppala, S. M., KÅllberg, P. W., Simmons, A. J., Andrae, U., Bechtold, V. D. C., Fiorino, M., et al. (2006). The ERA-40 re-analysis. *Q. J. R. Meteorol. Soc.* 131, 2961–3012. doi:10.1256/qj.04.176.

Yasutomi, N., Hamada, A., and Yatagai, A. (2011). Development of a Long-term Daily Gridded Temperature Dataset and Its Application to Rain/Snow Discrimination of Daily Precipitation. Available at: http://hydro.iis.u-tokyo.ac.jp/GAME-T.

Yatagai, A., Kamiguchi, K., Arakawa, O., Hamada, A., Yasutomi, N., and Kitoh, A. (2012). APHRODITE: Constructing a Long-Term Daily Gridded Precipitation Dataset for Asia Based on a Dense Network of Rain Gauges. *Bull. Am. Meteorol. Soc.* 93, 1401–1415. doi:10.1175/BAMS-D-11-00122.1.

Zhang, H.-M., Lawrimore, J., Huang, B., Menne, M., Yin, X., Sánchez-Lugo, A., et al. (2019). Updated Temperature Data Give a Sharper View of Climate Trends. *Eos (Washington. DC).* 100. doi:10.1029/2019EO128229.

ACCEPTED VERSION
SUBJECT TO FINAL EDITING

Chapter 11: Weather and climate extreme events in a changing climate

Coordinating Lead Authors:
Sonia I. Seneviratne (Switzerland), Xuebin Zhang (Canada)

Lead Authors:
Muhammad Adnan (Pakistan), Wafae Badi (Morocco), Claudine Dereczynski (Brazil), Alejandro Di Luca (Australia, Canada/Argentina), Subimal Ghosh (India), Iskhaq Iskandar (Indonesia), James Kossin (United States of America), Sophie Lewis (Australia), Friederike Otto (United Kingdom/Germany), Izidine Pinto (South Africa/Mozambique), Masaki Satoh (Japan), Sergio M. Vicente-Serrano (Spain), Michael Wehner (United States of America), Botao Zhou (China)

Contributing Authors:
Mathias Hauser (Switzerland), Megan Kirchmeier-Young (Canada/United States of America), Lisa V. Alexander (Australia), Richard P. Allan (United Kingdom), Mansour Almazroui (Saudi Arabia), Lincoln M. Alvez (Brazil), Margot Bador (Australia, France/France), Rondrotiana Barimalala (South Africa/Madagascar), Richard A. Betts (United Kingdom), Suzana J. Camargo (United States of America/Brazil, USA), Pep G. Canadell (Australia), Erika Coppola (Italy), Markus G. Donat (Spain/Germany, Australia), Hervé Douville (France), Robert J. H. Dunn (United Kingdom/Germany, United Kingdom), Erich Fischer (Switzerland), Hayley J. Fowler (United Kingdom), Nathan P. Gillett (Canada), Peter Greve (Austria/Germany), Michael Grose (Australia), Lukas Gudmundsson (Switzerland/Germany, Iceland), Jose Manuel Guttierez (Spain), Lofti Halimi (Algeria), Zhenyu Han (China), Kevin Hennessy (Australia), Richard G. Jones (United Kingdom), Yeon-Hee Kim (Republic of Korea), Thomas Knutson (United States of America), June-Yi Lee (Republic of Korea), Chao Li (China), Georges-Noel T. Longandjo (South Africa/Democratic Republic of Congo), Kathleen L. McInnes (Australia), Tim R. McVicar (Australia), Malte Meinshausen (Australia/Germany), Seung-Ki Min (Republic of Korea), Ryan S. Padron Flasher (Switzerland/Ecuador, United States of America), Christina M. Patricola (United States of America), Roshanka Ranasinghe (The Netherlands/Sri Lanka, Australia), Johan Reyns (The Netherlands/Belgium), Joeri Rogelj (United Kingdom/Belgium), Alex C. Ruane (United States of America), Daniel Ruiz Carrascal (United States of America/Colombia), Bjørn H. Samset (Norway), Jonathan Spinoni (Italy), Qiaohong Sun (Canada/China), Ying Sun (China), Mouhamadou Bamba Sylla (Rwanda/Senegal), Claudia Tebaldi (United States of America), Laurent Terray (France), Wim Thiery (Belgium), Jessica Tierney (United States of America), Maarten K. van Aalst (The Netherlands), Bart van den Hurk (The Netherlands), Robert Vautard (France), Wen Wang (China), Seth Westra (Australia), Jakob Zscheischler (Germany)

Review Editors:
Johnny Chan (China), Asgeir Sorteberg (Norway), Carolina Vera (Argentina)

Chapter Scientists:
Mathias Hauser (Switzerland), Megan Kirchmeier-Young (Canada/ United States of America), Hui Wan (Canada)

This Chapter should be cited as:
Seneviratne, S. I., X. Zhang, M. Adnan, W. Badi, C. Dereczynski, A. Di Luca, S. Ghosh, I. Iskandar, J. Kossin, S. Lewis, F. Otto, I. Pinto, M. Satoh, S. M. Vicente-Serrano, M. Wehner, B. Zhou, 2021, Weather and Climate Extreme Events in a Changing Climate. In: *Climate Change 2021: The Physical Science Basis. Contribution of Working Group I to the Sixth Assessment Report of the Intergovernmental Panel on Climate Change* [Masson-Delmotte, V., P. Zhai, A. Pirani, S. L. Connors, C. Péan, S. Berger, N. Caud, Y. Chen, L. Goldfarb, M. I. Gomis, M. Huang, K. Leitzell, E. Lonnoy, J. B. R. Matthews, T. K. Maycock, T. Waterfield, O. Yelekçi, R. Yu and B. Zhou (eds.)]. Cambridge University Press. In Press.

Date: August 2021

This document is subject to copy-editing, corrigenda and trickle backs.

ACCEPTED VERSION SUBJECT TO FINAL EDITING

Table Of Content

Executive Summary 6

11.1 Framing 11
11.1.1 Introduction to the chapter 11
11.1.2 What are extreme events and how are their changes studied? 11
11.1.3 Types of extremes assessed in this chapter 12
11.1.4 Effects of greenhouse gas and other external forcings on extremes 13

BOX 11.1: Thermodynamic and dynamic changes in extremes across scales 15

11.1.5 Effects of large-scale circulation on changes in extremes 17
11.1.6 Effects of regional-scale processes and forcings and feedbacks on changes in extremes 18
11.1.7 Global-scale synthesis 19

BOX 11.2: Low-likelihood high-impact changes in extremes 24

11.2 Data and Methods 26
11.2.1 Definition of extremes 26
11.2.2 Data 27

BOX 11.3: Extremes in paleoclimate archives compared to instrumental records 28

11.2.3 Attribution of extremes 31
11.2.4 Projecting changes in extremes as a function of global warming levels 32

Cross-Chapter Box 11.1: Translating between regional information at global warming levels vs scenarios for end users 34

11.3 Temperature extremes 38
11.3.1 Mechanisms and drivers 38
11.3.2 Observed trends 40
11.3.3 Model evaluation 43
11.3.4 Detection and attribution, event attribution 45
11.3.5 Projections 47

11.4 Heavy precipitation 51
11.4.1 Mechanisms and drivers 51
11.4.2 Observed Trends 52
11.4.3 Model evaluation 56
11.4.4 Detection and attribution, event attribution 57
11.4.5 Projections 59

ACCEPTED VERSION SUBJECT TO FINAL EDITING

11.5 Floods 63
11.5.1 Mechanisms and drivers 64
11.5.2 Observed trends 65
11.5.3 Model evaluation 65
11.5.4 Attribution 66
11.5.5 Future projections 67

11.6 Droughts 68
11.6.1 Mechanisms and drivers 68
11.6.1.1 Precipitation deficits 69
11.6.1.2 Atmospheric evaporative demand 69
11.6.1.3 Soil moisture deficits 70
11.6.1.4 Hydrological deficits 71
11.6.1.5 Atmospheric-based drought indices 71
11.6.1.6 Relation of assessed variables and metrics for changes in different drought types 71
11.6.2 Observed trends 72
11.6.2.1 Precipitation deficits 72
11.6.2.2 Atmospheric evaporative demand 72
11.6.2.3 Soil moisture deficits 73
11.6.2.4 Hydrological deficits 74
11.6.2.5 Atmospheric-based drought indices 74
11.6.2.6 Synthesis for different drought types 75
11.6.3 Model evaluation 75
11.6.3.1 Precipitation deficits 75
11.6.3.2 Atmospheric evaporative demand 75
11.6.3.3 Soil moisture deficits 76
11.6.3.4 Hydrological deficits 77
11.6.3.5 Atmospheric-based drought indices 77
11.6.3.6 Synthesis for different drought types 77
11.6.4 Detection and attribution, event attribution 78
11.6.4.1 Precipitation deficits 78
11.6.4.2 Soil moisture deficits 79
11.6.4.3 Hydrological deficits 79
11.6.4.4 Atmospheric-based drought indices 80
11.6.4.5 Synthesis for different drought types 80
11.6.5 Projections 81
11.6.5.1 Precipitation deficits 81
11.6.5.2 Atmospheric evaporative demand 82
11.6.5.3 Soil moisture deficits 83

ACCEPTED VERSION
SUBJECT TO FINAL EDITING

11.6.5.4 Hydrological deficits 84
11.6.5.5 Atmospheric-based drought indices 85
11.6.5.6 Synthesis for different drought types 86

11.7 Extreme storms 87
11.7.1 Tropical cyclones 88
11.7.1.1 Mechanisms and drivers 88
11.7.1.2 Observed trends 88
11.7.1.3 Model evaluation 90
11.7.1.4 Detection and attribution, event attribution 92
11.7.1.5 Projections 94
11.7.2 Extratropical storms 97
11.7.2.1 Observed trends 97
11.7.2.2 Model evaluation 98
11.7.2.3 Detection and attribution, event attribution 98
11.7.2.4 Projections 98
11.7.3 Severe convective storms 99
11.7.3.1 Mechanisms and drivers 100
11.7.3.2 Observed trends 101
11.7.3.3 Model evaluation 102
11.7.3.4 Detection and attribution, event attribution 103
11.7.3.5 Projections 103
11.7.4 Extreme winds 104

11.8 Compound events 106
11.8.1 Overview 106
11.8.2 Concurrent extremes in coastal and estuarine regions 107
11.8.3 Concurrent droughts and heat waves 108

BOX 11.4: Case study: Global-scale concurrent climate anomalies at the example of the 2015-2016 extreme El Niño and the 2018 boreal spring/summer extremes 109

11.9 Regional information on extremes 113
11.9.1 Overview 113
11.9.2 Temperature extremes 114
11.9.3 Heavy precipitation 114
11.9.4 Droughts 115

Frequently Asked Questions 117
FAQ 11.1: How do changes in climate extremes compare with changes in climate averages? 117
FAQ 11.2: Will unprecedented extremes occur as a result of human-induced climate change? 119

ACCEPTED VERSION SUBJECT TO FINAL EDITING

FAQ 11.3: Did climate change cause that recent extreme event in my country? 120

Large tables **122**

Acknowledgements **233**

References **234**

Appendix 11.A **314**

Figures **316**

ACCEPTED VERSION
SUBJECT TO FINAL EDITING

Executive Summary

This chapter assesses changes in weather and climate extremes on regional and global scales, including observed changes and their attribution, as well as projected changes. The extremes considered include temperature extremes, heavy precipitation and pluvial floods, river floods, droughts, storms (including tropical cyclones), as well as compound events (multivariate and concurrent extremes). Changes in marine extremes are addressed in Chapter 9 and Cross-Chapter Box 9.1. Assessments of past changes and their drivers are from 1950 onward, unless indicated otherwise. Projections for changes in extremes are presented for different levels of global warming, supplemented with information for the conversion to emission scenario-based projections (Cross-Chapter Box 11.1; Chapter 4, Table 4.2). Since AR5, there have been important new developments and knowledge advances on changes in weather and climate extremes, in particular regarding human influence on individual extreme events, on changes in droughts, tropical cyclones, and compound events, and on projections at different global warming levels (1.5°C–4°C). These, together with new evidence at regional scales, provide a stronger basis and more regional information for the AR6 assessment on weather and climate extremes.

It is an established fact that human-induced greenhouse gas emissions have led to an increased frequency and/or intensity of some weather and climate extremes since pre-industrial time, in particular for temperature extremes. Evidence of observed changes in extremes and their attribution to human influence (including greenhouse gas and aerosol emissions and land-use changes) has strengthened since AR5, in particular for extreme precipitation, droughts, tropical cyclones and compound extremes (including dry/hot events and fire weather). Some recent hot extreme events would have been *extremely unlikely* to occur without human influence on the climate system. {11.2, 11.3, 11.4, 11.6, 11.7, 11.8}

Regional changes in the intensity and frequency of climate extremes generally scale with global warming. New evidence strengthens the conclusion from SR1.5 that even relatively small incremental increases in global warming (+0.5°C) cause statistically significant changes in extremes on the global scale and for large regions (*high confidence*). In particular, this is the case for temperature extremes (*very likely*), the intensification of heavy precipitation (*high confidence*) including that associated with tropical cyclones (*medium confidence*), and the worsening of droughts in some regions (*high confidence*). The occurrence of extreme events unprecedented in the observed record will increase with increasing global warming, even at 1.5°C of global warming. Projected percentage changes in frequency are higher for the rarer extreme events (*high confidence*). {11.1, 11.2, 11.3, 11.4, 11.6, 11.9, CC-Box 11.1}

Methods and Data for Extremes

Since AR5, the confidence about past and future changes in weather and climate extremes has increased due to better physical understanding of processes, an increasing proportion of the scientific literature combining different lines of evidence, and improved accessibility to different types of climate models (*high confidence*). There have been improvements in some observation-based datasets, including reanalysis data (*high confidence*). Climate models can reproduce the sign of changes in temperature extremes observed globally and in most regions, although the magnitude of the trends may differ (*high confidence*). Models are able to capture the large-scale spatial distribution of precipitation extremes over land (*high confidence*). The intensity and frequency of extreme precipitation simulated by Coupled Model Intercomparison Project Phase 6 (CMIP6) models are similar to those simulated by CMIP5 models (*high confidence*). Higher horizontal model resolution improves the spatial representation of some extreme events (e.g., heavy precipitation events), in particular in regions with highly varying topography (*high confidence*). {11.2, 11.3, 11.4}

Temperature Extremes

The frequency and intensity of hot extremes have increased and those of cold extremes have decreased on the global scale since 1950 (*virtually certain*). This also applies at regional scale, with more than

ACCEPTED VERSION SUBJECT TO FINAL EDITING

80% of AR6 regions[1] showing similar changes assessed to be at least *likely*. In a few regions, *limited evidence* (data or literature) prevents the reliable estimation of trends. {11.3, 11.9}

Human-induced greenhouse gas forcing is the main driver of the observed changes in hot and cold extremes on the global scale (*virtually certain*) and on most continents (*very likely*). The effect of enhanced greenhouse gas concentrations on extreme temperatures is moderated or amplified at the regional scale by regional processes such as soil moisture or snow/ice-albedo feedbacks, by regional forcing from land use and land-cover changes, or aerosol concentrations, and decadal and multidecadal natural variability. Changes in anthropogenic aerosol concentrations have *likely* affected trends in hot extremes in some regions. Irrigation and crop expansion have attenuated increases in summer hot extremes in some regions, such as the U.S. Midwest (*medium confidence*). Urbanization has *likely* exacerbated changes in temperature extremes in cities, in particular for night-time extremes. {11.1, 11.2, 11.3}

The frequency and intensity of hot extremes will continue to increase and those of cold extremes will continue to decrease, at both global and continental scales and in nearly all inhabited regions[1] with increasing global warming levels. This will be the case even if global warming is stabilized at 1.5°C. Relative to present-day conditions, changes in the intensity of extremes would be at least double at 2°C, and quadruple at 3°C of global warming, compared to changes at 1.5°C of global warming. The number of hot days and hot nights and the length, frequency, and/or intensity of warm spells or heat waves will increase over most land areas (*virtually certain*). In most regions, future changes in the intensity of temperature extremes will *very likely* be proportional to changes in global warming, and up to 2–3 times larger (*high confidence*). The highest increase of temperature of hottest days is projected in some mid-latitude and semi-arid regions, at about 1.5 time to twice the rate of global warming (*high confidence*). The highest increase of temperature of coldest days is projected in Arctic regions, at about three times the rate of global warming (*high confidence*). The frequency of hot temperature extreme events will *very likely* increase non-linearly with increasing global warming, with larger percentage increases for rarer events. {11.2, 11.3, 11.9; Table 11.1; Figure 11.3}

Heavy Precipitation and Pluvial Floods

The frequency and intensity of heavy precipitation events have *likely* increased at the global scale over a majority of land regions with good observational coverage. Heavy precipitation has *likely* increased on the continental scale over three continents: North America, Europe, and Asia. Regional increases in the frequency and/or intensity of heavy precipitation have been observed with at least *medium confidence* for nearly half of AR6 regions, including WSAF, ESAF, WSB, SAS, ESB, REF, WCA, ECA, TIB, EAS, SEA, NAU, NEU, EEU, GIC, WCE, SES, CNA, and ENA. {11.4, 11.9}

Human influence, in particular greenhouse gas emissions, is *likely* the main driver of the observed global scale intensification of heavy precipitation in land regions. It is *likely* that human-induced climate change has contributed to the observed intensification of heavy precipitation at the continental scale in North America, Europe and Asia. Evidence of a human influence on heavy precipitation has emerged in some regions. {11.4, 11.9, Table 11.1}

Heavy precipitation will generally become more frequent and more intense with additional global warming. At global warming levels of 4°C relative to the pre-industrial, very rare (e.g., 1 in 10 or more

[1] See Figure 1.18 in Chapter 1 for definition of AR6 regions. Acronyms for inhabited regions: ARP: Arabian Peninsula; CAF: C. Africa; CAR : Caribbean; CAU: C. Australia; CNA: C. North America; EAS: E. Asia; EAU: E. Australia; ECA: E. Central Asia; EEU: E. Europe; ENA: E. North America; ESAF: E. Southern Africa; ESB: E. Siberia; GIC: Greenland/Iceland; MDG: Madagascar; MED: Mediterranean; NAU: N. Australia; NCA: N. Central America; NEAF: N.E. Africa; NEN: N.E. North America; NES: N.E. South America; NEU: N. Europe; NSA: N. South America; NWN: N.W. North America; NWS: N.W. South America; NZ: New Zealand; RAR: Russian Arctic; RFE: Russian Far East; SAH: Sahara; SAM: South American Monsoon; SAS: South Asia; SAU: Southern Australia; SCA: S. Central America; SEAF: S.E. Africa; SES: S.E. South America; SSA: S. South America; SWS: S.W. South America; TIB: Tibetan Plateau; WAF: Western Africa; WCA: W. Central Asia; WCE: Western & Central Europe; WNA: W. North America; WSAF: W. Southern Africa; WSB: W. Siberia.

ACCEPTED VERSION SUBJECT TO FINAL EDITING

years) heavy precipitation events would become more frequent and more intense than in the recent past, on the global scale (*virtually certain*) and in all continents and AR6 regions. The increase in frequency and intensity is *extremely likely* for most continents and *very likely* for most AR6 regions. At the global scale, the intensification of heavy precipitation will follow the rate of increase in the maximum amount of moisture that the atmosphere can hold as it warms (*high confidence*), of about 7% per 1°C of global warming. The increase in the frequency of heavy precipitation events will accelerate with more warming and will be higher for rarer events (*high confidence*), with a *likely* doubling and tripling in the frequency of 10-year and 50-year events, respectively, compared to the recent past at 4°C of global warming. Increases in the intensity of extreme precipitation at regional scales will vary, depending on the amount of regional warming, changes in atmospheric circulation and storm dynamics (*high confidence*). {11.4, Box 11.1}

The projected increase in the intensity of extreme precipitation translates to an increase in the frequency and magnitude of pluvial floods – surface water and flash floods – (*high confidence*), as pluvial flooding results from precipitation intensity exceeding the capacity of natural and artificial drainage systems. {11.4}

River Floods

Significant trends in peak streamflow have been observed in some regions over the past decades (*high confidence*). This includes increases in RAR, NSA, and parts of SES, NEU, ENA and decreases in NES, SAU, and parts of MED and EAS). The seasonality of river floods has changed in cold regions where snow-melt is involved, with an earlier occurrence of peak streamflow (*high confidence*). {11.5}

Global hydrological models project a larger fraction of land areas to be affected by an increase in river floods than by a decrease in river floods (*medium confidence*). River floods are projected to become more frequent and intense in some AR6 regions (RAR, SEA, SAS, NWS) (*high confidence*) and less frequent and intense in others (WCE, EEU, MED) (*high confidence*). Regional changes in river floods are more uncertain than changes in pluvial floods because complex hydrological processes and forcings, including land cover change and human water management, are involved. {11.5}

Droughts

Different drought types exist, and they are associated with different impacts and respond differently to increasing greenhouse gas concentrations. Precipitation deficits and changes in evapotranspiration (ET) govern net water availability. A lack of sufficient soil moisture, sometimes amplified by increased atmospheric evaporative demand (AED), results in agricultural and ecological drought. Lack of runoff and surface water result in hydrological drought. {11.6}

Human-induced climate change has contributed to decreases in water availability during the dry season over a predominant fraction of the land area due to evapotranspiration increases (*medium confidence*). Increases in evapotranspiration have been driven by AED increases induced by increased temperature, decreased relative humidity and increased net radiation (*high confidence*). Trends in precipitation are not a main driver in affecting global-scale trends in drought (*medium confidence*), but have induced drying trends in a few AR6 regions (NES: *high confidence*; WAF, CAF, ESAF, SAM, SWS, SSA, SAS: *medium confidence*). Increasing trends in agricultural and ecological droughts have been observed on all continents (WAF, CAF, WSAF, ESAF, WCA, ECA, EAS, SAU, MED, WCE, WNA, NES: *medium confidence*), but decreases only in one AR6 region (NAU: *medium confidence*). Increasing trends in hydrological droughts have been observed in a few AR6 regions (MED: *high confidence*; WAF, EAS, SAU: *medium confidence*). Regional-scale attribution shows that human-induced climate change has contributed to increased agricultural and ecological droughts (MED, WNA), and increased hydrological drought (MED) in some regions (*medium confidence*). {11.6, 11.9}

The land area affected by increasing drought frequency and severity expands with increasing global

ACCEPTED VERSION SUBJECT TO FINAL EDITING

warming (*high confidence*). Several regions will be affected by more severe agricultural and ecological droughts even if global warming is stabilized in a range of 1.5°C-2°C of global warming (*high confidence*), including WCE, MED, EAU, SAU, SCA, NSA, SAM, SWS, SSA, NCA, CAN, WSAF, ESAF and MDG (*medium confidence*). At 4°C of global warming, about 50% of all inhabited AR6 regions would be affected (WCE, MED, CAU, EAU, SAU, WCA, EAS, SCA, CAR, NSA, NES, SAM, SWS, SSA, NCA, CAN, ENA, WNA, WSAF, ESAF, MDG; *medium confidence* or higher), and only two regions (NEAF, SAS) would experience decreases in agricultural and ecological drought (*medium confidence*). There is *high confidence* that the projected increases in agricultural and ecological droughts are strongly affected by ET increases associated with enhanced AED**.** Several regions are projected to be more strongly affected by hydrological droughts with increasing global warming (at 4°C of global warming: NEU, WCE, EEU, MED, SAU, WCA, SCA, NSA, SAM, SWS, SSA, WNA, WSAF, ESAF, MDG; *medium confidence* or higher). There is *low confidence* that effects of enhanced atmospheric CO_2 concentrations on plant water-use efficiency alleviate extreme agricultural and ecological droughts in conditions characterized by limited soil moisture and enhanced AED. There is also *low confidence* that these effects will substantially reduce global plant transpiration and the severity of hydrological droughts. There is *high confidence* that the land carbon sink will become less efficient due to soil moisture limitations and associated drought conditions in some regions in higher-emission scenarios, in particular under global warming levels above 4°C. {11.6, 11.9, CC-Box 5.1}

Extreme Storms, Including Tropical Cyclones (TCs)

The average and maximum rain rates associated with TCs, extratropical cyclones and atmospheric rivers across the globe, and severe convective storms in some regions, increase in a warming world (*high confidence*). Available event attribution studies of observed strong TCs provide *medium confidence* for a human contribution to extreme TC rainfall. Peak TC rain rates increase with local warming at least at the rate of mean water vapour increase over oceans (about 7% per 1°C of warming) and in some cases exceeding this rate due to increased low-level moisture convergence caused by increases in TC wind intensity (*medium confidence*). {11.7, 11.4, Box 11.1}

It is *likely* that the global proportion of major TC (Category 3–5) intensities over the past four decades has increased. The average location where TCs reach their peak wind intensity has *very likely* migrated poleward in the western North Pacific Ocean since the 1940s, and TC translation speed has *likely* slowed over the conterminous USA since 1900. Evidence of similar trends in other regions is not robust. The global frequency of TC rapid intensification events has *likely* increased over the past four decades. None of these changes can be explained by natural variability alone (*medium confidence*).

The proportion of intense TCs, average peak TC wind speeds, and peak wind speeds of the most intense TCs will increase on the global scale with increasing global warming (*high confidence*). The total global frequency of TC formation will decrease or remain unchanged with increasing global warming (*medium confidence*). {11.7.1}

There is *low confidence* in past changes of maximum wind speeds and other measures of dynamical intensity of extratropical cyclones. Future wind speed changes are expected to be small, although poleward shifts in the storm tracks could lead to substantial changes in extreme wind speeds in some regions (*medium confidence*). There is *low confidence* in past trends in characteristics of severe convective storms, such as hail and severe winds, beyond an increase in precipitation rates. The frequency of springtime severe convective storms is projected to increase in the USA, leading to a lengthening of the severe convective storm season (*medium confidence*); evidence in other regions is limited. {11.7.2, 11.7.3}.

Compound Events, Including Dry/Hot events, Fire Weather, Compound Flooding, and Concurrent Extremes

The probability of compound events has *likely* increased in the past due to human-induced climate change and will *likely* continue to increase with further global warming. Concurrent heat waves and droughts have become more frequent and this trend will continue with higher global warming (*high confidence*). Fire weather conditions (compound hot, dry and windy events) have become more probable in

ACCEPTED VERSION SUBJECT TO FINAL EDITING

some regions (*medium confidence*) and there is *high confidence* that they will become more frequent in some regions at higher levels of global warming. The probability of compound flooding (storm surge, extreme rainfall and/or river flow) has increased in some locations, and will continue to increase due to both sea level rise and increases in heavy precipitation, including changes in precipitation intensity associated with TCs (*high confidence*). The land area affected by concurrent extremes has increased (*high confidence*). Concurrent extreme events at different locations, but possibly affecting similar sectors (e.g., critical crop-producing areas for global food supply) in different regions, will become more frequent with increasing global warming, in particular above 2°C of global warming (*high confidence*). {11.8, Box 11.3, Box 11.4}.

Low-Likelihood High-Impact (LLHI) Events Associated With Climate Extremes

The future occurrence of LLHI events linked to climate extremes is generally associated with *low confidence*, but cannot be excluded, especially at global warming levels above 4°C. Compound events, including concurrent extremes, are a factor increasing the probability of LLHI events (*high confidence*). With increasing global warming some compound events with low likelihood in past and current climate will become more frequent, and there is a higher chance of occurrence of historically unprecedented events and surprises (*high confidence*). However, even extreme events that do not have a particularly low probability in the present climate (at more than 1°C of global warming) can be perceived as surprises because of the pace of global warming (*high confidence*). {Box 11.2}

ACCEPTED VERSION
SUBJECT TO FINAL EDITING

11.1 Framing

11.1.1 Introduction to the chapter

This chapter provides assessments of changes in weather and climate extremes (collectively referred to as extremes) framed in terms of the relevance to the Working Group II assessment. It assesses observed changes in extremes, their attribution to causes, and future projections, at three global warming levels: 1.5°C, 2°C, 4°C. This chapter is also one of the four "regional chapters" of the WGI report (along with Chapters 10 and 12 and the Atlas). Consequently, while it encompasses assessments of changes in extremes at global and continental scales to provide a large-scale context, it also addresses changes in extremes at regional scales.

Extremes are climatic impact-drivers (Annex VII: Glossary, see Chapter 12 for a comprehensive assessment). The IPCC risk framework (Chapter 1) articulates clearly that the exposure and vulnerability to climatic impact-drivers, such as extremes, modulate the risk of adverse impacts of these drivers, and that adaptation that reduces exposure and vulnerability will increase resilience resulting in a reduction in impacts. Nonetheless, changes in extremes lead to changes in impacts not only as a direct consequence of changes in their magnitude and frequency, but also through their influence on exposure and resilience.

The Special Report on Managing the Risks of Extreme Events and Disasters to Advance Climate Change Adaptation (referred as the SREX report, IPCC, 2012) provided a comprehensive assessment on changes in extremes and how exposure and vulnerability to extremes determine the impacts and likelihood of disasters. Chapter 3 of that report (Seneviratne et al., 2012, hereafter also referred to as SREX Ch3) assessed physical aspects of extremes, and laid a foundation for the follow-up IPCC assessments. Several chapters of the WGI AR5 (IPCC AR5; IPCC, 2013) addressed climate extremes with respect to observed changes (Hartmann et al., 2013), model evaluation (Flato et al., 2013), attribution (Bindoff et al., 2013), and projected long-term changes (Collins et al., 2013). Assessments were also provided in the recent IPCC Special Reports on 1.5°C global warming (SR15, IPCC, 2018; Hoegh-Guldberg et al., 2018), on climate change and land (IPCC, 2019), and on oceans and the cryosphere (IPCC, 2019). These assessments are the starting point of the present assessment.

This chapter is structured as follows (Figure 11.1). This Section (11.1) provides the general framing and introduction to the chapter, highlighting key aspects that underlie the confidence and uncertainty in the assessment of changes in extremes, and introducing some main elements of the chapter. To provide readers a quick overview of past and future changes in extremes, a synthesis of global scale assessment for different types of extremes is included at the end of this Section (Tables 11.1 and 11.2). Section 11.2 introduces methodological aspects of research on climate extremes. Sections 11.3 to 11.7 assess past changes and their attribution to causes, and projected future changes in extremes, for different types of extremes, including temperature extremes, heavy precipitation and pluvial floods, river floods, droughts, and storms, in separate sections. Section 11.8 addresses compound events. Section 11.9 summarizes regional assessments of changes in temperature extremes, in precipitation extremes and in droughts by continents in tables. The chapter also includes several boxes and FAQs on more specific topics.

[START FIGURE 11.1 HERE]

Figure 11.1: Chapter 11 visual abstract of contents.

[END FIGURE 11.1 HERE]

11.1.2 What are extreme events and how are their changes studied?

Building on the SREX report and AR5, this Report defines an extreme weather event as "an event that is rare at a particular place and time of year" and an extreme climate event as "a pattern of extreme weather that

ACCEPTED VERSION SUBJECT TO FINAL EDITING

persists for some time, such as a season" (Annex VII: Glossary). The definitions of rare are wide ranging, depending on applications. Some studies consider an event as an extreme if it is unprecedented; on the other hand, other studies consider events that occur several times a year as moderate extreme events. Rarity of an event with a fixed magnitude also changes under human-induced climate change, making events that are unprecedented so far rather probable under present conditions, but unique in the observational record – and thus often considered as "surprises" (see Box 11.2).

Various approaches are used to define extremes. These are generally based on the determination of relative (e.g. 90th percentile) or absolute (e.g. 35°C for a hot day) thresholds above which conditions are considered extremes. Changes in extremes can be examined from two perspectives, either focusing on changes in frequency of given extremes, or on changes in their intensity. These considerations in the definition of extremes are further addressed in Section 11.2.1.

11.1.3 Types of extremes assessed in this chapter

The types of extremes assessed in this chapter include temperature extremes, heavy precipitation and pluvial floods, river floods, droughts, and storms. The drought assessment addresses meteorological droughts, agricultural and ecological droughts, and hydrological droughts (see Annex VII: Glossary). The storms assessment addresses tropical cyclones, extratropical cyclones, and severe convective storms. In addition, this chapter also assesses changes in compound events, that is, multivariate or concurrent extreme events, because of their relevance to impacts as well as the emergence of new literature on the subject. Most of the considered extremes were also assessed in the SREX and AR5. Compound events were not assessed in depth in past IPCC reports (SREX Ch3; Section 11.8). Marine-related extremes such as marine heat waves and extreme sea level, are assessed in Chapter 9 (Section 9.6.4 and Box 9.2) of this report.

Extremes and related phenomena are of various spatial and temporal scales. Tornadoes have a spatial scale as small as less than 100 meters and a temporal scale as short as a few minutes. In contrast, a drought can last for multiple years, affecting vast regions. The level of complexity of the involved processes differs from one type of extreme to another, affecting our capability to detect, attribute and project changes in weather and climate extremes. Temperature and precipitation extremes studied in the literature are often based on extremes derived from daily values. Studies of events on longer time scales for both temperature or precipitation, or on sub-daily extremes, are scarcer, which generally limits the assessment for such events. Nevertheless, extremes on time scales different from daily are assessed for temperature extremes and heavy precipitation, when possible (Sections 11.3, 11.4). Droughts, as well as tropical and extratropical cyclones, are assessed as phenomena in general, not limited by their extreme forms, because these phenomena are relevant to impacts (Sections 11.6, 11.7). Both precipitation and wind extremes associated with storms are considered.

Multiple concomitant extremes can lead to stronger impacts than those resulting from the same extremes had they happened in isolation. For this reason, the occurrence of multiple extremes that are multivariate and/or concurrent and/or happening in succession, also called "compound events" (SREX Ch3), are assessed in this chapter based on emerging literature on this topic (Section 11.8). Box 11.2 also provides an assessment on low-likelihood high-impact scenarios associated with extremes.

The assessment of projected future changes in extremes is presented as function of different global warming levels (Section 11.2.4 and CC-Box 11.1). On the one hand, this provides traceability and comparison to the SR15 assessment (Hoegh-Guldberg et al., 2018, hereafter referred to as SR15 Ch3). On the other hand, this is useful for decision makers as actionable information, as much of the mitigation policy discussion and adaptation planning can be tied to the level of global warming. For example, regional changes in extremes, and thus their impacts, can be linked to global mitigation efforts. Additionally, there is also an advantage of separating uncertainty in future projections due to regional responses as function of global warming levels from other factors such as differences in global climate sensitivity and emission scenarios (CC-Box 11.1). However, information is also provided on the translation between information provided at global warming levels and for single emissions scenarios (CC-Box 11.1) to facilitate easier comparison with the AR5

ACCEPTED VERSION SUBJECT TO FINAL EDITING

assessment and with some analyses provided in other chapters as function of emissions scenarios.

A global-scale synthesis of this chapter's assessments is provided in Section 11.1.7. In particular, Tables 11.1 and 11.2 provide a synthesis for observed and attributed changes, and projected changes in extremes, respectively, at different global warming levels (1.5°C, 2°C, 4°C). Tables on regional-scale assessments for changes in temperature extremes, heavy precipitation and droughts, are provided in Section 11.9.

11.1.4 Effects of greenhouse gas and other external forcings on extremes

SREX, AR5, and SR15 assessed that there is evidence from observations that some extremes have changed since the mid 20th century, that some of the changes are a result of anthropogenic influences, and that some observed changes are projected to continue into the future, while other changes are projected to emerge from natural climate variability under enhanced global warming (SREX Chapter 3, AR5 Chapter 10).

At the global scale but also at the regional scale to some extent, many of the changes in extremes are a direct consequence of enhanced radiative forcing, and the associated global warming and/or resultant increase in the water-holding capacity of the atmosphere, as well as changes in vertical stability and meridional temperature gradients that affect climate dynamics (see Box 11.1). Widespread observed and projected increases in the intensity and frequency of hot extremes, together with decreases in the intensity and frequency of cold extremes, are consistent with global and regional warming (Figure 11.2, Section 11.3). Extreme temperatures on land tend to increase more than the global mean temperature (Figure 11.2), due in large part to the land-sea contrast, and additionally to regional feedbacks in some regions (Section 11.1.6). Increases in the intensity of temperature extremes scale robustly and in general linearly with global warming across different geographical regions in projections up to 2100, with minimal dependence on emissions scenarios (Figures 11.3 and 11.A.1; Seneviratne et al., 2016; Wartenburger et al., 2017; Kharin et al., 2018; Section 11.2.4 and CC-Box 11.1). The frequency of hot temperature extremes (see Figure 11.6), the number of heat wave days and the length of heat wave seasons in various regions also scale well, but non-linearly (because of the threshold effect), with global mean temperatures (Wartenburger et al., 2017; Sun et al., 2018a).

Changes in annual maximum one-day precipitation (Rx1day) are proportional to mean global surface temperature changes, at about 7% increase per 1°C temperature increase, that is, following the Clausius-Clapeyron relationship (Box 11.1), both in observations (Westra et al., 2013) and in future projections (Kharin et al., 2013) at the global scale. Extreme short-duration precipitation in North America also scales with global surface temperature (Li et al., 2018a; Prein et al., 2016b). At the local and regional scales, changes in extremes are also strongly modulated and controlled by regional forcings and feedback mechanisms (Section 11.1.6), whereby some regional forcings, for example, associated with changes in land cover and land or aerosol emissions, can have non-local or some (non-homogeneous) global-scale effects. In general, there is *high confidence* in changes in extremes due to global-scale thermodynamic processes (i.e., global warming, mean moistening of the air) as the processes are well understood, while the confidence in those related to dynamic processes or regional and local forcing, including regional and local thermodynamic processes, is much lower due to multiple factors (see following sub-section and Box 11.1).

[START FIGURE 11.2 HERE]

Figure 11.2: Time series of observed temperature anomalies for global average annual mean temperature (black), land average annual mean temperature (green), land average annual hottest daily maximum temperature (TXx, purple), and land average annual coldest daily minimum temperature (TNn, blue). Global and land mean temperature anomalies are relative to their 1850-1900 means based on the multi-product mean annual time series assessed in Section 2.3.1.1.3 (see text for references). TXx and TNn anomalies are relative to their respective 1961-1990 means and are based on the HadEX3 dataset (Dunn et al., 2020) using values for grid boxes with at least 90% temporal completeness over 1961-2018. Further details on data sources and processing are available in the chapter data table (Table 11.SM.9).

ACCEPTED VERSION SUBJECT TO FINAL EDITING

[END FIGURE 11.2 HERE]

[START FIGURE 11.3 HERE]

Figure 11.3: Regional mean changes in annual hottest daily maximum temperature (TXx) for AR6 land regions and the global land, against changes in global mean surface air temperature (GSAT) as simulated by CMIP6 models under different forcing scenarios SSP1-1.9, SSP1-2.6, SSP2-4.5, SSP3-7.0, and SSP5-8.5. (a) shows individual models from the CMIP6 ensemble (grey), the multi-model median under three selected SSPs (colours), and the multi-model median (black). (b) to (l) show the multi-model-median for the pooled data for individual AR6 regions. Numbers in parantheses indicate the linear scaling between regional TXx and GSAT. The black line indicates the 1:1 reference scaling between TXx and GSAT. See Atlas.1.3.2 for the definition of regions. For details on the methods see Supplementary Material 11.SM.2.

[END FIGURE 11.3 HERE]

Since AR5, the attribution of extreme weather events, or the investigation of changes in the frequency and/or magnitude of individual and local- and regional-scale extreme weather events due to various drivers (see Cross-Working Group Box 1.1 (in Chapter 1) and Section 11.2.3) has provided evidence that greenhouse gases and other external forcings have affected individual extreme weather events. The events that have been studied are geographically uneven. A few events, for example, extreme rainfall events in the UK (Schaller et al., 2016; Vautard et al., 2016; Otto et al., 2018b) or heat waves in Australia (King et al., 2014; Perkins-Kirkpatrick et al., 2016; Lewis et al., 2017b), have spurred more studies than other events. Many highly impactful extreme weather events have not been studied in the event attribution framework. Studies in the developing world are also generally lacking. This is due to various reasons (Section 11.2) including lack of observational data, lack of reliable climate models, and lack of scientific capacity (Otto et al., 2020). While the events that have been studied are not representative of all extreme events that occurred and results from these studies may also be subject to selection bias, the large number of event attribution studies provide evidence that changes in the properties of these local and individual events are in line with expected consequences of human influence on the climate and can be attributed to external drivers (Section 11.9). Figure 11.4 summarizes assessments of observed changes in temperature extremes, in heavy precipitation and in droughts, and their attribution in a map form.

[START FIGURE 11.4 HERE]

Figure 11.4: Overview of observed changes for cold, hot, and wet extremes and their potential human contribution. Shown are the direction of change and the confidence in 1) the observed changes in how cold and hot as well as wet extremes have already changed across the world and 2) in the contribution of whether human-induced climate change contributed in causing to these changes (attribution). In each region changes in extremes are indicated by colour (orange – increase in the type of extreme, blue – decrease, both colours – there are changes of opposing direction within the region the signal depends on the exact event definition, grey – there are no changes observed, and no fill – the data/evidence is too sparse to make an assessment). The squares and dots next to the symbol indicate the level of confidence for observing the trend and the human contribution, respectively. The more black dots/squares the higher the level of confidence. The information on this figure is based on regional assessment of the literature on observed trends, detection and attribution and event attribution in section 11.9.

[END FIGURE 11.4 HERE]

ACCEPTED VERSION SUBJECT TO FINAL EDITING

[START BOX 11.1 HERE]

BOX 11.1: Thermodynamic and dynamic changes in extremes across scales

Changes in weather and climate extremes are determined by local exchanges in heat, moisture, and other related quantities (thermodynamic changes) and those associated with atmospheric and oceanic motions (dynamic changes). While thermodynamic and dynamic processes are interconnected, considering them separately helps to disentangle the roles of different processes contributing to changes in climate extremes (e.g. Shepherd, 2014).

Temperature extremes

An increase in the concentration of greenhouse gases in the atmosphere leads to the warming of tropospheric air and the Earth's surface. This direct thermodynamic effect leads to warmer temperatures everywhere with an increase in the frequency and intensity of warm extremes and a decrease in the frequency and intensity of cold extremes. The initial increase in temperature in turn leads to other thermodynamic responses and feedbacks affecting both the atmosphere and the surface. These include an increase in the water vapour content of the atmosphere (water vapour feedback, see Section 7.4.2.2) and a change in the vertical profile of temperature (e.g., lapse rate feedback, see Section 7.4.2.2). While the water vapour feedback always amplifies the initial temperature increases (positive feedback), the lapse rate feedback amplifies near-surface temperature increases (positive feedback) in mid- and high latitudes but reduces temperature increases (negative feedback) in tropical regions (Pithan and Mauritsen, 2014).

Thermodynamic responses and feedbacks also occur through surface processes. For instance, observations and model simulations show that temperature increases, including extreme temperatures, are amplified in areas where seasonal snow cover is reduced due to decreases in surface albedo (see Section 11.3.1). In some mid-latitude areas, temperature increases are amplified by the higher atmospheric evaporative demand (Fu and Feng, 2014; Vicente-Serrano et al., 2020b) that results in a drying of soils in some regions (Section 11.6), leading to increased sensible heat fluxes (soil-moisture temperature feedback, see Sections 11.1.6 and 11.3.1). Other thermodynamic feedback processes include changes in the water-use efficiency of plants under enhanced atmospheric CO_2 concentrations that can reduce the overall transpiration, and thus also enhance temperature in projections (Sections 8.2.3.3, 11.1.6, 11.3, and 11.6).

Changes in the spatial distribution of temperatures can also affect temperature extremes by modifying the characteristics of weather patterns (e.g., Suarez-Gutierrez et al., 2020). For example, a robust thermodynamic effect of polar amplification is a weakened north-south temperature gradient, which amplifies the warming of cold extremes in the Northern Hemisphere mid- and high latitudes because of the reduction of cold air advection (Holmes et al., 2015; Schneider et al., 2015; Gross et al., 2020). Much less robust is the dynamic effect of polar amplification (Section 7.4.4.1) and the reduced low-altitude meridional temperature gradient that has been linked to an increase in the persistence of weather patterns (e.g., heatwaves) and subsequent increases in temperature extremes (Francis and Vavrus, 2012; Coumou et al., 2015, 2018; Mann et al., 2017) (CC-Box 10.1).

Precipitation extremes

Changes in temperature also control changes in water vapour through increases in evaporation and in the water-holding capacity of the atmosphere (Section 8.2.1). At the global scale, column-integrated water vapour content increases roughly following the Clausius-Clapeyron (C-C) relation, with an increase of approximately 7% for every degree celsius of global-mean surface warming (Section 8.2.1). Nonetheless, at regional scales, water vapour increases differ from this C-C rate due to several reasons (Section 8.2.2), including a change in weather regimes and limitations in moisture transport from the ocean, which warms more slowly than land (Byrne and O'Gorman, 2018). Observational studies (Fischer and Knutti, 2016; Sun et al., 2020) have shown the observed rate of increase of precipitation extremes is similar to the C-C scaling at the global scale. Climate model projections show that the increase in water vapour leads to robust increases in precipitation extremes everywhere, with a magnitude that varies between 4% and 8% per degree celsius of surface warming (thermodynamic contribution, Box 11.1, Figure 1b). At regional scales, climate models show that the dynamic contribution (Box 11.1, Figure 1c) can be substantial and strongly modify the

ACCEPTED VERSION SUBJECT TO FINAL EDITING

projected rate of change of extreme precipitation (Box 11.1, Figure 1a) with large regions in the subtropics showing robust reductions and other areas (e.g., equatorial Pacific) showing robust amplifications (Box 11.1, Figure 1c). However, the dynamic contributions show large differences across models and are more uncertain than thermodynamic contributions (Shepherd, 2014; Trenberth et al., 2015; Pfahl et al., 2017; Box 11.1, Figure 1c).

Dynamic contributions can occur in response to changes in the vertical and horizontal distribution of temperature (thermodynamics) and can affect the frequency and intensity of synoptic and subsynoptic phenomena including tropical cyclones, extratropical cyclones, fronts, mesoscale-convective systems and thunderstorms. For example, the poleward shift and strengthening of the Southern Hemisphere mid-latitude storm tracks (Section 4.5.1) can modify the frequency/intensity of extreme precipitation. However, the precise way in which dynamic changes will affect precipitation extremes is unclear due to several competing effects (Shaw et al., 2016; Allan et al., 2020).

Extreme precipitation can also be enhanced by dynamic responses and feedbacks occurring within storms that result from the extra latent heat released from the thermodynamic increases in moisture (Lackmann, 2013; Willison et al., 2013; Marciano et al., 2015; Nie et al., 2018; Mizuta and Endo, 2020). The extra latent heat released within storms has been shown to increase precipitation extremes by strengthening convective updrafts and the intensity of the cyclonic circulation (e.g., Molnar et al., 2015; Nie et al., 2018), although weakening effects have also been found in mid-latitude cyclones (e.g., Kirshbaum et al., 2017). Additionally, the increase in latent heat can also suppress convection at larger scales due to atmospheric stabilization (Nie et al., 2018; Tandon et al., 2018; Kendon et al., 2019). As these dynamic effects result from feedback processes within storms where convective processes are crucial, their proper representation might require improving the horizontal/vertical resolution, the formulation of parameterizations, or both, in current climate models (i.e., Ban et al., 2015; Kendon et al., 2014; Meredith et al., 2015; Nie et al., 2018; Prein et al., 2015; Westra et al., 2014).

[START BOX 11.1, FIGURE 1 HERE]

Box 11.1, Figure 1: Multi-model (CMIP5) mean fractional changes (in % per degree of warming) for (a) annual maximum precipitation (Rx1day), (b) changes in Rx1day due to the thermodynamic contribution and (c) changes in Rx1day due to the dynamic contribution estimated as the difference between the total changes and the thermodynamic contribution. Changes were derived from a linear regression for the period 1950–2100. Uncertainty is represented using the simple approach: no overlay indicates regions with high model agreement, where ≥80% of models (n=22) agree on sign of change; diagonal lines indicate regions with low model agreement, where <80% of models agree on sign of change. For more information on the simple approach, please refer to the Cross-Chapter Box Atlas 1. A detailed description of the estimation of dynamic and thermodynamic contributions is given in Pfahl et al. (2017). Adapted from (Pfahl et al., 2017), originally published in Nature Climate Change/ Springer Nature. Further details on data sources and processing are available in the chapter data table (Table 11.SM.9).

[END BOX 11.1, FIGURE 1 HERE]

Droughts

Droughts are also affected by both thermodynamic and dynamic processes (Sections 8.2.3.3 and 11.6). Thermodynamic processes affect droughts by increasing atmospheric evaporative demand (Martin, 2018; Gebremeskel Haile et al., 2020; Vicente-Serrano et al., 2020b) through changes in air temperature, radiation, wind speed, and relative humidity. Dynamic processes affect droughts through changes in the occurrence, duration and intensity of weather anomalies, which are related to precipitation and the amount of sunlight (Section 11.6). While atmospheric evaporative demand increases with warming, regional changes in aridity are affected by increasing land-ocean warming contrast, vegetation feedbacks and responses to rising CO_2 concentrations and dynamic shifts in the location of the wet and dry parts of the atmospheric circulation in response to climate change as well as internal variability (Byrne and O'Gorman, 2015; Kumar et al., 2015;

ACCEPTED VERSION SUBJECT TO FINAL EDITING

Allan et al., 2020).

In summary, both thermodynamic and dynamic processes are involved in the changes of extremes in response to warming. Anthropogenic forcing (e.g., increases in greenhouse gas concentrations) directly affects thermodynamic variables, including overall increases in high temperatures and atmospheric evaporative demand, and regional changes in atmospheric moisture, which intensify heatwaves, droughts and heavy precipitation events when they occur (*high confidence*). Dynamic processes are often indirect responses to thermodynamic changes, are strongly affected by internal climate variability and are also less well understood. As such, there is *low confidence* in how dynamic changes affect the location and magnitude of extreme events in a warming climate.

[END BOX 11.1 HERE]

11.1.5 Effects of large-scale circulation on changes in extremes

Atmospheric large-scale circulation patterns and associated atmospheric dynamics are important determinants of the regional climate (Chapter 10). As a result, they are also important to the magnitude, frequency, and duration of extremes (Box 11.4). Aspects of changes in large-scale circulation patterns are assessed in Chapters 2, 3, 4, and 8 and representative atmospheric and oceanic modes are described in Annex IV. This subsection provides some general concepts, through a couple of examples, on why the uncertainty in the response of large-scale circulation patterns to external forcing can cascade to uncertainty in the response of extremes to external forcings. Details for specific types of extremes are covered in the relevant subsections. For example, the occurrence of the El Niño-Southern Oscillation (ENSO) influences precipitation regimes in many areas, favoring droughts in some regions and heavy rains in others (Box 11.4). The extent and strength of the Hadley circulation influences regions where tropical and extra-tropical cyclones occur, with important consequences for the characteristics of extreme precipitation, drought, and winds (Section 11.7). Changes in circulation patterns associated with land-ocean heat contrast, which affect the monsoon circulations (Section 8.4.2.4), lead to heavy precipitation along the coastal regions in East Asia (Freychet et al., 2015). As a result, changes in the spatial and/or temporal variability of the atmospheric circulation in response to warming affect characteristics of weather systems such as tropical cyclones (Sharmila and Walsh, 2018), storm tracks (Shaw et al., 2016), and atmospheric rivers (Waliser and Guan, 2017) (e.g. Section 11.7). Changes in weather systems come with changes in the frequency and intensity of extreme winds, extreme temperatures, and extreme precipitation, on the backdrop of thermodynamic responses of extremes to warming (Box 11.1). Floods are also affected by large-scale circulation modes, including ENSO, the North Atlantic Oscillation (NAO), the Atlantic Multi-decadal Variability (AMV), and the Pacific Decadal Variability (PDV) (Kundzewicz et al., 2018; Annex IV). Aerosol forcing, through changes in patterns of sea surface temperatures (SSTs), also affects circulation patterns and tropical cyclone activities (Takahashi et al., 2017).

Changes in atmospheric large-scale circulation due to external forcing are uncertain in general, but there are clear signals in some aspects (Chapter 2, 3, 4, and 8; Sections 2.3.1.4, 8.2.2.2). Among them, there has been a *very likely* widening of the Hadley circulation since the 1980s and the extratropical jets and cyclone tracks have *likely* been shifting poleward since the 1980s (Section 2.3.1.4). The poleward expansion affects drought occurrence in some regions (Section 11.6), and results in poleward shifts of tropical cyclones and storm tracks (Sections 11.7.1, 11.7.2). Although it is *very likely* that the amplitude of ENSO variability will not robustly change over the 21st century (Section 4.3.3.2), the frequency of extreme El Niños (Box 11.4), defined by precipitation threshold, is projected to increase with global warming (Section 6.5 of SROCC). This would have implications for projected changes in extreme events affected by ENSO, including droughts over wide areas (Section 11.6; Box 11.4) and tropical cyclones (Section 11.7.1). A case study is provided for extreme ENSOs in 2015/2016 in Box 11.4 to highlight the influence of ENSO on extremes.

In summary, large-scale atmospheric circulation patterns are important drivers for local and regional extremes. There is overall *low confidence* about future changes in the magnitude, frequency, and spatial distribution of these patterns, which contributes to uncertainty in projected responses of extremes, especially

ACCEPTED VERSION SUBJECT TO FINAL EDITING

in the near term.

11.1.6 Effects of regional-scale processes and forcings and feedbacks on changes in extremes

At the local and regional scales, changes in extremes are strongly modulated by regional and local feedbacks (SRCCL, Jia et al., 2019; Seneviratne et al., 2013; Miralles et al., 2014; Lorenz et al., 2016; Vogel et al., 2017), changes in large-scale circulation patterns (11.1.5), and regional forcings such as changes in land use or aerosol concentrations (Chapters 3 and 7; Hirsch et al., 2017, 2018; Thiery et al., 2017; Wang et al., 2017f; Findell et al., 2017). In some cases, such responses may also include non-local effects (e.g., Persad and Caldeira, 2018; Miralles et al., 2019; de Vrese et al., 2016; Schumacher et al., 2019). Regional-scale forcing and feedbacks often affect temperature distributions asymmetrically, with generally higher effects for the hottest percentiles (Section 11.3).

Land use can affect regional extremes, in particular hot extremes, in several ways (*high confidence*). This includes effects of land management (e.g. cropland intensification, irrigation, double cropping) and well as of land cover changes (deforestation) (Section 11.3.2; see also 11.6). Some of these processes are not well represented (e.g. effects of forest cover on diurnal temperature cycle) or not integrated (e.g. irrigation) in climate models (Sections 11.3.2, 11.3.3). Overall, the effects of land use forcing may be particularly relevant in the context of low-emissions scenarios, which include large land use modifications, for instance associated with the expansion of biofuels, biofuels with carbon capture and storage (BECCS), or re-afforestation to ensure negative emissions, as well as with the expansion of food production (e.g. SR15, Chapter 3; CC-Box 5.1; van Vuuren et al., 2011, Hirsch et al., 2018). There are also effects on the water cycle through freshwater use (CC-Box 5.1; Section 11.6).

Aerosol forcing also has a strong regional footprint associated with regional emissions, which affects temperature and precipitation extremes (*high confidence;* Sections 11.3, 11.4). From ca. the 1950s to 1980s, enhanced aerosol loadings led to regional cooling due to decreased global solar radiation ("global dimming") which was followed by a phase of "global brightening" due to a reduction in aerosol loadings (Chapters 3 and 7; Wild et al., 2005). King et al. (2016a) show that aerosol-induced cooling delayed the timing of a significant human contribution to record-breaking heat extremes in some regions. On the other hand, the decreased aerosol loading since the 1990s has led to an accelerated warming of hot extremes in some regions. Based on Earth System Model (ESM) simulations, Dong et al. (2017b) suggest that a substantial fraction of the warming of the annual hottest days in Western Europe since the mid-1990s has been due to decreases in aerosol concentrations in the region. Dong et al. (2016) also identify non-local effects of decreases in aerosol concentrations in Western Europe, which they estimate played a dominant role in the warming of the hottest daytime temperatures in Northeast Asia since the mid-1990s, via induced coupled atmosphere-land surface and cloud feedbacks, rather than a direct impact of anthropogenic aerosol changes on cloud condensation nuclei.

In addition to regional forcings, regional feedback mechanisms can also substantially affect extremes (*high confidence;* Sections 11.3, 11.4, 11.6). In particular, soil moisture feedbacks play an important role for extremes in several mid-latitude regions, leading in particular to a marked additional warming of hot extremes compared to mean global warming (Seneviratne et al., 2016; Bathiany et al., 2018; Miralles et al., 2019), which is superimposed on the known land-sea contrast in mean warming (Vogel et al., 2017). Soil moisture-atmosphere feedbacks also affect drought development (Section 11.6). Additionally, effects of land surface conditions on circulation patterns have also been reported (Koster et al., 2016; Sato and Nakamura, 2019). These regional feedbacks are also associated with substantial spread in models (Section 11.3), and contribute to the identified higher spread of regional projections of temperature extremes as function of global warming, compared with the spread resulting from the differences in projected global warming (global transient climate responses) in climate models (Seneviratne and Hauser, 2020). In addition, there are also feedbacks between soil moisture content and precipitation occurrence, generally characterized by negative spatial feedbacks and positive local feedbacks (Taylor et al., 2012; Guillod et al., 2015). Climate model projections suggest that these feedbacks are relevant for projected changes in heavy precipitation (Seneviratne et al., 2013), however, there is evidence that climate models do not capture the correct sign of

ACCEPTED VERSION SUBJECT TO FINAL EDITING

the soil moisture-precipitation feedbacks in several regions, in particular spatially and/or in some cases also temporally (Taylor et al., 2012; Moon et al., 2019). In the Northern Hemisphere high latitudes, the snow- and ice-albedo feedback, along with other factors, is projected to largely amplify temperature increases (e.g., Pithan and Mauritsen, 2014), although the effect on temperature extremes is still unclear. It is also still unclear whether snow-albedo feedbacks in mountainous regions might have an effect on temperature and precipitation extremes (e.g. Gobiet et al., 2014), however these feedbacks play an important role in projected changes in high-latitude warming (Hall and Qu, 2006), and, in particular, in changes in cold extremes in these regions (Section 11.3).

Finally, extreme events may also regionally amplify one another. This is, e.g., the case for heat waves and droughts, with high temperatures and stronger radiative forcing leading to drying tendencies on land due to increased evapotranspiration (Section 11.6), and drier soils then inducing decreased evapotranspiration and higher sensible heat flux and hot temperatures (Seneviratne et al., 2013; Miralles et al., 2014; Vogel et al., 2017; Zscheischler and Seneviratne, 2017; Zhou et al., 2019b; Kong et al., 2020; see Box 11.1, Section 11.8).

In summary, regional forcings and feedbacks, in particular associated with land use and aerosol forcings, and soil moisture-temperature, soil moisture-precipitation, and snow/ice-albedo-temperature feedbacks, play an important role in modulating regional changes in extremes. These can also lead to a higher warming of extreme temperatures compared to mean temperature (*high confidence*), and possibly cooling in some regions (*medium confidence*). However, there is only *medium confidence* in the representation of the associated processes in state-of-the-art Earth System Models.

11.1.7 Global-scale synthesis

Tables 11.1 and 11.2 provide a synthesis for observed and attributed changes in extremes, and projected changes in extremes, respectively, at different levels of global warming. This synthesis assessment focuses on the more likely range of observed and projected changes. However, some low-likelihood high-impact scenarios can also be of high relevance as addressed in Box 11.2.

Figure 11.5 provides a synthesis on the level of confidence in the attribution and projection of changes in extremes, building on the assessments from Tables 11.1 and 11.2. In the case where the physical processes underlying the changes in extremes in response to human forcing are well understood and the signal in the observations is still relatively weak, confidence in the projections would be higher than in the attribution because of an increase in the signal to noise ratio with higher global warming. On the other hand, when the observed signal is already strong and when observational evidence is consistent with model simulated responses, confidence in attribution may be higher than that in projections if certain physical processes could be expected to behave differently in a much warmer world and under much higher greenhouse gas forcing, and if such a behavior is poorly understood.

Further synthesis figures for regional assessments are provided in Figure 11.4 (event attribution), Figure 11.6 (projected change in hot temperature extremes) and Figure 11.7 (projected changes in precipitation extremes), and a synthesis on regional assessments for observed, attributed and projected changes in extremes is provided in Section 11.9 for all AR6 reference regions (See Chapter 1, section 1.4.5 and Figure 1.18 for definition of AR6 regions).

Confidence and likelihood of past changes and projected future changes at 2°C of global warming lon the global scale. The information in this figure is based on Tables 11.1 and 11.2.

[START FIGURE 11.5 HERE]

Figure 11.5: Confidence and likelihood of past changes and projected future changes at 2°C of global warming on the global scale. The information in this figure is based on Tables 11.1 and 11.2.

ACCEPTED VERSION SUBJECT TO FINAL EDITING

[END FIGURE 11.5 HERE]

[START FIGURE 11.6 HERE]

Figure 11.6: Projected changes in the frequency of extreme temperature events under 1°C, 1.5°C, 2°C, 3°C, and 4°C global warming levels relative to the 1851-1900 baseline. Extreme temperatures are defined as the maximum daily temperatures that were exceeded on average once during a 10-year period (10-year event, blue) and once during a 50-year period (50-year event, orange) during the 1851-1900 base period. Results are shown for the global land and the AR6 regions. For each box plot, the horizontal line and the box represent the median and central 66% uncertainty range, respectively, of the frequency changes across the multi model ensemble, and the whiskers extend to the 90% uncertainty range. The dotted line indicates no change in frequency. The results are based on the multi-model ensemble from simulations of global climate models contributing to the sixth phase of the Coupled Model Intercomparison Project (CMIP6) under different SSP forcing scenarios. Adapted from (Li et al., 2020a). Further details on data sources and processing are available in the chapter data table (Table 11.SM.9).

[END FIGURE 11.6 HERE]

[START FIGURE 11.7 HERE]

Figure 11.7: Projected changes in the frequency of extreme precipitation events under 1°C, 1.5°C, 2°C, 3°C, and 4°C global warming levels relative to the 1951-1990 baseline. Extreme precipitation is defined as the maximum daily precipitation (Rx1day) that was exceeded on average once during a 10-year period (10-year event, blue) and once during a 50-year period (50-year event, orange) during the 1851-1900 base period. Results are shown for the global land and the AR6 regions. For each box plot, the horizontal line and the box represent the median and central 66% uncertainty range, respectively, of the frequency changes across the multi model ensemble, and the whiskers extend to the 90% uncertainty range. The dotted line indicates no change in frequency. The results are based on the multi-model ensemble from simulations of global climate models contributing to the sixth phase of the Coupled Model Intercomparison Project (CMIP6) under different SSP forcing scenarios. Adapted from (Li et al., 2020a). Further details on data sources and processing are available in the chapter data table (Table 11.SM.9).

[END FIGURE 11.7 HERE]

[START TABLE 11.1 HERE]

Table 11.1: Synthesis table on observed changes in extremes and contribution by human influences. Note that observed changes in marine extremes are assessed in the Cross-Chapter Box 9.1 in Chapter 9.

Phenomenon and direction of trend	Observed/detected trends since 1950 (for +0.5°C global warming or higher)	Human contribution to the observed trends since 1950 (for +0.5°C global warming or higher)
Warmer and/or more frequent hot days and nights over most land areas Warmer and/or fewer cold days and nights over most land areas Warm spells/heat waves; Increases in frequency or intensity over most land areas Cold spells/cold waves: Decreases in frequency or	*Virtually certain* on global scale {11.3} *Continental-scale evidence:* Asia, Australasia, Europe, North America: *Very likely* Central and South America: *High confidence* Africa: *Medium confidence* {11.3, 11.9}	*Extremely likely* main contributor on global scale {11.3} *Continental-scale evidence:* North America, Europe, Australasia, Asia: *Very likely* Central and South America: *High confidence* Africa: *Medium confidence* {11.3, 11.9}

ACCEPTED VERSION SUBJECT TO FINAL EDITING

intensity over most land areas		
Heavy precipitation events: increase in the frequency, intensity, and/or amount of heavy precipitation	*Likely* on global scale, over majority of land regions with good observational coverage {11.3} *Continental-scale evidence:* Asia, Europe, North America: *Likely* Africa, Australasia, Central and South America: *Low confidence* {11.3, 11.9}	*Likely* main contributor to the observed intensification of heavy precipitation in land regions on global scale. {11.3} *Continental-scale evidence:* Asia, Europe, North America: *Likely* Africa, Australasia, Central and South America: *Low confidence* {11.3, 11.9}
Agricultural and ecological drought events: Enhanced drying in dry season	*Medium confidence,* in predominant fraction of land area Observed decrease in water availability in the dry season due to increased evapotranspiration (driven by increased atmospheric evaporative demand) in a predominant fraction of the land area (*medium confidence*) {11.6} Increasing trends in agricultural and ecological droughts have been observed in AR6 regions on all continents (*medium confidence*) {11.6, 11.9}	*Medium confidence*, in predominant fraction of land area Human contribution to decrease in water availability in the dry season in a predominant fraction of the land area (*medium confidence*) {11.6}
Increase in precipitation associated with tropical cyclones	*Medium confidence* {11.7}	*High confidence* {11.7}
Increase in likelihood that a TC will be at major TC intensity (Cat. 3-5)	*Likely* {11.7}	*Medium confidence* {11.7}
Changes in frequency of rapidly intensifying tropical cyclones	*Likely* {11.7}	*Medium confidence* {11.7}
Poleward migration of tropical cyclones in the western Pacific	*Medium confidence* {11.7}	*Medium confidence* {11.7}
Decrease in TC forward motion over the USA	It is *likely* that TC translation speed has slowed over the USA since 1900. {11.7}	It is *more likely than not* that the slowdown of TC translation speed over the USA has contributions from anthropogenic forcing. {11.7}
Severe convective storms (tornadoes, hail, rainfall, wind, lightning)	*Low confidence* in past trends in hail and winds and tornado activity due to short length of high-quality data records. {11.7}	*Low confidence.* {11.7}
Increase in compound events	*Likely* increase in the probability of compound events. *High confidence* that co-occurrent heat waves and droughts are becoming more frequent under enhanced greenhouse gas forcing at global scale. *Medium confidence* that fire weather, i.e. compound hot, dry and windy events, have become more frequent in some regions. *Medium confidence* that compound flooding risk has increased along the USA coastline. {11.8}	*Likely* that human-induced climate change has increased the probability of compound events. *High confidence* that human influence has increased the frequency of co-occurrent heat waves and droughts. *Medium confidence* that human influence has increased fire weather occurrence in some regions. *Low confidence* that human influences has contributed to changes in compound events leading to flooding. {11.8}

ACCEPTED VERSION SUBJECT TO FINAL EDITING

[END TABLE 11.1 HERE]

[START TABLE 11.2 HERE]

Table 11.2: Synthesis table on projected changes in extremes. Note that projected changes in marine extremes are assessed in Chapter 9 and the Cross-chapter box 9.1 (marine heat waves). Assessments are provided compared to pre-industrial conditions.

Phenomenon and direction of trend	Projected changes at +1.5°C global warming	Projected changes at +2°C global warming	Projected changes at +4°C global warming
Warmer and/or more frequent hot days and nights over most land areas Warmer and/or fewer cold days and nights over most land areas Warm spells/heat waves; Increases in frequency or intensity over most land areas Cold spells/cold waves: Decreases in frequency or intensity over most land areas	*Virtually certain* compared to pre-industrial on global scale. *Extremely likely* on all continents Highest increase of temperature of hottest days is projected in some mid-latitude and semi-arid regions, at about 1.5 times to twice the rate of global warming (*high confidence*) Highest increase of temperature of coldest days is projected in Arctic regions, at about three times the rate of global warming (*high confidence*) {11.3} *Continental-scale projections:* *Extremely likely:* Africa, Asia, Australasia, Central and South America, Europe, North America {11.3, 11.9}}	*Virtually certain* compared to pre-industrial on global scale. *Virtually certain* on all continents Highest increase of temperature of hottest days is projected in some mid-latitude and semi-arid regions, at about 1.5 times to twice the rate of global warming (*high confidence*) Highest increase of temperature of coldest days is projected in Arctic regions, at about three times the rate of global warming (*high confidence*) {11.3} *Continental-scale projections:* *Virtually certain:* Africa, Asia, Australasia, Central and South America, Europe, North America {11.3, 11.9}	*Virtually certain* compared to pre-industrial on global scale. *Virtually certain* on all continents Highest increase of temperature of hottest days is projected in some mid-latitude and semi-arid regions, at about 1.5 times to twice the rate of global warming (*high confidence*) Highest increase of temperature of coldest days is projected in Arctic regions, at about three times the rate of global warming (*high confidence*) {11.3} *Continental-scale projections:* *Virtually certain:* Africa, Asia, Australasia, Central and South America, Europe, North America {11.3, 11.9}
Heavy precipitation events: increase in the frequency, intensity, and/or amount of heavy precipitation	*High confidence* that increases take place in most land regions {11.4} *Very likely:* Asia, N. America *Likely:* Africa, Europe *High confidence:* Central and South America *Medium confidence:* Australasia {11.4, 11.9}	*Likely* that increases take place in most land regions {11.4} *Extremely likely:* Asia, N. America *Very likely:* Africa, Europe *Likely:* Australasia, Central and South America {11.4, 11.9}	*Very likely* that increases take place in most land regions {11.4} *Virtually certain:* Africa, Asia, N. America *Extremely likely:* Central and South America, Europe *Very likely* Australasia {11.4, 11.9}

ACCEPTED VERSION SUBJECT TO FINAL EDITING

Agricultural and ecological droughts: Increases in intensity and/or duration of drought events	*High confidence* over predominant fraction of land area Land area affected by increasing drought frequency and severity expands with increasing global warming *(high confidence).* {11.6, 11.9} Precipitation decreases is going to increase the severity of drought in some regions; atmospheric evaporative demand will continue to increase compared to pre-industrial conditions and lead to further increases in agricultural and ecological droughts due to increased evapotranspiration in some regions. (*high confidence*) {11.6, 11.9}	*Likely* over predominant fraction of land area Land area affected by increasing drought frequency and severity expands with increasing global warming *(likely).* {11.6, 11.9} Precipitation decreases is going to increase the severity of drought in some regions; atmospheric evaporative demand will continue to increase compared to pre-industrial conditions and lead to further increases in agricultural and ecological droughts due to increased evapotranspiration in some regions. (*high confidence*) {11.6, 11.9}	*Very likely* over predominant fraction of land area Land area affected by increasing drought frequency and severity expands with increasing global warming *(very likely).* {11.6, 11.9} Precipitation decreases is going to increase the severity of drought in several regions; atmospheric evaporative demand will continue to increase compared to pre-industrial conditions and lead to further increases in agricultural and ecological droughts due to increased evapotranspiration in several regions. (*high confidence*) {11.6, 11.9}
Increase in precipitation associated with tropical cyclones (TC)	*High confidence* in a projected increase of TC rain rates at the global scale; the median projected rate of increase due to human emissions is about 11%. {11.7} *Medium confidence* that rain rates will increase in every basin. {11.7}	*High confidence* in a projected increase of TC rain rates at the global scale; the median projected rate of increase due to human emissions is about 14%. {11.7} *Medium confidence* that rain rates will increase in every basin. {11.7}	*High confidence* in a projected increase of TC rain rates at the global scale; the median projected rate of increase due to human emissions is about 28%. {11.7} *Medium confidence* that rain rates will increase in every basin. {11.7}
Increase in mean tropical cyclone lifetime-maximum wind speed (intensity)	*Medium confidence* {11.7}	*High confidence* {11.7}	*High confidence* {11.7}
Increase in likelihood that a TC will be at major TC intensity (Cat. 4-5)	*High* confidence for an increase in the proportion of TCs that reach the strongest (Category 4-5) levels. The median projected increase in this proportion is about 10%. {11.7}	*High* confidence for an increase in the proportion of TCs that reach the strongest (Category 4-5) levels. The median projected increase in this proportion is about 13%. {11.7}	*High confidence* for an increase in the proportion of TCs that reach the strongest (Category 4-5) levels. The median projected increase in this proportion is about 20%. {11.7}
Severe convective storms	There is *medium confidence* that the frequency of severe convective storms increases in the spring with enhancement of convective available potential energy (CAPE), leading to extension of seasons of occurrence of severe convective storms. There is *high confidence* of future intensification of precipitation associated with severe convective storms. {11.7}		
Increase in compound events (frequency, intensity)	*Likely* that probability of compound events will continue to increase with global warming. *High confidence* that co-occurrent heat waves and droughts will continue to increase under higher levels of global warming, with higher frequency/intensity with every additional 0.5°C of global warming. *High confidence* that fire weather, i.e. compound hot, dry and windy events, will become more frequent in some regions at higher levels of global warming. *Medium confidence* that compound flooding at the coastal zone will increase under higher levels of global warming, with higher frequency/intensity with every additional 0.5°C of global warming. {11.8}		

ACCEPTED VERSION SUBJECT TO FINAL EDITING

[END TABLE 11.2 HERE]

[START BOX 11.2 HERE]

BOX 11.2: Low-likelihood high-impact changes in extremes

SREX (Chapter 3) assigned *low confidence* to low-probability high-impact (LLHI) events. Such events are often not anticipated and thus sometimes referred to as surprises. There are several types of LLHI events. Abrupt changes in mean climate are addressed in Chapter 4. Unanticipated LLHI events can either result from tipping points in the climate system (Section 1.4.4.3), such as the shutdown of the Atlantic thermohaline circulation (SROCC Ch6; Collins et al., 2019) or the drydown of the Amazonian rainforest (SR15 Ch3; Hoegh-Guldberg et al., 2018; Drijfhout et al. 2015), or from uncertainties in climate processes including climate feedbacks that may enhance or damp extremes either related to global or regional climate responses (Seneviratne et al., 2018b; Sutton, 2018). The *low confidence* does not by itself exclude the possibility of such events to occur, it is instead an indication of a poor state of knowledge. Such outcomes, while *unlikely*, could be associated with very high impacts, and are thus highly relevant from a risk perspective (see Chapter 1, Section 1.4.3, Box 11.4; Sutton, 2018, 2019). Alternatively, high impacts can occur when different extremes occur at the same time or in short succession at the same location or in several regions with shared vulnerability (e.g. food-basket regions Gaupp et al., 2019). These "compound events" are assessed in Section 11.8 and Box 11.4 provides a case-study example.

The difficulties in determining the likelihood of occurrence and time frame of potential tipping points and LLHI events persist. However, new literature has emerged on unanticipated and low-probability high-impact events more generally. There are events that are sufficiently rare that they have not been observed in meteorological records, but whose occurrence is nonetheless plausible within the current state of the climate system, see examples below and McCollum et al. (2020). The rare nature of such events and the limited availability of relevant data makes it difficult to estimate their occurrence probability and thus gives little evidence on whether to include such hypothetical events in planning decisions and risk assessments. The estimation of such potential surprises is often limited to events that have historical analogues (including before the instrumental records began, Wetter et al., 2014), albeit the magnitude of the event may differ. Additionally, there is also a limitation of available resources to exhaust all plausible trajectories of the climate system. As a result, there will still be events that cannot be anticipated. These events can be surprises to many in that the events have not been experienced, although their occurrence could be inferred by statistical means or physical modelling approaches (Chen et al., 2017; van Oldenborgh et al., 2017; Harrington and Otto, 2018a). Another approach focusing on the estimation of low-probability events and of events whose likelihood of occurrence is unknown consists in using physical climate models to create a physically self-consistent storyline of plausible extreme events and assessing their impacts and driving factors in past (Section 11.2.3) or future conditions (11.2.4) (Cheng et al., 2018; Schaller et al., 2020; Shepherd, 2016; Shepherd et al., 2018; Sutton, 2018; Zappa and Shepherd, 2017; Wehrli et al., 2020; Hazeleger et al., 2015).

In many parts of the world, observational data are limited to 50-60 years. This means that the chance to observe an extreme event that occurs once in several hundred or more years is small. Thus, when a very extreme event occurs, it becomes a surprise to many (Bao et al., 2017; McCollum et al., 2020), and very rare events are often associated with high impacts (van Oldenborgh et al., 2017; Philip et al., 2018b; Tozer et al., 2020). Attributing and projecting very rare events in a particular location by assessing their likelihood of occurrence within the same larger region and climate thus provides another way to make quantitative assessments regarding events that are extremely rare locally. Some examples of such events include for instance:

- Hurricane Harvey, that made landfall in Houston, TX in August 2017 (Section 11.7.1.4.)
- The 2010-2011 extreme floods in Queensland, Australia (Christidis et al., 2013a)
- The 2018 concurrent heat waves across the northern Hemisphere (Box 11.4)
- Tropical cyclone Idai in Mozambique (Cross-Chapter Box Disaster in WGII AR6 Chapter 4)

ACCEPTED VERSION SUBJECT TO FINAL EDITING

- The California fires in 2018 and 2019
- The 2019-2020 Australia fires (Cross-Chapter Box Disaster in WGII AR6 Chapter 4)

One factor making such events hard to anticipate is the fact that we now live in a non-stationary climate, and that the framework of reference for adaptation is continuously moving. As an example, the concurrent heat waves that occurred across the Northern Hemisphere in the summer of 2018 were considered very unusual and were indeed unprecedented given the total area that was concurrently affected (Toreti et al., 2019; Vogel et al., 2019; Drouard et al., 2019; Kornhuber et al., 2019); however, the probability of this event under 1°C global warming was found to be about 16% (Vogel et al., 2019), which is not particularly low. Similarly, the 2013 summer temperature over eastern China was the hottest on record at the time, but it had an estimated recurrence interval of about 4 years in the climate of 2013 (Sun et al., 2014). Furthermore, when other aspects of the risk, vulnerability, and exposure are historically high or have recently increased (see WGII, Chapter 16, Section 16.4), relatively moderate extremes can have very high impacts (Otto et al., 2015b; Philip et al., 2018b). As warming continues, the climate moves further away from its historical state with which we are familiar, resulting in an increased likelihood of unprecedented events and surprises. This is particularly the case under high global warming levels e.g. such as the climate of the late 21st century under high-emissions scenarios (above 4°C of global warming, CC-Box 11.1).

Another factor highlighted in Section 11.8 and Box 11.4 making events high-impact and difficult to anticipate is that several locations under moderate warming levels could be affected simultaneously, or very repeatedly by different types of extremes (Mora et al., 2018, Gaupp et al., 2019; Vogel et al., 2019). Box 11.4 shows that concurrent events at different locations, which can lead to major impacts across the world, can also result from the combination of anomalous circulation or natural variability (ENSO) patterns with amplification of resulting responses to human-induced global warming. Also multivariate extremes at single locations pose specific challenges to anticipation (Section 11.8), with low-likelihoods in the current climate but the probability of occurrence of such compound events strongly increasing with increasing global warming levels (Vogel et al., 2020a). Therefore, in order to estimate whether and at what level of global warming very high impacts arising from extremes would occur, the spatial extent of extremes and the potential of compounding extremes need to be assessed. Sections 11.3, 11.4, 11.7 and 11.8 highlight increasing evidence that temperature extremes, higher intensity precipitation accompanying tropical cyclones, and compound events such as dry/hot conditions conducive to wildfire or storm surges resulting from sea level rise and heavy precipitation events, pose widespread threats to societies already at relatively low warming levels. Studies have already shown that the probability for some recent extreme events is so small in the undisturbed world such that these events may not have been possible without human influence (Section 11.2.4). Box 11.2, Table 1, provides examples of projected changes in LLHI extremes (single extremes, compound events) of potential relevance for impact and adaptation assessments showing that today's very rare events can become commonplace in a warmer future.

In summary, the future occurrence of LLHI events linked to climate extremes is generally associated with *low confidence*, but cannot be excluded, especially at global warming levels above 4°C. Compound events, including concurrent extremes, are a factor increasing the probability of LLHI events (*high confidence*). With increasing global warming some compound events with low likelihood in past and current climate will become more frequent, and there is a higher chance of historically unprecedented events and surprises (*high confidence*). However, even extreme events that do not have a particularly low probability in the present climate (at more than 1°C of global warming) can be perceived as surprises because of the pace of global warming (*high confidence*).

Box 11.2, Table 1: Examples of changes in LLHI extreme conditions (single extremes, compound events) at different global warming levels

	+1°C (present-day)	+1.5°C	+2°C	+3°C and higher
Risk ratio for annual hottest daytime temperature (TXx) with 1% of probability under present-day warming (+1°C) (Kharin et	1	3.3 (i.e. 230% higher probability)	8.2 (i.e. 720% higher probability)	Not assessed

ACCEPTED VERSION SUBJECT TO FINAL EDITING

al., 2018): Global land				
Risk ratio for heavy precipitation events (Rx1day) with 1% of probability under present-day warming (+1°C) (Kharin et al., 2018): Global land	1	1.2 (i.e. 20% higher probability)	1.5 (i.e. 50% higher probability)	Not assessed
Risk ratio for 1- 5 day duration extreme floods with 1% of probability under present-day warming (+1°C) (Ali et al., 2019a)Indian subcontinent	Up to 3 in individual locations	Up to 5 in individual locations	2-6 in most locations	Up to 12 in individual locations (4°C)
Probability of "extremes extremes" hot days with 1/1000 probability at the end of 20th century (Vogel et al., 2020a): Global land	~20 days over 20 years in most locations	about ~50 days in 20 years in most locations	about ~150 days in 20 years in most locations	about ~500 days in 20 years in most locations (3°C)
Probability of co-occurrence in the same week of hot days with 1/1000 probability and dry days with 1/1000 probability at the end of 20th century (Vogel et al., 2020a): Amazon	0% probability	~1 week within 20 years	~4-5 weeks within 20 years	>9 weeks within 20 years (3°C)
Projected soil moisture drought duration per year (Samaniego et al., 2018): Mediterranean region	41 days (+46% compared to late 20th century)	58 days (+107% compared to late 20th century)	71 days (+154% compared to late 20th century)	125 days (+346% compared to late 20th century) (3°C)
Increase in days exposed to dangerous extreme heat (measured in Health Heat Index (HHI) (Sun et al., 2019c) global land	Not assessed, baseline is 1981-2000	1.6 times higher risk of experiencing heat > 40.6	2.3 times higher risk of experiencing heat > 40.6	~ 80% of land area exposed to dangerous heat, tropical regions 1/3 of the year (4°C)
Increase in regional mean fire season length (Sun et al., 2019c; Xu et al., 2020) global land	Not assessed, baseline is 1981-2000	6.2 days	9.5 days	~ 50 days (4°C)

[END BOX 11.2 HERE]

11.2 Data and Methods

This section provides an assessment of observational data and methods used in the analysis and attribution of climate change specific to weather and climate extremes, and also introduces some concepts used in presenting future projections of extremes in the chapter. The main focus is on extreme events over land, as extremes in the ocean are assessed in Chapter 9 of this Report. Later sections (11.3-11.8) also provide additional assessments on relevant observational datasets and model validation specific for the type of extremes to be assessed. General background on climate modelling is provided in Chapters 4 and 10.

11.2.1 Definition of extremes

In the literature, an event is generally considered extreme if the value of a variable exceeds (or lies below) a

ACCEPTED VERSION SUBJECT TO FINAL EDITING

threshold. The thresholds have been defined in different ways, leading to differences in the meaning of extremes that may share the same name. For example, two sets of frequency of hot/warm days have been used in the literature. One set counts the number of days when maximum daily temperature is above a relative threshold defined as the 90th or higher percentile of maximum daily temperature for the calendar day over a base period. An event based on such a definition can occur during any time of the year and the impact of such an event would differ depending on the season. The other set counts the number of days in which maximum daily temperature is above an absolute threshold such as 35°C, because exceedance of this temperature can sometimes cause health impacts (however, these impacts may depend on location and whether ecosystems and the population are adapted to such temperatures). While both types of hot extreme indices have been used to analyze changes in the frequency of hot/warm events, they represent different events that occur at different times of the year, possibly affected by different types of processes and mechanisms, and possibly also associated with different impacts.

Changes in extremes have also been examined from two perspectives: changes in the frequency for a given magnitude of extremes or changes in the magnitude for a particular return period (frequency). Changes in the probability of extremes (e.g., temperature extremes) depend on the rarity of the extreme event that is assessed, with a larger change in probability associated with a rarer event (e.g., Kharin et al., 2018). On the other hand, changes in the magnitude represented by the return levels of the extreme events may not be as sensitive to the rarity of the event. While the answers to the two different questions are related, their relevance to different audiences may differ. Conclusions regarding the respective contribution of greenhouse gas forcing to changes in magnitude versus frequency of extremes may also differ (Otto et al., 2012). Correspondingly, the sensitivity of changes in extremes to increasing global warming is also dependent on the definition of the considered extremes. In the case of temperature extremes, changes in magnitude have been shown to often depend linearly on global surface temperature (Seneviratne et al., 2016; Wartenburger et al., 2017), while changes in frequency tend to be non-linear and can, for example, be exponential for increasing global warming levels (Fischer and Knutti, 2015; Kharin et al., 2018). When similar damage occurs once a fixed threshold is exceeded, it is more important to ask a question regarding changes in the frequency. But when the exceedance of this fixed threshold becomes a normal occurrence in the future, this can lead to a saturation in the change of probability (Harrington and Otto, 2018a). On the other hand, if the impact of an event increases with the intensity of the event, it would be more relevant to examine changes in the magnitude. Finally, adaptation to climate change might change the relevant thresholds over time, although such aspects are still rarely integrated in the assessment of projected changes in extremes. Framing, including how extremes are defined and how the questions are asked in the literature, is considered when forming the assessments of this chapter.

11.2.2 Data

Studies of past and future changes in weather and climate extremes and in the mean state of the climate use the same original sources of weather and climate observations, including in-situ observations, remotely sensed data, and derived data products such as reanalyses. Chapter 2 (Section 2.3) and Chapter 10 (Section 10.2) assess various aspects of these data sources and data products from the perspective of their general use and in the analysis of changes in the mean state of the climate in particular. Building on these previous chapters, this subsection highlights particular aspects that are related to extremes and that are most relevant to the assessment of this chapter. The SREX (Chapter 3, Seneviratne et al., 2012) and AR5 (Chapter 2, Hartmann et al., 2013) addressed critical issues regarding the quality and availability of observed data and their relevance for the assessment of changes in extremes.

Extreme weather and climate events occur on time scales of hours (e.g., convective storms that produce heavy precipitation) to days (e.g., tropical cyclones, heat waves), to seasons and years (e.g., droughts). A robust determination of long-term changes in these events can have different requirements for the spatial and temporal scales and sample size of the data. In general, it is more difficult to determine long-term changes for events of fairly large temporal duration, such as “mega-droughts” that last several years or longer (e.g., Ault et al. 2014), because of the limitations of the observational sample size. Literature that study changes in extreme precipitation and temperature often use indices representing specifics of extremes that are derived

ACCEPTED VERSION SUBJECT TO FINAL EDITING

from daily precipitation and temperature values. Station-based indices would have the same issues as those for the mean climate regarding the quality, availability, and homogeneity of the data. For the purpose of constructing regional information and/or for comparison with model outputs, such as model evaluation, and detection and attribution, these station-based indices are often interpolated onto regular grids. Two different approaches, involving two different orders of operation, have been used in producing such gridded datasets.

In some cases, such as for the HadEX3 dataset (Dunn et al., 2020), indices of extremes are computed using time series directly derived from stations first and are then gridded over the space. As the indices are computed at the station level, the gridded data products represent point estimates of the indices averaged over the spatial scale of the grid box. In other instances, daily values of station observations are first gridded (e.g., Contractor et al., 2020), and the interpolated values can then be used to compute various indices by the users. Depending on the station density, values for extremes computed from data gridded this way represent extremes of spatial scales anywhere from the size of the grid box to a point. In regions with high station density (e.g., North America, Europe), the gridded values are closer to extremes of area means and are thus more appropriate for comparisons with extremes estimated from climate model output, which is often considered to represent areal means (Chen and Knutson, 2008; Gervais et al., 2014; Avila et al., 2015; Di Luca et al., 2020a). In regions with very limited station density (e.g., Africa), the gridded values are closer to point estimates of extremes. The difference in spatial scales among observational data products and model simulations needs to be carefully accounted for when interpreting the comparison among different data products. For example, the average annual maximum daily maximum temperature (TXx) over land computed from the original ERA-interim reanalysis (at 0.75° resolution) is about 0.4°C warmer than that computed when the ERA-interim dataset is upscaled to the resolution of 2.5° x 3.75° (Di Luca et al., 2020).

Extreme indices computed from various reanalysis data products have been used in some studies, but reanalysis extreme statistics have not been rigorously compared to observations (Donat et al., 2016a). In general, changes in temperature extremes from various reanalyses were most consistent with gridded observations after about 1980, but larger differences were found during the pre-satellite era (Donat et al., 2014b). Overall, lower agreement across reanalysis datasets was found for extreme precipitation changes, although temporal and spatial correlations against observations were found to be still significant. In regions with sparse observations (e.g., Africa and parts of South America), there is generally less agreement for extreme precipitation between different reanalysis products, indicating a consequence of the lack of an observational constraint in these regions (Donat et al., 2014b, 2016a). More recent reanalyses, such as ERA5 (Hersbach et al., 2020), seem to have improved over previous products, at least over some regions (e.g., Mahto and Mishra, 2019; Gleixner et al., 2020; Sheridan et al., 2020). Caution is needed when reanalysis data products are used to provide additional information about past changes in these extremes in regions where observations are generally lacking.

Satellite remote sensing data have been used to provide information about precipitation extremes because several products provide data at sub-daily resolution for precipitation (e.g., TRMM; Maggioni et al. 2016) and clouds (e.g., HIMAWARI; Bessho et al., 2016; Chen et al. 2019). However, satellites do not observe the primary atmospheric state variables directly and polar orbiting satellites do not observe any given place at all times. Hence, their utility as a substitute for high-frequency (i.e., daily) ground-based observations is limited. For instance, Timmermans et al. (2019) found little relationship between the timing of extreme daily and five-day precipitation in satellite and gridded station data products over the United States.

[START BOX 11.3 HERE]

BOX 11.3: Extremes in paleoclimate archives compared to instrumental records

Examining extremes in pre-instrumental information can help to put events occurring in the instrumental record (referred to as 'observed') in a longer-term context. This box focuses on extremes in the Common Era (CE, the last 2000 years), because there is generally higher confidence in pre-instrumental information gathered from the more recent archives from the Common Era than from earlier evidence. It addresses evidence of extreme events in paleo reconstructions, documentary evidence (such as grape harvest data, religious documents, newspapers, and logbooks) and model-based analyses, and whether observed extremes

ACCEPTED VERSION SUBJECT TO FINAL EDITING

have or have not been exceeded in the Common Era. This box provides overviews of i) AR5 assessments and ii) types of evidence assessed here, evidence of iii) droughts, iv) temperature extremes, v) paleofloods, and vi) paleotempests, and vii) a summary.

AR5 (Chapter 5, Masson-Delmotte et al., 2013) concluded with *high confidence* that droughts of greater magnitude and of longer duration than those observed in the instrumental period occurred in many regions during the preceding millennium. There was *high confidence* in evidence that floods during the past five centuries in northern and Central Europe, the western Mediterranean region, and eastern Asia were of a greater magnitude than those observed instrumentally, and *medium confidence* in evidence that floods in the near East, India and central North America were comparable to modern observed floods. While AR5 assessed 20th century summer temperatures compared to those reconstructed in the Common Era, it did not assess shorter duration temperature extremes.

Many factors affect confidence in information on pre-instrumental extremes. First, the geographical coverage of paleoclimate reconstructions of extremes is not spatially uniform (Smerdon and Pollack, 2016) and depends on both the availability of archives and records, which are environmentally dependent, and also the differing attention and focus from the scientific community. In Australia, for example, the paleoclimate network is sparser than for other regions, such as Asia, Europe and North America, and synthesised products rely on remote proxies and assumptions about the spatial coherence of precipitation between remote climates (Cook et al., 2016c; Freund et al., 2017). Second, pre-instrumental evidence of extremes may be focused on understanding archetypal extreme events, such as the climatic consequences of the 1815 eruption of Mount Tambora, Indonesia (Brohan et al., 2016; Veale and Endfield, 2016). These studies provide narrow evidence of extremes in response to specific forcings (Li, 2017) for specific epochs. Third, natural archives may provide information about extremes in one season only and may not represent all extremes of the same types.

Evidence of shorter duration extreme event types, such as floods and tropical storms, is further restricted by the comparatively low chronological controls and temporal resolution (e.g., monthly, seasonal, yearly, multiple years) of most archives compared to the events (e.g., minutes to days). Natural archives may be sensitive only to intense environmental disturbances, and so only sporadically record short-duration or small spatial scale extremes. Interpreting sedimentary records as evidence of past short-duration extremes is also complex and requires a clear understanding of natural processes. For example, paleoflood reconstructions of flood recurrence and intensity produced from geological evidence (e.g., river and lake sediments), speleothems (Denniston and Luetscher, 2017), botanical evidence (e.g., flood damage to trees, or tree ring reconstructions), and floral and faunal evidence (e.g., diatom fossil assemblages) require understanding of sediment sources and flood mechanisms. Pre-instrumental records of tropical storm intensity and frequency (also called paleotempest records) derived from overwash deposits of coastal lake and marsh sediments are difficult to interpret. Many factors impact whether disturbances are deposited in archives (Muller et al., 2017) and deposits may provide sporadic and incomplete preservation histories (e.g., Tamura et al., 2018).

Overall, the most complete pre-instrumental evidence of extremes occurs for long-duration, large-spatial-scale extremes, such as for multi-year meteorological droughts or seasonal- and regional-scale temperature extremes. Additionally, more precise insights into recent extremes emerge where multiple studies have been undertaken, compared to the confidence in extremes reported at single sites or in single studies, which may not necessarily be representative of large-scale changes, or for reconstructions that synthesise multiple proxies over large areas (e.g., drought atlases). Multiproxy synthesis products combine paleoclimate temperature reconstructions and cover sub-continental- to hemispheric-scale regions to provide continuous records of the Common Era (e.g. Ahmed et al., 2013; Neukom et al., 2014 for temperature).

There is *high confidence* in the occurrence of long-duration and severe drought events during the Common Era for many locations, although their severity compared to recent drought events differs between locations and the lengths of reconstruction provided. Recent observed drought extremes in some regions (such as the Levant (Cook et al., 2016a), California in the United States (Cook et al., 2014; Griffin and Anchukaitis, 2014), and the Andes (Domínguez-Castro et al., 2018)) do not have precedents within the multi-century periods reconstructed in these studies, in terms of duration and/or severity. In some regions (in Southwest North America (Asmerom et al., 2013; Cook et al., 2015), the Great Plains region (Cook et al., 2004), the

ACCEPTED VERSION SUBJECT TO FINAL EDITING

Middle East (Kaniewski et al., 2012), and China (Gou et al., 2015), recent drought extremes may have been exceeded in the Common Era. In further locations, there is conflicting evidence for the severity of pre-instrumental droughts compared to observed extremes, depending on the length of the reconstruction and the seasonal perspective provided (see Cook et al., 2016b; Freund et al., 2017 for Australia). There can also be differing conclusions for the severity, or even the occurrence, of specific individual pre-instrumental droughts when different evidence is compared (e.g., Büntgen et al., 2015; Wetter et al., 2014).

There is *medium confidence* that the magnitude of large-scale, seasonal-scale extreme high temperatures in observed records exceed those reconstructed over the Common Era in some locations, such as Central Europe. In one example, multiple studies have examined the unusualness of present-day European summer temperature records in a long-term context, particularly in comparison to the exceptionally warm year of 1540 CE in Central Europe. Several studies indicate recent extreme summers (2003 and 2010) in Europe have been unusually warm in the context of the last 500 years (Barriopedro et al., 2011; Wetter and Pfister, 2013; Wetter et al., 2014; Orth et al., 2016a), or longer (Luterbacher et al., 2016). Others studies show summer temperatures in Central Europe in 1540 were warmer than the present-day (1966–2015) mean, but note that it is difficult to assess whether or not the 1540 summer was for its part warmer than observed record extreme temperatures (Orth et al., 2016a).

There is *high confidence* that the magnitude of floods over the Common Era has exceeded observed records in some locations, including Central Europe and eastern Asia. Recent literature supports the AR5 assessments (Masson-Delmotte et al., 2013) of floods. High temporally resolved records provide evidence, for example, of Common Era floods exceeding the probable maximum flood levels in the Upper Colorado River, USA (Greenbaum et al., 2014) and peak discharges that are double gauge levels along the middle Yellow River, China (Liu et al., 2014). Further studies demonstrate pre-instrumental or early instrumental differences in flood frequency compared to the instrumental period, including reconstructions of high and low flood frequency in the European Alps (e.g., Swierczynski et al., 2013; Amann et al., 2015) and Himalayas (Ballesteros Cánovas et al., 2017). The combination of extreme historical flood episodes determined from documentary evidence also increases confidence in the determination of flood frequency and magnitude, compared to using geomorphological archives alone (Kjeldsen et al., 2014). In regions, such as Europe and China, that have rich historical flood documents, there is strong evidence of high magnitude flood events over pre-instrumental periods (Benito et al., 2015; Kjeldsen et al., 2014; Macdonald and Sangster, 2017). A key feature of paleoflood records is variability in flood recurrence at centennial timescales (Wilhelm et al., 2019), although constraining climate-flood relationships remains challenging. Pre-instrumental floods often occurred in considerably different contexts in terms of land use, irrigation, and infrastructure, and may not provide direct insight into modern river systems, which further prevents long-term assessments of flood changes being made based on these sources.

There is *medium confidence* that periods of both more and less tropical cyclone activity (frequency or intensity) than observed occurred over the Common Era in many regions. Paleotempest studies cover a limited number of locations that are predominantly coastal, and hence provide information on specific locations that cannot be extrapolated basin-wide (see Muller et al., 2017). In some locations, such as the Gulf of Mexico and the New England coast, similarly intense storms to those observed recently have occurred multiple times over centennial timescales (Donnelly et al., 2001; Bregy et al., 2018). Further research focused on the frequency of tropical storm activity. Extreme storms occurred considerably more frequently in particular periods of the Common Era, compared to the instrumental period in northeast Queensland, Australia (Nott et al., 2009; Haig et al., 2014), and the Gulf Coast (e.g., Brandon et al., 2013; Lin et al., 2014).

The probability of finding an unprecedented extreme event increases with an increased length of past record-keeping, in the absence of longer-term trends. Thus, as a record is extended to the past based on paleo-reconstruction, there is a higher chance of very rare extreme events having occurred at some time prior to instrumental records. Such an occurrence is not, in itself, evidence of a change, or lack of a change, in the magnitude or the likelihood of extremes in the past or in the instrumental period at regional and local scales. Yet, the systematic collection of paleoclimate records over wide areas may provide evidence of changes in extremes. In one study, extended evidence of the last millennium from observational data and paleoclimate

ACCEPTED VERSION SUBJECT TO FINAL EDITING

reconstructions using tree rings indicates human activities affected the worldwide occurrence of droughts as early as the beginning of the 20th century (Marvel et al., 2019).

In summary, there is *low confidence* in overall changes in extremes derived from paleo-archives. The most robust evidence is *high confidence* that high-duration and severe drought events occurred at many locations during the last 2000 years. There is also *high confidence* that high-magnitude flood events occurred at some locations during the last 2000 years, but overall changes in infrastructure and human water management make the comparison with present-day records difficult. But these isolated paleo-drought and paleo-flood events are not evidence of a change, or lack of a change, in the magnitude or the likelihood of relevant extremes.

[END BOX 11.3 HERE]

11.2.3 Attribution of extremes

Attribution science concerns the identification of causes for changes in characteristics of the climate system (e.g., trends, single extreme events). A general overview and summary of methods of attribution science is provided in the Cross-Working Group Box 1.1 (in Chapter 1). Trend detection using optimal fingerprinting methods is a well-established field, and has been assessed in the AR5 (Chapter 10, Bindoff et al., 2013), and Chapter 3 in this Report (Section 3.2.1). There are specific challenges when applying optimal fingerprinting to the detection and attribution of trends in extremes and on regional scales where the lower signal-to-noise ratio is a challenge. In particular, the method generally requires the data to follow a Normal (Gaussian) distribution, which is often not the case for extremes. Recent studies showed that extremes can, however, be transformed to a Gaussian distribution, for example by averaging over space, so that optimal fingerprinting techniques can still be used (Zhang et al., 2013; Wen et al., 2013; and Wan et al., 2019). Non-stationary extreme value distributions, which allow for the detailed detection and attribution of regional trends in temperature extremes, have also been used (Wang et al., 2017c).

Apart from the detection and attribution of trends in extremes, new approaches have been developed to answer the question of whether and to what extent external drivers have altered the probability and intensity of an individual extreme event (NASEM, 2016). In AR5, there was an emerging consensus that the role of external drivers of climate change in specific extreme weather events could be estimated and quantified in principle, but related assessments were still confined to particular case studies, often using a single model, and typically focusing on high-impact events with a clear attributable signal.

However, since AR5, the attribution of extreme weather events has emerged as a growing field of climate research with an increasing body of literature (see series of supplements to the annual State of the Climate report (Peterson et al., 2012, 2013b, Herring et al., 2014, 2015, 2016, 2018), including the number of approaches to examining extreme events (described in Easterling et al., 2016; Otto, 2017; Stott et al., 2016)). A commonly-used approach, often called the risk-based approach in the literature and referred to here as the "probability-based approach", produces statements such as 'anthropogenic climate change made this event type twice as likely' or 'anthropogenic climate change made this event 15% more intense'. This is done by estimating probability distributions of the index characterizing the event in today's climate, as well as in a counterfactual climate, and either comparing intensities for a given occurrence probability (e.g., 1-in-100 year event) or probabilities for a given magnitude (see FAQ 11.3). There are a number of different analytical methods encompassed in the probability-based approach building on observations and statistical analyses (e.g., van Oldenborgh et al., 2012), optimal fingerprint methods (Sun et al., 2014), regional climate and weather forecast models (e.g., Schaller et al., 2016), global climate models (GCMs) (e.g., Lewis and Karoly, 2013), and large ensembles of atmosphere-only GCMs (e.g., Lott et al., 2013). A key component in any event attribution analysis is the level of conditioning on the state of the climate system. In the least conditional approach, the combined effect of the overall warming and changes in the large-scale atmospheric circulation are considered and often utilize fully coupled climate models (Sun et al., 2014). Other more conditional approaches involve prescribing certain aspects of the climate system. These range from prescribing the pattern of the surface ocean change at the time of the event (e.g. Hoerling et al., 2013, 2014),

ACCEPTED VERSION SUBJECT TO FINAL EDITING

often using AMIP-style global models, where the choice of sea surface temperature and ice patterns influences the attribution results (Sparrow et al., 2018), to prescribing the large-scale circulation of the atmosphere and using weather forecasting models or methods (e.g., Pall et al., 2017; Patricola and Wehner, 2018; Wehner et al., 2018a). These highly conditional approaches have also been called "storylines" (Shepherd, 2016; Cross-Working Group Box 1.1 in Chapter 1) and can be useful when applied to extreme events that are too rare to otherwise analyse or where the specific atmospheric conditions were central to the impact. These methods are also used to enable the use of very-high-resolution simulations in cases were lower-resolution models do not simulate the regional atmospheric dynamics well (Shepherd, 2016; Shepherd et al., 2018). However, the imposed conditions limit an overall assessment of the anthropogenic influence on an event, as the fixed aspects of the analysis may also have been affected by climate change. For instance, the specified initial conditions in the highly conditional hindcast attribution approach often applied to tropical cyclones (e.g., Patricola and Wehner, 2018; Takayabu et al., 2015) permit only a conditional statement about the magnitude of the storm if similar large-scale meteorological patterns could have occurred in a world without climate change, thus precluding any attribution statement about the change in frequency if used in isolation. Combining conditional assessments of changes in the intensity with a multi-model approach does allow for the latter as well (Shepherd, 2016).

The outcome of event attribution is dependent on the definition of the event (Leach et al., 2020), as well as the framing (Christidis et al., 2018; Jézéquel et al., 2018; Otto et al., 2016) and uncertainties in observations and modelling. Observational uncertainties arise both in estimating the magnitude of an event as well as its rarity (Angélil et al., 2017). Results of attribution studies can also be very sensitive to the choice of climate variables (Sippel and Otto, 2014; Wehner et al., 2016). Attribution statements are also dependent on the spatial (Uhe et al., 2016; Cattiaux and Ribes, 2018; Kirchmeier-Young et al., 2019) and temporal (Harrington, 2017; Leach et al., 2020) extent of event definitions, as events of different scales involve different processes (Zhang et al., 2020d) and large-scale averages generally yield higher attributable changes in magnitude or probability due to the smoothing out of the noise. In general, confidence in attribution statements for large-scale heat and lengthy extreme precipitation events have higher confidence than shorter and more localized events, such as extreme storms, an aspect also relevant for determining the emergence of signals in extremes or the confidence in projections (see also Cross-Chapter Box Atlas.1)

The reliability of the representation of the event in question in the climate models used in a study is essential (Angélil et al., 2016; Herger et al., 2018). Extreme events characterized by atmospheric dynamics that stretch the capabilities of current-generation models (see Section 10.3.3.4, Shepherd, 2014; Woollings et al., 2018) limit the applicability of the probability-based approach of event attribution. The lack of model evaluation, in particular in early event attribution studies, has led to criticism of the emerging field of attribution science as a whole (Trenberth et al., 2015) and of individual studies (Angélil et al., 2017). In this regard, the storyline approach (Shepherd, 2016) provides an alternative option that does not depend on the model's ability to represent the circulation reliably. In addition, several ways of quantifying statistical uncertainty (Paciorek et al., 2018) and model evaluation (Lott and Stott, 2016; Philip et al., 2018b, 2020) have been employed to evaluate the robustness of event attribution results.-For the unconditional probability-based approach, multi-model and multi-approach (e.g., combining observational analyses and model experiments) methods have been used to improve the robustness of event attribution (Hauser et al., 2017; Otto et al., 2018a; Philip et al., 2018b, 2019, 2020; van Oldenborgh et al., 2018; Kew et al., 2019).

In the regional tables provided in Section 11.9, the different lines of evidence from event attribution studies and trend attributions are assessed alongside one another to provide an assessment of the human contribution to observed changes in extremes in all AR6 regions .

11.2.4 Projecting changes in extremes as a function of global warming levels

The most important quantity used to characterize past and future climate change is global warming relative to its pre-industrial level. On the one hand, changes in global warming are linked quasi-linearly to global cumulative CO_2 emissions (IPCC, 2013). On the other hand, changes in regional climate, including many types of extremes, scale quasi-linearly with changes in global warming, often independently of the

ACCEPTED VERSION SUBJECT TO FINAL EDITING

underlying emissions scenarios (SR15 Ch3; Seneviratne et al., 2016; Wartenburger et al., 2017; Matthews et al., 2017; Tebaldi and Knutti 2018, Sun et al., 2018a, Kharin et al., 2018, Beusch et al., 2020b; Li et al., 2020). Finally, the use of global warming levels in the context of global policy documents (in particular the 2015 Paris Agreement, UNFCCC 2015), implies that information on changes in the climate system, and in particular extremes, as a function of global warming are of particular policy relevance. Cross-Chapter Box 11.1 provides on overview on the translation between information at global warming levels (GWLs) and scenarios.

The assessment of projections of future changes in extremes as function of GWL has an advantage in separating uncertainty associated with the global warming response (see Chapter 4) from the uncertainty resulting from the regional climate response as a function of GWLs (Seneviratne and Hauser, 2020). If the interest is in the projection of regional changes at certain GWLs, such as those defined by the Paris Agreement, projections based on time periods and emission scenarios have unnecessarily larger uncertainty due to differences in model global transient climate responses. To take advantage of this feature and to provide easy comparison with SR15, assessments of projected changes in this chapter are largely provided in relation to future GWLs, with a focus on changes at +1.5°C, +2°C, and +4°C of global warming above pre-industrial levels (e.g. Tables 11.1, 11.2 and regional tables in Section 11.9). These encompass a scenario compatible with the aim of the Paris Agreement (+1.5°C), a scenario slightly overshooting the aims of the Paris Agreement (+2°C), and a "worst-case" scenario with no mitigation (+4°C). The CC-Box 11.1 provides a background on the GWL sampling approach used in the AR6, both for the computation of GWL projections from ESMs contributing to the 6th Phase of the Coupled Model Intercomparison Project (CMIP6) as well as for the mapping of existing scenario-based literature for CMIP6 and the 5th Phase of CMIP (CMIP5) to assessments as function of GWLs (see also Section 11.9. and Table 11.3 for an example).

While regional changes in many types of extremes do scale robustly with global surface temperature, generally irrespective of emission scenarios (Section 11.1.4; Figures 11.3, 11.6, 11.7; CC-Box 11.1), effects of local forcing can distort this relation. In particular, emission scenarios with the same radiative forcing can have different regional extreme precipitation responses resulting from different aerosol forcing (Wang et al., 2017d). Another example is related to forcing from land use and land cover changes (Section 11.1.6). Climate models often either overestimate or underestimate observed changes in annual maximum daily maximum temperature depending on the region and considered models (Donat et al., 2017; Vautard et al., 9999). Part of the discrepancies may be due to the lack of representation of some land forcings, in particular crop intensification and irrigation (Mueller et al., 2016b; Thiery et al., 2017; Findell et al., 2017; Thiery et al., 2020). Since these local forcings are not represented and their future changes are difficult to project, these can be important caveats when using GWL scaling to project future changes for these regions. However, these caveats also apply to the use of scenario-based projections.

SR15 (Chapter 3) assessed different climate responses at +1.5°C of global warming, including transient climate responses, short-term stabilization responses, and long-term equilibrium stabilization responses, and their implications for future projections of different extremes. Indeed, the temporal dimension, that is, when the given GWL occurs, also matters for projections, in particular beyond the 21st century and for some climate variables with large inertia (e.g., sea level rise and associated extremes). Nonetheless, for assessments focused on conditions within the next decades and for the main extremes considered in this chapter, derived projections are relatively insensitive to details of climate scenarios and can be well estimated based on transient simulations (CC-Box 11.1; see also SR15).

An important question is the identification of the GWL at which a given change in a climate extreme can begin to emerge from climate noise. Figure 11.8 displays analyses of the GWLs at which emergence in hot extremes (20-year return values of TXx, TXx_20yr) and heavy precipitation (20-year return values of Rx1day, Rx1day_20yr) is identified in AR6 regions for the whole CMIP5 and CMIP6 ensembles). Overall, signals for extremes emerge very early for TXx_20yr, already below 0.2°C in many regions (Fig. 11.8a,b), and at around 0.5°C in most regions. This is consistent with conclusions from the SR15 Ch3 for less-rare temperature extremes (TXx on the yearly time scale), which shows that a difference as small as 0.5°C of global warming, e.g. between +1.5°C and +2°C of global warming, leads to detectable differences in temperature extremes in TXx in most WGI AR6 regions in CMIP5 projections (e.g.,Wartenburger et al.,

ACCEPTED VERSION SUBJECT TO FINAL EDITING

2017; Seneviratne et al., 2018b). The GWL emergence for Rx1day_20yr is also largely consistent with analyses for less-extreme heavy precipitation events (Rx5day on the yearly time scale) in the SR15 (see Chapter 3).

To some extent, analyses as functions of GWLs replace the time axis with a global surface temperature axis. Nonetheless, information on the timing of given changes in extremes is obviously also relevant. Regarding this information, that is, the time frame at which given global warming levels are reached, the readers are referred to Chapter 4 (Section 4.6; see also CC-Box 11.1). Figure 11.5 provides a synthesis of attributed and projected changes in extremes as function of GWLs (see also Figs. 11.3, 11.6, and 11.7 for regional analyses).

[START FIGURE 11.8 HERE]

Figure 11.8: Global and regional-scale emergence of changes in temperature (a) and precipitation (b) extremes for the globe (glob.), global oceans (oc.), global lands (land), and the AR6 regions. Colours indicate the multi-model mean global warming level at which the difference in 20-year means of the annual maximum daily maximum temperature (TXx) and the annual maximum daily precipitation (Rx1day) become significantly different from their respective mean values during the 1851–1900 base period. Results are based on simulations from the CMIP5 and CMIP6 multi-model ensembles. See Atlas.1.3.2 for the definition of regions. Adapted from Seneviratne and Hauser, 2020) under the terms of the Creative Commons Attribution license.

[END FIGURE 11.8 HERE]

[START CROSS-CHAPTER BOX 11.1 HERE]

Cross-Chapter Box 11.1: Translating between regional information at global warming levels vs scenarios for end users

Contributors: Erich Fischer (Switzerland), Mathias Hauser (Switzerland), Sonia I. Seneviratne (Switzerland), Richard Betts (UK), José M. Gutiérrez (Spain), Richard G. Jones (UK), June-Yi Lee (Republic of Korea), Malte Meinshausen (Australia/Germany), Friederike Otto (UK/Germany), Izidine Pinto (Mozambique), Roshanka Ranasinghe (The Netherlands/Sri Lanka/Australia), Joeri Rogelj (Germany/Belgium), Bjørn Samset (Norway), Claudia Tebaldi (USA), Laurent Terray (France)

Background

Traditionally, projections of climate variables are summarized and communicated as function of time and scenario. Recently, quantifying global and regional climate at specific global warming levels (GWLs) has become widespread, motivated by the inclusion of explicit GWLs in the long-term temperature goal of the Paris Agreement (Section 1.6.2). GWLs, expressed as changes in global surface temperature relative to the 1850-1900 period (see CCBox 2.3), are used in the SR15 and in the assessment of Reasons for Concerns in the WGII reports (see also CCBox 12.1). CCB 11.1, Figure 1 illustrates how the assessment of the climate response at GWLs relates to the uncertainty in scenarios regarding the timing of the respective GWLs, as well as to the uncertainty in the associated regional climate responses, including extremes and other climatic impact-drivers (CIDs). For many (but not all) climate variables and CIDs the response pattern for a given GWL is consistent across different scenarios (Chapters 1, 4, 9, 11 and Atlas). GWLs are defined as long-term means (e.g. 20-year averages) compared to the pre-industrial period, are commonly used in the literature and were also underlying main assessments of SR15 (Chapter 3).

[START CROSS-CHAPTER BOX 11.1, FIGURE 1 HERE]

Cross-Chapter Box 11.1, Figure 1: Schematic representation of relationship between emission scenarios, global

ACCEPTED VERSION SUBJECT TO FINAL EDITING

warming levels (GWLs), regional climate responses, and impacts. The illustration shows the implied uncertainty problem associated with differentiating between 1.5, 2°C, and other GWLs. Focusing on GWL raises questions associated with emissions pathways to get to these temperatures (scenarios), as well as questions associated with regional climate responses and the associated impacts at the corresponding GWL (the impacts question). Adapted from (James et al., 2017) and (Rogelj, 2013) under the terms of the Creative Commons Attribution license.

[END CROSS-CHAPTER BOX 11.1, FIGURE 1 HERE]

Numerous studies have compared the regional response to anthropogenic forcing at GWLs in annual and seasonal mean values and extremes of different climate and impact variables across different multi-model ensembles and/or different scenarios (e.g. Frieler et al., 2012; Schewe et al., 2014; Schleussner et al., 2016; Seneviratne et al., 2016; Wartenburger et al., 2017; Dosio and Fischer, 2018; Tebaldi et al., 2020; (Herger et al., 2015; Betts et al., 2018; Samset et al., 2019), see Sections 4.6.1, 8.5.3, 9.3.1, 9.5, 9.6.3, 10.4.3 and 11.2.4 for further details). The regional response patterns at given GWLs have been found to be consistent across different scenarios for many climate variables (CC-Box 11.1 Fig.2) (Pendergrass et al., 2015; Seneviratne et al., 2016; Wartenburger et al., 2017; Seneviratne and Hauser, 2020). The consistency tends to be higher for temperature-related variables than for variables in the hydrological cycle or variables characterizing atmospheric dynamics, and for intermediate to high emission scenarios than for low-emission scenarios (e.g. for mean precipitation in the RCP2.6 scenario: Pendergrass et al., 2015; Wartenburger et al., 2017). Nonetheless, CCB 11.1 Figure 2 illustrates that even for mean precipitation, which is known to be forcing-dependent (Section 4.6.1 and Section 8.5.3), scenario differences in the response pattern at a given GWL are smaller than model uncertainty and internal variability in many regions (Herger et al., 2015). The response pattern is further found to be broadly consistent between models that reach a GWL relatively early and those that reach it later under a given SSP (see CC Box 11.1 Fig.2 g, h)

[START CROSS-CHAPTER 11.1, FIGURE 2 HERE]

Cross-Chapter Box 11.1, Figure 2: (a-c) CMIP6 multi-model mean precipitation change at 2°C GWL (20-yr mean) in three different SSP scenarios relative to 1850-1900. All models reaching the corresponding GWL in the corresponding scenario are averaged. The number of models averaged across is shown at the top right of the panel. The maps for the other two SSP scenarios SSP1-1.9 (five models only) and SSP3-7.0 (not shown) are consistent. (d-f) Same as (a-c) but for annual mean temperature. (g) Annual mean temperature change at 2°C in CMIP6 models with high warming rate reaching the GWL in the corresponding scenario before the earliest year of the assessed very likely range (section 4.3.4) (h) Climate response at 2°C GWL across all SSP1-1.9, SSP2-2.6, SSP2-4.5. SSP3-7.0 and SSP5-8.5 in all other models not shown in (g). The good agreement of (g) and (h) demonstrate that the mean temperature response at 2°C is not sensitive to the rate of warming and thereby the GSAT warming of the respective models in 2081-2100. Uncertainty is represented using the advanced approach: No overlay indicates regions with robust signal, where ≥66% of models show change greater than variability threshold and ≥80% of all models agree on sign of change; diagonal lines indicate regions with no change or no robust signal, where <66% of models show a change greater than the variability threshold; crossed lines indicate regions with conflicting signal, where ≥66% of models show change greater than variability threshold and <80% of all models agree on sign of change. For more information on the advanced approach, please refer to the Cross-Chapter Box Atlas.1.

ACCEPTED VERSION SUBJECT TO FINAL EDITING

[END CROSS-CHAPTER BOX 11.1, FIGURE 2 HERE]

In contrast to linear pattern scaling (Mitchell, 2003; Collins et al., 2013a), the use of GWLs as a dimension of integration does not require linearity in the response of a climate variable. It is thus even useful for metrics which do not show a linear response, such as the frequency of heat extremes over land and oceans (Fischer and Knutti, 2015; Perkins-Kirkpatrick and Gibson, 2017; Frölicher et al., 2018; Kharin et al., 2018) if the relationship of the variable of interest to the GWL is scenario independent. The latter means that the response is independent of the pathway and relative contribution of various radiative forcings. For some more complex indices like warm-spell duration or for regions with strong aerosol changes, discrepancies can be larger (Wang et al., 2017d; King et al., 2018; Tebaldi et al., 2020) (see also subsection below on GWLs vs scenarios for further caveats).

The limited scenario dependence of the GWL-based response for many variables implies that the regional response to emissions scenarios can be split in almost independent contributions of 1) the transient global warming response to scenarios (see Chapter 4), and 2) the regional response as function of a given GWL, which has also been referred to as "regional climate sensitivity" (Seneviratne and Hauser, 2020). This property has also been used to develop regionally-resolved emulators for global climate models, using global surface temperature as input (Beusch et al., 2020; Tebaldi et al., 2020). Analyses of the CMIP6 and CMIP5 multi-model ensembles shows that the GWL-based responses are very similar for temperature and precipitation extremes across the ensembles (Li et al., 2020a; Seneviratne and Hauser, 2020; Wehner, 2020). This is despite their difference in global warming response (Chapter 4), confirming a substantial decoupling between the two responses (global warming vs GWL-based regional response) for these variables. Thus, the GWL approach isolates the uncertainty in the regional climate response from the global warming uncertainty induced by scenario, global mean model response and internal variability (CCB Figure 1).

Mapping between GWL- and scenario-based responses in model analyses

To map scenario-based climate projections into changes at specific GWLs, first, all individual ESM simulations that reach a certain GWL are identified. Second, the climate response patterns at the respective GWL are calculated using an approach termed here "GWL-sampling approach" – sometimes also referred to as epoch analysis, time shift, or time sampling approach –, taking into account all models and scenarios (CCB Figure 3). Note that the range of years when a given GWL is reached in the CMIP6 ensemble is different from the AR6 assessed range of projected global surface temperature (Table 4.5; Section 4.3.4). The latter further takes into account different lines of evidence, including the assessed observed warming between pre-industrial and present day, information from observational constraints on CMIP6, and emulators using the assessed transient climate response (TCR) and equilibrium climate sensitivity (ECS) ranges (Section 4.3.4). Hence the Chapter 4 assessed range (Table 4.5) is the reference to determine when a given GWL is *likely* reached under given scenarios, while the mapping between scenarios/time frames and GWLs is used to assess the respective regional responses happening at these time frames (which also allows to account for the global surface temperature assessment rather than using scenarios analyses directly from CMIP6 output).

In the model-based asssessment of Chapters 4, 8, 10, 11, 12 and the Atlas, the estimation of changes at GWLs are generally defined as the 20-year time period in which the mean global surface air temperature (GSAT; CCBox 2.3) first exceeds a certain anomaly relative to 1850-1900 (for simulations that start after 1850, relative to all years up to 1900 CCB Figure 3). The years when each individual model reaches a given GWL for CMIP6 and CMIP5 can be found in Hauser et al. (2021). The changes at given GWLs are identified for each ensemble member (for all scenarios) individually. Thereby, a given GWL is potentially reached a few years earlier or later in different realizations of the same model due to internal variability, but the temperature averaged across the 20-year period analysed in any simulation is consistent with the GWL. Instead of blending the information from the different scenarios, the Interactive Atlas can be used to compare the GWL spatial patterns and timings across the different scenarios (see Section Atlas 1.3.1).

ACCEPTED VERSION SUBJECT TO FINAL EDITING

[START CROSS-CHAPTER BOX 11.1, FIGURE 3 HERE]

Cross-Chapter Box11.1, Figure 3: Illustration of the AR6 GWL sampling approach to derive the timing and the response at a given GWL for the case of CMIP6 data. For the mapping of scenarios/time slices into GWLs for CMIP6, please refer to Table 4.2. Respective numbers for the CMIP6 multi-model experiment are provided in the Chapter 11 Supplementary Material (11.SM.1). Note that the time frames used to derived the GWL time slices can also include different number of years (e.g. 30 years for some analyses).

[END CROSS-CHAPTER BOX 11.1, FIGURE 3 HERE]

Mapping between GWL- and scenario-based responses for literature

A large fraction of the literature considers scenario-based analyses for given time slices. When GWL-based information is required instead, an approximated mapping of the multi-model mean can be derived based on the known GWL in the given experiments for a particular time period. As a rough approximation, CMIP6 multi-model mean projections for the near-term (2021-2040) correspond to changes at about 1.5°C, and projections for the high-end scenario (SSP5-8.5) for the long-term (2081-2100) correspond to about 4-5°C of global warming (see Table 4.2 for changes in the CMIP6 ensemble and the Chapter 11 Supplementary Material (11.SM.1) and Hauser (2021) for details on other time periods and CMIP5). These approximated changes are for instance used for some of the GWL-based assessments provided in the Chapter 11 regional tables (Section 11.9; Table 11.3) when literature based on scenario projections is used to assessed estimated changes at given GWLs.

GWLs vs scenarios

The use of scenarios remains a key element to inform mitigation decisions (Chapter 1, CCB1.4), to assess which emission pathways are consistent with a certain GWL (CCB1.4 Figure1), to estimate when certain GWLs are reached (Section 4.3.4), and to assess for which variables it is meaningful to use GWLs as a dimension of integration. The use of scenarios is also essential for variables whose climate response strongly depends on the contribution of radiative forcing (e.g. aerosols) and land use and land management changes, and are time and warming rate dependent (e.g. sea level rise), or differ between transient and quasi-equilibrium states. Furthermore, the use of concentration or emission-driven scenario simulations is required if regional climate assessments need to account for the uncertainty in GSAT changes or climate-carbon feedbacks.

Forcing dependence of the GWL response is found for global mean precipitation (Section 8.4.3), but less for regional patterns of mean precipitation changes (CC-Box 11.1, Fig. 2). Limited dependence is found for extremes, as highlighted above. In the cryosphere, elements that are quick to respond to warming like sea ice area, permafrost, and snow show little scenario dependence (Chapter 9.3.1.1, 9.5.2.3, 9.5.3.3), whereas slow-responding variables such as ice volumes of glaciers and ice sheets respond with a substantial delay and due to their inertia, the response depends on when a certain GWL is reached. This also applies to some extent for sea level rise where, for example, the contributions of melting glaciers and ice sheets depend on the pathway followed to reach a given GWL (Chapter 9.6.3.4).

In addition to the lagged effect, the climate response at a given GWL may differ before and after a period of overshoot, for example in the Atlantic Meridional Overturning Circulation (e.g. Palter et al. 2018). Finally, as assessed in IPCC SR15, there is a difference in the response even for temperature-related variables if a GWL is reached in a rapidly warming transient state or in an equilibrium state when the land-sea warming contrast is less pronounced (e.g. King et al. 2020). However, in this report GWLs are used in the context of projections for the 21st century when the climate response is mostly not in equilibrium and where projections for many variables are less dependent on the pathway than for projections beyond 2100 (Section 9.6.3.4).

ACCEPTED VERSION SUBJECT TO FINAL EDITING

Key conclusions on assessments based on GWLs

GWL-based projections can inform society and policymakers on how climate would change under GWLs consistent with the aims of the Paris Agreement (stabilization at 1.5°C/well below 2°C), as well as on the consequences of missing these aims and reaching GWLs of 3°C or 4°C by the end of the century. The AR6 assessment shows that every bit of global warming matters and that changes in global warming of 0.5°C lead to statistically significant changes in mean climate and climate extremes on global scale and for large regions (Sections 4.6.2, 11.2.4, 11.3, 11.4, 11.6, 11.9; Figs 11.8, 11.9, Atlas, Interactive Atlas), as also assessed in the IPCC SR15.

[END CROSS-CHAPTER BOX 11.1 HERE]

11.3 Temperature extremes

This section assesses changes in temperature extremes at global, continental and regional scales. The main focus is on the changes in the magnitude and frequency of moderate extreme temperatures (those that occur several times a year) to very extreme temperatures (those that occur once-in-10-years or longer) of time scales from a day to a season, though there is a strong emphasis on the daily scale where literature is most concentrated.

11.3.1 Mechanisms and drivers

The SREX (IPCC, 2012) and AR5 (IPCC, 2014) concluded that greenhouse gas forcing is the dominant factor for the increases in the intensity, frequency, and duration of warm extremes and the decrease in those of cold extremes. This general global-scale warming is modulated by large-scale atmospheric circulation patterns, as well as by feedbacks such as soil moisture-evapotranspiration-temperature and snow/ice-albedo-temperature feedbacks, and local forcings such as land use change or changes in aerosol concentrations at the regional and local scales (Box 11.1, Sections 11.1.5, 11.1.6). Therefore, changes in temperature extremes at regional and local scales can have heterogeneous spatial distributions. Changes in the magnitudes (or intensities) of extreme temperatures are often larger than changes in global surface temperature, because of larger warming on land than on the ocean surface (2.3.1.1) and feedbacks, though they are of similar magnitude to changes in the local mean temperature (Fig 11.2).

Extreme temperature events are associated with large-scale meteorological patterns (Grotjahn et al., 2016). Quasi-stationary anticyclonic circulation anomalies or atmospheric blocking events are linked to temperature extremes in many regions, such as in Australia (Parker et al., 2014; Perkins-Kirkpatrick et al., 2016), Europe (Brunner et al., 2017, 2018; Schaller et al., 2018), Eurasia (Yao et al., 2017), Asia (Chen et al., 2016; Ratnam et al., 2016; Rohini et al., 2016), and North America (Yu et al., 2018, 2019b; Zhang and Luo, 2019). Mid-latitude planetary wave modulations affect short-duration temperature extremes such as heat waves (Perkins, 2015; Kornhuber et al., 2020). The large-scale modes of variability (Annex VI) affect the strength, frequency, and persistence of these meteorological patterns and, hence, temperature extremes. For example, cold and warm extremes in the mid-latitudes are associated with atmospheric circulation patterns such as the Pacific-North American (PNA) pattern, as well as atmosphere-ocean coupled modes such as Pacific Decadal Variability (PDV), the North Atlantic Oscillation (NAO), and Atlantic Multidecadal Variability (AMV) (Kamae et al., 2014; Johnson et al., 2018; Ruprich-Robert et al., 2018; Yu et al., 2018, 2019a; Müller et al., 2020; Section 11.1.5). Changes in the modes of variability in response to warming would therefore affect temperature extremes (Clark and Brown, 2013; Horton et al., 2015). The level of confidence in those changes, both in the observations and in future projections, varies, affecting the level of confidence in changes in temperature extremes in different regions. As highlighted in Chapters 2-4 of this Report, it is *likely* that there have been observational changes in the extratropical jets and mid-latitude jet meandering (Section 2.3.1.4.3; Cross-Chapter Box 10.1). There is *low confidence* in possible effects of Arctic warming

ACCEPTED VERSION SUBJECT TO FINAL EDITING

on mid-latitude temperature extremes (Cross-Chapter Box 10.1). A large portion of the multi-decadal changes in extreme temperature remains after the removal of the effect of these modes of variability and can be attributed to human influence (Kamae et al., 2017b; Wan et al., 2019). Thus, global warming dominates changes in temperature extremes at the regional scale and it is *very unlikely* that dynamic responses to greenhouse-gas induced warming would alter the direction of these changes.

Land-atmosphere feedbacks strongly modulate regional- and local-scale changes in temperature extremes (*high confidence*; Section 11.1.6; Seneviratne et al., 2013; Lemordant et al., 2016; Donat et al., 2017; Sillmann et al., 2017b; Hirsch et al., 2019). This effect is particularly notable in mid-latitude regions where the drying of soil moisture amplifies high temperatures, in particular through increases in sensible heat flux (Whan et al., 2015; Douville et al., 2016; Vogel et al., 2017). Land-atmosphere feedbacks amplifying temperature extremes also include boundary-layer feedbacks and effects on atmospheric circulation (Miralles et al., 2014a; Schumacher et al., 2019). Soil moisture-temperature feedbacks affect past and present-day heat waves in observations and model simulations, both locally (Miralles et al. 2014; Hauser et al. 2016; Meehl et al. 2016; Wehrli et al., 2019; Cowan et al., 2016) and beyond the regions of feedback occurrence through changes in regional circulation patterns (Koster et al., 2016; Sato and Nakamura, 2019; Stéfanon et al., 2014). The uncertainty due to the representation of land-atmosphere feedbacks in ESMs is a cause of discrepancy between observations and simulations (Clark et al., 2006; Mueller and Seneviratne, 2014; Meehl et al., 2016). The decrease of plant transpiration or the increase of stomata resistance under enhanced CO_2 concentrations is a direct CO_2 forcing of land temperatures (warming due to reduced evaporative cooling), which contributes to higher warming on land (Lemordant et al., 2016; Vicente-Serrano et al., 2020c). The snow/ice-albedo feedback plays an important role in amplifying temperature variability in the high latitudes (Diro et al. 2018) and can be the largest contributor to the rapid warming of cold extremes in the mid- and high latitudes of the Northern Hemisphere (Gross et al., 2020).

Regional external forcings, including land-use changes and emissions of anthropogenic aerosols, play an important role in the changes of temperature extremes in some regions (*high confidence*, Section 11.1.6). Deforestation may have contributed to about one third of the warming of hot extremes in some mid-latitude regions since the pre-industrial time (Lejeune et al., 2018). Aspects of agricultural practice, including no-till farming, irrigation, and overall cropland intensification, may cool hot temperature extremes (Davin et al., 2014; Mueller et al., 2016b). For instance, cropland intensification has been suggested to be responsible for a cooling of the highest temperature percentiles in the US Midwest (Mueller et al., 2016b). Irrigation has been shown to be responsible for a cooling of hot temperature extremes of up to 1-2°C in many mid-latitude regions in the present climate (Thiery et al., 2017; Thiery et al., 2020), a process not represented in most of state-of-the-art ESMs (CMIP5, CMIP6). Double cropping may have led to increased hot extremes in the inter-cropping season in part of China (Jeong et al., 2014). Rapid increases in summertime warming in western Europe and northeast Asia since the 1980s are linked to a reduction in anthropogenic aerosol precursor emissions over Europe (Dong et al., 2016, 2017; Nabat et al., 2014), in addition to the effect of increased greenhouse gas forcing (see also Chapter 10, Section 10.1.3.1). This effect of aerosols on temperature-related extremes is also noted for declines in short-lived anthropogenic aerosol emissions over North America (Mascioli et al., 2016). On the local scale, the urban heat island (UHI) effect results in higher temperatures in urban areas than in their surrounding regions and contributes to warming in regions of rapid urbanization, in particular for night-time temperature extremes (Box 10.3; Phelan et al., 2015; Chapman et al., 2017; Sun et al., 2019). But these local and regional forcings are generally not (well-) represented in the CMIP5 and CMIP6 simulations (see also Section 11.3.3), contributing to uncertainty in model simulated changes.

In summary, greenhouse gas forcing is the dominant driver leading to the warming of temperature extremes. At regional scales, changes in temperature extremes are modulated by changes in large-scale patterns and modes of variability, feedbacks including soil moisture-evapotranspiration-temperature or snow/ice-albedo-temperature feedbacks, and local and regional forcings such as land use and land cover changes, or aerosol concentrations, and decadal and multidecadal natural variability. This leads to heterogeneity in regional changes and their associated uncertainties (*high confidence*). Urbanization has exacerbated the effects of global warming in cities, in particular for night-time temperature extremes (*high confidence*).

ACCEPTED VERSION SUBJECT TO FINAL EDITING

11.3.2 Observed trends

The SREX (IPCC, 2012) reported a *very likely* decrease in the number of cold days and nights and increase in the number of warm days and nights at the global scale. Confidence in trends was assessed as regionally variable (*low to medium confidence*) due to either a lack of observations or varying signals in sub-regions.

Since SREX (IPCC, 2012) and AR5 (IPCC, 2014), many regional-scale studies have examined trends in temperature extremes using different metrics that are based on daily temperatures, such as the CCl/WCRP/JCOMM Expert Team on Climate Change Detection and Indices (ETCCDI) indices (Dunn et al., 2020). The additional observational records, along with a stronger warming signal, show very clearly that changes observed at the time of AR5 (IPCC, 2014) continued, providing strengthened evidence of an increase in the intensity and frequency of hot extremes and decrease in the intensity and frequency of cold extremes. While the magnitude of the observed trends in temperature-related extremes varies depending on the region, spatial and temporal scales, and metric assessed, evidence of a warming effect is overwhelming, robust, and consistent. In particular, an increase in the intensity and frequency of hot extremes is almost always associated with an increase in the hottest temperatures and in the number of heatwave days. It is also the case for changes in cold extremes. For this reason, and to simplify the presentation, the phrase "increase in the intensity and frequency of hot extremes" is used to represent, collectively, an increase in the magnitude of extreme day and/or night temperatures, in the number of warm days and/or nights, and in the number of heat wave days. Changes in cold extremes are assessed similarly.

On the global scale, evidence of an increase in the number of warm days and nights and a decrease in the number of cold days and nights, and an increase in the coldest and hottest extreme temperatures is very robust and consistent among all variables. Figure 11.2 displays timeseries of globally-averaged annual maximum daily maximum (TXx) and annual minimum daily minimum temperature (TNn) on land. Warming of land mean TXx is similar to the mean land warming, which is about 45% higher than global warming (Section 2.3.1). Warming of land mean TNn is even higher, with about 3°C of warming since 1960 (Figure 11.2). Figure 11.9 shows maps of linear trends over 1960-2018 in the annual maximum daily maximum (TXx), the annual minimum daily minimum temperature (TNn), and frequency of warm days (TX90p). The maps for TXx and TNn show trends consistent with overall warming in most regions, with a particularly high warming of TXx in Europe and north-western South America, and a particularly high warming of TNn in the Arctic. Consistent with the observed warming in global surface temperature (2.3.1.2) and the observed trends in TXx and TNn, the frequency of TX90p has increased while that of cold nights (TN10p) has decreased since the 1950s: Nearly all land regions showed statistically significant decreases in TN10p (Alexander, 2016; Dunn et al., 2020), though trends in TX90p are variable with some decreases in southern South America, mainly during austral summer (Rusticucci et al., 2017). A decrease in the number of cold spell days is also observed over nearly all land surface areas (Easterling et al., 2016) and in the northern mid-latitudes in particular (van Oldenborgh et al., 2019). These observed changes are also consistent when a new global land surface daily air temperature dataset is analyzed (Zhang et al., 2019c). Consistent warming trends in temperature extremes globally, and in most land areas, over the past century are also found in a range of observation-based data sets (Fischer and Knutti, 2014; Donat et al., 2016a; Dunn et al., 2020), with the extremes related to daily minimum temperatures changing faster than those related to daily maximum temperatures (Dunn et al., 2020) (Fig. 11.2). Seasonal variations in trends in temperature-related extremes have been demonstrated. A warming in warm-season temperature extremes is detected, even during the "slower surface global warming" period from the late 1990s to early 2010s (Cross-Chapter Box 3.1) (Kamae et al., 2014; Seneviratne et al., 2014; Imada et al., 2017). Many studies of past changes in temperature extremes for particular regions or countries show trends consistent with this global picture, as summarized below and in Tables 11.4, 11.7, 11.10, 11.13, 11.16 and 11.19 in Section 11.9.

[START FIGURE 11.9 HERE]

Figure 11.9: Linear trends over 1960-2018 in the annual maximum daily maximum temperature (TXx, a), the annual minimum daily minimum temperature (TNn, b), and the annual number of days when daily maximum

ACCEPTED VERSION SUBJECT TO FINAL EDITING

temperature exceeds its 90th percentile from a base period of 1961-1990 (TX90p, c), based on the HadEX3 data set (Dunn et al., 2020). Linear trends are calculated only for grid points with at least 66% of the annual values over the period and which extend to at least 2009. Areas without sufficient data are shown in grey. No overlay indicates regions where the trends are significant at p = 0.1 level. Crosses indicate regions where trends are not significant. For details on the methods see Supplementary Material 11.SM.2. Further details on data sources and processing are available in the chapter data table (Table 11.SM.9).

[END FIGURE 11.9 HERE]

In Africa (Table 11.4), while it is difficult to assess changes in temperature extremes in parts of the continent because of a lack of data, evidence of an increase in the intensity and frequency of hot extremes and decrease in the intensity and frequency of cold extremes is clear and robust in regions where data are available. These include an increase in the frequency of warm days and nights and a decrease in the frequency of cold days and nights with *high confidence* (Donat et al., 2013b, 2014b; Kruger and Sekele, 2013; Chaney et al., 2014; Filahi et al., 2016; Moron et al., 2016; Ringard et al., 2016; Barry et al., 2018; Gebrechorkos et al., 2018) and an increase in heat waves (Russo et al., 2016; Ceccherini et al., 2017). The increase in TNn is more notable than in TXx (Figure 11.9). Cold spells occasionally strike subtropical areas, but are *likely* to have decreased in frequency (Barry et al., 2018). The frequency of cold events has *likely* decreased in South Africa (Song et al., 2014; Kruger and Nxumalo, 2017), North Africa (Driouech et al., 2021; Filahi et al., 2016), and the Sahara (Donat et al., 2016a). Over the whole continent, there is *medium confidence* in an increase in the intensity and frequency of hot extremes and decrease in the intensity and frequency of cold extremes; it is *likely* that similar changes have also occurred in areas with poor data coverage, as warming is widespread and as projected future changes are similar over all regions (11.3.5).

In Asia (Table 11.7), there is very *robust evidence* for a *very likely* increase in the intensity and frequency of hot extremes and decrease in the intensity and frequency of cold extremes in recent decades. This is clear in global studies (e.g. Alexander, 2016; Dunn et al., 2020), as well as in numerous regional studies (Table 11.7). The area fraction with extreme warmth in Asia increased during 1951–2016 (Imada et al., 2018). The frequency of warm extremes increased and the frequency of cold extremes decreased in East Asia (Zhou et al., 2016a; Chen and Zhai, 2017; Yin et al., 2017; Lee et al., 2018c; Qian et al., 2019) and west Asia (Acar Deniz and Gönençgil, 2015; Erlat and Türkeş, 2016; Imada et al., 2017; Rahimi et al., 2018; Rahimi and Hejabi, 2018) with *high confidence*. The duration of heat extremes has also lengthened in some regions, for example, in southern China (Luo and Lau, 2016), but there is *medium confidence* of heat extremes increasing in frequency in South Asia (AlSarmi and Washington, 2014; Sheikh et al., 2015; Mazdiyasni et al., 2017; Zahid et al., 2017; Nasim et al., 2018; Khan et al., 2019; Roy, 2019). Warming trends in daily temperature extremes indices have also been observed in central Asia (Hu et al., 2016; Feng et al., 2018), the Hindu Kush Himalaya (Sun et al., 2017), and Southeast Asia (Supari et al., 2017; Cheong et al., 2018). The intensity and frequency of cold spells in all Asian regions have been decreasing since the beginning of the 20th century (*high confidence*) (Sheikh et al., 2015; Donat et al., 2016a; Dong et al., 2018; van Oldenborgh et al., 2019).

In Australasia (Table 11.10), there is very *robust evidence* for *very likely* increases in the number of warm days and warm nights and decrease in the number of cold days and cold nights since 1950 (Lewis and King, 2015; Jakob and Walland, 2016; Alexander and Arblaster, 2017). The increase in extreme minimum temperatures occurs in all seasons over most of Australia and typically exceeds the increase in extreme maximum temperatures (Wang et al., 2013b; Jakob and Walland, 2016). However, some parts of southern Australia have shown stable or increased numbers of frost days since the 1980s (Dittus et al., 2014) (see also Section 11.3.4). Similar positive trends in extreme minimum and maximum temperatures have been observed in New Zealand, in particular in the autumn-winter seasons, although they generally show higher spatial variability (Caloiero, 2017). In the tropical Western Pacific region, spatially coherent warming trends in maximum and minimum temperature extremes have been reported for the period of 1951–2011 (Whan et al., 2014; McGree et al., 2019).

In Central and South America (Table 11.13), there is *high confidence* that observed hot extremes (TN90p, TX90p) have increased and cold extremes (TN10p, TX10p) have decreased over recent decades, though

ACCEPTED VERSION SUBJECT TO FINAL EDITING

trends vary among different extremes types, datasets, and regions (Dereczynski et al., 2020; Dittus et al., 2016; Dunn et al., 2020; Meseguer-Ruiz et al., 2018; Olmo et al., 2020; Rusticucci et al., 2017; Salvador and de Brito, 2018; Skansi et al., 2013). An increase in the intensity and frequency of heatwave events was also observed between 1961 and 2014, in an area covering most of South America (Ceccherini et al., 2016; Geirinhas et al., 2018). However, there is *medium confidence* that warm extremes (TXx and TX90p) have decreased in the last decades over the central region of SES during austral summer (Tencer, B.; Rusticucci, 2012; Skansi et al., 2013; Rusticucci et al., 2017; Wu and Polvani, 2017). There is *medium confidence* that TNn extremes are increasing faster than TXx extremes, with the largest warming rates observed over Northeast Brazil (NEB) and North South America (NSA) for cold nights (Skansi et al., 2013).

In Europe (Table 11.16), there is very robust evidence for a *very likely* increase in maximum temperatures and the frequency of heat waves. The increase in the magnitude and frequency of high maximum temperatures has been observed consistently across regions including in central (Twardosz and Kossowska-Cezak, 2013; Christidis et al., 2015; Lorenz et al., 2019) and southern Europe (Croitoru and Piticar, 2013; El Kenawy et al., 2013; Christidis et al., 2015; Nastos and Kapsomenakis, 2015; Fioravanti et al., 2016; Ruml et al., 2017). In northern Europe, a strong increase in extreme winter warming events has been observed (Matthes et al., 2015; Vikhamar-Schuler et al., 2016). Temperature observations for wintertime cold spells show a long-term decreasing frequency in Europe (Brunner et al., 2018; van Oldenborgh et al., 2019), and typical cold spells such as that observed during the 2009/2010 winter had an occurrence probability that is twice smaller currently than if climate change had not occurred (Christiansen et al., 2018).

In North America (Table 11.19), there is very robust evidence for a *very likely* increase in the intensity and frequency of hot extremes and decrease in the intensity and frequency of cold extremes for the whole continent, though there are substantial spatial and seasonal variations in the trends. Minimum temperatures display warming consistently across the continent, while there are more contrasting trends in the annual maximum daily temperatures in parts of the USA (Figure 11.9) (Lee et al., 2014; van Oldenborgh et al., 2019; Dunn et al., 2020). In Canada, there is a clear increase in the intensity and frequency of hot extremes and decrease in the intensity and frequency of cold extremes (Vincent et al., 2018). In Mexico, a clear warming trend in TNn was found, particularly in the northern arid region (Montero-Martínez et al., 2018). The number of warm days has increased and the number of cold days has decreased (García-Cueto et al., 2019). Cold spells have undergone a reduction in magnitude and intensity in all regions of North America (Bennett and Walsh, 2015; Donat et al., 2016a; Grotjahn et al., 2016; Vose et al., 2017; García-Cueto et al., 2019; van Oldenborgh et al., 2019).

Extreme heat events have increased around the Arctic since 1979, particularly over Arctic North America and Greenland (Matthes et al., 2015; Dobricic et al., 2020), which is consistent with summer melt (9.4.1). Observations north of 60°N show increases in wintertime warm days and nights over 1979-2015, while cold days and nights declined (Sui et al., 2017). Extreme heat days are particularly strong in winter, with observations showing the warmest mid-winter temperatures at the North Pole rising at twice the rate of mean temperature (Moore, 2016), as well as increases in Arctic winter warm days (T>-10°C) (Vikhamar-Schuler et al., 2016; Graham et al., 2017). Arctic annual minimum temperatures have increased at about three times the rate of global surface temperature since the 1960s (Figs. 11.2, 11.9), consistent with the observed mean cold season (October-May) warming of 3.1°C in the region (Atlas 11.2).

Trends in some measures of heat waves are also observed at the global scale. Globally-averaged heat wave intensity, heat wave duration, and the number of heat wave days have significantly increased from 1950-2011 (Perkins, 2015). There are some regional differences in trends in characteristics of heat waves with significant increases reported in Europe (Russo et al., 2015; Forzieri et al., 2016; Sánchez-Benítez et al., 2020) and Australia (CSIRO and BOM, 2016; Alexander and Arblaster, 2017). In Africa, there is *medium confidence* that heat waves, regardless of the definition, have been becoming more frequent, longer-lasting, and hotter over more than three decades (Fontaine et al., 2013; Mouhamed et al., 2013; Ceccherini et al., 2016, 2017; Forzieri et al., 2016; Moron et al., 2016; Russo et al., 2016). The majority of heat wave characteristics examined in China between 1961-2014 show increases in heat wave days, consistent with warming (You et al., 2017; Xie et al., 2020). Increases in the frequency and duration of heat waves are also observed in Mongolia (Erdenebat and Sato, 2016) and India (Ratnam et al., 2016; Rohini et al., 2016). In the

ACCEPTED VERSION SUBJECT TO FINAL EDITING

UK, the lengths of short heat waves have increased since the 1970s, while the lengths of long heat waves (over 10 days) have decreased over some stations in the southeast of England (Sanderson et al., 2017b). In Central and South America, there are increases in the frequency of heat waves (Barros et al., 2015; Bitencourt et al., 2016; Ceccherini et al., 2016; Piticar, 2018), although decreases in Excess Heat Factor (EHF), which is a metric for heat wave intensity, are observed in South America in data derived from HadGHCND (Cavanaugh and Shen, 2015).

In summary, it is *virtually certain* that there has been an increase in the number of warm days and nights and a decrease in the number of cold days and nights on the global scale since 1950. Both the coldest extremes and hottest extremes display increasing temperatures. It is *very likely* that these changes have also occurred at the regional scale in Europe, Australasia, Asia, and North America. It is *virtually certain* that there has been increases in the intensity and duration of heat waves and in the number of heat wave days at the global scale. These trends *likely* occur in Europe, Asia, and Australia. There is *medium confidence* in similar changes in temperature extremes in Africa and *high confidence* in South America; the lower confidence is due to reduced data availability and fewer studies. Annual minimum temperatures on land have increased about three times more than global surface temperature since the 1960s, with particularly strong warming in the Arctic (*high confidence*).

11.3.3 Model evaluation

AR5 assessed that CMIP3 and CMIP5 models generally captured the observed spatial distributions of the mean state and that the inter-model range of simulated temperature extremes was similar to the spread estimated from different observational datasets; the models generally captured trends in the second half of the 20th century for indices of extreme temperature, although they tended to overestimate trends in hot extremes and underestimate trends in cold extremes (Flato et al., 2013). Post-AR5 studies on the CMIP5 models' performance in simulating mean and changes in temperature extremes continue to support the AR5 assessment (Fischer and Knutti, 2014; Sillmann et al., 2014; Ringard et al., 2016; Borodina et al., 2017b; Donat et al., 2017; Di Luca et al., 2020a). Over Africa, the observed warming in temperature extremes is captured by CMIP5 models, although it is underestimated in west and central Africa (Sherwood et al., 2014; Diedhiou et al., 2018). Over East Asia, the CMIP5 ensemble performs well in reproducing the observed trend in temperature extremes averaged over China (Dong et al., 2015). Over Australia, the multi-model mean performs better than individual models in capturing observed trends in gridded station based ETCCDI temperature indices (Alexander and Arblaster, 2017).

Initial analyses of CMIP6 simulations (Chen et al., 2020a; Di Luca et al., 2020b; Kim et al., 2020; Li et al., 2020a; Thorarinsdottir et al., 2020; Wehner et al., 2020) indicate the CMIP6 models perform similarly to the CMIP5 models regarding biases in hot and cold extremes. In general, CMIP5 and CMIP6 historical simulations are similar in their performance in simulating the observed climatology of extreme temperatures *(high confidence)*. The general warm bias in hot extremes and cold bias in cold extremes reported for CMIP5 models (Kharin et al., 2013; Sillmann et al., 2013a) remain in CMIP6 models (Di Luca et al., 2020b). However, there is some evidence that CMIP6 models better represent some of the underlying processes leading to extreme temperatures, such as seasonal and diurnal variability and synoptic-scale variability (Di Luca et al., 2020b). Whether these improvements are sufficient to enhance our understanding of past changes or to reduce uncertainties in future projections remains unclear. The relative error estimates in the simulation of various indices of temperature extremes in the available CMIP6 models show that no single model performs the best on all indices and the multi-model ensemble seems to out-perform any individual model due to its reduction in systematic bias (Kim et al., 2020). Figure 11.10 show errors in the 1979-2014 average annual TXx and annual TNn simulated by available CMIP6 models in comparison with HadEX3 and ERA5 (Li et al., 2020; Kim et al., 2020, Wehner et al., 2020). While the magnitude of the model error depends on the reference data set, the model evaluations drawn from different reference data sets are quite similar. In general, models reproduce the spatial patterns and magnitudes of both cold and hot temperature extremes quite well. There are also systematic biases. Hot extremes tend to be too cool in mountainous and high-latitude regions, but too warm in the eastern United States and South America. For cold extremes, CMIP6 models are too cool, except in northeastern Eurasia and the southern mid-latitudes. Errors in seasonal mean

ACCEPTED VERSION SUBJECT TO FINAL EDITING

temperatures are uncorrelated with errors in extreme temperatures and are often of opposite sign (Wehner et al., 2020).

[START FIGURE 11.10 HERE]

Figure 11.10: Multi-model mean bias in temperature extremes (°C) for the period 1979-2014, calculated as the difference between the CMIP6 multi-model mean and the average of observations from the values available in HadEX3 for (a) the annual hottest temperature (TXx) and (b) the annual coldest temperature (TNn). Areas without sufficient data are shown in grey. Adapted from Wehner et al. (2020) under the terms of the Creative Commons Attribution license. Further details on data sources and processing are available in the chapter data table (Table 11.SM.9).

[END FIGURE 11.10 HERE]

Atmospheric model (AMIP) simulations are often used in event attribution studies to assess the influence of global warming on observed temperature-related extremes. These simulations typically capture the observed trends in temperature extremes, though some regional features, such as the lack of warming in daytime warm temperature extremes over South America and parts of North America, are not reproduced in the model simulations (Dittus et al., 2018), possibly due to internal variability, deficiencies in local surface processes, or forcings that are not represented in the SSTs. Additionally, the AMIP models assessed tend to produce overly persistent heat wave events. This bias in the duration of the events does not impact the reliability of the models' positive trends (Freychet et al., 2018).

Several regional climate models (RCMs) have also been evaluated in terms of their performance in simulating the climatology of extremes in various regions of the Coordinated Regional Downscaling Experiment (CORDEX) (Giorgi et al., 2009), especially in East Asia (Ji and Kang, 2015; Yu et al., 2015; Park et al., 2016; Bucchignani et al., 2017; Gao et al., 2017a; Niu et al., 2018; Sun et al., 2018b; Wang et al., 2018a), Europe (Cardoso et al., 2019; Gaertner et al., 2018; Jacob et al., 2020; Kim et al., 2020; Lorenz et al., 2019; Smiatek et al., 2016; Vautard et al., 2013; Vautard et al., 2020b), and Africa (Kim et al., 2014b; Diallo et al., 2015; Dosio, 2017; Samouly et al., 2018; Mostafa et al., 2019). Compared to GCMs, RCM simulations show an added value in simulating temperature-related extremes, though this depends on topographical complexity and the parameters employed (see Section 10.3.3). The improvement with resolution is noted in East Asia (Park et al., 2016; Zhou et al., 2016b; Shi et al., 2017; Hui et al., 2018). However, in the European CORDEX ensemble, different aerosol climatologies with various degrees of complexity were used in projections (Bartók et al., 2017; Lorenz et al., 2019) and the land surface models used in the RCMs do not account for physiological CO_2 effects on photosynthesis leading to enhanced water-use efficiency and decreased evapotranspiration (Schwingshackl et al., 2019), which could lead to biases in the representation of temperature extremes in these projections (Boé et al., 2020). In addition, there are key cold biases in temperature extremes over areas with complex topography (Niu et al., 2018). Over North America, 12 RCMs were evaluated over the ARCTIC-CORDEX region (Diaconescu et al., 2018). Models were able to simulate well climate indices related to mean air temperature and hot extremes over most of the Canadian Arctic, with the exception of the Yukon region where models displayed the largest biases related to topographic effects. Two RCMs were evaluated against observed extremes indices over North America over the period 1989–2009, with a cool bias in minimum temperature extremes shown in both RCMs (Whan and Zwiers, 2016). The most significant biases are found in TXx and TNn, with fewer differences in the simulation of annual minimum daily maximum temperature (TXn) and annual maximum daily minimum temperature (TNx) in central and western North America. Over Central and South America, maximum temperatures from the Eta RCM are generally underestimated, although hot days, warm nights, and heat waves are increasing in the period 1961-1990, in agreement with observations (Chou et al., 2014b; Tencer et al., 2016; Bozkurt et al., 2019).

Some land forcings are not well represented in climate models. As highlighted in the IPCC SRCCL Ch2, there is *high agreement* that temperate deforestation leads to summer warming and winter cooling (Bright et al., 2017; Zhao and Jackson, 2014; Gálos et al., 2011, 2013; Wickham et al., 2013; Ahlswede and Thomas,

ACCEPTED VERSION SUBJECT TO FINAL EDITING

2017; Anderson-Teixeira et al., 2012; Anderson et al., 2011; Chen et al., 2012; Strandberg and Kjellström, 2019), which has substantially contributed to the warming of hot extremes in the northern mid-latitudes over the course of the 20th century (Lejeune et al., 2018) and in recent years (Strandberg and Kjellström, 2019). However, observed forest effects on the seasonal and diurnal cycle of temperature are not well captured in several ESMs: while observations show a cooling effect of forest cover compared to non-forest vegetation during daytime (Li et al., 2015), in particular in arid, temperate, and tropical regions (Alkama and Cescatti, 2016), several ESMs simulate a warming of daytime temperatures for regions with forest vs non-forest cover (Lejeune et al., 2017). Also irrigation effects, which can lead to regional cooling of temperature extremes, are generally not integrated in current-generations of ESMs (Section 11.3.1).

In summary, there is *high confidence* that climate models can reproduce the mean state and overall warming of temperature extremes observed globally and in most regions, although the magnitude of the trends may differ. The ability of models to capture observed trends in temperature-related extremes depends on the metric evaluated, the way indices are calculated, and the time periods and spatial scales considered. Regional climate models add value in simulating temperature-related extremes over GCMs in some regions. Some land forcings on temperature extremes are not well captured (effects of deforestation) or generally not representated (irrigation) in ESMs.

11.3.4 Detection and attribution, event attribution

SREX (IPCC, 2012) assessed that it is *likely* anthropogenic influences have led to the warming of extreme daily minimum and maximum temperatures at the global scale. AR5 concluded that human influence has *very likely* contributed to the observed changes in the intensity and frequency of daily temperature extremes on the global scale in the second half of the 20th century (IPCC, 2014). With regard to individual, or regionally- or locally-specific events, AR5 concluded that it is *likely* human influence has substantially increased the probability of occurrence of heat waves in some locations.

Studies since AR5 continue to attribute the observed increase in the frequency or intensity of hot extremes and the observed decrease in the frequency or intensity of cold extremes to human influence, dominated by anthropogenic greenhouse gas emissions, on global and continental scales, and for many AR6 regions. These include attribution of changes in the magnitude of annual TXx, TNx, TXn, and TNn, based on different observational data sets including, HadEX2 and HadEX3, CMIP5 and CMIP6 simulations, and different statistical methods (Kim et al., 2016; Wang et al., 2017c; Seong et al., 2020). As is the case for an increase in mean temperature (3.3.1), an increase in extreme temperature is mostly due to greenhouse gas forcing, off-set by aerosol forcing. The aerosols' cooling effect is clearly detectable over Europe and Asia (Seong et al., 2020). As much as 75% of the moderate daily hot extremes (above 99.9th percentile) over land are due to anthropogenic warming (Fischer and Knutti, 2015). New results are found to be more robust due to the extended period that improves the signal-to-noise ratio. The effect of anthropogenic forcing is clearly detectable and attributable in the observed changes in these indicators of temperature extremes, even at country and sub-country scales, such as in Canada (Wan et al., 2019). Changes in the number of warm nights, warm days, cold nights, and cold days, and other indicators such as the Warm Spell Duration Index (WSDI), are also attributed to anthropogenic influence (Hu et al., 2020; Christidis and Stott, 2016).

Regional studies, including for Asia (Dong et al., 2018; Lu et al., 2018), Australia (Alexander and Arblaster, 2017), and Europe (Christidis and Stott, 2016), found similar results. A clear anthropogenic signal is also found in the trends in the Combined Extreme Index (CEI) for North America, Asia, Australia, and Europe (Dittus et al., 2016). While various studies have described increasing trends in several heat wave metrics (HWD, HWA, EHF, etc.) in different regions (e.g., Bandyopadhyay et al., 2016; Cowan et al., 2014; Sanderson et al., 2017), few recent studies have explicitly attributed these changes to causes; most of them stated that observed trends are consistent with anthropogenic warming. The detected anthropogenic signals are clearly separable from the response to natural forcing, and the results are generally insensitive to the use of different model samples, as well as different data availability, indicating robust attribution. Studies of monthly, seasonal, and annual records in various regions (Kendon, 2014; Lewis and King, 2015; Bador et al., 2016; Meehl et al., 2016; Zhou et al., 2019a) and globally (King, 2017) show an increase in the breaking of

ACCEPTED VERSION SUBJECT TO FINAL EDITING

hot records and a decrease in the breaking of cold records (King, 2017). Changes in anthropogenically-attributable record-breaking rates are noted to be largest over the Northern Hemisphere land areas (Shiogama et al., 2016). Yin and Sun (2018) found clear evidence of an anthropogenic signal in the changes in the number of frost and icing days, when multiple model simulations were used. In some key wheat-producing regions of southern Australia, increases in frost days or frost season length have been reported (Dittus et al., 2014; Crimp et al., 2016); these changes are linked to decreases in rainfall, cloud-cover, and subtropical ridge strength, despite an overall increase in regional mean temperatures (Dittus et al., 2014; Pepler et al., 2018).

A significant advance since AR5 has been a large number of studies focusing on extreme temperature events at monthly and seasonal scales, using various extreme event attribution methods. Diffenbaugh et al. (2017) found anthropogenic warming has increased the severity and probability of the hottest month over >80% of the available observational area on the global scale. Christidis and Stott (2014) provide clear evidence that warm events have become more probable because of anthropogenic forcings. Sun et al. (2014) found human influence has caused a more than 60-fold increase in the probability of the extreme warm 2013 summer in eastern China since the 1950s. Human influence is found to have increased the probability of the historically hottest summers in many regions of the world, both in terms of mean temperature (Mueller et al., 2016a) and wet-bulb globe temperature (WBGT) (Li et al., 2017a). In most regions of the Northern Hemisphere, changes in the probability of extreme summer average WBGT were found to be about an order of magnitude larger than changes in the probability of extreme hot summers estimated by surface air temperature (Li et al., 2017a). In addition to these generalised, global-scale approaches, extreme event studies have found an attributable increase in the probability of hot annual and seasonal temperatures in many locations, including Australia (Knutson et al., 2014a; Lewis and Karoly, 2014), China (Sun et al., 2014; Sparrow et al., 2018; Zhou et al., 2020), Korea (Kim et al., 2018c) and Europe (King et al., 2015b).

There have also been many extreme event attribution studies that examined short duration temperature extremes, including daily temperatures, temperature indices, and heat wave metrics. Examples of these events from different regions are summarised in various annual Explaining Extreme Events supplements of the Bulletin of the American Meteorological Society (Peterson et al., 2012, 2013b, Herring et al., 2014, 2015, 2016, 2018, 2019, 2020), including a number of approaches to examine extreme events (described in Easterling et al., 2016; Otto, 2017; Stott et al., 2016). Several studies of recent events from 2016 onwards have determined an infinite risk ratio (fraction of attributable risk (FAR) of 1), indicating the occurrence probability for such events is close to zero in model simulations without anthropogenic influences (see Herring et al., 2018, 2019, 2020; Imada et al., 2019; Vogel et al., 2019). Though it is difficult to accurately estimate the lower bound of the uncertainty range of the FAR in these cases (Paciorek et al., 2018), the fact that those events are so far outside the envelop of the models with only natural forcing indicates that it is *extremely unlikely* for those events to occur without human influence.

Studies that focused on the attributable signal in observed cold extreme events show human influence reducing the probability of those events. Individual attribution studies on the extremely cold winter of 2011 in Europe (Peterson et al., 2012), in the eastern US during 2014 and 2015 (Trenary et al., 2015, 2016; Wolter et al., 2015; Bellprat et al., 2016), in the cold spring of 2013 in the United Kingdom (Christidis et al., 2014), and of 2016 in eastern China (Qian et al., 2018; Sun et al., 2018b) all showed a reduced probability due to human influence on the climate. An exception is the study of Grose et al. (2018), who found an increase in the probability of the severe western Australian frost of 2016 due to anthropogenically-driven changes in circulation patterns that drive cold outbreaks and frost probability.

Different event attribution studies can produce a wide range of changes in the probability of event occurrence because of different framing. The temperature event definition itself plays a crucial role in the attributable signal (Fischer and Knutti, 2015; Kirchmeier-Young et al., 2019). Large-scale, longer-duration events tend to have notably larger attributable risk ratios (Angélil et al., 2014, 2018; Uhe et al., 2016; Harrington, 2017; Kirchmeier-Young et al., 2019), as natural variability is smaller. While uncertainty in the best estimates of the risk ratios may be large, their lower bounds can be quite insensitive to uncertainties in observations or model descriptions, thus increasing confidence in conservative attribution statements (Jeon et al., 2016).

ACCEPTED VERSION SUBJECT TO FINAL EDITING

The relative strength of anthropogenic influences on temperature extremes is regionally variable, in part due to differences in changes in atmospheric circulation, land surface feedbacks, and other external drivers like aerosols. For example, in the Mediterranean and over western Europe, risk ratios on the order of 100 have been found (Kew et al., 2019; Vautard et al., 2020a), whereas in the US, changes are much less pronounced. This is probably a reflection of the land-surface feedback enhanced extreme 1930s temperatures that reduce the rarity of recent extremes, in addition to the definition of the events and framing of attribution analyses (e.g., spatial and temporal scales considered). Local forcing may mask or enhance the warming effect of greenhouse gases. In India, short-lived aerosols or an increase in irrigation may be masking the warming effect of greenhouse gases (Wehner et al., 2018c). Irrigation and crop intensification have been shown to lead to a cooling in some regions, in particular in North America, Europe, and India (Mueller et al., 2016b; Thiery et al., 2017, 2020; Chen and Dirmeyer, 2019),(*high confidence*). Deforestation has contributed about one third of the total warming of hot extremes in some mid-latitude regions since pre-industrial times (Lejeune et al., 2018). Despite all of these differences, and larger uncertainties at the regional scale, nearly all studies demonstrated that human influence has contributed to an increase in the frequency or intensity of hot extremes and to a decrease in the frequency or intensity of cold extremes.

In summary, long-term changes in various aspects of long- and short-duration extreme temperatures, including intensity, frequency, and duration have been detected in observations and attributed to human influence at global and continental scales. It is *extremely likely* that human influence is the main contributor to the observed increase in the intensity and frequency of hot extremes and the observed decrease in the intensity and frequency of cold extremes on the global scale. It is *very likely* that this applies on continental scales as well. Some specific recent hot extreme events would have been *extremely unlikely* to occur without human influence on the climate system. Changes in aerosol concentrations have affected trends in hot extremes in some regions, with the presence of aerosols leading to attenuated warming, in particular from 1950-1980. Crop intensification, irrigation and no-till farming have attenuated increases in summer hot extremes in some regions, such as central North America (*medium confidence*).

11.3.5 Projections

AR5 (Chapter12, Collins et al., 2013a) concluded it is *virtually certain* there will be more frequent hot extremes and fewer cold extremes at the global scale and over most land areas in a future warmer climate and it is *very likely* heat waves will occur with a higher frequency and longer duration . SR15 (Chapter 3, Hoegh-Guldberg et al., 2018) assessment on projected changes in hot extremes at 1.5°C and 2°C global warming is consistent with the AR5 assessment, concluding it is *very likely* a global warming of 2°C, when compared with a 1.5°C warming, would lead to more frequent and more intense hot extremes on land, as well as to longer warm spells, affecting many densely-inhabited regions. SR15 also assessed it is *very likely* the strongest increases in the frequency of hot extremes are projected for the rarest events, while cold extremes will become less intense and less frequent and cold spells will be shorter.

New studies since AR5 and SR15 confirm these assessments. New literature since AR5 includes projections of temperature-related extremes in relation to changes in mean temperatures, projections based on CMIP6 simulations, projections based on stabilized global warming levels, and the use of new metrics. Constraints for the projected changes in hot extremes were also provided (Borodina et al., 2017b; Sippel et al., 2017b; Vogel et al., 2017). Overall, projected changes in the magnitude of extreme temperatures over land are larger than changes in global mean temperature, over mid-latitude land regions in particular (Figures 11.3, 11.11), (Fischer et al., 2014; Seneviratne et al., 2016; Sanderson et al., 2017a; Wehner et al., 2018b; Di Luca et al., 2020a). Large warming in hot and cold extremes will occur even at the 1.5°C global warming level (Figure 11.11). At this level, widespread significant changes at the grid-box level occur for different temperature indices (Aerenson et al., 2018). In agreement with CMIP5 projections, CMIP6 simulations show that a 0.5°C increment in global warming will significantly increase the intensity and frequency of hot extremes and decrease the intensity and frequency of cold extremes on the global scale (Figures 11.6, 11.8, 11.12). It takes less than half of a degree for the changes in TXx to emerge above the level of natural variability (Figure 11.8) and the 66% ranges of the land medians of the 10-year or 50-year TXx events do not overlap between

ACCEPTED VERSION SUBJECT TO FINAL EDITING

1.0°C and 1.5°C in the CMIP6 multi-model ensemble simulations (Figure 11.6, Li et al., 2020).

[START FIGURE 11.11 HERE]

Figure 11.11: Projected changes in (a-c) annual maximum temperature (TXx) and (d-f) annual minimum temperature (TNn) at 1.5°C, 2°C, and 4°C of global warming compared to the 1851-1900 baseline. Results are based on simulations from the CMIP6 multi-model ensemble under the SSP1-1.9, SSP1-2.6, SSP2-4.5, SSP3-7.0, and SSP5-8.5 scenarios. The numbers in the top right indicate the number of simulations included. Uncertainty is represented using the simple approach: no overlay indicates regions with high model agreement, where ≥80% of models agree on sign of change; diagonal lines indicate regions with low model agreement, where <80% of models agree on sign of change. For more information on the simple approach, please refer to the Cross-Chapter Box Atlas 1. For details on the methods see Supplementary Material 11.SM.2. Further details on data sources and processing are available in the chapter data table (Table 11.SM.9).

[END FIGURE 11.11 HERE]

Projected warming is larger for TNn and exhibits strong equator-to-pole amplification similar to the warming of boreal winter mean temperatures. The warming of TXx is more uniform over land and does not exhibit this behaviour (Figure 11.11). The warming of temperature extremes on global and regional scales tends to scale linearly with global warming (Section 11.1.4) (Fischer et al., 2014; Seneviratne et al., 2016, Wartenburger et al., 2017; Li et al., 2020; see also SR15, Chapter 3). In the mid-latitudes, the rate of warming of hot extremes can be as large as twice the rate of global warming (Figure 11.11). In the Arctic winter, the rate of warming of the temperature of the coldest nights is about three times the rate of global warming (Appendix Figure 11.A.1). Projected changes in temperature extremes can deviate from projected changes in annual mean warming in the same regions (Figure 11.3, Figs. 11.A.1 and 11.A.2, Di Luca et al., 2020a; Wehner, 2020) due to the additional processes that control the response of regional extremes, including, in particular, soil moisture-evapotranspiration-temperature feedbacks for hot extremes in the mid-latitudes and subtropical regions, and snow/ice-albedo-temperature feedbacks in high-latitude regions.

[START FIGURE 11.12 HERE]

Figure 11.12: Projected changes in the intensity of extreme temperature events under 1°C, 1.5°C, 2°C, 3°C, and 4°C global warming levels relative to the 1851-1900 baseline. Extreme temperature events are defined as the daily maximum temperatures (TXx) that were exceeded on average once during a 10-year period (10-year event, blue) and that once during a 50-year period (50-year event, orange) during the 1851-1900 base period. Results are shown for the global land. For each box plot, the horizontal line and the box represent the median and central 66% uncertainty range, respectively, of the intensity changes across the space, and the whiskers extend to the 90% uncertainty range. The results are based on the multi-model ensemble median estimated from simulations of global climate models contributing to the sixth phase of the Coupled Model Intercomparison Project (CMIP6) under different SSP forcing scenarios. Adapted from (Li et al., 2020a). Further details on data sources and processing are available in the chapter data table (Table 11.SM.9).

[END FIGURE 11.12 HERE]

The probability of exceeding a certain hot extreme threshold will increase, while those for cold extreme will decrease with global warming (Mueller et al., 2016a; Lewis et al., 2017b; Suarez-Gutierrez et al., 2020b). The changes tend to scale nonlinearly with the level of global warming, with larger changes for more rare events (Section 11.2.4 and CCB 11.11; Figure. 11.6 and 11.12; e.g. Fischer and Knutti, 2015, Kharin et al., 2018; Li et al., 2020). For example, the CMIP5 ensemble projects the frequency of the present-day climate 20-year hottest daily temperature to increase by 80% at the 1.5°C global warming level and by 180% at the 2.0°C global warming level, and the frequency of the present-day climate 100-year hottest daily temperature

ACCEPTED VERSION SUBJECT TO FINAL EDITING

to increase by 200% and more than 700% at the 1.5°C and 2.0°C warming levels, respectively (Kharin et al., 2018). CMIP6 simulations project similar changes (Li et al., 2020a).

Tebaldi and Wehner (2018) showed that at the middle of the 21st century, 66% of the land surface area would experience the present-day 20-year return values of TXx and the running 3-day average of the daily maximum temperature every other year on average under the RCP8.5 scenario, as opposed to only 34% under RCP4.5. By the end of the century, these area fractions increase to 92% and 62%, respectively. Such nonlinearities in the characteristics of future regional extremes are shown, for instance, for Europe (Lionello and Scarascia, 2020; Spinoni et al., 2018a; Dosio and Fischer, 2018), Asia (Guo et al., 2017; Harrington and Otto, 2018b; King et al., 2018), and Australia (Lewis et al., 2017a) under various global warming thresholds. The non-linear increase in fixed-threshold indices (e.g., percentile-based for a given reference period or based on an absolute threshold) as a function of global warming is consistent with a linear warming of the absolute temperature of the temperature extremes (e.g., Whan et al., 2015). Compared to the historical climate, warming will result in strong increases in heat wave area, duration, and magnitude (Vogel et al., 2020b). These changes are mostly due to the increase in mean seasonal temperature, rather than changes in temperature variability, though the latter can have an effect in some regions (Di Luca et al., 2020a; Suarez-Gutierrez et al., 2020a; Brown, 2020).

Projections of temperature-related extremes in RCMs in the CORDEX regions demonstrate robust increases under future scenarios and can provide information on finer spatial scales than GCMs (e.g. Coppola et al., 2021). Five RCMs in the CORDEX-East Asia region project decreases in the 20-year return values of temperature extremes (summer maxima), with models that exhibit warm biases projecting stronger warming (Park and Min, 2018). Similarly, in the African domain, future increases in TX90p and TN90p are projected (Dosio, 2017; Mostafa et al., 2019). This regional-scale analysis provides fine scale information, such as distinguishing the increase in TX90p over sub-equatorial Africa (Democratic Republic of Congo, Angola and Zambia) with values over the Gulf of Guinea, Central African Republic, South Sudan, and Ethiopia. Empirical-statistical downscaling has also been used to produce more robust estimates for future heat waves compared to RCMs based on large multi-model ensembles (Furrer et al., 2010; Keellings and Waylen, 2014; Wang et al., 2015; Benestad et al., 2018).

In all continental regions, including Africa (Table 11.4), Asia (Table 11.7), Australasia (Table 11.10), Central and South America (Table 11.13), Europe (Table 11.16), North America (Table 11.19) and at the continental scale, it is *very likely* the intensity and frequency of hot extremes will increase and the intensity and frequency of cold extremes will decrease compared with the 1995-2014 baseline, even under 1.5°C global warming, and those changes are *virtually certain* to occur under 4°C global warming. At the regional scale and for almost all AR6 regions, it is *likely* the intensity and frequency of hot extremes will increase and the intensity and frequency of cold extremes will decrease compared with the 1995-2014 baseline, even under 1.5°C global warming and those changes will *virtually certain* to occur under 4°C global warming. Exceptions include lower confidence in the projected decrease in the intensity and frequency of cold extremes compared with the 1995-2014 baseline under 1.5°C of global warming (*medium confidence*) and 4°C of global warming (*very likely*) in North Central America, Central North America, and Western North America.

In Africa (Table 11.4), evidence includes increases in the intensity and frequency of hot extremes, such as warm days, warm nights, and heat waves, and decreases in the intensity and frequency of cold extremes, such as cold days and cold nights, over the continent as projected by CMIP5, CMIP6, and CORDEX simulations (Giorgi et al., 2014; Engelbrecht et al., 2015; Lelieveld et al., 2016; Russo et al., 2016; Dosio, 2017; Bathiany et al., 2018; Mba et al., 2018; Nangombe et al., 2018; Weber et al., 2018; Kruger et al., 2019; Coppola et al., 2021; Li et al., 2020). Cold spells are projected to decrease under all RCPs and even at low warming levels in West and Central Africa (Diedhiou et al., 2018) and the number of cold days is projected to decrease in East Africa (Ongoma et al., 2018b).

In Asia (Table 11.7), evidence includes increases in the intensity and frequency of hot extremes, such as warm days, warm nights, and heat waves, and decreases in the intensity and frequency of cold extremes, such as cold days and cold nights, over the continent as projected by CMIP5, CMIP6, and CORDEX

ACCEPTED VERSION SUBJECT TO FINAL EDITING

simulations (Gao et al., 2018; Han et al., 2018; Li et al., 2019b; Pal and Eltahir, 2016; Shin et al., 2018; Sillmann et al., 2013b; Singh and Goyal, 2016; Sui et al., 2018; Xu et al., 2017; Zhang et al., 2015c; Zhao et al., 2015; Zhou et al., 2014; Zhu et al., 2020). More intense heat waves of longer durations and occurring at a higher frequency are projected over India (Murari et al., 2015; Mishra et al., 2017) and Pakistan (Nasim et al., 2018). Future mid-latitude warm extremes, similar to those experienced during the 2010 event, are projected to become more extreme, with temperature extremes increasing potentially by 8.4°C (RCP8.5) over northwest Asia (van der Schrier et al., 2018). Over WSB, ESB and RFE, an increase in extreme heat durations is expected in all scenarios (Sillmann et al., 2013b; Kattsov et al., 2017; Reyer et al., 2017). In the MENA regions (ARP, WCA), extreme temperatures could increase by almost 7°C by 2100 under RCP8.5 (Lelieveld et al., 2016).

In Australasia (Table 11.10), evidence includes increases in the intensity and frequency of hot extremes, such as warm days, warm nights, and heat waves, and decreases in the intensity and frequency of cold extremes, such as cold days and cold nights, over the continent as projected by CMIP5, CMIP6, and CORDEX simulations (Coppola et al., 2021; Alexander and Arblaster, 2017; CSIRO and BOM, 2015; Herold et al., 2018; Lewis et al., 2017a; Evans et al., 2020). Over most of Australia, increases in the intensity and frequency of hot extremes are projected to be predominantly driven by the long-term increase in mean temperatures (Di Luca et al., 2020a). Future projections indicate a decrease in the number of frost days regardless of the region and season considered (Alexander and Arblaster, 2017; Herold et al., 2018).

In Central and South America (Table 11.13), evidence includes increases in the intensity and frequency of hot extremes, such as warm days, warm nights, and heat waves, and decreases in the intensity and frequency of cold extremes, such as cold days and cold nights, over the continent as projected by CMIP5, CMIP6, and CORDEX simulations (Chou et al., 2014a; Cabré et al., 2016; López-Franca et al., 2016; Stennett-Brown et al., 2017; Li et al., 2020a; Coppola et al., 2021b; Vichot-Llano et al., 2021). Over SES during the austral summer, the increase in the frequency of TN90p is larger than that projected for TX90p, consistent with observed past changes (López-Franca et al., 2016). Under RCP8.5, the number of heat wave days are projected to increase for the intra-Americas region for the end of the 21st century (Angeles-Malaspina et al., 2018). A general decrease in the frequency of cold spells and frost days is projected as indicated by several indices based on minimum temperature (López-Franca et al., 2016).

In Europe (Table 11.16), evidence includes increases in the intensity and frequency of hot extremes, such as warm days, warm nights, and heat waves, and decreases in the intensity and frequency of cold extremes, such as cold days and cold nights, over the continent as projected by CMIP5, CMIP6, and CORDEX simulations (Coppola et al., 2021; Cardoso et al., 2019; Jacob et al., 2018; Lau and Nath, 2014; Lhotka et al., 2018; Lionello and Scarascia, 2020; Molina et al., 2020; Ozturk et al., 2015; Rasmijn et al., 2018; Russo et al., 2015; Schoetter et al., 2015; Suarez-Gutierrez et al., 2018; Vogel et al., 2017; Winter et al., 2017; Li et al., 2020). Increases in heat waves are greater over the southern Mediterranean and Scandinavia (Forzieri et al., 2016; Abaurrea et al., 2018; Dosio and Fischer, 2018; Rohat et al., 2019). The biggest increases in the number of heat wave days are expected for southern European cities (Guerreiro et al., 2018a; Junk et al., 2019), and Central European cities will see the biggest increases in maximum heat wave temperatures (Guerreiro et al., 2018a).

In North America (Table 11.19), evidence includes increases in the intensity and frequency of hot extremes, such as warm days, warm nights, and heat waves, and decreases in the intensity and frequency of cold extremes, such as cold days and cold nights, over the continent as projected by CMIP5, CMIP6, and CORDEX simulations (Li et al., 2020; Coppola et al., 2021; Alexandru, 2018; Grotjahn et al., 2016; Li et al., 2018a; Vose et al., 2017a; Yang et al., 2018a; Zhang et al., 2019d). Projections of temperature extremes for the end of the 21st century show that warm days and nights are *very likely* to increase and cold days and nights are *very likely* to decrease in all regions. There is *medium confidence* in large increases in warm days and warm nights in summer, particularly over the United States, and in large decreases in cold days in Canada in fall and winter (Li et al., 2020; Coppola et al., 2021; Alexandru, 2018; Grotjahn et al., 2016; Li et al., 2018a; Vose et al., 2017a; Yang et al., 2018a; Zhang et al., 2019d). Minimum winter temperatures are projected to rise faster than mean winter temperatures (Underwood et al., 2017). Projections for the end of the century under RCP8.5 showed the 4-day cold spell that happens on average once every 5 years is

ACCEPTED VERSION SUBJECT TO FINAL EDITING

projected to warm by more than 10 ºC and CMIP5 models do not project current 1-in-20 year annual minimum temperature extremes to recur over much of the continent (Wuebbles et al., 2014).

In summary, it is *virtually certain* that further increases in the intensity and frequency of hot extremes and decreases in the intensity and frequency of cold extremes will occur throughout the 21st century and around the world. It is *virtually certain* the number of hot days and hot nights and the length, frequency, and/or intensity of warm spells or heat waves compared to 1995-2014 will increase over most land areas. In most regions, changes in the magnitude of temperature extremes are proportional to global warming levels (*high confidence*). The highest increase of temperature of hottest days is projected in some mid-latitude and semi-arid regions, at about 1.5 time to twice the rate of global warming (high confidence). The highest increase of temperature of coldest days is projected in Arctic regions, at about three times the rate of global warming (high confidence). The probability of temperature extremes generally increases non-linearly with increasing global warming levels (*high confidence*). Confidence in assessments depends on the spatial and temporal scales of the extreme in question, with *high confidence* in projections of temperature-related extremes at global and continental scales for daily to seasonal scales. There is *high confidence* that, on land, the magnitude of temperature extremes increases more strongly than global mean temperature.

11.4 Heavy precipitation

This section assesses changes in heavy precipitation at global and regional scales. The main focus is on extreme precipitation at a daily scale where literature is most concentrated, though extremes of shorter (sub-daily) and longer (five-day or more) durations are also assessed to the extent the literature allows.

11.4.1 Mechanisms and drivers

SREX (Chapter 3, Seneviratne et al., 2012) assessed changes in heavy precipitation in the context of the effects of thermodynamic and dynamic changes. Box 11.1 assesses thermodynamic and dynamic changes in a warming world to aid the understanding of changes in observations and projections in some extremes and the sources of uncertainties (See also Chapter 8, Section 8.2.3.2). In general, warming increases the atmospheric water-holding capacity following the Clausius-Clapeyron (C-C) relation. This thermodynamic effect results in an increase in extreme precipitation at a similar rate at the global scale. On a regional scale, changes in extreme precipitation are further modulated by dynamic changes (Box 11.1).

Large-scale modes of variability, such as the North Atlantic Oscillation (NAO), El Niño-Southern Oscillation (ENSO), Atlantic Multidecadal Variability (AMV), and Pacific Decadal Variability (PDV) (Annex VI), modulate precipitation extremes through changes in environmental conditions or embedded storms (Section 8.3.2). Latent heating can invigorate these storms (Nie et al., 2018; Zhang et al., 2019g); changes in dynamics can increase precipitation intensity above that expected from the C-C scaling rate (8.2.3.2, Box 11.1, and Section 11.7). Additionally, the efficiency of converting atmospheric moisture into precipitation can change as a result of cloud microphysical adjustment to warming, resulting in changes in the characteristics of extreme precipitation; but changes in precipitation efficiency in a warming world are highly uncertain (Sui et al., 2020).

It is difficult to separate the effect of global warming from internal variability in the observed changes in the modes of variability (Section 2.4). Future projections of modes of variability are highly uncertain (Section 4.3.3), resulting in uncertainty in regional projections of extreme precipitation. Future warming may amplify monsoonal extreme precipitation. Changes in extreme storms, including tropical/extratropical cyclones and severe convective storms, result in changes in extreme precipitation (Section 11.7). Also, changes in sea surface temperatures (SSTs) alter land-sea contrast, leading to changes in precipitation extremes near coastal regions. For example, the projected larger SST increase near the coasts of East Asia and India can result in heavier rainfall near these coastal areas from tropical cyclones (Mei and Xie, 2016) or torrential rains (Manda et al., 2014). The warming in the western Indian Ocean is associated with increases in moisture surges on the low-level monsoon westerlies towards the Indian subcontinent, which may lead to an increase

ACCEPTED VERSION SUBJECT TO FINAL EDITING

in the occurrence of precipitation extremes over central India (Krishnan et al., 2016; Roxy et al., 2017).

Decreases in atmospheric aerosols results in warming and thus an increase in extreme precipitation (Samset et al., 2018; Sillmann et al., 2019). Changes in atmospheric aerosols also result in dynamic changes such as changes in tropical cyclones (Takahashi et al., 2017; Strong et al., 2018). Uncertainty in the projections of future aerosol emissions results in additional uncertainty in the heavy precipitation projections of the 21st century (Lin et al., 2016).

There has been new evidence of the effect of local land use and land cover change on heavy precipitation. There is a growing set of literature linking increases in heavy precipitation in urban centres to urbanization (Argüeso et al., 2016; Zhang et al., 2019f). Urbanization intensifies extreme precipitation, especially in the afternoon and early evening, over the urban area and its downwind region *(medium confidence) (*Box 10.3). There are four possible mechanisms: a) increases in atmospheric moisture due to horizontal convergence of air associated with the urban heat island effect (Shastri et al., 2015; Argüeso et al., 2016); b) increases in condensation due to urban aerosol emissions (Han et al., 2011; Sarangi et al., 2017); c) aerosol pollution that impacts cloud microphysics (Schmid and Niyogi, 2017) (Box 8.1); and d) urban structures that impede atmospheric motion (Ganeshan and Murtugudde, 2015; Paul et al., 2018; Shepherd, 2013). Other local forcing, including reservoirs (Woldemichael et al., 2012), irrigation (Devanand et al., 2019), or large-scale land use and land cover change (Odoulami et al., 2019), can also affect local extreme precipitation.

In summary, precipitation extremes are controlled by both thermodynamic and dynamic processes. Warming-induced thermodynamic change results in an increase in extreme precipitation, at a rate that closely follows the Clausius-Clapeyron relationship at the global scale (*high confidence)*. The effects of warming-induced changes in dynamic drivers on extreme precipitation are more complicated, difficult to quantify and are an uncertain aspect of projections. Precipitation extremes are also affected by forcings other than changes in greenhouse gases, including changes in aerosols, land use and land cover change, and urbanization (*medium confidence*).

11.4.2 Observed Trends

Both SREX (Chapter 3, Seneviratne et al., 2012) and AR5 (IPCC, 2014 Chapter 2) concluded it was *likely* the number of heavy precipitation events over land had increased in more regions than it had decreased, though there were wide regional and seasonal variations, and trends in many locations were not statistically significant. This assessment has been strengthened with multiple studies finding robust evidence of the intensification of extreme precipitation at global and continental scales, regardless of spatial and temporal coverage of observations and the methods of data processing and analysis.

The average annual maximum precipitation amount in a day (Rx1day) has significantly increased since the mid-20th century over land (Du et al., 2019; Dunn et al., 2020) and in the humid and dry regions of the globe (Dunn et al., 2020). The percentage of observing stations with statistically significant increases in Rx1day is larger than expected by chance, while the percentage of stations with statistically significant decreases is smaller than expected by chance, over the global land as a whole and over North America, Europe, and Asia (Figure 11.13, Sun et al., 2020) and over global monsoon regions (Zhang and Zhou, 2019) where data coverage is relatively good. The addition of the past decade of observational data shows a more robust increase in Rx1day over the global land region (Sun et al., 2020). Light, moderate, and heavy daily precipitation has all intensified in a gridded daily precipitation data set (Contractor et al., 2020). Daily mean precipitation intensities have increased since the mid-20th century in a majority of land regions (*high confidence,* Section 8.3.1.3). The probability of precipitation exceeding 50 mm/day increased during 1961-2018 (Benestad et al., 2019). The globally averaged annual fraction of precipitation from days in the top 5% (R95pTOT) has also significantly increased (Dunn et al., 2020). The increase in the magnitude of Rx1day in the 20th century is estimated to be at a rate consistent with C-C scaling with respect to global mean temperature (Fischer and Knutti, 2016; Sun et al., 2020). Studies on past changes in extreme precipitation of durations longer than a day are more limited, though there are some studies examining long-term trends in annual maximum five-day precipitation (Rx5day). On global and continental scales, long-term changes in

ACCEPTED VERSION SUBJECT TO FINAL EDITING

Rx5day are similar to those of Rx1day in many aspects (Zhang and Zhou 2019; Sun et al., 2020). As discussed below, at the regional scale, changes in Rx5day are also similar to those of Rx1day where there are analyses of changes in both Rx1day and Rx5day.

Overall, there is a lack of systematic analysis of long-term trends in sub-daily extreme precipitation at the global scale. Often, sub-daily precipitation data have only sporadic spatial coverage and are of limited length. Additionally, the available data records are far shorter than needed for a robust quantification of past changes in sub-daily extreme precipitation (Li et al., 2018b). Despite these limitations, there are studies in regions of almost all continents that generally indicate intensification of sub-daily extreme precipitation, although *confidence* in an overall increase at the global scale remains *very low*. Studies include an increase in extreme sub-daily rainfall in summer over South Africa (Sen Roy and Rouault, 2013), annually in Australia (Guerreiro et al., 2018b), over 23 urban locations in India (Ali and Mishra, 2018), in Peninsular Malaysia (Syafrina et al., 2015), and in eastern China in the summer season during 1971-2013 (Xiao et al., 2016). In some regions in Italy (Arnone et al., 2013; Libertino et al., 2019) and in the US during 1950-2011 (Barbero et al., 2017), there is also an increase. In general, an increase in sub-daily heavy precipitation results in an increase in pluvial floods over smaller watersheds (Ghausi and Ghosh, 2020).

There is a considerable body of literature examining scaling of sub-daily precipitation extremes, conditional on day-to-day air or dew-point temperatures (Westra et al., 2014; Fowler et al., 2021). This scaling, termed apparent scaling (Fowler et al., 2020) is robust when different methodologies are used in different regions, ranging between the C-C and two-times the C-C rate (e.g. Burdanowitz et al., 2019; Formayer and Fritz, 2017; Lenderink et al., 2017). This is confirmed when sub-daily precipitation data collected from multiple continents (Lewis et al., 2019a) are analysed in a consistent manner using different methods (Ali et al., 2021). It has been hoped that apparent scaling might be used to help understand past and future changes in extreme sub-daily precipitation. However, apparent scaling samples multiple synoptic weather states, mixing thermodynamic and dynamic factors that are not directly relevant for climate change responses (8.2.3.2) (Prein et al., 2016b; Bao et al., 2017; Zhang et al., 2017c; Drobinski et al., 2018; Sun et al., 2019d). The spatial pattern of apparent scaling is different from those of projected changes over Australia (Bao et al., 2017) and North America (Sun et al., 2019) in regional climate model simulations. It thus remains difficult to use the knowledge about apparent scaling to infer past and future changes in extreme sub-daily precipitation according to observed and projected changes in local temperature.

In Africa (Table 11.5), evidence shows an increase in extreme daily precipitation for the late half of the 20th century over the continent where data are available; there is a larger percentage of stations showing significant increases in extreme daily precipitation than decreases (Sun et al., 2020). There are increases in different metrics relevant to extreme precipitation in various regions of the continent (Chaney et al., 2014; Harrison et al., 2019; Dunn et al., 2020; Sun et al., 2020). There is an increase in extreme precipitation events in southern Africa (Weldon and Reason, 2014; Kruger et al., 2019) and a general increase in heavy precipitation over East Africa, the Greater Horn of Africa (Omondi et al., 2014). Over sub-Saharan Africa, increases in the frequency and intensity of extreme precipitation have been observed over the well-gauged areas during 1950-2013; however, this covers only 15% of the total area of sub-Saharan Africa (Harrison et al., 2019). *Confidence* about the increase in extreme precipitation for some regions where observations are more abundant is *medium,* but for Africa as whole, it is *low* because of a general lack of continent-wide systematic analysis, the sporadic nature of available precipitation data over the continent, and spatially non-homogenous trends in places where data are available (Donat et al., 2014a; Mathbout et al., 2018; Alexander et al., 2019; Funk et al., 2020)

In Asia (Table 11.8), there is *robust evidence* that extreme precipitation has increased since the 1950s (*high confidence*), however this is dominated by high spatial variability. Increases in Rx1day and Rx5day during 1950-2018 are found over two thirds of stations and the percentage of stations with statistically significant trends is significantly larger than can be expected by chance (Sun et al., 2020, also Fig 11.13). An increase in extreme precipitation has also been observed in various regional studies based on different metrics of extreme precipitation and different spatial and temporal coverage of the data. These include an increase in daily precipitation extremes over central Asia (Hu et al., 2016), most of South Asia (Zahid and Rasul, 2012; Pai et al., 2015; Sheikh et al., 2015; Adnan et al., 2016; Malik et al., 2016; Dimri et al., 2017; Priya et al.,

ACCEPTED VERSION SUBJECT TO FINAL EDITING

2017; Roxy et al., 2017; Hunt et al., 2018; Kim et al., 2019; Wester et al., 2019), the Arabian Peninsula (Rahimi and Fatemi, 2019; Almazroui and Saeed, 2020; Atif et al., 2020), Southeast Asia (Siswanto et al., 2015; Supari et al., 2017; Cheong et al., 2018); the northwest Himalaya (Malik et al., 2016), parts of east Asia (Nayak et al., 2017; Baek et al., 2017; Ye and Li, 2017), the western Himalayas since the 1950s (Ridley et al., 2013; Dimri et al., 2015; Madhura et al., 2015), WSB, ESB and RFE (Donat et al., 2016a) and a decrease was found over the eastern Himalayas (Sheikh et al., 2015; Talchabhadel et al., 2018). Increases have been observed over Jakarta (Siswanto et al., 2015), but Rx1day over most parts of the Maritime Continent has decreased (Villafuerte and Matsumoto, 2015). Trends in extreme precipitation over China are mixed with increases and decreases (Fu et al., 2013a; Jiang et al., 2013; Ma et al., 2015; Yin et al., 2015; Xiao et al., 2016) and are not significant over China as whole (Li et al., 2018c; Ge et al., 2017; Hu et al., 2016; Jiang et al., 2013; Liu et al., 2019b; Chen et al., 2021; Deng et al., 2018; He and Zhai, 2018; Tao et al., 2018). With few exceptions, most Southeast Asian countries have experienced an increase in rainfall intensity, but with a reduced number of wet days (Donat et al., 2016a; Cheong et al., 2018; Naveendrakumar et al., 2019), though large differences in trends exists if the trends are estimated from different datasets including gauge-based, remotely-sensed, and reanalysis over a relatively short period (Kim et al. 2019). There is a significant increase in heavy rainfall (>100 mm day^{-1}) and a significant decrease in moderate rainfall (5–100 mm day^{-1}) in central India during the South Asian monsoon season (Deshpande et al., 2016; Roxy et al., 2017).

In Australasia (Table 11.11), available evidence has not shown an increase or a decrease in heavy precipitation over Australasia as a whole (*medium confidence*), but heavy precipitation tends to increase over northern Australia (particularly the northwest) and decrease over the eastern and southern regions (e.g., Jakob and Walland, 2016; Dey et al., 2018; Guerreiro et al., 2018; Dunn et al., 2020; Sun et al., 2020). Available studies that used long-term observations since the mid-20th century showed nearly as many stations with an increase as those with a decrease in heavy precipitation (Jakob and Walland, 2016) or slightly more stations with a decrease than with an increase in Rx1day and Rx5day (Sun et al., 2020), or strong differences in Rx1day trends with increases over northern Australia and central Australia in general but mostly decreases over southern Australia and eastern Australia (Dunn et al., 2020). Over New Zealand, decreases are observed for moderate-heavy precipitation events, but there are no significant trends for very heavy events (more than 64 mm in a day) for the period 1951-2012. The number of stations with an increase in very wet days is similar to that with a decrease during 1960-2019 (MfE and Stats NZ, 2020). Overall, there is *low confidence* in trends in the frequency of heavy rain days with mostly decreases over New Zealand (Caloiero, 2015; Harrington and Renwick, 2014).

In Central and South America (Table 11.14), evidence shows an increase in extreme precipitation, but in general there is *low confidence;* while continent-wide analyses produced wetting trends, trends are not robust. Rx1day increased at more stations than it decreased in South America between 1950-2018 (Sun et al., 2020). Over 1950-2010, both Rx5day and R99p increased over large regions of South America, including NWS, NSA, and SES (Skansi et al., 2013). There are large regional differences. A decrease in daily extreme precipitation is observed in northeastern Brazil (Bezerra et al., 2018; Dereczynski et al., 2020; Skansi et al., 2013). Trends in extreme precipitation indices were not statistically significant over the period 1947-2012 within the São Francisco River basin in the Brazilian semi-arid region (Bezerra et al., 2018). An increase in extreme rainfall is observed in AMZ with *medium confidence* (Skansi et al., 2013) and in SES with *high confidence* (Ávila et al., 2016; Barros et al., 2015; Lovino et al., 2018; Skansi et al., 2013; Wu and Polvani, 2017; Dereczynski et al., 2020; Valverde and Marengo, 2014). Among all sub-regions, SES shows the highest rate of increase for rainfall extremes, followed by AMZ (Skansi et al., 2013). Increases in the intensity of heavy daily rainfall events have been observed in the southern Pacific and in the Titicaca basin (Huerta and Lavado-Casimiro, 2020; Skansi et al., 2013). In SCA trends in annual precipitation are generally not significant, although small (but significant) increases are found in Guatemala, El Salvador, and Panama (Hidalgo et al., 2017). Small positive trends were found in multiple extreme precipitation indices over the Caribbean region over a short time period (1986-2010) (Stephenson et al., 2014; McLean et al., 2015)

In Europe (Table 11.17), there is robust evidence that the magnitude and intensity of extreme precipitation has *very likely* increased since the 1950s. There is a significant increase in Rx1day and Rx5day during 1950-2018 in Europe as whole (Sun et al., 2020, also Figure 11.13). The number of stations with increases far

ACCEPTED VERSION SUBJECT TO FINAL EDITING

exceeds those with decreases in the frequency of daily rainfall exceeding its 90th or 95th percentile in century-long series (Cioffi et al., 2015). The 5-, 10-, and 20-year events of one-day and five-day precipitation during 1951-1960 became more common since the 1950s (van den Besselaar et al., 2013). There can be large discrepancies among studies and regions and seasons (Croitoru et al., 2013; Willems, 2013; Casanueva et al., 2014; Roth et al., 2014; Fischer et al., 2015); evidence for increasing extreme precipitation is more frequently observed for summer and winter, but not in other seasons (Madsen et al., 2014; Helama et al., 2018). An increase is observed in central Europe (Volosciuk et al., 2016; Zeder and Fischer, 2020), and in Romania (Croitoru et al., 2016). Trends in the Mediterranean region are in general not spatially (Reale and Lionello, 2013), with decreases in the western Mediterranean and some increases in the eastern Mediterranean (Rajczak et al., 2013; Casanueva et al., 2014; de Lima et al., 2015; Gajić-Čapka et al., 2015; Sunyer et al., 2015; Pedron et al., 2017; Serrano-Notivoli et al., 2018; Ribes et al., 2019). In the Netherlands, the total precipitation contributed from extremes higher than the 99th percentile doubles per degree C increase in warming (Myhre et al., 2019), though extreme rainfall trends in northern Europe may differ in different seasons (Irannezhad et al., 2017).

In North America (Table 11.20), there is robust evidence that the magnitude and intensity of extreme precipitation has *very likely* increased since the 1950s. Both Rx1day and Rx5day have significantly increased in North America during 1950-2018 (Sun et al., 2020, also Figure 11.13). There is, however, regional diversity. In Canada, there is a lack of detectable trends in observed annual maximum daily (or shorter duration) precipitation (Shephard et al., 2014; Mekis et al., 2015; Vincent et al., 2018). In the United States, there is an overall increase in one-day heavy precipitation, both in terms of intensity and frequency (Sun et al., 2020; Donat et al., 2013; Huang et al., 2017; Villarini et al., 2012; Easterling et al., 2017; Wu, 2015; Howarth et al., 2019), except for the southern part of the US (Hoerling et al., 2016) where internal variability may have played a substantial role in the lack of observed increases. In Mexico, increases are observed in R10mm and R95p (Donat et al., 2016a), very wet days over the cities (García-Cueto et al., 2019) and in PRCPTOT and Rx1day (Donat et al., 2016b).

In Small Islands, there is a lack of evidence showing changes in heavy precipitation overall. There were increases in extreme precipitation in Tobago from 1985–2015 (Stephenson et al., 2014; Dookie et al., 2019) and decreases in southwestern French Polynesia and the southern subtropics (*low confidence*; Atlas.10; Table 11.5). Extreme precipitation leading to flooding in the small islands has been attributed in part to TCs, as well as being influenced by ENSO (Khouakhi et al., 2016; Hoegh-Guldberg et al., 2018) (Box 11.5).

[START FIGURE 11.13 HERE]

Figure 11.13: Signs and significance of the observed trends in annual maximum daily precipitation (Rx1day) during 1950–2018 at 8345 stations with sufficient data. (a) Percentage of stations with statistically significant trends in Rx1day; green dots show positive trends and brown dots negative trends. Box-and-whisker plots indicate the expected percentage of stations with significant trends due to chance estimated from 1000 bootstrap realizations under a no-trend null hypothesis. The boxes mark the median, 25th percentile, and 75th percentile. The upper and lower whiskers show the 97.5th and the 2.5th percentiles, respectively. Maps of stations with positive (b) and negative (c) trends. The light color indicates stations with non-significant trends and the dark color stations with significant trends. Significance is determined by a two-tailed test conducted at the 5% level. Adapted from Sun et al., (2020). © American Meteorological Society. Used with permission. Further details on data sources and processing are available in the chapter data table (Table 11.SM.9).

[END FIGURE 11.13 HERE]

In summary, the frequency and intensity of heavy precipitation have *likely* increased at the global scale over a majority of land regions with good observational coverage. Since 1950, the annual maximum amount of precipitation falling in a day or over five consecutive days has *likely* increased over land regions with sufficient observational coverage for assessment, with increases in more regions than there are decreases. Heavy precipitation has *likely* increased on the continental scale over three continents, including North America, Europe, and Asia where observational data are more abundant. There is *very low confidence* about

ACCEPTED VERSION SUBJECT TO FINAL EDITING

changes in sub-daily extreme precipitation due to a limited number of studies and the data used in these studies are often limited.

11.4.3 Model evaluation

The evaluation of the skill of climate models to simulate heavy precipitation extremes is challenging due to a number of factors, including the lack of reliable observations and the spatial scale mismatch between simulated and observed data (Avila et al., 2015, Alexander et al., 2019). Simulated precipitation represents areal means, but station-based observations are conducted at point locations and are often sparse. The areal-reduction factor, the ratio between pointwise station estimates of extreme precipitation and extremes of the areal mean, can be as large as 130% at CMIP6 resolutions (~100km) (Gervais et al., 2014). Hence, the order in which gridded station based extreme values are constructed (i.e., if the extreme values are extracted at the station first and then gridded or if the daily station values are gridded and then the extreme values are extracted) represents different spatial scales of extreme precipitation and needs to be taken into account in model evaluation (Wehner et al. 2020). This aspect has been considered in some studies. Reanalysis products are used in place of station observations for their spatial completeness as well as spatial-scale comparability (Sillmann et al., 2013a; Kim et al., 2020; Li et al., 2020). However, reanalyses share similar parameterizations to the models themselves, reducing the objectivity of the comparison.

Different generations of the Coupled Model Intercomparison Project (CMIP) models have improved over time, though quite modestly (Flato et al., 2013; Watterson et al., 2014). Improvements in the representation of the magnitude of the ETCCDI indices in CMIP5 over CMIP3 (Sillmann et al., 2013a; Chen and Sun, 2015a) have been attributed to higher resolution as higher-resolution models represent smaller areas at individual grid boxes. Additionally, the spatial distribution of extreme rainfall simulated by high-resolution models (CMIP5 median resolution ~ 180 ×96) is generally more comparable to observations (Sillmann et al., 2013b; Kusunoki, 2017, 2018b; Scher et al., 2017) as these models tend to produce more realistic storms compared to coarser models (11.7.2). Higher horizontal resolution alone improves simulation of extreme precipitation in some models (Wehner et al., 2014; Kusunoki, 2017, 2018), but this is insufficient in other models (Bador et al., 2020) as model parameterization also plays a significant role (Wu et al., 2020a). A simple comparison of climatology may not fully reflect the improvements of the new models that have more comprehensive formulations of processes (Di Luca et al., 2015). Dittus et al. (2016) found that many of the eight CMIP5 models they evaluated reproduced the observed increase in the difference between areas experiencing an extreme high (90%) and an extreme low (10%) proportion of the annual total precipitation from heavy precipitation (R95p/PRCPTOT) for Northern Hemisphere regions. Additionally, CMIP5 models reproduced the relation between changes in extreme and non-extreme precipitation: an increase in extreme precipitation is at the cost of a decrease in non-extreme precipitation (Thackeray et al., 2018), a characteristic found in the observational record (Gu and Adler, 2018).

CMIP6 models perform reasonably well in capturing large-scale features of precipitation extremes, including intense precipitation extremes in the intertropical convergence zone (ITCZ), and weak precipitation extremes in dry areas in the tropical regions (Li et al., 2020) but a double-ITCZ bias over the equatorial central and eastern Pacific that appeared in CMIP5 models remains (3.3.2.1). There are also regional biases in the magnitude of precipitation extremes (Kim et al., 2020). The models also have difficulties in reproducing detailed regional patterns of extreme precipitation such as over the northeast US (Agel and Barlow, 2020), though they performed better for summer extremes over the US (Akinsanola et al., 2020). The comparison between climatologies in the observations and in model simulations shows that the CMIP6 and CMIP5 models that have similar horizontal resolutions also have similar model evaluation scores and their error patterns are highly correlated (Wehner et al., 2020). In general, extreme precipitation in CMIP6 models tends to be somewhat larger than in CMIP5 models (Li et al., 2020a), reflecting smaller spatial scales of extreme precipitation represented by slightly higher resolution models (Gervais et al., 2014). This is confirmed by Kim et al. (2020), who showed that Rx1day and Rx5day simulated by CMIP6 models tend to be closer to point estimates of HadEX3 data (Dunn et al., 2020) than those simulated by CMIP5. Figure 11.14 shows the multi-model ensemble bias in mean Rx1day over the period 1979-2014 from 21 available CMIP6 models when compared with observations and reanalyses. Measured by global land root mean square error, the

ACCEPTED VERSION SUBJECT TO FINAL EDITING

model performance is generally consistent across different observed/reanalysis data products for the extreme precipitation metric (Figure 11.14). The magnitude of extreme area-mean precipitation simulated by the CMIP6 models is consistently smaller than the point estimates of HadEX3, but the model values are more comparable to those of areal-mean values (Figure 11.14) of the ERA5 reanalysis or REGEN (Contractor et al., 2020b). Taylor-plot-based performance metrics reveal strong similarities in the patterns of extreme precipitation errors over land regions between CMIP5 and CMIP6 (Srivastava et al., 2020; Wehner et al., 2020) and between annual mean precipitation errors and Rx1day errors for both generations of models (Wehner et al., 2020).

In general, there is *high confidence* that historical simulations by CMIP5 and CMIP6 models of similar horizontal resolutions are interchangeable in their performance in simulating the observed climatology of extreme precipitation.

[START FIGURE 11.14 HERE]

Figure 11.14: Multi-model mean bias in annual maximum daily precipitation (Rx1day, %) for the period 1979-2014, calculated as the difference between the CMIP6 multi-model mean and the average of available observational or reanalysis products including (a) ERA5, (b) HadEX3, and (c) and REGEN. Bias is expressed as the percent error relative to the long-term mean of the respective observational data products. Brown indicates that models are too dry, while green indicates that they are too wet. Areas without sufficient observational data are shown in grey. Adapted from Wehner et al. (2020) under the terms of the Creative Commons Attribution license. Further details on data sources and processing are available in the chapter data table (Table 11.SM.9).

[END FIGURE 11.14 HERE]

Studies using regional climate models (RCMs), for example, CORDEX (Giorgi et al., 2009) over Africa (Dosio et al., 2015; Klutse et al., 2016; Pinto et al., 2016; Gibba et al., 2019), Australia, East Asia (Park et al., 2016), Europe (Prein et al., 2016a; Fantini et al., 2018), and parts of North America (Diaconescu et al., 2018) suggest that extreme rainfall events are better captured in RCMs compared to their host GCMs due to their ability to address regional characteristics, for example, topography and coastlines. However, CORDEX simulations do not show good skill over south Asia for heavy precipitation and do not add value with respect to their GCM source of boundary conditions (Mishra et al., 2014a; Singh et al., 2017b). The evaluation of models in simulating regional processes is discussed in detail in Chapter 10 (Section 10.3.3.4). The high-resolution simulation of mid-latitude winter extreme precipitation over land is of similar magnitude to point observations. Simulation of summer extreme precipitation has a high bias when compared with observations at the same spatial scale. Simulated extreme precipitation in the tropics also appears to be too large, indicating possible deficiencies in the parameterization of cumulus convection at this resolution. Indeed, precipitation distributions at both daily and sub-daily time scales are much improved with a convection-permitting model (Belušić et al., 2020) over west Africa (Berthou et al., 2019b), East Africa (Finney et al., 2019), North America and Canada (Cannon and Innocenti, 2019; Innocenti et al., 2019) and over Belgium in Europe (Vanden Broucke et al., 2019).

In summary, there is *high confidence* in the ability of models to capture the large-scale spatial distribution of precipitation extremes over land. The magnitude and frequency of extreme precipitation simulated by CMIP6 models are similar to those simulated by CMIP5 models (*high confidence*).

11.4.4 Detection and attribution, event attribution

Both SREX (Chapter 3, Seneviratne et al., 2012) and AR5 (Chapter 10, IPCC, 2014) concluded with *medium confidence* that anthropogenic forcing has contributed to a global-scale intensification of heavy precipitation over the second half of the 20th century. These assessments were based on the evidence of anthropogenic influence on aspects of the global hydrological cycle, in particular, the human contribution to the warming-

ACCEPTED VERSION SUBJECT TO FINAL EDITING

induced observed increase in atmospheric moisture that leads to an increase in heavy precipitation, and limited evidence of anthropogenic influence on extreme precipitation of durations of one and five days.

Since AR5 there has been new and robust evidence and improved understanding of human influence on extreme precipitation. In particular, detection and attribution analyses have provided consistent and robust evidence of human influence on extreme precipitation of one- and five-day durations at global to continental scales. The observed increases in Rx1day and Rx5day over the Northern Hemisphere land area during 1951-2005 can be attributed to the effect of combined anthropogenic forcing, including greenhouse gases and anthropogenic aerosols, as simulated by CMIP5 models and the rate of intensification with regard to warming is consistent with C-C scaling (Zhang et al., 2013). This is confirmed to be robust when an additional nine years of observational data and the CMIP6 model simulations were used (Paik et al., 2020; CCB3.2, Figure 1). Additionally, the influence of greenhouse gases is attributed as the dominant contributor to the observed intensification. The global average of Rx1day in the observations is consistent with simulations by both CMIP5 and CMIP6 models under anthropogenic forcing, but not under natural forcing (CCB3.2, Figure 1). The observed increase in the fraction of annual total precipitation falling into the top 5th or top 1st percentiles of daily precipitation can also be attributed to human influence at the global scale (Dong et al., 2020). CMIP5 models were able to capture the fraction of land experiencing a strong intensification of heavy precipitation during 1960-2010 under anthropogenic forcing, but not in unforced simulations (Fischer et al., 2014)). But the models underestimated the observed trends (Borodina et al., 2017a). Human influence also significantly contributed to the historical changes in record-breaking one-day precipitation (Shiogama et al., 2016). There is also limited evidence of the influences of natural forcing. Substantial reductions in Rx5day and SDII (daily precipitation intensity) over the global summer monsoon regions occurred during 1957-2000 after explosive volcanic eruptions (Paik and Min, 2018). The reduction in post-volcanic eruption extreme precipitation in the simulations is closely linked to the decrease in mean precipitation, for which both thermodynamic effects (moisture reduction due to surface cooling) and dynamic effects (monsoon circulation weakening) play important roles.

There has been new evidence of human influence on extreme precipitation at continental scales, including the detection of the combined effect of greenhouse gases and aerosol forcing on Rx1day and Rx5day over North America, Eurasia, and mid-latitude land regions (Zhang et al., 2013) and of greenhouse gas forcing in Rx1day and Rx5day in the mid-to-high latitudes, western and eastern Eurasia, and the global dry regions (Paik et al., 2020). These findings are corroborated by the detection of human influence in the fraction of extreme precipitation in the total precipitation over Asia, Europe, and North America (Dong et al., 2020). Human influence was found to have contributed to the increase in frequency and intensity of regional precipitation extremes in North America during 1961-2010, based on both optimal fingerprinting and event attribution approaches (Kirchmeier-Young and Zhang, 2020). Tabari et al. (2020) found the observed latitudinal increase in extreme precipitation over Europe to be consistent with model-simulated responses to anthropogenic forcing.

Evidence of human influence on extreme precipitation at regional scales is more limited and less robust. In northwest Australia, the increase in extreme rainfall since 1950 can be related to increased monsoonal flow due to increased aerosol emissions, but cannot be attributed to an increase in greenhouse gases (Dey et al., 2019a). Anthropogenic influence on extreme precipitation in China was detected in one study (Li et al., 2017), but it was not detected in another study (Li et al., 2018e) using different detection and data-processing procedures, indicating the lack of robustness in the detection results. A still weak signal-to-noise ratio seems to be the main cause for the lack of robustness, as detection would become robust 20 years in the future (Li et al., 2018e). Krishnan et al. (2016) attributed the observed increase in heavy rain events (intensity > 100 mm/day) in the post-1950s over central India to the combined effects of greenhouse gases, aerosols, land use and land cover changes, and rapid warming of the equatorial Indian Ocean SSTs. Roxy et al. (2017) and Devanand et al. (2019) showed the increase in widespread extremes over the South Asian Monsoon during 1950-2015 is due to the combined impacts of the warming of the Western Indian Ocean (Arabian Sea) and the intensification of irrigation water management over India

Anthropogenic influence may have affected the large-scale meteorological processes necessary for extreme precipitation and the localized thermodynamic and dynamic processes, both contributing to changes in

ACCEPTED VERSION SUBJECT TO FINAL EDITING

extreme precipitation events. Several new methods have been proposed to disentangle these effects by either conditioning on the circulation state or attributing analogues. In particular, the extremely wet winter of 2013/2014 in the UK can be attributed, approximately to the same degree, to both temperature-induced increases in saturation vapour pressure and changes in the large-scale circulation (Vautard et al., 2016; Yiou et al., 2017). There are multiple cases indicating that very extreme precipitation may increase at a rate more than the C-C rate (6-7%/ °C) (Pall et al., 2017; Risser and Wehner, 2017; van der Wiel et al., 2017; van Oldenborgh et al., 2017;Wang et al., 2018).

Event attribution studies found an influence of anthropogenic activities on the probability or magnitude of observed extreme precipitation events, including European winters (Schaller et al., 2016; Otto et al., 2018b), extreme 2014 precipitation over the northern Mediterranean (Vautard et al., 2015), parts of the US for individual events (Knutson et al., 2014b; Szeto et al., 2015; Eden et al., 2016; van Oldenborgh et al., 2017), extreme rainfall in 2014 over Northland, New Zealand (Rosier et al., 2016) or China (Burke et al., 2016; Sun and Miao, 2018; Yuan et al., 2018b; Zhou et al., 2018). For other heavy rainfall events, however, studies identified a lack of evidence about anthropogenic influences (Imada et al., 2013; Schaller et al., 2014; Otto et al., 2015c; Siswanto et al., 2015). There are also studies whose results are inconclusive because of limited reliable simulations (Christidis et al., 2013b; Angélil et al., 2016). Overall, both the spatial and temporal scales on which extreme precipitation events are defined are important for attribution; events defined on larger scales have larger signal-to-noise ratios and thus the signal is more readily detectable. At the current level of global warming, there is a strong enough signal to be detectable for large-scale extreme precipitation events, but the chance to detect such signals for smaller-scale events becomes smaller (Kirchmeier-Young et al., 2019).

In summary, most of the observed intensification of heavy precipitation over land regions is *likely* due to anthropogenic influence, for which greenhouse gases emissions are the main contributor. New and robust evidence since AR5 includes attribution of the observed increase in annual maximum one-day and five-day precipitation and in the fraction of annual precipitation due to heavy events to human influence. It also includes a larger fraction of land showing enhanced extreme precipitation and a larger probability of record-breaking one-day precipitation than expected by chance, both of which can only be explained when anthropogenic greenhouse gas forcing is considered. Human influence has contributed to the intensification of heavy precipitation in three continents where observational data are more abundant, including North America, Europe and Asia (*high confidence*). On the spatial scale of AR6 regions, *evidence* of human influence on extreme precipitation is *limited*, but new evidence is emerging; in particular, studies attributing individual heavy precipitation events found that human influence was a significant driver of the events, particularly in the winter season.

11.4.5 Projections

AR5 concluded it is *very likely* that extreme precipitation events will be more frequent and more intense over most of the mid-latitude land masses and wet tropics in a warmer world (Collins et al., 2013). Post-AR5 studies provide more and *robust evidence* to support the previous assessments. These include an observed increase in extreme precipitation (11.4.3) and human causes of past changes (11.4.4), as well as projections based on either GCM and/or RCM simulations. CMIP5 models project the rate of increase in Rx1day with warming is independent of the forcing scenario (Pendergrass et al., 2015, Chapter 8, Section 8.5.3.1) or forcing mechanism (Sillmann et al., 2017). This is confirmed in CMIP6 simulations (Li et al., 2020, and Sillmann et al., 2019). In particular, for extreme precipitation that occurs once a year or less frequently, the magnitudes of the rates of change per 1°C change in global mean temperature are similar regardless of whether the temperature change is caused by increases in CO_2, CH_4, solar forcing, or SO4 (Sillmann et al., 2019). In some models, CESM1 in particular, the extreme precipitation response to warming may follow a quadratic relation (Pendergrass et al., 2019). Figure 11.15 shows changes in the 10-year and 50-year return values of Rx1day at different warming levels as simulated by the CMIP6 models. The median value of the scaling over land, across all SSP scenarios and all models, is close to 7%/°C for the 50-year return value of Rx1day. It is just slightly smaller for the 10-year and 50-year return values of Rx5day (Li et al., 2020a). The 90% ranges of the multi-model ensemble changes across all land grid boxes in the 50-yr return values for

ACCEPTED VERSION SUBJECT TO FINAL EDITING

Rx1day and Rx5day do not overlap between 1.5°C and 2°C warming levels (Li et al., 2020), indicating that a small increment such as 0.5°C in global warming can result in a significant increase in extreme precipitation. Projected long-period Rx1day return value changes are larger than changes in mean Rx1day and increase with increasing rarity (Pendergrass, 2018; Mizuta and Endo, 2020; Wehner, 2020). The rate of change of moderate extreme precipitation may depend more on the forcing agent, similar to the mean precipitation response to warming (Lin et al., 2016, 2018a). Thus, there is *high confidence* that extreme precipitation that occurs once a year or less frequently increases proportionally to the amount of surface warming and the rate of change in precipitation is not dependent on the underlying forcing agents of warming.

[START FIGURE 11.15 HERE]

Figure 11.15: Projected changes in the intensity of extreme precipitation events under 1°C, 1.5°C, 2°C, 3°C, and 4°C global warming levels relative to the 1851-1900 baseline. Extreme precipitation events are defined as the daily precipitation (Rx1day) that was exceeded on average once during a 10-year period (10-year event, blue) and once during a 50-year period (50-year event, orange) during the 1851-1900 base period. Results are shown for the global land. For each box plot, the horizontal line and the box represent the median and central 66% uncertainty range, respectively, of the intensity changes across the space, and the whiskers extend to the 90% uncertainty range. The results are based on the multi-model ensemble median estimated from simulations of global climate models contributing to the sixth phase of the Coupled Model Intercomparison Project (CMIP6) under different SSP forcing scenarios. Based on (Li et al., 2020a). Further details on data sources and processing are available in the chapter data table (Table 11.SM.9).

[END FIGURE 11.15 HERE]

The spatial patterns of the projected changes across different warming levels are quite similar, as shown in Figure 11.16 and confirmed by near-linear scaling between extreme precipitation and global warming levels at regional scales (Seneviratne and Hauser, 2020). Internal variability modulates changes in heavy rainfall (Wood and Ludwig, 2020), resulting in different changes in different regions (Seneviratne and Hauser, 2020). Extreme precipitation nearly always increases across land areas with larger increases at higher global warming levels, except in very few regions, such as southern Europe around the Mediterranean Basin in some seasons. The *very likely* ranges of the multi-model ensemble changes across all land grid boxes in the 50-yr return values for Rx1day and Rx5day between 1.5°C and 1°C warming levels are above zero for all continents expect Europe, with *likely* range above zero over Europe (Li et al., 2020). Decreases in extreme precipitation are confined mostly to subtropical ocean areas and are highly correlated to decreases in mean precipitation due to storm track shifts. These subtropical decreases can extend to nearby land areas in individual realizations.

Projected increases in the probability of extreme precipitation of fixed magnitudes are non-linear and show larger increases for more rare events (Figures 11.7 and 11.15, Fischer and Knutti, 2015, Li et al., 2020, Kharin et al., 2018). CMIP5-model-projected increases in the probability of high (99^{th} and 99.9^{th}) percentile precipitation between 1.5°C and 2°C warming scenarios are consistent with what can be expected based on observed changes (Fischer and Knutti, 2015), providing confidence in the projections. CMIP5 model simulations show that the frequency for present-day climate 20-year extreme precipitation is projected to increase by 10% at the 1.5°C global warming level and by 22% at the 2.0°C global warming level, while the increase in the frequency for present-day climate 100-year extreme precipitation is projected to increase by 20% and more than 45% at the 1.5°C and 2.0°C warming levels, respectively (Kharin et al., 2018). CMIP6 simulations with SSP scenarios show the frequency of 10-year and 50-year events will be approximately doubled and tripled, respectively, at a very high warming level of 4°C (Figure 11.7, Li et al., 2020).

The number of studies on the projections of extreme hourly precipitation are limited. The ability of GCMs to simulate hourly precipitation extremes is limited (Morrison et al., 2019) and very few modelling centres archive sub-daily and hourly precipitation prior to CMIP6 experiments. RCM simulations project an increase in extreme sub-daily precipitation in North America (Li et al., 2019a) and over Sweden (Olsson and Foster,

ACCEPTED VERSION SUBJECT TO FINAL EDITING

2013), but these models still do not explicitly resolve convective processes that are important for properly simulating extreme sub-daily precipitation. Simulations by RCMs that explicitly resolve convective processes (convection-permitting models) are limited in length and only available in a few regions because of high computing costs. Yet, a majority of the available convection-permitting simulations project increases in the intensities of extreme sub-daily precipitation events with the amount similar to or higher than the C-C scaling rate (Ban et al., 2015; Helsen et al., 2020; Kendon et al., 2014, 2019; Prein et al., 2016b; Fowler et al., 2020). An increase is projected in extreme sub-daily precipitation over Africa (Kendon et al., 2019); over East Africa (Finney et al., 2020) and West Africa (Berthou et al., 2019a; Fitzpatrick et al., 2020), even for areas where parameterized RCMs project a decrease; in Europe (Chan et al., 2020 and Hodnebrog et al., 2019); as well as in the continental US (Prein et al., 2016). Overall, available evidence, while limited, points to an increase in extreme sub-daily precipitation in the future. Studies on future changes in extreme precipitation for a month or longer are limited. One study projects an increase in extreme monthly precipitation in Japan under 4°C global warming for around 80% of stations in the summer (Hatsuzuka and Sato, 2019).

In Africa (Table 11.5), extreme precipitation will *likely* increase under warming levels of 2°C or below (compared to pre-industrial values) and *very likely* increase at higher warming levels. Simulations by CMIP5, CMIP6 and CORDEX regional models project an increase in daily extreme precipitation between 1.5°C and 2.0°C warming levels. The pattern of change in heavy precipitation under different scenarios or warming levels is similar with larger increases for higher warming levels (e.g., Nikulin et al., 2018; Li et al., 2020). With increases in warming, extreme precipitation is projected to increase in the majority of land regions in Africa (Mtongori et al., 2016; Pfahl et al., 2017; Diedhiou et al., 2018; Dunning et al., 2018; Akinyemi and Abiodun, 2019; Giorgi et al., 2019). Over southern Africa, heavy precipitation will *likely* increase by the end of the 21st century under RCP 8.5 (Dosio, 2016; Pinto et al., 2016; Abiodun et al., 2017; Dosio et al., 2019). However, heavy rainfall amounts are projected to decrease over western South Africa (Pinto et al., 2018) as a result of a projected decrease in the frequency of the prevailing westerly winds south of the continent that translates into fewer cold fronts and closed mid-latitudes cyclones (Engelbrecht et al., 2009; Pinto et al., 2018). Heavy precipitation will *likely* increase by the end of the century under RCP8.5 in West Africa (Diallo et al., 2016; Dosio, 2016; Sylla et al., 2016; Abiodun et al., 2017; Akinsanola and Zhou, 2018; Dosio et al., 2019) and is projected to increase (*medium confidence*) in central Africa (Fotso-Nguemo et al., 2018, 2019; Sonkoué et al., 2019) and eastern Africa (Thiery et al., 2016; Ongoma et al., 2018a). In northeast and central east Africa, extreme precipitation intensity is projected to increase across CMIP5, CMIP6 and CORDEX-CORE (*high confidence*) in most areas annually (Coppola et al., 2021a), but the trends differ from season to season in all future scenarios (Dosio et al., 2019). In northern Africa, there is *low confidence* in the projected changes in heavy precipitation, either due to a lack of agreement among studies on the sign of changes (Sillmann et al., 2013a; Giorgi et al., 2014) or due to insufficient evidence.

In Asia (Table 11.8), extreme precipitation will *likely* increase at global warming levels of 2°C and below, but *very likely* increase at higher warming levels for the region as whole. The CMIP6 multi-model median projects an increase in the 10- and 50-yr return values of Rx1day and Rx5day over more than 95% of regions, even at the 2°C warming level, with larger increases at higher warming levels, independent of emission scenarios (Li et al., 2020, also Figure 11.7). CMIP5 models produced similar projections. Both heavy rainfall and rainfall intensity are projected to increase (Endo et al., 2017; Guo et al., 2016, 2018; Han et al., 2018; Kim et al., 2018; Xu et al., 2016; Zhou et al., 2014). A half-degree difference in warming between the 1.5°C and 2.0°C warming levels can result in a detectable increase in extreme precipitation over the region (Li et al., 2020), in the Asian-Australian monsoon region (Chevuturi et al., 2018), and over South Asia and China (Lee et al., 2018b; Li et al., 2018f). While there are regional differences, extreme precipitation is projected to increase in almost all sub-regions, though there can be spatial heterogeneity within sub-regions, such as in India (Shashikanth et al., 2018) and Southeast Asia (Ohba and Sugimoto, 2019). In East and Southeast Asia, there is *high confidence* that extreme precipitation is projected to intensify (Guo et al., 2018; Li et al., 2018a; Seo et al., 2014; Sui et al., 2018; Wang et al., 2017b, 2017c; Xu et al., 2016; Zhou et al., 2014, Nayak et al., 2017; Mandapaka and Lo, 2018; Raghavan et al., 2018; Tangang et al., 2018; Supari et al., 2020). Extreme daily precipitation is also projected to increase in South Asia (Shashikanth et al., 2018; Han et al., 2018; Xu et al., 2017). The extreme precipitation indices, including Rx5day, R95p, and days of heavy precipitation (i.e., R10mm), are all projected to increase under the RCP4.5

ACCEPTED VERSION SUBJECT TO FINAL EDITING

and RCP8.5 scenarios in central and northern Asia (Xu et al., 2017; Han et al., 2018). A general wetting across the whole Tibetan Plateau and the Himalaya is projected, with increases in heavy precipitation in the 21st century (Zhou et al., 2014; Zhang et al., 2015c; Gao et al., 2018; Palazzi et al., 2013; Rajbhandari et al., 2015; Wu et al., 2017; Paltan et al., 2018). Agreement in projected changes by different models is low in regions of complex topography such as Hindu-Kush-Himalaya (Wester et al., 2019), but CMIP5, CMIP6 and CORDEX-CORE simulations consistently project an increase in heavy precipitation in higher latitude areas (WSB, ESB, RFE) (Coppola et al., 2021a) (*high confidence*).

In Australasia (Table 11.11), most CMIP5 models project an increase in Rx1day under RCP4.5 and RCP8.5 scenarios for the late 21st century (CSIRO and BOM, 2015; Alexander and Arblaster, 2017; Grose et al., 2020) and the CMIP6 multi-model median projects an increase in the 10- and 50-yr return values of Rx1day and Rx5day at a rate between 5-6% per degree celsius of near-surface global mean warming (Li et al., 2020, also Figure 11.7). Yet, there is large uncertainty in the increase because projected changes in dynamic processes lead to a decrease in Rx1day that can offsets the thermodynamic increase over a large portion of the region (Pfahl et al., 2017, see also Box 11.1 Figure 1). Projected changes in moderate extreme precipitation (the 99th percentile of daily precipitation) by RCMs under RCP8.5 for 2070-2099 are mixed, with more regions showing decreases than increases (Evans et al., 2020). It is *likely* that daily rainfall extremes such as Rx1day will increase at the continental scale for global warming levels at or above 3°C, daily rainfall extremes are projected to increase at the 2.0°C global warming level (*medium confidence*), and there is *low confidence* in changes at the 1.5°C. Projected changes show important regional differences with *very likely* increases over NAU (Alexander and Arblaster, 2017; Herold et al., 2018; Grose et al., 2020) and NZ (MfE, 2018) where projected dynamic contributions are small (Pfahl et al., 2017), see also Box 11.1 Figure 1) and *medium confidence* on increases over central, eastern, and southern Australia where dynamic contributions are substantial and can affect local phenomena (CSIRO and BOM, 2015; Pepler et al., 2016; Bell et al., 2019; Dowdy et al., 2019).

In Central and South America (Table 11.14), extreme precipitation will *likely* increase at global warming levels of 2°C and below, but *very likely* increase at higher warming levels for the region as whole. A larger increase in global surface temperature leads to a larger increase in extreme precipitation, independent of emission scenarios (Li et al., 2020a). But there are regional differences in the projection and projected changes for more moderate extreme precipitation are also more uncertain. Extreme precipitation, represented by the R_{50mm} and R_{90p} extreme indices, is projected to increase on the eastern coast of SCA, but to decrease along the Pacific coasts of El Salvador and Guatemala (Imbach et al., 2018). Chou et al. (2014) and Giorgi et al. (2014) projected an increase in extreme precipitation over southeastern South America and the Amazon. Projected changes in moderate extreme precipitation represented by the 99th percentile of daily precipitation by different models under different emission scenarios, even at high warming levels, are mixed, with increases projected for all regions by the CORDEX-CORE and CMIP5 simulations, but increases for some regions and decreases for other regions by CMIP6 simulations (Coppola et al., 2021a). Extreme precipitation is projected to increase in the La Plata basin (Cavalcanti et al., 2015; Carril et al., 2016). Taylor et al. (2018) projected a decrease in days with intense rainfall in the Caribbean under 2°C global warming by the 2050s under RCP4.5 relative to 1971-2000.

In Europe (Table 11.17), extreme precipitation will *likely* increase at global warming levels of 2°C and below, but *very likely* increase for higher warming levels for the region as whole. The CMIP6 multi-model median projects an increase in the 10- and 50-yr return values of Rx1day and Rx5day over a majority of the region at the 2°C global warming level, with more than 95% of the region showing an increase at higher warming levels (Li et al., 2020, also Figure 11.7). The most intense precipitation events observed today in Europe are projected to almost double in occurrence for each degree celsius of further global warming (Myhre et al., 2019). Extreme precipitation is projected to increase in both boreal winter and summer over Europe (Madsen et al., 2014; OB et al., 2015; Nissen and Ulbrich, 2017). There are regional differences, with decreases or no change for the southern part of Europe, such as the southern Mediterranean (Lionello and Scarascia, 2020; Tramblay and Somot, 2018; Coppola et al., 2020), uncertain changes over central Europe (Argüeso et al., 2012; Croitoru et al., 2013; Rajczak et al., 2013; Casanueva et al., 2014; Patarčić et al., 2014; Paxian et al., 2014; Roth et al., 2014; Fischer and Knutti, 2015; Monjo et al., 2016) and a strong increase in the remaining parts, including the Alps region (Gobiet et al., 2014; Donnelly et al., 2017),

ACCEPTED VERSION SUBJECT TO FINAL EDITING

particularly in winter (Fischer et al., 2015), and northern Europe. In a 3°C warmer world, there will be a robust increase in extreme rainfall over 80% of land areas in northern Europe (Madsen et al., 2014; Donnelly et al., 2017; Cardell et al., 2020).

In North America (Table 11.20), the intensity and frequency of extreme precipitation will *likely* increase at the global warming levels of 2°C and below and *very likely* increase at higher warming levels. An increase is projected by CMIP6 model simulations (Li et al., 2020) and by previous model generations (Easterling et al., 2017; Wu, 2015; Zhang et al. 2018f; Innocenti et al., 2019b), as well as by RCMs (Coppola et al., 2020). Projections of extreme precipitation over the southern portion of the continent and over Mexico in particular are more uncertain, with decreases possible (Alexandru, 2018; Sillmann et al., 2013b; Coppola et al., 2020).

[START FIGURE 11.16 HERE]

Figure 11.16: Projected changes in annual maximum daily precipitation at (a) 1.5°C, (b) 2°C, and (c) 4°C of global warming compared to the 1851-1900 baseline. Results are based on simulations from the CMIP6 multi-model ensemble under the SSP1-1.9, SSP1-2.6, SSP2-4.5, SSP3-7.0, and SSP5-8.5 scenarios. The numbers on the top right indicate the number of simulations included. Uncertainty is represented using the simple approach: no overlay indicates regions with high model agreement, where ≥80% of models agree on sign of change; diagonal lines indicate regions with low model agreement, where <80% of models agree on sign of change. For more information on the simple approach, please refer to the Cross-Chapter Box Atlas 1. For details on the methods see Supplementary Material 11.SM.2. Further details on data sources and processing are available in the chapter data table (Table 11.SM.9).

[END FIGURE 11.16 HERE]

In summary, heavy precipitation will generally become more frequent and more intense with additional global warming. At global warming levels of 4°C relative to the pre-industrial, very rare (e.g., 1 in 10 or more years) heavy precipitation events would become more frequent and more intense than in the recent past, on the global scale (*virtually certain*), and in all continents and AR6 regions: The increase in frequency and intensity is *extremely likely* for most continents and *very likely* for most AR6 regions. The likelihood is lower at lower global warming levels and for less-rare heavy precipitation events. At the global scale, the intensification of heavy precipitation will follow the rate of increase in the maximum amount of moisture that the atmosphere can hold as it warms (*high confidence*), of about 7% per °C of global warming.The increase in the frequency of heavy precipitation events will accelerate with more warming and will be higher for rarer events (*high confidence)*, with 10-year and 50-year events to be approximately double and triple, respectively, at the 4°C warming level. Increases in the intensity of extreme precipitation events at regional scales will depend on the amount of regional warming as well as changes in atmospheric circulation and storm dynamics leading to regional differences in the rate of heavy precipitation changes *(high confidence)*.

11.5 Floods

Floods are the inundation of normally dry land and are classified into types (e.g., pluvial floods, flash floods, river floods, groundwater floods, surge floods, coastal floods) depending on the space and time scales and the major factors and processes involved (Chapter 8, Section 8.2.3.2, Nied et al., 2014; Aerts et al., 2018). Flooded area is difficult to measure or quantify and, for this reason, many of the existing studies on changes in floods focus on streamflow. Thus, this section assesses changes in flow as a proxy for river floods, in addition to some types of flash floods. Pluvial and urban floods, types of flash floods resulting from the precipitation intensity exceeding the capacity of natural and artificial drainage systems, are directly linked to extreme precipitation. Because of this link, changes in extreme precipitation are the main proxy for inferring changes in pluvial and urban floods (see also Section 12.4, REF Chapter 12), assuming there is no additional change in the surface condition. Changes in these types of floods are not assessed in this section, but can be inferred from the assessment of changes in heavy precipitation in Section 11.4. Coastal floods due to extreme sea levels and flood changes at regional scales are assessed in Chapter 12 (12.4).

ACCEPTED VERSION SUBJECT TO FINAL EDITING

11.5.1 Mechanisms and drivers

Since AR5, the number of studies on understanding how floods may have changed and will change in the future has substantially increased. Floods are a complex interplay of hydrology, climate, and human management, and the relative importance of these factors is different for different flood types and regions.

In addition to the amount and intensity of precipitation, the main factors for river floods include antecedent soil moisture (Paschalis et al., 2014; Berghuijs et al., 2016; Grillakis et al., 2016; Woldemeskel and Sharma, 2016) and snow water-equivalent in cold regions (Sikorska et al., 2015; Berghuijs et al., 2016). Other factors are also important, including stream morphology (Borga et al., 2014; Slater et al., 2015), river and catchment engineering (Pisaniello et al., 2012; Nakayama and Shankman, 2013; Kim and Sanders, 2016), land-use and land-cover characteristics (Aich et al., 2016; Rogger et al., 2017) and changes (Knighton et al., 2019), and feedbacks between climate, soil, snow, vegetation, etc. (Hall et al., 2014; Ortega et al., 2014; Berghuijs et al., 2016; Buttle et al., 2016; Teufel et al., 2019). Water regulation and management have, in general, increased resilience to flooding (Formetta and Feyen, 2019), masking effects of an increase in extreme precipitation on flood probability in some regions, even though they do not eliminate very extreme floods (Vicente-Serrano et al., 2017). This means that an increase in precipitation extremes may not always result in an increase in river floods (Sharma et al., 2018; Do et al., 2020). Yet, as very extreme precipitation can become a dominant factor for river floods, there can then be some correspondence in the changes in very extreme precipitation and river floods (Ivancic and Shaw, 2015; Wasko and Sharma, 2017; Wasko and Nathan, 2019). This has been observed in the western Mediterranean (Llasat et al., 2016), in China (Zhang et al., 2015a) and in the US (Peterson et al., 2013a; Berghuijs et al., 2016; Slater and Villarini, 2016).

In regions with a seasonal snow cover, snowmelt is the main cause of extreme river flooding over large areas (Pall et al., 2019). Extensive snowmelt combined with heavy and/or long-duration precipitation can cause significant floods (Li et al., 2019b; Krug et al., 2020). Changes in floods in these regions can be uncertain because of the compounding and competing effects of the responses of snow and rain to warming that affect snowpack size: warming results in an increase in precipitation, but also a reduction in the time period of snowfall accumulation (Teufel et al., 2019). An increase in atmospheric CO_2 enhances water-use efficiency by plants (Roderick et al., 2015; Milly and Dunne, 2016; Swann et al., 2016; Swann, 2018); this could reduce evapotranspiration and contribute to the maintenance of soil moisture and streamflow levels under enhanced atmospheric CO_2 concentrations (Yang et al., 2019). This mechanism would suggest an increase in the magnitude of some floods in the future (Kooperman et al., 2018). But this effect is uncertain as an increase in leaf area index and vegetation coverage could also result in overall larger water consumption (Mátyás and Sun, 2014; Mankin et al., 2019; Teuling et al., 2019), and there are also other CO_2-related mechanisms that come into play (Chapter 5, CC Box 5.1).

Various factors, such as extreme precipitation (Cho et al., 2016; Archer and Fowler, 2018), glacier lake outbursts (Schneider et al., 2014; Schwanghart et al., 2016), or dam breaks (Biscarini et al., 2016) can cause flash floods. Very intense rainfall, along with a high fraction of impervious surfaces can result in flash floods in urban areas (Hettiarachchi et al., 2018). Because of this direct connection, changes in very intense precipitation can translate to changes in urban flood potential (Rosenzweig et al., 2018), though there can be a spectrum of urban flood responses to this flood potential (Smith et al., 2013), as many factors such as the overland flow rate and the design of urban (Falconer et al., 2009) and storm water drainage systems (Maksimović et al., 2009) can play an important role. Nevertheless, changes in extreme precipitation are the main proxy for inferring changes in some types of flash floods , which are addressed in Chapter 12 (Section 12.4)), given the relation between extreme precipitation and pluvial floods, the very limited literature on urban and pluvial floods (e.g., Skougaard Kaspersen et al., 2017), and limitations of existing methodologies for assessing changes in floods (Archer et al., 2016).

In summary, there is not always a one-to-one correspondence between an extreme precipitation event and a flood event, or between changes in extreme precipitation and changes in floods, because floods are affected by many factors in addition to heavy precipitation (*high confidence*). Changes in extreme precipitation may

ACCEPTED VERSION SUBJECT TO FINAL EDITING

be used as a proxy to infer changes in some types of flash floods that are more directly related to extreme precipitation (*high confidence*).

11.5.2 Observed trends

The SREX (Seneviratne et al., 2012) assessed *low confidence* for observed changes in the magnitude or frequency of floods at the global scale. This assessment was confirmed by the AR5 report (Hartmann et al., 2013). The SR15 (Hoegh-Guldberg et al., 2018) found increases in flood frequency and extreme streamflow in some regions, but decreases in other regions. While the number of studies on flood trends has increased since the AR5 report, and there were also new analyses after the release of SR15 (Berghuijs et al., 2017; Blöschl et al., 2019; Gudmundsson et al., 2019), hydrological literature on observed flood changes is heterogeneous, focusing at regional and sub-regional basin scales, making it difficult to synthesise at the global and sometimes regional scales. The vast majority of studies focus on river floods using streamflow as a proxy, with limited attention to urban floods. Streamflow measurements are not evenly distributed over space, with gaps in spatial coverage, and their coverage in many regions of Africa, South America, and parts of Asia is poor (e.g. Do et al., 2017), leading to difficulties in detecting long-term changes in floods (Slater and Villarini, 2017). See also Chapter 8, Section 8.3.1.5.

Peak flow trends are characterized by high regional variability and lack overall statistical significance of a decrease or an increase over the globe as a whole. Of more than 3500 streamflow stations in the US, central and northern Europe, Africa, Brazil, and Australia, 7.1% stations showed a significant increase and 11.9% stations showed a significant decrease in annual maximum peak flow during 1961-2005 (Do et al., 2017). This is in direct contrast to the global and continental scale intensification of short-duration extreme precipitation (11.4.2). There may be some consistency over large regions (see Gudmundsson et al., 2019), in high streamflows (> 90th percentile), including a decrease in some regions (e.g., in the Mediterranean) and an increase in others (e.g., northern Asia), but gauge coverage is often limited. On a continental scale, a decrease seems to dominate in Africa (Tramblay et al., 2020) and Australia (Ishak et al., 2013; Wasko and Nathan, 2019), an increase in the Amazon (Barichivich et al., 2018), and trends are spatially variable in other continents (Do et al., 2017; Hodgkins et al., 2017; Bai et al., 2016; Zhang et al., 2015b). In Europe, flow trends have large spatial differences (Hall et al., 2014; Mediero et al., 2015; Kundzewicz et al., 2018; Mangini et al., 2018), but there appears to be a pattern of increase in northwestern Europe and a decrease in southern and eastern Europe in annual peak flow during 1960-2000 (Blöschl et al., 2019). In North America, peak flow has increased in the northeast US and decreased in the southwest US (Peterson et al., 2013a; Armstrong et al., 2014; Mallakpour and Villarini, 2015; Archfield et al., 2016; Burn and Whitfield, 2016; Wehner et al., 2017; Neri et al., 2019). There are important changes in the seasonality of peak flows in regions where snowmelt dominates, such as northern North America (Burn and Whitfield, 2016; Dudley et al., 2017) and northern Europe (Blöschl et al., 2017), corresponding to strong winter and spring warming.

In summary, the seasonality of floods has changed in cold regions where snowmelt dominates the flow regime in response to warming (*high confidence*). *Confidence* about peak flow trends over past decades on the global scale is *low,* but there are regions experiencing increases, including parts of Asia, southern South America, the northeast USA, northwestern Europe, and the Amazon, and regions experiencing decreases, including parts of the Mediterranean, Australia, Africa, and the southwestern USA.

11.5.3 Model evaluation

Hydrological models used to simulate floods are structurally diverse (Dankers et al., 2014; Mateo et al., 2017; Şen, 2018), often requiring extensive calibration since sub-grid processes and land-surface properties need to be parameterized, irrespective of the spatial resolutions (Döll et al., 2016; Krysanova et al., 2017). The data that are used to drive and calibrate the models are usually of coarse resolution, necessitating the use of a wide variety of downscaling techniques (Muerth et al., 2013). This adds uncertainty not only to the models, but also to the reliability of the calibrations. The quality of the flood simulations also depends on the spatial scale, as flood processes are different for catchments of different sizes. It is more difficult to replicate

ACCEPTED VERSION SUBJECT TO FINAL EDITING

flood processes for large basins, as water management and water use are often more complex for these basins.

Studies that use different regional hydrological models show large spread in flood simulations (Dankers et al., 2014; Roudier et al., 2016; Trigg et al., 2016; Krysanova et al., 2017). Regional models reproduce moderate and high flows (0.02 – 0.1 flow annual exceedance probabilities) reasonably well, but there are large biases for the most extreme flows (0 - 0.02 annual flow exceedance probability), independent of the climatic and physiographic characteristics of the basins (Huang et al., 2017)). Global-scale hydrological models have even more challenges, as they struggle to reproduce the magnitude of the flood hazard (Trigg et al., 2016). Additionally, the ensemble mean of multiple models does not perform better than individual models (Zaherpour et al., 2018).

The use of hydrological models for assessing changes in floods, especially for future projections, adds another dimension of uncertainty on top of uncertainty in the driving climate projections, including emission scenarios, and uncertainty in the driving climate models (both RCMs and GCMs) (Arnell and Gosling, 2016; Hundecha et al., 2016; Krysanova et al., 2017). The differences in hydrological models (Roudier et al., 2016; Thober et al., 2018), as well as post-processing of climate model output for the hydrological models (Muerth et al., 2013; Maier et al., 2018), both add to uncertainty for flood projections.

In summary, there is *medium confidence* that simulations for the most extreme flows by regional hydrological models can have large biases. Global-scale hydrological models still struggle with reproducing the magnitude of floods. Projections of future floods are hampered by these difficulties and cascading uncertainties, including uncertainties in emission scenarios and the climate models that generate inputs.

11.5.4 Attribution

There are very few studies focused on the attribution of long-term changes in floods, but there are studies on changes in flood events. Most of the studies focus on flash floods and urban floods, which are closely related to intense precipitation events (Hannaford, 2015). In other cases, event attribution focused on runoff using hydrological models, and examples include river basins in the UK (Schaller et al., 2016; Kay et al., 2018) (See Section 11.4.4), the Okavango river in Africa (Wolski et al., 2014), and the Brahmaputra in Bangladesh (Philip et al., 2019). Findings about anthropogenic influences vary between different regions and basins. For some flood events, the probability of high floods in the current climate is lower than in a climate without an anthropogenic influence (Wolski et al., 2014), while in other cases anthropogenic influence leads to more intense floods (Cho et al., 2016; Pall et al., 2017; van der Wiel et al., 2017; Philip et al., 2018a; Teufel et al., 2019). Factors such as land cover change and river management can also increase the probability of high floods (Ji et al., 2020). These, along with model uncertainties and the lack of studies overall, suggest a *low confidence* in general statements to attribute changes in flood events to anthropogenic climate change. Some individual regions have been well studied, which allows for *high confidence* in the attribution of increased flooding in these cases (Section 11.9 table). For example, flooding in the UK following increased winter precipitation (Schaller et al., 2016; Kay et al., 2018) can be attributed to anthropogenic climate change (Schaller et al., 2016; Vautard et al., 2016; Yiou et al., 2017; Otto et al., 2018b).

Attributing changes in heavy precipitation to anthropogenic activities (Section 11.4.4) cannot be readily translated to attributing changes in floods to human activities, because precipitation is only one of the multiple factors, albeit an important one, that affect floods. For example, Teufel et al. (2017) showed that while human influence increased the odds of the flood-producing rainfall for the 2013 Alberta flood in Canada, it was not detected to have influenced the probability of the flood itself. Schaller et al. (2016) showed human influence on the increase in the probability of heavy precipitation translated linearly into an increase in the resulting river flow of the Thames in winter 2014, but its contribution to the inundation was inconclusive.

Gudmundsson et al. (2021) compared the spatial pattern of the observed regional trends in high river flows (> 90th percentile) over 1971-2010 with those simulated by global hydrological models driven by outputs of

ACCEPTED VERSION SUBJECT TO FINAL EDITING

climate models under all historical forcing and with pre-industrial climate model simulations. They found complex spatial patterns of extreme river flow trends. They also found the observed spatial patterns of trends can be reproduced only if anthropogenic climate change is considered and that simulated effects of water and land management cannot reproduce the observed spatial pattern of trends. As there is only one study and multiple caveats, including relatively poor observational data coverage, there is *low confidence* about human influence on the changes in high river flows on the global scale.

In summary there is *low confidence* in the human influence on the changes in high river flows on the global scale. *Confidence* is in general *low* in attributing changes in the probability or magnitude of flood events to human influence because of a limited number of studies and differences in the results of these studies, and large modelling uncertainties.

11.5.5 Future projections

The SREX report (Chapter 3, Seneviratne et al., 2012) stressed the low availability of studies on flood projections under different emission scenarios and concluded there was *low confidence* in projections of flood events given the complexity of the mechanisms driving floods at the regional scale. The AR5 WGII report (Chapter 3, Jimenez Cisneros et al., 2014) assessed with *medium confidence* the pattern of future flood changes, including flood hazards increasing over about half of the globe (parts of southern and Southeast Asia, tropical Africa, northeast Eurasia, and South America) and flood hazards decreasing in other parts of the world, despite uncertainties in GCMs and their coupling to hydrological models. SR15 (Chapter 3, Hoegh-Guldberg et al., 2018) assessed with *medium confidence* that global warming of 2°C would lead to an expansion of the fraction of global area affected by flood hazards, compared to conditions at 1.5°C of global warming, as a consequence of changes in heavy precipitation.

The majority of new studies that produce future flood projections based on hydrological models do not typically consider aspects that are also important to actual flood severity or damages, such as flood prevention measures (Neumann et al., 2015; Sen, 2018), flood control policies (Barraqué, 2017), and future changes in land cover (see also Chapter 8, Section 8.4.1.5). At the global scale, Alfieri et al. (2017a) used downscaled projections from seven GCMs as input to drive a hydrodynamic model. They found successive increases in the frequency of high floods in all continents except Europe, associated with increasing levels of global warming (1.5°C, 2°C, 4°C). These results are supported by Paltan et al. (2018), who applied a simplified runoff aggregation model forced by outputs from four GCMs. Huang et al. (2018b) used three hydrological models forced with bias-adjusted outputs from four GCMs to produce projections for four river basins including the Rhine, Upper Mississippi, Upper Yellow, and Upper Niger under 1.5ºC, 2ºC, and 3°C global warming. This study found diverse projections for different basins, including a shift towards earlier flooding for the Rhine and the Upper Mississippi, a substantial increase in flood frequency in the Rhine only under the 1.5ºC and 2°C scenarios, and a decrease in flood frequency in the Upper Mississippi under all scenarios.

At the continental and regional scales, the projected changes in floods are uneven in different parts of the world, but there is a larger fraction of regions with an increase than with a decrease over the 21st century (Hirabayashi et al., 2013; Dankers et al., 2014; Arnell and Gosling, 2016; Döll et al., 2018). These results suggest *medium confidence* in flood trends at the global scale, but *low confidence* in projected regional changes. Increases in flood frequency or magnitude are identified for southeastern and northern Asia and India (high agreement across studies), eastern and tropical Africa, and the high latitudes of North America (*medium agreement*), while decreasing frequency or magnitude is found for central and eastern Europe and the Mediterranean (*high confidence*), and parts of South America, southern and central North America, and southwest Africa (Hirabayashi et al., 2013; Dankers et al., 2014; Arnell and Gosling, 2016; Döll et al., 2018). Over South America, most studies based on global and regional hydrological models show an increase in the magnitude and frequency of high flows in the western Amazon (Sorribas et al., 2016; Langerwisch et al., 2013; Guimberteau et al., 2013; Zulkafli et al., 2016) and the Andes (Hirabayashi et al., 2013; Bozkurt et al., 2018). Chapter 12, Section 12.4, provides a detailed assessment of regional flood projections.

ACCEPTED VERSION SUBJECT TO FINAL EDITING

In summary, global hydrological models project a larger fraction of land areas to be affected by an increase in river floods than by a decrease in river floods (*medium confidence)*. There is *medium confidence* that river floods will increase in the western Amazon, the Andes, and southeastern and northern Asia. Regional changes in river floods are more uncertain than changes in pluvial floods because complex hydrological processes and forcings, including land cover change and human water management, are involved.

11.6 Droughts

Droughts refer to periods of time with substantially below-average moisture conditions, usually covering large areas, during which limitations in water availability result in negative impacts for various components of natural systems and economic sectors (Wilhite and Pulwarty, 2017; Ault, 2020). Depending on the variables used to characterize it and the systems or sectors being impacted, drought may be classified in different types (Figure 8.6; Table 11.A.1) such as **meteorological** (precipitation deficits), **agricultural** (e.g., crop yield reductions or failure, often related to soil moisture deficits), **ecological** (related to plant water stress that causes e.g., tree mortality), or **hydrological** droughts (e.g., water shortage in streams or storages such as reservoirs, lakes, lagoons, and groundwater) (See Annex VII: Glossary). The distinction of drought types is not absolute as drought can affect different sub-domains of the Earth system concomitantly, but sometimes also asynchronously, including propagation from one drought type to another (Brunner and Tallaksen, 2019). Because of this, drought cannot be characterized using a single universal definition (Lloyd-Hughes, 2014) or directly measured based on a single variable (SREX Chapter 3; Wilhite and Pulwarty, 2017). Drought can happen on a wide range of timescales - from "flash droughts" on a scale of weeks, and characterized by a sudden onset and rapid intensification of drought conditions (Hunt et al., 2014; Otkin et al., 2018; Pendergrass et al., 2020) to multi-year or decadal rainfall deficits (sometimes termed “megadroughts”; Annex VII: Glossary) (Ault et al., 2014; Cook et al., 2016b; Garreaud et al., 2017). Droughts are often analysed using indices that are measures of drought severity, duration and frequency (Table 11.A.1; Chapter 8, Sections 8.3.1.6, 8.4.1.6, Chapter 12, Sections 12.3.2.6 and 12.3.2.7). There are many drought indices published in the scientific literature, as also highlighted in the IPCC SREX report (SREX Chapter 3). These can range from anomalies in single variables (e.g., precipitation, soil moisture, runoff, evapotranspiration) to indices combining different atmospheric variables.

This assessment is focused on changes in physical conditions and metrics of direct relevance to droughts (Table 11.A.1): a) precipitation deficits, b) excess of atmospheric evaporative demand (AED), c) soil moisture deficits, d) hydrological deficits, and e) atmospheric-based indices combining precipitation and AED. In the regional tables (Section 11.9), the assessment is structured by drought types, addressing i) meteorological, ii) agricultural and ecological, and iii) hydrological droughts. Note that the latter two assessments are directly informing the Chapter 12 assessment on projected regional changes in these climatic impact-drivers (Chapter 12, Section 12.4). The text refers to AR6 regions acronyms (Section 11.9, see Chapter 1, Section 1.4.5) when referring to changes in AR6 regions.

11.6.1 Mechanisms and drivers

Similar to many other extreme events, droughts occur as a combination of thermodynamic and dynamic processes (Box 11.1). Thermodynamic processes contributing to drought, which are modified by greenhouse gas forcing both at global and regional scales, are mostly related to heat and moisture exchanges and also partly modulated by plant coverage and physiology. They affect, for instance, atmospheric humidity, temperature, and radiation, which in turn affect precipitation and/or evapotranspiration in some regions and time frames. On the other hand, dynamic processes are particularly important to explain drought variability on different time scales, from a few weeks (flash droughts) to multiannual (megadroughts). There is *low confidence* in the effects of greenhouse gas forcing on changes in atmospheric dynamic (Chapter 2, Section 2.4; Chapter 4, Section 4.3.3), and, hence, on associated changes in drought occurrence. Thermodynamic processes are thus the main driver of drought changes in a warming climate *(high confidence)*.

ACCEPTED VERSION SUBJECT TO FINAL EDITING

11.6.1.1 Precipitation deficits

Lack of precipitation is generally the main factor controlling drought onset. There is *high confidence* that atmospheric dynamics, which varies on interannual, decadal and longer time scales, is the dominant contributor to variations in precipitation deficits in the majority of the world regions (Dai, 2013; Seager and Hoerling, 2014; Miralles et al., 2014b; Burgman and Jang, 2015; Dong and Dai, 2015; Schubert et al., 2016; Raymond et al., 2018; Baek et al., 2019; Drumond et al., 2019; Herrera-Estrada et al., 2019; Gimeno et al., 2020; Mishra, 2020). Precipitation deficits are driven by dynamic mechanisms taking place on different spatial scales, including synoptic processes –atmospheric rivers and extratropical cyclones, blocking and ridges (Section 11.7; Sousa et al., 2017), dominant large-scale circulation patterns (Kingston et al., 2015), and global ocean-atmosphere coupled patterns such as IPO, AMO and ENSO (Dai and Zhao, 2017). These various mechanisms occur on different scales, are not independent, and substantially interact with one another. Also regional moisture recycling and land-atmosphere feedbacks play an important role for some precipitation anomalies (see below).

There is *high confidence* that land-atmosphere feedbacks play a substantial or dominant role in affecting precipitation deficits in some regions (SREX, Chapter3; Gimeno et al., 2012; Guillod et al., 2015; Haslinger et al., 2019; Herrera-Estrada et al., 2019; Koster et al., 2011; Santanello Jr. et al., 2018; Taylor et al., 2012; Tuttle and Salvucci, 2016). The sign of the feedbacks can be either positive or negative, as well as local or non-local (Taylor et al., 2012; Guillod et al., 2015; Tuttle and Salvucci, 2016). ESMs tend to underestimate non-local negative soil moisture-precipitation feedbacks (Taylor et al., 2012) and also show high variations in their representation in some regions (Berg et al., 2017a). Soil moisture-precipitation feedbacks contribute to changes in precipitation in climate model projections in some regions, but ESMs display substantial uncertainties in their representation, and there is thus only *low confidence* in these contributions (Berg et al., 2017a; Vogel et al., 2017, 2018).

11.6.1.2 Atmospheric evaporative demand

Atmospheric evaporative demand (AED) quantifies the maximum amount of actual evapotranspiration (ET) that can happen from land surfaces if they are not limited by water availability (Table 11.A.1). AED is affected by both radiative and aerodynamic components. For this reason, the atmospheric dryness, often quantified with the relative humidity or the vapor pressure deficit (VPD), is not equivalent to the AED, as other variables are also highly relevant, including solar radiation and wind speed (Hobbins et al., 2012; McVicar et al., 2012b; Sheffield et al., 2012). AED can be estimated using different methods (McMahon et al., 2013). Methods solely based on air temperature (e.g. Hargreaves, Thornthwaite) usually overestimate it in terms of magnitude and temporal trends (Sheffield et al., 2012), in particular in the context of substantial background warming. Physically-based combination methods such as the Penman-Monteith equation are more adequate and recommended since 1998 by the Food and Agriculture Oganization (Pereira et al., 2015). For this reason, the assessment of this chapter, when considering atmospheric-based drought indices, only includes AED estimates using the latter (see also Section 11.9). AED is generally higher than ET, since it represents an upper bound for it. Hence, an AED increase does not necessarily lead to increased ET (Milly and Dunne, 2016), in particular under drought conditions given soil moisture limitation (Bonan et al., 2014; Berg et al., 2016; Konings et al., 2017; Stocker et al., 2018). In general, AED is highest in regions where ET is lowest (e.g., desert areas), further illustrating the decoupling between the two variables under limited soil moisture.

The influence of AED on drought depends on the drought type, background climate, the environmental conditions and the moisture availability (Hobbins et al., 2016, 2017; Vicente-Serrano et al., 2020b). This influence also includes effects not related to increased ET. Under low soil moisture conditions, increased AED increases plant stress, enhancing the severity of agricultural and ecological droughts (Williams et al., 2013; Allen et al., 2015; McDowell et al., 2016; Grossiord et al., 2020). Moreover, high VPD impacts overall plant physiology; it affects the leaf and xylem safety margins, and decreases the sap velocity and plant hydraulic conductance (Fontes et al., 2018). VPD also affects the plant metabolism of carbon and if prolongued, it may cause plant mortality via carbon starvation (Breshears et al., 2013; Hartmann, 2015).

ACCEPTED VERSION SUBJECT TO FINAL EDITING

Drought projections based exclusively on AED metrics overestimate changes in soil moisture and runoff deficits. Nevertheless, AED also directly impacts hydrological drought, as ET from surface waters is not limited (Wurbs and Ayala, 2014; Friedrich et al., 2018; Hogeboom et al., 2018; Xiao et al., 2018a), and this effect increases under climate change projections (Wang et al., 2018c; Althoff et al., 2020). In addition, high AED increases crop water consumptions in irrigated lands (García-Garizábal et al., 2014), contributing to intensifying hydrological droughts downstream (Fazel et al., 2017; Vicente-Serrano et al., 2017).

On subseasonal to decadal scales, temporal variations in AED are strongly controlled by circulation variability (Williams et al., 2014; Chai et al., 2018; Martens et al., 2018), but thermodynamic processes also play a fundamental role and under human-induced climate change dominate the changes in AED. Atmospheric warming due to increased atmospheric CO_2 concentrations increases AED by means of enhanced VPD in the absence of other influences (Scheff and Frierson, 2015). Indeed, because of the greater warming over land than over oceans (Chapter 2, Section 2.3.1.1; Section 11.3), the saturation pressure of water vapor increases more over land than over oceans; oceanic air masses advected over land thus contain insufficient water vapour to keep pace with the greater increase in saturation vapour pressure over land (Sherwood and Fu, 2014; Byrne and O'Gorman, 2018; Findell et al., 2019). Land-atmosphere feedbacks are also important in affecting atmospheric moisture content and temperature, with resulting effects on relative humidity and VPD (Berg et al., 2016; Haslinger et al., 2019; Zhou et al., 2019; Box 11.1).

11.6.1.3 Soil moisture deficits

Soil moisture shows an important correlation with precipitation variability (Khong et al., 2015; Seager et al., 2019), but ET also plays a substantial role in further depleting moisture from soils, in particular in humid regions during periods of precipitation deficits (Padrón et al., 2020; Teuling et al., 2013). In addition, soil moisture plays a role in drought self-intensification under dry conditions in which ET is decreased and leads to higher AED (Miralles et al., 2019), an effect that can also contribute to trigger "flash droughts" (Otkin et al., 2016, 2018; DeAngelis et al., 2020; Pendergrass et al., 2020). If soil moisture becomes limited, ET is reduced, which on one hand may decrease the rate of soil drying, but on the other hand can lead to further atmospheric dryness through various feedback loops (Seneviratne et al., 2010; Miralles et al., 2014a, 2019; Teuling, 2018; Vogel et al., 2018; Zhou et al., 2019b; Liu et al., 2020). The process is complex since vegetation cover plays a role in modulating albedo and in providing access to deeper stores of water (both in the soil and groundwater), and changes in land cover and in plant phenology may alter ET (Sterling et al., 2013; Woodward et al., 2014; Frank et al., 2015; Döll et al., 2016; Ukkola et al., 2016; Trancoso et al., 2017; Hao et al., 2019; Lian et al., 2020). Snow depth has strong and direct impacts on soil moisture in many systems (Gergel et al., 2017; Williams et al., 2020).

Soil moisture directly affects plant water stress and ET. Soil moisture is the primary factor that controls xylem hydraulic conductance, i.e. plant water uptake in plants (Sperry et al., 2016; Hayat et al., 2019; Chen et al., 2020d). For this reason, soil moisture deficits are the main driver of xylem embolism, the primary mechanism of plant mortality (Anderegg et al., 2012, 2016; Rowland et al., 2015). Also carbon assimilation by plants strongly depend on soil moisture (Hartzell et al., 2017), with implications for carbon starvation and plant dying if soil moisture deficits are prolongued (Sevanto et al., 2014). These mechanisms explain that soil moisture deficits are usually more relevant than AED excess to explain gross primary production anomalies and vegetation stress, mostly in sub-humid and semi-arid regions (Stocker et al. 2018; Liu et al., 2020b). CO_2 concentrations are shown to potentially decrease plant ET and increase plant water-use efficiency, affecting soil moisture levels, although this effect interacts with other CO_2 physiological and radiative effects (Section 11.6.5.2; Chapter 5, CC Box 5.1), and has less relevance under low soil moisture (Morgan et al., 2011; Xu et al., 2016b; Nackley et al., 2018; Dikšaitytė et al., 2019). ESMs represent both surface (ca. 10cm) and total column soil moisture, whereby total soil moisture is of more direct relevance for root water uptake, in particular by trees. There is evidence that surface soil moisture projections are substantially drier than total soil moisture projections, and may thus overestimate drying of relevance for most vegetation (Berg et al., 2017b).

ACCEPTED VERSION SUBJECT TO FINAL EDITING

11.6.1.4 Hydrological deficits

Drivers of streamflow and surface water deficits are complex and strongly depend on the hydrological system analysed (e.g., streamflows in the headwaters, medium course of the rivers, groundwater, highly regulated hydrological basins). Soil hydrological processes, which control the propagation of meteorological droughts throughout different parts of the hydrological cycle (Van Loon and Van Lanen, 2012), are spatially and temporally complex (Herrera-Estrada et al., 2017; Huang et al., 2017c) and difficult to quantify (Van Lanen et al., 2016; Apurv et al., 2017; Caillouet et al., 2017; Konapala and Mishra, 2017; Hasan et al., 2019). The physiographic characteristics of the basins also affect how droughts propagate throughout the hydrological cycle (Van Loon and Van Lanen, 2012; Van Lanen et al., 2013; Van Loon, 2015; Konapala and Mishra, 2020; Valiya Veettil and Mishra, 2020). In addition, the assessment of groundwater deficits is very difficult given the complexity of processes that involve natural and human-driven feedbacks and interactions with the climate system (Taylor et al., 2013). Streamflow and surface water deficits are affected by land cover, groundwater and soil characteristics (Van Lanen et al., 2013; Van Loon and Laaha, 2015; Barker et al., 2016; Tijdeman et al., 2018), as well as human activities (water management and demand, damming) and land use changes (He et al., 2017; Jehanzaib et al., 2020; Van Loon et al., 2016; Veldkamp et al., 2017; Wu et al., 2018; Xu et al., 2019b; Section 11.6.4.3). Finally, snow and glaciers are relevant for water resources in some regions. For instance, warming affects snowpack levels (Dierauer et al., 2019; Huning and AghaKouchak, 2020), as well as the timing of snow melt, thus potentially affecting the seasonality and magnitude of low flows (Barnhart et al., 2016).

11.6.1.5 Atmospheric-based drought indices

Given difficulties of drought quantification and data constraints, atmospheric-based drought indices combining both precipitation and AED have been developed, as they can be derived from meteorological data that is available in most regions with few exceptions. These demand/supply indices are not intended to be metrics of soil moisture, streamflow or vegetation water stress. Because of their reliance on precipitation and AED, they are mostly related to the actual water balance in humid regions, in which ET is not limited by soil moisture and tends towards AED. In water-limited regions and in dry periods everywhere, they constitute an upper bound for overall water-balance deficits (e.g. of surface waters) but are also related to conditions conducive to vegetation stress, particularly under soil moisture limitation (Section 11.6.1.2).

Although there are many atmospheric-based drought indices, two are assessed in this chapter: the Palmer Drought Severity Index (PDSI) and the Standardized Precipitation Evapotranspiration Index (SPEI). The PDSI has been widely used to monitor and quantify drought severity (Dai et al., 2018), but is affected by some constraints (SREX Chapter 3; Mukherjee et al., 2018). Although the calculation of the PDSI is based on a soil water budget, the PDSI is essentially a climate drought index that mostly responds to the precipitation and the AED (van der Schrier et al., 2013; Vicente-Serrano et al., 2015; Dai et al., 2018). The SPEI also combines precipitation and AED, being equally sensitive to these two variables (Vicente-Serrano et al., 2015). The SPEI is more sensitive to AED than the PDSI (Cook et al., 2014a; Vicente-Serrano et al., 2015), although under humid and normal precipitation conditions, the effects of AED on the SPEI are small (Tomas-Burguera et al., 2020). Given the limitations associated with temperature-based AED estimates (Section 11.6.1.2), only studies using the Penman-Monteith-based SPEI and PDSI (hereafter SPEI-PM and PDSI-PM) are considered in this assessment and in the regional tables in Section 11.9.

11.6.1.6 Relation of assessed variables and metrics for changes in different drought types

This chapter assesses changes in meteorological drought, agricultural and ecological droughts, and hydrological droughts. Precipitation-based indices are used for the estimation of changes in meteorological droughts, such as the Standardized Precipitation Index (SPI) and the Consecutive Dry Days (CDD). Changes in total soil moisture and soil moisture-based drought events are used for the estimation of changes in agricultural and ecological droughts, complemented by changes in surface soil moisture, water-balance estimates (precipitation minus ET), and SPEI-PM and PDSI-PM. For hydrological droughts, changes in low

ACCEPTED VERSION SUBJECT TO FINAL EDITING

flows are assessed, sometimes complemented by changes in mean streamflow.

In summary, different drought types exist and they are associated with different impacts and respond differently to increasing greenhouse gas concentrations. Precipitation deficits and changes in evapotranspiration govern net water availability. A lack of sufficient soil moisture, sometimes amplified by increased atmospheric evaporative demand, result in agricultural and ecological drought. Lack of runoff and surface water result in hydrological drought. Drought events are both the result of dynamic and/or thermodynamic processes, with thermodynamic processes being the main driver of drought changes under human-induced climate change *(high confidence)*.

11.6.2 Observed trends

Evidence on observed drought trends at the time of the SREX (Chapter 3) and AR5 (Chapter 2) was limited. SREX concluded that "There is *medium confidence* that since the 1950s some regions of the world have experienced a trend to more intense and longer droughts, in particular in southern Europe and West Africa, but in some regions droughts have become less frequent, less intense, or shorter, for example, in central North America and northwestern Australia". The assessment at the time did not distinguish between different drought types. This chapter includes numerous updates on observed drought trends, associated with extensive new literature and longer datasets since the AR5.

11.6.2.1 Precipitation deficits

Strong precipitation deficits have been recorded in recent decades in the Amazon (2005, 2010), southwestern China (2009-2010), southwestern North America (2011-2014), Australia (1997-2009), California (2014), the middle East (2012-2016), Chile (2010-2015), the Great Horn of Africa (2011), among others (van Dijk et al., 2013; Mann and Gleick, 2015; Rowell et al., 2015; Marengo and Espinoza, 2016; Dai and Zhao, 2017; Garreaud et al., 2017, 2020; Marengo et al., 2017; Brito et al., 2018; Cook et al., 2018). Global studies generally show no significant trends in SPI time series (Orlowsky and Seneviratne, 2013; Spinoni et al., 2014), and in derived drought frequency and severity data (Spinoni et al., 2019), with very few regional exceptions (Figure 11.17 and Section 11.9). Long-term decreases in precipitation are found in some AR6 regions in Africa (CAF, ESAF), and several regions in South America (NES, SAM, SWS, SSA) (Section 11.9). Evidence of precipitation-based drying trends is also found in Western Africa (WAF), consistent with studies based on CDD trends (Chaney et al., 2014; Donat et al., 2014b; Barry et al., 2018; Dunn et al., 2020)(Figure 11.17), however there is a partial recovery of the rainfall trends since the 1980s in this region (Chapter 10, 10.4.2.1). Some AR6 regions show a decrease in meteorological drought, including NAU, CAU, NEU and CNA (Section 11.9). Other regions do not show substantial trends in long-term meteorological drought, or display mixed signals depending on the considered time frame and subregions, such as in Southern Australia (SAU; Gallant et al., 2013; Delworth and Zeng, 2014; Alexander and Arblaster, 2017; Spinoni et al., 2019; Dunn et al., 2020; Rauniyar and Power, 2020) and the Mediterranean (MED; Camuffo et al., 2013; Gudmundsson and Seneviratne, 2016; Spinoni et al., 2017; Stagge et al., 2017; Caloiero et al., 2018; Peña-Angulo et al., 2020) (see also Section 11.9 and Atlas 8.2).

11.6.2.2 Atmospheric evaporative demand

In several regions, AED increases have intensified recent drought events (Williams et al., 2014, 2020; Seager et al., 2015b; Basara et al., 2019; García-Herrera et al., 2019), enhanced vegetation stress (Allen et al., 2015; Sanginés de Cárcer et al., 2018; Yuan et al., 2019), or contributed to the depletion of soil moisture or runoff through enhanced ET (Teuling et al., 2013; Padrón et al., 2020) (*high confidence*). Trends in pan evaporation measurements and Penman-Monteith AED estimates provide an indication of possible trends in the influence of AED on drought. Given the observed global temperature increases (Chapter 2; Section 2.3.1.1; Section 11.3) and dominant decrease in relative humidity over land areas (Simmons et al., 2010; Willett et al., 2014), VPD has increased globally (Barkhordarian et al., 2019; Yuan et al., 2019). Pan evaporation has increased as

ACCEPTED VERSION SUBJECT TO FINAL EDITING

a consequence of VPD changes in several AR6 regions such as East Asia (EAS; Li et al., 2013; Sun et al., 2018; Yang et al., 2018a), West Central Europe (WCE; Mozny et al., 2020), MED; Azorin-Molina et al., 2015) and Central and Southern Australia (CAU, SAU; Stephens et al., 2018). Nevertheless, there is an important regional variability in observed trends, and in other AR6 regions pan evaporation has decreased (e.g. in North Central America, NCA (Breña-Naranjo et al., 2016) and in the Tibetan Plateau, TIB (Zhang et al., 2018a)). Physical models also show an important regional diversity, with an increase in New Zealand (NZ; Salinger, 2013) and the Mediterranean (MED; Gocic and Trajkovic, 2014; Azorin-Molina et al., 2015; Piticar et al., 2016), a decrease in SAS (Jhajharia et al., 2015), and strong spatial variability in North America (Seager et al., 2015b). This variability is driven by the role of other meteorological variables affecting AED. Changes in solar radiation as a consequence of solar dimming and brightening may affect trends (Kambezidis et al., 2012; Sanchez-Lorenzo et al., 2015; Wang and Yang, 2014; Chapter 7, Section 7.2.2.2). Wind speed is also relevant (McVicar et al., 2012a), and studies suggest a reduction of the wind speed in some regions (Zhang et al., 2019h) that could compensate the role of the VPD increase. Nevertheless, the VPD trend seems to dominate the overall AED trends, compared to the effects of trends in wind speed and solar radiation (Wang et al., 2012; Park Williams et al., 2017; Vicente-Serrano et al., 2020b).

11.6.2.3 Soil moisture deficits

There are limited long-term measurements of soil moisture from ground observations (Dorigo et al., 2011; Qiu et al., 2016; Quiring et al., 2016), which impedes their use in the analysis of trends. Among the few existing observational studies covering at least two decades, several studies have investigated trends in ground soil moisture in East Asia (Section 11.9; (Chen and Sun, 2015b; Liu et al., 2015; Qiu et al., 2016)). Alternatively, microwave-based satellite measurements of surface soil moisture have also been used to analyse trends (Dorigo et al., 2012; Jia et al., 2018). Although there is regional evidence that microwave-based soil moisture estimates can capture well drying trends in comparison with ground soil moisture observations (Jia et al., 2018), there is only *medium confidence* in the derived trends, since satellite soil moisture data are affected by inhomogeneities (Dorigo et al., 2015; Rodell et al., 2018; Preimesberger et al., 2020). Furthermore, microwave-based satellites only sense surface soil moisture, which differs from root-zone soil moisture (Berg et al., 2017b), although relationships can be derived between the two (Brocca et al., 2011). Several studies have also analysed long-term soil moisture timeseries from observations-driven land-surface or hydrological models, including land-based reanalysis products (Albergel et al., 2013; Jia et al., 2018; Gu et al., 2019b; Markonis et al., 2021). Such models have also been used to assess changes in land water availability, estimated as precipitation minus ET, which is equal to the sum of soil moisture and runoff (Greve et al., 2014; Padrón et al., 2020).

Overall, evidence from global studies suggests that several land regions have been affected by increased soil drying or water-balance in past decades, despite some spread among products (Albergel et al., 2013; Greve et al., 2014; Gu et al., 2019b; Padrón et al., 2020). Drying has not only occurred in dry regions, but also in humid regions (Greve et al., 2014). Some studies have specifically addressed changes in soil moisture at regional scale (Section 11.9). For AR6 regions, several studies suggest an increase in the frequency and areal extent of soil moisture deficits, with examples in East Asia (EAS; Cheng et al., 2015; Qin et al., 2015; Jia et al., 2018), Western and Central Europe (WCE; Trnka et al., 2015b), and the Mediterranean (MED; Hanel et al., 2018; Moravec et al., 2019; Markonis et al., 2021). Nonetheless, some analyses also show no long-term trends in soil drying in some AR6 regions, e.g. in Eastern (ENA; Park Williams et al., 2017) and Central North America (CNA; Seager et al., 2019), as well as in North-Eastern Africa (NEAF; Kew et al., 2021). The soil moisture drying trends identified in both global and regional studies are generally related to increases in ET (associated with higher AED) rather than decreases in precipitation, as identified on global land for trends in water-balance in the dry season (Padrón et al., 2020), as well as for some regions (Teuling et al., 2013; Cheng et al., 2015; Trnka et al., 2015a; Van Der Linden et al., 2019; Li et al., 2020c).

Evidence from observed or observations-derived trends in soil moisture and precipitation minus ET, are combined with evidence from SPEI and PDSI-PM studies to derive regional assessments of changes in agricultural and ecological droughts (Section 11.9). This assessment is summarized in Section 11.6.2.6.

ACCEPTED VERSION SUBJECT TO FINAL EDITING

11.6.2.4 Hydrological deficits

There is evidence based on streamflow records of increased hydrological droughts in East Asia (Zhang et al., 2018b) and southern Africa (Gudmundsson et al., 2019). In areas of Western and Central Europe and of Northern Europe, there is no evidence of changes in the severity of hydrological droughts since 1950 based on flow reconstructions (Caillouet et al., 2017; Barker et al., 2019) and observations (Vicente-Serrano et al., 2019). In the Mediterranean region, there is *high confidence* in hydrological drought intensification (Giuntoli et al., 2013; Gudmundsson et al., 2019; Lorenzo-Lacruz et al., 2013; Masseroni et al., 2020; Section 11.9). In Southeastern South America there is a decrease in the severity of hydrological droughts (Rivera and Penalba, 2018). In North America, depending on the methods, datasets and study periods, there are differences between studies that suggest an increase (Shukla et al., 2015; Udall and Overpeck, 2017) vs a decrease in hydrological drought frequency (Mo and Lettenmaier, 2018), but in general there is strong spatial variability (Poshtiri and Pal, 2016). Streamflow observation reference networks of near-natural catchments have also been used to isolate the effect of climate trends on hydrological drought trends in a few regions, but these show limited trends in Northern Europe and Western and Central Europe (Stahl et al., 2010; Bard et al., 2015; Harrigan et al., 2018), North America (Dudley et al., 2020) and most of Australia with the exception of Eastern and Southern Australia (Zhang et al., 2016c). Given the low availability of observations, there are few studies analysing trends of drought severity in the groundwater. Nevertheless, some studies suggest a noticeable response of groundwater droughts to climate variability (Lorenzo-Lacruz et al., 2017) and increased drought frequency and severity associated with warming, probably as a consequence of enhanced ET induced by higher AED (Maxwell and Condon, 2016). This is supported by studies in Northern Europe (Bloomfield et al., 2019) and North America (Condon et al., 2020).

11.6.2.5 Atmospheric-based drought indices

Globally, trends in SPEI-PM and PDSI-PM suggest slightly higher increases of drought frequency and severity in regions affected by drying over the last decades in comparison to the SPI (Dai and Zhao, 2017; Spinoni et al., 2019; Song et al., 2020), mainly in regions of West and Southern Africa, the Mediterranean and East Asia (Figure 11.17), which is consistent with observed soil moisture trends (Section 11.6.2.3). These indices suggest that AED has contributed to increase the severity of agricultural and ecological droughts compared to meteorological droughts (García-Herrera et al., 2019; Williams et al., 2020), reduce soil moisture during the dry season (Padrón et al., 2020), increase plant water stress (Allen et al., 2015; Grossiord et al., 2020; Solander et al., 2020) and trigger more severe forest fires (Abatzoglou and Williams, 2016; Turco et al., 2019; Nolan et al., 2020). A number of regional studies based on these drought indices have also shown stronger drying trends in comparison to trends in precipitation-based indices in the following AR6 regions (see also 11.9): NSA (Fu et al., 2013b; Marengo and Espinoza, 2016), SCA (Hidalgo et al., 2017), WCA (Tabari and Aghajanloo, 2013; Sharafati et al., 2020), SAS (Niranjan Kumar et al., 2013), NEAF (Zeleke et al., 2017), WSAF (Edossa et al., 2016), NWN and NEN (Bonsal et al., 2013), EAS (Yu et al., 2014; Chen and Sun, 2015b; Li et al., 2020b; Liang et al., 2020; Wu et al., 2020b) and MED (Kelley et al., 2015; Stagge et al., 2017; González-Hidalgo et al., 2018; Mathbout et al., 2018a).

[START FIGURE 11.17 HERE]

Figure 11.17: Observed linear trend for (a) consecutive dry days (CDD) during 1960-2018, (b) standardized precipitation index (SPI) and (c) standardized precipitation-evapotranspiration index (SPEI) during 1951-2016. CDD data are from the HadEx3 dataset (Dunn et al., 2020), trend calculation of CDD as in Figure 11.9 Drought severity is estimated using 12-month SPI (SPI-12) and 12-month SPEI (SPEI-12). SPI and SPEI datasets are from Spinoni et al. (2019). The threshold to identify drought episodes was set at -1 SPI/SPEI units. Areas without sufficient data are shown in grey. No overlay indicates regions where the trends are significant at p = 0.1 level. Crosses indicate regions where trends are not significant. For details on the methods see Supplementary Material 11.SM.2. Further details on data sources and processing are available in the chapter data table (Table 11.SM.9).

ACCEPTED VERSION SUBJECT TO FINAL EDITING

[END FIGURE 11.17 HERE]

11.6.2.6 Synthesis for different drought types

Few AR6 regions show observed increases in meteorological drought (Section 11.9), mostly in Africa and South America (NES: *high confidence*; WAF, CAF, ESAF, SAM, SWS, SSA, SAS: *medium confidence*); a few others show a decrease (WSB, ESB, NAU, CAU, NEU, CNA: *medium confidence*). There are stronger signals indicating observed increases in agricultural and ecological drought (Section 11.9), which highlights the role of increased ET, driven by increased AED, for these trends (Sections 11.6.2.3, 11.6.2.5). Past increases in agricultural and ecological droughts are found on all continents and several regions (WAF, CAF, WSAF, ESAF, WCA, ECA, EAS, SAU, MED, WCE, NES: *medium confidence*), while decreases are found only in one AR6 region (NAU: *medium confidence*). The more limited availability of datasets makes it more difficult to assess historical trends in hydrological drought at regional scale (Section 11.9). Increasing (MED: *high confidence*; WAF, EAS, SAU: *medium confidence*) and decreasing (NEU, SES: *medium confidence*) trends in hydrological droughts have only been observed in a few regions.

In summary, there is *high confidence* that AED has increased on average on continents, contributing to increased ET and resulting water stress during periods with precipitation deficits, in particular during dry seasons. There is *medium confidence* in increases in precipitation deficits in a few regions of Africa and South America. Based on multiple evidence, there is *medium confidence* that agricultural and ecological droughts have increased in several regions on all continents (WAF, CAF, WSAF, ESAF, WCA, ECA, EAS, SAU, MED, WCE, NES: *medium confidence*), while there is only *medium confidence* in decreases in one AR6 region (NAU). More frequent hydrological droughts are found in fewer regions (MED: *high confidence*; WAF, EAS, SAU: *medium confidence*).

11.6.3 Model evaluation

11.6.3.1 Precipitation deficits

ESMs generally show limited performance and large spread in identifying precipitation deficits and associated long-term trends in comparison with observations (Nasrollahi et al., 2015). Meteorological drought trends in the CMIP5 ensemble showed substantial disagreements compared with observations (Orlowsky and Seneviratne, 2013; Knutson and Zeng, 2018) including a tendency to overestimate drying, in particular in mid- to high latitudes (Knutson and Zeng, 2018). CMIP6 models display a better performance in reproducing long-term precipitation trends or seasonal dynamics in some studies in southern South America (Rivera and Arnould, 2020), East Asia (Xin et al., 2020), southern Asia (Gusain et al., 2020), and southwestern Europe (Peña-Angulo et al., 2020b), but there is still too *limited evidence* to allow for an assessment of possible differences in performance between CMIP5 and CMIP6. Furthermore, ESMs are generally found to underestimate the severity of precipitation deficits and the dry day frequencies in comparison to observations (Fantini et al., 2018; Ukkola et al., 2018). This is probably related to shortcomings in the simulation of persistent weather events in the mid-latitudes (Chapter 10, Section 10.3.3.3). In addition, ESMs also show a tendency to underestimate precipitation-based drought persistence at monthly to decadal time scales (Ault et al., 2014; Moon et al., 2018). The overall inter-model spread in the projected frequency of precipitation deficits is also substantial (Touma et al., 2015; Zhao et al., 2016; Engström and Keellings, 2018). Moreover, there are spatial differences in the spread, which is higher in the regions where enhanced drought conditions are projected and under high-emission scenarios (Orlowsky and Seneviratne, 2013). Nonetheless, some event attribution studies have concluded that droughts at regional scales can be adequately simulated by some climate models (Schaller et al., 2016; Otto et al., 2018c).

11.6.3.2 Atmospheric evaporative demand

There is only limited evidence on the evaluation of AED in state-of-the-art ESMs, which is performed on

ACCEPTED VERSION SUBJECT TO FINAL EDITING

externally computed AED based on model output (Scheff and Frierson, 2015; Liu and Sun, 2016, 2017). An evaluation of average AED in 17 CMIP5 ESMs for 1981-1999 based on potential evaporation show that the models' spatial patterns resemble the observations, but that the magnitude of potential evaporation displays strong divergence among models globally and regionally (Scheff and Frierson, 2015). The evaluation of AED in 12 CMIP5 ESMs with pan evaporation observations in East Asia for 1961-2000 (Liu and Sun, 2016, 2017) show that the ESMs capture seasonal cycles well, but that regional AED averages are underestimated due to biases in the meteorological variables controlling the aerodynamic and radiative components of AED. CMIP5 ESMs also show a strong underestimation of atmospheric drying trends compared to reanalysis data (Douville and Plazzotta, 2017).

11.6.3.3 Soil moisture deficits

The performance of climate models for representing soil moisture deficits shows more uncertainty than for precipitation deficits since in addition to the uncertainties related to cloud and precipitation processes, there is uncertainty related to the representation of complex soil hydrological and boundary-layer processes (Van Den Hurk et al., 2011; Lu et al., 2019; Quintana-Seguí et al., 2020). A limitation is also the lack of observations, and in particular soil moisture, in most regions (Section 11.6.2.3), and the paucity of land surface property data to parameterize land surface models, in particular soil types, soil properties and depth (Xia et al., 2015). The spatial resolution of models is an additional limitation since the representation of some land-atmosphere feedbacks and topographic effects requires detailed resolution (Nicolai-Shaw et al., 2015; Van Der Linden et al., 2019). Beside climate models, also land surface and hydrological models are used to derive historical and projected trends in soil moisture and related land water variables (Albergel et al., 2013; Cheng et al., 2015; Gu et al., 2019b; Padrón et al., 2020; Markonis et al., 2021; Pokhrel et al., 2021).

Overall, there are contrasting results on the performance of land surface models and climate models in representing soil moisture. Some studies suggest that soil moisture anomalies are well captured by land surface models driven with observation-based forcing (Dirmeyer et al., 2006; Albergel et al., 2013; Xia et al., 2014; Balsamo et al., 2015; Reichle et al., 2017; Spennemann et al., 2020), but other studies report limited agreement in the representation of interannual soil moisture variability (Stillman et al., 2016; Yuan and Quiring, 2017; Ford and Quiring, 2019) and noticeable seasonal differences in model skill (Xia et al., 2014, 2015) in some regions. Models with good skill can nonetheless display biases in absolute soil moisture (Xia et al., 2014; Gu et al., 2019a), but these are not necessarily of relevance for the simulation of surface water fluxes and drought anomalies (Koster et al., 2009). There is also substantial intermodel spread (Albergel et al. 2013), particularly for the root-zone soil moisture (Berg et al., 2017b).

Regarding the performance of regional and global climate models, an evaluation of an ensemble of RCM simulations for Europe (Stegehuis et al., 2013) shows that these models display too strong drying in early summer, resulting in an excessive decrease of latent heat fluxes, with potential implications for more severe droughts in dry environments (Teuling, 2018; Van Der Linden et al., 2019). Compared with a range of observational ET estimates, CMIP5 models show an overestimation of ET on annual scale, but an ET underestimation in boreal summer in many North-Hemisphere mid-latitude regions, also suggesting a tendency towards excessive soil drying (Mueller and Seneviratne, 2014), consistent with identified biases in soil moisture-temperature coupling (Donat et al., 2018; Vogel et al., 2018; Selten et al., 2020). Land surface models used in ESM display a bias in their representation of the sensitivity of interannual land carbon uptake to soil moisture conditions, which appears related to a limited range of soil moisture variations compared to observations (Humphrey et al., 2018).

For future projections, the spread of soil moisture outputs among different ESMs is more important than internal variability and scenario uncertainty, and the bias is strongly related to the sign of the projected change (Ukkola et al., 2018; Lu et al., 2019; Selten et al., 2020). CMIP5 ESMs that project more drying and warming in mid-latitude regions show a substantial bias in soil moisture-temperature coupling (Donat et al., 2018; Vogel et al., 2018). Although CMIP6 and CMIP5 simulations for soil moisture changes are overall similar, some differences are found in projections in a few regions (Cook et al., 2020)(see also Section 11.9).

ACCEPTED VERSION SUBJECT TO FINAL EDITING

There is still *limited evidence* to assess whether there are substantial differences in model performance in the two ensembles, but improvements in modeling aspects relevant for soil moisture have been reported for precipitation (11.6.3.2), and a better performance has been found in CMIP6 for the representation of long-term trends in soil moisture in the continental USA (Yuan et al., 2021). Despite the mentioned model limitations, the representation of soil moisture processes in ESMs uses physical and biological understanding of the underlying processes, which can represent well the temporal anomalies associated with temporal variability and trends in climate. In summary, there is *medium confidence* in the representation of soil moisture deficits in ESMs and related land surface and hydrological models.

11.6.3.4 Hydrological deficits

Streamflow and groundwater are not directly simulated by ESMs, which only simulate runoff, but they are generallyn represented in hydrological models (Prudhomme et al., 2014; Giuntoli et al., 2015), which are typically driven in a stand-alone manner by observed or simulated climate forcing. The simulation of hydrological deficits is much more problematic than the simulation of mean streamflow or peak flows (Fundel et al., 2013; Stoelzle et al., 2013; Velázquez et al., 2013; Staudinger et al., 2015), since models tend to be too responsive to the climate forcing and do not satisfactorily capture low flows (Tallaksen and Stahl, 2014). Simulations of hydrological drought metrics show uncertainties related to the contribution of both GCMs and hydrological models (Bosshard et al., 2013; Giuntoli et al., 2015; Samaniego et al., 2017; Vetter et al., 2017), but hydrological models forced by the same climate input data also show a large spread (Van Huijgevoort et al., 2013; Ukkola et al., 2018). At the catchment scale, the hydrological model uncertainty is higher than both GCM and downscaling uncertainty (Vidal et al., 2016), and the hydrological models show issues in representing drought propagation throughout the hydrological cycle (Barella-Ortiz and Quintana Seguí, 2019). A study on the evaluation of streamflow droughts in seven global (hydrological and land surface) models compared with observations in near-natural catchments of Europe showed a substantial spread among models, an overestimation of the number of drought events, and an underestimation of drought duration and drought-affected area (Tallaksen and Stahl, 2014).

11.6.3.5 Atmospheric-based drought indices

A number of studies have analysed the ability of models to capture drought severity and trends based on climatic drought indices. Given the limitations of ESMs in reproducing the dynamic of precipitation deficits and AED (11.6.3.1, 11.6.3.2), atmospheric-based drought indices derived from ESM data for these two variables are also affected by uncertainties and biases. A comparison of historical trends in PDSI-PM for 1950-2014 derived from CMIP3 and CMIP5 with respective estimates derived from observations (Dai and Zhao, 2017) show a similar behaviour at global scale (long-term decrease), but low spatial agreement in the trends except in a few regions (Mediterranean, South Asia, northwestern US). In future projections there is an important spread in PDSI-PM and SPEI-PM among different models (Cook et al., 2014a).

11.6.3.6 Synthesis for different drought types

The performance of ESMs used to assessed changes in variables related to meteorological droughts, agricultural and ecological droughts, and hydrological droughts, show the presence of biases and uncertainties compared to observations, but there is *medium confidence* in their overall performance for assessing drought projections given process understanding. Given the substantial inter-model spread documented for all related variables, the consideration of multi-model projections increases the confidence of model-based assessments, with only *low confidence* in assessments based on single models.

In summary, the evaluation of ESMs, land surface and hydrological models for the simulation of droughts is complex, due to the regional scale of drought trends, their overall low signal-to-noise ratio, and the lack of observations in several regions, in particular for soil moisture and streamflow. There is *medium confidence* in the ability of ESMs to simulate trends and anomalies in precipitation deficits and AED, and also *medium*

ACCEPTED VERSION SUBJECT TO FINAL EDITING

confidence in the ability of ESMs and hydrological models to simulate trends and anomalies in soil moisture and streamflow deficits, on global and regional scales.

11.6.4 Detection and attribution, event attribution

11.6.4.1 Precipitation deficits

There are only two AR6 regions in which there is at least *medium confidence* that human-induced climate change has contributed to changes in meteorological droughts (Section 11.9). In South-western South America (SSW), there is *medium confidence* that human-induced climate change has contributed to an increase in meteorological droughts (Boisier et al., 2016; Garreaud et al., 2020), while in Northern Europe (NEU), there is *medium confidence* that it has contributed to a decrease in meteorological droughts (Gudmundsson and Seneviratne, 2016) (Section 11.9). In other AR6 regions, there is inconclusive evidence in the attribution of long-term trends, but a human contribution to single meteorological events or subregional trends has been identified in some instances (Section 11.9; see also below). In the Mediterranean (MED) region, some studies have identified a precipitation decline or increase in meteorological drought probability for time frames since the early or mid 20th century and a possible human contribution to these trends (Hoerling et al., 2012; Gudmundsson and Seneviratne, 2016; Knutson and Zeng, 2018), also on subregional scale in Syria from 1930 to 2010 (Kelley et al., 2015). On the contrary, other studies have not identified precipitation and meteorological drought trends in the region for the long-term (Camuffo et al., 2013; Paulo et al., 2016; Vicente-Serrano et al., 2021) and also from the mid 20th century (Norrant and Douguédroit, 2006; Stagge et al., 2017). There is evidence of substantial internal variability in long-term precipitation trends in the region (Section 11.6.2.1), which limits the attribution of human influence on variability and trends of meteorological droughts from observational records (Kelley et al., 2012; Peña-Angulo et al., 2020b). In addition, there are important subregional trends showing mixed signals (MedECC, 2020)(Section 11.9). The evidence thus leads to an assessment of *low confidence* in the attribution of observed short-term changes in meteorological droughts in the region (Section 11.9). In North America, the human influence on precipitation deficits is complex (Wehner et al., 2017), with *low confidence* in the attribution of long-term changes in meteorological drought in AR6 regions (Lehner et al., 2018; Section 11.9). In Africa there is *low confidence* that human influence has contributed to the observed long-term meteorological drought increase in Western Africa (Section 11.9; Chapter 10, Section 10.6.2). There is *low confidence* in the attribution of the observed increasing trends in meteorological drought in Eastern Southern Africa, but evidence that human-induced climate change has affected recent meteorological drought events in the region (11.9).

Attribution studies for recent meteorological drought events are available for various regions. In Central and Western Europe, a multi-method and multi-model attribution study on the 2015 Central European drought did not find conclusive evidence for whether human-induced climate change was a driver of the rainfall deficit, as the results depended on model and method used (Hauser et al., 2017). In the Mediterranean region, a human contribution was found in the case of the 2014 meteorological drought in the southern Levant based on a single-model study (Bergaoui et al., 2015). In Africa, there is some evidence of a contribution of human emissions to single meteorological drought events, such as the 2015-2017 southern African drought (Funk et al., 2018a; Yuan et al., 2018a; Pascale et al., 2020), and the three-year 2015-2017 drought in the western Cape Town region of South Africa (Otto et al., 2018c). An attributable signal was not found in droughts that occurred in different years with different spatial extents in the last decade in Northern and Southern East Africa (Marthews et al., 2015; Uhe et al., 2017; Otto et al., 2018a; Philip et al., 2018b; Kew et al., 2021). However, an attributable increase in 2011 long rain failure was identified (Lott et al., 2013). Further studies have attributed some African meteorological drought events to large-scale modes of variability, such as the strong 2015 El Niño (Philip et al., 2018; Box 11.4) and increased SSTs overall (Funk et al., 2015b, 2018b). Natural variability was dominant in the California droughts of 2011/12-2013/14 (Seager et al., 2015a). In Asia, no climate change signal was found in the record dry spell over Singapore-Malaysia in 2014 (Mcbride et al., 2015) or the drought in central southwest Asia in 2013/2014 (Barlow and Hoell, 2015). Nevertheless, the South East Asia drought of 2015 has been attributed to anthropogenic warming effects (Shiogama et al., 2020). Recent droughts occurring in South America, specifically in the southern Amazon region in 2010

ACCEPTED VERSION SUBJECT TO FINAL EDITING

(Shiogama et al., 2013) and in Northeast South America in 2014 (Otto et al., 2015) and 2016 (Martins et al., 2018) were not attributed to anthropogenic climate change. Nevertheless, the central Chile drought between 2010 and 2018 has been suggested to be partly associated to global warming (Boisier et al., 2016; Garreaud et al., 2020). The 2013 New Zealand meteorological drought was attributed to human influence by Harrington et al. (2014, 2016) based on fully coupled CMIP5 models, but, no corresponding change in the dry end of simulated precipitation from a stand-alone atmospheric model was found by Angélil et al. (2017).

Event attribution studies also highlight a complex interplay of anthropogenic and non-anthropogenic climatological factors for some events. For example, anthropogenic warming contributed to the 2014 drought in North Eastern-Africa by increasing east African and west Pacific temperatures, and increasing the gradient between standardized western and central Pacific SSTs causing reduced rainfall (Funk et al., 2015b). As different methodologies, models and data sources have been used for the attribution of precipitation deficits, Angélil et al. (2017) reexamined several events using a single analytical approach and climate model and observational datasets. Their results showed a disagreement in the original anthropogenic attribution in a number of precipitation deficit events, which increased uncertainty in the attribution of meteorological droughts events.

11.6.4.2 Soil moisture deficits

There is a growing number of studies on the detection and attribution of long-term changes in soil moisture deficits. Mueller and Zhang (2016) concluded that anthropogenic forcing contributed significantly to an increase in the land surface area affected by soil moisture deficits, which can be reproduced by CMIP5 models only if anthropogenic forcings are involved. A similar assessment was provided globally by Gu et al. (2019b) also using CMIP5 models. Padrón et al. (2019) analyzed long-term reconstructed and CMIP5 simulated dry season water availability, defined as precipitation minus ET (i.e., equivalent to soil moisture and runoff availability), and found that patterns of changes in dry-season deficits in the recent three last decades can only be explained by anthropogenic forcing and are mostly related to changes in ET. Similarly Williams et al. (2020) concluded human-induced climate change contributed to the strong soil moisture deficits recorded in the last two decades in western North America through VPD increases associated with higher air temperatures and lower air humidity. There are few studies analysing the attribution of particular episodes of soil moisture deficits to anthropogenic influence. Nevertheless, the available modeling studies coincide in supporting an anthropogenic attribution associated with more extreme temperatures, exacerbating AED and increasing ET, and thus depleting soil moisture, as observed in southern Europe in 2017 (García-Herrera et al., 2019) and in Australia in 2018 (Lewis et al., 2019b) and 2019 (van Oldenborgh et al., 2021), the latter event having strong implications in the propagation of widespread mega-fires (Nolan et al., 2020).

11.6.4.3 Hydrological deficits

It is often difficult to separate the role of climate trends from changes in land use, water management and demand for changes in hydrological deficits, especially on regional scale. However, a global study based on a recent multi-model experiment with global hydrological models and covering several AR6 regions suggests a dominant role of anthropogenic radiative forcing for trends in low, mean and high flows, while simulated effects of water and land management do not suffice to reproduce the observed spatial pattern of trends (Gudmundsson et al., 2021). Regional studies also suggest that climate trends have been dominant compared to land use and human water management for explaining trends in hydrological droughts in some regions, for instance in Ethiopia (Fenta et al., 2017), in China (Xie et al., 2015), and in North America for the Missouri and Colorado basins, as well as in California (Shukla et al., 2015; Udall and Overpeck, 2017; Ficklin et al., 2018; Xiao et al., 2018a; Glas et al., 2019; Martin et al., 2020; Milly and Dunne, 2020).

In other regions the influence of human water uses can be more important to explain hydrological drought trends (Liu et al., 2016b; Mohammed and Scholz, 2016). There is *medium confidence* that human-induced climate change has contributed to an increase of hydrological droughts in the Mediterranean (Giuntoli et al., 2013; Vicente-Serrano et al., 2014; Gudmundsson et al., 2017), but also *medium confidence* that changes in

ACCEPTED VERSION SUBJECT TO FINAL EDITING

land use and terrestrial water management contributed to these trends as well (Teuling et al., 2019; Vicente-Serrano et al., 2019; Section 11.9). A global study with a single hydrological model estimated that human water consumption has intensified the magnitude of hydrological droughts by 20%-40% over the last 50 years, and that the human water use contribution to hydrological droughts was more important than climatic factors in the Mediterranean, and the central US, as well as in parts of Brazil (Wada et al., 2013). However, Gudmundsson et al. (2021) concluded that the contribution of human water use is smaller than that of anthropogenic climate change to explain spatial differences in the trends of low flows based on a multi-model analysis. There is still *limited evidence* and thus *low confidence* in assessing these trends at the scale of single regions, with few exceptions (Section 11.9).

11.6.4.4 Atmospheric-based drought indices

Different studies using atmospheric-based drought indices suggest an attributable anthropogenic signal, characterized by the increased frequency and severity of droughts (Cook et al., 2018), associated to increased AED (Section 11.6.4.2). The majority of studies are based on the PDSI-PM. Williams et al. (2015) and Griffin and Anchukaitis (2014) concluded that increased AED has had an increased contribution to drought severity over the last decades, and played a dominant role in the intensification of the 2012-2014 drought in California. The same temporal pattern and physical mechanism was stressed by Li et al. (2017) in Central Asia. Marvel et al. (2019) compared tree ring-based reconstructions of the PDSI-PM over the past millennium with PDSI-PM estimates based on output from CMIP5 models, suggesting a contribution of greenhouse gas forcing to the changes since the beginning of the 20th century, although characterized with temporal differences that could be driven by temporal variations in the aerosol forcing, in agreement with the dominant external forcings of aridification at global scale between 1950 and 2014 (Bonfils et al., 2020). In the Mediterranean region there is *medium confidence* of drying attributable to antropogenic forcing as a consequence of the strong AED increase (Gocic and Trajkovic, 2014; Liuzzo et al., 2014; Azorin-Molina et al., 2015; Maček et al., 2018), which has enhanced the severity of drought events (Vicente-Serrano et al., 2014; Stagge et al., 2017; González-Hidalgo et al., 2018). In particular, this effect was identified to be the main driver of the intensification of the 2017 drought that affected southwestern Europe, and was attributed to the human forcing (García-Herrera et al., 2019). Nangombe et al. (2020) and Zhang et al. (2020) concluded from differences between precipitation and AED that anthropogenic forcing contributed to 2018 droughts that affected southern Africa and southeastern China, respectively, principally as consequence of the high AED that characterised these two events.

11.6.4.5 Synthesis for different drought types

The regional evidence on attribution for single AR6 regions generally shows *low confidence* for a human contribution to observed trends in meteorological droughts at regional scale, with few exceptions (Section 11.9). There is *medium confidence* that human influence has contributed to changes in agricultural and ecological droughts and has led to an increase in the overall affected land area. At regional scales, there is *medium confidence* in a contribution of human-induced climate change to increases in agricultural and ecological droughts in the Mediterranean (MED) and Western North America (WNA) (Section 11.9). There *is medium confidence* that human-induced climate change has contributed to an increase in hydrological droughts in the Mediterranean region, but also *medium confidence* in contributions from other human influences, including water management and land use (Section 11.9). Several meteorological and agricultural and ecological drought events have been attributed to human-induced climate change, even in regions where no long-term changes are detected (*medium confidence*). However, a lack of attribution to human-induced climate change has also been shown for some events (*medium confidence*).

In summary, human influence has contributed to changes in water availability during the dry season over land areas, including decreases over several regions due to increases in evapotranspiration (*medium confidence*). The increases in evapotranspiration have been driven by increases in atmospheric evaporative demand induced by increased temperature, decreased relative humidity and increased net radiation over affected land areas (*high confidence*). There is *low confidence* that human influence has affected trends in

ACCEPTED VERSION SUBJECT TO FINAL EDITING

meteorological droughts in most regions, but *medium confidence* that they have contributed to the severity of some single events. There is *medium confidence* that human-induced climate change has contributed to increasing trends in the probability or intensity of recent agricultural and ecological droughts, leading to an increase of the affected land area. Human-induced climate change has contributed to global-scale change in low flow, but human water management and land use changes are also important drivers (*medium confidence*).

11.6.5 Projections

SREX (Chapter 3) asssessed with *medium confidence* projections of increased drought severity in some regions, including southern Europe and the Mediterranean, central Europe, Central America and Mexico, northeast Brazil, and southern Africa, and. *low confidence* elsewhere given large inter-model spread. AR5 (Chapters 11 and 12) also assessed large uncertainties in drought projections at the regional and global scales. The assessment of drought mechanisms under future climate change scenarios depends on the model used (Section 11.6.3). Moreover, uncertainties in drought projections are affected by the consideration of plant physiological responses to increasing atmospheric CO_2 (Greve et al., 2019; Mankin et al., 2019; Milly and Dunne, 2016; Yang et al., 2020; Chapter 5, Cross-Chapter Box 5.1), the role of soil moisture-atmosphere feedbacks for changes in water-balance and aridity (Berg et al., 2016; Zhou et al., 2021), and statistical issues related to considered drought time scales (Vicente-Serrano et al., 2020a). Nonetheless, the extensive literature available since AR5 allows a substantially more robust assessment of projected changes in droughts, also subdivided in different drought types (meteorological drought, agricultural and ecological drought, and hydrological drought). This includes assessments of projected changes in droughts, including changes at 1.5°C, 2°C and 4°C of global warming, for all AR6 regions (Section 11.9). Projected changes show increases in drought frequency and intensity in several regions as function of global warming (*high confidence*). There are also substantial increases in drought hazard probability from 1.5°C to 2°C global warming as well as for further additional increments of global warming (Figs. 11.18 and 11.19) (*high confidence*). These findings are based both on CMIP5 and CMIP6 analyses (Section 11.9; Greve et al., 2018; Wartenburger et al., 2017; Xu et al., 2019a), and strengthen the conclusions of the SR15 Ch3.

11.6.5.1 Precipitation deficits

Studies based on CMIP5, CMIP6 and CORDEX projections show a consistent signal in the sign and spatial pattern of projections of precipitation deficits. Global studies based on these multi-model ensemble projections (Orlowsky and Seneviratne, 2013; Martin, 2018; Spinoni et al., 2020; Ukkola et al., 2020; Coppola et al., 2021b) show particularly strong signal-to-noise ratios for increasing meteorological droughts in the following AR6 regions: MED, ESAF, WSAF, SAU, CAU, NCA, SCA, NSA and NES (Section 11.9). There is also substantial evidence of changes in meteorological droughts at 1.5°C vs 2°C of global warming from global studies (Wartenburger et al., 2017; Xu et al., 2019a). The patterns of projected changes in mean precipitation are consistent with the changes in the drought duration, but they are not consistent with the changes in drought intensity (Ukkola et al., 2020). In general, CMIP6 projections suggest a stronger increase of the probability of precipitation deficits than CMIP5 projections (Cook et al., 2020; Ukkola et al., 2020). Projections for the number of CDDs in CMIP6 (Figure 11.19) for different levels of global warming relative to 1850-1900 show similar spatial patterns as projected precipitation deficits. The robustness of the patterns in projected precipitation deficits identified in the global studies is also consistent with results from regional studies (Giorgi et al., 2014; Marengo and Espinoza, 2016; Pinto et al., 2016; Huang et al., 2018a; Maúre et al., 2018; Nangombe et al., 2018; Tabari and Willems, 2018; Abiodun et al., 2019; Dosio et al., 2019).

In Africa, a strong increase in the length of dry spells (CDD) is projected for 4°C of global warming over most of the continent with the exception of central and eastern Africa (Giorgi et al., 2014; Han et al., 2019; Sillmann et al., 2013; Section 11.9). In West Africa, a strong reduction of precipitation is projected (Sillmann et al., 2013a; Diallo et al., 2016; Akinsanola and Zhou, 2018; Han et al., 2019; Todzo et al., 2020) at 4°C of global warming, and CDD would increase with stronger global warming levels (Klutse et al., 2018). The regions most strongly affected are Southern Africa (ESAF, WSAF; (Nangombe et al., 2018;

ACCEPTED VERSION SUBJECT TO FINAL EDITING

Abiodun et al., 2019) and Northern Africa (part of MED region), with increases in meteorological droughts already at 1.5°C of global warming, and further increases with increasing global warming (Section 11.9). CDD is projected to increase more in the southern Mediterranean (northern Africa) than in the northern part of the Mediterranean region (Lionello and Scarascia, 2020).

In Asia, most AR6 regions show *low confidence* in projected changes in meteorological droughts at 1.5°C and 2°C of global warming, with a few regions displaying a decrease in meteorological droughts at 4°C of global warming (RAR, ESB, RFE, ECA; *medium confidence*), although there is a projected increase in meteorological droughts in Southeast Asia (SEA) at 4°C (*medium confidence*) (Section 11.9). In Southeast Asia, an increasing frequency of precipitation deficits is projected as a consequence of an increasing frequency of extreme El Niño (Cai et al., 2014a, 2015, 2018).

In central America, projections suggest an increase in mid-summer meteorological drought (Imbach et al., 2018) and increased CDD (Nakaegawa et al., 2013; Chou et al., 2014a; Giorgi et al., 2014). In the Amazon, there is also a projected increase in dryness (Marengo and Espinoza, 2016), which is the combination of a projected increase in the frequency and geographic extent of meteorological drought in the eastern Amazon, and an opposite trend in the West (Duffy et al., 2015). In southwestern South America, there is a projected increase of the CDD (Chou et al., 2014a; Giorgi et al., 2014) and in Chile, drying is projected to prevail (Boisier et al., 2018). In the South America monsoon region, an increase in CDD is projected (Chou et al., 2014a; Giorgi et al., 2014), but a decrease is projected in southeastern and southern South America (Giorgi et al., 2014). In Central America, mid summer meteorological drought is projected to intensify during 2071-2095 for the RCP8.5 scenario (Corrales-Suastegui et al., 2019).

An increase in the frequency, duration and intensity of meteorological droughts is projected in southwest, south and east Australia (Kirono et al., 2020; Shi et al., 2020). In Canada and most of the USA, and based on the SPI, Swain and Hayhoe (2015) identified drier summer conditions in projections over most of the region, and there is a consistent signal toward an increase in duration and intensity of droughts in southern North America (Pascale et al., 2016; Escalante-Sandoval and Nuñez-Garcia, 2017). In California, more precipitation variability is projected, characterised by increased frequency of consecutive drought and humid periods (Swain et al., 2018).

Substantial increases in meteorological drought are projected in Europe, in particular in the Mediterranean region already at 1.5°C of global warming (Section 11.9). In southern Europe, model projections display a consistent drying among models (Russo et al., 2013; Hertig and Tramblay, 2017; Guerreiro et al., 2018a; Raymond et al., 2019). In Western and Central Europe there is some spread in CMIP5 projections, with some models projecting very strong drying and others close to no trend (Vogel et al., 2018), although CDD is projected to increase in CMIP5 projections under the RCP 8.5 scenario (Hari et al., 2020). The overall evidence suggests an increase in meteorological drought at 4°C in the WCE region (*medium confidence;* Section 11.9).

Overall, based on both global and regional studies, several hot spot regions are identified displaying more frequent and severe meteorological droughts with increasing with global warming, including several AR6 regions at 1.5°C (WSAF, ESAF, SAU, MED, NES) and 2°C of global warming (WSAF, ESAF, EAU, SAU, MED, NCA, SCA, NSA, NES) (Section 11.9). At 4°C of global warming, there is also confidence in increases in meteorological droughts in further regions (WAF, WCE, ENA, CAR, NWS, SAM, SWS, SSA; Section 11.9), showing a geographical expansion of meteorological drought with increasing global warming. Only few regions are projected to have less intense or frequent meteorological droughts (Section 11.9).

11.6.5.2 Atmospheric evaporative demand

Effects of AED on droughts in future projections is under debate. CMIP5 models project an AED increase over the majority of the world with increasing global warming, mostly as a consequence of strong VPD increases (Scheff and Frierson, 2015; Vicente-Serrano et al., 2020b). However, ET is projected to increase less than AED in many regions, due to plant physiological responses related to i) CO_2 effects on plant

ACCEPTED VERSION SUBJECT TO FINAL EDITING

photosynthesis and ii) soil moisture control on ET.

Several studies suggest that increasing atmospheric CO_2 could lead to reduced leaf stomatal conductance, which would increase water-use efficiency and reduce plant water needs, thus limiting ET (Chapter 5, Cross-Chapter Box 5.1; Greve et al., 2017; Lemordant et al., 2018; Milly and Dunne, 2016; Roderick et al., 2015; Scheff et al., 2017; Swann, 2018; Swann et al., 2016). The implemention of a CO_2-dependent land resistance parameter has been suggested for the estimation of AED (Yang et al., 2019). Nevertheless, there are other relevant mechanisms, as soil moisture deficits and VPD also play an importantrole in the control of the leaf stomatal conductance (Xu et al., 2016b; Menezes-Silva et al., 2019; Grossiord et al., 2020) and a number of ecophysiological and anatomical processes affect the response of plant physiology under higheratmospheric CO_2 concentrations (Mankin et al., 2019; Menezes-Silva et al., 2019; Chapter 5, Cross-Chapter Box 5.1). The benefits of the atmospheric CO_2 for plant stress and agricultural and ecological droughts would be minimal precisely during dry periods given stomatal closure in response to limited soil moisture (Allen et al., 2015; Xu et al., 2016b). In addition, CO_2 effects on plant stomatal conductance could not entirely compensate the increased demand associated to warming (Liu and Sun, 2017); in large tropical and subtropical regions (e.g. southern Africa, the Amazon, the Mediterranean and southern North America), AED is projected to increase even considering the possible CO_2 effects on the land resistance (Vicente-Serrano et al., 2020b). Moreover, these CO_2 effects would not affect the direct evaporation from soils and water bodies, which is very relevant in the reservoirs of warm areas (Friedrich et al., 2018). Because of these uncertainties, there is *low confidence* whether increased CO_2-induced water-use efficiency in vegetation will substantially reduce global plant transpiration and will diminish the frequency and severity of soil moisture and streamflow deficits associated with the radiative effect of higher CO_2 concentrations (Chapter 5, CC Box 5.1).

Another mechanism reducing the ET response to increased AED in projections is the control of soil moisture limitations on ET, which leads to reduced stomatal conductance under water stress (Berg and Sheffield, 2018; Stocker et al., 2018; Zhou et al., 2021). This response may be further amplified through VPD-induced decreases in stomatal conductance (Anderegg et al., 2020). However, the decreased stomatal conductance in response to both soil moisture limitation and enhanced CO_2 would further enhance AED (Sherwood and Fu, 2014; Berg et al., 2016; Teuling, 2018; Miralles et al., 2019), whereby the overall effects on AED in ESMs are found to be of similar magnitude for soil moisture limitation and CO_2 physiological effects on stomatal conductance (Berg et al., 2016). Increased AED is thus both a driver and a feedback with respect to changes in ET, complicating the interpretation of its role on drought changes with increasing CO_2 concentrations and global warming.

11.6.5.3 Soil moisture deficits

Areas with projected soil moisture decreases do not fully coincide with areas with projected precipitation decreases, although there is substantial consistency in the respective patterns (Dirmeyer et al., 2013; Berg and Sheffield, 2018). There are, however, more regions affected by increased soil moisture deficits (Figure 11.19) than precipitation deficits (CC-Box 11.1, Figures 2a,b,c), as a consequence of enhanced AED and the associated increased ET, as highlighted by some studies (Dai et al., 2018; Orlowsky and Seneviratne, 2013; Chapter 8, Section 8.2.2.1). Moisture in the top soil layer is projected to decrease more than precipitation at all warming levels (Lu et al., 2019), extending the regions affected by severe soil moisture deficits over most of south and central Europe (Lehner et al., 2017; Ruosteenoja et al., 2018; Samaniego et al., 2018; Van Der Linden et al., 2019), southern North America (Cook et al., 2019), South America (Orlowsky and Seneviratne, 2013), southern Africa (Lu et al., 2019), East Africa (Rowell et al., 2015), southern Australia (Kirono et al., 2020), India (Mishra et al., 2014b) and East Asia (Cheng et al., 2015) (Figure 11.19). Projected changes in total soil moisture display less widespread drying than those for surface soil moisture (Berg et al., 2017b), but still more than for precipitation (CC-Box 11.1, Figures 2a,b,c). The severity of droughts based on surface soil moisture in future projections is stronger than projections based on precipitation and runoff (Dai et al., 2018; Vicente-Serrano et al., 2020a). Nevertheless, in many parts of the world in which soil moisture is projected to decrease, the signal to noise ratio among models is low and only in the Mediterranean, Europe, the southwestern United States, and southern Africa the projections show a

ACCEPTED VERSION SUBJECT TO FINAL EDITING

high signal to noise ratio in soil moisture projections (Lu et al., 2019; (Figure 11.19). Increases in soil moisture deficits are found to be statistically signicant at regional scale in the Mediterranean region, Southern Africa and Western South America for changes as small as 0.5°C in global warming, based on differences between +1.5°C and +2°C of global warming (Wartenburger et al., 2017). Several other regions are affected when considering changes in droughts for higher changes in global warming (Figure 11.19; Section 11.9). Seasonal projections of drought frequency for boreal winter (DJF) and summer (JJA), from CMIP6 multimodel ensemble for 1.5ºC, 2ºC and 4ºC global warming levels, show contrasting trends (Fig 11.19). In the boreal winter in the Northern Hemisphere, the areas affected by drying show high agreement with those characterized by increase in meteorological drought projections (Chapter 8, Figure 8.14; Chapter 12, Figure 12.4). On the contrary, in the boreal summer the drought frequency increases worldwide in comparison to meteorological drought projections, with large areas of the Northern Hemisphere displaying a high signal to noise ratio (low spead between models). This stresses the dominant influence of ET (as a result of increased AED) in intensifying agricultural and ecological droughts in the warm season in many locations, including mid- to high latitudes.

Increased soil moisture limitation and associated changes in droughts are projected to lead to increased vegetation stress affecting the global land carbon sink in ESM projections (Green et al., 2019), with implications for projected global warming (Cross-Chapter Box 5). There is *high confidence* that the global land sink will become less efficient due to soil moisture limitations and associated agricultural and ecological drought conditions in some regions in higher emission scenarios specially under global warming levels above 4°C ; however, there is *low confidence* on how these water cycle feedbacks will play out in lower emission scenarios (at 2°C global warming or lower) (Cross-Chapter Box5.1).

[START FIGURE 11.18 HERE]

Figure 11.18: Projected changes in the intensity (a) and frequency (b) of drought under 1°C, 1.5°C, 2°C, 3°C, and 4°C global warming levels relative to the 1850-1900 baseline. Summaries are computed for the AR6 regions in which there is at least medium confidence in increase in agriculture/ ecological drought at the 2°C warming level ("drying regions"), including W. North-America, C. North-America, N. Central-America, S. Central-America, N. South-America, N. E. South-America, South-American-Monsoon, S.W.South-America, S.South-America, West & Central-Europe, Mediterranean, W.Southern-Africa, E.Southern-Africa, Madagascar, E.Australia, S.Australia (c). A drought event is defined as a 10-year drought event whose annual mean soil moisture was below its 10th percentile from the 1850-1900 base period. For each box plot, the horizontal line and the box represent the median and central 66% uncertainty range, respectively, of the frequency or the intensity changes across the multi-model ensemble, and the whiskers extend to the 90% uncertainty range. The line of zero in (a) indicates no change in intensity, while the line of one in (b) indicates no change in frequency. The results are based on the multi-model ensemble estimated from simulations of global climate models contributing to the sixth phase of the Coupled Model Intercomparison Project (CMIP6) under different SSP forcing scenarios. Intensity changes in (a) are expressed as standard deviations of the interannualvariability in the period 1850-1900 of the corresponding modelFor details on the methods see Supplementary Material 11.SM.2. Further details on data sources and processing are available in the chapter data table (Table 11.SM.9).

[END FIGURE 11.18 HERE]

11.6.5.4 Hydrological deficits

Some studies support wetting tendencies as a response to a warmer climate when considering globally-averaged changes in runoff over land (Roderick et al., 2015; Greve et al., 2017; Yang et al., 2018e), and streamflow projections respond to enhanced CO_2 concentrations in CMIP5 models (Yang et al., 2019). Nevertheless, when focusing regionally on low-runoff periods, model projections also show an increase of hydrological droughts in large world regions (Wanders and Van Lanen, 2015; Dai et al., 2018; Vicente-Serrano et al., 2020a). In general, the frequency of hydrological deficits is projected to increase over most of the continents, although with regionally and seasonally differentiated effects (Section 11.9), with *medium confidence* of increase in the following AR6 regions:WCE, MED, SAU, WCA, WNA, SCA, NSA, SAM,

ACCEPTED VERSION SUBJECT TO FINAL EDITING

SWS, SSA, WSAF, ESAF and MDG (Section 11.9; Cook et al., 2019; Forzieri et al., 2014; Giuntoli et al., 2015; Marx et al., 2018; Prudhomme et al., 2014; Roudier et al., 2016; Wanders and Van Lanen, 2015; Zhao et al., 2020). There are, however, large uncertainties related to the hydrological/impact model used (Prudhomme et al., 2014; Schewe et al., 2014; Gosling et al., 2017), limited signal-to-noise ratio (due to model spread) in several regions (Giuntoli et al., 2015), and also uncertainties in the projection of future human activities including water demand and land cover changes, which may represent more than 50% of the projected changes in hydrological droughts in some regions (Wanders and Wada, 2015).

Regions dependent on mountainous snowpack as a temporary reservoir may be affected by severe hydrological droughts in a warmer world. In the southern European Alps, both winter and summer low flows are projected to be more severe, with a 25% decrease in the 2050s (Vidal et al., 2016). In the western United States, a 22% reduction in winter snow water equivalent is projected at around 2°C of global warming with a further decrease of a 70% reduction at 4°C global warming (Rhoades et al., 2018). This decline would cause less predictable hydrological droughts in snowmelt-dominated areas of North America (Livneh and Badger, 2020). The exact magnitude of the influence of higher temperatures on snow-related droughts is, however, difficult to estimate (Mote et al., 2016), since the streamflow changes could affect the timing of peak streamflows but not necessarily their magnitude. In addition, projected changes in hydrological droughts downstream of declining glaciers can be very complex to assess (Chapter 9, see also SROCC).

11.6.5.5 Atmospheric-based drought indices

Studies show a stronger drying in projections based on atmospheric-based drought indices compared to ESM projections of changes in soil moisture (Berg and Sheffield, 2018) and runoff (Yang et al., 2019). It has been suggested that this difference is due to physiological CO_2 effects (Greve et al., 2019; Lemordant et al., 2018; Milly and Dunne, 2016; Roderick et al., 2015; Scheff, 2018; Swann, 2018; Swann et al., 2016; Yang et al., 2020; Section 11.6.5.2). Nonetheless, there is evidence that differences in projections between atmospheric-based drought indices and water-balance metrics from ESMs are not alone due to CO_2-plant effects (Berg et al., 2016; Scheff et al., 2021), and can be also related to the fact that AED is an upper bound for ET in dry regions and conditions (Section 11.6.1.2) and that soil moisture stress limits increases in ET in projections (Berg et al., 2016; Zhou et al., 2021; Section 11.6.5.2). Atmospheric-based indices show in general more drying than total column soil moisture (Berg and Sheffield, 2018; Cook et al., 2020; Scheff et al., 2021), but are more consistent with projected increases in surface soil moisture deficits (Dirmeyer et al., 2013; Dai et al., 2018; Lu et al., 2019; Cook et al., 2020; Vicente-Serrano et al., 2020a).

Atmospheric-based drought indices are not metrics of soil moisture or runoff (11.6.1.5) so their projections may not necessarily reflect the same trend of online simulated soil moisture and runoff. Independently of effects on the land water balance, atmospheric-based drought indices will reflect the potential vegetation stress resulting from deficits between available water and enhanced AED, even in conditions with no or only low ET. Under dry conditions, the enhanced AED associated to the human forcing would increase plant water stress (Brodribb et al., 2020), with effects on widespread forest dieback and mortality (Anderegg et al., 2013; Williams et al., 2013; Allen et al., 2015; McDowell and Allen, 2015; McDowell et al., 2016, 2020), and stronger risk of megafires (Flannigan et al., 2016; Podschwit et al., 2018; Clarke and Evans, 2019; Varela et al., 2019). For these reasons, there is *high confidence* that the future projections of enhanced drought severity showed by the PDSI-PM and the SPEI-PM are representative of more frequent and severe plant stress episodes and more severe agricultural and ecological drought impacts in some regions.

Global tendencies towards more severe and frequent agricultural and ecological drought conditions are identified in future projections when focusing on atmospheric-based drought indices such as the PDSI-PM or the SPEI-PM. They expand the spatial extent of drought conditions compared to meteorological drought to most of North America, Europe, Africa, Central and East Asia and southern Australia (Cook et al., 2014a; Chen and Sun, 2017b, 2017a; Zhao and Dai, 2017; Gao et al., 2017b; Lehner et al., 2017; Dai et al., 2018; Naumann et al., 2018; Potopová et al., 2018; Vicente-Serrano et al., 2020a; Gu et al., 2020; Dai, 2021). Projections in PDSI-PM and SPEI-PM are used in complement to changes in total soil moisture for the assessed projected changes in agricultural and ecological drought (Section 11.9).

ACCEPTED VERSION SUBJECT TO FINAL EDITING

11.6.5.6 Synthesis for different drought types

The tables in Section 11.9 provide assessed projected changes in metorological drought, agricultural and ecological drought, and hydrological droughts. The assessment shows that several regions will be affected by more severe agricultural and ecological droughts even if global warming is stabilized at well below 2°C, and 1.5°C, within the bounds of the Paris Agreement (*high confidence*). The most affected regions include WCE, MED, EAU, SAU, SCA, NSA, SAM, SWS, SSA, NCA, CAN, WSAF, ESAF and MDG (*medium confidence*). At 4°C of global warming, even more regions would be affected by agricultural and ecological droughts (WCE, MED, CAU, EAU, SAU, WCA, EAS, SCA, CAR, NSA, NES, SAM, SWS, SSA, NCA, CAN, ENA, WNA, WSAF, ESAF and MDG). NEAF, SAS are also projected to experience less agricultural and ecological drought with global warming (*medium confidence*). Projected changes in meteorological droughts are overall less extended but also affect several AR6 regions, at 1.5°C and 2°C (MED, EAU, SAU, SCA, NSA, NCA, WSAF, ESAF, MDG) and 4ºC of global warming (WCE, MED, EAU, SAU, SEA, SCA, CAR, NWS, NSA, NES, SAM, SWS, SSA, NCA, ENA, WAF, WSAF, ESAF, MDG). Several regions are also projected to be affected by more hydrological droughts at 1.5°C and 2°C (WCE, MED, WNA, WSAF, ESAF) and 4ºC of global warming (NEU, WCE, EEU, MED, SAU, WCA, SCA, NSA, SAM, SWS, SSA, WNA, WSAF, ESAF, MDG). To illustrate the changes in both intensity and frequency of drought in the regions where strongest changes are projected, Figure 11.18 displays changes in the intensity and frequency of soil moisture drought under different global warming levels (1.5°C, 2°C, 4°C) relative to the 1851-1900 baseline based on CMIP6 simulations under different SSP forcing scenarios. The 90% uncertainty ranges for the projected changes in both intensity and frequency are above zero, indicating significant increase in both intensity and frequency of drought in these regions as whole.

In summary, the land area affected by increasing drought frequency and severity expands with increasing global warming (*high confidence*). New evidence strengthens the SR15 conclusion that even relatively small incremental increases in global warming (+0.5°C) cause a worsening of droughts in some regions (*high confidence).* Several regions will be affected by more frequent and severe agricultural and ecological droughts even if global warming is stabilized at 1.5-2°C (*high confidence*). The most affected regions include WCE, MED, EAU, SAU, SCA, NSA, SAM, SWS, SSA, NCA, CAN, WSAF, ESAF and MDG (*medium confidence*). At 4°C of global warming, even more regions would be affected by agricultural and ecological droughts (WCE, MED, CAU, EAU, SAU, WCA, EAS, SCA, CAR, NSA, NES, SAM, SWS, SSA, NCA, CAN, ENA, WNA, WSAF, ESAF and MDG). Some regions are also projected to experience less agricultural and ecological drought with global warming (*medium confidence;* (NEAF, SAS)). There is *high confidence* that the projected increases in agricultural and ecological droughts are strongly affected by AED increases in a warming climate, although ET increases are projected to be smaller than those in AED due to soil moisture limitations and CO_2 effects on leaf stomatal conductance. Enhanced atmospheric CO_2 concentrations lead to enhanced water-use efficiency in plants (*medium confidence*), but there is *low confidence* that it can ameliorate agricultural and ecological droughts, or hydrological droughts, at higher global warming levels characterized by limited soil moisture and enhanced AED.

Projected changes in meteorological droughts are overall less extended than for agricultural and ecological droughts, but also affect several AR6 regions, even at 1.5°C and 2°C of global warming. Several regions are also projected to be more strongly affected by hydrological droughts with increasing global warming (NEU, WCE, EEU, MED, SAU, WCA, SCA, NSA, SAM, SWS, SSA, WNA, WSAF, ESAF, MDG). Increased soil moisture limitation and associated changes in droughts are projected to lead to increased vegetation stress in many regions, with implications for the global land carbon sink (CC-Box 5). There is *high confidence* that the global land sink will become less efficient due to soil moisture limitations and associated drought conditions in some regions in higher emission scenarios specially under global warming levels above 4°C ; however, there is *low confidence* on how these water cycle feedbacks will play out in lower emission scenarios (at 2°C global warming or lower) (Cross-Chapter Box5.1).

[START FIGURE 11.19 HERE]

ACCEPTED VERSION SUBJECT TO FINAL EDITING

Figure 11.19: Projected changes in (a-c) the number of consecutive dry days (CDD), (d-f) annual mean soil moisture over the total column, and (g-l) the frequency and intensity of one-in-ten year soil moisture drought for the June-to-August and December-to-February seasons at 1.5°C, 2°C, and 4°C of global warming compared to the 1851-1900 baseline. Results are based on simulations from the CMIP6 multi-model ensemble under the SSP1-1.9, SSP1-2.6, SSP2-4.5, SSP3-7.0, and SSP5-8.5 scenarios. The numbers in the top right indicate the number of simulations included. Uncertainty is represented using the simple approach: no overlay indicates regions with high model agreement, where ≥80% of models agree on sign of change; diagonal lines indicate regions with low model agreement, where <80% of models agree on sign of change. For more information on the simple approach, please refer to the Cross-Chapter Box Atlas 1. For details on the methods see Supplementary Material 11.SM.2. Further details on data sources and processing are available in the chapter data table (Table 11.SM.9).

[END FIGURE 11.19 HERE]

11.7 Extreme storms

Extreme storms, such as tropical cyclones (TCs), extratropical cyclones (ETCs), and severe convective storms often have substantial societal impacts. Quantifying the effect of climate change on extreme storms is challenging, partly because extreme storms are rare, short-lived, and local, and individual events are largely influenced by stochastic variability. The high degree of random variability makes detection and attribution of extreme storm trends more uncertain than detection and attribution of trends in other aspects of the environment in which the storms evolve (e.g., larger-scale temperature trends). Projecting changes in extreme storms is also challenging because of constraints in the models' ability to accurately represent the small-scale physical processes that can drive these changes. Despite the challenges, progress has been made since AR5.

SREX (Chapter 3) concluded that there is *low confidence* in observed long-term (40 years or more) trends in TC intensity, frequency, and duration, and any observed trends in phenomena such as tornadoes and hail; it is *likely* that extratropical storm tracks have shifted poleward in both the Northern and Southern Hemispheres and that heavy rainfalls and mean maximum wind speeds associated with TCs will increase with continued greenhouse gas (GHG) warming; it is *likely* that the global frequency of TCs will either decrease or remain essentially unchanged, while it is *more likely than not* that the frequency of the most intense storms will increase substantially in some ocean basins; there is *low confidence* in projections of small-scale phenomena such as tornadoes and hail storms; and there is *medium confidence* that there will be a reduced frequency and a poleward shift of mid-latitude cyclones due to future anthropogenic climate change.

Since SREX, several IPCC assessments also assessed storms. AR5 (Chapter 2, Hartmann et al., 2013) assessment with *low confidence* observed long-term trends in TC metrics, but revised the statement from SREX to state that it is *virtually certain* that there are increasing trends in North Atlantic TC activity since the 1970s, with *medium confidence* that anthropogenic aerosol forcing has contributed to these trends. AR5 concluded that it is *likely* that TC precipitation and mean intensity will increase and *more likely than not* that the frequency of the strongest storms increases with continued GHG warming. *Confidence* in projected trends in overall TC frequency remained *low*. *Confidence* in observed and projected trends in hail storm and tornado events also remained *low*. SROCC (Chapter 6, Collins et al., 2019) assessed past and projected TCs and ETCs supporting the conclusions of AR5 with some additional detail. Literature subsequent to AR5 adds support to the likelihood of increasing trends in TC intensity, precipitation, and frequency of the most intense storms, while some newer studies have added uncertainty to projected trends in overall frequency. A growing body literature since AR5 on the poleward migration of TCs led to a new assessment in SROCC of *low confidence* that the migration in the western North Pacific represents a detectable climate change contribution from anthropogenic forcing. SR15 (Chapter 3, Hoegh-Guldberg et al., 2018) essentially confirmed the AR5 assessment of TCs and ETCs, adding that heavy precipitation associated with TCs is projected to be higher at 2°C compared to 1.5°C global warming (*medium confidence*).

ACCEPTED VERSION SUBJECT TO FINAL EDITING

SREX, AR5, SROCC, and SR15, do not provide assessments of the atmospheric rivers and SROCC and SR15 do not assess severe convective storms and extreme winds. This section assesses the state of knowledge on the four phenomena of TCs, ETCs, severe convective storms, and extreme winds. Atmospheric rivers are addressed in Chapter 8. In this respect, this assessment closely mirrors the SROCC assessment of TCs and ETCs, while updating SREX and AR5 assessments of severe convective storms and extreme winds.

11.7.1 Tropical cyclones

11.7.1.1 Mechanisms and drivers

The genesis, development, and tracks of TCs depend on conditions of the larger-scale circulations of the atmosphere and ocean (Christensen et al., 2013). Large-scale atmospheric circulations (Annex VI), such as the Hadley and Walker circulations and the monsoon circulations, and internal variability acting on various time-scales, from intra-seasonal (e.g., the Madden-Julian and Boreal Summer Intraseasonal oscillations (MJO, BSISO), and equatorial waves) and inter-annual (e.g., the El Niño-Southern Oscillation (ENSO) and Pacific and Atlantic Meridional Modes (PMM, AMM)), to inter-decadal (e.g., Atlantic Multidecadal Variability and Pacific Decadal Variability (PDV)) can all significantly affect TCs. This broad range of natural variability makes detection of anthropogenic effects difficult, and uncertainties in the projected changes of these modes of variability increase uncertainty in the projected changes in TC activity. Aerosol forcing also affects SST patterns and cloud microphysics, and it is *likely* that observed changes in TC activity are partly caused by changes in aerosol forcing (Evan et al., 2011; Ting et al., 2015; Sobel et al., 2016, 2019; Takahashi et al., 2017; Zhao et al., 2018; Reed et al., 2019). Among possible changes from these drivers, there is *medium confidence* that the Hadley cell has widened and will continue to widen in the future (Chapter 2.3, 3.3, 4.5). This *likely* causes latitudinal shifts of TC tracks (Sharmila and Walsh, 2018). Regional TC activity changes are also strongly affected by projected changes in SST warming patterns (Yoshida et al., 2017), which are highly uncertain (Chapter 4, 9).

11.7.1.2 Observed trends

Identifying past trends in TC metrics remains a challenge due to the heterogeneous character of the historical instrumental data, which are known as "best-track" data (Schreck et al., 2014). There is *low confidence* in most reported long-term (multidecadal to centennial) trends in TC frequency- or intensity-based metrics due to changes in the technology used to collect the best-track data. This should not be interpreted as implying that no physical (real) trends exist, but rather as indicating that either the quality or the temporal length of the data is not adequate to provide robust trend detection statements, particularly in the presence of multidecadal variability.

There are previous and ongoing efforts to homogenize the best-track data (Elsner et al., 2008; Kossin et al., 2013, 2020; Choy et al., 2015; Landsea, 2015; Emanuel et al., 2018) and there is substantial literature that finds positive trends in intensity-related metrics in the best-track during the "satellite period", which is generally limited to the past ~40 years (Kang and Elsner, 2012; Kishtawal et al., 2012; Kossin et al., 2013, 2020; Mei and Xie, 2016; Zhao et al., 2018; Tauvale and Tsuboki, 2019). When best-track trends are tested using homogenized data, the intensity trends generally remain positive, but are smaller in amplitude (Kossin et al., 2013; Holland and Bruyère, 2014). Kossin et al. (2020) extended the homogenized TC intensity record to the period 1979–2017 and identified significant global increases in major TC exceedance probability of about 6% per decade. In addition to trends in TC intensity, there is evidence that TC intensification rates and the frequency of rapid intensification events have increased within the satellite era (Kishtawal et al. 2012; Balaguru et al., 2018; Bhatia et al., 2018). The increase in intensification rates is found in the best-track as well as the homogenized intensity data.

A subset of the best-track data corresponding to hurricanes that have directly impacted the United States

ACCEPTED VERSION SUBJECT TO FINAL EDITING

since 1900 is considered to be reliable, and shows no trend in the frequency of U.S. landfall events (Knutson et al., 2019). However, in this period since 1900, an increasing trend in normalized U.S. hurricane damage, which accounts for temporal changes in exposed wealth (Grinsted et al., 2019), and a decreasing trend in TC translation speed over the U.S. (Kossin, 2019) have been identified. A similarly reliable subset of the data representing TC landfall frequency over Australia shows a decreasing trend in eastern Australia since the 1800s (Callaghan and Power, 2011), as well as in other parts of Australia since 1982 (Chand et al., 2019; Knutson et al., 2019), and a paleoclimate proxy reconstruction shows that recent levels of TC interactions along parts of the Australian coastline are the lowest in the past 550–1,500 years (Haig et al., 2014). Existing TC datasets show substantial interdecadal variations in basin-wide TC frequency and intensity in the western North Pacific, but a statistically significant northwestward shift in the western North Pacific TC tracks since the 1980s (Lee et al., 2020b). In the case of the North Indian Ocean, analyses of trends are highly dependent on the details of each analysis (e.g., pre- and/or post-monsoon season period, or Bay of Bengal and/or Arabian Sea region). The most consistent trends are an increase in the occurrence of the most intense TCs and a decrease in the overall TC frequency, in particular in the Bay of Bengal (Sahoo and Bhaskaran, 2016; Balaji et al., 2018; Singh et al., 2019; Baburaj et al., 2020). In the South Indian Ocean (SIO), an increase in the occurrence of the most intense TCs has been noted, however there are well-known data quality issues there (Kuleshov et al., 2010; Fitchett, 2018). When the SIO data are homogenized, a significant increase is found in the fractional proportion of global category 3-5 TC estimates to all category 1-5 estimates (Kossin et al., 2020).

As with all confined regional analyses of TC frequency, it is generally unclear whether any identified changes are due to a basin-wide change in TC frequency, or to systematic track shifts (or both). From an impacts perspective, however, these changes over land are highly relevant and emphasize that large-scale modifications in TC behaviour can have a broad spectrum of impacts on a regional scale.

Subsequent to AR5, two metrics that are argued to be comparatively less sensitive to data issues than frequency- and intensity-based metrics have been analysed. Trends in these metrics have been identified over the past ~70 years or more (Knutson et al., 2019). The first metric, the mean latitude where TCs reach their peak intensity, exhibits a global and regional poleward migration during the satellite period (Kossin et al., 2014). The poleward migration can influence TC hazard exposure and risk (Kossin et al., 2016a) and is consistent with the independently-observed expansion of the tropics (Lucas et al., 2014). The migration has been linked to changes in the Hadley circulation (Altman et al., 2018; Sharmila and Walsh, 2018; Studholme and Gulev, 2018). The migration is also apparent in the mean locations where TCs exhibit eyes (Knapp et al., 2018), which is when TCs are most intense. Part of the Northern Hemisphere poleward migration is due to inter-basin changes in TC frequency (Kossin et al., 2014, 2016b, Moon et al., 2015, 2016) and the trends, as expected, can be sensitive to the time period chosen (Tennille and Ellis, 2017; Kossin, 2018; Song and Klotzbach, 2018) and to subsetting of the data by intensity (Zhan and Wang, 2017). The poleward migration is particularly pronounced and well-documented in the western North Pacific basin (Kossin et al., 2016a; Oey and Chou, 2016; Liang et al., 2017; Nakamura et al., 2017; Altman et al., 2018; Daloz and Camargo, 2018; Sun et al., 2019b; Lee et al., 2020b; Yamaguchi and Maeda, 2020a; Kubota et al., 2021).

[START FIGURE 11.20 HERE]

Figure 11.20: Summary schematic of past and projected changes in tropical cyclone (TC), extratropical cyclone (ETC), atmospheric river (AR), and severe convective storm (SCS) behaviour. Global changes (blue shading) from top to bottom: 1) Increased mean and maximum rain-rates in TCs, ETCs, and ARs [past (*low confidence* due to lack of reliable data) & projected (*high confidence*)]. 2) Increased proportion of stronger TCs [past (*medium confidence*) & projected (*high confidence*)]. 3) Decrease or no change in global frequency of TC genesis [past (*low confidence* due to lack of reliable data) & projected (*medium confidence*)]. 4) Increased and decreased ETC wind-speed, depending on the region, as storm-tracks change [past (*low confidence* due to lack of reliable data) & projected (*medium confidence*)]. Regional changes, from left to right: 1) Poleward TC migration in the western North Pacific and subsequent changes in TC exposure [past (*medium confidence*) & projected (*medium confidence*)]. 2) Slowdown of TC forward translation speed over the contiguous US and subsequent increase in TC rainfall [past (*medium confidence*) & projected (*low confidence* due to lack of directed studies)]. 3) Increase in mean

ACCEPTED VERSION SUBJECT TO FINAL EDITING

and maximum SCS rain-rate and increase in springtime SCS frequency and season length over the contiguous US [past (*low confidence* due to lack of reliable data) & projected (*medium confidence*)].

[END FIGURE 11.20 HERE]

A second metric that is argued to be comparatively less sensitive to data issues than frequency- and intensity-based metrics is TC translation speed (Kossin, 2018), which exhibits a global slowdown in the best-track data over the period 1949-2016. TC translation speed is a measure of the speed at which TCs move across the Earth's surface and is very closely related to local rainfall amounts (i.e., a slower translation speed causes greater local rainfall). TC translation speed also affects structural wind damage and coastal storm surge by changing the hazard event duration. The slowdown is observed in the best-track data from all basins except the Northern Indian Ocean and is also found in a number of regions where TCs interact directly with land. The slowing trends identified in the best-track data by Kossin (2018) have been argued to be largely due to data heterogeneity. Moon et al. (2019) and Lanzante (2019) provide evidence that meridional TC track shifts project onto the slowing trends and argue that these shifts are due to the introduction of satellite data. Kossin (2019) provides evidence that the slowing trend is real by focusing on Atlantic TC track data over the contiguous United States in the 118-year period 1900–2017, which are generally considered reliable. In this period, mean TC translation speed has decreased by 17%. The slowing TC translation speed is expected to increase local rainfall amounts, which would increase coastal and inland flooding. In combination with slowing translation speed, abrupt TC track direction changes – that can be associated with track "meanders" or "stalls" – have become increasingly common along the North American coast since the mid-20th century, leading to more rainfall in the region (Hall and Kossin, 2019).

In summary, there is mounting evidence that a variety of TC characteristics have changed over various time periods. It is *likely* that the proportion of major TC intensities and the frequency of rapid intensification events have both increased globally over the past 40 years. It is *very likely* that the average location where TCs reach their peak wind-intensity has migrated poleward in the western North Pacific Ocean since the 1940s. It is *likely* that TC translation speed has slowed over the U.S. since 1900.

11.7.1.3 Model evaluation

Accurate projections of future TC activity have two principal requirements: accurate representation of changes in the relevant environmental factors (e.g., SSTs) that can affect TC activity, and accurate representation of actual TC activity in given environmental conditions. In particular, models' capacity to reproduce historical trends or interannual variabilities of TC activity is relevant to the confidence in future projections. One test of the models is to evaluate their ability to reproduce the dependency of the TC statistics in the different basins in the real world, in addition to their capability of reproducing atmospheric and ocean environmental conditions. For the evaluation of projections of TC-relevant environmental variables, AR5 confidence statements were based on global surface temperature and moisture, but not on the detailed regional structure of SST and atmospheric circulation changes such as steering flows and vertical shear, which affect characteristics of TCs (genesis, intensity, tracks, etc.). Various aspects of TC metrics are used to evaluate how capable models are of simulating present-day TC climatologies and variability (e.g. TC frequency, wind-intensity, precipitation, size, tracks, and their seasonal and interannual changes) (Camargo and Wing, 2016; Knutson et al., 2019, 2020; Walsh et al., 2015). Other examples of TC climatology/variability metrics are spatial distributions of TC occurrence and genesis (Walsh et al., 2015), seasonal cycles and interannual variability of basin-wide activity (Zhao et al., 2009; Shaevitz et al., 2014; Kodama et al., 2015; Murakami et al., 2015; Yamada et al., 2017) or landfalling activity (Lok and Chan, 2018), as well as newly developed process-diagnostics designed specifically for TCs in climate models (Kim et al., 2018a; Wing et al., 2019; Moon et al., 2020).

Confidence in the projection of intense TCs, such as those of Category 4-5, generally becomes higher as the resolution of the models becomes higher. CMIP5/6 class climate models (~100-200 km grid spacing) cannot simulate TCs of Category 4-5 intensity. They do simulate storms of relatively high vorticity that are at best

ACCEPTED VERSION SUBJECT TO FINAL EDITING

described as "TC-like", but metrics like storm counts are highly dependent on tracking algorithms (Wehner et al., 2015; Zarzycki and Ullrich, 2017; Roberts et al., 2020a). High-resolution global climate models (~10-60 km grid spacing) as used in HighResMIP (Haarsma et al., 2016; Roberts et al., 2020a) begin to capture some structures of TCs more realistically, as well as produce intense TCs of Category 4-5 despite the effects of parameterized deep cumulus convection processes (Murakami et al., 2015; Wehner et al., 2015; Yamada et al., 2017; Roberts et al., 2018; Moon et al., 2020). Convection-permitting models (~1-10 km grid-spacing), such as used in some dynamical downscaling studies, provide further realism with capturing eye wall structures (Tsuboki et al., 2015). Model characteristics besides resolution, especially details of convective parameterization, can influence a model's ability to simulate intense TCs (Reed and Jablonowski, 2011; Zhao et al., 2012; He and Posselt, 2015; Kim et al., 2018a; Zhang and Wang, 2018; Camargo et al., 2020). However, models' dynamical cores and other physics also affect simulated TC properties (Reed et al., 2015; Vidale et al., 2021). Both wide-area regional and global convection-permitting models without the need for parameterized convection are becoming more useful for TC regional model projection studies (Tsuboki et al., 2015; Kanada et al., 2017a; Gutmann et al., 2018) and global model projection studies (Satoh et al., 2015, 2017; Yamada et al., 2017), as they capture more realistic eye-wall structures of TCs (Kinter et al., 2013) and are becoming more useful for investigating changes in TC structures (Kanada et al., 2013; Yamada et al., 2017). Large ensemble simulations of global climate models with 60 km grid spacing provide TC statistics that allow more reliable detection of changes in the projections, which are not well captured in any single experiment (Yoshida et al., 2017; Yamaguchi et al., 2020). Variable resolution global models offer an alternative to regional models for individual TC or basin-wide simulations (Yanase et al., 2012; Zarzycki et al., 2014; Harris et al., 2016; Reed et al., 2020; Stansfield et al., 2020). Computationally less intense than equivalent uniform resolution global models, they also do not require lateral boundary conditions, thus reducing this source of error (Hashimoto et al., 2016). Confidence in the projection of TC statistics and properties is increased by the higher-resolution models with more realistic simulations.

Operational forecasting models also reproduce TCs and their use for climate projection studies shows promise. However, there is limited application for future projections as they are specifically developed for operational purposes and TC climatology is not necessarily well evaluated. Intercomparison of operational models indicates that enhancement of horizontal resolution can provide more credible projections of TCs (Nakano et al., 2017). Likewise, high-resolution climate models show promise as TC forecast tools (Zarzycki and Jablonowski, 2015; Reed et al., 2020), further narrowing the continuum of weather and climate models and increasing confidence in projections of future TC behaviour. However, higher horizontal resolution does not necessarily lead to an improved TC climatology (Camargo et al., 2020).

Atmosphere-ocean interaction is an important process in TC evolution. Atmosphere-ocean coupled models are generally better than atmosphere-only models at capturing realistic processes related to TCs (Murakami et al., 2015; Ogata et al., 2015, 2016; Zarzycki, 2016; Kanada et al., 2017b; Scoccimarro et al., 2017), although the basin-scale SST biases commonly found in atmosphere-ocean models can introduce substantial errors in the simulated TC number (Hsu et al., 2019). Higher-resolution ocean models improve the simulation of TCs by reducing the SST climatology bias (Li and Sriver, 2018; Roberts et al., 2020a). Coarse resolution atmospheric models may degrade coupled model performance as well. For example, in a case study of Hurricane Harvey, Trenberth et al. (2018) suggested that the lack of realistic hurricane activity within coupled climate models hampers the models' ability to simulate SST and ocean heat content and their changes.

Even with higher-resolution atmosphere-ocean coupled models, TC projection studies still rely on assumptions in experimental design that introduce uncertainties. Computational constraints often limit the number of simulations, resulting in relatively small ensemble sizes and incomplete analyses of possible future SST magnitude and pattern changes (Zhao and Held, 2011; Knutson et al., 2013a). Uncertainties in aerosol forcing also are reflected in TC projection uncertainty (Wang et al., 2014).

Regional climate models (RCM) with grid spacing around 15-50 km can be used to study the projection of TCs. RCMs are run with lateral and surface boundary conditions, which are specified by the atmospheric state and SSTs simulated by GCMs. Various combinations of the lateral and surface boundary conditions can be chosen for RCM studies, and uncertainties in the projection can be further examined in general. They are

ACCEPTED VERSION SUBJECT TO FINAL EDITING

used for studying changes in TC characteristics in a specific area, such as Vietnam (Redmond et al., 2015) and the Philippines (Gallo et al., 2019).

Less computationally-expensive downscaling approaches that allow larger ensembles and long-term studies are also used in the projection of TCs (Emanuel et al., 2006; Lee et al., 2018a). A statistical–dynamical TC downscaling method requires assumptions of the rate of seeding of random initial disturbances, which are generally assumed to not change with climate change (Emanuel et al., 2008; Emanuel, 2013). The results with the downscaling approach might depend on the assumptions which are required for the simplification of the methods.

In summary, various types of models are useful to study climate changes of TCs, and there is no unique solution for choosing a model type. However, higher-resolution models generally capture TC properties more realistically (*high confidence*). In particular, models with horizontal resolutions of 10-60 km are capable of reproducing strong TCs with Category 4-5 and those of 1-10km are capable of the eyewall structure of TCs. Uncertainties in TC simulations come from details of the model configuration of both dynamical and physical processes. Models with realistic atmosphere-ocean interactions are generally better than atmosphere-only models at reproducing realistic TC evolutions (*high confidence*).

11.7.1.4 Detection and attribution, event attribution

There is general agreement in the literature that anthropogenic greenhouse gases and aerosols have measurably affected observed oceanic and atmospheric variability in TC-prone regions (see Chapter 3). This underpinned the SROCC assessment of *medium confidence* that humans have contributed to the observed increase in Atlantic hurricane activity since the 1970s (Chapter 5, Bindoff et al., 2013). Literature subsequent to the AR5 lends further support to this statement (Knutson et al., 2019). However, there is still no consensus on the relative magnitude of human and natural influences on past changes in Atlantic hurricane activity, and particularly on which factor has dominated the observed increase (Ting et al., 2015) and it remains uncertain whether past changes in Atlantic TC activity are outside the range of natural variability. A recent result using high-resolution dynamical model experiments suggested that the observed spatial contrast in TC trends cannot be explained only by multi-decadal natural variability, and that external forcing plays an important role (Murakami et al., 2020). Observational evidence for significant global increases in the proportion of major TC intensities (Kossin et al., 2020) is consistent with both theory and numerical modeling simulations, which generally indicate an increase in mean TC peak intensity and the proportion of very intense TCs in a warming world (Knutson et al., 2015, 2020, Walsh et al., 2015, 2016). In addition, high-resolution coupled model simulations provide support that natural variability alone is *unlikely* to explain the magnitude of the observed increase in TC intensification rates and upward TC intensity trend in the Atlantic basin since the early 1980s (Bhatia et al., 2019; Murakami et al. 2020).

The cause of the observed slowdown in TC translation speed is not yet clear. Yamaguchi et al. (2020) used large ensemble simulations to argue that part of the slowdown is due to actual latitudinal shifts of TC tracks, rather than data artefacts, in addition to atmospheric circulation changes, while Zhang et al. (2020a) used large ensemble simulations to show that anthropogenic forcing can lead to a robust slowdown, particularly outside of the tropics at higher latitudes. Yamaguchi and Maeda (2020b) found a significant slowdown in the western North Pacific over the past 40 years and attributed the slowdown to a combination of natural variability and global warming. The slowing trend since 1900 over the U.S. is robust and significant after removing multidecadal variability from the time series (Kossin, 2019). Among the hypotheses discussed is the physical linkage between warming and slowing circulation (Held and Soden 2006, see also Section 8.2.2.2), with expectations of Arctic amplification and weakening circulation patterns through weakening meridional temperature gradients (Coumou et al., 2018; see also Cross-Chapter Box 10.1), or through changes in planetary wave dynamics (Mann et al., 2017). The tropics expansion and the poleward shift of the mid-latitude westerlies associated with warming is also suggested for the reason of the slowdown (Zhang et al., 2020a). However, the connection of these mechanisms to the slowdown has not been robustly shown yet. Furthermore, slowing trends have not been unambiguously observed in circulation patterns that steer TCs such as the Walker and Hadley circulations (Section 2.3.1.4), although these circulations generally slow

ACCEPTED VERSION SUBJECT TO FINAL EDITING

down in numerical simulations under global warming (Sections 4.5.1.6 and 8.4.2.2).

The observed poleward trend in western North Pacific TCs remains significant after accounting for the known modes of dominant interannual to decadal variability in the region (Kossin et al., 2016a), and is also found in CMIP5 model-simulated TCs (in the recent historical period 1980–2005), although it is weaker than observed and is not statistically significant (Kossin et al., 2016a). However, the trend is significant in 21st century CMIP5 projections under the RCP8.5 scenario, with a similar spatial pattern and magnitude to the past observed changes in that basin over the period 1945–2016, supporting a possible anthropogenic GHG contribution to the observed trends (Knutson et al., 2019; Kossin et al., 2016a).

The recent active TC seasons in some basins have been studied to determine whether there is anthropogenic influence. For 2015, Murakami et al. (2017) explored the unusually high TC frequency near Hawaii and in the eastern Pacific basin. Zhang et al. (2016) considered unusually high Accumulated Cyclone Energy (ACE) in the western North Pacific. Yang et al. (2018) and Yamada et al. (2019) looked at TC intensification in the western North Pacific. These studies suggest that the anomalous TC activity in 2015 was not solely explained by the effect of an extreme El Niño (see BOX 11.3), that there was also an anthropogenic contribution, mainly through the effects of SSTs in subtropical regions. In the post-monsoon seasons of 2014 and 2015, tropical storms with lifetime maximum winds greater than 46 m s^{-1} were first observed over the Arabian Sea, and Murakami et al. (2017b) showed that the probability of late-season severe tropical storms is increased by anthropogenic forcing compared to the preindustrial era. Murakami et al. (2018) concluded that the active 2017 Atlantic hurricane season was mainly caused by pronounced SSTs in the tropical North Atlantic and that these types of seasonal events will intensify with projected anthropogenic forcing. The trans-basin SST change, which might be driven by anthropogenic aerosol forcing, also affects TC activity. Takahashi et al. (2017) suggested that a decrease in sulfate aerosol emissions caused about half of the observed decreasing trends in TC genesis frequency in the south-eastern region of the western North Pacific during 1992–2011.

Event attribution is used in case studies of TCs to test whether the severities of recent intense TCs are explained without anthropogenic effects. In a case study of Hurricane Sandy (2012), Lackmann (2015) found no statistically significant impact of anthropogenic climate change on storm intensity, while projections in a warmer world showed significant strengthening. On the other hand, Magnusson et al. (2014) found that in ECMWF simulations, the simulated cyclone depth and intensity, as well as precipitation, were larger when the model was driven by the warmer actual SSTs than the climatological average SSTs. In super typhoon Haiyan, which struck the Philippines on 8 November 2013, Takayabu et al. (2015) took an event attribution approach with cloud system-resolving (~1km) downscaling ensemble experiments to evaluate the anthropogenic effect on typhoons, and showed that the intensity of the simulated worst case storm in the actual conditions was stronger than that in a hypothetical condition without historical anthropogenic forcing in the model. However, in a similar approach with two coarser parameterized convection models, Wehner et al. (2018) found conflicting human influences on Haiyan's intensity. Patricola and Wehner (2018) found little evidence of an attributable change in intensity of hurricanes Katrina (2005), Irma (2017), and Maria (2017) using a regional climate model configured between 3 and 4.5 km resolution. They did, however, find attributable increases in heavy precipitation totals. These results imply that higher resolution, such as in a convective permitting 5-km or less mesh model, is required to obtain a robust anthropogenic intensification of a strong TC by simulating realistic rapid intensification of a TC (Kanada and Wada, 2016; Kanada et al., 2017a), and that whether the intensification of TCs can be attributed to the recent warming depends on the case.

The dominant factor in the extreme rainfall amounts during Hurricane Harvey's passage onto the U.S. in 2017 was its slow translation speed. But studies published after the event have argued that anthropogenic climate change contributed to an increase in rain rate, which compounded the extreme local rainfall caused by the slow translation. Emanuel (2017) used a large set of synthetically-generated storms and concluded that the occurrence of extreme rainfall as observed in Harvey was substantially enhanced by anthropogenic changes to the larger-scale ocean and atmosphere characteristics. Trenberth et al. (2018) linked Harvey's rainfall totals to the anomalously large ocean heat content from the Gulf of Mexico. van Oldenborgh et al. (2017) and Risser and Wehner (2017) applied extreme value analysis to extreme rainfall records in the

ACCEPTED VERSION SUBJECT TO FINAL EDITING

Houston, Texas region and both attributed large increases to climate change. Large precipitation increases during Harvey due to global warming were also found using climate models (van Oldenborgh et al., 2017; Wang et al., 2018b). Harvey precipitation totals were estimated in these papers to be 3 to 10 times more probable due to climate change. A best estimate from a regional climate and flood model is that urbanization increased the risk of the Harvey flooding by a factor of 21 (Zhang et al., 2018c). Anthropogenic effects on precipitation increases were also predicted in advance from a forecast model for Hurricane Florence in 2018 (Reed et al., 2020).

In summary, it is *very likely* that the recent active TC seasons in the North Atlantic, the North Pacific, and Arabian basins cannot be explained without an anthropogenic influence. The anthropogenic influence on these changes is principally associated to aerosol forcing, with stronger contributions to the response in the North Atlantic. It is *more likely than not* that the slowdown of TC translation speed over the USA has contributions from anthropogenic forcing. It is *likely* that the poleward migration of TCs in the western North Pacific and the global increase in TC intensity rates cannot be explained entirely by natural variability. Event attribution studies of specific strong TCs provide limited evidence for anthropogenic effects on TC intensifications so far, but *high confidence* for increases in TC heavy precipitation. There is *high confidence* that anthropogenic climate change contributed to extreme rainfall amounts during Hurricane Harvey (2017) and other intense TCs.

11.7.1.5 Projections

A summary of studies on TC projections for the late 21st century, particularly studies since AR5, is given by Knutson et al. (2020), which is an assessment report mandated by the World Meteorological Organization (WMO). Studies subsequent to Knutson et al. (2020) are generally consistent and the confidence assessments here closely follow theirs (Cha et al., 2020), although there are some differences due to the different confidence calibrations between the IPCC and WMO reports.

There is not an established theory for the drivers of future changes in the frequency of TCs. Most, but not all, high-resolution global simulations project significant reductions in the total number of TCs, with the bulk of the reduction at the weaker end of the intensity spectrum as the climate warms (Knutson et al., 2020). Recent exceptions based on high-resolution coupled model results are noted in Bhatia et al. (2018) and Vecchi et al. (2019). Vecchi et al. (2019) showed that the representation of synoptic-scale seeds for TC genesis in their high-resolution model causes different projections of global TC frequency, and there is evidence for a decrease in seeds in some projected TC simulations (Sugi et al., 2020). However, other research indicates that TC seeds are not an independent control on climatological TC frequency, rather the seeds covary with the large-scale controls on TCs (Patricola et al., 2018). While empirical genesis indices derived from observations and reanalysis describe well the observed subseasonal and interannual variability of current TC frequency (Camargo et al., 2007, 2009; Tippett et al., 2011; Menkes et al., 2012), they fail to predict the decreased TC frequency found in most high-resolution model simulations (Zhang et al., 2010; Camargo, 2013; Wehner et al., 2015), as they generally project an increase as the climate warms. This suggests a limitation of the use of the empirical genesis indices for projections of TC genesis, in particular due to their sensitivity to the humidity variable considered in the genesis index for these projections (Camargo et al., 2014). In a different approach, a statistical-dynamical downscaling framework assuming a constant seeding rate with warming (Emanuel, 2013, 2021) exhibits increases in TC frequency consistent with genesis indices based projections, while downscaling with a different model leads to two different scenarios depending on the humidity variable considered (Lee et al., 2020a). This disparity in the sign of the projected change in global TC frequency and the difficulty in explaining the mechanisms behind the different signed responses further emphasizes the lack of process understanding of future changes in tropical cyclogenesis (Walsh et al., 2015; Hoogewind et al., 2020). Even within a single model, uncertainty in the pattern of future SST changes leads to large uncertainties (including the sign) in the projected change in TC frequency in individual ocean basins, although global TCs would appear to be less sensitive (Yoshida et al., 2017; Bacmeister et al., 2018).

Changes in SST and atmospheric temperature and moisture play a role in tropical cyclogenesis (Walsh et al., 2015). Reductions in vertical convective mass flux due to increased tropical stability have been associated

ACCEPTED VERSION SUBJECT TO FINAL EDITING

with a reduction in cyclogenesis (Held and Zhao, 2011; Sugi et al., 2012). Satoh et al. (2015) further posits that the robust simulated increase in the number of intense TCs, and hence increased vertical mass flux associated with intense TCs, must lead to a decrease in overall TC frequency because of this association. The Genesis Potential Index can be modified to mimic the TC frequency decreases of a model by altering the treatment of humidity (Camargo et al., 2014), supporting the idea that increased mid-tropospheric saturation deficit (Emanuel et al., 2008) controls TC frequency, but the approach remains empirical. Other possible controlling factors, such as a decline in the number of seeds (held constant in Emanuel's downscaling approach, or dependent on the genesis index formulation in the approach proposed by Lee et al., 2020) caused by increased atmospheric stability have been proposed, but questioned as an important factor (Patricola et al., 2018). The resolution of atmospheric models affects the number of seeds, hence TC genesis frequency (Vecchi et al., 2019; Sugi et al., 2020; Yamada et al., 2021). The diverse and sometimes inconsistent projected changes in global TC frequency by high-resolution models indicate that better process understanding and improvement of the models are needed to raise confidence in these changes.

Most TC-permitting model simulations (10-60 km or finer grid spacing) are consistent in their projection of increases in the proportion of intense TCs (Category 4-5), as well as an increase in the intensity of the strongest TCs defined by maximum wind speed or central pressure fall (Murakami et al., 2012; Tsuboki et al., 2015; Wehner et al., 2018a; Knutson et al., 2020). The general reduction in the total number of TCs, which is concentrated in storms weaker than or equal to Category 1, contributes to this increase. The models are somewhat less consistent in projecting an increase in the frequency of Category 4-5 TCs (Wehner et al., 2018a). The projected increase in the intensity of the strongest TCs is consistent with theoretical understanding (e.g., Emanuel, 1987) and observations (e.g., Kossin et al., 2020). For a 2°C global warming, the median proportion of Category 4–5 TCs increases by 13%, while the median global TC frequency decreases by 14%, which implies that the median of the global Category 4–5 TC frequency is slightly reduced by 1% or almost unchanged (Knutson et al., 2020). Murakami et al. (2020) projected a decrease in TC frequency over the coming century in the North Atlantic due to greenhouse warming, as consistent with Dunstone et al. (2013), and a reduction in TC frequency almost everywhere in the tropics in response to +1% CO_2 forcing; exceptions include the central North Pacific (Hawaii region), east of the Philippines in the North Pacific, and two relatively small regions in the northern Arabian Sea and Bay of Bengal. These projections can vary substantially between ocean basins, possibly due to differences in regional SST warming and warming patterns (Sugi et al., 2017; Yoshida et al., 2017; Bacmeister et al., 2018). A summary of projections of TC characteristics is schematically shown by Figure 11.20.

The increase in global TC maximum surface wind speeds is about 5% for a 2°C global warming across a number of high-resolution multi-decadal studies (Knutson et al., 2020). This indicates the deepening in global TC minimum surface pressure under the global warming conditions. A regional cloud-permitting model study shows that the strongest TC in the western North Pacific can be as strong as 857 hPa in minimum surface pressure with a wind speed of 88 m s^{-1} under warming conditions in 2074-2087 (Tsuboki et al., 2015). TCs are also measured by quantities such as Accumulated Cyclone Energy (ACE) and the power dissipation index (PDI), which conflate TC intensity, frequency, and duration (Murakami et al., 2014). Several TC modeling studies (Yamada et al., 2010; Kim et al., 2014a; Knutson et al., 2015) project little change or decreases in the globally-accumulated value of PDI or ACE, which is due to the decrease in the total number of TCs.

A projected increase in global average TC rainfall rates of about 12% for a 2°C global warming is consistent with the Clausius-Clapeyron scaling of saturation specific humidity (Knutson et al., 2020). Increases substantially greater than Clausius-Clapeyron scaling are projected in some regions, which is caused by increased low-level moisture convergence due to projected TC intensity increases in those regions (Knutson et al., 2015; Phibbs and Toumi, 2016; Patricola and Wehner, 2018; Liu et al., 2019c). Projections of TC precipitation using large-ensemble experiments (Kitoh and Endo, 2019) show that the annual maximum 1-day precipitation total is projected to increase, except for the western North Pacific where there is only a small change or even a reduction is projected, mainly due to a projected decrease of TC frequency. They also show that the 10-year return value of extreme Rx1day associated with TCs will greatly increase in a region extending from Hawaii to the south of Japan. TC tracks and the location of topography relative to TCs significantly affect precipitation, thus in general, areas on the eastern and southern faces of mountains have

ACCEPTED VERSION SUBJECT TO FINAL EDITING

more impacts of TC precipitation changes (Hatsuzuka et al., 2020). Projection studies using variable-resolution models in the North Atlantic (Stansfield et al., 2020) indicate that TC-related precipitation rates within North Atlantic TCs and the amount of hourly precipitation due to TC are projected to increase by the end of the century compared to a historical simulation. However, the annual average TC-related Rx5day over the eastern United States is projected to decrease because of a decrease in landfalling TCs. RCM studies with around 25-50 km grid spacing are used to study projected changes in TCs. The projected changes of TCs in Southeast Asia simulated by RCMs are consistent with those of most global climate models, showing a decrease in TC frequency and an increase in the amount of TC-associated precipitation or an increase in the frequency of intense TCs (Redmond et al., 2015; Gallo et al., 2019).

Projected changes in TC tracks or TC areas of occurrence in the late 21st century vary considerably among available studies, although there is better agreement in the western North Pacific. Several studies project either poleward or eastward expansion of TC occurrence over the western North Pacific region, and more TC occurrence in the central North Pacific (Yamada et al., 2017; Yoshida et al., 2017; Wehner et al., 2018a; Roberts et al., 2020b). The observed poleward expansion of the latitude of maximum TC intensity in the western North Pacific is consistently reproduced by the CMIP5 models and downscaled models and these models show further poleward expansion in the future; the projected mean migration rate of the mean latitude where TCs reach their lifetime-maximum intensity is 0.2±0.1° from CMIP5 model results, while it is 0.13±0.04° from downscaled models in the western North Pacific (Kossin et al., 2014, 2016a). In the North Atlantic, while the location of TC maximum intensity does not show clear poleward migration observationally (Kossin et al., 2014), it tends to migrate poleward in projections (Garner et al., 2017). The poleward migration is less robust among models and observations in the Indian Ocean, eastern North Pacific, and South Pacific (e.g., Tauvale and Tsuboki, 2019; Ramsay et al. 2018; Cattiaux et al. 2020). There is presently no clear consensus in projected changes in TC translation speed (Knutson et al., 2020), although recent studies suggest a slowdown outside of the tropics (Kossin, 2019; Yamaguchi et al., 2020; Zhang et al., 2020a), but regionally there can even be an acceleration of the storms (Hassanzadeh et al., 2020).

The spatial extent, or "size", of the TC wind-field is an important determinant of storm surge and damage. No detectable anthropogenic influences on TC size have been identified to date, because TCs in observations vary in size substantially (Chan and Chan, 2015) and there is no definite theory on what controls TC size, although this is an area of active research (Chavas and Emanuel, 2014; Chan and Chan, 2018). However, projections by high-resolution models indicate future broadening of TC wind-fields when compared to TCs of the same categories (Yamada et al., 2017), while Knutson et al. (2015) simulates a reasonable interbasin distribution of TC size climatology, but projects no statistically significant change in global average TC size. A plausible mechanism is that as the tropopause height becomes higher with global warming, the eye wall areas become wider because the eye walls are inclined outward with height to the tropopause. This effect is only reproduced in high-resolution convection-permitting models capturing eye walls, and such modeling studies are not common. Moreover, the projected TC size changes are generally on the order of 10% or less, and these size changes are still highly variable between basins and studies. Thus, the projected change in both magnitude and sign of TC size is uncertain.

The coastal effects of TCs depend on TC intensity, size, track, and translation speed. Projected increases in sea level, average TC intensity, and TC rainfall rates each generally act to further elevate future storm surge and fresh-water flooding (see Section 9.6.4.2). Changes in TC frequency could contribute toward increasing or decreasing future storm surge risk, depending on the net effects of changes in weaker vs stronger storms. Several studies (McInnes et al., 2014, 2016; Little et al., 2015; Garner et al., 2017; Timmermans et al., 2017, 2018) have explored future projections of storm surge in the context of anthropogenic climate change with the influence of both sea level rise and future TC changes. Garner et al. (2017) investigated the near future changes in the New York City coastal flood hazard, and suggested a small change in storm-surge height because effects of TC intensification are compensated by the offshore shifts in TC tracks, but concluded that the overall effect due to the rising sea levels would increase the flood hazard. Future projection studies of storm surge in East Asia, including China, Japan and Korea, also indicate that storm surge due to TCs become more severe (Yang et al., 2018b; Mori et al., 2019, 2021; Chen et al., 2020c). For the Pacific islands, McInnes et al. (2014) found that the future projected increase in storm surge in Fiji is dominated by sea level rise, and projected TC changes make only a minor contribution. Among various storm surge factors, there is

ACCEPTED VERSION SUBJECT TO FINAL EDITING

high confidence that sea level rise will lead to a higher possibility of extreme coastal water levels in most regions, with all other factors assumed equal.

In the North Atlantic, vertical wind shear, which inhibits TC genesis and intensification, varies in a quasi-dipole pattern with one center of action in the tropics and another along the U.S. southeast coast (Vimont and Kossin, 2007). This pattern of variability creates a protective barrier of high shear along the U.S. coast during periods of heightened TC activity in the tropics (Kossin, 2017), and appears to be a natural part of the Atlantic ocean-atmosphere climate system (Ting et al., 2019). Greenhouse gas forcing in CMIP5 and the Community Earth System Model Large Ensemble (CESM-LE; Kay et al., 2015) simulations, however, erodes the pattern and degrades the natural shear barrier along the U.S. coast. Following the Representative Concentration Pathway 8.5 (RCP8.5) emission scenario, the magnitude of the erosion of the barrier equals the amplitude of past natural variability (time of emergence) by the mid-twenty-first century (Ting et al., 2019). The projected reduction of shear along the U.S. East Coast with warming is consistent among studies (e.g., Vecchi and Soden, 2007).

In summary, average peak TC wind speeds and the proportion of Category 4-5 TCs will *very likely* increase globally with warming. It is *likely* that the frequency of Category 4-5 TCs will increase in limited regions over the western North Pacific. It is *very likely* that average TC rain-rates will increase with warming, and *likely* that the peak rain-rates will increase at greater than the Clausius-Clapeyron scaling rate of 7% per °C of warming in some regions due to increased low-level moisture convergence caused by regional increases in TC wind-intensity. It is *likely* that the average location where TCs reach their peak wind-intensity will migrate poleward in the western North Pacific Ocean as the tropics expand with warming, and that the global frequency of TCs over all categories will decrease or remain unchanged.

11.7.2 Extratropical storms

This section focuses on extratropical cyclones (ETCs) that are either classified as strong or extreme by using some measure of their intensity, or by being associated with the occurrence of extremes in variables such as precipitation or near-surface wind speed (Seneviratne et al., 2012). Since AR5, the high relevance of ETCs for extreme precipitation events has been well established (Pfahl and Wernli, 2012; Catto and Pfahl, 2013; Utsumi et al., 2017), with 80% or more of hourly and daily precipitation extremes being associated with either ETCs or fronts over oceanic mid-latitude regions, and somewhat smaller, but still very large, proportions of events over mid-latitude land regions (Utsumi et al., 2017). The emphasis in this section is on individual ETCs that have been identified using some detection and tracking algorithms. Mid-latitude atmospheric rivers are assessed in Section 8.3.2.8.

11.7.2.1 Observed trends

Chapter 2 (Section 2.3.1.4.3) concluded that there is overall *low confidence* in recent changes in the total number of ETCs over both hemispheres and that there is *medium confidence* in a poleward shift of the storm tracks over both hemispheres since the 1980s. Overall, there is also *low confidence* in past-century trends in the number and intensity of the strongest ETCs due to the large interannual and decadal variability (Feser et al., 2015; Reboita et al., 2015; Wang et al., 2016; Varino et al., 2018) and due to temporal and spatial heterogeneities in the number and type of assimilated data in reanalyses, particularly before the satellite era (Krueger et al., 2013; Tilinina et al., 2013; Befort et al., 2016; Chang and Yau, 2016; Wang et al., 2016). There is *medium confidence* that the agreement among reanalyses and among detection and tracking algorithms is higher when considering stronger cyclones (Neu et al., 2013; Pepler et al., 2015; Wang et al., 2016). Over the Southern Hemisphere, there is *high confidence* that the total number of ETCs with low central pressures (<980 hPa) has increased between 1979 and 2009, with all eight reanalyses considered by Wang et al. (2016), showing positive trends and five of them showing statistically significant trends. Similar results were found by (Reboita et al., 2015) using a different detection and tracking algorithm and a single reanalysis product. Over the Northern Hemisphere, there is *high agreement* among reanalyses that the number of cyclones with low central pressures (<970 hPa) has decreased in summer and winter during the

ACCEPTED VERSION SUBJECT TO FINAL EDITING

period 1979-2010 (Tilinina et al., 2013; Chang et al., 2016). However, changes exhibit substantial decadal variability and do not show monotonic trends since the 1980s. For example, over the Arctic and North Atlantic, Tilinina et al. (2013) showed the number of cyclones with very low central pressure (<960 hPa) increased from 1979 to 1990 and then declined until 2010 in all five reanalyses considered. Over the North Pacific, the number of cyclones with very low central pressure reached a peak around 2000 and then decreased until 2010 in the five reanalyses considered (Tilinina et al., 2013).

Overall, however, it should be noted that characterising trends in the dynamical intensity of ETCs (e.g., wind speeds) using the absolute central pressure is problematic because the central pressure depends on the background mean sea level pressure, which varies seasonally and regionally (e.g., Befort et al., 2016).

11.7.2.2 Model evaluation

There is *high confidence* that coarse-resolution climate models (e.g., CMIP5 and CMIP6) underestimate the dynamical intensity of ETCs, including the strongest ETCs, as measured using a variety of metrics, including mean pressure gradient, mean vorticity and near-surface winds, over most regions (Colle et al., 2013; Zappa et al., 2013a; Govekar et al., 2014; Di Luca et al., 2016; Trzeciak et al., 2016; Seiler et al., 2018; Priestley et al., 2020). There is also *high confidence* that most current climate models underestimate the number of explosive systems (i.e., systems showing a decrease in mean sea level pressure of at least 24 hPa in 24 hours) over both hemispheres (Seiler and Zwiers, 2016a; Gao et al., 2020; Priestley et al., 2020). There is *high confidence* that the underestimation of the intensity of ETCs is associated with the coarse horizontal resolution of climate models, with higher horizontal resolution models, including models from HighResMIP and CORDEX, usually showing better performance (Colle et al., 2013; Zappa et al., 2013a; Di Luca et al., 2016; Trzeciak et al., 2016; Seiler et al., 2018; Gao et al., 2020; Priestley et al., 2020). The improvement by higher-resolution models is found even when comparing models and reanalyses after postprocessing data to a common resolution (Zappa et al., 2013a; Di Luca et al., 2016; Priestley et al., 2020). The systematic bias in the intensity of ETCs has also been linked to the inability of current climate models to well resolve diabatic processes, particularly those related to the release of latent heat (Willison et al., 2013; Trzeciak et al., 2016) and the formation of clouds (Govekar et al., 2014). There is *medium confidence* that climate models simulate well the spatial distribution of precipitation associated with ETCs over the Northern Hemisphere, together with some of the main features of the ETC life cycle, including the maximum in precipitation occurring just before the peak in dynamical intensity (e.g., vorticity) as observed in a reanalysis and observations (Hawcroft et al., 2018). There is, however, large observational uncertainty in ETC-associated precipitation (Hawcroft et al., 2018) and limitations in the simulation of frontal precipitation, including too low rainfall intensity over mid-latitude oceanic areas in both hemispheres (Catto et al., 2015).

11.7.2.3 Detection and attribution, event attribution

Chapter 3 (Section 3.3.3.3) concluded that there is *low confidence* in the attribution of observed changes in the number of ETCs in the Northern Hemisphere and that there is *high confidence* that the poleward shift of storm tracks in the Southern Hemisphere is linked to human activity, mostly due to emissions of ozone-depleting substances. Specific studies attributing changes in the most extreme ETCs are not available. The human influence on individual extreme ETC events has been considered only a few times and there is overall *low confidence* in the attribution of these changes (NASEM, 2016; Vautard et al., 2019).

11.7.2.4 Projections

The frequency of ETCs is expected to change primarily following a poleward shift of the storm tracks as discussed in Chapters 4 (Section 4.5.1.6, see also Figure 4.31) and 8 (Section 8.4.2.8). There is *medium confidence* that changes in the dynamical intensity (e.g., wind speeds) of ETCs will be small, although changes in the location of storm tracks can lead to substantial changes in local extreme wind speeds (Zappa et al., 2013b; Chang, 2014; Li et al., 2014; Seiler and Zwiers, 2016b; Yettella and Kay, 2017; Barcikowska

ACCEPTED VERSION SUBJECT TO FINAL EDITING

et al., 2018; Kar-Man Chang, 2018). Yettella and Kay (2017) detected and tracked ETCs over both hemispheres in an ensemble of 30 CESM-LE simulations, differing only in their initial conditions, and found that changes in mean wind speeds around ETC centres are often negligible between present (1986-2005) and future (2081-2100) periods. Using 19 CMIP5 models, Zappa et al. (2013b) found an overall reduction in the number of cyclones associated with low-troposphere (850-hPa) wind speeds larger than 25 m s^{-1} over the North Atlantic and Europe with the number of the 10% strongest cyclones decreasing by about 8% and 6% in DJF and JJA according to the RCP4.5 scenario (2070-2099 vs. 1976-2005). Over the North Pacific, Chang (2014) showed that CMIP5 models project a decrease in the frequency of ETCs with the largest central pressure perturbation (i.e., the depth, strongly related with low-level wind speeds) by the end of the century according to simulations using the RCP8.5 scenario. Using projections from CMIP5 GCMs under the RCP8.5 scenario (1981-2000 to 2081-2100), Seiler and Zwiers (2016b) projected a northward shift in the number of explosive ETCs in the northern Pacific, with fewer and weaker events south, and more frequent and stronger events north of 45°N. Using 19 CMIP5 GCMs under the RCP8.5 scenario, (Kar-Man Chang, 2018) found a significant decrease in the number of ETCs associated with extreme wind speeds (2081–2100 vs. 1980–99) over the Northern Hemisphere (average decrease of 17%) and over some smaller regions, including the Pacific and Atlantic regions.

Over the Southern Hemisphere, future changes (RCP8.5 scenario; 1980-1999 to 2081-2100) in extreme ETCs were studied by Chang (2017) using 26 CMIP5 models and a variety of intensity metrics (850-hPa vorticity, 850-hPa wind speed, mean sea level pressure and near-surface wind speed). They found that the number of extreme cyclones is projected to increase by at least 20% and as much as 50%, depending on the specific metric used to define extreme ETCs. Increases in the number of strong cyclones appear to be robust across models and for most seasons, although they show strong regional variations with increases occurring mostly over the southern flank of the storm track, consistent with a shift and intensification of the storm track. Overall, there is *medium confidence* that projected changes in the dynamical intensity of ETCs depend on the resolution and formulation (e.g., explicit or implicit representation of convection) of climate models (Booth et al., 2013; Michaelis et al., 2017; Zhang and Colle, 2017).

As reported in AR5 and in Chapter 8 (Section 8.4.2.8), despite small changes in the dynamical intensity of ETCs, there is *high confidence* that the precipitation associated with ETCs will increase in the future (Zappa et al., 2013b; Marciano et al., 2015; Pepler et al., 2016; Zhang and Colle, 2017; Michaelis et al., 2017; Yettella and Kay, 2017; Barcikowska et al., 2018; Zarzycki, 2018; Hawcroft et al., 2018; Kodama et al., 2019; Bevacqua et al., 2020c; Reboita et al., 2020). There is *high confidence* that increases in precipitation will follow increases in low-level water vapour (i.e., about 7% per degree of surface warming; Box 11.1) and will be largest for higher warming levels (Zhang and Colle, 2017). There is *medium confidence* that precipitation changes will show regional and seasonal differences due to distinct changes in atmospheric humidity and dynamical conditions (Zappa et al., 2015; Hawcroft et al., 2018), with even decreases in some specific regions such as the Mediterranean (Zappa et al., 2015; Barcikowska et al., 2018). There is *high confidence* that snowfall associated with wintertime ETCs will decrease in the future, because increases in tropospheric temperatures lead to a lower proportion of precipitation falling as snow (O'Gorman, 2014; Rhoades et al., 2018; Zarzycki, 2018). However, there is *medium confidence* that extreme snowfall events associated with wintertime ETCs will change little in regions where snowfall will be supported in the future (O'Gorman, 2014; Zarzycki, 2018).

In summary, there is *low confidence* in past changes in the dynamical intensity (e.g., maximum wind speeds) of ETCs and *medium confidence* that in the future these changes will be small, although changes in the location of storm tracks could lead to substantial changes in local extreme wind speeds. There is *high confidence* that average and maximum ETC precipitation-rates will increase with warming, with the magnitude of the increases associated with increases in atmospheric water vapour. There is *medium confidence* that projected changes in the intensity of ETCs, including wind speeds and precipitation, depend on the resolution and formulation of climate models.

11.7.3 Severe convective storms

ACCEPTED VERSION SUBJECT TO FINAL EDITING

Severe convective storms are convective systems that are associated with extreme phenomena such as tornadoes, hail, heavy precipitation (rain or snow), strong winds, and lightning. The assessment of changes in severe convective storms in SREX (Chapter 3, Seneviratne et al., 2012) and AR5 (Chapter 12, Collins et al., 2013) is limited and focused mainly on tornadoes and hail storms. SREX assessed that there is *low confidence* in observed trends in tornadoes and hail because of data inhomogeneities and inadequacies in monitoring systems. Subsequent literature assessed in the Climate Science Special Report (Kossin et al., 2017) led to the assessment of the observed tornado activity over the 2000s in the United States with a decrease in the number of days per year with tornadoes and an increase in the number of tornadoes on these days (*medium confidence*). However, there is *low confidence* in past trends for hail and severe thunderstorm winds. Climate models consistently project environmental changes that would support an increase in the frequency and intensity of severe thunderstorms that combine tornadoes, hail, and winds (*high confidence*), but there is *low confidence* in the details of the projected increase. Regional aspects of severe convective storms and details of the assessment of tornadoes and hail are also assessed in Chapter 12 (Section 12.3.3.2 for tornadoes; Section 12.3.4.5 for hail; Section 12.4.5.3 for Europe, Section 12.4.6.3 for North America, and Section 12.7.2 for regional gaps and uncertainties).

11.7.3.1 Mechanisms and drivers

Severe convective storms are sometimes embedded in synoptic-scale weather systems, such as TCs, ETCs, and fronts (Kunkel et al., 2013). They are also generated as individual events as mesoscale convective systems (MCSs) and mesoscale convective complexes (MCCs) (a special type of a large,organized and long-lived MCS), without being clearly embedded within larger-scale weather systems. In addition to the general vigorousness of precipitation, hail, and winds associated with MCSs, characteristics of MCSs are viewed in new perspectives in recent years, probably because of both the development of dense mesoscale observing networks and advances in high-resolution mesoscale modelling (Sections 11.7.3.2 and 11.7.3.3). The horizontal scale of MCSs is discussed with their organization of the convective structure and it is examined with a concept of "convective aggregation" in recent years (Holloway et al., 2017). MCSs sometimes take a linear shape and stay almost stationary with successive production of cumulonimbus on the upstream side (back-building type convection), and cause heavy rainfall (Schumacher and Johnson, 2005). Many of the recent severe rainfall events in Japan are associated with band-shaped precipitation systems (Kunii et al., 2016; Oizumi et al., 2018; Tsuguti et al., 2018; Kato, 2020), suggesting common characteristics of severe precipitation, at least in East Asia. The convective modes of severe storms in the United States can be classified into rotating or linear modes and preferable environmental conditions for these modes, such as vertical shear, have been identified (Trapp et al., 2005; Smith et al., 2013; Allen, 2018). Cloud microphysics characteristics of MCSs were examined and the roles of warm rain processes on extreme precipitation were emphasized recently (Sohn et al., 2013; Hamada et al., 2015; Hamada and Takayabu, 2018). Idealized studies also suggest the importance of ice and mixed-phase processes of cloud microphysics on extreme precipitation (Sandvik et al., 2018; Bao and Sherwood, 2019). However, it is unknown whether the types of MCSs are changing in recent periods or observed ubiquitously all over the world.

Severe convective storms occur under conditions preferable for deep convection, that is, conditionally unstable stratification, sufficient moisture both in lower and middle levels of the atmosphere, and a strong vertical shear. These large-scale environmental conditions are viewed as necessary conditions for the occurrence of severe convective systems, or the resulting tornadoes and lightning, and the relevance of these factors strongly depends on the region (e.g., Antonescu et al., 2016a; Allen, 2018; Tochimoto and Niino, 2018). Frequently used metrics are atmospheric static stability, moisture content, convective available potential energy (CAPE) and convective inhibition (CIN), wind shear or helicity, including storm-relative environmental helicity (SREH) (Tochimoto and Niino, 2018; Elsner et al., 2019). These metrics, largely controlled by large-scale atmospheric circulations or synoptic weather systems, such as TCs and ETCs, are then generally used to examine severe convective systems. In particular, there is *high confidence* that CAPE in the tropics and the subtropics increases in response to global warming (Singh et al., 2017a), as supported by theoretical studies (Singh and O'Gorman, 2013; Seeley and Romps, 2015; Romps, 2016; Agard and Emanuel, 2017). The uncertainty, however, arises from the balance between factors affecting severe storm occurrence. For example, the warming of mid-tropospheric temperatures leads to an increase in the freezing

ACCEPTED VERSION SUBJECT TO FINAL EDITING

level, which leads to increased melting of smaller hailstones, while there may be some offset by stronger updrafts driven by increasing CAPE, which would favour the growth of larger hailstones, leading to less melting when falling (Allen, 2018; Mahoney, 2020).

There are few studies on relations between changes in severe convective storms and those of the large-scale circulation patterns. Tornado outbreaks in the United States are usually associated with ETCs with their frontal systems and TCs (Fuhrmann et al., 2014; Tochimoto and Niino, 2016). In early June in East Asia, associated with the Baiu/Changma/Mei-yu, severe precipitation events are frequently caused by MCSs. Severe precipitation events are also caused by remote effects of TCs, known as predecessor rain events (PREs) (Galarneau et al., 2010). Atmospheric rivers and other coherent types of enhanced water vapour flux also have the potential to induce severe convective systems (Kamae et al., 2017; Ralph et al., 2018; Waliser and Guan, 2017; see Section 8.3.2.8.1). Combined with the above drivers, topographic effects also enhance the intensity and duration of severe convective systems and the associated precipitation (Ducrocq et al., 2008; Piaget et al., 2015). However, the changes in these drivers are not generally significant, so their relations to severe convective storms are unclear.

In summary, severe convective storms are sometimes embedded in synoptic-scale weather systems, such as TCs, ETCs, and fronts, and modulated by large-scale atmospheric circulation patterns. The occurrence of severe convective storms and the associated severe events, including tornadoes, hail, and lightning, is affected by environmental conditions of the atmosphere, such as CAPE and vertical shear. The uncertainty, however, arises from the balance between these environmental factors affecting severe storm occurrence.

11.7.3.2 Observed trends

Observed trends in severe convective storms or MCSs are not well documented, but the climatology of MCSs has been analysed in specific regions (North America, South America, Europe, Asia; regional aspects of convective storms are separately assessed in Chapter 12). As the definition of severe convective storms varies depending on the literature, it is not straightforward to make a synthesizing view of observed trends in severe convective storms in different regions. However, analysis using satellite observations provides a global view of MCSs (Kossin et al., 2017). The global distribution of thunderstorms is captured (Zipser et al., 2006; Liu and Zipser, 2015) by using the satellite precipitation measurements by the Tropical Rainfall Measuring Mission (TRMM) and Global Precipitation Mission (GPM) (Hou et al., 2014). The climatological characteristics of MCSs are provided by satellite analyses in South America (Durkee and Mote, 2010; Rasmussen and Houze, 2011; Rehbein et al., 2018) and those of MCC in the Maritime Continent by Trismidianto and Satyawardhana (2018). Analysis of the environmental conditions favourable for severe convective events indirectly indicates the climatology and trends of severe convective events (Allen et al., 2018; Taszarek et al., 2018, 2019), though favourable conditions depend on the location, such as the difference for tornadoes associated with ETCs between the United States and Japan (Tochimoto and Niino, 2018).

Observed trends in severe convective storms are highly regionally dependent. In the United States, it is indicated that there is no significant increase in convective storms, and hail and severe thunderstorms (Kossin et al., 2017; Kunkel et al., 2013). There is an upward trend in the frequency and intensity of extreme precipitation events in the United States (*high confidence*) (Kunkel et al., 2013; Easterling et al., 2017), and MCSs have increased in occurrence and precipitation amounts since 1979 (*limited evidence*) (Feng et al., 2016). Significant interannual variability of hailstone occurrences is found in the Southern Great Plains of the United States (Jeong et al., 2020). The mean annual number of tornadoes has remained relatively constant, but their variability of occurrence has increased since the 1970s, particularly over the 2000s, with a decrease in the number of days per year, but an increase in the number of tornadoes on these days (Brooks et al., 2014; Elsner et al., 2015, 2019; Kossin et al., 2017; Allen, 2018). There has been a shift in the distribution of tornadoes, with increases in tornado occurrence in the mid-south of the US and decreases over the High Plains (Gensini and Brooks, 2018). Trends in MCSs are relatively more visible for particular aspects of MCSs, such as lengthening of active seasons and dependency on duration. MCSs have increased in occurrence and precipitation amounts since 1979 (Easterling et al., 2017). Feng et al. (2016) analysed that

ACCEPTED VERSION SUBJECT TO FINAL EDITING

the observed increases in springtime total and extreme rainfall in the central United States are dominated by MCSs, with increased frequency and intensity of long-lasting MCSs.

Studies on trends in severe convective storms and their ingredients outside of the United States are limited. Westra et al. (2014) found that there is an increase in the intensity of short-duration convective events (minutes to hours) over many regions of the world, except eastern China. In Europe, a climatology of tornadoes shows an increase in detected tornadoes between 1800 to 2014, but this trend might be affected by the density of observations (Antonescu et al., 2016b, 2016a). An increase in the trend in extreme daily rainfall is found in southeastern France, where MCSs play a key role in this type of event (Blanchet et al., 2018; Ribes et al., 2019). Trend analysis of the mean annual number of days with thunderstorms since 1979 in Europe indicates an increase over the Alps and central, southeastern, and eastern Europe, with a decrease over the southwest (Taszarek et al., 2019). In the Sahelian region, Taylor et al. (2017) analysed MCSs using satellite observations since 1982 and showed an increase in the frequency of extreme storms. In Bangladesh, the annual number of propagating MCSs decreased significantly during 1998-2015 based on TRMM precipitation data (Habib et al., 2019). Prein and Holland (2018) estimated the hail hazard from large-scale environmental conditions using a statistical approach and showed increasing trends in the United States, Europe, and Australia. However, trends in hail on regional scales are difficult to validate because of an insufficient length of observations and inhomogeneous records (Allen, 2018). The high spatial variability of hail suggests it is reasonable that there would be local signals of both positive and negative trends and the trends that are occurring in hail globally are uncertain. In China, the total number of days that have either a thunderstorm or hail have decreased by about 50% from 1961 to 2010, and the reduction in these severe weather occurrences correlates strongly with the weakening of the East Asian summer monsoon (Zhang et al., 2017b). More regional aspects of severe convective storms are detailed in Chapter 12.

In summary, because the definition of severe convective storms varies depending on the literature and the region, it is not straightforward to make a synthesizing view of observed trends in severe convective storms in different regions. In particular, observational trends in tornadoes, hail, and lightning associated with severe convective storms are not robustly detected due to insufficient coverage of the long-term observations. There is *medium confidence* that the mean annual number of tornadoes in the United States has remained relatively constant, but their variability of occurrence has increased since the 1970s, particularly over the 2000s, with a decrease in the number of days per year and an increase in the number of tornadoes on these days (*high confidence*). Detected tornadoes have also increased in Europe, but the trend depends on the density of observations.

11.7.3.3 Model evaluation

The explicit representation of severe convective storms requires non-hydrostatic models with horizontal grid spacings below 5 km, denoted as convection-permitting models or storm-resolving models (Section 10.3.1). Convection-permitting models are becoming available to run over a wide domain, such as a continental scale or even over the global area, and show realistic climatological characteristics of MCSs (Prein et al., 2015; Guichard and Couvreux, 2017; Satoh et al., 2019). Such high-resolution simulations are computationally too expensive to perform at the larger domain and for long periods and alternative methods by using an RCM with dynamical downscaling are generally used (Section 10.3.1). Convection-permitting models are used as the flagship project of CORDEX to particularly study projections of thunderstorms (Section 10.3.3). Simulations of North American MCSs by a convection-permitting model conducted by Prein et al. (2017a) were able to capture the main characteristics of the observed MCSs, such as their size, precipitation rate, propagation speed, and lifetime. Cloud-permitting model simulations in Europe also showed sub-daily precipitation realistically (Ban et al., 2014; Kendon et al., 2014). Evaluation of precipitation conducted using convection-permitting simulations around Japan showed that finer resolution improves intense precipitation (Murata et al., 2017). MCSs over Africa simulated using convection-permitting models showed better extreme rainfall (Kendon et al., 2019) and diurnal cycles and convective rainfall over land than the coarser-resolution RCMs or GCMs (Stratton et al., 2018; Crook et al., 2019).

The other modeling approach is the analysis of the environmental conditions that control characteristics of

ACCEPTED VERSION SUBJECT TO FINAL EDITING

severe convective storms using the typical climate model results in CMIP5/6 (Allen, 2018). Severe convective storms are generally formed in environments with large CAPE and tornadic storms are, in particular, formed with a combination of large CAPE and strong vertical wind shear. As the processes associated with severe convective storms occur over a wide range of spatial and temporal scales, some of which are poorly understood and are inadequately sampled by observational networks, the model calibration approaches are in general difficult and insufficiently validated. Therefore, model simulations and their interpretations should be done with much caution.

In summary, there are typically two kinds of modeling approaches for studying changes in severe convective storms. One is to use convection-permitting models in wider regions or the global domain in time-sliced downscaling methods to directly simulate severe convective storms. The other is the analysis of the environmental conditions that control characteristics of severe convective storms by using coarse-resolution GCMs. Even in finer-resolution convection-permitting models, it is difficult to directly simulate tornadoes, hail storms, and lightning, so modeling studies of these changes are limited.

11.7.3.4 Detection and attribution, event attribution

It is extremely difficult to detect differences in time and space of severe convective storms (Kunkel et al., 2013). Although some ingredients that are favourable for severe thunderstorms have increased over the years, others have not; thus, overall, changes in the frequency of environments favourable for severe thunderstorms have not been statistically significant. Event attribution studies on severe convective events have now been undertaken for some cases. For the case of the July 2018 heavy rainfall event in Japan (BOX 11.3), Kawase et al. (2019) took a storyline approach to show that the rainfall during this event in Japan was increased by approximately 7% due to the recent rapid warming around Japan. For the case of the December 2015 extreme rainfall event in Chennai, India, the extremity of the event was equally caused by the warming trend in the Bay of Bengal SSTs and the strong El Niño conditions (van Oldenborgh et al., 2016; Boyaj et al., 2018). For hailstorms, such as those that caused disasters in the United States in 2018, detection of the role of climate change in changing hail storms is more difficult, because hail storms are not, in general, directly simulated by convection-permitting models and not adequately represented by the environmental parameters of coarse-resolution GCMs (Mahoney, 2020).

In summary, it is extremely difficult to detect and attribute changes in severe convective storms, except for case study approaches by event attribution. There is *limited evidence* that extreme precipitation associated with severe convective storms has increased in some cases.

11.7.3.5 Projections

Future projections of severe convective storms are usually studied either by analysing the environmental conditions simulated by climate models or by a time slice approach with higher-resolution convection-permitting models by comparing simulations downscaled with climate model results under historical conditions and those under hypothesized future conditions (Kendon et al., 2017; Allen, 2018). Up to now, individual studies using convection-permitting models gave projections of extreme events associated with severe convective storms in local regions, and it is not generally possible to obtain global or general views of projected changes of severe convective storms. Prein et al. (2017b) investigated future projections of North American MCS simulations and showed an increase in MCS frequency and an increase in total MCS precipitation volume by the combined effect of increases in maximum precipitation rates associated with MCSs and increases in their size. Rasmussen et al. (2017) investigated future changes in the diurnal cycle of precipitation by capturing organized and propagating convection and showed that weak to moderate convection will decrease and strong convection will increase in frequency in the future. Ban et al. (2015) found the day-long and hour-long precipitation events in summer intensify in the European region covering the Alps. Kendon et al. (2019) showed future increases in extreme 3-hourly precipitation in Africa. Murata et al. (2015) investigated future projections of precipitation around Japan and showed a decrease in monthly mean precipitation in the eastern Japan Sea region in December, suggesting convective clouds become

ACCEPTED VERSION SUBJECT TO FINAL EDITING

shallower in the future in the winter over the Japan Sea.

The other approach is the projection of the environmental conditions that control characteristics of severe convective storms by analysing climate model results. There is *high confidence* that CAPE, particularly summertime mean CAPE and high percentiles of the CAPE in the tropics and subtropics, increases in response to global warming in an ensemble of climate models including those of CMIP5, mainly from increased low-level specific humidity (Sobel and Camargo, 2011; Singh et al., 2017a; Chen et al., 2020b). CIN becomes stronger over most land areas under global warming, resulting mainly from reduced low-level relative humidity over land (Chen et al., 2020b). However, there are large differences within the CMIP5 ensemble for environmental conditions, which contribute to some degree of uncertainty (Allen, 2018). Because the relation between simulated environments in models and the occurrence of severe convective storms are in general insufficiently validated, the confidence level of the projection of severe convective storms with the approach of the environmental conditions is generally *low*.

In the United States, projected changes in the environmental conditions show an increase in CAPE and no changes or decreases in the vertical wind shear, suggesting favourable conditions for an increase in severe convective storms in the future, but the interpretation of how tornadoes or hail will change is an open question because of the strong dependence on shear (Brooks, 2013). Diffenbaugh et al. (2013) showed robust increases in the occurrence of the favourable environments for severe convective storms with increased CAPE and stronger low-level wind shear in response to future global warming. A downscaling approach showed that the variability of the occurrence of severe convective storms increases in spring in late 21st century simulations (Gensini and Mote, 2015). Future changes in hail occurrence in the United States examined through convection-permitting dynamical downscaling suggested that the hail season may begin earlier in the year and exhibit more interannual variability with increases in the frequency of large hail in broad areas over the United States (Trapp et al., 2019). There is *medium confidence* that the frequency and variability of the favourable environments for severe convective storms will increase in spring, and *low confidence* for summer and autumn (Diffenbaugh et al., 2013; Gensini and Mote, 2015; Hoogewind et al., 2017). The occurrence of hail events in Colorado in the United States was examined by comparing both present-day and projected future climates using high-resolution model simulations capable of resolving hailstorms (Mahoney et al., 2012), which showed hail is almost eliminated at the surface in the future in most of the simulations, despite more intense future storms and significantly larger amounts of hail generated in-cloud.

Future changes in severe convection environments show enhancement of instability with less robust changes in the frequency of strong vertical wind shear in Europe (Púčik et al. 2017) and in Japan (Muramatsu et al. 2016). In Japan, the frequency of conditions favourable for strong tornadoes increases in spring and partly in summer.

In summary, the average and maximum rain rates associated with severe convective storms increase in a warming world in some regions including the USA (*high confidence*). There is *high confidence* from climate models that CAPE increases in response to global warming in the tropics and subtropics, suggesting more favourable environments for severe convective storms. The frequency of springtime severe convective storms is projected to increase in the USA leading to a lengthening of the severe convective storm season (*medium confidence*), evidence in other regions is limited. There is significant uncertainty about projected regional changes in tornadoes, hail, and lightning due to limited analysis of simulations using convection-permitting models (*high confidence*).

11.7.4 Extreme winds

Extreme winds are defined here in terms of the strongest near-surface wind speeds that are generally associated with extreme storms, such as TCs, ETCs, and severe convective storms. In previous IPCC reports, near-surface wind speed (including extremes), has not been assessed as a variable in its own right, but rather in the context of other extreme atmospheric or oceanic phenomena. The exception was the SREX report (Seneviratne et al., 2012), which specifically examined past changes and projections of mean and extreme

ACCEPTED VERSION SUBJECT TO FINAL EDITING

near-surface wind speeds. A strong decline in extreme winds compared to mean winds was reported for the continental northern mid-latitudes. Due to the small number of studies and uncertainties in terrestrial-based surface wind measurements, the findings were assigned *low confidence* in the SREX. AR5 reported a weakening of mean and maximum winds from the 1960s or 1970s to the early 2000s in the tropics and mid-latitudes and increases in high latitudes, but with *low confidence* in changes in the observed surface winds over land (Hartmann et al., 2013). Observed trends in mean wind speed over land and the ocean are assessed in Section 2.3.1.4.4. Aspects of climate impact-drivers for winds are addressed in Section 12.3.3 and 12.5.2.3 and their regional changes are assessed in Section 12.4.

Observationally, although not specifically addressing extreme wind speed changes, negative surface wind speed trends (stilling) were found in the tropics and mid-latitudes of both hemispheres of -0.014 m s^{-1} $year^{-1}$, while positive trends were reported at high latitudes poleward of 70 degrees, based on a review of 148 studies (McVicar et al., 2012a). An earlier study attributed the stilling to both changes in atmospheric circulation and an increase in surface roughness due to an overall increase in vegetation cover (Vautard et al., 2010). Since then, a number of additional studies have mostly confirmed these general negative mean-wind trends based on anemometer data for Spain (Azorin-Molina et al., 2017), Turkey, (Dadaser-Celik and Cengiz, 2014), the Netherlands, (Wever, 2012), Saudi Arabia, (Rehman, 2013), Romania, (Marin et al., 2014), and China (Chen et al., 2013). Lin et al. (2013) note that wind speed variability over China is greater at high elevation locations compared to those closer to mean sea level. Hande et al. (2012), using radiosonde data, found an increase in surface wind speed on Macquarie Island.

A number of new studies have examined surface wind speeds over the ocean based on ship-based measurements, satellite altimeters, and Special Sensor Microwave/Imagers (SSM/I) (Tokinaga and Xie, 2011; Zieger et al., 2014). It has been noted that wind speed trends tend to be stronger in altimeter measurements, although the spatial patterns of change are qualitatively similar in both instruments (Zieger et al., 2014). Liu et al. (2016) found positive trends in surface wind speeds over the Arctic Ocean in 20 years of satellite observations. Small positive trends in mean wind speed were found in 33 years of satellite data, together with larger trends in the 90th percentile values over global oceans (Ribal and Young, 2019). These results were consistent with an earlier study that found a positive trend in 1-in-100 year wind speeds (Young et al., 2012). A positive change in mean wind speeds was found for the Arabian Sea and the Bay of Bengal (Shanas and Kumar, 2015) and Zheng et al. (2017) found that positive wind speed trends over the ocean were larger during winter seasons than summer seasons.

Changes in extreme winds are associated with changes in the characteristics (locations, frequencies, and intensities) of extreme storms, including TCs, ETCs, and severe convective storms. For TCs, as assessed in Section 11.7.1.5, it is projected that the average peak TC wind speeds will increase globally with warming, while the global frequency of TCs over all categories will decrease or remain unchanged; the average location where TCs reach their peak wind-intensity will migrate poleward in the western North Pacific Ocean as the tropics expand with warming. Frequency, intensities, and geographical distributions of extreme wind events associated with TCs will change according to these TC changes. For ETCs, by the end of the century, CMIP5 models show the number of ETCs associated with extreme winds will significantly decrease in the mid- and high latitudes of the Northern Hemisphere in winter, with the projected decrease being larger over the Atlantic (Kar-Man Chang, 2018), while it will significantly increase irrespective of the season in the Southern Hemisphere (Chang, 2017)(Section 11.7.2.4). Over the ocean in the subtropics, a large ensemble of 60-km global model simulations indicated that extreme winds associated with storm surges will intensify over 15–35°N in the Northern Hemisphere (Mori et al., 2019). On the other hand, extreme surface wind speeds will mostly decrease due to decreases in the number and intensity of TCs over most tropical areas of the Southern Hemisphere (Mori et al., 2019). The projected changes in the frequency of extreme winds are associated with the future changes in TCs and ETCs.

Extreme cyclonic windstorms that share some characteristics with both TCs and ETCs occur regularly over the Mediterranean Sea and are often referred to as “medicanes” (Ragone et al., 2018; Miglietta and Rotunno, 2019; Ragone et al., 2018; Miglietta and Rotunno, 2019; Zhang et al., 2020e). Medicanes pose substantial threats to regional islands and coastal zones. A growing body of literature consistently found that the frequency of medicanes decreases under warming, while the strongest medicanes become stronger

ACCEPTED VERSION SUBJECT TO FINAL EDITING

(González-Alemán et al., 2019; Tous et al., 2016; Romero and Emanuel, 2017; Romera et al., 2017; Cavicchia et al., 2014; Romero and Emanuel, 2013; Gaertner et al., 2007). This is also consistent with expected global changes in TCs under warming (11.7.1). Based on the consistency of these studies, it is *likely* that medicanes will decrease in frequency, while the strongest medicanes become stronger under warming scenario projections (*medium confidence*).

In summary, the observed intensity of extreme winds is becoming less severe in the lower to mid-latitudes, while becoming more severe in higher latitudes poleward of 60 degrees (*low confidence*). Projected changes in the frequency and intensity of extreme winds are associated with projected changes in the frequency and intensity of TCs and ETCs (*medium confidence*).

11.8 Compound events

The IPCC SREX (SREX Ch3) first defined compound events as "(1) two or more extreme events occurring simultaneously or successively, (2) combinations of extreme events with underlying conditions that amplify the impact of the events, or (3) combinations of events that are not themselves extremes but lead to an extreme event or impact when combined". Further definitions of compound events have emerged since the SREX. Zscheischler et al. (2018) defined compound events broadly as "the combination of multiple drivers and/or hazards that contributes to societal or environmental risk". This definition is used in the present assessment, because of its clear focus on the risk framework established by the IPCC, and also highlighting that compound events may not necessarily result from dependent drivers. Compound events have been classified into preconditioned events, where a weather-driven or climate-driven precondition aggravates the impacts of a hazard; multivariate events, where multiple drivers and/or hazards lead to an impact; temporally compounding events, where a succession of hazards leads to an impact; and spatially compounding events, where hazards in multiple connected locations cause an aggregated impact (Zscheischler et al., 2020). Drivers include processes, variables, and phenomena in the climate and weather domain that may span over multiple spatial and temporal scales. Hazards (such as floods, heat waves, wildfires) are usually the immediate physical precursors to negative impacts, but can occasionally have positive outcomes (Flach et al., 2018).

11.8.1 Overview

The combination of two or more – not necessarily extreme – weather or climate events that occur i) at the same time, ii) in close succession, or iii) concurrently in different regions, can lead to extreme impacts that are much larger than the sum of the impacts due to the occurrence of individual extremes alone. This is because multiple stressors can exceed the coping capacity of a system more quickly. The contributing events can be of similar types (clustered multiple events) or of different types (Zscheischler et al., 2020). Many major weather- and climate-related catastrophes are inherently of a compound nature (Zscheischler et al., 2018). This has been highlighted for a broad range of hazards, such as droughts, heat waves, wildfires, coastal extremes, and floods (Westra et al., 2016; AghaKouchak et al., 2020; Ridder et al., 2020). Co-occurring extreme precipitation and extreme winds can result in infrastructural damage (Martius et al., 2016); the compounding of storm surge and precipitation extremes can cause coastal floods (Wahl et al., 2015); the combination of drought and heat can lead to tree mortality (Allen et al., 2015)(see also Section 11.6); wildfires increase occurrences of hailstorms and lightning (Zhang et al., 2019e). Compound storm types consisting of co-located cyclone, front and thunderstorm systems have a higher chance of causing extreme rainfall and extreme winds than individual storm types (Dowdy and Catto, 2017). Extremes may occur at similar times at different locations (De Luca et al., 2020a,b) but affect the same system, for instance, spatially-concurrent climate extremes affecting crop yields and food prices (Anderson et al., 2019; Singh et al., 2018). Studies also show an increasing risk for breadbasket regions to be concurrently affected by climate extremes with increasing global warming, even between 1.5°C and 2°C of global warming (Gaupp et al., 2019) (Box 11.2). Concomitant extreme conditions at different locations become more probable as changes in climate extremes are emerging over an increasing fraction of the land area (Sections 11.2.3, 11.2.4, 11.8.2, 11.8.3; Box 11.4).

ACCEPTED VERSION SUBJECT TO FINAL EDITING

Finally, impacts may occur because of large multivariate anomalies in the climate drivers, if systems are adapted to historical multivariate climate variability (Flach et al., 2017). For instance, ecosystems are typically adapted to the local covariability of temperature and precipitation such that a bivariate anomaly may have a large impact even though neither temperature nor precipitation may be extreme based on a univariate assessment (Mahony and Cannon, 2018). Given that almost all systems are affected by weather and climate phenomena at multiple space-time scales (Raymond et al., 2020), it is natural to consider extremes in a compound event framework. It should be noted, however, that multi-hazard dependencies can also decrease risk, for instance when hazards are negatively correlated (Hillier et al., 2020). Despite this recognition, the literature on past and future changes in compound events has been limited, but is growing. This section assesses examples of types of compound events in available literature.

In summary, compound events include the combination of two or more – not necessarily extreme – weather or climate events that occur i) at the same time, ii) in close succession, or iii) concurrently in different regions. The land area affected by concurrent extremes has increased (*high confidence*). Concurrent extreme events at different locations, but possibly affecting similar sectors (e.g., breadbaskets) in different regions, will become more frequent with increasing global warming, in particular above +2°C of global warming (*high confidence*).

11.8.2 Concurrent extremes in coastal and estuarine regions

Coastal and estuarine zones are prone to a number of meteorological extreme events and also to concurrent extremes. A major climati-impact driver in coastal regions around the world is floods (Chapter 12), and flood occurrence may be influenced by the dependence between storm surge, extreme rainfall, river flow, but also by sea level rise, waves and tides, as well as groundwater for estuaries. Floods with multiple drivers are often referred to as “compound floods” (Wahl et al., 2015; Moftakhari et al., 2017; Bevacqua et al., 2020b).

At US coasts, the probability of co-occurring storm surge and heavy precipitation is higher for the Atlantic/Gulf coast relative to the Pacific coast (Wahl et al., 2015). Furthermore, six studied locations on the US coast with long overlapping time series show an increase in the dependence between heavy precipitation and storm surge over the last century, leading to more frequent co-occurring storm surge and heavy precipitation events at the present day (Wahl et al., 2015). Storm surge and extreme rainfall are also dependent in most locations on the Australian coasts (Zheng et al., 2013) and in Europe along the Dutch coasts (Ridder et al., 2018), along the Mediterranean Sea, the Atlantic coast and the North Sea (Bevacqua et al., 2019). The probability of flood occurrence can be assessed via the dependence between storm surge and river flow (Bevacqua et al., 2020a, 2020b). For instance, the occurrence of a North Sea storm surge in close succession with an extreme Rhine or Meuse river discharge is much more probable due to their dependence, compared to if both events would be independent (Kew et al., 2013; Klerk et al., 2015). Significant dependence between high sea levels and high river discharge are found for more than half of the available station observations, which are mostly located around the coasts of North America, Europe, Australia, and Japan (Ward et al., 2018). Combining global river discharge with a global storm surge model, hotspots of compound flooding have been discovered that are not well covered by observations, including Madagascar, Northern Morocco, Vietnam, and Taiwan (Couasnon et al., 2020). In the Dutch Noorderzijlvest area, there is more than a two-fold increase in the frequency of exceeding the highest warning level compared to the case if storm surge and heavy precipitation were independent (van den Hurk et al., 2015). In other regions and seasons, the dependence can be insignificant (Wu et al., 2018b) and there can be significant seasonal and regional differences in the storm surge-heavy precipitation relationship. Assessments of flood probabilities are often not based on actual flood measurements and instead are estimated from its main drivers including astronomical tides, storm surge, heavy precipitation, and high streamflow. Such single driver analyses might underestimate flood probabilities if multiple correlated drivers contribute to flood occurrence (e.g., van den Hurk et al., 2015).

Many coastal areas are also prone to the occurrence of compound precipitation and wind extremes, which can cause damage, including to infrastructure and natural environments. A high percentage of co-occurring

ACCEPTED VERSION SUBJECT TO FINAL EDITING

wind and precipitation extremes are found in coastal regions and in areas with frequent tropical cyclones. Finally, the combination of extreme wave height and duration is also shown to influence coastal erosion processes (Corbella and Stretch, 2012).

Aspects of concurrent extremes in coastal and estuarine environments have increased in frequency and/or magnitude over the last century in some regions. These include an increase in the dependence between heavy precipitation and storm surge over the last century, leading to more frequent co-occurring storm surge and heavy precipitation events in the present day along US coastlines (Wahl et al., 2015). In Europe, the probability of compound flooding occurrence increases most strongly along the Atlantic coast and the North Sea under strong warming. This increase is mostly driven by an intensification of precipitation extremes and aggravated flooding probability due to sea level rise (Bevacqua et al., 2019). At the global scale and under a high emissions scenario, the concurrence probability of meteorological conditions driving compound flooding would increase by more than 25% on average along coastlines worldwide by 2100, compared to the present (Bevacqua et al., 2020b). Sea level extremes and their physical impacts in the coastal zone arise from a complex set of atmospheric, oceanic, and terrestrial processes that interact on a range of spatial and temporal scales and will be modified by a changing climate, including sea level rise (McInnes et al., 2016). Interactions between sea level rise and storm surges (Little et al., 2015), and sea level and fluvial flooding (Moftakhari et al., 2017) are projected to lead to more frequent and more intense compound coastal flooding events as sea levels continue to rise.

In summary, there is *medium confidence* that over the last century the probability of compound flooding has increased in some locations, including along the US coastline. There is *medium confidence* that the occurrence and magnitude of compound flooding in coastal regions will increase in the future due to both sea level rise and increases in heavy precipitation.

11.8.3 Concurrent droughts and heat waves

Concurrent droughts and heat waves have a number of negative impacts on human society and natural ecosystems. Studies since SREX and AR5 show several occurrences of observed combinations of drought and heat waves in various regions.

Over most land regions, temperature and precipitation are strongly negatively correlated during summer (Zscheischler and Seneviratne, 2017), mostly due to land-atmosphere feedbacks (Sections 11.1.6, 11.3.2), but also because synoptic-scale weather systems favourable for extreme heat are also unfavourable for rain (Berg et al., 2015). This leads to a strong correlation between droughts and heat waves (Zscheischler and Seneviratne, 2017). Drought events characterized by low precipitation and extreme high temperatures have occurred, for example, in California (AghaKouchak et al., 2014), inland eastern Australia (King et al., 2014), and large parts of Europe (Orth et al., 2016b). The 2018 growing season was both record-breaking dry and hot in Germany (Zscheischler and Fischer, 2020).

The probability of co-occurring meteorological droughts and heat waves has increased in the observational period in many regions and will continue to do so under unabated warming (Herrera-Estrada and Sheffield, 2017; Zscheischler and Seneviratne, 2017; Hao et al., 2018; Sarhadi et al., 2018; Alizadeh et al., 2020; Wu et al., 2021). Overall, projections of increases in co-occurring drought and heat waves are reported in northern Eurasia (Schubert et al., 2014), Europe ; Sedlmeier et al., 2018), southeast Australia (Kirono et al., 2017), multiple regions of the United States (Diffenbaugh et al., 2015; Herrera-Estrada and Sheffield 2017), northwest China (Li et al., 2019c; Kong et al., 2020) and India (Sharma and Mujumdar, 2017). The dominant signal is related to the increase in heat wave occurrence, which has been attributed to anthropogenic forcing (11.3.4). This means that even if drought occurrence is unaffected, compound hot and dry events will be more frequent (Sarhadi et al., 2018; Yu and Zhai, 2020).

Drought and heat waves are also associated with fire weather, related through high temperatures, low soil moisture, and low humidity. Fire weather refers to weather conditions conducive to triggering and sustaining wildfires, which generally include temperature, soil moisture, humidity, and wind (Chapter 12). Concurrent

ACCEPTED VERSION SUBJECT TO FINAL EDITING

hot and dry conditions amplify conditions that promote wildfires (Schubert et al., 2014; Littell et al., 2016; Hope et al., 2019, Dowdy, 2018). Burnt area extent in western US forests (Abatzoglou and Williams, 2016) and particularly in California (Williams et al., 2019) has been linked to anthropogenic climate change via a significant increase in vapour pressure deficit, a primary driver of wildfires. A study of the western US examined the correlation between historical water-balance deficits and annual area burned, across a range of vegetation types from temperate rainforest to desert (McKenzie and Littell, 2017). The relationship between temperature and dryness, and wildfire, varied with ecosystem type, and the fire-climate relationship was both nonstationary and vegetation-dependent. In many fire-prone regions, such as the Mediterranean and China's Daxing'anling region, projections for increased severity of future drought and heat waves may lead to an increased frequency of wildfires relative to observed (Ruffault et al., 2018; Tian et al., 2017). Observations show a long-term trend towards more dangerous weather conditions for bushfires in many regions of Australia, which is attributable at least in part to anthropogenic climate change (Dowdy, 2018). There is emerging evidence that recent regional surges in wildland fires are being driven by changing weather extremes (SRCCL Ch2, Cross-Chapter Box 3; Jia et al., 2019). Between 1979 and 2013, the global burnable area affected by long fire-weather seasons doubled, and the mean length of the fire-weather season increased by 19% (Jolly et al., 2015). However, at the global scale, the total burned area has been decreasing between 1998 and 2015 due to human activities mostly related to changes in land use (Andela et al., 2017). Given the projected *high confidence* increase in compound hot and dry conditions, there is *high confidence* that fire weather conditions will become more frequent at higher levels of global warming in some regions. This assessment is also consistent with assessments of Chapter 12 for regional projected changes in fire weather. The SRCCL Ch2 assessed with *high confidence* that future climate variability is expected to enhance the risk and severity of wildfires in many biomes such as tropical rainforests.

In summary, there is *high confidence* that concurrent heat waves and droughts have increased in frequency over the last century at the global scale due to human influence. There is *medium confidence* that weather conditions that promote wildfires (fire weather) have become more probable in southern Europe, northern Eurasia, the US, and Australia over the last century. There is *high confidence* that compound hot and dry conditions become more probable in nearly all land regions as global mean temperature increases. There is *high confidence* that fire weather conditions will become more frequent at higher levels of global warming in some regions.

[START BOX 11.4 HERE]

BOX 11.4: Case study: Global-scale concurrent climate anomalies at the example of the 2015-2016 extreme El Niño and the 2018 boreal spring/summer extremes

Occurrence of concurrent or near-concurrent extremes in different parts of a region, or in different locations around the world challenges adaptation and risk management capacity. This can occur as a result of natural climate variability, as climates in different parts of the world are inter-connected through teleconnections. In addition, in a warming climate, the probability of having several locations being affected simultaneously by e.g. hot extremes and heat waves increases strongly as a function of global warming, with detectable changes even for changes as small as +0.5°C of additional global warming (Sections 11.2.5 and 11.3, Cross-chapter Box 11.1). Recent articles have highlighted the risks associated with concurrent extremes over large spatial scales (e.g. Lehner and Stocker, 2015; Boers et al., 2019; Gaupp et al., 2019). There is evidence that such global-scale extremes associated with hot temperature extremes are increasing in occurrence (Sippel et al., 2015; Vogel et al., 2019). Hereafter, the focus is on two recent global-scale events that featured concurrent extremes in several regions across the world. The first focuses on concurrent extremes driven by variability in tropical Pacific SSTs associated with the 2015-2016 extreme El Niño, while the second is a case study of the impacts of global warming combined with abnormal atmospheric circulation patterns in the 2018 boreal spring/summer.

[START BOX 11.4, FIGURE 1 HERE]

ACCEPTED VERSION SUBJECT TO FINAL EDITING

Box 11.4, Figure 1: Analysis of the percentage of land area affected by temperature extremes larger than two (orange) or three (blue) standard deviations in June-July-August (JJA) between 30°N and 80°N using a normalization. The more appropriate estimate is the corrected normalization. These panels show for both estimates a substantial increase in the overall land area affected by very high hot extremes since 1990 onward. Adapted from Sippel et al. (2015)

[END BOX 11.4, FIGURE 1 HERE]

The extreme El Niño in 2015-2016

El Niño-Southern Oscillation (ENSO) is one of the phenomena that have the ability to bring multitudes of extremes in different parts of the world, especially in the extreme cases of El Niño (Annex VI.4). Additionally, the background climate warming associated with greenhouse gas forcing can significantly exacerbate extremes in parts of the world even under normal El Niño conditions. The 2015-2016 El Niño event was one of the three extreme El Nino events since 1980s since the availability of satellite rainfall observations. According to some measures, it was the strongest El Niño over the past 145 years (Barnard et al., 2017). The 2015-2016 warmth was unprecedented at the central equatorial Pacific (Niño4: 5°N–5°S, 150°E–150°W) and this exceptional warmth was *unlikely* to have occurred entirely naturally, appearing to reflect an anthropogenically forced trend (Newman et al., 2018)). In particular, its signal was seen in very high monthly Global Mean Surface Temperature (GMST) values in late 2015 and early 2016, contributing to the highest record of GMST in 2016 (Section 2.3.1.1). Both the ENSO amplitude and the frequency of high-magnitude events since 1950 is higher than over the pre-industrial period (*medium confidence*; Section 2.4.2), suggesting that global extremes similar to those associated with the 2015-2016 El Niño would occur more frequently under further increases in global warming. Hereafter, the 2015-2016 El Niño event is referred to as "the 2015-2016 extreme El Niño" (Annex VI.4.1). A brief summary of extreme events that happened in 2015-2016 is provided in Section 6.2.2, 6.5.1.1 of the Special Report on the Ocean and Cryosphere in a Changing Climate (SROCC's). We provide some highlights illustrating extremes that occurred in different parts of the world during the 2015-2016 extreme El Niño in BOX11.4-Table 1, as well as a short summary hereafter.

Several regions were strongly affected by droughts in 2015, including Indonesia, Australia, the Amazon region, Ethiopia, Southern Africa, and Europe. As a result, global measurements of land water anomalies were particularly low in that year (Humphrey et al., 2018). In 2015, Indonesia experienced a severe drought and forest fire causing pronounced impact on economy, ecology and human health due to haze crisis (Field et al., 2016; Huijnen et al., 2016; Patra et al., 2017; Hartmann et al., 2018). The northern part of Australia experienced high temperatures and low precipitation between late 2015 and early 2016, and the extensive mangrove trees were damaged along the Gulf of Carpentaria in northern Australia (Duke et al., 2017). The Amazon region experienced the most intense droughts of this century in 2015-2016. This drought was more severe than the previous major droughts that occurred in the Amazon in 2005 and 2010 (Lewis et al., 2011; Erfanian et al., 2017; Panisset et al., 2018). The 2015-2016 Amazon drought impacted the entirety of South America north of 20°S during the austral spring and summer (Erfanian et al., 2017). It also increased forest fire incidence by 36% compared to the preceding 12 years (Aragão et al., 2018) and as a consequence, increased the biomass burning outbreaks and the carbon monoxide (CO) concentration in the area, affecting air quality (Ribeiro et al., 2018). This out-of-season drought affected the water availability for human consumption and agricultural irrigation and it also left rivers with very low water levels, without conditions of ship transportation, due to large sandbanks, preventing the arrival of food, medicines, and fuels (INMET, 2017). Eastern African countries were impacted by drought in 2015. It was found that the drought in Ethiopia, which was the worst in several decades, was associated with the 2015-2016 extreme El Niño that developed early in the year (Blunden and Arndt, 2016; Philip et al., 2018b). It was suggested that anthropogenic warming contributed to the 2015 Ethiopian and southern African droughts by increasing SSTs and local air temperatures (Funk et al., 2016, 2018b; Yuan et al., 2018a). It has also been suggested that the 2015-2016 extreme El Niño affected circulation patterns in Europe during the 2015-2016 winter (Geng et al., 2017; Scaife et al., 2017).

ACCEPTED VERSION SUBJECT TO FINAL EDITING

It was identified that 2015 was a year of a particularly high CO_2 growth rate, possibly related to some of the mentioned droughts, in particular in Indonesia and the Amazon region, leading to higher CO_2 release in combination with less CO_2 uptake from land areas (Humphrey et al., 2018). The impact of the 2015-2016 extreme El Niño on vegetation systems via drought was also shown from satellite data (Kogan and Guo, 2017). Overall, tropical forests were a carbon source to the atmosphere during the 2015–2016 El Niño–related drought, with some estimates suggesting that up to 2.3 PgC were released (Brando et al., 2019).

The 2015-2016 extreme El Niño has induced extreme precipitation in some regions. Severe rainfall events were observed in Chennai city in India in Devember 2015 and Yangtze river region in China in June-July 2016, and it was shown that these rainfall events are partly attributed to the 2015-2016 extreme El Niño (van Oldenborgh et al., 2016; Boyaj et al., 2018; Sun and Miao, 2018; Yuan et al., 2018b; Zhou et al., 2018).

In 2015, the activity of tropical cyclones was notably high in the North Pacific (Blunden and Arndt, 2016). Over the western North Pacific, the number of category 4 and 5 Tropical Cyclones (TCs) was 13, which is more than twice its typical annual value of 6.3 (Zhang et al., 2016a). Similarly, a record-breaking number of TCs was observed in the eastern North Pacific, particularly in the western part of that domain (Collins et al., 2016; Murakami et al., 2017a). These extraordinary TC activities were related to the average SST anomaly during that year, which were associated with the 2015-2016 extreme El Niño and the positive phase of the Pacific Meridional Mode (PMM) (Murakami et al., 2017a; Hong et al., 2018; Yamada et al., 2019). However, it has been suggested that the intense TC activities in both the western and the eastern North Pacific in 2015 were not only due to the El Niño, but also to a contribution of anthropogenic forcing (Murakami et al., 2017a; Yang et al., 2018d). The impact of the Indian Ocean SST also was suggested to contribute to the extreme TC activity in the western North Pacific in 2015 (Zhan et al., 2018). In contrast, in Australia, it was the least active TC season since satellite records began in 1969-70 (Blunden and Arndt, 2017).

[START BOX 11.4, TABLE 1 HERE]

Box 11.4, Table 1: List of events related to the 2015-2016 Extreme El Niño in the literature.

Region	Period	Events	References
Indonesia	July 2015 to June 2016	droughts, forest fire	(Field et al., 2016; Huijnen et al., 2016; Patra et al., 2017; Hartmann et al., 2018)
Northern Australia	Between late 2015 and early 2016	high temperature and drought	(Duke et al., 2017)
Amazon	September 2015 to May 2016	droughts, forest fire	(Jiménez-Muñoz et al., 2016; Erfanian et al., 2017; Aragão et al., 2018; Panisset et al., 2018; Ribeiro et al., 2018)
The entirety of South America north of 20°S	Austral spring and 2015-2016 summer	droughts	(Erfanian et al., 2017)
Ethiopia	February-September 2015	droughts	(Blunden and Arndt, 2016; Philip et al., 2018b)
Southern Africa	November 2015–April 2016	droughts	(Funk et al., 2016, 2018a; Blamey et al., 2018; Yuan et al., 2018a)
Europe	Boreal 2015-2016 winter	effects on of circulation patterns	(Geng et al., 2017; Scaife et al., 2017)
India	May 2016	high temperature	(van Oldenborgh et al., 2018)
India	December 2015	extreme rainfall	(van Oldenborgh et al., 2016; Boyaj et al., 2018)
China	June-July 2016	extreme rainfall	(Sun and Miao, 2018; Yuan et al., 2018b; Zhou et al., 2018)
Western North Pacific	Boreal summer 2015	the large number (13) of category 4 and 5 tropical cyclones	(Blunden and Arndt, 2016; Mueller et al., 2016a; Zhang et al., 2016b; Hong et al., 2018; Yamada et al., 2019)
Eastern North Pacific	Boreal summer 2015	a record-breaking number of tropical cyclones	(Collins et al., 2016; Murakami et al., 2017a)
Global	2015-2016 El Niño	high CO_2 release to the atmosphere associated with	(Humphrey et al., 2018; Brando et al., 2019)

ACCEPTED VERSION SUBJECT TO FINAL EDITING

		droughts and fires in several affected regions	

[END BOX 11.4, TABLE 1 HERE]

Global-scale temperature extremes and concurrent precipitation extremes in boreal 2018 spring and summer

In the 2018 boreal spring-summer season (May-August), wide areas of the mid-latitudes in the Northern Hemisphere experienced heat extremes and in part enhanced drought (Kornhuber et al., 2019; Vogel et al., 2019; Box 11.3, Figure 2). The reported impacts included the following (Vogel et al., 2019): 90 deaths from heat strokes in Quebec (Canada), 1469 deaths from heat strokes in Japan (Shimpo et al., 2019a), 48 heat-related deaths in South Korea (Min et al., 2020), heat warning affecting 90,000 students in the USA, fires in numerous countries (Canada (British Columbia), USA (California), Lapland, Latvia), crop losses in the UK, Germany and Switzerland (Vogel et al., 2019) and overall in central and northern Europe (leading to yield reductions of up to 50% for the main crops; Toreti et al., 2019), fish deaths in Switzerland, and melting of roads in the Netherlands and the UK, among others. In addition to the numerous hot and dry extremes, an extremely heavy rainfall event occurred over wide areas of Japan from 28 June to 8 July 2018 (Tsuguti et al., 2018), which was followed by a heat wave (Shimpo et al., 2019b). The heavy precipitation event caused more than 230 deaths in Japan, and was named as “the Heavy Rain Event of July 2018”.

The heavy precipitation event was characterized by unusually widespread and persistent rainfall and locally anomalous total precipitation led by band-shaped precipitation systems, which are frequently associated with heavy precipitation events in East Asia (Kato, 2020; Section 11.7.3). The extreme rainfall in Japan was caused by anomalous moisture transport with a combination of abnormal jet condition (Takemi and Unuma, 2019; Takemura et al., 2019; Tsuji et al., 2019; Yokoyama et al., 2020), which can be viewed as an atmospheric river (Yatagai et al., 2019; Sections 8.2.2.8, 11.7.2) caused by intensified inflow velocity and high SST around Japan (Kawase et al., 2019; Sekizawa et al., 2019).

This precipitation event and the subsequent heat wave are related to abnormal condition of the jet and North Pacific Subtropical High in this month (Shimpo et al., 2019a; Ren et al., 2020), which caused extreme conditions from Europe, Eurasia, and North America (Kornhuber et al., 2019; Box 11.4, Figure 2). A role of Atlantic SST anomaly on the meandering jets and the subtropical high have been suggested (Liu et al., 2019a). These dynamic and thermodynamic components generally have substantial influence on extreme rainfall in East Asia (Oh et al., 2018), but it is under investigation whether these factors were due to anthropogenic forcing.

[START BOX 11.4, FIGURE 2 HERE]

Box 11.4, Figure 2: Meteorological conditions in July 2018. The color shading shows the monthly mean near-surface air temperature anomaly with respect to 1981 to 2010. Contour lines indicate the geopotential height in m, highlighted are the isolines on 12'000 m and 12'300 m, which indicate the approximate positions of the polar-front jet and subtropical jet, respectively. The light blue-green ellipse shows the approximate extent of the strong precipitation event that occurred at the beginning of July in the region of Japan and Korea. All data is from the global ECMWF Reanalysis v5 (ERA5, Hersbach et al., 2020).

[END BOX 11.4, FIGURE 2 HERE]

Regarding the hot extremes that occurred across the Northern Hemisphere in the 2018 boreal May-July time period, Vogel et al. (2019) found that the event was unprecedented in terms of the total area affected by hot extremes (on average about 22% of populated and agricultural areas in the Northern Hemisphere) for that

ACCEPTED VERSION SUBJECT TO FINAL EDITING

period, but was consistent with a +1°C climate which was the estimated global mean temperature anomaly around that time (for 2017; SR1.5). This study also found that events similar to the 2018 May-July temperature extremes would approximately occur 2 out of 3 years under +1.5°C of global warming, and every year under +2°C of global warming. Imada et al. (2019) also suggests that the mean annual occurrence of extremely hot days in Japan will be expected to increase by 1.8 times under a global warming level of 2°C above pre-industrial levels. Kawase et al. (2019) showed that the extreme rainfall in Japan during this event was increased by approximately 7% due to recent rapid warming around Japan. Hence, it is *virtually certain* that these 2018 concurrent events would not have occurred without human-induced global warming. Concurrent events of this type are also projected to happen more frequently under higher levels of global warming. On the other hand, there is currently *low confidence* in projected changes in the frequency or strength of the anomalous circulation patterns leading to concurrent extremes (e.g. Cross-Chapter Box 10.1).

The case studies presented in this Box illustrate the current state of knowledge regarding the contribution of human-induced climate change to recent concurrent extremes in the global domain. Recent years have seen a more frequent occurrence of such events. The heat wave in Europe in the 2019 boreal summer and its coverage in the global domain is an additional example (Vautard et al., 2020a). However, there are still very few studies investigating which types of concurrent extreme events could occur under increasing global warming. It has been noted that such events could also be of particular risk for concurrent impacts in the world's breadbaskets (Zampieri et al., 2017; Kornhuber et al., 2020).

In summary, the 2015-2016 extreme El Niño and the 2018 boreal spring/summer extremes were two examples of recent concurrent extremes. The El Niño event in 2015-2016 was one of the three extreme El Niño events since 1980s and there are many extreme events concurrently observed in this period including droughts, heavy precipitation, and more frequent intense tropical cyclones. Both the ENSO amplitude and the frequency of high-magnitude events since 1950 is higher than over the pre-industrial period (*medium confidence*), suggesting that global extremes similar to those associated with the 2015-2016 El Niño would occur more frequently under further increases in global warming. The 2018 boreal spring/summer extremes were characterized by heat extremes and enhanced droughts in wide areas of the mid-latitudes in the Northern Hemisphere and extremely heavy rainfall in East Asia. These concurrent events were generally related to abnormal condition of the jet and North Pacific Subtropical High, but also amplified by background global warming. It is *virtually certain* that these 2018 concurrent extreme events would not have occurred without human-induced global warming. Recent years have seen a more frequent occurrence of such concurrent events. However, it is still unknown which types of concurrent extreme events could occur under increasing global warming.

[END BOX 11.4 HERE]

11.9 Regional information on extremes

This section complements the assessments of changes in temperature extremes (Section 11.3), heavy precipitation (Section 11.4), and droughts (Section 11.6), by providing additional regional details. Owing to the large number of regions and space limitations, the regional assessment for each of the AR6 reference regions (see Section 1.5.2.2 for a description) is presented here in a set of tables. The tables are organized according to types of extremes (temperature, heavy precipitation, droughts) for Africa (Tables 11.4-11.6), Asia (Table 11.7-11.9), Australasia (Tables 11.10-11.12), Central and South America (Tables 11.13-11.15), Europe (Tables 11.16-11.18), and North America (Tables 11.19-11.21). Each table contains regional assessments for observed changes, the human contribution to the observed changes, and projections of changes in these extremes at 1.5°C, 2°C and 4°C of global warming. Expanded versions of the tables with full evidence and rationale for assessments are provided in the Chapter Appendix (Tables 11.A.4-11.A.21).

11.9.1 Overview

Sections 11.9.2, 11.9.3., and 11.9.4 provide brief summaries of the underlying evidence used to derive the

ACCEPTED VERSION SUBJECT TO FINAL EDITING

regional assessments for temperature extremes, heavy precipitation events, and droughts, respectively. The assessments take into account evidence from studies based on global datasets (global studies), as well as regional studies. Global studies include analyses for all continents and AR6 regions with sufficient data coverage, and provide an important basis for cross-region consistency, as the same data and methods are used for all regions. However, individual regional studies may include additional information that is missed in global studies and thus provide an important regional calibration for the assessment.

The assessments are presented using the calibrated confidence and likelihood language (Box 1.1). *Low confidence* is assessed when there is *limited evidence*, either because of a lack of available data in the region and/or a lack of relevant studies. *Low confidence* is also assessed when there is a lack of agreement on the evidence of a change, which may be due to large variability or inconsistent changes depending on the considered subregions, time frame, models, assessed metrics, or studies. In cases when the evidence is strongly contradictory, for example with substantial regional changes of opposite sign, "mixed signal" is indicated. With an assessment of *low confidence*, the direction of change is not indicated in the tables. A direction of change (increase or decrease) is provided with an assessment of *medium confidence*, *high confidence*, *likely*, or higher likelihood levels. Likelihood assessments are only provided in the case of *high confidence*. In some cases, there may be confidence in a small or no change.

For projections, changes are assessed at three global warming levels (GWLs, CC-Box 11.1): 1.5°C, 2°C and 4°C. Literature based both on GWL projections and on scenario-based projections is used for the assessments. In the case of literature on scenario-based projections, a mapping between scenarios/time frames and GWLs was performed as documented in CC-Box 11.1. Projections of changes in temperature and precipitation extremes are assessed relative to two different baselines: the recent past (1995-2014) and pre-industrial (1850-1900). With smaller changes relative to the variability, in particular because droughts happen on longer timescales compared to extremes of daily temperature and precipitation, it is more difficult to distinguish changes in drought relative to the recent past. As such, changes in droughts are assessed relative to the pre-industrial baseline, unless indicated otherwise.

11.9.2 Temperature extremes

Tables 11.4, 11.7, 11.10, 11.13, 11.16, and 11.19 include assessments for past chn temperature extremes and their attribution, as well as future projections. The evidence is mostly drawn from changes in metrics based on daily maximum and minimum temperatures, similar to those used in Section 11.3. The regional assessments start from global studies that used consistent analyses for all regions globally with sufficient data. This includes Dunn et al. (2020) for observed changes and Li et al. (2020) and the Chapter 11 Supplementary Material (11.SM) for projections with the CMIP6 multi-model ensemble. Evidence from regional studies, and those based on the CMIP5 multi-model ensemble or CORDEX simulations, are then used to refine the confidence assessments. For attribution, Seong et al. (2020) provide a consistent analysis for AR6 regions and Wang et al. (2017) for SREX regions. Additional regional studies, including event attribution analyses (Section 11.2), are used when available. In some regions that were not analysed in Seong et al. (2020) and with no known event attribution studies, *medium confidence* of a human contribution is assessed when there is strong evidence of changes from observations that are in the direction of model projected changes for the future, the magnitude of projected changes increases with global warming, and there is no other evidence to the contrary. Understanding of how temperature extremes change with the mean temperature and overwhelming evidence of a human contribution to the observed larger-scale changes in the mean temperature and temperature extremes further support this assessment.

11.9.3 Heavy precipitation

ACCEPTED VERSION SUBJECT TO FINAL EDITING

Tables 11.5, 11.8, 11.11, 11.14, 11.17, and 11.20 include assessments for past changes in heavy precipitation events and their attribution, as well as future projections. The evidence is mostly drawn from changes in metrics based on one-day or five-day precipitation amounts, as addressed in Section 11.4. Similar to temperature extremes, the assessment of changes in heavy precipitation uses global studies, including Dunn et al. (2020) and Sun et al. (2020) for observed changes, and Li et al. (2020) and the Chapter 11 Supplementary Material (11.SM) for projected changes using the CMIP6 multi-model ensemble. For attribution, Paik et al. (2020) provided continental analyses where data coverage was sufficient, but no attribution studies based on global data are available for the regional scale. For each region, regional studies, and studies based on the CMIP5 multi-model ensemble or CORDEX simulations, are also considered in the assessments for past changes, attribution, and projections.

11.9.4 Droughts

Tables 11.6, 11.9, 11.12, 11.15, 11.18, and 11.21 provide regional tables on past, attributed and projected changes in droughts. The assessment is subdivided in three drought categories corresponding to four drought types: i) meteorological droughts, ii) agricultural and ecological droughts, and iii) hydrological droughts (see Section 11.6). A list of metrics and global studies used for the assessments is provided below. The evidence from global studies is complemented in each continent with evidence from regional studies. An overview of studies considered for the assessments in projections is provided in Table 11.3.

Meteorological droughts are assessed based on observed and projected changes in precipitation-only metrics such as the Standardized Precipitation Index (SPI) and Consecutive Dry Days (CDD). Observed changes are assessed based on two global studies, Dunn et al. (2020) for CDD and Spinoni et al. (2019) for SPI. For projections, evidence for changes at 1.5°C and 2°C of global warming is drawn from Xu et al. (2019) and Touma et al. (2015) (based on RCP8.5 for 2010-2054 compared to 1961-2005) for SPI (CMIP5) and the Chapter 11 Supplementary Material (11.SM) for CDD (CMIP6). For projections at 4°C of global warming, evidence is drawn from several sources, including Touma et al. (2015) and Spinoni et al. (2020) for SPI (from CMIP5 and CORDEX, respectively), and the Chapter 11 Supplementary Material (11.SM) for CDD (CMIP6). No global-scale studies are available for the attribution of meteorological drought, and thus this assessment is based on regional detection and attribution or event attribution studies.

Agricultural and ecological droughts are assessed based on observed and projected changes in total column soil moisture, complemented by evidence on changes in surface soil moisture, water-balance (precipitation minus evapotranspiration (ET)) and metrics driven by precipitation and atmospheric evaporative demand (AED) such as the SPEI and PDSI (Section 11.6). In the case of the latter, only studies including estimates based on the Penman-Monteith equation (SPEI-PM and PDSI-PM) are considered because of biases associated with temperature-only approaches (Section 11.6). In arid regions in which AED-based metrics can increase strongly in projections, more weight is given to soil moisture projections. For observed changes, evidence is drawn from several sources: Padrón et al. (2020) for changes in precipitation minus ET, as well as soil moisture from the multi-model Land Surface Snow and Soil Moisture Model Intercomparison Project within CMIP6 (LS3MIP, Van Den Hurk et al., 2016; Chapter 11 Supplementary Material (11.SM)); Greve et al. (2014) for changes in precipitation minus ET, and precipitation minus AED; Spinoni et al. (2019) for changes in SPEI-PM; and Dai and Zhao (2017) for changes in PDSI-PM. For projections at 1.5°C of global warming, evidence is drawn from Xu et al. (2019) based on CMIP5 and the Chapter 11 Supplementary Material (11.SM) based on CMIP6 for changes in total column and surface soil moisture, and from Naumann et al. (2018) for changes in SPEI-PM, based on EC-Earth simulations driven with SSTs from seven CMIP5 ESMs. For projections at 2°C of global warming, evidence is drawn from Xu et al. (2019) based on CMIP5, and Cook et al. (2020) (SSP1-2.6, 2071-2100 compared to pre-industrial) and the Chapter 11 Supplementary Material (11.SM) based on CMIP6, for changes in total column and surface soil moisture; evidence is also drawn from Naumann et al. (2018) for changes in SPEI-PM. For projections at 4°C of global warming, evidence is mostly drawn from Cook et al. (2020) (SSP3-7.0, 2071-2100) and the Chapter 11 Supplementary Material (11.SM) based on CMIP6 for changes in total column and surface soil moisture, and from Vicente-Serrano et al. (2020) for changes in SPEI-PM based on CMIP5. No global-scale studies with regional-scale

ACCEPTED VERSION SUBJECT TO FINAL EDITING

information are available for the attribution of agricultural and ecological droughts, and thus this assessment is based on regional detection and attribution or event attribution studies.

Hydrological droughts are assessed based on observed and projected changes in low flows, complemented by information on changes in mean runoff. For observed changes, evidence is drawn from three studies (Dai and Zhao, 2017; Gudmundsson et al., 2019, 2021). For projected changes at 1.5°C of global warming, evidence is drawn from Touma et al. (2015) based on analyses of the Standardized Runoff Index (SRI) (CMIP5, based on 2010-2054 compared to 1961-2005), complemented with regional studies when available. For projected changes at 2°C of global warming, evidence is also drawn from Cook et al. (2020) for changes in runoff in CMIP6 (Scenario SSP1-2.6, 2071-2100), and from Zhai et al. (2020) for changes in low flows based on simulations with a single model. For projected changes at 4°C of global warming, evidence is drawn from Touma et al. (2015) based on CMIP5 analyses of SRI, Cook et al. (2020) for changes in surface and total runoff based on CMIP6, and Giuntoli et al. (2015) for changes in low flows based on the Inter-Sectoral Impact Model Intercomparison Project (ISI-MIP) based on six Global Hydrological Models (GHMs) and five GCMs, including an analysis of inter-model signal-to-noise ratio. One global-scale study with regional-scale information is available for the attribution of hydrological droughts (Gudmundsson et al., 2021), but only in a few AR6 regions. This information was complemented with evidence from regional detection and attribution, and event attribution studies when available.

[START TABLE 11.3 HERE]

Table 11.3: Global analyses considered for the assessments of drought projections. "MET" refers to meteorological droughts, "AGR/ECOL" to agricultural and ecological droughts, and "HYDR" to hydrological droughts

Reference	Model data	Index	Drought type	Projection horizon(s)	Baseline
Chapter 11 Suppl. Material (11.SM)	CMIP6	CDD, Soil moisture (total, surface)	MET	1.5°C, 2°C, 4°C	1850-1900
Cook et al. (2020)	CMIP6	Soil moisture (total, surface), Runoff (total, surface)	AGR/ECOL, HYDR	2071-2011, SSP1-2.6 (~2°C, CC-Box 11.1; Chapter 4, Table 4.2) 2071-2011, SSP3-7-3 (~4°C, CC-Box 11.1; Chapter 4, Table 4.2)	1850-1900
Xu et al. (2019)	CMIP5	SPI, Soil moisture (total, surface)	MET, AGR/ECOL	1.5°C, 2°C	1971-2000
Touma et al. (2015)	CMIP5	SPI, SRI	MET, HYDR	2010-2054, RCP8.5 (~1.5°C; CC-Box 11.1, 11.SM.1) 2055-2099, RCP8.5 (~3.5°C, CC-Box 11.1, 11.SM.1)	1961-2005
Spinoni et al. (2020)	CORDEX (CMIP5 driving GCMs, RCMs)	SPI	MET	2071-2100, RCP4.5 (~2.5°C, CC-Box 11.1, 11.SM.1) 2071-2100, RCP8.5 (~4.5°C, CC-Box 11.1, 11.SM.1)	1981-2010
Naumann et al. (2018)	1 GCM (EC-EARTH3-HR v3.1) driven with SST fields from 7 CMIP5 GCMs	SPEI-PM	AGR/ECOL	1.5°C, 2°C, (3°C)	0.6°C
Vicente-Serrano et al. (2020)	CMIP5	SPEI-PM	AGR/ECOL	2070-2100, RCP8.5 (~4.5°C, CC-Box 11.1, 11.SM.1)	1970-2000
Giuntoli et al. (2015)	ISI-MIP (6 GHMs and 5 CMIP5 GCMs)	Low-flows days	HYDR	2066-2099, RCP8-5 (~4°C, CC-Box 11.1, 11.SM.1)	1972-2005
Zhai et al. (2020)	1 GHM (VIC) driven by 4 CMIP5 GCMs	Extreme low runoff	HYDR	1.5°C, 2°C	2006-2015

[END TABLE 11.3 HERE]

ACCEPTED VERSION SUBJECT TO FINAL EDITING

Frequently Asked Questions

FAQ 11.1: How do changes in climate extremes compare with changes in climate averages?

Human-caused climate change alters the frequency and intensity of climate variables (e.g., surface temperature) and phenomena (e.g., tropical cyclones) in a variety of ways. We now know that the ways in which average and extreme conditions have changed (and will continue to change) depend on the variable and the phenomenon being considered. Changes in local surface temperature extremes follow closely the corresponding changes in local average surface temperatures. On the contrary, changes in precipitation extremes (heavy precipitation) generally do not follow those in average precipitation and can even move in the opposite direction (e.g., with average precipitation decreasing but extreme precipitation increasing).

Climate change will manifest very differently depending on which region, which season and which variable we are interested in. For example, over some parts of the Arctic, temperatures will warm at rates about 3-4 times higher during winter compared to summer months. And in summer, most of northern Europe will experience larger temperatures increases than most places in Southeast South America and Australasia, with differences that can be larger than 1°C depending on the level of global warming. In general, differences across regions and seasons arise because the underlying physical processes differ drastically across regions and seasons.

Climate change will also manifest differently for different weather regimes and can lead to contrasting changes in average and extreme conditions. Observations of the recent past and climate model projections show that, in most places, changes in daily temperatures are dominated by a general warming in which both the climatological average and extreme values are shifted towards higher temperatures, making warm extremes more frequent and cold extremes less frequent. The top panels in FAQ 11.1, Figure 1 show projected changes in surface temperature for long-term average conditions (left) and for extreme hot days (right) during the warm season (summer in mid- to high-latitudes). Projected increases in long-term average temperature differ substantially in different places, varying from less than 3°C in some places in central South Asia and southern South America to over 7°C in some places in North America, north Africa and the Middle East. Changes in extreme hot days follow changes in average conditions quite closely, although in some places the warming rates for extremes can be intensified (e.g., southern Europe and the Amazon basin) or weakened (e.g., northern Asia and Greenland) compared to average values.

Recent observations and global and regional climate model projections point to changes in precipitation extremes (including both rainfall and snowfall extremes) differing drastically from those in average precipitation. The bottom panels in FAQ 11.1, Figure 1 show projected changes in the long-term average precipitation (left) and in heavy precipitation (right). Averaged precipitation changes show striking regional differences, with substantial drying in places such as southern Europe and northern South America and wetting in places such as Middle East and southern South America. Changes in extreme heavy precipitation are much more uniform, with systematic increases over nearly all land regions. The physical reasons behind the different response of averaged and extreme precipitation are now well understood. The intensification of extreme precipitation is driven by the increase in atmospheric water vapour (about 7% per 1°C of warming near the surface), although this is modulated by various dynamical changes. In contrast, changes in average precipitation are driven not only by moisture increases but also by slower processes that constrain future changes to on be only about 2–3% per 1°C of warming near the surface.

In summary, the specific relationship between changes in average and extreme conditions strongly depends on the variable or phenomenon being considered. At the local scale, average and extreme surface temperature changes are strongly related, while average and extreme precipitation changes are often weakly related. For both variables, the changes in average and extreme conditions vary strongly across different places due to the effect of local and regional processes.

[START FAQ 11.1, FIGURE 1 HERE]

FAQ 11.1, Figure 1: Global maps of future changes in surface temperature (top panels) and precipitation (bottom panels) for long-term average (left) and extreme conditions (right). All changes were estimated using the CMIP6 ensemble mean for a scenario with a global warming of 4°C relative to 1850-

ACCEPTED VERSION SUBJECT TO FINAL EDITING

1900 temperatures. Average surface temperatures refer to the warmest three-month season (summer in mid- to high-latitudes) and extreme temperature refer to the hottest day in a year. Precipitation changes, which can include both rainfall and snowfall changes, are normalized by 1850-1900 values and shown in percentage; extreme precipitation refers to the largest daily rainfall in a year.

[END FAQ 11.1, FIGURE 1 HERE]

[END FAQ 11.1 HERE]

ACCEPTED VERSION
SUBJECT TO FINAL EDITING

[START FAQ 11.2 HERE]

FAQ 11.2: Will unprecedented extremes occur as a result of human-induced climate change?

Climate change has already increased the magnitude and frequency of extreme hot events and decreased the magnitude and frequency of extreme cold events, and, in some regions, intensified extreme precipitation events. As the climate moves away from its past and current states, we will experience extreme events that are unprecedented, either in magnitude, frequency, timing or location. The frequency of these unprecedented extreme events will increase with increasing global warming. Additionally, the combined occurrence of multiple unprecedented extremes may result in large and unprecedented impacts.

Human-induced climate change has already affected many aspects of the climate system. In addition to the increase in global surface temperature, many types of weather and climate extremes have changed. In most regions, the frequency and intensity of hot extremes have increased and those of cold extremes have decreased. The frequency and intensity of heavy precipitation events have increased at a global scale and over a majority of land regions. Although extreme events such as land and marine heatwaves, heavy precipitation, drought, tropical cyclones, and associated wildfires and coastal flooding have occurred in the past and will continue to occur in the future, they often come with different magnitudes or frequencies in a warmer world. For example, future heatwaves will last longer and have higher temperatures, and future extreme precipitation events will be more intense in several regions. Certain extremes, such as extreme cold, will be less intense and less frequent with increasing warming.

Unprecedented extremes – that is, events not experienced in the past – will occur in the future in five different ways (FAQ 11.2, Figure 1). First, events that are considered to be extreme in the current climate will occur in the future with unprecedented magnitudes. Second, future extreme events will also occur with unprecedented frequency. Third, certain types of extremes may occur in regions that have not previously encountered those types of events. For example, as the sea level rises, coastal flooding may occur in new locations, and wildfires are already occurring in areas, such as parts of the Arctic, where the probability of such events was previously low. Fourth, extreme events may also be unprecedented in their timing. For example, extremely hot temperatures may occur either earlier or later in the year than they have in the past.

Finally, compound events, where multiple extreme events of either different or similar types occur simultaneously and/or in succession, may be more probable or severe in the future. These compound events can often impact ecosystems and societies more strongly than when such events occur in isolation. For example, a drought along with extreme heat will increase the risk of wildfires and agriculture damages or losses. As individual extreme events become more severe as a result of climate change, the combined occurrence of these events will create unprecedented compound events. This could exacerbate the intensity and associated impacts of these extreme events.

Unprecedented extremes have already occurred in recent years, relative to the 20th century climate. Some recent extreme hot events would have had very little chance of occurring without human influence on the climate (see FAQ 11.3). In the future, unprecedented extremes will occur as the climate continues to warm. Those extremes will happen with larger magnitudes and at higher frequencies than previously experienced. Extreme events may also appear in new locations, at new times of the year, or as unprecedented compound events. Moreover, unprecedented events will become more frequent with higher levels of warming, for example at 3°C of global warming compared to 2°C of global warming.

[START FAQ 11.2, FIGURE 1 HERE]

FAQ 11.2, Figure 1: New types of unprecedented extremes that will occur as a result of climate change.

[END FAQ 11.2, FIGURE 1 HERE]

[END FAQ 11.2 HERE]

ACCEPTED VERSION SUBJECT TO FINAL EDITING

[START FAQ 11.3 HERE]

FAQ 11.3: Did climate change cause that recent extreme event in my country?

While it is difficult to identify the exact causes of a particular extreme event, the relatively new science of event attribution is able to quantify the role of climate change in altering the probability and magnitude of some types of weather and climate extremes. There is strong evidence that characteristics of many individual extreme events have already changed because of human-driven changes to the climate system. Some types of highly impactful extreme weather events have occurred more often and have become more severe due to these human influences. As the climate continues to warm, the observed changes in the probability and/or magnitude of some extreme weather events will continue as the human influences on these events increase.

It is common to question whether human-caused climate change caused a major weather- and climate-related disaster. When extreme weather and climate events do occur, both exposure and vulnerability play an important role in determining the magnitude and impacts of the resulting disaster. As such, it is difficult to attribute a specific disaster directly to climate change. However, the relatively new science of event attribution enables scientists to attribute aspects of specific extreme weather and climate events to certain causes. Scientists cannot answer directly whether a particular event was caused by climate change, as extremes do occur naturally and any specific weather and climate event is the result of a complex mix of human and natural factors. Instead, scientists quantify the relative importance of human and natural influences on the magnitude and/or probability of specific extreme weather events. Such information is important for disaster risk reduction planning, because improved knowledge about changes in the probability and magnitude of relevant extreme events enables better quantification of disaster risks.

On a case-by-case basis, scientists can now quantify the contribution of human influences to the magnitude and probability of many extreme events. This is done by estimating and comparing the probability or magnitude of the same type of event between the current climate – including the increases in greenhouse gas concentrations and other human influences – and an alternate world where the atmospheric greenhouse gases remained at pre-industrial levels. FAQ 11.3 Figure 1 illustrates this approach using differences in temperature and probability between the two scenarios as an example. Both the pre-industrial (blue) and current (red) climates experience hot extremes, but with different probabilities and magnitudes. Hot extremes of a given temperature have a higher probability of occurrence in the warmer current climate than in the cooler pre-industrial climate. Additionally, an extreme hot event of a particular probability will be warmer in the current climate than in the pre-industrial climate. Climate model simulations are often used to estimate the occurrence of a specific event in both climates. The change in the magnitude and/or probability of the extreme event in the current climate compared to the pre-industrial climate is attributed to the difference between the two scenarios, which is the human influence.

Attributable increases in probability and magnitude have been identified consistently for many hot extremes. Attributable increases have also been found for some extreme precipitation events, including hurricane rainfall events, but these results can vary among events. In some cases, large natural variations in the climate system prevent attributing changes in the probability or magnitude of a specific extreme to human influence. Additionally, attribution of certain classes of extreme weather (e.g., tornadoes) is beyond current modelling and theoretical capabilities. As the climate continues to warm, larger changes in probability and magnitude are expected, and as a result it will be possible to attribute future temperature and precipitation extremes in many locations to human influences. Attributable changes may emerge for other types of extremes as the warming signal increases.

In conclusion, human-caused global warming has resulted in changes in a wide variety of recent extreme weather events. Strong increases in probability and magnitude, attributable to human influence, have been found for many heat waves and hot extremes around the world.

[START FAQ11.3 FIGURE 1 HERE]

ACCEPTED VERSION SUBJECT TO FINAL EDITING

FAQ 11.3, Figure 1: Changes in climate result in changes in the magnitude and probability of extremes. Example of how temperature extremes differ between a climate with pre-industrial greenhouse gases (shown in blue) and the current climate (shown in orange) for a representative region. The horizontal axis shows the range of extreme temperatures, while the vertical axis shows the annual chance of each temperature event's occurrence. Moving towards the right indicates increasingly hotter extremes that are more rare (less probable). For hot extremes, an extreme event of a particular temperature in the pre-industrial climate would be more probable (vertical arrow) in the current climate. An event of a certain probability in the pre-industrial climate would be warmer (horizontal arrow) in the current climate. While the climate under greenhouse gases at the pre-industrial level experiences a range of hot extremes, such events are hotter and more frequent in the current climate.

[END FAQ11.3 FIGURE 1 HERE]

[END FAQ11.3 HERE]

ACCEPTED VERSION
SUBJECT TO FINAL EDITING

Large tables

Color scale for tables for changes in temperature extremes and heavy precipitation

	Fact	Virtually certain	Extremely likely	Very likely	Likely	High confidence	Medium confidence	Low confidence
Increasing hot extremes, decreasing cold extremes								
Decreasing hot extremes, increasing cold extremes								
Inconsistent sign								

Color scale for tables for changes in droughts

	Fact	Virtually certain	Extremely likely	Very likely	Likely	High confidence	Medium confidence	Low confidence
Increasing drought								
Decreasing drought								
Inconsistent sign								

[START TABLE 11.4 HERE]

Table 11.4: Observed trends, human contribution to observed trends, and projected changes at 1.5°C, 2°C and 4°C of global warming for temperature extremes in Africa, subdivided by AR6 regions. See Sections 11.9.1 and 11.9.2 for details

All Africa	Observed trends	Detection and attribution; event attribution	Projections		
			1.5 °C	2 °C	4 °C
	Insufficient data for the continent, but there is *high confidence* of an increase in the intensity and frequency of hot extremes and decrease in the intensity and frequency of cold extremes in all subregions with sufficient data	Limited evidence for the continent, but there is *medium confidence* in a human contribution to the observed increase in the intensity and frequency of hot extremes and decrease in the intensity and frequency of cold extremes for all subregions with sufficient data	CMIP6 models project a robust increase in the intensity and frequency of TXx events and a robust decrease in the intensity and frequency of TNn events (Li et al., 2020; Annex). Median increase of more than 0.5°C in the 50-year TXx and TNn events compared to the 1°C warming level (Li et al., 2020)	CMIP6 models project a robust increase in the intensity and frequency of TXx events and a robust decrease in the intensity and frequency of TNn events (Li et al., 2020; Annex). Median increase of more than 1°C in the 50-year TXx and TNn events compared to the 1°C warming level (Li et al., 2020)	CMIP6 models project a robust increase in the intensity and frequency of TXx events and a robust decrease in the intensity and frequency of TNn events (Li et al., 2020; Annex). Median increase of more than 3°C in the 50-year TXx and TNn events compared to the 1°C warming level ((Li et al., 2020)
	Medium confidence in the increase in the intensity and frequency of hot extremes and decrease in the intensity and frequency of cold extremes.	*Medium confidence* in a human contribution to the observed increase in the intensity and frequency of hot extremes and decrease in the intensity and	Increase in the intensity and frequency of hot extremes: *Very likely* (compared with the recent past (1995-2014)) *Extremely likely* (compared with pre-industrial)	Increase in the intensity and frequency of hot extremes: *Extremely likely* (compared with the recent past (1995-2014))	Increase in the intensity and frequency of hot extremes: *Virtually certain* (compared with the recent past (1995-2014))

ACCEPTED VERSION SUBJECT TO FINAL EDITING

		frequency of cold extremes.	Decrease in the intensity and frequency of cold extremes: *Very likely* (compared with the recent past (1995-2014)) *Extremely likely* (compared with pre-industrial)	*Virtually certain* (compared with pre-industrial) Decrease in the intensity and frequency of cold extremes: *Extremely likely* (compared with the recent past (1995-2014)) *Virtually certain* (compared with pre-industrial)	*Virtually certain* (compared with pre-industrial) Decrease in the intensity and frequency of cold extremes: *Virtually certain* (compared with the recent past (1995-2014)) *Virtually certain* (compared with pre-industrial)
Mediterranean (MED)[2]	Significant ncreases in the intensity and frequency of hot extremes and significant decreases in the intensity and frequency of cold extremes (Peña-Angulo et al., 2020; El Kenawy et al., 2013; Acero et al., 2014; Fioravanti et al., 2016; Ruml et al., 2017; Türkeș and Erlat, 2018; Donat et al., 2013, 2014, 2016; Filahi et al., 2016; Driouech et al., 2021; Dunn et al., 2020)	Robust evidence of a human contribution to the observed increase in the intensity and frequency of hot extremes and decrease in the intensity and frequency of cold extremes (Seong et al., 2020; Wang et al., 2017; Sippel and Otto, 2014; Wilcox et al., 2018)	CMIP6 models project a robust increase in the intensity and frequency of TXx events and a robust decrease in the intensity and frequency of TNn events (Li et al., 2020; Annex). Median increase of more than 0.5°C in the 50-year TXx and TNn events compared to the 1°C warming level (Li et al., 2020) and more than 2°C in annual TXx and TNn compared to pre-industrial (Annex). Additional evidence from CMIP5 and RCM simulations for an increase in the intensity and frequency of hot extremes and decrease in the intensity and frequency of cold extremes (Cardoso et al., 2019; Zollo et al., 2016; Weber et al., 2018)	CMIP6 models project a robust increase in the intensity and frequency of TXx events and a robust decrease in the intensity and frequency of TNn events (Li et al., 2020; Annex). Median increase of more than 1°C in the 50-year TXx and TNn events compared to the 1°C warming level (Li et al., 2020) and more than 2.5°C in annual TXx and TNn compred to pre-industrial (Annex). Additional evidence from CMIP5 and RCM simulations for an increase in the intensity and frequency of hot extremes and decrease in the intensity and frequency of cold extremes (Cardoso et al., 2019; Tomozeiu et al., 2014; Abaurrea et al., 2018; Nastos and Kapsomenakis, 2015; Cardell et al., 2020; Zollo et al., 2016; Weber et al., 2018; Coppola et al., 2021a)	CMIP6 models project a robust increase in the intensity and frequency of TXx events and a robust decrease in the intensity and frequency of TNn events (Li et al., 2020; Annex). Median increase of more than 3.5°C in the 50-year TXx and TNn events compared to the 1°C warming level (Li et al., 2020) and more than 5°C in annual TXx and TNn compared to pre-industrial (Annex). Additional evidence from CMIP5 and RCM simulations for an increase in the intensity and frequency of hot extremes and decrease in the intensity and frequency of cold extremes (Cardoso et al., 2019; Nastos and Kapsomenakis, 2015; Tomozeiu et al., 2014; Cardell et al., 2020; Zollo et al., 2016; Giorgi et al., 2014; Driouech et al., 2020; Coppola et al., 2021a; Engelbrecht et al., 2015)

[2] This region includes both northern Africa and southern Europe

ACCEPTED VERSION SUBJECT TO FINAL EDITING

	Very likely increase in the intensity and frequency of hot extremes and decrease in the intensity and frequency of cold extremes	Human influence *likely* contributed to the observed increase in the intensity and frequency of hot extremes and decrease in the intensity and frequency of cold extremes	Increase in the intensity and frequency of hot extremes: *Likely* (compared with the recent past (1995-2014)) *Very likely* (compared with pre-industrial) Decrease in the intensity and frequency of cold extremes: *Likely* (compared with the recent past (1995-2014)) *Very likely* (compared with pre-industrial)	Increase in the intensity and frequency of hot extremes: *Very likely* (compared with the recent past (1995-2014)) *Extremely likely* (compared with pre-industrial) Decrease in the intensity and frequency of cold extremes: *Very likely* (compared with the recent past (1995-2014)) *Extremely likely* (compared with pre-industrial)	Increase in the intensity and frequency of hot extremes: *Virtually certain* (compared with the recent past (1995-2014)) *Virtually certain* (compared with pre-industrial) Decrease in the intensity and frequency of cold extremes: *Virtually certain* (compared with the recent past (1995-2014)) *Virtually certain* (compared with pre-industrial)
Sahara (SAH)	Significant increases in the intensity and frequency of hot extremes and significant decreases in the intensity and frequency of cold extremes (Donat et al., 2014a; Moron et al., 2016; Dunn et al., 2020)	Strong evidence of changes from observations that are in the direction of model projected changes for the future. The magnitude of projected changes increases with global warming.	CMIP6 models project a robust increase in the intensity and frequency of TXx events and a robust decrease in the intensity and frequency of TNn events (Li et al., 2020; Annex). Median increase of more than 0.5°C in the 50-year TXx and TNn events compared to the 1°C warming level (Li et al., 2020) and more than 2°C in annual TXx and TNn compared to pre-industrial (Annex). Additional evidence from CMIP5 and CORDEX simulations for an increase in the intensity and frequency of hot extremes (Weber et al., 2018)	CMIP6 models project a robust increase in the intensity and frequency of TXx events and a robust decrease in the intensity and frequency of TNn events (Li et al., 2020; Annex). Median increase of more than 1°C in the 50-year TXx and TNn events compared to the 1°C warming level (Li et al., 2020) and more than 2.5°C in annual TXx and TNn compared to pre-industrial (Annex). Additional evidence from CMIP5 and CORDEX simulations for an increase in the intensity and frequency of hot extremes (Weber et al., 2018; Coppola et al., 2021a)	CMIP6 models project a robust increase in the intensity and frequency of TXx events and a robust decrease in the intensity and frequency of TNn events (Li et al., 2020; Annex). Median increase of more than 3.5°C in the 50-year TXx and TNn events compared to the 1°C warming level (Li et al., 2020) and more than 5°C in annual TXx and TNn compared to pre-industrial (Annex). Additional evidence from CMIP5/CMIP3 and CORDEX simulations for an increase in the intensity and frequency of hot extremes (Coppola et al., 2021a; Engelbrecht et al., 2015; Giorgi et al., 2014)
	Likely increase in the intensity and frequency of hot extremes and decrease in the intensity and frequency of cold extremes	*Medium* confidence in a human contribution to the observed increase in the intensity and frequency of hot extremes and decrease in the intensity and frequency of cold extremes.	Increase in the intensity and frequency of hot extremes: *Likely* (compared with the recent past (1995-2014)) *Very likely* (compared with pre-industrial) Decrease in the intensity and frequency of cold extremes: *Likely* (compared with the recent past (1995-2014))	Increase in the intensity and frequency of hot extremes: *Very likely* (compared with the recent past (1995-2014)) *Extremely likely* (compared with pre-industrial) Decrease in the intensity and frequency of cold extremes: *Very likely* (compared with the recent past (1995-2014))	Increase in the intensity and frequency of hot extremes: *Virtually certain* (compared with the recent past (1995-2014)) *Virtually certain* (compared with pre-industrial) Decrease in the intensity and frequency of cold extremes: *Virtually certain* (compared

ACCEPTED VERSION SUBJECT TO FINAL EDITING

			Very likely (compared with pre-industrial).	*Extremely likely* (compared with pre-industrial)	with the recent past (1995-2014)) *Virtually certain* (compared with pre-industrial)
Western Africa (WAF)	Significant increases in the intensity and frequency of hot extremes and significant decreases in the intensity and frequency of cold extremes (Barry et al., 2018; Chaney et al., 2014; Dunn et al., 2020; Mouhamed et al., 2013; Perkins-Kirkpatrick and Lewis, 2020)	Strong evidence of changes from observations that are in the direction of model projected changes for the future. The magnitude of projected changes increases with global warming.	CMIP6 models project a robust increase in the intensity and frequency of TXx events and a robust decrease in the intensity and frequency of TNn events (Li et al., 2020; Annex). Median increase of more than 0.5°C in the 50-year TXx and TNn events compared to the 1°C warming level (Li et al., 2020) and more than 1.5°C in annual TXx and TNn compared to pre-industrial (Annex). Additional evidence from CMIP5 and CORDEX simulations for an increase in the intensity and frequency of hot extremes (Weber et al., 2018)	CMIP6 models project a robust increase in the intensity and frequency of TXx events and a robust decrease in the intensity and frequency of TNn events (Li et al., 2020; Annex). Median increase of more than 1°C in the 50-year TXx and TNn events compared to the 1°C warming level (Li et al., 2020) and more than 2°C in annual TXx and TNn compared to pre-industrial (Annex). Additional evidence from CMIP5 and CORDEX simulations for an increase in the intensity and frequency of hot extremes (Weber et al., 2018; Coppola et al., 2021a)	CMIP6 models project a robust increase in the intensity and frequency of TXx events and a robust decrease in the intensity and frequency of TNn events (Li et al., 2020; Annex). Median increase of more than 3°C in the 50-year TXx and TNn events compared to the 1°C warming level (Li et al., 2020) and more than 4.5°C in annual TXx and TNn compared to pre-industrial (Annex). Additional evidence from CMIP5/CMIP3 and CORDEX simulations for an increase in the intensity and frequency of hot extremes (Coppola et al., 2021a; Engelbrecht et al., 2015; Giorgi et al., 2014)
	Likely increase in the intensity and frequency of hot extremes and decrease in the intensity and frequency of cold extremes	*Medium confidence* in a human contribution to the observed increase in the intensity and frequency of hot extremes and decrease in the intensity and frequency of cold extremes.	Increase in the intensity and frequency of hot extremes: *Likely* (compared with the recent past (1995-2014)) *Very likely* (compared with pre-industrial) Decrease in the intensity and frequency of cold extremes: *Likely* (compared with the recent past (1995-2014)) *Very likely* (compared with pre-industrial).	Increase in the intensity and frequency of hot extremes: *Very likely* (compared with the recent past (1995-2014)) *Extremely likely* (compared with pre-industrial) Decrease in the intensity and frequency of cold extremes: *Very likely* (compared with the recent past (1995-2014)) *Extremely likely* (compared with pre-industrial)	Increase in the intensity and frequency of hot extremes: *Virtually certain* (compared with the recent past (1995-2014)) *Virtually certain* (compared with pre-industrial) Decrease in the intensity and frequency of cold extremes: *Virtually certain* (compared with the recent past (1995-2014)) *Virtually certain* (compared with pre-industrial)
Northern Eastern Africa (NEAF)	Increases in the intensity and frequency of hot extremes and decreases in the intensity and frequency of cold extremes (Perkins-Kirkpatrick and Lewis, 2020; Chaney et al., 2014; Gebrechorkos et al.,	Evidence of a human contribution to the observed increase in the intensity and frequency of hot extremes and decrease in the intensity and frequency of cold	CMIP6 models project a robust increase in the intensity and frequency of TXx events and a robust decrease in the intensity and frequency of TNn events (Li et al., 2020; Annex). Median increase of more than 0.5°C in	CMIP6 models project a robust increase in the intensity and frequency of TXx events and a robust decrease in the intensity and frequency of TNn events (Li et al., 2020; Annex). Median increase of more than	CMIP6 models project a robust increase in the intensity and frequency of TXx events and a robust decrease in the intensity and frequency of TNn events (Li et al., 2020; Annex). Median increase of more than

ACCEPTED VERSION SUBJECT TO FINAL EDITING

	2018; Omondi et al., 2014; Dunn et al., 2020)	extremes (Otto et al., 2015; Philip et al., 2020; Marthews et al., 2015; Kew et al., 2021; Funk et al., 2015)	the 50-year TXx and TNn events compared to the 1°C warming level (Li et al., 2020) and more than 1.5°C in annual TXx and TNn compared to pre-industrial (Annex). Additional evidence from CMIP5 and CORDEX simulations for an increase in the intensity and frequency of hot extremes (Weber et al., 2018)	1°C in the 50-year TXx and TNn events compared to the 1°C warming level (Li et al., 2020) and more than 2°C in annual TXx and TNn compared to pre-industrial (Annex). Additional evidence from CMIP5 and CORDEX simulations for an increase in the intensity and frequency of hot extremes (Weber et al., 2018; Coppola et al., 2021a)	2.5°C in the 50-year TXx and TNn events compared to the 1°C warming level (Li et al., 2020) and more than 4°C in annual TXx and TNn compared to pre-industrial (Annex). Additional evidence from CMIP5/CMIP3 and CORDEX simulations for an increase in the intensity and frequency of hot extremes Coppola et al., 2021a; Engelbrecht et al., 2015; Giorgi et al., 2014)
	Medium confidence in the increase in the intensity and frequency of hot extremes	*Medium confidence* in a human contribution to the observed increase in the intensity and frequency of hot extremes	Increase in the intensity and frequency of hot extremes: *Likely* (compared with the recent past (1995-2014)) *Very likely* (compared with pre-industrial) Decrease in the intensity and frequency of cold extremes: *Likely* (compared with the recent past (1995-2014)) *Very likely* (compared with pre-industrial).	Increase in the intensity and frequency of hot extremes: *Very likely* (compared with the recent past (1995-2014)) *Extremely likely* (compared with pre-industrial) Decrease in the intensity and frequency of cold extremes: *Very likely* (compared with the recent past (1995-2014)) *Extremely likely* (compared with pre-industrial)	Increase in the intensity and frequency of hot extremes: *Virtually certain* (compared with the recent past (1995-2014)) *Virtually certain* (compared with pre-industrial) Decrease in the intensity and frequency of cold extremes: *Virtually certain* (compared with the recent past (1995-2014)) *Virtually certain* (compared with pre-industrial)
Central Africa (CAF)	Insufficient data to assess trends (Dunn et al., 2020)	Limited evidence	CMIP6 models project a robust increase in the intensity and frequency of TXx events and a robust decrease in the intensity and frequency of TNn events (Li et al., 2020; Annex). Median increase of more than 0C in the 50-year TXx and TNn events compared to the 1°C warming level (Li et al., 2020) and more than 1.5°C in annual TXx and TNn compared to pre-industrial (Annex). Additional evidence from CMIP5 and CORDEX simulations for an increase in the intensity and	CMIP6 models project a robust increase in the intensity and frequency of TXx events and a robust decrease in the intensity and frequency of TNn events (Li et al., 2020; Annex). Median increase of more than 1°C in the 50-year TXx and TNn events compared to the 1°C warming level (Li et al., 2020) and more than 2°C in annual TXx and TNn compared to pre-industrial (Annex). Additional evidence from CMIP5 and CORDEX simulations for an increase in the intensity and frequency of	CMIP6 models project a robust increase in the intensity and frequency of TXx events and a robust decrease in the intensity and frequency of TNn events (Li et al., 2020; Annex). Median increase of more than 3°C in the 50-year TXx and TNn events compared to the 1°C warming level (Li et al., 2020) and more than 4.5°C in annual TXx and TNn compared to pre-industrial (Annex). Additional evidence from CMIP5/CMIP3 and CORDEX simulations for an increase in the intensity and frequency of

ACCEPTED VERSION SUBJECT TO FINAL EDITING

			frequency of hot extremes (Weber et al., 2018)	hot extremes (Weber et al., 2018; Coppola et al., 2021a)	hot extremes (Coppola et al., 2021a; Engelbrecht et al., 2015; Giorgi et al., 2014)
	Low confidence	*Low confidence*	Increase in the intensity and frequency of hot extremes: *Likely* (compared with the recent past (1995-2014)) *Very likely* (compared with pre-industrial) Decrease in the intensity and frequency of cold extremes: *Likely* (compared with the recent past (1995-2014)) *Very likely* (compared with pre-industrial).	Increase in the intensity and frequency of hot extremes: *Very likely* (compared with the recent past (1995-2014)) *Extremely likely* (compared with pre-industrial) Decrease in the intensity and frequency of cold extremes: *Very likely* (compared with the recent past (1995-2014)) *Extremely likely* (compared with pre-industrial)	Increase in the intensity and frequency of hot extremes: *Virtually certain* (compared with the recent past (1995-2014)) *Virtually certain* (compared with pre-industrial) Decrease in the intensity and frequency of cold extremes: *Virtually certain* (compared with the recent past (1995-2014)) *Virtually certain* (compared with pre-industrial)
South Eastern Africa (SEAF)	Increases in the intensity and frequency of hot extremes and decreases in the intensity and frequency of cold extremes (Perkins-Kirkpatrick and Lewis, 2020; Gebrechorkos et al., 2018; Omondi et al., 2014; Chaney et al., 2014)	Evidence of a human contribution to the observed increase in the intensity and frequency of hot extremes and decrease in the intensity and frequency of cold extremes (Otto et al., 2015; Philip et al., 2020; Marthews et al., 2015; Kew et al., 2021; Funk et al., 2015)	CMIP6 models project a robust increase in the intensity and frequency of TXx events and a robust decrease in the intensity and frequency of TNn events (Li et al., 2020; Annex). Median increase of more than 0.5°C in the 50-year TXx and TNn events compared to the 1°C warming level (Li et al., 2020) and more than 1.5°C in annual TXx and TNn compared to pre-industrial (Annex). Additional evidence from CMIP5 and CORDEX simulations for an increase in the intensity and frequency of hot extremes (Weber et al., 2018)	CMIP6 models project a robust increase in the intensity and frequency of TXx events and a robust decrease in the intensity and frequency of TNn events (Li et al., 2020; Annex). Median increase of more than 1°C in the 50-year TXx and TNn events compared to the 1°C warming level (Li et al., 2020) and more than 2°C in annual TXx and TNn compared to pre-industrial (Annex). Additional evidence from CMIP5 and CORDEX simulations for an increase in the intensity and frequency of hot extremes (Weber et al., 2018; Coppola et al., 2021a)	CMIP6 models project a robust increase in the intensity and frequency of TXx events and a robust decrease in the intensity and frequency of TNn events (Li et al., 2020; Annex). Median increase of more than 2.5°C in the 50-year TXx and TNn events compared to the 1°C warming level (Li et al., 2020) and more than 4°C in annual TXx and TNn compared to pre-industrial (Annex). Additional evidence from CMIP5/CMIP3 and CORDEX simulations for an increase in the intensity and frequency of hot extremes (Coppola et al., 2021a; Engelbrecht et al., 2015; Giorgi et al., 2014)
	Medium confidence in the increase in the intensity and frequency of hot extremes	*Medium confidence* in a human contribution to the observed increase in the intensity and frequency of hot extremes	Increase in the intensity and frequency of hot extremes: *Likely* (compared with the recent past (1995-2014)) *Very likely* (compared with pre-industrial)	Increase in the intensity and frequency of hot extremes: *Very likely* (compared with the recent past (1995-2014)) *Extremely likely* (compared with pre-industrial)	Increase in the intensity and frequency of hot extremes: *Virtually certain* (compared with the recent past (1995-2014)) *Virtually certain* (compared with pre-industrial)

ACCEPTED VERSION SUBJECT TO FINAL EDITING

			Decrease in the intensity and frequency of cold extremes: *Likely* (compared with the recent past (1995-2014)) *Very likely* (compared with pre-industrial).	Decrease in the intensity and frequency of cold extremes: *Very likely* (compared with the recent past (1995-2014)) *Extremely likely* (compared with pre-industrial)	Decrease in the intensity and frequency of cold extremes: *Virtually certain* (compared with the recent past (1995-2014)) *Virtually certain* (compared with pre-industrial)
Western Southern Africa (WSAF)	Significant increases in the intensity and frequency of hot extremes and significant decreases in the intensity and frequency of cold extremes (Russo et al., 2016; Perkins-Kirkpatrick and Lewis, 2020; Kruger and Nxumalo, 2017; Mbokodo et al., 2020; Dunn et al., 2020)	Robust evidence of a human contribution to the observed increase in the intensity and frequency of hot extremes and decrease in the intensity and frequency of cold extremes (Seong et al., 2020; Wang et al., 2017)	CMIP6 models project a robust increase in the intensity and frequency of TXx events and a robust decrease in the intensity and frequency of TNn events (Li et al., 2020; Annex). Median increase of more than 0.5°C in the 50-year TXx and TNn events compared to the 1°C warming level (Li et al., 2020) and more than 1.5°C in annual TXx and TNn compared to pre-industrial (Annex). Additional evidence from CMIP5 and CORDEX simulations for an increase in the intensity and frequency of hot extremes (Weber et al., 2018)	CMIP6 models project a robust increase in the intensity and frequency of TXx events and a robust decrease in the intensity and frequency of TNn events (Li et al., 2020; Annex). Median increase of more than 1°C in the 50-year TXx and TNn events compared to the 1°C warming level (Li et al., 2020) and more than 2°C in annual TXx and TNn compared to pre-industrial (Annex). Additional evidence from CMIP5 and CORDEX simulations for an increase in the intensity and frequency of hot extremes (Weber et al., 2018; Coppola et al., 2021a)	CMIP6 models project a robust increase in the intensity and frequency of TXx events and a robust decrease in the intensity and frequency of TNn events (Li et al., 2020; Annex). Median increase of more than 2.5°C in the 50-year TXx and TNn events compared to the 1°C warming level (Li et al., 2020) and more than 4.5°C in annual TXx and TNn compared to pre-industrial (Annex). Additional evidence from CMIP5/CMIP3 and CORDEX simulations for an increase in the intensity and frequency of hot extremes (Coppola et al., 2021a; Engelbrecht et al., 2015; Giorgi et al., 2014)
	Likely increase in the intensity and frequency of hot extremes and decrease in the intensity and frequency of cold extremes	Human influence *likely* contributed to the observed increase in the intensity and frequency of hot extremes and decrease in the intensity and frequency of cold extremes	Increase in the intensity and frequency of hot extremes: *Likely* (compared with the recent past (1995-2014)) *Very likely* (compared with pre-industrial) Decrease in the intensity and frequency of cold extremes: *Likely* (compared with the recent past (1995-2014)) *Very likely* (compared with pre-industrial).	Increase in the intensity and frequency of hot extremes: *Very likely* (compared with the recent past (1995-2014)) *Extremely likely* (compared with pre-industrial) Decrease in the intensity and frequency of cold extremes: *Very likely* (compared with the recent past (1995-2014)) *Extremely likely* (compared with pre-industrial)	Increase in the intensity and frequency of hot extremes: *Virtually certain* (compared with the recent past (1995-2014)) *Virtually certain* (compared with pre-industrial) Decrease in the intensity and frequency of cold extremes: *Virtually certain* (compared with the recent past (1995-2014)) *Virtually certain* (compared with pre-industrial)
Eastearn Southern Africa (ESAF)	Significant increases in the intensity and frequency of hot extremes and significant decreases in the intensity and	Robust evidence of a human contribution to the observed increase in the intensity and frequency of	CMIP6 models project a robust increase in the intensity and frequency of TXx events and a robust decrease in the intensity	CMIP6 models project a robust increase in the intensity and frequency of TXx events and a robust decrease in the intensity	CMIP6 models project a robust increase in the intensity and frequency of TXx events and a robust decrease in the intensity

ACCEPTED VERSION SUBJECT TO FINAL EDITING

	frequency of cold extremes (Dunn et al., 2020; Russo et al., 2016; Perkins-Kirkpatrick and Lewis, 2020; Kruger and Nxumalo, 2017; Mbokodo et al., 2020)	hot extremes and decrease in the intensity and frequency of cold extremes (Seong et al., 2020; Wang et al., 2017)	and frequency of TNn events (Li et al., 2020; Annex). Median increase of more than 0.5°C in the 50-year TXx and TNn events compared to the 1°C warming level (Li et al., 2020) and more than 1.5°C in annual TXx and TNn compared to pre-industrial (Annex). Additional evidence from CMIP5 and CORDEX simulations for an increase in the intensity and frequency of hot extremes (Weber et al., 2018)	and frequency of TNn events (Li et al., 2020; Annex). Median increase of more than 0.5°C in the 50-year TXx and TNn events compared to the 1°C warming level (Li et al., 2020) and more than 2°C in annual TXx and TNn compared to pre-industrial (Annex). Additional evidence from CMIP5 and CORDEX simulations for an increase in the intensity and frequency of hot extremes (Weber et al., 2018; Coppola et al., 2021a)	and frequency of TNn events (Li et al., 2020; Annex). Median increase of more than 2.5°C in the 50-year TXx and TNn events compared to the 1°C warming level (Li et al., 2020) and more than 4°C in annual TXx and TNn compared to pre-industrial (Annex). Additional evidence from CMIP5/CMIP3 and CORDEX simulations for an increase in the intensity and frequency of hot extremes (Coppola et al., 2021a; Engelbrecht et al., 2015; Giorgi et al., 2014)
	Likely increase in the intensity and frequency of hot extremes and decrease in the intensity and frequency of cold extremes	*High confidence* in a human contribution to the observed increase in the intensity and frequency of hot extremes and decrease in the intensity and frequency of cold extremes	Increase in the intensity and frequency of hot extremes: *Likely* (compared with the recent past (1995-2014)) *Very likely* (compared with pre-industrial) Decrease in the intensity and frequency of cold extremes: *Likely* (compared with the recent past (1995-2014)) *Very likely* (compared with pre-industrial).	Increase in the intensity and frequency of hot extremes: *Very likely* (compared with the recent past (1995-2014)) *Extremely likely* (compared with pre-industrial) Decrease in the intensity and frequency of cold extremes: *Very likely* (compared with the recent past (1995-2014)) *Extremely likely* (compared with pre-industrial)	Increase in the intensity and frequency of hot extremes: *Virtually certain* (compared with the recent past (1995-2014)) *Virtually certain* (compared with pre-industrial) Decrease in the intensity and frequency of cold extremes: *Virtually certain* (compared with the recent past (1995-2014)) *Virtually certain* (compared with pre-industrial)
Madagascar (MDG)	Increases in the intensity and frequency of hot extremes and decreases in the intensity and frequency of cold extremes (Vincent et al., 2011; Donat et al., 2013)	Limited evidence	CMIP6 models project a robust increase in the intensity and frequency of TXx events and a robust decrease in the intensity and frequency of TNn events (Li et al., 2020; Annex). Median increase of more than 0.5°C in the 50-year TXx and TNn events compared to the 1°C warming level (Li et al., 2020) and more than 1.5°C in annual TXx and TNn compared to pre-industrial (Annex).	CMIP6 models project a robust increase in the intensity and frequency of TXx events and a robust decrease in the intensity and frequency of TNn events (Li et al., 2020; Annex). Median increase of more than 0.5°C in the 50-year TXx and TNn events compared to the 1°C warming level (Li et al., 2020) and more than 2°C in annual TXx and TNn compared to pre-industrial (Annex).	CMIP6 models project a robust increase in the intensity and frequency of TXx events and a robust decrease in the intensity and frequency of TNn events (Li et al., 2020; Annex). Median increase of more than 2°C in the 50-year TXx and TNn events compared to the 1°C warming level (Li et al., 2020) and more than 3.5°C in annual TXx and TNn compared to pre-industrial (Annex).

ACCEPTED VERSION SUBJECT TO FINAL EDITING

			Additional evidence from CMIP5 and CORDEX simulations for an increase in the intensity and frequency of hot extremes (Weber et al., 2018)	Additional evidence from CMIP5 and CORDEX simulations for an increase in the intensity and frequency of hot extremes (Weber et al., 2018; Coppola et al., 2021a)	Additional evidence from CMIP5/CMIP3 and CORDEX simulations for an increase in the intensity and frequency of hot extremes (Coppola et al., 2021a; Engelbrecht et al., 2015; Giorgi et al., 2014)
	Medium confidence in the increase in the intensity and frequency of hot extremes and decrease in the intensity and frequency of cold extremes	*Low confidence*	Increase in the intensity and frequency of hot extremes: *Likely* (compared with the recent past (1995-2014)) *Very likely* (compared with pre-industrial) Decrease in the intensity and frequency of cold extremes: *Likely* (compared with the recent past (1995-2014)) *Very likely* (compared with pre-industrial).	Increase in the intensity and frequency of hot extremes: *Very likely* (compared with the recent past (1995-2014)) *Extremely likely* (compared with pre-industrial) Decrease in the intensity and frequency of cold extremes: *Very likely* (compared with the recent past (1995-2014)) *Extremely likely* (compared with pre-industrial)	Increase in the intensity and frequency of hot extremes: *Virtually certain* (compared with the recent past (1995-2014)) *Virtually certain* (compared with pre-industrial) Decrease in the intensity and frequency of cold extremes: *Virtually certain* (compared with the recent past (1995-2014)) *Virtually certain* (compared with pre-industrial)

[END TABLE 11.4 HERE]

[START TABLE 11.5 HERE]

Table 11.5: Observed trends, human contribution to observed trends, and projected changes at 1.5°C, 2°C and 4°C of global warming for heavy precipitation in Africa, subdivided by AR6 regions. See Sections 11.9.1 and 11.9.3 for details.

Region	Observed trends	Detection and attribution: event attribution	Projections		
			1.5 °C	2 °C	4 °C
All Africa	Insufficient data to assess trends	Limited evidence	CMIP6 models project an increase in the intensity and frequency of heavy precipitation (Li et al., 2020a). Median increase of more than 2% in the 50-year Rx1day and Rx5day events compared to the 1°C warming level (Li et al., 2020a)	CMIP6 models project a robust increase in the intensity and frequency of heavy precipitation (Li et al., 2020a). Median increase of more than 6% in the 50-year Rx1day and Rx5day events compared to the 1°C warming level (Li et al., 2020a)	CMIP6 models project a robust increase in the intensity and frequency of heavy precipitation (Li et al., 2020a). Median increase of more than 20% in the 50-year Rx1day and Rx5day events compared to the 1°C warming level (Li et al., 2020a)
	Low confidence	*Low confidence*	Intensification of heavy precipitation: *High confidence* (compared with the recent past (1995-2014)) *Likely* (compared with pre-industrial)	Intensification of heavy precipitation: *Likely* (compared with the recent past (1995-2014)) *Very likely* (compared with pre-industrial)	Intensification of heavy precipitation:

ACCEPTED VERSION SUBJECT TO FINAL EDITING

					Extremely likely (compared with the recent past (1995-2014)) *Virtually certain* (compared with pre-industrial)
Mediterranean (MED)[3]	Lack of agreement on the evidence of trends (Sun et al., 2020; Casanueva et al., 2014; de Lima et al., 2015; Gajić-Čapka et al., 2015; Ribes et al., 2019; Peña-Angulo et al., 2020; Rajczak and Schär, 2017; Jacob et al., 2018; Coppola et al., 2021a; Donat et al., 2014; Mathbout et al., 2018; Dunn et al., 2020)	Limited evidence (Añel et al., 2014; U.S. Department of Agriculture Economic Research Service, 2016)	CMIP6 models, CMIP5 models, and RCMs project inconsistent changes in the region (Li et al., 2020; Cardell et al., 2020; Zollo et al., 2016; Samuels et al., 2018)	CMIP6 models project a robust increase in the intensity and frequency of heavy precipitation (Li et al., 2020; Annex). Median increase of more than 2% in the 50-year Rx1day and Rx5day events compared to the 1°C warming level (Li et al., 2020a) and more than 0% in annual Rx1day and Rx5day and less than -2% in annual Rx30day compared to pre-industrial (Annex). Additional evidence from CMIP5 and RCM simulations for an increase in the intensity of heavy precipitation (Cardell et al., 2020; Zollo et al., 2016; Samuels et al., 2018)	CMIP6 models project a robust increase in the intensity and frequency of heavy precipitation (Li et al., 2020; Annex). Median increase of more than 8% in the 50-year Rx1day and Rx5day events compared to the 1°C warming level (Li et al., 2020a) and more than 2% in annual Rx1day and Rx5day and less than -2% in annual Rx30day compared to pre-industrial (Annex). Additional evidence from CMIP5 and RCM simulations for an increase in the intensity of heavy precipitation (Cardell et al., 2020; Tramblay and Somot, 2018; Zollo et al., 2016; Samuels et al., 2018; Monjo et al., 2016; Rajczak et al., 2013; Coppola et al., 2021b; Driouech et al., 2020)
	Low confidence	*Low confidence*	Intensification of heavy precipitation: *Low confidence* (compared with the recent past (1995-2014)) *Medium confidence* (compared with pre-industrial)	Intensification of heavy precipitation: *Medium confidence* (compared with the recent past (1995-2014)) *High confidence* (compared with pre-industrial)	Intensification of heavy precipitation: *High confidence* (compared with the recent past (1995-2014)) *High confidence* (compared with pre-industrial)
Sahara (SAH)	Insufficient data to assess trends (Sun et al., 2020; Dunn et al., 2020)	Limited evidence	CMIP6 models project an increase in the intensity and frequency of heavy precipitation (Li et al., 2020; Annex). Median increase of more than 4% in the 50-year Rx1day and Rx5day events compared to the 1°C warming level (Li et al., 2020a) and more than 15% in	CMIP6 models project a robust increase in the intensity and frequency of heavy precipitation (Li et al., 2020; Annex). Median increase of more than 8% in the 50-year Rx1day and Rx5day events compared to the 1°C warming level (Li et al., 2020a) and more than 20% in annual Rx1day,	CMIP6 models project a robust increase in the intensity and frequency of heavy precipitation (Li et al., 2020; Annex). Median increase of more than 30% in the 50-year Rx1day and Rx5day events

[3] This region includes both northern Africa and southern Europe

ACCEPTED VERSION SUBJECT TO FINAL EDITING

			annual Rx1day, Rx5day, and Rx30day compared to pre-industrial (Annex).	Rx5day, and Rx30day compared to pre-industrial (Annex).	compared to the 1°C warming level (Li et al., 2020a) and more than 40% in annual Rx1day, Rx5day, and Rx30day compared to pre-industrial (Annex).
	Low confidence	*Low confidence*	Intensification of heavy precipitation: *High confidence* (compared with the recent past (1995-2014)) *Likely* (compared with pre-industrial)	Intensification of heavy precipitation: *Likely* (compared with the recent past (1995-2014)) *Very likely* (compared with pre-industrial)	Intensification of heavy precipitation: *Extremely likely* (compared with the recent past (1995-2014)) *Virtually certain* (compared with pre-industrial)
Western Africa (WAF)	Insufficient data and a lack of agreement on the evidence of trends (Mouhamed et al., 2013; Chaney et al., 2014; Sanogo et al., 2015; Zittis, 2017; Barry et al., 2018; Sun et al., 2020; Dunn et al., 2020)	Limited evidence (Parker et al., 2017)	CMIP6 models project an increase in the intensity and frequency of heavy precipitation (Li et al., 2020; Annex). Median increase of more than 4% in the 50-year Rx1day and Rx5day events compared to the 1°C warming level (Li et al., 2020a) and more than 10% in annual Rx1day and Rx5day and 8% in annual Rx30day compared to pre-industrial (Annex). Additional evidence from CMIP5 and CORDEX simulations for an increase in the intensity of heavy precipitation (Nikulin et al., 2018)	CMIP6 models project a robust increase in the intensity and frequency of heavy precipitation (Li et al., 2020; Annex). Median increase of more than 8% in the 50-year Rx1day and Rx5day events compared to the 1°C warming level (Li et al., 2020a) and more than 15% in annual Rx1day and Rx5day and 10% in annual Rx30day compared to pre-industrial (Annex). Additional evidence from CMIP5 and CORDEX simulations for an increase in the intensity of heavy precipitation (Nikulin et al., 2018; Déqué et al., 2017)	CMIP6 models project a robust increase in the intensity and frequency of heavy precipitation (Li et al., 2020; Annex). Median increase of more than 25% in the 50-year Rx1day and Rx5day events compared to the 1°C warming level (Li et al., 2020a) and more than 30% in annual Rx1day and Rx5day and 15% in annual Rx30day compared to pre-industrial (Annex). Additional evidence from CMIP5 and CORDEX simulations for an increase in the intensity of heavy precipitation (Giorgi et al., 2014; Dosio et al., 2019; Akinsanola and Zhou, 2018; Coppola et al., 2021b)
	Low confidence	*Low confidence*	Intensification of heavy precipitation: *High confidence* (compared with the recent past (1995-2014)) *Likely* (compared with pre-industrial)	Intensification of heavy precipitation: *Likely* (compared with the recent past (1995-2014)) *Very likely* (compared with pre-industrial)	Intensification of heavy precipitation: *Extremely likely* (compared with the recent past (1995-2014)) *Virtually certain* (compared with pre-industrial)
North Eastern Africa (NEAF)	Insufficient data to assess trends (Sun et al., 2020; Dunn et al., 2020)	Limited evidence	CMIP6 models project an increase in the intensity and frequency of heavy precipitation (Li et al., 2020; Annex). Median increase of more than 4% in the	CMIP6 models project a robust increase in the intensity and frequency of heavy precipitation (Li et al., 2020; Annex). Median increase of more than 8% in the 50-year Rx1day and Rx5day	CMIP6 models project a robust increase in the intensity and frequency of heavy precipitation (Li et al., 2020;

ACCEPTED VERSION SUBJECT TO FINAL EDITING

			50-year Rx1day and Rx5day events compared to the 1°C warming level (Li et al., 2020a) and more than 8% in annual Rx1day and Rx5day and 6% in annual Rx30day compared to pre-industrial (Annex).	events compared to the 1°C warming level (Li et al., 2020a) and more than 10% in annual Rx1day, Rx5day, and Rx30day compared to pre-industrial (Annex).	Annex). Median increase of more than 25% in the 50-year Rx1day and Rx5day events compared to the 1°C warming level (Li et al., 2020a) and more than 35% in annual Rx1day and Rx5day and 30% in annual Rx30day compared to pre-industrial (Annex).
	Low confidence	*Low confidence*	Intensification of heavy precipitation: *High confidence* (compared with the recent past (1995-2014)) *Likely* (compared with pre-industrial)	Intensification of heavy precipitation: *Likely* (compared with the recent past (1995-2014)) *Very likely* (compared with pre-industrial)	Intensification of heavy precipitation: *Extremely likely* (compared with the recent past (1995-2014)) *Virtually certain* (compared with pre-industrial)
Central Africa (CAF)	Insufficient data to assess trends (Sun et al., 2020; Dunn et al., 2020)	Limited evidence (Otto et al., 2013)	CMIP6 models project an increase in the intensity and frequency of heavy precipitation (Li et al., 2020; Annex). Median increase of more than 2% in the 50-year Rx1day and Rx5day events compared to the 1°C warming level (Li et al., 2020a) and more than 10% in annual Rx1day and Rx5day and 8% in annual Rx30day compared to pre-industrial (Annex). Additional evidence from CMIP5 and CORDEX simulations for an increase in the intensity of heavy precipitation (Nikulin et al., 2018)	CMIP6 models project a robust increase in the intensity and frequency of heavy precipitation (Li et al., 2020; Annex). Median increase of more than 6% in the 50-year Rx1day and Rx5day events compared to the 1°C warming level (Li et al., 2020a) and more than 10% in annual Rx1day, Rx5day, and Rx30day compared to pre-industrial (Annex). Additional evidence from CMIP5 and CORDEX simulations for an increase in the intensity of heavy precipitation (Nikulin et al., 2018; Déqué et al., 2017; Coppola et al., 2021b)	CMIP6 models project a robust increase in the intensity and frequency of heavy precipitation (Li et al., 2020; Annex). Median increase of more than 20% in the 50-year Rx1day and Rx5day events compared to the 1°C warming level (Li et al., 2020a) and more than 30% in annual Rx1day and Rx5day and 20% in annual Rx30day compared to pre-industrial (Annex). Additional evidence from CMIP5 and CORDEX simulations for an increase in the intensity of heavy precipitation (Diedhiou et al. 2018; Fotso-Nguemo et al. 2018; Sonkoué et al. 2019; Coppola et al., 2021b)
	Low confidence	*Low confidence*	Intensification of heavy precipitation: *High confidence* (compared with the recent past (1995-2014)) *Likely* (compared with pre-industrial)	Intensification of heavy precipitation: *Likely* (compared with the recent past (1995-2014)) *Very likely* (compared with pre-industrial)	Intensification of heavy precipitation: *Extremely likely* (compared with the recent past (1995-2014)) *Virtually certain* (compared with pre-industrial)

ACCEPTED VERSION SUBJECT TO FINAL EDITING

South Eastern Africa (SEAF)	Insufficient data to assess trends (Sun et al., 2020; Dunn et al., 2020)	Limited evidence	CMIP6 models project an increase in the intensity and frequency of heavy precipitation (Li et al., 2020; Annex). Median increase of more than 2% in the 50-year Rx1day and Rx5day events compared to the 1°C warming level (Li et al., 2020a) and more than 6% in annual Rx1day and Rx5day and 4% in annual Rx30day compared to pre-industrial (Annex).	CMIP6 models project a robust increase in the intensity and frequency of heavy precipitation (Li et al., 2020; Annex). Median increase of more than 4% in the 50-year Rx1day and Rx5day events compared to the 1°C warming level (Li et al., 2020a) and more than 8% in annual Rx1day and Rx5day and 6% in annual Rx30day compared to pre-industrial (Annex).	CMIP6 models project a robust increase in the intensity and frequency of heavy precipitation (Li et al., 2020; Annex). Median increase of more than 15% in the 50-year Rx1day and Rx5day events compared to the 1°C warming level (Li et al., 2020a) and more than 25% in annual Rx1day and Rx5day and 15% in annual Rx30day compared to pre-industrial (Annex).
	Low confidence	*Low confidence*	Intensification of heavy precipitation: *High confidence* (compared with the recent past (1995-2014)) *Likely* (compared with pre-industrial)	Intensification of heavy precipitation: *Likely* (compared with the recent past (1995-2014)) *Very likely* (compared with pre-industrial)	Intensification of heavy precipitation: *Extremely likely* (compared with the recent past (1995-2014)) *Virtually certain* (compared with pre-industrial)
West Southern Africa (WSAF)	Intensification of heavy precipitation (Sun et al., 2020; Donat et al., 2013)	Limited evidence	CMIP6 models project inconsistent changes in the region (Li et al., 2020, Annex)	CMIP6 models project inconsistent changes in the region (Li et al., 2020, Annex)	CMIP6 models project an increase in the intensity and frequency of heavy precipitation (Li et al., 2020; Annex). Median increase of more than 10% in the 50-year Rx1day and Rx5day events compared to the 1°C warming level (Li et al., 2020a) and more than 4% in annual Rx1day and Rx5day and 0% in annual Rx30day compared to pre-industrial (Annex). Additional evidence from CMIP5 and RCM simulations for an increase in the intensity of heavy precipitation (Pinto et al., 2016; Dosio et al., 2019; Giorgi et al., 2014; Coppola et al., 2021b)
	Medium confidence in the intensification of heavy precipitation.	*Low confidence*	Intensification of heavy precipitation: *Low confidence* (compared with the recent past (1995-2014)) *Low confidence* (compared with pre-industrial)	Intensification of heavy precipitation: *Low confidence* (compared with the recent past (1995-2014)) *Medium confidence* (compared with pre-industrial)	Intensification of heavy precipitation: *High confidence* (compared with the recent past (1995-2014))

ACCEPTED VERSION SUBJECT TO FINAL EDITING

					Likely (compared with pre-industrial)
East Southern Africa (ESAF)	Intensification of heavy precipitation (Sun et al., 2020; Donat et al., 2013)	Limited evidence	CMIP6 models project an increase in the intensity and frequency of heavy precipitation (Li et al., 2020; Annex). Median increase of more than 2% in the 50-year Rx1day and Rx5day events compared to the 1°C warming level (Li et al., 2020a) and more than 4% in annual Rx1day and Rx5day and 0% in annual Rx30day compared to pre-industrial (Annex).	CMIP6 models project an increase in the intensity and frequency of heavy precipitation (Li et al., 2020; Annex). Median increase of more than 2% in the 50-year Rx1day and Rx5day events compared to the 1°C warming level (Li et al., 2020a) and more than 6% in annual Rx1day and Rx5day and 2% in annual Rx30day compared to pre-industrial (Annex).	CMIP6 models project a robust increase in the intensity and frequency of heavy precipitation (Li et al., 2020; Annex). Median increase of more than 15% in the 50-year Rx1day and Rx5day events compared to the 1°C warming level (Li et al., 2020a) and more than 15% in annual Rx1day and Rx5day and 8% in annual Rx30day compared to pre-industrial (Annex). Additional evidence from CMIP5 and RCM simulations for an increase in the intensity of heavy precipitation (Pinto et al., 2016; Dosio et al., 2019; Giorgi et al., 2014; Coppola et al., 2021b)
	Medium confidence in the intensification of heavy precipitation.	*Low confidence*	Intensification of heavy precipitation: *Medium confidence* (compared with the recent past (1995-2014)) *High confidence* (compared with pre-industrial)	Intensification of heavy precipitation: *High confidence* (compared with the recent past (1995-2014)) *Likely* (compared with pre-industrial)	Intensification of heavy precipitation: *Very likely* (compared with the recent past (1995-2014)) *Extremely likely* (compared with pre-industrial)
Madagascar (MDG)	Insufficient data to assess trends and trends in available data are not significant (Sun et al., 2020; Dunn et al., 2020; Donat et al., 2013; Vincent et al., 2011)	Limited evidence	CMIP6 models project an increase in the intensity and frequency of heavy precipitation (Li et al., 2020; Annex). Median increase of more than 2% in the 50-year Rx1day and Rx5day events compared to the 1°C warming level (Li et al., 2020a) and more than 4% in annual Rx1day and Rx5day and 0% in annual Rx30day compared to pre-industrial (Annex). Additional evidence from CMIP5 and CORDEX simulations for an increase in the intensity of heavy precipitation (Weber et al., 2018)	CMIP6 models project an increase in the intensity and frequency of heavy precipitation (Li et al., 2020; Annex). Median increase of more than 2% in the 50-year Rx1day and Rx5day events compared to the 1°C warming level (Li et al., 2020a) and more than 4% in annual Rx1day and Rx5day and 2% in annual Rx30day compared to pre-industrial (Annex). Additional evidence from CMIP5 and CORDEX simulations for an increase in the intensity of heavy precipitation (Weber et al., 2018)	CMIP6 models project a robust increase in the intensity and frequency of heavy precipitation (Li et al., 2020; Annex). Median increase of more than 15% in the 50-year Rx1day and Rx5day events compared to the 1°C warming level (Li et al., 2020a) and more than 15% in annual Rx1day and Rx5day and 6% in annual Rx30day compared to pre-industrial (Annex).

ACCEPTED VERSION SUBJECT TO FINAL EDITING

					Additional evidence from CMIP5 and CORDEX simulations for an increase in the intensity of heavy precipitation (Weber et al., 2018)
	Low confidence	*Low confidence*	Intensification of heavy precipitation: *Medium confidence* (compared with the recent past (1995-2014)) *High confidence* (compared with pre-industrial)	Intensification of heavy precipitation: *High confidence* (compared with the recent past (1995-2014)) *Likely* (compared with pre-industrial)	Intensification of heavy precipitation: *Very likely* (compared with the recent past (1995-2014)) *Extremely likely* (compared with pre-industrial)

[END TABLE 11.5 HERE]

[START TABLE 11.6 HERE]

Table 11.6: Observed trends, human contribution to observed trends, and projected changes at 1.5°C, 2°C and 4°C of global warming for meteorological droughts (MET), agricultural and ecological droughts (AGR/ECOL), and hydrological droughts (HYDR) in Africa, subdivided by AR6 regions. See Sections 11.9.1 and 11.9.4 for details.

Region and drought type		Observed trends	Human contribution	Projections		
				1.5 °C	2 °C	4 °C
MED[4]	MET	ENTRY IDENTICAL TO EU-MED	ENTRY IDENTICAL TO EU-MED	ENTRY IDENTICAL TO EU-MED	ENTRY IDENTICAL TO EU-MED	ENTRY IDENTICAL TO EU-MED
	AGR ECOL	ENTRY IDENTICAL TO EU-MED	ENTRY IDENTICAL TO EU-MED	ENTRY IDENTICAL TO EU-MED	ENTRY IDENTICAL TO EU-MED	ENTRY IDENTICAL TO EU-MED
	HYDR	ENTRY IDENTICAL TO EU-MED	ENTRY IDENTICAL TO EU-MED	ENTRY IDENTICAL TO EU-MED	ENTRY IDENTICAL TO EU-MED	ENTRY IDENTICAL TO EU-MED
Sahara (SAH)	MET	***Low confidence*: Limited evidence**.	***Low confidence*: Limited evidence**	***Low confidence:* Mixed signals** (seasonally and geographically varying) and non-robust changes (Cook et al., 2020). Slightly reduced drying based on CDD (Chapter 11 Supplementary Material (11.SM)).	***Low confidence:* Mixed signals** (seasonally and geographically varying) and non-robust changes (Cook et al., 2020). Slightly reduced drying based on CDD (Chapter 11 Supplementary Material (11.SM)).	***Low confidence:* Mixed signals** (seasonally and geographically varying) and non-robust changes (Cook et al., 2020). Reduced drying based on CDD (Chapter 11 Supplementary Material (11.SM)).
	AGR ECOL	***Low confidence*; Limited evidence.**	***Low confidence*; Limited evidence.**	***Low confidence*: Limited evidence** and inconsistent signals in CMIP6 (Chapter 11 Supplementary Material (11.SM)).	***Low confidence*: Limited evidence and inconsistent signals** in CMIP6 (Chapter 11 Supplementary Material (11.SM)).	***Low confidence*: Limited evidence and inconsistent signals** in CMIP6. (Cook et al., 2020; Vicente-Serrano et al.,

[4] This region includes both northern Africa and southern Europe

ACCEPTED VERSION SUBJECT TO FINAL EDITING

						2020a)(Chapter 11 Supplementary Material (11.SM))
	HYDR	***Low confidence:*** **Limited evidence**	***Low confidence*: Limited evidence**	***Low confidence:*** **Limited evidence.** One study shows lack of signal (Touma et al., 2015)	***Low confidence:*** **Limited evidence.** One study shows lack of signal (Touma et al., 2015)	***Low confidence:*** **Inconsistent** trends (Touma et al., 2015; Cook et al., 2020)
Western Africa (WAF)	MET	***Medium confidence:*** Increased drying based on CDD and SPI (Chaney et al., 2014; Barry et al., 2018; Spinoni et al., 2019; Dunn et al., 2020)	***Low confidence:*** **Mixed signals** (Lawal et al., 2016; Knutson and Zeng, 2018). Drying attributable in fraction of region to climate change over 1901-2010 and 1951-2010 time frames, but trend reversal from 1981-2010 (Knutson and Zeng, 2018) No evidence that late onset of 2015 wet season in Nigeria was due to human contribution (Lawal et al., 2016)	***Low confidence*: Mixed signal.** Mean increase of CDD over larger part of Guinea Coast in 25 CORDEX AFR runs, 1.5°C minus 1971-2000 (Klutse et al., 2016); slight increase in SPI-based meteorological drought frequency and magntidue in the Niger and Volta river basin in CORDEX simulations (Oguntunde et al., 2020); but inconsistent changes in CDD in CMIP6 GCMs (Diedhiou et al., 2018)(Chapter 11 Supplementary Material (11.SM)), as well as in mean precipitation in CMIP6 GCMs (Cook et al., 2020)	***Low confidence*: Mixed signal.** Mean increase of CDD over larger part of Guinea Coast in 25 CORDEX AFR runs, 1.5°C minus 1971-2000 (Klutse et al., 2016); slight increase in SPI-based meteorological drought frequency and magntidue in the Niger and Volta river basin in CORDEX simulations (Oguntunde et al., 2020); but inconsistent changes in CDD in CMIP6 GCMs (Diedhiou et al., 2018)(Chapter 11 Supplementary Material (11.SM)), as well as in mean precipitation in CMIP6 GCMs (Cook et al., 2020)	***Medium confidence*: Increase** in meteorological droughts, mostly on seasonal time scale**.** Seasonal CDD increases in the region for MAM and JJA (Dosio et al., 2019), increase in SPI-based meteorological drought frequency and magnitude in Niger and Volta river basins (Oguntunde et al., 2020); and slight increase in SPI-based meteorological drought for overall region (Spinoni et al., 2020). Mixed signal in annual CDD (Akinsanola and Zhou, 2018; Dosio et al., 2019)(Chapter 11 Supplementary Material (11.SM)).
	AGR ECOL	***Medium confidence*: Increased** drying based on water-balance estimates and SPEI-PM, with stronger signals for SPEI-PM (Greve et al., 2014; Spinoni et al., 2019; Padrón et al., 2020)	***Low confidence*: Limited evidence**	***Low confidence*: Inconsistent** signals (geographical and inter-model variations) in soil moisture and SPEI-PM (Naumann et al., 2018; Xu et al., 2019a)(Chapter 11 Supplementary Material (11.SM))	***Low confidence*: Inconsistent** signals (geographical and inter-model variations) in soil moisture and SPEI-PM (Naumann et al., 2018; Xu et al., 2019a; Cook et al., 2020)(Chapter 11 Supplementary Material (11.SM))	***Low confidence*: Mixed signal.** Inconsistent changes depending on subregion, indices, and season (Naumann et al., 2018; Cook et al., 2020; Vicente-Serrano et al., 2020a)(Chapter 11 Supplementary Material (11.SM)). Most projections show a drying in Western half of domain.
	HYDR	***Medium confidence:*** Decrease in streamflow (Dai and Zhao, 2017; Tramblay et al., 2020).	***Low confidence*: LimitedLimited evidence**	***Low confidence*: Limited evidence.** One study shows lack of signal (Touma et al., 2015)	***Low confidence*:** Inconsistent signal (Touma et al., 2015; Cook et al., 2020)	***Low confidence*: Inconsistent** projections and/or non-robust changes (Giuntoli et al., 2015; Touma et al., 2015; Cook et al., 2020)
North Eastern Africa (NEAF)	MET	***Low confidence*: Mixed signals.** Increasing drought in part of the region, in particular in recent two decades; but decreasing drought trends in other part of domain (NOTE: wetting trend in Horn of Africa in Spinoni et al. 2019)(Funk	***Low confidence:*** **Limited evidence** on attribution of long-term trends. Robust evidence that recent meteorological drought events (in 2016 and 2017) are not attributable to anthropogenic climate	***Low confidence*: Inconsistent trends.** Inconsistent and weak signals in SPI (Nguvava et al., 2019; Xu et al., 2019a), with high spatial variation (Nguvava et al., 2019); inconsistent signals in CDD in CMIP6 (Chapter 11 Supplementary Material (11.SM)).	***Low confidence:*Inconsistent trends.** Inconsistent changes in CDD (Chapter 11 Supplementary Material (11.SM)) and SPI (Nguvava et al., 2019; Xu et al., 2019a); but tendency towards increase in mean precipitation (Cook et al., 2020).	***Medium confidence:*** **Decrease** in meteorological drought (Sillmann et al., 2013b; Dosio et al., 2019; Cook et al., 2020; Spinoni et al., 2020) Sillmann et al. (2013), (2081-2100)/1981-2000, rcp8.5, CMIP3-CMIP5

ACCEPTED VERSION SUBJECT TO FINAL EDITING

		et al., 2015a; Nicholson, 2017; Spinoni et al., 2019) "No trends in observations in Ethiopia"; "large variability" (Philip et al., 2018b)	change (Lott et al., 2013; Marthews et al., 2015; Uhe et al., 2017; Funk et al., 2018b; Otto et al., 2018a; Philip et al., 2018b; Kew et al., 2021)	Nguvava et al. (2019): projections at 1.5°C GWL in Cordex AFR data, compared to 1971-2000: non significant changes in SPI-12-based meteorological drought frequency and intensity.	Nguvava et al. (2019): projections at 2°C GWL in Cordex AFR data, compared to 1971-2000: non significant changes in SPI-12-based meteorological drought frequency and intensity.	Decrease of CDD Dosio et al. (2019), (2070-2099/1981-2010), rcp 8.5, 23 RCM: Decrease in CDD
	AGR ECOL	***Low confidence***: **Inconsistent trends** (Greve et al., 2014; Dai and Zhao, 2017; Spinoni et al., 2019; Padrón et al., 2020)	***Low confidence***: **Limited evidence** because of lack of studies	***Low confidence:*** **Inconsistent** trends (Naumann et al., 2018; Xu et al., 2019a)(Chapter 11 Supplementary Material (11.SM))	***Low confidence:*** **Inconsistent** trends, but tendency to wetting (Naumann et al., 2018; Xu et al., 2019a; Cook et al., 2020)(Chapter 11 Supplementary Material (11.SM))	***Medium confidence:*** **Decrease** in soil moisture-based drought (Cook et al., 2020; Vicente-Serrano et al., 2020a)(Chapter 11 Supplementary Material (11.SM))
	HYDR	***Low confidence:*** **Limited evidence**	***Low confidence:*** **Limited evidence on attribution of long-term trends** (Fenta et al., 2017)	***Low confidence:*** **Limited evidence. One study shows lack of signal** (Touma et al., 2015)	***Low confidence:*** **Limited evidence** due to lack of studies;inconsistent trends (Touma et al., 2015; Cook et al., 2020)	***Medium confidence:*** **Decrease** in hydrological drought compared to pre-industrial conditions and recent past (Giuntoli et al., 2015; Cook et al., 2020) but some inconsistent signals (Touma et al., 2015)
Central Africa (CAF)	MET	***Medium confidence*** **Decrease** in SPI (Spinoni et al., 2019) and mean rainfall. (Aguilar et al., 2009; Hua et al., 2016; Dai and Zhao, 2017)	***Low confidence:*** **Inconsistent** signal in observations vs models for 1951-2010 trends (Knutson and Zeng, 2018); no signal in single-model based study (Otto et al., 2013)	***Low confidence;*** Mixed signal. Drying tendency (increasing CDD) in CORDEX AFR simulations compared to 1971-2000 (Mba et al., 2018); but tendency towards less drying (CDD decrease) in CMIP6 GCMs (Chapter 11 Supplementary Material (11.SM)), consistent with increase in precipitation at higher warming levels (Cook et al., 2020). Inconsistent signals in SPI in CMIP5 GCMs (Xu et al., 2019a)	***Low confidence;*** **Mixed signal**. Robust drying tendency (increasing CDD) in CORDEX AFR simulations compared to 1971-2000 (Mba et al., 2018); but inconsistent signal in CMIP6 GCMs (with tendency towards CDD decrease (Chapter 11 Supplementary Material (11.SM)); consistent with projected increase in mean precipitation (Cook et al., 2020)); inconsistent signals in CDD in CMIP5 GCMs (Sonkoué et al., 2019). Decrease frequency of SPI-based droughts in CMIP5 (Xu et al., 2019a).	***Low confidence:*** **Mixed signal**, depending on multi-model experiment and considered index (Fotso-Nguemo et al., 2018; Dosio et al., 2019; Sonkoué et al., 2019; Spinoni et al., 2020)(Chapter 11 Supplementary Material (11.SM)). Increase in mean precipitation in CMIP6 GCMs (Cook et al., 2020). Increase in CDD (increase in meteorological drought) in CORDEX AFR simulations (Dosio et al., 2019; Fotso-Nguemo et al., 2019) but inconsistent CDD signals in CMIP6 (with tendency towards CDD decrease; Chapter 11 Supplementary Material (11.SM)) and CMIP5 GCMs (Sonkoué et al., 2019). Increase in SPI (less drying) in CMIP5 GCMs (Spinoni et al., 2020).
	AGR ECOL	***Medium confidence*** **Decrease** in water-balance availability or SPEI, but some regional variability and index dependency of trends (Greve et al., 2014;	***Low confidence:*** **Limited evidence** due to lack of studies	***Low confidence***: **Inconsistent** signals. Slight tendency towards soil moisture wetting in CMIP5 (Xu et al., 2019a) and CMIP6 (Chapter 11 Supplementary Material	***Low confidence***: **Inconsistent** signals. Inconsistent trends in duration vs frequency of soil moisture-based drought events in CMIP5 (Xu et al., 2019a); slight mean soil moisture wetting in CMIP6	***Low confidence.*** **Inconsistent** signals. Tendency towards wetting in CMIP6 soil moisture (Cook et al., 2020)(Chapter 11 Supplementary Material (11.SM));

ACCEPTED VERSION SUBJECT TO FINAL EDITING

		Dai and Zhao, 2017; Spinoni et al., 2019; Padrón et al., 2020)		(11.SM)); and slight increase (less drying in SPEI-PM (Naumann et al., 2018)	(Chapter 11 Supplementary Material (11.SM)); slight wetting of SPEI-PM based events (Naumann et al., 2018).	inconsistent signals in SPEI-PM (Vicente-Serrano et al., 2020a)
	HYDR	***Low confidence:*** **Limited evidence.** Decrease in streamflow from 1950-2012 in southern part of domain (Dai and Zhao, 2017)	***Low confidence:*** **Limited evidence**	***Low confidence*: Limited evidence.** One study shows lack of signal (Touma et al., 2015)	***Low confidence*: Limited evidence and inconsistent trends** in mean runoff in two studies (Touma et al., 2015; Cook et al., 2020)	***Low confidence***: **Inconsistent** projections and/or non-robust changes (Giuntoli et al., 2015; Touma et al., 2015; Cook et al., 2020)
South Eastern Africa (SEAF)	MET	***Low confidence:*** **Inconsistent trends** in SPI (Spinoni et al., 2019) but occurrence of strong drought events in recent years (Funk et al., 2015a; Nicholson, 2017)	***Low confidence:*** **Limited evidence** on attribution of long-term trends. Robust evidence that recent drought events are not attributable to anthropogenic climate change (Uhe et al., 2017; Funk et al., 2018b)	***Low confidence:*** **Inconsistent changes** (Osima et al., 2018; Xu et al., 2019a)(Chapter 11 Supplementary Material (11.SM)) and lack of signal (Nangombe et al., 2018) Xu et al. (2019): Inconsistent or weak trends in SPI Osima et al. (2018): Cordex AFR data,CTL 1971-2000, RCP8.5, consistent increase of CDD over southern part Chapter 11 Supplementary Material (11.SM): Inconsistent changes in CDD	***Low confidence*: Inconsistent changes** (Osima et al., 2018; Xu et al., 2019a)(Chapter 11 Supplementary Material (11.SM)) and lack of signal (Nangombe et al., 2018) Xu et al. (2019): Inconsistent or weak trends in SPI Osima et al. (2018): Cordex AFR data,CTL 1971-2000, RCP8.5, Robust increase of CDD over southern part. Chapter 11 Supplementary Material (11.SM): inconsistent changes in CDD	***Low confidence***: **Inconsistent trends** between studies and subregions (Sillmann et al., 2013b; Dosio et al., 2019; Vicente-Serrano et al., 2020a)(Chapter 11 Supplementary Material (11.SM)). Inconsistent or no changes in SPI (Vicente-Serrano et al., 2020a) Sillmann et al. (2013), (2081-2100)/1981-2000, rcp8.5, CMIP3-CMIP5: Decrease of CDD Dosio et al. (2019), (2070-2099/1981-2010), rcp 8.5, 23 RCM: Decrease in CDD Inconsistent trends in CDD in CMIP6 (Chapter 11 Supplementary Material (11.SM))
	AGR ECOL	***Low confidence:*** **Inconsistent** trends (Greve et al., 2014; Spinoni et al., 2019; Padrón et al., 2020)	***Low confidence*: Limited evidence** due to lack of studies	***Low confidence*: Inconsistent** trends (Xu et al., 2019a)(Chapter 11 Supplementary Material (11.SM))	***Low confidence*; Inconsistent** trends (Xu et al., 2019a; Cook et al., 2020) (Chapter 11 Supplementary Material (11.SM))	***Low confidence***: **Inconsistent** trends (Cook et al., 2020; Vicente-Serrano et al., 2020a)(Chapter 11 Supplementary Material (11.SM))
	HYDR	***Low confidence:*** **Inconsistent** trends (Dai and Zhao, 2017)	***Low confidence:*** **Limited evidence**	***Low confidence*; Limited evidence.** One study shows lack of signal (Touma et al., 2015)	***Low confidence:*** **Limited evidence**; inconsistent trends in runoff in two studies (Touma et al., 2015; Cook et al., 2020)	***Low confidence:*** **Inconsistent** trends. Increase in runoff in a study based on CMIP6 (Cook et al., 2020) but inconsistent or non-robust trends in studies based on ISIMIP and CMIP5 ensembles (Giuntoli et al., 2015; Touma et al., 2015)

ACCEPTED VERSION SUBJECT TO FINAL EDITING

Western Southern Africa (WSAF)	MET	***Low confidence:*** **Inconsistent** trends (Spinoni et al., 2019; Dunn et al., 2020) Dunn et al. (2020): Conflicting trends in CDD depending on time frame	***Low confidence:*** **Limited evidence and inconsistent observed trends.** But recent meteorological drought attributable to anthropogenic climate change (Bellprat et al., 2015) Recent meteorological drought (2015/2016 drought in southern Africa) attributable to anthropogenic climate change (Otto et al., 2018b; Funk et al., 2018a; Yuan et al., 2018; Pascale et al., 2020)	***Medium confidence:*** **Increase**. Increases in dryness (CDD) (Maúre et al., 2018)(Chapter 11 Supplementary Material (11.SM)) both compared to pre-industrial climate and recent past. Increase in CDD for changes of +0.5°C in global warming based on CMIP5 for overall SREX/AR5 South Africa region (Wartenburger et al., 2017), but only weak shift in mean precipitation in large-ensemble single-model experiment for +0.5°C of global warming (Nangombe et al., 2018). Slight but weaker increase in SPI compared to CDD (Abiodun et al., 2019; Xu et al., 2019a; Naik and Abiodun, 2020) Maúre et al. (2018): 25 Cordex AFR run, CTL 1971-2000, RCP8.5, -Increase of CDD NB: Weaker signals in SPI (Xu et al., 2019a) Cordex AFR data, CTL 1971-2000, RCP8.5, pre-industrial reference period (1861-1890) (Abiodun et al., 2019; Naik and Abiodun, 2020) Non-significant increase in SPI-based drought frequency and intensity	***High confidence***: **Increases** in dryness (CDD, DF, NDD) (Maúre et al., 2018; Coppola et al., 2021b) (Chapter 11 Supplementary Material (11.SM)); slight but weaker increase in SPI (Abiodun et al., 2019; Naik and Abiodun, 2019; Xu et al., 2019) Maúre et al. (2018): 25 Cordex AFR run ,CTL 1971-2000, RCP8.5, -Increase of CDD Coppola et al. (2021b), (2041-2060)/1995-2014, rcp 8.5, CMIP5-CORDEX-CMIP6 Increase in DF (drought frequency) and NDD (number of dry days) NB: Weaker signals in SPI (Xu et al., 2019a) Cordex AFR data, CTL 1971-2000, RCP8.5, pre-industrial reference period (1861-1890)) (Abiodun et al., 2019; Naik and Abiodun, 2020): Non-significant increase in SPI-based drought frequency and intensity.	***Likely:*** **Increase** (CDD amd SPI) (Sillmann et al., 2013b; Giorgi et al., 2014; Touma et al., 2015; Pinto et al., 2016; Abiodun et al., 2019; Dosio et al., 2019; Naik and Abiodun, 2020; Spinoni et al., 2020; Coppola et al., 2021b) Using Cordex , CTL :1981-2010,RCP 8.5 2071-2100 (Spinoni et al., 2020) Robust increase of drought frequency and severity (SPI-12) Based on Giorgi et al., 2014, 5GCM/1RCM, CTL: 1976-2005, rcp 8.5, 2071-2100: Increase of CDD Sillmann et al. (2013), (2081-2100)/1981-2000, rcp8.5, CMIP3-CMIP5 Increase of CDD Coppola et al. (2021b), (2080-2099)/1995-2014, rcp 8.5, CMIP5-CORDEX-CMIP6 Increase in DF (drought frequency) and NDD (number of dry days) Dosio et al. (2019) (2070-2099/1981-2010), rcp 8.5, 23 RCM: Increase in CDD Pinto et al. (2016): (2069-2098/1976-2005), rcp 8.5,4 GCM/2RCM: Increase in CDD.
	AGR ECOL	***Medium confidence:*** **Drought increase** based on water-balance estimates and SPEI (Greve et al., 2014; Spinoni et al., 2019; Padrón et al., 2020)	***Low confidence*: Limited evidence:** Given small number of studies based on soil moisture (Yuan et al., 2018a) and atmospheric drought indices (Nangombe et al., 2020)	***Medium confidence;*** **Drought increase.** Decrease in SM both compared to recent past (Xu et al., 2019) and pre-industrial (Chapter 11 Supplementary Material (11.SM)) baselines; butut conflicting changes of drought magnitude based on SPEI-PM compared to 0.6°C baseline (Naumann et al., 2018)	***High confidence:*** **Drought increase.** Decrease in SM (Xu et al., 2019) (Chapter 11 Supplementary Material (11.SM)) (Cook et al., 2020); but conflicting changes of drought magnitude based on SPEI-PM (Naumann et al., 2018)	***Likely*: Drought increase**. Decrease in SM (Chapter 11 Supplementary Material (11.SM)) (Cook et al., 2020) and SPEI-PM (Vicente-Serrano et al., 2020a)

ACCEPTED VERSION SUBJECT TO FINAL EDITING

	HYDR	***Low confidence:*** **Limited evidence.** Decrease in runoff in larger AR5 "Southern Africa" region, but weaker signal depending on time frame (Gudmundsson et al., 2019, 2021); non significant drying tendency (Dai and Zhao, 2017)	***Low confidence:*** **Limited evidence**	***Low confidence:*** **Limited evidence.** One study shows lack of signal (Touma et al., 2015)	***Medium confidence;*** **Increased drying** (Touma et al., 2015; Cook et al., 2020; Zhai et al., 2020a)	***Medium confidence:*** **Increased drying** (Giuntoli et al., 2015; Touma et al., 2015; Cook et al., 2020)
Eastern Southern Africa (ESAF)	MET	***Medium confidence:*** **Dominant increase in meteorological drought** in SPI and CDD (Spinoni et al., 2019; Dunn et al., 2020)	***Low confidence*****: Limited evidence** on attribution of long-term trends. *Medium confidence* that human-influence has contributed to stronger recent meteorological drought.(Bellprat et al., 2015; Funk et al., 2018a; Yuan et al., 2018a)	***Medium confidence:*** **Increases** in meteorological drought based on CDD (Maúre et al., 2018)(Chapter 11 Supplementary Material (11.SM)) both compared to pre-industrial climate and recent past. Non-significant increase in SPI-based drought (Abiodun et al., 2017); lack of signal in SPI compared to recent past (1970-2000) (Xu et al., 2019a). Increase in CDD for changes of +0.5°C in global warming based on CMIP5 for overall SREX/AR5 South Africa region (Wartenburger et al., 2017), but only weak shift in mean precipitation in large-ensemble single-model experiment for +0.5°C of global warming (Nangombe et al., 2018). Maúre et al. (2018): 25 Cordex AFR run ,CTL 1971-2000, RCP8.5, -Increase of CDD Cordex AFR data,CTL 1971-2000, RCP8.5, pre-industrial reference period (1861-1890) (Abiodun et al., 2019) SPI non-significant drought frequency & intensity increase	***High confidence****:* **Increase** in meteorological drought based on (CDD,DF,NDD) (Maúre et al., 2018; Coppola et al., 2021b)(Chapter 11 Supplementary Material (11.SM)) and SPI (Abiodun et al., 2019; Xu et al., 2019a) both compared to recent past and pre-industrial period. Maúre et al. (2018): 25 Cordex AFR run ,CTL 1971-2000, RCP8.5: Increase of CDD (Coppola et al., 2021b), (2041-2060)/1995-2014, rcp 8.5, CMIP5-CORDEX-CMIP6: Increase in DF (drought frequency) and NDD (number of dry days) Abiodun et al. (2019): Cordex AFR data,CTL 1971-2000, RCP8.5, pre-industrial reference period (1861-1890): increase in SPI-based meteorological drought frequency and intensity. Xu et al. (2019): Drying in SPI at 2°C compared to 1970-2000 conditions.	***Likely:*** **Increase** in meteorological drought (CDD amd SPI) (Sillmann et al., 2013b; Giorgi et al., 2014; Touma et al., 2015; Pinto et al., 2016; Dosio et al., 2019; Spinoni et al., 2020; Coppola et al., 2021b)(Chapter 11 Supplementary Material (11.SM)) Using Cordex, CTL :1981-2010,RCP 8.5, 2071-2100 (Spinoni et al., 2020) Robust increase of drought frequency and severity (SPI-12,SPEI-12) Based on Giorgi et al. (2014), 5GCM/1RCM, CTL: 1976-2005, rcp 8.5, 2071-2100: Increase of CDD Sillmann et al. (2013), (2081-2100)/1981-2000, rcp8.5, CMIP3-CMIP5 Increase of CDD (Coppola et al., 2021b), (2080-2099)/1995-2014, rcp 8.5, CMIP5-CORDEX-CMIP6 Increase in DF (drought frequency) and NDD (number of dry days) Dosio et al. (2019), (2070-2099/1981-2010), rcp 8.5, 23 RCM Increase in CDD Pinto et al. (2016): (2069-2098/1976-2005), rcp 8.5,4 GCM/2RCM: Increase in CDD

ACCEPTED VERSION SUBJECT TO FINAL EDITING

	AGR ECOL	***Medium confidence*** **Increase**, based on water-balances estimates, PDSI and SPEI-PM (Greve et al., 2014; Dai and Zhao, 2017; Spinoni et al., 2019; Padrón et al., 2020)	***Low confidence:*** **Limited evidence** (Yuan et al., 2018a)	***Medium confidence*****: Increase** in drought. Decrease in SM both compared to recent past (Xu et al., 2019) and pre-industrial (Chapter 11 Supplementary Material (11.SM)) baselines; but inconsistent changes of drought magnitude based on SPEI-PM compared to +0.6°C baseline (Naumann et al., 2018)	***Medium confidence:*** **Increase** in drought;decrease in SM (Xu et al., 2019a; Cook et al., 2020) (Chapter 11 Supplementary Material (11.SM)); but inconsistent changes of in drought magnitude based on SPEI-PM (Naumann et al., 2018)	***High confidence:*** **Increase** in drought**:** decrease in SM (Chapter 11 Supplementary Material (11.SM)) (Cook et al., 2020) and SPEI-PM (Vicente-Serrano et al., 2020a)
	HYDR	***Low confidence:*** **Limited evidence.** Decrease in runoff in larger AR5 "Southern Africa" region, but weaker signal depending on time frame (Gudmundsson et al., 2019, 2021); non significant drying tendency (Dai and Zhao, 2017)	***Low confidence:*** **Limited evidence**	***Low confidence*****: Limited evidence.** One study shows lack of signal (Touma et al., 2015)	***Medium confidence;*** **Increased drying** (Touma et al., 2015; Cook et al., 2020; Zhai et al., 2020a).	***Medium confidence:*** **Increased drying** (Giuntoli et al., 2015; Touma et al., 2015; Cook et al., 2020)
Mada-gascar (MDG)	MET	***Low confidence:*** **Inconsistent trends** (Vincent et al., 2011; Spinoni et al., 2019)	***Low confidence:*** **Limited evidence**	***Medium confidence***: **Increase** in meteorological drought based on SPI compared to recent past (Abiodun et al., 2019; Xu et al., 2019a) and CDD compared to pre-industrial baseline (Chapter 11 Supplementary Material (11.SM)). Abiodun et al. (2019): Cordex AFR data,CTL 1971-2000, RCP8.5, pre-industrial reference period (1861-1890) SPI (drought frequency & intensity increase)	***High confidence:*** **Increase** in meteoroloigcal drought based on several metrics, including SPI (Abiodun et al., 2019; Xu et al., 2019a), CDD (Chapter 11 Supplementary Material (11.SM)), and DF (drought frequency) and NDD (number of dry days) (Coppola et al., 2021b) (Coppola et al., 2021b), (2041-2060)/1995-2014, rcp 8.5, CMIP5-CORDEX-CMIP6 Increase in DF (drought frequency) and NDD (number of dry days) Abiodun et al. (2019): Cordex AFR data,CTL 1971-2000, RCP8.5, pre-industrial reference period (1861-1890): Increase in SPI-based drought frequency and intensity.	***Likely:*** **Increase** in meteorological drought based on CDD and SPI (Sillmann et al., 2013b; Giorgi et al., 2014; Touma et al., 2015; Pinto et al., 2016; Dosio et al., 2019; Spinoni et al., 2020; Coppola et al., 2021b) Sillmann et al. (2013), (2081-2100)/1981-2000, rcp8.5, CMIP3-CMIP5 Increase of CDD Spinoni et al. (2020): Using CORDEX, CTL:1981-2010,RCP 8.5, 2071-2100 Robust increase of drought frequency and severity (SPI-12) (Coppola et al., 2021b), (2080-2099)/1995-2014, rcp 8.5, CMIP5-CORDEX-CMIP6 Increase in DF (drought frequency) and NDD (number of dry days) Dosio et al. (2019), (2070-2099/1981-2010), rcp 8.5, 23 RCM: Increase in CDD

ACCEPTED VERSION SUBJECT TO FINAL EDITING

	AGR ECOL	***Low confidence:*** **Inconsistent trends** based on water-balance estimates, PDSI and SPEI (Greve et al., 2014; Dai and Zhao, 2017; Spinoni et al., 2019; Padrón et al., 2020)	***Low confidence:*** **Limited evidence**	***Low confidence*****: Inconsistent** or weak trends (Xu et al., 2019) (Chapter 11 Supplementary Material (11.SM)) (Naumann et al., 2018)	***Medium confidence*****: Increase** in drought. Decrease in SM (Chapter 11 Supplementary Material (11.SM); (Cook et al., 2020) and in SPEI-PM (Naumann et al., 2018)	***High confidence: Increase*** in drought. Robust decrease in SM (Chapter 11 Supplementary Material (11.SM)) (Cook et al., 2020) and SPEI-PM (Vicente-Serrano et al., 2020a)
	HYDR	***Low confidence*****: Limited evidence.** Inconsistent trends in one study (Dai and Zhao, 2017)	***Low confidence:*** **Limited evidence**	***Low confidence:*** **Limited evidence.** One study shows lack of signal (Touma et al., 2015)	***Low confidence*****: Inconsistent** trends. Inconsistent trends (Cook et al., 2020) or weak drying (Touma et al., 2015; Zhai et al., 2020b)	***Medium confidence:*** **Increase** in drought based on two studies based on CMIP5 (Giuntoli et al., 2015; Touma et al., 2015), but some inconsistent trends in CMIP6 mean runoff trends (Cook et al., 2020)

[END TABLE 11.6 HERE]

[START TABLE 11.7 HERE]

Table 11.7: Observed trends, human contribution to observed trends, and projected changes at 1.5°C, 2°C and 4°C of global warming for temperature extremes in Asia, subdivided by AR6 regions. See Sections 11.9.1 and 11.9.2 for details

Region	Observed trends	Detection and attribution; event attribution	Projections		
			1.5 °C	2 °C	4 °C
All Asia	Most subregions show a *very likely* increase in the intensity and frequency of hot extremes and decrease in the intensity and frequency of cold extremes	Robust evidence of a human contribution to the observed increase in the intensity and frequency of hot extremes and decrease in the intensity and frequency of cold extremes (Hu et al., 2020; Seong et al., 2020)	CMIP6 models project a robust increase in the intensity and frequency of TXx events and a robust decrease in the intensity and frequency of TNn events (Li et al., 2020). Median increase of more than 0.5°C in the 50-year TXx and TNn events compared to the 1°C warming level (Li et al., 2020)	CMIP6 models project a robust increase in the intensity and frequency of TXx events and a robust decrease in the intensity and frequency of TNn events (Li et al., 2020). Median increase of more than 1°C in the 50-year TXx and TNn events compared to the 1°C warming level (Li et al., 2020)	CMIP6 models project a robust increase in the intensity and frequency of TXx events and a robust decrease in the intensity and frequency of TNn events (Li et al., 2020). Median increase of more than 4.5°C in the 50-year TXx and TNn events compared to the 1°C warming level (Li et al., 2020)
	Very likely increase in the intensity and frequency of hot extremes and decrease in the intensity and frequency of cold extremes	Human influence *very likely* contributed to the observed increase in the intensity and frequency of hot extremes and decrease in the intensity and frequency of cold extremes	Increase in the intensity and frequency of hot extremes : *Very likely* (compared with the recent past (1995-2014)) *Extremely likely* (compared with pre-industrial) Decrease in the intensity and frequency of cold extremes:	Increase in the intensity and frequency of hot extremes: *Extremely likely* (compared with the recent past (1995-2014)) *Virtually certain* (compared with pre-industrial) Decrease in the intensity and	Increase in the intensity and frequency of hot extremes: *Virtually certain* (compared with the recent past (1995-2014)) *Virtually certain* (compared with pre-industrial) Decrease in the intensity and

SUBJECT TO FINAL EDITING COPYEDITED VERSION

			Very likely (compared with the recent past (1995-2014)) *Extremely likely* (compared with pre-industrial)	frequency of cold extremes: *Extremely likely* (compared with the recent past (1995-2014)) *Virtually certain* (compared with pre-industrial)	frequency of cold extremes: *Virtually certain* (compared with the recent past (1995-2014)) *Virtually certain* (compared with pre-industrial)
Russian Arctic (RAR)	Significant increases in the intensity and frequency of hot extremes and significant decreases in the intensity and frequency of cold extremes (Donat et al., 2016a; Sui et al., 2017; Dunn et al., 2020)	Evidence of a human contribution to the observed increase in the intensity and frequency of hot extremes and decrease in the intensity and frequency of cold extremes (Wang et al., 2017c)	CMIP6 models project a robust increase in the intensity and frequency of TXx events and a robust decrease in the intensity and frequency of TNn events (Li et al., 2020; Annex). Median increase of more than 0.5°C in the 50-year TXx and TNn events compared to the 1°C warming level (Li et al., 2020) and more than 1.5°C in annual TXx and TNn compared to pre-industrial (Annex). Additional evidence from CMIP5 and RCM simulations for an increase in the intensity and frequency of hot extremes and decrease in the intensity and frequency of cold extremes (Xu et al. 2017; Han et al. 2018; Khlebnikova et al. 2019)	CMIP6 models project a robust increase in the intensity and frequency of TXx events and a robust decrease in the intensity and frequency of TNn events (Li et al., 2020; Annex). Median increase of more than 1.5°C in the 50-year TXx and TNn events compared to the 1°C warming level (Li et al., 2020) and more than 2.5°C in annual TXx and TNn compared to pre-industrial (Annex). Additional evidence from CMIP5 and RCM simulations for an increase in the intensity and frequency of hot extremes and decrease in the intensity and frequency of cold extremes (Xu et al. 2017; Han et al. 2018; Khlebnikova et al. 2019)	CMIP6 models project a robust increase in the intensity and frequency of TXx events and a robust decrease in the intensity and frequency of TNn events (Li et al., 2020; Annex). Median increase of more than 4.5°C in the 50-year TXx and TNn events compared to the 1°C warming level (Li et al., 2020) and more than 5.5°C in annual TXx and TNn compared to pre-industrial (Annex). Additional evidence from CMIP5 and RCM simulations for an increase in the intensity and frequency of hot extremes and decrease in the intensity and frequency of cold extremes (Xu et al. 2017; Han et al. 2018; Khlebnikova et al. 2019)
	Very likely increase in the intensity and frequency of hot extremes and decrease in the intensity and frequency of cold extremes	*Medium confidence* in a human contribution to the observed increase in the intensity and frequency of hot extremes and decrease in the intensity and frequency of cold extremes.	Increase in the intensity and frequency of hot extremes: *Likely* (compared with the recent past (1995-2014)) *Very likely* (compared with pre-industrial) Decrease in the intensity and frequency of cold extremes: *Likely* (compared with the recent past (1995-2014)) *Very likely* (compared with pre-industrial).	Increase in the intensity and frequency of hot extremes: *Very likely* (compared with the recent past (1995-2014)) *Extremely likely* (compared with pre-industrial) Decrease in the intensity and frequency of cold extremes: *Very likely* (compared with the recent past (1995-2014)) *Extremely likely* (compared with pre-industrial)	Increase in the intensity and frequency of hot extremes: *Virtually certain* (compared with the recent past (1995-2014)) *Virtually certain* (compared with pre-industrial) Decrease in the intensity and frequency of cold extremes: *Virtually certain* (compared with the recent past (1995-2014)) *Virtually certain* (compared with pre-industrial)
Arabian Peninsula (ARP)	Significant increases in the intensity and frequency of hot extremes and significant decreases in the intensity and	Strong evidence of changes from observations that are in the direction of model projected changes for the	CMIP6 models project a robust increase in the intensity and frequency of TXx events and a robust decrease in the intensity	CMIP6 models project a robust increase in the intensity and frequency of TXx events and a robust decrease in the intensity	CMIP6 models project a robust increase in the intensity and frequency of TXx events and a robust decrease in the intensity

ACCEPTED VERSION SUBJECT TO EDITING

	frequency of cold extremes (Dunn et al., 2020; Almazroui et al., 2014; Barlow et al., 2016; Donat et al., 2014; Nazrul Islam et al., 2015; Rahimi and Hejabi, 2018; Donat et al., 2014; Rahimi et al., 2018)	future. The magnitude of projected changes increases with global warming.	and frequency of TNn events (Li et al., 2020; Annex). Median increase of more than 0.5°C in the 50-year TXx and TNn events compared to the 1°C warming level (Li et al., 2020) and more than 2°C in annual TXx and TNn compared to pre-industrial (Annex). Additional evidence from CMIP5 and RCM simulations for an increase in the intensity and frequency of hot extremes and decrease in the intensity and frequency of cold extremes (Almazroui, 2019b)	and frequency of TNn events (Li et al., 2020; Annex). Median increase of more than 1.5°C in the 50-year TXx and TNn events compared to the 1°C warming level (Li et al., 2020) and more than 2.5°C in annual TXx and TNn compared to pre-industrial (Annex). Additional evidence from CMIP5 and RCM simulations for an increase in the intensity and frequency of hot extremes and decrease in the intensity and frequency of cold extremes (Almazroui, 2019b)	and frequency of TNn events (Li et al., 2020; Annex). Median increase of more than 3.5°C in the 50-year TXx and TNn events compared to the 1°C warming level (Li et al., 2020) and more than 5.5°C in annual TXx and TNn compared to pre-industrial (Annex). Additional evidence from CMIP5 and RCM simulations for an increase in the intensity and frequency of hot extremes and decrease in the intensity and frequency of cold extremes (Almazroui, 2019b)
	Very likely increase in the intensity and frequency of hot extremes and decrease in the intensity and frequency of cold extremes	*Medium confidence* in a human contribution to the observed increase in the intensity and frequency of hot extremes and decrease in the intensity and frequency of cold extremes.	Increase in the intensity and frequency of hot extremes: *Likely* (compared with the recent past (1995-2014)) *Very likely* (compared with pre-industrial) Decrease in the intensity and frequency of cold extremes: *Likely* (compared with the recent past (1995-2014)) *Very likely* (compared with pre-industrial).	Increase in the intensity and frequency of hot extremes: *Very likely* (compared with the recent past (1995-2014)) *Extremely likely* (compared with pre-industrial) Decrease in the intensity and frequency of cold extremes: *Very likely* (compared with the recent past (1995-2014)) *Extremely likely* (compared with pre-industrial)	Increase in the intensity and frequency of hot extremes: *Virtually certain* (compared with the recent past (1995-2014)) *Virtually certain* (compared with pre-industrial) Decrease in the intensity and frequency of cold extremes: *Virtually certain* (compared with the recent past (1995-2014)) *Virtually certain* (compared with pre-industrial)
West Central Asia (WCA)	Significant increases in the intensity and frequency of hot extremes and significant decreases in the intensity and frequency of cold extremes (Hu et al., 2016; Jiang et al., 2013; Dunn et al., 2020)	Robust evidence of a human contribution to the observed increase in the intensity and frequency of hot extremes and decrease in the intensity and frequency of cold extremes (Seong et al., 2020; Wang et al., 2017; Dong et al., 2018; Kim et al., 2019)	CMIP6 models project a robust increase in the intensity and frequency of TXx events and a robust decrease in the intensity and frequency of TNn events (Li et al., 2020; Annex). Median increase of more than 0.5°C in the 50-year TXx and TNn events compared to the 1°C warming level (Li et al., 2020) and more than 2°C in annual TXx and TNn compared to pre-industrial (Annex). Additional evidence from	CMIP6 models project a robust increase in the intensity and frequency of TXx events and a robust decrease in the intensity and frequency of TNn events (Li et al., 2020; Annex). Median increase of more than 1.5°C in the 50-year TXx and TNn events compared to the 1°C warming level (Li et al., 2020) and more than 3°C in annual TXx and TNn compared to pre-industrial (Annex). Additional evidence from	CMIP6 models project a robust increase in the intensity and frequency of TXx events and a robust decrease in the intensity and frequency of TNn events (Li et al., 2020; Annex). Median increase of more than 5°C in the 50-year TXx and TNn events compared to the 1°C warming level (Li et al., 2020) and more than 6°C in annual TXx and TNn compared to pre-industrial (Annex). Additional evidence from

ACCEPTED VERSION SUBJECT TO FINAL EDITING

			CMIP5 simulations for an increase in the intensity and frequency of hot extremes and decrease in the intensity and frequency of cold extremes (Han et al., 2018)	CMIP5 simulations for an increase in the intensity and frequency of hot extremes and decrease in the intensity and frequency of cold extremes (Han et al., 2018)	CMIP5 simulations for an increase in the intensity and frequency of hot extremes and decrease in the intensity and frequency of cold extremes (Han et al., 2018)
	Very likely increase in the intensity and frequency of hot extremes and decrease in the intensity and frequency of cold extremes	*High confidence* in a human contribution to the observed increase in the intensity and frequency of hot extremes and decrease in the intensity and frequency of cold extremes.	Increase in the intensity and frequency of hot extremes: *Likely* (compared with the recent past (1995-2014)) *Very likely* (compared with pre-industrial) Decrease in the intensity and frequency of cold extremes: *Likely* (compared with the recent past (1995-2014)) *Very likely* (compared with pre-industrial).	Increase in the intensity and frequency of hot extremes: *Very likely* (compared with the recent past (1995-2014)) *Extremely likely* (compared with pre-industrial) Decrease in the intensity and frequency of cold extremes: *Very likely* (compared with the recent past (1995-2014)) *Extremely likely* (compared with pre-industrial)	Increase in the intensity and frequency of hot extremes: *Virtually certain* (compared with the recent past (1995-2014)) *Virtually certain* (compared with pre-industrial) Decrease in the intensity and frequency of cold extremes: *Virtually certain* (compared with the recent past (1995-2014)) *Virtually certain* (compared with pre-industrial)
West Siberia (WSB)	Significant increases in the intensity and frequency of hot extremes and significant decreases in the intensity and frequency of cold extremes (Degefie et al., 2014; Salnikov et al., 2015; Donat et al., 2016a; Zhang et al., 2019c, 2019b; Dunn et al., 2020)	Robust evidence of a human contribution to the observed increase in the intensity and frequency of hot extremes and decrease in the intensity and frequency of cold extremes (Wang et al., 2017; Seong et al., 2020; Dong et al., 2018)	CMIP6 models project a robust increase in the intensity and frequency of TXx events and a robust decrease in the intensity and frequency of TNn events (Li et al., 2020; Annex). Median increase of more than 0.5°C in the 50-year TXx and TNn events compared to the 1°C warming level (Li et al., 2020) and more than 2°C in annual TXx and TNn compared to pre-industrial (Annex). Additional evidence from CMIP5 and RCM simulations for an increase in the intensity and frequency of hot extremes and decrease in the intensity and frequency of cold extremes (Xu et al. 2017; Han et al. 2018; Khlebnikova et al. 2019)	CMIP6 models project a robust increase in the intensity and frequency of TXx events and a robust decrease in the intensity and frequency of TNn events (Li et al., 2020; Annex). Median increase of more than 1°C in the 50-year TXx and TNn events compared to the 1°C warming level (Li et al., 2020) and more than 2.5°C in annual TXx and TNn compared to pre-industrial (Annex). Additional evidence from CMIP5 and RCM simulations for an increase in the intensity and frequency of hot extremes and decrease in the intensity and frequency of cold extremes (Xu et al. 2017; Han et al. 2018; Khlebnikova et al. 2019)	CMIP6 models project a robust increase in the intensity and frequency of TXx events and a robust decrease in the intensity and frequency of TNn events (Li et al., 2020; Annex). Median increase of more than 4°C in the 50-year TXx and TNn events compared to the 1°C warming level (Li et al., 2020) and more than 5°C in annual TXx and TNn compared to pre-industrial (Annex). Additional evidence from CMIP5 and RCM simulations for an increase in the intensity and frequency of hot extremes and decrease in the intensity and frequency of cold extremes (Xu et al. 2017; Han et al. 2018; Khlebnikova et al. 2019)
	Very likely increase in the intensity and frequency of hot extremes and decrease in the	*High confidence* in a human contribution to the observed increase in the intensity and	Increase in the intensity and frequency of hot extremes: *Likely* (compared with the recent	Increase in the intensity and frequency of hot extremes: *Very likely* (compared with the	Increase in the intensity and frequency of hot extremes: *Virtually certain* (compared

ACCEPTED VERSION SUBJECT TO FINAL EDITING

	intensity and frequency of cold extremes	frequency of hot extremes and decrease in the intensity and frequency of cold extremes.	past (1995-2014)) *Very likely* (compared with pre-industrial) Decrease in the intensity and frequency of cold extremes: *Likely* (compared with the recent past (1995-2014)) *Very likely* (compared with pre-industrial).	recent past (1995-2014)) *Extremely likely* (compared with pre-industrial) Decrease in the intensity and frequency of cold extremes: *Very likely* (compared with the recent past (1995-2014)) *Extremely likely* (compared with pre-industrial)	with the recent past (1995-2014)) *Virtually certain* (compared with pre-industrial) Decrease in the intensity and frequency of cold extremes: *Virtually certain* (compared with the recent past (1995-2014)) *Virtually certain* (compared with pre-industrial)
East Siberia (ESB)	Significant increases in the intensity and frequency of hot extremes and significant decreases in the intensity and frequency of cold extremes (Dashkhuu et al., 2015; Donat et al., 2016a; Zhang et al., 2019c; Dunn et al., 2020)	Robust evidence of a human contribution to the observed increase in the intensity and frequency of hot extremes and decrease in the intensity and frequency of cold extremes (Wang et al., 2017; Seong et al., 2020; Dong et al., 2018)	CMIP6 models project a robust increase in the intensity and frequency of TXx events and a robust decrease in the intensity and frequency of TNn events (Li et al., 2020; Annex). Median increase of more than 0.5°C in the 50-year TXx and TNn events compared to the 1°C warming level (Li et al., 2020) and more than 2°C in annual TXx and TNn compared to pre-industrial (Annex). Additional evidence from CMIP5 and RCM simulations for an increase in the intensity and frequency of hot extremes and decrease in the intensity and frequency of cold extremes (Xu et al. 2017; Han et al. 2018; Khlebnikova et al. 2019)	CMIP6 models project a robust increase in the intensity and frequency of TXx events and a robust decrease in the intensity and frequency of TNn events (Li et al., 2020; Annex). Median increase of more than 1.5°C in the 50-year TXx and TNn events compared to the 1°C warming level (Li et al., 2020) and more than 2.5°C in annual TXx and TNn compared to pre-industrial (Annex). Additional evidence from CMIP5 and RCM simulations for an increase in the intensity and frequency of hot extremes and decrease in the intensity and frequency of cold extremes (Xu et al. 2017; Han et al. 2018; Khlebnikova et al. 2019)	CMIP6 models project a robust increase in the intensity and frequency of TXx events and a robust decrease in the intensity and frequency of TNn events (Li et al., 2020; Annex). Median increase of more than 4.5°C in the 50-year TXx and TNn events compared to the 1°C warming level (Li et al., 2020) and more than 5.5°C in annual TXx and TNn compared to pre-industrial (Annex). Additional evidence from CMIP5 and RCM simulations for an increase in the intensity and frequency of hot extremes and decrease in the intensity and frequency of cold extremes (Xu et al. 2017; Han et al. 2018; Khlebnikova et al. 2019)
	Very likely increase in the intensity and frequency of hot extremes and decrease in the intensity and frequency of cold extremes	*High confidence* in a human contribution to the observed increase in the intensity and frequency of hot extremes and decrease in the intensity and frequency of cold extremes.	Increase in the intensity and frequency of hot extremes: *Likely* (compared with the recent past (1995-2014)) *Very likely* (compared with pre-industrial) Decrease in the intensity and frequency of cold extremes: *Likely* (compared with the recent past (1995-2014)) *Very likely* (compared with pre-industrial).	Increase in the intensity and frequency of hot extremes: *Very likely* (compared with the recent past (1995-2014)) *Extremely likely* (compared with pre-industrial) Decrease in the intensity and frequency of cold extremes: *Very likely* (compared with the recent past (1995-2014)) *Extremely likely* (compared with pre-industrial)	Increase in the intensity and frequency of hot extremes: *Virtually certain* (compared with the recent past (1995-2014)) *Virtually certain* (compared with pre-industrial) Decrease in the intensity and frequency of cold extremes: *Virtually certain* (compared with the recent past (1995-2014))

ACCEPTED VERSION SUBJECT TO FINAL EDITING

					Virtually certain (compared with pre-industrial)
Russian Far East (RFE)	Significant increases in the intensity and frequency of hot extremes and significant decreases in the intensity and frequency of cold extremes (Donat et al., 2016; Dunn et al., 2020; Zhang et al., 2019b)	Robust evidence of a human contribution to the observed increase in the intensity and frequency of hot extremes and decrease in the intensity and frequency of cold extremes (Seong et al., 2020; Wang et al., 2017; Dong et al., 2018)	CMIP6 models project a robust increase in the intensity and frequency of TXx events and a robust decrease in the intensity and frequency of TNn events (Li et al., 2020; Annex). Median increase of more than 0.5°C in the 50-year TXx and TNn events compared to the 1°C warming level (Li et al., 2020) and more than 1.5°C in annual TXx and TNn compared to pre-industrial (Annex). Additional evidence from CMIP5 and RCM simulations for an increase in the intensity and frequency of hot extremes and decrease in the intensity and frequency of cold extremes (Xu et al. 2017; Han et al. 2018; Khlebnikova et al. 2019).	CMIP6 models project a robust increase in the intensity and frequency of TXx events and a robust decrease in the intensity and frequency of TNn events (Li et al., 2020; Annex). Median increase of more than 1°C in the 50-year TXx and TNn events compared to the 1°C warming level (Li et al., 2020) and more than 2.5°C in annual TXx and TNn compared to pre-industrial (Annex). Additional evidence from CMIP5 and RCM simulations for an increase in the intensity and frequency of hot extremes and decrease in the intensity and frequency of cold extremes (Xu et al. 2017; Han et al. 2018; Khlebnikova et al. 2019).	CMIP6 models project a robust increase in the intensity and frequency of TXx events and a robust decrease in the intensity and frequency of TNn events (Li et al., 2020; Annex). Median increase of more than 4.5°C in the 50-year TXx and TNn events compared to the 1°C warming level (Li et al., 2020) and more than 5°C in annual TXx and TNn compared to pre-industrial (Annex). Additional evidence from CMIP5 and RCM simulations for an increase in the intensity and frequency of hot extremes and decrease in the intensity and frequency of cold extremes (Xu et al. 2017; Han et al. 2018; Khlebnikova et al. 2019).
	Very likely increase in the intensity and frequency of hot extremes and decrease in the intensity and frequency of cold extremes	*High confidence* in a human contribution to the observed increase in the intensity and frequency of hot extremes and decrease in the intensity and frequency of cold extremes.	Increase in the intensity and frequency of hot extremes: *Likely* (compared with the recent past (1995-2014)) *Very likely* (compared with pre-industrial) Decrease in the intensity and frequency of cold extremes: *Likely* (compared with the recent past (1995-2014)) *Very likely* (compared with pre-industrial).	Increase in the intensity and frequency of hot extremes: *Very likely* (compared with the recent past (1995-2014)) *Extremely likely* (compared with pre-industrial) Decrease in the intensity and frequency of cold extremes: *Very likely* (compared with the recent past (1995-2014)) *Extremely likely* (compared with pre-industrial)	Increase in the intensity and frequency of hot extremes: *Virtually certain* (compared with the recent past (1995-2014)) *Virtually certain* (compared with pre-industrial) Decrease in the intensity and frequency of cold extremes: *Virtually certain* (compared with the recent past (1995-2014)) *Virtually certain* (compared with pre-industrial)
East Asia (EAS)	Significant increases in the intensity and frequency of hot extremes and significant decreases in the intensity and frequency of cold extremes (Lin et al., 2017; Lu et al., 2016, 2018; Wang et al.,	Robust evidence of a human contribution to the observed increase in the intensity and frequency of hot extremes and decrease in the intensity and frequency of cold extremes (Seong et al., 2020;	CMIP6 models project a robust increase in the intensity and frequency of TXx events and a robust decrease in the intensity and frequency of TNn events (Li et al., 2020; Annex). Median increase of more than 0.5°C in	CMIP6 models project a robust increase in the intensity and frequency of TXx events and a robust decrease in the intensity and frequency of TNn events (Li et al., 2020; Annex). Median increase of more than	CMIP6 models project a robust increase in the intensity and frequency of TXx events and a robust decrease in the intensity and frequency of TNn events (Li et al., 2020; Annex). Median increase of more than

ACCEPTED VERSION SUBJECT TO FINAL EDITING

	2013a; Yin et al., 2017; Zhou et al., 2016; Dunn et al., 2020)	Wang et al., 2017; Imada et al., 2014, 2019; Kim et al., 2018; Lu et al., 2016, 2018; Takahashi et al., 2016; Ye and Li, 2017; Zhou et al., 2016)	the 50-year TXx and TNn events compared to the 1°C warming level (Li et al., 2020) and more than 1.5°C in annual TXx and TNn compared to pre-industrial (Annex). Additional evidence from CMIP5 and RCM simulations for an increase in the intensity and frequency of hot extremes and decrease in the intensity and frequency of cold extremes (Guo et al., 2018; Imada et al., 2019; Li et al., 2018c; Seo et al., 2014; Sui et al., 2018; Wang et al., 2017a, 2017c; Xu et al., 2016a; Zhou et al., 2014; Shi et al., 2018; Sun et al., 2019a)	1°C in the 50-year TXx and TNn events compared to the 1°C warming level (Li et al., 2020) and more than 2°C in annual TXx and TNn compared to pre-industrial (Annex). Additional evidence from CMIP5 and RCM simulations for an increase in the intensity and frequency of hot extremes and decrease in the intensity and frequency of cold extremes (Guo et al., 2018; Imada et al., 2019; Li et al., 2018c; Seo et al., 2014; Sui et al., 2018; Wang et al., 2017a, 2017c; Xu et al., 2016a; Zhou et al., 2014; Shi et al., 2018; Sun et al., 2019a)	4°C in the 50-year TXx and TNn events compared to the 1°C warming level (Li et al., 2020) and more than 4.5°C in annual TXx and TNn compared to pre-industrial (Annex). Additional evidence from CMIP5 and RCM simulations for an increase in the intensity and frequency of hot extremes and decrease in the intensity and frequency of cold extremes (Guo et al., 2018; Imada et al., 2019; Li et al., 2018c; Seo et al., 2014; Sui et al., 2018; Wang et al., 2017a, 2017c; Xu et al., 2016a; Zhou et al., 2014; Shi et al., 2018; Sun et al., 2019a)
	Very likely increase in the intensity and frequency of hot extremes and decrease in the intensity and frequency of cold extremes	Human influence *likely* contributed to the observed increase in the intensity and frequency of hot extremes and decrease in the intensity and frequency of cold extremes	Increase in the intensity and frequency of hot extremes: *Likely* (compared with the recent past (1995-2014)) *Very likely* (compared with pre-industrial) Decrease in the intensity and frequency of cold extremes: *Likely* (compared with the recent past (1995-2014)) *Very likely* (compared with pre-industrial).	Increase in the intensity and frequency of hot extremes: *Very likely* (compared with the recent past (1995-2014)) *Extremely likely* (compared with pre-industrial) Decrease in the intensity and frequency of cold extremes: *Very likely* (compared with the recent past (1995-2014)) *Extremely likely* (compared with pre-industrial)	Increase in the intensity and frequency of hot extremes: *Virtually certain* (compared with the recent past (1995-2014)) *Virtually certain* (compared with pre-industrial) Decrease in the intensity and frequency of cold extremes: *Virtually certain* (compared with the recent past (1995-2014)) *Virtually certain* (compared with pre-industrial)
East Central Asia (ECA)	Significant increases in the intensity and frequency of hot extremes and significant decreases in the intensity and frequency of cold extremes (Dunn et al., 2020)	Robust evidence of a human contribution to the observed increase in the intensity and frequency of hot extremes and decrease in the intensity and frequency of cold extremes (Seong et al., 2020; Wang et al., 2017; Dong et al., 2018; Kim et al., 2019)	CMIP6 models project a robust increase in the intensity and frequency of TXx events and a robust decrease in the intensity and frequency of TNn events (Li et al., 2020; Annex). Median increase of more than 0.5°C in the 50-year TXx and TNn events compared to the 1°C warming level (Li et al., 2020) and more than 2°C in annual TXx and TNn	CMIP6 models project a robust increase in the intensity and frequency of TXx events and a robust decrease in the intensity and frequency of TNn events (Li et al., 2020; Annex). Median increase of more than 1°C in the 50-year TXx and TNn events compared to the 1°C warming level (Li et al., 2020) and more than 2.5°C in	CMIP6 models project a robust increase in the intensity and frequency of TXx events and a robust decrease in the intensity and frequency of TNn events (Li et al., 2020; Annex). Median increase of more than 3.5°C in the 50-year TXx and TNn events compared to the 1°C warming level (Li et al., 2020) and more than 5.5°C in

ACCEPTED VERSION SUBJECT TO FINAL EDITING

			compared to pre-industrial (Annex). Additional evidence from CMIP5 simulations for an increase in the intensity and frequency of hot extremes and decrease in the intensity and frequency of cold extremes (Han et al., 2018)	annual TXx and TNn compared to pre-industrial (Annex). Additional evidence from CMIP5 simulations for an increase in the intensity and frequency of hot extremes and decrease in the intensity and frequency of cold extremes (Han et al., 2018)	annual TXx and TNn compared to pre-industrial (Annex). Additional evidence from CMIP5 simulations for an increase in the intensity and frequency of hot extremes and decrease in the intensity and frequency of cold extremes (Han et al., 2018)
	Very likely increase in the intensity and frequency of hot extremes and decrease in the intensity and frequency of cold extremes	*High confidence* in a human contribution to the observed increase in the intensity and frequency of hot extremes and decrease in the intensity and frequency of cold extremes.	Increase in the intensity and frequency of hot extremes: *Likely* (compared with the recent past (1995-2014)) *Very likely* (compared with pre-industrial) Decrease in the intensity and frequency of cold extremes: *Likely* (compared with the recent past (1995-2014)) *Very likely* (compared with pre-industrial).	Increase in the intensity and frequency of hot extremes: *Very likely* (compared with the recent past (1995-2014)) *Extremely likely* (compared with pre-industrial) Decrease in the intensity and frequency of cold extremes: *Very likely* (compared with the recent past (1995-2014)) *Extremely likely* (compared with pre-industrial)	Increase in the intensity and frequency of hot extremes: *Virtually certain* (compared with the recent past (1995-2014)) *Virtually certain* (compared with pre-industrial) Decrease in the intensity and frequency of cold extremes: *Virtually certain* (compared with the recent past (1995-2014)) *Virtually certain* (compared with pre-industrial)
Tibetan Plateau (TIB)	Significant increases in the intensity and frequency of hot extremes and significant decreases in the intensity and frequency of cold extremes (Donat et al., 2016a; Hu et al., 2016; Sun et al., 2017; Yin et al., 2019; Zhang et al., 2019c; Dunn et al., 2020)	Robust evidence of a human contribution to the observed increase in the intensity and frequency of hot extremes and decrease in the intensity and frequency of cold extremes (Seong et al., 2020; Wang et al., 2017; Yin et al., 2019)	CMIP6 models project a robust increase in the intensity and frequency of TXx events and a robust decrease in the intensity and frequency of TNn events (Li et al., 2020; Annex). Median increase of more than 0.5°C in the 50-year TXx and TNn events compared to the 1°C warming level (Li et al., 2020) and more than 1.5°C in annual TXx and TNn compared to pre-industrial (Annex). Additional evidence from CMIP5 and RCM simulations for an increase in the intensity and frequency of hot extremes and decrease in the intensity and frequency of cold extremes (Zhou et al., 2014; Singh and Goyal, 2016; Zhang et al.,	CMIP6 models project a robust increase in the intensity and frequency of TXx events and a robust decrease in the intensity and frequency of TNn events (Li et al., 2020; Annex). Median increase of more than 1°C in the 50-year TXx and TNn events compared to the 1°C warming level (Li et al., 2020) and more than 2°C in annual TXx and TNn compared to pre-industrial (Annex). Additional evidence from CMIP5 and RCM simulations for an increase in the intensity and frequency of hot extremes and decrease in the intensity and frequency of cold extremes (Zhou et al., 2014; Singh and Goyal, 2016; Zhang et al.,	CMIP6 models project a robust increase in the intensity and frequency of TXx events and a robust decrease in the intensity and frequency of TNn events (Li et al., 2020; Annex). Median increase of more than 4°C in the 50-year TXx and TNn events compared to the 1°C warming level (Li et al., 2020) and more than 4.5°C in annual TXx and TNn compared to pre-industrial (Annex). Additional evidence from CMIP5 and RCM simulations for an increase in the intensity and frequency of hot extremes and decrease in the intensity and frequency of cold extremes (Zhou et al., 2014; Singh and Goyal, 2016; Zhang et al.,

ACCEPTED VERSION SUBJECT TO FINAL EDITING

			2016a; Xu et al., 2017; Han et al., 2018; Li et al., 2018a)	2016a; Xu et al., 2017; Han et al., 2018; Li et al., 2018a)	2016a; Xu et al., 2017; Han et al., 2018; Li et al., 2018a)
	Very likely increase in the intensity and frequency of hot extremes and decrease in the intensity and frequency of cold extremes	*High confidence* in a human contribution to the observed increase in the intensity and frequency of hot extremes and decrease in the intensity and frequency of cold extremes.	Increase in the intensity and frequency of hot extremes: *Likely* (compared with the recent past (1995-2014)) *Very likely* (compared with pre-industrial) Decrease in the intensity and frequency of cold extremes: *Likely* (compared with the recent past (1995-2014)) *Very likely* (compared with pre-industrial).	Increase in the intensity and frequency of hot extremes: *Very likely* (compared with the recent past (1995-2014)) *Extremely likely* (compared with pre-industrial) Decrease in the intensity and frequency of cold extremes: *Very likely* (compared with the recent past (1995-2014)) *Extremely likely* (compared with pre-industrial)	Increase in the intensity and frequency of hot extremes: *Virtually certain* (compared with the recent past (1995-2014)) *Virtually certain* (compared with pre-industrial) Decrease in the intensity and frequency of cold extremes: *Virtually certain* (compared with the recent past (1995-2014)) *Virtually certain* (compared with pre-industrial)
South Asia (SAS)	Significant increases in the intensity and frequency of hot extremes and significant decreases in the intensity and frequency of cold extremes (Chakraborty et al., 2018; Dimri, 2019; Donat et al., 2016; Dunn et al., 2020; Roy, 2019; Sheikh et al., 2015; Rohini et al., 2016; Zahid and Rasul, 2012)	Robust evidence of a human contribution to the observed increase in the intensity and frequency of hot extremes and decrease in the intensity and frequency of cold extremes (Seong et al., 2020; Wang et al., 2017; Wehner et al., 2016; Kumar, 2017; van Oldenborgh et al., 2018)	CMIP6 models project a robust increase in the intensity and frequency of TXx events and a robust decrease in the intensity and frequency of TNn events (Li et al., 2020; Annex). Median increase of more than 0C in the 50-year TXx and TNn events compared to the 1°C warming level (Li et al., 2020) and more than 1°C in annual TXx and TNn compared to pre-industrial (Annex). Additional evidence from CMIP5 and RCM simulations for an increase in the intensity and frequency of hot extremes and decrease in the intensity and frequency of cold extremes (Ali et al., 2019; Han et al., 2018; Kharin et al., 2018; Sillmann et al., 2013; Xu et al., 2017; Murari et al., 2015; Nasim et al., 2018)	CMIP6 models project a robust increase in the intensity and frequency of TXx events and a robust decrease in the intensity and frequency of TNn events (Li et al., 2020; Annex). Median increase of more than 1°C in the 50-year TXx and TNn events compared to the 1°C warming level (Li et al., 2020) and more than 1.5°C in annual TXx and TNn compared to pre-industrial (Annex). Additional evidence from CMIP5 and RCM simulations for an increase in the intensity and frequency of hot extremes and decrease in the intensity and frequency of cold extremes (Ali et al., 2019; Han et al., 2018; Kharin et al., 2018; Sillmann et al., 2013; Xu et al., 2017; Murari et al., 2015; Nasim et al., 2018)	CMIP6 models project a robust increase in the intensity and frequency of TXx events and a robust decrease in the intensity and frequency of TNn events (Li et al., 2020; Annex). Median increase of more than 3.5°C in the 50-year TXx and TNn events compared to the 1°C warming level (Li et al., 2020) and more than 4°C in annual TXx and TNn compared to pre-industrial (Annex). Additional evidence from CMIP5 and RCM simulations for an increase in the intensity and frequency of hot extremes and decrease in the intensity and frequency of cold extremes (Ali et al., 2019; Han et al., 2018; Kharin et al., 2018; Sillmann et al., 2013; Xu et al., 2017; Murari et al., 2015; Nasim et al., 2018)
	High confidence in the increase in the intensity and frequency of hot extremes and decrease in the intensity	*High confidence* in a human contribution to the observed increase in the intensity and frequency of hot extremes and decrease in the intensity	Increase in the intensity and frequency of hot extremes: *Likely* (compared with the recent past (1995-2014)) *Very likely* (compared with pre-	Increase in the intensity and frequency of hot extremes: *Very likely* (compared with the recent past (1995-2014)) *Extremely likely* (compared	Increase in the intensity and frequency of hot extremes: *Virtually certain* (compared with the recent past (1995-2014))

ACCEPTED VERSION SUBJECT TO FINAL EDITING

	and frequency of cold extremes	and frequency of cold extremes.	industrial) Decrease in the intensity and frequency of cold extremes: *Likely* (compared with the recent past (1995-2014)) *Very likely* (compared with pre-industrial).	with pre-industrial) Decrease in the intensity and frequency of cold extremes: *Very likely* (compared with the recent past (1995-2014)) *Extremely likely* (compared with pre-industrial)	*Virtually certain* (compared with pre-industrial) Decrease in the intensity and frequency of cold extremes: *Virtually certain* (compared with the recent past (1995-2014)) *Virtually certain* (compared with pre-industrial)
Southeast Asia (SEA)	Significant increases in the intensity and frequency of hot extremes and significant decreases in the intensity and frequency of cold extremes (Donat et al., 2016a; Supari et al., 2017; Cheong et al., 2018; Zhang et al., 2019c; Dunn et al., 2020)	Robust evidence of a human contribution to the observed increase in the intensity and frequency of hot extremes and decrease in the intensity and frequency of cold extremes (Seong et al., 2020; Wang et al., 2017; King et al., 2016; Min et al., 2020)	CMIP6 models project a robust increase in the intensity and frequency of TXx events and a robust decrease in the intensity and frequency of TNn events (Li et al., 2020; Annex). Median increase of more than 0C in the 50-year TXx and TNn events compared to the 1°C warming level (Li et al., 2020) and more than 1°C in annual TXx and TNn compared to pre-industrial (Annex). Additional evidence from CMIP5 simulations for an increase in the intensity and frequency of hot extremes and decrease in the intensity and frequency of cold extremes (Han et al., 2018; Kharin et al., 2018; Xu et al., 2017)	CMIP6 models project a robust increase in the intensity and frequency of TXx events and a robust decrease in the intensity and frequency of TNn events (Li et al., 2020; Annex). Median increase of more than 0.5°C in the 50-year TXx and TNn events compared to the 1°C warming level (Li et al., 2020) and more than 1.5°C in annual TXx and TNn compared to pre-industrial (Annex). Additional evidence from CMIP5 simulations for an increase in the intensity and frequency of hot extremes and decrease in the intensity and frequency of cold extremes (Kharin et al., 2018; Xu et al., 2017).	CMIP6 models project a robust increase in the intensity and frequency of TXx events and a robust decrease in the intensity and frequency of TNn events (Li et al., 2020; Annex). Median increase of more than 2.5°C in the 50-year TXx and TNn events compared to the 1°C warming level (Li et al., 2020) and more than 4°C in annual TXx and TNn compared to pre-industrial (Annex) Additional evidence from CMIP5 simulations for an increase in the intensity and frequency of hot extremes and decrease in the intensity and frequency of cold extremes (Kharin et al., 2018; Xu et al., 2017)..
	High confidence in the increase in the intensity and frequency of hot extremes and decrease in the intensity and frequency of cold extremes	*High confidence* in a human contribution to the observed increase in the intensity and frequency of hot extremes and decrease in the intensity and frequency of cold extremes.	Increase in the intensity and frequency of hot extremes: *Likely* (compared with the recent past (1995-2014)) *Very likely* (compared with pre-industrial) Decrease in the intensity and frequency of cold extremes: *Likely* (compared with the recent past (1995-2014)) *Very likely* (compared with pre-industrial).	Increase in the intensity and frequency of hot extremes: *Very likely* (compared with the recent past (1995-2014)) *Extremely likely* (compared with pre-industrial) Decrease in the intensity and frequency of cold extremes: *Very likely* (compared with the recent past (1995-2014)) *Extremely likely* (compared with pre-industrial)	Increase in the intensity and frequency of hot extremes: *Virtually certain* (compared with the recent past (1995-2014)) *Virtually certain* (compared with pre-industrial) Decrease in the intensity and frequency of cold extremes: *Virtually certain* (compared with the recent past (1995-2014)) *Virtually certain* (compared

ACCEPTED VERSION SUBJECT TO EDITING

					with pre-industrial)

[END TABLE 11.7 HERE]

[START TABLE 11.8 HERE]

Table 11.8: Observed trends, human contribution to observed trends, and projected changes at 1.5°C, 2°C and 4°C of global warming for heavy precipitation in Asia, subdivided by AR6 regions. See Sections 11.9.1 and 11.9.3 for details

Region	Observed trends	Detection and attribution; event attribution	Projections		
			1.5 °C	2 °C	4 °C
All Asia	Significant intensification of heavy precipitation (Sun et al., 2020)	Robust evidence of a human contribution to the observed intensification of heavy precipitation	CMIP6 models project a robust increase in the intensity and frequency of heavy precipitation (Li et al., 2020a). Median increase of more than 2% in the 50-year Rx1day and Rx5day events compared to the 1°C warming level (Li et al., 2020a)	CMIP6 models project a robust increase in the intensity and frequency of heavy precipitation (Li et al., 2020a). Median increase of more than 6% in the 50-year Rx1day and Rx5day events compared to the 1°C warming level (Li et al., 2020a)	CMIP6 models project a robust increase in the intensity and frequency of heavy precipitation ((Li et al., 2020a). Median increase of more than 15% in the 50-year Rx1day and Rx5day events compared to the 1°C warming level (Li et al., 2020a)
	Likely intensification of heavy precipitation	Human influence *likely* contributed to the observed intensification of heavy precipitation	Intensification of heavy precipitation: *Likely* (compared with the recent past (1995-2014)) *Very likely* (compared with pre-industrial)	Intensification of heavy precipitation: *Very likely* (compared with the recent past (1995-2014)) *Extremely likely* (compared with pre-industrial)	Intensification of heavy precipitation: *Virtually certain* (compared with the recent past (1995-2014)) *Virtually certain* (compared with pre-industrial)
Russian Arctic (RAR)	Insufficient data and a lack of agreement on the evidence of trends (Sun et al., 2020; Dunn et al., 2020)	Limited evidence	CMIP6 models project a robust increase in the intensity and frequency of heavy precipitation (Li et al., 2020; Annex). Median increase of more than 4% in the 50-year Rx1day and Rx5day events compared to the 1°C warming level (Li et al., 2020a) and more than 10% in annual Rx1day and Rx5day and 8% in annual Rx30day compared to pre-industrial (Annex). Additional evidence from CMIP5 simulations for an increase in the intensity of heavy precipitation (Sillmann et	CMIP6 models project a robust increase in the intensity and frequency of heavy precipitation (Li et al., 2020; Annex). Median increase of more than 8% in the 50-year Rx1day and Rx5day events compared to the 1°C warming level (Li et al., 2020a) and more than 10% in annual Rx1day, Rx5day, and Rx30day compared to pre-industrial (Annex). Additional evidence from CMIP5 simulations for an increase in the intensity of heavy precipitation (Sillmann et	CMIP6 models project a robust increase in the intensity and frequency of heavy precipitation (Li et al., 2020; Annex). Median increase of more than 25% in the 50-year Rx1day and Rx5day events compared to the 1°C warming level (Li et al., 2020a) and more than 25% in annual Rx1day and Rx5day and 20% in annual Rx30day compared to pre-industrial (Annex). Additional evidence from CMIP5 simulations for an increase in the intensity of heavy precipitation (Sillmann et

ACCEPTED VERSION SUBJECT TO FINAL EDITING

			al., 2013b; Han et al., 2018; Kharin et al., 2018; Khlebnikova et al., 2019b)	al., 2013b; Han et al., 2018; Kharin et al., 2018; Khlebnikova et al., 2019b)	al., 2013b; Han et al., 2018; Kharin et al., 2018; Khlebnikova et al., 2019b)
	Low confidence	*Low confidence*	Intensification of heavy precipitation: *Likely* (compared with the recent past (1995-2014)) *Very likely* (compared with pre-industrial)	Intensification of heavy precipitation: *Very likely* (compared with the recent past (1995-2014)) *Extremely likely* (compared with pre-industrial)	Intensification of heavy precipitation: *Virtually certain* (compared with the recent past (1995-2014)) *Virtually certain* (compared with pre-industrial)
Arabian Peninsula (ARP)	Insufficient data and a lack of agreement on the evidence of trends (Sun et al., 2020; Dunn et al., 2020; Atif et al., 2020; Donat et al., 2014; Rahimi and Fatemi, 2019)	Limited evidence		CMIP6 models project an increase in the intensity and frequency of heavy precipitation (Li et al., 2020; Annex). Median increase of more than 8% in the 50-year Rx1day and Rx5day events compared to the 1°C warming level (Li et al., 2020a) and more than 15% in annual Rx1day, Rx5day, and Rx30day compared to pre-industrial (Annex).	CMIP6 models project a robust increase in the intensity and frequency of heavy precipitation (Li et al., 2020; Annex). Median increase of more than 20% in the 50-year Rx1day and Rx5day events compared to the 1°C warming level (Li et al., 2020a) and more than 40% in annual Rx1day and Rx5day and 45% in annual Rx30day compared to pre-industrial (Annex).
	Low confidence	*Low confidence*	Intensification of heavy precipitation: *Low confidence* (compared with the recent past (1995-2014)) *Medium confidence* (compared with pre-industrial)	Intensification of heavy precipitation: *Medium confidence* (compared with the recent past (1995-2014)) *High confidence* (compared with pre-industrial)	Intensification of heavy precipitation: *Likely* (compared with the recent past (1995-2014)) *Very likely* (compared with pre-industrial)
West Central Asia (WCA)	Intensification of heavy precipitation (Sun et al., 2020; Hu et al., 2016; Zhang et al., 2017).	Limited evidence	CMIP6 models project a robust increase in the intensity and frequency of heavy precipitation (Li et al., 2020; Annex). Median increase of more than 2% in the 50-year Rx1day and Rx5day events compared to the 1°C warming level (Li et al., 2020a) and more than 6% in annual Rx1day and Rx5day and 4% in annual Rx30day compared to pre-industrial (Annex). Additional evidence from CMIP5 simulations for an increase in the intensity of	CMIP6 models project a robust increase in the intensity and frequency of heavy precipitation (Li et al., 2020; Annex). Median increase of more than 6% in the 50-year Rx1day and Rx5day events compared to the 1°C warming level (Li et al., 2020a) and more than 8% in annual Rx1day and Rx5day and 6% in annual Rx30day compared to pre-industrial (Annex). Additional evidence from CMIP5 simulations for an increase in the intensity of	CMIP6 models project a robust increase in the intensity and frequency of heavy precipitation (Li et al., 2020; Annex). Median increase of more than 15% in the 50-year Rx1day and Rx5day events compared to the 1°C warming level (Li et al., 2020a) and more than 20% in annual Rx1day and Rx5day and 15% in annual Rx30day compared to pre-industrial (Annex). Additional evidence from CMIP5 simulations for an increase in the intensity of

ACCEPTED VERSION SUBJECT TO FINAL EDITING

			heavy precipitation (Han et al., 2018)	heavy precipitation (Han et al., 2018)	heavy precipitation (Han et al., 2018)
	Medium confidence in the intensitification of heavy precipitation	*Low confidence*	Intensification of heavy precipitation: *Likely* (compared with the recent past (1995-2014)) *Very likely* (compared with pre-industrial)	Intensification of heavy precipitation: *Very likely* (compared with the recent past (1995-2014)) *Extremely likely* (compared with pre-industrial)	Intensification of heavy precipitation: *Virtually certain* (compared with the recent past (1995-2014)) *Virtually certain* (compared with pre-industrial)
West Siberia (WSB)	Significant intensification of heavy precipitation (Sun et al., 2020; Zhang et al., 2017)	Limited evidence	CMIP6 models project a robust increase in the intensity and frequency of heavy precipitation (Li et al., 2020; Annex). Median increase of more than 2% in the 50-year Rx1day and Rx5day events compared to the 1°C warming level (Li et al., 2020a) and more than 6% in annual Rx1day, Rx5day, and Rx30day compared to pre-industrial (Annex). Additional evidence from CMIP5 simulations for an increase in the intensity of heavy precipitation (Sillmann et al., 2013b; Xu et al., 2017; Han et al., 2018; Kharin et al., 2018; Khlebnikova et al., 2019b)	CMIP6 models project a robust increase in the intensity and frequency of heavy precipitation (Li et al., 2020; Annex). Median increase of more than 4% in the 50-year Rx1day and Rx5day events compared to the 1°C warming level (Li et al., 2020a) and more than 8% in annual Rx1day and Rx5day and 6% in annual Rx30day compared to pre-industrial (Annex). Additional evidence from CMIP5 simulations for an increase in the intensity of heavy precipitation (Sillmann et al., 2013b; Xu et al., 2017; Han et al., 2018; Kharin et al., 2018; Khlebnikova et al., 2019b)	CMIP6 models project a robust increase in the intensity and frequency of heavy precipitation (Li et al., 2020; Annex). Median increase of more than 15% in the 50-year Rx1day and Rx5day events compared to the 1°C warming level (Li et al., 2020a) and more than 15% in annual Rx1day, Rx5day, and Rx30day compared to pre-industrial (Annex). Additional evidence from CMIP5 simulations for an increase in the intensity of heavy precipitation (Sillmann et al., 2013b; Xu et al., 2017; Han et al., 2018; Kharin et al., 2018; Khlebnikova et al., 2019b)
	High confidence in the intensitification of heavy precipitation	*Low confidence*	Intensification of heavy precipitation: *Likely* (compared with the recent past (1995-2014)) *Very likely* (compared with pre-industrial)	Intensification of heavy precipitation: *Very likely* (compared with the recent past (1995-2014)) *Extremely likely* (compared with pre-industrial)	Intensification of heavy precipitation: *Virtually certain* (compared with the recent past (1995-2014)) *Virtually certain* (compared with pre-industrial)
East Siberia (ESB)	Intensification of heavy precipitation (Knutson and Zeng, 2018; Sun et al., 2020; Dunn et al., 2020)	Limited evidence	CMIP6 models project a robust increase in the intensity and frequency of heavy precipitation (Li et al., 2020; Annex). Median increase of more than 2% in the 50-year Rx1day and Rx5day events compared to the 1°C warming level (Li et al., 2020a) and more than 6% in annual Rx1day and	CMIP6 models project a robust increase in the intensity and frequency of heavy precipitation (Li et al., 2020; Annex). Median increase of more than 4% in the 50-year Rx1day and Rx5day events compared to the 1°C warming level (Li et al., 2020a) and more than 8% in annual Rx1day and	CMIP6 models project a robust increase in the intensity and frequency of heavy precipitation (Li et al., 2020; Annex). Median increase of more than 20% in the 50-year Rx1day and Rx5day events compared to the 1°C warming level (Li et al., 2020a) and more than 20% in annual Rx1day and

ACCEPTED VERSION SUBJECT TO EDITING

			Rx5day and 4% in annual Rx30day compared to pre-industrial (Annex). Additional evidence from CMIP5 simulations for an increase in the intensity of heavy precipitation (Sillmann et al., 2013b; Xu et al., 2017; Han et al., 2018; Kharin et al., 2018; Khlebnikova et al., 2019b)	Rx5day and 6% in annual Rx30day compared to pre-industrial (Annex). Additional evidence from CMIP5 simulations for an increase in the intensity of heavy precipitation (Sillmann et al., 2013b; Xu et al., 2017; Han et al., 2018; Kharin et al., 2018; Khlebnikova et al., 2019b)	Rx5day and 15% in annual Rx30day compared to pre-industrial (Annex). Additional evidence from CMIP5 simulations for an increase in the intensity of heavy precipitation (Sillmann et al., 2013b; Xu et al., 2017; Han et al., 2018; Kharin et al., 2018; Khlebnikova et al., 2019b)
	Medium confidence in the intensitification of heavy precipitation	*Low confidence*	Intensification of heavy precipitation: *Likely* (compared with the recent past (1995-2014)) *Very likely* (compared with pre-industrial)	Intensification of heavy precipitation: *Very likely* (compared with the recent past (1995-2014)) *Extremely likely* (compared with pre-industrial)	Intensification of heavy precipitation: *Virtually certain* (compared with the recent past (1995-2014)) *Virtually certain* (compared with pre-industrial)
Russian Far East (RFE)	Intensification of heavy precipitation (Sun et al., 2020)	Limited evidence	CMIP6 models project a robust increase in the intensity and frequency of heavy precipitation (Li et al., 2020; Annex). Median increase of more than 4% in the 50-year Rx1day and Rx5day events compared to the 1°C warming level (Li et al., 2020a) and more than 8% in annual Rx1day and Rx5day and 6% in annual Rx30day compared to pre-industrial (Annex). Additional evidence from CMIP5 simulations for an increase in the intensity of heavy precipitation (Sillmann et al., 2013b; Xu et al., 2017; Han et al., 2018; Kharin et al., 2018)	CMIP6 models project a robust increase in the intensity and frequency of heavy precipitation (Li et al., 2020; Annex). Median increase of more than 8% in the 50-year Rx1day and Rx5day events compared to the 1°C warming level (Li et al., 2020a) and more than 10% in annual Rx1day, Rx5day, and Rx30day compared to pre-industrial (Annex). Additional evidence from CMIP5 simulations for an increase in the intensity of heavy precipitation (Sillmann et al., 2013b; Xu et al., 2017; Han et al., 2018; Kharin et al., 2018)	CMIP6 models project a robust increase in the intensity and frequency of heavy precipitation (Li et al., 2020; Annex). Median increase of more than 25% in the 50-year Rx1day and Rx5day events compared to the 1°C warming level (Li et al., 2020a) and more than 25% in annual Rx1day and Rx5day and 20% in annual Rx30day compared to pre-industrial (Annex). Additional evidence from CMIP5 simulations for an increase in the intensity of heavy precipitation (Sillmann et al., 2013b; Xu et al., 2017; Han et al., 2018; Kharin et al., 2018)
	Medium confidence in the intensitification of heavy precipitation	*Low confidence*	Intensification of heavy precipitation: *Likely* (compared with the recent past (1995-2014)) *Very likely* (compared with pre-industrial)	Intensification of heavy precipitation: *Very likely* (compared with the recent past (1995-2014)) *Extremely likely* (compared with pre-industrial)	Intensification of heavy precipitation: *Virtually certain* (compared with the recent past (1995-2014)) *Virtually certain* (compared with pre-industrial)
East Asia (EAS)	Intensification of heavy precipitation (Sun et al.,	Disagreement among studies (Chen and Sun, 2017; Li et	CMIP6 models project an increase in the intensity and	CMIP6 models project a robust increase in the intensity and	CMIP6 models project a robust increase in the intensity and

ACCEPTED VERSION SUBJECT TO FINAL EDITING

	2020; Dunn et al., 2020; Baek et al., 2017; Nayak et al., 2017; Ye and Li, 2017; Zhou et al., 2016)	al., 2017; Burke et al., 2016; Zhou et al., 2013; Ma et al., 2017)	frequency of heavy precipitation (Li et al., 2020; Annex). Median increase of more than 2% in the 50-year Rx1day and Rx5day events compared to the 1°C warming level (Li et al., 2020a) and more than 4% in annual Rx1day and Rx5day and 0% in annual Rx30day compared to pre-industrial (Annex). Additional evidence from CMIP5 simulations for an increase in the intensity of heavy precipitation (Ahn et al., 2016; Guo et al., 2018; Hatsuzuka et al., 2020; Kawase et al., 2019; Kim et al., 2018; Kusunoki, 2018; Kusunoki and Mizuta, 2013; Li et al., 2018a; Nayak and Dairaku, 2016; Ohba and Sugimoto, 2020, 2019; Seo et al., 2014; Wang et al., 2017a, 2017b; Zhou et al., 2014; Li et al., 2018b)	frequency of heavy precipitation (Li et al., 2020; Annex). Median increase of more than 6% in the 50-year Rx1day and Rx5day events compared to the 1°C warming level (Li et al., 2020a) and more than 6% in annual Rx1day and Rx5day and 2% in annual Rx30day compared to pre-industrial (Annex). Additional evidence from CMIP5 simulations for an increase in the intensity of heavy precipitation (Ahn et al., 2016; Guo et al., 2018; Hatsuzuka et al., 2020; Kawase et al., 2019; Kim et al., 2018; Kusunoki, 2018; Kusunoki and Mizuta, 2013; Li et al., 2018a; Nayak and Dairaku, 2016; Ohba and Sugimoto, 2020, 2019; Seo et al., 2014; Wang et al., 2017a, 2017b; Zhou et al., 2014; Li et al., 2018b)	frequency of heavy precipitation (Li et al., 2020; Annex). Median increase of more than 20% in the 50-year Rx1day and Rx5day events compared to the 1°C warming level (Li et al., 2020a) and more than 20% in annual Rx1day and Rx5day and 10% in annual Rx30day compared to pre-industrial (Annex). Additional evidence from CMIP5 simulations for an increase in the intensity of heavy precipitation (Ahn et al., 2016; Guo et al., 2018; Hatsuzuka et al., 2020; Kawase et al., 2019; Kim et al., 2018; Kusunoki, 2018; Kusunoki and Mizuta, 2013; Li et al., 2018a; Nayak and Dairaku, 2016; Ohba and Sugimoto, 2020, 2019; Seo et al., 2014; Wang et al., 2017a, 2017b; Zhou et al., 2014; Li et al., 2018b)
	Medium confidence in the intensitification of heavy precipitation	*Low confidence*	Intensification of heavy precipitation: *High confidence* (compared with the recent past (1995-2014)) *Likely* (compared with pre-industrial)	Intensification of heavy precipitation: *Likely* (compared with the recent past (1995-2014)) *Very likely* (compared with pre-industrial)	Intensification of heavy precipitation: *Extremely likely* (compared with the recent past (1995-2014)) *Virtually certain* (compared with pre-industrial)
East Central Asia (ECA)	Intensification of heavy precipitation (Sun et al., 2020)	Limited evidence	CMIP6 models project a robust increase in the intensity and frequency of heavy precipitation (Li et al., 2020; Annex). Median increase of more than 4% in the 50-year Rx1day and Rx5day events compared to the 1°C warming level (Li et al., 2020a) and more than 8% in annual Rx1day and Rx5day and 6% in annual Rx30day compared to pre-industrial (Annex).	CMIP6 models project a robust increase in the intensity and frequency of heavy precipitation (Li et al., 2020; Annex). Median increase of more than 6% in the 50-year Rx1day and Rx5day events compared to the 1°C warming level (Li et al., 2020a) and more than 10% in annual Rx1day, Rx5day, and Rx30day compared to pre-industrial (Annex).	CMIP6 models project a robust increase in the intensity and frequency of heavy precipitation (Li et al., 2020; Annex). Median increase of more than 20% in the 50-year Rx1day and Rx5day events compared to the 1°C warming level (Li et al., 2020a) and more than 25% in annual Rx1day, Rx5day, and Rx30day compared to pre-industrial (Annex).

ACCEPTED VARSION SUBJECT TO FINAL EDITING

	Medium confidence in the intensitification of heavy precipitation	*Low confidence*	Intensification of heavy precipitation: *Likely* (compared with the recent past (1995-2014)) *Very likely* (compared with pre-industrial)	Intensification of heavy precipitation: *Very likely* (compared with the recent past (1995-2014)) *Extremely likely* (compared with pre-industrial)	Intensification of heavy precipitation: *Virtually certain* (compared with the recent past (1995-2014)) *Virtually certain* (compared with pre-industrial)
Tibetan Plateau (TIB)	Intensification of heavy precipitation (Sun et al., 2020; Jiang et al., 2013; Hu et al., 2016; Ge et al., 2017; Zhan et al., 2017; Liu et al., 2019)	Limited evidence	CMIP6 models project a robust increase in the intensity and frequency of heavy precipitation (Li et al., 2020; Annex). Median increase of more than 2% in the 50-year Rx1day and Rx5day events compared to the 1°C warming level (Li et al., 2020a) and more than 4% in annual Rx1day and Rx5day and 2% in annual Rx30day compared to pre-industrial (Annex). Additional evidence from CMIP5 simulations for an increase in the intensity of heavy precipitation (Zhou et al., 2014; Zhang et al., 2015c; Gao et al., 2018; Han et al., 2018)	CMIP6 models project a robust increase in the intensity and frequency of heavy precipitation (Li et al., 2020; Annex). Median increase of more than 4% in the 50-year Rx1day and Rx5day events compared to the 1°C warming level (Li et al., 2020a) and more than 8% in annual Rx1day and Rx5day and 6% in annual Rx30day compared to pre-industrial (Annex). Additional evidence from CMIP5 simulations for an increase in the intensity of heavy precipitation (Zhou et al., 2014; Zhang et al., 2015c; Gao et al., 2018; Han et al., 2018)	CMIP6 models project a robust increase in the intensity and frequency of heavy precipitation (Li et al., 2020; Annex). Median increase of more than 20% in the 50-year Rx1day and Rx5day events compared to the 1°C warming level (Li et al., 2020a) and more than 25% in annual Rx1day and Rx5day and 20% in annual Rx30day compared to pre-industrial (Annex). Additional evidence from CMIP5 simulations for an increase in the intensity of heavy precipitation (Zhou et al., 2014; Zhang et al., 2015c; Gao et al., 2018; Han et al., 2018)
	Medium confidence in the intensitification of heavy precipitation	*Low confidence*	Intensification of heavy precipitation: *Likely* (compared with the recent past (1995-2014)) *Very likely* (compared with pre-industrial)	Intensification of heavy precipitation: *Very likely* (compared with the recent past (1995-2014)) *Extremely likely* (compared with pre-industrial)	Intensification of heavy precipitation: *Virtually certain* (compared with the recent past (1995-2014)) *Virtually certain* (compared with pre-industrial)
South Asia (SAS)	Significant intensification of heavy precipitation (Kim et al., 2019; Malik et al., 2016; Pai et al., 2015; Rohini et al., 2016; Roxy et al., 2017; Sheikh et al., 2015; Singh et al., 2014; Dunn et al., 2020; Hussain and Lee, 2013; Kim et al., 2019; Malik et al., 2016)	Disagreement among studies (Mukherjee et al., 2018a) (Singh et al., 2014a; van Oldenborgh et al., 2016)	CMIP6 models project an increase in the intensity and frequency of heavy precipitation (Li et al., 2020; Annex). Median increase of more than 2% in the 50-year Rx1day and Rx5day events compared to the 1°C warming level (Li et al., 2020a) and more than 8% in annual Rx1day and Rx5day and 4% in annual Rx30day compared to pre-industrial (Annex).	CMIP6 models project an increase in the intensity and frequency of heavy precipitation (Li et al., 2020; Annex). Median increase of more than 6% in the 50-year Rx1day and Rx5day events compared to the 1°C warming level (Li et al., 2020a) and more than 10% in annual Rx1day and Rx5day and 8% in annual Rx30day compared to pre-industrial (Annex).	CMIP6 models project a robust increase in the intensity and frequency of heavy precipitation (Li et al., 2020; Annex). Median increase of more than 25% in the 50-year Rx1day and Rx5day events compared to the 1°C warming level (Li et al., 2020a) and more than 30% in annual Rx1day and Rx5day and 25% in annual Rx30day compared to pre-industrial (Annex).

ACCEPTED VERSION SUBJECT TO FINAL EDITING

			Additional evidence from CMIP5 simulations for an increase in the intensity of heavy precipitation (Sillmann et al., 2013b; Xu et al., 2017; Han et al., 2018; Mukherjee et al., 2018a; Ali et al., 2019b; Rai et al., 2019)	Additional evidence from CMIP5 simulations for an increase in the intensity of heavy precipitation (Sillmann et al., 2013b; Xu et al., 2017; Han et al., 2018; Mukherjee et al., 2018a; Ali et al., 2019b; Rai et al., 2019)	Additional evidence from CMIP5 simulations for an increase in the intensity of heavy precipitation (Sillmann et al., 2013b; Xu et al., 2017; Han et al., 2018; Mukherjee et al., 2018a; Ali et al., 2019b; Rai et al., 2019)
	High confidence in the intensitification of heavy precipitation	*Low confidence*	Intensification of heavy precipitation: *Medium confidence* (compared with the recent past (1995-2014)) *High confidence* (compared with pre-industrial)	Intensification of heavy precipitation: *High confidence* (compared with the recent past (1995-2014)) *Likely* (compared with pre-industrial)	Intensification of heavy precipitation: *Very likely* (compared with the recent past (1995-2014)) *Extremely likely* (compared with pre-industrial)
Southeast Asia (SEA)	Intensification of heavy precipitation (Sun et al., 2020; Cheong et al., 2018; Li et al., 2018c; Siswanto et al., 2015; Supari et al., 2017; Villafuerte and Matsumoto, 2015)	Evidence of a human contribution for some events (Otto et al., 2018a), but cannot be generalized	CMIP6 models project an increase in the intensity and frequency of heavy precipitation (Li et al., 2020; Annex). Median increase of more than 0% in the 50-year Rx1day and Rx5day events compared to the 1°C warming level (Li et al., 2020a) and more than 4% in annual Rx1day and Rx5day and 2% in annual Rx30day compared to pre-industrial (Annex). Additional evidence from CMIP5 and CORDEX simulations for an increase in the intensity of heavy precipitation (Xu et al., 2017; Han et al., 2018; Tangang et al., 2018; Trinh-Tuan et al., 2019; Basconcillo et al., 2016; Ge et al., 2017; Han et al., 2018; Marzin et al., 2015; Tangang et al., 2018; Trinh-Tuan et al., 2019; Xu et al., 2017)	CMIP6 models project an increase in the intensity and frequency of heavy precipitation (Li et al., 2020; Annex). Median increase of more than 4% in the 50-year Rx1day and Rx5day events compared to the 1°C warming level (Li et al., 2020a) and more than 6% in annual Rx1day and Rx5day and 4% in annual Rx30day compared to pre-industrial (Annex). Additional evidence from CMIP5 and CORDEX simulations for an increase in the intensity of heavy precipitation (Xu et al., 2017; Han et al., 2018; Tangang et al., 2018; Trinh-Tuan et al., 2019; Basconcillo et al., 2016; Ge et al., 2017; Han et al., 2018; Marzin et al., 2015; Tangang et al., 2018; Trinh-Tuan et al., 2019; Xu et al., 2017)	CMIP6 models project a robust increase in the intensity and frequency of heavy precipitation (Li et al., 2020; Annex). Median increase of more than 10% in the 50-year Rx1day and Rx5day events compared to the 1°C warming level (Li et al., 2020a) and more than 20% in annual Rx1day and Rx5day and 10% in annual Rx30day compared to pre-industrial (Annex). Additional evidence from CMIP5 and CORDEX simulations for an increase in the intensity of heavy precipitation (Xu et al., 2017; Han et al., 2018; Tangang et al., 2018; Trinh-Tuan et al., 2019; Basconcillo et al., 2016; Ge et al., 2017; Han et al., 2018; Marzin et al., 2015; Tangang et al., 2018; Trinh-Tuan et al., 2019; Xu et al., 2017)
	Medium confidence in the intensitification of heavy precipitation	*Low confidence*	Intensification of heavy precipitation: *Medium confidence* (compared with the recent	Intensification of heavy precipitation: *High confidence* (compared with the recent past (1995-	Intensification of heavy precipitation: *Very likely* (compared with the recent past (1995-2014))

ACCEPTED VERSION SUBJECT TO FINAL EDITING

			past (1995-2014)) *High confidence* (compared with pre-industrial)	2014)) *Likely* (compared with pre-industrial)	*Extremely likely* (compared with pre-industrial)

[END TABLE 11.8 HERE]

[START TABLE 11.9 HERE]

Table 11.9: Observed trends, human contribution to observed trends, and projected changes at 1.5°C, 2°C and 4°C of global warming for meteorological droughts (MET), agricultural and ecological droughts (AGR/ECOL), and hydrological droughts (HYDR) in Asia, subdivided by AR6 regions. See Sections 11.9.1 and 11.9.4 for details

Region/ Drought type		Observed trends	Human contribution	Projections		
				+1.5 °C	+2 °C	+4 °C
Russian Arctic (RAR)	MET	***Low confidence:*** **Limited evidence.** Tendency towards decrease in CDD (Dunn et al., 2020). Lack of data in (Spinoni et al., 2019).	***Low confidence:*** **Limited evidence**	***Low confidence:*** **Limited evidence**. Slight decrease in CDD in CMIP6 (Chapter 11 Supplementary Material (11.SM))	***Low confidence:*** **Limited evidence,** but some evidence of decrease in dry spell duration (Khlebnikova et al., 2019b)(Chapter 11 Supplementary Material (11.SM))	***Medium confidence:*** **Decrease in drought severity** based on SPI (Touma et al., 2015; Spinoni et al., 2020) and CDD (Chapter 11 Supplementary Material (11.SM)).
	AGR, ECOL	***Low confidence:*** **Inconsistent trends** (Greve et al., 2014; Padrón et al., 2020).	***Low confidence:*** **Limited evidence**	***Low confidence:*** **Inconsistent changes** in soil moisture (Xu et al., 2019a)(Chapter 11 Supplementary Material (11.SM)).	***Low confidence:*** **Inconsistent changes** in soil moisture, variations across subregions (Xu et al., 2019a) (Chapter 11 Supplementary Material (11.SM))	***Low confidence:*** **Inconsistent trends.** Inconsistent trends across models and subregions for surface and total soil moisture (Dai et al., 2018; Lu et al., 2019; Cook et al., 2020)(Chapter 11 Supplementary Material (11.SM)); Slight drying in PDSI (Dai et al., 2018); inconsistent trends or wetting in SPEI-PM in CMIP5 (Cook et al., 2014b; Vicente-Serrano et al., 2020a).

ACCEPTED VERSION SUBJECT TO FINAL EDITING

	HYDR	***Low confidence:*** **Limited evidence.**	***Low confidence:*** **Limited evidence**.	***Low confidence:*** **Limited evidence.** One study shows lack of signal (Touma et al., 2015)	***Low confidence: Inconsistent changes.*.** Increasing runoff in CMIP6 (Cook et al., 2020) , inconsistent signal in SRI depending on subregion in CMIP5(Touma et al., 2015), or lack of signal (Zhai et al., 2020b) in available studies. (Cook et al., 2020): Increasing runoff in one study based on CMIP6 GCMs (Zhai et al., 2020b): Lack of signal in one study based on single hydrological model driven by HAPPI-MIP GCM simulations Touma et al. (2015): Inconsistent signal in SRI depending on subregion (CMIP5 GCMs)	***Low confidence:*** **Mixed signals** among studies (Prudhomme et al., 2014; Giuntoli et al., 2015; Touma et al., 2015; Cook et al., 2020)
Arabian Peninsula (ARP)	MET	***Low confidence***: **Inconsistent or no signa**l (Almazroui, 2019a; Almazroui and Islam, 2019). (Dunn et al., 2020): Wetting based on CDD in part of domain, but missing data in large fraction of region. (Spinoni et al., 2019): Missing data in this region.	***Low confidence:*** **Limited evidence** (Barlow and Hoell, 2015; Barlow et al., 2016)	***Low confidence:*** **Limited evidence and inconsistent trends** (Xu et al., 2019a)(Chapter 11 Supplementary Material (11.SM)).	***Low confidence***: **Limited evidence and inconsistent trends** (Xu et al., 2019a)(Chapter 11 Supplementary Material (11.SM)).	***Low confidence***: **Limited evidence and inconsistent trends** (Touma et al., 2015; Tabari and Willems, 2018)(Chapter 11 Supplementary Material (11.SM)). (Touma et al., 2015): Inconsistant projections in CMIP5 (Tabari and Willems, 2018): Dominant lack of signal Chapter 11 Supplementary Material (11.SM)): decreasing dryness based on CDD
	AGR, ECOL	***Low confidence***: **Limited evidence.** Drying in fraction of region in one study, but missing data in rest of region (Greve et al., 2014). (Greve et al., 2014) : Drying in part of region, but missing data in large fraction of region. (Padrón et al., 2020) : Missing data. (Spinoni et al., 2019) : Missing data.	***Low confidence:*** **Limited evidence**	***Low confidence:*** **Limited evidence and inconsistent trends** (Xu et al., 2019a)(Chapter 11 Supplementary Material (11.SM)) (Naumann et al., 2018): Missing data	***Low confidence***: **Limited evidence and inconsistent trends** (Xu et al., 2019a; Cook et al., 2020)(Chapter 11 Supplementary Material (11.SM))	***Low confidence***: **Mixed signal** between different metrics. including total and surface soil moisture (Chapter 11 Supplementary Material (11.SM))(Rajsekhar and Gorelick, 2017; Dai et al., 2018; Lu et al., 2019; Cook et al., 2020), PDSI (Dai et al., 2018) and SPEI-PM (Cook et al., 2014b; Vicente-Serrano et al., 2020a).

ACCEPTED VERSION SUBJECT TO FINAL EDITING

	HYDR	***Low confidence:*** **Limited evidence** Drying in one study in northern part of region but missing data in rest of region (Dai and Zhao, 2017)	***Low confidence:*** **Limited evidence**	***Low confidence***: **Limited evidence.** One study shows lack of signal (Touma et al., 2015).	***Low confidence:*** **Limited evidence and inconsistent trends** (Touma et al., 2015; Cook et al., 2020; Zhai et al., 2020b)	***Low confidence***: **Inconsistent trends** between models and studies (Prudhomme et al., 2014; Giuntoli et al., 2015; Touma et al., 2015; Cook et al., 2020)
West Central Asia (WCA)	MET	***Low confidence*: Inconsistent trends**between subregions, based both on CDD and SPI (Spinoni et al., 2019; Dunn et al., 2020; Sharafati et al., 2020; Yao et al., 2020).	***Low confidence:*** **Limited evidence**	***Low confidence***: t **Limited evidence**. Inconsistent or weak trends in available analyses (Xu et al., 2019a)(Chapter 11 Supplementary Material (11.SM))	***Low confidence:*** **Inconsistent, weak and/or non-significant trends** in SPI and CDD (Xu et al., 2019a; Spinoni et al., 2020; Yao et al., 2020)(Chapter 11 Supplementary Material (11.SM)).	***Low confidence*: Mixed signals** between models and between regions (Touma et al., 2015; Han et al., 2018; Tabari and Willems, 2018; Spinoni et al., 2020; Yao et al., 2020)(Chapter 11 Supplementary Material (11.SM))
	AGR, ECOL	***Medium confidence***: **Increase in drought severity.** Dominant signal shows drying for soil moisture, water-balance (precipitation-evapotranspiration), PDSI-PM and SPEI-PM, but with some differences between subregions and studies (Greve et al., 2014; Dai and Zhao, 2017; Li et al., 2017c; Spinoni et al., 2019; Padrón et al., 2020).	***Low confidence:*** **Limited evidence**. One study by Li et al. (2017) concluded that anthropogenic forcing has increased AED and contributed to drought severity over the last decades.	***Low confidence***: **Mixed signals** in changes in drought severity, depending on model and index (Naumann et al., 2018; Xu et al., 2019a; Gu et al., 2020)(Chapter 11 Supplementary Material (11.SM)). Weak signals and inconsistent trends between models for total and surface soil moisture (Xu et al., 2019a)(Chapter 11 Supplementary Material (11.SM)), but increased drying based on SPEI-PM (Naumann et al., 2018; Gu et al., 2020).	***Low confidence***: **Mixed signals** in changes in drought severity, depending on model and index (Naumann et al., 2018; Xu et al., 2019a; Cook et al., 2020; Gu et al., 2020) (Chapter 11 Supplementary Material (11.SM)). Weak signals and inconsistent trends between models and subregions for total and surface soil moisture (Xu et al., 2019a; Cook et al., 2020)(Chapter 11 Supplementary Material (11.SM)), but increased drying based on SPEI-PM (Naumann et al., 2018; Gu et al., 2020).	***Medium confidence***: **Increased drying** in several metrics, but substantial intermodel spread and lack of signal for total soil moisture (Dai et al., 2018; Cook et al., 2020; Vicente-Serrano et al., 2020a)(Chapter 11 Supplementary Material (11.SM)). Increase in drought severity based on surface soil moisture (Dai et al., 2018; Lu et al., 2019; Cook et al., 2020). (Chapter 11 Supplementary Material (11.SM)): only median, not 83.5%ile), PDSI (Dai et al., 2018), and SPEI-PM (Cook et al., 2014b; Vicente-Serrano et al., 2020a); but increase in median response and substantial intermodel spread for total soil moisture (Cook et al., 2020)(Chapter 11 Supplementary Material (11.SM))
	HYDR	***Low confidence:*** **Limited evidence**.	***Low confidence:*** **Limited evidence**	***Low confidence***: **Limited evidence.** One study shows lack of signal (Touma et al., 2015).	***Low confidence***: **Inconsistent** trends in available studies (Touma et al., 2015; Cook et al., 2020; Zhai et al., 2020b)	***Medium confidence***: **Increase of hydrological drought severity** (Prudhomme et al., 2014; Giuntoli et al., 2015; Touma et al., 2015; Cook et al., 2020); but large intermodel spread (only 2/3 of models showing signal) (Touma et al., 2015) and weak signal-to-noise ratio in eastern half of domain (Giuntoli et al., 2015).

ACCEPTED VERSION SUBJECT TO FINAL EDITING

Western Siberia (WSB)	MET	***Medium confidence***: **Decrease in dryness** based on SPI and CDD, but some inconsistent trends in part of domain (Zhang et al., 2017a, 2019b; Khlebnikova et al., 2019b; Spinoni et al., 2019; Dunn et al., 2020). Khlebnikova et al. (2019): In part mixed signals within domain (Dunn et al., 2020): Mostly decreasing trend, including significant changes. (Spinoni et al., 2019): Mostly decreasing trends	***Low confidence:*** **Limited evidence**	***Low confidence:*** **Inconsistent evidence** in CMIP5 (Xu et al., 2019a) and CMIP6 projections (Chapter 11 Supplementary Material (11.SM)).	***Low confidence:*** **Inconsistent trends** (Chapter 11 Supplementary Material (11.SM)) or slight decrease in drought (Khlebnikova et al., 2019b; Xu et al., 2019a; Spinoni et al., 2020). (Khlebnikova et al., 2019b): Mostly decrease in CDD in a regional climate model driven by several CMIP5 models (RCP8.5, 2050-2059 relative to 1990-1999) Chapter 11 Supplementary Material (11.SM): Tendency towards decrease but lack of model agreement.	***Low confidence:*** **Inconsistent trends** , but slight decrease in some studies (Touma et al., 2015; Spinoni et al., 2020)(Chapter 11 Supplementary Material (11.SM)). Spinoni et al. (2020): Slight decrease Touma et al. (2015): Tendency towards decrease but partly lack of model agreement. Chapter 11 Supplementary Material (11.SM): Lack of model agreement
	AGR, ECOL	***Low confidence:*** **Inconsistent trends** according to subregions or indices based on soil moisture, PDSI-PM and SPEI-PM (Greve et al., 2014; Dai and Zhao, 2017; Li et al., 2017c; Spinoni et al., 2019; Padrón et al., 2020).	***Low confidence:*** **Limited evidence**	***Low confidence:*** **Inconsistent trends** among different metrics and models. Inconsistent soil moisture projections in CMIP5 (Xu et al., 2019a) and CMIP6 (Chapter 11 Supplementary Material (11.SM)), and decrease in drought severity based on SPEI-PM (Naumann et al., 2018; Gu et al., 2020).	***Low confidence:*** **Inconsistent trends** among different metrics. No signal with total soil moisture (Chapter 11 Supplementary Material (11.SM)) and SPEI-PM (Naumann et al., 2018; Gu et al., 2020), and wetting trend with surface soil moisture (Xu et al., 2019a).	***Low confidence:*** **Mixed signals** between different models and metrics, including total and surface soil moisture in CMIP6 (Chapter 11 Supplementary Material (11.SM))(Cook et al., 2020), surface soil moisture in CMIP5 (Dai et al., 2018; Lu et al., 2019), PDSI (Dai et al., 2018) and SPEI-PM (Cook et al., 2014b; Vicente-Serrano et al., 2020a). Difference in signal in CMIP6 vs CMIP5: CMIP6 models show drying in soil moisture, while CMIP5 models show wetting (Cook et al., 2020)

ACCEPTED VERSION SUBJECT TO FINAL EDITING

	HYDR	***Low confidence:*** **Limited evidence.** One study suggests increasing weak (wetting) trend in runoff (Dai and Zhao, 2017)**.** Some increase in runoff at stations from 1951-1990 and 1961-2000 (Gudmundsson et al., 2019)	***Low confidence:*** **Limited evidence**	***Low confidence:*** **Limited evidence.** One study shows drying (Touma et al., 2015).	***Low confidence:*** **Inconsistent trends** in available studies (Touma et al., 2015; Cook et al., 2020; Zhai et al., 2020b) (Cook et al., 2020): Inconsistent trends including large seasonal variations (Zhai et al., 2020b): Inconsistent trends in study with single hydrological model driven with HAPPI-MIP GCM simulations (Touma et al., 2015)**:** Increase in the frequency of hydrological droughts based on SRI in CMIP5	***Low confidence:*** **Inconsistent trends**. Mixed signal among studies and low signal to noise ratio (Prudhomme et al., 2014; Giuntoli et al., 2015; Touma et al., 2015; Cook et al., 2020)
Eastern Siberia (ESB)	MET	***Medium confidence:*** **Decrease** in the duration and frequency of meteorological droughts (Khlebnikova et al., 2019b; Spinoni et al., 2019; Dunn et al., 2020). (Khlebnikova et al., 2019b): Decrease in fraction of dry days and decrease in mean CDD, but inconsistent trends for maximum CDD, for 1991-2015 compared to 1966-1990 (Dunn et al., 2020): Significant CDD decrease (Spinoni et al., 2019): Mostly decrease in SPI, but partly mixed signals and inconsistent trends	***Low confidence:*** **Limited evidence**	***Low confidence***: **Limited evidence.** Tendency towards decrease in SPI in CMIP5 (Xu et al., 2019a) and CDD in CMIP6 (Chapter 11 Supplementary Material (11.SM)).	***Medium confidence:*** **Decrease** in frequency and severity of meteorological droughts (Khlebnikova et al., 2019b; Xu et al., 2019a; Spinoni et al., 2020)(Chapter 11 Supplementary Material (11.SM)). (Khlebnikova et al., 2019b): Projections with a regional climate model driven with several CMIP5 GCMs (RCP8.5, 2050-2059 compared with 1990-1999): Mostly decrease in CDD but increase in part of domain, in particular in the south	***Medium confidence:*** **Decrease** in meteorological drought severity (Touma et al., 2015; Spinoni et al., 2020)(Chapter 11 Supplementary Material (11.SM)).

ACCEPTED VERSION SUBJECT TO FINAL EDITING

	AGR, ECOL	***Low confidence:*** **Inconsistent trends** depending on subregion and index based on soil moisture, PDSI-PM and SPEI-PM (Greve et al., 2014; Dai and Zhao, 2017; Spinoni et al., 2019; Padrón et al., 2020).	***Low confidence:*** **Limited evidence**	***Low confidence:*** **Mixed signal** in changes in drought severity depending on models and metrics. Inconsistent trends in soil moisture (Xu et al., 2019a)(Chapter 11 Supplementary Material (11.SM)), , but wetting tendency for SPEI-PM (Naumann et al., 2018; Gu et al., 2020).	***Low confidence:*** **Mixed signal** in changes in drought severity depending on models and metrics. Inconsistent trends in soil moisture (Xu et al., 2019a)(Chapter 11 Supplementary Material (11.SM)) , but wetting tendency for SPEI-PM (Naumann et al., 2018; Gu et al., 2020).	***Low confidence:*** **Mixed signal** in drought changes depending on models and metrics, including total and surface soil moisture in CMIP6 (Chapter 11 Supplementary Material (11.SM))(Cook et al., 2020), surface soil moisture in CMIP5 (Dai et al., 2018; Lu et al., 2019), PDSI (Dai et al., 2018) and SPEI-PM (Cook et al., 2014b; Vicente-Serrano et al., 2020a). Difference in signal in CMIP6 vs CMIP5: CMIP6 models show drying in soil moisture, while CMIP5 models show wetting (Cook et al., 2020)
	HYDR	***Low confidence:*** **Limited evidence.** One study suggests increasing (wetting) trend in runoff (Dai and Zhao, 2017)**.** Some increase in runoff at stations from 1951-1990 and 1961-2000 (Gudmundsson et al., 2019)	***Low confidence:*** **Limited evidence**	***Low confidence***: **Limited evidence.** One study shows lack of signal (Touma et al., 2015).	***Low confidence:*** **Inconsistent trends** in available studies (Touma et al., 2015; Cook et al., 2020; Zhai et al., 2020b) (Cook et al., 2020): Inconsistent trends including large seasonal variations (Zhai et al., 2020b): Inconsistent trends in one study based on single hydrological model driven by HAPPI-MIP GCM simulations (Touma et al., 2015)**:** Mixed signal.	***Low confidence:*** **Mixed signal** among studies (Prudhomme et al., 2014; Giuntoli et al., 2015; Touma et al., 2015; Cook et al., 2020)
Russian Far East (RFE)	MET	***Low confidence:*** **Mixed signals** between subregions and studies (Knutson and Zeng, 2018; Khlebnikova et al., 2019b; Spinoni et al., 2019; Dunn et al., 2020).	***Low confidence:*** **Limited evidence.** One study, Wilcox et al. in (Herring et al., 2015), but mostly inconclusive.	***Low confidence***: **Limited evidence**. Weak decrease in available analyses (Xu et al., 2019a)(Chapter 11 Supplementary Material (11.SM)).	***Medium confidence***: **Decrease** (Khlebnikova et al., 2019b; Xu et al., 2019a)(Chapter 11 Supplementary Material (11.SM)). (Khlebnikova et al., 2019b): Regional climate model driven by several CMIP5 models (RCP8.5, 2050-2059 relative to 1990-1999): Mostly decrease in CDD but also increase in part of region (Kamtchatka Peninsual).	***Medium confidence:*** **Decrease** in drought severity (Touma et al., 2015; Han et al., 2018; Spinoni et al., 2020)(Chapter 11 Supplementary Material (11.SM)).

ACCEPTED VERSION SUBJECT TO FINAL EDITING

	AGR, ECOL	***Low confidence:*** **Inconsistent trends** depending on subregion based on soil moisture, PDSI-PM and SPEI-PM (Greve et al., 2014; Dai and Zhao, 2017; Spinoni et al., 2019; Padrón et al., 2020).	***Low confidence:*** **Limited evidence**	***Low confidence:*** **Inconsistent trends** depending on model and index. Inconsistent trends in total and surface soil moisture in CMIP6 (Chapter 11 Supplementary Material (11.SM)), but wetting trends from CMIP5-based surface soil moisture (Xu et al., 2019a) and SPEI-PM (Naumann et al., 2018; Gu et al., 2020). (Naumann et al., 2018) : EC-Earth driven by SSTs from several CMIP5 models.	***Low confidence:*** **Inconsistent trends** depending on model and index. Inconsistent trends in CMIP6 total and surface soil moisture (Chapter 11 Supplementary Material (11.SM))(Cook et al., 2020), but wetting trends from CMIP5-based surface soil moisture (Xu et al., 2019a) and SPEI-PM (Naumann et al., 2018; Gu et al., 2020).	***Low confidence:*** **Mixed signals** between different models and metrics, including CMIP6 total and surface soil moisture (Chapter 11 Supplementary Material (11.SM))(Cook et al., 2020), and CMIP5-based surface soil moisture (Dai et al., 2018; Lu et al., 2019), PDSI (Dai et al., 2018) and SPEI-PM (Cook et al., 2014b; Vicente-Serrano et al., 2020a). Difference in signal in CMIP6 vs CMIP5: CMIP6 models show drying in soil moisture, while CMIP5 models show wetting (Cook et al., 2020).
	HYDR	***Low confidence***: **Limited evidence.** One study suggests decreasing (drying) trend in runoff (Dai and Zhao, 2017)**.**	***Low confidence:*** **Limited evidence**	***Low confidence***: **Limited evidence.** One study shows lack of signal (Touma et al., 2015).	***Low confidence***: **Inconsistent trends**. Available studies show inconsistent signal with high seasonal variations (Cook et al., 2020) or weak signal (Touma et al., 2015; Zhai et al., 2020b).	***Low confidence:*** **Inconsistent signal** among studies and metrics, with generally weak drying trend in summer season (Prudhomme et al., 2014; Giuntoli et al., 2015; Touma et al., 2015; Cook et al., 2020)
East Asia (EAS)	MET	***Low confidence***: Lack of signal and mixed trends between subregions (Spinoni et al., 2019; Zhang et al., 2019a; Dunn et al., 2020; Li et al., 2020b). Drying trends in Southwestern China (Qin et al., 2015a) and Northern China (Qin et al., 2015b), but not for overall China (Li et al., 2020b).	***Low confidence:*** **Limited evidence** (Qin et al., 2015a; Herring et al., 2019).	***Low confidence***: **Limited evidence**. Inconsistent subregional trends (Xu et al., 2019a) or drying tendency (Chapter 11 Supplementary Material (11.SM)).	***Low confidence***: **Inconsistent trends** depending on model, region or index (Guo et al., 2018; Xu et al., 2019a; Spinoni et al., 2020)(Chapter 11 Supplementary Material (11.SM)). (Spinoni et al., 2020): Tendency towards decreased in drought severity based on SPI. (Huang et al., 2018a): Important subregional differences in SPI projections in a single GCM Chapter 11 Supplementary Material (11.SM): Tendency towards drying based on CDD (increasing CDD), but inconsistent trends depending on model. (Xu et al., 2019a): Inconsistent subregional trends based on SPI.	***Low confidence***: **Inconsistent trends** between different models and important spatial variability (Zhou et al., 2014; Touma et al., 2015; Kusunoki, 2018a; Spinoni et al., 2020)(Chapter 11 Supplementary Material (11.SM)). (Zhou et al., 2014): Tendency towards wetting in the north and drying in the south based on CDD. (Kusunoki, 2018a): Increasing CDD (drying trend) over Japan based on one GCM.

ACCEPTED VERSION SUBJECT TO FINAL EDITING

	AGR, ECOL	***Medium confidence:*** **Increase** in drying, especially since ca. 1990; but wetting tendency beforehand and partly inconsistent subregional trends. Large-scale studies based on observed soil moisture, modelled soil moisture or water balance driven by meteorological observations, and SPEI-PM, show drying in northern part of domain (northern China, Russian part of domain, Japan) as well as in Southwest China (east of Tibetan Plateau), but there are some inconsistent trends in part of region or some studies, as well as for different time frames (Greve et al., 2014; Chen and Sun, 2015b; Cheng et al., 2015; Qiu et al., 2016; Dai and Zhao, 2017; Jia et al., 2018; Spinoni et al., 2019; Li et al., 2020b; Padrón et al., 2020). Identified trends are also confirmed by regional studies (Liu et al., 2015; Qin et al., 2015b; Liang et al., 2020; Wang et al., 2020). Most of the drying trend took place since 1990, with wetting trend beforehand (Chen and Sun, 2015b; Wu et al., 2020b).	***Low confidence***: **Limited evidence**. Zhang et al. (2020) concluded that anthropogenic forcing contributed to 2018 drought, principally as consequence of enhanced AED. One study suggests that soil moisture drought conditions in northern China have been intensified by agriculture (Liu et al., 2015).	***Low confidence***: **Inconsistent trends** depending on model, subregion and index (Huang et al., 2018a; Naumann et al., 2018; Xu et al., 2019a; Gu et al., 2020)(Chapter 11 Supplementary Material (11.SM)) . (Huang et al., 2018a): Inconsistent projections in a study with a single GCM for the time frame 2016-2050 (for different scenarios) compared to 1960-2005, i.e corresponding to 1.5°C projections compared to recent past.	***Low confidence***: **Mixed signals** depending on model, subregion and index (Gao et al., 2017b; Naumann et al., 2018; Xu et al., 2019a; Cook et al., 2020; Gu et al., 2020)(Chapter 11 Supplementary Material (11.SM)). (Gao et al., 2017b): Study for very small region (Loess Plateau).	***Medium confidence***: **Increasing dryness** as dominant signal in projections and over larger part of domain, but also inconsistent signal for some indices and part of the domain (Cook et al., 2014b, 2020; Cheng et al., 2015; Dai et al., 2018; Naumann et al., 2018; Lu et al., 2019; Vicente-Serrano et al., 2020a)(Chapter 11 Supplementary Material (11.SM)).

ACCEPTED VERSION SUBJECT TO FINAL EDITING

	HYDR	***Medium confidence:*** **Increase** in hydrological drought in the region, in particular in northern China; inconsistent trends in part of the region (Liu et al., 2015; Dai and Zhao, 2017; Zhang et al., 2018b). Drying in large part of domain, in particular in northern China (Zhao and Dai, 2017) Increase of hydrological droughts in the Yangtze river (Zhang et al., 2018b).	***Low confidence***: **Limited evidence and mixed signals.** Available evidence suggests that a combination of change in climatic drivers (precipitation, Epot) and human drivers (agriculture, water management) are responsible for trends (Liu et al., 2015; Zhang et al., 2018b). Increasing hydrological droughts trends in the Yangtze river are dominantly driven by precipitation, but increases in potential evaporation and human activities also play a role (Zhang et al., 2018b). Drought conditions in northern China (soil moisture and runoff) have been intensified by agriculture (Liu et al., 2015).	***Low confidence:*** **Limited evidence.** One study shows lack of signal (Touma et al., 2015).	***Low confidence:*** **Limited evidence and inconsistent trends** in available studies (Touma et al., 2015; Cook et al., 2020; Zhai et al., 2020b).	***Low confidence***: **Inconsistent** trend between models and studies, and generally low signal-to-noise ratio (Prudhomme et al., 2014; Giuntoli et al., 2015; Touma et al., 2015; Cook et al., 2020) (Touma et al., 2015; Cook et al., 2020): Generally inconsistent trends between models, with low model agreement. (Giuntoli et al., 2015): Trend towards drying but generally low signal-to-noise ratio except in small subregion.

ACCEPTED VERSION SUBJECT TO FINAL EDITING

Eastern Central Asia (ECA)	MET	***Low confidence:*** **Inconsistent trends** between subregions, with overall tendency to decrease (Spinoni et al., 2019; Dunn et al., 2020).	***Low confidence:*** **Limited evidence**	***Low confidence. Limited evidence***; slight decrease in meteorological drought in available analyses (Xu et al., 2013) (Chapter 11 Supplementary Material (11.SM))	***Medium confidence:*** **Decrease** in drought severity, with weakly inconsistent changes for some indices (Xu et al., 2019a; Spinoni et al., 2020)(Chapter 11 Supplementary Material (11.SM)) (Spinoni et al., 2019): Strong decrease in drought for SPI-based metrics in RCP4.5 compared to 1981-2010 (Xu et al., 2019a): Decrease in frequency of SPI-based events but slight increase or inconsistent changes in duration of SPI-based events. Chapter 11 Supplementary Material (11.SM): substantial decrease in CDD	***Medium confidence:*** **Decrease** in drought severity (Touma et al., 2015; Spinoni et al., 2020)(Chapter 11 Supplementary Material (11.SM)).
	AGR, ECOL	***Medium confidence:*** **Increase** in drying, but some conflicting trends between drought metrics and sub-regions (Greve et al., 2014; Cheng et al., 2015; Dai and Zhao, 2017; Li et al., 2017c; Spinoni et al., 2019; Padrón et al., 2020; Zhang et al., 2020c).	***Low confidence:*** **Limited evidence**	***Low confidence:*** **Mixed signal** in changes in drought severity, lack of signal based in total column soil moisture (Xu et al., 2019a)(Chapter 11 Supplementary Material (11.SM)) and SPEI-PM (Naumann et al., 2018; Gu et al., 2020).	***Low confidence:*** **Mixed signal** in changes in drought severity. Inconsistent trends in total and surface soil moisture, with stronger tendency to wetting, (Xu et al., 2019a; Cook et al., 2020)(Chapter 11 Supplementary Material (11.SM)), and drying based on the SPEI-PM (Naumann et al., 2018; Gu et al., 2020).	***Low confidence:*** **Mixed trends** between different models and drought metrics (Chapter 11 Supplementary Material (11.SM))(Cook et al., 2014b, 2020; Dai et al., 2018; Lu et al., 2019; Vicente-Serrano et al., 2020a).
	HYDR	***Low confidence: Limited evidence***. Mostly inconsistent trends in one study (Dai and Zhao, 2017).	***Low confidence:*** **Limited evidence**	***Low confidence***: **Limited evidence.** One study shows lack of signal (Touma et al., 2015).	***Low confidence***: **Limited evidence and inconsistent trends** (Touma et al., 2015; Cook et al., 2020; Zhai et al., 2020b)	***Low confidence***: **Mixed trends.** Model disagreement and inconsistent changes among studies, seaons and metrics, with overall low signal-to-noise ratio (Prudhomme et al., 2014; Giuntoli et al., 2015; Touma et al., 2015; Cook et al., 2020).

ACCEPTED VERSION SUBJECT TO FINAL EDITING

Tibetan Plateau (TIB)	MET	***Low confidence***: Inconsistent trends (Jiang et al., 2013; Donat et al., 2016a; Hu et al., 2016; Dunn et al., 2020).	***Low confidence:*** **Limited evidence**	***Low confidence***: **Limited evidence**. Weak or inconsistent trends in available analyses (Xu et al., 2019a)(Chapter 11 Supplementary Material (11.SM))	***Low confidence***: **Inconsistent trends**, but tendency towards wetting (Xu et al., 2019a; Cook et al., 2020)(Chapter 11 Supplementary Material (11.SM)) (Spinoni et al., 2019): No data in the region (Cook et al., 2020): Only analysis of mean precipitation but tendency towards wetting in all seasons in the region (Xu et al., 2019a)(Chapter 11 Supplementary Material (11.SM)): Weak trends but tendency towards wetting.	***Low confidence***: **Inconsistent trends** between models, but tendency towards wetting and decrease in drought (Zhou et al., 2014; Touma et al., 2015)(Chapter 11 Supplementary Material (11.SM)). (Zhou et al., 2014): Decrease of CDD is projected but there is large uncertainty
	AGR, ECOL	***Low confidence***: **Inconsistent trends.** Spatially varying trends, with slight tendency to overall wetting(Cheng et al., 2015; Dai and Zhao, 2017; Jia et al., 2018; Zhang et al., 2018a; Li et al., 2020c; Wang et al., 2020). (Greve et al., 2014; Spinoni et al., 2019; Padrón et al., 2020): Missing data in most of region.	***Low confidence:*** **Limited evidence**	***Low confidence***: **Inconsistent trends** between models, indices and subregions (Naumann et al., 2018; Xu et al., 2019a; Gu et al., 2020)(Chapter 11 Supplementary Material (11.SM)).	***Low confidence***: **Inconsistent trends** between models, indices and subregions (Naumann et al., 2018; Xu et al., 2019a; Cook et al., 2020; Gu et al., 2020)(Chapter 11 Supplementary Material (11.SM)).	***Low confidence***: **Inconsistent trends** between models, indices and subregions (Cook et al., 2014b, 2020; Dai et al., 2018; Lu et al., 2019; Vicente-Serrano et al., 2020a)(Chapter 11 Supplementary Material (11.SM)).
	HYDR	***Low confidence:*** **Limited evidence**.	***Low confidence:*** **Limited evidence**	***Low confidence:*** **Limited evidence.** One study shows lack of signal (Touma et al., 2015).	***Low confidence:*** **Limited evidence and inconsistent trends** in available studies (Touma et al., 2015; Cook et al., 2020; Zhai et al., 2020b)	***Low confidence***: **Inconsistent trends** between models and studies, and low signal-to-nois ratio (Prudhomme et al., 2014; Giuntoli et al., 2015; Touma et al., 2015; Cook et al., 2020)

ACCEPTED VERSION SUBJECT TO FINAL EDITING

South Asia (SAS)	MET	***Medium confidence*: Increase in meteorological drought.** Subregional differences but drying is dominant (Mishra et al., 2014b; Malik et al., 2016; Guhathakurta et al., 2017; Spinoni et al., 2019; Dunn et al., 2020) (see also Section 10.6.3)	***Low confidence:* Limited evidence** (Fadnavis et al., 2019)	***Low confidence*: Limited evidence and inconsistent trends** (Xu et al., 2019a)(Chapter 11 Supplementary Material (11.SM)).	***Low confidence*: Inconsistent trends,** with light tendency to decreased drying (Xu et al., 2019a; Spinoni et al., 2020)(Chapter 11 Supplementary Material (11.SM))	***Low confidence*: Inconsistent trends** depending on model and subregion, with light tendency to decreases in meteorological drought in CMIP5 and CMIP6 (Mishra et al., 2014b; Touma et al., 2015; Salvi and Ghosh, 2016; Spinoni et al., 2020)(Chapter 11 Supplementary Material (11.SM)); light increased drying in NDD in CORDEX-CORE (Coppola et al., 2021b). Overall poor climate model performance for South Asia monsoon in CMIP5 and CORDEX (Mishra et al., 2014a; Saha et al., 2014; Sabeerali et al., 2015; Singh et al., 2017b). See also Section 10.6.3 for assessment for changes in Indian summer monsoon rainfall.
	AGR, ECOL	***Low confidence*: Lack of signal and inconsistent trends** depending on subregion based on soil moisture, PDSI-PM and SPEI-PM (Greve et al., 2014; Mishra et al., 2014b; Dai and Zhao, 2017; Spinoni et al., 2019; Padrón et al., 2020) and decrease of the drying effect of the atmospheric evaporative demand (Jhajharia et al., 2015).	***Low confidence:* Limited evidence**	***Low confidence*: Inconsistent trends in drought between models and subregions** (Naumann et al., 2018; Xu et al., 2019a; Gu et al., 2020)(Chapter 11 Supplementary Material (11.SM))	***Low confidence*: Inconsistent trends in drought between models, subregions and studies,** but slight dominant tendency towards wetting(Naumann et al., 2018; Xu et al., 2019a; Cook et al., 2020; Gu et al., 2020)(CMIP6.ANNEX-CH11)	***Medium confidence*: Decreased drying trend** (Chapter 11 Supplementary Material (11.SM))(Cook et al., 2014b, 2020; Mishra et al., 2014b; Dai et al., 2018; Lu et al., 2019; Vicente-Serrano et al., 2020a)(Chapter 11 Supplementary Material (11.SM))
	HYDR	***Low confidence*: Limited evidence.** Inconsistent trends or limited data in available studies (Zhao and Dai, 2017; Gudmundsson et al., 2019, 2021).	***Low confidence:* Limited evidence**	***Low confidence*: Limited evidence.** One study shows lack of signal (Touma et al., 2015).	***Low confidence:* Limited evidence.** Lack of signal in CMIP5 (Touma et al., 2015)**.** Decrease in dryness in CMIP6 (Cook et al., 2020); mostly inconsistent trends in HAPPI-MIP driven simulations with one hydrological model (Zhai et al., 2020b).	***Low confidence*: Inconsistent trends** between models and studies (Prudhomme et al., 2014; Giuntoli et al., 2015; Touma et al., 2015; Cook et al., 2020)

ACCEPTED VERSION SUBJECT TO FINAL EDITING

Southeast Asia (SEA)	MET	***Low confidence***: **Inconsistent trends** between subregions (Spinoni et al., 2019; Dunn et al., 2020).	***Low confidence:*** **Limited evidence** (Mcbride et al., 2015; King et al., 2016b) although the the equatorial Asia drought of 2015 has been attributed to anthropogenic warming effects (Shiogama et al., 2020).	***Low confidence:*** **Limited evidence** (Xu et al., 2019a)(Chapter 11 Supplementary Material (11.SM))	***Low confidence*****: Inconsistent** trends between models, subregions and studies (Tangang et al., 2018; Xu et al., 2019a; Spinoni et al., 2020)(Chapter 11 Supplementary Material (11.SM)) but with overall drying in CMIP6 and CORDEX simulations (Tangang et al., 2018; Cook et al., 2020; Coppola et al., 2021b) (Chapter 11 Supplementary Material (11.SM)). (Tangang et al., 2018): Projected drying based on CDD in CORDEX simulations for Indonesia (Xu et al., 2019a): Inconsistent trends across region based on SPI, but with slight drying over Indonesia (Spinoni et al., 2020): Wetting trend based on SPI (Chapter 11 Supplementary Material (11.SM)): Drying trend based on CDD	***Medium confidence***: **Increase** in drying in CMIP6 and CORDEX simulations (Cook et al., 2020; Supari et al., 2020; Coppola et al., 2021b) (Chapter 11 Supplementary Material (11.SM)). but inconsistent trends or wetting in CMIP5-based projections(Touma et al., 2015; Cook et al., 2020; Spinoni et al., 2020; Supari et al., 2020)((Supari et al., 2020): Strong drying trend based on CDD in CORDEX simulations for Indonesia (Coppola et al., 2021b): Drying based on number of dry days (NDD) in CORDEX-CORE projects (Cook et al., 2020): Decreasing trend in mean precipitation which is only found in CMIP6 and not in CMIP5. Chapter 11 Supplementary Material (11.SM): Strong projected drying trend based on CDD in CMIP6 projections (Touma et al., 2015): Inconsistent trends in SPI in CMIP5 projections (Spinoni et al., 2020): Wetting trend based on SPI in CMIP5 projections. (Cai et al., 2014a, 2015, 2018): An increasing frequency of precipitation deficits is projected as a consequence of an increasing frequency of extreme El Niño.

ACCEPTED VERSION SUBJECT TO FINAL EDITING

	AGR, ECOL	***Low confidence***: **Inconsistent trends** depending onsubregion and index based on soil moisture, PDSI-PM and SPEI-PM (Greve et al., 2014; Dai and Zhao, 2017; Spinoni et al., 2019; Padrón et al., 2020).	***Low confidence:*** **Limited evidence**	***Low confidence***: **Inconsistent trends** depending on model, subregion, index or study (Naumann et al., 2018; Xu et al., 2019a; Gu et al., 2020)(Chapter 11 Supplementary Material (11.SM))	***Low confidence***: **Inconsistent trends** depending on model, subregion, index or study (Naumann et al., 2018; Xu et al., 2019a; Cook et al., 2020; Gu et al., 2020)(Chapter 11 Supplementary Material (11.SM)).	***Low confidence***: **Mixed signal** depending on model and metric. Drying tendency based on CMIP6 soil moisture projections (Cook et al., 2020)(Chapter 11 Supplementary Material (11.SM)), inconsistent trends in CMIP5 surface soil moisture (Dai et al., 2018; Lu et al., 2019), but wetting trends with PDSI (Dai et al., 2018) and SPEI-PM (Cook et al., 2014b; Vicente-Serrano et al., 2020a) in studies driven with CMIP5 data. , (Cook et al., 2020): Drying trend in SEA in CMIP6), but not in CMIP5.
	HYDR	***Low confidence***: **Limited evidence**. Regionally inconsistent trends in one study (Dai and Zhao, 2017).	***Low confidence:*** **Limited evidence**	***Low confidence***: **Limited evidence.** One study shows decrease in hydrological drought (Touma et al., 2015).	***Low confidence:*** **Limited evidence and inconsistent trends** in available studies (Touma et al., 2015; Cook et al., 2020; Zhai et al., 2020b)	***Low confidence:*** Inconsistent trend between models and studies (Prudhomme et al., 2014; Giuntoli et al., 2015; Touma et al., 2015; Cook et al., 2020)

[END TABLE 11.9 HERE]

[START TABLE 11.10 HERE]

Table 11.10: Observed trends, human contribution to observed trends, and projected changes at 1.5°C, 2°C and 4°C of global warming for temperature extremes in Australasia, subdivided by AR6 regions. See Sections 11.9.1 and 11.9.2 for details.

Region	Observed trends	Detection and attribution; event attribution	Projections		
			1.5 °C	2 °C	4 °C
All Australasia	Significant increases in the intensity and frequency of hot extremes and decreases in the intensity and frequency of cold extremes (CSIRO and BOM, 2015; Jakob and Walland, 2016; Alexander and Arblaster, 2017)	Robust evidence of a human contribution to the observed increase in the intensity and frequency of hot extremes and decrease in the intensity and frequency of cold extremes (Seong et al., 2020; Hu et al., 2020; Wang et al., 2017).	CMIP6 models project a robust increase in the intensity and frequency of TXx events and a robust decrease in the intensity and frequency of TNn events (Li et al., 2020). Median increase of more than 0C in the 50-year TXx and TNn events compared to the 1°C warming level (Li et al., 2020) Additional evidence from CMIP5 simulations for an	CMIP6 models project a robust increase in the intensity and frequency of TXx events and a robust decrease in the intensity and frequency of TNn events (Li et al., 2020). Median increase of more than 0.5°C in the 50-year TXx and TNn events compared to the 1°C warming level (Li et al., 2020) Additional evidence from CMIP5 simulations for an	CMIP6 models project a robust increase in the intensity and frequency of TXx events and a robust decrease in the intensity and frequency of TNn events (Li et al., 2020). Median increase of more than 2.5°C in the 50-year TXx and TNn events compared to the 1°C warming level (Li et al., 2020) Additional evidence from CMIP5 simulations for an

ACCEPTED VERSION SUBJECT TO FINAL EDITING

			increase in the intensity and frequency of hot extremes and decrease in the intensity and frequency of cold extremes (Alexander and Arblaster, 2017; Herold et al., 2018; Evans et al., 2020; Grose et al., 2020)	increase in the intensity and frequency of hot extremes and decrease in the intensity and frequency of cold extremes (Alexander and Arblaster, 2017; Herold et al., 2018; Evans et al., 2020; Grose et al., 2020)	increase in the intensity and frequency of hot extremes and decrease in the intensity and frequency of cold extremes (Alexander and Arblaster, 2017; Herold et al., 2018; Evans et al., 2020; Grose et al., 2020)
	Very likely increase in the intensity and frequency of hot extremes and decrease in the intensity and frequency of cold extremes	Human influence *very likely* contributed to the observed increase in the intensity and frequency of hot extremes and decrease in the intensity and frequency of cold extremes	Increase in the intensity and frequency of hot extremes: *Very likely* (compared with the recent past (1995-2014)) *Extremely likely* (compared with pre-industrial) Decrease in the intensity and frequency of cold extremes: *Very likely* (compared with the recent past (1995-2014)) *Extremely likely* (compared with pre-industrial)	Increase in the intensity and frequency of hot extremes: *Extremely likely* (compared with the recent past (1995-2014)) *Virtually certain* (compared with pre-industrial) Decrease in the intensity and frequency of cold extremes: *Extremely likely* (compared with the recent past (1995-2014)) *Virtually certain* (compared with pre-industrial)	Increase in the intensity and frequency of hot extremes: *Virtually certain* (compared with the recent past (1995-2014)) *Virtually certain* (compared with pre-industrial) Decrease in the intensity and frequency of cold extremes: *Virtually certain* (compared with the recent past (1995-2014)) *Virtually certain* (compared with pre-industrial)
Northern Australia (NAU)	Significant increases in the intensity and frequency of hot extremes and significant decreases in the intensity and frequency of cold extremes (Perkins and Alexander, 2013; Wang et al., 2013c; CSIRO and BOM, 2015; Donat et al., 2016a; Alexander and Arblaster, 2017; Dunn et al., 2020)	Robust evidence of a human contribution to the observed increase in the intensity and frequency of hot extremes and decrease in the intensity and frequency of cold extremes (Wang et al., 2017; Hu et al., 2020; Seong et al., 2020; Knutson et al., 2014; Lewis and Karoly, 2014; Perkins et al., 2014; Arblaster et al., 2014; Hope et al., 2015, 2016; Perkins and Gibson, 2015)	CMIP6 models project a robust increase in the intensity and frequency of TXx events and a robust decrease in the intensity and frequency of TNn events (Li et al., 2020; Annex). Median increase of more than 0C in the 50-year TXx and TNn events compared to the 1°C warming level (Li et al., 2020) and more than 1.5°C in annual TXx and TNn compared to pre-industrial (Annex). Additional evidence from CMIP5 simulations for an increase in the intensity and frequency of hot extremes and decrease in the intensity and frequency of cold extremes (Alexander and Arblaster, 2017; Herold et al., 2018; Evans et al., 2020; Grose et al., 2020)	CMIP6 models project a robust increase in the intensity and frequency of TXx events and a robust decrease in the intensity and frequency of TNn events (Li et al., 2020; Annex). Median increase of more than 0.5°C in the 50-year TXx and TNn events compared to the 1°C warming level (Li et al., 2020) and more than 2°C in annual TXx and TNn compared to pre-industrial (Annex). Additional evidence from CMIP5 simulations for an increase in the intensity and frequency of hot extremes and decrease in the intensity and frequency of cold extremes (Alexander and Arblaster, 2017; Herold et al., 2018; Evans et al., 2020; Grose et al., 2020)	CMIP6 models project a robust increase in the intensity and frequency of TXx events and a robust decrease in the intensity and frequency of TNn events (Li et al., 2020; Annex). Median increase of more than 3°C in the 50-year TXx and TNn events compared to the 1°C warming level (Li et al., 2020) and more than 3.5°C in annual TXx and TNn compared to pre-industrial (Annex). Additional evidence from CMIP5 simulations for an increase in the intensity and frequency of hot extremes and decrease in the intensity and frequency of cold extremes (Alexander and Arblaster, 2017; Herold et al., 2018; Evans et al., 2020; Grose et al., 2020)
	High confidence in the increase in the intensity and	*High confidence* in a human contribution to the observed	Increase in the intensity and frequency of hot extremes:	Increase in the intensity and frequency of hot extremes:	Increase in the intensity and frequency of hot extremes:

ACCEPTED VERSION SUBJECT TO FINAL EDITING

	frequency of hot extremes and *likely* decrease in the intensity and frequency of cold extremes	increase in the intensity and frequency of hot extremes and decrease in the intensity and frequency of cold extremes	*Likely* (compared with the recent past (1995-2014)) *Very likely* (compared with pre-industrial) Decrease in the intensity and frequency of cold extremes: *Likely* (compared with the recent past (1995-2014)) *Very likely* (compared with pre-industrial)	*Very likely* (compared with the recent past (1995-2014)) *Extremely likely* (compared with pre-industrial) Decrease in the intensity and frequency of cold extremes: *Very likely* (compared with the recent past (1995-2014)) *Extremely likely* (compared with pre-industrial)	*Virtually certain* (compared with the recent past (1995-2014)) *Virtually certain* (compared with pre-industrial) Decrease in the intensity and frequency of cold extremes: *Virtually certain* (compared with the recent past (1995-2014)) *Virtually certain* (compared with pre-industrial)
Central Australia (CAU)	Significant increases in the intensity and frequency of hot extremes and significant decreases in the intensity and frequency of cold extremes (Perkins and Alexander, 2013; Wang et al., 2013c; CSIRO and BOM, 2015; Donat et al., 2016a; Alexander and Arblaster, 2017; Dunn et al., 2020)	Robust evidence of a human contribution to the observed increase in the intensity and frequency of hot extremes and decrease in the intensity and frequency of cold extremes ((Wang et al., 2017c; Hu et al., 2020; Seong et al., 2020; Knutson et al., 2014; Lewis and Karoly, 2014; Perkins et al., 2014; Arblaster et al., 2014; Hope et al., 2015, 2016; Perkins and Gibson, 2015; King et al., 2014)	CMIP6 models project a robust increase in the intensity and frequency of TXx events and a robust decrease in the intensity and frequency of TNn events (Li et al., 2020; Annex). Median increase of more than 0C in the 50-year TXx and TNn events compared to the 1°C warming level (Li et al., 2020) and more than 1.5°C in annual TXx and TNn compared to pre-industrial (Annex). Additional evidence from CMIP5 simulations for an increase in the intensity and frequency of hot extremes and decrease in the intensity and frequency of cold extremes (Alexander and Arblaster, 2017; Herold et al., 2018; Evans et al., 2020; Grose et al., 2020)	CMIP6 models project a robust increase in the intensity and frequency of TXx events and a robust decrease in the intensity and frequency of TNn events (Li et al., 2020; Annex). Median increase of more than 0.5°C in the 50-year TXx and TNn events compared to the 1°C warming level (Li et al., 2020) and more than 2°C in annual TXx and TNn compared to pre-industrial (Annex). Additional evidence from CMIP5 simulations for an increase in the intensity and frequency of hot extremes and decrease in the intensity and frequency of cold extremes (Alexander and Arblaster, 2017; Herold et al., 2018; Evans et al., 2020; Grose et al., 2020)	CMIP6 models project a robust increase in the intensity and frequency of TXx events and a robust decrease in the intensity and frequency of TNn events (Li et al., 2020; Annex). Median increase of more than 2.5°C in the 50-year TXx and TNn events compared to the 1°C warming level (Li et al., 2020) and more than 4°C in annual TXx and TNn compared to pre-industrial (Annex). Additional evidence from CMIP5 simulations for an increase in the intensity and frequency of hot extremes and decrease in the intensity and frequency of cold extremes (Alexander and Arblaster, 2017; Herold et al., 2018; Evans et al., 2020; Grose et al., 2020)
	Likely increase in the intensity and frequency of hot extremes and decrease in the intensity and frequency of cold extremes	Human influence *likely* contributed to the observed increase in the intensity and frequency of hot extremes and decrease in the intensity and frequency of cold extremes	Increase in the intensity and frequency of hot extremes: *Likely* (compared with the recent past (1995-2014)) *Very likely* (compared with pre-industrial) Decrease in the intensity and frequency of cold extremes: *Likely* (compared with the recent past (1995-2014))	Increase in the intensity and frequency of hot extremes: *Very likely* (compared with the recent past (1995-2014)) *Extremely likely* (compared with pre-industrial) Decrease in the intensity and frequency of cold extremes: *Very likely* (compared with the recent past (1995-2014))	Increase in the intensity and frequency of hot extremes: *Virtually certain* (compared with the recent past (1995-2014)) *Virtually certain* (compared with pre-industrial) Decrease in the intensity and frequency of cold extremes: *Virtually certain* (compared

ACCEPTED UNDER SUBJECT TO FINAL EDITING

			Very likely (compared with pre-industrial)	*Extremely likely* (compared with pre-industrial)	with the recent past (1995-2014)) *Virtually certain* (compared with pre-industrial)
Eastern Australia (EAU)	Significant increases in the intensity and frequency of hot extremes and significant decreases in the intensity and frequency of cold extremes (Perkins and Alexander, 2013; Wang et al., 2013c; CSIRO and BOM, 2015; Donat et al., 2016a; Alexander and Arblaster, 2017; Dunn et al., 2020)	Robust evidence of a human contribution to the observed increase in the intensity and frequency of hot extremes and decrease in the intensity and frequency of cold extremes ((Wang et al., 2017c; Hu et al., 2020; Seong et al., 2020; Knutson et al., 2014; Lewis and Karoly, 2014; Perkins et al., 2014; Arblaster et al., 2014; Hope et al., 2015, 2016; Perkins and Gibson, 2015; King et al., 2015)	CMIP6 models project a robust increase in the intensity and frequency of TXx events and a robust decrease in the intensity and frequency of TNn events (Li et al., 2020; Annex). Median increase of more than 0.5°C in the 50-year TXx and TNn events compared to the 1°C warming level (Li et al., 2020) and more than 1°C in annual TXx and TNn compared to pre-industrial (Annex). Additional evidence from CMIP5 simulations for an increase in the intensity and frequency of hot extremes and decrease in the intensity and frequency of cold extremes (Alexander and Arblaster, 2017; Herold et al., 2018; Evans et al., 2020; Grose et al., 2020)	CMIP6 models project a robust increase in the intensity and frequency of TXx events and a robust decrease in the intensity and frequency of TNn events (Li et al., 2020; Annex). Median increase of more than 0.5°C in the 50-year TXx and TNn events compared to the 1°C warming level (Li et al., 2020) and more than 1.5°C in annual TXx and TNn compared to pre-industrial (Annex). Additional evidence from CMIP5 simulations for an increase in the intensity and frequency of hot extremes and decrease in the intensity and frequency of cold extremes (Alexander and Arblaster, 2017; Herold et al., 2018; Evans et al., 2020; Grose et al., 2020)	CMIP6 models project a robust increase in the intensity and frequency of TXx events and a robust decrease in the intensity and frequency of TNn events (Li et al., 2020; Annex). Median increase of more than 2.5°C in the 50-year TXx and TNn events compared to the 1°C warming level (Li et al., 2020) and more than 3.5°C in annual TXx and TNn compared to pre-industrial (Annex). Additional evidence from CMIP5 simulations for an increase in the intensity and frequency of hot extremes and decrease in the intensity and frequency of cold extremes (Alexander and Arblaster, 2017; Herold et al., 2018; Evans et al., 2020; Grose et al., 2020)
	Likely increase in the intensity and frequency of hot extremes and decrease in the intensity and frequency of cold extremes	Human influence *likely* contributed to the observed increase in the intensity and frequency of hot extremes and decrease in the intensity and frequency of cold extremes	Increase in the intensity and frequency of hot extremes: *Likely* (compared with the recent past (1995-2014)) *Very likely* (compared with pre-industrial) Decrease in the intensity and frequency of cold extremes: *Likely* (compared with the recent past (1995-2014)) *Very likely* (compared with pre-industrial)	Increase in the intensity and frequency of hot extremes: *Very likely* (compared with the recent past (1995-2014)) *Extremely likely* (compared with pre-industrial) Decrease in the intensity and frequency of cold extremes: *Very likely* (compared with the recent past (1995-2014)) *Extremely likely* (compared with pre-industrial)	Increase in the intensity and frequency of hot extremes: *Virtually certain* (compared with the recent past (1995-2014)) *Virtually certain* (compared with pre-industrial) Decrease in the intensity and frequency of cold extremes: *Virtually certain* (compared with the recent past (1995-2014)) *Virtually certain* (compared with pre-industrial)
Southern Australia (SAU)	Significant increases in the intensity and frequency of hot extremes and significant decreases in the intensity and	Robust evidence of a human contribution to the observed increase in the intensity and frequency of hot extremes	CMIP6 models project a robust increase in the intensity and frequency of TXx events and a robust decrease in the intensity	CMIP6 models project a robust increase in the intensity and frequency of TXx events and a robust decrease in the intensity	CMIP6 models project a robust increase in the intensity and frequency of TXx events and a robust decrease in the intensity

ACCEPTED VERSION SUBJECT TO FINAL EDITING

	frequency of cold extremes (Perkins and Alexander, 2013; Wang et al., 2013c; Dittus et al., 2014; CSIRO and BOM, 2015; Crimp et al., 2016; Donat et al., 2016a; Alexander and Arblaster, 2017; Dunn et al., 2020)	and decrease in the intensity and frequency of cold extremes (Wang et al., 2017c; Hu et al., 2020; Seong et al., 2020; Black and Karoly, 2016; Knutson et al., 2014; Lewis and Karoly, 2014; Perkins et al., 2014; Arblaster et al., 2014; Hope et al., 2015, 2016; Perkins and Gibson, 2015)	and frequency of TNn events (Li et al., 2020; Annex). Median increase of more than 0C in the 50-year TXx and TNn events compared to the 1°C warming level (Li et al., 2020) and more than 1°C in annual TXx and TNn compared to pre-industrial (Annex). Additional evidence from CMIP5 simulations for an increase in the intensity and frequency of hot extremes and decrease in the intensity and frequency of cold extremes (Alexander and Arblaster, 2017; Herold et al., 2018; Evans et al., 2020; Grose et al., 2020)	and frequency of TNn events (Li et al., 2020; Annex). Median increase of more than 0.5°C in the 50-year TXx and TNn events compared to the 1°C warming level (Li et al., 2020) and more than 1.5°C in annual TXx and TNn compared to pre-industrial (Annex). Additional evidence from CMIP5 simulations for an increase in the intensity and frequency of hot extremes and decrease in the intensity and frequency of cold extremes (Alexander and Arblaster, 2017; Herold et al., 2018; Evans et al., 2020; Grose et al., 2020)	and frequency of TNn events (Li et al., 2020; Annex). Median increase of more than 2°C in the 50-year TXx and TNn events compared to the 1°C warming level (Li et al., 2020) and more than 2.5°C in annual TXx and TNn compared to pre-industrial (Annex). Additional evidence from CMIP5 simulations for an increase in the intensity and frequency of hot extremes and decrease in the intensity and frequency of cold extremes (Alexander and Arblaster, 2017; Herold et al., 2018; Evans et al., 2020; Grose et al., 2020)
	Likely increase in the intensity and frequency of hot extremes and decrease in the intensity and frequency of cold extremes	Human influence *likely* contributed to the observed increase in the intensity and frequency of hot extremes and decrease in the intensity and frequency of cold extremes	Increase in the intensity and frequency of hot extremes: *Likely* (compared with the recent past (1995-2014)) *Very likely* (compared with pre-industrial) Decrease in the intensity and frequency of cold extremes: *Likely* (compared with the recent past (1995-2014)) *Very likely* (compared with pre-industrial)	Increase in the intensity and frequency of hot extremes: *Very likely* (compared with the recent past (1995-2014)) *Extremely likely* (compared with pre-industrial) Decrease in the intensity and frequency of cold extremes: *Very likely* (compared with the recent past (1995-2014)) *Extremely likely* (compared with pre-industrial)	Increase in the intensity and frequency of hot extremes: *Virtually certain* (compared with the recent past (1995-2014)) *Virtually certain* (compared with pre-industrial) Decrease in the intensity and frequency of cold extremes: *Virtually certain* (compared with the recent past (1995-2014)) *Virtually certain* (compared with pre-industrial)
New Zealand (NZ)	Significant increases in the intensity and frequency of hot extremes and significant decreases in the intensity and frequency of cold extremes (Caloiero, 2017; Dunn et al., 2020; Ministry for the Environment & Stats NZ, 2020; Harrington, 2020)	Limited evidence (Seong et al., 2020; Wang et al., 2017)	CMIP6 models project an increase in the intensity and frequency of TXx events and a decrease in the intensity and frequency of TNn events (Li et al., 2020; Annex). Median increase of more than 0C in the 50-year TXx and TNn events compared to the 1°C warming level (Li et al., 2020) and more than 1°C in annual TXx and TNn compared to pre-industrial (Annex).	CMIP6 models project a robust increase in the intensity and frequency of TXx events and a robust decrease in the intensity and frequency of TNn events (Li et al., 2020; Annex). Median increase of more than 0.5°C in the 50-year TXx and TNn events compared to the 1°C warming level (Li et al., 2020) and more than 1.5°C in annual TXx and TNn compared to pre-industrial	CMIP6 models project a robust increase in the intensity and frequency of TXx events and a robust decrease in the intensity and frequency of TNn events (Li et al., 2020; Annex). Median increase of more than 2°C in the 50-year TXx and TNn events compared to the 1°C warming level (Li et al., 2020) and more than 3°C in annual TXx and TNn compared to pre-industrial

ACCEPTED VERSION SUBJECT TO FINAL EDITING

				(Annex).	(Annex).
	Likely increase in the intensity and frequency of hot extremes and decrease in the intensity and frequency of cold extremes	*Low confidence*	Increase in the intensity and frequency of hot extremes: *High confidence* (compared with the recent past (1995-2014)) *Likely* (compared with pre-industrial) Decrease in the intensity and frequency of cold extremes: *High confidence* (compared with rthe recent past (1995-2014)) *Likely* (compared with pre-industrial)	Increase in the intensity and frequency of hot extremes: *Likely* (compared with the recent past (1995-2014)) *Very likely* (compared with pre-industrial) Decrease in the intensity and frequency of cold extremes: *Likely* (compared with the recent past (1995-2014)) *Very likely* (compared with pre-industrial)	Increase in the intensity and frequency of hot extremes: *Extremely likely* (compared with the recent past (1995-2014)) *Virtually certain* (compared with pre-industrial) Decrease in the intensity and frequency of cold extremes: *Extremely likely* (compared with the recent past (1995-2014)) *Virtually certain* (compared with pre-industrial)

[END TABLE 11.10 HERE]

[START TABLE 11.11 HERE]

Table 11.11: Observed trends, human contribution to observed trends, and projected changes at 1.5°C, 2°C and 4°C of global warming for heavy precipitation in Australasia, subdivided by AR6 regions. See Sections 11.9.1 and 11.9.3 for details.

Region	Observed trends	Detection and attribution; event attribution	Projections		
			1.5 °C	2 °C	4 °C
All Australasia	Limited evidence (Jakob and Walland, 2016; Guerreiro et al., 2018b; Dey et al., 2019b; Dunn et al., 2020; Sun et al., 2020)	Limited evidence	CMIP6 models project inconsistent changes in the region (Li et al., 2020a)	CMIP6 models project an increase in the intensity and frequency of heavy precipitation (Li et al., 2020). Median increase of more than 4% in the 50-year Rx1day and Rx5day events compared to the 1°C warming level (Li et al., 2020a)	CMIP6 models project a robust increase in the intensity and frequency of heavy precipitation (Li et al., 2020a). Median increase of more than 10% in the 50-year Rx1day and Rx5day events compared to the 1°C warming level (Li et al., 2020a)
	Low confidence	*Low confidence*	Intensification of heavy precipitation: *Low confidence* (compared with the recent past (1995-2014)) *Medium confidence* (compared with pre-industrial)	Intensification of heavy precipitation: *Medium confidence* (compared with the recent past (1995-2014)) *Likely* (compared with pre-industrial)	Intensification of heavy precipitation: *Likely* (compared with the recent past (1995-2014)) *Very likely* (compared with pre-industrial)
Northern Australia (NAU)	Intensification of heavy	Limited evidence (Dey et al.,	CMIP6 models project	CMIP6 models project an	CMIP6 models project a robust

ACCEPTED VERSION SUBJECT TO FINAL EDITING

	precipitation (Donat et al., 2016a; Alexander and Arblaster, 2017; Evans et al., 2017; Dey et al., 2019b; Dunn et al., 2020; Sun et al., 2020)	2019a)	inconsistent changes in the region (Li et al., 2020a)	increase in the intensity and frequency of heavy precipitation (Li et al., 2020; Annex). Median increase of more than 4% in the 50-year Rx1day and Rx5day events compared to the 1°C warming level (Li et al., 2020a) and more than 6% in annual Rx1day and Rx5day and 2% in annual Rx30day compared to pre-industrial (Annex).	increase in the intensity and frequency of heavy precipitation (Li et al., 2020; Annex). Median increase of more than 10% in the 50-year Rx1day and Rx5day events compared to the 1°C warming level (Li et al., 2020a) and more than 20% in annual Rx1day and Rx5day and 10% in annual Rx30day compared to pre-industrial (Annex).
	Medium confidence in the intensitification of heavy precipitation	*Low confidence*	Intensification of heavy precipitation: *Low confidence* (compared with the recent past (1995-2014)) *Medium confidence* (compared with pre-industrial)	Intensification of heavy precipitation: *Medium confidence* (compared with the recent past (1995-2014)) *High confidence* (compared with pre-industrial)	Intensification of heavy precipitation: *Likely* (compared with the recent past (1995-2014)) *Very likely* (compared with pre-industrial)
Central Australia (CAU)	Limited evidence (Donat et al., 2016a; Alexander and Arblaster, 2017; Evans et al., 2017; Dey et al., 2019b; Dunn et al., 2020; Sun et al., 2020).	Limited evidence	CMIP6 models project inconsistent changes in the region (Li et al., 2020a)	CMIP6 models project an increase in the intensity and frequency of heavy precipitation (Li et al., 2020; Annex). Median increase of more than 4% in the 50-year Rx1day and Rx5day events compared to the 1°C warming level (Li et al., 2020a) and more than 4% in annual Rx1day and Rx5day and 2% in annual Rx30day compared to pre-industrial (Annex).	CMIP6 models project a robust increase in the intensity and frequency of heavy precipitation (Li et al., 2020; Annex). Median increase of more than 10% in the 50-year Rx1day and Rx5day events compared to the 1°C warming level (Li et al., 2020a) and more than 10% in annual Rx1day and Rx5day and 4% in annual Rx30day compared to pre-industrial (Annex).
	Low confidence	*Low confidence*	Intensification of heavy precipitation: *Low confidence* (compared with the recent past (1995-2014)) *Medium confidence* (compared with pre-industrial)	Intensification of heavy precipitation: *Medium confidence* (compared with the recent past (1995-2014)) *High confidence* (compared with pre-industrial)	Intensification of heavy precipitation: *Likely* (compared with the recent past (1995-2014)) *Very likely* (compared with pre-industrial)
Eastern Australia (EAU)	Lack of agreement on the evidence of trends (Donat et al., 2016a; Alexander and Arblaster, 2017; Evans et al.,	Limited evidence	CMIP6 models project inconsistent changes in the region (Li et al., 2020a)	CMIP6 models project inconsistent changes in the region (Li et al., 2020a)	CMIP6 models project an increase in the intensity and frequency of heavy precipitation (Li et al., 2020;

ACCEPTED VERSION SUBJECT TO FINAL EDITING

	2017; Dey et al., 2019b; Dunn et al., 2020; Sun et al., 2020)				Annex). Median increase of more than 10% in the 50-year Rx1day and Rx5day events compared to the 1°C warming level (Li et al., 2020a) and more than 10% in annual Rx1day and Rx5day and 8% in annual Rx30day compared to pre-industrial (Annex).
	Low confidence	*Low confidence*	Intensification of heavy precipitation: *Low confidence* (compared with the recent past (1995-2014)) *Low confidence* (compared with pre-industrial)	Intensification of heavy precipitation: *Low confidence* (compared with the recent past (1995-2014)) *Medium confidence* (compared with pre-industrial)	Intensification of heavy precipitation: *High confidence* (compared with the recent past (1995-2014)) *Likely* (compared with pre-industrial)
Southern Australia (SAU)	Limited evidence (Donat et al., 2016a; Alexander and Arblaster, 2017; Evans et al., 2017; Dey et al., 2019b; Dunn et al., 2020; Sun et al., 2020)	Limited evidence	CMIP6 models project inconsistent changes in the region (Li et al., 2020a)	CMIP6 models project inconsistent changes in the region (Li et al., 2020a)	CMIP6 models project an increase in the intensity and frequency of heavy precipitation (Li et al., 2020; Annex). Median increase of more than 10% in the 50-year Rx1day and Rx5day events compared to the 1°C warming level (Li et al., 2020a) and more than 8% in annual Rx1day and Rx5day and 4% in annual Rx30day compared to pre-industrial (Annex).
	Low confidence	*Low confidence*	Intensification of heavy precipitation: *Low confidence* (compared with the recent past (1995-2014)) *Low confidence* (compared with pre-industrial)	Intensification of heavy precipitation: *Low confidence* (compared with the recent past (1995-2014)) *Medium confidence* (compared with pre-industrial)	Intensification of heavy precipitation: *High confidence* (compared with the recent past (1995-2014)) *Likely* (compared with pre-industrial)
New Zealand (NZ)	Lack of agreement on the evidence of trends (Donat et al., 2016a; Dunn et al., 2020; MfE and Stats NZ, 2020)	Limited evidence (Rosier et al., 2016)	CMIP6 models project inconsistent changes in the region (Li et al., 2020a)	CMIP6 models project inconsistent changes in the region (Li et al., 2020a)	CMIP6 models project an increase in the intensity and frequency of heavy precipitation (Li et al., 2020; Annex). Median increase of more than 15% in the 50-year Rx1day and Rx5day events compared to the 1°C warming level (Li et al., 2020a) and

ACCEPTED VERSION SUBJECT TO FINAL EDITING

					more than 15% in annual Rx1day and Rx5day and 10% in annual Rx30day compared to pre-industrial (Annex).
	Low confidence	*Low confidence*	Intensification of heavy precipitation: *Low confidence* (compared with the recent past (1995-2014)) *Low confidence* (compared with pre-industrial)	Intensification of heavy precipitation: *Low confidence* (compared with the recent past (1995-2014)) *Medium confidence* (compared with pre-industrial)	Intensification of heavy precipitation: *High confidence* (compared with the recent past (1995-2014)) *Likely* (compared with pre-industrial)

[END TABLE 11.11 HERE]

[START TABLE 11.12 HERE]

Table 11.12: Observed trends, human contribution to observed trends, and projected changes at 1.5°C, 2°C and 4°C of global warming for meteorological droughts (MET), agricultural and ecological droughts (AGR/ECOL), and hydrological droughts (HYDR) in Australasia, subdivided by AR6 regions. See Sections 11.9.1 and 11.9.4 for details.

Region and drought type		Observed trends	Human contribution	Projections		
				+1.5 °C	+2 °C	+4 °C
Northern Australia (NAU)	MET	***Medium confidence:* Decrease** in the frequency and intensity of meteorological droughts (Gallant et al., 2013; Delworth and Zeng, 2014; Alexander and Arblaster, 2017; Knutson and Zeng, 2018; Dey et al., 2019a; Dunn et al., 2020)	***Low confidence*** in attribution (Delworth and Zeng, 2014; Knutson and Zeng, 2018; Dey et al., 2019a).	***Low confidence*: Increases or non-robust** changes in meteorological droughts (Alexander and Arblaster, 2017; Kirono et al., 2020; Spinoni et al., 2020)(Chapter 11 Supplementary Material (11.SM)). Model disagreement in SPI projections (Spinoni et al., 2020) Increase in CDD-based drought in CMIP5, but generally not significant (Alexander and Arblaster, 2017) Slight increase in CDD-based drought in CMIP6 (Chapter 11 Supplementary Material (11.SM))	***Low confidence*: Increases or non-robust** changes in meteorological droughts (Alexander and Arblaster, 2017; Kirono et al., 2020; Spinoni et al., 2020)(Chapter 11 Supplementary Material (11.SM)). Large intermodel spread in changes in SPI in CMIP5 projections (Kirono et al., 2020) Model disagreement in SPI projections (Spinoni et al., 2020) Increase in CDD-based drought in CMIP5, but generally not significant (Alexander and Arblaster, 2017) Slight increase in CDD-based	***Low confidence*: Increases or non-robust** changes in meteorological droughts (Alexander and Arblaster, 2017; Grose et al., 2020; Kirono et al., 2020; Spinoni et al., 2020; Ukkola et al., 2020)(Chapter 11 Supplementary Material (11.SM)). Large intermodel spread in changes in SPI in CMIP5 projectons, but slight drying for median (Kirono et al., 2020) Model disagreement in SPI projections (Spinoni et al., 2020) Increase in CDD-based drought in CMIP5, but generally not significant (Alexander and Arblaster, 2017)

ACCEPTED VERSION SUBJECT TO FINAL EDITING

					drought CMIP6 (Chapter 11 Supplementary Material (11.SM))	Increase in CDD-based drought in CMIP6 (Grose et al., 2020)(Chapter 11 Supplementary Material (11.SM)) Inconsistent trends in mean precipitation in CORDEX RCMs, but drying trend on annual scale at northern tip of region (Evans et al., 2020)
	AGR ECOL	***Medium confidence:*** **Decrease** in agricultural and ecological drought Decrease in frequency (but not intensity) of soil moisture-based droughts (Gallant et al., 2013). Inconsistent signals in changes in water-balance (Greve et al., 2014; Padrón et al., 2019). Decrease in agricultural and ecological drought based on SPEI-PM from 1950-2009 (Beguería et al., 2014; Spinoni et al., 2019) and PDSI_PM (Dai and Zhao, 2017)	***Low confidence*** **Limited evidence** Lack of studies although (Lewis et al., 2019b) supported an anthropogenic attribution of 2018 drought associated with more extreme temperatures that exacerbated AED and ET, and depleting soil moisture.	***Low confidence*****: Increase or non-robust** (Naumann et al., 2018; Xu et al., 2019a; Cook et al., 2020; Kirono et al., 2020).(Chapter 11 Supplementary Material (11.SM)) Cook et al. (2020): non-robust changes in surface and column soil moisture in both summer and winter half years (CMIP6 projections)	***Low confidence:*** **Increase or non-robust** (Naumann et al., 2018; Xu et al., 2019a; Cook et al., 2020; Kirono et al., 2020).(Chapter 11 Supplementary Material (11.SM)) Cook et al. (2020): non-robust changes in surface and column soil moisture in both summer and winter half years (CMIP6 projections) Kirono et al. (2020): Standardized soil moisture index based on surface soil moisture: drying trend for median in CMIP5 but large intermodal spread	***Low confidence*****: Increase or non-robust,** with higher increases in SPEI-PM but non-robust changes in CMIP6 soil moisture (Naumann et al., 2018; Cook et al., 2020; Kirono et al., 2020; Vicente-Serrano et al., 2020a)(Chapter 11 Supplementary Material (11.SM)). Cook et al. (2020): non-robust changes in surface and column soil moisture in both summer and winter half years (CMIP6 projections) Kirono et al. (2020): Standardized soil moisture index based on surface soil moisture : drying trend for median in CMIP5, but larger inter-model spread
	HYDR	***Low confidence*** because of **lack of data and studies**	***Low confidence*** **Limited evidence** because of lack of data and studies	***Low confidence:*** **Limited evidence.** One study shows lack of signal (Touma et al., 2015)	***Low confidence*****: Limited evidence** and generally **non-robust** change in two studies (Touma et al., 2015; Cook et al., 2020)	***Low confidence*****: Non-robust changes** or **high model disagreement** (Giuntoli et al., 2015; Touma et al., 2015; Cook et al., 2020)
Central Australia (CAU)	MET	***Medium confidence***: **decrease** in the frequency/intensity of droughts (Gallant et al., 2013; Beguería et al., 2014; Delworth and Zeng, 2014; Greve et al., 2014; Alexander and Arblaster, 2017; Knutson and Zeng, 2018).	***Low confidence*** in attribution (Delworth and Zeng, 2014; Knutson and Zeng, 2018).	***Low confidence*****: Inconsistent or non-robust** changes in meteorological droughts (Alexander and Arblaster, 2017; Kirono et al., 2020; Spinoni et al., 2020)(Chapter 11 Supplementary Material (11.SM)). Tendency to increasing SPI-based drought in CMIP6, but to decreasing SPI-based drought in CORDEX (Spinoni et al., 2020)	***Low confidence*****: Inconsistent or non-robust** changes in meteorological droughts (Alexander and Arblaster, 2017; Kirono et al., 2020; Spinoni et al., 2020)(Chapter 11 Supplementary Material (11.SM)). Tendency to increasing SPI-based drought in CMIP6, but to decreasing SPI-based drought in CORDEX (Spinoni et al., 2020) Kirono et al. (2020): CMIP6 models	***Low confidence*****: Inconsistent or non-robust** changes in meteorological droughts (Alexander and Arblaster, 2017; Grose et al., 2020; Kirono et al., 2020; Spinoni et al., 2020; Ukkola et al., 2020) (Chapter 11 Supplementary Material (11.SM)). Tendency to increasing SPI-based drought in CMIP6, but to decreasing SPI-based drought in CORDEX (Spinoni et al., 2020)

ACCEPTED VERSION SUBJECT TO FINAL EDITING

					project increased in SPI in much of region for 2006-2100 under RCP8.5	Kirono et al. (2020): CMIP6 models project increased in SPI in much of region for 2006-2100 under RCP8.5
	AGR ECOL	***Low confidence***: **Inconsistent** changes in frequency/intensity of droughts (Gallant et al., 2013; Beguería et al., 2014; Delworth and Zeng, 2014; Greve et al., 2014; Dai and Zhao, 2017; Knutson and Zeng, 2018; Padrón et al., 2019; Spinoni et al., 2019)	***Low confidence*** because of **lack of studies**	***Low confidence*: Inconsistent changes** both in soil moisture and SPEI-PM (Naumann et al., 2018; Xu et al., 2019a; Cook et al., 2020; Kirono et al., 2020)(Chapter 11 Supplementary Material (11.SM)) .	***Low confidence*: Inconsistent changes** both in soil moisture and SPEI-PM (Naumann et al., 2018; Xu et al., 2019a; Cook et al., 2020; Kirono et al., 2020)(Chapter 11 Supplementary Material (11.SM)).	***Medium confidence*: Increased drying** for some metrics or part of domain for soil moisture and SPEI-PM with stronger changes for SPEI-PM (Naumann et al., 2018; Cook et al., 2020; Kirono et al., 2020; Vicente-Serrano et al., 2020a)(Chapter 11 Supplementary Material (11.SM))
	HYDR	***Low confidence*** because of **lack of data and studies**	***Low confidence*** **Limited evidence**, because of lack of studies	***Low confidence:* Limited evidence.** One study shows lack of signal (Touma et al., 2015)	***Low confidence*: Limited evidence** and generally **non-robust** change in two studies (Touma et al., 2015; Cook et al., 2020)	***Low confidence*: Non-robust changes** or **high model disagreement** (Giuntoli et al., 2015; Touma et al., 2015; Cook et al., 2020)
Eastern Australia (EAU)	MET	***Low confidence:* Inconsistent** trends (Gallant et al., 2013; Delworth and Zeng, 2014; Alexander and Arblaster, 2017; Knutson and Zeng, 2018; Spinoni et al., 2019) Gallant et al. (2013): Inconsistent trends, wetting on average in MDB Delworth and Zeng (2014): no trend Knutson and Zeng (2018): no trend Alexander and Arblaster (2017); Dunn et al. (2020): no trends in CDD Spinoni et al. (2019): Inconsistent trends, some increased severity in part of the region	***Low confidence*** in attribution (Delworth and Zeng, 2014; King et al., 2014; Knutson and Zeng, 2018)	***Low confidence*: Increase** in meteorological droughs based on CDD (Chapter 11 Supplementary Material (11.SM)) and SPI (Kirono et al., 2020), but weak signals and lack of other studies at this GWL.	***Medium confidence*: Increases** in meteorological droughts (Alexander and Arblaster, 2017; Kirono et al., 2020; Spinoni et al., 2020)(Chapter 11 Supplementary Material (11.SM)) .	***Medium confidence*:** Increases in meteorological droughts (Alexander and Arblaster, 2017; Grose et al., 2020; Kirono et al., 2020; Spinoni et al., 2020; Ukkola et al., 2020)(Chapter 11 Supplementary Material (11.SM)).
	AGR ECOL	***Low confidence*: Inconsistent trends** (Gallant et al., 2013; Beguería et al., 2014; Greve et al., 2014; Dai and Zhao, 2017; Spinoni et al., 2019; Padrón et al., 2020)	***Low confidence*** because of lack of studies although enhanced AED driven by extreme temperatures increased the severity of the 2019 drought (van Oldenborgh et al., 2021)	***Low confidence*: Inconsistent changes** in soil moisture and SPEI-PM, but tendency to **increase** (Naumann et al., 2018; Xu et al., 2019a; Cook et al., 2020; Kirono et al., 2020)(Chapter 11 Supplementary Material (11.SM))	***Medium confidence*: Increase** in drought based on soil moisture and SPEI-PM, but partly inconsistent changes for some studies (Naumann et al., 2018; Xu et al., 2019a; Cook et al., 2020; Kirono et al., 2020)(Chapter 11 Supplementary Material (11.SM))	***High confidence*: Increased drying** for some metrics or part of domain for soil moisture and SPEI-PM with stronger changes for SPEI-PM (Naumann et al., 2018; Cook et al., 2020; Kirono et al., 2020; Vicente-Serrano et al., 2020a)(Chapter 11 Supplementary Material (11.SM))

ACCEPTED VERSION SUBJECT TO FINAL EDITING

	HYDR	***Low confidence*: Limited evidence** because of **lack of data and studies** (Zhang et al., 2016d)	***Low confidence:* Limited evidence,** because of lack of studies	***Low confidence:* Limited evidence.** One study shows lack of signal (Touma et al., 2015)	***Low confidence*: Lack of studies** and generally **non-robust** change in two studies (Touma et al., 2015; Cook et al., 2020)	***Low confidence*: Non-robust changes** or **high model disagreement** (Giuntoli et al., 2015; Touma et al., 2015; Cook et al., 2020)
Southern Australia (SAU)	MET	***Low confidence*: Mixed signal** depending on subregion, index and season (Gallant et al., 2013; Delworth and Zeng, 2014; Alexander and Arblaster, 2017; Spinoni et al., 2019; Dunn et al., 2020; Rauniyar and Power, 2020)(Dai and Zhao, 2017). Gallant et al. (2013): Wetting in eastern part, drying in eastern part Rauniyar and Power (2020): Recovery from Millenium drought Delworth and Zeng (2014): Only drying in the western part, not in the eastern part Alexander and Arblaster (2017); Dunn et al. (2020): Overall decreasing CDD trends Spinoni et al. (2019): Decreasing droughts in most of domain	***Low confidence:*** Mixed signal in observations. Increase in the frequency/intensity of meteorological droughts can be attributed to anthropogenic forcing (greenhouse gases, ozone and aerosols) (Delworth and Zeng, 2014; Karoly et al., 2016; Knutson and Zeng, 2018) (Cai et al., 2014b).	***Medium confidence*: Increase** overall in meteorological droughts based on CDD (Chapter 11 Supplementary Material (11.SM)) and SPI (Kirono et al., 2020); but weak signals and lack of other studies at this GWL.	***Medium confidence:* Increases** in meteorological droughts (Alexander and Arblaster, 2017; Kirono et al., 2020; Spinoni et al., 2020)(Chapter 11 Supplementary Material (11.SM)).	***Medium confidence*:** Increases in meteorological droughts (Alexander and Arblaster, 2017; Grose et al., 2020; Kirono et al., 2020; Spinoni et al., 2020; Ukkola et al., 2020)(Chapter 11 Supplementary Material (11.SM)).
	AGR ECOL	***Medium confidence*: Increase.** Dominant increasing drying signal but some inconsistent trends depending on subregion and index; strongest drying trend in Western SAU. (Gallant et al., 2013; Beguería et al., 2014; Greve et al., 2018; Spinoni et al., 2019; Padrón et al., 2020).	***Low confidence:* Limited evidence,** Enhanced AED driven by extreme temperatures increased the severity of the 2019 drought (van Oldenborgh et al., 2021)	***Medium confidence*: Increase** in soil moisture and SPEI-PM, but partly inconsistent changes for some studies (Naumann et al., 2018; Xu et al., 2019a; Kirono et al., 2020)(Chapter 11 Supplementary Material (11.SM)).	***Medium confidence*: Increase** in drought based on soil moisture and SPEI-PM, but partly inconsistent changes for some studies (Naumann et al., 2018; Xu et al., 2019a; Cook et al., 2020; Kirono et al., 2020)(Chapter 11 Supplementary Material (11.SM))	***High confidence*: Increased drying** for some metrics or part of domain for soil moisture and SPEI-PM with stronger changes for SPEI-PM (Naumann et al., 2018; Cook et al., 2020; Kirono et al., 2020; Vicente-Serrano et al., 2020a)(Chapter 11 Supplementary Material (11.SM))

ACCEPTED VERSION SUBJECT TO FINAL EDITING

	HYDR	***Medium confidence:*** **Increasing drying signal in the southeast and particularly the southwest. Some dependence on time frame** in available studies (Gudmundsson et al., 2019, 2021)(Zhang et al., 2016d)	***Low confidence :*** **Limited evidence** because of lack of studies (Cai and Cowan, 2008)	***Low confidence:*** **Limited evidence.** One study shows lack of signal (Touma et al., 2015)	***Medium confidence*****: Increase in drought**, but some Inconsistent and non-robust change including subregional/seasonal differences (Touma et al., 2015; Zheng et al., 2019; Cook et al., 2020)	***Medium confidence*****: Increase in drought**, but some inconsistent changes depending on season or study (Giuntoli et al., 2015; Touma et al., 2015; Cook et al., 2020)
New Zealand (NZ)	MET	***Low confidence:*** **Inconsistent** changes (Caloiero, 2015; Spinoni et al., 2015; Knutson and Zeng, 2018)	***Low confidence*** in attribution of trends (Harrington et al., 2014, 2016; Knutson and Zeng, 2018).	***Low confidence:*** **Lack of studies** and **lack of signal** for CDD in CMIP6 (Chapter 11 Supplementary Material (11.SM))	***Low confidence*****: Inconsistent** changes, but increase in Northern Island (MfE, 2018; MfE and Stats NZ, 2020; Spinoni et al., 2020).(Chapter 11 Supplementary Material (11.SM))	***Low confidence*****: Inconsistent** changes, but increase in Northern Island (MfE, 2018; MfE and Stats NZ, 2020; Spinoni et al., 2020).(Chapter 11 Supplementary Material (11.SM))
	AGR ECOL	***Low confidence:*** **Inconsistent** trends. Increase in drying in part of the country based on soil mosture and SPEI-PM (Beguería et al., 2014; Spinoni et al., 2019; MfE and Stats NZ, 2020); decrease in PDSI-PM (Dai and Zhao, 2017)	***Low confidence:*** **Limited evidence** because of lack of studies	***Low confidence:*** **Lack of studies** and **lack of signal** for soil moisture in CMIP6 (Chapter 11 Supplementary Material (11.SM))	***Low confidence*****: Inconsistent** changes, but increase in Northern Island (MfE, 2018; MfE and Stats NZ, 2020; Spinoni et al., 2020).	***Low confidence*****: Inconsistent** changes, but increase in Northern Island (MfE, 2018; MfE and Stats NZ, 2020; Spinoni et al., 2020).
	HYDR	***Low confidence:*** **Lack of data and studies**	***Low confidence:*** **Lack of studies**	***Low confidence:*** **Lack of studies**	***Low confidence:*** **Lack of studies**	***Low confidence:*** **Lack of studies**

[END TABLE 11.12 HERE]

[START TABLE 11.13 HERE]

Table 11.13: Observed trends, human contribution to observed trends, and projected changes at 1.5°C, 2°C and 4°C of global warming for temperature extremes in Central and South America, subdivided by AR6 regions. See Sections 11.9.1 and 11.9.2 for details.

Region	Observed trends	Detection and attribution; event attribution	Projections		
			1.5 °C	2 °C	4 °C
All Central and South America	Most subregions show a *likely* increase in the intensity and frequency of hot extremes and decrease in the intensity and frequency of cold extremes	Robust evidence of a human contribution to the observed increase in the intensity and frequency of hot extremes and decrease in the intensity and frequency of cold extremes (Hu et al., 2020; Seong et al., 2020)	CMIP6 models project a robust increase in the intensity and frequency of TXx events and a robust decrease in the intensity and frequency of TNn events (Li et al., 2020). Median increase of more than 0.5°C in the 50-year TXx and TNn events compared to the 1°C warming level (Li et al., 2020)	CMIP6 models project a robust increase in the intensity and frequency of TXx events and a robust decrease in the intensity and frequency of TNn events (Li et al., 2020). Median increase of more than 1°C in the 50-year TXx and TNn events compared to the 1°C warming level (Li et al., 2020)	CMIP6 models project a robust increase in the intensity and frequency of TXx events and a robust decrease in the intensity and frequency of TNn events (Li et al., 2020). Median increase of more than 2.5°C in the 50-year TXx and TNn events compared to the 1°C warming level (Li et al., 2020)

ACCEPTED VERSION SUBJECT TO FINAL EDITING

			Additional evidence from CMIP5 and RCM simulations for an increase in the intensity and frequency of hot extremes and decrease in the intensity and frequency of cold extremes (Chou et al., 2014a)	Additional evidence from CMIP5 and RCM simulations for an increase in the intensity and frequency of hot extremes and decrease in the intensity and frequency of cold extremes (Chou et al., 2014a)	Additional evidence from CMIP5 and RCM simulations for an increase in the intensity and frequency of hot extremes and decrease in the intensity and frequency of cold extremes (Chou et al., 2014a)
	High confidence in the increase in the intensity and frequency of hot extremes and decrease in the intensity and frequency of cold extremes	*High confidence* in a human contribution to the observed increase in the intensity and frequency of hot extremes and decrease in the intensity and frequency of cold extremes	Increase in the intensity and frequency of hot extremes: *Very likely* (compared with the recent past (1995-2014)) *Extremely likely* (compared with pre-industrial) Decrease in the intensity and frequency of cold extremes: *Very likely* (compared with the recent past (1995-2014)) *Extremely likely* (compared with pre-industrial)	Increase in the intensity and frequency of hot extremes: *Extremely likely* (compared with the recent past (1995-2014)) *Virtually certain* (compared with pre-industrial) Decrease in the intensity and frequency of cold extremes: *Extremely likely* (compared with the recent past (1995-2014)) *Virtually certain* (compared with pre-industrial)	Increase in the intensity and frequency of hot extremes: *Virtually certain* (compared with the recent past (1995-2014)) *Virtually certain* (compared with pre-industrial) Decrease in the intensity and frequency of cold extremes: *Virtually certain* (compared with the recent past (1995-2014)) *Virtually certain* (compared with pre-industrial)
South Central America (SCA)	Increases in the intensity and frequency of hot extremes and decreases in the intensity and frequency of cold extremes (Dunn et al. 2020; Aguilar et al. 2005)	Evidence of a human contribution to the observed increase in the intensity and frequency of hot extremes and decrease in the intensity and frequency of cold extremes (Wang et al. 2017, Seong et al. 2020)	CMIP6 models project a robust increase in the intensity and frequency of TXx events and a robust decrease in the intensity and frequency of TNn events (Li et al., 2020; Annex). Median increase of more than 0.5°C in the 50-year TXx and TNn events compared to the 1°C warming level (Li et al., 2020) and more than 1.5°C in annual TXx and TNn compared to pre-industrial (Annex). Additional evidence from CMIP5 and RCM simulations for an increase in the intensity and frequency of hot extremes and decrease in the intensity and frequency of cold extremes (Imbach et al., 2018; Angeles-Malaspina et al., 2018; Chou et al., 2014)	CMIP6 models project a robust increase in the intensity and frequency of TXx events and a robust decrease in the intensity and frequency of TNn events (Li et al., 2020; Annex). Median increase of more than 0.5°C in the 50-year TXx and TNn events compared to the 1°C warming level (Li et al., 2020) and more than 2°C in annual TXx and TNn compared to pre-industrial (Annex). Additional evidence from CMIP5 and RCM simulations for an increase in the intensity and frequency of hot extremes and decrease in the intensity and frequency of cold extremes (Chou et al., 2014a)	CMIP6 models project a robust increase in the intensity and frequency of TXx events and a robust decrease in the intensity and frequency of TNn events (Li et al., 2020; Annex). Median increase of more than 2.5°C in the 50-year TXx and TNn events compared to the 1°C warming level (Li et al., 2020) and more than 3.5°C in annual TXx and TNn compared to pre-industrial (Annex). Additional evidence from CMIP5 and RCM simulations for an increase in the intensity and frequency of hot extremes and decrease in the intensity and frequency of cold extremes (Coppola et al., 2021b; Angeles-Malaspina et al., 2018; Chou et al., 2014)
	Medium confidence in the	*Medium confidence* in a	Increase in the intensity and	Increase in the intensity and	Increase in the intensity and

ACCEPTED PROOF SUBJECT TO FINAL EDITING

	increase in the intensity and frequency of hot extremes and decrease in the intensity and frequency of cold extremes	human contribution to the observed increase in the intensity and frequency of hot extremes and decrease in the intensity and frequency of cold extremes.	frequency of hot extremes: *Likely* (compared with the recent past (1995-2014)) *Very likely* (compared with pre-industrial) Decrease in the intensity and frequency of cold extremes: *Likely* (compared with the recent past (1995-2014)) *Very likely* (compared with pre-industrial).	frequency of hot extremes: *Very likely* (compared with the recent past (1995-2014)) *Extremely likely* (compared with pre-industrial) Decrease in the intensity and frequency of cold extremes: *Very likely* (compared with the recent past (1995-2014)) *Extremely likely* (compared with pre-industrial)	frequency of hot extremes: *Virtually certain* (compared with the recent past (1995-2014)) *Virtually certain* (compared with pre-industrial) Decrease in the intensity and frequency of cold extremes: *Virtually certain* (compared with the recent past (1995-2014)) *Virtually certain* (compared with pre-industrial)
Caribbean (CAR)	Significant increases in the intensity and frequency of hot extremes and significant decreases in the intensity and frequency of cold extremes (Angeles-Malaspina, González-Cruz & Ramírez-Beltran; 2018; McLean et al., 2015; Dunn et al., 2020)	Strong evidence of changes from observations that are in the direction of model projected changes for the future. The magnitude of projected changes increases with global warming.	CMIP6 models project a robust increase in the intensity and frequency of TXx events and a robust decrease in the intensity and frequency of TNn events (Annex). Median increase of more than 1.5°C in annual TXx and TNn compared to pre-industrial (Annex). Additional evidence from CMIP5 and RCM simulations for an increase in the intensity and frequency of hot extremes and decrease in the intensity and frequency of cold extremes (Angeles-Malaspina, González-Cruz & Ramírez-Beltran; 2018; Chou et al., 2014)	CMIP6 models project a robust increase in the intensity and frequency of TXx events and a robust decrease in the intensity and frequency of TNn events (Li et al., 2020; Annex). Median increase of more than XC in the 50-year TXx and TNn events compared to the 1°C warming level (Li et al., 2020) and more than 2°C in annual TXx and TNn compared to pre-industrial (Annex). Additional evidence from CMIP5 and RCM simulations for an increase in the intensity and frequency of hot extremes and decrease in the intensity and frequency of cold extremes (Chou et al., 2014a)	CMIP6 models project a robust increase in the intensity and frequency of TXx events and a robust decrease in the intensity and frequency of TNn events (Li et al., 2020; Annex). Median increase of more than XC in the 50-year TXx and TNn events compared to the 1°C warming level (Li et al., 2020) and more than 3.5°C in annual TXx and TNn compared to pre-industrial (Annex). Additional evidence from CMIP5 and RCM simulations for an increase in the intensity and frequency of hot extremes and decrease in the intensity and frequency of cold extremes (Coppola et al., 2021b; Angeles-Malaspina, González-Cruz & Ramírez-Beltran; 2018; Chou et al., 2014; Hall et al., 2013)
	Likely increase in the intensity and frequency of hot extremes and decrease in the intensity and frequency of cold extremes	*Medium confidence* in a human contribution to the observed increase in the intensity and frequency of hot extremes and decrease in the intensity and frequency of cold extremes.	Increase in the intensity and frequency of hot extremes: *Likely* (compared with the recent past (1995-2014)) *Very likely* (compared with pre-industrial) Decrease in the intensity and	Increase in the intensity and frequency of hot extremes: *Very likely* (compared with the recent past (1995-2014)) *Extremely likely* (compared with pre-industrial) Decrease in the intensity and	Increase in the intensity and frequency of hot extremes: *Virtually certain* (compared with the recent past (1995-2014)) *Virtually certain* (compared with pre-industrial)

ACCEPTED VERSION SUBJECT TO EDITING

			frequency of cold extremes: *Likely* (compared with the recent past (1995-2014)) *Very likely* (compared with pre-industrial).	frequency of cold extremes: *Very likely* (compared with the recent past (1995-2014)) *Extremely likely* (compared with pre-industrial)	Decrease in the intensity and frequency of cold extremes: *Virtually certain* (compared with the recent past (1995-2014)) *Virtually certain* (compared with pre-industrial)
Northwestern South America (NWS)	Significant increases in the intensity and frequency of hot extremes and significant decreases in the intensity and frequency of cold extremes (Dereczynski et al., 2020; Dunn et al., 2020)	Robust evidence of a human contribution to the observed increase in the intensity and frequency of hot extremes and decrease in the intensity and frequency of cold extremes (Seong et al., 2020)	CMIP6 models project a robust increase in the intensity and frequency of TXx events and a robust decrease in the intensity and frequency of TNn events (Li et al., 2020; Annex). Median increase of more than 0C in the 50-year TXx and TNn events compared to the 1°C warming level (Li et al., 2020) and more than 1.5°C in annual TXx and TNn compared to pre-industrial (Annex). Additional evidence from CMIP5 and RCM simulations for an increase in the intensity and frequency of hot extremes and decrease in the intensity and frequency of cold extremes (Chou et al., 2014a).	CMIP6 models project a robust increase in the intensity and frequency of TXx events and a robust decrease in the intensity and frequency of TNn events (Li et al., 2020; Annex). Median increase of more than 0.5°C in the 50-year TXx and TNn events compared to the 1°C warming level (Li et al., 2020) and more than 2°C in annual TXx and TNn compared to pre-industrial (Annex). Additional evidence from CMIP5 and RCM simulations for an increase in the intensity and frequency of hot extremes and decrease in the intensity and frequency of cold extremes (Chou et al., 2014a).	CMIP6 models project a robust increase in the intensity and frequency of TXx events and a robust decrease in the intensity and frequency of TNn events (Li et al., 2020; Annex). Median increase of more than 2°C in the 50-year TXx and TNn events compared to the 1°C warming level (Li et al., 2020) and more than 4.5°C in annual TXx and TNn compared to pre-industrial (Annex). Additional evidence from CMIP5/CMIP3 and RCM simulations for an increase in the intensity and frequency of hot extremes and decrease in the intensity and frequency of cold extremes (López-Franca et al., 2016; Coppola et al., 2021b; Chou et al., 2014)
	Likely increase in the intensity and frequency of hot extremes and decrease in the intensity and frequency of cold extremes	*High confidence* in a human contribution to the observed increase in the intensity and frequency of hot extremes and decrease in the intensity and frequency of cold extremes.	Increase in the intensity and frequency of hot extremes: *Likely* (compared with the recent past (1995-2014)) *Very likely* (compared with pre-industrial) Decrease in the intensity and frequency of cold extremes: *Likely* (compared with the recent past (1995-2014)) *Very likely* (compared with pre-industrial).	Increase in the intensity and frequency of hot extremes: *Very likely* (compared with the recent past (1995-2014)) *Extremely likely* (compared with pre-industrial) Decrease in the intensity and frequency of cold extremes: *Very likely* (compared with the recent past (1995-2014)) *Extremely likely* (compared with pre-industrial)	Increase in the intensity and frequency of hot extremes: *Virtually certain* (compared with the recent past (1995-2014)) *Virtually certain* (compared with pre-industrial) Decrease in the intensity and frequency of cold extremes: *Virtually certain* (compared with the recent past (1995-2014)) *Virtually certain* (compared with pre-industrial)
Northern South America (NSA)	Significant increases in the intensity and frequency of hot	Evidence of a human contribution to the observed	CMIP6 models project a robust increase in the intensity and	CMIP6 models project a robust increase in the intensity and	CMIP6 models project a robust increase in the intensity and

ACCEPTED VERSION SUBJECT TO FINAL EDITING

	extremes and significant decreases in the intensity and frequency of cold extremes (Dereczynski et al., 2020), Avila-Diaz et al.; 2020; Geirinhas et al., 2018; Dunn et al., 2020)	increase in the intensity and frequency of hot extremes and decrease in the intensity and frequency of cold extremes (Seong et al., 2020)	frequency of TXx events and a robust decrease in the intensity and frequency of TNn events (Li et al., 2020; Annex). Median increase of more than 0.5°C in the 50-year TXx and TNn events compared to the 1°C warming level (Li et al., 2020) and more than 1.5°C in annual TXx and TNn compared to pre-industrial (Annex). Additional evidence from CMIP5 and RCM simulations for an increase in the intensity and frequency of hot extremes and decrease in the intensity and frequency of cold extremes (Chou et al., 2014a).	frequency of TXx events and a robust decrease in the intensity and frequency of TNn events (Li et al., 2020; Annex). Median increase of more than 1°C in the 50-year TXx and TNn events compared to the 1°C warming level (Li et al., 2020) and more than 2°C in annual TXx and TNn compared to pre-industrial (Annex). Additional evidence from CMIP5 and RCM simulations for an increase in the intensity and frequency of hot extremes and decrease in the intensity and frequency of cold extremes (Chou et al., 2014a).	frequency of TXx events and a robust decrease in the intensity and frequency of TNn events (Li et al., 2020; Annex). Median increase of more than 3°C in the 50-year TXx and TNn events compared to the 1°C warming level (Li et al., 2020) and more than 4.5°C in annual TXx and TNn compared to pre-industrial (Annex). Additional evidence from CMIP5/CMIP3 and RCM simulations for an increase in the intensity and frequency of hot extremes and decrease in the intensity and frequency of cold extremes (López-Franca et al., 2016; Coppola et al., 2021b; Chou et al., 2014)
	Likely increase in the intensity and frequency of hot extremes and decrease in the intensity and frequency of cold extremes	*Medium confidence* in a human contribution to the observed increase in the intensity and frequency of hot extremes and decrease in the intensity and frequency of cold extremes.	Increase in the intensity and frequency of hot extremes: *Likely* (compared with the recent past (1995-2014)) *Very likely* (compared with pre-industrial) Decrease in the intensity and frequency of cold extremes: *Likely* (compared with the recent past (1995-2014)) *Very likely* (compared with pre-industrial).	Increase in the intensity and frequency of hot extremes: *Very likely* (compared with the recent past (1995-2014)) *Extremely likely* (compared with pre-industrial) Decrease in the intensity and frequency of cold extremes: *Very likely* (compared with the recent past (1995-2014)) *Extremely likely* (compared with pre-industrial)	Increase in the intensity and frequency of hot extremes: *Virtually certain* (compared with the recent past (1995-2014)) *Virtually certain* (compared with pre-industrial) Decrease in the intensity and frequency of cold extremes: *Virtually certain* (compared with the recent past (1995-2014)) *Virtually certain* (compared with pre-industrial)
South American Monsoon (SAM)	Significant increases in the intensity and frequency of hot extremes and significant decreases in the intensity and frequency of cold extremes (Dereczynski et al., 2020; Avila-Diaz et al., 2020; Geirinhas et al., 2018; Dunn et al., 2020)	Evidence of a human contribution to the observed increase in the intensity and frequency of hot extremes and decrease in the intensity and frequency of cold extremes (Seong et al., 2020)	CMIP6 models project a robust increase in the intensity and frequency of TXx events and a robust decrease in the intensity and frequency of TNn events (Li et al., 2020; Annex). Median increase of more than 0.5°C in the 50-year TXx and TNn events compared to the 1°C warming level (Li et al., 2020) and more than 1.5°C in annual TXx and	CMIP6 models project a robust increase in the intensity and frequency of TXx events and a robust decrease in the intensity and frequency of TNn events (Li et al., 2020; Annex). Median increase of more than 1°C in the 50-year TXx and TNn events compared to the 1°C warming level (Li et al., 2020) and more than 2°C in	CMIP6 models project a robust increase in the intensity and frequency of TXx events and a robust decrease in the intensity and frequency of TNn events (Li et al., 2020; Annex). Median increase of more than 2.5°C in the 50-year TXx and TNn events compared to the 1°C warming level (Li et al., 2020) and more than 4.5°C in

ACCEPTED VERSION SUBJECT TO FINAL EDITING

			TNn compared to pre-industrial (Annex). Additional evidence from CMIP5 and RCM simulations for an increase in the intensity and frequency of hot extremes and decrease in the intensity and frequency of cold extremes (Chou et al., 2014a).	annual TXx and TNn compared to pre-industrial (Annex). Additional evidence from CMIP5 and RCM simulations for an increase in the intensity and frequency of hot extremes and decrease in the intensity and frequency of cold extremes (Chou et al., 2014a).	annual TXx and TNn compared to pre-industrial (Annex). Additional evidence from CMIP5/CMIP3 and RCM simulations for an increase in the intensity and frequency of hot extremes and decrease in the intensity and frequency of cold extremes (López-Franca et al., 2016; Coppola et al., 2021b; Chou et al., 2014)
	Likely increase in the intensity and frequency of hot extremes and decrease in the intensity and frequency of cold extremes	*Medium confidence* in a human contribution to the observed increase in the intensity and frequency of hot extremes and decrease in the intensity and frequency of cold extremes.	Increase in the intensity and frequency of hot extremes: *Likely* (compared with the recent past (1995-2014)) *Very likely* (compared with pre-industrial) Decrease in the intensity and frequency of cold extremes: *Likely* (compared with the recent past (1995-2014)) *Very likely* (compared with pre-industrial).	Increase in the intensity and frequency of hot extremes: *Very likely* (compared with the recent past (1995-2014)) *Extremely likely* (compared with pre-industrial) Decrease in the intensity and frequency of cold extremes: *Very likely* (compared with the recent past (1995-2014)) *Extremely likely* (compared with pre-industrial)	Increase in the intensity and frequency of hot extremes: *Virtually certain* (compared with the recent past (1995-2014)) *Virtually certain* (compared with pre-industrial) Decrease in the intensity and frequency of cold extremes: *Virtually certain* (compared with the recent past (1995-2014)) *Virtually certain* (compared with pre-industrial)
Northeastern South America (NES)	Significant increases in the intensity and frequency of hot extremes and significant decreases in the intensity and frequency of cold extremes (Dereczynski et al., 2020), Avila-Diaz et al.; 2020; Geirinhas et al., 2018; Dunn et al., 2020)	Evidence of a human contribution to the observed increase in the intensity and frequency of hot extremes and decrease in the intensity and frequency of cold extremes (Seong et al., 2020)	CMIP6 models project a robust increase in the intensity and frequency of TXx events and a robust decrease in the intensity and frequency of TNn events (Li et al., 2020; Annex). Median increase of more than 0.5°C in the 50-year TXx and TNn events compared to the 1°C warming level (Li et al., 2020) and more than 1.5°C in annual TXx and TNn compared to pre-industrial (Annex). Additional evidence from CMIP5 and RCM simulations for an increase in the intensity and frequency of hot extremes and decrease in the intensity and frequency of cold extremes	CMIP6 models project a robust increase in the intensity and frequency of TXx events and a robust decrease in the intensity and frequency of TNn events (Li et al., 2020; Annex). Median increase of more than 0.5°C in the 50-year TXx and TNn events compared to the 1°C warming level (Li et al., 2020) and more than 2°C in annual TXx and TNn compared to pre-industrial (Annex). Additional evidence from CMIP5 and RCM simulations for an increase in the intensity and frequency of hot extremes and decrease in the intensity and frequency of cold extremes	CMIP6 models project a robust increase in the intensity and frequency of TXx events and a robust decrease in the intensity and frequency of TNn events (Li et al., 2020; Annex). Median increase of more than 2.5°C in the 50-year TXx and TNn events compared to the 1°C warming level (Li et al., 2020) and more than 4°C in annual TXx and TNn compared to pre-industrial (Annex). Additional evidence from CMIP5/CMIP3 and RCM simulations for an increase in the intensity and frequency of hot extremes and decrease in the intensity and frequency of

ACCEPTED VERSION SUBJECT TO FINAL EDITING

			(Chou et al., 2014a).	(Chou et al., 2014a).	cold extremes (López-Franca et al., 2016; Coppola et al., 2021b; Chou et al., 2014)
	Likely increase in the intensity and frequency of hot extremes and decrease in the intensity and frequency of cold extremes	*Medium confidence* in a human contribution to the observed increase in the intensity and frequency of hot extremes and decrease in the intensity and frequency of cold extremes.	Increase in the intensity and frequency of hot extremes: *Likely* (compared with the recent past (1995-2014)) *Very likely* (compared with pre-industrial) Decrease in the intensity and frequency of cold extremes: *Likely* (compared with the recent past (1995-2014)) *Very likely* (compared with pre-industrial).	Increase in the intensity and frequency of hot extremes: *Very likely* (compared with the recent past (1995-2014)) *Extremely likely* (compared with pre-industrial) Decrease in the intensity and frequency of cold extremes: *Very likely* (compared with the recent past (1995-2014)) *Extremely likely* (compared with pre-industrial)	Increase in the intensity and frequency of hot extremes: *Virtually certain* (compared with the recent past (1995-2014)) *Virtually certain* (compared with pre-industrial) Decrease in the intensity and frequency of cold extremes: *Virtually certain* (compared with the recent past (1995-2014)) *Virtually certain* (compared with pre-industrial)
Southwestern South America (SWS)	Significant increases in the intensity and frequency of hot extremes and significant decreases in the intensity and frequency of cold extremes (Dereczynski et al., 2020; Olmo et al., 2020; Dunn et al., 2020)	Evidence of a human contribution to the observed increase in the intensity and frequency of hot extremes and decrease in the intensity and frequency of cold extremes (Seong et al., 2020)	CMIP6 models project a robust increase in the intensity and frequency of TXx events and a robust decrease in the intensity and frequency of TNn events (Li et al., 2020; Annex). Median increase of more than 0.5°C in the 50-year TXx and TNn events compared to the 1°C warming level (Li et al., 2020) and more than 1.5°C in annual TXx and TNn compared to pre-industrial (Annex). Additional evidence from CMIP5 and RCM simulations for an increase in the intensity and frequency of hot extremes and decrease in the intensity and frequency of cold extremes (Chou et al., 2014a).	CMIP6 models project a robust increase in the intensity and frequency of TXx events and a robust decrease in the intensity and frequency of TNn events (Li et al., 2020; Annex). Median increase of more than 1°C in the 50-year TXx and TNn events compared to the 1°C warming level (Li et al., 2020) and more than 2.5°C in annual TXx and TNn compared to pre-industrial (Annex). Additional evidence from CMIP5 and RCM simulations for an increase in the intensity and frequency of hot extremes and decrease in the intensity and frequency of cold extremes (Chou et al., 2014a).	CMIP6 models project a robust increase in the intensity and frequency of TXx events and a robust decrease in the intensity and frequency of TNn events (Li et al., 2020; Annex). Median increase of more than 3°C in the 50-year TXx and TNn events compared to the 1°C warming level (Li et al., 2020) and more than 4.5°C in annual TXx and TNn compared to pre-industrial (Annex). Additional evidence from CMIP5/CMIP3 and RCM simulations for an increase in the intensity and frequency of hot extremes and decrease in the intensity and frequency of cold extremes (López-Franca et al., 2016; Coppola et al., 2021b; Chou et al., 2014)
	Likely increase in the intensity and frequency of hot extremes and decrease in the intensity and frequency of cold extremes	*Medium confidence* in a human contribution to the observed increase in the intensity and frequency of hot extremes and decrease in the intensity and frequency of	Increase in the intensity and frequency of hot extremes: *Likely* (compared with the recent past (1995-2014)) *Very likely* (compared with pre-industrial)	Increase in the intensity and frequency of hot extremes: *Very likely* (compared with the recent past (1995-2014)) *Extremely likely* (compared with pre-industrial)	Increase in the intensity and frequency of hot extremes: *Virtually certain* (compared with the recent past (1995-2014)) *Virtually certain* (compared

ACCEPTED UNDER SUBJECT TO FINAL EDITING

		cold extremes.	Decrease in the intensity and frequency of cold extremes: *Likely* (compared with the recent past (1995-2014)) *Very likely* (compared with pre-industrial).	Decrease in the intensity and frequency of cold extremes: *Very likely* (compared with the recent past (1995-2014)) *Extremely likely* (compared with pre-industrial)	with pre-industrial) Decrease in the intensity and frequency of cold extremes: *Virtually certain* (compared with the recent past (1995-2014)) *Virtually certain* (compared with pre-industrial)
Southeastern South America (SES)	Significant increases in the intensity and frequency of hot extremes and significant decreases in the intensity and frequency of cold extremes (Dereczynski et al., 2020; Avila-Diaz et al., 2020; Geirinhas et al., 2018; Rusticucci et al., 2017; Dunn et al., 2020)	Robust evidence of a human contribution to the observed increase in the intensity and frequency of hot extremes and decrease in the intensity and frequency of cold extremes (Seong et al., 2020; Wang et al., 2017)	CMIP6 models project a robust increase in the intensity and frequency of TXx events and a robust decrease in the intensity and frequency of TNn events (Li et al., 2020; Annex). Median increase of more than 0.5°C in the 50-year TXx and TNn events compared to the 1°C warming level (Li et al., 2020) and more than 1°C in annual TXx and TNn compared to pre-industrial (Annex). Additional evidence from CMIP5 and RCM simulations for an increase in the intensity and frequency of hot extremes and decrease in the intensity and frequency of cold extremes (Chou et al., 2014a).	CMIP6 models project a robust increase in the intensity and frequency of TXx events and a robust decrease in the intensity and frequency of TNn events (Li et al., 2020; Annex). Median increase of more than 1°C in the 50-year TXx and TNn events compared to the 1°C warming level (Li et al., 2020) and more than 1.5°C in annual TXx and TNn compared to pre-industrial (Annex). Additional evidence from CMIP5 and RCM simulations for an increase in the intensity and frequency of hot extremes and decrease in the intensity and frequency of cold extremes (Chou et al., 2014a).	CMIP6 models project a robust increase in the intensity and frequency of TXx events and a robust decrease in the intensity and frequency of TNn events (Li et al., 2020; Annex). Median increase of more than 3.5°C in the 50-year TXx and TNn events compared to the 1°C warming level (Li et al., 2020) and more than 3.5°C in annual TXx and TNn compared to pre-industrial (Annex). Additional evidence from CMIP5/CMIP3 and RCM simulations for an increase in the intensity and frequency of hot extremes and decrease in the intensity and frequency of cold extremes (López-Franca et al., 2016; Coppola et al., 2021b; Chou et al., 2014).
	High confidence in the increase in the intensity and frequency of hot extremes and decrease in the intensity and frequency of cold extremes	*High confidence* in a human contribution to the observed increase in the intensity and frequency of hot extremes and decrease in the intensity and frequency of cold extremes.	Increase in the intensity and frequency of hot extremes: *Likely* (compared with the recent past (1995-2014)) *Very likely* (compared with pre-industrial) Decrease in the intensity and frequency of cold extremes: *Likely* (compared with the recent past (1995-2014)) *Very likely* (compared with pre-industrial).	Increase in the intensity and frequency of hot extremes: *Very likely* (compared with the recent past (1995-2014)) *Extremely likely* (compared with pre-industrial) Decrease in the intensity and frequency of cold extremes: *Very likely* (compared with the recent past (1995-2014)) *Extremely likely* (compared with pre-industrial)	Increase in the intensity and frequency of hot extremes: *Virtually certain* (compared with the recent past (1995-2014)) *Virtually certain* (compared with pre-industrial) Decrease in the intensity and frequency of cold extremes: *Virtually certain* (compared with the recent past (1995-2014)) *Virtually certain* (compared with pre-industrial)

ACCEPTED VERSION SUBJECT TO FINAL EDITING

Southern South America (SSA)	Inconsistent trends and insufficient data (Dereczynski et al., 2020; Ceccherini et al., 2016; (1980-2014) Dunn et al., 2020)		CMIP6 models project a robust increase in the intensity and frequency of TXx events and a robust decrease in the intensity and frequency of TNn events (Li et al., 2020; Annex). Median increase of more than 0.5°C in the 50-year TXx and TNn events compared to the 1°C warming level (Li et al., 2020) and more than 1.5°C in annual TXx and TNn compared to pre-industrial (Annex). Additional evidence from CMIP5 and RCM simulations for an increase in the intensity and frequency of hot extremes and decrease in the intensity and frequency of cold extremes (Chou et al., 2014a).	CMIP6 models project a robust increase in the intensity and frequency of TXx events and a robust decrease in the intensity and frequency of TNn events (Li et al., 2020; Annex). Median increase of more than 1°C in the 50-year TXx and TNn events compared to the 1°C warming level (Li et al., 2020) and more than 2°C in annual TXx and TNn compared to pre-industrial (Annex). Additional evidence from CMIP5 and RCM simulations for an increase in the intensity and frequency of hot extremes and decrease in the intensity and frequency of cold extremes (Chou et al., 2014a).	CMIP6 models project a robust increase in the intensity and frequency of TXx events and a robust decrease in the intensity and frequency of TNn events (Li et al., 2020; Annex). Median increase of more than 2.5°C in the 50-year TXx and TNn events compared to the 1°C warming level (Li et al., 2020) and more than 4.5°C in annual TXx and TNn compared to pre-industrial (Annex). Additional evidence from CMIP5/CMIP3 and RCM simulations for an increase in the intensity and frequency of hot extremes and decrease in the intensity and frequency of cold extremes (López-Franca et al., 2016; Coppola et al., 2021b; Chou et al., 2014).
	Low confidence	*Low confidence*	Increase in the intensity and frequency of hot extremes: *Likely* (compared with the recent past (1995-2014)) *Very likely* (compared with pre-industrial) Decrease in the intensity and frequency of cold extremes: *Likely* (compared with the recent past (1995-2014)) *Very likely* (compared with pre-industrial).	Increase in the intensity and frequency of hot extremes: *Very likely* (compared with the recent past (1995-2014)) *Extremely likely* (compared with pre-industrial) Decrease in the intensity and frequency of cold extremes: *Very likely* (compared with the recent past (1995-2014)) *Extremely likely* (compared with pre-industrial)	Increase in the intensity and frequency of hot extremes: *Virtually certain* (compared with the recent past (1995-2014)) *Virtually certain* (compared with pre-industrial) Decrease in the intensity and frequency of cold extremes: *Virtually certain* (compared with the recent past (1995-2014)) *Virtually certain* (compared with pre-industrial)

[END TABLE 11.13 HERE]

[START TABLE 11.14 HERE]

ACCEPTED VERSION SUBJECT TO FINAL EDITING

Table 11.14: Observed trends, human contribution to observed trends, and projected changes at 1.5°C, 2°C and 4°C of global warming for heavy precipitation in Central and South America, subdivided by AR6 regions. See Sections 11.9.1 and 11.9.3 for details.

Region	Observed trends	Detection and attribution; event attribution	Projections		
			1.5 °C	2 °C	4 °C
All Central and South America	Insufficient data to assess trends	Limited evidence	CMIP6 models project an increase in the intensity and frequency of heavy precipitation (Li et al., 2020a). Median increase of more than 0% in the 50-year Rx1day and Rx5day events compared to the 1°C warming level (Li et al., 2020a) Additional evidence from CMIP5 and RCM simulations for an increase in the intensity of heavy precipitation (Chou et al., 2014a)	CMIP6 models project an increase in the intensity and frequency of heavy precipitation (Li et al., 2020a). Median increase of more than 4% in the 50-year Rx1day and Rx5day events compared to the 1°C warming level (Li et al., 2020a) Additional evidence from CMIP5 and RCM simulations for an increase in the intensity of heavy precipitation (Chou et al., 2014a)	CMIP6 models project a robust increase in the intensity and frequency of heavy precipitation (Li et al., 2020a). Median increase of more than 10% in the 50-year Rx1day and Rx5day events compared to the 1°C warming level (Li et al., 2020a) Additional evidence from CMIP5 and RCM simulations for an increase in the intensity of heavy precipitation (Chou et al., 2014a)
	Low confidence	*Low confidence*	Intensification of heavy precipitation: *Medium confidence* (compared with the recent past (1995-2014)) *High confidence* (compared with pre-industrial)	Intensification of heavy precipitation: *High confidence* (compared with the recent past (1995-2014)) *Likely* (compared with pre-industrial)	Intensification of heavy precipitation: *Very likely* (compared with the recent past (1995-2014)) *Extremely likely* (compared with pre-industrial)
South Central America (SCA)	Insufficient data coverage and trends in available data are generally not significant (Sun et al., 2020; Dunn et al., 2020; Stephenson et al., 2014)	Limited evidence	CMIP6 models, CMIP5 models, and RCMs project inconsistent changes in the region (Li et al., 2020; Imbach et al., 2018; Chou et al., 2014).	CMIP6 models, CMIP5 models, and RCMs project inconsistent changes in the region (Li et al., 2020; Chou et al., 2014).	CMIP6 models, CMIP5 models, and RCMs project inconsistent changes in the region (Li et al., 2020; Chou et al., 2014; Coppola et al., 2021b; Kusunoki et al., 2019; Nakaegawa et al., 2013)
	Low confidence	*Low confidence*	Intensification of heavy precipitation: *Low confidence* (compared with the recent past (1995-2014)) *Low confidence* (compared with pre-industrial)	Intensification of heavy precipitation: *Low confidence* (compared with the recent past (1995-2014)) *Low confidence* (compared with pre-industrial)	Intensification of heavy precipitation: *Low confidence* (compared with the recent past (1995-2014)) *Medium confidence* (compared with pre-industrial)
Caribbean (CAR)	Insufficient data and a lack of agreement on the evidence of trends (Sun et al., 2020; Dunn et al., 2020; McLean et al., 2015; Stephenson et al., 2014)	Evidence of a human contribution for some events (Patricola and Wehner, 2018), but cannot be generalized	CMIP6 models, CMIP5 models, and RCMs project inconsistent changes in the region (Li et al., 2020; Chou et al., 2014)	CMIP6 models, CMIP5 models, and RCMs project inconsistent changes in the region (Li et al., 2020; Chou et al., 2014)	CMIP6 models, CMIP5 models, and RCMs project inconsistent changes in the region (Li et al., 2020; Coppola et al., 2021b; Chou et al., 2014; Nakaegawa et al.,

ACCEPTED VERSION SUBJECT TO FINAL EDITING

					2013; Hall et al., 2013)
	Low confidence	*Low confidence.*	*Low confidence*	*Low confidence*	*Low confidence*
Northwestern South America (NWS)	Insufficient data coverage and trends in available data are generally not significant (Sun et al., 2020; Dunn et al., 2020; Dereczynski et al., 2020)	Disagreement among studies (Li et al., 2019; Otto et al., 2018a)	CMIP6 models, CMIP5 models, and RCMs project inconsistent changes in the region (Li et al., 2020; Chou et al., 2014)	CMIP6 models, CMIP5 models, and RCMs project inconsistent changes in the region (Li et al., 2020; Chou et al., 2014)	CMIP6 models, CMIP5 models, and RCMs project inconsistent changes in the region (Li et al., 2020; Chou et al., 2014)
	Low confidence	*Low confidence*	*Low confidence*	*Low confidence*	*Low confidence*
Northern South America (NSA)	Insufficient data coverage and trends in available data are generally not significant (Sun et al., 2020; Dunn et al., 2020; Dereczynski et al., 2020; Avila-Diaz et al., 2020)	Evidence of a human contribution for some events (Li et al., 2019d), but cannot be generalized	Conflicting projections by the CMIP6 multi-model ensemble and limited RCM simulations; more weight is given to the CMIP6 results.	CMIP6 models project an increase in the intensity and frequency of heavy precipitation (Li et al., 2020; Annex). Median increase of more than 4% in the 50-year Rx1day and Rx5day events compared to the 1°C warming level (Li et al., 2020a) and more than 4% in annual Rx1day and Rx5day and 0% in annual Rx30day compared to pre-industrial (Annex). Conflicting projections by the CMIP6 multi-model ensemble and limited RCM simulations; more weight is given to the CMIP6 results.	CMIP6 models project an increase in the intensity and frequency of heavy precipitation (Li et al., 2020; Annex). Median increase of more than 15% in the 50-year Rx1day and Rx5day events compared to the 1°C warming level (Li et al., 2020a) and more than 10% in annual Rx1day and Rx5day and 0% in annual Rx30day compared to pre-industrial (Annex). Conflicting projections by the CMIP6 multi-model ensemble and limited RCM simulations; more weight is given to the CMIP6 results.
	Low confidence	*Low confidence*	Intensification of heavy precipitation: *Low confidence* (compared with the recent past (1995-2014)) *Medium confidence* (compared with pre-industrial)	Intensification of heavy precipitation: *Medium confidence* (compared with the recent past (1995-2014)) *Medium confidence* (compared with pre-industrial)	Intensification of heavy precipitation: *Medium confidence* (compared with the recent past (1995-2014)) *Medium confidence* (compared with pre-industrial)
South American Monsoon (SAM)	Insufficient data coverage and trends in available data are generally not significant (Sun et al., 2020; Dunn et al., 2020; Dereczynski et al., 2020; Avila-Diaz et al., 2020)	Evidence of a human contribution for some events (Li et al., 2019d), but cannot be generalized	CMIP6 models, CMIP5 models, and RCMs project inconsistent changes in the region (Li et al., 2020; Chou et al., 2014)	CMIP6 models project an increase in the intensity and frequency of heavy precipitation (Li et al., 2020; Annex). Median increase of more than 2% in the 50-year Rx1day and Rx5day events compared to the 1°C warming level (Li et al., 2020a) and more than 6% in annual Rx1day and Rx5day and 2% in annual Rx30day compared	CMIP6 models project an increase in the intensity and frequency of heavy precipitation (Li et al., 2020; Annex). Median increase of more than 10% in the 50-year Rx1day and Rx5day events compared to the 1°C warming level (Li et al., 2020a) and more than 10% in annual Rx1day and Rx5day and 4% in annual Rx30day compared

ACCEPTED VERSION SUBJECT TO FINAL EDITING

				to pre-industrial (Annex). Conflicting projections by the CMIP6 multi-model ensemble and limited RCM simulations; more weight is given to the CMIP6 results.	to pre-industrial (Annex). Conflicting projections by the CMIP6 multi-model ensemble and limited RCM simulations; more weight is given to the CMIP6 results.
	Low confidence	*Low confidence*	Intensification of heavy precipitation: *Low confidence* (compared with the recent past (1995-2014)) *Medium confidence* (compared with pre-industrial)	Intensification of heavy precipitation: *Medium confidence* (compared with the recent past (1995-2014)) *Medium confidence* (compared with pre-industrial)	Intensification of heavy precipitation: *Medium confidence* (compared with the recent past (1995-2014)) *Medium confidence* (compared with pre-industrial)
Northeastern South America (NES)	Insufficient data coverage and trends in available data are generally not significant (Sun et al., 2020; Dunn et al., 2020; Dereczynski et al., 2020; Avila-Diaz et al., 2020)	Evidence of a human contribution for some events (Li et al., 2019d), but cannot be generalized	CMIP6 models, CMIP5 models, and RCMs project inconsistent changes in the region (Li et al., 2020; Chou et al., 2014)	CMIP6 models project an increase in the intensity and frequency of heavy precipitation (Li et al., 2020; Annex). Median increase of more than 4% in the 50-year Rx1day and Rx5day events compared to the 1°C warming level (Li et al., 2020a) and more than 8% in annual Rx1day and Rx5day and 4% in annual Rx30day compared to pre-industrial (Annex). Conflicting projections by the CMIP6 multi-model ensemble and limited RCM simulations; more weight is given to the CMIP6 results.	CMIP6 models project an increase in the intensity and frequency of heavy precipitation (Li et al., 2020; Annex). Median increase of more than 15% in the 50-year Rx1day and Rx5day events compared to the 1°C warming level (Li et al., 2020a) and more than 20% in annual Rx1day and Rx5day and 10% in annual Rx30day compared to pre-industrial (Annex). Conflicting projections by the CMIP6 multi-model ensemble and limited RCM simulations; more weight is given to the CMIP6 results.
	Low confidence	*Low confidence*	Intensification of heavy precipitation: *Low confidence* (compared with the recent past (1995-2014)) *Medium confidence* (compared with pre-industrial)	Intensification of heavy precipitation: *Medium confidence* (compared with the recent past (1995-2014)) *Medium confidence* (compared with pre-industrial)	Intensification of heavy precipitation: *Medium confidence* (compared with the recent past (1995-2014)) *Medium confidence* (compared with pre-industrial)
Southwestern South America (SWS)	Insufficient data coverage and trends in available data are generally not significant (Sun et al., 2020; Dunn et al., 2020; Dereczynski et al., 2020; Olmo et al., 2020)	Evidence of a human contribution for some events (Li et al., 2019d), but cannot be generalized	CMIP6 models, CMIP5 models, and RCMs project inconsistent changes in the region (Li et al., 2020; Chou et al., 2014)	CMIP6 models, CMIP5 models, and RCMs project inconsistent changes in the region (Li et al., 2020; Chou et al., 2014)	CMIP6 models, CMIP5 models, and RCMs project inconsistent changes in the region (Li et al., 2020; Chou et al., 2014)

ACCEPTED VERSION SUBJECT TO FINAL EDITING

	Low confidence	*Low confidence*	*Low confidence*	*Low confidence*	*Low confidence*
Southeastern South America (SES)	Significant intensification of heavy precipitation Dunn et al., 2020; Dereczynski et al., 2020; Olmo et al., 2020; Avila-Diaz et al. (2020)	Evidence of a human contribution for some events (Li et al., 2019d), but cannot be generalized	CMIP6 models, CMIP5 models, and RCMs project inconsistent changes in the region (Li et al., 2020; Chou et al., 2014)	CMIP6 models project an increase in the intensity and frequency of heavy precipitation (Li et al., 2020; Annex). Median increase of more than 4% in the 50-year Rx1day and Rx5day events compared to the 1°C warming level (Li et al., 2020a) and more than 8% in annual Rx1day and Rx5day and 6% in annual Rx30day compared to pre-industrial (Annex). Additional evidence from CMIP5 and RCM simulations for an increase in the intensity of heavy precipitation (Chou et al., 2014a)	CMIP6 models project a robust increase in the intensity and frequency of heavy precipitation (Li et al., 2020; Annex). Median increase of more than 8% in the 50-year Rx1day and Rx5day events compared to the 1°C warming level (Li et al., 2020a) and more than 20% in annual Rx1day and Rx5day and 15% in annual Rx30day compared to pre-industrial (Annex). Additional evidence from CMIP5 and RCM simulations for an increase in the intensity of heavy precipitation (Chou et al., 2014a)
	High confidence inintensification of heavy precipitation	*Low confidence*	Intensification of heavy precipitation: *Low confidence* (compared with the recent past (1995-2014)) *Medium confidence* (compared with pre-industrial)	Intensification of heavy precipitation: *Medium confidence* (compared with the recent past (1995-2014)) *High confidence* (compared with pre-industrial)	Intensification of heavy precipitation: *Likely* (compared with the recent past (1995-2014)) *Likely* (compared with pre-industrial)
Southern South America (SSA)	Insufficient data coverage and trends are generally not significant (Sun et al., 2020; Dunn et al., 2020; Dereczynski et al., 2020)	Evidence of a human contribution for some events (Li et al., 2019d), but cannot be generalized	CMIP6 models, CMIP5 models, and RCMs project inconsistent changes in the region (Li et al., 2020; Chou et al., 2014)	CMIP6 models project an increase in the intensity and frequency of heavy precipitation (Li et al., 2020; Annex). Median increase of more than 4% in the 50-year Rx1day and Rx5day events compared to the 1°C warming level (Li et al., 2020a) and more than 2% in annual Rx1day and Rx5day and 0% in annual Rx30day compared to pre-industrial (Annex). Additional evidence from CMIP5 and RCM simulations for an increase in the intensity of heavy precipitation (Chou et al., 2014a)	CMIP6 models project a robust increase in the intensity and frequency of heavy precipitation (Li et al., 2020; Annex). Median increase of more than 15% in the 50-year Rx1day and Rx5day events compared to the 1°C warming level (Li et al., 2020a) and more than 8% in annual Rx1day and Rx5day and 2% in annual Rx30day compared to pre-industrial (Annex). Additional evidence from CMIP5 and RCM simulations for an increase in the intensity of heavy precipitation (Chou et al., 2014a)

ACCEPTED VERSION SUBJECT TO FINAL EDITING

	Low confidence	*Low confidence*	Intensification of heavy precipitation: *Low confidence* (compared with the recent past (1995-2014)) *Medium confidence* (compared with pre-industrial)	Intensification of heavy precipitation: *Medium confidence* (compared with the recent past (1995-2014)) *High confidence* (compared with pre-industrial)	Intensification of heavy precipitation: *Likely* (compared with the recent past (1995-2014)) *Very likely* (compared with pre-industrial)

[END TABLE 11.14 HERE]

[START TABLE 11.15 HERE]

Table 11.15: Observed trends, human contribution to observed trends, and projected changes at 1.5°C, 2°C and 4°C of global warming for meteorological droughts (MET), agricultural and ecological droughts (AGR/ECOL), and hydrological droughts (HYDR) in Central and South America, subdivided by AR6 regions. See Sections 11.9.1 and 11.9.4 for details.

Region		Observed trends	Human contribution	Projections		
				+1.5 °C	+2 °C	+4 °C
South Central America (SCA)	MET	***Low confidence:* Mixed signal**. Dominant decrease in drought duration but mixed trends between subregions (Aguilar et al., 2005; Spinoni et al., 2019; Dunn et al., 2020).	***Low confidence:* Limited evidence**.	***Low confidence:* Limited evidence**. Available evidence suggests increase in drought severity (Chapter 11 Supplementary Material (11.SM) (Chou et al., 2014a; Imbach et al., 2018) (Chou et al., 2014a): RCM simulations with Eta model driven with 2 different GCMs.	***Medium confidence:* Increase** in drought severity (Chou et al., 2014a; Imbach et al., 2018; Xu et al., 2019a; Spinoni et al., 2020)(Chapter 11 Supplementary Material (11.SM) (Chou et al., 2014a): RCM simulations with Eta model driven with 2 different GCMs.	***High confidence:* Increase** in drought severity (Nakaegawa et al., 2013; Chou et al., 2014a; Touma et al., 2015; Corrales-Suastegui et al., 2019; Kusunoki et al., 2019; Spinoni et al., 2020; Coppola et al., 2021b) (Chapter 11 Supplementary Material (11.SM) . (Chou et al., 2014a): RCM simulations with Eta model driven with 2 different GCMs.
	AGR ECOL	***Low confidence:* Mixed signal.** Mixed trends in different subregions and in different drought metrics, including soil moisture, PDSI-PM and SPEI-PM (Greve et al., 2014; Dai and Zhao, 2017; Spinoni et al., 2019; Padrón et al., 2020).	***Low confidence*: Limited evidence**.	***Low confidence:* Mixed signal** in drought trends. Inconsistent drying trend (but stronger tendency towards drying) based on total column soil moisture (Imbach et al., 2018; Xu et al., 2019a)**(Chapter 11 Supplementary Material (11.SM)** and SPEI-PM (Naumann et al., 2018; Gu et al., 2020).	***Medium confidence:* Increase** in drought based on total and surface soil moisture (Xu et al., 2019a; Cook et al., 2020)(Chapter 11 Supplementary Material (11.SM) and on SPEI-PM (Naumann et al., 2018; Xu et al., 2019a; Gu et al., 2020).	***High confidence:* Increase** in drought severity with different metrics and high agreement between studies (Chapter 11 Supplementary Material (11.SM) (Cook et al., 2014b, 2020; Dai et al., 2018; Lu et al., 2019; Vicente-Serrano et al., 2020a).
	HYDR	***Low confidence*: Insufficient evidence** (Dai and Zhao, 2017; Gudmundsson et al., 2021).	***Low confidence:* Limited evidence**.	***Low confidence:* Limited evidence.** One study shows inconsistent changes (Touma et al.,	***Low confidence:* Limited evidence.** Inconsistent changes (Touma et al., 2015) or drying in	***Medium confidence:* Increase** in drought severity (Prudhomme et al., 2014; Giuntoli et al., 2015; Touma et

ACCEPTED VERSION SUBJECT TO FINAL EDITING

				2015)	part of region (Cook et al., 2020)	al., 2015; Cook et al., 2020)
Caribbean (CAR)	MET	***Low confidence:*** **Mixed signal**. Mixed trends between subregions, but some evidence of increases in drought duration (Stephenson et al., 2014; McLean et al., 2015; Spinoni et al., 2019; Dunn et al., 2020).	***Low confidence:*** **Limited evidence**	***Low confidence:*** **Increase** in drought duration (Chou et al., 2014a)**;** inconsistent changes in CDD (Chapter 11 Supplementary Material (11.SM)	***Low confidence:*** **Limited evidence and inconsistent changes**. One study suggests increase in drought duration (Chou et al., 2014a), but CMIP6 projections show inconsistent changes in CDD (Chapter 11 Supplementary Material (11.SM)	***Medium confidence***: **Increase** in drought duration (Chapter 11 Supplementary Material (11.SM) (Nakaegawa et al., 2013; Chou et al., 2014a; Stennett-Brown et al., 2017; Coppola et al., 2021b)
	AGR ECOL	***Low confidence:*** **Mixed signal.** Mixed trends between subregions with PDSI-PM and SPEI-PM (Dai and Zhao, 2017; Spinoni et al., 2019).	***Low confidence:*** **Limited evidence**	***Low confidence:*** **Inconsistent trends** in total column and surface soil moisture (Chapter 11 Supplementary Material (11.SM) , and SPEI-PM (Naumann et al., 2018; Gu et al., 2020).	***Medium confidence:*** **Increase**, but including mixed signal in changes of drought severity, with inconsistent trends in total soil moisture, (Chapter 11 Supplementary Material (11.SM) , and drying trend based on SPEI-PM (Naumann et al., 2018; Gu et al., 2020). See also Chapter 12.	***Medium confidence:*** **Increase**. Drying trend with surface soil moisture (Dai et al., 2018; Lu et al., 2019), PDSI (Dai et al., 2018) and SPEI-PM (Cook et al., 2014b; Vicente-Serrano et al., 2020a). Total soil moisture shows weak (Chapter 11 Supplementary Material (11.SM) or no signal (Cook et al., 2020)
	HYDR	***Low confidence:*** **Limited evidence**.	***Low confidence:*** **Limited evidence**	***Low confidence:*** **Limited evidence.**	***Low confidence:*** **Limited evidence.**	***Low confidence:*** **Mixed signal** among studies (Prudhomme et al., 2014; Giuntoli et al., 2015; Touma et al., 2015; Cook et al., 2020)
North-western South America (NWS)	MET	***Low confidence:*** **Mixed signal.** Mixed trends between subregions (Skansi et al., 2013; Spinoni et al., 2019; Dereczynski et al., 2020; Dunn et al., 2020).	***Low confidence:*** **Limited evidence**	***Low confidence:*** **Inconsistent trends** (Chapter 11 Supplementary Material (11.SM) (Chou et al., 2014a; Touma et al., 2015; Xu et al., 2019a)	***Low confidence:*** **Mixed signal** between different studies and models (Chou et al., 2014a; Touma et al., 2015; Xu et al., 2019a; Spinoni et al., 2020) (Chapter 11 Supplementary Material (11.SM)	***Medium confidence***: **Increase.** Dominant signal is positive CDD trend (increasing dryness; Chapter 11 Supplementary Material (11.SM)); also some mixed signals between different studies (Chou et al., 2014a; Duffy et al., 2015; Touma et al., 2015; Spinoni et al., 2020; Coppola et al., 2021b)
	AGR ECOL	***Low confidence:*** **Mixed trends** between subregions and drought metrics, including soil moisture, PDSI-PM and SPEI-PM (Greve et al., 2014; Dai and Zhao, 2017; Spinoni et al., 2019; Padrón et al., 2020)	***Low confidence:*** **Limited evidence**	***Low confidence:*** **Mixed trends** based on different metrics, including decrease in total column soil moisture, (Chapter 11 Supplementary Material (11.SM) , weak drying with surface soil moisture (Xu et al., 2019a) and wetting based on the SPEI-PM (Naumann et al., 2018; Gu et al., 2020).	***Low confidence:*** **Mixed signal** in changes in drought severity with drying in total column soil moisture, (Chapter 11 Supplementary Material (11.SM) , lack of signal in the surface soil moisture (Xu et al., 2019a) and wetting trends with SPEI-PM (Naumann et al., 2018; Gu et al., 2020).	***Low confidence:*** **Mixed trend** between different drought metrics (Cook et al., 2014b, 2020; Dai et al., 2018; Lu et al., 2019; Vicente-Serrano et al., 2020a) (Chapter 11 Supplementary Material (11.SM).
	HYDR	***Low confidence:*** **Limited evidence.**	***Low confidence:*** **Limited evidence.**	***Low confidence:*** **Limited evidence.** One study shows inconsistent changes (Touma et al., 2015)	***Low confidence:*** **Limited evidence.** Inconsistent changes (Touma et al., 2015; Cook et al., 2020)	***Low confidence:*** **Lack of signal** (Prudhomme et al., 2014; Giuntoli et al., 2015; Touma et al., 2015; Cook et al., 2020)

ACCEPTED VERSION SUBJECT TO FINAL EDITING

Northern South America (NSA)	MET	***Low confidence:*** **Mixed trends** between subregions, but some evidence of increased drought duration (Skansi et al., 2013; Marengo and Espinoza, 2016; Spinoni et al., 2019; Avila-Diaz et al., 2020; Dereczynski et al., 2020; Dunn et al., 2020)	***Low confidence:*** **Limited evidence**	***Medium confidence:*** Available evidence suggests drying (Chapter 11 Supplementary Material (11.SM) (Chou et al., 2014a; Touma et al., 2015; Xu et al., 2019a)**.**	***Medium confidence:*** **Increase** in drought severity (Chou et al., 2014a; Touma et al., 2015; Xu et al., 2019a; Spinoni et al., 2020) (Chapter 11 Supplementary Material (11.SM).	***High confidence:*** **Increase** in drought severity (Chou et al., 2014a; Duffy et al., 2015; Touma et al., 2015; Marengo and Espinoza, 2016; Spinoni et al., 2020; Coppola et al., 2021b) (Chapter 11 Supplementary Material (11.SM).
	AGR ECOL	***Low confidence:*** **Mixed trends** between subregions and different drought metrics, including soil moisture, PDSI-PM and SPEI-PM, but some evidence of decrease in drought severity (Greve et al., 2014; Dai and Zhao, 2017; Spinoni et al., 2019; Padrón et al., 2020)	***Low confidence:*** **Limited evidence**	***Medium confidence:*** **Increase** in drying. Tendency towards increase in drought severity in total and surface soil moisture (Chapter 11 Supplementary Material (11.SM) (Xu et al., 2019a) inconsistent trends in studiesbased on the SPEI-PM (Naumann et al., 2018; Gu et al., 2020).	***Medium confidence:*** **Increase.** Tendency towards increase in drought severity in total soil moisture (Chapter 11 Supplementary Material (11.SM) , surface soil moisture (Xu et al., 2019a) and SPEI-PM (Naumann et al., 2018; Gu et al., 2020).	***High confidence:*** **Increase** in drought severity with different metrics and high agreement between studies (Chapter 11 Supplementary Material (11.SM) (Cook et al., 2014b, 2020; Dai et al., 2018; Lu et al., 2019; Vicente-Serrano et al., 2020a).
	HYDR	***Low confidence:*** **Limited evidence.** Available evidence suggests lack of signal (Marengo and Espinoza, 2016; Gudmundsson et al., 2021)	***Low confidence:*** **Limited evidence**	***Low confidence:*** **Limited evidence**. One study shows mixed trends (Touma et al., 2015)	***Low confidence***: **Limited evidence.** Tendency to drying in two studies (Touma et al., 2015; Cook et al., 2020)	***High confidence:*** **Increase** in drought severity (Prudhomme et al., 2014; Giuntoli et al., 2015; Touma et al., 2015; Cook et al., 2020)
South American Monsoon (SAM)	MET	***Medium confidence:*** **Increase** in the frequency and severity of meteorological droughts based on SPI and CDD (Spinoni et al., 2019; Avila-Diaz et al., 2020; Dereczynski et al., 2020).	***Low confidence:*** **Limited evidence** and recent droughts as in 2010 were not attributed to anthropogenic climate change (Shiogama et al., 2013).	***Medium confidence:*** **Increase** meteorological droughts (Chapter 11 Supplementary Material (11.SM) (Chou et al., 2014a; Touma et al., 2015; Xu et al., 2019a)**..** Drying trends in CDD in CMIP6 and SPI in CMIP5 (Touma et al., 2015; Xu et al., 2019a) but divergent trends in an RCM driven by two GCMs (Chou et al., 2014a)	***Medium confidence:*** **Increase** in meteorological droughts (Chou et al., 2014a; Touma et al., 2015; Xu et al., 2019a) (Chapter 11 Supplementary Material (11.SM). Drying trend in CDD in CMIP6 and SPI in CMIP5 (Touma et al., 2015; Xu et al., 2019a) but divergent trends in an RCM driven by two GCMs (Chou et al., 2014a) and weak trends in CMIP5-based SPI projections (Spinoni et al., 2020).	***High confidence:*** **Increase** in drought severity (Chou et al., 2014a; Touma et al., 2015; Spinoni et al., 2020; Coppola et al., 2021b) (Chapter 11 Supplementary Material (11.SM).
	AGR ECOL	***Low confidence:*** **Mixed trends** depending on subregions and drought metrics, including soil moisture, PDSI-PM and SPEI-PM (Greve et al., 2014; Dai and Zhao, 2017; Spinoni et al., 2019; Padrón et al., 2020)	***Low confidence:*** **Limited evidence**	***Medium confidence:*** **Increase** in agricultural and ecological droughts based on total column and surface soil moisture, (Chapter 11 Supplementary Material (11.SM) (Xu et al., 2019a), and inconsistent signal	***High confidence:*** **Increase** in drought severity with different metrics (Naumann et al., 2018; Xu et al., 2019a; Gu et al., 2020) (Chapter 11 Supplementary Material (11.SM).	***High confidence:*** **Increase** in drought severity with different metrics and high agreement between studies (Chapter 11 Supplementary Material (11.SM) (Cook et al., 2014b, 2020; Dai et al., 2018; Lu et al., 2019; Vicente-Serrano et al.,

ACCEPTED VERSION SUBJECT TO FINAL EDITING

				with SPEI-PM (Naumann et al., 2018; Gu et al., 2020).		2020a).
	HYDR	***Low confidence:*** **Limited evidence.** Available evidence suggests lack of signal (Gudmundsson et al., 2021)	***Low confidence:*** **Limited evidence**	***Low confidence:*** **Limited evidence.** One study shows mixed signal (Touma et al., 2015)	***Low confidence:*** **Limited evidence.** Mixed signal (Touma et al., 2015) or tendency to drying (Cook et al., 2020)	***High confidence:*** **Increase** in drought severity (Prudhomme et al., 2014; Giuntoli et al., 2015; Touma et al., 2015; Cook et al., 2020).
North-eastern South America (NES)	MET	***High confidence:*** **Increase** in drought duration (Marengo et al., 2017; Brito et al., 2018; Spinoni et al., 2019; Avila-Diaz et al., 2020; Dereczynski et al., 2020; Dunn et al., 2020)	***Low confidence:*** Low confidence in human influence on meteorological drought in the region (Otto et al., 2015b; Martins et al., 2018).	***Medium confidence:*** **Increase** of CDD (Chapter 11 Supplementary Material (11.SM)(Chou et al., 2014a) and SPI (Xu et al. 2019, Touma et al. 2015). Increase in CDD for change of +0.5°C in global warming based on CMIP5 (Wartenburger et al., 2017)(SR15, Ch3)	***Medium confidence:*** **Increase** in drought severity (Chou et al., 2014a; Touma et al., 2015; Xu et al., 2019a; Spinoni et al., 2020) (Chapter 11 Supplementary Material (11.SM).	***Medium confidence:*** **Increase** in drought severity (Chou et al., 2014a; Touma et al., 2015; Spinoni et al., 2020; Coppola et al., 2021b) (Chapter 11 Supplementary Material (11.SM).
	AGR ECOL	***Medium confidence:*** **Increase** in drought severity based on different drought metrics, including soil moisture, PDSI-PM and SPEI-PM (Greve et al., 2014; Dai and Zhao, 2017; Spinoni et al., 2019; Padrón et al., 2020)	***Low confidence:*** Limited evidence	***Low confidence:*** **Lack of signal** based on different metrics, including total and surface column soil moisture, (Chapter 11 Supplementary Material (11.SM) (Xu et al., 2019a), and SPEI-PM (Naumann et al., 2018; Gu et al., 2020).	***Medium confidence:*** **Increase.** Dominant increase in drying with some inconsistencies between different drought metrics and models (Naumann et al., 2018; Xu et al., 2019a; Gu et al., 2020) (Chapter 11 Supplementary Material (11.SM)	***Medium confidence:*** **Increase** in drought severity with different metrics and high agreement between different studies (Chapter 11 Supplementary Material (11.SM) (Cook et al., 2014b, 2020; Dai et al., 2018; Lu et al., 2019; Vicente-Serrano et al., 2020a).
	HYDR	***Low confidence:*** **Limited evidence.** One study shows an increase in drought severity (Gudmundsson et al., 2021)	***Low confidence:*** **Limited evidence**	***Low confidence:*** Limited evidence. One study shows a weak drying (Touma et al., 2015)	***Low confidence:*** **Limited evidence.** Weak drying (Touma et al., 2015) or inconsistent trends (Cook et al., 2020)	***Low confidence:*** **Mixed signal** among studies (Prudhomme et al., 2014; Giuntoli et al., 2015; Touma et al., 2015; Cook et al., 2020).
South-western South America (SWS)	MET	***Medium confidence:*** **Increase** in drought duration and severity (Skansi et al., 2013; Garreaud et al., 2017, 2020; Saurral et al., 2017; Boisier et al., 2018; Dereczynski et al., 2020; Dunn et al., 2020)	***Medium confidence*** that human-induced climate change has contributed to long-term trends and Central Chile drought between 2010 and 2018 (Boisier et al., 2016; Garreaud et al., 2020)	***Low confidence:*** **Inconsistent trends** Increase in meteorological drought based on CDD in CMIP6 GCMs (Chapter 11 Supplementary Material (11.SM), but inconsistent trends in SPI in CMIP5 (Touma et al., 2015; Xu et al., 2019a) and substantial model spread in Eta-RCM driven with two GCMs (Chou et al., 2014a).	***Low confidence:*** **Mixed trends** between studies and models. Increase in meteorological drought based on CDD in CMIP6 GCMs (Chapter 11 supplementary Material (11.SM) , but inconsistent trends in SPI in CMIP5 (Touma et al., 2015; Xu et al., 2019a) and substantial model spread in Eta-RCM driven with two GCMs (Chou et al., 2014a).	***Medium confidence:*** **Increase** in drought severity (Chou et al., 2014a; Touma et al., 2015; Spinoni et al., 2020).
	AGR ECOL	***Low confidence:*** **Mixed trends** according to subregions and different drought metrics, including soil moisture, PDSI-PM and SPEI-PM (Greve et al., 2014; Dai and Zhao, 2017; Spinoni et al., 2019; Padrón et al., 2020)	***Low confidence:*** **Limited evidence**	***Low confidence:*** **Mixed trends** based on different metrics, including decrease in total column and surface soil moisture in CMIP6 (Chapter 11 Supplementary Material (11.SM) , weak drying in total and surface soil moisture in CMIP5 (Xu et al., 2019a), and weak signal based on	***Medium confidence:*** **Increase** in drought severity based on total and surface soil moisture in CMIP6 (Chapter 11 Supplementary Material (11.SM) and CMIP5 (Xu et al., 2019a), and SPEI-PM (Naumann et al., 2018; Gu et al., 2020).	***High confidence:*** **Increase** in drought severity with different metrics and high agreement between studies (Chapter 11 Supplementary Material (11.SM) (Cook et al., 2014b, 2020; Dai et al., 2018; Lu et al., 2019; Vicente-Serrano et al., 2020a).

ACCEPTED VERSION SUBJECT TO FINAL EDITING

				the SPEI-PM (Naumann et al., 2018; Gu et al., 2020).		
	HYDR	***Low confidence:*** **Limited evidence**. General lack of signal in one study (Gudmundsson et al., 2021) but streamflow decrease in subregions in another study (Boisier et al. (2018)	***Low confidence:*** **Limited evidence**	***Low confidence:*** **Limited evidence.** One study shows drying (Touma et al., 2015)	***Low confidence:*** **Limited evidence.** Strong drying in (Cook et al., 2020); weak drying in (Touma et al., 2015)	***High confidence:*** **Increase** in drought severity (Prudhomme et al., 2014; Giuntoli et al., 2015; Touma et al., 2015; Cook et al., 2020).
South-eastern South America (SES)	MET	***Low confidence:*** **Mixed signals** in observed trends depending on subregion (Saurral et al., 2017; Knutson and Zeng, 2018; Spinoni et al., 2019; Dereczynski et al., 2020; Dunn et al., 2020)	***Low confidence:*** **Limited evidence.** Wetting trend in models and observations in part of region in one study (Knutson and Zeng, 2018)**.**	***Low confidence:*** **Inconsistent trends.** Weak drying trend based on CDDCMIP6 (Chapter 11 Supplementary Material (11.SM) , inconsistent trend between models based on SPI in CMIP5 (Touma et al., 2015; Xu et al., 2019a) and lack of signal in study with one RCM driven by two GCMs (Chou et al., 2014a)**.**	***Low confidence:*** **Mixed signals** between studies and models (Chou et al., 2014a; Touma et al., 2015; Xu et al., 2019a; Spinoni et al., 2020) (Chapter 11 Supplementary Material (11.SM) .	***Low confidence:*** **Mixed signals** between studies and models (Chou et al., 2014a; Touma et al., 2015; Spinoni et al., 2020; Coppola et al., 2021b) (Chapter 11 Supplementary Material (11.SM).
	AGR ECOL	***Low confidence:*** **Mixed trends** according to subregions and different drought metrics, including soil moisture, PDSI-PM and SPEI-PM (Greve et al., 2014; Dai and Zhao, 2017; Spinoni et al., 2019; Padrón et al., 2020)	***Low confidence:*** **Limited evidence**	***Low confidence:*** **Mixed trends** based on different metrics, including lack of signal in total column soil moisture, (Chapter 11 Supplementary Material (11.SM) , weak drying with surface soil moisture (Xu et al., 2019a) and wetting based on the SPEI-PM (Naumann et al., 2018; Gu et al., 2020).	***Low confidence:*** **Mixed signal** in changes in drought severity with different metrics, (Chapter 11 Supplementary Material (11.SM), (Naumann et al., 2018; Xu et al., 2019a; Gu et al., 2020).	***Low confidence:*** **Mixed signals** Inconsistent trends or lack of signal in total and surface soil moisture(Chapter 11 Supplementary Material (11.SM) (Dai et al., 2018; Lu et al., 2019; Cook et al., 2020); decreasing drought severity in PDSI and SPEI-PM (Cook et al., 2014b; Dai et al., 2018; Vicente-Serrano et al., 2020a).
	HYDR	***Medium confidence:*** **Decrease.** Reduction of hydrological droughts (Dai and Zhao, 2017; Rivera and Penalba, 2018)	***Low confidence:*** **Limited evidence**	***Low confidence:*** **Limited evidence.** One study shows mixed signal (Touma et al., 2015)	***Low confidence:*** **Limited evidence.** Mixed signal (Touma et al., 2015) or wetting (Cook et al., 2020)	***Low confidence:*** **Mixed signal** among studies (Prudhomme et al., 2014; Giuntoli et al., 2015; Touma et al., 2015; Cook et al., 2020).
Southern South America (SSA)	MET	***Medium confidence:*** **Increase** in the frequency of droughts (Skansi et al., 2013; Spinoni et al., 2019; Dereczynski et al., 2020; Dunn et al., 2020).	***Low confidence:*** **Limited evidence**	***Low confidence:*** **Lack of signal** (Chapter 11 Supplementary Material (11.SM) (Chou et al., 2014a)**.**	***Medium confidence:*** Increase in drought severity (Chou et al., 2014a; Touma et al., 2015; Xu et al., 2019a; Spinoni et al., 2020) (Chapter 11 Supplementary Material (11.SM).	***Medium confidence:*** Increase in drought severity (Chou et al., 2014a; Touma et al., 2015; Spinoni et al., 2020; Coppola et al., 2021b) (Chapter 11 Supplementary Material (11.SM)
	AGR ECOL	***Low confidence:*** **Mixed trends** depending on subregions and drought metrics, including soil moisture, PDSI-PM and SPEI-PM (Greve et al., 2014; Dai and Zhao, 2017; Spinoni et al., 2019; Padrón et al., 2020)	***Low confidence:*** **Limited evidence**	***Medium confidence:*** **Increase** in drought severity considering total column soil moisture, (Chapter 11 Supplementary Material (11.SM) , and surface soil moisture (Xu et al., 2019a) and weak drying with the SPEI-PM (Naumann et al., 2018; Gu et al., 2020).	***High confidence:*** **Increase** in drought severity (Naumann et al., 2018; Xu et al., 2019a; Gu et al., 2020) (Chapter 11 Supplementary Material (11.SM).	***High confidence:*** **Increase** in drought severity with different metrics and high agreement between studies (Chapter 11 Supplementary Material (11.SM) (Cook et al., 2014b, 2020; Dai et al., 2018; Lu et al., 2019; Vicente-Serrano et al., 2020a).
	HYDR	***Low confidence:*** **Limited**	***Low confidence:***	***Low confidence:*** **Limited**	***Low confidence:*** **Limited**	***High confidence:*** Increase in

ACCEPTED VERSION SUBJECT TO FINAL EDITING

		evidence and lack of signal (Gudmundsson et al., 2021)	**Limited evidence**	**evidence.** One study shows drying (Touma et al., 2015)	**evidence.** Drying (Touma et al., 2015; Cook et al., 2020) or inconsistent trend (Zhai et al., 2020b).	drought severity (Prudhomme et al., 2014; Giuntoli et al., 2015; Touma et al., 2015; Cook et al., 2020)

[END TABLE 11.15 HERE]

[START TABLE 11.16 HERE]

Table 11.16: Observed trends, human contribution to observed trends, and projected changes at 1.5°C, 2°C and 4°C of global warming for temperature extremes in Europe, subdivided by AR6 regions. See Sections 11.9.1 and 11.9.2 for details.

Region	Observed trends	Detection and attribution; event attribution	Projections		
			1.5 °C	2 °C	4 °C
All Europe	All subregions show a *very likely* increase in the intensity and frequency of hot extremes and decrease in the intensity and frequency of cold extremes	Robust evidence of a human contribution to the observed increase in the intensity and frequency of hot extremes and decrease in the intensity and frequency of cold extremes (Hu et al., 2020; Seong et al., 2020)	CMIP6 models project a robust increase in the intensity and frequency of TXx events and a robust decrease in the intensity and frequency of TNn events (Li et al., 2020). Median increase of more than 0.5°C in the 50-year TXx and TNn events compared to the 1°C warming level (Li et al., 2020)	CMIP6 models project a robust increase in the intensity and frequency of TXx events and a robust decrease in the intensity and frequency of TNn events (Li et al., 2020). Median increase of more than 1.5°C in the 50-year TXx and TNn events compared to the 1°C warming level (Li et al., 2020)	CMIP6 models project a robust increase in the intensity and frequency of TXx events and a robust decrease in the intensity and frequency of TNn events (Li et al., 2020). Median increase of more than 5°C in the 50-year TXx and TNn events compared to the 1°C warming level (Li et al., 2020)
	Very likely increase in the intensity and frequency of hot extremes and decrease in the intensity and frequency of cold extremes	Human influence *very likely* contributed to the observed increase in the intensity and frequency of hot extremes and decrease in the intensity and frequency of cold extremes	Increase in the intensity and frequency of hot extremes: *Very likely* (compared with the recent past (1995-2014)) *Extremely likely* (compared with pre-industrial) Decrease in the intensity and frequency of cold extremes: *Very likely* (compared with the recent past (1995-2014)) *Extremely likely* (compared with pre-industrial)	Increase in the intensity and frequency of hot extremes: *Extremely likely* (compared with the recent past (1995-2014)) *Virtually certain* (compared with pre-industrial) Decrease in the intensity and frequency of cold extremes: *Extremely likely* (compared with the recent past (1995-2014)) *Virtually certain* (compared with pre-industrial)	Increase in the intensity and frequency of hot extremes: *Virtually certain* (compared with the recent past (1995-2014)) *Virtually certain* (compared with pre-industrial) Decrease in the intensity and frequency of cold extremes: *Virtually certain* (compared with the recent past (1995-2014)) *Virtually certain* (compared with pre-industrial)
Greenland/Iceland (GIC)	Significant increases in the intensity and frequency of hot extremes and significant decreases in the intensity and frequency of cold extremes	Strong evidence of changes from observations that are in the direction of model projected changes for the future. The magnitude of	CMIP6 models project a robust increase in the intensity and frequency of TXx events and a robust decrease in the intensity and frequency of TNn events (Li	CMIP6 models project a robust increase in the intensity and frequency of TXx events and a robust decrease in the intensity and frequency of TNn events	CMIP6 models project a robust increase in the intensity and frequency of TXx events and a robust decrease in the intensity and frequency of TNn events

ACCEPTED VERSION SUBJECT TO COPYEDITING

	(Peña-Angulo et al., 2020; Mernild et al., 2014; Sui et al., 2017; Dunn et al., 2020)	projected changes increases with global warming.	et al., 2020; Annex). Median increase of more than 0C in the 50-year TXx and TNn events compared to the 1°C warming level (Li et al., 2020) and more than 1°C in annual TXx and TNn compared to pre-industrial (Annex). Additional evidence from CMIP5 and CORDEX simulations for an increase in the intensity and frequency of hot extremes and decrease in the intensity and frequency of cold extremes (Wehner et al., 2018; Cardell et al., 2020).	(Li et al., 2020; Annex). Median increase of more than 0.5°C in the 50-year TXx and TNn events compared to the 1°C warming level (Li et al., 2020) and more than 1.5°C in annual TXx and TNn compared to pre-industrial (Annex). Additional evidence from CMIP5 and CORDEX simulations for an increase in the intensity and frequency of hot extremes and decrease in the intensity and frequency of cold extremes (Wehner et al., 2018; Cardell et al., 2020).	(Li et al., 2020; Annex). Median increase of more than 1°C in the 50-year TXx and TNn events compared to the 1°C warming level (Li et al., 2020) and more than 2.5°C in annual TXx and TNn compared to pre-industrial (Annex). Additional evidence from CMIP5 and CORDEX simulations for an increase in the intensity and frequency of hot extremes and decrease in the intensity and frequency of cold extremes (Cardell et al., 2020; Sillmann et al., 2013).
	Very likely increase in the intensity and frequency of hot extremes and decrease in the intensity and frequency of cold extremes	*Medium confidence* in a human contribution to the observed increase in the intensity and frequency of hot extremes and decrease in the intensity and frequency of cold extremes.	Increase in the intensity and frequency of hot extremes: *Likely* (compared with the recent past (1995-2014)) *Very likely* (compared with pre-industrial) Decrease in the intensity and frequency of cold extremes: *Likely* (compared with the recent past (1995-2014)) *Very likely* (compared with pre-industrial)	Increase in the intensity and frequency of hot extremes: *Very likely* (compared with the recent past (1995-2014)) *Extremely likely* (compared with pre-industrial) Decrease in the intensity and frequency of cold extremes: *Very likely* (compared with the recent past (1995-2014)) *Extremely likely* (compared with pre-industrial)	Increase in the intensity and frequency of hot extremes: *Virtually certain* (compared with the recent past (1995-2014)) *Virtually certain* (compared with pre-industrial) Decrease in the intensity and frequency of cold extremes: *Virtually certain* (compared with the recent past (1995-2014)) *Virtually certain* (compared with pre-industrial)
Mediterranean (MED) [5]	Significant increases in the intensity and frequency of hot extremes and significant decreases in the intensity and frequency of cold extremes (Peña-Angulo et al., 2020; El Kenawy et al., 2013; for Spain, Acero et al., 2014; Fioravanti et al., 2016; Ruml et al., 2017; Türkeş and Erlat, 2018; Donat et al., 2013,	Robust evidence of a human contribution to the observed increase in the intensity and frequency of hot extremes and decrease in the intensity and frequency of cold extremes (Seong et al., 2020); (Wang et al., 2017c); (Sippel and Otto, 2014); (Wilcox et al., 2018)	CMIP6 models project a robust increase in the intensity and frequency of TXx events and a robust decrease in the intensity and frequency of TNn events (Li et al., 2020; Annex). Median increase of more than 0.5°C in the 50-year TXx and TNn events compared to the 1°C warming level (Li et al., 2020) and more than 2°C in annual TXx and TNn	CMIP6 models project a robust increase in the intensity and frequency of TXx events and a robust decrease in the intensity and frequency of TNn events (Li et al., 2020; Annex). Median increase of more than 1°C in the 50-year TXx and TNn events compared to the 1°C warming level (Li et al., 2020) and more than 2.5°C in	CMIP6 models project a robust increase in the intensity and frequency of TXx events and a robust decrease in the intensity and frequency of TNn events (Li et al., 2020; Annex). Median increase of more than 3.5°C in the 50-year TXx and TNn events compared to the 1°C warming level (Li et al., 2020) and more than 5°C in

[5] This region includes both northern Africa and southern Europe

SUBJECT TO FINAL EDITING ACCEPTED VERSION OF

	2014, 2016; Filahi et al., 2016; Driouech et al., 2020; Dunn et al.2020)		compared to pre-industrial (Annex). Additional evidence from CMIP5 and RCM simulations for an increase in the intensity and frequency of hot extremes and decrease in the intensity and frequency of cold extremes (Cardoso et al., 2019; Zollo et al., 2016); Weber et al., 2018)	annual TXx and TNn compared to pre-industrial (Annex). Additional evidence from CMIP5 and RCM simulations for an increase in the intensity and frequency of hot extremes and decrease in the intensity and frequency of cold extremes (Cardoso et al., 2019; Tomozeiu et al., 2014; Abaurrea et al., 2018; Nastos and Kapsomenakis, 2015; Cardell et al., 2020; Zollo et al., 2016; Weber et al., 2018; Coppola et al., 2021a)	annual TXx and TNn compared to pre-industrial (Annex). Additional evidence from CMIP5 and RCM simulations for an increase in the intensity and frequency of hot extremes and decrease in the intensity and frequency of cold extremes (Cardoso et al., 2019; Nastos and Kapsomenakis, 2015; Tomozeiu et al., 2014; Cardell et al., 2020; Zollo et al., 2016; Giorgi et al., 2014; Driouech et al., 2020; Coppola et al., 2021a; Engelbrecht et al., 2015)
	Very likely increase in the intensity and frequency of hot extremes and decrease in the intensity and frequency of cold extremes	Human influence *likely* contributed to the observed increase in the intensity and frequency of hot extremes and decrease in the intensity and frequency of cold extremes	Increase in the intensity and frequency of hot extremes: *Likely* (compared with the recent past (1995-2014)) *Very likely* (compared with pre-industrial) Decrease in the intensity and frequency of cold extremes: *Likely* (compared with the recent past (1995-2014)) *Very likely* (compared with pre-industrial)	Increase in the intensity and frequency of hot extremes: *Very likely* (compared with the recent past (1995-2014)) *Extremely likely* (compared with pre-industrial) Decrease in the intensity and frequency of cold extremes: *Very likely* (compared with the recent past (1995-2014)) *Extremely likely* (compared with pre-industrial)	Increase in the intensity and frequency of hot extremes: *Virtually certain* (compared with the recent past (1995-2014)) *Virtually certain* (compared with pre-industrial) Decrease in the intensity and frequency of cold extremes: *Virtually certain* (compared with the recent past (1995-2014)) *Virtually certain* (compared with pre-industrial)
Western and Central Europe (WCE)	Significant increases in the intensity and frequency of hot extremes and significant decreases in the intensity and frequency of cold extremes (Christidis et al., 2015; Scherrer et al., 2016; Shevchenko et al., 2014; Twardosz and Kossowska-Cezak, 2013; Dunn et al., 2020)	Robust evidence of a human contribution to the observed increase in the intensity and frequency of hot extremes and decrease in the intensity and frequency of cold extremes (Seong et al., 2020; Wang et al., 2017; Sippel et al., 2017, 2018; Dong et al., 2014, 2016; Sippel et al., 2016; Christidis et al., 2015; Cattiaux and Ribes, 2018; Leach et al., 2020)	CMIP6 models project a robust increase in the intensity and frequency of TXx events and a robust decrease in the intensity and frequency of TNn events (Li et al., 2020; Annex). Median increase of more than 0.5°C in the 50-year TXx and TNn events compared to the 1°C warming level (Li et al., 2020) and more than 2°C in annual TXx and TNn compared to pre-industrial (Annex). Additional evidence from	CMIP6 models project a robust increase in the intensity and frequency of TXx events and a robust decrease in the intensity and frequency of TNn events (Li et al., 2020; Annex). Median increase of more than 1.5°C in the 50-year TXx and TNn events compared to the 1°C warming level (Li et al., 2020) and more than 3°C in annual TXx and TNn compared to pre-industrial (Annex). Additional evidence from	CMIP6 models project a robust increase in the intensity and frequency of TXx events and a robust decrease in the intensity and frequency of TNn events (Li et al., 2020; Annex). Median increase of more than 5.5°C in the 50-year TXx and TNn events compared to the 1°C warming level (Li et al., 2020) and more than 6°C in annual TXx and TNn compared to pre-industrial (Annex). Additional evidence from

SUBJECT TO FINAL EDITING ACCEPTED VERSION

			CMIP5 and RCM simulations for an increase in the intensity and frequency of hot extremes (Lau and Nath, 2014; Lhotka et al., 2018)	CMIP5 and RCM simulations for an increase in the intensity and frequency of hot extremes (Russo et al., 2015; Lau and Nath, 2014; Lhotka et al., 2018)	CMIP5 and RCM simulations for an increase in the intensity and frequency of hot extremes (Lau and Nath, 2014; Lhotka et al., 2018)
	Very likely increase in the intensity and frequency of hot extremes and decrease in the intensity and frequency of cold extremes	Human influence *likely* contributed to the observed increase in the intensity and frequency of hot extremes and decrease in the intensity and frequency of cold extremes	Increase in the intensity and frequency of hot extremes: *Likely* (compared with the recent past (1995-2014)) *Very likely* (compared with pre-industrial) Decrease in the intensity and frequency of cold extremes: *Likely* (compared with the recent past (1995-2014)) *Very likely* (compared with pre-industrial)	Increase in the intensity and frequency of hot extremes: *Very likely* (compared with the recent past (1995-2014)) *Extremely likely* (compared with pre-industrial) Decrease in the intensity and frequency of cold extremes: *Very likely* (compared with the recent past (1995-2014)) *Extremely likely* (compared with pre-industrial)	Increase in the intensity and frequency of hot extremes: *Virtually certain* (compared with the recent past (1995-2014)) *Virtually certain* (compared with pre-industrial) Decrease in the intensity and frequency of cold extremes: *Virtually certain* (compared with the recent past (1995-2014)) *Virtually certain* (compared with pre-industrial)
Eastern Europe (EEU)	Significant increases in the intensity and frequency of hot extremes and significant decreases in the intensity and frequency of cold extremes (Peña-Angulo et al., 2020; Zhang et al., 2019b; Donat et al., 2016; Dunn et al., 2020)	Robust evidence of a human contribution to the observed increase in the intensity and frequency of hot extremes and decrease in the intensity and frequency of cold extremes (Seong et al., 2020; Wang et al., 2017; Sippel and Otto, 2014; Leach et al., 2020; Hauser et al., 2016)	CMIP6 models project a robust increase in the intensity and frequency of TXx events and a robust decrease in the intensity and frequency of TNn events (Li et al., 2020; Annex). Median increase of more than 0.5°C in the 50-year TXx and TNn events compared to the 1°C warming level (Li et al., 2020) and more than 2°C in annual TXx and TNn compared to pre-industrial (Annex). Additional evidence from CMIP5 and CORDEX simulations for an increase in the intensity and frequency of hot extremes and decrease in the intensity and frequency of cold extremes (Wehner et al., 2018; Cardell et al., 2020).	CMIP6 models project a robust increase in the intensity and frequency of TXx events and a robust decrease in the intensity and frequency of TNn events (Li et al., 2020; Annex). Median increase of more than 1.5°C in the 50-year TXx and TNn events compared to the 1°C warming level (Li et al., 2020) and more than 2.5°C in annual TXx and TNn compared to pre-industrial (Annex). Additional evidence from CMIP5 and CORDEX simulations for an increase in the intensity and frequency of hot extremes and decrease in the intensity and frequency of cold extremes (Wehner et al., 2018; Cardell et al., 2020; Khlebnikova et al., 2019).	CMIP6 models project a robust increase in the intensity and frequency of TXx events and a robust decrease in the intensity and frequency of TNn events (Li et al., 2020; Annex). Median increase of more than 4.5°C in the 50-year TXx and TNn events compared to the 1°C warming level (Li et al., 2020) and more than 5.5°C in annual TXx and TNn compared to pre-industrial (Annex). Additional evidence from CMIP5 and CORDEX simulations for an increase in the intensity and frequency of hot extremes and decrease in the intensity and frequency of cold extremes (Cardell et al., 2020; Khlebnikova et al., 2019; Sillmann et al., 2013)
	Very likely increase in the intensity and frequency of hot extremes and decrease in the	Human influence *likely* contributed to the observed increase in the intensity and frequency of hot extremes	Increase in the intensity and frequency of hot extremes: *Likely* (compared with the recent past (1995-2014))	Increase in the intensity and frequency of hot extremes: *Very likely* (compared with the recent past (1995-2014))	Increase in the intensity and frequency of hot extremes: *Virtually certain* (compared with the recent past (1995-

ACCEPTED VERSION SUBJECT TO FINAL EDITING

	intensity and frequency of cold extremes	and decrease in the intensity and frequency of cold extremes	*Very likely* (compared with pre-industrial) Decrease in the intensity and frequency of cold extremes: *Likely* (compared with the recent past (1995-2014)) *Very likely* (compared with pre-industrial)	*Extremely likely* (compared with pre-industrial) Decrease in the intensity and frequency of cold extremes: *Very likely* (compared with the recent past (1995-2014)) *Extremely likely* (compared with pre-industrial)	2014)) *Virtually certain* (compared with pre-industrial) Decrease in the intensity and frequency of cold extremes: *Virtually certain* (compared with the recent past (1995-2014)) *Virtually certain* (compared with pre-industrial)
Northern Europe (NEU)	Significant increases in the intensity and frequency of hot extremes and significant decreases in the intensity and frequency of cold extremes (Matthes et al., 2015; Vikhamar-Schuler et al., 2016; Dunn et al., 2020)	Robust evidence of a human contribution to the observed increase in the intensity and frequency of hot extremes and decrease in the intensity and frequency of cold extremes (Seong et al., 2020; Wang et al., 2017; Otto et al., 2012; Massey et al., 2012; Christiansen et al., 2018; King et al., 2015; Roth et al., 2018)	CMIP6 models project a robust increase in the intensity and frequency of TXx events and a robust decrease in the intensity and frequency of TNn events (Li et al., 2020; Annex). Median increase of more than 0.5°C in the 50-year TXx and TNn events compared to the 1°C warming level (Li et al., 2020) and more than 1.5°C in annual TXx and TNn compared to pre-industrial (Annex). Additional evidence from CMIP5 simulations for an increase in the intensity and frequency of hot extremes and decrease in the intensity and frequency of cold extremes (Jacob et al., 2018; Laliberté et al., 2015; Sigmond et al., 2018; Dosio and Fischer, 2018; Forzieri et al., 2016)	CMIP6 models project a robust increase in the intensity and frequency of TXx events and a robust decrease in the intensity and frequency of TNn events (Li et al., 2020; Annex). Median increase of more than 1.5°C in the 50-year TXx and TNn events compared to the 1°C warming level (Li et al., 2020) and more than 2.5°C in annual TXx and TNn compared to pre-industrial (Annex). Additional evidence from CMIP5 simulations for an increase in the intensity and frequency of hot extremes and decrease in the intensity and frequency of cold extremes (Jacob et al., 2018; Laliberté et al., 2015; Sigmond et al., 2018; Dosio and Fischer, 2018; Forzieri et al., 2016)	CMIP6 models project a robust increase in the intensity and frequency of TXx events and a robust decrease in the intensity and frequency of TNn events (Li et al., 2020; Annex). Median increase of more than 4.5°C in the 50-year TXx and TNn events compared to the 1°C warming level (Li et al., 2020) and more than 4.5°C in annual TXx and TNn compared to pre-industrial (Annex). Additional evidence from CMIP5 simulations for an increase in the intensity and frequency of hot extremes and decrease in the intensity and frequency of cold extremes (Jacob et al., 2018; Laliberté et al., 2015; Sigmond et al., 2018; Dosio and Fischer, 2018; Forzieri et al., 2016)
	Very likely increase in the intensity and frequency of hot extremes and decrease in the intensity and frequency of cold extremes	Human influence *likely* contributed to the observed increase in the intensity and frequency of hot extremes and decrease in the intensity and frequency of cold extremes	Increase in the intensity and frequency of hot extremes: *Likely* (compared with the recent past (1995-2014)) *Very likely* (compared with pre-industrial) Decrease in the intensity and frequency of cold extremes: *Likely* (compared with the recent past (1995-2014))	Increase in the intensity and frequency of hot extremes: *Very likely* (compared with the recent past (1995-2014)) *Extremely likely* (compared with pre-industrial) Decrease in the intensity and frequency of cold extremes: *Very likely* (compared with the recent past (1995-2014))	Increase in the intensity and frequency of hot extremes: *Virtually certain* (compared with the recent past (1995-2014)) *Virtually certain* (compared with pre-industrial) Decrease in the intensity and frequency of cold extremes: *Virtually certain* (compared

ACCEPTED SUBJECT TO FINAL EDITING

			Very likely (compared with pre-industrial)	*Extremely likely* (compared with pre-industrial)	with the recent past (1995-2014)) *Virtually certain* (compared with pre-industrial)

[END TABLE 11.16 HERE]

[START TABLE 11.17 HERE]

Table 11.17: Observed trends, human contribution to observed trends, and projected changes at 1.5°C, 2°C and 4°C of global warming for heavy precipitation in Europe, subdivided by AR6 regions. See Sections 11.9.1 and 11.9.3 for details.

Region	Observed trends	Detection and attribution; event attribution	Projections		
			1.5 °C	2 °C	4 °C
All Europe	Significant intensification of heavy precipitation (Sun et al., 2020)	Robust evidence of a human contribution to the observed intensification of heavy precipitation (Paik et al., 2020)	CMIP6 models project an increase in the intensity and frequency of heavy precipitation (Li et al., 2020a). Median increase of more than 0% in the 50-year Rx1day and Rx5day events compared to the 1°C warming level (Li et al., 2020a)	CMIP6 models project a robust increase in the intensity and frequency of heavy precipitation (Li et al., 2020a). Median increase of more than 2% in the 50-year Rx1day and Rx5day events compared to the 1°C warming level (Li et al., 2020a)	CMIP6 models project a robust increase in the intensity and frequency of heavy precipitation (Li et al., 2020a). Median increase of more than 8% in the 50-year Rx1day and Rx5day events compared to the 1°C warming level (Li et al., 2020a)
	Likely intensification of heavy precipitation	Human influence *likely* contributed to the observed intensification of heavy precipitation	Intensification of heavy precipitation: *High confidence* (compared with the recent past (1995-2014)) *Likely* (compared with pre-industrial)	Intensification of heavy precipitation: *Likely* (compared with the recent past (1995-2014)) *Very likely* (compared with pre-industrial)	Intensification of heavy precipitation: *Very likely* (compared with the recent past (1995-2014)) *Extremely likely* (compared with pre-industrial)
Greenland/Iceland (GIC)	Intensification of heavy precipitation (Peña-Angulo et al., 2020)	Limited evidence	CMIP6 models project an increase in the intensity and frequency of heavy precipitation (Li et al., 2020; Annex). Median increase of more than 2% in the 50-year Rx1day and Rx5day events compared to the 1°C warming level (Li et al., 2020a) and more than 10% in annual Rx1day, Rx5day, and Rx30day compared to pre-industrial (Annex).	CMIP6 models project a robust increase in the intensity and frequency of heavy precipitation (Li et al., 2020; Annex). Median increase of more than 8% in the 50-year Rx1day and Rx5day events compared to the 1°C warming level (Li et al., 2020a) and more than 15% in annual Rx1day, Rx5day, and Rx30day compared to pre-industrial (Annex).	CMIP6 models project a robust increase in the intensity and frequency of heavy precipitation (Li et al., 2020; Annex). Median increase of more than 30% in the 50-year Rx1day and Rx5day events compared to the 1°C warming level (Li et al., 2020a) and more than 30% in annual Rx1day and Rx5day and 35% in annual Rx30day compared to pre-industrial (Annex).

ACCEPTED VERSION SUBJECT TO FINAL EDITING

			Additional evidence from CMIP5 and CORDEX simulations for an increase in the intensity of heavy precipitation (Cardell et al., 2020)	Additional evidence from CMIP5 and CORDEX simulations for an increase in the intensity of heavy precipitation (Cardell et al., 2020)	Additional evidence from CMIP5 and CORDEX simulations for an increase in the intensity of heavy precipitation (Cardell et al., 2020)
	Medium confidence in the intensitification of heavy precipitation	*Low confidence*	Intensification of heavy precipitation: *High confidence* (compared with the recent past (1995-2014)) *Likely* (compared with pre-industrial)	Intensification of heavy precipitation: *Likely* (compared with the recent past (1995-2014)) *Very likely* (compared with pre-industrial)	Intensification of heavy precipitation: *Extremely likely* (compared with the recent past (1995-2014)) *Virtually certain* (compared with pre-industrial)
Mediterranean (MED)[6]	Lack of agreement on the evidence of trends (Sun et al., 2020; Dunn et al., 2020; Casanueva et al., 2014; de Lima et al., 2015; Gajić-Čapka et al., 2015; Ribes et al., 2019; Peña-Angulo et al., 2020; Jacob et al., 2018; Rajczak and Schär, 2017; Coppola et al., 2021a; Donat et al., 2014; Mathbout et al., 2018)	Limited evidence (Añel et al., 2014; U.S. Department of Agriculture Economic Research Service, 2016)	CMIP6 models, CMIP5 models, and RCMs project inconsistent changes in the region (Li et al., 2020; Cardell et al., 2020; Zollo et al., 2016; Samuels et al., 2018)	CMIP6 models project a robust increase in the intensity and frequency of heavy precipitation (Li et al., 2020; Annex). Median increase of more than 2% in the 50-year Rx1day and Rx5day events compared to the 1°C warming level (Li et al., 2020a) and more than 0% in annual Rx1day and Rx5day and less than -2% in annual Rx30day compared to pre-industrial (Annex). Additional evidence from CMIP5 and RCM simulations for an increase in the intensity of heavy precipitation (Cardell et al., 2020; Zollo et al., 2016; Samuels et al., 2018)	CMIP6 models project a robust increase in the intensity and frequency of heavy precipitation (Li et al., 2020; Annex). Median increase of more than 8% in the 50-year Rx1day and Rx5day events compared to the 1°C warming level (Li et al., 2020a) and more than 2% in annual Rx1day and Rx5day and less than -2% in annual Rx30day compared to pre-industrial (Annex). Additional evidence from CMIP5 and RCM simulations for an increase in the intensity of heavy precipitation (Cardell et al., 2020; Tramblay and Somot, 2018; Zollo et al., 2016; Samuels et al., 2018; Monjo et al., 2016; Rajczak et al., 2013; Coppola et al., 2021b; Driouech et al., 2020)
	Low confidence	*Low confidence*	Intensification of heavy precipitation: *Low confidence* (compared with the recent past (1995-2014))	Intensification of heavy precipitation: *Medium confidence* (compared with the recent past (1995-2014))	Intensification of heavy precipitation: *High confidence* (compared with the recent past (1995-2014))

[6] This region includes both northern Africa and southern Europe

ACCEPTED VERSION SUBJECT TO FINAL EDITING

			Medium confidence (compared with pre-industrial)	*High confidence* (compared with pre-industrial)	*High confidence* (compared with pre-industrial)
Western and Central Europe (WCE)	Intensification of heavy precipitation (Sun et al., 2020; Casanueva et al., 2014; Croitoru et al., 2013; Fischer et al., 2015; Roth et al., 2014; Willems, 2013).	Disagreement among studies (Wilcox et al., 2018; Philip et al., 2018; Schaller et al., 2014, Vautard et al., 2015)	CMIP6 models project an increase in the intensity and frequency of heavy precipitation (Li et al., 2020; Annex). Median increase of more than 0% in the 50-year Rx1day and Rx5day events compared to the 1°C warming level (Li et al., 2020a) and more than 6% in annual Rx1day and Rx5day and 4% in annual Rx30day compared to pre-industrial (Annex). Additional evidence from CMIP5 and RCM simulations for an increase in the intensity of heavy precipitation (Rajczak and Schär, 2017; Donnelly et al., 2017)	CMIP6 models project an increase in the intensity and frequency of heavy precipitation (Li et al., 2020; Annex). Median increase of more than 2% in the 50-year Rx1day and Rx5day events compared to the 1°C warming level (Li et al., 2020a) and more than 8% in annual Rx1day and Rx5day and 6% in annual Rx30day compared to pre-industrial (Annex). Additional evidence from CMIP5 and RCM simulations for an increase in the intensity of heavy precipitation (Rajczak and Schär, 2017; Donnelly et al., 2017)	CMIP6 models project a robust increase in the intensity and frequency of heavy precipitation (Li et al., 2020; Annex). Median increase of more than 10% in the 50-year Rx1day and Rx5day events compared to the 1°C warming level (Li et al., 2020a) and more than 15% in annual Rx1day and Rx5day and 10% in annual Rx30day compared to pre-industrial (Annex). Additional evidence from CMIP5 and RCM simulations for an increase in the intensity of heavy precipitation (Rajczak and Schär, 2017; Madsen et al., 2014)
	Medium confidence in the intensification of havy precipitation	*Low confidence*	Intensification of heavy precipitation: *Medium confidence* (compared with the recent past (1995-2014)) *High confidence* (compared with pre-industrial)	Intensification of heavy precipitation: *High confidence* (compared with the recent past (1995-2014)) *Likely* (compared with pre-industrial)	Intensification of heavy precipitation: *Very likely* (compared with the recent past (1995-2014)) *Extremely likely* (compared with pre-industrial)
Eastern Europe (EEU)	Significant intensification of heavy precipitation (Sun et al., 2020; Dunn et al., 2020; Ashabokov et al., 2017)	Limited evidence	CMIP6 models project an increase in the intensity and frequency of heavy precipitation (Li et al., 2020; Annex). Median increase of more than 2% in the 50-year Rx1day and Rx5day events compared to the 1°C warming level (Li et al., 2020a) and more than 6% in annual Rx1day and Rx5day and 4% in annual Rx30day compared to pre-industrial (Annex). Additional evidence from CMIP5 and CORDEX simulations for an increase in	CMIP6 models project an increase in the intensity and frequency of heavy precipitation (Li et al., 2020; Annex). Median increase of more than 4% in the 50-year Rx1day and Rx5day events compared to the 1°C warming level (Li et al., 2020a) and more than 8% in annual Rx1day and Rx5day and 6% in annual Rx30day compared to pre-industrial (Annex). Additional evidence from CMIP5 and CORDEX simulations for an increase in	CMIP6 models project a robust increase in the intensity and frequency of heavy precipitation (Li et al., 2020; Annex). Median increase of more than 15% in the 50-year Rx1day and Rx5day events compared to the 1°C warming level (Li et al., 2020a) and more than 15% in annual Rx1day and Rx5day and 10% in annual Rx30day compared to pre-industrial (Annex). Additional evidence from CMIP5/CMIP3 and CORDEX simulations for an increase in

ACCEPTED VERSION SUBJECT TO FINAL EDITING

			the intensity of heavy precipitation (Cardell et al., 2020)	the intensity of heavy precipitation (Cardell et al., 2020)	the intensity of heavy precipitation (Cardell et al., 2020; Rajczak et al., 2013)
	High confidence in the intensification of havy precipitation	*Low confidence*	Intensification of heavy precipitation: *Medium confidence* (compared with the recent past (1995-2014)) *High confidence* (compared with pre-industrial)	Intensification of heavy precipitation: *High confidence* (compared with the recent past (1995-2014)) *Likely* (compared with pre-industrial)	Intensification of heavy precipitation: *Very likely* (compared with the recent past (1995-2014)) *Extremely likely* (compared with pre-industrial)
Northern Europe (NEU)	Significant intensification of heavy precipitation (Sun et al., 2020; Dunn et al., 2020)	Robust evidence of a human contribution to the observed intensification of heavy precipitation in winter (Schaller et al., 2016; Vautard et al., 2016; Otto et al., 2018b), but not in summer (Schaller et al., 2014; Otto et al., 2015c; Wilcox et al., 2018)	CMIP6 models project an increase in the intensity and frequency of heavy precipitation (Li et al., 2020; Annex). Median increase of more than 0% in the 50-year Rx1day and Rx5day events compared to the 1°C warming level (Li et al., 2020a) and more than 6% in annual Rx1day, Rx5day, and Rx30day compared to pre-industrial (Annex). Additional evidence from CMIP5 and RCM simulations for an increase in the intensity of heavy precipitation (Donnelly et al., 2017)	CMIP6 models project an increase in the intensity and frequency of heavy precipitation (Li et al., 2020; Annex). Median increase of more than 4% in the 50-year Rx1day and Rx5day events compared to the 1°C warming level (Li et al., 2020a) and more than 8% in annual Rx1day and Rx5day and 6% in annual Rx30day compared to pre-industrial (Annex). Additional evidence from CMIP5 and RCM simulations for an increase in the intensity of heavy precipitation (Donnelly et al., 2017; Ramos et al., 2016; Romero and Emanuel, 2017)	CMIP6 models project a robust increase in the intensity and frequency of heavy precipitation (Li et al., 2020; Annex). Median increase of more than 15% in the 50-year Rx1day and Rx5day events compared to the 1°C warming level (Li et al., 2020a) and more than 15% in annual Rx1day, Rx5day, and Rx30day compared to pre-industrial (Annex). Additional evidence from CMIP5 and RCM simulations for an increase in the intensity of heavy precipitation (Madsen et al., 2014; Ramos et al., 2016; Romero and Emanuel, 2017; Donnelly et al., 2017)
	High confidence in the intensification of heavy precipitation *High confidence* in the changes in flood seasonality *High confidence* in the increase in extreme snow-melt events	*High confidence* in a human contribution to the observed intensification of heavy precipitation in winter.	Intensification of heavy precipitation: *Medium confidence* (compared with the recent past (1995-2014)) *High confidence* (compared with pre-industrial)	Intensification of heavy precipitation: *High confidence* (compared with the recent past (1995-2014)) *Likely* (compared with pre-industrial)	Intensification of heavy precipitation: *Very likely* (compared with the recent past (1995-2014)) *Extremely likely* (compared with pre-industrial)

[END TABLE 11.17 HERE]

ACCEPTED VERSION SUBJECT TO FINAL EDITING

[START TABLE 11.18 HERE]

Table 11.18: Observed trends, human contribution to observed trends, and projected changes at 1.5°C, 2°C and 4°C of global warming for meteorological droughts (MET), agricultural and ecological droughts (AGR/ECOL), and hydrological droughts (HYDR) in Europe, subdivided by AR6 regions. See Sections 11.9.1 and 11.9.4 for details.

Region and drought types		Observed trends	Detection and attribution; event attribution	Projections		
				+1.5 °C	+2 °C	+4 °C
Greenland/ Iceland (GIC)	MET	***Low confidence:*** **Limited evidence,** given **limited number of studies and limited data** (Walsh et al., 2020; Dunn et al., 2020)	***Low confidence:*** **Limited evidence** because of **lack of studies**	***Low confidence:*** **Limited evidence** given limited number of studies (Walsh et al., 2020); tendency to decrease in meteorological drought based on CDD (Chapter 11 Supplementary Material (11.SM)) and SPI (Touma et al., 2015)	***Low confidence:*** **Limited evidence** given limited number of studies (Walsh et al., 2020); tendency to decrease in meteorological drought based on CDD (Chapter 11 Supplementary Material (11.SM)) and SPI (Touma et al., 2015) ; also consistent with mixed index combining SPI and SPEI in Iceland (Spinoni et al., 2018b) Based on (Spinoni et al., 2018b) in Iceland [11 EUROCORDEX RCPs 4.5 AND 8.5] Based on the Standardized Precipitation Index: Decrease of drought frequency.	***Low confidence:*** **Limited evidence** given limited number of studies (Walsh et al., 2020) ; tendency to decrease in meteorological drought based on CDD (Chapter 11 Supplementary Material (11.SM)) and SPI (Touma et al., 2015); also consistent with mixed index combining SPI and SPEI in Iceland (Spinoni et al., 2018b) Based on (Spinoni et al., 2018b) in Iceland [11 EUROCORDEX RCPs 4.5 AND 8.5] Based on the Standardized Precipitation Index: Decrease of drought frequency.
	AGR ECOL	***Low confidence:*** **Limited evidence**, given **limited number of studies and limited data** (Walsh et al., 2020).	***Low confidence:*** **Limited evidence** because of lack of studies	***Low confidence:*** **Limited evidence** because of lack of studies (Walsh et al., 2020) and **inconsistent c**hanges in soil moisture in CMIP6 (Chapter 11 Supplementary Material (11.SM))	***Low confidence:*** **Limited evidence** because of lack of studies (Walsh et al., 2020) and **inconsistent** changes in soil moisture in CMIP6 (Chapter 11 Supplementary Material (11.SM))	***Low confidence:*** **Limited evidence** because of lack of studies (Walsh et al., 2020) and **inconsistent** changes in soil moisture in CMIP6 (Chapter 11 Supplementary Material (11.SM))
	HYDR	***Low confidence:*** **Limited evidence** given **limited number of studies and limited data** (Walsh et al., 2020)	***Low confidence:*** **Limited evidence** because of **lack of studies**	***Low confidence:*** **Limited evidence** because of **lack of studies**	***Low confidence:*** **Limited evidence** because of **lack of studies**	***Low confidence:*** **Limited evidence** because of **lack of studies**

ACCEPTED VERSION SUBJECT TO FINAL EDITING

Mediter-ranean (MED)[7]	MET	***Low confidence***: **Mixed signals.** Observed land precipitation trends show pronounced variability within the region, with magnitude and sign of trend in the past centrury depending on time period (Donat et al., 2014a; Stagge et al., 2017; Zittis, 2017; Mathbout et al., 2018a). There is *low confidence* in an increase of drought frequency and severity based on SPI (Spinoni et al., 2015; Gudmundsson and Seneviratne, 2016; Peña-Angulo et al., 2020; Vicente-Serrano et al., 2021; MedECC, 2020; Driouech et al., 2021)	***Low confidence***: **Mixed signals.** There are mixed signals within the region and *low confidence* in human influence on meteorological drought over MED (Kelley et al., 2015; Gudmundsson and Seneviratne, 2016; Knutson and Zeng, 2018; Wilcox et al., 2018)	***Medium confidence:*** **Increase.** With *medium confidence* both CMIP5 and CMIP6 show a decline in winter and summer total precipitation and increase in number of CDD (percentage precipitation change per degree of local warming is *with high confidence* larger in JJA than DJF) (Interactive Atlas, Cardell et al., 2020; Li et al., 2020)(Chapter 11 Supplementary Material (11.SM)). Also weak increase in meteorological drought based on SPI (Touma et al., 2015; Xu et al., 2019a).	***Medium confidence:*** **Increase.** With *medium confidence* both CMIP5 and CMIP6 show a decline in winter and summer total precipitation and increase in number of CDD (percentage precipitation change per degree of local warming is *with high confidence* larger in JJA than DJF) (Interactive Atlas, Cardell et al., 2020; Li et al., 2020)(Chapter 11 Supplementary Material (11.SM)). Also weak increase in meteorological drought based on SPI (Touma et al., 2015; Xu et al., 2019a).	***High confidence***: **Increase**. With *high confidence* both CMIP5 and CMIP6 (and EURO-CORDEX) show a decline in winter and summer total precipitation and increase in number of CDD. Drought intensity and frequency increase with *high confidence*, particularly in the southern Mediterranean (Samuels et al., 2018; Cardell et al., 2020; Cook et al., 2020; Li et al., 2020a; Spinoni et al., 2020; Coppola et al., 2021a)(Chapter 11 Supplementary Material (11.SM); Interactive Atlas) (Driouech et al., 2020)
	AGR ECOL	***Medium confidence:*** **Increase.** Increases in probability and intensity of agricultural and ecological droughts based on soil moisture and water-balance deficits, but weakers signals in some studies (Greve et al., 2014; Hanel et al., 2018; García-Herrera et al., 2019; Moravec et al., 2019; Padrón et al., 2020; Markonis et al., 2021). Also increases based on analyses using the Standardized Precipitation Evapotranspiration Index (SPEI) and the Palmer Drought Severity Index (PDSI). Increase of drought severity in South Europe (Stagge et al., 2017; Spinoni et al., 2019; Dai and Zhao, 2017), the Iberian Peninsula (Vicente-Serrano et al., 2014; González-Hidalgo et al., 2018). (Markonis et al., 2021): Increase in duration of agricultural droughts based on soil moisture déficits from 1901-2015.	***Medium confidence:*** of attribution of **increasing** trend in ecological and agricultural drought, based on soil moisture and water-balance metrics (Mariotti et al., 2015; García-Herrera et al., 2019; Marvel et al., 2019; Padrón et al., 2020) García-Herrera et al. (2019): Attribution of the 2016/2017 drought in southwestern Europe to climate change based on NCEP trends in soil moisture for weather anologues to 2016/2017 event. Mariotti et al. (2015): Attributable trend to CC: Decrease in soil moisture in summer that agrees with CMIP5 models.	***Medium confidence***: Drought **increase** for pre-industrial and recent past baselines. *Recent past baseline:* Decreasing soil water availability during drought events compared to 1971-2000, even when accounting for adaptation to mean conditions (Samaniego et al., 2018). Increasing drought duration and frequency compared to 1971-2000 (Xu et al., 2019a) Increasing drought magnitude based on SPEI-PM compared to +0.6°C baseline, using simulations within single ESM driven with sea surface temperature and sea ice conditions of 7 ESMs (Naumann et al., 2018)	***High confidence:*** Drought **increase** for pre-industrial and recent past baselines. *Recent past baseline:* Decreasing soil water availability during drought events compared to 1971-2000, even when accounting for adaptation to mean conditions; about twice larger signal compared to response at +1.5°C (Samaniego et al., 2018). Increasing drought duration and frequency compared to 1971-2000, with about twice larger signal compared to response at +1.5°C (Xu et al., 2019a) Increasing drought magnitude based on SPEI-PM compared to +0.6°C baseline, using simulations within single ESM driven with sea surface temperature and sea ice conditions of 7 ESMs (Naumann et al., 2018)	***Very likely***: Drought **increase** for pre-industrial and recent past baselines. *Recent past baseline:* Based on projections at +3°C: Large decreasing soil water availability during drought events compared to 1971-2000, even when accounting for adaptation to mean conditions; more than three times larger signal compared to response at +1.5°C (Samaniego et al., 2018). Based on projections at +3°C:About five-fold increase in drought magnitude based on SPEI-PM compared to +0.6°C baseline, using simulations within single ESM driven with sea surface temperature and sea ice conditions of 7 ESMs (Naumann et al., 2018) *Pre-industrial baseline:*

[7] This region includes both northern Africa and southern Europe

ACCEPTED VERSION SUBJECT TO FINAL EDITING

		(García-Herrera et al., 2019): Increase in soil moisture anomalies for weather analogues to 2016/2017 drought events in 1985-2018 vs 1948-1984. (Padrón et al., 2020): Weak signals in water-balance (precipitation-evapotranspiration) deficits in the dry season (1985-2014)-(1902-1950) (Greve et al., 2014): Increase in water-balance (precipitation-evapotranspiration) deficits on annual scale, (1985-2005) - (1948-1968) (Hanel et al., 2018): Significant decrease in soil moisture in Southern Europe from 1766-2015 from hydrological model driven with reconstructed meteorological data.	However: no emergence yet in soil moisture or P-E at grid cell scale (see CC-Box A.1. on Uncertainty). Padrón et al. (2020): Increasing drying trend in P-E during dry season over land areas, including in Mediterranean region (but attribution done at global scale, not regional scale) Marvel et al. (2019): Attributable drying trend in larger continental region with tree-ring data including strong signal in Mediterranean from 1900-1950 and currently increasing again after masking from aerosols.	*Pre-industrial baseline:* Decrease in soil moisture during drought events in CMIP6 models at +1.5°C vs pre-industrial baseline (Chapter 11 Supplementary Material (11.SM))	*Pre-industrial baseline:* Decreases of surface and total soil moisture, in both AMJJAS and ONDJFM half years (Cook et al., 2020) Decrease in soil moisture during drought events in CMIP6 models at +2°C vs pre-industrial baseline (Chapter 11 Supplementary Material (11.SM))	Strong decreases of surface and total soil moisture, in both spring-summer (AMJJAS) and fall-winter (ONDJFM) half years, with about twice larger response compared to +2°C (Cook et al., 2020) Very large decrease in soil moisture during drought events in CMIP6 models at +4°C vs pre-industrial baseline (Chapter 11 Supplementary Material (11.SM))
	HYDR	***High confidence***: **Increase** in frequency and severity of hydrological droughts, particularly in northern part of the domain (Lorenzo-Lacruz et al., 2013; Dai and Zhao, 2017; Gudmundsson et al., 2017, 2019, 2021) (Section 8.3.1.6).	***Medium confidence:*** **Increase.** Model-based assessment shows with *medium confidence* a human fingerprint on increased hydrological drought, related to rising temperature and atmospheric demand (Gudmundsson et al., 2017, 2021) and recent events. There is *medium confidence* that change in land use and terrestrial water management contribute to trends in hydrological drought (Teuling et al., 2019; Vicente-Serrano et al., 2019)	***Medium confidence***: **Increase** in hydrological drought for both pre-industrial and recent past baseline *Recent past baseline:* Forzieri et al. (2014): 20 yr deficit volumes are projected to increase by 50% by the 2020s compared to 1961-1990 (based on simulations with LISFLOOD model driven by 12 RCM simulations with different GCM-RCM pairs; CMIP3 GCMs, A1B scenario). Frequency of hydrological droughts is projected to increase (Touma et al., 2015).	***High confidence****:* **Increase.** *Recent past baseline:* Forzieri et al. (2014) [LISFLOOD simulations driven by 12 RCM-GCM pairs using CMIP3 GCMs]: Strong increase in the 20-yr return level minimum flow and deficit volumes in 2050 in A1B scenario compared to 1961-1990. Roudier et al. (2016) [11 RCMs]: Increase in the severity of the low flows at +2°C compared to 1971-2000 conditions in the Iberian Peninsula, Southern France and Greece. Schewe et al. (2014). Decrease between 30-50% of the annual runoff compared to 1980-2010.	***Very likely:*** **Increase** *Recent past baseline:* Forzieri et al. (2014) [LISFLOOD simulations driven by 12 RCM-GCM pairs using CMIP5 GCMs]: Strong increase in the 20-yr return level minimum flow and deficit volumes in 2080 in A1B scenario compared to 1961-1990 Prudhomme et al. (2014) [5 CMIP5 models driving 7 global impact models. RCP8.5, 2070-2099] Strong increase (40-60%) of dry days compared to 1976-2005 Giuntoli et al. (2015) (5 CMIP5 models driving 6 global hydrology models): 50-60% increase in frequency of days under low flow in 2066-2099 compared to 1972-2005. Strong signal to noise

ACCEPTED VERSION SUBJECT TO FINAL EDITING

					Touma et al. (2015)**:** Increase in the frequency of hydrological droughts relative to 1961-2005. *Pre-industrial baseline* Cook et al. (2020) [13 CMIP6 models and SSP1-2.6] Decrease in surface and total runoff, in both spring-summer (AMJJAS) and fall-winter (ONDJFM) half years, with strongest decreases for total runoff in spring-summer half -year-	ratio in terms of model agreement, strongest hot spot globally. *Pre-industrial baseline* Cook et al. (2020) [13 CMIP6 models and SSP3-7.0. Very strong decrease (40-60%) of total runoff in spring-summer half-year in southern Europe. Also strong decreases (>20%) for total runoff in fall-winter half-year, and for surface runoff in both half years (AMJJAS, ONDJFM).
Western and Central Europe (WCE)	MET	***Low confidence***: Limited evidence in change in severity. **Small and non-significant** changes and some dependency on season and location. Small and non significant changes in the frequency of dry spells (Zolina et al., 2013), CDD (Dunn et al., 2020), and in drought severity (SPI) (Orlowsky and Seneviratne, 2013; Stagge et al., 2017; Caloiero et al., 2018; Spinoni et al., 2019); but wet days decrease in summer (Gobiet et al., 2014).	***Low confidence***: **No signal or varying signal** depending on considered index (Gudmundsson and Seneviratne, 2016; Hauser et al., 2017)	***Low confidence***: I**nconsistent** signal in CDD in CMIP6 (Chapter 11 Supplementary Material (11.SM)) and in SPI in CMIP5 (Orlowsky and Seneviratne, 2013; Touma et al., 2015; Xu et al., 2019a).	***Low confidence:*** **Inconsistent** signal, but with weak tendency to drying in CDD in CMIP6 (Chapter 11 Supplementary Material (11.SM)) and SPI in CMIP5 (Orlowsky and Seneviratne, 2013; Touma et al., 2015; Xu et al., 2019a)	***Medium confidence:*** **Increase** based on CDD (Chapter 11 Supplementary Material (11.SM)). Also partial drying based on CMIP5 SPI, but strong geographical gradients and trends in part not signficant (Orlowsky and Seneviratne, 2013; Touma et al., 2015; Vicente-Serrano et al., 2020a). Summer decrease in wet day projected in Switzerland (Fischer et al., 2015).
	AGR ECOL	***Medium confidence:*** **Increase**. Dominant signal shows an increase in available studies based on soil moisture models and SPEI-PM (Greve et al., 2014; Trnka et al., 2015b; Hanel et al., 2018; Moravec et al., 2019; Spinoni et al., 2019; Padrón et al., 2020; Markonis et al., 2021), despitesome conflicting trends in some subregions (Spinoni et al., 2019; Padrón et al., 2020).	***Low confidence:*** **Limited evidence** due to limited number of studies; one study suggests attribution of the 2017 drought event to climate change due to decreasing trends in soil moisture (García-Herrera et al. 2019)	***Low confidence:*** **Inconsistent** signal in CMIP6 (Chapter 11 Supplementary Material (11.SM)) or **weak** (Xu et al., 2019a) or insignificant signal (Samaniego et al., 2018), mostly in summer season. A bit stronger signal based on SPEI-PM projections (Naumann et al., 2018)	***Medium confidence***: I**ncrease** of drought frequency and severity based on some AGR and ECOL drought metrics, for surface soil moisture and SPEI-PM (Chapter 11 Supplementary Material (11.SM))(Naumann et al., 2018; Samaniego et al., 2018; Xu et al., 2019a), mostly for summer season, but inconsistent trends for CMIP6 total soil moisture (Chapter 11 Supplementary Material (11.SM))(Cook et al., 2020)	***Medium confidence:*** **Increase** of drought frequency and severity based on some AGR and ECOL drought metrics, for CMIP6 surface soil moisture, root-zone soil moisture in hydrological models, and SPEI-PM (Chapter 11 Supplementary Material (11.SM))(Naumann et al., 2018; Samaniego et al., 2018; Xu et al., 2019a; Cook et al., 2020), mostly in summer season, but inconsistent trends for CMIP6 total soil moisture (Chapter 11 Supplementary Material (11.SM)) despite projected drying in substantial fraction of domain, in particular over France (Cook et al., 2020)
	HYDR	***Low confidence:*** **Weak or insignificant** trends (Stahl et al., 2010; Bard et al., 2015; Caillouet et al., 2017; Moravec et al., 2019; Vicente-Serrano et al., 2019;	***Low confidence:*** **Limited evidence** because of **lack of studies.**	***Low confidence***: **No or weak changes**; CORDEX simulations: no change in most of domain, slight wetting over the Alps (Forzieri et al., 2014; Touma et al., 2015; Marx et al.,	***Medium confidence:*** **Increase** in drying, mostly in western part of domain: summer season surface runoff compared to pre-industrial (Cook et al., 2020); annual discharge in substantial part of domain (Schewe et al.,	***Medium confidence:*** **Increase** based on several lignes of evidence: Tendency towards drying but geographical variations (Prudhomme et al., 2014; Giuntoli et al., 2015; Touma et al., 2015; Cook et al., 2020)

ACCEPTED VERSION SUBJECT TO FINAL EDITING

		Gudmundsson et al., 2021)		2018)	2014); increase in duration and magnitude of low flows over France, decrease in eastern part of domain (Touma et al., 2015; Roudier et al., 2016); CORDEX simulations. drying in western and southeastern parts of domain, but wetting over the Alps (Forzieri et al., 2014; Marx et al., 2018)	
Eastern Europe (EEU)	MET	***Low confidence***: **Inconsistent or insignificant changes.** Inconsistent or insignificant changes in CDD (Khlebnikova et al., 2019b; Dunn et al., 2020). No change or insignificant changes in SPI (Stagge et al., 2017; Caloiero et al., 2018; Spinoni et al., 2019)	***Low confidence:*** **Limited evidence** because of **lack of studies.**	***Low confidence***: **Inconsistent changes.** Inconsistent changes in CDD in CMIP6 (Chapter 11 Supplementary Material (11.SM)) and inSPI in CMIP5 (Touma et al., 2015; Xu et al., 2019a).	***Low confidence:*** **Inconsistent changes.** Inconsistent changes in CDD in CMIP6 (Chapter 11 Supplementary Material (11.SM)) and in SPI in CMIP5 (Touma et al., 2015; Xu et al., 2019a)	***Low confidence:*** **Inconsistent changes.** Inconsistent CDD changes in CMIP6 (Chapter 11 Supplementary Material (11.SM)) and weak decrease in drying or inconsistent changes in SPI projections (Touma et al., 2015; Spinoni et al., 2020; Vicente-Serrano et al., 2020a)
	AGR ECOL	***Low confidence:*** **Inconsistent or weak changes** (Greve et al., 2014; Spinoni et al., 2019; Padrón et al., 2020)	***Low confidence***: **Limited evidence** because of **lack of studies**	***Low confidence*** based on different metrics: **Inconsistent** trends in both CMIP6 surface and total soil moisture (Chapter 11 Supplementary Material (11.SM)); weak trends in CMIP5 soil moisture (Xu et al., 2019a) or SPEI-PM (Naumann et al., 2018) projections	***Low confidence*** based on different metrics : **Inconsistent** trends in both CMIP6 surface and total soil moisture (Chapter 11 Supplementary Material (11.SM)); weak trends in CMIP5 soil moisture (Xu et al., 2019a) or SPEI-PM (Naumann et al., 2018) projections	***Low confidence:*** **Inconsistent** trends based on different metrics: Slight wetting or inconsistent trends in total soil moisture (Chapter 11 Supplementary Material (11.SM)); (Cook et al., 2020); slight drying in surface soil moisture (Chapter 11 Supplementary Material (11.SM)); (Cook et al., 2020). Increasing drying of measures based on evaporative demand (Naumann et al., 2018)
	HYDR	***Low confidence***: **No enough data and limited studies** (Gudmundsson et al., 2021)	***Low confidence***: **Limited evidence** because of **lack of studies**	***Low confidence:*** **Limited evidence. One study shows lack of signal** (Touma et al., 2015)	***Low confidence***: **Inconsistent** changes. Some studies with increases in drought/decrease in runoff: (Forzieri et al., 2014) [11 RCMs forced with CMIP5 models and the LISFLOOD model] : Decrease in the 20 yr return level minimum flow and deficit volumes; (Cook et al., 2020): decrease in summer surface runoff in CMIP6 models. Some studies with no change in HYDR drought or runoff: (Touma et al., 2015; Roudier et al., 2016) [11 RCMs]: No substantial changes in the severity of the low flows; (Schewe et al., 2014): No substantial changes in the annual runoff.	***Medium confidence:*** **Weak increase**. (Forzieri et al., 2014) [11 RCMs forced with CMIP5 models and the LISFLOOD model] : Decrease in the 20 yr return level minimum flow and deficit. (Cook et al., 2020) [13 CMIP6 models and SSP3-7.0. Moderate decrease (20%) of total runoff in eastern Europe during the warm season.. (Prudhomme et al., 2014) [5 CMIP5 models and 7 global impact models. RCP8.5] Small increase (10%) of dry days. (Giuntoli et al., 2015): Weak increase in probability of low flow but low signal to noise ratio.

ACCEPTED VERSION SUBJECT TO FINAL EDITING

Northern Europe (NEU)	MET	***Medium confidence:* Decrease** in intensity and frequency; but dependence on considered index, time frame and region, including negligible trends over shorter periods or some subregions (Orlowsky and Seneviratne, 2013; Stagge et al., 2017; Spinoni et al., 2019; Dunn et al., 2020)	***Medium confidence:* Human contribution to decrease** (Gudmundsson and Seneviratne, 2016).	***Medium confidence:* Decrease** of drought frequency and severity based on SPI indices (Touma et al., 2015; Xu et al., 2019a), but unclear sign in CDD (Chapter 11 Supplementary Material (11.SM)).	***Medium confidence:* Decrease** of drought frequency and severity based on SPI indices (Touma et al., 2015; Xu et al., 2019a), but unclear sign in CDD (Chapter 11 Supplementary Material (11.SM)).	***Medium confidence: Decrease*** of drought frequency and severity based on SPI indices (Touma et al., 2015; Spinoni et al., 2020; Vicente-Serrano et al., 2020a) but unclear sign and drying tendency in CDD (Chapter 11 Supplementary Material (11.SM)). Same assessment for pre-industrial and recent past baselines.
	AGR ECOL	***Low confidence***: Overall **weak** signals and signs depend on considered season and index (Greve et al., 2014; Spinoni et al., 2019; Padrón et al., 2020; Markonis et al., 2021)	***Low confidence***: **Limited evidence** because of **lack of studies**	***Low confidence:* Inconsistent** signal in CMIP6 total soil moisture at +1.5°C compared to pre-industrial baseline (Chapter 11 Supplementary Material (11.SM)). Overall inconsistency of signals between studies for different indices (e.g. total soil moisture, surface soil moisture, SPEI-PM) independently of global warming level (Naumann et al., 2018; Xu et al., 2019a; Cook et al., 2020), but some spatial variations in trends and stronger signals in summer (Samaniego et al., 2018). Same assessment for pre-industrial and recent past baseline.	***Low confidence:* Inconsistent** signal in CMIP6 total soil moisture at +2°C compared to pre-industrial baseline (Chapter 11 Supplementary Material (11.SM)). Overall inconsistency of signals between studies for different indices (e.g. total soil moisture, surface soil moisture, SPEI-PM) independently of global warming level (Naumann et al., 2018; Xu et al., 2019a; Cook et al., 2020); but some spatial variations in trends and stronger signals in summer and over Scandinavia compared to UK (Samaniego et al., 2018). Same assessment for pre-industrial and recent past baseline.	***Low confidence:* Inconsistent** signal in CMIP6 total soil moisture at +4°C compared to pre-industrial baseline (Chapter 11 Supplementary Material (11.SM)). Overall inconsistency of signals between studies for different indices (e.g. total soil moisture, surface soil moisture, SPEI-PM) independently of global warming level (Naumann et al., 2018; Xu et al., 2019a; Cook et al., 2020; Vicente-Serrano et al., 2020a), but some spatial variations in trends and stronger signals in summer and over Scandinavia compared to UK (Samaniego et al., 2018). Same assessment for pre-industrial and recent past baseline.
	HYDR	***Medium confidence: D*ecrease** in hydrological drought for overall region, but trends are weak, can be of different sign in sub-regions, and are dependent on time frame (Harrigan et al., 2018; Kay et al., 2018; Barker et al., 2019; Gudmundsson et al., 2019, 2021; Vicente-Serrano et al., 2019)	***Low confidence***: **Limited evidence** because of **lack of studies**	***Low confidence*: Weak and inconsistent signals.** Slight increase in Scandinavia, slight decrease or no change in the UK (Forzieri et al., 2014; Touma et al., 2015; Marx et al., 2018)	***Low confidence***: **Inconsistent** changes, generally with drying in ESMs (CMIP5, CMIP6) and wetting in CORDEX (Forzieri et al., 2014; Touma et al., 2015; Roudier et al., 2016; Dai et al., 2018; Marx et al., 2018; Cook et al., 2020). Cook et al. (2020): Weak **i**ncrease in hydrological drought (decrease in runoff) in summer in Scandinavia.	***Medium confidence:*** Weak **increase** in hydrological drought in summer but low signal-to-noise ratio (Prudhomme et al., 2014; Giuntoli et al., 2015; Touma et al., 2015; Cook et al., 2020)

ACCEPTED VERSION SUBJECT TO FINAL EDITING

					Roudier et al. (2016): Decrease in magnitude and duration of low-flows (wetting trend) Dai et al. (2018): CMIP5, RCP4.5, (2070-2099)-(1970-1999): slight drying trend, but lack of model agreement. Forzieri et al. (2014), for (2050 compared to 1961-1990 baseline), CORDEX simulations: Decrease in magnitude of low-flow in Scandinavia no change in UK, Marx et al. (2018), CORDEX simulations: slight wetting in Scandinavia	

[START TABLE 11.19 HERE]

Table 11.19: Observed trends, human contribution to observed trends, and projected changes at 1.5°C, 2°C and 4°C of global warming for temperature extremes in North America, subdivided by AR6 regions. See Sections 11.9.1 and 11.9.2 for details

Region	Observed trends	Detection and attribution; event attribution	Projections		
			1.5 °C	2 °C	4 °C
All North America	Most subregions show a *likely* increase in the intensity and frequency of hot extremes and decrease in the intensity and frequency of cold extremes	Robust evidence of a human contribution to the observed increase in the intensity and frequency of hot extremes and decrease in the intensity and frequency of cold extremes (Seong et al., 2020)	CMIP6 models project a robust increase in the intensity and frequency of TXx events and a robust decrease in the intensity and frequency of TNn events (Li et al., 2020). Median increase of more than 0.5°C in the 50-year TXx and TNn events compared to the 1°C warming level (Li et al., 2020)	CMIP6 models project a robust increase in the intensity and frequency of TXx events and a robust decrease in the intensity and frequency of TNn events (Li et al., 2020). Median increase of more than 1°C in the 50-year TXx and TNn events compared to the 1°C warming level (Li et al., 2020)	CMIP6 models project a robust increase in the intensity and frequency of TXx events and a robust decrease in the intensity and frequency of TNn events (Li et al., 2020). Median increase of more than 4.5°C in the 50-year TXx and TNn events compared to the 1°C warming level (Li et al., 2020)
	Very likely increase in the intensity and frequency of hot extremes and decrease in the intensity and frequency of cold extremes	Human influence *very likely* contributed to the observed increase in the intensity and frequency of hot extremes and decrease in the intensity and frequency of cold extremes	Increase in the intensity and frequency of hot extremes: *Very likely* (compared with the recent past (1995-2014)) *Extremely likely* (compared with pre-industrial) Decrease in the intensity and frequency of cold extremes: *Very likely* (compared with the recent past (1995-2014)) *Extremely likely* (compared	Increase in the intensity and frequency of hot extremes: *Extremely likely* (compared with the recent past (1995-2014)) *Virtually certain* (compared with pre-industrial) Decrease in the intensity and frequency of cold extremes: *Extremely likely* (compared with the recent past (1995-	Increase in the intensity and frequency of hot extremes: *Virtually certain* (compared with the recent past (1995-2014)) *Virtually certain* (compared with pre-industrial) Decrease in the intensity and frequency of cold extremes: *Extremely likely* (compared with the recent past (1995-

ACCEPTED VERSION SUBJECT TO FINAL EDITING

			with pre-industrial)	2014)) *Virtually certain* (compared with pre-industrial)	2014)) *Virtually certain* (compared with pre-industrial)
North Central America (NCA)	Significant increases in the intensity and frequency of hot extremes and significant decreases in the intensity and frequency of cold extremes (García-Cueto et al., 2019; Martinez-Austria and Bandala, 2017; Montero-Martínez et al., 2018; Dunn et al., 2020)	Strong evidence of changes from observations that are in the direction of model projected changes for the future. The magnitude of projected changes increases with global warming.	CMIP6 models project an increase in the intensity and frequency of TXx events and a decrease in the intensity and frequency of TNn events (Li et al., 2020; Annex). Median increase of more than 0.5°C in the 50-year TXx and TNn events compared to the 1°C warming level (Li et al., 2020) and more than 1.5°C in annual TXx and TNn compared to pre-industrial (Annex). Additional evidence from CMIP5 and RCM simulations for an increase in the intensity and frequency of hot extremes and decrease in the intensity and frequency of cold extremes (Kharin et al., 2013; Sillmann et al., 2013b; Alexandru, 2018; Wehner et al., 2018b)	CMIP6 models project a robust increase in the intensity and frequency of TXx events and a decrease in the intensity and frequency of TNn events (Li et al., 2020; Annex). Median increase of more than 1°C in the 50-year TXx and TNn events compared to the 1°C warming level (Li et al., 2020) and more than 2°C in annual TXx and TNn compared to pre-industrial (Annex). Additional evidence from CMIP5 and RCM simulations for an increase in the intensity and frequency of hot extremes and decrease in the intensity and frequency of cold extremes (Kharin et al., 2013; Sillmann et al., 2013b; Alexandru, 2018; Wehner et al., 2018b)	CMIP6 models project a robust increase in the intensity and frequency of TXx events and a robust decrease in the intensity and frequency of TNn events (Li et al., 2020; Annex). Median increase of more than 3.5°C in the 50-year TXx and TNn events compared to the 1°C warming level (Li et al., 2020) and more than 4.5°C in annual TXx and TNn compared to pre-industrial (Annex). Additional evidence from CMIP5 and RCM simulations for an increase in the intensity and frequency of hot extremes and decrease in the intensity and frequency of cold extremes (Kharin et al., 2013; Sillmann et al., 2013b; Alexandru, 2018; Wehner et al., 2018b)
	Likely increase in the intensity and frequency of hot extremes and decrease in the intensity and frequency of cold extremes	*Medium confidence* in a human contribution to the observed increase in the intensity and frequency of hot extremes and decrease in the intensity and frequency of cold extremes	Increase in the intensity and frequency of hot extremes: *High confidence* (compared with the recent past (1995-2014)) *Likely* (compared with pre-industrial) Decrease in the intensity and frequency of cold extremes: *Medium confidence* (compared with the recent past (1995-2014)) *High confidence* (compared with pre-industrial)	Increase in the intensity and frequency of hot extremes: *Likely* (compared with the recent past (1995-2014)) *Very likely* (compared with pre-industrial) Decrease in the intensity and frequency of cold extremes: *High confidence* (compared with the recent past (1995-2014)) *Likely* (compared with pre-industrial)	Increase in the intensity and frequency of hot extremes: *Extremely likely* (compared with the recent past (1995-2014)) *Virtually certain* (compared with pre-industrial) Decrease in the intensity and frequency of cold extremes: *Very likely* (compared with the recent past (1995-2014)) *Extremely likely* (compared with pre-industrial)
W. North America (WNA)	Significant increases in the intensity and frequency of hot extremes and significant decreases in the intensity and	Evidence of a human contribution to the observed increase in the intensity and frequency of hot extremes	CMIP6 models project a robust increase in the intensity and frequency of TXx events and a decrease in	CMIP6 models project a robust increase in the intensity and frequency of TXx events and a decrease in	CMIP6 models project a robust increase in the intensity and frequency of TXx events and a robust

ACCEPTED PENDING SUBJECT TO FINAL EDITING

	frequency of cold extremes (Vose et al., 2017; Dunn et al., 2020)	and decrease in the intensity and frequency of cold extremes (Seager et al., 2015; Angélil et al., 2017)	the intensity and frequency of TNn events (Li et al., 2020; Annex). Median increase of more than 0C in the 50-year TXx and TNn events compared to the 1°C warming level (Li et al., 2020) and more than 2°C in annual TXx and TNn compared to pre-industrial (Annex). Additional evidence from CMIP5 and RCM simulations for an increase in the intensity and frequency of hot extremes and decrease in the intensity and frequency of cold extremes (Vose et al., 2017; Palipane and Grotjahn, 2018; Wehner et al., 2018b)	the intensity and frequency of TNn events (Li et al., 2020; Annex). Median increase of more than 1°C in the 50-year TXx and TNn events compared to the 1°C warming level (Li et al., 2020) and more than 3°C in annual TXx and TNn compared to pre-industrial (Annex). Additional evidence from CMIP5 and RCM simulations for an increase in the intensity and frequency of hot extremes and decrease in the intensity and frequency of cold extremes (Vose et al., 2017; Palipane and Grotjahn, 2018; Wehner et al., 2018b)	decrease in the intensity and frequency of TNn events (Li et al., 2020; Annex). Median increase of more than 5°C in the 50-year TXx and TNn events compared to the 1°C warming level (Li et al., 2020) and more than 5.5°C in annual TXx and TNn compared to pre-industrial (Annex). Additional evidence from CMIP5 and RCM simulations for an increase in the intensity and frequency of hot extremes and decrease in the intensity and frequency of cold extremes (Vose et al., 2017; Palipane and Grotjahn, 2018; Wehner et al., 2018b)
	Likely increase in the intensity and frequency of hot extremes and decrease in the intensity and frequency of cold extremes	*Medium confidence* in a human contribution to the observed increase in the intensity and frequency of hot extremes and decrease in the intensity and frequency of cold extremes	Increase in the intensity and frequency of hot extremes: *Likely* (compared with the recent past (1995-2014)) *Very likely* (compared with pre-industrial) Decrease in the intensity and frequency of cold extremes: *Medium confidence* (compared with the recent past (1995-2014)) *High confidence* (compared with pre-industrial)	Increase in the intensity and frequency of hot extremes: *Very likely* (compared with the recent past (1995-2014)) *Extremely likely* (compared with pre-industrial) Decrease in the intensity and frequency of cold extremes: *High confidence* (compared with the recent past (1995-2014)) *Likely* (compared with pre-industrial)	Increase in the intensity and frequency of hot extremes: *Virtually certain* (compared with the recent past (1995-2014)) *Virtually certain* (compared with pre-industrial) Decrease in the intensity and frequency of cold extremes: *Very likely* (compared with the recent past (1995-2014)) *Extremely likely* (compared with pre-industrial)
C. North America (CNA)	Weak and inconsistent trends (Dunn et al., 2020)	Evidence of a human contribution for some events but cannot be generalized	CMIP6 models project a robust increase in the intensity and frequency of TXx events and a decrease in the intensity and frequency of TNn events (Li et al., 2020; Annex). Median increase of more than 0.5°C in the 50-year TXx and TNn events compared to the 1°C warming level (Li et al., 2020) and more than 2°C in annual TXx and TNn compared to pre-	CMIP6 models project a robust increase in the intensity and frequency of TXx events and a decrease in the intensity and frequency of TNn events (Li et al., 2020; Annex). Median increase of more than 1.5°C in the 50-year TXx and TNn events compared to the 1°C warming level (Li et al., 2020) and more than 3°C in annual TXx and TNn compared to pre-	CMIP6 models project a robust increase in the intensity and frequency of TXx events and a robust decrease in the intensity and frequency of TNn events (Li et al., 2020; Annex). Median increase of more than 4.5°C in the 50-year TXx and TNn events compared to the 1°C warming level (Li et al., 2020) and more than 5.5°C in annual TXx and TNn

ACCEPTED VERSION SUBJECT TO FINAL EDITS

			industrial (Annex). Additional evidence from CMIP5 and RCM simulations for an increase in the intensity and frequency of hot extremes and decrease in the intensity and frequency of cold extremes (Vose et al., 2017; Wehner et al., 2018b)	industrial (Annex). Additional evidence from CMIP5 and RCM simulations for an increase in the intensity and frequency of hot extremes and decrease in the intensity and frequency of cold extremes (Vose et al., 2017; Wehner et al., 2018b)	compared to pre-industrial (Annex). Additional evidence from CMIP5 and RCM simulations for an increase in the intensity and frequency of hot extremes and decrease in the intensity and frequency of cold extremes (Vose et al., 2017; Wehner et al., 2018b)
	Low confidence	*Low confidence*	Increase in the intensity and frequency of hot extremes: *Likely* (compared with the recent past (1995-2014)) *Very likely* (compared with pre-industrial) Decrease in the intensity and frequency of cold extremes: *Medium confidence* (compared with the recent past (1995-2014)) *High confidence* (compared with pre-industrial)	Increase in the intensity and frequency of hot extremes: *Very likely* (compared with the recent past (1995-2014)) *Extremely likely* (compared with pre-industrial) Decrease in the intensity and frequency of cold extremes: *High confidence* (compared with the recent past (1995-2014)) *Very likely* (compared with pre-industrial)	Increase in the intensity and frequency of hot extremes: *Virtually certain* (compared with the recent past (1995-2014)) *Virtually certain* (compared with pre-industrial) Decrease in the intensity and frequency of cold extremes: *Very likely* (compared with the recent past (1995-2014)) *Extremely likely* (compared with pre-industrial)
E. North America (ENA)	Weak and inconsistent trends (Dunn et al., 2020)	Evidence of a human contribution for some events, but cannot be generalized	CMIP6 models project a robust increase in the intensity and frequency of TXx events and a robust decrease in the intensity and frequency of TNn events (Li et al., 2020; Annex). Median increase of more than 0.5°C in the 50-year TXx and TNn events compared to the 1°C warming level (Li et al., 2020) and more than 1.5°C in annual TXx and TNn compared to pre-industrial (Annex). Additional evidence from CMIP5 and RCM simulations for an increase in the intensity and frequency of hot extremes and decrease in the intensity and frequency of cold extremes (Vose et al.,	CMIP6 models project a robust increase in the intensity and frequency of TXx events and a robust decrease in the intensity and frequency of TNn events (Li et al., 2020; Annex). Median increase of more than 1.5°C in the 50-year TXx and TNn events compared to the 1°C warming level (Li et al., 2020) and more than 2.5°C in annual TXx and TNn compared to pre-industrial (Annex). Additional evidence from CMIP5 and RCM simulations for an increase in the intensity and frequency of hot extremes and decrease in the intensity and frequency of cold extremes (Vose et al.,	CMIP6 models project a robust increase in the intensity and frequency of TXx events and a robust decrease in the intensity and frequency of TNn events (Li et al., 2020; Annex). Median increase of more than 5°C in the 50-year TXx and TNn events compared to the 1°C warming level (Li et al., 2020) and more than 5.5°C in annual TXx and TNn compared to pre-industrial (Annex). Additional evidence from CMIP5 and RCM simulations for an increase in the intensity and frequency of hot extremes and decrease in the intensity and frequency of cold extremes (Vose et al.,

ACCEPTED VERSION SUBJECT TO FINAL EDITING

			2017; Wehner et al., 2018b; Zhang et al., 2019d).	2017; Wehner et al., 2018b; Zhang et al., 2019d).	2017; Wehner et al., 2018b; Zhang et al., 2019d).
	Low confidence	*Low confidence*	Increase in the intensity and frequency of hot extremes: *Likely* (compared with the recent past (1995-2014)) *Very likely* (compared with pre-industrial) Decrease in the intensity and frequency of cold extremes: *Likely* (compared with the recent past (1995-2014)) *Very likely* (compared with pre-industrial)	Increase in the intensity and frequency of hot extremes: *Very likely* (compared with the recent past (1995-2014)) *Extremely likely* (compared with pre-industrial) Decrease in the intensity and frequency of cold extremes: *Very likely* (compared with the recent past (1995-2014)) *Extremely likely* (compared with pre-industrial)	Increase in the intensity and frequency of hot extremes: *Virtually certain* (compared with the recent past (1995-2014)) *Virtually certain* (compared with pre-industrial) Decrease in the intensity and frequency of cold extremes: *Virtually certain* (compared with the recent past (1995-2014)) *Virtually certain* (compared with pre-industrial)
N. E. North America (NEN)	Significant increases in the intensity and frequency of hot extremes and significant decreases in the intensity and frequency of cold extremes (Vincent et al., 2018; Zhang et al., 2019c; Dunn et al., 2020)	Robust evidence of a human contribution to the observed increase in the intensity and frequency of hot extremes and decrease in the intensity and frequency of cold extremes (Wan et al., 2019)	CMIP6 models project a robust increase in the intensity and frequency of TXx events and a robust decrease in the intensity and frequency of TNn events (Li et al., 2020; Annex). Median increase of more than 0.5°C in the 50-year TXx and TNn events compared to the 1°C warming level (Li et al., 2020) and more than 2°C in annual TXx and TNn compared to pre-industrial (Annex). Additional evidence from CMIP5 and RCM simulations for an increase in the intensity and frequency of hot extremes and decrease in the intensity and frequency of cold extremes (Li et al., 2018d; Zhang et al., 2019d)	CMIP6 models project a robust increase in the intensity and frequency of TXx events and a robust decrease in the intensity and frequency of TNn events (Li et al., 2020; Annex). Median increase of more than 1.5°C in the 50-year TXx and TNn events compared to the 1°C warming level (Li et al., 2020) and more than 2.5°C in annual TXx and TNn compared to pre-industrial (Annex). Additional evidence from CMIP5 and RCM simulations for an increase in the intensity and frequency of hot extremes and decrease in the intensity and frequency of cold extremes (Li et al., 2018d; Zhang et al., 2019d)	CMIP6 models project a robust increase in the intensity and frequency of TXx events and a robust decrease in the intensity and frequency of TNn events (Li et al., 2020; Annex). Median increase of more than 5°C in the 50-year TXx and TNn events compared to the 1°C warming level (Li et al., 2020) and more than 5.5°C in annual TXx and TNn compared to pre-industrial (Annex). Additional evidence from CMIP5 and RCM simulations for an increase in the intensity and frequency of hot extremes and decrease in the intensity and frequency of cold extremes (Li et al., 2018d; Zhang et al., 2019d)
	Very likely increase in the intensity and frequency of hot extremes and decrease in the intensity and frequency of cold extremes	*High confidence* in a human contribution to the observed increase in the intensity and frequency of hot extremes and decrease in the intensity and frequency of cold extremes	Increase in the intensity and frequency of hot extremes: *Likely* (compared with the recent past (1995-2014)) *Very likely* (compared with pre-industrial) Decrease in the intensity and	Increase in the intensity and frequency of hot extremes: *Very likely* (compared with the recent past (1995-2014)) *Extremely likely* (compared with pre-industrial) Decrease in the intensity and	Increase in the intensity and frequency of hot extremes: *Virtually certain* (compared with the recent past (1995-2014)) *Virtually certain* (compared with pre-industrial)

ACCEPTED VERSION SUBJECT TO MINOR EDITING

			frequency of cold extremes: *Likely* (compared with the recent past (1995-2014)) *Very likely* (compared with pre-industrial)	frequency of cold extremes: *Very likely* (compared with the recent past (1995-2014)) *Extremely likely* (compared with pre-industrial)	Decrease in the intensity and frequency of cold extremes: *Virtually certain* (compared with the recent past (1995-2014)) *Virtually certain* (compared with pre-industrial)
N. W. North America (NWN)	Significant increases in the intensity and frequency of hot extremes and significant decreases in the intensity and frequency of cold extremes (Vincent et al., 2018; Zhang et al., 2019c; Dunn et al., 2020)	Robust evidence of a human contribution to the observed increase in the intensity and frequency of hot extremes and decrease in the intensity and frequency of cold extremes (Wan et al., 2019)	CMIP6 models project a robust increase in the intensity and frequency of TXx events and a robust decrease in the intensity and frequency of TNn events (Li et al., 2020; Annex). Median increase of more than 0.5°C in the 50-year TXx and TNn events compared to the 1°C warming level (Li et al., 2020) and more than 1.5°C in annual TXx and TNn compared to pre-industrial (Annex). Additional evidence from CMIP5 and RCM simulations for an increase in the intensity and frequency of hot extremes and decrease in the intensity and frequency of cold extremes (Bennett and Walsh, 2015; Li et al., 2018d; Zhang et al., 2019d).	CMIP6 models project a robust increase in the intensity and frequency of TXx events and a robust decrease in the intensity and frequency of TNn events (Li et al., 2020; Annex). Median increase of more than 1°C in the 50-year TXx and TNn events compared to the 1°C warming level (Li et al., 2020) and more than 2.5°C in annual TXx and TNn compared to pre-industrial (Annex). Additional evidence from CMIP5 and RCM simulations for an increase in the intensity and frequency of hot extremes and decrease in the intensity and frequency of cold extremes (Bennett and Walsh, 2015; Li et al., 2018d; Zhang et al., 2019d).	CMIP6 models project a robust increase in the intensity and frequency of TXx events and a robust decrease in the intensity and frequency of TNn events (Li et al., 2020; Annex). Median increase of more than 4°C in the 50-year TXx and TNn events compared to the 1°C warming level (Li et al., 2020) and more than 5°C in annual TXx and TNn compared to pre-industrial (Annex). Additional evidence from CMIP5 and RCM simulations for an increase in the intensity and frequency of hot extremes and decrease in the intensity and frequency of cold extremes (Bennett and Walsh, 2015; Li et al., 2018d; Zhang et al., 2019d).
	Very likely increase in the intensity and frequency of hot extremes and decrease in the intensity and frequency of cold extremes	*High confidence* in a human contribution to the observed increase in the intensity and frequency of hot extremes and decrease in the intensity and frequency of cold extremes	Increase in the intensity and frequency of hot extremes: *Likely* (compared with the recent past (1995-2014)) *Very likely* (compared with pre-industrial) Decrease in the intensity and frequency of cold extremes: *Likely* (compared with the recent past (1995-2014)) *Very likely* (compared with pre-industrial)	Increase in the intensity and frequency of hot extremes: *Very likely* (compared with the recent past (1995-2014)) *Extremely likely* (compared with pre-industrial) Decrease in the intensity and frequency of cold extremes: *Very likely* (compared with the recent past (1995-2014)) *Extremely likely* (compared with pre-industrial)	Increase in the intensity and frequency of hot extremes: *Virtually certain* (compared with the recent past (1995-2014)) *Virtually certain* (compared with pre-industrial) Decrease in the intensity and frequency of cold extremes: *Virtually certain* (compared with the recent past (1995-2014)) *Virtually certain* (compared with pre-industrial)

ACCEPTED VERSION SUBJECT TO FINAL EDITING

[END TABLE 11.19 HERE]

[START TABLE 11.20 HERE]

Table 11.20: Observed trends, human contribution to observed trends, and projected changes at 1.5°C, 2°C and 4°C of global warming for heavy precipitation in North America, subdivided by AR6 regions. See Sections 11.9.1 and 11.9.3 for details

Region	Observed trends	Detection and attribution; event attribution	Projections		
			1.5 °C	2 °C	4 °C
All North America	Significant intensification of heavy precipitation (Sun et al., 2020; Dunn et al., 2020)	Robust evidence of a human contribution to the observed intensification of heavy precipitation (Kirchmeier-Young and Zhang, 2020; Paik et al., 2020)	CMIP6 models project a robust increase in the intensity and frequency of heavy precipitation (Li et al., 2020a). Median increase of more than 2% in the 50-year Rx1day and Rx5day events compared to the 1°C warming level (Li et al., 2020a)	CMIP6 models project a robust increase in the intensity and frequency of heavy precipitation (Li et al., 2020a). Median increase of more than 6% in the 50-year Rx1day and Rx5day events compared to the 1°C warming level (Li et al., 2020a)	CMIP6 models project a robust increase in the intensity and frequency of heavy precipitation (Li et al., 2020a). Median increase of more than 15% in the 50-year Rx1day and Rx5day events compared to the 1°C warming level (Li et al., 2020a)
	Likely intensification of heavy precipitation	Human influence *likely* contributed to the observed intensification of heavy precipitation	Intensification of heavy precipitation: *Likely* (compared with the recent past (1995-2014)) *Very likely* (compared with pre-industrial)	Intensification of heavy precipitation: *Very likely* (compared with the recent past (1995-2014)) *Extremely likely* (compared with pre-industrial)	Intensification of heavy precipitation: *Virtually certain* (compared with the recent past (1995-2014)) *Virtually certain* (compared with pre-industrial)
North Central America (NCA)	Trends are generally not significant (Sun et al., 2020; Dunn et al., 2020; Donat et al., 2016; García-Cueto et al., 2019)	Disagreement among studies (Eden et al., 2016; Pall et al., 2017; Hoerling et al., 2014)	CMIP6 models project an increase in the intensity and frequency of heavy precipitation (Li et al., 2020; Annex). Median increase of more than 2% in the 50-year Rx1day and Rx5day events compared to the 1°C warming level (Li et al., 2020a) and more than 2% in annual Rx1day and Rx5day and 0% in annual Rx30day compared to pre-industrial (Annex).	CMIP6 models project an increase in the intensity and frequency of heavy precipitation (Li et al., 2020; Annex). Median increase of more than 4% in the 50-year Rx1day and Rx5day events compared to the 1°C warming level (Li et al., 2020a) and more than 4% in annual Rx1day and Rx5day and 0% in annual Rx30day compared to pre-industrial (Annex).	CMIP6 models project a robust increase in the intensity and frequency of heavy precipitation (Li et al., 2020; Annex). Median increase of more than 15% in the 50-year Rx1day and Rx5day events compared to the 1°C warming level (Li et al., 2020a) and more than 10% in annual Rx1day and Rx5day and 2% in annual Rx30day compared to pre-industrial (Annex).
	Low confidence	*Low confidence*	Intensification of heavy precipitation: *Medium confidence* (compared with the recent past (1995-2014)) *High confidence* (compared	Intensification of heavy precipitation: *High confidence* (compared with the recent past (1995-2014)) *Likely* (compared with pre-	Intensification of heavy precipitation: *Very likely* (compared with the recent past (1995-2014)) *Extremely likely* (compared with pre-industrial)

ACCEPTED VERSION SUBJECT TO FINAL EDITING

			with pre-industrial)	industrial)	
W. North America (WNA)	Lack of agreement on the evidence of trends (Sun et al., 2020; Dunn et al., 2020; Easterling et al. 2017; Wu 2015)	Evidence of a human contribution for some events (Easterling et al., 2017; Kirchmeier-Young and Zhang, 2020), but cannot be generalized	CMIP6 models project inconsistent changes in the region (Li et al., 2020a)	CMIP6 models project an increase in the intensity and frequency of heavy precipitation (Li et al., 2020; Annex). Median increase of more than 2% in the 50-year Rx1day and Rx5day events compared to the 1°C warming level (Li et al., 2020a) and more than 6% in annual Rx1day and Rx5day and 4% in annual Rx30day compared to pre-industrial (Annex). Additional evidence from CMIP5 and RCM simulations for an increase in the intensity of heavy precipitation (Easterling et al., 2017)	CMIP6 models project a robust increase in the intensity and frequency of heavy precipitation (Li et al., 2020; Annex). Median increase of more than 10% in the 50-year Rx1day and Rx5day events compared to the 1°C warming level (Li et al., 2020a) and more than 10% in annual Rx1day, Rx5day, and Rx30day compared to pre-industrial (Annex). Additional evidence from CMIP5 and RCM simulations for an increase in the intensity of heavy precipitation (Easterling et al., 2017)
	Low confidence	*Low confidence*	Intensification of heavy precipitation: *Low confidence* (compared with the recent past (1995-2014)) *Medium confidence* (compared with pre-industrial)	Intensification of heavy precipitation: *Medium confidence* (compared with the recent past (1995-2014)) *High confidence* (compared with pre-industrial)	Intensification of heavy precipitation: *Likely* (compared with the recent past (1995-2014)) *Very likely* (compared with pre-industrial)
C. North America (CNA)	Significant intensification of heavy precipitation (Dunn et al., 2020; Easterling et al., 2017; Wu, 2015; Emanuel, 2017; Risser and Wehner, 2017; Trenberth et al., 2018; van Oldenborgh et al., 2017; Wang et al., 2018).	Evidence of a human contribution to the observed intensification of heavy precipitation (Easterling et al., 2017; Kirchmeier-Young and Zhang, 2020; Emanuel, 2017; Risser and Wehner, 2017; Trenberth et al., 2018; van Oldenborgh et al., 2017; Wang et al., 2018)	CMIP6 models project an increase in the intensity and frequency of heavy precipitation (Li et al., 2020; Annex). Median increase of more than 2% in the 50-year Rx1day and Rx5day events compared to the 1°C warming level (Li et al., 2020a) and more than 4% in annual Rx1day and Rx5day and 2% in annual Rx30day compared to pre-industrial (Annex). Additional evidence from CMIP5 and RCM simulations for an increase in the intensity of heavy precipitation	CMIP6 models project an increase in the intensity and frequency of heavy precipitation (Li et al., 2020; Annex). Median increase of more than 4% in the 50-year Rx1day and Rx5day events compared to the 1°C warming level (Li et al., 2020a) and more than 6% in annual Rx1day, Rx5day, and Rx30day compared to pre-industrial (Annex). Additional evidence from CMIP5 and RCM simulations for an increase in the intensity of heavy precipitation	CMIP6 models project a robust increase in the intensity and frequency of heavy precipitation (Li et al., 2020; Annex). Median increase of more than 10% in the 50-year Rx1day and Rx5day events compared to the 1°C warming level (Li et al., 2020a) and more than 10% in annual Rx1day, Rx5day, and Rx30day compared to pre-industrial (Annex). Additional evidence from CMIP5 and RCM simulations for an increase in the intensity

ACCEPTED VERSION SUBJECT TO FINAL EDITING

			(Easterling et al., 2017)	(Easterling et al., 2017)	of heavy precipitation (Easterling et al., 2017; Knutson et al., 2015; Kossin et al., 2017)
	High confidence in the intensificationof heavy precipitation	*Medium confidence* in a human contribution to the intensification of heavy precipitation.	Intensification of heavy precipitation: *Medium confidence* (compared with the recent past (1995-2014)) *High confidence* (compared with pre-industrial)	Intensification of heavy precipitation: *High confidence* (compared with the recent past (1995-2014)) *Likely* (compared with pre-industrial)	Intensification of heavy precipitation: *Very likely* (compared with the recent past (1995-2014)) *Extremely likely* (compared with pre-industrial)
E. North America (ENA)	Significant intensification of heavy precipitation (Sun et al., 2020; Dunn et al., 2020; Easterling et al., 2017; Wu, 2015; Emanuel, 2017; Risser and Wehner, 2017; Trenberth et al., 2018; van Oldenborgh et al., 2017; Wang et al., 2018), but a lack of a significant trend over Canada (Shephard et al., 2014; Mekis et al., 2015; Vincent et al., 2018)	Evidence of a human contribution for some events (Easterling et al., 2017; Teufel et al., 2019; Kirchmeier-Young and Zhang, 2020), but cannot be generalized	CMIP6 models project an increase in the intensity and frequency of heavy precipitation (Li et al., 2020; Annex). Median increase of more than 2% in the 50-year Rx1day and Rx5day events compared to the 1°C warming level (Li et al., 2020a) and more than 6% in annual Rx1day and Rx5day and 4% in annual Rx30day compared to pre-industrial (Annex). Additional evidence from CMIP5 and RCM simulations for an increase in the intensity of heavy precipitation (Zhang et al., 2019; Easterling et al., 2017)	CMIP6 models project an increase in the intensity and frequency of heavy precipitation (Li et al., 2020; Annex). Median increase of more than 4% in the 50-year Rx1day and Rx5day events compared to the 1°C warming level (Li et al., 2020a) and more than 8% in annual Rx1day and Rx5day and 6% in annual Rx30day compared to pre-industrial (Annex). Additional evidence from CMIP5 and RCM simulations for an increase in the intensity of heavy precipitation (Zhang et al., 2019; Easterling et al., 2017)	CMIP6 models project a robust increase in the intensity and frequency of heavy precipitation (Li et al., 2020; Annex). Median increase of more than 15% in the 50-year Rx1day and Rx5day events compared to the 1°C warming level (Li et al., 2020a) and more than 15% in annual Rx1day and Rx5day and 10% in annual Rx30day compared to pre-industrial (Annex). Additional evidence from CMIP5 and RCM simulations for an increase in the intensity of heavy precipitation (Zhang et al., 2019; Easterling et al., 2017; Knutson et al., 2015; Kossin et al., 2017)
	High confidence in the intensification of heavy precipitation	*Low confidence*	Intensification of heavy precipitation: *Medium confidence* (compared with the recent past (1995-2014)) *High confidence* (compared with pre-industrial)	Intensification of heavy precipitation: *High confidence* (compared with the recent past (1995-2014)) *Likely* (compared with pre-industrial)	Intensification of heavy precipitation: *Very likely* (compared with the recent past (1995-2014)) *Extremely likely* (compared with pre-industrial)
N. E. North America (NEN)	Limited evidence (Shephard et al., 2014; Mekis et al., 2015; Vincent et al., 2018)	Evidence of a human contribution for some events (Szeto et al., 2015), but cannot be generalized	CMIP6 models project an increase in the intensity and frequency of heavy precipitation (Li et al., 2020; Annex). Median increase of more than 2% in the 50-year	CMIP6 models project a robust increase in the intensity and frequency of heavy precipitation (Li et al., 2020; Annex). Median increase of more than 6% in	CMIP6 models project a robust increase in the intensity and frequency of heavy precipitation (Li et al., 2020; Annex). Median increase of more than 20% in

ACCEPTED VERSION SUBJECT TO FINAL EDITING

			Rx1day and Rx5day events compared to the 1°C warming level (Li et al., 2020a) and more than 8% in annual Rx1day and Rx5day and 6% in annual Rx30day compared to pre-industrial (Annex). Additional evidence from CMIP5 and RCM simulations for an increase in the intensity of heavy precipitation (Zhang et al., 2019d)	the 50-year Rx1day and Rx5day events compared to the 1°C warming level (Li et al., 2020a) and more than 10% in annual Rx1day and Rx5day and 8% in annual Rx30day compared to pre-industrial (Annex). Additional evidence from CMIP5 and RCM simulations for an increase in the intensity of heavy precipitation (Zhang et al., 2019d)	the 50-year Rx1day and Rx5day events compared to the 1°C warming level (Li et al., 2020a) and more than 20% in annual Rx1day and Rx5day and 15% in annual Rx30day compared to pre-industrial (Annex). Additional evidence from CMIP5 and RCM simulations for an increase in the intensity of heavy precipitation (Zhang et al., 2019d)
	Low confidence	*Low confidence*	Intensification of heavy precipitation: *High confidence* (compared with the recent past (1995-2014)) *Likely* (compared with pre-industrial)	Intensification of heavy precipitation: *Likely* (compared with the recent past (1995-2014)) *Very likely* (compared with pre-industrial)	Intensification of heavy precipitation: *Extremely likely* (compared with the recent past (1995-2014)) *Virtually certain* (compared with pre-industrial)
N. W. North America (NWN)	Lack of agreement on the evidence of trends (Sun et al., 2020; Dunn et al., 2020; Mekis et al., 2015; Shephard et al., 2014; Vincent et al., 2018)	Evidence of a human contribution for some events (Teufel et al., 2017; Kirchmeier-Young and Zhang, 2020), but cannot be generalized	CMIP6 models project an increase in the intensity and frequency of heavy precipitation (Li et al., 2020; Annex). Median increase of more than 2% in the 50-year Rx1day and Rx5day events compared to the 1°C warming level (Li et al., 2020a) and more than 6% in annual Rx1day, Rx5day, and Rx30day compared to pre-industrial (Annex). Additional evidence from CMIP5 and RCM simulations for an increase in the intensity of heavy precipitation (Bennett and Walsh, 2015; Zhang et al., 2019d)	CMIP6 models project a robust increase in the intensity and frequency of heavy precipitation (Li et al., 2020; Annex). Median increase of more than 6% in the 50-year Rx1day and Rx5day events compared to the 1°C warming level (Li et al., 2020a) and more than 10% in annual Rx1day, Rx5day, and Rx30day compared to pre-industrial (Annex). Additional evidence from CMIP5 and RCM simulations for an increase in the intensity of heavy precipitation (Bennett and Walsh, 2015; Zhang et al., 2019d)	CMIP6 models project a robust increase in the intensity and frequency of heavy precipitation (Li et al., 2020; Annex). Median increase of more than 20% in the 50-year Rx1day and Rx5day events compared to the 1°C warming level (Li et al., 2020a) and more than 20% in annual Rx1day, Rx5day, and Rx30day compared to pre-industrial (Annex). Additional evidence from CMIP5 and RCM simulations for an increase in the intensity of heavy precipitation (Bennett and Walsh, 2015; Zhang et al., 2019d)
	Low confidence	*Low confidence*	Intensification of heavy precipitation: *High confidence* (compared with the recent past (1995-2014))	Intensification of heavy precipitation: *Likely* (compared with the recent past (1995-2014)) *Very likely* (compared with	Intensification of heavy precipitation: *Extremely likely* (compared with the recent past (1995-2014))

ACCEPTED VERSION SUBJECT TO FINAL EDITING

			Likely (compared with pre-industrial)	pre-industrial)	*Virtually certain* (compared with pre-industrial)

[END TABLE 11.20 HERE]

[START TABLE 11.21 HERE]

Table 11.21: Observed trends, human contribution to observed trends, and projected changes at 1.5°C, 2°C and 4°C of global warming for meteorological droughts (MET), agricultural and ecological droughts (AGR/ECOL), and hydrological droughts (HYDR) in North America, subdivided by AR6 regions. See Sections 11.9.1 and 11.9.4 for details.

Region anddrought types		Observed trends	Human contribution	Projections		
				+1.5 °C	+2 °C	+4 °C
North Central America (NCA)	MET	***Low confidence:*** **Inconsistent** changes in the duration and frequency of droughts, (Spinoni et al., 2019; Dunn et al., 2020).	***Low confidence:*** **No signal** in precipitation (Funk et al., 2014; Swain et al., 2014; Wang and Schubert, 2014)	***Low confidence:*** **Limited evidence.** Evidence suggests tendency towards drying (Xu et al., 2019a)(Chapter 11 Supplementary Material (11.SM)).	***Medium confidence:*** **Increase** in drought duration(Xu et al., 2019a; Spinoni et al., 2020)(Chapter 11 Supplementary Material (11.SM)). Xu et al. (2019): Strong drying signal for meteorological drought duration using SPI at 2°C compared to recent past. Spinoni et al. (2020): for RCP4.5 compared to recent past: SPI-based drying trends in CORDEX GCMs, but inconsistent signals in CORDEX RCMs.	***High confidence:*** **Increase** in meteorological drought severity in the majority of models (Sillmann et al., 2013b; Touma et al., 2015; Escalante-Sandoval and Nuñez-Garcia, 2017; Spinoni et al., 2020)(Chapter 11 Supplementary Material (11.SM)).
	AGR ECOL	***Low evidence***: No signal in the duration and severity of droughts based on soil moisture, PDSI and SPEI and conflicting trend depending of the subregion (Greve et al., 2014; Dai and Zhao, 2017; Spinoni et al., 2019; Padrón et al., 2020)	***Low confidence:*** **Limited evidence**	***Low evidence:*** **Mixed signal** between the different drought metrics including total column soil moisture, (Chapter 11 Supplementary Material (11.SM)), surface soil moisture (Xu et al., 2019a) and a weak drying by SPEI-PM (Naumann et al., 2018; Gu et al., 2020).	***Medium confidence:*** **Increase** of drought severity. This is consistent between the different drought metrics including total column soil moisture, (Chapter 11 Supplementary Material (11.SM)), surface soil moisture (Xu et al., 2019a) and SPEI-PM (Naumann et al., 2018; Gu et al., 2020).	***Likely:*** **Increase** of drought severity. This is consistent between the different drought metrics including total column soil moisture, (Chapter 11 Supplementary Material (11.SM)), surface soil moisture (Dai et al., 2018; Lu et al., 2019), PDSI (Dai et al., 2018) and SPEI-PM (Cook et al., 2014b; Vicente-Serrano et al., 2020a).
	HYDR	***Low confidence:*** **Limited evidence**	***Low confidence:*** **Limited evidence**	***Low confidence:*** **Limited evidence.** One study shows inconsistent trends(Touma et al., 2015)	***Low confidence:*** **Limited evidence** . Inconsistent trends in available studies (Touma et al., 2015; Cook et al., 2020; Zhai et al., 2020b)	***Low confidence***: **Mixed signal** among studies (Prudhomme et al., 2014; Giuntoli et al., 2015; Touma et al., 2015; Cook et al., 2020), but slight stronger

ACCEPTED VERSION SUBJECT TO FINAL EDITING

						tendency towards drying.
W. North America (WNA)	MET	***Low confidence***: **Inconsistent trends** depending on subregion (Swain and Hayhoe, 2015; Wehner et al., 2017; Spinoni et al., 2019; Dunn et al., 2020).	***Low confidence:*** **Limited evidence**	***Low confidence:*** **Limited evidence and inconsistent trends** depending on models and seasons (Swain and Hayhoe, 2015; Xu et al., 2019a)(Chapter 11 Supplementary Material (11.SM))	***Low confidence:*** **Limited evidence and inconsistent trends** depending on models and seasons (Swain and Hayhoe, 2015; Xu et al., 2019a; Spinoni et al., 2020).	***Low confidence***: **Mixed signal** among models, seasons, and studies (Swain and Hayhoe, 2015; Touma et al., 2015; Spinoni et al., 2020)(Chapter 11 Supplementary Material (11.SM)), with tendency towards drying in the spring and wetting in summer (Swain and Hayhoe, 2015).
	AGR ECOL	***Medium confidence***: **Increase**. Dominant increase but some inconsistent trends based on soil moisture, water-balance estimates, PDSI and SPEI, but some inconsistent trends depending study, index and the subregion (Greve et al., 2014; Griffin and Anchukaitis, 2014; Williams et al., 2015, 2020; Ahmadalipour and Moradkhani, 2017; Dai and Zhao, 2017; Spinoni et al., 2019; Padrón et al., 2020)	***Medium confidence:*** **Human contribution to observed trend.** Williams et al. (2020) concluded human-induced climate change contributed to the strong soil moisture deficits recorded in the last two decades in western North America through VPD (and AED) increases associated with higher air temperatures and lower air humidity. Williams et al. (2015) and Griffin and Anchukaitis (2014) concluded that increased AED has had an increased contribution to drought severity over the last decades, and played a dominant role in the intensification of the 2012-2014 drought in California	***Low evidence***: **Inconsistent signal** between models**,** with weak tendency to increased drying in total and surface soil moisture (Xu et al., 2019a)(Chapter 11 Supplementary Material (11.SM)) and the SPEI-PM (Naumann et al., 2018; Gu et al., 2020). Weak soil moisture drying projection for California (Louise et al., 2018)	***Medium confidence***: **Increase** of drought severity. There are differences depending on metrics and models. with weak median drying and substantial intermodel spread for total soil moisture (Cook et al., 2020)(Chapter 11 Supplementary Material (11.SM)) and larger drying for surface soil moisture (Xu et al., 2019a; Cook et al., 2020)(Chapter 11 Supplementary Material (11.SM)) and SPEI-PM (Naumann et al., 2018; Gu et al., 2020). Stronger soil moisture drying in southern part of domain (Cook et al., 2020).	***Medium confidence:*** **Increase** of drought severity. There are differences depending onmetrics and models, with weak drying in total column soil moisture (Cook et al., 2020)(Chapter 11 Supplementary Material (11.SM)), and substantial drying with surface soil moisture (Dai et al., 2018; Lu et al., 2019; Cook et al., 2020)(Chapter 11 Supplementary Material (11.SM)), PDSI (Dai et al., 2018) and SPEI-PM (Cook et al., 2014b; Vicente-Serrano et al., 2020a).
	HYDR	***Low confidence:*** **Mixed signal** between different time frames and subregions (Gudmundsson et al., 2019, 2021; Poshtiri and Pal, 2016; Dudley et al., 2020). Strong spatial variability in the recent trends of low flows in the region (Poshtiri and Pal,	***Low confidence***: **Mixed signal** for overall region in observations. But evidence that temperature increase has been the main driver of increased hydrological drought in California and in the Colorado basin	***Low confidence:*** **Limited evidence.** One study shows drying (Touma et al., 2015)	***Medium confidence***: **Increase** in hydrological drought (more intense low flows, less runoff and more frequent hydrological droughts) (Touma et al., 2015; Cook et al., 2020; Zhai et al., 2020b) Particularly strong evidence of increasing hydrological droughts in regions dependent on snow pack	***Medium confidence***: **Increase** in hydrological droughts (Prudhomme et al., 2014; Giuntoli et al., 2015; Touma et al., 2015; Cook et al., 2020) Particularly strong evidence of increasing hydrological droughts in regions dependent on snow pack reservoirs (Wehner et al., 2017; Ackerly et al., 2018; Rhoades et al.,

ACCEPTED VERSION SUBJECT TO FINAL EDITING

		2016) but dominant increase of hydrological drought in California and in the Colorado basin (Xiao et al., 2018b; Milly and Dunne, 2020).	(Milly and Dunne, 2020; Shukla et al., 2015; Xiao et al., 2018; Udall and Overpeck, 2017).		reservoirs (Wehner et al., 2017; Ackerly et al., 2018; Rhoades et al., 2018)	2018)
C. North America (CNA)	MET	***Medium confidence***: **Decrease** in the duration and frequency of meteorological droughts, (Wehner et al., 2017; Spinoni et al., 2019; Dunn et al., 2020).	***Low confidence:*** **Limited evidence** (Rupp et al., 2013; Easterling et al., 2017)	***Low confidence:*** **Limited evidence and inconsistent trends** (Xu et al., 2019a)(Chapter 11 Supplementary Material (11.SM)).	***Low confidence***: **Mixed signal** among different models (Sillmann et al., 2013b; Spinoni et al., 2020)(Chapter 11 Supplementary Material (11.SM)).	***Low confidence***: **Mixed signal** among different models (Sillmann et al., 2013b; Touma et al., 2015; Spinoni et al., 2020)(Chapter 11 Supplementary Material (11.SM)); drying trend in spring and summer (Swain and Hayhoe, 2015).
	AGR ECOL	***Low confidence***: **Mixed signal** based on soil moisture, water-balance estimates, PDSI and SPEI and conflicting trend depending of the subregion (Greve et al., 2014; Dai and Zhao, 2017; Seager et al., 2019; Spinoni et al., 2019; Padrón et al., 2020).	***Low confidence:*** **Limited evidence.** Human influence on surface soil moisture deficits due to increased evapotranspiration caused by higher temperatures. (Easterling et al., 2017)	***Medium confidence***: **Increase** in drought. Dominant signal shows drought increase based ontotal and surface soil moisture (Xu et al., 2019a)(Chapter 11 Supplementary Material (11.SM)) and SPEI-PM (Naumann et al., 2018; Gu et al., 2020).	***Medium confidence***: **Increase** in drought severity or frequency. Changes are consistent between different drought metrics including total column soil moisture, (Chapter 11 Supplementary Material (11.SM))(Cook et al., 2020), surface soil moisture (Xu et al., 2019a) and SPEI-PM (Naumann et al., 2018; Gu et al., 2020).	***High confidence:*** **Increase** of drought severity. Changes are consistent between different drought metrics including total column soil moisture, (Chapter 11 Supplementary Material (11.SM)) (Cook et al., 2020), surface soil moisture (Dai et al., 2018; Lu et al., 2019; Cook et al., 2020), PDSI (Dai et al., 2018), and SPEI-PM (Cook et al., 2014b; Feng et al., 2017; Vicente-Serrano et al., 2020a).
	HYDR	***Low confidence:*** **Mixed signal.** No signal in changes (Gudmundsson et al., 2021; Mo and Lettenmaier, 2018; Dudley et al., 2020). Poshtiri and Pal (2016) show strong spatial variability in the recent trends of low flows although there is an increase of hydrological droughts in the Missouri (Martin et al., 2020; Woodhouse and Wise, 2020) and in the Colorado basins (Xiao et al., 2018b; Milly and Dunne, 2020) Wetting trend in (Dai and Zhao, 2017)	***Low confidence***: **Inconsistent trends in observations.** Two studies suggest that emperature increase has been the main driver of increased hydrological drought in the Missouri basin (Martin et al., 2020; Woodhouse and Wise, 2020).	***Low confidence:*** **Limited evidence.** One study shows drying (Touma et al., 2015)	***Low confidence:*** **Limited evidence and inconsistent trends** (Touma et al., 2015; Cook et al., 2020; Zhai et al., 2020b).	***Low confidence***: **Mixed signal** among studies (Prudhomme et al., 2014; Giuntoli et al., 2015; Touma et al., 2015; Cook et al., 2020)
E. North America (ENA)	MET	***Low confidence***: **Inconsistent** trends depending on the region (Wehner et al., 2017; Spinoni et al., 2019; Dunn et al., 2020).	***Low confidence:*** **Limited evidence** (Easterling et al., 2017)	***Low confidence:*** **Limited evidence and inconsistent trends** (Xu et al., 2019a) (Chapter 11 Supplementary Material (11.SM)).	***Low confidence:*** **Limited evidence** (Xu et al., 2019a; Spinoni et al., 2020)(Chapter 11 Supplementary Material (11.SM)).	***Medium confidence:*** **Increase** in drought severity in the majority of models, but weaker or inconsistent trends in part of region (Sillmann et al., 2013b; Touma et al., 2015; Spinoni et al., 2020)(Chapter 11 Supplementary Material (11.SM)).
	AGR	***Low confidence***: **Mixed**	***Low confidence:***	***Low confidence***:	***Low confidence***: **Inconsistent**	***Medium confidence:*** **Increase** of

ACCEPTED VERSION SUBJECT TO FINAL EDITING

	ECOL	**signal**. Inconsistent trends depending on metric, subregion, time frame and studies, based on soil moisture, water-balance estimates, PDSI, and SPEI (Greve et al., 2014; Dai and Zhao, 2017; Park Williams et al., 2017; Spinoni et al., 2019; Padrón et al., 2020).	**Limited evidence**. Human influence on surface soil moisture deficits due to increased evapotranspiration caused by higher temperatures. (Easterling et al., 2017)	**Inconsistent** trends between models, metrics and studies based on total and surface soil moisture (Xu et al., 2019a)(Chapter 11 Supplementary Material (11.SM)) and SPEI-PM (Naumann et al., 2018; Gu et al., 2020).	trends between models, metrics and studies based on total and surface soil moisture (Xu et al., 2019a; Cook et al., 2020)(Chapter 11 Supplementary Material (11.SM)), and SPEI-PM (Naumann et al., 2018; Gu et al., 2020), but with stronger tendency towards drying.	drought severity. Consistent signal between different drought metrics including total column soil moisture, (Chapter 11 Supplementary Material (11.SM)) (Cook et al., 2020), surface soil moisture (Dai et al., 2018; Lu et al., 2019), PDSI (Dai et al., 2018) and SPEI-PM (Cook et al., 2014b; Vicente-Serrano et al., 2020a).
	HYDR	***Low confidence***: **Limited evidence.** Decrease in low flows from 1971-2020, but not since 1950 (Gudmundsson et al., 2019, 2021). Poshtiri and Pal, (2016) and Dudley et al., (2020) show strong spatial variability in the recent trends of low flows in the region.	***Low confidence:*** **Limited evidence**	***Low confidence:*** **Limited evidence.** One study shows lack of signal (Touma et al., 2015)	***Low confidence:*** **Limited evidence and inconsistent trends** (Touma et al., 2015; Cook et al., 2020; Zhai et al., 2020b)	***Low confidence***: **Mixed signal** among models and studies (Prudhomme et al., 2014; Giuntoli et al., 2015; Touma et al., 2015; Cook et al., 2020)
N. E. North America (NEN)	MET	***Low confidence*****: No or limited signal** in duration and frequency of droughts (Bonsal et al., 2019; Dunn et al., 2020)	***Low confidence:*** **Limited evidence**	***Low confidence:*** **Limited evidence.** Available evidence suggest decrease in meteorological drought (Xu et al., 2019a)(Chapter 11 Supplementary Material (11.SM)).	***Medium confidence:*** **Decrease** in meteorological drought (Sillmann et al., 2013b; Xu et al., 2019a; Spinoni et al., 2020)(Chapter 11 Supplementary Material (11.SM)).	***Medium confidence:*** **Decrease** in meteorological drought (Touma et al., 2015; Spinoni et al., 2020; Vicente-Serrano et al., 2020a)(Chapter 11 Supplementary Material (11.SM)).
	AGR ECOL	***Low confidence***: **Mixed signal** between different drought metrics and strong spatial differences (Greve et al., 2014; Dai and Zhao, 2017; Padrón et al., 2020).	***Low confidence:*** **Limited evidence**	***Low confidence***: **Mixed signal** between different models and metrics. Substantial intermodal variations and weak drying trend in soil moisture(Xu et al., 2019a)(Chapter 11 Supplementary Material (11.SM)) and slight decrease in drought severity in SPEI-PM (Naumann et al., 2018; Gu et al., 2020).	***Low confidence***: **Mixed signal** between different models and drought metrics. Substantial intermodel spread for total column soil moisture, with overall weak or no change (Chapter 11 Supplementary Material (11.SM))(Cook et al., 2020), slight drying in surface soil moisture (Xu et al., 2019a)(Chapter 11 Supplementary Material (11.SM)) and tendency to wetting trend in SPEI-PM (Naumann et al., 2018; Gu et al., 2020).	***Low confidence***: **Mixed signal** between models and different drought metrics, including total column soil moisture, which shows inconsistent changes (Chapter 11 Supplementary Material (11.SM)) (Cook et al., 2020), surface soil moisture, which suggest drying (Dai et al., 2018; Lu et al., 2019; Cook et al., 2020)(Chapter 11 Supplementary Material (11.SM)), and PDSI (Dai et al., 2018) and SPEI-PM (Cook et al., 2014b; Vicente-Serrano et al., 2020a), which show tendency fo wetting trend.
	HYDR	***Low confidence:*** **Limited evidence.** Inconsistent trends in one study (Dai and Zhao, 2017)	***Low confidence:*** **Limited evidence**	***Low confidence:*** **Limited evidence.** One study shows inconsistent signals (Touma et al., 2015)	***Low confidence:*** **Inconsistent trends and limited evidence**. Available studies suggest inconsistent trends in low flow (Zhai et al., 2020b) and the	***Low confidence***: **Mixed signal** among studies (Prudhomme et al., 2014; Giuntoli et al., 2015; Touma et al., 2015; Cook et al., 2020). Some evidence

ACCEPTED VERSION SUBJECT TO FINAL EDITING

					SRI (Touma et al., 2015), and seasonally inconsistent trends in runoff, with decrease in summer and increase in winter (Cook et al., 2020).	(*medium confidence*) for strong seasonality of trends, with decrease in summer and increase in winter (Giuntoli et al., 2015; Cook et al., 2020).
N. W. North America (NWN)	MET	***Low confidence***: **Mixed signal** with conflicting trends depending on the region (Bonsal et al., 2019; Spinoni et al., 2019; Dunn et al., 2020).	***Low confidence:*** **Limited evidence**	***Low confidence:*** **Limited and inconsistent evidence**. Some evidence points to decrease in meteorological drought severity or intensity based on SPI (Xu et al., 2019a) and CDD (Chapter 11 Supplementary Material (11.SM))	***Medium confidence:*** **Decrease** in meteorological drought severity or intensity (Sillmann et al., 2013b; Xu et al., 2019a; Spinoni et al., 2020)(Chapter 11 Supplementary Material (11.SM)).	***Medium confidence***: **Decrease** in meteorological drought severity in the majority of models (Sillmann et al., 2013b; Swain and Hayhoe, 2015; Touma et al., 2015; Spinoni et al., 2020)(Chapter 11 Supplementary Material (11.SM)).
	AGR ECOL	***Low confidence*: No signal or inconsistent signals** in the duration and severity of droughts based on soil moisture, PDSI and SPEI and conflicting trend depending of the subregion (Greve et al., 2014; Dai and Zhao, 2017; Park Williams et al., 2017; Spinoni et al., 2019; Padrón et al., 2020).	***Low confidence:*** **Limited evidence**	***Low evidence***: **Mixed signal** in changes in drought severity. Inconsistent changes between models in CMIP6 and CMIP5 total and surface soil moisture(Xu et al., 2019a)(Chapter 11 Supplementary Material (11.SM)); SPEI-PM also suggests inconsistent changes drought severity (Naumann et al., 2018; Gu et al., 2020).	***Low confidence***: **Mixed signal** between different models, drought metrics and studies, including total and surfacesoil moisture, as well as SPEI-PM(Chapter 11 Supplementary Material (11.SM))(Naumann et al., 2018; Xu et al., 2019a; Cook et al., 2020; Gu et al., 2020).	***Low confidence***: **Mixed signal** between different models and drought metrics, including total and surface soil moisture, PDSI and SPEI-PM (Chapter 11 Supplementary Material (11.SM)) (Cook et al., 2014b, 2020; Dai et al., 2018; Lu et al., 2019; Vicente-Serrano et al., 2020a), with slight larger tendency towards wetting.
	HYDR	***Low confidence:*** **Limited evidence**. Regionally inconsistent trends in one study (Dai and Zhao, 2017)	***Low confidence:*** **Limited evidence**	***Low confidence:*** **Limited evidence.** One study shows lack of signal (Touma et al., 2015)	***Low confidence:*** **Limited evidence and inconsistent** signals in available studies (Touma et al., 2015; Cook et al., 2020; Zhai et al., 2020b)	***Low confidence***: **Mixed signal** among studies (Prudhomme et al., 2014; Giuntoli et al., 2015; Touma et al., 2015; Cook et al., 2020), but slight stronger tendency towards wetting.

[END TABLE 11.21 HERE]

ACCEPTED VERSION SUBJECT TO FINAL EDIT

Acknowledgements

Nate McDowell, Alexis Berg, Jamie Hannaford, Jack Scheff, Lena Tallaksen, Tim Brodribb, Peter Stott, Peter Thorne, Francis Zwiers**.**

ACCEPTED VERSION
SUBJECT TO FINAL EDITING

References

Abatzoglou, J. T., and Williams, A. P. (2016). Impact of anthropogenic climate change on wildfire across western US forests. *Proc. Natl. Acad. Sci.*, 201607171. doi:10.1073/pnas.1607171113.

Abaurrea, J., Asín, J., and Cebrián, A. C. (2018). Modelling the occurrence of heat waves in maximum and minimum temperatures over Spain and projections for the period 2031-60. *Glob. Planet. Change* 161, 244–260. doi:10.1016/j.gloplacha.2017.11.015.

Abiodun, B. J., Adegoke, J., Abatan, A. A., Ibe, C. A., Egbebiyi, T. S., Engelbrecht, F., et al. (2017). Potential impacts of climate change on extreme precipitation over four African coastal cities. *Clim. Change* 143. doi:10.1007/s10584-017-2001-5.

Abiodun, B. J., Makhanya, N., Petja, B., Abatan, A. A., and Oguntunde, P. G. (2019). Future projection of droughts over major river basins in Southern Africa at specific global warming levels. *Theor. Appl. Climatol.* 137, 1785–1799. doi:10.1007/s00704-018-2693-0.

Acar Deniz, Z., and Gönençgil, B. (2015). Trends of summer daily maximum temperature extremes in Turkey. *Phys. Geogr.* 36, 268–281. doi:10.1080/02723646.2015.1045285.

Acero, F. J., García, J. A., Gallego, M. C., Parey, S., and Dacunha-Castelle, D. (2014). Trends in summer extreme temperatures over the Iberian Peninsula using nonurban station data. *J. Geophys. Res. Atmos.* 119, 39–53. doi:10.1002/2013JD020590.

Ackerly, D., Jones, A., Stacey, M., and Riordan, B. (2018). "San Francisco Bay Area Summary Report," in *California's Fourth Climate Change Assessment* SUM-CCCA4-2018-005. (Berkeley, CA, USA: University of California Berkeley). Available at: https://www.climateassessment.ca.gov/regions/.

Adnan, M., Rehman, N., and Shahbir, J. (2016). Predicting the Frequency and Intensity of Climate Extremes by Regression Models. *J. Climatol. Weather Forecast.* 04. doi:10.4172/2332-2594.1000185.

Aerenson, T., Tebaldi, C., Sanderson, B., and Lamarque, J.-F. (2018). Changes in a suite of indicators of extreme temperature and precipitation under 1.5 and 2 degrees warming. *Environ. Res. Lett.* 13, 035009. doi:10.1088/1748-9326/aaafd6.

Aerts, J. C. J. H., Botzen, W. J., Clarke, K. C., Cutter, S. L., Hall, J. W., Merz, B., et al. (2018). Integrating human behaviour dynamics into flood disaster risk assessment. *Nat. Clim. Chang.* 8, 193–199. doi:10.1038/s41558-018-0085-1.

Agard, V., and Emanuel, K. (2017). Clausius-Clapeyron scaling of peak CAPE in continental convective storm environments. *J. Atmos. Sci.* 74, 3043–3054. doi:10.1175/JAS-D-16-0352.1.

Agel, L., and Barlow, M. (2020). How well do CMIP6 historical runs match observed northeast U.S. precipitation and extreme precipitation–related circulation? *J. Clim.* 33, 9835–9848. doi:10.1175/JCLI-D-19-1025.1.

AghaKouchak, A. (2014). A baseline probabilistic drought forecasting framework using standardized soil moisture index: Application to the 2012 United States drought. *Hydrol. Earth Syst. Sci.* 18, 2485–2492. doi:10.5194/hess-18-2485-2014.

AghaKouchak, A., Cheng, L., Mazdiyasni, O., and Farahmand, A. (2014). Global warming and changes in risk of concurrent climate extremes: Insights from the 2014 California drought. *Geophys. Res. Lett.* 41, 8847–8852. doi:10.1002/2014GL062308.

AghaKouchak, A., Chiang, F., Huning, L. S., Love, C. A., Mallakpour, I., Mazdiyasni, O., et al. (2020). Climate Extremes and Compound Hazards in a Warming World. *Annu. Rev. Earth Planet. Sci.* 48, 519–548. doi:10.1146/annurev-earth-071719-055228.

Aguilar, E., Barry, A. A., Brunet, M., Ekang, L., Fernandes, A., Massoukina, M., et al. (2009). Changes in temperature and precipitation extremes in western central Africa, Guinea Conakry, and Zimbabwe, 1955-2006. *J. Geophys. Res. Atmos.* 114. doi:10.1029/2008JD011010.

Aguilar, E., Peterson, T. C., Obando, P. R., Frutos, R., Retana, J. A., Solera, M., et al. (2005). Changes in precipitation and temperature extremes in Central America and northern South America, 1961–2003. *J. Geophys. Res.* 110, D23107. doi:10.1029/2005JD006119.

Ahlswede, B., and Thomas, R. Q. (2017). Community Earth System Model Simulations Reveal the Relative Importance of Afforestation and Forest Management to Surface Temperature in Eastern North America. *Forests* 8, 499. doi:10.3390/f8120499.

Ahmadalipour, A., and Moradkhani, H. (2017). Analyzing the uncertainty of ensemble-based gridded observations in land surface simulations and drought assessment. *J. Hydrol.* 555, 557–568. doi:10.1016/j.jhydrol.2017.10.059.

Ahmed, M., Anchukaitis, K. J., Asrat, A., Borgaonkar, H. P., Braida, M., Buckley, B. M., et al. (2013). Continental-scale temperature variability during the past two millennia. *Nat. Geosci.* 6, 339–346. doi:10.1038/ngeo1797.

Ahn, J.-B., Jo, S., Suh, M.-S., Cha, D.-H., Lee, D.-K., Hong, S.-Y., et al. (2016). Changes of precipitation extremes over South Korea projected by the 5 RCMs under RCP scenarios. *Asia-Pacific J. Atmos. Sci.* 52, 223–236. doi:10.1007/s13143-016-0021-0.

Aich, V., Liersch, S., Vetter, T., Fournet, S., Andersson, J. C. M., Calmanti, S., et al. (2016). Flood projections within the Niger River Basin under future land use and climate change. *Sci. Total Environ.* 562, 666–677.

ACCEPTED VERSION SUBJECT TO FINAL EDITING

doi:10.1016/j.scitotenv.2016.04.021.
Akinsanola, A. A., Kooperman, G. J., Pendergrass, A. G., Hannah, W. M., and Reed, K. A. (2020). Seasonal representation of extreme precipitation indices over the United States in CMIP6 present-day simulations. *Environ. Res. Lett.* 15, 094003. doi:10.1088/1748-9326/ab92c1.
Akinsanola, A. A., and Zhou, W. (2018). Projections of West African summer monsoon rainfall extremes from two CORDEX models. *Clim. Dyn.* doi:10.1007/s00382-018-4238-8.
Akinyemi, F. O., and Abiodun, B. J. (2019). Potential impacts of global warming levels 1.5 °C and above on climate extremes in Botswana. *Clim. Change* 154, 387–400. doi:10.1007/s10584-019-02446-1.
Albergel, C., Dorigo, W., Reichle, R. H., Balsamo, G., de Rosnay, P., Muñoz-Sabater, J., et al. (2013). Skill and Global Trend Analysis of Soil Moisture from Reanalyses and Microwave Remote Sensing. *J. Hydrometeorol.* 14, 1259–1277. doi:10.1175/JHM-D-12-0161.1.
Alexander, L. V. (2016). Global observed long-term changes in temperature and precipitation extremes: A review of progress and limitations in IPCC assessments and beyond. *Weather Clim. Extrem.* 11, 4–16. doi:10.1016/J.WACE.2015.10.007.
Alexander, L. V, and Arblaster, J. M. (2017). Historical and projected trends in temperature and precipitation extremes in Australia in observations and CMIP5. *Weather Clim. Extrem.* 15, 34–56.
Alexander, L. V, Fowler, H. J., Bador, M., Behrangi, A., Donat, M. G., Dunn, R., et al. (2019). On the use of indices to study extreme precipitation on sub-daily and daily timescales. *Environ. Res. Lett.* 14, 125008. doi:10.1088/1748-9326/ab51b6.
Alexandru, A. (2018). Consideration of land-use and land-cover changes in the projection of climate extremes over North America by the end of the twenty-first century. *Clim. Dyn.* 50, 1949–1973. doi:10.1007/s00382-017-3730-x.
Alfieri, L., Bisselink, B., Dottori, F., Naumann, G., de Roo, A., Salamon, P., et al. (2017). Global projections of river flood risk in a warmer world. *Earth's Futur.* 5, 171–182. doi:10.1002/2016EF000485.
Ali, H., Fowler, H. J., Lenderink, G., Lewis, E., and Pritchard, D. (2021). Consistent large-scale response of hourly extreme precipitation to temperature variation over land. *Geophys. Res. Lett.* doi:10.1029/2020GL090317.
Ali, H., and Mishra, V. (2018). Contributions of Dynamic and Thermodynamic Scaling in Subdaily Precipitation Extremes in India. *Geophys. Res. Lett.* 45, 2352–2361. doi:10.1002/2018GL077065.
Ali, H., Modi, P., and Mishra, V. (2019a). Increased flood risk in Indian sub-continent under the warming climate. *Weather Clim. Extrem.* 25, 100212. doi:10.1016/j.wace.2019.100212.
Ali, S., Eum, H.-I., Cho, J., Dan, L., Khan, F., Dairaku, K., et al. (2019b). Assessment of climate extremes in future projections downscaled by multiple statistical downscaling methods over Pakistan. *Atmos. Res.* 222, 114–133. doi:10.1016/j.atmosres.2019.02.009.
Alizadeh, M. R., Adamowski, J., Nikoo, M. R., AghaKouchak, A., Dennison, P., and Sadegh, M. (2020). A century of observations reveals increasing likelihood of continental-scale compound dry-hot extremes. *Sci. Adv.* 6, eaaz4571. doi:10.1126/sciadv.aaz4571.
Alkama, R., and Cescatti, A. (2016). Biophysical climate impacts of recent changes in global forest cover. *Science (80-.).* 351, 600–604. doi:10.1126/science.aac8083.
Allan, R. P., Barlow, M., Byrne, M. P., Cherchi, A., Douville, H., Fowler, H. J., et al. (2020). Advances in understanding large-scale responses of the water cycle to climate change. *Ann. N. Y. Acad. Sci.* 1472, 49–75. doi:10.1111/nyas.14337.
Allen, C. D., Breshears, D. D., and McDowell, N. G. (2015). On underestimation of global vulnerability to tree mortality and forest die-off from hotter drought in the Anthropocene. *Ecosphere* 6, art129. doi:10.1890/ES15-00203.1.
Allen, J. T. (2018). "Climate Change and Severe Thunderstorms," in *Oxford Research Encyclopedia of Climate Science* (Oxford, UK: Oxford University Press), 1–65. doi:10.1093/acrefore/9780190228620.013.62.
Allen, M. R., Dube, O. P., Solecki, W., Aragón-Durand, F., Cramer, W., Humphreys, S., et al. (2018). "Framing and Context," in *Global Warming of 1.5°C. An IPCC Special Report on the impacts of global warming of 1.5°C above pre-industrial levels and related global greenhouse gas emission pathways, in the context of strengthening the global response to the threat of climate change,* eds. V. Masson-Delmotte, P. Zhai, H.-O. Pörtner, D. Roberts, J. Skea, P. R. Shukla, et al. (In Press), 49–92. Available at: https://www.ipcc.ch/sr15/chapter/chapter-1.
Almazroui, M. (2019a). Assessment of meteorological droughts over Saudi Arabia using surface rainfall observations during the period 1978–2017. *Arab. J. Geosci.* 12. doi:10.1007/s12517-019-4866-2.
Almazroui, M. (2019b). Temperature Changes over the CORDEX-MENA Domain in the 21st Century Using CMIP5 Data Downscaled with RegCM4: A Focus on the Arabian Peninsula. *Adv. Meteorol.* 2019. doi:10.1155/2019/5395676.
Almazroui, M., and Islam, M. N. (2019). Coupled Model Inter-comparison Project Database to Calculate Drought Indices for Saudi Arabia: A Preliminary Assessment. *Earth Syst. Environ.* 3, 419–428. doi:10.1007/s41748-019-00126-9.
Almazroui, M., Islam, M. N., Dambul, R., and Jones, P. D. (2014). Trends of temperature extremes in Saudi Arabia. *Int. J. Climatol.* 34, 808–826. doi:10.1002/joc.3722.

ACCEPTED VERSION SUBJECT TO FINAL EDITING

Almazroui, M., and Saeed, S. (2020). Contribution of extreme daily precipitation to total rainfall over the Arabian Peninsula. *Atmos. Res.* 231, 104672. doi:10.1016/j.atmosres.2019.104672.

Almeida, C. T., Oliveira-Júnior, J. F., Delgado, R. C., Cubo, P., and Ramos, M. C. (2017). Spatiotemporal rainfall and temperature trends throughout the Brazilian Legal Amazon, 1973-2013. *Int. J. Climatol.* 37, 2013–2026. doi:10.1002/joc.4831.

AlSarmi, S. H., and Washington, R. (2014). Changes in climate extremes in the Arabian Peninsula: analysis of daily data. *Int. J. Climatol.* 34, 1329–1345. doi:10.1002/joc.3772.

Althoff, D., Rodrigues, L. N., and da Silva, D. D. (2020). Impacts of climate change on the evaporation and availability of water in small reservoirs in the Brazilian savannah. *Clim. Change* 159, 215–232. doi:10.1007/s10584-020-02656-y.

Altman, J., Ukhvatkina, O. N., Omelko, A. M., Macek, M., Plener, T., Pejcha, V., et al. (2018). Poleward migration of the destructive effects of tropical cyclones during the 20th century. *Proc. Natl. Acad. Sci.* 115, 11543 LP-11548. doi:10.1073/pnas.1808979115.

Amann, B., Szidat, S., and Grosjean, M. (2015). A millennial-long record of warm season precipitation and flood frequency for the North-western Alps inferred from varved lake sediments: implications for the future. *Quat. Sci. Rev.* 115, 89–100. doi:10.1016/j.quascirev.2015.03.002.

Andela, N., Morton, D. C., Giglio, L., Chen, Y., van der Werf, G. R., Kasibhatla, P. S., et al. (2017). A human-driven decline in global burned area. *Science (80-.).* 356, 1356–1362. doi:10.1126/science.aal4108.

Anderegg, W. R. L., Berry, J. A., Smith, D. D., Sperry, J. S., Anderegg, L. D. L., and Field, C. B. (2012). The roles of hydraulic and carbon stress in a widespread climate-induced forest die-off. *Proc. Natl. Acad. Sci.* 109, 233–237. doi:10.1073/pnas.1107891109.

Anderegg, W. R. L., Kane, J. M., and Anderegg, L. D. L. (2013). Consequences of widespread tree mortality triggered by drought and temperature stress. *Nat. Clim. Chang.* 3, 30–36. doi:10.1038/nclimate1635.

Anderegg, W. R. L., Klein, T., Bartlett, M., Sack, L., Pellegrini, A. F. A., Choat, B., et al. (2016). Meta-analysis reveals that hydraulic traits explain cross-species patterns of drought-induced tree mortality across the globe. *Proc. Natl. Acad. Sci. U. S. A.* 113, 5024–5029. doi:10.1073/pnas.1525678113.

Anderegg, W. R. L., Trugman, A. T., Badgley, G., Konings, A. G., and Shaw, J. (2020). Divergent forest sensitivity to repeated extreme droughts. *Nat. Clim. Chang.* doi:10.1038/s41558-020-00919-1.

Anderson-Teixeira, K. J., Snyder, P. K., Twine, T. E., Cuadra, S. V., Costa, M. H., and DeLucia, E. H. (2012). Climate-regulation services of natural and agricultural ecoregions of the Americas. *Nat. Clim. Chang.* 2, 177–181. doi:10.1038/nclimate1346.

Anderson, R. G., Canadell, J. G., Randerson, J. T., Jackson, R. B., Hungate, B. A., Baldocchi, D. D., et al. (2011). Biophysical considerations in forestry for climate protection. *Front. Ecol. Environ.* 9, 174–182. doi:10.1890/090179.

Anderson, W. B., Seager, R., Baethgen, W., Cane, M., and You, L. (2019). Synchronous crop failures and climate-forced production variability. *Sci. Adv.* 5, eaaw1976. doi:10.1126/sciadv.aaw1976.

Añel, J. A., López-Moreno, J. I., Otto, F. E. L., Vicente-Serrano, S. M., Schaller, N., Massey, N., et al. (2014a). The extreme snow accumulation in the Western Spanish Pyrenees during winter and spring 2013 [in "Explaining Extreme Events of 2013 from a Climate Perspective"]. *Bull. Am. Meteorol. Soc.* 95, S73–S74. doi:10.1175/1520-0477-95.9.S1.1.

Añel, J. A., López-Moreno, J. I., Otto, F. E. L., Vicente Serrano, S. M., Schaller, Nathalie; Massey, N., Buisán, S. T., et al. (2014b). The extreme snow accumulation in the western Spanish Pyrenees during winter and spring 2013 [in "Explaining Extreme Events of 2013 from a Climate Perspective"]. *Bull. Am. Meteorol. Soc.* 95, S73–S76. doi:10.1175/1520-0477-95.9.S1.1.

Angeles-Malaspina, M., González-Cruz, J. E., and Ramírez-Beltran, N. (2018). Projections of Heat Waves Events in the Intra-Americas Region Using Multimodel Ensemble. *Adv. Meteorol.* 2018, 1–16. doi:10.1155/2018/7827984.

Angélil, O., Perkins-Kirkpatrick, S., Alexander, L. V, Stone, D., Donat, M. G., Wehner, M., et al. (2016). Comparing regional precipitation and temperature extremes in climate model and reanalysis products. *Weather Clim. Extrem.* 13, 35–43. doi:10.1016/j.wace.2016.07.001.

Angélil, O., Stone, D. A., Tadross, M., Tummon, F., Wehner, M., and Knutti, R. (2014). Attribution of extreme weather to anthropogenic greenhouse gas emissions: Sensitivity to spatial and temporal scales. *Geophys. Res. Lett.* 41, 2150–2155. doi:10.1002/2014GL059234.

Angélil, O., Stone, D., Perkins-Kirkpatrick, S., Alexander, L. V., Wehner, M., Shiogama, H., et al. (2018). On the nonlinearity of spatial scales in extreme weather attribution statements. *Clim. Dyn.* 50, 2739–2752. doi:10.1007/s00382-017-3768-9.

Angélil, O., Stone, D., Wehner, M., Paciorek, C. J., Krishnan, H., and Collins, W. (2017). An Independent Assessment of Anthropogenic Attribution Statements for Recent Extreme Temperature and Rainfall Events. *J. Clim.* 30, 5–16. doi:10.1175/JCLI-D-16-0077.1.

Antonescu, B., Schultz, D. M., Holzer, A., and Groenemeijer, P. (2016a). Tornadoes in Europe: An Underestimated Threat. *Bull. Am. Meteorol. Soc.* 98, 713–728. doi:10.1175/BAMS-D-16-0171.1.

Antonescu, B., Schultz, D. M., Lomas, F., and Kühne, T. (2016b). Tornadoes in Europe: Synthesis of the Observational

ACCEPTED VERSION SUBJECT TO FINAL EDITING

Datasets. *Mon. Weather Rev.* 144, 2445–2480. doi:10.1175/MWR-D-15-0298.1.
Apurv, T., Sivapalan, M., and Cai, X. (2017). Understanding the Role of Climate Characteristics in Drought Propagation. *Water Resour. Res.* 53, 9304–9329. doi:10.1002/2017WR021445.
Aragão, L. E. O. C., Anderson, L. O., Fonseca, M. G., Rosan, T. M., Vedovato, L. B., Wagner, F. H., et al. (2018). 21st Century drought-related fires counteract the decline of Amazon deforestation carbon emissions. *Nat. Commun.* 9, 536. doi:10.1038/s41467-017-02771-y.
Arblaster, J. M., Lim, E.-P., Hendon, H. H., Trewin, B., Wheeler, M. C., Liu, G., et al. (2014). Understanding Australia's hottest September on record [in "Explaining Extreme Events of 2013 from a Climate Perspective"]. *Bull. Am. Meteorol. Soc.* 95, S37–S41. doi:10.1175/1520-0477-95.9.S1.1.
Archer, D. R., and Fowler, H. J. (2018). Characterising flash flood response to intense rainfall and impacts using historical information and gauged data in Britain. *J. Flood Risk Manag.* 11, S121–S133. doi:10.1111/jfr3.12187.
Archer, D. R., Parkin, G., and Fowler, H. J. (2016). Assessing long term flash flooding frequency using historical information. *Hydrol. Res.* 48, 1–16. doi:10.2166/nh.2016.031.
Archfield, S. A., Hirsch, R. M., Viglione, A., and Blöschl, G. (2016). Fragmented patterns of flood change across the United States. *Geophys. Res. Lett.* 43, 10,232-10,239. doi:10.1002/2016GL070590.
Argüeso, D., Di Luca, A., and Evans, J. P. (2016). Precipitation over urban areas in the western Maritime Continent using a convection-permitting model. *Clim. Dyn.* 47, 1143–1159. doi:10.1007/s00382-015-2893-6.
Argüeso, D., Hidalgo-Muñoz, J. M., Ga´ Miz-Fortis, S. R., Esteban-Parra, M. J., and Castro-Díez, Y. (2012). Evaluation of WRF Mean and Extreme Precipitation over Spain: Present Climate (1970-99). *J. Clim.* 25, 4883–4895. doi:10.1175/JCLI-D-11-00276.1.
Armstrong, W. H., Collins, M. J., and Snyder, N. P. (2014). Hydroclimatic flood trends in the northeastern United States and linkages with large-scale atmospheric circulation patterns. *Hydrol. Sci. J.* 59, 1636–1655. doi:10.1080/02626667.2013.862339.
Arnell, N. W., and Gosling, S. N. (2016). The impacts of climate change on river flood risk at the global scale. *Clim. Change* 134, 387–401. doi:10.1007/s10584-014-1084-5.
Arnone, E., Pumo, D., Viola, F., Noto, L. V., and La Loggia, G. (2013). Rainfall statistics changes in Sicily. *Hydrol. Earth Syst. Sci.* 17, 2449–2458. doi:10.5194/hess-17-2449-2013.
Ashabokov, B. A., Tashilova, A. A., Kesheva, L. A., and Taubekova, Z. A. (2017). Trends in precipitation parameters in the climate zones of southern Russia (1961-2011). *Russ. Meteorol. Hydrol.* 42, 150–158. doi:10.3103/S1068373917030025.
Asmerom, Y., Polyak, V. J., Rasmussen, J. B. T., Burns, S. J., and Lachniet, M. (2013). Multidecadal to multicentury scale collapses of Northern Hemisphere monsoons over the past millennium. *Proc. Natl. Acad. Sci. U. S. A.* 110, 9651–9656. doi:10.1073/pnas.1214870110.
Atif, R. M., Almazroui, M., Saeed, S., Abid, M. A., Islam, M. N., and Ismail, M. (2020). Extreme precipitation events over Saudi Arabia during the wet season and their associated teleconnections. *Atmos. Res.* 231, 104655. doi:10.1016/j.atmosres.2019.104655.
Ault, T. R. (2020). On the essentials of drought in a changing climate. *Science (80-.).* 368, 256–260. doi:10.1126/science.aaz5492.
Ault, T. R., Cole, J. E., Overpeck, J. T., Pederson, G. T., and Meko, D. M. (2014). Assessing the Risk of Persistent Drought Using Climate Model Simulations and Paleoclimate Data. *J. Clim.* 27, 7529–7549. doi:10.1175/JCLI-D-12-00282.1.
Avila-Diaz, A., Benezoli, V., Justino, F., Torres, R., and Wilson, A. (2020). Assessing current and future trends of climate extremes across Brazil based on reanalyses and earth system model projections. *Clim. Dyn.* 55, 1403–1426. doi:10.1007/s00382-020-05333-z.
Ávila, A., Justino, F., Wilson, A., Bromwich, D., and Amorim, M. (2016). Recent precipitation trends, flash floods and landslides in southern Brazil. *Environ. Res. Lett.* 11, 114029. doi:10.1088/1748-9326/11/11/114029.
Avila, F. B., Dong, S., Menang, K. P., Rajczak, J., Renom, M., Donat, M. G., et al. (2015). Systematic investigation of gridding-related scaling effects on annual statistics of daily temperature and precipitation maxima: A case study for south-east Australia. *Weather Clim. Extrem.* 9, 6–16. doi:10.1016/j.wace.2015.06.003.
Azorin-Molina, C., Vicente-Serrano, S. M., McVicar, T. R., Revuelto, J., Jerez, S., and López-Moreno, J. I. (2017). Assessing the impact of measurement time interval when calculating wind speed means and trends under the stilling phenomenon. *Int. J. Climatol.* 37, 480–492. doi:10.1002/joc.4720.
Azorin-Molina, C., Vicente-Serrano, S. M., Sanchez-Lorenzo, A., McVicar, T. R., Morán-Tejeda, E., Revuelto, J., et al. (2015). Atmospheric evaporative demand observations, estimates and driving factors in Spain (1961-2011). *J. Hydrol.* 523, 262–277. doi:10.1016/j.jhydrol.2015.01.046.
Baburaj, P. P., Abhilash, S., Mohankumar, K., and Sahai, A. K. (2020). On the Epochal Variability in the Frequency of Cyclones during the Pre-Onset and Onset Phases of the Monsoon over the North Indian Ocean. *Adv. Atmos. Sci.* 37, 634–651. doi:10.1007/s00376-020-9070-5.
Bacmeister, J. T., Reed, K. A., Hannay, C., Lawrence, P., Bates, S., Truesdale, J. E., et al. (2018). Projected changes in tropical cyclone activity under future warming scenarios using a high-resolution climate model. *Clim. Change* 146, 547–560. doi:10.1007/s10584-016-1750-x.

ACCEPTED VERSION SUBJECT TO FINAL EDITING

Bador, M., Boé, J., Terray, L., Alexander, L. V., Baker, A., Bellucci, A., et al. (2020). Impact of Higher Spatial Atmospheric Resolution on Precipitation Extremes Over Land in Global Climate Models. *J. Geophys. Res. Atmos.* 125. doi:10.1029/2019JD032184.

Bador, M., Terray, L., and Boé, J. (2016). Detection of anthropogenic influence on the evolution of record-breaking temperatures over Europe. *Clim. Dyn.* 46, 2717–2735. doi:10.1007/s00382-015-2725-8.

Baek, H.-J., Kim, M.-K., and Kwon, W.-T. (2017). Observed short- and long-term changes in summer precipitation over South Korea and their links to large-scale circulation anomalies. *Int. J. Climatol.* 37, 972–986. doi:10.1002/joc.4753.

Baek, S. H., Steiger, N. J., Smerdon, J. E., and Seager, R. (2019). Oceanic Drivers of Widespread Summer Droughts in the United States Over the Common Era. *Geophys. Res. Lett.* 46, 8271–8280. doi:10.1029/2019GL082838.

Bai, P., Liu, X., Liang, K., and Liu, C. (2016). Investigation of changes in the annual maximum flood in the Yellow River basin, China. *Quat. Int.* 392, 168–177. doi:10.1016/j.quaint.2015.04.053.

Balaguru, K., Foltz, G. R., and Leung, L. R. (2018). Increasing Magnitude of Hurricane Rapid Intensification in the Central and Eastern Tropical Atlantic. *Geophys. Res. Lett.* 45, 4238–4247. doi:10.1029/2018GL077597.

Balaji, M., Chakraborty, A., and Mandal, M. (2018). Changes in tropical cyclone activity in north Indian Ocean during satellite era (1981–2014). *Int. J. Climatol.* 38, 2819–2837. doi:10.1002/joc.5463.

Ballesteros Cánovas, J. A., Trappmann, D., Shekhar, M., Bhattacharyya, A., and Stoffel, M. (2017). Regional flood-frequency reconstruction for Kullu district, Western Indian Himalayas. *J. Hydrol.* 546, 140–149. doi:10.1016/j.jhydrol.2016.12.059.

Balsamo, G., Albergel, C., Beljaars, A., Boussetta, S., Brun, E., Cloke, H., et al. (2015). ERA-Interim/Land: a global land surface reanalysis data set. *Hydrol. Earth Syst. Sci.* 19, 389–407. doi:10.5194/hess-19-389-2015.

Ban, N., Schmidli, J., and Schär, C. (2014). Evaluation of the new convective-resolving regional climate modeling approach in decade-long simulations. *J. Geophys. Res. Atmos.* 119, 7889–7907. doi:10.1002/2014JD021478.

Ban, N., Schmidli, J., and Schär, C. (2015). Heavy precipitation in a changing climate: Does short-term summer precipitation increase faster? *Geophys. Res. Lett.* 42, 1165–1172. doi:10.1002/2014GL062588.

Bandyopadhyay, N., Bhuiyan, C., and Saha, A. K. (2016). Heat waves, temperature extremes and their impacts on monsoon rainfall and meteorological drought in Gujarat, India. *Nat. Hazards* 82, 367–388. doi:10.1007/s11069-016-2205-4.

Bao, J., and Sherwood, S. C. (2019). The Role of Convective Self-Aggregation in Extreme Instantaneous Versus Daily Precipitation. *J. Adv. Model. Earth Syst.* 11, 19–33. doi:10.1029/2018MS001503.

Bao, J., Sherwood, S. C., Alexander, L. V, and Evans, J. P. (2017). Future increases in extreme precipitation exceed observed scaling rates. *Nat. Clim. Chang.* 7, 128–132. doi:10.1038/nclimate3201.

Barbero, R., Fowler, H. J., Lenderink, G., and Blenkinsop, S. (2017). Is the intensification of precipitation extremes with global warming better detected at hourly than daily resolutions? *Geophys. Res. Lett.* 44, 974–983. doi:10.1002/2016GL071917.

Barcikowska, M. J., Weaver, S. J., Feser, F., Russo, S., Schenk, F., Stone, D. A., et al. (2018). Euro-Atlantic winter storminess and precipitation extremes under 1.5° C vs. 2° C warming scenarios. *Earth Syst. Dyn.* 9. Available at: https://doi.org/10.5194/esd-9-679-2018.

Bard, A., Renard, B., Lang, M., Giuntoli, I., Korck, J., Koboltschnig, G., et al. (2015). Trends in the hydrologic regime of Alpine rivers. *J. Hydrol.* 529, 1823–1837. doi:10.1016/j.jhydrol.2015.07.052.

Barella-Ortiz, A., and Quintana Seguí, P. (2019). Evaluation of drought representation and propagation in regional climate model simulations across Spain. *Hydrol. Earth Syst. Sci.* 23, 5111–5131. doi:10.5194/hess-23-5111-2019.

Barichivich, J., Gloor, E., Peylin, P., Brienen, R. J. W., Schöngart, J., Espinoza, J. C., et al. (2018). Recent intensification of Amazon flooding extremes driven by strengthened Walker circulation. *Sci. Adv.* 4. doi:10.1126/sciadv.aat8785.

Barker, L. J., Hannaford, J., Chiverton, A., and Svensson, C. (2016). From meteorological to hydrological drought using standardised indicators. *Hydrol. Earth Syst. Sci.* 20, 2483–2505. doi:10.5194/hess-20-2483-2016.

Barker, L. J., Hannaford, J., Parry, S., Smith, K. A., Tanguy, M., and Prudhomme, C. (2019). Historic hydrological droughts 1891-2015: Systematic characterisation for a diverse set of catchments across the UK. *Hydrol. Earth Syst. Sci.* 23, 4583–4602. doi:10.5194/hess-23-4583-2019.

Barkhordarian, A., Saatchi, S. S., Behrangi, A., Loikith, P. C., and Mechoso, C. R. (2019). A Recent Systematic Increase in Vapor Pressure Deficit over Tropical South America. *Sci. Rep.* 9, 15331. doi:10.1038/s41598-019-51857-8.

Barlow, M., and Hoell, A. (2015). Drought in the Middle East and Central–Southwest Asia During Winter 2013/14. *Bull. Am. Meteorol. Soc.* 96, S71–S76. doi:10.1175/BAMS-D-15-00127.1.

Barlow, M., Zaitchik, B., Paz, S., Black, E., Evans, J., and Hoell, A. (2016). A review of drought in the Middle East and southwest Asia. *J. Clim.* 29, 8547–8574. doi:10.1175/JCLI-D-13-00692.1.

Barnard, P. L., Hoover, D., Hubbard, D. M., Snyder, A., Ludka, B. C., Allan, J., et al. (2017). Extreme oceanographic forcing and coastal response due to the 2015–2016 El Niño. *Nat. Commun.* 8, 14365. doi:10.1038/ncomms14365.

Barnhart, T. B., Molotch, N. P., Livneh, B., Harpold, A. A., Knowles, J. F., and Schneider, D. (2016). Snowmelt rate dictates streamflow. *Geophys. Res. Lett.* 43, 8006–8016. doi:10.1002/2016GL069690.

ACCEPTED VERSION SUBJECT TO FINAL EDITING

Barraqué, B. (2017). The common property issue in flood control through land use in France. *J. Flood Risk Manag.* 10, 182–194. doi:10.1111/jfr3.12092.

Barriopedro, D., Fischer, E. M., Luterbacher, J., Trigo, R. M., and Garcia-Herrera, R. (2011). The Hot Summer of 2010: Redrawing the Temperature Record Map of Europe. *Science (80-.).* 332, 220–224. doi:10.1126/science.1201224.

Barros, V. R., Boninsegna, J. A., Camilloni, I. A., Chidiak, M., Magrín, G. O., and Rusticucci, M. (2015). Climate change in Argentina: trends, projections, impacts and adaptation. *Wiley Interdiscip. Rev. Clim. Chang.* 6, 151–169. doi:10.1002/wcc.316.

Barry, A. A., Caesar, J., Klein Tank, A. M. G., Aguilar, E., McSweeney, C., Cyrille, A. M., et al. (2018). West Africa climate extremes and climate change indices. *Int. J. Climatol.* 38, e921–e938. doi:10.1002/joc.5420.

Bartók, B., Wild, M., Folini, D., Lüthi, D., Kotlarski, S., Schär, C., et al. (2017). Projected changes in surface solar radiation in CMIP5 global climate models and in EURO-CORDEX regional climate models for Europe. *Clim. Dyn.* 49, 2665–2683. doi:10.1007/s00382-016-3471-2.

Basara, J. B., Christian, J. I., Wakefield, R. A., Otkin, J. A., Hunt, E. H., and Brown, D. P. (2019). The evolution, propagation, and spread of flash drought in the Central United States during 2012. *Environ. Res. Lett.* 14, 084025. doi:10.1088/1748-9326/ab2cc0.

Basconcillo, J., Lucero, A., Solis, A., Sandoval Jr, R., Bautista, E., Koizumi, T., et al. (2016). Statistically downscaled projected changes in seasonal mean temperature and rainfall in Cagayan Valley, Philippines. *J. Meteorol. Soc. Japan. Ser. II* 94, 151–164.

Bathiany, S., Dakos, V., Scheffer, M., and Lenton, T. M. (2018). Climate models predict increasing temperature variability in poor countries. *Sci. Adv.* 4, eaar5809. doi:10.1126/sciadv.aar5809.

Befort, D. J., Wild, S., Kruschke, T., Ulbrich, U., and Leckebusch, G. C. (2016). Different long-term trends of extra-tropical cyclones and windstorms in ERA-20C and NOAA-20CR reanalyses. *Atmos. Sci. Lett.* 17, 586–595. doi:10.1002/asl.694.

Beguería, S., Vicente-Serrano, S. M., Reig, F., and Latorre, B. (2014). Standardized precipitation evapotranspiration index (SPEI) revisited: Parameter fitting, evapotranspiration models, tools, datasets and drought monitoring. *Int. J. Climatol.* 34. doi:10.1002/joc.3887.

Bell, S. S., Chand, S. S., Tory, K. J., Dowdy, A. J., Turville, C., and Ye, H. (2019). Projections of southern hemisphere tropical cyclone track density using CMIP5 models. *Clim. Dyn.* 52, 6065–6079. doi:10.1007/s00382-018-4497-4.

Bellprat, O., García-Serrano, J., Fučkar, N. S., Massonnet, F., Guemas, V., and Doblas-Reyes, F. J. (2016). The Role of Arctic Sea Ice and Sea Surface Temperatures on the Cold 2015 February Over North America. *Bull. Am. Meteorol. Soc.* 97, S36–S41. doi:10.1175/BAMS-D-16-0159.1.

Bellprat, O., Lott, F. C., Gulizia, C., Parker, H. R., Pampuch, L. A., Pinto, I., et al. (2015). Unusual past dry and wet rainy seasons over Southern Africa and South America from a climate perspective. *Weather Clim. Extrem.* 9, 36–46. doi:10.1016/J.WACE.2015.07.001.

Belušić, D., de Vries, H., Dobler, A., Landgren, O., Lind, P., Lindstedt, D., et al. (2020). HCLIM38: a flexible regional climate model applicable for different climate zones from coarse to convection-permitting scales. *Geosci. Model Dev.* 13, 1311–1333. doi:10.5194/gmd-13-1311-2020.

Benestad, R. E., Parding, K. M., Erlandsen, H. B., and Mezghani, A. (2019). A simple equation to study changes in rainfall statistics. *Environ. Res. Lett.* 14, 84017. doi:10.1088/1748-9326/ab2bb2.

Benestad, R. E., van Oort, B., Justino, F., Stordal, F., Parding, K. M., Mezghani, A., et al. (2018). Downscaling probability of long heatwaves based on seasonal mean daily maximum temperatures. *Adv. Stat. Climatol. Meteorol. Oceanogr.* 4, 37–52. doi:10.5194/ascmo-4-37-2018.

Benito, G., Brázdil, R., Herget, J., and Machado, M. J. (2015). Quantitative historical hydrology in Europe. *Hydrol. Earth Syst. Sci.* 19, 3517–3539. doi:10.5194/hess-19-3517-2015.

Bennett, K. E., and Walsh, J. E. (2015). Spatial and temporal changes in indices of extreme precipitation and temperature for Alaska. *Int. J. Climatol.* 35, 1434–1452. doi:10.1002/joc.4067.

Berg, A., Findell, K., Lintner, B., Giannini, A., Seneviratne, S. I., van den Hurk, B., et al. (2016). Land–atmosphere feedbacks amplify aridity increase over land under global warming. *Nat. Clim. Chang.* 6, 869–874. doi:10.1038/nclimate3029.

Berg, A., Lintner, B. R., Findell, K., and Giannini, A. (2017a). Uncertain soil moisture feedbacks in model projections of Sahel precipitation. *Geophys. Res. Lett.* 44, 6124–6133. doi:10.1002/2017GL073851.

Berg, A., Lintner, B. R., Findell, K., Seneviratne, S. I., van den Hurk, B., Ducharne, A., et al. (2015). Interannual Coupling between Summertime Surface Temperature and Precipitation over Land: Processes and Implications for Climate Change. *J. Clim.* 28, 1308–1328. doi:10.1175/JCLI-D-14-00324.1.

Berg, A., and Sheffield, J. (2018). Climate Change and Drought: the Soil Moisture Perspective. *Curr. Clim. Chang. Reports* 4, 180–191. doi:10.1007/s40641-018-0095-0.

Berg, A., Sheffield, J., and Milly, P. C. D. (2017b). Divergent surface and total soil moisture projections under global warming. *Geophys. Res. Lett.* 44, 236–244. doi:10.1002/2016GL071921.

Bergaoui, K., Mitchell, D., Otto, F., Allen, M., Zaaboul, R., McDonnell, R., et al. (2015). The Contribution of Human-Induced Climate Change to the Drought of 2014 in the Southern Levant Region. *Bull. Am. Meteorol. Soc.* 96, S66–S70. doi:10.1175/BAMS-D-15-00129.1.

SUBJECT TO FINAL EDITING ACCEPTED VERSION

Berghuijs, W. R., Aalbers, E. E., Larsen, J. R., Trancoso, R., and Woods, R. A. (2017). Recent changes in extreme floods across multiple continents. *Environ. Res. Lett.* 12, 114035. doi:10.1088/1748-9326/aa8847.

Berghuijs, W. R., Woods, R. A., Hutton, C. J., and Sivapalan, M. (2016). Dominant flood generating mechanisms across the United States. *Geophys. Res. Lett.* 43, 4382–4390. doi:10.1002/2016GL068070.

Berthou, S., Kendon, E. J., Rowell, D. P., Roberts, M. J., Tucker, S., and Stratton, R. A. (2019a). Larger Future Intensification of Rainfall in the West African Sahel in a Convection-Permitting Model. *Geophys. Res. Lett.* 46, 13299–13307. doi:10.1029/2019GL083544.

Berthou, S., Rowell, D. P., Kendon, E. J., Roberts, M. J., Stratton, R. A., Crook, J. A., et al. (2019b). Improved climatological precipitation characteristics over West Africa at convection-permitting scales. *Clim. Dyn.* 53, 1991–2011. doi:10.1007/s00382-019-04759-4.

Bessho, K., Date, K., Hayashi, M., Ikeda, A., Imai, T., Inoue, H., et al. (2016). An Introduction to Himawari-8/9--Japan's New-Generation Geostationary Meteorological Satellites. *J. Meteorol. Soc. Japan. Ser. II* 94, 151–183. doi:10.2151/jmsj.2016-009.

Betts, R. A., Alfieri, L., Bradshaw, C., Caesar, J., Feyen, L., Friedlingstein, P., et al. (2018). Changes in climate extremes, fresh water availability and vulnerability to food insecurity projected at 1.5°C and 2°C global warming with a higher-resolution global climate model. *Philos. Trans. R. Soc. A Math. Phys. Eng. Sci.* 376. doi:10.1098/rsta.2016.0452.

Beusch, L., Gudmundsson, L., and Seneviratne, S. I. (2020). Emulating Earth system model temperatures with MESMER: From global mean temperature trajectories to grid-point-level realizations on land. *Earth Syst. Dyn.* 11, 139–159. doi:10.5194/esd-11-139-2020.

Bevacqua, E., Maraun, D., Vousdoukas, M. I., Voukouvalas, E., Vrac, M., Mentaschi, L., et al. (2019). Higher probability of compound flooding from precipitation and storm surge in Europe under anthropogenic climate change. *Sci. Adv.* 5, eaaw5531. doi:10.1126/sciadv.aaw5531.

Bevacqua, E., Vousdoukas, M. I., Shepherd, T. G., and Vrac, M. (2020a). Brief communication: The role of using precipitation or river discharge data when assessing global coastal compound flooding. *Nat. Hazards Earth Syst. Sci.* 20, 1765–1782. doi:10.5194/nhess-20-1765-2020.

Bevacqua, E., Vousdoukas, M. I., Zappa, G., Hodges, K., Shepherd, T. G., Maraun, D., et al. (2020b). More meteorological events that drive compound coastal flooding are projected under climate change. *Commun. Earth Environ.* 1, 47. doi:10.1038/s43247-020-00044-z.

Bevacqua, E., Zappa, G., and Shepherd, T. G. (2020c). Shorter cyclone clusters modulate changes in European wintertime precipitation extremes. *Environ. Res. Lett.* 8, 808–812. doi:10.1088/1748-9326/abbde7.

Bezerra, B. G., Silva, L. L., Santos e Silva, C. M., and de Carvalho, G. G. (2018). Changes of precipitation extremes indices in São Francisco River Basin, Brazil from 1947 to 2012. *Theor. Appl. Climatol.* 135, 565–576. doi:10.1007/s00704-018-2396-6.

Bhatia, K. T., Vecchi, G. A., Knutson, T. R., Murakami, H., Kossin, J., Dixon, K. W., et al. (2019). Recent increases in tropical cyclone intensification rates. *Nat. Commun.* 10, 1–9. doi:10.1038/s41467-019-08471-z.

Bhatia, K., Vecchi, G., Murakami, H., Underwood, S., and Kossin, J. (2018). Projected response of tropical cyclone intensity and intensification in a global climate model. *J. Clim.* 31, 8281–8303. doi:10.1175/JCLI-D-17-0898.1.

Bindoff, N. L., Stott, P. A., AchutaRao, K., Allen, M. R., Gillett, N., Gutzler, D., et al. (2013). "Detection and Attribution of Climate Change: from Global to Regional," in *Climate Change 2013: The Physical Science Basis. Contribution of Working Group I to the Fifth Assessment Report of the Intergovernmental Panel on Climate Change*, eds. T. . Stocker, D. Qin, G.-K. Plattner, M. Tignor, S. K. Allen, J. Boschung, et al. (Cambridge, United Kingdom and New York, NY, USA: Cambridge University Press), 867–952. doi:10.1017/CBO9781107415324.022.

Biscarini, C., Francesco, S. D., Ridolfi, E., and Manciola, P. (2016). On the simulation of floods in a narrow bending valley: The malpasset dam break case study. *Water (Switzerland)* 8. doi:10.3390/w8110545.

Bitencourt, D. P., Fuentes, M. V., Maia, P. A., and Amorim, F. T. (2016). Frequência, Duração, Abrangência Espacial e Intensidadedas Ondas de Calor no Brasil. *Rev. Bras. Meteorol.* 31, 506–517. doi:10.1590/0102-77863123142015007 7.

Black, M. T., and Karoly, D. J. (2016). Southern Australia's Warmest October on Record: The Role of ENSO and Climate Change. *Bull. Am. Meteorol. Soc.* 97, S118–S121. doi:10.1175/BAMS-D-16-0124.1.

Blamey, R. C., Kolusu, S. R., Mahlalela, P., Todd, M. C., and Reason, C. J. C. (2018). The role of regional circulation features in regulating El Niño climate impacts over southern Africa: A comparison of the 2015/2016 drought with previous events. *Int. J. Climatol.* 38, 4276–4295. doi:10.1002/joc.5668.

Blanchet, J., Molinié, G., and Touati, J. (2018). Spatial analysis of trend in extreme daily rainfall in southern France. *Clim. Dyn.* 51, 799–812. doi:10.1007/s00382-016-3122-7.

Bloomfield, J. P., and Marchant, B. P. (2013). Analysis of groundwater drought building on the standardised precipitation index approach. *Hydrol. Earth Syst. Sci.* 17, 4769–4787. doi:10.5194/hess-17-4769-2013.

Bloomfield, J. P., Marchant, B. P., and McKenzie, A. A. (2019). Changes in groundwater drought associated with anthropogenic warming. *Hydrol. Earth Syst. Sci.* 23, 1393–1408. doi:10.5194/hess-23-1393-2019.

Blöschl, G., Hall, J., Parajka, J., Perdigão, R. A. P., Merz, B., Arheimer, B., et al. (2017). Changing climate shifts

ACCEPTED VERSION SUBJECT TO FINAL EDITING

timing of European floods. *Science (80-.).* 357, 588–590. doi:10.1126/science.aan2506.
Blöschl, G., Hall, J., Viglione, A., Perdigão, R. A. P., Parajka, J., Merz, B., et al. (2019). Changing climate both increases and decreases European river floods. *Nature* 573, 108–111. doi:10.1038/s41586-019-1495-6.
Blunden, J., and Arndt, D. S. (2016). State of the Climate in 2015. *Bull. Am. Meteorol. Soc.* 97, Si-S275. doi:10.1175/2016BAMSStateoftheClimate.1.
Blunden, J., and Arndt, D. S. (2017). State of the Climate in 2016. *Bull. Am. Meteorol. Soc.* 98, Si-S280. doi:10.1175/2017BAMSStateoftheClimate.1.
Boé, J., Somot, S., Corre, L., and Nabat, P. (2020). Large discrepancies in summer climate change over Europe as projected by global and regional climate models: causes and consequences. *Clim. Dyn.* 54, 2981–3002. doi:10.1007/s00382-020-05153-1.
Boers, N., Goswami, B., Rheinwalt, A., Bookhagen, B., Hoskins, B., and Kurths, J. (2019). Complex networks reveal global pattern of extreme-rainfall teleconnections. *Nature* 566, 373–377. doi:10.1038/s41586-018-0872-x.
Boisier, J. P., Alvarez-Garretón, C., Cordero, R. R., Damiani, A., Gallardo, L., Garreaud, R. D., et al. (2018). Anthropogenic drying in central-southern Chile evidenced by long-term observations and climate model simulations. *Elem Sci Anth* 6, 74. doi:10.1525/elementa.328.
Boisier, J. P., Rondanelli, R., Garreaud, R. D., and Muñoz, F. (2016). Anthropogenic and natural contributions to the Southeast Pacific precipitation decline and recent megadrought in central Chile. *Geophys. Res. Lett.* 43, 413–421. doi:10.1002/2015GL067265.
Bonan, G. B., Williams, M., Fisher, R. A., and Oleson, K. W. (2014). Modeling stomatal conductance in the earth system: linking leaf water-use efficiency and water transport along the soil–plant–atmosphere continuum. *Geosci. Model Dev.* 7, 2193–2222. doi:10.5194/gmd-7-2193-2014.
Bonfils, C. J. W., Santer, B. D., Fyfe, J. C., Marvel, K., Phillips, T. J., and Zimmerman, S. R. H. (2020). Human influence on joint changes in temperature, rainfall and continental aridity. *Nat. Clim. Chang.* 10, 726–731. doi:10.1038/s41558-020-0821-1.
Bonsal, B. R., Aider, R., Gachon, P., and Lapp, S. (2013). An assessment of Canadian prairie drought: Past, present, and future. *Clim. Dyn.* 41, 501–516. doi:10.1007/s00382-012-1422-0.
Bonsal, B. R., Peters, D. L., Seglenieks, F., Rivera, A., and Berg, A. (2019). Changes in freshwater availability across Canada. *Canada's Chang. Clim. Rep.*, 261–342.
Booth, J. F., Wang, S., and Polvani, L. (2013). Midlatitude storms in a moister world: lessons from idealized baroclinic life cycle experiments. *Clim. Dyn.* 41, 787–802. doi:10.1007/s00382-012-1472-3.
Borga, M., Stoffel, M., Marchi, L., Marra, F., and Jakob, M. (2014). Hydrogeomorphic response to extreme rainfall in headwater systems: Flash floods and debris flows. *J. Hydrol.* 518, 194–205. doi:10.1016/j.jhydrol.2014.05.022.
Borodina, A., Fischer, E. M., and Knutti, R. (2017a). Models are likely to underestimate increase in heavy rainfall in the extratropical regions with high rainfall intensity. *Geophys. Res. Lett.* 44, 7401–7409. doi:10.1002/2017GL074530.
Borodina, A., Fischer, E. M., and Knutti, R. (2017b). Potential to Constrain Projections of Hot Temperature Extremes. *J. Clim.* 30, 9949–9964. doi:10.1175/JCLI-D-16-0848.1.
Bosshard, T., Carambia, M., Goergen, K., Kotlarski, S., Krahe, P., Zappa, M., et al. (2013). Quantifying uncertainty sources in an ensemble of hydrological climate-impact projections. *Water Resour. Res.* 49, 1523–1536. doi:10.1029/2011WR011533.
Boyaj, A., Ashok, K., Ghosh, S., Devanand, A., and Dandu, G. (2018). The Chennai extreme rainfall event in 2015: The Bay of Bengal connection. *Clim. Dyn.* 50, 2867–2879. doi:10.1007/s00382-017-3778-7.
Bozkurt, D., Rojas, M., Boisier, J. P., Rondanelli, R., Garreaud, R., and Gallardo, L. (2019). Dynamical downscaling over the complex terrain of southwest South America: present climate conditions and added value analysis. *Clim. Dyn.* 53, 6745–6767. doi:10.1007/s00382-019-04959-y.
Bozkurt, D., Rojas, M., Boisier, J. P., and Valdivieso, J. (2018). Projected hydroclimate changes over Andean basins in central Chile from downscaled CMIP5 models under the low and high emission scenarios. *Clim. Change* 150, 131–147. doi:10.1007/s10584-018-2246-7.
Brando, P. M., Paolucci, L., Ummenhofer, C. C., Ordway, E. M., Hartmann, H., Cattau, M. E., et al. (2019). Droughts, Wildfires, and Forest Carbon Cycling: A Pantropical Synthesis. *Annu. Rev. Earth Planet. Sci.* 47, 555–581. doi:10.1146/annurev-earth-082517-010235.
Brandon, C. M., Woodruff, J. D., Lane, D. P., and Donnelly, J. P. (2013). Tropical cyclone wind speed constraints from resultant storm surge deposition: A 2500 year reconstruction of hurricane activity from St. Marks, FL. *Geochemistry, Geophys. Geosystems* 14, 2993–3008. doi:10.1002/ggge.20217.
Bregy, J. C., Wallace, D. J., Minzoni, R. T., and Cruz, V. J. (2018). 2500-year paleotempestological record of intense storms for the northern Gulf of Mexico, United States. *Mar. Geol.* 396, 26–42. doi:10.1016/j.margeo.2017.09.009.
Breña-Naranjo, J., Laverde B., M., and Pedrozo-Acuña, A. (2016). Changes in pan evaporation in Mexico from 1961 to 2010. *Int. J. Climatol.* 37. doi:10.1002/joc.4698.
Breshears, D. D., Adams, H. D., Eamus, D., Mcdowell, N. G., Law, D. J., Will, R. E., et al. (2013). The critical amplifying role of increasing atmospheric moisture demand on tree mortality and associated regional die-off.

ACCEPTED VERSION SUBJECT TO FINAL EDITING

Front. Plant Sci. 4. doi:10.3389/fpls.2013.00266.
Bright, R. M., Davin, E., O'Halloran, T., Pongratz, J., Zhao, K., and Cescatti, A. (2017). Local temperature response to land cover and management change driven by non-radiative processes. *Nat. Clim. Chang.* 7, 296–302. doi:10.1038/nclimate3250.
Brito, S. S. B., Cunha, A. P. M. A., Cunningham, C. C., Alvalá, R. C., Marengo, J. A., and Carvalho, M. A. (2018). Frequency, duration and severity of drought in the Semiarid Northeast Brazil region. *Int. J. Climatol.* 38, 517–529. doi:10.1002/joc.5225.
Brocca, L., Hasenauer, S., Lacava, T., Melone, F., Moramarco, T., Wagner, W., et al. (2011). Soil moisture estimation through ASCAT and AMSR-E sensors: An intercomparison and validation study across Europe. *Remote Sens. Environ.* 115, 3390–3408. doi:10.1016/j.rse.2011.08.003.
Brodribb, T. J., Powers, J., Cochard, H., and Choat, B. (2020). Hanging by a thread? Forests and drought. *Science (80-.).* 368, 261–266. doi:10.1126/science.aat7631.
Brohan, P., Compo, G. P., Brönnimann, S., Allan, R. J., Auchmann, R., Brugnara, Y., et al. (2016). The 1816 'year without a summer' in an atmospheric reanalysis. *Clim. Past Discuss.*, 1–11. doi:10.5194/cp-2016-78.
Brooks, H. E. (2013). Severe thunderstorms and climate change. *Atmos. Res.* 123, 129–138. doi:10.1016/j.atmosres.2012.04.002.
Brooks, H. E., Carbin, G. W., and Marsh, P. T. (2014). Increased variability of tornado occurrence in the United States. *Science (80-.).* 346, 349 LP-352. doi:10.1126/science.1257460.
Brown, S. J. (2020). Future changes in heatwave severity, duration and frequency due to climate change for the most populous cities. *Weather Clim. Extrem.* 30, 100278. doi:10.1016/j.wace.2020.100278.
Brunner, L., Hegerl, G. C., and Steiner, A. K. (2017). Connecting atmospheric blocking to European temperature extremes in spring. *J. Clim.* 30, 585–594. doi:10.1175/JCLI-D-16-0518.1.
Brunner, L., Schaller, N., Anstey, J., Sillmann, J., and Steiner, A. K. (2018). Dependence of Present and Future European Temperature Extremes on the Location of Atmospheric Blocking. *Geophys. Res. Lett.* 45, 6311–6320. doi:10.1029/2018GL077837.
Brunner, M. I., and Tallaksen, L. M. (2019). Proneness of European Catchments to Multiyear Streamflow Droughts. *Water Resour. Res.* doi:10.1029/2019WR025903.
Bucchignani, E., Zollo, A. L., Cattaneo, L., Montesarchio, M., and Mercogliano, P. (2017). Extreme weather events over China: assessment of COSMO-CLM simulations and future scenarios. *Int. J. Climatol.* 37, 1578–1594. doi:10.1002/joc.4798.
Büntgen, U., Tegel, W., Carrer, M., Krusic, P. J., Hayes, M., and Esper, J. (2015). Commentary to Wetter et al. (2014): Limited tree-ring evidence for a 1540 European 'Megadrought.' *Clim. Change* 131, 183–190. doi:10.1007/s10584-015-1423-1.
Burdanowitz, J., Buehler, S. A., Bakan, S., and Klepp, C. (2019). The sensitivity of oceanic precipitation to sea surface temperature. *Atmos. Chem. Phys.* 19, 9241–9252. doi:10.5194/acp-19-9241-2019.
Burgman, R. J., and Jang, Y. (2015). Simulated U.S. drought response to interannual and decadal pacific SST variability. *J. Clim.* 28, 4688–4705. doi:10.1175/JCLI-D-14-00247.1.
Burke, C., Stott, P., Ciavarella, A., and Sun, Y. (2016). Attribution of Extreme Rainfall in Southeast China During May 2015. *Bull. Am. Meteorol. Soc.* 97, S92–S96. doi:10.1175/BAMS-D-16-0144.1.
Burn, D. H., and Whitfield, P. H. (2016). Changes in floods and flood regimes in Canada. *Can. Water Resour. J.* 41, 139–150. doi:10.1080/07011784.2015.1026844.
Buttle, J. M., Allen, D. M., Caissie, D., Davison, B., Hayashi, M., Peters, D. L., et al. (2016). Flood processes in Canada: Regional and special aspects. *Can. Water Resour. J.* 41, 7–30. doi:10.1080/07011784.2015.1131629.
Byrne, M. P., and O'Gorman, P. A. (2015). The Response of Precipitation Minus Evapotranspiration to Climate Warming: Why the "Wet-Get-Wetter, Dry-Get-Drier" Scaling Does Not Hold over Land*. *J. Clim.* 28, 8078–8092. doi:10.1175/JCLI-D-15-0369.1.
Byrne, M. P., and O'Gorman, P. A. (2018). Trends in continental temperature and humidity directly linked to ocean warming. *Proc. Natl. Acad. Sci.* 115, 4863–4868. doi:10.1073/pnas.1722312115.
Cabré, M. F., Solman, S., and Núñez, M. (2016). Regional climate change scenarios over southern South America for future climate (2080-2099) using the MM5 Model. Mean, interannual variability and uncertainties. *Atmósfera* 29, 35–60. doi:10.20937/ATM.2016.29.01.04.
Cai, W., Borlace, S., Lengaigne, M., Van Rensch, P., Collins, M., Vecchi, G., et al. (2014a). Increasing frequency of extreme El Niño events due to greenhouse warming. *Nat. Clim. Chang.* 4, 111–116. doi:10.1038/nclimate2100.
Cai, W., and Cowan, T. (2008). Evidence of impacts from rising temperature on inflows to the Murray-Darling Basin. *Geophys. Res. Lett.* 35, 2–6. doi:10.1029/2008GL033390.
Cai, W., Purich, A., Cowan, T., Van Rensch, P., and Weller, E. (2014b). Did climate change-induced rainfall trends contribute to the australian millennium drought? *J. Clim.* 27, 3145–3168. doi:10.1175/JCLI-D-13-00322.1.
Cai, W., Santoso, A., Wang, G., Yeh, S. W., An, S. Il, Cobb, K. M., et al. (2015). ENSO and greenhouse warming. *Nat. Clim. Chang.* 5, 849–859. doi:10.1038/nclimate2743.
Cai, W., Wang, G., Gan, B., Wu, L., Santoso, A., Lin, X., et al. (2018). Stabilised frequency of extreme positive Indian Ocean Dipole under 1.5°C warming. *Nat. Commun.* 9, 4–11. doi:10.1038/s41467-018-03789-6.

ACCEPTED VERSION SUBJECT TO FINAL EDITING

Caillouet, L., Vidal, J.-P., Sauquet, E., Devers, A., and Graff, B. (2017). Ensemble reconstruction of spatio-temporal extreme low-flow events in France since 1871. *Hydrol. Earth Syst. Sci.* 21, 2923–2951. doi:10.5194/hess-21-2923-2017.

Callaghan, J., and Power, S. B. (2011). Variability and decline in the number of severe tropical cyclones making land-fall over eastern Australia since the late nineteenth century. *Clim. Dyn.* 37, 647–662. doi:10.1007/s00382-010-0883-2.

Caloiero, T. (2015). Analysis of rainfall trend in New Zealand. *Environ. Earth Sci.* 73, 6297–6310. doi:10.1007/s12665-014-3852-y.

Caloiero, T. (2017). Trend of monthly temperature and daily extreme temperature during 1951–2012 in New Zealand. *Theor. Appl. Climatol.* 129, 111–127. doi:10.1007/s00704-016-1764-3.

Caloiero, T., Veltri, S., Caloiero, P., and Frustaci, F. (2018). Drought Analysis in Europe and in the Mediterranean Basin Using the Standardized Precipitation Index. *Water* 10, 1043. doi:10.3390/w10081043.

Camargo, S. J. (2013). Global and regional aspects of tropical cyclone activity in the CMIP5 models. *J. Clim.* 26, 9880–9902. doi:10.1175/JCLI-D-12-00549.1.

Camargo, S. J., Emanuel, K. A., and Sobel, A. H. (2007). Use of a Genesis Potential Index to Diagnose ENSO Effects on Tropical Cyclone Genesis. *J. Clim.* 20, 4819–4834. doi:10.1175/JCLI4282.1.

Camargo, S. J., Giulivi, C. F., Sobel, A. H., Wing, A. A., Kim, D., Moon, Y., et al. (2020). Characteristics of Model Tropical Cyclone Climatology and the Large-Scale Environment. *J. Clim.* 33, 4463–4487. doi:10.1175/JCLI-D-19-0500.1.

Camargo, S. J., Tippett, M. K., Sobel, A. H., Vecchi, G. A., and Zhao, M. (2014). Testing the performance of tropical cyclone genesis indices in future climates using the HiRAM model. *J. Clim.* 27, 9171–9196. doi:10.1175/JCLI-D-13-00505.1.

Camargo, S. J., Wheeler, M. C., and Sobel, A. H. (2009). Diagnosis of the MJO modulation of tropical cyclogenesis using an empirical index. *J. Atmos. Sci.* 66, 3061–3074. doi:10.1175/2009JAS3101.1.

Camargo, S. J., and Wing, A. A. (2016). Tropical cyclones in climate models. *Wiley Interdiscip. Rev. Clim. Chang.* 7, 211–237. doi:10.1002/wcc.373.

Camuffo, D., Bertolin, C., Diodato, N., Cocheo, C., Barriendos, M., Dominguez-Castro, F., et al. (2013). Western Mediterranean precipitation over the last 300 years from instrumental observations. *Clim. Change* 117, 85–101. doi:10.1007/s10584-012-0539-9.

Cannon, A. J., and Innocenti, S. (2019). Projected intensification of sub-daily and daily rainfall extremes in convection-permitting climate model simulations over North America: implications for future intensity–duration–frequency curves. *Nat. Hazards Earth Syst. Sci.* 19, 421–440. doi:10.5194/nhess-19-421-2019.

Cardell, M. F., Amengual, A., Romero, R., and Ramis, C. (2020). Future extremes of temperature and precipitation in Europe derived from a combination of dynamical and statistical approaches. *Int. J. Climatol.* 40, 4800–4827. doi:10.1002/joc.6490.

Cardoso, R. M., Soares, P. M. M., Lima, D. C. A., and Miranda, P. M. A. (2019). Mean and extreme temperatures in a warming climate: EURO CORDEX and WRF regional climate high-resolution projections for Portugal. *Clim. Dyn.* 52, 129–157. doi:10.1007/s00382-018-4124-4.

Carril, A., Cavalcanti, I., Menéndez, C., Sörensson, A., López-Franca, N., Rivera, J., et al. (2016). Extreme events in the La Plata basin: a retrospective analysis of what we have learned during CLARIS-LPB project. *Clim. Res.* 68, 95–116. doi:10.3354/cr01374.

Carvalho, L. M. V (2020). Assessing precipitation trends in the Americas with historical data: A review. *WIREs Clim. Chang.* 11, e627. doi:10.1002/wcc.627.

Casanueva, A., Rodriguez-Puebla, C., Frías, M. D., and González-Reviriego, N. (2014). Variability of extreme precipitation over Europe and its relationships with teleconnection patterns. *Hydrol. Earth Syst. Sci.* 18, 709–725. doi:10.5194/hess-18-709-2014.

Cattiaux, J., and Ribes, A. (2018). Defining Single Extreme Weather Events in a Climate Perspective. *Bull. Am. Meteorol. Soc.* 99, 1557–1568. doi:10.1175/BAMS-D-17-0281.1.

Catto, J. L., Jakob, C., and Nicholls, N. (2015). Can the CMIP5 models represent winter frontal precipitation? *Geophys. Res. Lett.* doi:10.1002/2015GL066015.

Catto, J. L., and Pfahl, S. (2013). The importance of fronts for extreme precipitation. *J. Geophys. Res. Atmos.* 118, 10791–10801. doi:10.1002/jgrd.50852.

Cavalcanti, I. F. A., Carril, A. F., Penalba, O. C., Grimm, A. M., Menéndez, C. G., Sanchez, E., et al. (2015). Precipitation extremes over La Plata Basin – Review and new results from observations and climate simulations. *J. Hydrol.* 523, 211–230. doi:10.1016/j.jhydrol.2015.01.028.

Cavanaugh, N. R., and Shen, S. S. P. (2015). The Effects of Gridding Algorithms on the Statistical Moments and Their Trends of Daily Surface Air Temperature. *J. Clim.* 28, 9188–9205. doi:10.1175/JCLI-D-14-00668.1.

Cavicchia, L., von Storch, H., and Gualdi, S. (2014). Mediterranean Tropical-Like Cyclones in Present and Future Climate. *J. Clim.* 27, 7493–7501. doi:10.1175/JCLI-D-14-00339.1.

Ceccherini, G., Russo, S., Ameztoy, I., Marchese, A. F., and Carmona-Moreno, C. (2017). Heat waves in Africa 1981–2015, observations and reanalysis. *Nat. Hazards Earth Syst. Sci.* 17, 115–125. doi:10.5194/nhess-17-115-2017.

ACCEPTED VERSION SUBJECT TO FINAL EDITING

Ceccherini, G., Russo, S., Ameztoy, I., Romero, C. P., and Carmona-Moreno, C. (2016). Magnitude and frequency of heat and cold waves in recent decades: the case of South America. *Nat. Hazards Earth Syst. Sci.* 16, 821–831. doi:10.5194/nhess-16-821-2016.

Cha, E. J., Knutson, T. R., Lee, T.-C., Ying, M., and Nakaegawa, T. (2020). Third assessment on impacts of climate change on tropical cyclones in the Typhoon Committee Region – Part II: Future projections. *Trop. Cyclone Res. Rev.* 9, 75–86. doi:https://doi.org/10.1016/j.tcrr.2020.04.005.

Chai, R., Sun, S., Chen, H., and Zhou, S. (2018). Changes in reference evapotranspiration over China during 1960–2012: Attributions and relationships with atmospheric circulation. *Hydrol. Process.* 32, 3032–3048. doi:10.1002/hyp.13252.

Chakraborty, D., Sehgal, V. K., Dhakar, R., Varghese, E., Das, D. K., and Ray, M. (2018). Changes in daily maximum temperature extremes across India over 1951-2014 and their relation with cereal crop productivity. *Stoch. Environ. Res. Risk Assess.* 32. doi:10.1007/s00477-018-1604-3.

Chan, K. T. F., and Chan, J. C. L. (2015). Global climatology of tropical cyclone size as inferred from QuikSCAT data. *Int. J. Climatol.* 35, 4843–4848. doi:10.1002/joc.4307.

Chan, K. T. F., and Chan, J. C. L. (2018). The Outer-Core Wind Structure of Tropical Cyclones. *J. Meteorol. Soc. Japan. Ser. II* 96, 297–315. doi:10.2151/jmsj.2018-042.

Chan, S. C., Kendon, E. J., Berthou, S., Fosser, G., Lewis, E., and Fowler, H. J. (2020). Europe-wide precipitation projections at convection permitting scale with the Unified Model. *Clim. Dyn.* 55, 409–428. doi:10.1007/s00382-020-05192-8.

Chand, S. S., Dowdy, A. J., Ramsay, H. A., Walsh, K. J. E., Tory, K. J., Power, S. B., et al. (2019). Review of tropical cyclones in the Australian region: Climatology, variability, predictability, and trends. *WIREs Clim. Chang.* 10, e602. doi:10.1002/wcc.602.

Chaney, N. W., Sheffield, J., Villarini, G., and Wood, E. F. (2014). Development of a high-resolution gridded daily meteorological dataset over sub-Saharan Africa: Spatial analysis of trends in climate extremes. *J. Clim.* doi:10.1175/JCLI-D-13-00423.1.

Chang, E. K. M. (2014). Impacts of background field removal on CMIP5 projected changes in Pacific winter cyclone activity. *J. Geophys. Res. Atmos.* 119, 4626–4639. doi:10.1038/175238c0.

Chang, E. K. M. (2017). Projected Significant Increase in the Number of Extreme Extratropical Cyclones in the Southern Hemisphere. *J. Clim.* 30, 4915–4935. doi:10.1175/JCLI-D-16-0553.1.

Chang, E. K. M., Ma, C. G., Zheng, C., and Yau, A. M. W. (2016). Observed and projected decrease in Northern Hemisphere extratropical cyclone activity in summer and its impacts on maximum temperature. *Geophys. Res. Lett.* doi:10.1002/2016GL068172.

Chang, E. K. M., and Yau, A. M. W. (2016). Northern Hemisphere winter storm track trends since 1959 derived from multiple reanalysis datasets. *Clim. Dyn.* 47, 1435–1454. doi:10.1007/s00382-015-2911-8.

Chapman, S., Watson, J. E. M., Salazar, A., Thatcher, M., and McAlpine, C. A. (2017). The impact of urbanization and climate change on urban temperatures: a systematic review. *Landsc. Ecol.* 32, 1921–1935. doi:10.1007/s10980-017-0561-4.

Chavas, D. R., and Emanuel, K. (2014). Equilibrium tropical cyclone size in an idealized state of axisymmetric radiative-convective equilibrium. *J. Atmos. Sci.* 71, 1663–1680. doi:10.1175/JAS-D-13-0155.1.

Chen, C.-T., and Knutson, T. (2008). On the Verification and Comparison of Extreme Rainfall Indices from Climate Models. *J. Clim.* 21, 1605–1621. doi:10.1175/2007JCLI1494.1.

Chen, D., Guo, J., Yao, D., Lin, Y., Zhao, C., Min, M., et al. (2019). Mesoscale Convective Systems in the Asian Monsoon Region From Advanced Himawari Imager: Algorithms and Preliminary Results. *J. Geophys. Res. Atmos.* 124, 2210–2234. doi:10.1029/2018JD029707.

Chen, G.-S., Notaro, M., Liu, Z., and Liu, Y. (2012). Simulated Local and Remote Biophysical Effects of Afforestation over the Southeast United States in Boreal Summer. *J. Clim.* 25, 4511–4522. doi:10.1175/JCLI-D-11-00317.1.

Chen, H., and Sun, J. (2015a). Assessing model performance of climate extremes in China: an intercomparison between CMIP5 and CMIP3. *Clim. Change* 129, 197–211. doi:10.1007/s10584-014-1319-5.

Chen, H., and Sun, J. (2015b). Changes in Drought Characteristics over China Using the Standardized Precipitation Evapotranspiration Index. *J. Clim.* 28, 5430–5447. doi:10.1175/JCLI-D-14-00707.1.

Chen, H., and Sun, J. (2017a). Anthropogenic warming has caused hot droughts more frequently in China. *J. Hydrol.* 544, 306–318. doi:10.1016/j.jhydrol.2016.11.044.

Chen, H., and Sun, J. (2017b). Characterizing present and future drought changes over eastern China. *Int. J. Climatol.* 37, 138–156. doi:10.1002/joc.4987.

Chen, H., and Sun, J. (2017c). Contribution of human influence to increased daily precipitation extremes over China. *Geophys. Res. Lett.* doi:10.1002/2016GL072439.

Chen, H., Sun, J., Lin, W., and Xu, H. (2020a). Comparison of CMIP6 and CMIP5 models in simulating climate extremes. *Sci. Bull.* 65, 1415–1418. doi:10.1016/j.scib.2020.05.015.

Chen, J., Dai, A., Zhang, Y., and Rasmussen, K. L. (2020b). Changes in Convective Available Potential Energy and Convective Inhibition under Global Warming. *J. Clim.* 33, 2025–2050. doi:10.1175/JCLI-D-19-0461.1.

Chen, J., Wang, Z., Tam, C.-Y., Lau, N.-C., Lau, D.-S. D., and Mok, H.-Y. (2020c). Impacts of climate change on

ACCEPTED VERSION SUBJECT TO FINAL EDITING

tropical cyclones and induced storm surges in the Pearl River Delta region using pseudo-global-warming method. *Sci. Rep.* 10, 1965. doi:10.1038/s41598-020-58824-8.
Chen, L., and Dirmeyer, P. A. (2019). Global observed and modelled impacts of irrigation on surface temperature. *Int. J. Climatol.* 39, 2587–2600. doi:10.1002/joc.5973.
Chen, L., Li, D., and Pryor, S. C. (2013). Wind speed trends over China: Quantifying the magnitude and assessing causality. *Int. J. Climatol.* 33, 2579–2590. doi:10.1002/joc.3613.
Chen, R., Wen, Z., and Lu, R. (2016). Evolution of the circulation anomalies and the quasi-biweekly oscillations associated with extreme heat events in Southern China. *J. Clim.* 29, 6909–6921. doi:10.1175/JCLI-D-16-0160.1.
Chen, S., Li, Y., Kim, J., and Kim, S. W. (2017). Bayesian change point analysis for extreme daily precipitation. *Int. J. Climatol.* 37, 3123–3137. doi:10.1002/joc.4904.
Chen, X., Zhao, P., Ouyang, L., Zhu, L., Ni, G., and Schäfer, K. V. R. (2020d). Whole-plant water hydraulic integrity to predict drought-induced Eucalyptus urophylla mortality under drought stress. *For. Ecol. Manage.* 468. doi:10.1016/j.foreco.2020.118179.
Chen, Y., Li, W., Jiang, X., Zhai, P., and Luo, Y. (2021). Detectable Intensification of Hourly and Daily Scale Precipitation Extremes across Eastern China. *J. Clim.* 34, 1185–1201. doi:10.1175/JCLI-D-20-0462.1.
Chen, Y., and Zhai, P. (2017). Revisiting summertime hot extremes in China during 1961-2015: Overlooked compound extremes and significant changes. *Geophys. Res. Lett.* 44, 5096–5103. doi:10.1002/2016GL072281.
Cheng, L., Hoerling, M., Smith, L., and Eischeid, J. (2018). Diagnosing Human-Induced Dynamic and Thermodynamic Drivers of Extreme Rainfall. *J. Clim.* 31, 1029–1051. doi:10.1175/JCLI-D-16-0919.1.
Cheng, S., Guan, X., Huang, J., Ji, F., and Guo, R. (2015). Long-term trend and variability of soil moisture over East Asia. *J. Geophys. Res. Atmos.* 120, 8658–8670. doi:10.1002/2015JD023206.
Cheong, W. K., Timbal, B., Golding, N., Sirabaha, S., Kwan, K. F., Cinco, T. A., et al. (2018). Observed and modelled temperature and precipitation extremes over Southeast Asia from 1972 to 2010. *Int. J. Climatol.* 38, 3013–3027. doi:10.1002/joc.5479.
Chevuturi, A., Klingaman, N. P., Turner, A. G., and Hannah, S. (2018). Projected Changes in the Asian-Australian Monsoon Region in 1.5°C and 2.0°C Global-Warming Scenarios. *Earth's Futur.* 6, 339–358. doi:10.1002/2017EF000734.
Cho, C., Li, R., Wang, S.-Y., Yoon, J.-H., and Gillies, R. R. (2016). Anthropogenic footprint of climate change in the June 2013 northern India flood. *Clim. Dyn.* 46, 797–805. doi:10.1007/s00382-015-2613-2.
Chou, S. C., Lyra, A., Mourão, C., Dereczynski, C., Pilotto, I., Gomes, J., et al. (2014a). Assessment of Climate Change over South America under RCP 4.5 and 8.5 Downscaling Scenarios. *Am. J. Clim. Chang.* 03, 512–527. doi:10.4236/ajcc.2014.35043.
Chou, S. C., Lyra, A., Mourão, C., Dereczynski, C., Pilotto, I., Gomes, J., et al. (2014b). Evaluation of the Eta Simulations Nested in Three Global Climate Models. *Am. J. Clim. Chang.* 03, 438–454. doi:10.4236/ajcc.2014.35039.
Choy, C., Chong, S., Kong, D., and Cayanan, E. O. (2015). A Discussion of the Most Intense Tropical Cyclones in the Western North Pacific From 1978 to 2013. *Trop. Cyclone Res. Rev.* 4, 1–11. doi:https://doi.org/10.6057/2015TCRR01.01.
Christensen, J. H., Kumar Krishna, K., Aldrian, E., An, S.-I., Cavalcanti, I. F. A., Castro, M. de, et al. (2013). "Climate Phenomena and their Relevance for Future Regional Climate Change," in *Climate Change 2013: The Physical Science Basis. Contribution of Working Group I to the Fifth Assessment Report of the Intergovernmental Panel on Climate Change*, eds. T. . Stocker, D. Qin, G.-K. Plattner, M. Tignor, S. K. Allen, J. Boschung, et al. (Cambridge, United Kingdom and New York, NY, USA: Cambridge University Press), 1217–1308. doi:10.1017/CBO9781107415324.028.
Christiansen, B., Alvarez-Castro, C., Christidis, N., Ciavarella, A., Colfescu, I., Cowan, T., et al. (2018). Was the Cold European Winter of 2009/10 Modified by Anthropogenic Climate Change? An Attribution Study. *J. Clim.* 31, 3387–3410. doi:10.1175/JCLI-D-17-0589.1.
Christidis, N., Ciavarella, A., and Stott, P. A. (2018). Different Ways of Framing Event Attribution Questions: The Example of Warm and Wet Winters in the United Kingdom Similar to 2015/16. *J. Clim.* 31, 4827–4845. doi:10.1175/JCLI-D-17-0464.1.
Christidis, N., Jones, G. S., and Stott, P. A. (2015). Dramatically increasing chance of extremely hot summers since the 2003 European heatwave. *Nat. Clim. Chang.* 5, 46–50. doi:10.1038/nclimate2468.
Christidis, N., and Stott, P. A. (2014). Change in the Odds of Warm Years and Seasons Due to Anthropogenic Influence on the Climate. *J. Clim.* 27, 2607–2621.
Christidis, N., and Stott, P. A. (2016). Attribution analyses of temperature extremes using a set of 16 indices. *Weather Clim. Extrem.* 14, 24–35. doi:10.1016/j.wace.2016.10.003.
Christidis, N., Stott, P. A., and Ciavarella, A. (2014). The effect of anthropogenic climate change on the cold spring of 2013 in the United Kingdom. *Bull. Am. Meteorol. Soc.* 95, S15–S18. doi:10.1175/1520-0477-95.9.S1.1.
Christidis, N., Stott, P. A., Karoly, D. J., and Ciavarella, A. (2013a). An Attribution Study of the Heavy Rainfall Over Eastern Australia in March 2012 [in "Explaining Extreme Events of 2012 from a Climate Perspective"]. *Bull. Am. Meteorol. Soc.* 94, S58–S61. doi:10.1175/BAMS-D-13-00085.1.

ACCEPTED VERSION SUBJECT TO FINAL EDITING

Christidis, N., Stott, P. A., Scaife, A. A., Arribas, A., Jones, G. S., Copsey, D., et al. (2013b). A New HadGEM3-A-Based System for Attribution of Weather- and Climate-Related Extreme Events. *J. Clim.* 26, 2756–2783. doi:10.1175/JCLI-D-12-00169.1.

Cioffi, F., Lall, U., Rus, E., and Krishnamurthy, C. K. B. (2015). Space-time structure of extreme precipitation in Europe over the last century. *Int. J. Climatol.* 35, 1749–1760. doi:10.1002/joc.4116.

Clark, R. T., and Brown, S. J. (2013). Influences of Circulation and Climate Change on European Summer Heat Extremes. *J. Clim.* 26, 9621–9632. doi:10.1175/JCLI-D-12-00740.1.

Clark, R. T., Brown, S. J., and Murphy, J. M. (2006). Modeling Northern Hemisphere Summer Heat Extreme Changes and Their Uncertainties Using a Physics Ensemble of Climate Sensitivity Experiments. *J. Clim.* 19, 4418–4435. doi:10.1175/JCLI3877.1.

Clarke, H., and Evans, J. P. (2019). Exploring the future change space for fire weather in southeast Australia. *Theor. Appl. Climatol.* 136, 513–527. doi:10.1007/s00704-018-2507-4.

Colle, B. A., Zhang, Z., Lombardo, K. A., Chang, E., Liu, P., and Zhang, M. (2013). Historical evaluation and future prediction of eastern North American and Western Atlantic extratropical cyclones in the CMIP5 models during the cool season. *J. Clim.* doi:10.1175/JCLI-D-12-00498.1.

Collins, J. M., Klotzbach, P. J., Maue, R. N., Roache, D. R., Blake, E. S., Paxton, C. H., et al. (2016). The record-breaking 2015 hurricane season in the eastern North Pacific: An analysis of environmental conditions. *Geophys. Res. Lett.* 43, 9217–9224. doi:10.1002/2016GL070597.

Collins, M., Knutti, R., Arblaster, J., Dufresne, J.-L., Fichefet, T., Friedlingstein, P., et al. (2013). "Long-term Climate Change: Projections, Commitments and Irreversibility," in *Climate Change 2013: The Physical Science Basis. Contribution of Working Group I to the Fifth Assessment Report of the Intergovernmental Panel on Climate Change*, eds. T. . Stocker, D. Qin, G.-K. Plattner, M. Tignor, S. K. Allen, J. Boschung, et al. (Cambridge, United Kingdom and New York, NY, USA: Cambridge University Press), 1029–1136. doi:10.1017/CBO9781107415324.024.

Collins, M., Sutherland, M., Bouwer, L., Cheong, S.-M., and Frolicher, T. (2019). "Extremes, Abrupt Changes and Managing Risks," in *IPCC Special Report on the Ocean and Cryosphere in a Changing Climate*, eds. H.-O. Pörtner, D. C. Roberts, V. Masson-Delmotte, P. Zhai, M. Tignor, E. Poloczanska, et al. (In Press), 589–656. Available at: https://www.ipcc.ch/srocc/chapter/chapter-6.

Condon, L. E., Atchley, A. L., and Maxwell, R. M. (2020). Evapotranspiration depletes groundwater under warming over the contiguous United States. *Nat. Commun.* 11. doi:10.1038/s41467-020-14688-0.

Contractor, S., Donat, M. G., and Alexander, L. V (2020a). Changes in observed daily precipitation over global land areas since 1950. *J. Clim.*, 1–53. doi:10.1175/JCLI-D-19-0965.1.

Contractor, S., Donat, M. G., Alexander, L. V, Ziese, M., Meyer-Christoffer, A., Schneider, U., et al. (2020b). Rainfall Estimates on a Gridded Network (REGEN) – a global land-based gridded dataset of daily precipitation from 1950 to 2016. *Hydrol. Earth Syst. Sci.* 24, 919–943. doi:10.5194/hess-24-919-2020.

Cook, B. I., Anchukaitis, K. J., Touchan, R., Meko, D. M., and Cook, E. R. (2016a). Spatiotemporal drought variability in the Mediterranean over the last 900 years. *J. Geophys. Res. Atmos.* 121, 2060–2074. doi:10.1002/2015JD023929.

Cook, B. I., Ault, T. R., and Smerdon, J. E. (2015). Unprecedented 21st century drought risk in the American Southwest and Central Plains. *Sci. Adv.* 1, e1400082. doi:10.1126/sciadv.1400082.

Cook, B. I., Cook, E. R., Smerdon, J. E., Seager, R., Williams, A. P., Coats, S., et al. (2016b). North American megadroughts in the Common Era: Reconstructions and simulations. *Wiley Interdiscip. Rev. Clim. Chang.* 7, 411–432. doi:10.1002/wcc.394.

Cook, B. I., Mankin, J. S., and Anchukaitis, K. J. (2018). Climate Change and Drought: From Past to Future. *Curr. Clim. Chang. Reports* 4, 164–179. doi:10.1007/s40641-018-0093-2.

Cook, B. I., Mankin, J. S., Marvel, K., Williams, A. P., Smerdon, J. E., and Anchukaitis, K. J. (2020). Twenty-First Century Drought Projections in the CMIP6 Forcing Scenarios. *Earth's Futur.* 8, e2019EF001461. doi:10.1029/2019EF001461.

Cook, B. I., Palmer, J. G., Cook, E. R., Turney, C. S. M., Allen, K., Fenwick, P., et al. (2016c). The paleoclimate context and future trajectory of extreme summer hydroclimate in eastern Australia. *J. Geophys. Res.* 121, 12,812-820,838.

Cook, B. I., Seager, R., Williams, A. P., Puma, M. J., McDermid, S., Kelley, M., et al. (2019). Climate Change Amplification of Natural Drought Variability: The Historic Mid-Twentieth-Century North American Drought in a Warmer World. *J. Clim.* 32, 5417–5436. doi:10.1175/JCLI-D-18-0832.1.

Cook, B. I., Smerdon, J. E., Seager, R., and Coats, S. (2014a). Global warming and 21st century drying. *Clim. Dyn.* 43, 2607–2627. doi:10.1007/s00382-014-2075-y.

Cook, B. I., Smerdon, J. E., Seager, R., and Coats, S. (2014b). Global warming and 21stcentury drying. *Clim. Dyn.* 43, 2607–2627. doi:10.1007/s00382-014-2075-y.

Cook, B. I., Smerdon, J. E., Seager, R., and Cook, E. R. (2014c). Pan-Continental Droughts in North America over the Last Millennium. *J. Clim.* 27, 383–397. doi:10.1175/JCLI-D-13-00100.1.

Cook, E. R., Woodhouse, C. A., Mark Eakin, C., Meko, D. M., and Stahle, D. W. (2004). Long-Term Aridity Changes

ACCEPTED VERSION SUBJECT TO FINAL EDITING

in the Western United States. *Science (80-.).* 306, 1015–1018. doi:10.1126/science.1102586.
Coppola, E., Nogherotto, R., Ciarlo', J. M., Giorgi, F., Meijgaard, E., Kadygrov, N., et al. (2021a). Assessment of the European Climate Projections as Simulated by the Large EURO-CORDEX Regional and Global Climate Model Ensemble. *J. Geophys. Res. Atmos.* 126. doi:10.1029/2019JD032356.
Coppola, E., Raffaele, F., Giorgi, F., Giuliani, G., Xuejie, G., Ciarlo, J. M., et al. (2021b). Climate hazard indices projections based on CORDEX-CORE, CMIP5 and CMIP6 ensemble. *Clim. Dyn.* doi:10.1007/s00382-021-05640-z.
Corbella, S., and Stretch, D. D. (2012). Multivariate return periods of sea storms for coastal erosion risk assessment. *Nat. Hazards Earth Syst. Sci.* 12, 2699–2708. doi:10.5194/nhess-12-2699-2012.
Corrales-Suastegui, A., Fuentes-Franco, R., and Pavia, E. G. (2019). The mid-summer drought over Mexico and Central America in the 21st century. *Int. J. Climatol.* doi:10.1002/joc.6296.
Couasnon, A., Eilander, D., Muis, S., Veldkamp, T. I. E., Haigh, I. D., Wahl, T., et al. (2020). Measuring compound flood potential from river discharge and storm surge extremes at the global scale. *Nat. Hazards Earth Syst. Sci.* 20, 489–504. doi:10.5194/nhess-20-489-2020.
Coumou, D., Di Capua, G., Vavrus, S., Wang, L., and Wang, S. (2018). The influence of Arctic amplification on mid-latitude summer circulation. *Nat. Commun.* 9, 2959. doi:10.1038/s41467-018-05256-8.
Coumou, D., Lehmann, J., and Beckmann, J. (2015). The weakening summer circulation in the Northern Hemisphere mid-latitudes. *Science (80-.).* 348, 324–327. doi:10.1126/science.1261768.
Cowan, T., Hegerl, G. C., Colfescu, I., Bollasina, M., Purich, A., and Boschat, G. (2016). Factors Contributing to Record-Breaking Heat Waves over the Great Plains during the 1930s Dust Bowl. *J. Clim.* 30, 2437–2461. doi:10.1175/JCLI-D-16-0436.1.
Cowan, T., Purich, A., Perkins, S., Pezza, A., Boschat, G., and Sadler, K. (2014). More frequent, longer, and hotter heat waves for Australia in the Twenty-First Century. *J. Clim.* 27, 5851–5871. doi:10.1175/JCLI-D-14-00092.1.
Crimp, S. J., Zheng, B., Khimashia, N., Gobbett, D. L., Chapman, S., Howden, M., et al. (2016). Recent changes in southern Australian frost occurrence: Implications for wheat production risk. *Crop Pasture Sci.* 67, 801–811. doi:10.1071/CP16056.
Croitoru, A.-E., Chiotoroiu, B.-C., Ivanova Todorova, V., and Torică, V. (2013). Changes in precipitation extremes on the Black Sea Western Coast. *Glob. Planet. Change* 102, 10–19. doi:10.1016/j.gloplacha.2013.01.004.
Croitoru, A.-E., and Piticar, A. (2013). Changes in daily extreme temperatures in the extra-Carpathians regions of Romania. *Int. J. Climatol.* 33, 1987–2001. doi:10.1002/joc.3567.
Croitoru, A.-E., Piticar, A., and Burada, D. C. (2016). Changes in precipitation extremes in Romania. *Quat. Int.* 415, 325–335. doi:10.1016/J.QUAINT.2015.07.028.
Crook, J., Klein, C., Folwell, S., Taylor, C. M., Parker, D. J., Stratton, R., et al. (2019). Assessment of the Representation of West African Storm Lifecycles in Convection-Permitting Simulations. *Earth Sp. Sci.* 6, 818–835. doi:10.1029/2018EA000491.
CSIRO and BOM (2015). "Climate change in Australia: Projections for Australia's NRM regions," in *Climate Change in Australia: Information for Australia's Natural Resource Management Regions* (Australia: Commonwealth Scientific and Industrial Research Organisation (CSIRO) and Bureau of Meteorology (BOM)), 216. Available at: https://publications.csiro.au/rpr/download?pid=csiro:EP154327&dsid=DS2.
CSIRO, and BOM (2016). State of the Climate 2016. Australia: Commonwealth Scientific and Industrial Research Organisation (CSIRO) and Bureau of Meteorology (BOM) Available at: http://www.bom.gov.au/state-of-the-climate/State-of-the-Climate-2016.pdf.
Dadaser-Celik, F., and Cengiz, E. (2014). Wind speed trends over Turkey from 1975 to 2006. *Int. J. Climatol.* 34, 1913–1927. doi:10.1002/joc.3810.
Dai, A. (2013). Increasing drought under global warming in observations and models. *Nat. Clim. Chang.* 3, 52. doi:10.1038/nclimate1633.
Dai, A. (2021). Hydroclimatic trends during 1950–2018 over global land. *Clim. Dyn.* doi:10.1007/s00382-021-05684-1.
Dai, A., and Zhao, T. (2017). Uncertainties in historical changes and future projections of drought. Part I: estimates of historical drought changes. *Clim. Change* 144, 519–533. doi:10.1007/s10584-016-1705-2.
Dai, A., Zhao, T., and Chen, J. (2018). Climate Change and Drought: a Precipitation and Evaporation Perspective. *Curr. Clim. Chang. Reports* 4, 301–312. doi:10.1007/s40641-018-0101-6.
Daloz, A. S., and Camargo, S. J. (2018). Is the poleward migration of tropical cyclone maximum intensity associated with a poleward migration of tropical cyclone genesis? *Clim. Dyn.* 50, 705–715. doi:10.1007/s00382-017-3636-7.
Dankers, R., Arnell, N. W., Clark, D. B., Falloon, P. D., Fekete, B. M., Gosling, S. N., et al. (2014). First look at changes in flood hazard in the Inter-Sectoral Impact Model Intercomparison Project ensemble. *Proc. Natl. Acad. Sci.* 111, 3257–3261. doi:10.1073/pnas.1302078110.
Dashkhuu, D., Kim, J. P., Chun, J. A., and Lee, W.-S. (2015). Long-term trends in daily temperature extremes over Mongolia. *Weather Clim. Extrem.* 8, 26–33. doi:10.1016/j.wace.2014.11.003.
Davin, E. L., Seneviratne, S. I., Ciais, P., Olioso, A., and Wang, T. (2014). Preferential cooling of hot extremes from cropland albedo management. *Proc. Natl. Acad. Sci.* 111, 9757–9761. doi:10.1073/pnas.1317323111.
de Lima, M. I. P., Santo, F. E., Ramos, A. M., and Trigo, R. M. (2015). Trends and correlations in annual extreme

ACCEPTED VERSION SUBJECT TO FINAL EDITING

precipitation indices for mainland Portugal, 1941–2007. *Theor. Appl. Climatol.* 119, 55–75. doi:10.1007/s00704-013-1079-6.

De Luca, P., Messori, G., Pons, F. M. E., and Faranda, D. (2020a). Dynamical systems theory sheds new light on compound climate extremes in Europe and Eastern North America. *Q. J. R. Meteorol. Soc.* 146, 1636–1650. doi:10.1002/qj.3757.

De Luca, P., Messori, G., Wilby, R. L., Mazzoleni, M., and Di Baldassarre, G. (2020b). Concurrent wet and dry hydrological extremes at the global scale. *Earth Syst. Dyn.* 11, 251–266. doi:10.5194/esd-11-251-2020.

de Vrese, P., Hagemann, S., and Claussen, M. (2016). Asian irrigation, African rain: Remote impacts of irrigation. *Geophys. Res. Lett.* 43, 3737–3745. doi:10.1002/2016GL068146.

DeAngelis, A. M., Wang, H., Koster, R. D., Schubert, S. D., Chang, Y., and Marshak, J. (2020). Prediction Skill of the 2012 U.S. Great Plains Flash Drought in Subseasonal Experiment (SubX) Models. *J. Clim.* 33, 6229–6253. doi:10.1175/JCLI-D-19-0863.1.

Degefie, D. T., Fleischer, E., Klemm, O., Soromotin, A. V., Soromotina, O. V., Tolstikov, A. V., et al. (2014). Climate extremes in South Western Siberia: past and future. *Stoch. Environ. Res. Risk Assess.* 28, 2161–2173. doi:10.1007/s00477-014-0872-9.

Delworth, T. L., and Zeng, F. (2014). Regional rainfall decline in Australia attributed to anthropogenic greenhouse gases and ozone levels. *Nat. Geosci.* 7, 583–587. doi:10.1038/ngeo2201.

Deng, Y., Jiang, W., He, B., Chen, Z., and Jia, K. (2018). Change in Intensity and Frequency of Extreme Precipitation and its Possible Teleconnection With Large-Scale Climate Index Over the China From 1960 to 2015. *J. Geophys. Res. Atmos.* 123, 2068–2081. doi:10.1002/2017JD027078.

Denniston, R. F., and Luetscher, M. (2017). Speleothems as high-resolution paleoflood archives. *Quat. Sci. Rev.* 170, 1–13. doi:10.1016/j.quascirev.2017.05.006.

Déqué, M., Calmanti, S., Christensen, O. B., Dell Aquila, A., Maule, C. F., Haensler, A., et al. (2017). A multi-model climate response over tropical Africa at +2 °C. *Clim. Serv.* 7, 87–95. doi:10.1016/j.cliser.2016.06.002.

Dereczynski, C., Chan Chou, S., Lyra, A., Sondermann, M., Regoto, P., Tavares, P., et al. (2020). Downscaling of climate extremes over South America – Part I: Model evaluation in the reference climate. *Weather Clim. Extrem.* 29, 100273. doi:10.1016/j.wace.2020.100273.

Deshpande, N. R., Kothawale, D. R., and Kulkarni, A. (2016). Changes in climate extremes over major river basins of India. *Int. J. Climatol.* 36, 4548–4559. doi:10.1002/joc.4651.

Devanand, A., Huang, M., Ashfaq, M., Barik, B., and Ghosh, S. (2019). Choice of Irrigation Water Management Practice Affects Indian Summer Monsoon Rainfall and Its Extremes. *Geophys. Res. Lett.* 46, 9126–9135. doi:10.1029/2019GL083875.

Dey, R., Lewis, S. C., and Abram, N. J. (2019a). Investigating observed northwest Australian rainfall trends in Coupled Model Intercomparison Project phase 5 detection and attribution experiments. *Int. J. Climatol.* 39, 112–127. doi:10.1002/joc.5788.

Dey, R., Lewis, S. C., Arblaster, J. M., and Abram, N. J. (2019b). A review of past and projected changes in Australia's rainfall. *Wiley Interdiscip. Rev. Clim. Chang.* 10, e577. doi:10.1002/wcc.577.

Di Luca, A., de Elía, R., Bador, M., and Argüeso, D. (2020a). Contribution of mean climate to hot temperature extremes for present and future climates. *Weather Clim. Extrem.* 28, 100255. doi:10.1016/j.wace.2020.100255.

Di Luca, A., de Elía, R., and Laprise, R. (2015). Challenges in the Quest for Added Value of Regional Climate Dynamical Downscaling. *Curr. Clim. Chang. Reports* 1, 10–21. doi:10.1007/s40641-015-0003-9.

Di Luca, A., Evans, J. J. P., Pepler, A. S. A., Alexander, L. V. L., and Argüeso, D. (2016). Evaluating the representation of Australian East Coast Lows in a regional climate model ensemble. *J. South. Hemisph. Earth Syst. Sci.* 66, 108–124. doi:10.22499/3.6602.003.

Di Luca, A., Pitman, A. J., and de Elía, R. (2020b). Decomposing Temperature Extremes Errors in CMIP5 and CMIP6 Models. *Geophys. Res. Lett.* 47, 1–9. doi:10.1029/2020GL088031.

Diaconescu, E. P., Mailhot, A., Brown, R., and Chaumont, D. (2018). Evaluation of CORDEX-Arctic daily precipitation and temperature-based climate indices over Canadian Arctic land areas. *Clim. Dyn.* 50, 2061–2085. doi:10.1007/s00382-017-3736-4.

Diallo, I., Giorgi, F., Deme, A., Tall, M., Mariotti, L., and Gaye, A. T. (2016). Projected changes of summer monsoon extremes and hydroclimatic regimes over West Africa for the twenty-first century. *Clim. Dyn.* doi:10.1007/s00382-016-3052-4.

Diallo, I., Giorgi, F., Sukumaran, S., Stordal, F., and Giuliani, G. (2015). Evaluation of RegCM4 driven by CAM4 over Southern Africa: mean climatology, interannual variability and daily extremes of wet season temperature and precipitation. *Theor. Appl. Climatol.* 121, 749–766. doi:10.1007/s00704-014-1260-6.

Diedhiou, A., Bichet, A., Wartenburger, R., Seneviratne, S. I., Rowell, D. P., Sylla, M. B., et al. (2018). Changes in climate extremes over West and Central Africa at 1.5 °C and 2 °C global warming. *Environ. Res. Lett.* 13, 065020. doi:10.1088/1748-9326/aac3e5.

Dierauer, J. R., Allen, D. M., and Whitfield, P. H. (2019). Snow Drought Risk and Susceptibility in the Western United States and Southwestern Canada. *Water Resour. Res.* 55, 3076–3091. doi:10.1029/2018WR023229.

Diffenbaugh, N. S., Scherer, M., and Trapp, R. J. (2013). Robust increases in severe thunderstorm environments in

ACCEPTED VERSION SUBJECT TO FINAL EDITING

response to greenhouse forcing. *Proc. Natl. Acad. Sci.* 110, 16361 LP-16366. doi:10.1073/pnas.1307758110.
Diffenbaugh, N. S., Singh, D., Mankin, J. S., Horton, D. E., Swain, D. L., Touma, D., et al. (2017). Quantifying the influence of global warming on unprecedented extreme climate events. *Proc. Natl. Acad. Sci.* 114, 4881–4886.
Diffenbaugh, N. S., Swain, D. L., and Touma, D. (2015). Anthropogenic warming has increased drought risk in California. *Proc. Natl. Acad. Sci.* 112, 3931 LP-3936. doi:10.1073/pnas.1422385112.
Dikšaitytė, A., Viršilė, A., Žaltauskaitė, J., Januškaitienė, I., and Juozapaitienė, G. (2019). Growth and photosynthetic responses in Brassica napus differ during stress and recovery periods when exposed to combined heat, drought and elevated CO2. *Plant Physiol. Biochem.* 142, 59–72. doi:10.1016/j.plaphy.2019.06.026.
Dimri, A. P. (2019). Comparison of regional and seasonal changes and trends in daily surface temperature extremes over India and its subregions. *Theor. Appl. Climatol.* 136. doi:10.1007/s00704-018-2486-5.
Dimri, A. P., Chevuturi, A., Niyogi, D., Thayyen, R. J., Ray, K., Tripathi, S. N., et al. (2017). Cloudbursts in Indian Himalayas: A review. *Earth-Science Rev.* 168, 1–23. doi:10.1016/J.EARSCIREV.2017.03.006.
Dimri, A. P., Niyogi, D., Barros, A. P., Ridley, J., Mohanty, U. C., Yasunari, T., et al. (2015). Western Disturbances: A review. *Rev. Geophys.* 53, 225–246. doi:10.1002/2014RG000460.
Dirmeyer, P. A., Gao, X., Zhao, M., Guo, Z., Oki, T., and Hanasaki, N. (2006). GSWP-2: Multimodel Analysis and Implications for Our Perception of the Land Surface. *Bull. Am. Meteorol. Soc.* 87, 1381–1398. doi:10.1175/BAMS-87-10-1381.
Dirmeyer, P. A., Jin, Y., Singh, B., and Yan, X. (2013). Trends in land-atmosphere interactions from CMIP5 simulations. *J. Hydrometeorol.* 14, 829–849. doi:10.1175/JHM-D-12-0107.1.
Diro, G. T., Sushama, L., and Huziy, O. (2018). Snow-atmosphere coupling and its impact on temperature variability and extremes over North America. *Clim. Dyn.* 50, 2993–3007. doi:10.1007/s00382-017-3788-5.
Dittus, A. J., Karoly, D. J., Donat, M. G., Lewis, S. C., and Alexander, L. V (2018). Understanding the role of sea surface temperature-forcing for variability in global temperature and precipitation extremes. *Weather Clim. Extrem.* 21, 1–9. doi:10.1016/j.wace.2018.06.002.
Dittus, A. J., Karoly, D. J., Lewis, S. C., and Alexander, L. V. (2014). An investigation of some unexpected frost day increases in southern Australia. *Aust. Meteorol. Oceanogr. J.* 64, 261–271. doi:10.22499/2.6404.002.
Dittus, A. J., Karoly, D. J., Lewis, S. C., Alexander, L. V., and Donat, M. G. (2016). A multiregion model evaluation and attribution study of historical changes in the area affected by temperature and precipitation extremes. *J. Clim.* 29, 8285–8299. doi:10.1175/JCLI-D-16-0164.1.
Do, H. X., Mei, Y., and Gronewold, A. D. (2020). To What Extent Are Changes in Flood Magnitude Related to Changes in Precipitation Extremes? *Geophys. Res. Lett.* 47. doi:10.1029/2020GL088684.
Do, H. X., Westra, S., and Leonard, M. (2017). A global-scale investigation of trends in annual maximum streamflow. *J. Hydrol.* 552, 28–43. doi:10.1016/j.jhydrol.2017.06.015.
Dobricic, S., Russo, S., Pozzoli, L., Wilson, J., and Vignati, E. (2020). Increasing occurrence of heat waves in the terrestrial Arctic. *Environ. Res. Lett.* 15, 024022. doi:10.1088/1748-9326/ab6398.
Döll, P., Douville, H., Güntner, A., Müller Schmied, H., and Wada, Y. (2016). Modelling Freshwater Resources at the Global Scale: Challenges and Prospects. *Surv. Geophys.* 37, 195–221. doi:10.1007/s10712-015-9343-1.
Döll, P., Trautmann, T., Gerten, D., Schmied, H. M., Ostberg, S., Saaed, F., et al. (2018). Risks for the global freshwater system at 1.5 °C and 2 °C global warming. *Environ. Res. Lett.* 13, 044038. doi:10.1088/1748-9326/aab792.
Domínguez-Castro, F., García-Herrera, R., and Vicente-Serrano, S. M. (2018). Wet and dry extremes in Quito (Ecuador) since the 17th century. *Int. J. Climatol.* 38. doi:10.1002/joc.5312.
Donat, M. G., Alexander, L. V., Herold, N., and Dittus, A. J. (2016a). Temperature and precipitation extremes in century-long gridded observations, reanalyses, and atmospheric model simulations. *J. Geophys. Res. Atmos.* 121, 11,174-11,189. doi:10.1002/2016JD025480.
Donat, M. G., Alexander, L. V., Yang, H., Durre, I., Vose, R., Dunn, R. J. H. H., et al. (2013a). Updated analyses of temperature and precipitation extreme indices since the beginning of the twentieth century: The HadEX2 dataset. *J. Geophys. Res. Atmos.* 118, 2098–2118. doi:10.1002/jgrd.50150.
Donat, M. G., Alexander, L. V, Yang, H., Durre, I., Vose, R., and Caesar, J. (2013b). Global Land-Based Datasets for Monitoring Climatic Extremes. *Bull. Am. Meteorol. Soc.* 94, 997–1006. doi:10.1175/BAMS-D-12-00109.1.
Donat, M. G., Lowry, A. L., Alexander, L. V., O'Gorman, P. A., and Maher, N. (2016b). More extreme precipitation in the world's dry and wet regions. *Nat. Clim. Chang.* 6, 508–513. doi:10.1038/nclimate2941.
Donat, M. G., Peterson, T. C., Brunet, M., King, A. D., Almazroui, M., Kolli, R. K., et al. (2014a). Changes in extreme temperature and precipitation in the Arab region: long-term trends and variability related to ENSO and NAO. *Int. J. Climatol.* 34, 581–592. doi:10.1002/joc.3707.
Donat, M. G., Pitman, A. J., and Angélil, O. (2018). Understanding and Reducing Future Uncertainty in Midlatitude Daily Heat Extremes Via Land Surface Feedback Constraints. *Geophys. Res. Lett.* 45, 10,627-10,636. doi:10.1029/2018GL079128.
Donat, M. G., Pitman, A. J., and Seneviratne, S. I. (2017). Regional warming of hot extremes accelerated by surface energy fluxes. *Geophys. Res. Lett.* 44, 7011–7019.
Donat, M. G., Sillmann, J., Wild, S., Alexander, L. V., Lippmann, T., and Zwiers, F. W. (2014b). Consistency of

ACCEPTED VERSION SUBJECT TO FINAL EDITING

Temperature and Precipitation Extremes across Various Global Gridded In Situ and Reanalysis Datasets. *J. Clim.* 27, 5019–5035. doi:10.1175/JCLI-D-13-00405.1.
Dong, B., and Dai, A. (2015). The influence of the Interdecadal Pacific Oscillation on Temperature and Precipitation over the Globe. *Clim. Dyn.* 45, 2667–2681. doi:10.1007/s00382-015-2500-x.
Dong, B., Sutton, R., and Shaffrey, L. (2014). The 2013 hot, dry, summer in western Europe [in "Explaining Extreme Events of 2013 from a Climate Perspective"]. *Bull. Am. Meteorol. Soc.* 95, S62–S66.
Dong, B., Sutton, R., Shaffrey, L., and Wilcox, L. (2016a). The 2015 European Heat Wave. *Bull. Am. Meteorol. Soc.* 97, S57–S62. doi:10.1175/BAMS-D-16-0140.1.
Dong, B., Sutton, R. T., Chen, W., Liu, X., Lu, R., and Sun, Y. (2016b). Abrupt summer warming and changes in temperature extremes over Northeast Asia since the mid-1990s: Drivers and physical processes. *Adv. Atmos. Sci.* 33, 1005–1023. doi:10.1007/s00376-016-5247-3.
Dong, B., Sutton, R. T., and Shaffrey, L. (2017). Understanding the rapid summer warming and changes in temperature extremes since the mid-1990s over Western Europe. *Clim. Dyn.* 48, 1537–1554. doi:10.1007/s00382-016-3158-8.
Dong, S., Sun, Y., Aguilar, E., Zhang, X., Peterson, T. C., Song, L., et al. (2018). Observed changes in temperature extremes over Asia and their attribution. *Clim. Dyn.* 51, 339–353. doi:10.1007/s00382-017-3927-z.
Dong, S., Sun, Y., Li, C., Zhang, X., Min, S.-K., and Kim, Y.-H. (2021). Attribution of Extreme Precipitation with Updated Observations and CMIP6 Simulations. *J. Clim.* 34, 871–881. doi:10.1175/JCLI-D-19-1017.1.
Dong, S., Xu, Y., Zhou, B., and Shi, Y. (2015). Assessment of indices of temperature extremes simulated by multiple CMIP5 models over China. *Adv. Atmos. Sci.* 32, 1077–1091. doi:10.1007/s00376-015-4152-5.
Donnelly, C., Greuell, W., Andersson, J., Gerten, D., Pisacane, G., Roudier, P., et al. (2017). Impacts of climate change on European hydrology at 1.5, 2 and 3 degrees mean global warming above preindustrial level. *Clim. Change* 143, 13–26. doi:10.1007/s10584-017-1971-7.
Donnelly, J. P., Smith Bryant, S., Butler, J., Dowling, J., Fan, L., Hausmann, N., et al. (2001). 700 yr sedimentary record of intense hurricane landfalls in southern New England. *Geol. Soc. Am. Bull.* 113, 714–727. doi:10.1130/0016-7606(2001)113<0714:YSROIH>2.0.CO;2.
Dookie, N., Chadee, X. T., and Clarke, R. M. (2019). Trends in extreme temperature and precipitation indices for the Caribbean small islands: Trinidad and Tobago. *Theor. Appl. Climatol.* 136, 31–44. doi:10.1007/s00704-018-2463-z.
Dorigo, W. A., Gruber, A., De Jeu, R. A. M., Wagner, W., Stacke, T., Loew, A., et al. (2015). Evaluation of the ESA CCI soil moisture product using ground-based observations. *Remote Sens. Environ.* 162, 380–395. doi:10.1016/j.rse.2014.07.023.
Dorigo, W. A., Wagner, W., Hohensinn, R., Hahn, S., Paulik, C., Xaver, A., et al. (2011). The International Soil Moisture Network: a data hosting facility for global in situ soil moisture measurements. *Hydrol. Earth Syst. Sci.* 15, 1675–1698. doi:10.5194/hess-15-1675-2011.
Dorigo, W., de Jeu, R., Chung, D., Parinussa, R., Liu, Y., Wagner, W., et al. (2012). Evaluating global trends (1988-2010) in harmonized multi-satellite surface soil moisture. *Geophys. Res. Lett.* 39. doi:10.1029/2012GL052988.
Dorigo, W., Wagner, W., Albergel, C., Albrecht, F., Balsamo, G., Brocca, L., et al. (2017). ESA CCI Soil Moisture for improved Earth system understanding: State-of-the art and future directions. *Remote Sens. Environ.* 203, 185–215. doi:10.1016/j.rse.2017.07.001.
Dosio, A. (2016). Projections of climate change indices of temperature and precipitation from an ensemble of bias-adjusted high-resolution EURO-CORDEX regional climate models. *J. Geophys. Res. Atmos.* 121, 5488–5511. doi:10.1002/2015JD024411.
Dosio, A. (2017). Projection of temperature and heat waves for Africa with an ensemble of CORDEX Regional Climate Models. *Clim. Dyn.* 49, 493–519. doi:10.1007/s00382-016-3355-5.
Dosio, A., and Fischer, E. M. (2018). Will Half a Degree Make a Difference? Robust Projections of Indices of Mean and Extreme Climate in Europe Under 1.5°C, 2°C, and 3°C Global Warming. *Geophys. Res. Lett.* 45, 935–944. doi:10.1002/2017GL076222.
Dosio, A., Jones, R. G., Jack, C., Lennard, C., Nikulin, G., and Hewitson, B. (2019). What can we know about future precipitation in Africa? Robustness, significance and added value of projections from a large ensemble of regional climate models. *Clim. Dyn.*, 1–26. doi:10.1007/s00382-019-04900-3.
Dosio, A., Mentaschi, L., Fischer, E. M., and Wyser, K. (2018). Extreme heat waves under 1.5 °C and 2 °C global warming. *Environ. Res. Lett.* 13, 054006. doi:10.1088/1748-9326/aab827.
Dosio, A., Panitz, H.-J., Schubert-Frisius, M., and Lüthi, D. (2015). Dynamical downscaling of CMIP5 global circulation models over CORDEX-Africa with COSMO-CLM: evaluation over the present climate and analysis of the added value. *Clim. Dyn.* 44, 2637–2661. doi:10.1007/s00382-014-2262-x.
Douville, H., Colin, J., Krug, E., Cattiaux, J., and Thao, S. (2016). Midlatitude daily summer temperatures reshaped by soil moisture under climate change. *Geophys. Res. Lett.* 43, 812–818. doi:10.1002/2015GL066222.
Douville, H., and Plazzotta, M. (2017). Midlatitude Summer Drying: An Underestimated Threat in CMIP5 Models? *Geophys. Res. Lett.* 44, 9967–9975. doi:10.1002/2017GL075353.
Dowdy, A. J. (2018). Climatological Variability of Fire Weather in Australia. *J. Appl. Meteorol. Climatol.* 57, 221–234. doi:10.1175/JAMC-D-17-0167.1.

ACCEPTED VERSION
SUBJECT TO FINAL EDITING

Dowdy, A. J., and Catto, J. L. (2017). Extreme weather caused by concurrent cyclone, front and thunderstorm occurrences. *Sci. Rep.* 7, 1–8. doi:10.1038/srep40359.

Dowdy, A. J., Pepler, A., Di Luca, A., Cavicchia, L., Mills, G., Evans, J. P., et al. (2019). Review of Australian east coast low pressure systems and associated extremes. *Clim. Dyn.* doi:10.1007/s00382-019-04836-8.

Drijfhout, S., Bathiany, S., Beaulieu, C., Brovkin, V., Claussen, M., Huntingford, C., et al. (2015). Catalogue of abrupt shifts in Intergovernmental Panel on Climate Change climate models. *Proc. Natl. Acad. Sci.* 112, E5777–E5786. doi:10.1073/pnas.1511451112.

Driouech, F., ElRhaz, K., Moufouma-Okia, W., Arjdal, K., and Balhane, S. (2020). Assessing Future Changes of Climate Extreme Events in the CORDEX-MENA Region Using Regional Climate Model ALADIN-Climate. *Earth Syst. Environ.* 4, 477–492. doi:10.1007/s41748-020-00169-3.

Driouech, F., Stafi, H., Khouakhi, A., Moutia, S., Badi, W., ElRhaz, K., et al. (2021). Recent observed country-wide climate trends in Morocco. *Int. J. Climatol.* 41, 1–20. doi:10.1002/joc.6734.

Drobinski, P., Silva, N. Da, Panthou, G., Bastin, S., Muller, C., Ahrens, B., et al. (2018). Scaling precipitation extremes with temperature in the Mediterranean: past climate assessment and projection in anthropogenic scenarios. *Clim. Dyn.* 51, 1237–1257. doi:10.1007/s00382-016-3083-x.

Drouard, M., Kornhuber, K., and Woollings, T. (2019). Disentangling Dynamic Contributions to Summer 2018 Anomalous Weather Over Europe. *Geophys. Res. Lett.* 46, 12537–12546. doi:10.1029/2019GL084601.

Drumond, A., Stojanovic, M., Nieto, R., Vicente-Serrano, S. M., and Gimeno, L. (2019). Linking Anomalous Moisture Transport And Drought Episodes in the IPCC Reference Regions. *Bull. Am. Meteorol. Soc.* 100, 1481–1498. doi:10.1175/BAMS-D-18-0111.1.

Du, H., Alexander, L. V, Donat, M. G., Lippmann, T., Srivastava, A., Salinger, J., et al. (2019). Precipitation From Persistent Extremes is Increasing in Most Regions and Globally. *Geophys. Res. Lett.* 46, 6041–6049. doi:10.1029/2019GL081898.

Ducrocq, V., Nuissier, O., Ricard, D., Lebeaupin, C., and Thouvenin, T. (2008). A numerical study of three catastrophic precipitating events over southern France. II: Mesoscale triggering and stationarity factors. *Q. J. R. Meteorol. Soc.* 134, 131–145. doi:10.1002/qj.199.

Dudley, R. W., Hirsch, R. M., Archfield, S. A., Blum, A. G., and Renard, B. (2020). Low streamflow trends at human-impacted and reference basins in the United States. *J. Hydrol.* 580, 124254. doi:10.1016/j.jhydrol.2019.124254.

Dudley, R. W., Hodgkins, G. A., McHale, M. R., Kolian, M. J., and Renard, B. (2017). Trends in snowmelt-related streamflow timing in the conterminous United States. *J. Hydrol.* 547, 208–221. doi:10.1016/j.jhydrol.2017.01.051.

Duffy, P. B., Brando, P., Asner, G. P., and Field, C. B. (2015). Projections of future meteorological drought and wet periods in the Amazon. *Proc. Natl. Acad. Sci.* 112, 13172–13177. doi:10.1073/pnas.1421010112.

Duke, N. C., Kovacs, J. M., Griffiths, A. D., Preece, L., Hill, D. J. E., van Oosterzee, P., et al. (2017). Large-scale dieback of mangroves in Australia's Gulf of Carpentaria: a severe ecosystem response, coincidental with an unusually extreme weather event. *Mar. Freshw. Res.* 68, 1816–1829. doi:10.1071/MF16322.

Dunn, R. J. H., Alexander, L. V., Donat, M. G., Zhang, X., Bador, M., Herold, N., et al. (2020). Development of an Updated Global Land In Situ-Based Data Set of Temperature and Precipitation Extremes: HadEX3. *J. Geophys. Res. Atmos.* 125. doi:10.1029/2019JD032263.

Dunning, C. M., Black, E., and Allan, R. P. (2018). Later Wet Seasons with More Intense Rainfall over Africa under Future Climate Change. *J. Clim.* 31, 9719–9738. doi:10.1175/JCLI-D-18-0102.1.

Dunstone, N. J., Smith, D. M., Booth, B. B. B., Hermanson, L., and Eade, R. (2013). Anthropogenic aerosol forcing of Atlantic tropical storms. *Nat. Geosci.* 6, 534–539. doi:10.1038/ngeo1854.

Durkee, J. D., and Mote, T. L. (2010). A climatology of warm-season mesoscale convective complexes in subtropical South America. *Int. J. Climatol.* 30, 418–431. doi:10.1002/joc.1893.

Easterling, D. R., Arnold, J. R., Knutson, T., Kunkel, K. E., LeGrande, A. N., Leung, L. R., et al. (2017). Precipitation change in the United States. , eds. D. J. Wuebbles, D. W. Fahey, K. A. Hibbard, D. J. Dokken, B. C. Stewart, and T. K. Maycock Washington, DC, USA: U.S. Global Change Research Program doi:10.7930/J0H993CC.

Easterling, D. R., Kunkel, K. E., Wehner, M. F., and Sun, L. (2016). Detection and attribution of climate extremes in the observed record. *Weather Clim. Extrem.* 11, 17–27. doi:10.1016/j.wace.2016.01.001.

Eden, J. M., Wolter, K., Otto, F. E. L., and Jan van Oldenborgh, G. (2016). Multi-method attribution analysis of extreme precipitation in Boulder, Colorado. *Environ. Res. Lett.* 11, 124009. doi:10.1088/1748-9326/11/12/124009.

Edossa, D. C., Woyessa, Y. E., and Welderufael, W. A. (2016). Spatiotemporal analysis of droughts using self-calibrating Palmer's Drought Severity Index in the central region of South Africa. *Theor. Appl. Climatol.* 126, 643–657. doi:10.1007/s00704-015-1604-x.

El Kenawy, A., López-Moreno, J. I., and Vicente-Serrano, S. M. (2013). Summer temperature extremes in northeastern Spain: Spatial regionalization and links to atmospheric circulation (1960-2006). *Theor. Appl. Climatol.* 113, 387–405. doi:10.1007/s00704-012-0797-5.

Elsner, J. B., Elsner, S. C., and Jagger, T. H. (2015). The increasing efficiency of tornado days in the United States. *Clim. Dyn.* 45, 651–659. doi:10.1007/s00382-014-2277-3.

ACCEPTED VERSION SUBJECT TO FINAL EDITING

Elsner, J. B., Fricker, T., and Schroder, Z. (2019). Increasingly powerful tornadoes in the United States. *Geophys. Res. Lett.*, 1–10. doi:10.1029/2018GL080819.
Elsner, J. B., Kossin, J. P., and Jagger, T. H. (2008). The increasing intensity of the strongest tropical cyclones. *Nature* 455, 92–95. doi:10.1038/nature07234.
Emanuel, K. (2017). Assessing the present and future probability of Hurricane Harveys rainfall. *Proc. Natl. Acad. Sci.* 114, 12681–12684. doi:10.1073/pnas.1716222114.
Emanuel, K. (2021). Response of Global Tropical Cyclone Activity to Increasing CO2: Results from Downscaling CMIP6 Models. *J. Clim.* 34, 57–70. doi:10.1175/JCLI-D-20-0367.1.
Emanuel, K. A. (1987). The dependence of hurricane intensity on climate. *Nature* 326, 483–485. doi:10.1038/326483a0.
Emanuel, K. A. (2013). Downscaling CMIP5 climate models shows increased tropical cyclone activity over the 21st century. doi:10.1073/pnas.1301293110.
Emanuel, K., Caroff, P., Delgado, S., Guard, C. "Chip," Guishard, M., Hennon, C., et al. (2018). On the Desirability and Feasibility of a Global Reanalysis of Tropical Cyclones. *Bull. Am. Meteorol. Soc.* 99, 427–429. doi:10.1175/BAMS-D-17-0226.1.
Emanuel, K., Ravela, S., Vivant, E., and Risi, C. (2006). A statistical deterministic approach to hurricane risk assessment. *Bull. Am. Meteorol. Soc.* 87, 299–314. doi:10.1175/BAMS-87-3-299.
Emanuel, K., Sundararajan, R., and Williams, J. (2008). Hurricanes and global warming: Results from downscaling IPCC AR4 simulations. *Bull. Am. Meteorol. Soc.* 89, 347–367. doi:10.1175/BAMS-89-3-347.
Endo, H., Kitoh, A., Mizuta, R., and Ishii, M. (2017). Future Changes in Precipitation Extremes in East Asia and Their Uncertainty Based on Large Ensemble Simulations with a High-Resolution AGCM. 13, 0–5. doi:10.2151/sola.2017-002.
Engelbrecht, F. A., McGregor, J. L., and Engelbrecht, C. J. (2009). Dynamics of the Conformal-Cubic Atmospheric Model projected climate-change signal over southern Africa. *Int. J. Climatol.* 29, 1013–1033. doi:10.1002/joc.1742.
Engelbrecht, F., Adegoke, J., Bopape, M.-J., Naidoo, M., Garland, R., Thatcher, M., et al. (2015). Projections of rapidly rising surface temperatures over Africa under low mitigation. *Environ. Res. Lett.* 10, 085004. doi:10.1088/1748-9326/10/8/085004.
Engström, J., and Keellings, D. (2018). Drought in the Southeastern USA: an assessment of downscaled CMIP5 models. *Clim. Res.* 74, 251–262. doi:10.3354/cr01502.
Erdenebat, E., and Sato, T. (2016). Recent increase in heat wave frequency around Mongolia: role of atmospheric forcing and possible influence of soil moisture deficit. *Atmos. Sci. Lett.* 17, 135–140. doi:10.1002/asl.616.
Erfanian, A., Wang, G., and Fomenko, L. (2017). Unprecedented drought over tropical South America in 2016: significantly under-predicted by tropical SST. *Sci. Rep.* 7, 5811. doi:10.1038/s41598-017-05373-2.
Erlat, E., and Türkeş, M. (2016). Dates of frost onset, frost end and the frost-free season in Turkey: Trends, variability and links to the North Atlantic and Arctic Oscillation indices, 1950-2013. *Clim. Res.* 69, 155–176. doi:10.3354/cr01397.
Escalante-Sandoval, C., and Nuñez-Garcia, P. (2017). Meteorological drought features in northern and northwestern parts of Mexico under different climate change scenarios. *J. Arid Land* 9, 65–75. doi:10.1007/s40333-016-0022-y.
Evan, A. T., Kossin, J. P., Chung, C. E., and Ramanathan, V. (2011). Arabian Sea tropical cyclones intensified by emissions of black carbon and other aerosols. *Nature* 479, 94–97. doi:10.1038/nature10552.
Evans, J. P., Argueso, D., Olson, R., and Di Luca, A. (2017). Bias-corrected regional climate projections of extreme rainfall in south-east Australia. *Theor. Appl. Climatol.* 130, 1085–1098. doi:10.1007/s00704-016-1949-9.
Evans, J. P., Di Virgilio, G., Hirsch, A. L., Hoffmann, P., Remedio, A. R., Ji, F., et al. (2020). The CORDEX-Australasia ensemble: evaluation and future projections. *Clim. Dyn.* doi:10.1007/s00382-020-05459-0.
Fadnavis, S., Sabin, T. P., Roy, C., Rowlinson, M., Rap, A., Vernier, J.-P., et al. (2019). Elevated aerosol layer over South Asia worsens the Indian droughts. *Sci. Rep.* 9, 10268. doi:10.1038/s41598-019-46704-9.
Falconer, R. H., Cobby, D., Smyth, P., Astle, G., Dent, J., and Golding, B. (2009). Pluvial flooding: new approaches in flood warning, mapping and risk management. *J. Flood Risk Manag.* 2, 198–208. doi:10.1111/j.1753-318X.2009.01034.x.
Fantini, A., Raffaele, F., Torma, C., Bacer, S., Coppola, E., Giorgi, F., et al. (2018). Assessment of multiple daily precipitation statistics in ERA-Interim driven Med-CORDEX and EURO-CORDEX experiments against high resolution observations. *Clim. Dyn.* 51, 877–900. doi:10.1007/s00382-016-3453-4.
Fazel, N., Torabi Haghighi, A., and Kløve, B. (2017). Analysis of land use and climate change impacts by comparing river flow records for headwaters and lowland reaches. *Glob. Planet. Change* 158, 47–56. doi:10.1016/j.gloplacha.2017.09.014.
Feng, R., Yu, R., Zheng, H., and Gan, M. (2018). Spatial and temporal variations in extreme temperature in Central Asia. *Int. J. Climatol.* 38, e388–e400. doi:10.1002/joc.5379.
Feng, S., Trnka, M., Hayes, M., and Zhang, Y. (2017). Why Do Different Drought Indices Show Distinct Future Drought Risk Outcomes in the U.S. Great Plains? *J. Clim.* 30, 265–278. doi:10.1175/JCLI-D-15-0590.1.

ACCEPTED VERSION
SUBJECT TO FINAL EDITING

Feng, Z., Leung, L. R., Hagos, S., Houze, R. A., Burleyson, C. D., and Balaguru, K. (2016). More frequent intense and long-lived storms dominate the springtime trend in central US rainfall. *Nat. Commun.* 7, 13429. doi:10.1038/ncomms13429.

Fenta, A. A., Yasuda, H., Shimizu, K., and Haregeweyn, N. (2017). Response of streamflow to climate variability and changes in human activities in the semiarid highlands of northern Ethiopia. *Reg. Environ. Chang.* 17, 1229–1240. doi:10.1007/s10113-017-1103-y.

Feser, F., Barcikowska, M., Krueger, O., Schenk, F., Weisse, R., and Xia, L. (2015). Storminess over the North Atlantic and northwestern Europe – A review. *Q. J. R. Meteorol. Soc.* 141, 350–382. doi:10.1002/qj.2364.

Ficklin, D. L., Abatzoglou, J. T., Robeson, S. M., Null, S. E., and Knouft, J. H. (2018). Natural and managed watersheds show similar responses to recent climate change. *Proc. Natl. Acad. Sci.*, 201801026. doi:10.1073/PNAS.1801026115.

Field, R. D., van der Werf, G. R., Fanin, T., Fetzer, E. J., Fuller, R., Jethva, H., et al. (2016). Indonesian fire activity and smoke pollution in 2015 show persistent nonlinear sensitivity to El Niño-induced drought. *Proc. Natl. Acad. Sci.* 113, 9204–9209. doi:10.1073/pnas.1524888113.

Filahi, S., Tanarhte, M., Mouhir, L., El Morhit, M., and Tramblay, Y. (2016). Trends in indices of daily temperature and precipitations extremes in Morocco. *Theor. Appl. Climatol.* 124, 959–972. doi:10.1007/s00704-015-1472-4.

Findell, K. L., Berg, A., Gentine, P., Krasting, J. P., Lintner, B. R., Malyshev, S., et al. (2017). The impact of anthropogenic land use and land cover change on regional climate extremes. *Nat. Commun.* 8, 989. doi:10.1038/s41467-017-01038-w.

Findell, K. L., Keys, P. W., van der Ent, R. J., Lintner, B. R., Berg, A., and Krasting, J. P. (2019). Rising Temperatures Increase Importance of Oceanic Evaporation as a Source for Continental Precipitation. *J. Clim.* 32, 7713–7726. doi:10.1175/JCLI-D-19-0145.1.

Finney, D. L., Marsham, J. H., Jackson, L. S., Kendon, E. J., Rowell, D. P., Boorman, P. M., et al. (2019). Implications of Improved Representation of Convection for the East Africa Water Budget Using a Convection-Permitting Model. *J. Clim.* 32, 2109–2129. doi:10.1175/JCLI-D-18-0387.1.

Finney, D. L., Marsham, J. H., Rowell, D. P., Kendon, E. J., Tucker, S. O., Stratton, R. A., et al. (2020). Effects of Explicit Convection on Future Projections of Mesoscale Circulations, Rainfall, and Rainfall Extremes over Eastern Africa. *J. Clim.* 33, 2701–2718. doi:10.1175/JCLI-D-19-0328.1.

Fioravanti, G., Piervitali, E., and Desiato, F. (2016). Recent changes of temperature extremes over Italy: an index-based analysis. *Theor. Appl. Climatol.* 123, 473–486. doi:10.1007/s00704-014-1362-1.

Fischer, A. M., Keller, D. E., Liniger, M. A., Rajczak, J., Schär, C., and Appenzeller, C. (2015). Projected changes in precipitation intensity and frequency in Switzerland: a multi-model perspective. *Int. J. Climatol.* 35, 3204–3219. doi:10.1002/joc.4162.

Fischer, E. M., and Knutti, R. (2014). Detection of spatially aggregated changes in temperature and precipitation extremes. *Geophys. Res. Lett.* 41, 547–554. doi:10.1002/2013GL058499.

Fischer, E. M., and Knutti, R. (2015). Anthropogenic contribution to global occurrence of heavy-precipitation and high-temperature extremes. *Nat. Clim. Chang.* 5, 560–564. doi:10.1038/nclimate2617.

Fischer, E. M., and Knutti, R. (2016). Observed heavy precipitation increase confirms theory and early models. *Nat. Clim. Chang.* 6, 986–991. doi:10.1038/nclimate3110.

Fischer, E. M., Sedláček, J., Hawkins, E., and Knutti, R. (2014). Models agree on forced response pattern of precipitation and temperature extremes. *Geophys. Res. Lett.* 41, 8554–8562. doi:10.1002/2014GL062018.

Fitchett, J. M. (2018). Recent emergence of CAT5 tropical cyclones in the South Indian Ocean. *S. Afr. J. Sci.* 114. doi:10.17159/sajs.2018/4426.

Fitzpatrick, R. G. J., Parker, D. J., Marsham, J. H., Rowell, D. P., Guichard, F. M., Taylor, C. M., et al. (2020). What Drives the Intensification of Mesoscale Convective Systems over the West African Sahel under Climate Change? *J. Clim.* 33, 3151–3172. doi:10.1175/JCLI-D-19-0380.1.

Flach, M., Gans, F., Brenning, A., Denzler, J., Reichstein, M., Rodner, E., et al. (2017). Multivariate anomaly detection for Earth observations: a comparison of algorithms and feature extraction techniques. *Earth Syst. Dyn.* 8, 677–696. doi:10.5194/esd-8-677-2017.

Flach, M., Sippel, S., Gans, F., Bastos, A., Brenning, A., Reichstein, M., et al. (2018). Contrasting biosphere responses to hydrometeorological extremes: revisiting the 2010 western Russian heatwave. *Biogeosciences* 15, 6067–6085. doi:10.5194/bg-15-6067-2018.

Flannigan, M., Wotton, M., Marshall, G., Groot, W., Johnston, J., Jurko, N., et al. (2016). Fuel moisture sensitivity to temperature and precipitation: climate change implications. *Clim. Change* 134, 59–71. doi:10.1007/s10584-015-1521-0.

Flato, G., Marotzke, J., Abiodun, B., Braconnot, P., Chou, S. C., Collins, W., et al. (2013). "Evaluation of Climate Models," in *Climate Change 2013: The Physical Science Basis. Contribution of Working Group I to the Fifth Assessment Report of the Intergovernmental Panel on Climate Change*, eds. T. F. Stocker, D. Qin, G.-K. Plattner, M. Tignor, S. K. Allen, J. Boschung, et al. (Cambridge, United Kingdom and New York, NY, USA: Cambridge University Press), 741–866. doi:10.1017/CBO9781107415324.020.

Fontaine, B., Janicot, S., and Monerie, P.-A. (2013). Recent changes in air temperature, heat waves occurrences, and

ACCEPTED VERSION SUBJECT TO FINAL EDITING

atmospheric circulation in Northern Africa. *J. Geophys. Res. Atmos.* 118, 8536–8552. doi:10.1002/jgrd.50667.
Fontes, C. G., Dawson, T. E., Jardine, K., McDowell, N., Gimenez, B. O., Anderegg, L., et al. (2018). Dry and hot: The hydraulic consequences of a climate change–type drought for Amazonian trees. *Philos. Trans. R. Soc. B Biol. Sci.* 373. doi:10.1098/rstb.2018.0209.
Ford, T. W., and Quiring, S. M. (2019). Comparison of Contemporary In Situ, Model, and Satellite Remote Sensing Soil Moisture With a Focus on Drought Monitoring. *Water Resour. Res.* 55, 1565–1582. doi:10.1029/2018WR024039.
Formayer, H., and Fritz, A. (2017). Temperature dependency of hourly precipitation intensities – surface versus cloud layer temperature. *Int. J. Climatol.* 37, 1–10. doi:10.1002/joc.4678.
Formetta, G., and Feyen, L. (2019). Empirical evidence of declining global vulnerability to climate-related hazards. *Glob. Environ. Chang.* 57, 101920. doi:10.1016/j.gloenvcha.2019.05.004.
Forzieri, G., Feyen, L., Rojas, R., Flörke, M., Wimmer, F., and Bianchi, A. (2014). Ensemble projections of future streamflow droughts in Europe. *Hydrol. Earth Syst. Sci.* 18, 85–108. doi:10.5194/hess-18-85-2014.
Forzieri, G., Feyen, L., Russo, S., Vousdoukas, M., Alfieri, L., Outten, S., et al. (2016). Multi-hazard assessment in Europe under climate change. *Clim. Change* 137, 105–119. doi:10.1007/s10584-016-1661-x.
Fotso-Nguemo, T. C., Chamani, R., Yepdo, Z. D., Sonkoué, D., Matsaguim, C. N., Vondou, D. A., et al. (2018). Projected trends of extreme rainfall events from CMIP5 models over Central Africa. *Atmos. Sci. Lett.* 19, e803. doi:10.1002/asl.803.
Fotso-Nguemo, T. C., Diallo, I., Diakhaté, M., Vondou, D. A., Mbaye, M. L., Haensler, A., et al. (2019). Projected changes in the seasonal cycle of extreme rainfall events from CORDEX simulations over Central Africa. *Clim. Change* 155, 339–357.
Fowler, H. J., Lenderink, G., Prein, A. F., Westra, S., Allan, R. P., Ban, N., et al. (2021). Anthropogenic intensification of short-duration rainfall extremes. *Nat. Rev. Earth Environ.* 2, 107–122. doi:10.1038/s43017-020-00128-6.
Francis, J. A., and Vavrus, S. J. (2012). Evidence linking Arctic amplification to extreme weather in mid-latitudes. *Geophys. Res. Lett.* 39. doi:10.1029/2012GL051000.
Frank, D. C., Poulter, B., Saurer, M., Esper, J., Huntingford, C., Helle, G., et al. (2015). Water-use efficiency and transpiration across European forests during the Anthropocene. *Nat. Clim. Chang.* 5, 579–583. doi:10.1038/nclimate2614.
Freund, M., Henley, B. J., Karoly, D. J., Allen, K. J., and Baker, P. J. (2017). Multi-century cool- and warm-season rainfall reconstructions for Australia's major climatic regions. *Clim. Past* 13, 1751–1770. doi:10.5194/cp-13-1751-2017.
Freychet, N., Hsu, H.-H., Chou, C., and Wu, C.-H. (2015). Asian Summer Monsoon in CMIP5 Projections: A Link between the Change in Extreme Precipitation and Monsoon Dynamics. *J. Clim.* 28, 1477–1493. doi:10.1175/JCLI-D-14-00449.1.
Freychet, N., Tett, S. F. B., Hegerl, G. C., and Wang, J. (2018). Central-Eastern China Persistent Heat Waves: Evaluation of the AMIP Models. *J. Clim.* 31, 3609–3624. doi:10.1175/JCLI-D-17-0480.1.
Friedrich, K., Grossman, R. L., Huntington, J., Blanken, P. D., Lenters, J., Holman, K. D., et al. (2018). Reservoir evaporation in the Western United States. *Bull. Am. Meteorol. Soc.* 99, 167–187. doi:10.1175/BAMS-D-15-00224.1.
Frieler, K., Meinshausen, M., Mengel, M., Braun, N., and Hare, W. (2012). A Scaling Approach to Probabilistic Assessment of Regional Climate Change. *J. Clim.* 25, 3117–3144. doi:10.1175/JCLI-D-11-00199.1.
Frölicher, T. L., Fischer, E. M., and Gruber, N. (2018). Marine heatwaves under global warming. *Nature* 560, 360–364. doi:10.1038/s41586-018-0383-9.
Fu, G., Yu, J., Yu, X., Ouyang, R., Zhang, Y., Wang, P., et al. (2013a). Temporal variation of extreme rainfall events in China, 1961–2009. *J. Hydrol.* 487, 48–59. doi:10.1016/J.JHYDROL.2013.02.021.
Fu, Q., and Feng, S. (2014). Responses of terrestrial aridity to global warming. *J. Geophys. Res.* 119, 7863–7875. doi:10.1002/2014JD021608.
Fu, R., Yin, L., Li, W., Arias, P. A., Dickinson, R. E., Huang, L., et al. (2013b). Increased dry-season length over southern Amazonia in recent decades and its implication for future climate projection. *Proc. Natl. Acad. Sci. U. S. A.* 110, 18110–18115. doi:10.1073/pnas.1302584110.
Fuhrmann, C. M., Konrad II, C. E., Kovach, M. M., McLeod, J. T., Schmitz, W. G., and Dixon, P. G. (2014). Ranking of Tornado Outbreaks across the United States and Their Climatological Characteristics. *Weather Forecast.* 29, 684–701. doi:10.1175/WAF-D-13-00128.1.
Fundel, F., Jörg-Hess, S., and Zappa, M. (2013). Monthly hydrometeorological ensemble prediction of streamflow droughts and corresponding drought indices. *Hydrol. Earth Syst. Sci.* 17, 395–407. doi:10.5194/hess-17-395-2013.
Funk, C., Davenport, F., Harrison, L., Magadzire, T., Galu, G., Artan, G. A., et al. (2018a). Anthropogenic Enhancement of Moderate-to-Strong El Niño Events Likely Contributed to Drought and Poor Harvests in Southern Africa During 2016. *Bull. Am. Meteorol. Soc.* 99, S91–S96. doi:10.1175/BAMS-D-17-0112.1.
Funk, C., Harrison, L., Shukla, S., Korecha, D., Magadzire, T., Husak, G., et al. (2016). Assessing the Contributions of Local and East Pacific Warming to the 2015 Droughts in Ethiopia and Southern Africa. *Bull. Am. Meteorol. Soc.*

ACCEPTED VERSION
SUBJECT TO FINAL EDITING

97, S75–S80. doi:10.1175/BAMS-D-16-0167.1.
Funk, C., Harrison, L., Shukla, S., Pomposi, C., Galu, G., Korecha, D., et al. (2018b). Examining the role of unusually warm Indo-Pacific sea surface temperatures in recent African droughts. *Q. J. R. Meteorol. Soc.*, 1–20. doi:10.1002/acr.
Funk, C., Hoell, A., and Stone, D. (2014). Examining the contribution of the observed global warming trend to the California droughts of 2012/13 and 2013/14 [in "Explaining Extreme Events of 2013 from a Climate Perspective"]. *Bull. Amer. Meteor. Soc.* 95, S11–S13. doi:10.1175/1520-0477-95.9.S1.1.
Funk, C., Nicholson, S. E., Landsfeld, M., Klotter, D., Peterson, P., and Harrison, L. (2015a). The Centennial Trends Greater Horn of Africa precipitation dataset. *Sci. Data* 2, 150050. doi:10.1038/sdata.2015.50.
Funk, C., Peterson, P., Landsfeld, M., Davenport, F., Becker, A., Schneider, U., et al. (2020). "Algorithm and Data Improvements for Version 2.1 of the Climate Hazards Center's InfraRed Precipitation with Stations Data Set," in *Satellite Precipitation Measurement: Volume 1*, eds. V. Levizzani, C. Kidd, D. Kirschbaum, C. Kummerow, K. Nakamura, and F. Turk (Cham, Switzerland: Springer), 409–427. doi:10.1007/978-3-030-24568-9_23.
Funk, C., Shukla, S., Hoell, A., and Livneh, B. (2015b). Assessing the contributions of east African and west pacific warming to the 2014 boreal spring east African drought. *Bull. Am. Meteorol. Soc.* 96, S77–S82. doi:10.1175/BAMS-D-15-00106.1.
Furrer, E., Katz, R., Walter, M., and Furrer, R. (2010). Statistical modeling of hot spells and heat waves. *Clim. Res.* 43, 191–205. doi:10.3354/cr00924.
Gaertner, M. Á., González-Alemán, J. J., Romera, R., Domínguez, M., Gil, V., Sánchez, E., et al. (2018). Simulation of medicanes over the Mediterranean Sea in a regional climate model ensemble: impact of ocean–atmosphere coupling and increased resolution. *Clim. Dyn.* 51, 1041–1057. doi:10.1007/s00382-016-3456-1.
Gaertner, M. A., Jacob, D., Gil, V., Domínguez, M., Padorno, E., Sánchez, E., et al. (2007). Tropical cyclones over the Mediterranean Sea in climate change simulations. *Geophys. Res. Lett.* 34, L14711. doi:10.1029/2007GL029977.
Gajić-Čapka, M., Cindrić, K., and Pasarić, Z. (2015). Trends in precipitation indices in Croatia, 1961–2010. *Theor. Appl. Climatol.* 121, 167–177. doi:10.1007/s00704-014-1217-9.
Galarneau, T. J., Bosart, L. F., and Schumacher, R. S. (2010). Predecessor rain events ahead of tropical cyclones. *Mon. Weather Rev.* 138, 3272–3297. doi:10.1175/2010MWR3243.1.
Gallant, A. J. E., Reeder, M. J., Risbey, J. S., and Hennessy, K. J. (2013). The characteristics of seasonal-scale droughts in Australia, 1911-2009. *Int. J. Climatol.* 33, 1658–1672. doi:10.1002/joc.3540.
Gallo, F., Daron, J., Macadam, I., Cinco, T., Villafuerte II, M., Buonomo, E., et al. (2019). High-resolution regional climate model projections of future tropical cyclone activity in the Philippines. *Int. J. Climatol.* 39, 1181–1194. doi:10.1002/joc.5870.
Gálos, B., Hagemann, S., Hänsler, A., Kindermann, G., Rechid, D., Sieck, K., et al. (2013). Case study for the assessment of the biogeophysical effects of a potential afforestation in Europe. *Carbon Balance Manag.* 8, 3. doi:10.1186/1750-0680-8-3.
Gálos, B., Mátyás, C., and Jacob, D. (2011). Regional characteristics of climate change altering effects of afforestation. *Environ. Res. Lett.* 6, 044010. doi:10.1088/1748-9326/6/4/044010.
Gao, J., Shoshiro, M., Roberts, M. J., Haarsma, R., Putrasahan, D., Roberts, C. D., et al. (2020). Influence of model resolution on bomb cyclones revealed by HighResMIP-PRIMAVERA simulations. *Environ. Res. Lett.* 15, 084001. doi:10.1088/1748-9326/ab88fa.
Gao, X., Shi, Y., Han, Z., Wang, M., Wu, J., Zhang, D., et al. (2017a). Performance of RegCM4 over major river basins in China. *Adv. Atmos. Sci.* 34, 441–455. doi:10.1007/s00376-016-6179-7.
Gao, X., Zhao, Q., Zhao, X., Wu, P., Pan, W., Gao, X., et al. (2017b). Temporal and spatial evolution of the standardized precipitation evapotranspiration index (SPEI) in the Loess Plateau under climate change from 2001 to 2050. *Sci. Total Environ.* 595, 191–200. doi:10.1016/j.scitotenv.2017.03.226.
Gao, Y., Xiao, L., Chen, D., Xu, J., and Zhang, H. (2018). Comparison between past and future extreme precipitations simulated by global and regional climate models over the Tibetan Plateau. *Int. J. Climatol.* 38, 1285–1297. doi:10.1002/joc.5243.
García-Cueto, O. R., Santillán-Soto, N., López-Velázquez, E., Reyes-López, J., Cruz-Sotelo, S., and Ojeda-Benítez, S. (2019). Trends of climate change indices in some Mexican cities from 1980 to 2010. *Theor. Appl. Climatol.* 137, 775–790. doi:10.1007/s00704-018-2620-4.
García-Garizábal, I., Causapé, J., Abrahao, R., and Merchan, D. (2014). Impact of Climate Change on Mediterranean Irrigation Demand: Historical Dynamics of Climate and Future Projections. *Water Resour. Manag.* 28, 1449–1462. doi:10.1007/s11269-014-0565-7.
García-Herrera, R., Garrido-Pérez, J.M. Barriopedro, D., Ordóñez, C., Vicente-Serrano, S.M. Nieto, R., Gimeno, L., Sorí, R., et al. (2019). The European 2016/2017 drought. *J. Clim.* 32, 3169–3187.
Garner, A. J., Mann, M. E., Emanuel, K. A., Kopp, R. E., Lin, N., Alley, R. B., et al. (2017). Impact of climate change on New York City's coastal flood hazard: Increasing flood heights from the preindustrial to 2300 CE. *Proc. Natl. Acad. Sci.* 114, 11861 LP-11866. doi:10.1073/pnas.1703568114.
Garreaud, R. D., Alvarez-Garreton, C., Barichivich, J., Boisier, J. P., Christie, D., Galleguillos, M., et al. (2017). The 2010–2015 megadrought in central Chile: impacts on regional hydroclimate and vegetation. *Hydrol. Earth Syst.*

ACCEPTED VERSION SUBJECT TO FINAL EDITING

Sci. 21, 6307–6327. doi:10.5194/hess-21-6307-2017.
Garreaud, R. D., Boisier, J. P., Rondanelli, R., Montecinos, A., Sepúlveda, H. H., and Veloso-Aguila, D. (2020). The Central Chile Mega Drought (2010–2018): A climate dynamics perspective. *Int. J. Climatol.* 40, 421–439. doi:10.1002/joc.6219.
Gaupp, F., Hall, J., Mitchell, D., and Dadson, S. (2019). Increasing risks of multiple breadbasket failure under 1.5 and 2 °C global warming. *Agric. Syst.* 175, 34–45. doi:10.1016/j.agsy.2019.05.010.
Ge, G., Shi, Z., Yang, X., Hao, Y., Guo, H., Kossi, F., et al. (2017). Analysis of precipitation extremes in the Qinghai-Tibetan plateau, China: Spatio-temporal characteristics and topography effects. *Atmosphere (Basel).* 8, 1–16. doi:10.3390/atmos8070127.
Gebrechorkos, S. H., Hülsmann, S., and Bernhofer, C. (2018). Changes in temperature and precipitation extremes in Ethiopia, Kenya, and Tanzania. *Int. J. Climatol.* 39, 18–30. doi:10.1002/joc.5777.
Gebremeskel Haile, G., Tang, Q., Leng, G., Jia, G., Wang, J., Cai, D., et al. (2020). Long-term spatiotemporal variation of drought patterns over the Greater Horn of Africa. *Sci. Total Environ.* 704, 135299. doi:10.1016/j.scitotenv.2019.135299.
Geirinhas, J. L., Trigo, R. M., Libonati, R., Coelho, C. A. S., and Palmeira, A. C. (2018). Climatic and synoptic characterization of heat waves in Brazil. *Int. J. Climatol.* 38, 1760–1776. doi:10.1002/joc.5294.
Geng, X., Zhang, W., Stuecker, M. F., and Jin, F. F. (2017). Strong sub-seasonal wintertime cooling over East Asia and Northern Europe associated with super El Ninõ events. *Sci. Rep.* 7, 1–9. doi:10.1038/s41598-017-03977-2.
Gensini, V. A., and Brooks, H. E. (2018). Spatial trends in United States tornado frequency. *npj Clim. Atmos. Sci.* 1, 38. doi:10.1038/s41612-018-0048-2.
Gensini, V. A., and Mote, T. L. (2015). Downscaled estimates of late 21st century severe weather from CCSM3. *Clim. Change* 129, 307–321. doi:10.1007/s10584-014-1320-z.
Gergel, D. R., Nijssen, B., Abatzoglou, J. T., Lettenmaier, D. P., and Stumbaugh, M. R. (2017). Effects of climate change on snowpack and fire potential in the western USA. *Clim. Change* 141, 287–299. doi:10.1007/s10584-017-1899-y.
Gervais, M., Tremblay, L. B., Gyakum, J. R., and Atallah, E. (2014). Representing Extremes in a Daily Gridded Precipitation Analysis over the United States: Impacts of Station Density, Resolution, and Gridding Methods. *J. Clim.* 27, 5201–5218. doi:10.1175/JCLI-D-13-00319.1.
Ghausi, S. A., and Ghosh, S. (2020). Diametrically Opposite Scaling of Extreme Precipitation and Streamflow to Temperature in South and Central Asia. *Geophys. Res. Lett.* 47, e2020GL089386. doi:10.1029/2020GL089386.
Gibba, P., Sylla, M. B., Okogbue, E. C., Gaye, A. T., Nikiema, M., and Kebe, I. (2019). State-of-the-art climate modeling of extreme precipitation over Africa: analysis of CORDEX added-value over CMIP5. *Theor. Appl. Climatol.* 137, 1041–1057. doi:10.1007/s00704-018-2650-y.
Gimeno, L., Stohl, A., Trigo, R. M., Dominguez, F., Yoshimura, K., Yu, L., et al. (2012). Oceanic and terrestrial sources of continental precipitation. *Rev. Geophys.* 50. doi:10.1029/2012RG000389.
Gimeno, L., Vázquez, M., Eiras-Barca, J., Sorí, R., Stojanovic, M., Algarra, I., et al. (2020). Recent progress on the sources of continental precipitation as revealed by moisture transport analysis. *Earth-Science Rev.* 201. doi:10.1016/j.earscirev.2019.103070.
Giorgi, F., Coppola, E., Raffaele, F., Diro, G. T., Fuentes-Franco, R., Giuliani, G., et al. (2014). Changes in extremes and hydroclimatic regimes in the CREMA ensemble projections. *Clim. Change* 125, 39–51. doi:10.1007/s10584-014-1117-0.
Giorgi, F., Jones, C., and Asrar, G. (2009). Addressing climate information needs at the regional level: the CORDEX framework. *WMO Bull.* 58, 175.
Giorgi, F., Raffaele, F., and Coppola, E. (2019). The response of precipitation characteristics to global warming from climate projections. *Earth Syst. Dyn.* 10, 73–89. doi:10.5194/esd-10-73-2019.
Giuntoli, I., Renard, B., Vidal, J.-P., and Bard, A. (2013). Low flows in France and their relationship to large-scale climate indices. *J. Hydrol.* 482, 105–118. doi:10.1016/j.jhydrol.2012.12.038.
Giuntoli, I., Vidal, J.-P., Prudhomme, C., and Hannah, D. M. (2015). Future hydrological extremes: The uncertainty from multiple global climate and global hydrological models. *Earth Syst. Dyn.* 6, 267–285. doi:10.5194/esd-6-267-2015.
Glas, R., Burns, D., and Lautz, L. (2019). Historical changes in New York State streamflow: Attribution of temporal shifts and spatial patterns from 1961 to 2016. *J. Hydrol.* 574, 308–323. doi:10.1016/j.jhydrol.2019.04.060.
Gleixner, S., Demissie, T., and Diro, G. T. (2020). Did ERA5 Improve Temperature and Precipitation Reanalysis over East Africa? *Atmosphere (Basel).* 11, 996. doi:10.3390/atmos11090996.
Gobiet, A., Kotlarski, S., Beniston, M., Heinrich, G., Rajczak, J., and Stoffel, M. (2014). 21st century climate change in the European Alps – A review. *Sci. Total Environ.* 493, 1138–1151. doi:10.1016/j.scitotenv.2013.07.050.
Gocic, M., and Trajkovic, S. (2014). Analysis of trends in reference evapotranspiration data in a humid climate. *Hydrol. Sci. J.* 59, 165–180. doi:10.1080/02626667.2013.798659.
González-Alemán, J. J., Pascale, S., Gutierrez-Fernandez, J., Murakami, H., Gaertner, M. A., and Vecchi, G. A. (2019). Potential Increase in Hazard From Mediterranean Hurricane Activity With Global Warming. *Geophys. Res. Lett.* 46, 1754–1764. doi:10.1029/2018GL081253.

ACCEPTED VERSION
SUBJECT TO FINAL EDITING

González-Hidalgo, J. C., Vicente-Serrano, S. M., Peña-Angulo, D., Salinas, C., Tomas-Burguera, M., and Beguería, S. (2018). High-resolution spatio-temporal analyses of drought episodes in the western Mediterranean basin (Spanish mainland, Iberian Peninsula). *Acta Geophys.* 66, 381–392. doi:10.1007/s11600-018-0138-x.

Gosling, S. N., Zaherpour, J., Mount, N. J., Hattermann, F. F., Dankers, R., Arheimer, B., et al. (2017). A comparison of changes in river runoff from multiple global and catchment-scale hydrological models under global warming scenarios of 1 °C, 2 °C and 3 °C. *Clim. Change* 141, 577–595. doi:10.1007/s10584-016-1773-3.

Gou, X., Deng, Y., Gao, L., Chen, F., Cook, E., Yang, M., et al. (2015). Millennium tree-ring reconstruction of drought variability in the eastern Qilian Mountains, northwest China. *Clim. Dyn.* 45, 1761–1770. doi:10.1007/s00382-014-2431-y.

Govekar, P. D., Jakob, C., and Catto, J. (2014). The relationship between clouds and dynamics in Southern Hemisphere extratropical cyclones in the real world and a climate model. *J. Geophys. Res. Atmos.* doi:10.1002/2013JD020699.

Graham, R. M., Cohen, L., Petty, A. A., Boisvert, L. N., Rinke, A., Hudson, S. R., et al. (2017). Increasing frequency and duration of Arctic winter warming events. *Geophys. Res. Lett.* 44, 6974–6983. doi:10.1002/2017GL073395.

Green, J. K., Seneviratne, S. I., Berg, A. M., Findell, K. L., Hagemann, S., Lawrence, D. M., et al. (2019). Large influence of soil moisture on long-term terrestrial carbon uptake. *Nature* 565, 476–479. doi:10.1038/s41586-018-0848-x.

Greenbaum, N., Harden, T. M., Baker, V. R., Weisheit, J., Cline, M. L., Porat, N., et al. (2014). A 2000 year natural record of magnitudes and frequencies for the largest Upper Colorado River floods near Moab, Utah. *Water Resour. Res.* 50, 5249–5269. doi:10.1002/2013WR014835.

Greve, P., Gudmundsson, L., and Seneviratne, S. I. (2018). Regional scaling of annual mean precipitation and water availability with global temperature change. *Earth Syst. Dyn.* 9, 227–240. doi:10.3929/ethz-b-000251688.

Greve, P., Orlowsky, B., Mueller, B., Sheffield, J., Reichstein, M., and Seneviratne, S. I. (2014). Global assessment of trends in wetting and drying over land. *Nat. Geosci.* 7, 716–721. doi:10.1038/NGEO2247.

Greve, P., Roderick, M. L., and Seneviratne, S. I. (2017). Simulated changes in aridity from the last glacial maximum to 4xCO2. *Environ. Res. Lett.* 12, 114021. doi:10.1088/1748-9326/aa89a3.

Greve, P., Roderick, M. L., Ukkola, A. M., and Wada, Y. (2019). The aridity Index under global warming. *Environ. Res. Lett.* 14, 124006. doi:10.1088/1748-9326/ab5046.

Griffin, D., and Anchukaitis, K. J. (2014). How unusual is the 2012-2014 California drought? *Geophys. Res. Lett.* 41, 9017–9023. doi:10.1002/2014GL062433.

Grillakis, M. G., Koutroulis, A. G., Komma, J., Tsanis, I. K., Wagner, W., and Blöschl, G. (2016). Initial soil moisture effects on flash flood generation – A comparison between basins of contrasting hydro-climatic conditions. *J. Hydrol.* 541, 206–217. doi:10.1016/J.JHYDROL.2016.03.007.

Grinsted, A., Ditlevsen, P., and Christensen, J. H. (2019). Normalized US hurricane damage estimates using area of total destruction, 1900−2018. *Proc. Natl. Acad. Sci.* 116, 23942 LP-23946. doi:10.1073/pnas.1912277116.

Grose, M. R., Black, M., Risbey, J. S., Uhe, P., Hope, P. K., Haustein, K., et al. (2018). Severe Frosts in Western Australia in September 2016. *Bull. Am. Meteorol. Soc.* 99, S150–S154. doi:10.1175/BAMS-D-17-0088.1.

Grose, M. R., Narsey, S., Delage, F. P., Dowdy, A. J., Bador, M., Boschat, G., et al. (2020). Insights From CMIP6 for Australia's Future Climate. *Earth's Futur.* 8. doi:10.1029/2019EF001469.

Gross, M. H., Donat, M. G., Alexander, L. V, and Sherwood, S. C. (2020). Amplified warming of seasonal cold extremes relative to the mean in the Northern Hemisphere extratropics. *Earth Syst. Dyn.* 11, 97–111. doi:10.5194/esd-11-97-2020.

Grossiord, C., Buckley, T. N., Cernusak, L. A., Novick, K. A., Poulter, B., Siegwolf, R. T. W., et al. (2020). Plant responses to rising vapor pressure deficit. *New Phytol.* 226, 1550–1566. doi:10.1111/nph.16485.

Grotjahn, R., Black, R., Leung, R., Wehner, M. F., Barlow, M., Bosilovich, M., et al. (2016). North American extreme temperature events and related large scale meteorological patterns: a review of statistical methods, dynamics, modeling, and trends. *Clim. Dyn.* 46, 1151–1184. doi:10.1007/s00382-015-2638-6.

Gu, G., and Adler, R. F. (2018). Precipitation Intensity Changes in the Tropics from Observations and Models. *J. Clim.* 31, 4775–4790. doi:10.1175/JCLI-D-17-0550.1.

Gu, L., Chen, J., Yin, J., Sullivan, S. C., Wang, H.-M., Guo, S., et al. (2020). Projected increases in magnitude and socioeconomic exposure of global droughts in 1.5 and 2 °C warmer climates. *Hydrol. Earth Syst. Sci.* 24, 451–472. doi:10.5194/hess-24-451-2020.

Gu, X., Li, J., Chen, Y. D., Kong, D., and Liu, J. (2019a). Consistency and Discrepancy of Global Surface Soil Moisture Changes From Multiple Model-Based Data Sets Against Satellite Observations. *J. Geophys. Res. Atmos.* 124, 1474–1495. doi:10.1029/2018JD029304.

Gu, X., Zhang, Q., Li, J., Singh, V. P., Liu, J., Sun, P., et al. (2019b). Attribution of Global Soil Moisture Drying to Human Activities: A Quantitative Viewpoint. *Geophys. Res. Lett.* 46, 2573–2582. doi:10.1029/2018GL080768.

Gudmundsson, L., Boulange, J., Do, H. X., Gosling, S. N., Grillakis, M. G., Koutroulis, A. G., et al. (2021). Globally observed trends in mean and extreme river flow attribution to climate change. *Science (80-.).* doi:10.1126/science.aba3996.

Gudmundsson, L., Leonard, M., Do, H. X., Westra, S., and Seneviratne, S. I. (2019). Observed Trends in Global

ACCEPTED VERSION SUBJECT TO FINAL EDITING

Indicators of Mean and Extreme Streamflow. *Geophys. Res. Lett.* 46, 756–766. doi:10.1029/2018GL079725.
Gudmundsson, L., and Seneviratne, S. I. (2016). Anthropogenic climate change affects meteorological drought risk in Europe. *Environ. Res. Lett.* 11. doi:10.1088/1748-9326/11/4/044005.
Gudmundsson, L., Seneviratne, S. I., and Zhang, X. (2017). Anthropogenic climate change detected in European renewable freshwater resources. *Nat. Clim. Chang.* 7, 813–816. doi:10.1038/nclimate3416.
Guerreiro, S. B., Dawson, R. J., Kilsby, C., Lewis, E., and Ford, A. (2018a). Future heat-waves, droughts and floods in 571 European cities. *Environ. Res. Lett.* 13, 034009. doi:10.1088/1748-9326/aaaad3.
Guerreiro, S. B., Fowler, H. J., Barbero, R., Westra, S., Lenderink, G., Blenkinsop, S., et al. (2018b). Detection of continental-scale intensification of hourly rainfall extremes. *Nat. Clim. Chang.* 8, 803–807. doi:10.1038/s41558-018-0245-3.
Guhathakurta, P., Menon, P., Inkane, P. M., Krishnan, U., and Sable, S. T. (2017). Trends and variability of meteorological drought over the districts of India usting standardized precipitation index. *J. Earth Syst. Sci.* 126, 120. doi:10.1007/s12040-017-0896-x.
Guichard, F., and Couvreux, F. (2017). A short review of numerical cloud-resolving models. *Tellus, Ser. A Dyn. Meteorol. Oceanogr.* 69, 1–36. doi:10.1080/16000870.2017.1373578.
Guillod, B. P., Orlowsky, B., Miralles, D. G., Teuling, A. J., and Seneviratne, S. I. (2015). Reconciling spatial and temporal soil moisture effects on afternoon rainfall. *Nat. Commun.* 6, 6443. doi:10.1038/ncomms7443.
Guimberteau, M., Ronchail, J., Espinoza, J. C. C., Lengaigne, M., Sultan, B., Polcher, J., et al. (2013). Future changes in precipitation and impacts on extreme streamflow over Amazonian sub-basins. *Environ. Res. Lett.* 8, 014035. doi:10.1088/1748-9326/8/1/014035.
Guo, J., Huang, G., Wang, X., Li, Y., and Lin, Q. (2018). Dynamically-downscaled projections of changes in temperature extremes over China. *Clim. Dyn.* 50, 1045–1066. doi:10.1007/s00382-017-3660-7.
Guo, X., Huang, J., Luo, Y., Zhao, Z., and Xu, Y. (2016). Projection of precipitation extremes for eight global warming targets by 17 CMIP5 models. *Nat. Hazards* 84, 2299–2319. doi:10.1007/s11069-016-2553-0.
Guo, X., Huang, J., Luo, Y., Zhao, Z., and Xu, Y. (2017). Projection of heat waves over China for eight different global warming targets using 12 CMIP5 models. *Theor. Appl. Climatol.* 128, 507–522. doi:10.1007/s00704-015-1718-1.
Gusain, A., Ghosh, S., and Karmakar, S. (2020). Added value of CMIP6 over CMIP5 models in simulating Indian summer monsoon rainfall. *Atmos. Res.* 232, 104680. doi:10.1016/j.atmosres.2019.104680.
Gutmann, E. D., Rasmussen, R. M., Liu, C., Ikeda, K., Bruyere, C. L., Done, J. M., et al. (2018). Changes in hurricanes from a 13-Yr convection-permitting pseudo- global warming simulation. *J. Clim.* 31, 3643–3657. doi:10.1175/JCLI-D-17-0391.1.
Haarsma, R. J., Roberts, M. J., Vidale, P. L., Senior, C. A., Bellucci, A., Bao, Q., et al. (2016). High Resolution Model Intercomparison Project (HighResMIP v1.0) for CMIP6. *Geosci. Model Dev.* 9, 4185–4208. doi:10.5194/gmd-9-4185-2016.
Habib, S. M. A., Sato, T., and Hatsuzuka, D. (2019). Decreasing number of propagating mesoscale convective systems in Bangladesh and surrounding area during 1998–2015. *Atmos. Sci. Lett.* 20, e879. doi:10.1002/asl.879.
Haig, J., Nott, J., and Reichart, G.-J. (2014). Australian tropical cyclone activity lower than at any time over the past 550–1,500 years. *Nature* 505, 667–671. doi:10.1038/nature12882.
Hall, A., and Qu, X. (2006). Using the current seasonal cycle to constrain snow albedo feedback in future climate change. *Geophys. Res. Lett.* 33, L03502. doi:10.1029/2005GL025127.
Hall, J., Arheimer, B., Borga, M., Brázdil, R., Claps, P., Kiss, A., et al. (2014). Understanding flood regime changes in Europe: A state-of-the-art assessment. *Hydrol. Earth Syst. Sci.* 18, 2735–2772. doi:10.5194/hess-18-2735-2014.
Hall, T. C., Sealy, A. M., Stephenson, T. S., Kusunoki, S., Taylor, M. A., Chen, A. A., et al. (2013). Future climate of the Caribbean from a super-high-resolution atmospheric general circulation model. *Theor. Appl. Climatol.* 113, 271–287. doi:10.1007/s00704-012-0779-7.
Hall, T. M., and Kossin, J. P. (2019). Hurricane stalling along the North American coast and implications for rainfall. *npj Clim. Atmos. Sci.* 2, 1–9. doi:10.1038/s41612-019-0074-8.
Hamada, A., and Takayabu, Y. N. (2018). Large-scale environmental conditions related to midsummer extreme rainfall events around Japan in the TRMM region. *J. Clim.* 0, null. doi:10.1175/JCLI-D-17-0632.1.
Hamada, A., Takayabu, Y. N., Liu, C., and Zipser, E. J. (2015). Weak linkage between the heaviest rainfall and tallest storms. *Nat. Commun.* 6, 1–6. doi:10.1038/ncomms7213.
Han, F., Cook, K. H., and Vizy, E. K. (2019). Changes in intense rainfall events and dry periods across Africa in the twenty-first century. *Clim. Dyn.*, 1–21. doi:10.1007/s00382-019-04653-z.
Han, J.-Y., Baik, J.-J., and Khain, A. P. (2011). A Numerical Study of Urban Aerosol Impacts on Clouds and Precipitation. *J. Atmos. Sci.* 69, 504–520. doi:10.1175/JAS-D-11-071.1.
Han, T., Chen, H., Hao, X., and Wang, H. (2018). Projected changes in temperature and precipitation extremes over the Silk Road Economic Belt regions by the Coupled Model Intercomparison Project Phase 5 multi-model ensembles. *Int. J. Climatol.* 38, 4077–4091. doi:10.1002/joc.5553.
Hande, L. B., Siems, S. T., and Manton, M. J. (2012). Observed Trends in Wind Speed over the Southern Ocean. *Geophys. Res. Lett.* 39, 1–5. doi:10.1029/2012GL051734.
Hanel, M., Rakovec, O., Markonis, Y., Máca, P., Samaniego, L., Kyselý, J., et al. (2018). Revisiting the recent

ACCEPTED VERSION SUBJECT TO FINAL EDITING

European droughts from a long-term perspective. *Sci. Rep.* 8. doi:10.1038/s41598-018-27464-4.
Hannaford, J. (2015). Climate-driven changes in UK river flows. *Prog. Phys. Geogr. Earth Environ.* 39, 29–48. doi:10.1177/0309133314536755.
Hao, Y., Liu, Q., Li, C., Kharel, G., An, L., Stebler, E., et al. (2019). Interactive effect of meteorological drought and vegetation types on root zone soil moisture and runoff in Rangeland Watersheds. *Water (Switzerland)* 11. doi:10.3390/w11112357.
Hao, Z., Hao, F., Singh, V. P., and Zhang, X. (2018). Changes in the severity of compound drought and hot extremes over global land areas. *Environ. Res. Lett.* 13, 124022. doi:10.1088/1748-9326/aaee96.
Hari, V., Rakovec, O., Markonis, Y., Hanel, M., and Kumar, R. (2020). Increased future occurrences of the exceptional 2018–2019 Central European drought under global warming. *Sci. Rep.* 10, 12207. doi:10.1038/s41598-020-68872-9.
Harrigan, S., Hannaford, J., Muchan, K., and Marsh, T. J. (2018). Designation and trend analysis of the updated UK Benchmark Network of river flow stations: The UKBN2 dataset. *Hydrol. Res.* 49, 552–567. doi:10.2166/nh.2017.058.
Harrington, L. J. (2017). Investigating differences between event-as-class and probability density-based attribution statements with emerging climate change. *Clim. Change* 141, 641–654. doi:10.1007/s10584-017-1906-3.
Harrington, L. J. (2020). Rethinking extreme heat in a cool climate: a New Zealand case study. *Environ. Res. Lett.* doi:10.1088/1748-9326/abbd61.
Harrington, L. J., Gibson, P. B., Dean, S. M., Mitchell, D., Rosier, S. M., and Frame, D. J. (2016). Investigating event-specific drought attribution using self-organizing maps. *J. Geophys. Res. Atmos.* 121, 12,712-766,780. doi:10.1002/2016JD025602.
Harrington, L. J., and Otto, F. E. L. (2018a). Adapting attribution science to the climate extremes of tomorrow. *Environ. Res. Lett.* 13, 123006. doi:10.1088/1748-9326/aaf4cc.
Harrington, L. J., and Otto, F. E. L. (2018b). Changing population dynamics and uneven temperature emergence combine to exacerbate regional exposure to heat extremes under 1.5 °C and 2 °C of warming. *Environ. Res. Lett.* 13, 034011. doi:10.1088/1748-9326/aaaa99.
Harrington, L., Rosier, S., Dean, S. M., Stuart, S., and Scahill, A. (2014). The Role of Anthropogenic Climate Change in the 2013 Drought Over North Island, New Zealand [in "Explaining Extreme Events of 2013 from a Climate Perspective"]. *Bull. Am. Meteorol. Soc.* 95, S45–S48. doi:10.1175/1520-0477-95.9.S1.1.
Harrington, and Renwick (2014). Secular changes in New Zealand rainfall characteristics 1950-2009. *Weather Clim.* 34, 50. doi:10.2307/26169744.
Harris, L. M., Lin, S. J., and Tu, C. Y. (2016). High-resolution climate simulations using GFDL HiRAM with a stretched global grid. *J. Clim.* 29, 4293–4314. doi:10.1175/JCLI-D-15-0389.1.
Harrison, L., Funk, C., and Peterson, P. (2019). Identifying changing precipitation extremes in Sub-Saharan Africa with gauge and satellite products. *Environ. Res. Lett.* 14, 085007. doi:10.1088/1748-9326/ab2cae.
Hartmann, D. J., Klein Tank, A. M. G., Rusticucci, M., Alexander, L. V, Brönnimann, S., Charabi, Y. A.-R., et al. (2013). "Observations: Atmosphere and Surface," in *Climate Change 2013: The Physical Science Basis. Contribution of Working Group I to the Fifth Assessment Report of the Intergovernmental Panel on Climate Change*, eds. T. F. Stocker, D. Qin, G.-K. Plattner, M. Tignor, S. K. Allen, J. Boschung, et al. (Cambridge, United Kingdom and New York, NY, USA: Cambridge University Press), 159–254. doi:10.1017/CBO9781107415324.008.
Hartmann, F., Merten, J., Fink, M., and Faust, H. (2018). Indonesia's Fire Crisis 2015 A Twofold Perturbation on the Ground. *Pacific Geogr.* 49, 4–11. doi:10.23791/490411.
Hartmann, H. (2015). Carbon starvation during drought-induced tree mortality – are we chasing a myth? *J. Plant Hydraul.* 2, e005. doi:10.20870/jph.2015.e005.
Hartzell, S., Bartlett, M. S., and Porporato, A. (2017). The role of plant water storage and hydraulic strategies in relation to soil moisture availability. *Plant Soil* 419, 503–521. doi:10.1007/s11104-017-3341-7.
Hasan, H. H., Mohd Razali, S. F., Muhammad, N. S., and Ahmad, A. (2019). Research Trends of Hydrological Drought: A Systematic Review. *Water* 11. doi:10.3390/w11112252.
Hashimoto, A., Done, J. M., Fowler, L. D., and Bruyère, C. L. (2016). Tropical cyclone activity in nested regional and global grid-refined simulations. *Clim. Dyn.* 47, 497–508. doi:10.1007/s00382-015-2852-2.
Haslinger, K., Hofstätter, M., Kroisleitner, C., Schöner, W., Laaha, G., Holawe, F., et al. (2019). Disentangling Drivers of Meteorological Droughts in the European Greater Alpine Region During the Last Two Centuries. *J. Geophys. Res. Atmos.* doi:10.1029/2018JD029527.
Hassanzadeh, P., Lee, C.-Y., Nabizadeh, E., Camargo, S. J., Ma, D., and Yeung, L. Y. (2020). Effects of climate change on the movement of future landfalling Texas tropical cyclones. *Nat. Commun.* 11, 3319. doi:10.1038/s41467-020-17130-7.
Hatsuzuka, D., and Sato, T. (2019). Future Changes in Monthly Extreme Precipitation in Japan Using Large-Ensemble Regional Climate Simulations. *J. Hydrometeorol.* 20, 563–574. doi:10.1175/JHM-D-18-0095.1.
Hatsuzuka, D., Sato, T., Yoshida, K., Ishii, M., and Mizuta, R. (2020). Regional projection of tropical-cyclone-induced extreme precipitation around Japan based on large ensemble simulations. *SOLA* advpub, 23–29.

SUBMITTED VERSION ACCEPTED FOR FINAL EDITING

doi:10.2151/sola.2020-005.
Hauser, M. (2021). Mean temperature anomalies for CMIP5 and CMIP6 (Version v0.1.0). doi:10.5281/ZENODO.4600696.
Hauser, M., Engelbrecht, F., and Fischer, E. M. (2021). Transient global warming levels for CMIP5 and CMIP6 (Version v0.2.0). doi:10.5281/ZENODO.4600706.
Hauser, M., Gudmundsson, L., Orth, R., Jézéquel, A., Haustein, K., Vautard, R., et al. (2017). Methods and Model Dependency of Extreme Event Attribution: The 2015 European Drought. *Earth's Futur.* 5, 1034–1043. doi:10.1002/2017EF000612.
Hauser, M., Orth, R., and Seneviratne, S. I. (2016). Role of soil moisture versus recent climate change for the 2010 heat wave in western Russia. *Geophys. Res. Lett.* 43, 2819–2826. doi:10.1002/2016GL068036.
Hawcroft, M., Walsh, E., Hodges, K., and Zappa, G. (2018). Significantly increased extreme precipitation expected in Europe and North America from extratropical cyclones. *Environ. Res. Lett.* 13. doi:10.1088/1748-9326/aaed59.
Hayat, F., Ahmed, M. A., Zarebanadkouki, M., Cai, G., and Carminati, A. (2019). Measurements and simulation of leaf xylem water potential and root water uptake in heterogeneous soil water contents. *Adv. Water Resour.* 124, 96–105. doi:10.1016/j.advwatres.2018.12.009.
Hazeleger, W., van den Hurk, B. J. J. M., Min, E., van Oldenborgh, G. J., Petersen, A. C., Stainforth, D. A., et al. (2015). Tales of future weather. *Nat. Clim. Chang.* 5, 107–113. doi:10.1038/nclimate2450.
He, B.-R., and Zhai, P.-M. (2018). Changes in persistent and non-persistent extreme precipitation in China from 1961 to 2016. *Adv. Clim. Chang. Res.* 9, 177–184. doi:10.1016/j.accre.2018.08.002.
He, F., and Posselt, D. J. (2015). Impact of Parameterized Physical Processes on Simulated Tropical Cyclone Characteristics in the Community Atmosphere Model. *J. Clim.* 28, 9857–9872. doi:10.1175/JCLI-D-15-0255.1.
He, X., Wada, Y., Wanders, N., and Sheffield, J. (2017). Intensification of hydrological drought in California by human water management. *Geophys. Res. Lett.* 44, 1777–1785. doi:10.1002/2016GL071665.
Helama, S., Sohar, K., Läänelaid, A., Bijak, S., and Jaagus, J. (2018). Reconstruction of precipitation variability in Estonia since the eighteenth century, inferred from oak and spruce tree rings. *Clim. Dyn.* 50, 4083–4101. doi:10.1007/s00382-017-3862-z.
Held, I. M., and Soden, B. J. (2006). Robust responses of the hydrological cycle to global warming. *J. Clim.* 19, 5686–5699. doi:10.1175/JCLI3990.1.
Held, I. M., and Zhao, M. (2011). The Response of Tropical Cyclone Statistics to an Increase in CO2 with Fixed Sea Surface Temperatures. *J. Clim.* 24, 5353–5364. doi:10.1175/JCLI-D-11-00050.1.
Helsen, S., van Lipzig, N. P. M., Demuzere, M., Vanden Broucke, S., Caluwaerts, S., De Cruz, L., et al. (2020). Consistent scale-dependency of future increases in hourly extreme precipitation in two convection-permitting climate models. *Clim. Dyn.* 54, 1267–1280. doi:10.1007/s00382-019-05056-w.
Herger, N., Angélil, O., Abramowitz, G., Donat, M., Stone, D., and Lehmann, K. (2018). Calibrating Climate Model Ensembles for Assessing Extremes in a Changing Climate. *J. Geophys. Res. Atmos.* 123, 5988–6004. doi:10.1029/2018JD028549.
Herger, N., Sanderson, B. M., and Knutti, R. (2015). Improved pattern scaling approaches for the use in climate impact studies. *Geophys. Res. Lett.* 42, 3486–3494. doi:10.1002/2015GL063569.
Herold, N., Ekström, M., Kala, J., Goldie, J., and Evans, J. P. (2018). Australian climate extremes in the 21st century according to a regional climate model ensemble: Implications for health and agriculture. *Weather Clim. Extrem.* 20, 54–68. doi:10.1016/j.wace.2018.01.001.
Herrera-Estrada, J. E., Martinez, J. A., Dominguez, F., Findell, K. L., Wood, E. F., and Sheffield, J. (2019). Reduced Moisture Transport Linked to Drought Propagation Across North America. *Geophys. Res. Lett.* 46, 5243–5253. doi:10.1029/2019GL082475.
Herrera-Estrada, J. E., and Sheffield, J. (2017). Uncertainties in future projections of summer droughts and heat waves over the contiguous United States. *J. Clim.* 30, 6225–6246. doi:10.1175/JCLI-D-16-0491.1.
Herrera-Estrada, J. E., Satoh, Y., and Sheffield, J. (2017). Spatiotemporal dynamics of global drought. *Geophys. Res. Lett.* 44, 2254–2263. doi:10.1002/2016GL071768.
Herring, S. C., Christidis, N., Hoell, A., Hoerling, M. P., and Stott, P. A. (2019). Explaining Extreme Events of 2017 from a Climate Perspective. *Bull. Am. Meteorol. Soc.* 100, S1–S117. doi:10.1175/bams-explainingextremeevents2017.1.
Herring, S. C., Christidis, N., Hoell, A., Hoerling, M. P., and Stott, P. A. (2020). Explaining Extreme Events of 2018 from a Climate Perspective. *Bull. Am. Meteorol. Soc.* 101, S1–S140. doi:10.1175/BAMS-ExplainingExtremeEvents2018.1.
Herring, S. C., Christidis, N., Hoell, A., Kossin, J. P., Schreck, C. J., and Stott, P. A. (2018). Explaining Extreme Events of 2016 from a Climate Perspective. *Bull. Am. Meteorol. Soc.* 99, S1–S157. doi:10.1175/BAMS-ExplainingExtremeEvents2016.1.
Herring, S. C., Hoell, A., Hoerling, M. P., Kossin, J. P., Schreck, C. J., and Stott, P. A. (2016). Explaining Extreme Events of 2015 from a Climate Perspective. *Bull. Am. Meteorol. Soc.* 97, S1–S145. doi:10.1175/BAMS-ExplainingExtremeEvents2015.1.
Herring, S. C., Hoerling, M. P., Kossin, J. P., Peterson, T. C., and Stott, P. A. (2015). Explaining Extreme Events of

ACCEPTED VERSION SUBJECT TO FINAL EDITING

2014 from a Climate Perspective. *Bull. Am. Meteorol. Soc.* 96, S1–S172. doi:10.1175/BAMS-ExplainingExtremeEvents2014.1.

Herring, S. C., Hoerling, M. P., Peterson, T. C., and Stott, P. a. (2014). Explaining Extreme Events of 2013 from a Climate Perspective. *Bull. Am. Meteorol. Soc.* 95, S1–S104. doi:10.1175/1520-0477-95.9.S1.1.

Hersbach, H., Bell, B., Berrisford, P., Hirahara, S., Horányi, A., Muñoz-Sabater, J., et al. (2020). The ERA5 global reanalysis. *Q. J. R. Meteorol. Soc.* 146, 1999–2049. doi:10.1002/qj.3803.

Hertig, E., and Tramblay, Y. (2017). Regional downscaling of Mediterranean droughts under past and future climatic conditions. *Glob. Planet. Change* 151, 36–48. doi:10.1016/j.gloplacha.2016.10.015.

Hettiarachchi, S., Wasko, C., and Sharma, A. (2018). Increase in flood risk resulting from climate change in a developed urban watershed - The role of storm temporal patterns. *Hydrol. Earth Syst. Sci.* 22, 2041–2056. doi:10.5194/hess-22-2041-2018.

Hidalgo, H. G., Alfaro, E. J., and Quesada-Montano, B. (2017). Observed (1970–1999) climate variability in Central America using a high-resolution meteorological dataset with implication to climate change studies. *Clim. Change* 141, 13–28. doi:10.1007/s10584-016-1786-y.

Hillier, J. K., Matthews, T., Wilby, R. L., and Murphy, C. (2020). Multi-hazard dependencies can increase or decrease risk. *Nat. Clim. Chang.* 10, 595–598. doi:10.1038/s41558-020-0832-y.

Hirabayashi, Y., Mahendran, R., Koirala, S., Konoshima, L., Yamazaki, D., Watanabe, S., et al. (2013). Global flood risk under climate change. *Nat. Clim. Chang.* 3, 816–821. doi:10.1038/nclimate1911.

Hirsch, A. L., Evans, J. P., Di Virgilio, G., Perkins-Kirkpatrick, S. E., Argüeso, D., Pitman, A. J., et al. (2019). Amplification of Australian Heatwaves via Local Land-Atmosphere Coupling. *J. Geophys. Res. Atmos.* 124, 13625–13647. doi:10.1029/2019JD030665.

Hirsch, A. L., Guillod, B. P., Seneviratne, S. I., Beyerle, U., Boysen, L. R., Brovkin, V., et al. (2018). Biogeophysical Impacts of Land-Use Change on Climate Extremes in Low-Emission Scenarios: Results From HAPPI-Land. *Earth's Futur.* 6, 396–409. doi:10.1002/2017EF000744.

Hirsch, A. L., Wilhelm, M., Davin, E. L., Thiery, W., and Seneviratne, S. I. (2017). Can climate-effective land management reduce regional warming? *J. Geophys. Res. Atmos.* 122, 2269–2288. doi:10.1002/2016JD026125.

Hirschi, M., Seneviratne, S. I., Alexandrov, V., Boberg, F., Boroneant, C., Christensen, O. B., et al. (2011). Observational evidence for soil-moisture impact on hot extremes in southeastern Europe. *Nat. Geosci.* 4, 17–21. doi:10.1038/ngeo1032.

Hobbins, M., McEvoy, D., and Hain, C. (2017). "Evapotranspiration, Evaporative Demand, and Drought," in *Drought and Water Crises: Integrating Science, Management, and Policy*, 259–287.

Hobbins, M. T., Wood, A., McEvoy, D. J., Huntington, J. L., Morton, C., Anderson, M., et al. (2016). The evaporative demand drought index. Part I: Linking drought evolution to variations in evaporative demand. *J. Hydrometeorol.* 17, 1745–1761. doi:10.1175/JHM-D-15-0121.1.

Hobbins, M., Wood, A., Streubel, D., and Werner, K. (2012). What drives the variability of evaporative demand across the conterminous United States? *J. Hydrometeorol.* 13, 1195–1214. doi:10.1175/JHM-D-11-0101.1.

Hodgkins, G. A., Whitfield, P. H., Burn, D. H., Hannaford, J., Renard, B., Stahl, K., et al. (2017). Climate-driven variability in the occurrence of major floods across North America and Europe. *J. Hydrol.* 552, 704–717. doi:10.1016/j.jhydrol.2017.07.027.

Hodnebrog, Ø., Marelle, L., Alterskjær, K., Wood, R. R., Ludwig, R., Fischer, E. M., et al. (2019). Intensification of summer precipitation with shorter time-scales in Europe. *Environ. Res. Lett.* 14, 124050. doi:10.1088/1748-9326/ab549c.

Hoegh-Guldberg, O., Jacob, D., Taylor, M., Bindi, M., Brown, S., Camilloni, I., et al. (2018). "Impacts of 1.5°C Global Warming on Natural and Human Systems," in *Global Warming of 1.5°C. An IPCC Special Report on the impacts of global warming of 1.5°C above pre-industrial levels and related global greenhouse gas emission pathways, in the context of strengthening the global response to the threat of climate change,* eds. V. Masson-Delmotte, P. Zhai, H. O. Pörtner, D. Roberts, J. Skea, P. R. Shukla, et al. (In Press), 175–312. Available at: https://www.ipcc.ch/sr15/chapter/chapter-3.

Hoerling, M., Eischeid, J., Kumar, A., Leung, R., Mariotti, A., Mo, K., et al. (2014). Causes and Predictability of the 2012 Great Plains Drought. *Bull. Am. Meteorol. Soc.* 95, 269–282. doi:10.1175/BAMS-D-13-00055.1.

Hoerling, M., Eischeid, J., Perlwitz, J., Quan, X.-W., Wolter, K., and Cheng, L. (2016). Characterizing Recent Trends in U.S. Heavy Precipitation. *J. Clim.* 29, 2313–2332. doi:10.1175/JCLI-D-15-0441.1.

Hoerling, M., Eischeid, J., Perlwitz, J., Quan, X., Zhang, T., Pegion, P., et al. (2012). On the Increased Frequency of Mediterranean Drought. *J. Clim.* 25, 2146–2161. doi:10.1175/JCLI-D-11-00296.1.

Hoerling, M., Kumar, A., Dole, R., Nielsen-Gammon, J. W., Eischeid, J., Perlwitz, J., et al. (2013). Anatomy of an extreme event. *J. Clim.* 26, 2811–2832. doi:10.1175/JCLI-D-12-00270.1.

Hogeboom, R. J., Knook, L., and Hoekstra, A. Y. (2018). The blue water footprint of the world's artificial reservoirs for hydroelectricity, irrigation, residential and industrial water supply, flood protection, fishing and recreation. *Adv. Water Resour.* 113, 285–294. doi:10.1016/j.advwatres.2018.01.028.

Holland, G., and Bruyère, C. L. (2014). Recent intense hurricane response to global climate change. *Clim. Dyn.* 42, 617–627. doi:10.1007/s00382-013-1713-0.

ACCEPTED VERSION SUBJECT TO FINAL EDITING

Holloway, C. E., Wing, A. A., Bony, S., Muller, C., Masunaga, H., L'Ecuyer, T. S., et al. (2017). Observing Convective Aggregation. *Surv. Geophys.* 38, 1199–1236. doi:10.1007/s10712-017-9419-1.

Holmes, C. R., Woollings, T., Hawkins, E., and de Vries, H. (2015). Robust Future Changes in Temperature Variability under Greenhouse Gas Forcing and the Relationship with Thermal Advection. *J. Clim.* 29, 2221–2236. doi:10.1175/JCLI-D-14-00735.1.

Hong, C.-C., Lee, M.-Y., Hsu, H.-H., and Tseng, W.-L. (2018). Distinct Influences of the ENSO-Like and PMM-Like SST Anomalies on the Mean TC Genesis Location in the Western North Pacific: The 2015 Summer as an Extreme Example. *J. Clim.* 31, 3049–3059. doi:10.1175/JCLI-D-17-0504.1.

Hoogewind, K. A., Baldwin, M. E., and Trapp, R. J. (2017). The Impact of Climate Change on Hazardous Convective Weather in the United States: Insight from High-Resolution Dynamical Downscaling. *J. Clim.* 30, 10081–10100. doi:10.1175/JCLI-D-16-0885.1.

Hoogewind, K. A., Chavas, D. R., Schenkel, B. A., and O'Neill, M. E. (2020). Exploring Controls on Tropical Cyclone Count through the Geography of Environmental Favorability. *J. Clim.* 33, 1725–1745. doi:10.1175/JCLI-D-18-0862.1.

Hope, P., Black, M. T., Lim, E.-P., Dowdy, A., Wang, G., Fawcett, R. J. B., et al. (2019). On Determining the Impact of Increasing Atmospheric CO2 on the Record Fire Weather in Eastern Australia in February 2017. *Bull. Am. Meteorol. Soc.* 100, S111–S117. doi:10.1175/BAMS-D-18-0135.1.

Hope, P., Lim, E.-P., Wang, G., Hendon, H. H., and Arblaster, J. M. (2015). Contributors to the Record High Temperatures Across Australia in Late Spring 2014. *Bull. Am. Meteorol. Soc.* 96, S149–S153. doi:10.1175/BAMS-D-15-00096.1.

Hope, P., Wang, G., Lim, E.-P., Hendon, H. H., and Arblaster, J. M. (2016). What caused the record-breaking heat across Australia in October 2015? [in "Explaining Extreme Events of 2015 from a Climate Perspective"]. *Bull. Am. Meteorol. Soc.* 97, S122–S126. doi:10.1175/BAMS-ExplainingExtremeEvents2015.1.

Horton, D. E., Johnson, N. C., Singh, D., Swain, D. L., Rajaratnam, B., and Diffenbaugh, N. S. (2015). Contribution of changes in atmospheric circulation patterns to extreme temperature trends. *Nature* 522, 465–469. doi:10.1038/nature14550.

Hou, A. Y., Kakar, R. K., Neeck, S., Azarbarzin, A. A., Kummerow, C. D., Kojima, M., et al. (2014). The Global Precipitation Measurement Mission. *Bull. Am. Meteorol. Soc.* 95, 701–722. doi:10.1175/BAMS-D-13-00164.1.

Howarth, M. E., Thorncroft, C. D., and Bosart, L. F. (2019). Changes in Extreme Precipitation in the Northeast United States: 1979–2014. *J. Hydrometeorol.* 20, 673–689. doi:10.1175/JHM-D-18-0155.1.

Hsu, W.-C., Patricola, C. M., and Chang, P. (2019). The impact of climate model sea surface temperature biases on tropical cyclone simulations. *Clim. Dyn.* 53, 173–192. doi:10.1007/s00382-018-4577-5.

Hu, T., Sun, Y., Zhang, X., Min, S.-K., and Kim, Y.-H. (2020). Human influence on frequency of temperature extremes. *Environ. Res. Lett.* 15, 064014. doi:10.1088/1748-9326/ab8497.

Hu, Z., Li, Q., Chen, X., Teng, Z., Chen, C., Yin, G., et al. (2016). Climate changes in temperature and precipitation extremes in an alpine grassland of Central Asia. *Theor. Appl. Climatol.* 126, 519–531. doi:10.1007/s00704-015-1568-x.

Hua, W., Zhou, L., Chen, H., Nicholson, S. E., Raghavendra, A., and Jiang, Y. (2016). Possible causes of the Central Equatorial African long-term drought. *Environ. Res. Lett.* 11. doi:10.1088/1748-9326/11/12/124002.

Huang, H., Winter, J. M., Osterberg, E. C., Horton, R. M., and Beckage, B. (2017a). Total and Extreme Precipitation Changes over the Northeastern United States. *J. Hydrometeorol.* 18, 1783–1798. doi:10.1175/JHM-D-16-0195.1.

Huang, J., Zhai, J., Jiang, T., Wang, Y., Li, X., Wang, R., et al. (2018a). Analysis of future drought characteristics in China using the regional climate model CCLM. *Clim. Dyn.* 50, 507–525. doi:10.1007/s00382-017-3623-z.

Huang, S., Kumar, R., Flörke, M., Yang, T., Hundecha, Y., Kraft, P., et al. (2017b). Evaluation of an ensemble of regional hydrological models in 12 large-scale river basins worldwide. *Clim. Change* 141, 381–397. doi:10.1007/s10584-016-1841-8.

Huang, S., Kumar, R., Rakovec, O., Aich, V., Wang, X., Samaniego, L., et al. (2018b). Multimodel assessment of flood characteristics in four large river basins at global warming of 1.5, 2.0 and 3.0 K above the pre-industrial level. *Environ. Res. Lett.* 13, 124005. doi:10.1088/1748-9326/aae94b.

Huang, S., Li, P., Huang, Q., Leng, G., Hou, B., and Ma, L. (2017c). The propagation from meteorological to hydrological drought and its potential influence factors. *J. Hydrol.* 547, 184–195. doi:10.1016/J.JHYDROL.2017.01.041.

Huerta, A., and Lavado-Casimiro, W. (2020). Trends and variability of precipitation extremes in the Peruvian Altiplano (1971–2013). *Int. J. Climatol.* n/a. doi:10.1002/joc.6635.

Hui, P., Tang, J., Wang, S., Niu, X., Zong, P., and Dong, X. (2018). Climate change projections over China using regional climate models forced by two CMIP5 global models. Part I: evaluation of historical simulations. *Int. J. Climatol.* 38, e57–e77. doi:10.1002/joc.5351.

Huijnen, V., Wooster, M. J., Kaiser, J. W., Gaveau, D. L. A., Flemming, J., Parrington, M., et al. (2016). Fire carbon emissions over maritime southeast Asia in 2015 largest since 1997. *Sci. Rep.* 6, 1–8. doi:10.1038/srep26886.

Humphrey, V., Zscheischler, J., Ciais, P., Gudmundsson, L., Sitch, S., and Seneviratne, S. I. (2018). Sensitivity of atmospheric CO2 growth rate to observed changes in terrestrial water storage. *Nature* 560, 628–631.

ACCEPTED VERSION SUBJECT TO FINAL EDITING

doi:10.1038/s41586-018-0424-4.
Hundecha, Y., Sunyer, M. A., Lawrence, D., Madsen, H., Willems, P., Bürger, G., et al. (2016). Inter-comparison of statistical downscaling methods for projection of extreme flow indices across Europe. *J. Hydrol.* 541, 1273–1286. doi:10.1016/j.jhydrol.2016.08.033.
Huning, L. S., and AghaKouchak, A. (2020). Global snow drought hot spots and characteristics. *Proc. Natl. Acad. Sci. U. S. A.* 117, 19753–19759. doi:10.1073/pnas.1915921117.
Hunt, E. D., Svoboda, M., Wardlow, B., Hubbard, K., Hayes, M., and Arkebauer, T. (2014). Monitoring the effects of rapid onset of drought on non-irrigated maize with agronomic data and climate-based drought indices. *Agric. For. Meteorol.* 191, 1–11. doi:10.1016/j.agrformet.2014.02.001.
Hunt, K. M. R., Turner, A. G., and Shaffrey, L. C. (2018). Extreme Daily Rainfall in Pakistan and North India: Scale Interactions, Mechanisms, and Precursors. *Mon. Weather Rev.* 146, 1005–1022. doi:10.1175/MWR-D-17-0258.1.
Hussain, M. S., and Lee, S. (2013). The regional and the seasonal variability of extreme precipitation trends in Pakistan. *Asia-Pacific J. Atmos. Sci.* 49, 421–441. doi:10.1007/s13143-013-0039-5.
Imada, Y., Maeda, S., Watanabe, M., Shiogama, H., Mizuta, R., Ishii, M., et al. (2017). Recent enhanced seasonal temperature contrast in Japan from large ensemble high-resolution climate simulations. *Atmosphere (Basel).* 8. doi:10.3390/atmos8030057.
Imada, Y., Shiogama, H., Takahashi, C., Watanabe, M., Mori, M., Kamae, Y., et al. (2018). Climate Change Increased the Likelihood of the 2016 Heat Extremes in Asia [in "Explaining Extreme Events of 2016 from a Climate Perspective"]. *Bull. Am. Meteorol. Soc.* 99, S97–S101. doi:10.1175/BAMS-D-17-0109.1.
Imada, Y., Shiogama, H., Watanabe, M., Mori, M., Ishii, M., and Kimoto, M. (2014). The Contribution of anthropogenic forcing to the Japanese heat waves of 2013 [in "Explaining Extreme Events of 2013 from a Climate Perspective"]. *Bull. Am. Meteorol. Soc.* 95, S52–S54. doi:10.1175/1520-0477-95.9.S1.1.
Imada, Y., Watanabe, M., Kawase, H., Shiogama, H., and Arai, M. (2019). The July 2018 High Temperature Event in Japan Could Not Have Happened without Human-Induced Global Warming. *SOLA* 15A, 8–12. doi:10.2151/sola.15A-002.
Imada, Y., Watanabe, M., Mori, M., Kimoto, M., Shiogama, H., and Ishii, M. (2013). Contribution of Atmospheric Circulation Change to the 2012 Heavy Rainfall in Southwestern Japan. *Bull. Am. Meteorol. Soc.* 96, 52–54.
Imbach, P., Chou, S. C., Lyra, A., Rodrigues, D., Rodriguez, D., Latinovic, D., et al. (2018). Future climate change scenarios in Central America at high spatial resolution. *PLoS One* 13, e0193570. doi:10.1371/journal.pone.0193570.
INMET (2017). Situação da Seca Observada nas Regiões Norte e Nordeste do Brasil em 2016. Brasília, Brazil: Instituto Nacional de Meteorologia (INMET) Available at: https://portal.inmet.gov.br/uploads/notastecnicas/trabalho_tecnico_02-2017.pdf.
Innocenti, S., Mailhot, A., Leduc, M., Cannon, A. J., and Frigon, A. (2019). Projected Changes in the Probability Distributions, Seasonality, and Spatiotemporal Scaling of Daily and Subdaily Extreme Precipitation Simulated by a 50-Member Ensemble Over Northeastern North America. *J. Geophys. Res. Atmos.* 124, 10427–10449. doi:10.1029/2019JD031210.
IPCC (2012). Managing the Risks of Extreme Events and Disasters to Advance Climate Change Adaptation. A Special Report of Working Groups I and II of the Intergovernmental Panel on Climate Change. , eds. C. B. Field, V. Barros, T. F. Stocker, D. Qin, D. J. Dokken, K. L. Ebi, et al. Cambridge, United Kingdom and New York, NY , USA: Cambridge University Press Available at: https://www.ipcc.ch/report/managing-the-risks-of-extreme-events-and-disasters-to-advance-climate-change-adaptation.
IPCC (2013). Climate Change 2013: The Physical Science Basis. Contribution of Working Group I to the Fifth Assessment Report of the Intergovernmental Panel on Climate Change. , eds. T. F. Stocker, D. Qin, G.-K. Plattner, M. Tignor, S. K. Allen, J. Boschung, et al. Cambridge, United Kingdom and New York, NY, USA: Cambridge University Press doi:10.1017/CBO9781107415324.
IPCC (2014). *Climate Change 2014: Impacts, Adaptation, and Vulnerability. Part A: Global and Sectoral Aspects. Contribution of Working Group II to the FifthAssessment Report of the Intergovernmental Panel on Climate Change.* , eds. C. B. Field, V. R. Barros, D. J. Dokken, K. J. Mach, M. D. Mastrandrea, T. E. Bilir, et al. United Kingdom and New York, NY, USA,: ambridge UniversityPress, Cambridge.
IPCC (2018). "Summary for Policymakers," in *Global warming of 1.5°C. An IPCC Special Report on the impacts of global warming of 1.5°C above pre-industrial levels and related global greenhouse gas emission pathways, in the context of strengthening the global response to*, eds. V. Masson-Delmotte, P. Zhai, H.-O. Pörtner, D. Roberts, J. Skea, P. R. Shukla, et al. (In Press), 32. Available at: https://www.ipcc.ch/sr15/chapter/spm.
IPCC (2019). IPCC Special Report on the Ocean and Cryosphere in a Changing Climate. , eds. H.-O. Pörtner, D. C. Roberts, V. Masson-Delmotte, P. Zhai, M. Tignor, E. Poloczanska, et al. In Press Available at: https://www.ipcc.ch/srocc.
Irannezhad, M., Chen, D., Kløve, B., and Moradkhani, H. (2017). Analysing the variability and trends of precipitation extremes in Finland and their connection to atmospheric circulation patterns. *Int. J. Climatol.* 37, 1053–1066. doi:10.1002/joc.5059.
Ishak, E. H., Rahman, A., Westra, S., Sharma, A., and Kuczera, G. (2013). Evaluating the non-stationarity of australian

ACCEPTED VERSION SUBJECT TO FINAL EDITING

annual maximum flood. *J. Hydrol.* 494, 134–145. doi:10.1016/j.jhydrol.2013.04.021.
Ishiyama, T., Satoh, M., and Yamada, Y. (2018). Potential differences in North Pacific tropical cyclone activity between the super El Niño years of 1997 and 2015. *J. Meteorol. Soc. Japan*.
Ivancic, T. J., and Shaw, S. B. (2015). Examining why trends in very heavy precipitation should not be mistaken for trends in very high river discharge. *Clim. Change* 133, 681–693. doi:10.1007/s10584-015-1476-1.
Jacob, D., Kotova, L., Teichmann, C., Sobolowski, S. P., Vautard, R., Donnelly, C., et al. (2018). Climate Impacts in Europe Under +1.5°C Global Warming. *Earth's Futur.* 6, 264–285. doi:10.1002/2017EF000710.
Jacob, D., Teichmann, C., Sobolowski, S., Katragkou, E., Anders, I., Belda, M., et al. (2020). Regional climate downscaling over Europe: perspectives from the EURO-CORDEX community. *Reg. Environ. Chang.* 20, 51. doi:10.1007/s10113-020-01606-9.
Jakob, D., and Walland, D. (2016). Variability and long-term change in Australian temperature and precipitation extremes. *Weather Clim. Extrem.* 14, 36–55. doi:10.1016/j.wace.2016.11.001.
James, R., Washington, R., Schleussner, C.-F., Rogelj, J., and Conway, D. (2017). Characterizing half-a-degree difference: a review of methods for identifying regional climate responses to global warming targets. *Wiley Interdiscip. Rev. Clim. Chang.* 8, e457. doi:10.1002/wcc.457.
Jehanzaib, M., Shah, S. A., Yoo, J., and Kim, T.-W. (2020). Investigating the impacts of climate change and human activities on hydrological drought using non-stationary approaches. *J. Hydrol.* 588. doi:10.1016/j.jhydrol.2020.125052.
Jeon, S., Paciorek, C. J., and Wehner, M. F. (2016). Quantile-based bias correction and uncertainty quantification of extreme event attribution statements. *Weather Clim. Extrem.* 12, 24–32. doi:10.1016/j.wace.2016.02.001.
Jeong, J.-H., Fan, J., Homeyer, C. R., and Hou, Z. (2020). Understanding Hailstone Temporal Variability and Contributing Factors over the U.S. Southern Great Plains. *J. Clim.* 33, 3947–3966. doi:10.1175/JCLI-D-19-0606.1.
Jeong, S.-J., Ho, C.-H., Piao, S., Kim, J., Ciais, P., Lee, Y.-B., et al. (2014). Effects of double cropping on summer climate of the North China Plain and neighbouring regions. *Nat. Clim. Chang.* 4, 615–619. doi:10.1038/nclimate2266.
Jézéquel, A., Dépoues, V., Guillemot, H., Trolliet, M., Vanderlinden, J.-P., and Yiou, P. (2018). Behind the veil of extreme event attribution. *Clim. Change*. doi:10.1007/s10584-018-2252-9.
Jhajharia, D., Kumar, R., Dabral, P. P., Singh, V. P., Choudhary, R. R., and Dinpashoh, Y. (2015). Reference evapotranspiration under changing climate over the Thar Desert in India. *Meteorol. Appl.* 22, 425–435. doi:10.1002/met.1471.
Ji, P., Yuan, X., Jiao, Y., Wang, C., Han, S., and Shi, C. (2020). Anthropogenic contributions to the 2018 extreme flooding over upper Yellow River basin in China. *Bull. Am. Meteorol. Soc.* doi:10.1175/BAMS-D-19-0105.1.
Ji, Z., and Kang, S. (2015). Evaluation of extreme climate events using a regional climate model for China. *Int. J. Climatol.* 35, 888–902. doi:10.1002/joc.4024.
Jia, B., Liu, J., Xie, Z., and Shi, C. (2018). Interannual Variations and Trends in Remotely Sensed and Modeled Soil Moisture in China. *J. Hydrometeorol.* 19, 831–847. doi:10.1175/JHM-D-18-0003.1.
Jia, G., E. Shevliakova, Artaxo, P., Noblet-Ducoudré, N. De, Houghton, R., House, J., et al. (2019a). Land–climate interactions. In: Climate Change and Land: an IPCC special report on climate change, desertification, land degradation, sustainable land management, food security, and greenhouse gas fluxes in terrestrial ecosystems. , eds. P.R. Shukla, J. Skea, E. Calvo Buendia, V. Masson-Delmotte, H.-O. Pörtner, D. C. Roberts, et al.
Jia, G., Shevliakova, E., Artaxo, P., Noblet-Ducoudré, N. De, Houghton, R., House, J., et al. (2019b). "Land–climate interactions," in *Climate Change and Land: an IPCC special report on climate change, desertification, land degradation, sustainable land management, food security, and greenhouse gas fluxes in terrestrial ecosystems*, eds. P.R. Shukla, J. Skea, E. Calvo Buendia, V. Masson-Delmotte, H.-O. Pörtner, D. C. Roberts, et al. (In Press), 131–248. Available at: https://www.ipcc.ch/srccl/chapter/chapter-2.
Jiang, F., Hu, R.-J., Wang, S.-P., Zhang, Y.-W., and Tong, L. (2013). Trends of precipitation extremes during 1960–2008 in Xinjiang, the Northwest China. *Theor. Appl. Climatol.* 111, 133–148. doi:10.1007/s00704-012-0657-3.
Jiménez-Muñoz, J. C., Mattar, C., Barichivich, J., Santamaría-Artigas, A., Takahashi, K., Malhi, Y., et al. (2016). Record-breaking warming and extreme drought in the Amazon rainforest during the course of El Niño 2015–2016. *Sci. Rep.* 6, 33130. doi:10.1038/srep33130.
Jimenez Cisneros, B. E., Oki, T., Arnell, N. W., Benito, G., Cogley, J. G., Petra, D., et al. (2014). "IPCC WGIIAR5 Chapter 3 Freshwater resources," in *Climate Change 2014: Impacts,Adaptation, and Vulnerability. Part A: Global and Sectoral Aspects. Contribution of Working Group II to the Fifth Assessment Report of the Intergovernmental Panel on Climate Change*, eds. T. E. B. Field, C.B., V.R. Barros, D.J. Dokken, K.J. Mach, M.D. Mastrandrea, S. M. M. Chatterjee, K.L. Ebi, Y.O. Estrada, R.C. Genova, B. Girma, E.S. Kissel, A.N. Levy, and and L. L. W. P.R. Mastrandrea (Cambridge University Press, Cambridge, United Kingdom and New York, NY, USA), 229–269.
Johnson, N. C., Xie, S. P., Kosaka, Y., and Li, X. (2018). Increasing occurrence of cold and warm extremes during the recent global warming slowdown. *Nat. Commun.* 9, 4–6. doi:10.1038/s41467-018-04040-y.
Jolly, W. M., Cochrane, M. A., Freeborn, P. H., Holden, Z. A., Brown, T. J., Williamson, G. J., et al. (2015). Climate-

ACCEPTED VERSION SUBJECT TO FINAL EDITING

induced variations in global wildfire danger from 1979 to 2013. *Nat. Commun.* 6, 7537. doi:10.1038/ncomms8537.
Junk, J., Goergen, K., and Krein, A. (2019). Future Heat Waves in Different European Capitals Based on Climate Change Indicators. *Int. J. Environ. Res. Public Health* 16, 3959. doi:10.3390/ijerph16203959.
Kamae, Y., Mei, W., Xie, S. P., Naoi, M., and Ueda, H. (2017a). Atmospheric rivers over the Northwestern Pacific: Climatology and interannual variability. *J. Clim.* 30, 5605–5619. doi:10.1175/JCLI-D-16-0875.1.
Kamae, Y., Shiogama, H., Imada, Y., Mori, M., Arakawa, O., Mizuta, R., et al. (2017b). Forced response and internal variability of summer climate over western North America. *Clim. Dyn.* 49, 403–417. doi:10.1007/s00382-016-3350-x.
Kamae, Y., Shiogama, H., Watanabe, M., and Kimoto, M. (2014). Attributing the increase in Northern Hemisphere hot summers since the late 20th century. *Geophys. Res. Lett.* 41, 5192–5199. doi:10.1002/2014GL061062.
Kambezidis, H. D., Kaskaoutis, D. G., Kharol, S. K., Moorthy, K. K., Satheesh, S. K., Kalapureddy, M. C. R., et al. (2012). Multi-decadal variation of the net downward shortwave radiation over south Asia: The solar dimming effect. *Atmos. Environ.* 50, 360–372. doi:10.1016/j.atmosenv.2011.11.008.
Kanada, S., Takemi, T., Kato, M., Yamasaki, S., Fudeyasu, H., Tsuboki, K., et al. (2017a). A multimodel intercomparison of an intense typhoon in future, warmer climates by Four 5-km-Mesh models. *J. Clim.* 30, 6017–6036. doi:10.1175/JCLI-D-16-0715.1.
Kanada, S., Tsujino, S., Aiki, H., Yoshioka, M. K., Miyazawa, Y., Tsuboki, K., et al. (2017b). Impacts of SST Patterns on Rapid Intensification of Typhoon Megi (2010). *J. Geophys. Res. Atmos.* 122, 13,213-245,262. doi:10.1002/2017JD027252.
Kanada, S., and Wada, A. (2016). Sensitivity to Horizontal Resolution of the Simulated Intensifying Rate and Inner-Core Structure of Typhoon Ida, an Extremely Intense Typhoon. *J. Meteorol. Soc. Japan. Ser. II* 94A, 181–190. doi:10.2151/jmsj.2015-037.
Kanada, S., Wada, A., and Sugi, M. (2013). Future changes in structures of extremely intense tropical cyclones using a 2-km mesh nonhydrostatic model. *J. Clim.* 26, 9986–10005. doi:10.1175/JCLI-D-12-00477.1.
Kang, N. Y., and Elsner, J. B. (2012). Consensus on climate trends in Western North pacific tropical cyclones. *J. Clim.* 25, 7564–7573. doi:10.1175/JCLI-D-11-00735.1.
Kaniewski, D., Van Campo, E., and Weiss, H. (2012). Drought is a recurring challenge in the Middle East. *Proc. Natl. Acad. Sci. U. S. A.* 109, 3862–3867. doi:10.1073/pnas.1116304109.
Kar-Man Chang, E. (2018). CMIP5 Projected Change in Northern Hemisphere Winter Cyclones with Associated Extreme Winds. *J. Clim.* 31, 6527–6542. doi:10.1175/JCLI-D-17-0899.1.
Karoly, D. J., Black, M. T., Grose, M. R., and King, A. D. (2016). 25. The roles of climate change and El Niño in the record low rainfall in October 2015 in Tasmania, Australia. *Bull. Am. Meteorol. Soc.* 97, S127–S130. doi:10.1175/BAMS-D-16-0139.1.
Kato, T. (2020). Quasi-stationary band-shaped precipitation systems, named as “senjo-kousuitai”, causing localized heavy rainfall in Japan. *J. Meteorol. Soc. Japan* 98, 485–509. doi:10.2151/jmsj.2020-029.
Kattsov, V. M., Shkolnik, I. M., and Efimov, S. V. (2017). Climate change projections in Russian regions: The detailing in physical and probability spaces. *Russ. Meteorol. Hydrol.* 42, 452–460. doi:10.3103/S1068373917070044.
Kawase, H., Imada, Y., Tsuguti, H., Nakaegawa, T., Seinino, N., Murata, A., et al. (2019). The heavy rain event of July 2019 in Japan enhanced by historical warming. *Bull Am Meteorol Soc*. doi:10.1175/BAMS-D-19-0173.1.
Kay, A. L., Bell, V. A., Guillod, B. P., Jones, R. G., and Rudd, A. C. (2018). National-scale analysis of low flow frequency: historical trends and potential future changes. *Clim. Change* 147, 585–599. doi:10.1007/s10584-018-2145-y.
Kay, J. E., Deser, C., Phillips, A., Mai, A., Hannay, C., Strand, G., et al. (2015). The Community Earth System Model (CESM) Large Ensemble Project: A Community Resource for Studying Climate Change in the Presence of Internal Climate Variability. *Bull. Am. Meteorol. Soc.* 96, 1333–1349. doi:10.1175/BAMS-D-13-00255.1.
Keellings, D., and Waylen, P. (2014). Increased risk of heat waves in Florida: Characterizing changes in bivariate heat wave risk using extreme value analysis. *Appl. Geogr.* 46, 90–97. doi:10.1016/j.apgeog.2013.11.008.
Kelley, C. P., Mohtadi, S., Cane, M. A., Seager, R., and Kushnir, Y. (2015). Climate change in the Fertile Crescent and implications of the recent Syrian drought. *Proc. Natl. Acad. Sci. U. S. A.* 112, 3241–3246. doi:10.1073/pnas.1421533112.
Kelley, C., Ting, M., Seager, R., and Kushnir, Y. (2012). The relative contributions of radiative forcing and internal climate variability to the late 20th Century winter drying of the Mediterranean region. *Clim. Dyn.* 38, 2001–2015. doi:10.1007/s00382-011-1221-z.
Kendon, E. J., Ban, N., Roberts, N. M., Fowler, H. J., Roberts, M. J., Chan, S. C., et al. (2017). Do Convection-Permitting Regional Climate Models Improve Projections of Future Precipitation Change? *Bull. Am. Meteorol. Soc.* 98, 79–93. doi:10.1175/BAMS-D-15-0004.1.
Kendon, E. J., Roberts, N. M., Fowler, H. J., Roberts, M. J., Chan, S. C., and Senior, C. A. (2014). Heavier summer downpours with climate change revealed by weather forecast resolution model. *Nat. Clim. Chang.* 4, 570–576. doi:10.1038/nclimate2258.
Kendon, E. J., Stratton, R. A., Tucker, S., Marsham, J. H., Berthou, S., Rowell, D. P., et al. (2019). Enhanced future

ACCEPTED VERSION SUBJECT TO FINAL EDITING

changes in wet and dry extremes over Africa at convection-permitting scale. *Nat. Commun.* 10, 1794. doi:10.1038/s41467-019-09776-9.

Kendon, M. (2014). Has there been a recent increase in UK weather records? *Weather* 69, 327–332. doi:10.1002/wea.2439.

Kew, S. F., Philip, S. Y., Hauser, M., Hobbins, M., Wanders, N., van Oldenborgh, G. J., et al. (2021). Impact of precipitation and increasing temperatures on drought trends in eastern Africa. *Earth Syst. Dyn.* 12, 17–35. doi:10.5194/esd-12-17-2021.

Kew, S. F., Philip, S. Y., Jan van Oldenborgh, G., van der Schrier, G., Otto, F. E. L., and Vautard, R. (2019). The Exceptional Summer Heat Wave in Southern Europe 2017 [in "Explaining Extreme Events of 2017 from a Climate Perspective"]. *Bull. Am. Meteorol. Soc.* 100, S49–S53. doi:10.1175/BAMS-D-18-0109.1.

Kew, S. F., Selten, F. M., Lenderink, G., and Hazeleger, W. (2013). The simultaneous occurrence of surge and discharge extremes for the Rhine delta. *Nat. Hazards Earth Syst. Sci.* 13, 2017–2029. doi:10.5194/nhess-13-2017-2013.

Khan, N., Shahid, S., Ismail, T. bin, and Wang, X.-J. (2019). Spatial distribution of unidirectional trends in temperature and temperature extremes in Pakistan. *Theor. Appl. Climatol.* 136, 899–913. doi:10.1007/s00704-018-2520-7.

Kharin, V. V., Flato, G. M., Zhang, X., Gillett, N. P., Zwiers, F., and Anderson, K. J. (2018). Risks from Climate Extremes Change Differently from 1.5°C to 2.0°C Depending on Rarity. *Earth's Futur.* 6, 704–715. doi:10.1002/2018EF000813.

Kharin, V. V., Zwiers, F. W., Zhang, X., and Wehner, M. (2013). Changes in temperature and precipitation extremes in the CMIP5 ensemble. *Clim. Change* 119, 345–357. doi:10.1007/s10584-013-0705-8.

Khlebnikova, E. I., Rudakova, Y. L., Sall', I. A., Efimov, S. V., and Shkolnik, I. M. (2019a). Changes in indicators of temperature extremes in the 21st century: ensemble projections for the territory of Russia. *Russ. Meteorol. Hydrol.* 44, 159–168. doi:10.3103/S1068373919030014.

Khlebnikova, E. I., Rudakova, Y. L., and Shkolnik, I. M. (2019b). Changes in precipitation regime over the territory of Russia: Data of regional climate modeling and observations. *Russ. Meteorol. Hydrol.* 44, 431–439. doi:10.3103/S106837391907001X.

Khong, A., Wang, J. K., Quiring, S. M., and Ford, T. W. (2015). Soil moisture variability in Iowa. *Int. J. Climatol.* 35, 2837–2848. doi:10.1002/joc.4176.

Khouakhi, A., Villarini, G., and Vecchi, G. A. (2016). Contribution of Tropical Cyclones to Rainfall at the Global Scale. *J. Clim.* 30, 359–372. doi:10.1175/JCLI-D-16-0298.1.

Kim, B., and Sanders, B. F. (2016). Dam-Break Flood Model Uncertainty Assessment: Case Study of Extreme Flooding with Multiple Dam Failures in Gangneung, South Korea. *J. Hydraul. Eng.* 142, 05016002. doi:10.1061/(ASCE)HY.1943-7900.0001097.

Kim, D., Moon, Y., Camargo, S. J., Wing, A. A., Sobel, A. H., Murakami, H., et al. (2018a). Process-Oriented Diagnosis of Tropical Cyclones in High-Resolution GCMs. *J. Clim.* 31, 1685–1702. doi:10.1175/JCLI-D-17-0269.1.

Kim, G., Cha, D.-H., Park, C., Lee, G., Jin, C.-S., Lee, D.-K., et al. (2018b). Future changes in extreme precipitation indices over Korea. *Int. J. Climatol.* 38, e862–e874. doi:10.1002/joc.5414.

Kim, H. S., Vecchi, G. A., Knutson, T. R., Anderson, W. G., Delworth, T. L., Rosati, A., et al. (2014a). Tropical cyclone simulation and response to CO2 doubling in the GFDL CM2.5 high-resolution coupled climate model. *J. Clim.* 27, 8034–8054. doi:10.1175/JCLI-D-13-00475.1.

Kim, I.-W. W., Oh, J., Woo, S., and Kripalani, R. H. (2019). Evaluation of precipitation extremes over the Asian domain: observation and modelling studies. *Clim. Dyn.* 52, 1317–1342. doi:10.1007/s00382-018-4193-4.

Kim, J., Waliser, D. E., Mattmann, C. A., Goodale, C. E., Hart, A. F., Zimdars, P. A., et al. (2014b). Evaluation of the CORDEX-Africa multi-RCM hindcast: systematic model errors. *Clim. Dyn.* 42, 1189–1202. doi:10.1007/s00382-013-1751-7.

Kim, Y.-H., Min, S.-K., Stone, D. A. D. A., Shiogama, H., and Wolski, P. (2018c). Multi-model event attribution of the summer 2013 heat wave in Korea. *Weather Clim. Extrem.* 20, 33–44. doi:10.1016/j.wace.2018.03.004.

Kim, Y.-H., Min, S.-K., Zhang, X., Sillmann, J., and Sandstad, M. (2020). Evaluation of the CMIP6 multi-model ensemble for climate extreme indices. *Weather Clim. Extrem.* 29, 100269. doi:10.1016/j.wace.2020.100269.

Kim, Y. H., Min, S. K., Zhang, X., Zwiers, F., Alexander, L. V., Donat, M. G., et al. (2016). Attribution of extreme temperature changes during 1951–2010. *Clim. Dyn.* 46, 1769–1782. doi:10.1007/s00382-015-2674-2.

King, A. D. (2017). Attributing Changing Rates of Temperature Record Breaking to Anthropogenic Influences. *Earth's Futur.* 5, 1156–1168. doi:10.1002/2017EF000611.

King, A. D., Black, M. T., Karoly, D. J., and Donat, M. G. (2015a). Increased Likelihood of Brisbane, Australia, G20 Heat Event Due to Anthropogenic Climate Change. *Bull. Am. Meteorol. Soc.* 96, S141–S144. doi:10.1175/BAMS-D-15-00098.1.

King, A. D., Black, M. T., Min, S.-K., Fischer, E. M., Mitchell, D. M., Harrington, L. J., et al. (2016a). Emergence of heat extremes attributable to anthropogenic influences. *Geophys. Res. Lett.* 43, 3438–3443. doi:10.1002/2015GL067448.

King, A. D., Jan van Oldenborgh, G., Karoly, D. J., Lewis, S. C., and Cullen, H. (2015b). Attribution of the record high

ACCEPTED VERSION SUBJECT TO FINAL EDITING

Central England temperature of 2014 to anthropogenic influences. *Environ. Res. Lett.* 10, 054002. doi:10.1088/1748-9326/10/5/054002.

King, A. D., Karoly, D. J., Donat, M. G., and Alexander, L. V. (2014). Climate change turns Australia's 2013 big dry into a year of record-breaking heat [in "Explaining Extreme Events of 2013 from a Climate Perspective"]. *Bull. Am. Meteorol. Soc.* 95, S41–S45. doi:10.1175/1520-0477-95.9.S41.

King, A. D., Karoly, D. J., and van Oldenborgh, G. J. (2016b). Climate Change and El Niño Increase Likelihood of Indonesian Heat and Drought. *Bull. Am. Meteorol. Soc.* 97, S113–S117. doi:10.1175/BAMS-D-16-0164.1.

King, A. D., Knutti, R., Uhe, P., Mitchell, D. M., Lewis, S. C., Arblaster, J. M., et al. (2018). On the linearity of local and regional temperature changes from 1.5°C to 2°C of global warming. *J. Clim.*, JCLI-D-17-0649.1. doi:10.1175/JCLI-D-17-0649.1.

Kingston, D. G., Stagge, J. H., Tallaksen, L. M., and Hannah, D. M. (2015). European-scale drought: Understanding connections between atmospheric circulation and meteorological drought indices. *J. Clim.* 28, 505–516. doi:10.1175/JCLI-D-14-00001.1.

Kinter, J. L., Cash, B., Achuthavarier, D., Adams, J., Altshuler, E., Dirmeyer, P., et al. (2013). Revolutionizing climate modeling with project athena: A multi-institutional, international collaboration. *Bull. Am. Meteorol. Soc.* 94, 231–245. doi:10.1175/BAMS-D-11-00043.1.

Kirchmeier-Young, M. C., and Zhang, X. (2020). Human influence has intensified extreme precipitation in North America. *Proc. Natl. Acad. Sci.* 117, 13308–13313. doi:10.1073/pnas.1921628117.

Kirchmeier-Young, M. C., Wan, H., Zhang, X., and Seneviratne, S. I. (2019). Importance of Framing for Extreme Event Attribution: The Role of Spatial and Temporal Scales. *Earth's Futur.* 7, 1192–1204. doi:10.1029/2019EF001253.

Kirono, D. G. C., Hennessy, K. J., and Grose, M. R. (2017). Increasing risk of months with low rainfall and high temperature in southeast Australia for the past 150 years. *Clim. Risk Manag.* 16, 10–21. doi:10.1016/j.crm.2017.04.001.

Kirono, D. G. C., Round, V., Heady, C., Chiew, F. H. S., and Osbrough, S. (2020). Drought projections for Australia: Updated results and analysis of model simulations. *Weather Clim. Extrem.* 30, 100280. doi:10.1016/j.wace.2020.100280.

Kirshbaum, D. J., Merlis, T. M., Gyakum, J. R., and McTaggart-Cowan, R. (2017). Sensitivity of Idealized Moist Baroclinic Waves to Environmental Temperature and Moisture Content. *J. Atmos. Sci.* 75, 337–360. doi:10.1175/jas-d-17-0188.1.

Kishtawal, C. M., Jaiswal, N., Singh, R., and Niyogi, D. (2012). Tropical cyclone intensification trends during satellite era (1986-2010). *Geophys. Res. Lett.* 39, 1–6. doi:10.1029/2012GL051700.

Kitoh, A., and Endo, H. (2019). Future Changes in Precipitation Extremes Associated with Tropical Cyclones Projected by Large-Ensemble Simulations. *J. Meteorol. Soc. Japan. Ser. II* 97, 141–152. doi:10.2151/jmsj.2019-007.

Kjeldsen, T. R., Macdonald, N., Lang, M., Mediero, L., Albuquerque, T., Bogdanowicz, E., et al. (2014). Documentary evidence of past floods in Europe and their utility in flood frequency estimation. *J. Hydrol.* 517, 963–973. doi:10.1016/j.jhydrol.2014.06.038.

Klerk, W. J., Winsemius, H. C., van Verseveld, W. J., Bakker, A. M. R., and Diermanse, F. L. M. (2015). The co-incidence of storm surges and extreme discharges within the Rhine–Meuse Delta. *Environ. Res. Lett.* 10, 035005. doi:10.1088/1748-9326/10/3/035005.

Klutse, N. A. B., Ajayi, V. O., Gbobaniyi, E. O., Egbebiyi, T. S., Kouadio, K., Nkrumah, F., et al. (2018). Potential impact of 1.5 °C and 2 °C global warming on consecutive dry and wet days over West Africa. *Environ. Res. Lett.* 13, 055013. doi:10.1088/1748-9326/aab37b.

Klutse, N. A. B., Sylla, M. B., Diallo, I., Sarr, A., Dosio, A., Diedhiou, A., et al. (2016). Daily characteristics of West African summer monsoon precipitation in CORDEX simulations. *Theor. Appl. Climatol.* 123, 369–386. doi:10.1007/s00704-014-1352-3.

Knapp, K. R., Velden, C. S., Wimmers, A. J., Knapp, K. R., Velden, C. S., and Wimmers, A. J. (2018). A Global Climatology of Tropical Cyclone Eyes. *Mon. Weather Rev.* 146, 2089–2101. doi:10.1175/MWR-D-17-0343.1.

Knighton, J., Connely, J., and Walter, M. T. (2019). Possible Increases in Flood Frequency Due to the Loss of Eastern Hemlock in the Northeastern United States: Observational Insights and Predicted Impacts. *Water Resour. Res.* 55, 5342–5359. doi:10.1029/2018WR024395.

Knutson, T., Camargo, S. J., Chan, J. C. L., Emanuel, K., Ho, C.-H., Kossin, J., et al. (2019). Tropical Cyclones and Climate Change Assessment: Part I: Detection and Attribution. *Bull. Am. Meteorol. Soc.* 100, 1987–2007. doi:10.1175/BAMS-D-18-0189.1.

Knutson, T., Camargo, S. J., Chan, J. C. L., Emanuel, K., Ho, C.-H., Kossin, J., et al. (2020). Tropical Cyclones and Climate Change Assessment: Part II. Projected Response to Anthropogenic Warming. *Bull. Am. Meteorol. Soc.* 101, E303–E322. doi:10.1175/BAMS-D-18-0194.1.

Knutson, T. R., Sirutis, J. J., Vecchi, G. A., Garner, S., Zhao, M., Kim, H.-S., et al. (2013a). Dynamical Downscaling Projections of Twenty-First-Century Atlantic Hurricane Activity: CMIP3 and CMIP5 Model-Based Scenarios. *J. Clim.* 26, 6591–6617. doi:10.1175/JCLI-D-12-00539.1.

Knutson, T. R., Sirutis, J. J., Zhao, M., Tuleya, R. E., Bender, M., Vecchi, G. A., et al. (2015). Global Projections of

ACCEPTED VERSION SUBJECT TO FINAL EDITING

Intense Tropical Cyclone Activity for the Late Twenty-First Century from Dynamical Downscaling of CMIP5/RCP4.5 Scenarios. *J. Clim.* 28, 7203–7224. doi:10.1175/JCLI-D-15-0129.1.

Knutson, T. R., and Zeng, F. (2018). Model Assessment of Observed Precipitation Trends over Land Regions: Detectable Human Influences and Possible Low Bias in Model Trends. *J. Clim.* 31, 4617–4637. doi:10.1175/JCLI-D-17-0672.1.

Knutson, T. R., Zeng, F., and Wittenberg, A. T. (2013b). Multimodel assessment of regional surface temperature trends: CMIP3 and CMIP5 twentieth-century simulations. *J. Clim.* 26, 8709–8743. doi:10.1175/JCLI-D-12-00567.1.

Knutson, T. R., Zeng, F., and Wittenberg, A. T. (2014a). Multimodel assessment of extreme annual-mean warm anomalies during 2013 over regions of Australia and the western tropical Pacific [in "Explaining Extreme Events of 2013 from a Climate Perspective"]. *Bull. Am. Meteorol. Soc.* 95, S26–S30. doi:10.1175/1520-0477-95.9.S1.1.

Knutson, T., Zeng, F., and Wittenberg, A. (2014b). Seasonal and annual mean precipitation extremes during during 2013: A U.S. focused analysis [in "Explaining Extreme Events of 2013 from a Climate Perspective"]. *Bull. Am. Meteorol. Soc.* 95, S19–S23. doi:10.1175/1520-0477-95.9.S1.1.

Kodama, C., Stevens, B., Mauritsen, T., Seiki, T., and Satoh, M. (2019). A New Perspective for Future Precipitation Change from Intense Extratropical Cyclones. *Geophys. Res. Lett.* 46. doi:10.1029/2019GL084001.

Kodama, C., Yamada, Y., Noda, A. T., Kikuchi, K., Kajikawa, Y., Nasuno, T., et al. (2015). A 20-year climatology of a NICAM AMIP-type simulation. *J. Meteorol. Soc. Japan* 93, 393–424. doi:10.2151/jmsj.2015-024.

Kogan, F., and Guo, W. (2017). Strong 2015–2016 El Niño and implication to global ecosystems from space data. *Int. J. Remote Sens.* 38, 161–178. doi:10.1080/01431161.2016.1259679.

Konapala, G., and Mishra, A. (2017). Review of complex networks application in hydroclimatic extremes with an implementation to characterize spatio-temporal drought propagation in continental USA. *J. Hydrol.* 555, 600–620. doi:10.1016/j.jhydrol.2017.10.033.

Konapala, G., and Mishra, A. (2020). Quantifying Climate and Catchment Control on Hydrological Drought in the Continental United States. *Water Resour. Res.* 56. doi:10.1029/2018WR024620.

Kong, Q., Guerreiro, S. B., Blenkinsop, S., Li, X.-F., and Fowler, H. J. (2020). Increases in summertime concurrent drought and heatwave in Eastern China. *Weather Clim. Extrem.* 28, 100242. doi:10.1016/j.wace.2019.100242.

Konings, A. G., Williams, A. P., and Gentine, P. (2017). Sensitivity of grassland productivity to aridity controlled by stomatal and xylem regulation. *Nat. Geosci.* 10, 284. doi:10.1038/ngeo2903.

Kooperman, G. J., Fowler, M. D., Hoffman, F. M., Koven, C. D., Lindsay, K., Pritchard, M. S., et al. (2018). Plant Physiological Responses to Rising CO2 Modify Simulated Daily Runoff Intensity With Implications for Global-Scale Flood Risk Assessment. *Geophys. Res. Lett.* 45, 12,412-457,466. doi:10.1029/2018GL079901.

Kornhuber, K., Coumou, D., Vogel, E., Lesk, C., Donges, J. F., Lehmann, J., et al. (2020). Amplified Rossby waves enhance risk of concurrent heatwaves in major breadbasket regions. *Nat. Clim. Chang.* 10, 48–53. doi:10.1038/s41558-019-0637-z.

Kornhuber, K., Osprey, S., Coumou, D., Petri, S., Petoukhov, V., Rahmstorf, S., et al. (2019). Extreme weather events in early summer 2018 connected by a recurrent hemispheric wave-7 pattern. *Environ. Res. Lett.* 14, 54002. doi:10.1088/1748-9326/ab13bf.

Kossin, J. P. (2017). Hurricane intensification along United States coast suppressed during active hurricane periods. *Nature* 541, 390–393. doi:10.1038/nature20783.

Kossin, J. P. (2018). A global slowdown of tropical-cyclone translation speed. *Nature* 558, 104–107. doi:10.1038/s41586-018-0158-3.

Kossin, J. P. (2019). Reply to: Moon, I.-J. et al.; Lanzante, J. R. *Nature* 570, E16–E22. doi:10.1038/s41586-019-1224-1.

Kossin, J. P., Emanuel, K. A., and Camargo, S. J. (2016a). Past and Projected Changes in Western North Pacific Tropical Cyclone Exposure. *J. Clim.* 29, 5725–5739. doi:10.1175/JCLI-D-16-0076.1.

Kossin, J. P., Emanuel, K. A., and Vecchi, G. A. (2014). The poleward migration of the location of tropical cyclone maximum intensity. *Nature*, 4–7. doi:10.1038/nature13278.

Kossin, J. P., Emanuel, K. A., and Vecchi, G. A. (2016b). Comment on 'Roles of interbasin frequency changes in the poleward shifts of the maximum intensity location of tropical cyclones.' *Environ. Res. Lett.* 11, 068001. doi:10.1088/1748-9326/11/6/068001.

Kossin, J. P., Hall, T., Knutson, T., Kunkel, K. E., Trapp, R. J., Waliser, D. E., et al. (2017). "Extreme Storms. Climate Science Special Report: Fourth National Climate Assessment, Volume I," in *Climate Science Special Report: Fourth National Climate Assessment, Volume I*, eds. D. J. Wuebbles, D. W. Fahey, K. A. Hibbard, D. J. Dokken, B. C. Stewart, and T. K. Maycock (Washington, DC, USA: U.S. Global Change Research Program), 257–276. doi:10.7930/J07S7KXX.

Kossin, J. P., Knapp, K. R., Olander, T. L., and Velden, C. S. (2020). Global increase in major tropical cyclone exceedance probability over the past four decades. *Proc. Natl. Acad. Sci.* 117, 11975–11980. doi:10.1073/pnas.1920849117.

Kossin, J. P., Olander, T. L., and Knapp, K. R. (2013). Trend analysis with a new global record of tropical cyclone intensity. *J. Clim.* 26, 9960–9976. doi:10.1175/JCLI-D-13-00262.1.

Koster, R. D., Chang, Y., Wang, H., and Schubert, S. D. (2016). Impacts of Local Soil Moisture Anomalies on the

ACCEPTED VERSION SUBJECT TO FINAL EDITING

Atmospheric Circulation and on Remote Surface Meteorological Fields during Boreal Summer: A Comprehensive Analysis over North America. *J. Clim.* 29, 7345–7364. doi:10.1175/JCLI-D-16-0192.1.

Koster, R. D., Guo, Z., Yang, R., Dirmeyer, P. A., Mitchell, K., and Puma, M. J. (2009). On the Nature of Soil Moisture in Land Surface Models. *J. Clim.* 22, 4322–4335. doi:10.1175/2009JCLI2832.1.

Koster, R. D., Mahanama, S. P. P., Yamada, T. J., Balsamo, G., Berg, A. A., Boisserie, M., et al. (2011). The second phase of the global land-atmosphere coupling experiment: Soil moisture contributions to subseasonal forecast skill. *J. Hydrometeorol.* 12, 805–822. doi:10.1175/2011JHM1365.1.

Krishnan, R., Sabin, T. P., Vellore, R., Mujumdar, M., Sanjay, J., Goswami, B. N., et al. (2016). Deciphering the desiccation trend of the South Asian monsoon hydroclimate in a warming world. *Clim. Dyn.* 47, 1007–1027. doi:10.1007/s00382-015-2886-5.

Krueger, O., Schenk, F., Feser, F., and Weisse, R. (2013). Inconsistencies between long-term trends in storminess derived from the 20CR reanalysis and observations. *J. Clim.* 26, 868–874. doi:10.1175/JCLI-D-12-00309.1.

Krug, A., Primo, C., Fischer, S., Schumann, A., and Ahrens, B. (2020). On the temporal variability of widespread rain-on-snow floods. *Meteorol. Zeitschrift* 29, 147–163. doi:10.1127/METZ/2020/0989.

Kruger, A. C., and Nxumalo, M. (2017). Surface temperature trends from homogenized time series in South Africa: 1931--2015. *Int. J. Climatol.* 37, 2364–2377.

Kruger, A. C., Rautenbach, H., Mbatha, S., Ngwenya, S., and Makgoale, T. E. (2019). Historical and projected trends in near-surface temperature indices for 22 locations in South Africa. *S. Afr. J. Sci.* 115. doi:10.17159/sajs.2019/4846.

Kruger, A. C., and Sekele, S. S. (2013). Trends in extreme temperature indices in South Africa: 1962-2009. *Int. J. Climatol.* 33, 661–676. doi:10.1002/joc.3455.

Krysanova, V., Vetter, T., Eisner, S., Huang, S., Pechlivanidis, I., Strauch, M., et al. (2017). Intercomparison of regional-scale hydrological models and climate change impacts projected for 12 large river basins worldwide - A synthesis. *Environ. Res. Lett.* 12. doi:10.1088/1748-9326/aa8359.

Kubota, H., Matsumoto, J., Zaiki, M., Tsukahara, T., Mikami, T., Allan, R., et al. (2021). Tropical cyclones over the western north Pacific since the mid-nineteenth century. *Clim. Change* 164, 29. doi:10.1007/s10584-021-02984-7.

Kuleshov, Y., Fawcett, R., Qi, L., Trewin, B., Jones, D., McBride, J., et al. (2010). Trends in tropical cyclones in the South Indian Ocean and the South Pacific Ocean. *J. Geophys. Res. Atmos.* 115. doi:10.1029/2009JD012372.

Kumar, S., Allan, R. P., Zwiers, F., Lawrence, D. M., and Dirmeyer, P. A. (2015). Revisiting trends in wetness and dryness in the presence of internal climate variability and water limitations over land. *Geophys. Res. Lett.* 42, 10,867-10,875. doi:10.1002/2015GL066858.

Kumar, S. P. and R. S. N. and D. N. (2017). Linkage between global sea surface temperature and hydroclimatology of a major river basin of India before and after 1980. *Environ. Res. Lett.* 12, 124002. doi:10.1088/1748-9326/aa9664.

Kundzewicz, Z. W., Pin'skwar, I., and Brakenridge, G. R. (2018). Changes in river flood hazard in Europe: A review. *Hydrol. Res.* 49, 294–302. doi:10.2166/nh.2017.016.

Kunii, M., Otsuka, M., Shimoji, K., and Seko, H. (2016). Ensemble Data Assimilation and Forecast Experiments for the September 2015 Heavy Rainfall Event in Kanto and Tohoku Regions with Atmospheric Motion Vectors from Himawari-8. *SOLA* 12, 209–214. doi:10.2151/sola.2016-042.

Kunkel, K. E., Karl, T. R., Brooks, H., Kossin, J., Lawrimore, J. H., Arndt, D., et al. (2013). Monitoring and understanding trends in extreme storms: State of knowledge. *Bull. Am. Meteorol. Soc.* 94, 499–514. doi:10.1175/BAMS-D-11-00262.1.

Kusunoki, S. (2017). Future Changes in Global Precipitation Projected by the Atmospheric Model MRI-AGCM3.2H with a 60-km Size. *Atmos.* 8. doi:10.3390/atmos8050093.

Kusunoki, S. (2018a). Future changes in precipitation over East Asia projected by the global atmospheric model MRI-AGCM3.2. *Clim. Dyn.* 51, 4601–4617. doi:10.1007/s00382-016-3499-3.

Kusunoki, S. (2018b). Is the global atmospheric model MRI-AGCM3.2 better than the CMIP5 atmospheric models in simulating precipitation over East Asia? *Clim. Dyn.* 51, 4489–4510. doi:10.1007/s00382-016-3335-9.

Kusunoki, S., and Mizuta, R. (2013). Changes in precipitation intensity over East Asia during the 20th and 21st centuries simulated by a global atmospheric model with a 60 km grid size. *J. Geophys. Res. Atmos.* 118, 11,007-11,016. doi:10.1002/jgrd.50877.

Kusunoki, S., Nakaegawa, T., Pinzón, R., Sanchez-Galan, J. E., and Fábrega, J. R. (2019). Future precipitation changes over Panama projected with the atmospheric global model MRI-AGCM3.2. *Clim. Dyn.* 53, 5019–5034. doi:10.1007/s00382-019-04842-w.

Lackmann, G. M. (2013). The south-central U.S. flood of may 2010: Present and future. *J. Clim.* 26, 4688–4709. doi:10.1175/JCLI-D-12-00392.1.

Lackmann, G. M. (2015). Hurricane Sandy before 1900 and after 2100. *Bull. Am. Meteorol. Soc.* 96, 547–560. doi:10.1175/BAMS-D-14-00123.1.

Laliberté, F., Howell, S. E. L., and Kushner, P. J. (2015). Regional variability of a projected sea ice-free Arctic during the summer months. *Geophys. Res. Lett.* 43, 256–263. doi:10.1002/2015GL066855.

Landsea, C. W. (2015). Comments on "Monitoring and understanding trends in extreme storms: state of knowledge.". *Bull. Am. Meteorol. Soc.* 96, 1175–1182. doi:10.1175/1520-0477-96.7.1175.

ACCEPTED VERSION SUBJECT TO FINAL EDITING

Langerwisch, F., Rost, S., Gerten, D., Poulter, B., Rammig, A., and Cramer, W. (2013). Potential effects of climate change on inundation patterns in the Amazon Basin. *Hydrol. Earth Syst. Sci.* 17, 2247–2262. doi:10.5194/hess-17-2247-2013.

Lanzante, J. R. (2019). Uncertainties in tropical-cyclone translation speed. *Nature* 570, E6–E15. doi:10.1038/s41586-019-1223-2.

Lau, N.-C., and Nath, M. J. (2014). Model simulation and projection of European heat waves in present-day and future climates. *J. Clim.* 27, 3713–3730. doi:10.1175/JCLI-D-13-00284.1.

Lawal, K. A., Abatan, A. A., Angélil, O., Olaniyan, E., Olusoji, V. H., Oguntunde, P. G., et al. (2016). The Late Onset of the 2015 Wet Season in Nigeria. *Bull. Am. Meteorol. Soc.* 97, S63–S69. doi:10.1175/BAMS-D-16-0131.1.

Leach, N. J., Li, S., Sparrow, S., van Oldenborgh, G. J., Lott, F. C., Weisheimer, A., et al. (2020). Anthropogenic Influence on the 2018 Summer Warm Spell in Europe: The Impact of Different Spatio-Temporal Scales. *Bull. Am. Meteorol. Soc.* 101, S41–S46. doi:10.1175/BAMS-D-19-0201.1.

Lee, C.-Y., Camargo, S. J., Sobel, A. H., and Tippett, M. K. (2020a). Statistical–Dynamical Downscaling Projections of Tropical Cyclone Activity in a Warming Climate: Two Diverging Genesis Scenarios. *J. Clim.* 33, 4815–4834. doi:10.1175/JCLI-D-19-0452.1.

Lee, C. Y., Tippett, M. K., Sobel, A. H., and Camargo, S. J. (2018a). An environmentally forced tropical cyclone hazard model. *J. Adv. Model. Earth Syst.* 10, 223–241. doi:10.1002/2017MS001186.

Lee, D., Min, S., Fischer, E., Shiogama, H., and Bethke, I. (2018b). Impacts of half a degree additional warming on the Asian summer monsoon rainfall characteristics. *Environ. Res. Lett.* 13. doi:10.1088/1748-9326/aab55d.

Lee, J., Li, S., Lund, R., Lee, J., Li, S., and Lund, R. (2014). Trends in Extreme U.S. Temperatures. *J. Clim.* 27, 4209–4225. doi:10.1175/JCLI-D-13-00283.1.

Lee, T.-C., Knutson, T. R., Nakaegawa, T., Ying, M., and Cha, E. J. (2020b). Third assessment on impacts of climate change on tropical cyclones in the Typhoon Committee Region – Part I: Observed changes, detection and attribution. *Trop. Cyclone Res. Rev.* 9, 1–22. doi:10.1016/j.tcrr.2020.03.001.

Lee, W., Choi, H. M., Kim, D., Honda, Y., Guo, Y.-L. L., and Kim, H. (2018c). Temporal changes in mortality attributed to heat extremes for 57 cities in Northeast Asia. *Sci. Total Environ.* 616–617, 703–709. doi:10.1016/j.scitotenv.2017.10.258.

Lehner, F., Coats, S., Stocker, T. F., Pendergrass, A. G., Sanderson, B. M., Raible, C. C., et al. (2017). Projected drought risk in 1.5°C and 2°C warmer climates. *Geophys. Res. Lett.* 44, 7419–7428. doi:10.1002/2017GL074117.

Lehner, F., Deser, C., Simpson, I. R., and Terray, L. (2018). Attributing the U.S. Southwest's Recent Shift Into Drier Conditions. *Geophys. Res. Lett.* 45, 6251–6261. doi:10.1029/2018GL078312.

Lehner, F., and Stocker, T. F. (2015). From local perception to global perspective. *Nat. Clim. Chang.* 5, 731–734. doi:10.1038/nclimate2660.

Lejeune, Q., Davin, E. L., Gudmundsson, L., Winckler, J., and Seneviratne, S. I. (2018). Historical deforestation locally increased the intensity of hot days in northern mid-latitudes. *Nat. Clim. Chang.* 8, 386–390. doi:10.1038/s41558-018-0131-z.

Lejeune, Q., Seneviratne, S. I., and Davin, E. L. (2017). Historical Land-Cover Change Impacts on Climate: Comparative Assessment of LUCID and CMIP5 Multimodel Experiments. *J. Clim.* 30, 1439–1459. doi:10.1175/JCLI-D-16-0213.1.

Lelieveld, J., Proestos, Y., Hadjinicolaou, P., Tanarhte, M., Tyrlis, E., and Zittis, G. (2016). Strongly increasing heat extremes in the Middle East and North Africa (MENA) in the 21st century. *Clim. Change* 137, 245–260. doi:10.1007/s10584-016-1665-6.

Lemordant, L., Gentine, P., Stéfanon, M., Drobinski, P., and Fatichi, S. (2016). Modification of land-atmosphere interactions by CO2 effects: Implications for summer dryness and heat wave amplitude. *Geophys. Res. Lett.* 43, 10,240-10,248. doi:10.1002/2016GL069896.

Lemordant, L., Gentine, P., Swann, A. S., Cook, B. I., and Scheff, J. (2018). Critical impact of vegetation physiology on the continental hydrologic cycle in response to increasing CO2. *Proc. Natl. Acad. Sci.* 115, 4093–4098. doi:10.1073/pnas.1720712115.

Lenderink, G., Barbero, R., Loriaux, J. M., and Fowler, H. J. (2017). Super-Clausius–Clapeyron Scaling of Extreme Hourly Convective Precipitation and Its Relation to Large-Scale Atmospheric Conditions. *J. Clim.* 30, 6037–6052. doi:10.1175/JCLI-D-16-0808.1.

Lewis, E., Fowler, H., Alexander, L., Dunn, R., McClean, F., Barbero, R., et al. (2019a). GSDR: A Global Sub-Daily Rainfall Dataset. *J. Clim.* 32, 4715–4729. doi:10.1175/JCLI-D-18-0143.1.

Lewis, S. C., Blake, S. A. P., Trewin, B., Black, M. T., Dowdy, A. J., Perkins-Kirkpatrick, S. E., et al. (2019b). Deconstructing factors contributing to the 2018 fire weather in Queensland, Australia. *Bull. Am. Meteorol. Soc.*, BAMS-D-19-0144.1. doi:10.1175/BAMS-D-19-0144.1.

Lewis, S. C., and Karoly, D. J. (2013). Anthropogenic contributions to Australia's record summer temperatures of 2013. *Geophys. Res. Lett.* 40, 3705–3709. doi:10.1002/grl.50673.

Lewis, S. C., and Karoly, D. J. (2014). The Role of Anthropogenic Forcing in the Record 2013 Australia-Wide Annual and Spring Temperatures [in "Explaining Extreme Events of 2013 from a Climate Perspective"]. *Bull. Am. Meteorol. Soc.* 95, S31--S34. doi:10.1175/1520-0477-95.9.S1.1.

ACCEPTED VERSION SUBJECT TO FINAL EDITING

Lewis, S. C., and King, A. D. (2015). Dramatically increased rate of observed hot record breaking in recent Australian temperatures. *Geophys. Res. Lett.* 42, 7776–7784. doi:10.1002/2015GL065793.
Lewis, S. C., King, A. D., and Mitchell, D. M. (2017a). Australia's Unprecedented Future Temperature Extremes Under Paris Limits to Warming. *Geophys. Res. Lett.* 44, 9947–9956.
Lewis, S. C., King, A. D., and Perkins-Kirkpatrick, S. E. (2017b). Defining a New Normal for Extremes in a Warming World. *Bull. Am. Meteorol. Soc.* 98, 1139–1151. doi:10.1175/BAMS-D-16-0183.1.
Lewis, S. L., Brando, P. M., Phillips, O. L., van der Heijden, G. M. F., and Nepstad, D. (2011). The 2010 Amazon Drought. *Science (80-.).* 331, 554–554. doi:10.1126/science.1200807.
Lhotka, O., Kyselý, J., and Farda, A. (2018). Climate change scenarios of heat waves in Central Europe and their uncertainties. *Theor. Appl. Climatol.* 131, 1043–1054. doi:10.1007/s00704-016-2031-3.
Li, C., Fang, Y., Caldeira, K., Zhang, X., Diffenbaugh, N. S., and Michalak, A. M. (2018a). Widespread persistent changes to temperature extremes occurred earlier than predicted. *Sci. Rep.* 8, 1007. doi:10.1038/s41598-018-19288-z.
Li, C., Zhang, X., Zwiers, F., Fang, Y., and Michalak, A. M. (2017a). Recent Very Hot Summers in Northern Hemispheric Land Areas Measured by Wet Bulb Globe Temperature Will Be the Norm Within 20 Years. *Earth's Futur.* 5, 1203–1216. doi:10.1002/2017EF000639.
Li, C., Zwiers, F., Zhang, X., Chen, G., Lu, J., Li, G., et al. (2019a). Larger Increases in More Extreme Local Precipitation Events as Climate Warms. *Geophys. Res. Lett.* 46, 6885–6891. doi:10.1029/2019GL082908.
Li, C., Zwiers, F., Zhang, X., and Li, G. (2018b). How much information is required to well-constrain local estimates of future precipitation extremes? *Earth's Futur.*, 2018EF001001. doi:10.1029/2018EF001001.
Li, C., Zwiers, F., Zhang, X., Li, G., Sun, Y., and Wehner, M. (2020a). Changes in annual extremes of daily temperature and precipitation in CMIP6 models. *J. Clim.* (submitted, 1–61. doi:10.1175/JCLI-D-19-1013.1.
Li, D., Lettenmaier, D. P., Margulis, S. A., and Andreadis, K. (2019b). The Role of Rain-on-Snow in Flooding Over the Conterminous United States. *Water Resour. Res.* 55, 8492–8513. doi:10.1029/2019WR024950.
Li, D., Zhou, T., Zou, L., Zhang, W., and Zhang, L. (2018c). Extreme High-Temperature Events Over East Asia in 1.5°C and 2°C Warmer Futures: Analysis of NCAR CESM Low-Warming Experiments. *Geophys. Res. Lett.* 45, 1541–1550. doi:10.1002/2017GL076753.
Li, G., Zhang, X., Cannon, A. J., Murdock, T., Sobie, S., Zwiers, F., et al. (2018d). Indices of Canada's future climate for general and agricultural adaptation applications. *Clim. Change* 148, 249–263. doi:10.1007/s10584-018-2199-x.
Li, H., Chen, H., and Wang, H. (2017b). Effects of anthropogenic activity emerging as intensified extreme precipitation over China. *J. Geophys. Res. Atmos.* 122, 6899–6914. doi:10.1002/2016JD026251.
Li, H., and Sriver, R. L. (2018). Tropical Cyclone Activity in the High-Resolution Community Earth System Model and the Impact of Ocean Coupling. *J. Adv. Model. Earth Syst.* 10, 165–186. doi:10.1002/2017MS001199.
Li, L., She, D., Zheng, H., Lin, P., and Yang, Z.-L. (2020b). Elucidating diverse drought characteristics from two meteorological drought indices (SPI and SPEI) in China. *J. Hydrometeorol.* 21, 1513–1530. doi:10.1175/JHM-D-19-0290.s1.
Li, L., Yao, N., Li, Y., Liu, D. L., Wang, B., and Ayantobo, O. O. (2019c). Future projections of extreme temperature events in different sub-regions of China. *Atmos. Res.* 217, 150–164. doi:10.1016/j.atmosres.2018.10.019.
Li, M. (2017). Temperature reconstruction and volcanic eruption signal from tree-ring width and maximum latewood density over the past 304 years in the southeastern Tibetan Plateau. 2021–2032. doi:10.1007/s00484-017-1395-0.
Li, M., Woollings, T., Hodges, K., and Masato, G. (2014). Extratropical cyclones in a warmer, moister climate: A recent Atlantic analogue. *Geophys. Res. Lett.* 41, 8594–8601. doi:10.1002/2014GL062186.
Li, S., Otto, F. E. L., Harrington, L. J., Sparrow, S. N., Wallom, D., Wallom, S. L. and F. E. L. O. and L. J. H. and S. N. S. and D., et al. (2019d). A pan-South-America assessment of avoided exposure to dangerous extreme precipitation by limiting to 1.5 °C warming. *Environ. Res. Lett.* doi:10.1088/1748-9326/ab50a2.
Li, W., Jiang, Z., Zhang, X., and Li, L. (2018e). On the Emergence of Anthropogenic Signal in Extreme Precipitation Change Over China. *Geophys. Res. Lett.* doi:10.1029/2018GL079133.
Li, W., Jiang, Z., Zhang, X., Li, L., and Sun, Y. (2018f). Additional risk in extreme precipitation in China from 1.5 °C to 2.0 °C global warming levels. *Sci. Bull.* 63, 228–234. doi:10.1016/j.scib.2017.12.021.
Li, X., Liu, L., Li, H., Wang, S., and Heng, J. (2020c). Spatiotemporal soil moisture variations associated with hydro-meteorological factors over the Yarlung Zangbo River basin in Southeast Tibetan Plateau. *Int. J. Climatol.* 40, 188–206. doi:10.1002/joc.6202.
Li, X., Wang, X., and Babovic, V. (2018g). Analysis of variability and trends of precipitation extremes in Singapore during 1980–2013. *Int. J. Climatol.* 38, 125–141. doi:10.1002/joc.5165.
Li, X., You, Q., Ren, G., Wang, S., Zhang, Y., Yang, J., et al. (2019e). Concurrent droughts and hot extremes in northwest China from 1961 to 2017. *Int. J. Climatol.* 39, 2186–2196. doi:10.1002/joc.5944.
Li, Y., Zhao, M., Motesharrei, S., Mu, Q., Kalnay, E., and Li, S. (2015). Local cooling and warming effects of forests based on satellite observations. *Nat. Commun.* 6, 6603. doi:10.1038/ncomms7603.
Li, Z., Chen, Y., Fang, G., and Li, Y. (2017c). Multivariate assessment and attribution of droughts in Central Asia. *Sci. Rep.* 7, 1316. doi:10.1038/s41598-017-01473-1.

ACCEPTED VERSION SUBJECT TO FINAL EDITING

Li, Z., Chen, Y., Shen, Y., Liu, Y., and Zhang, S. (2013). Analysis of changing pan evaporation in the arid region of Northwest China. *Water Resour. Res.* 49, 2205–2212. doi:10.1002/wrcr.20202.
Lian, X., Piao, S., Li, L. Z. X., Li, Y., Huntingford, C., Ciais, P., et al. (2020). Summer soil drying exacerbated by earlier spring greening of northern vegetation. *Sci. Adv.* 6, eaax0255. doi:10.1126/sciadv.aax0255.
Liang, C., Chen, T., Dolman, H., Shi, T., Wei, X., Xu, J., et al. (2020). Drying and wetting trends and vegetation covariations in the drylands of China. *Water (Switzerland)* 12. doi:10.3390/W12040933.
Liang, J., Wang, C., and Hodges, K. I. (2017). Evaluation of tropical cyclones over the South China Sea simulated by the 12 km MetUM regional climate model. *Q. J. R. Meteorol. Soc.* 143, 1641–1656. doi:10.1002/qj.3035.
Libertino, A., Ganora, D., and Claps, P. (2019). Evidence for Increasing Rainfall Extremes Remains Elusive at Large Spatial Scales: The Case of Italy. *Geophys. Res. Lett.* 46, 7437–7446. doi:10.1029/2019GL083371.
Lin, C., Yang, K., Qin, J., and Fu, R. (2013). Observed Coherent Trends of Surface and Upper-Air Wind Speed over China since 1960. *J. Clim.* 26, 2891–2903. doi:10.1175/JCLI-D-12-00093.1.
Lin, L., Wang, Z., Xu, Y., and Fu, Q. (2016). Sensitivity of precipitation extremes to radiative forcing of greenhouse gases and aerosols. *Geophys. Res. Lett.* 43, 9860–9868. doi:10.1002/2016GL070869.
Lin, L., Wang, Z., Xu, Y., Fu, Q., and Dong, W. (2018). Larger Sensitivity of Precipitation Extremes to Aerosol Than Greenhouse Gas Forcing in CMIP5 Models. *J. Geophys. Res. Atmos.* doi:10.1029/2018JD028821.
Lin, N., Lane, P., Emanuel, K. A., Sullivan, R. M., and Donnelly, J. P. (2014). Heightened hurricane surge risk in northwest Florida revealed from climatological-hydrodynamic modeling and paleorecord reconstruction. *J. Geophys. Res. Atmos.* 119, 8606–8623. doi:10.1002/2014JD021584.
Lin, P., He, Z., Du, J., Chen, L., Zhu, X., and Li, J. (2017). Recent changes in daily climate extremes in an arid mountain region, a case study in northwestern China's Qilian Mountains. *Sci. Rep.* 7, 1–15. doi:10.1038/s41598-017-02345-4.
Lionello, P., and Scarascia, L. (2020). The relation of climate extremes with global warming in the Mediterranean region and its north versus south contrast. *Reg. Environ. Chang.* 20, 31. doi:10.1007/s10113-020-01610-z.
Littell, J. S., Peterson, D. L., Riley, K. L., Liu, Y., and Luce, C. H. (2016). A review of the relationships between drought and forest fire in the United States. *Glob. Chang. Biol.* 22, 2353–2369. doi:10.1111/gcb.13275.
Little, C. M., Horton, R. M., Kopp, R. E., Oppenheimer, M., Vecchi, G. A., and Villarini, G. (2015). Joint projections of US East Coast sea level and storm surge. *Nat. Clim. Chang.* 5, 1114. doi:10.1038/nclimate2801.
Liu, B., Zhu, C., Su, J., Ma, S., and Xu, K. (2019a). Record-Breaking Northward Shift of the Western North Pacific Subtropical High in July 2018. *J. Meteorol. Soc. Japan. Ser. II* 97, 913–925. doi:10.2151/jmsj.2019-047.
Liu, C., and Zipser, E. J. (2015). The global distribution of largest, deepest, and most intense precipitation systems. *Geophys. Res. Lett.* 42, 3591–3595. doi:10.1002/2015GL063776.
Liu, L., Gudmundsson, L., Hauser, M., Qin, D., Li, S., and Seneviratne, S. I. (2020). Soil moisture dominates dryness stress on ecosystem production globally. *Nat. Commun.* 11, 4892. doi:10.1038/s41467-020-18631-1.
Liu, M., Shen, Y., Qi, Y., Wang, Y., and Geng, X. (2019b). Changes in precipitation and drought extremes over the past half century in China. *Atmosphere (Basel).* 10. doi:10.3390/atmos10040203.
Liu, M., Vecchi, G. A., Smith, J. A., and Knutson, T. R. (2019c). Causes of large projected increases in hurricane precipitation rates with global warming. *npj Clim. Atmos. Sci.* 2, 1–5. doi:10.1038/s41612-019-0095-3.
Liu, Q., Babanin, A. V., Zieger, S., Young, I. R., and Guan, C. (2016a). Wind and wave climate in the Arctic Ocean as observed by altimeters. *J. Clim.* 29, 7957–7975. doi:10.1175/JCLI-D-16-0219.1.
Liu, T., Huang, C. C., Pang, J., Zhou, Y., Zhang, Y., Ji, L., et al. (2014). Extraordinary hydro-climatic events during 1800 – 1600 yr BP in the Jin – Shaan Gorges along the middle Yellow River , China. *Palaeogeogr. Palaeoclimatol. Palaeoecol.* 410, 143–152. doi:10.1016/j.palaeo.2014.05.039.
Liu, W., and Sun, F. (2016). Assessing estimates of evaporative demand in climate models using observed pan evaporation over China. *J. Geophys. Res.* 121, 8329–8349. doi:10.1002/2016JD025166.
Liu, W., and Sun, F. (2017). Projecting and attributing future changes of evaporative demand over china in CMIP5 climate models. *J. Hydrometeorol.* 18, 977–991. doi:10.1175/JHM-D-16-0204.1.
Liu, Y., Pan, Z., Zhuang, Q., Miralles, D. G., Teuling, A. J., Zhang, T., et al. (2015). Agriculture intensifies soil moisture decline in Northern China. *Sci. Rep.* 5, 11261. doi:10.1038/srep11261.
Liu, Y., Wu, G., Guo, R., and Wan, R. (2016b). Changing landscapes by damming: the Three Gorges Dam causes downstream lake shrinkage and severe droughts. *Landsc. Ecol.* 31, 1883–1890. doi:10.1007/s10980-016-0391-9.
Liuzzo, L., Viola, F., and Noto, L. (2014). Wind speed and temperature trends impacts on reference evapotranspiration in Southern Italy. *Theor. Appl. Climatol.* 123. doi:10.1007/s00704-014-1342-5.
Livneh, B., and Badger, A. M. (2020). Drought less predictable under declining future snowpack. *Nat. Clim. Chang.* 10, 452–458. doi:10.1038/s41558-020-0754-8.
Llasat, M. C., Marcos, R., Turco, M., Gilabert, J., and Llasat-Botija, M. (2016). Trends in flash flood events versus convective precipitation in the Mediterranean region: The case of Catalonia. *J. Hydrol.* 541, 24–37. doi:10.1016/j.jhydrol.2016.05.040.
Lloyd-Hughes, B. (2014). The impracticality of a universal drought definition. *Theor. Appl. Climatol.* 117, 607–611. doi:10.1007/s00704-013-1025-7.
Lok, C. C. F., and Chan, J. C. L. (2018). Changes of tropical cyclone landfalls in South China throughout the twenty-

ACCEPTED VERSION SUBJECT TO FINAL EDITING

first century. *Clim. Dyn.* 51, 2467–2483. doi:10.1007/s00382-017-4023-0.
López-Franca, N., Zaninelli, P., Carril, A., Menéndez, C., and Sánchez, E. (2016). Changes in temperature extremes for 21st century scenarios over South America derived from a multi-model ensemble of regional climate models. *Clim. Res.* 68, 151–167. doi:10.3354/cr01393.
Lorenz, R., Argüeso, D., Donat, M. G., Pitman, A. J., Hurk, B. Van Den, Berg, A., et al. (2016). Influence of land-atmosphere feedbacks on temperature and precipitation extremes in the GLACE-CMIP5 ensemble. *J. Geophys. Res.* 121, 607–623. doi:10.1002/2015JD024053.
Lorenz, R., Stalhandske, Z., and Fischer, E. M. (2019). Detection of a Climate Change Signal in Extreme Heat, Heat Stress, and Cold in Europe From Observations. *Geophys. Res. Lett.* 46, 8363–8374. doi:10.1029/2019GL082062.
Lorenzo-Lacruz, J., Garcia, C., and Morán-Tejeda, E. (2017). Groundwater level responses to precipitation variability in Mediterranean insular aquifers. *J. Hydrol.* 552, 516–531. doi:10.1016/j.jhydrol.2017.07.011.
Lorenzo-Lacruz, J., Moŕan-Tejeda, E., Vicente-Serrano, S. M., and Ĺopez-Moreno, J. I. (2013). Streamflow droughts in the Iberian Peninsula between 1945 and 2005: Spatial and temporal patterns. *Hydrol. Earth Syst. Sci.* 17. doi:10.5194/hess-17-119-2013.
Lott, F. C., Christidis, N., and Stott, P. A. (2013). Can the 2011 East African drought be attributed to human-induced climate change? *Geophys. Res. Lett.* 40, 1177–1181. doi:10.1002/grl.50235.
Lott, F. C., and Stott, P. A. (2016). Evaluating Simulated Fraction of Attributable Risk Using Climate Observations. *J. Clim.* 29, 4565–4575. doi:10.1175/JCLI-D-15-0566.1.
Louise, B., Cayan, D., Franco, G., Fisher, L., and Ziaja, S. (2018). Statewide Summary Report [in "California's Fourth Climate Change Assessment"]. Available at: https://www.energy.ca.gov/sites/default/files/2019-11/Statewide_Reports-SUM-CCCA4-2018-013_Statewide_Summary_Report_ADA.pdf.
Lovino, M. A., Müller, O. V., Berbery, E. H., and Müller, G. V. (2018). How have daily climate extremes changed in the recent past over northeastern Argentina? *Glob. Planet. Change* 168, 78–97. doi:10.1016/J.GLOPLACHA.2018.06.008.
Lu, C., Sun, Y., Wan, H., Zhang, X., and Yin, H. (2016). Anthropogenic influence on the frequency of extreme temperatures in China. *Geophys. Res. Lett.* 43, 6511–6518. doi:10.1002/2016GL069296.
Lu, C., Sun, Y., and Zhang, X. (2018). Multimodel detection and attribution of changes in warm and cold spell durations. *Environ. Res. Lett.* 13, 074013. doi:10.1088/1748-9326/aacb3e.
Lu, J., Carbone, G. J., and Grego, J. M. (2019). Uncertainty and hotspots in 21st century projections of agricultural drought from CMIP5 models. *Sci. Rep.* 9, 4922. doi:10.1038/s41598-019-41196-z.
Lucas, C., Timbal, B., and Nguyen, H. (2014). The expanding tropics: a critical assessment of the observational and modeling studies. *Wiley Interdiscip. Rev. Clim. Chang.* 5, 89–112. doi:10.1002/wcc.251.
Luiz Silva, W., Xavier, L. N. R., Maceira, M. E. P., and Rotunno, O. C. (2018). Climatological and hydrological patterns and verified trends in precipitation and streamflow in the basins of Brazilian hydroelectric plants. *Theor. Appl. Climatol.* doi:10.1007/s00704-018-2600-8.
Luo, M., and Lau, N.-C. (2016). Heat Waves in Southern China: Synoptic Behavior, Long-Term Change, and Urbanization Effects. *J. Clim.* 30, 703–720. doi:10.1175/JCLI-D-16-0269.1.
Luterbacher, J., Werner, J. P., Smerdon, J. E., Fernández-Donado, L., González-Rouco, F. J., Barriopedro, D., et al. (2016). European summer temperatures since Roman times. *Environ. Res. Lett.* 11, 024001. doi:10.1088/1748-9326/11/2/024001.
Ma, S., Zhou, T., Dai, A., and Han, Z. (2015). Observed Changes in the Distributions of Daily Precipitation Frequency and Amount over China from 1960 to 2013. *J. Clim.* 28, 6960–6978. doi:10.1175/JCLI-D-15-0011.1.
Ma, S., Zhou, T., Stone, D. A., Polson, D., Dai, A., Stott, P. A., et al. (2017). Detectable Anthropogenic Shift toward Heavy Precipitation over Eastern China. *J. Clim.* 30, 1381–1396. doi:10.1175/JCLI-D-16-0311.1.
Macdonald, N., and Sangster, H. (2017). High-magnitude flooding across Britain since AD 1750. *Hydrol. Earth Syst. Sci.* 21, 1631–1650. doi:10.5194/hess-21-1631-2017.
Maček, U., Bezak, N., and Šraj, M. (2018). Reference evapotranspiration changes in Slovenia, Europe. *Agric. For. Meteorol.* 260–261, 183–192. doi:10.1016/j.agrformet.2018.06.014.
Madhura, R. K., Krishnan, R., Revadekar, J. V, Mujumdar, M., and Goswami, B. N. (2015). Changes in western disturbances over the Western Himalayas in a warming environment. *Clim. Dyn.* 44, 1157–1168. doi:10.1007/s00382-014-2166-9.
Madsen, H., Lawrence, D., Lang, M., Martinkova, M., and Kjeldsen, T. R. (2014). Review of trend analysis and climate change projections of extreme precipitation and floods in Europe. *J. Hydrol.* 519, 3634–3650. doi:10.1016/j.jhydrol.2014.11.003.
Maggioni, V., Meyers, P. C., and Robinson, M. D. (2016). A Review of Merged High-Resolution Satellite Precipitation Product Accuracy during the Tropical Rainfall Measuring Mission (TRMM) Era. *J. Hydrometeorol.* 17, 1101–1117. doi:10.1175/JHM-D-15-0190.1.
Magnusson, L., Bidlot, J.-R., Lang, S. T. K., Thorpe, A., Wedi, N., and Yamaguchi, M. (2014). Evaluation of Medium-Range Forecasts for Hurricane Sandy. *Mon. Weather Rev.* 142, 1962–1981. doi:10.1175/MWR-D-13-00228.1.
Mahoney, K. (2020). Extreme Hail Storms and Climate Change: Foretelling the Future In Tiny, Turbulent Crystal Balls? *Bull. Am. Meteorol. Soc.* 95, S17–S22. doi:10.1175/BAMS-D-19-0233.1.

ACCEPTED VERSION SUBJECT TO FINAL EDITING

Mahoney, K., Alexander, M. A., Thompson, G., Barsugli, J. J., and Scott, J. D. (2012). Changes in hail and flood risk in high-resolution simulations over Colorado's mountains. *Nat. Clim. Chang.* 2, 125–131. doi:10.1038/nclimate1344.

Mahony, C. R., and Cannon, A. J. (2018). Wetter summers can intensify departures from natural variability in a warming climate. *Nat. Commun.* 9, 783. doi:10.1038/s41467-018-03132-z.

Mahto, S. S., and Mishra, V. (2019). Does ERA-5 Outperform Other Reanalysis Products for Hydrologic Applications in India? *J. Geophys. Res. Atmos.* 124, 9423–9441. doi:10.1029/2019JD031155.

Maier, N., Breuer, L., Chamorro, A., Kraft, P., and Houska, T. (2018). Multi-Source Uncertainty Analysis in Simulating Floodplain Inundation under Climate Change. *Water* 10, 809. doi:10.3390/w10060809.

Maksimović, Č., Prodanović, D., Boonya-Aroonnet, S., Leitão, J. P., Djordjević, S., and Allitt, R. (2009). Overland flow and pathway analysis for modelling of urban pluvial flooding. *J. Hydraul. Res.* 47, 512–523. doi:10.1080/00221686.2009.9522027.

Malik, N., Bookhagen, B., and Mucha, P. J. (2016). Spatiotemporal patterns and trends of Indian monsoonal rainfall extremes. *Geophys. Res. Lett.* 43, 1710–1717. doi:10.1002/2016GL067841.

Mallakpour, I., and Villarini, G. (2015). The changing nature of flooding across the central United States. *Nat. Clim. Chang.* 5, 250–254. doi:10.1038/nclimate2516.

Manda, A., Nakamura, H., Asano, N., Iizuka, S., Miyama, T., Moteki, Q., et al. (2014). Impacts of a warming marginal sea on torrential rainfall organized under the Asian summer monsoon. *Sci. Rep.* 4, 1–6. doi:10.1038/srep05741.

Mandapaka, P. V, and Lo, E. Y. M. (2018). Assessment of future changes in Southeast Asian precipitation using the NASA Earth Exchange Global Daily Downscaled Projections data set. *Int. J. Climatol.* 38, 5231–5244. doi:10.1002/joc.5724.

Mangini, W., Viglione, A., Hall, J., Hundecha, Y., Ceola, S., Montanari, A., et al. (2018). Detection of trends in magnitude and frequency of flood peaks across Europe. *Hydrol. Sci. J.* 63, 493–512. doi:10.1080/02626667.2018.1444766.

Mankin, J. S., Seager, R., Smerdon, J. E., Cook, B. I., and Williams, A. P. (2019). Mid-latitude freshwater availability reduced by projected vegetation responses to climate change. *Nat. Geosci.* 12, 983–988. doi:10.1038/s41561-019-0480-x.

Mann, M. E., and Gleick, P. H. (2015). Climate change and California drought in the 21st century. *Proc. Natl. Acad. Sci. U. S. A.* 112, 3858–3859. doi:10.1073/pnas.1503667112.

Mann, M. E., Rahmstorf, S., Kornhuber, K., Steinman, B. A., Miller, S. K., and Coumou, D. (2017). Influence of Anthropogenic Climate Change on Planetary Wave Resonance and Extreme Weather Events. *Sci. Rep.* 7, 45242. doi:10.1038/srep45242.

Marciano, C. G., Lackmann, G. M., and Robinson, W. A. (2015). Changes in U.S. East Coast cyclone dynamics with climate change. *J. Clim.* 28, 468–484. doi:10.1175/JCLI-D-14-00418.1.

Marengo, J. A., and Espinoza, J. C. (2016). Extreme seasonal droughts and floods in Amazonia: causes, trends and impacts. *Int. J. Climatol.* 36, 1033–1050. doi:10.1002/joc.4420.

Marengo, J. A., Torres, R. R., and Alves, L. M. (2017). Drought in Northeast Brazil – past, present, and future. *Theor. Appl. Climatol.* 129, 1189–1200. doi:10.1007/s00704-016-1840-8.

Marin, L., Birsan, M. V., Bojariu, R., Dumitrescu, A., Micu, D. M., and Manea, A. (2014). An overview of annual climatic changes in Romania: Trends in air temperature, precipitation, sunshine hours, cloud cover, relative humidity and wind speed during the 1961-2013 period. *Carpathian J. Earth Environ. Sci.* 9, 253–258. Available at: http://www.cjees.ro/viewTopic.php?topicId=489.

Mariotti, A., Pan, Y., Zeng, N., and Alessandri, A. (2015). Long-term climate change in the Mediterranean region in the midst of decadal variability. *Clim. Dyn.* 44, 1437–1456. doi:10.1007/s00382-015-2487-3.

Markonis, Y., Kumar, R., Hanel, M., Rakovec, O., Máca, P., and AghaKouchak, A. (2021). The rise of compound warm-season droughts in Europe. *Sci. Adv.* 7, eabb9668. doi:10.1126/sciadv.abb9668.

Martens, B., Waegeman, W., Dorigo, W. A., Verhoest, N. E. C., and Miralles, D. G. (2018). Terrestrial evaporation response to modes of climate variability. *npj Clim. Atmos. Sci.* 1, 43. doi:10.1038/s41612-018-0053-5.

Marthews, T. R., Otto, F. E. L., Mitchell, D., Dadson, S. J., and Jones, R. G. (2015). The 2014 Drought in the Horn of Africa: Attribution of Meteorological Drivers [in "Explaining Extreme Events of 2014 from a Climate Perspective"]. *Bull. Am. Meteorol. Soc.* 96, S83–S88. doi:10.1175/BAMS-D-15-00115.1.

Martin, E. R. (2018). Future Projections of Global Pluvial and Drought Event Characteristics. *Geophys. Res. Lett.* doi:10.1029/2018GL079807.

Martin, J. T., Pederson, G. T., Woodhouse, C. A., Cook, E. R., McCabe, G. J., Anchukaitis, K. J., et al. (2020). Increased drought severity tracks warming in the United States' largest river basin. *Proc. Natl. Acad. Sci. U. S. A.* 117. doi:10.1073/pnas.1916208117.

Martinez-Austria, P., and Bandala, E. (2017). Temperature and Heat-Related Mortality Trends in the Sonoran and Mojave Desert Region. *Atmosphere (Basel).* 8, 53. doi:10.3390/atmos8030053.

Martins, E. S. P. R., Coelho, C. A. S., Haarsma, R., Otto, F. E. L., King, A. D., Jan van Oldenborgh, G., et al. (2018). A Multimethod Attribution Analysis of the Prolonged Northeast Brazil Hydrometeorological Drought (2012–16). *Bull. Am. Meteorol. Soc.* 99, S65–S69. doi:10.1175/BAMS-D-17-0102.1.

ACCEPTED VERSION SUBJECT TO FINAL EDITING

Martius, O., Pfahl, S., and Chevalier, C. (2016). A global quantification of compound precipitation and wind extremes. *Geophys. Res. Lett.* 43, 7709–7717. doi:10.1002/2016GL070017.

Marvel, K., Cook, B. I., Bonfils, C. J. W., Durack, P. J., Smerdon, J. E., and Williams, A. P. (2019). Twentieth-century hydroclimate changes consistent with human influence. *Nature* 569, 59–65. doi:10.1038/s41586-019-1149-8.

Marx, A., Kumar, R., Thober, S., Rakovec, O., Wanders, N., Zink, M., et al. (2018). Climate change alters low flows in Europe under global warming of 1.5, 2, and 3°C. *Hydrol. Earth Syst. Sci.* 22, 1017–1032. doi:10.5194/hess-22-1017-2018.

Marzin, C., Rahmat, R., Bernie, D., Bricheno, L., Buonomo, E., Calvert, D., et al. (2015). Singapore 2nd National Climate Change Study – Phase 1. Singapore: Meteorological Service Singapore Available at: http://ccrs.weather.gov.sg/Publications-Second-National-Climate-Change-Study-Science-Reports/.

Mascioli, N. R., Fiore, A. M., Previdi, M., and Correa, G. (2016). Temperature and Precipitation Extremes in the United States: Quantifying the Responses to Anthropogenic Aerosols and Greenhouse Gases. *J. Clim.* 29, 2689–2701. doi:10.1175/JCLI-D-15-0478.1.

Masseroni, D., Camici, S., Cislaghi, A., Vacchiano, G., Massari, C., and Brocca, L. (2020). 65-year changes of annual streamflow volumes across Europe with a focus on the Mediterranean basin. *Hydrol. Earth Syst. Sci. Discuss.* 2020, 1–16. doi:10.5194/hess-2020-21.

Massey, N., Aina, T., Rye, C. J., Otto, F. E. L., Wilson, S., Jones, R. G., et al. (2012). Have the odds of warm November temperature and of cold December temperatures in central England changed? [in "Explaining Extreme Events of 2011 from a Climate Perspective"]. *Bull. Am. Meteorol. Soc.* 93, 1057–1059. doi:10.1175/BAMS-D-12-00021.1.

Masson-Delmotte, V., M, S., Abe-Ouchi, A., Beer, J., Ganopolski, A., Rouco, J. F. G., et al. (2013). "Information from Paleoclimate Archives," in *Climate Change 2013: The Physical Science Basis. Contribution of Working Group I to the Fifth Assessment Report of the Intergovernmental Panel on Climate Change*, eds. T. . Stocker, D. Qin, G.-K. Plattner, M. Tignor, S. K. Allen, J. Boschung, et al. (Cambridge, United Kingdom and New York, NY, USA: Cambridge University Press), 383–464. doi:10.1017/CBO9781107415324.013.

Mateo, C. M. R., Yamazaki, D., Kim, H., Champathong, A., Vaze, J., and Oki, T. (2017). Impacts of spatial resolution and representation of flow connectivity on large-scale simulation of floods. *Hydrol. Earth Syst. Sci.* 21, 5143–5163. doi:10.5194/hess-21-5143-2017.

Mathbout, S., Lopez-Bustins, J. A., Martin-Vide, J., Bech, J., and Rodrigo, F. S. (2018a). Spatial and temporal analysis of drought variability at several time scales in Syria during 1961–2012. *Atmos. Res.* 200, 153–168. doi:10.1016/j.atmosres.2017.09.016.

Mathbout, S., Lopez-Bustins, J. A., Royé, D., Martin-Vide, J., Bech, J., and Rodrigo, F. S. (2018b). Observed Changes in Daily Precipitation Extremes at Annual Timescale Over the Eastern Mediterranean During 1961–2012. *Pure Appl. Geophys.* 175, 3875–3890. doi:10.1007/s00024-017-1695-7.

Matthes, H., Rinke, A., and Dethloff, K. (2015). Recent changes in Arctic temperature extremes: Warm and cold spells during winter and summer. *Environ. Res. Lett.* 10. doi:10.1088/1748-9326/10/11/114020.

Matthews, T. K. R., Wilby, R. L., and Murphy, C. (2017). Communicating the deadly consequences of global warming for human heat stress. *Proc. Natl. Acad. Sci. U. S. A.* 114, 3861–3866. doi:10.1073/pnas.1617526114.

Mátyás, C., and Sun, G. (2014). Forests in a water limited world under climate change. *Environ. Res. Lett.* 9. doi:10.1088/1748-9326/9/8/085001.

Maúre, G., Pinto, I., Ndebele-Murisa, M., Muthige, M., Lennard, C., Nikulin, G., et al. (2018). The southern African climate under 1.5 °C and 2 °C of global warming as simulated by CORDEX regional climate models. *Environ. Res. Lett.* doi:10.1088/1748-9326/aab190.

Maxwell, R. M., and Condon, L. E. (2016). Connections between groundwater flow and transpiration partitioning. *Science (80-.).* 353, 377–380. doi:10.1126/science.aaf7891.

Mazdiyasni, O., AghaKouchak, A., Davis, S. J., Madadgar, S., Mehran, A., Ragno, E., et al. (2017). Increasing probability of mortality during Indian heat waves. *Sci. Adv.* 3, e1700066. doi:10.1126/sciadv.1700066.

Mba, W. P., Longandjo, G. N. T., Moufouma-Okia, W., Bell, J. P., James, R., Vondou, D. A., et al. (2018). Consequences of 1.5 °c and 2 °c global warming levels for temperature and precipitation changes over Central Africa. *Environ. Res. Lett.* 13. doi:10.1088/1748-9326/aab048.

Mbokodo, I., Bopape, M.-J., Chikoore, H., Engelbrecht, F., and Nethengwe, N. (2020). Heatwaves in the Future Warmer Climate of South Africa. *Atmosphere (Basel).* 11, 712.

Mcbride, J. L., Sahany, S., Hassim, M. E. E., Nguyen, C. M., Lim, S.-Y., Rahmat, R., et al. (2015). The 2014 Record Dry Spell at Singapore: An Intertropical Convergence Zone (ITCZ) Drought. *Bull. Am. Meteorol. Soc.* 96, S126–S130. doi:10.1175/BAMS-D-15-00117.1.

McCollum, D. L., Gambhir, A., Rogelj, J., and Wilson, C. (2020). Energy modellers should explore extremes more systematically in scenarios. *Nat. Energy* 5, 104–107. doi:10.1038/s41560-020-0555-3.

McDowell, N. G., and Allen, C. D. (2015). Darcy's law predicts widespread forest mortality under climate warming. *Nat. Clim. Chang.* 5, 669–672. doi:10.1038/nclimate2641.

McDowell, N. G., Allen, C. D., Anderson-Teixeira, K., Aukema, B. H., Bond-Lamberty, B., Chini, L., et al. (2020). Pervasive shifts in forest dynamics in a changing world. *Science (80-.).* 368. doi:10.1126/science.aaz9463.

ACCEPTED VERSION SUBJECT TO FINAL EDITING

McDowell, N. G., Williams, A. P., Xu, C., Pockman, W. T., Dickman, L. T., Sevanto, S., et al. (2016). Multi-scale predictions of massive conifer mortality due to chronic temperature rise. *Nat. Clim. Chang.* 6, 295–300. doi:10.1038/nclimate2873.

McEvoy, D. J., Huntington, J. L., Hobbins, M. T., Wood, A., Morton, C., Anderson, M., et al. (2016). The evaporative demand drought index. Part II: CONUS-wide assessment against common drought indicators. *J. Hydrometeorol.* 17, 1763–1779. doi:10.1175/JHM-D-15-0122.1.

McGree, S., Herold, N., Alexander, L., Schreider, S., Kuleshov, Y., Ene, E., et al. (2019). Recent changes in mean and extreme temperature and precipitation in the western Pacific Islands. *J. Clim.*, JCLI-D-18-0748.1. doi:10.1175/JCLI-D-18-0748.1.

McInnes, K. L., Walsh, K. J. E., Hoeke, R. K., O'Grady, J. G., Colberg, F., and Hubbert, G. D. (2014). Quantifying storm tide risk in Fiji due to climate variability and change. *Glob. Planet. Change* 116, 115–129. doi:10.1016/j.gloplacha.2014.02.004.

McInnes, K. L., White, C. J., Haigh, I. D., Hemer, M. A., Hoeke, R. K., Holbrook, N. J., et al. (2016). Natural hazards in Australia: sea level and coastal extremes. *Clim. Change* 139, 69–83. doi:10.1007/s10584-016-1647-8.

McKenzie, D., and Littell, J. S. (2017). Climate change and the eco-hydrology of fire: Will area burned increase in a warming western USA. *Ecol. Appl.* 27, 26–36. doi:10.1002/eap.1420.

McLean, N. M., Stephenson, T. S., Taylor, M. A., and Campbell, J. D. (2015). Characterization of Future Caribbean Rainfall and Temperature Extremes across Rainfall Zones. *Adv. Meteorol.* 2015, 1–18. doi:10.1155/2015/425987.

McMahon, T. A., Peel, M. C., Lowe, L., Srikanthan, R., and McVicar, T. R. (2013). Estimating actual, potential, reference crop and pan evaporation using standard meteorological data: A pragmatic synthesis. *Hydrol. Earth Syst. Sci.* 17, 1331–1363. doi:10.5194/hess-17-1331-2013.

McVicar, T. R., Roderick, M. L., Donohue, R. J., Li, L. T., Van Niel, T. G., Thomas, A., et al. (2012a). Global review and synthesis of trends in observed terrestrial near-surface wind speeds: Implications for evaporation. *J. Hydrol.* 416–417, 182–205. doi:10.1016/j.jhydrol.2011.10.024.

McVicar, T. R., Roderick, M. L., Donohue, R. J., and Van Niel, T. G. (2012b). Less bluster ahead? ecohydrological implications of global trends of terrestrial near-surface wind speeds. *Ecohydrology* 5, 381–388. doi:10.1002/eco.1298.

MedECC (2020). "MedECC 2020 Summary for Policymakers," in *Climate and Environmental Change in the Mediterranean Basin – Current Situation and Risks for the Future. First Mediterranean Assessment Report*, eds. W. Cramer, J. Guiot, K. Marini, M. V. Balzan, S. Cherif, E. Doblas-Miranda, et al. (Marseille, France: Union for the Mediterranean, Plan Bleu, UNEP/MAP), 34. Available at: https://www.medecc.org/first-mediterranean-assessment-report-mar1/.

Mediero, L., Kjeldsen, T. R., Macdonald, N., Kohnova, S., Merz, B., Vorogushyn, S., et al. (2015). Identification of coherent flood regions across Europe by using the longest streamflow records. *J. Hydrol.* 528, 341–360. doi:10.1016/j.jhydrol.2015.06.016.

Meehl, G. A., Tebaldi, C., and Adams-Smith, D. (2016). US daily temperature records past, present, and future. *Proc. Natl. Acad. Sci.* 113, 13977–13982. doi:10.1073/pnas.1606117113.

Mei, W., and Xie, S. P. (2016). Intensification of landfalling typhoons over the northwest Pacific since the late 1970s. *Nat. Geosci.* 9, 753–757. doi:10.1038/ngeo2792.

Mekis, É., Vincent, L. A., Shephard, M. W., and Zhang, X. (2015). Observed Trends in Severe Weather Conditions Based on Humidex, Wind Chill, and Heavy Rainfall Events in Canada for 1953–2012. *Atmosphere-Ocean* 53, 383–397. doi:10.1080/07055900.2015.1086970.

Menezes-Silva, P. E., Loram-Lourenço, L., Alves, R. D. F. B., Sousa, L. F., Almeida, S. E. da S., and Farnese, F. S. (2019). Different ways to die in a changing world: Consequences of climate change for tree species performance and survival through an ecophysiological perspective. *Ecol. Evol.* 0. doi:10.1002/ece3.5663.

Menkes, C. E., Lengaigne, M., Marchesiello, P., Jourdain, N. C., Vincent, E. M., Lefèvre, J., et al. (2012). Comparison of tropical cyclogenesis indices on seasonal to interannual timescales. *Clim. Dyn.* 38, 301–321. doi:10.1007/s00382-011-1126-x.

Meredith, E. P., Semenov, V. A., Maraun, D., Park, W., and Chernokulsky, A. V. (2015). Crucial role of Black Sea warming in amplifying the 2012 Krymsk precipitation extreme. *Nat. Geosci.* 8, 615–619. doi:10.1038/ngeo2483.

Mernild, S. H., Hanna, E., Yde, J. C., Cappelen, J., and Malmros, J. K. (2014). Coastal Greenland air temperature extremes and trends 1890-2010: annual and monthly analysis. *Int. J. Climatol.* 34. doi:10.1002/joc.3777.

Meseguer-Ruiz, O., Ponce-Philimon, P. I., Quispe-Jofré, A. S., Guijarro, J. A., and Sarricolea, P. (2018). Spatial behaviour of daily observed extreme temperatures in Northern Chile (1966–2015): data quality, warming trends, and its orographic and latitudinal effects. *Stoch. Environ. Res. Risk Assess.* 32, 3503–3523. doi:10.1007/s00477-018-1557-6.

MfE (2018). Climate Change Projections for New Zealand: Atmosphere Projections Based on Simulations from the IPCC Fifth Assessment, 2nd Edition. Wellington, NZ: New Zealand Ministry for the Environment (MfE) Available at: http://www.mfe.govt.nz/sites/default/files/media/Climate Change/climate-projections-snapshot.pdf.

MfE, and Stats NZ (2020). New Zealand's Environmental Reporting Series: Our atmosphere and climate 2020. New Zealand Ministry for the Environment (MfE) and Stats NZ Available at:

ACCEPTED VERSION SUBJECT TO FINAL EDITING

https://www.mfe.govt.nz/publications/environmental-reporting/our-atmosphere-and-climate-2020.
Michaelis, A. C., Willison, J., Lackmann, G. M., and Robinson, W. A. (2017). Changes in winter North Atlantic extratropical cyclones in high-resolution regional pseudo-global warming simulations. *J. Clim.* 30, 6905–6925. doi:10.1175/JCLI-D-16-0697.1.
Miglietta, M. M., and Rotunno, R. (2019). Development mechanisms for Mediterranean tropical-like cyclones (medicanes). *Q. J. R. Meteorol. Soc.* 145, 1444–1460. doi:10.1002/qj.3503.
Milly, P. C. D., and Dunne, K. A. (2016). Potential evapotranspiration and continental drying. *Nat. Clim. Chang.* 6, 946–949. doi:10.1038/nclimate3046.
Milly, P. C. D., and Dunne, K. A. (2020). Colorado River flow dwindles as warming-driven loss of reflective snow energizes evaporation. *Science (80-.).* 367, 1252–1255. doi:10.1126/science.aax0194.
Min, S., Kim, Y.-H., Lee, S.-M., Sparrow, S., Li, S., Lott, F. C., et al. (2020). Quantifying human impact on the 2018 summer longest heat wave in south korea. *Bull Am Meteorol Soc*. doi:10.1175/BAMS-D-19-0151.1.
Miralles, D. G., Gentine, P., Seneviratne, S. I., and Teuling, A. J. (2019). Land-atmospheric feedbacks during droughts and heatwaves: state of the science and current challenges. *Ann. N. Y. Acad. Sci.* 1436, 19–35. doi:10.1111/nyas.13912.
Miralles, D. G., Teuling, A. J., Van Heerwaarden, C. C., and De Arellano, J. V. G. (2014a). Mega-heatwave temperatures due to combined soil desiccation and atmospheric heat accumulation. *Nat. Geosci.* 7, 345–349. doi:10.1038/ngeo2141.
Miralles, D. G., van den Berg, M. J., Gash, J. H., Parinussa, R. M., de Jeu, R. A. M., Beck, H. E., et al. (2014b). El Niño–La Niña cycle and recent trends in continental evaporation. *Nat. Clim. Chang.* 4, 122–126. doi:10.1038/nclimate2068.
Mishra, V. (2020). Long-term (1870–2018) drought reconstruction in context of surface water security in India. *J. Hydrol.* 580. doi:10.1016/j.jhydrol.2019.124228.
Mishra, V., Kumar, D., Ganguly, A. R., Sanjay, J., Mujumdar, M., Krishnan, R., et al. (2014a). Reliability of regional and global climate models to simulate precipitation extremes over India. *J. Geophys. Res. Atmos.* 119, 9301–9323. doi:10.1002/2014JD021636.
Mishra, V., Mukherjee, S., Kumar, R., and Stone, D. A. (2017). Heat wave exposure in India in current, 1.5 °C, and 2.0 °C worlds. *Environ. Res. Lett.* 12, 124012. doi:10.1088/1748-9326/aa9388.
Mishra, V., Shah, R., and Thrasher, B. (2014b). Soil Moisture Droughts under the Retrospective and Projected Climate in India. *J. Hydrometeorol.* 15, 2267–2292. doi:10.1175/JHM-D-13-0177.1.
Mitchell, P. J., O'Grady, A. P., Hayes, K. R., and Pinkard, E. A. (2014). Exposure of trees to drought-induced die-off is defined by a common climatic threshold across different vegetation types. *Ecol. Evol.* 4, 1088–1101. doi:10.1002/ece3.1008.
Mitchell, T. D. (2003). Pattern Scaling. An Examination of the Accuracy of the Technique for Describing Future Climates. *Clim. Change* 60, 217–242. doi:10.1023/A:1026035305597.
Mizuta, R., and Endo, H. (2020). Projected Changes in Extreme Precipitation in a 60-km AGCM Large Ensemble and Their Dependence on Return Periods. *Geophys. Res. Lett.* 47, 1–8. doi:10.1029/2019GL086855.
Mo, K. C., and Lettenmaier, D. P. (2018). Drought variability and trends over the central United States in the instrumental record. *J. Hydrometeorol.* 19, 1149–1166. doi:10.1175/JHM-D-17-0225.1.
Moftakhari, H. R., Salvadori, G., AghaKouchak, A., Sanders, B. F., and Matthew, R. A. (2017). Compounding effects of sea level rise and fluvial flooding. *Proc. Natl. Acad. Sci.* 114, 9785–9790. doi:10.1073/pnas.1620325114.
Mohammed, R., and Scholz, M. (2016). Impact of climate variability and streamflow alteration on groundwater contribution to the base flow of the Lower Zab River (Iran and Iraq). *Environ. Earth Sci.* 75. doi:10.1007/s12665-016-6205-1.
Molina, M. O., Sánchez, E., and Gutiérrez, C. (2020). Future heat waves over the Mediterranean from an Euro-CORDEX regional climate model ensemble. *Sci. Rep.* 10, 8801. doi:10.1038/s41598-020-65663-0.
Molnar, P., Fatichi, S., Gaál, L., Szolgay, J., and Burlando, P. (2015). Storm type effects on super Clausius-Clapeyron scaling of intense rainstorm properties with air temperature. *Hydrol. Earth Syst. Sci.* 19, 1753–1766. doi:10.5194/hess-19-1753-2015.
Monjo, R., Gaitán, E., Pórtoles, J., Ribalaygua, J., and Torres, L. (2016). Changes in extreme precipitation over Spain using statistical downscaling of CMIP5 projections. *Int. J. Climatol.* 36, 757–769. doi:10.1002/joc.4380.
Montero-Martínez, M. J., Santana-Sepúlveda, J. S., Pérez-Ortiz, N. I., Pita-Díaz, Ó., and Castillo-Liñan, S. (2018). Comparing climate change indices between a northern (arid) and a southern (humid) basin in Mexico during the last decades. *Adv. Sci. Res.* 15, 231–237. doi:10.5194/asr-15-231-2018.
Moon, H., Gudmundsson, L., and Seneviratne, S. I. (2018). Drought Persistence Errors in Global Climate Models. *J. Geophys. Res. Atmos.* 123, 3483–3496. doi:10.1002/2017JD027577.
Moon, H., Guillod, B. P., Gudmundsson, L., and Seneviratne, S. I. (2019). Soil Moisture Effects on Afternoon Precipitation Occurrence in Current Climate Models. *Geophys. Res. Lett.* 46, 1861–1869. doi:10.1029/2018GL080879.
Moon, I.-J., Kim, S.-H., Klotzbach, P., and Chan, J. C. L. (2015). Roles of interbasin frequency changes in the poleward shifts of the maximum intensity location of tropical cyclones. *Environ. Res. Lett.* 10, 104004. doi:10.1088/1748-

ACCEPTED VERSION SUBJECT TO FINAL EDITING

9326/10/10/104004.
Moon, I.-J., Kim, S.-H., Klotzbach, P., and Chan, J. C. L. (2016). Reply to Comment on 'Roles of interbasin frequency changes in the poleward shifts of maximum intensity location of tropical cyclones.' *Environ. Res. Lett.* 11, 068002. doi:10.1088/1748-9326/11/6/068002.
Moon, Y., Kim, D., Camargo, S. J., Wing, A. A., Sobel, A. H., Murakami, H., et al. (2020). Azimuthally Averaged Wind and Thermodynamic Structures of Tropical Cyclones in Global Climate Models and Their Sensitivity to Horizontal Resolution. *J. Clim.* 33, 1575–1595. doi:10.1175/JCLI-D-19-0172.1.
Moore, G. W. K. (2016). The December 2015 North Pole Warming Event and the Increasing Occurrence of Such Events. *Sci. Rep.* 6. doi:10.1038/srep39084.
Mora, C., Spirandelli, D., Franklin, E. C., Lynham, J., Kantar, M. B., Miles, W., et al. (2018). Broad threat to humanity from cumulative climate hazards intensified by greenhouse gas emissions. *Nat. Clim. Chang.* 8, 1062–1071. doi:10.1038/s41558-018-0315-6.
Moravec, V., Markonis, Y., Rakovec, O., Kumar, R., and Hanel, M. (2019). A 250-Year European Drought Inventory Derived From Ensemble Hydrologic Modeling. *Geophys. Res. Lett.* 46, 5909–5917. doi:10.1029/2019GL082783.
Morgan, J. A., LeCain, D. R., Pendall, E., Blumenthal, D. M., Kimball, B. A., Carrillo, Y., et al. (2011). C4 grasses prosper as carbon dioxide eliminates desiccation in warmed semi-arid grassland. *Nature* 476, 202–205. doi:10.1038/nature10274.
Mori, N., Ariyoshi, N., Shimura, T., Miyashita, T., and Ninomiya, J. (2021). Future projection of maximum potential storm surge height at three major bays in Japan using the maximum potential intensity of a tropical cyclone. *Clim. Change* 164, 25. doi:10.1007/s10584-021-02980-x.
Mori, N., Shimura, T., Yoshida, K., Mizuta, R., Okada, Y., Fujita, M., et al. (2019). Future changes in extreme storm surges based on mega-ensemble projection using 60-km resolution atmospheric global circulation model. *Coast. Eng. J.* 61, 295–307. doi:10.1080/21664250.2019.1586290.
Moron, V., Oueslati, B., Pohl, B., Rome, S., and Janicot, S. (2016). Trends of mean temperatures and warm extremes in northern tropical Africa (1961-2014) from observed and PPCA-reconstructed time series. *J. Geophys. Res. Atmos.* 121, 5298–5319. doi:10.1002/2015JD024303.
Morrison, A., Villarini, G., Zhang, W., and Scoccimarro, E. (2019). Projected changes in extreme precipitation at sub-daily and daily time scales. *Glob. Planet. Change* 182, 103004. doi:10.1016/j.gloplacha.2019.103004.
Mostafa, A. N., Wheida, A., El Nazer, M., Adel, M., El Leithy, L., Siour, G., et al. (2019). Past (1950–2017) and future (−2100) temperature and precipitation trends in Egypt. *Weather Clim. Extrem.* 26, 100225. doi:10.1016/j.wace.2019.100225.
Mote, P. W., Rupp, D. E., Li, S., Sharp, D. J., Otto, F., Uhe, P. F., et al. (2016). Perspectives on the causes of exceptionally low 2015 snowpack in the western United States. *Geophys. Res. Lett.* 43, 10,910-980,988. doi:10.1002/2016GL069965.
Mouhamed, L., Traore, S. B., Alhassane, A., and Sarr, B. (2013). Evolution of some observed climate extremes in the West African Sahel. *Weather Clim. Extrem.* doi:10.1016/j.wace.2013.07.005.
Mozny, M., Trnka, M., Vlach, V., Vizina, A., Potopova, V., Zahradnicek, P., et al. (2020). Past (1971–2018) and future (2021–2100) pan evaporation rates in the Czech Republic. *J. Hydrol.* 590. doi:10.1016/j.jhydrol.2020.125390.
Mtongori, H. I., Stordal, F., and Benestad, R. E. (2016). Evaluation of Empirical Statistical Downscaling Models' Skill in Predicting Tanzanian Rainfall and Their Application in Providing Future Downscaled Scenarios. *J. Clim.* 29, 3231–3252. doi:10.1175/JCLI-D-15-0061.1.
Mueller, B., and Seneviratne, S. (2014). Systematic land climate and evapotranspiration biases in CMIP5 simulations. *Geophys. Res. Lett.* 41, 128–134. doi:10.1002/2013GL058055.
Mueller, B., and Seneviratne, S. I. (2012). Hot days induced by precipitation deficits at the global scale. *Proc. Natl. Acad. Sci.* 109, 12398–12403. doi:10.1073/pnas.1204330109.
Mueller, B., and Zhang, X. (2016). Causes of drying trends in northern hemispheric land areas in reconstructed soil moisture data. *Clim. Change* 134, 255–267. doi:10.1007/s10584-015-1499-7.
Mueller, B., Zhang, X., and Zwiers, F. W. (2016a). Historically hottest summers projected to be the norm for more than half of the world's population within 20 years. *Environ. Res. Lett.* 11, 1–15. doi:10.1088/1748-9326/11/4/044011.
Mueller, N. D., Butler, E. E., McKinnon, K. A., Rhines, A., Tingley, M., Holbrook, N. M., et al. (2016b). Cooling of US Midwest summer temperature extremes from cropland intensification. *Nat. Clim. Chang.* 6, 317–322. doi:10.1038/nclimate2825.
Muerth, M. J., Gauvin St-Denis, B., Ricard, S., Velázquez, J. A., Schmid, J., Minville, M., et al. (2013). On the need for bias correction in regional climate scenarios to assess climate change impacts on river runoff. *Hydrol. Earth Syst. Sci.* 17, 1189–1204. doi:10.5194/hess-17-1189-2013.
Mukherjee, S., Aadhar, S., Stone, D., and Mishra, V. (2018a). Increase in extreme precipitation events under anthropogenic warming in India. *Weather Clim. Extrem.* 20, 45–53. doi:10.1016/J.WACE.2018.03.005.
Mukherjee, S., Mishra, A., and Trenberth, K. E. (2018b). Climate Change and Drought: a Perspective on Drought Indices. *Curr. Clim. Chang. Reports* 4, 145–163. doi:10.1007/s40641-018-0098-x.
Muller, J., Collins, J. M., Gibson, S., and Paxton, L. (2017). "Recent Advances in the Emerging Field of Paleotempestology," in *Hurricanes and Climate Change: Volume 3*, eds. J. M. Collins and K. Walsh (Cham,

ACCEPTED VERSION SUBJECT TO FINAL EDITING

Switzerland: Springer), 1–33. doi:10.1007/978-3-319-47594-3_1.
Müller, W. A., Borchert, L., and Ghosh, R. (2020). Observed Subdecadal Variations of European Summer Temperatures. *Geophys. Res. Lett.* 47, e2019GL086043. doi:10.1029/2019GL086043.
Murakami, H., Delworth, T. L., Cooke, W. F., Zhao, M., Xiang, B., and Hsu, P.-C. (2020). Detected climatic change in global distribution of tropical cyclones. *Proc. Natl. Acad. Sci.* 117, 10706–10714. doi:10.1073/pnas.1922500117.
Murakami, H., Levin, E., Delworth, T. L., Gudgel, R., and Hsu, P.-C. (2018). Dominant effect of relative tropical Atlantic warming on major hurricane occurrence. *Science (80-.).* 362, 794–799. doi:10.1126/science.aat6711.
Murakami, H., Li, T., and Hsu, P. C. (2014). Contributing factors to the recent high level of accumulated cyclone energy (ACE) and power dissipation index (PDI) in the North Atlantic. *J. Clim.* 27, 3023–3034. doi:10.1175/JCLI-D-13-00394.1.
Murakami, H., Vecchi, G. A., Delworth, T. L., Wittenberg, A. T., Underwood, S., Gudgel, R., et al. (2017a). Dominant Role of Subtropical Pacific Warming in Extreme Eastern Pacific Hurricane Seasons: 2015 and the Future. *J. Clim.* 30, 243–264. doi:10.1175/JCLI-D-16-0424.1.
Murakami, H., Vecchi, G. A., and Underwood, S. (2017b). Increasing frequency of extremely severe cyclonic storms over the Arabian Sea. *Nat. Clim. Chang.* 7, 885–889. doi:10.1038/s41558-017-0008-6.
Murakami, H., Vecchi, G. A., Underwood, S., Delworth, T. L., Wittenberg, A. T., Anderson, W. G., et al. (2015). Simulation and prediction of category 4 and 5 hurricanes in the high-resolution GFDL HiFLOR coupled climate model. *J. Clim.* 28, 9058–9079. doi:10.1175/JCLI-D-15-0216.1.
Murakami, H., Wang, Y., Yoshimura, H., Mizuta, R., Sugi, M., Shindo, E., et al. (2012). Future changes in tropical cyclone activity projected by the new high-resolution MRI-AGCM. *J. Clim.* 25, 3237–3260. doi:10.1175/JCLI-D-11-00415.1.
Muramatsu, T., Kato, T., Nakazato, M., Endo, H., and Kitoh, A. (2016). Future Change of Tornadogenesis-Favorable Environmental Conditions in Japan Estimated by a 20-km-Mesh Atmospheric General Circulation Model. *J. Meteorol. Soc. Japan. Ser. II* 94A, 105–120. doi:10.2151/jmsj.2015-053.
Murari, K. K., Ghosh, S., Patwardhan, A., Daly, E., and Salvi, K. (2015). Intensification of future severe heat waves in India and their effect on heat stress and mortality. *Reg. Environ. Chang.* 15. doi:10.1007/s10113-014-0660-6.
Murata, A., Sasaki, H., Kawase, H., and Nosaka, M. (2017). Evaluation of precipitation over an oceanic region of Japan in convection-permitting regional climate model simulations. *Clim. Dyn.* 48, 1779–1792. doi:10.1007/s00382-016-3172-x.
Murata, A., Sasaki, H., Kawase, H., Nosaka, M., Oh'izumi, M., Kato, T., et al. (2015). Projection of Future Climate Change over Japan in Ensemble Simulations with a High-Resolution Regional Climate Model. *SOLA* 11, 90–94. doi:10.2151/sola.2015-022.
Myhre, G., Alterskjær, K., Stjern, C. W., Hodnebrog, Ø., Marelle, L., Samset, B. H., et al. (2019). Frequency of extreme precipitation increases extensively with event rareness under global warming. *Sci. Rep.* 9, 16063. doi:10.1038/s41598-019-52277-4.
Nabat, P., Somot, S., Mallet, M., Sanchez-Lorenzo, A., and Wild, M. (2014). Contribution of anthropogenic sulfate aerosols to the changing Euro-Mediterranean climate since 1980. *Geophys. Res. Lett.* 41, 5605–5611. doi:10.1002/2014GL060798.
Nackley, L. L., Betzelberger, A., Skowno, A., G. West, A., Ripley, B. S., Bond, W. J., et al. (2018). CO2 enrichment does not entirely ameliorate Vachellia karroo drought inhibition: A missing mechanism explaining savanna bush encroachment. *Environ. Exp. Bot.* 155, 98–106. doi:10.1016/j.envexpbot.2018.06.018.
Naik, M., and Abiodun, B. J. (2020). Projected changes in drought characteristics over the Western Cape, South Africa. *Meteorol. Appl.* 27. doi:10.1002/met.1802.
Nakaegawa, T., Kitoh, A., Murakami, H., and Kusunoki, S. (2013). Annual maximum 5-day rainfall total and maximum number of consecutive dry days over Central America and the Caribbean in the late twenty-first century projected by an atmospheric general circulation model with three different horizontal resolutions. *Theor. Appl. Climatol.* 116. doi:10.1007/s00704-013-0934-9.
Nakamura, J., Camargo, S. J., Sobel, A. H., Henderson, N., Emanuel, K. A., Kumar, A., et al. (2017). Western North Pacific Tropical Cyclone Model Tracks in Present and Future Climates. *J. Geophys. Res. Atmos.* 122, 9721–9744. doi:10.1002/2017JD027007.
Nakano, M., Wada, A., Sawada, M., Yoshimura, H., Onishi, R., Kawahara, S., et al. (2017). Global 7km mesh nonhydrostatic Model Intercomparison Project for improving TYphoon forecast (TYMIP-G7): Experimental design and preliminary results. *Geosci. Model Dev.* 10, 1368–1381. doi:10.5194/gmd-10-1363-2017.
Nakayama, T., and Shankman, D. (2013). Impact of the Three-Gorges Dam and water transfer project on Changjiang floods. *Glob. Planet. Change* 100, 38–50. doi:10.1016/j.gloplacha.2012.10.004.
Nangombe, S., Zho, T., Zhang, L., and Zhang, W. (2020). Attribution of the 2018 october-december drought over south southern africa. *Bull. Am. Meteorol. Soc.* 101, S135–S140. doi:10.1175/BAMS-D-19-0179.1.
Nangombe, S., Zhou, T., Zhang, W., Wu, B., Hu, S., Zou, L., et al. (2018). Record-breaking climate extremes in Africa under stabilized 1.5 °C and 2 °C global warming scenarios. *Nat. Clim. Chang.* 8, 375–380. doi:10.1038/s41558-018-0145-6.
NASEM (2016). Attribution of Extreme Weather Events in the Context of Climate Change. Washington, DC, USA:

ACCEPTED VERSION SUBJECT TO FINAL EDITING

National Academies of Sciences Engineering and Medicine (NASEM). The National Academies Press doi:10.17226/21852.
Nasim, W., Amin, A., Fahad, S., Awais, M., Khan, N., Mubeen, M., et al. (2018). Future risk assessment by estimating historical heat wave trends with projected heat accumulation using SimCLIM climate model in Pakistan. *Atmos. Res.* 205, 118–133. doi:10.1016/j.atmosres.2018.01.009.
Nasrollahi, N., Aghakouchak, A., Cheng, L., Damberg, L., Phillips, T. J., Miao, C., et al. (2015). How well do CMIP5 climate simulations replicate historical trends and patterns of meteorological droughts? *Water Resour. Res.* 51, 2847–2864. doi:10.1002/2014WR016318.
Nastos, P. T., and Kapsomenakis, J. (2015). Regional climate model simulations of extreme air temperature in Greece. Abnormal or common records in the future climate? *Atmos. Res.* 152, 43–60. doi:10.1016/j.atmosres.2014.02.005.
Naumann, G., Alfieri, L., Wyser, K., Mentaschi, L., Betts, R. A., Carrao, H., et al. (2018). Global Changes in Drought Conditions Under Different Levels of Warming. *Geophys. Res. Lett.* 45, 3285–3296. doi:10.1002/2017GL076521.
Naveendrakumar, G., Vithanage, M., Kwon, H.-H., Chandrasekara, S. S. K., Iqbal, M. C. M., Pathmarajah, S., et al. (2019). South Asian perspective on temperature and rainfall extremes: A review. *Atmos. Res.* 225, 110–120. doi:10.1016/j.atmosres.2019.03.021.
Nayak, S., and Dairaku, K. (2016). Future changes in extreme precipitation intensities associated with temperature under SRES A1B scenario. *Hydrol. Res. Lett.* 10, 139–144. doi:10.3178/hrl.10.139.
Nayak, S., Dairaku, K., Takayabu, I., Suzuki-Parker, A., and Ishizaki, N. N. (2017). Extreme precipitation linked to temperature over Japan: current evaluation and projected changes with multi-model ensemble downscaling. *Clim. Dyn.* 51, 1–17. doi:10.1007/s00382-017-3866-8.
Nazrul Islam, M., Almazroui, M., Dambul, R., Jones, P. D., and Alamoudi, A. O. (2015). Long-term changes in seasonal temperature extremes over Saudi Arabia during 1981-2010. *Int. J. Climatol.* 35, 1579–1592. doi:10.1002/joc.4078.
Neri, A., Villarini, G., Slater, L. J., and Napolitano, F. (2019). On the statistical attribution of the frequency of flood events across the U.S. Midwest. *Adv. Water Resour.* 127, 225–236. doi:10.1016/j.advwatres.2019.03.019.
Neu, U., Akperov, M. G., Bellenbaum, N., Benestad, R., Blender, R., Caballero, R., et al. (2013). Imilast: A community effort to intercompare extratropical cyclone detection and tracking algorithms. *Bull. Am. Meteorol. Soc.* doi:10.1175/BAMS-D-11-00154.1.
Neukom, R., Gergis, J., Karoly, D. J., Wanner, H., Curran, M., Elbert, J., et al. (2014). Inter-hemispheric temperature variability over the past millennium. *Nat. Clim. Chang.* 4, 362–367. doi:10.1038/nclimate2174.
Neumann, B., Vafeidis, A. T., Zimmermann, J., and Nicholls, R. J. (2015). Future Coastal Population Growth and Exposure to Sea-Level Rise and Coastal Flooding – A Global Assessment. *PLoS One* 10, e0118571. doi:10.1371/journal.pone.0118571.
Newman, M., Wittenberg, A. T., Cheng, L., Compo, G. P., and Smith, C. A. (2018). The Extreme 2015/16 El Niño, in the Context of Historical Climate Variability and Change. *Bull. Am. Meteorol. Soc.* 99, S16–S20. doi:10.1175/BAMS-D-17-0116.1.
Nguvava, M., Abiodun, B. J., and Otieno, F. (2019). Projecting drought characteristics over East African basins at specific global warming levels. *Atmos. Res.* 228, 41–54. doi:10.1016/j.atmosres.2019.05.008.
Nicholls, R. J., Brown, S., Goodwin, P., Wahl, T., Lowe, J., Solan, M., et al. (2018). Stabilization of global temperature at 1.5°C and 2.0°C: implications for coastal areas. *Philos. Trans. R. Soc. A Math. Phys. Eng. Sci.* 376, 20160448. doi:10.1098/rsta.2016.0448.
Nicholson, S. E. (2017). Climate and climatic variability of rainfall over eastern Africa. *Rev. Geophys.* 55, 590–635.
Nicolai-Shaw, N., Hirschi, M., Mittelbach, H., and Seneviratne, S. I. (2015). Spatial representativeness of soil moisture using in situ, remote sensing, and land reanalysis data. *J. Geophys. Res. Atmos.* 120, 9955–9964. doi:10.1002/2015JD023305.
Nie, J., Sobel, A. H., Shaevitz, D. A., and Wang, S. (2018). Dynamic amplification of extreme precipitation sensitivity. *Proc. Natl. Acad. Sci.* 115, 9467 LP-9472. doi:10.1073/pnas.1800357115.
Nied, M., Pardowitz, T., Nissen, K., Ulbrich, U., Hundecha, Y., and Merz, B. (2014). On the relationship between hydro-meteorological patterns and flood types. *J. Hydrol.* 519, 3249–3262. doi:10.1016/j.jhydrol.2014.09.089.
Nikulin, G., Lennard, C., Dosio, A., Kjellström, E., Chen, Y., Hänsler, A., et al. (2018). The effects of 1.5 and 2 degrees of global warming on Africa in the CORDEX ensemble. *Environ. Res. Lett.* 13, 065003. doi:10.1088/1748-9326/aab1b1.
Niranjan Kumar, K., Rajeevan, M., Pai, D. S., Srivastava, A. K., and Preethi, B. (2013). On the observed variability of monsoon droughts over India. *Weather Clim. Extrem.* 1, 42–50. doi:10.1016/J.WACE.2013.07.006.
Nissen, K. M., and Ulbrich, U. (2017). Increasing frequencies and changing characteristics of heavy precipitation events threatening infrastructure in Europe under climate change. *Nat. Hazards Earth Syst. Sci.* 17, 1177–1190. doi:10.5194/nhess-17-1177-2017.
Niu, X., Wang, S., Tang, J., Lee, D.-K., Gutowski, W., Dairaku, K., et al. (2018). Ensemble evaluation and projection of climate extremes in China using RMIP models. *Int. J. Climatol.* 38, 2039–2055. doi:10.1002/joc.5315.
Nolan, R. H., Boer, M. M., Collins, L., Resco de Dios, V., Clarke, H., Jenkins, M., et al. (2020). Causes and consequences of eastern Australia's 2019–20 season of mega-fires. *Glob. Chang. Biol.* 26, 1039–1041.

ACCEPTED VERSION SUBJECT TO FINAL EDITING

doi:10.1111/gcb.14987.
Norrant, C., and Douguédroit, A. (2006). Monthly and daily precipitation trends in the Mediterranean (1950-2000). *Theor. Appl. Climatol.* 83, 89–106. doi:10.1007/s00704-005-0163-y.
Nott, J., Smithers, S., Walsh, K., and Rhodes, E. (2009). Sand beach ridges record 6000 year history of extreme tropical cyclone activity in northeastern Australia. *Quat. Sci. Rev.* 28, 1511–1520. doi:10.1016/j.quascirev.2009.02.014.
O'Gorman, P. (2014). Contrasting responses of mean and extreme snowfall to climate change. *Nature* 512, 416–418.
OB, C., Yang, S., Boberg, F., C, F. M., Thejll, P., Olesen, M., et al. (2015). Scalability of regional climate change in Europe for high-end scenarios. *Clim. Res.* 64, 25–38. doi:10.3354/cr01286.
Odoulami, R. C., Abiodun, B. J., and Ajayi, A. E. (2019). Modelling the potential impacts of afforestation on extreme precipitation over West Africa. *Clim. Dyn.* 52, 2185–2198. doi:10.1007/s00382-018-4248-6.
Oey, L.-Y., and Chou, S. C. (2016). Evidence of rising and poleward shift of storm surge in western North Pacific in recent decades. *J. Geophys. Res. Ocean.* 121, 5181–5192. doi:10.1002/2015JC011516.
Ogata, T., Mizuta, R., Adachi, Y., Murakami, H., and Ose, T. (2015). Effect of air-sea coupling on the frequency distribution of intense tropical cyclones over the northwestern Pacific. *Geophys. Res. Lett.* 42, 10,410-415,421. doi:10.1002/2015GL066774.
Ogata, T., Mizuta, R., Adachi, Y., Murakami, H., and Ose, T. (2016). Atmosphere-Ocean Coupling Effect on Intense Tropical Cyclone Distribution and its Future Change with 60 km-AOGCM. *Sci. Rep.* 6, 29800. doi:10.1038/srep29800.
Oguntunde, P. G., Abiodun, B. J., Lischeid, G., and Abatan, A. A. (2020). Droughts projection over the Niger and Volta River basins of West Africa at specific global warming levels. *Int. J. Climatol.* 40, 5688–5699. doi:10.1002/joc.6544.
Oh, H., Ha, K.-J., and Timmermann, A. (2018). Disentangling Impacts of Dynamic and Thermodynamic Components on Late Summer Rainfall Anomalies in East Asia. *J. Geophys. Res. Atmos.* 123, 8623–8633. doi:10.1029/2018JD028652.
Ohba, M., and Sugimoto, S. (2019). Differences in climate change impacts between weather patterns: possible effects on spatial heterogeneous changes in future extreme rainfall. *Clim. Dyn.* 52, 4177–4191. doi:10.1007/s00382-018-4374-1.
Ohba, M., and Sugimoto, S. (2020). Impacts of climate change on heavy wet snowfall in Japan. *Clim. Dyn.* 54, 3151–3164. doi:10.1007/s00382-020-05163-z.
Oizumi, T., Saito, K., Ito, J., Kuroda, T., Doc, L., DUC, L., et al. (2018). Ultra-High-Resolution Numerical Weather Prediction with a Large Domain Using the K Computer: A Case Study of the Izu Oshima Heavy Rainfall Event on October 15-16, 2013. *J. Meteorol. Soc. Japan. Ser. II* 96, 25–54. doi:10.2151/jmsj.2018-006.
Olmo, M., Bettolli, M. L., and Rusticucci, M. (2020). Atmospheric circulation influence on temperature and precipitation individual and compound daily extreme events: Spatial variability and trends over southern South America. *Weather Clim. Extrem.* 29, 100267. doi:10.1016/j.wace.2020.100267.
Olsson, J., and Foster, K. (2013). Short-term precipitation extremes in regional climate simulations for Sweden. *Hydrol. Res.* 45, 479–489. doi:10.2166/nh.2013.206.
Omondi, P. A., Awange, J. L., Forootan, E., Ogallo, L. A., Barakiza, R., Girmaw, G. B., et al. (2014). Changes in temperature and precipitation extremes over the Greater Horn of Africa region from 1961 to 2010. *Int. J. Climatol.* 34, 1262–1277. doi:10.1002/joc.3763.
Ongoma, V., Chen, H., and Gao, C. (2018a). Projected changes in mean rainfall and temperature over East Africa based on CMIP5 models. *Int. J. Climatol.* 38, 1375–1392. doi:10.1002/joc.5252.
Ongoma, V., Chen, H., Gao, C., Nyongesa, A. M., and Polong, F. (2018b). Future changes in climate extremes over Equatorial East Africa based on CMIP5 multimodel ensemble. *Nat. Hazards* 90, 901–920. doi:10.1007/s11069-017-3079-9.
Orlowsky, B., and Seneviratne, S. I. (2013). Elusive drought: Uncertainty in observed trends and short-and long-term CMIP5 projections. *Hydrol. Earth Syst. Sci.* 17, 1765–1781. doi:10.5194/hess-17-1765-2013.
Ortega, J. A., Razola, L., and Garzón, G. (2014). Recent human impacts and change in dynamics and morphology of ephemeral rivers. *Nat. Hazards Earth Syst. Sci.* 14, 713–730. doi:10.5194/nhess-14-713-2014.
Orth, R., Vogel, M. M., Luterbacher, J., Pfister, C., and Seneviratne, S. I. (2016a). Did European temperatures in 1540 exceed present-day records? *Environ. Res. Lett.* 11, 114021. doi:10.1088/1748-9326/11/11/114021.
Orth, R., Zscheischler, J., and Seneviratne, S. I. (2016b). Record dry summer in 2015 challenges precipitation projections in Central Europe. *Sci. Rep.* 6, 28334. doi:10.1038/srep28334.
Osima, S., Indasi, V. S., Zaroug, M., Endris, H. S., Gudoshava, M., Misiani, H. O., et al. (2018). Projected climate over the Greater Horn of Africa under 1.5 °C and 2 °C global warming. *Environ. Res. Lett.* 13, 065004. doi:10.1088/1748-9326/aaba1b.
Otkin, J. A., Anderson, M. C., Hain, C., Svoboda, M., Johnson, D., Mueller, R., et al. (2016). Assessing the evolution of soil moisture and vegetation conditions during the 2012 United States flash drought. *Agric. For. Meteorol.* 218–219, 230–242. doi:10.1016/j.agrformet.2015.12.065.
Otkin, J. A., Svoboda, M., Hunt, E. D., Ford, T. W., Anderson, M. C., Hain, C., et al. (2018). Flash droughts: A review and assessment of the challenges imposed by rapid-onset droughts in the United States. *Bull. Am. Meteorol. Soc.*

ACCEPTED VERSION SUBJECT TO FINAL EDITING

99, 911–919. doi:10.1175/BAMS-D-17-0149.1.
Otto, F. E. L. (2017). Attribution of Weather and Climate Events. *Annu. Rev. Environ. Resour.* 42, null. doi:10.1146/annurev-environ-102016-060847.
Otto, F. E. L., Boyd, E., Jones, R. G., Cornforth, R. J., James, R., Parker, H. R., et al. (2015a). Attribution of extreme weather events in Africa: a preliminary exploration of the science and policy implications. *Clim. Change* 132, 531–543. doi:10.1007/s10584-015-1432-0.
Otto, F. E. L., Harrington, L., Schmitt, K., Philip, S., Kew, S., van Oldenborgh, G. J., et al. (2020). Challenges to Understanding Extreme Weather Changes in Lower Income Countries. *Bull. Am. Meteorol. Soc.* 101, E1851–E1860. doi:10.1175/BAMS-D-19-0317.1.
Otto, F. E. L., Haustein, K., Uhe, P., Coelho, C. A. S., Aravequia, J. A., Almeida, W., et al. (2015b). Factors Other Than Climate Change, Main Drivers of 2014/15 Water Shortage in Southeast Brazil. *Bull. Am. Meteorol. Soc.* 96, S35–S40. doi:10.1175/BAMS-D-15-00120.1.
Otto, F. E. L., Jones, R. G., Halladay, K., and Allen, M. R. (2013). Attribution of changes in precipitation patterns in African rainforests. *Philos. Trans. R. Soc. B Biol. Sci.* 368, 20120299. doi:10.1098/rstb.2012.0299.
Otto, F. E. L., Massey, N., van Oldenborgh, G. J., Jones, R. G., and Allen, M. R. (2012). Reconciling two approaches to attribution of the 2010 Russian heat wave. *Geophys. Res. Lett.* 39, n/a-n/a. doi:10.1029/2011GL050422.
Otto, F. E. L., Philip, S., Kew, S., Li, S., King, A., and Cullen, H. (2018a). Attributing high-impact extreme events across timescales – a case study of four different types of events. *Clim. Change* 149, 399–412. doi:10.1007/s10584-018-2258-3.
Otto, F. E. L., Rosier, S. M., Allen, M. R., Massey, N. R., Rye, C. J., and Quintana, J. I. (2015c). Attribution analysis of high precipitation events in summer in England and Wales over the last decade. *Clim. Change* 132, 77–91. doi:10.1007/s10584-014-1095-2.
Otto, F. E. L., van der Wiel, K., van Oldenborgh, G. J., Philip, S., Kew, S. F., Uhe, P., et al. (2018b). Climate change increases the probability of heavy rains in Northern England/Southern Scotland like those of storm Desmond—a real-time event attribution revisited. *Environ. Res. Lett.* 13, 024006. doi:10.1088/1748-9326/aa9663.
Otto, F. E. L., van Oldenborgh, G. J., Eden, J., Stott, P. A., Karoly, D. J., and Allen, M. R. (2016). The attribution question. *Nat. Clim. Chang.* 6, 813–816. doi:10.1038/nclimate3089.
Otto, F. E. L., Wolski, P., Lehner, F., Tebaldi, C., van Oldenborgh, G. J., Hogesteeger, S., et al. (2018c). Anthropogenic influence on the drivers of the Western Cape drought 2015–2017. *Environ. Res. Lett.* 13, 124010. doi:10.1088/1748-9326/aae9f9.
Ozturk, T., Ceber, Z. P., Türkeş, M., and Kurnaz, M. L. (2015). Projections of climate change in the Mediterranean Basin by using downscaled global climate model outputs. *Int. J. Climatol.* 35, 4276–4292. doi:10.1002/joc.4285.
Paciorek, C. J., Stone, D. A., and Wehner, M. F. (2018). Quantifying statistical uncertainty in the attribution of human influence on severe weather. *Weather Clim. Extrem.* 20, 69–80. doi:10.1016/j.wace.2018.01.002.
Padrón, R. S., Gudmundsson, L., Decharme, B., Ducharne, A., Lawrence, D. M., Mao, J., et al. (2020). Observed changes in dry-season water availability attributed to human-induced climate change. *Nat. Geosci.* 13, 477–481. doi:10.1038/s41561-020-0594-1.
Padrón, R. S., Gudmundsson, L., and Seneviratne, S. I. (2019). Observational Constraints Reduce Likelihood of Extreme Changes in Multidecadal Land Water Availability. *Geophys. Res. Lett.* 46, 736–744. doi:10.1029/2018GL080521.
Pai, D. S., Sridhar, L., Badwaik, M. R., and Rajeevan, M. (2015). Analysis of the daily rainfall events over India using a new long period (1901–2010) high resolution (0.25° × 0.25°) gridded rainfall data set. *Clim. Dyn.* 45, 755–776. doi:10.1007/s00382-014-2307-1.
Paik, S., and Min, S.-K. (2018). Assessing the Impact of Volcanic Eruptions on Climate Extremes Using CMIP5 Models. *J. Clim.* 31, 5333–5349. doi:10.1175/JCLI-D-17-0651.1.
Paik, S., Min, S., Zhang, X., Donat, M. G., King, A. D., and Sun, Q. (2020). Determining the Anthropogenic Greenhouse Gas Contribution to the Observed Intensification of Extreme Precipitation. *Geophys. Res. Lett.* 47, e2019GL086875. doi:10.1029/2019GL086875.
Pal, J. S., and Eltahir, E. A. B. (2016). Future temperature in southwest Asia projected to exceed a threshold for human adaptability. *Nat. Clim. Chang.* 6, 197–200. doi:10.1038/nclimate2833.
Palazzi, E., Hardenberg, J., and Provenzale, A. (2013). Precipitation in the Hindu-Kush Karakoram Himalaya: Observations and future scenarios. *J. Geophys. Res. Atmos.* 118, 85–100. doi:10.1029/2012JD018697.
Palipane, E., and Grotjahn, R. (2018). Future Projections of the Large-Scale Meteorology Associated with California Heat Waves in CMIP5 Models. *J. Geophys. Res. Atmos.* 123, 8500–8517. doi:10.1029/2018JD029000.
Pall, P., Patricola, C. M., Wehner, M. F., Stone, D. A., Paciorek, C. J., and Collins, W. D. (2017). Diagnosing conditional anthropogenic contributions to heavy Colorado rainfall in September 2013. *Weather Clim. Extrem.* 17, 1–6. doi:10.1016/j.wace.2017.03.004.
Pall, P., Tallaksen, L. M., and Stordal, F. (2019). A climatology of rain-on-snow events for Norway. *J. Clim.* 32, 6995–7016. doi:10.1175/JCLI-D-18-0529.1.
Paltan, H., Allen, M., Haustein, K., Fuldauer, L., and Dadson, S. (2018). Global implications of 1.5 °C and 2 °C warmer worlds on extreme river flows. *Environ. Res. Lett.* 13, 94003. doi:10.1088/1748-9326/aad985.

ACCEPTED VERSION SUBJECT TO FINAL EDITING

Panisset, J. S., Libonati, R., Gouveia, C. M. P., Machado-Silva, F., França, D. A., França, J. R. A., et al. (2018). Contrasting patterns of the extreme drought episodes of 2005, 2010 and 2015 in the Amazon Basin. *Int. J. Climatol.* 38, 1096–1104. doi:10.1002/joc.5224.

Park, C., and Min, S.-K. (2018). Multi-RCM near-term projections of summer climate extremes over East Asia. *Clim. Dyn.* 0, 1–16. doi:10.1007/s00382-018-4425-7.

Park, C., Min, S.-K., Lee, D., Cha, D.-H., Suh, M.-S., Kang, H.-S., et al. (2016). Evaluation of multiple regional climate models for summer climate extremes over East Asia. *Clim. Dyn.* 46, 2469–2486. doi:10.1007/s00382-015-2713-z.

Park Williams, A., Cook, B. I., Smerdon, J. E., Bishop, D. A., Seager, R., and Mankin, J. S. (2017). The 2016 Southeastern U.S. Drought: An Extreme Departure From Centennial Wetting and Cooling. *J. Geophys. Res. Atmos.* 122, 10,810-888,905. doi:10.1002/2017JD027523.

Parker, H. R., Lott, F. C., Cornforth, R. J., Mitchell, D. M., Sparrow, S., and Wallom, D. (2017). A comparison of model ensembles for attributing 2012 West African rainfall. *Environ. Res. Lett.* 12, 14019. doi:10.1088/1748-9326/aa5386.

Parker, T. J., Berry, G. J., Reeder, M. J., and Nicholls, N. (2014). Modes of climate variability and heat waves in Victoria, southeastern Australia. *Geophys. Res. Lett.* 41, 6926–6934. doi:10.1002/2014GL061736.

Pascale, S., Kapnick, S. B., Delworth, T. L., and Cooke, W. F. (2020). Increasing risk of another Cape Town "Day Zero" drought in the 21st century. *Proc. Natl. Acad. Sci.* 117, 29495 LP-29503. doi:10.1073/pnas.2009144117.

Pascale, S., Lucarini, V., Feng, X., Porporato, A., and ul Hasson, S. (2016). Projected changes of rainfall seasonality and dry spells in a high greenhouse gas emissions scenario. *Clim. Dyn.* 46, 1331–1350. doi:10.1007/s00382-015-2648-4.

Paschalis, A., Fatichi, S., Molnar, P., Rimkus, S., and Burlando, P. (2014). On the effects of small scale space-time variability of rainfall on basin flood response. *J. Hydrol.* 514, 313–327. doi:10.1016/j.jhydrol.2014.04.014.

Patarčić, M., Gajić-Čapka, M., Cindrić, K., and Branković, C. (2014). Recent and near-future changes in precipitationextreme indices over the Croatian Adriatic coast. *Clim. Res.* 61, 157–176. doi:10.3354/cr01250.

Patra, P. K., Crisp, D., Kaiser, J. W., Wunch, D., Saeki, T., Ichii, K., et al. (2017). The Orbiting Carbon Observatory (OCO-2) tracks 2-3 peta-gram increase in carbon release to the atmosphere during the 2014-2016 El Niño. *Sci. Rep.* 7, 1–12. doi:10.1038/s41598-017-13459-0.

Patricola, C. M., Saravanan, R., and Chang, P. (2018). The Response of Atlantic Tropical Cyclones to Suppression of African Easterly Waves. *Geophys. Res. Lett.* 45, 471–479. doi:10.1002/2017GL076081.

Patricola, C. M., and Wehner, M. F. (2018). Anthropogenic influences on major tropical cyclone events. *Nature* 563, 339–346. doi:10.1038/s41586-018-0673-2.

Paul, S., Ghosh, S., Mathew, M., Devanand, A., Karmakar, S., and Niyogi, D. (2018). Increased Spatial Variability and Intensification of Extreme Monsoon Rainfall due to Urbanization. *Sci. Rep.* 8, 3918. doi:10.1038/s41598-018-22322-9.

Paulo, A., Martins, D., and Pereira, L. S. (2016). Influence of Precipitation Changes on the SPI and Related Drought Severity. An Analysis Using Long-Term Data Series. *Water Resour. Manag.* 30, 5737–5757. doi:10.1007/s11269-016-1388-5.

Paxian, A., Hertig, E., Seubert, S., Vogt, G., Jacobeit, J., and Paeth, H. (2014). Present-day and future mediterranean precipitation extremes assessed by different statistical approaches. *Clim. Dyn.* 44, 845–860. doi:10.1007/s00382-014-2428-6.

Pedron, I. T., Silva Dias, M. A. F., de Paula Dias, S., Carvalho, L. M. V., and Freitas, E. D. (2017). Trends and variability in extremes of precipitation in Curitiba – Southern Brazil. *Int. J. Climatol.* 37, 1250–1264. doi:10.1002/joc.4773.

Peña-Angulo, D., Reig-Gracia, F., Domínguez-Castro, F., Revuelto, J., Aguilar, E., van der Schrier, G., et al. (2020a). ECTACI: European Climatology and Trend Atlas of Climate Indices (1979–2017). *J. Geophys. Res. Atmos.* 125. doi:10.1029/2020JD032798.

Peña-Angulo, D., Vicente-Serrano, S. M., Domínguez-Castro, F., Murphy, C., Reig, F., Tramblay, Y., et al. (2020b). Long-term precipitation in Southwestern Europe reveals no clear trend attributable to anthropogenic forcing. *Environ. Res. Lett.* 15, 094070. doi:10.1088/1748-9326/ab9c4f.

Pendergrass, A. G. (2018). What precipitation is extreme? *Science (80-.).* 360, 1072–1073. doi:10.1126/science.aat1871.

Pendergrass, A. G., Coleman, D. B., Deser, C., Lehner, F., Rosenbloom, N., and Simpson, I. R. (2019). Nonlinear Response of Extreme Precipitation to Warming in CESM1. *Geophys. Res. Lett.* 46, 10551–10560. doi:10.1029/2019GL084826.

Pendergrass, A. G., Lehner, F., Sanderson, B. M., and Xu, Y. (2015). Does extreme precipitation intensity depend on the emissions scenario? *Geophys. Res. Lett.* 42, 8767–8774. doi:10.1002/2015GL065854.

Pendergrass, A. G., Meehl, G. A., Pulwarty, R., Hobbins, M., Hoell, A., AghaKouchak, A., et al. (2020). Flash droughts present a new challenge for subseasonal-to-seasonal prediction. *Nat. Clim. Chang.* 10, 191–199. doi:10.1038/s41558-020-0709-0.

Pepler, A., Ashcroft, L., and Trewin, B. (2018). The relationship between the subtropical ridge and Australian temperatures. *J. South. Hemisph. Earth Syst. Sci.* 68, 201–214. doi:10.22499/3.6801.011.

ACCEPTED VERSION SUBJECT TO FINAL EDITING

Pepler, A. S., Di Luca, A., Ji, F., Alexander, L. V., Evans, J. P., and Sherwood, S. C. (2015). Impact of Identification Method on the Inferred Characteristics and Variability of Australian East Coast Lows. *Mon. Weather Rev.* 143, 864–877. doi:10.1175/MWR-D-14-00188.1.

Pepler, A. S., Luca, A. Di, Ji, F., Alexander, L. V, Evans, J. P., and Sherwood, S. C. (2016). Projected changes in east Australian midlatitude cyclones during the 21st century. *Geophys. Res. Lett.* 43, 334–340. doi:10.1002/2015GL067267.Received.

Pereira, L. S., Allen, R. G., Smith, M., and Raes, D. (2015). Crop evapotranspiration estimation with FAO56: Past and future. *Agric. Water Manag.* 147, 4–20. doi:10.1016/j.agwat.2014.07.031.

Perkins-Kirkpatrick, S. E., and Gibson, P. B. (2018). Changes in regional heatwave characteristics as a function of increasing global temperature. *Sci. Rep.* 7, 1–12. doi:10.1038/s41598-017-12520-2.

Perkins-Kirkpatrick, S. E., and Lewis, S. C. (2020). Increasing trends in regional heatwaves. *Nat. Commun.* 11, 1–8. doi:10.1038/s41467-020-16970-7.

Perkins-Kirkpatrick, S. E., White, C. J., Alexander, L. V, Argüeso, D., Boschat, G., Cowan, T., et al. (2016). Natural hazards in Australia: heatwaves. *Clim. Change* 139, 101–114. doi:10.1007/s10584-016-1650-0.

Perkins, S. E. (2015). A review on the scientific understanding of heatwaves – Their measurement, driving mechanisms, and changes at the global scale. *Atmos. Res.* 164–165, 242–267. doi:10.1016/j.atmosres.2015.05.014.

Perkins, S. E., and Alexander, L. V (2013). On the Measurement of Heat Waves. *J. Clim.* 26, 4500–4517. doi:10.1175/JCLI-D-12-00383.1.

Perkins, S. E., and Gibson, P. B. (2015). Increased Risk of the 2014 Australian May Heatwave Due to Anthropogenic Activity. *Bull. Am. Meteorol. Soc.* 96, S154–S157. doi:10.1175/BAMS-D-15-00074.1.

Perkins, S. E., Lewis, S. C., King, A. D., and Alexander, L. V (2014). Increased simulated risk of the hot Australian summer of 2012-2013 due to anthropogenic activity as measured by heatwave frequency and intensity [in "Explaining Extreme Events of 2013 from a Climate Perspective"]. *Bull. Am. Meteorol. Soc.* 95, S34--S37. doi:10.1175/1520-0477-95.9.S1.1.

Persad, G. G., and Caldeira, K. (2018). Divergent global-scale temperature effects from identical aerosols emitted in different regions. *Nat. Commun.* 9, 3289. doi:10.1038/s41467-018-05838-6.

Peterson, T. C., Heim, R. R., Hirsch, R., Kaiser, D. P., Brooks, H., Diffenbaugh, N. S., et al. (2013a). Monitoring and Understanding Changes in Heat Waves, Cold Waves, Floods, and Droughts in the United States: State of Knowledge. *Bull. Am. Meteorol. Soc.* 94, 821–834. doi:10.1175/BAMS-D-12-00066.1.

Peterson, T. C., Hoerling, M. P., Stott, P. A., and Herring, S. C. (2013b). Explaining Extreme Events of 2012 from a Climate Perspective. *Bull. Am. Meteorol. Soc.* 94, S1–S74. doi:10.1175/BAMS-D-13-00085.1.

Peterson, T. C., Stott, P. A., and Herring, S. (2012). Explaining Extreme Events of 2011 from a Climate Perspective. *Bull. Am. Meteorol. Soc.* 93, 1041–1067. doi:10.1175/BAMS-D-12-00021.1.

Pfahl, S., O'Gorman, P. A., and Fischer, E. M. (2017). Understanding the regional pattern of projected future changes in extreme precipitation. *Nat. Clim. Chang.* 7, 423. doi:10.1038/nclimate3287.

Pfahl, S., and Wernli, H. (2012). Quantifying the relevance of cyclones for precipitation extremes. *J. Clim.* 25, 6770–6780. doi:10.1175/JCLI-D-11-00705.1.

Phelan, P. E., Kaloush, K., Miner, M., Golden, J., Phelan, B., Silva, H., et al. (2015). Urban Heat Island: Mechanisms, Implications, and Possible Remedies. *Annu. Rev. Environ. Resour.* 40, 285–307. doi:10.1146/annurev-environ-102014-021155.

Phibbs, S., and Toumi, R. (2016). The dependence of precipitation and its footprint on atmospheric temperature in idealized extratropical cyclones. *J. Geophys. Res.* 121, 8743–8754. doi:10.1002/2015JD024286.

Philip, S., Kew, S. F., Jan van Oldenborgh, G., Aalbers, E., Vautard, R., Otto, F., et al. (2018a). Validation of a Rapid Attribution of the May/June 2016 Flood-Inducing Precipitation in France to Climate Change. *J. Hydrometeorol.* 19, 1881–1898. doi:10.1175/JHM-D-18-0074.1.

Philip, S., Kew, S. F., Jan van Oldenborgh, G., Otto, F., O'Keefe, S., Haustein, K., et al. (2018b). Attribution Analysis of the Ethiopian Drought of 2015. *J. Clim.* 31, 2465–2486. doi:10.1175/JCLI-D-17-0274.1.

Philip, S., Kew, S., van Oldenborgh, G. J., Otto, F., Vautard, R., van der Wiel, K., et al. (2020). A protocol for probabilistic extreme event attribution analyses. *Adv. Stat. Clim. Meteorol. Ocean.* 6, 177–203. doi:10.5194/ascmo-6-177-2020.

Philip, S., Sparrow, S., Kew, S. F., van der Wiel, K., Wanders, N., Singh, R., et al. (2019). Attributing the 2017 Bangladesh floods from meteorological and hydrological perspectives. *Hydrol. Earth Syst. Sci.* 23, 1409–1429. doi:10.5194/hess-23-1409-2019.

Piaget, N., Froidevaux, P., Giannakaki, P., Gierth, F., Martius, O., Riemer, M., et al. (2015). Dynamics of a local Alpine flooding event in October 2011: moisture source and large-scale circulation. *Q. J. R. Meteorol. Soc.* 141, 1922–1937. doi:10.1002/qj.2496.

Pinto, I., Jack, C., and Hewitson, B. (2018). Process-based model evaluation and projections over southern Africa from Coordinated Regional Climate Downscaling Experiment and Coupled Model Intercomparison Project Phase 5 models. *Int. J. Climatol.*, 1–11. doi:10.1002/joc.5666.

Pinto, I., Lennard, C., Tadross, M., Hewitson, B., Dosio, A., Nikulin, G., et al. (2016). Evaluation and projections of extreme precipitation over southern Africa from two CORDEX models. *Clim. Change* 135. doi:10.1007/s10584-

SUBJECT TO FINAL EDITING
ACCEPTED VERSION

015-1573-1.
Pisaniello, J. D., Tingey-Holyoak, J., and Burritt, R. L. (2012). Appropriate small dam management for minimizing catchment-wide safety threats: International benchmarked guidelines and demonstrative cases studies. *Water Resour. Res.* 48. doi:10.1029/2011WR011155.
Pithan, F., and Mauritsen, T. (2014). Arctic amplification dominated by temperature feedbacks in contemporary climate models. *Nat. Geosci.* 7, 181–184. doi:10.1038/ngeo2071.
Piticar, A. (2018). Changes in heat waves in Chile. *Glob. Planet. Change* 169, 234–246. doi:10.1016/j.gloplacha.2018.08.007.
Piticar, A., Mihăilă, D., Lazurca, L. G., Bistricean, P.-I., Puţuntică, A., and Briciu, A.-E. (2016). Spatiotemporal distribution of reference evapotranspiration in the Republic of Moldova. *Theor. Appl. Climatol.* 124, 1133–1144. doi:10.1007/s00704-015-1490-2.
Podschwit, H. R., Larkin, N. K., Steel, E. A., Cullen, A., and Alvarado, E. (2018). Multi-model forecasts of very-large fire occurences during the end of the 21st century. *Climate* 6, 1–21. doi:10.3390/cli6040100.
Pokhrel, Y., Felfelani, F., Satoh, Y., Boulange, J., Burek, P., Gädeke, A., et al. (2021). Global terrestrial water storage and drought severity under climate change. *Nat. Clim. Chang.* doi:10.1038/s41558-020-00972-w.
Poshtiri, M. P., and Pal, I. (2016). Patterns of hydrological drought indicators in major U.S. River basins. *Clim. Change* 134, 549–563. doi:10.1007/s10584-015-1542-8.
Potopová, V., Štěpánek, P., Zahradníček, P., Farda, A., Türkott, L., and Soukup, J. (2018). Projected changes in the evolution of drought on various timescales over the Czech Republic according to Euro-CORDEX models. *Int. J. Climatol.* 38, e939–e954. doi:10.1002/joc.5421.
Preimesberger, W., Scanlon, T., Su, C.-H., Gruber, A., and Dorigo, W. (2020). Homogenization of Structural Breaks in the Global ESA CCI Soil Moisture Multisatellite Climate Data Record. *IEEE Trans. Geosci. Remote Sens.*, 1–18. doi:10.1109/tgrs.2020.3012896.
Prein, A. F., Gobiet, A., Truhetz, H., Keuler, K., Goergen, K., Teichmann, C., et al. (2016a). Precipitation in the EURO-CORDEX 0.11∘ and 0.44∘ simulations: high resolution, high benefits? *Clim. Dyn.* 46, 383–412. doi:10.1007/s00382-015-2589-y.
Prein, A. F., and Holland, G. J. (2018). Global estimates of damaging hail hazard. *Weather Clim. Extrem.* 22, 10–23. doi:10.1016/j.wace.2018.10.004.
Prein, A. F., Langhans, W., Fosser, G., Ferrone, A., Ban, N., Goergen, K., et al. (2015). A review on regional convection-permitting climate modeling: Demonstrations, prospects, and challenges. *Rev. Geophys.* 53, 323–361. doi:10.1002/2014RG000475.
Prein, A. F., Liu, C., Ikeda, K., Bullock, R., Rasmussen, R. M., Holland, G. J., et al. (2017a). Simulating North American mesoscale convective systems with a convection-permitting climate model. *Clim. Dyn.* 0, 1–16. doi:10.1007/s00382-017-3993-2.
Prein, A. F., Liu, C., Ikeda, K., Trier, S. B., Rasmussen, R. M., Holland, G. J., et al. (2017b). Increased rainfall volume from future convective storms in the US. *Nat. Clim. Chang.* 7, 880–884. doi:10.1038/s41558-017-0007-7.
Prein, A. F., Rasmussen, R. M., Ikeda, K., Liu, C., Clark, M. P., and Holland, G. J. (2016b). The future intensification of hourly precipitation extremes. *Nat. Clim. Chang.* 7, 48. doi:10.1038/nclimate3168.
Priestley, M. D. K. K., Ackerley, D., Catto, J. L., Hodges, K. I., McDonald, R. E., and Lee, R. W. (2020). An Overview of the Extratropical Storm Tracks in CMIP6 Historical Simulations. *J. Clim.* 33, 6315–6343. doi:10.1175/JCLI-D-19-0928.1.
Priya, P., Krishnan, R., Mujumdar, M., and Houze, R. A. (2017). Changing monsoon and midlatitude circulation interactions over the Western Himalayas and possible links to occurrences of extreme precipitation. *Clim. Dyn.* 49, 2351–2364. doi:10.1007/s00382-016-3458-z.
Prudhomme, C., Giuntoli, I., Robinson, E. L., Clark, D. B., Arnell, N. W., Dankers, R., et al. (2014). Hydrological droughts in the 21st century, hotspots and uncertainties from a global multimodel ensemble experiment. *Proc. Natl. Acad. Sci. U. S. A.* 111, 3262–3267. doi:10.1073/pnas.1222473110.
Púčik, T., Groenemeijer, P., Rädler, A. T., Tijssen, L., Nikulin, G., Prein, A. F., et al. (2017). Future Changes in European Severe Convection Environments in a Regional Climate Model Ensemble. *J. Clim.* 30, 6771–6794. doi:10.1175/JCLI-D-16-0777.1.
Qian, C., Wang, J., Dong, S., Yin, H., Burke, C., Ciavarella, A., et al. (2018). Human Influence on the Record-breaking Cold Event in January of 2016 in Eastern China [in "Explaining Extreme Events of 2016 from a Climate Perspective"]. *Bull. Am. Meteorol. Soc.* 99, S118–S122. doi:10.1175/BAMS-D-17-0095.1.
Qian, C., Zhang, X., and Li, Z. (2019). Linear trends in temperature extremes in China, with an emphasis on non-Gaussian and serially dependent characteristics. *Clim. Dyn.* 53, 533–550. doi:10.1007/s00382-018-4600-x.
Qin, N., Wang, J., Yang, G., Chen, X., Liang, H., and Zhang, J. (2015a). Spatial and temporal variations of extreme precipitation and temperature events for the Southwest China in 1960–2009. *Geoenvironmental Disasters* 2. doi:10.1186/s40677-015-0014-9.
Qin, Y., Yang, D., Lei, H., Xu, K., and Xu, X. (2015b). Comparative analysis of drought based on precipitation and soil moisture indices in Haihe basin of North China during the period of 1960–2010. *J. Hydrol.* 526, 55–67. doi:10.1016/j.jhydrol.2014.09.068.

ACCEPTED VERSION
SUBJECT TO FINAL EDITING

Qiu, J., Gao, Q., Wang, S., and Su, Z. (2016). Comparison of temporal trends from multiple soil moisture data sets and precipitation: The implication of irrigation on regional soil moisture trend. *Int. J. Appl. Earth Obs. Geoinf.* 48, 17–27. doi:10.1016/j.jag.2015.11.012.

Quesada, B., Vautard, R., Yiou, P., Hirschi, M., and Seneviratne, S. I. (2012). Asymmetric European summer heat predictability from wet and dry southern winters and springs. *Nat. Clim. Chang.* 2, 736–741. doi:10.1038/nclimate1536.

Quintana-Seguí, P., Barella-Ortiz, A., Regueiro-Sanfiz, S., and Miguez-Macho, G. (2020). The Utility of Land-Surface Model Simulations to Provide Drought Information in a Water Management Context Using Global and Local Forcing Datasets. *Water Resour. Manag.* 34, 2135–2156. doi:10.1007/s11269-018-2160-9.

Quiring, S. M., Ford, T. W., Wang, J. K., Khong, A., Harris, E., Lindgren, T., et al. (2016). The North American Soil Moisture Database: Development and Applications. *Bull. Am. Meteorol. Soc.* 97, 1441–1459. doi:10.1175/BAMS-D-13-00263.1.

Raghavan, S. V, Hur, J., and Liong, S.-Y. (2018). Evaluations of NASA NEX-GDDP data over Southeast Asia: present and future climates. *Clim. Change* 148, 503–518. doi:10.1007/s10584-018-2213-3.

Ragone, F., Mariotti, M., Parodi, A., von Hardenberg, J., and Pasquero, C. (2018). A Climatological Study of Western Mediterranean Medicanes in Numerical Simulations with Explicit and Parameterized Convection. *Atmosphere (Basel).* 9, 397. doi:10.3390/atmos9100397.

Rahimi, M., and Fatemi, S. S. (2019). Mean versus Extreme Precipitation Trends in Iran over the Period 1960–2017. *Pure Appl. Geophys.* 176, 3717–3735. doi:10.1007/s00024-019-02165-9.

Rahimi, M., and Hejabi, S. (2018). Spatial and temporal analysis of trends in extreme temperature indices in Iran over the period 1960–2014. *Int. J. Climatol.* 38, 272–282. doi:10.1002/joc.5175.

Rahimi, M., Mohammadian, N., Vanashi, A. R., and Whan, K. (2018). Trends in Indices of Extreme Temperature and Precipitation in Iran over the Period 1960-2014. *Open J. Ecol.* 08, 396–415. doi:10.4236/oje.2018.87024.

Rai, P., Choudhary, A., and Dimri, A. P. (2019). Future precipitation extremes over India from the CORDEX-South Asia experiments. *Theor. Appl. Climatol.* doi:10.1007/s00704-019-02784-1.

Rajbhandari, R., Shrestha, A. B., Kulkarni, A., Patwardhan, S. K., and Bajracharya, S. R. (2015). Projected changes in climate over the Indus river basin using a high resolution regional climate model (PRECIS). *Clim. Dyn.* 44, 339–357. doi:10.1007/s00382-014-2183-8.

Rajczak, J., Pall, P., and Schär, C. (2013). Projections of extreme precipitation events in regional climate simulations for Europe and the Alpine Region. *J. Geophys. Res. Atmos.* 118, 3610–3626. doi:10.1002/jgrd.502972013.

Rajczak, J., and Schär, C. (2017). Projections of Future Precipitation Extremes Over Europe: A Multimodel Assessment of Climate Simulations. *J. Geophys. Res. Atmos.* 122, 10,773-10,800. doi:10.1002/2017JD027176.

Rajsekhar, D., and Gorelick, S. M. (2017). Increasing drought in Jordan: Climate change and cascading Syrian land-use impacts on reducing transboundary flow. *Sci. Adv.* 3, 1–15. doi:10.1126/sciadv.1700581.

Ralph, F. M., Dettinger, M. D., Cairns, M. M., Galarneau, T. J., and Eylander, J. (2018). Defining "Atmospheric River": How the Glossary of Meteorology Helped Resolve a Debate. *Bull. Am. Meteorol. Soc.* 99, 837–839. doi:10.1175/BAMS-D-17-0157.1.

Ramos, A. M., Tomé, R., Trigo, R. M., Liberato, M. L. R., and Pinto, J. G. (2016). Projected changes in atmospheric rivers affecting Europe in CMIP5 models. *Geophys. Res. Lett.* 43, 9315–9323. doi:10.1002/2016GL070634.

Rasmijn, L. M., Van Der Schrier, G., Bintanja, R., Barkmeijer, J., Sterl, A., and Hazeleger, W. (2018). Future equivalent of 2010 Russian heatwave intensified by weakening soil moisture constraints. *Nat. Clim. Chang.* 8, 381–385. doi:10.1038/s41558-018-0114-0.

Rasmussen, K. L., and Houze, R. A. (2011). Orogenic Convection in Subtropical South America as Seen by the TRMM Satellite. *Mon. Weather Rev.* 139, 2399–2420. doi:10.1175/MWR-D-10-05006.1.

Rasmussen, K. L., Prein, A. F., Rasmussen, R. M., Ikeda, K., and Liu, C. (2017). Changes in the convective population and thermodynamic environments in convection-permitting regional climate simulations over the United States. *Clim. Dyn.* doi:10.1007/s00382-017-4000-7.

Ratnam, J. V., Behera, S. K., Ratna, S. B., Rajeevan, M., and Yamagata, T. (2016). Anatomy of Indian heatwaves. *Sci. Rep.* 6, 1–11. doi:10.1038/srep24395.

Rauniyar, S. P., and Power, S. B. (2020). The impact of anthropogenic forcing and natural processes on past, present, and future rainfall over Victoria, Australia. *J. Clim.* 33, 8087–8106. doi:10.1175/JCLI-D-19-0759.1.

Raymond, C., Horton, R. M., Zscheischler, J., Martius, O., AghaKouchak, A., Balch, J., et al. (2020). Understanding and managing connected extreme events. *Nat. Clim. Chang.* 10, 611–621. doi:10.1038/s41558-020-0790-4.

Raymond, F., Ullmann, A., Camberlin, P., Oueslati, B., and Drobinski, P. (2018). Atmospheric conditions and weather regimes associated with extreme winter dry spells over the Mediterranean basin. *Clim. Dyn.* 50, 4437–4453. doi:10.1007/s00382-017-3884-6.

Raymond, F., Ullmann, A., Tramblay, Y., Drobinski, P., and Camberlin, P. (2019). Evolution of Mediterranean extreme dry spells during the wet season under climate change. *Reg. Environ. Chang.* 19, 2339–2351. doi:10.1007/s10113-019-01526-3.

Reale, M., and Lionello, P. (2013). Synoptic climatology of winter intense precipitation events along the Mediterranean coasts. *Nat. Hazards Earth Syst. Sci.* 13, 1707–1722. doi:10.5194/nhess-13-1707-2013.

ACCEPTED VERSION SUBJECT TO FINAL EDITING

Reboita, M. S., da Rocha, R. P., Ambrizzi, T., and Gouveia, C. D. (2015). Trend and teleconnection patterns in the climatology of extratropical cyclones over the Southern Hemisphere. *Clim. Dyn.* 45, 1929–1944. doi:10.1007/s00382-014-2447-3.

Reboita, M. S., Reale, M., da Rocha, R. P., Giorgi, F., Giuliani, G., Coppola, E., et al. (2020). Future changes in the wintertime cyclonic activity over the CORDEX-CORE southern hemisphere domains in a multi-model approach. *Clim. Dyn.* doi:10.1007/s00382-020-05317-z.

Redmond, G., Hodges, K. I., Mcsweeney, C., Jones, R., and Hein, D. (2015). Projected changes in tropical cyclones over Vietnam and the South China Sea using a 25 km regional climate model perturbed physics ensemble. *Clim. Dyn.* 45, 1983–2000. doi:10.1007/s00382-014-2450-8.

Reed, K. A., Bacmeister, J. T., Huff, J. J. A., Wu, X., Bates, S. C., and Rosenbloom, N. A. (2019). Exploring the Impact of Dust on North Atlantic Hurricanes in a High-Resolution Climate Model. *Geophys. Res. Lett.* 46, 1105–1112. doi:10.1029/2018GL080642.

Reed, K. A., Bacmeister, J. T., Rosenbloom, N. A., Wehner, M. F., Bates, S. C., Lauritzen, P. H., et al. (2015). Impact of the dynamical core on the direct simulation of tropical cyclones in a high-resolution global model. *Geophys. Res. Lett.* 42, 3603–3608. doi:10.1002/2015GL063974.

Reed, K. A., and Jablonowski, C. (2011). Impact of physical parameterizations on idealized tropical cyclones in the Community Atmosphere Model. *Geophys. Res. Lett.* 38. doi:10.1029/2010GL046297.

Reed, K. A., Stansfield, A. M., Wehner, M. F., and Zarzycki, C. M. (2020). Forecasted attribution of the human influence on Hurricane Florence. *Sci. Adv.* 6, eaaw9253. doi:10.1126/sciadv.aaw9253.

Rehbein, A., Ambrizzi, T., and Mechoso, C. R. (2018). Mesoscale convective systems over the Amazon basin. Part I: climatological aspects. *Int. J. Climatol.* 38, 215–229. doi:10.1002/joc.5171.

Rehman, S. (2013). Long-term wind speed analysis and detection of its trends using Mann-Kendall test and linear regression method. *Arab. J. Sci. Eng.* 38, 421–437. doi:10.1007/s13369-012-0445-5.

Reichle, R. H., Draper, C. S., Liu, Q., Girotto, M., Mahanama, S. P. P., Koster, R. D., et al. (2017). Assessment of MERRA-2 Land Surface Hydrology Estimates. *J. Clim.* 30, 2937–2960. doi:10.1175/JCLI-D-16-0720.1.

Ren, L., Ren, L., Zhou, T., Zhou, T., Zhou, T., and Zhang, W. (2020). Attribution of the record-breaking heat event over Northeast Asia in summer 2018: The role of circulation. *Environ. Res. Lett.* 15. doi:10.1088/1748-9326/ab8032.

Reyer, C. P. ., Otto, I. M., Adams, S., Albrecht, T., Baarsch, F., Cartsburg, M., et al. (2017). Climate change impacts in Central Asia and their implications for development. *Reg. Environ. Chang.* 17, 1639–1650. doi:10.1007/s10113-015-0893-z.

Rhoades, A. M., Ullrich, P. A., and Zarzycki, C. M. (2018). Projecting 21st century snowpack trends in western USA mountains using variable-resolution CESM. *Clim. Dyn.* 50, 261–288. doi:10.1007/s00382-017-3606-0.

Ribal, A., and Young, I. R. (2019). 33 Years of Globally Calibrated Wave Height and Wind Speed Data Based on Altimeter Observations. *Sci. data* 6, 77. doi:10.1038/s41597-019-0083-9.

Ribeiro, I. O., Andreoli, R. V., Kayano, M. T., Sousa, T. R., Medeiros, A. S., Godoi, R. H. M., et al. (2018). Biomass burning and carbon monoxide patterns in Brazil during the extreme drought years of 2005, 2010, and 2015. *Environ. Pollut.* 243, 1008–1014. doi:10.1016/j.envpol.2018.09.022.

Ribes, A., Thao, S., Vautard, R., Dubuisson, B., Somot, S., Colin, J., et al. (2019). Observed increase in extreme daily rainfall in the French Mediterranean. *Clim. Dyn.* 52, 1095–1114. doi:10.1007/s00382-018-4179-2.

Ridder, N., de Vries, H., and Drijfhout, S. (2018). The role of atmospheric rivers in compound events consisting of heavy precipitation and high storm surges along the Dutch coast. *Nat. Hazards Earth Syst. Sci.* 18, 3311–3326. doi:10.5194/nhess-18-3311-2018.

Ridder, N. N., Pitman, A. J., Westra, S., Ukkola, A., Do, H. X., Bador, M., et al. (2020). Global hotspots for the occurrence of compound events. *Nat. Commun.* 11, 5956. doi:10.1038/s41467-020-19639-3.

Ridley, J., Wiltshire, A., and Mathison, C. (2013). More frequent occurrence of westerly disturbances in Karakoram up to 2100. *Sci. Total Environ.* 468–469, S31–S35. doi:10.1016/J.SCITOTENV.2013.03.074.

Ringard, J., Dieppois, B., Rome, S., Diedhiou, A., Pellarin, T., Konaré, A., et al. (2016). The intensification of thermal extremes in west Africa. *Glob. Planet. Change* 139, 66–77. doi:10.1016/j.gloplacha.2015.12.009.

Risser, M. D., and Wehner, M. F. (2017). Attributable Human-Induced Changes in the Likelihood and Magnitude of the Observed Extreme Precipitation during Hurricane Harvey. *Geophys. Res. Lett.* 44, 12,412-457,464. doi:10.1002/2017GL075888.

Rivera, J. A., and Arnould, G. (2020). Evaluation of the ability of CMIP6 models to simulate precipitation over Southwestern South America: Climatic features and long-term trends (1901–2014). *Atmos. Res.* 241, 104953. doi:https://doi.org/10.1016/j.atmosres.2020.104953.

Rivera, J. A., and Penalba, O. C. (2018). Spatio-temporal assessment of streamflow droughts over Southern South America: 1961–2006. *Theor. Appl. Climatol.* 133, 1021–1033. doi:10.1007/s00704-017-2243-1.

Roberts, M. J., Camp, J., Seddon, J., Vidale, P. L., Hodges, K., Vanniere, B., et al. (2020a). Impact of model resolution on tropical cyclone simulation using the HighResMIP PRIMAVERA multi-model ensemble. *J. Clim.* 33, 2557–2583. doi:10.1175/JCLI-D-19-0639.1.

Roberts, M. J., Camp, J., Seddon, J., Vidale, P. L., Hodges, K., Vanniere, B., et al. (2020b). Projected Future changes of

ACCEPTED VERSION SUBJECT TO FINAL EDITING

tropical cyclones using the CMIP6 HighResMIP multi-model ensemble. *Geophys. Res. Lett.* 47, e2020GL088662. doi:10.1029/2020GL088662.
Roberts, M. J., Vidale, P. L., Senior, C., Hewitt, H. T., Bates, C., Berthou, S., et al. (2018). The Benefits of Global High Resolution for Climate Simulation: Process Understanding and the Enabling of Stakeholder Decisions at the Regional Scale. *Bull. Am. Meteorol. Soc.* 99, 2341–2359. doi:10.1175/BAMS-D-15-00320.1.
Rodell, M., Famiglietti, J. S., Wiese, D. N., Reager, J. T., Beaudoing, H. K., Landerer, F. W., et al. (2018). Emerging trends in global freshwater availability. *Nature* 557, 651–659. doi:10.1038/s41586-018-0123-1.
Roderick, M. L., Greve, P., and Farquhar, G. D. (2015). On the assessment of aridity with changes in atmospheric CO2. *Water Resour. Res.* 51, 5450–5463. doi:10.1002/2015WR017031.
Rogelj, J. (2013). Uncertainties of low greenhouse gas emission scenarios. doi:doi.org/10.3929/ethz-a-009915210.
Rogger, M., Agnoletti, M., Alaoui, A., Bathurst, J. C., Bodner, G., Borga, M., et al. (2017). Land use change impacts on floods at the catchment scale: Challenges and opportunities for future research. *Water Resour. Res.* 53, 5209–5219. doi:10.1002/2017WR020723.
Rohat, G., Flacke, J., Dosio, A., Pedde, S., Dao, H., and van Maarseveen, M. (2019). Influence of changes in socioeconomic and climatic conditions on future heat-related health challenges in Europe. *Glob. Planet. Change* 172, 45–59. doi:10.1016/j.gloplacha.2018.09.013.
Rohini, P., Rajeevan, M., and Srivastava, A. K. (2016). On the Variability and Increasing Trends of Heat Waves over India. *Sci. Rep.*, 1–9.
Romera, R., Gaertner, M. Á., Sánchez, E., Domínguez, M., González-Alemán, J. J., and Miglietta, M. M. (2017). Climate change projections of medicanes with a large multi-model ensemble of regional climate models. *Glob. Planet. Change* 151, 134–143. doi:10.1016/j.gloplacha.2016.10.008.
Romero, R., and Emanuel, K. (2013). Medicane risk in a changing climate. *J. Geophys. Res. Atmos.* 118, 5992–6001. doi:10.1002/jgrd.50475.
Romero, R., and Emanuel, K. (2017). Climate change and hurricane-like extratropical cyclones: Projections for North Atlantic polar lows and medicanes based on CMIP5 models. *J. Clim.* 30, 279–299. doi:10.1175/JCLI-D-16-0255.1.
Romps, D. M. (2016). Clausius-clapeyron scaling of CAPE from analytical solutions to RCE. *J. Atmos. Sci.* 73, 3719–3737. doi:10.1175/JAS-D-15-0327.1.
Rosenzweig, B. R., McPhillips, L., Chang, H., Cheng, C., Welty, C., Matsler, M., et al. (2018). Pluvial flood risk and opportunities for resilience. *WIREs Water* 5, e1302. doi:10.1002/wat2.1302.
Rosier, S., Dean, S., Stuart, S., Carey-Smith, T., Black, M. T., and Massey, N. (2016). Extreme rainfall in early July 2014 in northland, New Zealand-was there an anthropogenic influence? *Bull. Am. Meteorol. Soc.* 96, S136–S140. doi:10.1175/BAMS-D-15-00105.1.
Roth, M., Buishand, T. A., Jongbloed, G., Klein Tank, A. M. G., and van Zanten, J. H. (2014). Projections of precipitation extremes based on a regional, non-stationary peaks-over-threshold approach: A case study for the Netherlands and north-western Germany. *Weather Clim. Extrem.* 4, 1–10. doi:10.1016/j.wace.2014.01.001.
Roth, M., Jongbloed, G., and Buishand, A. (2018). Monotone trends in the distribution of climate extremes. *Theor. Appl. Climatol.* doi:10.1007/s00704-018-2546-x.
Roudier, P., Andersson, J. C. M., Donnelly, C., Feyen, L., Greuell, W., and Ludwig, F. (2016). Projections of future floods and hydrological droughts in Europe under a +2°C global warming. *Clim. Change* 135, 341–355. doi:10.1007/s10584-015-1570-4.
Rowell, D. P., Booth, B. B. B., Nicholson, S. E., and Good, P. (2015). Reconciling Past and Future Rainfall Trends over East Africa. *J. Clim.* 28, 9768–9788. doi:10.1175/JCLI-D-15-0140.1.
Rowland, L., Da Costa, A. C. L., Galbraith, D. R., Oliveira, R. S., Binks, O. J., Oliveira, A. A. R., et al. (2015). Death from drought in tropical forests is triggered by hydraulics not carbon starvation. *Nature* 528, 119–122. doi:10.1038/nature15539.
Roxy, M. K. K., Ghosh, S., Pathak, A., Athulya, R., Mujumdar, M., Murtugudde, R., et al. (2017). A threefold rise in widespread extreme rain events over central India. *Nat. Commun.* 8, 708. doi:10.1038/s41467-017-00744-9.
Roy, S. Sen (2019). Spatial patterns of trends in seasonal extreme temperatures in India during 1980–2010. *Weather Clim. Extrem.* 24, 100203. doi:10.1016/j.wace.2019.100203.
Ruffault, J., Curt, T., Martin-Stpaul, N. K., Moron, V., and Trigo, R. M. (2018). Extreme wildfire events are linked to global-change-type droughts in the northern Mediterranean. *Nat. Hazards Earth Syst. Sci.* 18, 847–856. doi:10.5194/nhess-18-847-2018.
Ruml, M., Gregorić, E., Vujadinović, M., Radovanović, S., Matović, G., Vuković, A., et al. (2017). Observed changes of temperature extremes in Serbia over the period 1961 − 2010. *Atmos. Res.* 183, 26–41. doi:10.1016/j.atmosres.2016.08.013.
Ruosteenoja, K., Markkanen, T., Venäläinen, A., Räisänen, P., and Peltola, H. (2018). Seasonal soil moisture and drought occurrence in Europe in CMIP5 projections for the 21st century. *Clim. Dyn.* 50, 1177–1192. doi:10.1007/s00382-017-3671-4.
Rupp, D. E., Mote, P. W., Massey, N., Otto, F. E. L., and Allen, M. R. (2013). Human influence on the probability of low precipitation in the central United States in 2012 [in "Explaining Extreme Events of 2012 from a Climate

ACCEPTED VERSION SUBJECT TO FINAL EDITING

Perspective"]. *Bull. Am. Meteorol. Soc.* 94, S2–S6. doi:10.1175/BAMS-D-13-00085.1.
Ruprich-Robert, Y., Delworth, T., Msadek, R., Castruccio, F., Yeager, S., and Danabasoglu, G. (2018). Impacts of the Atlantic Multidecadal Variability on North American Summer Climate and Heat Waves. *J. Clim.* 31, 3679–3700. doi:10.1175/JCLI-D-17-0270.1.
Russo, S., Dosio, A., Sterl, A., Barbosa, P., and Vogt, J. (2013). Projection of occurrence of extreme dry-wet years and seasons in Europe with stationary and nonstationary Standardized Precipitation Indices. *J. Geophys. Res. Atmos.* 118, 7628–7639. doi:10.1002/jgrd.50571.
Russo, S., Marchese, A. F., Sillmann, J., and Immé, G. (2016). When will unusual heat waves become normal in a warming Africa? *Environ. Res. Lett.* 11, 054016. doi:10.1088/1748-9326/11/5/054016.
Russo, S., Sillmann, J., and Fischer, E. M. (2015). Top ten European heatwaves since 1950 and their occurrence in the coming decades. *Environ. Res. Lett.* 10, 124003. doi:10.1088/1748-9326/10/12/124003.
Rusticucci, M., Barrucand, M., and Collazo, S. (2017). Temperature extremes in the Argentina central region and their monthly relationship with the mean circulation and ENSO phases. *Int. J. Climatol.* 37, 3003–3017. doi:10.1002/joc.4895.
Sabeerali, C. T., Rao, S. A., Dhakate, A. R., Salunke, K., and Goswami, B. N. (2015). Why ensemble mean projection of south Asian monsoon rainfall by CMIP5 models is not reliable? *Clim. Dyn.* 45, 161–174. doi:10.1007/s00382-014-2269-3.
Saha, A., Ghosh, S., Sahana, A. S., and Rao, E. P. (2014). Failure of CMIP5 climate models in simulating post-1950 decreasing trend of Indian monsoon. *Geophys. Res. Lett.* 41, 7323–7330. doi:10.1002/2014GL061573.
Sahoo, B., and Bhaskaran, P. K. (2016). Assessment on historical cyclone tracks in the Bay of Bengal, east coast of India. *Int. J. Climatol.* 36, 95–109. doi:10.1002/joc.4331.
Salinger, M. J., and Porteous, A. S. (2014). New Zealand Climate: Patterns of Drought 1941/42 – 2012/13. *Weather Clim.* 34, 2–19. doi:10.2307/26169741.
Salnikov, V., Tutulina, G., Polyakova, S., Petrova, Y., and Skakova, A. (2015). Climate change in Kazakhstan during the past 70 years. *Quat. Int.* 358, 77–82. doi:10.1016/j.quaint.2014.09.008.
Salvador, M. de A., and de Brito, J. I. B. (2018). Trend of annual temperature and frequency of extreme events in the MATOPIBA region of Brazil. *Theor. Appl. Climatol.* 133, 253–261. doi:10.1007/s00704-017-2179-5.
Salvi, K., and Ghosh, S. (2016). Projections of Extreme Dry and Wet Spells in the 21st Century India Using Stationary and Non-stationary Standardized Precipitation Indices. *Clim. Change* 139, 667–681. doi:10.1007/s10584-016-1824-9.
Samaniego, L., Kumar, R., Breuer, L., Chamorro, A., Flörke, M., Pechlivanidis, I. G., et al. (2017). Propagation of forcing and model uncertainties on to hydrological drought characteristics in a multi-model century-long experiment in large river basins. *Clim. Change* 141, 435–449. doi:10.1007/s10584-016-1778-y.
Samaniego, L., Thober, S., Kumar, R., Wanders, N., Rakovec, O., Pan, M., et al. (2018). Anthropogenic warming exacerbates European soil moisture droughts. *Nat. Clim. Chang.* 8, 421–426. doi:10.1038/s41558-018-0138-5.
Samouly, A. Al, Luong, C. N., Li, Z., Smith, S., Baetz, B., and Ghaith, M. (2018). Performance of multi-model ensembles for the simulation of temperature variability over Ontario, Canada. *Environ. Earth Sci.* 77, 524. doi:10.1007/s12665-018-7701-2.
Samset, B. H., Sand, M., Smith, C. J., Bauer, S. E., Forster, P. M., Fuglestvedt, J. S., et al. (2018). Climate Impacts From a Removal of Anthropogenic Aerosol Emissions. *Geophys. Res. Lett.* 45, 1020–1029. doi:10.1002/2017GL076079.
Samset, B. H., Stjern, C. W., Lund, M. T., Mohr, C. W., Sand, M., and Daloz, A. S. (2019). How Daily Temperature and Precipitation Distributions Evolve With Global Surface Temperature. *Earth's Futur.* 7, 1323–1336. doi:10.1029/2019EF001160.
Samuels, R., Hochman, A., Baharad, A., Givati, A., Levi, Y., Yosef, Y., et al. (2018). Evaluation and projection of extreme precipitation indices in the Eastern Mediterranean based on CMIP5 multi-model ensemble. *Int. J. Climatol.* 38, 2280–2297. doi:10.1002/joc.5334.
Sánchez-Benítez, A., Barriopedro, D., and García-Herrera, R. (2020). Tracking Iberian heatwaves from a new perspective. *Weather Clim. Extrem.* 28, 100238. doi:10.1016/j.wace.2019.100238.
Sanchez-Lorenzo, A., Wild, M., Brunetti, M., Guijarro, J. A., Hakuba, M. Z., Calbó, J., et al. (2015). Reassessment and update of long-term trends in downward surface shortwave radiation over Europe (1939-2012). *J. Geophys. Res.* 120, 9555–9569. doi:10.1002/2015JD023321.
Sanderson, B. M., Xu, Y., Tebaldi, C., Wehner, M., O'Neill, B., Jahn, A., et al. (2017a). Community climate simulations to assess avoided impacts in 1.5 and 2C futures. *Earth Syst. Dyn.* 8, 827–847. doi:10.5194/esd-8-827-2017.
Sanderson, M., Economou, T., Salmon, K., and Jones, S. (2017b). Historical Trends and Variability in Heat Waves in the United Kingdom. *Atmosphere (Basel).* 8, 117–191. doi:10.3390/atmos8100191.
Sandvik, M. I., Sorteberg, A., and Rasmussen, R. (2018). Sensitivity of historical orographically enhanced extreme precipitation events to idealized temperature perturbations. *Clim. Dyn.* 50, 143–157. doi:10.1007/s00382-017-3593-1.
Sanginés de Cárcer, P., Vitasse, Y., Peñuelas, J., Jassey, V. E. J., Buttler, A., and Signarbieux, C. (2018). Vapor–

ACCEPTED VERSION SUBJECT TO FINAL EDITING

pressure deficit and extreme climatic variables limit tree growth. *Glob. Chang. Biol.* 24, 1108–1122. doi:10.1111/gcb.13973.
Sanogo, S., Fink, A. H., Omotosho, J. A., Ba, A., Redl, R., and Ermert, V. (2015). Spatio-temporal characteristics of the recent rainfall recovery in West Africa. *Int. J. Climatol.* 35, 4589–4605. doi:10.1002/joc.4309.
Santanello Jr., J. A., Dirmeyer, P. A., Ferguson, C. R., Findell, K. L., Tawfik, A. B., Berg, A., et al. (2018). Land–Atmosphere Interactions: The LoCo Perspective. *Bull. Am. Meteorol. Soc.* 99, 1253–1272. doi:10.1175/BAMS-D-17-0001.1.
Sarangi, C., Tripathi, S. N., Kanawade, V. P., Koren, I., and Pai, D. S. (2017). Investigation of the aerosol–cloud–rainfall association over the Indian summer monsoon region. *Atmos. Chem. Phys.* 17, 5185–5204. doi:10.5194/acp-17-5185-2017.
Sarhadi, A., Ausín, M. C., Wiper, M. P., Touma, D., and Diffenbaugh, N. S. (2018). Multidimensional risk in a nonstationary climate: Joint probability of increasingly severe warm and dry conditions. *Sci. Adv.* 4, eaau3487. doi:10.1126/sciadv.aau3487.
Sato, T., and Nakamura, T. (2019). Intensification of hot Eurasian summers by climate change and land–atmosphere interactions. *Sci. Rep.* 9, 10866. doi:10.1038/s41598-019-47291-5.
Satoh, M., Stevens, B., Judt, F., Khairoutdinov, M., Lin, S., and Putman, W. M. (2019). Global Cloud-Resolving Models. *Curr. Clim. Chang. Reports*. doi:10.1007/s40641-019-00131-0.
Satoh, M., Tomita, H., Yashiro, H., Kajikawa, Y., Miyamoto, Y., Yamaura, T., et al. (2017). Outcomes and challenges of global high-resolution non-hydrostatic atmospheric simulations using the K computer. *Prog. Earth Planet. Sci.* 4, 13. doi:10.1186/s40645-017-0127-8.
Satoh, M., Yamada, Y., Sugi, M., Komada, C., and Noda, A. T. (2015). Constraint on Future Change in Global Frequency of Tropical Cyclones due to Global Warming. *J. Meteorol. Soc. Japan. Ser. II* 93, 489–500. doi:10.2151/jmsj.2015-025.
Saurral, R. I., Camilloni, I. A., and Barros, V. R. (2017). Low-frequency variability and trends in centennial precipitation stations in southern South America. *Int. J. Climatol.* 37, 1774–1793. doi:10.1002/joc.4810.
Scaife, A. A., Comer, R., Dunstone, N., Fereday, D., Folland, C., Good, E., et al. (2017). Predictability of European winter 2015/2016. *Atmos. Sci. Lett.* 18, 38–44. doi:10.1002/asl.721.
Schaller, N., Kay, A. L., Lamb, R., Massey, N. R., van Oldenborgh, G. J., Otto, F. E. L., et al. (2016). Human influence on climate in the 2014 southern England winter floods and their impacts. *Nat. Clim. Chang.* 6, 627–634. doi:10.1038/nclimate2927.
Schaller, N., Otto, F. E. L., van Oldenborgh, G. J., Massey, N. R., Sparrow, S., and Allen, M. R. (2014). The heavy precipitation event of May-June 2013 in the upper Danube and Elbe basins. *Bull. Amer. Meteor. Soc.* 95, S69–S72.
Schaller, N., Sillmann, J., Anstey, J., Fischer, E. M., Grams, C. M., and Russo, S. (2018). Influence of blocking on Northern European and Western Russian heatwaves in large climate model ensembles. *Environ. Res. Lett.* 13. doi:10.1088/1748-9326/aaba55.
Schaller, N., Sillmann, J., Müller, M., Haarsma, R., Hazeleger, W., Hegdahl, T. J., et al. (2020). The role of spatial and temporal model resolution in a flood event storyline approach in western Norway. *Weather Clim. Extrem.* 29, 100259. doi:10.1016/j.wace.2020.100259.
Scheff, J. (2018). Drought Indices, Drought Impacts, CO2, and Warming: a Historical and Geologic Perspective. *Curr. Clim. Chang. Reports* 4, 202–209. doi:10.1007/s40641-018-0094-1.
Scheff, J., and Frierson, D. M. W. (2015). Terrestrial aridity and its response to greenhouse warming across CMIP5 climate models. *J. Clim.* 28, 5583–5600. doi:10.1175/JCLI-D-14-00480.1.
Scheff, J., Mankin, J. S., Coats, S., and Liu, H. (2021). CO2-plant effects do not account for the gap between dryness indices and projected dryness impacts in CMIP6 or CMIP5. *Environ. Res. Lett.* 16, 34018. doi:10.1088/1748-9326/abd8fd.
Scheff, J., Seager, R., Liu, H., and Coats, S. (2017). Are glacials dry? Consequences for paleoclimatology and for greenhouse warming. *J. Clim.* 30, 6593–6609. doi:10.1175/JCLI-D-16-0854.1.
Scher, S., Haarsma, R. J., de Vries, H., Drijfhout, S. S., and van Delden, A. J. (2017). Resolution dependence of extreme precipitation and deep convection over the Gulf Stream. *J. Adv. Model. Earth Syst.* 9, 1186–1194. doi:10.1002/2016MS000903.
Scherrer, S. C., Fischer, E. M., Posselt, R., Liniger, M. A., Croci-Maspoli, M., and Knutti, R. (2016). Emerging trends in heavy precipitation and hot temperature extremes in Switzerland. *J. Geophys. Res. Atmos.* 121, 2626–2637. doi:10.1002/2015JD024634.
Schewe, J., Heinke, J., Gerten, D., Haddeland, I., Arnell, N. W., Clark, D. B., et al. (2014). Multimodel assessment of water scarcity under climate change. *Proc. Natl. Acad. Sci.* 111, 3245–3250. doi:10.1073/pnas.1222460110.
Schleussner, C.-F., Lissner, T. K., Fischer, E. M., Wohland, J., Perrette, M., Golly, A., et al. (2016). Differential climate impacts for policy-relevant limits to global warming: the case of 1.5 °C and 2 °C. *Earth Syst. Dyn.* 7, 327–351. doi:10.5194/esd-7-327-2016.
Schmid, P. E., and Niyogi, D. (2017). Modeling Urban Precipitation Modification by Spatially Heterogeneous Aerosols. *J. Appl. Meteorol. Climatol.* 56, 2141–2153. doi:10.1175/JAMC-D-16-0320.1.

ACCEPTED VERSION SUBJECT TO FINAL EDITING

Schneider, D., Huggel, C., Cochachin, A., Guillén, S., and García, J. (2014). Mapping hazards from glacier lake outburst floods based on modelling of process cascades at Lake 513, Carhuaz, Peru. *Adv. Geosci.* 35, 145–155. doi:10.5194/adgeo-35-145-2014.

Schneider, T., Bischoff, T., and Płotka, H. (2015). Physics of changes in synoptic midlatitude temperature variability. *J. Clim.* 28, 2312–2331. doi:10.1175/JCLI-D-14-00632.1.

Schoetter, R., Cattiaux, J., and Douville, H. (2015). Changes of western European heat wave characteristics projected by the CMIP5 ensemble. *Clim. Dyn.* 45, 1601–1616. doi:10.1007/s00382-014-2434-8.

Schreck, C. J., Knapp, K. R., and Kossin, J. P. (2014). The impact of best track discrepancies on global tropical cyclone climatologies using IBTrACS. *Mon. Weather Rev.* 142, 3881–3899. doi:10.1175/MWR-D-14-00021.1.

Schubert, S. D., Stewart, R. E., Wang, H., Barlow, M., Berbery, E. H., Cai, W., et al. (2016). Global Meteorological Drought: A Synthesis of Current Understanding with a Focus on SST Drivers of Precipitation Deficits. *J. Clim.* 29, 3989–4019. doi:10.1175/JCLI-D-15-0452.1.

Schubert, S. D., Wang, H., Koster, R. D., Suarez, M. J., and Groisman, P. Y. (2014). Northern Eurasian heat waves and droughts. *J. Clim.* 27, 3169–3207. doi:10.1175/JCLI-D-13-00360.1.

Schumacher, D. L., Keune, J., van Heerwaarden, C. C., Vilà-Guerau de Arellano, J., Teuling, A. J., and Miralles, D. G. (2019). Amplification of mega-heatwaves through heat torrents fuelled by upwind drought. *Nat. Geosci.* 12, 712–717. doi:10.1038/s41561-019-0431-6.

Schumacher, R. S., and Johnson, R. H. (2005). Organization and Environmental Properties of Extreme-Rain-Producing Mesoscale Convective Systems. *Mon. Weather Rev.* 133, 961–976. doi:10.1175/MWR2899.1.

Schwanghart, W., Worni, R., Huggel, C., Stoffel, M., and Korup, O. (2016). Uncertainty in the Himalayan energy–water nexus: estimating regional exposure to glacial lake outburst floods. *Environ. Res. Lett.* 11, 074005. doi:10.1088/1748-9326/11/7/074005.

Schwingshackl, C., Davin, E. L., Hirschi, M., Sørland, S. L., Wartenburger, R., and Seneviratne, S. I. (2019). Regional climate model projections underestimate future warming due to missing plant physiological CO2 response. *Environ. Res. Lett.* 14, 114019. doi:10.1088/1748-9326/ab4949.

Scoccimarro, E., Fogli, P. G., Reed, K. A., Gualdi, S., Masina, S., and Navarra, A. (2017). Tropical cyclone interaction with the ocean: The role of high-frequency (subdaily) coupled processes. *J. Clim.* 30, 145–162. doi:10.1175/JCLI-D-16-0292.1.

Seager, R., and Hoerling, M. (2014). Atmosphere and ocean origins of North American droughts. *J. Clim.* 27, 4581–4606. doi:10.1175/JCLI-D-13-00329.1.

Seager, R., Hoerling, M., Schubert, S., Wang, H., Lyon, B., Kumar, A., et al. (2015a). Causes of the 2011-14 California drought. *J. Clim.* 28, 6997–7024. doi:10.1175/JCLI-D-14-00860.1.

Seager, R., Hooks, A., Williams, A. P., Cook, B., Nakamura, J., and Henderson, N. (2015b). Climatology, Variability, and Trends in the U.S. Vapor Pressure Deficit, an Important Fire-Related Meteorological Quantity. *J. Appl. Meteorol. Climatol.* 54, 1121–1141. doi:10.1175/JAMC-D-14-0321.1.

Seager, R., Nakamura, J., and Ting, M. (2019). Mechanisms of seasonal soil moisture drought onset and termination in the southern Great Plains. *J. Hydrometeorol.* 20, 751–771. doi:10.1175/JHM-D-18-0191.1.

Sedlmeier, K., Feldmann, H., and Schädler, G. (2018). Compound summer temperature and precipitation extremes over central Europe. *Theor. Appl. Climatol.* 131, 1493–1501. doi:10.1007/s00704-017-2061-5.

Seeley, J. T., and Romps, D. M. (2015). Why does tropical convective available potential energy (CAPE) increase with warming? *Geophys. Res. Lett.* 42, 10,410-429,437. doi:10.1002/2015GL066199.

Seiler, C., and Zwiers, F. W. (2016a). How well do CMIP5 climate models reproduce explosive cyclones in the extratropics of the Northern Hemisphere? *Clim. Dyn.* 46, 1241–1256. doi:10.1007/s00382-015-2642-x.

Seiler, C., and Zwiers, F. W. (2016b). How will climate change affect explosive cyclones in the extratropics of the Northern Hemisphere? *Clim. Dyn.* 46, 3633–3644. doi:10.1007/s00382-015-2791-y.

Seiler, C., Zwiers, F. W., Hodges, K. I., and Scinocca, J. F. (2018). How does dynamical downscaling affect model biases and future projections of explosive extratropical cyclones along North America's Atlantic coast? *Clim. Dyn.* 50, 677–692. doi:10.1007/s00382-017-3634-9.

Sekizawa, S., Miyasaka, T., Nakamura, H., Shimpo, A., Takemura, K., and Maeda, S. (2019). Anomalous Moisture Transport and Oceanic Evaporation during a Torrential Rainfall Event over Western Japan in Early July 2018. *SOLA* 15A, 25–30. doi:10.2151/sola.15A-005.

Selten, F. M., Bintanja, R., Vautard, R., and van den Hurk, B. J. J. M. (2020). Future continental summer warming constrained by the present-day seasonal cycle of surface hydrology. *Sci. Rep.* 10, 4721. doi:10.1038/s41598-020-61721-9.

Sen Roy, S., and Rouault, M. (2013). Spatial patterns of seasonal scale trends in extreme hourly precipitation in South Africa. *Appl. Geogr.* 39, 151–157. doi:10.1016/j.apgeog.2012.11.022.

Şen, Z. (2018). *Flood Modeling, Prediction and Mitigation*. Cham, Switzerland: Springer doi:10.1007/978-3-319-52356-9.

Seneviratne, S. I., Corti, T., Davin, E. L., Hirschi, M., Jaeger, E. B., Lehner, I., et al. (2010). Investigating soil moisture-climate interactions in a changing climate: A review. *Earth-Science Rev.* 99, 125–161. doi:10.1016/j.earscirev.2010.02.004.

ACCEPTED VERSION SUBJECT TO FINAL EDITING

Seneviratne, S. I., Donat, M. G., Mueller, B., and Alexander, L. V. (2014). No pause in the increase of hot temperature extremes. *Nat. Clim. Chang.* 4, 161–163. doi:10.1038/nclimate2145.
Seneviratne, S. I., Donat, M. G., Pitman, A. J., Knutti, R., and Wilby, R. L. (2016). Allowable CO2 emissions based on regional and impact-related climate targets. *Nature* 529, 477–483. doi:10.1038/nature16542.
Seneviratne, S. I., and Hauser, M. (2020). Regional climate sensitivity of climate extremes in CMIP6 vs CMIP5 multi-model ensembles. *Earth's Futur.* doi:10.1029/2019EF001474.
Seneviratne, S. I., Nicholls, N., Easterling, D., Goodess, C. M., Kanae, S., Kossin, J., et al. (2012). "Changes in Climate Extremes and their Impacts on the Natural Physical Environment," in *Managing the Risks of Extreme Events and Disasters to Advance Climate Change Adaptation*, eds. C. B. Field, V. Barros, T. F. Stocker, and Q. Dahe (Cambridge, United Kingdom and New York, NY, USA: Cambridge University Press), 109–230. doi:10.1017/CBO9781139177245.006.
Seneviratne, S. I., Rogelj, J., Séférian, R., Wartenburger, R., Allen, M. R., Cain, M., et al. (2018a). The many possible climates from the Paris Agreement's aim of 1.5 °C warming. *Nature* 558, 41–49. doi:10.1038/s41586-018-0181-4.
Seneviratne, S. I., Wartenburger, R., Guillod, B. P., Hirsch, A. L., Vogel, M. M., Brovkin, V., et al. (2018b). Climate extremes, land–climate feedbacks and land-use forcing at 1.5°C. *Philos. Trans. R. Soc. A Math. Phys. Eng. Sci.* 376, 20160450. doi:10.1098/rsta.2016.0450.
Seneviratne, S. I., Wilhelm, M., Stanelle, T., Van Den Hurk, B., Hagemann, S., Berg, A., et al. (2013). Impact of soil moisture-climate feedbacks on CMIP5 projections: First results from the GLACE-CMIP5 experiment. *Geophys. Res. Lett.* 40, 5212–5217. doi:10.1002/grl.50956.
Seo, Y.-W., Kim, H., Yun, K.-S., Lee, J.-Y., Ha, K.-J., and Moon, J.-Y. (2014). Future change of extreme temperature climate indices over East Asia with uncertainties estimation in the CMIP5. *Asia-Pacific J. Atmos. Sci.* 50, 609–624. doi:10.1007/s13143-014-0050-5.
Seong, M.-G., Min, S.-K., Kim, Y.-H., Zhang, X., and Sun, Y. (2020). Anthropogenic Greenhouse Gas and Aerosol Contributions to Extreme Temperature Changes During 1951-2015. *J. Clim.*, 1–41. doi:10.1175/JCLI-D-19-1023.1.
Serrano-Notivoli, R., Beguería, S., Saz, M. Á., and de Luis, M. (2018). Recent trends reveal decreasing intensity of daily precipitation in Spain. *Int. J. Climatol.* 38, 4211–4224. doi:10.1002/joc.5562.
Sevanto, S., Mcdowell, N. G., Dickman, L. T., Pangle, R., and Pockman, W. T. (2014). How do trees die? A test of the hydraulic failure and carbon starvation hypotheses. *Plant, Cell Environ.* 37, 153–161. doi:10.1111/pce.12141.
Shaevitz, D. A., Camargo, S. J., Sobel, A. H., Jonas, J. A., Kim, D., Kumar, A., et al. (2014). Characteristics of tropical cyclones in high-resolution models in the present climate. *J. Adv. Model. Earth Syst.* 6, 1154–1172. doi:10.1002/2014MS000372.
Shanas, P. R., and Kumar, V. S. (2015). Trends in surface wind speed and significant wave height as revealed by ERA-Interim wind wave hindcast in the Central Bay of Bengal. *Int. J. Climatol.* 35, 2654–2663. doi:10.1002/joc.4164.
Sharafati, A., Nabaei, S., and Shahid, S. (2020). Spatial assessment of meteorological drought features over different climate regions in Iran. *Int. J. Climatol.* 40, 1864–1884. doi:10.1002/joc.6307.
Sharma, A., Wasko, C., and Lettenmaier, D. P. (2018). If precipitation extremes are increasing, why aren't floods? *Water Resour. Res.* 54, 8545–8551. doi:10.1029/2018WR023749.
Sharma, S., and Mujumdar, P. (2017). Increasing frequency and spatial extent of concurrent meteorological droughts and heatwaves in India. *Sci. Rep.* 7, 15582. doi:10.1038/s41598-017-15896-3.
Sharmila, S., and Walsh, K. J. E. (2018). Recent poleward shift of tropical cyclone formation linked to Hadley cell expansion. *Nat. Clim. Chang.* doi:10.1038/s41558-018-0227-5.
Shashikanth, K., Ghosh, S., H. V., and Karmakar, S. (2018). Future projections of Indian summer monsoon rainfall extremes over India with statistical downscaling and its consistency with observed characteristics. *Clim. Dyn.* 51, 1–15. doi:10.1007/s00382-017-3604-2.
Shastri, H., Paul, S., Ghosh, S., and Karmakar, S. (2015). Impacts of urbanization on Indian summer monsoon rainfall extremes. *J. Geophys. Res. Atmos.* 120, 496–516. doi:10.1002/2014JD022061.
Shaw, T. A., Baldwin, M., Barnes, E. A., Caballero, R., Garfinkel, C. I., Hwang, Y.-T., et al. (2016). Storm track processes and the opposing influences of climate change. *Nat. Geosci.* 9, 656–664. doi:10.1038/ngeo2783.
Sheffield, J., Wood, E. F., and Roderick, M. L. (2012). Little change in global drought over the past 60 years. *Nature* 491, 435–438. doi:10.1038/nature11575.
Sheikh, M. M., Manzoor, N., Ashraf, J., Adnan, M., Collins, D., Hameed, S., et al. (2015). Trends in extreme daily rainfall and temperature indices over South Asia. *Int. J. Climatol.* 35, 1625–1637. doi:10.1002/joc.4081.
Shephard, M. W., Mekis, E., Morris, R. J., Feng, Y., Zhang, X., Kilcup, K., et al. (2014). Trends in Canadian Short-Duration Extreme Rainfall: Including an Intensity–Duration–Frequency Perspective. *Atmosphere-Ocean* 52, 398–417. doi:10.1080/07055900.2014.969677.
Shepherd, J. M. (2013). Impacts of Urbanization on Precipitation and Storms: Physical Insights and Vulnerabilities. *Clim. Vulnerability*, 109–125. doi:10.1016/B978-0-12-384703-4.00503-7.
Shepherd, T. G. (2014). Atmospheric circulation as a source of uncertainty in climate change projections. *Nat. Geosci.* 7, 703–708. doi:10.1038/NGEO2253.

ACCEPTED VERSION SUBJECT TO FINAL EDITING

Shepherd, T. G. (2016). A Common Framework for Approaches to Extreme Event Attribution. *Curr. Clim. Chang. Reports* 2, 28–38. doi:10.1007/s40641-016-0033-y.
Shepherd, T. G., Boyd, E., Calel, R. A., Chapman, S. C., Dessai, S., Dima-West, I. M., et al. (2018). Storylines: an alternative approach to representing uncertainty in physical aspects of climate change. *Clim. Change* 151, 555–571. doi:10.1007/s10584-018-2317-9.
Sheridan, S. C., Lee, C. C., and Smith, E. T. (2020). A Comparison Between Station Observations and Reanalysis Data in the Identification of Extreme Temperature Events. *Geophys. Res. Lett.* 47. doi:10.1029/2020GL088120.
Sherwood, S. C., Bony, S., and Dufresne, J.-L. (2014). Spread in model climate sensitivity traced to atmospheric convective mixing. *Nature* 505, 37–42. doi:10.1038/nature12829.
Sherwood, S., and Fu, Q. (2014). A Drier Future? *Science (80-.).* 343, 737–739. doi:10.1126/science.1247620.
Shevchenko, O., Lee, H., Snizhko, S., and Mayer, H. (2014). Long-term analysis of heat waves in Ukraine. *Int. J. Climatol.* 34, 1642–1650. doi:10.1002/joc.3792.
Shi, C., Jiang, Z.-H., Chen, W.-L., and Li, L. (2018). Changes in temperature extremes over China under 1.5 °C and 2 °C global warming targets. *Adv. Clim. Chang. Res.* 9, 120–129. doi:10.1016/j.accre.2017.11.003.
Shi, L., Feng, P., Wang, B., Liu, D. L., and Yu, Q. (2020). Quantifying future drought change and associated uncertainty in southeastern Australia with multiple potential evapotranspiration models. *J. Hydrol.* 590, 125394. doi:https://doi.org/10.1016/j.jhydrol.2020.125394.
Shi, Y., Wang, G., and Gao, X. (2017). Role of resolution in regional climate change projections over China. *Clim. Dyn.* 51, 2375–2396. doi:10.1007/s00382-017-4018-x.
Shimpo, A., Takemura, K., Wakamatsu, S., Togawa, H., Mochizuki, Y., Takekawa, M., et al. (2019a). Primary Factors behind the Heavy Rain Event of July 2018 and the Subsequent Heat Wave in Japan. *SOLA* 15A, 13–18. doi:10.2151/sola.15A-003.
Shimpo, A., Takemura, K., Wakamatsu, S., Togawa, H., Mochizuki, Y., Takekawa, M., et al. (2019b). Primary Factors behind the Heavy Rain Event of July 2018 and the Subsequent Heat Wave in Japan. *SOLA* 15A, 13–18. doi:10.2151/sola.15A-003.
Shin, J., Olson, R., and An, S.-I. (2018). Projected Heat Wave Characteristics over the Korean Peninsula During the Twenty-First Century. *Asia-Pacific J. Atmos. Sci.* 54, 53–61. doi:10.1007/s13143-017-0059-7.
Shiogama, H., Hirata, R., Hasegawa, T., Fujimori, S., Ishizaki, N. N., Chatani, S., et al. (2020). Historical and future anthropogenic warming effects on droughts, fires and fire emissions of CO2 and PM2.5 in equatorial Asia when 2015-like El Niño events occur. *Earth Syst. Dyn.* 11, 435–445. doi:10.5194/esd-11-435-2020.
Shiogama, H., Imada, Y., Mori, M., Mizuta, R., Stone, D., Yoshida, K., et al. (2016). Attributing Historical Changes in Probabilities of Record-Breaking Daily Temperature and Precipitation Extreme Events. *SOLA* 12, 225–231. doi:10.2151/sola.2016-045.
Shiogama, H., Watanabe, M., Imada, Y., Mori, M., Ishii, M., and Kimoto, M. (2013). An event attribution of the 2010 drought in the South Amazon region using the MIROC5 model. *Atmos. Sci. Lett.* 14, 170–175. doi:10.1002/asl2.435.
Shukla, S., Safeeq, M., AghaKouchak, A., Guan, K., and Funk, C. (2015). Temperature impacts on the water year 2014 drought in California. *Geophys. Res. Lett.* 42, 4384–4393. doi:10.1002/2015GL063666.
Sigmond, M., Fyfe, J. C., and Swart, N. C. (2018). Ice-free Arctic projections under the Paris Agreement. *Nat. Clim. Chang.* 8, 404–408. doi:10.1038/s41558-018-0124-y.
Sikorska, A. E., Viviroli, D., and Seibert, J. (2015). Flood-type classification in mountainous catchments using crisp and fuzzy decision trees. *Water Resour. Res.* 51, 7959–7976. doi:10.1002/2015WR017326.
Sillmann, J., Donat, M. G., Fyfe, J. C., and Zwiers, F. W. (2014). Observed and simulated temperature extremes during the recent warming hiatus. *Environ. Res. Lett.* 9, 64023–64029. doi:10.1088/1748-9326/9/6/064023.
Sillmann, J., Kharin, V. V., Zhang, X., Zwiers, F. W., and Bronaugh, D. (2013a). Climate extremes indices in the CMIP5 multimodel ensemble: Part 1. Model evaluation in the present climate. *J. Geophys. Res. Atmos.* 118, 1716–1733. doi:10.1002/jgrd.50203.
Sillmann, J., Kharin, V. V., Zwiers, F. W., Zhang, X., and Bronaugh, D. (2013b). Climate extremes indices in the CMIP5 multimodel ensemble: Part 2. Future climate projections. *J. Geophys. Res. Atmos.* 118, 2473–2493. doi:10.1002/jgrd.50188.
Sillmann, J., Stjern, C. W., Myhre, G., and Forster, P. M. (2017a). Slow and fast responses of mean and extreme precipitation to different forcing in CMIP5 simulations. *Geophys. Res. Lett.* 44, 6383–6390. doi:10.1002/2017GL073229.
Sillmann, J., Stjern, C. W., Myhre, G., Samset, B. H., Hodnebrog, Ø., Andrews, T., et al. (2019). Extreme wet and dry conditions affected differently by greenhouse gases and aerosols. *npj Clim. Atmos. Sci.* 2, 24. doi:10.1038/s41612-019-0079-3.
Sillmann, J., Thorarinsdottir, T., Keenlyside, N., Schaller, N., Alexander, L. V., Hegerl, G., et al. (2017b). Understanding, modeling and predicting weather and climate extremes: Challenges and opportunities. *Weather Clim. Extrem.* 18, 65–74. doi:10.1016/j.wace.2017.10.003.
Simmons, A. J., Willett, K. M., Jones, P. D., Thorne, P. W., and Dee, D. P. (2010). Low-frequency variations in surface atmospheric humidity, temperature, and precipitation: Inferences from reanalyses and monthly gridded

ACCEPTED VERSION SUBJECT TO FINAL EDITING

observational data sets. *J. Geophys. Res. Atmos.* 115. doi:10.1029/2009JD012442.
Singh, D., Horton, D. E., Tsiang, M., Haugen, M., Ashfaq, M., Mei, R., et al. (2014a). Severe precipitaiton in northern India in June 2013: Causes, historical context, and changes in probability [in "Explaining Extreme Events of 2013 from a Climate Perspective"]. *Bull. Am. Meteorol. Soc.* 95, S58–S61. doi:10.1175/1520-0477-95.9.S1.1.
Singh, D., Seager, R., Cook, B. I., Cane, M., Ting, M., Cook, E., et al. (2018). Climate and the Global Famine of 1876–78. *J. Clim.* 31, 9445–9467. doi:10.1175/JCLI-D-18-0159.1.
Singh, D., Tsiang, M., Rajaratnam, B., and Diffenbaugh, N. S. (2014b). Observed changes in extreme wet and dry spells during the South Asian summer monsoon season. *Nat. Clim. Chang.* 4, 456–461. doi:10.1038/nclimate2208.
Singh, K., Panda, J., Sahoo, M., and Mohapatra, M. (2019). Variability in Tropical Cyclone Climatology over North Indian Ocean during the Period 1891 to 2015. *Asia-Pacific J. Atmos. Sci.* 55, 269–287. doi:10.1007/s13143-018-0069-0.
Singh, M. S., Kuang, Z., Maloney, E. D., Hannah, W. M., and Wolding, B. O. (2017a). Increasing potential for intense tropical and subtropical thunderstorms under global warming. *Proc. Natl. Acad. Sci.* 114, 11657 LP-11662. doi:10.1073/pnas.1707603114.
Singh, M. S., and O'Gorman, P. A. (2013). Influence of entrainment on the thermal stratification in simulations of radiative-convective equilibrium. *Geophys. Res. Lett.* 40, 4398–4403. doi:10.1002/grl.50796.
Singh, S., Ghosh, S., Sahana, A. S., Vittal, H., and Karmakar, S. (2017b). Do dynamic regional models add value to the global model projections of Indian monsoon? *Clim. Dyn.* 48, 1375–1397. doi:10.1007/s00382-016-3147-y.
Singh, V., and Goyal, M. K. (2016). Changes in climate extremes by the use of CMIP5 coupled climate models over eastern Himalayas. *Environ. Earth Sci.* 75, 839. doi:10.1007/s12665-016-5651-0.
Sippel, S., El-Madany, T. S., Migliavacca, M., Mahecha, M. D., Carrara, A., Flach, M., et al. (2018). Warm Winter, Wet Spring, and an Extreme Response in Ecosystem Functioning on the Iberian Peninsula. *Bull. Am. Meteorol. Soc.* 99, S80–S85. doi:10.1175/BAMS-D-17-0135.1.
Sippel, S., and Otto, F. E. L. (2014). Beyond climatological extremes – assessing how the odds of hydrometeorological extreme events in South-East Europe change in a warming climate. *Clim. Change* 125, 381–398. doi:10.1007/s10584-014-1153-9.
Sippel, S., Otto, F. E. L., Flach, M., and van Oldenborgh, G. J. (2016). The role of anthropogenic warming in 2015 central european heat waves. *Bull. Am. Meteorol. Soc.* 97, S51–S56. doi:10.1175/BAMS-D-16-0150.1.
Sippel, S., Zscheischler, J., Heimann, M., Lange, H., Mahecha, M. D., van Oldenborgh, G. J., et al. (2017a). Have precipitation extremes and annual totals been increasing in the world's dry regions over the last 60 years? *Hydrol. Earth Syst. Sci.* 21, 441–458. doi:10.5194/hess-21-441-2017.
Sippel, S., Zscheischler, J., Heimann, M., Otto, F. E. L., Peters, J., and Mahecha, M. D. (2015). Quantifying changes in climate variability and extremes: Pitfalls and their overcoming. *Geophys. Res. Lett.* 42, 9990–9998. doi:10.1002/2015GL066307.
Sippel, S., Zscheischler, J., Mahecha, M. D., Orth, R., Reichstein, M., Vogel, M., et al. (2017b). Refining multi-model projections of temperature extremes by evaluation against land–atmosphere coupling diagnostics. *Earth Syst. Dyn.* 8, 387–403. doi:10.5194/esd-8-387-2017.
Siswanto, Jan van Oldenborgh, G., van der Schrier, G., Lenderink, G., and van den Hurk, B. (2015). Trends in High-Daily Precipitation Events in Jakarta and the Flooding of January 2014. *Bull. Am. Meteorol. Soc.* 96, S131–S135. doi:10.1175/BAMS-D-15-00128.1.
Skansi, M. de los M., Brunet, M., Sigró, J., Aguilar, E., Arevalo Groening, J. A., Bentancur, O. J., et al. (2013). Warming and wetting signals emerging from analysis of changes in climate extreme indices over South America. *Glob. Planet. Change* 100, 295–307. doi:10.1016/j.gloplacha.2012.11.004.
Skougaard Kaspersen, P., Høegh Ravn, N., Arnbjerg-Nielsen, K., Madsen, H., and Drews, M. (2017). Comparison of the impacts of urban development and climate change on exposing European cities to pluvial flooding. *Hydrol. Earth Syst. Sci.* 21, 4131–4147. doi:10.5194/hess-21-4131-2017.
Slater, L. J., Singer, M. B., and Kirchner, J. W. (2015). Hydrologic versus geomorphic drivers of trends in flood hazard. *Geophys. Res. Lett.* 42, 370–376. doi:10.1002/2014GL062482.
Slater, L. J., and Villarini, G. (2016). Recent trends in U.S. flood risk. *Geophys. Res. Lett.* 43, 12,428-12,436. doi:10.1002/2016GL071199.
Slater, L., and Villarini, G. (2017). On the impact of gaps on trend detection in extreme streamflow time series. *Int. J. Climatol.* 37, 3976–3983. doi:10.1002/joc.4954.
Smerdon, J. E., and Pollack, H. N. (2016). Reconstructing Earth's surface temperature over the past 2000 years: the science behind the headlines. *Wiley Interdiscip. Rev. Clim. Chang.* 7, 746–771. doi:10.1002/wcc.418.
Smiatek, G., Kunstmann, H., and Senatore, A. (2016). EURO-CORDEX regional climate model analysis for the Greater Alpine Region: Performance and expected future change. *J. Geophys. Res. Atmos.* 121, 7710–7728. doi:10.1002/2015JD024727.
Smith, B. K., Smith, J. A., Baeck, M. L., Villarini, G., and Wright, D. B. (2013). Spectrum of storm event hydrologic response in urban watersheds. *Water Resour. Res.* 49, 2649–2663. doi:10.1002/wrcr.20223.
Sobel, A. H., and Camargo, S. J. (2011). Projected Future Seasonal Changes in Tropical Summer Climate. *J. Clim.* 24,

ACCEPTED VERSION
SUBJECT TO FINAL EDITING

473–487. doi:10.1175/2010JCLI3748.1.
Sobel, A. H., Camargo, S. J., Hall, T. M., Lee, C.-Y., Tippett, M. K., and Wing, A. A. (2016). Human influence on tropical cyclone intensity. *Science (80-.).* 353, 242 LP-246. doi:10.1126/science.aaf6574.
Sobel, A. H., Camargo, S. J., and Previdi, M. (2019). Aerosol versus greenhouse gas effects on tropical cyclone potential intensity and the hydrologic cycle. *J. Clim.* 32, 5511–5527. doi:10.1175/JCLI-D-18-0357.1.
Sohn, B. J., Ryu, G.-H., Song, H.-J., and Ou, M.-L. (2013). Characteristic Features of Warm-Type Rain Producing Heavy Rainfall over the Korean Peninsula Inferred from TRMM Measurements. *Mon. Weather Rev.* 141, 3873–3888. doi:10.1175/MWR-D-13-00075.1.
Sohrabi, M. M., Ryu, J. H., Abatzoglou, J., and Tracy, J. (2015). Development of soil moisture drought index to characterize droughts. *J. Hydrol. Eng.* 20. doi:10.1061/(ASCE)HE.1943-5584.0001213.
Solander, K. C., Newman, B. D., de Araujo, A., Barnard, H. R., Berry, Z. C., Bonal, D., et al. (2020). The pantropical response of soil moisture to El Niño. *Hydrol. Earth Syst. Sci.* 24, 2303–2322. doi:10.5194/hess-24-2303-2020.
Song, J., and Klotzbach, P. J. (2018). What Has Controlled the Poleward Migration of Annual Averaged Location of Tropical Cyclone Lifetime Maximum Intensity Over the Western North Pacific Since 1961? *Geophys. Res. Lett.* 45, 1148–1156. doi:10.1002/2017GL076883.
Song, X., Song, Y., and Chen, Y. (2020). Secular trend of global drought since 1950. *Environ. Res. Lett.* 15, 094073. doi:10.1088/1748-9326/aba20d.
Song, X., Zhang, Z., Chen, Y., Wang, P., Xiang, M., Shi, P., et al. (2014). Spatiotemporal changes of global extreme temperature events (ETEs) since 1981 and the meteorological causes. 70, 975–994. doi:10.1007/s11069-013-0856-y.
Sonkoué, D., Monkam, D., Fotso-Nguemo, T. C., Yepdo, Z. D., and Vondou, D. A. (2019). Evaluation and projected changes in daily rainfall characteristics over Central Africa based on a multi-model ensemble mean of CMIP5 simulations. *Theor. Appl. Climatol.* 137, 2167–2186. doi:10.1007/s00704-018-2729-5.
Sorribas, M. V., Paiva, R. C. D., Melack, J. M., Bravo, J. M., Jones, C., Carvalho, L., et al. (2016). Projections of climate change effects on discharge and inundation in the Amazon basin. *Clim. Change* 136, 555–570. doi:10.1007/s10584-016-1640-2.
Sousa, P. M., Trigo, R. M., Barriopedro, D., Soares, P. M. M., Ramos, A. M., and Liberato, M. L. R. (2017). Responses of European precipitation distributions and regimes to different blocking locations. *Clim. Dyn.* 48, 1141–1160. doi:10.1007/s00382-016-3132-5.
Sparrow, S., Su, Q., Tian, F., Li, S., Chen, Y., Chen, W., et al. (2018). Attributing human influence on the July 2017 Chinese heatwave: the influence of sea-surface temperatures. *Environ. Res. Lett.* 13, 114004. doi:10.1088/1748-9326/aae356.
Spennemann, P. C., Fernández-Long, M. E., Gattinoni, N. N., Cammalleri, C., and Naumann, G. (2020). Soil moisture evaluation over the Argentine Pampas using models, satellite estimations and in-situ measurements. *J. Hydrol. Reg. Stud.* 31. doi:10.1016/j.ejrh.2020.100723.
Sperry, J. S., Wang, Y., Wolfe, B. T., Mackay, D. S., Anderegg, W. R. L., McDowell, N. G., et al. (2016). Pragmatic hydraulic theory predicts stomatal responses to climatic water deficits. *New Phytol.* 212, 577–589. doi:10.1111/nph.14059.
Spinoni, J., Barbosa, P., Bucchignani, E., Cassano, J., Cavazos, T., Christensen, J. H., et al. (2020). Future Global Meteorological Drought Hot Spots: A Study Based on CORDEX Data. *J. Clim.* 33, 3635–3661. doi:10.1175/JCLI-D-19-0084.1.
Spinoni, J., Barbosa, P., De Jager, A., McCormick, N., Naumann, G., Vogt, J. V., et al. (2019). A new global database of meteorological drought events from 1951 to 2016. *J. Hydrol. Reg. Stud.* 22, 100593. doi:10.1016/J.EJRH.2019.100593.
Spinoni, J., Naumann, G., Carrao, H., Barbosa, P., and Vogt, J. (2014). World drought frequency, duration, and severity for 1951-2010. *Int. J. Climatol.* 34, 2792–2804. doi:10.1002/joc.3875.
Spinoni, J., Naumann, G., and Vogt, J. V. (2017). Pan-European seasonal trends and recent changes of drought frequency and severity. *Glob. Planet. Change* 148, 113–130. doi:10.1016/j.gloplacha.2016.11.013.
Spinoni, J., Naumann, G., Vogt, J. V., and Barbosa, P. (2015). The biggest drought events in Europe from 1950 to 2012. *J. Hydrol. Reg. Stud.* 3, 509–524. doi:10.1016/j.ejrh.2015.01.001.
Spinoni, J., Vogt, J. V, Barbosa, P., Dosio, A., McCormick, N., Bigano, A., et al. (2018a). Changes of heating and cooling degree-days in Europe from 1981 to 2100. *Int. J. Climatol.* 38, e191–e208. doi:10.1002/joc.5362.
Spinoni, J., Vogt, J. V, Naumann, G., Barbosa, P., and Dosio, A. (2018b). Will drought events become more frequent and severe in Europe? *Int. J. Climatol.* 38, 1718–1736. doi:10.1002/joc.5291.
Srivastava, A., Grotjahn, R., and Ullrich, P. A. (2020). Evaluation of historical CMIP6 model simulations of extreme precipitation over contiguous US regions. *Weather Clim. Extrem.* 29, 100268. doi:10.1016/j.wace.2020.100268.
Stagge, J. H., Kingston, D. G., Tallaksen, L. M., and Hannah, D. M. (2017). Observed drought indices show increasing divergence across Europe. *Sci. Rep.* 7. doi:10.1038/s41598-017-14283-2.
Stagge, J. H., Tallaksen, L. M., Gudmundsson, L., Van Loon, A. F., and Stahl, K. (2015). Candidate Distributions for Climatological Drought Indices (SPI and SPEI). *Int. J. Climatol.* 35, 4027–4040. doi:10.1002/joc.4267.
Stahl, K., Hisdal, H., Hannaford, J., Tallaksen, L. M., Van Lanen, H. A. J., Sauquet, E., et al. (2010). Streamflow trends

ACCEPTED VERSION SUBJECT TO FINAL EDITING

in Europe: Evidence from a dataset of near-natural catchments. *Hydrol. Earth Syst. Sci.* 14, 2367–2382. doi:10.5194/hess-14-2367-2010.

Stansfield, A. M., Reed, K. A., and Zarzycki, C. M. (2020). Changes in Precipitation From North Atlantic Tropical Cyclones Under RCP Scenarios in the Variable-Resolution Community Atmosphere Model. *Geophys. Res. Lett.* 47, e2019GL086930. doi:10.1029/2019GL086930.

Staudinger, M., Weiler, M., and Seibert, J. (2015). Quantifying sensitivity to droughts-an experimental modeling approach. *Hydrol. Earth Syst. Sci.* 19, 1371–1384. doi:10.5194/hess-19-1371-2015.

Stéfanon, M., Drobinski, P., D'Andrea, F., Lebeaupin-Brossier, C., and Bastin, S. (2014). Soil moisture-temperature feedbacks at meso-scale during summer heat waves over Western Europe. *Clim. Dyn.* 42, 1309–1324. doi:10.1007/s00382-013-1794-9.

Stegehuis, A. I., Vautard, R., Ciais, P., Teuling, A. J., Jung, M., and Yiou, P. (2013). Summer temperatures in Europe and land heat fluxes in observation-based data and regional climate model simulations. *Clim. Dyn.* 41, 455–477. doi:10.1007/s00382-012-1559-x.

Stennett-Brown, R. K., Jones, J. J. P., Stephenson, T. S., and Taylor, M. A. (2017). Future Caribbean temperature and rainfall extremes from statistical downscaling. *Int. J. Climatol.* 37, 4828–4845. doi:10.1002/joc.5126.

Stephens, C. M., McVicar, T. R., Johnson, F. M., and Marshall, L. A. (2018). Revisiting Pan Evaporation Trends in Australia a Decade on. *Geophys. Res. Lett.* 45, 11,111-164,172. doi:10.1029/2018GL079332.

Stephenson, T. S., Vincent, L. A., Allen, T., Van Meerbeeck, C. J., McLean, N., Peterson, T. C., et al. (2014). Changes in extreme temperature and precipitation in the Caribbean region, 1961–2010. *Int. J. Climatol.* 34, 2957–2971. doi:10.1002/joc.3889.

Sterling, S. M., Ducharne, A., and Polcher, J. (2013). The impact of global land-cover change on the terrestrial water cycle. *Nat. Clim. Chang.* 3, 385–390. doi:10.1038/nclimate1690.

Stillman, S., Zeng, X., and Bosilovich, M. G. (2016). Evaluation of 22 Precipitation and 23 Soil Moisture Products over a Semiarid Area in Southeastern Arizona. *J. Hydrometeorol.* 17, 211–230. doi:10.1175/JHM-D-15-0007.1.

Stocker, B. D., Zscheischler, J., Keenan, T. F., Prentice, I. C., Peñuelas, J., and Seneviratne, S. I. (2018). Quantifying soil moisture impacts on light use efficiency across biomes. *New Phytol.* 218, 1430–1449. doi:10.1111/nph.15123.

Stoelzle, M., Stahl, K., and Weiler, M. (2013). Are streamflow recession characteristics really characteristic? *Hydrol. Earth Syst. Sci.* 17, 817–828. doi:10.5194/hess-17-817-2013.

Stott, P. A., Christidis, N., Otto, F. E. L., Sun, Y., Vanderlinden, J.-P., van Oldenborgh, G. J., et al. (2016). Attribution of extreme weather and climate-related events. *Wiley Interdiscip. Rev. Clim. Chang.* 7, 23–41. doi:10.1002/wcc.380.

Strandberg, G., and Kjellström, E. (2019). Climate Impacts from Afforestation and Deforestation in Europe. *Earth Interact.* 23, 1–27. doi:10.1175/EI-D-17-0033.1.

Stratton, R. A., Senior, C. A., Vosper, S. B., Folwell, S. S., Boutle, I. A., Earnshaw, P. D., et al. (2018). A Pan-African Convection-Permitting Regional Climate Simulation with the Met Office Unified Model: CP4-Africa. *J. Clim.* 31, 3485–3508. doi:10.1175/JCLI-D-17-0503.1.

Strong, J. D. O., Vecchi, G. A., and Ginoux, P. (2018). The Climatological Effect of Saharan Dust on Global Tropical Cyclones in a Fully Coupled GCM. *J. Geophys. Res. Atmos.* 123, 5538–5559. doi:10.1029/2017JD027808.

Studholme, J., and Gulev, S. (2018). Concurrent Changes to Hadley Circulation and the Meridional Distribution of Tropical Cyclones. *J. Clim.* 31, 4367–4389. doi:10.1175/JCLI-D-17-0852.1.

Suarez-Gutierrez, L., Li, C., Müller, W. A., and Marotzke, J. (2018). Internal variability in European summer temperatures at 1.5 °C and 2 °C of global warming. *Environ. Res. Lett.* 13, 064026. doi:10.1088/1748-9326/aaba58.

Suarez-Gutierrez, L., Müller, W. A., Li, C., and Marotzke, J. (2020a). Dynamical and thermodynamical drivers of variability in European summer heat extremes. *Clim. Dyn.* 54, 4351–4366. doi:10.1007/s00382-020-05233-2.

Suarez-Gutierrez, L., Müller, W. A., Li, C., and Marotzke, J. (2020b). Hotspots of extreme heat under global warming. *Clim. Dyn.* doi:10.1007/s00382-020-05263-w.

Sugi, M., Murakami, H., and Yoshida, K. (2017). Projection of future changes in the frequency of intense tropical cyclones. *Clim. Dyn.* 49, 619–632. doi:10.1007/s00382-016-3361-7.

Sugi, M., Murakami, H., and Yoshimura, J. (2012). On the Mechanism of Tropical Cyclone Frequency Changes Due to Global Warming. *J. Meteorol. Soc. Japan* 90A, 397–408. doi:10.2151/jmsj.2012-A24.

Sugi, M., Yamada, Y., Yoshida, K., Mizuta, R., Nakano, M., Kodama, C., et al. (2020). Future changes in frequency of tropical cyclone seeds. *SOLA* 16, 70–74. doi:10.2151/sola.2020-012.

Sui, C. H., Satoh, M., and Suzuki, K. (2020). Precipitation efficiency and its role in cloud-radiative feedbacks to climate variability. *J. Meteorol. Soc. Japan* 98, 261–282. doi:10.2151/jmsj.2020-024.

Sui, C., Zhang, Z., Yu, L., Li, Y., and Song, M. (2017). Investigation of Arctic air temperature extremes at north of 60N in winter. *Acta Oceanol. Sin.* 36, 51–60. doi:10.1007/s13131-017-1137-5.

Sui, Y., Lang, X., and Jiang, D. (2018). Projected signals in climate extremes over China associated with a 2 °C global warming under two RCP scenarios. *Int. J. Climatol.* 38, e678–e697. doi:10.1002/joc.5399.

Sun, C., Jiang, Z., Li, W., Hou, Q., and Li, L. (2019a). Changes in extreme temperature over China when global

ACCEPTED VERSION SUBJECT TO FINAL EDITING

warming stabilized at 1.5 °C and 2.0 °C. *Sci. Rep.* 9, 14982. doi:10.1038/s41598-019-50036-z.
Sun, J., Wang, D., Hu, X., Ling, Z., and Wang, L. (2019b). Ongoing Poleward Migration of Tropical Cyclone Occurrence Over the Western North Pacific Ocean. *Geophys. Res. Lett.* 46, 9110–9117. doi:10.1029/2019GL084260.
Sun, Q., and Miao, C. (2018). Extreme Rainfall (R20mm, RX5day) in Yangtze–Huai, China, in June–July 2016: The Role of ENSO and Anthropogenic Climate Change. *Bull. Am. Meteorol. Soc.* 99, S102–S106. doi:10.1175/BAMS-D-17-0091.1.
Sun, Q., Miao, C., Hanel, M., Borthwick, A. G. L., Duan, Q., Ji, D., et al. (2019c). Global heat stress on health, wildfires, and agricultural crops under different levels of climate warming. *Environ. Int.* 128, 125–136. doi:10.1016/j.envint.2019.04.025.
Sun, Q., Zhang, X., Zwiers, F., Westra, S., and Alexander, L. V (2020). A global, continental and regional analysis of changes in extreme precipitation. *J. Clim.*, 1–52. doi:10.1175/JCLI-D-19-0892.1.
Sun, Q., Zwiers, F., Zhang, X., and Li, G. (2019d). A comparison of intra-annual and long-term trend scaling of extreme precipitation with temperature in a large-ensemble regional climate simulation. *J. Clim.* Under Revi.
Sun, X. B., Ren, G. Y., Shrestha, A. B., Ren, Y. Y., You, Q. L., Zhan, Y. J., et al. (2017). Changes in extreme temperature events over the Hindu Kush Himalaya during 1961–2015. *Adv. Clim. Chang. Res.* 8, 157–165. doi:10.1016/j.accre.2017.07.001.
Sun, Y., Hu, T., and Zhang, X. (2018a). Substantial Increase in Heat Wave Risks in China in a Future Warmer World. *Earth's Futur.* 6, 1528–1538. doi:10.1029/2018EF000963.
Sun, Y., Hu, T., Zhang, X., Li, C., Lu, C., Ren, G., et al. (2019e). Contribution of Global warming and Urbanization to Changes in Temperature Extremes in Eastern China. *Geophys. Res. Lett.* 46, 11426–11434. doi:10.1029/2019GL084281.
Sun, Y., Hu, T., Zhang, X., Wan, H., Stott, P., and Lu, C. (2018b). Anthropogenic Influence on the Eastern China 2016 Super Cold Surge. *Bull. Am. Meteorol. Soc.* 99, S123–S127. doi:10.1175/BAMS-D-17-0092.1.
Sun, Y., Zhang, X., Zwiers, F. W., Song, L., Wan, H., Hu, T., et al. (2014). Rapid increase in the risk of extreme summer heat in Eastern China. *Nat. Clim. Chang.* 4, 1082–1085. doi:10.1038/nclimate2410.
Sun, Z., Ouyang, Z., Zhao, J., Li, S., Zhang, X., and Ren, W. (2018c). Recent rebound in observational large-pan evaporation driven by heat wave and droughts by the Lower Yellow River. *J. Hydrol.* 565, 237–247. doi:10.1016/J.JHYDROL.2018.08.014.
Sunyer, M. A., Hundecha, Y., Lawrence, D., Madsen, H., Willems, P., Martinkova, M., et al. (2015). Inter-comparison of statistical downscaling methods for projection of extreme precipitation in Europe. *Hydrol. Earth Syst. Sci.* 19, 1827–1847. doi:10.5194/hess-19-1827-2015.
Supari, Tangang, F., Juneng, L., and Aldrian, E. (2017). Observed changes in extreme temperature and precipitation over Indonesia. *Int. J. Climatol.* 37, 1979–1997. doi:10.1002/joc.4829.
Supari, Tangang, F., Juneng, L., Cruz, F., Chung, J. X., Ngai, S. T., et al. (2020). Multi-model projections of precipitation extremes in Southeast Asia based on CORDEX-Southeast Asia simulations. *Environ. Res.* 184, 109350. doi:10.1016/j.envres.2020.109350.
Sutton, R. T. (2018). ESD Ideas: a simple proposal to improve the contribution of IPCC WGI to the assessment and communication of climate change risks. *Earth Syst. Dynam.* 9, 1155–1158. doi:10.5194/esd-9-1155-2018.
Sutton, R. T. (2019). Climate Science Needs to Take Risk Assessment Much More Seriously. *Bull. Am. Meteorol. Soc.* 100, 1637–1642. doi:10.1175/BAMS-D-18-0280.1.
Swain, D. L., Langenbrunner, B., Neelin, J. D., and Hall, A. (2018). Increasing precipitation volatility in twenty-first-century California. *Nat. Clim. Chang.* 8, 427–433. doi:10.1038/s41558-018-0140-y.
Swain, D. L., Tsiang, M., Haugen, M., Singh, D., Charland, A., Rajaratnam, B., et al. (2014). The Extraordinary California Drought of 2013/2014: Character, Context, and the Role of Climate Change [in "Explaining Extreme Events of 2013 from a Climate Perspective"]. *Bull. Am. Meteorol. Soc.* 95, S3–S7. doi:10.1175/1520-0477-95.9.S1.1.
Swain, S., and Hayhoe, K. (2015). CMIP5 projected changes in spring and summer drought and wet conditions over North America. *Clim. Dyn.* 44, 2737–2750. doi:10.1007/s00382-014-2255-9.
Swann, A. L. S. (2018). Plants and Drought in a Changing Climate. *Curr. Clim. Chang. Reports* 4, 192–201. doi:10.1007/s40641-018-0097-y.
Swann, A. L. S., Hoffman, F. M., Koven, C. D., and Randerson, J. T. (2016). Plant responses to increasing CO2 reduce estimates of climate impacts on drought severity. *Proc. Natl. Acad. Sci.* 113, 10019–10024. doi:10.1073/pnas.1604581113.
Swierczynski, T., Lauterbach, S., Dulski, P., Delgado, J., Merz, B., and Brauer, A. (2013). Mid- to late Holocene flood frequency changes in the northeastern Alps as recorded in varved sediments of Lake Mondsee (Upper Austria). *Quat. Sci. Rev.* 80, 78–90. doi:10.1016/j.quascirev.2013.08.018.
Syafrina, A. H., Zalina, M. D., and Juneng, L. (2015). Historical trend of hourly extreme rainfall in Peninsular Malaysia. *Theor. Appl. Climatol.* 120, 259–285. doi:10.1007/s00704-014-1145-8.
Sylla, M. B., Elguindi, N., Giorgi, F., and Wisser, D. (2016). Projected robust shift of climate zones over West Africa in response to anthropogenic climate change for the late 21st century. *Clim. Change* 134, 241–253.

ACCEPTED VERSION SUBJECT TO FINAL EDITING

doi:10.1007/s10584-015-1522-z.
Szeto, K., Gysbers, P., Brimelow, J., and Stewart, R. (2015). The 2014 Extreme Flood on the Southeastern Canadian Prairies. *Bull. Am. Meteorol. Soc.* 96, S20–S24. doi:10.1175/BAMS-D-15-00110.1.
Tabari, H., and Aghajanloo, M.-B. (2013). Temporal pattern of aridity index in Iran with considering precipitation and evapotranspiration trends. *Int. J. Climatol.* 33, 396–409. doi:10.1002/joc.3432.
Tabari, H., Madani, K., and Willems, P. (2020). The contribution of anthropogenic influence to more anomalous extreme precipitation in Europe. *Environ. Res. Lett.* 15, 104077. doi:10.1088/1748-9326/abb268.
Tabari, H., and Willems, P. (2018). More prolonged droughts by the end of the century in the Middle East. *Environ. Res. Lett.* 13. doi:10.1088/1748-9326/aae09c.
Takahashi, C., Watanabe, M., and Mori, M. (2017). Significant Aerosol Influence on the Recent Decadal Decrease in Tropical Cyclone Activity Over the Western North Pacific. *Geophys. Res. Lett.* 44, 9496–9504. doi:10.1002/2017GL075369.
Takahashi, C., Watanabe, M., Shiogama, H., Imada, Y., and Mori, M. (2016). A Persistent Japanese Heat Wave in Early August 2015: Roles of Natural Variability and Human-Induced Warming. *Bull. Am. Meteorol. Soc.* 97, S107–S112. doi:10.1175/BAMS-D-16-0157.1.
Takayabu, I., Hibino, K., Sasaki, H., Shiogama, H., Mori, N., Shibutani, Y., et al. (2015). Climate change effects on the worst-case storm surge: a case study of Typhoon Haiyan. *Environ. Res. Lett.* 10, 064011. doi:10.1088/1748-9326/10/6/064011.
Takemi, T., and Unuma, T. (2019). Diagnosing Environmental Properties of the July 2018 Heavy Rainfall Event in Japan. *SOLA* 15A, 60–65. doi:10.2151/sola.15A-011.
Takemura, K., Wakamatsu, S., Togawa, H., Shimpo, A., Kobayashi, C., Maeda, S., et al. (2019). Extreme Moisture Flux Convergence over Western Japan during the Heavy Rain Event of July 2018. *SOLA* 15A, 49–54. doi:10.2151/sola.15A-009.
Talchabhadel, R., Karki, R., Thapa, B. R., Maharjan, M., and Parajuli, B. (2018). Spatio-temporal variability of extreme precipitation in Nepal. *Int. J. Climatol.* 38, 4296–4313. doi:10.1002/joc.5669.
Tallaksen, L. M., and Stahl, K. (2014). Spatial and temporal patterns of large-scale droughts in Europe: Model dispersion and performance. *Geophys. Res. Lett.* 41, 429–434. doi:10.1002/2013GL058573.
Tamura, T., Nicholas, W. A., Oliver, T. S. N., and Brooke, B. P. (2018). Coarse-sand beach ridges at Cowley Beach, north-eastern Australia: Their formative processes and potential as records of tropical cyclone history. *Sedimentology* 65, 721–744. doi:10.1111/sed.12402.
Tandon, N. F., Zhang, X., and Sobel, A. H. (2018). Understanding the Dynamics of Future Changes in Extreme Precipitation Intensity. *Geophys. Res. Lett.* 45, 2870–2878. doi:10.1002/2017GL076361.
Tangang, F., Supari, S., Chung, J. X., Cruz, F., Salimun, E., Ngai, S. T., et al. (2018). Future changes in annual precipitation extremes over Southeast Asia under global warming of 2°C. *APN Sci. Bull.* 8, 6–11. doi:10.30852/sb.2018.436.
Tao, Y., Wang, W., Song, S., and Ma, J. (2018). Spatial and Temporal Variations of Precipitation Extremes and Seasonality over China from 1961~2013. *Water* 10, 719. doi:10.3390/w10060719.
Taszarek, M., Allen, J., Púčik, T., Groenemeijer, P., Czernecki, B., Kolendowicz, L., et al. (2019). A Climatology of Thunderstorms across Europe from a Synthesis of Multiple Data Sources. *J. Clim.* 32, 1813–1837. doi:10.1175/JCLI-D-18-0372.1.
Taszarek, M., Brooks, H. E., Czernecki, B., Szuster, P., and Fortuniak, K. (2018). Climatological Aspects of Convective Parameters over Europe: A Comparison of ERA-Interim and Sounding Data. *J. Clim.* 31, 4281–4308. doi:10.1175/JCLI-D-17-0596.1.
Tauvale, L., and Tsuboki, K. (2019). Characteristics of Tropical Cyclones in the Southwest Pacific. *J. Meteorol. Soc. Japan. Ser. II* 97, 711–731. doi:10.2151/jmsj.2019-042.
Taylor, C. M., Belusic, D., Guichard, F., Parker, D. J., Vischel, T., Bock, O., et al. (2017). Frequency of extreme Sahelian storms tripled since 1982 in satellite observations. *Nature* 544, 475–478. doi:10.1038/nature22069.
Taylor, C. M., de Jeu, R. A. M., Guichard, F., Harris, P. P., and Dorigo, W. A. (2012). Afternoon rain more likely over drier soils. *Nature* 489, 423–426. doi:10.1038/nature11377.
Taylor, M. A., Clarke, L. A., Centella, A., Bezanilla, A., Stephenson, T. S., Jones, J. J., et al. (2018). Future Caribbean Climates in a World of Rising Temperatures: The 1.5 vs 2.0 Dilemma. *J. Clim.* 31, 2907–2926. doi:10.1175/JCLI-D-17-0074.1.
Taylor, R. G., Scanlon, B., Döll, P., Rodell, M., Van Beek, R., Wada, Y., et al. (2013). Ground water and climate change. *Nat. Clim. Chang.* 3, 322–329. doi:10.1038/nclimate1744.
Tebaldi, C., Armbruster, A., Engler, H. P., and Link, R. (2020). Emulating climate extreme indices. *Environ. Res. Lett.* 15. doi:10.1088/1748-9326/ab8332.
Tebaldi, C., and Knutti, R. (2018). Evaluating the accuracy of climate change pattern emulation for low warming targets. *Environ. Res. Lett.* 13, 055006. doi:10.1088/1748-9326/aabef2.
Tebaldi, C., and Wehner, M. F. (2018). Benefits of mitigation for future heat extremes under RCP4.5 compared to RCP8.5. *Clim. Change* 146, 349–361. doi:10.1007/s10584-016-1605-5.
Tencer, B.; Rusticucci, M. (2012). Analysis of interdecadal variability of temperature extreme events in Argentina

ACCEPTED VERSION
SUBJECT TO FINAL EDITING

applying EVT. *Atmósfera* 25, 327–337.
Tencer, B., Bettolli, M., and Rusticucci, M. (2016). Compound temperature and precipitation extreme events in southern South America: associated atmospheric circulation, and simulations by a multi-RCM ensemble. *Clim. Res.* 68, 183–199. doi:10.3354/cr01396.
Tennille, S. A., and Ellis, K. N. (2017). Spatial and temporal trends in the location of the lifetime maximum intensity of tropical cyclones. *Atmosphere (Basel).* 8, 1–9. doi:10.3390/atmos8100198.
Teufel, B., Diro, G. T., Whan, K., Milrad, S. M., Jeong, D. I., Ganji, A., et al. (2017). Investigation of the 2013 Alberta flood from weather and climate perspectives. *Clim. Dyn.* 48, 2881–2899. doi:10.1007/s00382-016-3239-8.
Teufel, B., Sushama, L., Huziy, O., Diro, G. T., Jeong, D. I., Winger, K., et al. (2019). Investigation of the mechanisms leading to the 2017 Montreal flood. *Clim. Dyn.* 52, 4193–4206. doi:10.1007/s00382-018-4375-0.
Teuling, A. J. (2018). A hot future for European droughts. *Nat. Clim. Chang.* 8, 364–365. doi:10.1038/s41558-018-0154-5.
Teuling, A. J., de Badts, E., Jansen, F. A., Fuchs, R., Buitink, J., van Dijke, A. J., et al. (2019). Climate change, reforestation/afforestation, and urbanisation impacts on evapotranspiration and streamflow in Europe. *Hydrol. Earth Syst. Sci.* 23, 3631–3652. doi:10.5194/hess-2018-634.
Teuling, A. J., Van Loon, A. F., Seneviratne, S. I., Lehner, I., Aubinet, M., Heinesch, B., et al. (2013). Evapotranspiration amplifies European summer drought. *Geophys. Res. Lett.* 40, 2071–2075. doi:10.1002/grl.50495.
Thackeray, C. W., DeAngelis, A. M., Hall, A., Swain, D. L., and Qu, X. (2018). On the Connection Between Global Hydrologic Sensitivity and Regional Wet Extremes. *Geophys. Res. Lett.* 45. doi:10.1029/2018GL079698.
Thiery, W., Davin, E. L., Lawrence, D. M., Hirsch, A. L., Hauser, M., and Seneviratne, S. I. (2017). Present-day irrigation mitigates heat extremes. *J. Geophys. Res. Atmos.* 122, 1403–1422. doi:10.1002/2016JD025740.
Thiery, W., Davin, E. L., Seneviratne, S. I., Bedka, K., Lhermitte, S., and van Lipzig, N. P. M. (2016). Hazardous thunderstorm intensification over Lake Victoria. *Nat. Commun.* 7, 12786. doi:10.1038/ncomms12786.
Thiery, W., Visser, A. J., Fischer, E. M., Hauser, M., Hirsch, A. L., Lawrence, D. M., et al. (2020). Warming of hot extremes alleviated by expanding irrigation. *Nat. Commun.* 11, 290. doi:10.1038/s41467-019-14075-4.
Thober, S., Kumar, R., Wanders, N., Marx, A., Pan, M., Rakovec, O., et al. (2018). Multi-model ensemble projections of European river floods and high flows at 1.5, 2, and 3 degrees global warming. *Environ. Res. Lett.* 13, 014003. doi:10.1088/1748-9326/aa9e35.
Thorarinsdottir, T. L., Sillmann, J., Haugen, M., Gissibl, N., and Sandstad, M. (2020). Evaluation of CMIP5 and CMIP6 simulations of historical surface air temperature extremes using proper evaluation methods. *Environ. Res. Lett.* 15, 124041. doi:10.1088/1748-9326/abc778.
Tian, X., Shu, L., Wang, M., and Zhao, F. (2017). The impact of climate change on fire risk in Daxing'anling, China. *J. For. Res.* 28, 997–1006. doi:10.1007/s11676-017-0383-x.
Tijdeman, E., Hannaford, J., and Stahl, K. (2018). Human influences on streamflow drought characteristics in England and Wales. *Hydrol. Earth Syst. Sci.* 22, 1051–1064. doi:10.5194/hess-22-1051-2018.
Tilinina, N., Gulev, S. K., Rudeva, I., and Koltermann, P. (2013). Comparing cyclone life cycle characteristics and their interannual variability in different reanalyses. *J. Clim.* doi:10.1175/JCLI-D-12-00777.1.
Timmermans, B., Patricola, C., and Wehner, M. (2018). Simulation and analysis of extremehurricane-drivenwave climate under two ocean warming scenarios. *Oceanography* 31, 88–99. doi:10.5670/oceanog.2018.218.
Timmermans, B., Stone, D., Wehner, M., and Krishnan, H. (2017). Impact of tropical cyclones on modeled extreme wind-wave climate. *Geophys. Res. Lett.* 44, 1393–1401. doi:10.1002/2016GL071681.
Timmermans, B., Wehner, M., Cooley, D., O'Brien, T., and Krishnan, H. (2019). An evaluation of the consistency of extremes in gridded precipitation data sets. *Clim. Dyn.* 52, 6651–6670. doi:10.1007/s00382-018-4537-0.
Ting, M., Camargo, S. J., Li, C., and Kushnir, Y. (2015). Natural and Forced North Atlantic Hurricane Potential Intensity Change in CMIP5 Models. *J. Clim.* 28, 3926–3942. doi:10.1175/JCLI-D-14-00520.1.
Ting, M., Kossin, J. P., Camargo, S. J., and Li, C. (2019). Past and Future Hurricane Intensity Change along the U.S. East Coast. *Sci. Rep.* 9, 7795. doi:10.1038/s41598-019-44252-w.
Tippett, M. K., Camargo, S. J., and Sobel, A. H. (2011). A Poisson Regression Index for Tropical Cyclone Genesis and the Role of Large-Scale Vorticity in Genesis. *J. Clim.* 24, 2335–2357. doi:10.1175/2010JCLI3811.1.
Tochimoto, E., and Niino, H. (2016). Structural and Environmental Characteristics of Extratropical Cyclones that Cause Tornado Outbreaks in the Warm Sector: A Composite Study. *Mon. Weather Rev.* 144, 945–969. doi:10.1175/MWR-D-15-0015.1.
Tochimoto, E., and Niino, H. (2018). Structure and Environment of Tornado-Spawning Extratropical Cyclones around Japan. *J. Meteorol. Soc. Japan* 96, 355–380. doi:10.2151/jmsj.2018-043.
Todzo, S., Bichet, A., and Diedhiou, A. (2020). Intensification of the hydrological cycle expected in West Africa over the 21st century. *Earth Syst. Dyn.* 11, 319–328. doi:10.5194/esd-11-319-2020.
Tokinaga, H., and Xie, S.-P. (2011). Wave- and Anemometer-Based Sea Surface Wind (WASWind) for Climate Change Analysis. *J. Clim.* 24, 267–285. doi:10.1175/2010JCLI3789.1.
Tölle, M. H., Schefczyk, L., and Gutjahr, O. (2018). Scale dependency of regional climate modeling of current and future climate extremes in Germany. *Theor. Appl. Climatol.* 134, 829–848. doi:10.1007/s00704-017-2303-6.

ACCEPTED VERSION SUBJECT TO FINAL EDITING

Tomas-Burguera, M., Vicente-Serrano, S. M., Peña-Angulo, D., Domínguez-Castro, F., Noguera, I., and El Kenawy, A. (2020). Global characterization of the varying responses of the Standardized Evapotranspiration Index (SPEI) to atmospheric evaporative demand (AED). *J. Geophys. Res. Atmos.* 125, e2020JD0330178. doi:10.1029/2020JD033017.

Tomozeiu, R., Agrillo, G., Cacciamani, C., and Pavan, V. (2014). Statistically downscaled climate change projections of surface temperature over Northern Italy for the periods 2021-2050 and 2070-2099. *Nat. Hazards* 72, 143–168. doi:10.1007/s11069-013-0552-y.

Toreti, A., Belward, A., Perez-Dominguez, I., Naumann, G., Luterbacher, J., Cronie, O., et al. (2019). The Exceptional 2018 European Water Seesaw Calls for Action on Adaptation. *Earth's Futur.* 7, 652–663. doi:10.1029/2019EF001170.

Touma, D., Ashfaq, M., Nayak, M. A., Kao, S.-C., and Diffenbaugh, N. S. (2015). A multi-model and multi-index evaluation of drought characteristics in the 21st century. *J. Hydrol.* 526, 196–207. doi:10.1016/j.jhydrol.2014.12.011.

Tous, M., Zappa, G., Romero, R., Shaffrey, L., and Vidale, P. L. (2016). Projected changes in medicanes in the HadGEM3 N512 high-resolution global climate model. *Clim. Dyn.* 47, 1913–1924. doi:10.1007/s00382-015-2941-2.

Tozer, C. R., Risbey, J. S., Grose, M., Monselesan, D. P., Squire, D. T., Black, A. S., et al. (2020). A 1-Day Extreme Rainfall Event in Tasmania: Process Evaluation and Long Tail Attribution [in "Explaining Extreme Events of 2018 from a Climate Perspective"]. *Bull. Am. Meteorol. Soc.* 101, S123–S128. doi:10.1175/BAMS-D-19-0219.1.

Tramblay, Y., and Somot, S. (2018). Future evolution of extreme precipitation in the Mediterranean. *Clim. Change* 151, 289–302. doi:10.1007/s10584-018-2300-5.

Tramblay, Y., Villarini, G., and Zhang, W. (2020). Observed Changes in Flood Hazard in Africa. *Environ. Res. Lett.* doi:10.1088/1748-9326/abb90b.

Trancoso, R., Larsen, J. R., McVicar, T. R., Phinn, S. R., and McAlpine, C. A. (2017). CO2-vegetation feedbacks and other climate changes implicated in reducing base flow. *Geophys. Res. Lett.* 44, 2310–2318. doi:10.1002/2017GL072759.

Trapp, R. J., Hoogewind, K. A., and Lasher-Trapp, S. (2019). Future Changes in Hail Occurrence in the United States Determined through Convection-Permitting Dynamical Downscaling. *J. Clim.* 32, 5493–5509. doi:10.1175/JCLI-D-18-0740.1.

Trapp, R. J., Tessendorf, S. A., Godfrey, E. S., and Brooks, H. E. (2005). Tornadoes from Squall Lines and Bow Echoes. Part I: Climatological Distribution. *Weather Forecast.* 20, 23–34. doi:10.1175/WAF-835.1.

Trenary, L., DelSole, T., Doty, B., and Tippett, M. K. (2015). Was the Cold Eastern US Winter of 2014 Due to Increased Variability? *Bull. Am. Meteorol. Soc.* 96, S15–S19. doi:10.1175/BAMS-D-15-00138.1.

Trenary, L., DelSole, T., Tippett, M. K., and Doty, B. (2016). Extreme Eastern U.S. Winter of 2015 Not Symptomatic of Climate Change. *Bull. Am. Meteorol. Soc.* 97, S31–S35. doi:10.1175/BAMS-D-16-0156.1.

Trenberth, K. E., Fasullo, J. T., and Shepherd, T. G. (2015). Attribution of climate extreme events. *Nat. Clim. Chang.* 5, 725–730. doi:10.1038/nclimate2657.

Trenberth, K., Lijing, C., Peter, J., Yongxin, Z., and John, F. (2018). Hurricane Harvey Links to Ocean Heat Content and Climate Change Adaptation. *Earth's Futur.* 6, 730–744. doi:10.1029/2018EF000825.

Trigg, M. A., Birch, C. E., Neal, J. C., Bates, P. D., Smith, A., Sampson, C. C., et al. (2016). The credibility challenge for global fluvial flood risk analysis. *Environ. Res. Lett.* 11, 094014. doi:10.1088/1748-9326/11/9/094014.

Trinh-Tuan, L., Matsumoto, J., Tangang, F. T., Juneng, L., Cruz, F., Narisma, G., et al. (2019). Application of Quantile Mapping bias correction for mid-future precipitation projections over Vietnam. *Sci. Online Lett. Atmos.* 15, 1–6. doi:10.2151/SOLA.2019-001.

Trismidianto, and Satyawardhana, H. (2018). Mesoscale Convective Complexes (MCCs) over the Indonesian Maritime Continent during the ENSO events. *IOP Conf. Ser. Earth Environ. Sci.* 149, 012025. doi:10.1088/1755-1315/149/1/012025.

Trnka, M., Brázdil, R., Balek, J., Semerádová, D., Hlavinka, P., Možný, M., et al. (2015a). Drivers of soil drying in the Czech Republic between 1961 and 2012. *Int. J. Climatol.* 35, 2664–2675. doi:10.1002/joc.4167.

Trnka, M., Brázdil, R., Možný, M., Štěpánek, P., Dobrovolný, P., Zahradníček, P., et al. (2015b). Soil moisture trends in the Czech Republic between 1961 and 2012. *Int. J. Climatol.* 35, 3733–3747. doi:10.1002/joc.4242.

Trzeciak, T. M., Knippertz, P., Pirret, J. S. R., and Williams, K. D. (2016). Can we trust climate models to realistically represent severe European windstorms? *Clim. Dyn.* 46, 3431–3451. doi:10.1007/s00382-015-2777-9.

Tsuboki, K., Yoshioka, M. K., Shinoda, T., Kato, M., Kanada, S., and Kitoh, A. (2015). Future increase of supertyphoon intensity associated with climate change. *Geophys. Res. Lett.* 42, 646–652. doi:10.1002/2014GL061793.

Tsuguti, H., Seino, N., Kawase, H., Imada, Y., Nakaegawa, T., and Takayabu, I. (2018). Meteorological overview and mesoscale characteristics of the Heavy Rain Event of July 2018 in Japan. *Landslides* 16, 363–371. doi:10.1007/s10346-018-1098-6.

Tsuji, H., Yokoyama, C., and Takayabu, Y. N. (2019). Contrasting features of the July 2018 heavy rainfall event and the 2017 Northern Kyushu rainfall event in Japan. *J. Meteorol. Soc. Japan* in review.

ACCEPTED VERSION SUBJECT TO FINAL EDITING

Turco, M., Jerez, S., Augusto, S., Tarín-Carrasco, P., Ratola, N., Jiménez-Guerrero, P., et al. (2019). Climate drivers of the 2017 devastating fires in Portugal. *Sci. Rep.* 9. doi:10.1038/s41598-019-50281-2.

Türkeş, M., and Erlat, E. (2018). Variability and trends in record air temperature events of Turkey and their associations with atmospheric oscillations and anomalous circulation patterns. *Int. J. Climatol.* 38, 5182–5204. doi:10.1002/joc.5720.

Tuttle, S., and Salvucci, G. (2016). Atmospheric science: Empirical evidence of contrasting soil moisture-precipitation feedbacks across the United States. *Science (80-.).* 352, 825–828. doi:10.1126/science.aaa7185.

Twardosz, R., and Kossowska-Cezak, U. (2013). Exceptionally hot summers in Central and Eastern Europe (1951-2010). *Theor. Appl. Climatol.* 112, 617–628. doi:10.1007/s00704-012-0757-0.

Udall, B., and Overpeck, J. (2017). The twenty-first century Colorado River hot drought and implications for the future. *Water Resour. Res.* 53, 2404–2418. doi:10.1002/2016WR019638.

Uhe, P., Otto, F. E. L., Haustein, K., van Oldenborgh, G. J., King, A. D., Wallom, D. C. H., et al. (2016). Comparison of methods: Attributing the 2014 record European temperatures to human influences. *Geophys. Res. Lett.* 43, 8685–8693. doi:10.1002/2016GL069568.

Uhe, P., Sjoukje, P., Sarah, K., Kasturi, S., Joyce, K., Emmah, M., et al. (2017). Attributing drivers of the 2016 Kenyan drought. *Int. J. Climatol.* 38, e554–e568. doi:10.1002/joc.5389.

Ukkola, A. M., De Kauwe, M. G., Roderick, M. L., Abramowitz, G., and Pitman, A. J. (2020). Robust Future Changes in Meteorological Drought in CMIP6 Projections Despite Uncertainty in Precipitation. *Geophys. Res. Lett.* 47, e2020GL087820. doi:10.1029/2020GL087820.

Ukkola, A. M., Pitman, A. J., De Kauwe, M. G., Abramowitz, G., Herger, N., Evans, J. P., et al. (2018). Evaluating CMIP5 model agreement for multiple drought metrics. *J. Hydrometeorol.* 19, 969–988. doi:10.1175/JHM-D-17-0099.1.

Ukkola, A. M., Prentice, I. C., Keenan, T. F., Van Dijk, A. I. J. M., Viney, N. R., Myneni, R. B., et al. (2016). Reduced streamflow in water-stressed climates consistent with CO2 effects on vegetation. *Nat. Clim. Chang.* 6, 75–78. doi:10.1038/nclimate2831.

Underwood, B. S., Guido, Z., Gudipudi, P., and Feinberg, Y. (2017). Increased costs to US pavement infrastructure from future temperature rise. *Nat. Clim. Chang.* 7, 704–707. doi:10.1038/nclimate3390.

UNFCCC (2015). "Decision 1/CP.21: Adoption of the Paris Agreement," in *Report of the Conference of the Parties on its twenty-first session, held in Paris from 30 November to 13 December 2015. Addendum: Part two: Action taken by the Conference of the Parties at its twenty-first session* FCCC/CP/2015/10/Add.1. (United Nations Framework Convention on Climate Change (UNFCCC)), 1–36. Available at: https://unfccc.int/documents/9097.

Utsumi, N., Kim, H., Kanae, S., and Oki, T. (2017). Relative contributions of weather systems to mean and extreme global precipitation. *J. Geophys. Res.* 122, 152–167. doi:10.1002/2016JD025222.

Valiya Veettil, A., and Mishra, A. K. (2020). Multiscale hydrological drought analysis: Role of climate, catchment and morphological variables and associated thresholds. *J. Hydrol.* 582. doi:10.1016/j.jhydrol.2019.124533.

Valverde, M. C., and Marengo, J. A. (2014). Extreme Rainfall Indices in the Hydrographic Basins of Brazil. *Open J. Mod. Hydrol.* 04, 10–26. doi:10.4236/ojmh.2014.41002.

van den Besselaar, E. J. M., Klein Tank, A. M. G., and Buishand, T. A. (2013). Trends in European precipitation extremes over 1951–2010. *Int. J. Climatol.* 33, 2682–2689. doi:10.1002/joc.3619.

Van Den Hurk, B., Best, M., Dirmeyer, P., Pitman, A., Polcher, J., and Santanello, J. (2011). Acceleration of land surface model development over a decade of glass. *Bull. Am. Meteorol. Soc.* 92, 1593–1600. doi:10.1175/BAMS-D-11-00007.1.

Van Den Hurk, B., Kim, H., Krinner, G., Seneviratne, S. I., Derksen, C., Oki, T., et al. (2016). LS3MIP (v1.0) contribution to CMIP6: The Land Surface, Snow and Soil moisture Model Intercomparison Project - Aims, setup and expected outcome. *Geosci. Model Dev.* 9, 2809–2832. doi:10.5194/gmd-9-2809-2016.

van den Hurk, B., Meijgaard, E. van, Valk, P. de, Heeringen, K.-J. van, and Gooijer, J. (2015). Analysis of a compounding surge and precipitation event in the Netherlands. *Environ. Res. Lett.* 10. doi:10.1088/1748-9326/10/3/035001.

Van Der Linden, E. C., Haarsma, R. J., and Van Der Schrier, G. (2019). Impact of climate model resolution on soil moisture projections in central-western Europe. *Hydrol. Earth Syst. Sci.* 23, 191–206. doi:10.5194/hess-23-191-2019.

van der Schrier, G., Barichivich, J., Briffa, K. R., and Jones, P. D. (2013). A scPDSI-based global data set of dry and wet spells for 1901-2009. *J. Geophys. Res. Atmos.* 118, 4025–4048. doi:10.1002/jgrd.50355.

van der Schrier, G., Rasmijn, L. M., Barkmeijer, J., Sterl, A., and Hazeleger, W. (2018). The 2010 Pakistan floods in a future climate. *Clim. Change* 148, 205–218. doi:10.1007/s10584-018-2173-7.

van der Wiel, K., Kapnick, S. B., van Oldenborgh, G. J., Whan, K., Philip, S., Vecchi, G. A., et al. (2017). Rapid attribution of the August 2016 flood-inducing extreme precipitation in south Louisiana to climate change. *Hydrol. Earth Syst. Sci.* 21, 897–921. doi:10.5194/hess-21-897-2017.

van Dijk, A. I. J. M., Beck, H. E., Crosbie, R. S., de Jeu, R. A. M., Liu, Y. Y., Podger, G. M., et al. (2013). The Millennium Drought in southeast Australia (2001-2009): Natural and human causes and implications for water resources, ecosystems, economy, and society. *Water Resour. Res.* 49, 1040–1057. doi:10.1002/wrcr.20123.

ACCEPTED VERSION SUBJECT TO FINAL EDITING

Van Huijgevoort, M. H. J., Hazenberg, P., Van Lanen, H. A. J., Teuling, A. J., Clark, D. B., Folwell, S., et al. (2013). Global multimodel analysis of drought in runofffor the second half of the twentieth century. *J. Hydrometeorol.* 14, 1535–1552. doi:10.1175/JHM-D-12-0186.1.

Van Lanen, H. A. J., Laaha, G., Kingston, D. G., Gauster, T., Ionita, M., Vidal, J.-P., et al. (2016). Hydrology needed to manage droughts: the 2015 European case. *Hydrol. Process.* 30, 3097–3104. doi:10.1002/hyp.10838.

Van Lanen, H. A. J., Wanders, N., Tallaksen, L. M., and Van Loon, A. F. (2013). Hydrological drought across the world: Impact of climate and physical catchment structure. *Hydrol. Earth Syst. Sci.* 17, 1715–1732. doi:10.5194/hess-17-1715-2013.

Van Loon, A. F. (2015). Hydrological drought explained. *Wiley Interdiscip. Rev. Water* 2, 359–392. doi:10.1002/wat2.1085.

Van Loon, A. F., and Laaha, G. (2015). Hydrological drought severity explained by climate and catchment characteristics. *J. Hydrol.* 526, 3–14. doi:10.1016/j.jhydrol.2014.10.059.

Van Loon, A. F., Stahl, K., Di Baldassarre, G., Clark, J., Rangecroft, S., Wanders, N., et al. (2016). Drought in a human-modified world: Reframing drought definitions, understanding, and analysis approaches. *Hydrol. Earth Syst. Sci.* 20, 3631–3650. doi:10.5194/hess-20-3631-2016.

Van Loon, A. F., and Van Lanen, H. A. J. (2012). A process-based typology of hydrological drought. *Hydrol. Earth Syst. Sci.* 16, 1915–1946. doi:10.5194/hess-16-1915-2012.

van Oldenborgh, G. J., Krikken, F., Lewis, S., Leach, N. J., Lehner, F., Saunders, K. R., et al. (2021). Attribution of the Australian bushfire risk to anthropogenic climate change. *Nat. Hazards Earth Syst. Sci.* 21, 941–960. doi:10.5194/nhess-21-941-2021.

van Oldenborgh, G. J., Mitchell-Larson, E., Vecchi, G. A., de Vries, H., Vautard, R., and Otto, F. (2019). Cold waves are getting milder in the northern midlatitudes. *Environ. Res. Lett.* 14, 114004. doi:10.1088/1748-9326/ab4867.

van Oldenborgh, G. J., Otto, F. E. L., Haustein, K., and AchutaRao, K. (2016). The Heavy Precipitation Event of December 2015 in Chennai, India. *Bull. Am. Meteorol. Soc.* 97, S87–S91. doi:10.1175/BAMS-D-16-0129.1.

van Oldenborgh, G. J., Philip, S., Kew, S., van Weele, M., Uhe, P., Otto, F., et al. (2018). Extreme heat in India and anthropogenic climate change. *Nat. Hazards Earth Syst. Sci.* 18, 365–381. doi:10.5194/nhess-18-365-2018.

van Oldenborgh, G. J., van der Wiel, K., Sebastian, A., Singh, R., Arrighi, J., Otto, F., et al. (2017). Attribution of extreme rainfall from Hurricane Harvey, August 2017. *Environ. Res. Lett.* 12, 124009. doi:10.1088/1748-9326/aa9ef2.

van Vuuren, D. P., Stehfest, E., den Elzen, M. G. J., Kram, T., van Vliet, J., Deetman, S., et al. (2011). RCP2.6: Exploring the possibility to keep global mean temperature increase below 2°C. *Clim. Change* 109, 95–116. doi:10.1007/s10584-011-0152-3.

Vanden Broucke, S., Wouters, H., Demuzere, M., and van Lipzig, N. P. M. (2019). The influence of convection-permitting regional climate modeling on future projections of extreme precipitation: dependency on topography and timescale. *Clim. Dyn.* 52, 5303–5324. doi:10.1007/s00382-018-4454-2.

Varela, V., Vlachogiannis, D., Sfetsos, A., Karozis, S., Politi, N., and Giroud, F. (2019). Projection of forest fire danger due to climate change in the French Mediterranean region. *Sustain.* 11. doi:10.3390/su11164284.

Varino, F., Arbogast, P., Joly, B., Riviere, G., Fandeur, M. L., Bovy, H., et al. (2018). Northern Hemisphere extratropical winter cyclones variability over the 20th century derived from ERA-20C reanalysis. *Clim. Dyn.* doi:10.1007/s00382-018-4176-5.

Vautard, R., Aalst, M., Boucher, O., Drouin, A., Haustein, K., Kreienkamp, F., et al. (2020a). Human contribution to the record-breaking June and July 2019 heat waves in Western Europe. *Environ. Res. Lett.* doi:10.1088/1748-9326/aba3d4.

Vautard, R., Cattiaux, J., Yiou, P., Thépaut, J.-N., and Ciais, P. (2010). Northern Hemisphere atmospheric stilling partly attributed to an increase in surface roughness. *Nat. Geosci.* 3, 756–761. doi:10.1038/ngeo979.

Vautard, R., Gobiet, A., Jacob, D., Belda, M., Colette, A., Déqué, M., et al. (2013). The simulation of European heat waves from an ensemble of regional climate models within the EURO-CORDEX project. *Clim. Dyn.* 41, 2555–2575. doi:10.1007/s00382-013-1714-z.

Vautard, R., Kadygrov, N., Iles, C., Boberg, F., Buonomo, E., Bülow, K., et al. (2020b). Evaluation of the large EURO-CORDEX regional climate model ensemble. *J. Geophys. Res. Atmos.* doi:10.1029/2019JD032344.

Vautard, R., van Oldenborgh, G. J., Otto, F. E. L., Yiou, P., de Vries, H., van Meijgaard, E., et al. (2019). Human influence on European winter wind storms such as those of January 2018. *Earth Syst. Dynam.* 10, 271–286. doi:10.5194/esd-10-271-2019.

Vautard, R., Yiou, P., D'Andrea, F., de Noblet, N., Viovy, N., Cassou, C., et al. (2007). Summertime European heat and drought waves induced by wintertime Mediterranean rainfall deficit. *Geophys. Res. Lett.* 34. doi:10.1029/2006GL028001.

Vautard, R., Yiou, P., Otto, F., Stott, P., Christidis, N., Oldenborgh, G. J. van, et al. (2016). Attribution of human-induced dynamical and thermodynamical contributions in extreme weather events. *Environ. Res. Lett.* 11, 114009. doi:10.1088/1748-9326/11/11/114009.

Vautard, R., Yiou, P., van Oldenborgh, G.-J., Lenderink, G., Thao, S., Ribes, A., et al. (2015). Extreme Fall 2014 Precipitation in the Cévennes Mountains. *Bull. Am. Meteorol. Soc.* 96, S56–S60. doi:10.1175/BAMS-D-15-

ACCEPTED VERSION SUBJECT TO FINAL EDITING

00088.1.
Veale, L., and Endfield, G. H. (2016). Situating 1816, the 'year without summer', in the UK. *Geogr. J.* 182, 318–330. doi:10.1111/geoj.12191.
Vecchi, G. A., Delworth, T. L., Murakami, H., Underwood, S. D., Wittenberg, A. T., Zeng, F., et al. (2019). Tropical cyclone sensitivities to CO2 doubling: roles of atmospheric resolution, synoptic variability and background climate changes. *Clim. Dyn.* doi:10.1007/s00382-019-04913-y.
Vecchi, G. A., and Soden, B. J. (2007). Increased tropical Atlantic wind shear in model projections of global warming. *Geophys. Res. Lett.* 34. doi:10.1029/2006GL028905.
Velázquez, J. A., Schmid, J., Ricard, S., Muerth, M. J., Gauvin St-Denis, B., Minville, M., et al. (2013). An ensemble approach to assess hydrological models' contribution to uncertainties in the analysis of climate change impact on water resources. *Hydrol. Earth Syst. Sci.* 17, 565–578. doi:10.5194/hess-17-565-2013.
Veldkamp, T. I. E., Wada, Y., Aerts, J. C. J. H., Döll, P., Gosling, S. N. N., Liu, J., et al. (2017). Water scarcity hotspots travel downstream due to human interventions in the 20th and 21st century. *Nat. Commun.* 8, 15697. doi:10.1038/ncomms15697.
Vetter, T., Reinhardt, J., Flörke, M., van Griensven, A., Hattermann, F., Huang, S., et al. (2017). Evaluation of sources of uncertainty in projected hydrological changes under climate change in 12 large-scale river basins. *Clim. Change* 141, 419–433. doi:10.1007/s10584-016-1794-y.
Vicente-Serrano, S. M., Domínguez-Castro, F., McVicar, T. R., Tomas-Burguera, M., Peña-Gallardo, M., Noguera, I., et al. (2020a). Global characterization of hydrological and meteorological droughts under future climate change: The importance of timescales, vegetation-CO2 feedbacks and changes to distribution functions. *Int. J. Climatol.* 40, 2557–2567. doi:10.1002/joc.6350.
Vicente-Serrano, S. M., Lopez-Moreno, J.-I., Beguería, S., Lorenzo-Lacruz, J., Sanchez-Lorenzo, A., García-Ruiz, J. M., et al. (2014). Evidence of increasing drought severity caused by temperature rise in southern Europe. *Environ. Res. Lett.* 9, 044001. doi:10.1088/1748-9326/9/4/044001.
Vicente-Serrano, S. M., McVicar, T. R., Miralles, D. G., Yang, Y., and Tomas-Burguera, M. (2020b). Unraveling the influence of atmospheric evaporative demand on drought and its response to climate change. *WIREs Clim. Chang.* 11, e632. doi:10.1002/wcc.632.
Vicente-Serrano, S. M., Peña-Gallardo, M., Hannaford, J., Murphy, C., Lorenzo-Lacruz, J., Dominguez-Castro, F., et al. (2019). Climate, Irrigation, and Land Cover Change Explain Streamflow Trends in Countries Bordering the Northeast Atlantic. *Geophys. Res. Lett.* 46, 10821–10833. doi:10.1029/2019GL084084.
Vicente-Serrano, S. M., Quiring, S. M., Peña-Gallardo, M., Yuan, S., and Domínguez-Castro, F. (2020c). A review of environmental droughts: Increased risk under global warming? *Earth-Science Rev.* 201, 102953. doi:10.1016/j.earscirev.2019.102953.
Vicente-Serrano, S. M., Van der Schrier, G., Beguería, S., Azorin-Molina, C., Lopez-Moreno, J.-I. J.-I., der Schrier, G., et al. (2015). Contribution of precipitation and reference evapotranspiration to drought indices under different climates. *J. Hydrol.* 526, 42–54. doi:10.1016/j.jhydrol.2014.11.025.
Vicente-Serrano, S. M., Zabalza-Martínez, J., Borràs, G., López-Moreno, J. I., Pla, E., Pascual, D., et al. (2017). Effect of reservoirs on streamflow and river regimes in a heavily regulated river basin of Northeast Spain. *Catena* 149. doi:10.1016/j.catena.2016.03.042.
Vicente-Serrano, S. M., Domínguez-Castro, F., Murphy, C., Hannaford, J., Reig, F., Peña-Angulo, D., et al. (2021). Long-term variability and trends in meteorological droughts in Western Europe (1851–2018). *Int. J. Climatol.* 41, E690–E717. doi:10.1002/joc.6719.
Vichot-Llano, A., Martinez-Castro, D., Bezanilla-Morlot, A., Centella-Artola, A., and Giorgi, F. (2021). Projected changes in precipitation and temperature regimes and extremes over the Caribbean and Central America using a multiparameter ensemble of RegCM4. *Int. J. Climatol.* 41, 1328–1350. doi:10.1002/joc.6811.
Vidal, J.-P., Hingray, B., Magand, C., Sauquet, E., and Ducharne, A. (2016). Hierarchy of climate and hydrological uncertainties in transient low-flow projections. *Hydrol. Earth Syst. Sci.* 20, 3651–3672. doi:10.5194/hess-20-3651-2016.
Vidale, P. L., Hodges, K., Vannière, B., Davini, P., Roberts, M. J., Strommen, K., et al. (2021). Impact of stochastic physics and model resolution on the simulation of Tropical Cyclones in climate GCMs. *J. Clim.*, 1–85. doi:10.1175/JCLI-D-20-0507.1.
Vikhamar-Schuler, D., Isaksen, K., Haugen, J. E., Tømmervik, H., Luks, B., Schuler, T. V., et al. (2016). Changes in Winter Warming Events in the Nordic Arctic Region. *J. Clim.* 29, 6223–6244. doi:10.1175/JCLI-D-15-0763.1.
Villafuerte, M. Q., and Matsumoto, J. (2015). Significant Influences of Global Mean Temperature and ENSO on Extreme Rainfall in Southeast Asia. *J. Clim.* 28, 1905–1919. doi:10.1175/JCLI-D-14-00531.1.
Villarini, G., Smith, J. A., and Vecchi, G. A. (2012). Changing Frequency of Heavy Rainfall over the Central United States. *J. Clim.* 26, 351–357. doi:10.1175/JCLI-D-12-00043.1.
Vimont, D. J., and Kossin, J. P. (2007). The Atlantic Meridional Mode and hurricane activity. *Geophys. Res. Lett.* 34. doi:10.1029/2007GL029683.
Vincent, L. A., Aguilar, E., Saindou, M., Hassane, A. F., Jumaux, G., Roy, D., et al. (2011). Observed trends in indices of daily and extreme temperature and precipitation for the countries of the western Indian Ocean, 1961–2008. *J.*

ACCEPTED VERSION SUBJECT TO FINAL EDITING

Geophys. Res. 116, D10108. doi:10.1029/2010JD015303.
Vincent, L. A., Zhang, X., Mekis, É., Wan, H., and Bush, E. J. (2018). Changes in Canada's Climate: Trends in Indices Based on Daily Temperature and Precipitation Data. *Atmosphere-Ocean* 56, 332–349. doi:10.1080/07055900.2018.1514579.
Vogel, M. M., Hauser, M., and Seneviratne, S. I. (2020a). Projected changes in hot, dry and wet extreme events' clusters in CMIP6 multi-model ensemble. *Environ. Res. Lett.* 15, 094021. doi:10.1088/1748-9326/ab90a7.
Vogel, M. M., Orth, R., Cheruy, F., Hagemann, S., Lorenz, R., van den Hurk, B. J. J. M., et al. (2017). Regional amplification of projected changes in extreme temperatures strongly controlled by soil moisture-temperature feedbacks. *Geophys. Res. Lett.* 44, 1511–1519. doi:10.1002/2016GL071235.
Vogel, M. M., Zscheischler, J., Fischer, E. M., and Seneviratne, S. I. (2020b). Development of Future Heatwaves for Different Hazard Thresholds. *J. Geophys. Res. Atmos.* 125. doi:10.1029/2019JD032070.
Vogel, M. M., Zscheischler, J., and Seneviratne, S. I. (2018). Varying soil moisture–atmosphere feedbacks explain divergent temperature extremes and precipitation projections in central Europe. *Earth Syst. Dyn.* 9, 1107–1125. doi:10.5194/esd-9-1107-2018.
Vogel, M. M., Zscheischler, J., Wartenburger, R., Dee, D., and Seneviratne, S. I. (2019). Concurrent 2018 Hot Extremes Across Northern Hemisphere Due to Human-Induced Climate Change. *Earth's Futur.* 7, 2019EF001189. doi:10.1029/2019EF001189.
Volosciuk, C., Maraun, D., Semenov, V. A., Tilinina, N., Gulev, S. K., and Latif, M. (2016). Rising Mediterranean Sea Surface Temperatures Amplify Extreme Summer Precipitation in Central Europe. *Sci. Rep.* 6, 32450. doi:10.1038/srep32450.
Vose, R. S., Easterling, D. R., Kunkel, K. E., LeGrande, A. N., and Wehner, M. F. (2017). "Temperature Changes in the United States," in *Climate Science Special Report: Fourth National Climate Assessment, Volume I*, eds. D. J. Wuebbles, D. W. Fahey, K. A. Hibbard, D. J. Dokken, B. C. Stewart, and T. K. Maycock (Washington, DC, USA: U.S. Global Change Research Program), 185–206. doi:10.7930/J0N29V45.
Wada, Y., van Beek, L. P. H., Wanders, N., and Bierkens, M. F. P. (2013). Human water consumption intensifies hydrological drought worldwide. *Environ. Res. Lett.* 8, 034036. doi:10.1088/1748-9326/8/3/034036.
Wahl, T., Jain, S., Bender, J., Meyers, S. D., and Luther, M. E. (2015). Increasing risk of compound flooding from storm surge and rainfall for major US cities. *Nat. Clim. Chang.* 5, 1093. doi:10.1038/nclimate2736.
Waliser, D., and Guan, B. (2017). Extreme winds and precipitation during landfall of atmospheric rivers. *Nat. Geosci.* 10, 179. doi:10.1038/ngeo2894.
Walsh, J. E., Ballinger, T. J., Euskirchen, E. S., Hanna, E., Mård, J., Overland, J. E., et al. (2020). Extreme weather and climate events in northern areas: A review. *Earth-Science Rev.* 209, 103324. doi:10.1016/j.earscirev.2020.103324.
Walsh, K. J. E. E., Camargo, S. J., Vecchi, G. A., Daloz, A. S., Elsner, J., Emanuel, K., et al. (2015). Hurricanes and climate: The U.S. Clivar working group on hurricanes. *Bull. Am. Meteorol. Soc.* 96, 997–1017. doi:10.1175/BAMS-D-13-00242.1.
Walsh, K. J. E., McBride, J. L., Klotzbach, P. J., Balachandran, S., Camargo, S. J., Holland, G., et al. (2016). Tropical cyclones and climate change. *Wiley Interdiscip. Rev. Clim. Chang.* 7, 65–89. doi:10.1002/wcc.371.
Wan, H., Zhang, X., and Zwiers, F. (2019). Human influence on Canadian temperatures. *Clim. Dyn.* 52, 479–494. doi:10.1007/s00382-018-4145-z.
Wanders, N., and Van Lanen, H. A. J. (2015). Future discharge drought across climate regions around the world modelled with a synthetic hydrological modelling approach forced by three general circulation models. *Nat. Hazards Earth Syst. Sci.* 15, 487–504. doi:10.5194/nhess-15-487-2015.
Wanders, N., and Wada, Y. (2015). Human and climate impacts on the 21st century hydrological drought. *J. Hydrol.* 526, 208–220. doi:10.1016/j.jhydrol.2014.10.047.
Wang, H., Chen, Y., Xun, S., Lai, D., Fan, Y., and Li, Z. (2013a). Changes in daily climate extremes in the arid area of northwestern China. *Theor. Appl. Climatol.* 112, 15–28. doi:10.1007/s00704-012-0698-7.
Wang, H., and Schubert, S. (2014). Causes of the extreme dry conditions over California during early 2013 [in "Explaining Extreme Events of 2013 from a Climate Perspective"]. *Bull. Amer. Meteor. Soc.* 95, S7–S11.
Wang, K., Dickinson, R. E., and Liang, S. (2012). Global atmospheric evaporative demand over land from 1973 to 2008. *J. Clim.* 25, 8353–8361. doi:10.1175/JCLI-D-11-00492.1.
Wang, P., Tang, J., Sun, X., Liu, J., and Juan, F. (2018a). Spatiotemporal characteristics of heat waves over China in regional climate simulations within the CORDEX-EA project. *Clim. Dyn.* doi:10.1007/s00382-018-4167-6.
Wang, P., Wu, X., Hao, Y., Wu, C., and Zhang, J. (2020). Is Southwest China drying or wetting? Spatiotemporal patterns and potential causes. *Theor. Appl. Climatol.* 139, 1–15. doi:10.1007/s00704-019-02935-4.
Wang, S.-Y. S., Zhao, L., Yoon, J.-H., Klotzbach, P., and Gillies, R. R. (2018b). Quantitative attribution of climate effects on Hurricane Harvey's extreme rainfall in Texas. *Environ. Res. Lett.* 13, 54014. doi:10.1088/1748-9326/aabb85.
Wang, W., Lee, X., Xiao, W., Liu, S., Schultz, N., Wang, Y., et al. (2018c). Global lake evaporation accelerated by changes in surface energy allocation in a warmer climate. *Nat. Geosci.* 11, 410–414. doi:10.1038/s41561-018-0114-8.

ACCEPTED VERSION SUBJECT TO FINAL EDITING

Wang, W., Zhou, W., Li, Y., Wang, X., and Wang, D. (2015). Statistical modeling and CMIP5 simulations of hot spell changes in China. *Clim. Dyn.* 44, 2859–2872. doi:10.1007/s00382-014-2287-1.

Wang, X., Jiang, D., and Lang, X. (2017a). Future extreme climate changes linked to global warming intensity. *Sci. Bull.* 62, 1673–1680. doi:10.1016/j.scib.2017.11.004.

Wang, X. L., Feng, Y., Chan, R., and Isaac, V. (2016). Inter-comparison of extra-tropical cyclone activity in nine reanalysis datasets. *Atmos. Res.* doi:10.1016/j.atmosres.2016.06.010.

Wang, X. L., Feng, Y., Compo, G. P., Swail, V. R., Zwiers, F. W., Allan, R. J., et al. (2013b). Trends and low frequency variability of extra-tropical cyclone activity in the ensemble of twentieth century reanalysis. *Clim. Dyn.* 40, 2775–2800. doi:10.1007/s00382-012-1450-9.

Wang, X. L., Trewin, B., Feng, Y., and Jones, D. (2013c). Historical changes in Australian temperature extremes as inferred from extreme value distribution analysis. *Geophys. Res. Lett.* 40, 573–578. doi:10.1002/grl.50132.

Wang, Y., Lee, K.-H., Lin, Y., Levy, M., and Zhang, R. (2014). Distinct effects of anthropogenic aerosols on tropical cyclones. *Nat. Clim. Chang.* 4, 368. doi:10.1038/nclimate2144.

Wang, Y. W., and Yang, Y. H. (2014). China's dimming and brightening: Evidence, causes and hydrological implications. *Ann. Geophys.* 32, 41–55. doi:10.5194/angeo-32-41-2014.

Wang, Y., Zhou, B., Qin, D., Wu, J., Gao, R., and Song, L. (2017b). Changes in mean and extreme temperature and precipitation over the arid region of northwestern China: Observation and projection. *Adv. Atmos. Sci.* 34, 289–305. doi:10.1007/s00376-016-6160-5.

Wang, Z., Jiang, Y., Wan, H., Yan, J., and Zhang, X. (2017c). Detection and Attribution of Changes in Extreme Temperatures at Regional Scale. *J. Clim.* 30, 7035–7047. doi:10.1175/JCLI-D-15-0835.1.

Wang, Z., Lin, L., Zhang, X., Zhang, H., Liu, L., and Xu, Y. (2017d). Scenario dependence of future changes in climate extremes under 1.5 °C and 2 °C global warming. *Sci. Rep.* 7, 46432. doi:10.1038/srep46432.

Ward, P. J., Couasnon, A., Eilander, D., Haigh, I. D., Hendry, A., Muis, S., et al. (2018). Dependence between high sea-level and high river discharge increases flood hazard in global deltas and estuaries. *Environ. Res. Lett.* 13, 084012. doi:10.1088/1748-9326/aad400.

Wartenburger, R., Hirschi, M., Donat, M. G., Greve, P., Pitman, A. J., and Seneviratne, S. I. (2017). Changes in regional climate extremes as a function of global mean temperature: an interactive plotting framework. *Geosci. Model Dev. Discuss.*, 1–30. doi:10.5194/gmd-2017-33.

Wasko, C., and Nathan, R. (2019). Influence of changes in rainfall and soil moisture on trends in flooding. *J. Hydrol.* 575, 432–441. doi:https://doi.org/10.1016/j.jhydrol.2019.05.054.

Wasko, C., and Sharma, A. (2017). Global assessment of flood and storm extremes with increased temperatures. *Sci. Rep.* 7, 7945. doi:10.1038/s41598-017-08481-1.

Watterson, I. G., J. Bathols, and Heady, C. (2014). What influences the skill of climate models over the continents? *Bull. Am. Meteorol. Soc.* 95, 689–700. doi:10.1175/BAMS-D-12-00136.1.

Weber, T., Haensler, A., Rechid, D., Pfeifer, S., Eggert, B., and Jacob, D. (2018). Analyzing Regional Climate Change in Africa in a 1.5, 2, and 3°C Global Warming World. *Earth's Futur.* 6, 643–655. doi:10.1002/2017EF000714.

Wehner, M. F. (2020). Characterization of long period return values of extreme daily temperature and precipitation in the CMIP6 models: Part 2, projections of future change. *Weather Clim. Extrem.* 30, 100284. doi:10.1016/j.wace.2020.100284.

Wehner, M. F., Arnold, J. R., Knutson, T., Kunkel, K. E., and LeGrande, A. N. (2017). "Droughts, Floods, and Wildfires," in *Climate Science Special Report: Fourth National Climate Assessment, Volume I*, eds. D. J. Wuebbles, D. W. Fahey, K. A. Hibbard, D. J. Dokken, B. C. Stewart, and T. K. Maycock (Washington, DC, USA: U.S. Global Change Research Program), 231–256. doi:10.7930/J0CJ8BNN.

Wehner, M. F., Reed, K. A., Li, F., Prabhat, Bacmeister, J., Chen, C.-T., et al. (2014). The effect of horizontal resolution on simulation quality in the Community Atmospheric Model, CAM5.1. *J. Adv. Model. Earth Syst.* 6, 980–997. doi:10.1002/2013MS000276.

Wehner, M. F., Reed, K. A., Loring, B., Stone, D., and Krishnan, H. (2018a). Changes in tropical cyclones under stabilized 1.5 and 2.0 °C global warming scenarios as simulated by the Community Atmospheric Model under the HAPPI protocols. *Earth Syst. Dyn.* 9, 187–195. doi:10.5194/esd-9-187-2018.

Wehner, M. F., Zarzycki, C., and Patricola, C. (2019). "Estimating the Human Influence on Tropical Cyclone Intensity as the Climate Changes," in *Hurricane Risk*, eds. J. Collins and K. Walsh (Cham, Switzerland: Springer), 235–260. doi:10.1007/978-3-030-02402-4_12.

Wehner, M., Gleckler, P., and Lee, J. (2020). Characterization of long period return values of extreme daily temperature and precipitation in the CMIP6 models: Part 1, model evaluation. *Weather Clim. Extrem.* 30, 100283. doi:10.1016/j.wace.2020.100283.

Wehner, M., Prabhat, Reed, K. A., Stone, D., Collins, W. D., and Bacmeister, J. (2015). Resolution Dependence of Future Tropical Cyclone Projections of CAM5.1 in the U.S. CLIVAR Hurricane Working Group Idealized Configurations. *J. Clim.* 28, 3905–3925. doi:10.1175/JCLI-D-14-00311.1.

Wehner, M., Stone, D., Krishnan, H., AchutaRao, K., and Castillo, F. (2016). The Deadly Combination of Heat and Humidity in India and Pakistan in Summer 2015. *Bull. Am. Meteorol. Soc.* 97, S81–S86. doi:10.1175/BAMS-D-16-0145.1.

ACCEPTED VERSION SUBJECT TO FINAL EDITING

Wehner, M., Stone, D., Mitchell, D., Shiogama, H., Fischer, E., Graff, L. S., et al. (2018b). Changes in extremely hot days under stabilized 1.5 and 2.0°C global warming scenarios as simulated by the HAPPI multi-model ensemble. *Earth Syst. Dyn.* 9, 299–311. doi:10.5194/esd-9-299-2018.

Wehner, M., Stone, D., Shiogama, H., Wolski, P., Ciavarella, A., Christidis, N., et al. (2018c). Early 21st century anthropogenic changes in extremely hot days as simulated by the C20C+ detection and attribution multi-model ensemble. *Weather Clim. Extrem.* 20, 1–8. doi:10.1016/j.wace.2018.03.001.

Wehrli, K., Guillod, B. P., Hauser, M., Leclair, M., and Seneviratne, S. I. (2019). Identifying Key Driving Processes of Major Recent Heat Waves. *J. Geophys. Res. Atmos.* 124, 11746–11765. doi:10.1029/2019JD030635.

Wehrli, K., Hauser, M., and Seneviratne, S. I. (2020). Storylines of the 2018 Northern Hemisphere heatwave at pre-industrial and higher global warming levels. *Earth Syst. Dyn.* 11, 855–873. doi:10.5194/esd-11-855-2020.

Weldon, D., and Reason, C. J. C. (2014). Variability of rainfall characteristics over the South Coast region of South Africa. *Theor. Appl. Climatol.* 115, 177–185. doi:10.1007/s00704-013-0882-4.

Wen, Q. H., Zhang, X., Xu, Y., and Wang, B. (2013). Detecting human influence on extreme temperatures in China. *Geophys. Res. Lett.* 40, 1171–1176. doi:10.1002/grl.50285.

Wester, P., Mishra, A., Mukherji, A., and Shrestha, A. B. eds. (2019). *The Hindu Kush Himalaya Assessment: Mountains, Climate Change, Sustainability and People*. Cham, Switzerland: Springer doi:10.1007/978-3-319-92288-1.

Westra, S., Alexander, L. V., and Zwiers, F. W. (2013). Global Increasing Trends in Annual Maximum Daily Precipitation. *J. Clim.* 26, 3904–3918. doi:10.1175/JCLI-D-12-00502.1.

Westra, S., Fowler, H. J., Evans, J. P., Alexander, L. V, Berg, P., Johnson, F., et al. (2014). Future changes to the intensity and frequency of short-duration extreme rainfall. *Rev. Geophys.* 52, 522–555. doi:10.1002/2014RG000464.

Westra, S., White, C. J., and Kiem, A. S. (2016). Introduction to the special issue: historical and projected climatic changes to Australian natural hazards. *Clim. Change* 139, 1–19. doi:10.1007/s10584-016-1826-7.

Wetter, O., and Pfister, C. (2013). An underestimated record breaking event – why summer 1540 was likely warmer than 2003. 41–56. doi:10.5194/cp-9-41-2013.

Wetter, O., Pfister, C., Werner, J. P., Zorita, E., Wagner, S., Seneviratne, S. I., et al. (2014). The year-long unprecedented European heat and drought of 1540 – a worst case. *Clim. Change* 125, 349–363. doi:10.1007/s10584-014-1184-2.

Wever, N. (2012). Quantifying trends in surface roughness and the effect on surface wind speed observations. *J. Geophys. Res. Atmos.* 117, 1–14. doi:10.1029/2011JD017118.

Whan, K., Alexander, L. V., Imielska, A., Mcgree, S., Jones, D., Ene, E., et al. (2014). Trends and variability of temperature extremes in the tropical Western Pacific. *Int. J. Climatol.* 34, 2585–2603. doi:10.1002/joc.3861.

Whan, K., Zscheischler, J., Orth, R., Shongwe, M., Rahimi, M., Asare, E. O., et al. (2015). Impact of soil moisture on extreme maximum temperatures in Europe. *Weather Clim. Extrem.* 9, 57–67. doi:10.1016/j.wace.2015.05.001.

Whan, K., and Zwiers, F. (2016). Evaluation of extreme rainfall and temperature over North America in CanRCM4 and CRCM5. *Clim. Dyn.* 46, 3821–3843. doi:10.1007/s00382-015-2807-7.

Wickham, J. D., Wade, T. G., and Riitters, K. H. (2013). Empirical analysis of the influence of forest extent on annual and seasonal surface temperatures for the continental United States. *Glob. Ecol. Biogeogr.* 22, 620–629. doi:10.1111/geb.12013.

Wilcox, L. J., Yiou, P., Hauser, M., Lott, F. C., van Oldenborgh, G. J., Colfescu, I., et al. (2018). Multiple perspectives on the attribution of the extreme European summer of 2012 to climate change. *Clim. Dyn.* 50, 3537–3555. doi:10.1007/s00382-017-3822-7.

Wild, M., Gilgen, H., Roesch, A., Ohmura, A., Long, C. N., Dutton, E. G., et al. (2005). From Dimming to Brightening: Decadal Changes in Solar Radiation at Earth's Surface. *Science (80-.).* 308, 847–850. doi:10.1126/science.1103215.

Wilhelm, B., Ballesteros Cánovas, J. A., Macdonald, N., Toonen, W. H. J., Baker, V., Barriendos, M., et al. (2019). Interpreting historical, botanical, and geological evidence to aid preparations for future floods. *Wiley Interdiscip. Rev. Water* 6, e1318. doi:10.1002/wat2.1318.

Wilhite, D. A., and Pulwarty, R. S. (2017). "Drought as Hazard: Understanding the Natural and Social Context," in *Drought and Water Crises: Integrating Science, Management, and Policy (2nd Edition)* (Boca Raton, FL, USA: CRC Press), 3–22. doi:10.1201/b22009.

Willems, P. (2013). Multidecadal oscillatory behaviour of rainfall extremes in Europe. *Clim. Change* 120, 931–944. doi:10.1007/s10584-013-0837-x.

Willett, K. M., Dunn, R. J. H., Thorne, P. W., Bell, S., de Podesta, M., Parker, D. E., et al. (2014). HadISDH land surface multi-variable humidity and temperature record for climate monitoring. *Clim. Past* 10, 1983–2006. doi:10.5194/cp-10-1983-2014.

Williams, A. P., Abatzoglou, J. T., Gershunov, A., Guzman-Morales, J., Bishop, D. A., Balch, J. K., et al. (2019). Observed Impacts of Anthropogenic Climate Change on Wildfire in California. *Earth's Futur.* 7, 892–910. doi:10.1029/2019EF001210.

Williams, A. P., Allen, C. D., Macalady, A. K., Griffin, D., Woodhouse, C. A., Meko, D. M., et al. (2013). Temperature

ACCEPTED VERSION SUBJECT TO FINAL EDITING

as a potent driver of regional forest drought stress and tree mortality. *Nat. Clim. Chang.* 3, 292–297. doi:10.1038/nclimate1693.
Williams, A. P., Cook, E. R., Smerdon, J. E., Cook, B. I., Abatzoglou, J. T., Bolles, K., et al. (2020). Large contribution from anthropogenic warming to an emerging North American megadrought. *Science (80-.).* 368, 314–318. doi:10.1126/science.aaz9600.
Williams, A. P., Seager, R., Abatzoglou, J. T., Cook, B. I., Smerdon, J. E., and Cook, E. R. (2015). Contribution of anthropogenic warming to California drought during 2012-2014. *Geophys. Res. Lett.* 42, 6819–6828. doi:10.1002/2015GL064924.
Williams, A. P., Seager, R., Berkelhammer, M., Macalady, A. K., Crimmins, M. A., Swetnam, T. W., et al. (2014). Causes and Implications of Extreme Atmospheric Moisture Demand during the Record-Breaking 2011 Wildfire Season in the Southwestern United States. *J. Appl. Meteorol. Climatol.* 53, 2671–2684. doi:10.1175/JAMC-D-14-0053.1.
Willison, J., Robinson, W. A., and Lackmann, G. M. (2013). The Importance of Resolving Mesoscale Latent Heating in the North Atlantic Storm Track. *J. Atmos. Sci.* 70, 2234–2250. doi:10.1175/JAS-D-12-0226.1.
Wing, A. A., Camargo, S. J., Sobel, A. H., Kim, D., Moon, Y., Murakami, H., et al. (2019). Moist Static Energy Budget Analysis of Tropical Cyclone Intensification in High-Resolution Climate Models. *J. Clim.* 32, 6071–6095. doi:10.1175/JCLI-D-18-0599.1.
Winter, H. C., Brown, S. J., and Tawn, J. A. (2017). Characterising the changing behaviour of heatwaves with climate change. *Dyn. Stat. Clim. Syst.*, dzw006. doi:10.1093/climsys/dzw006.
Woldemeskel, F., and Sharma, A. (2016). Should flood regimes change in a warming climate? The role of antecedent moisture conditions. *Geophys. Res. Lett.* 43, 7556–7563. doi:10.1002/2016GL069448.
Woldemichael , Abel, T., Hossain, F., Pielke, R., and Beltrán-Przekurat, A. (2012). Understanding the impact of dam-triggered land use/land cover change on the modification of extreme precipitation. *Water Resour. Res.* 48. doi:10.1029/2011WR011684.
Wolski, P., Stone, D., Tadross, M., Wehner, M., and Hewitson, B. (2014). Attribution of floods in the Okavango basin, Southern Africa. *J. Hydrol.* 511, 350–358. doi:10.1016/j.jhydrol.2014.01.055.
Wolter, K., Eischeid, J. K., Quan, X.-W., Chase, T. n., Hoerling, M., Dole, R. M., et al. (2015). How Unusual was the Cold Winter of 2013/14 in the Upper Midwest? *Bull. Am. Meteorol. Soc.* 96, S10–S14. doi:10.1175/BAMS-D-15-00126.1.
Wood, R. R., and Ludwig, R. (2020). Analyzing Internal Variability and Forced Response of Subdaily and Daily Extreme Precipitation Over Europe. *Geophys. Res. Lett.* 47, e2020GL089300. doi:10.1029/2020GL089300.
Woodhouse, C. A., and Wise, E. K. (2020). The changing relationship between the upper and lower Missouri River basins during drought. *Int. J. Climatol.* 40, 5011–5028. doi:10.1002/joc.6502.
Woodward, C., Shulmeister, J., Larsen, J., Jacobsen, G. E., and Zawadzki, A. (2014). The hydrological legacy of deforestation on global wetlands. *Science (80-.).* 346, 844–847. doi:10.1126/science.1260510.
Woollings, T., Barriopedro, D., Methven, J., Son, S. W., Martius, O., Harvey, B., et al. (2018). Blocking and its Response to Climate Change. *Curr. Clim. Chang. Reports* 4, 287–300. doi:10.1007/s40641-018-0108-z.
Wu, J., Liu, Z., Yao, H., Chen, X., Chen, X., Zheng, Y., et al. (2018a). Impacts of reservoir operations on multi-scale correlations between hydrological drought and meteorological drought. *J. Hydrol.* 563, 726–736. doi:10.1016/j.jhydrol.2018.06.053.
Wu, J., Xu, Y., and Gao, X.-J. (2017). Projected changes in mean and extreme climates over Hindu Kush Himalayan region by 21 CMIP5 models. *Adv. Clim. Chang. Res.* 8, 176–184. doi:10.1016/j.accre.2017.03.001.
Wu, M., Nikulin, G., Kjellström, E., Belušić, D., Jones, C., and Lindstedt, D. (2020a). The impact of regional climate model formulation and resolution on simulated precipitation in Africa. *Earth Syst. Dyn.* 11, 377–394. doi:10.5194/esd-11-377-2020.
Wu, S.-Y. (2015). Changing characteristics of precipitation for the contiguous United States. *Clim. Change* 132, 677–692. doi:10.1007/s10584-015-1453-8.
Wu, W., McInnes, K., O'Grady, J., Hoeke, R., Leonard, M., and Westra, S. (2018b). Mapping Dependence Between Extreme Rainfall and Storm Surge. *J. Geophys. Res. Ocean.* 123, 2461–2474. doi:10.1002/2017JC013472.
Wu, X., Hao, Z., Tang, Q., Singh, V. P., Zhang, X., and Hao, F. (2021). Projected increase in compound dry and hot events over global land areas. *Int. J. Climatol.* 41, 393–403. doi:10.1002/joc.6626.
Wu, Y., and Polvani, L. M. (2017). Recent Trends in Extreme Precipitation and Temperature over Southeastern South America: The Dominant Role of Stratospheric Ozone Depletion in the CESM Large Ensemble. *J. Clim.* 30, 6433–6441. doi:10.1175/JCLI-D-17-0124.1.
Wu, Z., Yu, L., Du, Z., Zhang, H., Fan, X., and Lei, T. (2020b). Recent changes in the drought of China from 1960 to 2014. *Int. J. Climatol.* 40, 3281–3296. doi:10.1002/joc.6397.
Wuebbles, D., Meehl, G., Hayhoe, K., Karl, T. R., Kunkel, K., Santer, B., et al. (2014). CMIP5 Climate Model Analyses: Climate Extremes in the United States. *Bull. Am. Meteorol. Soc.* 95, 571–583. doi:10.1175/BAMS-D-12-00172.1.
Wurbs, R. A., and Ayala, R. A. (2014). Reservoir evaporation in Texas, USA. *J. Hydrol.* 510, 1–9. doi:10.1016/j.jhydrol.2013.12.011.

ACCEPTED VERSION
SUBJECT TO FINAL EDITING

Xia, Y., Ek, M. B., Wu, Y., Ford, T., and Quiring, S. M. (2015). Comparison of NLDAS-2 Simulated and NASMD Observed Daily Soil Moisture. Part I: Comparison and Analysis. *J. Hydrometeorol.* 16, 1962–1980. doi:10.1175/JHM-D-14-0096.1.

Xia, Y., Sheffield, J., Ek, M. B., Dong, J., Chaney, N., Wei, H., et al. (2014). Evaluation of multi-model simulated soil moisture in NLDAS-2. *J. Hydrol.* 512, 107–125. doi:10.1016/j.jhydrol.2014.02.027.

Xiao, C., Wu, P., Zhang, L., and Song, L. (2016). Robust increase in extreme summer rainfall intensity during the past four decades observed in China. *Sci. Rep.* 6, 38506. doi:10.1038/srep38506.

Xiao, K., Griffis, T. J., Baker, J. M., Bolstad, P. V, Erickson, M. D., Lee, X., et al. (2018a). Evaporation from a temperate closed-basin lake and its impact on present, past, and future water level. *J. Hydrol.* 561, 59–75. doi:10.1016/j.jhydrol.2018.03.059.

Xiao, M., Udall, B., and Lettenmaier, D. P. (2018b). On the Causes of Declining Colorado River Streamflows. *Water Resour. Res.* 54, 6739–6756. doi:10.1029/2018WR023153.

Xie, W., Zhou, B., You, Q., Zhang, Y., and Ullah, S. (2020). Observed changes in heat waves with different severities in China during 1961–2015. *Theor. Appl. Climatol.* 141, 1529–1540. doi:10.1007/s00704-020-03285-2.

Xie, X., Liang, S., Yao, Y., Jia, K., Meng, S., and Li, J. (2015). Detection and attribution of changes in hydrological cycle over the Three-North region of China: Climate change versus afforestation effect. *Agric. For. Meteorol.* 203, 74–87. doi:10.1016/j.agrformet.2015.01.003.

Xin, X., Wu, T., Zhang, J., Yao, J., and Fang, Y. (2020). Comparison of CMIP6 and CMIP5 simulations of precipitation in China and the East Asian summer monsoon. *Int. J. Climatol.* doi:10.1002/joc.6590.

Xu, L., Chen, N., and Zhang, X. (2019a). Global drought trends under 1.5 and 2 °C warming. *Int. J. Climatol.* 39, 2375–2385. doi:10.1002/joc.5958.

Xu, R., Yu, P., Abramson, M. J., Johnston, F. H., Samet, J. M., Bell, M. L., et al. (2020). Wildfires, Global Climate Change, and Human Health. *N. Engl. J. Med.* 383, 2173–2181. doi:10.1056/NEJMsr2028985.

Xu, W., Yuan, W., Dong, W., Xia, J., Liu, D., and Chen, Y. (2013). A meta-analysis of the response of soil moisture to experimental warming. *Environ. Res. Lett.* 8, 044027. doi:10.1088/1748-9326/8/4/044027.

Xu, Y., Wu, J., Shi, Y., Zhou, B., Li, R., and Wu, J. (2016a). Change in Extreme Climate Events over China Based on CMIP5 Change in Extreme Climate Events over China Based on CMIP5. *Atmos. Ocean. Sci. Lett.* 8, 185–192. doi:10.3878/AOSL20150006.

Xu, Y., Zhang, X., Wang, X., Hao, Z., Singh, V. P., and Hao, F. (2019b). Propagation from meteorological drought to hydrological drought under the impact of human activities: A case study in northern China. *J. Hydrol.* 579. doi:10.1016/j.jhydrol.2019.124147.

Xu, Y., Zhou, B. T., Wu, J., Han, Z. Y., Zhang, Y. X., and Wu, J. (2017). Asian climate change under 1.5–4 °C warming targets. *Adv. Clim. Chang. Res.* 8, 99–107. doi:10.1016/j.accre.2017.05.004.

Xu, Z., Jiang, Y., Jia, B., and Zhou, G. (2016b). Elevated-CO2 Response of Stomata and Its Dependence on Environmental Factors. *Front. Plant Sci.* 7, 657. doi:10.3389/fpls.2016.00657.

Yamada, Y., Kodama, C., Satoh, M., Nakano, M., Nasuno, T., and Sugi, M. (2019). High-Resolution Ensemble Simulations of Intense Tropical Cyclones and Their Internal Variability During the El Niños of 1997 and 2015. *Geophys. Res. Lett.* 46, 7592–7601. doi:10.1029/2019GL082086.

Yamada, Y., Kodama, C., Satoh, M., Sugi, M., Roberts, M. J., Mizuta, R., et al. (2021). Evaluation of the contribution of tropical cyclone seeds to changes in tropical cyclone frequency due to global warming in high-resolution multi-model ensemble simulations. *Prog. Earth Planet. Sci.* 8, 11. doi:10.1186/s40645-020-00397-1.

Yamada, Y., Oouchi, K., Satoh, M., Tomita, H., and Yanase, W. (2010). Projection of changes in tropical cyclone activity and cloud height due to greenhouse warming: global cloud-system-resolving approach. *Geophys Res Lett* 37.

Yamada, Y., Satoh, M., Sugi, M., Kodama, C., Noda, A. T., Nakano, M., et al. (2017). Response of Tropical Cyclone Activity and Structure to Global Warming in a High-Resolution Global Nonhydrostatic Model. *J. Clim.* 30, 9703–9724. doi:10.1175/JCLI-D-17-0068.1.

Yamaguchi, M., Chan, J. C. L., Moon, I.-J., Yoshida, K., and Mizuta, R. (2020). Global warming changes tropical cyclone translation speed. *Nat. Commun.* 11, 47. doi:10.1038/s41467-019-13902-y.

Yamaguchi, M., and Maeda, S. (2020a). Increase in the Number of Tropical Cyclones Approaching Tokyo since 1980. *J. Meteorol. Soc. Japan. Ser. II* 98, 775–786. doi:10.2151/jmsj.2020-039.

Yamaguchi, M., and Maeda, S. (2020b). Slowdown of typhoon translation speeds in mid-latitudes in September influenced by the Pacific Decadal Oscillation and global warming. *J. Meteor. Soc. Japan* 98. doi:10.2151/jmsj.2020-068.

Yanase, W., Satoh, M., Taniguchi, H., and Fujinami, H. (2012). Seasonal and intraseasonal modulation of tropical cyclogenesis environment over the bay of bengal during the extended summer monsoon. *J. Clim.* 25, 2914–2930. doi:10.1175/JCLI-D-11-00208.1.

Yang, C., Li, L., and Xu, J. (2018a). Changing temperature extremes based on CMIP5 output via semi-parametric quantile regression approach. *Int. J. Climatol.* 38, 3736–3748. doi:10.1002/joc.5524.

Yang, J. A., Kim, S., Mori, N., and Mase, H. (2018b). Assessment of long-term impact of storm surges around the Korean Peninsula based on a large ensemble of climate projections. *Coast. Eng.* 142, 1–8.

ACCEPTED VERSION SUBJECT TO FINAL EDITING

doi:10.1016/j.coastaleng.2018.09.008.
Yang, M.-Z., Zhong, P. A., Li, J.-Y., Chen, J., Wang, W.-Z., Zhu, F.-L., et al. (2018c). Spatial and temporal characteristics of pan evaporation in the Huaihe river basin during 1951-2015. *Appl. Ecol. Environ. Res.* 16, 7635–7655. doi:10.15666/aeer/1606_76357655.
Yang, S.-H., Kang, N.-Y., Elsner, J. B., and Chun, Y. (2018d). Influence of Global Warming on Western North Pacific Tropical Cyclone Intensities during 2015. *J. Clim.* 31, 919–925. doi:10.1175/JCLI-D-17-0143.1.
Yang, Y., Roderick, M. L., Zhang, S., McVicar, T. R., and Donohue, R. J. (2019). Hydrologic implications of vegetation response to elevated CO2 in climate projections. *Nat. Clim. Chang.* 9, 44–48. doi:10.1038/s41558-018-0361-0.
Yang, Y., Zhang, S., McVicar, T. R., Beck, H. E., Zhang, Y., and Liu, B. (2018e). Disconnection Between Trends of Atmospheric Drying and Continental Runoff. *Water Resour. Res.* 54, 4700–4713. doi:10.1029/2018WR022593.
Yang, Y., Zhang, S., Roderick, M. L., McVicar, T. R., Yang, D., Liu, W., et al. (2020). Comparing Palmer Drought Severity Index drought assessments using the traditional offline approach with direct climate model outputs. *Hydrol. Earth Syst. Sci.* 24, 2921–2930. doi:10.5194/hess-24-2921-2020.
Yao, J., Chen, Y., Chen, J., Zhao, Y., Tuoliewubieke, D., Li, J., et al. (2020). Intensification of extreme precipitation in arid Central Asia. *J. Hydrol.*, 125760. doi:10.1016/j.jhydrol.2020.125760.
Yao, Y., Luo, D., Dai, A., and Simmonds, I. (2017). Increased Quasi Stationarity and Persistence of Winter Ural Blocking and Eurasian Extreme Cold Events in Response to Arctic Warming. Part I: Insights from Observational Analyses. *J. Clim.* 30, 3549–3568. doi:10.1175/JCLI-D-16-0261.1.
Yatagai, A., Minami, K., Masuda, M., and Sueto, N. (2019). Development of Intensive APHRODITE Hourly Precipitation Data for Assessment of the Moisture Transport That Caused Heavy Precipitation Events. *SOLA* 15A, 43–48. doi:10.2151/sola.15A-008.
Ye, Z., and Li, Z. (2017). Spatiotemporal variability and trends of extreme precipitation in the Huaihe river basin, a climatic transitional zone in East China. *Adv. Meteorol.* 2017. doi:10.1155/2017/3197435.
Yettella, V., and Kay, J. E. (2017). How will precipitation change in extratropical cyclones as the planet warms? Insights from a large initial condition climate model ensemble. *Clim. Dyn.* 49, 1765–1781. doi:10.1007/s00382-016-3410-2.
Yin, H., Donat, M. G., Alexander, L. V, and Sun, Y. (2015). Multi-dataset comparison of gridded observed temperature and precipitation extremes over China. *Int. J. Climatol.* 35, 2809–2827. doi:10.1002/joc.4174.
Yin, H., and Sun, Y. (2018). Detection of Anthropogenic Influence on Fixed Threshold Indices of Extreme Temperature. *J. Clim.* 31, 6341–6352. doi:10.1175/JCLI-D-17-0853.1.
Yin, H., Sun, Y., and Donat, M. G. (2019). Changes in temperature extremes on the Tibetan Plateau and their attribution. *Environ. Res. Lett.* 14, 124015. doi:10.1088/1748-9326/ab503c.
Yin, H., Sun, Y., Wan, H., Zhang, X., and Lu, C. (2017). Detection of anthropogenic influence on the intensity of extreme temperatures in China. *Int. J. Climatol.* 37, 1229–1237. doi:10.1002/joc.4771.
Yiou, P., Jézéquel, A., Naveau, P., Otto, F. E. L., Vautard, R., and Vrac, M. (2017). A statistical framework for conditional extreme event attribution. *Adv. Stat. Climatol. Meteorol. Oceanogr.* 3, 17–31. doi:10.5194/ascmo-3-17-2017.
Yokoyama, C., Tsuji, H., and Takayabu, Y. N. (2020). The Effects of an Upper-Tropospheric Trough on the Heavy Rainfall Event in July 2018 over Japan. *J. Meteorol. Soc. Japan. Ser. II* 98, 235–255. doi:10.2151/jmsj.2020-013.
Yoshida, K., Sugi, M., Mizuta, R., Murakami, H., and Ishii, M. (2017). Future Changes in Tropical Cyclone Activity in High-Resolution Large-Ensemble Simulations. *Geophys. Res. Lett.* 44, 9910–9917. doi:10.1002/2017GL075058.
You, Q., Jiang, Z., Kong, L., Wu, Z., Bo, Y., Kang, S., et al. (2017). A comparison of heat wave climatologies and trends in China based on multiple definitions. *Clim. Dyn.* 48, 3975–3989. doi:10.1007/s00382-016-3315-0.
Young, I. R., Vinoth, J., Zieger, S., and Babanin, A. V. (2012). Investigation of trends in extreme value wave height and wind speed. *J. Geophys. Res. Ocean.* 117, 1–13. doi:10.1029/2011JC007753.
Yu, B., Lin, H., Kharin, V. V., and Wang, X. L. (2019a). Interannual variability of North American winter temperature extremes and its associated circulation anomalies in observations and CMIP5 simulations. *J. Clim.*, JCLI-D-19-0404.1. doi:10.1175/JCLI-D-19-0404.1.
Yu, B., Lin, H., and Soulard, N. (2019b). A Comparison of North American Surface Temperature and Temperature Extreme Anomalies in Association with Various Atmospheric Teleconnection Patterns. *Atmos.* 10. doi:10.3390/atmos10040172.
Yu, B., Lin, H., Wu, Z. W., and Merryfield, W. J. (2018). The Asian–Bering–North American teleconnection: seasonality, maintenance, and climate impact on North America. *Clim. Dyn.* 50, 2023–2038. doi:10.1007/s00382-017-3734-6.
Yu, E., Sun, J., Chen, H., and Xiang, W. (2015). Evaluation of a high-resolution historical simulation over China: climatology and extremes. *Clim. Dyn.* 45, 2013–2031. doi:10.1007/s00382-014-2452-6.
Yu, M., Li, Q., Hayes, M. J., Svoboda, M. D., and Heim, R. R. (2014). Are droughts becoming more frequent or severe in China based on the Standardized Precipitation Evapotranspiration Index: 1951-2010? *Int. J. Climatol.* 34, 545–558. doi:10.1002/joc.3701.
Yu, R., and Zhai, P. (2020). Changes in compound drought and hot extreme events in summer over populated eastern

ACCEPTED VERSION
SUBJECT TO FINAL EDITING

China. *Weather Clim. Extrem.* 30, 100295. doi:10.1016/j.wace.2020.100295.
Yuan, S., and Quiring, S. M. (2017). Evaluation of soil moisture in CMIP5 simulations over the contiguous United States using in situ and satellite observations. *Hydrol. Earth Syst. Sci.* 21, 2203–2218. doi:10.5194/hess-21-2203-2017.
Yuan, S., Quiring, S. M., and Leasor, Z. T. (2021). Historical Changes in Surface Soil Moisture Over the Contiguous United States: An Assessment of CMIP6. *Geophys. Res. Lett.* 48, 1–9. doi:10.1029/2020GL089991.
Yuan, W., Zheng, Y., Piao, S., Ciais, P., Lombardozzi, D., Wang, Y., et al. (2019). Increased atmospheric vapor pressure deficit reduces global vegetation growth. *Sci. Adv.* 5, eaax1396. doi:10.1126/sciadv.aax1396.
Yuan, X., Wang, L., and Wood, E. F. (2018a). Anthropogenic Intensification of Southern African Flash Droughts as Exemplified by the 2015/16 Season [in "Explaining Extreme Events of 2016 from a Climate Perspective"]. *Bull. Am. Meteorol. Soc.* 99, S86–S90. doi:10.1175/BAMS-D-17-0077.1.
Yuan, X., Wang, S., and Hu, Z.-Z. (2018b). Do Climate Change and El Niño Increase Likelihood of Yangtze River Extreme Rainfall? [in "Explaining Extreme Events of 2016 from a Climate Perspective"]. *Bull. Am. Meteorol. Soc.* 99, S113–S117. doi:10.1175/BAMS-D-17-0089.1.
Zaherpour, J., Gosling, S. N., Mount, N., Schmied, H. M., Veldkamp, T. I. E., Dankers, R., et al. (2018). Worldwide evaluation of mean and extreme runoff from six global-scale hydrological models that account for human impacts. *Environ. Res. Lett.* 13, 065015. doi:10.1088/1748-9326/aac547.
Zahid, M., Blender, R., Lucarini, V., and Bramati, M. C. (2017). Return levels of temperature extremes in southern Pakistan. *Earth Syst. Dyn.* 8, 1263–1278. doi:10.5194/esd-8-1263-2017.
Zahid, M., and Rasul, G. (2012). Changing trends of thermal extremes in Pakistan. *Clim. Change*. doi:10.1007/s10584-011-0390-4.
Zampieri, M., Ceglar, A., Dentener, F., and Toreti, A. (2017). Wheat yield loss attributable to heat waves, drought and water excess at the global, national and subnational scales. *Environ. Res. Lett.* 12, 064008. doi:10.1088/1748-9326/aa723b.
Zampieri, M., D'Andrea, F., Vautard, R., Ciais, P., de Noblet-Ducoudré, N., and Yiou, P. (2009). Hot European Summers and the Role of Soil Moisture in the Propagation of Mediterranean Drought. *J. Clim.* 22, 4747–4758. doi:10.1175/2009JCLI2568.1.
Zappa, G., Hawcroft, M. K., Shaffrey, L., Black, E., and Brayshaw, D. J. (2015). Extratropical cyclones and the projected decline of winter Mediterranean precipitation in the CMIP5 models. *Clim. Dyn.* doi:10.1007/s00382-014-2426-8.
Zappa, G., Shaffrey, L. C., and Hodges, K. I. (2013a). The Ability of CMIP5 Models to Simulate North Atlantic Extratropical Cyclones. *J. Clim.* 26, 5379–5396. doi:10.1175/JCLI-D-12-00501.1.
Zappa, G., Shaffrey, L. C., Hodges, K. I., Sansom, P. G., and Stephenson, D. B. (2013b). A multimodel assessment of future projections of north atlantic and european extratropical cyclones in the CMIP5 climate models. *J. Clim.* 26, 5846–5862. doi:10.1175/JCLI-D-12-00573.1.
Zappa, G., and Shepherd, T. G. (2017). Storylines of Atmospheric Circulation Change for European Regional Climate Impact Assessment. *J. Clim.* 30, 6561–6577. doi:10.1175/JCLI-D-16-0807.1.
Zarzycki, C. M. (2016). Tropical Cyclone Intensity Errors Associated with Lack of Two-Way Ocean Coupling in High-Resolution Global Simulations. *J. Clim.* 29, 8589–8610. doi:10.1175/JCLI-D-16-0273.1.
Zarzycki, C. M. (2018). Projecting Changes in Societally Impactful Northeastern U.S. Snowstorms. *Geophys. Res. Lett.* 45, 12,067-12,075. doi:10.1029/2018GL079820.
Zarzycki, C. M., and Jablonowski, C. (2015). Experimental Tropical Cyclone Forecasts Using a Variable-Resolution Global Model. *Mon. Weather Rev.* 143, 4012–4037. doi:10.1175/MWR-D-15-0159.1.
Zarzycki, C. M., Jablonowski, C., and Taylor, M. A. (2014). Using Variable-Resolution Meshes to Model Tropical Cyclones in the Community Atmosphere Model. *Mon. Weather Rev.* 142, 1221–1239. doi:10.1175/MWR-D-13-00179.1.
Zarzycki, C. M., and Ullrich, P. A. (2017). Assessing sensitivities in algorithmic detection of tropical cyclones in climate data. *Geophys. Res. Lett.* 44, 1141–1149. doi:10.1002/2016GL071606.
Zeder, J., and Fischer, E. M. (2020). Observed extreme precipitation trends and scaling in Central Europe. *Weather Clim. Extrem.* 29, 100266. doi:10.1016/j.wace.2020.100266.
Zeleke, T. T., Giorgi, F., Diro, G. T., and Zaitchik, B. F. (2017). Trend and periodicity of drought over Ethiopia. *Int. J. Climatol.* 37, 4733–4748. doi:10.1002/joc.5122.
Zhai, J., Mondal, S. K., Fischer, T., Wang, Y., Su, B., Huang, J., et al. (2020a). Future drought characteristics through a multi-model ensemble from CMIP6 over South Asia. *Atmos. Res.* 246. doi:10.1016/j.atmosres.2020.105111.
Zhai, R., Tao, F., Lall, U., Fu, B., Elliott, J., and Jägermeyr, J. (2020b). Larger Drought and Flood Hazards and Adverse Impacts on Population and Economic Productivity Under 2.0 than 1.5°C Warming. *Earth's Futur.* 8. doi:10.1029/2019EF001398.
Zhan, R., Chen, B., and Ding, Y. (2018). Impacts of SST anomalies in the Indian-Pacific basin on Northwest Pacific tropical cyclone activities during three super El Niño years. *J. Oceanol. Limnol.* 36, 20–32. doi:10.1007/s00343-018-6321-8.
Zhan, R., and Wang, Y. (2017). Weak Tropical Cyclones Dominate the Poleward Migration of the Annual Mean

ACCEPTED VERSION SUBJECT TO FINAL EDITING

Location of Lifetime Maximum Intensity of Northwest Pacific Tropical Cyclones since 1980. *J. Clim.* 30, 6873–6882. doi:10.1175/JCLI-D-17-0019.1.

Zhan, Y. J., Ren, G. Y., Shrestha, A. B., Rajbhandari, R., Ren, Y. Y., Sanjay, J., et al. (2017). Changes in extreme precipitation events over the Hindu Kush Himalayan region during 1961–2012. *Adv. Clim. Chang. Res.* 8, 166–175. doi:10.1016/j.accre.2017.08.002.

Zhang, C., Liu, F., and Shen, Y. (2018a). Attribution analysis of changing pan evaporation in the Qinghai-Tibetan Plateau, China: Pan Evaporation in the Qinghai-Tibetan Plateau. *Int. J. Climatol.* 38. doi:10.1002/joc.5431.

Zhang, C., and Wang, Y. (2018). Why is the simulated climatology of tropical cyclones so sensitive to the choice of cumulus parameterization scheme in the WRF model? *Clim. Dyn.* 51, 3613–3633. doi:10.1007/s00382-018-4099-1.

Zhang, D., Zhang, Q., Qiu, J., Bai, P., Liang, K., and Li, X. (2018b). Intensification of hydrological drought due to human activity in the middle reaches of the Yangtze River, China. *Sci. Total Environ.* 637–638, 1432–1442. doi:10.1016/j.scitotenv.2018.05.121.

Zhang, G., Murakami, H., Knutson, T. R., Mizuta, R., and Yoshida, K. (2020a). Tropical cyclone motion in a changing climate. *Sci. Adv.* 6, eaaz7610. doi:10.1126/sciadv.aaz7610.

Zhang, J., Chen, H., and Zhang, Q. (2019a). Extreme drought in the recent two decades in northern China resulting from Eurasian warming. *Clim. Dyn.* 52, 2885–2902. doi:10.1007/s00382-018-4312-2.

Zhang, L., Zhou, T., Chen, X., Wu, P., Christidis, N., and Lott, F. C. (2020b). The late spring drought of 2018 in South China. *Bull. Am. Meteorol. Soc.* 101, S59–S64. doi:10.1175/BAMS-D-19-0202.1.

Zhang, M., Chen, Y., Shen, Y., and Li, B. (2019b). Tracking climate change in Central Asia through temperature and precipitation extremes. *J. Geogr. Sci.* 29, 3–28. doi:10.1007/s11442-019-1581-6.

Zhang, M., Chen, Y., Shen, Y., and Li, Y. (2017a). Changes of precipitation extremes in arid Central Asia. *Quat. Int.* 436, 16–27. doi:10.1016/j.quaint.2016.12.024.

Zhang, P., Jeong, J. H., Yoon, J. H., Kim, H., Simon Wang, S. Y., Linderholm, H. W., et al. (2020c). Abrupt shift to hotter and drier climate over inner East Asia beyond the tipping point. *Science (80-.).* 370, 1095–1099. doi:10.1126/science.abb3368.

Zhang, P., Ren, G., Xu, Y., Wang, X. L., Qin, Y., Sun, X., et al. (2019c). Observed Changes in Extreme Temperature over the Global Land Based on a Newly Developed Station Daily Dataset. *J. Clim.* 32, 8489–8509. doi:10.1175/JCLI-D-18-0733.1.

Zhang, Q., Gu, X., Singh, V. P., Kong, D., and Chen, X. (2015a). Spatiotemporal behavior of floods and droughts and their impacts on agriculture in China. *Glob. Planet. Change* 131, 63–72. doi:10.1016/j.gloplacha.2015.05.007.

Zhang, Q., Gu, X., Singh, V. P., Xiao, M., and Xu, C.-Y. (2015b). Flood frequency under the influence of trends in the Pearl River basin, China: Changing patterns, causes and implications. *Hydrol. Process.* 29, 1406–1417. doi:10.1002/hyp.10278.

Zhang, Q., Ni, X., and Zhang, F. (2017b). Decreasing trend in severe weather occurrence over China during the past 50 years. *Sci. Rep.* 7, 42310. doi:10.1038/srep42310.

Zhang, R., Su, F., Jiang, Z., Gao, X., Guo, D., Ni, J., et al. (2015c). An overview of projected climate and environmental changes across the Tibetan Plateau in the 21st century. *Chinese Sci. Bull.* doi:10.1360/N972014-01296.

Zhang, W., Li, W., Zhu, L., Ma, Y., Yang, L., Lott, F. C., et al. (2020d). Anthropogenic Influence on 2018 Summer Persistent Heavy Rainfall in Central Western China. *Bull. Am. Meteorol. Soc.* 101, S65–S70. doi:10.1175/BAMS-D-19-0147.1.

Zhang, W., and Luo, D. (2019). A Nonlinear Theory of Atmospheric Blocking: An Application to Greenland Blocking Changes Linked to Winter Arctic Sea Ice Loss. *J. Atmos. Sci.* 77, 723–751. doi:10.1175/JAS-D-19-0198.1.

Zhang, W., Vecchi, G. A., Murakami, H., Delworth, T. L., Paffendorf, K., Jia, L., et al. (2016a). Influences of Natural Variability and Anthropogenic Forcing on the Extreme 2015 Accumulated Cyclone Energy in the Western North Pacific. *Bull. Am. Meteorol. Soc.* 97, S131–S135. doi:10.1175/BAMS-D-16-0146.1.

Zhang, W., Vecchi, G. A., Murakami, H., Villarini, G., and Jia, L. (2016b). The Pacific meridional mode and the occurrence of tropical Cyclones in the western North Pacific. *J. Clim.* 29, 381–398. doi:10.1175/JCLI-D-15-0282.1.

Zhang, W., Villarini, G., Scoccimarro, E., and Napolitano, F. (2020e). Examining the precipitation associated with medicanes in the high-resolution ERA-5 reanalysis data. *Int. J. Climatol.* n/a. doi:10.1002/joc.6669.

Zhang, W., Villarini, G., Vecchi, G. A., and Smith, J. A. (2018c). Urbanization exacerbated the rainfall and flooding caused by hurricane Harvey in Houston. *Nature* 563, 384–388. doi:10.1038/s41586-018-0676-z.

Zhang, W., and Zhou, T. (2019). Significant Increases in Extreme Precipitation and the Associations with Global Warming over the Global Land Monsoon Regions. *J. Clim.* 32, 8465–8488. doi:10.1175/JCLI-D-18-0662.1.

Zhang, X., Flato, G., Kirchmeier-Young, M., Vincent, L., Wan, H., Wang, X., et al. (2019d). "Changes in Temperature and Precipitation Across Canada," in *Canada's Changing Climate Report*, eds. E. Bush and D. S. Lemmen (Ottawa, ON, Canada: Government of Canada), 112–193. Available at: https://changingclimate.ca/CCCR2019/.

Zhang, X. S., Amirthanathan, G. E., Bari, M. A., Laugesen, R. M., Shin, D., Kent, D. M., et al. (2016c). How streamflow has changed across Australia since the 1950s: evidence from the network of hydrologic reference

ACCEPTED VERSION SUBJECT TO FINAL EDITING

stations. *Hydrol. Earth Syst. Sci.* 20, 3947–3965. doi:10.5194/hess-20-3947-2016.
Zhang, X. S., Amirthanathan, G. E., Bari, M. A., Laugesen, R. M., Shin, D., Kent, D. M., et al. (2016d). How streamflow has changed across Australia since the 1950s: evidence from the network of hydrologic reference stations. *Hydrol. Earth Syst. Sci.* 20, 3947–3965. doi:10.5194/hess-20-3947-2016.
Zhang, X., Wan, H., Zwiers, F. W., Hegerl, G. C., and Min, S.-K. (2013). Attributing intensification of precipitation extremes to human influence. *Geophys. Res. Lett.* 40, 5252–5257. doi:10.1002/grl.51010.
Zhang, X., Zwiers, F. W., Li, G., Wan, H., and Cannon, A. J. (2017c). Complexity in estimating past and future extreme short-duration rainfall. *Nat. Geosci.* 10, 255. doi:10.1038/ngeo2911.
Zhang, Y., Fan, J., Logan, T., Li, Z., and Homeyer, C. R. (2019e). Wildfire Impact on Environmental Thermodynamics and Severe Convective Storms. *Geophys. Res. Lett.* 46, 10082–10093. doi:10.1029/2019GL084534.
Zhang, Y., Pang, X., Xia, J., Shao, Q., Yu, E., Zhao, T., et al. (2019f). Regional Patterns of Extreme Precipitation and Urban Signatures in Metropolitan Areas. *J. Geophys. Res. Atmos.* 124, 641–663. doi:10.1029/2018JD029718.
Zhang, Y., Wang, H., Sun, J., and Drange, H. (2010). Changes in the tropical cyclone genesis potential index over the western north pacific in the SRES A2 scenario. *Adv. Atmos. Sci.* 27, 1246–1258. doi:10.1007/s00376-010-9096-1.
Zhang, Z., and Colle, B. A. (2017). Changes in Extratropical Cyclone Precipitation and Associated Processes during the Twenty-First Century over Eastern North America and the Western Atlantic Using a Cyclone-Relative Approach. *J. Clim.* 30, 8633–8656. doi:10.1175/JCLI-D-16-0906.1.
Zhang, Z., Ralph, F. M., and Zheng, M. (2019g). The Relationship Between Extratropical Cyclone Strength and Atmospheric River Intensity and Position. *Geophys. Res. Lett.* 46, 1814–1823. doi:10.1029/2018GL079071.
Zhang, Z., Wang, K., Chen, D., Li, J., and Dickinson, R. (2019h). Increase in Surface Friction Dominates the Observed Surface Wind Speed Decline during 1973–2014 in the Northern Hemisphere Lands. *J. Clim.* 32, 7421–7435. doi:10.1175/JCLI-D-18-0691.1.
Zhao, C., Brissette, F., Chen, J., and Martel, J. L. J.-L. (2020). Frequency change of future extreme summer meteorological and hydrological droughts over North America. *J. Hydrol.* 584, 124316. doi:10.1016/j.jhydrol.2019.124316.
Zhao, C., Lin, Y., Wu, F., Wang, Y. Y., Li, Z., Rosenfeld, D., et al. (2018). Enlarging Rainfall Area of Tropical Cyclones by Atmospheric Aerosols. *Geophys. Res. Lett.* 45, 8604–8611. doi:10.1029/2018GL079427.
Zhao, K., and Jackson, R. B. (2014). Biophysical forcings of land-use changes from potential forestry activities in North America. *Ecol. Monogr.* 84, 329–353. doi:10.1890/12-1705.1.
Zhao, M., and Held, I. M. (2011). TC-Permitting GCM Simulations of Hurricane Frequency Response to Sea Surface Temperature Anomalies Projected for the Late-Twenty-First Century. *J. Clim.* 25, 2995–3009. doi:10.1175/JCLI-D-11-00313.1.
Zhao, M., Held, I. M., and Lin, S.-J. (2012). Some Counterintuitive Dependencies of Tropical Cyclone Frequency on Parameters in a GCM. *J. Atmos. Sci.* 69, 2272–2283. doi:10.1175/JAS-D-11-0238.1.
Zhao, M., Held, I. M., Lin, S. J., and Vecchi, G. A. (2009). Simulations of global hurricane climatology, interannual variability, and response to global warming using a 50-km resolution GCM. *J. Clim.* 22, 6653–6678. doi:10.1175/2009JCLI3049.1.
Zhao, S., Deng, Y., and Black, R. X. (2016). Warm Season Dry Spells in the Central and Eastern United States: Diverging Skill in Climate Model Representation. *J. Clim.* 29, 5617–5624. doi:10.1175/JCLI-D-16-0321.1.
Zhao, T., and Dai, A. (2015). The magnitude and causes of global drought changes in the twenty-first century under a low-moderate emissions scenario. *J. Clim.* 28, 4490–4512. doi:10.1175/JCLI-D-14-00363.1.
Zhao, T., and Dai, A. (2017). Uncertainties in historical changes and future projections of drought. Part II: model-simulated historical and future drought changes. *Clim. Change* 144, 535–548. doi:10.1007/s10584-016-1742-x.
Zhao, Y., Ducharne, A., Sultan, B., Braconnot, P., and Vautard, R. (2015). Estimating heat stress from climate-based indicators: present-day biases and future spreads in the CMIP5 global climate model ensemble. *Environ. Res. Lett.* 10, 084013. doi:10.1088/1748-9326/10/8/084013.
Zheng, C., Zhang, R., Shi, W., Li, X., and Chen, X. (2017). Trends in significant wave height and surface wind speed in the China Seas between 1988 and 2011. *J. Ocean Univ. China* 16, 717–726. doi:10.1007/s11802-017-3213-z.
Zheng, F., Westra, S., and Sisson, S. A. (2013). Quantifying the dependence between extreme rainfall and storm surge in the coastal zone. *J. Hydrol.* 505, 172–187. doi:10.1016/j.jhydrol.2013.09.054.
Zheng, H., Chiew, F. H. S., Potter, N. J., and Kirono, D. G. C. (2019). Projections of water futures for Australia: An update. in *23rd International Congress on Modelling and Simulation – Supporting Evidence-Based Decision Making: The Role of Modelling and Simulation, MODSIM 2019*, 1000–1006. doi:10.36334/modsim.2019.k7.zhengh.
Zhou, B., Wen, Q. H., Xu, Y., Song, L., and Zhang, X. (2014). Projected changes in temperature and precipitation extremes in China by the CMIP5 multimodel ensembles. *J. Clim.* 27, 6591–6611. doi:10.1175/JCLI-D-13-00761.1.
Zhou, B., Xu, Y., Wu, J., Dong, S., and Shi, Y. (2016a). Changes in temperature and precipitation extreme indices over China: Analysis of a high-resolution grid dataset. *Int. J. Climatol.* 36, 1051–1066. doi:10.1002/joc.4400.
Zhou, C., Chen, D., Wang, K., Dai, A., and Qi, D. (2020). Conditional Attribution of the 2018 Summer Extreme Heat over Northeast China: Roles of Urbanization, Global Warming, and Warming-Induced Circulation Changes. *Bull.*

ACCEPTED VERSION SUBJECT TO FINAL EDITING

Am. Meteorol. Soc. 101, S71–S76. doi:10.1175/BAMS-D-19-0197.1.
Zhou, C., Wang, K., and Qi, D. (2018). Attribution of the July 2016 Extreme Precipitation Event Over China's Wuhang [in "Explaining Extreme Events of 2016 from a Climate Perspective"]. *Bull. Am. Meteorol. Soc.* 99, S107–S111. doi:10.1175/BAMS-D-17-0090.1.
Zhou, C., Wang, K., Qi, D., and Tan, J. (2019a). Attribution of a Record-Breaking Heatwave Event in Summer 2017 over the Yangtze River Delta [in "Explaining Extreme Events of 2017 from a Climate Perspective"]. *Bull. Am. Meteorol. Soc.* 100, S97–S103. doi:10.1175/BAMS-D-18-0134.1.
Zhou, S., Williams, A. P., Berg, A. M., Cook, B. I., Zhang, Y., Hagemann, S., et al. (2019b). Land–atmosphere feedbacks exacerbate concurrent soil drought and atmospheric aridity. *Proc. Natl. Acad. Sci.* 116, 18848–18853. doi:10.1073/pnas.1904955116.
Zhou, S., Williams, A. P., Lintner, B. R., Berg, A. M., Zhang, Y., Keenan, T. F., et al. (2021). Soil moisture–atmosphere feedbacks mitigate declining water availability in drylands. *Nat. Clim. Chang.* 11, 38–44. doi:10.1038/s41558-020-00945-z.
Zhou, T., Song, F., Lin, R., Chen, X., and Chen, X. (2013). The 2012 north China floods: explaining an extreme rainfall event in the context of a longer-term drying tendency [in "Explaining Extreme Events of 2012 from a Climate Perspective"]. *Bull. Am. Meteorol. Soc.* 94, S49–S52. doi:10.1175/BAMS-D-13-00085.1.
Zhou, W., Tang, J., Wang, X., Wang, S., Niu, X., and Wang, Y. (2016b). Evaluation of regional climate simulations over the CORDEX-EA-II domain using the COSMO-CLM model. *Asia-Pacific J. Atmos. Sci.* 52, 107–127. doi:10.1007/s13143-016-0013-0.
Zhu, S., Ge, F., Fan, Y., Zhang, L., Sielmann, F., Fraedrich, K., et al. (2020). Conspicuous temperature extremes over Southeast Asia: seasonal variations under 1.5 °C and 2 °C global warming. *Clim. Change* 160, 343–360. doi:10.1007/s10584-019-02640-1.
Zieger, S., Babanin, A. V., and Young, I. R. (2014). Changes in ocean surface wind with a focus on trends in regional and monthly mean values. *Deep. Res. Part I Oceanogr. Res. Pap.* 86, 56–67. doi:10.1016/j.dsr.2014.01.004.
Zipser, E. J., Cecil, D. J., Liu, C., Nesbitt, S. W., and Yorty, D. P. (2006). Where are the most: Intense thunderstorms on Earth? *Bull. Am. Meteorol. Soc.* 87, 1057–1071. doi:10.1175/BAMS-87-8-1057.
Zittis, G. (2017). Observed rainfall trends and precipitation uncertainty in the vicinity of the Mediterranean, Middle East and North Africa. *Theor. Appl. Climatol.* doi:10.1007/s00704-017-2333-0.
Zolina, O., Simmer, C., Belyaev, K., Gulev, S. K., and Koltermann, P. (2013). Changes in the duration of European wet and dry spells during the last 60 years. *J. Clim.* 26, 2022–2047. doi:10.1175/JCLI-D-11-00498.1.
Zollo, A. L., Rillo, V., Bucchignani, E., Montesarchio, M., and Mercogliano, P. (2016). Extreme temperature and precipitation events over Italy: assessment of high-resolution simulations with COSMO-CLM and future scenarios. *Int. J. Climatol.* 36, 987–1004. doi:10.1002/joc.4401.
Zscheischler, J., and Fischer, E. M. (2020). The record-breaking compound hot and dry 2018 growing season in Germany. *Weather Clim. Extrem.* 29, 100270. doi:10.1016/j.wace.2020.100270.
Zscheischler, J., Fischer, E. M., and Lange, S. (2018a). The effect of bias adjustment on impact modeling. *Earth Syst. Dyn. Discuss.*, 1–17. doi:10.5194/esd-2018-68.
Zscheischler, J., Martius, O., Westra, S., Bevacqua, E., Raymond, C., Horton, R. M., et al. (2020). A typology of compound weather and climate events. *Nat. Rev. Earth Environ.* 1, 333–347. doi:10.1038/s43017-020-0060-z.
Zscheischler, J., and Seneviratne, S. I. (2017). Dependence of drivers affects risks associated with compound events. *Sci. Adv.* 3, e1700263. doi:10.1126/sciadv.1700263.
Zscheischler, J., Westra, S., van den Hurk, B. J. J. M., Seneviratne, S. I., Ward, P. J., Pitman, A., et al. (2018b). Future climate risk from compound events. *Nat. Clim. Chang.* 8, 469–477. doi:10.1038/s41558-018-0156-3.
Zulkafli, Z., Buytaert, W., Manz, B., Rosas, C. V., Willems, P., Lavado-Casimiro, W., et al. (2016). Projected increases in the annual flood pulse of the Western Amazon. *Environ. Res. Lett.* 11, 014013. doi:10.1088/1748-9326/11/1/014013.

ACCEPTED VERSION SUBJECT TO FINAL EDITING

Appendix 11.A

[START TABLE 11.A.1 HERE]

Table 11.A.1: Common drought metrics, associated drought types, drought indices, general description and associated references

Drought metric	Associated drought type	Drought indices	Comments	Representative references
Precipitation deficit	Referred to as "meteorological drought"	Standardized Precipitation Index (SPI), Consecutive Dry Days (CDD), Precipitation deciles and percentiles.	SPI is defined for given time scales in order to identify precipitation deficits over different periods. The SPI shows flexibility to account for different time scales by summing precipitation over *k* months, termed accumulation periods. CDD is usually based on daily precipitation records. Dry-spell length is another commonly used term. The number of dry days (NDD) is also used in some publications.	(Donat et al., 2013a; Orlowsky and Seneviratne, 2013; Sillmann et al., 2013a; Spinoni et al., 2014; Kingston et al., 2015; Stagge et al., 2017; Coppola et al., 2021b)
Excess atmospheric evaporative demand (AED)	Driver for agricultural and ecological drought, together with precipitation through its impact on evapotrans-piration and vegetation stress under soil moisture deficits	Potential evaporation anomalies, Evaporative Demand Drought Index (EDDI).	AED can be measured locally by means of evaporation pans. Physically-based models (e.g., Penman-Monteith) using all aerodynamic and radiative drivers from observations produce robust estimates of the the observed magnitude and variability of the evaporative demand. On the contrary, empirical estimates based on air temperature are affected by more uncertainties (Section 11.6.1.2), especially when applied to climate change projections. AED is an upper bound for actual evapotranspiration (ET) but also induces additional vegetation stress under dry conditions (Section 11.6.1.2).	(Hobbins et al., 2012, 2016; Sheffield et al., 2012; Wang et al., 2012; McEvoy et al., 2016; Roberts et al., 2018; Stephens et al., 2018; Sun et al., 2018c; Vicente-Serrano et al., 2020b)
Soil moisture deficits	Usually referred to as "agricultural drought". Also relevant for ecological droughts.	Soil moisture anomalies (SMA), Standardized Soil Moisture Index (SSMI)	Networks of ground-based soil moisture measurements are available in different regions, but are very sparse and cover very short periods. Surface soil moisture can be monitored from satellites, but only since the 1980s at the earliest. Physically-based land surface models retrieve soil moisture using meteorological variables (precipitation, radiation, wind, temperature, humidity) as input.	(Dorigo et al., 2011, 2015, 2017; Seneviratne et al., 2013; Orlowsky and Seneviratne, 2013; AghaKouchak, 2014; Sohrabi et al., 2015; Zhao and Dai, 2015; Stillman et al., 2016; Yuan and Quiring, 2017; Berg and Sheffield, 2018; Hanel et al., 2018; Samaniego et al., 2018; Seager et al., 2019; Ford and Quiring, 2019; Moravec et al., 2019)
Streamflow and surface waterdeficits	Usually referred to as "hydrological drought"	SRI (Standardized Runoff Index), SSI (Standardized Streamflow Index), threshold level methods, SGI (Standardized Grounwater Index)	Usually based on monthly records of hydrological variables (e.g., streamflow, groundwater, reservoir storages), although daily streamflow is also used using threshold level methods. Observational data is available but not in all regions.	(Bloomfield and Marchant, 2013; Van Lanen et al., 2013; Wada et al., 2013; Forzieri et al., 2014; Prudhomme et al., 2014; Schewe et al., 2014; Van Loon, 2015; Van Loon and Laaha, 2015; Gosling et al., 2017)

ACCEPTED VERSION SUBJECT TO FINAL EDITING

Atmospheri-based drought indices	Metrics of drought severity based on meteorological variables, combining precipitation and AED as drivers.	Standardized-Precipitation Evapotranspiration Index (SPEI), Palmer Drought Severity Index (PDSI)	These drought indices are generated using precipitation and AED. The quality of the outputs depend on the method used to determine the AED. They are widely used for drought monitoring and early warning. These indices are not intended to be a soil moisture or water-balance proxy.	(Dai, 2013; Beguería et al., 2014; Cook et al., 2014a; Mitchell et al., 2014; Stagge et al., 2015; Vicente-Serrano et al., 2015; Dai et al., 2018; Mukherjee et al., 2018b; Yang et al., 2020)

[END TABLE 11.A.1 HERE]

ACCEPTED VERSION
SUBJECT TO FINAL EDITING

Figures

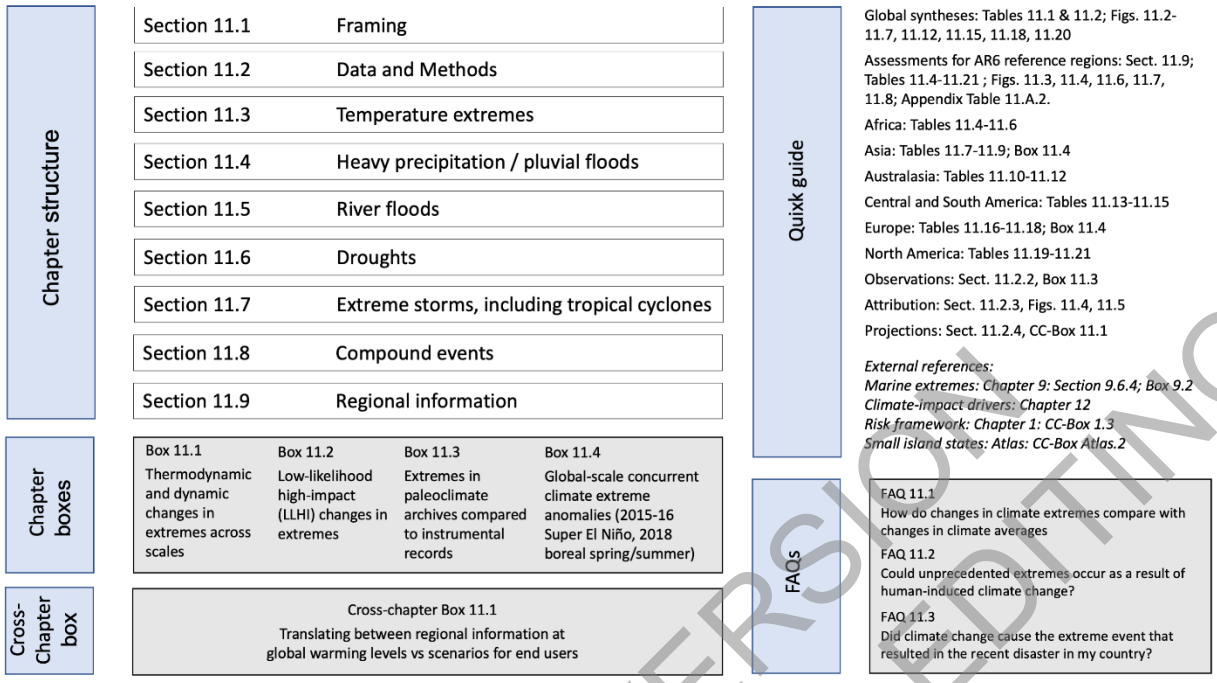


Figure 11.1: Chapter 11 visual abstract of contents.

ACCEPTED VERSION SUBJECT TO FINAL EDITING

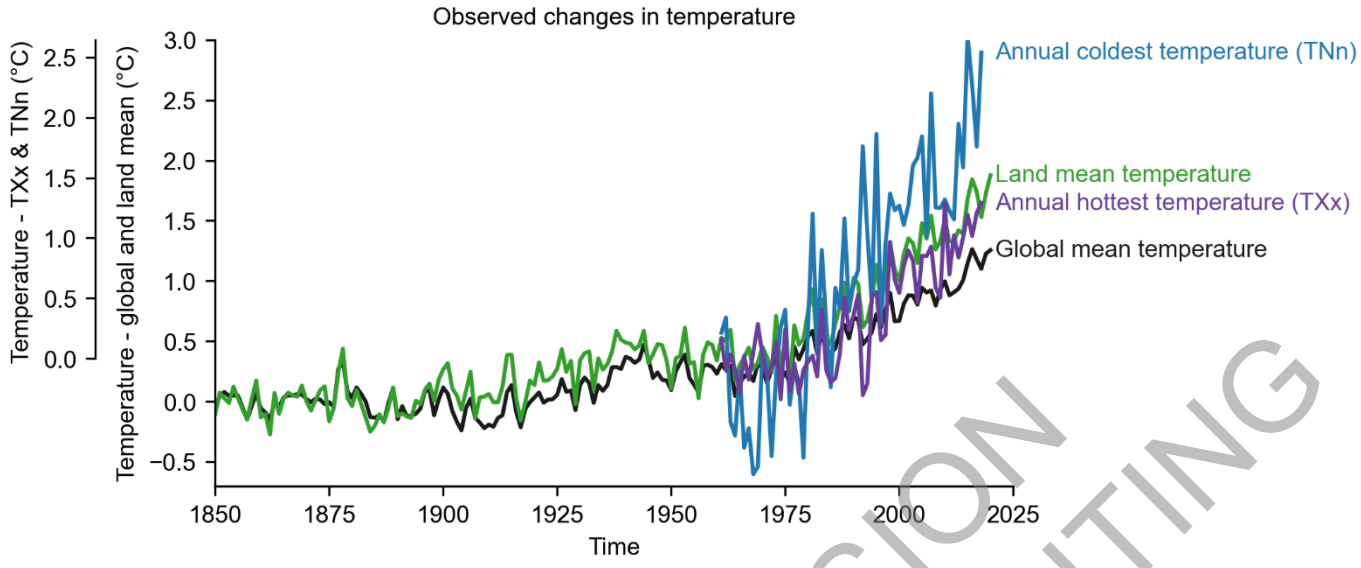
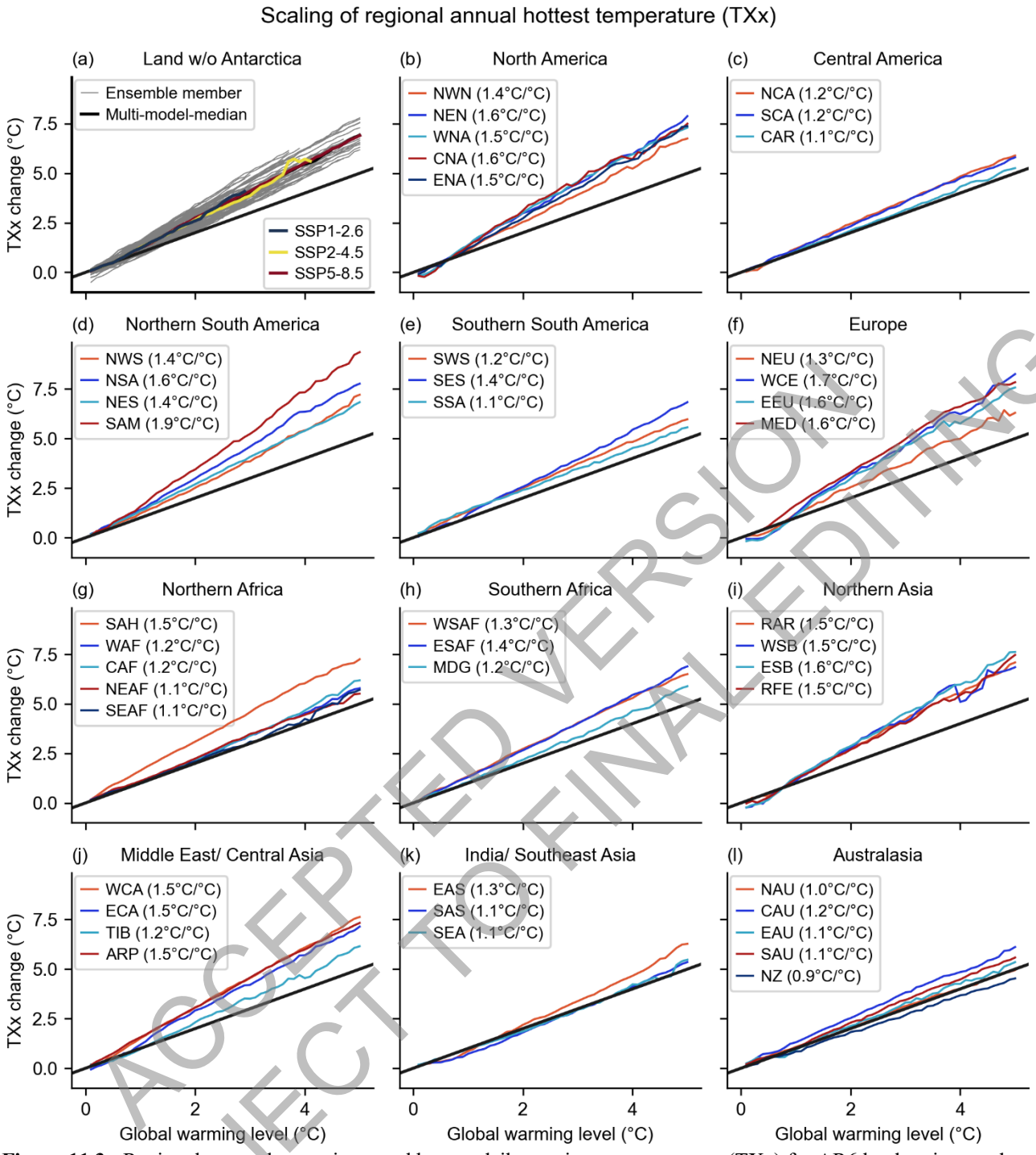


Figure 11.2: Time series of observed temperature anomalies for global average annual mean temperature (black), land average annual mean temperature (green), land average annual hottest daily maximum temperature (TXx, purple), and land average annual coldest daily minimum temperature (TNn, blue). Global and land mean temperature anomalies are relative to their 1850-1900 means based on the multi-product mean annual time series assessed in Section 2.3.1.1.3 (see text for references). TXx and TNn anomalies are relative to their respective 1961-1990 means and are based on the HadEX3 dataset (Dunn et al., 2020) using values for grid boxes with at least 90% temporal completeness over 1961-2018. Further details on data sources and processing are available in the chapter data table (Table 11.SM.9).

ACCEPTED VERSION SUBJECT TO FINAL EDITING



ACCEPTED VERSION SUBJECT TO FINAL EDITING

Figure 11.3: Regional mean changes in annual hottest daily maximum temperature (TXx) for AR6 land regions and the global land, against changes in global mean surface air temperature (GSAT) as simulated by CMIP6 models under different forcing scenarios SSP1-1.9, SSP1-2.6, SSP2-4.5, SSP3-7.0, and SSP5-8.5. (a) shows individual models from the CMIP6 ensemble (grey), the multi-model median under three selected SSPs (colours), and the multi-model median (black). (b) to (l) show the multi-model-median for the pooled data for individual AR6 regions. Numbers in parantheses indicate the linear scaling between regional TXx and GSAT. The black line indicates the 1:1 reference scaling between TXx and GSAT. See Atlas.1.3.2 for the definition of regions. For details on the methods see Supplementary Material 11.SM.2.

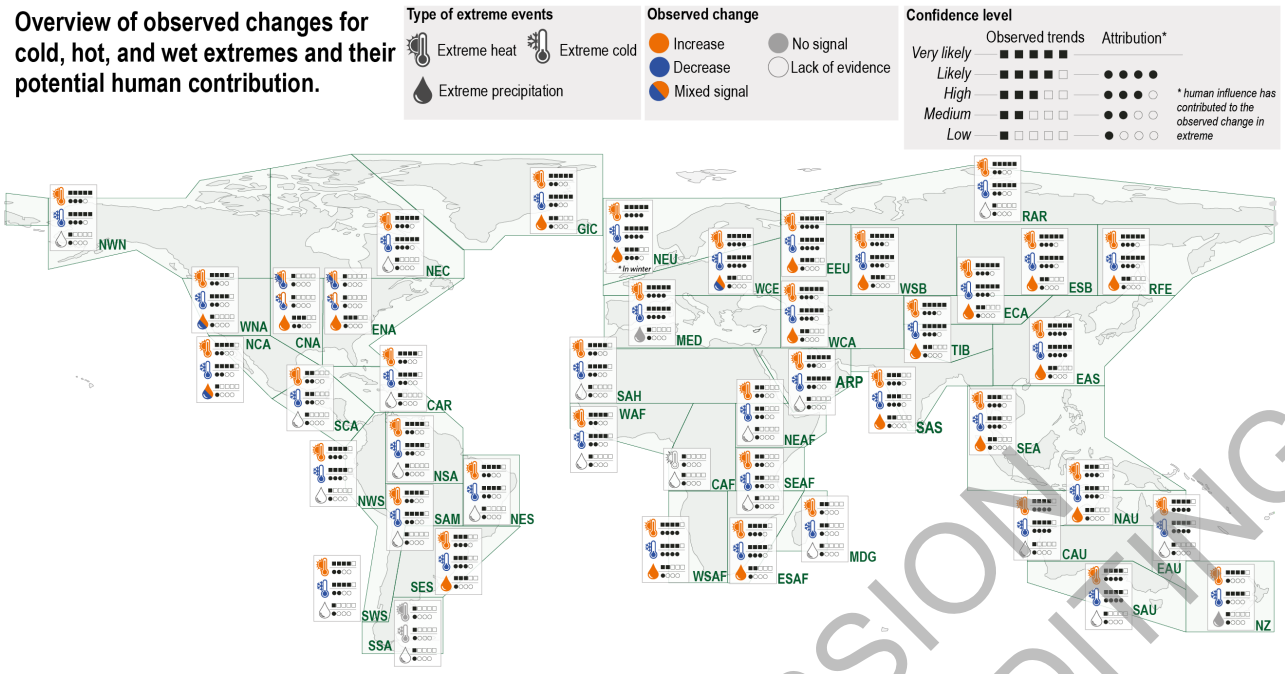
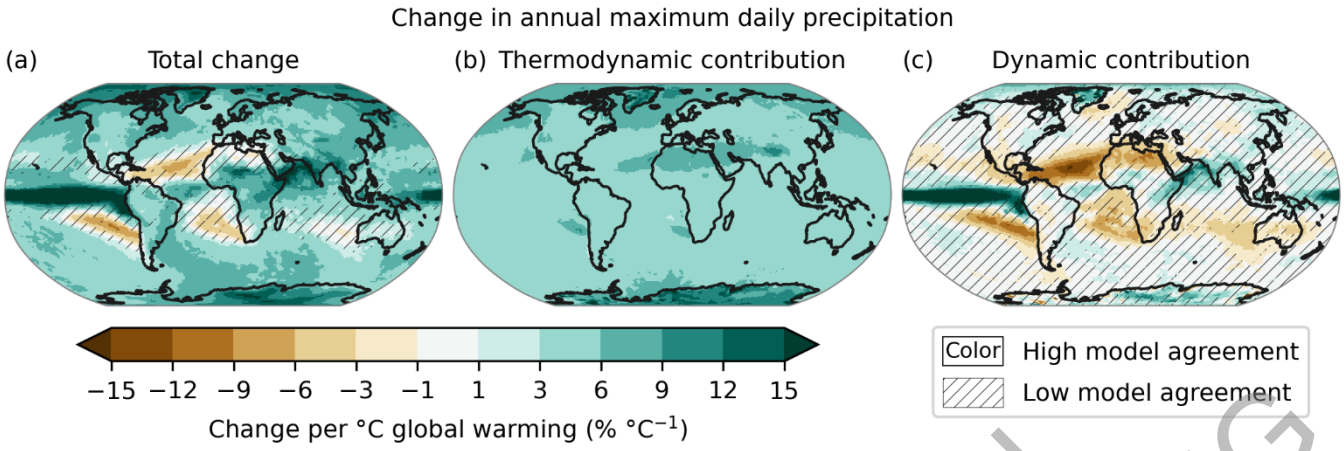


Figure 11.4: *Overview of observed changes for cold, hot, and wet extremes and* **their potential human contribution**. *Shown are the direction of* **change** *and the confidence in* **1)** *the observed changes in how cold and hot as well as wet extremes have already changed across the world and* **2)** *in the contribution of whether human-induced climate change contributed in causing to these changes (***attribution***). In each region changes in extremes are indicated by colour (orange – increase in the type of extreme, blue – decrease, both colours – there are changes of opposing direction within the region the signal depends on the exact event definition, grey – there are no changes observed,* **and no fill –** *the data/evidence is too sparse to make an assessment). The* **squares and dots next to** *the symbol indicate the level of confidence for observing the trend and the human contribution,* **respectively**. *The more* **black** *dots/***squares** *the higher the level of confidence. The information on this figure is based on regional assessment of the literature on observed trends, detection and attribution and event attribution in section 11.9.*

ACCEPTED VERSION SUBJECT TO FINAL EDITING



Box 11.1, Figure 1: Multi-model (CMIP5) mean fractional changes (in % per degree of warming) for (a) annual maximum precipitation (Rx1day), (b) changes in Rx1day due to the thermodynamic contribution and (c) changes in Rx1day due to the dynamic contribution estimated as the difference between the total changes and the thermodynamic contribution. Changes were derivefd from a linear regression for the period 1950–2100. Uncertainty is represented using the simple approach: no overlay indicates regions with high model agreement, where ≥80% of models (n=22) agree on sign of change; diagonal lines indicate regions with low model agreement, where <80% of models agree on sign of change. For more information on the simple approach, please refer to the Cross-Chapter Box Atlas 1. A detailed description of the estimation of dynamic and thermodynamic contributions is given in Pfahl et al. (2017). Adapted from (Pfahl et al., 2017), originally published in Nature Climate Change/ Springer Nature. Further details on data sources and processing are available in the chapter data table (Table 11.SM.9).

ACCEPTED VERSION SUBJECT TO FINAL EDITING

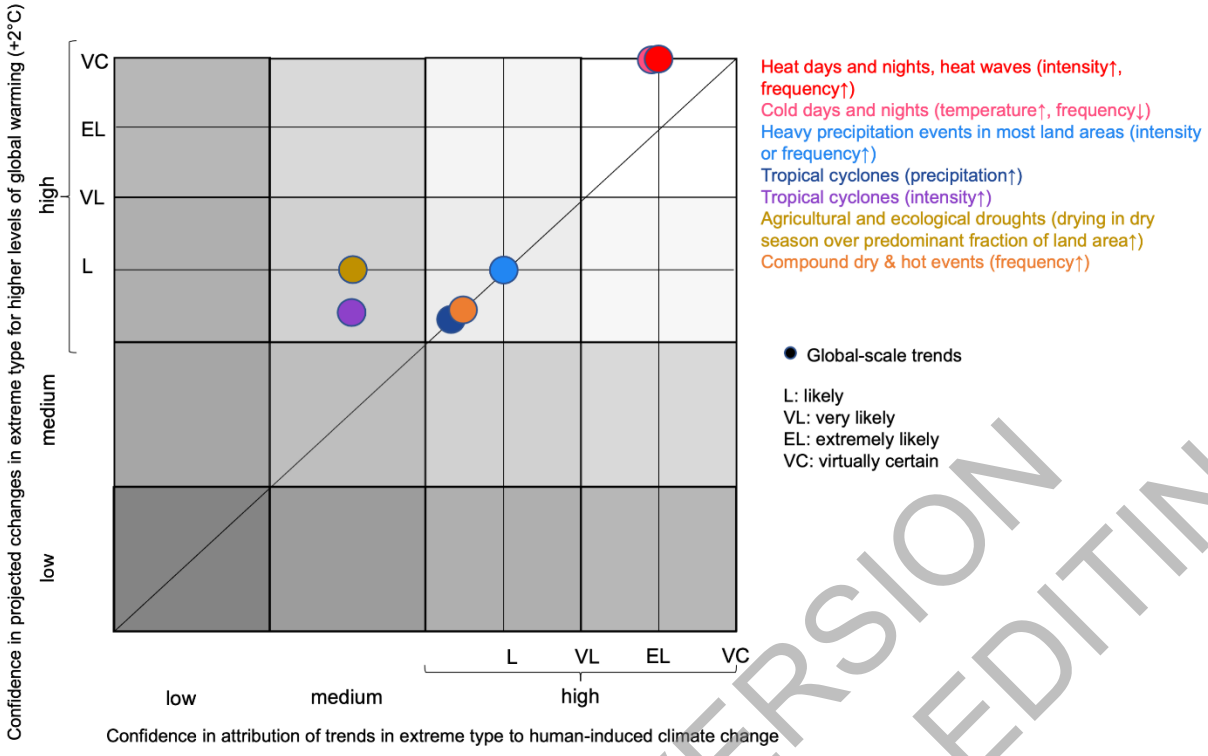


Figure 11.5: Confidence and likelihood of past changes and projected future changes at 2°C of global warming on the global scale. The information in this figure is based on Tables 11.1 and 11.2.

ACCEPTED VERSION
SUBJECT TO FINAL EDITING

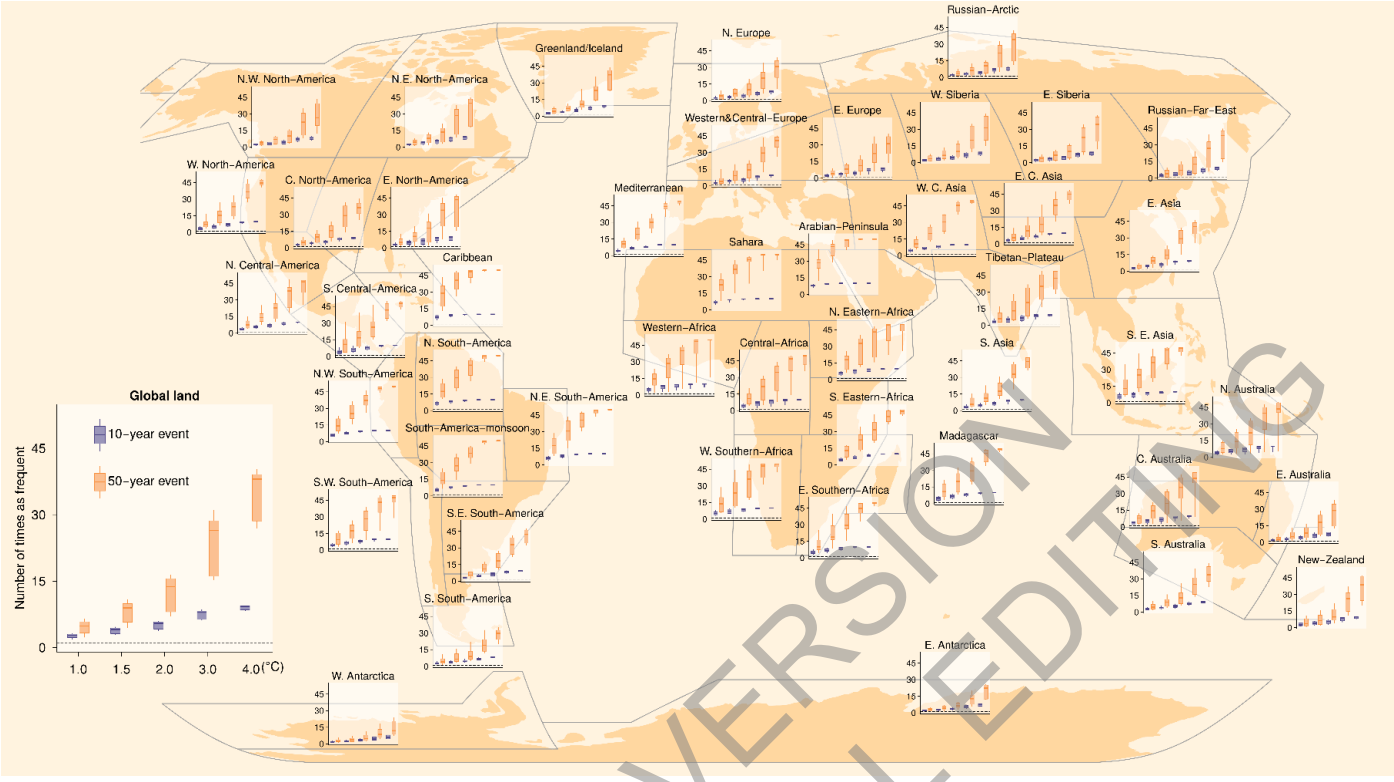


Figure 11.6: Projected changes in the frequency of extreme temperature events under 1°C, 1.5°C, 2°C, 3°C, and 4°C global warming levels relative to the 1851-1900 baseline. Extreme temperatures are defined as the maximum daily temperatures that were exceeded on average once during a 10-year period (10-year event, blue) and once during a 50-year period (50-year event, orange) during the 1851-1900 base period. Results are shown for the global land and the AR6 regions. For each box plot, the horizontal line and the box represent the median and central 66% uncertainty range, respectively, of the frequency changes across the multi model ensemble, and the whiskers extend to the 90% uncertainty range. The dotted line indicates no change in frequency. The results are based on the multi-model ensemble from simulations of global climate models contributing to the sixth phase of the Coupled Model Intercomparison Project (CMIP6) under different SSP forcing scenarios. Adapted from (Li et al., 2020a). Further details on data sources and processing are available in the chapter data table (Table 11.SM.9).

.

ACCEPTED VERSION SUBJECT TO FINAL EDITING

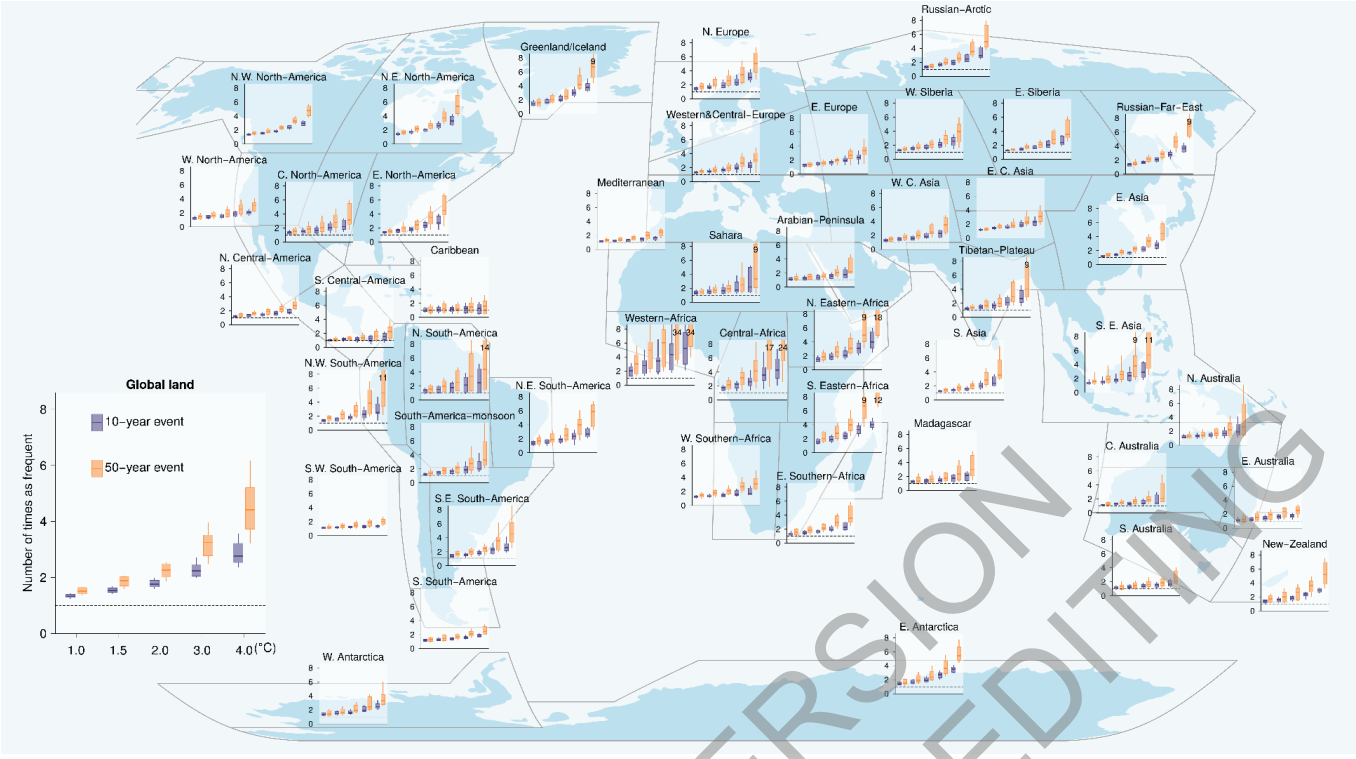


Figure 11.7: Projected changes in the frequency of extreme precipitation events under 1°C, 1.5°C, 2°C, 3°C, and 4°C global warming levels relative to the 1951-1990 baseline. Extreme precipitation is defined as the maximum daily precipitation (Rx1day) that was exceeded on average once during a 10-year period (10-year event, blue) and once during a 50-year period (50-year event, orange) during the 1851-1900 base period. Results are shown for the global land and the AR6 regions. For each box plot, the horizontal line and the box represent the median and central 66% uncertainty range, respectively, of the frequency changes across the multi model ensemble, and the whiskers extend to the 90% uncertainty range. The dotted line indicates no change in frequency. The results are based on the multi-model ensemble from simulations of global climate models contributing to the sixth phase of the Coupled Model Intercomparison Project (CMIP6) under different SSP forcing scenarios. Adapted from (Li et al., 2020a). Further details on data sources and processing are available in the chapter data table (Table 11.SM.9).

ACCEPTED VERSION SUBJECT TO FINAL EDITING

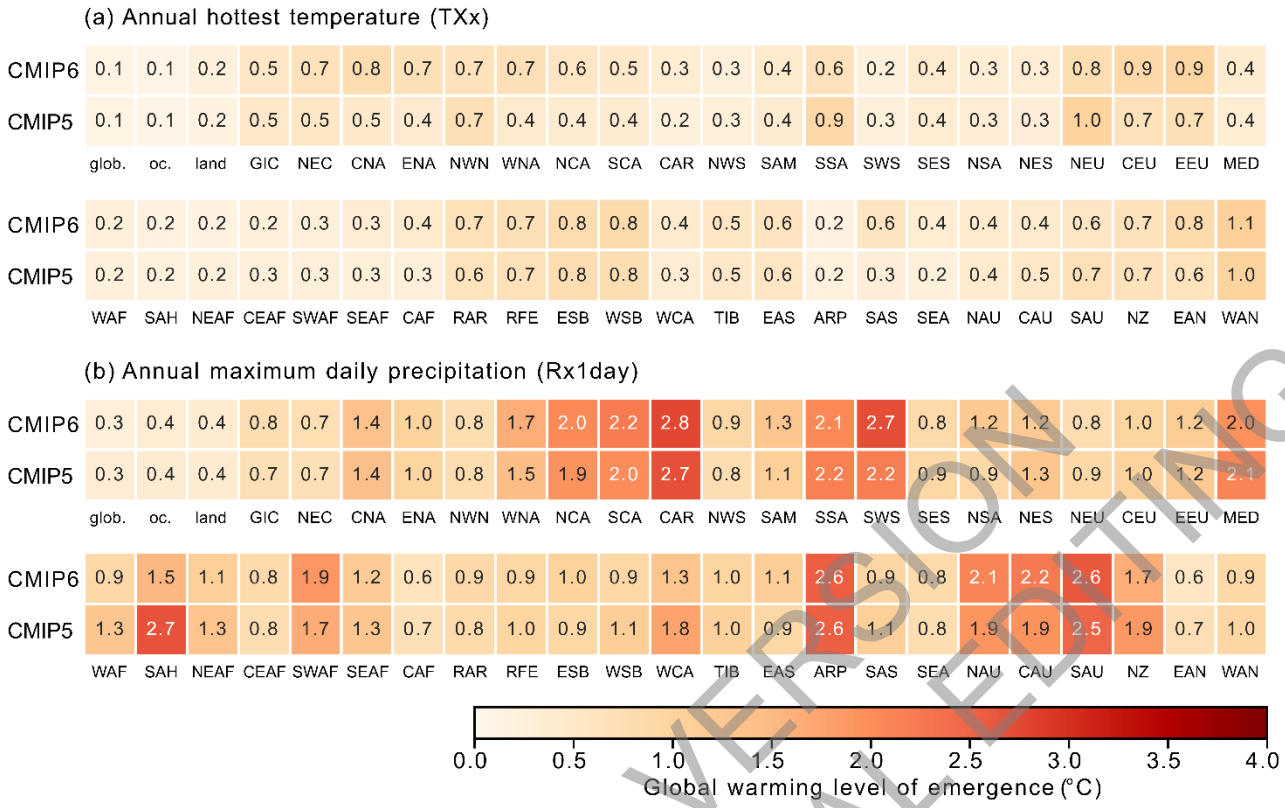
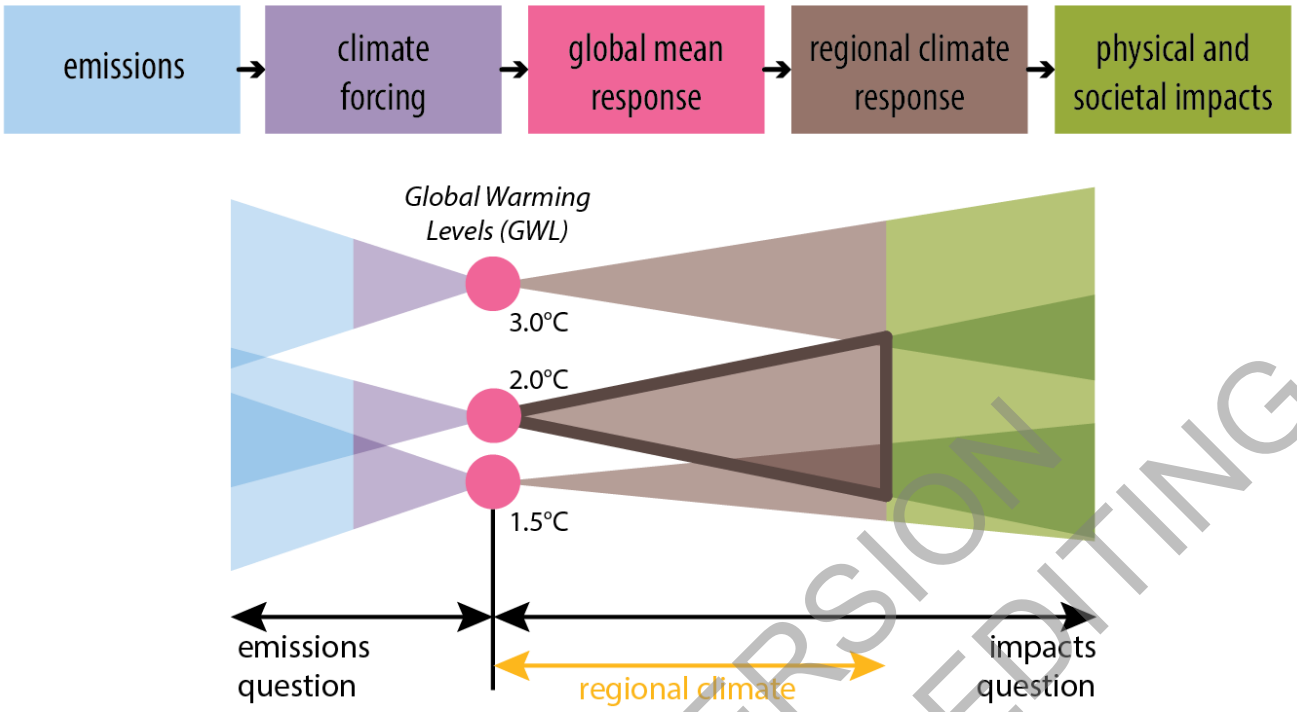


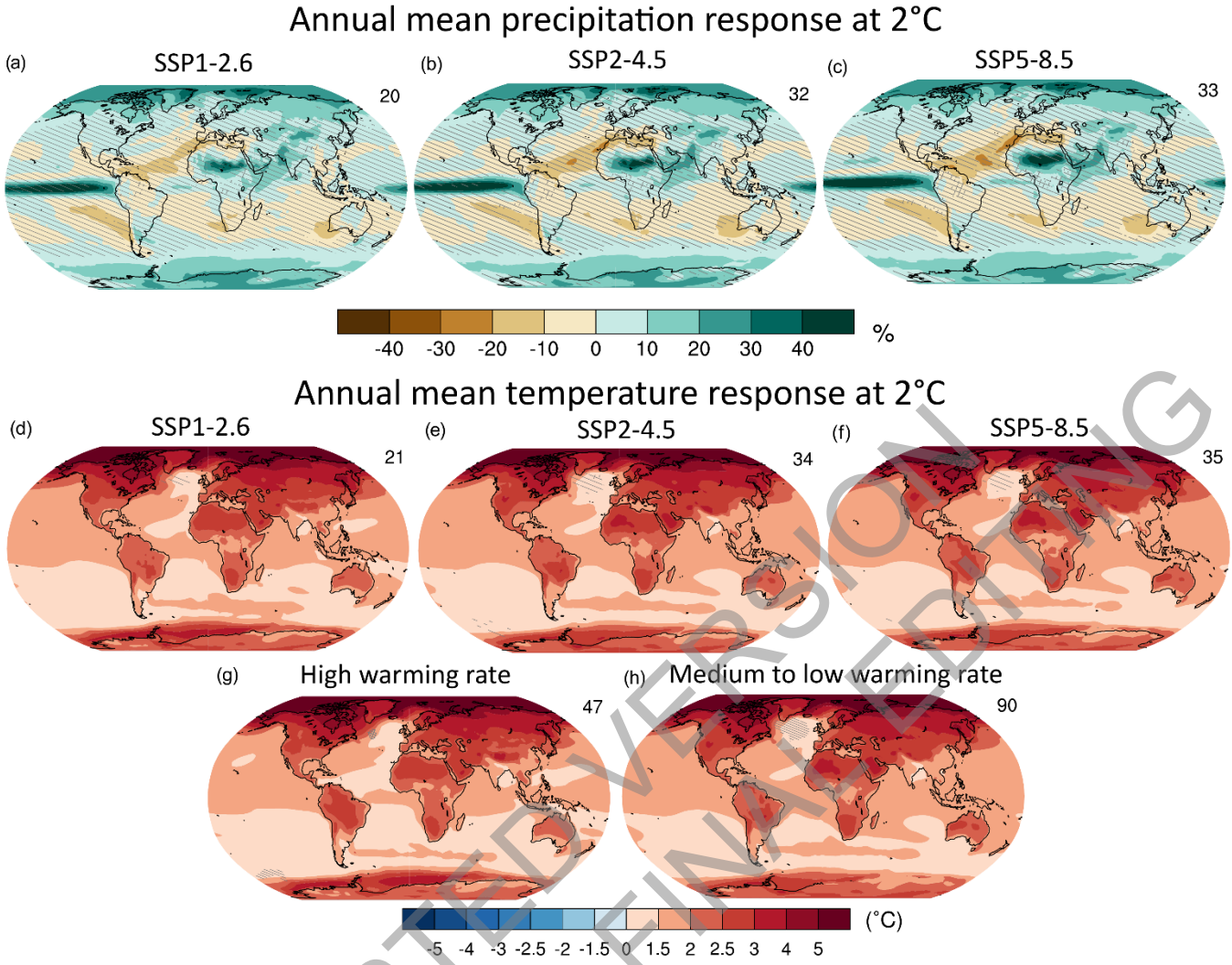
Figure 11.8: Global and regional-scale emergence of changes in temperature (a) and precipitation (b) extremes for the globe (glob.), global oceans (oc.), global lands (land), and the AR6 regions. Colours indicate the multi-model mean global warming level at which the difference in 20-year means of the annual maximum daily maximum temperature (TXx) and the annual maximum daily precipitation (Rx1day) become significantly different from their respective mean values during the 1851–1900 base period. Results are based on simulations from the CMIP5 and CMIP6 multi-model ensembles. See Atlas.1.3.2 for the definition of regions. Adapted from Seneviratne and Hauser, 2020) under the terms of the Creative Commons Attribution license.

ACCEPTED VERSION SUBJECT TO FINAL EDITING



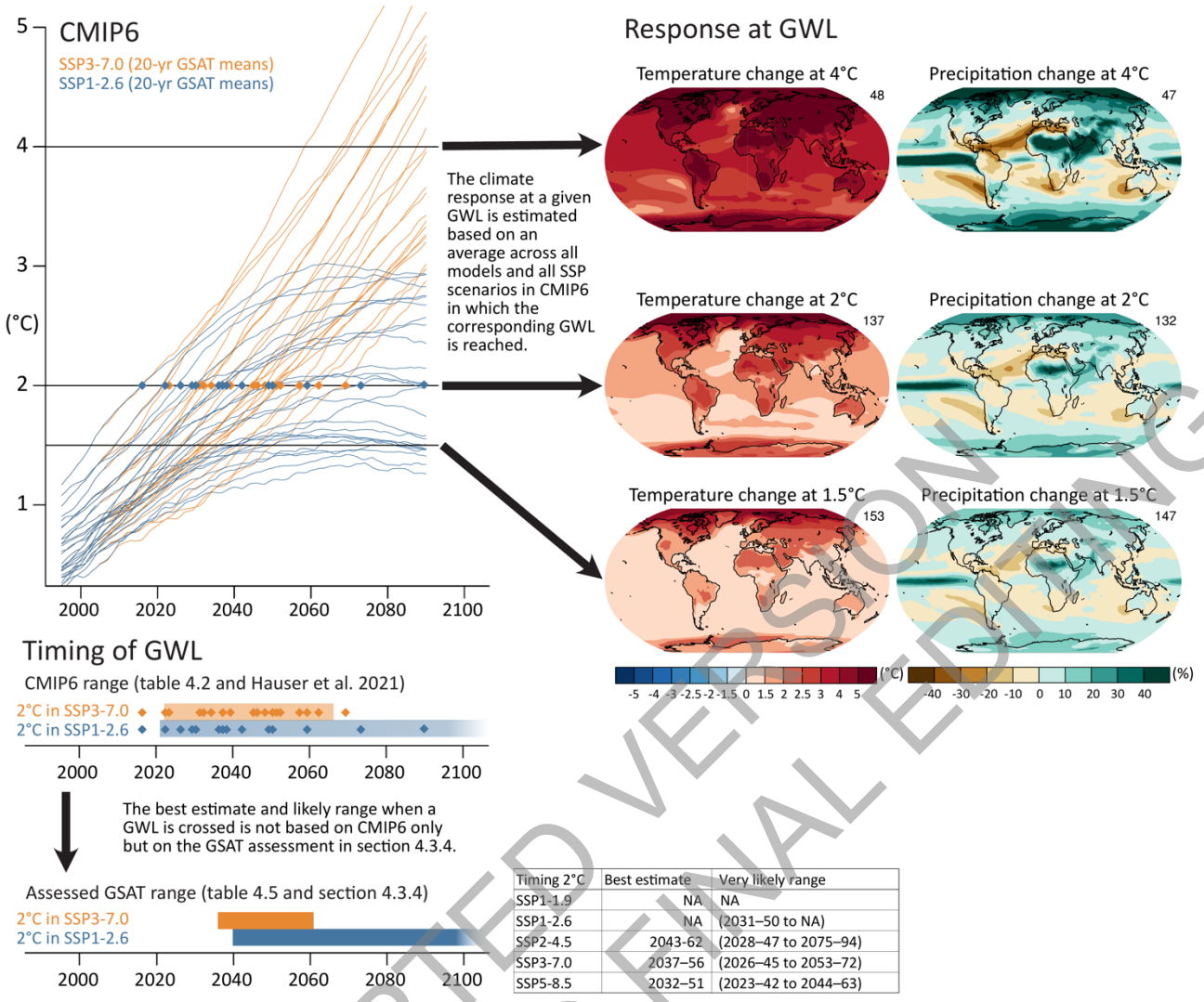
Cross-Chapter Box 11.1, Figure 1: Schematic representation of relationship between emission scenarios, global warming levels (GWLs), regional climate responses, and impacts. The illustration shows the implied uncertainty problem associated with differentiating between 1.5, 2°C, and other GWLs. Focusing on GWL raises questions associated with emissions pathways to get to these temperatures (scenarios), as well as questions associated with regional climate responses and the associated impacts at the corresponding GWL (the impacts question). Adapted from (James, Washington, Schleussner, Rogelj, & Conway, 2017) and (Rogelj, 2013) under the terms of the Creative Commons Attribution license.

ACCEPTED VERSION SUBJECT TO FINAL EDITING



Cross-Chapter Box 11.1, Figure 2: (a-c) CMIP6 multi-model mean precipitation change at 2°C GWL (20-yr mean) in three different SSP scenarios relative to 1850-1900. All models reaching the corresponding GWL in the corresponding scenario are averaged. The number of models averaged across is shown at the top right of the panel. The maps for the other two SSP scenarios SSP1-1.9 (five models only) and SSP3-7.0 (not shown) are consistent. (d-f) Same as (a-c) but for annual mean temperature. (g) Annual mean temperature change at 2°C in CMIP6 models with high warming rate reaching the GWL in the corresponding scenario before the earliest year of the assessed very likely range (section 4.3.4) (h) Climate response at 2°C GWL across all SSP1-1.9, SSP2-2.6, SSP2-4.5. SSP3-7.0 and SSP5-8.5 in all other models not shown in (g). The good agreement of (g) and (h) demonstrate that the mean temperature response at 2°C is not sensitive to the rate of warming and thereby the GSAT warming of the respective models in 2081-2100. Uncertainty is represented using the advanced approach: No overlay indicates regions with robust signal, where ≥66% of models show change greater than variability threshold and ≥80% of all models agree on sign of change; diagonal lines indicate regions with no change or no robust signal, where <66% of models show a change greater than the variability threshold; crossed lines indicate regions with conflicting signal, where ≥66% of models show change greater than variability threshold and <80% of all models agree on sign of change. For more information on the advanced approach, please refer to the Cross-Chapter Box Atlas.1.

ACCEPTED VERSION SUBJECT TO FINAL EDITING



Timing 2°C	Best estimate	Very likely range
SSP1-1.9	NA	NA
SSP1-2.6	NA	(2031–50 to NA)
SSP2-4.5	2043-62	(2028–47 to 2075–94)
SSP3-7.0	2037–56	(2026–45 to 2053–72)
SSP5-8.5	2032–51	(2023–42 to 2044–63)

Cross-Chapter Box 11.1, Figure. 3: Illustration of the AR6 GWL sampling approach to derive the timing and the response at a given GWL for the case of CMIP6 data. For the mapping of scenarios/time slices into GWLs for CMIP6, please refer to Table 4.2. Respective numbers for the CMIP6 multi-model experiment are provided in the Chapter 11 Supplementary Material (11.SM.1). Note that the time frames used to derived the GWL time slices can also include different number of years (e.g. 30 years for some analyses).

ACCEPTED VERSION SUBJECT TO FINAL EDITING

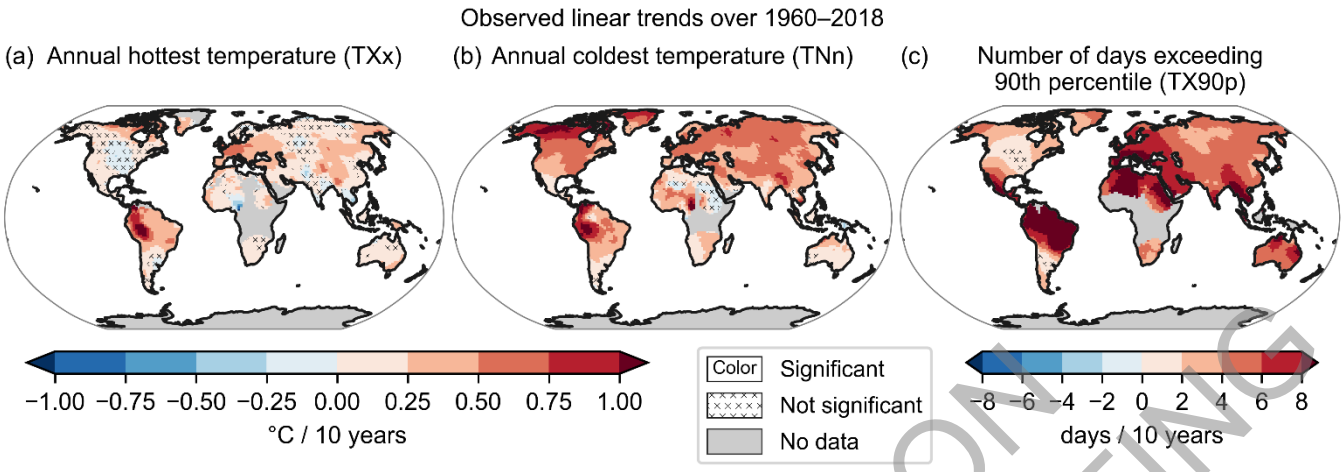


Figure 11.9: Linear trends over 1960-2018 in the annual maximum daily maximum temperature (TXx, a), the annual minimum daily minimum temperature (TNn, b), and the annual number of days when daily maximum temperature exceeds its 90th percentile from a base period of 1961-1990 (TX90p, c), based on the HadEX3 data set (Dunn et al., 2020). Linear trends are calculated only for grid points with at least 66% of the annual values over the period and which extend to at least 2009. Areas without sufficient data are shown in grey. No overlay indicates regions where the trends are significant at p = 0.1 level. Crosses indicate regions where trends are not significant. Further details on data sources and processing are available in the chapter data table (Table 11.SM.9).

ACCEPTED VERSION SUBJECT TO FINAL EDITING

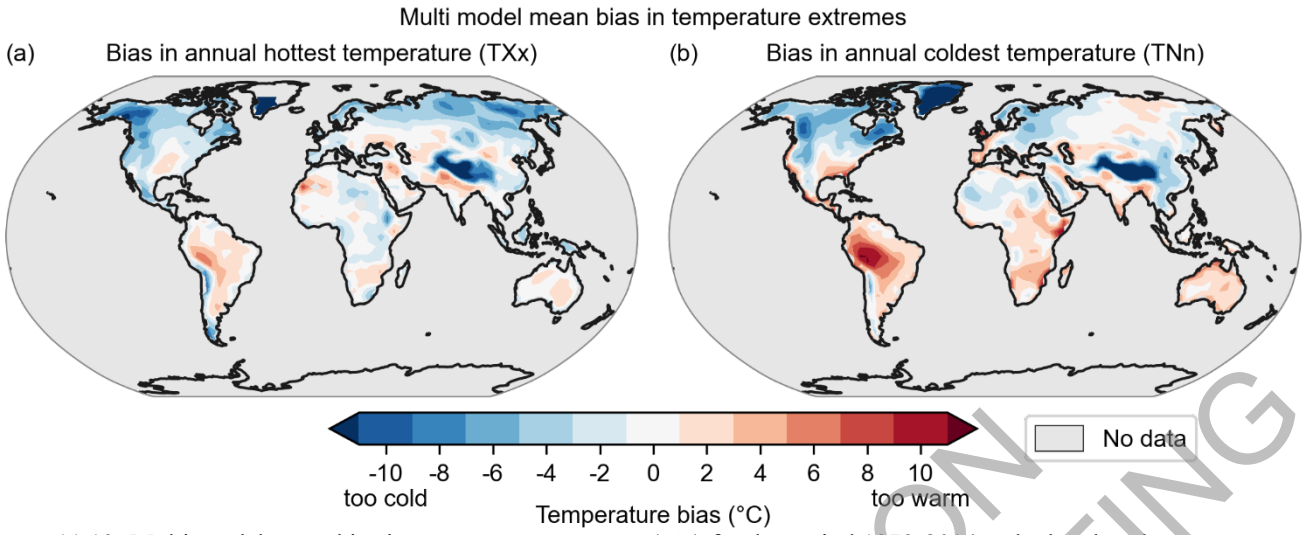


Figure 11.10: Multi-model mean bias in temperature extremes (°C) for the period 1979-2014, calculated as the difference between the CMIP6 multi-model mean and the average of observations from the values available in HadEX3 for (a) the annual hottest temperature (TXx) and (b) the annual coldest temperature (TNn). Areas without sufficient data are shown in grey. Adapted from Wehner et al. (2020) under the terms of the Creative Commons Attribution license. Further details on data sources and processing are available in the chapter data table (Table 11.SM.9).

ACCEPTED VERSION SUBJECT TO FINAL EDITING

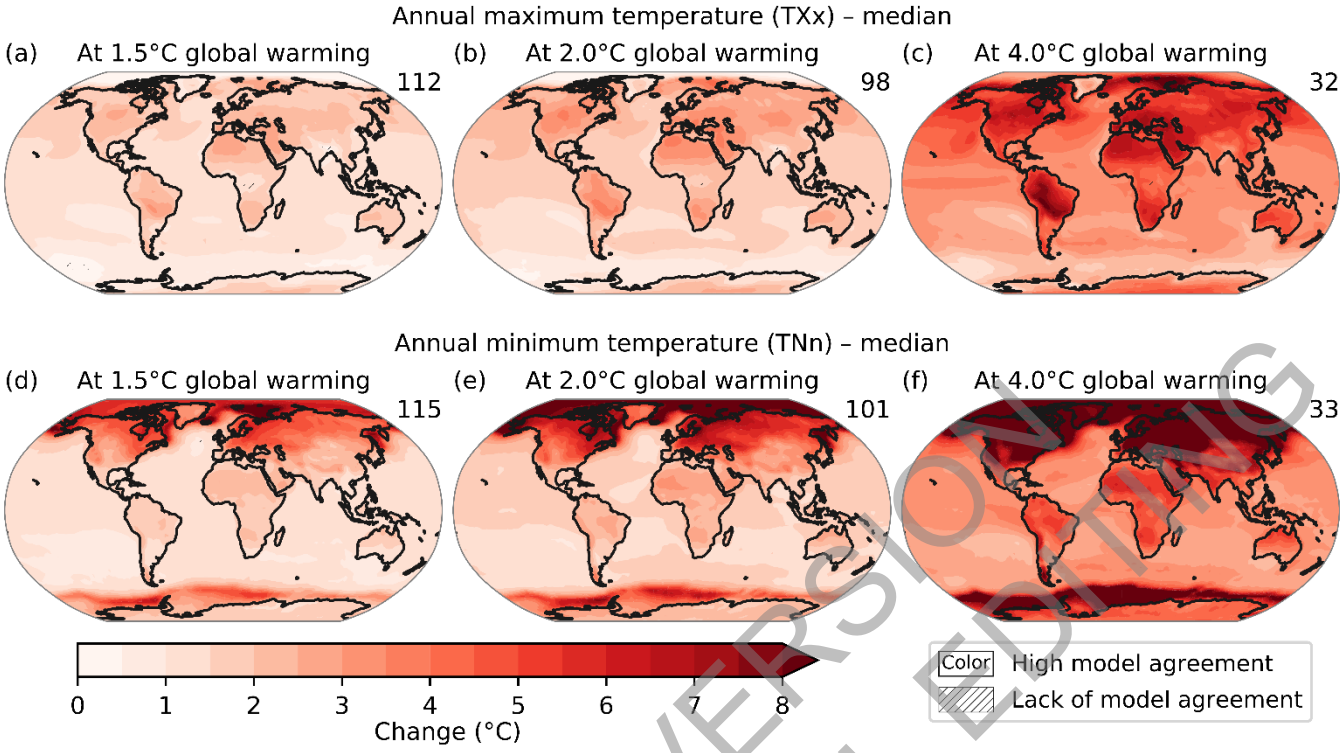


Figure 11.11: Projected changes in (a-c) annual maximum temperature (TXx) and (d-f) annual minimum temperature (TNn) at 1.5°C, 2°C, and 4°C of global warming compared to the 1851-1900 baseline. Results are based on simulations from the CMIP6 multi-model ensemble under the SSP1-1.9, SSP1-2.6, SSP2-4.5, SSP3-7.0, and SSP5-8.5 scenarios. The numbers in the top right indicate the number of simulations included. Uncertainty is represented using the simple approach: no overlay indicates regions with high model agreement, where ≥80% of models agree on sign of change; diagonal lines indicate regions with low model agreement, where <80% of models agree on sign of change. For more information on the simple approach, please refer to the Cross-Chapter Box Atlas 1. For details on the methods see Supplementary Material 11.SM.2. Further details on data sources and processing are available in the chapter data table (Table 11.SM.9).

ACCEPTED VERSION SUBJECT TO FINAL EDITING

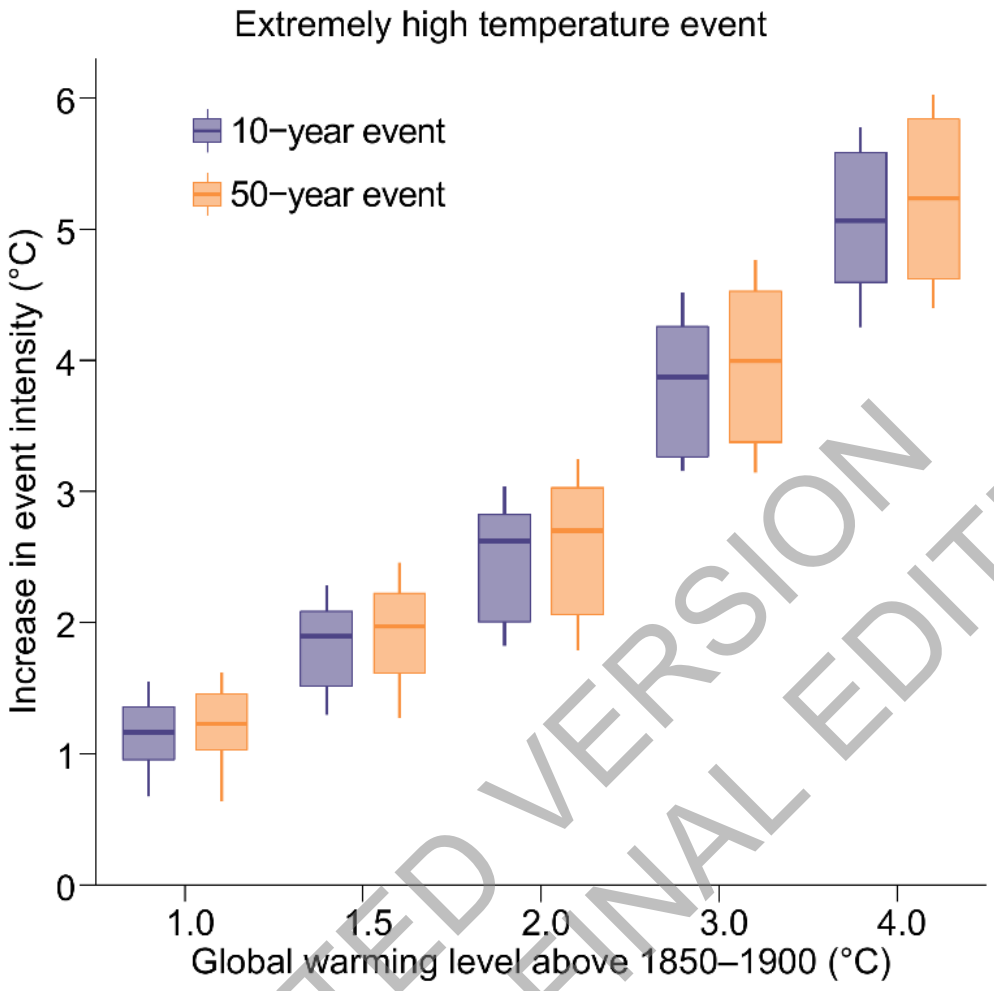


Figure 11.12: Projected changes in the intensity of extreme temperature events under 1°C, 1.5°C, 2°C, 3°C, and 4°C global warming levels relative to the 1851-1900 baseline. Extreme temperature events are defined as the daily maximum temperatures (TXx) that were exceeded on average once during a 10-year period (10-year event, blue) and that once during a 50-year period (50-year event, orange) during the 1851-1900 base period. Results are shown for the global land. For each box plot, the horizontal line and the box represent the median and central 66% uncertainty range, respectively, of the intensity changes across the multi model ensemble, and the whiskers extend to the 90% uncertainty range. The results are based on the multi-model ensemble from simulations of global climate models contributing to the sixth phase of the Coupled Model Intercomparison Project (CMIP6) under different SSP forcing scenarios. Based on (Li et al., 2020a). Further details on data sources and processing are available in the chapter data table (Table 11.SM.9).

ACCEPTED VERSION SUBJECT TO FINAL EDITING

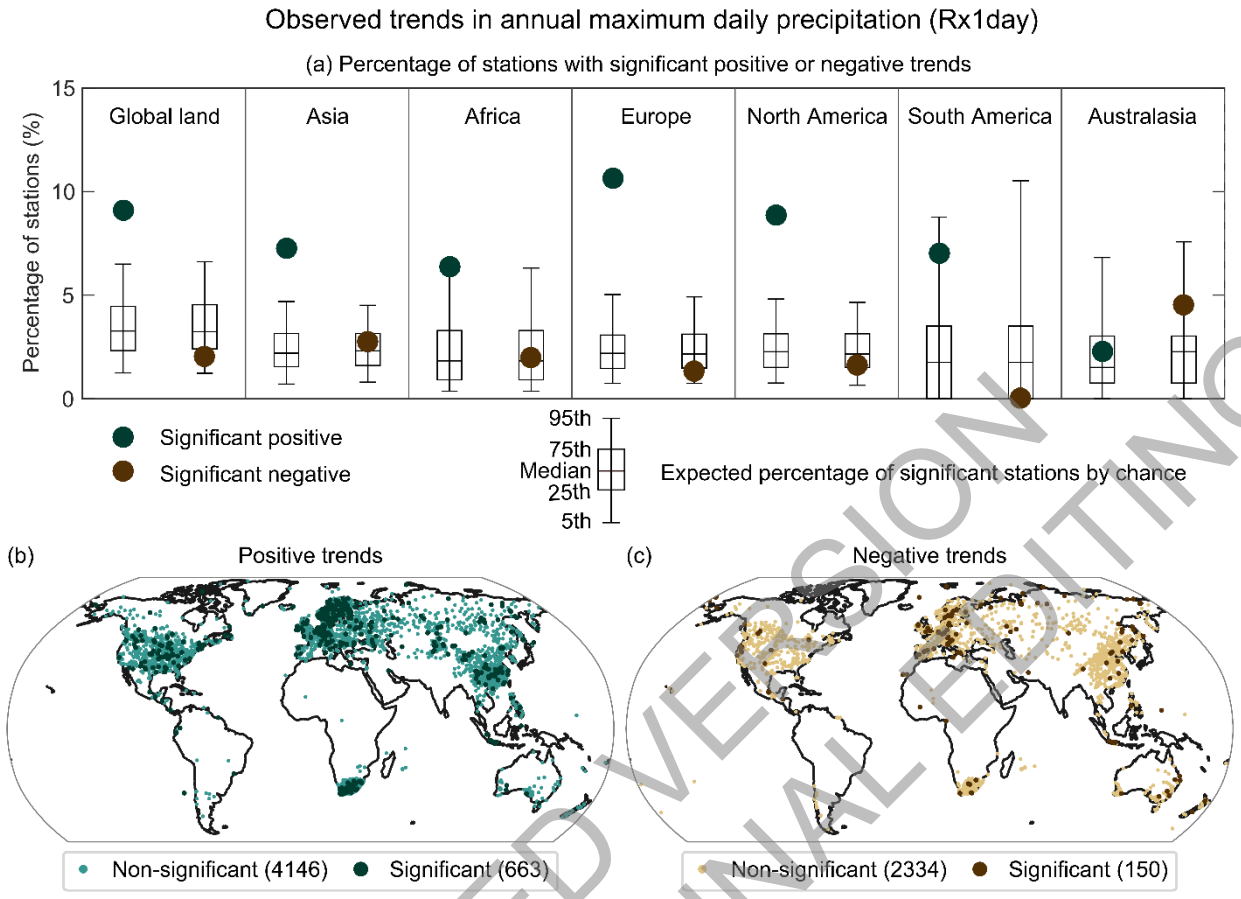


Figure 11.13: Signs and significance of the observed trends in annual maximum daily precipitation (Rx1day) during 1950–2018 at 8345 stations with sufficient data. (a) Percentage of stations with statistically significant trends in Rx1day; green dots show positive trends and brown dots negative trends. Box-and-whisker plots indicate the expected percentage of stations with significant trends due to chance estimated from 1000 bootstrap realizations under a no-trend null hypothesis. The boxes mark the median, 25th percentile, and 75th percentile. The upper and lower whiskers show the 97.5th and the 2.5th percentiles, respectively. Maps of stations with positive (b) and negative (c) trends. The light color indicates stations with non-significant trends and the dark color stations with significant trends. Significance is determined by a two-tailed test conducted at the 5% level. Adapted from Sun et al. (2020). © American Meteorological Society. Used with permission. Further details on data sources and processing are available in the chapter data table (Table 11.SM.9).

ACCEPTED VERSION SUBJECT TO FINAL EDITING

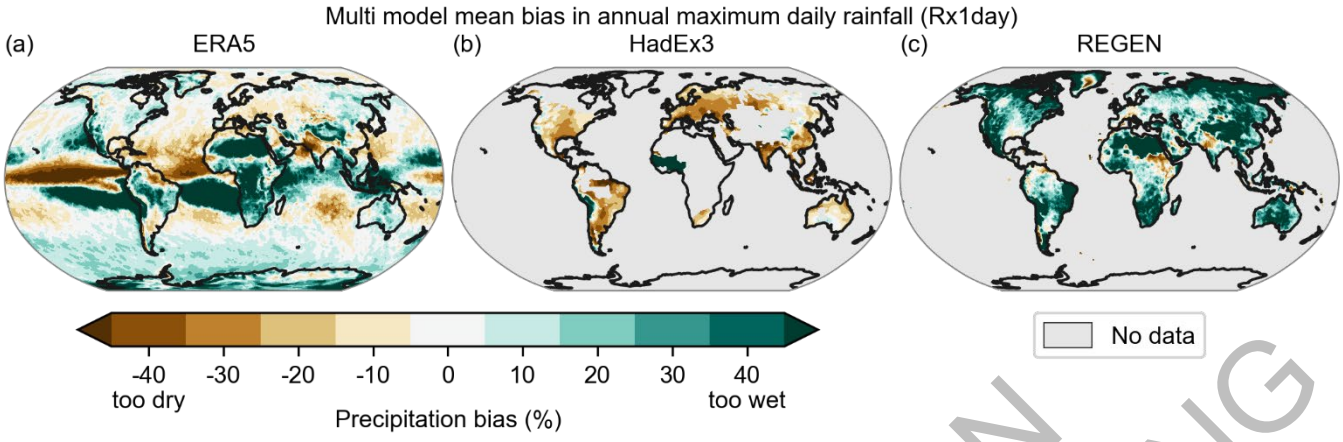


Figure 11.14: Multi-model mean bias in annual maximum daily precipitation (Rx1day, %) for the period 1979-2014, calculated as the difference between the CMIP6 multi-model mean and the average of available observational or reanalysis products including (a) ERA5, (b) HadEX3, and (c) and REGEN. Bias is expressed as the percent error relative to the long-term mean of the respective observational data products. Brown indicates that models are too dry, while green indicates that they are too wet. Areas without sufficient observational data are shown in grey. Adapted from Wehner et al. (2020) under the terms of the Creative Commons Attribution license. Further details on data sources and processing are available in the chapter data table (Table 11.SM.9).

ACCEPTED VERSION
SUBJECT TO FINAL EDITING

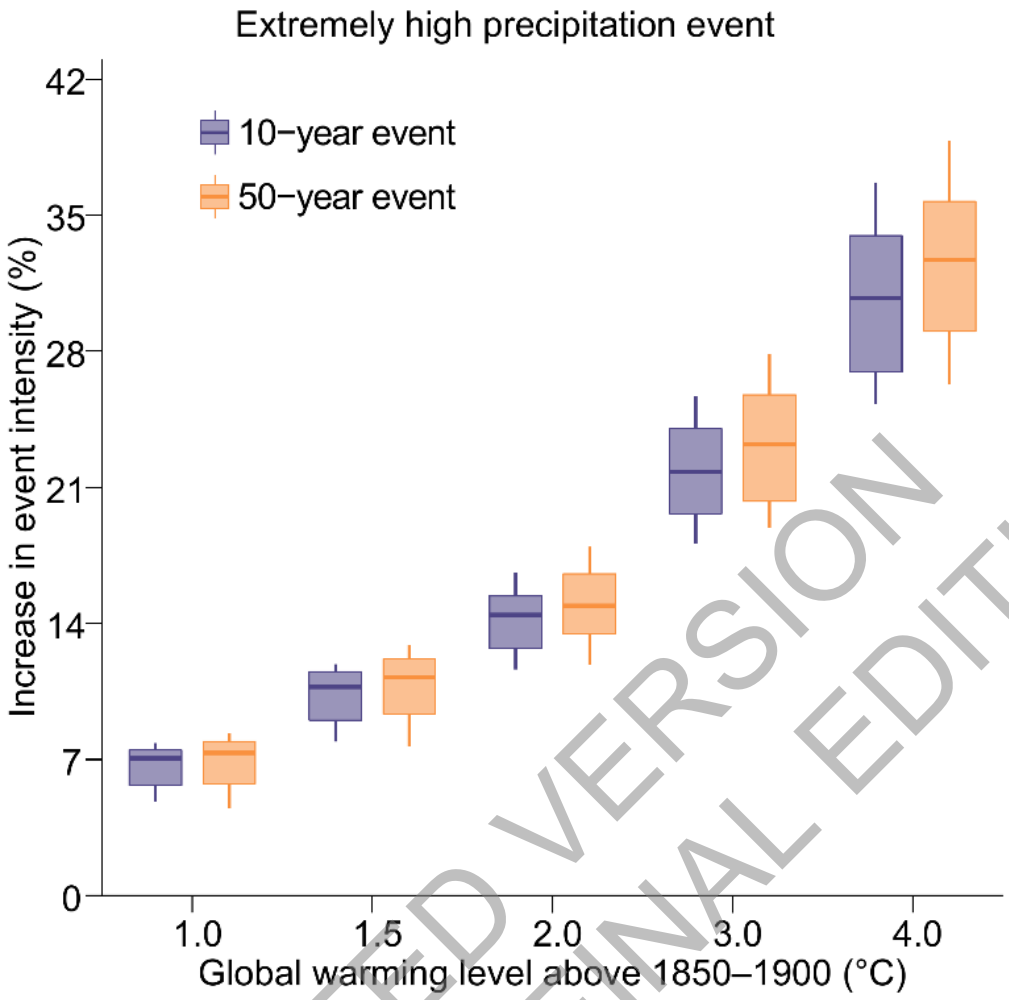


Figure 11.15: Projected changes in the intensity of extreme precipitation events under 1°C, 1.5°C, 2°C, 3°C, and 4°C global warming levels relative to the 1851-1900 baseline. Extreme precipitation events are defined as the daily precipitation (Rx1day) that was exceeded on average once during a 10-year period (10-year event, blue) and once during a 50-year period (50-year event, orange) during the 1851-1900 base period. Results are shown for the global land. For each box plot, the horizontal line and the box represent the median and central 66% uncertainty range, respectively, of the intensity changes across the multi model median, and the whiskers extend to the 90% uncertainty range. The results are based on the multi-model ensemble estimated from simulations of global climate models contributing to the sixth phase of the Coupled Model Intercomparison Project (CMIP6) under different SSP forcing scenarios. Based on Li et al. (2020a). Further details on data sources and processing are available in the chapter data table (Table 11.SM.9).

ACCEPTED VERSION SUBJECT TO FINAL EDITING

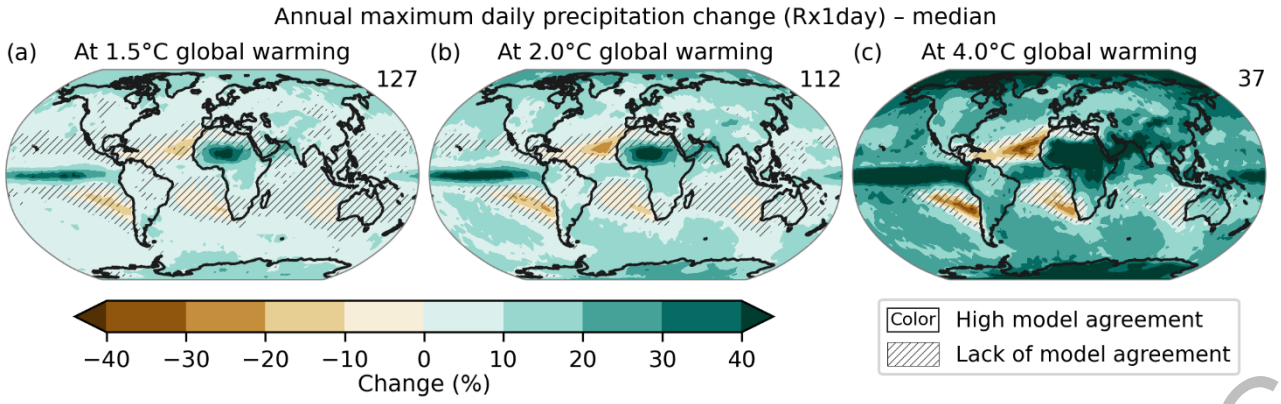


Figure 11.16: Projected changes in annual maximum daily precipitation at (a) 1.5°C, (b) 2°C, and (c) 4°C of global warming compared to the 1851-1900 baseline. Results are based on simulations from the CMIP6 multi-model ensemble under the SSP1-1.9, SSP1-2.6, SSP2-4.5, SSP3-7.0, and SSP5-8.5 scenarios. The numbers on the top right indicate the number of simulations included. Uncertainty is represented using the simple approach: no overlay indicates regions with high model agreement, where ≥80% of models agree on sign of change; diagonal lines indicate regions with low model agreement, where <80% of models agree on sign of change. For more information on the simple approach, please refer to the Cross-Chapter Box Atlas 1. For details on the methods see Supplementary Material 11.SM.2. Further details on data sources and processing are available in the chapter data table (Table 11.SM.9).

ACCEPTED VERSION SUBJECT TO FINAL EDITING

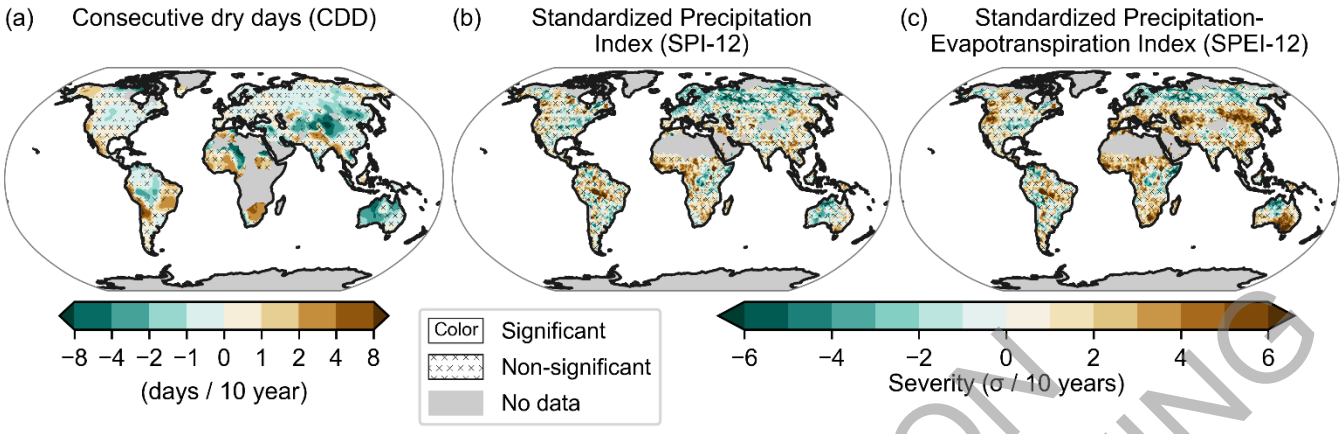


Figure 11.17: Observed linear trend for (a) consecutive dry days (CDD) during 1960-2018, (b) standardized precipitation index (SPI) and (c) standardized precipitation-evapotranspiration index (SPEI) during 1951-2016. CDD data are from the HadEx3 dataset (Dunn et al., 2020), trend calculation of CDD as in Figure 11.9 Drought severity is estimated using 12-month SPI (SPI-12) and 12-month SPEI (SPEI-12). SPI and SPEI datasets are from Spinoni et al. (2019). The threshold to identify drought episodes was set at -1 SPI/SPEI units. Areas without sufficient data are shown in grey. No overlay indicates regions where the trends are significant at p = 0.1 level. Crosses indicate regions where trends are not significant. For details on the methods see Supplementary Material 11.SM.2. Further details on data sources and processing are available in the chapter data table (Table 11.SM.9).

ACCEPTED VERSION SUBJECT TO FINAL EDITING

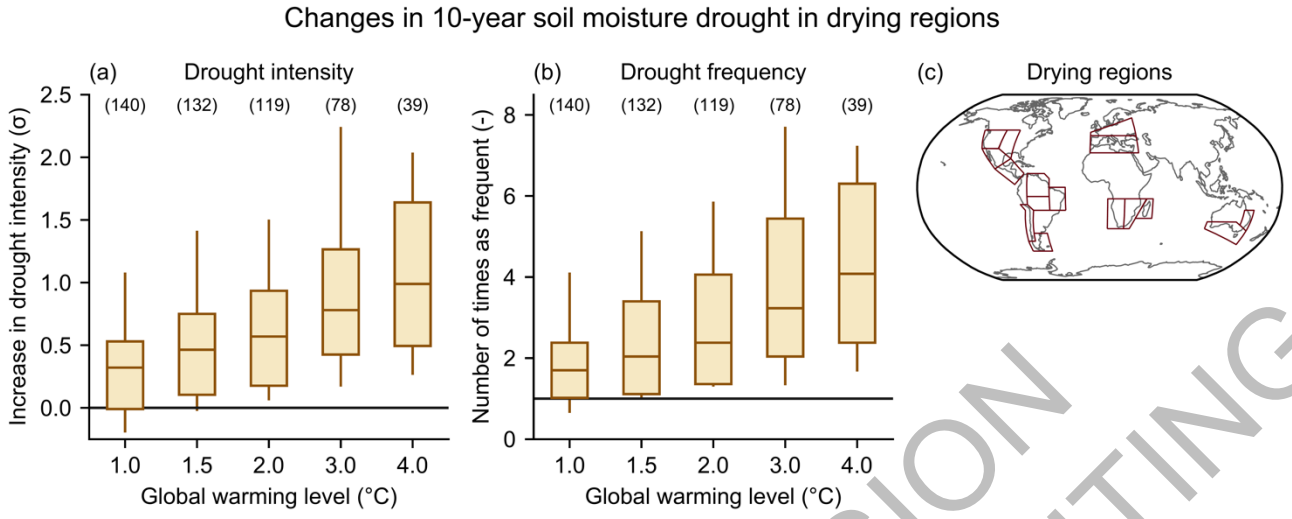
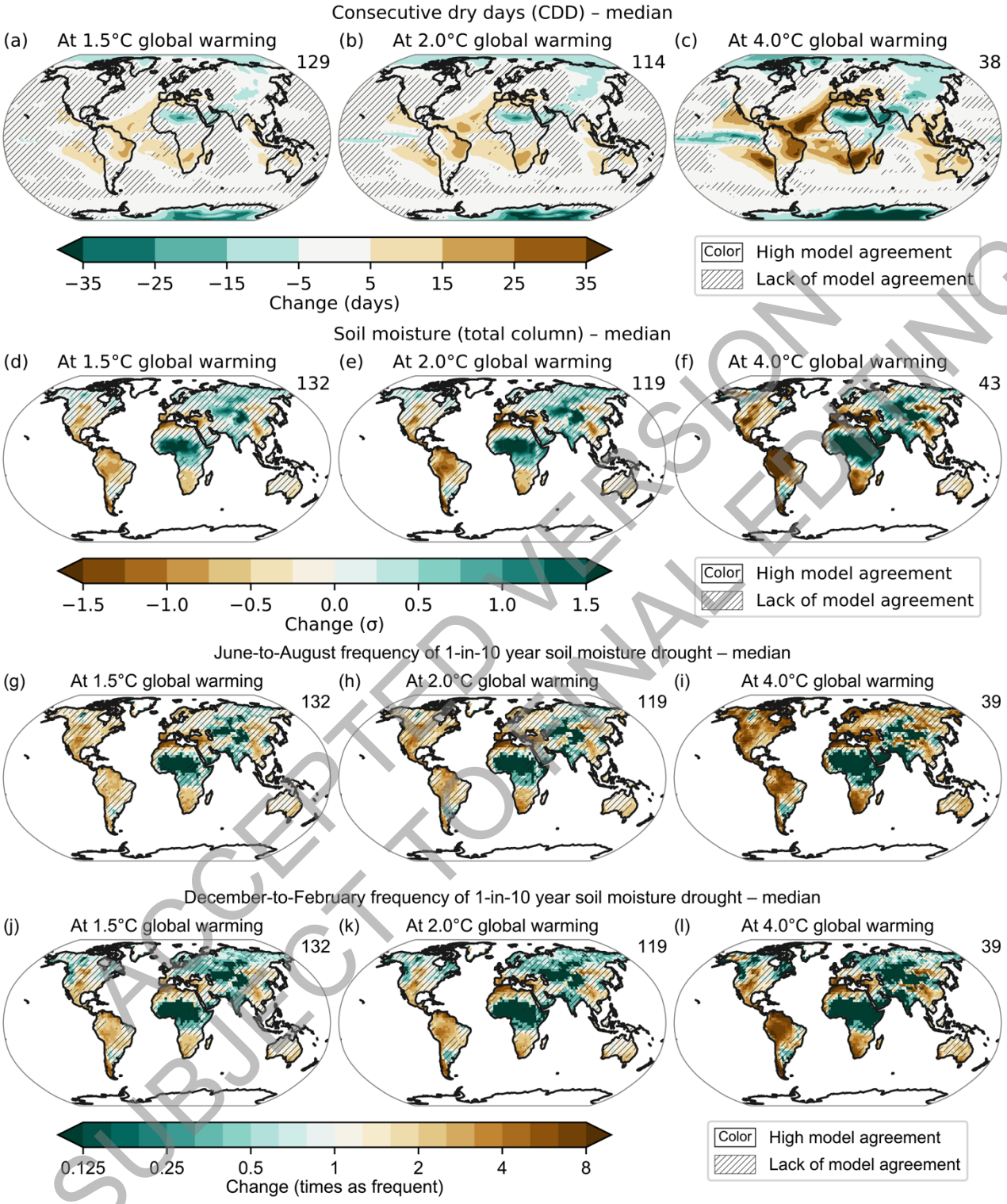


Figure 11.18: Projected changes in the intensity (a) and frequency (b) of drought under 1°C, 1.5°C, 2°C, 3°C, and 4°C global warming levels relative to the 1850-1900 baseline. Summaries are computed for the AR6 regions in which there is at least medium confidence in increase in agriculture/ ecological drought at the 2°C warming level ("drying regions"), including W. North-America, C. North-America, N. Central-America, S. Central-America, N. South-America, N. E. South-America, South-American-Monsoon, S.W.South-America, S.South-America, West & Central-Europe, Mediterranean, W.Southern-Africa, E.Southern-Africa, Madagascar, E.Australia, S.Australia (c). A drought event is defined as a 10-year drought event whose annual mean soil moisture was below its 10th percentile from the 1850-1900 base period. For each box plot, the horizontal line and the box represent the median and central 66% uncertainty range, respectively, of the frequency or the intensity changes across the multi-model ensemble, and the whiskers extend to the 90% uncertainty range. The line of zero in (a) indicates no change in intensity, while the line of one in (b) indicates no change in frequency. The results are based on the multi-model ensemble estimated from simulations of global climate models contributing to the sixth phase of the Coupled Model Intercomparison Project (CMIP6) under different SSP forcing scenarios. Intensity changes in (a) are expressed as standard deviations of the interannualvariability in the period 1850-1900 of the corresponding modelFor details on the methods see Supplementary Material 11.SM.2. Further details on data sources and processing are available in the chapter data table (Table 11.SM.9).

ACCEPTED VERSION SUBJECT TO FINAL EDITING



ACCEPTED VERSION SUBJECT TO FINAL EDITING

Figure 11.19: Projected changes in (a-c) the number of consecutive dry days (CDD), (d-f) annual mean soil moisture over the total column, and (g-l) the frequency and intensity of one-in-ten year soil moisture drought for the June-to-August and December-to-February seasons at 1.5°C, 2°C, and 4°C of global warming compared to the 1851-1900 baseline. Results are based on simulations from the CMIP6 multi-model ensemble under the SSP1-1.9, SSP1-2.6, SSP2-4.5, SSP3-7.0, and SSP5-8.5 scenarios. The numbers in the top right indicate the number of simulations included. Uncertainty is represented using the simple

approach: no overlay indicates regions with high model agreement, where ≥80% of models agree on sign of change; diagonal lines indicate regions with low model agreement, where <80% of models agree on sign of change. For more information on the simple approach, please refer to the Cross-Chapter Box Atlas 1. For details on the methods see Supplementary Material 11.SM.2. Further details on data sources and processing are available in the chapter data table (Table 11.SM.9).

ACCEPTED VERSION
SUBJECT TO FINAL EDITING

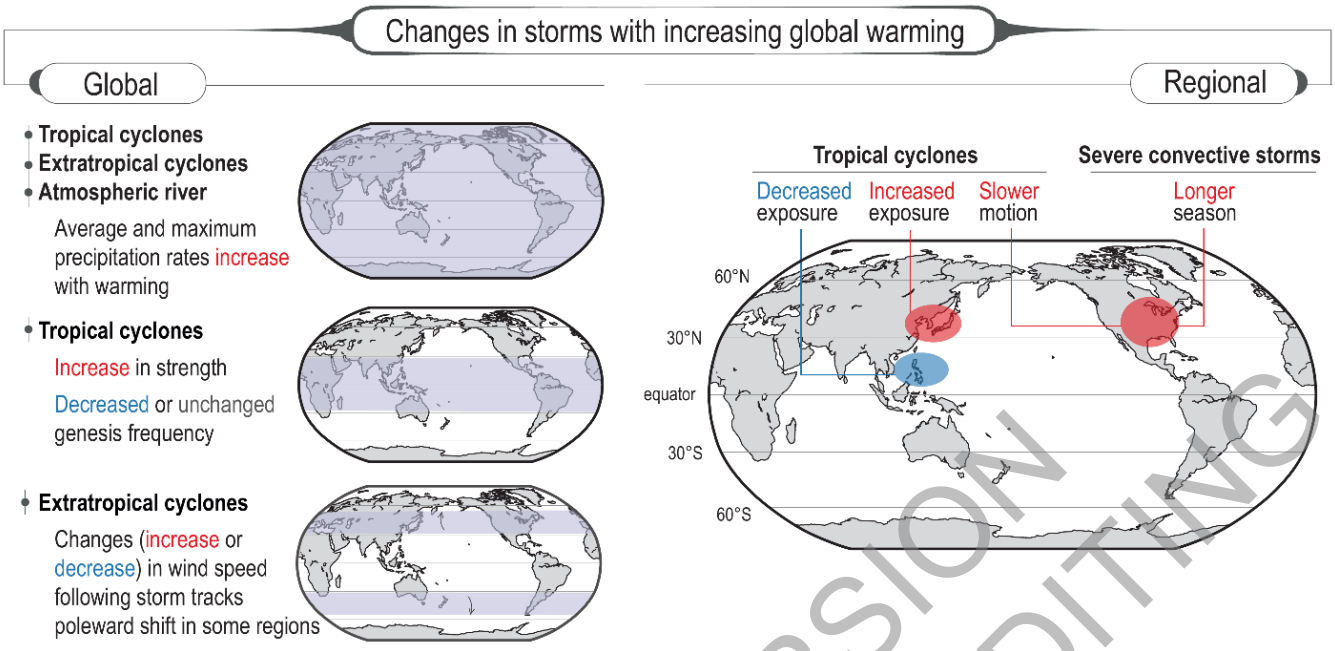
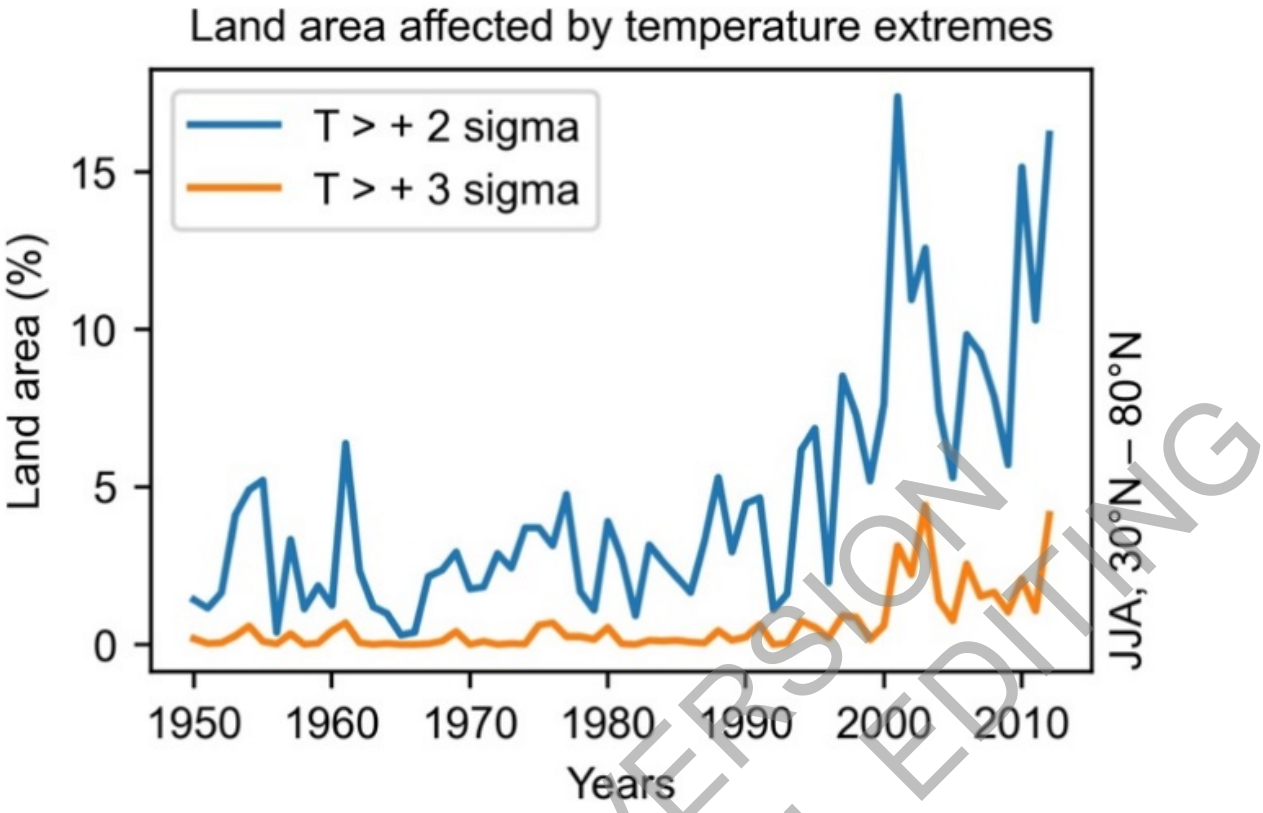


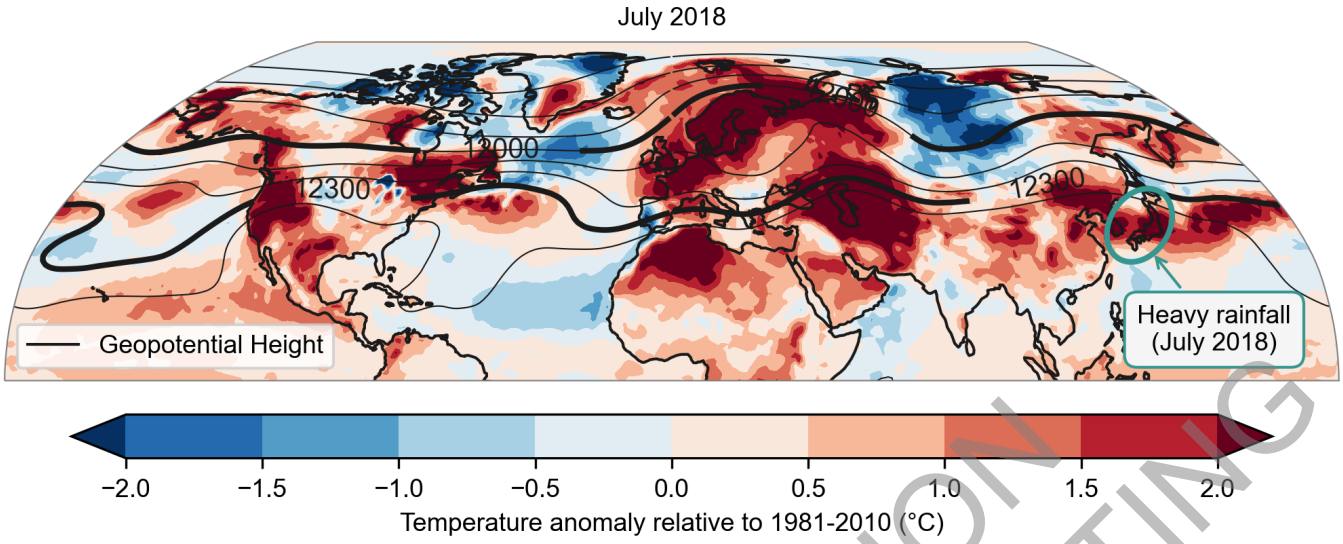
Figure 11.20: Summary schematic of past and projected changes in tropical cyclone (TC), extratropical cyclone (ETC), atmospheric river (AR), and severe convective storm (SCS) behaviour. Global changes (blue shading) from top to bottom: 1) Increased mean and maximum rain-rates in TCs, ETCs, and ARs [past (*low confidence* due to lack of reliable data) & projected (*high confidence*)]. 2) Increased proportion of stronger TCs [past (*medium confidence*) & projected (*high confidence*)]. 3) Decrease or no change in global frequency of TC genesis [past (*low confidence* due to lack of reliable data) & projected (*medium confidence*)]. 4) Increased and decreased ETC wind-speed, depending on the region, as storm-tracks change [past (*low confidence* due to lack of reliable data) & projected (*medium confidence*)]. Regional changes, from left to right: 1) Poleward TC migration in the western North Pacific and subsequent changes in TC exposure [past (*medium confidence*) & projected (*medium confidence*)]. 2) Slowdown of TC forward translation speed over the contiguous US and subsequent increase in TC rainfall [past (*medium confidence*) & projected (*low confidence* due to lack of directed studies)]. 3) Increase in mean and maximum SCS rain-rate and increase in springtime SCS frequency and season length over the contiguous US [past (*low confidence* due to lack of reliable data) & projected (*medium confidence*)].

ACCEPTED VERSION SUBJECT TO FINAL EDITING



Box 11.4, Figure 1: Analysis of the percentage of land area affected by temperature extremes larger than two (orange) or three (blue) standard deviations in June-July-August (JJA) between 30°N and 80°N using a normalization. The more appropriate estimate is the corrected normalization. These panels show for both estimates a substantial increase in the overall land area affected by very high hot extremes since 1990 onward. Adapted from Sippel et al. (2015) .

ACCEPTED VERSION
SUBJECT TO FINAL EDITING

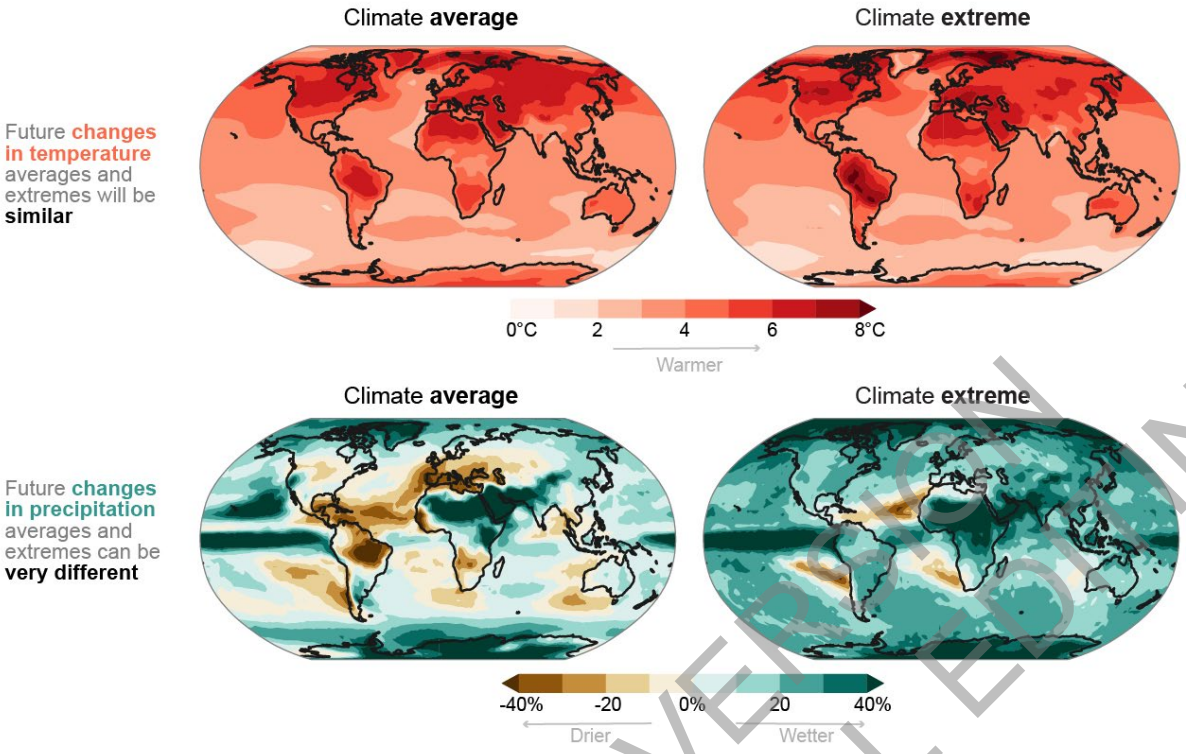


Box 11.4, Figure 2: Meteorological conditions in July 2018. The color shading shows the monthly mean near-surface air temperature anomaly with respect to 1981 to 2010. Contour lines indicate the geopotential height in m, highlighted are the isolines on 12'000 m and 12'300 m, which indicate the approximate positions of the polar-front jet and subtropical jet, respectively. The light blue-green ellipse shows the approximate extent of the strong precipitation event that occurred at the beginning of July in the region of Japan and Korea. All data is from the global ECMWF Reanalysis v5 (ERA5, Hersbach et al., 2020).

ACCEPTED VERSION
SUBJECT TO FINAL EDITING

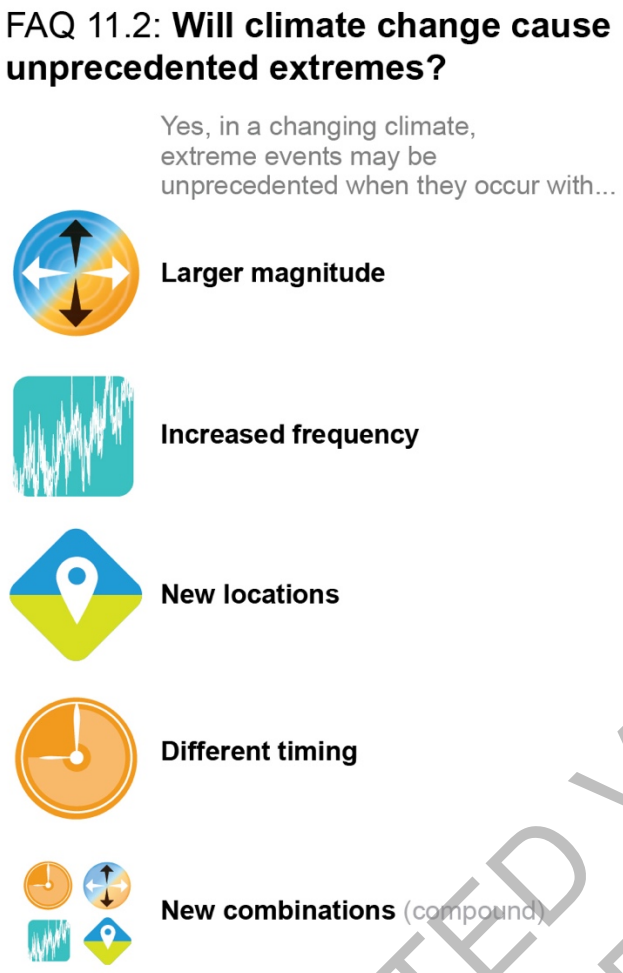
FAQ 11.1: **How will changes in climate extremes compare with changes in climate averages?**

The direction and magnitude of future changes in climate extremes and averages depend on the variable considered.



FAQ 11.1, Figure 1: Global maps of future changes in surface temperature (top panels) and precipitation (bottom panels) for long-term average (left) and extreme conditions (right). All changes were estimated using the CMIP6 ensemble mean for a scenario with a global warming of 4°C relative to 1850-1900 temperatures. Average surface temperatures refer to the warmest three-month season (summer in mid- to high-latitudes) and extreme temperature refer to the hottest day in a year. Precipitation changes, which can include both rainfall and snowfall changes, are normalized by 1850-1900 values and shown in percentage; extreme precipitation refers to the largest daily rainfall in a year.

ACCEPTED VERSION SUBJECT TO FINAL EDITING

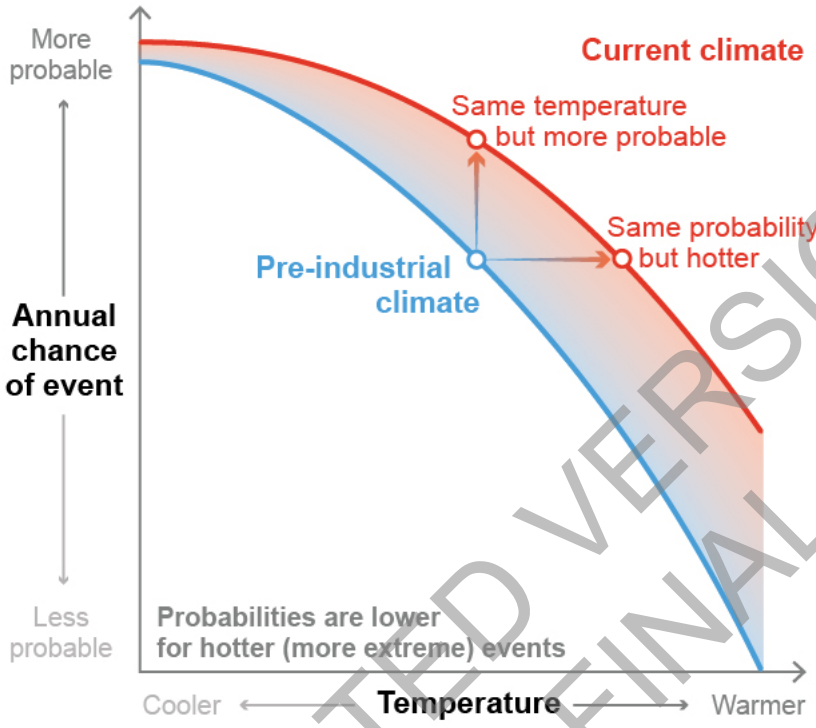


FAQ 11.2, Figure 1: New types of unprecedented extremes that will occur as a result of climate change.

ACCEPTED VERSION SUBJECT TO FINAL EDITING

FAQ 11.3: **Climate change and extreme events**

Extreme events have become more probable and more intense. Many of these changes can be attributed to human influence on the climate.



FAQ 11.3, Figure 1: Changes in climate result in changes in the magnitude and probability of extremes. Example of how temperature extremes differ between a climate with pre-industrial greenhouse gases (shown in blue) and the current climate (shown in orange) for a representative region. The horizontal axis shows the range of extreme temperatures, while the vertical axis shows the annual chance of each temperature event's occurrence. Moving towards the right indicates increasingly hotter extremes that are more rare (less probable). For hot extremes, an extreme event of a particular temperature in the pre-industrial climate would be more probable (vertical arrow) in the current climate. An event of a certain probability in the pre-industrial climate would be warmer (horizontal arrow) in the current climate. While the climate under greenhouse gases at the pre-industrial level experiences a range of hot extremes, such events are hotter and more frequent in the current climate.

ACCEPTED VERSION SUBJECT TO FINAL EDITING

11.SM Chapter 11: Weather and climate extreme events in a changing climate – Supplementary Material

Coordinating Lead Authors:
Sonia I. Seneviratne (Switzerland), Xuebin Zhang (Canada)

Lead Authors:
Muhammad Adnan (Pakistan), Wafae Badi (Morocco), Claudine Dereczynski (Brazil), Alejandro Di Luca (Australia, Canada/Argentina), Subimal Ghosh (India), Iskhaq Iskandar (Indonesia), James Kossin (United States of America), Sophie Lewis (Australia), Friederike Otto (United Kingdom/Germany), Izidine Pinto (South Africa/Mozambique), Masaki Satoh (Japan), Sergio M. Vicente-Serrano (Spain), Michael Wehner (United States of America), Botao Zhou (China)

Contributing Authors:
Mathias Hauser (Switzerland), Megan Kirchmeier-Young (Canada/United States of America), Lisa V. Alexander (Australia), Richard P. Allan (United Kingdom), Mansour Almazroui (Saudi Arabia), Lincoln M. Alvez (Brazil), Margot Bador (Australia, France/France), Rondrotiana Barimalala (South Africa/Madagascar), Richard A. Betts (United Kingdom), Suzana J. Camargo (United States of America/Brazil, USA), Pep G. Canadell (Australia), Erika Coppola (Italy), Markus G. Donat (Spain/Germany, Australia), Hervé Douville (France), Robert J. H. Dunn (United Kingdom/Germany, United Kingdom), Erich Fischer (Switzerland), Hayley J. Fowler (United Kingdom), Nathan P. Gillett (Canada), Peter Greve (Austria/Germany), Michael Grose (Australia), Lukas Gudmundsson (Switzerland/Germany, Iceland), Jose Manuel Guttierez (Spain), Lofti Halimi (Algeria), Zhenyu Han (China), Kevin Hennessy (Australia), Richard G. Jones (United Kingdom), Yeon-Hee Kim (Republic of Korea), Thomas Knutson (United States of America), June-Yi Lee (Republic of Korea), Chao Li (China), Georges-Noel T. Longandjo (South Africa/Democratic Republic of Congo), Kathleen L. McInnes (Australia), Tim R. McVicar (Australia), Malte Meinshausen (Australia/Germany), Seung-Ki Min (Republic of Korea), Ryan S. Padron Flasher (Switzerland/Ecuador, United States of America), Christina M. Patricola (United States of America), Roshanka Ranasinghe (The Netherlands/Sri Lanka, Australia), Johan Reyns (The Netherlands/Belgium), Joeri Rogelj (United Kingdom/Belgium), Alex C. Ruane (United States of America), Daniel Ruiz Carrascal (United States of America/Colombia), Bjørn H. Samset (Norway), Jonathan Spinoni (Italy), Qiaohong Sun (Canada/China), Ying Sun (China), Mouhamadou Bamba Sylla (Rwanda/Senegal), Claudia Tebaldi (United States of America), Laurent Terray (France), Wim Thiery (Belgium), Jessica Tierney (United States of America), Maarten K. van Aalst (The Netherlands), Bart van den Hurk (The Netherlands), Robert Vautard (France), Wen Wang (China), Seth Westra (Australia), Jakob Zscheischler (Germany)

Review Editors:
Johnny Chan (China), Asgeir Sorteberg (Norway), Carolina Vera (Argentina)

Chapter Scientists:
Mathias Hauser (Switzerland), Megan Kirchmeier-Young (Canada/ United States of America), Hui Wan (Canada)

ACCEPTED VERSION SUBJECT TO FINAL EDITING

This Supplementary Material should be cited as:
Seneviratne, S. I., X. Zhang, M. Adnan, W. Badi, C. Dereczynski, A. Di Luca, S. Ghosh, I. Iskandar, J. Kossin, S. Lewis, F. Otto, I. Pinto, M. Satoh, S. M. Vicente-Serrano, M. Wehner, B. Zhou, 2021, Weather and Climate Extreme Events in a Changing Climate Supplementary Material. In: *Climate Change 2021: The Physical Science Basis. Contribution of Working Group I to the Sixth Assessment Report of the Intergovernmental Panel on Climate Change* [Masson-Delmotte, V., P. Zhai, A. Pirani, S. L. Connors, C. Péan, S. Berger, N. Caud, Y. Chen, L. Goldfarb, M. I. Gomis, M. Huang, K. Leitzell, E. Lonnoy, J. B. R. Matthews, T. K. Maycock, T. Waterfield, O. Yelekçi, R. Yu and B. Zhou (eds.)]. Available from https://ipcc.ch/static/ar6/wg1

Date: August 2021

This document is subject to copy-editing, corrigenda and trickle backs.

ACCEPTED VERSION
SUBJECT TO FINAL EDITING

11.SM.1 Mean temperature anomalies for CMIP5 model output 3
11.SM.2 Methods used for the figures 3
11.SM.2.1 Overview 3
11.SM.2.2 Climate indices 3
11.SM.2.2.1 Soil-moisture based drought indices 4
11.SM.2.3 Observed trends in TXx, TNn, TX90p, and CDD 4
11.SM.2.4 Observed trends in SPI and SPEI 4
11.SM.2.5 CMIP6 data 4
11.SM.2.6 Global warming levels 5
11.SM.2.7 Scaling of regional climate indices 5
11.SM.2.8 Maps at global warming levels 5
11.SM.2.9 Warmest three-month season 5
11.SM.3 Multi-model-median regional means at warming levels for selected indices 5
11.SM.4 Data Table 19
References 26

ACCEPTED VERSION
SUBJECT TO FINAL EDITING

11.SM.1 Mean temperature anomalies for CMIP5 model output

Table 11.SM.1 lists mean annual mean global surface air temperature anomalies for CMIP5 model output for selected time periods and all RCPs, in a similar format as Table 4.2 (Chapter 4). See (Hauser, 2021b) for respective numbers for individual CMIP5 and CMIP6 models.

[START TABLE 11.SM.1 HERE]

Table 11.SM.1: CMIP5 annual mean global surface air temperature anomalies (°C) from the 1850–1900 reference period for selected time periods, regions and all RCPs. Displayed are multi-model averages and 5–95% ranges. Numbers in brackets in the top row indicate the number of models.

	RCP2.6 (21)	RCP4.5 (30)	RCP6.0 (14)	RCP8.5 (32)
near-term (2021-2040)	1.5 (1.1-2.0)	1.6 (1.2-2.0)	1.5 (1.0-1.9)	1.7 (1.2-2.3)
mid-term (2041-2060)	1.7 (1.3-2.2)	2.0 (1.5-2.6)	1.9 (1.4-2.4)	2.5 (1.9-3.2)
long-term (2081-2100)	1.7 (1.1-2.3)	2.5 (1.8-3.2)	2.8 (2.3-3.6)	4.4 (3.2-5.5)
AR5 “near-term” (2016-2035)	1.4 (1.0-1.9)	1.4 (1.1-1.9)	1.4 (0.9-1.8)	1.5 (1.1-2.1)
AR5 “mid-term” (2046-2065)	1.7 (1.2-2.2)	2.1 (1.6-2.7)	2.0 (1.5-2.5)	2.7 (2.1-3.5)
2020 (2011-2030)	1.4 (1.0-1.8)	1.3 (0.9-1.7)	1.3 (0.9-1.7)	1.4 (1.0-1.8)
2030 (2021-2040)	1.5 (1.1-2.0)	1.6 (1.2-2.0)	1.5 (1.0-1.9)	1.7 (1.2-2.3)
2040 (2031-2050)	1.7 (1.2-2.2)	1.8 (1.4-2.3)	1.7 (1.2-2.1)	2.1 (1.6-2.7)
2050 (2041-2060)	1.7 (1.3-2.2)	2.0 (1.5-2.6)	1.9 (1.4-2.4)	2.5 (1.9-3.2)
2060 (2051-2070)	1.7 (1.2-2.3)	2.2 (1.6-2.8)	2.1 (1.6-2.6)	2.9 (2.3-3.8)
2070 (2061-2080)	1.7 (1.2-2.3)	2.3 (1.7-3.0)	2.3 (1.9-2.9)	3.4 (2.6-4.3)
2080 (2071-2090)	1.7 (1.1-2.3)	2.4 (1.8-3.1)	2.6 (2.1-3.3)	3.9 (2.9-4.9)
2090 (2081-2100)	1.7 (1.1-2.3)	2.5 (1.8-3.2)	2.8 (2.3-3.6)	4.4 (3.2-5.5)
2100 (2091-2100)	1.7 (1.0-2.3)	2.5 (1.9-3.2)	2.9 (2.4-3.7)	4.6 (3.4-5.7)

[END TABLE 11.SM.1 HERE]

11.SM.2 Methods used for the figures

11.SM.2.1 Overview

This section provides additional methods used for the figures produced specifically for Chapter 11. These figures are either based on published observational data or data from the sixth phase of the Coupled Model Intercomparison Project (CMIP6) (Eyring et al., 2016). See also Appendix 11.A for additional information on the used data.

11.SM.2.2 Climate indices

Figure 11.11 and Figure 11.17 show trends of observed climate indices. Most of the shown climate indices are defined by the expert group on Climate Change Detection and Indices (ETCCDI) (Karl, Nicholls, &

ACCEPTED VERSION SUBJECT TO FINAL EDITING

Ghazi, 1999; Peterson et al., 2001), which were calculated on an annual basis according to the standard procedure. The used ETCCDI indices include hottest daily maximum temperature (TXx), hottest daily minimum temperature (TNn), the annual number of days when daily maximum temperature exceeds its 90th percentile from a base period (TX90p), and consecutive dry days (CDD). Further, trends in the Standardized Precipitation Index (SPI) and the Standardized Precipitation-Evapotranspiration Index (SPEI) at an accumulation scale of 12 months (SPI-12 and SPEI-12) are shown.

Model data from CMIP6 is shown in Figure 11.2, Figure 11.9, Figure 11.16, Figure 11.18, and Figure 11.19 (all other figures showing CMIP6 data are taken from publications). The following indices were computed for the figures: TXx, TNn, annual maximum daily precipitation (Rx1day), and CDD. In addition, total soil moisture (summed over the whole column), a soil-moisture based drought frequency index and a soil-moisture based drought intensity index were analyzed. For soil moisture data from CMIP6 all values are masked over the ocean, land ice, Antarctica, and Greenland.

11.SM.2.2.1 Soil-moisture based drought indices

The soil moisture-based drought indices are displayed in Figure 11.18 and Figure 11.19. Both drought indices are calculated for annual mean and seasonal mean data. First, soil moisture is normalized subtracting the mean over 1850-1900 and dividing it by the standard deviation over the same time period. For the drought frequency the 10^{th} quantile over the period 1850-1900 is calculated and all soil moisture values below this threshold are defined as drought. Finally, the drought frequency for a certain time period is given as fraction of years or season under drought. Time periods are selected for certain global warming levels (see below), where 30-year periods are used. For the drought intensity we calculate the 10^{th} quantile over the period 1850-1900 and for certain global warming levels.

11.SM.2.3 Observed trends in TXx, TNn, TX90p, and CDD

Observed trends in TXx, TNn, TX90p, and CDD are shown in Figure 11.9 and Figure 11.17 (a). The data is obtained from (Dunn et al., 2020) and the calculation of the trends and the selection of valid grid points follows the method outlined in (Dunn et al., 2020). In contrast to (Dunn et al., 2020), however, we show trends for the time period 1960-2018 and the significance was calculated the p = 0.1 level.

11.SM.2.4 Observed trends in SPI and SPEI

Trend in SPI and SPEI are shown in Figure 11.17 (b) and (c). The data is obtained from (Spinoni et al., 2019) and trends were calculated by linear regression analysis. Time was the independent variable and the drought severity the dependent variable. The slope of the regression indicates the amount of change. Data was available for 5-year periods. Significance was analyzed by means of the nonparametric Mann–Kendall statistic that measures the degree to which a trend is consistently increasing or decreasing. Autocorrelation was considered in the trend analysis returning the corrected p values after accounting for temporal pseudo replication (Hamed & Ramachandra Rao, 1998).

11.SM.2.5 CMIP6 data

CMIP6 data is specifically analysed for Chapter 11 in Figure 11.3, Figure 11.11, Figure 11.16, Figure 11.18, Figure 11.19, and FAQ 11.1 Figure 1 (all other figures showing CMIP6 data are taken from publications). For these figures historical simulations (1850 to 2015) are combined with the shared socioeconomic pathways (SSPs) projections (O'Neill et al., 2016). The following SSPs were chosen: SSP1-1.9, SSP1-2.6, SSP2-4.5, SSP3-7.0, and SSP5-8.5. This subset of SSPs includes all Tier 1 scenarios (SSP1-2.6, SSP2-4.5, SSP3-7.0, and SSP5-8.5) and additionally the scenario most consistent with a stabilisation at +1.5°C at the end of the 21st century as aimed in the Paris Agreement (SSP1-1.9) (O'Neill et al., 2016).

ACCEPTED VERSION SUBJECT TO FINAL EDITING

A "ensemble of opportunity" is used, including all available models that pass very basic checks. Only the first ensemble member of each model is used, and all models are weighted equally. In order to be used, models must (i) provide the corresponding variable, (ii) run from 1850 to 2099, (iii) must not have duplicate time steps or missing time steps, and (iv) must not have any obvious data errors (e.g., negative soil moisture, or an inconsistency between historical simulation and projection). The exact model ensemble used for each figure is given in Appendix 11.

11.SM.2.6 Global warming levels

Global warming levels expressed as changes in global mean surface air temperature (GSAT) relative to the 1850-1900 period are used to display changes in climate indices in Chapter 12. See Cross-Chapter Box 11.1 for details. Global warming levels are computed as outlined in (Hauser, Engelbrecht, & Fischer, 2021) using 20-year periods, except for the soil moisture-based drought indices where 30-year periods are used.

11.SM.2.7 Scaling of regional climate indices

Figure 11.3 shows regional mean changes in TXx as function of GWL. To obtain regional averages of climate indices they are first calculated on the original model grid. Then regional averages are computed, weighting each grid cell with its area (if available, else the grid cells are weighted by the cosine of the latitude). Finally, the mean of the climate index is calculated at GWLs between 0.1°C and 5°C in steps of 0.1°C. In Figure 11.3 TXx scaling is shown for individual models (panel a), as multi-model mean for selected SSPs (panel a), or as multi model mean over all used SSPs (see Section 11.SM.1.5; all panels).

11.SM.2.8 Maps at global warming levels

Maps of climate indices at global warming levels are shown in Figure 11.11, Figure 11.16, and Figure 11.19. The response of the climate indices is calculated at three different global warming levels: 1.5°C, 2°C, and 4°C. The model data is interpolated on a common 2.5° x 2.5° latitude-longitude grid using a conservative regridding scheme. All models from each of the five used SSPs (see Section 11.SM.1.5) that reaches the warming level is included in the ensemble, thus each model can contribute more than one data point for a given warming level. Finally, the median over all models is calculated.

11.SM.2.9 Warmest three-month season

FAQ 11.1, Figure 1 displays changes in mean precipitation and temperatures for the warmest three consecutive months, which corresponds to summer in mid- to high-latitudes. The warmest months were determined for each model and grid point individually from the period 1850-1900. The warmest-three month season was kept constant over the whole period of the simulation.

11.SM.3 Multi-model-median regional means at warming levels for selected indices

[START TABLE 11.SM.2 HERE]

Table 11.SM.2: Multi model median regional changes in annual hottest daily maximum temperature (TXx) for the globe, global ocean, global land, global land excluding Antarctica, and the AR6 land regions for three global warming levels (GWL) as simulated by CMIP6 models under the forcing scenarios SSP1-1.9, SSP1-2.6, SSP2-4.5, SSP3-7.0, and SSP5-8.5. Regional averages are calculated from the original model grid using the grid cell area as weights if available, else the grid cells where weighted with the cosine of the latitude. See also Hauser (2021).

ACCEPTED VERSION SUBJECT TO FINAL EDITING

	Projections		
	+1.5°C GWL	+2.0°C GWL	+4.0°C GWL
Global (global)	1.40°C	1.90°C	3.93°C
Ocean (ocean)	1.22°C	1.64°C	3.40°C
Land (land)	1.88°C	2.55°C	5.25°C
Land w/o Antarctica (land_wo_antarctica)	1.94°C	2.65°C	5.47°C
Greenland/Iceland (GIC)	1.21°C	1.54°C	2.97°C
N.W.North-America (NWN)	1.93°C	2.55°C	5.23°C
N.E.North-America (NEN)	2.22°C	2.99°C	5.96°C
W.North-America (WNA)	2.24°C	3.01°C	5.95°C
C.North-America (CNA)	2.33°C	3.12°C	5.71°C
E.North-America (ENA)	1.97°C	2.72°C	5.68°C
N.Central-America (NCA)	1.81°C	2.45°C	4.84°C
S.Central-America (SCA)	1.77°C	2.32°C	4.76°C
Caribbean (CAR)	1.59°C	2.11°C	4.33°C
N.W.South-America (NWS)	1.87°C	2.52°C	5.41°C
N.South-America (NSA)	2.24°C	2.98°C	6.35°C
N.E.South-America (NES)	2.04°C	2.69°C	5.39°C
South-American-Monsoon (SAM)	2.58°C	3.44°C	7.33°C
S.W.South-America (SWS)	1.91°C	2.50°C	4.83°C
S.E.South-America (SES)	1.95°C	2.57°C	5.45°C
S.South-America (SSA)	1.91°C	2.41°C	4.52°C
N.Europe (NEU)	1.81°C	2.54°C	4.99°C
West&Central-Europe (WCE)	2.33°C	3.20°C	6.23°C
E.Europe (EEU)	2.20°C	2.97°C	5.76°C
Mediterranean (MED)	2.50°C	3.30°C	6.61°C
Sahara (SAH)	2.39°C	3.09°C	6.03°C
Western-Africa (WAF)	1.62°C	2.19°C	4.53°C
Central-Africa (CAF)	1.56°C	2.12°C	4.67°C
N.Eastern-Africa (NEAF)	1.66°C	2.24°C	4.45°C
S.Eastern-Africa (SEAF)	1.59°C	2.08°C	4.24°C
W.Southern-Africa (WSAF)	2.03°C	2.73°C	5.29°C
E.Southern-Africa (ESAF)	1.93°C	2.66°C	5.45°C
Madagascar (MDG)	1.63°C	2.17°C	4.65°C
Russian-Arctic (RAR)	1.99°C	2.77°C	5.52°C

ACCEPTED VERSION SUBJECT TO FINAL EDITING

W.Siberia (WSB)	2.11°C	2.80°C	5.09°C
E.Siberia (ESB)	2.09°C	2.87°C	5.97°C
Russian-Far-East (RFE)	1.93°C	2.69°C	5.45°C
W.C.Asia (WCA)	2.34°C	3.08°C	6.09°C
E.C.Asia (ECA)	2.17°C	2.92°C	5.70°C
Tibetan-Plateau (TIB)	1.65°C	2.32°C	4.55°C
E.Asia (EAS)	1.50°C	2.19°C	4.66°C
Arabian-Peninsula (ARP)	2.29°C	3.06°C	5.99°C
S.Asia (SAS)	1.20°C	1.81°C	4.12°C
S.E.Asia (SEA)	1.40°C	1.85°C	4.23°C
N.Australia (NAU)	1.59°C	2.03°C	3.99°C
C.Australia (CAU)	1.95°C	2.53°C	4.85°C
E.Australia (EAU)	1.60°C	2.13°C	4.25°C
S.Australia (SAU)	1.71°C	2.30°C	4.48°C
New-Zealand (NZ)	1.36°C	1.82°C	3.68°C
E.Antarctica (EAN)	1.18°C	1.65°C	3.22°C
W.Antarctica (WAN)	0.62°C	0.84°C	1.81°C

[END TABLE 11.SM.2 HERE]

[START TABLE 11.SM.3 HERE]

Table 11.SM.3: As Table 11.SM.2 but for changes in the annual hottest daily minimum temperature (TNn).

	Projections		
	+1.5°C GWL	+2.0°C GWL	+4.0°C GWL
Global (global)	1.99°C	2.63°C	5.19°C
Ocean (ocean)	1.74°C	2.28°C	4.53°C
Land (land)	2.64°C	3.48°C	6.80°C
Land w/o Antarctica (land_wo_antarctica)	2.73°C	3.59°C	7.05°C
Greenland/Iceland (GIC)	3.88°C	4.99°C	9.90°C
N.W.North-America (NWN)	4.46°C	6.01°C	12.38°C
N.E.North-America (NEN)	4.85°C	6.37°C	13.22°C
W.North-America (WNA)	2.80°C	3.92°C	7.80°C
C.North-America (CNA)	2.54°C	3.76°C	7.82°C
E.North-America (ENA)	3.67°C	4.99°C	9.72°C
N.Central-America (NCA)	1.79°C	2.36°C	5.03°C

ACCEPTED VERSION SUBJECT TO FINAL EDITING

S.Central-America (SCA)	1.59°C	2.08°C	3.87°C
Caribbean (CAR)	1.51°C	2.02°C	3.74°C
N.W.South-America (NWS)	1.87°C	2.43°C	4.89°C
N.South-America (NSA)	1.81°C	2.36°C	4.62°C
N.E.South-America (NES)	1.79°C	2.35°C	4.40°C
South-American-Monsoon (SAM)	1.78°C	2.41°C	4.79°C
S.W.South-America (SWS)	2.04°C	2.66°C	5.90°C
S.E.South-America (SES)	1.42°C	1.80°C	3.75°C
S.South-America (SSA)	2.14°C	2.79°C	6.40°C
N.Europe (NEU)	5.08°C	6.46°C	10.59°C
West&Central-Europe (WCE)	4.80°C	6.06°C	11.04°C
E.Europe (EEU)	4.90°C	6.16°C	11.33°C
Mediterranean (MED)	2.20°C	2.79°C	5.28°C
Sahara (SAH)	2.15°C	2.74°C	5.35°C
Western-Africa (WAF)	2.04°C	2.65°C	4.63°C
Central-Africa (CAF)	1.89°C	2.52°C	4.94°C
N.Eastern-Africa (NEAF)	1.95°C	2.51°C	4.90°C
S.Eastern-Africa (SEAF)	1.83°C	2.36°C	4.54°C
W.Southern-Africa (WSAF)	1.77°C	2.40°C	4.75°C
E.Southern-Africa (ESAF)	1.78°C	2.28°C	4.42°C
Madagascar (MDG)	1.63°C	2.08°C	3.93°C
Russian-Arctic (RAR)	4.81°C	6.44°C	12.78°C
W.Siberia (WSB)	4.05°C	5.52°C	10.26°C
E.Siberia (ESB)	3.42°C	4.55°C	8.62°C
Russian-Far-East (RFE)	4.10°C	5.56°C	11.17°C
W.C.Asia (WCA)	2.75°C	3.56°C	7.32°C
E.C.Asia (ECA)	2.26°C	2.97°C	5.77°C
Tibetan-Plateau (TIB)	2.42°C	2.97°C	5.74°C
E.Asia (EAS)	2.11°C	2.95°C	5.83°C
Arabian-Peninsula (ARP)	2.30°C	2.84°C	5.96°C
S.Asia (SAS)	1.79°C	2.48°C	5.23°C
S.E.Asia (SEA)	1.46°C	1.96°C	4.10°C
N.Australia (NAU)	1.97°C	2.57°C	5.08°C
C.Australia (CAU)	1.62°C	2.06°C	4.22°C
E.Australia (EAU)	1.37°C	1.89°C	3.76°C

ACCEPTED VERSION
SUBJECT TO FINAL EDITING

S.Australia (SAU)	1.10°C	1.52°C	2.95°C
New-Zealand (NZ)	1.33°C	1.74°C	3.41°C
E.Antarctica (EAN)	1.64°C	2.17°C	4.38°C
W.Antarctica (WAN)	2.26°C	2.95°C	5.58°C

[END TABLE 11.SM.3 HERE]

[START TABLE 11.SM.4 HERE]

Table 11.SM.4: As Table 11.SM.2 but for changes in annual maximum daily precipitation (Rx1day).

	Projections		
	+1.5°C GWL	+2.0°C GWL	+4.0°C GWL
Global (global)	6.96%	9.96%	24.02%
Ocean (ocean)	6.49%	9.12%	22.81%
Land (land)	8.42%	11.42%	26.58%
Land w/o Antarctica (land_wo_antarctica)	8.37%	11.30%	26.56%
Greenland/Iceland (GIC)	11.76%	15.66%	33.77%
N.W.North-America (NWN)	9.06%	12.49%	27.28%
N.E.North-America (NEN)	9.99%	13.29%	26.54%
W.North-America (WNA)	7.09%	8.01%	16.89%
C.North-America (CNA)	7.39%	9.91%	17.93%
E.North-America (ENA)	8.05%	10.67%	22.03%
N.Central-America (NCA)	5.28%	7.29%	15.89%
S.Central-America (SCA)	2.24%	4.55%	8.36%
Caribbean (CAR)	3.38%	2.56%	4.17%
N.W.South-America (NWS)	8.05%	11.05%	26.81%
N.South-America (NSA)	6.26%	8.31%	17.42%
N.E.South-America (NES)	7.26%	9.35%	27.46%
South-American-Monsoon (SAM)	5.73%	9.06%	18.72%
S.W.South-America (SWS)	1.64%	2.50%	3.15%
S.E.South-America (SES)	8.45%	11.91%	24.59%
S.South-America (SSA)	4.87%	7.09%	14.37%
N.Europe (NEU)	9.33%	11.55%	23.21%
West&Central-Europe (WCE)	7.48%	9.51%	18.37%
E.Europe (EEU)	7.28%	8.78%	18.88%
Mediterranean (MED)	3.61%	4.42%	8.88%

ACCEPTED VERSION SUBJECT TO FINAL EDITING

Sahara (SAH)	19.43%	24.07%	45.50%
Western-Africa (WAF)	18.26%	19.74%	46.24%
Central-Africa (CAF)	14.36%	18.24%	47.14%
N.Eastern-Africa (NEAF)	13.38%	17.42%	46.12%
S.Eastern-Africa (SEAF)	11.23%	15.66%	41.36%
W.Southern-Africa (WSAF)	4.68%	6.40%	9.36%
E.Southern-Africa (ESAF)	5.95%	9.25%	20.87%
Madagascar (MDG)	6.28%	8.18%	22.26%
Russian-Arctic (RAR)	10.95%	15.89%	31.50%
W.Siberia (WSB)	8.22%	10.53%	19.17%
E.Siberia (ESB)	8.11%	11.36%	24.80%
Russian-Far-East (RFE)	10.54%	15.40%	35.29%
W.C.Asia (WCA)	9.14%	11.48%	24.16%
E.C.Asia (ECA)	9.10%	12.75%	29.93%
Tibetan-Plateau (TIB)	8.80%	12.46%	30.70%
E.Asia (EAS)	7.28%	10.76%	28.69%
Arabian-Peninsula (ARP)	11.07%	17.46%	43.04%
S.Asia (SAS)	10.39%	15.84%	41.56%
S.E.Asia (SEA)	6.77%	10.57%	33.37%
N.Australia (NAU)	6.97%	9.33%	28.35%
C.Australia (CAU)	5.82%	7.06%	15.27%
E.Australia (EAU)	4.01%	5.97%	14.73%
S.Australia (SAU)	5.84%	6.53%	14.18%
New-Zealand (NZ)	8.21%	12.11%	25.55%
E.Antarctica (EAN)	11.68%	15.56%	35.98%
W.Antarctica (WAN)	8.42%	11.47%	23.65%

[END TABLE 11.SM.4 HERE]

[START TABLE 11.SM.5 HERE]

Table 11.SM.5: As Table 11.SM.2 but for changes in annual maximum five-day precipitation (Rx5day).

	Projections		
	+1.5°C GWL	+2.0°C GWL	+4.0°C GWL
Global (global)	5.24%	7.45%	18.94%
Ocean (ocean)	4.77%	6.74%	17.92%
Land (land)	6.13%	8.54%	20.76%

ACCEPTED VERSION SUBJECT TO FINAL EDITING

Land w/o Antarctica (land_wo_antarctica)	6.07%	8.42%	20.52%
Greenland/Iceland (GIC)	11.38%	15.12%	34.24%
N.W.North-America (NWN)	7.87%	11.44%	24.67%
N.E.North-America (NEN)	8.83%	11.51%	22.90%
W.North-America (WNA)	5.08%	6.24%	11.99%
C.North-America (CNA)	5.04%	7.74%	14.33%
E.North-America (ENA)	6.06%	8.47%	18.41%
N.Central-America (NCA)	3.30%	4.34%	10.77%
S.Central-America (SCA)	0.23%	1.02%	1.72%
Caribbean (CAR)	0.21%	-0.18%	-1.94%
N.W.South-America (NWS)	5.65%	7.47%	17.66%
N.South-America (NSA)	3.91%	5.48%	11.10%
N.E.South-America (NES)	6.19%	8.32%	20.24%
South-American-Monsoon (SAM)	4.56%	7.04%	11.26%
S.W.South-America (SWS)	-0.96%	-0.24%	-1.75%
S.E.South-America (SES)	6.75%	9.53%	21.74%
S.South-America (SSA)	2.71%	3.92%	8.37%
N.Europe (NEU)	7.44%	9.42%	18.64%
West&Central-Europe (WCE)	6.26%	8.05%	15.30%
E.Europe (EEU)	6.20%	8.10%	16.22%
Mediterranean (MED)	1.02%	1.36%	2.24%
Sahara (SAH)	17.35%	21.19%	42.94%
Western-Africa (WAF)	13.91%	16.20%	31.56%
Central-Africa (CAF)	11.01%	14.67%	33.88%
N.Eastern-Africa (NEAF)	9.63%	14.11%	35.71%
S.Eastern-Africa (SEAF)	7.35%	9.84%	29.05%
W.Southern-Africa (WSAF)	2.33%	3.13%	4.53%
E.Southern-Africa (ESAF)	4.40%	6.25%	16.42%
Madagascar (MDG)	4.93%	5.46%	15.03%
Russian-Arctic (RAR)	10.02%	14.39%	29.14%
W.Siberia (WSB)	7.18%	9.21%	16.93%
E.Siberia (ESB)	6.32%	9.03%	21.07%
Russian-Far-East (RFE)	8.74%	12.76%	28.94%
W.C.Asia (WCA)	7.42%	9.60%	20.98%
E.C.Asia (ECA)	8.48%	11.50%	26.81%

ACCEPTED VERSION SUBJECT TO FINAL EDITING

Tibetan-Plateau (TIB)	5.78%	9.01%	26.12%
E.Asia (EAS)	4.08%	6.38%	22.49%
Arabian-Peninsula (ARP)	10.86%	16.94%	45.56%
S.Asia (SAS)	8.55%	13.32%	34.05%
S.E.Asia (SEA)	4.56%	7.44%	23.12%
N.Australia (NAU)	5.98%	7.14%	21.51%
C.Australia (CAU)	4.55%	5.50%	11.15%
E.Australia (EAU)	2.48%	3.81%	10.23%
S.Australia (SAU)	3.04%	2.80%	8.64%
New-Zealand (NZ)	5.85%	8.08%	18.04%
E.Antarctica (EAN)	10.74%	14.50%	34.17%
W.Antarctica (WAN)	7.75%	10.22%	21.85%

[END TABLE 11.SM.5 HERE]

[START TABLE 11.SM.6 HERE]

Table 11.SM.6: As Table 11.SM.2 but for changes in annual mean total soil moisture (summed over the whole soil column).

	Projections		
	+1.5°C GWL	+2.0°C GWL	+4.0°C GWL
Global (global)	-	-	-
Ocean (ocean)	-	-	-
Land (land)	-	-	-
Land w/o Antarctica (land_wo_antarctica)	-0.93σ	-1.63σ	-3.53σ
Greenland/Iceland (GIC)	-0.54σ	-0.50σ	-2.04σ
N.W.North-America (NWN)	-0.02σ	0.34σ	-2.72σ
N.E.North-America (NEN)	-1.00σ	-0.77σ	-2.21σ
W.North-America (WNA)	-0.53σ	-0.72σ	-1.63σ
C.North-America (CNA)	-1.28σ	-1.14σ	-1.59σ
E.North-America (ENA)	-0.35σ	-0.32σ	-0.76σ
N.Central-America (NCA)	-0.94σ	-1.04σ	-1.52σ
S.Central-America (SCA)	-1.40σ	-1.40σ	-3.42σ
Caribbean (CAR)	-0.54σ	-0.69σ	-1.22σ
N.W.South-America (NWS)	-1.20σ	-1.33σ	-3.50σ
N.South-America (NSA)	-1.21σ	-1.66σ	-3.05σ

ACCEPTED VERSION SUBJECT TO FINAL EDITING

N.E.South-America (NES)	-0.38σ	-0.31σ	-0.50σ
South-American-Monsoon (SAM)	-1.34σ	-1.71σ	-3.81σ
S.W.South-America (SWS)	-2.33σ	-2.91σ	-4.83σ
S.E.South-America (SES)	0.16σ	0.32σ	-0.11σ
S.South-America (SSA)	-1.22σ	-1.58σ	-2.10σ
N.Europe (NEU)	0.42σ	0.16σ	-0.28σ
West&Central-Europe (WCE)	0.05σ	-0.11σ	-0.72σ
E.Europe (EEU)	0.55σ	0.38σ	0.59σ
Mediterranean (MED)	-2.03σ	-2.75σ	-4.18σ
Sahara (SAH)	1.31σ	1.59σ	3.59σ
Western-Africa (WAF)	2.14σ	2.44σ	2.68σ
Central-Africa (CAF)	1.76σ	2.03σ	2.57σ
N.Eastern-Africa (NEAF)	1.40σ	2.27σ	3.78σ
S.Eastern-Africa (SEAF)	0.70σ	1.14σ	2.08σ
W.Southern-Africa (WSAF)	-0.93σ	-1.21σ	-2.54σ
E.Southern-Africa (ESAF)	-0.66σ	-0.82σ	-1.89σ
Madagascar (MDG)	-0.09σ	-0.28σ	-1.01σ
Russian-Arctic (RAR)	0.80σ	0.88σ	-1.28σ
W.Siberia (WSB)	1.22σ	1.24σ	1.43σ
E.Siberia (ESB)	0.09σ	0.11σ	0.99σ
Russian-Far-East (RFE)	-0.20σ	0.00σ	-0.04σ
W.C.Asia (WCA)	0.04σ	0.25σ	0.15σ
E.C.Asia (ECA)	0.13σ	0.29σ	1.27σ
Tibetan-Plateau (TIB)	-0.16σ	-0.48σ	-1.39σ
E.Asia (EAS)	-0.30σ	-0.23σ	-0.35σ
Arabian-Peninsula (ARP)	0.47σ	0.74σ	3.12σ
S.Asia (SAS)	1.03σ	1.33σ	2.26σ
S.E.Asia (SEA)	-0.16σ	-0.07σ	-0.72σ
N.Australia (NAU)	-0.03σ	-0.03σ	-0.20σ
C.Australia (CAU)	-0.16σ	-0.21σ	-0.46σ
E.Australia (EAU)	-0.41σ	-0.46σ	-0.68σ
S.Australia (SAU)	-0.61σ	-0.96σ	-1.14σ
New-Zealand (NZ)	-0.23σ	-0.10σ	-0.17σ
E.Antarctica (EAN)	-	-	-
W.Antarctica (WAN)	-	-	-

ACCEPTED VERSION SUBJECT TO FINAL EDITING

[END TABLE 11.SM.6 HERE]

[START TABLE 11.SM.7 HERE]

Table 11.SM.7: As Table 11.SM.2 but for changes in annual mean soil moisture in the upper 10 cm of the soil column.

	Projections		
	+1.5°C GWL	+2.0°C GWL	+4.0°C GWL
Global (global)	-	-	-
Ocean (ocean)	-	-	-
Land (land)	-	-	-
Land w/o Antarctica (land_wo_antarctica)	-1.40σ	-2.38σ	-6.72σ
Greenland/Iceland (GIC)	-0.92σ	-1.12σ	-3.14σ
N.W.North-America (NWN)	-0.00σ	-0.01σ	-0.93σ
N.E.North-America (NEN)	-0.45σ	-0.63σ	-2.14σ
W.North-America (WNA)	-0.70σ	-0.97σ	-1.66σ
C.North-America (CNA)	-0.59σ	-0.83σ	-1.50σ
E.North-America (ENA)	-0.78σ	-1.14σ	-2.64σ
N.Central-America (NCA)	-0.62σ	-0.76σ	-1.20σ
S.Central-America (SCA)	-1.04σ	-1.36σ	-3.43σ
Caribbean (CAR)	-0.54σ	-0.66σ	-1.44σ
N.W.South-America (NWS)	-0.95σ	-1.23σ	-3.22σ
N.South-America (NSA)	-1.06σ	-1.44σ	-2.92σ
N.E.South-America (NES)	-1.01σ	-1.25σ	-2.59σ
South-American-Monsoon (SAM)	-1.58σ	-1.92σ	-3.36σ
S.W.South-America (SWS)	-1.53σ	-1.87σ	-2.89σ
S.E.South-America (SES)	-0.39σ	-0.37σ	-0.96σ
S.South-America (SSA)	-1.25σ	-1.32σ	-2.46σ
N.Europe (NEU)	-0.88σ	-1.39σ	-3.79σ
West&Central-Europe (WCE)	-0.81σ	-1.23σ	-1.97σ
E.Europe (EEU)	-0.48σ	-0.77σ	-1.59σ
Mediterranean (MED)	-1.45σ	-2.03σ	-3.62σ
Sahara (SAH)	0.70σ	0.69σ	1.35σ
Western-Africa (WAF)	1.33σ	1.24σ	1.54σ
Central-Africa (CAF)	0.92σ	1.11σ	1.52σ
N.Eastern-Africa (NEAF)	0.56σ	0.74σ	2.22σ

ACCEPTED VERSION SUBJECT TO FINAL EDITING

S.Eastern-Africa (SEAF)	0.17σ	0.29σ	0.62σ
W.Southern-Africa (WSAF)	-0.93σ	-1.16σ	-2.08σ
E.Southern-Africa (ESAF)	-0.86σ	-1.11σ	-2.41σ
Madagascar (MDG)	-0.51σ	-0.82σ	-1.68σ
Russian-Arctic (RAR)	0.44σ	0.37σ	-1.21σ
W.Siberia (WSB)	0.21σ	0.08σ	-0.06σ
E.Siberia (ESB)	0.62σ	0.65σ	1.06σ
Russian-Far-East (RFE)	-0.07σ	-0.39σ	-1.51σ
W.C.Asia (WCA)	-0.21σ	-0.38σ	-0.55σ
E.C.Asia (ECA)	0.66σ	0.97σ	2.38σ
Tibetan-Plateau (TIB)	0.15σ	0.25σ	-0.00σ
E.Asia (EAS)	-0.43σ	-0.49σ	-0.81σ
Arabian-Peninsula (ARP)	0.20σ	0.25σ	0.64σ
S.Asia (SAS)	0.71σ	0.80σ	1.41σ
S.E.Asia (SEA)	-0.51σ	-0.34σ	-1.12σ
N.Australia (NAU)	-0.14σ	-0.14σ	-0.24σ
C.Australia (CAU)	-0.16σ	-0.21σ	-0.54σ
E.Australia (EAU)	-0.42σ	-0.41σ	-0.67σ
S.Australia (SAU)	-0.57σ	-0.62σ	-0.98σ
New-Zealand (NZ)	-0.37σ	-0.39σ	-0.37σ
E.Antarctica (EAN)	-	-	-
W.Antarctica (WAN)	-	-	-

[END TABLE 11.SM.7 HERE]

[START TABLE 11.SM.8 HERE]

Table 11.SM.8: As Table 11.SM.2 but for changes in consecutive dry days (CDD).

	Projections		
	+1.5°C GWL	+2.0°C GWL	+4.0°C GWL
Global (global)	0.91day	0.96day	1.48day
Ocean (ocean)	1.65day	1.80day	3.24day
Land (land)	-0.61day	-0.71day	-2.11day
Land w/o Antarctica (land_wo_antarctica)	0.37day	0.46day	0.73day
Greenland/Iceland (GIC)	-3.46day	-4.85day	-8.52day
N.W.North-America (NWN)	-0.91day	-1.47day	-2.51day

ACCEPTED VERSION SUBJECT TO FINAL EDITING

N.E.North-America (NEN)	-1.94day	-2.51day	-5.16day
W.North-America (WNA)	0.92day	1.00day	0.25day
C.North-America (CNA)	0.37day	0.32day	1.20day
E.North-America (ENA)	0.19day	0.27day	0.84day
N.Central-America (NCA)	3.46day	4.04day	8.48day
S.Central-America (SCA)	2.63day	4.01day	9.50day
Caribbean (CAR)	1.27day	1.56day	3.29day
N.W.South-America (NWS)	1.48day	1.78day	3.99day
N.South-America (NSA)	6.65day	9.37day	19.56day
N.E.South-America (NES)	15.14day	18.63day	28.44day
South-American-Monsoon (SAM)	8.90day	10.34day	19.05day
S.W.South-America (SWS)	4.11day	5.90day	10.09day
S.E.South-America (SES)	2.54day	2.90day	3.99day
S.South-America (SSA)	0.91day	1.16day	2.09day
N.Europe (NEU)	-0.27day	-0.06day	0.25day
West&Central-Europe (WCE)	1.03day	1.82day	4.09day
E.Europe (EEU)	0.33day	1.08day	1.83day
Mediterranean (MED)	4.96day	7.13day	16.07day
Sahara (SAH)	-8.12day	-7.92day	-15.07day
Western-Africa (WAF)	-1.07day	-0.43day	-0.79day
Central-Africa (CAF)	-1.39day	-1.05day	-1.29day
N.Eastern-Africa (NEAF)	-1.89day	-2.63day	-9.28day
S.Eastern-Africa (SEAF)	2.11day	2.50day	0.89day
W.Southern-Africa (WSAF)	9.81day	14.63day	28.84day
E.Southern-Africa (ESAF)	8.76day	11.29day	23.51day
Madagascar (MDG)	5.98day	8.23day	17.35day
Russian-Arctic (RAR)	-3.73day	-4.75day	-7.41day
W.Siberia (WSB)	-0.83day	-1.02day	-0.16day
E.Siberia (ESB)	-3.46day	-4.73day	-8.75day
Russian-Far-East (RFE)	-2.55day	-3.25day	-5.71day
W.C.Asia (WCA)	-1.07day	-0.42day	-0.55day
E.C.Asia (ECA)	-6.75day	-8.59day	-14.95day
Tibetan-Plateau (TIB)	-1.48day	-1.66day	-5.48day
E.Asia (EAS)	1.42day	0.93day	1.08day
Arabian-Peninsula (ARP)	-6.79day	-8.04day	-19.71day

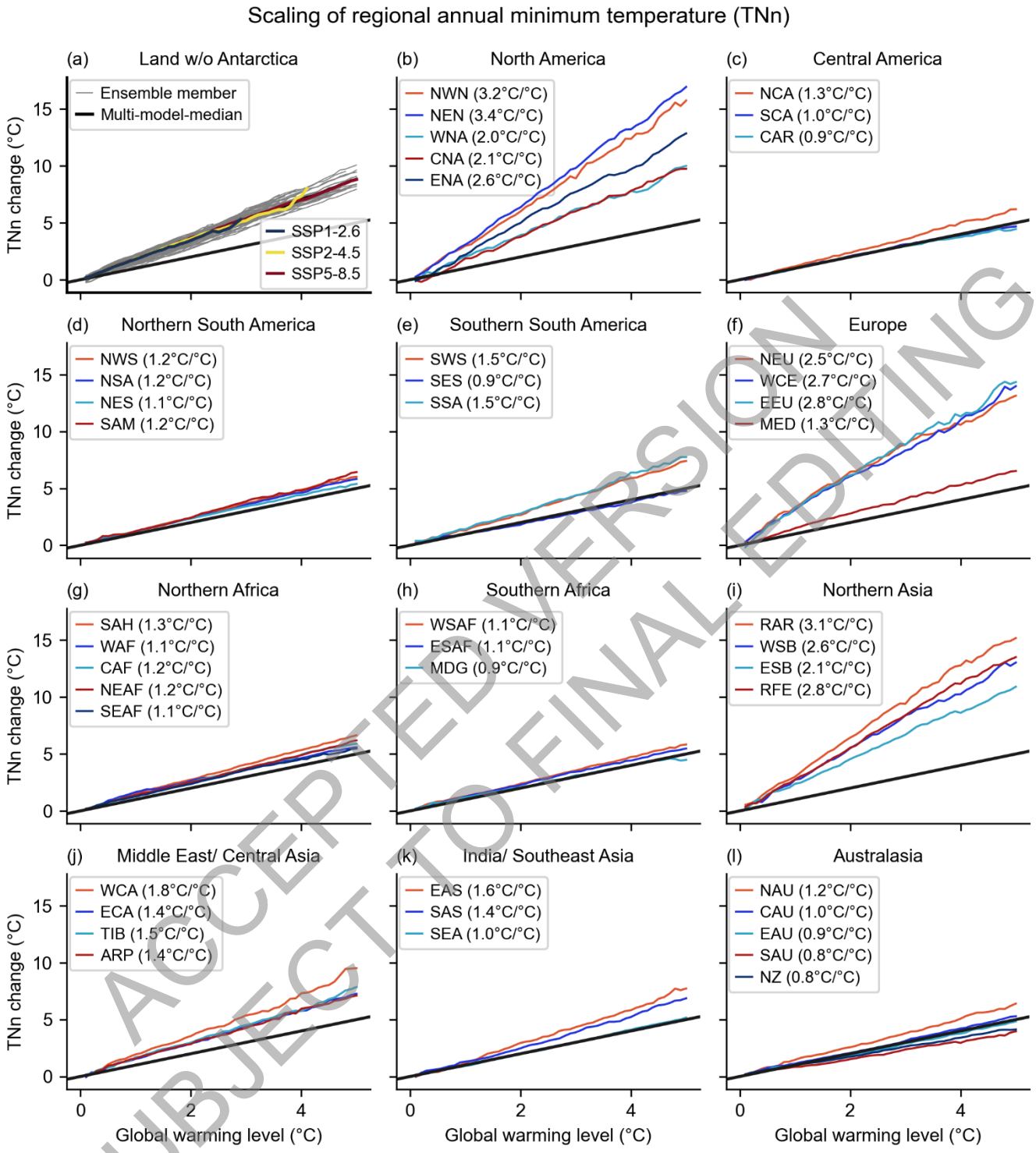
ACCEPTED VERSION SUBJECT TO FINAL EDITING

S.Asia (SAS)	-2.13day	-2.13day	-8.97day
S.E.Asia (SEA)	3.11day	3.29day	7.74day
N.Australia (NAU)	6.61day	5.46day	8.13day
C.Australia (CAU)	3.76day	4.06day	9.81day
E.Australia (EAU)	4.46day	4.37day	9.06day
S.Australia (SAU)	2.93day	3.38day	7.07day
New-Zealand (NZ)	0.11day	0.17day	0.32day
E.Antarctica (EAN)	-12.44day	-16.04day	-34.35day
W.Antarctica (WAN)	-2.09day	-2.79day	-5.22day

[END TABLE 11.SM.8 HERE]

ACCEPTED VERSION
SUBJECT TO FINAL EDITING

[START FIGURE 11.SM.1 HERE]



ACCEPTED VERSION SUBJECT TO FINAL EDITING

Figure 11.SM.1: As Figure 11.2 but for the annual minimum temperature (TNn).

[END FIGURE 11.SM.1 HERE]

11.SM.4 Data Table

[START TABLE 11.SM.9 HERE]

Table 11.SM.9: Input Data Table. Input datasets and code used to create chapter figures.

Figure number	Dataset / Code name	Type	Filename / Specificities	License type	Dataset / Code citation	Dataset / Code URL	Related publications / Software used	Notes
Figure 11.2	HadEX3 (v3.0.2) - TXx	Input dataset	HadEX3_TXx_1901-2018_ADW_61-90_1.25x1.875deg.nc	Open Government License http://www.nationalarchives.gov.uk/doc/open-government-licence/version/3/		https://www.metoffice.gov.uk/hadobs/hadex3/	(Dunn et	
	HadEX3 (v3.0.2) - TNn	Input dataset	HadEX3_TNn_1901-2018_ADW_61-90_1.25x1.875deg.nc	Open Government License		https://www.metoffice.gov.uk/hadobs/hadex3/	(Dunn et	
	Global average annual mean temperature	Input dataset	glob_temp.csv				Section 2.3.1.1.3	Data provided by from Chapter 2.
	Land average annual mean temperature	Input dataset	land_temp.csv				Section 2.3.1.1.3	Data provided by from Chapter 2.

ACCEPTED VERSION SUBJECT TO FINAL EDITING

	Figure 11.2 code	Code	Figure_11.2_obs_ts_plots.ipynb					
Figure 11.3	Figure 11.3 code	Code	Figure_11.3_TXx_scaling.ipynb					
Box 11.1, Figure 1	Changes in annual maximum precipitation	Input dataset	pfahl_2017.nc				(Pfahl,	Data provided by Stephan Pfahl.
	Box 11.1, Figure 1 code	Code	Box_11.1_Figure_1_Pfahl_2017.ipynb					
Figure 11.6	Figure 11.6 input dataset	Input dataset	Changes in txx_baseline0deg.xlsx				(Li et al., 2020)	Figure created by Chao Li.
Figure 11.7	Figure 11.7 input dataset	Input dataset	Changes in rx1day_baseline0deg.xlsx				(Li et al., 2020)	Figure created by Chao Li.
Figure 11.9	HadEX3 (v3.0.2) - TXx	Input dataset	HadEX3_TXx_1901-2018_ADW_61-	Open Government License		https://www.metoffice.gov.uk/hadobs/hadex3/	(Dunn et al., 2020)	

ACCEPTED VERSION SUBJECT TO FINAL EDITING

			90_1.25x1.875deg.nc					
	HadEX3 (v3.0.2) – TX90p	Input dataset	HadEX3_TX90p_1901-2018_ADW_61-90_1.25x1.875deg.nc	Open Government License		https://www.metoffice.gov.uk/hadobs/hadex3/	(Dunn et al., 2020)	Converted from % to days per year.
	HadEX3 (v3.0.2) - TNn	Input dataset	HadEX3_TNn_1901-2018_ADW_61-90_1.25x1.875deg.nc	Open Government License		https://www.metoffice.gov.uk/hadobs/hadex3/	(Dunn et	
	Figure 11.9 code	Code	Figure_11.9_HadEX3_maps.ipynb					
Figure 11.10	CMIP6 data	Input dataset	TXx_TNn_error_CMIP6.nc				(Wehner, Gleckler, & Lee, 2020)	Data provided by Michael Wehner..
	Figure 11.10	Code	Figure_11.10_Wehner_temperature_bias.ipynb					
Figure 11.11	Figure 11.11 code for annual maximum temperature (TXx)	Code	Figure_11.11_TXx_map.ipynb					
	Figure 11.11 code for annual maximum temperature (TNn)	Code	Figure_11.11_TNn_map.ipynb					

ACCEPTED VERSION SUBJECT TO FINAL EDITING

Figure 11.12	Figure 11.12 input dataset	Input dataset	Changes in txx_baseline 0deg.xlsx				(Li et al., 2020)	Figure created by Chao Li.
Figure 11.13	Figure 11.13a	Input dataset					(Sun,	Panel a created by Qiaohong Sun
	Figure 11.13 b and c	Input dataset	station_MK_1950_2018.csv				(Sun et al.,	Data provided by Qiaohong Sun.

ACCEPTED VERSION
SUBJECT TO FINAL EDITING

	Code for Figure 11.13 b and c	Code	Figure_11.13_Rx1day_trend_maps_Sun.ipynb					
Figure 11.14	Bias of CMIP6 w.r.t ERA5	Input dataset	Rx_CMIP6_errors_ERA5.nc				(Wehner et al., 2020)	Data provided by Michael Wehner.
	Bias of CMIP6 w.r.t HadEX3	Input dataset	Rx_CMIP6_errors_HadEx3.nc				(Wehner et al., 2020)	Data provided by Michael Wehner.
	Bias of CMIP6 w.r.t REGEN	Input dataset	Rx_CMIP6_errors_REGEN.nc				(Wehner et al., 2020)	Data provided by Michael Wehner.
	Figure 11.14 code	Code	Figure_11.14_Wehner_precipitation_bias.ipynb					
Figure 11.15	Figure 11.15 input dataset	Input dataset	Changes in rx1day_baseline0deg.xlsx				(Li et al., 2020)	Figure created by Chao Li.
Figure 11.16	Figure 11.16 code	Code	Figure_11.16_Rx1day_map.ipynb					
Figure 11.17	HadEX3 (v3.0.2) - CDD	Input dataset	HadEX3_CDD_1901-2018_ADW_61-90_1.25x1.875deg.nc	Open Government License		https://www.metoffice.gov.uk/hadobs/hadex3/	(Dunn et al., 2020)	
	SPI-12 and SPEI-12 trends	Input dataset	results_spinoni_01.nc				(Spinoni et al., 2019)	SPI & SPEI data from (Spinoni et al., 2019) processed by Sergio Vincente Serrano.
	Figure 11.17 code	Code	Figure_11.17_CDD_SPI_SPEI.ipynb					

ACCEPTED VERSION SUBJECT TO FINAL EDITING

Figure 11.18	Figure 11.18 code	Code	SMDroughtIndex.ipynb					
Figure 11.19	code for CDD	Code	Figure_11.19_CDD_map.ipynb					
	code for total soil moisture	Code	Figure_11.19_SM_map.ipynb					
	code for soil moisture based drought frequency	Code	SMDroughtIndex.ipynb					
Box 11.4, Figure 1	Input dataset Box 11.4 Figure 2	Input dataset	sippel_2015_fig3.txt				(Sippel et al., 2015)	Data provided by Sebsatian Sippel..
	Box 11.4, Figure 1 code	Code	Box_11.4_Figure_1_Sippel_2015.ipynb					
Box 11.4 Figure 2	Global ECMWF Reanalysis v5 (ERA5) - temperature	Input dataset	era5_deterministic_recent.t2m.025deg.1m.*.nc	Copernicus License https://cds.climate.copernicus.eu/api/v2/terms/static/licence-to-use-copernicus-products.pdf			(Hersbach et al., 2020)	
	Global ECMWF Reanalysis v5 (ERA5) - geopotential	Input dataset	era5_deterministic_recent.z200.025deg.1m.2018.nc	Copernicus License			(Hersbach et al., 2020)	
	Box 11.4, Figure 2 code	Code	Box_11.4_Figure_2_2018.ipynb					

ACCEPTED VERSION SUBJECT TO FINAL EDITING

FAQ 11.1, Figure 1	FAQ 11.1 Figure 1	Code	FAQ_11.1_Figure_1_mean_vs_extreme.ipynb					

[END TABLE 11.SM.9 HERE]

ACCEPTED VERSION
SUBJECT TO FINAL EDITING

References

Dunn, R. J. H., Alexander, L. V., Donat, M. G., Zhang, X., Bador, M., Herold, N., … Bin Hj Yussof, M. N. (2020). Development of an Updated Global Land In Situ-Based Data Set of Temperature and Precipitation Extremes: HadEX3. *Journal of Geophysical Research: Atmospheres*, *125*(16). http://doi.org/10.1029/2019JD032263

Eyring, V., Bony, S., Meehl, G. A., Senior, C. A., Stevens, B., Stouffer, R. J., & Taylor, K. E. (2016). Overview of the Coupled Model Intercomparison Project Phase 6 (CMIP6) experimental design and organization. *Geoscientific Model Development*, *9*(5). http://doi.org/10.5194/gmd-9-1937-2016

Hamed, K. H., & Ramachandra Rao, A. (1998). A modified Mann-Kendall trend test for autocorrelated data. *Journal of Hydrology*, *204*(1–4). http://doi.org/10.1016/S0022-1694(97)00125-X

Hauser, M. (2021a). Multi-model-median regional means at warming levels for selected indices (CMIP6). http://doi.org/10.5281/ZENODO.4603428

Hauser, M. (2021b, March 12). Mean temperature anomalies for CMIP5 and CMIP6 (Version v0.1.0). http://doi.org/10.5281/ZENODO.4600696

Hauser, M., Engelbrecht, F., & Fischer, E. M. (2021, March 12). Transient global warming levels for CMIP5 and CMIP6 (Version v0.2.0). http://doi.org/10.5281/ZENODO.4600706

Hersbach, H., Bell, B., Berrisford, P., Hirahara, S., Horányi, A., Muñoz-Sabater, J., … Thépaut, J. (2020). The ERA5 global reanalysis. *Quarterly Journal of the Royal Meteorological Society*, *146*(730), 1999–2049. http://doi.org/10.1002/qj.3803

Karl, T. R., Nicholls, N., & Ghazi, A. (1999). CLIVAR/GCOS/WMO Workshop on Indices and Indicators for Climate Extremes - Workshop summary. In S1755 (Trans.), *Climatic Change*. http://doi.org/10.1023/A:1005491526870

Li, C., Zwiers, F., Zhang, X., Li, G., Sun, Y., & Wehner, M. (2020). Changes in annual extremes of daily temperature and precipitation in CMIP6 models. *Journal of Climate*, 1–61. http://doi.org/10.1175/JCLI-D-19-1013.1

O'Neill, B. C., Tebaldi, C., Van Vuuren, D. P., Eyring, V., Friedlingstein, P., Hurtt, G., … Sanderson, B. M. (2016). The Scenario Model Intercomparison Project (ScenarioMIP) for CMIP6. *Geoscientific Model Development*, *9*(9). http://doi.org/10.5194/gmd-9-3461-2016

Peterson, T. C., Folland, C., Gruza, G., Hogg, W., Mokssit, A., & Plummer, N. (2001). *Report on the activities of the Working Group on Climate Change Detection and Related Rapporteurs 1998–2001*. (S1754, Trans.)*Climate Change Detection*.

Pfahl, S., O'Gorman, P. A., & Fischer, E. M. (2017). Understanding the regional pattern of projected future changes in extreme precipitation. *Nature Climate Change*, *7*, 423. http://doi.org/10.1038/nclimate3287

Sippel, S., Zscheischler, J., Heimann, M., Otto, F. E. L., Peters, J., & Mahecha, M. D. (2015). Quantifying changes in climate variability and extremes: Pitfalls and their overcoming. *Geophysical Research Letters*, *42*(22), 9990–9998. http://doi.org/10.1002/2015GL066307

Spinoni, J., Barbosa, P., De Jager, A., McCormick, N., Naumann, G., Vogt, J. V., … Mazzeschi, M. (2019). A new global database of meteorological drought events from 1951 to 2016. *Journal of Hydrology: Regional Studies*, *22*, 100593. http://doi.org/10.1016/J.EJRH.2019.100593

Sun, Q., Zhang, X., Zwiers, F., Westra, S., & Alexander, L. V. (2020). A global, continental and regional analysis of changes in extreme precipitation. *Journal of Climate*, 1–52. http://doi.org/10.1175/JCLI-D-19-0892.1

Wehner, M., Gleckler, P., & Lee, J. (2020). Characterization of long period return values of extreme daily temperature and precipitation in the CMIP6 models: Part 1, model evaluation. *Weather and Climate Extremes*, *30*, 100283. http://doi.org/10.1016/j.wace.2020.100283

ACCEPTED VERSION SUBJECT TO FINAL EDITING

Chapter 12: Climate change information for regional impact and for risk assessment

Coordinating Lead Authors:
Roshanka Ranasinghe (The Netherlands/Sri Lanka, Australia), Alex C. Ruane (United States of America), Robert Vautard (France)

Lead Authors:
Nigel Arnell (United Kingdom), Erika Coppola (Italy), Faye Abigail Cruz (Philippines), Suraje Dessai (United Kingdom/Portugal), Akm Saiful Islam (Bangladesh), Mohammad Rahimi (Iran), Daniel Ruiz Carrascal (United States of America/Columbia), Jana Sillmann (Norway/Germany), Mouhamadou Bamba Sylla (Rwanda/Senegal), Claudia Tebaldi (United States of America), Wen Wang (China), Rashyd Zaaboul (United Arab Emirates/Morocco)

Contributing Authors:
Carley E. Iles (Norway, France/ United Kingdom), Jérôme Servonnat (France), Guðfinna Aðalgeirsdóttir (Iceland), Rita Adrian (Germany), Roxana Bojariu (Romania), Laurent Bopp (France), Audrey Brouillet (France), Carlo Buontempo (United Kingdom/Italy), Winston Chow (Singapore), Augustin Colette (France), Cecilia Conde (Mexico), Leticia Cotrim da Cunha (Brazil), Claudine Dereczynski (Brazil), Alejandro Di Luca (Australia, Canada/Argentina), Fabio Di Sante (Italy), Arona Diedhiou (Côte d'Ivoire/Senegal), Aida Diongue-Niang (Senegal), Francisco J. Doblas-Reyes (Spain), Pariva Dobriyal (India), Sybren S. Drijfhout (The Netherlands), John P. Dunne (United States of America), Tamsin L. Edwards (United Kingdom), Aidan D. Farrell (Trinidad and Tobago/Ireland), Erich Fischer (Switzerland), John C. Fyfe (Canada), Alexander Gelfan (Russian Federation), Subimal Ghosh (India), Irina V. Gorodetskaya (Portugal/Belgium, Russian Federation), Michael Grose (Australia), José Manuel Gutiérrez (Spain), David S. Gutzler (United States of America), Rebecca Harris (Australia), Matthias Hauser (Switzerland), Mark Hemer (Australia), Kevin Hennessy (Australia), Helene T. Hewitt (United Kingdom), Masao Ishii (Japan), Maialen Iturbide (Spain), Christopher D. Jack (South Africa), Richard G. Jones (United Kingdom), Nikolay Kadygrov (France/Russian Federation), Ebru Kirezci (Australia/Turkey), Nana Ama Browne Klutse (Ghana), Robert E. Kopp (United States of America), James Kossin (United States of America), Charles Koven (United States of America), Svitlana Krakovska (Ukraine), Gerhard Krinner (France/Germany, France), Benjamin L. Lamptey (Niger, Ghana/Ghana), Christopher Lennard (South Africa), Xianfu Lu (United Kingdom/China), Douglas Maraun (Austria/Germany), Simon McGree (Australia/Fiji, Australia), Glenn McGregor (United Kingdom/New Zealand, United Kingdom), Kathleen L. McInnes (Australia), Dirk Notz (Germany), Brian O'Neill (United States of America), Ben Orlove (United States of America), Friederike Otto (United Kingdom/Germany), Carlos Pérez García-Pando (Spain), Franz Prettenthaler (Austria), Francesca Raffaele (Italy), Srivatsan Raghavan (Singapore/India), Christophe F. Randin (Switzerland/France, Switzerland), Johan Reyns (The Netherlands/Belgium), Lucas Ruiz (Argentina), Fahad Saeed (Germany/Pakistan), Jean-Baptiste Sallee (France), Marit Sandstad (Norway), Clemens Schwingshackl (Norway, Germany/Italy), Sonia I. Seneviratne (Switzerland), Aimée B. A. Slangen (The Netherlands), Tannecia S. Stephenson (Jamaica), Anna Steynor (South Africa), Markus Stoffel (Switzerland), Benjamin Sultan (France), William V. Sweet (United States of America), Sophie Szopa (France), Izuru Takayabu (Japan), Moustapha Tall (Rwanda/Senegal), N'Datchoh Evelyne Touré N'Datchoh (Cote d'Ivoire), Bart van den Hurk (The Netherlands), Sergio M. Vicente-Serrano (Spain), Michalis Vousdoukas (Italy, Greece/Greece), Morgan Wairiu (Fiji), Prodromos Zanis (Greece), Xuebin Zhang (Canada)

Review Editors:
Edvin Aldrian (Indonesia), David Karoly (Australia), Murat Türkeş (Turkey)

ACCEPTED VERSION SUBJECT TO FINAL EDITS

Chapter Scientists:
Carley Iles (Norway, France/ United Kingdom), Jérôme Servonnat (France)

This Chapter should be cited as:
Ranasinghe, R., A. C. Ruane, R. Vautard, N. Arnell, E. Coppola, F. A. Cruz, S. Dessai, A. S. Islam, M. Rahimi, D. Ruiz Carrascal, J. Sillmann, M. B. Sylla, C. Tebaldi, W. Wang, R. Zaaboul, 2021, Climate Change Information for Regional Impact and for Risk Assessment. In: *Climate Change 2021: The Physical Science Basis. Contribution of Working Group I to the Sixth Assessment Report of the Intergovernmental Panel on Climate Change* [Masson-Delmotte, V., P. Zhai, A. Pirani, S. L. Connors, C. Péan, S. Berger, N. Caud, Y. Chen, L. Goldfarb, M. I. Gomis, M. Huang, K. Leitzell, E. Lonnoy, J. B. R. Matthews, T. K. Maycock, T. Waterfield, O. Yelekçi, R. Yu and B. Zhou (eds.)]. Cambridge University Press. In Press.

Date: August 2021

This document is subject to copy-editing, corrigenda and trickle backs.

ACCEPTED VERSION
SUBJECT TO FINAL EDITS

Table of content

Executive Summary **6**
12.1 Framing **9**
12.2 Methodological approach **11**
12.3 Climatic impact-drivers for sectors **14**
12.3.1 Heat and cold 16
12.3.1.1 Mean air temperature 16
12.3.1.2 Extreme heat 17
12.3.1.3 Cold spells 18
12.3.1.4 Frost 18
12.3.2 Wet and dry 19
12.3.2.1 Mean precipitation 19
12.3.2.2 River flood 20
12.3.2.3 Heavy precipitation and pluvial flood 20
12.3.2.4 Landslide 20
12.3.2.5 Aridity 21
12.3.2.6 Hydrological drought 21
12.3.2.7 Agricultural and ecological drought 21
12.3.2.8 Fire weather 22
12.3.3 Wind 22
12.3.3.1 Mean wind speed 22
12.3.3.2 Severe wind storm 22
12.3.3.3 Tropical cyclone 22
12.3.3.4 Sand and dust storm 23
12.3.4 Snow and ice 23
12.3.4.1 Snow, glacier and ice sheet 23
12.3.4.2 Permafrost 24
12.3.4.3 Lake, river and sea ice 24
12.3.4.4 Heavy snowfall and ice storm 24
12.3.4.5 Hail 24
12.3.4.6 Snow avalanche 24
12.3.5 Coastal 25
12.3.5.1 Relative sea level 25
12.3.5.2 Coastal flood 25
12.3.5.3 Coastal erosion 25
12.3.6 Oceanic 26

ACCEPTED VERSION
SUBJECT TO FINAL EDITS

12.3.6.1 Mean ocean temperature 26
12.3.6.2 Marine heatwave 26
12.3.6.3 Ocean acidity 26
12.3.6.4 Ocean Salinity 27
12.3.6.5 Dissolved oxygen 27
12.3.7 Other climatic impact-drivers 27
12.3.7.1 Air pollution weather 27
12.3.7.2 Atmospheric Carbon Dioxide (CO_2) at surface 27
12.3.7.3 Radiation at surface 28
12.3.7.4 Additional relevant climatic impact-drivers 28
12.4 Regional information on changing climate 29
12.4.1 Africa 32
12.4.1.1 Heat and cold 32
12.4.1.2 Wet and dry 33
12.4.1.3 Wind 36
12.4.1.4 Snow and Ice 37
12.4.1.5 Coastal and Oceanic 37
12.4.2 Asia 39
12.4.2.1 Heat and cold 40
12.4.2.2 Wet and dry 41
12.4.2.3 Wind 43
12.4.2.4 Snow and Ice 45
12.4.2.5 Coastal and oceanic 46
12.4.3 Australasia 48
12.4.3.1 Heat and Cold 49
12.4.3.2 Wet and Dry 51
12.4.3.3 Wind 54
12.4.3.4 Snow and Ice 55
12.4.3.5 Coastal and Oceanic 55
12.4.4 Central and South America 58
12.4.4.1 Heat and cold 59
12.4.4.2 Wet and dry 60
12.4.4.3 Wind 62
12.4.4.4 Snow and ice 63
12.4.4.5 Coastal and oceanic 64
12.4.5 Europe 66

ACCEPTED VERSION
SUBJECT TO FINAL EDITS

12.4.5.1 Heat and Cold 67
12.4.5.2 Wet and Dry 68
12.4.5.3 Wind 71
12.4.5.4 Snow and ice 72
12.4.5.5 Coastal and Oceanic 73
12.4.5.6 Other 75
12.4.6 North America 76
12.4.6.1 Heat and cold 77
12.4.6.2 Wet and dry 78
12.4.6.3 Wind 81
12.4.6.4 Snow and ice 82
12.4.6.5 Coastal and oceanic 84
12.4.7 Small islands 86
12.4.7.1 Heat and Cold 87
12.4.7.2 Wet and Dry 88
12.4.7.3 Wind 90
12.4.7.4 Coastal and Oceanic 90
12.4.8 Open and deep ocean 93
12.4.9 Polar terrestrial regions 96
12.4.9.1 Heat and cold 96
12.4.9.2 Wet and dry 97
12.4.9.3 Wind 97
12.4.9.4 Snow and ice 98
12.4.9.5 Coastal and oceanic 99
12.4.10 Specific zones and hotspots 101
12.4.10.1 Hotspots of biodiversity (land, coasts and oceans) 101
12.4.10.2 Cities and settlements by the sea 102
12.4.10.3 Deserts and semi-arid areas 103
12.4.10.4 Mountains 104
12.4.10.5 Tropical forests 105
12.5 Global perspective on climatic impact-drivers 106
12.5.1 A global synthesis 106
12.5.2 The emergence of climatic impact-drivers across time and scenarios 108
Cross-Chapter Box 12.1: Projections by warming levels of hazards relevant to the assessment of Representative Key Risks and Reasons for Concern 113
12.6 Climate change information in climate services 120

ACCEPTED VERSION
SUBJECT TO FINAL EDITS

12.6.1 Context of climate services 120
12.6.2 Assessment of climate services practice and products related to climate change information 121
12.6.3 Challenges 123
Cross-Chapter Box 12.2: Climate services and climate change information 124
12.7 Final Remarks 128
Frequently Asked Questions 129
References 135
Figures 205

ACCEPTED VERSION
SUBJECT TO FINAL EDITS

Executive Summary

Climate change information is increasingly available and robust at regional scale for impacts and risk assessment. Climate services and vulnerability, impacts, and adaptation studies require regional scale multi-decadal climate observations and projections. Since AR5, the increased availability of coordinated ensemble regional climate model projections and improvements in the level of sophistication and resolution of global and regional climate models, completed by attribution and sectoral vulnerability studies, have enabled the investigation of past and future evolution of a range of climatic quantities that are relevant to socio-economic sectors and natural systems. Chapter 12 consolidates core physical knowledge from preceding AR6 WGI chapters and post-AR5 climate impact assessment literature to assess the spatio-temporal evolution of the climatic conditions that may lead to regional scale impacts and risks (following the sectoral classes adopted by AR6 WGII) in the world's regions (presented in Chapter 1) {12.1}

The Climatic Impact-Driver (CID) framework adopted in Chapter 12 allows for assessment of changing climate conditions that are relevant for sectoral impacts and risks assessment. CIDs are physical climate system conditions (e.g., means, events, extremes) that affect an element of society or ecosystems and are thus a priority for climate information provision. Depending on system tolerance, CIDs and their changes can be detrimental, beneficial, neutral, or a mixture of each across interacting system elements, regions and society sectors. Each sector is affected by multiple CIDs, and each CID affects multiple sectors. A CID can be measured by indices to represent related tolerance thresholds. {12.1-12.3}

The current climate in most regions is already different from the climate of the early or mid 20th century with respect to several CIDs. Climate change has already altered CID profiles and resulted in shifts in the magnitude, frequency, duration, seasonality, and spatial extent of associated indices (*high confidence*). Changes in temperature-related CIDs such as mean temperatures, growing season length, extreme heat, frost, have already occurred and many of these changes have been attributed to human activities (*medium confidence*). Mean temperatures and heat extremes have emerged above natural variability in all land regions with *high confidence*. In tropical regions, recent past temperature distributions have already shifted to a range different to that of the early 20th century (*high confidence*). Ocean acidification and deoxygenation have already emerged over most of the global open ocean, as has reduction in Arctic sea ice (*high confidence*). Using CID index distributions and event probabilities accurately in both current and future risk assessments requires taking into account the climate change–induced shifts in distributions that have already occurred {12.4, 12.5}

Several impact-relevant changes have not yet emerged from the natural variability, but will emerge sooner or later in this century depending on the emission scenario (*high confidence*). Increasing precipitation is projected to emerge before the middle of the century in the high latitudes of the Northern hemisphere (*high confidence*). Decreasing precipitation will emerge in a very few regions (Mediterranean, South Africa, South Western Australia) (*medium confidence*) by the mid-century (*medium confidence*). The anthropogenic forced signal in near-coast relative sea-level rise will emerge by mid-century RCP8.5 in all regions with coasts, except in the West Antarctic region where emergence is projected to occur before 2100 (*medium confidence*). The signal of ocean acidification in the surface ocean is projected to emerge before 2050 in every ocean basin (*high confidence*). However, there is *low evidence* of emerging drought trends above natural variability in the 21st century {12.5}.

Every region of the world will experience concurrent changes in multiple CIDs by mid-century (*high confidence*), challenging the resilience and adaptation capacity of the region. Heat, cold, snow and ice, coastal oceanic, and CO_2 at surface CID changes are projected with *high confidence* in most regions, indicating worldwide challenges, while additional region-specific changes are projected in other CIDs that may lead to more regional challenges. *High confidence* increases in some of the drought, aridity, and fire weather CIDs will challenge, for example, agriculture, forestry, water systems, health and ecosystems in Southern Africa, the Mediterranean, North Central America, Western North America, the Amazon regions, South-western South America, and Australia. *High confidence* changes in snow, ice and pluvial or river flooding changes will pose challenges for, for example, energy production, river transportation, ecosystems, infrastructure and winter tourism in North America, Arctic regions, Andes regions, Europe, Siberia, Central,

ACCEPTED VERSION SUBJECT TO FINAL EDITS

South and East Asia, Southern Australia and New Zealand. Only a few CIDs are projected to change with *high confidence* in the Sahara, Madagascar, Arabian Peninsula, Western Africa, Small Islands; however, the lower confidence levels for CID changes in these regions can originate from knowledge gaps or model uncertainties, and does not necessarily mean that these regions have relatively low risk. {12.5}

Worldwide changes in heat, cold, snow and ice, coastal, oceanic and CO_2-related CIDs will continue over the 21st century, albeit with regionally varying rates of change, regardless of the climate scenario (*high confidence*). In all regions, there is *high confidence* that, by 2050, mean temperature and heat extremes will increase, and there is *high confidence* that sea surface temperature will increase in all oceanic regions, excepting the North Atlantic. With the exception of a few regions with substantial land uplift, relative sea-level rise is *very likely to virtually certain* (depending on the region) to continue along the 21st century, contributing to increased coastal flooding in most low-lying coastal areas (*high confidence*) and coastal erosion along most sandy coasts (*high confidence*), while ocean acidification is *virtually certain* to increase. It is *virtually certain* that atmospheric CO_2 at the surface will increase in all emissions scenarios until net-zero emissions are achieved. Glaciers will continue to shrink and permafrost to thaw in all regions where they are present (*high confidence*). These changes will lead to climate states with no recent analogue that are of particular importance for specific regions such as tropical forests or biodiversity hotspots. {12.4}

A wide range of region-specific CID changes relative to recent past are expected with *high* or *medium confidence*, by 2050 and beyond. Most of these changes are concerning CIDs related to the water cycle and storms. Agricultural and ecological drought changes are generally of higher confidence than hydrological drought changes, with increases projected in North and Southern Africa, Madagascar, Southern and Eastern Australia, some regions of Central and South America, Mediterranean Europe, Western North America and North Central America (*medium to high confidence*). Fire weather conditions will increase by 2050 under RCP4.5 or above in several regions in Africa, Australia, several regions of South America, Mediterranean Europe, and North America (*medium to high confidence*). Extreme precipitation and pluvial flooding will increase in many regions around the world (*high confidence*). Increases in river flooding are also expected in Western and Central Europe and in polar regions (*high confidence*), most of Asia, Australasia and North America, South American Monsoon and Southeastern South America (*medium confidence*). Mean winds are projected to slightly decrease by 2050 over much of Europe, Asia, and Western North America, and increase in many parts of South America except Patagonia, West and South Africa and Eastern Mediterranean (*medium confidence*). Storms are expected to have a decreasing frequency but increasing intensity over the Mediterranean, most of North America, and increase over most of Europe. Enhanced convective conditions are expected in North America (*medium confidence*). Tropical cyclones are expected to increase in intensity despite a decrease in frequency in most tropical regions (*medium confidence*). Climate change will modify multiple CIDs for small islands in all ocean basins, most notably those related to heat, aridity and droughts, tropical cyclones and coastal impacts. {12.4}

The level of confidence in the projected direction of change in CIDs and the intensity of the signal depend on mitigation efforts over the 21st century, as reflected by the differences between end-century projections for different climate scenarios. Dangerous humid heat thresholds, such as the NOAA HI of 41°C, will be exceeded much more frequently under SSP5-8.5 scenario than under SSP1-2.6 and will affect many regions (*high confidence*). In many tropical regions, the number of days per year where a HI of 41°C is exceeded will increase by more than 100 days relative to the recent past under SSP5-8.5, while this increase will be limited to less than 50 days under SSP1-2.6 (*high confidence*). The number of days per year where temperature exceeds 35°C will increase by more than 150 days in many tropical areas, such as the Amazon basin and South-east Asia under SSP5-8.5, while it is expected to increase by less than 2 months in these areas under SSP1-2.6 (except for the Amazon Basin). There is *high confidence* that the total length of sandy shorelines around the world that are projected to retreat by more than 100 m will be 35% greater under RCP8.5 (~130,000 km) compared to RCP4.5 (~ 95,000 km) by the end of the century. The frequency of the present-day 1-in-100-yr extreme sea level (represented here by extreme total water level) event, in a globally averaged sense, is projected to become an event that occurs multiple times per year under RCP8.5, while under RCP 4.5 it is projected to become a 1-in-5-yr event, representing a 5 fold difference between the two RCPs (*high confidence*).{12.4, 12.5}

ACCEPTED VERSION SUBJECT TO FINAL EDITS

There is *low confidence* in past and future changes of several CIDs. In nearly all regions there is *low confidence* in changes in hail, ice storms, severe storms, dust storms, heavy snowfall, and avalanches, although this does not indicate that these CIDs will not be affected by climate change. For such CIDs, observations are short-term or lack homogeneity, and models often do not have sufficient resolution or accurate parametrizations to adequately simulate them over climate change time scales. {12.4}.

Many global- and regional-scale CIDs have a direct relation to global warming levels (GWLs) and can thus inform the hazard component of 'Representative Key Risks' and 'Reasons for Concern' assessed by AR6 WGII. These include heat, cold, wet and dry hazards, both mean and extremes; cryospheric hazards (snow cover, ice extent, permafrost) and oceanic hazards (marine heatwaves) *(high confidence)*. For some of these, a quantitative relation can be drawn *(high confidence)*. For example, with each degree of GSAT warming, the magnitude and intensity of many heat extremes show a linear change, while some changes in frequency of threshold exceedances are exponential; arctic temperatures warm about twice as fast as GSAT; global SSTs increase by ~80% of GSAT change; Northern Hemisphere spring snow cover decreases by ~8% per 1°C. For other hazards (e.g., ice sheet behaviour, glacier mass loss, global mean sea-level rise, coastal floods and coastal erosion) the time and/or scenario dimensions remain critical and a simple relation with GWLs cannot be drawn *(high confidence)*, but still quantitative estimates assuming specific time frames, and/or stabilized GWLs can be derived *(medium confidence)*. Model uncertainty challenges the link between specific GWLs and tipping points and irreversible behavior, but their occurrence cannot be excluded and their chances increase with warming levels *(medium confidence)* {CCB 12.1}.

Since AR5, climate change information produced in climate service contexts has increased significantly due to scientific and technological advancements and growing user demand *(very high confidence*)**.** Climate services involve the provision of climate information in such a way as to assist decision-making. These services include appropriate engagement from users and providers, are based on scientifically credible information and expertise, have an effective access mechanism, and respond to user needs.. Climate services are being developed across regions, sectors, timescales and target users. {12.6}

Climate services are growing rapidly and are highly diverse in their practices and products (*very high confidence*). The decision-making context, level of user engagement and co-production between scientists, practitioners and intended users are important determinants of the type of climate service developed and its utility supporting adaptation, mitigation and risk management decisions. User needs and decision-making contexts are very diverse and there is no universal approach to climate services. {12.6}

Realization of the full potential of climate services is often hindered by limited resources for the co-design and co-production process, including sustained engagement between scientists, service providers and users (*high confidence*). Further challenges relate to climate services development, provision of climate services, generation of climate service products, communication with users, and evaluation of the quality and socio-economic value of climate services. The development of climate services often uncovers and presents new research challenges to the scientific community. {12.6}

ACCEPTED VERSION SUBJECT TO FINAL EDITS

12.1 Framing

Climate change is already resulting in significant societal and environmental impacts and will induce major socio-economic damages in the future (AR5 WGII). The society, at large, benefits from information related to climate change risks, which enables the development of options to protect lives, preserve nature, build resilience and prevent avoidable loss and damage. Climate change can also lead to beneficial conditions which can be taken into account in adaptation strategies.

This chapter assesses climate information relevant to regional impact and risk assessment. It complements other WG1 chapters which focus on the physical processes determining changes in the climate system and on methods for estimating regional changes.

Impacts of climate change are driven not only by changes in climate conditions, but also by changes in exposure and vulnerability (Cross-Chapter Box 1.3). This chapter concentrates on drivers of impacts that are of climatic origin (see also SR1.5 (IPCC, 2018), and Section 1.3.2), referred to in WGI as "climatic impact-drivers" (CIDs). CIDs are physical climate system conditions (e.g., means, events, extremes) that affect an element of society or ecosystems. Depending on system tolerance, CIDs and their changes can be detrimental, beneficial, neutral, or a mixture of each across interacting system elements and regions. However, this chapter largely focuses on drivers commonly connected to hazards, and adopts the IPCC risk framework (Chapter 1, Cross-Chapter Box 1.3) since the main objective of the UNFCCC convention is to "prevent dangerous anthropogenic interference with the climate system" (Article 2).

In some cases, risk assessments may require climate information beyond the CIDs identified in this chapter, with further impacts or risk modelling often driven by historical climate forcing datasets (e.g., Ruane et al., 2021) and full climate scenario time series (e.g., Lange, 2019) produced using methods described in Chapter 10. Chapter 12 focuses on the assessment of a finite number of drivers and how they are projected to evolve with climate change, in order to inform impact and risk assessments.

This chapter is new IPCC WGI assessment reports, in that it represents a contribution to the "IPCC Risk Framework". Within this framework, climate-related impacts and risks are determined through an interplay between the occurrence of climate hazards and their consequences depending on the exposure of the affected human or natural system and its vulnerability to the hazardous conditions. In Chapter 12, we are assessing climatic impact-drivers that could lead to hazards or to opportunities, from the literature and model results since AR5. This will particularly support the assessment of key risks related to climate change by WGII (Chapter 16). Despite the fact that impacts may also be induced by climate adaptation and mitigation policies themselves, as well as by socioeconomic trends, changes in vulnerability or exposure, and external geophysical hazards such as volcanoes, the focus here is only on 'climatic' impacts and risks induced by shifts in physical climate phenomena that directly influence human and ecological systems.

This chapter follows the terminology associated with the framing introduced in Chapter 1 (Cross-chapter Box 1.2: Baseline and reference periods in AR6) and as found in the AR6 Glossary. The highlighted terms below are introduced and used extensively in this chapter:

- **Indices for climatic impact-drivers**: numerically computable indices using one or a combination of climate variables designed to measure the intensity of the climatic impact-driver, or the probability of exceedance of a threshold. For instance, an index of heat inducing human health stress is the Heat Index (HI) that combines temperature and relative humidity (e.g., Burkart et al., 2011; Lin et al., 2012; Kent et al., 2014) and is used by the US National Oceanic and Atmospheric Administration (NOAA) for issuing heat warnings.
- **Thresholds for climatic impact-drivers**: an identified index value beyond which a climatic impact-driver interacts with vulnerability or exposure to create, increase or reduce an impact, risk or opportunity. Thresholds can be used to measure various aspects of the climatic impact-driver (magnitude or intensity, duration, frequency, timing, and spatial extent of threshold exceedance). For instance, a threshold of daily maximum temperature above 35ºC is considered critical for maize pollination and production (e.g., Schauberger et al., 2017; Tesfaye et al., 2017).

ACCEPTED VERSION SUBJECT TO FINAL EDITS

The approach adopted here is consistent with the United Nations 'Sendai Framework for Disaster Risk Reduction 2015-2030', which aims to face disaster consequences (including, but not limited to climate disasters) and reduce risks in natural, managed, and built environments (Aitsi-Selmi et al., 2015; UNISDR, 2015). The classification of climatic impact-drivers in this chapter is largely consistent with the classification of hazards used in the Sendai Framework, however, the UNISDR hazard list spans a wider range of hazards inducing damage to society, including hazards that are not directly related to climate (such as volcanoes and earthquakes), which are excluded from the assessment herein. Furthermore, the UNISDR classification of hazards does not include mean climatic conditions which are also discussed as climatic impact-drivers in this chapter. The first priority mentioned in the Sendai Framework is understanding disaster risk as a necessary step for action. Facilitating such an understanding is a clear goal of this chapter.

The chapter adopts a regional perspective (continental regions as defined in Chapter 1 and used in WGII, see Figure 1.18) on climatic impact-drivers to support decision making across a wide audience of global and regional stakeholders in addition to governments (e.g., civil society organizations, public and private sectors, academia). While the focus here is on future changes, it also describes current levels and observed trends of CIDs as an important point of reference for informing adaptation strategies.

Figure 12.1 summarizes the rationale behind Chapter 12 as the linkage (also referred to as a handshake) between WGI and WGII, illustrating how the changing profile of risk may be informed by an assessment of climatic impact-drivers, aligning WGI findings on physical climate change with WGII needs. The implementation of mitigation policy shifts may modulate hazard probability changes (i.e., by reducing emissions to limit global warming) as well as regional vulnerability and exposure. The assessment herein is organized around regional climatic impact-drivers, but also relates key indices and thresholds to increasing global drivers (such as mean surface warming) as a contribution to the assessment of 'Reasons for Concern' in WGII (O'Neill et al., 2017).

[START FIGURE 12.1 HERE]

Figure 12.1: Schematic diagram showing the use of climate change information (WGI chapters) for typical impacts or risk assessment (WGII chapters) and the role of Chapter 12, via an illustration of the assessment of property damage or loss in a particular region when extreme sea level exceeds dike height.

[END FIGURE 12.1 HERE]

The narrative in Chapter 12 is illustrated in Figure 12.2. First, Section 12.2 defines a range of climatic impact-driver categories that are relevant for regional and sectoral impacts and the associated ECVs. Next, Section 12.3 identifies climatic impact-drivers and their relevant indices that are frequently used in the context of climate impacts in the WGII focus sectors (Chapters 2-8). The assessment of changes in regional-scale climatic impact-drivers is then developed within Section 12.4 by continent, following the structure of the WGII assessment report regional chapters (Chapters 9-15), and adding the polar regions, open/deep ocean and other specific zones corresponding to the WGII cross-chapter papers. Section 12.5 then presents a global perspective (both bottom-up and top-down) on the change of regional climatic impact-drivers, including an assessment of the "emergence" of climatic impact-drivers. Section 12.6 discusses how climate information is used in 'climate services', which encompasses a range of activities bridging climate science and its use for adaptation and mitigation decision making (see also AR6 WGII Chapter 17). The chapter concludes with final remarks in Section 12.7.

ACCEPTED VERSION SUBJECT TO FINAL EDITS

[START FIGURE 12.2 HERE]

Figure 12.2: Narrative and structure of Chapter 12.

[END FIGURE 12.2 HERE]

The chapter includes two Cross-Chapter boxes. Cross-chapter Box 12.1 connects climatic impact-drivers them to global climate drivers and levels of warming as an element of the 'Reasons for Concern' framework (AR6 WGII Chapter 16). An additional cross-chapter box, including three case studies from Europe, Asia and Africa, describes how climate services draw upon and apply regional climate information to support stakeholder decisions (Cross-Chapter Box 12.2).

12.2 Methodological approach

This section details the methodological approach followed in Chapter 12 and discusses the underlying rationale for the assessments presented herein. Scientific literature on vulnerability, impacts, and adaptation (as typically asssessed in IPCC WGII) is examined to identify relevant climatic impact-drivers (CIDs) that contribute to sectoral risks and opportunities. Projected changes in corresponding CID indices are then derived from existing literature on changes in the physical climate system, results of other AR6 WGI chapters, and direct calculations based on climate projections from several model ensembles.

The classification of climatic impact-drivers, the ways that they change (e.g., their magnitude or intensity, duration, frequency, timing, and spatial extent) is described in this section. It is emphasized that this chapter only assesses literature relating to physical climatic impact-drivers, not their impacts on human systems or the environment. Thus, here we do not consider indicators including exposure or vulnerability as assessed by WGII, although the selection of climatic impact-drivers is informed by literature feeding into WGII.

Chapter 12 assesses climate information relevant for impact and for risk assessment in the seven main sectors corresponding to Chapters 2-8 of the WGII assessment report:

- Terrestrial and freshwater ecosystems and their services (WGII Chapter 2);
- Ocean and coastal ecosystems and their services (WGII Chapter 3);
- Water (WGII Chapter 4);
- Food, fibre and other ecosystem products (WGII Chapter 5);
- Cities, settlements and key infrastructure (WGII Chapter 6);
- Health, wellbeing and the changing structure of communities (WGII Chapter 7);
- Poverty, livelihoods and sustainable development (WGII Chapter 8).

Many of these sectors also include assets affected by climate change that are important for recreation and tourism, including elements of ecosystems services, health and wellbeing, communities, livelihoods, and sustainable development (see also Chapter 1 on the Intergovernmental Science-Policy Platform on Biodiversity and Ecosystem Services (IPBES), and the IPCC Special Report on climate change, desertification, land degradation, sustainable land management, food security, and greenhouse gas fluxes in terrestrial ecosystems (Hurlbert et al., 2019; IPCC, 2019c).

CIDs can be captured in seven main types: heat and cold, wet and dry, wind, snow and ice, coastal, oceanic and others. Table 12.1 provides an overview of the seven CID types and the CID categories associated with each type. The type "Other" comprises additional CIDs that are not encompassed with the above six CID types, including air pollution weather (e.g., meteorological conditions that favour high concentrations of surface ozone, particulate matter, or other air pollutants), near-surface atmospheric CO_2 concentrations, and mean radiation forcing at the surface, for instance relevant for plant growth. Icebergs, fog and lightning are also noted in this chapter but are not broadly assessed across all sub-sections. In addition, there can be changes in impacts associated with earthquakes that interact with climate variables and climate change, such as liquefaction (e.g., Yasuhara et al., 2012) during earthquakes, or earthquakes caused by snow and water

ACCEPTED VERSION SUBJECT TO FINAL EDITS

changes (Amos et al., 2014; Johnson et al., 2017), which are secondary effects on geophysical hazards that are not further assessed in this chapter. The characteristics and physical description of the climate phenomena or essential climate variables associated with each of these CID categories are assessed and described in previous Chapters 2-11 or Chapter 12 directly as indicated in Table 12.1. The CID categories are further mapped onto different sectors in section 12.3 (Table 12.2).

[START TABLE 12.1 HERE]

Table 12.1: Overview of the main Climatic impact-driver (CID) types and related CID categories with a short description and their link to other chapters where the underlying climatic phenomenon and its associated essential climate variables are assessed and described.

CID Type	CID Category	Brief Description	Physical Description of Phenomena
Heat and Cold	**Mean air temperature**	Mean surface air temperature and its diurnal and seasonal cycles.	CH2, CH3, CH4, Atlas
	Extreme heat	Episodic high surface air temperature events potentially exacerbated by humidity.	CH11
	Cold spell	Episodic cold surface air temperature events potentially exacerbated by wind.	CH11
	Frost	Freeze and thaw events near the land surface and their seasonality.	CH12
Wet and Dry	**Mean precipitation**	Mean precipitation, its diurnal and seasonal cycles, and associated soil moisture and humidity conditions.	CH2, CH8, Atlas
	River flood	Episodic high water levels in streams and rivers driven by basin runoff and the expected seasonal cycle of flooding.	CH8, CH11
	Heavy precipitation and pluvial flood	High rates of precipitation and resulting episodic, localized flooding of streams and flat lands.	CH11
	Landslide	Ground and atmospheric conditions that lead to geological mass movements, including landslide, mudslide, and rockfall.	CH12
	Aridity	Mean conditions of precipitation and evapotranspiration compared to potential atmospheric and surface water demand, resulting in low mean surface water, low soil moisture and/or low relative humidity.	CH8, CH11, Atlas
	Hydrological drought	Episodic combination of runoff deficit and evaporative demand that lead to dry soil.	CH8, CH11
	Agricultural and ecological drought	Episodic combination of soil moisture supply deficit and atmospheric demand requirements that challenge the vegetation's ability to meet its water needs for transpiration and growth. *Note: 'agricultural' vs. 'ecological' term depends on affected biome.*	CH8, CH11
	Fire weather	Weather conditions conducive to triggering and sustaining wildfires, usually based on a set of indicators and combinations of indicators including temperature, soil moisture, humidity, and wind. Fire weather does not include the presence or absence of fuel load. *Note: distinct from wildfire occurrence and area burned.*	CH11, CH12
Wind	**Mean wind speed**	Mean wind speeds and transport patterns and their diurnal and seasonal cycles.	CH2, CH12
	Severe wind storm	Severe storms including thunderstorms, wind gusts, derechos, and tornados.	CH11, CH12
	Tropical cyclone	Strong, rotating storm originating over tropical oceans accompanied by high winds, rainfall, and storm surge.	CH11
	Sand and dust storm	Storms causing the transport of soil and fine dust particles.	CH8, CH12
Snow and Ice	**Snow, glacier and ice sheet**	Snowpack seasonality and characteristics of glaciers and ice sheets including calving events and meltwater.	CH2, CH9, Atlas
	Permafrost	Permanently frozen deep soil layers, their ice characteristics, and the characteristics of seasonally frozen soils above.	CH2, CH9
	Lake, river and sea ice	The seasonality and characteristics of ice formations on the ocean and freshwater bodies of water.	CH2, CH9
	Heavy snowfall and ice storm	High snowfall and ice storm events including freezing rain and rain-on-snow conditions.	CH11, CH12
	Hail	Storms producing solid hailstones.	CH11, CH12

ACCEPTED VERSION SUBJECT TO FINAL EDITS

	Snow avalanche	Cryospheric mass movements and the conditions of collapsing snowpack.	CH12
Coastal	**Relative sea level**	The local mean sea surface height relative to the local solid surface.	CH9
	Coastal flood	Flooding driven by episodic high coastal water levels that result from a combination of relative sea level rise, tides, storm surge, and wave setup.	CH9, CH12
	Coastal erosion	Long term or episodic change in shoreline position caused by relative sea level rise, nearshore currents, waves, and storm surges.	CH12
Open Ocean	**Mean ocean temperature**	Mean temperature profile of ocean through the seasons, including heat content at different depths and associated stratification.	CH2, CH9
	Marine heatwave	Episodic extreme ocean temperatures.	CH9, CH12
	Ocean acidity	Profile of ocean water pH and accompanying concentrations of carbonate and bicarbonate ions.	CH5
	Ocean salinity	Profile of ocean salinity and associated seasonal stratification. *Note: distinct from salinization of freshwater resources.*	CH2, CH5
	Dissolved oxygen	Profile of ocean water dissolved oxygen and episodic low oxygen events.	CH5
Other	**Air pollution weather**	Atmospheric conditions that increase the likelihood of high particulate matter or ozone concentrations or chemical processes generating air pollutants. *Note: distinct from aerosol emissions or air pollution concentrations themselves.*	CH6
	Atmospheric CO_2 at surface	Concentration of atmospheric carbon dioxide [CO_2] at the surface. *Note: distinct from overall radiative effect of CO_2 as greenhouse gas.*	CH5
	Radiation at surface	Balance of net shortwave, longwave and ultraviolet radiation at the earth's surface and their diurnal and seasonal patterns.	CH7

[END TABLE 12.1 HERE]

Potential changes in the seasonality of CIDs or the length and characteristics of seasons (e.g. changes in growing season length or pollen season) are also important as they may shift the timing of many CIDs with broad implications for sectors and regional stakeholders (Wanders and Wada, 2015; Cassou and Cattiaux, 2016; Hansen and Sato, 2016; Brönnimann et al., 2018; Marelle et al., 2018; Unterberger et al., 2018; Kuriqi et al., 2020). Episodic CIDs characterize impact-relevant conditions persisting from short to long time frames but eventually returning to normal conditions.

In some situations, phenomena causing severe impacts go well beyond a single extreme event or a single climate variable, and can include interaction of climatic conditions, such as sea level rise and storm surges (Wahl et al., 2015), precipitation in combination with strong winds (Martius et al., 2016) or flooding quickly followed by a heat wave (Wang et al., 2019c) (see also section 10.5.2.4). Such compound events, particularly in context of climate extremes, are assessed in section 11.8. A combination of non-extreme climatic impact-drivers in time or space can also lead to severe impacts (Cutter, 2018).

Several climatic impact-drivers are reliant on many factors beyond their associated primary climatic phenomenon. For example, river flooding is heavily dependent on river management and engineering and could also be affected by tidal water levels due to sea level rise and/or storm surge. Coastal flooding could be affected by coastal protection structures, port and harbour structures as well as river flows (on inlet-interrupted coasts). Coastal erosion could be influenced by coastal protection measures as well as fluvial sediment supply to the coast. Furthermore, air pollution weather is not the only or dominant driver, for instance, of surface ozone pollution, but precursor emissions from anthropogenic sources can play a significant role (see section 6.5). Chapter 12 focuses only on the influence of the atmospheric, land and oceanic conditions associated with the climatic impact-drivers and the confidence in the direction of CID changes given here does not take into account existing or potential future adaptation measures, unless otherwise stated.

For each CID category there can be a range of indices that capture the sector- or application-relevant characteristics of a climatic impact-driver as described in sections 12.3 and 12.4. Indices for climatic impact-drivers that are based on absolute or percentile thresholds (e.g. daily maximum temperature above 35ºC) can be affected by biases in climate model simulations, such as local or regional deviations of a simulated

ACCEPTED VERSION SUBJECT TO FINAL EDITS

climate variable from observed values (Sillmann et al., 2014; Dosio, 2016). Where sensible (i.e., where reliable observational data is available and a climate model that fits for the desired purpose), the output of climate model simulations can be bias-adjusted, potentially involving advanced methods to account for multiple variables and extreme value statistics as assessed in detail in Cross-chapter box 10.2. Yet, there is no general agreement about which bias adjustment methods to apply, as artefacts can arise both from the climate model and from the bias adjustment method, and the number of available methods has considerably grown in recent years (see a detailed discussion of available methods and their performance in Chapter 10 sections 10.3.1.3 and 10.3.3.7 and in Cross-chapter box 10.2). The WGI Interactive Atlas illustrates original and bias-adjusted CIDs (see Atlas.1.4.5) and underlying methods are further described in Technical Annex VI.

A global perspective on climatic impact-drivers related to their evolution for different global warming levels (see section 1.6) is provided in section 12.5.1. Section 12.5.2 focuses on assessing evidence for the emergence (see section 1.4.2.2) of an anthropogenic climate change signal on the change in CIDs beyond natural climate variability, based on the literature assessed in other chapters and additional literature, at both global and regional scales. The process of generating user-relevant regional climate information in context of co-production and climate services is assessed in sections 10.5, 12.6, Box 10.2 and Cross-chapter boxes 10.3 and 12.2.

12.3 Climatic impact-drivers for sectors

Climate change becomes relevant for regional impact management and for risk assessment when changes in mean conditions or episodic events affect natural and societal assets (system components with socioeconomic, cultural, or intrinsic value) positively or negatively (Table 12.2). Decision makers, policy makers, risk managers and engineers therefore benefit from climate information that tracks key trends and exceedance of thresholds that represent crucial challenges for natural and human systems. While useful indices can vary widely for a given sector and precise tolerance threshold values are often unknown, common metrics, categories and progressions of threshold levels allow experts to recognize coherent messages concerning altered regional impacts and risk profiles under climate change.

This section surveys the links between CIDs and affected sectors; not to perform specific climate change impact or risk assessments (see AR6 WGII), but to describe key indices (among many) that quantify these links as guidance for stakeholders seeking applicable climate information. This survey builds on the work of the World Meteorological Organization Expert Team on Sector-Specific Climate Indices (ET-SCI) and previous IPCC assessments, notably AR5 WGII (Birkmann et al., 2014; IPCC, 2014a) and IPCC Special Reports (IPCC, 2018, 2019b, 2019c) that have assessed climate hazards affecting sectors but is organized from a CID perspective drawing also upon recent summaries of sectoral hazards (Mora et al., 2018; ICOMOS, 2019; Yokohata et al., 2019). Impacts, risks, and opportunities are rarely attributable to a single CID index or threshold, but climate shifts that push conditions outside of expected conditions and beyond tolerance levels are indicative of impact, risk, or benefit given vulnerability and exposure. Focus is on direct sectoral connections of a CID (Hallegatte and Przyluski, 2010) rather than cascading or secondary effects (e.g., water-borne diseases following a flood, mental health challenges following a severe storm, or the effects of drought on poverty), as these are strongly affected by exposure, vulnerability, and response, as discussed in WGII report.

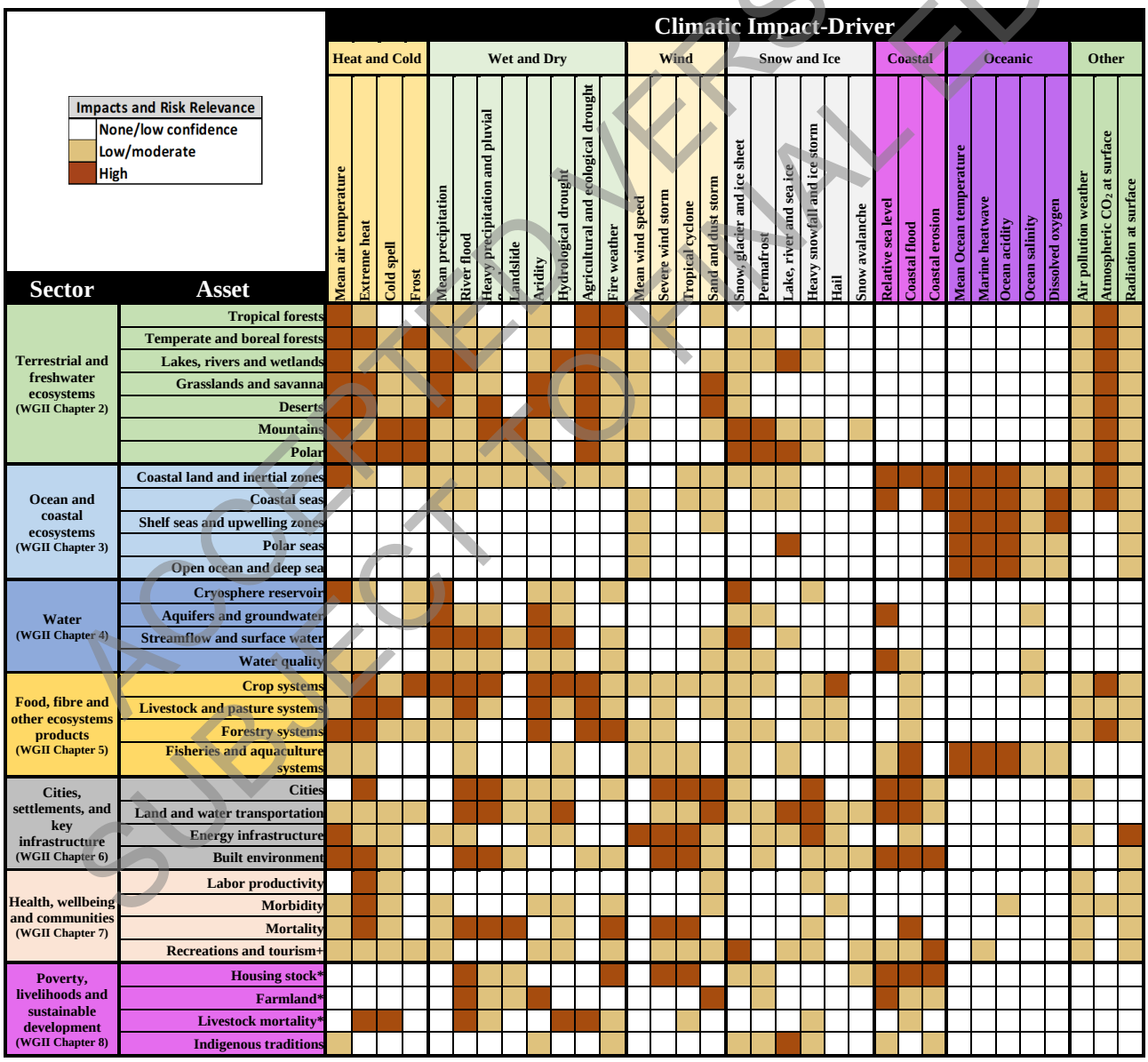
Table 12.2 presents a summary of Section 12.3 connections between CIDs as defined in Table 12.1 and key sectoral assets, utilizing the WGII organization of sectors (corresponding to WGII chapters 2-8). Colours are shown for connections with at least *medium confidence* as assessed from sectoral impacts and risk literature, with relevance assessed according to the prominence of that specific CID/asset connection in analyses of current and future impacts and risk. Within each sector there is a multitude of specific sectoral systems that may be affected by CID increases and decreases, with consequences further distinguished by region, background climate, and socioeconomic or ecological context of the affected asset. Our aim is therefore to recognize important drivers and the common attributes of change within each CID that scientists and practitioners monitor to understand current and future challenges for important asset groups, thereby pointing

ACCEPTED VERSION SUBJECT TO FINAL EDITS

to the climate information that needs to be tailored and analysed for impacts and for risk assessment (Section 12.6). Additional effects whereby CIDs affect each other (across Table 12.2 columns) are discussed as climatic phenomena within WGI. The ways sectoral assets affect each other (across Table 12.2 rows) are described throughout WGII, for example with information about the suitability of future climate zones and climate velocity challenges for a given asset potentially drawing from multiple CIDs and associated system tolerance thresholds (Hamann et al., 2015). Some broad connections indicated as *low confidence* may be under-represented in the literature or could be acute under specific circumstances.

[START TABLE 12.2 HERE]

Table 12.2: Relevance of key climatic impact-drivers (and their respective changes in intensity, frequency, duration, timing, and spatial extent) for major categories of sectoral assets, as assessed with at least *medium confidence* in Section 12.3 across many studies and applications. 'High relevance' indicates climatic impact-drivers that are most prominent and widely studied for their direct connection to assets, while lower relevance indicates weaker linkages and less commonly-studied driving behaviours. Specific levels of risk and opportunity depend on the changing character of regional hazards, vulnerability, and exposure as assessed in WGII.



ACCEPTED VERSION SUBJECT TO FINAL EDITS

*The Recreation and tourism asset category includes outdoor exercise and the tourism industry (including ecosystem services) assessed in many WGII chapters
*This asset category is distinguished by the threat of a full loss of key investments and living environments rather than a recoverable damage or loss of productivity or profit

[END TABLE 12.2 HERE]

12.3.1 Heat and cold

12.3.1.1 Mean air temperature

Information about increasing mean annual and seasonal air temperature is relevant in the determination of suitable species range for terrestrial, freshwater, and intertidal species (Thomas et al., 2004; Elith et al., 2010; Hincapie and Caicedo, 2013; Cooper, 2014; Krist et al., 2014; Lindner et al., 2014; Saintilan et al., 2014; Urban, 2015; Lenoir and Svenning, 2015; Myers-Smith et al., 2015; Thorne et al., 2017). Ocean ecosystems are affected by the ocean temperature CID (described in Section 12.3.6.1). Species redistribution and extinction studies also need information about climate velocity, a comparison of the pace of warming to geographical temperature gradients that indicates the rate at which a species would have to move to maintain its climatological temperature (Thomas et al., 2004; Loarie et al., 2009; Dobrowski et al., 2013; Burrows et al., 2014; Dobrowski and Parks, 2016; Sittaro et al., 2017) with some studies incorporating additional variables beyond temperature (Hamann et al., 2015). Many freshwater ecosystems are strongly constrained by stream and lake temperatures (Scheurer et al., 2009; Comte and Grenouillet, 2013; Contador et al., 2014; Knouft and Ficklin, 2017). Warmer and more stratified lake temperatures are more conducive to cyanobacteria blooms with implications for ecosystem health and water resource quality (Whitehead et al., 2009; Moss, 2011; Jones and Brett, 2014; Chapra et al., 2017; Shatwell et al., 2019). Consideration of night-time and daytime temperature trends also elucidates different biophysical effects on vegetation (Peng et al., 2013). Changes in the seasonal timing caused by warming trends are critical to species ranges and ecosystem function (Pearce-Higgins et al., 2015; Hughes et al., 2017b), and indices that characterise the onset of spring shed light on plant emergence and development (Ault et al., 2015).

Mean air temperature dictates many aspects of crop cultivation, livestock production, agroforestry, and output from freshwater aquaculture and fisheries as well as the potential for food contamination. Mean warming alters suitable cultivation zones for crop species (Bragança et al., 2016; Gendron St-Marseille et al., 2019; IPCC, 2019c) and tree species (Hanewinkel et al., 2013; Fei et al., 2017). Crop and ecosystem service productivity often responds directly to mean temperatures, although this is dependent on farming system (Bassu et al., 2014; Challinor et al., 2014; Lobell and Tebaldi, 2014; Rosenzweig et al., 2014; Asseng et al., 2015; Li et al., 2015; Fleisher et al., 2017; Zhao et al., 2017; Smith and Fazil, 2019). Many studies relate plant development (phenology), insect generation cycles, and pest outbreaks to growing degree days, an aggregation of daily thermal units above a threshold (e.g., Tmean>5°C) that accelerates with warmer conditions (Hof and Svahlin, 2016; Ruosteenoja et al., 2016; Tripathi et al., 2016). Many plants respond to changes in night-time temperatures that affect respiration and transpiration rates (Narayanan et al., 2015; Chen et al., 2019b), and warming of the soil column is also relevant to determine plant sprouting (Grotjahn, 2021). A number of indices have been developed to represent the length of the viable local growing season, including a count of days where Tmax > 5°C (Mueller et al., 2015) or the period between a year's first and last set of 5 consecutive days with a weighted Tmean ≥ 10°C (Li et al., 2018b). Warmer conditions and altered seasonality modify the range and metabolism of some pollinators, pests, diseases and weeds (Wolfe et al., 2008; Bebber, 2015; Aljaryian and Kumar, 2016; IPBES, 2016; Ramesh et al., 2017; Deutsch et al., 2018; Nyangiwe et al., 2018) and may reduce the effectiveness of winter storage for farmers and caching species (Sutton et al., 2016).

Warming raises accumulated seasonal heat indices used in livestock production, especially when humidity is high (Key et al., 2014; Lallo et al., 2018), determines aquaculture suitability and is important for wild fish species migration (Tripathi et al., 2016; Brander et al., 2017). Agricultural planners may also calculate how overall warming trends alter the accumulation of vernalization units or chilling hours for agricultural or horticultural crops (often accumulated temperature deficit below a given daily or hourly threshold) (Dennis and Peacock, 2009; Luedeling, 2012; Tripathi et al., 2016; Grotjahn, 2021). Warming in the post-harvest is

ACCEPTED VERSION SUBJECT TO FINAL EDITS

also important for the determination of spoilage and waste (Stathers et al., 2013) as well as food-borne diseases (Kovats et al., 2004; Mbow et al., 2019).

Warming affects road degradation rates (Chinowsky and Arndt, 2012; Espinet et al., 2016) and warming rates informs designs for long-term energy efficiency of buildings (Kalvelage et al., 2014). Mean temperature drives seasonal energy demand, often expressed using wintertime heating degree days (the accumulated deficit of daily temperatures below a 'comfortable' indoor temperature, e.g., 15.5°C) and summertime cooling degree days (the accumulated excess of temperature above a 'comfortable' level, e.g., 18°C) (Spinoni et al., 2015; Arnell et al., 2019). Energy resources may also need information on warming trends to determine suitable zones and overall productivity for biofuels and solar panels whose efficiency decreases with higher temperatures (Schaeffer et al., 2012; Wild et al., 2015; Solaun and Cerdá, 2019).

Health impacts and risk studies compare seasonal temperature conditions to limiting thresholds to understand range shifts and incubation rates for pathogens, disease vectors, and zoonotic hosts (e.g., mosquitos, ticks; Caminade et al., 2012, 2014; Eisen and Moore, 2013; Lima et al., 2016; Ogden, 2017; Monaghan et al., 2018) and warming of surface ocean and lake waters conducive to bacterial outbreaks (Baker-Austin et al., 2013; Jacobs et al., 2015; Vezzulli et al., 2015). Warmer conditions can also affect tourism (Kovács et al., 2017) and impact human health by lengthening the allergy season and increasing pollen concentration (Hamaoui-Laguel et al., 2015; Kinney et al., 2015a; Lake et al., 2017; Upperman et al., 2017; Sapkota et al., 2019; Ziska et al., 2019).

12.3.1.2 Extreme heat

Impacts and risk assessments utilize a large variety of indices and approaches tailored to evaluate heat impacts on human health (Sanderson et al., 2017; Gao et al., 2018a; McGregor and Vanos, 2018; Staiger et al., 2019; Zhu et al., 2019; Schwingshackl et al., 2021). A mixture of simple and complex heat stress indices often combine extreme temperatures and high humidity to capture human health challenges (Aström et al., 2013; Chow et al., 2016; Dahl et al., 2017a; Im et al., 2017; Coffel et al., 2018; Li et al., 2018c; Vanos et al., 2020). Different optimum temperatures and extreme heat thresholds based on local distributions are needed to reflect acclimation of different locations and populations (Cheng et al., 2018; Dosio, 2017; Hajat et al., 2014; Kinney et al., 2015b; Lay et al., 2018; Petitti et al., 2016; Russo et al., 2015; Schwingshackl et al., 2021; WHO, 2014). Hot and humid heat episodes can be deadly (Mora et al., 2017), are associated with elevated hospital intake (Goldie et al., 2017) and lower safety and productivity of outdoor labourers (Dunne et al., 2013; Graff Zivin and Neidell, 2014; Kjellstrom et al., 2016; Pal and Eltahir, 2016; Zhao et al., 2016b; Mora et al., 2017; Watts et al., 2018; Orlov et al., 2019). Elevated night-time temperatures prevent the human body from experiencing relief from heat stress (Zhang et al., 2012) and can be tracked over extended periods of sequential day and night heat extremes (Murage et al., 2017; Mukherjee and Mishra, 2018). Extreme heat also exacerbates asthma, respiratory difficulties, and response to airborne allergens such as hay fever (Upperman et al., 2017). Extreme heat affects outdoor exercise such as the use of bike-share facilities (Heaney et al., 2019; Vanos et al., 2020). Large-scale recreational and sporting events such as marathons and tennis tournaments monitor heat extremes when determining the viability of host cities (Smith et al., 2016, 2018).

Short-term exposure of crops to temperatures beyond a critical temperature threshold can lead to lower yields and above a limiting temperature threshold, crops may fail altogether (Schlenker and Roberts, 2009; Lobell et al., 2012, 2013; Gourdji et al., 2013; Deryng et al., 2014; Schauberger et al., 2017; Tesfaye et al., 2017; Vogel et al., 2019). The exact level of these thresholds depends on species, cultivar, and farm management (Hatfield and Prueger, 2015; Hatfield et al., 2015; Bisbis et al., 2018; Grotjahn, 2021). The timing of heatwaves is particularly important, as extreme heat is more damaging during critical phenological stages (Eyshi Rezaei et al., 2015; Fontana et al., 2015; Mäkinen et al., 2018; Wang et al., 2017). Extreme canopy temperatures, rather than 2 m air temperatures, may be a more robust biophysical indicator of heat impacts on crop production (Siebert et al., 2017). Heat stress indices based upon temperature and humidity determine livestock productivity as well as conception and mortality rates (Dash et al., 2016; Key et al., 2014; Pragna et al., 2017; Rojas-Downing et al., 2017).

ACCEPTED VERSION SUBJECT TO FINAL EDITS

Heat extremes factor in mortality, morbidity and the range of some thermally sensitive ecosystem species (Smith and Nagy, 2015; Ratnayake et al., 2019; Thomsen et al., 2019). Combined heat and drought stress can reduce forest and grassland primary productivity (Ciais et al., 2005; De Boeck et al., 2018) and even cause tree mortality at higher extremes (Teskey et al., 2015).

Extreme heat events raise temperatures in buildings and cities already warmed by the urban heat-island effect (Gaffin et al., 2012; Oleson et al., 2018; Zhao et al., 2018; Mauree et al., 2019; Box 10.3) and can induce disruptions in critical infrastructure networks (Chapman et al., 2013). Heat affects transportation infrastructure by warping roads and airport runways (Chinowsky and Arndt, 2012) or buckling railways (Dobney et al., 2010; Dépoues, 2017; Chinowsky et al., 2019), and high temperatures reduce air density leading to aircraft take-off weight restrictions (Coffel et al., 2017; Palko, 2017; Zhou et al., 2018b). Heat extremes increase peak cooling demand and challenge transmission and transformer capacity (Sathaye et al., 2013; Russo et al., 2016; Craig et al., 2018; Gao et al., 2018b) and may cause transmission lines to sag or fail (Gupta et al., 2012). Thermal and nuclear electricity plants may be challenged when using warmer river waters for cooling or when mixing waste waters back into waterways without causing ecosystem impacts (Kopytko and Perkins, 2011; van Vliet et al., 2016; Tobin et al., 2018). Extreme temperature can also reduce solar photovoltaic efficiency (Jerez et al., 2015).

12.3.1.3 Cold spells

The magnitude and timing (relative to developmental stages) of cold extremes (such as the typical coldest day of the year) set limits in the range of species habitat for ecosystems as well as for agricultural and forest pests (Osland et al., 2013; Cavanaugh et al., 2014; Parker and Abatzoglou, 2016; Brunner et al., 2018; Unterberger et al., 2018). Cold air outbreaks can lead to chilling injuries for crops (even above 0°C) and may kill outdoor livestock (particularly young animals) (Mader et al., 2010; Liu et al., 2013; Grotjahn, 2021), but are often necessary for crop chill requirements (Dennis and Peacock, 2009).

Increases in human mortality can occur on exceptionally cold days (e.g., <1st percentile of temperatures in winter) although thresholds and human-perceived temperatures linked to wind speed (i.e., 'wind chill') vary geographically due to acclimatization (Li et al., 2013b, 2018c; Gao et al., 2015; Zhu et al., 2019a). The timing of 'unseasonal' cold spells also affect human health (Kinney et al., 2015b). Extreme cold can increase heat and electricity demand (Stuivenvolt-Allen and Wang, 2019), cause water pipes to burst , and mechanically alter roads, railroads and buildings (Underwood et al., 2017).

12.3.1.4 Frost

Frost (T_{min} < 0 °C) is a natural and fundamental aspect of many ecosystems, with more extreme conditions defined as ice (or icing) days (T_{max} < 0 °C) (Vincent et al., 2018c). Agricultural systems planning (e.g., planting calendars, seed selection, or the opportunity to double-crop) requires information about the start and end of the frost-free season (Wypych et al., 2017; Wolfe et al., 2018). Crops and wild plants can be directly damaged by frost, but hard or killing frosts (at a threshold several degrees below freezing) can kill crops or lower harvest quality depending on duration (which relates to soil temperature penetration) and plant developmental stage (Crimp et al., 2016; Cradock-Henry, 2017; Li et al., 2018c; Mäkinen et al., 2018; Grotjahn, 2021). Earlier disappearance of snow cover reduces natural insulation that protects plants and burrowing animals from hard frost damages (Trnka et al., 2014; Mäkinen et al., 2018). In some cases an early season warm spell may reduce plant hardiness or induce fruit tree flowering that exposes plants to devastating subsequent frost impacts (Hufkens et al., 2012; Hatfield et al., 2014; Tripathi et al., 2016; Brunner et al., 2018; DeGaetano, 2018; Unterberger et al., 2018; Wolfe et al., 2018). Shifts in the seasonality of frozen soils also affect groundwater recharge and surface streamflow for water resource applications, particularly when peak precipitation is shifted to a season that no longer has frozen soils (Jyrkama and Sykes, 2007).

ACCEPTED VERSION SUBJECT TO FINAL EDITS

Regional information about the spring and autumn seasonal periods in which freeze-thaw cycles are common (such as the dates of first spring thaw and last spring frost, or the number of days where $T_{max} > 0$ °C and $T_{min} < 0$ °C) are particularly useful in estimating the rate of potential road and building damages or determining seasonal truck weight restrictions (Kvande and Lisø, 2009; Chinowsky and Arndt, 2012; Palko, 2017; Daniel et al., 2018). The altitude of the freezing level also identifies portions of mountain slopes where freeze/thaw transitions or changes in snowpack condition can influence landslide and snow avalanche hazards (Coe et al., 2018). The geographical distribution of frost is also a determining factor in the range of vectors for human diseases such as malaria (Zhao et al., 2016a; Smith et al., 2020).

Figure 12.3 illustrates how successive heat and cold hazards can potentially affect important natural and human systems, with climatic pressures reaching new sectoral assets or becoming increasingly severe as conditions become more extreme. While the precise value of any CID threshold may depend strongly on local environmental and system characteristics, there are common patterns and interdependencies in the types of thresholds encountered. Changes in the regional profile of CIDs can thus substantially alter threshold exceedance likelihoods.

[START FIGURE 12.3 HERE]

Figure 12.3: Conceptual illustration of representative climatic impact-driver thresholds showing how graduating thresholds affect successive sectoral assets and lead to potentially more acute hazards as conditions become more extreme (exact values are not shown as these must be tailored to reflect diverse vulnerabilities of regional assets). Representative threshold definitions (T = instantaneous temperature; $\bar{T}$ = mean temperature): **Cities and Infrastructure**: T_{trans} = temperature at which energy transmission lines efficiency reduced; $T_{aircraft}$ = temperature at which aircraft become weight-restricted for takeoff; $T_{hotroads}$ = temperature above which roads begin to warp; T_{stream} = temperature at which streams are not capable of adequately cooling thermal plants; CDD_{min} = Minimum temperature for calculating cooling degree days; HDD_{min} = maximum temperature for calculating heating degree days; T_{ice} = temperature at which ice threatens transportation; $\bar{T}_{permafrost}$ = mean seasonal temperature above which permafrost thaws at critical depths; $T_{coldroads}$ = temperature below which road asphalt performance suffers. **Health**: T_{deadly} = temperatures above which prolonged exposure may be deadly (often combined with humidity for heat indices); T_{severe} = temperatures above which prolonged exposure may cause elevated morbidity; $\bar{T}_{blooms}$ = mean temperature for harmful algal or cyanobacteria blooms; T_{danger} = level of dangerous cold temperatures (often combined with wind for chill indices); $T_{overwinter}$ = temperature below which disease vector species cannot survive winter. **Ecosystems** (CID indices for air and ocean temperature): T_{hotlim} and $T_{coldlim}$ = limiting hot and cold temperatures for a given species range; T_{frost} = frost threshold; $\bar{T}_{max}$ and $\bar{T}_{min}$ = maximum and minimum suitable annual mean temperatures for a given species; T_{crit} = critical temperature above which a given species is stressed. **Agriculture**: T_{hotlim}= temperature above which a crop or livestock species dies; $T_{hotpest}$ = maximum (or 'lethal') temperature above which an agricultural pest/disease/weed cannot survive; T_{crit} = temperature at which productivity for a given crop is depressed; $\bar{T}_{opt}$ = optimal mean temperature for a given plant's productivity; GDD_{min} = threshold temperature for growing degree days determining plant development; T_{chill} = temperature below which chilling units are accumulated; T_{frost} = temperature below which frost occurs; T_{hfrost} = temperature below which a hard frost threatens crops or livestock; $T_{coldpest}$ = minimum wintertime temperature below which a given agricultural pest cannot survive; $T_{coldlim}$ = minimum temperature below which a given crop cannot survive.

[END FIGURE 12.3 HERE]

12.3.2 Wet and dry

12.3.2.1 Mean precipitation

Changes in mean precipitation alter total water resources and long-term surface, snowpack, and groundwater reservoirs (Schewe et al., 2014a). Annual and seasonal wet trends can alter the suitable geographic range of species, with implications for biodiversity and vector borne disaeses (Knouft and Ficklin, 2017; Smith et al.,

ACCEPTED VERSION SUBJECT TO FINAL EDITS

2020). The rate at which higher total stream flow increases river erosion and changes sediment loading is relevant for fish breeding (Scheurer et al., 2009), the location of riverine salt fronts that affect coastal agriculture and ecosystems (Chun et al., 2018; Vu et al., 2018), coastal freshwater stratification (Baker-Austin et al., 2013; Bell et al., 2013), and the accretion of sediment in estuaries and beaches (Syvitski and Milliman, 2007). Wetter conditions may shift tourist appeal (Kovács et al., 2017) and alter the pace of degradation for paved and especially unpaved roads (Chinowsky and Arndt, 2012).

Many agricultural systems require minimum rainfall totals or rely upon irrigation (Mbow et al., 2019). The length of the wet season helps determine the potential for multiple cropping seasons, but inconsistency of wet season arrival times poses challenges for farm management (Waha et al., 2020). Wetter growing season conditions increase the chance of water logging, which can delay planting or damage planted seeds (Rosenzweig et al., 2002; Ben-Ari et al., 2018; Mäkinen et al., 2018; Wolfe et al., 2018; Kolberg et al., 2019; Grotjahn, 2021). Tomasek et al. (2017) calculated 'workable days' for agricultural machinery around planting and harvest time set in part by limits in soil moisture saturation below which farmers can utilize critical machinery with less rutting or soil compaction. Wetter conditions may also increase canopy moisture that is conducive to crop pathogens (Garrett et al., 2006; Kilroy, 2015; Grotjahn, 2021).

12.3.2.2 River flood

A large variety of climate indices and models are utilized to understand how river flooding affects both natural or built environments with highly variable hazard thresholds, given unique local topography and engineered defences such as dams and polders (Arnell and Gosling, 2016; Ekström et al., 2018).. Key transportation routes, built infrastructure, and agricultural lands are threatened when floods exceed design standards commonly based around flood magnitudes of a given historic return period (e.g., 1-in-100 yr flood event), an annual exceedance probability, or precipitation intensity-duration-frequency relationships with key indices (e.g., 10-day cumulative precipitation) related to catchment size and properties (Hirabayashi et al., 2013; Arnell and Lloyd-Hughes, 2014; Kundzewicz et al., 2014; Arnell and Gosling, 2016; Dikanski et al., 2016; Gosling and Arnell, 2016; Forzieri et al., 2017; Fluixá-Sanmartín et al., 2018; Koks et al., 2019). Floods and high flow events can scour river beds and elevate silt loads, reducing water quality and accelerating deposition in estuaries and reservoirs (Khan et al., 2018; Parasiewicz et al., 2019). Floods can knock down, drown, or wash away crops and livestock, and partially-submerged plants can have yield reduction depending on water turbidity and their development stage (Ruane et al., 2013; Shrestha et al., 2019). Basin snowpack properties may also be important during heavy rain events, as rain-on-snow events can lead to rapid acceleration of flood stages that threaten wildlife and society (Hansen et al., 2014).

12.3.2.3 Heavy precipitation and pluvial flood

Heavy downpours can lead to pluvial flooding in cities, roadways, farmland, subway tunnels and buildings (particularly those with basements) (Grahn and Nyberg, 2017; Palko, 2017; Pregnolato et al., 2017; Orr et al., 2018). Heavy precipitation may overwhelm city transportation and storm water drainage systems, which are typically designed using intensity-duration-frequency information such as the return periods for 1-, 6- or 24-hour rainfall totals (Kermanshah et al., 2017; Depietri and McPhearson, 2018; Rosenzweig et al., 2018; Courty et al., 2019). Heavy rain events can directly cause leaf loss and damage or knock over crops, also driving pollutant entrainment and erosion hazards in terrestrial ecosystems and farmland with downstream ramifications for water quality (Hatfield et al., 2014; Segura et al., 2014; Li and Fang, 2016; Chhetri et al., 2019). The proportion of total precipitation that falls in heavy events also affects the percentage that is retained in the soil column, altering groundwater recharge and deep soil moisture content for agricultural use (Fishman, 2016; Lesk et al., 2020).

12.3.2.4 Landslide

Landslides, mudslides, rock falls, and other mass movements can lead to fatalities, destroy infrastructure and

ACCEPTED VERSION SUBJECT TO FINAL EDITS

housing stock, and block critical transportation routes. Climate models cannot resolve these complex slope failure processes (nor triggering mechanisms such as earthquakes), so most studies rely on proxies or conditions conducive to slope failure (Gariano and Guzzetti, 2016; Ho et al., 2017). Common indices include precipitation intensity-duration thresholds (Brunetti et al., 2010; Khan et al., 2012; Melchiorre and Frattini, 2012) and thresholds related to antecedent wet periods and extreme rainfall intensities (Alvioli et al., 2018; Monsieurs et al., 2019). Landslides and rockfalls may also be exacerbated by permafrost thaw and receding glaciers in polar and mountain areas (Cook et al., 2016; Haeberli et al., 2017a; Patton et al., 2019).

12.3.2.5 Aridity

Aridity indices may track long-term changes in precipitation, evapotranspiration demand, surface water, groundwater, or soil moisture (Sherwood and Fu, 2014; Herrera-Pantoja and Hiscock, 2015; Cook et al., 2020a). Changes in soil moisture and surface water can shift the rate of carbon uptake by ecosystems (Humphrey et al., 2018) and alter suitable climate zones for wild species and agricultural cultivation (Feng and Fu, 2013; Garcia et al., 2014; Huang et al., 2016b; Schlaepfer et al., 2017; Fatemi et al., 2018; IPCC, 2019c) as well as the prevalence of related pests and pathogen-carrying vectors (Paritsis and Veblen, 2011; Smith et al., 2020). Water table depth, in relation to rooting depth, is also important for farms and forests under dry conditions (Feng et al., 2006). A reduction in water availability (via aridity or hydrological drought) challenges water supplies needed for for municipal, industrial, agriculture and hydropower use (Schaeffer et al., 2012; Arnell and Lloyd-Hughes, 2014; Schewe et al., 2014b; Gosling and Arnell, 2016; van Vliet et al., 2016).

12.3.2.6 Hydrological drought

Water managers often utilize a variety of hydrological drought indices and hydrological models to characterize water resources, low flow conditions and the potential for irrigation (Wanders and Wada, 2015; Mukherjee et al., 2018) (11.9). Low flow volume and intermittency thresholds can indicate reductions in dissolved oxygen, more concentrated pollutants, and higher stream temperatures relevant for ecosystems, water resource quality, and thermal power plant cooling (Feeley et al., 2008; Döll and Schmied, 2012; Schaeffer et al., 2012; Prudhomme et al., 2014; van Vliet et al., 2016). Low water levels may also restrict waterway navigation for commerce and recreation (Forzieri et al., 2018).

12.3.2.7 Agricultural and ecological drought

Agricultural and ecological drought indices relate to the ability of plants to meet growth and transpiration needs (Zargar et al., 2011; Lobell et al., 2015; Pedro-Monzonís et al., 2015; Bachmair et al., 2016; Wehner et al., 2017; Naumann et al., 2018; Table 11.3) and the timing and duration of droughts can lead to substantially different impacts (Peña-Gallardo et al., 2019). Drought stress for agriculture and ecosystems is difficult to directly observe, and therefore, scientists use a variety of drought indices (Table 11.3), proxy information about changes in precipitation supply and reference evapotranspiration demand, the ratio of actual/potential evapotranspiration or a deficit in available soil water content, particularly at rooting level (Williams et al., 2013; Trnka et al., 2014; Allen et al., 2015a; Svoboda and Fuchs, 2017; Mäkinen et al., 2018; Otkin et al., 2018). Severe water stress can lead to crop failure, in particular when droughts persist for an extended period or occur during key plant developmental stages (Hatfield et al., 2014; Jolly et al., 2015; Leng and Hall, 2019). Projections of high wind speed and low humidity (even for just a portion of the day) can also inform studies examining fruit desiccation and rice cracking (Grotjahn, 2021). Drought also raises disease infection rates for West Nile Virus (Paull et al., 2017), and the alternation of dry and wet spells induces swelling and shrinkage of clay soils that can lead to sinkholes and destabilize buildings (Hadji et al., 2014).

ACCEPTED VERSION SUBJECT TO FINAL EDITS

12.3.2.8 Fire weather

Complex fire weather indices shed light on conditions that increase the likelihood of wildfire and shifts in the fire season (Flannigan et al., 2013; Bedia et al., 2015; Jolly et al., 2015; Harvey, 2016; Littell et al., 2016; Westerling, 2016; Abatzoglou et al., 2019) which pose particularly acute challenges for indigenous communities (Christianson and McGee, 2019). Projection of future lightning frequency provides information on an important natural triggering mechanism, particularly when coupled with long-term warming and drying trends (Romps et al., 2014; Jin et al., 2015; Veraverbeke et al., 2017). Fuel aridity metrics also help determine vegetative fuel desiccation and therefore the ignitability, flammability, and spread of fires when they occur (Abatzoglou and Williams, 2016). The presence of snow cover can influence the length of the fire season and the penetration of fire danger into new portions of the Arctic tundra (Young et al., 2017; Abatzoglou et al., 2019). Data on the changing characteristics of local wind circulations like the *Santa Ana* in California shed light on future intensity and spread patterns for fires (Jin et al., 2015). Fires also produce smoke plumes that reduce air and water quality (via deposition), adversely affecting health, visibility and water resources both near and far downwind (Dennekamp and Abramson, 2011; McKenzie et al., 2014; Dreessen et al., 2016; Liu et al., 2016; Martin, 2016).

12.3.3 Wind

12.3.3.1 Mean wind speed

Changes in the speed and direction of prevailing winds can alter the profile of seed dispersal, windblown pest and disease vectors, animal activities, and dust or pollen dispersal affecting ecosystems, agriculture, and human health (Reid and Gamble, 2009; Bullock et al., 2012; Hellberg and Chu, 2016; Nourani et al., 2017). Seasonal winds influence algal blooms, ecosystems and fisheries via lake mixing, ocean currents and coastal upwelling (Bakun et al., 2015; Townhill et al., 2018; Woolway et al., 2020). Changes to wind density also modify a region's wind and wave renewable energy endowment (Schaeffer et al., 2012; Sierra et al., 2017; Craig et al., 2018; Devis et al., 2018; Tobin et al., 2018; Yalew et al., 2020). Li et al. (2020) and Karnauskas et al. (2018) evaluated wind thresholds at turbine height (~80-100 m above ground) including periods outside of cut-in (2.5-3 m s^{-1}) and cut-out (~25 m s^{-1}) levels beyond which given turbines could not operate.

12.3.3.2 Severe wind storm

High winds associated with severe storms can level trees and houses, break plant stems and knock fruits, nuts and grains to the ground, with tolerance thresholds depending on crop species and developmental stage (Seidl et al., 2017; Lai, 2018; Elsner et al., 2019; Grotjahn, 2021). Severe storms particularly threaten energy infrastructure, with maximum wind speed associated with treefall and breaking of above-ground electrical transmission lines (Ward, 2013; Nik et al., 2020) . The profile of heavy wind gusts is also required in the design of skyscrapers (Wang et al., 2013a) and bridges (Mondoro et al., 2018). Severe storms are difficult to simulate at the relatively coarse spatial scales of earth system models, thus scientists often project changes by noting areas with increased convective available potential energy (CAPE) and strong low-level wind shear as these are conducive to tornado formation (Diffenbaugh et al., 2013; Tippett et al., 2016; Glazer et al., 2020).

12.3.3.3 Tropical cyclone

Tropical cyclones and severe coastal storms can deliver wind, water, and coastal hazards with the potential for widespread mortality and damages to cities, housing, transportation and energy infrastructure, ecosystems, and agricultural lands (Burkett, 2011; NASEM, 2012; Bell et al., 2013; Wehof et al., 2014; Ward et al., 2016; Cheal et al., 2017; Godoi et al., 2018; Koks et al., 2019; Pinnegar et al., 2019). Storm planning is often tied to the Saffir-Simpson scale related to peak sustained wind speed (Izaguirre et al., 2021), with several indices focusing on storms' overall power and energy, size and translation speed to

ACCEPTED VERSION SUBJECT TO FINAL EDITS

anticipate destructive potential (Knutson et al., 2015; Wang and Toumi, 2016; Parker et al., 2018; Hassanzadeh et al., 2020).

12.3.3.4 Sand and dust storm

Sand and dust storms erode topsoils, damage crops and induce problems for health, transportation, mechanical equipment and built infrastructure corresponding to the magnitude and duration of high winds and particulate matter concentrations (Goudie, 2014; O'Loingsigh et al., 2014; Crooks et al., 2016; Barreau et al., 2017; Bhattachan et al., 2018; Al Ameri et al., 2019; Middleton et al., 2019). Dust events may be represented as the number of dust hours per dust storm year and by particulate matter (PM) concentrations (Leys et al., 2011; Spickett et al., 2011; Hand et al., 2016). Photovoltaic panels can lose energy production efficiency with dust accumulation (Patt et al., 2013; Javed et al., 2017). It is also useful to track dust storm deposition of nutrients necessary for coral and tropical forest systems, but they may also feed algal blooms harming lake and coastal ecosystems, health, and recreation (Jickells et al., 2005; Hallegraeff et al., 2014; Gabric et al., 2016). Dust storms also cause air pollution and redistribute the soil-based fungus associated with Valley Fever (Barreau et al., 2017; Coopersmith et al., 2017; Tong et al., 2017; Gorris et al., 2018).

12.3.4 Snow and ice

Cryospheric changes are a focus of Chapter 9 and were central to the recent IPCC Special Report on the Ocean and Cryosphere in a Changing Climate (IPCC, 2019b). Here we focus on the ways that scientists use snow and ice CIDs to understand current and future societal impacts and risks.

12.3.4.1 Snow, glacier and ice sheet

A large number of indices have been used in water resource and ecosystem studies to track changes in snow under current and future climate conditions, including measurements of the snow water equivalent at key seasonal dates, the fraction of precipitation falling as snow, the first and last days of snow cover, and cold season temperatures (Mills et al., 2013; Pierce and Cayan, 2013; Berghuijs et al., 2014; Klos et al., 2014; Musselman et al., 2017; Rhoades et al., 2018). Applications also examine shifts in seasonal streamflow for snow-fed river basins (Mote et al., 2005; Pederson et al., 2011; Beniston and Stoffel, 2014; Coppola et al., 2014, Fyfe et al., 2017; Coppola et al., 2018; Islam et al., 2017; Knouft and Ficklin, 2017) as well as the geographic extent of snow cover and the depth of frosts when snow cover's natural insulation is absent (Scheurer et al., 2009; Millar and Stephenson, 2015). Studies examining the impact of snow changes on winter recreation and transportation have used thresholds of ~30 cm snow depth or snow water equivalent > 10 cm to determine the length of the season for alpine and cross-country skiing and snowmobiling (Damm et al., 2017; Wobus et al., 2017b; Spandre et al., 2019; Steiger et al., 2019; Abegg et al., 2020). Changes in snow quality also affect recreational activities (Rutty et al., 2017), and artificial snowmaking can augment recreational snowpack depending on the number of suitable snowmaking hours (e.g., where WBGT < -2.2 °C; Wobus et al., 2017). Local detail may also be provided by tracking the seasonal rain-snow transition line across space and elevation (Berghuijs et al., 2014).

Change in ice sheet and glacier spatial extent and surface mass balance is relevant for polar and high mountain ecosystems and downstream assets that rely on glacial water resources (Lee et al., 2017a; Milner et al., 2017; Huss and Hock, 2018; Schaefli et al., 2019). The loss of glaciers reduces the thermal consistency of cold streams suitable for some freshwater species (Giersch et al., 2017), and parks and recreation areas may lose appeal as glaciers and seasonal snow cover retreat (Gonzalez et al., 2018; Wang and Zhou, 2019). Rapid glacial retreat can lead to glacial lakes and outburst floods that endanger downstream communities (Carrivick and Tweed, 2016; Cook et al., 2016; Harrison et al., 2018).

ACCEPTED VERSION SUBJECT TO FINAL EDITS

12.3.4.2 Permafrost

Changes in permafrost temperature, extent, and active layer thickness are metrics that track how permafrost thaw below for e.g. roads, airstrips, rails, and building foundations in high-latitude and mountain regions may destabilize settlements and critical infrastructure (Pendakur, 2016; Derksen et al., 2018; Duvillard et al., 2019; Olsson et al., 2019; Streletskiy et al., 2019). Warmer conditions can also affect ecosystems, built infrastructure, and water resources through thawing of especially ice-rich permafrost (≥ 20% ice content) and by thawing of ice wedges (Shiklomanov et al., 2017; Hjort et al., 2018), creation of thermokarst ponds and increased subsurface drainage for polar and high-mountain wetlands (Walvoord and Kurylyk, 2016; Farquharson et al., 2019) and the release of water pollutants such as mercury (Burkett, 2011; Schaeffer et al., 2012; Schuster et al., 2018) .

12.3.4.3 Lake, river and sea ice

Reductions in the duration of thick sea, lake and river ice influence ecosystems as well as ice fishing, hunting, dog sledding, and snowmobiling; which are recreation activities for some but vital aspects of many traditional indigenous communities (Durkalec et al., 2015; AMAP, 2017a; Baztan et al., 2017; Arp et al., 2018; Rokaya et al., 2018; Knoll et al., 2019; Meredith et al., 2019; Sharma et al., 2019). The seasonal extent of thin ice and iceberg density also determines the viability of shipping lanes and seasonal roads (Valsson and Ulfarsson, 2011; Pizzolato et al., 2016; AMAP, 2017; Mullan et al., 2017; Sturm et al., 2017), oil and gas exploration timing (Schaeffer et al., 2012) and the seasonality of phytoplankton blooms (Oziel et al., 2017). Sea ice is a critical aspect of some ecosystems and fisheries (Massom and Stammerjohn, 2010; Jenouvrier et al., 2014; Bindoff et al., 2019; Meredith et al., 2019). Various definitions of 'ice free' Arctic Ocean conditions can be tailored to represent transportation needs, including thresholds of ice coverage (< 5% or < 30% or < 1 million km^2) in September or over a 4-month period (Laliberté et al., 2016; Jahn, 2018).

12.3.4.4 Heavy snowfall and ice storm

Heavy snowfall is a substantial concern for cities, settlements, and key transportation and energy infrastructure (Ward, 2013; Palko, 2017; Janoski et al., 2018; Collins et al., 2019). Heavy snowfall can interfere with transportation (Herring et al., 2018) and cause a loss of both work and school days depending on local snow removal infrastructure. Freezing rain and ice storms can be treacherous for road and air travel (Tamerius et al., 2016), and can knock down power and telecommunication lines if ice accumulation is high (Degelia et al., 2016). Rain-on-snow events can create a solid barrier that hinders wildlife and livestock grazing that is important to indigenous communities (Forbes et al., 2016). Shifts in the frequency, seasonal timing and regions susceptible to ice storms shift risks for agriculture and infrastructure (Lambert and Hansen, 2011; Klima and Morgan, 2015; Ning and Bradley, 2015; Groisman et al., 2016).

12.3.4.5 Hail

Information on the changing frequency and size distribution of hail can help stakeholders build resilience for agriculture, vehicles, transportation infrastructure and buildings, solar panels, and wild species that see critical damage at particular hail size thresholds (Dessens et al., 2007; Webb et al., 2009; Patt et al., 2013; Fiss et al., 2019). Most climate models do not directly resolve hail and therefore studies often examine proxies associated with severe mesoscale storms (Tippett et al., 2015; Prein and Holland, 2018) although some regional studies now utilize hail-resolving models (Mahoney et al., 2012; Brimelow et al., 2017).

12.3.4.6 Snow avalanche

Information about the changing frequency and seasonal timing of snow avalanches is important to assess threats to transportation routes, infrastructure, recreational skiing, and people living in alpine communities

ACCEPTED VERSION SUBJECT TO FINAL EDITS

(Lazar and Williams, 2008; Mock et al., 2017; Ballesteros-Cánovas et al., 2018; Hock et al., 2019). Like landslides and other mass movements, snow avalanches are not directly resolved by climate models and are thus tracked using proxy climate information describing snow avalanche susceptibility, particularly the snow water equivalent, and triggering mechanisms such as heatwaves, high winds, rain-on-snow and heavy precipitation (Hock et al., 2019). The quality of snow also provides insight into avalanche hazards (Mock et al., 2017), with the seasonal altitude of wet snowpack (>0 .5% liquid water by volume) particularly important in determining characteristics of potential avalanches (Castebrunet et al., 2014).

12.3.5 Coastal

The recent IPCC Special Report on the Ocean and Cryosphere in a Changing Climate included in-depth discussions of threats facing the world's coastlines (IPCC, 2019b) and Section 9.6 provides further discussion on coastal processes. Here we note major connections between coastal CIDs and ecosystem and societal assets near coastlines.

12.3.5.1 Relative sea level

Sea level rise hazards for coastal ecosystems, infrastructure, farmland, cities and settlements in a particular region are often driven by regional changes in relative sea level (RSL) that accounts for land uplift or subsidence and thus represents local asset vulnerability better than global mean sea level (Hallegatte et al., 2013; Hinkel et al., 2013; McInnes et al., 2016; Weatherdon et al., 2016; Brown et al., 2018; IPCC, 2019b; Rasoulkhani et al., 2020) (Box 9.1). Vertical land motion (i.e. land subsidence) caused by local fluid (gas or groundwater) extraction can also have a large influence on relative sea levels (Minderhoud et al., 2020). Several indices have been suggested to signify coastal inundation, including a threshold when the local land elevation falls below the local mean higher-high water (MHHW) that is close to the 'high tide' level (Kulp and Strauss, 2019) or a threshold when flooding occurs about once every two weeks (Sweet and Park, 2014; Dahl et al., 2017b). RSL rise (or RSLR) can drive increased inland penetration of above-ground and subterranean salt water fronts (i.e., salinity intrusion) affecting coastal ecosystems, agriculture, and water resources (Ferguson and Gleeson, 2012; Kirwan and Megonigal, 2013; Rotzoll and Fletcher, 2013; Chen et al., 2016; Colombani et al., 2016; Holding et al., 2016; Sawyer et al., 2016; Mohammed and Scholz, 2018). The rate of RSLR can determine the survival and net pressure on niche coastal ecosystems such as mangroves, tidal flats, sea grasses and coral reefs (Hubbard et al., 2008; Craft et al., 2009; Bell et al., 2013; Kirwan and Megonigal, 2013; Alongi, 2015; Ellison, 2015; Lovelock et al., 2015; Ward et al., 2016; Lee et al., 2018).

12.3.5.2 Coastal flood

Episodic coastal flooding of coastal communities, farmland, buildings, transportation routes, industry and other infrastructure is caused by Extreme Total Water Levels (ETWL), which is the combination of RSL, tides, storm surge and high wave setup at the shoreline (Vitousek et al., 2017; Melet et al., 2018; Vousdoukas et al., 2018, 2020a; Koks et al., 2019; Kirezci et al., 2020). Coastal settlement and infrastructure design often uses coastal flooding metrics such as the ETWL frequency distribution or the 100-year average return interval storm tide (storm surge + high tide) level (McInnes et al., 2016; Mills et al., 2016; Walsh et al., 2016b; Zheng et al., 2017). The duration of floods that overtop coastal protection, due to Extreme Coastal Water Levels (ECWL) is important for port and harbour operations and coastal energy infrastructure thresholds (Bilskie et al., 2016; Camus et al., 2017). Frequent inundation by salt water can also have significant impacts on water resources, crops, aquaculture and transportation systems due to corrosion and undercutting of coastal roads, bridges, and rails (Zimmerman and Faris, 2010; Ahmed et al., 2019b; Gopalakrishnan et al., 2019).

12.3.5.3 Coastal erosion

ACCEPTED VERSION SUBJECT TO FINAL EDITS

Effective management of coastal ecosystems, cities, settlements, beaches and infrastructure requires information about coastal erosion driven by storm surge, waves, and sea level rise (Dawson et al., 2009; Harley et al., 2017; Mentaschi et al., 2017 Hinkel et al., 2013). Coastal erosion is generally accompanied by shoreline retreat, which can occur as a gradual process (e.g., due to sea level rise) or as an episodic event due to storm surge and/or extreme waves, especially when combined with high tide (Ranasinghe, 2016). The most commonly used shoreline retreat index is the magnitude of shoreline retreat by a pre-determined planning horizon such as 50 or 100 years into the future. Commonly used metrics for episodic coastal erosion include the beach erosion volume due to the 100 yr recurrence storm wave height, the full exceedance probability distribution of coastal erosion volume (Li et al., 2014; Pender et al., 2015; Ranasinghe and Callaghan, 2017) and the cumulative storm energy and storm power index (Godoi et al., 2018). The destruction or overtopping of barrier islands may lead to irreversible changes in the physical system as well as in coastal ecosystems (Carrasco et al., 2016; Zinnert et al., 2019). Shoreline position change rates along inlet-interrupted coasts may also be affected by changes in river flows and fluvial sediment supply (Hinkel et al., 2013; Bamunawala et al., 2018; Ranasinghe et al., 2019). Permafrost thaw and Arctic sea ice decline also reduce natural coastal protection from wave erosion for communities and industry (Forbes, 2011; Melvin et al., 2017).

12.3.6 Oceanic

Oceanic changes and impacts were a substantial focus of the recent IPCC Special Report on the Ocean and Cryosphere in a Changing Climate (IPCC, 2019b). Chapter 9 assesses changes in ocean processes, and here we note major connections used by scientists to understand how oceanic CIDs affect ecosystems and society.

12.3.6.1 Mean ocean temperature

Shifts in thermal zones affect the suitability of fisheries and marine and coastal species habitat and migration routes (Hoegh-Guldberg and Bruno, 2010; Doney et al., 2012; Burrows et al., 2014; Urban, 2015; Hixson and Arts, 2016; Tripathi et al., 2016; Ahmed et al., 2019b; Bindoff et al., 2019). Intertidal species are particularly dependent on suitable conditions for both air and sea surface temperatures (Monaco and McQuaid, 2019). The structure of ocean warming also affects the intensity of upper-ocean stratification and the timing and strength of coastal upwelling (driven also by mean wind changes), which alters the vertical transport of oxygen- and nutrient-rich waters affecting fishery and marine ecosystem productivity (Wang et al., 2015).

12.3.6.2 Marine heatwave

Marine heatwaves (MHW) push water temperatures above key thresholds and have been associated with coral bleaching episodes, species shifts, and harmful algal blooms that can disrupt ecosystems, tourism and human health (see Box 9.2; Wernberg et al., 2016; Arias-Ortiz et al., 2018; Oliver et al., 2018; Frölicher, 2019; Smale et al., 2019; Sully et al., 2019). The duration and return period of marine heatwaves provide insight into aggregate stresses on marine species, fisheries and ecosystems, with various indices gauging cumulative intensity or the number of days, weeks or months exceeding critical thresholds (Frieler et al., 2013; Frölicher et al., 2018; Hughes et al., 2018b; Cheung and Frölicher, 2020). Hobday et al. (2016) defined marine heatwaves as the exceedance of the 30-year 90th percentile of the sea surface temperature (SST) distribution on a given Julian day during 5 or more consecutive days, while Box 9.2, Figure 1 shows MHW as an exceedance of 99th-percentile 11-day de-seasonalised SSTs. The return period of marine heatwaves is also critical in determining a coral system's ability to recover before the next event (Hughes et al., 2018a).

12.3.6.3 Ocean acidity

Uptake of atmospheric CO_2 and subsequent increases in dissolved CO_2 lowers ocean pH and can reduce

ACCEPTED VERSION SUBJECT TO FINAL EDITS

carbonate ion concentrations below critical calcium carbonate saturation thresholds for marine and aquatic organisms growth, reproduction and/or survival with extended implications for marine ecosystems including fisheries (Bell et al., 2013; Kroeker et al., 2013; Barange et al., 2014; Mathis et al., 2015a; Nagelkerken and Connell, 2015; Dutkiewicz et al., 2015; Ekstrom et al., 2015; Gattuso et al., 2015; Nagelkerken and Munday, 2016; Tripathi et al., 2016; Behrenfeld et al., 2016b; Weiss et al., 2018; Jiang et al., 2018; Ahmed et al., 2019b; Bindoff et al., 2019). Lower pH may provide more favourable conditions for toxic algal blooms (Riebesell et al., 2018) and can interact with hypoxic zones to impact ecosystems (Gobler and Baumann, 2016; Cai et al., 2017).

12.3.6.4 Ocean Salinity

Changes in currents, sea ice brine rejection and net freshwater flux in the ocean can alter salinity with effects on mixed layer structure, density stratification, and the vertical movement of nutrients and marine organisms (Freeland, 2013; Haumann et al., 2016).

12.3.6.5 Dissolved oxygen

Ocean warming and increased stratification decrease the oxygen content of the ocean (Griffiths et al., 2017; Schmidtko et al., 2017; Bindoff et al., 2019), lead to an expansion of oxygen minimum zones in the open ocean (Stramma et al., 2012; Zhang et al., 2013) and exacerbate the creation of anoxic "dead zones" in the coastal oceans (Breitburg et al., 2018). Such a decline (characterized by successive dissolved oxygen concentration thresholds) could affect a wide range of marine organisms and reduce marine habitats (Chan et al., 2008; Vaquer-Sunyer and Duarte, 2008; Hoegh-Guldberg and Bruno, 2010; Altieri and Gedan, 2015; Breitburg et al., 2018) and can also lead to further local acidification (Zhang and Gao, 2016; Laurent et al., 2017).

12.3.7 Other climatic impact-drivers

12.3.7.1 Air pollution weather

Although future air pollution will be strongly driven by air quality policies, anthropogenically-driven changes to temperature, humidity, precipitation, and synoptic patterns have the potential to affect the emissions, production, concentration and transport of particulate matter (e.g., from dust, fires, pollen), and gaseous pollutants such as sulphur dioxide, tropospheric ozone, and nitrogen dioxide (see Section 6.5) with resulting impacts on human health, agriculture and ecosystems (Ren et al., 2011; Fiore et al., 2015; Kinney et al., 2015a; Tian et al., 2016; Orru et al., 2017; Emberson et al., 2018; Hayes et al., 2020). Information about conditions leading to poor air quality is also important for visibility in natural parks and tourist locations (Yue et al., 2013; Val Martin et al., 2015), as well as the efficiency of solar photovoltaic panels (Sweerts et al., 2019). Relevant information about conditions favouring air pollution includes tracking warmer conditions that accelerate ozone formation (Peel et al., 2013; Schnell et al., 2016) and the frequency and duration of stagnant air events (Horton et al., 2014; Fann et al., 2015; Lelieveld et al., 2015; Vautard et al., 2018), although no regional index has proven sufficient to capture regional changes or acute events (Kerr and Waugh, 2018; Schnell et al., 2018) whereas precipitation and moister air tend to reduce pollution (Section 6.5).

12.3.7.2 Atmospheric Carbon Dioxide (CO_2) at surface

CO_2 is a well-mixed greenhouse gas with global repercussions on the Earth's energy balance; however, atmospheric CO_2 concentration changes at the land surface also affect plant functions within ecosystems and agriculture (see also Chapter 5). High CO_2 concentration can increase photosynthesis rates and primary production within natural ecosystems (Norby et al., 2010; Ratliff et al., 2015; Zhu et al., 2016) and

ACCEPTED VERSION SUBJECT TO FINAL EDITS

agricultural crops (Hatfield et al., 2011; Leakey et al., 2012; Bell et al., 2013; Glenn et al., 2014; Nagelkerken and Connell, 2015; Behrenfeld et al., 2016a; Deryng et al., 2016; Kimball, 2016). High CO_2 concentration affects total biomass and plant sugar content important to bioenergy production (Schaeffer et al., 2012), but also helps some pests and weeds flourish (Hamilton et al., 2005; Wolfe et al., 2008; Valerio et al., 2013; Korres et al., 2016; Stinson et al., 2016; Ramesh et al., 2017) while potentially shifting the effectiveness of herbicides (Varanasi et al., 2016; Refatti et al., 2019). Higher CO_2 concentration reduces transpiration losses during drought conditions (Cammarano et al., 2016; Deryng et al., 2016; Swann et al., 2016; Durand et al., 2018), which also changes the energy balance within the plant canopy (Webber et al., 2017). Higher CO_2 reduces the nutritional density of crops and forage lands (Loladze, 2014; Müller et al., 2014; Myers et al., 2014, 2017; Li et al., 2016c; Lee et al., 2017b; Smith and Myers, 2018; Zhu et al., 2018; Beach et al., 2019) and can increase the production of toxins (Ziska et al., 2007) and allergenic pollen (Schmidt, 2016).

12.3.7.3 Radiation at surface

Changes in surface solar and longwave radiation fluxes alter photosynthesis rates and potential evapotranspiration for natural ecosystems and food, fibre, and energy crops (Mäkinen et al., 2018) and shift solar energy resources (Schaeffer et al., 2012; Jerez et al., 2015; Wild et al., 2015; Fant et al., 2016; Craig et al., 2018). Plants and aquatic systems particularly respond to changes in photosynthetically-active radiation (PAR) and the fraction of diffuse radiation (Proctor et al., 2018; Ren et al., 2018; Ryu et al., 2018). Increases in ultraviolet radiation can also detrimentally affect ecosystems and human health (Barnes et al., 2019).

12.3.7.4 Additional relevant climatic impact-drivers

Additional CIDs may be relevant for regional studies but are not the focus of assessment in this report. For example, information about changes in the frequency and seasonal timing of fog helps anticipate airport delays and cool beach days, and is also important for water delivery and retention in coastal ecological and agricultural systems (Torregrosa et al., 2014).

Threats to many sectoral assets and associated systems may also be compounded when multiple hazards occur simultaneously in the same place, affect multiple regions at the same time, or occur in a sequence that may amplify overall impact (see Section 11.8; Clarke et al., 2018; IPCC, 2012a; Raymond et al., 2020; Zscheischler et al., 2018). There is emerging literature on many connected extremes and their associated hazards (e.g., climatic conditions that could drive multi-breadbasket failures; Kornhuber et al., 2019; Trnka et al., 2019), but a full accounting is not practical here especially considering the many possible CID combinations and the need to assess how exposed systems would be vulnerable to compound CIDs (assessed in Working Group II). Table 12.2 is once again instructive here in considering hazard-related storylines, as the multiple CIDs affecting a given sectoral asset (assessing across a row of Table 12.2) point to potentially dangerous hazard combinations. Similarly, change in a single CID has the potential to affect multiple sectoral assets (assessing down a column of Table 12.2) in a manner with broader systemic implications (see AR6 WGII).

Recent literature defines CID indices to represent trends and thresholds that influence sectoral assets, albeit with considerable variation owing to the unique characteristics of regional and sectoral assets. Indices include direct information about the CID's profile (magnitude, frequency, duration, timing, spatial extent) or utilize atmospheric conditions as a proxy for CIDs that are more difficult to directly observe or simulate. Each sector is affected by multiple CIDs, and each CID affects multiple sectors. Assets within the same sector may require different or tailored indices even for the same CID. These indices may be defined to capture graduated thresholds associated with tipping points or inflection points in a particular sectoral vulnerability, with commonalities in the types of processes these thresholds represent even as their precise magnitude may vary by specific sectoral system and asset.

ACCEPTED VERSION SUBJECT TO FINAL EDITS

12.4 Regional information on changing climate

This section describes the historical and projected changes in commonly used indices and thresholds associated with the main climatic impact-drivers (see 12.2 and 12.3) at the scale of AR6 regions described in (Figure 1.18a). The section is organised by continents (12.4.1-12.4.6) with a specific assessment for small islands (12.4.7), open and deep ocean (12.4.8), and Polar regions (12.4.9) as defined in Chapter 1 (Figure 1.18c). In addition, CID indices and thresholds relevant to and *Specific zones*, as defined in WGII AR6 "Cross-Chapter Papers", are assessed in Section 12.4.10 except for the Mediterranean, which is addressed both under Africa and Europe (12.4.1 and 12.4.5) and is a focus in 10.6.4.

Regional assessment method and tables: In each section herein (12.4.1 – 12.4.10), we assess changes in sector-relevant CIDs following the main CID categories defined in Section 12.2 through commonly used indices and thresholds relevant for sectors described in 12.3. Sections 12.4.1-12.4.9 each include a summary qualitative CID assessment table (Tables 12.3-12.11) showing the confidence levels associated with the direction of projected CID changes (i,e increasing or decreasing) for the mid-century period (2041-2060) relative to the recent past, for scenarios RCP4.5, SSP2-4.5, SRES A1B, or above (RCP6.0, RCP8.5, SSP3-7.0, SSP5-8.5, SRES A2), which approximately encompasses Global Warming Levels of 2.0°C to 2.4°C (as best estimate, see Chapter 4, Table 4.5). For Scenarios RCP2.6, SSP1-2.6 or SSP1-1.9, the signal may have lower confidence levels in some cases due to smaller overall changes, embedded in a similar internal variability, and to the availability of relatively few studies that account for these scenarios. Nevertheless, CID changes under these lower emissions scenarios are included in the text whenever information is available. For each cell in Tables 12.3-12.11, literature is assessed, aided by global Figure 12.4 or regional Figures 12.5-12.10. Confidence in projections is established considering evidence emerging from observations, attribution and projections, as explained in CCBox 10.3 while considering the amount of evidence and agreement across models and studies and model generations.

The confidence levels associated with the directions of projected CID changes are synthesized assessments based on literature that may utilize different indices and baseline periods or projections by global warming levels. For extreme heat, cold spell, heavy precipitation and drought CIDs that are assessed in Chapter 11, here we draw projections from the 2°C global warming level tables in Section 11.9. In some cases, more details are needed in order to emphasize one aspect of projected CID change. For instance, the change in a CID may be different for intensity, duration, frequency; or there can be strong sub-regional or seasonal signals; or different CID indices may have conflicting signals. A footnote is added in such cases, but a confidence level for a direction of projected change is given based on the 12.3 assessment of aspects of regional CID change that are most relevant for impacts and for risks. As an example, tropical cyclones are increasing in intensity but decreasing in frequency in some regions. Here, in assessing the confidence of the direction of projected change in the Tropical cyclone CID (i.e. the colour of the table cell), we assign more weight to the "intensity" rather than the "frequency", corresponding to the higher relevance of the intensity major tropical cyclones for risk assessment. Low confidence of changes, arising from lack of evidence, strong spatial or seasonal heterogeneity, or lack of agreement are represented by colour-less cells, and, for the sake of simplicity, only two categories of confidence are given: "*medium confidence*" and "*high confidence*" (and higher). In addition, CID assessment tables also indicate observed or projected emergence of the CID change signal from the natural inter-annual variability if assessed with at least *medium confidence* in Section 12.5.2, using as a basis a criterion of S/N > 1, noise being defined as the interannual variability. The time of emergence (ToE) is given as either: (i) already emerged in the historical period, or (ii) emerging by 2050 at least for RCP8.5/SSP5-8.5, or (iii) emerging after 2050 but before 2100 at least for scenarios RCP8.5 or SSP5-8.5. Table cells that do not include emergence information are indicative of "*low confidence* of emergence in the 21st century", which includes situations where assessment indicates emergence will not occur before 2100 or that evidence is not available or insufficient for a confidence assessment of time of emergence.

Figures: The assessment of changes in CIDs is based on literature, physical understanding (Chapters 2-11), and global and regional climate projections of indices and thresholds presented in the Atlas, as well as in the global and regional figures in 12.4 (Figures 12.4-12.10) showing the future evolution of 9 key CID indices/thresholds used in this assessment (see also Cross-Chapter Box 10.3). The figure indices and

ACCEPTED VERSION SUBJECT TO FINAL EDITS

impacts-relevant thresholds are described in the Technical Annex VI on Climatic impact-drivers and Extreme Indices.

Figure 12.4 shows changes in 6 CID indices. These global maps are derived from CMIP6 simulations for different time periods and scenarios (except for Extreme Total Water Level where CMIP5 is used). The uncertainty due to climate models, time, scenarios and regional downscaling is illustrated in Supplementary Figures SM.12.1 to SM.12.6 which show the distribution of the spatial average of the index among models over each land region for CMIP5, CMIP6 and CORDEX ensembles for the recent past, mid- and end-21st century, and for GWLs +1.5ºC, +2ºC and +4ºC. The hatching in the figure covers areas where less than 80% of models agree on the sign of change.

[START FIGURE 12.4 HERE]

Figure 12.4: Median projected changes in selected climatic impact-driver indices based on CMIP6 models. (a-c) mean number of days per year with maximum temperature exceeding 35°C, (d-f) mean number of days per year with the NOAA Heat Index (HI) exceeding 41°C, (g-i) number of negative precipitation anomaly events per decade using the 6-month Standardised Precipitation Index, (j-l) mean soil moisture (%) and (m-o) mean wind speed (%). (p-r) shows change in extreme sea level (1:100 yr return period total water level from Vousdoukas et al. (2018)'s CMIP5 based dataset; meters). Left column is for SSP1-2.6, 2081-2100, middle column is for SSP5-8.5 2041-2060, and right column SSP5-8.5, 2081-2100, all expressed as changes relative to 1995-2014. Exception is extreme total water level which is for (p) RCP4.5 2100, (q) RCP8.5 2050 and (r) RCP8.5 2100, each relative to 1980-2014. Bias correction is applied to daily maximum temperature and HI data (see Technical Annex VI and Atlas.1.4.5). Uncertainty is represented using the simple approach: No overlay indicates regions with high model agreement, where ≥80% of models agree on sign of change; diagonal lines indicate regions with low model agreement, where <80% of models agree on sign of change. For more information on the simple approach, please refer to the Cross-Chapter Box Atlas.1. See Technical Annex VI for details of indices. Figures SM 12.1-12.6 show regionally averaged values of these indices for the WGI reference AR6 regions for various model ensembles, scenarios, time horizons and global warming levels. Further details on data sources and processing are available in the chapter data table (Table 12.SM.1).

[END FIGURE 12.4 HERE]

Further regional detail is provided for the remaining indices in each continental section in the form of continental maps accompanied by regional box plots displaying changes calculated for AR6 region averages, and the associated regionally averaged uncertainty.

Climatic impact-drivers changing in a globally coherent way: For the sake of conciseness, assessments pertaining to ocean acidity and the 'Other' CID type in 12.2 and 12.3 are not provided per region in Sections 12.4.1-9 but are summarised here given the globally coherent way in which they change.

Ocean acidity: Observations show increasing ocean acidification (*robust evidence, high agreement*), and it is *virtually certain* that future ocean acidification will increase given future increases in greenhouse gases (5.4). Areas below calcium carbonate saturation thresholds expanded from the 1990s-2010 and Meredith et al. (2019) indicated that both the Southern and Arctic Oceans will experience year-round under-saturation conditions by 2100 under RCP8.5. The vertical level of the aragonite saturation horizon off the Pacific coast of North America has risen toward the surface by 30-50 m since pre-industrial times (Mathis et al., 2015b; Feely et al., 2016). In a study of US coastlines, Ekstrom et al. (2015) mapped out the projected year when aragonite saturation state drops below 1.5 (a sublethal threshold for bivalve mollusk larvae), finding hazardous conditions before 2030 from northern Oregon to Alaska and before 2100 for the Pacific coast and Atlantic coastline north of New Jersey. Mathis et al. (2015a) found that surface waters in the Beaufort Sea have already dropped below aragonite saturation thresholds, projecting further declines and the Chukchi Sea also dropping below saturation by ~2030.

Air pollution weather: The effect of climate change on air quality is assessed in Section 6.5 with limitations

ACCEPTED VERSION SUBJECT TO FINAL EDITS

for local planning explained in 6.1.3, and only a brief summary is given here. Section 6.5 notes that climate change will have a small burden on particulate matter (PM) pollution (*medium confidence*) while the main controlling factor in determining future concentrations will be future emissions policy for PM and their precursors (*high confidence*). Surface ozone is sensitive to temperature and water vapor changes, but future levels depend on precursor emissions. Although there is *low confidence* in precise regional changes (Section 6.5), climate change will generally introduce a surface O_3 penalty (increasing concentrations with increasing warming levels) over regions with high anthropogenic and/or natural ozone precursor emissions, while in less polluted regions higher temperatures and humidity favor destruction of ozone (Schnell et al., 2016). There is *low confidence* in changes to future stagnation events given the lack of robust projections of related atmospheric conditions, such as future atmospheric blocking events (Sections 3.3.3, 8.4.2). The response of regional air pollution to climate change will also be affected by other CIDs like fire weather, as well as by ecosystem responses such as shifts in emissions by vegetation (Fiore et al., 2015). Section 6.5 assessed *medium confidence* that climate driven changes to meteorological conditions generally favor extreme air pollution episodes in heavily polluted environments, but noted strong regional and metric dependencies. Given the dominant influence of future air quality policies, uncertainties around stagnation or blocking events, and the potential contrasting regional changes of conditions favoring ozone and PM formation, accumulation and destruction, cells in Tables 12.3-12.11 for air pollution weather are marked as *low confidence*, and the reader is referred to Section 6.5 for further details.

Atmospheric CO_2 at surface: Observations show rising atmospheric CO_2 concentrations at the surface over all earth regions *(robust evidence, high agreement*) (Sections 2.2, 5.1.1), and it is *virtually certain* that surface atmospheric CO_2 concentrations will continue to increase absent substantial changes to emissions (Section 5.4).

Radiation at surface: Radiation has undergone decadal variations in past observations which are mostly responding to the so-called dimming and brightening phenomenon driven by the increase and decrease of aerosols. Over the last two decades or so, brightening continues in Europe and Northern America and dimming stabilizes over South and East Asia and increases in some other areas (7.2.2.3). Future regional shortwave radiation projections depend mostly on cloud trends, aerosol and water vapour trends, and stratospheric ozone when considering UV radiation. Over Africa in 2050 and beyond, there is *medium confidence* that radiation will increase in North and South Africa and decrease over the Sahara, North-East Africa and West Africa (Wild et al., 2015, 2017; Soares et al., 2019; Tang et al., 2019b; Sawadogo et al., 2020a, 2020b). Over Asia, the CMIP5 multi-model-mean response shows that solar radiation will decrease in South Asia and increase in East Asia (*medium confidence*) by the mid-century RCP8.5 (Wild et al., 2015, 2017; Ruosteenoja et al., 2019a). Projected solar resources show an increasing trend throughout the 21st century in east Asia under RCP2.6 and RCP8.5 scenarios in CMIP5 simulations (Wild et al., 2015; Zhang et al., 2018a; Shiogama et al., 2020) (*medium confidence*). More sunshine is projected over Australia in winter and spring by the end of the century (*medium confidence*) with the increases in southern Australia exceeding 10% (CSIRO and BOM, 2015; Wild et al., 2015). In Central and South America, there is *medium confidence* of increasing solar radiation over the Amazon Basin and the Northern part of South America (Wild et al., 2015, 2017; de Jong et al., 2019) (*medium confidence*). There is *low confidence* for an increase in surface radiation in Central Europe, owing in particular to disagreement in cloud cover across global and regional models (Jerez et al., 2015; Bartók et al., 2017; Craig et al., 2018), as well as water vapor. The treatment of aerosol appears to be key in explaining these differences (Boé, 2016; Undorf et al., 2018; Boé et al., 2020; Gutiérrez et al., 2020). Regional and global studies however indicate that there is *medium confidence* in increasing radiation over Southern Europe and decreasing radiation over Northern Europe. Increasing radiation trends are also found over Southern and Eastern U.S.A., and decreasing trends over North Western North America (Wild et al., 2015; Losada Carreño et al., 2020), despite large differences between responses from RCMs and GCMs over South and Eastern U.S.A. (*low confidence*), where, as for central Europe, the role of aerosols appears important (Chen, 2021). Over polar regions there is *medium confidence* of a decrease in radiation due to increasing moisture in the atmosphere and clouds (Wild et al., 2015).

ACCEPTED VERSION SUBJECT TO FINAL EDITS

12.4.1 Africa

Previous IPCC assessments results are summarized in the Atlas section 4.1.1 For the purpose of this assessment the Africa region has been divided in 9 sub regions of which 8 Sahara (SAH), Western Africa (WAF), Central Africa (CAF), North East Africa (NEAF), South East Africa (SEAF), West Southern Africa (WSAF), East Southern Africa (ESAF) and Madagascar (MDG) are the official AR6 regions (see Figure Atlas.2) and one North Africa is used in this assessment to indicate the African portion of the Mediterranean region.

Quite a large body of new literature is now available for the African climate as a result of regionally downscaled CORDEX Africa outputs, in particular, providing projections of both the mean climate (Mariotti et al., 2014; Nikulin et al., 2018; Dosio et al., 2019; Teichmann et al., 2020) and extreme climate phenomena (Giorgi et al., 2014; Nikulin et al., 2018; Dosio et al., 2019; Coppola et al., 2021b). CORDEX Africa simulations are assessed in the Atlas, which finds reasonable skill in mean temperature and precipitation as well as important features of regional climate (e.g., timing of monsoon onset in West Africa) although lower performance in Central Africa.

[START FIGURE 12.5 HERE]

Figure 12.5: Projected changes in selected climatic impact-driver indices for Africa. (a) Mean change in 1-in-100 year river discharge per unit catchment area (Q100, $m^3\ s^{-1}\ km^{-2}$) from CORDEX models for 2041-2060 relative to 1995-2014 for RCP8.5. (b) Shoreline position change along sandy coasts by the year 2100 relative to 2010 (meters; negative values indicate shoreline retreat) from the CMIP5 based data set presented by Vousdoukas et al., (2020). (c) Bar plots for Q100 ($m^3\ s^{-1}\ km^{-2}$) averaged over land areas for the WGI reference AR6 regions (defined in Chapter 1). The left column within each panel (associated with the left y-axis) shows the 'recent past' (1995-2014) Q100 absolute values in grey shades. The other columns (associated with the right y-axis) show the Q100 changes relative to the recent past values for two time periods ('mid' 2041-2060 and 'long' 2081-2100) and for three global warming levels (defined relative to the preindustrial period 1850-1900): 1.5°C (purple), 2°C (yellow) and 4°C (brown). The bars show the median (dots) and the 10^{th}-90^{th} percentile range of model ensemble values across each model ensemble. CMIP6 is shown by the darkest colors, CMIP5 by medium, and CORDEX by light. SSP5-8.5/RCP8.5 is shown in red and SSP1-2.6/RCP2.6 in blue. (d) Bar plots for shoreline position change show CMIP5 based projections of shoreline position change along sandy coasts for 2050 and 2100 relative to 2010 for RCP8.5 (red) and RCP4.5 (blue) from Vousdoukas et al., (2020). Dots indicate regional mean change estimates and bars the 5^{th}-95^{th} percentile range of associated uncertainty. Note that these shoreline position change projections assume that there are no additional sediment sinks/sources or any physical barriers to shoreline retreat. See Technical Annex VI for details of indices. Further details on data sources and processing are available in the chapter data table (Table 12.SM.1).

[END FIGURE 12.5 HERE]

12.4.1.1 Heat and cold

Mean air temperature: The African continent has experienced increased warming since the beginning of the 20th century in regions where measurements allow a sufficient homogeneous observation coverage to estimate trends (*high confidence*) (Figure Atlas.11). This warming is *very likely* attributable to human influence (Chapter 3, Atlas.4.2) at continental scale. Mean annual temperature have increased in recent decades at a high rate since the mid-20th century, reaching 0.2-0.5°C/decade in some regions such as north, north-eastern, west and south-western Africa (*high confidence*) (Atlas.4.2, Figure Atlas.11).

It is *very likely* that temperatures will increase in all future emission scenarios and all regions of Africa (Atlas.4.4). By the end of century under RCP8.5 or SSP5-8.5, all African regions will *very likely* experience a warming larger than 3°C except Central Africa where warming is *very likely* expected above 2.5°C under, while under RCP2.6 or SSP1-2.6, the warming remains *very likely* limited to below 2°C (Figure Atlas.19). A *very likely* warming with ranges between 0.5°C and 2.5°C is projected by the mid-century for all scenarios

ACCEPTED VERSION SUBJECT TO FINAL EDITS

depending on the region *(high confidence)*. Mean temperature for all regions are projected to increase with increasing global warming (*virtually certain*) (Figure Atlas.19).

Extreme heat: Warm extremes have increased in most of the regions (*high confidence*), NEAF and MDG (*medium confidence*) and with *low confidence* in CAF and SEAF (Chapter 11, Table 11.4). Despite the increasing mean temperature, there is *low confidence* (*limited evidence*) that Africa has experienced increased extreme heat stress trend for agriculture or human health in the last two decades of the 20th century in a few regions such as West Africa, South Africa and North Africa considering the period from 1973 to 2012 (Knutson and Ploshay, 2016).

A substantial increase in heatwave magnitude and frequency over most of the Africa domain is projected for even 2°C global warming (*high confidence*) (Chapter 11, 11.3,11.9, Table 11.4,), with potential effects on health and agriculture. The number of days with maximum temperature exceeding 35°C is projected to increase (Coppola et al., 2021b) in the range of 50-100 days by 2050 under SSP5-8.5 in WAF, ESAF and WSAF and NEAF (*high confidence*) (Figure 12.4b). Under SSP1-2.6, the change in the number of exceedance days remains limited to about 40-50 days per year at the end of the Century, at the end of the century in these regions, while it increases by 150 days or more in WAF, CAF, NEAF for SSP5-8.5 (Figure 12.4a,c).

Mortality-related heat stress levels and deadly temperatures are *very likely* to become more frequent in the future in RCP8.5/SSP5-8.5 and RCP4.5/SSP2-4.5 and for a 2°C global warming (Mora et al., 2017; Nangombe et al., 2018; Sylla et al., 2018; Rohat et al., 2019; Sun et al., 2019b). In particular the equatorial regions where heat is combined with higher humidity levels, but also North Africa, the Sahel and Southern Africa (Figure 12.4d-f) are among the regions with largest increases of heat stress (Zhao et al., 2015; Ahmadalipour and Moradkhani, 2018; Coffel et al., 2018). Mitigation scenario make a large difference in frequency of exceedance of high heat stress indices thresholds (e.g., HI>41°C) by the end of the century (Figure 12.4d-f) (Schwingshackl et al., 2021). In West Africa and Central Africa, under SSP5-8.5, the expected number of days per year with HI>41°C will increase by around 200 days while in SSP1-2.6 such exceedances are expected to increase by less than 50 days per year (Figure 12.4).

Cold spell and frost: Africa experiences cold events and frost days that can affect agriculture, infrastructure, health and ecosystems, especially in South and North Africa, which have marked cold seasons, and mountainous areas. Cold spells have *likely* decreased in frequency over subtropical areas. In particular, in North and Southern Africa, the frequency of cold events has *likely* decreased in the last few decades (Chapter 11,11.3,11.9). There is a *high confidence* that cold spells and low target temperatures will decrease in future climates under all scenarios in West, Central and East Africa. Heating degree days will have a substantial decrease by the end of century for up to about one month under RCP8.5 in North and South Africa(Coppola et al., 2021b) (*high confidence*).

There is *high confidence* that extreme heat has increased in frequency and intensity in most African regions. Heatwaves and deadly heat stress and the frequency of exceedance of hot temperature thresholds (e.g., 35°C) will drastically increase by the end of the century (*high confidence*) under SSP5-8.5, but limited increases are expected in SSP1-2.6. Dangerous heat stress thresholds (HI>41°C) are projected to be crossed more than 200 days more in West and Central Africa under SSP5-8.5 while this increase remains limited to a few tens of days more for SSP1-2.6. Cold spells and frost days are projected to occur less frequently in all scenarios.

12.4.1.2 Wet and dry

Mean precipitation: Since the mid-20th century, precipitation trends have varied in Africa but notable drying trends are found in east, central and north eastern part of South Africa, Central Africa, and in the Horn of Africa (Atlas 4.2).

There is *high confidence* in projected mean precipitation decreases in North Africa and West Southern

ACCEPTED VERSION SUBJECT TO FINAL EDITS

Africa and *medium confidence* in East Southern Africa by the end of the 21st century (see also Dosio et al., 2019; Gebrechorkos et al., 2019; Teichmann et al., 2020) (Atlas.4.5). The West Africa and Northern and Southern East Africa regions each feature a gradient in which precipitation decreases in the west and increases in the east (*medium confidence*) (Atlas.4.5), with trends in West Africa affecting the boreal summer monsoon (Chen et al., 2020). Increasing precipitation for a 1.5°C and 2°C global warming levels are found in central and eastern Sahel with *low confidence* and the wet signal is getting stronger and more extended for a 3°C and 4°C warmer world (Atlas 1.1.5).

A change in monsoon seasonality is also reported in West Africa and Sahel (*low confidence*) with a forward shift in time (later onset and end) (Mariotti et al., 2011; Seth et al., 2013; Ashfaq et al., 2020) (Chapter 8.2). This shift has been associated with a precipitation decrease during the monsoon season attributed to a decrease of African Easterly Wave activity in the 6-9 day regime (Mariotti et al., 2014) and a soil precipitation feedback reported in Mariotti et al. (2011).

River flood: Generally in Africa from 1990 through 2014, annual flood frequencies have fluctuated and there is *medium confidence* in an upward trend in flood events occurrences (Li et al., 2016a). In particular, over West Africa, upward trends in hydrological extremes such as maximum peak discharge have *likely* occurred during the last few decades (i.e., after 1980) and have caused increased flood events in riparian countries of rivers such as Niger, Senegal and Volta (Nka et al., 2015; Aich et al., 2016; Wilcox et al., 2018; Tramblay et al., 2020) (*high confidence*). In Southern Africa, trends in flood occurrences are decreasing prior to 1980 and increasing afterwards (*medium confidence)* (Tramblay et al., 2020).

Under future climate scenarios, the extreme river discharge as characterized by the 30 year return period of 5-day average peak flow, is projected to increase by end of century for the RCP8.5 (more than 10% relative to 1960-1999 period) for most of the tropical African river basins (Dankers et al., 2014) and a consistent increase of flood magnitude across humid tropical Africa by 2050 for the AIB scenario (Arnell et al, 2014) (*medium confidence*) (Figure 12.5). Specifically, in West Africa there is not univocal pattern of change for future projections (Roudier et al., 2014) however under RCP8.5, there is a *medium confidence* of projected increase of 20-year flood magnitudes by 2050 in countries within the Niger river basin (Aich et al., 2016) and a *low confidence* (limited evidence) of an increase in extreme peak flows and their duration in countries of the Volta river basin by 2050 and 2090 (Jin et al., 2018). A significant median change of flood magnitude for the Gambia river (-4.5%) and for the Sessandra (+14.4%) and Niger (+6.1%) are projected under several scenario between mid and end of century (Roudier et al., 2014). In East Africa, extreme flows are projected to increase for region within the Blue Nile with *low confidence* (*limited evidence*) (Aich et al., 2014). However, uncertainty due to the climate scenario dominates the projection of extreme flows (Aich et al., 2014; Krysanova et al., 2017) for the Blue Nile and Niger river basins. Averaged over the African continent for different levels of global warming, the present-day 100-year return period flood levels will have a return period of 40 years in 1.5°C and 2°C (Alfieri et al., 2017) and 21 years for 4°C warmer climate (Hirabayashi et al., 2013b; Alfieri et al., 2017).

Heavy precipitation and pluvial flood: Chapter 11 found that heavy precipitation intensity and frequency has *likely* increased over West Southern Africa but there is no evidence due to a lack of studies that any significant trend is observed in any other region. In addition, East Africa has experienced strong precipitation variability and intense wet spells leading to widespread pluvial flooding events hitting most countries including Ethiopia, Somalia, Kenya and Tanzania (*medium confidence*). Finally, with respect to Southern Africa, heavy precipitations events have increased in frequency (*medium confidence*).

In West Africa and Central Africa, there is *high confidence* that the intensity of extreme precipitation will increase in future climate under both RCP4.5 and RCP8.5 scenarios and 1.5°C and 2°C global warming levels threatening for widespread flood occurrences before, during and after the mature monsoon season. Extreme precipitation is also increasing in several other regions like SAH, NEAF, SEAF, ESAF and Madagascar (*high confidence*) for 2°C GWL and higher (Chapter 11).

Landslide: There is an increase in reported landslides in WAF, CAF, NEAF and SEAF in the past decades but low evidence of significant trends (Gariano and Guzzetti, 2016; Haque et al., 2019). There is *low*

ACCEPTED VERSION SUBJECT TO FINAL EDITS

confidence (*limited evidence*) of a future increase in landslides in Central-Eastern Africa, and literature is largely missing to assess this important hazard (Gariano and Guzzetti, 2016).

Aridity: Section 11.9 assesses *medium confidence* in observed long-term declines of soil moisture and aridity indices in several African regions (NAF, WSAF, ESAF, MDG). Trends in East Africa are not definitive given uncertain balances between precipitation and potential evaporation (Kew et al., 2021). Projected declines in precipitation and soil moisture trends indicate *high confidence* in increased aridity over the 21st century in NAF, WSAF, ESAF, and MDG but *low confidence* elsewhere in Africa (Section 11.9; see also Figure 12.4j-l; Gizaw and Gan, 2017). A growing number of studies provide further regional context on expanding aridity in several places in East and West Africa, respectively (Sylla et al., 2016; Liu et al., 2018b; Haile et al., 2020).

Hydrological drought: Section 11.9 noted observed decreases in hydrological drought over the Mediterranean (*high confidence*) and diminished summertime river flows in West Africa (*medium confidence*). Recent regional modeling studies project substantial increases in hydrological drought affecting major West African river basins under 1.5ºC and 2ºC global warming levels and RCP4.5 and RCP8.5 scenarios; however there remains *low confidence* in future projections given disagreement with global model runoff projections (e.g., Cook et al., 2020) (*low confidence*). There is *high confidence* that a 2 ºC global warming level would see an increase in hydrological droughts in the Mediterranean region, and *medium confidence* in increasing hydrological drought conditions in the Southern Africa regions (Section 11.9).

Agricultural and ecological drought: Farmers and food security experts in East Africa have noted spatial extensions in seasonal agricultural droughts in recent decades (Elagib, 2014), but it is difficult to disentangle these trends from climate variability. In Ethiopia, past severe agricultural drought conditions in the northern regions are moderately common events in recent years (Zeleke et al., 2017). In Southern Africa, the number of "flash" droughts (with rapid onset and durations from a few days to couple of months) have increased by 220% between 1961 and 2016 as a result of anthropogenic warming (Yuan et al., 2018). Section 11.9 notes *medium confidence* increases in agricultural and ecological drought trends in North, West and Central Africa as well as both Southern Africa regions. The most striking drought is the Western Cape drought in 2015-2018, a prolonged drought which resulted in acute water shortages (Wolski, 2018; Burls et al., 2019) (Section 10.6.2). Anthropogenic climate change caused a threefold increase in the probability of such a drought to occur (Botai et al., 2017; Otto et al., 2018) (see also Chapters 10 and 11). Section 11.9 assesses increases in agricultural and ecological drought at 2°C global warming level for North Africa and West Southern Africa (*high confidence*) and for East Southern Africa and Madagascar (*medium confidence*), with confidence generally rising for higher emissions scenarios (see also Sylla et al., 2016; Zhao and Dai, 2017; Diedhiou et al., 2018; Abiodun et al., 2019; Todzo et al., 2020; Coppola et al., 2021). Liu et al. (2018) identified the Southern Africa region as the drought 'hottest spot' in Africa in 1.5 and 2 ºC global warming scenarios.

Fire weather: There is *low confidence* (*low agreement*) in recent reductions in fire activity given soil moisture increases in some regions and substantial land use changes (Andela et al., 2017; Forkel et al., 2019; Zubkova et al., 2019). Days prone to fire conditions are going to increase in all extratropical Africa for end of century and fire weather indices are projected to largely increase in North and South Africa, where increasing aridity trends occur (*high confidence*), with an emerging signal well before the middle of the century where drought and heat increase will combine (Chapter 11) (Engelbrecht et al., 2015; Abatzoglou et al., 2019). There is *low confidence (low evidence)* of fire weather changes for other African regions.

Total precipitation is projected to decrease in the northernmost (*high confidence*) and southernmost regions of Africa (*medium confidence*), with West and East Africa regions each having a west-to-east pattern of decreasing-to-increasing precipitation (*medium confidence*). Most African regions will undergo an increase in heavy precipitation that can lead to pluvial floods (*high confidence*), even as increasing dry climatic impact-drivers (aridity, hydrological, agricultural and ecological droughts, fire weather) are generally projected in the North Africa and Southern African regions (*high confidence*) and western portions of West Africa (*medium confidence*).

ACCEPTED VERSION SUBJECT TO FINAL EDITS

12.4.1.3 Wind

Mean wind speed: Decreasing trends in wind speeds have occurred in many parts of Africa (McVicar et al., 2012; AR5 WGI) (*low confidence* due to observations with limited homogeneity). There is *high confidence* in climate-change induced future decreasing mean wind, wind energy potential and strong winds in North Africa and Mediterranean regions as a consequence of the poleward shift of the Hadley cell (Karnauskas et al., 2018a; Kjellström et al., 2018; Sivakumar and Lucio, 2018; Tobin et al., 2018; Jung and Schindler, 2019) in the RCP4.5 and RCP8.5 scenarios by the middle of the century or beyond, and for a global warming level of 2°C or higher. Over West Africa and South Africa a future significant increase in wind speeds and wind energy potential is expected (*medium confidence*) (Karnauskas et al., 2018a; Jung and Schindler, 2019) (see also Figure 12.4m-o).

Severe wind storm: A limited number of studies allow an assessment of past trends in wind storms. In West Africa and specifically in the Sahel band, more intense storms have occurred since the 1980s (*low confidence, limited evidence*). A persistent and large increase of frequency of Sahelian mesoscale convective storms has been found in several studies (Panthou et al., 2014; Taylor et al., 2017b), with consequences for extreme rainfalls, and potentially on extreme winds (*low confidence, limited evidence*). There is *low confidence* of a general increasing trend in extreme winds across West, Central, East and South Africa in a majority of regions by the middle of the century even in high-end scenarios. The frequency of Mediterranean wind storms reaching North Africa, including Medicanes, is projected to decrease, but their intensities are projected to increase, by the mid-century and beyond under SRES A1B, A2 and RCP8.5, (Cavicchia et al.; Walsh et al., 2014; Tous et al., 2016; Romera et al., 2017; Romero and Emanuel, 2017; González-Alemán et al., 2019) (Chapter 11) (*medium confidence*).

Tropical cyclone. In the Southern Indian ocean, an increase of Category 5 cyclones has been observed in recent decades (Fitchett, 2018) as in other basins (Section 11.7). However, there is a projected decrease in the frequency of tropical cyclones making landfall over Madagascar, South Eastern Africa and East South Africa in a 1°C, 2°C and 3ºC warmer world (*medium confidence*) (Malherbe et al., 2013; Roberts et al., 2015, 2020; Muthige et al., 2018; Knutson et al., 2020). There is *medium confidence* in general increasing intensities for cyclones in such studies for African regions.

Sand and dust storm: North Africa and the Sahel, and to a lesser extent South Africa, are prone to dust storms, having consequences on health (Querol et al., 2019), transmission of infectious diseases (Agier et al., 2013; Wu et al., 2016), and solar power generation and related maintenance costs. There is *limited evidence* and *low agreement* of secular 20th century trends in wind speeds or dust emissions (limited length of data records, large variability). Dust variations are controlled by changes in surface winds, precipitation and vegetation, which in turn are modulated at multiple time scales by dominant modes of internal climate variability (see Chapter 10). In North Africa, wind variability explains both the observed high concentrations between the 1970s and 1980s and lower concentrations thereafter (Ridley et al., 2014; Evan et al., 2016). Yet, the effect of vegetation changes may not be negligible (Pu and Ginoux, 2017, 2018).

Changes to the frequency and intensity of dust storms also remain largely uncertain due to uncertainty in future regional wind and precipitation as the climate warms, CO_2 fertilization effects on vegetation (Huang et al., 2017), and anthropogenic land use and land cover change due to land management and invasive species (Ginoux et al., 2012; Webb and Pierre, 2018). Dust loadings and related air pollution hazards (from fine particles that affect health) are projected to generally decrease in many regions of the Sahara and Sahel due to the changing winds (Evan et al., 2016) and slightly increase over the Guinea Coast and West Africa (*low confidence*) (Ji et al., 2018).

In summary, there is *high confidence* of a decrease in mean wind speed and wind energy potential in North Africa and *medium confidence* of an increase in South and West Africa, by the middle of the century regardless of climate scenario or global warming level equal or superior to 2°C, *high confidence* of a decrease in frequency of cyclones landing in SEAF, ESAF and MDG, and *low confidence* of a general increase in wind storms in most of African regions located Southward of Sahel. The evolution of dust storms remains largely uncertain.

ACCEPTED VERSION SUBJECT TO FINAL EDITS

12.4.1.4 Snow and Ice

Snow and glacier: African glaciers are located in East Africa and more specifically on Mount Kenya, the Rwenzori Mountains and Mount Kilimanjaro, with glaciers reducing substantially in each region (*high confidence*) (Taylor et al., 2006; Cullen et al., 2013; Chen et al., 2018; Prinz et al., 2018; Wang and Zhou, 2019). Observation and future projection of African glacier mass changes are assessed in Section 9.5.1 within the Low Latitude glacier region, which is one of the regions with the largest mass loss even under low-emission scenarios (assessment of this region is dominated by glaciers in the South American Andes, however) (*high confidence*). Glaciers in the Low Latitude region will lose 67 ± 42%, 86 ± 24% and 94 ± 13% of their mass in 2015 by the end of the century for RCP4.5, RCP6.0 and RCP8.5 scenarios, respectively (Marzeion et al., 2020). Cullen et al., (2013) calculated that even imbalances between the Mount Kilimanjaro glaciers and present-day climate would be enough to eliminate the mountain's glaciers by 2060. Snow water equivalent and snow cover season duration also decline in the East African mountains, Ethiopian Highlands, and Atlas Mountains with climate change (*high confidence*) (López-Moreno et al., 2017).

In conclusion, there is *high confidence* that African snow and glaciers have very significantly decreased in the last decades and that this trend will continue over the 21st century.

12.4.1.5 Coastal and Oceanic

Relative sea level: Around Africa, over 1900-2018, a new tide-gauge based reconstruction finds a regional-mean RSL change of 2.07 [1.36–2.77] mm yr^{-1} in the South Atlantic and 1.33 [0.80-1.86] mm yr^{-1} in the Indian Ocean (Frederikse et al., 2020), compared to a GMSL change of around 1.7 mm yr^{-1} (Section 2.3.3.3; Table 9.5). For the period 1993-2018, these RSLR rates, based on satellite altimetry, increased to 3.45 [3.04-3.86] mm yr^{-1} and 3.65 [3.23-4.08] mm yr^{-1}, respectively (Frederikse et al., 2020), compared to a GMSL change of 3.25 mm yr^{-1} (Section 2.3.3.3; Table 9.5).

Relative sea-level rise is *virtually certain* to continue in the oceans around Africa. Regional-mean RSLR projections for the oceans around Africa range from 0.4 m–0.5 m under SSP1-2.6 to 0.8 m–0.9 m under SSP5-8.5 for 2081-2100 relative to 1995-2014 (median values), which is within the range of projected GMSL change {Section 9.6.3.3}. These RSLR projections may however be underestimated due to potential partial representation of land subsidence in their assessment (Section 9.6.3.2).

Coastal flood: The present day 1:100 yr Extreme Total Water Level is between 0.1 m – 1.2 m around Africa, with values around 1 m or above along the South West, South East and Central East coasts (Vousdoukas et al., 2018).

Extreme total water level (ETWL) magnitude and occurrence frequency are expected to increase throughout the region (*high confidence*) (see Figure 12.4p-r and Figure SM 12.6). Across the region, the 5th – 95th percentile range of the 1:100 yr ETWL is projected increase (relative to 1980 – 2014) by 7 cm – 36 cm and by 14 cm – 42 cm by 2050 under RCP4.5 and RCP8.5, respectively. By 2100, this range is projected to be 28 cm – 86 cm and 43 cm – 190 cm under RCP4.5 and RCP8.5, respectively (Vousdoukas et al., 2018; Kirezci et al., 2020). In terms of ETWL occurrence frequencies, the present day 1:100 yr ETWL is projected to have median return periods of around 1:10-1:20 yrs by 2050 and 1:1-1:5 yrs by 2100 in Southern and North Africa and occur more than once per year by 2050 and 2100 in most of East and West Africa under RCP4.5 (Vousdoukas et al., 2018). The present day 1:50 yr ETWL is projected to occur around 3 times a year by 2100 with a SLR of 1 m in Africa (Vitousek et al., 2017).

Coastal erosion: Shoreline retreat rates upto 1 m yr^{-1} have been observed around the continent during 1984 – 2015, except in ESAF which has experienced a shoreline progration rate of 0.1 m/r over the same period (Luijendijk et al., 2018; Mentaschi et al., 2018). (Mentaschi et al., 2018) report a coastal area losses of 160 km^2 and 460 km^2 over a 30 year period (1984-2015) along the Atlantic and Indian ocean coasts of the continent. At the more regional level, in Ghana along the Gulf of Guinea, about 79% of the shoreline was found to be retreating while 21% was found to be stable or prograding over the period 1974–1996 (Addo and

ACCEPTED VERSION SUBJECT TO FINAL EDITS

Addo, 2016).

Projections indicate that a vast majority of sandy coasts in the region will experience shoreline retreat throughout the 21st century (*high confidence*), while parts of the ESAF and west MDG coastline are projected to prograde over the 21st century, if present ambient trends continue. Median shoreline change projections (CMIP5), relative to 2010, presented by Vousdoukas et al. (2020) show that, under RCP4.5, shorelines in Africa will retreat by between 30 m (SAH, NEAF, WSAF, ESAF, MDG) and 55 m (WAF, CAF), by mid-century. By the same period but under RCP8.5, the median shoreline retreat is projected to be between 35 m (SAH, NEAF, WSAF, ESAF) and 65 m (WAF, CAF). By 2100, more than 100 m of median retreat is projected in WAF, CAF and SEAF under RCP4.5, while under RCP8.5, more than 100 m of shoreline retreat is projected in all regions except NEAF and WSAF. Under RCP8.5 especially, the projected retreat by 2100 is greater than 150 m in WAF and CAF. The total length of sandy coasts in Africa that is projected to retreat by more than a median of 100 m by 2100 under RCP4.5 and RCP8.5 is about 13,000 km and 17,000 km respectively, an increase of approximately 33%.

Marine heatwave: Over 1982-2016, the coastal oceans of Africa has experienced on average 2.0–3.0 MHW per year, with the coastal oceans around the southern half of the continent experiencing on average 2.5–3 MHWs per year. The average duration was between 5 and 15 days (Oliver et al., 2018). Changes over the 20th century, derived from MHW proxies, show an increase in frequency between 0.5 and 2.0 MHW per decade over the region, especially off the Horn of Africa; an increase in intensity per event around South Africa; and an increase in MHW duration along the North African coastlines (Oliver et al., 2018).

There is *high confidence* that MHWs will increase around Africa. Mean SST, a common proxy for MHWs, is projected to increase by 1 ºC (2ºC) around Africa by 2100, with a hotspot of around 2 ºC (5ºC) along the coastlines of South Africa under RCP4.5 (RCP8.5) (see Interactive Atlas). Under global warming conditions, MHW intensity and duration will increase in the coastal zones of all subregions of Africa (Frölicher et al., 2018). Projections for SSP1-2.6 and SSP5-8.5 both show an increase in MHWs around Australasia by 2081 – 2100, relative to 1985 – 2014 (Box 9.2, Figure 1).

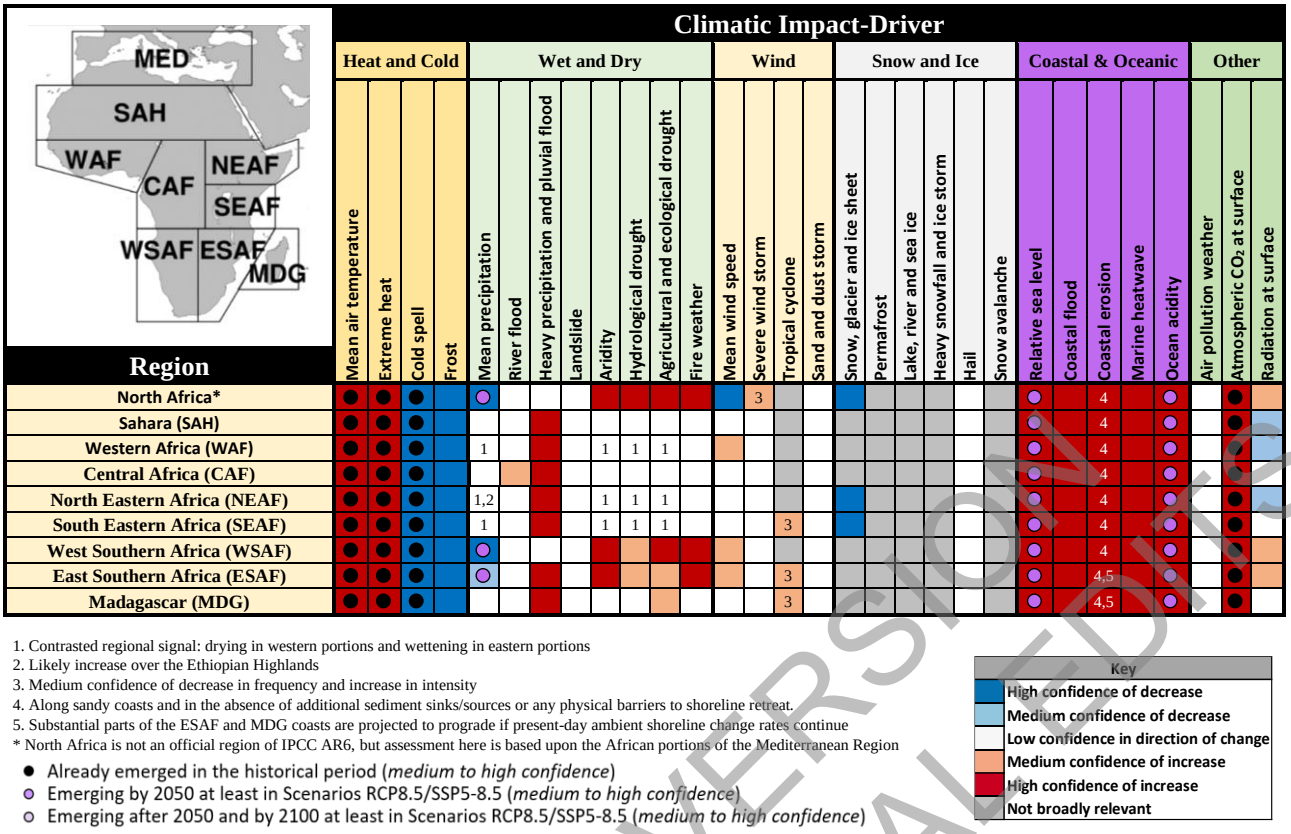
In general, there is *high confidence* that most coastal and ocean related hazards in Africa will increase over the 21st century. Relative sea-level rise is *virtually certain* to continue around Africa, contributing to increased coastal flooding in low-lying areas (*high confidence*) and shoreline retreat along most sandy coasts (*high confidence*). Marine Heatwaves are also expected to increase around the region over the 21st century (*high confidence*).

The assessed direction of change in CIDs for Africa and associated confidence levels are illustrated in Table 12.3. No relevant literature could be found for permafrost and hail, although these phenomena may be relevant in parts of the continent.

[START TABLE 12.3 HERE]

Table 12.3: Summary of confidence in direction of projected change in climatic impact-drivers in Africa, representing their aggregate characteristic changes for mid-century for scenarios RCP4.5, SSP3-4.5, SRES A1B, or above within each AR6 region (defined in Chapter 1), approximately corresponding (for CIDs that are independent of sea-level rise) to global warming levels between 2°C and 2.4°C (see 12.4 for more details of the assessment method). The table also includes the assessment of observed or projected time-of-emergence of the CID change signal from the natural inter-annual variability if found with at least *medium confidence* in Section 12.5.2.

ACCEPTED VERSION SUBJECT TO FINAL EDITS



1. Contrasted regional signal: drying in western portions and wettening in eastern portions
2. Likely increase over the Ethiopian Highlands
3. Medium confidence of decrease in frequency and increase in intensity
4. Along sandy coasts and in the absence of additional sediment sinks/sources or any physical barriers to shoreline retreat.
5. Substantial parts of the ESAF and MDG coasts are projected to prograde if present-day ambient shoreline change rates continue

* North Africa is not an official region of IPCC AR6, but assessment here is based upon the African portions of the Mediterranean Region

● Already emerged in the historical period (*medium to high confidence*)
○ Emerging by 2050 at least in Scenarios RCP8.5/SSP5-8.5 (*medium to high confidence*)
○ Emerging after 2050 and by 2100 at least in Scenarios RCP8.5/SSP5-8.5 (*medium to high confidence*)

ACCEPTED VERSION SUBJECT TO FINAL EDITS

[END TABLE 12.3 HERE]

12.4.2 Asia

According to the region definitions given in Chapter 1, Asia is divided into 11 regions: the Arabian Peninsula (ARP), Western Central Asia (WCA), West Siberia (WSB), East Siberia (ESB), the Russian Far East (RFE), East Asia (EAS), East Central Asia (ECA), the Tibetan Plateau (TIB), South Asia (SAS), South-East Asia (SEA) and the Russian Arctic Region (RAR). CID changes in RAR are assessed in the Polar Region section (12.4.9). As assessed in previous IPCC reports, major concerns in Asia are associated particularly with droughts and floods in all regions, heat extremes in SAS and EAS, sand-dust storms in WCA, tropical cyclones in SEA and EAS, snow cover and glacier changes in ECA and the Hindu Kush Himalaya (HKH) region, and sea ice and permafrost thawing in North Asia.

Since AR5, a large body of new literature is now available relevant to climate change in Asia, which includes projections of both mean climate and extreme climate phenomena from global and regional ensembles of climate simulations such as CMIP6 and CORDEX (see Chapter 10 and the Atlas). Literature has also considerably grown on several climate topics relevant to Asia such as the mountain climate (see in particular Chapter 3 of the SROCC), and the novel regional assessments such as the Hindu Kush Himalaya Assessment (Wester et al., 2019). Figure 12.6 shows the regional changes in indices related to floods, and coastal erosion over Asia, which are assessed on a regional basis along with other climatic impact-driver indices below.

[START FIGURE 12.6 HERE]

Figure 12.6: Projected changes in selected climatic impact-driver indices for Asia. (a) Mean change in 1-in-100 year river discharge per unit catchment area (Q100, $m^3 s^{-1} km^{-2}$) from CORDEX models for 2041-2060 relative to 1995-2014 for RCP8.5. (b) Shoreline position change along sandy coasts by the year 2100 relative to 2010 (meters; negative values indicate shoreline retreat) from the CMIP5 based data set

presented by Vousdoukas et al., (2020). (c) Bar plots for Q100 ($m^3 s^{-1} km^{-2}$) averaged over land areas for the WGI reference AR6 regions (defined in Chapter 1). The left column within each panel (associated with the left y-axis) shows the 'recent past' (1995-2014) Q100 absolute values in grey shades. The other columns (associated with the right y-axis) show the Q100 changes relative to the recent past values for two time periods ('mid' 2041-2060 and 'long' 2081-2100) and for three global warming levels (defined relative to the preindustrial period 1850-1900): 1.5°C (purple), 2°C (yellow) and 4°C (brown). The bars show the median (dots) and the 10^{th}-90^{th} percentile range of model ensemble values across each model ensemble. CMIP6 is shown by the darkest colors, CMIP5 by medium, and CORDEX by light. SSP5-8.5/RCP8.5 is shown in red and SSP1-2.6/RCP2.6 in blue. (d) Bar plots for shoreline position change show CMIP5 based projections of shoreline position change along sandy coasts for 2050 and 2100 relative to 2010 for RCP8.5 (red) and RCP4.5 (blue) from Vousdoukas et al., (2020). Dots indicate regional mean change estimates and bars the 5^{th}-95^{th} percentiles ranges of associated uncertainty. Note that these shoreline position change projections assume that there are no additional sediment sinks/sources or any physical barriers to shoreline retreat. See Technical Annex VI for details of indices. Further details on data sources and processing are available in the chapter data table (Table 12.SM.1).

[END FIGURE 12.6 HERE]

12.4.2.1 Heat and cold

Mean air temperature: A long-term warming trend in annual mean surface temperature has been observed across Asia during 1960-2015, and the warming accelerated after the 1970s (*high confidence*) (Davi et al., 2015; Aich et al., 2017; Cheong et al., 2018; Dong et al., 2018a; IPCC, 2018; Krishnan et al., 2019; Zhang et al., 2019a). Records also indicate a higher rate of warming in minimum temperatures than maximum temperatures in Asia, leading to more frequent warm nights and warm days, and less frequent cold days and cold nights (*high confidence*) (Supari et al., 2017; Akperov et al., 2018; Cheong et al., 2018; Rahimi et al., 2018; Khan et al., 2019a; Li et al., 2019a; Zhang et al., 2019a).

Projections show continued warming over Asia in the future with contrasted regional patterns across the continent (*high confidence*) (see Chapter 4 Figure 4.19). For RCP8.5/SSP5-8.5 at the end of the century, the mean estimated warming exceeds 5°C in WSB, ESB and RFE and 7°C in some parts (*high confidence*). In most areas of ARP and WCA, 5°C is exceded (Ozturk et al., 2017), but EAS, SAS and SEA have a lower projected warming of less than 5°C (Basha et al., 2017; Lu et al., 2019a; Almazroui et al., 2020) (see also Atlas.5). Under SSP1-2.6, the warming remains limited to 2°C in most areas except Arctic regions where it exceeds 2°C (Chapter 4 Figure 4.19).

Extreme heat: There are increased evidences and *high confidence* of more frequent heat extremes in the recent decades than in previous ones in most of Asia (Acar Deniz and Gönençgil, 2015; Rohini et al., 2016; Mishra et al., 2017a; You et al., 2017; Imada et al., 2018; Khan et al., 2019b; Krishnan et al., 2019; Rahimi et al., 2019; Yin et al., 2019) (Chapter 11) due to the effects of anthropogenic global warming, El Niño and urbanization (Luo and Lau, 2017; Thirumalai et al., 2017; Imada et al., 2019; Sun et al., 2019c; Zhou et al., 2019). But there is *medium confidence* of heat extremes increasing frequency in many parts of India (Rohini et al., 2016; Mazdiyasni et al., 2017; van Oldenborgh et al., 2018; Roy, 2019; Kumar et al., 2020) partly due to the alleviation of anthropogenic warming by increased air pollution with aerosols and expanding irrigation (van Oldenborgh et al., 2018; Thiery et al., 2020).

Extreme heat events are *very likely* to become more intense and/or more frequent in SAS, WCA, ARP, EAS, and SEA by the end of 21st century, especially under RCP6.0 and RCP8.5 (Lelieveld et al., 2016; Pal and Eltahir, 2016; Guo et al., 2017; Mishra et al., 2017a; Dosio et al., 2018; Shin et al., 2018; Lin et al., 2018; Nasim et al., 2018; Su and Dong, 2019; Hong et al., 2019; Khan et al., 2020; Kumar et al., 2020) (see Figure 12.4a-c, and Chapter 11). The exceedance of the dangerous heat stress 41°C threshold of the HI is expected to increase by about 250 days in SEA and by 50-150 days in SAS, WCA, ARP and EAS for SSP5-8.5 at the end of century. Under SSP1-2.6, the increase would be restricted to less than 30 days in many of these regions except SEA where the number of exceedance days increases by about 100 days in some areas. Such increases are already present in the middle of the century (see Figure 12.4d-f) (Schwingshackl et al., 2021).

ACCEPTED VERSION SUBJECT TO FINAL EDITS

In these regions, the increase in number of days with exceedance of 35°C of high heat stress is also expected to increase substantially for the mid-century under SSP5-8.5 (typically by 10-50 days except in Arctic and Siberian regions), and by more than 60 days in areas of SEA, and a large difference is found between low and high-end scenarios in the end of the century (*high confidence*) (Figure 12.4b). Over WSB, ESB and RFE also, an increase of extreme heat durations and frequency is expected in all scenarios (Kattsov et al., 2017; Khlebnikova et al., 2019a) (*high confidence*).

Cold spell and frost: Cold spells intensity and frequency, as well as the number of frost days, in most Asian regions have been decreasing since the beginning of the 20th century (*high confidence*) (Sheikh et al., 2015; Donat et al., 2016; Erlat and Türkeş, 2016; Dong et al., 2018a; Liao et al., 2018, 2020; Lu et al., 2018; van Oldenborgh et al., 2019) (Chapter 11), except for the central Eurasian regions where there was a cooling trend during 1995–2014 which is linked to sea-ice loss in the Barents–Kara Seas (*medium confidence*) (Wegmann et al., 2018; Blackport et al., 2019; Mori et al., 2019) (Atlas.5.2).

It is *very likely* that cold spells will have a decreasing frequency in all future scenarios across Asian regions (Guo et al., 2018b; Sui et al., 2018; Li et al., 2019a), as well as frost days (Wang et al., 2017c; Fallah-Ghalhari et al., 2019) except in tropical Asia (Chapter 11).

In Asia, temperatures have warmed along the last century (*high confidence*) and extreme heat episodes have become more frequent in most regions (*high confidence*), and are *very likely* projected to increase in all regions of Asia under all warming scenarios along this century. Dangerous heat stress thresholds such as HI>41°C will be crossed much more often (typically 50-150 days per year more than recent past) in many Southern Asia regions at the end of century under SSP5-8.5 while these numbers should remain limited to a few tens under SSP1-2.6 (*high confidence*). It is *very likely* that cold spells and frost days will decrease in frequency in all future scenarios across Asian regions along the century.

12.4.2.2 Wet and dry

Mean precipitation: The most prominent features about changes in precipitation over Asia (1901-2010) are the increasing precipitation trends across higher latitudes, along with some scattered smaller regions of detectable increases and decreases (Knutson and Zeng, 2018); however, spatial variability remains high (Wang et al., 2015b, 2019a; Limsakul and Singhruck, 2016; Supari et al., 2017; Rahimi et al., 2018, 2019; Sein et al., 2018; Kumar et al., 2019) (*medium confidence*) (see also Atlas.5).

Mean precipitation is *likely* to increase in most areas of Northern (WSB, ESB, RFE), Southern (ECA, TIB, SAS) and East Asia (EAS) in different scenarios (Huang et al., 2014; Xu et al., 2017; Kusunoki, 2018; Mandapaka and Lo, 2018; Luo et al., 2019; Wu et al., 2019; Zhu et al., 2019b; Almazroui et al., 2020; Jiang et al., 2020; Rai et al., 2020) (*high confidence*) (see Atlas.5). Monsoon circulation will also increase seasonal contrasts, with SAS seeing wetter wet seasons and drier dry seasons (Atlas.5.3). Higher uncertainty between CMIP5 and CMIP6 as well as spatial differences lend *low confidence* to model projections in ARP and WCA (Atlas.5.5), with large seasonal differences (Zhu et al., 2020) and some models projecting decreases in precipitation in Central Asia (Ozturk et al., 2017), Pakistan (Nabeel and Athar, 2020) and SEA (Supari et al., 2020).

River flood: Flood risk has grown in many places in China from 1961 to 2017 (Kundzewicz et al., 2019) (*low confidence*). In SAS, the numbers of flood events and human fatalities have increased in India during 1978–2006 (Singh and Kumar, 2013), whereas the average country-wide inundation depth has been decreasing during 2002 to 2010 in Bangladesh attributed to improved flood management (Sciance and Nooner, 2018) (*low confidence*).

Given the increase of heavy precipitation in most Asian regions the river flood frequency and intensities will change consequently in Asia. Over China floods will increase with different levels under different warming scenarios (Lin et al., 2018; Kundzewicz et al., 2019; Liang et al., 2019; Gu et al., 2020) (*medium confidence*). Monsoon floods will be more intense in SAS (*medium confidence*) (Nowreen et al., 2015; Babur

ACCEPTED VERSION SUBJECT TO FINAL EDITS

et al., 2016; Mohammed et al., 2018). The total flood damage will increase greatly in river basins in SEA countries under the conditions of climate change and rapid urbanization in the near future (Dahal et al., 2018; Kefi et al., 2020). A changing snowmelt regime in the mountains may contribute to a shift of spring floods to earlier periods in Central Asia in future (Reyer et al., 2017b) (*medium confidence*). The annual maximum river discharge can almost double by the mid-21st century in major Siberian rivers, and annual maximum flood area is projected to increase across Siberia mostly by 2–5% relative to the baseline period (1990–1999) under RCP8.5 scenario (Shkolnik et al., 2018) (*medium confidence*).

Heavy precipitation and pluvial flood

Pluvial floods are driven by extreme precipitation and land use. Observed changes in extreme precipitation vary considerably by region (see also Chapter 11). Heavy precipitation is *very likely* to become more intense and frequent in all areas of Asia except in ARP (*medium confidence*) for a 2ºC GWL or higher (see Chapter 11).

Landslide: The majority of non-seismic fatal landslide events were triggered by rainfall, and Asia is the dominant geographical area of landslide distribution (Froude and Petley, 2018). Floods and landslides are the most frequently occurring natural hazards in the eastern Himalaya and hilly regions, particularly caused by torrential rain during the monsoon season (Gaire et al., 2015; Syed and Al Amin, 2016). They accounted for nearly half of the events recorded in the countries of the HKH region (Vaidya et al., 2019). Intense monsoon rainfall in northern India and western Nepal in 2013, which led to landslides and one of the worst floods in history, has been linked to increased loading of GHG and aerosols (Cho et al., 2016). Due to an increase of heavy precipitation and permafrost thawing an increase in landslides is expected in some areas of Asia, such as northern Taiwan of China, some South Korea mountains, Himalaya Mountains, and permafrost territories of Siberia, and the increase is expected to be the greatest over areas covered by current glaciers and glacial lakes (Kim et al., 2015; Kharuk et al., 2016; Chen et al., 2019a; Kirschbaum et al., 2020) (*medium confidence, medium evidence*).

Aridity: Aridity in West Central Asia and parts of South Asia increased in recent decades (*medium confidence*), as documented in Afghanistan (Qutbudin et al., 2019), Iran (Zarei et al., 2016; Zolfaghari et al., 2016; Pour et al., 2020), most parts of Pakistan (Ahmed et al., 2018, 2019a), and many parts of India (Roxy et al., 2015; Mallya et al., 2016; Matin and Behera, 2017; Ramarao et al., 2019). Some spatial and seasonal differences within these regions remain, with Ambika and Mishra (2020) noting significant aridity declines over the Indo-Gangetic Plain in India during 1979–2018 due in part to the effect of irrigation and Araghi et al. (2018) found that many parts of Iran show no significant trends in aridity. There was slight drying in dry season and significant wetting in wet season in Philippines during 1951–2010 (Villafuerte et al., 2014), and slight wetting in Viet Nam during 1980-2017 (Stojanovic et al., 2020) (*low confidence*). In EAS there is *low confidence* of broad aridity changes, as the frequency of droughts have increased (especially in spring) along a strip extending from southwest China to the western part of northeast China; however, there is no evidence of a significant increase in drought severity over China as a whole and many parts in the arid northwest China got wetter during 1961-2012 (Wang et al., 2015b, 2019a; Zhai et al., 2017; Zhang and Shen, 2019). In Siberia, the number of dry days has decreased for much of the region, but increased in its southern parts (Khlebnikova et al., 2019b).

The counteracting factors of projected increases in precipitation and temperature across most of Asia (Atlas.5; Section 11.9) leads to *low confidence* (*limited evidence, inconsistent trends*) for broad, long-term aridity changes with *medium confidence* only for aridity increases in West Central Asia and East Asia. A growing number of studies highlight the potential for more localized aridity trends, including projection ensembles indicating significant increase in aridity and more frequent and intense droughts in most parts of China (Li et al., 2019b; Yao et al., 2020) and India under RCP4.5 and RCP8.5 for 2020-2100 period (Gupta and Jain, 2018; Bisht et al., 2019; Preethi et al., 2019).

Hydrological drought: Section 11.9 indicates that *limited evidence* and inconsistent regional trends gives *low confidence* to observed and projected changes in hydrological drought in all Asian regions at a 2°C GWL (approximately mid-century), although West Central Asia hydrological droughts increase at the 4°C global warming level (approximately end-of-century under higher emissions scenarios) (*medium confidence*).

ACCEPTED VERSION SUBJECT TO FINAL EDITS

Human activities such as reservoir operation and water abstraction have had a profound effect on low river flow characteristics and drought impacts in many Asian regions (Kazemzadeh and Malekian, 2016; Yang et al., 2020b). There was no observed overall long-term change of both meteorological droughts and hydrological droughts over India during 1870-2018 (Mishra, 2020), but there were strong trends toward drying of soil moisture in north-central India (Ganeshi et al., 2020) and intensified droughts in northwest India, parts of Peninsular India, and Myanmar (Malik et al., 2016). The frequency of water scarcity connected with hydrological droughts has increased significantly in southern Russia since the beginning of twenty-first century (Frolova et al., 2017). Higher future temperatures are expected to alter the seasonal profile of hydrologic droughts given reduced summertime snowmelt (*medium confidence*) downstream of mountains such as the Himalayas and the Tibetan Plateau (Sorg et al., 2014). Several studies project more severe future hydrological drought in the Weihe River basin in northern China (Yuan et al., 2016; Sun and Zhou, 2020).

Agricultural and ecological drought: Section 11.9 assesses *medium confidence* in observed increases to agricultural and ecological droughts in West Central Asia, East Central Asia, and East Asia. Persistent droughts were the main factor for grassland degradation and desertification in Central Asia in the early 21st century (Zhang et al., 2018b; Emadodin et al., 2019). Compound meteorological drought and heat events, which lead to water stress conditions for agricultural and ecological systems, have become more frequent, widespread and persistent in China especially since the late 1990s (Yu and Zhai, 2020). There were more agricultural droughts in north China than in south China, and the intensity of agricultural drought increased during 1951-2018 (Zhao et al., 2021).

Studies examining a 2°C global warming level give *low confidence* for projected broad changes to agricultural and ecological drought across all Asia regions, although at the 4°C global warming level agricultural and ecological drought increases are projected for West Central Asia and East Asia along with a decrease in South Asia (*medium confidence*) (Section 11.9). Summertime temperature increase will enhance evapotranspiration, facilitating ecological and agricultural drought over Central Asia towards the latter half of this century (Ozturk et al., 2017; Reyer et al., 2017b; Senatore et al., 2019) (see also Figure 12.4 for soil moisture and DF indices) (see also Chapter 11). However, broader changes in droughts could not be determined in Asia due to the mixture of total precipitation signals together with temperature increase patterns (Section 11.9; Atlas.5).

Fire weather: Under the global warming scenario of 2°C, the magnitude of length and frequency of fire seasons are projected to increase with strong effects in India, China and Russia (Sun et al., 2019b) (*medium confidence*). (Abatzoglou et al., 2019) found that higher fire weather conditions due to climate change emerge in the first part of the 21st century in South China, WCA as well as in boreal areas of Siberia and RFE. The potential burned areas in five Central Asian countries (Kazakhstan, Kyrgyzstan, Tajikistan, Uzbekistan, and Turkmenistan) will increase by 2%-8% in the 2030s and 3%-13% in the 2080s compared with the baseline (1971-2000) (Zong et al., 2020) (*medium confidence*).

In conclusion, there is *medium confidence* in that extreme precipitation, mean precipitation and river floods will increase across most Asian regions. There is *low confidence* for projected changes in aridity and drought given overall increases in precipitation and regional inconsistencies, with medium increases for West Central Asia and East Asia especially beyond the middle of the century and global warming levels beyond 2°C. Fire weather seasons are projected to lengthen and intensify particularly in the northern regions (*medium confidence*).

12.4.2.3 Wind

Mean wind speed: There is *high confidence* of the slowdown in terrestrial near-surface wind speed (SWS) in Asia by approximately -0.1 m s^{-1} per decade since 1950s based on observations and reanalysis data, with the significant decreases in Central Asia among the highest in the world followed by EAS and SAS (Tian et al., 2019; Wu et al., 2018b; Zhang et al., 2019b). But a short-term strengthening in SWS was observed during the winter since 2000 in Eastern China (Zeng et al., 2019; Zha et al., 2019) (*medium confidence*).

ACCEPTED VERSION SUBJECT TO FINAL EDITS

There is *medium confidence* of future declining mean SWS in Asia, except in SAS and SEA, as global projections indicate a decreasing trend in all climate scenarios for most of North Asia, TIB and East Asia by the mid-century (Karnauskas et al., 2018a; Fedotova, 2019; Jung and Schindler, 2019; Ohba, 2019; Wu et al., 2020a; Zha et al., 2020) (see also Figure 12.4m-o), with negative effects on wind energy potential. Decreases in North Asia are generally modest, not exceeding 10% for the mid-century and 20% for the end of century for the RCP8.5 and RCP4.5 scenarios (Figure 12.4m-o).

Severe wind storms: Consistent with the general mean decreasing surface winds, there is *medium confidence* that strong winds declined faster than weak winds in the past few decades in Asia in general (Vautard et al., 2010; Tian et al., 2019), but evidence is lacking for spatial patterns. There is *low confidence* that extra-tropical cyclones will decline in number in future climate scenarios over WCA, TIB, WSB and ESB, and intensify over the Arctic regions as a result of the poleward shift of storm-tracks (Basu et al., 2018) (see also Chapter 11). There is *limited evidence* for projection of changes in severe winds occurring in convective storms in Asia.

Tropical cyclone: There was an increase in the number and intensification rate of intense tropical cyclones (TC), such as category 4-5 (wind speeds greater than 58 m s^{-1}), in the Western North Pacific (WNP) and Bay of Bengal since the mid-1980s (Kim et al., 2016; Mei and Xie, 2016; Walsh et al., 2016a; Knutson et al., 2019) (*medium confidence*) (see also Section 11.7). There is *medium confidence* that there has been a significant north-westward shift in TC tracks and a poleward shift in the average latitude where TCs reach their peak intensity in the WNP since the 1980s (Knutson et al., 2019; Sun et al., 2019a; Lee et al., 2020), increasing exposure to TC passage and more destructive landfall over east China, Japan, and Korea in the last few decades (Kossin et al., 2016; Li et al., 2017; Altman et al., 2018; Liu and Chan, 2019), and decreasing exposure in the region of SAS and southern China (Kossin et al., 2016; Cinco et al., 2016) (see also Chapter 11). However, while the analysis shows fewer typhoons, more extreme TCs have affected the Philippines (Cinco et al., 2016; Takagi and Esteban, 2016) (*low confidence*). The frequency and duration of tropical cyclones has significantly increased over time over the Arabian Sea and insignificantly decreased over the Bay of Bengal during 1977-2018 (Fan et al., 2020) (*low confidence*).

There is *medium confidence* that future TC numbers will decrease but the maximum TC wind intensities will increase in the Western Pacific as elsewhere (Choi et al., 2019; Cha et al., 2020; Knutson et al., 2020) (Chapter 11, see Figure 11.24). The simulations for the late 21st century for the RCP8.5 scenario yield considerably more TCs in the WNP that exceed 49.4 m s^{-1} (Category 3) intensity (Mclay et al., 2019). There is *medium confidence* that the average location of the maximum wind will migrate poleward (see Chapter 11), and TC translation speeds at the higher latitudes would decrease (Yamaguchi et al., 2020). As a consequence, the intensity of TCs affecting the Japan Islands would increase in the future under the RCP8.5 scenario (Yoshida et al., 2017), whereas the frequency of TCs affecting the Philippine region and Vietnam is projected to decrease (Kieu-Thi et al., 2016; Wang et al., 2017b; Gallo et al., 2019) (*low confidence*).

Sand and dust storm: The Asia-Pacific region contributes 26.8 per cent to global dust emissions as of 2012 (UNESCAP, 2018). In West Asia, the frequency of dust events has increased markedly in some areas (east and northeast of Saudi Arabia, northwest of Iraq and east of Syria) from 1980 to the present (Nabavi et al., 2016; Alobaidi et al., 2017). This marked dust increase has been associated to drought conditions in the Fertile Crescent (Notaro et al., 2015; Yu et al., 2015) *likely* amplified by anthropogenic warming (Kelley et al., 2015) (see Chapter 10). Dust storm frequency in most regions of northern China show a decreasing trend since the 1960s due to the decrease in surface wind speed (Guan et al., 2017) (*medium confidence*).

While dust activity has decreased greatly over EAS, current climate models are unable to reproduce the trends (Guan et al., 2015, 2017; Zha et al., 2017; Wu et al., 2018a). Thus, there is *limited evidence* for future trends of sand and dust storms in Asia.

In conclusion, surface wind speeds have been decreasing in Asia (*high confidence*), but there is a large uncertainty in future trends. There is *medium confidence* that mean wind speeds will decrease in Central and Northern Asia, and that tropical cyclones will have decreasing frequency and increasing intensity overall.

ACCEPTED VERSION SUBJECT TO FINAL EDITS

12.4.2.4 Snow and Ice

Snow: There is no significant interannual trend of total snow cover from 2000 to 2016 over Eurasia (Wang et al., 2017e; Sun et al., 2020). Observations do show significant changes in the seasonal timing of Eurasian snow cover extent (especially for earlier spring snowmelt) since the 1970s, with seasonal changes expected to continue in the future (*high confidence*) (Yeo et al., 2017; Zhong et al., 2021). By 2100, snowline elevations are projected to rise between 400 and 900 m (4.4 to 10.0 m yr^{-1}) in the Indus, Ganges, and Brahmaputra basins under RCP8.5 scenario (Viste and Sorteberg, 2015).

Glacier: Observation and future projection of glacier mass changes in Asia are assessed in Section 9.5.1 grouped in three main regions: North Asia, High Mountains of Asia, and Caucuses and Middle East. All regions show continuing decline in glacier mass and area in the coming century (*high confidence*). Under RCP2.6 the pace of glacier loss slows, but glacier losses increase in RCP8.5 and peak in the mid to late 21st century. GlacierMIP projections indicate that glaciers in the High Mountains of Asia lose 42 ± 25%, 56 ± 24%, and 71 ± 21% of their 2015 mass by the end of the century for RCP4.5, RCP6.0 and RCP8.5 scenarios, respectively. Under the same scenarios, glaciers in North Asia would lose 57 ± 40%, 72 ± 38%, and 85 ± 30% of their mass, and glaciers in the Caucuses and the Middle East would lose 68 ± 32%, 83 ± 19%, and 94 ± 13% of their mass (see also Kraaijenbrink et al., 2017; Rounce et al., 2020).

Although enhanced melt water from snow and glaciers largely offsets hydrological drought-like conditions (Pritchard, 2019), this effect is unsustainable and may reverse as these cryospheric buffers disappear (Gan et al., 2015; Dong et al., 2018b; Huss and Hock, 2018) (*medium confidence*). In the Himalayas and the TIB region higher temperatures will lead to higher glacier melt rates and significant glacier shrinkage and a summer runoff decrease (Sorg et al., 2014) (*medium confidence*). Glacier runoff in the Asian high mountains will increase up to mid-century, and after that runoff might decrease due to the loss of glacier storage (Lutz et al., 2014; Huss and Hock, 2018; Rounce et al., 2020) (*medium confidence*).

Compared with 1990s, the number of lakes in TIB in the 2010s decreased by 2%, whereas total lake area expanded by 25% (Wang et al., 2020a) due to the joint effect of precipitation increase and glacier retreat. Many new lakes are predicted to form as a consequence of continued glacier retreat in the Himalaya-Karakoram region (Linsbauer et al., 2016). As many of these lakes will develop at the immediate foot of steep icy peaks with degrading permafrost and decreasing slope stability, the risk of glacier lake outburst floods and floods from landslides into moraine-dammed lakes is increasing in Asian high mountains (Haeberli et al., 2017b; Kapitsa et al., 2017; Bajracharya et al., 2018; Narama et al., 2018; Wang et al., 2020a) (*high confidence*).

Permafrost: Permafrost is thawing in Asia (*high confidence*). Temperatures in the cold continuous permafrost of northeastern ESB rose from the 1980s up to 2017, and the active layer thicknesses in Siberia and RFE generally increased from late 1990s to 2017 (Romanovsky et al., 2018). The change in mean annual ground temperature for north Siberia is about +0.1 – 0.3 °C per decade since 2000 (Romanovsky et al., 2018). Ground temperature in the permafrost regions of TIB (taking 40% of TIB currently) increased (0.02~0.26°C per decade for different boreholes) during 1980 to 2018, and the active layer thickened at a rate of 19.5 cm per decade (Zhao et al., 2020b). There is *high confidence* that permafrost in Asian high mountains will continue to thaw and the active layer thickness will increase (Bolch et al., 2019). The permafrost area is projected to decline by 13.4–27.7% and 60–90% in TIB (Zhao et al., 2020b), and 32% ± 11% and 76% ± 12% in Russia (Guo and Wang, 2016) by the end of the 21st century under the RCP2.6 and RCP8.5 scenario respectively (*high confidence*).

Lake and river ice: Lake ice cover duration got shorter in many lakes in TIB (Yao et al., 2016; Cai et al., 2019; Guo et al., 2020) and some other areas such as northwest China (Cai et al., 2020) and northeast China (Yang et al., 2019) in last two decades (*high confidence*). River ice cover extent decreased in TIB as well (Li et al., 2020d; Yang et al., 2020a). Climate warming also leads to a significant reduction in the period with ice phenomena and the decrement of ice regime hazard in Russian lowland rivers (Agafonova et al., 2017), and the Inner Mongolia reach of the Yellow River in north China (Wan et al., 2020) (*high confidence*). Lake ice and river ice in Asia are expected to decline with projected increases in surface air temperature towards the

ACCEPTED VERSION SUBJECT TO FINAL EDITS

end of this century (Guo et al., 2020; Yang et al., 2020a) (*high confidence*).

Heavy snowfall and ice storm: Observed trends in heavy snowfall and ice storms are uncertain. Annual maximum snow depth decreased for the period between 1962 and 2016 on the western side of both eastern and western Japan, at rates of 12.3% and 14.6% per decade, respectively (Ministry of the Environment et al., 2018). Observational results generally show a decrease in the frequency and an increase in the mean intensity of snowfalls in most Chinese regions (Zhou et al., 2018) (*medium confidence*). Because of the decrease in the snow frequency, the occurrence of large-scale snow disasters in TIB decreased (Qiu et al., 2018; Wang et al., 2019d) (*low confidence*). Large parts of northern high-latitude continents (including Siberia and RFE) have experienced cold snaps and heavy snowfalls in the past few winters, and the reduction of Arctic sea ice would increase the chance of heavy snowfall events in those regions in coming decades (Song and Liu, 2017) (*medium confidence*). Heavy snowfall is projected to occur more frequently in Japan's Northern Alps, the inland areas of Honshu Island and Hokkaido Island (Kawase et al., 2016, 2020; MOE et al., 2018), and the heavy wet snowfall can be enhanced over the mountainous regions in central Japan and northern part of Japan (Ohba and Sugimoto, 2020) (*medium confidence*).

Hail: The hailstorm in the Asian region shows a decreasing trend in several regions (*low confidence, limited evidence*). In China severe weather days including thunderstorm, hail and/or damaging wind have decreased by 50% from 1961 to 2010 (Li et al., 2016b; Zhang et al., 2017), and the hail size decreased since 1980 (Ni et al., 2017). A rate of decrease of 0.214 hail days per decade has also been reported for Mongolia between 1984-2013, where the annual number of hail days averaged is 0.74 (Lkhamjav et al., 2017).

Snow avalanche: There is as yet *limited evidence* for the evolution of avalanches in Asia. Tree-ring–based snow avalanche reconstructions in the Indian Himalayas show an increase in avalanche occurrence and runout distances in recent decades (Ballesteros-Cánovas et al., 2018).

In summary, snowpack and glaciers are projected to continue decreasing and permafrost to continue thawing in Asia (*high confidence*). There is *medium confidence* of increasing heavy snowfall in some regions, but *limited evidence* on future changes in hail and snow avalanches.

12.4.2.5 Coastal and oceanic

Relative sea level: Around Asia, over 1900-2018, a new tide-gauge based reconstruction finds a regional-mean RSL change of 1.33 (0.80-1.86) mm yr^{-1} in the Indian Ocean-Southern Pacific and 1.68 [1.27 to 2.09] mm yr^{-1} in the Northwest Pacific (Frederikse et al., 2020), compared to a GMSL change of around 1.7 mm yr^{-1} (Section 2.3.3.3; Table 9.5). For the period 1993-2018, the RSLR rates, based on satellite altimetry, increased to 3.65 [3.23 to 4.08] mm yr^{-1} and 3.53 [2.64 to 4.45] mm yr^{-1}, respectively (Frederikse et al., 2020), compared to a GMSL change of 3.25 mm yr^{-1} (Section 2.3.3.3; Table 9.5). The rate of RSL rise along the coastline of China ranges from -2.3 ± 1.9 to 5.7 ± 0.4 mm yr^{-1} during 1980–2016; after removing the vertical land movement, the average rate of sea level rise is 2.9 ± 0.8 mm yr^{-1} over 1980-2016 and 3.2 ± 1.1 mm yr^{-1} since 1993 (Qu et al., 2019). However, the rates of land subsidence reported by (Minderhoud et al., 2017) are substantially higher than those reported by Qu et al. (2019). RSL change in many coastal areas in Asia, especially in EAS, is affected by land subsidence due to sediment compaction under building mass and groundwater extraction (Erban et al., 2014; Nicholls, 2015; Minderhoud et al., 2019; Qu et al., 2019) (*high confidence*). During 1991- 2016, the Mekong delta in Vietnam sank on average ~18 cm as a consequence of groundwater withdrawal, and the subsidence related to groundwater extraction has gradually increased with highest sinking rates estimated to be 11 mm yr^{-1} in 2015 (Minderhoud et al., 2017).

Relative sea-level rise is *very likely* to continue in the oceans around Asia. Regional-mean RSLR projections for the oceans around Asia range from 0.3 m–0.5 m under SSP1-RCP2.6 to 0.7 m–0.8 m under SSP5-RCP8.5 for 2081-2100 relative to 1995-2014 (median values), which means local RSL change ranges from just below mean projected GMSL change to above-average values {Section 9.6.3.3}. These RSLR projections may however be underestimated due to potential partial representation of land subsidence in their assessment (Section 9.6.3.2).

ACCEPTED VERSION SUBJECT TO FINAL EDITS

Coastal flood: The present day 1:100 yr ETWL is between 0.5 m – 8 m around Asia, with values above 2.5 m or above common along the Central and North East coasts of Asia (Vousdoukas et al., 2018; Kirezci et al., 2020). Sea level rise and land subsidence will jointly lead to more flooding in delta areas in Asia (Takagi et al., 2016; Wang et al., 2018a) (*high confidence*).

Extreme total water level magnitude and occurrence frequency are expected to increase throughout the region (*high confidence*) (see Figure 12.4p-r and Figure SM 12.6). Across the region, the 5^{th} – 95^{th} percentile range of the 1:100 yr ETWL is projected to increase (relative to 1980 – 2014) by 7 cm – 44 cm and by 10 cm – 42 cm by 2050 under RCP4.5 and RCP8.5, respectively. By 2100, this range is projected to be 11 cm – 91 cm and 28 cm – 187 cm under RCP4.5 and RCP8.5, respectively (Vousdoukas et al., 2018; Kirezci et al., 2020). Furthermore, the present day 1:100 yr ETWL is projected to have median return periods of around 1:50 yrs by 2050 and 1:10 yrs by 2100 under RCP in most of Asia, except SEA and ARP, in which the present day 1:100 yr ETWL is projected occur once per year or more, both by 2050 and 2100 (Vousdoukas et al., 2018). The present day 1:50 yr ETWL is projected to occur around 3 times a year by 2100 with a SLR of 1 m across Asia (Vitousek et al., 2017). Compound impacts of precipitation change, land subsidence, sea-level rise, upstream hydropower development, and local water infrastructure development may lead to larger flood extent and prolonged inundation in the Vietnamese Mekong Delta (Triet et al., 2020).

Coastal erosion: Over the past 30 years, South, Southeast and East Asia exhibit the most pronounced delta changes globally due to strong human-induced changes to the fluvial sediment flux (Nienhuis et al., 2020). Satellite derived shoreline change estimates over 1984 – 2015 indicate shoreline retreat rates between 0.5 m yr^{-1} and 1 m yr^{-1} along the coasts of WCA and ARP, increasing to 3 m yr^{-1} in SAS. Over the same period, shoreline progradation has been observed along the coasts of RFE (0.2 m yr^{-1}), SEA (0.1 m yr^{-1}) and EAS (0.5 m yr^{-1}) (Luijendijk et al., 2018; Mentaschi et al., 2018). Meanwhile, there has been a gross coastal area loss of 3,590 km^2 in South Asia, and a loss of 2,350 km^2 in Pacific Asia, over a 30 year period (1984-2015) (Mentaschi et al., 2018).

Projections indicate that a majority of sandy coasts in the Asia region will experience shoreline retreat (Udo and Takeda, 2017; Ritphring et al., 2018; Vousdoukas et al., 2020b) (*high confidence*), while parts of the RFE, EAS, SEA and WCA coastline are projected to prograde over the 21st century, if present ambient shoreline change trends continue. Median shoreline change projections (CMIP5), relative to 2010, presented by Vousdoukas et al. (2020) show that, by mid-century, sandy shorelines in Asia will retreat by between 10 m – 50 m, except in SAS where shoreline retreat is projected to exceed 100 m, under both RCP4.5 and RCP8.5. By 2100, and under RCP4.5, shoreline retreats of around 85 m, 100 m and 300 m are projected along the sandy coastlines of SEA and WCA, ARP and SAS respectively (50 m or less in other Asian regions), while under RCP8.5, over the same period, sandy shorelines along all regions with coastlines, except RFE and EAS, are projected to retreat by more than 100 m, with the retreat in SAS reaching 350 m (2100 RCP8.5 projections for RFE and EAS are ~ 60 m and ~ 85 m respectively) (see Figure 12.6).

Marine heatwave: There have been frequent marine heatwaves (MHW) in the coastal oceans of Asia, connected to the increase between 0.25°C and 1°C in mean SST of the coastal oceans since 1982-1998 (Oliver et al., 2018). There is *high confidence* that MHWs will increase around most of Asia. Mean SST is projected to increase by 1ºC (2ºC) around Asia by 2100, with a hotspot of around 2 ºC (5 ºC) along the coastlines of the East Sea and the RFE under RCP4.5 (RCP8.5) (see Interactive Atlas). Under global warming conditions, MHW intensity and duration are projected to increase in the coastal zones of all sub-regions of Asia, but most notably in SEA and SAS (Frölicher et al., 2018). Projections for SSP1-2.6 and SSP5-8.5 both show an increase in MHWs around Asia by 2081 – 2100, relative to 1985 – 2014 (Box 9.2, Figure 1).

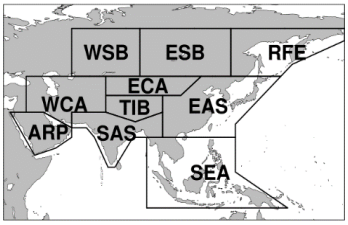
In general, there is *high confidence* that most coastal/ocean related hazards in Asia will increase over the 21^{st} century. Relative sea-level rise is *very likely* to continue around Asia contributing to increased coastal flooding in low-lying areas (*high confidence*) and shoreline retreat along most sandy coasts (*high confidence*). Marine heatwaves are also expected to increase around the region over the 21^{st} century (*high confidence*).

ACCEPTED VERSION SUBJECT TO FINAL EDITS

The assessed direction of change in climatic impact-drivers for Asia and associated confidence levels are illustrated in Table 12.4.

[START TABLE 12.4 HERE]

Table 12.4: Summary of confidence in direction of projected change in climatic impact-drivers in Asia, representing their aggregate characteristic changes for mid-century for scenarios RCP4.5, SSP3-4.5, SRES A1B, or above within each AR6 region (defined in Chapter 1), approximately corresponding (for CIDs that are independent of sea-level rise) to global warming levels between 2°C and 2.4°C (see 12.4 for more details of the assessment method). The table also includes the assessment of observed or projected time-of-emergence of the CID change signal from the natural inter-annual variability if found with at least *medium confidence* in Section 12.5.2.



Region	Heat and Cold: Mean air temperature	Heat and Cold: Extreme heat	Heat and Cold: Cold spell	Heat and Cold: Frost	Wet and Dry: Mean precipitation	Wet and Dry: River flood	Wet and Dry: Heavy precipitation and pluvial flood	Wet and Dry: Landslide	Wet and Dry: Aridity	Wet and Dry: Hydrological drought	Wet and Dry: Agricultural and ecological drought	Wet and Dry: Fire weather	Wind: Mean wind speed	Wind: Severe wind storm	Wind: Tropical cyclone	Wind: Sand and dust storm	Snow and Ice: Snow, glacier and ice sheet	Snow and Ice: Permafrost	Snow and Ice: Lake, river and sea ice	Snow and Ice: Heavy snowfall and ice storm	Snow and Ice: Hail	Snow and Ice: Snow avalanche	Coastal & Oceanic: Relative sea level	Coastal & Oceanic: Coastal flood	Coastal & Oceanic: Coastal erosion	Coastal & Oceanic: Marine heatwave	Coastal & Oceanic: Ocean acidity	Other: Air pollution weather	Other: Atmospheric CO_2 at surface	Other: Radiation at surface
Arabian Peninsula (ARP)	●	●	○															○							1		○		●	
West Central Asia (WCA)	●	●	○		5																		○		1,2		○		●	
West Siberia (WSB)	●	●	○		○		○											●											●	
East Siberia (ESB)	●	●	○		○		○											●											●	
Russian Far East (RFE)	●	●	○		○		○											●					○		1,2		○		●	
East Asia (EAS)	●	●	○				○								3								○		1,2		○		●	
East Central Asia (ECA)	●	●	○															●											●	
Tibetan Plateau (TIB)	●	○	○															●											●	
South Asia (SAS)	●	●	○															●					○		1		○		●	
South East Asia (SEA)	●	●	○		4										3								○		1,2		○		●	

1. Along sandy coasts and in the absence of additional sediment sinks/sources or any physical barriers to shoreline retreat.
2. Substantial parts of the EAS and SEA coasts are projected to prograde if present-day ambient shoreline change rates continue
3. Tropical cyclones decrease in number but increase in intensity
4. High confidence of decrease in Indonesia (Atlas.5.4.5)
5. Medium confidence of decreasing in summer and increasing in winter

● Already emerged in the historical period (*medium to high confidence*)
○ Emerging by 2050 at least in Scenarios RCP8.5/SSP5-8.5 (*medium to high confidence*)
○ Emerging after 2050 and by 2100 at least in Scenarios RCP8.5/SSP5-8.5 (*medium to high confidence*)

Key
High confidence of decrease
Medium confidence of decrease
Low confidence in direction of change
Medium confidence of increase
High confidence of increase
Not broadly relevant

[END TABLE 12.4 HERE]

12.4.3 Australasia

For the purpose of this assessment, Australasia is sub-divided into five sub-regions as defined in Section 1.4.5: Northern Australia (NAU), Central Australia (CAU), Eastern Australia (EAU), Southern Australia (SAU) and New Zealand (NZ).

Previous IPCC Assessment reports 4 and 5 identify the most damaging historical hazards in this region to be inland flooding, drought, wildfire, and episodic coastal erosion due to storms (Hennessy et al., 2007; Reisinger et al., 2014). The IPCC Special Report on 1.5°C warming (Hoegh-Guldberg et al., 2018) projects *very likely* increases in the intensity and frequency of warm days and warm nights and decreases in the intensity and frequency of cold days and cold nights in Australasia. Furthermore, a *likely* increase in the frequency and duration of warm spells is also projected for Australia. The IPCC Special Report on the Ocean

ACCEPTED VERSION SUBJECT TO FINAL EDITS

and Cryosphere (IPCC, 2019) projects a *likely* global mean sea level rise (RCP8.5) that is up to 0.1 m higher than corresponding AR5 projections. IPCC SROCC also projects an increase of mean significant wave height across the Southern Ocean (*high confidence*) and an increase in the occurrence of historically rare (1:100 yr) extreme sea levels to 1:1 yr or more frequent events all around the Australasian region by 2100 under RCP8.5.

A detailed national scale climate change assessment of observed and projected climate change, based on over 40 CMIP5 models and high resolution downscaling (CSIRO and BOM, 2015) and bi-annual short updates thereafter are available for Australia (CSIRO and BOM, 2016, 2018, 2020). Similar national assessments for New Zealand are also available (Ministry for the Environment & Stats NZ (2017), Ministry for the Environment (2018) and Ministry for the Environment (2020)). The severe extreme events such as heat waves and river floods that have occurred in Australasia, especially over the last decade, have enabled a number of attribution studies, improving the understanding of regional climate change mechanisms that drive such extreme events (see Chapter 11).

Figure 12.7 illustrates projected changes in two selected hazard indices for Australasia.

[START FIGURE 12.7 HERE]

Figure 12.7: Projected changes in selected climatic impact-driver indices for Australasia. (a) Mean change in 1-in-100 year river discharge per unit catchment area (Q100, $m^3 s^{-1} km^{-2}$) from CORDEX models for 2041-2060 relative to 1995-2014 for RCP8.5. (b) Shoreline position change along sandy coasts by the year 2100 relative to 2010 (meters; negative values indicate shoreline retreat) from the CMIP5 based data set presented by Vousdoukas et al. (2020). (c) Bar plots for Q100 ($m^3 s^{-1} km^{-2}$) averaged over land areas for the WGI reference AR6 regions (defined in Chapter 1). The left column within each panel (associated with the left y-axis) shows the 'recent past' (1995-2014) Q100 absolute values in grey shades. The other columns (associated with the right y-axis) show the Q100 changes relative to the recent past values for two time periods ('mid' 2041-2060 and 'long' 2081-2100) and for three global warming levels (defined relative to the preindustrial period 1850-1900): 1.5°C (purple), 2°C (yellow) and 4°C (brown). The bars show the median (dots) and the 10^{th}-90^{th} percentile range of model ensemble values across each model ensemble. CMIP6 is shown by the darkest colours, CMIP5 by medium, and CORDEX by light. SSP5-8.5/RCP8.5 is shown in red and SSP1-2.6/RCP2.6 in blue. (d) Bar plots for shoreline position change show CMIP5 based projections of shoreline position change along sandy coasts for 2050 and 2100 relative to 2010 for RCP8.5 (red) and RCP4.5 (blue) from Vousdoukas et al. (2020). Dots indicate regional mean change estimates and bars the 5^{th}-95^{th} percentiles ranges of associated uncertainty. Note that these shoreline position change projections assume that there are no additional sediment sinks/sources or any physical barriers to shoreline retreat. See Technical Annex VI for details of indices. Further details on data sources and processing are available in the chapter data table (Table 12.SM.1).

[END FIGURE 12.7 HERE]

12.4.3.1 Heat and Cold

Mean air temperature: Across Australia mean temperatures have increased by 1.44±0.24 °C during the period 1910-2019, with most of the warming occurring since 1950 (Section Atlas.6.2; CSIRO and BOM, 2020; Trewin et al., 2020). In New Zealand, an increase of 1.1°C has been measured from 1909-2016 (Section Atlas.6.2; Ministry for the Environment, 2020). In the period 1980 – 2014 a rate of increase of 0.1º – 0.3º per decade has been observed (Figure Atlas.11 and Figure Atlas.23).

Mean temperature in Australasia is projected to continue to rise through the 21st century (*virtually certain*) (Section Atlas.6.4). Projections for Australia indicate that the average temperature will increase by +1.1°C (0.84-1.52°C 10^{th} -90^{th} percentile range) by 2041-2060 (mid-century), and by +1.9°C (1.29 to 2.58°C) by 2081-2100 (end-century), relative to the baseline period of 1995-2014, under SSP2-4.5 (Interactive Atlas). For SSP5-8.5, the projected changes are up to +1.5°C (1.17 to 1.96°C) and +3.7°C (2.75 to 4.91°C) for mid and end century respectively. For SSP1-2.6, mean temperature is projected to rise by +0.9°C (0.55 to 1.26

ACCEPTED VERSION SUBJECT TO FINAL EDITS

°C) and +1.0°C (0.55 to 1.54 °C) relative to 1995-2014 by mid and end century, respectively (Interactive Atlas). In New Zealand, an increase of mean temperature of +1.0°C (0.60-1.32°C) relative to 1995-2014 is projected by mid-century, and an increase of +1.6°C (1.03 to 2.26°C) by end century under SSP2-4.5. For SSP5-8.5, the projected increase in mean temperature is +1.3°C (0.91 to 1.66°C) and +3.1°C (2.20 to 4.05°C 10-90 percentile range) relative to 1995-2014 by mid and end century, respectively. For SSP1-2.6, the projected increase in mean temperature is +0.75°C (0.39 to 1.06°C) and +0.8°C (0.47 to 1.46°C) relative to 1995-2014 by mid and end century, respectively (Interactive Atlas).

Extreme heat: The region has a *very likely* trend of increasing frequency and severity of hot extremes since the 1950s (Table 11.6). Extreme minimum temperatures have increased in all seasons over most of Australia and exceeds the increase in extreme maximum temperatures (Wang et al., 2013b; Jakob and Walland, 2016). Heatwave characteristics and hot extremes have increased across many Australian regions since the mid-20th century (Table 11.6; BOM and CSIRO, 2020)). The number of days per year with maximum temperature greater than 35°C has increased over most parts of Australia from 1957 – 2015, with the largest increasing trends of 0.4-1 days/year occurring in north western, northern, north eastern and parts of central Australia (CSIRO and BOM, 2016). Long term changes of hot extremes in Australia have been attributed to anthropogenic influence (Table 11.6). In New Zealand, the number of annual heatwave days increased at 18 of 30 sites during the period 1972–2019 (MfE and Stats NZ, 2020).

More frequent hot extremes and heatwaves are expected over the 21st century in Australia (*virtually certain*) (Table 11.6). Heat thresholds potentially affecting agriculture and health, such as 35°C or 40°C, are also projected to be exceeded more frequently over the 21st century in Australia under all RCPs (*high confidence*). By 2090 under RCP4.5, the average number of days per year with maximum temperatures above 35°C is highly spatially variable and is expected to increase by 50%–100%, while the number of days per year with maximum temperatures above 40°C is expected to increase by 200%, relative to 1985 2005 (CSIRO and BOM, 2015). Under RCP8.5 the corresponding projected increases are even greater, with a greater than 100% increase in most of Australia, and far greater increases (up to a 20-fold increase in Darwin) in central and northern Australia. Projections for NZ indicate more frequent hot extremes (*virtually certain*) (Table 11.6). Figure 12.4b, c shows CMIP6 projections of mean number of days per year with maximum temperature exceeding 35°C under SSP5-8.5, which are consistent with the above assessed literature and across the two CMIP generations, and indicate a strong difference depending on the mitigation scenario (e.g. over 100 days more per year under SSP5-8.5 in NAU, but, in general, less than 60 days more per year under SSP1-2.6 in NAU) (see also Figure SM 12.1)

The projected frequency of exceeding dangerous humid heat thresholds is increasing in Australia, with a strong increase in Northern Australia for RCP8.5 (*high confidence*) (Zhao et al., 2015; Mora et al., 2017; Brouillet and Joussaume, 2019), consistently across CMIP5, CMIP6 and CORDEX simulations (Figure 12.4d-f and Figure SM 12.2). Using the HI index, by end-century, the average number of days exceeding 41°C is projected to increase in NAU by about 100 days and by about 25 days under SSP5-8.5 and SSP1-2.6, respectively. The projections for New Zealand indicate no appreciable increase in the number of days with HI > 41°C across SSPs, time periods and CMIP generations (Figure 12.4d-f and Figure SM 12.2).

Cold spell and frost: Excepting parts of southern Australia, the Australasian region has a significant trend of decreasing frequency in cold extremes since the 1950s (*high confidence*) (Table 11.6) and there is *high confidence* that such trends are attributable to anthropogenic influence (Table 11.6). The number of frost days per year in Australia has on average declined at a rate of 0.15 days/decade in the past century (Alexander and Arblaster, 2017), except in some regions of southern Australia, where an increase in both number and season length has been reported (Dittus et al., 2014; Crimp et al., 2016b). The number of frost days has decreased at 12 of 30 monitoring sites around New Zealand over the period 1972–2019 (MfE and Stats NZ, 2020).

Less frequent cold extremes are *virtually certain* in Australasia (Table 11.6) while a decrease of frost days is projected with *high confidence* for the region. Projections, relative to 1986–2005, for the number of frost days per year in Australia indicate declines of 0.9 days by mid-century and 1.1 days by end of the century for RCP4.5, while for RCP8.5, the projected declines are 1.0 days and 1.3 days by mid- and end century

ACCEPTED VERSION SUBJECT TO FINAL EDITS

respectively (Alexander and Arblaster, 2017; Herold et al., 2018). Projections for New Zealand indicate that the number of frost days will decrease by 30% (RCP2.6) to 50% (RCP8.5) by 2040, relative to 1986–2005. By 2090, the decrease ranges from 30% (RCP2.6) to 90% (RCP8.5) (MfE and Stats NZ, 2017).

In general, there is *high confidence* that most heat hazards in Australasia will increase and that cold hazards will decrease over the 21st century. The mean temperature in Australasia is *virtually certain* to continue to rise through the 21st century, accompanied by less frequent cold extremes (*virtually certain*) and frost days (*high confidence*), and more frequent hot extremes (*virtually certain*). Heat stress is projected to increase in Australia (*high confidence*).

12.4.3.2 Wet and Dry

Mean precipitation: Here, only increases in precipitation (under *Wet*) are addressed, with decreases (under *Dry*) are addressed in *Aridity* below.

In terms of wet climatic impact-drivers, detectable anthropogenic increases in precipitation in Australia have been reported particularly for north central Australia for the period 1901-2010 (Knutson and Zeng, 2018). Figure Atlas.11 indicates no significant trend in precipitation over the region during the baseline period 1960 – 2015, except for the GPCP dataset which shows an increasing trend in north central Australia. In New Zealand, increases in annual rainfall have been observed between 1960-2019 in the south and west of the South Island and east of the North Island. Note however, for the most part, the above reported trends in New Zealand have been classified as statistically not significant (Figure Atlas.23).

Annual mean precipitation is projected to increase in central and north east Australia (*low confidence*) and in the south and west of New Zealand (*medium confidence*) (Section Atlas.6.4). Liu et al. (2018a) show that under 1.5°C warming, central and northeast Australia will become wetter. In New Zealand, projected patterns in annual precipitation exhibit increases in the west and south of New Zealand (Section Atlas.6.4).(Liu et al., 2018a) project that the South Island will be wetter under both 1.5°C and 2°C warming. However, there is limited model agreement for projected rainfall changes in Australasia as shown in the Atlas.

River flood: Streamflow observations in Australia have shown that negative trends dominate in annual maximum flow and that stations with significant negative trends were mostly located in the southeast and southwest (Gu et al., 2020). The observed peak flow trend in southern Australia is attributed to the decrease of soil moisture, although an increase of flood magnitude is possible for very rare events. For the more frequent flood events, the increase of extreme precipitation is balanced by the decrease of soil moisture. (Wasko and Nathan, 2019).

While median annual runoff is projected to decrease in most of Australia (Chiew et al., 2017), consistent with projected decreases in average rainfall (CSIRO and BOM, 2015; Alexander and Arblaster, 2017), river floods are projected to increase due to more intense extreme rainfall events and associated increase in runoff (*medium confidence*). Asadieh and Krakauer (2017) found a decrease in the value of the 95% percentile of mean streamflow with RCP8.5 by the end of the century in all of Australia, except in a small part in centre of the country. In terms of relative increases, flooding is expected to increase more in the northern Australia (driven by convective rainfall systems) than in southern Australia (where more intense extreme rainfall may be compensated by drier antecedent moisture conditions) (Alexander and Arblaster, 2017; Dey et al., 2019) with flood frequency increasing in northern Australia and along parts of the east coast and decreasing in south-western Western Australia (Hirabayashi et al. 2013). Gu et al. (2020) project larger flood magnitude and volumes under both RCP2.6 and RCP8.5 in northern Australia, and smaller flood magnitudes and volumes in southern Australia under the same RCPs. These findings are in general agreement with the patterns in peak flow, corresponding to the 1:100 yr return period streamflow, shown in Figure 12.7a,c for mid-21st century under RCP8.5.

There is *medium confidence* that river flooding will increase in New Zealand. Projections for New Zealand

ACCEPTED VERSION SUBJECT TO FINAL EDITS

indicate that the 1:50 yr and 1:100 yr flood peaks for rivers in many parts of the country may increase by 5 to 10% by 2050 and more by 2100 (with large variation between models and emissions scenarios), with a corresponding decrease in return periods for specific flood levels (Gray et al., 2005; Carey-Smith et al., 2010; McMillan et al., 2010, 2012; Ballinger et al., 2011).

Heavy precipitation and pluvial flood: Rainfall extremes have been detected to increase in Australasia, with *low confidence* (Table 11.6). There is *high confidence* that Rx1day and Rx5day precipitation extremes will increase for 2ºC or lower warming for the region as a whole, but on a sub-regional basis there is only *medium confidence* of increases in NAU and CAU and *low confidence* of increases on EAU, SAU and NZ. For warming levels exceeding 2ºC, these extremes are *very likely* to increase in NAU and CAU and they are *likely* to increase elsewhere in the region (Section 11.9).

Landslide: Based on local slope characteristics, lithology and seismic activity, the South Island and the eastern half of the North Island of New Zealand are vulnerable to landslide occurrence (Broeckx et al., 2020). The potential for land and rockslides increases with, amongst other factors, total precipitation rates, precipitation intensity, mountain permafrost thaw rates, glacier retreat and air temperature (Allen and Huggel, 2013; Crozier, 2010; Gariano and Guzzetti, 2016; IPCC, 2019). Given the increase of the magnitude of these physical variables in areas that are already highly susceptible to mass movements (MfE, 2018), there is *low confidence* that the occurrence of landslides will increase under future climate conditions.

Aridity: In terms of dry climatic impact-drivers, a substantial decrease in precipitation has been observed across southern Australia during the cool season (April–October) (*medium confidence*). The drying trend has been particularly strong over southwest Western Australia between May and July, with rainfall since 1970 being around 20% less than the 1900-1969 average (CSIRO and BOM, 2020). Detectable decreases in mean precipitation, attributable at least in part to anthropogenic forcing, have been reported for parts of southwest Australia (Delworth and Zeng, 2014; Knutson and Zeng, 2018), southeast Australia, and Tasmania (Knutson and Zeng, 2018; see also case study in Section 10.4.1.2.3). In New Zealand, the northeast of the South Island and western and the northern parts of the North Island show decreasing precipitation trends during 1960-2019 (MfE and Stats NZ, 2020).

Aridity is projected to increase, especially during winter and spring, with *medium confidence* in SAU but with *high confidence* in southwest Western Australia (Section Atlas.6.4, Table 11.6). In EAU and in the north and east of NZ, aridity is projected to increase with *medium confidence*, while a decrease is projected with *medium confidence* in the south and west of NZ (Section Atlas.6.4). Although there is only *low confidence* in the projected decrease of mean annual precipitation in south western and eastern Australia and the north and east of New Zealand, there is *high confidence* of reduced winter and spring precipitation in Australia in future, mostly in southwestern and eastern Australia (Section Atlas.6.4). Liu et al. (2018b) show that under 2°C warming, most of Australia is projected to become drier based on PDSI, with the exception of the tropical northeast. Ferguson et al. (2018) project that between 1976-2005 and 2070-2099, winters will become drier (mainly in southern Australia) under RCP8.5. (Liu et al., 2018c) project that the north island of New Zealand will be drier under both 1.5°C and 2°C warming.

Hydrological Drought: There is *low confidence* of observed changes in hydrological droughts in Australasia, except in SAU where there is *medium comfidence* of an observed increase in the south-east and south-west. Future projections indicate *medium confidence* in further hydrological drought increases for Southern Australia for warming levels of 2°C or higher (Section 11.9). Mean annual runoff in far south-east and far south-west Australia are projected to decline by median values of 20% and 50%, respectively, by mid-century under RCP8.5 (Chiew et al., 2017). Prudhomme et al. (2014) assess changes in the Drought Index (DI), defined as areal runoff less than the 10^{th} percentile over the reference period 1976 – 2005, and project DI increases for both Australia and New Zealand by 10%–20% by 2070-2099 under RCP8.5 with the greatest effects being in the southern parts of the Australian continent. Those projections are consistent with the trends shown in Figure 12.4g-i (see also Figure SM 12.3). The SPI drought frequency is projected to increase in SAU and particularly in southwest Western Australia by mid- century, while by the end of the century SPI drought frequency is projected to increase all over Australia, and particularly strongly in southwest Western Australia as well as southern Victoria (see Figure 12.4g-i). For the Murray-Darling basin,

ACCEPTED VERSION SUBJECT TO FINAL EDITS

Ferguson et al. (2018) project effectively no change (-1%) in mean precipitation, a 27% decrease in P-E, and 30% increase in runoff in 2070-2099 relative to 1976-2005 with RCP8.5.

Agricultural and ecological Drought: There is *medium confidence* in observations of Agricultural and ecological droughts increasing in SAU and decreasing in NAU, while there is *low confidence* of changes elsewhere in the region (Section 11.9). More regional studies have observed an increase in agricultural and ecological drought intensity in southwest Australia and an increase in drought intensity in parts of southeast Australia, while the length of droughts therein has increased (Section 11.9). In New Zealand, since 1972/73, soils at 7 of 30 monitored sites became drier, while the 2012–13 drought was one of the most extreme in the previous 41 years (MfE and Stats NZ, 2017). Future evaporative demand is projected to lead to *medium confidence* increases in agricultural and ecological droughts for a 2° global warming level in SAU and EAU and *low confidence* for changes in CAU, NAU and NZ although there is *medium confidence* of CAU increases at the 4°C global warming level (Section 11.9). There is *medium confidence* for more time in agricultural and ecological drought in SAU by mid-21st century (Coppola et al., 2021b) as well as by the end of the 21st century (Herold et al., 2018). The SPEI shows a springtime intensification in SAU with moderate and severe droughts in the southwest and moderate droughts in the southeast (Herold et al., 2018). There is consensus among the different model ensembles (CORDEX-CORE, CMIP5 and CMIP6) that the drought frequency (DF), one of several proxies for agricultural and ecological drought, will increase in all four Australian regions for both mid-century (NAU 0.2 to 2 DF increase, CEU 0.5 to 2 DF increase, SAU 1 to 3 DF increase and EAU 0.8 to 3 DF increase) and end-century (0.8–2.7 DF increase for NAU, 1.2–2 DF increase for CAU, 2.2–3.8 for SAU, and 0.2–3 for EAU) for both RCP8.5 and SSP5-85, with CMIP6 showing the lowest increase (see Figure 12.4g-l and Figure SM 12.4) (Coppola et al., 2021b).

Fire weather: Dowdy and Pepler (2018) examined atmospheric conditions conducive to pyroconvection in the period 1979-2016, and found an increased risk in southeast Australia during spring and summer, due to changes in vertical atmospheric stability and humidity, in combination with adverse near-surface fire weather conditions. CSIRO and BOM (2018) and Dowdy (2018) found that the annual 90th percentile daily Forest Fire Danger Index (FFDI) has increased from 1950-2016 in parts of Australia, especially in southern Australia (1 to 2.5 decade^{-1}) and in spring and summer. These studies indicate an increase in the frequency and magnitude of FFDI extreme quantiles, as well as a shift of the fire season start toward spring, lengthening the fire season. The unprecedented large fires of austral spring and summer of 2019 in SE Australia were a result of extreme hot and dry weather in significantly drier than average conditions that had persisted since 2017, in combination with consistently stronger than average winds, resulting in above average to highest on record FFDI values in much of the country (Abram et al., 2021). These fires have been attributed to climate change through the temperature component of fire weather indices (van Oldenborgh et al., 2021). In New Zealand, days with very high and extreme fire weather increased in 12 out of 28 monitored sites, and decreased in 8, in the period 1997 to 2019 (MfE and Stats NZ, 2020). Attribution studies indicate that there is *medium confidence* of an anthropogenically-driven past increase in fire weather conditions, essentially due to increase in frequency of extreme heat waves. (Hope et al., 2019; Lewis et al., 2020; van Oldenborgh et al., 2021).

Fire weather indices are projected to increase in most of Australia (*high confidence*) and many parts of New Zealand (*medium confidence*), in particular with respect to extreme fire and induced pyroconvection (Dowdy et al., 2019b). Increasing mean temperature, cool season rainfall decline, and changes in tropical climate variability all contribute to a future increase in extreme fire risk in Australia (Abram et al., 2021). Projections indicate that the annual cumulative FFDI will increase by 31-33% in southern and eastern Australia, and by 17-25% in northern Australia and the Rangelands by 2090 (relative to 1995) under RCP8.5 (CSIRO and BOM, 2015). Using a CMIP5 ensemble of 17 models, Abatzoglou et al. (2019) found a statistically significant positive trend for fire weather intensity and fire season length for future mid-century conditions under RCP8.5, including a detectable anthropogenic influence on fire risk magnitude and fire season length by 2040 in Western Australia and along the Queensland coastline. Using the C-Haines and FFDI indices with A2 and RCP8.5 respectively, Di Virgilio et al. (2019) and Clarke et al. (2019) have shown that extreme fire weather frequency will increase in south eastern Australia by the end of the 21st century. Most of these projections indicate that the biggest increases in fire weather conditions will be in late spring, effectively resulting in longer (stronger) fire seasons in areas where spring is the shoulder (peak) season.

ACCEPTED VERSION SUBJECT TO FINAL EDITS

In New Zealand, Watt et al. (2019) projected that the number of days with very high to extreme fire risk will increase by 71 per cent by 2040, and by a further 12 per cent by 2090, for the A1B scenario, with fire risk increase all along the east coast. The most marked relative changes by 2090 were projected for Wellington and Dunedin where very high to extreme fire risk is projected to increase by, respectively, 89% to 32 days and 207% to 18 days, compared to the baseline period 1970-1999.

Annual mean precipitation is projected to increase in central and north east Australia (*low confidence*) and in the south and west of New Zealand (*medium confidence*), while it is projected to decrease in southern Australia (*medium confidence*), albeit with *high confidence* in southwest western Australia, in eastern Australia (*medium confidence*), and in the north and east of New Zealand (*medium confidence*). Heavy precipitation and pluvial flooding are projected to increase with *medium confidence* in northern Australia and central Australia. There is *medium confidence* that river flooding will increase in New Zealand and Australia, with higher increases in northern Australia. Aridity is projected to increase with *medium confidence* in southern Australia (*high confidence* in southwest Western Australia), eastern Australia *(medium confidence*), and in the north and east of New Zealand (*medium confidence*). Hydrological droughts are projected to increase in Southern Australia (*medium confidence*), while Agricultural and ecological droughts are projected to increase with *medium confidence* in Southern Australia and Eastern Australia. Fire weather is projected to increase throughout Australia *(high confidence)* and New Zealand (*medium confidence)*.

12.4.3.3 Wind

Mean wind speed: There is *low confidence* of a mean wind-speed trend in the last decades (*low agreement*) (McVicar et al., 2012; Troccoli et al., 2012; Azorin-Molina et al., 2018; Wu et al., 2018b), as long-term measurements are not homogeneous.

In future climate scenarios wind speed trends exhibit generally weak amplitudes with *low agreement* among models (Figure 12.4m-o and Figure SM 12.5) in Australia with uncertain consequences on wind power potential (CSIRO and BOM, 2015; Karnauskas et al., 2018a; Jung and Schindler, 2019). However, there is *medium confidence* that, by the end of the century, annual mean wind power will significantly increase in northeastern Australia under RCP8.5, but there is *low confidence* of an increase by end-century under RCP4.5, and for any scenario by mid-century (Karnauskas et al., 2018). In New Zealand, mean wind patterns are projected to become more north-easterly in summer, and westerlies to become more intense in winter (*low confidence*), in agreement with the strengthening of the southern hemisphere storm tracks (Section 4.5.1).

Severe wind storm: There is generally *low confidence* in observed changes in extreme winds and extratropical storms in Australasia (Section 11.7.2). CMIP5 projections of severe winds indicate a general increase in north eastern Australia, and decrease in some parts in southern and central Australia (*medium confidence*) by the end of the century under RCP8.5 (CSIRO and BOM, 2015; Kumar et al., 2015; Jung and Schindler, 2019). Elsewhere trends are diverse and vary across simulations with *low agreement*. Projections of changes in the 1:25 yr return period winds (based on annual maxima) for 2074–2100 relative to 1979–2005 for RCP8.5 show an increase in tropical areas of northern Australia (Kumar et al., 2015).

In New Zealand, the frequency and magnitude of extreme wind have decreased (from 1980 – 2019) at 12 of 14 monitored sites and increased at two monitored sites (MfE and Stats NZ, 2020). Due to the intensification and the shift of the Austral storm track by the end of the century (Yin, 2005), a continuous increase in extreme wind speed in New Zealand is projected over the South Island and the southern part of the North Island by mid- and end of century for all RCP's (*low confidence*) (MfE, 2018).

Tropical cyclone: In Australia, the number of TCs has generally declined since 1982, and the frequency of intense TCs that make landfall in north eastern Australia has declined significantly since the 19th century (*medium confidence*) (Kuleshov et al., 2010; Callaghan and Power, 2011; Holland and Bruyère, 2014; Knutson et al., 2019; CSIRO and BOM, 2020). There is *high confidence* that cyclones making landfall along

ACCEPTED VERSION SUBJECT TO FINAL EDITS

north eastern and north Australian coastlines will decrease in number and *low confidence* of an increase in their intensities for a 2°C global warming level as well as for the mid-century period with scenarios RCP4.5 and above (Roberts et al., 2015, 2020; Bacmeister et al., 2018; Knutson et al., 2020) , with the amplitude of changes increasing from RCP4.5 to RCP8.5 (Bacmeister et al., 2018). Decreases in frequency are projected for "east coast lows" (Walsh et al., 2016b; Dowdy et al., 2019a).

Sand and dust storm: Australia is recognized to be the largest dust source in the Southern Hemisphere (Zheng et al., 2016). Land use and land cover change have increase dust emissions in Australia in the past 200 years (Marx et al., 2014). While projections suggest a decrease in severe winds in central and southern Australia, changes in vegetation due to increased aridity and hydrological drought could be expected to result in increased wind erosion and dust emission across the country *(medium confidence*) (Webb et al., 2020).

In Australasia, there is *low confidence* in projected mean wind speeds and wind power potential, with a *medium confidence* increase projected only in northeastern Australia under high emission scenarios and by the end of the 21st century. Tropical cyclones in north eastern and north Australia are projected to decrease in number (*high confidence*) while their intensity is projected to increase (*low confidence*).

12.4.3.4 Snow and Ice

Snow: The snow season length in Australia has decreased by 5% during 2000-2013 relative to 1954-1999, especially in spring (Pepler et al., 2015). A shift in the date of peak snowfall has also been observed with an 11 day advance over the same period (Pepler et al., 2015). A decreasing trend in maximum snow depth has been observed for Australian alpine regions since the late 1950s, with the largest declines during spring and at lower altitudes. Maximum snow depth is highly variable and is strongly influenced by rare heavy snowfall days, which have no observed trends in frequency (CSIRO and BOM, 2020).

Projections for Southern Australia and New Zealand show a continuing reduction in snowfall during the 21st century (*high confidence*). The magnitude of decrease varies with the altitude of the region and the emission scenario. At elevations lower than 1500 m, years without snowfall are projected from 2030 in some models. By 2090, and under RCP8.5, such years are projected to become common (CSIRO and BOM, 2015). The number of annual snow days in New Zealand is projected to decrease under all RCP's, by up to 30 days or more by 2090 under RCP8.5, relative to 1986 – 2005 (MfE, 2018).

Glacier: Glacier mass and areal extent in New Zealand is projected to continue to decease over the 21st century (*high confidence*) (Section 9.5.1.3). Glacier ice volume from 1977 to 2018 in New Zealand has decreased from 26.6 km^3 to 17.9 km^3 (a loss of 33%) (Salinger et al., 2019). Relative to 2015, glaciers in New Zealand are projected to lose $36 \pm 44\%$, $53 \pm 33\%$, and $77 \pm 27\%$ of their mass by the end of the century under RCP2.6, RCP4.5, and RCP8.5, respectively, with the loss rates decreasing over time under RCP2.6 and increasing under RCP8.5 (Marzeion et al., 2020).

In summary, snowfall is expected to decrease throughout the region at high altitudes in both Australia (*high confidence*) and New Zealand (*medium confidence*). In New Zealand, glacier ice mass and extent are expected to decrease over the 21st century for all scenarios (*high confidence*).

12.4.3.5 Coastal and Oceanic

Relative sea level: Around Australasia, over 1900-2018, a new tide-gauge based reconstruction finds a regional-mean RSL change of 1.33 [0.80-1.86] $^{mm\ yr\text{-}1}$ in the Indian ocean - South Pacific region (Frederikse et al., 2020), compared to a GMSL change of around 1.7 mm yr^{-1} (Section 2.3.3.3; Table 9.5). For the period 1993-2018, the RSLR rates, based on satellite altimetry, increased to 3.65 [3.23-4.08] mm yr^{-1} (Frederikse et al., 2020), compared to a GMSL change of 3.25 mm yr^{-1} (Section 2.3.3.3; Table 9.5).

ACCEPTED VERSION SUBJECT TO FINAL EDITS

Relative sea level is *virtually certain* to increase throughout the region over the 21st century (Section 9.6.3, Figure 9.28). Regional-mean RSLR projections for the oceans around Australasia range from 0.4 m–0.5 m under SSP1-RCP2.6 to 0.7 m–0.9 m under SSP5-RCP8.5 for 2081-2100 relative to 1995-2014 (median values), which means local RSL change falls within the range of mean projected GMSL change (Section 9.6.3.3). However these RSLR projections may be underestimated due to potential partial representation of land subsidence (Section 9.6.3.2).

Coastal flood: The most commonly used index for episodic coastal inundation in Australia is the summation of a high end SLR and the 1:100 yr storm tide level (the combined sea level due to storm surge and tide) (CSIRO and BOM, 2016; McInnes et al., 2016). However, episodic coastal flooding is caused by Extreme Total Water Levels (ETWL), which is the combination of SLR, tides, surge and wave setup (12.3.5.2). The present day 1:100 yr ETWL is between 0.5 m – 2.5 m around most of Australia, except the northwestern coast where 1:100 yr ETWL can be as large as 6 m–7 m (Vousdoukas et al., 2018; O'Grady et al., 2019; Kirezci et al., 2020).

Extreme total water level magnitude and occurrence frequency are expected to increase throughout the region (*high confidence*) (see Figure 12.4p-r and Figure SM 12.6). Across the region, the 5th – 95th percentile range of the 1:100 yr ETWL is projected increase (relative to 1980 – 2014) by 5 cm – 35 cm and by 10 cm – 40 cm by 2050 under RCP4.5 and RCP8.5, respectively (Figure 12.4q). By 2100 (Figure 12.4p,r), this range is projected to be 25 cm – 80 cm and 50 cm – 190 cm under RCP4.5 and RCP8.5, respectively (Vousdoukas et al., 2018; Kirezci et al., 2020). Furthermore, the present day 1:100 yr ETWL is projected to have median return periods of around 1:20 yrs by 2050 and 1:1 yrs by 2100 in SAU and NZ and return periods of around 1:50 yrs by 2050 and 1:20 yrs by 2100 in NAU under RCP4.5 (Vousdoukas et al., 2018), while the present day 1:50 yr ETWL is projected to occur around 3 times a year by 2100 with a SLR of 1 m around Australasia (Vitousek et al., 2017).

Coastal erosion: Satellite derived shoreline retreat rates for the period between 1984 – 2015 show retreat rates between 0.5 m yr^{-1} and 1 m yr^{-1} around the region, except in SAU where a shoreline progradation rate of 0.1 m yr^{-1} has been observed (Luijendijk et al., 2018; Mentaschi et al., 2018). Mentaschi et al. (2018) report a coastal area loss of 350 km^2 over the same period in West Australia from satellite observations.

Projections indicate that a majority of sandy coasts in the region will experience shoreline retreat, throughout the 21st century (*high confidence*) (Figure 12.7b,d). Median shoreline change projections (CMIP5) under both RCP4.5 and RCP8.5 presented by Vousdoukas et al. (2020) show that, by mid-century, sandy shorelines will retreat (relative to 2010) by between 50 m and 80 m all around Australasia, except in SAU and NZ where the projected retreat (relative to 2010) is between 35 m and 50 m. By 2100, median shoreline retreats exceeding 100 m (relative to 2010) are projected along the sandy coasts of NAU (~ 150 m), CAU (~ 160 m), and EAU (~ 110 m) under RCP4.5m, while projections for SAU and NZ are around 80 m – 90 m. Under RCP8.5, shoreline retreat exceeding 100 m is projected all around the region by 2100 (relative to 2010) with retreats as high as 220 m in NAU and CAU (~ 170 m in EAU and around 130 m in SAU and NZ) (Figure 12.7b, d). The total length of sandy coasts in Australasia that is projected to retreat by more than a median of 100 m by 2100 under RCP4.5 and RCP8.5 is about 12,500 km and 16,000 km respectively, an increase of approximately 30%.

Distinct from long term coastline recession, storms and storm surges also result in episodic coastal erosion. In general, the historically measured maximum episodic coastal erosion (either eroded volume or coastline retreat distance) or that due to a 1:100 yr return period storm wave height is used as a design criterion for coastal zone management and planning in Australia (Wainwright et al., 2014; Mortlock et al., 2017).

While there is wide recognition in Australia that the combined effect of SLR, changing storm surge and wave climates will directly affect future episodic coastal erosion (Harley et al., 2017; McInnes et al., 2016; Ranasinghe, 2016) only a few projections of how this hazard may evolve are available for Australia. In one such study, Jongejan et al. (2016) provide projections of how the full exceedance probability curve of the maximum erosion per year may evolve over the 21st century (due to the combined action of SLR, storm surge and storm waves). Their results show that, for example, the 0.01 exceedance probability maximum

ACCEPTED VERSION SUBJECT TO FINAL EDITS

coastline retreat in 2025 will have an exceedance probability of 0.015 by 2050 and 0.07 by 2100.

Marine heatwave: The mean SST of the ocean around Australia and east of New Zealand has warmed at a rate of about 0.22ºC per decade between 1992 and 2016 (Wijffels et al., 2018), which is higher than the global average SST increase of 0.16ºC per decade (Oliver et al., 2018). This mean ocean surface warming is connected to longer and more frequent marine heatwaves in the region (Oliver et al., 2018). Over the period 1982-2016, the coastal ocean of Australia experienced on average more than 1.5 MHW per year, with the north coast of Western Australia and the Tasman Sea experiencing on average 2.5-3 MHWs per year. The average duration was between 10 and 15 days, with somewhat longer and hotter MHWs in the Tasman Sea. In New Zealand, the SE coast of the South Island experiences the most MHWs (2.5-3.0 per year). The duration of MHW in New Zealand is on average 10-15 days (Oliver et al., 2018). Changes over the 20th century, derived from MHW proxies, show an increase in frequency between 0.3 and 1.5 MHW per decade, except along the south east coast of New Zealand (Box 9.1); an increase in duration per event; and the total number of MHW days per decade, with the change being stronger in the Tasman Sea than elsewhere (Oliver et al., 2018).

There is *high confidence* that MHWs will increase around most of Australasia. Under RCP4.5 and RCP8.5 respectively, mean SST is projected to increase by 1ºC and 2 ºC around Australia by 2100, with a hotspot of around 2 ºC for RCP4.5 and of 4ºC for RCP8.5 along the southeast coast between Sydney and Tasmania (see Interactive Atlas). Under all RCPs, the mean SST around Australia is expected to increase in the future, with median values of around 0.4-1.0 ºC by 2030 under RCP4.5, and 2-4 ºC by 2090 under RCP8.5 (CSIRO and BOM, 2015). Warming is expected to be largest along the north-west coast of Australia, southern Western Australia, and along the east coast of Tasmania (CSIRO and BOM, 2018). More frequent, extensive, intense and longer-lasting MHWs are projected around Australia and New Zealand for GWLs of 1.5 ºC, 2 ºC and 3.5 ºC relative to the modelled reference value for 1861-1880 (Frölicher et al., 2018) Projections for SSP1-2.6 and SSP5-8.5 both show an increase in MHWs around Australasia by 2081 – 2100, relative to 1985 – 2014 (Box 9.2, Figure 1).

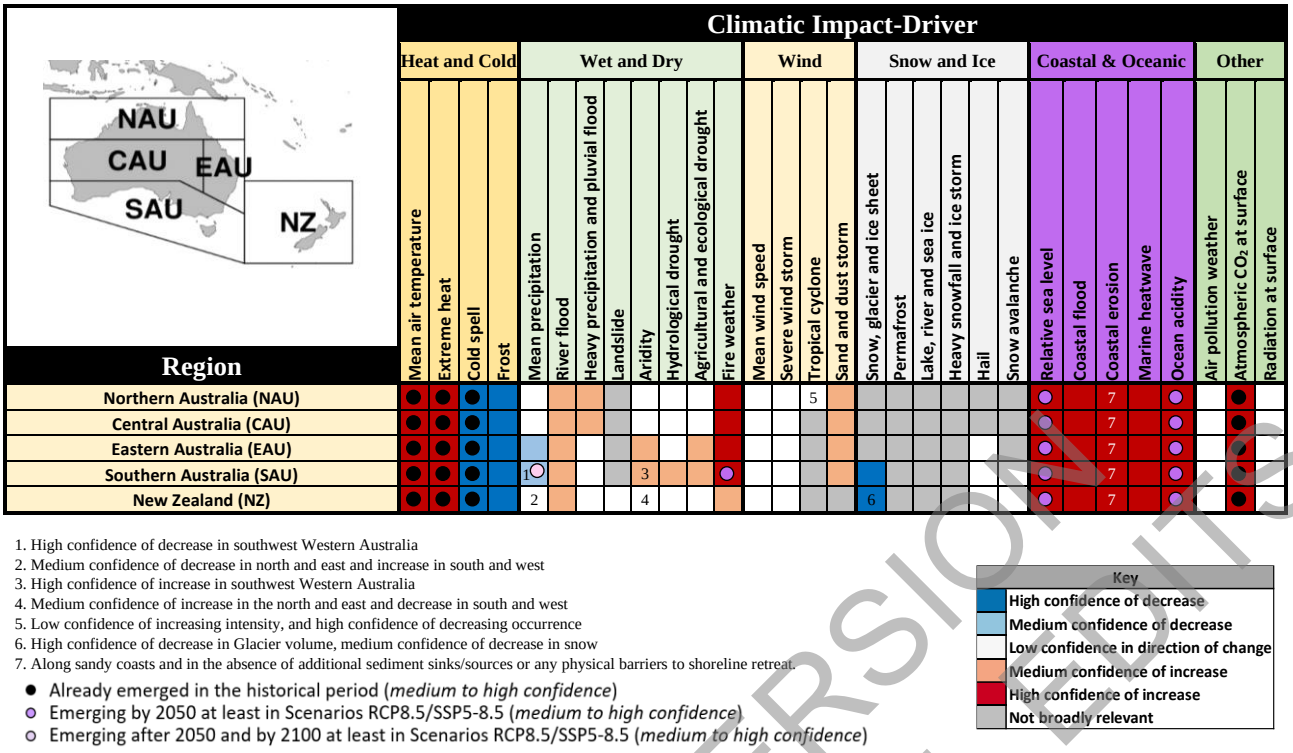
In general, there is *high confidence* that most coastal/ocean related hazards in Australasia will increase over the 21st century. Relative sea-level rise is *virtually certain* to continue in the oceans around Australasia, contributing to increased coastal flooding in low-lying areas (*high confidence*) and shoreline retreat along most sandy coasts (*high confidence*). Marine heatwaves are also expected to increase around the region over the 21st century (*high confidence*).

The assessed direction of change in climatic impact-drivers for Australasia and associated confidence levels are illustrated in Table 12.5, together with emergence time information (see Section 12.5.2). No assessable literature could be found for Hail and Snow avalanches, although these phenomena may be relevant in parts of the region.

[START TABLE 12.5 HERE]

Table 12.5: Summary of confidence in direction of projected change in climatic impact-drivers in Australasia, representing their aggregate characteristic changes for mid-century for scenarios RCP4.5, SSP3-4.5, SRES A1B, or above within each AR6 region (defined in Chapter 1), approximately corresponding (for CIDs that are independent of sea-level rise) to global warming levels between 2°C and 2.4°C (see 12.4 for more details of the assessment method). The table also includes the assessment of observed or projected time-of-emergence of the CID change signal from the natural inter-annual variability if found with at least *medium confidence* in Section 12.5.2.

ACCEPTED VERSION SUBJECT TO FINAL EDITS



[END TABLE 12.5 HERE]

12.4.4 Central and South America

For the purpose of this assessment, Central and South America is sub-divided into eight sub-regions, as defined in Chapter 1: southern Central America (SCA), north western South America (NWS), northern South America (NSA), South American Monsoon (SAM), north eastern South America (NES), south western South America (SWS), south eastern South America (SES), and southern South America (SSA). The Caribbean is placed under the Small Islands section (12.4.7) of this chapter.

Previous assessments have documented ongoing and projected changes in several CIDs. IPCC AR5 projections (IPCC, 2014b) pointed to increases in mean temperature between 2-6ºC by end of the century (*high confidence*) and increases in the occurrence of warm days and nights under various future climate scenarios (*medium confidence*). AR5 also pointed to patterns of changes in precipitation (*medium confidence*), changes in the duration of dry spells (*medium confidence*), and decreases in water supply (*high confidence*). IPCC SR1.5 projections indicated expected increases in river flooding and extreme runoff at 2°C warming in parts of South America, and decreases in runoff in Central America, central and southern South America, and the Amazon basin. The IPCC SROCC reported an increased number of landslides, a decreased volume of lahars from ice and snow-clad volcanoes, and increased frequency of Glacier Lake Outburst Floods. SROCC also indicated that regional and local-scale projections point to decreasing trends in glacier runoff.

New literature is now available for the regional climate as a result of observational research and coordinated modelling outputs of CORDEX South America (Solman, 2013; Sánchez et al., 2015) and CORDEX-CORE (Giorgi et al., 2018; Teichmann et al., 2019; Coppola et al., 2021b). Of particular interest are the new projections of both mean climate and extremes. This new regional climate information is key to main sectors sensitive to climate change in Central and South America such as water resources, infrastructure, agriculture, livestock, forestry, silviculture, and fisheries (Magrin, 2015; López Feldman and Hernández Cortés, 2016), human health (changes in morbidity and mortality, and emergence of diseases in previously non-endemic areas; (Núñez et al., 2016)) and biodiversity (Uribe Botero, 2015), urban planning, navigation and tourism.

ACCEPTED VERSION SUBJECT TO FINAL EDITS

[START FIGURE 12.8 HERE]

Figure 12.8: Projected changes in selected climatic impact-driver indices for Central and South America. (a) Mean change in 1-in-100 year river discharge per unit catchment area (Q100, $m^3 s^{-1} km^{-2}$) from CORDEX models for 2041-2060 relative to 1995-2014 for RCP8.5. (b) Shoreline position change along sandy coasts by the year 2100 relative to 2010 (meters; negative values indicate shoreline retreat) from the CMIP5 based data set presented by Vousdoukas et al. (2020). (c) Bar plots for Q100 ($m^3 s^{-1} km^{-2}$) averaged over land areas for the WGI reference AR6 regions (defined in Chapter 1). The left column within each panel (associated with the left y-axis) shows the 'recent past' (1995-2014) Q100 absolute values in grey shades. The other columns (associated with the right y-axis) show the Q100 changes relative to the recent past values for two time periods ('mid' 2041-2060 and 'long' 2081-2100) and for three global warming levels (defined relative to the preindustrial period 1850-1900): 1.5°C (purple), 2°C (yellow) and 4°C (brown). The bars show the median (dots) and the 10^{th}-90^{th} percentile range of model ensemble values across each model ensemble. CMIP6 is shown by the darkest colours, CMIP5 by medium, and CORDEX by light. SSP5-8.5/RCP8.5 is shown in red and SSP1-2.6/RCP2.6 in blue. (d) Bar plots for shoreline position change show CMIP5 based projections of shoreline position change along sandy coasts for 2050 and 2100 relative to 2010 for RCP8.5 (red) and RCP4.5 (blue) from Vousdoukas et al. (2020). Dots indicate regional mean change estimates and bars the 5^{th}-95^{th} percentiles ranges of associated uncertainty. Note that these shoreline position change projections assume that there are no additional sediment sinks/sources or any physical barriers to shoreline retreat. See Technical Annex VI for details of indices. Further details on data sources and processing are available in the chapter data table (Table 12.SM.1).

[END FIGURE 12.8 HERE]

12.4.4.1 Heat and cold

Mean air temperature: New literature confirms a continuous warming since the beginning of the 20^{th} century in the majority of the eight sub-regions (Atlas.7). However, observational datasets in several areas are still short and trend estimation is hindered by year-to-year and interannual variability. Atlas projections point to a *virtually certain* warming across all sub-regions, with the largest increases taking place in the Amazon Basin (NSA and SAM) (Atlas.7.2.4). A consistent increase in temperature-related indices linked to several climate-sensitive sectors (GDD, CDD) is found across CMIP5, CMIP6 and CORDEX-CORE projections, with lesser increase for CDD in mid-latitude regions than in SCA and the Amazon (Coppola et al., 2021b). Daily mean temperature exceedances of a typical 21.5°C threshold for a successful incubation of disease pathogens inside many mosquito vectors (Lambrechts et al., 2011; Blanford et al., 2013; Mordecai et al., 2013, 2017) will be crossed much more frequently, potentially driving increases in the incidence of vector-borne diseases (Laporta et al., 2015; Messina et al., 2019).

Extreme heat: Chapter 11 found *high confidence* of increased heat waves in all regions but SSA over the past decades. There is evidence of increasing heat stress over summertime in much of SES and SWS using the WBGT index for the period 1973-2012, and this has been attributed to human influence on the climate system (Knutson and Ploshay, 2016). Climate change projections point to major increases in several heat indices across the region for all scenarios (*high confidence*). Largest increases in the frequency of hot days (maximum temperatures, Tx > 35°C) are projected for the Amazon basin under SSP5-8.5 with more than 200 days per year at the end of the century under SSP5-8.5, while such increases remain moderate (50-100 days) in SSP1-2.6. For the dangerous heat threshold of HI>41°C, increases in frequency are similar to that in Tx>35°C (Figure 12.4 and Figure SM 1.1 and 1.2) (Coppola et al., 2021b; Schwingshackl et al., 2021).

Cold spell and frost: A decreasing frequency of cold days and nights has been observed in many sub-regions (Chapter 11). There is *medium confidence* (limited agreement) of a decrease in frost days in SWS, SES and SSA. Projections consistently suggest a general decrease in the frequency of cold spells and frost days in all sub-regions as indicated by several indices based on minimum temperature (Chou et al., 2014; López-Franca et al., 2016; Li et al., 2020b). Heating Degree Days are consistently projected to decrease by 5 degree days per year in the Amazon region, and up to 20-30 degree days in NSA, SWS and SES, under future RCP8.5/SSP5-8.5 (Coppola et al., 2021b).

ACCEPTED VERSION SUBJECT TO FINAL EDITS

In conclusion, it is *virtually certain* that warming will continue everywhere in Central and South America and there is *high confidence* that by the end of century most regions will undergo extreme heat stress conditions much more often than in recent past (e.g., increase of dangerous heat HI>41°C, or Tx>35°C) with more than 200 additional days per year under SSP5-8.5, while such conditions will be met up typically 50-100 more days per year under SSP1-2.6 over the same regions. Cold spells and frost days will have a decreasing trend (*high confidence*).

12.4.4.2 Wet and dry

Mean precipitation: The Atlas documents diverse historical precipitation trends in the region, including: a small but not significant increasing trend in SCA, a decreasing trend in south-eastern and north-eastern Brazil, and an increasing trend in SSA. Projections indicate a drying signal for SCA (*medium confidence*) (Coppola et al., 2014; Nakaegawa et al., 2014), NES and SWS (*high confidence*) (Atlas 7.2.5) and the well-known dipole for South America, meaning increasing precipitation over subtropical regions like the Río de La Plata basin (SES) (*high confidence*) and decreased precipitation in the Amazon (NSA) (*medium confidence*) (Chou et al., 2014; Llopart et al., 2014; Reboita et al., 2014; Sánchez et al., 2015b; Teichmann et al., 2019). These features are consistent among observations (Sena et al., 2018) and are consistently evident in regional and global model projections by mid- and end-of-century for both RCP4.5 and RCP8.5 (Jones and Carvalho, 2013) .

River flood: Emerging literature in the region documents ongoing changes in river floods: (Mernild et al., 2018) report decreases and increases in annual runoff on the west of the Andes Cordillera's continental divide, with the greatest decreases in the number of low ($<10^{th}$ percentile) runoff and the greatest increases in high ($>90^{th}$ percentile) runoff conditions. In coastal northeast Peru, extreme precipitation events recently caused devastating river floods and landslides (Son et al., 2020). In Brazil, floods are becoming more (less) frequent and intense in wet (drier) regions (Bartiko et al., 2019; Borges de Amorim and Chaffe, 2019), with higher propagation of hydrological changes through anthropogenically-modified agricultural basins (Chagas and Chaffe, 2018). Record, catastrophic, unprecedented, and once-in-a-century flooding events have also been reported in recent decades in the tributaries of the Amazon river or along its mainstream (Sena et al., 2012; Espinoza et al., 2013; Marengo et al., 2013; Filizola et al., 2014), in Argentinean rural and urban areas (Barros et al., 2015), in the lower reaches of the Atrato, Cauca and Magdalena rivers in Colombia (Hoyos et al., 2013; Ávila et al., 2019), in basins whose mainstreams flow through important metropolitan areas such as Concepción, Chile (Rojas et al., 2017), and even in one of Earth's driest regions, the Atacama Desert (Wilcox et al., 2016). In the Amazon basin, the significant increase in extreme flow was associated with the strengthening of the Walker circulation (Barichivich et al., 2018).

Emerging literature in the region documents projected increases for river floods in SES and SAM (*medium confidence*). Projections indicate that SES and the coasts of Ecuador and Peru will experience a tendency toward wetter conditions that can be a proxy for longer periods of flooding and enhanced river discharges (Zaninelli et al., 2019). CORDEX models project the strongest changes for the peak flow with a return period of 100 years in SES by mid-century and under RCP8.5. (Figure 12.8). At the continental scale, on the contrary, (Alfieri et al., 2017) suggest that 100-yr river floods are projected to decrease under RCP8.5. Regional projections of river floods have high uncertainty, however; owing to differences in hydrological models (Reyer et al., 2017a) (*low confidence*). Fábrega et al. (2013) projected increases in surface runoff for Panamá, while Zulkafli et al. (2016) identified increases in 100-yr floods of 7.5% and 12.0% in projections for the Peruvian Amazon wet season under RCPs 4.5 and 8.5, respectively. Wetter conditions and ±20% variations in annual mean streamflow are also projected for the Río de La Plata under the warming levels of 1.5°C, 2°C and 3°C above pre-industrial conditions (Montroull et al., 2018). In central Chile, 50-yr peak flows are expected to be greater by mid-century than 100-yr peak flows observed over the reference period (Bozkurt et al., 2018).

Heavy precipitation and pluvial flood: Chapter 11 indicated that there is *low confidence* due to limited evidence of extreme precipitation trends in almost all Central and South America, except in SES where increases in the magnitude and frequency of heavy precipitation have been observed (*high confidence*). In

ACCEPTED VERSION SUBJECT TO FINAL EDITS

general, data scarcity persists for a representative continental assessment. Chapter 11 projections indicate *low confidence* of increase, compared to the modern period, in the intensity and frequency of heavy precipitation in SCA and SWS for all GWLs, a *medium confidence* of increase in NSA, NES, SSA, SAM and SES for GWL of 4°C. In NWS, a wide range of changes is projected (*low confidence*).

Landslide: Several regions in Central America, as well as Colombia and southeastern Brazil, are considered areas of high incidence of observed fatal landslides. In these areas, ENSO-driven fluctuations in rainfall amounts (Sepúlveda and Petley, 2015) and climate change (Nehren et al., 2019) seem to be key factors. Rock falls, ice- and rock-ice avalanches, lahars, and landslides have been reported in frequent number in the southern, extratropical Andes in the last decades (Gariano and Guzzetti, 2016). A large number of ice- and moraine-dammed lakes have consequently failed, causing floods that rank amongst the largest events ever recorded (Iribarren Anacona et al., 2015). However, due to research deficit, evidence is largely missing for a reliable assessment of past and future trends of such hazards.

Aridity: Several new regional studies suggest positive trends in the frequency and length of droughts in the region, such as: over NWS (Domínguez-Castro et al., 2018), NSA (Marengo and Espinoza, 2016; Cunha et al., 2019) and NES (Marengo and Bernasconi, 2015), over southern Amazonia (Fu et al., 2013; Boisier et al., 2015), in the São Francisco River Basin and the capital city Distrito Federal in Brazil (Borges et al., 2018; Bezerra et al., 2019), in the southern Andes (Vera and Díaz, 2015), in central southern Chile (Boisier et al., 2018), in SES (Rivera and Penalba, 2014), and during recent years in SSA (Rivera and Penalba, 2014). Chapter 8 indicated *medium confidence* of anthropogenic forcing on observed drying trends in central Chile. Additional discussion on droughts and aridity trends in South America is presented in Chapter 8 (Sections 8.3.1.6, 8.4.1.6, 8.6.2.1).

Chapter 8 projections point to two important drying hotspots in South America with long-term soil moisture decline and precipitation declines, namely the Amazon basin (SAM and NSA) and SWS (*medium confidence*) (see also Figure 12.4). End-of-century RCP8.5 projections show a longer dry season in the central part of South America and decreased precipitation over the Amazon and central Brazil (Coppola et al., 2014; Giorgi et al., 2014b; Llopart et al., 2014; Teichmann et al. 2013) (Atlas.7). Seasonal changes are also apparent, with decreases in June-July-August rainfall projected for NSA, the coastal region of SES, SAM and the southern portion of the SWS (Marengo et al., 2016). Decreases in December-January-February rainfall are projected for the central part of South America in the near term (Kitoh et al., 2011; Chou et al., 2014; Cabré et al., 2016). Regional projections for Central and South America also indicate an increase in dryness in SCA and NES by mid to end of the century (*medium confidence*) (Chou et al., 2014; Marengo and Bernasconi, 2015).

Hydrological drought: Chapter 11 assessed mostly *low confidence* in observed changes in hydrological droughts given a lack of studies and clear evidence, with *medium confidence* only for a streamflow decrease in subregions of SWS. Some trends are becoming more clear, such as the ones reported for Colombia (NWS) by Carmona and Poveda (2014), who indicated that 62% of the 25- to 50-year long monthly average streamflow time series exhibited significant decreasing trends. However, studies of discharge changes indicate that uncertainty is still large, as argued by Pabón-Caicedo et al. (2020) for the full extent of the Andes.

A number of studies project decreases in runoff and river discharge for SCA, Colombia, Brazil and the southern part of South America by the end of this century (Nakaegawa and Vergara, 2010; Arnell and Gosling, 2013; van Vliet et al., 2013). Section 11.9 assessed *high confidence* in projections of increases in hydrological droughts in NSA, SAM, SWS, and SSA under a +4°C GWL, *medium confidence* in SCA, and *low confidence* in the rest of the sub-regions given insufficient evidence, lack of signal or mixed signals among the available studies. Signals are much more uncertain for the middle of the century (or for a 2°C GWL), with only SAM projected to have increased hydrological droughts with *medium confidence*.

Agricultural and ecological drought: Section 11.9 assessed *low confidence* in observed changes to agricultural and ecological drought across Central and South America due to regional heterogeneity and differences depending on the drought metrics used, except in NES which has seen a dominant increase in

ACCEPTED VERSION SUBJECT TO FINAL EDITS

drought severity (*medium confidence*).

NSA and SAM are the two regions where the strongest signal of increasing number of dry days (NDD) and drought frequency (DF) is projected compared to other regions of the world (Coppola et al., 2021b). By the end of this century and under RCP8.5, the NSA area average value for NDD reaches 43, 32 and 27, within the CORDEX-CORE, CMIP5 and CMIP6 ensembles, respectively. For the frequency of droughts, the NSA area average value is of about 4.6, 3.4 and 3.8. The SAM region shows NDD and DF values of 29, 20 and 21, and of 4, 3 and 3.5, respectively (see also Figure 12.4j-l). In Central America, a significantly drier northern region and a wetter southern region were projected for mid-century by (Hidalgo et al., 2017), whilst Fuentes-Franco et al. (2015) pointed to more pronounced dry periods during the rainy season in SCA by the end of this century under RCP8.5. Increases in the frequency of meteorological droughts that may initiate other drought types are projected for the eastern part of the Amazon and the opposite for the west under RCP8.5 (Duffy et al., 2015). In central Chile, the occurrence of extended droughts, such as the recently-experienced 2010-2015 mega-drought (which is still driving impacts), is projected to increase from one to up to five events per 100 years under RCP8.5 (Bozkurt et al., 2018). Section 11.9 highlights change in confidence in increases in drought severity in SCA, NSA, NES, SAM, SWS, and SSA from *low* to *high* under the three GWLs of +1.5°C, +2°C and +4°C. NES and SES change from *low confidence* to *medium confidence* increases in agricultural and ecological drought severity by +4°C GWL with different metrics and high agreement between studies. Only SAM and SSA have projections of agricultural and ecological drought increasing with *high confidence* for the middle of the century, or for a +2°C GWL, and NSA, NES and SCA are increasing with *medium confidence*.

Fire weather: There is evidence of increases in forest fire activity (number of fires, burned area and fire duration) such as in central and south-central Chile, where more conducive fire weather conditions have been proposed as the main driver (González et al., 2018; Urrutia-Jalabert et al., 2018). Projections indicate that the Amazon is one of the regions in the world with the highest increase in fire weather indices over the 21st century and under all RCPs (*high confidence*) (Betts et al., 2015; Abatzoglou et al., 2019; Sun et al., 2019b). This is consistent with the large increase in the frequency of joint occurrence of extreme hot and dry days for a 2°C warming level or more (Vogel et al., 2020). Projections of fire weather indices also show an increased risk in SWS (*high confidence*), SSA and SCA (*medium confidence*). However, wildfires highly depend on land-use and appropriate management may help mitigate future increases in fire risk (Fonseca et al., 2019).

Mean precipitation is projected to change in a dipole pattern with increases in NWS and SES and decreases in NES and SWS (*high confidence*) with further decreases in NSA and SCA (*medium confidence*). There is *medium confidence* of an increase in river floods in SAM and SES. There is *high confidence* of a dominant increase in drought duration in NES, an in the number of dry days and drought frequency in NSA and SAM. Dry climatic impact-drivers have more prevalent regional increases with higher global warming levels, with strongest projections of agricultural and ecological drought (*high confidence*) and aridity and fire changes (*medium confidence*) over the Amazon and with both drought types increasing over the SWS (*medium confidence*).

12.4.4.3 Wind

Mean wind speed: Due to the lack of long-term homogeneous records or limited observations in the region, past wind speed trends are difficult to establish. Global climate models project an increase in wind speeds, under all future scenarios, augmenting wind power potential in most parts of Central and South America, especially in NES where changes lie in the range 0-20% by 2050 under RCP8.5 and 0-40% under RCP8.5 (*medium confidence*) (Karnauskas et al., 2018a; Reboita et al., 2018; Jung and Schindler, 2019). In Patagonia, wind speeds are projected to decrease. For RCP4.5 changes remain marginal and have *low confidence (low agreement)*. Further information in (Figure 12.4m-o).

Severe wind storm: Similar observational limitations inhibit an assessment of long-term extreme wind trends. However, (Pes et al., 2017) found extreme wind increases in most of Brazil over the past decades. Future projections indicate a slight decrease in the number of extra-tropical cyclones in mid latitudes (*limited*

ACCEPTED VERSION SUBJECT TO FINAL EDITS

evidence, low confidence) (Reboita et al., 2018), and an increase of extreme winds in tropical areas (*limited evidence, low confidence*) (Kumar et al., 2015). Climate models project a shift and an intensification of southern storm tracks, with most effects offshore over the Southern ocean (Chapter 4), with *low confidence (low agreement)* of significant extreme wind changes over land and coastal areas across the 21st century (Chang, 2017; Augusto Sanabria and Carril, 2018; Reboita et al., 2020).

Tropical cyclone: CMIP5 and CMIP6 simulations, including the new HighResMIP, project a decrease in the frequency of tropical cyclones in the Atlantic and Pacific coasts of Central America for the mid-century or under a 2°C global warming level, accompanied with an increased frequency of intense cyclones (*medium confidence*) (Diro et al., 2014; Knutson et al., 2020; Roberts et al., 2020) (Chapter 11).

In summary, there is *limited evidence* of current trends in observed wind speed and wind storms in South America. Climate projections indicate a decrease in frequency of tropical cyclones in Central America accompanied with an increased frequency of intense cyclones, and an increase in mean wind speed and wind power potential in NES, NSA and SAM (*medium confidence*).

12.4.4.4 Snow and ice

Snow: Studies on seasonal snow cover are limited and restricted to the Andes Cordillera. Mernild et al. (2017) indicated that much of the area north of 23°S experienced a decrease in the number of snow cover days, while the southern half experienced the opposite. A reduction in snow cover of about 15% was simulated for areas in the range [3000-5000 m], whereas in regions with altitude below 1000 m (Patagonia) snow cover extent increased. The reduced snowfall over the Chilean and Argentinean Andes mountains, which has resulted in unprecedented reductions in river flow, reservoir volumes and groundwater levels, led to the most severe and long-lasting hydrological drought (2010-2015) reported in the adjacent semi-arid foothills of the central Andes (Garreaud et al., 2017; Rivera et al., 2017; Masiokas et al., 2020). Projections (based on process understanding) in Chapter 9 point to decreases in seasonal snow cover extent and duration across South America as global climate continues to warm (*high confidence*).

Glacier: Observation and future projection of Central and South America glacier mass changes are assessed in Section 9.5.1, grouped in two main regions: Low Latitude region (98% of which is glaciers in the Andes) and the Southern Andes region. An increase in the number and areal extent of glacial lakes in the Southern Andes was reported for the period 1986-2016 (Wilson et al., 2018). Similar changes are being observed in the central Andes (Colonia et al., 2017). Since 1800 at least 15 ice-dammed lakes and 16 moraine-dammed lakes have failed in the extratropical Andes, causing high-magnitude Glacial Lake Outburst Floods (Rojas et al., 2014; Cook et al., 2016; Wilson et al., 2018; Drenkhan et al., 2019). Partially due to glaciers shrinkage and lake growth, the frequency of outburst floods has increased in the last 30-40 years (Carey et al., 2012; Iribarren Anacona et al., 2015).

Glaciers across South America are expected to continue to lose mass and glacier area in the coming century (*high confidence*) (Section 9.5). In term of their mass, glaciers in the Low Latitude region are projected by GlacierMIP to lose 67 ± 42%, 86 ± 24% and 94 ± 13%, of their 2015 baseline by the end of the century under RCP2.6, RCP4.5 and RCP8.5 scenarios, respectively (Marzeion et al., 2020). Glaciers in the Southern Andes show decreasing mass loss rates for RCP2.6, and increasing rates for RCP8.5, which peak in the mid to late 21st century. Glaciers in the Southern Andes are projected to lose 26 ± 27%, 33 ± 26%, and 47 ± 26% of their mass in 2015 by the end of the century under RCP2.6, RCP4.5 and RCP8.5 scenarios, respectively. Details in (Section 9.5.1.3).

Permafrost: There is limited information on the ongoing changes and projections of permafrost conditions in the region. Based on model projections under the IPCC A1B scenario, permafrost areas in the Bolivian Andes will eventually be lost, but this could take years to decades or longer depending on permafrost thickness (Rangecroft et al., 2016). The central Andes will experience the highest disturbance to the thermal regime of the twenty-first century. As a consequence, in the Argentinian Andes up to 95% of rock glaciers in the southern Desert Andes and in the central Andes will rest in areas above 0 °C under the worst case

ACCEPTED VERSION SUBJECT TO FINAL EDITS

scenario of warming (the freezing level might move up more than twice as much as during the entire Holocene) (Drewes et al., 2018).

In conclusion, glacier volume loss and permafrost thawing will *likely* continue in the Andes Cordillera under all climate scenarios, causing important reductions in river flow and potentially high-magnitude Glacial Lake Outburst Floods.

12.4.4.5 Coastal and oceanic

Relative sea level: Around Central and South America, over 1900-2018, a new tide-gauge based reconstruction finds a regional-mean relative sea level (RSL) change of 2.07 [1.36 to 2.77] mm yr^{-1} in the South Atlantic, 2.49 [1.89 to 3.06] mm yr^{-1} in the subtropical North Atlantic and 1.20 [0.76 to1.62] mm yr^{-1} in the East Pacific (Frederikse et al., 2020), compared to a global mean sea level (GMSL) change of around 1.7 mm yr^{-1} (Section 2.3.3.3; Table 9.5). For the period 1993-2018, these RSLR rates, based on satellite altimetry, increased to 3.45 [3.04to 3.86)] mm yr^{-1}, 4.04 [2.77 to 5.24] mm yr^{-1} and 2.35 [0.70 to 4.06] mm yr^{-1}, respectively (Frederikse et al., 2020), compared to a GMSL change of 3.25 mm yr^{-1} (Section 2.3.3.3; Table 9.5).

Relative sea-level rise is *extremely likely* to continue in the oceans around CSA. Regional-mean RSLR projections for the oceans around Central and South America range from 0.3 m–0.5 m under SSP1-RCP2.6 to 0.5 m–0.9 m under SSP5-RCP8.5 for 2081-2100 relative to 1995-2014 (median values), which is around the projected GMSL change {Section 9.6.3.3}. These RSLR projections may however be underestimated due to potential partial representation of land subsidence in their assessment (Section 9.6.3.2).

Coastal flood: Present day 1:100 yr Extreme Total Water Level (ETWL) ranges from 0.5 to 2.5 m around most of Central and South America, except in SSA and SWS subregions where 1:100 yr ETWLs can be as large as 5 to 6 m (Vousdoukas et al., 2018). ETWL magnitude and occurrence frequency are expected to increase throughout the region (*high confidence*) (see Figure 12.4p-r and Figure SM 12.6). Across the region, the 5^{th} – 95^{th} percentile range of the 1:100 yr ETWL is projected increase (relative to 1980 – 2014) by 8 cm – 34 cm and by 10 cm – 43 cm by 2050 under RCP4.5 and RCP8.5, respectively (Vousdoukas et al., 2018; Kirezci et al., 2020). By 2100, this range is projected to be 21 cm – 93 cm and 34 cm – 190 cm under RCP4.5 and RCP8.5, respectively (Vousdoukas et al., 2018; Kirezci et al., 2020). Furthermore, under RCP4.5, the present day 1:100 yr ETWL is projected to have median return periods of 1:10 yrs – 1:50 yrs by 2050 and 1:1 yr by 2100 in SES, SSA and SWS. In other regions of Central and South America, the present day 1:100 yr ETWL is projected to occur once per year or more by both 2050 and 2100 under RCP4.5. The present day 1:50 yr ETWL is projected to occur around 3 times a year by 2100 with a SLR of 1 m (Vitousek et al., 2017).

Coastal erosion: According to satellite data, shoreline retreat rates of around 1 m yr^{-1} have been observed along the sandy coasts of SCA, SES and SSA over the period 1984-2015, while shoreline progradation rates of around 0.25 m /yr has been observed in NWS and NSA. The sandy shorelines in NES and SWS have remained more or less stable over the same period (Luijendijk et al., 2018; Mentaschi et al., 2018). Using satellite observations, Mentaschi et al. (2018) report a coastal area loss of 250 km^2 over a 30-year period (1984-2015) along the Pacific coast of South America, and of 780 km^2 along the Atlantic coastlines.

Projections indicate that a majority of sandy coasts in the region will experience shoreline retreat throughout the 21^{st} century (*high confidence*). Median shoreline change projections (CMIP5) for the mid-century period show that, relative to 2010, presented by Vousdoukas et al. (2020) show that sandy shorelines will retreat by between 30 m and 75 m in SCA, NES, SES and SSA under both RCP4.5 and RCP8.5, while the projected mid-century retreats are less than 30 m in NSA, NWS and SWS for both RCPs (Vousdoukas et al., 2020). Parts of the coastline in these latter three regions projected to prograde over the 21st century, if present ambient shoreline change trends continue (Vousdoukas et al., 2020). By 2100, median retreats of more than 100 m are projected in SCA, NES, SES and SSA under both RCPs, while retreats between 50 m – 100 m are projected for NSA, NWS, and SWS under both RCPs (Figure 12.8). Notably, the projected shoreline retreats

ACCEPTED VERSION SUBJECT TO FINAL EDITS

in SCA and SES approach 150 m by 2100 under RCP4.5 and 200 m under RCP8.5. The total length of sandy coasts in Central and South America that is projected to retreat by more than a median of 100 m by 2100 under RCP4.5 and RCP8.5 is about 15,000 km and 12,000 km respectively, an increase of approximately 30%.

Marine heatwave: The mean sea surface temperature (SST) of the Atlantic Ocean and the Caribbean around Central and South America increased from 0.25°C to 1°C over the period 1982-1998 (Oliver et al., 2018). This mean ocean surface warming is connected to longer and more frequent marine heatwaves (MHW) in the region (Oliver et al., 2018). Over the period 1982-2016, the coastlines experienced on average more than 1.0 MHW per year, with the Pacific coast of North Central America and the coast of SES (Atlantic) experiencing on average 2.5-3.0 MHWs per year. The average duration was between 10 and 15 days, with the notable exception of the Equatorial Pacific coastline, which experiences MHWs with >30 days average duration related to ENSO conditions. In the Southwestern Atlantic shelf (32-38°S), more than half of the days with MHWs have occurred since 2014, and the most intense event (1.7°C above previous maximum) took place in the austral summer of 2017 (Manta et al., 2018). Changes over the 20th century, derived from MHW proxies, show an increase in frequency between 0.5 and 2.0 MHW per decade in the South Atlantic, the Caribbean and the Pacific coast of North Central America, an increase in intensity per event in the South Atlantic, and a decrease along the Equatorial Pacific coastline. The total number of MHW days per year increases around Central and South America, with the exception of the Equatorial Pacific coastline (Oliver et al., 2018).

There is *high confidence* that MHWs will increase around Central and South America. Mean SST is projected to increase by 1ºC (2ºC) by 2100, with a hotspot of about 2ºC (4ºC) along the coast of South East South America and North West South America under RCP4.5 (RCP8.5). (See Interactive Atlas). More frequent, MHWs are projected around the region for GWLs of 1.5 ºC, 2 ºC and 3.5 ºC relative to the modelled reference value for 1861-1880 (Frölicher et al., 2018). Projections for SSP1-2.6 and SSP5-8.5 both show an increase in MHWs around Central and South America by 2081 – 2100, relative to 1985 – 2014 (Box 9.2, Figure 1).

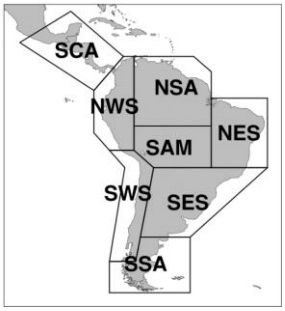
In summary, relative sea-level rise is *extremely likely* to continue in the oceans around Central and South America, contributing to increased coastal flooding in low-lying areas (*high confidence*) and shoreline retreat along most sandy coasts (*high confidence*). Marine heatwaves are also expected to increase around the region over the 21st century (*high confidence*).

The assessed direction of change in climatic impact-drivers for Central and South America and associated confidence levels are illustrated in Table 12.6. No assessable literature could be found for sand and dust storm, lake and sea ice, heavy snowfall and ice storms, hail, and snow avalanches, although these phenomena may be relevant in parts of the region.

[START TABLE 12.6 HERE]

Table 12.6: Summary of confidence in direction of projected change in climatic impact-drivers in Central and South America, representing their aggregate characteristic changes for mid-century for scenarios RCP4.5, SSP3-4.5, SRES A1B, or above within each AR6 region (defined in Chapter 1), approximately corresponding (for CIDs that are independent of sea-level rise) to global warming levels between 2°C and 2.4°C (see 12.4 for more details of the assessment method). The table also includes the assessment of observed or projected time-of-emergence of the CID change signal from the natural inter-annual variability if found with at least *medium confidence* in Section 12.5.2.

ACCEPTED VERSION SUBJECT TO FINAL EDITS



Region	Heat and Cold				Wet and Dry								Wind				Snow and Ice						Coastal & Oceanic					Other		
	Mean air temperature	Extreme heat	Cold spell	Frost	Mean precipitation	River flood	Heavy precipitation and pluvial flood	Landslide	Aridity	Hydrological drought	Agricultural and ecological drought	Fire weather	Mean wind speed	Severe wind storm	Tropical cyclone	Sand and dust storm	Snow, glacier and ice sheet	Permafrost	Lake, river and sea ice	Heavy snowfall and ice storm	Hail	Snow avalanche	Relative sea level	Coastal flood	Coastal erosion	Marine heatwave	Ocean acidity	Air pollution weather	Atmospheric CO_2 at surface	Radiation at surface
Southern Central America (SCA)	●	●	○												2								○		3		○		●	
Northwestern South America (NWS)	●	●	●																				○		3,4		○		●	
Northern South America (NSA)	●	●	●												2										3,4				●	
South American Monsoon (SAM)	●	●	●			1																							●	
Northeastern South America (NES)	●	●	●																				○		3		○		●	
Southwestern South America (SWS)	●	●	●																				○		3,4		○		●	
Southeastern South America (SES)	●	●	○																				○		3		○		●	
Southern South America (SSA)	●		○																				○		3		○		●	

1. Increase in extreme flow in the Amazon basin.
2. Tropical cyclones decrease in number but increase in intensity
3. Along sandy coasts and in the absence of additional sediment sinks/sources or any physical barriers to shoreline retreat.
4. Substantial parts of the NWS, NSA and NES coasts are projected to prograde if present-day ambient shoreline change rates continue.

● Already emerged in the historical period (*medium to high confidence*)
○ Emerging by 2050 at least in Scenarios RCP8.5/SSP5-8.5 (*medium to high confidence*)
○ Emerging after 2050 and by 2100 at least in Scenarios RCP8.5/SSP5-8.5 (*medium to high confidence*)

Key
High confidence of decrease
Medium confidence of decrease
Low confidence in direction of change
Medium confidence of increase
High confidence of increase
Not broadly relevant

[END TABLE 12.6 HERE]

12.4.5 Europe

The regional European climate and main hazards have been previously assessed in SREX, AR5 (WGII), SR1.5, SROCC and SRCCL and a summary of key findings can be found in the Europe section of the Atlas 8.1. For the purpose of these assessment Europe is divided in four climatic regions North Europe (NEU), Western and Central Europe (WCE), Eastern Europe (EE) and Mediterranean (MED) (see Figure Atlas.27).

Since AR5 and SR1.5, a large body of literature that uses the EURO-CORDEX and MED-CORDEX ensembles of high-resolution simulations (Jacob et al., 2014; Ruti et al., 2016; Kjellström et al., 2018; Vautard et al., 2020; Coppola et al., 2021a) to assess signals of climate change in Europe has emerged. These scenario simulations have been the basis of a number of impact studies (see e.g., Jacob et al., 2014b, 2018; Somot et al., 2018; Faggian and Decimi, 2019)) highlighting the use of the climatic impact-drivers. The development of the science of attribution of weather events (Stott et al., 2016) has provided evidence of links between climate change and hazard changes such as the 2017 Mediterranean heat wave (Kew et al., 2019) and many others (see Chapter 11).

The ability of global and regional models to reproduce the observed changes in mean and extreme temperature and precipitation in Europe is assessed in the literature (see Atlas 8.3). In summary, both GCMs and RCMs have their limitations but, in general, the increased resolution of RCMs is shown to clearly add valued in terms of resolving spatial patterns and seasonal cycles of precipitation and precipitation extremes in many European regions, especially in regions of complex topography such as the Alps and for quantities such as snowmelt driven runoff, regional winds and Mediterranean hurricanes (Medicanes).

Examples of projected hazard thresholds are illustrated in Figures 12.4 and 12.9 based on the most recently updated Euro-CORDEX RCM projections, CMIP5 and CMIP6 GCMs for comparison. For a more comprehensive representation of other hazard index trends assessed in this section the reader is referred to the interactive Atlas.

ACCEPTED VERSION SUBJECT TO FINAL EDITS

[START FIGURE 12.9 HERE]

Figure 12.9: Projected changes in selected climatic impact-driver indices for Europe. (a) Mean change in 1-in-100 year river discharge per unit catchment area (Q100, $m^3 s^{-1} km^{-2}$), and (b) median change in the number of days with snow water equivalent (SWE) over 100 mm (from November to March), from EURO-CORDEX models for 2041-2060 relative to 1995-2014 and RCP8.5. Diagonal lines indicate where less than 80% of models agree on the sign of change. (c) Bar plots for Q100 ($m^3 s^{-1} km^{-2}$) averaged over land areas for the WGI reference AR6 regions (defined in Chapter 1). The left column within each panel (associated with the left y-axis) shows the 'recent past' (1995-2014) Q100 absolute values in grey shades. The other columns (associated with the right y-axis) show the Q100 changes relative to the recent past values for two time periods ('mid' 2041-2060 and 'long' 2081-2100) and for three global warming levels (defined relative to the preindustrial period 1850-1900): 1.5°C (purple), 2°C (yellow) and 4°C (brown). The bars show the median (dots) and the 10^{th}-90^{th} percentile range of model ensemble values across each model ensemble. CMIP6 is shown by the darkest colours, CMIP5 by medium, and CORDEX by light. SSP5-8.5/RCP8.5 is shown in red and SSP1-2.6/RCP2.6 in blue. (d) As for (c) but showing absolute values for number of days with SWE > 100mm, masked to grid cells with at least 14 such days in the recent-past. See Technical Annex VI for details of indices. Further details on data sources and processing are available in the chapter data table (Table 12.SM.1).

[END FIGURE 12.9 HERE]

12.4.5.1 Heat and Cold

Mean air temperature: Since AR5, studies have confirmed that the mean warming trend in Europe is increasing (Atlas.8.2). The observed warming trend patterns are largely consistent with those simulated by global and regional climate models and it is *very likely* that such trends are, in large part, due to human influence on climate (Chapter 3).

All temperature trends are *very likely* to continue for a global warming of 1.5°C or 2°C and 3°C (Atlas 8.4). Future warming leads to the exceedance of different temperature thresholds relevant for vector-borne diseases (*medium confidence*) (Caminade et al., 2012; Medlock et al., 2013), invasive allergens (*medium confidence*) (Storkey et al., 2014; Hamaoui-Laguel et al., 2015), SST thresholds in the Mediterranean (*likely* to exceed 20°C), or relevant for the vibrio bacteria development (Vezzulli et al., 2015). Future warming is also projected to lead to the exceedance of cooling degree-day index (>22°C) thresholds, characterizing a potential increase in energy demand for cooling in Southern Europe with increases *likely* exceeding 40% in some areas (Spinoni et al., 2015) by 2050 under RCP8.5 (*high confidence*) (Coppola et al., 2021a) (see also Atlas and Section 12.3).

Extreme heat: The frequency of heat waves observed in Europe has *very likely* increased in recent decades due to human-induced change in atmospheric composition (see Chapter 11) and a detectable anthropogenic increase in a summertime heat stress index over all regions of Europe has been identified based on wet bulb globe temperature (WBGT) index trends for 1973-2012 (*medium confidence, limited evidence*) (Knutson and Ploshay, 2016).

It is *very likely* that the frequency of heat waves will increase during the 21^{st} century regardless of the emission scenario in each European region, and for 1.5°C and 2°C global warming levels (GWLs) (Chapter 11). Heat stress due to both high temperature and humidity, affecting morbidity, mortality and labor capacity (see Section 12.3) is projected to increase under all emission scenarios and GWLs by the middle of the century (Figure 12.4a-f). Under RCP8.5, the expected number of days with WBGT larger than 31°C of about 25, 30 and 40 days per year, projected by EURO-CORDEX, CMIP5 and CMIP6 respectively on average over the Mediterranean region, and specifically of 30, 40 and 60 days per year in low coastal plain areas such as the Po Valley, the Italian, Greek and Spanish coasts and the Mediterranean islands in (Coppola et al., 2021a). An average increase of a few days per year of maximum daily temperature exceeding 35°C, a typical critical threshold for crop productivity, is expected by the mid-century in Central Europe, and a further increase of 10-20 days is expected for the Mediterranean areas (see Figure 12.4b) (Coppola et al., 2021a). By

ACCEPTED VERSION SUBJECT TO FINAL EDITS

contrast, under SSP1-2.6, the increase in this number of days remain limited to less than about 10 days, and confined to the Mediterranean regions. Mitigation is expected to have a strong effect: by the end of century, and under SSP5-8.5, dangerous heat threshold of HI>41°C is projected to be crossed 5-10 days more per year in the Mediterranean regions and a few days per year more in WCE and EEU while these increases would virtually be absent under SSP1-2.6 (Figure 12.4d-f).

Cold spell and frost: Temperature observations for winter cold spells in Europe show a long-term decreasing frequency (Brunner et al., 2018), with their probability of occurrence projected to decrease in the future (*high confidence*) and virtually disappear by the end of the century (Chapter 11). The frequency of frost days will *very likely* decrease for all scenario and all time horizons (Lindner et al., 2014; Coppola et al, 2021) with consequences on agriculture and forests. A simple heating degree-day index, characterizing heating demand, shows a large observed decreasing trend for winter heating energy demand in Europe (Spinoni et al., 2015),. This trend is *very likely* to continue through the 21st century, with decreases in the range of 20-30% for Northern Europe, about 20% for Central Europe and 35% for Southern Europe, by mid-century under RCP8.5 (Spinoni et al., 2018b; Coppola et al., 2021a) (See also the interactive Atlas).

In summary, irrespective of the scenario, it is *virtually certain* that warming will continue in Europe, and there is *high confidence* that the observed increase in heat extremes is due to human activities. It is *very likely* that the frequency of heat extremes will increase over the 21st century with an increasing gradient toward the Southern regions. Extreme heat will exceed critical thresholds for health, agriculture and other sectors more frequently (*high confidence*), with strong differences between mitigation scenarios. It is *very likely* that the frequency of cold spells and frost days will keep decreasing over the course of this century and it is *likely* that cold spells will virtually disappear towards the end of the century.

12.4.5.2 Wet and Dry

Mean precipitation: Precipitation has generally increased in Northern Europe and decreased in Southern Europe, especially in winter (Fischer and Knutti, 2016, Knutson and Zeng, 2018) but in the latter precipitation trends are strongly dependent on the examined period (Chapter 11). The trend in precipitation increase in the north and decreasing in the south is also represented by global and regional climate simulations (Jacob et al., 2014; Rajczak and Schär, 2017; Lionello and Scarascia, 2018; Coppola et al., 2021a) (see Atlas.8.2) and has been attributed to climate change (Chapter 3, Chapter 8).

Studies since AR5, together with EURO-CORDEX and MED-CORDEX experiments and the latest CMIP6 ensemble, have increased confidence in regional projections of mean and extreme precipitation (Prein et al., 2016) despite their wet bias, and show that it is *very likely* that precipitation will increase in Northern Europe in DJF and decrease in the Mediterranean in JJA under all climate scenarios except RCP2.6/SSP1-2.6 and for both mid and end century periods (Coppola et al., 2021a). (Atlas 8.5).

River flood: There is *high confidence* of an observed increasing trend of river floods in Central and Western Europe (WCE) and *medium confidence* of a decrease in northern (NEU) and Southern Europe (MED).

SR1.5 shows evidence of an increase in reported floods in the UK over the period 1884-2013, and increasing trends in annual maximum daily streamflow data over 1966–2005 in parts of Europe. Although, high flow does not show uniform trends for the entire region (Hall et al., 2014; Mediero et al., 2015) or specific region (Mudersbach et al., 2017; Tramblay et al., 2019; Vicente-Serrano et al., 2017), regional patterns of significant flood trends do exist. Based on the most extended river flow database spanning the period 1960-2010, an increase in floods frequency in northwestern Europe, decreasing in medium and large catchments in southern Europe and decreasing floods in eastern Europe has been detected (Blöschl et al., 2019) in line with (Mediero et al., 2014; Arheimer and Lindström, 2015; Gudmundsson et al., 2017; Krysanova et al., 2017; Kundzewicz et al., 2018; Mangini et al., 2018)

There is *high confidence* of river floods increasing in Central and Western Europe (WCE) and *medium*

ACCEPTED VERSION SUBJECT TO FINAL EDITS

confidence of a decrease in northern (NEU) Eastern (EE) and Southern Europe (MED) for mid and end of century under RCP8.5 and *low confidence* under RCP2.6. The projected increase in WCE is roughly 10% (18% by end of century) and the projected decrease in NEU is of 5% (11% by end of century) for the peak flow with a return period of 100 years for mid-century, under RCP8.5 (Di Sante et al., 2021) (See Figure 12.9a for mid of century Q(100) projections of flood discharges per unit catchment area (Blöschl et al., 2019) based on EURO-CORDEX models).

Using frequency analysis of extreme peak flow events above a 100-year return period as a threshold, which is the average protection level of the European river network (Rojas et al., 2013), Alfieri et al. (2017) and Alfieri et al. (2015) show that Europe is *likely* to be one of the regions where the largest increases in flood risk may occur, with only few countries in Eastern Europe showing a decrease (Poland Lithuania, Belarus) (Osuch et al., 2017). They find a significant increase of events with peak discharge above 100-year return period (Q100) in most of Europe in line with (Rojas et al., 2012; Hirabayashi et al., 2013; Dankers et al., 2014; Forzieri et al., 2016; Roudier et al., 2016; Thober et al., 2018) and an increase in the magnitude of floods in southern Europe, although (Giuntoli et al., 2015) projects no change. A modest but significant decrease in the 100-year return period river flood is projected for Southern (due to reduction of precipitation) and north Eastern European regions the latter because of the strong reduction in snowmelt induced river floods (Thober et al., 2018; Di Sante et al., 2021).

Heavy precipitation and pluvial flood: Heavy precipitation frequency trends have been detected in Europe with *high confidence* for the NEU and Alpine regions and with *medium confidence* in WCE, and also attributed to climate change with *high confidence* in NEU (Section 11.9).

Projections based on multiple lines of evidence from global to convective permitting model scales show *high confidence* in extreme precipitation increase in the northern, central and eastern European regions (NEU, WCE, EEU and in the Alpine area, Increases with *medium confidence* are projected for the Mediterranean basin (with a negative gradient toward the south) for mid and end of century under RCP8.5, RCP4.5, and SSP5-8.5 (Section 11.9) (MedECC, 2020). Guerreiro et al. (2017), based on observations, showed that 20% of city areas in WCE and MED regions is affected by pluvial flooding and less than 10% of city areas in the Northern and Western coastal cities.

Landslide: Increase of rainfall periods connected to landslides are projected to increase in central Europe by up to 1 more period per year in flat areas in low altitudes and by up to 14 more periods per year at higher altitudes by mid-century, becoming even more evident by end of the century (Schlögl and Matulla, 2018). An increase of landslides by up to + 45.7% and + 21.2% is also projected for Southern Italy (Calabria region) by mid of century under both RCP4.5 and RCP8.5 (Gariano and Guzzetti, 2016) and by up to 40% in Central Italy (Umbria) during the winter season (Ciabatta et al., 2016). A decrease of landslides is projected in the Peloritani Mountains in Southern Italy (RCP4.5 and 8.5) by mid of the century (Peres and Cancelliere, (2018)). A slight increase (10 year return period) in landslides is projected in the Eastern Carpathians, the Moldavian Subcarpathian and the northern part of the Moldavian Tableland and higher increase in the western hilly and plateau areas of Romania (100 year return period) (Jurchescu et al., 2017).

Aridity: The Mediterranean region shows evidence of large-scale decreasing precipitation trends over 1901-2010, which are at least partly attributable to anthropogenic forcing according to CMIP5 models (Knutson and Zeng (2018). Nevertheless, there is *low agreement* among studies on observed precipitation trend in the Mediterranean region. (Chapter 11; Atlas 8.2).

The precipitation is projected to decrease by mid and end of century for the RCP8.5 and SSP5-85 with *strong agreement* among CMIP5, CMIP6 and CORDEX regional climate ensemble models on the direction of change. With both temperature increase and precipitation decrease there is *high confidence* on increase aridity in the MED region. (Coppola et al., 2021 Atlas.8.2; Chapter 4; Chapter 8).

Hydrological drought: There is *high confidence* that hydrological droughts have increased in the Mediterranean basin with *medium confidence* in anthropogenic attribution of the signal, and *high confidence* that they will continue to increase through the 21st century for 2°C GWL and higher and all scenarios.

ACCEPTED VERSION SUBJECT TO FINAL EDITS

(Section 11.9; Chapter 8). There is *medium confidence* in hydrological drought increase in WCE and *low confidence* in direction of change for EEU and NEU from mid-century onward and for 2°C GWL and higher and all scenarios (Section 11.9) (see Figure 12.4g-i)

Streamflow droughts are projected become more severe and persistent in Mediterranean and Western Europe (current 100-year events could occur approximately every 2 to 5 years by 2080) (Forzieri et al., 2016). The opposite tendency is projected in Northern, Eastern and Central Europe where higher precipitation that outweigh the effects of increased evapotranspiration is expected to result in a decrease in streamflow drought frequency (Forzieri et al. 2014). For a 2ºC GWL droughts will become more intense in the MED and in France and longer mainly due to less rainfall and higher evapotranspiration. A reduction of drought length and magnitude is projected for NEU and EEU (Roudier et al., 2016). In the Southern Alps, both winter and summer low flows are projected to be more severe, with a 25% decrease in the 2050s (Vidal et al., 2016).

Agricultural and ecological drought: There is *medium confidence* that agricultural and ecological droughts have increased in Western and Central Europe and in the Mediterranean region, and *medium confidence* that anthropogenic drivers contributed to the Mediterranean increase (Section 11.9, Chapter 8).

Chapter 11 assesses that agricultural and ecological droughts will increase in the Mediterranean regions (*high confidence*) and Western and Central Europe (*medium confidence*) by mid-century with *high confidence* by the end of century for the MED for 2ºC GWL and higher and all scenarios. *Low confidence* in direction of change is assessed for EEU and NEU (see Figure 12.4k).

Recent local studies provide additional risk-relevant context to changes in European drought. Agricultural and ecological drought conditions are expected to intensify in Southern Europe by end-of-century based on the 12-month rainfall Drought Severity Index (a soil moisture indicator), precipitation deficit SPI and SPEI indices. There will be regions in Southern Europe where this type of drought could be up to 14 times worse than the worst drought in the historical period (Guerreiro et al., 2018). One-in-10 year drought events are projected to happen every second year (Mora et al., 2018; Ruosteenoja et al., 2018). The Mediterranean region will have 100 additional stress years (years with three consecutive months of precipitation deficits greater than 25%) (Giorgi et al., 2018); an increase of both drought frequency (up to 2 events per decade) and severity (Spinoni et al., 2014, 2019a) and an increase of consecutive dry day (CDD) in the southern part of the MED region (Lionello and Scarascia, 2020). In contrast, droughts are expected to decrease in winter in Northern Europe (Spinoni et al., 2018a; Section 11.9). These findings are confirmed by the EURO-CORDEX, CMIP5 and CMIP6 ensemble that show a change of frequency of drought events in the MED between 2 and 3 events per decade for mid of the century RCP8.5 scenario (Coppola et al., 2021a) (see also Figure SM 1.3)

Fire weather: Fire weather conditions have been increasing since about 1980 over a few regions in Europe including Mediterranean areas (*low confidence*) (Venäläinen et al., 2014; Urbieta et al., 2019; Barbero et al., 2020; Giannaros et al., 2021). However beyond a few studies, evidence is largely missing about attribution of these trends to anthropogenic climate change (Forzieri et al., 2016). An increase in fire weather is projected for most of Europe, especially Western, Eastern and Central regions, by 2080 (current 100-yr. events will occur every 5 to 50 years), with a progressive increase in confidence and model agreement along the 21st century (*medium confidence*) (Forzieri et al., 2016; Abatzoglou et al., 2019). With increased drying and heat combined, in Mediterranean areas, an increase in fire weather indices is projected under RCP4.5 and RCP8.5, or SRES A1B, as early as by the mid century (Bedia et al., 2014; Abatzoglou et al., 2019; Dupuy et al., 2020; Fargeon et al., 2020; Ruffault et al., 2020) (*high confidence*) and an increase in burned area of 40% and 100% for a 2ºC and 3ºC respectively (Turco et al., 2018).

In summary, there is *high confidence* that river floods will increase in Central and Western Europe and *medium confidence* that they will decrease in Northern, Eastern and Southern Europe, for mid and end of century under RCP8.5 and with *low confidence* under RCP2.6. There is *high confidence* that aridity will increase by mid and end of century for the RCP8.5 and SSP5-85, and *high confidence* that agricultural, ecological and hydrological droughts will increase in the Mediterranean region by mid and far end of century under all RCPs except RCP2.6/SSP1-2.6 and also for 2ºC and higher

ACCEPTED VERSION SUBJECT TO FINAL EDITS

GWLs. There is *high confidence* in fire weather increase in the Mediterranean region.

12.4.5.3 Wind

Mean wind speed: Mean surface wind speeds have decreased in Europe as in many other areas of the Northern Hemisphere over the past four decades (AR5, WGI) (*medium confidence*), with a reversal to an increasing trend in the last decade (*low confidence*) that is however not fully consistent across studies (Tian et al., 2019; Zeng et al., 2019; Zhang et al., 2019d; Deng et al., 2021) (Chapter 2). Reanalyses also show declining winds in Europe (Deng et al., 2021) with large interdecadal variability (Laurila et al., 2020). The declining trend has induced a corresponding decline in wind power potential indices across Europe (*low confidence)* (Tian et al., 2019). However, there is *low agreement* and *low evidence* that climate model historical trends are consistent with observed trends (Tian et al., 2019; Deng et al., 2021) . Several factors have been attributed to these trends, including forest growth, urbanization, local changes in wind measurement exposure and aerosols (Bichet et al., 2012), as well as natural variability (Zeng et al., 2019).

Due to changes in mean surface wind speed patterns (Li et al., 2018a) and the poleward shift of the North Atlantic jet stream exit, mean surface wind speeds are projected to decrease in the Mediterranean areas under RCP4.5 and RCP8.5 by the middle of the century and beyond, or for global warming levels of 2 degrees and higher (*high confidence*), with a subsequent decrease in wind power potential (*medium confidence*) (Hueging et al., 2013; Tobin et al., 2015, 2018; Davy et al., 2018; Karnauskas et al., 2018a; Kjellström et al., 2018; Moemken et al., 2018) (see also Fig. 12.4). However, subregional patterns of change are present from regional climate models such as an increase in wind speeds in the Aegean Sea and in the northern Adriatic Sea where a reduction of Bora events and an increase of Scirocco events are projected for mid-century and beyond under RCP4.5 and RCP8.5 (*medium confidence*) (Tobin et al., 2016; Davy et al., 2018; Belušić Vozila et al., 2019). Projections (as cited above) also indicate a decrease in mean wind speed in Northern Europe (*medium confidence, medium agreement*) (Karnauskas et al., 2018a; Tobin et al., 2018; Jung and Schindler, 2019). Daily and interannual wind variability is projected to increase under RCP8.5 (only) Northern Europe (Moemken et al., 2018) (*low confidence*), which can influence electrical grid management and wind energy production (*low confidence*). Wind speeds are projected to shift towards more frequent occurrences below thresholds inhibiting wind power production (Weber et al., 2018). Wind stagnation events may become more frequent in future climate scenarios in some areas of Europe in the second half of the 21st century (Horton et al., 2014; Vautard et al., 2018), with potential consequences on air quality (*low confidence*).

Severe wind storm: There are large uncertainties in past evolutions of windstorms and extreme winds in Europe. Extreme near-surface winds have been decreasing in the past decades (Smits et al., 2005; Tian et al., 2019; Vautard et al., 2019) according to near-surface observations. Significant negative trends of cyclone frequency in spring and positive trends in summer have been found in the Mediterranean basin for the period 1979-2008 (Lionello et al., 2016). By contrast increasing trands have been found in Arctic ocean areas (Wickström et al., 2020). These trends are not associated with significant trends in extratropical cyclones (Chapter 2), and are consistent with the mean wind decreasing trends.

There is *medium confidence* that serial clustering of storms, inducing cumulated economic losses, in future climate will increase in many areas in Europe under climate projections over Europe (Karremann et al., 2014; Economou et al., 2015). Strong winds and extra-tropical storms are projected to have a slightly increasing frequency and amplitude in the future in Northern, Western and central Europe (Outten and Esau, 2013; Feser et al., 2015; Forzieri et al., 2016; Mölter et al., 2016; Ruosteenoja et al., 2019b; Vautard et al., 2019) in RCP8.5 and SRES A1B by the end of the century (*medium confidence*), as well as off the European coasts (Martínez-Alvarado et al., 2018) due to the increase of intensity of extratropical storms at a 2°C global warming level or above (Zappa et al., 2013) in these areas. The frequency of storms, including Medicanes, is projected to decrease in Mediterranean regions, and their intensities are projected to increase, by the middle of the century and beyond for SRES A1B, A2 and RCP8.5 (*medium confidence*) (Nissen et al., 2014; Feser et al., 2015; Forzieri et al., 2016; Mölter et al., 2016; Tous et al., 2016; Romera et al., 2017; González-Alemán et al., 2019) (MedECC, 2020)(Chapter 11).

ACCEPTED VERSION SUBJECT TO FINAL EDITS

Projections of smaller-scale hazard phenomena such as tornadoes, wind gusts, hail storms and lightning are currently not directly available partly due to the inability of climate models to simulate such phenomena. Observational networks for such phenomena usually lack homogeneity over long climate periods, hindering clear trends to be detected. For instance, while no robust trends have been identified (Hermida et al., 2015; Mohr et al., 2015a; Burcea et al., 2016; Ćurić and Janc, 2016), hail storm environments (favourable atmospheric configurations) have increased in frequency (Sanchez et al., 2017) (*low confidence, low evidence*). In future climate periods it is *more likely than not* that severe convection environments will become more frequent by the end of the century under scenario RCP8.5 (Mohr et al., 2015b; Púčik et al., 2017), and there is *medium confidence* that such environments become more frequent by the 2050s in scenario RCP4.5. There is no evidence for changes in tornado frequencies in Europe in the observations (Groenemeijer and Kühne, 2014) as well as in future climate projections. Insufficient observational record length for lightning numbers does not allow an assessment of trends.

There is *high confidence* that mean wind speeds will decrease in Mediterranean areas and *medium confidence* of such decreases in Northern Europe for global warming levels of 2°C or more and beyond the middle of the century. A slightly increased frequency and amplitude of extratropical cyclones, strong winds and extra-tropical storms is projected for Northern, Central and Western Europe by the middle of the century and beyond and for global warming levels of 2°C or more (*medium confidence*). The frequency of Medicanes is projected to decrease (*medium confidence*), but their intensity is projected to increase. Proxies of intense convection indicate that the large-scale conditions conducive to severe convection will tend to increase in the future climate *(low confidence)*.

12.4.5.4 Snow and ice

Snow: Widespread and accelerated declines of snow depth are currently observed in Europe (Fontrodona Bach et al., 2018) and snow water equivalent (Marty et al., 2017b) (see also Figures 12.9b) for a typical range of altitudes of higher settlement elevation and ski resorts. In the Pyrenees a slow snow cover decline has been observed starting from the industrial period with a sharp increase since 1955 (López-Moreno et al., 2020). Under the RCP2.6, RCP4.5 and RCP8.5 scenario the reliability elevation using snowmaking will rise of 200-300 m in the Alps and 400-600 in the Pyrenees by mid century. By end of century projections are highly dependent from the scenario being stationary for the RCP2.6 and continuously decreasing under the RCP8.5 up to not have anymore natural snow conditions for any of the locations in the French Alps and Pyrenees (Spandre et al., 2019). Similarly also Norway and Austria will see a rising of the natural snow elevation with consequences for the ski season (Scott et al., 2020; Steiger and Scott, 2020). In the Alps, recent simulations project a reduction in Snow Water Equivalent (SWE) at 1500 m a.s.l. of 80–90% by 2100 under the A1B scenario and a snow season that would start 2-4 weeks later and end 5-10 weeks earlier than in the 1992-2012 average (Schmucki et al., 2015), which is equivalent to a shift in elevation of about 700 m (Marty et al., 2017a). For elevations above 3000 m a.s.l., a decline in SWE of at least 10% is expected by the end of the century even when assuming the largest projected precipitation increase. Similar trends are observed for the Pyrenees and Scandinavia (López-Moreno et al., 2009; Räisänen and Eklund, 2012). For the Northern French Alps above 1500 m and the Ötztal locations in the Austrian alps SWE has a similar decreasing trend altitudinal dependent for all 3 scenarios (RCP2.6, RPC4.5 and RCP8.5) until mid of century and with significant differentiation among them in the second half of the century up to free snow condition for the RCP8.5 scenario (Hanzer et al., 2018; Verfaillie et al., 2018).

Glacier: Observation and future projections of European glacier mass changes are assessed in Section 9.5.1 grouped in two main regions: Scandinavia and Central Europe regions. It is *virtually certain* that glaciers will shrink in the future and there is medium confidence in the timing and mass change rates (Chapter 9). Central Europe is one of the regions where glaciers are projected to lose substantial mass even under low-emission scenarios (Section 9.5.1.3) (MedECC, 2020). GlacierMIP projections indicate that glaciers in the Central Europe region lose 63 ± 31%, 80 ± 22% and 93 ± 13% of their 2015 mass by the end of the century for RCP2.6, RCP4.5 and RCP8.5, respectively (Marzeion et al., 2020). In those same scenarios, glaciers in Scandinavia are projected to lose 55 ± 33%, 66 ± 34% and 82 ± 24% of their 2015 mass. The *virtually certain* shrink in glaciers is bolstered by RCM simulations from the EURO-CORDEX ensemble, with the

ACCEPTED VERSION SUBJECT TO FINAL EDITS

Global Glacier Evolution Model (GloGEM) indicating a substantial reduction of glacier ice volumes in the European Alps by 2050 (47–52% with respect to 2017 for RCP2.6, 4.5 and 8.5). Under RCP2.6, about two-thirds (63 ± 11%) of the present-day (2017) ice volume is projected to be lost by 2100. In contrast, under the strong warming of RCP8.5, glaciers in the European Alps are projected to largely disappear by 2100 (94 ± 4% volume loss compared to 2017; Zekollari et al., 2019).

Permafrost: In Europe, permafrost is found in high mountains and in Scandinavia, as well as in Arctic Islands (e.g., Iceland, Novaya Zemlia or Svalbard). In recent decade permafrost has been lost (Chapter 9) and accelerated warming at high altitudes and latitudes has favored an increase of permafrost temperatures in the order of 0.2 ± 0.1°C between 2007 and 2016 (Romanovsky et al., 2018; Noetzli et al., 2019). Over the 21st century, permafrost is *very likely* to undergo increasing thaw and degradation (Hock et al., 2019) and it is *virtually certain* that permafrost extent and volume with decrease with increase of global warming (Chapter 9).

Permafrost thawing is projected to affect the frequency and magnitude of high-mountain mass wasting processes (Stoffel and Huggel, 2012). The temporal frequency of periglacial debris flows in the Alps is *unlikely* to change significantly by the mid-21st century but is *likely* to decrease during the second part of the century, especially in summer (Stoffel et al., 2011, 2014; Lane et al., 2017). There is *medium confidence* that most of the Northern Europe periglacial processes will disappear by the end of the century, even in the RCP2.6 scenario (Aalto et al., 2017). The magnitude of debris flow events might increase (Lugon and Stoffel, 2010) (*low confidence*) and the debris-flow season may last longer in a warming climate (Stoffel and Corona, 2018) *(medium confidence).* Quantitative data for the European Alps is highly site dependent (Haeberli, 2013).

Heavy Snowfall, ice storms and hail: There is *low confidence* that climate change will affect ice and snow episodic hazards (*limited evidence*). The change in snowpack in the Alps is expected to lead to a possible reduction in overall avalanche activity (*low confidence*), except possibly in winter and at high altitudes (Castebrunet et al., 2014).

For ice storms, or freezing rainstorms, there is also limited evidence due to a limited number of studies. Heavy snowfalls have decreased in frequency in the past decades and this is expected to continue in the future climate (Beniston et al., 2018) (*low confidence*). Freezing rain is projected to increase in western, central and southern Europe (Kämäräinen et al., 2018) (*low confidence*). Rain-on-snow events, are decreasing in northern regions (Pall et al., 2019) and by 48% on average in southern Scandinavia (Poschlod et al., 2020) due to decreases in snowfall.

In summary, in the future snow cover extent and seasonal duration will reduce (*high confidence*) and it is *virtually certain* that glaciers will continue to shrink. A reduction of glacier ice volume is projected in the European Alps and Scandinavia (*high confidence*). There is *high confidence* that permafrost will undergo increasing thaw and degradation over the 21st century. Most of the Northern Europe periglacial will disappear by the end of the century even for a lower emissions scenario (*medium confidence*) and the debris-flow season may last longer in a warming climate (*medium confidence*).

12.4.5.5 Coastal and Oceanic

Relative sea level: Around Europe, over 1900-2018, a new tide-gauge based reconstruction finds a regional-mean RSL change of 1.08 [0.79 to 1.38] mm yr^{-1} in the subpolar North Atlantic (Frederikse et al., 2020), compared to a GMSL change of around 1.7 mm yr^{-1} (Section 2.3.3.3; Table 9.5). For the period 1993-2018, the RSLR rates, based on satellite altimetry, increased to 2.17 [1.66 to 2.66] mm yr^{-1} (Frederikse et al., 2020), compared to a GMSL change of 3.25 mm yr^{-1} (Section 2.3.3.3; Table 9.5).

Relative sea level rise is *extremely likely* to continue in the oceans around Europe. Regional-mean RSLR projections for the oceans around Europe range from 0.4 m–0.5 m under SSP1-RCP2.6 to 0.7 m–0.8 m under SSP5-RCP8.5 for 2081-2100 relative to 1995-2014 (median values), which means that there are locally large

ACCEPTED VERSION SUBJECT TO FINAL EDITS

deviations from the projected GMSL change {Section 9.6.3.3}. These RSLR projections may however be underestimated due to potential partial representation of land subsidence in their assessment (Section 9.6.3.2). The signal is strongest for the North Sea and Atlantic coasts, followed by the Black Sea. The Baltic Sea on the contrary shows the lowest increase due to land uplift (Vousdoukas et al., 2017). The model agreement is higher for the Mediterranean and in line with the previous findings by Gualdi et al. (2013).

Coastal flood: The present day 1:100 yr ETWL is between 0.5-1.5m in the MED basin and 2.5-5.0 m in the western Atlantic European coasts, around the UK and along the North Sea coast, and lower at 1.5-2.5m along the Baltic Sea coast. (Kirezci et al 2020). Similar values are reported by Vousdoukas et al., (2018).

There is *high confidence* that extreme total water level (ETWL) magnitude and occurrence frequency will increase throughout Europe (see Figure 12.4p-r), except in the northern Baltic Sea. Across the region, the 5th – 95th percentile range of the 1:100 yr ETWL is projected to increase (relative to 1980 – 2014) by 4 cm – 40 cm and by 6 cm – 47 cm by 2050 under RCP4.5 and RCP8.5, respectively. By 2100, this range is projected to be 6 cm – 88 cm and 25 cm – 186 cm under RCP4.5 and RCP8.5, respectively (Vousdoukas et al., 2018; Kirezci et al., 2020) (see Figure SM 12.6). Mass addition across the Gibraltar Strait may play a role even if this is quite unclear to which extent (Lionello et al., 2017). Furthermore, under RCP4.5, the present day 1:100 yr ETWL is projected to have median return periods of between 1:5 and 1:20 yrs by 2050 and occur once per year or more by 2100 in the Mediterranean and Black Sea, while in the rest of Europe it is mostly projected to have median return periods of between 1:20 yrs and 1:50 yrs by 2050 and between 1:5 yrs and 1:20 yrs by 2100 (Vousdoukas et al., 2018). Under RCP8.5, occurrence of the present day 1:100 yr ETWL is projected to increase further to median return periods of 1:1 yr to 1:5 yrs by 2050 and occur more than once per year by 2100 in the Mediterranean and Black Sea, while in the rest of Europe it is mostly projected to have median return periods between 1:5 yrs and more than once per year by 2100.

Coastal erosion: Satellite derived shoreline change estimates over 1984 – 2015 indicate shoreline retreat rates of around 0.5 m yr^{-1} along the sandy coasts of CEU and MED, around 4 m yr^{-1} in EEU (Caspian Sea region) and more or less stable shorelines in NEU (Luijendijk et al., 2018; Mentaschi et al., 2018). Mentaschi et al. (2018) report a coastal area loss of 270 km^2 over a 30 year period (1984-2015) along the Atlantic coastlines of Europe.

Projections indicate that sandy coasts throughout the continent (except those bordering the northern Baltic Sea) will experience shoreline retreat through the 21st century (*high confidence*). Median shoreline change projections (CMIP5) relative to 2010, show that, by mid-century, shorelines will retreat by between 25 m and 60 m along sandy coasts in CEU and MED under both RCP4.5 and RCP8.5 (Vousdoukas et al., 2020; Athanasiou et al., 2020). Mid-century median projections for NEU indicate virtually no shoreline retreat under RCP4.5, but a retreat of around 40 m under RCP8.5. By 2100, median shoreline retreats of around 50 m are projected in NEU and MED under RCP4.5, increasing to around 80 m under RCP8.5. End century median projections for CEU are far higher at 100 m (RCP4.5) and 160 m (RCP8.5). The total length of sandy coasts in Europe that is projected to retreat by more than a median of 100 m by 2100 under RCP4.5 and RCP8.5 is about 12,000 km and 18,000 km respectively, an increase of approximately 54% (Vousdoukas et al., 2020)

Local assessments of both long term shoreline retreat and episodic coastal erosion are given by (Li et al., 2013a; Toimil et al., 2017; Bon de Sousa et al., 2018; Le Cozannet et al., 2019). In terms of episodic coastal erosion, 31%–88% of all Aegean beaches are projected to experience complete erosion, with a RCP4.5 sea level rise of 0.5 m and a surge of 0.6 m, but with substantial uncertainty (Monioudi et al., 2017).

Marine heatwave: The mean SST of the Atlantic Ocean and the Mediterranean has increased between 0.25°C and 1°C since 1982-1998. This mean ocean surface warming is correlated to longer and more frequent marine heatwaves in the region (Oliver et al., 2018). Over the period 1982-2016, the coastlines of Europe experienced on average more than 2.0 MHW per year, with the eastern Mediterranean and Scandinavia experiencing 2.5–3 MHWs per year. The average duration was between 10 and 15 days. Changes over the 20th century, derived from MHW proxies, show an increase in frequency of between 1.0 and 2.0 MHWs per decade in Europe, although the trend is not statistically significant; with an increase in

ACCEPTED VERSION SUBJECT TO FINAL EDITS

intensity per event in the North Atlantic and the Mediterranean, and a decrease in the Atlantic off the British Isles. The total number of MHW days per decade has increased in the Mediterranean (Oliver et al., 2018).

Mean SST is projected to increase by 1 ºC to 3ºC around Europe by 2100, with a hotspot of around 4 ºC to 5 ºC along the Arctic coastline of Europe under RCP4.5 and RCP8.5 scenarios (see Interactive Atlas), leading to a continued increase in MHW frequency, magnitude and duration (Oliver et al., 2018; MedECC, 2020). Projections for SSP1-2.6 and SSP5-8.5 both show an increase in MHWs around Europe by 2081 – 2100, relative to 1985 – 2014 (Box 9.2, Figure 1). Darmaraki et al. (2019) project that, by the end of the 21st century and under RCP8.5, there will be one MHW occurring every year in the Northern Mediterranean sea, and that these MHWs would be 3 months longer, 4 times more intense, and 42 times more severe than present day MHWs in the region. Frölicher et al., (2018) show that, in Europe, the change in the probability for the number of days of MHWs exceeding the 99th percentile of the pre-industrial level is 4%, 15% and 30% for global warming levels of 1ºC, 2ºC and 3.5ºC, respectively. MHW increase in the Mediterranean will impact on many species that live in shallow waters and have reduced motility, with consequences for the related economic activities (Galli et al., 2017).

In general, there is *high confidence* that most coastal/ocean related climatic impact-drivers in Europe will increase over the 21st century for all scenarios and time horizons. Relative sea level rise is *extremely likely* to continue around Europe (except in the northern Baltic Sea), contributing to increased coastal flooding in low-lying areas and shoreline retreat along most sandy coasts (*high confidence*). Marine Heatwaves are also expected to increase around the region over the 21st century (*high confidence*).

12.4.5.6 Other

Compound events. One typical compound event that is observed in the European area is compound flooding due to the combination of extreme sea level events and extreme precipitation events associated with high level of runoff. In the present climate, the Mediterranean coasts are exposed to a higher probability of this type of compound flooding events (Bevacqua et al., 2019). Under RCP8.5, the probability of these events are projected to increase along northern European coasts (west coast of UK, northern France, the east and south coast of the North Sea, and the eastern half of the Black Sea) with the percentage of coastline currently experiencing such events with a return period lower than 6 years will increasing from 3% to 11% by the end of the 21st century (Bevacqua et al., 2019).

Under RCP8.5, regions in Russia, France and Germany are projected to experience an increase in the frequency and the length of wet and cold compound events, while Spain and Bulgaria are projected to stay longer in the hot and dry state by mid-century (Sedlmeier et al., 2016).

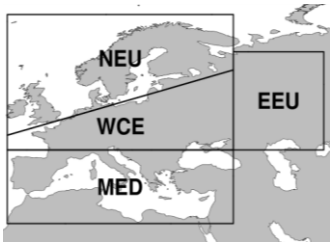
Compound events of dry and hot summers have increased in Europe. (Manning et al., 2019) found that the probability of such compound events has increased across much of Europe between 1950–1979 and 1984–2013, notably in southern, eastern and western Europe. Compound hot and dry extremes are projected to increase in Europe by mid-century for the SRES A1B and RCP8.5 but a particularly strong signal is projected in southern and eastern Germany and the Czech Republic (Sedlmeier et al., 2016).

The assessed direction of change in climatic impact-drivers for Europe and associated confidence levels are illustrated in Table 12.7, together with emergence time information (see Section 12.5.2). No assessable literature could be found for Sand and dust storms, although these phenomena may be relevant in parts of the region.

ACCEPTED VERSION SUBJECT TO FINAL EDITS

[START TABLE 12.7 HERE]

Table 12.7: Summary of confidence in direction of projected change in climatic impact-drivers in Europe, representing their aggregate characteristic changes for mid-century for scenarios RCP4.5, SSP3-4.5, SRES A1B, or above within each AR6 region (defined in Chapter 1), approximately corresponding (for CIDs that are independent of sea-level rise) to global warming levels between 2°C and 2.4°C (see 12.4 for more details of the assessment method). The table also includes the assessment of observed or projected time-of-emergence of the CID change signal from the natural inter-annual variability if found with at least *medium confidence* in Section 12.5.2.



Region	Heat and Cold				Wet and Dry							Wind				Snow and Ice					Coastal & Oceanic					Other		
	Mean air temperature	Extreme heat	Cold spell	Frost	Mean precipitation	River flood	Heavy precipitation and pluvial flood	Landslide	Aridity	Hydrological drought	Agricultural and ecological drought	Fire weather	Mean wind speed	Severe wind storm	Tropical cyclone	Sand and dust storm	Snow, glacier and ice sheet	Permafrost	Lake, river and sea ice	Heavy snowfall and ice storm	Hail	Snow avalanche	Relative sea level	Coastal flood	Coastal erosion	Marine heatwave	Ocean acidity	Air pollution weather	Atmospheric CO_2 at surface	Radiation at surface
Mediterranean (MED)	●	●	○		○		5						6	7					●				○		2		○		●	
Western and Central Europe (WCE)	●	●	○					4									○		●				○		2		○		●	
Eastern Europe (EEU)	●	●	○														○												●	
Northern Europe (NEU)	●	●	●		○	1											○		●				○	8	2,3		○		●	

1. Excluding southern UK.
2. Along sandy coasts and in the absence of additional sediment sinks/sources or any physical barriers to shoreline retreat.
3. The Baltic sea shoreline is projected prograde if present-day ambient shoreline change rates continue.
4. For the Alps landslide risk is likely to increase.
5. Low confidence of decrease in the southernmost part of the region.
6. General decrease except in Aegean Sea exhibiting increase.
7. Medium confidence of decrease in frequency and increase in intensities.
8. Except in the Northern Baltic Sea region.

● Already emerged in the historical period (*medium to high confidence*)
○ Emerging by 2050 at least in Scenarios RCP8.5/SSP5-8.5 (*medium to high confidence*)
○ Emerging after 2050 and by 2100 at least in Scenarios RCP8.5/SSP5-8.5 (*medium to high confidence*)

Key
High confidence of decrease
Medium confidence of decrease
Low confidence in direction of change
Medium confidence of increase
High confidence of increase
Not broadly relevant

[END TABLE 12.7 HERE]

12.4.6 *North America*

Major changes in North American CIDs were assessed in WGII AR5 Chapter 26 (Romero-Lankao et al., 2014), with additional detail on connections to warming levels provided by SR1.5 (IPCC, 2018), and climate information related to land degradation and land use suitability in SRCCL (IPCC, 2019c), and ocean and coastal hazards in the SROCC (IPCC, 2019b). Recent national assessments in the United States (USGCRP, 2017, 2018) and Canada (Bush and Lemmen, 2019) enhance the local perspective and assessments across a number of CIDs and their sectoral connections. For the purpose of this assessment, North America is sub-divided into six sub-regions as defined in Chapter 1: Central North America (CNA), Western North America (WNA), Central North America (CAN), Eastern North America (ENA), Northeast North America (NEN), and Northwest North America (NWN). Greenland and Arctic regions of Northeast and Northwest North America are further assessed in 12.4.9, and the Caribbean and Hawaiian Islands are assessed in 12.4.7.

[START FIGURE 12.10 HERE]

Figure 12.10: Projected changes in selected climatic impact-driver indices for North America. (a) Mean change in 1-in-100 year river discharge per unit catchment area (Q100, $m^3 s^{-1} km^{-2}$), and (b) median change in the

ACCEPTED VERSION SUBJECT TO FINAL EDITS

number of days with snow water equivalent (SWE) over 100 mm (from November to March), from CORDEX-North America models for 2041-2060 relative to 1995-2014 and RCP8.5. Diagonal lines indicate where less than 80% of models agree on the sign of change. (c) Bar plots for Q100 ($m^3 s^{-1} km^{-2}$) averaged over land areas for the WGI reference AR6 regions (defined in Chapter 1). The left column within each panel (associated with the left y-axis) shows the 'recent past' (1995-2014) Q100 absolute values in grey shades. The other columns (associated with the right y-axis) show the Q100 changes relative to the recent past values for two time periods ('mid' 2041-2060 and 'long' 2081-2100) and for three global warming levels (defined relative to the preindustrial period 1850-1900): 1.5°C (purple), 2°C (yellow) and 4°C (brown). The bars show the median (dots) and the 10^{th}-90^{th} percentile range of model ensemble values across each model ensemble. CMIP6 is shown by the darkest colours, CMIP5 by medium, and CORDEX by light. SSP5-8.5/RCP8.5 is shown in red and SSP1-2.6/RCP2.6 in blue. (d) As for (c) but showing absolute values for number of days with SWE > 100mm, masked to grid cells with at least 14 such days in the recent-past. See Technical Annex VI for details of indices. A Caribbean Q100 bar plot is included here but assessed in the Small islands section (12.4.7). Further details on data sources and processing are available in the chapter data table (Table 12.SM.1).

[END FIGURE 12.10 HERE]

12.4.6.1 Heat and cold

Mean air temperature: Section Atlas.9.2 assessed *very likely* mean warming in observations across North America with highest increases at higher latitudes and in the winter season. Section Atlas.9.4 assessed *very likely* mean warming in future decades in all North American regions, with CMIP and CORDEX models showing median increases exceeding 2°C in much of the continental interior under RCP8.5 (2041-2060 compared to 1995-2014) and higher increases toward the north. Mean temperatures at the end of century show strong scenario dependence, rising between 1°C and 2.5°C in RCP2.6 and about 4 to 8°C in RCP8.5 (Figures Atlas.15, Atlas.32, Atlas.33). Warming also raises stream temperatures across the continent (DOE, 2015; Trtanj et al., 2016; van Vliet et al., 2016; Chapra et al., 2017), and Hill et al. (2014) projected US stream warming by 0.6°C (±0.3°C) per 1°C increase in local air temperature. Mean warming drives shifts in the seasonal timing of temperature thresholds, including increasing growing degree-days (Mu et al., 2017), longer growing seasons (Gowda et al., 2018; Li et al., 2018b; Vincent et al., 2018c), reduced chill hours (Luedeling, 2012; Lee and Sumner, 2015; Xie et al., 2015; Parker and Abatzoglou, 2019), and longer pollen and allergy seasons (Fann et al., 2016; Anenberg et al., 2017; Sapkota et al., 2019). Warmer temperatures will *very likely* reduce heating degree days and increase cooling degree days (Bartos et al., 2016; US EPA, 2016; Craig et al., 2018; Zhang et al., 2019c; Coppola et al., 2021b).

Extreme heat: Section 11.9 assessed that extreme temperatures in North America have increased in recent decades (*medium evidence, medium agreement*) other than Central and Eastern North America (*low confidence*), and extreme heat in all regions is projected to increase with climate change (*high confidence*). Observed trends in extreme heat are more positive for heat extreme indices that include temperature and humidity given historical expansion of irrigation and intensification of agriculture (Mueller et al., 2017; Grotjahn and Huynh, 2018; Thiery et al., 2020). Several studies noted statistically significant increases in intensity and particularly the frequency, duration, and seasonal length of the physiologically-hazardous extreme heat conditions across North American (Grineski et al., 2015; Habeeb et al., 2015; Martínez-Austria et al., 2016; Petitti et al., 2016; Vincent et al., 2018c; García-Cueto et al., 2019).

Figure 12.4b shows over a month of additional days at CMIP6 SSP5-8.5 mid-century where temperatures exceed 35°C across much of southern Mexico and regions near the US-Mexico border and these extreme temperatures occur at least once per year up to southern Canada. (Coppola et al., 2021b) found similar patterns in CMIP5 and CORDEX-Core. Using locally-tailored heat thresholds, Maxwell et al. (2018) found that "very hot" days in 5 US cities will occur a median of 3 to 5 times more often by RCP8.5 2036-2065 (2 to 3.5x in RCP4.5), Oleson et al. (2018) projected that annual heatwave duration will exceed one month in Houston in RCP8.5 2061-2080, and Anderson et al. (2018) projected 7 to 12 times more exceedances of thresholds associated with high-mortality in RCP8.5 2061-2080 (6 to 7x in RCP4.5). (Schwingshackl et al., 2021) found that Central and Eastern North America are among the regions with the strongest trend in heat

ACCEPTED VERSION SUBJECT TO FINAL EDITS

stress indicators. Studies also project increasingly surpassed heat extreme thresholds for North American crops (Gourdji et al., 2013), airplane weight restrictions (Coffel et al., 2017), and peak load energy systems (Auffhammer et al., 2017).

The number of days crossing dangerous heat thresholds such as HI>41°C will be very sensitive to the mitigation scenario at the end of century (Wuebbles et al., 2014; Zhao et al., 2015; Dahl et al., 2019; Schwingshackl et al., 2021). At the end of the century under SSP5-8.5, a CMIP6 median increase of exceedances of 75-150 days per year is projected over much of North Central America, Central North America and the U.S. Southwest while this increase is projected to remain limited below 60 days under SSP1-2.6 (Figure 12.4d,f and Figure SM 1.2). Steinberg et al. (2018) also projected more frequent and longer 'heat-health' events in California extending into October.

Cold spell: Chapter 11 assessed *high confidence* in decreasing frequency and intensity of cold spells over North America (Section 11.9). The number of days with extreme wind chill hours (humidex<-30) decreased at 76% of examined Canadian stations from 1953-2012 (Mekis et al., 2015) and cold days and coldest nights decreased in Mexico from 1980-2010 (García-Cueto et al., 2019).

Cold spells are projected to decrease over North America under climate change, with the largest decreases most common in the winter season (*high confidence*) (Section 11.9). Minimum winter temperatures are projected to rise faster than the mean wintertime temperature (Underwood et al., 2017) and alter cold hardiness zones used to determine agricultural suitability (Parker and Abatzoglou, 2016). Wuebbles et al. (2014) projections for RCP8.5 end-of-century found that the 4-day cold spell that happens on average once every 5 years is projected to warm by more than 10 ºC and CMIP5 models do not project current 1-in-20 year annual minimum temperature extremes to recur over much of the continent. Multiple studies have shown that Arctic warming can alter large-scale variability and change the frequency and duration of mid-latitude cold air outbreaks, potentially leading to increasing cold hazards in some regions (Barcikowska et al., 2019; Cohen et al., 2019; Zhou et al., 2021) (*low agreement*).

Frost: An expansion of the frost-free season is underway and projections for North America indicate a continuation of this trend in the future (*high confidence*). Significant decreases in frost days, consecutive frost days, and ice days were identified in 1948-2016 station observations across Canada, along with a resulting lengthening of the frost-free season by more than a month in many regions (Vincent et al., 2018c). Frost days also declined in nearly all Mexican cities from 1980-2010 (García-Cueto et al., 2019), and a 1917-2016 decline of about 3 weeks in frigid winter conditions challenges ecosystems in the Northeast US and Southeast Canada (Contosta et al., 2020). Studies connect projections of a longer frost-free season in North America to a longer outdoor construction season, orchard production, and weight restrictions on runways (Daniel et al., 2018; DeGaetano, 2018; Jacobs et al., 2018). Frosts are projected to persist as an episodic hazard in many regions given natural variability and cold air outbreaks even as mean temperature rises (*high confidence*).

Climate change is *virtually certain* to shift the balance of temperature toward warming trends and away from cold extremes, with increases in the magnitude, frequency, duration and seasonal and spatial extent of heat extremes driving impacts across North America. There is a particular sensitivity to scenario pathway in resulting changes to the frequency of exceeding dangerous heat thresholds such as HI>41°C in NCA, CNA and the US Southwest, with 75-150 days more under SSP5-8.5 but less than 60 days more under SSP1-2.6 in the end of the century.

12.4.6.2 Wet and dry

Mean precipitation: Atlas.9.2 found that trends in annual precipitation over 1960–2015 are generally non-significant though there are consistent positive trends over parts of ENA and CNA, together with significant decreases in precipitation in parts of south-western US and north-western Mexico.

Atlas.9.4 assessed *very high confidence* in increases in precipitation over most of Northern and Eastern

ACCEPTED VERSION SUBJECT TO FINAL EDITS

North America, with *medium confidence* of decrease over Northern Central America and *low confidence* elsewhere (see Figure Atlas.33, Cross-Chapter Box Atlas.1 Figure 1). Changes are most dramatic in the Spring and Winter, when wet conditions are projected to extend from the northern portions of the continent as far south as the central Great Plains while Mexico becomes drier; in contrast, summertime changes are uncertain across most of the continent other than wetter conditions in Northern Canada (Easterling et al., 2017; Bukovsky and Mearns, 2020; Teichmann et al., 2020; Almazroui et al., 2021) .

River flood: There is *limited evidence and low agreement* on observed climate change influences for river floods in North America (see also Section 11.5). Trends in streamflow indices are mixed and difficult to separate from river engineering influences, with large changes but little spatial coherence across the US, making it difficult to identify trends with confidence (Villarini and Slater; Peterson et al., 2013; Mallakpour and Villarini, 2015; Archfield et al., 2016; Wehner et al., 2017; Hodgkins et al., 2019; Neri et al., 2019). There is *high confidence* in historical shifts in the timing of peak streamflow toward higher winter and earlier spring flows in snowmelt-driven basins in Canada (Burn and Whitfield, 2016; Bonsal et al., 2019) and the United States (Dudley et al., 2017; Wehner et al., 2017). Some rivers show ice-jam floods occurring a week earlier, but changes are mixed given localized positive and negative changes across the continent (Rokaya et al., 2018). There is *medium confidence* that climate change will increase river floods over the United States and Canada but *low confidence* for changes in Mexico. Wobus et al. (2017a) used a regional hydrologic model for 57000 streams to project more than a doubling in the frequency of current 100 yr flow events in many portions of the United States for RCP8.5 2050 with additional contributions from earlier snowmelt. CMIP6 projections for SSP5-8.5 2065-2099 show strongest peak United States runoff increases in the East (Villarini and Zhang, 2020); however, several studies applying global hydrological models disagree with regional streamflow projections, indicating a decrease in the magnitude or frequency of floods over a large portion of North America (e.g., Hirabayashi et al., 2013; Arnell and Gosling, 2016) (Figure 12.10a,c).

Heavy precipitation and pluvial flood: Section 11.4 assessed *high confidence* in observed increases in extreme precipitation events (including hourly totals) in Central and Eastern North America with *low confidence* in broad trends elsewhere in the continent despite observational increases in some portions of each region (Vincent et al., 2018c; García-Cueto et al., 2019; Zhang et al., 2019c).

Section 11.4 found that high precipitation is projected to increase across North America (*high confidence*) except for portions of Western North America where projections are mixed (*medium confidence* of increase). Maxwell et al. (2018) identified regional "heavy precipitation day" thresholds for 5 cities across the US and projected that a tripling (or more) of these events is possible by RCP8.5 mid-century. Projections indicate changes to intensity-duration-frequency (IDF) curves typically used for construction design and automobile hazards, as well as increases in the 10 year recurrence level of 24 hour rainfall intensities that challenge storm water drainage systems (Hambly et al., 2013; Cheng and AghaKouchak, 2015; Neumann et al., 2015b; Prein et al., 2017b; Hettiarachchi et al., 2018; Ragno et al., 2018). Precise levels of regional IDF characteristics may still depend substantially on the method and resolution of downscaling applied (DeGaetano and Castellano, 2017; Cook et al., 2020b).

Landslide: There is growing but yet *limited evidence* for unique climate-driven changes in landslide and rockfall hazards in North America, even as theory suggests decreases in slope and rockface stability due to more intense rainfall, rain-on-snow events, mean warming, permafrost thaw, glacier retreat, and coastal erosion (Cloutier et al., 2017; Coe et al., 2018; Handwerger et al., 2019; Hock et al., 2019; Patton et al., 2019) although dry trends can decelerate mass movements (Bennett et al., 2016). Landslide frequency has *likely* increased in British Columbia (Geertsema et al., 2006) and is expected to increase in Northwest North America given the combination of these factors (*medium confidence*) (Gariano and Guzzetti, 2016). Cloutier et al. (2017) projected an increase in landslides in Western Canada due to wetter overall conditions and reduced return period for extreme rainfall. Robinson et al. (2017) used scenarios based upon projection of 50 yr recurrence of 7 d precipitation periods to highlight the potential for increased landslide hazards near Seattle. Broad US projections are more uncertain given increases in evapotranspiration that will counteract precipitation changes over much of the country (Coe, 2016).

Aridity: Chapter 8 showed that aridity in North America generally moves opposite to mean precipitation

ACCEPTED VERSION SUBJECT TO FINAL EDITS

change with an added evaporative demand from warmer temperatures (*high confidence* in aridity increase for North Central America, *medium confidence* increase in Central North America; *high confidence* decrease in Northeast North America, *medium confidence* decrease in Eastern and Northwest North America; see also Section 11.9). Projected soil moisture declines (Figure 12.4j-l) are most widespread across North America during the summertime, with largest declines in Mexico and the southern Great Plains but also extending into Canada (Section 8.4.1.6; Swain and Hayhoe, 2015; Easterling et al., 2017; Bonsal et al., 2019; Lu et al., 2019). Yoon et al. (2018) found net reduction in southern Great Plains groundwater storage in RCP8.5 mid-century projections despite increases in mean precipitation and both wet and dry extremes. Soil moisture drying could reach unprecedented levels by the CMIP6 RCP8.5 end of century, even when evaluating deeper soil columns relevant for crop rooting depth (Cook et al., 2020a). Projected changes in the aridity index portray a shift the geographic range of temperate drylands northward and eastward in Central and Western North America (Schlaepfer et al., 2017; Seager et al., 2018) which also diminishes aquifer recharge rates in the southern Great Plains and in some Western regions where snowpack is reduced (Meixner et al., 2016).

Hydrological drought: Section 11.9 asssessed *low confidence* of significant observational trends and projected future changes in the characteristics of episodic hydrological drought in North America given *limited evidence* and *low agreement* in modeled changes. Zhao et al. (2020) found that increases in hydrological drought frequency (particularly the 100 yr drought) were far more prevalent than for meteorological drought across 5797 watersheds in the US and Canada, indicating a strong influence of evaporative demand. Reductions in the overall supply of meltwater from a declining snowpack also increase the potential for intermittent hydrological droughts in the Western US (Mote et al., 2018; Livneh and Badger, 2020).

Agricultural and ecological drought: Section 11.9 assessed medium confidence for an increase in agricultural and ecological drought in Western North America but otherwise found *limited evidence* for broadly observed changes in North American agricultural and ecological drought even as increasing evaporative demand intensified vegetation stress and soil moisture deficits in recent events (Sections 11.6, 11.9). Section 11.9 asssessed *medium confidence* for more intense agricultural and ecological drought conditions over North Central America, Western North America and Central North America in a 2°C global warming level (about mid-century), with medium confidence extending to Eastern North America and *high confidence* for North Central America and Central North America under a 4°C global warming level associated with higher emissions scenarios past 2050. Figure 12.4g-i shows that the frequency of meteorological droughts (which often initiate hydrological, agricultural and ecological drought) is largely projected to increase in North American areas where total precipitation decreases (and vice versa; see Section 11.9 and Coppola et al., 2021b), and higher evaporative demand will extend the regions where more intense ecological and agricultural droughts develop when meteorological droughts occur (Wehner et al., 2017; Cook et al., 2019). Studies utilizing a variety of drought indices and soil moisture projections consistently project increased drought extending from Mexico into the southern Canadian Plains during the summer (Swain and Hayhoe, 2015; Ahmadalipour et al., 2017; Feng et al., 2017; Bonsal et al., 2019; Tam et al., 2019; Cook et al., 2020a).

Fire weather: Climatic conditions conducive to wildfire have increased in Mexico, Western and Northwest North America, essentially due to warming (*high confidence*). Abatzoglou and Williams (2016) found climate changes led to higher values for 8 fuel aridity indices over the Western US in recent decades, with 2000-2015 changes exposing 75% more forested area to high fuel aridity and adding 9 more high fire potential days each year, similar to 1979-2013 Western US and Mexico fire season expansion in Jolly et al., 2015). Increases in lightning-initiated fires have been distinguished from trends in man-made fire in Western Canada and the United States (Balch et al., 2017; Hanes et al., 2019). Jain et al. (2017) identified a 1979-2015 expansion in fire weather season in Eastern Canada and the southwestern United States (with a smaller reduction in the northern mountain West) along with regional shifts in the 99th percentile Canadian Fire Weather Index (FWI) and potential fire spread days. Girardin and Wotton (2009) noted that 1951-2002 trends in the Monthly Drought Code fire index in Eastern Canada could hardly be distinguished from decadal variability.

Climate change drives future increases in North American fire weather, particularly in the Southwest (*high*

ACCEPTED VERSION SUBJECT TO FINAL EDITS

confidence), although shifts in exposure and vulnerability are needed to understand overall fire risks (see WGII Chapter 14). A significant increase of FWI is apparent before RCP8.5 2050 in much of North America, including the frequency of 95th percentile FWI days, peak seasonal FWI average, fire weather season length, and maximum fire weather index (Abatzoglou et al., 2019), and fire season across North America expands dramatically beyond 2°C global warming levels (Sun et al., 2019b; Jain et al., 2020). Wang et al. (2017) simulated fire spread days across Canada and found median increases by 2071-2100 of -20 to 140% (RCP2.6), -20 to 250% (RCP4.5) and 40 to 360% (RCP8.5) compared to 1976-2015. Prestemon et al. (2016) found more conducive conditions for lightning-ignited fires in the Southeastern US by mid-century, while warming conditions in Alaska increasingly push July temperatures above 13.4 ºC, a threshold for fire danger across Alaska's tundra and boreal forest (Partain et al., 2016; Young et al., 2017). Longer and more intense fire seasons would also raise particulate matter and black carbon concentrations in the Western United States, reducing visibility at many National Parks (Yue et al., 2013; Val Martin et al., 2015).

Changes in North American wet and dry climatic impact-drivers are largely organized by the northeast (more wet) to southwest (more dry) pattern of mean precipitation change, although heavy precipitation increases are widespread and increasing evaporative demand expands aridity, agricultural and ecological drought, and fire weather (particularly in summertime) (*high confidence*).

12.4.6.3 Wind

Mean wind speed: Mean wind speeds have declined in past decades in North America as in other Northern Hemisphere areas over the past four decades (AR5, WGI) (*medium confidence*) with a reversal in the last decade (*low confidence*) not fully consistent across studies (Tian et al., 2019; Zeng et al., 2019; Zhang et al., 2019d) (Chapter 2). Tian et al. (2019) found a corresponding reduction in the wind power potential across the eastern parts of North America.

Mean wind speeds are expected to decline over much of North America (Figure 12.4m-o), but the only broad signal of consistent change across model types is a reduction in wind speed in Western North America (*high confidence*). These declines reduce wind power endowment by 2050 and as early as the 2020-2040 near-term period in the US Mountain West, while there is disagreement between global and regional model change projections in the upper and lower Great Plains, Ohio River Valley, Mexico and Eastern Canada (Karnauskas et al., 2018a; Jung and Schindler, 2019; Chen, 2020).

Severe wind storm: There is *limited evidence* and *low agreement* in observed changes in North American CID indices associated with extratropical cyclones (Chapter 11), severe thunderstorms, severe wind bursts (*derechos*), tornadoes, or lightning strikes (Vose et al., 2014; Easterling et al., 2017; Kossin et al., 2017). Observational studies have indicated a reduction in the number of tornado days in the US, but increases in outbreaks with 30 or more tornados in one day (Brooks et al., 2014), the density of tornado clusters (Elsner et al., 2015), and overall tornado power (Elsner et al., 2019).

There is *medium confidence* of a general decrease in the number of extratropical cyclones producing high wind speeds in North America, except over northernmost parts, for a global warming level of 2°C or by the end of the century in under RCP4.5 and RCP8.5 (Kumar et al., 2015; Jeong and Sushama, 2018; Li et al., 2018a). GCMs cannot directly resolve tornadoes and severe thunderstorms, however projections of favorable environments for severe storms (based on convective available potential energy and wind shear) indicate *medium confidence* for more severe storms and a longer convective storm season in the United States weaker increases extending north and east (Seeley and Romps, 2015; Glazer et al., 2020) and a corresponding increase in fall and winter tornadic storms (Brooks, 2013a; Diffenbaugh et al., 2013; Brooks et al., 2014) (see also Section 11.7.1). Prein et al. (2017a) used a convection-permitting model to project a tripling of mesoscale convective systems over the United States for end-of-century RCP8.5.

Tropical cyclone: Section 11.7.1 identified recent reductions in tropical cyclone translation speed and higher tropical cyclone rainfall totals over the North Atlantic as well as substantial natural variability. Projections indicate *low confidence* in change in North Atlantic tropical cyclone numbers, but *medium confidence* in

ACCEPTED VERSION SUBJECT TO FINAL EDITS

Mexico and the US Gulf and Atlantic coasts for more intense storms with higher wind, precipitation, and storm surge totals when they do occur (Diro et al., 2014; DOE, 2015; Walsh et al., 2016a; Kossin et al., 2017; Marsooli et al., 2019; Ting et al., 2019; Knutson et al., 2020) (see Section 11.7.1). A more rapid intensification of tropical cyclone winds and destructive power also heightens the tropical cyclone hazard (Bhatia et al., 2019). Greenhouse gas forcing is projected to shift tropical cyclones poleward (Kossin et al., 2016), while also holding the potential for higher precipitation totals (Risser and Wehner, 2017; Knutson et al., 2020) particularly given evidence that storms increasingly stall near North American coastlines (Hall and Kossin, 2019).

Sand and dust storm: Land use change has increased dust emission in the western U.S. in the past 200 years (Neff et al., 2008). However, there is *medium confidence* for observed increases in Western North American sand and dust storm activity since 1980. In their study of Valley Fever spread, Tong et al. (2017) identified a rapid intensification of dust storm activity using PM_{10} and $PM_{2.5}$ observations from 1980-2011 across 29 monitoring sites in the Southwestern US, similar to contiguous US observations by Brahney et al. (2013). Hand et al. (2016) attributed the earlier onset of spring dusts in the Southwest in large part to the Pacific Decadal Oscillation, however. The increasing trend in dust since the 1990s in the southwest US can be explained by precipitation deficit and surface bareness (Pu and Ginoux, 2018). Projections of future sand and dust storms over North America are based on aridity as a primary proxy for conducive conditions which lends *medium confidence* of an increase over Mexico and the Southwest US. Pu and Ginoux (2017) project about 5 more dusty days in spring and summer in the southern Great Plains under RCP8.5 at the end of the century, while dusty days decrease in northern regions where mean precipitation tends toward wetter conditions.

Tropical cyclones, severe wind and dust storms in North America are shifting toward more extreme characteristics, with a stronger signal toward heightened intensity than increased frequency, although specific regional patterns are more uncertain (*medium confidence*). Mean wind speed and wind power potential are projected to decrease in Western North America (*medium confidence*) with differences between global and regional models lending *low confidence* elsewhere.

12.4.6.4 Snow and ice

Snow: The seasonal extent of snow cover has reduced over North America in recent decades (*robust evidence, high agreement*) (see also Section 2.3.2.2, Section 9.5.3 and Atlas). The average North America area covered by snow decreased at a rate of about 8500 km^2 per year over the 1972-2015 period, reducing the average snow cover season by two weeks primarily due to earlier spring melt (US EPA, 2016). Observations indicate earlier spring snowpack melting (Dudley et al., 2017) and a reduction in end-of-season snowpack metrics important to water resources over the Rockies (particularly since 1980) and Pacific Northwest (Pederson et al., 2013; Kormos et al., 2016; Kunkel et al., 2016; Fyfe et al., 2017; Mote et al., 2018). In situ measurements in Canada show more heterogenous trends in snow amount and density (Brown et al., 2019).

Climate change is expected to reduce the total snow amount and the length of the snow cover season over most of North America, with a corresponding decrease in the proportion of total precipitation falling as snow and a reduction in end-of-season snowpack (*high confidence*) (see Atlas.9). Changes include a reduction in days with snowfall in all but Northern Canada (Danco et al., 2016; McCrary and Mearns, 2019), a delay of about a week in first snowfall in the US West in RCP8.5 2050 (Pierce and Cayan, 2013), and more prominent reductions in Canadian snow cover in the October-December period (Mudryk et al., 2018). Reduced total snowpack and earlier snowmelt lower dry season streamflow (Kormos et al., 2016; Rhoades et al., 2018). Figure 12.10b shows a reduction in days suitable for skiing (SWE>10 cm; Wobus et al., 2017b) across the US and Southern Canada, although some portions of Northern Central Canada see an increase.

Glacier: Section 9.5.1 assessed that glaciers in Alaska, Western Canada and the Western United States are expected to continue to lose mass and areal extent (*high confidence*). Compared to their 2015 state, glaciers in the Western Canada and the United States region will lose 62 ± 30%, 75 ± 29% and 85 ± 23%, of their

ACCEPTED VERSION SUBJECT TO FINAL EDITS

mass by the end of the century for RCP2.6, RCP4.5 and RCP8.5 scenarios, respectively (Marzeion et al., 2020). Meanwhile glaciers in Alaska will lose 26 ± 21%, 31 ± 24% and 44 ± 27%, of their mass in 2015 under the same scenarios. The overall loss of glacial mass can act as a meltwater supply for freshwater resources, although this is expected to peak in the middle of the century and then fade as glaciers disappear (Fyfe et al., 2017; Derksen et al., 2018). Continued shrinkage of glaciers is projected to create further glacial lakes (*medium confidence*) similar to those that have led to outburst floods in Alaska and Canada (Carrivick and Tweed, 2016; Harrison et al., 2018).

Permafrost: Warmer ground temperatures are expected to extend the geographical extent and depth of permafrost thaw across northern North America (*very high confidence*) (see also Section 9.5.2). Observations across Canada show that permafrost temperature is increasing and the active layer is getting thicker (Chapter 2.3.2.5; Biskaborn et al., 2019; Derksen et al., 2019; Romanovsky et al., 2020). Slater and Lawrence (2013) note that end-of-century RCP8.5 in North America only has shallow permafrost as the most probable condition in the Canadian Archipelago. Melvin et al. (2017) noted the loss of shallow permafrost in 5 RCP8.5 CMIP5 models across a wide swath of southern Alaska by 2050 along with increases of active layer thickness. There is *high confidence* in continued reductions in mountain near-surface permafrost area with high spatial variability given local snow and temperature changes (Chapter 9.5.2; Peng et al., 2018; Hock et al., 2019).

Lake, river and sea ice: Anthropogenic warming reduces the seasonal extent of lake and river ice over many North American freshwater systems, with ice-free winter conditions pushing further north with rising temperatures (*high confidence*). Observations in Central and Eastern North America show reduced average seasonal lake ice cover duration (Benson et al., 2012; Mason et al., 2016; US EPA, 2016). Satellite observations show declines in lake ice (Du et al., 2017) and loss of more than 20% of winter river ice length in much of Alaska (2008-2018 compared to 1984-1994; Yang et al., 2020). Spring lake and river ice in Canada is projected to break up 10-25 days earlier while fall freeze-up occurs 5-15 days later by mid-century, with larger declines in lake ice season by the coasts (Dibike et al., 2012) and for rivers in the Rockies and Northeastern United States (Yang et al., 2020a) although global models have difficulty with frozen freshwater system dynamics (Derksen et al., 2018). Substantial ice loss is projected over the Laurentian Great Lakes (Hewer and Gough, 2019; Matsumoto et al., 2019). The southern extent of lakes experiencing intermittent winter ice cover moves northward with rising temperature, pushing nearly out of the continental United States at low elevations when GMT increases by 4.5℃ (Sharma et al., 2019). Higher spring flows and the potential for winter thaws are also projected to heighten the threat of ice jams (Rokaya et al., 2018; Bonsal et al., 2019) while reducing the seasonal viability of ice roads and recreational use (Pendakur, 2016; Mullan et al., 2017; Knoll et al., 2019).

Seasonal sea ice coverage along the majority of Canadian and Alaskan coastlines is declining (*robust evidence, high agreement*) and there is *high confidence* that hazards associated with a loss of sea ice increase under climate change, as further assessed in Section 12.4.9.

Heavy snowfall: There is *low agreement (limited evidence)* for observed changes in heavy snowfall in North America. Kluver and Leathers (2015) noted a 1930-2008 frequency increase for all snow intensities in the Northern Great Plains but declines in heavier snow events in the Pacific Northwest and declines in the Southeastern US. Changnon (2018) found that most extreme 30-day high snowfall periods in the 1900-2016 record over the Eastern US occurred in the 1959-1987 period that lies between the Dust Bowl and recent warming. There is *low agreement* and *medium evidence* for broad projected changes to heavy snowfall over North America given increased heavy precipitation and warmer winter temperatures. Several recent regional studies have projected that low-intensity events decrease more rapidly than heavy snowfall events, resulting in an increase in the snowfall proportion from heavy snowfall events even as the number of such events decreases (O'Gorman, 2014; Lute et al., 2015; Zarzycki, 2016; Janoski et al., 2018; Ashley et al., 2020)

Ice storm: There is *limited evidence* in the literature of unique changes in ice storms observed or projected over North America. Groisman et al. (2016) examined 40 years of observations and found weak decreases in freezing rain events over the Southeastern US in the most recent decade. Ning and Bradley (2015) project that the average snow-rain transition line, which is associated with mixed precipitation, moves 2˚ latitude

ACCEPTED VERSION SUBJECT TO FINAL EDITS

northward over Eastern North America by the end of the 21st century under RCP4.5 (4˚under RCP8.5) (see also Klima and Morgan, 2015)..

Hail: There is *limited evidence* and *low agreement* for observed changes in the frequency or intensity of North American hail storms. Allen et al., (2015) and Allen (2018) found that temporal inconsistencies in the US and Canadian hail records made long-term climate analysis difficult, although Tang et al. (2019) identified increasing environments conducive for hail ≥ 5 cm over the Central and Eastern United States. There is *limited evidence* and *medium agreement* in projections of increased hail damage potential over North America. Some regional and convective-permitting model projections indicate a longer hail season with fewer events and larger hail sizes that result in higher hail damage potential (Brimelow et al., 2017; Trapp et al., 2019).

Snow avalanche: There is *limited evidence* of directional changes in snow avalanches over North America. Mock and Birkeland (2000) identified a 1969-1995 decrease in snow avalanches over the Western United States, although they note the heavy influence of natural variability. A similar decline was observed over Western Canada (Bellaire et al., 2016; Sinickas et al., 2016), but clear trends are difficult to discern given sparse observations and shifts in avalanche management. We concur with the SROCC assessment of *medium confidence* and *high agreement* that snow avalanche hazards generally decrease at low elevations given lower snowpack even as high elevations are increasingly susceptible to wet snow avalanches (Hock et al., 2019; see also Lazar and Williams, 2008).

Observations and projections agree that snow and ice CIDs over North America are characterized by reduction in glaciers and the seasonality of snow and ice formation, loss of shallow permafrost, and shifts in the rain/snow transition line that alters the seasonal and geographic range of snow and ice conditions in the coming decades (*very high confidence*).

12.4.6.5 Coastal and oceanic

Relative sea level: Chapter 9 found that observations indicate increasing sea levels along most North American coasts (*robust evidence, high agreement*), although there is substantial regional variation in relative sea level rise (*robust evidence, high agreement*). Around North America, over 1900-2018, a new tide-gauge based reconstruction finds a regional-mean RSL change of 1.08 [0.79-1.38] mm yr^{-1} in the subpolar North Atlantic, 2.49 [1.89-3.06] mm yr^{-1} in the subtropical North Atlantic, and 1.20 [0.76-1.62] in the East Pacific (Frederikse et al., 2020), compared to a GMSL change of around 1.7 mm yr^{-1} (Section 2.3.3.3; Table 9.5). For the period 1993-2018, these RSLR rates, based on satellite altimetry, increased to 2.17 [1.66-2.66] mm yr^{-1}, 4.04 [2.77-5.24] mm yr^{-1} and 2.35 [0.70-4.06] mm yr^{-1}, respectively (Frederikse et al., 2020), compared to a GMSL change of 3.25 mm yr^{-1} (Section 2.3.3.3; Table 9.5). Relative sea level (RSL) is falling in portions of southern Alaska (Sweet et al., 2018) and much of northern Northeastern Canada and around Hudson Bay (where land is rising by >10 mm/year; Greenan et al., 2019).

Relative sea-level rise is *virtually certain* to continue in the oceans around North America, except in northern Northeastern Canada and potions of Southern Alaska. Regional-mean RSLR projections for the oceans around North America range from 0.4 m -1.0 m under SSP1-RCP2.6 to 0.7 m -1.4 m under SSP5-RCP8.5 for 2081-2100 relative to 1995-2014 (median values), which means that there are locally large deviations from the projected GMSL change {Section 9.6.3.3}, including decreases in RSL in northern Northeastern Canada from land uplift (see also Sweet et al., 2017; Greenan et al., 2019; Oppenheimer et al., 2019). The RSLR projections here may however be underestimated due to potential partial representation of land subsidence in their assessment (Section 9.6.3.2).

Coastal flood: Observations indicate that episodic coastal flooding is increasing along many coastlines in North America (*robust evidence, high agreement*), and this episodic coastal flooding will increase in many North American regions under future climate change (*high confidence*) although land uplift from glacial isostatic adjustment in northern and Hudson Bay portions of Northeast North America leads to only *medium confidence* of coastal flood increases in that region. Sweet et al. (2018) found 2000-2015 observed increases

ACCEPTED VERSION SUBJECT TO FINAL EDITS

of about 125% in high tide flooding frequencies along the southern Atlantic US coastline, with 75% increases along the US Gulf Coast and US northern Atlantic coastlines. That same study noted that a GMSL of 0.5m in 2100 would increase high tide ('nuisance') flooding from current rates of about once a month for most coastal regions to about once every other day along the US Atlantic and Gulf Coasts and smaller frequency increases along the Pacific coast, and Dahl et al. (2017) found similar trends on the US East Coast prior to mid-century (see also . The present day 1:50 yr ETWL is projected to occur around 3 times a year by 2100 with a SLR of 1 m all around the region, except in most of Eastern North America where it is expected to have return periods of 1:1 yr – 1:2 yrs (Vitousek et al., 2017). Ghanbari et al. (2019) projected corresponding shifts toward higher frequencies of major flooding events for 20 US cities. Figure 12.4r and Figure SM.12.6 show increases of 70 cm or more in the 100-yr return period extreme total water level (ETWL) over much of the US East Coast, British Columbia, Alaska, and the Hudson Bay under RCP8.5 by 2100 (relative to 1980–2014), with lower increases in Northern Mexico, Northern Canada, Labrador, and the Pacific and Gulf Coasts of the US (Vousdoukas et al., 2018). Projected coastal flooding increases generally follow patterns of RSL change although sea ice loss in the north also increases open water storm surge (Greenan et al., 2019).

Coastal erosion: There is *limited evidence* of changes in North American episodic storm erosion caused by waves and storm surges. Observations show increased extreme wave energy on the Pacific coast, but no clear trend on other US coasts given substantial natural variability (Bromirski et al., 2013; Vose et al., 2014). In terms of long term coastal erosion, shoreline retreat rates of around 1 m yr^{-1} have been observed during 1984-2015 along the sandy coasts of NWN and NCA while portions of the US Gulf Coast have seen a retreat rate approaching 2.5 m yr^{-1} (Luijendijk et al., 2018; Mentaschi et al., 2018).Sandy shorelines along ENA and WNA have remained more or less stable during 1984 – 2014, but a shoreline progradation rate of around 0.5 m yr^{-1} has been observed in NEN Mentaschi et al. (2018) report 1984-2015 coastal area land losses of 630 km^2 and 1,260 km^2 along the Pacific and Atlantic coasts of USA, respectively.

Projections indicate that sandy coasts in most of the region will experience shoreline retreat through the 21st century (*high confidence*). Median shoreline change projections presented by Vousdoukas et al. (2020) compated CMIP5 projections show that sandy shorelines in NWN, ENA, and NCA will retreat by between 40 m – 80 m by mid-century (relative to 2010) under both RCP4.5 and RCP8.5. Projections for NEN and WNA are lower at 20 m – 30 m under the same RCPs. The highest median mid-century projection in the region is for CNA at around 125 m under both RCPs. RCP4.5 projections for 2100 show shoreline retreats of 100 m or more along the sandy coasts of NWN, CNA, and NCA, while retreats of between 40 m – 80 m are projected in other regions. Under RCP8.5, retreats exceeding 100 m are projected in all regions except NEN and WNA (approximately 80 m) by 2100, with particularly high retreats in NWN (160 m), CNA (330 m) and SCA (200 m). The total length of sandy coasts in North America that are projected to retreat by more than a median of 100 m by 2100 under RCP4.5 and RCP8.5 is about 15,000 km and 25,000 km respectively, an increase of approximately 70%.

Marine heatwave: There is *high confidence* in observed increases in marine heatwave frequency and future increases in marine heatwaves are *very likely* around North America (Box 9.2). The total number of MHW days per decade increased in the North American coastal zone, albeit somewhat more in the Pacific (Oliver et al., 2018; Smale et al., 2019). Projected increases in degree heating weeks (Heron et al., 2016) and degree heating months (Frieler et al., 2013) indicate increasing bleaching-level and mortality-level heating stress threshold events for reefs in Florida and Mexico.

Mean SST is projected to increase by 1 ºC (3 ºC) around North America by 2100, with a hotspot of around 4 ºC (5 ºC) off the North America Atlantic coastline under RCP4.5 (RCP8.5) conditions (see Interactive Atlas). Frölicher et al. (2018) projected increasing MHW frequency and spatial extent at a 2ºC global warming level with the largest increases in the Gulf of Mexico and off the southern US East Coast (>20x) as well as off the coast of the Pacific Northwest (>15x). Projections for SSP1-2.6 and SSP5-8.5 both show an increase in MHWs around North America by 2081 – 2100, relative to 1985 – 2014 (Box 9.2, Figure 1).

There is *high confidence* that most coastal CIDs in North America will continue to increase in the future with climate change. An observed increase in relative sea level rise is *virtually certain* to

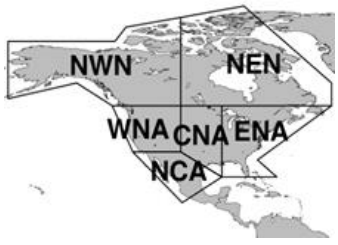
ACCEPTED VERSION SUBJECT TO FINAL EDITS

continue in North America (other than around the Hudson Bay and Southern Alaska) contributing to more frequent and severe coastal flooding in low-lying areas (*high confidence*) and shoreline retreat along most sandy coasts (*high confidence*). Marine heatwaves are also expected to increase all around the region over the 21st century (*high confidence*).

The assessed direction of change in climatic impact-drivers for North America and associated confidence levels are illustrated in Table 12.8.

[START TABLE 12.8 HERE]

Table 12.8: Summary of confidence in direction of projected change in climatic impact-drivers in North America, representing their aggregate characteristic changes for mid-century for scenarios RCP4.5, SSP3-4.5, SRES A1B, or above within each AR6 region (defined in Chapter 1), approximately corresponding (for CIDs that are independent of sea-level rise) to global warming levels between 2°C and 2.4°C (see 12.4 for more details of the assessment method). The table also includes the assessment of observed or projected time-of-emergence of the CID change signal from the natural inter-annual variability if found with at least *medium confidence* in Section 12.5.2.



Region	Heat and Cold: Mean air temperature	Heat and Cold: Extreme heat	Heat and Cold: Cold spell	Heat and Cold: Frost	Wet and Dry: Mean precipitation	Wet and Dry: River flood	Wet and Dry: Heavy precipitation and pluvial flood	Wet and Dry: Landslide	Wet and Dry: Aridity	Wet and Dry: Hydrological drought	Wet and Dry: Agricultural and ecological drought	Wet and Dry: Fire weather	Wind: Mean wind speed	Wind: Severe wind storm	Wind: Tropical cyclone	Wind: Sand and dust storm	Snow and Ice: Snow, glacier and ice sheet	Snow and Ice: Permafrost	Snow and Ice: Lake, river and sea ice	Snow and Ice: Heavy snowfall and ice storm	Snow and Ice: Hail	Snow and Ice: Snow avalanche	Coastal & Oceanic: Relative sea level	Coastal & Oceanic: Coastal flood	Coastal & Oceanic: Coastal erosion	Coastal & Oceanic: Marine heatwave	Coastal & Oceanic: Ocean acidity	Other: Air pollution weather	Other: Atmospheric CO_2 at surface	Other: Radiation at surface
North Central America (NCA)	●	◑	○																				○		2		○		●	
Western North America (WNA)	●	●	○		3		5	5	4,7		6,7	6,7		8		6	○		●	1		1	○	5	2		○		●	
Central North America (CNA)	●	○	○						7		7	7		8		4			●				○		2		○		●	
Eastern North America (ENA)	●	○	○		5							7		8			1○		●	1		1	○		2		○		●	
Northeast North America (NEN)	◑	●	○		5○				5		6,7	6,7		8			1,6○	●	●			1	4	4,6	2,6		○		●	
Northwest North America (NWN)	●	◑	○		5○			6	5		6,7	6,7		8			1○	●	●			1,6	9○		2		○		●	

1. Snow may increase in some high elevations and during the cold season and decrease in other seasons and at lower elevations.
2. Along sandy coasts and in the absence of additional sediment sinks/sources or any physical barriers to shoreline retreat.
3. Increasing in northern regions and decreasing toward south.
4. Decreasing in northern regions and increasing toward south.
5. Higher confidence in northern regions and lower toward south.
6. Higher confidence in southern regions and lower toward north.
7. Higher confidence in increase for some climatic impact driver indices during summertime.
8. Increase in convective conditions but decrease in winter extratropical cyclones.
9. Relative sea level rise reduced given land uplift in Southern Alaska.

● Already emerged in the historical period (*medium to high confidence*)
○ Emerging by 2050 at least in Scenarios RCP8.5/SSP5-8.5 (*medium to high confidence*)
○ Emerging after 2050 and by 2100 at least in Scenarios RCP8.5/SSP5-8.5 (*medium to high confidence*)

Key
High confidence of decrease
Medium confidence of decrease
Low confidence in direction of change
Medium confidence of increase
High confidence of increase
Not broadly relevant

[END TABLE 12.8 HERE

12.4.7 Small islands

This section covers the climatic impact-drivers affecting small islands around the world (see definition of SIDS in the Glossary; Cross-Chapter Box Atlas.2) with a particular focus on small islands in the Caribbean (CAR) Sea and the Pacific Ocean. Caribbean and Pacific small islands have mostly tropical climates and local conditions are also influenced by diverse topography ranging from low-lying islands and atolls to volcanic and mountainous terrain. Climate variability in these islands is influenced by the trade winds, the

APPROVED VERSION SUBJECT TO FINAL EDITS

easterly waves, tropical cyclones (TC), and the migrations of the Inter-Tropical Convergence Zone (ITCZ), the North Atlantic Subtropical High, and the South Pacific Convergence Zone (SPCZ), and other modes of climate variability as discussed in Cross-Chapter Box Atlas.2. Furthermore, changes in the ocean temperature and chemistry, and relative sea level have strong impacts on these small islands given their geographical location and dependence on coastal and marine ecosystem services.

IPCC AR5 recognized the heterogeneity in these small islands in terms of physical geography, socio-economic and cultural backgrounds, as well as their vulnerability to the impacts of climate change. Similar to previous reports, these regions have been assessed together in this section given similarities in the challenges they face in addressing climate change impacts and risk, which was thought to be dominated by sea level rise until IPCC AR4 (Nurse et al., 2014; Betzold, 2015). Since then there has been a substantial increase in the number and complexity of the literature on the drivers and impacts of climate change on small islands (BOM and CSIRO, 2011, 2014; Nurse et al., 2014; Gould et al., 2018; Keener et al., 2018). There are also increasing efforts in producing higher resolution climate projections for the small islands through downscaling methods (Elison Timm et al., 2015; McLean et al., 2015; Khalyani et al., 2016; Zhang et al., 2016a; Stennett-Brown et al., 2017; Bhardwaj et al., 2018; Bowden et al., 2021).

IPCC AR5 identified the key climate and ocean-related hazards affecting the small islands, which occur at different timescales and have diverse impacts on multiple sectors (Christensen et al., 2013; Nurse et al., 2014). Recent findings from IPCC SR1.5 and IPCC SROCC emphasize that the multiple interrelated climate hazards currently faced by low-lying islands and coastal areas will be amplified in the future, especially at higher global warming levels (Hoegh-Guldberg et al., 2018; IPCC, 2019b).

12.4.7.1 Heat and Cold

Mean air temperature: Significant warming trends are clearly evident in the small islands, such as those in the Pacific, CAR, and Western Indian Ocean, particularly over the latter half of the 20th century (see Figure Atlas.11; Section Atlas.10.2; Cross-Chapter Box Atlas.2, Table 1). This observed warming signal in the tropical western Pacific has been attributed to anthropogenic forcing (Wang et al., 2016). There is *high confidence* of warming over small islands even at 1.5°C global warming level (GWL) (Section Atlas.10.4; Figure Atlas.31) (Hoegh-Guldberg et al., 2018). Mean temperature is *very likely* to increase by 1°C–2°C (2°C–4°C) by 2041–2060 (2081–2100) under RCP8.5 (BOM and CSIRO, 2014) and SSP3-7.0 (Figure 4.19 and Figure Atlas.13) (Section Atlas.10.4) (Almazroui et al., 2021).

Extreme heat: Observation records indicate warming trends in the temperature extremes since the 1950s in CAR and the Pacific small islands (*high confidence*) (Section 11.3.2; Section 11.9, Table 11.7). A detectable anthropogenic increase in summertime heat stress index has been identified over a number of island regions in CAR, western tropical Pacific, and tropical Indian Ocean, based on wet bulb globe temperature (WBGT) index trends for 1973–2012 (*medium confidence*) (Knutson and Ploshay, 2016). An increasing trend in the maximum daytime heat index is also noted in CAR during the 1980–2014 period, as well as more extreme heat events since 1991 (Ramirez-Beltran et al., 2017).

Compared with the recent past, it is *likely* that the intensity and frequency of hot (cold) temperature extremes will increase (decrease) in the small islands (Section 11.9, Table 11.7) (BOM and CSIRO, 2014). Warm spell conditions will occur up to half the year in CAR at 1.5°C GWL with an additional 70 days at 2°C (Taylor et al., 2018), with livestock temperature-humidity tolerance thresholds increasingly surpassed (Lallo et al., 2018). In CAR, a median increase of almost a month where temperatures exceed 35°C is projected by end of the 21st century under SSP5-8.5 (Figure 12.4a.c and Figure SM 12.1). Heat waves are projected to increase in CAR by the mid- and end of the 21st century under RCP8.5 (Section 11.3.5; Section 11.9, Table 11.7). Figure 12.4d-f and Figure SM 12.2 also show an increase of about 30-60 days with HI exceeding 41°C by 2041-2060 under SSP5-8.5 relative to 1995-2014 in CAR, with an additional increase of about days by end of the 21st century for RCP8.5/SSP5-8.5, but this increase remains below 50 days for RCP2.6/SSP1-2.6. The Pacific Islands is also among regions projected to have an increase in number of days with mean HI exceeding 41°C by 2091-2100 under RCP8.5/SSP5-8.5, increasing the risk of heat stress in the region

ACCEPTED VERSION SUBJECT TO FINAL EDITS

(Newth and Gunasekera, 2018).

It is *very likely* that the significant recent warming trends observed in the small islands will continue in the 21st century, which will *likely* further increase heat stress in these regions.

12.4.7.2 Wet and Dry

Mean precipitation: Observational datasets have generally revealed no significant long-term trends in rainfall in the Caribbean over the 20th century when analysed at seasonal and inter-decadal timescales, except for some areas where there is evidence for decreasing trends for the period 1901-2010 but not for the period 1951-2010 (Knutson and Zeng, 2018; Section Atlas.10.2; Cross-Chapter Box Atlas.2, Table 1). Although there are spatial variations, annual rainfall trends in the Western Indian Ocean are mostly decreasing, with generally non-significant trends in the Western tropical Pacific since the 1950s (*low confidence*). Significant drying trends are noted in the southern Pacific subtropics and southwestern French Polynesia during the 1951-2015 period (McGree et al., 2019), and in some areas of Hawaii during the 1920-2012 period (*medium confidence*) (Section Atlas.10.2; Cross-Chapter Box Atlas.2, Table 1).

Atlas.10.4 projects precipitation reduction over the Caribbean (*high confidence*) and parts of the Atlantic and Indian Oceans, particularly in June to August by end of 21st century. Precipitation is generally projected to increase in the small islands in parts of the western and equatorial Pacific, but there is low confidence in broad changes givend drier conditionsprojected for the southern sub-tropical and eastern Pacific Ocean (*limited agreement* given spatial and seasonal variability; Section Atlas.10.4; Figure Atlas.31) (Almazroui et al., 2021).

River flood: There is *limited evidence* on observed changes in river flooding in small islands. Long-term records in Hawaii indicate no clear trends in peak flow, except for the significant decrease in peak streamflow in Hawaii Island over the period 1967-2016 (Bassiouni and Oki, 2013; Clilverd et al., 2019). Similarly, there is no significant trend in the frequency and height (after adjusting for average sea level rise) of river flood in Fiji over the period 1892-2013 (McAneney et al., 2017). There is *low confidence* on the direction of future change of river flooding in the small islands due to the limited currently available literature. In Oahu, Hawaii, extreme peak flow events with high return periods are projected to increase by end of 21st century under RCP8.5, but there is also high uncertainty in these projections (Leta et al., 2018).

Heavy precipitation and pluvial flood: Heavy precipitation days in CAR have increased in magnitude, and have been more frequent in the northern part during the latter part of the 20th century (*low confidence*) (Section 11.4.2; Table 11.7). The direction of change in extreme precipitation varies across the Pacific and depends on the season (*low confidence*) (Section 11.4.2; Cross-Chapter Box Atlas.2, Table 1). Although pluvial flooding events have been observed in some islands, there is *limited evidence* for an assessment on past changes in pluvial flooding unlike in other regions. There is *low confidence* in the projected increase in magnitude of very heavy precipitation days in CAR across different GWLs (Table 11.7). On the other hand, there is *high confidence* in the increase in frequency and intensity of extreme rainfall events (i.e. 1-in-20 year rainfall events) in the western tropical Pacific in the 21st century even for RCP2.6 scenario based on model agreement and mechanistic understanding but *low confidence* in the magnitude of change in extreme rainfall due to model bias (BOM and CSIRO, 2014).

Landslide: Heavy rainfall, such as from tropical cyclones, can trigger landslides over steep terrain in the small islands (Bessette-Kirton et al., 2019). There is *limited evidence* to determine long-term trends in rainfall-induced landslides in the small islands (Kirschbaum et al., 2015; Sepúlveda and Petley, 2015; Froude and Petley, 2018; Bessette-Kirton et al., 2019). There is *low confidence* in the future change in landslides in the small islands. The direction of change may depend on future changes in precipitation, tropical cyclones, climate modes (e.g., El Niño-Southern Oscillation (ENSO)), as well as human disturbance, but more data and understanding of the complexity of these relationships are needed, especially in these vulnerable areas (Sepúlveda and Petley, 2015; Gariano and Guzzetti, 2016; Froude and Petley, 2018).

ACCEPTED VERSION SUBJECT TO FINAL EDITS

Aridity: Current estimates identify many small islands as being under water stress and thus particularly sensitive to variations in rainfall and groundwater, population growth and demand, land use change, among others (Holding et al., 2016) (Cross-Chapter Box Atlas.2). From 1950 to 2016, a heterogeneous but prevalent drying trend is found in CAR (*medium confidence*), where drought variability is modulated by the tropical Pacific and North Atlantic oceans (Herrera and Ault, 2017) (Table 11.7, Cross-Chapter Box Atlas.2, Table 1). In the future, increased aridity and decreased freshwater availability are projected in many small islands due to higher evapotranspiration in a warmer climate that partially offsets increases or exacerbates reductions in precipitation (Karnauskas et al., 2016, 2018b; Hoegh-Guldberg et al., 2018). Increased aridity is projected for the majority of the small islands, such as in CAR, southern Pacific and Western Indian Ocean, by 2041-2059 relative to 1981-1999, and at 1.5°C and 2.0°C GWLs, under RCP8.5, which will further intensify by 2081-2099 (Karnauskas et al., 2016, 2018b) (*medium confidence*). Groundwater recharge is projected to increase in Maui, Hawaii except on the leeward sides of the island, which underscores the importance of topography and elevation on freshwater availability in different island microclimates (Brewington et al., 2019; Mair et al., 2019).

Hydrological drought: There is *low confidence* of widespread changes to hydrological drought in the Caribbean or Pacific small islands in recent decades, although an increasing number of studies document local changes. Records in Hawaii indicate downward trends in low streamflow and base flow from 1913 to 2008 (Bassiouni and Oki, 2013). Decadal variability of Hawaiian streamflow coincides with rainfall fluctuations associated with the Pacific Decadal Variability although significant average declines in surface and baseflow runoff of about 8% and 11% per decade, respectively, have been noted during the 1987-2016 period (Clilverd et al., 2019).

There is *low confidence* in hydrological drought change projections given low signal to noise ratios and the challenge in representing island scales in global analyses. Prudhomme et al. (2014) recognized the Caribbean as one of the regions with highest increase in regional deficit index (RDI; a measure of the fraction of area in hydrological drought conditions) by end of the 21st century under RCP8.5. Daily streamflow and extreme low flows in two watersheds in Oahu, Hawaii are projected to decline by mid- and end of the 21st century under RCP4.5 and RCP8.5, which would result in more frequent hydrological droughts in this area (Leta et al., 2018).

Agricultural and ecological drought: Recent trends toward more frequent and severe droughts have been noted in the small islands but only generate *low confidence* in broad trend patterns given high spatial variability including heightened drought on the leeward side of islands (e.g., Frazier and Giambelluca, 2017; Herrera and Ault, 2017; McGree et al., 2019; Table 11.7, Cross-Chapter Box Atlas.2, Table 1). There is *medium confidence* that agricultural and ecological droughts will increase in frequency, duration, magnitude, and extent in the small islands, such as in CAR and parts of the Pacific, particularly where there are future declines in precipitation compounded by higher evapotranspiration, under increasing levels of warming (Naumann et al., 2018; Taylor et al., 2018; Vichot-Llano et al., 2021). Relative to the period 1985-2014, decreases in annual surface and total column soil moisture becomes more robust in more areas in CAR by 2071-2100 under SSP3-7.0 and SSP5-8.5 scenarios (Cook et al., 2020a), but global simulations are challenged to represent drought features in small island domains (see also Section 11.9).

Fire weather: There is *limited evidence* on trends in wildfire in CAR and the Pacific. Records of wildfire in Hawaii from 2005-2011 indicate a peak in area burned during the hot and dry summer months, but Trauernicht et al. (2015) note the difficulty in establishing the link between past climate and wildfire trends due to human activities and vegetation changes. Availability of literature limits assessment on future fire weather in the small islands (*low confidence*). Drying and warming trends tend to increase fire probability aside from the climate impact on fuel loading, e.g., grassland fires in Hawaii (Trauernicht, 2019), and wildfires in Puerto Rico (Van Beusekom et al., 2018).

Observed and projected rainfall trends vary spatially across the small islands. Higher evapotranspiration under a warming climate can partially offset future increases or amplify future reductions in rainfall resulting in drier conditions and increase water stress in the small islands (*medium confidence*).

ACCEPTED VERSION SUBJECT TO FINAL EDITS

12.4.7.3 Wind

Mean wind speed: Scarcity of observations limits assessment of long-term changes in winds over the small islands in the Pacific and CAR. Records indicate that average daily wind speeds have slowly declined in Hawaii, but trends have remained constant across western and south Pacific sites since the mid-20th century (Marra and Kruk, 2017). Recent studies of reanalyses and hindcast simulations indicate an intensification of the Pacific trade winds during the 1992-2011 period, which contributed to the ocean cooling in the tropical central and eastern Pacific (England et al., 2014; Takahashi and Watanabe, 2016). Projections estimate up to 0.4 m s^{-1} (8%) increase in annual winds in CAR under RCP8.5, which is associated with changes in the extension of the North Atlantic Subtropical High that enhances the Caribbean low-level jet during the wet season, and stronger local easterlies due to enhanced land-ocean temperature differences in the dry season (Costoya et al., 2019) (*low confidence*).

Tropical cyclone: Tropical cyclones have devastating impacts on the small islands due to intense winds, storm surge, and rainfall, although the associated rainfall can also be beneficial for freshwater resources. It is *likely* that tropical cyclone intensity and intensification rates at a global scale have increased in the past 40 years but it is not clear if regional-scale changes are basin-wide or due to shifts in tracks (Section 11.7.1.2). Other features are less sensitive to these issues, such as the poleward migration where tropical cyclones reach peak intensity in the western North Pacific and the slowdown in tropical cyclone translational speed in most basins in the latter half of the 20th century (*low confidence*), which can enhance rainfall and flooding events, including over small islands in CAR and the Pacific (Section 11.7.1.2).

Future global changes in tropical cyclones include more frequent Category 4-5 storms (*high confidence*) and increased rain rates (*very high confidence*) (Knutson et al., 2020), with relative sea level rise exacerbating storm surge potential but large differences per region depending also on changes to future storm tracks (see Section 11.7.1.5). By the late 21st century, tropical cyclones are projected to be less frequent in the basins of the western and eastern North Pacific, Bay of Bengal, Caribbean Sea and in the Southern Hemisphere, but will be more frequent in the subtropical central Pacific (Murakami et al., 2014; Yoshida et al., 2017; Bell et al., 2019; Knutson et al., 2020). Over CAR, tropical cyclone intensity is expected to increase due to higher sea surface temperatures but can be inhibited by increases in vertical wind shear in the region (*medium confidence*) (Kossin, 2017; Ting et al., 2019). The poleward movement of the area where tropical cyclones reach peak intensity in the western North Pacific is *likely* to continue, which affects the tropical cyclone frequency over the small islands in the area (Kossin et al., 2016) (Section 11.7.1.5). Projections also indicate an increase (decrease) in the tropical cyclone frequency during El Niño (La Niña) events in the Pacific at the end of the 21st century (Chand et al., 2017). RCP8.5 2080-2099 projections indicate an increase in tropical cyclone number by 2% in the North Central Pacific relative to 1980-1999, with tracks shifting northward towards Hawaii (Li et al., 2018d). Given projected reductions to the overall number of storms but increases in storm intensity, total rainfall and storm surge potential, we assess *medium confidence* of overall changes to tropical cyclones affecting the Caribbean and Pacific small islands.

Global changes indicate that small islands will generally face fewer but more intense tropical cyclones (*medium confidence*) although there is substantial variability across small island regions given projected regional shifts in storm tracks.

12.4.7.4 Coastal and Oceanic

Relative sea level: Relative sea level rise (SLR) continues to be a major threat to small islands and atolls, since it can exacerbate the impacts of other climate hazards on low-lying coastal communities and infrastructures, ecosystems, and freshwater resources (Nurse et al., 2014; Hoegh-Guldberg et al., 2018). In the Indian Ocean- South Pacific region, a new tide-gauge based reconstruction finds a regional-mean RSL change of 1.33 [0.80 to 1.86] mm yr^{-1} over 1900-2018 (Frederikse et al., 2020) compared to a GMSL change of around 1.7 mm yr^{-1} (Section 2.3.3.3; Table 9.5). RSLR rates based on satellite altimetry for the period 1993-2018 increased to 3.65 [3.23 to 4.08] mm yr^{-1} (Frederikse et al., 2020), compared to a GMSL change of 3.25 mm yr^{-1} (Section 2.3.3.3; Table 9.5).

ACCEPTED VERSION SUBJECT TO FINAL EDITS

Relative sea-level rise is *very likely* to continue in the oceans in the Small Island States. Around the small islands, regional-mean RSLR projections vary widely, from 0.4 m–0.6 m under SSP1-RCP2.6 to 0.7 m–1.6 m under SSP5-RCP8.5 for 2081–2100 relative to 1995–2014 (median values), but in general they are situated in areas with RSL changes ranging from the mean projected GMSL change to above-average values {Section 9.6.3.3}. These RSLR projections may however be underestimated due to potential partial representation of land subsidence in their assessment (Section 9.6.3.2).

Coastal flood: Relative sea-level rise, storm surges, and swells contribute to coastal inundation in the small islands, where studies on historical trends in coastal flooding are currently limited. For example, a swell event due to distant extra-tropical cyclones in December 2008 raised extreme water levels leading to flooding affecting five Pacific island nations: Marshall Islands, Micronesia, Papua New Guinea, Kiribati and Solomon Islands (Hoeke et al., 2013; Merrifield et al., 2014). Over low-lying atoll islands in the northwest tropical Pacific, potential increases in the areal extent in coastal flooding with reduced return periods, especially at higher SLR scenarios, are expected to have negative consequences on freshwater resources and island habitability (Storlazzi et al., 2015, 2018). Select tide gauges across the Pacific also indicate increasing trends in the frequency of minor flooding since the 1960s (Marra and Kruk, 2017).

As relative sea levels increase, the potential for coastal flooding increases in the small islands (*high confidence*). Across the Pacific and CAR small islands, the 5th – 95th percentile range of the 1:100 yr ETWL is projected to increase (relative to 1980 – 2014) by 10 cm – 35 cm and by 14 cm – 41 cm by 2050 under RCP4.5 and RCP8.5, respectively (Figure 12.4q). By 2100, this range is projected to be 27 cm – 81 cm and 44 cm – 188 cm under RCP4.5 and RCP8.5, respectively (Figure 12.4p,r) (Vousdoukas et al., 2018; Kirezci et al., 2020). Furthermore, by 2050, the present day 1:100 yr ETWL is projected to have median return periods of between 1:1 yr and 1:50 yr in both the Pacific and CAR small islands, with some Pacific islands projected to experience the present day 1:100 yr ETWL more than once a year (Vousdoukas et al., 2018; Oppenheimer et al., 2019). By 2100, the present day 1:50 yr ETWL is projected to occur around 3 times a year by 2100 with a SLR of 1 m at Pacific and CAR small islands (Vitousek et al., 2017). In the Western Tropical Pacific, the magnitude and frequency of coastal flooding due to SLR can be modulated by changes in the wave climate (Shope et al., 2016).

Coastal erosion: Recent studies have indicated variable and dynamic changes in shorelines of reef islands (*medium confidence*), including both erosion and accretion, which suggest factors other than SLR affecting shoreline changes, such as in the central and western Pacific within the past 50 to 60 year timeframe (Webb and Kench, 2010; Le Cozannet et al., 2014; Ford and Kench, 2015; Duvat and Pillet, 2017). For example, islands on atolls in the central and western Pacific have not substantially eroded or reduced in size in the past decades when sea level has increased but rather have changed their position and morphology due to anthropogenic factors (e.g., seawalls, reclamation) and climate-ocean processes (Biribo and Woodroffe, 2013; McLean and Kench, 2015). Analysis of aerial and satellite imagery revealed severe shoreline retreat in six islands and the disappearance of five vegetated reef islands in Solomon Islands in the western Pacific between 1947 to 2014, which may be due to the interaction between SLR and waves (Albert et al., 2016). In French Polynesia, changes in shoreline and island area have been observed since the 1960s, partly due to the effect of TCs on sediment changes and human activities (Duvat and Pillet, 2017; Duvat et al., 2017). Coastal erosion have also been noted over the small, low-lying, sandy islands, such as in French Polynesia and Solomon Islands, among others, due to high relative sea level rise and storms (Luijendijk et al., 2018a; Mentaschi et al., 2018). Average shoreline retreat rates between 1 m yr^{-1} and 2 m yr^{-1} are estimated for the islands in the Equatorial Pacific and in CAR, while a retreat rate of 0.5 m is estimated for islands in the south Pacific, based on satellite observations from 1984-2016 (Luijendijk et al., 2018a; Mentaschi et al., 2018). There was also a loss of 610 km^2 vs. a gain of 520 km^2 in coastal area in Oceania during the 1984-2015 period (Mentaschi et al., 2018).

Projections indicate that shoreline retreat will occur over most of the small islands in the Pacific and CAR throughout the 21st century with spatial variability (*high confidence*). Median shoreline change projections (CMIP5), relative to 2010, presented by Vousdoukas et al. (2020) show that, by mid-century, shorelines in the islands in the equatorial Pacific and south Pacific will retreat by around 40 m, under both RCP4.5 and RCP8.5. In CAR islands, sandy shorelines are projected to retreat by about 80 m by mid-century under both

ACCEPTED VERSION SUBJECT TO FINAL EDITS

RCPs. By 2100, more than 100 m of median shoreline retreat is projected for all small islands under both RCPs; notably in CAR where retreats approaching 200 m (relative to 2010) are projected under both RCPs. The total length of sandy coasts in CAR and Pacific small islands that is projected to retreat by more than a median of 100 m by 2100 under RCP4.5 and RCP8.5 is about 1,100 km and 1,200 km respectively, an increase of approximately 14%.

Marine heatwave: Ocean temperatures from satellite observations noted a moderate increase of 1–4 annual marine heat wave (MHW) events between 1982–1988 and 2000–2016 over some areas in the Indian Ocean, subtropical parts of the North and South Atlantic, and central and western parts of the North and South Pacific, but a decrease in frequency (2 annual events) over the eastern Pacific Ocean (Oliver et al., 2018) (see Box 9.2). The intensity of MHWs has also increased between 0.2°C and 0.5°C over the equatorial portions of the North Atlantic, and the South Pacific. Over the eastern tropical Pacific, the decrease in intensity and duration of MHW is between 0.5–1.0 °C and between 30–75 days, respectively (Oliver et al., 2018) (see Box 9.2). There is *high confidence* that MHWs will increase around all small island nations. Marine heatwaves are projected to be more intense and prolonged where the largest changes are noted in the equatorial region with maximum annual intensities up to 1.2°C (1.8°C) and annual mean duration reaching 100 days (200 days) at 1.5°C (2.0 °C) warming levels (Frölicher et al., 2018). Projections for SSP1-2.6 and SSP5-8.5 both show an increase in MHWs around all small island nations by 2081–2100, relative to 1985–2014 (Box 9.2, Figure 1).

In summary, relative sea level rise is *very likely* in the oceans around small islands, and along with storm surges and waves will exacerbate coastal inundation in small islands. Shoreline retreat is projected along sandy coasts of most small islands (*high confidence*). There is *high confidence* that MHWs will increase around all small island nations.

The assessed direction of change in climatic impact-drivers for CAR and Pacific small islands and associated confidence levels are illustrated in Table 12.9. Cold, Snow, Ice related climatic impact-drivers, and sand and dust storms are not broadly relevant in small islands.

[START TABLE 12.9 HERE]

Table 12.9: Summary of confidence in direction of projected change in climatic impact-drivers in the small islands, representing their aggregate characteristic changes for mid-century for scenarios RCP4.5, SSP3-4.5, SRES A1B, or above within each AR6 region (defined in Chapter 1), approximately corresponding (for CIDs that are independent of sea-level rise) to global warming levels between 2°C and 2.4°C (see 12.4 for more details of the assessment method). The table also includes the assessment of observed or projected time-of-emergence of the CID change signal from the natural inter-annual variability if found with at least *medium confidence* in Section 12.5.2.

ACCEPTED VERSION SUBJECT TO FINAL EDITS

Region	Climatic Impact-Driver																								
	Heat and Cold				Wet and Dry							Wind				Snow and Ice						Coastal & Oceanic					Other		
	Mean air temperature	Extreme heat	Cold spell	Frost	Mean precipitation	River flood	Heavy precipitation and pluvial flood	Landslide	Aridity	Hydrological drought	Agricultural and ecological drought	Fire weather	Mean wind speed	Severe wind storm	Tropical cyclone	Sand and dust storm	Snow, glacier and ice sheet	Permafrost	Lake, river and sea ice	Heavy snowfall and ice storm	Hail	Snow avalanche	Relative sea level	Coastal flood	Coastal erosion	Marine heatwave	Ocean acidity	Air pollution weather	Atmospheric CO_2 at surface	Radiation at surface
Caribbean (CAR)	●														6								○		7		○		●	
Pacific Islands	●	1			2		3		4		5				6								○		7		○		●	

1. Very high confidence in the direction of change, but low to medium confidence in the magnitude of change due to model uncertainty.
2. Decrease in eastern Pacific and southern Pacific subtropics, but Increase in parts of western and equatorial Pacific; with seasonal variation in future changes.
3. High confidence in increase in extreme rain frequency and intensity in western tropical Pacific; low confidence in magnitude of change due to model bias.
4. Increase in southern Pacific.
5. Particularly in parts of the Pacific with projected rainfall declines.
6. Increase in intensity; decrease in frequency except over central north Pacific.
7. Along sandy coasts and in the absence of additional sediment sinks/sources or any physical barriers to shoreline retreat.

● Already emerged in the historical period (*medium to high confidence*)
○ Emerging by 2050 at least in Scenarios RCP8.5/SSP5-8.5 (*medium to high confidence*)
○ Emerging after 2050 and by 2100 at least in Scenarios RCP8.5/SSP5-8.5 (*medium to high confidence*)

Key
High confidence of decrease
Medium confidence of decrease
Low confidence in direction of change
Medium confidence of increase
High confidence of increase
Not broadly relevant

[END TABLE 12.9 HERE]

12.4.8 Open and deep ocean

Oceans face challenges from anthropogenic perturbations to the global Earth system, which cause increasing ocean warming, carbon dioxide induced acidification and oxygen loss (Bindoff et al., 2019). Climate change will affect the major oceanic CIDs described in Section 12.2; mean ocean temperature, marine heatwaves, ocean acidity, ocean salinity, dissolved oxygen (O_2), severe wind storms and sea ice melting. These changes result in a shifting profile of hazards relevant to impact and risk assessments (Section 12.3). New evidence, the IPCC (2019b) and advances in the new CMIP6 climate simulations reinforce confidence in projected changes in climatic impact-drivers in the global oceans. As the ocean has taken up about 90% of the global warming for the period 1971-2018 (Section 7.2.2.2), the emergence of the sea surface temperature increase signal has already been observed in global oceans over the last century (Hawkins et al., 2020). The emergence signal in in sea ice extent decrease has already emerged in the Arctic Ocean (Landrum and Holland, 2020), while ocean acidification and low oxygen have also already emerged in many ocenic regions and will emerge in all global oceans by 2050 under RCP8.5 (see Section 12.5.2; Table 12.10). This section assesses key hazards that can be linked with sectoral and regional vulnerability and exposure in open and deep oceans, drawing from previous Chapters (2,3,4, 5, and 9).

Mean ocean temperature: It is *very likely* that global mean sea surface temperature global mean SST has increased by 0.88°C [0.68 to 1.01°C] from 1850-1900 to 2011-2020, and 0.60°C [0.44 to 0.74°C] from 1980-2020 (Section 2.3.1.1.6; Table 2.4). There is *very high confidence* that the Indian Ocean, western equatorial the Pacific Ocean, and western boundary currents have warmed faster than the global average, while the Southern Ocean, the eastern equatorial Pacific, and the North Atlantic Ocean have warmed more slowly or slightly cooled (Section 9.2.1.1). It is *virtually certain* that SST will continue to increase in the 21st century at a rate depending on future emission scenario, while the global mean ocean surface temperature will continue to increase throughout the 21st century (*very high confidence*), with CMIP6 projections indicating an increase of 0.86°C (*likely* range: 0.43-1.47°C) under SSP1-2.6 and 2.89°C (2.01-4.07°C) under SSP5-8.5, by 2081-2100, relative to 1995-2014 (Section 9.2.1.1). Global warming of 2°C above pre-industrial levels is projected to increase sea surface temperature, resulting in the exceedance of numerous hazard thresholds for pathogens, seagrasses, mangroves, kelp forests, rocky shores, coral reefs and other marine ecosystems (Poloczanska et al., 2013b, 2016, 2013a; Pörtner et al., 2014; Liu et al., 2014; Graham et

ACCEPTED VERSION SUBJECT TO FINAL EDITS

al., 2015; Schoepf et al., 2015; Gobler et al., 2017; Henson et al., 2017; Hoegh-Guldberg et al., 2017; Krueger et al., 2017; Hughes et al., 2018b, 2018a; Perry et al., 2018) (*medium confidence*). It is *virtually certain* that upper ocean stratification has increased at a rate of 4.9±1.5% during 1970-2018 and that this will continue to increase in the 21st century (Section 9.2.1.3), potentially leading to reduced nutrient supply and total productivity (Moore et al., 2018) (*low confidence*).

Marine heatwave: Marine heaywaves have increased in frequency over the 20th century, with an approximate doubling since the 1980s (*high confidence*), and their intensity and duration have also increased (*medium confidence*) (Box 9.2). Projections show that this increasing trend *likely* continues with 2-9 times more frequent marine heatwaves (at global scale) projected by 2081-2100, relative to 1995-2014 under SSP1-2.6, and 4-18 times more frequent under SSP5-8.5. The largest changes in MHW frequency *likely* to occur in the tropical ocean and the Arctic, while there is *medium confidence* of moderate increases in the mid-latitudes, and of small increases in the Southern Ocean (Box 9.2). Permanent MHWs (more than 360 days per year, relative to the historical climate conditions) are projected to occur in the 21st century in parts of the tropical ocean, in the Arctic Ocean and around latitude 45°S, under SSP5-8.5 (Box 9.2). The occurrence of such permanent MHWs can be largely avoided under SSP1-2.6 scenario (Box 9.2). MHW can have devastating and long-term impacts on ecosystems (Oliver et al., 2018), making them an emerging hazard for marine ecosystems (Frölicher and Laufkötter, 2018; Smale et al., 2019). A series of marine heatwaves that occurred in 2010-2011 had consequences for seagrass in Western Australia (Wernberg et al., 2013; Arias-Ortiz et al., 2018), and for loster fishery in the Gulf of Maine (Pershing et al., 2018). The MHWs that occured Western Australia in 2015/2016 lead to the third-highest mass bleaching globally (Le Nohaïc et al., 2017).

Ocean acidity: With the increasing CO_2 concentration, the global mean ocean surface pH is decreasing and is now the lowest it has been for at least a thousand years (*very high confidence*) (Section 2.3.3.5). It is *very likely* that, since the 1980s, ocean surface pH has changed at a rate of –0.016 to –0.019 per decade in the subtropical open oceans, at –0.010 to –0.026 per decade in the tropical Pacific, and at –0.003 to –0.026 per decade in open subpolar and polar zones (Section 2.3.3.5; Section 5.3.3.2). Over the period 1870–1899 to 2080–2099, ocean surface pH is projected to decline by -0.16 ± 0.002 under SSP1–2.6, and by -0.44 ± 0.005 under SSP5–8.5 (Section 4.3.2.5; Section 5.3.4.1). Declining ocean pH will exacerbate negative impacts on marine species (Albright et al., 2016; Kwiatkowski et al., 2016; Watson et al., 2017) (*medium confidence*).

Ocean salinity: Salinity contrasts have increased since the 1950s, near the ocean surface (*virtually certain*) and in the sub-surface (*very likely*), with high salinity regions becoming more saline and low salinity regions becoming fresher (Section 2.3.3.2). At the basin scale, it is *very likely* that the Pacific and the Southern Oceans have freshened, and the Atlantic has become more saline (Section 2.3.3.2). The IPCC (2019) assessment that fresh ocean regions get fresher and salty ocean regions get saltier will continue in the 21st century is confirmed in Section 9.2.2.2.

At the regional scale, by 2100, the average Arctic surface salinity is projected to decrease by 1.5 ± 1.1 psu, and the liquid freshwater column in the Arctic Ocean is projected increase by 5.4 ± 3.8 m under RCP8.5, (Shu et al., 2018). In the Indian Ocean, sea surface salinity is projected to decrease by 0.49 psu and 0.75 psu by 2080, compared to 2015, under RCP2.6 and RCP2.6, respectively (Akhiljith et al., 2019). Projections for the North and South Atlantic Oceans indicate increasing salinity in the upper layer (0 – 500 m) under both RCP4.5 and RCP8.5, due to the decreasing freshwater input from the Equator and increasing net evaporation (Skliris et al., 2020). There is *medium confidence* that fresh ocean regions (Pacific, Southern and Indian oceans) will get fresher and salty ocean regions (Atlantic ocean) will get saltier over the 21st century (IPCC, 2019; Section 9.2.2.2). Ocean warming and high-latitude surface freshening is projected to continue to increase upper ocean stratification in the 21st century (Section 9.2.1.3).

Dissolved oxygen: Since the middle of the last century, oxygen concentrations of open and coastal waters have been declining, and such deoxygenation affects biological and biogeochemical processes in the ocean (Schmidtko et al., 2017). In recent decades, low oxygen zones in ocean ecosystems have expanded, and projections indicate an acceleration with global warming (Diaz and Rosenberg, 2008; Gilly et al., 2013; Gobler et al., 2014) (*medium confidence*). A 2% loss (4.8 ± 2.1 Pmoles O_2) in total dissolved oxygen in the

ACCEPTED VERSION SUBJECT TO FINAL EDITS

upper ocean layer (100–600 m) has been observed during 1970–2010 (Section 2.3.4.2), with the highest oxygen loss of up to 30 mol m-2 per decade in the equatorial and North Pacific, the Southern Ocean and the South Atlantic Ocean (Section 5.3.3.2). Global mean ocean oxygen concentration is projected to decrease by 6.36 ± 2.92 mmol m^{-3} under SSP1-2.6 and by 13.27 ± 5.28 mmol m^{-3} under SSP5-8.5 in the subsurface (100-600 m) by 2080–2099, compared to 1870–1899, which is respectively 71% and 40% greater than previous estimates based on CMIP5 models (Section 5.3.3.2). In the benthic ocean, projected future losses of dissolved oxygen concentration by 2080–2099, compared to 1870– 1899, are −5.14 ± 2.04 mmol m^{-3} under SSP1-2.6 and −6.04 ± 2.19 mmol m^{-3} under SSP5-8.5 (Kwiatkowski et al., 2020). Section 5.3.3.2 assessed *very likely* global decreases in ocean oxygen concentrations although there is *medium confidence* in specific regional declines that are expected to expand both anoxic and hypoxic zones, with such reductions of oxygen expected to persist for thousands of years (Yamamoto et al., 2015; Frölicher et al., 2020).

Sea ice: The Arctic sea ice area for September has decreased from 6.23 to 3.76 million km^2 and for March from 14.52 to 13.42 million km^2 between 1979-1988 and 2010-19 (Section 2.3.2.1.1). There is *high confidence* that sea ice in the Arctic will further decrease in the future under all emission scenarios (Section 9.3.1.1). In contrast, there is no clear observed trend in the Antarctic sea ice area over the past few decades and there is *low confidence* of future changes therein (Section 9.3.1.1). The duration of the summer season in the Arctic has increased by 5 to 20 weeks between 1979 and 2013, with a significant trend ranging from 5 to 17 days/decade for earlier spring retreat and from 5 to 25 days/decade for later fall advance, with consequences for Arctic marine mammals (AMMs) due to sea ice habitat loss (Laidre et al., 2015). The Arctic is projected to be ice-free more often during summer under 2°C global warming compared to 1.5°C global warming (Section 9.3.1.1; see also Section 12.4.9 and Section 4.4.2.1), opening new shipping lanes for international commerce (Valsson and Ulfarsson, 2011) and lengthening the season for offshore resource extraction (Schaeffer et al., 2012). Iceberg numbers are expected to increase as a result of global warming, forming an elevated hazard to shipping and offshore facilities (Bigg et al., 2018).

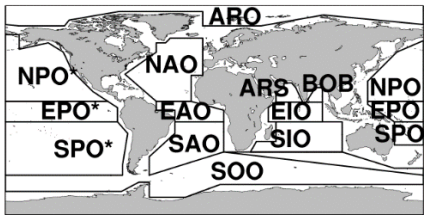
It is *virtually certain* that global mean SST will continue to increase throughout the 21st century, resulting in the exceedance of numerous hazard thresholds relevant to marine ecosystems (*medium confidence*). Marine heatwaves day are projected to increase in global oceans with a larger increase in the tropical ocean and Arctic Ocean (*high confidence*). It is *virtually certain* that upper ocean stratification will continue to increase in the 21st century. Future Ocean warming will *very likely* assist the development of both anoxic and hypoxic zones, with such reductions of oxygen expected to persist for thousands of years. Future projections also indicate freshening of the Pacific, Southern and Indian Oceans and a saltier Atlantic Ocean (*medium confidence*).

The assessed direction of change in climatic impact-drivers for open and deep ocean regions and associated confidence levels are illustrated in Table 12.10, following the AR6 WGI ocean reference regions as proposed by the Atlas (Figure Atlas.2b).

[START TABLE 12.10 HERE]

Table 12.10: Summary of confidence in direction of projected change in climatic impact-drivers in open and deep ocean regions, representing their aggregate characteristic changes for mid-century for scenarios RCP4.5, SSP3-4.5, SRES A1B, or above within each AR6 region (defined in Chapter 1), approximately corresponding (for CIDs that are independent of sea-level rise) to global warming levels between 2°C and 2.4°C (see 12.4 for more details of the assessment method). The table also includes the assessment of observed or projected time-of-emergence of the CID change signal from the natural inter-annual variability if found with at least *medium confidence* in Section 12.5.2.

ACCEPTED VERSION SUBJECT TO FINAL EDITS



Region	Mean Ocean Temperature	Marine Heatwave	Ocean acidity	Salinity	Dissolved Oxygen	Sea Ice
Arctic Ocean (ARO)	●		○	○	○	●
South Pacific Ocean (SPO)	●		○	○	●	
Equatorial Pacific Ocean (EPO)	●		○		●	
North Pacific Ocean (NPO)	●		○	○	●	
South Atlantic Ocean (SAO)	●		○	○	○	
Equatorial Atlantic Ocean (EAO)	●		○		○	
North Atlantic Ocean (NAO)	●		○	○	○	
Equatorial Indian Ocean (EIO)	●		○	○	○	
South Indian Ocean (SIO)	●		○	○	○	
Arabian Sea (ARS)	●		○		○	
Bay of Bengal (BOB)	●		○	○	○	
Southern Ocean (SOO)	●		○	○	●	

Climatic Impact-Driver

● Already emerged in the historical period (*medium to high confidence*)
○ Emerging by 2050 at least in Scenarios RCP8.5/SSP5-8.5 (*medium to high confidence*)
○ Emerging after 2050 and by 2100 at least in Scenarios RCP8.5/SSP5-8.5 (*medium to high confidence*)

Key
High confidence of decrease
Medium confidence of decrease
Low confidence in direction of change
Medium confidence of increase
High confidence of increase
Not broadly relevant

[END TABLE 12.10 HERE]

12.4.9 Polar terrestrial regions

Several recent climate assessments on polar regions describe robust patterns of recent and future climatic changes driving impacts and risk for polar environmental, societal, and economic assets, including the IPCC SROCC (Meredith et al., 2019), the Report on Snow, Water, Ice and Permafrost in the Arctic (AMAP, 2017b), and national assessments for the United States (Markon et al., 2018) and Canada (Derksen et al., 2018). This section examines Greenland and Iceland, the Russian Arctic, Antarctica, and the arctic portions of Northern Europe and North America (Figure 1.18c).

12.4.9.1 Heat and cold

Mean air temperature: Atlas.11.2 shows *high confidence* in warming of the Arctic in observations and projections, measuring among the fastest-warming places at more than twice the global mean, with substantially higher temperature increases in the cold season (see also AMAP, 2017; Meredith et al., 2019). Atlas.11.1 assessed *very likely* warming in observations of West Antarctica from 1957-2016, but *limited evidence* of mean air temperature change across East Antarctica even as there is *high confidence* in future warming across the continent (Meredith et al., 2019) (Figures Atlas.32, Atlas.33).

Extreme heat, cold spell and frost: Ecosystem and societal temperature thresholds in polar regions often reflect lower tolerance to heat and higher tolerance to cold. Extreme heat events have increased around the Arctic and Iceland since 1979, including increases in cold season warm days and nights, melt days, and Arctic winter warm events (T>-10°C) as well as decreases in cold days and nights (Mernild et al., 2014; Matthes et al., 2015; Vikhamar-Schuler et al., 2016; Graham et al., 2017; Sui et al., 2017; Dobricic et al., 2020; Peña-Angulo et al., 2020). Heatwaves causing high temperature records have been recently documented in West and East Antarctica (Wille et al., 2019; Robinson et al., 2020). There is *high confidence* that polar amplification will drive increases in Arctic heat extremes as well as continuing declines in the

ACCEPTED VERSION SUBJECT TO FINAL EDITS

magnitude and frequency of cold extremes (Matthes et al., 2015; Kharin et al., 2018), although dynamical effects will still bring substantial cold air anomalies over the Arctic (Wu and Francis, 2019). There is *medium confidence* for equivalent changes in extreme heat in Antarctica based primarily on higher mean temperatures, with Lee et al. (2017) projecting more than 50 additional degree days above freezing (2098 RCP8.5 vs. 2014) over parts of the Antarctic Peninsula but smaller changes over mainland Antarctica.

12.4.9.2 Wet and dry

Mean precipitation: Atlas.11.2 indicated *medium confidence* in observed increases in Arctic precipitation with the largest rises in the cold season. Antarctic precipitation showed no significant overall trend since the 1970s, with a positive trend over the 20th century (Atlas.11.1, 9.4.2.1). Increases in Arctic and Antarctic precipitation during the 21st century are *very likely* with projected percentage increases that are much higher than most sub-polar regions of the world (Figure Atlas.32).

Floods and heavy precipitation: Observations and model projections indicate *high confidence* in increasing Arctic river runoff in response to increasing total precipitation (Box et al., 2019; Durocher et al., 2019; Meredith et al., 2019) with a shift toward earlier meltwater flooding (AMAP, 2017b). Higher Arctic precipitable water totals are also connected with observed increases in heavy precipitation and convective activity (*high confidence*) (Ye et al., 2015; Kharin et al., 2018; Chernokulsky et al., 2019). Higher flood magnitudes are also driven by future increases in rain-on-snow event days, amounts, and runoff, which are more significant in the Arctic than in mid-latitudes (where seasonal snow cover is often further reduced) (AMAP, 2017b; Il Jeong and Sushama, 2018).

Landslide and snow avalanche: There is a growing number of studies on mass movements in polar regions. Although there is *low confidence* in widespread observational trends for landslides or snow avalanches, a rise in the number of future landslides is supported by strong links to increases in heavy precipitation, glacier retreat, and thawing of ice-rich permafrost that can lead to retrogressive thaw slumps in Arctic regions (Kokelj et al., 2015; Derksen et al., 2018; Lewkowicz and Way, 2019; Patton et al., 2019; Ward Jones et al., 2019) (Section 2.3.2.5).

Aridity and drought: Recent decades have seen a general decrease in Arctic aridity with projections indicating a continuing trend toward reduced aridity (*high confidence*) as increased moisture transport leads to higher precipitation, humidity and streamflow (Meredith et al., 2019) and a corresponding decrease in dry days (Khlebnikova et al., 2019b). There is *low confidence* overall of recent or projected drought changes in polar regions (Section 11.9) even as increasing evidence shows that drainage from permafrost thaw, higher potential evapotranspiration, and changing seasonal patterns of melt have caused lake reduction and soil moisture deficits in several areas that match with projections of future drought increase despite overall precipitation increases (Andresen and Lougheed, 2015; Bring et al., 2016; Spinoni et al., 2018a; Feng et al., 2019; Finger Higgens et al., 2019).

Fire weather: Fire season lengthened from 1979-2015 over Arctic portions of North America (Jain et al., 2017), corresponding also to a 1975-2015 increase in lightning-ignited fires in Northwestern North America (Girardin et al., 2013; Veraverbeke et al., 2017). Abatzoglou et al. (2019) climate model simulations project significant fire weather index increases in boreal forests of Arctic Europe, Arctic Russia and Northeast North America (*medium confidence*). Trends toward more frequent fires in tundra regions are expected to continue, driven in particular by increasing potential evapotranspiration and changes in vegetation (*high confidence*) (Hu et al., 2015; AMAP, 2017b; Young et al., 2017).

12.4.9.3 Wind

Mean wind speed and severe storm: There is *medium confidence* of mean wind decrease over the Russian Arctic, Greenland and Iceland and Arctic Northeast North America (Karnauskas et al., 2018a; Jung and Schindler, 2019), but *low confidence* of changes in the other Arctic regions and Antarctica. Bintanja et al.

ACCEPTED VERSION SUBJECT TO FINAL EDITS

(2014) projected that a strengthening of the Southern Annular Mode would decrease easterlies along Antarctica's coasts with only small changes in katabatic winds (although this effect may diminish with stratospheric ozone recovery). In contrast, Gorter et al. (2014) regional climate model projections indicated a reduction in mean winds over the interior of Greenland by RCP4.5 2100 while coastal winds increase. Reanalysis data and climate models indicate few coherent regional trends of polar cyclone frequency or relationships with cyclone depth and size (Akperov et al., 2018, 2019; Day and Hodges, 2018; Zahn et al., 2018).

12.4.9.4 Snow and ice

Snow: Atlas.11.1 identified *likely* increases in surface mass balance (driven by snowfall) across Antarctica in the 20th century (*medium confidence*). In the Arctic, overall snow extent and seasonal duration are projected to continue recent declines (*high confidence*), although mid-winter snowpack increases in some of the coldest and high-elevation locations given higher precipitation totals (*medium confidence*) (Bring et al., 2016; Danco et al., 2016; AMAP, 2017; Meredith et al., 2019) (9.5.3; Atlas.11.2; Atlas.9). Higher temperatures result in a higher percentage of Arctic precipitation falling as rain (particularly in fall and spring) (*high confidence*), with most land regions (outside of Greenland and Antarctica) becoming dominated by rainfall (more than 50% of total precipitation) by RCP8.5 2100 (Bintanja and Andry, 2017; Irannezhad et al., 2017).

Glacier and ice sheet: Section 9.5.1 and Section 2.3.2.3 found that glaciers have lost mass in all polar regions since 2000 (*high confidence*), and Section 9.4 assessed *high confidence* in Greenland ice sheet mass losses since 1980 and Antarctic Ice Sheet losses since 1992 (dominated by West Antarctica with losses in parts of East Antarctica in the past two decades). New simulations from GlacierMIP (Marzeion et al., 2020) indicate glaciers in Iceland will lose 31 ± 35%, 41 ± 46% and 53 ± 45% of their mass in 2015 by the end of the century for RCP2.6, RCP4.5 and RCP8.5 scenarios, respectively. Marzeion et al. (2020) projected mass losses (*high confidence*) for those same scenarios in the Greenland Periphery: 22 ± 23%, 29 ± 26%, and 42 ± 28%; Svalbard: 35 ± 34%, 50 ± 36%, and 66 ± 35%; Russian Arctic: 26 ± 26%, 38 ± 28%, and 52 ± 30%; Northern Arctic Canada: 12 ± 13%, 18 ± 12%, and 27 ± 18%; Southern Arctic Canada: 23 ± 27%, 33 ± 29%, and 48 ± 32%; and Antarctic Periphery: 7 ± 12%, 13 ± 10%, and 16 ± 19%. Areas with receding glaciers are also potentially vulnerable to glacial lake outburst floods (Harrison et al., 2018).

Permafrost: Observations from recent decades (assessed in Section 9.5.2 and Section 2.3.2.5) show increases in permafrost temperature (*very high confidence*) and active layer thickness (*medium confidence*) across the Arctic (AMAP, 2017; Markon et al., 2018; Biskaborn et al., 2019; Derksen et al., 2019; Farquharson et al., 2019; Meredith et al., 2019; Romanovsky et al., 2020). Section 9.5.2 noted that observations of active layer thickness in Antarctica are too limited to assess long-term trends (see also Biskaborn et al., 2019; Hrbáček et al., 2018). Future projections indicate continuing increases in permafrost temperature and active layer thickness with loss of permafrost across the Arctic (Section 9.5.2). Streletskiy et al. (2019) noted that changes to Russian permafrost temperature and active layer thickness are most pronounced in areas where permafrost is continuous (underlying >90% of landmass). CMIP5 analyses by Slater and Lawrence (2013) projected that, by RCP8.5 2100, shallow (<3 m) permafrost would be most probable only in portions of the Canadian Arctic Archipelago and the Russian Arctic coastal and eastern upland regions.

Sea ice: Consistent with the SROCC (Meredith et al., 2019), Section 9.3.1 and Section 2.3.2.1.1 assess *very high confidence* that Arctic sea ice thickness, extent, and average age have significantly decreased over the past four decades with largest declines in September (when sea ice is at an annual minimum). Declines in landfast ice are most rapid in the Laptev Sea (Selyuzhenok et al., 2015), are breaking perennial landfast ice blocking ocean channels ('ice plugs') in the Canadian Archipelago (Pope et al., 2017), and declining in the cold season by 7% decade^{-1} across the Arctic (1976-2007) (Yu et al., 2014). Observed trends and projections suggest that perennial sea ice is being replaced by thin, seasonal ice, although multi-year ice will persist above the Canadian Archipelago and drift into sea transportation lanes (Howell et al., 2016; Derksen et al., 2018). Trends from 1979-2013 show slightly earlier spring melt for Arctic sea ice, but substantially-delayed

ACCEPTED VERSION SUBJECT TO FINAL EDITS

fall freeze up and a melt season lengthened by more than 3 days decade^{-1} off northern Alaska and Canada with the exception of portions of the Bering Sea (Parkinson, 2014; Stroeve et al., 2014). Section 9.3.2 assessed *low confidence* in long-term trends in sea ice extent or thickness near Antarctica.

Future declines in Arctic sea ice are *virtually certain*, although there is *low confidence* in declines of Antarctic sea ice given dynamical processes in the Southern Ocean and the recovery of stratospheric ozone (Section 9.3; Meredith et al., 2019). Projections of an 'ice-free' Arctic vary depending on definitions representing transportation needs, however Laliberté et al. (2016) noted that the median of 42 CMIP5 models projected <5% sea ice for the month of September by 2050, with equivalent conditions for the entirety of the August-October period by 2090. Section 9.3.1 assessed *high confidence* that practically ice-free conditions (<1 million km^2 in the September mean) would *likely* first appear before 2050 even under strong mitigation scenarios (Sigmond et al., 2018; Stroeve and Notz, 2018; Notz and SIMIP, 2020).

Lake and river ice: There is *high confidence* in observations of significant declines in seasonal ice cover thickness and duration over most Arctic lakes, with many lakes projected to lose more than month of ice cover by mid-century (*medium confidence*) (Meredith et al., 2019; Sharma et al., 2019). Some lakes that previously froze to the bottom ('bedfast') now maintain liquid bottom water year round, and others shift from perennial to seasonal ice cover (Surdu et al., 2016; Engram et al., 2018). Yang et al. (2020) identified a decline in Arctic cold-season river ice extent in satellite observations (particularly in Alaska) and projected reductions in average Northern Hemisphere seasonal river ice duration of 6.10 ± 0.08 days per degree global surface air temperature.

Heavy snowfall and ice storm: There is *limited evidence* of changes in heavy snowfall due to competing influences of shortened snowfall seasonality with more intense (and larger overall) precipitation in the Arctic. Episodic heavy snowfall trends in Antarctica are difficult to separate from large interannual variability (*limited evidence*) (Gorodetskaya et al., 2014, Turner et al., 2020). *Limited evidence* also hinders clear signals in ice storms, although warming shifts the freezing line (around which ice storms occur) poleward and upslope (Bintanja and Andry, 2017). Groisman et al. (2016) used 40 years of observations to identify an increase of freezing rain events in Norway, North America, and Eastern and Western Russia. Increases in wintertime rainfall have led to more frequent development of difficult wildlife and livestock grazing conditions as basal ice conditions coat the ground below snowpack (Peeters et al., 2019).

12.4.9.5 Coastal and oceanic

Relative sea level: Satellite altimetry and tide data show that relative sea levels (with glacial isostatic adjustment) are rising in Arctic Europe and Northwest North America, declining in portions of Southern Alaska and Arctic Northeast North America and no clear trend in Greenland and Arctic Russia (Sweet et al., 2018; Rose et al., 2019), which is broadly consistent with findings in Oppenheimer et al. (2019). Areas with low or negative change have substantial land uplift counteracting the global mean sea level trend (Greenan et al., 2018; Sweet et al., 2018; Madsen et al., 2019). SROCC projections indicate *high confidence* in future rises in relative sea level for all Arctic regions other than areas of substantial land uplift in Northeastern Canada, the west coast of Greenland, and narrow portions of West Antarctica (Oppenheimer et al., 2019).

Coastal flooding and erosion: Higher sea levels and reduced coastal sea ice protection will increase future extreme sea levels in the Arctic (*high confidence* for Arcitc NEU, RAR, and Arctic NWN; *medium confidence* for GIC and Arctic NEN given glacial isostatic adjustment). Vousdoukas et al. (2018) project that the current 1:100 yr extreme total water level would have median return periods of 1:20 yrs – 1:50 yrs by 2050, increasing to 1:5 yrs – 1:20 yrs by 2100 under RCP4.5 along nearly the entire Arctic coastline by 2100 (excluding GIC for which projections are not available). Projections for RCP8.5 indicate that the present day 1:100 yr ETWL would have median return periods of 1:10 yrs – 1:50 yrs 2050 and would occur once every 5 years (or more frequently). Arctic coastal erosion is also expected to increase with climate change (*medium confidence*; *high agreement* but *limited evidence* of projections), accelerated in some regions by subsurface permafrost thaw and increased wave energy (Gibbs and Richmond, 2015; Fritz et al., 2017; Oppenheimer et al., 2019; Casas-Prat and Wang, 2020). A longer ice-free season for the RCP8.5

ACCEPTED VERSION SUBJECT TO FINAL EDITS

2080s is projected to help drive more than 100 m of shoreline retreat in Northwest North America Arctic coastal communities (Melvin et al., 2017; Greenan et al., 2019; Magnan et al., 2019). Assessment of coastal flooding and erosion changes in Antarctica are limited by a lack of studies.

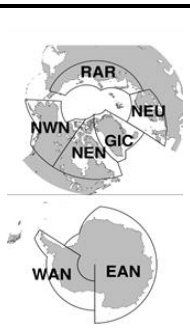
Marine heatwave: Recent years have seen marine heatwaves and increasing extreme coastal SSTs in Arctic systems (Lima and Wethey, 2012; Collins et al., 2019; Frölicher, 2019). Projections show increases in marine heatwave intensity, frequency, and duration will be larger over the Arctic Ocean than mid-latitude oceans due in part to low interannual variability under current sea ice (*high confidence*). Frölicher et al. (2018) used 12 CMIP5 models to project median MHW days increasing about 25-fold and 50-fold at the 2°C and 3.5°C GWLs in response to mean ocean warming and sea ice loss, and the smallest global changes still being increases in the Southern Ocean around Antarctica (see also Cross-chapter Box 9.1).

Climate change has caused and will continue to induce enhanced warming trend, increasing heat-related extremes and decreasing cold spells and frosts in the Arctic (*high confidence*), with similar changes in Antarctica but *medium confidence* for extreme heat increases and West Antarctic frost change decreases and *low confidence* for cold spell changes and East Antarctica frost. The water cycle is projected to intensify in polar regions, leading to more rainfall, higher river flood potential and more intense precipitation (*high confidence*). Projections indicate reductions in glaciers and sea ice at both poles, with enhanced permafrost warming, decreasing permafrost extent, and decreasing seasonal duration and extent of snow cover in the Arctic (*high confidence*) even as some of the coldest regions will see higher total snowfall given increased precipitation (*medium confidence*). Projections indicate relative sea level rises in Polar regions *(high confidence)*, with the exception of regions with substantial land uplift including Northeast North America *(high confidence)*, Western Greenland, the Northern Baltic Sea, and portions of West Antarctica. Higher sea levels also contribute to *high confidence* for projected increases of Arctic coastal flooding and higher coastal erosion (aided by sea ice loss) (*medium confidence*) with lower confidence for those CIDs in regions with substantial land uplift (Arctic Northeast North America and Greenland).

[START TABLE 12.11 HERE]

Table 12.11: Summary of confidence in direction of projected change in climatic impact-drivers in the polar regions, representing their aggregate characteristic changes for mid-century for scenarios RCP4.5, SSP3-4.5, SRES A1B, or above within each AR6 region (defined in Chapter 1), approximately corresponding (for CIDs that are independent of sea-level rise) to global warming levels between 2°C and 2.4°C (see 12.4 for more details of the assessment method). The table also includes the assessment of observed or projected time-of-emergence of the CID change signal from the natural inter-annual variability if found with at least *medium confidence* in Section 12.5.2. Note that the Arctic portions of the NEU, NEN, and NWN differ from the full AR6 regions assessed in the Europe and North America sections above (see also Figure 1.18c).

ACCEPTED VERSION SUBJECT TO FINAL EDITS



Region	Heat and Cold				Wet and Dry								Wind				Snow and Ice						Coastal & Oceanic					Other		
	Mean air temperature	Extreme heat	Cold spell	Frost	Mean precipitation	River flood	Heavy precipitation and pluvial flood	Landslide	Aridity	Hydrological drought	Agricultural and ecological drought	Fire weather	Mean wind speed	Severe wind storm	Tropical cyclone	Sand and dust storm	Snow, glacier and ice sheet	Permafrost	Lake, river and sea ice	Heavy snowfall and ice storm	Hail	Snow avalanche	Relative sea level	Coastal flood	Coastal erosion	Marine heatwave	Ocean acidity	Air pollution weather	Atmospheric CO_2 at surface	Radiation at surface
Greenland and Iceland (GIC)	●	●	●		○		○					2,3					1						5				○		●	
Arctic Northern Europe (aNEU)	●	●	●		○		○					2,3					1						6		7		○		●	
Russian Arctic (RAR)	●	●	●		○		○					2,3					1,4						○		7		○		●	
Arctic Northwest North America (aNWN)	●	●	●		○							2,3					1						○		7		○		●	
Arctic Northeast North America (aNEN)	●	●	●		○							2,3					1,4										○		●	
West Antarctica (WAN)	●																1,4										○		●	
East Antarctica (EAN)	●																						○				○		●	

1. Snow may increase in some high elevations and during the cold season and decrease in other seasons and at lower elevations
2. Higher confidence in southern regions and lower toward north
3. Higher confidence in increase for some climatic impact-driver indices during summertime
4. Glaciers decline even as some regional snow climatic impact-driver indices increase
5. Decreasing in west and increasing in east
6. Except for Northern Baltic Sea coasts where relative sea levels fall
7. Along sandy coasts and in the absence of additional sediment sinks/sources or any physical barriers to shoreline retreat.

● Already emerged in the historical period (*medium to high confidence*)
○ Emerging by 2050 at least in Scenarios RCP8.5/SSP5-8.5 (*medium to high confidence*)
○ Emerging after 2050 and by 2100 at least in Scenarios RCP8.5/SSP5-8.5 (*medium to high confidence*)

Key
High confidence of decrease
Medium confidence of decrease
Low confidence in direction of change
Medium confidence of increase
High confidence of increase
Not broadly relevant

[END TABLE 12.11 HERE]

12.4.10 Specific zones and hotspots

This section focuses on CIDs affecting specific zones heightened vulnerability and coherent characteristics that cut across traditional continental regions (see also Section 12.3). It is designed to match the structure of the cross-chapter papers in the WGII report, although polar regions were addressed in more extensive detail in 12.4.8 and 12.4.9 and the Mediterranean Region will not be handled separately given that its climatic impact-drivers are discussed in Sections 12.4.1 and 12.4.5 as well as in Cross-Chapter Box 10.3.

12.4.10.1 Hotspots of biodiversity (land, coasts and oceans)

Hotspots of biodiversity are defined by the AR6 WGII as "geographic areas with exceptionally high richness of species, including rare (endemic) species" (WGII Cross-Chapter Paper 1). The AR6 assessment is based on 238 distinctive regions often called the "Global 200 ecoregions" (Olson and Dinerstein, 2002).

Mean temperature increase is a major climatic impact-driver for biodiversity hotspots, and it is *very likely* that it will affect all hotspot areas identified in the literature, at various rates in all climate scenarios, except those located in the North Atlantic where warming is uncertain (see Chapter 4). Terrestrial ecosystems will experience an enhanced warming compared to ocean ecosystems, because land temperatures are warming faster than ocean temperatures (Chapter 4). Marine ecoregions will experience ocean acidification and temperatures that increase faster in high latitudes (*high confidence*), but critical temperature and oxygen thresholds are projected to be crossed earlier (by mid-century RCP8.5) in tropical areas (Hughes et al., 2017a; Bruno et al., 2018). A warming trend is also expected for freshwater ecosystems, with different local magnitudes due to combined effects of groundwater system inertia as well as hydrology changes (Knouft and Ficklin, 2017). In tropical land areas, because interannual temperature variability is weak compared to changes, the temperature distribution range is *likely* to be shifted to a very different range in all projection scenarios, with unprecedented values relative to preindustrial. High climate velocities are particularly

ACCEPTED VERSION SUBJECT TO FINAL EDITS

noteworthy for biodiversity hotspots given complex ecosystem dynamics and niche climates not easily replicated under shifted geographies (Burrows et al., 2014; Halpern et al., 2015; Dobrowski and Parks, 2016). In some regions (Central Africa, Amazon, South East Asia) the mean temperature change is already beyond the normal range of variations as it has reached levels higher than 3 (and up to 6) times larger than the standard deviation of the interannual variations (Hawkins et al., 2020). Together with global warming, land and marine heat waves are *very likely* to increase in the future climate in biodiversity hotspots (Sections 12.4.1-12.4.7).

There is *low confidence* in broad patterns of future drying or wet trends across the land and freshwater biodiversity hotspots from the humid tropics, although drying trends have been detected and predicted in parts of the Amazon (Fu et al., 2013; Boisier et al., 2015). There is *medium confidence* (*limited evidence, high agreement*) that in several regions the length of the dry season has already increased and is projected to further increase in some parts of the Mediterranean, Amazonia and sub-Saharan Africa (S. Debortoli et al., 2015; Dunning et al., 2018; Hochman et al., 2018; Saeed et al., 2018). Longer dry seasons also extend the seasonal length and geographical extent of fire weather in all future scenarios (*medium confidence*) (Jolly et al., 2015; Abatzoglou et al., 2019).

In conclusion, biodiversity hotspots located around the world will each face unique challenges in climatic impact-drivers changes. However, heat, drought and length of dry season, wildfire weather, sea surface temperature and deoxygenation are relevant drivers to terrestrial and freshwater ecosystems, and have marked increasing trends.

12.4.10.2 Cities and settlements by the sea

Cities and settlements (C&S) by the sea are exposed to specific climate and climate change patterns and to compound coastal hazard risks (AR6 WGII Cross-chapter paper 2). AR5 WGII found that, in general, "urban climate change-related risks are increasing (including rising sea levels and storm surges, heat stress, extreme precipitation, inland and coastal flooding, landslides, drought, increased aridity, water scarcity, and air pollution)". Since AR5 a number of studies have been carried out to understand urban climate and its change. Box 10.3 identified a continuing strong role of the urban heat island in amplifying heat extremes in cities, although changes in the urban heat island are an order of magnitude smaller than projected localized warming trends (*very high confidence*).

Coastal cities' proximity to the sea somewhat mitigates the effect of urban heat islands (*high confidence*) (Salvati et al., 2017; Santamouris et al., 2017; Wang et al., 2018b; Martinelli et al., 2020). Cities and settlements by the sea typically experience higher humidity levels than inland regions, combining with heat to enhance heat stress and induce exceedance of critical heat stress thresholds for outdoor activities, with potential enhanced exposure to heat for informal settlements (Wang et al., 2019b). Such threshold exceedances are projected to increase for many coastal areas (*high confidence*), including the Persian Gulf where heat stress is projected to be extreme (Pal and Eltahir, 2016; Ahmadalipour and Moradkhani, 2018), and some low-lying areas in Europe such as the Po Valley and coastal Mediterranean areas (Coppola et al., 2021a) (Schwingshackl et al., 2021) (see also the heat stress index shown in Figure 12.4d-f).

Climate change related variations in oceanic drivers (e.g., relative sea level, storm surge, ocean waves), combined with tropical cyclones, extreme precipitation and river flooding, are expected to lead to more frequent and more intense coastal flooding and erosion (*very high confidence*) impacting C&S located especially in low elevation coastal zones and mega-deltas (Chan et al., 2012, 2018; Karymbalis et al., 2012; Hemer et al., 2013; Aerts et al., 2014; Neumann et al., 2015a; Ranasinghe, 2016; Hauer et al., 2016; Hinkel et al., 2018; Mavromatidi et al., 2018; Marcos et al., 2019) (See also Sections 12.3, 12.4.1-12.4.7 and 12.4.9). Coastal erosion and flooding also pose challenges to critical infrastructure such as roads, subway tunnels, electricity and phone networks, wastewater management plants and buildings (Grahn and Nyberg, 2017; Pregnolato et al., 2017). Compound flooding due to simultaneous storm surges and high river flows have been found to be increasingly frequent in several cities and/or low-lying areas in Europe and the U.S.A. (Wahl et al., 2015; Paprotny et al., 2018; Bevacqua et al., 2019; Ganguli and Merz, 2019) (*high confidence*).

ACCEPTED VERSION SUBJECT TO FINAL EDITS

Chapter 11 found that the frequency of such compound flood events is projected to increase (*high confidence*). In addition to sea level rise induced changes, many C&S by the sea are in regions where tropical cyclones are projected to become more intense and frequent (*high confidence*) (Section 11.7).

The SROCC report highlighted coastal settlements in the Arctic as being particularly exposed to several CID changes (Magnan et al., 2019). Enhanced waves due to extended season of sea ice retreat are projected to foster coastal flooding and erosion (Gudmestad, 2018; Casas-Prat and Wang, 2020) (Section 12.4.9). Climate change is also affecting sea ice quality and season length along coasts of the Arctic ocean where populations depend on sea ice for hunting or transportation (Pearce et al., 2015) (Section 12.4.9).

In summary, coastal cities and settlements are particularly affected by a number of climatic impact-drivers that have already changed and will continue to change whatever the emission scenario. These include increases in extreme heat, pluvial floods, coastal erosion and coastal flood (*high confidence*). Increasing relative sea level compounding with increasing tropical cyclone storm surge and rainfall intensity will increase the probability of coastal city flooding (*high confidence*). Arctic coastal settlements are particularly exposed to climate change due to sea ice retreat (*high confidence*).

12.4.10.3 Deserts and semi-arid areas

Drylands, which include hyper arid, arid, semi-arid and dry sub-humid areas (IPCC, 2019c), lie on all continents and cover 46% of the global land area and host over a third of the current population (Olsson et al., 2019) . Huang et al. (2016) found that aridity changes have helped expand dryland area by ~4% from 1948 to 2004, with the largest expansion of drylands occurring in semi-arid regions since the early 1960s. Section 4.5.1 assessed *high confidence* of a future poleward expansion of the Hadley cell, leading to a poleward shift of dryland areas in all scenarios considered. There is no evidence of a future global trend in aridification of drylands (IPCC, 2019a), but *high confidence* of aridification in some areas (Mediterranean, Central America, South Africa) (IPCC, 2019a) (see also Figure 12.4j-l). However, drivers of desertification largely include land cover changes and land use management, along with climate change (IPCC, 2019a).

Warming temperatures and extreme heat are major climatic impact-drivers with multiple potential impacts on societies, health, and habitability in semi-arid and arid regions that are already near physiological limits for outdoor activities. Semi-arid regions will *very likely* undergo a warming in all future scenarios (Chapter 4; Atlas) and *likely* undergo an increase in duration, magnitude and frequency of heatwaves (Chapter 11) (see also Figure 12.4a-c). It is *likely* that heat stress will be much more intense by the end of the century in many areas under all scenarios, such as deserts and semi-arid zones in Asia (Murari et al., 2015; Mishra et al., 2017b), Australia and Africa (Dosio et al., 2018; Guo et al., 2017; Schwingshackl et al., 2021; Xia et al., 2016; Zhao et al., 2015a), with consequences on labour productivity with respect to very heat-humidity conditions (see also Figure 12.4d-f).

Drought is another major climatic impact-driver for semi-arid areas, imposing major challenges on agriculture given existing water availability constraints (Kusunose and Lybbert, 2014; Barlow et al., 2016; Wolski et al., 2018). Over the period 1961-2013, the annual area of drylands in drought has increased, on average by slightly more than 1% per year, with large inter-annual variability (Olsson et al., 2019). In general, droughts have increased in several arid and semi-arid areas over the last decades (*medium confidence*), and are *likely* to increase in the future as indicated by a number of indices calculated from climate (Liu et al., 2018b; Zkhiri et al., 2019; Coppola et al., 2021b; Driouech et al., 2021)(see also Figure 12.4j-l).

Deserts and semi-arid areas are prone to dust storms, which can drive impacts on health and several other sectors (Zhang et al., 2016b; Tong et al., 2017). SRCCL indicated that the evolution of dust under climate change is uncertain (Mirzabaev et al., 2019), and there is a lack of evidence and agreement of a change in their frequency or intensity so far in most regions (Sections 12.4.1-12.4.9). Model projections of future changes in dust are hindered by the uncertainties in future regional wind and precipitation as the climate warms (Evan et al., 2016), in the effect of CO_2 fertilization on source extent (Huang et al., 2017), and in the

ACCEPTED VERSION SUBJECT TO FINAL EDITS

impact of human activities upon the land surface (Ginoux et al., 2012) (see Chapter 10). Projected trends on dust storms and dust loads in deserts and semi-arid areas vary from region to region. Dust loadings are expected to decrease over most of the Sahara and Sahel (*low confidence*) (Section 12.4.1), increase over Mexico and Southwestern U.S. (*medium confidence*) (Section 12.4.6), and there is *low confidence* of a future trend due to climate change in other continents (Sections 12.4.2-12.4.5).

In conclusion, desert and semi-arid areas are strongly affected by climatic impact-drivers such as extreme heat, drought and dust storms. Heat hazards are *very likely* increasing in all future climate scenarios, but broadly consistent desert and semi-arid region changes for other climatic impact-drivers' future evolution remains uncertain.

12.4.10.4 Mountains

Mountains cover about 30% of the land areas on Earth (not counting Antarctica) and deliver a number of vital services to humanity (IPCC, 2019b) (WGII Cross-chapter paper 5). Climate change in high mountains was addressed in the SROCC, which emphasized changes in several climatic impact-drivers, such as: an observed general decline in low-elevation snow cover, glaciers and permafrost (*high confidence*), which induced changes in natural hazards such as decrease in slope stability (*high confidence*), changes to the frequency of glacial lake outbursts (*limited evidence*), and climate effects on other hazards (avalanche, rain-on-snow floods) with various degrees of confidence (Hock et al., 2019).

There is a growing body of literature indicating elevation-dependent warming (EDW; different rates of warming by altitude although not necessarily increasing with altitude) in several mountain regions but not globally (Hock et al., 2019; Pepin et al., 2019; Ahmed et al., 2020; Li et al., 2020a; Williamson et al., 2020; You et al., 2020; Micu et al., 2021). Statistically significant elevational enhancement to long-term trends in maximum near-surface air temperatures and diurnal temperature range were observed in southern central Himalaya and in the Swiss Alps (Rottler et al., 2019; Thakuri et al., 2019). Aguilar-Lome et al. (2019) reported that winter daytime land surface temperatures in the Andean region between 7°S and 20°S show the strongest trends at higher elevations: +1.7°C per decade above 5000 masl. Palazzi et al. (2019) identified changes in albedo and downward thermal radiation as key drivers of EDW according to the simulation outputs of a high-spatial resolution model in three important mountainous areas: the Colorado Rocky Mountains, the Greater Alpine Region and the Himalayas-Tibetan Plateau, but mechanisms for EDW remain complex (Hock et al., 2019). Warming is also affecting mountain lake surface temperatures, increasing probabilities of ice-free winters and the frequency and duration of "lake heatwaves" (O'Reilly et al., 2015; Woolway et al., 2020, 2021) (*high confidence*) with a high variability from lake to lake.

EDW could speed up the observed, rapid upward shifts of the Freezing Level Height (FLH) in several mountainous regions of the world and lead to faster changes in the snowline, the glacier equilibrium-line altitude and the snow/rain transition height (*high confidence*). In the Indus, Ganges and Brahmaputra basins in Asia, the FLH is projected to rise at a rate of 4.4 to 10.0 m yr^{-1} under RCP8.5 (Viste and Sorteberg, 2015). In the Argentinian Andes, FLH is projected under RCP8.5 to move up more than twice as much by 2070 as during the entire Holocene under the worst case scenario (Drewes et al., 2018). On the western slope of the subtropical Andes (30°-38°S) in central Chile, the mean value of the free tropospheric height of the 0°C isotherm under wet conditions is projected to be close to or higher than the upper quartile of the distribution in the current climate, towards the end of the century and under RCP8.5 (Mardones and Garreaud, 2020). In the Alps and the Pyrenees, Spandre et al. (2019) projected a rise in the natural snow elevation of 200 to 300 m and 400 to 600 m by mid-century under RCP2.6 and RCP8.5, respectively. In the same region, the environmental equilibrium-line altitude is projected to exceed the maximum elevation of 69%, 81% and 92% of the glaciers by the end of the century under RCPs 2.6, 4.5 and 8.5, respectively (Žebre et al., 2021).

Orographic effects enhance convection and stratiform heavy precipitation (due to uplift) and make mountains prone to extreme precipitation events. These events are projected to increase in major mountainous regions (Alps, parts of the Andes, British Columbia, Northwest North America, Calabria, Carpathian, Hindu-Kush-Himalaya, Rockies, Umbria; *medium to high confidence* depending on location),

ACCEPTED VERSION SUBJECT TO FINAL EDITS

with potential cascading consequences of floods, landslides and lake outbursts in mountainous areas in all scenarios (*medium confidence*) (Geertsema et al., 2006; Kim et al., 2015; Gaire et al., 2015; Kharuk et al., 2016; Syed and Al Amin, 2016; Ciabatta et al., 2016; Gariano and Guzzetti, 2016; Jurchescu et al., 2017; Rajczak and Schär, 2017; Cloutier et al., 2017; Gądek et al., 2017; Alvioli et al., 2018; Schlögl and Matulla, 2018; Coe et al., 2018; Chen et al., 2019a; Handwerger et al., 2019; Hock et al., 2019; Patton et al., 2019; Vaidya et al., 2019; Kirschbaum et al., 2020; Coppola et al., 2021b) (Sections 12.4.1-12.4.9, Chapter 11).

Declines in low-elevation snow depth and seasonal extent are projected for all SSP-RCPs (see Sections 12.4.1-6), along with reductions in mountain glacier surface area, increases in permafrost temperature, decreases in permafrost thickness, changes in lake and river ice, changes in the amount and seasonality of streamflows and hydrologic droughts in snow-dominated and glacier-fed river basins (e.g., in Central Asia; Sorg et al., 2014; Reyer et al., 2017) (*medium confidence*), and decreases in the stability of mountain slopes and snowfields. Glacier recession could lead to the creation of new glacial lakes in places like the Himalaya-Karakoram region; (Linsbauer et al., 2016) and in Alaska and Canada (Carrivick and Tweed, 2016; Harrison et al., 2018) (*medium confidence*). With increasing temperature and precipitation these can increase the occurrence of glacier lake outburst floods and landslides over moraine-dammed lakes (Carey et al., 2012; Rojas et al., 2014; Iribarren Anacona et al., 2015; Cook et al., 2016; Haeberli et al., 2017a; Kapitsa et al., 2017; Narama et al., 2018; Wilson et al., 2018; Drenkhan et al., 2019; Wang et al., 2020a) (*high confidence*).

In conclusion, mountains face complex challenges from specific climatic impact-drivers drastically influenced by climate change: regional elevation-dependent warming (*high confidence*), low-to-mid-altitude snow cover and snow-season decrease even as some high elevations see more snow (*high confidence*), glacier mass reduction and permafrost thawing (*high confidence*), and increases in extreme precipitation and floods in most parts of major mountain ranges (*medium confidence*).

12.4.10.5 Tropical forests

Tropical forests, which are among the world's most biologically diverse ecosystems, are essentially located in Central and South America, Africa and South-East Asia. AR5 and SR1.5 indicated several specific climatic impact-driver changes that are particularly important to tropical forests: mean temperature increase, long-term drying trends (including shifts in the length of the dry season), prolonged drought, wildfires and surface CO_2 increase for inland forests (IPCC, 2013, 2018). SRCCL assessed an enhanced risk and severity of wildfires in tropical rainforests (*high confidence*), but fires are not only natural and also due to deforestation and other human influences (IPCC, 2019a).

Temperature is rising in all tropical regions covered with forests and will *very likely* continue to rise, reaching levels unprecendented in recent decades as the temperature trends rapidly emerge from weak historical interannual variability (12.4.1-4; 12.5.2) (see Chapter 4, Atlas).

Regional patterns of increasing drought or unusual wet and dry periods are predicted with agreement over many climate models such as over the Amazon basin (Boisier et al., 2015; Duffy et al., 2015; Zulkafli et al., 2016; Coppola et al., 2021b). There is *medium confidence* (*limited evidence, high agreement*) that in several tropical-forest regions the dry season length has increased (Amazonia, West Africa) (Fu et al., 2013; S. Debortoli et al., 2015; Saeed et al., 2017; Dunning et al., 2018; Wadsworth et al., 2019), and *low confidence* (*limited evidence*) that deforestation influences the shift in the onset of the wet season in South Amazonia (Leite-Filho et al., 2019). In contrast, the wet season is increasing in Northern Australia Tropical Forests (Catto et al., 2012).

Tropical forests typically reach peak fire weather conditions in the dry season (Taufik et al., 2017), in particular during long-lived droughts (Brando et al., 2014; Marengo et al., 2018), with consequences on tree mortality, forest and carbon sink loss (Brando et al., 2019), and on the hydrological cycle in South America (Martinez and Dominguez, 2014; Espinoza et al., 2020). Observations and reanalyses over the past 3-4 decades, combined into fire risk indices, show that the fire weather season length has been increasing by about 20% globally (Jolly et al., 2015), and this index exhibits particularly high trend values over tropical

ACCEPTED VERSION SUBJECT TO FINAL EDITS

forest areas of South and Central America and Africa. There is generally *low confidence* in future projections of general fire weather risk evolution in tropical forests and evolutions depend on the region (Abatzoglou et al., 2019). Over the Amazon basin the fire risk increase is emerging well before 2050 while for other equatorial forests no significant evolution is found. In Savanna areas the risk increase is found to be more general.

In conclusion, most tropical forests are challenged by a mix of emerging warming trends that are particularly large in comparison to historical variability (*medium confidence*). Water cycle changes bring prolonged drought, longer dry seasons, and increased fire weather to many tropical forests, with plants also responding to CO_2 increases (*medium confidence*).

12.5 Global perspective on climatic impact-drivers

12.5.1 A global synthesis

Section 12.4 assessed changes in climatic impact-drivers by region, primarily based on a large number of local, regional-scale studies (even though global studies are also used). This section presents an assessment of changes in CID at the global scale. It is based on both a bottom-up synthesis of the results in 12.4, and a top-down assessment from global-scale studies undertaken here. Box 12.1 summarizes global-scale CIDs with levels of warming.

Global-scale studies use similar indices of climatic impact-drivers across space, although these indices may not be always those used at the local or regional scale. Most published global-scale studies concentrate on single sectors or climatic impact-drivers, but some take a multi-sectoral perspective (e.g., Warszawski et al., 2014; Arnell et al., 2016; Mitchell et al., 2017; O'Neill et al., 2018; Arnell et al., 2019a; Schleussner et al., 2016; Betts et al., 2018; Byers et al., 2018; Mora et al., 2018; O'Neill et al., 2018; Zscheischler et al., 2018). Only a few published global-scale studies (e.g., Coppola et al., 2021; Schwingshackl et al., 2021) have used CMIP6 scenarios to date. Box 12.1 summarizes global-scale CIDs with levels of warming.

All regions will experience, before 2050, increased warming, an increase of extreme heat and a decrease in cold spells, regardless of the emissions trajectory (*high confidence*). Tropical regions, but also mid latitude regions to a lesser extent, will experience an increasing number of days with heat indices crossing dangerous thresholds used to characterize heat stress, such as HI>41°C (Figure 12.4). The increase, by the end of century, exceeds 100 days per year in most tropical areas under SSP5-8.5 but remains much more limited to almost half under SSP1-2.6. Several global-scale studies have shown that high temperature extremes will increase everywhere (*high confidence*)) (Gourdji et al., 2013; Perkins-Kirkpatrick and Gibson, 2017; Harrington et al., 2018; Jones et al., 2018; Lehner et al., 2018; Shi et al., 2018; Tebaldi and Wehner, 2018; Arnell et al., 2019; Russo et al., 2019; Schwingshackl et al., 2021), although the change depends on the indicator (see also Chapter 11). For example, by 2080, at least 80% of the land surface is expected to experience average summer temperatures greater than the historical (1920-2014) maximum with high RCP8.5 emissions (Lehner et al., 2018). The areas of rice and maize cropland with damaging extreme temperatures during the reproductive season will increase by a factor of three under RCP8.5 (Gourdji et al., 2013). Heatwaves that are currently considered rare become the norm almost everywhere with high emissions by the end of the century (Russo et al., 2014). Heat stress as a combined function of temperature and humidity also increases at the global scale, especially with high emissions (e.g. Matthews et al., 2017). Growing degree-days and cooling degree-days also increase everywhere (Arnell et al., 2019) with the absolute and proportional changes depending on temperature threshold. Increases in temperatures will result in reductions in heating degree-days (Arnell et al., 2019; Coppola et al., 2021b) and a widespread reduced frequency of cold extremes (*high confidence*).

Integrating the results of the regional assessments in 12.4 shows that changes in CIDs linked with the water cycle or atmospheric dynamics (e.g. storms) vary more among regions, largely due to the spatial pattern of changes in atmospheric circulation and changes in precipitation and evaporation (Chapters 8 and 11). There is *high confidence* that heavy precipitation and pluvial floods will be increasing in a majority of land regions,

ACCEPTED VERSION SUBJECT TO FINAL EDITS

primarily due to the well-understood Clausius-Clapeyron relationship describing the increase in moisture content with air temperature (Chapters 8 and 11), but there is a large spatial variability in fluvial flood hazards. Top-down global-scale studies show that although fluvial flood hazards are projected to decrease in regions where there are large reductions in seasonal rainfall totals or where warmer temperatures mean less accumulated snow, at the global scale, fluvial flood hazard (characterized as the area affected, size of peak or likelihood of an event) is projected to increase substantially through the century (Giuntoli et al., 2015; Arnell and Gosling, 2016; Winsemius et al., 2016; Alfieri et al., 2017; Dottori et al., 2018; Arnell et al., 2019). Projected changes in agricultural and hydrological drought characteristics are dependent on the indicator used to define drought (Section 12.3; Chapter 11), but there is at least *medium confidence* of an increase in the drought hazard in many parts of the world. This is also reflected in global scale studies, with for example Naumann et al. (2018) showing that the global mean average drought duration (based on the SPEI index which is calculated from the difference between precipitation and potential evaporation) increased from 7 months with the current climate to 18.5 months for a global warming level of 3ºC. The apparent global increase in drought occurrence is greater when evaporation is captured in the drought indicator (e.g. SPEI) than when the indicator is based on precipitation alone (as in SPI) (Carrão et al., 2018). There is evidence that the likelihood of simultaneous events in several locations will increase: (Trnka et al., 2019) found that the proportion of wheat-growing areas experiencing simultaneous severe water stress events (based on SPEI) in a year increased from 15% under current conditions to up to 60% at the end of the 21st century under high emissions.

The regional assessment in 12.4 shows that fire weather is projected in increase with *medium or high confidence* in every continent of the world, including Arctic polar regions. Globally, fire weather is projected to increase in future, primarily due to higher temperatures and exacerbated where precipitation reduces. By 2050, 60% of the global land area would see a significant increase in fire weather under RCP8.5 (Abatzoglou et al., 2019). There is less confidence in the projected distribution of change in fire weather across regions in global scale studies. For example, (Moritz et al., 2012) projected an increase in fire weather in mid and high latitudes but a reduction in the tropics, whilst Yu et al. (2019) and Bedia et al. (2015) projected an increase in the tropics. These differences reflect differences in methodologies and fire weather indices adopted in different studies.

Integration of the results of 12.4 shows that the total number of tropical cyclones is projected to decrease through the 21st century, particularly with high emissions, but the number of very intense tropical cyclones is projected to increase in most areas (at least *medium confidence*) (e.g. Bacmeister et al., 2018) (Chapter 11). Furthermore, regions with glaciers will lose glacier mass and regions concerned with snow cover will see a reduction in snow depth, the duration, or extent of cover (*medium confidence* in Polar regions, *high confidence* elsewhere).

Relative sea-level rise is projected in all regions (excepting a few Arctic polar regions) with likelihoods varying from *very likely* to *virtually certain* depending on the region. This will increase the frequency of extreme sea levels and, depending on the level of coastal flood protection, coastal flooding (Vousdoukas et al., 2018; Kirezci et al., 2020).. In terms of globally averaged extreme total water level (ETWL) frequency changes, the present-day 1:100 yr event is projected to become 1:30 yr and 1:20 yr events by 2050 under RCP4.5 and RCP8.5 respectively. By 2100 the present day 1:100 yr ETWL is projected to become a 1:5 yr event under RCP4.5, while under RCP8.5, such events are projected to occur more than once a year (Vousdoukas et al., 2018).

There is *high confidence* that most of the world's sandy coasts will experience shoreline retreat, in the absence of terrestrial or offshore sediment sources. Median projections presented by (Vousdoukas et al., 2020b) indicate that 13.6% (36,097 km) and 15.2% (40,511 km) of the world's sandy beaches could retreat by more than 100 m by 2050 (relative to 2010) under RCP4.5 and RCP8.5 respectively, implying a 12% increase in severely threatened shoreline length under RCP8.5, relative to RCP4.5. These median projections increase to 35.7% (RCP4.5)–49.5% (RCP8.5) (or 95,061 km–131,745 km) by the end of the century, implying a 38% increase in severely threatened shoreline length under RCP8.5, relative to RCP4.5.

Figure 12.11 highlights that each region will, with *high confidence*, experience changes in multiple CIDs,

ACCEPTED VERSION SUBJECT TO FINAL EDITS

challenging the vulnerability of the region and its adaptation and mitigation capacity. All non-polar regions with a coastline will see an increase in relative sea level, extreme sea level and coastal erosion, and will also see an increase in hot extremes, a decrease in cold extremes, and many will experience an increase in heavy precipitation. One cluster of regions – South eastern and western Africa regions, the Mediterranean, North Central America, West North America, the Amazon regions, Western South America, and Australia – will experience, in addition to the aforementioned globally changing CIDs, increases in either drought/aridity or fire weather with *high confidence*. This will impact upon agricultural resources, infrastructure and health and ecosystems. A second cluster of regions including mountainous areas or regions with seasonal snow cover will experience (in addition to increases in heat extremes, more intense short-duration rainfall, and increases in coastal hazards where coasts exist) reductions in snow and ice cover and/or increases in river flooding in many cases (Western, Northwestern, Central and Eastern North America, Arctic regions, Andes regions, Europe, Siberia, central and East Asia, Southern Australia and New Zealand) (*high confidence*). These are places where energy production, ski tourism, river transportation, infrastructure could in particular face increased risks.

In a few other regions, only a few CIDs are projected to change with *high confidence* (e.g., Sahara, Central Africa, Western Africa, Madagascar, Arabian Peninsula, South eastern South America, New Zealand, Small Islands). The lower confidence levels associated with changes in CIDs in these regions can be due either to weaker change signals compared to natural variability, or due to *limited evidence* and model uncertainties leading to *low agreement*, and does not mean that climate change may affect these regions any less than in other regions.

In summary, there is *high confidence* that all regions of the world will experience changes in several climatic impact-drivers by mid-century, albeit at region specific rates of change and confidence levels per CID. Consequently, changing CIDs have the potential to affect climate-related risks in all regions of the world.

[START FIGURE 12.11 HERE]

Figure 12.11: Synthesis of the CID changes projected by 2050 (2041-2060) with *high confidence*, relative to reference period (1995-2014), together with the sign of change. Information is taken from the CID tables in Section 12.4. Some CIDs are grouped in order to streamline the information in order to fit in all information in the figure. Mean temperature, extreme heat, cold spells and frost are grouped under a single icon "heat", as they are projected to change simultaneously, albeit heat and cold are changing in opposite directions. Coastal CIDs (relative sea level, coastal flooding and coastal erosion at sandy beaches) are also grouped. In the figure, the "coastal" icon indicates regions where at least two of the three individual coastal CIDs are projected to change with *high confidence*. Cases where only two of the three CIDs increase with high confidence are in Arctic North Europe, Russian Arctic and Arctic North West North America. A single icon is used for aridity, hydrological drought, and agricultural and ecological drought, and only the number of drought types that change is indicated. For the "Snow, ice" icon, information is taken from the evolution of the "Snow, Glacier and ice sheet" CID, and in most regions also have similar changes for "permafrost" and "lake, river and sea ice". Exceptions are for NEN, RAR and Arctic NWN where snow is decreasing with *medium confidence* (thus not appearing in the figure), while permafrost and Lake, river and sea ice is decreasing with *high confidence*. The location of the icon within the regions is arbitrary. Further details on data sources and processing are available in the chapter data table (Table 12.SM.1). Icon sources: https://www.flaticon.com/authors/freepik

[END FIGURE 12.11 HERE]

12.5.2 The emergence of climatic impact-drivers across time and scenarios

The emergence of a climate change signal occurs when that signal exceeds some critical threshold (usually taken to be a measure of natural variability, see e.g. Hawkins and Sutton, 2012) or when the probability distribution of an indicator becomes significantly different to that over a reference period (e.g. Chadwick et al., 2019) (see also Section 1.4.2, Chapter 10), in which case external anthropogenic forcings can be detected

ACCEPTED VERSION SUBJECT TO FINAL EDITS

as causal factors. The "time of emergence" (ToE) or "temperature of emergence" is the time or global warming level thresholds associated with this exceedance. Emergence is particularly relevant to impacts, risks assessment and adaptation because human and natural systems are largely adapted to natural variability but may be vulnerable if exposed to changes that go beyond this variability range; this is not to say that changes within natural variability have no impact, as occurrence of damaging extremes proves. Emergence also informs the timing of adaptation measures. The emergence of a change is always relative to a reference period (e.g. the pre-industrial period or a recent past), depending on the framing question. In the former case, the goal is to estimate the amplitude of an anthropogenically driven change while in the latter, it is to estimate the amplitude of change relative to a baseline that is familiar to stakeholders. Both questions are important for risk assessment, but the former may be more directly interpretable in a mitigation context. The variability also refers to a time scale, generally interannual to interdecadal. The reader is referred to Section 1.4.2 and Chapter 10 for more details about how emergence is defined and used in the literature.

Changes in climatic impact-drivers may remain within the range of natural variability or have a time of emergence that varies by region and scenario. This section assesses the evidence for the effects of anthropogenic climate change on the emergence of changes in CID index, past, resent and future, as evidenced by the literature assessed in other chapters, as well as additional literature assessed here, at both global and regional scales. In many cases, however, sufficient literature for a robust region by region assessment of times of emergence is lacking. The assessment herein is made by CID. Regional emergence assessment is reported in Tables 12.3-11 but is undertaken in this section.

ToE estimation must be done with caution given the many sources of inherent uncertainties, such as observations representing only a single realization of climate history, internal variability (whose frequency -- e.g., annual or decadal -- needs to be precisely defined), model biases, and potential low-frequency changes in variability (Chapter 10) (Lehner et al., 2017). In addition, a homogeneous interpretation of multiple studies is hampered by heterogeneous methodologies used to calculate emergence. In this section, we assess emergence and its confidence level based on such multiple methods as provided by the literature, and unless specified otherwise, emergence here refers to S/N>1 (S/N= signal to noise ratio) relative to a preindustrial baseline and interannual variability (the "noise"). Furthermore, observed trends and attribution are taken into account in combination with climate simulations (historical or projections) for assessing whether a trend has already emerged in the historical period.

Mean air temperature: Warming of mean annual temperatures has already emerged in all land regions as obtained from past observations and confirmed by historical simulations (*high confidence*) (King et al., 2015; Hawkins et al., 2020) (Figure 1.13), with S/N ratios larger than 2. In the current climate, the highest S/N ratios exceed 5 over Central Africa, Amazonia, East and South East Asia. Seasonal warming emergence depends on the season. Because the temperature variability in the mid-latitudes is higher in winter than in summer, the emergence of seasonal warming occurs for summer but not for winter in most of this part of the world. In Europe, summer warming has emerged in all regions (*medium confidence, medium agreement*), and in North America, it has emerged only over Eastern and Western regions while in winter there is *low confidence* of an emergence in warming in all regions for both Europe and North America (Lehner et al., 2017; Hawkins et al., 2020). When considering the climate of the end of the 20th century (i.e. recent past) as a baseline, the emergence of mean temperature is projected at very different times depending on the scenario. For instance, emergence is reached by 2050 under RCP8.5 in most areas of Europe, Australia or East Asia, but it does not occur within the 21st century under RCP2.6 (*medium confidence*) (Sui et al., 2014; Im et al., 2020). This means that RCP2.6 is efficient to keep mean temperatures within the recent climate range in the mid-latitudes. However, even under RCP2.6, mean temperatures in tropical regions that have not already emerged are projected to emerge before 2050 (*medium confidence*).

Extreme heat and cold: Increase in heat extremes have emerged or will emerge in the coming 3 decades in most land regions (*high confidence*) (King et al., 2015; Seneviratne and Hauser, 2020) (Chapter 11), relative to the pre-inudtrial period, as found by testing significance of differences in distributions of yearly temperature maxima in simulated 20-year periods. In tropical regions, wherever observed changes can be established with statistical significance, and in most mid-latitude regions, there is *high confidence* that hot and cold extremes have emerged in the historical period, but only *medium confidence* elsewhere. In other

ACCEPTED VERSION SUBJECT TO FINAL EDITS

regions emergence is projected at the latest in the first half of the 21st century (*high confidence*) under RCP8.5 at least (King et al., 2015; Seneviratne and Hauser, 2020). Relative to the end of 20th-century conditions, changes in humid heat stress as characterized by wet bulb temperature, indicates a ToE as early as in the first two decades of the 21st century in RCP8.5 at least in many tropical regions (most of Africa in the band [20°S-20°N], South Asia and South-East Asia) (Im et al., 2020) (*medium confidence*) . By 2050 and under RCP8.5, wet bulb temperature is projected to emerge in many other areas such as South Africa, North Africa, Europe, and most of Central, Southern, Eastern Asia and Northern and Eastern Australia, while under RCP2.6, emergence is either reached later in the century (Europe, Central Asia, Northern Australia), or never reached in the century (Im et al., 2020). Decrease of cold spells has already emerged above the interannual variability in Australasia, Africa and most of northern South America, and they are projected to emerge before 2050 in the Northern mid-latitudes and in southern South America (King et al., 2015) under RCP8.5 *(medium confidence, low evidence and high agreement)*.

Mean precipitation: Over only a few regions mean precipitation changes have emerged in the historical period (increase in Northern and Eastern Europe and decrease in West Africa, Amazonia) from observations with an S/N ratio larger than 1 (Hawkins et al., 2020) (*low confidence*). The emergence of increasing precipitation before the middle of the 21st century is found across scenarios in Siberian regions, Russian far east, northern Europe, Arctic regions and the northernmost parts of North America (*high confidence*) and later in other Northern mid-latitude areas, depending on the scenario, albeit with different methods and emergence definitions used in climate projections (Chapter 8) (Giorgi and Bi, 2009; Maraun, 2013; King et al., 2015; Akhter et al., 2018; Kumar and Ganguly, 2018; Nguyen et al., 2018; Barrow and Sauchyn, 2019; Rojas et al., 2019; Kusunoki et al., 2020; Pohl et al., 2020; Li et al., 2021). Decreases in mean precipitation are projected to emerge in parts of Africa by the middle of trhe century, and later in the Mediterranean and southern Australia, but the emergence depends on the scenario, and specific seasons for crop growth (Nguyen et al., 2018; Rojas et al., 2019). Mean precipitation does not emerge in any of these regions at anytime in the 21st century under RCP2.6, but emerges in all under RCP8.5. ToE under RCP4.5 is projected to be around 25 years later relative to RCP8.5 in many of the early emergence regions, highlighting the importance of mitigation to gain more time for adaptation.

Heavy precipitation and floods: There is *low confidence* in the emergence of heavy precipitation and pluvial and fluvial flood frequency in observations, despite trends that have been found in a few regions (Chapter 8, Chapter 11, and across Section 12.4). In climate projections, the emergence of increase in heavy precipitation strongly depends on the scale of aggregation (Kirchmeier-Young et al., 2019), with, in general, no emergence before a 1.5°C or 2°C warming level, and before the middle of the century (*medium confidence*), but results depend on the method used for the calculation of the ToE (Maraun, 2013; King et al., 2015; Kusunoki et al., 2020). Emergent increases in heavy precipitation are found in several regions when aggregated at a regional scale in Northern Europe, Northern Asia and East Asia, at latest by the end of the century in SRES A1B or RCP8.5 scenarios or when considering the decadal variability as a reference (*medium confidence*) (Maraun, 2013; Li et al., 2018e, 2021; Kusunoki et al., 2020). There have been few emergence studies for streamflow and flooding, although one study showed emergence of different hydrological regimes at different times during the 21st century across the United States (Leng et al., 2016). Variability in extreme streamflows from year to year can be high relative to a trend (Zhuan et al., 2018). Given the heterogeneity of methods and results, there is only *low confidence* in the emergence of heavy precipitation and flood signals in any region when considering the S/N ratio.

Droughts, aridity and fire weather: There is *low confidence* in the emergence of drought frequency in observations, for any type of drought, in all regions. Even though significant drought trends are observed in several regions with at least *medium confidence* (Section 12.4), agricultural and ecological drought indices have interannual variability that dominates trends, as can be seen from their time series (Guo et al., 2018a; Spinoni et al., 2019b; Haile et al., 2020; Wu et al., 2020b) (*medium confidence*). Studies of the emergence of drought with systematic comparisons between trends and variability of indices are lacking, precluding a comprehensive assessment of future drought emergence. Historical climate simulations indicate that fire weather indices have already emerged in several regions (the Amazon basin, Mediterranean, Central America, West and South Africa) (*low confidence, low evidence*) (Abatzoglou et al., 2019), and emergence is projected with *low confidence* by the middle of the century in several other regions (Southern Australia,

ACCEPTED VERSION SUBJECT TO FINAL EDITS

Siberia, most of Northern America and Europe) when considering several indices together.

Wind: Observed mean surface wind speed trends are present in many areas (12.4), but the emergence of these trends from the interannual natural variability and their attribution to human-induced climate change remains of *low confidence* due to various factors such as changes in the type and exposure of recording instruments, and their relation to climate change is not established. For future conditions, there is *limited evidence* of the emergence of trends in mean wind speeds due to the lack of studies quantifying wind speed changes and their interannual variability. The same limitation also holds for wind extremes (severe storms, cyclones, dust and sandstorms).

Snow and ice: The decrease in the Northern Hemisphere snow cover extent in spring has already emerged from natural variability (Section 3.4.2). The snow cover duration period is projected to emerge over large parts of Eastern and Western North America and Europe by the mid-century both in spring and autumn, and emergence is expected in the second half of the 21st century in the Arctic regions in the high RCP8.5 scenario (Chapter 9, SROCC) (*medium confidence*). For snow depth or snow water equivalent, there is *low confidence (limited evidence)* of the emergence of a decrease before 2050 because climate change also increases the variability of the snow depth signal, in Europe (Willibald et al., 2020) (Section 3.4.2). Terrestrial permafrost is warming worldwide due to climate change (Sections 2.3.2.5, 9.5.2). Due to weak interannual variability of permafrost temperatures, terrestrial permafrost warming has emerged above natural variability in almost all observed time series of the Northern Hemisphere (Biskaborn et al., 2019) (*medium confidence, limited evidence, high agreement*), but the active layer thickness exhibits considerable interannual variability inhibiting evidence for emergence (Chapter 9).

Sea ice: Sea ice area decrease in the Arctic in all seasons has already emerged from the interannual variability (*high confidence*) (Chapter 9). By contrast, the Antarctic sea ice area shows no significant trend, and therefore no emergence.

For other snow and ice CIDs (heavy snowfall and ice storm, hail, snow avalanche), there is *limited evidence* of emerging signals.

Relative sea level, coastal flood and coastal erosion: Near-coast RSLR will emerge before 2050 for RCP4.5 along the coasts of all AR6 regions (with coasts) except EAS, RFE, MDG, the southern part of ENA and the Antarctic regions (9.6.1.4) (Bilbao et al., 2015) (*medium confidence*). Under RCP8.5, emergence of near-coast RSLR is projected by mid-century along the coasts of all AR6 regions (with coasts), except WAN where emergence is projected to occur before 2100 (Section 9.6.1.4) (Lyu et al., 2014) (*medium confidencce*). Emergence studies for ETWL and coastal erosion are lacking and hence it is not currently possible to robustly assess emergence in these CIDs.

Mean ocean temperature and marine heatwave: The emergence of the sea surface temperature increase signal has been observed in global oceans over the last century, and the largest S/N values are found in the tropical Atlantic and tropical Indian Oceans (Hawkins et al., 2020). There is *high confidence* in the widespread occurrence of marine heatwaves in all basins and marginal seas over the last decades (Chapter 9), but the emergence of this signal above the natural variability has not yet been addressed in detail.

Ocean acidity, ocean salinity and dissolved oxygen: The global ocean pH has *very likely* emerged from natural variability for more than 95% of the global open ocean (SROCC, Chapter 2). The regional signals are more variable, but in all ocean basins, the signal of ocean acidification in the surface ocean is projected to emerge in the early 21st century (Chapter 5). The mean time of emergence for acidity in the coastal subtropical to temperate northeast Pacific and northwest Atlantic is above two decades (5.3.5.2) (*high agreement, medium evidence*). Salinity change signals have already emerged with 20–45% of the zonally averaged basin in the Atlantic, 20–55% in the Pacific and 25–50% in the Indian Oceans and will be reaching 35–55% in the Atlantic in 2050 to 55–65% in 2080; 45–65% to 60–75% in the Pacific; 45–65% to 60–80% in the Indian Oceans (Silvy et al., 2020) (Chapter 9). Deoxygenization has already emerged in many open oceans. The signal is most evident in the Pacific and Southern Oceans but not evident in the North Atlantic Ocean (Andrews et al., 2013; Levin, 2018). However, there is *medium confidence* in the emergence of the

ACCEPTED VERSION SUBJECT TO FINAL EDITS

anthropogenic signal in many other oceanic regions by 2050 (Henson et al., 2017; Levin, 2018).

There is *high confidence* that several CID changes have already emerged above natural variability in the historical period in many regions (e.g. mean temperature in most regions, heat extremes in tropical areas, sea ice, salinity). Heat and cold CIDs (excluding frost) that have not already emerged will emerge by 2050 whatever the scenario (*medium confidence*) in almost all land regions. The emergence of increasing precipitation before the middle of the century is also projected in in Siberian regions, Russian far east, northern Europe and the northernmost parts of North America and Arctic regions across scenarios with the various methods and emergence definitions used (*high confidence*). Studies are missing to properly assess S/N emergence for droughts and for wind CIDs. Arctic sea ice extent declines have mostly emerged above noise level (*medium to high confidence*), and the emergence of declining snow cover is expected by the end of the century under RCP8.5. There is *medium confidence* that, under RCP8.5, the anthropogenic forced signal in near coast relative sea-level change will emerge by mid-century in all regions with coasts, except in the West Antarctic region where emergence is projected to occur before 2100. In all ocean basins, the signal of ocean acidification in the surface ocean is projected to emerge before 2050 (*high confidence*).

[START TABLE 12.12 HERE]

Table 12.12: Emergence of CIDs in different time periods, as assessed in this section; the colour corresponds to the confidence of the region with the highest confidence; White cells indicate where evidence is lacking or the signal is not present, leading to overall *low confidence* of an emerging signal.

High Confidence (decreasing)	*Medium Confidence* (decreasing)	*Low confidence*	*Medium Confidence* (increasing)	*High Confidence* (increasing)

Climatic Impact-Driver Type	Climatic Impact-Driver Category	Already emerged in historical period	Emerging by 2050 at least for RCP8.5/SSP5-8.5	Emerging between 2050 and 2100 for at least RC8.5/SSP5-8.5
Heat and Cold	Mean air temperature	1		
	Extreme heat	2	3	
	Cold spell	4	5	
	Frost			
Wet and Dry	Mean precipitation		6 7	
	River flood			
	Heavy precipitation and pluvial flood			8
	Landslide			
	Aridity			
	Hydrological drought			
	Agricultural and ecological drought			
	Fire weather			
Wind	Mean wind speed			
	Severe wind storm			
	Tropical cyclone			
	Sand and dust storm			
Snow and Ice	Snow, glacier and ice sheet		9	10
	Permafrost			
	Lake, river and sea ice	11		

1 *High confidence* except over a few regions (CNA and NWS) where there is *low agreement* across observation datasets
2 *High confidence* in tropical regions where observations allow trend estimation and in most regions in the mid-latitudes, *medium confidence* elsewhere
3 *High confidence* in all land regions
4 Emergence in Australia, Africa and most of northern South America where observations allow trend estimation
5 Emergence in other regions
6 Increase (Most Northern mid-latitudes, Siberia, Arctic regions by mid-century, other later in the century)
7 decrease in the Mediterranean area, South Africa, South West Australia
8 Northern Europe, Northern Asia and East Asia under RCP8.5 and not in low-end scenarios
9 Europe, Eastern and Western North America (snow)

ACCEPTED VERSION SUBJECT TO FINAL EDITS

	Heavy snowfall and ice storm				**10** Arctic (snow) **11** Arctic sea ice only **12** Everywhere except WAN under RCP8.5 **13** With varying area fraction depending on basin **14** Pacific and Southern Ocean then many other regions by 2050
	Hail				
	Snow avalanche				
Coastal	Relative sea level		**12**		
	Coastal flood				
	Coastal erosion				
Oceanic	Mean ocean temperature				
	Marine heatwave				
	Ocean acidity				
	Ocean salinity	**13**			
	Dissolved oxygen	**14**			
Other	Air pollution weather				
	Atmospheric CO_2 at surface				
	Radiation at surface				

[END TABLE 12.12 HERE]

[START CROSS-CHAPTER BOX 12.1 HERE]

Cross-Chapter Box 12.1: Projections by warming levels of hazards relevant to the assessment of Representative Key Risks and Reasons for Concern

Contributors:
Claudia Tebaldi (USA), Guofinna Aoalgeirsdottir (Iceland), Sybren Drijfhout (UK), John Dunne (USA), Tamsin Edwards (UK), Erich Fischer (Switzerland), John Fyfe (Canada), Richard Jones (UK), Robert Kopp (USA), Charles Koven (USA), Gerhard Krinner (France), Friederike Otto (UK/Germany), Alex C. Ruane (USA), Sonia I. Seneviratne (Switzerland), Jana Sillmann (Norway/Germany), Sophie Szopa (France), Prodromos Zanis (Greece).

A consistent risk framework (Reisinger et al., 2020) has been adopted across the three Working Groups (WG) in IPCC AR6 while recognizing the diversity of risk concepts across disciplines. WGI is assessing changes in climatic impact-drivers (CIDs), which are physical climate system conditions (e.g., means, events and extremes) that affect an element of society or ecosystems. Depending on system tolerance, CIDs and their changes can be detrimental, beneficial, neutral, or a mixture of each across interacting system elements and regions (Sections 12.1-12.3). In the assessment of Representative Key Risk (RKR) categories and Reasons for Concerns (RFCs) in WGII Chapter 16, the focus lies on the adverse consequences of climate change, for which many types of CIDs (i.e., 'hazards' in the context of identified risks) play a key role. This box synthesizes the assessment of such hazards according to global warming levels (GWLs) from various chapters of WGI to inform understanding of their potential changes and associated risks with temperature levels in general, and in particular to facilitate WGII integrated assessments of RKRs and RFCs. Another cross-chapter box, CCB 11.1, connects the organization of regional information according to GWLs to the other common dimension along which future projections are organized, i.e., scenarios. Section 1.6 describes all dimensions of integration adopted in this report, adding cumulative carbon emissions to GWLs and scenarios.

Eight RKRs are identified within WGII Chapter 16:
RKR-A: risk to the integrity of low-lying coastal socio-ecological systems;
RKR-B: risk to terrestrial and ocean ecosystems;
RKR-C: risk to critical infrastructure and networks;
RKR-D: risk to living standards;
RKR-E: risk to human health;
RKR-F: risk to food security;
RKR-G: risk to water security; and
RKR-H: risk to peace and migration.

ACCEPTED VERSION SUBJECT TO FINAL EDITS

RFCs further synthesize the landscape of risks from climatic changes into five categories (from IPCC TAR onward; Smith et al., 2001):
RFC1: Risks to unique and threatened systems;
RFC2: Risks associated with extreme weather events;
RFC3: Risks associated with the distribution of impacts;
RFC4: Risks associated with global aggregate impacts; and
RFC5: Risks associated with large-scale singular events.
Importantly, the assessment of risk in WGII considers hazards as only one component of an integrated assessment that involves their complex interaction with exposure and vulnerability of the systems at risk (Reisinger et al., 2020).

Hazards relevant to RKRs and RFCs are identified among aspects of the climate system that have an episodic, short term nature, like extreme events (particularly relevant to RFC2 but contributing to many other risk categories). Increasing GWLs translate into changing characteristics of frequency, duration, intensity, seasonality and spatial extent for many of these hazards also apparent in scenario-based results (Chapter 11, Chapter 12, Sections 12.4 and 12.5.1). Also, increasing GWLs increase the likelihood of compound temporal or spatial occurrence of similar or different hazards (Chapter 11, Section 11.8). Other relevant hazards coincide with long-term trends embodying a gradual change that may result in unfavorable environmental conditions. Furthermore, RFC5's focus on singular events includes concern surrounding potential tipping points and irreversible behavior in the physical climate system.

Cross-Chapter Box12.2 Table 1 organizes information by hazard and presents current state and future change assessments with increasing GWLs (defined by increasing GSAT, see CCB2.3). We draw on individual chapters across the WG1 report for the assessment of how these hazards vary with GWL. Hazards for which a relation to GWLs has not been assessed are not reported in the table.

[START CROSS-CHAPTER BOX 12.1, TABLE 1 HERE]

Cross-chapter Box 12.1 Table 1: Summary of CIDs/hazards that are identified as driving RKRs and RFCs. The behavior of each (in most cases considered at the global scale, but for some types in terms of spatially resolved patterns) as a function of GWLs is described and when possible quantified (in which case the cell is colored), together with the level of confidence of the assessment, to be found in more detail in the chapter/sections indicated in the corresponding column. For the relation with GSAT levels, two columns detail current state, which can be associated to ~1C of global warming, and future behavior. Tipping Points and Irreversibility is comprehensively assessed with CMIP6 models up to GWL = 3C with fewer studies and lower confidence at higher GWLs up to 5C.

ACCEPTED VERSION SUBJECT TO FINAL EDITS

Hazard Category Sub-category	RKR/RFC relevance	Behavior at ~1C (present)	Behavior as a function of GWL (future)	WGI Chapter references
Extreme events				
Hot and Cold extremes	All RKRs; RFC2, RFC3	Frequency and intensity of hot extremes increased and cold extremes decreased at the global scale and in most regions since 1950 (GSAT change ~0.6C) (*virtually certain*). Number of warm days and nights increased; intensity and duration of heat waves increased; number of cold days and nights decreased (*virtually certain*). Regional-to-continental scale trends generally consistent global-scale trends (*high confidence*). Limited data in a few regions (esp. of Africa) hampers trend assessment.	Strong linear relation between magnitude and intensity of heat and cold extremes and GSAT, detectable from warming as low as 1.5C; changes in the extreme metrics twice as large (in mid-latitude regions) or more (in high latitude regions) than GSAT warming (*very likely*); metrics related to frequency of exceedance may show stronger than linear relationships (exponential) (*very likely*).Compared to today, changes in extremes at +2°C at least two times larger than at +1.5°C, and four times larger at +3°C.	Sections 11.3, 11.9, 12.4; Figures 11.4, 11.5, 11.9; Table 11.2.
Extreme precipitation events	All RKRs; RFC2, RFC3	Frequency and intensity of heavy precipitation events increased at the global scale over a majority of land regions with good observational coverage (*high confidence*) and at the continental scale in North America, Europe, and Asia. Larger percentage increases in heavy precipitation observed in the northern high latitudes in all seasons, and in the mid latitudes in the cold season (*high confidence*). Regional increases in the frequency and/or the intensity of heavy rainfall also observed in most parts of Asia, northwest Australia, northern Europe, southeastern South America, and most of the United States (*high confidence*), and west and southern Africa, central Europe, the eastern Mediterranean region, Mexico, and northwestern South America (*medium confidence*). GHGs *likely* the main cause.	Precipitation events - including those associated with Tropical Cyclones (TCs) - increase with GSAT. For GWLs >2°C very rare (e.g., 1 in 10 or more years) heavy precipitation events more frequent and more intense over all continents (*virtually certain*) and nearly all AR6 regions (*likely*). Likelihood lower at lower GWLs and for less rare events. At the global scale, intensification of heavy precipitation generally follows Clausius-Clapeyron (~6-7% per degree C of GSAT warming; *high confidence*). Increase in frequency of heavy precipitation events accelerates with warming, higher for rarer events (*high confidence*), with approximately a doubling and tripling frequency of 10-year and 50-year events, respectively, at 4°C of global warming.	Sections 11.4, 11.7, 12.4; Figure 11.5, 11.13, 11.14; Table 11.2.
Drought	All RKRs; RFC2, RFC3	Increased atmospheric evaporative demand in dry seasons over a majority of land areas due to human induced climate change (*medium confidence*). Esp. observed in dry summer climates in Europe, North America and Africa (*high confidence).*	Upward trend with GSAT (*high confidence*).	Sections 11.6, 12.4; Figure 11.18; Table 11.2.
Inland floods	All RKRs; RFC2, RFC3		Upward trend with GSAT for flooded area extent, starting from 2C vs. 1.5C and higher levels. Increase in the frequency and magnitude of pluvial floods (*high confidence*). Increasing flood potential in urban areas where heavy precipitation projected to increase, especially at high GWLs (*high confidence*).	Sections 11.5, 12.4; Table 11.2.
Tropical Cyclones	All RKRs; RFC2, RFC3	Human contribution to extreme rainfall amount from specific TC events *(high confidence*). Global proportion of major TC intensities *likely* increased over the past four decades.	Increase in precipitation from TC with GSAT; Average peak TC wind speeds, proportion of intense TCs, and peak wind speeds of most intense TCs increase globally with GSAT (*high confidence*). Decrease or lack of change in global frequency of TCs (all categories) with GSAT (*medium confidence*).	Sections 11.7.1, 12.4; Table 11.2.
Marine Heatwaves	RKR A,B,F; RFC1,2,3;	*High confidence* that MHWs have increased in frequency over the 20th century, with an approximate doubling from 1982-2016, and *medium confidence* that they have become more intense and longer since the 1980s.	MHWs *very likely* become 2-9 times more frequent in 2081-2100 compare to 1985-2014 under SSP2.1.6 corresponding to a GWL of 2.1°C (1.3°C -2.8°C 95%CI), or 3-15 times more frequent under SSP5-8.5 corresponding to a GWL of 5°C (3.6-	Section 12.4; Box 9.2.

ACCEPTED VERSION SUBJECT TO FINAL EDITS

			6.9 95%CI). Spatial heterogeneity with larger changes in the tropical oceans and Arctic Ocean (*medium confidence*)	
Concurrent Events in Time and Space	All RKRs; RFC2, RFC3	Higher frequency already detected: More frequent concurrent heat waves and droughts. Increased compound flooding risk (storm surge, extreme rainfall and/or river flow) in some locations; the probability of concurring events *likely* increased.	Higher frequency with increasing GSAT. Increasing trend in more frequent concurrent heat waves and droughts with GSAT (*high confidence*). More frequent concurrent (in time) extreme events at different locations with increasing GSAT, for GWLs > 2°C (*high confidence*). Compound flooding risk (storm surge, extreme rainfall and/or river flow) increasing with GSAT (*high confidence*).	Section 11.8; Table 11.2; Boxes 11.3, 11.4.
Trends				
Fire Weather trends	RKR-B, C; RFC1,2,3	Weather conditions that promote wildfire (compound hot, dry and windy events) more probable in some regions over the last century (*medium confidence*).	Weather conditions promoting wildfire (compound hot, dry and windy events) *likely* more frequent with GSAT.	Section 12.4; Table 11.2.
Air Pollution weather	RKR-E; RFC3	Not discernible.	Behavior to first order controlled by emissions and policies, not by meteorology. Ozone decreases with GSAT in low polluted regions (-0.2 to -2 ppbv per degree C). Ozone increases with GSAT in regions close to sources of precursors (0.2 to 2 ppbv per degree C).	Sections 6.5, 12.4.
Patterns of mean warming	RKR-B, D, F, RFC1,3,4	Spatial patterns of temperature changes associated with the 0.5°C difference in GMST warming between 1991–2010 and 1960–1970 consistent with projected changes under 1.5°C and 2°C of global warming.	Temperatures scale approximately linearly with GSAT, largely independently of scenario *(high confidence*). High latitudes of Northern Hemisphere warm faster (*virtually certain*). Antarctic polar amplification smaller than Arctic (*high confidence*). Arctic annual mean temperatures warm between 2 and 2.4 times faster for GWLs between 1.5°C-4°C. In the Southern Hemisphere relatively high rates of warming in subtropical continental areas of South America, southern Africa, Australia (*high confidence*).	Sections 4.6.1.1, 12.4, Atlas; Figure 4.36. Figure.Atlas.15 and all Atlas sections' figures for mean temperature changes.
Arctic Warming trends	RKR-A,C,G,H; RFC1, RFC3	Emerged already from internal variability.	*Very likely* more pronounced (2–2.4 times faster) than the global average over the 21st century (*high confidence*).	Sections 4.6.1, 7.4.4.1, 12.4.9; Atlas.11; Figures 4.22, Atlas.32; Table 4.2.
Patterns of Precipitation Change	RKR-B, D, F, RFC1, RFC3	Regional patterns of recent trends, over at least the past three decades, consistent with documented increase in precipitation over tropical wet regions and decrease over dry areas.	Changes in large-scale atmospheric circulation and precipitation with each half degree of warming (*high confidence*). Stable pattern of change over time and scenarios. Some departures from linearity possible at regional scale (*medium confidence*). Precipitation increase on land higher at 3°C and 4°C compared to 1.5°C and 2°C. Precipitation increases in large parts of the monsoon regions, tropics and high latitudes, decreases in the Mediterranean and large parts of the subtropics (*high confidence*).	Sections 2.3.1.3.4, 4.5.1, 4.6.1, 12.4; Figures 2.14, 4.37, Atlas.15.
SST warming	RKR-A, B, D; RFC1, RFC4	Increased 0.81 (0.65-0.94) per degree C of GSAT (1850-1900 average vs. 2009-2018 average).	Model and observations show globally averaged SSTs warming at a lower rate of ~80% than GSAT. It is *virtually certain* that SST will continue to increase at a rate depending on future emission scenario ranging from 0.4 – 1.5°C in 2081-2100 relative to 1995-2014 under SSP1-2.6 correspomding to a GWL of 2.1°C (1.3°C - 2.8°C 95%CI), to 2–4°C under SSP5-8.5 correspomding to a GWL of 5°C (3.6°C - 6.9°C 95%CI).	Sections 2.3.1.1.6, 9.2.1, 12.4

ACCEPTED VERSION SUBJECT TO FINAL EDITS

Ocean Acidification/pH	RKR-A,B; RFC1, RFC4	*Virtually certain* decline of surface pH globally over the last 40 years at a rate of 0.017–0.027 pH units per decade, decline also in the subsurface over the past 2-3 decades (*medium confidence*). Surface pH now the lowest of at least the last 26 thousand years (*very high confidence*).	Increase of net ocean carbon flux throughout the century irrespectively of the emission scenario considered (*high confidence*). Decrease of ocean surface pH through the 21st century, except for SSP1-1.9 and SSP1-2.6 where values increase slightly starting from 2070 to 2100 (*high confidence*).	Sections 2.3.3.5, 4.3.2.4, 5.3.4, 5.4.2, 12.4; Figure 4.6.
SPEI index Global	RKR-B,F,G,H; RFC3	9.4% chance of at least 3 months of drought in a year at current levels (~1C)	Increase at the global scale in the chance of at least 3 months of drought in a year to about 20% (15-30%) at 1.5°C, 35%(20-45%) at 2°C to 60% (45-75%) at 4°C.	Sections 12.4, 12.5.1.
ENSO Variability	RKR-B,D,F,G; RFC2,3,5	*Medium confidence* that both ENSO amplitude and frequency of high-magnitude events since 1950 higher than over the pre-industrial period (before 1850) but *low confidence* of this being outside the range of internal variability. No clear evidence shifts in ENSO or associated features or its teleconnections.	No change in the amplitude of ENSO variability (*medium confidence*); enhanced ENSO-related variability of precipitation under SSP2-4.5 and higher (*high confidence*). *Likely* shift eastward of the pattern of teleconnection over N.Pacific and N. America.	Sections 2.4.2, 4.3.3.1, 4.5.3.2; Figure 4.10.
Sea-Ice Loss	RKR-A, B, H; RFC1,3,5	Arctic Sea Ice Area decreased for all months since 1970s; strongest decrease in summer (*very high confidence*). Arctic sea-ice younger, thinner and faster moving (*very high confidence*). Current pan-Arctic sea ice levels unprecedented since 1850 (*high confidence)*. *Low confidence* in all aspects of Antarctic sea-ice prior to the satellite era. Antarctic SIA experienced little net change since 1979 (*high confidence*).	The Arctic Ocean will *likely* become sea ice–free in September before 2050 in all considered SSP scenarios; such disappearance consistently occurring in most-years at 2-3°C (*medium confidence*) and including several months in most years at 3-5°C (*high confidence*).	Sections 2.3.2, 4.3.2.1, 9.3.1, 9.3.2, 12.4.9; Figures 4.2c, 4.5.
Permafrost Thaw	RKR-A,C; RFC3,5	Increases in permafrost temperatures in the upper 30 m over the past three to four decades throughout the permafrost regions (*high confidence*).	Global permafrost volume in the top 3 m decreasing by about 25±5% per °C for GWLs < 4°C. Relative to 1995-2014: at 1.5 and 2 °C decreasing by less than 40% (*medium confidence*), at 2 and 3 °C by less than 75% (*medium confidence*), at 3 and 5 °C by more than at least 60% loss (*medium confidence*).	Sections 2.3.2.5, 9.5.2, 12.4.9.
Sea-Level Change over the 21st century	RKR-A,C,D,E,F,G, H; RFC1,3,4	GMSL is rising with accelerated rate since the 19th century (*high confidence),* almost doubled during past 2 decades (about 0.1 mm yr^{-2}). GMSL increase over the 20th century faster than over any preceding century in at least the last three millennia (*high confidence*).	Up to 2050, limited scenario/GWL dependency (*likely* SLR=~0.15-0.30 m). By 2100, *likely* GMSL rise wrt 1995-2014 of 0.51 (0.40-0.69) m, 0.62 (0.50-0.81) m and 0.70 (0.58-0.91) m for, respectively, GWLs of 2.0°C, 3.0°C, and 4.0°C (*medium confidence*). Deep uncertainty in projections for GWLs> 3°C because of Ice Sheet behavior. For example, incorporation of *low confidence* ice-sheet processes under SSP5-8.5 (approximately 5°C) leads to a rise of 0.6-1.6 m rather than 0.7-1.1 m.	Sections 9.6.1.2, 9.6.3.3, 9.6.3.4, 12.4.
Sea-Level Change Commitment (2,000 years after peak GWL)	RFC5		Global Mean Sea Level commitment (over the 2000-year-long period following peak warming) of 2-6 m for 2°C peak warming, 4-10 m for 3°C peak warming, 12-16 m for 4°C peak warming, and 19-22 m for 5°C peak warming (*medium agreement, limited evidence*).	Section 9.6.3.5.
Northern Hemisphere Spring Snow Cover	RKR-G, RFC1,3	Substantial reductions in spring snow cover extent in the NH since 1978 (*very high confidence).* Since 1981, general decline in NH spring snow water equivalent (*high confidence*).	Linear change of NH snow cover in Spring of about 8% (area) per °C of (for GWLs <4°C). Relative to 1995-2014: at 1.5-2 °C NH spring snow cover extent *likely* decreases by less than 20% (*medium confidence*); at 2-3 °C *likely* decreases by less than 30%; At 3-5 °C, *likely* decreases by more than 25%.	Sections 2.3.2.2, 9.5.3, 12.4.
Mass Loss of Glaciers	RKR-B,G; RFC1, RFC3	*Very high confidence* global glaciers continuing retreat since ~1850. Current global glacier mass loss highly unusual over at least the last 2000 years (*medium confidence*). Increased rate of glacier mass loss over the last 3-4 decades (*high confidence*).). Glaciers not in balance with respect to current climate conditions and will continue to lose mass for at least several decades.	For 1.5- 2 °C about 50-60% (*low confidence*) of glacier mass outside the two ice sheets and excluding peripheral glaciers in Antarctica remaining, predominantly in the polar regions. At 2- 3 °C about 40-50% (*low confidence)* of current glacier mass outside Antarctica remaining. At sustained 3–5 °C 25-40% (*low confidence*).of current glacier mass outside Antarctica remaining. likely nearly all glacier mass lost in low latitudes, Central Europe, Caucasus, Western Canada and USA, North Asia, Scandinavia and New Zealand.	Sections 2.3.2.3, 9.5.1, 12.4.

ACCEPTED VERSION SUBJECT TO FINAL EDITS

Tipping Points / Irreversibility				
Amazon Forest Dieback	RFC1, RFC5	Highly dependent on human disturbance	Amazon drying and deforestation expected to cause a rapid change in the regional water cycle, possibly linked to the crossing of a climate threshold. *Low confidence* change will occur by 2100.	Sections 5.4.3, 5.4.8, 8.6.2.1, 12.4.10; Table 4.11.
Boreal Forest Dieback	RFC1, RFC5	Highly dependent on human disturbance	Possible if climate threshold is exceeded, but counteracted by poleward expansion.	Section 5.4.8.
Ice Sheets	RFC5	Greenland Ice Sheet mass loss rate increased substantially since the turn of the 21st century (*high confidence*). The Antarctic Ice Sheet has lost mass between 1992 and 2017 (*very high confidence*), with an increasing mass-loss rate over this period (*medium confidence*)	At sustained warming levels between 1.5°C and 2°C, the ice sheets will continue to lose mass (*high confidence*); on time scales of multiple centuries, the Greenland and West Antarctic Ice Sheets will partially be lost (*medium confidence*); there is *limited evidence* that the Greenland and West Antarctic Ice Sheets will be lost almost completely and irreversibly over multiple millennia; At sustained warming levels between 2°C and 3°C, there is *limited evidence* that the Greenland and West Antarctic Ice Sheets will be lost almost completely and irreversibly over multiple millennia, and *high confidence* in increasing risk of complete loss and increasing rate of mass loss for higher warming; At sustained warming levels between 3°C and 5°C, near-complete loss of the Greenland Ice Sheet and complete loss of the West Antarctic Ice Sheet will occur irreversibly over multiple millennia (*medium confidence*); substantial parts or all of Wilkes Subglacial Basin in East Antarctica will be lost over multiple millennia (*low confidence*).	Sections 2.3.2.4, 9.4.1, 9.4.2; Table 4.11.
Glaciers	RFC5	See Trends section of this table	Continuing substantial global mass loss.	Sections 9.5.1, 12.4.9; Table 4.11
Global Ocean Temperature	RFC5	See Trends section of this table	Centennial-scale irreversibility of ocean warming.	Sections 4.7.2, 9.6.3; Table 4.11.
SLR	RFC5	See Trends section of this table	Centennial-scale irreversibility of sea level rise. Tipping point linked to ice-sheet behavior. Deep uncertainty on SLR above 3°C warming	Sections 4.7.2, 9.6.3; Table 4.11.
Atlantic Meridional Overturning Circulation (AMOC)	RFC5	Low agreement on 20th century trend between models and most reconstructions. Observed decline since the mid-2000s cannot be distinguished from internal variability (*high confidence*).	There is *medium confidence* an abrupt collapse will not occur before 2100; for 1.5-2, 2-3, 3-5°C warming in 2100, AMOC decline is 29, 32 and 39%, respectively, of its pre-industrial strength.	Sections 2.3.3.4.1, 9.2.3.1; Table 4.11.
Permafrost Carbon	RFC5	See Trends section of this table	Will contribute as a feedback with warming, of approximately 18 +/- 12 Pg C per °C. Possibly nonlinear but *low confidence* in the value of any threshold for such behavior. Likely irreversible at centennial time scales.	Section 5.4.8; Table 4.11; Box 5.1.
Arctic Sea Ice	RFC5	Abrupt change already observed	Reversible within years to decades; No tipping point or threshold beyond which loss of ice becomes irreversible (*high confidence*)	Sections 4.3.2, 9.3.1; Table 4.11.
Snow Cover of Northern Hemisphere	RFC5	See Trends section of the table	Not anticipated to present tipping point/irreversible behavior.	Sections 8.6.2.3, 9.5.3; Table 4.11.

ACCEPTED VERSION SUBJECT TO FINAL EDITS

Global Monsoon	RFC5	Has *likely* increased over the last 40 years (*medium confidence*) and can be explained by a phase change in Atlantic Multidecadal Variability.	Not anticipated to present tipping point/irreversible behaviour, unless AMOC collapse occurs.	Sections 4.4.1.4, 4.5.1.5, 8.6.1; Table 4.11.
ENSO	RFC5	See Trends section of the table	Not anticipated to present tipping point/irreversible behavior.	Section 4.5.3.2; Table 4.11.
Methane Clathrates	RFC5	Methane release from shelf clathrates is <10 $TgCH_4\ yr^{-1}$	Not anticipated to present tipping point/irreversible behavior.	Section 5.4.8; Table 4.11.

[END CROSS-CHAPTER BOX 12.1, TABLE 1 HERE]

[END CROSS-CHAPTER BOX 12.1]

ACCEPTED VERSION
SUBJECT TO FINAL EDITS

12.6 Climate change information in climate services

Climate services are a significantly evolving source for climate change information to support adaptation, mitigation and risk management decisions. As an evolving field, there are multiple definitions of climate services (cf. Brasseur and Gallardo, 2016). The Global Framework for Climate Services defines a climate service as the provision of climate information to assist decision-making. The service includes appropriate engagement from users and providers, is based on scientifically credible information and expertise, has an effective access mechanism, and responds to user needs (Hewitt et al., 2012)

IPCC AR5 WGII introduced climate services as bridging the generation and application of climate knowledge, also describing their history and concepts (Jones et al., 2014). Since then, this transdisciplinary field has been growing rapidly (Brasseur and Gallardo, 2016; Hewitt et al., 2020a) with the social sciences in particular pointing out knowledge requirements for co-design and co-development of climate services (Larosa and Mysiak, 2019; Daniels et al., 2020; Steynor et al., 2020). Climate services differ from more research-driven vulnerability, impacts, and adaptation research in their orientation toward decision support (Stone and Meinke, 2005; Ruane et al., 2016; Golding et al., 2019), but overlaps exist (Bruno Soares and Buontempo, 2019). Climate services are often targeted at building resilience to climate-related hazards from near real-time to seasonal and multi-decadal time horizons, to inform adaptation to climate variability and change (Hewitt et al., 2012), widely recognized as an important challenge for sustainable development and risk management (Moss et al., 2010; Jones et al., 2014; Vaughan et al., 2018). This section focuses largely on climate change timescales (past, present and future), which are the focus of AR6 WGI.

This section introduces the current climate services landscape, assesses climate services practices and products related to climate change information and associated challenges. Cross-chapter box 12.2 provides concrete examples of climate services. The section builds on the introduction to climate services in Section 1.6.1.4 and the assessment of regional climate information construction including storylines discussed in sections 10.3.4.2, 10.5.3 and Box 10.2. The Atlas supports the provision of climate information across WGs by providing interactive maps and further details to the material made publicly accessible for use in climate services. WGII (Chapter 17) further elaborates on climate services as enablers for climate risk management.

12.6.1 Context of climate services

The idea of climate services is not new and has its roots in meteorology and climatology (Larosa and Mysiak, 2019). It can be traced back to the late 1970s and the US National Climate Program Act of 1978 (Henderson et al., 2016). The development of the Global Framework for Climate Services (GFCS) after the World Climate Conference-3 in Geneva brought international attention and renewed impetus to the climate services field (Hewitt et al., 2012). As a result, large investments have been made globally and regionally in the development of user-driven climate services. WMO has created Regional Climate Centres (RCCs) to facilitate climate service development by regional and national providers (Hewitt et al., 2020a). The European Union declared its ambition to stimulate "*the creation of a community of climate services application developers and users that matches supply and demand for climate information and prediction*", giving primacy to climate services that are user-driven and science-informed (Lourenço et al., 2016), thus embracing concepts of co-design, co-development and co-evaluation of climate services (Street, 2016). Diverse and action-driven international initiatives allowed climate services to progressively shift from mitigation towards adaptation (Larosa and Mysiak, 2019). Opportunities for the development of climate services have emerged through the 2015 Agendas (Paris Agreement, Sustainable Development Goals and Sendai Framework), Nationally Determined Contributions, National Adaptation Plans, Multilateral Development Banks and Task Force on Climate-related Financial Disclosure (see Chapter 1.2.2).

Scientific advancements in climate services related to meteorology and climatology are still closely linked to essential climate variables (Larosa and Mysiak, 2019) and benefit from consistently growing computational power, infrastructure and storage capacity to meet the demands of higher spatially and temporally resolved climate information (Buontempo et al., 2020). Climate services also focus on impact chains providing decision-makers with information on climate change with cross-sectoral impact assessments for adaptation

ACCEPTED VERSION SUBJECT TO FINAL EDITS

(Jacob and Solman, 2017). Today there is a diversity of climate services that involve interpretation, analysis, and communication of different sources of climate data, ideally combining different types of knowledge (scientific/technical, experiential, indigenous, etc.), to a targeted group of decision-makers (Parris et al., 2016; Olazabal et al., 2018; Pezij et al., 2019). (Jacobs and Street, 2020) argue that climate services should be expanded to also address societal challenges, such as system transformation that includes climate in the context of other risks and development challenges.

Climate services are undertaken in public and private sectors at global, regional, national, and local scales (Hewitt et al., 2012, 2020b; Cortekar et al., 2020). Intermediaries such as private sector consulting companies, national climate service providers as well as research organizations, government agencies or academic institutions provide climate services that translate aspects of climate research to the specific context of decision-makers (see also Chapter 10.5). The EU Roadmap for Climate Services (

an Commission, 2015; Street, 2016) focuses on developing a market for climate services comprising of both public and private domains. The GFCS, under the leadership of several United Nations Agencies, emphasizes the public domain by supporting national and regional capacity building and development of climate services mainly through National Meteorological and Hydrological Services (Hewitt et al., 2012; Domingos et al., 2016; Sivakumar and Lucio, 2018; WMO, 2018). There are on-going debates about the commercialization of climate services (Brooks, 2013b; WMO, 2015; Webber and Donner, 2017; Hoa, 2018; Troccoli et al., 2018; Bruno Soares and Buontempo, 2019; Hewitt et al., 2020a). Some argue that the commercialization of climate services is needed to meet the diverse needs of specific clients and to drive innovation in the field (Brooks, 2013b; Troccoli, 2018a). Others argue that if climate services shift incentives for climate science away from the public interest towards profit-seeking, this will result in less publicly accessible and transparent climate information and more private knowledge (Keele, 2019; Tart et al., 2020).

Some climate adaptation planning already use climate information as provided by the IPCC, however, depending on the decision context, this information may be too coarse, too broad or too disciplinary to directly inform decision-making at the scale where adaptation measures are taken (Howarth and Painter, 2016; Nissan et al., 2019). Thus, while the role of IPCC is clearly felt as a reference, authoritative, starting point, there is a need for complementary information to translate the assessments at the national, local or sectoral level (Howarth and Painter, 2016; Kjellström et al., 2016; van den Hurk et al., 2018; Vaughan et al., 2018). The AR6 Interactive Atlas (see section Atlas.2) does provide a collection of observational data and global and regional climate projections. It is designed as a climate service towards the WGI needs and beyond to assess the state of the climate by offering data, maps and a level of expert analysis by aggregation of results to regions, scenarios and warming levels.

12.6.2 Assessment of climate services practice and products related to climate change information

The climate services landscape is fast growing and very broad as reflected in the vast diversity of practices and products that can be found in the peer-reviewed literature (*very high confidence*). However, a large part of climate services practices and products is published in ‘grey’ literature (i.e. non-peer reviewed or non-academic) by private consultancy and non-scientific civil organizations of which many are not in the public domain. In addition, the respective climate service context of a specific stakeholder in a sector dictates what climate information is required and on what scales and in what format it is most usefully provided. The extent and type of engagement between scientists and users is another critical aspect of climate services (see Cross-chapter box 12.2 Fig 1, and2section 10.5). The assessment here can thus only provide a partial and rather general representation of available practices and products of the evolving climate services field.

User needs and decision making contexts are very diverse and there is no “one size fits all” solution to climate services (*very high confidence*) (Hewitt et al., 2017a; Vincent et al., 2018b). In many cases this requires recognizing that stakeholders make decisions through a combination of scientific information and additional values (Vanderlinden et al., 2017; Parker and Lusk, 2019) (see also Section 1.2.3 and Section 10.5.4). The emerging climate service literature may clarify some features of climate information requested by users, for instance climatic impact-driver identification and prioritization through stakeholder

ACCEPTED VERSION SUBJECT TO FINAL EDITS

engagement; the specification of thresholds for various regions/sectors; the types of metrics (magnitude/intensity, frequency, duration, timing, spatial extent) that are of primary interest; and decision support systems where informatics allow stakeholders to custom-make impact-relevant thresholds and then query databases to understand current and future characteristics (Bachmair et al., 2016; Buontempo et al., 2020). However, users also ask for capacity building activities related to basic knowledge in climate change sciences and climate-related risks (De Bruin et al., 2020; Sultan et al., 2020).

Since AR5 and SROCC (Chapter 2) there has been considerable progress in understanding climate information user needs (Baztan et al., 2017; Golding et al., 2017b, 2017a, 2019; Bruno Soares et al., 2018a; Hewitt and Golding, 2018; Singh et al., 2018; Sivakumar and Lucio, 2018; Bessembinder et al., 2019; Sultan et al., 2020; Wang et al., 2020b; Hewitt et al., 2020b), better facilitation of user engagement (Buontempo et al., 2014, 2018; Buontempo and Hewitt, 2018) and an appreciation of climate scientists to involve communication specialists and social scientists to support the co-design and co-development process that is fundamental to a successful climate service (Buontempo et al., 2014; Gregow et al., 2016; Damm et al., 2019).

Climate services require user engagement and can take various forms in which climate information and data is delivered or communicated to the users (*very high confidence*). Different levels of user engagement exist, which can range from passive engagement, interactive group activities, to focused relationships between climate service provider and users, and which result in different types of climate service products including websites, capacity building, and co-design of tailored climate indices (Hewitt et al., 2017b) (see Cross-Chapter Box 12.2, Figure 1). The fundamental basis for climate service development is the co-production process between climate services provider and user (Valiela, 2006; Briley et al., 2015; Golding et al., 2017a; Vincent et al., 2018a; Bruno Soares and Buontempo, 2019; Schipper et al., 2019), which can be very resource intensive (Buontempo et al., 2018; Falloon et al., 2018; Kolstad et al., 2019) and varies strongly from case to case (Reinecke, 2015; Bremer et al., 2019; Goodess et al., 2019; Jung and Schindler, 2019). Climate services scholars and practitioners can better facilitate and embrace the knowledge co-production process if it is recognized as a multi-faceted phenomenon with several dimensions (e.g., constitutive, interactional, institutional, pedagogical, empowerment) (Kruk et al., 2017; Knaggård et al., 2019; Weichselgartner and Arheimer, 2019).

Information moves from useful to usable only when users effectively incorporate this information into a decision process (Lemos et al., 2012; Bruno Soares and Dessai, 2016; Prokopy et al., 2017) (see also WGII, Chapter 17). Climate services include a range of knowledge brokerage activities such as: identify knowledge needs; dissemination of knowledge; coordinate and network; compile and translate; build capacity through informed decision-making; analyse, evaluate and develop policy; and personal consultation (e.g., (De Bruin et al., 2020). When analysing four European climate services, (Reinecke, 2015) found that different climate services emphasized different knowledge brokerage activities.

There are various types of providers and products of climate services related to the key sectors and regions such as those described in previous sections (Hewitt et al., 2017a). For instance, studies have described sectoral climate services in support of agriculture (Falloon et al., 2018; Hansen et al., 2019), health (Jancloes et al., 2014; Lowe et al., 2017), tourism (Morin et al., 2018; Damm et al., 2019; Matthews et al., 2020), energy (Troccoli, 2018b; Goodess et al., 2019; Soret et al., 2019), disaster risk reduction (Golding et al., 2019; Street et al., 2019), water (van den Hurk et al., 2016; Vano et al., 2018), ocean and coastal ecosystems (Weisse et al., 2015; Le Cozannet et al., 2017), cities (Rosenzweig and Solecki, 2014; Rosenzweig et al., 2015; Gidhagen et al., 2020), and cultural heritage (ICOMOS, 2019). Many countries (including almost every country in Europe – see Atlas.5.6.3.4) have established a climate service centre, which follow different practices of user engagement and provide different products (e.g., Kjellström et al., 2016; Kolstad, 2019; Skelton et al., 2017). Climate services in other countries may be distributed across agencies and programs, although these are often not centrally coordinated (Parris et al., 2016). One of the key pillars of the GFCS is the Climate Services Information System (CSIS), which is the principal mechanism through which information about past, present and future climate is archived, analysed, modelled, exchanged and processed for users (Hewitt et al., 2020a). Some national governments also have organized national climate projections to be used for official planning (e.g.,(EEA, 2018). A list of available national products (e.g., observational

ACCEPTED VERSION SUBJECT TO FINAL EDITS

datasets) and projections can be found in the Atlas (e.g., Section Atlas.1.1.3 and 2.3).

Figure 12.12 maps a general categorization of practices and products that have emerged from reviewing the climate service literature and user interviews (Visscher et al., 2020). The categories range from very generic products or expert analysis focused particularly on climate information (climate-centric approaches) to more integrated products that include shared open-source products and capacity building as well as tailored products that treat climate information as part of a larger decision-making context (climate-inclusive approaches). Three specific examples that elaborate in more detail on specific practices and products related to those general categories are provided in the Cross-chapter box 12.2.

[START FIGURE 12.12 HERE]

Figure 12.12: Illustration of different types of climate services. Products, for instance, can focus only on climate-related information or can be designed to integrate climate information with other decision-relevant context (vertical axis) and they can be very generic in terms of relevance to a wide range of sectors or stakeholders or customized to fit the needs of a specific sector or stakeholder (horizontal axis). Source: Adapted from (Visscher et al., 2020).

[END FIGURE 12.12 HERE]

12.6.3 Challenges

Climate services set new scientific challenges to physical climate research (*high confidence*). Over at least the last decade, for instance, many questions have appeared in terms of optimal estimation of changes and uncertainties from projections of model ensembles, ensemble optimization, or adjustment of model biases while preserving essential information on trends and cross-variable, time and space consistencies, downscaling information at the local scale (Benestad et al., 2017; Hewitt et al., 2017a; Marotzke et al., 2017; Hewitt and Lowe, 2018; Knutti, 2019) (see also Section 10.5). Other challenges related to climate services are the inter-operability of data (Giuliani et al., 2017), access to data (open/FAIR Guiding principles (Wilkinson et al., 2016; Georgeson et al., 2017)), format of data (including moving away from percentile-based probabilistic forecasts (e.g., Haines, 2019) and funding mechanisms (Bruno Soares and Buontempo, 2019).

Understanding and modeling of weather and climate extremes is of great relevance for climate services and is continuing to set challenges for research, such as modeling changes in impact-relevant threshold exceedance and return periods for a variety of extremes (Maraun et al., 2015; Sillmann et al., 2017; Hewitt et al., 2020c; Schwingshackl et al., 2021) (see also Chapter 11). Extreme event attribution has also been used in context of climate services (Philip et al., 2020) as it is of interest to some stakeholder groups (Sippel et al., 2015; Marjanac and Patton, 2018; Jézéquel et al., 2019, 2020). The usefulness or applicability of available extreme event attribution methods (see Cross-chapter box 1.4 and section 11.2.4) for assessing climate-related risks remains subject to debate (Shepherd, 2016; Mann et al., 2017; Lloyd and Oreskes, 2018).

The design of climate services involves key challenges, such as a domain challenge where users, tasks and data may be unknown; and an informational challenge related to the use and adoption of novel and complex scientific data (Christel et al., 2018). This includes challenges in the uptake of climate information in terms of coordinated delivery of data, information, expertise and training by public research institutes, the inclusion of climate change adaptation in public and private regulation, and uncertainties and confidence in climate projections (Cavelier et al., 2017). Quality control and quality assurance are still weak elements in the development of climate service products (Jacob, 2020). Quality criteria or standards (that go beyond good practice) will have to be developed and agreed (cf. (Pacchetti et al., 2021). These challenges reflect the dilemma that exists at the interface between the climate modelling community and climate services regarding: 1) the purposes of the models for climate research versus service development; 2) the gap between the spatial and temporal scales of the models versus the scales needed in applications; and 3) tailoring

ACCEPTED VERSION SUBJECT TO FINAL EDITS

climate model results to real-world applications (Benestad et al., 2017; Hackenbruch et al., 2017; van den Hurk et al., 2018).

Climate services require a sustained engagement between scientists, service providers and users that is often hindered by limited resources for the co-design and co-production process (*high confidence*). There are recurring challenges related to successful climate service applications: 1) climate services are not visible and poorly understood by 'end users' (Weichselgartner and Arheimer, 2019); 2) data can be of unknown or poor quality, data formats can be hard to access or process, and it can be difficult to choose from large databases (e.g. Section 1.5.4) without appropriate user guidance; 3) users are unsure how to choose from available climate services to meet their needs (Rössler et al., 2019); 4) building trust between climate service users and providers (Baztan et al., 2020); 5) the lack of understanding of users and their contexts by the climate science and service community (Porter and Dessai, 2017); 6) the difficulty in scaling up services (Tall et al., 2014; van Huysen et al., 2018); 7) the lack of trained scientists skilled at conducting societally-relevant research (Rozance et al., 2020).

Challenges also arise in determining the effectiveness and added value of climate services, particularly in terms of providing quantitative estimates of economic benefits and making a business case for climate services (Bruno Soares, 2017). The market for climate services is still in its infancy (Cavelier et al., 2017; Bruno Soares et al., 2018b; Tall et al., 2018; Damm et al., 2019). One form of value may be determined by a particular user community's willingness to pay (Acquah and Onumah, 2011; Ouédraogo et al., 2018; Antwi-Agyei et al., 2021), which however cannot reflect the value of climate services as a public good and for society as a whole (Hewitt et al., 2012). Literature is only recently emerging on the socio-economic benefits of weather and climate services (Vaughan et al., 2019). Early studies and guidelines from the WMO focus on cost-benefit ratios (Perrels et al., 2013; WMO, 2015). Issues related to demand-driven versus supply-driven climate services (Lourenço et al., 2016; Street, 2016; Daniels et al., 2020), public versus private climate services (Hewitt et al., 2020a) and business models for climate services (Hoa, 2018) have been raised. A large share of climate services documented in peer-reviewed literature is currently provided in non-market frameworks (e.g., public service obligations and R&D grants) (Hoa, 2018; Kolstad et al., 2019; Cortekar et al., 2020).

Other challenges related to governance and dealing with complex systems are sometimes acknowledged but less well described in the climate services domain (Hewitt et al., 2020a). Importantly, decision contexts are strongly rooted in past practice (which often does not even make optimal use of past climate information), stakeholder experience and history. Even important emerging concepts of co-production, entry points, and champions do not always fall naturally into these realities without significant effort. The social sciences have an important role in helping understand and tackle these challenges (Bruno Soares and Buontempo, 2019).

[START CROSS-CHAPTER BOX 12.2 HERE]

Cross-Chapter Box 12.2: Climate services and climate change information

Contributing Authors:
Suraje Dessai (UK/Portugal), Jana Sillmann (Norway/Germany), Carlo Buontempo (UK/Italy), Cecilia Conde (Mexico), Aida Diongue-Niang (Senegal), Francisco J. Doblas-Reyes (Spain), Christopher Jack (South Africa), Richard Jones (UK), Benjamin Lamptey (Niger/Ghana), Xianfu Lu (UK/China), Douglas Maraun (Austria/Germany), Ben Orlove (USA), Roshanka Ranasinghe (Netherlands/Sri Lanka/Australia), Alex C. Ruane (USA), Anna Steynor (South Africa), Bart van den Hurk (Netherlands), Robert Vautard (France)

Climate services involve the provision of climate information in such a way as to assist decision-making. The service needs to have appropriate engagement from users and providers, be based on scientifically credible information and expertise, have an effective access mechanism, and meet the users' needs (Hewitt et al., 2012). Predominantly, climate services are targeted at informing and enabling risk management in adaptation to climate variability and change (Jones et al., 2014; Vaughan et al., 2018). Chapter 1 introduces

ACCEPTED VERSION SUBJECT TO FINAL EDITS

climate services in a broader context of interaction between science and society, including how climate information can be tailored and co-produced for greatest utility in specific contexts. Chapter 10 assesses the key foundations for the generation of climate information about regional climate change. Chapters 11, 12 and Atlas comprehensively assess regional climate change information. The Interactive Atlas gives access to various repositories of quantitative climate information. In WG2, Chapter 17 assesses climate services in the context of climate risk management.

Climate services contexts are diverse and complex. They can be characterised using different factors such as sectors, regions, purposes, time horizons, data sources, level of processing of climate data, background knowledge, type of climate services providers, as well as the nature of the interactions between providers, users and other stakeholders (Bessembinder et al., 2019). To illustrate the wide diversity of climate change information in climate services, a useful categorisation is by user-provider engagement of climate services (Cross-Chapter Box 12.2, Figure 1). One broad category includes *Websites and web tools* which generally focuses on data and information provision (Hewitson et al., 2017). Websites are generally able to reach many users, but engagement is passive through one-way transfer of information. The second broad category involves *Interactive group activities,* such as workshops, meetings and interactive forums, which create a stronger dialogue between climate service providers and decision-makers. Multi-way communication and regular interaction enable building of trust, co-learning and co-production of products and services. The third broad category involves *Focused relationships* which are tailored, targeted and address very specific needs of the user. Effective engagement arises from an iterative process between the provider and user to ensure the user's needs are being addressed appropriately (Hewitt et al., 2017b).

The diversity of climate services practices and products is illustrated here using three case studies that represent each of the broad categories of provider-user engagement (Cross-chapter box Figure 1).

[START CROSS-CHAPTER BOX 12.2, FIGURE 1 HERE]

Cross-Chapter Box 12.2, Figure 1: Schematic of three broad categories of engagement between users and providers of climate services (adapted from Hewitt et al., (2017b).

[END CROSS-CHAPTER BOX 12.2, FIGURE 1 HERE]

Case study 1 – Websites and web tools. The Copernicus Climate Change Service (C3S) provides free and open access to climate data, tools and information through a website. It also includes demonstration projects that show how C3S data can be used in practice through case studies, training sessions and workshops (Thepaut et al., 2018). A large audience of the service is composed of intermediate users, loosely defined as the community of operators in one of the intermediate steps between the primary producers of climate data and the ultimate beneficiaries.

To address this audience, the strategy of C3S is to provide free and open access climate data and tools such as historical observations (both satellite and ground-based), climate data records relevant for a number of Essential Climate Variables (Bojinski et al., 2014), global and regional reanalyses, climate monitoring bulletins, seasonal predictions, as well as both global (a selection of simulations from the Coupled Model Intercomparison Project (CMIP (Taylor et al., 2012; Eyring et al., 2016)) and regional climate projections from the Coordinated Regional Downscaling Experiment (Euro- and Med-CORDEX (Jacob et al., 2014; Ruti et al., 2016)). A number of indices for various sectors can be calculated through cloud-based tools. For instance, in order to address the specific needs of key sectoral users, climate impact indicators for common variables such as "heating degree-days" can be calculated by the users and made available to others (Buontempo et al., 2020). All this material is quality controlled following a standardised, transparent and traceable framework.

C3S also facilitates the tailoring process, by providing a series of working open-source on-the-cloud demonstrators which show how climate data can be transformed into actionable information to meet specific

ACCEPTED VERSION SUBJECT TO FINAL EDITS

user requirements. This tailoring process covers the chain between the definition of key indicators all the way to the user interface. The C3S products definition and production involve scientists that produced and assessed the data. A variety of potential users are involved in the definition of indicators and other products.

Through its quality assurance process and demonstrators, C3S provides a basic evaluation of all climate data it provides access, and it encourages the users to develop their own case-specific analysis within the C3S infrastructure. Trustworthiness and relevance of such an analysis are substantially strengthened through a distillation process, co-designed by the user and data provider, and drawing upon multiple lines of evidence and process-based evaluation of model fitness (Section 10.5).

Case study 2 – Interactive group activities. Science-application engagement is extremely challenging especially in critically important but complex contexts such as rapidly growing cities in developing nations (Culwick and Patel, 2017). The publicly funded Future Resilience for African CiTies And Lands (FRACTAL) project was conceived and designed in response to extensive and strong evidence and experience that useful and useable climate services require strong mutual relationships across the science-application interface that can be built using supportive processes and structures (Taylor et al., 2017).

Informed by this understanding, FRACTAL was grounded in a very reflexive and context guided approach with city decision making at its core (Taylor et al., 2017a). Representatives from selected southern African cities were included in the proposal design and, throughout the project, a core principle was to allow the city partners to lead and guide the process.

Two important elements were deployed in FRACTAL: "embedded researchers" and "learning labs". Embedded Researchers were seconded into the municipality and served as the essential connection for the learning process within each city (Steynor et al., 2020). Learning Labs (Arrighi et al., 2016) were interactive structures in which participants from academia, local city government and councils, state-owned enterprises, communities and community development institutions, etc could interact. Embedded Researchers and Learning Labs were the backbone of ongoing learning processes within each city and resulted in more focused small-group dialogues, capacity development and training processes, and within-city research and engagement activities. Each Learning Lab focused initially on identifying "burning issues" without a requirement that they involve strong climate linkages. However, with the over-arching focus on resilience, discussions evolved in that direction and the burning issues identified often centered around water in peri-urban areas e.g., in Windhoek (Scott et al., 2018).

The learning labs also introduced and developed the concept of Climate Risk Narratives as a process and product (CRN; see Cross-Chapter Box 12.2, Figure 2 and Chapter 10 Box 10.2 on storylines) to generate and integrate climate and socio-economic information relevant to adaptation and resilience (Jack et al., 2020). The first CRNs were informed primarily by climate evidence, but also included some tentative socio-economic impact elements gleaned from literature and other studies. Their content was intentionally provocative and designed to promote debate and discussion, and subsequent iteration. Many participants noted that this was the first time that various important conversations across governance structures and disciplinary areas had occurred around what climate change may actually mean. This demonstrates the engagement value of CRNs as a key element in an iterative co-production process to ensure important details are included correctly, such as the local context, terms and names as well as providing reality checks on the impacts and societal responses (Jack et al., 2020).

This case study emphasises the positive contributions of the fit, tailoring and contextualization of climate information with respect to the specific decision-making needs of particular users (10.5 and WG2 17.4.4.2.2), the importance of participatory planning for risk management in urban areas (WG2 6.1.5 and 6.4.2) and the importance of networks and organizations which link researchers, policy-makers and end-users to promote adaptation in African cities (WG2 9.8.5.1). Upscaling this type of interactive activity to cater for the large number of user demands remains a challenge.

ACCEPTED VERSION SUBJECT TO FINAL EDITS

[START CROSS-CHAPTER BOX 12.2, FIGURE 2 HERE]

Cross-Chapter Box 12.2, Figure 2: Climate Risk Narrative infographic developed through the FRACTAL Windhoek Learning Lab process (adapted from Jack et al., (2020)).

[END CROSS-CHAPTER BOX 12.2, FIGURE 2 HERE]

Case study 3 – Focused relationships. This broad category involves one-to-one engagement between a provider and a user with very specific needs. One such user is the Asian Development Bank (ADB) who has committed to making all its investments climate resilient by implementing a climate risk management framework (ADB, 2014, 2018; Lu, 2019). The climate risk management framework mandates all climate-sensitive investment projects undertake a climate risk and adaptation assessment, to identify material risks of a changing climate to the proposed project and potential adaptive measures to be incorporated into project design, implementation, maintenance and/or monitoring. Typically, loan project processing teams procure consulting services for a bespoke climate risk and adaptation assessment (CRA) for a specific project. The user-provider engagement is highly targeted and goal-oriented. An example of such a focused user-provider engagement is the CRA carried out as part of an investment project in Viet Nam, the Water Efficiency Improvement in Drought-Affected Provinces (WEIDAP) project.

In the wake of the El Niño-induced 2015-2016 severe drought causing major damage to agricultural land in the Central Highlands of Viet Nam, the WEIDAP project was initiated to improve water productivity of irrigated agriculture. Proposed project interventions include a package of both "soft" (e.g., policy, institutional and capacity building, on-farm water efficiency practices) and "hard" (modernized irrigation schemes) activities. To ensure that the project delivers expected benefits under a changing climate, consultants were recruited to carry out a detailed CRA, working as part of the overall project processing team. Through extensive consultations with the rest of the project team and review of literature including relevant climate projections, the CRA consultants chose to construct three broad climate scenarios for the 2050s (a time frame appropriate for the lifetime of the irrigation schemes being proposed under the project): a warm-and-wet, a hot-and-wet, and a hotter future. Outputs from a selection of CMIP5 models were analysed under these three scenarios, to derive changes in temperature, rainfall and potential evapotranspiration, which in turn were used as inputs to hydrological, crop and agro-economics models to assess the impacts of climate change on the overall project performance. Table 1 presents the summary of the key parameters under the three scenarios. Recommendations from the CRA included (largely minor) refinements and additional activities for drought planning, detailed engineering design of the relevant project components (such as access roads, river crossings and foundations), and support for poorer farmers who may not be able to afford access to water and climate-resilient technologies.

This case study illustrates that climate information distillation including a sustained iterative engagement between climate information users, producers and translators can improve the quality of the information and the decision-making (Section 10.5, WG2 17.4.4.2.2).

[START CROSS-CHAPTER BOX 12.2, TABLE 1 HERE]

Cross-Chapter Box 12.2, Table 1: Summary of Annual Province-Level Changes in Temperature, Precipitation and Evapotranspiration under the Three Broad Scenarios in Southern Viet Nam (Scenario 1: warm-and-wet; Scenario 2: hot-and-wet; Scenario 3: hotter) *(Source: Table 3 in* (ADB, 2020)*)*

ACCEPTED VERSION SUBJECT TO FINAL EDITS

Item	Province and Scenario Number														
	Binh Thuan			Dak Lak			Dak Nong			Khanh Hoa			Ninh Thuan		
	1	2	3	1	2	3	1	2	3	1	2	3	1	2	3
ΔT (°C)	1.1	1.8	2.6	1.1	1.5	2.0	1.2	2.1	2.7	1.1	1.8	2.6	1.1	1.5	2.6
ΔP (%)	28	-12	4	8	17	-8	8	-8	7	3	-10	7	27	1	5
ΔPET (%)	3	6	8	4	5	7	4	7	9	3	6	8	3	5	8

ΔP = change in precipitation, ΔPET = change in potential evapotranspiration, ΔT = change in temperature.
Note: Color scale indicates significance of changes for the water balance. Gray = no significant change, green = medium positive impact, blue = high positive impact, yellow = medium negative impact, orange = high negative impact

[END CROSS-CHAPTER BOX 12.2, TABLE 1 HERE]

[END CROSS-CHAPTER BOX 12.2 HERE]

12.7 Final Remarks

The assessment in this chapter is based on a rapidly growing body of new evidence from the peer-reviewed literature, direct calculations of climate projections from several new model ensembles, and results from other AR6 WGI chapters. Although a large amount a new information on CID changes and their uptake in climate services has become available since AR5, some challenges still remain. This section summarizes some of these main challenges, with a view to facilitating improved assessments in future. The section is organized following the order of chapter sections and consolidated according to key assessment components.

- The adoption of the climatic impact-driver (CID) framework could benefit more from stronger connections across physical climate and impact scientists, and between the science community and practitioners/stakeholders on the ground. Co-development of CID index definitions with impact scientists or stakeholders helps ensure their salience and utility {12.1, 12.2, 12.3, 12.6}.

- The ability to project all aspects of shifting CID profiles and their effects at fine, local scales is often reliant on dynamical downscaling and additional impact modelling steps, making a robust and full quantification of the uncertainties involved more challenging. Availability of multiple models and ease of connecting physical climate models at different scales can facilitate assessment {12.2, 12.3, 12.4, 12.5}.

- Regional and sub-regional differences in coverage and access of homogeneous historical records, in the deployment of regional model ensembles and the exploration of scenarios, and ultimately in peer-reviewed studies addressing the full range of past and current behavior, detection and attribution, and future projections challenge a uniformly robust assessment across all CIDs and regions of the world {12.4, 12.5}.

- Efforts to assess a consistent global, large scale view of CID changes across regions and sectors would benefit from additional coordinated studies adopting common CID indices, model protocols, time horizons and scenarios or global warming levels {12.3, 12.5}.

- Even though the body of peer-reviewed literature regarding climate services practices and products is growing, a large part is still documented only in grey literature arising from commercial consultancy, and thus not publicly and freely accessible {12.6}.

ACCEPTED VERSION SUBJECT TO FINAL EDITS

Frequently Asked Questions

FAQ 12.1: What is a climatic impact-driver (CID)?

A climatic impact-driver is a physical climate condition that directly affects society or ecosystems. Climatic impact-drivers may represent a long-term average condition (such as the average winter temperatures that affect indoor heating requirements), a common event (such as a frost that kills off warm-season plants), or an extreme event (such as a coastal flood that destroys homes). A single climatic impact-driver may lead to detrimental effects for one part of society while benefiting another, while others are not affected at all. A climatic impact-driver (or its change caused by climate change) is therefore not universally hazardous or beneficial, but we refer to it as a 'hazard' when experts determine it is detrimental to a specific system.

Climate change can alter many aspects of the climate system, but efforts to identify impacts and risks usually focus on a smaller set of changes known to affect, or potentially affect, things that society cares about. These *climatic impact-drivers* (CIDs) are formally defined in this Report as 'physical climate system conditions (e.g., means, events, extremes) that affect an element of society or ecosystems. Depending on system tolerance, CIDs and their changes can be detrimental, beneficial, neutral, or a mixture of each across interacting system elements and regions'. Because people, infrastructure and ecosystems interact directly with their immediate environment, climate experts assess CIDs locally and regionally. CIDs may relate to temperature, the water cycle, wind and storms, snow and ice, oceanic and coastal processes or the chemistry and energy balance of the climate system. Future impacts and risk may also be directly affected by factors unrelated to the climate (such as socio-economic development, population growth, or a viral outbreak) that may also alter the vulnerability or exposure of systems.

CIDs capture important characteristics of the average climate and both common and extreme events that shape society and nature (see FAQ 12.2). Some CIDs focus on aspects of the average climate (such as the seasonal progression of temperature and precipitation, average winds and the chemistry of the ocean) that determine, for example, species distribution, farming systems, the location of tourist resorts, the availability of water resources and the expected heating and cooling needs for buildings in an average year. CIDs also include common episodic events that are particularly important to systems, such as thaw events that can trigger springtime plant development, cold spells that are important for fruit crop chill requirements, or frost events that eliminate summer vegetation as winter sets in. Finally, CIDs include many extreme events connected to impacts such as hailstorms that damage vehicles, coastal floods that destroy shoreline property, tornadoes that damage infrastructure, droughts that increase competition for water resources, and heatwaves that can strain the health of outdoor laborers.

Many aspects of our daily lives, businesses and natural systems depend on weather and climate, and there is great interest in anticipating the impacts of climate change on the things we care about. To meet these needs, scientists engage with companies and authorities to provide climate services – meaningful and possibly actionable climate information designed to assist decision-making. Climate science and services can focus on CIDs that substantially disrupt systems to support broader risk management approaches. A single CID change can have dramatically different implications for different sectors or even elements of the same sector, so engagement between climate scientists and stakeholders is important to contextualize the climate changes that will come. Climate services responding to planning and optimization of an activity can focus on more gradual changes in climate operating conditions.

FAQ 12.1, Figure 1 tracks example outcomes of seasonal snow cover changes that connect climate science to the need for mitigation, adaptation and regional risk management. The length of the season with snow on the ground is just one of many regional climate conditions that may change in the future, and it becomes a CID because there are many elements of society and ecosystems that rely on an expected seasonality of snow cover. Climate scientists and climate service providers examining human-driven climate change may identify different regions where the length of the season with snow cover could increase, decrease, or stay relatively unaffected. In each region, change in seasonal snow cover in turn may affect different systems in beneficial or detrimental ways (in the latter case, changing seasonal snow cover would be a 'hazard'), although systems such as coastal aquaculture remain relatively unaffected. The changing profile of benefits

ACCEPTED VERSION SUBJECT TO FINAL EDITS

and hazards connected to these changes in the seasonal snow cover CID in turn affects the profile of impacts, risks and benefits that stakeholder in the region manage in response to climate change.

[START FAQ12.1, FIGURE 1 HERE]

FAQ 12.1, Figure 1: A single climatic impact-driver can affect ecosystems and society in different ways. A variety of impacts from the same climatic impact-driver change, illustrated with the example of regional seasonal snow cover.

[END FAQ12.1, FIGURE 1 HERE]

ACCEPTED VERSION
SUBJECT TO FINAL EDITS

FAQ 12.2: What are climatic thresholds and why are they important?

Climatic thresholds tell us about the tolerance of society and ecosystems so that we can better scrutinize the types of climate changes that are expected to impact things we care about. Many systems have natural or structural thresholds. If conditions exceed those thresholds, the result can be sudden changes or even collapses in health, productivity, utility or behavior. Adaptation and risk management efforts can change these thresholds, altering the profile of climate conditions that would be problematic and increasing overall system resilience.

Decision makers have long observed that certain weather and climate conditions can be problematic, or hazardous, for things they care about (i.e., things with socio-economic, cultural or intrinsic value). Many elements of society and ecosystems operate in a suitable climate zone selected naturally or by stakeholders considering the expected climate conditions. However, as climate change moves conditions beyond expected ranges, they may cross a climatic 'threshold' – a level beyond which there are either gradual changes in system behaviour or abrupt, non-linear and potentially irreversible impacts.

Climatic thresholds can be associated with either natural or structural tolerance levels. Natural thresholds, for instance, include heat and humidity conditions above which humans cannot regulate their internal temperatures through sweat, drought durations that heighten competition between species, and winter temperatures that are lethal for pests or disease-carrying vector species. Structural thresholds include engineered limits of drainage systems, extreme wind speeds that limit wind turbine operation, the height of coastal protection infrastructure, and the locations of irrigation infrastructure or tropical cyclone sheltering facilities.

Thresholds may be defined according to raw values (such as maximum temperature exceeding 35°C) or percentiles (such as the local 99th percentile daily rainfall total). They also often have strong seasonal dependence (see FAQ 12.3). For example, the amount of snowfall that a deciduous tree can withstand depends on whether the snowfall occurs before or after the tree sheds its leaves. Most systems respond to changes in complex ways, and those responses are not determined solely or precisely by specific thresholds of a single climate variable. Nonetheless, thresholds can be useful indicators of system behaviours, and an understanding of these thresholds can help inform risk management decisions.

FAQ 12.2 Figure 1 illustrates how threshold conditions can help us understand climate conditions that are suitable for normal system operation and the thresholds beyond which impacts occur. Crops tend to grow most optimally within a suitable range of daily temperatures that is influenced by the varieties being cultivated and the way the farm is managed. As daily temperatures rise above a 'critical' temperature threshold, plants begin to experience heat stress that reduces growth and may lower resulting yields. If temperatures reach a higher 'limiting' temperature threshold, crops may suffer leaf loss, pollen sterility, or tissue damage that can lead to crop failure. Farmers typically select a cropping system with some consideration to the probability of extreme temperature events that may occur within a typical season, and so identifying hot temperature thresholds helps farmers select their seed and field management strategies as part of their overall risk management. Climate experts may therefore aim to assist farm planning by providing information about the climate change-induced shifts to the expected frequency of daily heat extremes that exceed crop tolerance thresholds.

Adaptation and other changes in societies and environment can shift climatic thresholds by modifying vulnerability and exposure. For example, adaptation efforts may include breeding new crops with higher heat tolerance levels so that corresponding dangerous thresholds occur less frequently. Likewise, increasing the height of a flood embankment protecting a given community can increase the level of river flow that may be tolerated without flooding, reducing the frequency of damaging floods. Stakeholders therefore benefit from climate services that are based on a co-development process, with scientists identifying system-relevant thresholds and developing tailored climatic impact-driver indices that represent these thresholds (FAQ 12.1). These thresholds help focus the provision of action-relevant climate information for adaptation and risk management.

ACCEPTED VERSION SUBJECT TO FINAL EDITS

[START FAQ12.2, FIGURE 1 HERE]

FAQ12.2, Figure 1: Crop response to maximum temperature thresholds. Crop growth rate responds to daily maximum temperature increases, leading to reduced growth and crop failure as temperatures exceed critical and limiting temperature thresholds, respectively. Note that changes in other environmental factors (such as carbon dioxide and water) may increase the tolerance of plants to increasing temperatures.

[END FAQ12.2, FIGURE 1 HERE]

ACCEPTED VERSION
SUBJECT TO FINAL EDITS

FAQ 12.3: How will climate change affect the regional characteristics of a climate hazard?

Human-driven climate change can alter the regional characteristics of climate hazard by changing the magnitude or intensity of a climate hazard, the frequency with which it occurs, the duration that hazardous conditions persist, the timing when a hazard occurs, or the spatial extent threatened by a hazard. By examining each of these aspects of a hazard's profile change, climate services may provide climate risk information that allows decision makers to better tailor adaptation, mitigation and risk management strategies.

A *climate hazard* is a climate condition with the potential to harm natural systems or society. Examples include heatwaves, droughts, heavy snowfall events and sea level rise. Climate scientists look for patterns in climatic impact-drivers to detect the signature of changing hazards that may influence stakeholder planning (FAQ 12.1). Climate service providers work with stakeholders and impacts experts to identify key system responses and tolerance thresholds (FAQ 12.2) and then examine historical observations and future climate projections to identify associated changes to the characteristics of a regional hazard's profile. Climate change can alter at least five different characteristics of the hazard profile of a region (FAQ 12.3, Figure 1):

Magnitude or intensity is the raw value of a climate hazard, such as an increase in the maximum yearly temperature or in the depth of flooding that results from a coastal storm with a 1% change of occurring each year.

Frequency is the number of times that a climate hazard reaches or surpasses a threshold over a given period. For example, increases to the number of heavy snowfall events, tornadoes, or floods experienced in a year or in a decade.

Duration is the length of time over which hazardous conditions persist beyond a threshold, such as an increase in the number of consecutive days where maximum air temperature exceeds 35°C, the number of consecutive months of drought conditions, or the number of days that a tropical cyclone affects a location.

Timing captures the occurrence of a hazardous event in relation to the course of a day, season, year, or other period in which sectoral elements are evolving or co-dependent (such as the time of year when migrating animals expect to find a seasonal food supply). Examples include a shift toward an earlier day of the year when the last spring frost occurs or a delay in the typical arrival date for the first seasonal rains, the length of the winter period when the ground is typically covered by snow, or a reduction in the typical time needed for soil moisture to move from normal to drought conditions.

Spatial extent is the region in which a hazardous condition is expected, such as the area currently threatened by tropical cyclones, geographical areas where the coldest day of the year restricts a particular pest or pathogen, terrain where permafrost is present, the area that would flood following a common storm, zones where climate conditions are conducive to outdoor labour, or the size of a marine heatwave.

Hazard profile changes are often intertwined or stem from related physical changes to the climate system. For example, changes in the frequency and magnitude of extreme events are often directly related to each other as a result of atmospheric dynamics and chemical processes. In many cases, one aspect of hazard change is more apparent than others, which may provide a first emergent signal indicating a larger set of changes to come (FAQ1.2).

Information about how a hazard has changed or will change helps stakeholders prioritize more robust adaptation, mitigation and risk management strategies. For example, allocation of limited disaster relief resources may be designed to recognize that tropical cyclones are projected to become more intense even as the frequency of those storms may not change. Planning may also factor in the fact that even heatwaves that are not record-breaking in their intensity can still be problematic for vulnerable populations when they persist over a long period. Likewise, firefighters recognize new logistical challenges in the lengthening of the fire weather season and an expansion of fire conditions into parts of the world where fires were not previously a great concern. Strong engagement between climate scientists and stakeholders therefore helps

ACCEPTED VERSION SUBJECT TO FINAL EDITS

climate services tailor and communicate clear information about the types of changing climate hazards to be addressed in resilience efforts.

[START FAQ12.3, FIGURE 1 HERE]

FAQ 12.3, Figure 1: Types of changes to a region's hazard profile. The first five panels illustrate how climate changes can alter a hazard's intensity (or magnitude), frequency, duration, and timing (by seasonality and speed of onset) in relation to a hazard threshold (horizontal grey line). The difference between the historical climate (blue) and future climate (red) shows the changing aspects of climate change that stakeholders will have to manage. The bottom-right panel shows how a given climate hazard (such as a once-in-100-year river flood) may reach new geographical areas under a future climate change.

[END FAQ12.3, FIGURE 1 HERE]

ACCEPTED VERSION
SUBJECT TO FINAL EDITS

References

Aalto, J., S. Harrison, and M. Luoto, 2017: Statistical modelling predicts almost complete loss of major periglacial processes in Northern Europe by 2100. *Nature Communications*, **8(1)**, 515, doi:10.1038/s41467-017-00669-3.

Abatzoglou, J.T. and A.P. Williams, 2016: Impact of anthropogenic climate change on wildfire across western US forests. *Proceedings of the National Academy of Sciences*, **113(42)**, 11770–11775, doi:10.1073/pnas.1607171113.

Abatzoglou, J.T., A.P. Williams, and R. Barbero, 2019: Global Emergence of Anthropogenic Climate Change in Fire Weather Indices. *Geophysical Research Letters*, **46(1)**, 326–336, doi:10.1029/2018gl080959.

Abegg, B. et al., 2020: Overloaded! Critical revision and a new conceptual approach for snow indicators in ski tourism. *International Journal of Biometeorology*, 1–11, doi:10.1007/s00484-020-01867-3.

Abiodun, B.J., N. Makhanya, B. Petja, A.A. Abatan, and P.G. Oguntunde, 2019: Future projection of droughts over major river basins in Southern Africa at specific global warming levels. *Theoretical and Applied Climatology*, **137(3–4)**, 1785–1799, doi:10.1007/s00704-018-2693-0.

Abram, N.J. et al., 2021: Connections of climate change and variability to large and extreme forest fires in southeast Australia. *Communications Earth & Environment*, **2(1)**, 8, doi:10.1038/s43247-020-00065-8.

Acar Deniz, Z. and B. Gönençgil, 2015: Trends of summer daily maximum temperature extremes in Turkey. *Physical Geography*, **36(4)**, 268–281, doi:10.1080/02723646.2015.1045285.

Acquah, H.-G. and E.E. Onumah, 2011: Farmers Perception and Adaptation to Climate Change: An Estimation of Willingness to Pay. *AGRIS on-line Papers in Economics and Informatics*, **3**, 31–39, doi:10.22004/ag.econ.120241.

ADB, 2014: *Climate Risk Management in ADB Projects*. Publication Stock No. ARM146926-2, Asian Development Bank (ADB), Manila, Philippines, 6 pp.

ADB, 2018: *Strategy 2030: Achieving a Prosperous, Inclusive, Resilient, and Sustainable Asia and the Pacific*. Publication Stock No. TCS189401-2, Asian Development Bank (ADB), Manila, Philippines, 34 pp., doi:10.22617/tcs189401-2.

ADB, 2020: *Climate Change Risk and Adaptation Assessment for Irrigation in Southern Viet Nam: Water Efficiency Improvements in Drought-Affected Provinces*. Publication Stock No. TCS200351-2, Asian Development Bank (ADB), Manila, Philippines, 80 pp., doi:10.22617/tcs200351-2.

Addo, K.A. and I.A. Addo, 2016: Coastal erosion management in Accra: Combining local knowledge and empirical research. *Journal of Disaster Risk Studies*, **8(1)**, 274, doi:10.4102/jamba.v8i1.274.

Aerts, J.C.J.H. et al., 2014: Evaluating Flood Resilience Strategies for Coastal Megacities. *Science*, **344(6183)**, 473–475, doi:10.1126/science.1248222.

Agafonova, S.A., N.L. Frolova, I.N. Krylenko, A.A. Sazonov, and P.P. Golovlyov, 2017: Dangerous ice phenomena on the lowland rivers of European Russia. *Natural Hazards*, **88(S1)**, 171–188, doi:10.1007/s11069-016-2580-x.

Agier, L. et al., 2013: Seasonality of meningitis in Africa and climate forcing: aerosols stand out. *Journal of The Royal Society Interface*, **10(79)**, 20120814, doi:10.1098/rsif.2012.0814.

Aguilar-Lome, J. et al., 2019: Elevation-dependent warming of land surface temperatures in the Andes assessed using MODIS LST time series (2000–2017). *International Journal of Applied Earth Observation and Geoinformation*, **77**, 119–128, doi:10.1016/j.jag.2018.12.013.

Ahmadalipour, A. and H. Moradkhani, 2018: Escalating heat-stress mortality risk due to global warming in the Middle East and North Africa (MENA). *Environment International*, **117**, 215–225, doi:10.1016/j.envint.2018.05.014.

Ahmadalipour, A., H. Moradkhani, and M.C. Demirel, 2017: A comparative assessment of projected meteorological and hydrological droughts: Elucidating the role of temperature. *Journal of Hydrology*, **553**, 785–797, doi:10.1016/j.jhydrol.2017.08.047.

Ahmed, K., S. Shahid, and N. Nawaz, 2018: Impacts of climate variability and change on seasonal drought characteristics of Pakistan. *Atmospheric Research*, **214**, 364–374, doi:10.1016/j.atmosres.2018.08.020.

Ahmed, K., S. Shahid, X. Wang, N. Nawaz, and N. Khan, 2019: Spatiotemporal changes in aridity of Pakistan during 1901-2016. *Hydrology and Earth System Sciences*, **23(7)**, 3081–3096, doi:10.5194/hess-23-3081-2019.

Ahmed, N., S. Thompson, and M. Glaser, 2019: Global Aquaculture Productivity, Environmental Sustainability, and Climate Change Adaptability. *Environmental Management*, **63(2)**, 159–172, doi:10.1007/s00267-018-1117-3.

Ahmed, N. et al., 2020: Temperature trends and elevation dependent warming during 1965–2014 in headwaters of Yangtze River, Qinghai Tibetan Plateau. *Journal of Mountain Science*, **17(3)**, 556–571, doi:10.1007/s11629-019-5438-3.

Aich, V. et al., 2014: Comparing impacts of climate change on streamflow in four large African river basins. *Hydrology and Earth System Sciences*, **18(4)**, 1305–1321.

Aich, V. et al., 2017: Climate Change in Afghanistan Deduced from Reanalysis and Coordinated Regional Climate Downscaling Experiment (CORDEX)-South Asia Simulations. *Climate*, **5(2)**, 38, doi:10.3390/cli5020038.

Aitsi-Selmi, A., S. Egawa, H. Sasaki, C. Wannous, and V. Murray, 2015: The Sendai Framework for Disaster Risk Reduction: Renewing the Global Commitment to People's Resilience, Health, and Well-being. *International*

ACCEPTED VERSION SUBJECT TO FINAL EDITS

Journal of Disaster Risk Science, **6(2)**, 164–176, doi:10.1007/s13753-015-0050-9.
Akhiljith, P.J. et al., 2019: Climatic Projections of Indian Ocean During 2030, 2050, 2080 with Implications on Fisheries Sector. *BRAQCON 2019: World Brackishwater Aquaculture Conference. Journal of Coastal Research*, **Special Is**, 198–208, doi:10.2112/si86-030.1.
Akhter, J., L. Das, J.K. Meher, and A. Deb, 2018: Uncertainties and time of emergence of multi-model precipitation projection over homogeneous rainfall zones of India. *Climate Dynamics*, **50(9)**, 3813–3831, doi:10.1007/s00382-017-3847-y.
Akperov, M. et al., 2018: Cyclone Activity in the Arctic From an Ensemble of Regional Climate Models (Arctic CORDEX). *Journal of Geophysical Research: Atmospheres*, **123(5)**, 2537–2554, doi:10.1002/2017jd027703.
Akperov, M. et al., 2019: Future projections of cyclone activity in the Arctic for the 21st century from regional climate models (Arctic-CORDEX). *Global and Planetary Change*, **182**, 103005, doi:10.1016/j.gloplacha.2019.103005.
Al Ameri, I.D.S., R.M. Briant, and S. Engels, 2019: Drought severity and increased dust storm frequency in the Middle East: a case study from the Tigris–Euphrates alluvial plain, central Iraq. *Weather*, **74(12)**, 416–426, doi:10.1002/wea.3445.
Albert, S. et al., 2016: Interactions between sea-level rise and wave exposure on reef island dynamics in the Solomon Islands. *Environmental Research Letters*, **11(5)**, 54011, doi:10.1088/1748-9326/11/5/054011.
Albright, R. et al., 2016: Reversal of ocean acidification enhances net coral reef calcification. *Nature*, **531(7594)**, 362–365, doi:10.1038/nature17155.
Alexander, L. and J.M. Arblaster, 2017: Historical and projected trends in temperature and precipitation extremes in Australia in observations and CMIP5. *Weather and Climate Extremes*, **15**, 34–56, doi:10.1016/j.wace.2017.02.001.
Alfieri, L., L. Feyen, F. Dottori, and A. Bianchi, 2015: Ensemble flood risk assessment in Europe under high end climate scenarios. *Global Environmental Change*, **35**, 199–212, doi:10.1016/j.gloenvcha.2015.09.004.
Alfieri, L. et al., 2017: Global projections of river flood risk in a warmer world. *Earth's Future*, **5(2)**, 171–182, doi:10.1002/2016ef000485.
Aljaryian, R. and L. Kumar, 2016: Changing global risk of invading greenbug Schizaphis graminum under climate change. *Crop Protection*, **88**, 137–148, doi:10.1016/j.cropro.2016.06.008.
Allen, C.D., D.D. Breshears, and N.G. McDowell, 2015: On underestimation of global vulnerability to tree mortality and forest die-off from hotter drought in the Anthropocene. *Ecosphere*, **6(8)**, art129, doi:10.1890/es15-00203.1.
Allen, J.T., 2018: Climate Change and Severe Thunderstorms. In: *Oxford Research Encyclopedia of Climate Science*. Oxford University Press, Oxford, UK, doi:10.1093/acrefore/9780190228620.013.62.
Allen, J.T., M.K. Tippett, and A.H. Sobel, 2015: An empirical model relating U.S. monthly hail occurrence to large-scale meteorological environment. *Journal of Advances in Modeling Earth Systems*, **7(1)**, 226–243, doi:10.1002/2014ms000397.
Allen, S. and C. Huggel, 2013: Extremely warm temperatures as a potential cause of recent high mountain rockfall. *Global and Planetary Change*, **107**, 59–69, doi:10.1016/j.gloplacha.2013.04.007.
Almazroui, M., S. Saeed, F. Saeed, M.N. Islam, and M. Ismail, 2020: Projections of Precipitation and Temperature over the South Asian Countries in CMIP6. *Earth Systems and Environment*, **4(2)**, 297–320, doi:10.1007/s41748-020-00157-7.
Almazroui, M. et al., 2021: Projected Changes in Temperature and Precipitation Over the United States, Central America, and the Caribbean in CMIP6 GCMs. *Earth Systems and Environment*, **5(1)**, 1–24, doi:10.1007/s41748-021-00199-5.
Alobaidi, M., M. Almazroui, A. Mashat, and P.D. Jones, 2017: Arabian Peninsula wet season dust storm distribution: regionalization and trends analysis (1983–2013). *International Journal of Climatology*, **37(3)**, 1356–1373, doi:10.1002/joc.4782.
Alongi, D.M., 2015: The Impact of Climate Change on Mangrove Forests. *Current Climate Change Reports*, **1(1)**, 30–39, doi:10.1007/s40641-015-0002-x.
Altieri, A.H. and K.B. Gedan, 2015: Climate change and dead zones. *Global Change Biology*, **21(4)**, 1395–1406, doi:10.1111/gcb.12754.
Altman, J. et al., 2018: Poleward migration of the destructive effects of tropical cyclones during the 20th century. *Proceedings of the National Academy of Sciences of the United States of America*, **115(45)**, 11543–11548, doi:10.1073/pnas.1808979115.
Alvioli, M. et al., 2018: Implications of climate change on landslide hazard in Central Italy. *Science of The Total Environment*, **630**, 1528–1543, doi:10.1016/j.scitotenv.2018.02.315.
AMAP, 2017a: *Snow, Water, Ice and Permafrost in the Arctic (SWIPA) 2017*. Arctic Monitoring and Assessment Programme (AMAP), Oslo, Norway, 269 pp.
AMAP, 2017b: *Snow, Water, Ice and Permafrost in the Arctic: Summary for Policy-makers*. Arctic Monitoring and Assessment Programme (AMAP), Oslo, Norway, 20 pp.
Ambika, A.K. and V. Mishra, 2020: Substantial decline in atmospheric aridity due to irrigation in India. *Environmental*

ACCEPTED VERSION SUBJECT TO FINAL EDITS

Research Letters, **15(12)**, 124060, doi:10.1088/1748-9326/abc8bc.
Amos, C.B. et al., 2014: Uplift and seismicity driven by groundwater depletion in central California. *Nature*, **509(7501)**, 483–486, doi:10.1038/nature13275.
Andela, N. et al., 2017: A human-driven decline in global burned area. *Science*, **356(6345)**, 1356–1362, doi:10.1126/science.aal4108.
Anderson, G.B., K.W. Oleson, B. Jones, and R.D. Peng, 2018: Projected trends in high-mortality heatwaves under different scenarios of climate, population, and adaptation in 82 US communities. *Climatic Change*, **146(3–4)**, 455–470, doi:10.1007/s10584-016-1779-x.
Andresen, C.G. and V.L. Lougheed, 2015: Disappearing Arctic tundra ponds: Fine-scale analysis of surface hydrology in drained thaw lake basins over a 65 year period (1948-2013). *Journal of Geophysical Research: Biogeosciences*, **120(3)**, 466–479, doi:10.1002/2014jg002778.
Andrews, O.D., N.L. Bindoff, P.R. Halloran, T. Ilyina, and C. Quéré, 2013: Detecting an external influence on recent changes in oceanic oxygen using an optimal fingerprinting method. *Biogeosciences*, **10(3)**, 1799–1813, doi:10.5194/bg-10-1799-2013.
Anenberg, S.C. et al., 2017: Impacts of oak pollen on allergic asthma in the United States and potential influence of future climate change. *GeoHealth*, **1(3)**, 80–92, doi:10.1002/2017gh000055.
Antwi-Agyei, P., K. Amanor, J.N. Hogarh, and A.J. Dougill, 2021: Predictors of access to and willingness to pay for climate information services in north-eastern Ghana: A gendered perspective. *Environmental Development*, **37**, 100580, doi:10.1016/j.envdev.2020.100580.
Araghi, A., C.J. Martinez, J. Adamowski, and J.E. Olesen, 2018: Spatiotemporal variations of aridity in Iran using high-resolution gridded data. *International Journal of Climatology*, **38(6)**, 2701–2717, doi:10.1002/joc.5454.
Archfield, S.A., R.M. Hirsch, A. Viglione, and G. Blöschl, 2016: Fragmented patterns of flood change across the United States. *Geophysical Research Letters*, **43(19)**, 10232–10239, doi:10.1002/2016gl070590.
Arheimer, B. and G. Lindström, 2015: Climate impact on floods: Changes in high flows in Sweden in the past and the future (1911-2100). *Hydrology and Earth System Sciences*, **19(2)**, 771–784, doi:10.5194/hess-19-771-2015.
Arias-Ortiz, A. et al., 2018: A marine heatwave drives massive losses from the world's largest seagrass carbon stocks. *Nature Climate Change*, **8(4)**, 338–344, doi:10.1038/s41558-018-0096-y.
Arnell, N.W. and S.N. Gosling, 2013: The impacts of climate change on river flow regimes at the global scale. *Journal of Hydrology*, **486**, 351–364, doi:10.1016/j.jhydrol.2013.02.010.
Arnell, N.W. and B. Lloyd-Hughes, 2014: The global-scale impacts of climate change on water resources and flooding under new climate and socio-economic scenarios. *Climatic Change*, **122(1–2)**, 127–140, doi:10.1007/s10584-013-0948-4.
Arnell, N.W. and S.N. Gosling, 2016: The impacts of climate change on river flood risk at the global scale. *Climatic Change*, **134(3)**, 387–401, doi:10.1007/s10584-014-1084-5.
Arnell, N.W. et al., 2016: The impacts of climate change across the globe: A multi-sectoral assessment. *Climatic Change*, **134(3)**, 457–474, doi:10.1007/s10584-014-1281-2.
Arnell, N.W. et al., 2019: The global and regional impacts of climate change under representative concentration pathway forcings and shared socioeconomic pathway socioeconomic scenarios. *Environmental Research Letters*, **14(8)**, 084046, doi:10.1088/1748-9326/ab35a6.
Arp, C.D. et al., 2018: Contrasting lake ice responses to winter climate indicate future variability and trends on the Alaskan Arctic Coastal Plain. *Environmental Research Letters*, **13(12)**, 125001, doi:10.1088/1748-9326/aae994.
Arrighi, J. et al., 2016: *Unpacking the 'City Learning Lab' approach*. Working Paper Series No. 7, Red Cross/Red Crescent Climate Centre, International Federation of Red Cross and Red Crescent Societies, The Hague, Netherlands, 15 pp.
Asadieh, B. and N.Y. Krakauer, 2017: Global change in streamflow extremes under climate change over the 21st century. *Hydrology and Earth System Sciences*, **21(11)**, 5863–5874, doi:10.5194/hess-21-5863-2017.
Ashfaq, M. et al., 2020: Robust late twenty-first century shift in the regional monsoons in RegCM-CORDEX simulations. *Climate Dynamics*, doi:10.1007/s00382-020-05306-2.
Ashley, W.S., A.M. Haberlie, and V.A. Gensini, 2020: Reduced frequency and size of late-twenty-first-century snowstorms over North America. *Nature Climate Change*, **10(6)**, 539–544, doi:10.1038/s41558-020-0774-4.
Asseng, S. et al., 2015: Rising temperatures reduce global wheat production. *Nature Climate Change*, **5(2)**, 143–147, doi:10.1038/nclimate2470.
Aström, C. et al., 2013: Heat-related respiratory hospital admissions in Europe in a changing climate: a health impact assessment.. *BMJ open*, **3(1)**, e001842, doi:10.1136/bmjopen-2012-001842.
Auffhammer, M., P. Baylis, and C.H. Hausman, 2017: Climate change is projected to have severe impacts on the frequency and intensity of peak electricity demand across the United States.. *Proceedings of the National Academy of Sciences of the United States of America*, **114(8)**, 1886–1891, doi:10.1073/pnas.1613193114.
Augusto Sanabria, L. and A.F. Carril, 2018: Maps of wind hazard over South Eastern South America considering climate change. *Climatic Change*, **148(1–2)**, 235–247, doi:10.1007/s10584-018-2174-6.
Ault, T.R., M.D. Schwartz, R. Zurita-Milla, J.F. Weltzin, and J.L. Betancourt, 2015: Trends and Natural Variability of

ACCEPTED VERSION SUBJECT TO FINAL EDITS

Spring Onset in the Coterminous United States as Evaluated by a New Gridded Dataset of Spring Indices. *Journal of Climate*, **28(21)**, 8363–8378, doi:10.1175/jcli-d-14-00736.1.

Ávila, F. Guerrero, Y. Escobar, and F. Justino, 2019: Recent Precipitation Trends and Floods in the Colombian Andes. *Water*, **11(2)**, 379, doi:10.3390/w11020379.

Azorin-Molina, C., J.H. Dunn, C.A. Mears, P. Berrisford, and T.R. McVicar, 2018: Surface winds [in "State of the Climate in 2017"]. *Bulletin of the American Meteorological Society*, **99 (8)**, S41–S44, oi:10.1175/2018bamsstateoftheclimate.1.

Babur, M., M. Babel, S. Shrestha, A. Kawasaki, and N. Tripathi, 2016: Assessment of Climate Change Impact on Reservoir Inflows Using Multi Climate-Models under RCPs – The Case of Mangla Dam in Pakistan. *Water*, **8(9)**, 389, doi:10.3390/w8090389.

Bachmair, S. et al., 2016: Drought indicators revisited: the need for a wider consideration of environment and society. *Wiley Interdisciplinary Reviews: Water*, **3(4)**, 516–536, doi:10.1002/wat2.1154.

Bacmeister, J.T. et al., 2018: Projected changes in tropical cyclone activity under future warming scenarios using a high-resolution climate model. *Climatic Change*, **146(3)**, 547–560, doi:10.1007/s10584-016-1750-x.

Bajracharya, A.R., S.R. Bajracharya, A.B. Shrestha, and S.B. Maharjan, 2018: Climate change impact assessment on the hydrological regime of the Kaligandaki Basin, Nepal. *Science of the Total Environment*, **625**, 837–848, doi:10.1016/j.scitotenv.2017.12.332.

Baker-Austin, C. et al., 2013: Emerging Vibrio risk at high latitudes in response to ocean warming. *Nature Climate Change*, **3(1)**, 73–77, doi:10.1038/nclimate1628.

Bakun, A. et al., 2015: Anticipated Effects of Climate Change on Coastal Upwelling Ecosystems. *Current Climate Change Reports*, **1(2)**, 85–93, doi:10.1007/s40641-015-0008-4.

Balch, J.K. et al., 2017: Human-started wildfires expand the fire niche across the United States. *Proceedings of the National Academy of Sciences of the United States of America*, **114(11)**, 2946–2951, doi:10.1073/pnas.1617394114.

Ballesteros-Cánovas, J.A., D. Trappmann, J. Madrigal-González, N. Eckert, and M. Stoffel, 2018: Climate warming enhances snow avalanche risk in the Western Himalayas. *Proceedings of the National Academy of Sciences of the United States of America*, **115(13)**, 3410–3415, doi:10.1073/pnas.1716913115.

Ballinger, J., B. Jackson, I. Pechlivanidis, and W. Ries, 2011: *Potential flooding and inundation on the Hutt River*. School of Geography, Environment and Earth Sciences, and Climate Change Research Institute, Victoria University of Wellington, Wellington, New Zealand, 37 pp.

Bamunawala, J., S. Maskey, T. Duong, and A. van der Spek, 2018: Significance of Fluvial Sediment Supply in Coastline Modelling at Tidal Inlets. *Journal of Marine Science and Engineering*, **6(3)**, 79, doi:10.3390/jmse6030079.

Barange, M. et al., 2014: Impacts of climate change on marine ecosystem production in societies dependent on fisheries. *Nature Climate Change*, **4(3)**, 211–216, doi:10.1038/nclimate2119.

Barbero, R., J.T. Abatzoglou, F. Pimont, J. Ruffault, and T. Curt, 2020: Attributing Increases in Fire Weather to Anthropogenic Climate Change Over France. *Frontiers in Earth Science*, **8**, 527278832, doi:10.3389/feart.2020.00104.

Barcikowska, M.J., G. Muñoz, S.J. Weaver, S. Russo, and M. Wehner, 2019: On the potential impact of a half-degree warming on cold and warm temperature extremes in mid-latitude North America. *Environmental Research Letters*, **14(12)**, 124040, doi:10.1088/1748-9326/ab4dea.

Barlow, M. et al., 2016: A Review of Drought in the Middle East and Southwest Asia. *Journal of Climate*, **29(23)**, 8547–8574, doi:10.1175/jcli-d-13-00692.1.

Barnes, P.W. et al., 2019: Ozone depletion, ultraviolet radiation, climate change and prospects for a sustainable future. *Nature Sustainability*, **2(7)**, 569–579, doi:10.1038/s41893-019-0314-2.

Barreau, T. et al., 2017: Physical, Mental, and Financial Impacts From Drought in Two California Counties, 2015. *American Journal of Public Health*, **107(5)**, 783–790, doi:10.2105/ajph.2017.303695.

Barros, V.R. et al., 2015: Climate change in Argentina: trends, projections, impacts and adaptation. *Wiley Interdisciplinary Reviews: Climate Change*, **6(2)**, 151–169, doi:10.1002/wcc.316.

Barrow, E.M. and D.J. Sauchyn, 2019: Uncertainty in climate projections and time of emergence of climate signals in the western Canadian Prairies. *International Journal of Climatology*, **39(11)**, 4358–4371, doi:10.1002/joc.6079.

Bartiko, D., D.Y. Oliveira, N.B. Bonumá, and P.L.B. Chaffe, 2019: Spatial and seasonal patterns of flood change across Brazil. *Hydrological Sciences Journal*, **64(9)**, 1071–1079, doi:10.1080/02626667.2019.1619081.

Bartók, B. et al., 2017: Projected changes in surface solar radiation in CMIP5 global climate models and in EURO-CORDEX regional climate models for Europe. *Climate Dynamics*, **49(7–8)**, 2665–2683, doi:10.1007/s00382-016-3471-2.

Bartos, M. et al., 2016: Impacts of rising air temperatures on electric transmission ampacity and peak electricity load in the United States. *Environmental Research Letters*, **11(11)**, 114008, doi:10.1088/1748-9326/11/11/114008.

Basha, G. et al., 2017: Historical and Projected Surface Temperature over India during the 20th and 21st century. *Scientific Reports*, **7(1)**, 2987, doi:10.1038/s41598-017-02130-3.

ACCEPTED VERSION SUBJECT TO FINAL EDITS

Bassiouni, M. and D.S. Oki, 2013: Trends and shifts in streamflow in Hawai'i, 1913-2008. *Hydrological Processes*, **27(10)**, 1484–1500, doi:10.1002/hyp.9298.
Bassu, S. et al., 2014: How do various maize crop models vary in their responses to climate change factors? *Global Change Biology*, **20(7)**, 2301–2320, doi:10.1111/gcb.12520.
Basu, S., X. Zhang, and Z. Wang, 2018: Eurasian Winter Storm Activity at the End of the Century: A CMIP5 Multi-model Ensemble Projection. *Earth's Future*, **6(1)**, 61–70, doi:10.1002/2017ef000670.
Baztan, J., M. Cordier, J.-M. Huctin, Z. Zhu, and J.-P. Vanderlinden, 2017: Life on thin ice: Insights from Uummannaq, Greenland for connecting climate science with Arctic communities. *Polar Science*, **13**, 100–108, doi:10.1016/j.polar.2017.05.002.
Baztan, J., J.-P. Vanderlinden, L. Jaffrès, B. Jorgensen, and Z. Zhu, 2020: Facing climate injustices: Community trust-building for climate services through arts and sciences narrative co-production. *Climate Risk Management*, **30**, 100253, doi:10.1016/j.crm.2020.100253.
Beach, R.H. et al., 2019: Combining the effects of increased atmospheric carbon dioxide on protein, iron, and zinc availability and projected climate change on global diets: a modelling study. *The Lancet Planetary Health*, **3(7)**, e307–e317, doi:10.1016/s2542-5196(19)30094-4.
Bebber, D.P., 2015: Range-Expanding Pests and Pathogens in a Warming World. *Annual Review of Phytopathology*, **53(1)**, 335–356, doi:10.1146/annurev-phyto-080614-120207.
Bedia, J., S. Herrera, A. Camia, J.M. Moreno, and J.M. Gutiérrez, 2014: Forest fire danger projections in the Mediterranean using ENSEMBLES regional climate change scenarios. *Climatic Change*, **122(1–2)**, 185–199, doi:10.1007/s10584-013-1005-z.
Bedia, J. et al., 2015: Global patterns in the sensitivity of burned area to fire-weather: Implications for climate change. *Agricultural and Forest Meteorology*, **214–215**, 369–379, doi:10.1016/j.agrformet.2015.09.002.
Behrenfeld, M.J. et al., 2016a: Revaluating ocean warming impacts on global phytoplankton. *Nature Climate Change*, **6(3)**, 323–330, doi:10.1038/nclimate2838.
Behrenfeld, M.J. et al., 2016b: Revaluating ocean warming impacts on global phytoplankton. *Nature Climate Change*, **6(3)**, 323–330, doi:10.1038/nclimate2838.
Bell, J.D. et al., 2013: Mixed responses of tropical Pacific fisheries and aquaculture to climate change. *Nature Climate Change*, **3(6)**, 591–599, doi:10.1038/nclimate1838.
Bell, S.S. et al., 2019: Projections of southern hemisphere tropical cyclone track density using CMIP5 models. *Climate Dynamics*, **52(9–10)**, 6065–6079, doi:10.1007/s00382-018-4497-4.
Bellaire, S., B. Jamieson, S. Thumlert, J. Goodrich, and G. Statham, 2016: Analysis of long-term weather, snow and avalanche data at Glacier National Park, B.C., Canada. *Cold Regions Science and Technology*, **121**, 118–125, doi:10.1016/j.coldregions.2015.10.010.
Belušić Vozila, A., I. Güttler, B. Ahrens, A. Obermann-Hellhund, and M. Telišman Prtenjak, 2019: Wind Over the Adriatic Region in CORDEX Climate Change Scenarios. *Journal of Geophysical Research: Atmospheres*, **124(1)**, 110–130, doi:10.1029/2018jd028552.
Ben-Ari, T. et al., 2018: Causes and implications of the unforeseen 2016 extreme yield loss in the breadbasket of France. *Nature Communications*, **9(1)**, 1627, doi:10.1038/s41467-018-04087-x.
Benestad, R. et al., 2017: New vigour involving statisticians to overcome ensemble fatigue. *Nature Climate Change*, **7(10)**, 697–703, doi:10.1038/nclimate3393.
Beniston, M. et al., 2018: The European mountain cryosphere: a review of its current state, trends, and future challenges. *The Cryosphere*, **12(2)**, 759–794, doi:10.5194/tc-12-759-2018.
Bennett, G.L. et al., 2016: Historic drought puts the brakes on earthflows in Northern California. *Geophysical Research Letters*, **43(11)**, 5725–5731, doi:10.1002/2016gl068378.
Benson, B.J. et al., 2012: Extreme events, trends, and variability in Northern Hemisphere lake-ice phenology (1855-2005). *Climatic Change*, **112(2)**, 299–323, doi:10.1007/s10584-011-0212-8.
Berghuijs, W.R., R.A. Woods, and M. Hrachowitz, 2014: A precipitation shift from snow towards rain leads to a decrease in streamflow. *Nature Climate Change*, **4(7)**, 583–586, doi:10.1038/nclimate2246.
Bessembinder, J. et al., 2019: Need for a common typology of climate services. *Climate Services*, **16**, 100135, doi:10.1016/j.cliser.2019.100135.
Bessette-Kirton, E.K. et al., 2019: Landslides Triggered by Hurricane Maria: Assessment of an Extreme Event in Puerto Rico. *GSA Today*, **29(6)**, 4–10, doi:10.1130/gsatg383a.1.
Betts, R.A. et al., 2015: Climate and land use change impacts on global terrestrial ecosystems and river flows in the HadGEM2-ES Earth system model using the representative concentration pathways. *Biogeosciences*, **12(5)**, 1317–1338, doi:10.5194/bg-12-1317-2015.
Betzold, C., 2015: Adapting to climate change in small island developing states. *Climatic Change*, **133(3)**, 481–489, doi:10.1007/s10584-015-1408-0.
Bevacqua, E. et al., 2019: Higher probability of compound flooding from precipitation and storm surge in Europe under anthropogenic climate change. *Science Advances*, **5(9)**, eaaw5531, doi:10.1126/sciadv.aaw5531.
Bezerra, B.G., L.L. Silva, C.M. Santos e Silva, and G.G. de Carvalho, 2019: Changes of precipitation extremes indices in São Francisco River Basin, Brazil from 1947 to 2012. *Theoretical and Applied Climatology*, **135(1–2)**, 565–

ACCEPTED VERSION SUBJECT TO FINAL EDITS

576, doi:10.1007/s00704-018-2396-6.
Bhardwaj, A. et al., 2018: Downscaling future climate change projections over Puerto Rico using a non-hydrostatic atmospheric model. *Climatic Change*, **147(1–2)**, 133–147, doi:10.1007/s10584-017-2130-x.
Bhatia, K.T. et al., 2019: Recent increases in tropical cyclone intensification rates. *Nature Communications*, **10(1)**, 635, doi:10.1038/s41467-019-08471-z.
Bhattachan, A. et al., 2018: Evaluating the effects of land-use change and future climate change on vulnerability of coastal landscapes to saltwater intrusion. *Elementa*, doi:10.1525/elementa.316.
Bichet, A., M. Wild, D. Folini, and C. Schär, 2012: Causes for decadal variations of wind speed over land: Sensitivity studies with a global climate model. *Geophysical Research Letters*, **39(11)**, L11701, doi:10.1029/2012gl051685.
Bigg, G.R. et al., 2018: A model for assessing iceberg hazard. *Natural Hazards*, **92(2)**, 1113–1136, doi:10.1007/s11069-018-3243-x.
Bilbao, R.A.F., J.M. Gregory, and N. Bouttes, 2015: Analysis of the regional pattern of sea level change due to ocean dynamics and density change for 1993–2099 in observations and CMIP5 AOGCMs. *Climate Dynamics*, **45(9)**, 2647–2666.
Bilskie, M. et al., 2016: Dynamic simulation and numerical analysis of hurricane storm surge under sea level rise with geomorphologic changes along the northern Gulf of Mexico. *Earth's Future*, **4(5)**, 177–193, doi:10.1002/2015ef000347.
Bindoff, N. et al., 2019: Changing Ocean, Marine Ecosystems, and Dependent Communities. In: *IPCC Special Report on the Ocean and Cryosphere in a Changing Climate* [Pörtner, H.-O., D.C. Roberts, V. Masson-Delmotte, P. Zhai, M. Tignor, E. Poloczanska, K. Mintenbeck, A. Alegría, M. Nicolai, A. Okem, J. Petzold, B. Rama, and N.M. Weyer (eds.)]. In Press, pp. 447–588.
Bintanja, R. and O. Andry, 2017: Towards a rain-dominated Arctic. *Nature Climate Change*, **7(4)**, 263–267, doi:10.1038/nclimate3240.
Bintanja, R., C. Severijns, R. Haarsma, and W. Hazeleger, 2014: The future of Antarctica's surface winds simulated by a high-resolution global climate model: 2. Drivers of 21st century changes. *Journal of Geophysical Research: Atmospheres*, **119(12)**, 7160–7178, doi:10.1002/2013jd020848.
Biribo, N. and C.D. Woodroffe, 2013: Historical area and shoreline change of reef islands around Tarawa Atoll, Kiribati. *Sustainability Science*, **8(3)**, 345–362, doi:10.1007/s11625-013-0210-z.
Birkmann, J. et al., 2014: Cross-chapter box on a selection of the hazards, key vulnerabilities, key risks, and emergent risks identified in the WGII contribution to the fifth assessment report. In: *Climate Change 2014: Impacts, Adaptation, and Vulnerability. Part A: Global and Sectoral Aspects. Contribution of Working Group II to the Fifth Assessment Report of the Intergovernmental Panel on Climate Change* [Field, C.B., V.R. Barros, D.J. Dokken, K.J. Mach, M.D. Mastrandrea, T.E. Bilir, M. Chatterjee, K.L. Ebi, Y.O. Estrada, R.C. Genova, B. Girma, E.S. Kissel, A.N. Levy, S. MacCracken, P.R. Mastrandrea, and L.L. White (eds.)]. Cambridge University Press, Cambridge, United Kingdom and New York, NY, USA, pp. 113–121, doi:10.1017/cbo9781107415379.005.
Bisbis, M.B., N. Gruda, and M. Blanke, 2018: Potential impacts of climate change on vegetable production and product quality – A review. *Journal of Cleaner Production*, **170**, 1602–1620, doi:10.1016/j.jclepro.2017.09.224.
Bisht, D.S., V. Sridhar, A. Mishra, C. Chatterjee, and N.S. Raghuwanshi, 2019: Drought characterization over India under projected climate scenario. *International Journal of Climatology*, **39(4)**, 1889–1911, doi:10.1002/joc.5922.
Biskaborn, B.K. et al., 2019: Permafrost is warming at a global scale. *Nature Communications*, **10(1)**, 264, doi:10.1038/s41467-018-08240-4.
Blackport, R., J.A. Screen, K. van der Wiel, and R. Bintanja, 2019: Minimal influence of reduced Arctic sea ice on coincident cold winters in mid-latitudes. *Nature Climate Change*, **9**, 697–704, doi:10.1038/s41558-019-0551-4.
Blanford, J.I. et al., 2013: Implications of temperature variation for malaria parasite development across Africa. *Scientific Reports*, **3**, 1300, doi:10.1038/srep01300.
Blöschl, G. et al., 2019: Changing climate both increases and decreases European river floods. *Nature*, **573(7772)**, 108–111, doi:10.1038/s41586-019-1495-6.
Boé, J., 2016: Modulation of the summer hydrological cycle evolution over western Europe by anthropogenic aerosols and soil-atmosphere interactions. *Geophysical Research Letters*, **43(14)**, 7678–7685, doi:10.1002/2016gl069394.
Boé, J., S. Somot, L. Corre, and P. Nabat, 2020: Large discrepancies in summer climate change over Europe as projected by global and regional climate models: causes and consequences. *Climate Dynamics*, **54(5–6)**, 2981–3002, doi:10.1007/s00382-020-05153-1.
Boisier, J.P., P. Ciais, A. Ducharne, and M. Guimberteau, 2015: Projected strengthening of Amazonian dry season by constrained climate model simulations. *Nature Climate Change*, **5(7)**, 656–660, doi:10.1038/nclimate2658.
Boisier, J.P. et al., 2018: Anthropogenic drying in central-southern Chile evidenced by long-term observations and climate model simulations. *Elem Sci Anth*, **6(1)**, 74, doi:10.1525/elementa.328.

ACCEPTED VERSION SUBJECT TO FINAL EDITS

Bojinski, S. et al., 2014: The Concept of Essential Climate Variables in Support of Climate Research, Applications, and Policy. *Bulletin of the American Meteorological Society*, **95(9)**, 1431–1443, doi:10.1175/bams-d-13-00047.1.

Bolch, T. et al., 2019: Status and Change of the Cryosphere in the Extended Hindu Kush Himalaya Region. In: *The Hindu Kush Himalaya Assessment: Mountains, Climate Change, Sustainability and People* [Wester, P., A. Mishra, A. Mukherji, and A.B. Shrestha (eds.)]. Springer, Cham, Switzerland, pp. 209–255, doi:10.1007/978-3-319-92288-1_7.

BOM and CSIRO, 2011: *Climate Change in the Pacific: Scientific Assessment and New Research. Volume 1: Regional Overview. Volume 2: Country Reports*. Australian Bureau of Meteorology (BoM) and Commonwealth Scientific and Industrial Research Organisation (CSIRO), 257 pp.

BOM and CSIRO, 2014: *Climate Variability, Extremes and Change in the Western Tropical Pacific: New Science and Updated Country Reports*. Pacific-Australia Climate Change Science and Adaptation Planning Program Technical Report, Australian Bureau of Meteorology (BoM) and Commonwealth Scientific and Industrial Research Organisation (CSIRO), Melbourne, Australia, 372 pp.

Bon de Sousa, L., C. Loureiro, and O. Ferreira, 2018: Morphological and economic impacts of rising sea levels on cliff-backed platform beaches in southern Portugal. *Applied Geography*, **99**, 31–43, doi:10.1016/j.apgeog.2018.07.023.

Bonsal, B.R., D.L. Peters, F. Seglenieks, A. Rivera, and A. Berg, 2019: Changes in freshwater availability across Canada, Chapter 6. In: *Canada's Changing Climate Report* [Bush, E. and D.S. Lemmen (eds.)]. Government of Canada, Ottawa, ON, Canada, pp. 261–342.

Borges, P.A., C. Bernhofer, and R. Rodrigues, 2018: Extreme rainfall indices in Distrito Federal, Brazil: Trends and links with El Niño southern oscillation and Madden-Julian oscillation. *International Journal of Climatology*, **38(12)**, 4550–4567, doi:10.1002/joc.5686.

Borges de Amorim, P. and P.B. Chaffe, 2019: Towards a comprehensive characterization of evidence in synthesis assessments: the climate change impacts on the Brazilian water resources. *Climatic Change*, **155(1)**, 37–57, doi:10.1007/s10584-019-02430-9.

Botai, C., J. Botai, J. de Wit, K. Ncongwane, and A. Adeola, 2017: Drought Characteristics over the Western Cape Province, South Africa. *Water*, **9(11)**, 876, doi:10.3390/w9110876.

Bowden, J.H. et al., 2021: High-resolution dynamically downscaled rainfall and temperature projections for ecological life zones within Puerto Rico and for the U.S. Virgin Islands. *International Journal of Climatology*, **41(2)**, 1305–1327, doi:10.1002/joc.6810.

Box, J.E. et al., 2019: Key indicators of Arctic climate change: 1971–2017. *Environmental Research Letters*, **14(4)**, 045010, doi:10.1088/1748-9326/aafc1b.

Bozkurt, D., M. Rojas, J.P. Boisier, and J. Valdivieso, 2018: Projected hydroclimate changes over Andean basins in central Chile from downscaled CMIP5 models under the low and high emission scenarios. *Climatic Change*, doi:10.1007/s10584-018-2246-7.

Bragança, R. et al., 2016: Impactos das mudanças climáticas no zoneamento agroclimatológico do café arábica no Espírito Santo. *REVISTA AGRO@MBIENTE ON-LINE*, **10(1)**, 77, doi:10.18227/1982-8470ragro.v10i1.2809.

Brahney, J., A.P. Ballantyne, C. Sievers, and J.C. Neff, 2013: Increasing Ca2+ deposition in the western US: The role of mineral aerosols. *Aeolian Research*, **10**, 77–87, doi:10.1016/j.aeolia.2013.04.003.

Brander, K., K. Cochrane, M. Barange, and D. Soto, 2017: Climate Change Implications for Fisheries and Aquaculture. In: *Climate Change Impacts on Fisheries and Aquaculture: A Global Analysis, I* [Phillips, B.F. and M. Pérez-Ramírez (eds.)]. John Wiley & Sons, Ltd, Chichester, UK, pp. 45–62, doi:10.1002/9781119154051.ch3.

Brando, P.M. et al., 2014: Abrupt increases in Amazonian tree mortality due to drought-fire interactions. *Proceedings of the National Academy of Sciences*, **111(17)**, 6347–6352, doi:10.1073/pnas.1305499111.

Brando, P.M. et al., 2019: Droughts, Wildfires, and Forest Carbon Cycling: A Pantropical Synthesis. *Annual Review of Earth and Planetary Sciences*, **47(1)**, 555–581, doi:10.1146/annurev-earth-082517-010235.

Brasseur, G.P. and L. Gallardo, 2016: Climate services: Lessons learned and future prospects. *Earth's Future*, **4(3)**, 79–89, doi:10.1002/2015ef000338.

Breitburg, D. et al., 2018: Declining oxygen in the global ocean and coastal waters. *Science*, **359(6371)**, eaam7240, doi:10.1126/science.aam7240.

Bremer, S. et al., 2019: Toward a multi-faceted conception of co-production of climate services. *Climate Services*, **13**, 42–50, doi:10.1016/j.cliser.2019.01.003.

Brewington, L., V. Keener, and A. Mair, 2019: Simulating Land Cover Change Impacts on Groundwater Recharge under Selected Climate Projections, Maui, Hawai'i. *Remote Sensing*, **11(24)**, 3048, doi:10.3390/rs11243048.

Briley, L., D. Brown, and S.E. Kalafatis, 2015: Overcoming barriers during the co-production of climate information for decision-making. *Climate Risk Management*, **9**, 41–49, doi:10.1016/j.crm.2015.04.004.

Brimelow, J.C., W.R. Burrows, and J.M. Hanesiak, 2017: The changing hail threat over North America in response to anthropogenic climate change. *Nature Climate Change*, **7(7)**, 516–522, doi:10.1038/nclimate3321.

Bring, A. et al., 2016: Arctic terrestrial hydrology: A synthesis of processes, regional effects, and research challenges. *Journal of Geophysical Research G: Biogeosciences*, **121(3)**, 621–649, doi:10.1002/2015jg003131.

Broeckx, J. et al., 2020: Landslide mobilization rates: A global analysis and model. *Earth-Science Reviews*, **201**,

ACCEPTED VERSION SUBJECT TO FINAL EDITS

102972, doi:10.1016/j.earscirev.2019.102972.
Bromirski, P.D., D.R. Cayan, J. Helly, and P. Wittmann, 2013: Wave power variability and trends across the North Pacific. *Journal of Geophysical Research: Oceans*, **118(12)**, 6329–6348, doi:10.1002/2013jc009189.
Brönnimann, S. et al., 2018: Changing seasonality of moderate and extreme precipitation events in the Alps. *Natural Hazards and Earth System Sciences*, **18(7)**, 2047–2056, doi:10.5194/nhess-18-2047-2018.
Brooks, H.E., 2013: Severe thunderstorms and climate change. *Atmospheric Research*, **123**, 129–138, doi:10.1016/j.atmosres.2012.04.002.
Brooks, H.E., G.W. Carbin, and P.T. Marsh, 2014: Increased variability of tornado occurrence in the United States.. *Science (New York, N.Y.)*, **346(6207)**, 349–52, doi:10.1126/science.1257460.
Brooks, M.S., 2013: Accelerating Innovation in Climate Services: The 3 E's for Climate Service Providers. *Bulletin of the American Meteorological Society*, **94(6)**, 807–819, doi:10.1175/bams-d-12-00087.1.
Brouillet, A. and S. Joussaume, 2019: Investigating the Role of the Relative Humidity in the Co-Occurrence of Temperature and Heat Stress Extremes in CMIP5 Projections. *Geophysical Research Letters*, **46(20)**, 11435–11443, doi:10.1029/2019gl084156.
Brown, R.D., B. Fang, and L. Mudryk, 2019: Update of Canadian Historical Snow Survey Data and Analysis of Snow Water Equivalent Trends, 1967–2016. *Atmosphere - Ocean*, **57(2)**, 149–156, doi:10.1080/07055900.2019.1598843.
Brown, S. et al., 2018: Quantifying Land and People Exposed to Sea-Level Rise with No Mitigation and 1.5°C and 2.0°C Rise in Global Temperatures to Year 2300. *Earth's Future*, **6(3)**, 583–600, doi:10.1002/2017ef000738.
Brunetti, M.T. et al., 2010: Rainfall thresholds for the possible occurrence of landslides in Italy. *Natural Hazards and Earth System Science*, **10(3)**, 447–458, doi:10.5194/nhess-10-447-2010.
Brunner, L., N. Schaller, J. Anstey, J. Sillmann, and A.K. Steiner, 2018: Dependence of Present and Future European Temperature Extremes on the Location of Atmospheric Blocking. *Geophysical Research Letters*, **45(12)**, 6311– 6320, doi:10.1029/2018gl077837.
Bruno, J.F. et al., 2018: Climate change threatens the world's marine protected areas. *Nature Climate Change*, **8(6)**, 499–503, doi:10.1038/s41558-018-0149-2.
Bruno Soares, M., 2017: Assessing the usability and potential value of seasonal climate forecasts in land management decisions in the southwest UK: challenges and reflections. *Advances in Science and Research*, **14**, 175–180, doi:10.5194/asr-14-175-2017.
Bruno Soares, M. and S. Dessai, 2016: Barriers and enablers to the use of seasonal climate forecasts amongst organisations in Europe. *Climatic Change*, **137(1)**, 89–103, doi:10.1007/s10584-016-1671-8.
Bruno Soares, M. and C. Buontempo, 2019: Challenges to the sustainability of climate services in Europe. *Wiley Interdisciplinary Reviews: Climate Change*, **10(4)**, e587, doi:10.1002/wcc.587.
Bruno Soares, M., M. Alexander, and S. Dessai, 2018a: Sectoral use of climate information in Europe: A synoptic overview. *Climate Services*, **9**, 5–20, doi:10.1016/j.cliser.2017.06.001.
Bruno Soares, M., M. Daly, and S. Dessai, 2018b: Assessing the value of seasonal climate forecasts for decision-making. *Wiley Interdisciplinary Reviews: Climate Change*, **9(4)**, e523, doi:10.1002/wcc.523.
Bukovsky, M.S. and L.O. Mearns, 2020: Regional climate change projections from NA-CORDEX and their relation to climate sensitivity. *Climatic Change*, **162(2)**, 645–665, doi:10.1007/s10584-020-02835-x.
Bullock, J.M. et al., 2012: Modelling spread of British wind-dispersed plants under future wind speeds in a changing climate. *Journal of Ecology*, **100(1)**, 104–115, doi:10.1111/j.1365-2745.2011.01910.x.
Buontempo, C. and C. Hewitt, 2018: EUPORIAS and the development of climate services. *Climate Services*, **9**, 1–4, doi:10.1016/j.cliser.2017.06.011.
Buontempo, C., C.D. Hewitt, F.J. Doblas-Reyes, and S. Dessai, 2014: Climate service development, delivery and use in Europe at monthly to inter-annual timescales. *Climate Risk Management*, **6**, 1–5, doi:10.1016/j.crm.2014.10.002.
Buontempo, C. et al., 2018: What have we learnt from EUPORIAS climate service prototypes? *Climate Services*, **9**, 21–32, doi:10.1016/j.cliser.2017.06.003.
Buontempo, C. et al., 2020: Fostering the development of climate services through Copernicus Climate Change Service (C3S) for agriculture applications. *Weather and Climate Extremes*, **27**, 100226, doi:10.1016/j.wace.2019.100226.
Burcea, S., R. Cică, and R. Bojariu, 2016: Hail Climatology and Trends in Romania: 1961–2014. *Monthly Weather Review*, **144(11)**, 4289–4299, doi:10.1175/mwr-d-16-0126.1.
Burkart, K. et al., 2011: The effect of atmospheric thermal conditions and urban thermal pollution on all-cause and cardiovascular mortality in Bangladesh. *Environmental Pollution*, **159(8)**, 2035–2043, doi:10.1016/j.envpol.2011.02.005.
Burkett, V., 2011: Global climate change implications for coastal and offshore oil and gas development. *Energy Policy*, **39(12)**, 7719–7725, doi:10.1016/j.enpol.2011.09.016.
Burls, N.J. et al., 2019: The Cape Town "Day Zero" drought and Hadley cell expansion. *npj Climate and Atmospheric Science*, **2(1)**, 1–8, doi:10.1038/s41612-019-0084-6.
Burn, D.H. and P.H. Whitfield, 2016: Changes in floods and flood regimes in Canada. *Canadian Water Resources*

ACCEPTED VERSION SUBJECT TO FINAL EDITS

Journal, **41(1–2)**, 139–150, doi:10.1080/07011784.2015.1026844.
Burrows, M.T. et al., 2014: Geographical limits to species-range shifts are suggested by climate velocity. *Nature*, **507(7493)**, 492–495, doi:10.1038/nature12976.
Bush, E. and D.S. Lemmen (eds.), 2019: *Canada's Changing Climate Report*. Government of Canada, Ottawa, ON, Canada, 444 pp.
Cabré, M.F., S. Solman, and M. Núñez, 2016: Regional climate change scenarios over southern South America for future climate (2080-2099) using the MM5 Model. Mean, interannual variability and uncertainties. *Atmósfera*, **29(1)**, 35–60, doi:10.20937/atm.2016.29.01.04.
Cai, W.-J. et al., 2017: Redox reactions and weak buffering capacity lead to acidification in the Chesapeake Bay. *Nature Communications*, **8(1)**, 369, doi:10.1038/s41467-017-00417-7.
Cai, Y., C.-Q. Ke, G. Yao, and X. Shen, 2020: MODIS-observed variations of lake ice phenology in Xinjiang, China. *Climatic Change*, **158(3)**, 575–592, doi:10.1007/s10584-019-02623-2.
Cai, Y. et al., 2019: Variations of Lake Ice Phenology on the Tibetan Plateau From 2001 to 2017 Based on MODIS Data. *Journal of Geophysical Research: Atmospheres*, **124(2)**, 825–843, doi:10.1029/2018jd028993.
Callaghan, J. and S.B. Power, 2011: Variability and decline in the number of severe tropical cyclones making land-fall over eastern Australia since the late nineteenth century. *Climate Dynamics*, **37(3–4)**, 647–662, doi:10.1007/s00382-010-0883-2.
Caminade, C. et al., 2012: Suitability of European climate for the Asian tiger mosquito Aedes albopictus: recent trends and future scenarios. *Journal of The Royal Society Interface*, **9(75)**, 2708–2717, doi:10.1098/rsif.2012.0138.
Caminade, C. et al., 2014: Impact of climate change on global malaria distribution. *Proceedings of the National Academy of Sciences*, **111(9)**, 3286–3291, doi:10.1073/pnas.1302089111.
Cammarano, D. et al., 2016: Uncertainty of wheat water use: Simulated patterns and sensitivity to temperature and CO2. *Field Crops Research*, **198**, 80–92, doi:10.1016/j.fcr.2016.08.015.
Camus, P. et al., 2017: Statistical wave climate projections for coastal impact assessments. *Earth's Future*, **5(9)**, 918–933, doi:10.1002/2017ef000609.
Carey, M., C. Huggel, J. Bury, C. Portocarrero, and W. Haeberli, 2012: An integrated socio-environmental framework for glacier hazard management and climate change adaptation: lessons from Lake 513, Cordillera Blanca, Peru. *Climatic Change*, **112(3–4)**, 733–767, doi:10.1007/s10584-011-0249-8.
Carey-Smith, T., S. Deana, J. Vialb, and C. Thompsona, 2010: Changes in precipitation extremes for New Zealand: climate model predictions. *Weather and Climate*, **30**, 23–48, doi:10.2307/26169712.
Carmona, A.M. and G. Poveda, 2014: Detection of long-term trends in monthly hydro-climatic series of Colombia through Empirical Mode Decomposition. *Climatic Change*, doi:10.1007/s10584-013-1046-3.
Carrão, H., G. Naumann, and P. Barbosa, 2018: Global projections of drought hazard in a warming climate: a prime for disaster risk management. *Climate Dynamics*, **50(5–6)**, 2137–2155, doi:10.1007/s00382-017-3740-8.
Carrasco, A.R., O. Ferreira, and D. Roelvink, 2016: Coastal lagoons and rising sea level: A review. *Earth-Science Reviews*, **154**, 356–368, doi:10.1016/j.earscirev.2015.11.007.
Carrivick, J.L. and F.S. Tweed, 2016: A global assessment of the societal impacts of glacier outburst floods. *Global and Planetary Change*, **144**, 1–16, doi:10.1016/j.gloplacha.2016.07.001.
Casas-Prat, M. and X.L. Wang, 2020: Projections of extreme ocean waves in the Arctic and potential implications for coastal inundation and erosion. *Journal of Geophysical Research: Oceans*, **125(8)**, e2019JC015745, doi:10.1029/2019jc015745.
Cassou, C. and J. Cattiaux, 2016: Disruption of the European climate seasonal clock in a warming world. *Nature Climate Change*, **6(6)**, 589–594, doi:10.1038/nclimate2969.
Castebrunet, H., N. Eckert, G. Giraud, Y. Durand, and S. Morin, 2014: Projected changes of snow conditions and avalanche activity in a warming climate: the French Alps over the 2020-2050 and 2070-2100 periods. *The Cryosphere*, **8(5)**, 1673–1697, doi:10.5194/tc-8-1673-2014.
Catto, J.L., C. Jakob, and N. Nicholls, 2012: The influence of changes in synoptic regimes on north Australian wet season rainfall trends. *Journal of Geophysical Research: Atmospheres*, **117**, D10102, doi:10.1029/2012jd017472.
Cavalcanti, I.F.A. et al., 2015: Precipitation extremes over La Plata Basin – Review and new results from observations and climate simulations. *Journal of Hydrology*, **523**, 211–230, doi:10.1016/j.jhydrol.2015.01.028.
Cavanaugh, K.C. et al., 2014: Poleward expansion of mangroves is a threshold response to decreased frequency of extreme cold events. *Proceedings of the National Academy of Sciences*, **111(2)**, 723–727, doi:10.1073/pnas.1315800111.
Cavelier, R. et al., 2017: Conditions for a market uptake of climate services for adaptation in France. *Climate Services*, **6**, 34–40, doi:10.1016/j.cliser.2017.06.010.
Cavicchia, L., H. von Storch, and S. Gualdi, : Mediterranean Tropical-Like Cyclones in Present and Future Climate. *Journal of Climate*, **27(19)**, 7493–7501, doi:10.1175/jcli-d-14-00339.1.
Cha, E.J., T.R. Knutson, T.-C. Lee, M. Ying, and T. Nakaegawa, 2020: Third assessment on impacts of climate change on tropical cyclones in the Typhoon Committee Region – Part II: Future projections. *Tropical Cyclone Research and Review*, **9(2)**, 75–86, doi:10.1016/j.tcrr.2020.04.005.

ACCEPTED VERSION SUBJECT TO FINAL EDITS

Chadwick, C., J. Gironás, S. Vicuña, and F. Meza, 2019: Estimating the Local Time of Emergence of Climatic Variables Using an Unbiased Mapping of GCMs: An Application in Semiarid and Mediterranean Chile. *Journal of Hydrometeorology*, **20(8)**, 1635–1647, doi:10.1175/jhm-d-19-0006.1.

Chagas, V.B.P. and P.L.B. Chaffe, 2018: The Role of Land Cover in the Propagation of Rainfall Into Streamflow Trends. *Water Resources Research*, **54(9)**, 5986–6004, doi:10.1029/2018wr022947.

Challinor, A.J. et al., 2014: A meta-analysis of crop yield under climate change and adaptation. *Nature Climate Change*, **4(4)**, 287–291, doi:10.1038/nclimate2153.

Chan, F. et al., 2008: Emergence of Anoxia in the California Current Large Marine Ecosystem. *Science*, **319(5865)**, 920–920, doi:10.1126/science.1149016.

Chan, F.K.S., G. Mitchell, O. Adekola, and A. McDonald, 2012: Flood Risk in Asia's Urban Mega-deltas: Drivers, Impacts and Response. *Environment and Urbanization ASIA*, **3(1)**, 41–61, doi:10.1177/097542531200300103.

Chan, F.K.S., C.J. Chuah, A.D. Ziegler, M. Dąbrowski, and O. Varis, 2018: Towards resilient flood risk management for Asian coastal cities: Lessons learned from Hong Kong and Singapore. *Journal of Cleaner Production*, **187**, 576–589, doi:10.1016/j.jclepro.2018.03.217.

Chand, S.S., K.J. Tory, H. Ye, and K.J.E. Walsh, 2017: Projected increase in El Niño-driven tropical cyclone frequency in the Pacific. *Nature Climate Change*, **7(2)**, 123–127, doi:10.1038/nclimate3181.

Chang, E.K.M., 2017: Projected Significant Increase in the Number of Extreme Extratropical Cyclones in the Southern Hemisphere. *Journal of Climate*, **30(13)**, 4915–4935, doi:10.1175/jcli-d-16-0553.1.

Changnon, D., 2018: A Spatial and Temporal Analysis of 30-Day Heavy Snowfall Amounts in the Eastern United States, 1900–2016. *Journal of Applied Meteorology and Climatology*, **57(2)**, 319–331, doi:10.1175/jamc-d-17-0217.1.

Chapman, L., J.A. Azevedo, and T. Prieto-Lopez, 2013: Urban heat & critical infrastructure networks: A viewpoint. *Urban Climate*, **3**, 7–12, doi:10.1016/j.uclim.2013.04.001.

Chapra, S.C. et al., 2017: Climate Change Impacts on Harmful Algal Blooms in U.S. Freshwaters: A Screening-Level Assessment. *Environmental Science & Technology*, **51(16)**, 8933–8943, doi:10.1021/acs.est.7b01498.

Cheal, A.J., M.A. MacNeil, M.J. Emslie, and H. Sweatman, 2017: The threat to coral reefs from more intense cyclones under climate change. *Global Change Biology*, **23(4)**, 1511–1524, doi:10.1111/gcb.13593.

Chen, A.-, N.- Wang, Z.- Guo, Y.- Wu, and H.- Wu, 2018: Glacier variations and rising temperature in the Mt. Kenya since the Last Glacial Maximum. *Journal of Mountain Science*, **15(6)**, 1268–1282, doi:10.1007/s11629-017-4600-z.

Chen, C.-W. et al., 2019: Assessing landslide characteristics in a changing climate in northern Taiwan. *CATENA*, **175**, 263–277, doi:10.1016/j.catena.2018.12.023.

Chen, L., 2020: Impacts of climate change on wind resources over North America based on NA-CORDEX. *Renewable Energy*, **153**, 1428–1438, doi:10.1016/j.renene.2020.02.090.

Chen, L., 2021: Uncertainties in solar radiation assessment in the United States using climate models. *Climate Dynamics*, **56(1)**, 665–678, doi:10.1007/s00382-020-05498-7.

Chen, W. et al., 2016: Influence of sea level rise on saline water intrusion in the Yangtze River Estuary, China. *Applied Ocean Research*, **54**, 12–25, doi:10.1016/j.apor.2015.11.002.

Chen, X., G. Tian, Z. Qin, and X. Bi, 2019: High Daytime and Nighttime Temperatures Exert Large and Opposing Impacts on Winter Wheat Yield in China. *Weather, Climate, and Society*, **11(4)**, 777–790, doi:10.1175/wcas-d-19-0026.1.

Chen, Z. et al., 2020: Global Land Monsoon Precipitation Changes in CMIP6 Projections. *Geophysical Research Letters*, **47(14)**, e2019GL086902, doi:10.1029/2019gl086902.

Cheng, J. et al., 2018: Heatwave and elderly mortality: An evaluation of death burden and health costs considering short-term mortality displacement. *Environment International*, **115**, 334–342, doi:10.1016/j.envint.2018.03.041.

Cheng, L. and A. AghaKouchak, 2015: Nonstationary Precipitation Intensity-Duration-Frequency Curves for Infrastructure Design in a Changing Climate. *Scientific Reports*, **4(1)**, 7093, doi:10.1038/srep07093.

Cheong, W.K. et al., 2018: Observed and modelled temperature and precipitation extremes over Southeast Asia from 1972 to 2010. *International Journal of Climatology*, **38(7)**, 3013–3027, doi:10.1002/joc.5479.

Chernokulsky, A. et al., 2019: Observed changes in convective and stratiform precipitation in Northern Eurasia over the last five decades. *Environmental Research Letters*, **14(4)**, doi:10.1088/1748-9326/aafb82.

Cheung, W.W.L. and T.L. Frölicher, 2020: Marine heatwaves exacerbate climate change impacts for fisheries in the northeast Pacific. *Scientific Reports*, **10(1)**, 6678, doi:10.1038/s41598-020-63650-z.

Chhetri, B.K. et al., 2019: Projected local rain events due to climate change and the impacts on waterborne diseases in Vancouver, British Columbia, Canada. *Environmental Health: A Global Access Science Source*, **18(1)**, 116, doi:10.1186/s12940-019-0550-y.

Chiew, F.H.S. et al., 2017: Future runoff projections for Australia and science challenges in producing next generation projections. In: *MODSIM2017, 22nd International Congress on Modelling and Simulation* [Syme, G., D.H. MacDonald, B. Fulton, and J. Piantadosi (eds.)]. Modelling and Simulation Society of Australia and New Zealand, Hobart, TAS, Australia, 1745–1751 pp.

ACCEPTED VERSION SUBJECT TO FINAL EDITS

Chinowsky, P. and C. Arndt, 2012: Climate Change and Roads: A Dynamic Stressor-Response Model. *Review of Development Economics*, **16(3)**, 448–462, doi:10.1111/j.1467-9361.2012.00673.x.

Chinowsky, P., J. Helman, S. Gulati, J. Neumann, and J. Martinich, 2019: Impacts of climate change on operation of the US rail network. *Transport Policy*, **75**, 183–191, doi:10.1016/j.tranpol.2017.05.007.

Cho, C., R. Li, S.Y. Wang, J.-H. Yoon, and R.R. Gillies, 2016: Anthropogenic footprint of climate change in the June 2013 northern India flood. *Climate Dynamics*, **46(3–4)**, 797–805, doi:10.1007/s00382-015-2613-2.

Choi, W., C.-H. Ho, J. Kim, and J.C.L. Chan, 2019: Near-future tropical cyclone predictions in the western North Pacific: fewer tropical storms but more typhoons. *Climate Dynamics*, **53(3–4)**, 1341–1356, doi:10.1007/s00382-019-04647-x.

Chou, S.C. et al., 2014: Assessment of Climate Change over South America under RCP 4.5 and 8.5 Downscaling Scenarios. *American Journal of Climate Change*, **03(05)**, 512–527, doi:10.4236/ajcc.2014.35043.

Chow, W.T.L., S.N.A.B.A. Akbar, S.L. Heng, and M. Roth, 2016: Assessment of measured and perceived microclimates within a tropical urban forest. *Urban Forestry & Urban Greening*, **16**, 62–75, doi:10.1016/j.ufug.2016.01.010.

Christel, I. et al., 2018: Introducing design in the development of effective climate services. *Climate Services*, **9**, 111–121, doi:10.1016/j.cliser.2017.06.002.

Christensen, J.H. et al., 2013: Climate Phenomena and their Relevance for Future Regional Climate Change. In: *Climate Change 2013: The Physical Science Basis. Contribution of Working Group I to the Fifth Assessment Report of the Intergovernmental Panel on Climate Change* [Stocker, T.F., D. Qin, G.-K. Plattner, M. Tignor, S.K. Allen, J. Boschung, A. Nauels, Y. Xia, V. Bex, and P.M. Midgley (eds.)]. Cambridge University Press, Cambridge, United Kingdom and New York, NY, USA, pp. 1217–1308, doi:10.1017/cbo9781107415324.028.

Christianson, A.C. and T.K. McGee, 2019: Wildfire evacuation experiences of band members of Whitefish Lake First Nation 459, Alberta, Canada. *Natural Hazards*, **98(1)**, 9–29, doi:10.1007/s11069-018-3556-9.

Chun, J., C. Lim, D. Kim, and J. Kim, 2018: Assessing Impacts of Climate Change and Sea-Level Rise on Seawater Intrusion in a Coastal Aquifer. *Water*, **10(4)**, 357, doi:10.3390/w10040357.

Ciabatta, L. et al., 2016: Assessing the impact of climate-change scenarios on landslide occurrence in Umbria Region, Italy. *Journal of Hydrology*, **541**, 285–295, doi:10.1016/j.jhydrol.2016.02.007.

Ciais, P. et al., 2005: Europe-wide reduction in primary productivity caused by the heat and drought in 2003. *Nature*, **437(7058)**, 529–533, doi:10.1038/nature03972.

Cinco, T.A. et al., 2016: Observed trends and impacts of tropical cyclones in the Philippines. *International Journal of Climatology*, **36(14)**, 4638–4650, doi:10.1002/joc.4659.

Clarke, H. et al., 2019: Climate change effects on the frequency, seasonality and interannual variability of suitable prescribed burning weather conditions in south-eastern Australia. *Agricultural and Forest Meteorology*, **271**, 148–157, doi:10.1016/j.agrformet.2019.03.005.

Clarke, L. et al., 2018: Sector Interactions, Multiple Stressors, and Complex Systems. In: *Impacts, Risks, and Adaptation in the United States: Fourth National Climate Assessment, Volume II* [Reidmiller, D.R., C.W. Avery, D.R. Easterling, K.E. Kunkel, K.L.M. Lewis, T.K. Maycock, and B.C. Stewart (eds.)]. U.S. Global Change Research Program, Washington, DC, USA, pp. 638–668, doi:10.7930/nca4.2018.ch17.

Clilverd, H.M., Y.-P. Tsang, D.M. Infante, A.J. Lynch, and A.M. Strauch, 2019: Long-term streamflow trends in Hawai'i and implications for native stream fauna. *Hydrological Processes*, **33(5)**, 699–719, doi:10.1002/hyp.13356.

Cloutier, C., J. Locat, M. Geertsema, M. Jakob, and M. Schnorbus, 2017: Potential impacts of climate change on landslides occurrence in Canada. In: *Slope Safety Preparedness for Impact of Climate Change (1st edition)* [Ho, K., S. Lacasse, and L. Picarelli (eds.)]. CRC Press, London, UK, pp. 34, doi:10.1201/9781315387789.

Coe, J., 2016: Landslide Hazards and Climate Change: A Perspective from the United States. In: *Slope Safety Preparedness for Impact of Climate Change (1st edition)* [Ho, K., S. Lacasse, and L. Picarelli (eds.)]. CRC Press, London, UK, pp. 479–523, doi:10.1201/9781315387789-16.

Coe, J.A., E.K. Bessette-Kirton, and M. Geertsema, 2018: Increasing rock-avalanche size and mobility in Glacier Bay National Park and Preserve, Alaska detected from 1984 to 2016 Landsat imagery. *Landslides*, **15(3)**, 393–407, doi:10.1007/s10346-017-0879-7.

Coffel, E.D., T.R. Thompson, and R.M. Horton, 2017: The impacts of rising temperatures on aircraft takeoff performance. *Climatic Change*, **144(2)**, 381–388, doi:10.1007/s10584-017-2018-9.

Coffel, E.D., R.M. Horton, and A. de Sherbinin, 2018: Temperature and humidity based projections of a rapid rise in global heat stress exposure during the 21st century. *Environmental Research Letters*, **13(1)**, 014001, doi:10.1088/1748-9326/aaa00e.

Cohen, J. et al., 2019: Divergent consensuses on Arctic amplification influence on midlatitude severe winter weather. *Nature Climate Change*, 1–10.

Collins, M. et al., 2019: Extremes, Abrupt Changes and Managing Risks. In: *IPCC Special Report on the Ocean and Cryosphere in a Changing Climate* [Pörtner, H.-O., D.C. Roberts, V. Masson-Delmotte, P. Zhai, M. Tignor, E. Poloczanska, K. Mintenbeck, A. Alegría, M. Nicolai, A. Okem, J. Petzold, B. Rama, and N.M. Weyer (eds.)]. In Press, pp. 3–63.

ACCEPTED VERSION SUBJECT TO FINAL EDITS

Colombani, N., A. Osti, G. Volta, and M. Mastrocicco, 2016: Impact of Climate Change on Salinization of Coastal Water Resources. *Water Resources Management*, **30(7)**, 2483–2496, doi:10.1007/s11269-016-1292-z.

Colonia, D. et al., 2017: Compiling an Inventory of Glacier-Bed Overdeepenings and Potential New Lakes in De-Glaciating Areas of the Peruvian Andes: Approach, First Results, and Perspectives for Adaptation to Climate Change. *Water*, **9(5)**, 336, doi:10.3390/w9050336.

Comte, L. and G. Grenouillet, 2013: Do stream fish track climate change? Assessing distribution shifts in recent decades. *Ecography*, **36(11)**, 1236–1246, doi:10.1111/j.1600-0587.2013.00282.x.

Contador, T., J. Kennedy, J. Ojeda, P. Feinsinger, and R. Rozzi, 2014: Ciclos de vida de insectos dulceacuícolas y cambio climático global en la ecorregión subantártica de Magallanes: investigaciones ecológicas a largo plazo en el Parque Etnobotánico Omora, Reserva de Biosfera Cabo de Hornos (55° S). *Bosque (Valdivia)*, **35(3)**, 429–437, doi:10.4067/s0717-92002014000300018.

Contosta, A.R., N.J. Casson, S.J. Nelson, and S. Garlick, 2020: Defining frigid winter illuminates its loss across seasonally snow-covered areas of eastern North America. *Environmental Research Letters*, **15(3)**, 034020, doi:10.1088/1748-9326/ab54f3.

Cook, B.I. et al., 2019: Climate change amplification of natural drought variability: The historic mid-twentieth-century North American drought in a warmer world. *Journal of Climate*, **32(17)**, 5417–5436, doi:10.1175/jcli-d-18-0832.1.

Cook, B.I. et al., 2020: Twenty-First Century Drought Projections in the CMIP6 Forcing Scenarios. *Earth's Future*, **8(6)**, e2019EF001461, doi:10.1029/2019ef001461.

Cook, L.M., S. McGinnis, and C. Samaras, 2020: The effect of modeling choices on updating intensity-duration-frequency curves and stormwater infrastructure designs for climate change. *Climatic Change*, **159(2)**, 289–308, doi:10.1007/s10584-019-02649-6.

Cook, S.J., I. Kougkoulos, L.A. Edwards, J. Dortch, and D. Hoffmann, 2016: Glacier change and glacial lake outburst flood risk in the Bolivian Andes. *The Cryosphere*, **10(5)**, 2399–2413, doi:10.5194/tc-10-2399-2016.

Cooper, E.J., 2014: Warmer Shorter Winters Disrupt Arctic Terrestrial Ecosystems. *Annual Review of Ecology, Evolution, and Systematics*, **45(1)**, 271–295, doi:10.1146/annurev-ecolsys-120213-091620.

Coopersmith, E.J. et al., 2017: Relating coccidioidomycosis (valley fever) incidence to soil moisture conditions. *GeoHealth*, **1(1)**, 51–63, doi:10.1002/2016gh000033.

Coppola, E. et al., 2014: Present and future climatologies in the phase I CREMA experiment. *Climatic Change*, **125(1)**, 23–38, doi:10.1007/s10584-014-1137-9.

Coppola, E. et al., 2021a: Assessment of the European Climate Projections as Simulated by the Large EURO-CORDEX Regional and Global Climate Model Ensemble. *Journal of Geophysical Research: Atmospheres*, **126(4)**, e2019JD032356, doi:10.1029/2019jd032356.

Coppola, E. et al., 2021b: Climate hazard indices projections based on CORDEX-CORE, CMIP5 and CMIP6 ensemble. *Climate Dynamics*, doi:10.1007/s00382-021-05640-z.

Cortekar, J., M. Themessl, and K. Lamich, 2020: Systematic analysis of EU-based climate service providers. *Climate Services*, **17**, 100125, doi:10.1016/j.cliser.2019.100125.

Costoya, X., M. de Castro, F. Santos, M.C. Sousa, and M. Gómez-Gesteira, 2019: Projections of wind energy resources in the Caribbean for the 21st century. *Energy*, **178**, 356–367, doi:10.1016/j.energy.2019.04/121.

Courty, L.G., R.L. Wilby, J.K. Hillier, and L.J. Slater, 2019: Intensity-duration-frequency curves at the global scale. *Environmental Research Letters*, **14(8)**, 084045, doi:10.1088/1748-9326/ab370a.

Cradock-Henry, N.A., 2017: New Zealand kiwifruit growers' vulnerability to climate and other stressors. *Regional Environmental Change*, **17(1)**, 245–259, doi:10.1007/s10113-016-1000-9.

Craft, C. et al., 2009: Forecasting the effects of accelerated sea-level rise on tidal marsh ecosystem services. *Frontiers in Ecology and the Environment*, **7(2)**, 73–78, doi:10.1890/070219.

Craig, M.T. et al., 2018: A review of the potential impacts of climate change on bulk power system planning and operations in the United States. *Renewable and Sustainable Energy Reviews*, **98**, 255–267, doi:10.1016/j.rser.2018.09.022.

Crimp, S.J. et al., 2016a: Recent seasonal and long-term changes in southern Australian frost occurrence. *Climatic Change*, **139(1)**, 115–128, doi:10.1007/s10584-016-1763-5.

Crimp, S.J. et al., 2016b: Recent changes in southern Australian frost occurrence: implications for wheat production risk. *Crop and Pasture Science*, **67(8)**, 801, doi:10.1071/cp16056.

Crooks, J.L. et al., 2016: The Association between Dust Storms and Daily Non-Accidental Mortality in the United States, 1993–2005. *Environmental Health Perspectives*, **124(11)**, 1735–1743, doi:10.1289/ehp216.

Crozier, M.J., 2010: Deciphering the effect of climate change on landslide activity: A review. *Geomorphology*, **124(3–4)**, 260–267, doi:10.1016/j.geomorph.2010.04.009.

CSIRO and BOM, 2015: *Climate Change in Australia Information for Australia's Natural Resource Management Regions*. Commonwealth Scientific and Industrial Research Organisation (CSIRO) and Bureau of Meteorology (BOM), Australia, 216 pp., doi:10.4225/08/58518c08c4ce8.

CSIRO and BOM, 2016: *State of the Climate 2016*. Commonwealth Scientific and Industrial Research Organisation (CSIRO) and Bureau of Meteorology (BOM), Australia, 22 pp.

ACCEPTED VERSION SUBJECT TO FINAL EDITS

CSIRO and BOM, 2018: *State of the Climate 2018*. Commonwealth Scientific and Industrial Research Organisation (CSIRO) and Bureau of Meteorology (BOM), Australia, 24 pp.
CSIRO and BOM, 2020: *State of the Climate 2020*. Commonwealth Scientific and Industrial Research Organisation (CSIRO) and Bureau of Meteorology (BOM), Australia, 23 pp.
Cullen, N.J. et al., 2013: A century of ice retreat on Kilimanjaro: the mapping reloaded. *The Cryosphere*, **7(2)**, 419–431, doi:10.5194/tc-7-419-2013.
Culwick, C. and Z. Patel, 2017: United and divided responses to complex urban issues: insights on the value of a transdisciplinary approach to flooding risk. *Area*, **49(1)**, 43–51, doi:10.1111/area.12282.
Cunha, A.P.M.A. et al., 2019: Extreme Drought Events over Brazil from 2011 to 2019. *Atmosphere*, **10(11)**, 642, doi:10.3390/atmos10110642.
Ćurić, M. and D. Janc, 2016: Hail climatology in Serbia. *International Journal of Climatology*, **36(9)**, 3270–3279, doi:10.1002/joc.4554.
Cutter, S.L., 2018: Compound, Cascading, or Complex Disasters: What's in a Name? *Environment: Science and Policy for Sustainable Development*, **60(6)**, 16–25, doi:10.1080/00139157.2018.1517518.
Dahal, N., U. Shrestha, A. Tuitui, and H. Ojha, 2018: Temporal Changes in Precipitation and Temperature and their Implications on the Streamflow of Rosi River, Central Nepal. *Climate*, **7(1)**, 3, doi:10.3390/cli7010003.
Dahl, K., R. Licker, J.T. Abatzoglou, and J. Declet-Barreto, 2019: Increased frequency of and population exposure to extreme heat index days in the United States during the 21st century. *Environmental Research Communications*, **1(7)**, 075002, doi:10.1088/2515-7620/ab27cf.
Dahl, K.A., M.F. Fitzpatrick, and E. Spanger-Siegfried, 2017a: Sea level rise drives increased tidal flooding frequency at tide gauges along the U.S. East and Gulf Coasts: Projections for 2030 and 2045. *PLoS ONE*, **12(2)**, e0170949, doi:10.1371/journal.pone.0170949.
Dahl, K.A., E. Spanger-Siegfried, A. Caldas, and S. Udvardy, 2017b: Effective inundation of continental United States communities with 21st century sea level rise. *Elementa: Science of the Anthropocene*, **5**, 37, doi:10.1525/elementa.234.
Damm, A., W. Greuell, O. Landgren, and F. Prettenthaler, 2017: Impacts of +2°C global warming on winter tourism demand in Europe. *Climate Services*, **7**, 31–46, doi:10.1016/j.cliser.2016.07.003.
Damm, A., J. Köberl, P. Stegmaier, E. Jiménez Alonso, and A. Harjanne, 2019: The market for climate services in the tourism sector – An analysis of Austrian stakeholders' perceptions. *Climate Services*, 100094, doi:10.1016/j.cliser.2019.02.001.
Danco, J.F., A.M. DeAngelis, B.K. Raney, and A.J. Broccoli, 2016: Effects of a Warming Climate on Daily Snowfall Events in the Northern Hemisphere. *Journal of Climate*, **29(17)**, 6295–6318, doi:10.1175/jcli-d-15-0687.1.
Daniel, J.S. et al., 2018: Climate change: potential impacts on frost–thaw conditions and seasonal load restriction timing for low-volume roadways. *Road Materials and Pavement Design*, **19(5)**, 1126–1146, doi:10.1080/14680629.2017.1302355.
Daniels, E., S. Bharwani, Gerger Swartling, G. Vulturius, and K. Brandon, 2020: Refocusing the climate services lens: Introducing a framework for co-designing "transdisciplinary knowledge integration processes" to build climate resilience. *Climate Services*, **19**, 100181, doi:10.1016/j.cliser.2020.100181.
Dankers, R. et al., 2014: First look at changes in flood hazard in the Inter-Sectoral Impact Model Intercomparison Project ensemble. *Proceedings of the National Academy of Sciences*, **111(9)**, 3257–3261, doi:10.1073/pnas.1302078110.
Darmaraki, S. et al., 2019: Future evolution of Marine Heatwaves in the Mediterranean Sea. *Climate Dynamics*, **53(3–4)**, 1371–1392, doi:10.1007/s00382-019-04661-z.
Dash, S. et al., 2016: Effect of heat stress on reproductive performances of dairy cattle and buffaloes: A review. *Veterinary World*, **9(3)**, 235–244, doi:10.14202/vetworld.2016.235-244.
Davi, N.K. et al., 2015: A long-term context (931-2005 C.E.) for rapid warming over Central Asia. *Quaternary Science Reviews*, **121**, 89–97, doi:10.1016/j.quascirev.2015.05.020.
Davy, R., N. Gnatiuk, L. Pettersson, and L. Bobylev, 2018: Climate change impacts on wind energy potential in the European domain with a focus on the Black Sea. *Renewable and Sustainable Energy Reviews*, **81**, 1652–1659, doi:10.1016/j.rser.2017.05.253.
Dawson, R.J. et al., 2009: Integrated analysis of risks of coastal flooding and cliff erosion under scenarios of long term change. *Climatic Change*, **95(1–2)**, 249–288, doi:10.1007/s10584-008-9532-8.
Day, J.J. and K.I. Hodges, 2018: Growing Land-Sea Temperature Contrast and the Intensification of Arctic Cyclones. *Geophysical Research Letters*, **45(8)**, 3673–3681, doi:10.1029/2018gl077587.
De Boeck, H.J., E. Hiltbrunner, M. Verlinden, S. Bassin, and M. Zeiter, 2018: Legacy Effects of Climate Extremes in Alpine Grassland. *Frontiers in Plant Science*, **9**, 1586, doi:10.3389/fpls.2018.01586.
De Bruin, K. et al., 2020: Physical climate risks and the financial sector – Synthesis of investors' climate information needs. In: *Handbook of Climate Services: Climate Change Management* [Leal Filho, W. and D. Jacob (eds.)]. Springer, Cham, Switzerland, pp. 135–156, doi:10.1007/978-3-030-36875-3_8.
de Jong, P. et al., 2019: Estimating the impact of climate change on wind and solar energy in Brazil using a South American regional climate model. *Renewable Energy*, **141**, 390–401, doi:10.1016/j.renene.2019.03.086.

ACCEPTED VERSION SUBJECT TO FINAL EDITS

DeGaetano, A.T., 2018: Regional Influences of Mean Temperature and Variance Changes on Freeze Risk in Apples. *HortScience*, **53(1)**, 90–96, doi:10.21273/hortsci11546-16.
DeGaetano, A.T. and C.M. Castellano, 2017: Future projections of extreme precipitation intensity-duration-frequency curves for climate adaptation planning in New York State. *Climate Services*, **5**, 23–35, doi:10.1016/j.cliser.2017.03.003.
Degelia, S.K. et al., 2016: An overview of ice storms and their impact in the United States. *International Journal of Climatology*, **36(8)**, 2811–2822, doi:10.1002/joc.4525.
Delworth, T.L. and F. Zeng, 2014: Regional rainfall decline in Australia attributed to anthropogenic greenhouse gases and ozone levels. *Nature Geoscience*, **7(8)**, 583–587, doi:10.1038/ngeo2201.
Deng, K., C. Azorin-Molina, L. Minola, G. Zhang, and D. Chen, 2021: Global Near-Surface Wind Speed Changes over the Last Decades Revealed by Reanalyses and CMIP6 Model Simulations. *Journal of Climate*, **34(6)**, 2219–2234, doi:10.1175/jcli-d-20-0310.1.
Dennekamp, M. and M.J. Abramson, 2011: The effects of bushfire smoke on respiratory health. *Respirology*, **16(2)**, 198–209, doi:10.1111/j.1440-1843.2010.01868.x.
Dennis, E.S. and W.J. Peacock, 2009: Vernalization in cereals.. *Journal of biology*, **8(6)**, 57, doi:10.1186/jbiol156.
Depietri, Y. and T. McPhearson, 2018: Changing urban risk: 140 years of climatic hazards in New York City. *Climatic Change*, **148(1–2)**, 95–108, doi:10.1007/s10584-018-2194-2.
Dépoues, V., 2017: Organisational uptake of scientific information about climate change by infrastructure managers: the case of adaptation of the French railway company. *Climatic Change*, **143(3–4)**, 473–486, doi:10.1007/s10584-017-2016-y.
Derksen, C. et al., 2018: Changes in Snow, Ice, and Permafrost Across Canada. In: *Canada's Changing Climate Report* [Bush, E. and D.S. Lemmen (eds.)]. Government of Canada, Ottawa, ON, Canada, pp. 194–260.
Deryng, D., D. Conway, N. Ramankutty, J. Price, and R. Warren, 2014: Global crop yield response to extreme heat stress under multiple climate change futures. *Environmental Research Letters*, **9(3)**, 034011, doi:10.1088/1748-9326/9/3/034011.
Deryng, D. et al., 2016: Regional disparities in the beneficial effects of rising CO2 concentrations on crop water productivity. *Nature Climate Change*, **6(8)**, 786–790, doi:10.1038/nclimate2995.
Dessens, J., C. Berthet, and J.L. Sanchez, 2007: A point hailfall classification based on hailpad measurements: The ANELFA scale. *Atmospheric Research*, **83(2–4)**, 132–139, doi:10.1016/j.atmosres.2006.02.029.
Deutsch, C.A. et al., 2018: Increase in crop losses to insect pests in a warming climate.. *Science (New York, N.Y.)*, **361(6405)**, 916–919, doi:10.1126/science.aat3466.
Devis, A., N.P.M. Van Lipzig, and M. Demuzere, 2018: Should future wind speed changes be taken into account in wind farm development? *Environmental Research Letters*, **13(6)**, 064012, doi:10.1088/1748-9326/aabff7.
Dey, R., S.C. Lewis, and N.J. Abram, 2019: Investigating observed northwest Australian rainfall trends in Coupled Model Intercomparison Project phase 5 detection and attribution experiments. *International Journal of Climatology*, **39(1)**, 112–127, doi:10.1002/joc.5788.
Di Sante, F., E. Coppola, and F. Giorgi, 2021: Projections of river floods in Europe using EURO-CORDEX, CMIP5 and CMIP6 simulations. *International Journal of Climatology*, **41(5)**, 3203–3221, doi:10.1002/joc.7014.
Di Virgilio, G. et al., 2019: Climate Change Increases the Potential for Extreme Wildfires. *Geophysical Research Letters*, **46(14)**, 8517–8526, doi:10.1029/2019gl083699.
Diaz, R.J. and R. Rosenberg, 2008: Spreading Dead Zones and Consequences for Marine Ecosystems. *Science*, **321(5891)**, 926–929, doi:10.1126/science.1156401.
Dibike, Y., T. Prowse, B. Bonsal, L. Rham, and T. Saloranta, 2012: Simulation of North American lake-ice cover characteristics under contemporary and future climate conditions. *International Journal of Climatology*, **32(5)**, 695–709, doi:10.1002/joc.2300.
Diedhiou, A. et al., 2018: Changes in climate extremes over West and Central Africa at 1.5 °C and 2 °C global warming. *Environmental Research Letters*, **13(6)**, 065020, doi:10.1088/1748-9326/aac3e5.
Diffenbaugh, N.S., M. Scherer, and R.J. Trapp, 2013: Robust increases in severe thunderstorm environments in response to greenhouse forcing. *Proceedings of the National Academy of Sciences*, **110(41)**, 16361–16366, doi:10.1073/pnas.1307758110.
Dikanski, H., A. Hagen-Zanker, B. Imam, and K. Avery, 2016: Climate change impacts on railway structures: bridge scour. *Proceedings of the Institution of Civil Engineers - Engineering Sustainability*, **170(5)**, 237–248, doi:10.1680/jensu.15.00021.
Diro, G.T. et al., 2014: Tropical cyclones in a regional climate change projection with RegCM4 over the CORDEX Central America domain. *Climatic Change*, **125(1)**, 79–94, doi:10.1007/s10584-014-1155-7.
Dittus, A., D. Karoly, S. Lewis, and L. Alexander, 2014: An investigation of some unexpected frost day increases in southern Australia. *Australian Meteorological and Oceanographic Journal*, **64(4)**, 261–271, doi:10.22499/2.6404.002.
Dobney, K., C.J. Baker, L. Chapman, and A.D. Quinn, 2010: The future cost to the United Kingdom's railway network of heat-related delays and buckles caused by the predicted increase in high summer temperatures owing to climate change. *Proceedings of the Institution of Mechanical Engineers, Part F: Journal of Rail and Rapid*

ACCEPTED VERSION SUBJECT TO FINAL EDITS

Transit, **224(1)**, 25–34, doi:10.1243/09544097jrrt292.
Dobricic, S., S. Russo, L. Pozzoli, J. Wilson, and E. Vignati, 2020: Increasing occurrence of heat waves in the terrestrial Arctic. *Environmental Research Letters*, **15(2)**, 024022, doi:10.1088/1748-9326/ab6398.
Dobrowski, S.Z. and S.A. Parks, 2016: Climate change velocity underestimates climate change exposure in mountainous regions. *Nature Communications*, **7(1)**, 12349, doi:10.1038/ncomms12349.
Dobrowski, S.Z. et al., 2013: The climate velocity of the contiguous United States during the 20th century. *Global Change Biology*, **19(1)**, 241–251, doi:10.1111/gcb.12026.
DOE, 2015: *Climate Change and the U.S. Energy Sector: Regional Vulnerabilities and Resilience Solutions*. DOE/EPSA-0005, U.S. Department of Energy (DOE), 193 pp.
Döll, P. and H.M. Schmied, 2012: How is the impact of climate change on river flow regimes related to the impact on mean annual runoff? A global-scale analysis. *Environmental Research Letters*, **7(1)**, 014037, doi:10.1088/1748-9326/7/1/014037.
Domingos, F., F. Lúcio, and V. Grasso, 2016: The Global Framework for Climate Services (GFCS). *Climate Services*, **2–3**, 52–53, doi:10.1016/j.cliser.2016.09.001.
Domínguez-Castro, F., R. García-Herrera, and S.M. Vicente-Serrano, 2018: Wet and dry extremes in Quito (Ecuador) since the 17th century. *International Journal of Climatology*, **38(4)**, 2006–2014, doi:10.1002/joc.5312.
Donat, M.G., L. Alexander, N. Herold, and A.J. Dittus, 2016: Temperature and precipitation extremes in century-long gridded observations, reanalyses, and atmospheric model simulations. *Journal of Geophysical Research: Atmospheres*, **121(19)**, 11,174–11,189, doi:10.1002/2016jd025480.
Doney, S.C. et al., 2012: Climate Change Impacts on Marine Ecosystems. *Annual Review of Marine Science*, **4(1)**, 11–37, doi:10.1146/annurev-marine-041911-111611.
Dong, S. et al., 2018: Observed changes in temperature extremes over Asia and their attribution. *Climate Dynamics*, **51(1–2)**, 339–353, doi:10.1007/s00382-017-3927-z.
Dong, W. et al., 2018: Regional disparities in warm season rainfall changes over arid eastern–central Asia. *Scientific Reports*, **8(1)**, 13051, doi:10.1038/s41598-018-31246-3.
Dosio, A., 2016: Projections of climate change indices of temperature and precipitation from an ensemble of bias-adjusted high-resolution EURO-CORDEX regional climate models. *Journal of Geophysical Research: Atmospheres*, **121(10)**, 5488–5511, doi:10.1002/2015jd024411.
Dosio, A., 2017: Projection of temperature and heat waves for Africa with an ensemble of CORDEX Regional Climate Models. *Climate Dynamics*, **49(1–2)**, 493–519, doi:10.1007/s00382-016-3355-5.
Dosio, A., L. Mentaschi, E.M. Fischer, and K. Wyser, 2018: Extreme heat waves under 1.5°C and 2°C global warming. *Environmental Research Letters*, **13(5)**, 054006, doi:10.1088/1748-9326/aab827.
Dosio, A. et al., 2019: What can we know about future precipitation in Africa? Robustness, significance and added value of projections from a large ensemble of regional climate models. *Climate Dynamics*, **53(9)**, 5833–5858, doi:10.1007/s00382-019-04900-3.
Dottori, F. et al., 2018: Increased human and economic losses from river flooding with anthropogenic warming. *Nature Climate Change*, **8(9)**, 781–786, doi:10.1038/s41558-018-0257-z.
Dowdy, A.J., 2018: Climatological Variability of Fire Weather in Australia. *Journal of Applied Meteorology and Climatology*, **57(2)**, 221–234, doi:10.1175/jamc-d-17-0167.1.
Dowdy, A.J. and A. Pepler, 2018: Pyroconvection Risk in Australia: Climatological Changes in Atmospheric Stability and Surface Fire Weather Conditions. *Geophysical Research Letters*, **45(4)**, 2005–2013, doi:10.1002/2017gl076654.
Dowdy, A.J. et al., 2019a: Review of Australian east coast low pressure systems and associated extremes. *Climate Dynamics*, **53(7)**, 4887–4910, doi:10.1007/s00382-019-04836-8.
Dowdy, A.J. et al., 2019b: Future changes in extreme weather and pyroconvection risk factors for Australian wildfires. *Scientific Reports*, **9(1)**, 10073, doi:10.1038/s41598-019-46362-x.
Dreessen, J., J. Sullivan, and R. Delgado, 2016: Observations and impacts of transported Canadian wildfire smoke on ozone and aerosol air quality in the Maryland region on June 9–12, 2015. *Journal of the Air & Waste Management Association*, **66(9)**, 842–862, doi:10.1080/10962247.2016.1161674.
Drenkhan, F., C. Huggel, L. Guardamino, and W. Haeberli, 2019: Managing risks and future options from new lakes in the deglaciating Andes of Peru: The example of the Vilcanota-Urubamba basin. *Science of The Total Environment*, **665**, 465–483, doi:10.1016/j.scitotenv.2019.02.070.
Drewes, J., S. Moreiras, and O. Korup, 2018: Permafrost activity and atmospheric warming in the Argentinian Andes. *Geomorphology*, **323**, 13–24, doi:10.1016/j.geomorph.2018.09.005.
Driouech, F. et al., 2021: Recent observed country-wide climate trends in Morocco. *International Journal of Climatology*, **41(S1)**, E855– E874, doi:10.1002/joc.6734.
Du, J., J.S. Kimball, C. Duguay, Y. Kim, and J.D. Watts, 2017: Satellite microwave assessment of Northern Hemisphere lake ice phenology from 2002 to 2015. *The Cryosphere*, **11(1)**, 47–63, doi:10.5194/tc-11-47-2017.
Dudley, R.W., G.A. Hodgkins, M.R. McHale, M.J. Kolian, and B. Renard, 2017: Trends in snowmelt-related streamflow timing in the conterminous United States. *Journal of Hydrology*, **547**, 208–221, doi:10.1016/j.jhydrol.2017.01.051.

ACCEPTED VERSION SUBJECT TO FINAL EDITS

Duffy, P.B., P. Brando, G.P. Asner, and C.B. Field, 2015: Projections of future meteorological drought and wet periods in the Amazon. *Proceedings of the National Academy of Sciences*, **112(43)**, 13172–13177, doi:10.1073/pnas.1421010112.

Dunne, J.P., R.J. Stouffer, and J.G. John, 2013: Reductions in labour capacity from heat stress under climate warming. *Nature Climate Change*, **3(6)**, 563–566, doi:10.1038/nclimate1827.

Dunning, C.M., E. Black, and R.P. Allan, 2018: Later Wet Seasons with More Intense Rainfall over Africa under Future Climate Change. *Journal of Climate*, **31(23)**, 9719–9738, doi:10.1175/jcli-d-18-0102.1.

Dupuy, J.- et al., 2020: Climate change impact on future wildfire danger and activity in southern Europe: a review. *Annals of Forest Science*, **77(2)**, 35, doi:10.1007/s13595-020-00933-5.

Durand, J.-L. et al., 2018: How accurately do maize crop models simulate the interactions of atmospheric CO2 concentration levels with limited water supply on water use and yield? *European Journal of Agronomy*, **100**, 67–75, doi:10.1016/j.eja.2017.01.002.

Durkalec, A., C. Furgal, M.W. Skinner, and T. Sheldon, 2015: Climate change influences on environment as a determinant of Indigenous health: Relationships to place, sea ice, and health in an Inuit community. *Social Science & Medicine*, **136–137**, 17–26, doi:10.1016/j.socscimed.2015.04.026.

Durocher, M., A.I. Requena, D.H. Burn, and J. Pellerin, 2019: Analysis of trends in annual streamflow to the Arctic Ocean. *Hydrological Processes*, **33(7)**, 1143–1151, doi:10.1002/hyp.13392.

Dutkiewicz, S. et al., 2015: Impact of ocean acidification on the structure of future phytoplankton communities. *Nature Climate Change*, **5(11)**, 1002–1006, doi:10.1038/nclimate2722.

Duvat, V.K.E. and V. Pillet, 2017: Shoreline changes in reef islands of the Central Pacific: Takapoto Atoll, Northern Tuamotu, French Polynesia. *Geomorphology*, **282**, 96–118, doi:10.1016/j.geomorph.2017.01.002.

Duvat, V.K.E., B. Salvat, and C. Salmon, 2017: Drivers of shoreline change in atoll reef islands of the Tuamotu Archipelago, French Polynesia. *Global and Planetary Change*, **158**, 134–154, doi:10.1016/j.gloplacha.2017.09.016.

Duvillard, P.A., L. Ravanel, M. Marcer, and P. Schoeneich, 2019: Recent evolution of damage to infrastructure on permafrost in the French Alps. *Regional Environmental Change*, **19(5)**, 1281–1293, doi:10.1007/s10113-019-01465-z.

Easterling, D.R. et al., 2017: Precipitation change in the United States. In: *Climate Science Special Report: Fourth National Climate Assessment, Volume I* [Wuebbles, D.J., D.W. Fahey, K.A. Hibbard, D.J. Dokken, B.C. Stewart, and T.K. Maycock (eds.)]. U.S. Global Change Research Program, Washington, DC, USA, pp. 207–230, doi:10.7930/j0h993cc.

EC, 2015: *A European research and innovation Roadmap for Climate Services*. KI0614177ENN, European Commission (EC) Directorate-General for Research and Innovation (DG RTD), Brussels, Belgium, 56 pp., doi:10.2777/702151.

Economou, T., D.B. Stephenson, J.G. Pinto, L.C. Shaffrey, and G. Zappa, 2015: Serial clustering of extratropical cyclones in a multi-model ensemble of historical and future simulations. *Quarterly Journal of the Royal Meteorological Society*, **141(693)**, 3076–3087, doi:10.1002/qj.2591.

EEA, 2018: *National climate change vulnerability and risk assessments in Europe, 2018*. EEA Report No 1/2018, European Environment Agency (EEA), Copenhagen, Denmark, 79 pp., doi:10.2800/348489.

Eisen, L. and C.G. Moore, 2013: Aedes (Stegomyia) aegypti in the Continental United States: A Vector at the Cool Margin of Its Geographic Range. *Journal of Medical Entomology*, **50(3)**, 467–478, doi:10.1603/me12245.

Ekstrom, J.A. et al., 2015: Vulnerability and adaptation of US shellfisheries to ocean acidification. *Nature Climate Change*, **5(3)**, 207–214, doi:10.1038/nclimate2508.

Ekström, M., E.D. Gutmann, R.L. Wilby, M.R. Tye, and D.G.C. Kirono, 2018: Robustness of hydroclimate metrics for climate change impact research. *Wiley Interdisciplinary Reviews: Water*, **5(4)**, e1288, doi:10.1002/wat2.1288.

Elagib, N.A., 2014: Development and application of a drought risk index for food crop yield in Eastern Sahel. *Ecological Indicators*, **43**, 114–125, doi:10.1016/j.ecolind.2014.02.033.

Elison Timm, O., T.W. Giambelluca, and H.F. Diaz, 2015: Statistical downscaling of rainfall changes in Hawai'i based on the CMIP5 global model projections. *Journal of Geophysical Research: Atmospheres*, **120(1)**, 92–112, doi:10.1002/2014jd022059.

Elith, J., M. Kearney, and S. Phillips, 2010: The art of modelling range-shifting species. *Methods in Ecology and Evolution*, **1(4)**, 330–342, doi:10.1111/j.2041-210x.2010.00036.x.

Ellison, J.C., 2015: Vulnerability assessment of mangroves to climate change and sea-level rise impacts. *Wetlands Ecology and Management*, **23(2)**, 115–137, doi:10.1007/s11273-014-9397-8.

Elsner, J.B., S.C. Elsner, and T.H. Jagger, 2015: The increasing efficiency of tornado days in the United States. *Climate Dynamics*, **45(3–4)**, 651–659, doi:10.1007/s00382-014-2277-3.

Elsner, J.B., T. Fricker, and Z. Schroder, 2019: Increasingly Powerful Tornadoes in the United States. *Geophysical Research Letters*, **46(1)**, 392–398, doi:10.1029/2018gl080819.

Emadodin, I., T. Reinsch, and F. Taube, 2019: Drought and Desertification in Iran. *Hydrology*, **6(3)**, 66, doi:10.3390/hydrology6030066.

Emberson, L.D. et al., 2018: Ozone effects on crops and consideration in crop models. *European Journal of Agronomy*,

ACCEPTED VERSION SUBJECT TO FINAL EDITS

100, 19–34, doi:10.1016/j.eja.2018.06.002.
Engelbrecht, F. et al., 2015: Projections of rapidly rising surface temperatures over Africa under low mitigation. *Environmental Research Letters*, **10(8)**, 085004, doi:10.1088/1748-9326/10/8/085004.
England, M.H. et al., 2014: Recent intensification of wind-driven circulation in the Pacific and the ongoing warming hiatus. *Nature Climate Change*, **4(3)**, 222–227, doi:10.1038/nclimate2106.
Engram, M., C.D. Arp, B.M. Jones, O.A. Ajadi, and F.J. Meyer, 2018: Analyzing floating and bedfast lake ice regimes across Arctic Alaska using 25 years of space-borne SAR imagery. *Remote Sensing of Environment*, **209**, 660–676, doi:10.1016/j.rse.2018.02.022.
Erban, L.E., S.M. Gorelick, and H.A. Zebker, 2014: Groundwater extraction, land subsidence, and sea-level rise in the Mekong Delta, Vietnam. *Environmental Research Letters*, **9(8)**, 84010, doi:10.1088/1748-9326/9/8/084010.
Erlat, E. and M. Türkeş, 2016: Dates of frost onset, frost end and the frost-free season in Turkey: trends, variability and links to the North Atlantic and Arctic Oscillation indices, 1950-2013. *Climate Research*, **69(2)**, 155–176, doi:10.3354/cr01397.
Espinet, X., A. Schweikert, N. van den Heever, and P. Chinowsky, 2016: Planning resilient roads for the future environment and climate change: Quantifying the vulnerability of the primary transport infrastructure system in Mexico. *Transport Policy*, **50**, 78–86, doi:10.1016/j.tranpol.2016.06.003.
Espinoza, J.C. et al., 2013: The Major Floods in the Amazonas River and Tributaries (Western Amazon Basin) during the 1970–2012 Period: A Focus on the 2012 Flood. *Journal of Hydrometeorology*, **14(3)**, 1000–1008, doi:10.1175/jhm-d-12-0100.1.
Espinoza, J.C. et al., 2020: Hydroclimate of the Andes Part I: Main Climatic Features. *Frontiers in Earth Science*, **8**, 64, doi:10.3389/feart.2020.00064.
Evan, A.T., C. Flamant, M. Gaetani, and F. Guichard, 2016: The past, present and future of African dust. *Nature*, **531(7595)**, 493–495, doi:10.1038/nature17149.
Eyring, V. et al., 2016: Overview of the Coupled Model Intercomparison Project Phase 6 (CMIP6) experimental design and organization. *Geoscientific Model Development*, **9(5)**, 1937–1958, doi:10.5194/gmd-9-1937-2016.
Eyshi Rezaei, E., H. Webber, T. Gaiser, J. Naab, and F. Ewert, 2015: Heat stress in cereals: Mechanisms and modelling. *European Journal of Agronomy*, **64**, 98–113, doi:10.1016/j.eja.2014.10.003.
Fábrega, J. et al., 2013: Hydroclimate projections for Panama in the late 21st Century. *Hydrological Research Letters*, **7(2)**, 23–29, doi:10.3178/hrl.7.23.
Faggian, P. and G. Decimi, 2019: An updated investigation about climate-change hazards that might impact electric infrastructures. In: *2019 AEIT International Annual Conference (AEIT)*. IEEE, pp. 1–5, doi:10.23919/aeit.2019.8893297.
Fallah-Ghalhari, G., F. Shakeri, and A. Dadashi-Roudbari, 2019: Impacts of climate changes on the maximum and minimum temperature in Iran. *Theoretical and Applied Climatology*, **138(3–4)**, 1539–1562, doi:10.1007/s00704-019-02906-9.
Falloon, P. et al., 2018: The land management tool: Developing a climate service in Southwest UK. *Climate Services*, **9**, 86–100, doi:10.1016/j.cliser.2017.08.002.
Fan, X.-T., Y. Li, A.-M. Lyu, and L.-S. Liu, 2020: Statistical and Comparative Analysis of Tropical Cyclone Activity over the Arabian Sea and Bay of Bengal (1977-2018). *Journal of tropical meteorology*, **26(4)**, 441–452, doi:10.46267/j.1006-8775.2020.038.
Fann, N. et al., 2015: The geographic distribution and economic value of climate change-related ozone health impacts in the United States in 2030. *Journal of the Air & Waste Management Association*, **65(5)**, 570–580, doi:10.1080/10962247.2014.996270.
Fann, N. et al., 2016: Ch. 3: Air Quality Impacts. In: *The Impacts of Climate Change on Human Health in the United States: A Scientific Assessment*. U.S. Global Change Research Program, Washington, DC, USA, pp. 69–98, doi:10.7930/j0gq6vp6.
Fant, C., C. Adam Schlosser, and K. Strzepek, 2016: The impact of climate change on wind and solar resources in southern Africa. *Applied Energy*, **161**, 556–564, doi:10.1016/j.apenergy.2015.03.042.
Fargeon, H. et al., 2020: Projections of fire danger under climate change over France: where do the greatest uncertainties lie? *Climatic Change*, **160(3)**, 479–493, doi:10.1007/s10584-019-02629-w.
Farquharson, L.M. et al., 2019: Climate Change Drives Widespread and Rapid Thermokarst Development in Very Cold Permafrost in the Canadian High Arctic. *Geophysical Research Letters*, **46(12)**, 6681–6689, doi:10.1029/2019gl082187.
Fatemi, S.S., M. Rahimi, M. Tarkesh, and H. Ravanbakhsh, 2018: Predicting the impacts of climate change on the distribution of Juniperus excelsa M. Bieb. in the central and eastern Alborz Mountains, Iran. *iForest - Biogeosciences and Forestry*, **11(5)**, 643–650, doi:10.3832/ifor2559-011.
Fedotova, E., 2019: Wind projections for the territory of Russia considering the development of wind power. *IOP Conference Series: Earth and Environmental Science*, **386**, 12042, doi:10.1088/1755-1315/386/1/012042.
Feeley, T.J. et al., 2008: Water: A critical resource in the thermoelectric power industry. *Energy*, **33(1)**, 1–11, doi:10.1016/j.energy.2007.08.007.
Feely, R.A. et al., 2016: Chemical and biological impacts of ocean acidification along the west coast of North America.

ACCEPTED VERSION SUBJECT TO FINAL EDITS

Estuarine, Coastal and Shelf Science, **183**, 260–270, doi:10.1016/j.ecss.2016.08.043.
Fei, S. et al., 2017: Divergence of species responses to climate change. *Science Advances*, **3(5)**, e1603055, doi:10.1126/sciadv.1603055.
Feng, J., T. Wang, and C. Xie, 2006: Eco-Environmental Degradation in the Source Region of the Yellow River, Northeast Qinghai-Xizang Plateau. *Environmental Monitoring and Assessment*, **122(1–3)**, 125–143, doi:10.1007/s10661-005-9169-2.
Feng, S. and Q. Fu, 2013: Expansion of global drylands under a warming climate. *Atmospheric Chemistry and Physics*, **13(19)**, 10081–10094, doi:10.5194/acp-13-10081-2013.
Feng, S., M. Trnka, M. Hayes, and Y. Zhang, 2017: Why Do Different Drought Indices Show Distinct Future Drought Risk Outcomes in the U.S. Great Plains? *Journal of Climate*, **30(1)**, 265–278, doi:10.1175/jcli-d-15-0590.1.
Feng, T., T. Su, R. Zhi, G. Tu, and F. Ji, 2019: Assessment of actual evapotranspiration variability over global land derived from seven reanalysis datasets. *International Journal of Climatology*, **39(6)**, 2919–2932, doi:10.1002/joc.5992.
Ferguson, C.R., M. Pan, and T. Oki, 2018: The Effect of Global Warming on Future Water Availability: CMIP5 Synthesis. *Water Resources Research*, **54(10)**, 7791–7819, doi:10.1029/2018wr022792.
Ferguson, G. and T. Gleeson, 2012: Vulnerability of coastal aquifers to groundwater use and climate change. *Nature Climate Change*, **2(5)**, 342–345, doi:10.1038/nclimate1413.
Feser, F. et al., 2015: Storminess over the North Atlantic and northwestern Europe-A review. *Quarterly Journal of the Royal Meteorological Society*, **141(687)**, 350–382, doi:10.1002/qj.2364.
Filizola, N. et al., 2014: Was the 2009 flood the most hazardous or the largest ever recorded in the Amazon? *Geomorphology*, **215**, 99–105, doi:10.1016/j.geomorph.2013.05.028.
Finger Higgens, R.A. et al., 2019: Changing Lake Dynamics Indicate a Drier Arctic in Western Greenland. *Journal of Geophysical Research: Biogeosciences*, **124(4)**, 870–883, doi:10.1029/2018jg004879.
Fiore, A.M., V. Naik, and E.M. Leibensperger, 2015: Air quality and climate connections. *Journal of the Air and Waste Management Association*, **65(6)**, 645–685, doi:10.1080/10962247.2015.1040526.
Fischer, E.M. and R. Knutti, 2016: Observed heavy precipitation increase confirms theory and early models. *Nature Climate Change*, **6(11)**, 986–991, doi:10.1038/nclimate3110.
Fishman, R., 2016: More uneven distributions overturn benefits of higher precipitation for crop yields. *Environmental Research Letters*, **11(2)**, 024004, doi:10.1088/1748-9326/11/2/024004.
Fiss, C.J., D.J. McNeil, F. Rodríguez, A.D. Rodewald, and J.L. Larkin, 2019: Hail-induced nest failure and adult mortality in a declining ground-nesting forest songbird. *The Wilson Journal of Ornithology*, **131(1)**, 165, doi:10.1676/18-15.
Fitchett, J.M., 2018: Recent emergence of CAT5 tropical cyclones in the South Indian Ocean. *South African Journal of Science*, **114(11/12)**, 1–6, doi:10.17159/sajs.2018/4426.
Flannigan, M. et al., 2013: Global wildland fire season severity in the 21st century. *Forest Ecology and Management*, **294**, 54–61, doi:10.1016/j.foreco.2012.10.022.
Fleisher, D.H. et al., 2017: A potato model intercomparison across varying climates and productivity levels. *Global Change Biology*, **23(3)**, 1258–1281, doi:10.1111/gcb.13411.
Fluixá-Sanmartín, J., L. Altarejos-García, A. Morales-Torres, and I. Escuder-Bueno, 2018: Review article: Climate change impacts on dam safety. *Natural Hazards and Earth System Sciences*, **18(9)**, 2471–2488, doi:10.5194/nhess-18-2471-2018.
Fonseca, M.G. et al., 2019: Effects of climate and land-use change scenarios on fire probability during the 21st century in the Brazilian Amazon. *Global Change Biology*, **25(9)**, 2931–2946, doi:10.1111/gcb.14709.
Fontana, G., A. Toreti, A. Ceglar, and G. De Sanctis, 2015: Early heat waves over Italy and their impacts on durum wheat yields. *Natural Hazards and Earth System Sciences*, **15(7)**, 1631–1637, doi:10.5194/nhess-15-1631-2015.
Fontrodona Bach, A., G. Schrier, L.A. Melsen, A.M.G. Klein Tank, and A.J. Teuling, 2018: Widespread and Accelerated Decrease of Observed Mean and Extreme Snow Depth Over Europe. *Geophysical Research Letters*, **45(22)**, 12,312–12,319, doi:10.1029/2018gl079799.
Forbes, B.C. et al., 2016: Sea ice, rain-on-snow and tundra reindeer nomadism in Arctic Russia. *Biology Letters*, **12(11)**, 20160466, doi:10.1098/rsbl.2016.0466.
Forbes, D.L. (ed.), 2011: *State of the Arctic Coast 2010 – Scientific Review and Outlook*. 178 pp.
Ford, M.R. and P.S. Kench, 2015: Multi-decadal shoreline changes in response to sea level rise in the Marshall Islands. *Anthropocene*, **11**, 14–24, doi:10.1016/j.ancene.2015.11.002.
Forkel, M. et al., 2019: Recent global and regional trends in burned area and their compensating environmental controls. *Environmental Research Communications*, **1(5)**, 051005, doi:10.1088/2515-7620/ab25d2.
Forzieri, G., A. Cescatti, F.B. e Silva, and L. Feyen, 2017: Increasing risk over time of weather-related hazards to the European population: a data-driven prognostic study. *The Lancet Planetary Health*, **1(5)**, e200–e208, doi:10.1016/s2542-5196(17)30082-7.
Forzieri, G. et al., 2014: Ensemble projections of future streamflow droughts in Europe. *Hydrology and Earth System Sciences*, **18(1)**, 85–108, doi:10.5194/hess-18-85-2014.

ACCEPTED VERSION SUBJECT TO FINAL EDITS

Forzieri, G. et al., 2016: Multi-hazard assessment in Europe under climate change. *Climatic Change*, **137(1–2)**, 105–119, doi:10.1007/s10584-016-1661-x.
Forzieri, G. et al., 2018: Escalating impacts of climate extremes on critical infrastructures in Europe. *Global Environmental Change*, **48**, 97–107, doi:10.1016/j.gloenvcha.2017.11.007.
Frazier, A.G. and T.W. Giambelluca, 2017: Spatial trend analysis of Hawaiian rainfall from 1920 to 2012. *International Journal of Climatology*, **37(5)**, 2522–2531, doi:10.1002/joc.4862.
Frederikse, T. et al., 2020: The causes of sea-level rise since 1900. *Nature*, **584(7821)**, 393–397, doi:10.1038/s41586-020-2591-3.
Freeland, H.J., 2013: Evidence of Change in the Winter Mixed Layer in the Northeast Pacific Ocean: A Problem Revisited. *Atmosphere-Ocean*, **51(1)**, 126–133, doi:10.1080/07055900.2012.754330.
Frieler, K. et al., 2013: Limiting global warming to 2°C is unlikely to save most coral reefs. *Nature Climate Change*, **3(2)**, 165–170, doi:10.1038/nclimate1674.
Fritz, M., J.E. Vonk, and H. Lantuit, 2017: Collapsing Arctic coastlines. *Nature Climate Change*, **7(1)**, 6–7, doi:10.1038/nclimate3188.
Frölicher, T.L., 2019: Chapter 5 – Extreme climatic events in the ocean. In: *Predicting Future Oceans* [Cisneros-Montemayor, A.M., W.W.L. Cheung, and Y. Ota (eds.)]. Elsevier, pp. 53–60, doi:10.1016/b978-0-12-817945-1.00005-8.
Frölicher, T.L. and C. Laufkötter, 2018: Emerging risks from marine heat waves. *Nature Communications*, **9(1)**, 650, doi:10.1038/s41467-018-03163-6.
Frölicher, T.L., E.M. Fischer, and N. Gruber, 2018: Marine heatwaves under global warming. *Nature*, **560(7718)**, 360–364, doi:10.1038/s41586-018-0383-9.
Frölicher, T.L. et al., 2020: Contrasting Upper and Deep Ocean Oxygen Response to Protracted Global Warming. *Global Biogeochemical Cycles*, **34(8)**, e2020GB006601, doi:10.1029/2020gb006601.
Frolova, N.L. et al., 2017: Hydrological hazards in Russia: origin, classification, changes and risk assessment. *Natural Hazards*, **88(1)**, 103–131, doi:10.1007/s11069-016-2632-2.
Froude, M.J. and D.N. Petley, 2018: Global fatal landslide occurrence from 2004 to 2016. *Natural Hazards and Earth System Sciences*, **18**, 2161–2181, doi:10.5194/nhess-18-2161-2018.
Fu, R. et al., 2013: Increased dry-season length over southern Amazonia in recent decades and its implication for future climate projection. *Proceedings of the National Academy of Sciences*, **110(45)**, 18110–18115, doi:10.1073/pnas.1302584110.
Fuentes-Franco, R. et al., 2015: Inter-annual variability of precipitation over Southern Mexico and Central America and its relationship to sea surface temperature from a set of future projections from CMIP5 GCMs and RegCM4 CORDEX simulations. *Climate Dynamics*, **45(1–2)**, 425–440, doi:10.1007/s00382-014-2258-6.
Fyfe, J.C. et al., 2017: Large near-term projected snowpack loss over the western United States. *Nature Communications*, **8**, 14996, doi:10.1038/ncomms14996.
Gabric, A.J. et al., 2016: Tasman Sea biological response to dust storm events during the austral spring of 2009. *Marine and Freshwater Research*, **67(8)**, 1090, doi:10.1071/mf14321.
Gądek, B. et al., 2017: Snow avalanche activity in Żleb Żandarmerii in a time of climate change (Tatra Mts., Poland). *CATENA*, **158**, 201–212, doi:10.1016/j.catena.2017.07.005.
Gaffin, S.R. et al., 2012: Bright is the new black – multi-year performance of high-albedo roofs in an urban climate. *Environmental Research Letters*, **7(1)**, 014029, doi:10.1088/1748-9326/7/1/014029.
Gaire, S., R. Castro Delgado, and P. Arcos González, 2015: Disaster risk profile and existing legal framework of Nepal: floods and landslides.. *Risk management and healthcare policy*, **8**, 139–149, doi:10.2147/rmhp.s90238.
Galli, G., C. Solidoro, and T. Lovato, 2017: Marine Heat Waves Hazard 3D Maps and the Risk for Low Motility Organisms in a Warming Mediterranean Sea. *Frontiers in Marine Science*, **4**, 136, doi:10.3389/fmars.2017.00136.
Gallo, F. et al., 2019: High-resolution regional climate model projections of future tropical cyclone activity in the Philippines. *International Journal of Climatology*, **39(3)**, 1181–1194, doi:10.1002/joc.5870.
Gan, R., Y. Luo, Q. Zuo, and L. Sun, 2015: Effects of projected climate change on the glacier and runoff generation in the Naryn River Basin, Central Asia. *Journal of Hydrology*, **523**, 240–251, doi:10.1016/j.jhydrol.2015.01.057.
Ganeshi, N.G., M. Mujumdar, R. Krishnan, and M. Goswami, 2020: Understanding the linkage between soil moisture variability and temperature extremes over the Indian region. *Journal of Hydrology*, **589**, 125183, doi:10.1016/j.jhydrol.2020.125183.
Ganguli, P. and B. Merz, 2019: Trends in Compound Flooding in Northwestern Europe During 1901–2014. *Geophysical Research Letters*, **46(19)**, 10810–10820, doi:10.1029/2019gl084220.
Gao, C., K. Kuklane, P.O. Östergren, and T. Kjellstrom, 2018: Occupational heat stress assessment and protective strategies in the context of climate change. *International Journal of Biometeorology*, **62(3)**, 359–371, doi:10.1007/s00484-017-1352-y.
Gao, X., C.A. Schlosser, and E.R. Morgan, 2018: Potential impacts of climate warming and increased summer heat stress on the electric grid: a case study for a large power transformer (LPT) in the Northeast United States. *CLIMATIC CHANGE*, **147(1–2)**, 107–118, doi:10.1007/s10584-017-2114-x.

ACCEPTED VERSION
SUBJECT TO FINAL EDITS

Gao, Y., L.R. Leung, J. Lu, and G. Masato, 2015: Persistent cold air outbreaks over North America in a warming climate. *Environmental Research Letters*, **10(4)**, 044001, doi:10.1088/1748-9326/10/4/044001.
Garcia, R.A., M. Cabeza, C. Rahbek, and M.B. Araujo, 2014: Multiple Dimensions of Climate Change and Their Implications for Biodiversity. *Science*, **344(6183)**, 1247579, doi:10.1126/science.1247579.
García-Cueto, O.R. et al., 2019: Trends of climate change indices in some Mexican cities from 1980 to 2010. *Theoretical and Applied Climatology*, **137(1)**, 775–790, doi:10.1007/s00704-018-2620-4.
Gariano, S.L. and F. Guzzetti, 2016: Landslides in a changing climate. *Earth-Science Reviews*, **162**, 227–252, doi:10.1016/j.earscirev.2016.08.011.
Garreaud, R.D. et al., 2017: The 2010–2015 megadrought in central Chile: impacts on regional hydroclimate and vegetation. *Hydrology and Earth System Sciences*, **21(12)**, 6307–6327, doi:10.5194/hess-21-6307-2017.
Garrett, K.A., S.P. Dendy, E.E. Frank, M.N. Rouse, and S.E. Travers, 2006: Climate Change Effects on Plant Disease: Genomes to Ecosystems. *Annual Review of Phytopathology*, **44(1)**, 489–509, doi:10.1146/annurev.phyto.44.070505.143420.
Gattuso, J.-P. et al., 2015: Contrasting futures for ocean and society from different anthropogenic CO2 emissions scenarios. *Science*, **349(6243)**, aac4722, doi:10.1126/science.aac4722.
Gebrechorkos, S.H., S. Hülsmann, and C. Bernhofer, 2019: Regional climate projections for impact assessment studies in East Africa. *Environmental Research Letters*, **14(4)**, 044031, doi:10.1088/1748-9326/ab055a.
Geertsema, M., J.J. Clague, J.W. Schwab, and S.G. Evans, 2006: An overview of recent large catastrophic landslides in northern British Columbia, Canada. *Engineering Geology*, **83(1–3)**, 120–143, doi:10.1016/j.enggeo.2005.06.028.
Gendron St-Marseille, A.-F., G. Bourgeois, J. Brodeur, and B. Mimee, 2019: Simulating the impacts of climate change on soybean cyst nematode and the distribution of soybean. *Agricultural and Forest Meteorology*, **264**, 178–187, doi:10.1016/j.agrformet.2018.10.008.
Georgeson, L., M. Maslin, and M. Poessinouw, 2017: Global disparity in the supply of commercial weather and climate information services. *Science Advances*, **3(5)**, e1602632, doi:10.1126/sciadv.1602632.
Ghanbari, M., M. Arabi, J. Obeysekera, and W. Sweet, 2019: A Coherent Statistical Model for Coastal Flood Frequency Analysis Under Nonstationary Sea Level Conditions. *Earth's Future*, **7(2)**, 162–177, doi:10.1029/2018ef001089.
Giannaros, T.M., V. Kotroni, and K. Lagouvardos, 2021: Climatology and trend analysis (1987–2016) of fire weather in the Euro-Mediterranean. *International Journal of Climatology*, **41(S1)**, E491–E508, doi:10.1002/joc.6701.
Gibbs, A.E. and B.M. Richmond, 2015: *National Assessment of Shoreline Change – Historical Shoreline Change Along the North Coast of Alaska, U.S.-Canadian Border to Icy Cape*. USGS Open-File Report 2015-1048, U.S. Geological Survey (USGS), Reston, VA, USA, 96 pp., doi:10.3133/ofr20151048.
Gidhagen, L. et al., 2020: Towards climate services for European cities: Lessons learnt from the Copernicus project Urban SIS. *Urban Climate*, **31**, 100549, doi:10.1016/j.uclim.2019.100549.
Giersch, J.J., S. Hotaling, R.P. Kovach, L.A. Jones, and C.C. Muhlfeld, 2017: Climate-induced glacier and snow loss imperils alpine stream insects. *Global Change Biology*, **23(7)**, 2577–2589, doi:10.1111/gcb.13565.
Gilly, W.F., J.M. Beman, S.Y. Litvin, and B.H. Robison, 2013: Oceanographic and Biological Effects of Shoaling of the Oxygen Minimum Zone. *Annual Review of Marine Science*, **5(1)**, 393–420, doi:10.1146/annurev-marine-120710-100849.
Ginoux, P., J.M. Prospero, T.E. Gill, N.C. Hsu, and M. Zhao, 2012: Global-scale attribution of anthropogenic and natural dust sources and their emission rates based on MODIS Deep Blue aerosol products. *Reviews of Geophysics*, **50(3)**, RG3005, doi:10.1029/2012rg000388.
Giorgi, F. and X. Bi, 2009: Time of emergence (TOE) of GHG-forced precipitation change hot-spots. *Geophysical Research Letters*, **36(6)**, L06709, doi:10.1029/2009gl037593.
Giorgi, F., E. Coppola, and F. Raffaele, 2018: Threatening levels of cumulative stress due to hydroclimatic extremes in the 21st century. *npj Climate and Atmospheric Science*, **1(1)**, 18, doi:10.1038/s41612-018-0028-6.
Giorgi, F. et al., 2014: Changes in extremes and hydroclimatic regimes in the CREMA ensemble projections. *Climatic Change*, **125(1)**, 39–51, doi:10.1007/s10584-014-1117-0.
Girardin, M.P. and B.M. Wotton, 2009: Summer moisture and wildfire risks across Canada. *Journal of Applied Meteorology and Climatology*, **48(3)**, 517–533, doi:10.1175/2008jamc1996.1.
Girardin, M.P. et al., 2013: Fire in managed forests of eastern Canada: Risks and options. *Forest Ecology and Management*, **294**, 238–249, doi:10.1016/j.foreco.2012.07.005.
Giuliani, G., S. Nativi, A. Obregon, M. Beniston, and A. Lehmann, 2017: Spatially enabling the Global Framework for Climate Services: Reviewing geospatial solutions to efficiently share and integrate climate data & information. *Climate Services*, **8**, 44–58, doi:10.1016/j.cliser.2017.08.003.
Giuntoli, I., J.-P. Vidal, C. Prudhomme, and D.M. Hannah, 2015: Future hydrological extremes: The uncertainty from multiple global climate and global hydrological models. *Earth System Dynamics*, **6(1)**, 267–285, doi:10.5194/esd-6-267-2015.
Gizaw, M.S. and T.Y. Gan, 2017: Impact of climate change and El Niño episodes on droughts in sub-Saharan Africa. *Climate Dynamics*, **49(1–2)**, 665–682, doi:10.1007/s00382-016-3366-2.

ACCEPTED VERSION SUBJECT TO FINAL EDITS

Glazer, R.H. et al., 2020: Projected changes to severe thunderstorm environments as a result of twenty-first century warming from RegCM CORDEX-CORE simulations. *Climate Dynamics*, doi:10.1007/s00382-020-05439-4.
Glenn, D.M., S.-H. Kim, J. Ramirez-Villegas, and P. Läderach, 2014: Response of Perennial Horticultural Crops to Climate Change. In: *Horticultural Reviews Volume 41* [Janick, J. (ed.)]. John Wiley & Sons, Inc., Hoboken, NJ, USA, pp. 47–130, doi:10.1002/9781118707418.ch02.
Gobler, C.J. and H. Baumann, 2016: Hypoxia and acidification in ocean ecosystems: coupled dynamics and effects on marine life. *Biology Letters*, **12(5)**, 20150976, doi:10.1098/rsbl.2015.0976.
Gobler, C.J., E.L. DePasquale, A.W. Griffith, and H. Baumann, 2014: Hypoxia and Acidification Have Additive and Synergistic Negative Effects on the Growth, Survival, and Metamorphosis of Early Life Stage Bivalves. *PLoS ONE*, **9(1)**, e83648, doi:10.1371/journal.pone.0083648.
Gobler, C.J. et al., 2017: Ocean warming since 1982 has expanded the niche of toxic algal blooms in the North Atlantic and North Pacific oceans. *Proceedings of the National Academy of Sciences*, **114(19)**, 4975–4980, doi:10.1073/pnas.1619575114.
Godoi, V.A., K.R. Bryan, and R.M. Gorman, 2018: Storm wave clustering around New Zealand and its connection to climatic patterns. *International Journal of Climatology*, **38**, e401–e417, doi:10.1002/joc.5380.
Goldie, J., L. Alexander, S.C. Lewis, and S. Sherwood, 2017: Comparative evaluation of human heat stress indices on selected hospital admissions in Sydney, Australia. *Australian and New Zealand Journal of Public Health*, **41(4)**, 381–387, doi:10.1111/1753-6405.12692.
Golding, N., C. Hewitt, and P. Zhang, 2017a: Effective engagement for climate services: Methods in practice in China. *Climate Services*, **8**, 72–76, doi:10.1016/j.cliser.2017.11.002.
Golding, N. et al., 2017b: Improving user engagement and uptake of climate services in China. *Climate Services*, **5**, 39–45, doi:10.1016/j.cliser.2017.03.004.
Golding, N. et al., 2019: Co-development of a seasonal rainfall forecast service: Supporting flood risk management for the Yangtze River basin. *Climate Risk Management*, **23**, 43–49, doi:10.1016/j.crm.2019.01.002.
Gonzalez, P., F. Wang, M. Notaro, D.J. Vimont, and J.W. Williams, 2018: Disproportionate magnitude of climate change in United States national parks. *Environmental Research Letters*, **13(10)**, 104001, doi:10.1088/1748-9326/aade09.
González, M.E., S. Gómez-González, A. Lara, R. Garreaud, and I. Díaz-Hormazábal, 2018: The 2010-2015 Megadrought and its influence on the fire regime in central and south-central Chile. *Ecosphere*, **9(8)**, e02300, doi:10.1002/ecs2.2300.
González-Alemán, J.J. et al., 2019: Potential Increase in Hazard From Mediterranean Hurricane Activity With Global Warming. *Geophysical Research Letters*, **46(3)**, 1754–1764, doi:10.1029/2018gl081253.
Goodess, C.M. et al., 2019: Advancing climate services for the European renewable energy sector through capacity building and user engagement. *Climate Services*, **16**, 100139, doi:10.1016/j.cliser.2019.100139.
Gopalakrishnan, T., M. Hasan, A. Haque, S. Jayasinghe, and L. Kumar, 2019: Sustainability of Coastal Agriculture under Climate Change. *Sustainability*, **11(24)**, 7200, doi:10.3390/su11247200.
Gorris, M.E., L.A. Cat, C.S. Zender, K.K. Treseder, and J.T. Randerson, 2018: Coccidioidomycosis Dynamics in Relation to Climate in the Southwestern United States. *GeoHealth*, **2(1)**, 6–24, doi:10.1002/2017gh000095.
Gorter, W., J.H. van Angelen, J.T.M. Lenaerts, and M.R. van den Broeke, 2014: Present and future near-surface wind climate of Greenland from high resolution regional climate modelling. *Climate Dynamics*, **42(5–6)**, 1595–1611, doi:10.1007/s00382-013-1861-2.
Gosling, S.N. and N.W. Arnell, 2016: A global assessment of the impact of climate change on water scarcity. *Climatic Change*, **134(3)**, 371–385, doi:10.1007/s10584-013-0853-x.
Goudie, A.S., 2014: Desert dust and human health disorders. *Environment International*, **63**, 101–113, doi:10.1016/j.envint.2013.10.011.
Gould, W.A. et al., 2018: U.S. Caribbean. In: *Impacts, Risks, and Adaptation in the United States: Fourth National Climate Assessment, Volume II* [Reidmiller, D.R., C.W. Avery, D.R. Easterling, K.E. Kunkel, K.L.M. Lewis, T.K. Maycock, and B.C. Stewart (eds.)]. U.S. Global Change Research Program, Washington, DC, USA, pp. 809–871, doi:10.7930/nca4.2018.ch20.
Gourdji, S.M., A.M. Sibley, and D.B. Lobell, 2013: Global crop exposure to critical high temperatures in the reproductive period: historical trends and future projections. *Environmental Research Letters*, **8(2)**, 024041, doi:10.1088/1748-9326/8/2/024041.
Gowda, P.H. et al., 2018: Agriculture and Rural Communities. In: *Impacts, Risks, and Adaptation in the United States: Fourth National Climate Assessment, Volume II* [Reidmiller, D.R., C.W. Avery, D.R. Easterling, K.E. Kunkel, K.L.M. Lewis, T.K. Maycock, and B.C. Stewart (eds.)]. pp. 391–437, doi:10.7930/nca4.2018.ch10.
Graff Zivin, J. and M. Neidell, 2014: Temperature and the Allocation of Time: Implications for Climate Change. *Journal of Labor Economics*, **32(1)**, 1–26, doi:10.1086/671766.
Graham, N.A.J., S. Jennings, M.A. MacNeil, D. Mouillot, and S.K. Wilson, 2015: Predicting climate-driven regime shifts versus rebound potential in coral reefs. *Nature*, **518(7537)**, 94–97, doi:10.1038/nature14140.
Graham, R.M. et al., 2017: Increasing frequency and duration of Arctic winter warming events. *Geophysical Research Letters*, **44(13)**, 6974–6983, doi:10.1002/2017gl073395.

ACCEPTED VERSION SUBJECT TO FINAL EDITS

Grahn, T. and L. Nyberg, 2017: Assessment of pluvial flood exposure and vulnerability of residential areas. *International Journal of Disaster Risk Reduction*, **21**, 367–375, doi:10.1016/j.ijdrr.2017.01.016.
Gray, W., R. Ibbitt, R. Turner, M. Duncan, and M. Hollis, 2005: *A Methodology to Assess the Impacts of Climate Change on Flood Risk in New Zealand*. New Zealand Climate Change Office, Ministry for the Environment, New Zealand, 40 pp.
Greenan, B.J.W. et al., 2018: Changes in Oceans Surrounding Canada. In: *Canada's Changing Climate Report* [Lemmen and Bush (eds.)]. Government of Canada, Ottawa, ON, Canada, pp. 343–423.
Gregow, H. et al., 2016: Worldwide survey of awareness and needs concerning reanalyses and respondents views on climate services. *Bulletin of the American Meteorological Society*, **97(8)**, 1461–1474, doi:10.1175/bams-d-14-00271.1.
Griffiths, J.R. et al., 2017: The importance of benthic-pelagic coupling for marine ecosystem functioning in a changing world. *Global Change Biology*, **23(6)**, 2179–2196, doi:10.1111/gcb.13642.
Grineski, S.E. et al., 2015: Double exposure and the climate gap: changing demographics and extreme heat in Ciudad Juárez, Mexico. *Local Environment*, **20(2)**, 180–201, doi:10.1080/13549839.2013.839644.
Groenemeijer, P. and T. Kühne, 2014: A Climatology of Tornadoes in Europe: Results from the European Severe Weather Database. *Monthly Weather Review*, **142(12)**, 4775–4790, doi:10.1175/mwr-d-14-00107.1.
Groisman, P.Y. et al., 2016: Recent changes in the frequency of freezing precipitation in North America and Northern Eurasia. *Environmental Research Letters*, **11(4)**, 045007, doi:10.1088/1748-9326/11/4/045007.
Grotjahn, R., 2021: Weather extremes that impact various agricultural commodities. In: *Extreme Events and Climate Change: A Multidisciplinary Approach* [Castillo, F., M. Wehner, and D. Stone (eds.)]. John Wiley & Sons, Inc. pp. 23–48.
Grotjahn, R. and J. Huynh, 2018: Contiguous US summer maximum temperature and heat stress trends in CRU and NOAA Climate Division data plus comparisons to reanalyses. *Scientific Reports*, **8(1)**, 11146, doi:10.1038/s41598-018-29286-w.
Gu, X. et al., 2020: The changing nature and projection of floods across Australia. *Journal of Hydrology*, **584**, 124703, doi:10.1016/j.jhydrol.2020.124703.
Gualdi, S. et al., 2013: Future Climate Projections. In: *Regional Assessment of Climate Change in the Mediterranean: Volume 1: Air, Sea and Precipitation and Water* [Navarra, A. and L. Tubiana (eds.)]. Advances in Global Change Research vol. 50, Springer, Dordrecht, The Netherlands, pp. 53–118, doi:10.1007/978-94-007-5781-3_3.
Guan, Q. et al., 2015: Climatological analysis of dust storms in the area surrounding the Tengger Desert during 1960–2007. *Climate Dynamics*, **45(3–4)**, 903–913, doi:10.1007/s00382-014-2321-3.
Guan, Q. et al., 2017: Dust Storms in Northern China: Long-Term Spatiotemporal Characteristics and Climate Controls. *Journal of Climate*, **30(17)**, 6683–6700, doi:10.1175/jcli-d-16-0795.1.
Gudmestad, O.T., 2018: The changing climate and the arctic coastal settlements. *International Journal of Environmental Impacts: Management, Mitigation and Recovery*, **1(4)**, 411–419, doi:10.2495/ei-v1-n4-411-419.
Gudmundsson, L., S.I. Seneviratne, and X. Zhang, 2017: Anthropogenic climate change detected in European renewable freshwater resources. *Nature Climate Change*, **7(11)**, 813–816, doi:10.1038/nclimate3416.
Guerreiro, S., V. Glenis, R. Dawson, and C. Kilsby, 2017: Pluvial Flooding in European Cities – A Continental Approach to Urban Flood Modelling. *Water*, **9(4)**, 296, doi:10.3390/w9040296.
Guerreiro, S.B., R.J. Dawson, C. Kilsby, E. Lewis, and A. Ford, 2018: Future heat-waves, droughts and floods in 571 European cities. *Environmental Research Letters*, **13(3)**, 034009, doi:10.1088/1748-9326/aaaad3.
Guo, D. and H. Wang, 2016: CMIP5 permafrost degradation projection:A comparison among different regions. *Journal of Geophysical Research: Atmospheres*, **121(9)**, 4499–4517, doi:10.1002/2015jd024108.
Guo, H. et al., 2018: Spatial and temporal characteristics of droughts in Central Asia during 1966–2015. *Science of the Total Environment*, **624**, 1523–1538, doi:10.1016/j.scitotenv.2017.12.120.
Guo, J., G. Huang, X. Wang, Y. Li, and Q. Lin, 2018: Dynamically-downscaled projections of changes in temperature extremes over China. *Climate Dynamics*, **50(3–4)**, 1045–1066, doi:10.1007/s00382-017-3660-7.
Guo, L. et al., 2020: Responses of Lake Ice Phenology to Climate Change at Tibetan Plateau. *IEEE Journal of Selected Topics in Applied Earth Observations and Remote Sensing*, **13**, 3856–3861, doi:10.1109/jstars.2020.3006270.
Guo, X., J. Huang, Y. Luo, Z. Zhao, and Y. Xu, 2017: Projection of heat waves over China for eight different global warming targets using 12 CMIP5 models. *Theoretical and Applied Climatology*, **128(3–4)**, 507–522, doi:10.1007/s00704-015-1718-1.
Gupta, S., S. Kundu, and A. Mallik, 2012: Monitoring of Sag & Temperature in the Electrical Power Transmission lines. *International Journal of Recent Technology and Engineering (IJRTE)*, **1(4)**, 43–45.
Gupta, V. and M.K. Jain, 2018: Investigation of multi-model spatiotemporal mesoscale drought projections over India under climate change scenario. *Journal of Hydrology*, **567**, 489–509, doi:10.1016/j.jhydrol.2018.10.012.
Gutiérrez, C. et al., 2020: Future evolution of surface solar radiation and photovoltaic potential in Europe: investigating the role of aerosols. *Environmental Research Letters*, **15(3)**, 34035, doi:10.1088/1748-9326/ab6666.
Habeeb, D., J. Vargo, and B. Stone, 2015: Rising heat wave trends in large US cities. *Natural Hazards*, **76(3)**, 1651–

ACCEPTED VERSION SUBJECT TO FINAL EDITS

1665, doi:10.1007/s11069-014-1563-z.
Hackenbruch, J., T. Kunz-Plapp, S. Müller, and J. Schipper, 2017: Tailoring Climate Parameters to Information Needs for Local Adaptation to Climate Change. *Climate*, **5(2)**, 25, doi:10.3390/cli5020025.
Hadji, R. et al., 2014: Climate change and its influence on shrinkage–swelling clays susceptibility in a semi-arid zone: a case study of Souk Ahras municipality, NE-Algeria. *Desalination and Water Treatment*, **52(10–12)**, 2057–2072, doi:10.1080/19443994.2013.812989.
Haeberli, W., 2013: Mountain permafrost - research frontiers and a special long-term challenge. *Cold Regions Science and Technology*, **96**, 71–76, doi:10.1016/j.coldregions.2013.02.004.
Haeberli, W., Y. Schaub, and C. Huggel, 2017a: Increasing risks related to landslides from degrading permafrost into new lakes in de-glaciating mountain ranges. *Geomorphology*, **293**, 405–417, doi:10.1016/j.geomorph.2016.02.009.
Haeberli, W., Y. Schaub, and C. Huggel, 2017b: Increasing risks related to landslides from degrading permafrost into new lakes in de-glaciating mountain ranges. *Geomorphology*, **293**, 405–417, doi:10.1016/j.geomorph.2016.02.009.
Haile, G.G. et al., 2020: Long-term spatiotemporal variation of drought patterns over the Greater Horn of Africa. *Science of The Total Environment*, **704**, 135299, doi:10.1016/j.scitotenv.2019.135299.
Haines, S., 2019: Managing expectations: articulating expertise in climate services for agriculture in Belize. *Climatic Change*, **157(1)**, 43–59, doi:10.1007/s10584-018-2357-1.
Hajat, S., S. Vardoulakis, C. Heaviside, and B. Eggen, 2014: Climate change effects on human health: projections of temperature-related mortality for the UK during the 2020s, 2050s and 2080s. *Journal of Epidemiology and Community Health*, **68(7)**, 641–648, doi:10.1136/jech-2013-202449.
Hall, J. et al., 2014: Understanding flood regime changes in Europe: A state-of-the-art assessment. *Hydrology and Earth System Sciences*, **18(7)**, 2735–2772, doi:10.5194/hess-18-2735-2014.
Hall, T.M. and J.P. Kossin, 2019: Hurricane stalling along the North American coast and implications for rainfall. *npj Climate and Atmospheric Science*, **2(1)**, 17, doi:10.1038/s41612-019-0074-8.
Hallegatte, S. and V. Przyluski, 2010: The economics of natural disasters: Concepts and methods. , 31, doi:10.1596/1813-9450-5507.
Hallegatte, S., C. Green, R.J. Nicholls, and J. Corfee-Morlot, 2013: Future flood losses in major coastal cities. *Nature Climate Change*, **3(9)**, 802–806, doi:10.1038/nclimate1979.
Hallegraeff, G. et al., 2014: Australian Dust Storm Associated with Extensive Aspergillus sydowii Fungal "Bloom" in Coastal Waters. *Applied and Environmental Microbiology*, **80(11)**, 3315–3320, doi:10.1128/aem.04118-13.
Halpern, B.S. et al., 2015: Climate velocity and the future global redistribution of marine biodiversity. *Nature Climate Change*, **6(1)**, 83–88, doi:10.1038/nclimate2769.
Hamann, A., D.R. Roberts, Q.E. Barber, C. Carroll, and S.E. Nielsen, 2015: Velocity of climate change algorithms for guiding conservation and management. *Global Change Biology*, **21(2)**, 997–1004, doi:10.1111/gcb.12736.
Hamaoui-Laguel, L. et al., 2015: Effects of climate change and seed dispersal on airborne ragweed pollen loads in Europe. *Nature Climate Change*, **5(8)**, 766–771, doi:10.1038/nclimate2652.
Hambly, D., J. Andrey, B. Mills, and C. Fletcher, 2013: Projected implications of climate change for road safety in Greater Vancouver, Canada. *Climatic Change*, **116(3–4)**, 613–629, doi:10.1007/s10584-012-0499-0.
Hamilton, J.G. et al., 2005: Anthropogenic Changes in Tropospheric Composition Increase Susceptibility of Soybean to Insect Herbivory. *Environmental Entomology*, **34(2)**, 479–485, doi:10.1603/0046-225x-34.2.479.
Hand, J.L. et al., 2016: Earlier onset of the spring fine dust season in the southwestern United States. *Geophysical Research Letters*, **43(8)**, 4001–4009, doi:10.1002/2016gl068519.
Handwerger, A.L., M.-H. Huang, E.J. Fielding, A.M. Booth, and R. Bürgmann, 2019: A shift from drought to extreme rainfall drives a stable landslide to catastrophic failure. *Scientific Reports*, **9(1)**, 1569, doi:10.1038/s41598-018-38300-0.
Hanes, C.C. et al., 2019: Fire-regime changes in canada over the last half century. *Canadian Journal of Forest Research*, **49(3)**, 256–269, doi:10.1139/cjfr-2018-0293.
Hanewinkel, M., D.A. Cullmann, M.-J. Schelhaas, G.-J. Nabuurs, and N.E. Zimmermann, 2013: Climate change may cause severe loss in the economic value of European forest land. *Nature Climate Change*, **3(3)**, 203–207, doi:10.1038/nclimate1687.
Hansen, B.B. et al., 2014: Warmer and wetter winters: characteristics and implications of an extreme weather event in the High Arctic. *Environmental Research Letters*, **9(11)**, 114021, doi:10.1088/1748-9326/9/11/114021.
Hansen, J. and M. Sato, 2016: Regional climate change and national responsibilities. *Environmental Research Letters*, **11(3)**, 034009, doi:10.1088/1748-9326/11/3/034009.
Hansen, J.W. et al., 2019: Climate Services Can Support African Farmers' Context-Specific Adaptation Needs at Scale. *Frontiers in Sustainable Food Systems*, **3**, 21, doi:10.3389/fsufs.2019.00021.
Hanzer, F., K. Förster, J. Nemec, and U. Strasser, 2018: Projected cryospheric and hydrological impacts of 21st century climate change in the Ötztal Alps (Austria) simulated using a physically based approach. *Hydrology and Earth System Sciences*, **22(2)**, 1593–1614, doi:10.5194/hess-22-1593-2018.
Haque, U. et al., 2019: The human cost of global warming: Deadly landslides and their triggers (1995–2014). *Science of*

ACCEPTED VERSION SUBJECT TO FINAL EDITS

The Total Environment, **682**, 673–684, doi:10.1016/j.scitotenv.2019.03.415.
Harley, M.D. et al., 2017: Extreme coastal erosion enhanced by anomalous extratropical storm wave direction. *Scientific Reports*, **7(1)**, 6033, doi:10.1038/s41598-017-05792-1.
Harrington, L.J., D. Frame, A.D. King, and F.E.L. Otto, 2018: How Uneven Are Changes to Impact-Relevant Climate Hazards in a 1.5°C World and Beyond? *Geophysical Research Letters*, **45(13)**, 6672–6680, doi:10.1029/2018gl078888.
Harrison, S. et al., 2018: Climate change and the global pattern of moraine-dammed glacial lake outburst floods. *The Cryosphere*, **12(4)**, 1195–1209, doi:10.5194/tc-12-1195-2018.
Harvey, B.J., 2016: Human-caused climate change is now a key driver of forest fire activity in the western United States. *Proceedings of the National Academy of Sciences*, **113(42)**, 11649–11650, doi:10.1073/pnas.1612926113.
Hassanzadeh, P. et al., 2020: Effects of climate change on the movement of future landfalling Texas tropical cyclones. *Nature Communications*, **11(1)**, 3319, doi:10.1038/s41467-020-17130-7.
Anderson, T. (ed.), 2015: *USDA Midwest and Northern Forests Regional Climate Hub: Assessment of Climate Change Vulnerability and Adaptation and Mitigation Strategies*. U.S. Department of Agriculture, USA, 55 pp.
Hatfield, J. et al., 2014: Ch. 6: Agriculture. In: *Climate Change Impacts in the United States: The Third National Climate Assessment* [Melillo, J.M., T.C. Richmond, and G.W. Yohe (eds.)]. U.S Global Change Research Program, pp. 150–174, doi:10.7930/j02z13fr.
Hatfield, J.L. and J.H. Prueger, 2015: Temperature extremes: Effect on plant growth and development. *Weather and Climate Extremes*, **10**, 4–10, doi:10.1016/j.wace.2015.08.001.
Hatfield, J.L. et al., 2011: Climate Impacts on Agriculture: Implications for Crop Production. *Agronomy Journal*, **103(2)**, 351, doi:10.2134/agronj2010.0303.
Hauer, M.E., J.M. Evans, and D.R. Mishra, 2016: Millions projected to be at risk from sea-level rise in the continental United States. *Nature Climate Change*, **6(7)**, 691–695, doi:10.1038/nclimate2961.
Haumann, F.A., N. Gruber, M. Münnich, I. Frenger, and S. Kern, 2016: Sea-ice transport driving Southern Ocean salinity and its recent trends. *Nature*, **537(7618)**, 89–92, doi:10.1038/nature19101.
Hawkins, E. and R. Sutton, 2012: Time of emergence of climate signals. *Geophysical Research Letters*, **39(1)**, L01702, doi:10.1029/2011gl050087.
Hawkins, E. et al., 2020: Observed Emergence of the Climate Change Signal: From the Familiar to the Unknown. *Geophysical Research Letters*, **47(6)**, e2019GL086259, doi:10.1029/2019gl086259.
Hayes, F., K. Sharps, H. Harmens, I. Roberts, and G. Mills, 2020: Tropospheric ozone pollution reduces the yield of African crops. *Journal of Agronomy and Crop Science*, **206(2)**, 214–228, doi:10.1111/jac.12376.
Heaney, A.K., D. Carrión, K. Burkart, C. Lesk, and D. Jack, 2019: Climate change and physical activity: Estimated impacts of ambient temperatures on bikeshare usage in new york city. *Environmental Health Perspectives*, **127(3)**, 037002–1–037002–10, doi:10.1289/ehp4039.
Hellberg, R.S. and E. Chu, 2016: Effects of climate change on the persistence and dispersal of foodborne bacterial pathogens in the outdoor environment: A review. *Critical Reviews in Microbiology*, **42(4)**, 548–572, doi:10.3109/1040841x.2014.972335.
Hemer, M.A., K.L. McInnes, and R. Ranasinghe, 2013: Projections of climate change-driven variations in the offshore wave climate off south eastern Australia. *International Journal of Climatology*, **33(7)**, 1615–1632, doi:10.1002/joc.3537.
Henderson, R., S. Reinert, P. Dekhtyar, and A. Migdal, 2016: *Climate Change in 2017: Implications for Business*. 9-317-032, Harvard Business School, Boston, MA, USA, 39 pp.
Hennessy, K. et al., 2007: Australia and New Zealand. In: *Climate Change 2007: Impacts, Adaptation and Vulnerability. Contribution of Working Group II to the Fourth Assessment Report of the Intergovernmental Panel on Climate Change* [Parry, M.L., O.F. Canziani, J.P. Palutikof, P.J. Linden, and C.E. Hanson (eds.)]. Cambridge University Press, Cambridge, United Kingdom and New York, NY, USA, pp. 507–540.
Henson, S.A. et al., 2017: Rapid emergence of climate change in environmental drivers of marine ecosystems. *Nature Communications*, **8(1)**, 14682, doi:10.1038/ncomms14682.
Hermida, L. et al., 2015: Hailfall in southwest France: Relationship with precipitation, trends and wavelet analysis. *Atmospheric Research*, **156**, 174–188, doi:10.1016/j.atmosres.2015.01.005.
Herold, N., M. Ekström, J. Kala, J. Goldie, and J.P. Evans, 2018: Australian climate extremes in the 21st century according to a regional climate model ensemble: Implications for health and agriculture. *Weather and Climate Extremes*, **20**, 54–68, doi:10.1016/j.wace.2018.01.001.
Heron, S.F., J.A. Maynard, R. van Hooidonk, and C.M. Eakin, 2016: Warming Trends and Bleaching Stress of the World's Coral Reefs 1985–2012. *Scientific Reports*, **6(1)**, 38402, doi:10.1038/srep38402.
Herrera, D. and T. Ault, 2017: Insights from a New High-Resolution Drought Atlas for the Caribbean Spanning 1950 – 2016. *Journal of Climate*, **30**, 7801–7825, doi:10.1175/jcli-d-16-0838.1.
Herrera-Pantoja, M. and K.M. Hiscock, 2015: Projected impacts of climate change on water availability indicators in a semi-arid region of central Mexico. *Environmental Science & Policy*, **54**, 81–89, doi:10.1016/j.envsci.2015.06.020.

ACCEPTED VERSION SUBJECT TO FINAL EDITS

Herring, S.C. et al., 2018: Explaining Extreme Events of 2016 from a Climate Perspective. *Bulletin of the American Meteorological Society*, **99(1)**, S1–S157, doi:10.1175/bams-explainingextremeevents2016.1.
Hettiarachchi, S., C. Wasko, and A. Sharma, 2018: Increase in flood risk resulting from climate change in a developed urban watershed – the role of storm temporal patterns. *Hydrology and Earth System Sciences*, **22(3)**, 2041–2056, doi:10.5194/hess-22-2041-2018.
Hewer, M.J. and W.A. Gough, 2019: Lake Ontario ice coverage: Past, present and future. *Journal of Great Lakes Research*, **45(6)**, 1080–1089, doi:10.1016/j.jglr.2019.10.006.
Hewitson, B., K. Waagsaether, J. Wohland, K. Kloppers, and T. Kara, 2017: Climate information websites: an evolving landscape. *WIREs Climate Change*, **8(5)**, e470, doi:10.1002/wcc.470.
Hewitt, C. and N. Golding, 2018: Development and Pull-through of Climate Science to Services in China. *Advances in Atmospheric Sciences*, **35(8)**, 905–908, doi:10.1007/s00376-018-7255-y.
Hewitt, C., S. Mason, and D. Walland, 2012: The Global Framework for Climate Services. *Nature Climate Change*, **2(12)**, 831–832, doi:10.1038/nclimate1745.
Hewitt, C. et al., 2017: Climate Observations, Climate Modeling, and Climate Services. *Bulletin of the American Meteorological Society*, **98(7)**, 1503–1506, doi:10.1175/bams-d-17-0012.1.
Hewitt, C.D. and J.A. Lowe, 2018: Toward a European Climate Prediction System. *Bulletin of the American Meteorological Society*, **99(10)**, 1997–2001, doi:10.1175/bams-d-18-0022.1.
Hewitt, C.D., R.C. Stone, and A.B. Tait, 2017: Improving the use of climate information in decision-making. *Nature Climate Change*, **7(9)**, 614–616, doi:10.1038/nclimate3378.
Hewitt, C.D. et al., 2020a: Making Society Climate Resilient: International Progress under the Global Framework for Climate Services. *Bulletin of the American Meteorological Society*, **101(2)**, E237–E252, doi:10.1175/bams-d-18-0211.1.
Hewitt, C.D. et al., 2020b: The Process and Benefits of Developing Prototype Climate Services-Examples in China. *Journal of Meteorological Research*, **34(5)**, 893–903, doi:10.1007/s13351-020-0042-6.
Hewitt, C.D. et al., 2020c: Recommendations for future research priorities for climate modelling and climate services. *Bulletin of the American Meteorological Society*, 1–26, doi:10.1175/bams-d-20-0103.1.
Hidalgo, H.G., E.J. Alfaro, and B. Quesada-Montano, 2017: Observed (1970–1999) climate variability in Central America using a high-resolution meteorological dataset with implication to climate change studies. *Climatic Change*, **141(1)**, 13–28, doi:10.1007/s10584-016-1786-y.
Hill, R.A., C.P. Hawkins, and J. Jin, 2014: Predicting thermal vulnerability of stream and river ecosystems to climate change. *Climatic Change*, **125(3–4)**, 399–412, doi:10.1007/s10584-014-1174-4.
Hincapie, J.C.A. and J.D.P. Caicedo, 2013: El cambio climático y la distribución espacial de las formaciones vegetales en Colombia. *Colombia forestal*, **16(2)**, 171–185, doi:10.14483/udistrital.jour.colomb.for.2013.2.a04.
Hinkel, J. et al., 2013: A global analysis of erosion of sandy beaches and sea-level rise: An application of DIVA. *Global and Planetary Change*, **111**, 150–158, doi:10.1016/j.gloplacha.2013.09.002.
Hinkel, J. et al., 2018: The ability of societies to adapt to twenty-first-century sea-level rise. *Nature Climate Change*, **8(7)**, 570–578, doi:10.1038/s41558-018-0176-z.
Hirabayashi, Y. et al., 2013: Global flood risk under climate change. *Nature Climate Change*, **3(9)**, 816–821, doi:10.1038/nclimate1911.
Hixson, S.M. and M.T. Arts, 2016: Climate warming is predicted to reduce omega-3, long-chain, polyunsaturated fatty acid production in phytoplankton. *Global Change Biology*, **22(8)**, 2744–2755, doi:10.1111/gcb.13295.
Hjort, J. et al., 2018: Degrading permafrost puts Arctic infrastructure at risk by mid-century. *Nature Communications*, **9(1)**, 5147, doi:10.1038/s41467-018-07557-4.
Ho, K., S. Lacasse, and L. Picarelli (eds.), 2017: *Slope Safety Preparedness for Impact of Climate Change*. CRC Press, London, UK, 590 pp., doi:10.1201/9781315387789.
Hoa, E., 2018: From generating to using climate services – how the EU-MACS and MARCO projects help to unlock the market potential. *Climate Services*, **11**, 86–88, doi:10.1016/j.cliser.2018.08.001.
Hobday, A.J. et al., 2016: A hierarchical approach to defining marine heatwaves. *Progress in Oceanography*, **141**, 227–238, doi:10.1016/j.pocean.2015.12.014.
Hochman, A., T. Harpaz, H. Saaroni, and P. Alpert, 2018: The seasons' length in 21st century CMIP5 projections over the eastern Mediterranean. *International Journal of Climatology*, **38(6)**, 2627–2637, doi:10.1002/joc.5448.
Hock, R. et al., 2019: High Mountain Areas. In: *IPCC Special Report on the Ocean and Cryosphere in a Changing Climate* [Pörtner, H.-O., D.C. Roberts, V. Masson-Delmotte, P. Zhai, M. Tignor, E. Poloczanska, K. Mintenbeck, A. Alegría, M. Nicolai, A. Okem, J. Petzold, B. Rama, and N.M. Weyer (eds.)]. In Press, pp. 131–202.
Hodgkins, G.A., R.W. Dudley, S.A. Archfield, and B. Renard, 2019: Effects of climate, regulation, and urbanization on historical flood trends in the United States. *Journal of Hydrology*, **573**, 697–709, doi:10.1016/j.jhydrol.2019.03.102.
Hoegh-Guldberg, O. and J.F. Bruno, 2010: The impact of climate change on the world's marine ecosystems.. *Science (New York, N.Y.)*, **328(5985)**, 1523–8, doi:10.1126/science.1189930.
Hoegh-Guldberg, O., E.S. Poloczanska, W. Skirving, and S. Dove, 2017: Coral Reef Ecosystems under Climate Change

ACCEPTED VERSION SUBJECT TO FINAL EDITS

and Ocean Acidification. *Frontiers in Marine Science*, **4**, 158, doi:10.3389/fmars.2017.00158.
Hoegh-Guldberg, O. et al., 2018: Impacts of 1.5°C Global Warming on Natural and Human Systems. In: *Global Warming of 1.5°C. An IPCC Special Report on the impacts of global warming of 1.5°C above pre-industrial levels and related global greenhouse gas emission pathways, in the context of strengthening the global response to the threat of climate change*, [Masson-Delmotte, V., P. Zhai, H.-O. Pörtner, D. Roberts, J. Skea, P.R. Shukla, A. Pirani, W. Moufouma-Okia, C. Péan, R. Pidcock, S. Connors, J.B.R. Matthews, Y. Chen, X. Zhou, M.I. Gomis, E. Lonnoy, T. Maycock, M. Tignor, and T. Waterfield (eds.)]. In Press, pp. 175–312.
Hoeke, R.K. et al., 2013: Widespread inundation of Pacific islands triggered by distant-source wind-waves. *Global and Planetary Change*, **108**, 128–138, doi:10.1016/j.gloplacha.2013.06.006.
Hof, A.R. and A. Svahlin, 2016: The potential effect of climate change on the geographical distribution of insect pest species in the Swedish boreal forest. *Scandinavian Journal of Forest Research*, **31(1)**, 29–39, doi:10.1080/02827581.2015.1052751.
Holding, S. et al., 2016: Groundwater vulnerability on small islands. *Nature Climate Change*, **6(12)**, 1100–1103, doi:10.1038/nclimate3128.
Holland, G. and C.L. Bruyère, 2014: Recent intense hurricane response to global climate change. *Climate Dynamics*, **42(3–4)**, 617–627, doi:10.1007/s00382-013-1713-0.
Hong, J.-W., J. Hong, E.E. Kwon, and D.K. Yoon, 2019: Temporal dynamics of urban heat island correlated with the socio-economic development over the past half-century in Seoul, Korea. *Environmental Pollution*, **254**, 112934, doi:10.1016/j.envpol.2019.07.102.
Hope, P. et al., 2019: On Determining the Impact of Increasing Atmospheric CO2 on the Record Fire Weather in Eastern Australia in February 2017. *Bulletin of the American Meteorological Society*, **100(1)**, S111–S117, doi:10.1175/bams-d-18-0135.1.
Horton, D.E., C.B. Skinner, D. Singh, and N.S. Diffenbaugh, 2014: Occurrence and persistence of future atmospheric stagnation events. *Nature Climate Change*, **4(8)**, 698–703, doi:10.1038/nclimate2272.
Howarth, C. and J. Painter, 2016: Exploring the Science – Policy Interface on Climate Change: The Role of the IPCC in Informing Local Decision-Making in the UK. *SSRN*, doi:10.1057/palcomms.2016.58.
Howell, S.E.L., F. Laliberté, R. Kwok, C. Derksen, and J. King, 2016: Landfast ice thickness in the Canadian Arctic Archipelago from observations and models. *The Cryosphere*, **10(4)**, 1463–1475, doi:10.5194/tc-10-1463-2016.
Hoyos, N., J. Escobar, J.C. Restrepo, A.M. Arango, and J.C. Ortiz, 2013: Impact of the 2010–2011 La Niña phenomenon in Colombia, South America: The human toll of an extreme weather event. *Applied Geography*, **39**, 16–25, doi:10.1016/j.apgeog.2012.11.018.
Hrbáček, F. et al., 2018: Active layer monitoring in Antarctica: an overview of results from 2006 to 2015. *Polar Geography*, 1–15, doi:10.1080/1088937x.2017.1420105.
Hu, F.S. et al., 2015: Arctic tundra fires: natural variability and responses to climate change. *Frontiers in Ecology and the Environment*, **13(7)**, 369–377, doi:10.1890/150063.
Huang, A. et al., 2014: Changes of the Annual Precipitation over Central Asia in the Twenty-First Century Projected by Multimodels of CMIP5. *Journal of Climate*, **27(17)**, 6627–6646, doi:10.1175/jcli-d-14-00070.1.
Huang, J., H. Yu, X. Guan, G. Wang, and R. Guo, 2016a: Accelerated dryland expansion under climate change. *Nature Climate Change*, **6(2)**, 166–171, doi:10.1038/nclimate2837.
Huang, J. et al., 2016b: Global semi-arid climate change over last 60 years. *Climate Dynamics*, **46(3–4)**, 1131–1150, doi:10.1007/s00382-015-2636-8.
Huang, J. et al., 2017: Dryland climate change: Recent progress and challenges. *Reviews of Geophysics*, **55(3)**, 719–778, doi:10.1002/2016rg000550.
Hubbard, D.K., R.B. Burke, and I.P. Gill, 2008: Coral-reef geology: Puerto Rico and the US Virgin islands. *Coral Reefs of the USA*, 263–302, doi:10.1007/978-1-4020-6847-8_7.
Hueging, H., R. Haas, K. Born, D. Jacob, and J.G. Pinto, 2013: Regional Changes in Wind Energy Potential over Europe Using Regional Climate Model Ensemble Projections. *Journal of Applied Meteorology and Climatology*, **52(4)**, 903–917, doi:10.1175/jamc-d-12-086.1.
Hufkens, K. et al., 2012: Ecological impacts of a widespread frost event following early spring leaf-out. *Global Change Biology*, **18(7)**, 2365–2377, doi:10.1111/j.1365-2486.2012.02712.x.
Hughes, T.P. et al., 2017a: Coral reefs in the Anthropocene. *Nature*, **546(7656)**, 82–90, doi:10.1038/nature22901.
Hughes, T.P. et al., 2017b: Global warming and recurrent mass bleaching of corals. *Nature*, **543(7645)**, 373–377, doi:10.1038/nature21707.
Hughes, T.P. et al., 2018a: Spatial and temporal patterns of mass bleaching of corals in the Anthropocene. *Science*, **359(6371)**, 80–83, doi:10.1126/science.aan8048.
Hughes, T.P. et al., 2018b: Global warming transforms coral reef assemblages. *Nature*, **556(7702)**, 492–496, doi:10.1038/s41586-018-0041-2.
Humphrey, V. et al., 2018: Sensitivity of atmospheric CO2 growth rate to observed changes in terrestrial water storage. *Nature*, **560(7720)**, 628–631, doi:10.1038/s41586-018-0424-4.
Hurlbert, M. et al., 2019: Risk management and decision making in relation to sustainable development. In: *Climate Change and Land: an IPCC special report on climate change, desertification, land degradation, sustainable*

ACCEPTED VERSION SUBJECT TO FINAL EDITS

land management, food security, and greenhouse gas fluxes in terrestrial ecosystems [P.R. Shukla, J. Skea, E.C. Buendia, V. Masson-Delmotte, H.-O. Pörtner, D.C. Roberts, P. Zhai, R. Slade, S. Connors, R. Diemen, M. Ferrat, E. Haughey, S. Luz, S. Neogi, M. Pathak, J. Petzold, J.P. Pereira, P. Vyas, E. Huntley, K. Kissick, M. Belkacemi, and J. Malley (eds.)]. In Press, pp. 673–800.

Huss, M. and R. Hock, 2018: Global-scale hydrological response to future glacier mass loss. *Nature Climate Change*, **8(2)**, 135–140, doi:10.1038/s41558-017-0049-x.

ICOMOS, 2019: *The Future of Our Pasts: Engaging cultural heritage in climate action*. International Council on Monuments and Sites (ICOMOS) Climate Change and Heritage Working Group, Paris, France, 110 pp.

Il Jeong, D. and L. Sushama, 2018: Rain-on-snow events over North America based on two Canadian regional climate models. *Climate Dynamics*, **50(1–2)**, 303–316, doi:10.1007/s00382-017-3609-x.

Im, E.-S., J.S. Pal, and E.A.B. Eltahir, 2017: Deadly heat waves projected in the densely populated agricultural regions of South Asia. *Science Advances*, **3(8)**, e1603322, doi:10.1126/sciadv.1603322.

Im, E.-S. et al., 2020: Emergence of robust anthropogenic increase of heat stress-related variables projected from CORDEX-CORE climate simulations. *Climate Dynamics*, doi:10.1007/s00382-020-05398-w.

Imada, Y., M. Watanabe, H. Kawase, H. Shiogama, and M. Arai, 2019: The July 2018 High Temperature Event in Japan Could Not Have Happened without Human-Induced Global Warming. *SOLA*, **15A**, 8–12, doi:10.2151/sola.15a-002.

Imada, Y. et al., 2018: Climate Change Increased the Likelihood of the 2016 Heat Extremes in Asia. *Bulletin of the American Meteorological Society*, **99(1)**, S97–S101, doi:10.1175/bams-d-17-0109.1.

Potts, S.G., V.L. Imperatriz-Fonseca, and H.T. Ngo (eds.), 2016: *The assessment report of the Intergovernmental Science-Policy Platform on Biodiversity and Ecosystem Services on pollinators, pollination and food production*. Secretariat of the Intergovernmental Science-Policy Platform on Biodiversity and Ecosystem Services, Bonn, Germany, 552 pp., doi:10.5281/zenodo.3402856.

IPCC, 2012: Summary for Policymakers. In: *Managing the Risks of Extreme Events and Disasters to Advance Climate Change Adaptation* [Field, C.B., V. Barros, T.F. Stocker, D. Qin, D.J. Dokken, K.L. Ebi, M.D. Mastrandrea, K.J. Mach, G.-K. Plattner, S.K. Allen, M. Tignor, and P.M. Midgle (eds.)]. Cambridge University Press, Cambridge, United Kingdom and New York, NY, USA, pp. 3–22, doi:10.1017/cbo9781139177245.003.

IPCC, 2013: Climate Change 2013: The Physical Science Basis. Contribution of Working Group I to the Fifth Assessment Report of the Intergovernmental Panel on Climate Change. [Stocker, T.F., D. Qin, G.-K. Plattner, M. Tignor, S.K. Allen, J. Boschung, A. Nauels, Y. Xia, V. Bex, and P.M. Midgley (eds.)]. Cambridge University Press, Cambridge, United Kingdom and New York, NY, USA, 1535 pp., doi:10.1017/cbo9781107415324.

IPCC, 2014a: Climate Change 2014: Impacts, Adaptation, and Vulnerability. Part A: Global and Sectoral Aspects. Contribution of Working Group II to the Fifth Assessment Report of the Intergovernmental Panel on Climate Change. [Field, C.B., V.R. Barros, D.J. Dokken, K.J. Mach, M.D. Mastrandrea, T.E. Bilir, M. Chatterjee, K.L. Ebi, Y.O. Estrada, R.C. Genova, B. Girma, E.S. Kissel, A.N. Levy, S. MacCracken, P.R. Mastrandrea, and L.L. White (eds.)]. Cambridge University Press, Cambridge, UK and New York, NY, USA,, 1132 pp., doi:10.1017/cbo9781107415379.

IPCC, 2014b: Climate Change 2014: Impacts, Adaptation, and Vulnerability. Part B: Regional Aspects. Contribution of Working Group II to the Fifth Assessment Report of the Intergovernmental Panel on Climate Change. [Barros, V.R., C.B. Field, D.J. Dokken, M.D. Mastrandrea, K.J. Mach, T.E. Bilir, M. Chatterjee, K.L. Ebi, Y.O. Estrada, R.C. Genova, B. Girma, E.S. Kissel, A.N. Levy, S. MacCracken, P.R. Mastrandrea, and L.L. White (eds.)]. Cambridge University Press, Cambridge, United Kingdom and New York, NY, USA, 688 pp., doi:10.1017/cbo9781107415386.

IPCC, 2018: Global warming of 1.5°C. An IPCC Special Report on the impacts of global warming of 1.5°C above pre-industrial levels and related global greenhouse gas emission pathways, in the context of strengthening the global response to the threat of climate change. [Masson-Delmotte, V., P. Zhai, H.-O. Pörtner, D. Roberts, J. Skea, P.R. Shukla, A. Pirani, W. Moufouma-Okia, C. Péan, R. Pidcock, S. Connors, J.B.R. Matthews, Y. Chen, X. Zhou, M.I. Gomis, E. Lonnoy, T. Maycock, M. Tignor, and T. Waterfield (eds.)]. In Press, 616 pp.

IPCC, 2019a: Climate Change and Land: an IPCC special report on climate change, desertification, land degradation, sustainable land management, food security, and greenhouse gas fluxes in terrestrial ecosystems. [Shukla, P.R., J. Skea, E.C. Buendia, V. Masson-Delmotte, H.-O. Pörtner, D.C. Roberts, P. Zhai, R. Slade, S. Connors, R. Diemen, M. Ferrat, E. Haughey, S. Luz, S. Neogi, M. Pathak, J. Petzold, J.P. Pereira, P. Vyas, E. Huntley, K. Kissick, M. Belkacemi, and J. Malley (eds.)]. In Press, 896 pp.

IPCC, 2019b: IPCC Special Report on the Ocean and Cryosphere in a Changing Climate. [Pörtner, H.-O., D.C. Roberts, V. Masson-Delmotte, P. Zhai, M. Tignor, E. Poloczanska, K. Mintenbeck, A. Alegría, M. Nicolai, A. Okem, J. Petzold, B. Rama, and N.M. Weyer (eds.)]. In Press, 755 pp.

IPCC, 2019c: Summary for Policymakers. In: *Climate Change and Land: an IPCC special report on climate change, desertification, land degradation, sustainable land management, food security, and greenhouse gas fluxes in terrestrial ecosystems* [Shukla, P.R., J. Skea, E.C. Buendia, V. Masson-Delmotte, H.-O. Pörtner, D.C. Roberts, P. Zhai, R. Slade, S. Connors, R. Diemen, M. Ferrat, E. Haughey, S. Luz, S. Neogi, M. Pathak, J. Petzold, J.P.

ACCEPTED VERSION SUBJECT TO FINAL EDITS

Pereira, P. Vyas, E. Huntley, K. Kissick, M. Belkacemi, and J. Malley (eds.)]. In Press, pp. 3–36.
Irannezhad, M., A.K. Ronkanen, S. Kiani, D. Chen, and B. Kløve, 2017: Long-term variability and trends in annual snowfall/total precipitation ratio in Finland and the role of atmospheric circulation patterns. *Cold Regions Science and Technology*, **143**, 23–31, doi:10.1016/j.coldregions.2017.08.008.
Iribarren Anacona, P., A. Mackintosh, and K.P. Norton, 2015: Hazardous processes and events from glacier and permafrost areas: lessons from the Chilean and Argentinean Andes. *Earth Surface Processes and Landforms*, **40(1)**, 2–21, doi:10.1002/esp.3524.
Islam, S., S.J. Déry, and A.T. Werner, 2017: Future Climate Change Impacts on Snow and Water Resources of the Fraser River Basin, British Columbia. *Journal of Hydrometeorology*, **18(2)**, 473–496, doi:10.1175/jhm-d-16-0012.1.
Izaguirre, C., I.J. Losada, P. Camus, J.L. Vigh, and V. Stenek, 2021: Climate change risk to global port operations. *Nature Climate Change*, **11(1)**, 14–20, doi:10.1038/s41558-020-00937-z.
Jack, C.D., R. Jones, L. Burgin, and J. Daron, 2020: Climate risk narratives: An iterative reflective process for co-producing and integrating climate knowledge. *Climate Risk Management*, **29**, 100239, doi:10.1016/j.crm.2020.100239.
Jacob, D., 2020: Future Trends in Climate Services. In: *Handbook of Climate Services* [Leal Filho, W. and D. Jacob (eds.)]. Springer, Cham, Switzerland, pp. 515–519, doi:10.1007/978-3-030-36875-3_26.
Jacob, D. and S. Solman, 2017: IMPACT2C – An introduction. *Climate Services*, **7**, 1–2, doi:10.1016/j.cliser.2017.07.006.
Jacob, D. et al., 2014: EURO-CORDEX: new high-resolution climate change projections for European impact research. *Regional Environmental Change*, **14(2)**, 563–578, doi:10.1007/s10113-013-0499-2.
Jacob, D. et al., 2018: Climate Impacts in Europe Under +1.5°C Global Warming. *Earth's Future*, **6(2)**, 264–285, doi:10.1002/2017ef000710.
Jacobs, J., S.K. Moore, K.E. Kunkel, and L. Sun, 2015: A framework for examining climate-driven changes to the seasonality and geographical range of coastal pathogens and harmful algae. *Climate Risk Management*, **8**, 16–27, doi:10.1016/j.crm.2015.03.002.
Jacobs, J.M. et al., 2018: Transportation. In: *Impacts, Risks, and Adaptation in the United States: Fourth National Climate Assessment, Volume II* [Reidmiller, D.R., C.W. Avery, D.R. Easterling, K.E. Kunkel, K.L.M. Lewis, T.K. Maycock, and B.C. Stewar (eds.)]. U.S. Global Change Research Program, Washington, DC, USA, pp. 479–511, doi:10.7930/nca4.2018.ch12.
Jacobs, K.L. and R.B. Street, 2020: The next generation of climate services. *Climate Services*, **20**, 100199, doi:10.1016/j.cliser.2020.100199.
Jahn, A., 2018: Reduced probability of ice-free summers for 1.5°C compared to 2°C warming. *Nature Climate Change*, **8(5)**, 409–413, doi:10.1038/s41558-018-0127-8.
Jain, P., X. Wang, and M.D. Flannigan, 2017: Trend analysis of fire season length and extreme fire weather in North America between 1979 and 2015. *International Journal of Wildland Fire*, **26(12)**, 1009, doi:10.1071/wf17008.
Jain, P., M.R. Tye, D. Paimazumder, and M. Flannigan, 2020: Downscaling fire weather extremes from historical and projected climate models. *Climatic Change*, **163(1)**, 189–216, doi:10.1007/s10584-020-02865-5.
Jakob, D. and D. Walland, 2016: Variability and long-term change in Australian temperature and precipitation extremes. *Weather and Climate Extremes*, **14**, 36–55, doi:10.1016/j.wace.2016.11.001.
Jancloes, M. et al., 2014: Climate services to improve public health. *International Journal of Environmental Research and Public Health*, **11(5)**, 4555–4559, doi:10.3390/ijerph110504555.
Janoski, T.P., A.J. Broccoli, S.B. Kapnick, and N.C. Johnson, 2018: Effects of Climate Change on Wind-Driven Heavy-Snowfall Events over Eastern North America. *Journal of Climate*, **31(22)**, 9037–9054, doi:10.1175/jcli-d-17-0756.1.
Javed, W., Y. Wubulikasimu, B. Figgis, and B. Guo, 2017: Characterization of dust accumulated on photovoltaic panels in Doha, Qatar. *Solar Energy*, **142**, 123–135, doi:10.1016/j.solener.2016.11.053.
Jenouvrier, S. et al., 2014: Projected continent-wide declines of the emperor penguin under climate change. *Nature Climate Change*, **4(8)**, 715–718, doi:10.1038/nclimate2280.
Jeong, D. and L. Sushama, 2018: Projected changes to extreme wind and snow environmental loads for buildings and infrastructure across Canada. *Sustainable Cities and Society*, **36**, 225–236, doi:10.1016/j.scs.2017.10.004.
Jerez, S. et al., 2015: The impact of climate change on photovoltaic power generation in Europe. *Nature Communications*, **6(1)**, 10014, doi:10.1038/ncomms10014.
Jézéquel, A., P. Yiou, and J.-P. Vanderlinden, 2019: Comparing scientists and delegates perspectives on the use of extreme event attribution for loss and damage. *Weather and Climate Extremes*, **26**, 100231, doi:10.1016/j.wace.2019.100231.
Jézéquel, A. et al., 2020: Singular Extreme Events and Their Attribution to Climate Change: A Climate Service-Centered Analysis. *Weather, Climate, and Society*, **12(1)**, 89–101, doi:10.1175/wcas-d-19-0048.1.
Ji, Z., G. Wang, M. Yu, and J.S. Pal, 2018: Potential climate effect of mineral aerosols over West Africa: Part II – contribution of dust and land cover to future climate change. *Climate Dynamics*, **50(7–8)**, 2335–2353, doi:10.1007/s00382-015-2792-x.

ACCEPTED VERSION SUBJECT TO FINAL EDITS

Jiang, J., T. Zhou, X. Chen, and L. Zhang, 2020: Future changes in precipitation over Central Asia based on CMIP6 projections. *Environmental Research Letters*, **15(5)**, 54009, doi:10.1088/1748-9326/ab7d03.
Jiang, L. et al., 2018: Increased temperature mitigates the effects of ocean acidification on the calcification of juvenile Pocillopora damicornis, but at a cost. *Coral Reefs*, **37(1)**, 71–79, doi:10.1007/s00338-017-1634-1.
Jickells, T.D. et al., 2005: Global iron connections between desert dust, ocean biogeochemistry, and climate. *Science*, **308(5718)**, 67–71, doi:10.1126/science.1105959.
Jin, Y. et al., 2015: Identification of two distinct fire regimes in Southern California: implications for economic impact and future change. *Environmental Research Letters*, **10(9)**, 094005, doi:10.1088/1748-9326/10/9/094005.
Johnson, C.W., Y. Fu, and R. Bürgmann, 2017: Seasonal water storage, stress modulation, and California seismicity. *Science*, **356(6343)**, 1161–1164, doi:10.1126/science.aak9547.
Jolly, W.M. et al., 2015: Climate-induced variations in global wildfire danger from 1979 to 2013. *Nature Communications*, **6(1)**, 7537, doi:10.1038/ncomms8537.
Jones, B., C. Tebaldi, B.C. O'Neill, K. Oleson, and J. Gao, 2018: Avoiding population exposure to heat-related extremes: demographic change vs climate change. *Climatic Change*, **146(3–4)**, 423–437, doi:10.1007/s10584-017-2133-7.
Jones, C. and L.M. Carvalho, 2013: Climate Change in the South American Monsoon System: Present Climate and CMIP5 Projections. *Journal of Climate*, **26(17)**, 6660–6678, doi:10.1175/jcli-d-12-00412.1.
Jones, J. and M.T. Brett, 2014: Lake Nutrients, Eutrophication, and Climate Change. In: *Global Environmental Change* [Freedman, B. (ed.)]. Springer, Dordrecht, The Netherlands, pp. 273–279, doi:10.1007/978-94-007-5784-4_109.
Jones, R.N. et al., 2014: Foundations for decision making. In: *Climate Change 2014: Impacts, Adaptation, and Vulnerability. Part A: Global and Sectoral Aspects. Contribution of Working Group II to the Fifth Assessment Report of the Intergovernmental Panel on Climate Change* [Field, C.B., V.R. Barros, D.J. Dokken, K.J. Mach, M.D. Mastrandrea, T.E. Bilir, M. Chatterjee, K.L. Ebi, Y.O. Estrada, R.C. Genova, B. Girma, E.S. Kissel, A.N. Levy, S. MacCracken, P.R. Mastrandrea, and L.L. White (eds.)]. Cambridge University Press, Cambridge, United Kingdom and New York, NY, USA, pp. 195–228, doi:10.1017/cbo9781107415379.007.
Jongejan, R., R. Ranasinghe, D. Wainwright, D.P. Callaghan, and J. Reyns, 2016: Drawing the line on coastline recession risk. *Ocean & Coastal Management*, **122**, 87–94, doi:10.1016/j.ocecoaman.2016.01.006.
Jung, C. and D. Schindler, 2019: Changing wind speed distributions under future global climate. *Energy Conversion and Management*, **198**, 111841, doi:10.1016/j.enconman.2019.111841.
Jurchescu, M. et al., 2017: An approach to investigate the effects of climate change on landslide hazard at a national scale (Romania). In: *Proceedings of the 33rd Romanian Geomorphology Symposium*. Alexandru Ioan Cuza University of Iași Press, Iași, pp. 121–124, doi:10.15551/prgs.2017.121.
Jyrkama, M.I. and J.F. Sykes, 2007: The impact of climate change on spatially varying groundwater recharge in the grand river watershed (Ontario). *Journal of Hydrology*, **338(3–4)**, 237–250, doi:10.1016/j.jhydrol.2007.02.036.
Kalvelage, K., U. Passe, S. Rabideau, and E.S. Takle, 2014: Changing climate: The effects on energy demand and human comfort. *Energy and Buildings*, **76**, 373–380, doi:10.1016/j.enbuild.2014.03.009.
Kämäräinen, M. et al., 2018: Estimates of Present-Day and Future Climatologies of Freezing Rain in Europe Based on CORDEX Regional Climate Models. *Journal of Geophysical Research: Atmospheres*, **123(23)**, 13,291–13,304, doi:10.1029/2018jd029131.
Kapitsa, V., M. Shahgedanova, H. Machguth, I. Severskiy, and A. Medeu, 2017: Assessment of evolution and risks of glacier lake outbursts in the Djungarskiy Alatau, Central Asia, using Landsat imagery and glacier bed topography modelling. *Natural Hazards and Earth System Sciences*, **17(10)**, 1837–1856, doi:10.5194/nhess-17-1837-2017.
Karnauskas, K.B., J.P. Donnelly, and K.J. Anchukaitis, 2016: Future freshwater stress for island populations. *Nature Climate Change*, **6(7)**, 720–725, doi:10.1038/nclimate2987.
Karnauskas, K.B., J.K. Lundquist, and L. Zhang, 2018a: Southward shift of the global wind energy resource under high carbon dioxide emissions. *Nature Geoscience*, **11(1)**, 38–43, doi:10.1038/s41561-017-0029-9.
Karnauskas, K.B., C.-F. Schleussner, J.P. Donnelly, and K.J. Anchukaitis, 2018b: Freshwater stress on small island developing states: population projections and aridity changes at 1.5 and 2°C. *Regional Environmental Change*, **18**, 2273–2282, doi:10.1007/s10113-018-1331-9.
Karremann, M.K., J.G. Pinto, M. Reyers, and M. Klawa, 2014: Return periods of losses associated with European windstorm series in a changing climate. *Environmental Research Letters*, **9(12)**, 124016, doi:10.1088/1748-9326/9/12/124016.
Karymbalis, E. et al., 2012: Assessment of the sensitivity of the southern coast of the Gulf of Corinth (Peloponnese, Greece) to sea-level rise. *Open Geosciences*, **4(4)**, 561–577, doi:10.2478/s13533-012-0101-3.
Kattsov, V.M., I.M. Shkolnik, and S. Efimov, 2017: Climate change projections in Russian regions: The detailing in physical and probability spaces. *Russian Meteorology and Hydrology*, **42(7)**, 452–460, doi:10.3103/s1068373917070044.
Kawase, H. et al., 2016: Enhancement of heavy daily snowfall in central Japan due to global warming as projected by large ensemble of regional climate simulations. *Climatic Change*, **139(2)**, 265–278, doi:10.1007/s10584-016-

ACCEPTED VERSION SUBJECT TO FINAL EDITS

1781-3.
Kawase, H. et al., 2020: Changes in extremely heavy and light snow-cover winters due to global warming over high mountainous areas in central Japan. *Progress in Earth and Planetary Science*, **7(1)**, 10, doi:10.1186/s40645-020-0322-x.
Kazemzadeh, M. and A. Malekian, 2016: Spatial characteristics and temporal trends of meteorological and hydrological droughts in northwestern Iran. *Natural Hazards*, **80(1)**, 191–210, doi:10.1007/s11069-015-1964-7.
Keele, S., 2019: Consultants and the business of climate services: implications of shifting from public to private science. *Climatic Change*, **157(1)**, 9–26, doi:10.1007/s10584-019-02385-x.
Keener, V. et al., 2018: Hawai'i and U.S.-Affiliated Pacific Islands. In: *Impacts, Risks, and Adaptation in the United States: Fourth National Climate Assessment, Volume II* [Reidmiller, D.R., C.W. Avery, D.R. Easterling, K.E. Kunkel, K.L.M. Lewis, T.K. Maycock, and B.C. Stewart (eds.)]. U.S. Global Change Research Program, Washington, DC, USA, pp. 1242–1308, doi:10.7930/nca4.2018.ch27.
Kefi, M., B.K. Mishra, Y. Masago, and K. Fukushi, 2020: Analysis of flood damage and influencing factors in urban catchments: case studies in Manila, Philippines, and Jakarta, Indonesia. *Natural Hazards*, **104(3)**, 2461–2487, doi:10.1007/s11069-020-04281-5.
Kelley, C.P., S. Mohtadi, M.A. Cane, R. Seager, and Y. Kushnir, 2015: Climate change in the Fertile Crescent and implications of the recent Syrian drought. *Proceedings of the National Academy of Sciences*, **112(11)**, 3241–3246, doi:10.1073/pnas.1421533112.
Kent, S.T., L.A. McClure, B.F. Zaitchik, T.T. Smith, and J.M. Gohlke, 2014: Heat Waves and Health Outcomes in Alabama (USA): The Importance of Heat Wave Definition. *Environmental Health Perspectives*, **122(2)**, 151–158, doi:10.1289/ehp.1307262.
Kermanshah, A., S. Derrible, and M. Berkelhammer, 2017: Using Climate Models to Estimate Urban Vulnerability to Flash Floods. *Journal of Applied Meteorology and Climatology*, **56(9)**, 2637–2650, doi:10.1175/jamc-d-17-0083.1.
Kerr, G.H. and D.W. Waugh, 2018: Connections between summer air pollution and stagnation. *Environmental Research Letters*, **13(8)**, 84001, doi:10.1088/1748-9326/aad2e2.
Kew, S.F. et al., 2019: The Exceptional Summer Heat Wave in Southern Europe 2017. *Bulletin of the American Meteorological Society*, **100(1)**, S49–S53, doi:10.1175/bams-d-18-0109.1.
Kew, S.F. et al., 2021: Impact of precipitation and increasing temperatures on drought trends in eastern Africa. *Earth System Dynamics*, **12(1)**, 17–35, doi:10.5194/esd-12-17-2021.
Key, N., S. Sneeringer, and D. Marquardt, 2014: Climate Change, Heat Stress, and U.S. Dairy Production. *SSRN Electronic Journal*, doi:10.2139/ssrn.2506668.
Khalyani, A.H. et al., 2016: Climate change implications for tropical islands: Interpolating and interpreting statistically downscaled GCM projections for management and planning. *Journal of Applied Meteorology and Climatology*, **55(2)**, 265–282, doi:10.1175/jamc-d-15-0182.1.
Khan, N., S. Shahid, T. Ismail, and X.-Wang, 2019a: Spatial distribution of unidirectional trends in temperature and temperature extremes in Pakistan. *Theoretical and Applied Climatology*, **136(3–4)**, 899–913, doi:10.1007/s00704-018-2520-7.
Khan, N., S. Shahid, T. Ismail, K. Ahmed, and N. Nawaz, 2019b: Trends in heat wave related indices in Pakistan. *Stochastic Environmental Research and Risk Assessment*, **33(1)**, 287–302, doi:10.1007/s00477-018-1605-2.
Khan, N. et al., 2020: Selection of GCMs for the projection of spatial distribution of heat waves in Pakistan. *Atmospheric Research*, **233**, 104688, doi:10.1016/j.atmosres.2019.104688.
Khan, S. et al., 2018: Flows and sediment dynamics in the Ganga River under present and future climate scenarios. *Hydrological Sciences Journal*, **63(5)**, 763–782, doi:10.1080/02626667.2018.1447113.
Khan, Y.A., H. Lateh, M.A. Baten, and A.A. Kamil, 2012: Critical antecedent rainfall conditions for shallow landslides in Chittagong City of Bangladesh. *Environmental Earth Sciences*, **67(1)**, 97–106, doi:10.1007/s12665-011-1483-0.
Kharin, V. et al., 2018: Risks from Climate Extremes Change Differently from 1.5°C to 2.0°C Depending on Rarity. *Earth's Future*, **6(5)**, 704–715, doi:10.1002/2018ef000813.
Kharuk, V.I., A.S. Shushpanov, S.T. Im, and K.J. Ranson, 2016: Climate-induced landsliding within the larch dominant permafrost zone of central Siberia. *Environmental Research Letters*, **11(4)**, 45004, doi:10.1088/1748-9326/11/4/045004.
Khlebnikova, E.I., Y.L. Rudakova, and I.M. Shkolnik, 2019a: Changes in Precipitation Regime over the Territory of Russia: Data of Regional Climate Modeling and Observations. *Russian Meteorology and Hydrology*, **44(7)**, 431–439, doi:10.3103/s106837391907001x.
Khlebnikova, E.I., Y.L. Rudakova, I.A. Sall', S. Efimov, and I.M. Shkolnik, 2019b: Changes in Indicators of Temperature Extremes in the 21st Century: Ensemble Projections for the Territory of Russia. *Russian Meteorology and Hydrology*, **44(3)**, 159–168, doi:10.3103/s1068373919030014.
Kieu-Thi, X. et al., 2016: Rainfall and Tropical Cyclone Activity over Vietnam Simulated and Projected by the Non-Hydrostatic Regional Climate Model – NHRCM. *Journal of the Meteorological Society of Japan. Ser. II*, **94A**, 135–150, doi:10.2151/jmsj.2015-057.

ACCEPTED VERSION SUBJECT TO FINAL EDITS

Kilroy, G., 2015: A review of the biophysical impacts of climate change in three hotspot regions in Africa and Asia. *Regional Environmental Change*, **15(5)**, 771–782, doi:10.1007/s10113-014-0709-6.
Kim, H.G. et al., 2015: Evaluating landslide hazards using RCP 4.5 and 8.5 scenarios. *Environmental Earth Sciences*, **73(3)**, 1385–1400, doi:10.1007/s12665-014-3775-7.
Kim, J., H. Kang, C. Son, and Y. Moon, 2016: Spatial variations in typhoon activities and precipitation trends over the Korean Peninsula. *Journal of Hydro-environment Research*, **13**, 144–151, doi:10.1016/j.jher.2014.12.005.
Kimball, B.A., 2016: Crop responses to elevated CO2 and interactions with H2O, N, and temperature. *Current Opinion in Plant Biology*, **31**, 36–43, doi:10.1016/j.pbi.2016.03.006.
King, A.D. et al., 2015: The timing of anthropogenic emergence in simulated climate extremes. *Environmental Research Letters*, **10(9)**, 094015, doi:10.1088/1748-9326/10/9/094015.
Kinney, P.L. et al., 2015a: New York City Panel on Climate Change 2015 Report. Chapter 5: Public Health Impacts and Resiliency. *Annals of the New York Academy of Sciences*, **1336(1)**, 67–88, doi:10.1111/nyas.12588.
Kinney, P.L. et al., 2015b: Winter season mortality: Will climate warming bring benefits? *Environmental Research Letters*, **10(6)**, 064016, doi:10.1088/1748-9326/10/6/064016.
Kirchmeier-Young, M.C., H. Wan, X. Zhang, and S.I. Seneviratne, 2019: Importance of Framing for Extreme Event Attribution: The Role of Spatial and Temporal Scales. *Earth's Future*, **7(10)**, 1192–1204, doi:10.1029/2019ef001253.
Kirezci, E. et al., 2020: Projections of global-scale extreme sea levels and resulting episodic coastal flooding over the 21st Century. *Scientific Reports*, **10(1)**, 11629, doi:10.1038/s41598-020-67736-6.
Kirschbaum, D., T. Stanley, and Y. Zhou, 2015: Spatial and temporal analysis of a global landslide catalog. *Geomorphology*, **249**, 4–15, doi:10.1016/j.geomorph.2015.03.016.
Kirschbaum, D., S.B. Kapnick, T. Stanley, and S. Pascale, 2020: Changes in Extreme Precipitation and Landslides Over High Mountain Asia. *Geophysical Research Letters*, **47(4)**, e2019GL085347, doi:10.1029/2019gl085347.
Kirwan, M.L. and J.P. Megonigal, 2013: Tidal wetland stability in the face of human impacts and sea-level rise. *Nature*, **504(7478)**, 53–60, doi:10.1038/nature12856.
Kitoh, A., S. Kusunoki, and T. Nakaegawa, 2011: Climate change projections over South America in the late 21st century with the 20 and 60 km mesh Meteorological Research Institute atmospheric general circulation model (MRI-AGCM). *Journal of Geophysical Research*, **116(D6)**, D06105, doi:10.1029/2010jd014920.
Kjellstrom, T. et al., 2016: Heat, Human Performance, and Occupational Health: A Key Issue for the Assessment of Global Climate Change Impacts. *Annual Review of Public Health*, **37(1)**, 97–112, doi:10.1146/annurev-publhealth-032315-021740.
Kjellström, E. et al., 2016: Production and use of regional climate model projections – A Swedish perspective on building climate services. *Climate Services*, **2–3**, 15–29, doi:10.1016/j.cliser.2016.06.004.
Kjellström, E. et al., 2018: European climate change at global mean temperature increases of 1.5 and 2°C above pre-industrial conditions as simulated by the EURO-CORDEX regional climate models. *Earth System Dynamics*, **9(2)**, 459–478, doi:10.5194/esd-9-459-2018.
Klima, K. and M.G. Morgan, 2015: Ice storm frequencies in a warmer climate. *Climatic Change*, **133(2)**, 209–222, doi:10.1007/s10584-015-1460-9.
Klos, P.Z., T.E. Link, and J.T. Abatzoglou, 2014: Extent of the rain-snow transition zone in the western U.S. under historic and projected climate. *Geophysical Research Letters*, **41(13)**, 4560–4568, doi:10.1002/2014gl060500.
Kluver, D. and D. Leathers, 2015: Regionalization of snowfall frequency and trends over the contiguous United States. *International Journal of Climatology*, **35(14)**, 4348–4358, doi:10.1002/joc.4292.
Knaggård, D. Slunge, A. Ekbom, M. Göthberg, and U. Sahlin, 2019: Researchers' approaches to stakeholders: Interaction or transfer of knowledge? *Environmental Science and Policy*, **97**, 25–35, doi:10.1016/j.envsci.2019.03.008.
Knoll, L.B. et al., 2019: Consequences of lake and river ice loss on cultural ecosystem services. *Limnology and Oceanography Letters*, **4(5)**, 119–131, doi:10.1002/lol2.10116.
Knouft, J.H. and D.L. Ficklin, 2017: The Potential Impacts of Climate Change on Biodiversity in Flowing Freshwater Systems. *Annual Review of Ecology, Evolution, and Systematics*, **48(1)**, 111–133, doi:10.1146/annurev-ecolsys-110316-022803.
Knutson, T. et al., 2019: Tropical Cyclones and Climate Change Assessment: Part I: Detection and Attribution. *Bulletin of the American Meteorological Society*, **100(10)**, 1987–2007, doi:10.1175/bams-d-18-0189.1.
Knutson, T. et al., 2020: Tropical Cyclones and Climate Change Assessment: Part II: Projected Response to Anthropogenic Warming. *Bulletin of the American Meteorological Society*, **101(3)**, E303–E322, doi:10.1175/bams-d-18-0194.1.
Knutson, T.R. and J.J. Ploshay, 2016: Detection of anthropogenic influence on a summertime heat stress index. *Climatic Change*, **138(1–2)**, 25–39, doi:10.1007/s10584-016-1708-z.
Knutson, T.R. and F. Zeng, 2018: Model assessment of observed precipitation trends over land regions: Detectable human influences and possible low bias in model trends. *Journal of Climate*, **31(12)**, 4617–4637, doi:10.1175/jcli-d-17-0672.1.
Knutson, T.R. et al., 2015: Global projections of intense tropical cyclone activity for the late twenty-first century from

ACCEPTED VERSION SUBJECT TO FINAL EDITS

dynamical downscaling of CMIP5/RCP4.5 scenarios. *Journal of Climate*, **28(18)**, 7203–7224, doi:10.1175/jcli-d-15-0129.1.
Knutti, R., 2019: Closing the Knowledge-Action Gap in Climate Change. *One Earth*, **1(1)**, 21–23, doi:10.1016/j.oneear.2019.09.001.
Kokelj, S. et al., 2015: Increased precipitation drives mega slump development and destabilization of ice-rich permafrost terrain, northwestern Canada. *Global and Planetary Change*, **129**, 56–68, doi:10.1016/j.gloplacha.2015.02.008.
Koks, E.E. et al., 2019: A global multi-hazard risk analysis of road and railway infrastructure assets. *Nature Communications*, **10(1)**, 2677, doi:10.1038/s41467-019-10442-3.
Kolberg, D., T. Persson, K. Mangerud, and H. Riley, 2019: Impact of projected climate change on workability, attainable yield, profitability and farm mechanization in Norwegian spring cereals. *Soil and Tillage Research*, **185**, 122–138, doi:10.1016/j.still.2018.09.002.
Kolstad, E.W. et al., 2019: Trials, Errors, and Improvements in Coproduction of Climate Services. *Bulletin of the American Meteorological Society*, **100(8)**, 1419–1428, doi:10.1175/bams-d-18-0201.1.
Kopytko, N. and J. Perkins, 2011: Climate change, nuclear power, and the adaptation–mitigation dilemma. *Energy Policy*, **39(1)**, 318–333, doi:10.1016/j.enpol.2010.09.046.
Kormos, P.R., C.H. Luce, S.J. Wenger, and W.R. Berghuijs, 2016: Trends and sensitivities of low streamflow extremes to discharge timing and magnitude in Pacific Northwest mountain streams. *Water Resources Research*, **52(7)**, 4990–5007, doi:10.1002/2015wr018125.
Kornhuber, K. et al., 2020: Amplified Rossby waves enhance risk of concurrent heatwaves in major breadbasket regions. *Nature Climate Change*, **10(1)**, 48–53, doi:10.1038/s41558-019-0637-z.
Korres, N.E. et al., 2016: Cultivars to face climate change effects on crops and weeds: a review. *Agronomy for Sustainable Development*, **36(1)**, 12, doi:10.1007/s13593-016-0350-5.
Kossin, J.P., 2017: Hurricane intensification along United States coast suppressed during active hurricane periods. *Nature*, **541**, 390–393, doi:10.1038/nature20783.
Kossin, J.P., K.A. Emanuel, and S.J. Camargo, 2016: Past and Projected Changes in Western North Pacific Tropical Cyclone Exposure. *Journal of Climate*, **29(16)**, 5725–5739, doi:10.1175/jcli-d-16-0076.1.
Kossin, J.P. et al., 2017: Extreme storms. In: *Climate Science Special Report: Fourth National Climate Assessment, Volume I* [Wuebbles, D.J., D.W. Fahey, K.A. Hibbard, D.J. Dokken, B.C. Stewart, and T.K. Maycock (eds.)]. U.S. Global Change Research Program, Washington, DC, USA, pp. 257–276, doi:10.7930/j07s7kxx.
Kovács, A., A. Nemeth, J. Unger, and N. Kántor, 2017: Tourism climatic conditions of Hungary – Present situation and assessment of future changes. *Idojaras, Quarterly Journal of the Hungarian Meteorological Service*, **121(1)**, 79–99.
Kovats, R.S. et al., 2004: The effect of temperature on food poisoning: a time-series analysis of salmonellosis in ten European countries. *Epidemiology and Infection*, **132(3)**, 443–453, doi:10.1017/s0950268804001992.
Kraaijenbrink, P.D.A., M.F.P. Bierkens, A.F. Lutz, and W.W. Immerzeel, 2017: Impact of a global temperature rise of 1.5 degrees Celsius on Asia's glaciers. *Nature*, **549(7671)**, 257–260, doi:10.1038/nature23878.
Krishnan, R. et al., 2019: Unravelling Climate Change in the Hindu Kush Himalaya: Rapid Warming in the Mountains and Increasing Extremese. In: *The Hindu Kush Himalaya Assessment: Mountains, Climate Change, Sustainability and Peopl* [Wester, P., A. Mishra, A. Mukherji, and A.B. Shrestha (eds.)]. Springer, Cham, Switzerland, pp. 57–97, doi:10.1007/978-3-319-92288-1_3.
Krist, F.J. et al., 2014: *2013-2027 National insect and disease forest risk assessment*. FHTET-14-01, Forest Health Technology Enterprise Team (FHTET), United States Forest Service, Fort Collins, CO, USA, 209 pp.
Kroeker, K.J. et al., 2013: Impacts of ocean acidification on marine organisms: quantifying sensitivities and interaction with warming. *Global Change Biology*, **19(6)**, 1884–1896, doi:10.1111/gcb.12179.
Krueger, T. et al., 2017: Common reef-building coral in the Northern Red Sea resistant to elevated temperature and acidification. *Royal Society Open Science*, **4(5)**, 170038, doi:10.1098/rsos.170038.
Kruk, M.C. et al., 2017: Engaging with users of climate information and the coproduction of knowledge. *Weather, Climate, and Society*, **9(4)**, 839–849, doi:10.1175/wcas-d-16-0127.1.
Krysanova, V. et al., 2017: Intercomparison of regional-scale hydrological models and climate change impacts projected for 12 large river basins worldwide-a synthesis. *Environmental Research Letters*, **12(10)**, 105002, doi:10.1088/1748-9326/aa8359.
Kubota, H. and J.C.L. Chan, 2009: Interdecadal variability of tropical cyclone landfall in the Philippines from 1902 to 2005. *Geophysical Research Letters*, **36(12)**, L12802, doi:10.1029/2009gl038108.
Kuleshov, Y. et al., 2010: Trends in tropical cyclones in the South Indian Ocean and the South Pacific Ocean. *Journal of Geophysical Research*, **115(D1)**, D01101, doi:10.1029/2009jd012372.
Kulp, S.A. and B.H. Strauss, 2019: New elevation data triple estimates of global vulnerability to sea-level rise and coastal flooding. *Nature Communications*, **10(1)**, 4844, doi:10.1038/s41467-019-12808-z.
Kumar, D. and A.R. Ganguly, 2018: Intercomparison of model response and internal variability across climate model ensembles. *Climate Dynamics*, **51(1–2)**, 207–219, doi:10.1007/s00382-017-3914-4.
Kumar, D., V. Mishra, and A.R. Ganguly, 2015: Evaluating wind extremes in CMIP5 climate models. *Climate*

ACCEPTED VERSION SUBJECT TO FINAL EDITS

Dynamics, **45(1)**, 441–453, doi:10.1007/s00382-014-2306-2.
Kumar, S., K. Chanda, and S. Pasupuleti, 2020: Spatiotemporal analysis of extreme indices derived from daily precipitation and temperature for climate change detection over India. *Theoretical and Applied Climatology*, **140(1)**, 343–357, doi:10.1007/s00704-020-03088-5.
Kumar, S. et al., 2019: Characteristics of Observed Meteorological Drought and its Linkage with Low-Level Easterly Wind Over India. *Pure and Applied Geophysics*, **176(6)**, 2679–2696, doi:10.1007/s00024-019-02118-2.
Kundzewicz, Z.W., I. Pin'skwar, and G.R. Brakenridge, 2018: Changes in river flood hazard in Europe: A review. *Hydrology Research*, **49(2)**, 294–302, doi:10.2166/nh.2017.016.
Kundzewicz, Z.W. et al., 2014: Flood risk and climate change: global and regional perspectives. *Hydrological Sciences Journal*, **59(1)**, 1–28, doi:10.1080/02626667.2013.857411.
Kundzewicz, Z.W. et al., 2019: Flood risk and its reduction in China. *Advances in Water Resources*, **130**, 37–45, doi:10.1016/j.advwatres.2019.05.020.
Kunkel, K.E. et al., 2016: Trends and Extremes in Northern Hemisphere Snow Characteristics. *Current Climate Change Reports*, **2(2)**, 65–73, doi:10.1007/s40641-016-0036-8.
Kuriqi, A. et al., 2020: Seasonality shift and streamflow flow variability trends in central India. *Acta Geophysica*, **68(5)**, 1461–1475, doi:10.1007/s11600-020-00475-4.
Kusunoki, S., 2018: Future changes in precipitation over East Asia projected by the global atmospheric model MRI-AGCM3.2. *Climate Dynamics*, **51**, 4601–4617, doi:10.1007/s00382-016-3499-3.
Kusunoki, S., T. Ose, and M. Hosaka, 2020: Emergence of unprecedented climate change in projected future precipitation. *Scientific Reports*, **10(1)**, 4802, doi:10.1038/s41598-020-61792-8.
Kusunose, Y. and T.J. Lybbert, 2014: Coping with drought by adjusting land tenancy contracts: A model and evidence from rural Morocco. *World Development*, **61**, 114–126, doi:10.1016/j.worlddev.2014.04.006.
Kvande, T. and K.R. Lisø, 2009: Climate adapted design of masonry structures. *Building and Environment*, **44(12)**, 2442–2450, doi:10.1016/j.buildenv.2009.04.007.
Kwiatkowski, L. et al., 2016: Nighttime dissolution in a temperate coastal ocean ecosystem increases under acidification. *Scientific Reports*, **6**, 22984, doi:10.1038/srep22984.
Kwiatkowski, L. et al., 2020: Twenty-first century ocean warming, acidification, deoxygenation, and upper-ocean nutrient and primary production decline from CMIP6 model projections. *Biogeosciences*, **17(13)**, 3439–3470, doi:10.5194/bg-17-3439-2020.
Lai, L.-W., 2018: The relationship between extreme weather events and crop losses in central Taiwan. *Theoretical and Applied Climatology*, **134(1–2)**, 107–119, doi:10.1007/s00704-017-2261-z.
Laidre, K.L. et al., 2015: Arctic marine mammal population status, sea ice habitat loss, and conservation recommendations for the 21st century. *Conservation Biology*, **29(3)**, 724–737, doi:10.1111/cobi.12474.
Lake, I.R. et al., 2017: Climate Change and Future Pollen Allergy in Europe. *Environmental Health Perspectives*, **125(3)**, 385–391, doi:10.1289/ehp173.
Laliberté, F., S.E.L. Howell, and P.J. Kushner, 2016: Regional variability of a projected sea ice-free Arctic during the summer months. *Geophysical Research Letters*, **43(1)**, 256–263, doi:10.1002/2015gl066855.
Lallo, C.H.O. et al., 2018: Characterizing heat stress on livestock using the temperature humidity index (THI) – prospects for a warmer Caribbean. *Regional Environmental Change*, **18(8)**, 2329–2340, doi:10.1007/s10113-018-1359-x.
Lambert, S.J. and B.K. Hansen, 2011: Simulated Changes in the Freezing Rain Climatology of North America under Global Warming Using a Coupled Climate Model. *Atmosphere-Ocean*, **49(3)**, 289–295, doi:10.1080/07055900.2011.607492.
Lambrechts, L. et al., 2011: Impact of daily temperature fluctuations on dengue virus transmission by Aedes aegypti. *Proceedings of the National Academy of Sciences*, **108(18)**, 7460–7465, doi:10.1073/pnas.1101377108.
Landrum, L. and M.M. Holland, 2020: Extremes become routine in an emerging new Arctic. *Nature Climate Change*, **10(12)**, 1108–1115, doi:10.1038/s41558-020-0892-z.
Lane, S.N., M. Bakker, C. Gabbud, N. Micheletti, and J.-N. Saugy, 2017: Sediment export, transient landscape response and catchment-scale connectivity following rapid climate warming and Alpine glacier recession. *Geomorphology*, **277**, 210–227, doi:10.1016/j.geomorph.2016.02.015.
Lange, S., 2019: Trend-preserving bias adjustment and statistical downscaling with ISIMIP3BASD (v1.0). *Geoscientific Model Development*, **12(7)**, 3055–3070, doi:10.5194/gmd-12-3055-2019.
Laporta, G.Z. et al., 2015: Malaria vectors in South America: current and future scenarios. *Parasites & Vectors*, **8(1)**, 426, doi:10.1186/s13071-015-1038-4.
Larosa, F. and J. Mysiak, 2019: Mapping the landscape of climate services. *Environmental Research Letters*, **14(9)**, 93006, doi:10.1088/1748-9326/ab304d.
Laurent, A. et al., 2017: Eutrophication-induced acidification of coastal waters in the northern Gulf of Mexico: Insights into origin and processes from a coupled physical-biogeochemical model. *Geophysical Research Letters*, **44(2)**, 946–956, doi:10.1002/2016gl071881.
Laurila, T.K., V.A. Sinclair, and H. Gregow, 2020: Climatology, variability, and trends in near-surface wind speeds over the North Atlantic and Europe during 1979–2018 based on ERA5. *International Journal of Climatology*,

ACCEPTED VERSION SUBJECT TO FINAL EDITS

1–26, doi:10.1002/joc.6957.
Lay, C.R. et al., 2018: Emergency Department Visits and Ambient Temperature: Evaluating the Connection and Projecting Future Outcomes. *GeoHealth*, **2(6)**, 182–194, doi:10.1002/2018gh000129.
Lazar, B. and M. Williams, 2008: Climate change in western ski areas: Potential changes in the timing of wet avalanches and snow quality for the Aspen ski area in the years 2030 and 2100. *Cold Regions Science and Technology*, **51(2–3)**, 219–228, doi:10.1016/j.coldregions.2007.03.015.
Le Cozannet, G., M. Garcin, M. Yates, D. Idier, and B. Meyssignac, 2014: Approaches to evaluate the recent impacts of sea-level rise on shoreline changes. *Earth-Science Reviews*, **138**, 47–60, doi:10.1016/j.earscirev.2014.08.005.
Le Cozannet, G. et al., 2017: Sea Level Change and Coastal Climate Services: The Way Forward. *Journal of Marine Science and Engineering*, **5(4)**, 49, doi:10.3390/jmse5040049.
Le Cozannet, G. et al., 2019: Quantifying uncertainties of sandy shoreline change projections as sea level rises. *Scientific Reports*, **9(1)**, 42, doi:10.1038/s41598-018-37017-4.
Le Nohaïc, M. et al., 2017: Marine heatwave causes unprecedented regional mass bleaching of thermally resistant corals in northwestern Australia. *Scientific Reports*, **7(1)**, 14999, doi:10.1038/s41598-017-14794-y.
Leakey, A.D.B., K.A. Bishop, and E.A. Ainsworth, 2012: A multi-biome gap in understanding of crop and ecosystem responses to elevated CO2. *Current Opinion in Plant Biology*, **15(3)**, 228–236, doi:10.1016/j.pbi.2012.01.009.
Lee, C.K.F., C. Duncan, H.J.F. Owen, and N. Pettorelli, 2018: A New Framework to Assess Relative Ecosystem Vulnerability to Climate Change. *Conservation Letters*, **11(2)**, e12372, doi:10.1111/conl.12372.
Lee, H. and D.A. Sumner, 2015: Economics of downscaled climate-induced changes in cropland, with projections to 2050: evidence from Yolo County California. *Climatic Change*, **132(4)**, 723–737, doi:10.1007/s10584-015-1436-9.
Lee, J.R. et al., 2017: Climate change drives expansion of Antarctic ice-free habitat. *Nature*, **547(7661)**, 49–54, doi:10.1038/nature22996.
Lee, M.A., A.P. Davis, M.G.G. Chagunda, and P. Manning, 2017: Forage quality declines with rising temperatures, with implications for livestock production and methane emissions. *Biogeosciences*, **14(6)**, 1403–1417, doi:10.5194/bg-14-1403-2017.
Lee, T.-C., T.R. Knutson, T. Nakaegawa, M. Ying, and E.J. Cha, 2020: Third assessment on impacts of climate change on tropical cyclones in the Typhoon Committee Region – Part I: Observed changes, detection and attribution. *Tropical Cyclone Research and Review*, **9(1)**, 1–22, doi:10.1016/j.tcrr.2020.03.001.
Lehner, F., C. Deser, and L. Terray, 2017: Toward a New Estimate of "Time of Emergence" of Anthropogenic Warming: Insights from Dynamical Adjustment and a Large Initial-Condition Model Ensemble. *Journal of Climate*, **30(19)**, 7739–7756, doi:10.1175/jcli-d-16-0792.1.
Lehner, F., C. Deser, and B.M. Sanderson, 2018: Future risk of record-breaking summer temperatures and its mitigation. *Climatic Change*, **146(3–4)**, 363–375, doi:10.1007/s10584-016-1616-2.
Leite-Filho, A.T., V.Y. de Sousa Pontes, and M.H. Costa, 2019: Effects of Deforestation on the Onset of the Rainy Season and the Duration of Dry Spells in Southern Amazonia. *Journal of Geophysical Research: Atmospheres*, **124(10)**, 5268–5281, doi:10.1029/2018jd029537.
Lelieveld, J., J.S. Evans, M. Fnais, D. Giannadaki, and A. Pozzer, 2015: The contribution of outdoor air pollution sources to premature mortality on a global scale. *Nature*, **525(7569)**, 367–371, doi:10.1038/nature15371.
Lelieveld, J. et al., 2016: Strongly increasing heat extremes in the Middle East and North Africa (MENA) in the 21st century. *Climatic Change*, **137(1–2)**, 245–260, doi:10.1007/s10584-016-1665-6.
Lemos, M.C., C.J. Kirchhoff, and V. Ramprasad, 2012: Narrowing the climate information usability gap. *Nature Climate Change*, **2(11)**, 789–794, doi:10.1038/nclimate1614.
Leng, G. and J. Hall, 2019: Crop yield sensitivity of global major agricultural countries to droughts and the projected changes in the future. *Science of the Total Environment*, **654**, 811–821, doi:10.1016/j.scitotenv.2018.10.434.
Leng, G. et al., 2016: Emergence of new hydrologic regimes of surface water resources in the conterminous United States under future warming. *Environmental Research Letters*, **11(11)**, 114003, doi:10.1088/1748-9326/11/11/114003.
Lenoir, J. and J.-C. Svenning, 2015: Climate-related range shifts - a global multidimensional synthesis and new research directions. *Ecography*, **38(1)**, 15–28, doi:10.1111/ecog.00967.
Lesk, C., E. Coffel, and R. Horton, 2020: Net benefits to US soy and maize yields from intensifying hourly rainfall. *Nature Climate Change*, **10(9)**, 819–822, doi:10.1038/s41558-020-0830-0.
Leta, O., A. El-Kadi, and H. Dulai, 2018: Impact of Climate Change on Daily Streamflow and Its Extreme Values in Pacific Island Watersheds. *Sustainability*, **10(6)**, 2057, doi:10.3390/su10062057.
Levin, L.A., 2018: Manifestation, Drivers, and Emergence of Open Ocean Deoxygenation. *Annual Review of Marine Science*, **10(1)**, 229–260, doi:10.1146/annurev-marine-121916-063359.
Lewis, S.C. et al., 2020: Deconstructing Factors Contributing to the 2018 Fire Weather in Queensland, Australia. *Bulletin of the American Meteorological Society*, **101(1)**, S115–S122, doi:10.1175/bams-d-19-0144.1.
Lewkowicz, A.G. and R.G. Way, 2019: Extremes of summer climate trigger thousands of thermokarst landslides in a High Arctic environment. *Nature Communications*, **10(1)**, 1329, doi:10.1038/s41467-019-09314-7.
Leys, J.F., S.K. Heidenreich, C.L. Strong, G.H. McTainsh, and S. Quigley, 2011: PM10 concentrations and mass

ACCEPTED VERSION SUBJECT TO FINAL EDITS

transport during “Red Dawn” – Sydney 23 September 2009. *Aeolian Research*, **3(3)**, 327–342, doi:10.1016/j.aeolia.2011.06.003.
Li, B., Y. Chen, and X. Shi, 2020: Does elevation dependent warming exist in high mountain Asia? *Environmental Research Letters*, **15(2)**, 024012, doi:10.1088/1748-9326/ab6d7f.
Li, C. et al., 2018: Midlatitude atmospheric circulation responses under 1.5 and 2.0°C warming and implications for regional impacts. *Earth System Dynamics*, **9(2)**, 359–382, doi:10.5194/esd-9-359-2018.
Li, C. et al., 2020: Changes in annual extremes of daily temperature and precipitation in CMIP6 models. *Journal of Climate*, doi:10.1175/jcli-d-19-1013.1.
Li, C.-, Y.- Chai, L.- Yang, and H.- Li, 2016: Spatio-temporal distribution of flood disasters and analysis of influencing factors in Africa. *Natural Hazards*, **82(1)**, 721–731.
Li, D. et al., 2020: Historical Evaluation and Future Projections of 100-m Wind Energy Potentials Over CORDEX-East Asia. *Journal of Geophysical Research: Atmospheres*, **125(15)**, e2020JD032874, doi:10.1029/2020jd032874.
Li, F., P.H.A.J.M. van Gelder, R. Ranasinghe, D.P. Callaghan, and R.B. Jongejan, 2014: Probabilistic modelling of extreme storms along the Dutch coast. *Coastal Engineering*, **86**, 1–13, doi:10.1016/j.coastaleng.2013.12.009.
Li, F. et al., 2013: Probabilistic modeling of wave climate and predicting dune erosion. *Journal of Coastal Research*, **65**, 760–765, doi:10.2112/si65-129.1.
Li, G. et al., 2018: Indices of Canada’s future climate for general and agricultural adaptation applications. *Climatic Change*, **148(1–2)**, 249–263, doi:10.1007/s10584-018-2199-x.
Li, H., H. Li, J. Wang, and X. Hao, 2020: Monitoring high-altitude river ice distribution at the basin scale in the northeastern Tibetan Plateau from a Landsat time-series spanning 1999–2018. *Remote Sensing of Environment*, **247**, 111915, doi:10.1016/j.rse.2020.111915.
Li, J., Y.D. Chen, T.Y. Gan, and N.C. Lau, 2018: Elevated increases in human-perceived temperature under climate warming. *Nature Climate Change*, **8(1)**, 43–47, doi:10.1038/s41558-017-0036-2.
Li, L. et al., 2019: Future projections of extreme temperature events in different sub-regions of China. *Atmospheric Research*, **217**, 150–164, doi:10.1016/j.atmosres.2018.10.019.
Li, M., Q. Zhang, and F. Zhang, 2016: Hail Day Frequency Trends and Associated Atmospheric Circulation Patterns over China during 1960–2012. *Journal of Climate*, **29(19)**, 7027–7044, doi:10.1175/jcli-d-15-0500.1.
Li, N., Y. Yamazaki, V. Roeber, K.F. Cheung, and G. Chock, 2018: Probabilistic mapping of storm-induced coastal inundation for climate change adaptation. *Coastal Engineering*, **133**, 126–141, doi:10.1016/j.coastaleng.2017.12.013.
Li, R.C.Y., W. Zhou, C.M. Shun, and T.C. Lee, 2017: Change in destructiveness of landfalling tropical cyclones over China in recent decades. *Journal of Climate*, **30(9)**, 3367–3379, doi:10.1175/jcli-d-16-0258.1.
Li, T., R.M. Horton, and P.L. Kinney, 2013: Projections of seasonal patterns in temperature- related deaths for Manhattan, New York. *Nature Climate Change*, **3(8)**, 717–721, doi:10.1038/nclimate1902.
Li, T. et al., 2015: Uncertainties in predicting rice yield by current crop models under a wide range of climatic conditions. *Global Change Biology*, **21(3)**, 1328–1341, doi:10.1111/gcb.12758.
Li, W., Y. Chen, and W. Chen, 2021: The emergence of anthropogenic signal in mean and extreme precipitation trend over China by using two large ensembles. *Environmental Research Letters*, **16(1)**, 14052, doi:10.1088/1748-9326/abd26d.
Li, W., Z. Jiang, X. Zhang, and L. Li, 2018: On the Emergence of Anthropogenic Signal in Extreme Precipitation Change Over China. *Geophysical Research Letters*, **45(17)**, 9179–9185, doi:10.1029/2018gl079133.
Li, X., D. Jiang, and F. Liu, 2016: Dynamics of amino acid carbon and nitrogen and relationship with grain protein in wheat under elevated CO2 and soil warming. *Environmental and Experimental Botany*, **132**, 121–129, doi:10.1016/j.envexpbot.2016.08.013.
Li, Y., W. Yu, K. Wang, and X. Ma, 2019: Comparison of the aridity index and its drivers in eight climatic regions in China in recent years and in future projections. *International Journal of Climatology*, **39(14)**, 5256–5272, doi:10.1002/joc.6137.
Li, Z. and H. Fang, 2016: Impacts of climate change on water erosion: A review. *Earth-Science Reviews*, **163**, 94–117, doi:10.1016/j.earscirev.2016.10.004.
Liang, Y., Y. Wang, Y. Zhao, Y. Lu, and X. Liu, 2019: Analysis and Projection of Flood Hazards over China. *Water*, **11(5)**, 1022, doi:10.3390/w11051022.
Liao, Z., P. Zhai, Y. Chen, and H. Lu, 2018: Atmospheric circulation patterns associated with persistent wet-freezing events over southern China. *International Journal of Climatology*, **38(10)**, 3976–3990, doi:10.1002/joc.5548.
Liao, Z., P. Zhai, Y. Chen, and H. Lu, 2020: Differing mechanisms for the 2008 and 2016 wintertime cold events in southern China. *International Journal of Climatology*, **40(11)**, 4944–4955, doi:10.1002/joc.6498.
Lima, A., D.D. Lovin, P. Hickner, and D.W. Severson, 2016: Evidence for an overwintering population of aedes aegypti in capitol hill Neighborhood, Washington, DC. *American Journal of Tropical Medicine and Hygiene*, **94(1)**, 231–235, doi:10.4269/ajtmh.15-0351.
Lima, F.P. and D.S. Wethey, 2012: Three decades of high-resolution coastal sea surface temperatures reveal more than warming. *Nature Communications*, **3(1)**, 704, doi:10.1038/ncomms1713.
Limsakul, A. and P. Singhruck, 2016: Long-term trends and variability of total and extreme precipitation in Thailand.

ACCEPTED VERSION SUBJECT TO FINAL EDITS

Atmospheric Research, **169**, 301–317, doi:10.1016/j.atmosres.2015.10.015.
Lin, L. et al., 2018: Additional Intensification of Seasonal Heat and Flooding Extreme Over China in a 2°C Warmer World Compared to 1.5°C. *Earth's Future*, **6(7)**, 968–978, doi:10.1029/2018ef000862.
Lin, Y.-K., C.-K. Chang, M.-H. Li, Y.-C. Wu, and Y.-C. Wang, 2012: High-temperature indices associated with mortality and outpatient visits: Characterizing the association with elevated temperature. *Science of The Total Environment*, **427–428**, 41–49, doi:10.1016/j.scitotenv.2012.04.039.
Lindner, M. et al., 2014: Climate change and European forests: What do we know, what are the uncertainties, and what are the implications for forest management? *Journal of Environmental Management*, **146**, 69–83, doi:10.1016/j.jenvman.2014.07.030.
Linsbauer, A. et al., 2016: Modelling glacier-bed overdeepenings and possible future lakes for the glaciers in the Himalaya-Karakoram region. *Annals of Glaciology*, **57(71)**, 119–130, doi: 10.3189/2016aog71a627.
Lionello, P. and L. Scarascia, 2018: The relation between climate change in the Mediterranean region and global warming. *Regional Environmental Change*, **18(5)**, 1481–1493, doi:10.1007/s10113-018-1290-1.
Lionello, P. and L. Scarascia, 2020: The relation of climate extremes with global warming in the Mediterranean region and its north versus south contrast. *Regional Environmental Change*, **20(1)**, 31, doi:10.1007/s10113-020-01610-z.
Lionello, P., D. Conte, L. Marzo, and L. Scarascia, 2017: The contrasting effect of increasing mean sea level and decreasing storminess on the maximum water level during storms along the coast of the Mediterranean Sea in the mid 21st century. *Global and Planetary Change*, **151**, 80–91, doi:10.1016/j.gloplacha.2016.06.012.
Lionello, P. et al., 2016: Objective climatology of cyclones in the Mediterranean region: a consensus view among methods with different system identification and tracking criteria. *Tellus A: Dynamic Meteorology and Oceanography*, **68(1)**, 29391, doi:10.3402/tellusa.v68.29391.
Littell, J.S., D.L. Peterson, K.L. Riley, Y. Liu, and C.H. Luce, 2016: A review of the relationships between drought and forest fire in the United States. *Global Change Biology*, **22(7)**, 2353–2369, doi:10.1111/gcb.13275.
Liu, G. et al., 2014: Reef-Scale Thermal Stress Monitoring of Coral Ecosystems: New 5-km Global Products from NOAA Coral Reef Watch. *Remote Sensing*, **6(11)**, 11579–11606, doi:10.3390/rs61111579.
Liu, J.C. et al., 2016: Future respiratory hospital admissions from wildfire smoke under climate change in the Western US. *Environmental Research Letters*, **11(12)**, 124018, doi:10.1088/1748-9326/11/12/124018.
Liu, K.S. and J.C.L. Chan, 2019: Inter-decadal variability of the location of maximum intensity of category 4–5 typhoons and its implication on landfall intensity in East Asia. *International Journal of Climatology*, **39(4)**, 1839–1852, doi:10.1002/joc.5919.
Liu, W. et al., 2018a: Global Freshwater Availability Below Normal Conditions and Population Impact Under 1.5 and 2 °C Stabilization Scenarios. *Geophysical Research Letters*, **45(18)**, 9803–9813, doi:10.1029/2018gl078789.
Liu, W. et al., 2018b: Global drought and severe drought-affected populations in 1.5 and 2°C warmer worlds. *Earth System Dynamics*, **9(1)**, 267–283, doi:10.5194/esd-9-267-2018.
Liu, W. et al., 2018c: Global drought and severe drought-affected populations in 1.5 and 2°C warmer worlds. *Earth System Dynamics*, **9(1)**, 267–283, doi:10.5194/esd-9-267-2018.
Liu, X. et al., 2013: Impact of chilling injury and global warming on rice yield in Heilongjiang Province. *Journal of Geographical Sciences*, **23(1)**, 85–97, doi:10.1007/s11442-013-0995-9.
Livneh, B. and A.M. Badger, 2020: Drought less predictable under declining future snowpack. *Nature Climate Change*, **10(5)**, 452–458, doi:10.1038/s41558-020-0754-8.
Lkhamjav, J., H.-G. Jin, H. Lee, and J.-J. Baik, 2017: A hail climatology in Mongolia. *Asia-Pacific Journal of Atmospheric Sciences*, **53(4)**, 501–509, doi:10.1007/s13143-017-0052-1.
Llopart, M., E. Coppola, F. Giorgi, R.P. da Rocha, and S. Cuadra, 2014: Climate change impact on precipitation for the Amazon and La Plata basins. *Climatic Change*, **125(1)**, 111–125, doi:10.1007/s10584-014-1140-1.
Lloyd, E.A. and N. Oreskes, 2018: Climate Change Attribution: When Is It Appropriate to Accept New Methods? *Earth's Future*, **6(3)**, 311–325, doi:10.1002/2017ef000665.
Loarie, S.R. et al., 2009: The velocity of climate change. *Nature*, **462(7276)**, 1052–1055, doi:10.1038/nature08649.
Lobell, D.B. and C. Tebaldi, 2014: Getting caught with our plants down: the risks of a global crop yield slowdown from climate trends in the next two decades. *Environmental Research Letters*, **9(7)**, 074003, doi:10.1088/1748-9326/9/7/074003.
Lobell, D.B., A. Sibley, and J. Ivan Ortiz-Monasterio, 2012: Extreme heat effects on wheat senescence in India. *Nature Climate Change*, **2(3)**, 186–189, doi:10.1038/nclimate1356.
Lobell, D.B. et al., 2013: The critical role of extreme heat for maize production in the United States. *Nature Climate Change*, **3(5)**, 497–501, doi:10.1038/nclimate1832.
Lobell, D.B. et al., 2015: The shifting influence of drought and heat stress for crops in northeast Australia. *Global Change Biology*, **21(11)**, 4115–4127, doi:10.1111/gcb.13022.
Loladze, I., 2014: Hidden shift of the ionome of plants exposed to elevated CO2 depletes minerals at the base of human nutrition. *eLife*, **3**, e02245, doi:10.7554/elife.02245.
López Feldman, A.J. and D. Hernández Cortés, 2016: Cambio climático y agricultura: una revisión de la literatura con énfasis en América Latina. *El Trimestre Económico*, **83(332)**, 459, doi:10.20430/ete.v83i332.231.

ACCEPTED VERSION SUBJECT TO FINAL EDITS

López-Franca, N., P.G. Zaninelli, A.F. Carril, C.G. Menéndez, and E. Sánchez, 2016: Changes in temperature extremes for 21st century scenarios over South America derived from a multi-model ensemble of regional climate models. *Climate Research*, **68(2–3)**, 151–167, doi:10.3354/cr01393.

López-Moreno, J.I., S. Goyette, and M. Beniston, 2009: Impact of climate change on snowpack in the Pyrenees: Horizontal spatial variability and vertical gradients. *Journal of Hydrology*, **374(3–4)**, 384–396, doi:10.1016/j.jhydrol.2009.06.049.

López-Moreno, J.I. et al., 2017: Different sensitivities of snowpacks to warming in Mediterranean climate mountain areas. *Environmental Research Letters*, **12(7)**, 74006, doi:10.1088/1748-9326/aa70cb.

López-Moreno, J.I. et al., 2020: Long-term trends (1958–2017) in snow cover duration and depth in the Pyrenees. *International Journal of Climatology*, **40(14)**, 6122–6136, doi:10.1002/joc.6571.

Losada Carreño, I. et al., 2020: Potential impacts of climate change on wind and solar electricity generation in Texas. *Climatic Change*, **163(2)**, 745–766, doi:10.1007/s10584-020-02891-3.

Lourenço, T.C., R. Swart, H. Goosen, and R. Street, 2016: The rise of demand-driven climate services. *Nature Climate Change*, **6(1)**, 13–14, doi:10.1038/nclimate2836.

Lovelock, C.E. et al., 2015: The vulnerability of Indo-Pacific mangrove forests to sea-level rise. *Nature*, **526(7574)**, 559–563, doi:10.1038/nature15538.

Lowe, R. et al., 2017: Climate services for health: predicting the evolution of the 2016 dengue season in Machala, Ecuador. *The Lancet Planetary Health*, **1(4)**, e142–e151, doi:10.1016/s2542-5196(17)30064-5.

Lu, C., Y. Sun, and X. Zhang, 2018: Multimodel detection and attribution of changes in warm and cold spell durations. *Environmental Research Letters*, **13(7)**, 74013, doi:10.1088/1748-9326/aacb3e.

Lu, C., G. Huang, and X. Wang, 2019: Projected changes in temperature, precipitation, and their extremes over China through the RegCM. *Climate Dynamics*, **53(9)**, 5859–5880, doi:10.1007/s00382-019-04899-7.

Lu, J., G.J. Carbone, and J.M. Grego, 2019: Uncertainty and hotspots in 21st century projections of agricultural drought from CMIP5 models. *Scientific Reports*, **9(1)**, 4922, doi:10.1038/s41598-019-41196-z.

Lu, X., 2019: *Building Resilient Infrastructure for the Future: Background paper for the G20 Climate Sustainability Working Group*. ADB Sustainable Development Working Paper Series No .61, Asian Development Bank (ADB), Manila, Philippines, 38 pp., doi:10.22617/wps190340-2.

Luedeling, E., 2012: Climate change impacts on winter chill for temperate fruit and nut production: A review. *Scientia Horticulturae*, **144**, 218–229, doi:10.1016/j.scienta.2012.07.011.

Lugon, R. and M. Stoffel, 2010: Rock-glacier dynamics and magnitude–frequency relations of debris flows in a high-elevation watershed: Ritigraben, Swiss Alps. *Global and Planetary Change*, **73(3–4)**, 202–210, doi:10.1016/j.gloplacha.2010.06.004.

Luijendijk, A. et al., 2018a: The State of the World's Beaches. *Scientific Reports*, **8(1)**, 6641, doi:10.1038/s41598-018-24630-6.

Luijendijk, A. et al., 2018b: The State of the World's Beaches. *Scientific Reports*, **8(1)**, 6641, doi:10.1038/s41598-018-24630-6.

Luo, M. and N.-C. Lau, 2017: Heat Waves in Southern China: Synoptic Behavior, Long-Term Change, and Urbanization Effects. *Journal of Climate*, **30(2)**, 703–720, doi:10.1175/jcli-d-16-0269.1.

Luo, M. et al., 2019: Spatiotemporal characteristics of future changes in precipitation and temperature in Central Asia. *International Journal of Climatology*, **39(3)**, 1571–1588, doi:10.1002/joc.5901.

Lute, A.C., J.T. Abatzoglou, and K.C. Hegewisch, 2015: Projected changes in snowfall extremes and interannual variability of snowfall in the western United States. *Water Resources Research*, **51(2)**, 960–972, doi:10.1002/2014wr016267.

Lutz, A.F., W.W. Immerzeel, A.B. Shrestha, and M.F.P. Bierkens, 2014: Consistent increase in High Asia's runoff due to increasing glacier melt and precipitation. *Nature Climate Change*, **4(7)**, 587–592, doi:10.1038/nclimate2237.

Lyu, K., X. Zhang, J.A. Church, A.B.A. Slangen, and J. Hu, 2014: Time of emergence for regional sea-level change. *Nature Climate Change*, **4(11)**, 1006–1010, doi:10.1038/nclimate2397.

Mader, T.L., L.J. Johnson, and J.B. Gaughan, 2010: A comprehensive index for assessing environmental stress in animals. *Journal of Animal Science*, **88(6)**, 2153–2165, doi:10.2527/jas.2009-2586.

Madsen, K.S., J.L. Høyer, Suursaar, J. She, and P. Knudsen, 2019: Sea Level Trends and Variability of the Baltic Sea From 2D Statistical Reconstruction and Altimetry. *Frontiers in Earth Science*, **7**, 243, doi:10.3389/feart.2019.00243.

Magnan, A.K. et al., 2019: Cross.Chapter Box 9: Integrative Cross-Chapter Box on Low-Lying Islands and Coasts. *IPCC Special Report on the Ocean and Cryosphere in a Changing Climate*.

Magrin, G., 2015: *Adaptación al cambio climático en América Latina y el Caribe*. Comisión Económica para América Latina y el Caribe (CEPAL), 80 pp.

Mahoney, K., M.A. Alexander, G. Thompson, J.J. Barsugli, and J.D. Scott, 2012: Changes in hail and flood risk in high-resolution simulations over Colorado's mountains. *Nature Climate Change*, **2(2)**, 125–131, doi:10.1038/nclimate1344.

Mair, A., A.G. Johnson, K. Rotzoll, and D.S. Oki, 2019: Estimated groundwater recharge from a water-budget model

ACCEPTED VERSION SUBJECT TO FINAL EDITS

incorporating selected climate projections, Island of Maui, Hawai'i. , 46, doi:10.3133/sir20195064.
Mäkinen, H. et al., 2018: Sensitivity of European wheat to extreme weather. *Field Crops Research*, **222**, 209–217, doi:10.1016/j.fcr.2017.11.008.
Malherbe, J., F.A. Engelbrecht, and W.A. Landman, 2013: Projected changes in tropical cyclone climatology and landfall in the Southwest Indian Ocean region under enhanced anthropogenic forcing. *Climate Dynamics*, **40(11–12)**, 2867–2886, doi:10.1007/s00382-012-1635-2.
Malik, N., B. Bookhagen, and P.J. Mucha, 2016: Spatiotemporal patterns and trends of Indian monsoonal rainfall extremes. *Geophysical Research Letters*, **43(4)**, 1710–1717, doi:10.1002/2016gl067841.
Mallakpour, I. and G. Villarini, 2015: The changing nature of flooding across the central United States. *Nature Climate Change*, **5(3)**, 250–254, doi:10.1038/nclimate2516.
Mallya, G., V. Mishra, D. Niyogi, S. Tripathi, and R.S. Govindaraju, 2016: Trends and variability of droughts over the Indian monsoon region. *Weather and Climate Extremes*, **12**, 43–68, doi:10.1016/j.wace.2016.01.002.
Mandapaka, P. and E.Y.M. Lo, 2018: Assessment of future changes in Southeast Asian precipitation using the NASA Earth Exchange Global Daily Downscaled Projections data set. *International Journal of Climatology*, **38(14)**, 5231–5244, doi:10.1002/joc.5724.
Mangini, W. et al., 2018: Detection of trends in magnitude and frequency of flood peaks across Europe. *Hydrological Sciences Journal*, **63(4)**, 493–512, doi:10.1080/02626667.2018.1444766.
Mann, M.E., E.A. Lloyd, and N. Oreskes, 2017: Assessing climate change impacts on extreme weather events: the case for an alternative (Bayesian) approach. *Climatic Change*, **144(2)**, 131–142, doi:10.1007/s10584-017-2048-3.
Manning, C. et al., 2019: Increased probability of compound long-duration dry and hot events in Europe during summer (1950-2013). *Environmental Research Letters*, **14(9)**, 094006, doi:10.1088/1748-9326/ab23bf.
Manta, G., S. Mello, R. Trinchin, J. Badagian, and M. Barreiro, 2018: The 2017 Record Marine Heatwave in the Southwestern Atlantic Shelf. *Geophysical Research Letters*, **45(22)**, 12,449–12,456, doi:10.1029/2018gl081070.
Maraun, D., 2013: When will trends in European mean and heavy daily precipitation emerge? *Environmental Research Letters*, **8(1)**, 014004, doi:10.1088/1748-9326/8/1/014004.
Maraun, D. et al., 2015: VALUE: A framework to validate downscaling approaches for climate change studies. *Earth's Future*, **3(1)**, 1–14, doi:10.1002/2014ef000259.
Marcos, M. et al., 2019: Increased Extreme Coastal Water Levels Due to the Combined Action of Storm Surges and Wind Waves. *Geophysical Research Letters*, **46(8)**, 4356–4364, doi:10.1029/2019gl082599.
Mardones, P. and R.D. Garreaud, 2020: Future Changes in the Free Tropospheric Freezing Level and Rain–Snow Limit: The Case of Central Chile. *Atmosphere*, **11(11)**, 1259, doi:10.3390/atmos11111259.
Marelle, L., G. Myhre, Hodnebrog, J. Sillmann, and B.H. Samset, 2018: The Changing Seasonality of Extreme Daily Precipitation. *Geophysical Research Letters*, **45(20)**, 11,352– 11,360, doi:10.1029/2018gl079567.
Marengo, J.A. and M. Bernasconi, 2015: Regional differences in aridity/drought conditions over Northeast Brazil: present state and future projections. *Climatic Change*, **129(1–2)**, 103–115, doi:10.1007/s10584-014-1310-1.
Marengo, J.A. and J.C. Espinoza, 2016: Extreme seasonal droughts and floods in Amazonia: causes, trends and impacts. *International Journal of Climatology*, **36(3)**, 1033–1050, doi:10.1002/joc.4420.
Marengo, J.A., L.M. Alves, and R.R. Torres, 2016: Regional climate change scenarios in the Brazilian Pantanal watershed. *Climate Research*, **68(2–3)**, 201–213, doi:10.3354/cr01324.
Marengo, J.A. et al., 2013: Recent Extremes of Drought and Flooding in Amazonia: Vulnerabilities and Human Adaptation. *American Journal of Climate Change*, **02(02)**, 87–96, doi:10.4236/ajcc.2013.22009.
Marengo, J.A. et al., 2018: Changes in Climate and Land Use Over the Amazon Region: Current and Future Variability and Trends. *Frontiers in Earth Science*, **6**, 228, doi:10.3389/feart.2018.00228.
Mariotti, L., I. Diallo, E. Coppola, and F. Giorgi, 2014: Seasonal and intraseasonal changes of African monsoon climates in 21st century CORDEX projections. *Climatic Change*, **125(1)**, 53–65, doi:10.1007/s10584-014-1097-0.
Mariotti, L., E. Coppola, M.B. Sylla, F. Giorgi, and C. Piani, 2011: Regional climate model simulation of projected 21st century climate change over an all-Africa domain: Comparison analysis of nested and driving model results. *Journal of Geophysical Research*, **116(D15)**, D15111, doi:10.1029/2010jd015068.
Marjanac, S. and L. Patton, 2018: Extreme weather event attribution science and climate change litigation: an essential step in the causal chain? *Journal of Energy & Natural Resources Law*, **36(3)**, 265–298, doi:10.1080/02646811.2018.1451020.
Markon, C. et al., 2018: Alaska. In: *Impacts, Risks, and Adaptation in the United States: Fourth National Climate Assessment, Volume II* [Reidmiller, D.R., C.W. Avery, D.R. Easterling, K.E. Kunkel, K.L.M. Lewis, T.K. Maycock, and B.C. Stewart (eds.)]. U.S. Global Change Research Program, Washington, DC, USA, pp. 1185–1241, doi:10.7930/nca4.2018.ch26.
Marotzke, J. et al., 2017: Climate research must sharpen its view. *Nature Climate Change*, **7(2)**, 89–91, doi:10.1038/nclimate3206.
Marra, J.J. and M.C. Kruk, 2017: *State of Environmental Conditions in Hawaii and the U.S. Affiliated Pacific Islands under a Changing Climate: 2017*. National Oceanic and Atmospheric Administration (NOAA) National

ACCEPTED VERSION SUBJECT TO FINAL EDITS

Centers for Environmental Information (NCEI), 93 pp.
Marsooli, R., N. Lin, K. Emanuel, and K. Feng, 2019: Climate change exacerbates hurricane flood hazards along US Atlantic and Gulf Coasts in spatially varying patterns. *Nature Communications*, **10(1)**, 3785, doi:10.1038/s41467-019-11755-z.
Martin, D.A., 2016: At the nexus of fire, water and society. *Philosophical Transactions of the Royal Society B: Biological Sciences*, **371(1696)**, 20150172, doi:10.1098/rstb.2015.0172.
Martinelli, A., D.-D. Kolokotsa, and F. Fiorito, 2020: Urban heat island in Mediterranean coastal cities: The case of Bari (Italy). *Climate*, **8(6)**, 79, doi:10.3390/cli8060079.
Martinez, J.A. and F. Dominguez, 2014: Sources of Atmospheric Moisture for the La Plata River Basin. *Journal of Climate*, **27(17)**, 6737–6753, doi:10.1175/jcli-d-14-00022.1.
Martínez-Alvarado, O. et al., 2018: Increased wind risk from sting-jet windstorms with climate change. *Environmental Research Letters*, **13(4)**, 044002, doi:10.1088/1748-9326/aaae3a.
Martínez-Austria, P.F., E.R. Bandala, and C. Patiño-Gómez, 2016: Temperature and heat wave trends in northwest Mexico. *Physics and Chemistry of the Earth, Parts A/B/C*, **91**, 20–26, doi:10.1016/j.pce.2015.07.005.
Martius, O., S. Pfahl, and C. Chevalier, 2016: A global quantification of compound precipitation and wind extremes. *Geophysical Research Letters*, **43(14)**, 7709–7717, doi:10.1002/2016gl070017.
Marty, C., A.-M. Tilg, and T. Jonas, 2017a: Recent Evidence of Large-Scale Receding Snow Water Equivalents in the European Alps. *Journal of Hydrometeorology*, **18(4)**, 1021–1031, doi:10.1175/jhm-d-16-0188.1.
Marty, C., S. Schlögl, M. Bavay, and M. Lehning, 2017b: How much can we save? Impact of different emission scenarios on future snow cover in the Alps. *The Cryosphere*, **11(1)**, 517–529, doi:10.5194/tc-11-517-2017.
Marx, S.K. et al., 2014: Unprecedented wind erosion and perturbation of surface geochemistry marks the Anthropocene in Australia. *Journal of Geophysical Research: Earth Surface*, **119(1)**, 45–61, doi:10.1002/2013jf002948.
Marzeion, B. et al., 2020: Partitioning the Uncertainty of Ensemble Projections of Global Glacier Mass Change. *Earth's Future*, **8(7)**, e2019EF001470, doi:10.1029/2019ef001470.
Masiokas, M.H. et al., 2020: A Review of the Current State and Recent Changes of the Andean Cryosphere. *Frontiers in Earth Science*, **8**, 99, doi:10.3389/feart.2020.00099.
Mason, L.A. et al., 2016: Fine-scale spatial variation in ice cover and surface temperature trends across the surface of the Laurentian Great Lakes. *Climatic Change*, **138(1–2)**, 71–83, doi:10.1007/s10584-016-1721-2.
Massom, R.A. and S.E. Stammerjohn, 2010: Antarctic sea ice change and variability – Physical and ecological implications. *Polar Science*, **4(2)**, 149–186, doi:10.1016/j.polar.2010.05.001.
Mathis, J., J. Cross, W. Evans, and S. Doney, 2015: Ocean Acidification in the Surface Waters of the Pacific-Arctic Boundary Regions. *Oceanography*, **25(2)**, 122–135, doi:10.5670/oceanog.2015.36.
Mathis, J.T. et al., 2015: Ocean acidification risk assessment for Alaska's fishery sector. *Progress in Oceanography*, **136**, 71–91, doi:10.1016/j.pocean.2014.07.001.
Matin, S. and M. Behera, 2017: Alarming rise in aridity in the Ganga river basin, India, in past 3.5 decades. *Current science*, **112(2)**, 229–230.
Matsumoto, K., K.S. Tokos, and J. Rippke, 2019: Climate projection of lake superior under a future warming scenario. *Journal of Limnology*, **78(3)**, 296–309, doi:10.4081/jlimnol.2019.1902.
Matthes, H., A. Rinke, and K. Dethloff, 2015: Recent changes in Arctic temperature extremes: warm and cold spells during winter and summer. *Environmental Research Letters*, **10(11)**, 114020, doi:10.1088/1748-9326/10/11/114020.
Matthews, L. et al., 2020: Developing climate services for Caribbean tourism: a comparative analysis of climate push and pull influences using climate indices. *Current Issues in Tourism*, 1–19, doi:10.1080/13683500.2020.1816928.
Matthews, T.K.R., R.L. Wilby, and C. Murphy, 2017: Communicating the deadly consequences of global warming for human heat stress. *Proceedings of the National Academy of Sciences*, **114(15)**, 3861–3866, doi:10.1073/pnas.1617526114.
Mauree, D. et al., 2019: A review of assessment methods for the urban environment and its energy sustainability to guarantee climate adaptation of future cities. *Renewable and Sustainable Energy Reviews*, **112**, 733–746, doi:10.1016/j.rser.2019.06.005.
Mavromatidi, A., E. Briche, and C. Claeys, 2018: Mapping and analyzing socio-environmental vulnerability to coastal hazards induced by climate change: An application to coastal Mediterranean cities in France. *Cities*, **72**, 189–200, doi:10.1016/j.cities.2017.08.007.
Maxwell, K.B. et al., 2018: Built Environment, Urban Systems, and Cities.. In: *Impacts, Risks, and Adaptation in the United States: Fourth National Climate Assessment, Volume II* [Reidmiller, D.R., C.W. Avery, D.R. Easterling, K.E. Kunkel, K.L.M. Lewis, T.K. Maycock, and B.C. Stewart (eds.)]. U.S. Global Change Research Program, Washington, DC, USA, pp. 438–478, doi:10.7930/nca4.2018.ch11.
Mazdiyasni, O. et al., 2017: Increasing probability of mortality during Indian heat waves. *Science Advances*, **3(6)**, e1700066, doi:10.1126/sciadv.1700066.
Mbow, C. et al., 2019: Food Security. In: *Climate Change and Land: an IPCC special report on climate change, desertification, land degradation, sustainable land management, food security, and greenhouse gas fluxes in*

ACCEPTED VERSION SUBJECT TO FINAL EDITS

terrestrial ecosystems [Shukla, P.R., J. Skea, E.C. Buendia, V. Masson-Delmotte, H.-O. Pörtner, D.C. Roberts, P. Zhai, R. Slade, S. Connors, R. Diemen, M. Ferrat, E. Haughey, S. Luz, S. Neogi, M. Pathak, J. Petzold, J.P. Pereira, P. Vyas, E. Huntley, K. Kissick, M. Belkacemi, and J. Malley (eds.)]. In Press, pp. 437–550.

McAneney, J., R. van den Honert, and S. Yeo, 2017: Stationarity of major flood frequencies and heights on the Ba River, Fiji, over a 122-year record. *International Journal of Climatology*, **37**, 171–178, doi:10.1002/joc.4989.

McCrary, R.R. and L.O. Mearns, 2019: Quantifying and Diagnosing Sources of Uncertainty in Midcentury Changes in North American Snowpack from NARCCAP. *Journal of Hydrometeorology*, **20(11)**, 2229–2252, doi:10.1175/jhm-d-18-0248.1.

McGree, S. et al., 2019: Recent Changes in Mean and Extreme Temperature and Precipitation in the Western Pacific Islands. *Journal of Climate*, **32(16)**, 4919–4941, doi:10.1175/jcli-d-18-0748.1.

McGregor, G.R. and J.K. Vanos, 2018: Heat: a primer for public health researchers. *Public Health*, **161**, 138–146, doi:10.1016/j.puhe.2017.11.005.

McInnes, K.L. et al., 2016: Natural hazards in Australia: sea level and coastal extremes. *Climatic Change*, **139(1)**, 69–83, doi:10.1007/s10584-016-1647-8.

McKenzie, D. et al., 2014: Smoke consequences of new wildfire regimes driven by climate change. *Earth's Future*, **2(2)**, 35–59, doi:10.1002/2013ef000180.

Mclay, J.G., E.A. Hendricks, and J.R. Moskaitis, 2019: High-resolution seeded simulations of western North Pacific Ocean tropical cyclones in two future extreme climates. *Journal of Climate*, **32(2)**, 309–334, doi:10.1175/jcli-d-18-0353.1.

McLean, N.M., T.S. Stephenson, M.A. Taylor, and J.D. Campbell, 2015: Characterization of Future Caribbean Rainfall and Temperature Extremes across Rainfall Zones. *Advances in Meteorology*, **2015**, 425987, doi:10.1155/2015/425987.

McLean, R. and P. Kench, 2015: Destruction or persistence of coral atoll islands in the face of 20th and 21st century sea-level rise? *Wiley Interdisciplinary Reviews: Climate Change*, **6(5)**, 445–463, doi:10.1002/wcc.350.

McMillan et al., 2012: The Urban Impacts Toolbox. *Weather and Climate*, **32(2)**, 21, doi:10.2307/26169731.

McMillan, H., B. Jackson, and S. Poyck, 2010: *Flood Risk Under Climate Change: A framework for assessing the impacts of climate change on river flow and floods, using dynamically-downscaled climate scenarios. A case study for the Uawa (East Cape) and Waihou (Northland) catchments*. National Institute of Water and Atmospheric Research (NIWA), Christchurch, New Zealand, 63 pp.

McVicar, T.R. et al., 2012: Global review and synthesis of trends in observed terrestrial near-surface wind speeds: Implications for evaporation. *Journal of Hydrology*, **416–417**, 182–205, doi:10.1016/j.jhydrol.2011.10.024.

Cramer, W., J. Guiot, and K. Marini (eds.), 2020: *Climate and Environmental Change in the Mediterranean Basin – Current Situation and Risks for the Future. First Mediterranean Assessment Report*. Union for the Mediterranean, Plan Bleu, UNEP/MAP, Marseille, France, 600 pp.

Mediero, L., D. Santillán, L. Garrote, and A. Granados, 2014: Detection and attribution of trends in magnitude, frequency and timing of floods in Spain. *Journal of Hydrology*, **517**, 1072–1088, doi:10.1016/j.jhydrol.2014.06.040.

Medlock, J.M. et al., 2013: Driving forces for changes in geographical distribution of Ixodes ricinus ticks in Europe. *Parasites & Vectors*, **6(1)**, 1, doi:10.1186/1756-3305-6-1.

Mei, W. and S.P. Xie, 2016: Intensification of landfalling typhoons over the northwest Pacific since the late 1970s. *Nature Geoscience*, **9(10)**, 753–757, doi:10.1038/ngeo2792.

Meixner, T. et al., 2016: Implications of projected climate change for groundwater recharge in the western United States. *Journal of Hydrology*, **534**, 124–138, doi:10.1016/j.jhydrol.2015.12.027.

Mekis, L.A. Vincent, M.W. Shephard, and X. Zhang, 2015: Observed Trends in Severe Weather Conditions Based on Humidex, Wind Chill, and Heavy Rainfall Events in Canada for 1953–2012. *Atmosphere-Ocean*, **53(4)**, 383–397, doi:10.1080/07055900.2015.1086970.

Melchiorre, C. and P. Frattini, 2012: Modelling probability of rainfall-induced shallow landslides in a changing climate, Otta, Central Norway. *Climatic Change*, **113(2)**, 413–436, doi:10.1007/s10584-011-0325-0.

Melet, A., B. Meyssignac, R. Almar, and G. Le Cozannet, 2018: Under-estimated wave contribution to coastal sea-level rise. *Nature Climate Change*, **8(3)**, 234–239, doi:10.1038/s41558-018-0088-y.

Melvin, A.M. et al., 2017: Climate change damages to Alaska public infrastructure and the economics of proactive adaptation. *Proceedings of the National Academy of Sciences*, **114(2)**, E122–E131, doi:10.1073/pnas.1611056113.

Mentaschi, L., M.I. Vousdoukas, E. Voukouvalas, A. Dosio, and L. Feyen, 2017: Global changes of extreme coastal wave energy fluxes triggered by intensified teleconnection patterns. *Geophysical Research Letters*, **44(5)**, 2416–2426, doi:10.1002/2016gl072488.

Mentaschi, L., M.I. Vousdoukas, J.-F. Pekel, E. Voukouvalas, and L. Feyen, 2018: Global long-term observations of coastal erosion and accretion. *Scientific Reports*, **8(1)**, 12876, doi:10.1038/s41598-018-30904-w.

Meredith, M. et al., 2019: Polar Regions. In: *IPCC Special Report on the Ocean and Cryosphere in a Changing Climate* [Pörtner, H.-O., D.C. Roberts, V. Masson-Delmotte, P. Zhai, M. Tignor, E. Poloczanska, K. Mintenbeck, A. Alegría, M. Nicolai, A. Okem, J. Petzold, B. Rama, and N.M. Weyer (eds.)]. In Press, pp. 203–320.

ACCEPTED VERSION SUBJECT TO FINAL EDITS

Mernild, S.H., E. Hanna, J.C. Yde, J. Cappelen, and J.K. Malmros, 2014: Coastal Greenland air temperature extremes and trends 1890-2010: annual and monthly analysis. *International Journal of Climatology*, **34(5)**, 1472–1487, doi:10.1002/joc.3777.

Mernild, S.H., G.E. Liston, C.A. Hiemstra, J.C. Yde, and G. Casassa, 2018: Annual River Runoff Variations and Trends for the Andes Cordillera. *Journal of Hydrometeorology*, **19(7)**, 1167–1189, doi:10.1175/jhm-d-17-0094.1.

Mernild, S.H. et al., 2017: The Andes Cordillera. Part I: snow distribution, properties, and trends (1979-2014). *International Journal of Climatology*, **37(4)**, 1680–1698, doi:10.1002/joc.4804.

Merrifield, M.A., J.M. Becker, M. Ford, and Y. Yao, 2014: Observations and estimates of wave-driven water level extremes at the Marshall Islands. *Geophysical Research Letters*, **41(20)**, 7245–7253, doi:10.1002/2014gl061005.

Messina, J.P. et al., 2019: The current and future global distribution and population at risk of dengue. *Nature Microbiology*, **4(9)**, 1508–1515, doi:10.1038/s41564-019-0476-8.

MfE, 2018: *Climate Change Projections for New Zealand: Atmosphere Projections Based on Simulations from the IPCC Fifth Assessment, 2nd Edition*. Ministry for the Environment (MfE), Wellington, New Zealand, 131 pp.

MfE and Stats NZ, 2017: *Our atmosphere and climate 2017*. New Zealand's Environmental Reporting Series, Ministry for the Environment (MfE) and Stats NZ, New Zealand, 58 pp.

MfE and Stats NZ, 2020: *Our atmosphere and climate 2020*. New Zealand's Environmental Reporting Series, Ministry for the Environment (MfE) and Stats NZ, New Zealand, 79 pp.

Miao, H. et al., 2020: Evaluation of Northern Hemisphere surface wind speed and wind power density in multiple reanalysis datasets. *Energy*, **200**, 117382, doi:10.1016/j.energy.2020.117382.

Micu, D.M., A. Dumitrescu, S. Cheval, I.-A. Nita, and M.-V. Birsan, 2021: Temperature changes and elevation-warming relationships in the Carpathian Mountains. *International Journal of Climatology*, **41(3)**, 2154–2172, doi:10.1002/joc.6952.

Middleton, N., P. Tozer, and B. Tozer, 2019: Sand and dust storms: underrated natural hazards. *Disasters*, **43(2)**, 390–409, doi:10.1111/disa.12320.

Millar, C.I. and N.L. Stephenson, 2015: Temperate forest health in an era of emerging megadisturbance. *Science*, **349(6250)**, 823–826, doi:10.1126/science.aaa9933.

Mills, L.S. et al., 2013: Camouflage mismatch in seasonal coat color due to decreased snow duration. *Proceedings of the National Academy of Sciences*, **110(18)**, 7360–7365, doi:10.1073/pnas.1222724110.

Mills, M. et al., 2016: Perceived and projected flood risk and adaptation in coastal Southeast Queensland, Australia. *Climatic Change*, **136(3–4)**, 523–537, doi:10.1007/s10584-016-1644-y.

Milner, A.M. et al., 2017: Glacier shrinkage driving global changes in downstream systems. *Proceedings of the National Academy of Sciences of the United States of America*, **114(37)**, 9770–9778, doi:10.1073/pnas.1619807114.

Minderhoud, P.S.J., H. Middelkoop, G. Erkens, and E. Stouthamer, 2020: Groundwater extraction may drown mega-delta: projections of extraction-induced subsidence and elevation of the Mekong delta for the 21st century. *Environmental Research Communications*, **2(1)**, 011005, doi:10.1088/2515-7620/ab5e21.

Minderhoud, P.S.J., L. Coumou, G. Erkens, H. Middelkoop, and E. Stouthamer, 2019: Mekong delta much lower than previously assumed in sea-level rise impact assessments. *Nature Communications*, **10(1)**, 3847, doi:10.1038/s41467-019-11602-1.

Minderhoud, P.S.J. et al., 2017: Impacts of 25 years of groundwater extraction on subsidence in the Mekong delta, Vietnam. *Environmental Research Letters*, **12(6)**, 64006, doi:10.1088/1748-9326/aa7146.

Mirzabaev, A. et al., 2019: Chapter 3: Desertification. *Climate Change and Land: an IPCC special report on climate change, desertification, land degradation, sustainable land management, food security, and greenhouse gas fluxes in terrestrial ecosystems [P.R. Shukla, J. Skea, E. Calvo Buendia, V. Masson-Delmot.*

Mishra, V., 2020: Long-term (1870–2018) drought reconstruction in context of surface water security in India. *Journal of Hydrology*, **580**, 124228, doi:10.1016/j.jhydrol.2019.124228.

Mishra, V., S. Mukherjee, R. Kumar, and D.A. Stone, 2017a: Heat wave exposure in India in current, 1.5 °C, and 2.0 °C worlds. *Environmental Research Letters*, **12(12)**, 124012, doi:10.1088/1748-9326/aa9388.

Mishra, V., S. Mukherjee, R. Kumar, and D.A. Stone, 2017b: Heat wave exposure in India in current, 1.5°C, and 2.0°C worlds. *Environmental Research Letters*, **12(12)**, 124012, doi:10.1088/1748-9326/aa9388.

Mitchell, D. et al., 2017: Half a degree additional warming, prognosis and projected impacts (HAPPI): background and experimental design. *Geoscientific Model Development*, **10(2)**, 571–583, doi:10.5194/gmd-10-571-2017.

Mock, C.J. and K.W. Birkeland, 2000: Snow Avalanche Climatology of the Western United States Mountain Ranges. *Bulletin of the American Meteorological Society*, **81(10)**, 2367–2392, doi:10.1175/1520-0477(2000)081<2367:sacotw>2.3.co;2.

Mock, C.J., K.C. Carter, and K.W. Birkeland, 2017: Some Perspectives on Avalanche Climatology. *Annals of the American Association of Geographers*, **107(2)**, 299–308, doi:10.1080/24694452.2016.1203285.

MOE, MEXT, MAFF, MLIT, and JMA, 2018: *Climate Change in Japan and Its Impacts*. Ministry of the Environment (MOE), Ministry of Education, Culture, Sports, Science and Technology (MEXT), Ministry of Agriculture,

ACCEPTED VERSION SUBJECT TO FINAL EDITS

Forestry and Fisheries (MAFF), Ministry of Land, Infrastructure, Transport and Tourism (MLIT) and Japan Meteorological Agenc, Japan, 8 pp.
Moemken, J., M. Reyers, H. Feldmann, and J.G. Pinto, 2018: Future Changes of Wind Speed and Wind Energy Potentials in EURO-CORDEX Ensemble Simulations. *Journal of Geophysical Research: Atmospheres*, **123(12)**, 6373–6389, doi:10.1029/2018jd028473.
Mohammed, K. et al., 2018: Future Floods in Bangladesh under 1.5° C, 2° C, and 4° C Global Warming Scenarios. *Journal of Hydrologic Engineering*, **23(12)**, 04018050, doi:10.1061/(asce)he.1943-5584.0001705.
Mohammed, R. and M. Scholz, 2018: Critical review of salinity intrusion in rivers and estuaries. *Journal of Water and Climate Change*, **9(1)**, 1–16, doi:10.2166/wcc.2017.334.
Mohr, S., M. Kunz, and B. Geyer, 2015a: Hail potential in Europe based on a regional climate model hindcast. *Geophysical Research Letters*, **42(24)**, 10,904–10,912, doi:10.1002/2015gl067118.
Mohr, S., M. Kunz, and K. Keuler, 2015b: Development and application of a logistic model to estimate the past and future hail potential in Germany. *Journal of Geophysical Research: Atmospheres*, **120(9)**, 3939–3956, doi:10.1002/2014jd022959.
Mölter, T., D. Schindler, A. Albrecht, and U. Kohnle, 2016: Review on the Projections of Future Storminess over the North Atlantic European Region. *Atmosphere*, **7(4)**, 60, doi:10.3390/atmos7040060.
Monaco, C.J. and C.D. McQuaid, 2019: Climate warming reduces the reproductive advantage of a globally invasive intertidal mussel. *Biological Invasions*, **21(7)**, 2503–2516, doi:10.1007/s10530-019-01990-2.
Monaghan, A.J. et al., 2018: The potential impacts of 21st century climatic and population changes on human exposure to the virus vector mosquito Aedes aegypti. *Climatic Change*, **146(3–4)**, 487–500, doi:10.1007/s10584-016-1679-0.
Mondoro, A., D.M. Frangopol, and L. Liu, 2018: Bridge Adaptation and Management under Climate Change Uncertainties: A Review. *Natural Hazards Review*, **19(1)**, 04017023, doi:10.1061/(asce)nh.1527-6996.0000270.
Monioudi, I.N. et al., 2017: Assessment of island beach erosion due to sea level rise: the case of the Aegean archipelago (Eastern Mediterranean). *Natural Hazards and Earth System Sciences*, **17(3)**, 449–466, doi:10.5194/nhess-17-449-2017.
Monsieurs, E., O. Dewitte, and A. Demoulin, 2019: A susceptibility-based rainfall threshold approach for landslide occurrence. *Natural Hazards and Earth System Sciences*, **19(4)**, 775–789, doi:10.5194/nhess-19-775-2019.
Montroull, N.B., R.I. Saurral, and I.A. Camilloni, 2018: Hydrological impacts in La Plata basin under 1.5, 2 and 3°C global warming above the pre-industrial level. *International Journal of Climatology*, **38(8)**, 3355–3368, doi:10.1002/joc.5505.
Moore, J.K. et al., 2018: Sustained climate warming drives declining marine biological productivity. *Science*, **359(6380)**, 1139–1143, doi:10.1126/science.aao6379.
Mora, C. et al., 2017: Global risk of deadly heat. *Nature Climate Change*, **7(7)**, 501–506, doi:10.1038/nclimate3322.
Mora, C. et al., 2018: Broad threat to humanity from cumulative climate hazards intensified by greenhouse gas emissions. *Nature Climate Change*, **8(12)**, 1062–1071, doi:10.1038/s41558-018-0315-6.
Mordecai, E.A. et al., 2013: Optimal temperature for malaria transmission is dramatically lower than previously predicted. *Ecology Letters*, **16(1)**, 22–30, doi:10.1111/ele.12015.
Mordecai, E.A. et al., 2017: Detecting the impact of temperature on transmission of Zika, dengue, and chikungunya using mechanistic models. *PLOS Neglected Tropical Diseases*, **11(4)**, e0005568, doi:10.1371/journal.pntd.0005568.
Mori, M., Y. Kosaka, M. Watanabe, H. Nakamura, and M. Kimoto, 2019: A reconciled estimate of the influence of Arctic sea-ice loss on recent Eurasian cooling. *Nature Climate Change*, **9(2)**, 123–129, doi:10.1038/s41558-018-0379-3.
Morin, S. et al., 2018: The mountain component of the Copernicus Climate Change Services – Sectoral Information Service "European Tourism": towards pan-European analysis and projections of natural and managed snow conditions. In: *Proceedings, International Snow Science Workshop, Innsbruck, Austria, 2018*. pp. 542–547.
Moritz, M.A. et al., 2012: Climate change and disruptions to global fire activity. *Ecosphere*, **3(6)**, art49, doi:10.1890/es11-00345.1.
Mortlock, T., I. Goodwin, J. McAneney, and K. Roche, 2017: The June 2016 Australian East Coast Low: Importance of Wave Direction for Coastal Erosion Assessment. *Water*, **9(2)**, 121, doi:10.3390/w9020121.
Moss, B., 2011: Allied attack: climate change and eutrophication. *Inland Waters*, **1(2)**, 101–105, doi:10.5268/iw-1.2.359.
Moss, R.H. et al., 2010: The next generation of scenarios for climate change research and assessment. *Nature*, **463(7282)**, 747–756, doi:10.1038/nature08823.
Mote, P.W., A.F. Hamlet, M.P. Clark, and D.P. Lettenmaier, 2005: Declining Mountain Snowpack in Western North America. *Bulletin of the American Meteorological Society*, **86(1)**, 39–50, doi:10.1175/bams-86-1-39.
Mote, P.W., S. Li, D.P. Lettenmaier, M. Xiao, and R. Engel, 2018: Dramatic declines in snowpack in the western US. *npj Climate and Atmospheric Science*, **1(1)**, 2, doi:10.1038/s41612-018-0012-1.
Mu, J.E., B.M. Sleeter, J.T. Abatzoglou, and J.M. Antle, 2017: Climate impacts on agricultural land use in the USA: the

ACCEPTED VERSION SUBJECT TO FINAL EDITS

role of socio-economic scenarios. *Climatic Change*, **144(2)**, 329–345, doi:10.1007/s10584-017-2033-x.
Mudersbach, C., J. Bender, and F. Netzel, 2017: An analysis of changes in flood quantiles at the gauge Neu Darchau (Elbe River) from 1875 to 2013. *Stochastic Environmental Research and Risk Assessment*, **31(1)**, 145–157, doi:10.1007/s00477-015-1173-7.
Mudryk, L.R. et al., 2018: Canadian snow and sea ice: historical trends and projections. *The Cryosphere*, **12(4)**, 1157–1176, doi:10.5194/tc-12-1157-2018.
Mueller, B. et al., 2015: Lengthening of the growing season in wheat and maize producing regions. *Weather and Climate Extremes*, **9**, 47–56, doi:10.1016/j.wace.2015.04.001.
Mueller, N.D. et al., 2017: Global Relationships between Cropland Intensification and Summer Temperature Extremes over the Last 50 Years. *Journal of Climate*, **30(18)**, 7505–7528, doi:10.1175/jcli-d-17-0096.1.
Mukherjee, S. and V. Mishra, 2018: A sixfold rise in concurrent day and night-time heatwaves in India under 2°C warming.. *Scientific reports*, **8(1)**, 16922, doi:10.1038/s41598-018-35348-w.
Mukherjee, S., A. Mishra, and K.E. Trenberth, 2018: Climate Change and Drought: a Perspective on Drought Indices. *Current Climate Change Reports*, **4(2)**, 145–163, doi:10.1007/s40641-018-0098-x.
Mullan, D. et al., 2017: Climate change and the long-term viability of the World's busiest heavy haul ice road. *Theoretical and Applied Climatology*, **129(3–4)**, 1089–1108, doi:10.1007/s00704-016-1830-x.
Müller, C., J. Elliott, and A. Levermann, 2014: Fertilizing hidden hunger. *Nature Climate Change*, **4(7)**, 540–541, doi:10.1038/nclimate2290.
Murage, P., S. Hajat, and R.S. Kovats, 2017: Effect of night-time temperatures on cause and age-specific mortality in London. *Environmental Epidemiology*, **1(2)**, e005, doi:10.1097/ee9.0000000000000005.
Murakami, H., P.C. Hsu, O. Arakawa, and T. Li, 2014: Influence of model biases on projected future changes in tropical cyclone frequency of occurrence. *Journal of Climate*, **27(5)**, 2159–2181, doi:10.1175/jcli-d-13-00436.1.
Murari, K., S. Ghosh, A. Patwardhan, E. Daly, and K. Salvi, 2015: Intensification of future severe heat waves in India and their effect on heat stress and mortality Intensification of future severe heat waves in India and their effect on heat stress and mortality. *Regional Environmental Change*, doi:10.1007/s10113-014-0660-6.
Musselman, K.N., M.P. Clark, C. Liu, K. Ikeda, and R. Rasmussen, 2017: Slower snowmelt in a warmer world. *Nature Climate Change*, **7(3)**, 214–219, doi:10.1038/nclimate3225.
Muthige, M.S. et al., 2018: Projected changes in tropical cyclones over the South West Indian Ocean under different extents of global warming. *Environmental Research Letters*, **13(6)**, 065019, doi:10.1088/1748-9326/aabc60.
Myers, S.S. et al., 2014: Increasing CO2 threatens human nutrition. *Nature*, **510(7503)**, 139–142, doi:10.1038/nature13179.
Myers, S.S. et al., 2017: Climate Change and Global Food Systems: Potential Impacts on Food Security and Undernutrition. *Annual Review of Public Health*, **38(1)**, 259–277, doi:10.1146/annurev-publhealth-031816-044356.
Myers-Smith, I.H. et al., 2015: Climate sensitivity of shrub growth across the tundra biome. *Nature Climate Change*, **5(9)**, 887–891, doi:10.1038/nclimate2697.
Nabavi, S.O., L. Haimberger, and C. Samimi, 2016: Climatology of dust distribution over West Asia from homogenized remote sensing data. *Aeolian Research*, **21**, 93–107, doi:10.1016/j.aeolia.2016.04.002.
Nabeel, A. and H. Athar, 2020: Stochastic projection of precipitation and wet and dry spells over Pakistan using IPCC AR5 based AOGCMs. *Atmospheric Research*, **234**, 104742, doi:10.1016/j.atmosres.2019.104742.
Nagelkerken, I. and S.D. Connell, 2015: Global alteration of ocean ecosystem functioning due to increasing human CO 2 emissions. *Proceedings of the National Academy of Sciences*, **112(43)**, 13272–13277, doi:10.1073/pnas.1510856112.
Nagelkerken, I. and P.L. Munday, 2016: Animal behaviour shapes the ecological effects of ocean acidification and warming: Moving from individual to community-level responses. *Global Change Biology*, **22(3)**, 974–989, doi:10.1111/gcb.13167.
Nakaegawa, T. and W. Vergara, 2010: First Projection of Climatological Mean River Discharges in the Magdalena River Basin, Colombia, in a Changing Climate during the 21st Century. *Hydrological Research Letters*, **4**, doi:10.3178/hrl.4.50.
Nakaegawa, T., A. Kitoh, S. Kusunoki, H. Murakami, and O. Arakawa, 2014: Hydroclimate changes over Central America and the Caribbean in a global warming climate projected with 20-km and 60-km mesh MRI atmospheric general circulation models. *Papers in Meteorology and Geophysics*, **65**, 15–33, doi:10.2467/mripapers.65.15.
Nangombe, S. et al., 2018: Record-breaking climate extremes in Africa under stabilized 1.5 °C and 2 °C global warming scenarios. *Nature Climate Change*, **8(5)**, 375–380, doi:10.1038/s41558-018-0145-6.
Narama, C. et al., 2018: Large drainages from short-lived glacial lakes in the Teskey Range, Tien Shan Mountains, Central Asia. *Natural Hazards and Earth System Sciences*, **18(4)**, 983–995, doi:10.5194/nhess-18-983-2018.
Narayanan, S., P.V. Prasad, A.K. Fritz, D.L. Boyle, and B.S. Gill, 2015: Impact of High Night-Time and High Daytime Temperature Stress on Winter Wheat. *Journal of Agronomy and Crop Science*, **201(3)**, 206–218, doi:10.1111/jac.12101.

ACCEPTED VERSION SUBJECT TO FINAL EDITS

NASEM, 2012: *Airport Climate Adaptation and Resilience*. National Academies of Sciences, Engineering, and Medicine (NASEM). The National Academies Press, Washington, DC, USA, 87 pp., doi:10.17226/22773.
Nasim, W. et al., 2018: Future risk assessment by estimating historical heat wave trends with projected heat accumulation using SimCLIM climate model in Pakistan. *Atmospheric Research*, **205**, 118–133, doi:10.1016/j.atmosres.2018.01.009.
Naumann, G. et al., 2018: Global Changes in Drought Conditions Under Different Levels of Warming. *Geophysical Research Letters*, **45(7)**, 3285–3296, doi:10.1002/2017gl076521.
Neff, J.C. et al., 2008: Recent increase in eolian dust deposition related to human activity in the Western United States. *Nature Geosciences*, **1**, 189–195.
Nehren, U., A. Kirchner, W. Lange, M. Follador, and D. Anhuf, 2019: Natural Hazards and Climate Change Impacts in the State of Rio de Janeiro: A Landscape Historical Analysis. *Strategies and Tools for a Sustainable Rural Rio de Janeiro*, 313–330, doi:10.1007/978-3-319-89644-1_20.
Neri, A., G. Villarini, L.J. Slater, and F. Napolitano, 2019: On the statistical attribution of the frequency of flood events across the U.S. Midwest. *Advances in Water Resources*, **127**, 225–236, doi:10.1016/j.advwatres.2019.03.019.
Neumann, B., A.T. Vafeidis, J. Zimmermann, and R.J. Nicholls, 2015: Future Coastal Population Growth and Exposure to Sea-Level Rise and Coastal Flooding – A Global Assessment. *PLOS ONE*, **10(3)**, e0118571, doi:10.1371/journal.pone.0118571.
Neumann, J.E. et al., 2015: Climate change risks to US infrastructure: impacts on roads, bridges, coastal development, and urban drainage. *Climatic Change*, **131(1)**, 97–109, doi:10.1007/s10584-013-1037-4.
Newth, D. and D. Gunasekera, 2018: Projected Changes in Wet-Bulb Globe Temperature under Alternative Climate Scenarios. *Atmosphere*, **9(5)**, 187, doi:10.3390/atmos9050187.
Nguyen, T.-H., S.-K. Min, S. Paik, and D. Lee, 2018: Time of emergence in regional precipitation changes: an updated assessment using the CMIP5 multi-model ensemble. *Climate Dynamics*, **51(9)**, 3179–3193, doi:10.1007/s00382-018-4073-y.
Ni, X. et al., 2017: Decreased hail size in China since 1980. *Scientific Reports*, **7(1)**, 10913, doi:10.1038/s41598-017-11395-7.
Nicholls, R.J., 2015: Chapter 9 – Adapting to Sea Level Rise. In: *Coastal and Marine Hazards, Risks, and Disasters* [Shroder, J.F., J.T. Ellis, and D.J. Sherman (eds.)]. Elsevier, Boston, MA, USA, pp. 243–270, doi:10.1016/b978-0-12-396483-0.00009-1.
Nienhuis, J.H. et al., 2020: Global-scale human impact on delta morphology has led to net land area gain. *Nature*, **577(7791)**, 514–518, doi:10.1038/s41586-019-1905-9.
Nik, V.M., A.T.D. Perera, and D. Chen, 2020: Towards climate resilient urban energy systems: a review. *National Science Review*, nwaa134, doi:10.1093/nsr/nwaa134.
Nikulin, G. et al., 2018: The effects of 1.5 and 2 degrees of global warming on Africa in the CORDEX ensemble. *Environmental Research Letters*, **13(6)**, 065003, doi:10.1088/1748-9326/aab1b1.
Ning, L. and R.S. Bradley, 2015: Snow occurrence changes over the central and eastern United States under future warming scenarios.. *Scientific reports*, **5**, 17073, doi:10.1038/srep17073.
Nissan, H. et al., 2019: On the use and misuse of climate change projections in international development. *Wiley Interdisciplinary Reviews: Climate Change*, **10(3)**, e579, doi:10.1002/wcc.579.
Nissen, K.M., G.C. Leckebusch, J.G. Pinto, and U. Ulbrich, 2014: Mediterranean cyclones and windstorms in a changing climate. *Regional Environmental Change*, **14(5)**, 1873–1890, doi:10.1007/s10113-012-0400-8.
Noetzli, J. et al., 2019: Permafrost thermal state [in "State of the Climate in 2018"]. *Bulletin of the American Meteorological Society*, **100(9)**, S21–22, doi:10.1175/2019bamsstateoftheclimate.1.
Norby, R.J., J.M. Warren, C.M. Iversen, B.E. Medlyn, and R.E. McMurtrie, 2010: CO2 enhancement of forest productivity constrained by limited nitrogen availability. *Proceedings of the National Academy of Sciences*, **107(45)**, 19368–19373, doi:10.1073/pnas.1006463107.
Notaro, M., Y. Yu, and O. Kalashnikova, 2015: Regime shift in Arabian dust activity, triggered by persistent Fertile Crescent drought. *Journal of Geophysical Research: Atmospheres*, **120(19)**, 10229–10249, doi:10.1002/2015jd023855.
Notz, D. and SIMIP, 2020: Arctic Sea Ice in CMIP6. *Geophysical Research Letters*, **47(10)**, e2019GL086749, doi:10.1029/2019gl086749.
Nourani, E., N.M. Yamaguchi, and H. Higuchi, 2017: Climate change alters the optimal wind-dependent flight routes of an avian migrant. *Proceedings of the Royal Society B: Biological Sciences*, **284(1854)**, doi:10.1098/rspb.2017.0149.
Nowreen, S., S.B. Murshed, A.K.M.S. Islam, B. Bhaskaran, and M.A. Hasan, 2015: Changes of rainfall extremes around the haor basin areas of Bangladesh using multi-member ensemble RCM. *Theoretical and Applied Climatology*, **119(1–2)**, 363–377, doi:10.1007/s00704-014-1101-7.
Núñez, E., M. Vásquez, B. Beltrán-Luque, and D. Padgett, 2016: Virus Zika en Centroamérica y sus complicaciones (Zika virus in Central America and its complications). *Acta Médica Peruana*, **33(1)**, 42–49.
Nurse, L.A. et al., 2014: Small Islands. In: *Climate Change 2014: Impacts, Adaptation, and Vulnerability. Part B: Regional Aspects. Contribution of working Group II to the Fifth Assessment Report of the Intergovernmental*

ACCEPTED VERSION SUBJECT TO FINAL EDITS

Panel on Climate Change [Barros, V.R., C.B. Field, D.J. Dokken, M.D. Mastrandrea, K.J. Mach, T.E. Bilir, M. Chatterjee, K.L. Ebi, Y.O. Estrada, R.C. Genova, B. Girma, E.S. Kissel, A.N. Levy, S. MacCracken, P.R. Mastrandrea, and L.L. White (eds.)]. Cambridge University Press, Cambridge, United Kingdom and New York, NY, USA, pp. 1613–1654, doi:10.1017/cbo9781107415386.009.

Nyangiwe, N., M. Yawa, and V. Muchenje, 2018: Driving forces for changes in geographic range of cattle ticks (Acari: Ixodidae) in Africa: A review. *South African Journal of Animal Science*, **48(5)**, 829, doi:10.4314/sajas.v48i5.4.

O'Gorman, P.A., 2014: Contrasting responses of mean and extreme snowfall to climate change. *Nature*, **512(7515)**, 416–418, doi:10.1038/nature13625.

O'Grady, J.G. et al., 2019: Extreme Water Levels for Australian Beaches Using Empirical Equations for Shoreline Wave Setup. *Journal of Geophysical Research: Oceans*, **124(8)**, 5468–5484, doi:10.1029/2018jc014871.

O'Loingsigh, T. et al., 2014: The Dust Storm Index (DSI): A method for monitoring broadscale wind erosion using meteorological records. *Aeolian Research*, **12**, 29–40, doi:10.1016/j.aeolia.2013.10.004.

O'Neill, B.C. et al., 2017: IPCC reasons for concern regarding climate change risks. *Nature Climate Change*, **7(1)**, 28–37, doi:10.1038/nclimate3179.

O'Neill, B.C. et al., 2018: The Benefits of Reduced Anthropogenic Climate changE (BRACE): a synthesis. *Climatic Change*, **146(3–4)**, 287–301, doi:10.1007/s10584-017-2009-x.

O'Reilly, C.M. et al., 2015: Rapid and highly variable warming of lake surface waters around the globe. *Geophysical Research Letters*, **42(24)**, 10,710–773,781, doi:10.1002/2015gl066235.

Ogden, N.H., 2017: Climate change and vector-borne diseases of public health significance. *FEMS Microbiology Letters*, **364(19)**, fnx186, doi:10.1093/femsle/fnx186.

Ohba, M., 2019: The Impact of Global Warming on Wind Energy Resources and Ramp Events in Japan. *Atmosphere*, **10(5)**, 265, doi:10.3390/atmos10050265.

Ohba, M. and S. Sugimoto, 2020: Impacts of climate change on heavy wet snowfall in Japan. *Climate Dynamics*, **54(5)**, 3151–3164, doi:10.1007/s00382-020-05163-z.

Olazabal, M., A. Chiabai, S. Foudi, and M.B. Neumann, 2018: Emergence of new knowledge for climate change adaptation. *Environmental Science and Policy*, **83**, 46–53, doi:10.1016/j.envsci.2018.01.017.

Oleson, K.W., G.B. Anderson, B. Jones, S.A. McGinnis, and B. Sanderson, 2018: Avoided climate impacts of urban and rural heat and cold waves over the U.S. using large climate model ensembles for RCP8.5 and RCP4.5. *Climatic Change*, **146(3–4)**, 377–392, doi:10.1007/s10584-015-1504-1.

Oliver, E.C.J. et al., 2018: Longer and more frequent marine heatwaves over the past century. *Nature Communications*, **9(1)**, 1324, doi:10.1038/s41467-018-03732-9.

Olson, D.M. and E. Dinerstein, 2002: The Global 200: Priority Ecoregions for Global Conservation. *Annals of the Missouri Botanical Garden*, **89(2)**, 199–224, doi:10.2307/3298564.

Olsson, L. et al., 2019: Land Degradation. In: *Climate Change and Land: an IPCC special report on climate change, desertification, land degradation, sustainable land management, food security, and greenhouse gas fluxes in terrestrial ecosystems* [Shukla, P.R., J. Skea, E.C. Buendia, V. Masson-Delmotte, H.-O. Pörtner, D.C. Roberts, P. Zhai, R. Slade, S. Connors, R. Diemen, M. Ferrat, E. Haughey, S. Luz, S. Neogi, M. Pathak, J. Petzold, J.P. Pereira, P. Vyas, E. Huntley, K. Kissick, M. Belkacemi, and J. Malley (eds.)]. In Press, pp. 345–436.

Oppenheimer, M. et al., 2019: Sea Level Rise and Implications for Low Lying Islands, Coasts and Communities. In: *IPCC Special Report for the Ocean and Cryosphere in the Changing Climate* [Pörtner, H.-O., D.C. Roberts, V. Masson-Delmotte, P. Zhai, M. Tignor, E. Poloczanska, K. Mintenbeck, A. Alegría, M. Nicolai, A. Okem, J. Petzold, B. Rama, and N.M. Weyer (eds.)]. In Press, pp. 321–446.

Orlov, A., J. Sillmann, A. Aaheim, K. Aunan, and K. de Bruin, 2019: Economic Losses of Heat-Induced Reductions in Outdoor Worker Productivity: a Case Study of Europe. *Economics of Disasters and Climate Change*, **3(3)**, 191–211, doi:10.1007/s41885-019-00044-0.

Orr, S.A., M. Young, D. Stelfox, J. Curran, and H. Viles, 2018: Wind-driven rain and future risk to built heritage in the United Kingdom: Novel metrics for characterising rain spells. *Science of the Total Environment*, **640–641**, 1098–1111, doi:10.1016/j.scitotenv.2018.05.354.

Orru, H., K.L. Ebi, and B. Forsberg, 2017: The Interplay of Climate Change and Air Pollution on Health. *Current environmental health reports*, **4(4)**, 504–513, doi:10.1007/s40572-017-0168-6.

Osland, M.J., N. Enwright, R.H. Day, and T.W. Doyle, 2013: Winter climate change and coastal wetland foundation species: salt marshes vs. mangrove forests in the southeastern United States. *Global Change Biology*, **19(5)**, 1482–1494, doi:10.1111/gcb.12126.

Osuch, M., D. Lawrence, H.K. Meresa, J.J. Napiorkowski, and R.J. Romanowicz, 2017: Projected changes in flood indices in selected catchments in Poland in the 21st century. *Stochastic Environmental Research and Risk Assessment*, **31(9)**, 2435–2457, doi:10.1007/s00477-016-1296-5.

Otkin, J.A. et al., 2018: Flash Droughts: A Review and Assessment of the Challenges Imposed by Rapid-Onset Droughts in the United States. *Bulletin of the American Meteorological Society*, **99(5)**, 911–919, doi:10.1175/bams-d-17-0149.1.

Otto, F.E.L. et al., 2018: Anthropogenic influence on the drivers of the Western Cape drought 2015–2017. *Environmental Research Letters*, **13(12)**, 124010, doi:10.1088/1748-9326/aae9f9.

ACCEPTED VERSION SUBJECT TO FINAL EDITS

Ouédraogo, M. et al., 2018: Farmers' Willingness to Pay for Climate Information Services: Evidence from Cowpea and Sesame Producers in Northern Burkina Faso. *Sustainability*, **10(3)**, 611, doi:10.3390/su10030611.
Outten, S.D. and I. Esau, 2013: Extreme winds over Europe in the ENSEMBLES regional climate models. *Atmospheric Chemistry and Physics*, **13(10)**, 5163–5172, doi:10.5194/acp-13-5163-2013.
Oziel, L. et al., 2017: Role for Atlantic inflows and sea ice loss on shifting phytoplankton blooms in the Barents Sea. *Journal of Geophysical Research: Oceans*, **122(6)**, 5121–5139, doi:10.1002/2016jc012582.
Ozturk, T., M.T. Turp, M. Türkeş, and M.L. Kurnaz, 2017: Projected changes in temperature and precipitation climatology of Central Asia CORDEX Region by using RegCM4.3.5. *Atmospheric Research*, **183**, 296–307, doi:10.1016/j.atmosres.2016.09.008.
Pabón-Caicedo, J.D. et al., 2020: Observed and Projected Hydroclimate Changes in the Andes. *Frontiers in Earth Science*, **8**, 61, doi:10.3389/feart.2020.00061.
Pacchetti, M.B., S. Dessai, S. Bradley, and D.A. Stainforth, 2021: Assessing the Quality of Regional Climate Information. *Bulletin of the American Meteorological Society*, **102(3)**, E476–E491, doi:10.1175/bams-d-20-0008.1.
Pal, J.S. and E.A.B. Eltahir, 2016: Future temperature in southwest Asia projected to exceed a threshold for human adaptability. *Nature Climate Change*, **6(2)**, 197–200, doi:10.1038/nclimate2833.
Palazzi, E., L. Mortarini, S. Terzago, and J. von Hardenberg, 2019: Elevation-dependent warming in global climate model simulations at high spatial resolution. *Climate Dynamics*, **52(5–6)**, 2685–2702, doi:10.1007/s00382-018-4287-z.
Palko, K.G., 2017: Synthesis. In: *Climate risks and adaptation practices for the Canadian transportation sector 2016* [Palko, K. and D.S. Lemmen (eds.)]. Government of Canada, Ottawa, ON, Canada, pp. 12–25.
Pall, P., L.M. Tallaksen, and F. Stordal, 2019: A climatology of rain-on-snow events for Norway. *Journal of Climate*, **32(20)**, 6995–7016, doi:10.1175/jcli-d-18-0529.1.
Panthou, G., A. Mailhot, E. Laurence, and G. Talbot, 2014: Relationship between Surface Temperature and Extreme Rainfalls: A Multi-Time-Scale and Event-Based Analysis. *Journal of Hydrometeorology*, **15(5)**, 1999–2011, doi:10.1175/jhm-d-14-0020.1.
Paprotny, D., M.I. Vousdoukas, O. Morales-Nápoles, S.N. Jonkman, and L. Feyen, 2018: Compound flood potential in Europe. *Hydrol. Earth Syst. Sci. Discuss*, 1–34, doi:10.5194/hess-2018-132.
Parasiewicz, P. et al., 2019: The role of floods and droughts on riverine ecosystems under a changing climate. *Fisheries Management and Ecology*, **26(6)**, 461–473, doi:10.1111/fme.12388.
Paritsis, J. and T.T. Veblen, 2011: Dendroecological analysis of defoliator outbreaks on Nothofagus pumilio and their relation to climate variability in the Patagonian Andes. *Global Change Biology*, **17(1)**, 239–253, doi:10.1111/j.1365-2486.2010.02255.x.
Park Williams, A. et al., 2013: Temperature as a potent driver of regional forest drought stress and tree mortality. *Nature Climate Change*, **3(3)**, 292–297, doi:10.1038/nclimate1693.
Parker, C.L., C.L. Bruyère, P.A. Mooney, and A.H. Lynch, 2018: The response of land-falling tropical cyclone characteristics to projected climate change in northeast Australia. *Climate Dynamics*, **51(9–10)**, 3467–3485, doi:10.1007/s00382-018-4091-9.
Parker, L.E. and J.T. Abatzoglou, 2016: Projected changes in cold hardiness zones and suitable overwinter ranges of perennial crops over the United States. *Environmental Research Letters*, **11(3)**, 034001, doi:10.1088/1748-9326/11/3/034001.
Parker, L.E. and J.T. Abatzoglou, 2019: Warming Winters Reduce Chill Accumulation for Peach Production in the Southeastern United States. *Climate*, **7(8)**, 94, doi:10.3390/cli7080094.
Parker, W.S. and G. Lusk, 2019: Incorporating User Values into Climate Services. *Bulletin of the American Meteorological Society*, **100(9)**, 1643–1650, doi:10.1175/bams-d-17-0325.1.
Parkinson, C.L., 2014: Spatially mapped reductions in the length of the Arctic sea ice season. *Geophysical Research Letters*, **41(12)**, 4316–4322, doi:10.1002/2014gl060434.
Parris, A., S.L. Close, R. Meyer, K. Dow, and G. Garfin, 2016: Evolving the practice of Regional Integrated Sciences and Assessments. In: *Climate in Context: Science and Society Partnering for Adaptation* [Parris, A.S., G.M. Garfin, K. Dow, R. Meyer, and S.L. Close (eds.)]. Wiley Online Books, John Wiley & Sons, Ltd, Chichester, UK, pp. 255–262, doi:10.1002/9781118474785.ch12.
Partain, J.L. et al., 2016: An Assessment of the Role of Anthropogenic Climate Change in the Alaska Fire Season of 2015. *Bulletin of the American Meteorological Society*, **97(12)**, S14–S18, doi:10.1175/bams-d-16-0149.1.
Patt, A., S. Pfenninger, and J. Lilliestam, 2013: Vulnerability of solar energy infrastructure and output to climate change. *Climatic Change*, **121(1)**, 93–102, doi:10.1007/s10584-013-0887-0.
Patton, A.I., S.L. Rathburn, and D.M. Capps, 2019: Landslide response to climate change in permafrost regions. *Geomorphology*, **340**, 116–128, doi:10.1016/j.geomorph.2019.04.029.
Paull, S.H. et al., 2017: Drought and immunity determine the intensity of west nile virus epidemics and climate change impacts. *Proceedings of the Royal Society B: Biological Sciences*, **284(1848)**, 20162078, doi:10.1098/rspb.2016.2078.
Pearce, T., J. Ford, A.C. Willox, and B. Smit, 2015: Inuit Traditional Ecological Knowledge (TEK), Subsistence

ACCEPTED VERSION SUBJECT TO FINAL EDITS

Hunting and Adaptation to Climate Change in the Canadian Arctic. *Arctic*, **68(2)**, 233–245.
Pearce-Higgins, J.W., S.M. Eglington, B. Martay, and D.E. Chamberlain, 2015: Drivers of climate change impacts on bird communities. *Journal of Animal Ecology*, **84(4)**, 943–954, doi:10.1111/1365-2656.12364.
Pederson, G.T. et al., 2011: The Unusual Nature of Recent Snowpack Declines in the North American Cordillera. *Science*, **333(6040)**, 332–335, doi:10.1126/science.1201570.
Pederson, N. et al., 2013: Three centuries of shifting hydroclimatic regimes across the Mongolian Breadbasket. *Agricultural and Forest Meteorology*, **178–179**, 10–20, doi:10.1016/j.agrformet.2012.07.003.
Pedro-Monzonís, M., A. Solera, J. Ferrer, T. Estrela, and J. Paredes-Arquiola, 2015: A review of water scarcity and drought indexes in water resources planning and management. *Journal of Hydrology*, **527**, 482–493, doi:10.1016/j.jhydrol.2015.05.003.
Peel, J.L., R. Haeuber, V. Garcia, A.G. Russell, and L. Neas, 2013: Impact of nitrogen and climate change interactions on ambient air pollution and human health. *Biogeochemistry*, **114(1–3)**, 121–134, doi:10.1007/s10533-012-9782-4.
Peeters, B. et al., 2019: Spatiotemporal patterns of rain-on-snow and basal ice in high Arctic Svalbard: detection of a climate-cryosphere regime shift. *Environmental Research Letters*, **14(1)**, 015002, doi:10.1088/1748-9326/aaefb3.
Peña-Angulo, D. et al., 2020: ECTACI: European Climatology and Trend Atlas of Climate Indices (1979–2017). *Journal of Geophysical Research: Atmospheres*, **125(16)**, e2020JD032798, doi:10.1029/2020jd032798.
Peña-Gallardo, M. et al., 2019: Response of crop yield to different time-scales of drought in the United States: Spatio-temporal patterns and climatic and environmental drivers. *Agricultural and Forest Meteorology*, **264**, 40–55, doi:10.1016/j.agrformet.2018.09.019.
Pendakur, K., 2016: Northern Territories. In: *Climate risks and adaptation practices for the Canadian transportation sector 2016* [Palko, K. and D.S. Lemmen (eds.)]. Government of Canada, Ottawa, ON, Canada, pp. 27–64.
Pender, D., D.P. Callaghan, and H. Karunarathna, 2015: An evaluation of methods available for quantifying extreme beach erosion. *Journal of Ocean Engineering and Marine Energy*, **1(1)**, 31–43, doi:10.1007/s40722-014-0003-1.
Peng, S. et al., 2013: Asymmetric effects of daytime and night-time warming on Northern Hemisphere vegetation. *Nature*, **501(7465)**, 88–92, doi:10.1038/nature12434.
Peng, X. et al., 2018: Spatiotemporal changes in active layer thickness under contemporary and projected climate in the Northern Hemisphere. *Journal of Climate*, **31(1)**, 251–266, doi:10.1175/jcli-d-16-0721.1.
Pepin, N. et al., 2019: An Examination of Temperature Trends at High Elevations Across the Tibetan Plateau: The Use of MODIS LST to Understand Patterns of Elevation-Dependent Warming. *Journal of Geophysical Research: Atmospheres*, **124(11)**, 5738–5756, doi:10.1029/2018jd029798.
Pepler, A.S., B. Trewin, and C. Ganter, 2015: The influences of climate drivers on the Australian snow season. *Australian Meteorological and Oceanographic Journal*, **65(2)**, doi:10.22499/2.6502.002.
Peres, D.J. and A. Cancelliere, 2018: Modeling impacts of climate change on return period of landslide triggering. *Journal of Hydrology*, **567**, 420–434, doi:10.1016/j.jhydrol.2018.10.036.
Perkins-Kirkpatrick, S.E. and P.B. Gibson, 2017: Changes in regional heatwave characteristics as a function of increasing global temperature. *Scientific Reports*, **7(1)**, 12256, doi:10.1038/s41598-017-12520-2.
Perrels, A., T. Frei, F. Espejo, L. Jamin, and A. Thomalla, 2013: Socio-economic benefits of weather and climate services in Europe. *Advances in Science and Research*, **10(1)**, 65–70, doi:10.5194/asr-10-65-2013.
Perry, C.T. et al., 2018: Loss of coral reef growth capacity to track future increases in sea level. *Nature*, **558(7710)**, 396–400, doi:10.1038/s41586-018-0194-z.
Pershing, A., K. Mills, A. Dayton, B. Franklin, and B. Kennedy, 2018: Evidence for Adaptation from the 2016 Marine Heatwave in the Northwest Atlantic Ocean. *Oceanography*, **31(2)**, 152–161, doi:10.5670/oceanog.2018.213.
Pes, M.P. et al., 2017: Climate trends on the extreme winds in Brazil. *Renewable Energy*, **109**, 110–120, doi:10.1016/j.renene.2016.12.101.
Peterson, T.C. et al., 2013: Monitoring and Understanding Changes in Heat Waves, Cold Waves, Floods, and Droughts in the United States: State of Knowledge. *Bulletin of the American Meteorological Society*, **94(6)**, 821–834, doi:10.1175/bams-d-12-00066.1.
Petitti, D.B., D.M. Hondula, S. Yang, S.L. Harlan, and G. Chowell, 2016: Multiple Trigger Points for Quantifying Heat-Health Impacts: New Evidence from a Hot Climate. *Environmental Health Perspectives*, **124(2)**, 176–183, doi:10.1289/ehp.1409119.
Pezij, M., D.C.M. Augustijn, D.M.D. Hendriks, and S.J.M.H. Hulscher, 2019: The role of evidence-based information in regional operational water management in the Netherlands. *Environmental Science and Policy*, **93**, 75–82, doi:10.1016/j.envsci.2018.12.025.
Philip, S. et al., 2020: A protocol for probabilistic extreme event attribution analyses. *Advances in Statistical Climatology, Meteorology and Oceanography*, **6(2)**, 177–203, doi:10.5194/ascmo-6-177-2020.
Pierce, D.W. and D.R. Cayan, 2013: The Uneven Response of Different Snow Measures to Human-Induced Climate Warming. *Journal of Climate*, **26(12)**, 4148–4167, doi:10.1175/jcli-d-12-00534.1.
Pinnegar, J.K., G.H. Engelhard, N.J. Norris, D. Theophille, and R.D. Sebastien, 2019: Assessing vulnerability and

ACCEPTED VERSION SUBJECT TO FINAL EDITS

adaptive capacity of the fisheries sector in Dominica: long-term climate change and catastrophic hurricanes. *ICES Journal of Marine Science*, **76(5)**, 1353–1367, doi:10.1093/icesjms/fsz052.

Pizzolato, L., S.E.L. Howell, J. Dawson, F. Laliberté, and L. Copland, 2016: The influence of declining sea ice on shipping activity in the Canadian Arctic. *Geophysical Research Letters*, **43(23)**, 12,146–12,154, doi:10.1002/2016gl071489.

Pohl, E., C. Grenier, M. Vrac, and M. Kageyama, 2020: Emerging climate signals in the Lena River catchment: a non-parametric statistical approach. *Hydrology and Earth System Sciences*, **24(5)**, 2817–2839, doi:10.5194/hess-24-2817-2020.

Poloczanska, E., O. Hoegh-Guldberg, W. Cheung, H.-O. Pörtner, and M.T. Burrows, 2013: Cross-chapter box on observed Global Responses of Marine Biogeography, Abundance, and Phenology to Climate Change. In: *Climate Change 2014: Impacts, Adaptation, and Vulnerability. Part A: Global and Sectoral Aspects. Contribution of Working Group II to the Fifth Assessment Report of the Intergovernmental Panel on Climate Change* [Field, C.B., V.R. Barros, D.J. Dokken, K.J. Mach, M.D. Mastrandrea, T.E. Bilir, M. Chatterjee, K.L. Ebi, Y.O. Estrada, R.C. Genova, B. Girma, E.S. Kissel, A.N. Levy, S. MacCracken, P.R. Mastrandrea, and L.L. White (eds.)]. Cambridge University Press, Cambridge, United Kingdom and New York, NY, USA, pp. 123–127, doi:10.1017/cbo9781107415379.005.

Poloczanska, E.S. et al., 2013: Global imprint of climate change on marine life. *Nature Climate Change*, **3(10)**, 919–925, doi:10.1038/nclimate1958.

Poloczanska, E.S. et al., 2016: Responses of Marine Organisms to Climate Change across Oceans. *Frontiers in Marine Science*, **3**, 62, doi:10.3389/fmars.2016.00062.

Pope, S., L. Copland, and B. Alt, 2017: Recent Changes in Sea Ice Plugs Along the Northern Canadian Arctic Archipelago. In: *Arctic Ice Shelves and Ice Islands* [Copland, L. and D. Mueller (eds.)]. Springer, Dordrecht, The Netherlands, pp. 317–342, doi:10.1007/978-94-024-1101-0_12.

Porter, J.J. and S. Dessai, 2017: Mini-me: Why do climate scientists' misunderstand users and their needs? *Environmental Science & Policy*, **77**, 9–14, doi:10.1016/j.envsci.2017.07.004.

Pörtner, H.-O. et al., 2014: Ocean systems. In: *Climate Change 2014: Impacts, Adaptation, and Vulnerability. Part A: Global andSectoral Aspects. Contribution of Working Group II to the Fifth Assessment Report of the IntergovernmentalPanel on Climate Change* [Field, C.B., V.R. Barros, D.J. Dokken, K.J. Mach, M.D. Mastrandrea, T.E. Bilir, M. Chatterjee, K.L. Ebi, Y.O. Estrada, R.C. Genova, B. Girma, E.S. Kissel, A.N. Levy, S. MacCracken, P.R. Mastrandrea, and L.L. White (eds.)]. Cambridge University Press, Cambridge, United Kingdom and New York, NY, USA, pp. 411–484, doi:10.1017/cbo9781107415379.011.

Poschlod, B., J. Zscheischler, J. Sillmann, R.R. Wood, and R. Ludwig, 2020: Climate change effects on hydrometeorological compound events over southern Norway. *Weather and Climate Extremes*, **28**, 100253, doi:10.1016/j.wace.2020.100253.

Pour, S.H., A.K.A. Wahab, and S. Shahid, 2020: Spatiotemporal changes in aridity and the shift of drylands in Iran. *Atmospheric Research*, **233**, 104704, doi:10.1016/j.atmosres.2019.104704.

Pragna, P. et al., 2016: Heat Stress and Dairy Cow: Impact on Both Milk Yield and Composition. *International Journal of Dairy Science*, **12(1)**, 1–11, doi:10.3923/ijds.2017.1.11.

Preethi, B., R. Ramya, S.K. Patwardhan, M. Mujumdar, and R.H. Kripalani, 2019: Variability of Indian summer monsoon droughts in CMIP5 climate models. *Climate Dynamics*, **53(3–4)**, 1937–1962, doi:10.1007/s00382-019-04752-x.

Pregnolato, M., A. Ford, V. Glenis, S. Wilkinson, and R. Dawson, 2017: Impact of Climate Change on Disruption to Urban Transport Networks from Pluvial Flooding. *Journal of Infrastructure Systems*, **23(4)**, 04017015, doi:10.1061/(asce)is.1943-555x.0000372.

Prein, A.F. and G.J. Holland, 2018: Global estimates of damaging hail hazard. *Weather and Climate Extremes*, **22**, 10–23, doi:10.1016/j.wace.2018.10.004.

Prein, A.F. et al., 2016: Precipitation in the EURO-CORDEX 0.11° and 0.44° simulations: high resolution, high benefits? *Climate Dynamics*, **46(1–2)**, 383–412, doi:10.1007/s00382-015-2589-y.

Prein, A.F. et al., 2017a: Increased rainfall volume from future convective storms in the US. *Nature Climate Change*, **7(12)**, 880–884, doi:10.1038/s41558-017-0007-7.

Prein, A.F. et al., 2017b: The future intensification of hourly precipitation extremes. *Nature Climate Change*, **7(1)**, 48–52, doi:10.1038/nclimate3168.

Prestemon, J.P. et al., 2016: Projecting wildfire area burned in the south-eastern United States, 2011–60. *International Journal of Wildland Fire*, **25(7)**, 715–729, doi:10.1071/wf15124.

Prinz, R., A. Heller, M. Ladner, L. Nicholson, and G. Kaser, 2018: Mapping the Loss of Mt. Kenya's Glaciers: An Example of the Challenges of Satellite Monitoring of Very Small Glaciers. *Geosciences*, **8(5)**, 174, doi:10.3390/geosciences8050174.

Pritchard, H.D., 2017: Asia's glaciers are a regionally important buffer against drought. *Nature*, **545(7653)**, 169–174, doi:10.1038/nature22062.

Proctor, J., S. Hsiang, J. Burney, M. Burke, and W. Schlenker, 2018: Estimating global agricultural effects of geoengineering using volcanic eruptions. *Nature*, **560(7719)**, 480–483, doi:10.1038/s41586-018-0417-3.

ACCEPTED VERSION SUBJECT TO FINAL EDITS

Prokopy, L.S. et al., 2017: Useful to Usable: Developing usable climate science for agriculture. *Climate Risk Management*, **15**, 1–7, doi:10.1016/j.crm.2016.10.004.
Prudhomme, C. et al., 2014: Hydrological droughts in the 21st century, hotspots and uncertainties from a global multimodel ensemble experiment. *Proceedings of the National Academy of Sciences*, **111(9)**, 3262–3267, doi:10.1073/pnas.1222473110.
Pu, B. and P. Ginoux, 2017: Projection of American dustiness in the late 21st century due to climate change. *Scientific Reports*, **7(1)**, 5553, doi:10.1038/s41598-017-05431-9.
Pu, B. and P. Ginoux, 2018: Climatic factors contributing to long-term variations in surface fine dust concentration in the United States. *Atmospheric Chemistry and Physics*, **18(6)**, 4201–4215, doi:10.5194/acp-18-4201-2018.
Púčik, T. et al., 2017: Future Changes in European Severe Convection Environments in a Regional Climate Model Ensemble. *Journal of Climate*, **30(17)**, 6771–6794, doi:10.1175/jcli-d-16-0777.1.
Qiu, X., X. Yang, Y. Fang, Y. Xu, and F. Zhu, 2018: Impacts of snow disaster on rural livelihoods in southern Tibet-Qinghai Plateau. *International Journal of Disaster Risk Reduction*, **31**, 143–152, doi:10.1016/j.ijdrr.2018.05.007.
Qu, Y., S. Jevrejeva, L.P. Jackson, and J.C. Moore, 2019: Coastal Sea level rise around the China Seas. *Global and Planetary Change*, **172**, 454–463, doi:10.1016/j.gloplacha.2018.11.005.
Querol, X. et al., 2019: Monitoring the impact of desert dust outbreaks for air quality for health studies. *Environment International*, **130**, 104867, doi:10.1016/j.envint.2019.05.061.
Qutbudin, I. et al., 2019: Seasonal Drought Pattern Changes Due to Climate Variability: Case Study in Afghanistan. *Water*, **11(5)**, 1096, doi:10.3390/w11051096.
Ragno, E. et al., 2018: Quantifying Changes in Future Intensity-Duration-Frequency Curves Using Multimodel Ensemble Simulations. *Water Resources Research*, **54(3)**, 1751–1764, doi:10.1002/2017wr021975.
Rahimi, J., A. Malekian, and A. Khalili, 2019: Climate change impacts in Iran: assessing our current knowledge. *Theoretical and Applied Climatology*, **135(1)**, 545–564, doi:10.1007/s00704-018-2395-7.
Rahimi, M., N. Mohammadian, A.R. Vanashi, and K. Whan, 2018: Trends in Indices of Extreme Temperature and Precipitation in Iran over the Period 1960-2014. *Open Journal of Ecology*, **08(07)**, 396–415, doi:10.4236/oje.2018.87024.
Rai, P.K., G.P. Singh, and S.K. Dash, 2020: Projected changes in extreme precipitation events over various subdivisions of India using RegCM4. *Climate Dynamics*, **54(1)**, 247–272, doi:10.1007/s00382-019-04997-6.
Räisänen, J. and J. Eklund, 2012: 21st Century changes in snow climate in Northern Europe: a high-resolution view from ENSEMBLES regional climate models. *Climate Dynamics*, **38(11–12)**, 2575–2591, doi:10.1007/s00382-011-1076-3.
Rajczak, J. and C. Schär, 2017: Projections of Future Precipitation Extremes Over Europe: A Multimodel Assessment of Climate Simulations. *Journal of Geophysical Research: Atmospheres*, **122(20)**, 10,773–10,800, doi:10.1002/2017jd027176.
Ramarao, M.V.S. et al., 2019: On observed aridity changes over the semiarid regions of India in a warming climate. *Theoretical and Applied Climatology*, **136(1)**, 693–702, doi:10.1007/s00704-018-2513-6.
Ramesh, K., A. Matloob, F. Aslam, S.K. Florentine, and B.S. Chauhan, 2017: Weeds in a Changing Climate: Vulnerabilities, Consequences, and Implications for Future Weed Management. *Frontiers in Plant Science*, **8**, 95, doi:10.3389/fpls.2017.00095.
Ramirez-Beltran, N.D. et al., 2017: Analysis of the Heat Index in the Mesoamerica and Caribbean Region. *Journal of Applied Meteorology and Climatology*, **56**, 2905–2925, doi:10.1175/jamc-d-16-0167.1.
Ranasinghe, R., 2016: Assessing climate change impacts on open sandy coasts: A review. *Earth-Science Reviews*, **160**, 320–332, doi:10.1016/j.earscirev.2016.07.011.
Ranasinghe, R. and D. Callaghan, 2017: Assessing Storm Erosion Hazards. In: *Coastal Storms: Processes and Impacts* [Ciavola, P. and G. Coco (eds.)]. John Wiley & Sons, Ltd, Chichester, UK, pp. 241–256, doi:10.1002/9781118937099.ch12.
Ranasinghe, R., C.S. Wu, J. Conallin, T.M. Duong, and E.J. Anthony, 2019: Disentangling the relative impacts of climate change and human activities on fluvial sediment supply to the coast by the world's large rivers: Pearl River Basin, China. *Scientific Reports*, **9(1)**, 9236, doi:10.1038/s41598-019-45442-2.
Rangecroft, S., A.J. Suggitt, K. Anderson, and S. Harrison, 2016: Future climate warming and changes to mountain permafrost in the Bolivian Andes. *Climatic Change*, **137(1–2)**, 231–243, doi:10.1007/s10584-016-1655-8.
Rasoulkhani, K., A. Mostafavi, M.P. Reyes, and M. Batouli, 2020: Resilience planning in hazards-humans-infrastructure nexus: A multi-agent simulation for exploratory assessment of coastal water supply infrastructure adaptation to sea-level rise. *Environmental Modelling and Software*, **125**, 104636, doi:10.1016/j.envsoft.2020.104636.
Ratliff, K.M., A.E. Braswell, and M. Marani, 2015: Spatial response of coastal marshes to increased atmospheric CO2. *Proceedings of the National Academy of Sciences of the United States of America*, **112(51)**, 15580–15584, doi:10.1073/pnas.1516286112.
Ratnayake, H.U., M.R. Kearney, P. Govekar, D. Karoly, and J.A. Welbergen, 2019: Forecasting wildlife die-offs from extreme heat events. *Animal Conservation*, **22(4)**, 386–395, doi:10.1111/acv.12476.

ACCEPTED VERSION SUBJECT TO FINAL EDITS

Raymond, C. et al., 2020: Understanding and managing connected extreme events. *Nature Climate Change*, **10(7)**, 611–621, doi:10.1038/s41558-020-0790-4.
Reboita, M.S., R.P. da Rocha, C.G. Dias, and R.Y. Ynoue, 2014: Climate Projections for South America: RegCM3 Driven by HadCM3 and ECHAM5. *Advances in Meteorology*, **2014**, 1–17, doi:10.1155/2014/376738.
Reboita, M.S., R.P. da Rocha, M.R. de Souza, and M. Llopart, 2018: Extratropical cyclones over the southwestern South Atlantic Ocean: HadGEM2-ES and RegCM4 projections. *International Journal of Climatology*, **38(6)**, 2866–2879, doi:10.1002/joc.5468.
Reboita, M.S. et al., 2020: Future changes in the wintertime cyclonic activity over the CORDEX-CORE southern hemisphere domains in a multi-model approach. *Climate Dynamics*, 1–17, doi:10.1007/s00382-020-05317-z.
Refatti, J.P. et al., 2019: High [CO2] and Temperature Increase Resistance to Cyhalofop-Butyl in Multiple-Resistant Echinochloa colona. *Frontiers in Plant Science*, **10**, 529, doi:10.3389/fpls.2019.00529.
Reid, C.E. and J.L. Gamble, 2009: Aeroallergens, allergic disease, and climate change: Impacts and adaptation. *EcoHealth*, **6(3)**, 458–470, doi:10.1007/s10393-009-0261-x.
Reinecke, S., 2015: Knowledge brokerage designs and practices in four european climate services: A role model for biodiversity policies? *Environmental Science and Policy*, doi:10.1016/j.envsci.2015.08.007.
Reisinger, A. et al., 2014: Australasia. In: *Climate Change 2014: Impacts, Adaptation, and Vulnerability. Part B: Regional Aspects. Contribution of Working Group II to the Fifth Assessment Report of the Intergovernmental Panel on Climate Change* [Barros, V.R., C.B. Field, D.J. Dokken, M.D. Mastrandrea, K.J. Mach, T.E. Bilir, M. Chatterjee, K.L. Ebi, Y.O. Estrada, R.C. Genova, B. Girma, E.S. Kissel, A.N. Levy, S. MacCracken, P.R. Mastrandrea, and L.L.White (eds.)]. Cambridge University Press, Cambridge, United Kingdom and New York, NY, USA, pp. 1371–1438, doi:10.1017/cbo9781107415386.005.
Reisinger, A. et al., 2020: *The Concept of Risk in the IPCC Sixth Assessment Report: A Summary of Cross-Working Group Discussions*. Intergovernmental Panel on Climate Change, Geneva, Switzerland, 15 pp.
Ren, W. et al., 2011: Impacts of tropospheric ozone and climate change on net primary productivity and net carbon exchange of China's forest ecosystems. *Global Ecology and Biogeography*, **20(3)**, 391–406, doi:10.1111/j.1466-8238.2010.00606.x.
Ren, X., H. He, L. Zhang, and G. Yu, 2018: Global radiation, photosynthetically active radiation, and the diffuse component dataset of China, 1981–2010. *Earth System Science Data*, **10(3)**, 1217–1226, doi:10.5194/essd-10-1217-2018.
Reyer, C.P.O. et al., 2017a: Climate change impacts in Latin America and the Caribbean and their implications for development. *Regional Environmental Change*, **17(6)**, 1601–1621, doi:10.1007/s10113-015-0854-6.
Reyer, C.P.O. et al., 2017b: Climate change impacts in Central Asia and their implications for development. *Regional Environmental Change*, **17(6)**, 1639–1650, doi:10.1007/s10113-015-0893-z.
Rhoades, A.M., P.A. Ullrich, and C.M. Zarzycki, 2018: Projecting 21st century snowpack trends in western USA mountains using variable-resolution CESM. *Climate Dynamics*, **50(1–2)**, 261–288, doi:10.1007/s00382-017-3606-0.
Ridley, D.A., C.L. Heald, and J.M. Prospero, 2014: What controls the recent changes in African mineral dust aerosol across the Atlantic? *Atmospheric Chemistry and Physics*, **14(11)**, 5735–5747, doi:10.5194/acp-14-5735-2014.
Riebesell, U. et al., 2018: Toxic algal bloom induced by ocean acidification disrupts the pelagic food web. *Nature Climate Change*, **8(12)**, 1082–1086, doi:10.1038/s41558-018-0344-1.
Risser, M.D. and M.F. Wehner, 2017: Attributable Human-Induced Changes in the Likelihood and Magnitude of the Observed Extreme Precipitation during Hurricane Harvey. *Geophysical Research Letters*, **44(24)**, 12,457–12,464, doi:10.1002/2017gl075888.
Ritphring, S., C. Somphong, K. Udo, and S. Kazama, 2018: Projections of Future Beach Loss due to Sea Level Rise for Sandy Beaches along Thailand's Coastlines. *Journal of Coastal Research*, **85**, 541–545, doi:10.2112/si85-109.1.
Rivera, J. and O. Penalba, 2014: Trends and Spatial Patterns of Drought Affected Area in Southern South America. *Climate*, **2(4)**, 264–278, doi:10.3390/cli2040264.
Rivera, J., O. Penalba, R. Villalba, and D. Araneo, 2017: Spatio-Temporal Patterns of the 2010–2015 Extreme Hydrological Drought across the Central Andes, Argentina. *Water*, **9(9)**, 652, doi:10.3390/w9090652.
Roberts, M.J. et al., 2015: Tropical Cyclones in the UPSCALE Ensemble of High-Resolution Global Climate Models. *Journal of Climate*, **28(2)**, 574–596, doi:10.1175/jcli-d-14-00131.1.
Roberts, M.J. et al., 2020: Projected Future Changes in Tropical Cyclones Using the CMIP6 HighResMIP Multimodel Ensemble. *Geophysical Research Letters*, **47(14)**, e2020GL088662, doi:10.1029/2020gl088662.
Robinson, J.D., F. Vahedifard, and A. AghaKouchak, 2017: Rainfall-triggered slope instabilities under a changing climate: comparative study using historical and projected precipitation extremes. *Canadian Geotechnical Journal*, **54(1)**, 117–127, doi:10.1139/cgj-2015-0602.
Robinson, S.A. et al., 2020: The 2019/2020 summer of Antarctic heatwaves. *Global Change Biology*, **26(6)**, 3178–3180, doi:10.1111/gcb.15083.
Rohat, G. et al., 2019: Influence of changes in socioeconomic and climatic conditions on future heat-related health challenges in Europe. *Global and Planetary Change*, **172**, 45–59, doi:10.1016/j.gloplacha.2018.09.013.

ACCEPTED VERSION SUBJECT TO FINAL EDITS

Rohini, P., M. Rajeevan, and A.K. Srivastava, 2016: On the Variability and Increasing Trends of Heat Waves over India. *Scientific Reports*, **6(1)**, 26153, doi:10.1038/srep26153.
Rojas, M., F. Lambert, J. Ramirez-Villegas, and A.J. Challinor, 2019: Emergence of robust precipitation changes across crop production areas in the 21st century. *Proceedings of the National Academy of Sciences of the United States of America*, **116(14)**, 6673–6678, doi:10.1073/pnas.1811463116.
Rojas, O., M. Mardones, J.L. Arumí, and M. Aguayo, 2014: Una revisión de inundaciones fluviales en Chile, período 1574-2012: causas, recurrencia y efectos geográficos. *Revista de geografía Norte Grande*, 177–192, doi:10.4067/s0718-34022014000100012.
Rojas, O., M. Mardones, C. Rojas, C. Martínez, and L. Flores, 2017: Urban Growth and Flood Disasters in the Coastal River Basin of South-Central Chile (1943–2011). *Sustainability*, **9(2)**, 195, doi:10.3390/su9020195.
Rojas, R., L. Feyen, and P. Watkiss, 2013: Climate change and river floods in the European Union: Socio-economic consequences and the costs and benefits of adaptation. *Global Environmental Change*, **23(6)**, 1737–1751, doi:10.1016/j.gloenvcha.2013.08.006.
Rojas, R., L. Feyen, A. Bianchi, and A. Dosio, 2012: Assessment of future flood hazard in Europe using a large ensemble of bias-corrected regional climate simulations. *Journal of Geophysical Research: Atmospheres*, **117**, D17109, doi:10.1029/2012jd017461.
Rojas-Downing, M.M., A.P. Nejadhashemi, T. Harrigan, and S.A. Woznicki, 2017: Climate change and livestock: Impacts, adaptation, and mitigation. *Climate Risk Management*, **16**, 145–163, doi:10.1016/j.crm.2017.02.001.
Rokaya, P., S. Budhathoki, and K.-E. Lindenschmidt, 2018: Trends in the Timing and Magnitude of Ice-Jam Floods in Canada. *Scientific Reports*, **8(1)**, 5834, doi:10.1038/s41598-018-24057-z.
Romanovsky, V. et al., 2018: Terrestrial Permafrost [in "State of the Climate in 2017"]. *Bulletin of the American Meteorological Society*, **99(8)**, S161—S165, doi:10.1175/2018bamsstateoftheclimate.1.
Romanovsky, V.E., Smith, S.L., Isaksen, K., Nyland, K. E., Kholodov, A. L, Shiklomanov, N. I., Streletskiy, D. A., Farquharson, L. M., Drozdov, D. S., Malkova, G. V., Christiansen, G., 2020: Terrestrial permafrost [in "State of the Climate in 2019"]. *Bulletin of the American Meteorological Society*, **101(8)**, S265–S271, doi:10.1175/bams-d-20-0086.1.
Romera, R. et al., 2017: Climate change projections of medicanes with a large multi-model ensemble of regional climate models. *Global and Planetary Change*, **151**, 134–143, doi:10.1016/j.gloplacha.2016.10.008.
Romero, R. and K. Emanuel, 2017: Climate Change and Hurricane-Like Extratropical Cyclones: Projections for North Atlantic Polar Lows and Medicanes Based on CMIP5 Models. *Journal of Climate*, **30(1)**, 279–299, doi:10.1175/jcli-d-16-0255.1.
Romero-Lankao, P. et al., 2014: North America. In: *Climate Change 2014: Impacts, Adaptation, and Vulnerability. Part B: Regional Aspects. Contribution of Working Group II to the Fifth Assessment Report of the Intergovernmental Panel on Climate Change* [Barros, V.R., C.B. Field, D.J. Dokken, M.D. Mastrandrea, K.J. Mach, T.E. Bilir, M. Chatterjee, K.L. Ebi, Y.O. Estrada, R.C. Genova, B. Girma, E.S. Kissel, A.N. Levy, S. MacCracken, P.R. Mastrandrea, and L.L.White (eds.)]. Cambridge University Press, Cambridge, United Kingdom and New York, NY, USA, pp. 1439–1498, doi:10.1017/cbo9781107415386.006.
Romps, D.M., J.T. Seeley, D. Vollaro, and J. Molinari, 2014: Projected increase in lightning strikes in the United States due to global warming. *Science*, **346(6211)**, 851–854, doi:10.1126/science.1259100.
Rose, S.K., O.B. Andersen, M. Passaro, C.A. Ludwigsen, and C. Schwatke, 2019: Arctic Ocean Sea Level Record from the Complete Radar Altimetry Era: 1991–2018. *Remote Sensing*, **11(14)**, 1672, doi:10.3390/rs11141672.
Rosenzweig, B.R. et al., 2018: Pluvial flood risk and opportunities for resilience. *Wiley Interdisciplinary Reviews: Water*, **5(6)**, e1302, doi:10.1002/wat2.1302.
Rosenzweig, C. and W. Solecki, 2014: Hurricane Sandy and adaptation pathways in New York: Lessons from a first-responder city. *Global Environmental Change*, **28**, 395–408, doi:10.1016/j.gloenvcha.2014.05.003.
Rosenzweig, C., F.N. Tubiello, R. Goldberg, E. Mills, and J. Bloomfield, 2002: Increased crop damage in the US from excess precipitation under climate change. *Global Environmental Change*, **12(3)**, 197–202, doi:10.1016/s0959-3780(02)00008-0.
Rosenzweig, C. et al., 2014: Assessing agricultural risks of climate change in the 21st century in a global gridded crop model intercomparison. *Proceedings of the National Academy of Sciences*, **111(9)**, 3268–3273, doi:10.1073/pnas.1222463110.
Rosenzweig, C. et al., 2015: *ARC3.2 Summary for City Leaders*. Urban Climate Change Research Network. Columbia University, New York, NY, USA, 25 pp.
Rössler, O. et al., 2019: Challenges to link climate change data provision and user needs: Perspective from the COST-action VALUE. *International Journal of Climatology*, **39(9)**, 3704–3716, doi:10.1002/joc.5060.
Rottler, E., C. Kormann, T. Francke, and A. Bronstert, 2019: Elevation-dependent warming in the Swiss Alps 1981–2017: Features, forcings and feedbacks. *International Journal of Climatology*, **39(5)**, 2556–2568, doi:10.1002/joc.5970.
Rotzoll, K. and C.H. Fletcher, 2013: Assessment of groundwater inundation as a consequence of sea-level rise. *Nature Climate Change*, **3(5)**, 477–481, doi:10.1038/nclimate1725.
Roudier, P., A. Ducharne, and L. Feyen, 2014: Climate change impacts on runoff in West Africa: a review. *Hydrology*

ACCEPTED VERSION SUBJECT TO FINAL EDITS

and Earth System Sciences, **18(7)**, 2789–2801, doi:10.5194/hess-18-2789-2014.
Roudier, P. et al., 2016: Projections of future floods and hydrological droughts in Europe under a +2°C global warming. *Climatic Change*, **135(2)**, 341–355, doi:10.1007/s10584-015-1570-4.
Rounce, D.R., R. Hock, and D.E. Shean, 2020: Glacier Mass Change in High Mountain Asia Through 2100 Using the Open-Source Python Glacier Evolution Model (PyGEM). *Frontiers in Earth Science*, **7**, 331, doi:10.3389/feart.2019.00331.
Roxy, M.K. et al., 2015: Drying of Indian subcontinent by rapid Indian ocean warming and a weakening land-sea thermal gradient. *Nature Communications*, **6(1)**, 7423, doi:10.1038/ncomms8423.
Roy, S., 2019: Spatial patterns of trends in seasonal extreme temperatures in India during 1980–2010. *Weather and Climate Extremes*, **24**, 100203, doi:10.1016/j.wace.2019.100203.
Rozance, M.A. et al., 2020: Building capacity for societally engaged climate science by transforming science training. *Environmental Research Letters*, **15(12)**, 125008, doi:10.1088/1748-9326/abc27a.
Ruane, A.C. et al., 2013: Multi-factor impact analysis of agricultural production in Bangladesh with climate change. *Global Environmental Change*, **23(1)**, 338–350, doi:10.1016/j.gloenvcha.2012.09.001.
Ruane, A.C. et al., 2016: The Vulnerability, Impacts, Adaptation and Climate Services Advisory Board (VIACS AB v1.0) contribution to CMIP6. *Geoscientific Model Development*, **9(9)**, 3493–3515, doi:10.5194/gmd-9-3493-2016.
Ruane, A.C. et al., 2021: Strong regional influence of climatic forcing datasets on global crop model ensembles. *Agricultural and Forest Meteorology*, **300**, 108313, doi:10.1016/j.agrformet.2020.108313.
Ruffault, J. et al., 2020: Increased likelihood of heat-induced large wildfires in the Mediterranean Basin. *Scientific Reports*, **10(1)**, 13790, doi:10.1038/s41598-020-70069-z.
Ruosteenoja, K., T. Vihma, and A. Venäläinen, 2019a: Projected Changes in European and North Atlantic Seasonal Wind Climate Derived from CMIP5 Simulations. *Journal of Climate*, **32(19)**, 6467–6490, doi:10.1175/jcli-d-19-0023.1.
Ruosteenoja, K., J. Räisänen, A. Venäläinen, and M. Kämäräinen, 2016: Projections for the duration and degree days of the thermal growing season in Europe derived from CMIP5 model output. *International Journal of Climatology*, **36(8)**, 3039–3055, doi:10.1002/joc.4535.
Ruosteenoja, K., T. Markkanen, A. Venäläinen, P. Räisänen, and H. Peltola, 2018: Seasonal soil moisture and drought occurrence in Europe in CMIP5 projections for the 21st century. *Climate Dynamics*, **50(3–4)**, 1177–1192, doi:10.1007/s00382-017-3671-4.
Ruosteenoja, K., P. Räisänen, S. Devraj, S.S. Garud, and A. Lindfors, 2019b: Future changes in incident surface solar radiation and contributing factors in India in CMIP5 climate model simulations. *Journal of Applied Meteorology and Climatology*, **58(1)**, 19–35, doi:10.1175/jamc-d-18-0013.1.
Russo, S., J. Sillmann, and E.M. Fischer, 2015: Top ten European heatwaves since 1950 and their occurrence in the coming decades. *Environmental Research Letters*, **10(12)**, 124003, doi:10.1088/1748-9326/10/12/124003.
Russo, S., A.F. Marchese, J. Sillmann, and G. Immé, 2016: When will unusual heat waves become normal in a warming Africa? *Environmental Research Letters*, **11(5)**, 054016, doi:10.1088/1748-9326/11/5/054016.
Russo, S. et al., 2014: Magnitude of extreme heat waves in present climate and their projection in a warming world. *Journal of Geophysical Research: Atmospheres*, **119(22)**, 12,500–12,512, doi:10.1002/2014jd022098.
Russo, S. et al., 2019: Half a degree and rapid socioeconomic development matter for heatwave risk. *Nature Communications*, **10(1)**, 136, doi:10.1038/s41467-018-08070-4.
Ruti, P.M. et al., 2016: Med-CORDEX Initiative for Mediterranean Climate Studies. *Bulletin of the American Meteorological Society*, **97(7)**, 1187–1208, doi:10.1175/bams-d-14-00176.1.
Rutty, M. et al., 2017: Using ski industry response to climatic variability to assess climate change risk: An analogue study in Eastern Canada. *Tourism Management*, **58**, 196–204, doi:10.1016/j.tourman.2016.10.020.
Ryu, Y., C. Jiang, H. Kobayashi, and M. Detto, 2018: MODIS-derived global land products of shortwave radiation and diffuse and total photosynthetically active radiation at 5 km resolution from 2000. *Remote Sensing of Environment*, **204**, 812–825, doi:10.1016/j.rse.2017.09.021.
S. Debortoli, N. et al., 2015: Rainfall patterns in the Southern Amazon: a chronological perspective (1971–2010). *Climatic Change*, **132(2)**, 251–264, doi:10.1007/s10584-015-1415-1.
Saeed, F., M. Almazroui, N. Islam, and M.S. Khan, 2017: Intensification of future heat waves in Pakistan: a study using CORDEX regional climate models ensemble. *Natural Hazards*, **87(3)**, 1635–1647, doi:10.1007/s11069-017-2837-z.
Saeed, F. et al., 2018: Robust changes in tropical rainy season length at 1.5 °C and 2 °C. *Environmental Research Letters*, **13(6)**, 64024, doi:10.1088/1748-9326/aab797.
Saintilan, N., N.C. Wilson, K. Rogers, A. Rajkaran, and K.W. Krauss, 2014: Mangrove expansion and salt marsh decline at mangrove poleward limits. *Global Change Biology*, **20(1)**, 147–157, doi:10.1111/gcb.12341.
Salinger, M.J., B.B. Fitzharris, and T. Chinn, 2019: Atmospheric circulation and ice volume changes for the small and medium glaciers of New Zealand's Southern Alps mountain range 1977–2018. *International Journal of Climatology*, **39(11)**, 4274–4287, doi:10.1002/joc.6072.
Salvati, A., H. Coch Roura, and C. Cecere, 2017: Assessing the urban heat island and its energy impact on residential

ACCEPTED VERSION
SUBJECT TO FINAL EDITS

buildings in Mediterranean climate: Barcelona case study. *Energy and Buildings*, **146**, 38–54, doi:10.1016/j.enbuild.2017.04.025.
Sanchez, J.L. et al., 2017: Are meteorological conditions favoring hail precipitation change in Southern Europe? Analysis of the period 1948–2015. *Atmospheric Research*, **198**, 1–10, doi:10.1016/j.atmosres.2017.08.003.
Sánchez, E. et al., 2015: Regional climate modelling in CLARIS-LPB: a concerted approach towards twentyfirst century projections of regional temperature and precipitation over South America. *Climate Dynamics*, **45(7–8)**, 2193–2212, doi:10.1007/s00382-014-2466-0.
Sanderson, M., K. Arbuthnott, S. Kovats, S. Hajat, and P. Falloon, 2017: The use of climate information to estimate future mortality from high ambient temperature: A systematic literature review. *PLOS ONE*, **12(7)**, e0180369, doi:10.1371/journal.pone.0180369.
Santamouris, M. et al., 2017: Urban heat island and overheating characteristics in Sydney, Australia. An analysis of multiyear measurements. *Sustainability*, **9(5)**, 712, doi:10.3390/su9050712.
Sapkota, A. et al., 2019: Associations between alteration in plant phenology and hay fever prevalence among US adults: Implication for changing climate. *PLOS ONE*, **14(3)**, e0212010, doi:10.1371/journal.pone.0212010.
Sathaye, J.A. et al., 2013: Estimating impacts of warming temperatures on California's electricity system. *Global Environmental Change*, **23(2)**, 499–511, doi:10.1016/j.gloenvcha.2012.12.005.
Sawadogo, W., B.J. Abiodun, and E.C. Okogbue, 2020a: Impacts of global warming on photovoltaic power generation over West Africa. *Renewable Energy*, **151**, 263–277, doi:10.1016/j.renene.2019.11.032.
Sawadogo, W. et al., 2020b: Current and future potential of solar and wind energy over Africa using the RegCM4 CORDEX-CORE ensemble. *Climate Dynamics*, doi:10.1007/s00382-020-05377-1.
Sawyer, A.H., C.H. David, and J.S. Famiglietti, 2016: Continental patterns of submarine groundwater discharge reveal coastal vulnerabilities.. *Science (New York, N.Y.)*, **353(6300)**, 705–7, doi:10.1126/science.aag1058.
Schaeffer, R. et al., 2012: Energy sector vulnerability to climate change: A review. *Energy*, **38(1)**, 1–12, doi:10.1016/j.energy.2011.11.056.
Schaefli, B., P. Manso, M. Fischer, M. Huss, and D. Farinotti, 2019: The role of glacier retreat for Swiss hydropower production. *Renewable Energy*, **132**, 615–627, doi:10.1016/j.renene.2018.07.104.
Schauberger, B. et al., 2017: Consistent negative response of US crops to high temperatures in observations and crop models. *Nature Communications*, **8**, 13931, doi:10.1038/ncomms13931.
Scheurer, K., C. Alewell, D. Bänninger, and P. Burkhardt-Holm, 2009: Climate and land-use changes affecting river sediment and brown trout in alpine countries-a review. *Environmental Science and Pollution Research*, **16(2)**, 232–242, doi:10.1007/s11356-008-0075-3.
Schewe, J. et al., 2014a: Multimodel assessment of water scarcity under climate change. *Proceedings of the National Academy of Sciences of the United States of America*, **111(9)**, 3245–3250, doi:10.1073/pnas.1222460110.
Schewe, J. et al., 2014b: Multimodel assessment of water scarcity under climate change. *Proceedings of the National Academy of Sciences*, **111(9)**, 3245–3250, doi:10.1073/pnas.1222460110.
Schipper, J.W., J. Hackenbruch, H.S. Lentink, and K. Sedlmeier, 2019: Integrating Adaptation Expertise into Regional Climate Data Analyses through Tailored Climate Parameters. *Meteorologische Zeitschrift*, **28(1)**, 41–57, doi:10.1127/metz/2019/0878.
Schlaepfer, D.R. et al., 2017: Climate change reduces extent of temperate drylands and intensifies drought in deep soils. *Nature Communications*, **8(1)**, 14196, doi:10.1038/ncomms14196.
Schlenker, W. and M.J. Roberts, 2009: Nonlinear temperature effects indicate severe damages to U.S. crop yields under climate change. *Proceedings of the National Academy of Sciences*, **106(37)**, 15594–15598, doi:10.1073/pnas.0906865106.
Schlögl, M. and C. Matulla, 2018: Potential future exposure of European land transport infrastructure to rainfall-induced landslides throughout the 21st century. *Natural Hazards and Earth System Sciences*, **18(4)**, 1121–1132, doi:10.5194/nhess-18-1121-2018.
Schmidt, C.W., 2016: Pollen Overload: Seasonal Allergies in a Changing Climate. *Environmental Health Perspectives*, **124(4)**, A71–A75, doi:10.1289/ehp.124-a70.
Schmidtko, S., L. Stramma, and M. Visbeck, 2017: Decline in global oceanic oxygen content during the past five decades. *Nature*, **542(7641)**, 335–339, doi:10.1038/nature21399.
Schmucki, E., C. Marty, C. Fierz, and M. Lehning, 2015: Simulations of 21st century snow response to climate change in Switzerland from a set of RCMs. *International Journal of Climatology*, **35(11)**, 3262–3273, doi:10.1002/joc.4205.
Schnell, J.L. et al., 2016: Effect of climate change on surface ozone over North America, Europe, and East Asia. *Geophysical Research Letters*, **43(7)**, 3509–3518, doi:10.1002/2016gl068060.
Schnell, J.L. et al., 2018: Exploring the relationship between surface PM2.5 and meteorology in Northern India. *Atmospheric Chemistry and Physics*, **18(14)**, 10157–10175, doi:10.5194/acp-18-10157-2018.
Schoepf, V. et al., 2015: Annual coral bleaching and the long-term recovery capacity of coral. *Proceedings of the Royal Society B: Biological Sciences*, **282(1819)**, 20151887, doi:10.1098/rspb.2015.1887.
Schuster, P.F. et al., 2018: Permafrost Stores a Globally Significant Amount of Mercury. *Geophysical Research Letters*, **45(3)**, 1463–1471, doi:10.1002/2017gl075571.

ACCEPTED VERSION SUBJECT TO FINAL EDITS

Schwingshackl, C., J. Sillmann, A.M. Vicedo-Cabrera, M. Sandstad, and K. Aunan, 2021: Heat Stress Indicators in CMIP6: Estimating Future Trends and Exceedances of Impact-Relevant Thresholds. *Earth's Future*, **9**, e2020EF001885, doi:10.1029/2020ef001885.

Sciance, M.B. and S.L. Nooner, 2018: Decadal flood trends in Bangladesh from extensive hydrographic data. *Natural Hazards*, **90(1)**, 115–135, doi:10.1007/s11069-017-3036-7.

Scott, D., R. Steiger, H. Dannevig, and C. Aall, 2020: Climate change and the future of the Norwegian alpine ski industry. *Current Issues in Tourism*, **23(19)**, 2396–2409, doi:10.1080/13683500.2019.1608919.

Scott, D. et al., 2018: The Story of Water in Windhoek: A Narrative Approach to Interpreting a Transdisciplinary Process. *Water*, **10(10)**, 1366, doi:10.3390/w10101366.

Seager, R. et al., 2018: Whither the 100th Meridian? The Once and Future Physical and Human Geography of America's Arid–Humid Divide. Part II: The Meridian Moves East. *Earth Interactions*, **22(5)**, 1–24, doi:10.1175/ei-d-17-0012.1.

Sedlmeier, K., S. Mieruch, G. Schädler, and C. Kottmeier, 2016: Compound extremes in a changing climate-a Markov chain approach. *Nonlin. Processes Geophys*, **23**, 375–390, doi:10.5194/npg-23-375-2016.

Seeley, J.T. and D.M. Romps, 2015: The effect of global warming on severe thunderstorms in the United States. *Journal of Climate*, **28(6)**, 2443–2458, doi:10.1175/jcli-d-14-00382.1.

Segura, C., G. Sun, S. McNulty, and Y. Zhang, 2014: Potential impacts of climate change on soil erosion vulnerability across the conterminous United States. *Journal of Soil and Water Conservation*, **69(2)**, 171–181, doi:10.2489/jswc.69.2.171.

Seidl, R. et al., 2017: Forest disturbances under climate change. *Nature Climate Change*, **7(6)**, 395–402, doi:10.1038/nclimate3303.

Sein, K.K., A. Chidthaisong, and K.L. Oo, 2018: Observed Trends and Changes in Temperature and Precipitation Extreme Indices over Myanmar. *Atmosphere*, **9(12)**, 477, doi:10.3390/atmos9120477.

Selyuzhenok, V., T. Krumpen, A. Mahoney, M. Janout, and R. Gerdes, 2015: Seasonal and interannual variability of fast ice extent in the southeastern Laptev Sea between 1999 and 2013. *Journal of Geophysical Research: Oceans*, **120(12)**, 7791–7806, doi:10.1002/2015jc011135.

Sena, E.T., M.A.F.S. Dias, L.M. Carvalho, and P.L.S. Dias, 2018: Reduced Wet-Season Length Detected by Satellite Retrievals of Cloudiness over Brazilian Amazonia: A New Methodology. *Journal of Climate*, **31(24)**, 9941–9964, doi:10.1175/jcli-d-17-0702.1.

Sena, J.A., L.A. Beser de Deus, M.A. Freitas, and L. Costa, 2012: Extreme Events of Droughts and Floods in Amazonia: 2005 and 2009. *Water Resources Management*, **26(6)**, 1665–1676, doi:10.1007/s11269-012-9978-3.

Senatore, A., S. Hejabi, G. Mendicino, J. Bazrafshan, and P. Irannejad, 2019: Climate conditions and drought assessment with the Palmer Drought Severity Index in Iran: evaluation of CORDEX South Asia climate projections (2070–2099). *Climate Dynamics*, **52(1–2)**, 865–891, doi:10.1007/s00382-018-4171-x.

Seneviratne, S.I. and M. Hauser, 2020: Regional Climate Sensitivity of Climate Extremes in CMIP6 Versus CMIP5 Multimodel Ensembles. *Earth's Future*, **8(9)**, e2019EF001474, doi:10.1029/2019ef001474.

Sepúlveda, S.A. and D.N. Petley, 2015: Regional trends and controlling factors of fatal landslides in Latin America and the Caribbean. *Natural Hazards and Earth System Sciences*, **15(8)**, 1821–1833, doi:10.5194/nhess-15-1821-2015.

Seth, A. et al., 2013: CMIP5 Projected Changes in the Annual Cycle of Precipitation in Monsoon Regions. *Journal of Climate*, **26(19)**, 7328–7351, doi:10.1175/jcli-d-12-00726.1.

Sharma, S. et al., 2019: Widespread loss of lake ice around the Northern Hemisphere in a warming world. *Nature Climate Change*, **9(3)**, 227–231, doi:10.1038/s41558-018-0393-5.

Shatwell, T., W. Thiery, and G. Kirillin, 2019: Future projections of temperature and mixing regime of European temperate lakes. *Hydrology and Earth System Sciences*, **23(3)**, 1533–1551, doi:10.5194/hess-23-1533-2019.

Sheikh, M.M. et al., 2015: Trends in extreme daily rainfall and temperature indices over South Asia. *International Journal of Climatology*, **35(7)**, 1625–1637, doi:10.1002/joc.4081.

Shepherd, T.G., 2016: A Common Framework for Approaches to Extreme Event Attribution. *Current Climate Change Reports*, **2(1)**, 28–38, doi:10.1007/s40641-016-0033-y.

Sherwood, S. and Q. Fu, 2014: A Drier Future? *Science*, **343(6172)**, 737–739, doi:10.1126/science.1247620.

Shi, C., Z.-H. Jiang, W.-L. Chen, and L. Li, 2018: Changes in temperature extremes over China under 1.5°C and 2°C global warming targets. *Advances in Climate Change Research*, **9(2)**, 120–129, doi:10.1016/j.accre.2017.11.003.

Shiklomanov, N.I., D.A. Streletskiy, T.B. Swales, and V.A. Kokorev, 2017: Climate Change and Stability of Urban Infrastructure in Russian Permafrost Regions: Prognostic Assessment based on GCM Climate Projections. *Geographical Review*, **107(1)**, 125–142, doi:10.1111/gere.12214.

Shin, J., R. Olson, and S.-I. An, 2018: Projected Heat Wave Characteristics over the Korean Peninsula During the Twenty-First Century. *Asia-Pacific Journal of Atmospheric Sciences*, **54(1)**, 53–61, doi:10.1007/s13143-017-0059-7.

Shiogama, H. et al., 2020: Selecting Future Climate Projections of Surface Solar Radiation in Japan. *SOLA*, **16**, 75–79,

ACCEPTED VERSION SUBJECT TO FINAL EDITS

doi:10.2151/sola.2020-013.
Shkolnik, I., T. Pavlova, S. Efimov, and S. Zhuravlev, 2018: Future changes in peak river flows across northern Eurasia as inferred from an ensemble of regional climate projections under the IPCC RCP8.5 scenario. *Climate Dynamics*, **50(1–2)**, 215–230, doi:10.1007/s00382-017-3600-6.
Shope, J.B., C.D. Storlazzi, L.H. Erikson, and C.A. Hegermiller, 2016: Changes to extreme wave climates of islands within the Western Tropical Pacific throughout the 21st century under RCP 4.5 and RCP 8.5, with implications for island vulnerability and sustainability. *Global and Planetary Change*, **141**, 25–38, doi:10.1016/j.gloplacha.2016.03.009.
Shrestha, B.B. et al., 2019: Assessing flood disaster impacts in agriculture under climate change in the river basins of Southeast Asia. *Natural Hazards*, **97(1)**, 157–192, doi:10.1007/s11069-019-03632-1.
Shu, Q., F. Qiao, Z. Song, J. Zhao, and X. Li, 2018: Projected Freshening of the Arctic Ocean in the 21st Century. *Journal of Geophysical Research: Oceans*, **123(12)**, 9232–9244, doi:10.1029/2018jc014036.
Siebert, S., H. Webber, G. Zhao, and F. Ewert, 2017: Heat stress is overestimated in climate impact studies for irrigated agriculture. *Environmental Research Letters*, **12(5)**, 054023, doi:10.1088/1748-9326/aa702f.
Sierra, J.P., M. Casas-Prat, and E. Campins, 2017: Impact of climate change on wave energy resource: The case of Menorca (Spain). *Renewable Energy*, **101**, 275–285, doi:10.1016/j.renene.2016.08.060.
Sigmond, M., J.C. Fyfe, and N.C. Swart, 2018: Ice-free Arctic projections under the Paris Agreement. *Nature Climate Change*, **8(5)**, 404–408, doi:10.1038/s41558-018-0124-y.
Sillmann, J. et al., 2014: Evaluating model-simulated variability in temperature extremes using modified percentile indices. *International Journal of Climatology*, **34(11)**, 3304–3311, doi:10.1002/joc.3899.
Sillmann, J. et al., 2017: Understanding, modeling and predicting weather and climate extremes: Challenges and opportunities. *Weather and Climate Extremes*, **18**, 65–74, doi:10.1016/j.wace.2017.10.003.
Silvy, Y., E. Guilyardi, J.-B. Sallée, and P.J. Durack, 2020: Human-induced changes to the global ocean water masses and their time of emergence. *Nature Climate Change*, **10(11)**, 1030–1036, doi:10.1038/s41558-020-0878-x.
Singh, C. et al., 2018: The utility of weather and climate information for adaptation decision-making: current uses and future prospects in Africa and India. *Climate and Development*, **10(5)**, 389–405, doi:10.1080/17565529.2017.1318744.
Singh, O. and M. Kumar, 2013: Flood events, fatalities and damages in India from 1978 to 2006. *Natural Hazards*, **69(3)**, 1815–1834, doi:10.1007/s11069-013-0781-0.
Sinickas, A., B. Jamieson, and M.A. Maes, 2016: Snow avalanches in western Canada: investigating change in occurrence rates and implications for risk assessment and mitigation. *Structure and Infrastructure Engineering*, **12(4)**, 490–498, doi:10.1080/15732479.2015.1020495.
Sippel, S., P. Walton, and F.E.L. Otto, 2015: Stakeholder Perspectives on the Attribution of Extreme Weather Events: An Explorative Enquiry. *Weather, Climate, and Society*, **7(3)**, 224–237, doi:10.1175/wcas-d-14-00045.1.
Sittaro, F., A. Paquette, C. Messier, and C.A. Nock, 2017: Tree range expansion in eastern North America fails to keep pace with climate warming at northern range limits. *Global Change Biology*, **23(8)**, 3292–3301, doi:10.1111/gcb.13622.
Sivakumar, M.V.K. and F. Lucio, 2018: Climate Services for Sustainable Development. In: *Bridging Science and Policy Implication for Managing Climate Extremes* [Jung, H.-S. and B. Wang (eds.)]. World Scientific, pp. 81–100, doi:10.1142/9789813235663_0006.
Skelton, M., J.J. Porter, S. Dessai, D.N. Bresch, and R. Knutti, 2017: The social and scientific values that shape national climate scenarios: a comparison of the Netherlands, Switzerland and the UK. *Regional Environmental Change*, **17(8)**, 2325–2338, doi:10.1007/s10113-017-1155-z.
Skliris, N., R. Marsh, J. Mecking, and J.D. Zika, 2020: Changing water cycle and freshwater transports in the Atlantic Ocean in observations and CMIP5 models. *Climate Dynamics*, **54**, 4971–4989, doi:10.1007/s00382-020-05261-y.
Slater, A.G. and D.M. Lawrence, 2013: Diagnosing Present and Future Permafrost from Climate Models. *Journal of Climate*, **26(15)**, 5608–5623, doi:10.1175/jcli-d-12-00341.1.
Smale, D.A. et al., 2019: Marine heatwaves threaten global biodiversity and the provision of ecosystem services. *Nature Climate Change*, **9(4)**, 306–312, doi:10.1038/s41558-019-0412-1.
Smith, A.T. and J.D. Nagy, 2015: Population resilience in an American pika (Ochotona princeps) metapopulation. *Journal of Mammalogy*, **96(2)**, 394–404, doi:10.1093/jmammal/gyv040.
Smith, B.A. and A. Fazil, 2019: How will climate change impact microbial foodborne disease in Canada? *Canada Communicable Disease Report*, **45(4)**, 108–113, doi:10.14745/ccdr.v45i04a05.
Smith, K.R. et al., 2016: The last Summer Olympics? Climate change, health, and work outdoors. *The Lancet*, **388(10045)**, 642–644, doi:10.1016/s0140-6736(16)31335-6.
Smith, M.R. and S.S. Myers, 2018: Impact of anthropogenic CO2 emissions on global human nutrition. *Nature Climate Change*, **8(9)**, 834–839, doi:10.1038/s41558-018-0253-3.
Smith, M.T., M. Reid, S. Kovalchik, T.O. Woods, and R. Duffield, 2018: Heat stress incident prevalence and tennis matchplay performance at the Australian Open. *Journal of Science and Medicine in Sport*, **21(5)**, 467–472, doi:10.1016/j.jsams.2017.08.019.

ACCEPTED VERSION SUBJECT TO FINAL EDITS

Smith, M.W. et al., 2020: Incorporating hydrology into climate suitability models changes projections of malaria transmission in Africa. *Nature Communications*, **11(1)**, 4353, doi:10.1038/s41467-020-18239-5.

Smith., J. et al., 2001: Vulnerability to Climate Change and Reasons for Concern: A Synthesis Contents. In: *Climate Change 2001: Impacts, Adaptation, and Vulnerability. Contribution of Working Group II to the Third Assessment Report of the Intergovernmental Panel on Climate Change* [McCarthy, J.J., O.F. Canziani, N.A. Leary, D.J. Dokken, and K.S. White (eds.)]. Cambridge University Press, Cambridge, United Kingdom and NewYork, NY, USA, pp. 915–969.

Smits, A., A.M.G. Klein Tank, and G.P. Können, 2005: Trends in storminess over the Netherlands, 1962-2002. *International Journal of Climatology*, **25(10)**, 1331–1344, doi:10.1002/joc.1195.

Soares, P.M.M., M.C. Brito, and J.A.M. Careto, 2019: Persistence of the high solar potential in Africa in a changing climate. *Environmental Research Letters*, **14(12)**, 124036, doi:10.1088/1748-9326/ab51a1.

Solaun, K. and E. Cerdá, 2019: Climate change impacts on renewable energy generation. A review of quantitative projections. *Renewable and Sustainable Energy Reviews*, **116**, 109415, doi:10.1016/j.rser.2019.109415.

Solman, S.A., 2013: Regional Climate Modeling over South America: A Review. *Advances in Meteorology*, **2013**, 504357, doi:10.1155/2013/504357.

Somot, S. et al., 2018: Editorial for the Med-CORDEX special issue. *Climate Dynamics*, **51(3)**, 771–777, doi:10.1007/s00382-018-4325-x.

Son, R. et al., 2020: Climate diagnostics of the extreme floods in Peru during early 2017. *Climate Dynamics*, **54(1–2)**, 935–945, doi:10.1007/s00382-019-05038-y.

Song, M. and J. Liu, 2017: The role of diminishing Arctic sea ice in increased winter snowfall over northern high-latitude continents in a warming environment. *Acta Oceanologica Sinica*, **36(8)**, 34–41, doi:10.1007/s13131-017-1021-3.

Soret, A. et al., 2019: Sub-seasonal to seasonal climate predictions for wind energy forecasting. *Journal of Physics: Conference Series*, **1222**, 12009, doi:10.1088/1742-6596/1222/1/012009.

Sorg, A., M. Huss, M. Rohrer, and M. Stoffel, 2014: The days of plenty might soon be over in glacierized Central Asian catchments. *Environmental Research Letters*, **9(10)**, 104018, doi:10.1088/1748-9326/9/10/104018.

Spandre, P. et al., 2019: Winter tourism under climate change in the Pyrenees and the French Alps: relevance of snowmaking as a technical adaptation. *The Cryosphere*, **13(4)**, 1325–1347, doi:10.5194/tc-13-1325-2019.

Spickett, J.T., H.L. Brown, and K. Rumchev, 2011: Climate Change and Air Quality: The Potential Impact on Health. *Asia Pacific Journal of Public Health*, **23(2_suppl)**, 37S–45S, doi:10.1177/1010539511398114.

Spinoni, J., J. Vogt, and P. Barbosa, 2015: European degree-day climatologies and trends for the period 1951-2011. *International Journal of Climatology*, **35(1)**, 25–36, doi:10.1002/joc.3959.

Spinoni, J., G. Naumann, H. Carrao, P. Barbosa, and J. Vogt, 2014: World drought frequency, duration, and severity for 1951-2010. *International Journal of Climatology*, **34(8)**, 2792–2804, doi:10.1002/joc.3875.

Spinoni, J., J. Vogt, G. Naumann, P. Barbosa, and A. Dosio, 2018a: Will drought events become more frequent and severe in Europe? *International Journal of Climatology*, **38(4)**, 1718–1736, doi:10.1002/joc.5291.

Spinoni, J. et al., 2018b: Changes of heating and cooling degree-days in Europe from 1981 to 2100. *International Journal of Climatology*, **38(S1)**, e191–e208, doi:10.1002/joc.5362.

Spinoni, J. et al., 2019a: Future global meteorological drought hotspots: a study based on CORDEX data. *Journal of Climate*, JCLI–D–19–0084.1, doi:10.1175/jcli-d-19-0084.1.

Spinoni, J. et al., 2019b: A new global database of meteorological drought events from 1951 to 2016. *Journal of Hydrology: Regional Studies*, **22**, 100593, doi:10.1016/j.ejrh.2019.100593.

Staiger, H., G. Laschewski, and A. Matzarakis, 2019: Selection of Appropriate Thermal Indices for Applications in Human Biometeorological Studies. *Atmosphere*, **10(1)**, 18, doi:10.3390/atmos10010018.

Stathers, T., R. Lamboll, and B.M. Mvumi, 2013: Postharvest agriculture in changing climates: its importance to African smallholder farmers. *Food Security*, **5(3)**, 361–392, doi:10.1007/s12571-013-0262-z.

Steiger, R. and D. Scott, 2020: Ski tourism in a warmer world: Increased adaptation and regional economic impacts in Austria. *Tourism Management*, **77**, 104032, doi:10.1016/j.tourman.2019.104032.

Steiger, R., D. Scott, B. Abegg, M. Pons, and C. Aall, 2019: A critical review of climate change risk for ski tourism. *Current Issues in Tourism*, **22(11)**, 1343–1379, doi:10.1080/13683500.2017.1410110.

Steinberg, N. et al., 2018: *Preparing Public Health Officials for Climate Change: A Decision Support Tool. A report for California's Fourth Climate Change Assessment*. CCCA4-CNRA-2018-012, California Natural Resources Agency, CA, USA, 74 pp.

Stennett-Brown, R.K., J.J.P. Jones, T.S. Stephenson, and M.A. Taylor, 2017: Future Caribbean temperature and rainfall extremes from statistical downscaling. *International Journal of Climatology*, **37(14)**, 4828–4845, doi:10.1002/joc.5126.

Steynor, A., J. Lee, and A. Davison, 2020: Transdisciplinary co-production of climate services: a focus on process. *Social Dynamics*, **46(3)**, 414–433, doi:10.1080/02533952.2020.1853961.

Stinson, K.A., J.M. Albertine, L.M.S. Hancock, T.G. Seidler, and C.A. Rogers, 2016: Northern ragweed ecotypes flower earlier and longer in response to elevated CO2: what are you sneezing at? *Oecologia*, **182(2)**, 587–594, doi:10.1007/s00442-016-3670-x.

ACCEPTED VERSION SUBJECT TO FINAL EDITS

Stoffel, M. and C. Huggel, 2012: Effects of climate change on mass movements in mountain environments. *Progress in Physical Geography: Earth and Environment*, **36(3)**, 421–439, doi:10.1177/0309133312441010.
Stoffel, M., M. Bollschweiler, and M. Beniston, 2011: Rainfall characteristics for periglacial debris flows in the Swiss Alps: past incidences–potential future evolutions. *Climatic Change*, **105(1–2)**, 263–280, doi:10.1007/s10584-011-0036-6.
Stoffel, M., T. Mendlik, M. Schneuwly-Bollschweiler, and A. Gobiet, 2014: Possible impacts of climate change on debris-flow activity in the Swiss Alps. *Climatic Change*, **122(1–2)**, 141–155, doi:10.1007/s10584-013-0993-z.
Stojanovic, M. et al., 2020: Trends and Extremes of Drought Episodes in Vietnam Sub-Regions during 1980–2017 at Different Timescales. *Water*, **12(3)**, 813, doi:10.3390/w12030813.
Stone, R.C. and H. Meinke, 2005: Operational seasonal forecasting of crop performance. *Philosophical Transactions of the Royal Society B: Biological Sciences*, **360(1463)**, 2109–2124, doi:10.1098/rstb.2005.1753.
Storkey, J., P. Stratonovitch, D.S. Chapman, F. Vidotto, and M.A. Semenov, 2014: A Process-Based Approach to Predicting the Effect of Climate Change on the Distribution of an Invasive Allergenic Plant in Europe. *PLoS ONE*, **9(2)**, e88156, doi:10.1371/journal.pone.0088156.
Storlazzi, C.D., E.P.L. Elias, and P. Berkowitz, 2015: Many Atolls May be Uninhabitable Within Decades Due to Climate Change. *Scientific Reports*, **5(1)**, 14546, doi:10.1038/srep14546.
Storlazzi, C.D. et al., 2018: Most atolls will be uninhabitable by the mid-21st century because of sea-level rise exacerbating wave-driven flooding. *Science Advances*, **4(4)**, eaap9741, doi:10.1126/sciadv.aap9741.
Stott, P.A. et al., 2016: Attribution of extreme weather and climate-related events. *Wiley Interdisciplinary Reviews: Climate Change*, **7(1)**, 23–41, doi:10.1002/wcc.380.
Stramma, L. et al., 2012: Expansion of oxygen minimum zones may reduce available habitat for tropical pelagic fishes. *Nature Climate Change*, **2(1)**, 33–37, doi:10.1038/nclimate1304.
Street, R.B., 2016: Towards a leading role on climate services in Europe: A research and innovation roadmap. *Climate Services*, **1**, 2–5, doi:10.1016/j.cliser.2015.12.001.
Street, R.B.B. et al., 2019: How could climate services support disaster risk reduction in the 21st century. *International Journal of Disaster Risk Reduction*, **34**, 28–33, doi:10.1016/j.ijdrr.2018.12.001.
Streletskiy, D.A., L.J. Suter, N.I. Shiklomanov, B.N. Porfiriev, and D.O. Eliseev, 2019: Assessment of climate change impacts on buildings, structures and infrastructure in the Russian regions on permafrost. *Environmental Research Letters*, **14(2)**, 025003, doi:10.1088/1748-9326/aaf5e6.
Stroeve, J. and D. Notz, 2018: Changing state of Arctic sea ice across all seasons. *Environmental Research Letters*, **13(10)**, 103001, doi:10.1088/1748-9326/aade56.
Stroeve, J.C., T. Markus, L. Boisvert, J. Miller, and A. Barrett, 2014: Changes in Arctic melt season and implications for sea ice loss. *Geophysical Research Letters*, **41(4)**, 1216–1225, doi:10.1002/2013gl058951.
Stuivenvolt-Allen, J. and S.S.-Y. Wang, 2019: Data Mining Climate Variability as an Indicator of U.S. Natural Gas. *Frontiers in Big Data*, **2**, 20, doi:10.3389/fdata.2019.00020.
Sturm, M., M.A. Goldstein, H. Huntington, and T.A. Douglas, 2017: Using an option pricing approach to evaluate strategic decisions in a rapidly changing climate: Black–Scholes and climate change. *Climatic Change*, **140(3–4)**, 437–449, doi:10.1007/s10584-016-1860-5.
Su, Q. and B. Dong, 2019: Projected near-term changes in three types of heat waves over China under RCP4.5. *Climate Dynamics*, **53(7)**, 3751–3769, doi:10.1007/s00382-019-04743-y.
Sui, C., Z. Zhang, L. Yu, Y. Li, and M. Song, 2017: Investigation of Arctic air temperature extremes at north of 60N in winter. *Acta Oceanologica Sinica*, **36(11)**, 51–60, doi:10.1007/s13131-017-1137-5.
Sui, Y., X. Lang, and D. Jiang, 2014: Time of emergence of climate signals over China under the RCP4.5 scenario. *Climatic Change*, **125(2)**, 265–276, doi:10.1007/s10584-014-1151-y.
Sui, Y., X. Lang, and D. Jiang, 2018: Projected signals in climate extremes over China associated with a 2°C global warming under two RCP scenarios. *International Journal of Climatology*, **38(S1)**, e678–e697, doi:10.1002/joc.5399.
Sully, S., D.E. Burkepile, M.K. Donovan, G. Hodgson, and R. van Woesik, 2019: A global analysis of coral bleaching over the past two decades. *Nature Communications*, **10(1)**, 1264, doi:10.1038/s41467-019-09238-2.
Sultan, B. et al., 2020: Current needs for climate services in West Africa: Results from two stakeholder surveys. *Climate Services*, **18**, 100166, doi:10.1016/j.cliser.2020.100166.
Sun, C. and X. Zhou, 2020: Characterizing Hydrological Drought and Water Scarcity Changes in the Future: A Case Study in the Jinghe River Basin of China. *Water*, **12(6)**, 1605, doi:10.3390/w12061605.
Sun, J., D. Wang, X. Hu, Z. Ling, and L. Wang, 2019: Ongoing Poleward Migration of Tropical Cyclone Occurrence Over the Western North Pacific Ocean. *Geophysical Research Letters*, **46(15)**, 9110–9117, doi:10.1029/2019gl084260.
Sun, Q. et al., 2019: Global heat stress on health, wildfires, and agricultural crops under different levels of climate warming. *Environment International*, **128**, 125–136, doi:10.1016/j.envint.2019.04.025.
Sun, Y., T. Zhang, Y. Liu, W. Zhao, and X. Huang, 2020: Assessing Snow Phenology over the Large Part of Eurasia Using Satellite Observations from 2000 to 2016. *Remote Sensing*, **12(12)**, 2060, doi:10.3390/rs12122060.
Sun, Y. et al., 2017: Impact of Ocean Warming on Tropical Cyclone Size and Its Destructiveness. *Scientific Reports*,

ACCEPTED VERSION SUBJECT TO FINAL EDITS

7(1), 8154, doi:10.1038/s41598-017-08533-6.
Sun, Y. et al., 2019: Contribution of Global warming and Urbanization to Changes in Temperature Extremes in Eastern China. *Geophysical Research Letters*, **46(20)**, 11426–11434, doi:10.1029/2019gl084281.
Supari, F. Tangang, L. Juneng, and E. Aldrian, 2017: Observed changes in extreme temperature and precipitation over Indonesia. *International Journal of Climatology*, **37(4)**, 1979–1997, doi:10.1002/joc.4829.
Supari et al., 2020: Multi-model projections of precipitation extremes in Southeast Asia based on CORDEX-Southeast Asia simulations. *Environmental Research*, **184**, 109350, doi:10.1016/j.envres.2020.109350.
Surdu, C.M., C.R. Duguay, and D. Fernández Prieto, 2016: Evidence of recent changes in the ice regime of lakes in the Canadian High Arctic from spaceborne satellite observations. *The Cryosphere*, **10(3)**, 941–960, doi:10.5194/tc-10-941-2016.
Sutton, A.O., D. Strickland, and D.R. Norris, 2016: Food storage in a changing world: implications of climate change for food-caching species. *Climate Change Responses*, **3(1)**, doi:10.1186/s40665-016-0025-0.
Svoboda, M.D. and B.A. Fuchs, 2017: Handbook of drought indicators and indices. In: *Drought and Water Crises: Integrating Science, Management, and Policy (Second Edition) (2nd edition)* [Wilhite, D.A. and R.S. Pulwarty (eds.)]. CRC Press, Boca Raton, FL, USA, pp. 155–208, doi:10.1201/b22009.
Swain, S. and K. Hayhoe, 2015: CMIP5 projected changes in spring and summer drought and wet conditions over North America. *Climate Dynamics*, **44(9–10)**, 2737–2750, doi:10.1007/s00382-014-2255-9.
Swann, A.L.S., F.M. Hoffman, C.D. Koven, and J.T. Randerson, 2016: Plant responses to increasing CO2 reduce estimates of climate impacts on drought severity. *Proceedings of the National Academy of Sciences*, **113(36)**, 10019–10024, doi:10.1073/pnas.1604581113.
Sweerts, B. et al., 2019: Estimation of losses in solar energy production from air pollution in China since 1960 using surface radiation data. *Nature Energy*, **4(8)**, 657–663, doi:10.1038/s41560-019-0412-4.
Sweet, W. and J. Park, 2014: From the extreme to the mean: Acceleration and tipping points of coastal inundation from sea level rise. *Earth's Future*, **2(12)**, 579–600, doi:10.1002/2014ef000272.
Sweet, W., G. Dusek, J. Obeysekera, and J.J. Marra, 2018: *Patterns and projections of high tide flooding along the U.S. coastline using a common impact threshold*. NOAA Technical Report NOS CO-OPS 086, National Oceanic and Atmospheric Administration (NOAA), National Ocean Service (NOS) Center for Operational Oceanographic Products and Services (COOPS), Silver Spring, MD, USA, 56 pp., doi:10.7289/v5/tr-nos-coops-086.
Sweet, W.V., R. Horton, R.E. Kopp, A.N. LeGrande, and A. Romanou, 2017: Sea Level Rise. In: *Climate Science Special Report: Fourth National Climate Assessment, Volume I* [Wuebbles, D.J., D.W. Fahey, K.A. Hibbard, D.J. Dokken, B.C. Stewart, and T.K. Maycock (eds.)]. U.S. Global Change Research Program, Washington, DC, USA, pp. 333–363, doi:10.7930/j0vm49f2.
Syed, M. and M. Al Amin, 2016: Geospatial Modeling for Investigating Spatial Pattern and Change Trend of Temperature and Rainfall. *Climate*, **4(2)**, 21, doi:10.3390/cli4020021.
Sylla, M.B., P.M. Nikiema, P. Gibba, I. Kebe, and N.A.B. Klutse, 2016: Climate Change over West Africa: Recent Trends and Future Projections. In: *Adaptation to Climate Change and Variability in Rural West Africa* [Yaro, J.A. and J. Hesselberg (eds.)]. Springer, Cham, Switzerland, pp. 25–40, doi:10.1007/978-3-319-31499-0_3.
Sylla, M.B., A. Faye, F. Giorgi, A. Diedhiou, and H. Kunstmann, 2018: Projected Heat Stress Under 1.5°C and 2°C Global Warming Scenarios Creates Unprecedented Discomfort for Humans in West Africa. *Earth's Future*, **6(7)**, 1029–1044, doi:10.1029/2018ef000873.
Syvitski, J.P.M. and J.D. Milliman, 2007: Geology, Geography, and Humans Battle for Dominance over the Delivery of Fluvial Sediment to the Coastal Ocean. *The Journal of Geology*, **115(1)**, 1–19, doi:10.1086/509246.
Takagi, H. and M. Esteban, 2016: Statistics of tropical cyclone landfalls in the Philippines: unusual characteristics of 2013 Typhoon Haiyan. *Natural Hazards*, **80(1)**, 211–222, doi:10.1007/s11069-015-1965-6.
Takagi, H., N. Thao, and L. Anh, 2016: Sea-Level Rise and Land Subsidence: Impacts on Flood Projections for the Mekong Delta's Largest City. *Sustainability*, **8(9)**, 959, doi:10.3390/su8090959.
Takahashi, C. and M. Watanabe, 2016: Pacific trade winds accelerated by aerosol forcing over the past two decades. *Nature Climate Change*, **6(8)**, 768–772, doi:10.1038/nclimate2996.
Tall, A., J.Y. Coulibaly, and M. Diop, 2018: Do climate services make a difference? A review of evaluation methodologies and practices to assess the value of climate information services for farmers: Implications for Africa. *Climate Services*, **11**, 1–12, doi:10.1016/j.cliser.2018.06.001.
Tall, A. et al., 2014: *Scaling up climate services for farmers: Mission Possible. Learning from good practice in Africa and South Asia*. CCAFS Report No. 13, CGIAR Research Program on Climate Change, Agriculture and Food Security (CCAFS), Copenhagen, Denmark, 44 pp.
Tam, B.Y. et al., 2019: CMIP5 drought projections in Canada based on the Standardized Precipitation Evapotranspiration Index. *Canadian Water Resources Journal*, **44(1)**, 90–107, doi:10.1080/07011784.2018.1537812.
Tamerius, J.D., X. Zhou, R. Mantilla, and T. Greenfield-Huitt, 2016: Precipitation Effects on Motor Vehicle Crashes Vary by Space, Time, and Environmental Conditions. *Weather, Climate, and Society*, **8(4)**, 399–407, doi:10.1175/wcas-d-16-0009.1.

ACCEPTED VERSION SUBJECT TO FINAL EDITS

Tang, B.H., V.A. Gensini, and C.R. Homeyer, 2019: Trends in United States large hail environments and observations. *npj Climate and Atmospheric Science*, **2(1)**, 45, doi:10.1038/s41612-019-0103-7.

Tang, C. et al., 2019: Numerical simulation of surface solar radiation over Southern Africa. Part 2: projections of regional and global climate models. *Climate Dynamics*, **53(3–4)**, 2197–2227, doi:10.1007/s00382-019-04817-x.

Tart, S., M. Groth, and P. Seipold, 2020: Market demand for climate services: An assessment of users' needs. *Climate Services*, **17**, 100109, doi:10.1016/j.cliser.2019.100109.

Taufik, M. et al., 2017: Amplification of wildfire area burnt by hydrological drought in the humid tropics. *Nature Climate Change*, **7(6)**, 428–431, doi:10.1038/nclimate3280.

Taylor, A., D. Scott, A. Steynor, and A. Mcclure, 2017: *Transdisciplinary, co-production and co-exploration: integrating knowledge across science, policy and practice in FRACTAL*. Future Resilience for African CiTies and Lands (FRACTAL), 22 pp.

Taylor, C.M. et al., 2017: Frequency of extreme Sahelian storms tripled since 1982 in satellite observations. *Nature*, **544(7651)**, 475–478, doi:10.1038/nature22069.

Taylor, K.E., R.J. Stouffer, and G.A. Meehl, 2012: An Overview of CMIP5 and the Experiment Design. *Bulletin of the American Meteorological Society*, **93(4)**, 485–498, doi:10.1175/bams-d-11-00094.1.

Taylor, M.A. et al., 2018: Future Caribbean Climates in a World of Rising Temperatures: The 1.5 vs 2.0 Dilemma. *Journal of Climate*, **31(7)**, 2907–2926, doi:10.1175/jcli-d-17-0074.1.

Taylor, R.G. et al., 2006: Recent glacial recession in the Rwenzori Mountains of East Africa due to rising air temperature. *Geophysical Research Letters*, **33(10)**, L10402, doi:10.1029/2006gl025962.

Tebaldi, C. and M.F. Wehner, 2018: Benefits of mitigation for future heat extremes under RCP4.5 compared to RCP8.5. *Climatic Change*, **146(3–4)**, 349–361, doi:10.1007/s10584-016-1605-5.

Teichmann, C. et al., 2013: How Does a Regional Climate Model Modify the Projected Climate Change Signal of the Driving GCM: A Study over Different CORDEX Regions Using REMO. *Atmosphere*, **4(2)**, 214–236, doi:10.3390/atmos4020214.

Teichmann, C. et al., 2019: Assessing mean climate change signals in the global CORDEX-CORE ensemble. *Climate Dynamics*, **(submitted**.

Teichmann, C. et al., 2020: Assessing mean climate change signals in the global CORDEX-CORE ensemble. *Climate Dynamics*, doi:10.1007/s00382-020-05494-x.

Teixeira, E.I., G. Fischer, H. van Velthuizen, C. Walter, and F. Ewert, 2013: Global hot-spots of heat stress on agricultural crops due to climate change. *Agricultural and Forest Meteorology*, **170**, 206–215, doi:10.1016/j.agrformet.2011.09.002.

Tesfaye, K. et al., 2017: Climate change impacts and potential benefits of heat-tolerant maize in South Asia. *Theoretical and Applied Climatology*, **130(3–4)**, 959–970, doi:10.1007/s00704-016-1931-6.

Teskey, R. et al., 2015: Responses of tree species to heat waves and extreme heat events. *Plant, Cell & Environment*, **38(9)**, 1699–1712, doi:10.1111/pce.12417.

Thakuri, S. et al., 2019: Elevation-dependent warming of maximum air temperature in Nepal during 1976–2015. *Atmospheric Research*, **228**, 261–269, doi:10.1016/j.atmosres.2019.06.006.

Thepaut, J.-N., D. Dee, R. Engelen, and B. Pinty, 2018: The Copernicus Programme and its Climate Change Service. In: *IGARSS 2018 – 2018 IEEE International Geoscience and Remote Sensing Symposium*. IEEE, pp. 1591–1593, doi:10.1109/igarss.2018.8518067.

Thiery, W. et al., 2020: Warming of hot extremes alleviated by expanding irrigation. *Nature communications*, **11(1)**, 290, doi:10.1038/s41467-019-14075-4.

Thirumalai, K., P.N. DiNezio, Y. Okumura, and C. Deser, 2017: Extreme temperatures in Southeast Asia caused by El Niño and worsened by global warming. *Nature Communications*, **8(1)**, 15531, doi:10.1038/ncomms15531.

Thober, S. et al., 2018: Multi-model ensemble projections of European river floods and high flows at 1.5, 2, and 3 degrees global warming. *Environmental Research Letters*, **13(1)**, 014003, doi:10.1088/1748-9326/aa9e35.

Thomas, C.D. et al., 2004: Extinction risk from climate change. *Nature*, **427(6970)**, 145–148, doi:10.1038/nature02121.

Thomsen, M.S. et al., 2019: Local Extinction of Bull Kelp (Durvillaea spp.) Due to a Marine Heatwave. *Frontiers in Marine Science*, **6**, 84, doi:10.3389/fmars.2019.00084.

Thorne, J.H. et al., 2017: The impact of climate change uncertainty on California's vegetation and adaptation management. *Ecosphere*, **8(12)**, e02021, doi:10.1002/ecs2.2021.

Tian, H. et al., 2016: Climate extremes and ozone pollution: a growing threat to China's food security. *Ecosystem Health and Sustainability*, **2(1)**, e01203, doi:10.1002/ehs2.1203.

Tian, Q., G. Huang, K. Hu, and D. Niyogi, 2019: Observed and global climate model based changes in wind power potential over the Northern Hemisphere during 1979–2016. *Energy*, **167**, 1224–1235, doi:10.1016/j.energy.2018.11.027.

Ting, M., J.P. Kossin, S.J. Camargo, and C. Li, 2019: Past and Future Hurricane Intensity Change along the U.S. East Coast. *Scientific Reports*, **9(1)**, 7795, doi:10.1038/s41598-019-44252-w.

Tippett, M.K., C. Lepore, and J.E. Cohen, 2016: More tornadoes in the most extreme U.S. tornado outbreaks.. *Science (New York, N.Y.)*, **354(6318)**, 1419–1423, doi:10.1126/science.aah7393.

ACCEPTED VERSION SUBJECT TO FINAL EDITS

Tippett, M.K., J.T. Allen, V.A. Gensini, and H.E. Brooks, 2015: Climate and Hazardous Convective Weather. *Current Climate Change Reports*, **1(2)**, 60–73, doi:10.1007/s40641-015-0006-6.

Tobin, I. et al., 2015: Assessing climate change impacts on European wind energy from ENSEMBLES high-resolution climate projections. *Climatic Change*, **128(1–2)**, 99–112, doi:10.1007/s10584-014-1291-0.

Tobin, I. et al., 2016: Climate change impacts on the power generation potential of a European mid-century wind farms scenario. *Environmental Research Letters*, **11(3)**, 034013, doi:10.1088/1748-9326/11/3/034013.

Tobin, I. et al., 2018: Vulnerabilities and resilience of European power generation to 1.5°C, 2°C and 3°C warming. *Environmental Research Letters*, **13(4)**, 044024, doi:10.1088/1748-9326/aab211.

Todzo, S., A. Bichet, and A. Diedhiou, 2020: Intensification of the hydrological cycle expected in West Africa over the 21st century. *Earth System Dynamics*, **11(1)**, 319–328, doi:10.5194/esd-11-319-2020.

Toimil, A., I.J. Losada, P. Camus, and P. Díaz-Simal, 2017: Managing coastal erosion under climate change at the regional scale. *Coastal Engineering*, **128**, 106–122, doi:10.1016/j.coastaleng.2017.08.004.

Tomasek, B.J., M.M. Williams, and A.S. Davis, 2017: Changes in field workability and drought risk from projected climate change drive spatially variable risks in Illinois cropping systems. *PLOS ONE*, **12(2)**, e0172301, doi:10.1371/journal.pone.0172301.

Tong, D.Q., J.X.L. Wang, T.E. Gill, H. Lei, and B. Wang, 2017: Intensified dust storm activity and Valley fever infection in the southwestern United States. *Geophysical Research Letters*, **44(9)**, 4304–4312, doi:10.1002/2017gl073524.

Torregrosa, A., T.A. O'Brien, and I.C. Faloona, 2014: Coastal Fog, Climate Change, and the Environment. *Eos, Transactions American Geophysical Union*, **95(50)**, 473–474, doi:10.1002/2014eo500001.

Tous, M., G. Zappa, R. Romero, L. Shaffrey, and P.L. Vidale, 2016: Projected changes in medicanes in the HadGEM3 N512 high-resolution global climate model. *Climate Dynamics*, **47(5–6)**, 1913–1924, doi:10.1007/s00382-015-2941-2.

Townhill, B.L. et al., 2018: Harmful algal blooms and climate change: exploring future distribution changes. *ICES Journal of Marine Science*, **75(6)**, 1882–1893, doi:10.1093/icesjms/fsy113.

Trapp, R.J., K.A. Hoogewind, and S. Lasher-Trapp, 2019: Future Changes in Hail Occurrence in the United States Determined through Convection-Permitting Dynamical Downscaling. *Journal of Climate*, **32(17)**, 5493–5509, doi:10.1175/jcli-d-18-0740.1.

Trauernicht, C., 2019: Vegetation-Rainfall interactions reveal how climate variability and climate change alter spatial patterns of wildland fire probability on Big Island, Hawaii. *Science of the Total Environment*, **650**, 459–469, doi:10.1016/j.scitotenv.2018.08.347.

Trauernicht, C. et al., 2015: The Contemporary Scale and Context of Wildfire in Hawai'i. *Pacific Science*, **69(4)**, 427–444, doi:10.2984/69.4.1.

Trewin, B. et al., 2020: An updated long-term homogenized daily temperature data set for Australia. *Geoscience Data Journal*, **7(2)**, 149–169, doi:10.1002/gdj3.95.

Triet, N.V.K. et al., 2020: Future projections of flood dynamics in the Vietnamese Mekong Delta. *Science of The Total Environment*, **742**, 140596, doi:10.1016/j.scitotenv.2020.140596.

Tripathi, A., D.K. Tripathi, D.K. Chauhan, N. Kumar, and G.S. Singh, 2016: Paradigms of climate change impacts on some major food sources of the world: A review on current knowledge and future prospects. *Agriculture, Ecosystems & Environment*, **216**, 356–373, doi:10.1016/j.agee.2015.09.034.

Trnka, M. et al., 2014: Adverse weather conditions for European wheat production will become more frequent with climate change. *Nature Climate Change*, **4(7)**, 637–643, doi:10.1038/nclimate2242.

Trnka, M. et al., 2019: Mitigation efforts will not fully alleviate the increase in water scarcity occurrence probability in wheat-producing areas. *Science Advances*, **5(9)**, eaau2406, doi:10.1126/sciadv.aau2406.

Troccoli, A., 2018a: Achieving Valuable Weather and Climate Services. In: *Weather & Climate Services for the Energy Industry* [Troccoli, A. (ed.)]. Palgrave Macmillan, Cham, Switzerland, pp. 13–25, doi:10.1007/978-3-319-68418-5_2.

Troccoli, A. (ed.), 2018b: *Weather & Climate Services for the Energy Industry*. Palgrave Macmillan, Cham, Switzerland, 197 pp., doi:10.1007/978-3-319-68418-5.

Troccoli, A. et al., 2012: Long-term wind speed trends over Australia. *Journal of Climate*, **25(1)**, 170–183, doi:10.1175/2011jcli4198.1.

Troccoli, A. et al., 2018: Creating a proof-of-concept climate service to assess future renewable energy mixes in Europe: An overview of the C3S ECEM project. *Advances in Science and Research*, **15**, 191–205, doi:10.5194/asr-15-191-2018.

Trtanj, J. et al., 2016: Ch. 6: Climate Impacts on Water-Related Illness. In: *The Impacts of Climate Change on Human Health in the United States: A Scientific Assessment*. U.S. Global Change Research Program, Washington, DC, USA, pp. 157–188, doi:10.7930/j03f4mh4.

Turco, M. et al., 2018: Exacerbated fires in Mediterranean Europe due to anthropogenic warming projected with non-stationary climate-fire models. *Nature Communications*, **9(1)**, 3821, doi:10.1038/s41467-018-06358-z.

Udo, K. and Y. Takeda, 2017: Projections of Future Beach Loss in Japan Due to Sea-Level Rise and Uncertainties in Projected Beach Loss. *Coastal Engineering Journal*, **59(2)**, 1740006–1740016,

ACCEPTED VERSION SUBJECT TO FINAL EDITS

doi:10.1142/s057856341740006x.
Underwood, B.S., Z. Guido, P. Gudipudi, and Y. Feinberg, 2017: Increased costs to US pavement infrastructure from future temperature rise. *Nature Climate Change*, **7(10)**, 704–707, doi:10.1038/nclimate3390.
Undorf, S., M.A. Bollasina, B.B.B. Booth, and G.C. Hegerl, 2018: Contrasting the Effects of the 1850-1975 Increase in Sulphate Aerosols from North America and Europe on the Atlantic in the CESM. *Geophysical Research Letters*, **45(21)**, 11,930–11,940, doi:10.1029/2018gl079970.
UNESCAP, 2018: *Sand and Dust Storms in Asia and the Pacific: Opportunities for Regional Cooperation and Action*. ST/ESCAP/2837, United Nations Economic and Social Commission for Asia and the Pacific (UNESCAP), Bangkok, Thailand, 112 pp.
UNISDR, 2015: *Making Development Sustainable: The Future of Disaster Risk Management. Global Assessment Report on Disaster Risk Reduction*. United Nations Office for Disaster Risk Reduction (UNISDR), Geneva, Switzerland, 316 pp.
Unterberger, C. et al., 2018: Spring frost risk for regional apple production under a warmer climate. *PLOS ONE*, **13(7)**, e0200201, doi:10.1371/journal.pone.0200201.
Upperman, C.R. et al., 2017: Exposure to Extreme Heat Events Is Associated with Increased Hay Fever Prevalence among Nationally Representative Sample of US Adults: 1997-2013. *The Journal of Allergy and Clinical Immunology: In Practice*, **5(2)**, 435–441.e2, doi:10.1016/j.jaip.2016.09.016.
Urban, M.C., 2015: Accelerating extinction risk from climate change. *Science*, **348(6234)**, 571–573, doi:10.1126/science.aaa4984.
Urbieta, I.R., M. Franquesa, O. Viedma, and J.M. Moreno, 2019: Fire activity and burned forest lands decreased during the last three decades in Spain. *Annals of Forest Science*, **76(3)**, 90, doi:10.1007/s13595-019-0874-3.
Uribe Botero, E., 2015: *El cambio climático y sus efectos en la biodiversidad en América Latina*. Comisión Económica para América Latina y el Caribe (CEPAL), 84 pp.
Urrutia-Jalabert, R., M.E. González, González-Reyes, A. Lara, and R. Garreaud, 2018: Climate variability and forest fires in central and south-central Chile. *Ecosphere*, **9(4)**, doi:10.1002/ecs2.2171.
US EPA, 2016: *Climate change indicators in the United States 2016. 4th Edition*. EPA 430-R-16-004, United States Envirnomental Protection Agency (US EPA), 92 pp.
Wuebbles, D.J., D.W. Fahey, K.A. Hibbard, D.J. Dokken, B.C. Stewart, and T.K. Maycock (eds.), 2017: *Climate Science Special Report: Fourth National Climate Assessment, Volume I*. U.S. Global Change Research Program, Washington, DC, USA, 470 pp., doi:10.7930/j0j964j6.
Reidmiller, D.R., C.W. Avery, D.R. Easterling, K.E. Kunkel, K.L.M. Lewis, T.K. Maycock, and B.C. Stewart (eds.), 2018: *Impacts, Risks, and Adaptation in the United States: Fourth National Climate Assessment, Volume II*. US. Global Change Research Program, Washington, DC, USA, 1515 pp., doi:10.7930/nca4.2018.
Vaidya, R.A. et al., 2019: Disaster Risk Reduction and Building Resilience in the Hindu Kush Himalaya. In: *The Hindu Kush Himalaya Assessment: Mountains, Climate Change, Sustainability and People* [Wester, P., A. Mishra, A. Mukherji, and A.B. Shrestha (eds.)]. Springer, Cham, pp. 389–419, doi:10.1007/978-3-319-92288-1_11.
Val Martin, M. et al., 2015: How emissions, climate, and land use change will impact mid-century air quality over the United States: a focus on effects at national parks. *Atmospheric Chemistry and Physics*, **15(5)**, 2805–2823, doi:10.5194/acp-15-2805-2015.
Valerio, M., M. Tomecek, S. Lovelli, and L. Ziska, 2013: Assessing the impact of increasing carbon dioxide and temperature on crop-weed interactions for tomato and a C3 and C4 weed species. *European Journal of Agronomy*, **50**, 60–65, doi:10.1016/j.eja.2013.05.006.
Valiela, I., 2006: Global Coastal Change. , 368.
Valsson, T. and G.F. Ulfarsson, 2011: Future changes in activity structures of the globe under a receding Arctic ice scenario. *Futures*, **43(4)**, 450–459, doi:10.1016/j.futures.2010.12.002.
Van Beusekom, A.E. et al., 2018: Fire weather and likelihood: characterizing climate space for fire occurrence and extent in Puerto Rico. *Climatic Change*, **146(1–2)**, 117–131, doi:10.1007/s10584-017-2045-6.
van den Hurk, B. et al., 2018: The match between climate services demands and Earth System Models supplies. *Climate Services*, **12**, 59–63, doi:10.1016/j.cliser.2018.11.002.
van den Hurk, B.J.J.M. et al., 2016: Improving predictions and management of hydrological extremes through climate services. *Climate Services*, **1**, 6–11, doi:10.1016/j.cliser.2016.01.001.
van Huysen, T., J. Hansen, and A. Tall, 2018: Scaling up climate services for smallholder farmers: Learning from practice. *Climate Risk Management*, **22**, 1–3, doi:10.1016/j.crm.2018.10.002.
van Oldenborgh, G.J. et al., 2018: Extreme heat in India and anthropogenic climate change. *Natural Hazards and Earth System Sciences*, **18(1)**, 365–381, doi:10.5194/nhess-18-365-2018.
van Oldenborgh, G.J. et al., 2019: Cold waves are getting milder in the northern midlatitudes. *Environmental Research Letters*, **14(11)**, 114004, doi:10.1088/1748-9326/ab4867.
van Oldenborgh, G.J. et al., 2021: Attribution of the Australian bushfire risk to anthropogenic climate change. *Natural Hazards and Earth System Sciences*, **21(3)**, 941–960, doi:10.5194/nhess-21-941-2021.
van Vliet, M.T.H., D. Wiberg, S. Leduc, and K. Riahi, 2016: Power-generation system vulnerability and adaptation to changes in climate and water resources. *Nature Climate Change*, **6(4)**, 375–380, doi:10.1038/nclimate2903.

ACCEPTED VERSION SUBJECT TO FINAL EDITS

van Vliet, M.T.H. et al., 2013: Global river discharge and water temperature under climate change. *Global Environmental Change*, **23(2)**, 450–464, doi:10.1016/j.gloenvcha.2012.11.002.
Vanderlinden, J.-P. et al., 2017: Coastal Flooding, Uncertainty and Climate Change: Science as a Solution to (mis) Perceptions? A Qualitative Enquiry in Three Coastal European Settings. *Journal of Coastal Research*, **77**, 127–133, doi:10.2112/si77-013.1.
Vano, J.A. et al., 2018: DOs and DON'Ts for using climate change information for water resource planning and management: guidelines for study design. *Climate Services*, **12**, 1–13, doi:10.1016/j.cliser.2018.07.002.
Vanos, J.K., J.W. Baldwin, O. Jay, and K.L. Ebi, 2020: Simplicity lacks robustness when projecting heat-health outcomes in a changing climate. *Nature Communications*, **11(1)**, 6079, doi:10.1038/s41467-020-19994-1.
Vaquer-Sunyer, R. and C.M. Duarte, 2008: Thresholds of hypoxia for marine biodiversity. *Proceedings of the National Academy of Sciences*, **105(40)**, 15452–15457, doi:10.1073/pnas.0803833105.
Varanasi, A., P.V.V. Prasad, and M. Jugulam, 2016: Impact of Climate Change Factors on Weeds and Herbicide Efficacy. *Advances in Agronomy*, **135**, 107–146, doi:10.1016/bs.agron.2015.09.002.
Vaughan, C., S. Dessai, and C. Hewitt, 2018: Surveying Climate Services: What Can We Learn from a Bird's-Eye View? *Weather, Climate, and Society*, **10(2)**, 373–395, doi:10.1175/wcas-d-17-0030.1.
Vaughan, C., J. Hansen, P. Roudier, P. Watkiss, and E. Carr, 2019: Evaluating agricultural weather and climate services in Africa: Evidence, methods, and a learning agenda. *WIREs Climate Change*, **10(4)**, e586, doi:10.1002/wcc.586.
Vautard, R., J. Cattiaux, P. Yiou, J.-N. Thépaut, and P. Ciais, 2010: Northern Hemisphere atmospheric stilling partly attributed to an increase in surface roughness. *Nature Geoscience*, **3(11)**, doi:10.1038/ngeo979.
Vautard, R. et al., 2018: Attribution of Wintertime Anticyclonic Stagnation Contributing to Air Pollution in Western Europe. *Bulletin of the American Meteorological Society*, **99(1)**, S70–S75, doi:10.1175/bams-d-17-0113.1.
Vautard, R. et al., 2019: Human influence on European winter wind storms such as those of January 2018. *Earth System Dynamics*, **10(2)**, 271–286, doi:10.5194/esd-10-271-2019.
Vautard, R. et al., 2020: Evaluation of the large EURO-CORDEX regional climate model ensemble. *Journal of Geophysical Research: Atmospheres*, **125**, e2019JD032344, doi:10.1029/2019jd032344.
Veettil and Kamp, 2019: Global Disappearance of Tropical Mountain Glaciers: Observations, Causes, and Challenges. *Geosciences*, **9(5)**, 196, doi:10.3390/geosciences9050196.
Venäläinen, A. et al., 2014: Temporal variations and change in forest fire danger in Europe for 1960–2012. *Natural Hazards and Earth System Sciences*, **14(6)**, 1477–1490, doi:10.5194/nhess-14-1477-2014.
Vera, C.S. and L. Díaz, 2015: Anthropogenic influence on summer precipitation trends over South America in CMIP5 models. *International Journal of Climatology*, **35(10)**, 3172–3177, doi:10.1002/joc.4153.
Veraverbeke, S. et al., 2017: Lightning as a major driver of recent large fire years in North American boreal forests. *Nature Climate Change*, **7(7)**, 529–534, doi:10.1038/nclimate3329.
Verfaillie, D. et al., 2018: Multi-component ensembles of future meteorological and natural snow conditions for 1500 m altitude in the Chartreuse mountain range, Northern French Alps. *Cryosphere*, **12(4)**, 1249–1271, doi:10.5194/tc-12-1249-2018.
Vezzulli, L., E. Pezzati, I. Brettar, M. Höfle, and C. Pruzzo, 2015: Effects of Global Warming on Vibrio Ecology. *Microbiology Spectrum*, **3(3)**, doi:10.1128/microbiolspec.ve-0004-2014.
Vichot-Llano, A., D. Martinez-Castro, A. Bezanilla-Morlot, A. Centella-Artola, and F. Giorgi, 2021: Projected changes in precipitation and temperature regimes and extremes over the Caribbean and Central America using a multiparameter ensemble of <scp>RegCM4</scp>. *International Journal of Climatology*, **41(2)**, 1328–1350, doi:10.1002/joc.6811.
Vidal, J.-P., B. Hingray, C. Magand, E. Sauquet, and A. Ducharne, 2016: Hierarchy of climate and hydrological uncertainties in transient low-flow projections. *Hydrology and Earth System Sciences*, **20(9)**, 3651–3672, doi:10.5194/hess-20-3651-2016.
Vikhamar-Schuler, D. et al., 2016: Changes in Winter Warming Events in the Nordic Arctic Region. *Journal of Climate*, **29(17)**, 6223–6244, doi:10.1175/jcli-d-15-0763.1.
Villafuerte, M.Q. et al., 2014: Long-term trends and variability of rainfall extremes in the Philippines. *Atmospheric Research*, **137**, 1–13, doi:10.1016/j.atmosres.2013.09.021.
Villarini, G. and L.J. Slater, : Examination of Changes in Annual Maximum Gauge Height in the Continental United States Using Quantile Regression. *Journal of Hydrologic Engineering*, **23(3)**, 06017010, doi:10.1061/(asce)he.1943-5584.0001620.
Villarini, G. and W. Zhang, 2020: Projected changes in flooding: a continental U.S. perspective. *Annals of the New York Academy of Sciences*, **1472(1)**, 95–103, doi:10.1111/nyas.14359.
Vincent, K., M. Daly, C. Scannell, and B. Leathes, 2018a: What can climate services learn from theory and practice of co-production? *Climate Services*, **12**, 48–58, doi:10.1016/j.cliser.2018.11.001.
Vincent, K., A. Steynor, K. Waagsaether, and T. Cull, 2018b: Communities of practice: One size does not fit all. *Climate Services*, **11**, 72–77, doi:10.1016/j.cliser.2018.05.004.
Vincent, L.A., X. Zhang, Mekis, H. Wan, and E.J. Bush, 2018: Changes in Canada's Climate: Trends in Indices Based on Daily Temperature and Precipitation Data. *Atmosphere-Ocean*, **56(5)**, 332–349,

ACCEPTED VERSION SUBJECT TO FINAL EDITS

doi:10.1080/07055900.2018.1514579.
Visscher, K. et al., 2020: Matching supply and demand: A typology of climate services. *Climate Services*, **17**, 100136, doi:10.1016/j.cliser.2019.100136.
Viste, E. and A. Sorteberg, 2015: Snowfall in the Himalayas: an uncertain future from a little-known past. *The Cryosphere*, **9(3)**, 1147–1167, doi:10.5194/tc-9-1147-2015.
Vitousek, S. et al., 2017: Doubling of coastal flooding frequency within decades due to sea-level rise. *Scientific Reports*, **7(1)**, 1399, doi:10.1038/s41598-017-01362-7.
Vogel, E. et al., 2019: The effects of climate extremes on global agricultural yields. *Environmental Research Letters*, **14(5)**, 054010, doi:10.1088/1748-9326/ab154b.
Vogel, M.M., M. Hauser, and S.I. Seneviratne, 2020: Projected changes in hot, dry and wet extreme events' clusters in CMIP6 multi-model ensemble. *Environmental Research Letters*, **15(9)**, 94021, doi:10.1088/1748-9326/ab90a7.
Vose, R.S. et al., 2014: Monitoring and Understanding Changes in Extremes: Extratropical Storms, Winds, and Waves. *Bulletin of the American Meteorological Society*, **95(3)**, 377–386, doi:10.1175/bams-d-12-00162.1.
Vousdoukas, M.I., L. Mentaschi, E. Voukouvalas, M. Verlaan, and L. Feyen, 2017: Extreme sea levels on the rise along Europe's coasts. *Earth's Future*, **5(3)**, 304–323, doi:10.1002/2016ef000505.
Vousdoukas, M.I. et al., 2018: Global probabilistic projections of extreme sea levels show intensification of coastal flood hazard. *Nature Communications*, **9(1)**, 2360, doi:10.1038/s41467-018-04692-w.
Vousdoukas, M.I. et al., 2020a: Economic motivation for raising coastal flood defenses in Europe. *Nature Communications*, **11(1)**, 1–11, doi:10.1038/s41467-020-15665-3.
Vousdoukas, M.I. et al., 2020b: Sandy coastlines under threat of erosion. *Nature Climate Change*, **10(3)**, 260–263, doi:10.1038/s41558-020-0697-0.
Vu, D.T., T. Yamada, and H. Ishidaira, 2018: Assessing the impact of sea level rise due to climate change on seawater intrusion in Mekong Delta, Vietnam. *Water Science and Technology*, **77(6)**, 1632–1639, doi:10.2166/wst.2018.038.
Wadsworth, R., A. Jalloh, and A. Lebbie, 2019: Changes in Rainfall in Sierra Leone: 1981–2018. *Climate*, **7(12)**, 144, doi:10.3390/cli7120144.
Waha, K. et al., 2020: Multiple cropping systems of the world and the potential for increasing cropping intensity. *Global Environmental Change*, **64**, 102131, doi:10.1016/j.gloenvcha.2020.102131.
Wahl, T., S. Jain, J. Bender, S.D. Meyers, and M.E. Luther, 2015: Increasing risk of compound flooding from storm surge and rainfall for major US cities. *Nature Climate Change*, **5(12)**, 1093–1097, doi:10.1038/nclimate2736.
Wainwright, D.J. et al., 2014: An argument for probabilistic coastal hazard assessment: Retrospective examination of practice in New South Wales, Australia. *Ocean & Coastal Management*, **95**, 147–155, doi:10.1016/j.ocecoaman.2014.04.009.
Walsh, K., F. Giorgi, and E. Coppola, 2014: Mediterranean warm-core cyclones in a warmer world. *Climate Dynamics*, **42(3–4)**, 1053–1066, doi:10.1007/s00382-013-1723-y.
Walsh, K. et al., 2016: Natural hazards in Australia: storms, wind and hail. *Climatic Change*, **139(1)**, 55–67, doi:10.1007/s10584-016-1737-7.
Walsh, K.J.E. et al., 2016: Tropical cyclones and climate change. *Wiley Interdisciplinary Reviews: Climate Change*, **7(1)**, 65–89, doi:10.1002/wcc.371.
Walvoord, M.A. and B.L. Kurylyk, 2016: Hydrologic Impacts of Thawing Permafrost – A Review. *Vadose Zone Journal*, **15(6)**, vzj2016.01.0010, doi:10.2136/vzj2016.01.0010.
Wan, Z., H. Shi, X. Liu, and H. Liu, 2020: Analysis on the Ice Regime Change Characteristics in the Inner Mongolia Reach of the Yellow River from 1950 to 2010. *Journal of Coastal Research*, **115(sp1)**, 405–408, doi:10.2112/jcr-si115-115.1.
Wanders, N. and Y. Wada, 2015: Human and climate impacts on the 21st century hydrological drought. *Journal of Hydrology*, **526**, 208–220, doi:10.1016/j.jhydrol.2014.10.047.
Wang, B., D.L. Liu, S. Asseng, I. Macadam, and Q. Yu, 2017: Modelling wheat yield change under CO2 increase, heat and water stress in relation to plant available water capacity in eastern Australia. *European Journal of Agronomy*, **90**, 152–161, doi:10.1016/j.eja.2017.08.005.
Wang, C., J. Liang, and K.I. Hodges, 2017: Projections of tropical cyclones affecting Vietnam under climate change: downscaled HadGEM2-ES using PRECIS 2.1. *Quarterly Journal of the Royal Meteorological Society*, **143(705)**, 1844–1859, doi:10.1002/qj.3046.
Wang, C.-H., X. Wang, and Y.B. Khoo, 2013: Extreme wind gust hazard in Australia and its sensitivity to climate change. *Natural Hazards*, **67(2)**, 549–567, doi:10.1007/s11069-013-0582-5.
Wang, D., T.C. Gouhier, B.A. Menge, and A.R. Ganguly, 2015: Intensification and spatial homogenization of coastal upwelling under climate change. *Nature*, **518(7539)**, 390, doi:10.1038/nature14235.
Wang, G., S.B. Power, and S. Mcgree, 2016: Unambiguous warming in the western tropical Pacific primarily caused by anthropogenic forcing. *International Journal of Climatology*, **36(2)**, 933–944, doi:10.1002/joc.4395.
Wang, H., T. Gao, and L. Xie, 2019: Extreme precipitation events during 1960–2011 for the Northwest China: space-time changes and possible causes. *Theoretical and Applied Climatology*, **137(1)**, 977–995,

ACCEPTED VERSION SUBJECT TO FINAL EDITS

doi:10.1007/s00704-018-2645-8.
Wang, J., M. Kuffer, R. Sliuzas, and D. Kohli, 2019: The exposure of slums to high temperature: Morphology-based local scale thermal patterns. *Science of The Total Environment*, **650**, 1805–1817, doi:10.1016/j.scitotenv.2018.09.324.
Wang, J., S. Yi, M. Li, L. Wang, and C. Song, 2018: Effects of sea level rise, land subsidence, bathymetric change and typhoon tracks on storm flooding in the coastal areas of Shanghai. *Science of The Total Environment*, **621**, 228–234, doi:10.1016/j.scitotenv.2017.11.224.
Wang, L. et al., 2017: Changes in start, end, and length of frost-free season across Northeast China. *International Journal of Climatology*, **37**, 271–283, doi:10.1002/joc.5002.
Wang, S. and R. Toumi, 2016: On the relationship between hurricane cost and the integrated wind profile. *Environmental Research Letters*, **11(11)**, 114005, doi:10.1088/1748-9326/11/11/114005.
Wang, S., L. Zhou, and Y. Wei, 2019: Integrated risk assessment of snow disaster over the Qinghai-Tibet Plateau. *Geomatics, Natural Hazards and Risk*, **10(1)**, 740–757, doi:10.1080/19475705.2018.1543211.
Wang, S., Y. Che, and M. Xinggang, 2020: Integrated risk assessment of glacier lake outburst flood (GLOF) disaster over the Qinghai–Tibetan Plateau (QTP). *Landslides*, **17(12)**, 2849–2863, doi:10.1007/s10346-020-01443-1.
Wang, S.-J. and L.-Y. Zhou, 2019: Integrated impacts of climate change on glacier tourism. *Advances in Climate Change Research*, **10(2)**, 71–79, doi:10.1016/j.accre.2019.06.006.
Wang, S.S.-Y. et al., 2019: Consecutive extreme flooding and heat wave in Japan: Are they becoming a norm? *Atmospheric Science Letters*, **20(10)**, e933, doi:10.1002/asl.933.
Wang, W., Y. Zhu, R. Xu, and J. Liu, 2015: Drought severity change in China during 1961–2012 indicated by SPI and SPEI. *Natural Hazards*, **75(3)**, 2437–2451, doi:10.1007/s11069-014-1436-5.
Wang, X., C. Wu, H. Wang, A. Gonsamo, and Z. Liu, 2017a: No evidence of widespread decline of snow cover on the Tibetan Plateau over 2000–2015. *Scientific Reports*, **7(1)**, 14645, doi:10.1038/s41598-017-15208-9.
Wang, X. et al., 2017b: Projected changes in daily fire spread across Canada over the next century. *Environmental Research Letters*, **12(2)**, 025005, doi:10.1088/1748-9326/aa5835.
Wang, X.L., B. Trewin, Y. Feng, and D. Jones, 2013: Historical changes in Australian temperature extremes as inferred from extreme value distribution analysis. *Geophysical Research Letters*, **40(3)**, 573–578, doi:10.1002/grl.50132.
Wang, Y., L. Song, C. Hewitt, N. Golding, and Z. Huang, 2020: Improving China's Resilience to Climate-Related Risks: The China Framework for Climate Services. *Weather, Climate, and Society*, **12(4)**, 729–744, doi:10.1175/wcas-d-19-0121.1.
Wang, Y. et al., 2018: Temporal and spatial variation relationship and influence factors on surface urban heat island and ozone pollution in the Yangtze River Delta, China. *Science of The Total Environment*, **631–632**, 921–933, doi:10.1016/j.scitotenv.2018.03.050.
Ward, D.M., 2013: The effect of weather on grid systems and the reliability of electricity supply. *Climatic Change*, **121(1)**, 103–113, doi:10.1007/s10584-013-0916-z.
Ward, R.D., D.A. Friess, R.H. Day, and R.A. Mackenzie, 2016: Impacts of climate change on mangrove ecosystems: a region by region overview. *Ecosystem Health and Sustainability*, **2(4)**, e01211, doi:10.1002/ehs2.1211.
Ward Jones, M.K., W.H. Pollard, and B.M. Jones, 2019: Rapid initialization of retrogressive thaw slumps in the Canadian high Arctic and their response to climate and terrain factors. *Environmental Research Letters*, **14(5)**, 055006, doi:10.1088/1748-9326/ab12fd.
Warszawski, L. et al., 2014: The Inter-Sectoral Impact Model Intercomparison Project (ISI–MIP): Project framework. *Proceedings of the National Academy of Sciences*, **111(9)**, 3228–3232, doi:10.1073/pnas.1312330110.
Wasko, C. and R. Nathan, 2019: Influence of changes in rainfall and soil moisture on trends in flooding. *Journal of Hydrology*, **575**, 432–441, doi:10.1016/j.jhydrol.2019.05.054.
Watson, S.-A., J.B. Fields, and P.L. Munday, 2017: Ocean acidification alters predator behaviour and reduces predation rate. *Biology Letters*, **13(2)**, 20160797, doi:10.1098/rsbl.2016.0797.
Watt, M.S. et al., 2019: Assessment of multiple climate change effects on plantation forests in New Zealand. *Forestry: An International Journal of Forest Research*, **92(1)**, 1–15, doi:10.1093/forestry/cpy024.
Watts, N. et al., 2018: The 2018 report of the Lancet Countdown on health and climate change: shaping the health of nations for centuries to come. *The Lancet*, **392(10163)**, 2479–2514, doi:10.1016/s0140-6736(18)32594-7.
Weatherdon, L., A.K. Magnan, A.D. Rogers, U.R. Sumaila, and W.W.L. Cheung, 2016: Observed and Projected Impacts of Climate Change on Marine Fisheries, Aquaculture, Coastal Tourism, and Human Health: An Update. *Frontiers in Marine Science*, **3**, 48, doi:10.3389/fmars.2016.00048.
Webb, A.P. and P.S. Kench, 2010: The dynamic response of reef islands to sea-level rise: Evidence from multi-decadal analysis of island change in the Central Pacific. *Global and Planetary Change*, **72(3)**, 234–246, doi:10.1016/j.gloplacha.2010.05.003.
Webb, J.D.C., D.M. Elsom, and G.T. Meaden, 2009: Severe hailstorms in Britain and Ireland, a climatological survey and hazard assessment. *Atmospheric Research*, **93(1–3)**, 587–606, doi:10.1016/j.atmosres.2008.10.034.
Webb, N.P. and C. Pierre, 2018: Quantifying Anthropogenic Dust Emissions. *Earth's Future*, **6(2)**, 286–295, doi:10.1002/2017ef000766.

ACCEPTED VERSION SUBJECT TO FINAL EDITS

Webb, N.P. et al., 2020: Indicators and benchmarks for wind erosion monitoring, assessment and management. *Ecological Indicators*, **110**, 105881, doi:10.1016/j.ecolind.2019.105881.
Webber, H. et al., 2017: Canopy temperature for simulation of heat stress in irrigated wheat in a semi-arid environment: A multi-model comparison. *Field Crops Research*, **202**, 21–35, doi:10.1016/j.fcr.2015.10.009.
Webber, S. and S.D. Donner, 2017: Climate service warnings: cautions about commercializing climate science for adaptation in the developing world. *Wiley Interdisciplinary Reviews: Climate Change*, **8(1)**, e424, doi:10.1002/wcc.424.
Weber, J., F. Gotzens, and D. Witthaut, 2018: Impact of strong climate change on the statistics of wind power generation in Europe. *Energy Procedia*, **153**, 22–28, doi:10.1016/j.egypro.2018.10.004.
Wegmann, M., Y. Orsolini, and O. Zolina, 2018: Warm Arctic-cold Siberia: comparing the recent and the early 20th-century Arctic warmings. *Environmental Research Letters*, **13(2)**, 25009, doi:10.1088/1748-9326/aaa0b7.
Wehner, M.F., J.R. Arnold, T. Knutson, K.E. Kunkel, and A.N. LeGrande, 2017: Droughts, Floods, and Wildfires. In: *Climate Science Special Report: Fourth National Climate Assessment, Volume I* [Wuebbles, D.J., D.W. Fahey, K.A. Hibbard, D.J. Dokken, B.C. Stewart, and T.K. Maycock (eds.)]. U.S. Global Change Research Program, Washington, DC, USA, pp. 231–256, doi:10.7930/j0cj8bnn.
Wehof, J., J.K. Miller, and J. Engle, 2014: Application of the storm erosion index (SEI) to three unique storms. *Coastal Engineering Proceedings*, **1(34)**, 39, doi:10.9753/icce.v34.management.39.
Weichselgartner, J. and B. Arheimer, 2019: Evolving Climate Services into Knowledge–Action Systems. *Weather, Climate, and Society*, **11(2)**, 385–399, doi:10.1175/wcas-d-18-0087.1.
Weiss, L.C. et al., 2018: Rising pCO2 in Freshwater Ecosystems Has the Potential to Negatively Affect Predator-Induced Defenses in Daphnia.. *Current biology : CB*, **28(2)**, 327–332.e3, doi:10.1016/j.cub.2017.12.022.
Weisse, R. et al., 2015: Climate services for marine applications in Europe. *Earth Perspectives*, **2(1)**, 3, doi:10.1186/s40322-015-0029-0.
Wernberg, T. et al., 2013: An extreme climatic event alters marine ecosystem structure in a global biodiversity hotspot. *Nature Climate Change*, **3(1)**, 78–82, doi:10.1038/nclimate1627.
Wernberg, T. et al., 2016: Climate-driven regime shift of a temperate marine ecosystem. *Science*, **353(6295)**, 169–172, doi:10.1126/science.aad8745.
Wester, P., A. Mishra, A. Mukherji, and A. Shrestha, 2019: The Hindu Kush Himalaya Assessment. , doi:10.1007/978-3-319-92288-1.
Westerling, A.L.R., 2016: Increasing western US forest wildfire activity: sensitivity to changes in the timing of spring. *Philosophical Transactions of the Royal Society B: Biological Sciences*, **371(1696)**, 20150178, doi:10.1098/rstb.2015.0178.
Whitehead, P.G., R.L. Wilby, R.W. Battarbee, M. Kernan, and A.J. Wade, 2009: A review of the potential impacts of climate change on surface water quality. *Hydrological Sciences Journal*, **54(1)**, 101–123, doi:10.1623/hysj.54.1.101.
Hales, S., S. Kovats, S. Lloyd, and D. Campbell-Lendrum (eds.), 2014: *Quantitative risk assessment of the effects of climate change on selected causes of death, 2030s and 2050s*. World Health Organization (WHO), Geneva, Switzerland, 115 pp.
Wickström, S., M.O. Jonassen, T. Vihma, and P. Uotila, 2020: Trends in cyclones in the high-latitude North Atlantic during 1979–2016. *Quarterly Journal of the Royal Meteorological Society*, **146(727)**, 762–779, doi:10.1002/qj.3707.
Wijffels, S.E. et al., 2018: A fine spatial-scale sea surface temperature atlas of the Australian regional seas (SSTAARS): Seasonal variability and trends around Australasia and New Zealand revisited. *Journal of Marine Systems*, **187**, 156–196, doi:10.1016/j.jmarsys.2018.07.005.
Wilcox, A.C. et al., 2016: An integrated analysis of the March 2015 Atacama floods. *Geophysical Research Letters*, **43(15)**, 8035–8043, doi:10.1002/2016gl069751.
Wild, M., D. Folini, and F. Henschel, 2017: Impact of climate change on future concentrated solar power (CSP) production. In: *AIP Conference Proceedings*. AIP Publishing, pp. 100007, doi:10.1063/1.4975562.
Wild, M., D. Folini, F. Henschel, N. Fischer, and B. Müller, 2015: Projections of long-term changes in solar radiation based on CMIP5 climate models and their influence on energy yields of photovoltaic systems. *Solar Energy*, **116**, 12–24, doi:10.1016/j.solener.2015.03.039.
Wilkinson, M.D. et al., 2016: The FAIR Guiding Principles for scientific data management and stewardship. *Scientific Data*, **3(1)**, 160018, doi:10.1038/sdata.2016.18.
Wille, J.D. et al., 2019: West Antarctic surface melt triggered by atmospheric rivers. *Nature Geoscience*, **12(11)**, 911–916, doi:10.1038/s41561-019-0460-1.
Williamson, S.N. et al., 2020: Evidence for Elevation-Dependent Warming in the St. Elias Mountains, Yukon, Canada. *Journal of Climate*, **33(8)**, 3253–3269, doi:10.1175/jcli-d-19-0405.1.
Willibald, F., S. Kotlarski, A. Grêt-Regamey, and R. Ludwig, 2020: Anthropogenic climate change versus internal climate variability: impacts on snow cover in the Swiss Alps. *The Cryosphere*, **14(9)**, 2909–2924, doi:10.5194/tc-14-2909-2020.
Wilson, R. et al., 2018: Glacial lakes of the Central and Patagonian Andes. *Global and Planetary Change*, **162**, 275–

ACCEPTED VERSION SUBJECT TO FINAL EDITS

291, doi:10.1016/j.gloplacha.2018.01.004.
Winsemius, H.C. et al., 2016: Global drivers of future river flood risk. *Nature Climate Change*, **6(4)**, 381–385, doi:10.1038/nclimate2893.
WMO, 2015: *Valuing Weather and Climate: Economic Assessment of Meteorological and Hydrological Services*. WMO-No. 1153, World Meteorological Organization (WMO), Geneva, Switzerland, 286 pp.
WMO, 2018: Climate Change: Science and solutions. *WMO Bulletin*, **67(2)**, 76.
Wobus, C. et al., 2017a: Climate change impacts on flood risk and asset damages within mapped 100-year floodplains of the contiguous United States. *Natural Hazards and Earth System Sciences*, **17(12)**, 2199–2211, doi:10.5194/nhess-17-2199-2017.
Wobus, C. et al., 2017b: Projected climate change impacts on skiing and snowmobiling: A case study of the United States. *Global Environmental Change*, **45**, 1–14, doi:10.1016/j.gloenvcha.2017.04.006.
Wolfe, D.W. et al., 2008: Projected change in climate thresholds in the Northeastern U.S.: implications for crops, pests, livestock, and farmers. *Mitigation and Adaptation Strategies for Global Change*, **13(5–6)**, 555–575, doi:10.1007/s11027-007-9125-2.
Wolfe, D.W. et al., 2018: Unique challenges and opportunities for northeastern US crop production in a changing climate. *Climatic Change*, **146(1–2)**, 231–245, doi:10.1007/s10584-017-2109-7.
Wolski, P., 2018: How severe is Cape Town's "Day Zero" drought? *Significance*, **15(2)**, 24–27, doi:10.1111/j.1740-9713.2018.01127.x.
Wolski, P. et al., 2018: Attributing 2015-2017 drought in Western Cape , South Africa. In: *20th EGU General Assembly, EGU2018, Proceedings from the conference held 4-13 April, 2018 in Vienna, Austria,*. pp. 13705.
Woolway, R.I. et al., 2020: Global lake responses to climate change. *Nature Reviews Earth & Environment*, **1(8)**, 388–403, doi:10.1038/s43017-020-0067-5.
Woolway, R.I. et al., 2021: Lake heatwaves under climate change. *Nature*, **589(7842)**, 402–407, doi:10.1038/s41586-020-03119-1.
Wu, B. and J.A. Francis, 2019: Summer Arctic Cold Anomaly Dynamically Linked to East Asian Heat Waves. *Journal of Climate*, **32(4)**, 1137–1150, doi:10.1175/jcli-d-18-0370.1.
Wu, C. et al., 2018: Can Climate Models Reproduce the Decadal Change of Dust Aerosol in East Asia. *Geophysical Research Letters*, **45(18)**, 9953–9962, doi:10.1029/2018gl079376.
Wu, J., Y. Shi, and Y. Xu, 2020: Evaluation and Projection of Surface Wind Speed Over China Based on CMIP6 GCMs. *Journal of Geophysical Research: Atmospheres*, **125(22)**, e2020JD033611, doi:10.1029/2020jd033611.
Wu, J., J. Zha, D. Zhao, and Q. Yang, 2018: Changes in terrestrial near-surface wind speed and their possible causes: an overview. *Climate Dynamics*, **51(5–6)**, 2039–2078, doi:10.1007/s00382-017-3997-y.
Wu, M. et al., 2020: Spatiotemporal variability of standardized precipitation evapotranspiration index in mainland China over 1961–2016. *International Journal of Climatology*, **40(11)**, 4781–4799, doi:10.1002/joc.6489.
Wu, S., Y. Wu, and J. Wen, 2019: Future changes in precipitation characteristics in China. *International Journal of Climatology*, **39(8)**, 3558–3573, doi:10.1002/joc.6038.
Wu, X., Y. Lu, S. Zhou, L. Chen, and B. Xu, 2016: Impact of climate change on human infectious diseases: Empirical evidence and human adaptation. *Environment International*, **86**, 14–23, doi:10.1016/j.envint.2015.09.007.
Wuebbles, D. et al., 2014: CMIP5 Climate Model Analyses: Climate Extremes in the United States. *Bulletin of the American Meteorological Society*, **95(4)**, 571–583, doi:10.1175/bams-d-12-00172.1.
Wypych, A., Z. Ustrnul, A. Sulikowska, F.-M. Chmielewski, and B. Bochenek, 2017: Spatial and temporal variability of the frost-free season in Central Europe and its circulation background. *International Journal of Climatology*, **37(8)**, 3340–3352, doi:10.1002/joc.4920.
Xia, J., K. Tu, Z. Yan, and Y. Qi, 2016: The super-heat wave in eastern China during July-August 2013: a perspective of climate change. *International Journal of Climatology*, **36(3)**, 1291–1298, doi:10.1002/joc.4424.
Xie, Y., K.F. Ahmed, J.M. Allen, A.M. Wilson, and J.A. Silander, 2015: Green-up of deciduous forest communities of northeastern North America in response to climate variation and climate change. *Landscape Ecology*, **30(1)**, 109–123, doi:10.1007/s10980-014-0099-7.
Xu, Y. et al., 2017: Asian climate change under 1.5–4 °C warming targets. *Advances in Climate Change Research*, **8(2)**, 99–107, doi:10.1016/j.accre.2017.05.004.
Yalew, S.G. et al., 2020: Impacts of climate change on energy systems in global and regional scenarios. *Nature Energy*, **5(10)**, 794–802, doi:10.1038/s41560-020-0664-z.
Yamaguchi, M., J.C.L. Chan, I.-J. Moon, K. Yoshida, and R. Mizuta, 2020: Global warming changes tropical cyclone translation speed. *Nature Communications*, **11(1)**, 47, doi:10.1038/s41467-019-13902-y.
Yamamoto, A. et al., 2015: Global deep ocean oxygenation by enhanced ventilation in the Southern Ocean under long-term global warming. *Global Biogeochemical Cycles*, **29(10)**, 1801–1815, doi:10.1002/2015gb005181.
Yang, Q., K. Song, Z. Wen, X. Hao, and C. Fang, 2019: Recent trends of ice phenology for eight large lakes using MODIS products in Northeast China. *International Journal of Remote Sensing*, **40(14)**, 5388–5410, doi:10.1080/01431161.2019.1579939.
Yang, X., T.M. Pavelsky, and G.H. Allen, 2020a: The past and future of global river ice. *Nature*, **577(7788)**, 69–73,

ACCEPTED VERSION SUBJECT TO FINAL EDITS

doi:10.1038/s41586-019-1848-1.
Yang, X. et al., 2020b: Contrasting Influences of Human Activities on Hydrological Drought Regimes Over China Based on High-Resolution Simulations. *Water Resources Research*, **56(6)**, e2019WR025843, doi:10.1029/2019wr025843.
Yao, N. et al., 2020: Projections of drought characteristics in China based on a standardized precipitation and evapotranspiration index and multiple GCMs. *Science of The Total Environment*, **704**, 135245, doi:10.1016/j.scitotenv.2019.135245.
Yao, X. et al., 2016: Spatial-temporal variations of lake ice phenology in the Hoh Xil region from 2000 to 2011. *Journal of Geographical Sciences*, **26(1)**, 70–82, doi:10.1007/s11442-016-1255-6.
Yasuhara, K. et al., 2012: Effects of climate change on geo-disasters in coastal zones and their adaptation. *Geotextiles and Geomembranes*, **30**, 24–34, doi:10.1016/j.geotexmem.2011.01.005.
Ye, H. et al., 2015: Increasing atmospheric water vapor and higher daily precipitation intensity over northern Eurasia. *Geophysical Research Letters*, **42(21)**, 9404–9410, doi:10.1002/2015gl066104.
Yeo, S.-R., W.M. Kim, and K.-Y. Kim, 2017: Eurasian snow cover variability in relation to warming trend and Arctic Oscillation. *Climate Dynamics*, **48(1)**, 499–511, doi:10.1007/s00382-016-3089-4.
Yin, H., Y. Sun, and M.G. Donat, 2019: Changes in temperature extremes on the Tibetan Plateau and their attribution. *Environmental Research Letters*, **14(12)**, 124015, doi:10.1088/1748-9326/ab503c.
Yin, J.H., 2005: A consistent poleward shift of the storm tracks in simulations of 21st century climate. *Geophysical Research Letters*, **32**, L18701, doi:10.1029/2005gl023684.
Yokohata, T. et al., 2019: Visualizing the Interconnections Among Climate Risks. *Earth's Future*, **7(2)**, 85–100, doi:10.1029/2018ef000945.
Yoon, J.H., S.Y.S. Wang, M.H. Lo, and W.Y. Wu, 2018: Concurrent increases in wet and dry extremes projected in Texas and combined effects on groundwater. *Environmental Research Letters*, **13(5)**, 054002, doi:10.1088/1748-9326/aab96b.
Yoshida, K., M. Sugi, R. Mizuta, H. Murakami, and M. Ishii, 2017: Future Changes in Tropical Cyclone Activity in High-Resolution Large-Ensemble Simulations. *Geophysical Research Letters*, **44(19)**, 9910–9917, doi:10.1002/2017gl075058.
You, Q. et al., 2017: A comparison of heat wave climatologies and trends in China based on multiple definitions. *Climate Dynamics*, **48(11–12)**, 3975–3989, doi:10.1007/s00382-016-3315-0.
You, Q. et al., 2020: Elevation dependent warming over the Tibetan Plateau: Patterns, mechanisms and perspectives. *Earth-Science Reviews*, **210**, 103349, doi:10.1016/j.earscirev.2020.103349.
Young, A.M., P.E. Higuera, P.A. Duffy, and F.S. Hu, 2017: Climatic thresholds shape northern high-latitude fire regimes and imply vulnerability to future climate change. *Ecography*, **40(5)**, 606–617, doi:10.1111/ecog.02205.
Yu, D., Y. Liu, P. Shi, and J. Wu, 2019: Projecting impacts of climate change on global terrestrial ecoregions. *Ecological Indicators*, **103**, 114–123, doi:10.1016/j.ecolind.2019.04.006.
Yu, R. and P. Zhai, 2020: More frequent and widespread persistent compound drought and heat event observed in China. *Scientific Reports*, **10(1)**, doi:10.1038/s41598-020-71312-3.
Yu, Y., H. Stern, C. Fowler, F. Fetterer, and J. Maslanik, 2014: Interannual Variability of Arctic Landfast Ice between 1976 and 2007. *Journal of Climate*, **27(1)**, 227–243, doi:10.1175/jcli-d-13-00178.1.
Yu, Y. et al., 2015: Climatic controls on the interannual to decadal variability in Saudi Arabian dust activity: Toward the development of a seasonal dust prediction model. *Journal of Geophysical Research: Atmospheres*, **120(5)**, 1739–1758, doi:10.1002/2014jd022611.
Yuan, F. et al., 2016: Possible Future Climate Change Impacts on the Hydrological Drought Events in the Weihe River Basin, China. *Advances in Meteorology*, **2016**, 2905198, doi:10.1155/2016/2905198.
Yuan, X., L. Wang, and E.F. Wood, 2018: Anthropogenic Intensification of Southern African Flash Droughts as Exemplified by the 2015/16 Season. *Bulletin of the American Meteorological Society*, **99(1)**, S86–S90, doi:10.1175/bams-d-17-0077.1.
Yue, X., L.J. Mickley, J.A. Logan, and J.O. Kaplan, 2013: Ensemble projections of wildfire activity and carbonaceous aerosol concentrations over the western United States in the mid-21st century. *Atmospheric Environment*, **77**, 767–780, doi:10.1016/j.atmosenv.2013.06.003.
Zahn, M., M. Akperov, A. Rinke, F. Feser, and I.I. Mokhov, 2018: Trends of Cyclone Characteristics in the Arctic and Their Patterns From Different Reanalysis Data. *Journal of Geophysical Research: Atmospheres*, **123(5)**, 2737–2751, doi:10.1002/2017jd027439.
Zaninelli, P.G., C.G. Menéndez, M. Falco, N. López-Franca, and A.F. Carril, 2019: Future hydroclimatological changes in South America based on an ensemble of regional climate models. *Climate Dynamics*, **52(1–2)**, 819–830, doi:10.1007/s00382-018-4225-0.
Zappa, G., L.C. Shaffrey, K.I. Hodges, P.G. Sansom, and D.B. Stephenson, 2013: A Multimodel Assessment of Future Projections of North Atlantic and European Extratropical Cyclones in the CMIP5 Climate Models. *Journal of Climate*, **26(16)**, 5846–5862, doi:10.1175/jcli-d-12-00573.1.
Zarei, A.R., M.M. Moghimi, and M.R. Mahmoudi, 2016: Parametric and Non-Parametric Trend of Drought in Arid and

ACCEPTED VERSION SUBJECT TO FINAL EDITS

Semi-Arid Regions Using RDI Index. *Water Resources Management*, **30(14)**, 5479–5500, doi:10.1007/s11269-016-1501-9.
Zargar, A., R. Sadiq, B. Naser, and F.I. Khan, 2011: A review of drought indices. *Environmental Reviews*, **19(NA)**, 333–349, doi:10.1139/a11-013.
Zarzycki, C.M., 2016: Tropical cyclone intensity errors associated with lack of two-way ocean coupling in high-resolution global simulations. *Journal of Climate*, **29(23)**, 8589–8610, doi:10.1175/jcli-d-16-0273.1.
Žebre, M. et al., 2021: 200 years of equilibrium-line altitude variability across the European Alps (1901-2100). *Climate Dynamics*, **56(3–4)**, 1183–1201, doi:10.1007/s00382-020-05525-7.
Zekollari, H., M. Huss, and D. Farinotti, 2019: Modelling the future evolution of glaciers in the European Alps under the EURO-CORDEX RCM ensemble. *The Cryosphere*, **13(4)**, 1125–1146, doi:10.5194/tc-13-1125-2019.
Zeleke, T.T., F. Giorgi, G.T. Diro, and B.F. Zaitchik, 2017: Trend and periodicity of drought over Ethiopia. *International Journal of Climatology*, **37(13)**, 4733–4748, doi:10.1002/joc.5122.
Zeng, Z. et al., 2019: A reversal in global terrestrial stilling and its implications for wind energy production. *Nature Climate Change*, **9(12)**, 979–985, doi:10.1038/s41558-019-0622-6.
Zha, J., J. Wu, D. Zhao, and Q. Yang, 2017: Changes of the probabilities in different ranges of near-surface wind speed in China during the period for 1970 – 2011. *Journal of Wind Engineering & Industrial Aerodynamics*, **169**, 156–167, doi:10.1016/j.jweia.2017.07.019.
Zha, J., J. Wu, D. Zhao, and J. Tang, 2019: A possible recovery of the near-surface wind speed in Eastern China during winter after 2000 and the potential causes. *Theoretical and Applied Climatology*, **136(1)**, 119–134, doi:10.1007/s00704-018-2471-z.
Zha, J., J. Wu, D. Zhao, and W. Fan, 2020: Future projections of the near-surface wind speed over eastern China based on CMIP5 datasets. *Climate Dynamics*, **54(3)**, 2361–2385, doi:10.1007/s00382-020-05118-4.
Zhai, J. et al., 2017: Intensity–area–duration analysis of droughts in China 1960–2013. *Climate Dynamics*, **48(1)**, 151–168, doi:10.1007/s00382-016-3066-y.
Zhang, C., Y. Wang, K. Hamilton, and A. Lauer, 2016: Dynamical downscaling of the climate for the Hawaiian islands. Part II: Projection for the late twenty-first century. *Journal of Climate*, **29(23)**, 8333–8354, doi:10.1175/jcli-d-16-0038.1.
Zhang, F. et al., 2018: Projection of global wind and solar resources over land in the 21st century. *Global Energy Interconnection*, **1(4)**, 443–451, doi:10.14171/j.2096-5117.gei.2018.04.004.
Zhang, G. et al., 2018: Exacerbated grassland degradation and desertification in Central Asia during 2000–2014. *Ecological Applications*, **28(2)**, 442–456, doi:10.1002/eap.1660.
Zhang, J. and X. Gao, 2016: Nutrient distribution and structure affect the acidification of eutrophic ocean margins: A case study in southwestern coast of the Laizhou Bay, China. *Marine Pollution Bulletin*, **111(1–2)**, 295–304, doi:10.1016/j.marpolbul.2016.06.095.
Zhang, J. and Y. Shen, 2019: Spatio-temporal variations in extreme drought in China during 1961–2015. *Journal of Geographical Sciences*, **29(1)**, 67–83, doi:10.1007/s11442-019-1584-3.
Zhang, J., G. Cowie, and S.W.A. Naqvi, 2013: Hypoxia in the changing marine environment. *Environmental Research Letters*, **8(1)**, 015025, doi:10.1088/1748-9326/8/1/015025.
Zhang, K. et al., 2012: Comparing exposure metrics for classifying 'dangerous heat' in heat wave and health warning systems. *Environment International*, **46**, 23–29, doi:10.1016/j.envint.2012.05.001.
Zhang, M., Y. Chen, Y. Shen, and B. Li, 2019: Tracking climate change in Central Asia through temperature and precipitation extremes. *Journal of Geographical Sciences*, **29(1)**, 3–28, doi:10.1007/s11442-019-1581-6.
Zhang, Q., X. Ni, and F. Zhang, 2017: Decreasing trend in severe weather occurrence over China during the past 50 years. *Scientific Reports*, **7(1)**, 42310, doi:10.1038/srep42310.
Zhang, R., S. Zhang, J. Luo, Y. Han, and J. Zhang, 2019: Analysis of near-surface wind speed change in China during 1958–2015. *Theoretical and Applied Climatology*, **137(3)**, 2785–2801, doi:10.1007/s00704-019-02769-0.
Zhang, X. et al., 2016: A Systematic Review of Global Desert Dust and Associated Human Health Effects. *Atmosphere*, **7(12)**, 158, doi:10.3390/atmos7120158.
Zhang, X. et al., 2019: Changes in Temperature and Precipitation Across Canada. In: *Canada's Changing Climate Report* [Bush, E. and D.S. Lemmen (eds.)]. Government of Canada, Ottawa, ON, Canada, pp. 112–193.
Zhang, Z., K. Wang, D. Chen, J. Li, and R. Dickinson, 2019: Increase in Surface Friction Dominates the Observed Surface Wind Speed Decline during 1973–2014 in the Northern Hemisphere Lands. *Journal of Climate*, **32(21)**, 7421–7435, doi:10.1175/jcli-d-18-0691.1.
Zhao, C., F. Brissette, J. Chen, and J.L. Martel, 2020: Frequency change of future extreme summer meteorological and hydrological droughts over North America. *Journal of Hydrology*, **584**, 124316, doi:10.1016/j.jhydrol.2019.124316.
Zhao, C. et al., 2017: Temperature increase reduces global yields of major crops in four independent estimates. *Proceedings of the National Academy of Sciences*, **114(35)**, 9326–9331, doi:10.1073/pnas.1701762114.
Zhao, H.- et al., 2021: Temporal and Spatial Characteristics of Drought in China under Climate Change. *Chinese Journal of Agrometeorology*, **42(1)**, 69–79, doi:10.3969/j.issn.1000-6362.2021.01.007.
Zhao, L. et al., 2018: Interactions between urban heat islands and heat waves. *Environmental Research Letters*, **13(3)**,

ACCEPTED VERSION SUBJECT TO FINAL EDITS

34003, doi:10.1088/1748-9326/aa9f73.
Zhao, L. et al., 2020: Changing climate and the permafrost environment on the Qinghai-Tibet (Xizang) plateau. *PERMAFROST AND PERIGLACIAL PROCESSES*, **31(3, SI)**, 396–405, doi:10.1002/ppp.2056.
Zhao, T. and A. Dai, 2017: Uncertainties in historical changes and future projections of drought. Part II: model-simulated historical and future drought changes. *Climatic Change*, **144(3)**, 535–548, doi:10.1007/s10584-016-1742-x.
Zhao, X., D.L. Smith, and A.J. Tatem, 2016: Exploring the spatiotemporal drivers of malaria elimination in Europe. *Malaria Journal*, **15(1)**, 122, doi:10.1186/s12936-016-1175-z.
Zhao, Y., A. Ducharne, B. Sultan, P. Braconnot, and R. Vautard, 2015: Estimating heat stress from climate-based indicators: present-day biases and future spreads in the CMIP5 global climate model ensemble. *Environmental Research Letters*, **10(8)**, 084013, doi:10.1088/1748-9326/10/8/084013.
Zhao, Y. et al., 2016: Potential escalation of heat-related working costs with climate and socioeconomic changes in China. *Proceedings of the National Academy of Sciences*, **113(17)**, 4640–4645, doi:10.1073/pnas.1521828113.
Zheng, F., M. Leonard, and S. Westra, 2017: Application of the design variable method to estimate coastal flood risk. *Journal of Flood Risk Management*, **10(4)**, 522–534, doi:10.1111/jfr3.12180.
Zheng, Y. et al., 2016: A 20-year simulated climatology of global dust aerosol deposition. *Science of the Total Environment*, **557–558**, 861–868, doi:10.1016/j.scitotenv.2016.03.086.
Zhong, X., T. Zhang, S. Kang, and J. Wang, 2021: Spatiotemporal variability of snow cover timing and duration over the Eurasian continent during 1966–2012. *Science of The Total Environment*, **750**, 141670, doi:10.1016/j.scitotenv.2020.141670.
Zhou, B., Z. Wang, Y. Shi, Y. Xu, and Z. Han, 2018: Historical and Future Changes of Snowfall Events in China under a Warming Background. *Journal of Climate*, **31(15)**, 5873–5889, doi:10.1175/jcli-d-17-0428.1.
Zhou, C., K. Wang, D. Qi, and J. Tan, 2019: Attribution of a Record-Breaking Heatwave Event in Summer 2017 over the Yangtze River Delta [in "Explaining Extremes of 2017 from a Climate Perspective"]. *Bulletin of the American Meteorological Society*, **100(1)**, S97–S103, doi:10.1175/bams-d-18-0134.1.
Zhou, C., A. Dai, J. Wang, and D. Chen, 2021: Quantifying Human-Induced Dynamic and Thermodynamic Contributions to Severe Cold Outbreaks Like November 2019 in the Eastern United States [in "Explaining Extremes of 2019 from a Climate Perspective"]. *Bulletin of the American Meteorological Society*, **102(1)**, S17–S23, doi:10.1175/bams-d-20-0171.1.
Zhou, T., L. Ren, H. Liu, and J. Lu, 2018: Impact of 1.5°C and 2.0°C global warming on aircraft takeoff performance in China. *Science Bulletin*, **63(11)**, 700–707, doi:10.1016/j.scib.2018.03.018.
Zhu, C. et al., 2018: Carbon dioxide (CO2) levels this century will alter the protein, micronutrients, and vitamin content of rice grains with potential health consequences for the poorest rice-dependent countries. *Science Advances*, **4(5)**, eaaq1012, doi:10.1126/sciadv.aaq1012.
Zhu, J., S. Wang, and G. Huang, 2019: Assessing Climate Change Impacts on Human-Perceived Temperature Extremes and Underlying Uncertainties. *Journal of Geophysical Research: Atmospheres*, **124(7)**, 3800–3821, doi:10.1029/2018jd029444.
Zhu, X. et al., 2019: Projected temperature and precipitation changes on the Tibetan Plateau: results from dynamical downscaling and CCSM4. *Theoretical and Applied Climatology*, **138(1)**, 861–875, doi:10.1007/s00704-019-02841-9.
Zhu, X. et al., 2020: Dynamical downscaling simulation and projection for mean and extreme temperature and precipitation over central Asia. *Climate Dynamics*, **54(7–8)**, 3279–3306, doi:10.1007/s00382-020-05170-0.
Zhu, Z. et al., 2016: Greening of the Earth and its drivers. *Nature Climate Change*, **6(8)**, 791–795, doi:10.1038/nclimate3004.
Zhuan, M.-J. et al., 2018: Timing of human-induced climate change emergence from internal climate variability for hydrological impact studies. *Hydrology Research*, **49(2)**, 421–437, doi:10.2166/nh.2018.059.
Zimmerman, R. and C. Faris, 2010: Chapter 4: Infrastructure impacts and adaptation challenges. *Annals of the New York Academy of Sciences*, **1196(1)**, 63–86, doi:10.1111/j.1749-6632.2009.05318.x.
Zinnert, J.C. et al., 2019: Connectivity in coastal systems: Barrier island vegetation influences upland migration in a changing climate. *Global Change Biology*, gcb.14635, doi:10.1111/gcb.14635.
Ziska, L.H., R.C. Sicher, K. George, and J.E. Mohan, 2007: Rising Atmospheric Carbon Dioxide and Potential Impacts on the Growth and Toxicity of Poison Ivy (Toxicodendron radicans). *Weed Science*, **55(4)**, 288–292, doi:10.1614/ws-06-190.
Ziska, L.H. et al., 2019: Temperature-related changes in airborne allergenic pollen abundance and seasonality across the northern hemisphere: a retrospective data analysis. *The Lancet Planetary Health*, **3(3)**, e124–e131, doi:10.1016/s2542-5196(19)30015-4.
Zkhiri, W., Y. Tramblay, L. Hanich, L. Jarlan, and D. Ruelland, 2019: Spatiotemporal characterization of current and future droughts in the High Atlas basins (Morocco). *Theoretical and Applied Climatology*, **135(1–2)**, 593–605, doi:10.1007/s00704-018-2388-6.
Zolfaghari, H., J. Masoompour, M. Yeganefar, and M. Akbary, 2016: Studying spatial and temporal changes of aridity in Iran. *Arabian Journal of Geosciences*, **9(5)**, 375, doi:10.1007/s12517-016-2379-9.

ACCEPTED VERSION SUBJECT TO FINAL EDITS

Zong, X., X. Tian, and Y. Yin, 2020: Impacts of Climate Change on Wildfires in Central Asia. *Forests*, **11(8)**, 802, doi:10.3390/f11080802.
Zscheischler, J. et al., 2018: Future climate risk from compound events. *Nature Climate Change*, **8(6)**, 469–477, doi:10.1038/s41558-018-0156-3.
Zubkova, M., L. Boschetti, J.T. Abatzoglou, and L. Giglio, 2019: Changes in Fire Activity in Africa from 2002 to 2016 and Their Potential Drivers. *Geophysical Research Letters*, **46(13)**, 7643–7653, doi:10.1029/2019gl083469.
Zulkafli, Z. et al., 2016: Projected increases in the annual flood pulse of the Western Amazon. *Environmental Research Letters*, **11(1)**, 14013, doi:10.1088/1748-9326/11/1/014013.

ACCEPTED VERSION
SUBJECT TO FINAL EDITS

Figures

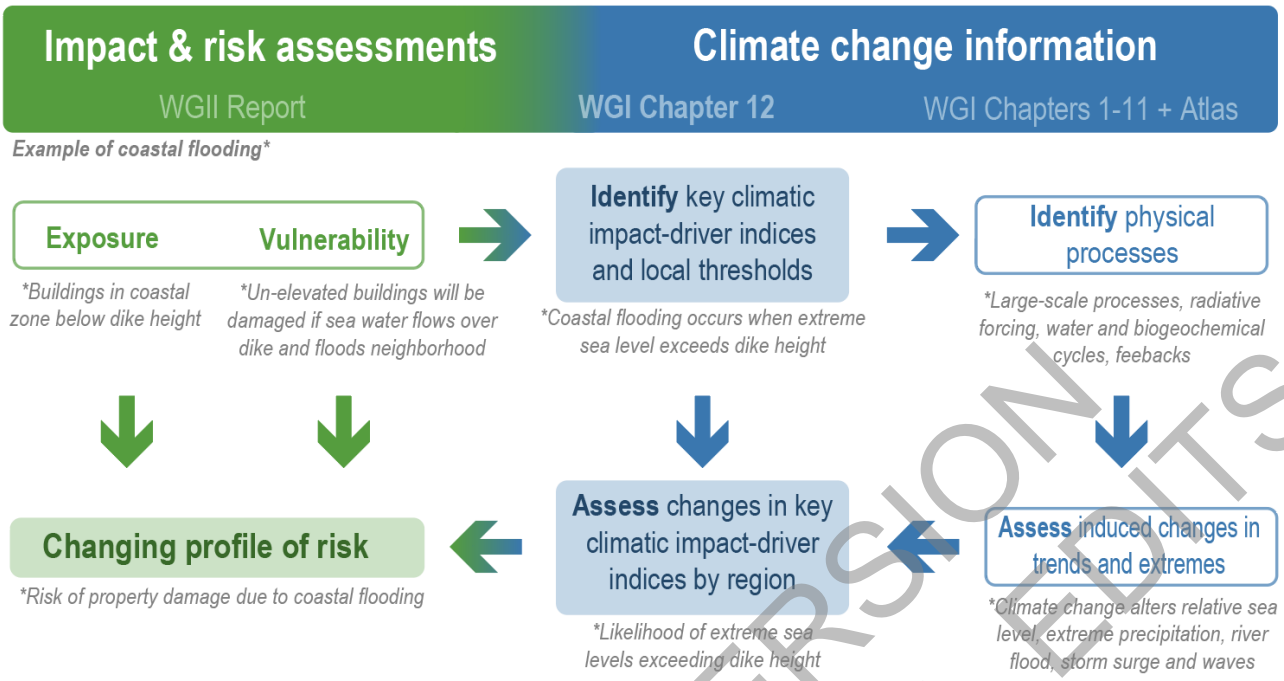


Figure 12.1: **Schematic diagram showing the use of climate change information (WGI chapters) for typical impacts or risk assessment (WGII chapters) and the role of Chapter 12, via an illustration of the assessment of property damage or loss in a particular region when extreme sea level exceeds dike height.**

ACCEPTED VERSION
SUBJECT TO FINAL EDITS

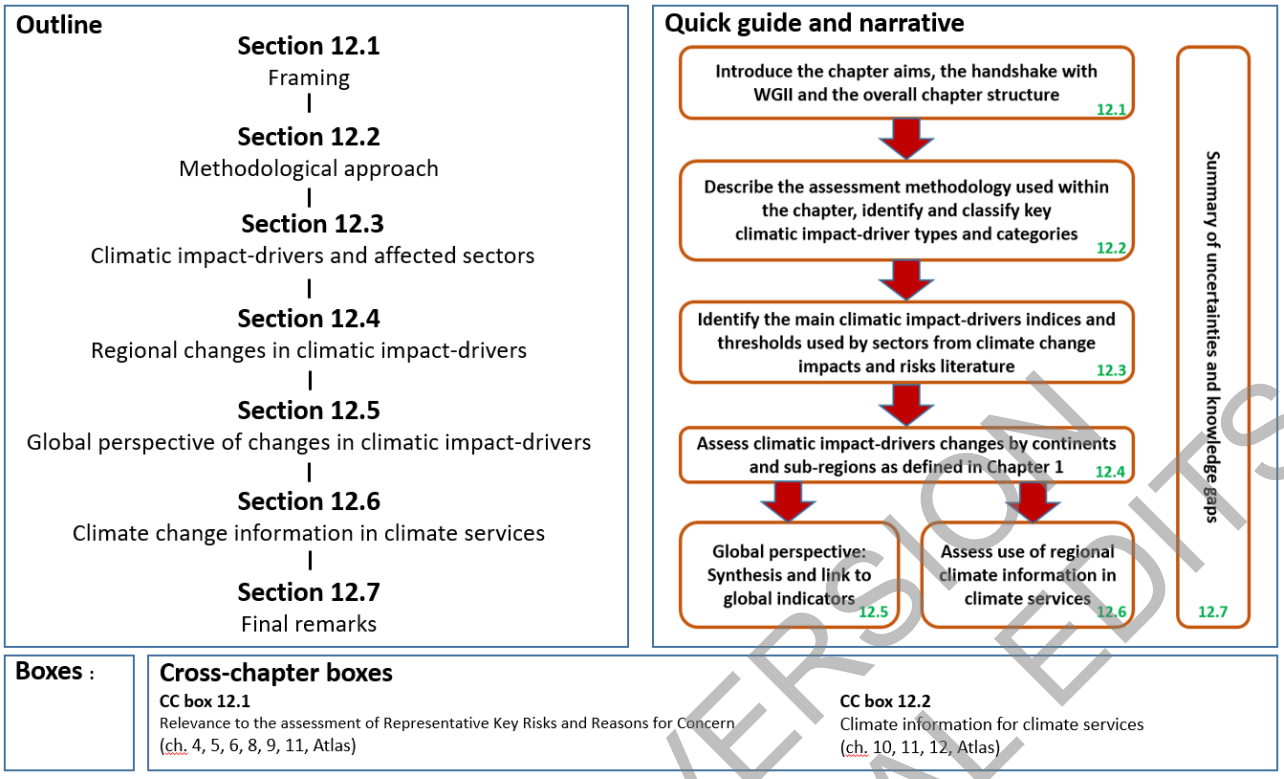


Figure 12.2: Narrative and structure of Chapter 12.

ACCEPTED VERSION SUBJECT TO FINAL EDITS

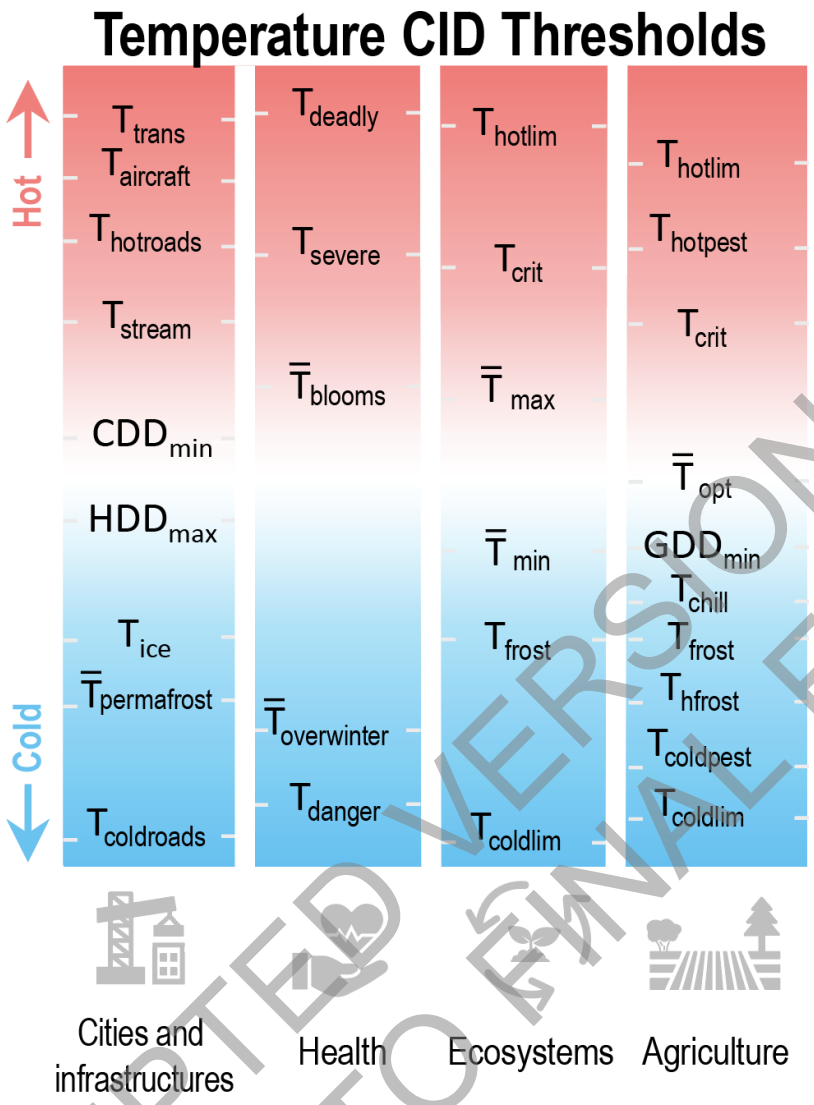
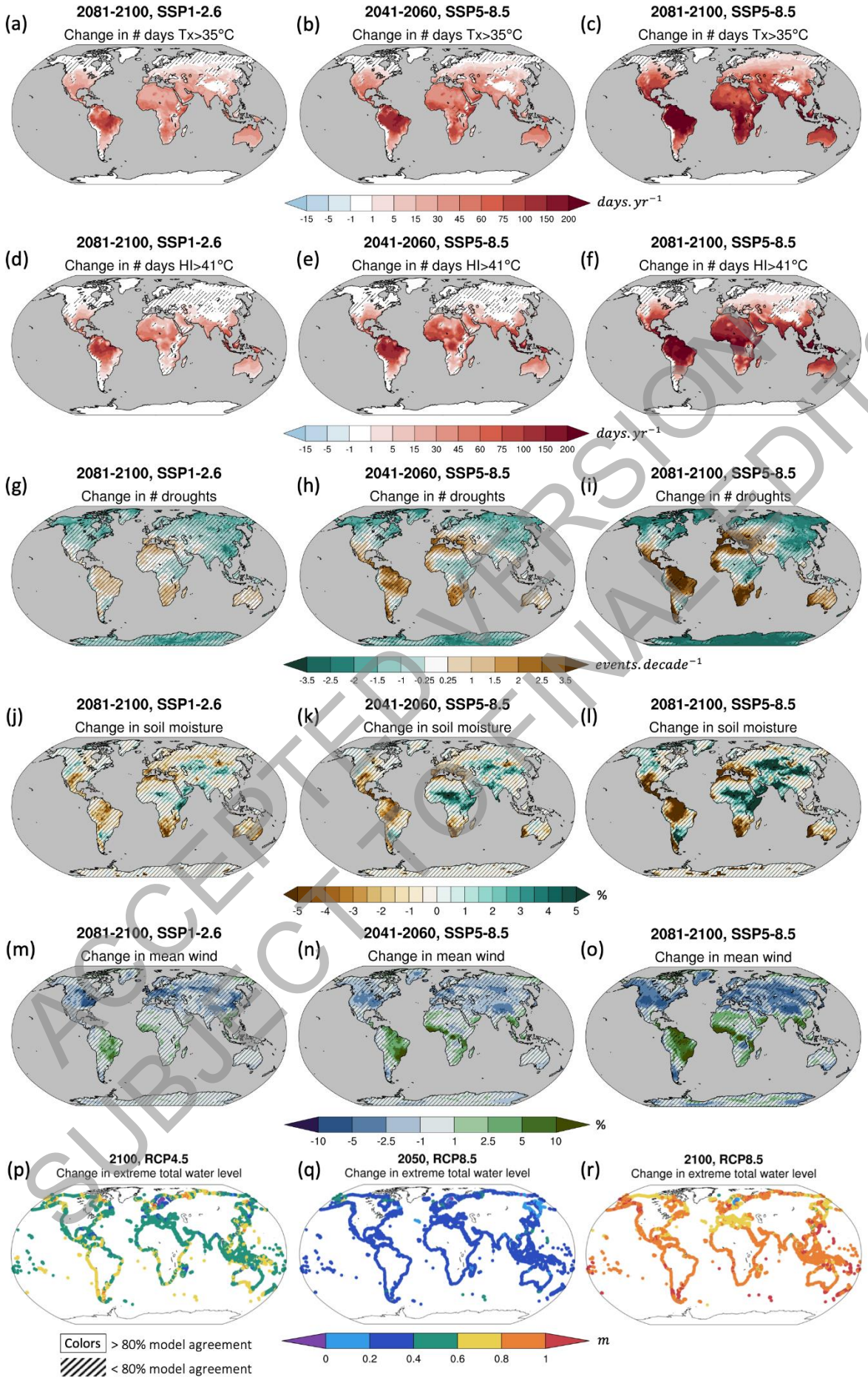


Figure 12.3: Conceptual illustration of representative climatic impact-driver thresholds showing how graduating thresholds affect successive sectoral assets and lead to potentially more acute hazards as conditions become more extreme (exact values are not shown as these must be tailored to reflect diverse vulnerabilities of regional assets). Representative threshold definitions (T = instantaneous temperature; $\bar{T}$ = mean temperature). **Cities and Infrastructure**: T_{trans} = temperature at which energy transmission lines efficiency reduced; $T_{aircraft}$ = temperature at which aircraft become weight-restricted for takeoff; $T_{hotroads}$ = temperature above which roads begin to warp; T_{stream} = temperature at which streams are not capable of adequately cooling thermal plants; CDD_{min} = Minimum temperature for calculating cooling degree days; HDD_{min} = maximum temperature for calculating heating degree days; T_{ice} = temperature at which ice threatens transportation; $\bar{T}_{permafrost}$ = mean seasonal temperature above which permafrost thaws at critical depths; $T_{coldroads}$ = temperature below which road asphalt performance suffers. **Health**: T_{deadly} = temperatures above which prolonged exposure may be deadly (often combined with humidity for heat indices); T_{severe} = temperatures above which prolonged exposure may cause elevated morbidity; $\bar{T}_{blooms}$ = mean temperature for harmful algal or cyanobacteria blooms; T_{danger} = level of dangerous cold temperatures (often combined with wind for chill indices); $T_{overwinter}$ = temperature below which disease vector species cannot survive winter. **Ecosystems** (CID indices for air and ocean temperature): T_{hotlim} and $T_{coldlim}$ = limiting hot and cold temperatures for a given species range; T_{frost} = frost threshold; $\bar{T}_{max}$ and $\bar{T}_{min}$ = maximum and minimum suitable annual mean temperatures for a given species; T_{crit} = critical temperature above which a given species is stressed. **Agriculture**: T_{hotlim}= temperature above which a crop or livestock species dies; $T_{hotpest}$ = maximum (or 'lethal') temperature above which an agricultural pest/disease/weed cannot survive; T_{crit} = temperature at which productivity for a given crop is depressed; $\bar{T}_{opt}$ = optimal mean temperature for a given plant's productivity; GDD_{min} = threshold temperature for growing degree days determining plant development; T_{chill} = temperature below which chilling units are accumulated; T_{frost} = temperature below which frost occurs; T_{hfrost} = temperature

ACCEPTED VERSION SUBJECT TO FINAL EDITS

below which a hard frost threatens crops or livestock; $T_{coldpest}$ = minimum wintertime temperature below which a given agricultural pest cannot survive; $T_{coldlim}$ = minimum temperature below which a given crop cannot survive.

ACCEPTED VERSION
SUBJECT TO FINAL EDITS

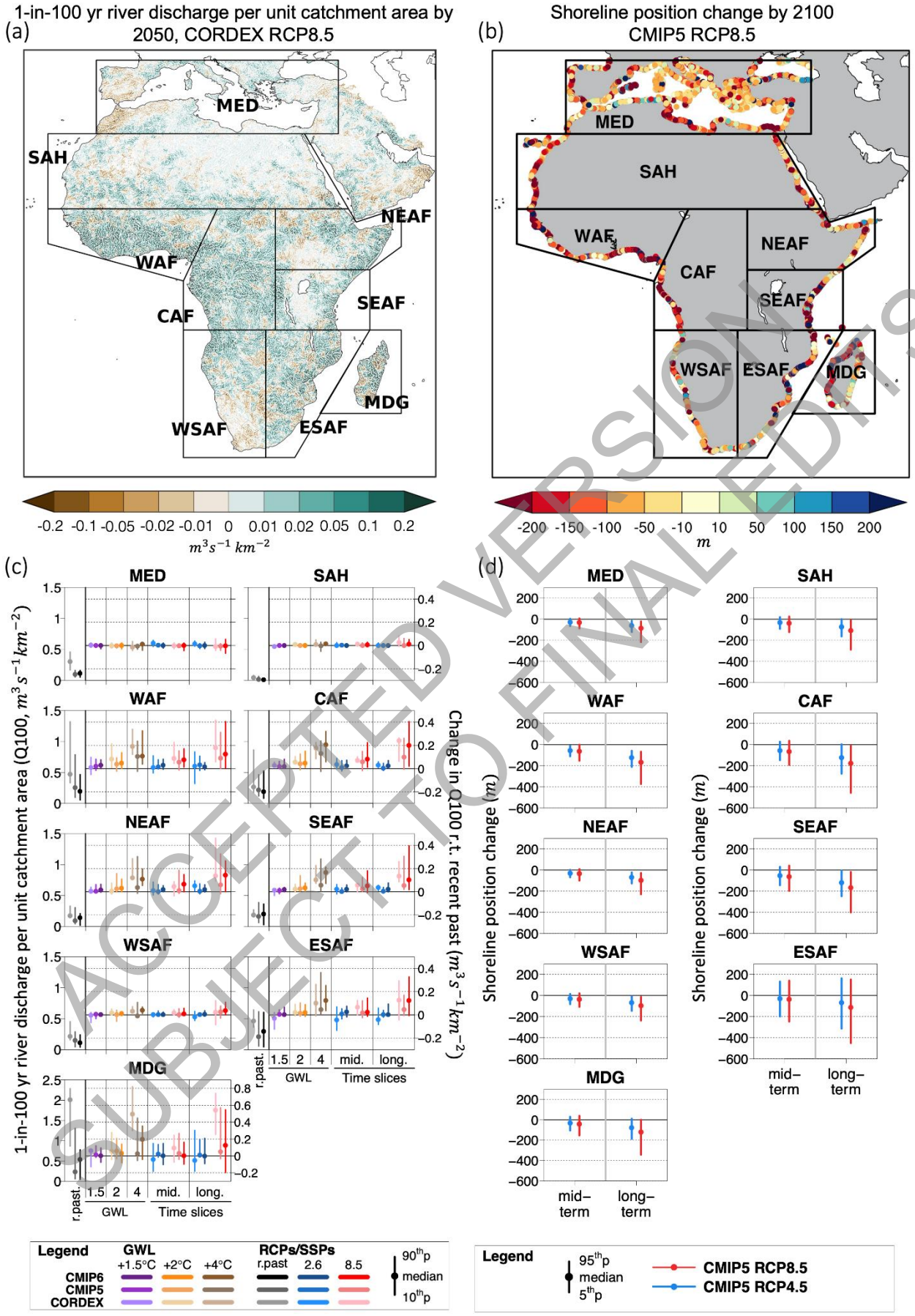


ACCEPTED VERSION SUBJECT TO FINAL EDITS

1

Figure 12.4: Median projected changes in selected climatic impact-driver indices based on CMIP6 models. (a-c) mean number of days per year with maximum temperature exceeding 35°C, (d-f) mean number of days per year with the NOAA Heat Index (HI) exceeding 41°C, (g-i) number of negative precipitation anomaly events per decade using the 6-month Standardised Precipitation Index, (j-l) mean soil moisture (%) and (m-o) mean wind speed (%). (p-r) shows change in extreme sea level (1:100 yr return period total water level from Vousdoukas et al. (2018)'s CMIP5 based dataset; meters). Left column is for SSP1-2.6, 2081-2100, middle column is for SSP5-8.5 2041-2060, and right column SSP5-8.5, 2081-2100, all expressed as changes relative to 1995-2014. Exception is extreme total water level which is for (p) RCP4.5 2100, (q) RCP8.5 2050 and (r) RCP8.5 2100, each relative to 1980-2014. Bias correction is applied to daily maximum temperature and HI data (see Technical Annex VI and Atlas.1.4.5). Uncertainty is represented using the simple approach: No overlay indicates regions with high model agreement, where ≥80% of models agree on sign of change; diagonal lines indicate regions with low model agreement, where <80% of models agree on sign of change. For more information on the simple approach, please refer to the Cross-Chapter Box Atlas.1. See Technical Annex VI for details of indices. Figures SM 12.1-12.6 show regionally averaged values of these indices for the WGI reference AR6 regions for various model ensembles, scenarios, time horizons and global warming levels. Further details on data sources and processing are available in the chapter data table (Table 12.SM.1).

ACCEPTED VERSION
SUBJECT TO FINAL EDITS



ACCEPTED VERSION SUBJECT TO FINAL EDITS

Figure 12.5: Projected changes in selected climatic impact-driver indices for Africa. (a) Mean change in 1-in-100 year river discharge per unit catchment area (Q100, $m^3 s^{-1} km^{-2}$) from CORDEX models for 2041-2060 relative to 1995-2014 for RCP8.5. (b) Shoreline position change along sandy coasts by the year 2100 relative to 2010 (meters; negative values indicate shoreline retreat) from the CMIP5 based data set presented by Vousdoukas et al., (2020). (c) Bar plots for Q100 ($m^3 s^{-1} km^{-2}$) averaged over land areas for the WGI reference AR6 regions (defined in Chapter 1). The left column within each panel (associated with the left y-axis) shows the 'recent past' (1995-2014) Q100 absolute values in grey shades. The other columns (associated with the right y-axis) show the Q100 changes relative to the recent past values for two time periods ('mid' 2041-2060 and 'long' 2081-2100) and for three global warming levels (defined relative to the preindustrial period 1850-1900): 1.5°C (purple), 2°C (yellow) and 4°C (brown). The bars show the median (dots) and the 10^{th}-90^{th} percentile range of model ensemble values across each model ensemble. CMIP6 is shown by the darkest colors, CMIP5 by medium, and CORDEX by light. SSP5-8.5/RCP8.5 is shown in red and SSP1-2.6/RCP2.6 in blue. (d) Bar plots for shoreline position change show CMIP5 based projections of shoreline position change along sandy coasts for 2050 and 2100 relative to 2010 for RCP8.5 (red) and RCP4.5 (blue) from Vousdoukas et al., (2020). Dots indicate regional mean change estimates and bars the 5^{th}-95^{th} percentile range of associated uncertainty. Note that these shoreline position change projections assume that there are no additional sediment sinks/sources or any physical barriers to shoreline retreat. See Technical Annex VI for details of indices. Further details on data sources and processing are available in the chapter data table (Table 12.SM.1).

ACCEPTED VERSION
SUBJECT TO FINAL EDITS

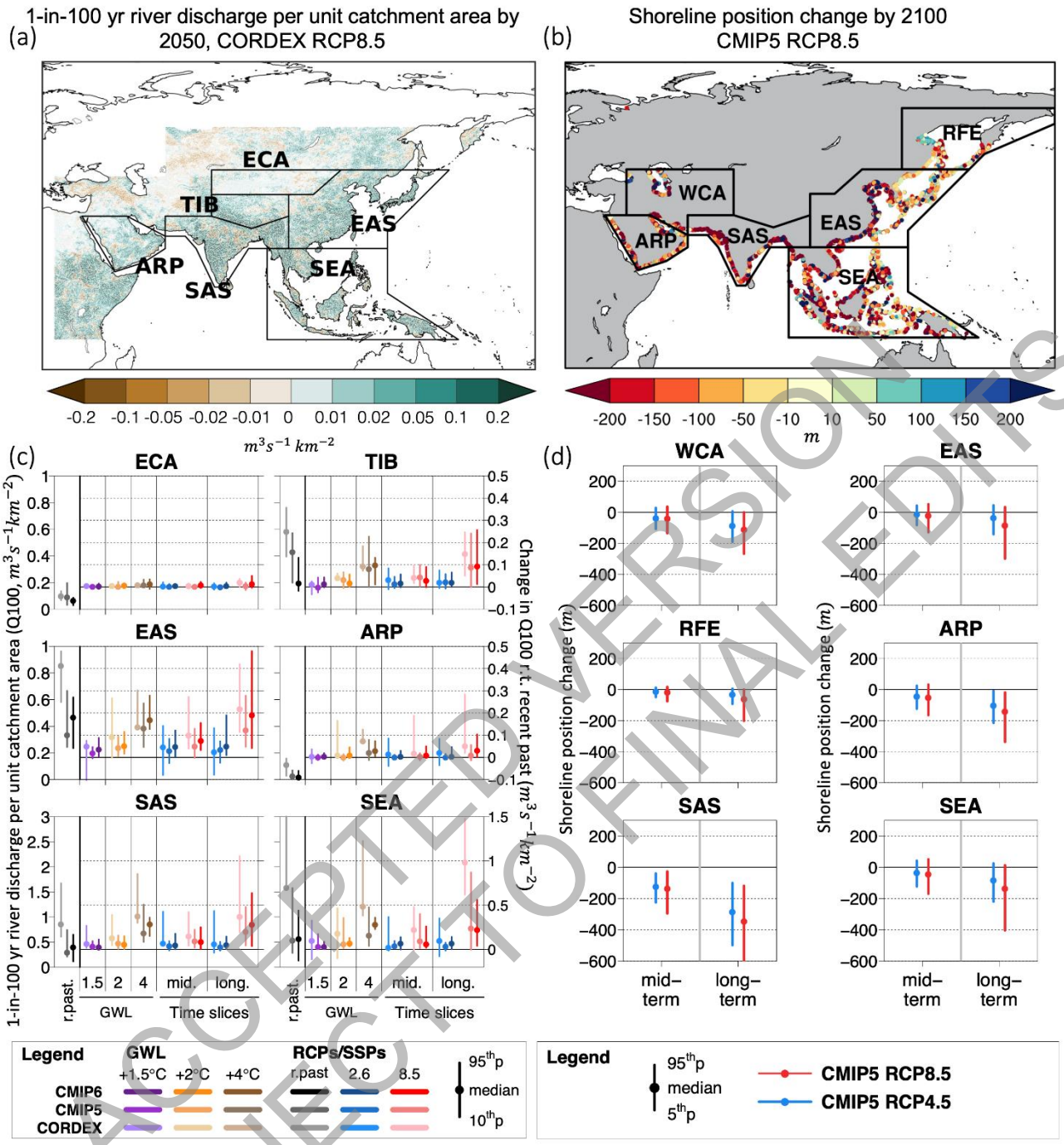
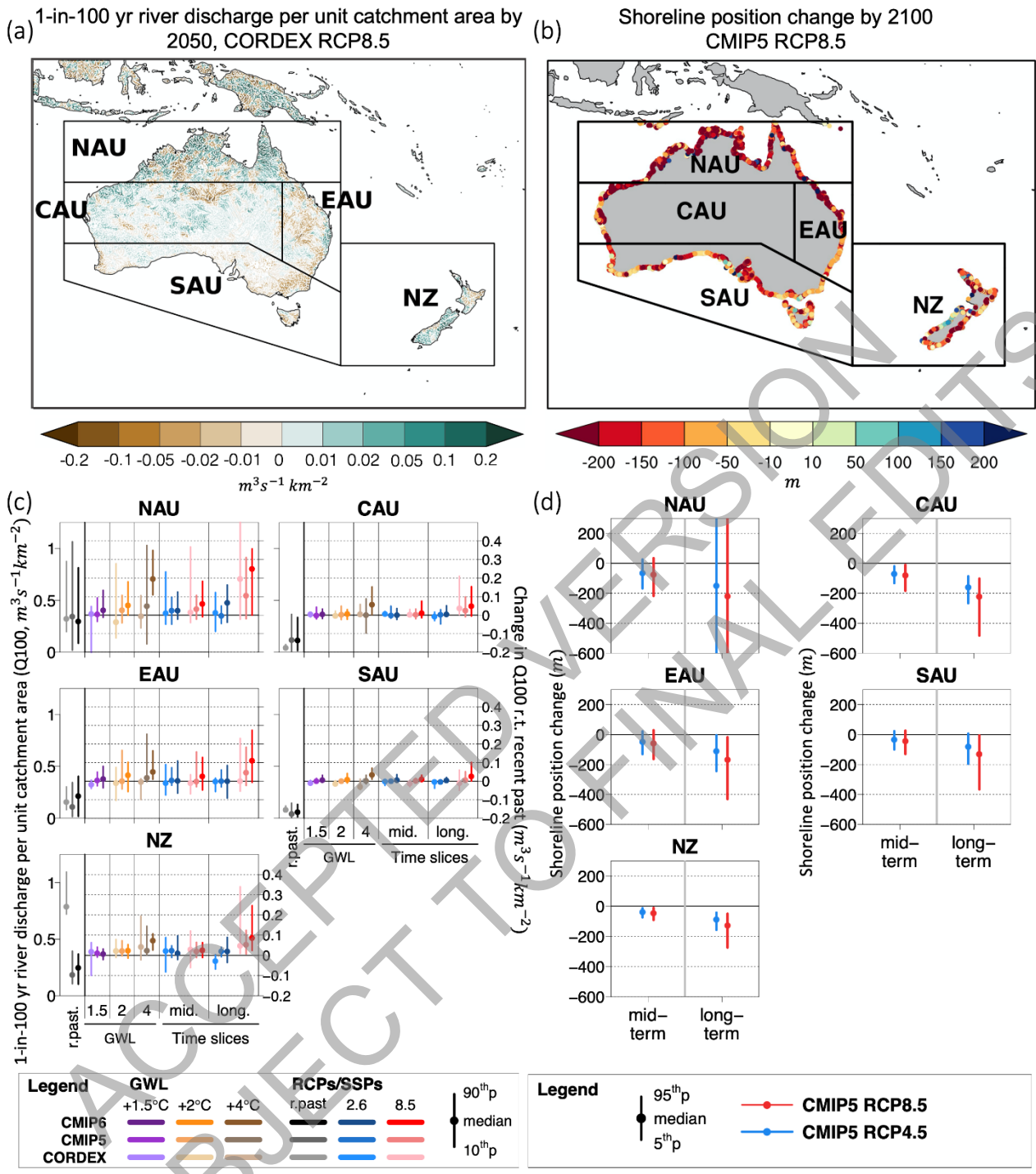


Figure 12.6: Projected changes in selected climatic impact-driver indices for Asia. (a) Mean change in 1-in-100 year river discharge per unit catchment area (Q100, $m^3 s^{-1} km^{-2}$) from CORDEX models for 2041-2060 relative to 1995-2014 for RCP8.5. (b) Shoreline position change along sandy coasts by the year 2100 relative to 2010 (meters; negative values indicate shoreline retreat) from the CMIP5 based data set presented by Vousdoukas et al., (2020). (c) Bar plots for Q100 ($m^3 s^{-1} km^{-2}$) averaged over land areas for the WGI reference AR6 regions (defined in Chapter 1). The left column within each panel (associated with the left y-axis) shows the 'recent past' (1995-2014) Q100 absolute values in grey shades. The other columns (associated with the right y-axis) show the Q100 changes relative to the recent past values for two time periods ('mid' 2041-2060 and 'long' 2081-2100) and for three global warming levels (defined relative to the preindustrial period 1850-1900): 1.5°C (purple), 2°C (yellow) and 4°C (brown). The bars show the median (dots) and the 10th-90th percentile range of model ensemble values across each model ensemble. CMIP6 is shown by the darkest colors, CMIP5 by medium, and CORDEX by light. SSP5-8.5/RCP8.5 is shown in red and SSP1-2.6/RCP2.6 in blue. (d) Bar plots for shoreline position change

ACCEPTED VERSION SUBJECT TO FINAL EDITS

show CMIP5 based projections of shoreline position change along sandy coasts for 2050 and 2100 relative to 2010 for RCP8.5 (red) and RCP4.5 (blue) from Vousdoukas et al., (2020). Dots indicate regional mean change estimates and bars the 5^{th}-95^{th} percentiles ranges of associated uncertainty. Note that these shoreline position change projections assume that there are no additional sediment sinks/sources or any physical barriers to shoreline retreat. See Technical Annex VI for details of indices. Further details on data sources and processing are available in the chapter data table (Table 12.SM.1).

ACCEPTED VERSION
SUBJECT TO FINAL EDITS

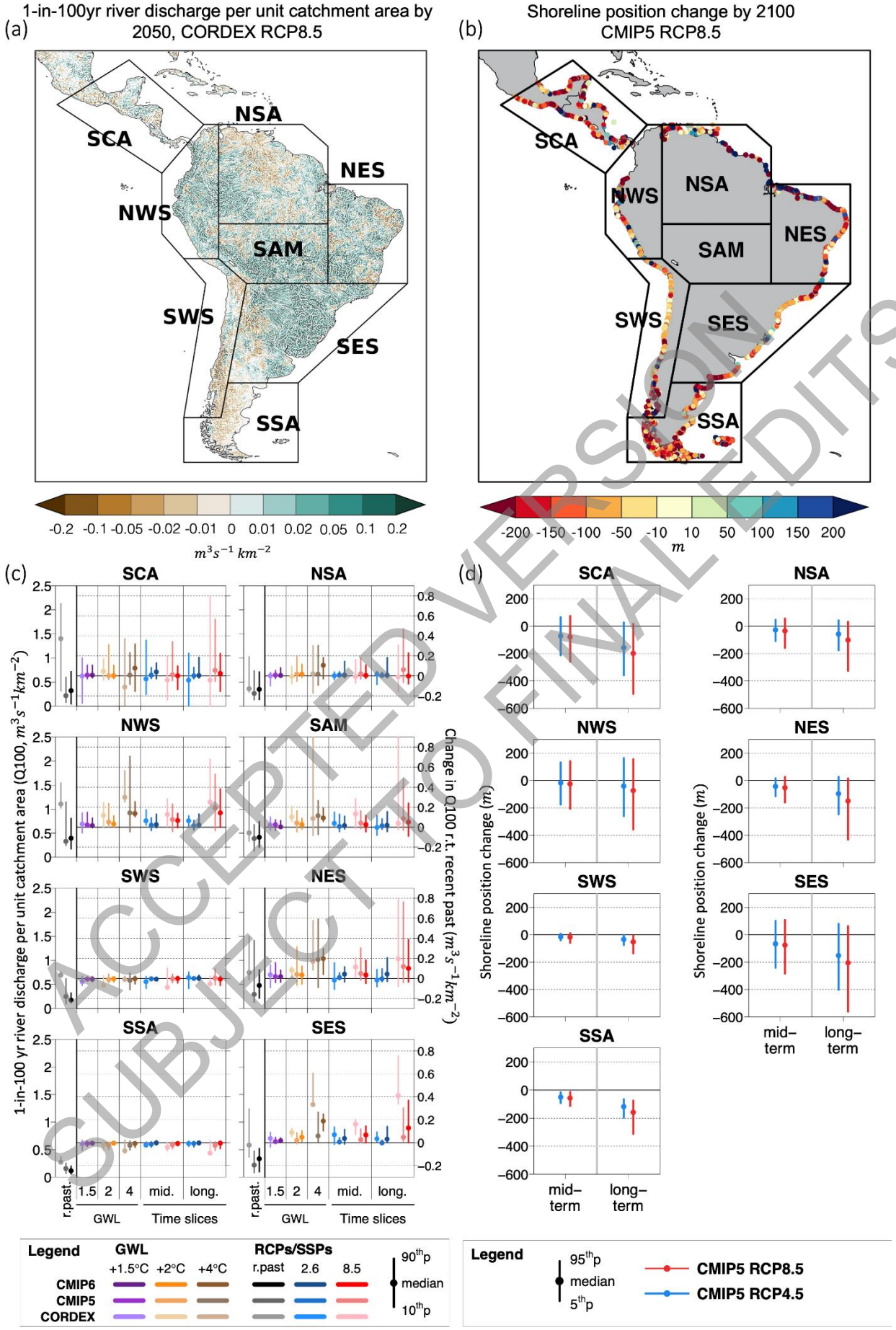


ACCEPTED VERSION SUBJECT TO FINAL EDITS

Figure 12.7: Projected changes in selected climatic impact-driver indices for Australasia. (a) Mean change in 1-in-100 year river discharge per unit catchment area (Q100, $m^3 s^{-1} km^{-2}$) from CORDEX models for 2041-2060 relative to 1995-2014 for RCP8.5. (b) Shoreline position change along sandy coasts by the year 2100 relative to 2010 (meters; negative values indicate shoreline retreat) from the CMIP5 based data set presented by Vousdoukas et al. (2020). (c) Bar plots for Q100 ($m^3 s^{-1} km^{-2}$) averaged over land areas for the WGI reference AR6 regions (defined in Chapter 1). The left column within each panel (associated with the left y-axis) shows the 'recent past' (1995-2014) Q100 absolute values in grey shades. The other columns (associated with the right y-axis) show the Q100 changes relative to the recent past values for two time periods ('mid' 2041-2060 and 'long' 2081-2100) and for three global warming levels (defined relative to the preindustrial period 1850-1900): 1.5°C (purple), 2°C (yellow) and 4°C (brown). The bars show the median (dots) and the 10th-90th percentile range of model ensemble values across each model

ensemble. CMIP6 is shown by the darkest colours, CMIP5 by medium, and CORDEX by light. SSP5-8.5/RCP8.5 is shown in red and SSP1-2.6/RCP2.6 in blue. (d) Bar plots for shoreline position change show CMIP5 based projections of shoreline position change along sandy coasts for 2050 and 2100 relative to 2010 for RCP8.5 (red) and RCP4.5 (blue) from Vousdoukas et al. (2020). Dots indicate regional mean change estimates and bars the 5^{th}-95^{th} percentiles ranges of associated uncertainty. Note that these shoreline position change projections assume that there are no additional sediment sinks/sources or any physical barriers to shoreline retreat. See Technical Annex VI for details of indices. Further details on data sources and processing are available in the chapter data table (Table 12.SM.1).

ACCEPTED VERSION
SUBJECT TO FINAL EDITS



ACCEPTED VERSION SUBJECT TO FINAL EDITS

1

Figure 12.8: Projected changes in selected climatic impact-driver indices for Central and South America. (a) Mean change in 1-in-100 year river discharge per unit catchment area (Q100, $m^3 s^{-1} km^{-2}$) from CORDEX models for 2041-2060 relative to 1995-2014 for RCP8.5. (b) Shoreline position change along sandy coasts by the year 2100 relative to 2010 (meters; negative values indicate shoreline retreat) from the CMIP5 based data set presented by Vousdoukas et al. (2020). (c) Bar plots for Q100 ($m^3 s^{-1} km^{-2}$) averaged over land areas for the WGI reference AR6 regions (defined in Chapter 1). The left column within each panel (associated with the left y-axis) shows the 'recent past' (1995-2014) Q100 absolute values in grey shades. The other columns (associated with the right y-axis) show the Q100 changes relative to the recent past values for two time periods ('mid' 2041-2060 and 'long' 2081-2100) and for three global warming levels (defined relative to the preindustrial period 1850-1900): 1.5°C (purple), 2°C (yellow) and 4°C (brown). The bars show the median (dots) and the 10^{th}-90^{th} percentile range of model ensemble values across each model ensemble. CMIP6 is shown by the darkest colours, CMIP5 by medium, and CORDEX by light. SSP5-8.5/RCP8.5 is shown in red and SSP1-2.6/RCP2.6 in blue. (d) Bar plots for shoreline position change show CMIP5 based projections of shoreline position change along sandy coasts for 2050 and 2100 relative to 2010 for RCP8.5 (red) and RCP4.5 (blue) from Vousdoukas et al. (2020). Dots indicate regional mean change estimates and bars the 5^{th}-95^{th} percentiles ranges of associated uncertainty. Note that these shoreline position change projections assume that there are no additional sediment sinks/sources or any physical barriers to shoreline retreat. See Technical Annex VI for details of indices. Further details on data sources and processing are available in the chapter data table (Table 12.SM.1).

ACCEPTED VERSION
SUBJECT TO FINAL EDITS

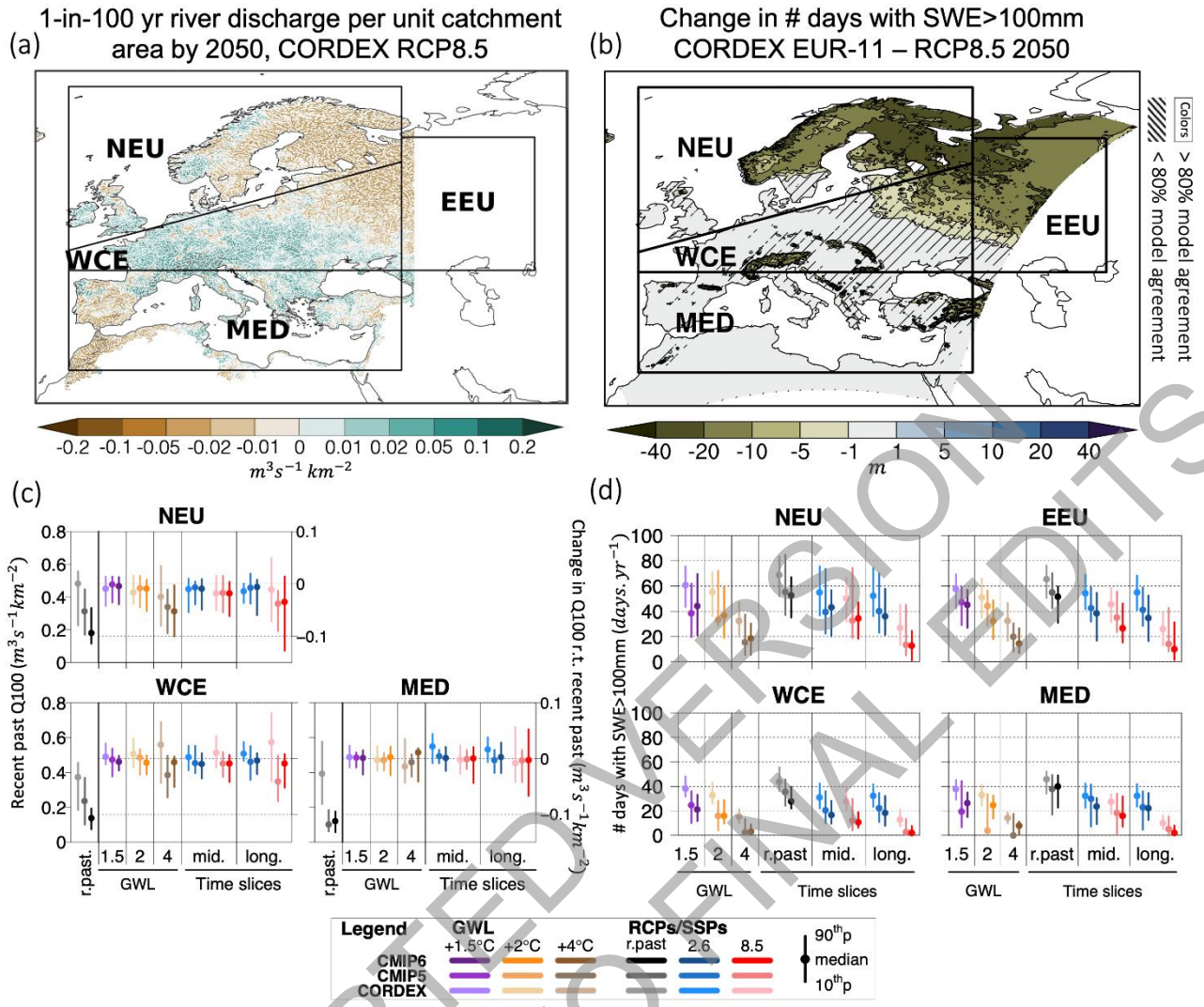
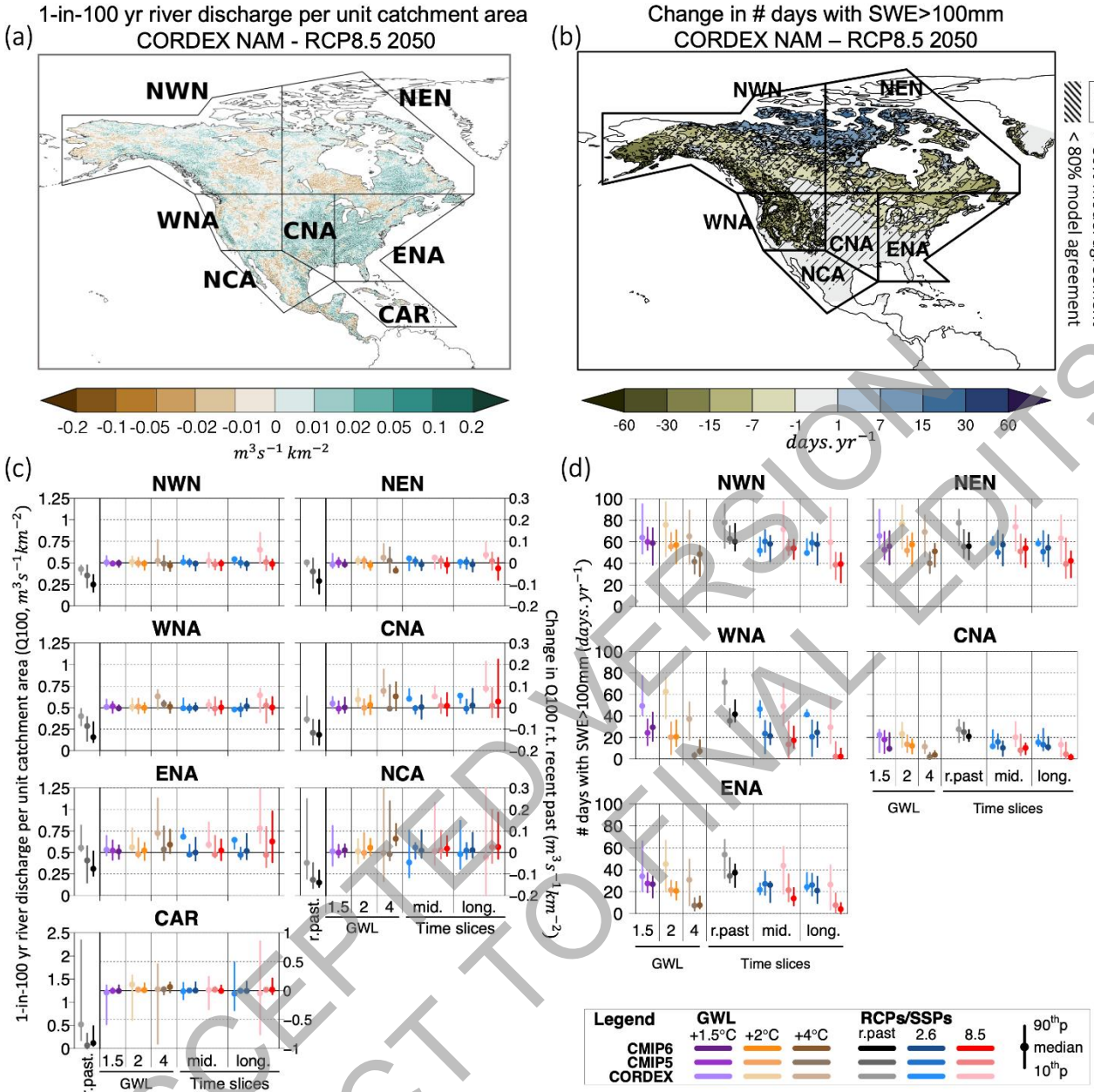


Figure 12.9: Projected changes in selected climatic impact-driver indices for Europe. (a) Mean change in 1-in-100 year river discharge per unit catchment area (Q100, $m^3 s^{-1} km^{-2}$), and (b) median change in the number of days with snow water equivalent (SWE) over 100 mm (from November to March), from EURO-CORDEX models for 2041-2060 relative to 1995-2014 and RCP8.5. Diagonal lines indicate where less than 80% of models agree on the sign of change. (c) Bar plots for Q100 ($m^3 s^{-1} km^{-2}$) averaged over land areas for the WGI reference AR6 regions (defined in Chapter 1). The left column within each panel (associated with the left y-axis) shows the 'recent past' (1995-2014) Q100 absolute values in grey shades. The other columns (associated with the right y-axis) show the Q100 changes relative to the recent past values for two time periods ('mid' 2041-2060 and 'long' 2081-2100) and for three global warming levels (defined relative to the preindustrial period 1850-1900): 1.5°C (purple), 2°C (yellow) and 4°C (brown). The bars show the median (dots) and the 10th-90th percentile range of model ensemble values across each model ensemble. CMIP6 is shown by the darkest colours, CMIP5 by medium, and CORDEX by light. SSP5-8.5/RCP8.5 is shown in red and SSP1-2.6/RCP2.6 in blue. (d) As for (c) but showing absolute values for number of days with SWE > 100mm, masked to grid cells with at least 14 such days in the recent-past. See Technical Annex VI for details of indices. Further details on data sources and processing are available in the chapter data table (Table 12.SM.1).

ACCEPTED VERSION SUBJECT TO FINAL EDITS



ACCEPTED VERSION SUBJECT TO FINAL EDITS

Figure 12.10:Projected changes in selected climatic impact-driver indices for North America. (a) Mean change in 1-in-100 year river discharge per unit catchment area (Q100, $m^3 s^{-1} km^{-2}$), and (b) median change in the number of days with snow water equivalent (SWE) over 100 mm (from November to March), from CORDEX-North America models for 2041-2060 relative to 1995-2014 and RCP8.5. Diagonal lines indicate where less than 80% of models agree on the sign of change. (c) Bar plots for Q100 ($m^3 s^{-1} km^{-2}$) averaged over land areas for the WGI reference AR6 regions (defined in Chapter 1). The left column within each panel (associated with the left y-axis) shows the 'recent past' (1995-2014) Q100 absolute values in grey shades. The other columns (associated with the right y-axis) show the Q100 changes relative to the recent past values for two time periods ('mid' 2041-2060 and 'long' 2081-2100) and for three global warming levels (defined relative to the preindustrial period 1850-1900): 1.5°C (purple), 2°C (yellow) and 4°C (brown). The bars show the median (dots) and the 10th-90th percentile range of model ensemble values across each model ensemble. CMIP6 is shown by the darkest colours, CMIP5 by medium, and CORDEX by light. SSP5-8.5/RCP8.5 is shown in red and SSP1-2.6/RCP2.6 in blue. (d) As for (c) but showing absolute values for number of days with SWE > 100mm, masked to grid cells with at least 14 such days in the recent-past. See Technical Annex VI for details of indices. A Caribbean Q100 bar plot is included here but assessed in the Small islands section (12.4.7). Further details on data sources and processing are available in the chapter data table (Table 12.SM.1).

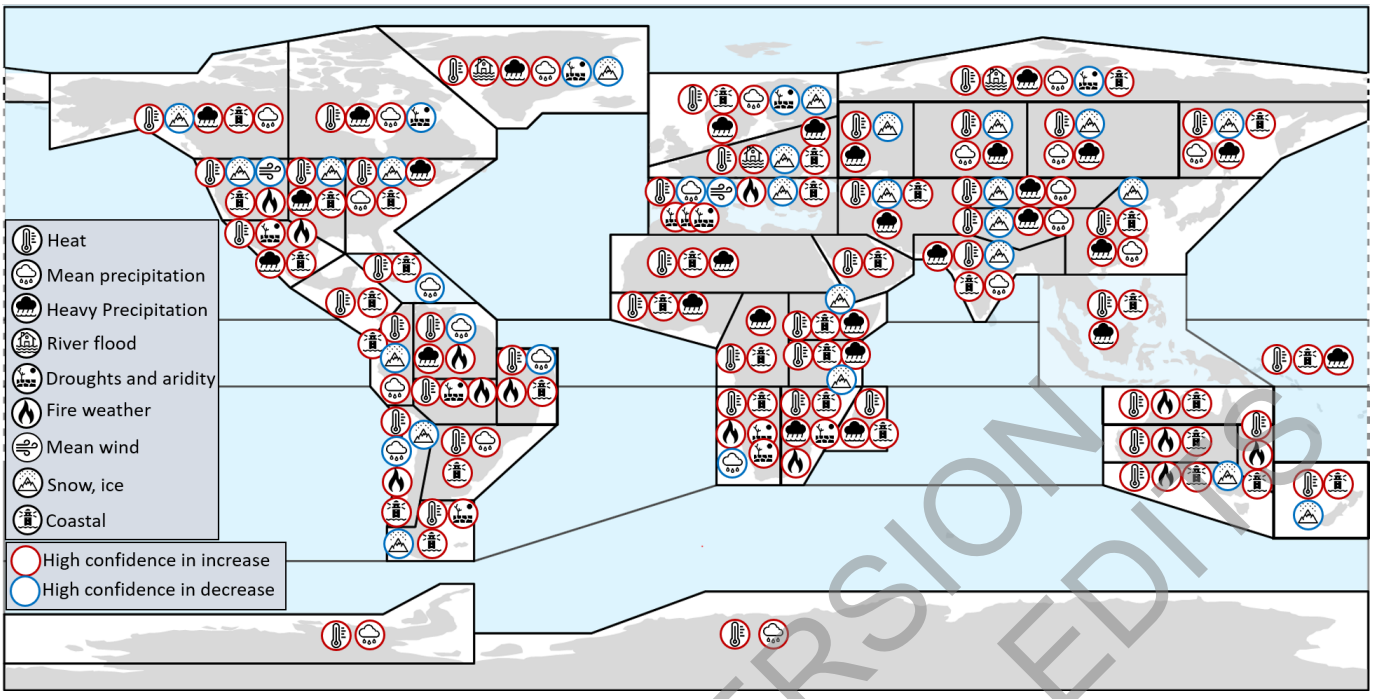


Figure 12.11: Synthesis of the CID changes projected by 2050 (2041-2060) with *high confidence*, relative to reference period (1995-2014), together with the sign of change. Information is taken from the CID tables in Section 12.4. Some CIDs are grouped in order to streamline the information in order to fit in all information in the figure. Mean temperature, extreme heat, cold spells and frost are grouped under a single icon "heat", as they are projected to change simultaneously, albeit heat and cold are changing in opposite directions. Coastal CIDs (relative sea level, coastal flooding and coastal erosion at sandy beaches) are also grouped. In the figure, the "coastal" icon indicates regions where at least two of the three individual coastal CIDs are projected to change with *high confidence*. Cases where only two of the three CIDs increase with high confidence are in Arctic North Europe, Russian Arctic and Arctic North West North America. A single icon is used for aridity, hydrological drought, and agricultural and ecological drought, and only the number of drought types that change is indicated. For the "Snow, ice" icon, information is taken from the evolution of the "Snow, Glacier and ice sheet" CID, and in most regions also have similar changes for "permafrost" and "lake, river and sea ice". Exceptions are for NEN, RAR and Arctic NWN where snow is decreasing with *medium confidence* (thus not appearing in the figure), while permafrost and Lake, river and sea ice is decreasing with *high confidence*. The location of the icon within the regions is arbitrary. Further details on data sources and processing are available in the chapter data table (Table 12.SM.1). Icon sources: https://www.flaticon.com/authors/freepik

ACCEPTED VERSION SUBJECT TO FINAL EDITS

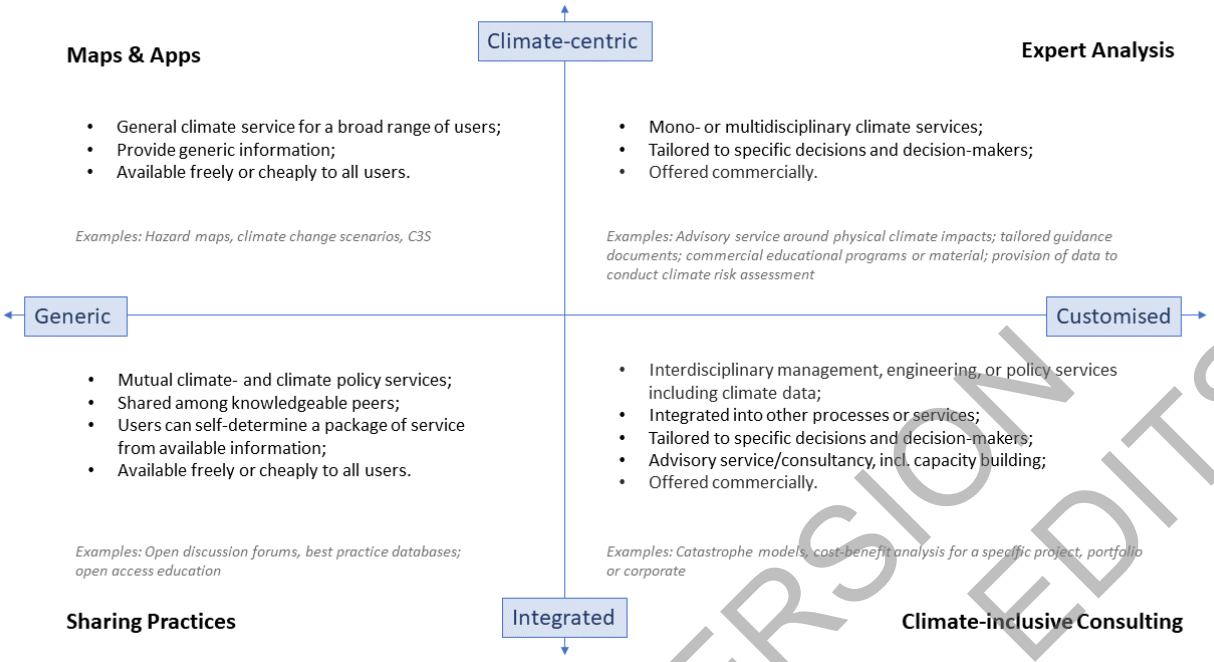
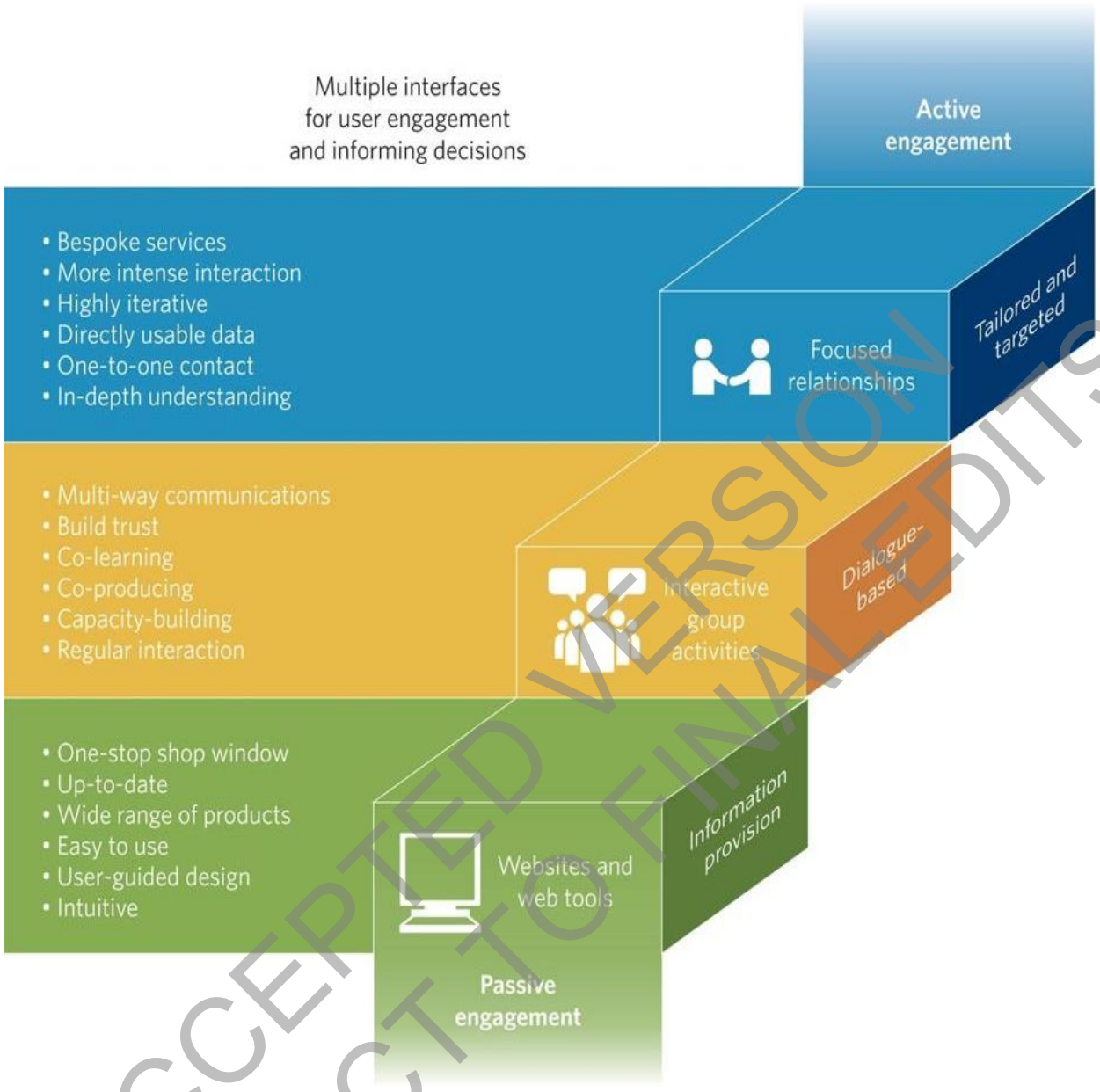


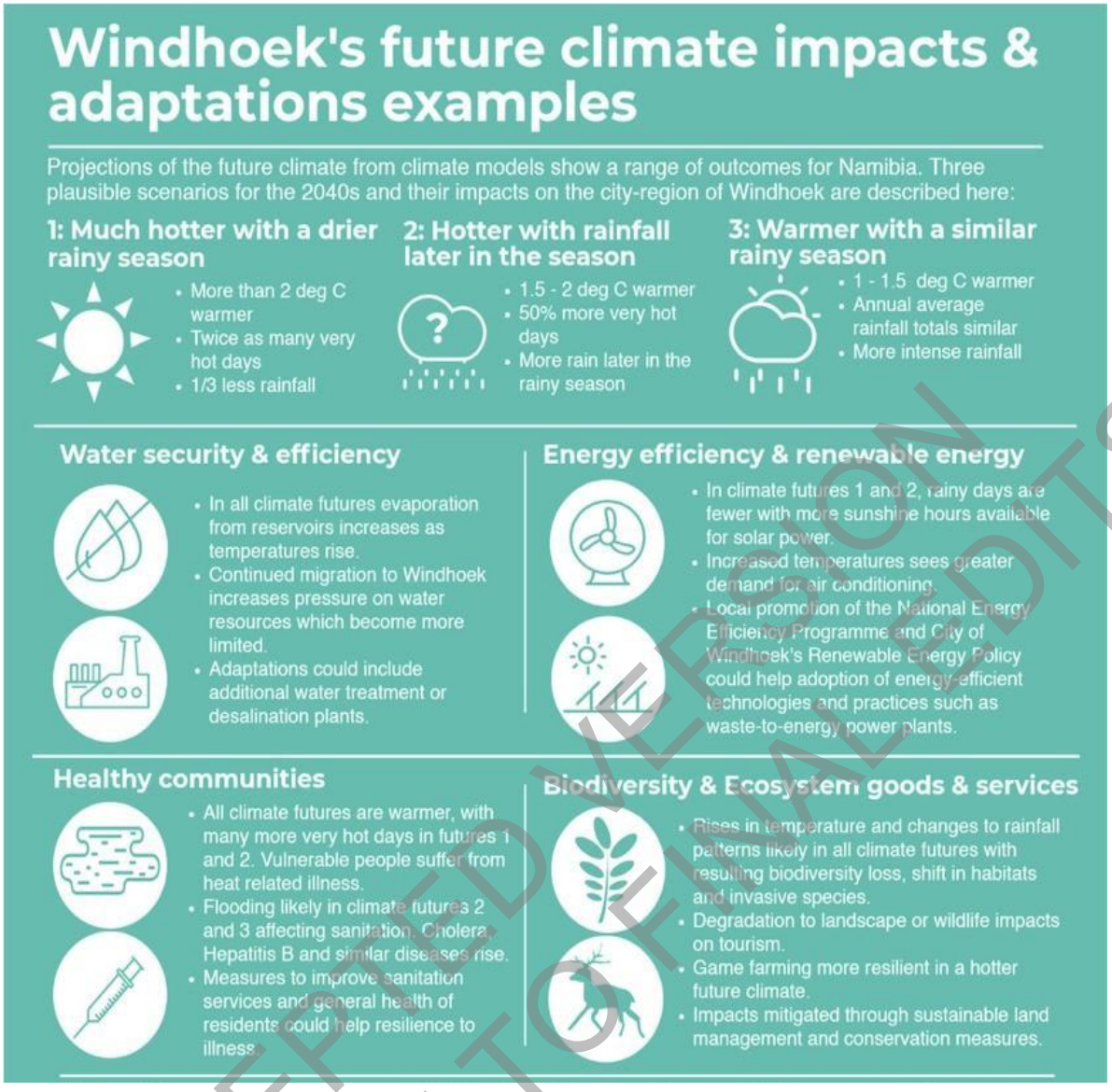
Figure 12.12: Illustration of different types of climate services. Products, for instance, can focus only on climate-related information or can be designed to integrate climate information with other decision-relevant context (vertical axis) and they can be very generic in terms of relevance to a wide range of sectors or stakeholders or customized to fit the needs of a specific sector or stakeholder (horizontal axis). Source: Adapted from (Visscher et al., 2020).

ACCEPTED VERSION
SUBJECT TO FINAL EDITS



Cross-Chapter Box 12.2, Figure 1: Schematic of three broad categories of engagement between users and providers of climate services (adapted from Hewitt et al., 2017b).

ACCEPTED VERSION
SUBJECT TO FINAL EDITS

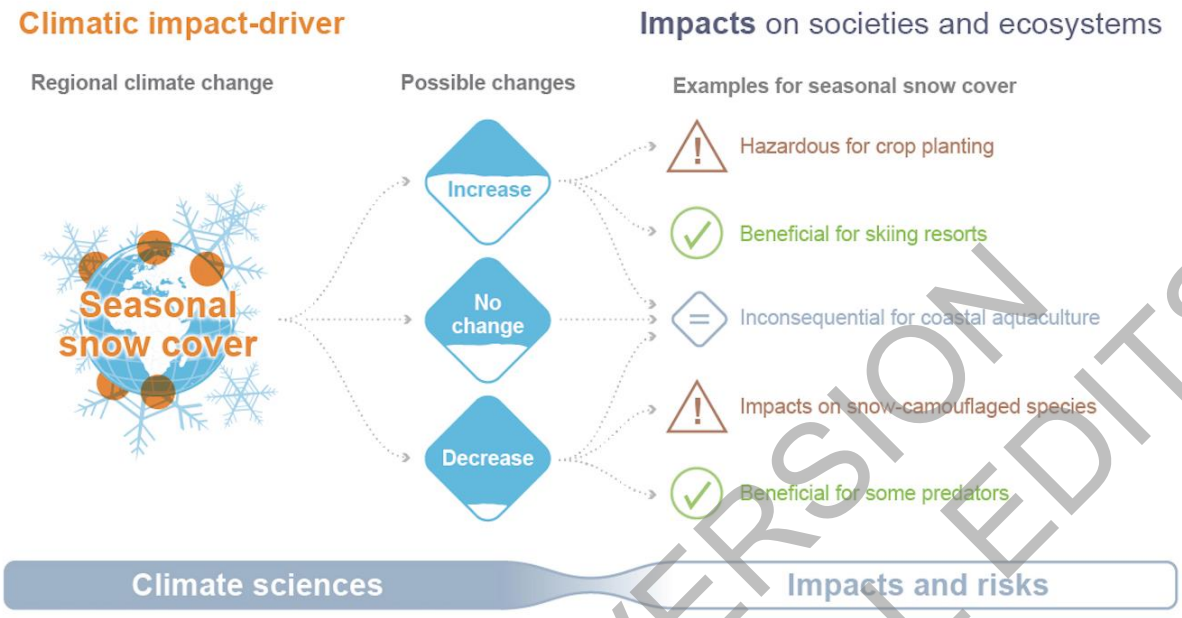


Cross-Chapter Box 12.2, Figure 2: Climate Risk Narrative infographic developed through the FRACTAL Windhoek Learning Lab process (adapted from Jack et al., (2020)).

ACCEPTED VERSION SUBJECT TO FINAL EDITS

FAQ 12.1: **What is a climatic impact-driver (CID)?**

A climatic impact-driver (CID) is a climate condition that directly affects elements of society or ecosystems. Climatic impact-drivers and their changes can lead to positive, negative, or inconsequential outcomes (or a mixture).

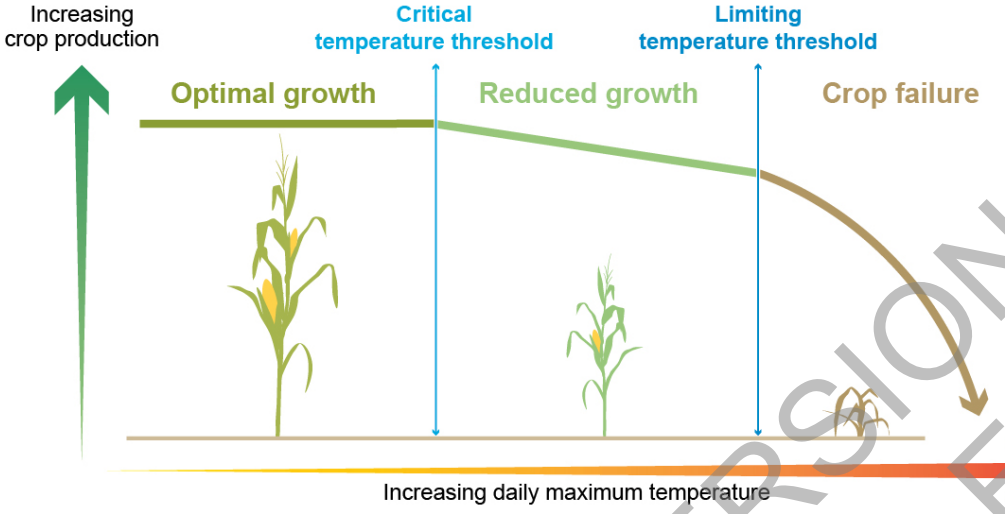


FAQ 12.1, Figure 1: A single climatic impact-driver can affect ecosystems and society in different ways. A variety of impacts from the same climatic impact-driver change, illustrated with the example of regional seasonal snow cover.

ACCEPTED VERSION SUBJECT TO FINAL EDITS

FAQ 12.2: **What are climatic thresholds and why are they important?**

Many systems have thresholds that can lead to sudden changes, if climate conditions exceed them. Adaptation and risk management efforts can increase overall system resilience by identifying and changing tolerance thresholds.

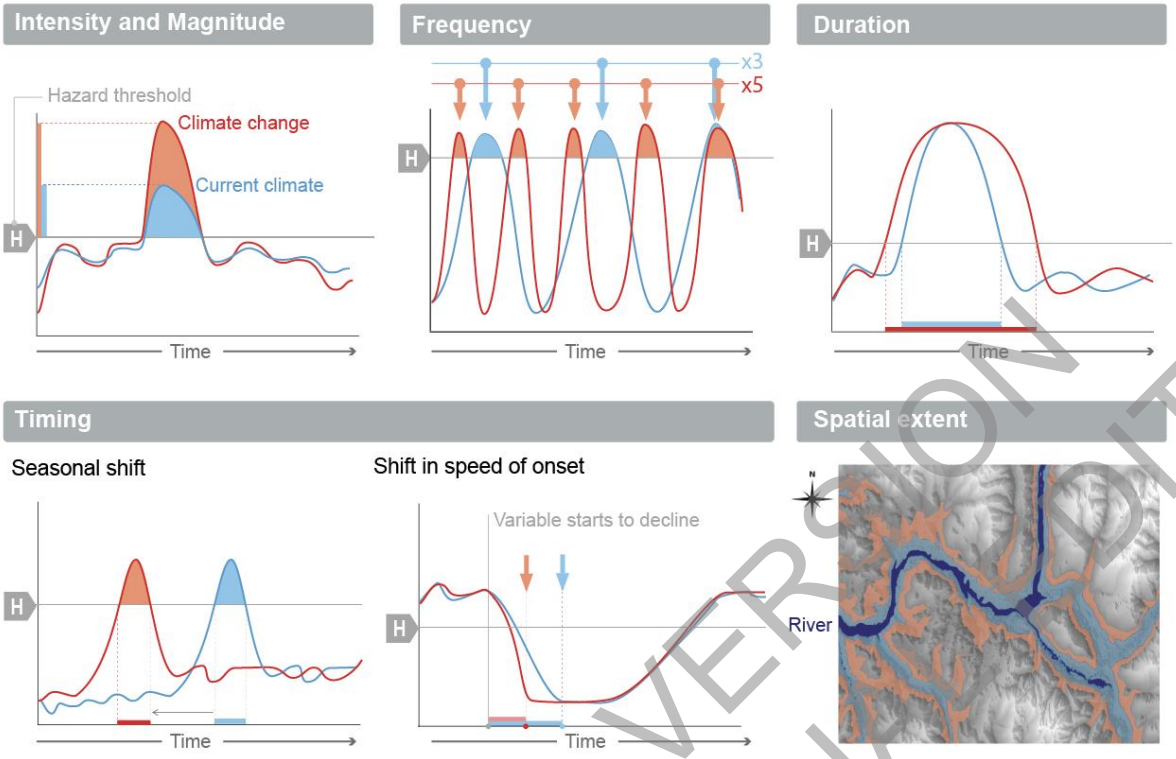


FAQ12.2, Figure 1: **Crop response to maximum temperature thresholds.** Crop growth rate responds to daily maximum temperature increases, leading to reduced growth and crop failure as temperatures exceed critical and limiting temperature thresholds, respectively. Note that changes in other environmental factors (such as carbon dioxide and water) may increase the tolerance of plants to increasing temperatures.

ACCEPTED VERSION SUBJECT TO FINAL EDITS

FAQ 12.3: **How will climate change affect climate hazards?**

Climate change can alter the intensity and magnitude, frequency, duration, timing and spatial extent of a region's climate hazards.



FAQ 12.3, Figure 1: Types of changes to a region's hazard profile. The first five panels illustrate how climate changes can alter a hazard's intensity (or magnitude), frequency, duration, and timing (by seasonality and speed of onset) in relation to a hazard threshold (horizontal grey line). The difference between the historical climate (blue) and future climate (red) shows the changing aspects of climate change that stakeholders will have to manage. The bottom-right panel shows how a given climate hazard (such as a once-in-100-year river flood) may reach new geographical areas under a future climate change.

ACCEPTED VERSION SUBJECT TO FINAL EDITS

Chapter 12: Climate change information for regional impact and for risk assessment - Supplementary Material

Coordinating Lead Authors:
Roshanka Ranasinghe (The Netherlands/Sri Lanka, Australia), Alex C. Ruane (United States of America), Robert Vautard (France)

Lead Authors:
Nigel Arnell (United Kingdom), Erika Coppola (Italy), Faye Abigail Cruz (Philippines), Suraje Dessai (United Kingdom/Portugal), Akm Saiful Islam (Bangladesh), Mohammad Rahimi (Iran), Daniel Ruiz Carrascal (United States of America/Columbia), Jana Sillmann (Norway/Germany), Mouhamadou Bamba Sylla (Rwanda/Senegal), Claudia Tebaldi (United States of America), Wen Wang (China), Rashyd Zaaboul (United Arab Emirates/Morocco)

Contributing Authors:
Carley E. Iles (Norway, France/ United Kingdom), Jérôme Servonnat (France), Guðfinna Aðalgeirsdóttir (Iceland), Rita Adrian (Germany), Roxana Bojariu (Romania), Laurent Bopp (France), Audrey Brouillet (France), Carlo Buontempo (United Kingdom/Italy), Winston Chow (Singapore), Augustin Colette (France), Cecilia Conde (Mexico), Leticia Cotrim da Cunha (Brazil), Claudine Dereczynski (Brazil), Alejandro Di Luca (Australia, Canada/Argentina), Fabio Di Sante (Italy), Arona Diedhiou (Côte d'Ivoire/Senegal), Aida Diongue-Niang (Senegal), Francisco J. Doblas-Reyes (Spain), Pariva Dobriyal (India), Sybren S. Drijfhout (The Netherlands), John P. Dunne (United States of America), Tamsin L. Edwards (United Kingdom), Aidan D. Farrell (Trinidad and Tobago/Ireland), Erich Fischer (Switzerland), John C. Fyfe (Canada), Alexander Gelfan (Russian Federation), Subimal Ghosh (India), Irina V. Gorodetskaya (Portugal/Belgium, Russian Federation), Michael Grose (Australia), José Manuel Gutiérrez (Spain), David S. Gutzler (United States of America), Rebecca Harris (Australia), Matthias Hauser (Switzerland), Mark Hemer (Australia), Kevin Hennessy (Australia), Helene T. Hewitt (United Kingdom), Masao Ishii (Japan), Maialen Iturbide (Spain), Christopher D. Jack (South Africa), Richard G. Jones (United Kingdom), Nikolay Kadygrov (France/Russian Federation), Ebru Kirezci (Australia/Turkey), Nana Ama Browne Klutse (Ghana), Robert E. Kopp (United States of America), James Kossin (United States of America), Charles Koven (United States of America), Svitlana Krakovska (Ukraine), Gerhard Krinner (France/Germany, France), Benjamin L. Lamptey (Niger, Ghana/Ghana), Christopher Lennard (South Africa), Xianfu Lu (United Kingdom/China), Douglas Maraun (Austria/Germany), Simon McGree (Australia/Fiji, Australia), Glenn McGregor (United Kingdom/New Zealand, United Kingdom), Kathleen L. McInnes (Australia), Dirk Notz (Germany), Brian O'Neill (United States of America), Ben Orlove (United States of America), Friederike Otto (United Kingdom/Germany), Carlos Pérez García-Pando (Spain), Franz Prettenthaler (Austria), Francesca Raffaele (Italy), Srivatsan Raghavan (Singapore/India), Christophe F. Randin (Switzerland/France, Switzerland), Johan Reyns (The Netherlands/Belgium), Lucas Ruiz (Argentina), Fahad Saeed (Germany/Pakistan), Jean-Baptiste Sallee (France), Marit Sandstad (Norway), Clemens Schwingshackl (Norway, Germany/Italy), Sonia I. Seneviratne (Switzerland), Aimée B. A. Slangen (The Netherlands), Tannecia S. Stephenson (Jamaica), Anna Steynor (South Africa), Markus Stoffel (Switzerland), Benjamin Sultan (France), William V. Sweet (United States of America), Sophie Szopa (France), Izuru Takayabu (Japan), Moustapha Tall (Rwanda/Senegal), N'Datchoh Evelyne Touré N'Datchoh (Cote d'Ivoire), Bart van den Hurk (The Netherlands), Sergio M. Vicente-Serrano (Spain), Michalis Vousdoukas (Italy, Greece/Greece), Morgan Wairiu (Fiji), Prodromos Zanis (Greece), Xuebin Zhang (Canada)

ACCEPTED VERSION SUBJECT TO FINAL EDITS

Review Editors:
Edvin Aldrian (Indonesia), David Karoly (Australia), Murat Türkeş (Turkey)

Chapter Scientists:
Carley Iles (Norway, France/ United Kingdom), Jérôme Servonnat (France)

This Supplementary Material should be cited as:
Ranasinghe, R., A. C. Ruane, R. Vautard, N. Arnell, E. Coppola, F. A. Cruz, S. Dessai, A. S. Islam, M. Rahimi, D. Ruiz Carrascal, J. Sillmann, M. B. Sylla, C. Tebaldi, W. Wang, R. Zaaboul, 2021, Climate Change Information for Regional Impact and for Risk Assessment Supplementary Material. In: *Climate Change 2021: The Physical Science Basis. Contribution of Working Group I to the Sixth Assessment Report of the Intergovernmental Panel on Climate Change* [Masson-Delmotte, V., P. Zhai, A. Pirani, S. L. Connors, C. Péan, S. Berger, N. Caud, Y. Chen, L. Goldfarb, M. I. Gomis, M. Huang, K. Leitzell, E. Lonnoy, J. B. R. Matthews, T. K. Maycock, T. Waterfield, O. Yelekçi, R. Yu and B. Zhou (eds.)]. Available from https://ipcc.ch/static/ar6/wg1

Date: August 2021

This document is subject to copy-editing, corrigenda and trickle backs.

ACCEPTED VERSION
SUBJECT TO FINAL EDITS

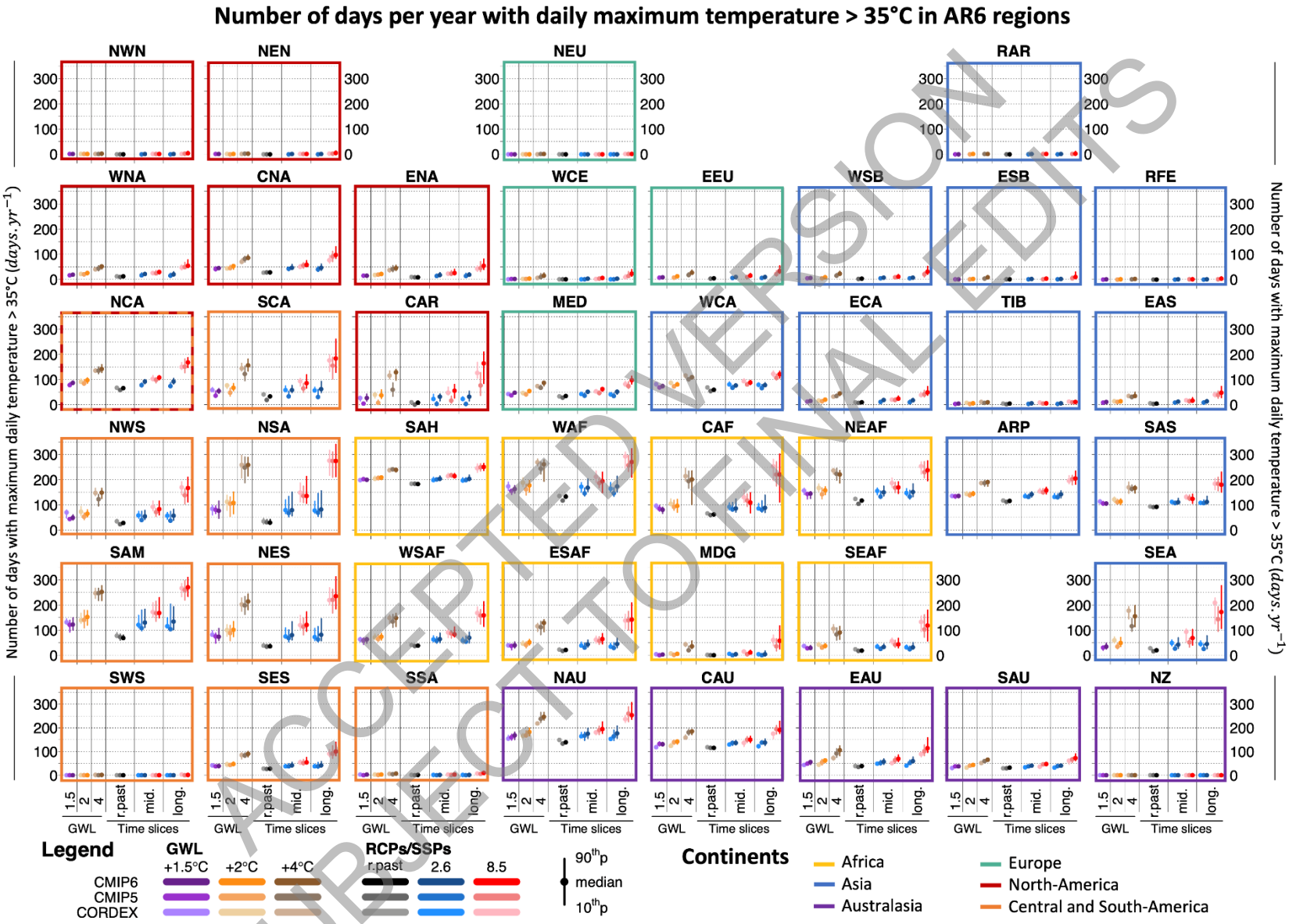
Table of Contents

12.SM.1 Figures 3
12.SM.2 Data Table 16
References 80

ACCEPTED VERSION
SUBJECT TO FINAL EDITS

12.SM.1 Figures

ACCEPTED VERSION
SUBJECT TO FINAL EDITS

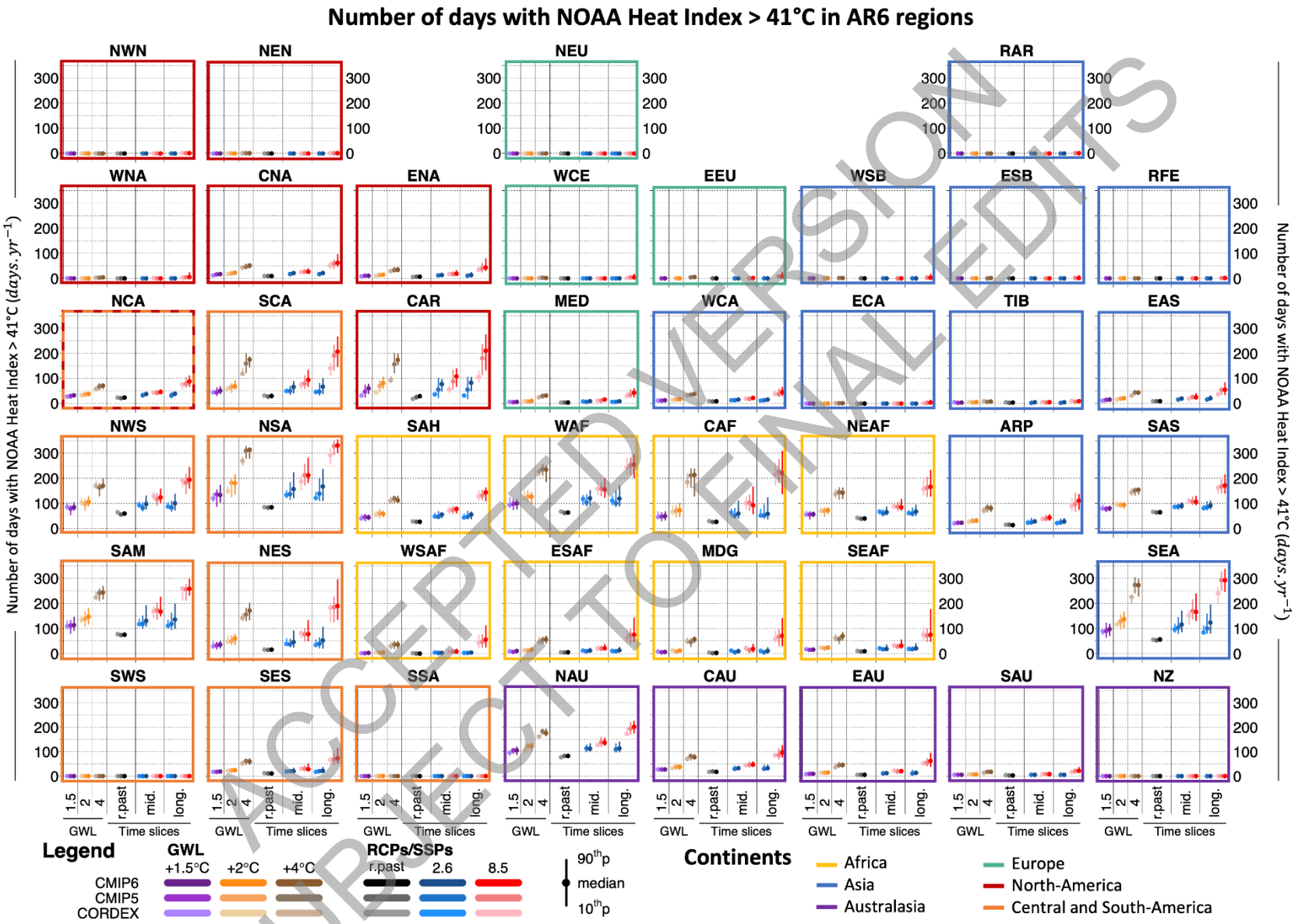


ACCEPTED VERSION SUBJECT TO FINAL EDITS

1

Figure 12.SM.1: Regional projections for the number of days per year with maximum temperature exceeding 35°C for different scenarios, time horizons and global warming levels. The bar plots show projections from CMIP6 (darkest colours), CMIP5 (medium colours) and CORDEX (lightest colours) ensembles, for RCP8.5/SSP5-8.5 (red) and RCP2.6/SSP1-2.6 (blue), for the mid-term (2041-2060), long-term (2081-2100), and the recent past (grey, 1995-2014). Results for global warming levels (defined relative to the pre-industrial period 1850-1900) are shown in purple for 1.5°C, yellow for 2°C and brown for 4°C. The median (dots) and the 10^{th}-90^{th} percentile range of model ensemble values across each model ensemble and each time period are shown for the regional mean over land areas for the WGI reference AR6 regions (defined in Chapter 1). Bias adjustment is applied (see Atlas.1.4.5). The CORDEX ensemble is missing in regions that are not fully covered by the CORDEX domain (EEU, ESB, RAR, RFE and WSB). See Technical Annex VI for details of indices. Further details on data sources and processing are available in the chapter data table (Table 12.SM.1).

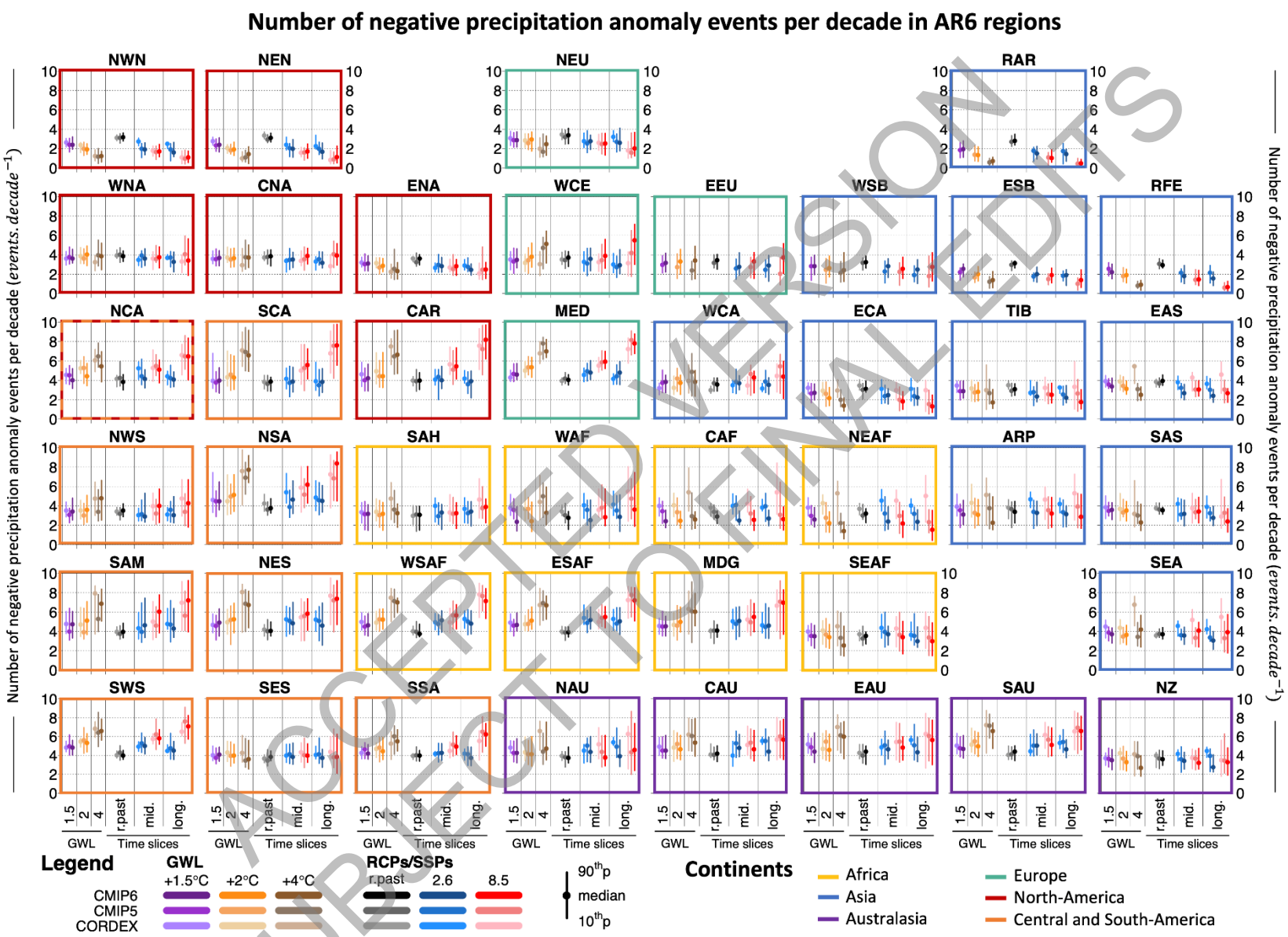
ACCEPTED VERSION
SUBJECT TO FINAL EDITS



ACCEPTED VERSION SUBJECT TO FINAL EDITS

Figure 12.SM.2: **Regional projections for the number of days per year with the NOAA Heat Index exceeding 41°C for different scenarios, time horizons and global warming levels.** 41°C corresponds to conditions that the US National Weather Service classifies into the category of "Danger" (Blazejczyk et al., 2012). The bar plots show projections from CMIP6 (darkest colours), CMIP5 (medium colours) and CORDEX (lightest colours) ensembles, for RCP8.5/SSP5-8.5 (red) and RCP2.6/SSP1-2.6 (blue), for the mid-term (2041-2060), long-term (2081-2100), and the recent past (grey, 1995-2014). Results for global warming levels (defined relative to the pre-industrial period 1850-1900) are shown in purple for 1.5°C, yellow for 2°C and brown for 4°C. The median (dots) and the 10^{th}-90^{th} percentile range of model ensemble values across each model ensemble and each time period are shown for the regional mean over land areas for the WGI reference AR6 regions (defined in Chapter 1). Bias adjustment is applied. The CORDEX ensemble is missing in regions that are not fully covered by the CORDEX domain (EEU, ESB, RAR, RFE and WSB). See Technical Annex VI for details of indices and bias adjustment. Further details on data sources and processing are available in the chapter data table (Table 12.SM.1).

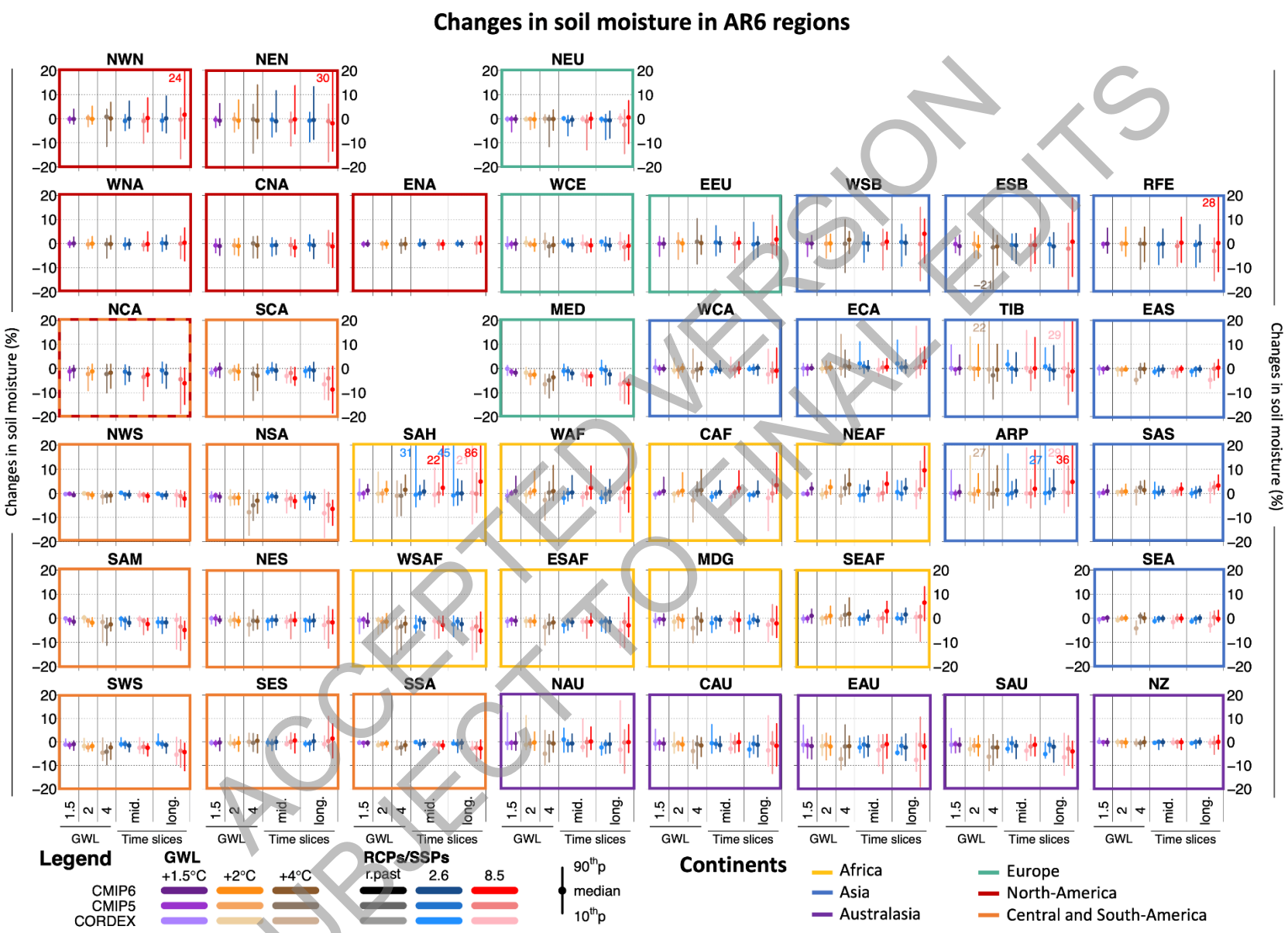
ACCEPTED VERSION
SUBJECT TO FINAL EDITS



ACCEPTED VERSION SUBJECT TO FINAL EDITS

Figure 12.SM.3: Regional projections for the number of negative precipitation anomaly events per decade using the 6-month Standardised Precipitation Index for different scenarios, time horizons and global warming levels. The bar plots show projections from CMIP6 (darkest colours), CMIP5 (medium colours) and CORDEX (lightest colours) ensembles, for RCP8.5/SSP5-8.5 (red) and RCP2.6/SSP1-2.6 (blue), for the mid-term (2041-2060), long-term (2081-2100), and the recent past (grey, 1995-2014). Results for global warming levels (defined relative to the pre-industrial period 1850-1900) are shown in purple for 1.5°C, yellow for 2°C and brown for 4°C. The median (dots) and the 10^{th}-90^{th} percentile range of model ensemble values across each model ensemble and each time period are shown for the regional mean over land areas for the WGI reference AR6 regions (defined in Chapter 1). Units are events per decade. The CORDEX ensemble is missing in regions that are not fully covered by the CORDEX domain (EEU, ESB, RAR, RFE and WSB). See Technical Annex VI for details of indices. Further details on data sources and processing are available in the chapter data table (Table 12.SM.1).

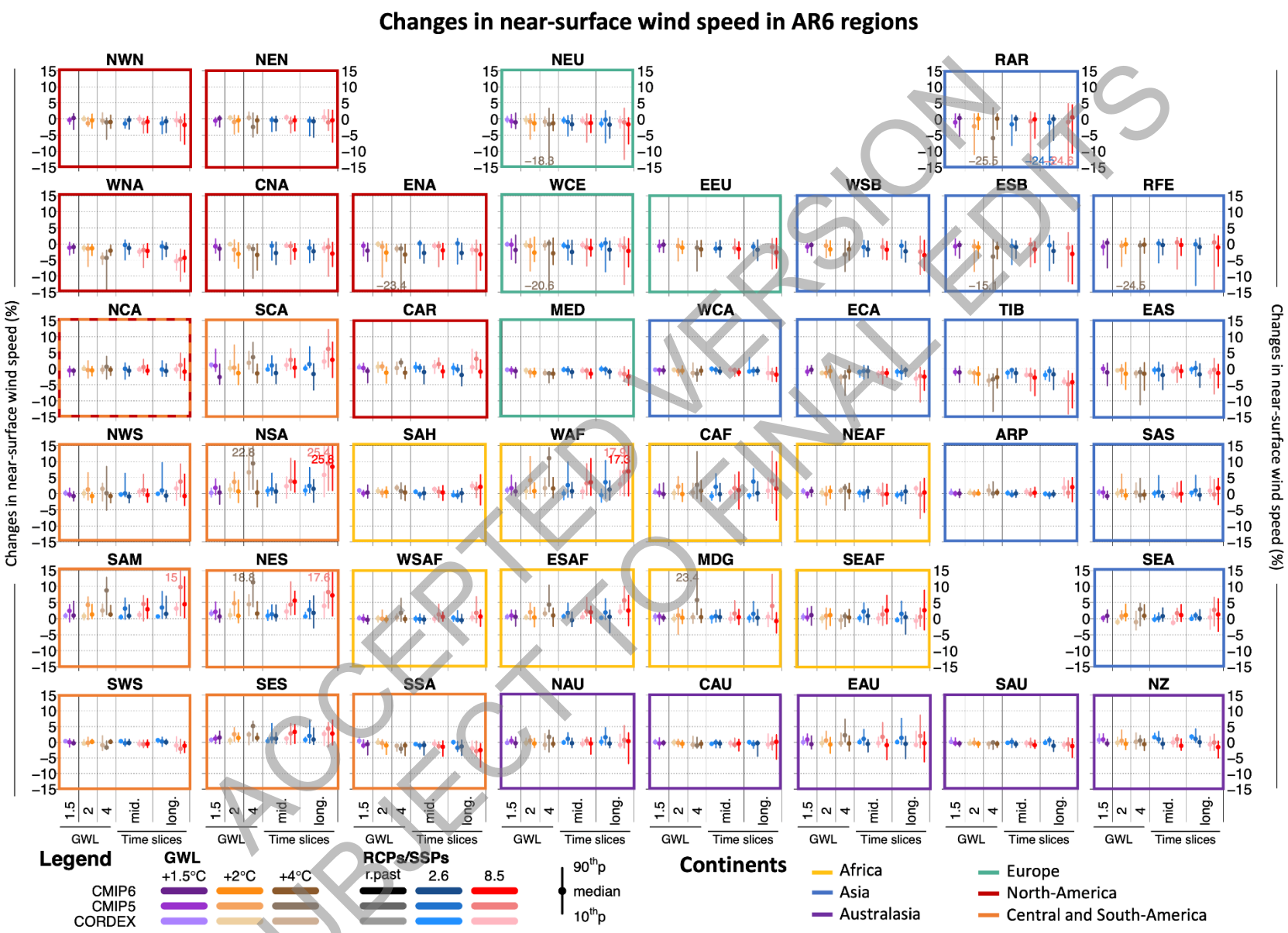
ACCEPTED VERSION
SUBJECT TO FINAL EDITS



ACCEPTED VERSION SUBJECT TO FINAL EDITS

Figure 12.SM.4: Regional projections for changes in soil moisture for different scenarios, time horizons and global warming levels. The bar plots show projections of soil moisture as percentage changes relative to the recent-past (1994-2015) for the mid-term (2041-2060) and long-term (2081-2100) and for three global warming levels (defined relative to the preindustrial period 1850-1900): 1.5°C (purple), 2°C (yellow) and 4°C (brown), using CMIP6 (darkest colours), CMIP5 (medium colours) and CORDEX (lightest colours) ensembles. RCP8.5/SSP5-8.5 is shown in red and RCP2.6/SSP1-2.6 in blue.. The median (dots) and the 10^{th}-90^{th} percentile range of model ensemble values across each model ensemble and each time period are shown for the regional mean over land areas for the WGI reference AR6 regions (defined in Chapter 1). The CORDEX ensemble is missing in regions that are not fully covered by the CORDEX domain (EEU, ESB, RAR, RFE and WSB) or because less than five simulations were available (NWN, NEN, WNA, CAN, ENA and NCA). See Technical Annex VI for details of indices. Further details on data sources and processing are available in the chapter data table (Table 12.SM.1).

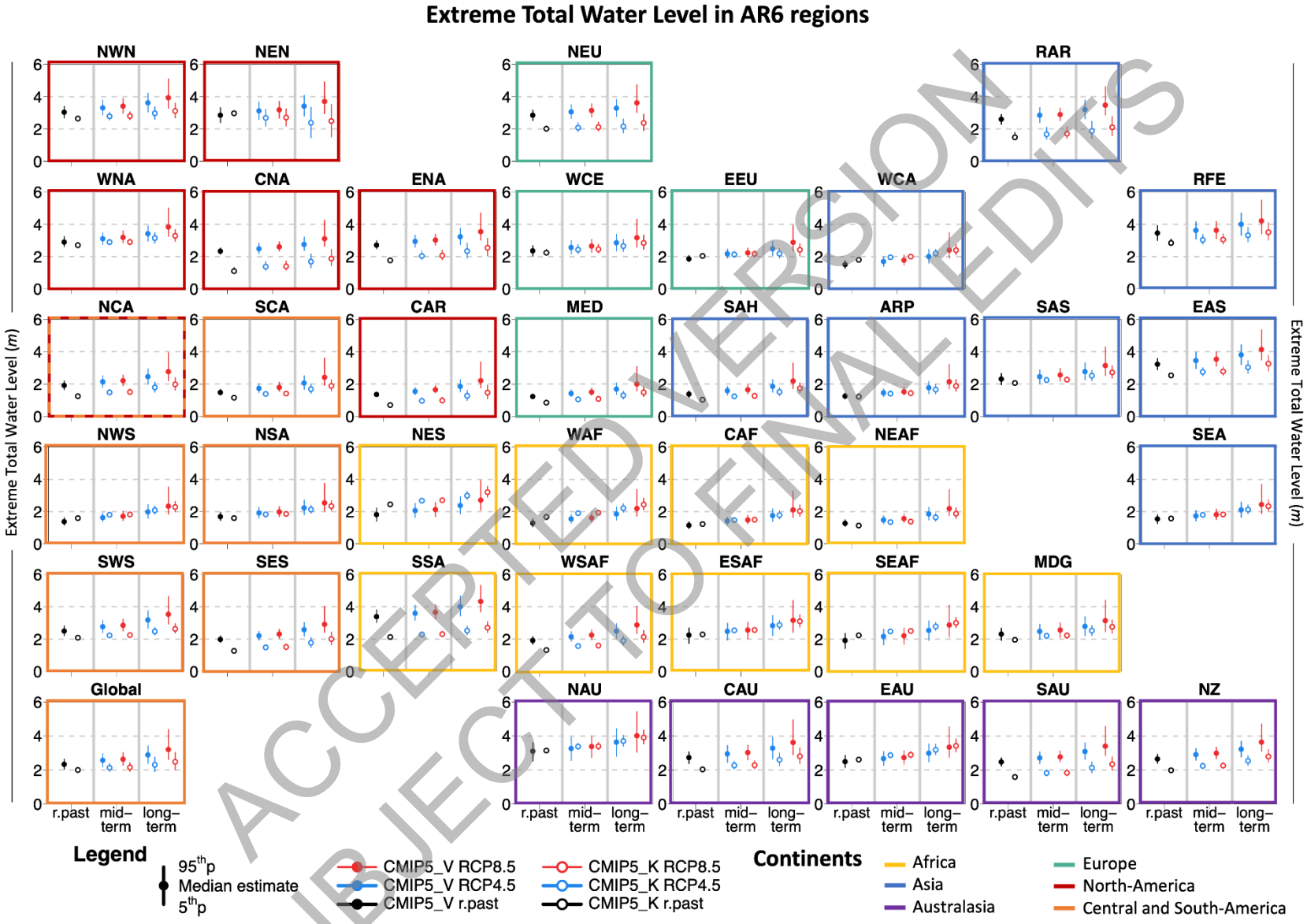
ACCEPTED VERSION
SUBJECT TO FINAL EDITS



ACCEPTED VERSION SUBJECT TO FINAL EDITS

Figure 12.SM.5: Regional projections for changes in mean wind speed for different scenarios, time horizons and global warming levels. The bar plots show projections of wind speed as percentage changes relative to the recent-past (1994-2015) for the mid-term (2041-2060) and long-term (2081-2100) and for three global warming levels (defined relative to the preindustrial period 1850-1900): 1.5°C (purple), 2°C (yellow) and 4°C (brown), using CMIP6 (darkest colours), CMIP5 (medium colours) and CORDEX (lightest colours) ensembles. RCP8.5/SSP5-8.5 is shown in red and RCP2.6/SSP1-2.6 in blue. The median (dots) and the 10^{th}-90^{th} percentile range of model ensemble values across each model ensemble and each time period are shown for the regional mean over land areas for the WGI reference AR6 regions (defined in Chapter 1). The CORDEX ensemble is missing in regions that are not fully covered by the CORDEX domain (EEU, ESB, RAR, RFE and WSB). See Technical Annex VI for details of indices. Further details on data sources and processing are available in the chapter data table (Table 12.SM.1).

ACCEPTED VERSION
SUBJECT TO FINAL EDITS



ACCEPTED VERSION SUBJECT TO FINAL EDITS

Figure 12.SM.6: Regional projections of extreme sea level (1-in-100 year return period extreme total water level (ETWL)). The bar plots show projections of regionally averaged ETWL from the CMIP5 based datasets presented in Vousdoukas et al. (2018) (filled circles, 'V' in legend), and the Kirezci et al., (2020) (open circles, 'K' in legend), for the WGI reference AR6 regions, for RCP8.5 (red) and RCP4.5 (blue). Dots represent the median estimate, and bars the 5th-95th percentiles representing the uncertainty associated with the projections for the mid-term (2050), long-term (2100) and the recent past (black, 1979/1980-2014). Units are meters. See Technical Annex VI for details about the index. Further details on data sources and processing are available in the chapter data table (Table 12.SM.1).

ACCEPTED VERSION
SUBJECT TO FINAL EDITS

12.SM.2 Data Table

[START TABLE 12.SM.1 HERE]

Table 12.SM.1: Input Data Table. Input datasets and code used to create chapter figures.

Figure number	Dataset / Code name	Type	Filename / Specificities	License type	Dataset / Code citation	Dataset / Code URL	Related publications / Software used	Notes
Figure 12.4, a, b, c	CMIP6 multi-model ensemble mean of tx35 – ssp126 long term minus recent past – panel a	Final plotted data	tx35_panel_a_ssp126_2081-2100_minus_baseline.nc			https://github.com/IPCC-WG1/Chapter-12/tree/main/Figures/data/Figure_12.4/tx35/	CliMAF, CDO, Xarray	
	Mask for hatching – showing more than 80% agreement in sign of change (or no change) – panel a	Final plotted data	mask_80perc-agreement_tx35_panel_a_ssp126_2081-2100_minus_baseline.nc			https://github.com/IPCC-WG1/Chapter-12/tree/main/Figures/data/Figure_12.4/tx35/	CliMAF, CDO, Xarray	
	CMIP6 multi-model ensemble mean of tx35 – ssp585 mid term minus recent past – panel b	Final plotted data	tx35_panel_b_ssp585_2041-2060_minus_baseline.nc			https://github.com/IPCC-WG1/Chapter-12/tree/main/Figures/data/Figure_12.4/tx35/	CliMAF, CDO, Xarray	
	Mask for hatching – showing more than 80% agreement in sign of change (or no change) – panel b	Final plotted data	mask_80perc-agreement_tx35_panel_b_ssp585_2041-2060_minus_baseline.nc			https://github.com/IPCC-WG1/Chapter-12/tree/main/Figures/data/Figure_12.4/tx35/	CliMAF, CDO, Xarray	
	CMIP6 multi-model ensemble mean of tx35 – ssp585 long term minus	Final plotted data	tx35_panel_c_ssp585_2081-2100_minus_base			https://github.com/IPCC-WG1/Chapter-	CliMAF, CDO, Xarray	

ACCEPTED VERSION SUBJECT TO FINAL EDITS

	recent past – panel b		line.nc			12/tree/main/Figures/data/Figure_12.4/tx35/		
	Mask for hatching – showing more than 80% agreement in sign of change (or no change) – panel c	Final plotted data	mask_80perc-agreement_tx35_panel_c_ssp585_2081-2100_minus_baseline.nc			https://github.com/IPCC-WG1/Chapter-12/tree/main/Figures/data/Figure_12.4/tx35/	CliMAF, CDO, Xarray	
	Script to do the bias correction on tasmax (before extracting the number of days with tasmax > 35°C)	Code	bias_correction_isimip3.R (data processing routine)			https://github.com/IPCC-WG1/Atlas/tree/master/scripts/ATLAS-data/bias-correction/	R	
	Computing averages + ensemble statistics + model agreement + plotting for panel a, b and c	Code	tx35_individual_figures.ipynb (plotting code)			https://github.com/IPCC-WG1/Chapter-12/tree/main/Figures/scripts/global_figure_12.4	CliMAF, ncl, CDO, Xarray	
	Datasets used for panels a, b and c, with the list of the panels at the end of each line	Metadata file	CMIP6_day_tx35isimip_withpanels.csv			https://github.com/IPCC-WG1/Chapter-12/tree/main/Figures/data/Figure_12.4/tx35/		
Figure 12.4, d, e, f	Datasets used for panels d, e and f, with the list of the panels at the end of each line	Metadata file	Fig12-4_md_cmip6.txt			https://github.com/IPCC-WG1/Chapter-12/tree/main/data/Figure_12.4/DF6		
	Figure 12.4d-f processing code	Code	EXE0_create_model_overview.ipynb (data			https://github.com/IPCC-WG1/Chapter-	(Schwingshackl et al., 2021)	

ACCEPTED VERSION SUBJECT TO FINAL EDITS

			processing routine) EXE1_calcHI_performBC_CMIP6.ipynb (data processing routine) EXE2_Prepare_data_for_IPCC.ipynb (data processing routine)			12/tree/main/HIcalculation		
	CMIP6 multi-model ensemble mean of NOAA Heat Index > 41°C – ssp126 long term minus recent past – panel d	Final plotted data	HI41_panel_d_ssp126_2081-2100_minus_baseline.nc			https://github.com/IPCC-WG1/Chapter-12/tree/main/Figures/data/Figure_12.4/HI41/	CliMAF, CDO, Xarray	
	Mask for hatching – showing more than 80% agreement in sign of change (or no change) – panel d	Final plotted data	mask_80perc-agreement_HI41_panel_d_ssp126_2081-2100_minus_baseline.nc			https://github.com/IPCC-WG1/Chapter-12/tree/main/Figures/data/Figure_12.4/HI41/	CliMAF, CDO, Xarray	
	CMIP6 multi-model ensemble mean of NOAA Heat Index > 41°C – ssp585 mid term minus recent past – panel e	Final plotted data	HI41_panel_e_ssp585_2041-2060_minus_baseline.nc			https://github.com/IPCC-WG1/Chapter-12/tree/main/Figures/data/Figure_12.4/HI41/	CliMAF, CDO, Xarray	
	Mask for hatching – showing more than 80% agreement in sign of change (or no change) – panel e	Final plotted data	mask_80perc-agreement_HI41_panel_e_ssp585_2041-2060_minus_baseline.nc			https://github.com/IPCC-WG1/Chapter-12/tree/main/Figures/data/Figure_12.4/HI41/	CliMAF, CDO, Xarray	

ACCEPTED VERSION SUBJECT TO FINAL EDITS

	CMIP6 multi-model ensemble mean of NOAA Heat Index > 41°C – ssp585 long term minus recent past – panel f	Final plotted data	HI41_panel_f_ssp585_2081-2100_minus_baseline.nc			https://github.com/IPCC-WG1/Chapter-12/tree/main/Figures/data/Figure_12.4/HI41/	CliMAF, CDO, Xarray	
	Mask for hatching – showing more than 80% agreement in sign of change (or no change) – panel f	Final plotted data	mask_80perc-agreement_HI41_panel_f_ssp585_2081-2100_minus_baseline.nc			https://github.com/IPCC-WG1/Chapter-12/tree/main/Figures/data/Figure_12.4/HI41/	CliMAF, CDO, Xarray	
	Computing averages + ensemble statistics + model agreement + plotting for panel d, e and f	Code	HI_NOAA_individual_figures.ipynb (plotting routine)			https://github.com/IPCC-WG1/Chapter-12/tree/main/Figures/scripts/global_figure_12.4	CliMAF, CDO, Ncl, Xarray	
Figure 12.4, g, h, i	Datasets used for panels g, h and i, with the list of the panels at the end of each line	Metadata file	CMIP6_day_spi6_withpanels.csv			https://github.com/IPCC-WG1/Chapter-12/tree/main/data/Figure_12.4/DF6		
	Drought events calculation	Code	calculate_SPELL_multy.sh, dspell_minter19.x (data processing routine)			https://github.com/fraffael/DFscripts/tree/main/CMIP6		
	Drought Frequency calculation for each timeslice	Code	far-mid-hist.sh (data processing routine)			https://github.com/fraffael/DFscripts/tree/main/CMIP6		
	CMIP6 multi-model ensemble mean of DF6	Final plotted data	DF6_panel_g_ssp126_farch_minus			https://github.com/IPCC-	CliMAF, CDO, Xarray	

ACCEPTED VERSION SUBJECT TO FINAL EDITS

	Index – ssp126 log term minus recent past – panel g		_baseline.nc			WG1/Chapter-12/tree/main/Figures/data/Figure_12.4/DF6		
	Mask for hatching – showing more than 80% agreement in sign of change (or no change) – panel g	Final plotted data	mask_80perc-agreement_DF6_panel_g_ssp126_farch_minus_baseline.nc			https://github.com/IPCC-WG1/Chapter-12/tree/main/Figures/data/Figure_12.4/DF6	CliMAF, CDO, Xarray	
	CMIP6 multi-model ensemble mean of DF6 Index – ssp585 mid term minus recent past – panel h	Final plotted data	DF6_panel_h_ssp585_midch_minus_baseline.nc			https://github.com/IPCC-WG1/Chapter-12/tree/main/Figures/data/Figure_12.4/DF6	CliMAF, CDO, Xarray	
	Mask for hatching – showing more than 80% agreement in sign of change (or no change) – panel h	Final plotted data	mask_80perc-agreement_DF6_panel_h_ssp585_midch_minus_baseline.nc			https://github.com/IPCC-WG1/Chapter-12/tree/main/Figures/data/Figure_12.4/DF6	CliMAF, CDO, Xarray	
	CMIP6 multi-model ensemble mean of DF6 Index - ssp585 long term minus recent past – panel i	Final plotted data	DF6_panel_i_ssp585_farch_minus_baseline.nc			https://github.com/IPCC-WG1/Chapter-12/tree/main/Figures/data/Figure_12.4/DF6	CliMAF, CDO, Xarray	
	Mask for hatching showing more than 80% agreement in sign of change (or no change) – panel i	Final plotted data	mask_80perc-agreement_DF6_panel_i_ssp585_farch_minus_baseline.nc			https://github.com/IPCC-WG1/Chapter-12/tree/main/Figures/data/Figure_1	CliMAF, CDO, Xarray	

ACCEPTED VERSION SUBJECT TO FINAL EDITS

						2.4/DF6		
	Script to compute ensemble statistics + model agreement + plotting for panel g, h and i	Code	DF6_individual_figures.ipynb (plotting routine)			https://github.com/IPCC-WG1/Chapter-12/tree/main/Figures/scripts/global_figure_12.4	CliMAF, CDO, Ncl, Xarray	
Figure 12.4, j, k, l	Datasets used for panels j, k and l, with the list of the panels at the end of each line	Metadata file	cmip6_SM_tot_at_w_md cmip6_SM_tot_time_ave_md			https://github.com/IPCC-WG1/Chapter-12/tree/main/data/Figure_12.4/SM		
	CMIP6 multi-model ensemble mean of soil moisture – ssp126 long term minus recent past - % of recent past climatology – panel j	Final plotted data	SM_panel_j_ssp126_2081-2100_minus_baseline.nc			https://github.com/IPCC-WG1/Chapter-12/tree/main/Figures/data/Figure_12.4/SM	CliMAF, CDO, Xarray	
	Mask for hatching – showing more than 80% agreement in sign of change (or no change) – panel j	Final plotted data	mask_80perc-agreement_SM_panel_j_ssp126_2081-2100_minus_baseline.nc			https://github.com/IPCC-WG1/Chapter-12/tree/main/Figures/data/Figure_12.4/SM/	CliMAF, CDO, Xarray	
	CMIP6 multi-model ensemble mean of soil moisture – ssp585 mid term minus recent past - % of recent past climatology – panel k	Final plotted data	SM_panel_k_ssp585_2041-2060_minus_baseline.nc			https://github.com/IPCC-WG1/Chapter-12/tree/main/Figures/data/Figure_12.4/SM	CliMAF, CDO, Xarray	
	Mask for hatching – showing more than 80% agreement in sign of change (or no change) –	Final plotted data	mask_80perc-agreement_SM_panel_j_ssp585_2041-			https://github.com/IPCC-WG1/Chapter-12/tree/main/F	CliMAF, CDO, Xarray	

ACCEPTED VERSION SUBJECT TO FINAL EDITS

	panel k		2060_minus_baseline.nc			igures/ data/Figure_12.4/SM/		
	CMIP6 multi-model ensemble mean of soil moisture – ssp585 long term minus recent past - % of recent past climatology – panel k	Final plotted data	SM_panel_k_ssp585_2081-2100_minus_baseline.nc			https://github.com/IPCC-WG1/Chapter-12/tree/main/Figures/data/Figure_12.4/SM	CliMAF, CDO, Xarray	
	Mask for hatching – showing more than 80% agreement in sign of change (or no change) – panel l	Final plotted data	mask_80perc-agreement_SM_panel_l_ssp585_2081-2100_minus_baseline.nc			https://github.com/IPCC-WG1/Chapter-12/tree/main/Figures/data/Figure_12.4/SM/	CliMAF, CDO, Xarray	
	Script to compute ensemble statistics + model agreement + plotting for panel j, k and l	Code	SoilMoisture_individual_figures.ipynb (plotting routine)			https://github.com/IPCC-WG1/Chapter-12/tree/main/Figures/scripts/global_figure_12.4	CliMAF, CDO, Ncl, Xarray	
Figure 12.4, m, n, o	Datasets used for panels m, n and o, with the list of the panels at the end of each line	Metadata file	CMIP6_Amon_sfcWind_withpanels.csv			https://github.com/IPCC-WG1/Chapter-12/tree/main/data/Figure_12.4/sfcWind		
	CMIP6 multi-model ensemble mean of near surface wind – ssp126 long term minus recent past - % of recent past climatology – panel m	Final plotted data	sfcWind_panel_m_ssp126_2081-2100_minus_baseline.nc			https://github.com/IPCC-WG1/Chapter-12/tree/main/Figures/data/Figure_12.4/sfcWind	CliMAF, CDO, Xarray	
	Mask for hatching – showing more than 80%	Final plotted data	mask_80perc-agreement_sfcWi			https://github.com/IPCC-	CliMAF, CDO, Xarray	

ACCEPTED VERSION SUBJECT TO FINAL EDITS

	agreement in sign of change (or no change) – panel m		nd_panel_m_ssp126_2081-2100_minus_baseline.nc			WG1/Chapter-12/tree/main/Figures/data/Figure_12.4/ sfcWind/		
	CMIP6 multi-model ensemble mean of near surface wind – ssp585 mid term minus recent past - % of recent past climatology – panel n	Final plotted data	sfcWind_panel_n_ssp585_2041-2060_minus_baseline.nc			https://github.com/IPCC-WG1/Chapter-12/tree/main/Figures/data/Figure_12.4/sfcWind/	CliMAF, CDO, Xarray	
	Mask for hatching – showing more than 80% agreement in sign of change (or no change) – panel n	Final plotted data	mask_80perc-agreement_sfcWind_panel_n_ssp585_2041-2060_minus_baseline.nc			https://github.com/IPCC-WG1/Chapter-12/tree/main/Figures/data/Figure_12.4/sfcWind	CliMAF, CDO, Xarray	
	CMIP6 multi-model ensemble mean of near surface wind – ssp585 long term minus recent past - % of recent past climatology – panel o	Final plotted data	sfcWind_panel_o_ssp585_2081-2100_minus_baseline.nc			https://github.com/IPCC-WG1/Chapter-12/tree/main/Figures/data/Figure_12.4/sfcWind	CliMAF, CDO, Xarray	
	Mask for hatching – showing more than 80% agreement in sign of change (or no change) – panel o	Final plotted data	mask_80perc-agreement_sfcWind_panel_o_ssp585_2081-2100_minus_baseline.nc			https://github.com/IPCC-WG1/Chapter-12/tree/main/Figures/data/Figure_12.4/sfcWind	CliMAF, CDO, Xarray	
	Script to compute ensemble statistics + model agreement + plotting for panel m, n and o	Code	wind_perc-baseline_individual_figures.ipynb (plotting routine)			https://github.com/IPCC-WG1/Chapter-12/tree/main/Figures/scripts/global_figure_	CliMAF, CDO, Ncl, Xarray	

ACCEPTED VERSION SUBJECT TO FINAL EDITS

						12.4		
Figure 12.4, p, q, r	Global Extreme Sea Level projections	Input dataset	globalTWL_RCP45.nc globalTWL_RCP85.nc both expressed as changes relative to globalTWL_baseline.nc	Creative Commons Attribution 4.0 International (CC BY 4.0) licence	Vousdoukas, Michail; Mentaschi, Lorenzo; Voukouvalas, Evangelos; Verlaan, Martin; Jevrejeva, Svetlana; Jackson, Luke; Feyen, Luc (2018): Global Extreme Sea Level projections. European Commission, Joint Research Centre (JRC) [Dataset] doi:10.2905/jrc-liscoast-10012 PID: http://data.europa.eu/89h/jrc-liscoast-10012	https://data.jrc.ec.europa.eu/dataset/jrc-liscoast-10012	(Vousdoukas et al., 2018)	
	Plotting for panel p, q and r	Code	ETWL_individual_figures.ipynb (plotting routine)			https://github.com/IPCC-WG1/Chapter-12/tree/main/Figures/scripts/global_figure_12.4	pyNgl	

ACCEPTED VERSION SUBJECT TO FINAL EDITS

Figure 12.5, a	List of CORDEX datasets used as boundary conditions for the hydro model	Metadata file	Fig12-5_md_cordex.csv			https://github.com/IPCC-WG1/Chapter-12/tree/main/data/Figure_12.5/		
	Plotting code to do the map	Code	ch12_fig12.5_plotting_code_Q100_AFR.py (plotting routine)			https://github.com/fdisante/IPCC-ch12/tree/main/CORDEX/AFR	matplotlib	
	Csv file creation for plotting	Code	dranetwrite (plotting subroutine)			https://github.com/ictp-esp/CHyM/tree/master/utility/dranetwrite		
	Data processing routine: forcing fields remapping to CHyM grid	Code	create_input.sh (data processing routine)			https://github.com/fdisante/IPCC-ch12/tree/main/common		
	parallel MPI execution for CHyM	Code	run_simulations.sh (script to run the simulations)			https://github.com/fdisante/IPCC-ch12/tree/main/common		
	River routing model CHyM	Code	CHyM-roff (model)			https://github.com/fdisante/CHyM-roff		
	Q100 calculations	Code	create_Qx_regcm.R (data processing routine)			https://github.com/fdisante/IPCC-ch12/tree/main/common		
	Ensemble mean modern time slice calculation	Code	calculate_ensMean_1995-2014.sh (data processing routine)			https://github.com/fdisante/IPCC-ch12/tree/main		

ACCEPTED VERSION SUBJECT TO FINAL EDITS

						/common		
	Ensemble mean mid time slice calculation	Code	calculate_ensMean_2041-2060.sh (data processing routine)			https://github.com/fdisante/IPCC-ch12/tree/main/common		
	Q100 changes for CORDEX domains AFR and EUR, RCP8.5, mid term	Final plotted data	Q100_map_panel_a_AFR_less_MED_divdra.nc and Q100_map_panel_a_MED_for_AFR_from_EUR_divdra.nc			https://github.com/IPCC-WG1/Chapter-12/tree/main/data/Figure_12.5		
Figure 12.5, b	Global shoreline change projections	Input dataset	globalErosionProjections_Long_Term_Change_RCP85_2100.csv	Creative Commons Attribution 4.0 International (CC BY 4.0) licence	European Commission, Joint Research Centre (2019): Global shoreline change projections. European Commission, Joint Research Centre (JRC) [Dataset] doi:10.2905/18EB5F19-B916-454F-B2F5-88881931587E PID: http://data.europa.eu/89h/	https://data.jrc.ec.europa.eu/dataset/18eb5f19-b916-454f-b2f5-88881931587e	(Vousdoukas et al., 2020)	

ACCEPTED VERSION SUBJECT TO FINAL EDITS

					18eb5f19-b916-454f-b2f5-88881931587e			
	Plotting script to do the map	Code	CoastalRecession_map_AR6regions_AFRICA.ipynb (plotting routine)			https://github.com/IPCC-WG1/Chapter-12/tree/main/scripts/AFRICA_regional_figure/	pyNgl	
Figure 12.5, c	List of CORDEX datasets used as boundary conditions for ChyM	Metadata file	Fig12-5_md_cordex.csv			https://github.com/IPCC-WG1/Chapter-12/tree/main/data/Figure_12.5/		
	List of CMIP5 datasets used as boundary conditions for ChyM	Metadata file	Fig12-5_10_md_cmip5.csv			https://github.com/IPCC-WG1/Chapter-12/tree/main/data/Figure_12.5/		
	List of CMIP6 datasets used as boundary conditions for ChyM	Metadata file	Fig12-5_10_md_cmip6.csv			https://github.com/IPCC-WG1/Chapter-12/tree/main/data/Figure_12.5/		
	Data processing routine: forcing fields remapping to ChyM grid	Code	create_input.sh (data processing routine)			https://github.com/fdisante/IPCC-ch12/tree/main/common		
	parallel MPI execution for ChyM	Code	run_simulations.sh (script to run the simulations)			https://github.com/fdisante/IPCC-ch12/tree/main		

ACCEPTED VERSION SUBJECT TO FINAL EDITS

						/common		
	River routing model ChyM	Code	ChyM-roff (model)			https://github.com/fdisante/CHyM-roff		
	Q100 calculations	Code	create_Qx_regcm.R (data processing routine)			https://github.com/fdisante/IPCC-ch12/tree/main/common		
	Ensemble mean modern time slice calculation	Code	calculate_ensMean_1995-2014.sh (data processing routine)			https://github.com/fdisante/IPCC-ch12/tree/main/common		
	Ensemble mean mid time slice calculation	Code	calculate_ensMean_2041-2060.sh (data processing routine)			https://github.com/fdisante/IPCC-ch12/tree/main/common		
	Ensemble mean far time slice calculation	Code	calculate_ensMean_2080-2099.sh (data processing routine)			https://github.com/fdisante/IPCC-ch12/tree/main/common		
	Ensemble mean warming levels rcp26 calculations for EUR (1850-1900)	Code	calculate_WarmingLevels_ensMean_EUR_rcp26.sh (data processing routine)			https://github.com/fdisante/IPCC-ch12/tree/main/CORDEX/EUR		
	Ensemble mean warming levels rcp26 calculations for EUR (1861-1900)	Code	calculate_WarmingLevels_ensMean_EUR_rcp26_1861.sh (data processing routine)			https://github.com/fdisante/IPCC-ch12/tree/main/CORDEX/EUR		
	Ensemble mean warming levels rcp85 calculations for EUR (1850-1900)	Code	calculate_WarmingLevels_ensMean_EUR_rcp85.sh			https://github.com/fdisante/IPCC-		

ACCEPTED VERSION SUBJECT TO FINAL EDITS

			(data processing routine)			ch12/tree/main/CORDEX/EUR		
	Ensemble mean warming levels rcp85 calculations for EUR (1861-1900)	Code	calculate_WarmingLevels_ensMean_EUR_rcp85_1861.sh (data processing routine)			https://github.com/fdisante/IPCC-ch12/tree/main/CORDEX/EUR		
	Ensemble mean warming levels calculations for all domains (EUR excluded) (1850-1900)	Code	calculate_WarmingLevels_ensMean.sh (data processing routine)			https://github.com/fdisante/IPCC-ch12/tree/main/common		
	Ensemble mean warming levels calculations for all domains (EUR excluded) (1861-1900)	Code	calculate_WarmingLevels_ensMean_1861-1900.sh (data processing routine)			https://github.com/fdisante/IPCC-ch12/tree/main/common		
	Regional averages per CORDEX domain, per scenario and per period; ${CORDEX_domain} = AFR or EUR ${scenario} = rcp26 or rcp85 ${period} = 1995-2014 (baseline), 2041-2060 (mid-term), or 2080-2099 (long-term)	Final plotted data	Q100_${scenario}_${period}.nc_${CORDEX_domain}.txt			https://github.com/IPCC-WG1/Chapter-12/tree/main/data/Figure_12.5/Q100_${ensemble}, with ${ensemble} = CMIP5, CMIP6 or CORDEX-core		
	Regional averages per CORDEX domain per global warming level, with: ${CORDEX_domain} = AFR or EUR ${GWL} = 1.5, 2 or 4	Final plotted data	${GWL}_${CORDEX_domain}.txt			https://github.com/IPCC-WG1/Chapter-12/tree/main/data/Figure_12.5/Q100_${ensemble}, with ${ensemble}		

ACCEPTED VERSION SUBJECT TO FINAL EDITS

						= CMIP5, CMIP6 or CORDEX-core		
	Plotting script to do the Q100 barplots	Code	Q100_Quantile_plot_region.ipynb (plotting routine)			https://github.com/IPCC-WG1/Chapter-12/tree/main/scripts/AFRICA_regional_figure_1	R	
Figure 12.5, d	Script to compute the regional averages by AR6 region	Code	Compute_averages_AR6_regions_Coastal_recession.py (data processing routine)			https://github.com/IPCC-WG1/Chapter-12/tree/main/scripts/Coastal_recession_by_AR6_region	CliMAF (https://climaf.readthedocs.io/en/master/) regionmask (https://github.com/mathause/regionmask)	
	Global shoreline change projections for experiments RCP4.5 and RCP8.5 (${scenario} = RCP45 or RCP85) and for future mid and long term periods (${horizon} in 2050 or 2100)	Input dataset	globalErosionProjections_Long_Term_Change_${scenario}_${horizon}.csv	Creative Commons Attribution 4.0 International (CC BY 4.0) licence	European Commission, Joint Research Centre (2019): Global shoreline change projections. European Commission, Joint Research Centre (JRC) [Dataset] doi:10.2905/18EB5F19-B916-454F-B2F5-	https://data.jrc.ec.europa.eu/dataset/18eb5f19-b916-454f-b2f5-88881931587e	(Vousdoukas et al., 2020)	

ACCEPTED VERSION SUBJECT TO FINAL EDITS

					8888193158 7E PID: http://data.europa.eu/89h/18eb5f19-b916-454f-b2f5-8888193158 7e			
	Regional averages of shoreline position change for RCP8.5, long term	Final plotted data	CoastalRecession _AFRICA_RCP8 5_2100.json			https://github.com/IPCC-WG1/Chapter-12/tree/main/data/Figure_12.5		
	Plotting script to do the barplots of shoreline position changes	Code	Barplots_coastalrecession.ipynb (plotting routine)			https://github.com/IPCC-WG1/Chapter-12/tree/main/scripts/AFRICA_regional_figure	R	
Figure 12.6 Panel, a	List of CORDEX datasets used as boundary conditions for the hydro model	Metadata file	Fig12-5_md_cordex.csv			https://github.com/IPCC-WG1/Chapter-12/tree/main/data/Figure_12.6/		
	Plotting code to do the map	Code	ch12_fig12.6_plotting_code_Q100_ASIA.py (plotting routine)			https://github.com/fdisante/IPCC-ch12/tree/main/CORDEX/ASIA	matplotlib	
	Csv file creation for plotting	Code	dranetwrite (plotting subroutine)			https://github.com/ictp-esp/CHyM/tree/master/utility/dranetwrite		

ACCEPTED VERSION SUBJECT TO FINAL EDITS

	Data processing routine: forcing fields remapping to CHyM grid	Code	create_input.sh (data processing routine)			https://github.com/fdisante/IPCC-ch12/tree/main/common		
	parallel MPI execution for CHyM	Code	run_simulations.sh (script to run the simulations)			https://github.com/fdisante/IPCC-ch12/tree/main/common		
	River routing model CHyM	Code	CHyM-roff (model)			https://github.com/fdisante/CHyM-roff		
	Q100 calculations	Code	create_Qx_regcm.R (data processing routine)			https://github.com/fdisante/IPCC-ch12/tree/main/common		
	Ensemble mean modern time slice calculation	Code	calculate_ensMean_1995-2014.sh (data processing routine)			https://github.com/fdisante/IPCC-ch12/tree/main/common		
	Ensemble mean mid time slice calculation	Code	calculate_ensMean_2041-2060.sh (data processing routine)			https://github.com/fdisante/IPCC-ch12/tree/main/common		
	Q100 changes for CORDEX domains EAS, WAS and SEA, RCP8.5, mid term	Final plotted data	Q100_map_panel_a_${CORDEX_domain}_for_ASIA_divdra.nc With ${CORDEX_domain} in EAS, WAS, SEA			https://github.com/IPCC-WG1/Chapter-12/tree/main/data/Figure_12.6		
Figure 12.6, b	Global shoreline change projections	Input dataset	globalErosionProjections_Long_Term_Change_RCP8	Creative Commons Attribution	European Commission, Joint	https://data.jrc.ec.europa.eu/dataset/18eb5f1	(Vousdoukas et al., 2020)	

ACCEPTED VERSION SUBJECT TO FINAL EDITS

			5_2100.csv	4.0 International (CC BY 4.0) licence	Research Centre (2019): Global shoreline change projections. European Commission, Joint Research Centre (JRC) [Dataset] doi:10.2905/18EB5F19-B916-454F-B2F5-8888193158 7E PID: http://data.europa.eu/89h/18eb5f19-b916-454f-b2f5-8888193158 7e	9-b916-454f-b2f5-88881931587e		
	Plotting script to do the map	Code	CoastalRecession_map_AR6regions_ASIA.ipynb (plotting routine)			https://github.com/IPCC-WG1/Chapter-12/tree/main/scripts/ASIA_regional_figure/	pyNgl	
Figure 12.6, c	List of CORDEX datasets used as boundary conditions for ChyM	Metadata file	Fig12-6_md_cordex.csv			https://github.com/IPCC-WG1/Chapter-12/tree/main/data/Figure_12.		

ACCEPTED VERSION SUBJECT TO FINAL EDITS

						6/		
	List of CMIP5 datasets used as boundary conditions for ChyM	Metadata file	Fig12-5_10_md_cmip5.csv			https://github.com/IPCC-WG1/Chapter-12/tree/main/data/Figure_12.6/		
	List of CMIP6 datasets used as boundary conditions for ChyM	Metadata file	Fig12-5_10_md_cmip6.csv			https://github.com/IPCC-WG1/Chapter-12/tree/main/data/Figure_12.6		
	Data processing routine: forcing fields remapping to ChyM grid	Code	create_input.sh (data processing routine)			https://github.com/fdisante/IPCC-ch12/tree/main/common		
	parallel MPI execution for ChyM	Code	run_simulations.sh (script to run the simulations)			https://github.com/fdisante/IPCC-ch12/tree/main/common		
	River routing model ChyM	Code	ChyM-roff (model)			https://github.com/fdisante/CHyM-roff		
	Q100 calculations	Code	create_Qx_regcm.R (data processing routine)			https://github.com/fdisante/IPCC-ch12/tree/main/common		
	Ensemble mean modern time slice calculation	Code	calculate_ensMean_1995-2014.sh (data processing routine)			https://github.com/fdisante/IPCC-ch12/tree/main/common		
	Ensemble mean mid time slice calculation	Code	calculate_ensMean_2041-2060.sh (data processing			https://github.com/fdisante/IPCC-		

ACCEPTED VERSION SUBJECT TO FINAL EDITS

			routine)			ch12/tree/main/common		
	Ensemble mean far time slice calculation	Code	calculate_ensMean_2080-2099.sh (data processing routine)			https://github.com/fdisante/IPCC-ch12/tree/main/common		
	Ensemble mean warming levels calculations for all domains (EUR excluded) (1850-1900)	Code	calculate_WarmingLevels_ensMean.sh (data processing routine)			https://github.com/fdisante/IPCC-ch12/tree/main/common		
	Ensemble mean warming levels calculations for all domains (EUR excluded) (1861-1900)	Code	calculate_WarmingLevels_ensMean_1861-1900.sh (data processing routine)			https://github.com/fdisante/IPCC-ch12/tree/main/common		
	Regional averages per CORDEX domain, per scenario and per period; ${CORDEX_domain} = EAS, WAS, SEA ${scenario} = rcp26 or rcp85 ${period} = 1995-2014 (baseline), 2041-2060 (mid-term), or 2080-2099 (long-term)	Final plotted data	Q100_${scenario}_${period}.nc_${CORDEX_domain}.txt			https://github.com/IPCC-WG1/Chapter-12/tree/main/data/Figure_12.6/Q100_${ensemble}, with ${ensemble} = CMIP5, CMIP6 or CORDEX-core		
	Regional averages per CORDEX domain per global warming level, with: ${CORDEX_domain} = EAS, WAS, SEA ${GWL} = 1.5, 2 or 4	Final plotted data	${GWL}_${CORDEX_domain}.txt			https://github.com/IPCC-WG1/Chapter-12/tree/main/data/Figure_12.6/Q100_${ensemble}, with ${ensemble} = CMIP5, CMIP6 or		

ACCEPTED VERSION SUBJECT TO FINAL EDITS

						CORDEX-core		
	Plotting script to do the Q100 barplots	Code	Q100_Quantile_plot_region.ipynb (plotting routine)			https://github.com/IPCC-WG1/Chapter-12/tree/main/scripts/ASIA_regional_figure}	R	
Figure 12.6, d	Script to compute the regional averages by AR6 region	Code	Compute_averages_AR6_regions_Coastal_recession.py (data processing routine)			https://github.com/IPCC-WG1/Chapter-12/tree/main/scripts/Coastal_recession_by_AR6_region	CliMAF (https://climaf.readthedocs.io/en/master/) regionmask (https://github.com/mathause/regionmask)	
	Global shoreline change projections for experiments RCP4.5 and RCP8.5 (${scenario} = RCP45 or RCP85) and for future mid and long term periods (${horizon} in 2050 or 2100)	Input dataset	globalErosionProjections_Long_Term_Change_${scenario}_${horizon}.csv	Creative Commons Attribution 4.0 International (CC BY 4.0) licence	European Commission, Joint Research Centre (2019): Global shoreline change projections. European Commission, Joint Research Centre (JRC) [Dataset] doi:10.2905/18EB5F19-B916-454F-B2F5-88881931587E PID:	https://data.jrc.ec.europa.eu/dataset/18eb5f19-b916-454f-b2f5-88881931587e	(Vousdoukas et al., 2020)	

ACCEPTED VERSION SUBJECT TO FINAL EDITS

					http://data.europa.eu/89h/18eb5f19-b916-454f-b2f5-88881931587e			
	Regional averages of shoreline position change for RCP8.5, long term	Final plotted data	CoastalRecession_ASIA_RCP85_2100.json			https://github.com/IPCC-WG1/Chapter-12/tree/main/data/Figure_12.7		
	Plotting script to do the barplots of shoreline position changes	Code	Barplots_coastalrecession.ipynb (plotting routine)			https://github.com/IPCC-WG1/Chapter-12/tree/main/scripts/ASIA_regional_figure	R	
Figure 12.7, a	List of CORDEX datasets used as boundary conditions for the hydro model	Metadata file	Fig12-7_md_cordex.csv			https://github.com/IPCC-WG1/Chapter-12/tree/main/data/Figure_12.7/		
	Plotting code to do the map	Code	ch12_fig12.7_plotting_code_Q100_AUS.py (plotting routine)			https://github.com/fdisante/IPCC-ch12/tree/main/CORDEX/ASIA	matplotlib	
	Csv file creation for plotting	Code	dranetwrite (plotting subroutine)			https://github.com/ictp-esp/CHyM/tree/master/utility/dranetwrite		
	Data processing routine: forcing fields remapping to CHyM grid	Code	create_input.sh (data processing routine)			https://github.com/fdisante/IPCC-		

ACCEPTED VERSION SUBJECT TO FINAL EDITS

						ch12/tree/main/common		
	parallel MPI execution for CHyM	Code	run_simulations.sh (script to run the simulations)			https://github.com/fdisante/IPCC-ch12/tree/main/common		
	River routing model CHyM	Code	CHyM-roff (model)			https://github.com/fdisante/CHyM-roff		
	Q100 calculations	Code	create_Qx_regcm.R			https://github.com/fdisante/IPCC-ch12/tree/main/common		
	Ensemble mean modern time slice calculation	Code	calculate_ensMean_1995-2014.sh (data processing routine)			https://github.com/fdisante/IPCC-ch12/tree/main/common		
	Ensemble mean mid time slice calculation	Code	calculate_ensMean_2041-2060.sh (data processing routine)			https://github.com/fdisante/IPCC-ch12/tree/main/common		
	Q100 changes for CORDEX domains AUS, RCP8.5, mid term	Final plotted data	Q100_map_panel_a_AUS_divdra.nc			https://github.com/IPCC-WG1/Chapter-12/tree/main/data/Figure_12.7		
Figure 12.7, b	Global shoreline change projections	Input dataset	globalErosionProjections_Long_Term_Change_RCP85_2100.csv	Creative Commons Attribution 4.0 International (CC BY 4.0) licence	European Commission, Joint Research Centre (2019): Global shoreline	https://data.jrc.ec.europa.eu/dataset/18eb5f19-b916-454f-b2f5-88881931587e	(Vousdoukas et al., 2020)	

ACCEPTED VERSION SUBJECT TO FINAL EDITS

					change projections. European Commission, Joint Research Centre (JRC) [Dataset] doi:10.2905/18EB5F19-B916-454F-B2F5-88881931587E PID: http://data.europa.eu/89h/18eb5f19-b916-454f-b2f5-88881931587e			
	Plotting script to do the map	Code	CoastalRecession_map_AR6regions_Australasia.ipynb (plotting routine)			https://github.com/IPCC-WG1/Chapter-12/tree/main/scripts/Australasia_regional_figure/	pyNgl	
Figure 12.7, c	List of CORDEX datasets used as boundary conditions for ChyM	Metadata file	Fig12-7_md_cordex.csv			https://github.com/IPCC-WG1/Chapter-12/tree/main/data/Figure_12.7/		
	List of CMIP5 datasets used as boundary conditions for ChyM	Metadata file	Fig12-5_10_md_cmip5.csv			https://github.com/IPCC-WG1/Chapter-12/tree/main/d		

ACCEPTED VERSION SUBJECT TO FINAL EDITS

						ata/Figure_12.7/		
	List of CMIP6 datasets used as boundary conditions for ChyM	Metadata file	Fig12-5_10_md_cmip6.csv			https://github.com/IPCC-WG1/Chapter-12/tree/main/data/Figure_12.7		
	Data processing routine: forcing fields remapping to ChyM grid	Code	create_input.sh (data processing routine)			https://github.com/fdisante/IPCC-ch12/tree/main/common		
	parallel MPI execution for ChyM	Code	run_simulations.sh (script to run the simulations)			https://github.com/fdisante/IPCC-ch12/tree/main/common		
	River routing model ChyM	Code	ChyM-roff (model)			https://github.com/fdisante/CHyM-roff		
	Q100 calculations	Code	create_Qx_regcm.R (data processing routine)			https://github.com/fdisante/IPCC-ch12/tree/main/common		
	Ensemble mean modern time slice calculation	Code	calculate_ensMean_1995-2014.sh (data processing routine)			https://github.com/fdisante/IPCC-ch12/tree/main/common		
	Ensemble mean mid time slice calculation	Code	calculate_ensMean_2041-2060.sh (data processing routine)			https://github.com/fdisante/IPCC-ch12/tree/main/common		
	Ensemble mean far time slice calculation	Code	calculate_ensMean_2080-2099.sh (data processing			https://github.com/fdisante/IPCC-		

ACCEPTED VERSION SUBJECT TO FINAL EDITS

			routine)			ch12/tree/main/common		
	Ensemble mean warming levels calculations for all domains (EUR excluded) (1850-1900)	Code	calculate_WarmingLevels_ensMean.sh (data processing routine)			https://github.com/fdisante/IPCC-ch12/tree/main/common		
	Ensemble mean warming levels calculations for all domains (EUR excluded) (1861-1900)	Code	calculate_WarmingLevels_ensMean_1861-1900.sh (data processing routine)			https://github.com/fdisante/IPCC-ch12/tree/main/common		
	Regional averages per CORDEX domain, per scenario and per period; ${CORDEX_domain} = AUS ${scenario} = rcp26 or rcp85 ${period} = 1995-2014 (baseline), 2041-2060 (mid-term), or 2080-2099 (long-term)	Final plotted data	Q100_${scenario}_${period}.nc_${CORDEX_domain}.txt			https://github.com/IPCC-WG1/Chapter-12/tree/main/data/Figure_12.7/Q100_${ensemble}, with ${ensemble} = CMIP5, CMIP6 or CORDEX-core		
	Regional averages per CORDEX domain per global warming level, with: ${CORDEX_domain} = AUS ${GWL} = 1.5, 2 or 4	Final plotted data	${GWL}_${CORDEX_domain}.txt			https://github.com/IPCC-WG1/Chapter-12/tree/main/data/Figure_12.7/Q100_${ensemble}, with ${ensemble} = CMIP5, CMIP6 or CORDEX-core		
	Plotting script to do the Q100 barplots	Code	Q100_Quantile_plot_region.ipynb (plotting routine)			https://github.com/IPCC-WG1/Chapter-	R	

ACCEPTED VERSION SUBJECT TO FINAL EDITS

						12/tree/main/scripts/Australasia_regional_figure_1		
Figure 12.7, d	Script to compute the regional averages by AR6 region	Code	Compute_averages_AR6_regions_Coastal_recession.py (data processing routine)			https://github.com/IPCC-WG1/Chapter-12/tree/main/scripts/Coastal_recession_by_AR6_region	CliMAF (https://climaf.readthedocs.io/en/master/) regionmask (https://github.com/mathause/regionmask)	
	Global shoreline change projections for experiments RCP4.5 and RCP8.5 (${scenario} = RCP45 or RCP85) and for future mid and long term periods (${horizon} in 2050 or 2100)	Input dataset	globalErosionProjections_Long_Term_Change_${scenario}_${horizon}.csv	Creative Commons Attribution 4.0 International (CC BY 4.0) licence	European Commission, Joint Research Centre (2019): Global shoreline change projections. European Commission, Joint Research Centre (JRC) [Dataset] doi:10.2905/18EB5F19-B916-454F-B2F5-88881931587E PID: http://data.europa.eu/89h/18eb5f19-b916-454f-b2f5-	https://data.jrc.ec.europa.eu/dataset/18eb5f19-b916-454f-b2f5-88881931587e	(Vousdoukas et al., 2020)	

ACCEPTED VERSION SUBJECT TO FINAL EDITS

					88881931587e			
	Regional averages of shoreline position change for RCP8.5, long term	Final plotted data	CoastalRecession_Australasia_RCP85_2100.json			https://github.com/IPCC-WG1/Chapter-12/tree/main/data/Figure_12.7		
	Plotting script to do the barplots of shoreline position changes	Code	Barplots_coastalrecession.ipynb (plotting routine)			https://github.com/IPCC-WG1/Chapter-12/tree/main/scripts/Australasia_regional_figure	pyNgl	
Figure 12.8, a	List of CORDEX datasets used as boundary conditions for the hydro model	Metadata file	Fig12-8_md_cordex.csv			https://github.com/IPCC-WG1/Chapter-12/tree/main/data/Figure_12.8/		
	Plotting code to do the map	Code	ch12_fig12.8_plotting_code_Q100_SAM.py (plotting routine)			https://github.com/fdisante/IPCC-ch12/tree/main/CORDEX/SAM	matplotlib	
	Csv file creation for plotting	Code	dranetwrite (plotting subroutine)			https://github.com/ictp-esp/CHyM/tree/master/utility/dranetwrite		
	Data processing routine: forcing fields remapping to CHyM grid	Code	create_input.sh (data processing routine)			https://github.com/fdisante/IPCC-ch12/tree/main/common		
	parallel MPI execution for CHyM	Code	run_simulations.sh			https://github.com/fdisante/I		

ACCEPTED VERSION SUBJECT TO FINAL EDITS

						PCC-ch12/tree/main/common		
	River routing model CHyM	Code	CHyM-roff (model)			https://github.com/fdisante/CHyM-roff		
	Q100 calculations	Code	create_Qx_regcm.R (data processing routine)			https://github.com/fdisante/IPCC-ch12/tree/main/common		
	Ensemble mean modern time slice calculation	Code	calculate_ensMean_1995-2014.sh (data processing routine)			https://github.com/fdisante/IPCC-ch12/tree/main/common		
	Ensemble mean mid time slice calculation	Code	calculate_ensMean_2041-2060.sh (data processing routine)			https://github.com/fdisante/IPCC-ch12/tree/main/common		
	Q100 changes for CORDEX domains SAM and CAM, RCP8.5, mid term	Final plotted data	Q100_map_panel_a_SAM_divdra.nc And Q100_map_panel_a_CAM_for_SAM_divdra.nc			https://github.com/IPCC-WG1/Chapter-12/tree/main/data/Figure_12.8		
Figure 12.8, b	Global shoreline change projections	Input dataset	globalErosionProjections_Long_Term_Change_RCP85_2100.csv	Creative Commons Attribution 4.0 International (CC BY 4.0) licence	European Commission, Joint Research Centre (2019): Global shoreline change projections. European	https://data.jrc.ec.europa.eu/dataset/18eb5f19-b916-454f-b2f5-88881931587e	(Vousdoukas et al., 2020)	

ACCEPTED VERSION SUBJECT TO FINAL EDITS

					Commission, Joint Research Centre (JRC) [Dataset] doi:10.2905/18EB5F19-B916-454F-B2F5-88881931587E PID: http://data.europa.eu/89h/18eb5f19-b916-454f-b2f5-88881931587e			
	Plotting script to do the map	Code	CoastalRecession_map_AR6regions_SOUTH-AMERICA.ipynb (plotting routine)			https://github.com/IPCC-WG1/Chapter-12/tree/main/scripts/SOUTH-AMERICA_regional_figure/	pyNgl	
Figure 12.8, c	List of CORDEX datasets used as boundary conditions for ChyM	Metadata file	Fig12-8_md_cordex.csv			https://github.com/IPCC-WG1/Chapter-12/tree/main/data/Figure_12.8/		
	List of CMIP5 datasets used as boundary conditions for ChyM	Metadata file	Fig12-5_10_md_cmip5.csv			https://github.com/IPCC-WG1/Chapter-12/tree/main/data/Figure_12.8/		

ACCEPTED VERSION SUBJECT TO FINAL EDITS

	List of CMIP6 datasets used as boundary conditions for ChyM	Metadata file	Fig12-5_10_md_cmip6.csv			https://github.com/IPCC-WG1/Chapter-12/tree/main/data/Figure_12.8		
	Data processing routine: forcing fields remapping to ChyM grid	Code	create_input.sh (data processing routine)			https://github.com/fdisante/IPCC-ch12/tree/main/common		
	parallel MPI execution for ChyM	Code	run_simulations.sh (script to run the simulations)			https://github.com/fdisante/IPCC-ch12/tree/main/common		
	River routing model ChyM	Code	ChyM-roff (model)			https://github.com/fdisante/CHyM-roff		
	Q100 calculations	Code	create_Qx_regcm.R (data processing routine)			https://github.com/fdisante/IPCC-ch12/tree/main/common		
	Ensemble mean modern time slice calculation	Code	calculate_ensMean_1995-2014.sh (data processing routine)			https://github.com/fdisante/IPCC-ch12/tree/main/common		
	Ensemble mean mid time slice calculation	Code	calculate_ensMean_2041-2060.sh (data processing routine)			https://github.com/fdisante/IPCC-ch12/tree/main/common		
	Ensemble mean far time slice calculation	Code	calculate_ensMean_2080-2099.sh (data processing routine)			https://github.com/fdisante/IPCC-ch12/tree/main/common		

ACCEPTED VERSION SUBJECT TO FINAL EDITS

	Ensemble mean warming levels calculations for all domains (EUR excluded) (1850-1900)	Code	calculate_WarmingLevels_ensMean.sh (data processing routine)			https://github.com/fdisante/IPCC-ch12/tree/main/common		
	Ensemble mean warming levels calculations for all domains (EUR excluded) (1861-1900)	Code	calculate_WarmingLevels_ensMean_1861-1900.sh (data processing routine)			https://github.com/fdisante/IPCC-ch12/tree/main/common		
	Regional averages per CORDEX domain, per scenario and per period; ${CORDEX_domain} = SAM, CAM ${scenario} = rcp26 or rcp85 ${period} = 1995-2014 (baseline), 2041-2060 (mid-term), or 2080-2099 (long-term)	Final plotted data	Q100_${scenario}_${period}.nc_${CORDEX_domain}.txt			https://github.com/IPCC-WG1/Chapter-12/tree/main/data/Figure_12.8/Q100_${ensemble}, with ${ensemble} = CMIP5, CMIP6 or CORDEX-core		
	Regional averages per CORDEX domain per global warming level, with: ${CORDEX_domain} = SAM, CAM ${GWL} = 1.5, 2 or 4	Final plotted data	${GWL}_${CORDEX_domain}.txt			https://github.com/IPCC-WG1/Chapter-12/tree/main/data/Figure_12.8/Q100_${ensemble}, with ${ensemble} = CMIP5, CMIP6 or CORDEX-core		
	Plotting script to do the Q100 barplots	Code	Q100_Quantile_plot_region.ipynb (plotting routine)			https://github.com/IPCC-WG1/Chapter-12/tree/main/scripts/SOUTH	R	

ACCEPTED VERSION SUBJECT TO FINAL EDITS

						- AMERICA_regional_figure }		
Figure 12.8, d	Script to compute the regional averages by AR6 region	Code	Compute_averages_AR6_regions_Coastal_recession.py (data processing routine)			https://github.com/IPCC-WG1/Chapter-12/tree/main/scripts/Coastal_recession_by_AR6_region	CliMAF (https://climaf.readthedocs.io/en/master/) regionmask (https://github.com/mathause/regionmask)	
	Global shoreline change projections for experiments RCP4.5 and RCP8.5 (${scenario} = RCP45 or RCP85) and for future mid and long term periods (${horizon} in 2050 or 2100)	Input dataset	globalErosionProjections_Long_Term_Change_${scenario}_${horizon}.csv	Creative Commons Attribution 4.0 International (CC BY 4.0) licence	European Commission, Joint Research Centre (2019): Global shoreline change projections. European Commission, Joint Research Centre (JRC) [Dataset] doi:10.2905/18EB5F19-B916-454F-B2F5-88881931587E PID: http://data.europa.eu/89h/18eb5f19-b916-454f-b2f5-	https://data.jrc.ec.europa.eu/dataset/18eb5f19-b916-454f-b2f5-88881931587e	(Vousdoukas et al., 2020)	

ACCEPTED VERSION SUBJECT TO FINAL EDITS

					8888193158 7e			
	Regional averages of shoreline position change for RCP8.5, long term	Final plotted data	CoastalRecession _SOUTH-AMERICA_RCP 85_2100.json			https://github. com/IPCC-WG1/Chapter-12/tree/main/data/Figure_12.8		
	Plotting script to do the barplots of shoreline position changes	Code	Barplots_coastalrecession.ipynb (plotting routine)			https://github. com/IPCC-WG1/Chapter-12/tree/main/scripts/SOUTH-AMERICA_regional_figure	R	
Figure 12.9, a	List of CORDEX datasets used as boundary conditions for the hydro model	Metadata file	Fig12-9_md_cordex.csv			https://github. com/IPCC-WG1/Chapter-12/tree/main/data/Figure_12.9/		
	Plotting code to do the map	Code	ch12_fig12.9_plotting_code_Q100_EUR.py (plotting routine)			https://github. com/fdisante/IPCC-ch12/tree/main/CORDEX/EUR	matplotlib	
	Csv file creation for plotting	Code	dranetwrite (plotting subroutine)			https://github. com/ictp-esp/CHyM/tree/master/utility/dranetwrite		
	Data processing routine: forcing fields remapping to CHyM grid	Code	create_input.sh (data processing routine)			https://github. com/fdisante/IPCC-ch12/tree/main/common		
	parallel MPI execution	Code	run_simulations.s			https://github.		

ACCEPTED VERSION SUBJECT TO FINAL EDITS

	for CHyM		h (script to run the simulations)			com/fdisante/IPCC-ch12/tree/main/common		
	River routing model CHyM	Code	CHyM-roff (model)			https://github.com/fdisante/CHyM-roff		
	Q100 calculations	Code	create_Qx_regcm.R (data processing routine)			https://github.com/fdisante/IPCC-ch12/tree/main/common		
	Ensemble mean modern time slice calculation	Code	calculate_ensMean_1995-2014.sh (data processing routine)			https://github.com/fdisante/IPCC-ch12/tree/main/common		
	Ensemble mean mid time slice calculation	Code	calculate_ensMean_2041-2060.sh (data processing routine)			https://github.com/fdisante/IPCC-ch12/tree/main/common		
	Q100 changes for CORDEX domains EUR, RCP8.5, mid term	Final plotted data	Q100_map_panel_a_EUR_divdra.nc			https://github.com/IPCC-WG1/Chapter-12/tree/main/data/Figure_12.9		
Figure 12.9 b	CORDEX datasets for SWE index, RCP8.5 mid-term	Metadata file	EURO_CORDEX_snw_time_periods.csv			https://github.com/IPCC-WG1/Chapter-12/tree/main/data/Figure_12.9		
	Computing ensemble median and model agreement	Code	snow_map_Europe.ipynb (data processing routine)			https://github.com/IPCC-WG1/Chapter-12/tree/main/scripts/EUROP	CliMAF (https://climaf.readthedocs.io/en/master/) CDO, Xarray	

ACCEPTED VERSION SUBJECT TO FINAL EDITS

						E_regional_figure		
	CORDEX multi-model ensemble mean of number of days with SWE > 100mm – rcp85 mid term minus recent past	Final plotted data	SWE_panel_b_RCP85_mce_minus_baseline.nc			https://github.com/IPCC-WG1/Chapter-12/tree/main/data/Figure_12.9		
	Mask for hatching – showing more than 80% agreement in sign of change (or no change)	Final plotted data	mask_80perc-agreement_SWE_panel_b_RCP85_mce_minus_baseline.nc			https://github.com/IPCC-WG1/Chapter-12/tree/main/data/Figure_12.9		
	Plotting script for the SWE map	Code	pyNGL_AR6regions_SWE_EUROPE.ipynb (plotting routine)			https://github.com/IPCC-WG1/Chapter-12/tree/main/scripts/EUROPE_regional_figure	pyNgl	
Figure 12.9, c	List of CORDEX datasets used as boundary conditions for ChyM	Metadata file	Fig12-9_md_cordex.csv			https://github.com/IPCC-WG1/Chapter-12/tree/main/data/Figure_12.9/		
	List of CMIP5 datasets used as boundary conditions for ChyM	Metadata file	Fig12-5_10_md_cmip5.csv			https://github.com/IPCC-WG1/Chapter-12/tree/main/data/Figure_12.9/		
	List of CMIP6 datasets used as boundary conditions for ChyM	Metadata file	Fig12-5_10_md_cmip6.csv			https://github.com/IPCC-WG1/Chapter-12/tree/main/data/Figure_12.9		

ACCEPTED VERSION SUBJECT TO FINAL EDITS

	Data processing routine: forcing fields remapping to ChyM grid	Code	create_input.sh (data processing routine)			https://github.com/fdisante/IPCC-ch12/tree/main/common		
	parallel MPI execution for ChyM	Code	run_simulations.sh (script to run the simulations)			https://github.com/fdisante/IPCC-ch12/tree/main/common		
	River routing model ChyM	Code	ChyM-roff (model)			https://github.com/fdisante/CHyM-roff		
	Q100 calculations	Code	create_Qx_regcm.R (data processing routine)			https://github.com/fdisante/IPCC-ch12/tree/main/common		
	Ensemble mean modern time slice calculation	Code	calculate_ensMean_1995-2014.sh (data processing routine)			https://github.com/fdisante/IPCC-ch12/tree/main/common		
	Ensemble mean mid time slice calculation	Code	calculate_ensMean_2041-2060.sh (data processing routine)			https://github.com/fdisante/IPCC-ch12/tree/main/common		
	Ensemble mean far time slice calculation	Code	calculate_ensMean_2080-2099.sh (data processing routine)			https://github.com/fdisante/IPCC-ch12/tree/main/common		
	Regional averages per CORDEX domain, per scenario and per period; ${CORDEX_domain} = EUR ${scenario} = rcp26 or	Final plotted data	Q100_${scenario}_${period}.nc_${CORDEX_domain}.txt			https://github.com/IPCC-WG1/Chapter-12/tree/main/data/Figure_12.9/Q100_${ens		

ACCEPTED VERSION SUBJECT TO FINAL EDITS

	rcp85 ${period} = 1995-2014 (baseline), 2041-2060 (mid-term), or 2080-2099 (long-term)					emble}, with ${ensemble} = CMIP5, CMIP6 or CORDEX-core		
	Regional averages per CORDEX domain per global warming level, with: ${CORDEX_domain} = EUR ${GWL} = 1.5, 2 or 4	Final plotted data	${GWL}_${CORDEX_domain}.txt			https://github.com/IPCC-WG1/Chapter-12/tree/main/data/Figure_12.9/Q100_${ensemble}, with ${ensemble} = CMIP5, CMIP6 or CORDEX-core		
	Plotting script to do the Q100 barplots	Code	Q100_Quantile_plot_region.ipynb (plotting routine)			https://github.com/IPCC-WG1/Chapter-12/tree/main/scripts/EUROPE_regional_figure	R	
Figure 12.9 d	CMIP6 snow datasets	Metadata file	Fig12-9_md_cmip6_snow.txt			https://github.com/IPCC-WG1/Chapter-12/tree/main/data/Figure_12.9		
	CMIP5 snow datasets	Metadata file	Fig12-9_md_cmip5_snow.txt			https://github.com/IPCC-WG1/Chapter-12/tree/main/data/Figure_12.9		
	EURO CORDEX snow datasets	Metadata file	EURO_CORDEX_snw_time_period			https://github.com/IPCC-		

ACCEPTED VERSION SUBJECT TO FINAL EDITS

			s.csv and EURO_CORDEX_snw_gwls.csv			WG1/Chapter-12/tree/main/data/Figure_12.9		
	Computing SWE climatologies for future time periods and GWLs	Code	snow_CMIP5.sh (data processing routine) snow_CMIP6.sh (data processing routine) Snow_CMIP5_GWLs.ipyn (data processing routine) Snow_CMIP6_GWLs.ipyn (data processing routine)			https://github.com/IPCC-WG1/Chapter-12/tree/main/snow		
	Computing regional averages for SWE + ensemble statistics, for CMIP6, CMIP5 and EURO-CORDEX	Code	snw_Average_over_AR6_region_EUROPE.ipynb (data processing routine)			https://github.com/IPCC-WG1/Chapter-12/tree/main/scripts/EUROPE_regional_figure	CliMAF (https://climaf.readthedocs.io/en/master/) regionmask (https://github.com/mathause/regionmask)	
	Ensemble statistics of SWE regional averages over AR6 regions for CMIP6	Final plotted data	CMIP6_EUR-11_snw_mask14_AR6_regional_averages.json			https://github.com/IPCC-WG1/Chapter-12/tree/main/data/Figure_12.9		
	Ensemble statistics of SWE regional averages over AR6 regions for CMIP5	Final plotted data	CMIP5_EUR-11_snw_mask14_AR6_regional_averages.json			https://github.com/IPCC-WG1/Chapter-12/tree/main/data/Figure_12.9		
	Ensemble statistics of	Final plotted	EURO-			https://github.		

ACCEPTED VERSION SUBJECT TO FINAL EDITS

	SWE regional averages over AR6 regions for CORDEX	data	CORDEX_snw_mask14_AR6_regional_averages.json			com/IPCC-WG1/Chapter-12/tree/main/data/Figure_12.9		
	Plotting scripts for the SWE barplots	Code	SWE_Quantile_plot_region.ipynb (plotting routine)			https://github.com/IPCC-WG1/Chapter-12/tree/main/scripts/EUROPE_regional_figure	R	
Figure 12.10, a	List of CORDEX datasets used as boundary conditions for the hydro model	Metadata file	Fig12-10_md_cordex.csv			https://github.com/IPCC-WG1/Chapter-12/tree/main/data/Figure_12.10/		
	Plotting code to do the map	Code	ch12_fig12.10_plotting_code_Q100_NAM.py (plotting routine)			https://github.com/fdisante/IPCC-ch12/tree/main/CORDEX/NAM	pyNgl	
	Csv file creation for plotting	Code	dranetwrite (plotting subroutine)			https://github.com/ictp-esp/CHyM/tree/master/utility/dranetwrite		
	Data processing routine: forcing fields remapping to CHyM grid	Code	create_input.sh (data processing routine)			https://github.com/fdisante/IPCC-ch12/tree/main/common		
	parallel MPI execution for CHyM	Code	run_simulations.sh (script to run the simulations)			https://github.com/fdisante/IPCC-ch12/tree/main/common		

ACCEPTED VERSION SUBJECT TO FINAL EDITS

	River routing model CHyM	Code	CHyM-roff (model)			https://github.com/fdisante/CHyM-roff		
	Q100 calculations	Code	create_Qx_regcm.R (data processing routine)			https://github.com/fdisante/IPCC-ch12/tree/main/common		
	Ensemble mean modern time slice calculation	Code	calculate_ensMean_1995-2014.sh (data processing routine)			https://github.com/fdisante/IPCC-ch12/tree/main/common		
	Ensemble mean mid time slice calculation	Code	calculate_ensMean_2041-2060.sh (data processing routine)			https://github.com/fdisante/IPCC-ch12/tree/main/common		
	Q100 changes for CORDEX domains NAM and CAM, RCP8.5, mid term	Final plotted data	Q100_map_panel_a_NAM_divdra.nc And Q100_map_panel_a_CAM_for_NAM_divdra.nc			https://github.com/IPCC-WG1/Chapter-12/tree/main/data/Figure_12.10		
Figure 12.10, b	CORDEX datasets for SWE index, RCP8.5 mid-term	Metadata file	Fig12-10_md_CORDEX_snow.txt			https://github.com/IPCC-WG1/Chapter-12/tree/main/data/Figure_12.10		
	Computing ensemble median and model agreement	Code	NORTH-AMERICA_prepare_snw_map.ipynb (data processing routine)			https://github.com/IPCC-WG1/Chapter-12/tree/main/scripts/NORTH-	CliMAF (https://climaf.readthedocs.io/en/master/) CDO	

ACCEPTED VERSION SUBJECT TO FINAL EDITS

						AMERICA_regional_figure		
	CORDEX multi-model ensemble mean of number of days with SWE > 100mm – rcp85 mid term minus recent past	Final plotted data	SWE_panel_b_RCP85_mce_minus_baseline.nc			https://github.com/IPCC-WG1/Chapter-12/tree/main/data/Figure_12.10		
	Mask for hatching – showing more than 80% agreement in sign of change (or no change)	Final plotted data	mask_80perc-agreement_SWE_panel_b_RCP85_mce_minus_baseline.nc			https://github.com/IPCC-WG1/Chapter-12/tree/main/data/Figure_12.10		
	Plotting script for the SWE map	Code	pyNGL_AR6regions_SWE_NORTH-AMERICA.ipynb (plotting routine)			https://github.com/IPCC-WG1/Chapter-12/tree/main/scripts/NORTH-AMERICA_regional_figure	pyNgl	
Figure 12.10, c	List of CORDEX datasets used as boundary conditions for ChyM	Metadata file	Fig12-10_md_cordex.csv			https://github.com/IPCC-WG1/Chapter-12/tree/main/data/Figure_12.10/		
	List of CMIP5 datasets used as boundary conditions for ChyM	Metadata file	Fig12-5_10_md_cmip5.csv			https://github.com/IPCC-WG1/Chapter-12/tree/main/data/Figure_12.10/		
	List of CMIP6 datasets used as boundary conditions for ChyM	Metadata file	Fig12-5_10_md_cmip6.csv			https://github.com/IPCC-WG1/Chapter-12/tree/main/data/Figure_12.		

ACCEPTED VERSION SUBJECT TO FINAL EDITS

						10		
	Data processing routine: forcing fields remapping to ChyM grid	Code	create_input.sh (data processing routine)			https://github.com/fdisante/IPCC-ch12/tree/main/common		
	parallel MPI execution for ChyM	Code	run_simulations.sh (script to run the simulations)			https://github.com/fdisante/IPCC-ch12/tree/main/common		
	River routing model ChyM	Code	ChyM-roff (model)			https://github.com/fdisante/CHyM-roff		
	Q100 calculations	Code	create_Qx_regcm.R (data processing routine)			https://github.com/fdisante/IPCC-ch12/tree/main/common		
	Ensemble mean modern time slice calculation	Code	calculate_ensMean_1995-2014.sh (data processing routine)			https://github.com/fdisante/IPCC-ch12/tree/main/common		
	Ensemble mean mid time slice calculation	Code	calculate_ensMean_2041-2060.sh (data processing routine)			https://github.com/fdisante/IPCC-ch12/tree/main/common		
	Ensemble mean far time slice calculation	Code	calculate_ensMean_2080-2099.sh (data processing routine)			https://github.com/fdisante/IPCC-ch12/tree/main/common		
	Regional averages per CORDEX domain, per scenario and per period; ${CORDEX_domain} = NAM, CAM	Final plotted data	Q100_${scenario}_${period}.nc_${CORDEX_domain}.txt			https://github.com/IPCC-WG1/Chapter-12/tree/main/data/Figure_12.		

ACCEPTED VERSION SUBJECT TO FINAL EDITS

	${scenario} = rcp26 or rcp85 ${period} = 1995-2014 (baseline), 2041-2060 (mid-term), or 2080-2099 (long-term)					10/Q100_${ensemble}, with ${ensemble} = CMIP5, CMIP6 or CORDEX-core		
	Regional averages per CORDEX domain per global warming level, with: ${CORDEX_domain} = NAM, CAM ${GWL} = 1.5, 2 or 4	Final plotted data	${GWL}_${CORDEX_domain}.txt			https://github.com/IPCC-WG1/Chapter-12/tree/main/data/Figure_12.10/Q100_${ensemble}, with ${ensemble} = CMIP5, CMIP6 or CORDEX-core		
	Plotting script to do the Q100 barplots	Code	Q100_Quantile_plot_region.ipynb (plotting routine)			https://github.com/IPCC-WG1/Chapter-12/tree/main/scripts/NORTH-AMERICA_regional_figure	R	
Figure 12.10, d	CMIP6 snow datasets	Metadata file	Fig12-10_md_cmip6_snow.txt			https://github.com/IPCC-WG1/Chapter-12/tree/main/data/Figure_12.10		
	CMIP5 snow datasets	Metadata file	Fig12-10_md_cmip5_snow.txt			https://github.com/IPCC-WG1/Chapter-12/tree/main/data/Figure_12.10		

ACCEPTED VERSION SUBJECT TO FINAL EDITS

	CORDEX snow datasets	Metadata file	Fig12-10_md_cordex_snow.txt			https://github.com/IPCC-WG1/Chapter-12/tree/main/data/Figure_12.10		
	Computing SWE climatologies for future time periods and GWLs	Code	snow_CMIP5.sh (data processing routine) snow_CMIP6.sh (data processing routine) Snow_CMIP5_GWLs.ipyn (data processing routine) Snow_CMIP6_GWLs.ipyn (data processing routine)			https://github.com/IPCC-WG1/Chapter-12/tree/main/snow	CliMAF (https://climaf.readthedocs.io/en/master/) CDO Xarray	
	Computing regional averages for SWE + ensemble statistics, for CMIP6, CMIP5 and CORDEX	Code	snw_Average_over_AR6_region_NORTH-AMERICA.ipynb (data processing routine)			https://github.com/IPCC-WG1/Chapter-12/tree/main/scripts/NORTH-AMERICA_regional_figure	CliMAF (https://climaf.readthedocs.io/en/master/) regionmask (https://github.com/mathause/regionmask)	
	Ensemble statistics of SWE regional averages over AR6 regions for CMIP6	Final plotted data	CMIP6_NORTH-AMERICA_snw_mask14_AR6_regional_averages.json			https://github.com/IPCC-WG1/Chapter-12/tree/main/data/Figure_12.10		
	Ensemble statistics of SWE regional averages over AR6 regions for CMIP5	Final plotted data	CMIP5_NORTH-AMERICA_snw_mask14_AR6_regional_averages.jso			https://github.com/IPCC-WG1/Chapter-12/tree/main/d		

ACCEPTED VERSION SUBJECT TO FINAL EDITS

			n			ata/Figure_12.10		
	Ensemble statistics of SWE regional averages over AR6 regions for CORDEX	Final plotted data	NAM-22-CORDEX_snw_mask14_AR6_regional_averages.json			https://github.com/IPCC-WG1/Chapter-12/tree/main/data/Figure_12.10		
	Plotting scripts for the SWE barplots	Code	SWE_Quantile_plot_region.ipynb (plotting routine)			https://github.com/IPCC-WG1/Chapter-12/tree/main/scripts/NORTH-AMERICA_regional_figure	R	
Figure 12.SM.1	CMIP6 input datasets for tx35isimip	Metadata file	CMIP6_day_tx35isimip_md.csv			https://github.com/IPCC-WG1/Chapter-12/tree/main/data/Figure_S12.1		
	CMIP5 input datasets for tx35isimip	Metadata file	CMIP5_day_tx35isimip_md.csv			https://github.com/IPCC-WG1/Chapter-12/tree/main/data/Figure_S12.1		
	CORDEX input datasets for tx35isimip for ${CORDEX_domain} in AFR, AUS, CAM, SAM, NAM, EUR, EAS, WAS, SEA	Metadata file	CORDEX-${CORDEX_domain}_day_tx35isimip_md.csv			https://github.com/IPCC-WG1/Chapter-12/tree/main/data/Figure_S12.1		
	Script to do the bias correction on tasmax (before extracting the number of days with	Code	bias_correction_isimip3.R (data processing routine)			https://github.com/IPCC-WG1/Atlas/tree/master/script	R	

ACCEPTED VERSION SUBJECT TO FINAL EDITS

	tasmax > 35°C)					s/ATLAS-data/bias-correction/		
	Computation of the tx35 index							
	Computing the climatologies for CMIP5 over the periods and global warming levels + computing the regional averages + ensemble statistics	Code	compute_regional_averages_CMIP5.py (data processing routine)			https://github.com/IPCC-WG1/Chapter-12/tree/main/scripts/tx35_satellites	CliMAF (https://climaf.readthedocs.io/en/master/) regionmask (https://github.com/mathause/regionmask)	
	Computing the climatologies for CMIP6 over the periods and global warming levels + computing the regional averages + ensemble statistics	Code	compute_regional_averages_CMIP6.py (data processing routine)			https://github.com/IPCC-WG1/Chapter-12/tree/main/scripts/tx35_satellites	CliMAF (https://climaf.readthedocs.io/en/master/) regionmask (https://github.com/mathause/regionmask)	
	Computing the climatologies for CORDEX over the periods and global warming levels + computing the regional averages + ensemble statistics	Code	compute_regional_averages_CORDEX.py (data processing routine)			https://github.com/IPCC-WG1/Chapter-12/tree/main/scripts/tx35_satellites	CliMAF (https://climaf.readthedocs.io/en/master/) regionmask (https://github.com/mathause/regionmask)	
	CMIP6 regional averages over the AR6 regions for the periods (baseline, mid-term and long-term) and the global warming levels (1.5, 2 and 4)	Final plotted data	CMIP6_tx35isimip_AR6_regional_averages.json			https://github.com/IPCC-WG1/Chapter-12/tree/main/data/Figure_S12.1		
	CMIP5 regional averages over the AR6 regions for the periods (baseline, mid-term and long-term) and the global warming	Final plotted data	CMIP5_tx35isimip_AR6_regional_averages.json			https://github.com/IPCC-WG1/Chapter-12/tree/main/data/Figure_S1		

ACCEPTED VERSION SUBJECT TO FINAL EDITS

	levels (1.5, 2 and 4)					2.1		
	CORDEX regional averages over the AR6 regions for the periods (baseline, mid-term and long-term) and the global warming levels (1.5, 2 and 4)	Final plotted data	CORDEX_tx35isimip_AR6_regional_averages.json			https://github.com/IPCC-WG1/Chapter-12/tree/main/data/Figure_S12.1		
	Plotting script to do the barplots for tx35	Code	Quantile_plot_region.ipynb (plotting routine)			https://github.com/IPCC-WG1/Chapter-12/tree/main/scripts/tx35_satellites	R	
Figure 12.SM.2	CMIP6 input datasets for NOAA Heat Index (HI)	Metadata file	FigSM12-2_cmip6.txt			https://github.com/IPCC-WG1/Chapter-12/tree/main/data/Figure_S12.2		
	CMIP5 input datasets for NOAA Heat Index (HI)	Metadata file	FigSM12-2_cmip5.txt			https://github.com/IPCC-WG1/Chapter-12/tree/main/data/Figure_S12.2		
	CORDEX input datasets for NOAA Heat Index (HI) for ${CORDEX_domain} in AFR, AUS, CAM, SAM, NAM, EUR, EAS, WAS, SEA	Metadata file	FigSM12-2_cordex.txt			https://github.com/IPCC-WG1/Chapter-12/tree/main/data/Figure_S12.2		
	Computing NOAA HI for figure S12.2 for CMIP5, CMIP6 and each CORDEX domain (AFR,	code	EXE0_create_model_overview.ipynb (data processing			https://github.com/IPCC-WG1/Chapter-12/tree/main/	(Schwingshackl et al., 2021)	

ACCEPTED VERSION SUBJECT TO FINAL EDITS

	AUS, EUR, CAM, SAM, NAM, WAS, EAS, SEA)		routine) EXE1_calcHI_performBC_CMIP5.ipynb (data processing routine) EXE1_calcHI_performBC_CMIP6.ipynb (data processing routine) EXE1_calcHI_performBC_CORDEX_AFR-22.ipynb (data processing routine) EXE1_calcHI_performBC_CORDEX_AFR-44.ipynb (data processing routine) EXE1_calcHI_performBC_CORDEX_AUS-22.ipynb (data processing routine) EXE1_calcHI_performBC_CORDEX_AUS-44.ipynb (data processing routine) EXE1_calcHI_performBC_CORDEX_CAM-22.ipynb (data processing routine) EXE1_calcHI_performBC_CORDEX_CAM-44.ipynb			Hicalculation		

ACCEPTED VERSION SUBJECT TO FINAL EDITS

			(data processing routine) EXE1_calcHI_performBC_CORDEX_EAS-22.ipynb (data processing routine) EXE1_calcHI_performBC_CORDEX_EAS-44.ipynb (data processing routine) EXE1_calcHI_performBC_CORDEX_EUR-11.ipynb (data processing routine) EXE1_calcHI_performBC_CORDEX_NAM-22.ipynb (data processing routine) EXE1_calcHI_performBC_CORDEX_NAM-44.ipynb (data processing routine) EXE1_calcHI_performBC_CORDEX_SAM-22.ipynb (data processing routine) EXE1_calcHI_performBC_CORDEX_SAM-44.ipynb (data processing routine) EXE1_calcHI_performBC_CORDE					

ACCEPTED VERSION SUBJECT TO FINAL EDITS

			X_SEA-22.ipynb (data processing routine) EXE1_calcHI_performBC_CORDEX_WAS-22.ipynb (data processing routine) EXE1_calcHI_performBC_CORDEX_WAS-44.ipynb (data processing routine) EXE2_Prepare_data_for_IPCC.ipynb (data processing routine)					
	Computing the climatologies for CMIP5 over the periods and global warming levels + computing the regional averages + ensemble statistics	Code	Average_over_AR6_region.ipynb (data processing routine)			https://github.com/IPCC-WG1/Chapter-12/tree/main/scripts/HI_satellites	CliMAF (https://climaf.readthedocs.io/en/master/) regionmask (https://github.com/mathause/regionmask)	
	Computing the climatologies for CMIP6 over the periods and global warming levels + computing the regional averages + ensemble statistics	Code	Average_over_AR6_region.ipynb (data processing routine)			https://github.com/IPCC-WG1/Chapter-12/tree/main/scripts/HI_satellites	CliMAF (https://climaf.readthedocs.io/en/master/) regionmask (https://github.com/mathause/regionmask)	
	Computing the climatologies for CORDEX over the periods and global warming levels + computing the regional averages + ensemble statistics	Code	Average_over_AR6_region.ipynb (data processing routine)			https://github.com/IPCC-WG1/Chapter-12/tree/main/scripts/HI_satellites	CliMAF (https://climaf.readthedocs.io/en/master/) regionmask (https://github.com/mathause/regionmask)	

ACCEPTED VERSION SUBJECT TO FINAL EDITS

	CMIP6 regional averages over the AR6 regions for the periods (baseline, mid-term and long-term) and the global warming levels (1.5, 2 and 4)	Final plotted data	CMIP6_HI41_AR6_regional_averages.json			https://github.com/IPCC-WG1/Chapter-12/tree/main/data/Figure_S12.2		
	CMIP5 regional averages over the AR6 regions for the periods (baseline, mid-term and long-term) and the global warming levels (1.5, 2 and 4)	Final plotted data	CMIP5_HI41_AR6_regional_averages.json			https://github.com/IPCC-WG1/Chapter-12/tree/main/data/Figure_S12.2		
	CORDEX regional averages over the AR6 regions for the periods (baseline, mid-term and long-term) and the global warming levels (1.5, 2 and 4)	Final plotted data	CORDEX_HI41_AR6_regional_averages.json			https://github.com/IPCC-WG1/Chapter-12/tree/main/data/Figure_S12.2		
	Plotting script to do the barplots for NOAA HI	Code	Quantile_plot_region.ipynb (plotting routine)			https://github.com/IPCC-WG1/Chapter-12/tree/main/scripts/HI_satellites	R	
Figure 12.SM.3	CMIP6 precipitation datasets used to compute the drought frequency index DF6	Metadata file	CMIP6_day_pr_md.csv			https://github.com/IPCC-WG1/Chapter-12/tree/main/data/Figure_S12.3		
	CMIP5 precipitation datasets used to compute the drought frequency index DF6	Metadata file	CMIP5_day_pr_md.csv			https://github.com/IPCC-WG1/Chapter-12/tree/main/data/Figure_S12.3		
	CORDEX precipitation datasets used to compute	Metadata file	CORDEX-${CORDEX_dom			https://github.com/IPCC-		

ACCEPTED VERSION SUBJECT TO FINAL EDITS

	the drought frequency index DF6		ain}_day_pr_md.csv ${CORDEX_doain}: AUS, AFR, CAM, SAM, NAM, WAS, EAS, SEA, EUR			WG1/Chapter-12/tree/main/data/Figure_S12.3		
	Drought events calculation (for CMIP6, CMIP5 and CORDEX)	Code	calculate_SPELL_multy.sh, dspell_minter19.x (data processing routine)			https://github.com/fraffael/Dfscripts/${ENS}, with ${ENS} in CMIP6, CMIP5 and https://github.com/fraffael/Dfscripts/${CORDEX_domain}, with ${CORDEX_domain} in AFR-22, AUS-22, CAM-22, EUR-11, NAM-22, SAM-22, WAS-22, EAS-22, SEA-22		
	Drought Frequency calculation for each timeslice	Code	far-mid-hist.sh (data processing routine)			https://github.com/fraffael/Dfscripts/${ENS}, with ${ENS} in CMIP6,		

ACCEPTED VERSION SUBJECT TO FINAL EDITS

						CMIP5 and https://github.com/fraffael/Dfscripts/${CORDEX_domain}, with ${CORDEX_domain} in AFR-22, AUS-22, CAM-22, EUR-11, NAM-22, SAM-22, WAS-22, EAS-22, SEA-22		
	Global Warming Levels calculation for rcp26 for CMIP5 and CMIP6	Code	lancio_warmlev.sh, warming-levels-match26-${ENS} (data processing routine)			https://github.com/fraffael/Dfscripts/${ENS}, with ${ENS} in CMIP6, CMIP5		
	Global Warming Levels calculation for rcp85 for CMIP5 and CMIP6	Code	lancio_warmlev.sh, warming-levels-match85-${ENS}, with ${ENS} in CMIP6, CMIP5			https://github.com/fraffael/Dfscripts/${ENS}, with ${ENS} in CMIP6, CMIP5		
	Ensemble mean calculation for far and mid timeslices, far and	Code	ensembleDF.sh (processing routine)			https://github.com/fraffael/Dfscripts/${EN		

ACCEPTED VERSION SUBJECT TO FINAL EDITS

	mid change and GWLs ensemble means for CMIP5, CMIP6 and CORDEX					S}, with ${ENS} in CMIP6, CMIP5 and https://github.com/fraffael/Dfscripts/${CORDEX_domain}, with ${CORDEX_domain} in AFR-22, AUS-22, CAM-22, EUR-11, NAM-22, SAM-22, WAS-22, EAS		
	Global Warming Levels calculation for rcp26 for CORDEX	Code	lancio_warmlev.sh, warming-levels-match26-${CORDEX_domain}, with ${CORDEX_domain} in AFR22, AUS22, CAM22, EUR11, NAM22, SAM22, WAS22, EAS22, SEA22			https://github.com/fraffael/Dfscripts/${CORDEX_domain}, with ${CORDEX_domain} in AFR-22, AUS-22, CAM-22, EUR-11, NAM-22, SAM-22, WAS-22, EAS-22, SEA-22		
	Global Warming Levels calculation for rcp85 for	Code	lancio_warmlev.sh, warming-			https://github.com/fraffael/D		

ACCEPTED VERSION SUBJECT TO FINAL EDITS

	CORDEX		levels-match85-${CORDEX_domain }, with ${CORDEX_domain} in AFR22, AUS22, CAM22, EUR11, NAM22, SAM22, WAS22, EAS22, SEA22			Fscripts/${CORDEX_domain}, with ${CORDEX_domain} in AFR-22, AUS-22, CAM-22, EUR-11, NAM-22, SAM-22, WAS-22, EAS-22, SEA-22		
	Drought Frequency calculation for each timeslice (for CMIP6, CMIP5 and CORDEX)	Code	far-mid-hist.sh (data processing routine)			https://github.com/fraffael/Dfscripts/${ENS}, with ${ENS} in CMIP6, CMIP5 and https://github.com/fraffael/Dfscripts/${CORDEX_domain}, with ${CORDEX_domain} in AFR-22, AUS-22, CAM-22, EUR-11, NAM-22, SAM-22, WAS-22, EAS		
	Computing regional	Code	Average_over_A			https://github.	CliMAF	

ACCEPTED VERSION SUBJECT TO FINAL EDITS

	averages		R6_region.ipynb (data processing routine)			com/IPCC-WG1/Chapter-12/tree/main/scripts/DF6_satellites	(https://climaf.readthedocs.io/en/master/) regionmask (https://github.com/mathause/regionmask)	
	DF6 regional averages over AR6 regions fro CORDEX	Final plotted data	CORDEX_DF6_AR6_regional_averages.json			https://github.com/IPCC-WG1/Chapter-12/tree/main/data/Figure_S12.3		
	DF6 regional averages over AR6 regions fro CORDEX	Final plotted data	CORDEX_DF6_AR6_regional_averages.json			https://github.com/IPCC-WG1/Chapter-12/tree/main/data/Figure_S12.3		
	DF6 regional averages over AR6 regions fro CORDEX	Final plotted data	CORDEX_DF6_AR6_regional_averages.json			https://github.com/IPCC-WG1/Chapter-12/tree/main/data/Figure_S12.3		
	Plotting script for the satellite barplots	Code	Quantile_plot_region.ipynb (plotting routine)			https://github.com/IPCC-WG1/Chapter-12/tree/main/scripts/DF6_satellites	R	
Figure 12.SM.4	CMIP6 soil moisture datasets used to compute the climatologies over the time periods	Metadata file	cmip6_SM_tot_time_ave_md			https://github.com/IPCC-WG1/Chapter-12/tree/main/data/Figure_S12.4		
	CMIP6 soil moisture datasets used to compute the climatologies over	Metadata file	cmip6_SM_tot_at_w_md			https://github.com/IPCC-WG1/Chapter-		

ACCEPTED VERSION SUBJECT TO FINAL EDITS

	the global warming levels					12/tree/main/data/Figure_S12.4		
	CMIP5 soil moisture datasets used to compute the climatologies over the time periods	Metadata file	CMIP5_mrso_time_periods.csv			https://github.com/IPCC-WG1/Chapter-12/tree/main/data/Figure_S12.4		
	CMIP5 soil moisture datasets used to compute the climatologies over the global warming levels	Metadata file	CMIP5_mrso_gwl.csv			https://github.com/IPCC-WG1/Chapter-12/tree/main/data/Figure_S12.4		
	CORDEX soil moisture datasets used to compute the climatologies over the time periods	Metadata file	CORDEX_mrso_time_periods.csv			https://github.com/IPCC-WG1/Chapter-12/tree/main/data/Figure_S12.4		
	CORDEX soil moisture datasets used to compute the climatologies over the global warming levels	Metadata file	CORDEX_mrso_GWL.csv			https://github.com/IPCC-WG1/Chapter-12/tree/main/data/Figure_S12.4		
	Compute averages over time periods and GWLs for CMIP6 + ensemble statistics	Code	Compute_CMIP6_time_averages_GWLs_on_regional_averages_MathiasHauser.ipynb (data processing routine)			https://github.com/IPCC-WG1/Chapter-12/tree/main/scripts/SM_satellites	CliMAF (https://climaf.readthedocs.io/en/master/) regionmask (https://github.com/mathause/regionmask)	
	Compute averages and regional averages + ensemble statistics for CMIP5	Code	Prepare_time_slices_GWLs_soilmoisture_CMIP5.ipynb (data processing			https://github.com/IPCC-WG1/Chapter-12/tree/main/scripts/SM_sate	CliMAF (https://climaf.readthedocs.io/en/master/) regionmask	

ACCEPTED VERSION SUBJECT TO FINAL EDITS

			routine)			llites	(https://github.com/mathause/regionmask)	
	Compute averages and regional averages + ensemble statistics for CORDEX	Code	Prepare_time_slices_GWLs_soilmoisture_CORDEX.ipynb (data processing routine)			https://github.com/IPCC-WG1/Chapter-12/tree/main/scripts/SM_satellites	CliMAF (https://climaf.readthedocs.io/en/master/) regionmask (https://github.com/mathause/regionmask)	
	Differences between the regional averages over the AR6 regions between the future periods and GWLs and the baseline, expressed as % of the baseline value for CMIP6	Final plotted data	CMIP6_SM_diff_perc2020_AR6_regional_averages.json			https://github.com/IPCC-WG1/Chapter-12/tree/main/data/Figure_S12.4		
	Differences between the regional averages over the AR6 regions between the future periods and GWLs and the baseline, expressed as % of the baseline value for CMIP5	Final plotted data	CMIP5_SM_diff_perc2020_AR6_regional_averages.json			https://github.com/IPCC-WG1/Chapter-12/tree/main/data/Figure_S12.4		
	Differences between the regional averages over the AR6 regions between the future periods and GWLs and the baseline, expressed as % of the baseline value for CORDEX	Final plotted data	CORDEX_SM_diff_perc2020_AR6_regional_averages.json			https://github.com/IPCC-WG1/Chapter-12/tree/main/data/Figure_S12.4		
	Plotting script for the satellite barplots	Code	Quantile_plot_region.ipynb (plotting routine)			https://github.com/IPCC-WG1/Chapter-12/tree/main/scripts/DF6_satellites	R	

ACCEPTED VERSION SUBJECT TO FINAL EDITS

Figure 12.SM.5	CMIP6 sfcWind datasets	Metadata file	CMIP6_Amon_sfcWind_withpanels.csv			https://github.com/IPCC-WG1/Chapter-12/tree/main/data/Figure_S12.5		
	CMIP5 sfcWind datasets	Metadata file	CMIP5_sfcWind_time_periods.csv And CMIP5_sfcWind_gwl.csv			https://github.com/IPCC-WG1/Chapter-12/tree/main/data/Figure_S12.5		
	CORDEX sfcWind datasets (for ${CORDEX_domain} in AUS, AFR, NAM, SAM, CAM, EAS, WAS, SEA)	Metadata file	CORDEX-${CORDEX_domain}_day_sfcWind_md.csv			https://github.com/IPCC-WG1/Chapter-12/tree/main/data/Figure_S12.5		
	EURO CORDEX sfcWind datasets	Metadata file	EURO_CORDEX_sfcWind_gwls.csv And EURO_CORDEX_sfcWind_time_periods.csv			https://github.com/IPCC-WG1/Chapter-12/tree/main/data/Figure_S12.5		
	Computing the regional averages for near-surface wind over the AR6 regions + difference against baseline (in % of the baseline value) + ensemble statistics for CMIP5	Code	compute_regional_averages_CMIP5.py (data processing routine)			https://github.com/IPCC-WG1/Chapter-12/tree/main/scripts/wind_satellites	CliMAF (https://climaf.readthedocs.io/en/master/) regionmask (https://github.com/mathause/regionmask)	
	Computing the regional averages for near-surface wind over the AR6 regions + difference against baseline (in % of the	Code	Prepare_time_slices_GWLs_wind_CMIP6.ipynb			https://github.com/IPCC-WG1/Chapter-12/tree/main/scripts/wind_satellites		

ACCEPTED VERSION SUBJECT TO FINAL EDITS

	baseline value) + ensemble statistics for CMIP6							
	Computing the regional averages for near-surface wind over the AR6 regions + difference against baseline (in % of the baseline value) + ensemble statistics for CORDEX	Code	compute_regional_averages_CORDEX.py (data processing routine)			https://github.com/IPCC-WG1/Chapter-12/tree/main/scripts/wind_satellites	CliMAF (https://climaf.readthedocs.io/en/master/) regionmask (https://github.com/mathause/regionmask)	
	Differences between the regional averages over the AR6 regions between the future periods and GWLs and the baseline, expressed as % of the baseline value for CMIP6	Final plotted data	CMIP6_sfcWind_diff-perc-baseline_AR6_regional_averages.json			https://github.com/IPCC-WG1/Chapter-12/tree/main/data/Figure_S12.5		
	Differences between the regional averages over the AR6 regions between the future periods and GWLs and the baseline, expressed as % of the baseline value for CMIP5	Final plotted data	CMIP5_sfcWind_diff-perc-baseline_AR6_regional_averages.json			https://github.com/IPCC-WG1/Chapter-12/tree/main/data/Figure_S12.5		
	Differences between the regional averages over the AR6 regions between the future periods and GWLs and the baseline, expressed as % of the baseline value for CORDEX	Final plotted data	CORDEX_sfcWind_diff-perc-baseline_AR6_regional_averages.json			https://github.com/IPCC-WG1/Chapter-12/tree/main/data/Figure_S12.5		
	Plotting script for the satellite barplots	Code	Quantile_plot_region_diff.ipynb (plotting routine)			https://github.com/IPCC-WG1/Chapter-12/tree/main/s	R	

ACCEPTED VERSION SUBJECT TO FINAL EDITS

						cripts/DF6_satellites		
Figure 12.SM.6	Global Extreme Sea Level projections	Input dataset	globalTWL_baseline.nc globalTWL_RCP45.nc globalTWL_RCP85.nc	Creative Commons Attribution 4.0 International (CC BY 4.0) licence	Vousdoukas, Michail; Mentaschi, Lorenzo; Voukouvalas, Evangelos; Verlaan, Martin; Jevrejeva, Svetlana; Jackson, Luke; Feyen, Luc (2018): Global Extreme Sea Level projections. European Commission, Joint Research Centre (JRC) [Dataset] doi:10.2905/jrc-liscoast-10012 PID: http://data.europa.eu/89h/jrc-liscoast-10012	https://data.jrc.ec.europa.eu/dataset/jrc-liscoast-10012	(Vousdoukas et al., 2018)	
	Extreme sea level projections	Input dataset	41598_2020_67736_MOESM2_ESM			https://www.nature.com/articles/s41598-020-67736-6#Sec23 (Supplementar	(Kirezci et al., 2020)	

ACCEPTED VERSION SUBJECT TO FINAL EDITS

						y data file 2)		
	Computing regional averages of AR6 regions on the Kirezci et al (2020) dataset	Code	IPCC_ESLs_AR6_Regions_Kirezci.m (data processing routine)			https://github.com/IPCC-WG1/Chapter-12/tree/main/scripts/ETWL_satellites/Kirezci_IPCC_AR6_MatlabCodes/	matlab	
	Computing regional averages over 1R6 regions on the Vousdoukas et al (2018) dataset	Code	Compute_averages_AR6_regions_ETWL.ipynb (data processing routine)			https://github.com/IPCC-WG1/Chapter-12/tree/main/scripts/ETWL_satellites	CliMAF (https://climaf.readthedocs.io/en/master/) regionmask (https://github.com/mathause/regionmask)	
	Regional averages of Extreme Total Water Level estimates from Vousdoukas et al 2018	Final plotted data	Vousdoukas_ETWL_by_AR6_region_modern.json Vousdoukas_ETWL_by_AR6_region_RCP45_2050.json Vousdoukas_ETWL_by_AR6_region_RCP45_2100.json Vousdoukas_ETWL_by_AR6_region_RCP85_2050.json Vousdoukas_ETWL_by_AR6_region_RCP85_2100.json			https://github.com/IPCC-WG1/Chapter-12/tree/main/data/Figure_S12.6		
	Regional averages of Extreme Total Water Level estimates from	Final plotted data	Kirezci_ESL.csv			https://github.com/IPCC-WG1/Chapter-		

ACCEPTED VERSION SUBJECT TO FINAL EDITS

	Kirezci et al., 2020					12/tree/main/data/Figure_S12.6		
	Plotting script for the ETWL satellite barplots	Code	Barplots_ETWL.ipynb (plotting routine)			https://github.com/IPCC-WG1/Chapter-12/tree/main/scripts/ETWL_satellites		

[END TABLE 12.SM.1 HERE]

ACCEPTED VERSION
SUBJECT TO FINAL EDITS

References

Blazejczyk, K., Epstein, Y., Jendritzky, G., Staiger, H., and Tinz, B. (2012). Comparison of UTCI to selected thermal indices. *Int. J. Biometeorol.* 56, 515–535. doi:10.1007/s00484-011-0453-2.

Kirezci, E., Young, I. R., Ranasinghe, R., Muis, S., Nicholls, R. J., Lincke, D., et al. (2020). Projections of global-scale extreme sea levels and resulting episodic coastal flooding over the 21st Century. *Sci. Rep.* 10, 11629. doi:10.1038/s41598-020-67736-6.

Schwingshackl, C., Sillmann, J., Vicedo-Cabrera, A. M., Sandstad, M., and Aunan, K. (2021). Heat Stress Indicators in CMIP6: Estimating Future Trends and Exceedances of Impact-Relevant Thresholds. *Earth's Futur.* 9, e2020EF001885. doi:10.1029/2020EF001885.

Vousdoukas, M. I., Mentaschi, L., Voukouvalas, E., Verlaan, M., Jevrejeva, S., Jackson, L. P., et al. (2018). Global probabilistic projections of extreme sea levels show intensification of coastal flood hazard. *Nat. Commun.* 9, 2360. doi:10.1038/s41467-018-04692-w.

Vousdoukas, M. I., Ranasinghe, R., Mentaschi, L., Plomaritis, T. A., Athanasiou, P., Luijendijk, A., et al. (2020). Sandy coastlines under threat of erosion. *Nat. Clim. Chang.* 10, 260–263. doi:10.1038/s41558-020-0697-0.

ACCEPTED VERSION
SUBJECT TO FINAL EDITS

Atlas

Coordinating Lead Authors:
José Manuel Gutiérrez (Spain), Richard G. Jones (United Kingdom), Gemma Teresa Narisma (Philippines)

Lead Authors:
Lincoln M. Alves (Brazil), Muhammad Amjad (Pakistan), Irina V. Gorodetskaya (Portugal/Belgium, Russian Federation), Michael Grose (Australia), Nana Ama Browne Klutse (Ghana), Svitlana Krakovska (Ukraine), Jian Li (China), Daniel Martínez-Castro (Cuba, Peru/Cuba), Linda O. Mearns (United States of America), Sebastian H. Mernild (Denmark, Norway/Denmark), Thanh Ngo-Duc (Vietnam), Bart van den Hurk (The Netherlands), Jin-Ho Yoon (Republic of Korea)

Contributing Authors (Atlas chapter):
Maialen Iturbide (Spain), Ma. Laurice Preciado Jamero (Philippines), Émilie Vanvyve United Kingdom/ Belgium), Guðfinna Aðalgeirsdóttir (Iceland), Cécile Agosta (France), Mansour Almazroui (Saudi Arabia), Jorge Baño-Medina (Spain), Joaquín Bedia (Spain), María Laura Bettolli (Argentina), Donovan Campbell (Jamaica), Ana Casanueva (Spain), Christophe Cassou (France), Tereza Cavazos (Mexico), Abel Centella-Artola (Cuba), Ruth Cerezo-Mota (Mexico), Haoming Chen (China), Annalisa Cherchi (Italy), Erika Coppola (Italy), Faye Abigail Cruz (Philippines), Joseph D. Daron (United Kingdom), Chirag Dhara (India), Alejandro di Luca (Australia, Canada/Argentina), Arona Diedhiou (Ivory Coast/Senegal), Javier Díez Sierra (Spain), Alessandro Dosio (Italy), Jason Evans (Australia), Vincent Favier (France), Erich Fischer (Switzerland), Sebastian Gerland (Norway/Germany), Subimal Ghosh (India), Natalia Gnatiuk (Russian Federation/Ukraine), Melissa I. Gomis (France/Switzerland), Patrick Grenier (Canada), David S. Gutzler (United States of America), Rein Haarsma (The Netherlands), Rafiq Hamdi (Belgium), Cédric Hananel (Belgium/France), Ed Hawkins (United Kingdom), Mark Hemer (Australia), Kevin Hennessy (Australia), Nazrul Islam (Bangladesh/Saudi Arabia), Sanjay Jayanarayanan (India), Liew Juneng (Malaysia), Eleni Katragkou (Greece), Elena Kharyutkina (Russian Federation), Megan Kirchmeier-Young (Canada/ United States of America), Akio Kitoh (Japan), Erik Kjellström (Sweden), Yu Kosaka (Japan), James Kossin (United States of America), Kenneth Kunkel (United States of America), June-Yi Lee (Republic of Korea), Christopher Lennard (South Africa), Piero Lionello (Italy), Marta Pereira Llopart (Brazil), Ian Macadam (Australia/ United Kingdom), Douglas Maraun (Austria/Germany), Seth McGinnis (United States of America), Simon McGree (Australia/Fiji, Australia), Wilfran Moufouma-Okia (France), Gregory Nikulin (Sweden/Russian Federation), Francis Nkrumah (Ghana), Dirk Notz (Germany), Andrew Orr (United Kingdom), Sarah Osima (Tanzania), Tugba Ozturk (Turkey), Mohammad Rahimi (Iran), Mehwish Ramzan (Pakistan), Rosh Ranasinghe (The Netherlands/Sri Lanka, Australia), Johan Reyns (The Netherlands/Belgium), Annette Rinke (Germany), Daniela Schmidt (United Kingdom), Stéphane Sénési (France), Sonia I. Seneviratne (Switzerland), Chris Shaw (United Kingdom), Stefan Sobolowski (Norway/ United States of America), Samuel Somot (France), Anna A. Sörensson (Argentina), Tannecia S. Stephenson (Jamaica), Mouhamadou Bamba Sylla (Rwanda/Senegal), Fredolin Tangang (Malaysia), Claas Teichmann (Germany), Peter W. Thorne (Ireland/United Kingdom), Blair Trewin (Australia), Geert-Jan van Oldenborgh (The Netherlands), Jan Melchior van Wessem (The Netherlands), Robert Vautard (France), Sergio M. Vicente-Serrano (Spain), Alejandro Vichot-Llano (Cuba), Etienne Vignon (France), Yu Xiaoyong (China, Germany), Xuebin Zhang (Canada)

Contributing Authors (Interactive Atlas):
Maialen Iturbide (Spain), Jorge Baño-Medina (Spain), Joaquín Bedia (Spain), Ana Casanueva (Spain), Ezequiel Cimadevilla (Spain), Antonio S. Cofiño (Spain), Javier Díez Sierra (Spain), Jesús Fernández (Spain), Markel García (Spain), Sixto Herrera (Spain), Rodrigo Manzanas (Spain), Josipa Milovac (Spain/Croatia), Juan José Sáenz de la Torre (Spain), Daniel San Martín (Spain), Iván Sánchez (Spain), Elena Suárez (Spain), Max Tuni (Spain)

Review Editors:
Inés Camilloni (Argentina), Jens Hesselbjerg Christensen (Denmark), Fatima Driouech (Morocco)

ACCEPTED VERSION SUBJECT TO FINAL EDITS

Chapter Scientists:
Maialen Iturbide (Spain), Ma. Laurice Preciado Jamero (Philippines), Émilie Vanvyve (United Kingdom/Belgium)

Gemma Teresa Narisma, *in memoriam*.

This Atlas should be cited as:
Gutiérrez, J. M., R. G. Jones, G. T. Narisma, L. M. Alves, M. Amjad, I. V. Gorodetskaya, M. Grose, N. A. B. Klutse, S. Krakovska, J. Li, D. Martínez-Castro, L. O. Mearns, S. H. Mernild, T. Ngo-Duc, B. van den Hurk, J-H. Yoon, 2021, Atlas. In: *Climate Change 2021: The Physical Science Basis. Contribution of Working Group I to the Sixth Assessment Report of the Intergovernmental Panel on Climate Change* [Masson-Delmotte, V., P. Zhai, A. Pirani, S. L. Connors, C. Péan, S. Berger, N. Caud, Y. Chen, L. Goldfarb, M. I. Gomis, M. Huang, K. Leitzell, E. Lonnoy, J. B. R. Matthews, T. K. Maycock, T. Waterfield, O. Yelekçi, R. Yu and B. Zhou (eds.)]. Cambridge University Press. In Press.

Date: August 2021

This document is subject to copy-editing, corrigenda and trickle backs.

ACCEPTED VERSION
SUBJECT TO FINAL EDITS

Access to the Interactive Atlas

To access the Interactive Atlas, please copy http://interactive-atlas.ipcc.ch in any web browser.

Table of Contents

Executive summary **8**

Atlas.1 Introduction **11**

Atlas.1.1 Purpose 11
Atlas.1.2 Context and framing 11
Atlas.1.3 Defining temporal and spatial scales and regions 12
Atlas.1.3.1 Baselines and temporal scales of analysis for projections across scenarios 12
Atlas.1.3.2 Global warming levels 13
Atlas.1.3.3 Spatial scales and reference regions 14
Atlas.1.3.4 Typological and socio-economic regions 15
Atlas.1.4 Combining multiple sources of information for regions 16
Atlas.1.4.1 Observations 16
Atlas.1.4.2 Reanalysis 17
Atlas.1.4.3 Global model data (CMIP5 and CMIP6) 17
Atlas.1.4.4 Regional model data (CORDEX) 18

BOX ATLAS.1: ..... CORDEX-CORE 20

Atlas.1.4.5 Bias adjustment 21

Cross-Chapter Box Atlas.1: ..... Displaying robustness and uncertainty in maps 21

Atlas.2 The online 'Interactive Atlas' **26**

Atlas.2.1 Why an interactive online Atlas in AR6? 27
Atlas.2.2 Description of the Interactive Atlas: functionalities and datasets 27
Atlas.2.3 Accessibility, reproducibility and reusability (FAIR principles) 29
Atlas.2.4 Guidance for users 31
Atlas.2.4.1 Purpose of the Interactive Atlas 31
Atlas.2.4.2 Guidelines for the Interactive Atlas 31
Atlas.2.4.2.1 Quantitative support for assessments 31
Atlas.2.4.2.2 Insights from physical understanding 32
Atlas.2.4.2.3 Construction of storylines 32
Atlas.2.4.2.4 Visual information 32
Atlas.2.4.2.5 Dedicated climate change assessment programs 33

Atlas.3 Global synthesis **33**

Atlas.3.1 Global atmosphere and land surface 34
Atlas.3.2 Global ocean 40

Atlas.4 Africa **41**

ACCEPTED VERSION SUBJECT TO FINAL EDITS

Atlas.4.1 Key features of the regional climate and findings from previous IPCC assessments 41
Atlas.4.1.1 Key features of the regional climate 41
Atlas.4.1.2 Findings from previous IPCC assessments 41
Atlas.4.2 Assessment and synthesis of observations, trends and attribution 42
Atlas.4.3 Assessment of model performance 43
Atlas.4.4 Assessment and synthesis of projections 44
Atlas.4.5 Summary 45
Atlas.5 Asia 46
Atlas.5.1 East Asia 47
Atlas.5.1.1 Key features of the regional climate and findings from previous IPCC assessments 47
Atlas.5.1.1.1 Key features of the regional climate 47
Atlas.5.1.1.2 Findings from previous IPCC assessments 47
Atlas.5.1.2 Assessment and synthesis of observations, trends and attribution 47
Atlas.5.1.3 Assessment of model performance 48
Atlas.5.1.4 Assessment and synthesis of projections 49
Atlas.5.1.5 Summary 50
Atlas.5.2 North Asia 51
Atlas.5.2.1 Key features of the regional climate and findings from previous IPCC assessments 51
Atlas.5.2.1.1 Key features of the regional climate 51
Atlas.5.2.1.2 Findings from previous IPCC assessments 51
Atlas.5.2.2 Assessment and synthesis of observations, trends and attribution 51
Atlas.5.2.3 Assessment of model performance 52
Atlas.5.2.4 Assessment and synthesis of projections 53
Atlas.5.2.5 Summary 54
Atlas.5.3 South Asia 54
Atlas.5.3.1 Key features of the regional climate and findings from IPCC previous assessments 54
Atlas.5.3.1.1 Key features of the regional climate 54
Atlas.5.3.1.2 Findings from previous IPCC assessments 55
Atlas.5.3.2 Assessment and synthesis of observations, trends and attribution 55
Atlas.5.3.3 Assessment of model performance 56
Atlas.5.3.4 Assessment and synthesis of projections 57
Atlas.5.3.5 Summary 58
Atlas.5.4 Southeast Asia 58
Atlas.5.4.1 Key features of the regional climate and findings from previous IPCC assessments 58
Atlas.5.4.1.1 Key features of the regional climate 58
Atlas.5.4.1.2 Findings from previous IPCC assessments 59
Atlas.5.4.2 Assessment and synthesis of observations, trends and attribution 59
Atlas.5.4.3 Assessment of model performance 60
Atlas.5.4.4 Assessment and synthesis of projections 60

ACCEPTED VERSION SUBJECT TO FINAL EDITS

Atlas.5.4.5 Summary 61
Atlas.5.5 Southwest Asia 61
Atlas.5.5.1 Key features of the regional climate and findings from previous IPCC assessments 61
Atlas.5.5.1.1 Key features of the regional climate 61
Atlas.5.5.1.2 Findings from previous IPCC assessments 62
Atlas.5.5.2 Assessment and synthesis of observations, trends and attribution 62
Atlas.5.5.3 Assessment of model performance 63
Atlas.5.5.4 Assessment and synthesis of projections 64
Atlas.5.5.5 Summary 65
Atlas.6 Australasia 66
Atlas.6.1 Key features of the regional climate and findings from previous IPCC assessments 66
Atlas.6.1.1 Key features of the regional climate 66
Atlas.6.1.2 Findings from previous IPCC assessments 66
Atlas.6.2 Assessment and synthesis of observations, trends and attribution 67
Atlas.6.3 Assessment of climate model performance 68
Atlas.6.4 Assessment and synthesis of projections 68
Atlas.6.5 Summary 70
Atlas.7 Central and South America 70
Atlas.7.1 Central America and the Caribbean 71
Atlas.7.1.1 Key features of the regional climate and findings from previous IPCC assessments 71
Atlas.7.1.1.1 Key features of the regional climate 71
Atlas.7.1.1.2 Findings from previous IPCC assessments 72
Atlas.7.1.2 Assessment and synthesis of observations, trends and attribution 72
Atlas.7.1.3 Assessment of model performance 72
Atlas.7.1.4 Assessment and synthesis of projections 73
Atlas.7.1.5 Summary 74
Atlas.7.2 South America 75
Atlas.7.2.1 Key features of the regional climate and findings from previous IPCC assessments 75
Atlas.7.2.1.1 Key features of the regional climate 75
Atlas.7.2.1.2 Findings from previous IPCC assessments 75
Atlas.7.2.2 Assessment and synthesis of observations, trends and attribution 76
Atlas.7.2.3 Assessment of model performance 77
Atlas.7.2.4 Assessment and synthesis of projections 78
Atlas.7.2.5 Summary 79
Atlas.8 Europe 79
Atlas.8.1 Key features of the regional climate and findings from previous IPCC assessments 80
Atlas.8.1.1 Key features of the regional climate 80
Atlas.8.1.2 Findings from previous IPCC assessments 80

ACCEPTED VERSION
SUBJECT TO FINAL EDITS

Atlas.8.2 Assessment and synthesis of observations, trends and attribution....81
Atlas.8.3 Assessment of model performance....83
Atlas.8.4 Assessment and synthesis of projections....84
Atlas.8.5 Summary....86

Atlas.9 North America....86

Atlas.9.1 Key features of the regional climate and findings from previous IPCC assessments....87
Atlas.9.1.1 Key features of the regional climate....87
Atlas.9.1.2 Findings from previous IPCC assessments....87
Atlas.9.2 Assessment and synthesis of observations, trends, and attribution....88
Atlas.9.3 Assessment of model performance....89
Atlas.9.4 Assessment and synthesis of projections....90
Atlas.9.5 Summary....92

Atlas.10 Small islands....93

Atlas.10.1 Key features of the regional climate and findings from previous IPCC assessments....93
Atlas.10.1.1 Key features of the regional climate....93
Atlas.10.1.2 Findings from previous IPCC assessments....93
Atlas.10.2 Assessment and synthesis of observations, trends and attribution....93
Atlas.10.3 Assessment of model performance....95
Atlas.10.4 Assessment and synthesis of projections....95
Atlas.10.5 Summary....97

Cross-Chapter Box Atlas.2: Climate information relevant to water resources in Small Islands....97

Atlas.11 Polar regions....101

Atlas.11.1 Antarctica....102
Atlas.11.1.1 Key features of the regional climate and findings from previous IPCC assessments....102
Atlas.11.1.1.1 Key features of the regional climate....102
Atlas.11.1.1.2 Findings from previous IPCC assessments....103
Atlas.11.1.2 Assessment and synthesis of observations, trends and attribution....103
Atlas.11.1.3 Assessment of model performance....105
Atlas.11.1.4 Assessment and synthesis of projections....107
Atlas.11.1.5 Summary....108
Atlas.11.2 Arctic....109
Atlas.11.2.1 Key features of the regional climate and findings from previous IPCC assessments....109
Atlas.11.2.1.1 Key features of the regional climate....109
Atlas.11.2.1.2 Findings from previous IPCC assessments....109
Atlas.11.2.2 Assessment and synthesis of observations, trends and attribution....110
Atlas.11.2.3 Assessment of model performance....111
Atlas.11.2.4 Assessment and synthesis of projections....112

ACCEPTED VERSION SUBJECT TO FINAL EDITS

Atlas.11.2.5 Summary 114

Atlas.12 Final remarks 114

References 116

Figures 161

ACCEPTED VERSION
SUBJECT TO FINAL EDITS

Executive summary

This Atlas chapter assesses changes in mean climate at regional scales, in particular observed trends and their attribution and projected future changes. The main focus is on changes in temperature and precipitation (including snow and derived variables in polar regions) over land regions, though other variables, including for oceanic regions, are also discussed. Projected changes are presented both as relative to levels of global warming and for future time periods under a range of emissions scenarios. In order to facilitate summarizing assessment findings, a new set of WGI reference regions is used within the chapter which were derived following broad consultation and peer review. These are used in other chapters for summarizing regional information. This includes the assessment of climatic impact-driver changes in Chapter 12, which incorporates the changes in mean climate assessed in the Atlas. Another important new development since AR5 is the AR6 WGI Interactive Atlas, which is described in this chapter and is used to generate results both for the Atlas and other regional chapters. It is also a resource allowing exploration of datasets underpinning assessment findings in other chapters of the report.

Observed trends and projections in regional climate

Most land areas have warmed faster than the global average (*high confidence*) and *very likely* by at least 0.1°C per decade since 1960. A surface temperature change signal has *likely* emerged over all land areas. Many areas *very likely* warmed faster since the 1980s, including areas of northern, eastern and south-western Africa, Australia, Central America, Amazonia and West Antarctica (0.2°C–0.3°C per decade), the Arabian Peninsula, Central and East Asia and Europe (0.3°C–0.5°C per decade) and Arctic and near-Arctic land regions (up to 1°C per decade, or more in a few areas). {Figure Atlas.11, Interactive Atlas, Sections Atlas.3.1, Atlas.4.2, Atlas.5.1.2, Atlas.5.2.2, Atlas.5.3.2, Atlas.5.4.2, Atlas.5.5.2, Atlas.6.1.2, Atlas.6.2.2, Atlas.7.2, Atlas.8.2, Atlas.9.2, Atlas.10.2, Atlas.11.1.2, Atlas.11.2.2}

Significant positive trends in precipitation have been observed in most of North Asia, parts of West Central Asia, South-eastern South America, Northern Europe, Eastern North America, Western Antarctica and the Arctic (*medium confidence*). Significant negative trends have been observed in the Horn of Africa and southwest Western Australia (*high confidence*), parts of the Russian Far East, some parts of the Mediterranean and of the Caribbean, Southeast and Northeast Brazil and southern Africa (*medium confidence*), with the last attributed to anthropogenic warming of the Indian Ocean. In the many other land areas there are no significant trends in annual precipitation over the period 1960–2015 though increases in average precipitation intensity have been observed in the Sahel and Southeast Asia (*medium confidence*). {Figure Atlas.11, Interactive Atlas, Sections Atlas.3.1, Atlas.4.2, Atlas.5.1.2, Atlas.5.2.2, Atlas.5.3.2, Atlas.5.4.2, Atlas.5.5.2, Atlas.6.1.2, Atlas.6.2.2, Atlas.7.2, Atlas.8.2, Atlas.9.2, Atlas.10.2, Atlas.11.1.2, Atlas.11.2.2}.

The observed warming trends are projected to continue over the 21st century (*high confidence*) and over most land regions at a rate higher than the global average. At a global warming level of 4°C (i.e. relative to an 1850-1900 baseline) it is *likely* that most land areas will experience a further warming (from a 1995–2014 baseline) of at least 3°C and in some areas significantly more, including increases of 4°C–6°C in the Sahara/Sahel, Southwest, Central and Northern Asia; Northern South America and Amazonia, West Central and Eastern Europe; and Western, Central and Eastern North America, and up to 8°C or more in some Arctic regions. Across each of the continents, higher warming is *likely* to occur in northern Africa, the central interior of southern and Western Africa; in northern Asia; in Central Australia; in Amazonia; in northern Europe and northern North America (*high confidence*). Ranges of regional warming for global warming levels of 1.5ºC, 2ºC, 3ºC and 4ºC and for other time periods and emissions scenarios are available in the Interactive Atlas from Coupled Model Intercomparison Project Phases 5 and 6 (CMIP5, CMIP6) and Coordinated Regional Climate Downscaling Experiment (CORDEX) projections. {Figure Atlas.12, Interactive Atlas, Sections Atlas.4.4, Atlas.5.1.4, Atlas.5.2.4, Atlas.5.3.4, Atlas.5.4.4, Atlas.5.5.4, Atlas.6.4, Atlas.7.4, Atlas.8.4, Atlas.9.4, Atlas.10.4, Atlas.11.4}

For given global warming levels, model projections from CMIP6 show future regional warming and precipitation changes that are similar to those projected by CMIP5. However, the larger climate

ACCEPTED VERSION SUBJECT TO FINAL EDITS

sensitivity in some CMIP6 models and differences in the model forcings lead to a wider range of and higher projected regional warming in CMIP6 compared to CMIP5 projections for given time periods and emissions scenarios. {Figure Atlas.13, Sections Atlas.4.4, Atlas.5.1.4, Atlas.5.2.4, Atlas.5.3.4, Atlas.5.4.4, Atlas.5.5.4, Atlas.6.1.4, Atlas.6.2.4, Atlas.7.4, Atlas.8.4, Atlas.9.4, Atlas.10.4, Atlas.11.1.4, Atlas.11.2.4}

Precipitation will change in most regions, either through changes in mean values or the characteristics of rainy seasons or daily precipitation statistics (*high confidence*). Regions where annual precipitation is *likely* to increase include the Ethiopian Highlands; East, South and North Asia; Southeast South America; northern Europe; northern and eastern North America and the polar regions. Regions where annual precipitation is *likely* to decrease include northern and southwest southern Africa and the Sahel, Indonesia, northern Arabian Peninsula, southwest Australia, Central America, southwest South America and southern Europe. Changes in monsoons are *likely* to result in increased precipitation in northern China and in South Asia in summer (*high confidence*). Precipitation intensity will increase in many areas, including in some where annual mean reductions are *likely* (e.g., Southern Africa) (*high confidence*). Ranges of regional mean precipitation change for global warming levels of 1.5°C, 2°C, 3°C and 4°C and for other time periods and emissions scenarios are available in Interactive Atlas from CMIP5, CORDEX and CMIP6 projections. {Figure Atlas.13, Interactive Atlas, Sections Atlas.4.4, Atlas.5.1.4, Atlas.5.2.4, Atlas.5.3.4, Atlas.5.4.4, Atlas.5.5.4, Atlas.6.1.4, Atlas.6.2.4, Atlas.7.4, Atlas.8.4, Atlas.9.4, Atlas.10.4, Atlas.11.1.4, Atlas.11.2.4}

Cryosphere, Polar Regions and Small Islands

Many aspects of the cryosphere either have seen significant changes in the recent past or will see them during the 21st century (*high confidence*). Snow cover duration has *very likely* reduced over Siberia and Eastern and Northern Europe. Also, it is *virtually certain* that snow cover will experience a decline in these regions and over most of North America during the 21st century, in terms of water equivalent, extent and annual duration. Over the Hindu Kush-Himalaya, glacier mass is *likely* to decrease considerably (nearly 50%) under the RCP4.5 and RCP8.5 scenarios. Snow cover has declined over Australia as has annual maximum snow mass over North America (*medium confidence*). Some high-latitude regions have experienced increases in winter snow (parts of northern Asia, *medium confidence*) or will do so in the future (*very likely* in parts of northern North America) due to the effect of increased snowfall prevailing over warming-induced increased snowmelt. {Sections 2.3.2.2, 3.4.2, Atlas.5.2.2, Atlas.5.3.4, Altas.6.2, Atlas.8.2, Atlas.8.4, Atlas.9.2, Atlas.9.4}

It is *very likely* that the Arctic has warmed at more than twice the global rate over the past 50 years and that the Antarctic Peninsula experienced a strong warming trend starting in 1950s. It is *likely* that Arctic annual precipitation has increased, with the highest increases during the cold season. Antarctic precipitation and surface mass balance showed a significant positive trend over the 20th century, while strong interannual variability masks any existing trend over recent decades[1] (*medium confidence*). Significant warming trends are observed in other West Antarctic regions and at selected stations in East Antarctica since the 1950s (*medium confidence*). Under all assessed emission scenarios, both Polar regions are *very likely* to have higher annual mean surface air temperatures and more precipitation, with temperature increases higher than the global mean, most prominently in the Arctic. {Sections Atlas.11.1.2, Atlas.11.1.4, Atlas.11.2.2, Atlas.11.2.4}

It is *very likely* that most Small Islands have warmed over the period of instrumental records. Precipitation has *likely* decreased since the mid-20th century in some parts of the Pacific poleward of 20° latitude in both hemispheres and in the Caribbean in June-July-August. It is *very likely* that sea levels will continue to rise in Small Island regions and that this will result in increased coastal flooding.

[1] The term 'recent decades' refers to a period of approximately 30 to 40 years which ends within the period 2010–2020. This is used as many studies in the literature will analyse datasets over a range of climatologically significant periods (i.e., 30 years or more) with precise start and end dates and periods depending on data availability and the year of the study. An equivalent approximate description using specific years would be 'since the 1980s'.

ACCEPTED VERSION SUBJECT TO FINAL EDITS

Observed temperature trends are generally in the range of 0.15°C–0.2°C per decade. Rainfall trends in most other Pacific and Indian Ocean Small Islands are mixed and largely non-significant. There is *limited evidence* and *low agreement* on the cause of the Caribbean drying trend, though it is *likely* that both this and the Pacific drying trends will continue in coming decades with drying also projected in the part of the West Indian and Atlantic Oceans. Small Islands regions in the Western and equatorial Pacific and North Indian Ocean are *likely* to be wetter in the future. {Cross-Chapter Box Atlas.2, Sections Atlas.10.2, Atlas.10.4}

Model Evaluation, Technical Infrastructure and the Interactive Atlas

The regional performance of CMIP6 global climate models (GCMs) has improved overall compared to CMIP5 in simulating mean temperature and precipitation, though large errors still exist in some regions. In particular, improvements have been seen over Africa which has belatedly become a focus for GCM model development. Other specific improvement include over East Asia for temperature and the winter monsoon, over parts of South Asia for the summer monsoon, over Australia (including influences of modes of variability), in simulation of Antarctic temperatures and Arctic sea ice. Notable errors include large cold biases in mountain ranges in South Asia, a significant wet bias over Central Asia, in the East Asia summer monsoon and in Antarctic precipitation. An in-depth evaluation of CMIP6 models is lacking for several regions (North and Southeast Asia, parts of West Central Asia, Central and South America), though CMIP5 models have been evaluated for many of these. {Sections Atlas.4.3, Atlas.5.1.3, Atlas.5.2.3, Atlas.5.3.3, Atlas.5.4.3, Atlas.5.5.3, Atlas.6.1.3, Atlas.6.2.3, Atlas.7.3, Atlas.8.3, Atlas.9.3, Atlas.10.3, Atlas.11.1.3, Atlas.11.2.3}

Since AR5, the improvement in regional climate modelling and the growing availability of regional simulations through coordinated dynamical downscaling initiatives such as CORDEX, have advanced the understanding of regional climate variability, adding value to CMIP global models, particularly in complex topography zones, coastal areas and small islands, and in the representation of extremes (*high confidence*). In particular, regional climate models with polar-optimized physics are important for estimating the regional and local surface mass balance and are improved compared to reanalyses and GCMs when evaluated with observations (*high confidence*). There is still a lack of high-quality and high-resolution observational data to assess observational uncertainty in climate studies, and this compromises the ability to evaluate models (*high confidence*). {Sections Atlas.4.3, Atlas.5.1.3, Atlas.5.2.3, Atlas.5.3.3, Atlas.5.4.3, Atlas.5.5.3, Atlas.6.1.3, Atlas.6.2.3, Atlas.7.3, Atlas.8.3, Atlas.9.3, Atlas.10.3, Atlas.11.1.3, Atlas.11.2.3}

Significant improvements in technical infrastructure, open tools and methodologies for accessing and analysing observed and simulated climate data, and the progressive adoption of FAIR (findability, accessibility, interoperability, and reusability) data principles have *very likely* broadened the ability to interact with these data for a wide range of activities, including fundamental climate research, providing inputs into assessments of impacts, building resilience and developing adaptations. Tools to analyse and assess climate information have improved to allow development of information that goes beyond averages (e.g., on future climate thresholds and extremes) and that is relevant for regional climate risk assessments. {Sections Atlas.2.2, Atlas.2.3}

The Interactive Atlas is a new WGI product developed to take advantage of the interactivity offered by web applications by allowing flexible and expanded exploration of some key products underpinning the assessment (including extreme indices and climatic impact-drivers). This provides a transparent interface for access to authoritative IPCC results, facilitating their use in applications and climate services. The Interactive Atlas implements FAIR principles and builds on open tools and therefore is an important step towards making IPCC results more reproducible and reusable. {Section Atlas.2 and Interactive Atlas}

ACCEPTED VERSION SUBJECT TO FINAL EDITS

Atlas.1 Introduction

Atlas.1.1 Purpose

The Atlas is the final chapter of this Working Group I (WGI) Sixth Assessment Report (AR6) and comprises the Atlas Chapter and an online interactive tool, the Interactive Atlas. The Atlas assesses fundamental aspects of observed, attributed and projected changes in regional climate in coordination with other WGI chapters (Chapters 2, 3, 4, 6, 8, 9, 10, 11, 12). In particular, it provides analyses and assessments of regional changes in mean climate (specifically surface temperature, precipitation and some cryospheric variables, such as snow cover and surface mass balance) and expands on and integrates results from other chapters across different spatial and temporal scales. The Atlas considers multiple lines of evidence including assessment of different global and regional observational datasets, attribution of observed trends and multiple model simulations from the Coupled Model Intercomparison Projects CMIP5 (Taylor et al., 2012a) and CMIP6 (Eyring et al., 2016; O'Neill et al., 2016), and the COordinated Regional Downscaling EXperiment (CORDEX) (Gutowski Jr. et al., 2016). The Atlas chapter also assesses model performance and summarizes cross-referenced findings from other chapters relevant for the different regions.

The Interactive Atlas allows for a flexible spatial and temporal analysis of the results presented in the Atlas and other Chapters, supporting and expanding on their assessments. In particular, the Interactive Atlas includes information from global observational datasets (and paleoclimate information) assessed in Chapter 2, and projections of relevant extreme indices (used in Chapter 11) and climatic impact-drivers (used in Chapter 12) allowing for a regional analysis of the results (Section Atlas.2.2). It provides information on climatic impact-drivers relevant to sectoral and regional chapters of the Working Group II (WGII) report, being informed by and complementing the work of Chapter 12 in creating a bridge to WGII. Similarly, a specific aim of the integration is synthesising information drawn from across multiple chapters that is relevant to the WGII report and the mitigation and sectoral chapters of the Working Group III (WGIII) report.

An overview of the main components of the Atlas chapter is provided in Figure Atlas.1. The Interactive Atlas is described in Section Atlas.2 and is available online at http://ipcc-atlas.ifca.es.

[START FIGURE ATLAS.1 HERE]

Figure Atlas.1: The main components of the Atlas chapter with, upper right, a screenshot from the online Interactive Atlas.

[END FIGURE ATLAS.1 HERE]

Atlas.1.2 Context and framing

Information on global and regional climate change in the form of maps, tables, graphs and infographics has always been a key output of IPCC reports. With the consensus that climate has changed and will continue to do so, policymakers are focusing more on understanding its implications, which often requires an increase in regional and temporal details of observed and future climate. The WGI contribution of the AR5 included a globally comprehensive coverage of land regions and some oceanic regions in the Atlas of Global and Regional Climate Projections (IPCC, 2013a), focusing on projected changes in temperature and precipitation. In the WGII contribution, Chapter 21, Regional Context (Hewitson et al., 2014) included continental scale maps of observed and future temperature and precipitation changes, subcontinental changes in high percentiles of daily temperature and precipitation, and a table of changes in extremes over subcontinental regions (updating an assessment in the Special Report on Managing the Risks of Extreme Events and Disasters to Advance Climate Change Adaptation; SREX). However, there was only limited coordination between these two contributions despite the largely common data sources and their relevance across the two working groups and to wider communities of climate change-related policy and practice. This

ACCEPTED VERSION SUBJECT TO FINAL EDITS

resulted in inefficiencies and the potential for confusing or inconsistent information. The Atlas, with its links with other WGI/II/III chapters, has been designed to help address this.

Given the aims of the Atlas, there are several important factors to consider. There is a clear requirement for climate change information over a wide range of 'regions', and classes thereof, and temporal scales. There is also often the need for integrated information relevant for policy, practice and awareness raising. However, most other chapters in WGI are disciplinary, focusing on specific processes in the climate system or on its past or future behaviour, and have limited space to be spatially and temporally comprehensive. The Atlas provides an opportunity to facilitate this integration and exploration of information.

Developing this information often requires a broad range of data sources (various observations, global and regionally downscaled baselines and projections) to be analysed and combined and, where appropriate, reconciled. This is a topic which is assessed from a methodological perspective in Chapter 10 using a limited set of examples (see also Cross-Chapter Box 10.3). The Atlas then builds on this work with a more comprehensive treatment of the available results, largely (but not exclusively) based on CMIP5, CMIP6, and CORDEX, to provide wider coverage and to further demonstrate techniques and issues. These multiple lines of evidence are integrated in the Interactive Atlas, a new AR6 WGI product described in Section Atlas.2 allowing for flexible spatial and temporal analysis of this information with a predefined granularity (e.g., flexible seasons, regions, and baselines and future periods of analysis including time-slices and warming levels).

Generating information relevant to policy or practice requires understanding the context of the systems that they focus on. In addition to the hazards these systems face, their vulnerability and exposure, and the related socio-economic and other physical drivers, also need to be understood. To ensure this relevance, the Atlas is informed by the assessments in Chapter 12 and the regional and thematic chapters and cross-chapter papers of WGII. Therefore, it focuses on generating information on climatic impact-drivers and hazards applicable to assessing impacts on and risks to human and ecological systems whilst noting the potential relevance of these to related contexts such as the Sustainable Development Goals and the Sendai Framework for Disaster Risk Reduction.

Transparency and reproducibility are promoted in the Atlas chapter implementing FAIR principles for Findability, Accessibility, Interoperability, and Reusability of data (Wilkinson et al., 2016). More specifically, the Interactive Atlas provides full metadata of the displayed products (describing both the underlying datasets and the applied postprocessing) and most of the figures included in the Atlas chapter can be reproduced using the scripts and data provided in the WGI-Atlas repository (see Iturbide et al., 2021 and https://github.com/IPCC-WG1/Atlas).

Atlas.1.3 Defining temporal and spatial scales and regions

Over the past decades scientists have engaged in a wide array of investigations aimed at quantifying and understanding the state of the components of the land surface-ocean-atmosphere system, the complex nature of their interactions and impacts over different temporal and spatial scales. As a result, a great deal has been learned about the importance of an appropriate choice of these scales when estimating changes due to internal climate variability, trends, characterization of the spatiotemporal variability and quantifying the range of and establishing confidence in climate projections. It is therefore important to be able to explore a whole range of spatial and temporal scales and this section presents the basic definitions of those, and the domains of analysis, used by the Atlas accounting for potential synergies between WGI and WGII.

Atlas.1.3.1 Baselines and temporal scales of analysis for projections across scenarios

Chapter 1 has extensively explored this topic in Section 1.4.1 and Cross-Chapter Box 1.2. A summary of the main points relevant to the Atlas chapter and the Interactive Atlas are provided here.

ACCEPTED VERSION SUBJECT TO FINAL EDITS

There is no standard baseline in the literature although the World Meteorological Organization (WMO) recommends a 30-year baseline approach such as the climate normal period 1981–2010. However, it retains the 1961–1990 period as the historical baseline for the sake of supporting long-term climate change assessments (WMO, 2017). Using the WMO standards also provides sample sizes relevant to calculating changes in statistics other than the mean. The AR6 WGI has established the 1995–2014 period as recent past baseline period – for similar reasons to the 1986–2005 period used in AR5 WGI (IPCC, 2013b) – since 2014 (2005) is the final year of the historical simulations of the models (more details in Cross-Chapter Box 1.2).

The choice of a baseline can significantly influence the analysis results for future changes in mean climate (Hawkins and Sutton, 2016) (Cross-Chapter Box 1.2) as well as its variability and extremes. Thus, assessing the sensitivity of results to the baseline period is important. The Interactive Atlas (see Section Atlas.2) allows users to explore and investigate a wide range of different baseline periods when analysing changes for future time-slices or global warming levels:

- 1995–2014 period (AR6 20-year baseline),
- 1986–2005 period (AR5 20-year baseline),
- 1981–2010 period (WMO 30-year climate normal),
- 1961–1990 period (WMO 30-year long-term climate normal).
- 1850–1900 period (baseline used in the calculation of global warming levels).

This promotes cross-Working Group consistency and facilitates comparability with previous reports and across datasets. For instance, the AR5 and long-term WMO baselines facilitate the intercomparison of CMIP5, CORDEX and CMIP6 projections since all have historical simulations in these periods. Using more recent baselines introduces discontinuity for the CMIP5 and CORDEX models, since historical simulations end in 2005. A pragmatic approximation to deal with this issue is to use scenario data to fill the missing segment, for example for 2006 to 2014 use the first years of RCP8.5-driven transient projections in which the emissions are close to those observed. This approach is used in the Atlas chapter and Chapter 12.

When assessing changes over the recent past, many studies analyse datasets using a range of climatologically significant periods (i.e., 30 years or more) with precise start and end dates depending on data availability and the year of the study. To account for this, when generating assessments from this literature the term ‘recent decades’ is used to refer to a period of approximately 30 to 40 years which ends within the period 2010–2020. An equivalent approximate description using specific years would be ‘since the 1980s’.

Regarding the future reference periods, the Interactive Atlas presents projected global and regional climate changes at near-, mid- and long-term periods, respectively 2021–2040, 2041–2060 and 2081–2100, for a range of emissions scenarios (Section Atlas.1.4.3, Cross-Chapter Box 1.4).

Atlas.1.3.2 Global warming levels

Noting the approach taken in the recent IPCC Special Report on Global Warming of 1.5°C (SR1.5) above 1850–1900 levels (IPCC, 2018b), the Atlas also presents global and regional climate change information at different Global Warming Levels (GWLs, see Cross-Chapter Box 11.1). In particular, to provide policy-relevant climate information and represent the range of outcomes from the emissions scenario and time periods considered, GWLs of 1.5°C, 2°C, 3°C and 4°C are considered. The information is computed from all available scenarios (e.g. only 1.5°C and 2°C GWL information can be computed from projections under the SSP1-2.6 scenario). The Interactive Atlas allows comparison of timings for global warming across the different scenarios and of spatial patterns of change, for example information at 2°C GWL is calculated from SSP1-2.6, SSP2-4.5, SSP3-7.0 and SSP5-8.5 projections (Section 4.2.4).

To calculate GWL information for the datasets used in the Atlas (CMIP6 and CMIP5; see Section Atlas.1.4), this chapter adopted the procedure used in Cross-Chapter Box 11.1. A model future climate simulation reaches the defined GWL of 1.5°C, 2°C, 3°C or 4°C when its global near-surface air temperature change averaged over successive 20-year periods first attains that level of warming relative to its simulation of the

ACCEPTED VERSION SUBJECT TO FINAL EDITS

1851-1900 climate. (1851–1900 defines the pre-industrial baseline period for calculating the required global surface temperature baseline, Cross-Chapter Box 1.2). Note that this process is different from the one used in the SR1.5 report which used 30-year future periods. If a projection stabilizes before reaching the required threshold it is unable to simulate climate at that GWL and is thus discarded. For CORDEX simulations, the periods of the driving GCM are used, as in Nikulin et al. (2018). Detailed reproducible information on the GWLs used in the Atlas is provided in the Atlas repository (Iturbide et al., 2021).

Climate information at many temporal scales and over a wide range of temporal averaging periods is required for the assessment of climate change and its implications. These range from annual to multi-decadal averages required to characterise low-frequency variability and trends in climate to hourly or instantaneous maximum or minimum values of impactful climate variables. In between, information on, for example, seasonal rainfall is important and implies the need to include averaging periods whose relevance are geographically dependent. As a result, the Atlas chapter presents results over a wide range of timescales, from daily to decadal, and averaging periods with the Interactive Atlas allowing a choice of user-defined seasons and a range of predefined daily to multi-day climate indices.

Atlas.1.3.3 Spatial scales and reference regions

Many factors influence the spatial scales and regions over which climate information is required and can be reliably generated. Despite all efforts in researching, analysing and understanding climate and climate change, a key factor in determining spatial scales at which analysis can be undertaken is the availability and reliability of data, both observational and from model simulations. In addition, information is required over a wide range of spatial domains defined either from a climatological or geographical perspective (e.g., a region affected by monsoon rainfall or a river basin) or from a socio-economic or political perspective (e.g., least-developed countries or nation states). Chapter 1 provides an overview of these topics (Section 1.5.2). This subsection discusses some relevant issues, summarizes recent advances in defining domains and spatial scales used by AR6 analyses and how these can be explored with the Interactive Atlas.

Recent IPCC reports – AR5 Chapter 14 (Christensen et al., 2013) and SR1.5 Chapter 3 (Hoegh-Guldberg et al., 2018) – have summarized information on projected future climate changes over subcontinental regions defined in the SREX report (Seneviratne et al., 2012) and later extended in the AR5 from the 26 regions in SREX to include the polar, Caribbean, two Indian Ocean, and three Pacific Ocean regions (hereafter known as the AR5 WGI reference regions) (Figure Atlas.2a). In recent literature, new subregions have been used, for example for North and South America, Africa and Central America, together with the new definition of reference oceanic regions. Iturbide et al. (2020) describes an updated version of the reference regions which is used in this report (hereafter known as AR6 WGI reference regions) and is shown in Figure Atlas.2b. The goal of these subsequent revisions was to improve the climatic consistency of the regions so they represented sub-continental areas of greater climatic coherency.

[START FIGURE ATLAS.2 HERE]

Figure Atlas.2: WGI reference regions used in the (a) AR5 and (b) AR6 reports (Iturbide et al., 2020). The latter includes both land and ocean regions and it is used as the standard for the regional analysis of atmospheric variables in the Atlas chapter and the Interactive Atlas. The definition of the regions and companion notebooks and scripts are available at the Atlas repository (Iturbide et al., 2021).

[END FIGURE ATLAS.2 HERE]

The rationale followed for the definition of the reference regions was guided by two basic principles: 1) climatic consistency and better representation of regional climate features and 2) representativeness of model results (i.e., sufficient number of model grid boxes). The finer resolution of CMIP6 models (as compared, on average, to CMIP5) yields better model representation of the reference regions allowing them to be revised

ACCEPTED VERSION SUBJECT TO FINAL EDITS

for better climatic consistency (e.g., dividing heterogeneous regions) while preserving the model representation. Figure Atlas.3 illustrates this issue displaying the number of grid boxes (over land for land regions) in the AR6 reference regions for two Interactive Atlas reference grids of horizontal resolutions of 1° and 2°, representative of the typical resolution of CMIP6 and CMIP5 models respectively. This figure shows that the new reference regions are well suited for the assessment of model results, with poorest model coverage for the New Zealand (NZ), Caribbean (CAR) and Madagascar (MAD) regions.

[START FIGURE ATLAS.3: HERE]

Figure Atlas.3: Number of land grid boxes (blue numbers) for the AR6 WGI reference regions for the reference grids representative of (a) CMIP6 and (b) CMIP5, at horizontal resolutions of 1° and 2°respectively. Colour shading indicate regions with fewer than 250 grid boxes indicating the number of grid boxes (darkest shading if fewer than 20 grid boxes). The polygons show the AR6 WGI reference regions of Figure Atlas.2.

[END FIGURE ATLAS.3 HERE]

AR6 WGI (land and open ocean) reference regions are used in the Interactive Atlas as the default regionalization for atmospheric variables. However, these regions are not optimum for the analysis of oceanic variables since, for instance, the five upwelling regions (Canary, California, Peru, Benguela and Somali) are mostly included in 'land' regions. Therefore, the alternative set of oceanic regions defined by their biological activity (Figure Atlas.4) is used in the Interactive Atlas for the regional analysis of oceanic variables (see Fay and McKinley, 2014; Gregor et al., 2019). Due to the many potential definitions of the regions relevant for WGI and WGII, some additional typological and socio-economic regions have also been included in the Interactive Atlas.

Atlas.1.3.4 Typological and socio-economic regions

In addition to contiguous spatial domains discussed in the previous section, some domains are defined by specific climatological, geographical, ecological or socio-economic properties where climate is an important determinant or influencer. In these cases the domains are subject to particular physical processes that are important for its climatology or that involve systems affected by the climate in a way that observations and climate model simulations can be used to understand. Many of these are the basis of the chapters and cross-chapter papers of the AR6 WGII report, namely river basins, biodiversity hotspots, tropical forests, cities, coastal settlements, deserts and semi-arid areas, the Mediterranean, mountains and polar regions. It is therefore important to generate climate information relevant to these typological domains and some examples of these used in the Interactive Atlas are shown in Figure Atlas.4.

[START FIGURE ATLAS.4 HERE]

Figure Atlas.4: Typological and socio-economic regions used in the Interactive Atlas. (a) Eleven ocean regions defined by their biological activity used for the regional analysis of oceanic variables; (b) ocean regions for small islands, including the Caribbean (CAR) and the North Indian Ocean (ARS and BOB); (c) land monsoon regions of North America, South America, Africa, Asia and Australasia; (d) major river basins; (e) mountain regions; (f) WGII continental regions. These regions can be used alternatively to the reference regions for the regional analysis of climatic variables in the Interactive Atlas. The definition of the regions and companion notebooks and scripts are available at the Atlas repository (Iturbide et al., 2021).

[END FIGURE ATLAS.4 HERE]

ACCEPTED VERSION SUBJECT TO FINAL EDITS

Atlas.1.4 Combining multiple sources of information for regions

This section introduces the observational data sources and reanalyses that are used in the assessment of regional climate change and for evaluating and bias-adjusting the results of models (more information on observational reference datasets is available in Annex I). It also introduces the different global and regional climate model outputs that are used for regional climate assessment considering both historical and future climate projections (Annex II). Many of these models are run as part of coordinated Model Intercomparison Projects (MIPs), including CMIP5, CMIP6 and CORDEX, described below. Combining information from these multiple data sources is a significant challenge (see Section 10.5 for an in-depth treatment of the problem) though if they can be used to generate robust information on regional climate change it can guide policy and support decisions responding to these changes. An important and necessary part of this process is to check for consistency amongst the data sources which is discussed in the final section.

Atlas.1.4.1 Observations

There are various sources of observational information available for global and regional analysis. Observational uncertainty is a key factor when assessing and attributing historical trends, so assessment should build on integrated analyses from different datasets (disparity, inadequacy and contradictions in existing datasets are assessed in Section 10.2). The Atlas chapter can supplement and complement Chapter 10 by providing the opportunity to visualise and expand on its assessment. This includes displaying maps of density of stations observations (including those that are used in the different datasets) and assessing observational uncertainty by using multiple datasets.

Two of the most commonly used variables in climate studies are gridded surface air temperature and precipitation. There are many datasets available (Annex I) and Chapter 2 provides an assessment of key global datasets, including blended land-air and sea-surface temperature datasets to assess Global Mean Surface Temperature (GMST). The Atlas analyses separately atmospheric and oceanic variables and for the former a number of common global datasets supporting the assessment done in other chapters is used, including those selected in Chapter 2, but considering land-only information for the blended products. In particular, for air temperature the Atlas uses CRUTEM5 – the land component of the HadCRUT5 dataset – (Osborn et al., 2021), Berkeley Earth (Rohde and Hausfather, 2020) and the Climatic Research Unit CRU TS4 (version 4.04 used here) (Harris et al., 2020). For precipitation the Atlas includes CRU TS4, the Global Precipitation Climatology Centre (GPCC, v2018 used here) (Schneider et al., 2011), and Global Precipitation Climatology Project (GPCP; monthly version 2.3 used here) (Adler et al., 2018). Although the ultimate source of these datasets is surface station reported values (GPCP also includes satellite information), each has access to different numbers of stations and lengths of records and employs different ways of creating the gridded product and ensuring quality control. For oceanic variables, the most widely used sea surface temperature (SST) datasets are HadSST4 (Kennedy et al., 2019), which is the oceanic component of the HadCRUT5 dataset, ERSST (Huang et al., 2017a), and KaplanSST (Kaplan et al., 1998).

Figure Atlas.5 shows the spatial coverage of the total number of observation stations for different periods (1901–1910, 1971–1980, and 2001–2010) for two illustrative datasets: the CRU TS4.0 dataset for precipitation and the SST data in HadSST4. The former illustrates spatially the declining trend of station observation data used in the precipitation datasets for certain regions (South America, Africa) after the 1990s. This demonstrates the regional inhomogeneity and temporal change in station density, which is in part a consequence of many stations not reporting to the WMO networks and their data being held domestically or regionally. During early years a limited number of observations are available. This information is used in the Interactive Atlas to blank out regions not constrained with observations in those datasets providing station density information.

ACCEPTED VERSION SUBJECT TO FINAL EDITS

[START FIGURE ATLAS.5 HERE]

Figure Atlas.5: Number of stations per 0.5° x 0.5° grid cell reported over the periods of 1901–1910, 1971–1980, and 2001–2010 (rows 1–3) and global total number of stations reported over the entire globe (bottom row) for precipitation in the CRU TS4.0 dataset (left) and the HadSST4 dataset (right). Further details on data sources and processing are available in the chapter data table (Table Atlas.SM.15).

[END FIGURE ATLAS.5 HERE]

In addition to surface observations, satellites have been widely used to produce rainfall estimates. The advantage of satellite-based rainfall products is their global coverage including remote areas but there is significant uncertainty in these products over complex terrain (Rahmawati and Lubczynski, 2018; Satgé et al., 2019). Another recent development has been on gridded datasets for climate extremes based on surface stations, such as HadEX3 (Dunn et al., 2020).

There are some studies assessing observational datasets globally (Beck et al., 2017; Sun et al., 2018b) and regionally (Manzanas et al., 2014; Salio et al., 2015; Prakash, 2019), reporting large differences among them and stressing the importance of considering observational uncertainty in regional climate assessment studies. Uncertainty in observations is also a key limitation for the evaluation of climate models, particularly over regions with low station density (Kalognomou et al., 2013; Kotlarski et al., 2019). More detailed information on these issues is provided in Section 10.2.

For regional studies, observational datasets with global coverage are complemented by a range of regional observational analyses and gridded products, such as E-OBS (Cornes et al., 2018) over Europe, Daymet (Thornton et al., 2016) over North America, or APHRODITE (Yatagai et al., 2012) over Asia. These are highlighted in various other chapters and the Atlas expands on their treatment, complementing discussions on discrepancies/conflicts in observations presented in Chapter 10 and expanding on and replicating their results for other regions. In particular, the Interactive Atlas includes the global and regional observational products described here to assess observational uncertainty over the different regions analysed.

Atlas.1.4.2 Reanalysis

There are currently many atmospheric reanalysis datasets with different spatial resolution and assimilation algorithms (see Annex I and Section 1.5.2). There are also substantial differences among these datasets due to the types of observations assimilated into the reanalyses, the assimilation techniques that are used, and the resolution of the outputs, amongst other reasons. For example, 20CR (Slivinski et al., 2019) only assimilates surface pressure and sea surface temperature to achieve the longest record but at relatively low resolution, while ERA-20C (Poli et al., 2016) only assimilates surface pressure and surface marine winds. At the other extreme, very sophisticated assimilation systems using multiple surface, upper air and Earth observation data sources are employed, for example ERA5 (Hersbach et al., 2020) and JRA-55 (Harada et al., 2016), which also have much higher resolutions. Most reanalysis datasets cover the entire globe, but there are also high-resolution regional reanalysis datasets which provide further regional detail (Kaiser-Weiss et al., 2019).

The Atlas and Interactive Atlas use information from ERA5 and from the bias-adjusted version WFDE5 (Cucchi et al., 2020) which is combined with ERA5 information over the ocean and used as the ISIMIP observational reference dataset W5E5 (Lange, 2019b). This reference is also used in the Atlas for model evaluation (Section Atlas.1.4.4) and for bias-adjusting model outputs (Section Atlas.1.4.5).

Atlas.1.4.3 Global model data (CMIP5 and CMIP6)

The Atlas chapter (and the Interactive Atlas) uses global model simulations from both CMIP5 and CMIP6, mainly historical and future projections performed under ScenarioMIP (O'Neill et al., 2016). This facilitates

ACCEPTED VERSION SUBJECT TO FINAL EDITS

backwards comparability and thus the detection of new salient features and findings from recent science and the latest CMIP6 ensemble. The selection of the models is based on availability of scenario data for the variables assessed in the Atlas chapter and for those included in the Interactive Atlas (Section Atlas.2.2). In particular, in order to harmonize the results obtained from the different scenarios as much as possible, only models providing data for the historical scenario and at least two emission scenarios, RCP2.6, RCP4.5 and/or RCP8.5 (for CMIP5) and SSP1-2.6, SSP2-4.5, SSP3-7.0 and/or SSP5-8.5 (for CMIP6), were chosen, resulting in 29 and 35 models, respectively (see Cross-Chapter Box 1.4 for a description of the scenarios). In the Atlas chapter (similarly to the regional Chapters 11 and 12) a single simulation is taken from each model (see Section Atlas.12 for limitations of this choice). Since the RCP and SSP emission scenarios are not directly comparable due to different regional forcing (Section 4.2.2), the Atlas includes Global Warming Levels (GWLs) as an alternative dimension of analysis (see Cross-Chapter Box 11.1), which allows intercomparison of results from different scenarios as an alternative to the standard analysis based on time-slices for particular scenarios (Section Atlas.1.3.1). This dimension allows for enhanced comparability of CMIP5 and CMIP6, since it constrains the regional patterns to the same global warming level for both datasets.

Building on this information, the Interactive Atlas displays a number of (mean and extreme) indices and climatic impact-drivers (CIDs) considering both atmospheric and oceanic variables (see Section Atlas.2.2). Some of these indices have been selected in coordination with Chapters 11 and 12, in order to support and extend the assessment performed in these chapters (see Annex VI for details on the indices). In order to harmonize this information, the indices have been computed for each individual model on the original model grids and the results have been interpolated to a common 2° (for CMIP5) and 1° (CMIP6) horizontal resolution grids. In addition, for the sake of comparability with CMIP6 results (in particular when using baselines going beyond 2005), the historical period of the CMIP5 and CORDEX datasets has been extended to 2006–2014 using the first years of RCP8.5-driven transient projections (see Section Atlas.1.3.1). Tables listing the CMIP5 and CMIP6 models used in the Atlas and in the Interactive Atlas for different scenarios and variables are included as Supplementary Material (Tables Atlas.SM.1 and Atlas.SM.2, respectively); moreover, full inventories including details on the specific ESGF versions are given in the Atlas GitHub repository (Iturbide et al., 2021).

Chapter 3 and Flato et al. (2013) describe the evaluation of CMIP6 and CMIP5 models, respectively, assessing surface variables and large-scale indicators. Section 10.3.3, assesses the general capability of GCMs to produce climate output for regions.

Information from the existing CMIP5 and CMIP6 datasets is supplemented with downscaled regional climate simulations from CORDEX. This facilitates an assessment of the effects from higher resolution including whether this modifies the projected climate change signals compared to global models and adds any value, especially in terms of high-resolution features and extremes.

Atlas.1.4.4 Regional model data (CORDEX)

Global model data, as generated by the CMIP ensembles, although available globally, have spatial resolutions that are limited for reproducing certain processes and phenomena relevant for regional analysis (around 2° and 1° for CMIP5 and CMIP6, respectively). The Coordinated Regional Climate Downscaling Experiment (CORDEX) (Gutowski Jr. et al., 2016) facilitates worldwide application of Regional Climate Models (RCMs, see Section 10.3.1.2), focusing on a number of regions (see Figure Atlas.6) with a typical resolution of 0.44° (but also at 0.22° and 0.11° over some domains, such as Europe). However, only a few simulations are available for some domains (Annex II, Tables AII.1 and AII.2), thus limiting the level of analysis and assessment that can be performed using CORDEX data in some regions. Moreover, there are regions where several domains overlap, thus providing additional lines of evidence. The use of multi-domain grand ensembles to work globally with CORDEX data have recently been proposed (Legasa et al., 2020; Spinoni et al., 2020). Ongoing efforts, such as the multi-domain CORDEX-CORE simulations are promoting more homogeneous coverage and thus more systematic treatment of CORDEX domains (see Box Atlas.1).

ACCEPTED VERSION SUBJECT TO FINAL EDITS

[START FIGURE ATLAS.6 HERE]

Figure Atlas.6: CORDEX domains showing the curvilinear domain boundaries resulting from the original rotated domains. The topography corresponding to the standard CORDEX 0.44° resolution is shown to illustrate the orographic gradients over the different regions.

[END FIGURE ATLAS.6 HERE]

A lot of progress has been made by the regional climate modelling community since AR5 (Table AII.2) to produce and make available evaluation (reanalysis-driven) simulations over the different CORDEX domains along with downscaled CMIP5 historical and future climate projection information under a range of emission scenarios, mainly RCP2.6, RCP4.5 and RCP8.5 (Tables AII.3 and AII.4). However, these ensembles cover only a fraction of the uncertainty range spanned by the full CMIP5 ensemble in the different domains (e.g., Ito et al., 2020b), Figure Atlas.16, Figure Atlas.17, Figure Atlas.21, Figure Atlas.22, Figure Atlas.24, Figure Atlas.26, Figure Atlas.28 and Figure Atlas.29). Therefore, comparison of CMIP5 and CORDEX results should be performed carefully, providing results not only for the full CMIP5 ensemble but also for the sub-ensemble formed by the driving models since results can diverge (Fernández et al., 2019; Iles et al., 2020).

The Atlas chapter and the Interactive Atlas use CORDEX information for the following eleven individual CORDEX domains (out of the fourteen domains shown in Figure Atlas.6): Northern, Central and South America, Europe, Africa, South, East and Southeast Asia, Australasia, Arctic and Antarctica; in addition, oceanic information has been used from the Mediterranean domain, which provides simulations from coupled atmosphere-ocean regional climate models. In order to harmonize the information across domains and to maximize the size of the resulting ensembles, all the available simulations for each individual CORDEX domain (including the standard 0.44° CORDEX and the 0.22° CORDEX-CORE) have been interpolated to a common regular 0.5°-resolution grid to provide a grand ensemble covering the historical and future emission RCP2.6, RCP4.5 and RCP8.5 scenarios, and also the reanalysis-driven simulations for evaluation purposes. In the case of the European domain, the dataset considered is the 0.11° simulations (CORDEX EUR-11, the same dataset as used in Chapter 12) which has been interpolated to a regular 0.25° resolution grid (the same used for the regional observations). In the case of the Mediterranean domain, oceanic information (sea surface temperature) is interpolated to a regular 0.11º grid. In all cases, the indices are computed on the original grids and the interpolation process is applied to the resulting indices. Moreover, for the sake of comparability with CMIP6 results (in particular when using baseline periods beyond 2005), the historical period of the CORDEX datasets has been extended to 2006–2014 using the first years of RCP8.5-driven transient projections in which the emissions are close to those observed (see Section Atlas.1.3.1); note that this procedure is also applied to CMIP5 simulations.

For the different CORDEX domains, the full ensembles of models (GCM-RCM matrix) used in the Atlas for the different scenarios and variables are described in the Supplementary Material (Tables Atlas.SM.3 to Atlas.SM.14) and in the Atlas repository (Iturbide et al., 2021), including full metadata relative to ESGF versions used and the periods with data available for the different simulations. In particular, the historical scenario information is only available from 1970 onwards for some models and therefore the common period 1970–2005 is used for historical CORDEX data in the Atlas. As a result, the WMO baseline period 1961–1990 is not available in the Interactive Atlas for CORDEX data.

Sections Atlas.4 to Atlas.11 assess research on CORDEX simulations over different regions, analysing past and present climate as well as future climate projections. They also focus on regional model evaluation in order to extend and complement the validation of global models done in Chapter 3, considering the specific regional climate and relevant large-scale and regional phenomena, drivers and feedbacks (Section 10.3.3). Besides the literature assessment, some simple evaluation diagnostics have been computed for the simulations used in the Atlas chapter to provide some basic information on model performance across regions. In particular biases for mean temperature and precipitation have been calculated for the eleven CORDEX domains analysed.

ACCEPTED VERSION SUBJECT TO FINAL EDITS

Figure Atlas.7 shows mean temperature and precipitation biases over the North American domain in RCM simulations driven by reanalysis and historical GCM simulations (see Section 10.3.2.5). Annual and seasonal (DJF and JJA) biases are computed for both the RCMs and driving GCMs. Biases in the reanalysis-driven RCMs result from intrinsic model errors, with the results displayed being spatially aggregated for each reference region. This same analysis is performed for the GCM-driven RCM simulations over the historical period 1986–2005. This allows comparison of the intrinsic bias of the RCMs with the biases resulting when driven by the different GCMs and patterns of behaviour in the RCMs, for example intrinsic warm and dry biases in ENA and WNA respectively or reduced RCM warm biases compared to the CCCma GCM in NEN and ENA. Similar results for the other CORDEX domains are included as Supplementary Material (Figures Atlas.SM.1 to Atlas.SM.10).

[START FIGURE ATLAS.7 HERE]

Figure Atlas.7: Evaluation of annual and seasonal air temperature and precipitation for the six North America subregions NWN, NEN, WNA, CNA, ENA and NCA (land only), for CORDEX-NAM RCM simulations driven by reanalysis or historical GCMs. Seasons are June-July-August (JJA) and December-January-February (DJF). Rows represent subregions and columns correspond to the models. Magenta text indicates the driving historical CMIP5 GCMs (including ERA-Interim in first set of slightly separated columns) and the black text to the right of the magenta text represents the driven RCMs. The colour matrices show the mean spatial biases; all biases have been computed for the period 1985–2005 relative to the observational reference (E5W5, see Section Atlas.1.4.2). Further details on data sources and processing are available in the chapter data table (Table Atlas.SM.15).

[END FIGURE ATLAS.7 HERE]

[START BOX ATLAS.1 HERE]

BOX ATLAS.1: CORDEX-CORE

The main objective of CORDEX-CORE is to provide a global homogeneous foundation of high-resolution RCM projections to improve understanding of local phenomena and facilitate impact and adaptation research worldwide (Gutowski Jr. et al., 2016). The experimental framework is designed to produce homogeneous regional projections for most inhabited land regions using nine CORDEX domains at 0.22° resolution (Figure Atlas.6): North, Central and South America (NAM, CAM, SAM), Europe (EUR), Africa (AFR), East, South and Southeast Asia (EAS, WAS, SEA) and Australasia (AUS). Due to computational requirements, three GCMs were selected to drive the simulations, HADGEM2-ES, MPI-ESM, and NorESM covering, respectively the spread of high, medium and low equilibrium climate sensitivities from the CMIP5 ensemble at a global scale (with MIROC5, EC-Earth, GFDL-ES2M as secondary GCMs) focusing on two scenarios RCP2.6 and RCP8.5 (see Box Atlas.1, Figure 1). Two RCMs have contributed so far to this initiative (REMO and RegCM4) constituting an initial homogeneous downscaled ensemble to analyse mean climate change signals and hazards (Teichmann et al., 2020; Coppola et al., 2021), and there are ongoing efforts to extend the CORDEX-CORE ensemble with additional regional simulations (e.g., the COSMO-CLM community) to increase the ensemble size. CORDEX-CORE simulations are distributed as part of the information available for the different CORDEX domains at the Earth System Grid Federation (ESGF).

CORDEX-CORE spans the spread of the CMIP5 climate change signals for interquartile ranges of annual mean temperature and precipitation for most of the reference regions covered (Teichmann et al., 2020)(see Box Atlas.1, Figure 1). However, it is still a small ensemble and for other variables like extremes or climatic impact-drivers has only been partially investigated in Coppola et al. (2021) and needs further analysis.

ACCEPTED VERSION SUBJECT TO FINAL EDITS

[START BOX ATLAS.1, FIGURE 1 HERE]

Box Atlas.1, Figure 1: Temperature (left) and precipitation (right) climate change signals at the end of the century (2070–2099) for the entire CMIP5 ensemble (box-whisker plots) and the CORDEX-CORE driving GCMs (grey symbols) of the respective CORDEX-CORE results (non-grey symbols) in the South Asia (SAS) reference region. The shape of the grey symbols represents the climate sensitivity of the driving GCMs: triangles pointing upwards (low ECS), circles (medium ECS), triangles pointing downwards (high ECS). The corresponding RCM results are drawn using the same symbols, but in orange for REMO and in blue for RegCM. The bottom panels show the warming signal by 2070–2099 over the CORDEX regions for RCP2.6 (left) and RCP8.5 (right) (Teichmann et al., 2020).

[END BOX ATLAS.1, FIGURE 1 HERE]

[END BOX ATLAS.1 HERE]

Atlas.1.4.5 Bias adjustment

Bias adjustment is often applied to data from climate model simulations to improve their applicability for assessing climate impacts and risk (for instance in the Inter-Sectoral Impact Model Intercomparison Project, ISIMIP (Rosenzweig et al., 2017). Bias-adjustment approaches (Section 10.3.1.3) are particularly beneficial when threshold-based indices are used, but they can introduce other biases, in particular when applied directly to coarse-resolution GCMs (Cross-Chapter Box 10.2). Bias-adjustment techniques should be chosen carefully for a particular application. In the Atlas, bias adjustment is not applied systematically (in particular it is not applied for the variables assessed in the Atlas chapter), and only the threshold-dependent extreme indices and climatic impact-drivers (CIDs) included in the Interactive Atlas are bias-adjusted (in particular frost days, and TX35, TX40 in coordination with Chapter 12). To facilitate integration with WGII, the Atlas uses the same bias-adjustment method as in ISIMIP3 (Lange, 2019a) and the same observational reference (W5E5, see Section Atlas.1.4.2), upscaled to the same resolution as the model to avoid downscaling artefacts (Cross-Chapter Box 10.2). The ISIMIP3 bias-adjustment method is a trend-preserving approach that is recommended for general applications, as it reduces biases while preserving the original climate change signal (Casanueva et al., 2020). Following the recommendations given in Chapter 10, results in the Interactive Atlas are displayed for both the adjusted and the raw model output.

[START CROSS-CHAPTER BOX ATLAS.1 HERE]

Cross-Chapter Box Atlas.1: Displaying robustness and uncertainty in maps

Coordinators: José Manuel Gutiérrez (Spain), Erich Fischer (Switzerland)
Contributors: Alessandro Dosio (Italy), Melissa I. Gomis (France/Switzerland), Richard G. Jones (UK), Maialen Iturbide (Spain), Megan Kirchmeier-Young (Canada/USA), June-Yi Lee (Republic of Korea), Stéphane Sénési (France), Sonia I. Seneviratne (Switzerland), Peter W. Thorne (Ireland/UK), Xuebin Zhang (Canada)

Spatial information on observed and projected future climate changes has always been a key output of IPCC reports. This information is typically represented in the form of maps of historical trends (from observational datasets) and of projected changes for future reference periods and scenarios relative to baseline periods (from multi-model ensembles). These maps usually include information on the robustness or uncertainty of the results such as the significance of trends or the consistency of the change across models. Visualization of this information combines two aspects that are intertwined: the core methodology (measures and thresholds) and its visual implementation. For observed trends, robustness can be simply ascertained by using an appropriate statistical significance test. However, for multi-model mean changes, the consistency across models for the sign of change (model agreement) and the magnitude of change relative to unforced climate variability (signal-to-noise ratio) provide two complementary measures allowing for simple or more

ACCEPTED VERSION SUBJECT TO FINAL EDITS

comprehensive approaches to represent robustness and uncertainty. While they can be visually represented in various ways with more or less complexity (Retchless and Brewer, 2016), the most common implementation for maps in the climate science community remains the overlay of symbols and/or masking of the primary variable. This Cross-Chapter Box reviews the approaches followed in previous IPCC reports and describes the methods used across this WGI report, presenting the rationale and discussing its relative merits and limitations.

The objectives in AR6 for representing robustness and uncertainty in maps are 1) adopting a method that can be as coherent as possible across the different global/regional chapters while accommodating different needs, 2) being visually consistent across WGs, and 3) making the different layers of information on the maps as accessible as possible for the reader. As a result, a single approach is selected for observations and two alternative approaches (simple and advanced) are adopted for projected future changes. It is important to highlight that, as in previous reports, these approaches are implemented in maps at a grid-box level and, therefore, are not informative for larger spatial scales (e.g., over AR6 reference regions) where the aggregated signals are less affected by small-scale variability leading to an increase in robustness. This is particularly relevant for the AR6 regional assessments and approaches (e.g., for trend detection and attribution, Cross-Chapter Box 1.4, Section 11.2.4) which are performed for climatological regions and not at grid-box scale (Chapters 11, 12, Atlas). Both small and large scales are relevant (e.g., adaptation occurs at the smaller scales but also at the level of countries, which are typically larger than a few grid boxes). They are both addressed in the Interactive Atlas, which implements the above approaches for representing robustness in maps at the grid-box level, but also allows analysing region-wide signals (e.g., AR6 WG I reference regions, monsoon regions, etc.), helping to isolate background changes happening at larger scales (Section Atlas.2.2).

Approaches used in previous reports

Recent IPCC reports adopted different approaches for mapping uncertainty/robustness, including their calculation method and/or their visual implementation. In AR5 WGI '+' symbols were used to represent significant trends in observations at grid-box level. For future projections, different methods for mapping robustness were assessed (AR5 Box 12.1, Collins et al., 2013), while proposing as a reference an approach based on relating the multi-model mean climate change signal to internal variability, calculated as the standard deviation of non-overlapping 20-year means in the pre-industrial control runs. Regions where the multi-model mean change exceeded two standard deviations of the internal variability and where at least 90% of the models agreed on the sign of change were stippled (as an indication of a robust signal). Regions where the multi-model change was less than one standard deviation were hatched (small multi-model mean signal). However, this category did not distinguish areas with consistent small changes from areas of significant but opposing/divergent signals. In addition, the unstippled/unhatched areas were left undefined, since the categories were not mutually exclusive.

AR5 WGII (Hewitson et al., 2014) used hatching to represent non-significant trends in observations. For future projections, an elaborated approach with four mutually exclusive and exhaustive categories was proposed (to avoid some of the limitations of the AR5 WGI approach): very strong agreement (same as in WGI); strong agreement; divergent change; and little or no change. These depended on the percentage of models showing change greater than the baseline variability and/or agreeing on sign of change (using a 66% agreement threshold). Leaving the robust regions uncovered minimized any interference with the perception of underlying colours that encoded the primary information of the figure.

The two special reports IPCC SR1.5 (Hoegh-Guldberg et al., 2018) and SROCC (IPCC, 2019a, 2019c) adopted a simplified approach, using only model agreement (≥66% of models agree on sign of change) to characterize robustness. However, cross-hatching was used in SR1.5 to highlight robust areas where models agree, whereas the SROCC used hatching/shading to represent regions where models disagree. Similarly, stippling was used in SR1.5 to indicate regions with significant trends, whereas it was used in SROCC to represent regions where the trends were not significant.

Recent methodologies

ACCEPTED VERSION SUBJECT TO FINAL EDITS

Since AR5 there has been a growing interest for disentangling small consistent climate change signals from significant divergent opposite changes resulting in conflicting information (Tebaldi et al., 2011), and different statistical tests have been applied to assess the significance of signals working with the individual models forming the ensemble (Dosio and Fischer, 2018; Yang et al., 2018; Morim et al., 2019). Moreover, new approaches have been proposed to identify large changes of opposite sign that compensate in the mean (Zappa et al., 2021). Recent literature has also highlighted the respective risks of Type I vs Type II errors, which can be associated with the determination of robustness in analysed signals (Lloyd and Oreskes, 2018; Knutson et al., 2019). Type I errors are identifying signals when there are none, while Type II errors are concluding there is no signal when there is one. In the case of grid-box level analysis, the focus on small-scale features with inherently large signal-to-noise ratio may emphasize noise even though signals are present when aggregated at larger scale (Sections 11.2.4 and 11.2.5). Consequently, changes averaged over regions or a number of grid-boxes emerge from internal variability at a lower level of warming than at the grid-box level (e.g., Cross-Chapter Box Atlas.1, Figure 2). Hence, focus on grid-box significance enhances the risk of Type II errors for overlooking signals significant at the level of AR6 regions. The significance of signals is also affected by interdependence of single simulations considered in a given ensemble, for example when several come from the same modelling group and share parameterizations or model components (Knutti et al., 2013; Maher et al., 2021). The risk of Type II errors increases when a model ensemble includes several related simulations showing no signal.

The AR6 WGI approach

AR6 WGI adapts the approaches applied in previous IPCC reports into a comprehensive framework based on the two general principles followed by AR5 WGII: 1) not obscuring (with stippling or hatching) the areas where relevant/robust information needs to be highlighted (since stippling and hatching obstruct the visualisation of the colours, which can affect the perception/interpretation of the underlying data); 2) using mutually exclusive and exhaustive categories to avoid leaving areas undefined. The three adopted approaches (one for observations and two for model projections) are described in Cross-Chapter Box Atlas.1, Table 1. This framework integrates as much as possible the specificities of each WGI Chapter, proposing in some cases alternative thresholds.

Approach A is intended for observations and consists of two categories, one for areas with significant trends (colour, no overlay) and one for non-significant ones (coloured areas overlaid with 'x'), typically using a two-sided test for a significance level of 0.1; Chapter 2 and Atlas trends have been calculated using OLS regression accounting for serial correlation (Santer et al., 2008).

Approach B is the simple alternative for model projections. It consists of two categories, one for model agreement (at least 80% of the models agree on the sign of change; colour, no overlay) and the other one for non-agreement (hatching). It is noted that model agreement is computed using 'model democracy' (i.e. without discarding/weighting models), since quantifying and accounting for model interdependence (shared building blocks) still remain challenging (Section 4.2.6). Different thresholds have been used in previous reports and in the literature. 80% has been widely used in CORDEX studies (Dosio and Fischer, 2018; Kjellström et al., 2018; Nikulin et al., 2018; Yang et al., 2018; Akperov et al., 2019; Rana et al., 2020) partially due to the small ensemble sizes available in some cases; this also helps to reduce the impact of model interdependence in the final results. Although 90% (used in AR5 WGI) provides high confidence on the forced change, it is deemed too stringent for precipitation-like variables and regional assessments and was therefore not included (see Cross-Chapter Box Atlas.1, Figure 1). The 66% threshold, which has been used in previous reports (e.g., SR1.5 and SROCC) and in the literature, is not used to avoid communicating weak confidence. Cross-Chapter Box Atlas.1, Figure 1 illustrates the application of this approach.

Approach C is a more advanced alternative for model projections, extending the AR5 WGI and simplifying the AR5 WGII approaches (fewer categories). It consists of three categories: 'robust change', 'conflicting change', and 'no change or no robust change' (see the details in Cross-Chapter Box Atlas.1, Table 1). The first two categories can be interpreted as areas where the climate change signal likely emerges from internal variability (i.e., it exceeds the variability threshold in ≥66% of the models). The variability threshold is defined as $\gamma = \sqrt{2} \cdot 1.645 \cdot \sigma_{20yr}$, where σ_{20yr} is the standard deviation of 20-year means, computed from

ACCEPTED VERSION SUBJECT TO FINAL EDITS

non-overlapping periods in the pre-industrial control (after detrending with a quadratic fit as in AR5 WG1); in cases where this information is not available (e.g., for CORDEX or HighResMIP), the following approximation is used instead: $\gamma = \sqrt{2/20} \cdot 1.645 \cdot \sigma_{1yr}$, where σ_{1yr} is the interannual standard deviation measured in a linearly detrended modern period (note that for white noise $\sigma_{20yr} = \sigma_{1yr}/\sqrt{20}$). The factor $\sqrt{2}$ is used as in the AR5 WGI approach to account for the fact that the variability of a difference in means (the climate change signal) is of interest. This approach is an evolution of AR5 WGI method with three notable differences: (a) AR6 uses a lower threshold for internal variability (1.645 corresponding to a 90% confidence level, instead of 2 as used in AR5 WG1); (b) the threshold on agreement in sign is lowered from ≥90% to ≥80%, leading to more grid boxes classified as robust as opposed to conflicting signal; (c) the AR6 method compares signal to variability in each individual model and consequently introduces a 66% cut-off on significant changes implying that the climate change signal *likely* emerges from internal variability in the baseline period. This change is motivated by the criticisms of internal variability of the models, while it can differ largely across models.

Cross-Chapter Box Atlas.1, Figure 1 illustrates the application of this method considering the effect of the baseline period (1850–1900 versus 1995–2014) and shows that it provides similar results to related approaches proposed in the literature (Zappa et al., 2021).

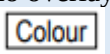
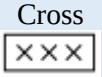
The two alternative approaches discussed above allow visualisation of different level of detail of information on the projected change and are intended for different communication purposes. Approach B just informs on the consistency of the sign of change independent of its significance relative to internal variability, whereas approach C puts the projected changes into context of internal variability and allows highlighting of areas of conflicting signals. It is important to note that different approaches can be applied to the same variable between different chapters for different communication purposes. For example, in maps showing multi-model mean changes of precipitation, Chapter 4 adopts the approach C but Chapter 8 applies the approach B.

In terms of visual implementation, the approach follows recommendations resulting from conversations with IPCC national delegations: 1) having a consistent approach across WGs would aid consistency and reduce the risk of confusion; 2) defining 'hatching' as 'diagonal lines' in the caption would aid accessibility for non-expert audiences; 3) a clear and concise legend that explains what these patterns represent should be included directly in the figure; 4) information about model uncertainty should be overlaid such that it does not detract from the data underneath.

Since stippling is commonly used to represent statistical significance, hatching was chosen to 'obscure' the problematic categories in the above approaches; it also facilitates the visualisation of uncertainty in the Interactive Atlas when zooming in. To avoid confusion, methods or thresholds that were unrelated to the three approaches hereby presented were visualised with a different pattern (i.e., model improvement between low- and high-resolution simulations in Chapter 3; agreement between observation-based products in Chapter 5; correlation between two variables in Chapter 6).

[START CROSS-CHAPTER BOX ATLAS.1, TABLE 1 HERE]

Cross-Chapter Box Atlas.1, Table 1: Approaches for representing robustness (uncertainty) in maps of observed (approach A) and projected (approaches B and C) climate changes.

Approach	Category	Definition	Visual Code
A. Observations (significance)	**A.1. Significant**	Significant (0.1 level) trend	Colour (no overlay) 
	A.2. Non significant	Non-significant trend	Cross 
B. Model	**B.1. High model**	≥80% of models agree on sign of change.	Colour

ACCEPTED VERSION SUBJECT TO FINAL EDITS

projections. Simple approach (agreement)	**agreement**	For Chapter 6 (<5 model ensembles): more than (n-1)/n models agree on the sign of change	(no overlay) Colour
	B.2. Low model agreement	<80% agree on sign of change. For Chapter 6: fewer than (n-1)/n models agree on the sign of change	Diagonal
C. Model projections. Advanced approach (significant change and agreement)	**C.1. Robust signal** (significant change and high agreement)	≥66% of models show change greater than variability threshold γ and ≥80% of all models agree on sign of change	Colour (no overlay) Color
	C.2. No change or no robust signal	<66% of models show change greater than variability threshold	Reverse diagonal
	C.3. Conflicting signals (significant change but low agreement)	≥66% of models show change greater than variability threshold γ and <80% of all models agree on sign of change	Crossed lines

[END CROSS-CHAPTER BOX ATLAS.1, TABLE 1 HERE]

[START CROSS-CHAPTER BOX ATLAS.1, FIGURE 1 HERE]

Cross-Chapter Box Atlas.1, Figure 1: Illustration of the simple (top) and advanced (bottom) approaches (B and C in Cross-Chapter Box Atlas.1, Table 1) for uncertainty representation in maps of future projections. Annual multi-model mean projected relative precipitation change (%) from CMIP6 for the period 2040–2060 (left) and 2080–2100 (right) relative to the baseline periods 1995–2014 (a–d) and 1850–1900 (e–g) under a high-emission (SSP3-7.0) future. Diagonal and crossed lines follow the indications in Cross-Chapter Box Atlas.1, Table 1. Further details on data sources and processing are available in the chapter data table (Table Atlas.SM.15).

[END CROSS-CHAPTER BOX ATLAS.1, FIGURE 1 HERE]

Uncertainty at the grid-box and regional scales: interpreting hatched areas

There is no one-size-fits-all method for representing robustness or uncertainty in future climate projections from a multi-model ensemble. One of the main challenges is the dependence of the significance on the spatial scale of interest: while a significant trend may not be detected at every location, a fraction of locations showing significant trends can be sufficient to indicate a significant change over a region, particularly for extremes (e.g., it is *likely* that annual maximum 1-day precipitation has intensified over the land regions globally even though there are only about 10% of weather stations showing significant trends; Figure 11.13). The approach adopted in WGI works at a grid-box level and, therefore, is not informative for assessing climate change signals over larger spatial scales. For instance, an assessment of the amount of warming required for a robust climate change signal to emerge can strongly depend on the considered spatial scale. A robust change in the precipitation extremes averaged over a region or a number of grid-boxes emerge at a lower level of warming than at the grid-box level because of larger variability at the smaller scale (Cross-Chapter Box Atlas.1, Figure 2).

[START CROSS-CHAPTER BOX ATLAS.1, FIGURE 2 HERE]

Cross-Chapter Box Atlas.1, Figure 2: Climate change signals are more separable from noise at larger spatial scales. The figure is showing the global warming level associated with the

ACCEPTED VERSION SUBJECT TO FINAL EDITS

emergence of a significant increase in the probability due to anthropogenic forcing in the 1-in-20-year daily precipitation event using a 500-year sample from the CanESM2 large ensemble simulations. The left panel uses data analysed over a single grid box, with no spatial aggregation, while the right box uses data averaged over 25 grid boxes to represent moderate spatial aggregation. Aggregation over 25 grid boxes reduces natural variability, resulting in a smaller warming required for a clear separation between the signal and noise. Adapted from Kirchmeier-Young et al. (2019).

[END CROSS-CHAPTER BOX ATLAS.1, FIGURE 2 HERE]

[END CROSS-CHAPTER BOX ATLAS.1 HERE]

Atlas.2 The online 'Interactive Atlas'

The WGI Interactive Atlas is a new AR6 product developed as part of the Atlas in consultation with other chapters to facilitate flexible synthesis information for regions, and to support the Technical Summary (TS) and the Summary for Policymakers (SPM), as well as the handshake with WGII. It includes multiple lines of evidence to support the assessment of observed and projected climate change by offering information for regions using both time-slices across scenarios and Global Warming Levels (GWLs). Coordination has been established with other chapters (particularly the regional chapters) adopting their methodological recommendations (Chapter 10) and using common datasets and agreed extreme indices and climatic impact-drivers (CIDs) to support and expand their assessment (Chapters 11 and 12).

The Interactive Atlas allows for flexible spatial and temporal analysis (Section Atlas.1.3) with a predefined granularity (predefined climatological and typological regions and user-defined seasons) through a wide range of maps, graphs and tables generated in an interactive manner building on a collection of global and regional observational datasets and climate projections (including CMIP5, CMIP6 and CORDEX; Section Atlas.1.4). In particular, the Interactive Atlas provides trends and changes for observations and projections in the form of interactive maps for predefined historical and future periods of analysis, the former including recent-past and paleoclimate (see Cross-Chapter Box 2.1) and the latter including future time-slices (near, medium and long term) across scenarios (RCPs and SSPs; see Cross-Chapter Box 1.4) and GWLs (1.5°C, 2°C, 3°C and 4°C; see Cross-Chapter Box 11.1). It also provides regional information (aggregated spatial values) for a number of predefined (reference and typological) regions in the form of time series, annual cycle plots, scatter plots (e.g., temperature versus precipitation), table summaries, and ensemble and seasonal stripe plots. This allows for a comprehensive analysis (and intercomparison, particularly using GWLs as a dimension of integration) of the different datasets at a global and regional scale.

The Interactive Atlas can be consulted online at http://ipcc-atlas.ifca.es. Figure Atlas.8 illustrates the main functionalities available: the controls at the top of the window allow the interactive selection of the dataset, variable, period (reference and baseline) and season which define a particular product of interest (e.g., annual temperature change from CMIP6 under SSP3-7.0 for the long-term 2081–2100 period relative to 1995–2104 in this illustrative case). Regionally aggregated information can be obtained interactively by clicking on one or several subregions on the map and by selecting one of the several options available for visuals (time series, annual-cycle plots, scatter and stripe plots) and tables.

[START FIGURE ATLAS.8 HERE]

Figure Atlas.8: Screenshots from the Interactive Atlas. (a) The main interface includes a global map and controls to define a particular choice of dataset, variable, period (reference and baseline) and season (in this example, annual temperature change from CMIP6 for SSP3-7.0 for the long-term 2081–2100 period relative to 1995–2104). (b–e) Various visuals and summary tables for the regionally averaged information for the selected reference regions.

ACCEPTED VERSION SUBJECT TO FINAL EDITS

[END FIGURE ATLAS.8 HERE]

A major goal during the development of the Interactive Atlas has been ensuring transparency and reproducibility of results, and promoting open science and Findability, Accessibility, Interoperability, and Reuse (FAIR) principles (Wilkinson et al., 2016) described in Atlas.2.3. As a result, full metadata are provided in the Interactive Atlas for each of the products, and the scripts used to generate the intermediated products (e.g., extreme indices and CIDs) and figures are available online in a public repository (Iturbide et al., 2021), which also includes simple notebooks illustrating key parts of the code suitable for reusability. These scripts are based on the climate4R open-source framework (Iturbide et al., 2019) and full metadata have been generated for all final products using the METACLIP framework (Bedia et al., 2019), which builds on standards and describes provenance of the datasets as well as the post-processing workflow.

Atlas.2.1 Why an interactive online Atlas in AR6?

The idea of an interactive online Atlas was first discussed in the IPCC Expert Meeting on Assessing Climate Information for the Regions (IPCC, 2018a). The meeting stressed the need for the AR6 regional Atlas to go beyond the AR5 experience in supporting and expanding the assessment of key variables/indices and datasets conducted in all chapters, ensuring traceability, and facilitating the 'handshake' between WGI and WGII. One of the main limitations of previous products, including the AR5 WGI Atlas (IPCC, 2013a), is their static nature with inherent limited options and flexibility to provide comprehensive regional climate information for different regions and applications. For instance, the use of standard seasons limits the assessment in many cases, such as regions affected by monsoons or seasonal rainband migrations or other phenomena-driven seasons. The limited number of variables which can be treated on a printed Atlas also prevents the inclusion of relevant extreme indices and CIDs. The development of an online Interactive Atlas for AR6 was proposed as a solution to overcome these obstacles, facilitating the flexible exploration of key variables/indices and datasets assessed in all chapters through a wide range of maps, graphs and tables generated in an interactive manner, and thus also providing support to the TS and SPM. One of the main concerns raised by this new online interactive product was the potential danger of having an unmanageable number of final products impossible to assess following the IPCC review process. This was addressed by designing the Interactive Atlas with limited and predefined functionality and granularity thus facilitating the review process and including use of open-source tools and code for traceability and reproducibility of results.

Atlas.2.2 Description of the Interactive Atlas: functionalities and datasets

The Interactive Atlas builds on the work done in the context of the Spanish National Adaptation Plan (PNACC – AdapteCCa; http://escenarios.adaptecca.es) to develop an interactive online application centralizing and providing key regional climate change information to assist the Spanish climate change impact and adaptation community. The functionalities included in the AR6 WGI Interactive Atlas are an evolution of those implemented in AdapteCCa and have been adapted and extended to cope with the particular requirements of the datasets and functionalities it includes. In particular, the Interactive Atlas allows analysis of global and regional information on past trends and future climate changes through a wide range of maps, graphs and tables generated in an interactive manner and building on six basic products (see Figure Atlas.8):

1. Global maps of variables averaged over time-slices across scenarios and GWLs, with robustness represented using the approaches described in Cross-Chapter Box Atlas.1.
2. Temporal series, displaying all individual ensemble members and the multi-model mean, with robustness represented as ranges across the ensemble (25th–75th and 10th–90th percentile ranges). The selected reference period of analysis is also displayed as context information, either a time-slice (near-, mid- or long-term) or a GWL (defined for a given model as the first 20-year period where its average surface temperature change first reaches the GWL relative to its 1850–1900 temperature).
3. Annual cycle plots representing individual models, the multi-model mean and ranges across the ensemble.

ACCEPTED VERSION SUBJECT TO FINAL EDITS

4. Stripe and seasonal stripe plots, providing visual information on changes across the ensemble (different models in rows with the multi-model mean on the top) and across seasons (months in rows, using the signal from the multi-model mean), respectively.
5. Two-variable scatter plots (e.g., temperature versus precipitation).
6. Tables with summary information.

The first of these products provides spatial information about the ensemble mean, while the latter five convey (spatially) aggregated information of the multi-model ensemble for particular region(s) selected by the user from a number of predefined alternatives (see Sections Atlas.1.3.3 and Atlas.1.3.4 for reference and typological regions, respectively).

The Interactive Atlas includes both atmospheric (daily mean, minimum and maximum temperatures, precipitation, snowfall and wind) and oceanic (sea surface temperature, pH, sea ice, and sea level rise) essential variables assessed in the Atlas chapter and Chapters 4, 8 and 9, as well as some derived extreme indices used in Chapter 11 and a selection of CIDs used in Chapter 12 (see Annex VI):

- Maximum of maximum temperatures (TXx) – see Chapter 11.
- Minimum of minimum temperatures (TNn) – see Chapter 11.
- Maximum 1-day precipitation (RX1day) – see Chapter 11.
- Maximum 5-day precipitation (RX5day) – see Chapter 11.
- Consecutive Dry Days (CDD) – see Chapter 11.
- Standardized Precipitation Index (SPI-6) – see Chapters 11 and 12.
- Frost days (FD), both raw and bias adjusted – see Chapters 11 and 12.
- Heating Degree Days (HD) – see Chapter 12.
- Cooling Degree Days (CD) – see Chapter 12.
- Days with maximum temperature above 35°C (TX35), both raw and bias adjusted – see Chapter 12.
- Days with maximum temperature above 40°C (TX40), both raw and bias adjusted – see Chapter 12.

The essential variables are computed for observations and reanalysis datasets as described in Sections Atlas.1.4.1 and Atlas.1.4.2 (note that the Atlas does not include observational datasets for extremes). Trend analyses are available for two alternative baseline periods (1961–2015 and 1980–2015, selected according to data availability). This expands the information available in Chapter 2 for global observational datasets, including new periods of analysis and new regional observational datasets which provide further insight into observational uncertainty.

Both essential variables and indices/CIDs are computed for CMIP5, CMIP6 and CORDEX model projections (Sections Atlas.1.4.3 and Atlas.1.4.4). The calculations are performed on the original model grids and results are interpolated to the reference regular grids at horizontal resolutions of 2° (CMIP5), 1° (CMIP6) and 0.5° (CORDEX) (Iturbide et al., 2021). Information is available for the historical, SSP1-2.6, SSP2-4.5, SSP3-7.0 and SSP5-8.5 scenarios for CMIP6, and historical, RCP2.6, RCP4.5 and RCP8.5 for CMIP5 and CORDEX, as documented in Annex II Tables 1-2 (for CMIP5/CMIP6) and Annex II Tables 3-14 (for the different CORDEX domains). All products (maps, graphs and tables) are available for different reference periods of analysis, either time-slices (2021–2040, 2041–2060 and 2081–2100 for near-, mid- and long-term future periods, respectively; see Section Atlas.1.3.1), or GWLs (1.5°C, 2°C, 3°C or 4°C; see Section Atlas.1.3.2), with changes relative to a number of alternative baselines (including 1850–1900 pre-industrial, and 1995–2014 recent past; see Section Atlas.1.3.1). Note that instead of blending the information from the different scenarios, the Interactive Atlas allows comparison of the GWL spatial patterns and timings across the different scenarios (see Cross Chapter Box 11.1).

Some of the above indices (in particular TX35 and TX40) are highly sensitive to model biases and the application of bias-adjustment techniques is recommended to alleviate this problem (see Cross-Chapter Box 10.2). Bias adjustment is performed as explained in Section Atlas.1.4.5.

The Interactive Atlas implements the approaches for representing robustness in maps at the grid-box level described in Cross-Chapter Box Atlas.1. These approaches are not necessarily informative for assessing

ACCEPTED VERSION SUBJECT TO FINAL EDITS

trends and climate change signals over larger spatial scales where signals are less affected by small-scale variability leading to an increase in robustness. For regional analysis, the Interactive Atlas allows the analysis of aggregated region-wide signals and assessing their robustness at a regional scale thus complementing the previous approach for grid-box robustness representation. For example, Figure Atlas.9 shows large hatched areas for maximum 5-day precipitation in the South Asia region. When aggregated spatially, the region exhibits a robust wetting signal, with most ensemble members agreeing on the sign. This highlights that signals may not have emerged at the station- or grid-box scale but have clearly at aggregated scales, particularly for variables with high variability (e.g., extreme precipitation or cold extremes; see Cross-Chapter Box Atlas.1).

The advanced approach for representing robustness includes a new category for identifying conflicting signals, where models are projecting significant changes but of opposite signs. This is demonstrated in Figure Atlas.9 which shows a region of central Africa where models have significant changes in surface winds with some projecting increases and others decreases. This is clearly demonstrated in the time-series below the map which shows these wind-speed changes aggregated over the CAF reference region for each of the CMIP6 models and the opposing signals in many of these.

[START FIGURE ATLAS.9 HERE]

Figure Atlas.9: Analysing robustness and uncertainty in climate change signals across spatial scales using the Interactive Atlas. The left panel shows projected annual relative changes for maximum 5-day precipitation from CMIP6 at 3°C of global warming level relative to the 1850–1900 baseline, through a map of the ensemble mean changes (panel top) and information on the regional aggregated signal over the South Asia reference region as time series (panel bottom). This shows non-robust changes (diagonal lines) at the grid-box level (due to the large local variability), but a robust aggregated signal over the region. The right panel shows projected surface wind speed changes from CMIP6 models for 2041–2060 relative to a 1995–2014 baseline under the SSP5-8.5 scenario, again with the ensemble mean changes in the map (panel top) and regionally aggregated time series over Central Africa for each model (panel bottom). This shows conflicting changes (crossed lines) at the grid-box level due to signals of opposite sign in the individual models displayed in the time series.

[END FIGURE ATLAS.9 HERE]

Atlas.2.3 Accessibility, reproducibility and reusability (FAIR principles)

The accessibility and reproducibility of scientific results have become a major concern in all scientific disciplines (Baker, 2016). During the design and development of the Interactive Atlas, special attention was paid to these issues in order to ensure the transparency of the products feeding into the Interactive Atlas (which are all publicly available). Accessibility is implemented in collaboration with the IPCC Data Distribution Centre (DDC), since all products underpinning the Interactive Atlas, including the intermediate products required for the indices and CIDs (monthly aggregated data), are curated and distributed by the IPCC-DDC and include full provenance information as part of their metadata. Atlas products are generated using the open source climate4R framework (Iturbide et al., 2019) for data processing (e.g. regridding, aggregation, index calculation, bias adjustment), evaluation and quality control (when applicable). Full metadata are generated for all final products using the METACLIP framework (Bedia et al., 2019), based on the Resource Description Framework (RDF) standard to describe the datasets and data-processing workflow.

In summary, a number of actions have been conducted in order to implement open access, reproducibility and reusability of results, including:

- Use of standards and open-source tools.
- Open access to raw data and derived Atlas products via the IPCC-DDC.
- Provision of full provenance metadata describing the product generation workflow.
- Access to code through an online repository (Iturbide et al., 2021), including the scripts needed for calculating the intermediate datasets and for reproducing some of the figures of the Atlas chapter.

ACCEPTED VERSION SUBJECT TO FINAL EDITS

- Provision of annotated (Jupyter) notebooks describing key elements of the code to provide guidance and facilitate reusability.

All final products visualized in the Interactive Atlas can be exported in a variety of formats, including PNG and PDF for bitmap and vector information, respectively. Moreover, in the case of the global maps, the final data underlying these products can be downloaded in GIS format (GeoTIFF), thus facilitating reusability of the information. Note that the images are final IPCC products (covered by the IPCC terms of use), whereas the underlying data are distributed by the IPCC-DDC under a more flexible license which facilitates reusability. Moreover, a comprehensive provenance metadata description has been generated, including all details needed for reproducibility, from the data sources to the different post-processes applied to obtain the final product. In these cases, there is also the possibility to download a PNG file augmented with attached metadata information (in JSON format). This metadata information (including the source code generating the product) can be accessed and interpreted automatically using specific JSON software/libraries. However, for the sake of simplicity, a human-readable version of the metadata is accessible directly from the Interactive Atlas describing the key information along the workflow.

Provenance is defined as a 'record that describes the people, institutions, entities, and activities involved in producing, influencing, or delivering a piece of data or a thing'. This information can be used to form assessments about their quality, reliability or trustworthiness. In the context of the outcomes of the Interactive Atlas, having an effective way of dealing with data provenance is a necessary condition to ensure not only the reproducibility of results, but also to build trust on the information provided. However, the relative complexity of the data and the post-processing workflows involved may prevent a proper communication of data provenance with full details for reproducibility. Therefore, a special effort was made in order to build a comprehensive provenance metadata model for the Interactive Atlas products.

Provenance frameworks are typically based on RDF (Resource Description Framework), a family of World Wide Web Consortium (W3C) specifications originally designed as a metadata model (Candan et al., 2001). It is an abstract model that has become a general method for conceptual description of information for the Web, using a variety of syntax notations and serialization formats. METACLIP (Bedia et al., 2019) exploits RDF through specific vocabularies, written in the OWL ontology language, describing different aspects involved in climate product generation, from the data source to the post-processing workflow, extending international standard vocabularies such as PROV-O (Moreau et al., 2015). The METACLIP vocabularies are publicly available in the METACLIP repository (http://github.com/metaclip/vocabularies).

METACLIP emphasises the delivery of 'final products' (understood as any piece of information that is stored in a file, such as a plot or a map) with a full semantic description of its origin and meaning attached. METACLIP ensures 'machine readability' through reuse of well-defined, standard metadata vocabularies, providing semantic interoperability and the possibility of developing database engines supporting advanced provenance analytics. Therefore, this framework has been adopted to generate provenance information and attach it as metadata to the products generated by the Interactive Atlas. A specific vocabulary ('ipcc_terms') is created alongside the inclusion of new products in the Interactive Atlas and uses the controlled vocabularies existing from CMIP and CORDEX experiments. As an example, Figure Atlas.10 shows the semantic vocabularies needed to encode the information of the typical workflow for computing (from bias-adjusted data) any of the climate indices (extreme or CIDs) included in the Interactive Atlas.

[START FIGURE ATLAS.10 HERE]

Figure Atlas.10: Schematic representation of the Interactive Atlas workflow, from database description, subsetting and data transformation to final graphical product generation (maps and plots). Product-dependent workflow steps are depicted with dashed borders. METACLIP specifically considers the different intermediate steps consisting of various data transformations, bias adjustment, climate index calculation and graphical product generation, providing a semantic description of each stage and the different elements involved. The different controlled vocabularies describing each stage are indicated by the colours, with gradients indicating several vocabularies involved, usually meaning that specific individual instances are defined in 'ipcc_terms' extending generic classes of

ACCEPTED VERSION SUBJECT TO FINAL EDITS

'datasource'. These two vocabularies, dealing with the primary data sources have specific annotation properties linking their own features with the CMIP5, CMIP6 and CORDEX Data Reference Syntax, taking as reference their respective controlled vocabularies. All products generated by the Interactive Atlas provide a METACLIP provenance description, including a persistent link to a reproducible source code under version control.

[END FIGURE ATLAS.10 HERE]

Atlas.2.4 Guidance for users

Atlas.2.4.1 Purpose of the Interactive Atlas

The primary purpose of the IPCC is to provide a policy relevant, non-prescriptive assessment of the state of knowledge on climate change and its impacts. This purpose is different from the provision of information targeted to implement climate policies, which is the focus of climate services and national climate change assessment communities. IPCC assessments are based on quantitative observational and model-generated data that are also used in many activities supporting the development of climate policies. However, the functionality of the Interactive Atlas is primarily aimed at supporting the knowledge assessment.

Much of the assessment in this report is based on multiple lines of evidence (Cross Chapter Box 10.3). The Interactive Atlas facilitates combining multiple observational and model-generated datasets and spatial and temporal analyses that combine to support statements on the characteristics of the climate system. The use of predefined spatial and temporal aggregations imposes constraints on the ability to make specific or tailored assessments but does provide essential background and uncertainty information to generate broad findings and provide confidence statements on these. Also, the inclusion of a selection of extremes and CIDs is a new element in the Interactive Atlas and facilitates broader application including the handshake with WGII. Below, some guidelines on the use, interpretation and limitations of the Interactive Atlas are given.

Atlas.2.4.2 Guidelines for the Interactive Atlas

Atlas.2.4.2.1 Quantitative support for assessments

Many assessment statements make use of evidence derived from observed changes, model projections, and process-oriented attribution of changes to human interventions. The Interactive Atlas shows a small subset of available observations that document climate change, namely surface air temperature and total precipitation (and thus not including observations of other atmospheric and Earth system components used as part of the evidence base for the report). Only datasets that have (near) global or large regional gridded spatial coverage and go back multiple decades are used. For each variable multiple datasets are included, but some of these have overlapping native ground-station observations and so are not independent (see Section Atlas.1.4.1). The datasets show patterns of substantial spatial and temporal variability, and the empirical evidence of a non-stationary climatology needs to be filtered from this information. Issues with quality, representativity, and mutual consistency lead to constraints on their use for attribution of causes of trends (see Section 10.4.1.2 for examples). The practice of attributing trends and extreme events to human causes gives confidence that these trends are expected to continue in the (near) future, provided the human drivers of climate change remain unchanged. However, large internal variability at decadal time scales can be mis-interpreted as an anthropogenic influence on the likelihood of extreme events, and in that case extrapolation of trends cannot be expected to be a reliable predictor for the future (Schiermeier, 2018).

The Interactive Atlas gives access to a specific set of climate variables from a large number of climate model simulations, particularly the (global) CMIP5, CMIP6 and (regional) CORDEX archives. The global model outputs generally give a relatively coarse picture of climate change, which is an important line of evidence for the detection and attribution of climate change, but is rarely directly applicable for local climate change assessment or support of policy design (van den Hurk et al., 2018). To provide additional detail, downscaling global projections with regional climate models (RCMs) or statistical downscaling can be undertaken but

ACCEPTED VERSION SUBJECT TO FINAL EDITS

also adds a source of uncertainty as it involves additional modelling (see Section 10.3).

The information displayed in the Interactive Atlas allows a number of sources of uncertainty to be quantified. 'Observational uncertainty' is represented by the use of multiple (albeit often not completely independent) observational datasets. 'Uncertainty due to internal variability' cannot be quantified directly since multiple realizations from historic and future projections are not accessible (the Interactive Atlas uses a single realization of each model). The use of a large collection of model systems allows for an elaborate quantification of 'model uncertainty'. In addition, a comparison of CMIP5 and CMIP6 supports evidence of progress in model quality since the AR5, while the evaluation of the added value of RCMs reveals model uncertainty related to spatial resolution (see Section 10.3). Finally, the assessment of 'scenario uncertainty' is supported by the inclusion of multiple emission scenarios for both CMIP5, CORDEX and CMIP6.

The communication of uncertainty has a profound influence on the perception of information that is exchanged during the communication process. An assessment of uncertainty communication and the barriers to climate information construction is given in Section 10.5.4.

Atlas.2.4.2.2 Insights from physical understanding

The detailed technical findings in IPCC reports also serve as an important benchmark resource for the research community. The Interactive Atlas complements the IPCC assessment report as a repository of scientific information on global and regional climate and its representation in coordinated model ensemble experiments. Regional climate is governed by a mixture of drivers, such as circulation patterns, seasonal monsoons, annual cycles of snow and regional land-atmosphere feedbacks. Global warming may affect regional climate characteristics by altering the dynamics of their drivers. The Interactive Atlas allows the comparison of different levels of global warming on specific regional climate features but is not designed for advanced analysis of the relationship between drivers and regional climate characteristics. For this, tailored analysis protocols need to be applied, such as the aggregation of climate change information from ensembles of regional climate projections, and stratification according to drivers of regional climate such as patterns of atmospheric circulation (Lenderink et al., 2014). The analysis of complex regional climate characteristics resulting from compound drivers also require additional expert knowledge and data processing (Thompson et al., 2016). Section 12.6.2 assesses various categories of climate services, including tailored analysis of regional climate processes.

Atlas.2.4.2.3 Construction of storylines

Communicating the full extent of available information on future climate for a region, including a quantification of uncertainties, can act as a barrier to the uptake and use of such information (Lemos et al., 2012; Daron et al., 2018). To address the need to simplify and increase the relevance of information for specific contexts, recent studies have adopted narrative and storyline approaches (Hazeleger et al., 2015; Shepherd et al., 2018) (see Sections 1.4.4 and 10.5.3 for definitions and further discussion on these concepts). The use of region-specific climate storylines, including a role for local mechanisms, drivers and societal impacts generally requires detailed information that is typically not provided by the Interactive Atlas. However, background information and basic (scenario) assumptions can be derived from the Interactive Atlas which can be considered to provide an expert knowledge base from which to build targeted storylines and climate information.

Atlas.2.4.2.4 Visual information

The visual communication of climate information can take many forms. Besides the standard visual products typically used for communicating global and regional climate information to practitioners (e.g., maps, time series or scatter plots), the Interactive Atlas incorporates new visuals, for example 'stripes' (RMetS, 2019), facilitating the communication of key messages (e.g., warming and consistency across models) to a less technical audience. The various tabular and graphical representation alternatives included as options in the Interactive Atlas (Figure Atlas.8) facilitate exploring the information interactively from different perspectives and for different levels of detail, thus favouring the communication with the larger and diverse

ACCEPTED VERSION SUBJECT TO FINAL EDITS

audience of IPCC products.

To support the use of visuals provided in the Interactive Atlas for application to different audiences, new insights since the AR5 have emerged from a range of scientific disciplines, including the cognitive and psychological sciences (Harold et al., 2016). Studies have used interviews and online surveys to assess interpretations of visuals used to communicate climate information and uncertainties (Daron et al., 2015; Lorenz et al., 2015; McMahon et al., 2015; Retchless and Brewer, 2016). They commonly find wide-ranging interpretations and varied understandings of climate information amongst respondents due to the choice of visuals. In addition, Taylor et al. (2015) found that preferences for a particular visualization approach do not always align with approaches that achieve greatest accuracy in interpretation. Choosing appropriate visuals for a particular purpose and audience can be informed by testing and evaluation with target groups.

Atlas.2.4.2.5 Dedicated climate change assessment programs

Communication aimed at informing the general public about assessed scientific findings on climate change have a different purpose and format than if intended to inform a specific target audience to support adaptation or mitigation policies (Whetton et al., 2016). The growing societal engagement with climate change means IPCC reports are increasingly used directly by businesses, the financial sector, health practitioners, civil society, the media, and educators at all levels. The IPCC reports could effectively be considered a tiered set of products with information relevant to a range of audiences.

The Interactive Atlas does provide access to a collection of observational and modelling datasets, presented in a form that supports the distillation of information on observed and projected climate trends at the regional scale. Access to the repository of underlying datasets enables further processing for particular purposes. As noted above, it is not the intention nor the ambition of this IPCC assessment and the Interactive Atlas component to provide a climate service for supporting targeted policies. For this an increasing number of dedicated climate change assessment programs have been carried out, aiming at mapping climate change information relevant for adaptation and mitigation decision support.

For instance, the European Environment Agency (2018) provides an overview of European national climate change scenario programs. Most of these use CMIP5 (or earlier) global climate change ensembles driven by an agreed set of greenhouse-gas emission scenarios, followed by downscaling using RCMs and/or statistical methods, in order to generate regionally representative hydrometeorological indicators of climate change. In some cases, output of selected downscaled global and regional models is provided to users (Whetton et al., 2012; Daron et al., 2018). Uptake by users is strongly dependent on providing justification of the selection or for the downscaling procedure and if further steps are needed to tailor the information to local scales (Lemos et al., 2012). More comprehensive programs provide probabilistic climate information by careful analysis and interpretation of ensembles of model outputs (Lowe et al., 2018). The information is generally tailored to professional practitioners with expertise to interpret and process this probabilistic data. This top-down probabilistic information chain is not always able to highlight the essential climate change information for users, and alternative bottom-up approaches are encouraged (Frigg et al., 2013). Section 12.6.2 assesses climate services including the national climate assessments and user uptake.

Atlas.3 Global synthesis

Most other chapters in WGI assess past or future behaviour of specific aspects of the global climate system and this section introduces some of the key results, specifically from Chapters 2, 4 and 9. This provides a global overview on observations and information from the CMIP5 and CMIP6 ensembles to underpin the regional assessments in the rest of the Atlas Chapter and the results displayed in the Interactive Atlas. Thus, its aim is not to generate an assessment of regional climate change directly but to provide the global context for this information derived later in the Atlas. Section Atlas.3.1 considers global atmospheric and land-surface information with global ocean information in Section Atlas.3.2.

ACCEPTED VERSION SUBJECT TO FINAL EDITS

Atlas.3.1 Global atmosphere and land surface

The principal atmospheric quantities of interest for understanding how climate change may impact human and ecological systems, as well as being key global indicators of change, are surface air temperature and precipitation. They are therefore a significant focus of the regional climate assessments in the following regional sections of the chapter (Atlas.4 to Atlas.11) and of the Interactive Atlas. Changes in these variables over land during the recent past (1960–2015) are shown in Figure Atlas.11 using results from two global datasets (assessed in Chapter 2) to illustrate both where there is robust information on observed trends and observational uncertainty.

For temperature, a clear signal of warming is seen over most land areas with an amplification at high latitudes, though all continents apart from Europe also have regions where trends are not significant. Significant changes in annual mean precipitation are seen over much more limited areas though with consistent increasing trends over some northern high-latitude regions and decreasing trends over smaller regions in tropical Africa, the Americas and Southwest Asia. The information conveyed in Figure Atlas.11 on both consensus in the signal of change and on observational uncertainty is used in this chapter as a line of evidence to assess historical observed trends.

As an alternative way of viewing and summarising information in the observational data, the panels (c) and (d) in Figure Atlas.11 show the time at which any significant temperature trends from the Berkeley Earth and CRUTEM5 datasets, averaged over the reference regions, emerged from interannual variability – with a signal to noise ratio greater than two (Hawkins et al., 2020). In the former a regionally averaged warming signal has emerged over all of the land reference regions. In the latter, emergence times are only calculated for those regions which have data available in more than 50% of the land area (unlike Berkeley Earth, CRUTEM does not include spatial interpolation, see Section 2.3.1.1.3) and these are similar for all but one of the regions indicating that observational uncertainty does not change the main conclusion of widespread emergence of surface temperature signals over land regions.

[START FIGURE ATLAS.11 HERE]

Figure Atlas.11: Observed linear trends of signals in annual mean surface air temperature (a, b) and precipitation (e, f) in the Berkeley Earth, CRU TS and GPCC datasets (see Section Atlas.1 for dataset details). Trends are calculated for the common 1960–2015 period and are expressed as ºC per decade for temperature and relative change (with respect to the climatological mean) per decade for precipitation. Crosses indicate regions where trends are not significant (at a 0.1 significance level) and the black lines mark out the reference regions defined in Section Atlas.1. Panels c and d display the period in which the signals of temperature change in data aggregated over the reference regions emerged from the noise of annual variability in the respective aggregated data. Emergence time is calculated for (c) Berkeley Earth (as used in (a)) and CRUTEM5. Regions in the CRUTEM5 map are shaded grey when data are available over less than 50% of the land area of the region. Further details on data sources and processing are available in the chapter data table (Table Atlas.SM.15).

[END FIGURE ATLAS.11 HERE]

As described earlier, information on projected future changes is required both at different time periods in the future under a range of emissions scenarios but also for different global warming levels. Figure Atlas.12 shows the global surface air temperature change projection calculated from the CMIP6 ensemble mean of for the middle of the century under the SSP1-2.6 and SSP3-7.0 emissions scenarios compared to the end of the century warming under SSP3-7.0 and for a global warming level of 2°C. The patterns of changes are similar to the observed warming and there is a high level of consistency with CMIP5 in terms of both patterns and magnitude of change (Interactive Atlas). However, for the long-term future, warming in the CMIP6 ensemble is generally higher, reflecting the increase in the top end of the range of climate sensitivities amongst the CMIP6 GCMs (Figure Atlas.13).

ACCEPTED VERSION SUBJECT TO FINAL EDITS

[START FIGURE ATLAS.12 HERE]

Figure Atlas.12: Global temperature changes projected for the mid-century under SSP1-2.6 (left, top) and SSP3-7.0 (left, bottom) compared with a 2°C global warming level (right, top) and the end of the century under SSP3-7.0 (right, bottom) from the CMIP6 ensemble. Note that the future period warmings are calculated against a baseline period of 1995–2014 whereas the global mean warming level is defined with respect to the baseline period of 1851–1900 used to define global warming levels. The other three SSP-based maps would show greater warmings with respect to this earlier baseline. Further details on data sources and processing are available in the chapter data table (Table Atlas.SM.15).

[END FIGURE ATLAS.12 HERE]

Figure Atlas.12 demonstrates how temperature is projected to increase for all regions, and at a greater rate than the global average over many land regions and with significant amplification in the Arctic. It also shows the higher mid-century warming and significantly higher end of century warming under the high-emission SSP3-7.0 scenario compared to the low-emission SSP1-2.6 scenario. Conversely, comparing the projected 2°C Global Warming Level change with that projected additional warming compared to the recent past under the SSP1-2.6 scenario demonstrates the much smaller additional warming projected under this low-emission scenario. Finally, the maps display the CMIP6 ensemble mean projection but it is important to explore the full range of outcomes from the ensemble, for example when undertaking a comprehensive risk assessment in which temperature is an important hazard. This can be explored regionally in the Interactive Atlas (Section Atlas.2) by viewing the timeseries of changes for all of the models within the ensemble over the AR6 WGI reference regions (Figure Atlas.2:).

Changes in annual mean precipitation present a more complex picture with regions of decrease as well as increase and areas where there is model disagreement on the sign of the change, even when the signal is strong in the long-term future period as shown in Cross-Chapter Box Atlas.1, Figure 1. However, as with the temperature changes, there is a high level of consistency in the patterns and magnitude of the precipitation changes, with changes in some areas being larger in the long-term future period. Considering changes over land, Cross-Chapter Box Atlas.1, Figure 1 also shows that at lower warming levels there are many regions, especially in the southern hemisphere, where there is no robust signal of change from the models.

In addition to displaying results from global model ensembles as maps of projected changes and their robustness or as timeseries of the projected temporal evolution of the median and range of a climate statistic, it is often useful to generate area-averaged summaries of these statistics under different future emission scenarios or at specific global warming levels. This is demonstrated in Figure Atlas.13 and forms the basis of a common set of analyses which are presented for the reference regions in the regional assessments in the following Sections Atlas.4 to Atlas.11. It shows the range of projected changes compared to the 1850–1900 and the recent past 1995–2014 baseline periods for the CMIP5 and CMIP6 ensembles. The first four panels show: annual mean changes in temperature globally and over land only for various global warming levels and emission scenarios and time periods (left pair) and then again globally and for global land, changes in precipitation and temperature at the same global warming levels (right pair). The second four panels provide the same temperature and precipitation information globally and for global land only in the December–February and July–August seasons. These results demonstrate the consensus between the two ensembles for increased warming over land areas and increases in global precipitation at all warming levels and that global land precipitation increases more. They also show the increased precipitation response in DJF reflecting the large precipitation increases in the northern hemisphere higher latitudes in winter. Finally, they demonstrate the greater warming projected by the CMIP6 ensemble, as an average over the ensemble and the upper end of the range. See Chapter 4 for an in-depth assessment of these results.

ACCEPTED VERSION SUBJECT TO FINAL EDITS

[START FIGURE ATLAS.13 HERE]

Figure Atlas.13: Changes in annual mean surface air temperature and precipitation averaged over the global (left) and global land areas (right) in each horizontal pair of panels. The top left two panels show the median (dots) and 10th–90th percentile range across each model ensemble for temperature change, for two datasets (CMIP5 and CMIP6) and two scenarios (SSP1-2.6/RCP2.6 and SSP5-8.5/RCP8.5). The first twelve bars represent the projected changes over three time periods (near-term 2021–2040, mid-term 2041–2060 and long-term 2081–2100) compared to the baseline period of 1995–2014 and the remaining four bars represent the additional warming projected relative to the same baseline to reach four global warming levels (GWL; 1.5°C, 2°C, 3°C and 4°C). The top right two panels show scatter diagrams of temperature against precipitation changes, displaying the median (dots) and 10th–90th percentile ranges for the same four GWLs, again representing the additional changes for the global temperature to reach the respective GWL from the baseline period of 1995–2014. In all panels the dark (light) grey lines or dots represent the CMIP6 (CMIP5) simulated changes in temperature and precipitation between the 1850–1900 baseline used for calculating GWLs and the recent past baseline of 1995–2014 used to calculate the changes in the bar diagrams and scatter-plots. Changes are absolute for temperature and relative for precipitation. The script used to generate this figure is available online (Iturbide et al., 2021) and similar results can be generated in the Interactive Atlas for flexibly defined seasonal periods. Further details on data sources and processing are available in the chapter data table (Table Atlas.SM.15).

[END FIGURE ATLAS.13 HERE]

Global warming leads to systematic changes in regional climate variability via various mechanisms such as thermodynamic responses via altered lapse rates (Kröner et al., 2017; Brogli et al., 2019) and land-atmosphere feedbacks (Boé and Terray, 2014). These can modify temporal and spatial variability of temperature and precipitation, including an altered seasonal and diurnal cycle and return frequency of extremes. Regional influences from and feedbacks with sea surface, clouds, radiation and other processes also modulate the regional response to enhanced warming, both locally and, via teleconnections, remotely.

Given their potential to influence extremes in temperature, precipitation and other climatic impact-drivers and hazards, and thus risks to human and ecological systems, it is important to understand these links for developing adaptations in response to clear anthropogenic influences on individual hazards. This will also support the related fields of disaster risk reduction and global sustainable development efforts (Steptoe et al., 2018). They demonstrated that 15 regional hazards shared connections via the El Niño–Southern Oscillation, with the Indian Ocean Dipole, North Atlantic Oscillation and the Southern Annular Mode (see Annex IV) being secondary sources of significant regional interconnectivity (Figure Atlas.14). Understanding these connections and quantifying the concurrence of resulting hazards can support adaptation planning as well as multi-hazard resilience and disaster risk reduction goals.

[START FIGURE ATLAS.14 HERE]

Figure Atlas.14: Influence of major modes of variability (see Annex IV) on regional extreme events relevant to assessing multi-hazard resilience. Ribbon colours define the driver from which they originate and their width is proportional to the correlation. Crossed lines represent where there is conflicting evidence for a correlation or where the driver is not directly related to the hazard and dots represent drivers that have both a positive and negative correlation with the hazard. Figure is copied from Steptoe et al. (2018) / CCBY4.0.

[END FIGURE ATLAS.14 HERE]

The main modes of variability influencing global and regional climate are comprehensively described in Annex IV. In the context of the assessment in the Atlas chapter, they are important because of their influence on the variability of temperature (Part A) and precipitation (Part B) in regions around the world. This is

ACCEPTED VERSION SUBJECT TO FINAL EDITS

quantified in Table Atlas.1: which lists the fraction of interannual variance in seasonal mean temperature and precipitation explained by variability in these modes. The table provides information on the influence of the teleconnections for selected seasons for the interannual to decadal modes and at an annual scale for the multi-decadal. The columns related to the interannual to decadal modes focus on the seasons where these connections are strongest but each mode of variability will often have influences in other seasons (for more details see Annex IV). The table shows that for many regions, seasonal temperature and precipitation is substantially modulated by these modes of variability, all regions feel some influence and variability in ocean basins often has influence in multiple remote regions.

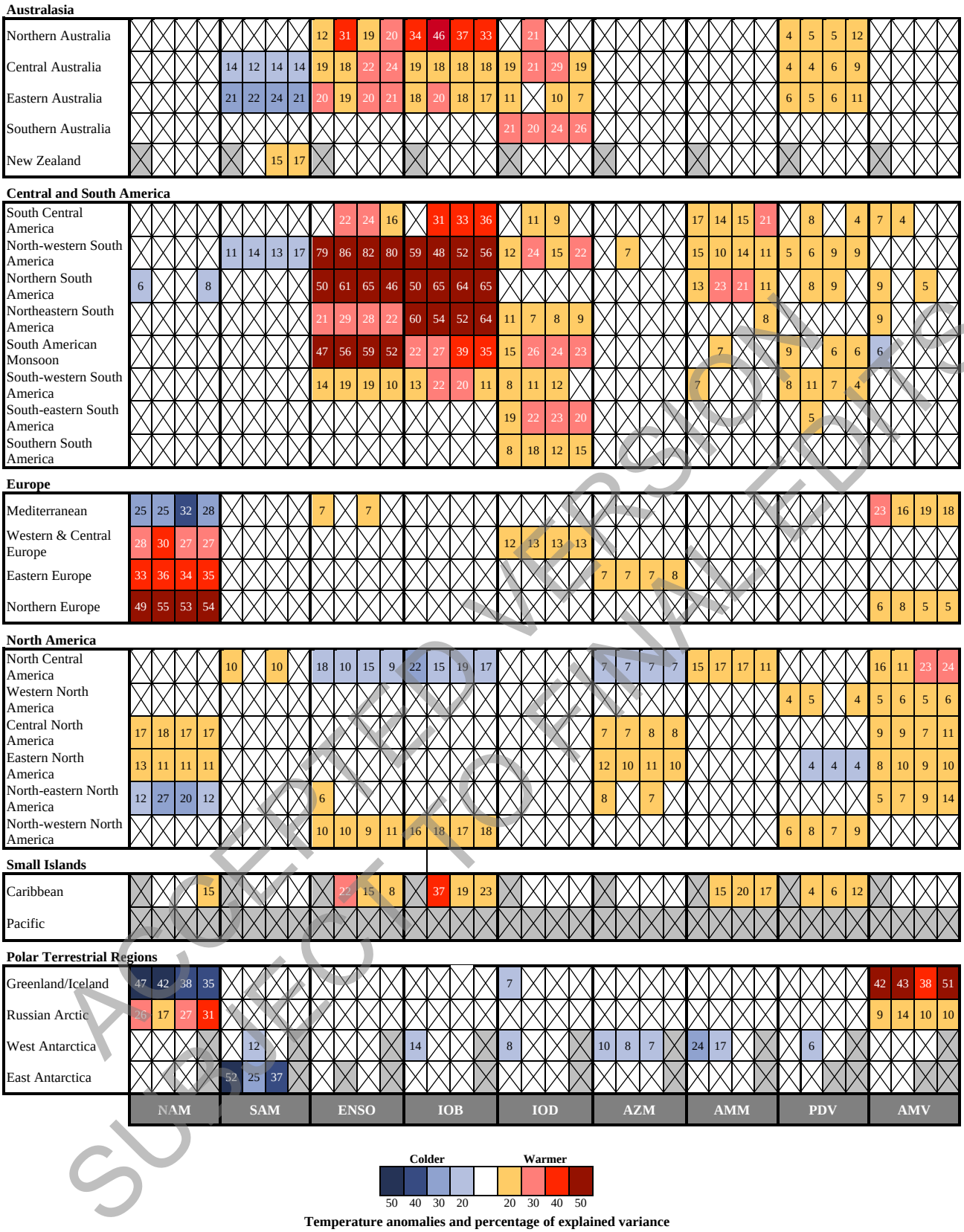
[START TABLE ATLAS.1 HERE]

Table Atlas.1: Regional mapping of the teleconnections associated with the main modes of variability (Annex IV). Fraction of surface air temperature and precipitation variance explained at interannual timescale by each mode of variability (columns) for each AR6 region (rows) based on the coefficient of determination R^2. Units are in percent and non-significant values based on t-statistics at the 95% level confidence are indicated by a cross. HadCRUT (HAD), GISTEMP (GIS), BerkeleyEarth (BE), and CRU-TS (CRU) observed datasets are used to assess the strength of the teleconnection for surface air temperature and GPCC and CRU-TS are used for precipitation. The colour scale given on label bars shown at the bottom quantifies the values of the explained variance and also stands for the sign of the teleconnection for the positive phase of the mode. All data are linearly detrended prior the computation of the regression. Note that results are sensitive to the choice of the detrending function (linear, loess filter, 3-order polynomial function) but by few percent at most, which is well below the range of the observational uncertainty assessed here through the use of several observational products.

2-meter temperature

	NAM				SAM				ENSO				IOB				IOD				AZM				AMM				PDV				AMV			
	DJF 1959-2019				DJF 1979-2019				DJF 1959-2019				MAM 1958-2019				SON 1958-2019				JJA 1958-2019				JJA 1958-2019				Annual 1900-2014				Annual 1900-2014			
Africa	HAD	GIS	BE	CRU	HAD	GIS	BE	CRU	HAD	GIS	BE	CRU	HAD	GIS	BE	CRU	HAD	GIS	BE	CRU	HAD	GIS	BE	CRU	HAD	GIS	BE	CRU	HAD	GIS	BE	CRU	HAD	GIS	BE	CRU
Sahara	60	56	60	57									9	15	14	16					8	10	12	9						7			13	5	15	14
Western Africa	24	22	26	28				11					43	50	45	40					18	29	20	15	8	13	8			8			5		4	9
Central Africa	16	22	17	19					14			13	50	41	56	58					13	16	9	12		11							15	13	13	13
North-eastern Africa	19	20	16	21									40	34	41	28														8		5	5		9	
South-eastern Africa				9					17	11	12	17	37	36	42	29									7	8	17	6		8				12	5	
West-southern Africa									43	45	56	53	17	27	32	32	7	8													4	4		5		5
East-southern Africa						12		13	72	71	75	73	32	40	36	32													4	3						
Madagascar									12	35	22	25	16	33	22	26	9	14	7	13						10	10	8						4	5	
Asia																																				
West Siberia	45	47	45	44																																
East Siberia	52	54	53	50												7														3	3	4				
Russian Far East	7			8					8	14	12	9	6	6	6																	7	4	5	
West Central Asia																																				
East Central Asia		7																																		
Tibetan Plateau																	19	11	15	14									8	5	4	5	6	8	5	17
East Asia		8								8		6																					13	12	14	14
South Asia	9	9	8	10						7			11	14	12	11									9	7		8					4	6		5
Southeast Asia									34	46	36	41	71	76	73	73									7					4		6			5	
Arabian Peninsula	30	33	29	35									12		11	7																	21	10	11	11

ACCEPTED VERSION SUBJECT TO FINAL EDITS



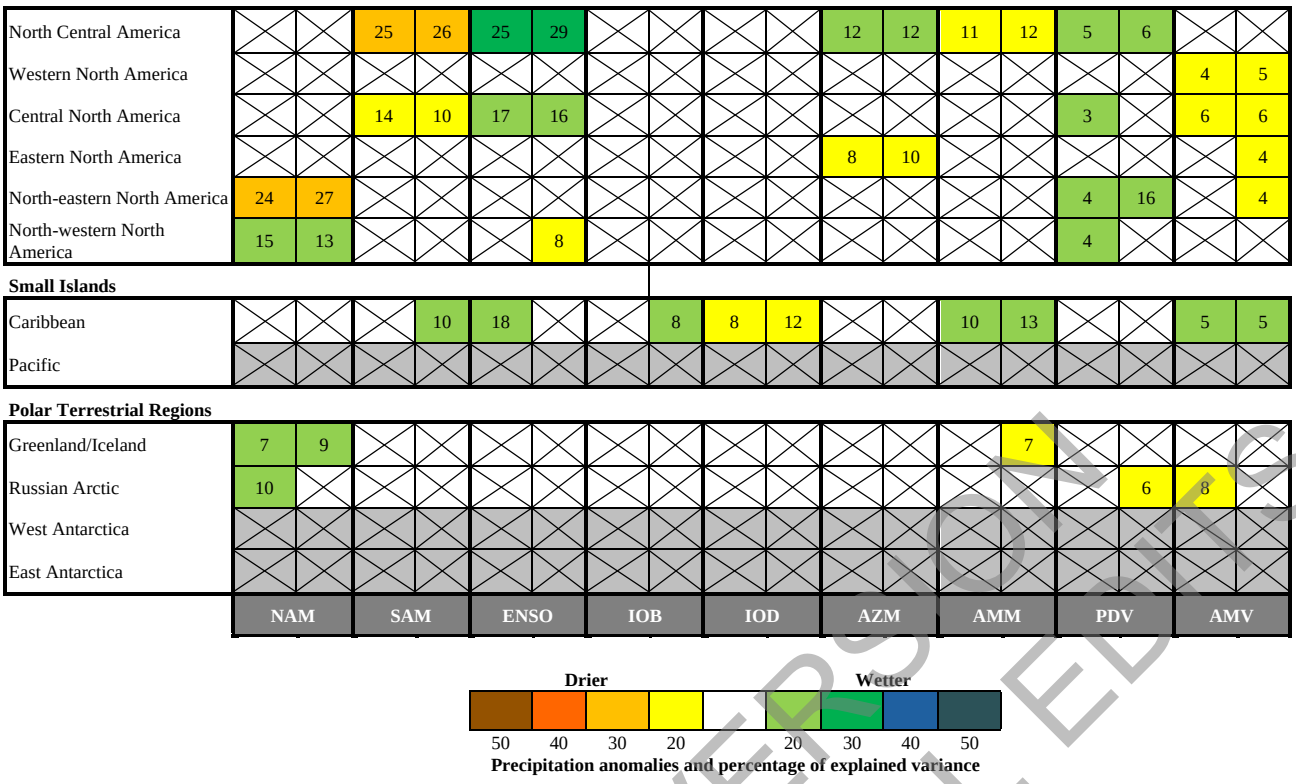
Temperature anomalies and percentage of explained variance

ACCEPTED VERSION SUBJECT TO WAIVER

Precipitation

	NAM		SAM		ENSO		IOB		IOD		AZM		AMM		PDV		AMV	
	DJF 1959-2019		DJF 1979-2019		DJF 1959-2019		MAM 1958-2019		SON 1958-2019		JJA 1958-2019		JJA 1958-2019		Annual 1900-2014		Annual 1900-2014	
Africa	GPCC	CRU	GPCC	CRU	GPCC	CRU	GPCC	CRU	GPCC	CRU	GPCC	CRU	GPCC	CRU	GPCC	CRU	GPCC	CRU
Sahara											20	17	14	10	7	10	25	24
Western Africa					17	13									4	7	19	27
Central Africa	**8**			10											9	11	13	9
North-eastern Africa		**7**			16	11			**32**	**31**								
South-eastern Africa					24	20			**59**	**55**					4			
West-southern Africa					30	22	17	14							11	13		
East-southern Africa					36	31	7	7							6	5		
Madagascar								7	12	8								
Asia																		
West Siberia					7						8	9					11	
East Siberia																		11
Russian Far East	**9**	**10**															5	
West Central Asia							13	17	27	14					4			
East Central Asia							**39**	**36**										
Tibetan Plateau	16	13							7		9	13			4	6		
East Asia					19	21	26	20			8	9			9	8		
South Asia									8									
Southeast Asia					31	31		6	51	45					9	14	8	6
Arabian Peninsula								24	20						5		7	
Australasia																		
Northern Australia					14	12			19	18			7		7			
Central Australia					13	11			19	21		7		7	5	4		
Eastern Australia					14	10				8	7				8	7		
Southern Australia					10	11			41	38		8			3			
New Zealand																		
Central and South America																		
South Central America					16				15	7							7	
North-western South America	7		16		11	23							16			8		
Northern South America					64	51					22	22	31	16	11	12		
North-eastern South America							20	17	12	11			7	8				
South American Monsoon									7					6				
South-western South America				10	16	12			19	12								
South-eastern South America					22	19	13	13	10		13	10			6	4	6	5
Southern South America			13	33						7							9	
Europe																		
Mediterranean	58	58																
Western & Central Europe	15	20							10	9					4		8	
Eastern Europe																		
Northern Europe	**35**	**29**																
North America																		

ACCEPTED VERSION SUBJECT TO FINAL EDITS



[END TABLE ATLAS.1 HERE]

Atlas.3.2 Global ocean

As with the atmosphere, there are several key ocean-related quantities which are relevant for understanding how climate change may impact human and ecological systems and/or key global indicators of change. These include ocean surface temperature and heat content, sea-surface height, sea ice cover and thickness, and certain chemical properties such as ocean acidity and oxygen concentration. For example, there is growing awareness of the threat presented by ocean acidification to ecosystem services and its socio-economic consequences are becoming increasingly apparent and quantifiable (Hurd et al., 2018) and SR1.5 (IPCC, 2018c) noted a significant impact of low levels of global warming on the state of the global oceanic ecosystems and food security. For instance, 70–90% of coral reefs are projected to decline at a warming level of 1.5°C, with larger losses at 2°C.

Thus, because of their importance to coastal populations and infrastructure and ocean ecosystems, the Interactive Atlas focuses on change in sea-surface temperature, sea level and pH. Figure Atlas.15:shows projected changes sea-surface temperature and sea level at the end of the century under SSP1-2.6 and SSP5-8.5 emissions, demonstrating the much larger changes seen with the higher-emission scenario. The projected changes in sea level show the significantly greater increases, of up to 1 m locally, under a high-emissions future. Regional details of these projected changes under a range of emission scenarios and time periods can be explored in the Interactive Atlas. An in-depth assessment of these changes is presented in Section 5.3 and Chapter 9.

[START FIGURE ATLAS.15 HERE]

Figure Atlas.15: Projected changes in sea surface temperature (top), sea level rise (bottom) for 2081–2100 under the SSP1-2.6 (left) and SSP5-8.5 (right) emission scenarios compared to a 1995–2014 baseline period from the CMIP6 ensemble. For sea surface temperature, diagonal lines indicate regions where 80% of the models do not agree on the sign of the projected changes. Further details on data

ACCEPTED VERSION SUBJECT TO FINAL EDITS

sources and processing are available in the chapter data table (Table Atlas.SM.15).

[END FIGURE ATLAS.15 HERE]

Atlas.4 Africa

The assessment in this section focuses on changes in average temperature and precipitation (rainfall and snow), including the most recent years of observations, updates to observed datasets, the consideration of recent studies using CMIP5 and those using CMIP6 and CORDEX simulations. Assessment of changes in extremes are in Chapter 11 (Table 11.4–11.6) and climatic impact-drivers in Chapter 12 (Table 12.1-12.12).

Atlas.4.1 Key features of the regional climate and findings from previous IPCC assessments

Atlas.4.1.1 Key features of the regional climate

Africa has many varied climates which can be categorized as dry regime in the Saharan region, tropical humid regime in West and East Africa except for parts of the Greater Horn of Africa (alpine) and the Sahel (semi-arid), and a dry/wet season regime in the northern and southern African region including the Namibian desert; each climate region has its local variations resulting in very high spatial and temporal variations (Peel et al., 2007). Based on the varied climates, nine subregions are defined for Africa (see Figure Atlas.16:) the Mediterranean region (MED) including North Africa, Sahara including parts of the Sahel (SAH), West Africa (WAF), Central Africa (CAF), North Eastern Africa (NEAF), South Eastern Africa (SEAF), West Southern Africa (WSAF), East Southern Africa (ESAF) and Madagascar (MDG).

The climatic features that characterize the intra-seasonal and inter-annual variability of Africa are mainly the Madden-Julian Oscillation (MJO) which is confined to the deep tropics during boreal winter, Pacific Decadal Variability (PDV), and the shift of the Atlantic Inter Tropical Convergence Zone in response to changes in the meridional SST gradient. A positive phase of the PDV weakens African monsoons (Meehl and Hu, 2006)(Figure AIV.8d) and MJO phase 4 suppresses convection over the equatorial Africa (Figure AIV.10a) (see Annex IV). Other features influence specific subregions. For instance, El Niño events increase precipitation in eastern Africa and decreases precipitation in southern Africa. Over southern Africa there is a strong link between ENSO and droughts (Meque and Abiodun, 2015). The positive phase of the IOD increases rainfall in eastern tropical Africa in boreal autumn to early winter (Figure AIV.5d), while the negative phase induces the reduction in rainfall. West African monsoon is influenced by Atlantic Zonal Mode (AZM) with decreased rainfall over the Sahel and increased rainfall over Guinea (Losada et al., 2010). Positive Atlantic Multidecadal Variability (AMV) influences positive anomalies all year round over a broad Mediterranean region, including North Africa.

Atlas.4.1.2 Findings from previous IPCC assessments

The most recent IPCC reports, AR5 and SR1.5 (Christensen et al., 2013; Hoegh-Guldberg et al., 2018), state that over most parts of Africa, minimum temperatures have warmed more rapidly than maximum temperatures during the last 50 to 100 years (*medium confidence*). In the same period minimum and maximum temperatures have increased by more than 0.5°C relative to 1850-1900 (*high confidence*). While the quality of ground observational temperature measurements tends to be high compared to that of measurements for other climate variables, Africa remains an under-represented region as reported in SR1.5 (Hoegh-Guldberg et al., 2018; IPCC, 2018c). Based on the Coupled Model Intercomparison Project Phase 5 (CMIP5) ensemble and reported in IPCC AR5 and SR1.5, surface air temperatures in Africa are projected to rise faster than the global average increase and *likely* to increase by more than 2°C and up to 6°C by the end of the century relative to the late 20th century if global warming reaches 2°C (Bindoff et al., 2013; Niang et al., 2014; Hoegh-Guldberg et al., 2018). The higher temperature magnitudes are projected during boreal summer. Southern Africa is *likely* to exceed the global mean land surface temperature increase in all seasons

ACCEPTED VERSION SUBJECT TO FINAL EDITS

by the end of the century. Temperature projections for East Africa indicate considerable warming under RCP8.5 where average warming across all models is approximately 4°C by the end of the century. According to SROCC, eastern Africa like other regions with smaller glaciers is projected to lose more than 80% of its glaciers by 2100 under RCP8.5 (*medium confidence*) (Hock et al., 2019b).

West Africa has also experienced an overall reduction of rainfall over the 20th century, with a recovery towards the last 20 years of the century (Christensen et al., 2013). Over the last three decades rainfall has decreased over East Africa especially between March and May/June. Projected rainfall changes over Africa in the mid and late 21st century is uncertain. In regions of high or complex topography such as the Ethiopian Highlands, downscaled projections indicate *likely* increases in rainfall and extreme rainfall by the end of the 21st century. However, Northern Africa and the south-western parts of South Africa are *likely* to have a reduction in precipitation.

The consequence of increased temperature and evapotranspiration, and decreased precipitation amount, in interaction with climate variability and human activities, have contributed to desertification in dryland areas in Sub-Saharan Africa (*medium confidence*) as reported in SRCCL (Mirzabaev et al., 2019).

Atlas.4.2 Assessment and synthesis of observations, trends and attribution

Figure Atlas.11: shows observed trends in annual mean surface temperature and indicates it has been rising rapidly over Africa over 1960–2015 and with significant increases in all regions of 0.1°C–0.2°C per decade and higher over some northern, eastern and south-western regions (*high confidence*) (see also Interactive Atlas). This is confirmed by an independent analysis performed for a longer period (1961–2018) over areas where long-term homogeneous temperature time-series are available (Engelbrecht et al., 2015). More specifically over the Horn of East Africa, the long-term mean annual temperature change between 1930 and 2014 showed two distinct but contrary trends: significant decreases between 1930 and 1969 and increases from 1970 to 2014 (Ghebrezgabher et al., 2016). North Africa has an overall warming in observed seasonal temperature (Barkhordarian et al., 2012; Lelieveld et al., 2016) with positive trends in annual minimum and maximum temperatures (Vizy and Cook, 2012). Temperatures over West Africa have increased over the last 50 years (Mouhamed et al., 2013; Niang et al., 2014) with a spatially variable warming reaching 0.5°C per decade from 1983 to 2010 (Sylla et al., 2016). West Africa has also experienced a decrease in the number of cool nights as well as more frequent warm days and warm spells (Mouhamed et al., 2013; Ringard et al., 2016). Similarly, East Africa has experienced a significant increase in temperature since the beginning of the early 1980s (Anyah and Qiu, 2012) with an increase in seasonal mean temperature. Over South Africa, positive trends were found in the annual mean, maximum and minimum temperatures for 1960–2003 in all seasons, except for the central interior (Kruger and Shongwe, 2004; Zhou et al., 2010; Collins, 2011; Kruger and Sekele, 2013; MacKellar et al., 2014), where minimum temperatures have decreased significantly (MacKellar et al., 2014). Inland southern Africa, minimum temperatures have increased more rapidly than maximum temperatures (New et al., 2006).

Most areas lack enough observational data to draw conclusions about trends in annual precipitation over the past century. In addition, many regions of Africa have discrepancies between different observed precipitation datasets (Sylla et al., 2013; Panitz et al., 2014). A statistically significant (95% confidence level) decrease in rainfall and the number of rainy days is reported in autumn over the east, central and north-eastern parts of South Africa in spring and summer during 1960–2010 (MacKellar et al., 2014; Kruger and Nxumalo, 2017). Central Africa has experienced a significant decrease in total precipitation which is likely associated with a significant decrease of the length of the maximum number of consecutive wet days (Aguilar et al., 2009). Furthermore, rainfall decreased significantly in the Horn of Africa (Tierney et al., 2015) with the largest reductions during the long rains season March to May (Lyon and Dewitt, 2012; Viste et al., 2013; Rowell et al., 2015). Over mountainous areas significant increases are found in the number of rain days around the southern Drakensberg in spring and summer during the period 1960–2010 (MacKellar et al., 2014). Similarly, southern West Africa is observed to have had more intense rainfall from 1950 to 2014 during the second rainy season of September to November (Nkrumah et al., 2019). The Sahel region also had more intense rainfall throughout the rainy season (Panthou et al., 2014, 2018b, 2018a; Sanogo et al., 2015; Gaetani

ACCEPTED VERSION SUBJECT TO FINAL EDITS

et al., 2017; Taylor et al., 2017; Biasutti, 2019) during the period 1980–2010. Southern African rainfall shows a significant downtrend of –0.013 mm day^{-1} year^{-1} in recent decades and –0.003 mm day^{-1} year^{-1} for longer periods during 1900–2010 (Jury, 2013) (*low confidence*).

Temperature increases over Africa in the 20th century can be attributed to the strong evidence of a continent-wide anthropogenic signal in the warming (Hoerling et al., 2006; Min and Hense, 2007; Stott et al., 2010, 2011; Niang et al., 2014)(Figure 3.8). More specifically over West Africa, the clear emergence of temperature change (Figure Atlas.11:) is due to the relatively small natural climate variability in the region which generates narrow climate bounds that can be easily surpassed by relatively small climate changes (Niang et al., 2014). Warming over North Africa is largely due to anthropogenic climate forcing (Knippertz et al., 2003; Barkhordarian et al., 2012; Diffenbaugh et al., 2017).

The drying observed over the Sahel in the 1960s to 1970s has been attributed to warming of the South Atlantic SST and southern African drying as a response to Indian Ocean warming (Hoerling et al., 2006; Dai, 2011). Enhanced rainfall intensity since the mid-1980s over the Sahel (Maidment et al., 2015; Sanogo et al., 2015) is associated with increased greenhouse gases suggesting an anthropogenic influence (Biasutti, 2019) (*medium confidence*). In the last decade, the changes in the timing of onset and cessation of rainfall over Africa have been linked to changes in the progression of the tropical rainband and the Saharan Heat Low (Dunning et al., 2018; Wainwright et al., 2019). Moreover, later onset and earlier cessation of Eastern Africa rainfall is associated with a delayed and then faster movement of the tropical rainband northwards during the boreal spring and northward shift of the Saharan Heat Low (Wainwright et al., 2019) driven by anthropogenic carbon emissions and changing aerosol forcings (*medium confidence*). Over East Africa, the drying trend is associated with an anthropogenic-forced relatively rapid warming of Indian Ocean SSTs (Williams and Funk, 2011; Hoell et al., 2017); a shift to warmer SSTs over the western tropical Pacific and cooler SSTs over the central and eastern tropical Pacific (Lyon and Dewitt, 2012); multidecadal variability of SSTs in the tropical Pacific, with cooling in the east and warming in the west (Lyon, 2014); and the strengthening of the 200-mb easterlies (Liebmann et al., 2017). However, decadal natural variability from SST variations over the Pacific Ocean has also been associated with the drying trend of the East Africa (Wang et al., 2014; Hoell et al., 2017) with an anthropogenic-forced rapid warming of Indian Ocean SSTs (*medium confidence*).

Atlas.4.3 Assessment of model performance

Model development has advanced in the world, but Africa still lags as a focus and in its contribution (James et al., 2018). None of the current generation of general circulation models (GCMs) was developed in Africa (Watterson et al., 2014), and the relevant processes in the continent have not been the priority for model development but treated in a one-size-fit-all approach (James et al., 2018) except for a few studies that focused on convective-permitting climate projections (Stratton et al., 2018; Kendon et al., 2019). However, there are growing efforts to boost African climate science by running and evaluating climate models over Africa (Endris et al., 2013; Kalognomou et al., 2013; Gbobaniyi et al., 2014; Engelbrecht et al., 2015; Klutse et al., 2016; Gibba et al., 2019).

The CMIP project previously did not result in improved performance for Africa (Flato et al., 2013; Rowell, 2013; Whittleston et al., 2017) and culling ensembles based on existing metrics for Africa fails to reduce the range of uncertainty in precipitation projections (Roehrig et al., 2013; Yang et al., 2015; Rowell et al., 2016) but biases over Africa are lower in CMIP6 compared to CMIP5 (Almazroui et al., 2020b). Nonetheless, the CMIP5 ensemble has been evaluated over Africa to advance its application for climate research (Biasutti, 2013; Rowell, 2013; Dike et al., 2015; McSweeney and Jones, 2016; Onyutha et al., 2016; Wainwright et al., 2019) as has, more recently, the CMIP6 ensemble (Almazroui et al., 2020b).

Coordinated Regional Downscaling Experiment (CORDEX) regional climate models have been widely evaluated over Africa. They capture the occurrence of the West African Monsoon jump and the timing and amplitude of mean annual cycle of precipitation and temperature over the homogeneous subregions of West Africa (Gbobaniyi et al., 2014), simulate eastern Africa rainfall adequately (Endris et al., 2013) and over

ACCEPTED VERSION SUBJECT TO FINAL EDITS

Southern Africa capture the observed climatological spatial patterns of extreme precipitation (Pinto et al., 2016). They simulate also the phasing and amplitude of monthly rainfall evolution and the spatial progression of the wet season onset well over Southern Africa (Shongwe et al., 2015). However, discrepancies and biases in present-day rainfall are reported over Uganda from the RCM-simulated rainfall compared to three gridded observational datasets (Kisembe et al., 2018). Specifically, they reported that the CORDEX models underestimate annual rainfall of Uganda and struggle to reproduce the variability of the long and short rainy seasons.

Atlas.4.4 Assessment and synthesis of projections

Research over Africa has improved since AR5 and though SR1.5 (de Coninck et al., 2018) has synthesised new information for the continent, there is still not enough literature on specific areas for assessment. CMIP5 and CMIP6 projections (Figure Atlas.16:) are for continued warming, with median projected regional warming for 2080–2100 compared to 1995–2014 of between 1°C and 2°C under SSP1-2.6/RCP2.6 emissions and exceeding 4°C and in some regions 5°C under SSP5-8.5/RCP8.5 emissions. The central interior of Southern and Northern Africa are *likely* to warm faster than equatorial and tropical regions (Interactive Atlas). Projections from CMIP5 show that East Africa is *likely* to warm by 1.7°C–2.8 °C and 2.2°C–5.4°C under the RCP4.5 and RCP8.5 scenarios respectively in the period 2071–2100 relative to 1961–1990 (Ongoma et al., 2018). Over southern Africa, areas in the south-western region of the subcontinent, covering South Africa and parts of Namibia and Botswana, are projected to experience the largest increase in temperature, which are expected to be greater than the global mean warming (Maúre et al., 2018). A large ensemble of CORDEX Africa simulations have been used to project the impact of 1.5°C and 2°C global warming levels (GWLs) (Klutse et al., 2018; Lennard et al., 2018; Maúre et al., 2018; Mba et al., 2018; Nikulin et al., 2018; Osima et al., 2018). While a few studies addressed the whole African continent (Lennard et al., 2018; Nikulin et al., 2018), some focused on specific regions of Africa (Diedhiou et al., 2018; Klutse et al., 2018; Kumi and Abiodun, 2018; Maúre et al., 2018; Mba et al., 2018). CORDEX simulations project robust warming over Africa in excess of the global mean (Lennard et al., 2018; Nikulin et al., 2018) and over West Africa the magnitude of regional warming reaches the 2080–2100 global warming level one to two decades earlier (Mora et al., 2013; Niang et al., 2014; Sylla et al., 2016; Klutse et al., 2018). Temperature increases projected under RCP8.5 over Sudan and northern Ethiopia implying that the Greater Horn of Africa would warm faster than the global mean relative to 1971–2000 (Osima et al., 2018). Over North Africa, summer mean temperatures from CORDEX, CMIP5 (RCP8.5) and CMIP6 (SSP5-8.5) are projected to increase beyond 6.0°C by the end of the century with respect to the period 1970–2000 (Schilling et al., 2012; Ozturk et al., 2018; Almazroui et al., 2020b), see also the Interactive Atlas. Note that results for the CORDEX-AFR over the Mediterranean (MED) are consistent with those reported from the CORDEX-EUR dataset (Figure Atlas.24:; Section Atlas.1.3), in agreement with Legasa et al. (2020).

[START FIGURE ATLAS.16 HERE]

Figure Atlas.16: Regional mean changes in annual mean surface air temperature and precipitation relative to the 1995–2014 baseline for the reference regions in Africa (warming since the 1850–1900 pre-industrial baseline is also provided as an offset). Bar plots in the left panel of each region triplet show the median (dots) and 10th–90th percentile range (bars) across each model ensemble for annual mean temperature changes for four datasets (CMIP5 in intermediate colours; subset of CMIP5 used to drive CORDEX in light colours; CORDEX overlying the CMIP5 subset with dashed bars; and CMIP6 in solid colours); the first six groups of bars represent the regional warming over two time periods (near-term 2021–2040 and long-term 2081–2100) for three scenarios (SSP1-2.6/RCP2.6, SSP2-4.5/RCP4.5, and SSP5-8.5/RCP8.5), and the remaining bars correspond to four global warming levels (GWL: 1.5°C, 2°C, 3°C, and 4°C). The scatter diagrams of temperature against precipitation changes display the median (dots) and 10th–90th percentile ranges for the above four warming levels for December-January-February-March (DJFM; middle panel) and June-July-August-September (JJAS; right panel), respectively; for the CMIP5 subset only the percentile range of temperature is shown, and only for 3°C and 4°C GWLs. Changes are absolute for temperature (in °C) and relative (as %) for precipitation. See Section Atlas.1.3 for more details on reference regions (Iturbide et al., 2020) and

ACCEPTED VERSION SUBJECT TO FINAL EDITS

Section Atlas.1.4 for details on model data selection and processing. The script used to generate this figure is available online (Iturbide et al., 2021) and similar results can be generated in the Interactive Atlas for flexibly defined seasonal period. Further details on data sources and processing are available in the chapter data table (Table Atlas.SM.15).

[END FIGURE ATLAS.16 HERE]

Projected rainfall changes over Africa in the mid and late 21st century are uncertain in many regions, highly variable spatially and with differing levels of model agreements (Figure Atlas.16:) though with robust projections of decreases in MED and WSAF and increases in NEAF and SEAF by 2080–2100 under high emissions (Interactive Atlas). Some uncertainties are reported over parts of Africa from CORDEX projections (Dosio and Panitz, 2016; Endris et al., 2016; Klutse et al., 2018). For example, large uncertainties are associated with projections at 1.5°C and 2°C of global warming over Central Africa (Mba et al., 2018) and over the Sahel (Gbobaniyi et al., 2014; Sylla et al., 2016). Over southern Africa, enhanced warming is projected to result in a reduction in mean rainfall across the region (Maúre et al., 2018) and in particular over the Limpopo Basin and smaller areas of the Zambezi Basin in Zambia, and also parts of Western Cape, South Africa, under a global warming of 2°C. The projections of reduced precipitation in summer rainfall regions of southern Africa are associated with delayed wet season onset in spring (Dunning et al., 2018) due to a northward shift and delayed breakdown of the Congo Air Boundary (Howard and Washington, 2020). However, projected rainfall intensity over southern Africa is *likely* to increase and be magnified under RCP8.5 compared with RCP4.5 for the period 2069–2098 relative to the reference period (1976–2005) (Pinto et al., 2018). For West Africa, rainfall projection is uncertain because of the contrasting signals from models (Dosio et al., 2019). Nonetheless, West Africa river basin-scale irrigation potential would decline under 2°C of global warming even for areas where water availability increases (Sylla et al., 2018). The western and eastern Sahel are projected as hotspots for delayed rainfall onset dates of about four days and six days causing reduced length of rainy season in the 1.5°C to 2°C warmer climates under RCP4.5 and RCP8.5 scenarios (Kumi and Abiodun, 2018). Projected delay in rainfall cessation dates and a longer length of rainy season over the western part of the Guinea coast is *likely* under the same scenarios (Sellami et al., 2016; Kumi and Abiodun, 2018)(Figure Atlas.16:). There is a tendency towards an increase in annual mean precipitation over central Sahel and eastern Africa (Figure Atlas.16, (Nikulin et al., 2018) especially over the Ethiopian highlands with up to 0.5 mm day^{-1} (Osima et al., 2018).

Atlas.4.5 Summary

The rate of surface temperature increase has generally been more rapid in Africa than the global average and by at least 0.1°C–0.2°C during 1960–2015 (*high confidence*). Minimum temperatures have increased more rapidly than maximum temperatures over inland southern Africa (*medium confidence*). Since 1970, mean temperature over East Africa has shown an increasing trend but showed a decreasing trend in the previous 40 years (*medium confidence*).

The Horn of Africa has experienced significantly decreased rainfall during the long rain season from March to May (*high confidence*) and drying trends in this and other parts of Africa are attributable to oceanic influences (*high confidence*), resulting from both internal variability and anthropogenic causes. Drying over the Sahel in the last century was attributed to an increase in the South Atlantic SST and more recently over southern African as a response to anthropogenic-forced Indian Ocean warming. Drying over East Africa is associated with decadal natural variability in SSTs over the Pacific Ocean. The enhanced rainfall intensity over the Sahel in the last two decades is associated with increased greenhouse gases indicating an anthropogenic influence (*medium confidence*).

Relative to the late 20th century, annual mean temperature over Africa is projected to rise faster than the global average (*very high confidence*) with the increase *likely* to exceed 4°C by the end of the century under RCP8.5 emissions. The central interior of Southern and Northern Africa are *likely* to warm faster than equatorial and tropical regions (*high confidence*).

ACCEPTED VERSION SUBJECT TO FINAL EDITS

There are contrasting signals in the projections of rainfall over some parts of Africa until the end of the 21st century (*high confidence*) though changes in any given region are generally projected with *medium confidence.* In regions of high or complex topography such as the Ethiopian Highlands, downscaled projections indicate increases in rainfall by the end of the 21st century. However, Northern Africa and the south-western parts of South Africa are *likely* to have a reduction in precipitation under higher warming levels (*high confidence*). Over West Africa, rainfall is projected to decrease in the Western Sahel subregion (*medium confidence*) and increase in the central Sahel subregion (*low confidence*) and along the Guinea Coast subregion (*medium confidence*). Rainfall amounts are projected to reduce over the western part of East Africa, but to increase in the eastern part of the region (*medium confidence*). Southern Africa is projected to have a reduction in annual mean rainfall but increases in rainfall intensity by 2100 (*medium confidence*).

Atlas.5 Asia

The assessment in this section focuses on changes in average temperature and precipitation (rainfall and snow), including the most recent years of observations, updates to observed datasets, the consideration of recent studies using CMIP5 and those using CMIP6 and CORDEX simulations. Assessment of changes in extremes are in Chapter 11 (Table 11.7–11.9) and climatic impact-drivers in Chapter 12 (Table 12.4). It covers most Asian territories of the region (Figure Atlas.17:) with the exception of the Russian Arctic, RAR, which is assessed as part of the Arctic in section 11.2. These include West and East Siberia (WSB, ESB) and the Russian Far East (RFE) in the north; West and East Central Asia (WCA, ECA), the Tibetan Plateau (TIB) and East Asia (EAS); and the Arabian Peninsula (ARP), South and Southeast Asia (SAS, SEA) in the south. Figure Atlas.17: supports the assessment of regional mean changes in annual mean surface air temperature and precipitation over Asia. Due to the high climatological and geographical heterogeneity of Asia, the assessment is performed over five sub-continental areas: East Asia (EAS+ECA), North Asia (WSB+ESB+RFE), South Asia (SAS+TIB), Southeast Asia (SEA) and Southwest Asia (ARP+WCA).

[START FIGURE ATLAS.17 HERE]

Figure Atlas.17: Regional mean changes in annual mean surface air temperature and precipitation relative to the 1995–2014 baseline for the reference regions in Asia (warming since the 1850–1900 pre-industrial baseline is also provided as an offset). Bar plots in the left panel of each region triplet show the median (dots) and 10th–90th percentile range (bars) across each model ensemble for annual mean temperature changes for four datasets (CMIP5 in intermediate colours; subset of CMIP5 used to drive CORDEX in light colours; CORDEX overlying the CMIP5 subset with dashed bars; and CMIP6 in solid colours); the first six groups of bars represent the regional warming over two time periods (near-term 2021–2040 and long-term 2081–2100) for three scenarios (SSP1-2.6/RCP2.6, SSP2-4.5/RCP4.5, and SSP5-8.5/RCP8.5), and the remaining bars correspond to four global warming levels (GWL: 1.5°C, 2°C, 3°C, and 4°C). The scatter diagrams of temperature against precipitation changes display the median (dots) and 10th–90th percentile ranges for the above four warming levels for December-January-February (DJF; middle panel) and June-July-August (JJA; right panel), respectively; for the CMIP5 subset only the percentile range of temperature is shown, and only for 3°C and 4°C GWLs. Changes are absolute for temperature (in °C) and relative (as %) for precipitation. See Section Atlas.1.3 for more details on reference regions (Iturbide et al., 2020) and Section Atlas.1.4 for details on model data selection and processing. Further details on data sources and processing are available in the chapter data table (Table Atlas.SM.15).

[END FIGURE ATLAS.17 HERE]

ACCEPTED VERSION SUBJECT TO FINAL EDITS

Atlas.5.1 East Asia

Atlas.5.1.1 Key features of the regional climate and findings from previous IPCC assessments

Atlas.5.1.1.1 Key features of the regional climate

The climatic regions defined for East Asia include central and eastern China, Japan and Korea Peninsula (regions ECA and EAS in Figure Atlas.17:). East Asia is significantly influenced by monsoon systems (see Section 8.3.2.4.2). The seasonal advance or retreat of the East Asian summer monsoon (EASM) rain band is crucial to local climate. The East Asian winter monsoon (EAWM) has significant influence on the weather and climate over East Asia and plays an important role in regulating winter temperatures including strong cold events and snowstorms (Wang and Chen, 2014; Wang and Lu, 2016). The East Asian monsoons exhibit considerable variability on a wide range of time scales, including notable interannual variabilities that includes an effect of the El Niño Southern Oscillation (ENSO) (Wang et al., 2000) and the Indian Ocean Dipole (IOD) (Takaya et al., 2020), and significant inter-decadal variabilities in the 20th century resulted from the effect of Pacific Decadal Variability (PDV) (Zhou et al., 2009), see also Annex IV and Table Atlas.1:. The thermal conditions of both the Tibetan Plateau and related ocean regions play key roles in modulating the intensity of the monsoon circulation. The East Asian monsoons are mainly driven by land-sea thermal contrast and, thus, are deeply affected by global climate change (Ding et al., 2014; Gong et al., 2018).

Atlas.5.1.1.2 Findings from previous IPCC assessments

The findings of the IPCC AR5 (Christensen et al., 2013) stated that the EASM and EAWM circulations have experienced an inter-decadal scale weakening since the 1970s, leading to a warmer climate in winter and enhanced mean precipitation along the Yangtze River Valley (30°N) but deficient mean precipitation in North China in summer. Since the middle of the 20th century, it is *likely* that there has been an increasing trend in winter temperatures across much of Asia (Christensen et al., 2013). The numbers of cold days and nights have decreased and the numbers of warm days and nights have increased over Asia (Hartmann et al., 2013). It is *likely* that there are decreasing numbers of snowfall events where increased winter temperatures have been observed (Hartmann et al., 2013). The SRCCL reports a land-use change induced cooling as large as –1.5°C in eastern China between 1871 and 2007 (Hartmann et al., 2013). The summer rainfall amount over East Asia shows no clear trend during the 20th century.

The IPCC AR5 (Christensen et al., 2013) reports a significant increase in mean temperatures in southeastern China, associated with a decrease in the number of frost days under the SRES A2 scenario. The CMIP5 model projections indicate an increase of temperature in both boreal winter and summer over East Asia for RCP4.5. Based on CMIP5 model projections, there is *medium confidence* in an intensified EASM and increased summer precipitation over East Asia. More than 85% of CMIP5 models show an increase in mean precipitation of the EASM, while more than 95% of models project an increase in heavy precipitation events (Christensen et al., 2013). SROCC states that future projections of annual precipitation indicate increases of the order of 5% to 20% over the 21st century in many mountain regions, including the Himalaya and East Asia (Hock et al., 2019b). SR1.5 reports that statistically significant changes in heavy precipitation between 1.5°C and 2°C of global warming are found in East Asia (Hoegh-Guldberg et al., 2018).

Atlas.5.1.2 Assessment and synthesis of observations, trends and attribution

Summer (June–August) mean temperature in Eastern China has increased by 0.82°C since reliable observations were established in the 1950s (Sun et al., 2014). Based on historical meteorological observations, the best estimate of the linear trend of annual mean surface air temperature (SAT) for China with 95% uncertainty ranges is 0.38 ± 0.05°C per decade for 1979–2015 (Li et al., 2017). From 1960 to 2010, the increasing trend of temperature was about 0.34°C per decade in the arid region of northwest China, higher than the average over China (Li et al., 2012a; Xu et al., 2015). Over South Korea, warming is 1.4–2.6 times larger than global trends. The increase is 1.90°C during 1912–2014 and 0.99°C during 1973–2014 (Park et al., 2017) with a 25–45% urbanization contribution. The annual temperature increased in large cities

ACCEPTED VERSION SUBJECT TO FINAL EDITS

at a rate of 0.29 ± 0.08°C per decade compared with 0.11 ± 0.08°C per decade in other stations in South Korea from 1960 to 2010 (Kim et al., 2016a). A relatively high increase in annual mean temperature at the rate of 3.0°C per century was detected in the Tokyo metropolitan area for the period 1901–2015 (Matsumoto et al., 2017). Trends of annual temperature for the period of 1960–2015 are shown in Figure Atlas.11:. Most areas of East Asia have significant warming trends exceeding 0.1°C per decade, and the strongest warming (0.3°C–0.4°C per decade) occurs in northern China.

Observational studies indicated significant decadal variations in the EAWM (Wang and Lu, 2016; He et al., 2017). It weakened significantly around the late 1980s, being relatively strong during 1976–1987 and weaker during 1988–2001. The EAWM has recovered in intensity after 2004 and caused frequent and prevalent severe cold spells, as well as a number of unusually harsh cold winters in many parts of East Asia during the period 2004–2012 (Wang and Chen, 2014; Kug et al., 2015; Ge et al., 2016; Gong et al., 2018). Negative zonal mean winter SAT anomalies were observed over the whole of East Asia from 1980 to 1988, with positive anomalies observed over high and low latitudes from 1988 to 2010 (Miao and Wang, 2020).

Precipitation trends over East Asia show considerable regional differences (*medium confidence*). Mean precipitation has shown negligible sensitivity to the warming trend with consequently limited overall trends in China though summer rainfall daily frequency and intensity show respectively decreasing and increasing trends from 1961 to 2014 (Zhou and Wang, 2017). The summer precipitation trends over eastern China display a dipole pattern, characterized by positive anomalies in the central-eastern China along the Yangtze River Valley and negative anomalies in the north China since the 1950s (Section 8.3.2.4.2). This pattern has changed with the enhanced rainfall in the Huaihe River Valley and decreased in the regions south of the middle and lower reaches of the Yangtze River Valley since the 2000s (Liu et al., 2012; Zhao et al., 2015). The climate in northwest China changed from 'warm-dry' to 'warm-wet' condition in the mid-1980s (Peng and Zhou, 2017; Wang et al., 2020), with an increases rate of annual precipitation of about 3.7% per decade from 1961 to 2015 (Wu et al., 2019a) and 11.2 mm per decade between 1960 and 2011 in northern Xinjiang (Xu et al., 2015). Mean rainfall and the number of rainy days during the Meiyu-Baiu-Changma period from June to September have increased during 1973–2015 in Korea (Lee et al., 2017). The precipitation trend has caused a large increase in summer precipitation at a rate of 40.6 ± 4.3 mm per decade, resulting in an increase of annual precipitation of 27.7 ± 5.5 mm per decade in South Korea from 1960 to 2010 (Kim et al., 2016a). Precipitation amounts exhibited a slight decrease at both the annual and seasonal scales in Japan for the period 1901–2012 (Duan et al., 2015).

Agriculture intensification through oasis expansion in Xinjiang region has increased summer precipitation in the Tianshan mountains (Zhang et al., 2009, 2019b; Deng et al., 2015; Guo and Li, 2015; Yao et al., 2016; Xu et al., 2018; Cai et al., 2019) (*high confidence* from *medium evidence* with *high agreement)*. However, there is *very low confidence* of the effect of oasis expansion on the temperature warming trend (Han and Yang, 2013; Li et al., 2013; Yuan et al., 2017).

In the context of climate warming, intense snowfalls have hit China frequently in recent winters and have caused severe damages to the sustainability of the society (Sun et al., 2019). Observations generally show a decrease in the frequency and an increase in the mean intensity of snowfalls in north-western, north-eastern and south-eastern China and the eastern Tibetan Plateau since the 1960s (Zhou et al., 2018), but the results may depend on the objective criteria for identifying wintertime snowfall (Luo et al., 2020a).

Atlas.5.1.3 Assessment of model performance

Current climate models perform poorly in simulating the mean precipitation in East Asia, including the phase of the northward progression of the seasonal rain band (Zhang et al., 2018b). Although there has been an improvement in the simulation of mean states, interannual variability, and past climate changes in the progression from CMIP3 to CMIP5, some previously documented biases (such as the ridge position of the western North Pacific Subtropical High and the associated rainfall bias) are still evident in CMIP5 models (Sperber et al., 2013; Zhou et al., 2017). Most models capture the main characteristics of the winter mean circulation over East Asia reasonably well, but they still suffer from difficulty in predicting the interannual

ACCEPTED VERSION SUBJECT TO FINAL EDITS

variability of the EAWM (Shin and Moon, 2018). Models have improved from CMIP5 to CMIP6 for climatological temperature and EAWM (Jiang et al., 2020a). Some CMIP6 models also show improvements in simulating the annual mean and interannual variation of precipitation (Sellar et al., 2019; Tatebe et al., 2019; Wu et al., 2019b). The performance of models is sensitive to cumulus convection schemes and horizontal resolution (Haarsma et al., 2016; Wu et al., 2017; Kusunoki, 2018b). High-resolution atmospheric general circulation models (AGCM) successfully reproduce the intensity and the spatial pattern of the EASM rainfall (Li et al., 2015; Yao et al., 2017; Ito et al., 2020a) and improve the simulation of the diurnal cycle of precipitation rates and the probability density distributions of daily precipitation over Korea, Japan and northern China (Lin et al., 2019), but increasing horizontal resolution (at the typical scales used in GCMs) is not always a panacea for solving model biases (Roberts et al., 2018).

Recent studies using CORDEX-EA models with resolution about 12–25 km showed that the RCMs produce relatively more detailed regional features of the temperature distribution compared with the driving GCMs (Tang et al., 2016). Over China, RCMs provide more spatial details and in general reduce the biases of their driving GCMs, in particular in DJF (December–January–February) and over areas with complex topography (Wu and Gao, 2020). However, RCMs also show biases in simulating East Asian precipitation and its variability (Park et al., 2016; Zhou et al., 2016; Zou and Zhou, 2016), and do not always show added value compared to the driving GCMs (Li et al., 2018a). For example, by comparing inter-GCM and inter-RCM differences around the Japan archipelago, it was found that RCM generate relatively large differences in precipitation (Suzuki-Parker et al., 2018). The RCM multi-model ensemble produces superior simulation compared to that of a single model (Jin et al., 2016; Guo et al., 2018a). A comparative study of RCMs at different spatial resolutions showed with coarse-resolution they present some limitations and high-resolution RCMs offer added value for several evaluation metrics (Park et al., 2020).

Atlas.5.1.4 Assessment and synthesis of projections

The development of climate models provides a solid basis for projection of future monsoon changes under different global warming scenarios. Coupled model simulations indicate that East Asia will *likely* experience higher warming than the global mean conditions across all global warming levels (Figure Atlas.17:) and with the projected warming greater in ECA than EAS. Also, in the CMIP6 ensemble, the multi-model mean and 90th percentile warming for a given period and emissions scenario are consistently greater than in the CMIP5 ensemble. Larger warming magnitudes are projected to occur in the southern, north-western, and north-eastern regions of China, parts of Mongolia, the Korean Peninsula, and Japan than in other regions (Li et al., 2018b). Projections indicated that the winter SAT increases over the East Asian continent, and the precipitation increases over the northern East Asian continent in winter reaching 1.5°C and 2.0°C global warming under the RCP4.5 and RCP8.5 scenarios (Miao et al., 2020).

Projected annual precipitation changes in the CMIP5 and CMIP6 ensembles are positive for all warming levels in ECA and for the higher warming levels in EAS. Changes in precipitation per degree Celsius global warming are larger in DJF than in JJA in ECA but show smaller seasonal difference in EAS (Figure Atlas.17). The EASM precipitation is projected to increase but with a complex spatial structure (Kitoh, 2017; Moon and Ha, 2017). Simulations from CMIP5 models show that compared with the current summer climate, both SAT and precipitation increase significantly over the East Asian continent during the 1.5°C warming period (Chen et al., 2019a), and the main mode of EASM precipitation changing from tripolar to dipolar (Wang et al., 2018). The increase in precipitable water in the wet EASM region is only slightly greater than global average but the increase in precipitation is much greater (Li et al., 2019b). The monsoon circulation in the lower troposphere is projected to strengthen due to the enhanced thermal forcing by the Tibetan Plateau (He et al., 2019; He and Zhou, 2020), which causes the increased summer precipitation over the East Asian continent. Precipitation over eastern China increases for almost all months under global warming in projections from GCMs with different horizontal resolutions (Kusunoki, 2018a). Also, under RCP scenarios, in the 21st century, mean precipitation is projected to increase (Kim et al., 2020) especially in the late afternoons (Oh and Suh, 2018) over the Korean Peninsula due to global warming and associated changes in EASM. Increase in JJA mean precipitation is projected in northern East Asia consistently among the CMIP models, while northward migration of early summer East Asian rain band such as the Meiyu-Baiu-

ACCEPTED VERSION SUBJECT TO FINAL EDITS

Changma is delayed along with that of the mid-latitude westerly jet in the future (Horinouchi et al., 2019). However, the geographical distribution of precipitation change tends to depend more on the cumulus convection scheme (Ose, 2017) and horizontal resolution of models rather than on SST distributions. Under the RCP4.5 and the RCP8.5 scenarios, the interannual variability in EASM rainfall is projected by the multi-model ensemble mean to increase in the 21st century (Ren et al., 2017). Further studies showed a projected increase in heavy rainfall together with increases in rainfall intensity (Endo et al., 2017). Multi-model intercomparison indicates significant uncertainties in future projections of climate change in East Asia, although precipitation increases consistently across models (Zhou et al., 2017). Simulations under RCP4.5 scenario project that the number of snow days will be reduced by the end of the 21st century relative to 1986–2005, primarily owing to the decline of light snowfall events. The total amount is projected to increase in north-western China but decrease in the other subregions (Zhou et al., 2018).

The increasing temperature trends under RCP scenarios were consistently reproduced in projections using CORDEX-EA models (Kim et al., 2016b) as reported in AR5 using GCMs. However, changes in annual and seasonal mean precipitation exhibit significant inter-RCM differences with larger magnitudes and variability than in the GCMs (Ham et al., 2016; Ozturk et al., 2017; Sun et al., 2018a; Zhang et al., 2018a). RCM simulations project that the Meiyu-Baiu-Changma heavy rainfall will significantly increase in northern Japan at the end of the 21st century under the RCP8.5 scenario (Osakada and Nakakita, 2018), but projected precipitation amount and number of precipitation days in summer around and over Japan differ as a result of RCM uncertainty (Suzuki-Parker et al., 2018). Annual total snowfall is projected to decrease in most parts of Japan except for Japan's northern island under RCP2.6 (Kawase et al., 2021).

Statistically downscaling of 37 CMIP5 GCMs for Xinjiang, China projected pronounced temperature increase of 0.27℃ to 0.51℃ per decade from 2021 to 2060 while precipitation change was projected to be between –1.7% to 6.8% per decade and varying seasonally and spatially (Luo et al., 2018). A decrease of precipitation was projected in the western region of Xinjiang during summer. More extreme rainfall events were projected to occur during summer and autumn.

Atlas.5.1.5 Summary

In East Asia annual mean temperature has been increasing since the 1950s (*high confidence*). The linear trend of annual mean surface air temperature *likely* exceeded 0.1°C per decade over most of East Asia from 1960 to 2015. Trends of annual precipitation show considerable regional differences with areas of both increases and decreases (*medium confidence*) and with increases over northwest China and South Korea (*high confidence*). Agricultural intensification through oasis expansion in Xinjiang region has increased summer precipitation in the Tianshan mountains (*high confidence*).

GCMs still show poor performance in simulating the mean rainfall and its variability over East Asia, especially over regions characterized by complex topography. The CMIP6 models have improved from CMIP5 for climatological temperature and winter monsoon but show little improvements for the summer monsoon. The RCMs produce relatively more detailed regional features, but do not always produce superior simulations compared with the driving GCMs.

The annual mean surface temperature over East Asia will *very likely* increase under all emissions scenarios and global warming levels. Larger warming magnitudes will *likely* occur in the northern part of EAS and in ECA. Precipitation is *likely* to increase over land in most of EAS at the end of the 21st century under higher emissions scenario (SSP3-7.0, RCP8.5, SSP5-8.5) and global warming levels and in ECA under all emissions scenarios and global warming levels. Summer precipitation increase is *likely* to occur in East Asia, corresponding to the strengthened summer monsoon circulation.

ACCEPTED VERSION SUBJECT TO FINAL EDITS

Atlas.5.2 North Asia

Atlas.5.2.1 Key features of the regional climate and findings from previous IPCC assessments

Atlas.5.2.1.1 Key features of the regional climate

North Asia extends from the Ural Mountains in the west to the Pacific Ocean in the east and from the Russian Arctic in the north to Southwest Asia and East Asia in the south. Its most recognizable features are boreal forests and permafrost. In AR6 North Asia is divided into three reference regions (Figure Atlas.17:): West Siberia (WSB) with a continental climate, warm summers and cold winters, many waterlogged areas and several natural zones due to a large extent from south to north and heterogeneity in regional climates; East Siberia (ESB) which is mainly highland with extensive permafrost and a more severe continental climate characterised by harsh, long winters and short, hot summers, and by less precipitation and snow cover than in neighbouring regions; and the Russian Far East (RFE) with a monsoon-influenced climate, cold winters and wet summers in the south and cold winters and cool summers almost without precipitation in the north. WSB and ESB are mainly influenced by NAO and NAM (Annex IV.2.1) and AO with associated atmospheric blocking by the Siberian High that exhibits a pronounced decadal-to-multidecadal variability (see also Table Atlas.1). RFE is under the influence of the ENSO (Annex IV.2.3) and the PDV (Annex IV.2.6) that mostly affect rainfall variability.

Atlas.5.2.1.2 Findings from previous IPCC assessments

In the previous IPCC assessment cycles, the three subregions comprising North Asia in this section along with Eastern Europe and the Asian Arctic were considered as either Northern Eurasia or Russia in AR4 and AR5. WGI AR5 stated that for North and Central Asia CMIP5 models had difficulty in representing climatological means of both temperature and precipitation, which is partly related to the scarceness of observational data in northern parts of the region and to issues related to the estimation of biases with coarse resolution models (Christensen et al., 2013). In CMIP3 projections under different RCP scenarios, North Asia temperatures increase more in winter (DJF) than summer (JJA) (Seneviratne et al., 2012). With most models projecting increased precipitation significantly above the 20-year natural variability, it was concluded that precipitation in northern Asia will *very likely* increase (Christensen et al., 2013).

SRCCL identified aridisation of the climate in southern Eastern Siberia between 1976 and 2016 as causing an extension of the steppes polewards whilst climate change also extended the vegetation season, increasing forest productivity in most of boreal Siberia, but increasing risk of wildfire and tree mortality (Mirzabaev et al., 2019). SROCC noted the warming climate has caused permafrost thaw and loss of ground ice, and thus land subsidence and collapse, disturbing ecosystems and human infrastructure. Permafrost stability, hydrology and vegetation were also impacted by recent extensive fires burning into the organic soil layer (Meredith et al., 2019). SR1.5 noted that future, higher levels of warming lead to greater impacts in key systems such as the Siberian ecosystems, identified as one of the threatened systems (‘Reason for Concern 1 – RFC1’) (Hoegh-Guldberg et al., 2018) with impacts at 2°C expected to be greater than those at 1.5°C (*medium confidence)*.

Atlas.5.2.2 Assessment and synthesis of observations, trends and attribution

Increases in surface air temperature (SAT) have been observed since the mid-1970s over the whole of North Asia (Frolov et al., 2014), and particularly over the north-eastern part (Gruza et al., 2015) (see also Figure Atlas.18). Trends of annual SAT in the northern part of the region during the last decades were *very likely* twice as strong as the global average (Figure Atlas.11) (Frolov et al., 2014; Mokhov, 2015; Sherstyukov, 2016) with trends in RFE of 0.8°C–1.2°C per decade for the 1976–2014 period and more intense warming strengthening from south to north observed in spring in ESB (Frolov et al., 2014; Ippolitov et al., 2014; Kokorev and Sherstiukov, 2015).

Recent strong warming in polar regions (Section Atlas.11.2) was accompanied by cooling in winter in mid-latitude regions particularly in the southern part of WSB and ESB (Cohen et al., 2014; Ippolitov et al., 2014;

ACCEPTED VERSION SUBJECT TO FINAL EDITS

Gruza et al., 2015; Kharyutkina et al., 2016; Overland et al., 2016; Perevedentsev et al., 2017; Wegmann et al., 2018). These temperature decreases were strongly correlated with significant warming over the Barents-Kara Sea (greater than 2.5°C per decade during 2003–2017) and sea-ice loss suggesting a causal link (Outten and Esau, 2012; Semenov et al., 2012; Overland et al., 2016; Semenov, 2016; Wegmann et al., 2018; Meleshko et al., 2019; Susskind et al., 2019) though recent studies (Blackport et al., 2019; Clark and Lee, 2019) have shown that both phenomena result from mid-latitude circulation variability (see also Cross-Chapter Box 10.1). In addition, significant warming in the last decade has halved the cooling trend in southern WSB from –0.6°C per decade during 1976–2012 to –0.3°C per decade during 1976–2018 (Frolov et al., 2014; Roshydromet, 2019) (*high confidence*).

Annual precipitation totals *very likely* increased over North Asia in the last half century along with more heavy and less light precipitation, more freezing rain and less freezing drizzle (Wen et al., 2014; Groisman et al., 2016; Ye et al., 2017; Chernokulsky et al., 2019)(see Figure Atlas.11 and Interactive Atlas). The highest increase was observed over regions of Siberia and RFE with estimated trends of 10–25 mm per decade for the 1976–2014 period (Kokorev and Sherstiukov, 2015) or 5% per decade for the 1976–2018 period (Roshydromet, 2019). Increases over southern RFE are the largest (over 50 mm per decade) and mostly due to positive changes in convective precipitation intensity in the region in summer season (JJA) during 1966–2016 (*medium confidence*) (Chernokulsky et al., 2019). A decreasing trend was observed in central WSB, northern ESB, the Baikal and Transbaikal regions, the Amur River region, and Primorie territories of RFE (the Kamchatka and Chukchi Peninsulas) with up to –20 mm per decade for the 1976–2014 period (Kokorev and Sherstiukov, 2015) or 15–20% per decade for the 1976–2018 period (Roshydromet, 2019). Overall, solid precipitation predominantly decreased in North Asia and *very likely* caused both less Snow Cover Extent (SCE) and Snow Water Equivalent (SWE), attributable to the anthropogenic influence with *high confidence* (Sections 2.3.2.2, 3.4.2).

Snow characteristics depend on both temperature and precipitation, and observed trends over North Asia show large spatial heterogeneity and interannual variability (Figure Atlas.18:) leading to *medium confidence* that maximum snow depth has increased over Siberia, the Okhotsk sea coast and in southern RFE since 1960s (Callaghan et al., 2011; Loginov et al., 2014), with trends during 1976–2016 of 1.8 cm (in WBS), 1.1 cm (in ESB), and 4.6 cm (in RFE) per decade (Bulygina et al., 2017). Snow cover duration increased in Yakutia, Sakhalin Island and some other coastal areas of the Pacific Ocean in RFE during 1980–2009 (Callaghan et al., 2011) and decreased in WSB and ESB (Bulygina et al., 2017; Roshydromet, 2019). However, Gorbatenko et al. (2019) reported that in southeastern WSB maximal snow depth has increased by 5–20 cm and duration of steady snow cover by between 4 and 10 days during 1989–2016 (Figure Atlas.18).

[START FIGURE ATLAS.18 HERE]

Figure Atlas.18: Linear trends for the 1980–2015 period based on station data from the World Data Centre of the Russian Institute for Hydrometeorological Information (RIHMI-WDC) (Bulygina et al., 2014). (a) Snow season duration from 1 July to 31 December (days per decade); (b) snow season duration from 1 January to 30 June (days per decade); (c) maximum annual height of snow cover (mm per decade). Trends have been calculated using ordinary least squares regression and the crosses indicate nonsignificant trend values (at the 0.1 level) following the method of Santer et al. (2008) to account for serial correlation. Further details on data sources and processing are available in the chapter data table (Table Atlas.SM.15).

[END FIGURE ATLAS.18 HERE]

Atlas.5.2.3 Assessment of model performance

Temperature trends and means derived from reanalysis datasets (JRA-25, MERRA) correctly represented temperature variability shown in observational data over the Asian territory of Russia for the 1976–2010 period (Loginov et al., 2014). Assessment of CRU TS 3.22, CRUTEMP4, ERA-Interim and NCEP2 datasets against station data over North Asia for annual and seasonal air temperature has shown that the ERA-Interim

ACCEPTED VERSION SUBJECT TO FINAL EDITS

reanalysis outperforms others for the 1981–2005 period (Kokorev and Sherstiukov, 2015). The latter reanalysis also underestimates summer precipitation and shows large wet biases over Northeast Asia during spring and underestimates mean seasonal temperature over northeast Asia in spring (MAM), autumn (SON), and winter (DJF) but overestimate it in summer (JJA) compared with the CRU dataset (*medium confidence*) (Ozturk et al., 2017; Top et al., 2021).

GCMs capture the main synoptic processes affecting North Asia and the CMIP5 ensemble simulates the temporal evolution of the magnitude and position of the Siberian High (SH) over the period 1872–2005 (Fei and Yong-Qi, 2015). CMIP5 models simulate a weakened intensity of the winter SH and a strengthened interannual variability compared to observations (Fei and Yong-Qi, 2015). The characteristics of blocking events over the region (number, duration, intensity and frequency) were reasonably well reproduced by GCMs (Mokhov et al., 2014) and most overestimate the annual mean temperature over northern Eurasia (Interactive Atlas). Biases in simulated annual surface air temperature simulation primarily come from winter (DJF) season and are relatively smaller in other seasons (Miao et al., 2014; Peng et al., 2019). Most GCMs capture the main decadal SAT trend (Miao et al., 2014) though CMIP5 GCMs fail to capture the decreasing temperature trend over East Siberia (Fei and Yong-Qi, 2015). Possible causes of GCMs inability to represent the recent slowdown of warming is discussed more in Cross-Chapter Box 3.1. For CMIP5, models with higher resolution do not always perform better than those with lower resolutions (*medium confidence*) (Miao et al., 2014).

Sixteen CMIP5 model simulations of SAT variability over Eurasia were evaluated against CRU observations for permafrost subregions (Peng et al., 2019), showing a warm bias in northwest Eurasia capturing the climate warming over the 20th century and its acceleration during the late 20th century. CMIP5 GCMs generally underestimate daily temperature range compared with observations over north-eastern Russia (Sillmann et al., 2013; Lindvall and Svensson, 2015). Currently there is no literature on the CMIP6 ensemble over the region though a few single-model studies are available (Voldoire et al., 2019; Wu et al., 2019b).

There is very limited use of RCMs for North Asia. CORDEX-CAS covers North Asia except parts of RFE and ARCTIC-CORDEX the northern regions (Figure Atlas.6:). For CORDEX-CAS three RCMs (REMO, ALARO-0 and CLMcom) have been used and have warm biases for maximum temperatures, cold biases for minimum temperatures and a wet bias in the north during the winter (Top et al., 2021). Rain gauges, however, are known to have problems in terms of measuring properly solid precipitation (e.g., drifting snow) which can greatly affect the accuracy of precipitation observations over North Asia (Harris et al., 2014).

Atlas.5.2.4 Assessment and synthesis of projections

CMIP5 and CMIP6 projections are consistent in the direction and ranges of surface temperature change which are higher than the global average and with ensemble mean warming of around 6°C for the 4°C GWL. Projected precipitation changes are also consistent with significant increases in winter, of up to 40% in the ensemble mean for the highest warming levels, and lower increases in summer except for WSB where changes are small and suggest drying at the 4°C GWL (Figure Atlas.17:, Interactive Atlas).

The CMIP5 ensemble projects a warming of the annual mean SAT over northern Eurasia in the 21st century, *likely* in the range of 0.8°C–1.0°C (RCP2.6), 2.3°C–3.1°C (RCP4.5) and up to 7.2°C (RCP8.5) (Miao et al., 2014; Peng et al., 2019). Mid-latitude permafrost subregions in Eurasia are projected to warm more than the global mean and non-permafrost territories, with ensemble area-averaged changes of 1.7°C (RCP2.6), 3.2°C (RCP4.5) or 6.4°C (RCP8.5) in 2081–2100 relative to 1986–2005 (Peng et al., 2019).

Over the Central Asia CORDEX domain, RegCM4.3.5 simulations driven by two different CMIP5 GCMs (HadGEM2-ES and MPI-ESM-MR) project SAT warming for 2071–2100 relative to 1971–2000 of about 3°C–4°C during the summer for RCP4.5 to over 7°C for all seasons for RCP8.5. Projected warming is most evident on the large continental Siberian Plateau with boreal and sub-boreal climates and biomes (i.e., taiga forests and tundra) during the winter season (Ozturk et al., 2017). The Voeikov Main Geophysical Observatory (MGO) RCM, driven by five CMIP5 GCMs for the RCP8.5 scenario, projects a faster increase

ACCEPTED VERSION SUBJECT TO FINAL EDITS

in annual minimum temperature as compared with maximum temperature over the whole territory of Russia (Kattsov et al., 2017), and the smallest change in growing season lengths (i.e., periods with daily temperatures over 5°C, 10°C and 15°C) in the area of northern taiga in WSB and ESB comparable with other territories of Russia during the 21st century (Torzhkov et al., 2019).

For precipitation, MGO RCM projections for the Arctic-CORDEX domain under the RCP8.5 scenario are for increases in annual totals for northern North Asia, a decrease in summer over ESB for 2006–2100 relative to 1951–2005 and significant increases in the upper limit of intense precipitation over most of the region in winter (Kattsov et al., 2017; Khlebnikova et al., 2018). Other RCM projections show that in most seasons and for all future periods, precipitation in Siberia is not projected to change with respect to the 1971–2000 period, except under the RCP8.5 scenario for the winter and autumn (Ozturk et al., 2017). This very limited and controversial evidence leads to *low confidence* in RCM precipitation projections for North Asia and since the projections of GCMs and ESMs are more physically consistent, assessment of future precipitation changes is based on CMIP5/CMIP6 presented in Figure Atlas.17: and the Interactive Atlas.

Atlas.5.2.5 Summary

Annual surface air temperature and precipitation have *very likely* increased and maximum snow depth has *likely* increased over most of North Asia since the mid-1970s. The highest warming has been found in spring in ESB and RFE, strengthening from south to north with linear trends of 0.8°C–1.2°C per decade over the 1976–2014 period (*high confidence*). A temperature decrease was identified just in winter in the southern part of WSB and ESB as a result of natural variability, but halved from –0.6°C per decade in 1976–2012 to –0.3°C per decade for the longer 1976–2018 period due to recent warmer winters (*high confidence*). Over North Asia annual precipitation increases with estimated trends of 5–15 mm per decade in the 1976–2014 period have been recorded with an exception over the Kamchatka and the Chukchi Peninsulas where decreases up to –20 mm per decade in the same period have been found (*medium confidence*). Snow cover duration has *very likely* decreased over Siberia and increases in maximum snow depths of 1.8 cm, 1.1 cm, and 4.6 cm per decade have been observed for WSB, ESB, and RFE respectively from 1976 to 2016 (*limited evidence*).

Most of the CMIP5 and some CMIP6 GCMs overestimate the annual mean air temperature and precipitation over North Asia region (*medium confidence*). GCMs generally represent the observed decadal temperature trend (*medium confidence*) and biases primarily come from the winter (DJF) season (*high confidence*). Results of a very limited number of RCMs applied over the whole region show that they have warmer biases for maximum and colder biases for minimum temperatures (*medium agreement, limited evidence*). Sparsity of observational data particularly in the northern part of ESB and the whole of the RFE results in *low confidence* in the assessments of model performance in North Asia.

Surface air temperature and precipitation in North Asia are projected to increase further (*high confidence*) with warming higher than the global average and around 6°C at the 4°C GWL. Temperature change in 2080–2099 relative to 1981–2000 is *likely* in the range of 3°C in summer to 4.9°C in winter under the RCP4.5 scenario, and 5.6°C in summer to 9.7°C in winter under the RCP8.5 scenario. Precipitation is projected to increase with ensemble mean changes of 9% in summer under both RCP4.5 and RCP8.5 and of 22% and 56% in winter respectively.

Atlas.5.3 South Asia

Atlas.5.3.1 Key features of the regional climate and findings from IPCC previous assessments

Atlas.5.3.1.1 Key features of the regional climate

The countries in this region are mostly semi-arid to arid and therefore depend heavily on the summer monsoon (June–September, JJAS) which is when most of the precipitation falls over the South Asia region (SAS) (Figure Atlas.17:). The topographic mechanical effect of the Tibetan Plateau (TIB) promotes moisture

ACCEPTED VERSION SUBJECT TO FINAL EDITS

convergence downstream which triggers the early summer monsoon onset particularly over the Bay of Bengal and South China. In winter, Westerly Disturbances (WD) bring moisture from the Atlantic Ocean. The WD interaction with Himalayas causes precipitation over northern and western parts of South Asia that is crucial to maintain the glacier mass balance. The observed teleconnection patterns over SAS for temperature shows cooling effects during NAM and warming effect when in positive phase with ENSO, IOB, AMM and AMV (Annex IV). IOD also influences South Asian precipitation (Annex IV).

Atlas.5.3.1.2 Findings from previous IPCC assessments

Recent IPCC reports assessed that it is *very likely* that the mean annual temperature over South Asia has increased during the past century (Figure 2.21 in Hartmann et al., 2013, Figure 24-2 in Hijioka et al., 2014), and the frequency of cold (warm) days and nights have decreased (increased) across most of Asia since about 1950 (Figure 2.32 in Hartmann et al., 2013). AR5 assessed that there is *high confidence* that the large-scale patterns of surface temperature are generally well simulated by the CMIP5 models though with problems in some regions, particularly at higher elevations over the Himalayas (Flato et al., 2013). CMIP5 models projected for the 21st century a significant increase in temperature over South Asia (*high confidence* from *robust evidence*) and in projections of increased summer monsoon precipitation (*medium confidence*) (Collins et al., 2013). AR5 assessed there is *high confidence* that high-resolution regional downscaling, which generate results complementary to those from global climate models, adds value to the simulation of spatial variations in climate in regions with highly variable topography (e.g., distinct orography, coastlines), and for mesoscale phenomena and extremes (Flato et al., 2013).

Inconsistent evidence was found on the declining trends in mean precipitation and increasing droughts from 1950 onwards considering 1960–1990 as the baseline period. Similarly, SREX (Table 3-3 in Seneviratne et al., 2012) reported *low confidence* (due to lack of literature) in trends in climate indices related to extreme precipitation events. The Indian summer monsoon circulation was found to have weakened, but this was compensated by increased local atmospheric moisture content leading to more rainfall (*medium confidence*). It is *likely* that the occurrence of snowfall events is decreasing in South Asia along with other regions due to an increase in winter temperatures (Hock et al., 2019b). Based on satellite- and surface-based remote sensing it is *very likely* that aerosol optical depth has increased over southern Asia since 2000.

Atlas.5.3.2 Assessment and synthesis of observations, trends and attribution

Recent studies show that annual mean land temperatures over India warmed at a rate of around 0.6°C per century during 1901–2018, which was primarily contributed by a significant increase in annual maximum temperature of 1.0°C per century, while the annual minimum temperature showed a lesser increasing trend of 0.18°C per century during this period, with significant rise only in the recent few decades (1981–2010) at a rate of 0.17°C per decade (Srivastava et al., 2017, 2019). The annual average of daily maximum and minimum temperatures has increased over almost all Pakistan with a faster increasing trend in the south (*high confidence*). Minimum temperatures have increased faster (0.17°C–0.37°C per decade) than maximum temperatures (0.17°C–0.29°C per decade) with the diurnal temperature range reduced (–0.15°C to –0.08°C per decade) in some regions (Khan et al., 2019).

There has been a noticeable declining trend in rainfall with monsoon deficits occurring with higher frequency in different regions in South Asia (see also Section 8.3.2.4 on the South Asian monsoon). Concurrently, the frequency of heavy precipitation events has increased over India, while the frequency of moderate rain events has decreased since 1950 (*high confidence*) (Goswami et al., 2006; Dash et al., 2009; Christensen et al., 2013; Krishnan et al., 2016; Kulkarni et al., 2017; Roxy et al., 2017). There is a considerable spread in the seasonal and annual mean precipitation climatology and interannual variability among the different observed precipitation datasets over India (Collins et al., 2013; Prakash et al., 2014; Kim et al., 2018; Ramarao et al., 2018). Yet, the regions of agreement among datasets lend *high confidence* that there has been a decrease in mean rainfall over most parts of the eastern and central north regions of India (Singh et al., 2014; Roxy et al., 2015; Juneng et al., 2016; Krishnan et al., 2016; Guhathakurta and Revadekar, 2017; Jin and Wang, 2017; Latif et al., 2017). A global modelling study with high resolution

ACCEPTED VERSION SUBJECT TO FINAL EDITS

over South Asia (Sabin et al., 2013) indicated that a juxtaposition of regional land-use changes, anthropogenic-aerosol forcing and the rapid warming signal of the equatorial Indian Ocean was crucial to simulate the observed Indian summer monsoon weakening in recent decades (*medium confidence*).

A dipole-like structure in summer monsoon rainfall trends is observed over the northern Indo-Pakistan area with significant increases over Pakistan and decreases over central north India resulting from strengthening (weakening) of vertically integrated meridional moisture transport over the Arabian Sea (Bay of Bengal) (*low confidence*) (Latif et al., 2017). Positive annual precipitation trends are observed in global and regional datasets (Figure Atlas.11: and Interactive Atlas) during 1960–2015 and over arid provinces of Pakistan (for Rabi and Kharif cropping seasons) during 1951–2015 of 2.8–34.8 mm per decade (Khan et al., 2020) imply *high confidence* for increased precipitation in Pakistan. Observations located in the monsoon-dominated strip in Pakistan indicate that the mean monsoon onset became earlier during 1971–2010 (Ali et al., 2020).

Snow and glaciers are the main water resources of all countries in South Asia. Glacier melting is mainly controlled by natural phenomena but anthropogenic emissions of black carbon (BC) are now making a significant contributing to total glacial melting in the Hindu Kush Himalaya (HKH) region (Menon, 2002; Ramanathan et al., 2007; Ramanathan and Carmichael, 2008). BC concentration is seven to ten times higher in mid-altitudes (1000–4000 metres above sea level) than at high altitudes (>4000 metres above sea level). The concentration of BC sampled from the surface of snow/ice samples as well as ice core records shows decreasing ice albedo and an acceleration in glacier melting (Wester et al., 2019) (see also Cross-Chapter Box 10.4). Karakoram and western HKH snow cover is increasing, a phenomena known as the 'Karakoram anomaly', and partially attributed to an increase in strength of westerly disturbances (Wester et al., 2019).

Significant glacier retreat has been observed since 1960 in TIB with lower rates in the interior of the region (Yao et al., 2007). A large interdecadal variation in snow cover is also observed from 1960 to 2010. Observations and model simulations showed that the increasing temperature of frozen grounds is leading to thawing and reduced depth of permafrost, with further significant reductions projected under future global warming scenarios (Yang et al., 2019) (*medium confidence*).

Atlas.5.3.3 Assessment of model performance

Whilst simulations of Indian summer monsoon rainfall (ISMR) have improved in CMIP5 compared to CMIP3 in terms of northward propagation, time for peak monsoon and withdrawal (Sperber et al., 2013) they fail to simulate the trends in monsoon rainfall and the post-1950 weakening of monsoon circulation (Saha et al., 2014). This is partially attributed to the failure of coarse resolution CMIP5 models to simulate fine-resolution processes such as orographic effects or land surface feedback, and problems in cloud parameterization result in an overestimation of convective precipitation fraction (Singh et al., 2017a). In CMIP6, a significant improvement is found in capturing the monsoon spatiotemporal patterns over India, particularly in the Western Ghats and north-eastern Himalayan foothills (Gusain et al., 2020). Over Pakistan the CMIP6 models simulate surface temperature better in JJA than DJF (Karim et al., 2020). The CMIP6 ensemble underestimates annual mean temperature over all of South Asian with mixed results for precipitation (Almazroui et al., 2020c). The CMIP6 GCMs have a large cold bias in both mean annual maximum and minimum temperatures in the complex Karakorum and Himalayan mountain ranges but exhibit warm biases in mean annual minimum temperature in most of the rest of South Asia.

Regional climate model (RCM) downscaling of CMIP5 models as part of CORDEX South Asia uses higher resolution (50 km) and improved surface fields such as topography and coastlines to resolve better the complexities of the monsoon and other hydrological processes (Giorgi et al., 2009). The added value of their simulations, relative to the driving GCMs, presents a complex picture. CORDEX RCMs better represent spatial patterns of temperature (Sanjay et al., 2017), the spatial features of precipitation distribution associated with the Indian summer monsoon (Choudhary and Dimri, 2018) and the simulation of monsoon active- and break-phase composite precipitation (Karmacharya et al., 2016). The RCMs follow the driving GCMs in underestimating seasonal mean surface air temperature and overestimating spatial variability in precipitation. They amplify CMIP5 cold biases over almost the entire region, including over the HKH

ACCEPTED VERSION SUBJECT TO FINAL EDITS

region, Afghanistan and southwest Pakistan during winter (Iqbal et al., 2017) and substantial cold biases of 6°C–10°C are found over the Himalayan watersheds of the Indus Basin (Nengker et al., 2018; Hasson et al., 2019). Neither RCMs nor their driving CMIP5 GCMs reproduce well the region's precipitation climatology (Mishra, 2015). In addition, important characteristics of ISMR such as northward and eastward propagation, onset, seasonal rainfall patterns, intra-seasonal oscillations and patterns of extremes did not show consistent improvement (Singh et al., 2017b). Also, these RCM simulations have not demonstrated added value in capturing the observed changes in ISMR characteristics over recent decades though RegCM4 simulations at 25 km showed high accuracy in capturing monsoon precipitation characteristics and atmospheric dynamics in historical simulations (Ashfaq et al., 2020).

Evaluation of four global reanalysis products (ERA5 and ERA-Interim, JRA-55 and MERRA-2, Section Atlas.1.4.2) for snow depth and snow cover over the TIB was performed against 33 in situ station observations, Interactive Multisensor Snow and Ice Mapping System (IMS) snow cover and a satellite microwave snow depth dataset (Orsolini et al., 2019). Most of the reanalyses showed a systematic overestimation. Only ERA-Interim assimilated IMS snow cover at high altitudes, whereas ERA5 did not and the excessive snowfall, snow depth and snow cover in ERA5 was attributed to this difference. The analysis of annual maximum consecutive snow-covered days for the period 1980–2018 over TIB using JRA-55 and Passive Microwave satellite observations showed decreasing trend in all time periods and in recent snow seasons for MERRA-2 (Bian et al., 2020). The uncertainty assessment of model physics in snow modelling over TIB using ground-based observations and high-resolution snow-cover satellite products from the Moderate Resolution Imaging Spectroradiometer (MODIS) and FengYun-3B (FY3B) suggests that errors can be overcome by optimizing parameterizations of the snow cover fraction rather than optimizing physics-scheme options (Jiang et al., 2020b).

Atlas.5.3.4 Assessment and synthesis of projections

CMIP5 and CMIP6 surface temperature projections are consistent across the range of global warming levels with increases greater than the global average, more so over TIB (Figure Atlas.17:). CMIP6 models show higher sensitivity to greenhouse gas emissions, projecting higher warming for a given emission scenario. The north-western parts of South Asia, mainly covering Karakorum and Himalayan mountain ranges, are projected to warm more (over 6°C under SSP5-8.5, with higher warming in winters than in summer, see Interactive Atlas) and this will accelerate glacier melting in the region. The warming pattern of maximum and minimum temperatures are projected to intensify in higher latitudes compared with mid-latitudes of South Asia in CMIP5 simulations for all RCP scenarios (Ullah et al., 2020).

Seasonal precipitation projections show increased winter precipitation over the western Himalayas and decreased precipitation over the eastern Himalayas. On the other hand, summer precipitation projections show a robust increase over most of South Asia, with the largest over the arid region of southern Pakistan and adjacent areas of India, under SSP5-8.5 (Almazroui et al., 2020c). Daily bias-adjusted projections from 13 CMIP6 GCMs using all emission scenarios project a warmer (3°C–5°C) and wetter (13–30%) climate in South Asia in the 21st century (Mishra et al., 2020).

With continued global warming and anticipated reductions in anthropogenic aerosol emissions in the future, CMIP5 models project an increase in the mean and variability of summer monsoon precipitation over India by the end of the 21st century, together with substantial increases in daily precipitation extremes (*medium confidence*) (Gnanaseelan et al., 2020), see also Section 8.4.2.4 on changes in the South Asian monsoon. The CMIP5 GCMs consistently project an increase in the moisture transport over the Arabian Sea and Bay of Bengal towards the end of 21st century, an increase in moisture convergence and consequent increases in monsoon rainfall over the Indo-Pakistan region which are higher under RCP8.5 thanRCP4.5 (Srivastava and Delsole, 2014; Mei et al., 2015; Latif, 2017). Out of 20 CMIP5 GCMs, four showed an increase in magnitude and lengthening of all-India summer monsoon under RCP8.5. The intensity of both strong and weak monsoons is projected to increase during the period 2051–2099 (Srivastava and Delsole, 2014).

Summer precipitation changes in South Asia are consistent between CMIP3 and CMIP5 projections, but the

ACCEPTED VERSION SUBJECT TO FINAL EDITS

model spread is large for winter precipitation changes. Changes in summer monsoon rainfall will dominate annual changes over South Asia (Woo et al., 2019). CMIP3 GCMs project a gradual increase in annual precipitation over monsoon-dominated areas of Pakistan throughout the 21st Century and increases in humid and semi-arid climate areas (Saeed and Athar, 2018).

Warming of 2.5°C to 5°C is projected over northern Pakistan and India (Syed et al., 2014). CORDEX-South Asia projections over northeast India under RCP4.5 for the period 2011–2060, show increasing trends for both seasonal maximum and minimum temperature over northeast India (Interactive Atlas). The future projections of South Asian monsoon from the CORDEX-CORE exhibit a spatially robust delay in the monsoon onset, an increase in seasonality, and a reduction in the rainy season length over parts of South Asia at higher levels of radiative forcing (Ashfaq et al., 2020).

With the TIB continuing to warm, snow cover and snow water equivalent are projected to decrease but with regional differences due to synoptic influences (Wester et al., 2019) and Cross-Chapter Box 10.4. There is *limited evidence* on whether the 'Karakoram Anomaly' will persist in coming decades, but its long-term persistence is *unlikely* with continued projected warming (*high confidence*) (Section 9.5.1.1). It is projected that peak river flow at higher altitudes will commence earlier, due to warming influences on snow cover area and snow/glacier melt rates and with more precipitation falling as rain rather than snow, and the magnitude and seasonality of flow will change over South Asia (Charles et al., 2016).

Atlas.5.3.5 Summary

Mean, minimum and maximum daily temperatures in South Asia are increasing and winters are getting warmer faster than summers (*high confidence*). The South Asian monsoon has shown contrasting behaviour over India and Pakistan. There is *high confidence* that there has been a decrease in mean rainfall over most parts of the eastern and central north regions of India and an increase in precipitation in Pakistan.

Global model performance over the region has improved from CMIP3 to CMIP5 to CMIP6 in the multi-model ensemble mean simulation of the amplitude and phase of the seasonal cycles of temperature and precipitation. However, there was no appreciable improvement in regions with steep orography, and there has remained substantial inter-model spread in seasonal and annual mean temperatures over South Asia with generally cold biases which are largest in the complex Karakorum and Himalayan mountain ranges. CMIP6 GCMs also show a dry bias (15–20%) in mean annual precipitation in the majority of South Asia region with a wet bias in Nepal, Pakistan and northern India.

It is *likely* that surface temperatures over South Asia (SAS and TIB) will increase greater than the global average, more so over TIB, and with projected increases of 4.6°C (3.4°C– 6.0°C) during 2081–2100 compared with 1995–2014 under SSP5-8.5 and 1.3°C (0.7°C– 2.0°C) under SSP1-2.6 (Interactive Atlas). Summer monsoon precipitation in South Asia is *likely* to increase by the end of the 21st century while winter monsoons are projected to be drier. Over the same time periods CMIP6 models project an increase in annual precipitation in the range 14–36% under SSP5-8.5 and 0.4–16% under SSP1-2.6 (*medium confidence*).

With continued warming, TIB snow cover and snow water equivalent are *likely* to decrease and with more precipitation falling as rain rather than snow in SAS. It is projected that the peak river flow at higher altitudes will commence earlier due to the effect of warming on snow cover and snow/glacier melt rates, causing changes in magnitude and seasonality of flow.

Atlas.5.4 Southeast Asia

Atlas.5.4.1 Key features of the regional climate and findings from previous IPCC assessments

Atlas.5.4.1.1 Key features of the regional climate

The Southeast Asia region is composed of countries that are part of Indochina (or mainland Southeast Asia)

ACCEPTED VERSION SUBJECT TO FINAL EDITS

and countries that are very archipelagic in nature and have strong land-ocean-atmosphere interactions, including those that are part of the Maritime Continent and the Philippines. Its climate is mainly tropical (i.e., hot and humid with abundant rainfall). Rainfall seasonal variability in the region is mainly affected by the synoptic-scale monsoon systems, the north-south migration of the ITCZ and tropical cyclones (mainly for the Philippines and Indochina) while intraseasonal variability can be influenced by the MJO (Annex IV). Temperature and especially rainfall are also interannually affected by ENSO and Indian Ocean Basin and Dipole (IOB/IOD) modes (Annex IV, Table Atlas.1).

Atlas.5.4.1.2 Findings from previous IPCC assessments

WGI AR5 showed that the mean annual temperature of Southeast Asia has been increasing at a rate of 0.14°C to 0.20°C per decade since the 1960s, along with an increasing number of warm days and nights, and a decreasing number of cold days and nights (Christensen et al., 2013). AR5 also reported the lack of sufficient observational records to allow for a full understanding of past precipitation trends in most of the Asian region, including Southeast Asia, and that precipitation trends that were available differed considerably across the region and between seasons (Christensen et al., 2013).

On projected changes, findings from AR5 showed that warming is *very likely* to continue with substantial subregional variations over Southeast Asia (Christensen et al., 2013). The median increase in temperature over land projected by the CMIP5 ensemble mean ranges from 0.8°C in RCP2.6 to 3.2°C in RCP8.5 by the end of the 21st century. Moderate future increases in precipitation are *very likely*, with projected ensemble mean increases of 1% in RCP2.6 to 8% in RCP8.5 by 2100. In the SR1.5, there is a projected increase in flooding and runoff over Southeast Asia for a 1.5°C to 2°C global warming, and these will increase even more for a greater than 2°C level of warming (Hoegh-Guldberg et al., 2018).

Atlas.5.4.2 Assessment and synthesis of observations, trends and attribution

Within the last decade, there has been an increasing number of studies on climatic trends over Southeast Asia, carried out on a regional basis (Thirumalai et al., 2017; Cheong et al., 2018) or focused on specific countries (Cinco et al., 2014; Villafuerte et al., 2014; Mayowa et al., 2015; Villafuerte and Matsumoto, 2015; Guo et al., 2017a; Sa'adi et al., 2017; Supari et al., 2017; Tan et al., 2021). They document *virtually certain* significant increases in mean as well as extreme temperature. The minimum temperature extremes *very likely* warmed faster compared to the maximum temperature. Temperatures, including extremes, are strongly influenced by ENSO in the region (Cinco et al., 2014; Thirumalai et al., 2017; Cheong et al., 2018). Over much of the regions, extreme high temperature occurred mostly in April and almost all April extreme temperatures occur in El Niño years (Thirumalai et al., 2017). In most of Southeast Asia (except for the north-eastern areas), there was *likely* an increase in the number of warm nights with El Niño episodes within the period 1972–2010 (Cheong et al., 2018).

Changes in mean precipitation are less spatially coherent over Southeast Asia. Over Thailand, the average number of rain days has decreased by 1.3 to 5.9 days per decade while average daily rainfall intensity has increased by 0.24–0.73 mm day^{-1} per decade (Limsakul and Singhruck, 2016). Precipitation is also affected by ENSO events (Tangang et al., 2017; Supari et al., 2018). Over Southeast Asia, there has been a significant increase in the amount of precipitation and its extremes with La Niña episodes in the past decades, especially during the winter monsoon period (*high confidence*) (Villafuerte and Matsumoto, 2015; Limsakul and Singhruck, 2016; Cheong et al., 2018).

Figure Atlas.11 shows trends in mean temperature and precipitation during 1960–2015 for two global datasets, indicating a significant overall warming over Southeast Asia (*high confidence*), with higher rates of warming in Malaysia, Indonesia, and the southern areas of mainland Southeast Asia (*low confidence*). Annual mean precipitation trends (see also Interactive Atlas which includes the regional dataset Aphrodite, see section Atlas.1.4.1) over the region are mostly not significant except for increases over parts of Malaysia, Vietnam and southern Philippines (*medium confidence*).

ACCEPTED VERSION SUBJECT TO FINAL EDITS

It is important to note that the availability, quality, and temporal and spatial density of observation data may lead to uncertainties and varying results in Southeast Asia (Juneng et al., 2016). Some efforts have been made to produce better observationally-based gridded datasets for the region (e.g., Nguyen-Xuan et al., 2016; van den Besselaar et al., 2017; Yatagai et al., 2020).

Atlas.5.4.3 Assessment of model performance

Performance in simulating rainfall over Southeast Asia varies among CMIP5 GCMs (*high confidence*). Only some are capable of reasonably simulating the rainfall seasonal cycle and spatial pattern (Siew et al., 2013; Raghavan et al., 2018). Over mainland Southeast Asia, the performance of CMIP5 GCMs in simulating rainfall during wet season was superior to that for annual and dry season precipitation (Li et al., 2019a).

RCMs have been intensively used over the region in recent years in a series of single or multi-model experiments and there is *medium confidence* that they reproduce reasonably well seasonal climate patterns of temperature, precipitation and large-scale circulation over the different subregions of Southeast Asia with added values compared to their host GCMs (Van Khiem et al., 2014; Kwan et al., 2014; Ngo-Duc et al., 2014, 2017; Juneng et al., 2016; Katzfey et al., 2016; Loh et al., 2016; Raghavan et al., 2016; Cruz et al., 2017; Ratna et al., 2017; Trinh-Tuan et al., 2018; Nguyen-Thuy et al., 2021). RCM ensemble means tend to outperform the individual models in representing the climatological mean state (Ngo-Duc et al., 2014; Trinh-Tuan et al., 2018; Nguyen-Thi et al., 2020). There is relatively high consistency among the simulations of historical climate over mainland Southeast Asia compared to those over the Maritime Continent for both seasonal and inter-annual variability (Ngo-Duc et al., 2017). The consistency in rainfall simulations was lower than for temperature simulations.

Some RCMs showed a systematic cold bias (Manomaiphiboon et al., 2013; Kwan et al., 2014; Ngo-Duc et al., 2014; Loh et al., 2016; Cruz and Sasaki, 2017; Cruz et al., 2017) that was mainly due to model physics (Manomaiphiboon et al., 2013; Kwan et al., 2014) and/or the biases in the SST forcing (Ngo-Duc et al., 2014). A few simulations revealed a warm bias over some areas such as in the Maritime Continent (Cruz et al., 2017) or Vietnam (Van Khiem et al., 2014). The biases for rainfall in GCMs and RCMs over Southeast Asia were found to be less systematic with wet or dry biases depending on the subregions (Manomaiphiboon et al., 2013; Kwan et al., 2014; Van Khiem et al., 2014; Juneng et al., 2016; Nguyen-Thi et al., 2020; Supari et al., 2020; Tangang et al., 2020) although wet biases were more pronounced in RCMs (Kwan et al., 2014; Van Khiem et al., 2014; Kirono et al., 2015; Juneng et al., 2016; Supari et al., 2020; Tangang et al., 2020). Some RCMs overestimated rainfall interannual variability (Juneng et al., 2016) while some others underestimated it (Kirono et al., 2015). Simulated rainfall amount is sensitive to the choice of convective scheme (Juneng et al., 2016; Ngo-Duc et al., 2017) and the choice of land-surface scheme (Chung et al., 2018). Rainfall biases in current climate simulations can be greatly reduced if a bias correction method such as quantile mapping is applied (Trinh-Tuan et al., 2018). The pattern of tropical cyclone numbers in the region were reasonable represented by RCM outputs (Van Khiem et al., 2014; Kieu-Thi et al., 2016; Herrmann et al., 2020).

Atlas.5.4.4 Assessment and synthesis of projections

Mean temperature in Southeast Asia is projected to continue to rise through the 21st century (*virtually certain, very high confidence*). Projections by multi-model regional climate simulations of CORDEX-SEA showed a temperature increment over land under RCP8.5 to range from 3°C to 5°C by the end of 21st century relative to pre-1986–2005 period (Tangang et al., 2018). For the same periods, the average mean temperature increase over land projected by CMIP5 (CMIP6) varies from 0.9 ± 0.3°C (1.2 ± 0.4°C) under RCP2.6 (SSP1-2.6) to 3.5 ± 0.7°C (3.8 ± 0.9°C) under RCP8.5 (SSP5-8.5) (Interactive Atlas). For all Global Warming Levels (GWLs) the land region is projected to warm by a slightly smaller amount than the global average, with 10th–90th percentile ranges for CMIP5 (CMIP6) of 1.2°C to 1.6°C (1.2°C to 1.5°C) for the 1.5°C GWL and of 3.3°C to 4.0°C (3.3°C to 3.9°C) for the 4°C GWL relative to the 1850–1900 baseline (calculated from RCP8.5 (SSP5-8.5) projections). Changes for other warming levels, periods, and emissions

ACCEPTED VERSION SUBJECT TO FINAL EDITS

pathways are shown in Figure Atlas.17 and can be explored in the Interactive Atlas.

Projections of future rainfall changes are highly variable among sub-regions of Southeast Asia and among the models (*high confidence*). The CMIP5 and CMIP6 ensembles showed an increase in annual mean precipitation over most land areas by the mid and late 21st century, although only with a strong model agreement for higher warming levels (Interactive Atlas, Figure Atlas.17), while CORDEX produces a general decrease in projected precipitation (Figure Atlas.17). Based on CORDEX Southeast Asia multi-model simulations, significant and robust increases of mean rainfall over Indochina and the Philippines were projected while there is a drying tendency over the Maritime Continent during DJF for the early, mid and end of the 21st century periods under both RCP4.5 and RCP8.5 (Tangang et al., 2020) (Figure Atlas.19). At the end of the 21st century during DJF and under RCP8.5, an increase of 20% in mean rainfall is projected over Myanmar, northern central Thailand and northern Laos, and of 5–10% over the eastern Philippines and northern Vietnam. During JJA, significant drier conditions are projected over almost the entire Southeast Asia except over Myanmar and northern Borneo. Over the Indonesian region, especially Java, Sumatra and Kalimantan, as much as a 20–30% decrease in mean rainfall is projected during JJA by the end of the 21st century. The projected drier condition over Indonesia from CORDEX is consistent with that of (Kusunoki, 2017; Giorgi et al., 2019; Kang et al., 2019; Supari et al., 2020) and is associated with enhanced subsidence over the region (Kang et al., 2019; Tangang et al., 2020).

[START FIGURE ATLAS.19 HERE]

Figure Atlas.19: The RCM projected changes in mean precipitation between the early (2011–2040), mid (2041–2070) and late (2071–2099) 21st century and the historical period 1976–2005. Data are obtained from the CORDEX-SEA downscaling simulations. Diagonal lines indicate areas with low model agreement (less than 80%). Adapted from Tangang et al. (2020).

[END FIGURE ATLAS.19 HERE]

Atlas.5.4.5 Summary

It is *virtually certain* that annual mean temperature has been increasing in Southeast Asia in the past decades while changes in annual mean precipitation are less spatially coherent though with some increasing trends over parts of Malaysia, Vietnam and southern Philippines (*medium confidence*).

Although various biases still exist, there is *high confidence* that the models can reproduce seasonal climate patterns well over the different subregions of Southeast Asia. There is *medium confidence* that the RCMs show added value compared to their host GCMs over the region.

Projections show continued warming over Southeast Asia, but *likely* by a slightly smaller amount than the global average. Projected changes in rainfall over Southeast Asia vary, depending on model, subregion and season (*high confidence*) with consistent projections of increases in annual mean rainfall from CMIP5 and CMIP6 over most land areas (*medium confidence*) and decreases in summer rainfall from CORDEX projections over much of Indonesia (*medium confidence*).

Atlas.5.5 Southwest Asia

Atlas.5.5.1 Key features of the regional climate and findings from previous IPCC assessments

Atlas.5.5.1.1 Key features of the regional climate

Southwest Asia includes the Arabian Peninsula (ARP) and West Central Asia (WCA) reference regions (Figure Atlas.17). ARP has a semi-arid or arid desert climate with very low annual mean precipitation and very high temperature. Its temperature is influenced by SST variations over the tropical ocean (e.g., ENSO)

ACCEPTED VERSION SUBJECT TO FINAL EDITS

and the NAO and AO (Attada et al., 2019) (see Annex IV for these and subsequent modes of variability). Rainfall is influenced by the IOD and ENSO with more rainfall during El Niño (Kang et al., 2015; Kumar et al., 2015; Abid et al., 2018; Kamil et al., 2019) and less during La Niña (Atif et al., 2020). The wet season in ARP is mainly from November to April and the dry season is from June to August. Rainfall is confined mostly to the south-western part of the Peninsula and contribution of extreme events to the total rainfall varies within 20–70% from region to region and season to season (Almazroui, 2020b; Almazroui and Saeed, 2020). WCA is separated from Eastern Europe by the Caucasus Mountains, is adjacent to ARP, with South Asia (SAS) to the south and West Siberia (WSB) to the north, and lies between the Mediterranean (MED), Tibetan Plateau (TIB) and East Central Asia (ECA) regions. WCA is heterogeneous in terrain with the Zagros Mountains and Iranian Plateau in the west and southwest, the Caspian Sea and lowland with deserts in the north and northeast. The regional climate of WCA is influenced by the NAO and ENSO and it is typically semi-arid or arid with a strong gradient in both precipitation and temperature from the mountains to the plains and from north to south.

Atlas.5.5.1.2 Findings from previous IPCC assessments

The IPCC AR5 established it is *very likely* that temperatures will continue to increase over WCA in all seasons whilst projections of decreased annual mean precipitation had *medium confidence* due to *medium agreement* resulting from model-dependent subregional and seasonal changes (Christensen et al., 2013). AR5 also concluded that for a better understanding of the climate of the region, results of high-resolution regional climate models also need to be assessed and CMIP5 models generally had difficulties simulating the mean temperature and precipitation climatology for Southwest Asia. This is partly related to the poor spatial resolution of the models not resolving the complex mountainous terrain and the influence of different drivers of the European, Asian and African climates. However, observational data scarsity and issues related to the comparison of observations with coarse-resolution models added to the uncertainty and remained poorly analysed in peer-reviewed literature on climate model performance (Christensen et al., 2013).

SR1.5 stated that even for 1.5°C and 2°C of global warming, Southwest Asia is among the regions with the strongest projected increase in hot extremes with more urban populations exposed to severe droughts in West Asia, while an increase of heavy precipitation events is projected in mountainous regions of Central Asia (Hoegh-Guldberg et al., 2018; IPCC, 2018c). Higher temperatures with less precipitation will *likely* result in higher risks of desertification, wildfire and dust storms exacerbated by land-use and land-cover changes in the region with consequent effects on human health. Further drying of the Aral Sea in Central Asia will *likely* have negative effects on the regional microclimate adding to the growing wind erosion in adjacent deltaic areas and deserts that is already resulting in a reduction of the vegetation productivity including croplands. There is also a projected increase of precipitation intensity in the Arabian Peninsula which is *likely* to lead to higher soil erosion particularly in winter and spring due to floods (Mirzabaev et al., 2019). WCA includes high mountains with enhanced warming above 500 m where, regardless of the emissions scenario, decreases in snow cover are projected due to increased winter snowmelt and more precipitation falling as rain (*high confidence*). A very strong interannual and decadal variability, as well as scarce in situ records for mountain snow cover, have prevented a quantification of recent trends in High Mountain Asia (Hock et al., 2019b).

Atlas.5.5.2 Assessment and synthesis of observations, trends and attribution

Since the AR5, there has been an increasing number of studies on past climate change in Southwest Asia though meteorological stations are sparsely scattered in the region. They are mainly located in the plains below 2 km of altitude, very scarce in mountainous areas and have declined in number in WCA since the end of the Soviet Union in 1991. This increases the uncertainty in both temperature and precipitation trends particularly for elevated areas (Christensen et al., 2013; Huang et al., 2014) (*high confidence*). So researchers use other sources of climate data in the region, particularly freely available gridded data (see Annex I).

Globally drylands showed an enhanced warming over the past century of 1.2°C to 1.3°C, significantly higher than the warming over humid lands (0.8°C to 1.0°C) (Huang et al., 2017b). A strong increase in annual surface air temperature of 0.27°C to 0.47°C per decade has been found over WCA between 1960 and 2013

ACCEPTED VERSION SUBJECT TO FINAL EDITS

(*very high confidence*) (Han and Yang, 2013; Li et al., 2013; Hu et al., 2014, 2017; Huang et al., 2014; Deng and Chen, 2017; Zhang et al., 2019a, 2017; Guo et al., 2018b; Haag et al., 2019; Yu et al., 2019). Warming is most prominent in the spring based on the CRU dataset with rates *likely* ranging from 0.64°C to 0.82°C per decade (Hu et al., 2014). Analysis of seasonal temperature trends based on high-resolution 1 km x 1 km downscaled dataset CHELSA and 20 stations in Uzbekistan has confirmed the maximum significant trend in temperature of from 0.6°C up to 1°C per decade in spring from 1979 to 2013 and no significant trend in winter (Khaydarov and Gerlitz, 2019). There is *very high confidence* (*robust evidence*, *high agreement*) that the shrinking of the Aral Sea has induced an increase in surface air temperature around the Aral Sea region in the range of 2°C to 6°C (Baidya Roy et al., 2014; McDermid and Winter, 2017; Sharma et al., 2018). The plateau of Iran has experienced significant increases in the average monthly values of daily maximum and minimum temperatures with spatially varying rates of 0.1°C–0.3°C up to 0.3°C–0.4°C per decade and greater spatial variation in minimum temperatures (*high confidence*) (Mahmoudi et al., 2019; Fathian et al., 2020; Sharafi and Mir Karim, 2020).

Observed warming over northern ARP is higher than over the south, where minimum temperatures are increasing faster than maximum temperatures (Almazroui, 2020a). The rate of mean temperature increase is estimated at 0.10°C per decade over 1901–2010 (Attada et al., 2019), while it has reached 0.63°C (*likely* in the range of 0.24°C to 0.81°C) per decade for the more recent period of 1978–2019 (Almazroui, 2020a).

An overall increasing trend of annual precipitation (0.66 mm per decade) was found over Central Asia based on GPCC V7 data for the period 1901–2013 (Hu et al., 2017), but annual trends were found not significant over the shorter period 1960–2013 (see also Figure Atlas.11 and Interactive Atlas). Winter precipitation saw a significant increase of 1.1 mm per decade (Song and Bai, 2016). These estimates have *low* to *medium confidence* since the satellite precipitation products have large systematic and random errors in mountainous regions. Moreover CMORPH and TRMM products fail to capture the precipitation events in the ice/snow-covered regions in winter and show a substantial false-alarm percentage in summer, but the gauge-corrected GSMAP performs better than other products (Song and Bai, 2016; Guo et al., 2017b; Hu et al., 2017; Chen et al., 2019b). Over the elevated part of eastern WCA precipitation increases in the range of 1.3–4.8 mm per decade during 1960–2013 were observed (*very high confidence*) (Han and Yang, 2013; Li et al., 2013; Hu et al., 2014, 2017; Huang et al., 2014; Deng and Chen, 2017; Zhang et al., 2019a, 2017; Guo et al., 2018b; Haag et al., 2019; Yu et al., 2019). Reductions in spring precipitation and increases in winter have been reported for Uzbekistan over the period 1979–2013 based on station data but these are not significant (Khaydarov and Gerlitz, 2019). There is *very low confidence* of impact of the Aral Sea shrinking on precipitation (Chen et al., 2011; Jin et al., 2017).

A decreasing trend of precipitation is reported for ARP with the mean value of –6.3 mm per decade (range of –30 mm to 16 mm) for the period 1978–2019 (*low confidence*) with large interannual variability over Saudi Arabia, which covers 80% of the region (AlSarmi and Washington, 2011; Almazroui et al., 2012; Donat et al., 2014). The same decreasing trend in precipitation totals and an increasing trend in the number of consecutive dry days are found for most of the Iranian plateau (*medium confidence*) (Rahimi and Fatemi, 2019; Fathian et al., 2020; Sharafi and Mir Karim, 2020). January-to-March mean snow cover and depth over mountainous areas decreased between 2000 and 2019 (*low* to *medium confidence* due to *limited evidence*) (Safarianzengir et al., 2020).

Atlas.5.5.3 Assessment of model performance

There is *limited evidence* about the performance of GCMs and RCMs in representing the current climate of Southwest Asia due to very few studies evaluating models over this region, but literature is now emerging particularly on CMIP5/CMIP6 and CORDEX simulations.

Over ARP, surface temperature biases for 18 of 30 CMIP5 models are within one standard deviation of the observed variability (Almazroui et al., 2017). A warm bias in summer and a cold bias for others months along with an underestimation of wet season precipitation and an overestimation in the dry season have been reported in 26 CMIP5 models (Lelieveld et al., 2016). 30 CMIP6 GCMs have limited skill in simulating

ACCEPTED VERSION SUBJECT TO FINAL EDITS

annual precipitation patterns, annual cycle statistics and long-term precipitation trends over Central Asia partially due to considerable wet biases of up to 100% in the Southern Xinjiang and Hexi Corridor regions (Guo et al., 2021). Also, CMIP6 models display a wide range of performance in reproducing ENSO teleconnections that influences the region (Barlow et al., 2021).

RCM simulations using the CORDEX-MENA domain reproduce the main features of the mean surface climatology over ARP with moderate biases (*high confidence*). RegCM4 driven by five GCMs (HadGEM2, GFDL, CNRM, CanESM2, and ECHAM6) showed an ensemble mean cold bias of about –0.7°C and dry bias of –13% over ARP (Almazroui, 2016) with a cold (warm) bias over western (south-eastern) areas (Syed et al., 2019). Temperature biases in 30-year historical simulations with WRF using three different radiation parameterizations were within ±2°C and mostly caused by surface long-wave radiation errors which affected night-time minimum temperatures over 70% of the domain (Zittis and Hadjinicolaou, 2017). Mean absolute errors in COSMO-CLM driven by ERA-Interim were about 1.2°C for temperature, 15 mm per month for precipitation and 9% for total cloud cover, and with new parameterizations of albedo and aerosols optimized for the region the RCM simulated the main climate features of this very complex area (Bucchignani et al., 2016). RegCM4.4 also simulated the main features of the observed climatology (especially for dry regions) with temperature biases within ±3.0°C. Annual precipitation was overestimated with winter and spring underestimated (Ozturk et al., 2018).

Four RCMs (REMO, RegCM4.3.5, ALARO-0, and COSMO-CLM5.0) driven by ERA-Interim, NCEP2 reanalyses and two different GCMs reproduced reasonably well the spatio-temporal patterns for temperature and precipitation though underestimated diurnal temperature range and had cold biases over mountainous and high plateau regions in all seasons. There is *low confidence* in this result because of low station density and a lack of high-elevation stations and with biases dependent on the choice of the observational dataset. However, the performance of both GCMs and RCMs is better than reanalyses when compared to available observations (Mannig et al., 2013; Ozturk et al., 2017; Russo et al., 2019; Top et al., 2021).

Atlas.5.5.4 Assessment and synthesis of projections

Temperature and precipitation projections from CMIP5/CMIP6 and CORDEX for different global warming levels, SSP and RCP scenarios, time periods and baselines are shown in Figure Atlas.17 and further details can be explored in the Interactive Atlas.

In WCA, projections for different GWLs are consistent not only in annual and seasonal warming but in ranges of the projections. Under RCP8.5, annual mean temperature will *likely* exceed 2°C by mid-century (compared with 1995–2014) and reach up to 4.8°C–6°C by the end of the century (Yang et al., 2017) with faster warming projected by the CMIP6 ensemble under SSP5-8.5. In individual county-level studies on GCM future climate projections temperatures increased by up to 7°C by the end of the century, depending on season and emission scenario (Allaberdiyev, 2010; MENRPG, 2015; Vermishev, 2015; Gevorgyan et al., 2016; Osborn et al., 2016; Aalto et al., 2017; IDOE, 2017; Salman et al., 2017). Statistical downscaling of 18 CMIP5 GCMs projected an annual temperature increase of 0.37°C per decade (under RCP4.5) with the maximum in northern WCA and warming most conspicuous in summer (Luo et al., 2019). RCM downscaling of GCMs over Central Asia projected a larger increase of temperature under RCP8.5 for the 2071–2100 period, ranging from 5°C to 8°C (Ozturk et al., 2017).

In ARP, the projected change in ensemble mean annual temperature from 30 CMIP6 models is from 1.6°C (SSP1-2.6) to 5.3°C (SSP5-8.5) by 2070–2099 compared to 1981–2010 (Almazroui et al., 2020a). The projected warming is the highest in the north, reaching 5.9°C and lowest in the south (4.7°C). COSMO-CLM projections over the CORDEX-MENA domain show for ARP and WCA a strong warming with marked seasonality for the end of the 21st century, ranging from 2.5°C in winter under RCP4.5 to 8°C in summer under RCP8.5 and with large increases found over high-altitude areas in winter and spring (Bucchignani et al., 2018; Ozturk et al., 2018). The CMIP5 multi-model mean warming in boreal summer in 2070–2099, compared with 1951–1980, is projected to be about 2.5°C and 6.5°C at the 2°C and 4°C global warming levels respectively (Huang et al., 2014).

ACCEPTED VERSION SUBJECT TO FINAL EDITS

Future projections of precipitation in Southwest Asia have large uncertainties and thus *low confidence*. There are few significant changes, little consensus on the sign and with a tendency for reduction in CMIP5 being reversed in CMIP6 across all warming levels (Ozturk et al., 2018). Statistical downscaling of 18 CMIP5 GCMs under RCP4.5 projected an increase in precipitation of 4.6 mm per decade in Southwest Asia during 2021–2060 relative to 1965–2004 (Luo et al., 2019). CMIP5 simulations project a general decrease in precipitation over lowlands in Turkey, Iran, Afghanistan and Pakistan (Ozturk et al., 2017) and increase over high-mountain regions (Aalto et al., 2017; Salman et al., 2018). At a 4°C global warming level, the multi-model mean annual precipitation for Turkmenistan and parts of Tajikistan and Uzbekistan is projected to decrease by 20%, with somewhat stronger relative decreases in summer (Reyer et al., 2017). Over northern WCA, the CMIP5 ensemble mean projects increases of over 3 mm per decade under RCP2.6 and over 6 mm per decade under RCP4.5 and RCP8.5 over the 21st century (Huang et al., 2014). Mean annual precipitation is projected to rise by 5.2% at the end of the 21st century (2070–2099) under RCP8.5, compared to 1976–2005, while mean annual snowfall is projected to decrease by 26.5% in Central Asia (Yang et al., 2017). However, regardless of the sign of the precipitation change in the high-mountain regions of Central Asia, the influence of the warming on the snowpack will *very likely* cause important changes in the timing and amount of the spring melt (Diffenbaugh et al., 2013).

In ARP, the projected change in ensemble mean annual precipitation from 30 CMIP6 models ranges from 3.8% (–2.6% to 28.8%) to 31.8% (12.0% to 106.5%) under SSP1-2.6 and SSP5-8.5 emissions for the period 2080–2100 compared with 1995–2014 (Almazroui et al., 2020a). Northwest ARP precipitation is projected to decrease between –6% to –27% per decade and in the south precipitation to increase by up to 8.6% per decade. CMIP6 projections are in line with those from CMIP3 and CMIP5, however they are less variable in the central area in CMIP6. The uncertainty associated with precipitation over ARP is large because of very low annual amounts and high variability.

Atlas.5.5.5 Summary

Increase in annual surface air temperature over Southwest Asia are *very likely* in the range of 0.24°C to 0.81°C per decade over the last 50–60 years. Annual precipitation change over ARP since 1970 is estimated at –6.3 mm per decade (and in the range of –30 to 16 mm per decade) and over WCA is generally not significant except over the elevated part of eastern WCA where increases between 1.3 mm and 4.8 mm per decade during 1960–2013 have been observed (*very high confidence*). In mountainous areas, the scarcity and decline of the number of observation sites since the end of the former Soviet Union from 1991 increase the uncertainty of the long-term temperature and precipitation estimates (*high confidence*).

Mean temperature biases in RCMs are within ±3°C in Southwest Asia, and annual precipitation biases are positive in almost all parts of the region except over the ARP where they are negative in the wet season (November to April) and over WCA in winter and spring (from December to May) (*medium confidence*). Since regional model evaluation literature has only recently emerged there is *medium evidence* about the performance of RCMs in Southwest Asia though with *medium* to *high agreement* on mean temperature and precipitation biases. RCMs simulate colder temperatures than observed over mountainous and high plateau regions (*limited evidence, high agreement*).

Further warming over Southwest Asia is projected in the 21st century to be greater than the global average, with rates varying from 0.25°C to 0.8°C per decade depending on the season and scenario and maximum rates found in the northern part of the region in summer (*high confidence*). The influence of the warming on the snowpack will *very likely* cause changes in the timing and amount of the spring melt. CMIP6 projected changes in annual precipitation totals are in the range of –3% to 29% (SSP1-2.6) and 12% to 107% (SSP5-8.5) in ARP (*medium confidence*). Strong spatio-temporal differences with overall precipitation decreases projected in the central and northern parts of WCA in summer (JJA) with increases in winter (DJF) (*medium confidence*).

ACCEPTED VERSION SUBJECT TO FINAL EDITS

Atlas.6 Australasia

The assessment in this section focuses on changes in average temperature and precipitation (rainfall and snow), including the most recent years of observations, updates to observed datasets, the consideration of recent studies using CMIP5 and those using CMIP6 and CORDEX simulations. Assessment of changes in extremes are in Chapter 11 (Table 11.10–12) and climatic impact-drivers in Chapter 12 (Table 12.5).

Atlas.6.1 Key features of the regional climate and findings from previous IPCC assessments

Atlas.6.1.1 Key features of the regional climate

Australasia is divided into five regions for the Atlas (Figure Atlas.21), as follows: New Zealand (NZ), with a varied climate with diverse landscapes, mainly maritime temperate with four distinct seasons; Northern Australia (NAU) which is mainly tropical with monsoonal summer-dominated rainfall (monsoon season December to March, see Annex V), but with a hot, semi-arid climate in the south of the region; Central Australia (CAU) with a predominantly hot, dry desert climate; Eastern Australia (EAU) with a temperate oceanic climate at the coast to semi-arid inland; and Southern Australia (SAU) which ranges from Mediterranean and semi-arid in the west to mainly cool temperate maritime climate in the southeast. Various remote drivers have notable teleconnections to regions within Australasia, including an effect of the El Niño Southern Oscillation and the Indian Ocean Dipole (Table Atlas.1, Annex IV). Much of southern NZ and SAU are affected by systems within the westerly mid-latitude circulation, in turn affected by the Southern Annular Mode. The monsoon and the Madden-Julian Oscillation affect rainfall variability in northern Australia.

Atlas.6.1.2 Findings from previous IPCC assessments

The AR5 WGI and WGII reports (IPCC, 2013c; Stocker et al., 2013; Reisinger et al., 2014) give *very high confidence* that air and sea temperatures in the region have warmed, cool extremes have become rarer in Australia and New Zealand since 1950, while hot extremes have become more frequent and intense (e.g., it is *very likely* that the number of warm days and nights have increased). The AR5 reported it is *virtually certain* that mean air and sea temperatures will continue to increase, with *very high confidence* that the greatest increase will be experienced by inland Australia and the smallest increase by coastal areas and New Zealand. The AR5 reported a range of different precipitation trends within the region. For example, while annual rainfall has been significantly increasing in north-western Australia since the 1950s (*very high confidence*), it has been decreasing in the northeast of the South Island of New Zealand over 1950–2004 (*very high confidence*) and over southwest of Western Australia. In line with these trends, WGI reported it is *likely* that drought has decreased in northwest Australia. Future projections for precipitation extremes indicate an increase in most of Australia and New Zealand, in terms of rare daily rainfall extremes (i.e., current 20-year return period events) and of short duration (sub-daily) extremes (*medium confidence*). Likewise, however, there is a projected increase the frequency of drought in southern Australia (*medium confidence*) and in many parts of New Zealand (*medium confidence*). Owing to hotter and drier conditions there is *high confidence* that the occurrence of fire weather will increase in most of southern Australia, and *medium confidence* that the fire danger index will increase in many parts of New Zealand.

AR5 reported mean sea levels have also increased in Australia and New Zealand at average rates of relative sea-level rise of 1.4 ± 0.6 mm yr^{-1} from 1900 to 2011, and 1.7 ± 0.1 mm yr^{-1} from 1900 to 2009, respectively (*very high confidence*). The assessment found that the volume of ice in New Zealand has declined by 36–61% from the mid-late 1800s to the late 1900s (*high confidence*), while late-season significant snow depth has also declined in three out of four Snowy Mountain sites in Australia between 1957 and 2002 (*high confidence*). As mean sea-level rise is projected to continue for at least several more centuries, there is *very high confidence* that this will lead to large increases in the frequency of extreme sea-level events in Australia and New Zealand. On the other hand, the volume of winter snow and the number of days with low-elevation snow cover in New Zealand are projected to decrease in the future (*very high confidence*), while both snow

ACCEPTED VERSION SUBJECT TO FINAL EDITS

depth and area are projected to decline in Australia (*very high confidence*).

SROCC (Hock et al., 2019b) reports on the observed and projected decline in snow cover in Australasia, as well as the retreat of New Zealand glaciers following an advance in 1983–2008 due to enhanced snowfall. It also reports on the vulnerability of some Australian communities and ecosystems to sea level rise, increases in the intensity and duration of marine heatwaves driven by human influence (*high confidence*), the decrease in frequency of tropical cyclones landfall on eastern Australia since the late 1800s (*low confidence* in an anthropogenic signal), and presented a case study on the multiple hazards, compound risk and cascading impacts from climate extremes in Tasmania in 2015/2016 (including an attributable human influence on some events). SRCCL (Mirzabaev et al., 2019) found widespread vegetation 'greening' has occurred in parts of Australia, and an increase in the desertification and drought risk in future in southern Australia.

Atlas.6.2 Assessment and synthesis of observations, trends and attribution

Reliable station observations are available from around 1900 in Australasia, but in some regions the coverage was and remains poor. Australia and New Zealand have continued to warm, and many rainfall trends have continued since the AR5. Changes and trends in temperature and precipitation from 1961 to 2015 from three different global data sets are displayed in Figure Atlas.11 and the Interactive Atlas and show significant (at 0.1 significance level) warming trends over the southern and eastern Australia. Most of the observed changes in precipitation over the region are not significant over this period. Although observed datasets (e.g. GPCC and GPCP) generally agree on a significant drying trend in the southern regions of New Zealand during the shorter 1980 to 2015 period, this is in fact the reverse of the longer-term trends in 1961 to 2015 (Interactive Atlas).

For a longer-term perspective based on high-quality regional datasets, Figure Atlas.20 shows Australasia has warmed over the last century (*very high confidence*). Australian mean temperature has increased by 1.44 ± 0.24°C during the period 1910–2019 using the updated observed temperature dataset ACORN-SATv2.1, with 2019 Australia's hottest year on record and nine out of ten warmest years on record occurring since 2005 (Trewin et al., 2020). Much of the warming has occurred since 1960, there is clear anthropogenic attribution of this change and emergence of the signal from the1850-1900 climate (BOM and CSIRO, 2020; Hawkins et al., 2020).Warming has been more rapid than the national average in central and eastern Australia, with a warming minimum and non-significant trends since the 1960s in the northwest (CSIRO and BOM, 2015; BOM and CSIRO, 2020). The National Institute of Water and Atmospheric Research temperature record, NIWA NZ, shows a warming of 1.13 ± 0.27°C during the period 1909–2019, although several stations show non-significant trends since 1960 (Figure Atlas.20), including a warming minimum in the southeast at least partly due to a persistent shift in atmospheric circulation (Sturman and Quénol, 2013; MfE and Stats NZ, 2017, 2020).

[START FIGURE ATLAS.20 HERE]

Figure Atlas.20: Observed trends in mean annual temperature (a–b) and summer (DJF) and inter (JJA) precipitation (c–d) for Australia and New Zealand from high-quality regional datasets. Time series show anomalies from 1961–1990 average and 10-year running mean; maps show annual linear trends for 1960–2019; rainfall trends are shown in % per decade, crosses show areas and stations with a lack of significant trend and regions of seasonally dry conditions (<0.25 mm day^{-1}) are masked and outlined in red. Datasets are Australian Climate Observation Reference Network – Surface Air Temperature version 2.1 (ACORN-SATv2.1) for Australian temperature, the Australian Gridded Climate Data (AGCD) for Australian rainfall (Evans et al., 2020a), and the 30-station high-quality network for New Zealand temperature and rainfall. Further details on data sources and processing are available in the chapter data table (Table Atlas.SM.15).

[END FIGURE ATLAS.20 HERE]

ACCEPTED VERSION SUBJECT TO FINAL EDITS

Since 1960, precipitation has increased in much of mainland Australia in austral summer and decreased in many regions of southern and eastern Australia in austral winter (Figure Atlas.20). A detectable anthropogenic signal of increases in precipitation in Australia has been reported particularly for north central Australia and for a few regions along the south-central coast for the period 1901–2010 (Knutson and Zeng, 2018). Seasonally, there is a significant decline in winter rainfall in southwest Western Australia (Figure Atlas.20), with an attributable human influence with *high confidence* (*robust evidence* and *medium agreement*) (Delworth and Zeng, 2014, and others)(see Section 10.4). Rainfall trends in the southeast are not significant since 1960 but have shown a notable reduction since the 1990s, and there is *limited evidence* for the attribution of this change to human influence (e.g., Rauniyar and Power, 2020). In New Zealand between 1960 and 2019 in both summer and winter, rainfall increased in some stations in the South Island and decreased at many stations in the North Island, however most station trends are not statistically significant (Figure Atlas.20)(MfE and Stats NZ, 2020). In JJA, Milford Sound (increasing) and Whangaparaoa (decreasing) trends are significant.

In Australia, there has been a decrease in snow depth and area since the late 1950s, especially in spring (BOM and CSIRO, 2018). Based on a reconstructed snow cover record, the recent rapid decrease in the past five decades has been shown to be larger by more than an order of magnitude than the maximum loss for any 5-decade period over the past 2000 years (McGowan et al., 2018). In New Zealand, from 1977 to 2018, glacier ice volume decreased from 26.6 km^3 to 17.9 km^3 (a loss of 33%) (Salinger et al., 2019).

Atlas.6.3 Assessment of climate model performance

Most studies assessed in WGII AR5 were based on Coupled Model Inter-comparison Project Phase 3 (CMIP3) models and Special Report on Emission Scenarios (SRES) scenarios and CMIP5 models whenever available. WGI AR5 reported that model biases in annual temperature and rainfall are similar to or lower than other continental regions outside the tropics, with temperature biases generally <1°C in the multi-model mean and <2°C in most models over Australia compared to reanalysis, and with a wet bias over the Australian inland region but a dry bias near coasts and mountain regions of both Australia and New Zealand.

Early results from CMIP6 suggest incremental improvements compared to CMIP5 in the simulation of the mean annual climatology of temperature and precipitation of the Indo-Pacific region surrounding Australasia, the teleconnection between ENSO and IOD and Australian rainfall and other relevant climate features (Grose et al., 2020). These assessments suggest that confidence in projections is similar to AR5 or incrementally improved. The CORDEX Australasia simulations are found to have cold biases in daily maximum temperature and an overestimation of precipitation but overall showed added value in the simulation of the current climate (Di Virgilio et al., 2019; Evans et al., 2020b).

Atlas.6.4 Assessment and synthesis of projections

Similar to the global average (Chapter 4), mean temperature in Australasia is projected to continue to rise through the 21st century at a magnitude proportional to the cumulative greenhouse-gas emissions (*virtually certain, very high confidence, robust evidence*), CMIP5 and CMIP6 results are shown in Figure Atlas.21. A higher end to the range of temperature projections is found in CMIP6 compared to CMIP5 (Grose et al., 2020), produced by a group of models with high climate sensitivity (Forster et al., 2019), and this creates a higher multi-model-mean change. For example, projections for Australasia including ocean between 1995–2014 and 2081–2100 are 1.4°C (1.1°C to 1.8°C 10th–90th percentile range) in CMIP5 under RCP4.5, but 1.8°C (1.3°C to 2.5°C) in CMIP6 under SSP2-4.5.

Using warming levels, the results can be directly compared accounting for the different distribution of climate sensitivities in the two ensembles. In this framework, Australasia (land only) is projected to warm by a similar amount to the global average: 1.4°C to 1.8°C for the 1.5°C warming level, through to 3.9°C to 4.8°C for the 4°C warming level from the 1850–1900 baseline in CMIP6 using SSP5-8.5 (results using other SSPs and from CMIP5 are similar). Projected warming is greater over land than ocean, greater in Australia

ACCEPTED VERSION SUBJECT TO FINAL EDITS

than in New Zealand, and greater over inland Australia than coastal regions. Due to historical warming, projected temperature change from the AR6 baseline of 1995–2014 is lower: 0.3°C to 1.0°C for the 1.5°C warming level, through to 2.9°C to 4.0°C for the 4°C warming level. Changes for other warming levels, subregions and emissions pathways are shown in Figure Atlas.21 and can be explored in the Interactive Atlas. Regional modelling suggests projected temperature increase is higher in mountainous areas than surrounding low-elevation areas in New Zealand and Australia (Olson et al., 2016; MfE, 2018).

[START FIGURE ATLAS.21 HERE]

Figure Atlas.21: Regional mean changes in annual mean surface air temperature and precipitation relative to the 1995–2014 baseline for the reference regions in Australasia (warming since the 1850–1900 pre-industrial baseline is also provided as an offset). Bar plots in the left panel of each region triplet show the median (dots) and 10th–90th percentile range (bars) across each model ensemble for annual mean temperature changes for four datasets (CMIP5 in intermediate colours; subset of CMIP5 used to drive CORDEX in light colours; CORDEX overlying the CMIP5 subset with dashed bars; and CMIP6 in solid colours); the first six groups of bars represent the regional warming over two time periods (near-term 2021–2040 and long-term 2081–2100) for three scenarios (SSP1-2.6/RCP2.6, SSP2-4.5/RCP4.5, and SSP5-8.5/RCP8.5), and the remaining bars correspond to four global warming levels (GWL: 1.5°C, 2°C, 3°C, and 4°C). The scatter diagrams of temperature against precipitation changes display the median (dots) and 10th–90th percentile ranges for the above four warming levels for December-January-February (DJF; middle panel) and June-July-August (JJA; right panel), respectively; for the CMIP5 subset only the percentile range of temperature is shown, and only for 3°C and 4°C GWLs. Changes are absolute for temperature (in °C) and relative (as %) for precipitation. See Section Atlas.1.3 for more details on reference regions (Iturbide et al., 2020) and Section Atlas.1.4 for details on model data selection and processing. The script used to generate this figure is available online (Iturbide et al., 2021) and similar results can be generated in the Interactive Atlas for flexibly defined seasonal periods. Further details on data sources and processing are available in the chapter data table (Table Atlas.SM.15).

[END FIGURE ATLAS.21 HERE]

In line with recent trends, a significant reduction in annual mean rainfall in southwest Australia is projected, with the greatest reduction in winter and spring (*very likely*, *high confidence*). There is more than 80% model agreement for projected mean annual rainfall decrease in southwest Western Australia for both mid (2041–2060) and far (2081–2100) future, and for all warming levels (Interactive Atlas). Rainfall decreases, mainly in winter and spring, are also projected for other regions within southern Australia with only *medium confidence* (*medium evidence* and *medium agreement*). Almost all models project continued drying in SAU in winter (JJA) and also in spring (SON), but a few models show little change. CMIP5 and CMIP6 results are similar or with a slightly narrower range in the latter (Figure Atlas.21). CORDEX produces a similar range of change in winter rainfall change for SAU as a whole. Circulation change is the dominant driver of these projected reductions, explaining the range of model results for southern Australia (CSIRO and BOM, 2015; Mindlin et al., 2020). Studies of winter rainfall change and circulation in southern Australia suggest the wettest changes in winter rainfall change may possibly be rejected (Grose et al., 2017, 2019a).

The model mean projection of northern Australian wet season precipitation (a period including DJF) is for little change under all SSPs and warming levels, with *low confidence* in the direction of change as the projections include both large and significant decrease and increases (Figure Atlas.21, Interactive Atlas). Evidence from warming patterns suggests a constraint on the dry end of projections (Brown et al., 2016), and the CMIP6 ensemble suggests that the projection follows the zonally-averaged rainfall response in the southern hemisphere rather than changes in the western Pacific (Narsey et al., 2020). There is also evidence for a projected increase in rainfall variability in northern Australia in scales from days to decades (Brown et al., 2017). Liu et al. (2018) find that under 1.5°C warming, central and northeast Australia is projected to become wetter, however this projection has *low confidence*. There are similar projections from CMIP5 and CMIP6 (Figure Atlas.21).

ACCEPTED VERSION SUBJECT TO FINAL EDITS

Projections for EAU vary by season, with moderate model agreement on a decrease in rainfall in winter and spring, but with lower agreement in CMIP6 compared to CMIP5, and low model agreement on the direction of change in summer (Figure Atlas.21). CAU shows a similar range of change as EAU, with low model agreement on the direction of change in DJF, moderate agreement on direction of change in JJA, but significant changes are projected by some models. Other seasonal and regional rainfall changes in Australia are reviewed in Dey et al. (2019).

For the NZ reference region, precipitation is projected to increase in winter and annual rainfall, with some differences in magnitude between CMIP5, CMIP6 and CORDEX (Figure Atlas.21). This projection of rainfall increase is a function of changes in the southern extent of the region, and notable regional differences are expected. Regional modelling suggests precipitation increases in the west and south of New Zealand and decreases in the north and east (MfE, 2018), with *medium confidence*, and with notable differences by season. Liu et al. (2018) project that the North Island will be drier, while the South Island will be wetter under both 1.5°C and 2°C warming levels. The projected increase in precipitation in the far future (2081–2100) for the southern regions of NZ has *high agreement* (Interactive Atlas). Other seasonal and regional rainfall changes in Australia can be explored in the Interactive Atlas.

The CORDEX Australasia simulations produce some regional detail in projected precipitation change associated with important features such as orography. Areas where there is coincident 'added value' in the simulation of the current climate and 'potential added value' as new information in the projected climate change signal (collectively termed 'realised added value') in Australia include the Australian Alps, Tasmania and parts of northern Australia (Di Virgilio et al., 2020). There have been several studies of regional climate change for New Zealand and states within Australia at fine resolution (5–12 km) that have produced important insights. One is enhanced drying in cool seasons on the windward slopes of the southern Australian Alps (decreases of 20–30% compared to 10–15% in the driving models), and conversely a chance of enhanced rainfall increase on the peaks of mountains in summer (Grose et al., 2019b), with the summer finding in line with those for the European Alps (Giorgi et al., 2016).

Under future warming, the snowpack in Australia is projected to decrease by approximately 15% and 60% by 2030 and 2070 respectively under the SRES A2 scenario (Di Luca et al., 2018), while in New Zealand the number of annual snow days is projected to decrease by 30 days or more by 2090 under RCP8.5 (MfE, 2018). New Zealand is also projected to lose up to 88 ± 5% of its glacier volume by the end of the 21st century (Chinn et al., 2012; Hock et al., 2019a).

Atlas.6.5 Summary

There is *very high confidence* that the climate of Australia warmed by around 1.4°C and New Zealand by around 1.1°C since reliable records began in 1910 and 1909 respectively, with human influence the dominant driver. Warming is *virtually certain* to continue, with a magnitude roughly equal to the global average temperature. A significant decrease in April to October rainfall in southwest Western Australia is observed from 1910 to 2019, is attributable to human influence with *high confidence* and is *very likely* to continue in future noting consistent projections in CMIP5 and CMIP6. Other observed and projected rainfall trends are less significant or less certain. Model representation of the climatology of Australasian temperature and rainfall has improved since AR5, through an incremental improvement between CMIP5 and CMIP6 and the development of coordinated regional modelling through CORDEX-Australasia. Snow cover is *likely* to decrease throughout the region at high altitudes in both Australia and New Zealand (*high confidence*).

Atlas.7 Central and South America

The assessment in this section focuses on changes in average surface temperature and precipitation (rainfall and snow), including the most recent years of observations, updates to observed datasets, the consideration of recent studies using CMIP5 and those using CMIP6 and CORDEX simulations. Assessment of changes in extremes are in Chapter 11 (Table 11.13–15) and climatic impact-drivers in Chapter 12 (Table 12.6). It

ACCEPTED VERSION SUBJECT TO FINAL EDITS

considers climate change over the regions show in Figure Atlas.22, extending to all territories from Mexico to South America, including the Caribbean islands. This figure supports the assessment of regional mean changes over the region which, due to the high climatological and geographical heterogeneity, has been split into two subregions: Central America and the Caribbean, and South America.

[START FIGURE ATLAS.22 HERE]

Figure Atlas.22: Regional mean changes in annual mean surface air temperature and precipitation relative to the 1995–2014 baseline for the reference regions in Central America, the Caribbean and South America (warming since the 1850–1900 pre-industrial baseline is also provided as an offset). Bar plots in the left panel of each region triplet show the median (dots) and 10th–90th percentile range (bars) across each model ensemble for annual mean temperature changes for four datasets (CMIP5 in intermediate colours; subset of CMIP5 used to drive CORDEX in light colours; CORDEX overlying the CMIP5 subset with dashed bars; and CMIP6 in solid colours); the first six groups of bars represent the regional warming over two time periods (near-term 2021–2040 and long-term 2081–2100) for three scenarios (SSP1-2.6/RCP2.6, SSP2-4.5/RCP4.5, and SSP5-8.5/RCP8.5), and the remaining bars correspond to four global warming levels (GWL: 1.5°C, 2°C, 3°C, and 4°C). The scatter diagrams of temperature against precipitation changes display the median (dots) and 10th–90th percentile ranges for the above four warming levels for December-January-February (DJF; middle panel) and June-July-August (JJA; right panel), respectively; for the CMIP5 subset only the percentile range of temperature is shown, and only for 3°C and 4°C GWLs. Changes are absolute for temperature (in °C) and relative (as %) for precipitation. See Section Atlas.1.3 for more details on reference regions (Iturbide et al., 2020) and Section Atlas.1.4 for details on model data selection and processing. The script used to generate this figure is available online (Iturbide et al., 2021) and similar results can be generated in the Interactive Atlas for flexibly defined seasonal periods. Further details on data sources and processing are available in the chapter data table (Table Atlas.SM.15).

[END FIGURE ATLAS.22 HERE]

Atlas.7.1 Central America and the Caribbean

Atlas.7.1.1 Key features of the regional climate and findings from previous IPCC assessments

Atlas.7.1.1.1 Key features of the regional climate

The Central America and Caribbean region is assessed considering three reference regions South Central America (SCA), including the isthmus and the Yucatan peninsula; North Central America (NCA), including Mexico (centre and north); and the Caribbean (CAR), including the Greater Antilles, the Lesser Antilles, the Bahamas and other small islands (see Figure Atlas.22); NCA is also covered in Section Atlas.9 North America.

Precipitation in most of SCA is characterized by two maxima in June and September, an extended dry season from November to May, and a shorter relatively dry season between July and August known as the midsummer drought (MSD) (Magaña et al., 1999; Perdigón-Morales et al., 2018) (see Chapter 10). To some extent, precipitation seasonality is explained by the migration of the Intertropical Convergence Zone (ITCZ) (Taylor and Alfaro, 2005). The climate of NCA is temperate to the north of the Tropic of Cancer, with marked difference between winter and summer, modulated by the North American monsoon (NAmerM, Section 8.3.2.4.4). CAR has two main seasons, characterized by differences in temperature and precipitation. The wet or rainy season, with higher values of temperature and accumulated precipitation, occurs during the boreal summer and part of spring and autumn (Gouirand et al., 2020). The MSD is also present in the Greater Antilles and the Bahamas (Taylor and Alfaro, 2005), influenced by the oscillations of the North Atlantic Subtropical High (NASH), interacting with the Pacific and Atlantic branches of the ITCZ and modulated by the Atlantic Warm Pool and the Caribbean Low-Level Jet (CLLJ), while the Atlantic ITCZ is responsible for the unimodal rainfall cycle of the central and southern Lesser Antilles (Martinez et al., 2019). The CLLJ is a persistent climatological feature of the low-level circulation in the Central Caribbean, with a characteristic semi-annual cycle with maxima in the summer (main) and winter (secondary) (Amador, 1998; Magaña et al.,

ACCEPTED VERSION SUBJECT TO FINAL EDITS

1999; Whyte et al., 2008). Temporal variability is influenced by several large-scale atmospheric modes (see Annex IV and Table Atlas.1). A significant positive correlation between precipitation rates in CAR and the Atlantic Multidecadal Variability was found (Enfield et al., 2001). A similar result was found in southern Mexico (north of SCA) in the MSD region (Méndez and Magaña, 2010; Cavazos et al., 2020) (see case-study discussion in Section 10.4.2.3). On the other hand, ENSO favours wet conditions in NCA, but its effect is modulated by Pacific Decadal Variability (Maldonado et al., 2016).

One of the most prominent features of the regional climate is the incidence of tropical cyclones (TCs), which represent an important hazard for almost all the countries of the region between June and November. A detailed assessment is given in Chapter 11.

Atlas.7.1.1.2 Findings from previous IPCC assessments

According to the AR5 (Christensen et al., 2013), significant positive trends of temperature have been observed in Central America (*high confidence*), while significant precipitation trends are regionally dependent, especially during the summer. In addition, changes in climate variability and in extreme events have severely affected the region (*medium confidence*). A decrease in mean precipitation is projected in SCA and NCA. El Niño and La Niña teleconnections are projected to move eastwards in the future (*medium confidence*), while changes in their effects on other regions, including Central America and the Caribbean is uncertain (*medium confidence*). There is *medium confidence* in projections showing an increase in seasonal mean precipitation on the equatorial flank of the ITCZ affecting parts of Central America and the Caribbean.

In relation to the 1986–2005 baseline period, temperatures are *very likely* to increase by the end of the century, even for the RCP2.6 scenario, with changes of more than 5°C in some regions for the RCP8.5 scenario. Precipitation change is projected to vary between +10% and –25% (*medium confidence*) (Christensen et al., 2013). SR1.5 (Hoegh-Guldberg et al., 2018) states there is a *high agreement* and *robust evidence* that at the 1.5°C global warming level the Caribbean region will experience a 0.5°C to 1.5°C warming compared to the 1971–2000 baseline period, with greatest warming over larger land masses.

Atlas.7.1.2 Assessment and synthesis of observations, trends and attribution

Significant warming trends between 0.2°C and 0.3°C per decade have been observed in the three reference regions of Central America in the last 30 years (Planos Gutiérrez et al., 2012; Jones et al., 2016c; Hidalgo et al., 2017), with the largest increases in the North America monsoon region (*high confidence*) (Cavazos et al., 2020) (see also Figure Atlas.11 and the Interactive Atlas). There is *high confidence* of increasing temperature over parts of NCA, reaching 0.5°C per decade in Mexico and southern Baja California. with a lower rate (0.2°C per decade) in the Yucatan Peninsula and the Guatemala Pacific coastal region (Cueto et al., 2010; García Cueto et al., 2013; Martínez-Austria et al., 2016; Martínez-Austria and Bandala, 2017; Navarro-Estupiñan et al., 2018; Cavazos et al., 2020) and CAR (McLean et al., 2015) over the last 30 to 40 years. Cooling trends have been detected in limited areas of Honduras and northern Panama (Hidalgo et al., 2017).

Changes in mean precipitation rates are less consistent and long-term trends are generally weak. Different databases show significant differences depending mainly on the type and resolution of data (Centella-Artola et al., 2020). Small positive trends were observed in the total annual precipitation (Stephenson et al., 2014). In SCA and CAR, trends in annual precipitation are generally non-significant, with the exception of small significant positive trends for subregions or limited periods (Planos Gutiérrez et al., 2012; Hidalgo et al., 2017) and the 1970–1999 trends in precipitation in SCA are generally non-significant (Jones et al., 2016a; Hidalgo et al., 2017). Positive trends in the duration of the MSD have been found in this region over the past four decades (Anderson et al., 2019) (*low confidence*). For CAR see also Section Atlas.10 Small Islands.

Atlas.7.1.3 Assessment of model performance

The ability of climate models to simulate the climate in this region has improved in many key aspects

ACCEPTED VERSION SUBJECT TO FINAL EDITS

(Karmalkar et al., 2013; Fuentes-Franco et al., 2014, 2015, 2017; Vichot-Llano et al., 2014; Vichot-Llano and Martínez-Castro, 2017; Martínez-Castro et al., 2018a). Particularly relevant for this region are increased model resolution and a better representation of the land-surface processes (*high confidence*).

Regional climate models (RCMs) forced with reanalyses and atmosphere-only global climate models provide simulations with a reasonably good performance over the core North American monsoon, mostly in NCA (*high confidence*) (Bukovsky et al., 2013; Cerezo-Mota et al., 2015). RCMs also reproduce the seasonal spatial patterns of temperature and the bimodal rainfall characteristics of the NCA, SCA and CAR (*high confidence*) (Karmalkar et al., 2013; Centella-Artola et al., 2015; Martínez-Castro et al., 2018b; Cavazos et al., 2020; Vichot-Llano et al., 2020) though in some subregions specific models overestimate and shift the month of the maxima. RCM simulations in the region do not necessarily improve with the size of the domain, as important features of the regional circulation and key rainfall climate features, such as the CLLJ and MSD, are well represented for a variety of domains of different sizes (Centella-Artola et al., 2015; Cabos et al., 2018; Martínez-Castro et al., 2018b; Cavazos et al., 2020; Vichot-Llano et al., 2020) (*high confidence*).

Atlas.7.1.4 Assessment and synthesis of projections

Figure Atlas.22 and the Interactive Atlas synthesize regional mean changes in annual mean surface air temperature and precipitation for the Central America reference regions for CMIP6, CMIP5 and CORDEX for different warming levels and time periods. At the 1.5°C GWL, it is *very likely* that average annual temperature in Central America over land surpasses 1.3°C (CAR), 1.7°C (NCA) and 1.6°C (SCA). For the 3°C GWL, the corresponding projected ensemble mean regional warming values are 2.7°C (CAR), 3.5°C (NCA) and 3.1°C (SCA). CAR average annual warming is below the level of global warming, while the two continental reference regions are close to the global warming level with CMIP6 and CMIP5 showing very consistent results (Figure Atlas.22). However, when focusing in time slices instead of warming levels, the CMIP6 projections show systematically higher median values than CMIP5. CORDEX results are also consistent with the previous findings, though the subset of driving models spans a smaller range of uncertainty, particularly over CAR. Results have also been reported for this region based on CMIP5, CMIP6 and downscaled simulations over the CORDEX CAM domain or similar smaller domains (Taylor et al., 2013a; Nakaegawa et al., 2014; Imbach et al., 2018; Vichot-Llano et al., 2019; Almazroui et al., 2021). Statistical downscaling methods have been also applied to CMIP5 projections to obtain bias-adjusted regional projections (Colorado-Ruiz et al., 2018; Taylor et al., 2018; Vichot-Llano et al., 2019).

Global and regional models consistently project warming in the whole region for the end of the century, under RCP4.5 and RCP8.5 for CMIP5 projections with greater warming for continental compared to insular territories, *likely* reaching values between 2°C and 4°C (*high confidence*) (Campbell et al., 2011; Karmalkar et al., 2011; Cavazos and Arriaga-Ramírez, 2012; Cantet et al., 2014; Chou et al., 2014; Coppola et al., 2014; Hidalgo et al., 2017; Colorado-Ruiz et al., 2018; Imbach et al., 2018). The greatest warming of 5.8°C for the end of the century was projected for northern Mexico under RCP8.5 (Colorado-Ruiz et al., 2018), using an ensemble of CMIP5 GCMs (see also the Interactive Atlas).

Regarding precipitation, it is *likely* that the annual average precipitation changes for the 1.5°C GWL will be in the ranges of –11% to 0% in CAR, from –12% to 0% in SCA, and from –10% to +3% in NCA (Interactive Atlas). For the 3°C GWL, the corresponding annual average precipitation changes will be from –17% to –2% in CAR, from –16% to +2% in NCA, and from –23% to 0% in SCA. A clear drying tendency is observed for the 3°C GWL relative to the 1.5°C GWL. Maloney et al. (2014) examined 21st-century climate projections of North American climate in CMIP5 models under RCP8.5, including Central America and the Caribbean. Summertime drying was projected in CAR and SCA for most of the models, with good agreement. The strongest drying is projected to occur during July and August which are the months when the MSD occurs in many subregions (Figure Atlas.22 and the Interactive Atlas). Intensification of the MSD in SCA was also projected by using the Rossby Centre Regional Climate Model (RCA4) (Corrales-Suastegui et al., 2020), but with future decrease in area and frequency (see Cross-Chapter Box Atlas.2). They also found a projected intensification of CLLJ and drying for the future time slice of 2071–2095, relative to their baseline of 1981–

ACCEPTED VERSION SUBJECT TO FINAL EDITS

2005. Decreased precipitation was also projected for SCA (Imbach et al., 2018) with the 8-km resolution Eta RCM during the rainy season, including an intensification of the MSD, although no significant change was projected for the CLLJ.

Colorado-Ruiz et al. (2018) assessed an ensemble of 14 GCMs from CMIP5 for a 1971–2000 baseline period, projecting precipitation decreases of between 5% and 10% by the end of the century for the RCP4.5 and RCP8.5 scenarios respectively. The greatest decrease in precipitation is projected during summer reaching 13%, especially in southern Mexico, Central America and the Caribbean. Dynamically downscaled simulations (Bukovsky et al., 2015) also projected a decrease of precipitation for the middle of the century (2041–2069) relative to 1971–1999 for the north of Mexico, though despite good agreement amongst the models, these results must be considered of *low confidence*, because of their poor simulation of important monsoon physical processes. Vichot-Llano et al. (2021) used a multiparameter ensemble of RegCM4, driven by the CMIP5 global model HagGEM2-ES projections to conclude that, relative to the 1975–2004 baseline, in the near (2020–2049) and more prominently in the far (2070–2099) future, drier conditions will prevail at over the eastern Caribbean. The projected future warming trend was statistically significant at the 95% confidence level over CAR and SCA. Almazroui et al. (2021) used an ensemble of 31 CMIP6 models to estimate climate change signals of temperature and precipitation in six reference regions in North, Central America and the Caribbean, finding a decrease in precipitation (10–30 %) over Central America and the Caribbean under three scenarios with regional and seasonal variations.

There is *high agreement* and *high confidence* in the projected decrease of precipitation by the end of the century for most of the region particularly for annual and summer precipitation, but there is *low confidence* on the magnitude of this decrease which varies between 5% and 50% for different projections and different subregions (see extended information in the Interactive Atlas).

The status of climate extreme trends and projections for the region has been assessed in Chapter 11 and the main findings are synthesized here. There is *high confidence* in the projections of significant heatwave events at the end of the century in SCA (Angeles-Malaspina et al., 2018) and an increase in warm days and warm nights over this region and CAR (Stennett-Brown et al., 2017). For CAR islands, using dynamically downscaled CMIP3 models, Karmalkar et al. (2013) projected increase in drought severity at the end of the century, mainly due to precipitation decrease during the early wet season. In SCA projections suggest an increase in the MSD (Imbach et al., 2018) and increase in consecutive dry days (Chou et al., 2014), consistent with the projections of Stennett-Brown et al. (2017).

Atlas.7.1.5 Summary

Significant warming trends between 0.2°C and 0.3°C per decade have been observed in the three reference regions of Central America in the last 30 years, with the largest increases in the North America monsoon region (*high confidence*). Changes in mean precipitation rates are less consistent and long-term trends are generally weak. Small positive trends were observed in the total annual precipitation in part of the region.

Warming in the continental part of the region is projected to increase in the range of the mean global values for GWL of 1.5°C and 3°C, but in the Caribbean regional warming will be lower. Precipitation is projected to decrease with increasing GWLs especially for CAR and SCA.

Projected change in mean annual precipitation shows a large spatial variability across Central America and the Caribbean. Under moderate future emissions overall negative but non-significant precipitation trends are projected for the 21st century (*low confidence*). Under higher emissions scenarios and at higher GWLs, average precipitation is *likely* to decrease in most of the region, particularly in the north-western and central Caribbean and part of continental Central America, especially in SCA.

ACCEPTED VERSION SUBJECT TO FINAL EDITS

Atlas.7.2 South America

Atlas.7.2.1 Key features of the regional climate and findings from previous IPCC assessments

Atlas.7.2.1.1 Key features of the regional climate

Regional synthesis of observed and modelled climate in South America is challenging due to the latitudinal extent of the continent, the Andes mountains, and local to regional climatic features, which are influenced by multiple drivers. The main large-scale drivers include many modes of natural variability (Annex IV.2): the interdecadal modes, Atlantic Multidecadal Variability (AMV) and Pacific Decadal Variability (PDV); the interannual-to-annual modes, El Niño-Southern Oscillation (ENSO), the Indian Ocean Dipole (IOD), the Southern Annular Mode (SAM) and the North Atlantic Oscillation (NAO); seasonal variability driven by the meridional migration of the Intertropical Convergence Zone and the timing and intensity of the South American Monsoon System (SAmerM, Section 8.3.2.4.5), the Madden-Julian Oscillation sub-seasonal mode of natural variability (MJO) and the behaviour at finer scales of the tropical easterly waves.

The regional assessment in this section emphasizes the seven new South American reference regions (Figure Atlas.22) (Iturbide et al., 2020) that have a largely consistent climate and response to climate change and can be used for analysis and impact studies (Solman et al., 2008; Neukom et al., 2010; Barros et al., 2015; Nobre et al., 2016). At the subregional scale, several phenomena drive climate variability. Brazil's northeast (North-Eastern South America; NES) is the most densely populated dryland globally and recurrently affected by climatic extremes. The climate variability, particularly the precipitation, is marked by strong interannual variability related to ENSO, the ITCZ, and the North Tropical Atlantic Ocean SSTs (Marengo et al., 2018a). Northern (NSA) and North-Western South America (NWS) are part of the Amazonia region. Its most recognizable features are the high rainfall, high humidity, and high temperatures that prevail in the region. Rainfall variability in these regions results from the interplay between regional atmospheric circulation, the SSTs variations in both the Pacific and Atlantic ocean, among other regional-to-local interactions (Marengo and Espinoza, 2016; Espinoza et al., 2020). The South America monsoon (SAM) region has distinct wet (summer) and dry (winter) periods. Key drivers include the South Atlantic Convergence Zone (Marengo et al., 2012), the Bolivian High the 40- to 60-day intraseasonal oscillation, and the forcing of the high Andes Mountains to the west (Almeida et al., 2017). The geographic position of South-Western South America (SWS) results in very specific climatic characteristics since SWS contains subtropical climates as well as sub-Antarctic and Antarctic climates. The climate of SWS is driven by seasonal changes in the position of subtropical high-pressure air masses in the South Atlantic and South Pacific ocean, the Southern Annular Mode, the dynamics of the cold Humboldt ocean current, and the icy cold fronts and mid-latitude westerlies (Valdés-Pineda et al., 2016). The densely populated, highly productive subregion of South-Eastern South America (SES) has cool winters and hot summers typical of the temperate zone, and climatic conditions are strongly tied to ENSO, whose influence is moderated by local air-sea thermodynamics in the South Atlantic (Barreiro, 2010). Lastly, the climate of the southern tip of South America (SSA) is cold and dry, and is influenced by the Southern Annular Mode, and the interaction between the wetter Pacific winds and the Andean Cordillera (Aceituno, 1988; Silvestri and Vera, 2009).

Atlas.7.2.1.2 Findings from previous IPCC assessments

According to WGII AR5 Chapter 27 (Magrin et al., 2014), during the last decades of the 20th century, observational studies identified significant trends in precipitation and temperature in South America (*high confidence*). Increasing trends in annual rainfall in south-eastern South America contrast with decreasing trends in central southern Chile and some regions of Brazil. Warming has been detected throughout South America (near 0.7°C to 1°C in the 40 years since the mid-1970s), except for a cooling off the Chilean coast of about –1°C over the same period.

WGI AR5 (Flato et al., 2013) noted that climate simulations from CMIP3 and CMIP5 models were able to represent well the main climatological features, such as seasonal mean and annual cycle (*high confidence*), although some biases remained over the Andes, Amazon basin and for the South America Monsoon. On the other hand, climate models from CMIP5 showed better results when compared to CMIP3.

ACCEPTED VERSION SUBJECT TO FINAL EDITS

The SR1.5 (Hoegh-Guldberg et al., 2018) assessed that a further increase of 0.5°C or 1°C is likely to have detectable effects on mean temperature and precipitation in South America, particularly in tropical regions (NWS, NAS, SAM and NES), as well as in SES given that changes in mean temperatures and precipitation have already been attributed in the last decades for global warming of less than 1°C.

Atlas.7.2.2 Assessment and synthesis of observations, trends and attribution

Studies on climatic trends in South America indicate that mean temperature and extremely warm maximum and minimum temperatures have shown an increasing trend (*high confidence*), particularly for a large region in northern South America and the south-western Andes (NSA, SAM, NES, SWS and the north of SES) (Skansi et al., 2013; de Barros Soares et al., 2017). Also, the trend of the difference between the annual mean of the daily maximum temperature and the annual mean of the daily minimum temperature was positive – up to 1°C per decade – over the extra-tropics with the maximum temperature generally increasing faster than the minimum temperature, while a negative trend – up to –0.5°C per decade – was observed over the tropics.

Regionally, analyses of temperatures point to an increased warming trend (*high confidence*) over Amazonia over the last 40 years, which reached approximately 0.6°C–0.7°C (Figure Atlas.11 and the Interactive Atlas) and with stronger warming during the dry season and over the southeast. The analyses also showed that 2016 was the warmest year since at least 1950 (Marengo et al., 2018b). Andean temperatures showed significant warming trends, especially at inland and higher-elevation sites, while trends are non-significant or negative at coastal sites (Vuille et al., 2015; Burger et al., 2018; Vicente-Serrano et al., 2018; Pabón-Caicedo et al., 2020) (*high confidence*). Over central Chile, positive trends are largely restricted to austral spring, summer and autumn seasons for mean, maximum and minimum temperatures (Burger et al., 2018; Vicente-Serrano et al., 2018). Over Peru trends of maximum air temperature were mainly amplified during the austral summer, but trends of cold season minimum air temperature showed an opposite pattern, with the strongest warming being recorded in the austral winter (Vicente-Serrano et al., 2018).

In general, the spatial patterns of observed trends in temperature are more consistent than for precipitation across the whole South America (Interactive Atlas) (de Barros Soares et al., 2017) (*medium confidence*). In southeast Brazil there is a region of highly significant decrease of rainfall in both wet and dry seasons recorded in the period 1979–2011 (Rao et al., 2016) (Interactive Atlas). The most consistent evidence of positive rainfall trend occurs in the southern part of the La Plata Basin (southern Brazil, Uruguay, and north-eastern Argentina) (de Barros Soares et al., 2017) (*high confidence*). By contrast, there is *high confidence* that annual rainfall has decreased over northeast Brazil during the last decades (Carvalho et al., 2020). Contrary to temperature changes, trends in annual precipitation exhibit different signs across sectors in the Andes. For instance, annual precipitation trends in north tropical (north of 8°S) and south tropical (8°S–27°S) Andes do not show a homogeneous pattern. Over the subtropical Andes, central Chile shows a robust signal of declining precipitation since 1970 (Pabón-Caicedo et al., 2020) (*high confidence*).

Observational studies show that the dry-season length over southern Amazonia has increased significantly since 1979 (Fu et al., 2013; Alves, 2016) (*high confidence*). In the Peruvian Amazon-Andes basin, there is no trend in mean rainfall during the period 1965–2007 (Lavado Casimiro et al., 2012) though statistically significant decreases in total annual rainfall in the central and southern Peruvian Andes from 1966 to 2010 were found (Heidinger et al., 2018). Despite that, recent analyses of Amazon hydrological and precipitation data suggest an intensification of the hydrological cycle over the past few decades (Gloor et al., 2015). In general, these changes are attributed mainly to decadal climate fluctuations (*high confidence*), ENSO, the Atlantic SST north-south gradient, feedbacks between fire and land-use change mainly across southern south-eastern Amazon and changes in the frequency of organized deep convection (Fernandes et al., 2015a; Sánchez et al., 2015; Tan et al., 2015).

Since AR5, there has been limited attribution literature in the South America. Recent publications based on observational and modelling evidence assessed that anthropogenic forcing in CMIP5 models explains with the overall warming (*high confidence*) over the entire South American continent, including the increase in the frequency of extreme temperature events (Hannart et al., 2015) such as the Argentinian heatwave of

ACCEPTED VERSION SUBJECT TO FINAL EDITS

December 2013 (Chapter 11). It has a detectable influence in explaining positive and negative precipitation trends observed in regions such as SES and the Southern Andes (Vera and Díaz, 2015; de Barros Soares et al., 2017; Boisier et al., 2018; de Abreu et al., 2019). Despite that, there is *limited evidence* that human-induced greenhouse gas emissions had an influence on the 2014/2015 water shortage in Southeast Brazil (Otto et al., 2015). Extreme event attribution on sub-continental scales is assessed in Chapter 11 and continental-scale attribution in Chapter 3.

In summary, analyses of historical temperature time series point strongly to an increased warming trend (*high confidence*) across many South American regions, except for a cooling off the Chilean coast. Annual rainfall has increased over south-eastern South America and decreased in most tropical land regions, particularly in central Chile (*high confidence*). The number and strength of extreme events, such as extreme temperatures, droughts and floods, have already increased (*medium confidence*) (see Table 11.7).

It is noted that the major barrier to the study of climate change in many regions of South America is still the absence or insufficiency of long time series of observational data (Carvalho, 2020; Condom et al., 2020). Most national datasets were created in the 1970s and 1980s, preventing a more comprehensive long-term trend analysis. To fulfil the users' demand for climatological and meteorological data products covering the whole region, several interpolation techniques have been used with reanalysis and gridded gauge-analysis products to add the necessary spatial detail to the climate analyses over land and for climate variability and trend studies but these are subject to uncertainties (Skansi et al., 2013; Rozante et al., 2020).

Atlas.7.2.3 Assessment of model performance

Since AR5 the number of publications on climate model performance and their projections in South America has increased, particularly for regional climate modelling studies (Giorgi et al., 2009; Boulanger et al., 2016; Ambrizzi et al., 2019) and the understanding of their strengths and weaknesses (*high confidence*).

Most global and regional climate models can simulate reasonably well the current climatological features of South America, such as seasonal mean and annual cycles. However, significant biases persist mainly at regional scales (*high confidence*) (Torres and Marengo, 2013; Blázquez and Nuñez, 2013b; Gulizia et al., 2013; Joetzjer et al., 2013; Jones and Carvalho, 2013; Gulizia and Camilloni, 2015; Zazulie et al., 2017a; Abadi et al., 2018; Barros and Doyle, 2018; Solman and Blázquez, 2019; Teichmann et al., 2020; Fan et al., 2020; Rivera and Arnould, 2020). During the dry season, precipitation is underestimated in most models over Amazonia (*medium evidence and high agreement*) (Torres and Marengo, 2013; Yin et al., 2013; Solman and Blázquez, 2019). Over regions with complex orography, such as the tropical Andes of NWS, CMIP5 models tend to underestimate precipitation which is associated with the misrepresentation of the Pacific ITCZ and the local low-level jets (Sierra et al., 2015, 2018), whereas over the subtropical central Andes in SWS, the models are found to overestimate both mean temperature and precipitation values (*limited evidence* and *high agreement*) (Zazulie et al., 2017b; Rivera and Arnould, 2020; Díaz et al., 2021). Most models show a dry bias over SES (Díaz and Vera, 2017; Barros and Doyle, 2018; Solman and Blázquez, 2019; Díaz et al., 2021) associated with an underestimation of the northern flow that brings water vapour into the region (*medium confidence*) (Gulizia et al., 2013; Zazulie et al., 2017a; Barros and Doyle, 2018). The biases in seasonal precipitation, annual precipitation and climate extremes over several regions of South America were reduced, including the Amazon, central South America, Bolivia, eastern Argentina and Uruguay, in the CMIP5 models when compared to those of CMIP3 (*medium confidence*) (Joetzjer et al., 2013; Gulizia and Camilloni, 2015; Díaz and Vera, 2017). The evidence is still insufficient to determine whether CMIP6 biases are reduced when compared with CMIP5 simulations regarding precipitation and its variability in South America. The temperature and precipitation patterns of anomalies associated with ENSO in the tropical South America (NWS, NSA and NES) are better captured by GCMs in tropical South America (NWS, NSA and NES) than in extra-tropical South America (SES), particularly during austral summer and autumn (*limited evidence* and *high agreement*) (Tedeschi and Collins, 2016; Perry et al., 2020).

Based on regional simulations, studies showed that some RCMs improve the quality of the simulated climate when compared with the driving GCM (*medium evidence* and *high agreement*) (Llopart et al., 2014; Sánchez

ACCEPTED VERSION SUBJECT TO FINAL EDITS

et al., 2015; Falco et al., 2019; Solman and Blázquez, 2019; Ciarlo et al., 2020; Teichmann et al., 2020). Regional climate model (RCM) simulations over South America can reproduce the main features of temperature and precipitation in terms of both spatial distributions (Solman et al., 2013; Falco et al., 2019) and seasonal cycles over the different climate regimes, including the main SAmerM features (*high confidence*) (Jacob et al., 2012; Solman, 2013; Llopart et al., 2014; Reboita et al., 2014a; de Jesus et al., 2016; Lyra et al., 2018; Bozkurt et al., 2019; Ashfaq et al., 2020). However, RCMs showed systematic biases such as precipitation overestimations and temperature underestimations along the Andes throughout the (*high confidence*) although these biases may be artificially amplified by the lack of a dense observational station network (Jacob et al., 2012; Solman et al., 2013; Bozkurt et al., 2019; Falco et al., 2019). RCMs tended to show dry biases over the Amazon and the northern part of the continent (SAM, NSA) during DJF and during the maximum precipitation associated with the intertropical convergence zone (ITCZ) over NSA during JJA (*medium evidence and high agreement*) (Solman et al., 2013; Falco et al., 2019). Temperature overestimation and precipitation underestimation over La Plata Basin (in SES) are also RCM common biases with the warm bias amplified for austral summer and the dry bias amplified for the rainy season (*high confidence*) (Solman et al., 2013; Reboita et al., 2014a; Solman, 2016; Falco et al., 2019). Despite their relevance RCM simulations at very high resolution (less than 10 km) are still few in South America (*high confidence*) and are mainly designed for specific regions or purposes (Lyra et al., 2018; Bozkurt et al., 2019; Bettolli et al., 2021).

The evaluation of statistical downscaling models (ESD) in representing regional climate features in South America has increased since the AR5, however there are still few ESD studies over the different subregions. Precipitation simulations based on ESD models are able to reproduce mean precipitation over tropical and subtropical South American regions, especially over maximum precipitation areas in western Colombia, south-eastern Peru, central Bolivia, Chile and the La Plata basin (*medium confidence*) (Souvignet et al., 2010; Mendes et al., 2014; Palomino-Lemus et al., 2015, 2017, 2018; Troin et al., 2016; Soares dos Santos et al., 2016; Borges et al., 2017; Bettolli and Penalba, 2018; Araya-Osses et al., 2020; Bettolli et al., 2021). Temperature simulations are fewer but show added value to GCM simulations (*medium evidence* and *high agreement*) (Souvignet et al., 2010; Borges et al., 2017; Bettolli and Penalba, 2018; Araya-Osses et al., 2020).

Overall, climate modelling has made some progress in the past decade but there is no model that performs well in simulating all aspects of the present climate over South America (*high confidence*). The performance of the models varies according to the region, time scale, and variables analysed (Abadi et al., 2018). There is also a fairly narrow spread in the representation of temperature and precipitation over South America by the CMIP5 GCMs and also the RCMs, with biases that can be associated with the parametrizations and schemes of surface, boundary layer, microphysics and radiation used by the models. Finally, observational reference datasets, such as reanalysis products, used in the calibration and validation of climate models also can be quite uncertain and may explain part of the apparent biases present in climate models (*high confidence*).

Atlas.7.2.4 Assessment and synthesis of projections

It is *very likely* that annual mean temperature will increase over South America, with a wide range of projected changes of 1.0°C to 6.0°C by the end of the 21st century (from RCP2.6/SSP1-2.6 to RCP8.5/SSP5-8.5 emissions, Figure Atlas.22). Overall, GCMs project higher temperature change than RCMs in austral summer and winter over all subregions and in winter mainly over the central part of the continent (Coppola et al., 2014; Llopart et al., 2020; Teichmann et al., 2020) (see also the Interactive Atlas). The largest warmings over the South American continent are projected for the Amazon basin (SAM and NSA) and the central Andes range (southern SAM, northern SWS and south-eastern NWS), Figure Atlas.22, especially during the dry and dry-to-wet transition seasons (austral winter and spring) (Blázquez and Nuñez, 2013a; Coppola et al., 2014; Pabón-Caicedo et al., 2020; Teichmann et al., 2020) (*high confidence*).

Using warming levels (Figure Atlas.22), the temperature is projected to increase at or above the level of global warming in all regions apart from SSA with additional warming (compared to a 1995–2014 baseline) of over 4°C for the 4°C warming level in NSA and SAM. Changes for other warming levels, subregions and

ACCEPTED VERSION SUBJECT TO FINAL EDITS

emissions pathways are shown in Figure Atlas.22 and can be explored with the Interactive Atlas.

In general, models show a wide regional range in the direction and the magnitude of mean precipitation change in many South American regions, with large significant increases and decreases (Figure Atlas.22, Interactive Atlas). In the medium and long term, under the high-emission scenario, the CMIP5 multi-model ensemble projected an increase in precipitation (generally greater than 10%) in SES and NWS and a decrease (less 10%) in NSA across seasons (*high confidence*, *robust evidence*) (Solman, 2013; Chou et al., 2014; Coppola et al., 2014; Llopart et al., 2014, 2020, Reboita et al., 2014b, 2020; Sánchez et al., 2015; Menéndez et al., 2016; Ruscica et al., 2016; Bozkurt et al., 2018a; Zaninelli et al., 2019). Also, in parts of SWS, annual precipitation is projected to decrease (up 30%) by the late 21st century (Souvignet et al., 2010; Palomino-Lemus et al., 2017, 2018; Bozkurt et al., 2018a). Under high RCPs, the CMIP5 ensemble projects that all Brazilian regions will experience more rainfall variability in the future, so drier dry periods and wetter wet periods on daily, weekly, monthly and seasonal timescales, despite the future changes in mean rainfall being currently uncertain (*medium confidence*) (Alves et al., 2020). Regarding the SAmerM, it is *very likely* that the monsoon will experience changes in its life cycle by the end of the 21st century for both RCP4.5 and RCP8.5 emissions and, in particular, delayed onset. However there is *low agreement* on the projected changes in terms of extreme and total precipitation of the monsoon season in South America (Llopart et al., 2014; Ashfaq et al., 2020). Changes in the SAmerM are assessed in Section 8.3.2.4.5.

Projected changes in seasonal precipitation and their uncertainties generally agree with the annual changes, particularly for the decreases in SWS (Figure Atlas.22). DJF precipitation changes in NSA and SAM are largely uncertain, with weak agreements in the projections, particularly for CMIP5 and CMIP6 ensembles, which project almost no change and decreasing precipitation for NSA and a narrow range from slight increases to no change respectively for SAM.

Atlas.7.2.5 Summary

In summary, it is *virtually certain* that the climate of South America has warmed. Studies on climate trends in South America indicate that mean temperature, maximum and minimum temperatures have increased over the last 40 years. Long-term observed precipitation trends show an increase over south-eastern South America and decreases in most tropical land regions (*high confidence*).

Evaluation of global and regional climate model simulations have increased over South America in the past decade and shown improved performance. However, the results reveal that no model performs well in simulating all aspects of the present climate (*very likely*). On the other hand, there is still a lack of high-quality and high-resolution observational data that may explain part of the important biases present in climate models (*high confidence*).

Climate model projections show a general increase in annual mean surface temperature over the coming century for all emission scenarios (RCPs and SSPs) (*high confidence*) consistent with the observed warming and with all regions except SSA warming faster than the global average. Unlike temperature, annual precipitation has patterns of decrease in North-eastern South America (NES) and South-western South America (SWS) and increase in southern South America (SES) and North-western South America (NWS) (*high confidence*), with small changes projected under a low-emission scenario. However, there is *low confidence* in the magnitude because of the large spread among models, both GCMs and RCMs.

Atlas.8 Europe

The assessment in this section focuses on changes in average temperature and precipitation (rainfall and snow), including the most recent years of observations, updates to observed datasets, the consideration of recent studies using CMIP5 and those using CMIP6 and CORDEX simulations. Assessment of changes in extremes are in Chapter 11 (Table 11.16–11.18) and climatic impact-drivers in Chapter 12 (Table 12.7).

ACCEPTED VERSION SUBJECT TO FINAL EDITS

Atlas.8.1 Key features of the regional climate and findings from previous IPCC assessments

Atlas.8.1.1 Key features of the regional climate

Westerly winds and the accompanying Atlantic storm track with cyclones and anticyclones travelling from the Atlantic towards inland Europe are the main climatic features that characterize daily to inter-annual variability in the European region. The Siberian High in winter determines cold weather in East Europe and can affect other regions with cold outbreaks. Intra-seasonal and inter-annual variations are driven by modes of climate variability such as the North Atlantic Oscillation (see Table Atlas.1 and Annex IV.2). Global warming can lead to systematic changes in regional climate variability via thermodynamic responses such as altered lapse rates (Kröner et al., 2017; Brogli et al., 2019) and land-atmosphere feedbacks (Zampieri and Lionello, 2011; Boé and Terray, 2014). Regional feedbacks involving the land-sea contrast, sea surface, land surface, clouds, aerosols, radiation and other processes modulate the regional response to enhanced warming.

Four climatic regions are defined for Europe (see Figure Atlas.24). The Mediterranean region (MED) in the south is characterized by mild winters and hot and dry summers (Mediterranean climate; see Section 10.6.4.2). It covers both Europe and Africa, and MED assessments in this section generally imply the entire MED domain unless stated otherwise. The Western and Central Europe region (WCE) has distinct summer and winter seasons with increasing continentality of climate eastwards. The northern region (NEU), close to the Atlantic Ocean, is characterized by high humidity and relatively mild winters, and strong exposure to the Atlantic storm track. Eastern Europe (EEU) covers the western part of Russia and neighbouring territories and has continental characteristics. Many regional datasets and model projections assessed here do not sufficiently cover the EEU region.

Atlas.8.1.2 Findings from previous IPCC assessments

AR5 WG II (Kovats et al., 2014) reports with *high confidence* that observed climate trends show regionally varying changes in temperature and rainfall in Europe. The average temperature in Europe has continued to increase, with seasonally different rates of warming being greatest in high latitudes in Northern Europe. Annual precipitation has increased in Northern Europe and decreased in parts of Southern Europe. SROCC (Hock et al., 2019b) reports with *high confidence* that a reduction in snow cover at low elevation and glacier extent is observed in recent decades, with consequent changes in annual and seasonal runoff patterns. According to the SRCCL report (IPCC, 2019b) there is *high agreement* that observed vegetation greening and forestation in the last 30 years cools summertime surface temperature and warms winter temperature due to decreased snow cover and increased snow shading in forested areas. It is *very likely* that aerosol column amounts have declined over Europe since the mid-1980s.

AR5 (Collins et al., 2013) reports that the ability of models to simulate the climate in Europe has improved in many important aspects. Particularly relevant for this region are increased model resolution and a better representation of the land-surface processes in many of the models that participated in CMIP5. The spread in climate model projections is still substantial, partly due to pronounced internal variability in this region (particularly NAO and AMO). In the winter half year, NEU and WCE are *likely* to have increased mean precipitation associated with increased atmospheric moisture and moisture convergence and intensification in extratropical cyclone activity. No change or a moderate reduction is projected for MED. In the summer half year, it is *likely* that NEU and WCE mean precipitation will have only small changes with a notable reduction in MED. According to SR1.5 (Hoegh-Guldberg et al., 2018), these precipitation changes are more pronounced at 2°C than at 1.5°C of global warming. For a 2°C global warming, an increase in runoff is projected for north-eastern Europe while decreases are projected in the Mediterranean region, where runoff differences between 1.5°C and 2°C global warming will be most prominent (*medium confidence*). According to SROCC (Hock et al., 2019b) the RCP8.5 projections lead to a loss of more than 80% of the ice mass from small glaciers by the end of century in Central Europe (*high confidence*). Snow cover and glaciers are projected to decrease all along the 21st century.

ACCEPTED VERSION SUBJECT TO FINAL EDITS

Atlas.8.2 Assessment and synthesis of observations, trends and attribution

To support climatological analyses and model evaluation, national meteorological and hydrological services are increasingly making available high spatial and temporal resolution gridded and in situ homogenized and quality-checked datasets (Déqué and Somot, 2008; Vidal et al., 2010; Rauthe et al., 2013; Noël et al., 2015; Spinoni et al., 2015b; Ruti et al., 2016; Fantini et al., 2018; Lussana et al., 2018; Herrera et al., 2019; Skrynyk et al., 2020). The inclusion of additional station data and data rescue activities lead to a better representation of extreme precipitation statistics than the global- or continental-scale datasets (see Section Atlas.1.4.1). Recent gridded products merging radar and station data allow higher spatial and temporal resolutions to be reached (Haiden et al., 2011; Tabary et al., 2011; Berg et al., 2016; Fumière et al., 2020). A number of regional reanalysis products has become available for the European region (Bollmeyer et al., 2015; Bach et al., 2016; Dahlgren et al., 2016; Landelius et al., 2016). A European ensemble of regional reanalyses from 1961 to 2019 is shown to add accuracy and reliability in comparison to global reanalysis products, but also introduces additional uncertainties, especially for threshold-based climate indices (Kaiser-Weiss et al., 2019). However, gridded European datasets are unreliable over data-sparse regions. Also, many datasets employ different approaches to interpolation and gridding, which adds to their uncertainty and complicates comparative evaluations (Berthou et al., 2018; Fantini et al., 2018; Kotlarski et al., 2019). For some subregions and performance metrics differences between datasets have been shown to be of the same magnitude as errors in regional climate models (Prein et al., 2016; Prein and Gobiet, 2017; Fantini et al., 2018), but observational uncertainty is substantially reduced when datasets of similar nature and representativeness are used (Kotlarski et al., 2019).

In addition to the global display of observed temperature and precipitation trends in Figure Atlas.11, annual mean temperature and precipitation trends between 1980 and 2015 calculated from the gridded ensemble E-OBS dataset (Cornes et al., 2018) are shown in Figure Atlas.23, together with time series of temperature and precipitation anomalies relative to the 1980–2015 mean value from E-OBS, CRU, EWEMBI and Berkeley for temperature, and E-OBS, CRU, GPCC and GPCP for precipitation (see also Figure 2.11 for global mean values, and Section Atlas.1.4.1 for description of global datasets).

In NEU continued warming has been observed, particularly during spring. An annual mean temperature increase of 0.4°C per decade was reported between 1970 and 2008 (Rutgersson et al., 2015). In WCE temperature increases since the mid 20th century have been documented for Poland (Degirmendžić et al., 2004) and Ukraine (Boychenko et al., 2016; Balabukh and Malitskaya, 2017). Land-only observations indicate a rapid increase in summer (JJA) mean surface air temperature since the mid-1990s (Dong et al., 2017). In Eastern Europe no significant trend in winter mean air temperatures was found between 1881 and 2016 in Belarus (Loginov et al., 2018). In parts of the European area of the MED spring and summer temperatures are reported to increase faster than in the other seasons (Brunetti et al., 2006; Homar et al., 2009; Lionello et al., 2012; Philandras et al., 2015; Gonzalez-Hidalgo et al., 2016; Vicente-Serrano et al., 2017) (see also the Mediterranean case study in Section 10.6.4 and Figure 10.18). Figure Atlas.23 shows that since 1980 in each European region all datasets show a consistent warming of annual mean temperature of 0.04°C yr^{-1} to 0.05°C yr^{-1}. Trends in European land temperature cannot be explained without accounting for anthropogenic warming offset by anthropogenic aerosol emissions (see Section 8.3.1.1 and Figure 3.8). It is *virtually certain* that annual mean temperature continues to increase in each European subdomain.

Multidecadal trends in mean precipitation are generally small and non-significant. Apart from difficulties related to observational coverage (Prein and Gobiet, 2017), gauge undercatch (e.g., Murphy et al., 2019) and data inhomogeneity (e.g., Camuffo et al., 2013), strong interannual and multidecadal variability is dominant over at least the last two centuries. However, significant precipitation trends have been recorded for recent periods, for example in south-western Europe between 1960 and 2000 (Peña-Angulo et al., 2020) and between 1961 and 2015 in NEU (Interactive Atlas). Also, some studies suggest that in the MED precipitation has declined and more frequent and severe meteorological droughts have occurred between 1960 and 2000 (Spinoni et al., 2015a; Gudmundsson and Seneviratne, 2016), and in some regions cannot be explained without anthropogenic forcing (Knutson and Zeng, 2018) (see also Section 10.4.1.2). Other studies suggest that this trend can be seen as an expression of multidecadal internal variability driven mainly by the North Atlantic Oscillation (Table Atlas.1) (Kelley et al., 2012; Zittis, 2018). Global dimming and brightening also

ACCEPTED VERSION SUBJECT TO FINAL EDITS

are reported to affect precipitation trends in the Mediterranean region (see Section 8.3.1.6 and Figure 8.7).

The large-scale spatial patterns of the E-OBS annual mean precipitation trend between 1980 and 2015 shown in Figure Atlas.23 is broadly consistent with trends derived from CRU, GPCP and GPCC (Figure Atlas.11) but with more explicit spatial detail. Trends calculated for regional averages are sensitive to the selection of the time window: for 1980–2015 annual mean precipitation averaged over the regions shows a positive trend (not significant at $p = 0.05$), while for CRU and GPCC the trend calculated over 1901–2015 is positive for NEU, EEU and WCE, and non-significant for MED. Precipitation trends in the MED are significant only in selected areas (Lionello et al., 2012; MedECC, 2020). Also the NEU trends show large spatial variability and are subject to decadal variability related to NAO (Heikkilä and Sorteberg, 2012), but are generally positive over the 20th century (Figure Atlas.23). There is *medium confidence* that annual mean precipitation in NEU, WCE and EEU has increased since the early 20th century. In the European Mediterranean observed land precipitation trends show pronounced variability within the region, with magnitude and sign of trend in the past century depending on time period and exact study region (*medium confidence*).

Trends in snowfall and snow melt are related to seasonal changes in both temperature and precipitation. In EEU melt onset dates have advanced by 1–2 weeks in the 1979–2012 period (Mioduszewski et al., 2015). Over Eurasia, trends in spring and early summer snow cover extent increased over the 1971–2014 period (Hernández-Henríquez et al., 2015). Between 1966 and 2012, averaged over entire Eurasia, monthly mean snow depth decreased in autumn and increased in winter and spring (Zhong et al., 2018), while the snow cover extent was reported to have decreased during the past 40 years (Bulygina et al., 2011). In NEU late winter and early spring snow depth and snow cover decreases since the early 1960s are reported over Finland (Luomaranta et al., 2019) and Norway (Rizzi et al., 2018) with a dependence on altitude (Skaugen et al., 2012), while winter snow depth increased in northern Sweden (Kohler et al., 2006). It is *very likely* that since the early 1980s in snow-dominant areas in NEU and EEU the length of the snowfall season is reduced with regional warming, and the melt onset dates have advanced.

[START FIGURE ATLAS.23 HERE]

Figure Atlas.23: (a) Mean 1980–2015 trend of annual mean surface air temperature (°C per decade) from E-OBS (Cornes et al., 2018). Data for non-European countries in the MED area are masked out. (b) Time series of mean annual temperature anomaly relative to the 1980–2015 period (shown with grey shading) aggregated for the land area in each of the four European subregions, from E-OBS, CRU, Berkeley and ERA5 (see Section Atlas.1.4.1 for description of global datasets). Mean trends for 1901–2015, 1961–2015 and 1980–2015 are shown for each data set in corresponding colours in the same units as panel (a) (see legend in upper panel). (c) As panel (a) for annual mean precipitation (mm day^{-1} per decade). (d) as panel (b) for annual mean precipitation, and data sets E-OBS, CRU, GPCC and GPCP. Note that E-OBS data are not shown in panels b and d for region EEU. For the MED region data are aggregated over the European countries alone. Trends have been calculated using ordinary least squares regression and the crosses indicate non-significant trend values (at the 0.1 level) following the method of Santer et al. (2008) to account for serial correlation. Further details on data sources and processing are available in the chapter data table (Table Atlas.SM.15).

[END FIGURE ATLAS.23 HERE]

The increasing trend in surface shortwave radiation, documented in AR5 (Hartmann et al., 2013) to have occurred since the 1980s and referred to as a brightening effect, is substantiated over Europe and the Mediterranean region (Nabat et al., 2014; Sanchez-Lorenzo et al., 2015; Cherif et al., 2020). This increasing trend has been attributed to the decrease in anthropogenic sulphate aerosols over the 1980–2012 period (Nabat et al., 2014). In model sensitivity experiments, the aerosol trend has been quantified to explain 81 ± 16% of the European surface shortwave trend and 23 ± 5% of the European surface temperature warming. It is *likely* that trends in anthropogenic aerosols in Europe have generated positive trends in shortwave radiation and surface temperature since the 1980s (see also Sections 6.3.3.1, 8.3.1.6 and 10.6.4).

ACCEPTED VERSION SUBJECT TO FINAL EDITS

Assessments of observed European trends in meteorological extremes and CIDs are reported elsewhere in this report. Section 11.3.5 documents and attributes an increase in the frequency and extent of heatwaves and daily maximum temperatures, and Section 11.6.2 discusses the uncertainty concerning the detection of trends in meteorological droughts, and the role of increasing atmospheric evaporative demand on hydrological and ecological/agricultural droughts. Section 8.3.1.8 reports on increasing aridity trends in the Mediterranean related to soil moisture declines and increases in atmospheric water vapor demand. Section 11.4.2 reports on the increased likelihood and intensity of daily precipitation extremes, while Sections 11.5.2 and 12.4.5.2 discuss implications for peak streamflow. Section 12.4.5.5 discusses the increased likelihood of wildfires, while Section 12.4.5.3 discusses the substantial decadal variability in mean wind speed and the trends in wind storms and gusts. The acceleration of sea level rise in the Atlantic and European seas has been discussed in Section 12.4.5.5.

Atlas.8.3 Assessment of model performance

A global evaluation of annual mean temperature and precipitation from the CMIP6 ensemble is presented in Sections 3.3.1 and 3.3.2 respectively. In general, annual mean temperature is slightly underestimated at high latitudes and overestimated in the MED area. Temporal evolution of decadal temperature oscillations in Europe simulated by the CMIP6 historical simulations is well reproduced (Fan et al., 2020). Fernandez-Granja et al. (2021) report an overall improvement of CMIP6 compared to CMIP5 to reproduce atmospheric weather patterns over Europe.

Regional climate models (RCMs; Section 10.3.1.2) have been extensively evaluated for a range of climate features over Europe (Casanueva et al., 2016; Vaittinada Ayar et al., 2016; Ivanov et al., 2017; Krakovska et al., 2017; Terzago et al., 2017; Cavicchia et al., 2018; Drobinski et al., 2018; Fantini et al., 2018; Harzallah et al., 2018; Panthou et al., 2018b). Standard assessments of RCMs driven by reanalyses, typically run at 12–25 km spatial resolution, confirm that the Euro-CORDEX and Med-CORDEX ensembles are capable of reproducing the salient features of European climate (Kotlarski et al., 2014; Krakovska, 2018) and represent European circulation features realistically (Cardoso et al., 2016; Drobinski et al., 2018; Flaounas et al., 2018; Sanchez-Gomez and Somot, 2018). Seasonal and regionally averaged temperature biases generally do not exceed 1.5°C, while precipitation biases can be up to ±40% (Kotlarski et al., 2014). Extensive evaluation of a large collection of RCM-GCM combinations show a general wet, cold and windy bias compared to observations and reanalyses, but none of the models is systematically performing best or worst (Vautard et al., 2020). Higher-resolution simulations do show improved performance in reproducing the spatial patterns and seasonal cycle of not only extreme precipitation but also mean precipitation over all European regions (Mayer et al., 2015; Fantini et al., 2018; Soares and Cardoso, 2018; Ciarlo et al., 2020)(see also Sections 10.3.3.4 and 10.3.3.5 for an extensive evaluation of the added value of increased simulation resolution).

In line with findings reported in Section 10.3.3.8, several studies argue that both GCMs and RCMs underestimate the observed trend in European summer temperature (Dosio, 2016; Boé et al., 2020b), indicating that essential processes are missing or that the natural variability is not correctly sampled (Dell'Aquila et al., 2018). Nabat et al. (2014) argued that including realistic aerosol variations enables climate models to correctly reproduce the summer warming trend (as is required for attributing continental annual temperature trends, Section 8.3.1.1). However, other studies showed models to be sensitive also to local effects, such as land-surface processes, convection, microphysics, and snow albedo (Vautard et al., 2013; Davin et al., 2016). In Euro-CORDEX the warm and dry summer bias over southern and south-eastern Europe is reduced compared to the previous ENSEMBLES simulations (Katragkou et al., 2015; Giot et al., 2016; Prein and Gobiet, 2017; Dell'Aquila et al., 2018). Natural variability has strongly affected the historical warming and large ensembles are necessary for a correct estimation of the forced signal versus natural variability (Aalbers et al., 2018; Lehner et al., 2020).

Specific assessments of Convection Permitting RCMs (CPRCMs, running at a resolution of typically 1 to 3 km and designed for extreme precipitation characteristics) is undertaken in Section 10.3.3.4.1. A unique CPRCM ensemble has been applied over the great Alpine domain and improves representation of mean and extreme precipitation compared to coarser resolution models (Ban et al., 2021; Pichelli et al., 2021).

ACCEPTED VERSION SUBJECT TO FINAL EDITS

The role of aerosol forcing is increasingly analysed as new and more realistic aerosol datasets become available (Nabat et al., 2013; Pavlidis et al., 2020), and as RCMs begin to include interactive aerosols (Nabat et al., 2012, 2015, 2020; Drugé et al., 2019). Explicitly accounting for aerosol effects in RCMs leads to improved representation of the surface shortwave radiation at various scales: long-term means (Gutiérrez et al., 2018), day-to-day variability (Nabat et al., 2015), and long-term trends (Nabat et al., 2014).

New, or updated, higher-resolution, coupled atmosphere-ocean-ice model systems have been found to improve simulations of observed climate features over the Baltic area compared to atmosphere-only model versions, including correlation between precipitation and SST, between surface heat-flux components and SST, and weather events like convective snow bands over the Baltic Sea (e.g., Tian et al., 2013; Van Pham et al., 2014; Gröger et al., 2015; Wang et al., 2015a; Pham et al., 2017). Coupled atmosphere-land-river-ocean Regional Climate System Models (RCSMs) from Med-CORDEX have similar skill as the ENSEMBLES and the Euro-CORDEX ensembles to represent decadal variability of Mediterranean climate and its extremes (Cavicchia et al., 2018; Dell'Aquila et al., 2018; Gaertner et al., 2018). Panthou et al. (2018b) showed that, over land, differences between atmosphere-only and coupled RCMs are confined to coastal areas that are directly influenced by SST anomalies. In contrast, Van Pham et al. (2014) showed significant differences in seasonal mean temperature across a widespread continental domain.

Statistical downscaling methods are assessed in Section 10.3.3.7, including the intercomparison and evaluation activities performed in the framework of VALUE and Euro-CORDEX over Europe.

Atlas.8.4 Assessment and synthesis of projections

Simulations from CMIP5 and CMIP6 indicate pronounced geographical patterns and scenario dependence of the projections of mean temperature and precipitation. Global warming projected under SSP5-8.5 emissions in CMIP6 exceeds the warming projected by RCP8.5 emissions in CMIP5 (Forster et al., 2019) (see also Section 4.3). In selected regions in Europe CMIP6 also projects a systematically higher mean temperature than CMIP5 (Seneviratne and Hauser, 2020). The annual mean projections from CMIP5, CMIP6 and 0.11° resolution EURO-CORDEX contained in the Interactive Atlas are shown for the four European regions in Figure Atlas.24. For each region and season a warming offset between the preindustrial (1850–1900) and the recent past (1995–2014) baselines is also shown. The results confirm higher CMIP6 long-term annual mean warming rates for WCE, EEU and MED and a larger inter-model spread for each region. For given global warming levels, regional annual mean temperature change in CMIP5 and CMIP6 are largely consistent and higher than the global average, most prominently in EEU. For high warming levels the CMIP5 subset of 8 GCMs used to drive the EURO-CORDEX simulations show a lower annual mean temperature change than the full CMIP5 ensemble in each of the European subregions. This illustrates the large inter-model spread and implications for subsampling a relatively small subset from the full ensemble. Regional warming is strongest in continental EEU away from the Atlantic and in MED during summer (Lionello and Scarascia, 2018). The assessment of EURO-CORDEX projections for levels of global warming of 1.5°C and 2.0°C indicate enhanced local warming even at relatively low global warming levels, particularly towards the north in winter (Schaller et al., 2016; Dosio and Fischer, 2018; Kjellström et al., 2018; Teichmann et al., 2018).

Some signatures of climate change projected by GCMs are modified by RCMs and CPRCMs. Projections of temperature, precipitation and wind in RCMs may deviate from GCM signals dependent on the dominant atmospheric circulation (Kjellström et al., 2018). In many areas RCMs produce lower warming rates and higher precipitation (less drying) in summer (Fernández et al., 2019; Boé et al., 2020a). Also for mean surface shortwave radiation systematic differences between GCM and RCM outputs are found (Bartók et al., 2017; Gutiérrez et al., 2020). Although RCMs generally have a smaller bias for the present climate (Sørland et al., 2018) and better cloud representation (Bartók et al., 2017), the representation of aerosol forcing (Boé et al., 2020a; Gutiérrez et al., 2020), air-sea coupling (Boé et al., 2020a) or vegetation response to elevated atmospheric CO_2 (Schwingshackl et al., 2019) give rise to systematic biases in RCM projections. The comparison between EURO-CORDEX and the CMIP5 subset shown in Figure Atlas.24 illustrates that the RCMs primarily modify the climate change warming signal from the driving GCMs for MED and WCE in summer (Boé et al., 2020a).

ACCEPTED VERSION SUBJECT TO FINAL EDITS

Changes in precipitation clearly show a seasonal signature and a meridional gradient over Europe. Mean precipitation increases by 4% to 5% per °C of global warming in NEU, EEU and WCE in DJF, and decreases in summer in WCE and MED (Jacob et al., 2018) (see Figure Atlas.24). CMIP5 projections of precipitation change in MED are strongest in DJF in the south, while changes in JJA are dominant in the northern (European) part of MED, Lionello and Scarascia (2018). The European north-south gradient in precipitation response is confirmed by the EURO-CORDEX experiment (Coppola et al., 2020), but Figure Atlas.24 shows that the JJA precipitation reduction in WCE projected by CMIP5 and CMIP6 at higher warming levels has *low confidence* in the CORDEX simulations. Precipitation in JJA in EEU is reduced in CMIP6, while little change is shown in CMIP5. Quantitative estimations of climate change features from regional climate projections in Eastern Europe (Partasenok et al., 2015; Kattsov et al., 2017) have *low confidence* due to the use of relatively small ensembles of GCMs and/or RCMs, and limited evaluation of model performance in the region.

Over specific geographic features such as high mountains, RCMs further modify the climate change signal of precipitation simulated by the low-resolution GCMs (Giorgi et al., 2016; Torma and Giorgi, 2020). This is especially true for summer precipitation over the Alps where opposite signs of changes in mean and extreme precipitation are generated by the CMIP5 GCM ensemble and the 12-km Med-CORDEX and EURO-CORDEX RCM ensembles (Giorgi et al., 2016) (see also Section 10.6.4.7).

[START FIGURE ATLAS.24 HERE]

Figure Atlas.24: Regional mean changes in annual mean surface air temperature and precipitation relative to the 1995–2014 baseline for the reference regions in Europe (warming since the 1850–1900 pre-industrial baseline is also provided as an offset). Bar plots in the left panel of each region triplet show the median (dots) and 10th–90th percentile range (bars) across each model ensemble for annual mean temperature changes for four datasets (CMIP5 in intermediate colours; subset of CMIP5 used to drive CORDEX in light colours; CORDEX overlying the CMIP5 subset with dashed bars; and CMIP6 in solid colours); the first six groups of bars represent the regional warming over two time periods (near-term 2021–2040 and long-term 2081–2100) for three scenarios (SSP1-2.6/RCP2.6, SSP2-4.5/RCP4.5, and SSP5-8.5/RCP8.5), and the remaining bars correspond to four global warming levels (GWL: 1.5°C, 2°C, 3°C, and 4°C). The scatter diagrams of temperature against precipitation changes display the median (dots) and 10th–90th percentile ranges for the above four warming levels for December-January-February (DJF; middle panel) and June-July-August (JJA; right panel), respectively; for the CMIP5 subset only the percentile range of temperature is shown, and only for 3°C and 4°C GWLs. Changes are absolute for temperature (in °C) and relative (as %) for precipitation. See Section Atlas.1.3 for more details on reference regions (Iturbide et al., 2020) and Section Atlas.1.4 for details on model data selection and processing. The script used to generate this figure is available online (Iturbide et al., 2021) and similar results can be generated in the Interactive Atlas for flexibly defined seasonal periods. Further details on data sources and processing are available in the chapter data table (Table Atlas.SM.15).

[END FIGURE ATLAS.24 HERE]

Regional warming is *virtually certain* to extend the observed downward trends in snow accumulation, snow water equivalent and length of the snow cover season in NEU and low altitudes in mountainous areas in the Alps and Pyrenees (*very high confidence*). This is supported by regional and global multi-model and/or single-model ensemble projections including CMIP5, PRUDENCE, ENSEMBLES and EURO-CORDEX (Jylhä et al., 2008; Steger et al., 2013; Mankin and Diffenbaugh, 2015; Schmucki et al., 2015; Marty et al., 2017; Frei et al., 2018) and attributed to changes in the snowfall fraction of precipitation and to increased snow melt. In mountain areas a strong dependence of projected snow trends on altitude is shown, with most pronounced effects below 1500 m (López-Moreno et al., 2009). Terzago et al. (2017) showed a large positive bias in the amplitude of the annual snow cycle of EURO-CORDEX 0.11° simulations driven by GCM projections, while reanalysis-driven RCMs showed good agreement with in-situ observations.

Regional ocean warming in projections with RCSMs for the Baltic and North Sea (Gröger et al., 2015) and

ACCEPTED VERSION SUBJECT TO FINAL EDITS

for the Mediterranean (Darmaraki et al., 2019) is associated with increased intensity and frequency of marine heatwaves in the Mediterranean (see Section 12.4.5.5), strong freshening in the Baltic, and, for some simulations, changes in the circulation in response to non-uniform changes in air-sea interaction (Dieterich et al., 2019). Med-CORDEX RCSM and CMIP5 GCM results agree well on the Mediterranean SST warming rate (Mariotti et al., 2015; Darmaraki et al., 2019); see also the Interactive Atlas.

Assessments of projected changes in meteorological extremes and CIDs are reported elsewhere in this report. Extreme precipitation and temperature often exhibit a different response to global warming than mean values. Increased intensity and frequency of extreme temperatures and heatwaves is assessed in Sections 11.3.5 and 12.4.5.1. Changes in the hydrological cycle include enhanced soil moisture decline in southern Europe, drying in summer and autumn in central Europe, and spring drought due to early snow melt in northern Europe (Sections 8.4.1, 11.6.5 and 12.4.5.2). Changes in mean and extreme wind are very uncertain (Section 12.4.5.3), while sea level rise will increase the frequency of occurrence of extreme sea level at most European coasts (Section 12.4.5.5).

Atlas.8.5 Summary

An assessment of recent literature largely confirms the findings of previous IPCC reports but with additional detail and (in some cases) higher confidence due to improvements in observations, reanalyses and methods. Observational data sets with global coverage are complemented by the E-OBS gridded ensemble temperature and precipitation dataset, a range of regional observational analyses, and regional reanalysis products. New RCM experiments, including CPRCMs and regional coupled climate system models, mostly coordinated under the umbrella of CORDEX, have generated many new projections and process studies.

The representation of mean European climate features by GCMs and RCMs is improved compared to previous IPCC assessments (*medium confidence*), in spite of persisting biases in annual mean and seasonal temperature and precipitation characteristics. The added value of regional downscaling of GCMs by RCM projections for summer mean temperature, precipitation and shortwave radiation is constrained by the representation of processes that lead to a systematic difference between RCM and driving GCM, such as aerosol forcing (*medium confidence*).

It is *virtually certain* that annual mean temperature continues to increase in each European region. There is *medium confidence* that annual mean precipitation in NEU, WCE and EEU has increased since the early 20th century. In the European Mediterranean trends in annual mean precipitation contain substantial spatial and temporal variability (*medium confidence*). It is *very likely* that since the early 1980s in snow-dominant areas in NEU and EEU the length of the snowfall season is reduced with regional warming, and the melt onset dates have advanced. It is *likely* that decreasing trends in anthropogenic aerosols in Europe have generated positive trends in shortwave radiation and surface temperature since the 1980s.

At increasing levels of global warming, there is *very high confidence* that temperature will increase in all European areas at a rate exceeding global mean temperature increases, while increased mean precipitation amounts at high latitudes in DJF and reduced JJA precipitation in southern Europe will occur with *medium confidence* for global warming levels of 2°C or less, and with *high confidence* for higher warming levels. At high latitudes and low-altitude mountain areas in Europe strong declines in snow accumulation are *virtually certain* to occur with further increasing regional temperatures (*very high confidence*).

Atlas.9 North America

The assessment in this section focuses on changes in average temperature and precipitation (rainfall and snow) for North America, including the most recent years of observations, updates to observed datasets, the consideration of recent studies using CMIP5 and those using CMIP6 and CORDEX simulations. Assessment of changes in extremes are in Chapter 11 (Table 11.19–21) and climatic impact-drivers in Chapter 12 (Table 12.8).

ACCEPTED VERSION SUBJECT TO FINAL EDITS

Atlas.9.1 Key features of the regional climate and findings from previous IPCC assessments

Atlas.9.1.1 Key features of the regional climate

The recent-past climate of North America is characterized by high spatial heterogeneity and by variability at diverse temporal scales. Considering the traditional Köppen-Geiger classification, North America covers all main climate types (see reference region descriptions below). Important geographical features influence local climates over various distances, like the Rocky Mountains through cyclogenesis (Grise et al., 2013) and the Great Lakes through lake-effect snowfall (Wright et al., 2013). The cryosphere is an important component of the climate system in North America, with fundamental roles for sea ice cover, snow cover and permafrost. The ocean surrounding the continent also influence its climate, with water temperatures strongly influencing hurricane activity which impacts the coasts of eastern Mexico and south-eastern USA (Walsh et al., 2010). Temporal variability is influenced by several large-scale atmospheric modes (Annex IV, Table Atlas.1) with the North Atlantic Oscillation (NAO) affecting north-eastern USA and eastern Canada precipitation (Whan and Zwiers, 2017), and El Niño–Southern Oscillation (ENSO) affecting temperature and precipitation in California, although in a complex and not yet fully understood manner (Yoon et al., 2015; Yeh et al., 2018).

The reference regions defined for summarising North America climate change (Figure Atlas.26) include: North-Western North America (NWN), characterized by a subarctic climate with cool summers and rainfall all year round; North-Eastern North America (NEN), which also has a subarctic climate with sections of tundra climate in the far north (these two northern regions are also discussed in Section Atlas.11.2, Polar Arctic; Western North America (WNA), which has a complex but mainly cold semi-arid climate; the Central North America (CNA) with a mainly by continental climate in the northern part of the region and humid subtropical in the southern portion; Eastern North America (ENA) with a humid continental climate in the northern half and a humid subtropical climate to the south; Northern Central America (northern Mexico) (NCA), has a temperate climate to the north of the Tropic of Cancer, with marked differences between winter and summer, modulated by the North American monsoon (Peel et al., 2007). NCA, also covered in Section Atlas.7.1 Central America, has a temperate climate to the north of the Tropic of Cancer, with marked differences between winter and summer, modulated by the North American monsoon (Peel et al., 2007).

Atlas.9.1.2 Findings from previous IPCC assessments

The IPCC AR5 (Bindoff et al., 2013; Hartmann et al., 2013) found that the climate of North America has changed due to anthropogenic causes (*high confidence*), in particular with primarily increasing annual precipitation and annual temperature (*very high confidence*). Assessment of CMIP5 ensemble projections concluded that mean annual temperature over North America and annual precipitation north of 45N will *very likely* continue to increase in the future. Also, CMIP5 projects increases in winter precipitation over Canada and Alaska and decreases in winter precipitation over the southwestern USA and much of Mexico.

The CMIP5 multi-model ensemble generally reproduces the observed spatial patterns but somewhat underestimates the extent and intensity of the North American Monsoon, and also underestimates wetting over Central North America over the period of 1950–2012 during winter season according to AR5 (Flato et al., 2013). In the long-term (2081–2100), the largest changes of precipitation over North America are projected to occur in the mid and high latitudes and during winter (Kirtman et al., 2013).

SR1.5 (Hoegh-Guldberg et al., 2018) reported a stronger warming compared to the global mean over Central and eastern North America, and a weakening of storm activity over North America under 1.5°C of global warming. SROCC (Hock et al., 2019b) reported that snow depth or mass is projected to decline by 25% mainly at lower elevations over the high mountains in Western North America. SRCCL (Mirzabaev et al., 2019) observed vegetation greening in central North America with *high confidence*.

ACCEPTED VERSION SUBJECT TO FINAL EDITS

Atlas.9.2 Assessment and synthesis of observations, trends, and attribution

The observed trends in annual mean surface temperature (see Figure Atlas.11 and the Interactive Atlas) across near-Arctic latitudes are exceptionally pronounced (>0.5°C per decade), significant and consistent across datasets except for far northeast Canada where trends are not significant in the CRU dataset. Significant positive trends are seen across the rest of North America during 1960–2015 (Figure Atlas.11) though over the shorter 1980–2015 period the regional dataset Daymet (Thornton et al., 2016) records non-significant changes over southern Alaska, western and south-central Canada, and north-central USA (Interactive Atlas). An analysis of annual mean surface temperature in the Berkeley Earth dataset aggregated over the reference regions (Figure Atlas.11) demonstrates that a temperature change signal has emerged over all regions of North America. There is a detectable anthropogenic influence (*medium confidence*) on the observed upward annual temperature trends in western and northern North America (Vose et al., 2017; Wang et al., 2017b; Smith et al., 2018).

Compared to temperature, trends in annual precipitation over 1960–2015 are generally non-significant though there are consistent positive trends over parts of ENA and CNA (Figure Atlas.11) and Daymet (Interactive Atlas) (*high confidence*). The global and regional datasets in Figure Atlas.11 and Interactive Atlas also indicate significant decreases in precipitation in parts of south-western US and north-western Mexico (see also Figure 2.15) though these are not all spatially coherent so there is only *medium confidence* in a drying trend over this region.

Several factors account for the differences in temperature and precipitation trend significance. Observed trends in precipitation are relatively modest compared to the very large natural interannual variability of precipitation. Furthermore, the precipitation observing network is spatially inadequate (see Section 10.2.2.3) and temporally inconsistent (see Section 10.2.2.2) over some regions of North America, particularly over Arctic and mountainous areas. So detection of multidecadal trends is difficult, especially for regions with summertime convective precipitation maxima that may be spatially patchy (Easterling et al., 2017). See Section 2.3 for further discussion of precipitation trends.

There is evidence of a recent decline in the overall North American annual maximum snow mass, with a trend for non-alpine regions above 40°N during 1980–2018 estimated from the bias-corrected GlobSnow 3.0 data (Pulliainen et al., 2020) (*medium confidence*). This is despite technical challenges with in situ measurements and remote sensing retrievals of snow variables (Larue et al., 2017; Smith et al., 2017; Wang et al., 2017a; Zeng et al., 2018), spatial heterogeneity and interpolation assumptions that affect gridded reference products, notably over alpine and forested areas (Mudryk et al., 2015; Dozier et al., 2016; Cantet et al., 2019) and breaks in instruments and procedures (Kunkel et al., 2007; Mortimer et al., 2020). Changes in snow cover have evolved in a complex way, with both positive and negative trends and differing from one metric to another (Knowles, 2015; Brown et al., 2019). Evidence of large-area snow cover decline includes decreases in annual maximum snow depth and in snow water equivalent (Vincent et al., 2015; Kunkel et al., 2016; Mote et al., 2018), as well as a shortening of the snow season duration (Knowles, 2015; Vincent et al., 2015). However, reported snow decline trends are statistically significant only for a fraction of the concerned areas or locations (see Figure Atlas.25) (*low confidence*). See also Sections 2.3.2.2 and 9.5.3.1.

Rupp et al. (2013) applied a standard finger-printing approach to CMIP5 models and determined that the decline in Northern Hemisphere spring snow cover extent could only be explained by simulations that included natural and anthropogenic forcing. In an attribution study focusing on direct physical causes, it was found that increased spring snowmelt in northern Canada was driven by warming-induced high latitudes changes such as atmospheric moisture, cloud cover, and energy advection (Mioduszewski et al., 2014). In an analysis of drivers of the record low snow water equivalent (SWE) values of spring 2015 in the western US, it was found that the relative importance of greenhouse gases varies spatially (Mote et al., 2016). See also Section 3.4.2 for further discussion of anthropogenic influences on snow extent.

ACCEPTED VERSION SUBJECT TO FINAL EDITS

[START FIGURE ATLAS.25 HERE]

Figure Atlas.25: Grid-box trends (mm yr^{-1}) in annual maximum snow depth for cold season periods of 1960/1961 to 2014/2015. (Left) Numbers indicate number of stations available in that grid box. (Right) Boxes with 'x' indicate non-significant trends (at the $p < 0.05$ level of significance) (Kunkel et al., 2016).

[END FIGURE ATLAS.25 HERE]

Atlas.9.3 Assessment of model performance

CMIP6 models have been evaluated in the literature, although these studies have not included the full set of CMIP6 simulations. Fan et al. (2020) established on a continental basis for North America that temperature pattern correlations were quite accurate. Thorarinsdottir et al. (2020) compared maximum and minimum temperatures over Europe and North America with several observational datasets and found that the CMIP6 ensemble agreed better with ERA5 data than did CMIP5. Srivastava et al. (2020) evaluated historical CMIP6 simulations for precipitation, comparing them with several observational datasets over the continental US. Most models show a wet bias over the eastern half of continental USA and the northeast region while dry biases persist in the central part of the country (Akinsanola et al. (2020a) and Almazroui et al. (2021)). The spatial structure of biases is similar in CMIP5 and CMIP6, but with lower magnitudes in CMIP6. Agel and Barlow (2020) examined 16 CMIP6 models over the north-eastern US for precipitation and did not find a distinct improvement over CMIP5, although they did find the higher resolution models tended to perform better. On the basis of the evidence so far, there is *medium confidence* that CMIP6 models are improved compared to CMIP5 in terms of biases in mean temperature and precipitation over North America.

North America has been extensively used as a testbed for regional climate model (RCM) experiments, such as the North American Regional Climate Change Assessment Program (NARCCAP) (Mearns et al., 2009), the MultiRCM Ensemble Downscaling (MRED) (Yoon et al., 2012), and NA-CORDEX (Bukovsky and Mearns, 2020). Therefore, much performance evaluation has been conducted with a focus on specific climate features in North America. For the North American monsoon region, multi-model performance evaluation (Bukovsky et al., 2013; Tripathi and Dominguez, 2013; Cerezo-Mota et al., 2015) or a single member performance (Lucas-Picher et al., 2013; Martynov et al., 2013; Šeparović et al., 2013) demonstrated the added value of RCMs, particularly more recent CORDEX simulations, through improved simulation of summertime precipitation and the climatological wintertime storm tracks across the western United States. NA-CORDEX simulations were more successful at reproducing weather types compared to a single model-based large perturbed-physics ensemble (Prein et al., 2019). The application of a complex evaluation tool to the full suite of NA-CORDEX simulations found that the higher resolution simulations (25 km vs 50 km) of precipitation were improved, particularly for daily intensity (Gibson et al., 2019).

However, deficiencies have also been reported. For example, storm occurrence over the East Coast of North America was found (Poan et al., 2018), and amplitude in the simulated annual cycle was generally excessive in NA-CORDEX simulations. RCMs tend to produce more (less) precipitation over mountains (the coastal plains) (Cerezo-Mota et al., 2015) and winter precipitation in the western US had large positive biases in all RegCM simulations, regardless of the driving GCM (Mahoney et al., 2021).

Recently, convective-permitting RCMs have been used to simulate North American climate features and generated better simulations of precipitation. For example, summer precipitation over the south-western USA was improved due to better representation of organized mesoscale convective systems at the sub-daily scale (Castro et al., 2012; Liu et al., 2017; Prein et al., 2017b; Pal et al., 2019), the diurnal cycle of convection (Nesbitt et al., 2008), and in terms of means (and extremes) for the north-eastern United States (Komurcu et al., 2018).

Recent studies have examined RCMs simulation of SWE, a quantity of primary importance notably for hydrological modelling though its ground measurements are restricted by relatively high time and monetary costs (Smith et al., 2017; Odry et al., 2020) which limit model assessment. Also, studies often emphasize that

ACCEPTED VERSION SUBJECT TO FINAL EDITS

a false impression of model skill for SWE can be obtained by compensating temperature and precipitation biases. Assessment frameworks have dealt with these issues by considering observational uncertainty (Mccrary et al., 2017) and by decomposing SWE biases into their contributing processes (Rhoades et al., 2018; Xu et al., 2019). SWE biases exceed observational uncertainty in several 50-km reanalysis-driven NARCCAP simulations over several regions, for all cold months (Mccrary et al., 2017). Analyses of NA-CORDEX simulations show that refining spatial resolution from 50 to 12 km improves certain (but not all) aspects of SWE, stemming from improved mean precipitation and topography-related temperature (Xu et al., 2019). Similarly an assessment of RCM simulations of freezing rain over Eastern Canada found a mix of improved and deteriorated aspects from higher resolution (St-Pierre et al., 2019).

Atlas.9.4 Assessment and synthesis of projections

[START FIGURE ATLAS.26 HERE]

Figure Atlas.26: Regional mean changes in annual mean surface air temperature and precipitation relative to the 1995–2014 baseline for the reference regions in North America (warming since the 1850–1900 pre-industrial baseline is also provided as an offset). Bar plots in the left panel of each region triplet show the median (dots) and 10th–90th percentile range (bars) across each model ensemble for annual mean temperature changes for four datasets (CMIP5 in intermediate colours; subset of CMIP5 used to drive CORDEX in light colours; CORDEX overlying the CMIP5 subset with dashed bars; and CMIP6 in solid colours); the first six groups of bars represent the regional warming over two time periods (near-term 2021–2040 and long-term 2081–2100) for three scenarios (SSP1-2.6/RCP2.6, SSP2-4.5/RCP4.5, and SSP5-8.5/RCP8.5), and the remaining bars correspond to four global warming levels (GWL: 1.5°C, 2°C, 3°C, and 4°C). The scatter diagrams of temperature against precipitation changes display the median (dots) and 10th–90th percentile ranges for the above four warming levels for December-January-February (DJF; middle panel) and June-July-August (JJA; right panel), respectively; for the CMIP5 subset only the percentile range of temperature is shown, and only for 3°C and 4°C GWLs. Changes are absolute for temperature (in °C) and relative (as %) for precipitation. See Section Atlas.1.3 for more details on reference regions (Iturbide et al., 2020) and Section Atlas.1.4 for details on model data selection and processing. The script used to generate this figure is available online (Iturbide et al., 2021) and similar results can be generated in the Interactive Atlas for flexibly defined seasonal periods. Further details on data sources and processing are available in the chapter data table (Table Atlas.SM.15).

[END FIGURE ATLAS.26 HERE]

CMIP5 and CMIP6 surface temperature and precipitation projections over the region are similar, with all regions warming more than the global average, most prominently those in the north most (Figure Atlas.26). CMIP6 projects, for scenarios and time-periods, higher temperature changes (see also Chapter 4) with this contrast more accentuated in the long-term future and at higher global warming levels. The higher warming in the north (also see the Interactive Atlas) is clear when comparing NEN, with increases from 2.5°C to over 11°C on an annual basis for SSP5-8.5 (near-term to long-term compared to a 1995–2014 baseline), to NCA, where changes range from 1.5°C to 6°C across the same periods. Maps showing changes in temperature and precipitation, and their robustness, are available in the Interactive Atlas. The number of model results (i.e., ensemble size used to generate these figures) differs, and this sample size difference may affect the results, but the patterns and magnitudes of change are generally consistent and thus it is *very likely* that temperatures will increase throughout the 21st century in all land areas, with stronger warming in the far north.

CMIP5 results have been analysed extensively (e.g., Maloney et al., 2014) and used in major climate change assessments. The most recent US National Climate Assessment analysis of CMIP5 focusing on RCP4.5 and RCP8.5 for two future time periods stated that the USA would continue to warm regardless of scenario but is *likely* to be higher with higher emissions scenarios (e.g., RCP8.5). Projected changes in precipitation are somewhat complex, but increased precipitation dominates in winter and spring, whereas in summer changes are more variable and uncertain. Canada's Changing Climate Report (Bush and Lemmen, 2019) presents changes in temperature and precipitation, as well as other variables, such as snow, for future periods in

ACCEPTED VERSION SUBJECT TO FINAL EDITS

Canada using results from CMIP5. It indicates that annual and winter precipitation is projected to increase everywhere in Canada over the 21st century with larger percentage increases in the north. Temperature is also projected to increase, regardless of scenario, and with larger changes occurring in the north.

To provide the basis for generating additional information compared to that derived from CMIP5 the NA-CORDEX experiments were designed to involve a GCM-RCM matrix which included multiple GCMs that sampled the full range of climate sensitivity, multiple RCMs, at two different spatial resolutions (25 and 50 km) and a range of emissions scenarios (in most cases RCP4.5 and RCP8.5) (Mearns et al., 2017). Karmalkar (2018) noted that the NA-CORDEX model covers subregional ranges of temperature change from the CMIP5 GCMs better than NARCCAP did for the CMIP3 models. This structural design shift provides greater confidence in the NA-CORDEX results in terms of sampling the uncertainty across the CMIP5 models (Figure Atlas.27) (Bukovsky and Mearns, 2020). The pattern of warming is as seen in CMIP5 and CMIP6 which also builds confidence that the RCMs generate high-resolution results consistent with CMIP5 on large scales whilst providing added value over regions such as the complex topography of the Rocky Mountains in the US West, which are not well resolved in the GCMs. There is *high confidence* that downscaling a subset of CMIP models that spans the range of climate sensitivities in the full ensemble is critical for producing a representative range of dynamically downscaled projections.

[START FIGURE ATLAS.27 HERE]

Figure Atlas.27: Changes (2070–2099 relative to 1970–1999) in the annual mean surface air temperature by three GCMs (GFDL ESM2M, MPI ESM-LR, HadGEM2-ES) and two RCMs (WRF and RegCM4) nested in the GCMs, for the RCP8.5 scenario (after Bukovsky and Mearns, 2020).

[END FIGURE ATLAS.27 HERE]

There are striking contrasts in the seasonal results for precipitation for the subregions (Figure Atlas.26). The northern regions and ENA all show steady increases with the global warming levels (*very high confidence*). For example, the projected increases in NEN region range from 7% in the near term to 40% at the end of the 21st century for the SSP5-8.5 scenario. In contrast, projected changes for NCA are for significant decreases both on an annual basis (Interactive Atlas) and in winter and which become greater as warming increases (Akinsanola et al., 2020b; Almazroui et al., 2021). The other two regions (WNA and CNA) exhibit mainly increases in winter. In summer, distributions are in general less uniform except for NWN and NEN which display steady increases with global warming levels (but smaller than in winter). WNA and CNA mainly show decreases (based on the median values) but with some models projecting increases. Projections from the NA-CORDEX ensemble are consistent with those from the GCMs whilst providing greater detail of precipitation changes over the mountains and along the coasts (Bukovsky and Mearns, 2020)(Interactive Atlas). Similar results are found in other analyses of RCM projections (Wang and Kotamarthi, 2015; Ashfaq et al., 2016; Teichmann et al., 2020). Also, further analysis of the NA-CORDEX projections showed substantial changes in weather types related to increased monsoonal flow frequency and drying of the northern Great Plains in summer (Prein et al., 2019).

In summary, NEN, NWN and most of ENA will *very likely* experience increased annual mean precipitation, with greater increases at higher levels of warming (*very high confidence*). In NCA decreases predominate on an annual basis and particularly in winter (*high confidence*). Projected changes in summer are highly uncertain throughout other regions apart from the far northern parts of NEN and NWN which will *likely* experience increases (*high confidence*).

As discussed in Section 10.3.3.4 an important advance in regional modelling over the past decade or so is the use of convection-permitting regional models (CPMs) (Prein et al., 2015, 2017b). There have been a number of experiments using CPMs over North America (e.g., Rasmussen et al., 2014; Prein et al., 2015, 2019; Liu et al., 2017; Komurcu et al., 2018). A CPM study over North America that investigated changes in Mesoscale Convective Systems projected that by the end of the century, assuming an RCP8.5 scenario, their

ACCEPTED VERSION SUBJECT TO FINAL EDITS

frequency more than tripled and associated precipitation increased by 80% (Prein et al., 2017a). A multiple nesting of WRF over north-eastern US downscaling to 3 km a CESM GCM climate projection assuming an RCP8.5 scenario, found a different pattern of precipitation change of mixed increases and decreases compared to the GCM projection of increases every month (Komurcu et al., 2018). These investigations demonstrate the potential of very high-resolution simulations to add important dimensions to our understanding of regional climate change, though not necessarily to reduce uncertainty (*high confidence*).

It is *virtually certain* that snow cover will experience a general decline across North America during the 21st century, in terms of extent, annual duration and SWE, based on CMIP5 (Maloney et al., 2014), CMIP6 (Mudryk et al., 2020), NA-CORDEX (Mahoney et al., 2021) and NARCCAP (e.g., McCrary and Mearns, 2019) simulations. For some regions the decline could be discernible over the next few decades, for example in western USA (Fyfe et al., 2017). It is, however, *likely* that some high-latitude regions will rather experience an increase in certain winter snow cover properties (Mudryk et al., 2018; McCrary and Mearns, 2019), due to snowfall increase (Krasting et al., 2013a) prevailing over the warming effect. Discussion of changes in snow in the future is also covered in Section 9.5.3, but for larger regions.

The fraction of precipitation falling as snow is projected to decrease practically everywhere over North America, including over western USA and south-western Canada (Mahoney et al., 2021), and in the Great Lakes basin where lake-effect precipitation is important (Suriano and Leathers, 2016). In this basin, the frequency of heavy lake-effect snowstorms is expected to decrease during the 21st century, except for a possible temporary increase around Lake Superior by mid-century, if local air temperatures remain low enough (Notaro et al., 2015). CMIP5 simulations of the periods 1981–2000 and 2081–2100 over central and eastern US suggest a northward shift in the transition zone between rain-dominated and snow-dominated areas, by about 2° latitude under the RCP4.5 scenario and 4° latitude under the RCP8.5 scenario (Ning and Bradley, 2015). Rain-on-snow event properties over North America should also evolve during the 21st century, with non-trivial dependencies on the positioning relative to the freezing line (Jeong and Sushama, 2018) and on elevation (Musselman et al., 2018).

Atlas.9.5 Summary

Across North America it is *very likely* that positive surface temperature trends are persistent**.** Across near-Arctic latitudes of North America increases are exceptionally pronounced, greater than 0.5°C per decade (*high confidence*). In parts of eastern and central North America it is *likely* that annual precipitation has increased over the period of 1960 to 2015 but with no clear trends in other regions except for parts of south-western US and north-western Mexico where there is *medium confidence* in drying.

Model representation of the climatology of mean temperature and precipitation has *likely* improved compared to the AR5 over North America. This is aided by continuous model development, and the existence of new coordinated modelling initiatives such as NA-CORDEX. There is *high confidence* that downscaling a subset of CMIP models that spans the range of climate sensitivities in the full ensemble is critical for producing a representative range of dynamically downscaled projections.

It is *virtually certain* that annual and seasonal surface temperatures over all of North America will continue to increase at a rate greater than the global average, with greater increases in the far north. It is *very likely*, based on global and regional model future projections, that on an annual time scale precipitation will increase over most of North America north of about 45°N and in eastern North America, and it is *likely* that it will decrease in the southwest US and northern Mexico, particularly in winter. Elsewhere the direction of change of precipitation is uncertain. It is *virtually certain* that snow cover will experience a decline over most regions of North America during the 21st century, in terms of water equivalent, extent and annual duration**.** It is however *very likely* that some high-latitude regions will rather experience an increase in winter snow water equivalent, due to the snowfall increase prevailing over the warming effect.

ACCEPTED VERSION SUBJECT TO FINAL EDITS

Atlas.10 Small islands

Atlas.10.1 Key features of the regional climate and findings from previous IPCC assessments

Atlas.10.1.1 Key features of the regional climate

Many small islands lie in tropical regions and their climate varies depending on a range of factors with location, extent and topography having major influences. In general, their climate is determined by that of the broader region in which they lie as they have little influence on the regional climate although steep topography can induce higher rainfall totals locally. Temperature variability tends to be low due to the influence of the surrounding ocean, most marked in the tropics where oceanic temperature ranges are small. However, seasonal rainfall variability can often be significant, both through the annual cycle and also interannually through the influence of many modes of variability (for more details see Cross-Chapter Box Atlas.2:, Annex IV and Section Atlas.7.1 for the Caribbean). Many small islands are exposed to tropical cyclones and the associated hazards of high winds, storm surges and extreme rainfall, and many low-lying islands are exposed to regular flooding from natural high tide and wave activity. In the Pacific, phases of the El Niño Southern Oscillation result in periods of warmer or cooler than average temperatures following the upper ocean warming of El Niño events or cooling of La Niña events, and respectively weaker and stronger trade winds. El Niño conditions also lead to drought in Melanesian islands and increased typhoons and storm surges in French Polynesia with La Niña conditions causing drought in Kiribati. Other islands experience increased rainfall during these periods.

Atlas.10.1.2 Findings from previous IPCC assessments

The AR5 noted observed temperature increases of 0.1°C–0.2°C per decade in Pacific Islands and that warming was *very likely* to continue across all Small Island regions (Christensen et al., 2013; IPCC, 2013a). It also reported decreased rainfall over the Caribbean, increases over the Seychelles, streamflow reductions over the Hawaiian Islands and projections of reduced rainfall over the Caribbean and drier rainy season for many of the southwest Pacific Islands (Christensen et al., 2013; IPCC, 2013a; Nurse et al., 2014). The remaining findings are derived from the SROCC (IPCC, 2019a). Ocean warming rates have *likely* increased in recent decades with marine heatwaves increasing and *very likely* to have become longer-lasting, more intense and extensive as a result of anthropogenic warming. Open ocean oxygen levels have *very likely* decreased and oxygen minimum zones have *likely* increased in extent. There is *very high confidence* that global mean sea level rise has accelerated in recent decades which, combined with increases in tropical cyclone winds and rainfall and increases in extreme waves, has exacerbated extreme sea level events and coastal hazards (*high confidence*). It is *virtually certain* that during the 21st century, the ocean will transition to unprecedented conditions with further warming and acidification *virtually certain*, increased upper ocean stratification *very likely* and continued oxygen decline (*medium confidence*). There is *very high confidence* that marine heatwaves and *medium confidence* that extreme El Niño and La Niña events will become more frequent. It is *very likely* that these changes will be smaller under scenarios with low greenhouse-gas emissions. Global mean sea level will continue to rise and there is *high confidence* that the consequent increases in extreme levels will result in local sea levels in most locations that historically occurred once per century occurring at least annually by the end of the century under all RCP scenarios (*high confidence*). In particular, many small islands are projected to experience historical centennial events at least annually by 2050 under RCP2.6 and higher emissions. The proportion of Category 4 and 5 tropical cyclones, and associated precipitation rates and storm surges, along with average tropical cyclone intensity are projected to increase with a 2°C global temperature rise, thereby exacerbating coastal hazards.

Atlas.10.2 Assessment and synthesis of observations, trends and attribution

Significant positive trends in temperature ranging from 0.15°C per decade (over the period 1953–2010) to 0.18°C per decade (over the period 1961–2011) are noted in the tropical Western Pacific, where the significant increasing trends in the warm and cool extremes are also spatially homogeneous (Jones et al.,

ACCEPTED VERSION SUBJECT TO FINAL EDITS

2013; Whan et al., 2014; Wang et al., 2016). Similarly, much of the Caribbean region showed statistically significant warming (at the 95% level) over the 1901–2010 period (Jones et al., 2016b). Observation records in the Caribbean region indicate a significant warming trend of 0.19°C per decade and 0.28°C per decade in daily maximum and minimum temperatures, respectively, with statistically significant increases (at the 5% level) in the number of warm days and warm nights during 1961–2010 (Taylor et al., 2012b; Stephenson et al., 2014; Beharry et al., 2015).

A weather station-based annual precipitation trend analysis over 1901–2010 in the Caribbean region indicated some locations with detectable decreasing trends (Knutson and Zeng, 2018), which were attributable in part to anthropogenic forcing. These include southern Cuba, the northern Bahamas, and the Windward Islands although significant trends were not found over the shorter periods of 1951–2010 and 1981–2010. In Caribbean Islands, a Palmer Drought Severity Index dataset from 1950 to 2016 showed a clear drying trend in the region (Herrera and Ault, 2017). The 2013–2016 period showed the most severe drought during the period and was strongly related to anthropogenic warming, which would have increased the severity of the event by 17% and its spatial extent by 7% (Herrera et al., 2018). However, a seasonal analysis of observations grouped into large subregions of the Caribbean revealed no significant long-term trends in rainfall over 1901–2012 but significant inter-decadal variability (Jones et al., 2016b). Declines in summer rainfall (–4.4% per decade) and maximum five-day rainfall (–32.6 mm per decade) over 1960–2005 were reported for Jamaica (CSGM, 2012) and an insignificant decrease in summer precipitation was observed for Cuba for 1960 to 1995 (Naranjo-Diaz and Centella, 1998). Three of four stations examined for Puerto Rico exhibited declining JJA rainfall over 1955–2009 with the trend statistically significant at the 95% level for Canóvana (Méndez-Lázaro et al., 2014). In the Caribbean, positive regional trends in precipitation of 2% and trends in extremes during 1961 to 2010 were found to be not statistically significant (at the 5% level) (Stephenson et al., 2014; Beharry et al., 2015). Positive trends in JJA rainfall over Cuba and Jamaica are seen in the CRU, whereas they are negative over Cuba for GPCC; over eastern Hispaniola they are positive in CRU and negative in CHIRPS (Cavazos et al., 2020).

In Hawai'i, between 1920 and 2012, over 90% of the islands showed reduced rainfall and streamflow, an increase in the frequency of days with zero flow (Strauch et al., 2015; Frazier and Giambelluca, 2017) and robust positive trends in the drought frequency and severity (McGree et al., 2016). Over the western Pacific, interannual and decadal variabilities also drive long-term trends in rainfall. Recent analysis of station data showed spatial variations in the mostly decreasing but non-significant trends in annual and extreme rainfall over the Western Pacific from 1961–2011 (*low confidence*) (McGree et al., 2014). Over the southern subtropical Pacific decreases in annual, JJA, SON and extreme rainfall and increasing drought frequency in western region has been observed since 1951 (Jovanovic et al., 2012; McGree et al., 2016, 2019).

Over the Western Indian Ocean significant warming trends have been reported for Mauritius (1.2°C during 1951–2016 (MESDDBM, 2016)), La Réunion (0.18°C per decade over 1968–2019 (Météo-France, 2020)) and Maldives (MEE, 2016). Both Mauritius and La Réunion have experienced rainfall decreases of 8% during 1951–2016 and 1.2% per decade during 1961–2019 with generally weak, non-significant rainfall trends during 1967–2012.

Assessing observed climate change for Small Islands is often constrained by low station density (Ryu and Hayhoe, 2014; Jones et al., 2016c), digitization requirements or data sharing limitations (Jones et al., 2016c). Station data typically have longer temporal coverage relative to satellite products but are limited in spatial coverage (Cavazos et al., 2020). For Small Island nations, spatial gaps between observations can be very large due to isolation of the islands (Wright et al., 2016). Additionally over past decades, the number of station observations has declined substantially in Mauritius (Dhurmea et al., 2019), Hawai'i (Bassiouni and Oki, 2013; Frazier and Giambelluca, 2017) and most Pacific Island countries since the 1980s (Jones et al., 2013; McGree et al., 2014, 2016). In Fiji, meteorological stations were located on or by the coast and sparse in the interior (Kumar et al., 2013). Notable topography and land use may result in changes in climatic conditions over small distances (Foley, 2018), making the observational density particularly relevant.

Moreover, many stations have little metadata available, including those in Vanuatu, the Solomon Islands and Papua New Guinea (Whan et al., 2014). Compared to earlier decades, little metadata are currently being

ACCEPTED VERSION SUBJECT TO FINAL EDITS

documented in the western Pacific islands (McGree et al., 2014), which will challenge the homogenization of long-term observational records. Challenges in the Caribbean include maintaining continuous daily time series with metadata, converting climatological data into digital formats and making them freely available (Stephenson et al., 2014; Beharry et al., 2015; Jones et al., 2016c). This is also an issue in the Pacific as many data are kept in national (local) databases, with only a fraction having been incorporated into global datasets (Whan et al., 2014).

Because of the small number of stations used for interpolation and the complex mountainous topography, gridded product for these small islands should be interpreted with caution (Frazier and Giambelluca, 2017). For the Antilles, the error in estimating CRU2.0 monthly precipitation can stand locally between 20% and 40%. Over the Caribbean, (Cavazos et al., 2020) found a discrepancy across gridded observational datasets (CRU, CHIRPS, and GPCP) in detecting orographic precipitation especially during boreal summer making their use in climate model evaluation challenging (Herrera and Ault, 2017). Furthermore, some reanalysis products such as the 0.7° x 0.7° ERA-Interim reanalysis are not adequate as many of the smaller Caribbean islands are not represented as land (Jones et al., 2016c).

Atlas.10.3 Assessment of model performance

An assessment of model performance for the Caribbean region is contained in Section Atlas.7.1 on Central America. In summary, the ability of climate models to simulate the climate over the region has improved in many key respects with the application of increased model resolution and a better representation of the land-surface processes of particular importance in these advances (*high confidence*). Regional climate models (RCMs) simulate realistically seasonal surface temperature and precipitation patterns including the bimodal rainfall in the precipitation annual cycle although with some timing biases in some regions (*high confidence*). The important regional circulation and precipitation features, the Caribbean Low-Level Jet and the mid-summer drought, are well represented over a variety of RCM domains covering the region (*high confidence*).

Over the tropical Pacific, surface temperature biases in CMIP6 models remain similar to those in CMIP5, although are reduced in the higher resolution models in the HiResMIP ensemble. CMIP6 models generally represents trends in sea surface temperatures better than CMIP5 (see Section 9.2.1 for more details). For precipitation, the persistent tropical Pacific bias of the double ITCZ (erronious bands of excessive rainfall both sides of the equatorial Pacific) is still present in CMIP6 models although is slightly improved compared to those in CMIP3 and CMIP5 models (Section 3.3.2.2). Application of downscaling techniques (RCMs and stretched-grid GCMs) using resolutions finer than 10 km over the Pacific can capture topographic influences on wind and rainfall to generate realistic simulations of island climates – for example over Fiji and New Caledonia, (Chattopadhyay and Katzfey, 2015; Dutheil et al., 2019). In both cases applying bias adjustment to the sea surface temperatures used as a lower boundary condition for the downscaling models was important to generate realistic simulations.

Atlas.10.4 Assessment and synthesis of projections

Projected median temperature increases for Small Islands from the CMIP5 ensemble range from 1°C (RCP4.5) to 1.5°C (RCP8.5) in the period 2046–2065, and from 1.3°C (RCP4.5) to 2.8°C (RCP8.5) by 2081–2100 relative to 1986–2005 (Harter et al., 2015). Spatial variations in the warming trend are projected to increase by the end of the 21st century, with relatively higher increases in the Arctic and sub-Arctic islands, and in the equatorial regions compared with islands in the Southern Ocean (Harter et al., 2015). In the western Pacific, temperatures are projected to increase by 2.0°C to 4.5°C by the end of the 21st century relative to 1961–1990 (Wang et al., 2016). The warming over land in the Lesser Antilles is estimated to be about 1.6°C (3.0°C) by 2071–2100 for the RCP4.5 (RCP8.5) scenario, relative to 1971–2000 (Cantet et al., 2014). Projections from the CMIP6 ensemble support these findings (Figure Atlas.28) and across global warming levels from 1.5°C to 4°C CMIP5 and CMIP6 consistently project lower levels of warming for Small Islands than the global average (see also the Interactive Atlas).

ACCEPTED VERSION SUBJECT TO FINAL EDITS

[START FIGURE ATLAS.28 HERE]

Figure Atlas.28: Regional mean changes in annual mean surface air temperature, precipitation and sea level rise relative to the 1995–2014 baseline for the reference regions in Small Islands (warming since the 1850–1900 pre-industrial baseline is also provided as an offset). Bar plots in the left panel of each region triplet show the median (dots) and 10th–90th percentile range (bars) across each model ensemble for annual mean temperature changes for four datasets (CMIP5 in intermediate colours; subset of CMIP5 used to drive CORDEX in light colours; CORDEX overlying the CMIP5 subset with dashed bars; and CMIP6 in solid colours); the first six groups of bars represent the regional warming over two time periods (near-term 2021–2040 and long-term 2081–2100) for three scenarios (SSP1-2.6/RCP2.6, SSP2-4.5/RCP4.5, and SSP5-8.5/RCP8.5), and the remaining bars correspond to four global warming levels (GWL: 1.5°C, 2°C, 3°C, and 4°C). Bar plots in the right panel show the median (dots) and 5th–95th percentile range (bars) sea level rise from the CMIP6 ensemble (see Chapter 9 for details) for the same time periods and scenarios. The scatter diagrams of temperature against precipitation changes display the median (dots) and 10th–90th percentile ranges for the above four warming levels for December-January-February (DJF; middle panel) and June-July-August (JJA; right panel), respectively; for the CMIP5 subset only the percentile range of temperature is shown, and only for 3°C and 4°C GWLs. Changes are absolute for temperature (in °C) and relative (as %) for precipitation. See Section Atlas.1.3 for more details on reference regions (Iturbide et al., 2020) and Section Atlas.1.4 for details on model data selection and processing. The script used to generate this figure is available online (Iturbide et al., 2021) and similar results can be generated in the Interactive Atlas for flexibly defined seasonal periods. Further details on data sources and processing are available in the chapter data table (Table Atlas.SM.15).

[END FIGURE ATLAS.28 HERE]

The CMIP5 ensemble median projected a precipitation decreases of up to –16% over the Caribbean, parts of the Atlantic and Indian Oceans and southern sub-tropical and eastern Pacific Ocean, and increases of up to 10% over parts of the western Pacific and Southern Ocean, and up to 55% in the equatorial Pacific islands under RCP6.0 in the period 2081–2100 relative to 1986–2005 (Harter et al., 2015). A projected decrease in annual precipitation is also noted over the Lesser Antilles under the RCP4.5 and RCP8.5 scenarios (Cantet et al., 2014). Seasonal rainfall is projected to decrease in most areas in Hawai'i, except for the climatically wet windward side of the mountains, which would increase the wet and dry gradient over the area (Timm et al., 2015). The average precipitation changes in Hawai'i are estimated to be about –11% to –28% under RCP4.5 during the wet season, and about –4% to –28% under RCP4.5 during the dry season in the period 2041–2071 relative to 1975–2005, with larger changes under RCP8.5 (Timm et al., 2015). There are still uncertainties in the projected changes, which have been attributed to factors including insufficient model skill in representing topography in the small islands, and high variability in climate drivers. However, the broad-scale pattern of projected wetter conditions in the western and equatorial Pacific, North Indian and Southern Oceans and of drier conditions over the Caribbean, parts of the Atlantic, West Indian and the southern sub-tropical and eastern Pacific Oceans are further strengthened in the CMIP6 ensemble (Figure Atlas.28) which are thus *likely* regional responses as the climate continues to warm.

The negative trend in future summer rainfall in the Caribbean and Central America is projected to be strongest during the mid-summer (June–August) based on studies using GCMs (Rauscher et al., 2008; Karmalkar et al., 2013; Karmacharya et al., 2017; Taylor et al., 2018). The future summer drying over the Caribbean is associated with a projected future strengthening of the Caribbean Low-Level Jet (Taylor et al., 2013b). Rauscher et al. (2008) hypothesized that the simulated 21st century drying over Central America represents an early onset and intensification of the mid-summer drought. The westward expansion and intensification of the NASH associated with the mid-summer drought occurs earlier under A1B, with stronger low-level easterlies. Rauscher et al. (2008) further suggested that the eastern Pacific ITCZ is also located further southward and that there are some indications that these changes could be forced by ENSO-like warming of the tropical eastern Pacific and increased land-ocean heating contrasts over the North American continent. Other studies also suggest a future intensification of the NASH due to changes in land-sea temperature contrast resulting from increased greenhouse-gas concentrations (Li et al., 2012b).

ACCEPTED VERSION SUBJECT TO FINAL EDITS

Atlas.10.5 Summary

It is *very likely* that all Small Island regions have warmed with significant trends recorded from at least the 1960s in all territories or nations. Trends include 0.15°C–0.18°C per decade in the tropical Western Pacific (1953 to 2011), significant warming over the Caribbean (1901–2010) with trends of 0.19°C (0.28°C) per decade in daily maximum (minimum temperatures) (1961–2010) and in La Réunion of 0.18°C per decade (1968–2019). There are fewer significant trends in precipitation in these regions though several locations in the Caribbean have detectable decreasing trends (*high confidence*), in part attributable to anthropogenic forcing (*limited evidence*). Also, it is *likely* that drying has occurred since the mid-20th century in some parts of the Western Indian Ocean, and in the Pacific poleward of 20° latitude in both the northern and southern hemispheres.

It is *very likely* that Small Island regions will continue to warm in the coming decades at a level slightly lower than the global mean. Small Island regions in the Western and equatorial Pacific, North Indian and Southern Ocean are *likely* to be wetter in the future and those in the Caribbean, parts of the Atlantic and West Indian Oceans and the southern sub-tropical and eastern Pacific Ocean drier.

[START CROSS-CHAPTER BOX ATLAS.2 HERE]

Cross-Chapter Box Atlas.2: Climate information relevant to water resources in Small Islands

Coordinators: Tannecia Stephenson (Jamaica), Faye Abigail Cruz (Philippines)
Contributors: Donovan Campbell (Jamaica), Subimal Ghosh (India), Rafiq Hamdi (Belgium), Mark Hemer (Australia), Richard G. Jones (UK), James Kossin (USA), Simon McGree (Australia/Fiji), Blair Trewin (Australia), Sergio M. Vicente-Serrano (Spain)

Constructing regional climate information for Small Islands involves synthesis from multiple sources. This cross-chapter box presents information relevant to water resources, drawing on several chapters in AR6 and Section Atlas.10. It introduces the context and current evidence base followed by an assessment of trends and projections in rainfall, temperature and sea levels across Small Islands and highlight key findings.

Regional context

Small Islands are predominantly located in the Pacific, Atlantic and Indian Oceans, and in the Caribbean (Nurse et al., 2014; Shultz et al., 2019). They are characterized by their small physical size, being surrounded by large ocean expanses, vulnerability to natural disasters and extreme events and relative isolation (Nurse et al., 2014) (Section 12.4.7, Section Atlas.10, Glossary). These and nearby larger islands (e.g., Madagascar, Cuba) are often water-scarce with low water volumes due to increasing demand (from population growth and tourism), aging and poorly designed infrastructure (Burns, 2002) and decreasing supply (from pollution, changes in precipitation patterns, drought, saltwater intrusion, regional sea level rise, inadequate water governance (Belmar et al., 2016; Mycoo, 2018) and competing and conflicting uses (Cashman, 2014; Gheuens et al., 2019) (Section 8.1.1.1). In the Caribbean, groundwater is the main freshwater source and depends strongly on rainfall variability (Post et al., 2018) while rain, ground or surface water are the primary sources for the Pacific islands depending on island type (volcanic or atoll), size and quality of groundwater reserves (Burns, 2002). Groundwater pumping and increasing sea levels also affect water availability by increasing the salinity of the aquifer (e.g., Bailey et al., 2015, 2016) thus reinforcing negative drought effects from reduced rainfall and increased evaporative demand from higher temperatures. For example, in 54% of the Marshall Islands, groundwater is highly vulnerable to droughts (Barkey and Bailey, 2017).

The climate of Small Islands and findings from previous IPCC assessments

Intraseasonal to interannual rainfall in the Caribbean and in the Indian and Pacific Ocean is influenced by the trade winds, the passage of tropical cyclones (TCs), Madden-Julian Oscillation (MJO), easterly waves, migrations of the Inter-Tropical Convergence Zone (ITCZ) and the North Atlantic Subtropical High (NASH)

ACCEPTED VERSION SUBJECT TO FINAL EDITS

for the Caribbean, the South Pacific Convergence Zone (SPCZ) and western North Pacific summer monsoon for the Pacific and the South Asian monsoons for the Indian Ocean. The relevant dominant modes of climate variability (Annex IV, Section 8.3.2.9) are El Niño-Southern Oscillation (ENSO) and the Indian Ocean Dipole (IOD) which have been associated with extreme events in the islands (Stephenson et al., 2014; Kruk et al., 2015; Frazier et al., 2018)(Annex IV). The modes of climate variability are modulated by Pacific Decadal Variability (PDV), Interdecadal Pacific Oscillation (IPO) and Atlantic Multidecadal Variability (AMV). These modes show no sustained trend since the late 19th century (*high confidence*) (Section 2.4).

The AR5 WGI reports observed temperature increases of 0.1°C–0.2°C per decade in Pacific Islands with these trends *very likely* to continue under high emissions, and projects a drier rainy season for many islands in the southwest Pacific (Christensen et al., 2013). AR5 WGII reports rainfall reductions over the Caribbean, increases over the Seychelles, streamflow reductions over the Hawaiian Islands and salt-water intrusion into groundwater reserves in Pacific Islands resulting from storm surges and high tides (Nurse et al., 2014). SROCC (IPCC, 2019a) finds *very high confidence* that global mean sea level rise has accelerated in recent decades which has exacerbated extreme sea level events and flooding (*high confidence*). It will continue to rise with consequent increases in extreme levels so that the historical one-in-a-century extreme local sea level will become an annual event by the end of the century under all RCP scenarios (*high confidence*). In particular, many Small Islands are projected to experience historical centennial events at least annually by 2050 under RCP2.6, RCP4.5 and RCP8.5 emissions. The proportion of Category 4 and 5 TCs and associated precipitation rates along with their average intensity are projected to increase with a 2°C global temperature rise which will further increase the magnitude of resultant storm surges and flooding. The SROCC cross-chapter box on Low-lying Islands and Coasts (Magnan et al., 2019) focused on sea level rise and oceanic changes and their impacts, therefore the assessment presented here on climate changes relevant to water resources, including precipitation and temperature, is complementary.

Observations and attribution of changes

Cross-Chapter Box Atlas.2: presents an overview of observed subregional trends relevant to water resources in some Small Islands and island regions largely from 1951. Some general observed climate trends include higher magnitude and frequency of temperatures including warm extremes (*medium* to *high confidence*; Table 11.7, Sections 12.4.7.1, Atlas.10.2), declines in high intensity rainfall events (*low* to *medium confidence*; Table 11.7), regional sea level rise with strong storm surge and waves resulting in increased coastal flood intensity (*high confidence*, Section 12.4.7.4, Section Atlas.10.2), and increased intensity and intensification rates of tropical cyclones at global scale (*medium confidence*, Sections 11.7.1.2, 12.4.7.3) and ocean acidification (*virtually certain*, Chapters 2, 6 and 9, Section Atlas.3.2).

No significant long-term trends are observed for annual Caribbean rainfall over the 20th century (*low confidence*; Section Atlas.10.2). Over the western Pacific, generally decreasing but non-significant trends are noted in annual total rainfall from 1961 to 2011 (*low confidence*; Section Atlas.10.2; Table 11.5). June-July-August (JJA) rainfall over the Caribbean shows some drying tendencies that may be linked to the combined effect of warm ENSO events and a positive NAO phase (Giannini et al., 2000; Méndez-Lázaro et al., 2014; Fernandes et al., 2015b), or to warm ENSO events and a positive PDV (Maldonado et al., 2016). The work of Herrera et al. (2018) however suggests that anthropogenic influences may also be possible though proposed mechanisms to date have not decoupled the influence of anthropogenic trends versus natural decadal variability (Vecchi et al., 2006; Vecchi and Soden, 2007; DiNezio et al., 2009).

Southern hemisphere subtropical Pacific June–November drying has been associated with intensification of the subtropical ridge and associated declines in baroclinicity (Whan et al., 2014). Austral summer drying in the southwest French Polynesia subregion has been linked with increased greenhouse-gas and ozone changes (Fyfe et al., 2012). The southern hemisphere jet stream has *likely* shifted polewards (Section 2.3.1.4.3) which is attributed largely to a trend in the Southern Annular Mode (Section 3.7.2).

These assessments are constrained by limited availability of observational datasets and of scientific studies. Assessment of observed climate change for Small Islands is often constrained by low station density (Ryu and Hayhoe, 2014; Jones et al., 2016c), short periods of record, digitization requirements or data sharing

ACCEPTED VERSION SUBJECT TO FINAL EDITS

limitations (Jones et al., 2016c), availability of metadata (McGree et al., 2014; Stephenson et al., 2014; Jones et al., 2016b), challenges in some gridded product representations of variability, for example for complex topography (Frazier and Giambelluca, 2017), and challenges characterizing the impact of vertical land motion on sea level rise (Wöppelmann and Marcos, 2016) (see also Section Atlas.10.2).

[START CROSS-CHAPTER BOX ATLAS.2, TABLE 1 HERE]

Cross-Chapter Box Atlas.2, Table 1: Summary of observed trends for Small Island regions. SLR = sea level rise; TC = tropical cyclone; SPCZ = South Pacific Convergence Zone.

Region	Subregion	Temperature	Rainfall	Other
Caribbean			*Low confidence* in drought intensity increasing over 2013–2016 (Herrera and Ault, 2017; Herrera et al., 2018)	
	Jamaica, Cuba, Puerto Rico		*Low confidence* in declining JJA rainfall (CSGM, 2012) and decreasing trend Puerto Rico 1955–2009 (Méndez-Lázaro et al., 2014). Mixed trends 1980–2010 (Cavazos et al., 2020);	No attributable JJA rainfall trends 1951–2010 (Knutson and Zeng, 2018)
	Eastern Caribbean	*Medium confidence* in increased frequency of hot extremes	*Low confidence* in an increase in periods of drought since 1999 (Van Meerbeeck, 2020)	*Medium confidence* in SLR of 1–2.5 mm yr^{-1} since 1950 (Van Meerbeeck, 2020)
Pacific	Midway-Hawaiian Islands	*High confidence* in the increase in mean temperature since 1917 and stronger increase in minimum temperature since 1905 (Keener et al., 2018; McKenzie et al., 2019; Kagawa-Viviani and Giambelluca, 2020)	*Medium confidence* in rainfall decreasing since 1920, drought frequency and severity increasing since 1951 and exceptional aridity since 2008; (McGree et al., 2016; Frazier and Giambelluca, 2017; Luo et al., 2020b). *Low confidence* in extreme rainfall increasing (Kruk et al., 2015)	*Medium confidence* in relative SLR of 2.1 mm yr^{-1} (Mokuoloe Is. and Honolulu, Oahu Is.) over 1993–2017
	Northwest Tropics	*High confidence* in the increase in mean and extreme temperature at most locations since 1951 (Whan et al., 2014; McGree et al., 2019)	*Low confidence* in JJA and SON total and extreme rainfall decreasing, increasing drought in east Micronesia and marginal increase in rainfall for western islands since 1951 (Kruk et al., 2015; McGree et al., 2019)	*Low confidence* in decrease in total TC numbers. Depends on dataset/period (Choi and Cha, 2015; Lee et al., 2020) *Medium confidence* in relative SLR of 2.8 mm yr^{-1} (Majuro, Marshall Is.) over 1994–2015 (Ford et al., 2018)
	Equatorial Pacific		*Low confidence* in increasing annual and JJA extreme rainfall, decreasing consecutive dry days in the central region since 1951 (McGree et al.,	*Low* to *medium confidence* in relative SLR of 5.3 (Nauru), 0.8 (Kanton, Kiribati)

ACCEPTED VERSION SUBJECT TO FINAL EDITS

			2019) and increasing DJF total rainfall (BOM and CSIRO, 2014) *Low confidence* in decreasing SON total rainfall, increasing JJA and SON extreme rainfall and fewer consecutive wet days in western region since 1951 (BOM and CSIRO, 2014; McGree et al., 2019)	mm yr^{-1} over 1993–2015 (Albrecht et al., 2019; Martínez-Asensio et al., 2019)
	Southwest SPCZ		*Low confidence* in change in mean and extreme rainfall at most locations since 1951 (Keener et al., 2012; McGree et al., 2016, 2019)	*Medium confidence* in decrease in total TC numbers and *low confidence* in decrease in numbers of intense TCs since 1981 (Kuleshov et al., 2020). *Low confidence* in shift in mean SPCZ position since 1911 (Salinger et al., 2014) *Medium confidence* in increase in relative SLR of 1.7–7.7 mm yr^{-1} across southern Pacific Islands over period 1993–2015 (Martínez-Asensio et al., 2019)
	Northeast SPCZ		*Low confidence* in change in mean and extreme rainfall at most locations since 1951 (BOM and CSIRO, 2014; McGree et al., 2016, 2019)	
	Southern Subtropics		*Medium confidence* in annual, JJA and SON total and extreme rainfall decreasing and increasing drought frequency in western region since 1951 (Jovanovic et al., 2012; McGree et al., 2016, 2019) *Low confidence* in annual, SON, DJF, MAM total and extreme rainfall decreasing, increases in drought, JJA rain days and consecutive dry days in Southwest French Polynesia since 1951 (McGree et al., 2016, 2019)	
Western Indian Ocean	Mauritius	Warming of 1.2°C over 1951–2016 (MESDDBM, 2016)	Rainfall decrease of 8% over 1951–2016 (MESDDBM, 2016)	Relative SLR at 5.6 mm yr^{-1} over 2007–2016 (MESDDBM, 2016)
	La Réunion	Temperature increase 0.18°C per decade over 1968–2019 (Météo-France, 2020)	Rainfall decrease of 1.2% per decade over 1961–2019 (Météo-France, 2020)	
	Maldives	Generally warming trends from the 1970s to 2012 (MEE, 2016)	Generally weak, non-significant rainfall trends over 1967–2012 (MEE, 2016)	SLR of 2.9–3.7 mm yr^{-1} over 1991–2012 (MEE, 2016)

[END CROSS-CHAPTER BOX ATLAS.2, TABLE 1 HERE]

Information on future climate changes

Small Islands will *very likely* continue to warm this century, though at a rate less than the global average (Figure Atlas.28), with consequent increased frequency of warm extremes for the Caribbean and Western Pacific islands, and heatwave events for the Caribbean (*high confidence*) (Table 11.7). Annual and JJA rainfall declines are *likely* for some Indian and southern Pacific regions with drying over southern French

ACCEPTED VERSION SUBJECT TO FINAL EDITS

Polynesia (attributed partially to greenhouse-gas increases) and farther east clearly evident in CMIP5 and CMIP6 projections (Figure Atlas.28) (*high confidence*). See also Section Atlas.10.4.

Rainfall is *very likely* to decline over the Caribbean, in the annual mean and especially in JJA, with a stronger and more coherent signal in CMIP6 compared to CMIP5 (Figure Atlas.28, Interactive Atlas) and reductions of 20–30% by the end of the century under high future emissions (SSP5-8.5). This JJA drying has been linked to a future strengthening of the Caribbean Low Level Jet (CLLJ) (Taylor et al., 2013b), a westward expansion and intensification of the NASH, stronger low-level easterlies over the region, a southwardly placed eastern Pacific ITCZ (Rauscher et al., 2008), and changing dynamics due to increased greenhouse-gas concentrations (Li et al., 2012b) (*very high confidence*). Projections from 15 GCM and two RCM experiments for 2080–2089 relative to 1970–1989 were for a generally drier Caribbean and a robust summer drying (Karmalkar et al., 2013). More recent downscaling studies (e.g., Taylor et al., 2018; Vichot-Llano et al., 2021) also project a drier Caribbean and longer dry spells (Van Meerbeeck, 2020).

Sea level rise is *very likely* to continue in all Small Island regions (Figure Atlas.28, see also Sections 9.6.3.3 and 12.4.7.4) and its the effects will be compounded by TC surge events. In general, the most intense TCs are *likely* to intensify and produce more flood rains with warming, however detailed effects of climate change on TCs will vary by region (Knutson et al., 2019)(Section 11.7.1). Bailey et al. (2016) projected a 20% decline in groundwater availability by 2050 in Coral Atoll islands of the Federal States of Micronesia and stressed that under higher sea level rise the decrease could be higher than 50% due to marine water intrusion into aquifers, as well as drought events.

Summary of information distilled from multiple lines of evidence

It is *very likely* that most Small Islands have warmed over the period of instrumental records. The clearest precipitation trend is a *likely* decrease in JJA rainfall over the Caribbean since 1950. There is *limited evidence* and *low agreement* for the cause of the observed drying trend, whether it is mainly caused by decadal-scale internal variability or anthropogenic forcing, but it is *likely* that it will continue over coming decades. It is *likely* that drying has occurred since the mid-20th century in some parts of the Pacific poleward of 20° latitude in both the northern and southern hemispheres and that these will continue over coming decades. Rainfall trends in most other Pacific and Indian Ocean Small Islands are mixed and largely non-significant. It is *very likely* that sea levels will continue to rise in all Small Island regions and this will result in increased coastal flooding with the potential to increase salt-water intrusion into aquifers in Small Islands.

Whilst this assessment demonstrates that the climate of Small Islands has and will continue to change in diverse ways, constructing climate information for Small Islands is challenging. This is due to observational issues, incomplete understanding of some modes of variability and their representation by climate models and the lack of availability of large ensembles of regional climate model simulations and limited studies to decouple internal variability and anthropogenic influences.

[END CROSS-CHAPTER BOX ATLAS.2 HERE]

Atlas.11 Polar regions

The assessment in this section focuses on changes in average temperature, precipitation (rainfall and snow) and surface mass balance over the polar regions, Antarctica and the Arctic, including the most recent years of observations, updates to observed datasets, the consideration of recent studies using CMIP5 simulations and those using CMIP6 and CORDEX simulations. Findings are presented for West Antarctica (WAN), East Antarctica (EAN) and three Arctic regions, Arctic Ocean (ARO), Greenland/Iceland (GIC) and Russian Arctic (RAR) (Figure Atlas.29) with some reference also to North-Eastern North America (NEN), North-Western North America (NWN) and Northern Europe (NEU), which are covered more extensively in Sections Atlas.9 and Atlas.8 respectively. Subregional changes are discussed when relevant, for example the Antarctic Peninsula (AP) as a subregion of WAN. The Southern Ocean (SOO) region is assessed in Chapter 9 with changes in climatic impact-drivers assessed in Chapter 12 (12.4.9, Table 12.11) and some extremes in

ACCEPTED VERSION SUBJECT TO FINAL EDITS

Chapter 11 (Table 11.7–9 for RAR). Chapter 9 provides an overall assessment of the ice sheet processes and changes, as part of the cryosphere, ocean and sea level change assessment.

[START FIGURE ATLAS.29 HERE]

Figure Atlas.29: Regional mean changes in annual mean surface air temperature and precipitation relative to the 1995–2014 baseline for the reference regions in Arctic and Antarctica (warming since the 1850–1900 pre-industrial baseline is also provided as an offset). Bar plots in the left panel of each region triplet show the median (dots) and 10th–90th percentile range (bars) across each model ensemble for annual mean temperature changes for four datasets (CMIP5 in intermediate colours; subset of CMIP5 used to drive CORDEX in light colours; CORDEX overlying the CMIP5 subset with dashed bars; and CMIP6 in solid colours); the first six groups of bars represent the regional warming over two time periods (near-term 2021–2040 and long-term 2081–2100) for three scenarios (SSP1-2.6/RCP2.6, SSP2-4.5/RCP4.5, and SSP5-8.5/RCP8.5), and the remaining bars correspond to four global warming levels (GWL: 1.5°C, 2°C, 3°C, and 4°C). The scatter diagrams of temperature against precipitation changes display the median (dots) and 10th–90th percentile ranges for the above four warming levels for December-January-February (DJF; middle panel) and June-July-August (JJA; right panel), respectively; for the CMIP5 subset only the percentile range of temperature is shown, and only for 3°C and 4°C GWLs. Changes are absolute for temperature (in °C) and relative (as %) for precipitation. See Section Atlas.1.3 for more details on reference regions (Iturbide et al., 2020) and Section Atlas.1.4 for details on model data selection and processing. The script used to generate this figure is available online (Iturbide et al., 2021) and similar results can be generated in the Interactive Atlas for flexibly defined seasonal periods. Further details on data sources and processing are available in the chapter data table (Table Atlas.SM.15).

[END FIGURE ATLAS.29 HERE]

Atlas.11.1 Antarctica

Atlas.11.1.1 Key features of the regional climate and findings from previous IPCC assessments

Atlas.11.1.1.1 Key features of the regional climate

The Antarctic region, covered by an ice sheet and surrounded by the Southern Ocean, is characterized by polar climate. It is the coldest, windiest and driest continent on Earth and plays a pivotal role in regulating the global climate and hydrological cycle. Antarctica has a mean temperature of –35°C (Lenaerts et al., 2016) and receives 171 mm yr^{-1} water equivalent of snowfall (north of 82°S, estimate based on satellite measurements during 2006–2011) (Palerme et al., 2014). Precipitation in Antarctica occurs mostly in the form of snowfall and diamond dust, with sporadic coastal rainfall during the summer over the Antarctic Peninsula and sub-Antarctic islands. Drizzle events sometimes occur during warm air intrusions (Nicolas et al., 2017) at relatively low temperatures (Silber et al., 2019). Precipitation constitutes the largest component of the surface mass balance (SMB), which also includes sublimation (from the surface or drifting snow), meltwater runoff and redistribution by wind (Lenaerts et al., 2019). SMB can be considered as a proxy of precipitation if averaged over an annual cycle (Gorodetskaya et al., 2015; Bracegirdle et al., 2019). Precipitation and SMB exhibit spatial and temporal variability controlled by atmospheric large-scale low-pressure systems and moisture advection from lower latitudes. SMB is an important component of the total ice-sheet mass balance (Section 9.4.2.1). The Antarctic contribution to sea level results from the imbalance between net snow accumulation and ice discharge into the ocean (Box 9.1). Ice shelves buttress the ice sheet and are influenced by oceanic and atmospheric drivers (Box 9.1).

Antarctic climate variability is influenced by the Southern Annular Mode (SAM) and regionally by other modes, including ENSO, Pacific-South American Pattern, Pacific Decadal Variability, Indian Ocean Dipole and Zonal Wave 3 (Annex IV). Climate change in Antarctica and the Southern Ocean is influenced by interactions between the ice sheet, ocean, sea ice, and atmosphere (Meredith et al., 2019) (Sections 9.2.3.2, 9.3.2 and 9.4.2). In addition to Chapter 9, Antarctica is discussed across the report: global climate links (Chapters 2 and 10), attribution (Chapter 3), global water cycle (Chapter 8), extremes (Chapter 11), and

ACCEPTED VERSION SUBJECT TO FINAL EDITS

climatic impact-drivers (Chapter 12).

Atlas.11.1.1.2 Findings from previous IPCC assessments

AR5 (Vaughan et al., 2013) reported warming over Antarctica since 1950s, mostly over AP and WAN, attributed to the positive trend in the SAM. These trends in the Antarctic temperature were given *low confidence* due to substantial multi-annual to multi-decadal variability, as well as uncertainties in magnitude and spatial trend structure. AR5 reported *low confidence* that anthropogenic forcing has contributed to the temperature change in Antarctica. AR5 highlighted a large interannual variability in snow accumulation with no significant trend since 1979 around Antarctica, and *high confidence* in the overall mass loss from Antarctica, accelerated since 1990s.

In this and the following paragraphs findings are from SROCC (Meredith et al., 2019) unless otherwise stated. Warming trends were reported over parts of WAN with record surface warmth over WAN during the 1990s compared to the past 200 years, and AP surface melting intensifying since the mid-20th century. No significant temperature trends were reported over EAN and there was *low confidence* in both WAN and EAN trend estimates due to sparse in situ records and large interannual to interdecadal variability. In the AP, concomitant increase in temperature and foehn winds due to positive SAM caused increased surface melting over the Larsen ice shelves (*medium confidence*). Strong warming between the mid-1950s and the late 1990s led to the collapse of the Larsen B ice shelf in 2002, which had been intact for the 11,000 years (*medium confidence*).

Snowfall increased over the Antarctic ice sheet over AP and WAN, offsetting some of the 20th century sea level rise (*medium confidence*). Longer records suggest either a decrease in snowfall over the Antarctic ice sheet over the last 1000 years or a statistically negligible change over the last 800 years (*low confidence*).

Recent warming in the AP and consequent ice-shelf collapse are *likely* linked to anthropogenic ozone and greenhouse-gas forcing via the SAM and anthropogenically-driven Atlantic sea surface. Also, there is *high confidence* in the influence of tropical sea surface temperature on the Antarctic temperature and Southern Hemisphere mid-latitude circulation, as well as the SAM. There is *medium agreement* but *limited evidence* of an anthropogenic forcing effect on Antarctic ice-sheet mass balance (*low confidence*) and partitioning between natural and human drivers of atmospheric and ocean circulation changes remains very uncertain.

In AR5 Church et al. (2013) gave *medium confidence* in model projections of a future Antarctic SMB increase, implying a negative contribution to global mean sea level rise, consistent with a projection of significant Antarctic warming. Church et al. (2013) also gave *high confidence* to the relationship between future temperature and precipitation increases in Antarctica on physical grounds and from ice core evidence. In Meredith et al. (2019), the total mass balance projections derived from ice sheet models were reported without separating the SMB though projections were reported of increased precipitation and continued strengthening of the westerly winds in the Southern Ocean.

Atlas.11.1.2 Assessment and synthesis of observations, trends and attribution

Figure Atlas.30 (Antarctic map inset) shows near surface air temperature trends for 1957-2016 and 1979-2016 at the stations where observations are available for at least 50 years and the detected trends have statistical significance of at least 90% according to the most recent (after SROCC) studies (Jones et al., 2019; Turner et al., 2020). It is *very likely* that the western and northern AP has been warming significantly since 1950s (0.49 ± 0.28°C per decade during 1957–2016 and 0.46 ± 0.15°C during 1951–2018 at Faraday-Vernadsky station; 0.29 ± 0.16°C per decade during 1957–2016 at Esperanza station), with no significant trends reported in the eastern AP during the same period (Gonzalez and Fortuny, 2018; Jones et al., 2019; Turner et al., 2020). Short-term cooling trends, strongest during austral summer, have been reported at AP stations during 1999–2016 but the absence of warming and cooling at some stations during 1999–2016 is consistent with natural variability and there is no evidence of a shift in the overall warming trend observed since 1950s (Turner et al., 2016, 2020; Gonzalez and Fortuny, 2018; Jones et al., 2019; Bozkurt et al., 2020).

ACCEPTED VERSION SUBJECT TO FINAL EDITS

Significant warming at the Byrd station (0.29 ± 0.19°C per decade during 1957–2016) confirms and extends earlier trend estimates (0.42 ± 0.24°C per decade during 1958–2010) and is representative of the entire WAN warming (0.22 ± 0.12°C per decade from 1958 to 2012 averaged over WAN excluding AP, *medium confidence* due to lack of observations) (Bromwich et al., 2013, 2014; Jones et al., 2019). WAN and AP show statistically significant warming in the HadCRUTv5 observational dataset (Figure 2.11b). There is a *high confidence* in the long-term warming trend at the AP and WAN also at the century scale based on reconstructions (Zagorodnov et al., 2012; Stenni et al., 2017; Lyu et al., 2020) confirming the trends estimated by earlier studies assessed in the SROCC (Meredith et al., 2019). The century-scale warming trend in the AP is *very likely* an emerging signal compared to natural variability, while the WAN warming trend falls in the high end of century-scale trends over the last 2000 years (Stenni et al., 2017) (*medium confidence*).

In EAN, during 1957-2016, three stations showed significant warming (Scott base 0.22 ± 0.15, Novolazarevskaya 0.13 ± 0.09 and Vostok 0.15 ± 0.13°C per decade), while other stations with long-term observations indicated no statistically significant trends (Figure Atlas.30). During 1979-2016, three coastal stations showed cooling, while at South Pole a warming trend was detected, increasing to 0.61±0.34 °C per decade during 1989-2018) (Jones et al., 2019; Clem et al., 2020; Turner et al., 2020) (Figure Atlas.30). The century-scale warming in Queen Maud Land Coast based on the ice-core reconstructions is within the range of centennial internal variability (Stenni et al., 2017).

While a trend towards a positive phase of the SAM since the 1970s *likely* explains a significant part of the warming at the northern AP, it had a cooling effect on the continental WAN and EAN (particularly strong in DJF, Table.Atlas.1). Warming in western AP and over WAN during 1957–2016 (Figure.Atlas.30) and through to 2020 (Figure 2.11) is *likely* due to significant contribution of other factors, such as tropical Pacific forcing through PDV, ENSO, Amundsen Sea Low position/strength and also anthropogenic climate change (Jones et al., 2019; Scott et al., 2019; Wille et al., 2019; Donat-Magnin et al., 2020; Turner et al., 2020). Since SROCC, new studies confirmed the influence of foehn wind and cloud radiative forcing on Larsen C surface melt (Elvidge et al., 2020; Gilbert et al., 2020; Turton et al., 2020). In the WAN, summer surface-melt occurrence over ice shelves may have increased since the late 2000s (Scott et al., 2019). It is *likely* that increased meltwater ponding and resulting hydrofracturing have been important mechanisms of the rapid disintegration of the Larsen B ice shelf (Banwell et al., 2013; MacAyeal and Sergienko, 2013; Robel and Banwell, 2019). Ice shelf disintegration and relevant processes are discussed in Sections 9.4.2.1 and 9.4.2.3.

Direct observations of snowfall in Antarctica using traditional gauges are highly uncertain and records from precipitation radars (Gorodetskaya et al., 2015; Grazioli et al., 2017; Scarchilli et al., 2020) are not long enough to assess trends. Estimates of precipitation and SMB are largely model-based due to the paucity of in situ observations in Antarctica (Lenaerts et al., 2019; Hanna et al., 2020). Antarctic SMB is dominated by precipitation and removal by sublimation with very small amounts of melt mostly important only on the ice shelves. Climate models and satellite records (IMBIE team et al., 2018; Rignot et al., 2019; Mottram et al., 2021) suggest that strong interannual variability of Antarctic-wide SMB over the satellite period currently masks any existing trend (Figure Atlas.30) in spite of a possible ozone depletion-related precipitation increase over the 1991–2005 period (Lenaerts et al., 2018). No significant Antarctic-wide SMB trend continent-wide SMB trend is inferred since 1979 (IMBIE team et al., 2018; Medley and Thomas, 2019). While ice core reconstructions show a significant increase in the western AP SMB since 1950s (Thomas et al., 2017; Medley and Thomas, 2019; Wang et al., 2019), this trend is not reproduced by regional climate models or reanalyses used to drive them (Figure Atlas.30) (van Wessem et al., 2016; Wang et al., 2019).

According to the ice core reconstructions, SMB over WAN (including AP) has *likely* increased during the 20th century with trends of 5.4 ± 2.9 Gt yr^{-1} per decade (1900–2010) (Wang et al., 2019) mitigating global mean sea level rise by, respectively, 0.28 ± 0.17 mm per decade (WAN excluding AP, during 1901–2000) and 0.62 ± 0.17 mm per decade (AP, during 1979–2000) (Medley and Thomas, 2019). Significant spatial heterogeneity in SMB trends has been observed over AP and WAN:

- western AP has *likely* experienced a significant increase in SMB beginning around 1930 and accelerating during 1970–2010, which is outside of the natural variability range of the past 300 years (Thomas et al., 2017; Medley and Thomas, 2019; Wang et al., 2019);

ACCEPTED VERSION SUBJECT TO FINAL EDITS

- eastern AP has no significant SMB trends during the same period (*low confidence*, observations limited to one ice core and large interannual variability) (Thomas et al., 2017; Engel et al., 2018);
- overall WAN SMB (excluding AP) was stable during 1980–2009 but exhibited high regional variability (Medley et al., 2013): significant increases (5–15 mm per decade during 1957–2000) to the east of the West Antarctic ice sheet divide and significant decrease (–1 to –5 mm per decade during 1901–1956, and –5 to –15 mm per decade during 1957–2000) to the west (Medley and Thomas, 2019; Wang et al., 2019).

The SMB of EAN increased during the 20th century which mitigated global mean sea level rise by 0.77 ± 0.40 mm per decade during 1901–2000 (Medley and Thomas, 2019) (*medium confidence*). EAN SMB has been increasing at a much lower rate since 1979 as shown by observations, while regional climate models show strong interannual variability masking any trend (Medley and Thomas, 2019; Rignot et al., 2019) (Figure Atlas.30) (*low confidence* due to limited observations). EAN SMB changes during the 20th century and recent decades showed large spatial heterogeneity:

- With significant increases *likely* in Queen Maud Land (QML): 5.2 ± 3.7% per decade during 1920–2011 measured in ice core near the Kohnen station (Medley et al., 2018), an increase on the plateau (Altnau et al., 2015), and stable conditions during 1993–2010 along the annual stake line from Syowa (coast) to Dome F (plateau) (Wang et al., 2015b); increases during 1911–2010 (Thomas et al., 2017) with anomalously high SMB observed in 2009 and 2011 (Boening et al., 2012; Lenaerts et al., 2013; Gorodetskaya et al., 2014);
- increases in Wilkes Land and Queen Mary Land during 1957–2000 (Thomas et al., 2017; Medley and Thomas, 2019) (*low confidence* due to limited observations and strong spatial variability);
- a *likely* stable SMB in the interior of the East Antarctic plateau during the 1901–2000 period and the last decades (Thomas et al., 2017; Medley and Thomas, 2019);
- stable in Adelie Land (annual stake line during 1971–2008) (Agosta et al., 2012) (*low confidence* due to *limited evidence*).

Regional trends of the last 50 years (1961–2010) and 100 years (1911–2010) are within centennial variability of the past 1000 years, except for coastal QML (unusual 100-year increase in accumulation) and for coastal Victoria Land (unusual 100-year decrease in accumulation) (Thomas et al., 2017). Nevertheless, the current EAN SMB is not unusual compared to the past 800 years (Frezzotti et al., 2013).

The geographic pattern of accumulation changes since the 1950s bears a strong imprint of a trend towards a more positive phase of the SAM (e.g., Medley and Thomas, 2019), which could be linked to ozone depletion (Lenaerts et al., 2018) or large-scale atmospheric warming (Frieler et al., 2015; Medley and Thomas, 2019). More evidence has emerged showing the importance of the Pacific-South American Pattern, ENSO and Pacific Ocean convection, and large-scale blocking causing warm-air intrusions and both extreme precipitation and melt events, responsible for large interannual SMB variability (*high confidence*) (Gorodetskaya et al., 2014; Bodart and Bingham, 2019; Scott et al., 2019; Turner et al., 2019; Wille et al., 2019; Adusumilli et al., 2021). This strengthens evidence for an important connection between Antarctic climate and tropical sea surface temperature stated by SROCC (Meredith et al., 2019). Section 3.4.3 and SROCC (Meredith et al., 2019) provide a discussion of attribution of Antarctic ice sheet changes.

Atlas.11.1.3 Assessment of model performance

This section provides evaluation of atmospheric global and regional climate models, including reanalyses. Evaluation of the ice sheet models and relevant processes, including selection of the atmospheric models used to drive ice sheet models, is given in Section 9.4.2.2.

One of the major systematic biases in CMIP5 and earlier GCMs was an equatorward bias in the latitude of the Southern Hemisphere mid-latitude westerly jet, which is significantly reduced in the CMIP6 ensemble (Bracegirdle et al., 2020a). GCM Southern Ocean sea-ice biases are also of importance as they influence 21st century temperature projections in Antarctica and simulation of present day temperatures are highly sensitive to these biases (Agosta et al., 2015; Bracegirdle et al., 2015). A positive bias in near-surface temperature

ACCEPTED VERSION SUBJECT TO FINAL EDITS

over the Antarctic plateau is seen in CMIP5 models (Lenaerts et al., 2016).

CMIP6 GCMs showed an improved representation of the Antarctic near-surface temperature compared to CMIP5 but little improvement (maintaining positive bias) in Antarctic precipitation estimates (Palerme et al., 2017; Roussel et al., 2020). An analysis of the 1850–2000 SMB mean, trends and interannual and spatial variability suggests slightly worse agreement with ice-core-based reanalyses in CMIP6 than CMIP5 (Gorte et al., 2020). Comparison of CMIP5 models with CloudSat satellite products and an ice-core-based SMB reconstruction showed almost all the models overestimate current Antarctic precipitation, some by more than 100% (Palerme et al., 2017; Gorte et al., 2020). GCM simulations of surface snow-melt processes are of variable quality, with extremely simple representatons, or non-existent (Agosta et al., 2015; Trusel et al., 2015). Though most meltwater refreezes in the snowpack in current climate simulations this may be an issue in the future climate simulations under global warming as run-off is projected to increase (Kittel et al., 2021). Since CMIP5, representation of snow (Lenaerts et al., 2016) and stable surface boundary layers (Vignon et al., 2018) has improved in some atmospheric GCMs. In one example, the CMIP6 model CESM2 simulation of cloud and precipitation showed substantial improvements (Schneider et al., 2020) though surface melting is still considerably overestimated compared to RCMs and satellite products (Trusel et al., 2015; Lenaerts et al., 2016).

Assimilation of observations in reanalysis products yields realistic temperature patterns and seasonal variations, with the recent ERA5 reanalysis showing improved performance compared to others for mean and extreme temperature, wind and humidity, though a warm bias in the near-surface air temperatures remains (Retamales-Muñoz et al., 2019; Tetzner et al., 2019; Dong et al., 2020; Gorodetskaya et al., 2020). The ability of the reanalyses to simulate precipitation and SMB is more variable; they generally overestimate the latter (Gossart et al., 2019; Roussel et al., 2020), but are well suited to provide atmospheric and sea surface boundary conditions to drive RCMs.

Recent higher-resolution simulations covering the entire Antarctic ice sheet with a grid spacing of 12 to 50 km include five Polar-CORDEX RCMs – RACMO2 (van Wessem et al., 2018), MAR (Agosta et al., 2019; Kittel et al., 2021), COSMO-CLM2 (Souverijns et al., 2019), HIRHAM5 (Lucas-Picher et al., 2012), and MetUM (Walters et al., 2017; Mottram et al., 2021) – and one stretched-grid GCM – ARPEGE (Beaumet et al., 2019). RCM simulations forced by ERA-Interim agree well with automatic weather station temperatures, with high correlation ($R^2 > 0.9$) and low bias (<1.5°C) except for high resolution HIRHAM5 (–2.1°C) and MetUM (–3.4°C), which are not internally nudged models (Mottram et al., 2021). RCMs generally underestimate the observed SMB but with biases lower than 20%, except for COSMO-CLM2 at lower elevations (<1200 m) and HIRHAM5 and MetUM at higher elevations (>2200 m) (Mottram et al., 2021). These RCM simulations lead to estimates of the grounded Antarctic ice sheet SMB ranging from 2133 Gt yr^{-1} to 2328 Gt yr^{-1} when considering the four simulations compatible with the IMBIE2 Antarctic total mass budget (IMBIE team et al., 2018; Mottram et al., 2021). However, the simulated spatial pattern of SMB differs widely between models suggesting the importance of missing or under-represented processes in the models, such as drifting-snow transport and sublimation (Agosta et al., 2019), cloud-precipitation microphysical processes (van Wessem et al., 2018) and snowpack modelling (Mottram et al., 2021). Comparisons of integrated SMB estimates between models are also complicated by different resolutions and continental ice masks, with models showing large differences in the absolute SMB (Mottram et al., 2021) but better agreement for SMB annual rates (Figure Atlas.30)

Finer resolution RCM studies demonstrate improved representation of precipitation and temperature gradients (van Wessem et al., 2018; Bozkurt et al., 2020; Donat-Magnin et al., 2020; Elvidge et al., 2020), and strength of katabatic winds (Bintanja et al., 2014; Souverijns et al., 2019) in coastal and mountainous regions. Adequate representation of some processes is still lacking, including drifting snow, sublimation of falling snow or the spectral dependency of snow albedo (Lenaerts et al., 2019). Non-hydrostatic regional models, for example Polar-WRF, MetUM or HARMONIE-AROME at spatial resolutions up to 2 km further improve regional RCM simulations, but are still often unable to resolve relevant feedbacks and foehn processes (Grosvenor et al., 2014; Elvidge et al., 2015, 2020; Elvidge and Renfrew, 2016; King et al., 2017; Turton et al., 2017; Bozkurt et al., 2018b; Hines et al., 2019; Vignon et al., 2019; Gilbert et al., 2020).

ACCEPTED VERSION SUBJECT TO FINAL EDITS

Existing uncertainties in the Antarctic climate representation by both GCMs and RCMs cause significant spread in the future Antarctic climate and SMB projections (Gorte et al., 2020; Kittel et al., 2021). Run-time bias adjustment in atmospheric GCMs (Krinner et al., 2019, 2020) (see also Cross-Chapter Box 10.2) has been proposed to provide low-bias present and consistently-corrected future RCM forcing (reducing the need for coupled model selection), which could be used directly for Antarctic climate projections (Krinner et al., 2019).

[START FIGURE ATLAS.30 HERE]

Figure Atlas.30: (Upper panels) Time series of annual surface mass balance (SMB) rates (in Gt a^{-1}) for Greenland ice sheet and its regions (shown in the inset map) for the periods 1972–2018 (Mouginot et al., 2019) and 1980–2012 (Fettweis et al., 2020) using 13 different models. (Lower panels) Time series of annual SMB rates (in Gt a^{-1}) for the grounded Antarctic ice sheet (excluding ice shelves) and its regions (shown in the inset map) for the periods 1979–2019 (Rignot et al., 2019) and 1980–2016 (Mottram et al., 2021) using five Polar-CORDEX regional climate models. The Antarctic inset map also shows the location of the stations discussed in section Atlas.11.1.2 where observations are available for at least 50 years. Colors indicate near surface air temperature trends for 1957-2016 (circles) and 1979-2016 (diamonds) statistically significant at 90% (Jones et al., 2019; Turner et al., 2020). Stations with an asterisk (*) are where significance estimates disagree between the two publications. Further details on data sources and processing are available in the chapter data table (Table Atlas.SM.15).

[END FIGURE ATLAS.30 HERE]

Atlas.11.1.4 Assessment and synthesis of projections

This section provides an assessment of projections in temperature, precipitation and SMB. See Section 9.4.2 for projected changes in the ice sheet total mass balance and relevant processes and see Section 4.3.1 (Table 4.2) and Section 4.5.1 for Antarctic temperature projections relative to other regions.

The Antarctic region is *very likely* to experience a significant increase in annual mean temperature and precipitation by the end of this century under all emission scenarios used in CMIP5 and CMIP6 (Bracegirdle et al., 2015, 2020b; Frieler et al., 2015; Lenaerts et al., 2016; Previdi and Polvani, 2016; Palerme et al., 2017)(Figure Atlas.29). Ensemble means (and 10th–90th percentile ranges) of end-of-century (2081–2100) projected Antarctic surface air temperature change from 35 CMIP6 models and relative to 1995–2014 are 1.2°C (0.5°C–2.0°C) for the SSP1-2.6 emissions scenarios, 2.3°C (1.3°C–3.4°C) for SSP2-4.5, 3.5°C (2.0°C–5°C) for SSP3-7.0 and 4.4°C (2.8°C–6.4°C) for SSP5-8.5 (Interactive Atlas). Both temperature and precipitation projections are characterised by a relatively large multi-model range (Figure Atlas.29, Interactive Atlas). A strong regional variability is present with the projected changes over coastal Antarctica not scaling linearly with global forcing. While continental mean temperatures are linearly related to global mean temperatures in CMIP6 models, the relative increase in coastal temperatures are higher for low-emissions scenarios due to stronger relative Southern Ocean warming and relatively stronger effects of ozone recovery (Bracegirdle et al., 2020b). A higher multi-model average increase in temperature is projected by CMIP6 models compared to CMIP5, with a 1.3°C higher mean Antarctic near-surface temperature at the end of 21st century (Kittel et al., 2021). While similar median temperature changes are projected for WAN and EAN, the former shows larger spread and higher projected temperature range in both CMIP5 and CMIP6 models and for all scenarios (Figure Atlas.29). CORDEX-Antarctica simulations show a mean and range in the future temperature changes similar to the subset of CMIP5 models used to drive them for the RCP8.5 scenario and 1.5°C, 2°C and 3°C global warming levels (GWL) (Figure Atlas.29).

There is *high confidence* that projected future surface-air temperature increase over Antarctica will be accompanied by precipitation increase (Figure Atlas.29). CMIP6 models show a similar or larger but more constrained increase in precipitation (more models agreeing with larger precipitation increase) for the same GWLs compared to CMIP5. For example, over WAN during JJA for 3°C GWL, CMIP6 and CMIP5 models project a median 15% increase in precipitation with a 10th–90th percentile range of 7–25% in CMIP6

ACCEPTED VERSION SUBJECT TO FINAL EDITS

models and of 3–24% in CMIP5. Average precipitation changes relative to 1995–2014 over WAN and EAN are largely similar, and show projected increases for SSP2-4.5 (SSP5-8.5) of around 5% (5%) for 2021–2040, 7% (10%) for 2041–2060, and 12% (25%) for 2081–2100 with smaller increases projected for SSP1-2.6 emissions, reaching around 5% in 2081–2100. Regionally, the largest relative precipitation increase is projected (under all scenarios) for the eastern part of WAN, the western AP, large parts of EAN plateau and over coastal EAN within 0°E–90°E longitudinal sector (Interactive Atlas). The largest increase in absolute precipitation amount is projected along the coastal regions, with the largest increase over coastal WAN and the western AP, and is projected to be largely driven by the increase in maximum 5-day precipitation (Interactive Atlas), which is in line with the dominant contribution of extreme snowfall events to the total annual precipitation in the present Antarctic climate (Boening et al., 2012; Gorodetskaya et al., 2014; Turner et al., 2020). Under all emission scenarios, the coastal precipitation increase corresponds to the snowfall increase, except for the northern and central part of the western AP, where snowfall is projected to decrease and rainfall to increase (similarly to the tendency towards increased precipitation, decreased snowfall and increase in rainfall over the Southern Ocean) (Interactive Atlas).

From 2000 to 2100, the grounded Antarctic SMB is projected to mitigate sea level rise for RCP4.5 (RCP8.5) by the following sea level equivalents (SLE), 0.03 ± 0.02 m (0.08 ± 0.04 m SLE) from 30 CMIP5 models and for SSP2-4.5 (SSP5-8.5) by 0.03 ± 0.03 m SLE (0.07 ± 0.04 m SLE) from 24 CMIP6 models (Gorte et al., 2020). Subsets or downscaling of CMIP AOGCMs lead to 21st century cumulative projections in the range of 0.05 ± 0.03 m SLE for CMIP5 RCP8.5 and 0.08 ± 0.04 m SLE for CMIP6 SSP5-8.5 (Gorte et al., 2020; Nowicki et al., 2020; Seroussi et al., 2020; Kittel et al., 2021). Use of model subsets reduces spread leading to either lower or higher climate sensitivity in the Antarctic depending on the selection method. For example, models selected by Gorte et al. (2020) based on SMB ice-core reconstruction from Medley and Thomas (2019) tend to underestimate strongly winter sea ice area (Agosta et al., 2015; Roach et al., 2020) and show reduced 21st century increase in Antarctic SMB compared to the full ensembles (Agosta et al., 2015; Bracegirdle et al., 2015). A different subset of models is used for ISMIP6 (Section 9.4.2.3) which gives a lower increase in Antarctic SMB than the full ensemble for CMIP5 but a larger increase for CMIP6.

Polar-CORDEX RCMs show higher variability in precipitation projections compared to CMIP5 models with a similar spatial pattern of the areas with precipitation increase over continental Antarctica but with higher local magnitude and also showing a larger increase over the Weddell Sea ice shelves (Interactive Atlas). CMIP5 and CMIP6 models, bias-adjusted based on regional climate model simulations, showed that the projected warming is expected to result in increased surface melting over the Antarctic ice shelves, with meltwater runoff under RCP8.5 and SSP5-8.5 becoming larger than precipitation over ice shelves over the period 2045–2050, surpassing intensities that were linked with the collapse of Larsen A and B ice shelves (Trusel et al., 2015; Kittel et al., 2021). Given the existing uncertainty in the present precipitation and SMB simulations and the significant range in the projected precipitation increase under various emissions scenarios in CMIP5, CMIP6 and CORDEX models, there is *medium confidence* that the future Antarctic SMB will have a negative contribution to sea level during the 21st century under all emissions scenarios (see Section 9.4.2.3 for assessment of the drivers of future Antarctic ice sheet change and Section 9.4.2.6 for longer time scales).

Atlas.11.1.5 Summary

Observations show a *very likely* widespread, strong warming trend starting in 1950s in the Antarctic Peninsula. Significant warming trends are observed in other West Antarctic regions and at selected stations in East Antarctica (*medium confidence*). Antarctic precipitation and SMB showed a significant positive trend over the 20th century according to the ice cores, while large interannual variability masks any existing trend over the satellite period since the end of 1970s (*medium confidence*).

An assessment of model performance for the present day shows that high-resolution regional climate models with polar-optimised physics are important for estimating SMB and generating climate information, and show improved realizations compared to reanalyses and GCMs when evaluated against observations. At the same time, CMIP6 GCMs showed an improved representation of the Antarctic near-surface temperature

ACCEPTED VERSION SUBJECT TO FINAL EDITS

compared to CMIP5, though still struggle with the representation of precipitation. There is therefore *medium confidence* in the capacity of climate models to simulate Antarctic climate and SMB changes.

Under all assessed emission scenarios, both West and East Antarctica are *very likely* to have higher annual mean surface air temperatures and more precipitation, which will have a dominant influence on determining future changes in the SMB (*high confidence*). However, due to the challenges of model evaluation over the region and the possibility of increased meltwater runoff described above, there is only *medium confidence* that the future contribution of the Antarctic SMB to sea level this century will be negative under all greenhouse-gas emission scenarios.

Atlas.11.2 Arctic

Atlas.11.2.1 Key features of the regional climate and findings from previous IPCC assessments

Atlas.11.2.1.1 Key features of the regional climate

The Arctic region comprises the Arctic Ocean (ARO), Russian Arctic (RAR), Greenland and Iceland (GIC) and other surrounding land areas in Europe (NEW) and North America (NEN, NWN) (Figure Atlas.29). The region is one of the coldest and driest regions on Earth and plays a key role influencing global and regional climates and the hydrological cycle. A number of physical processes contribute to amplified Arctic temperature variations as compared to the global temperature, in particular thermodynamic changes that include the increase in surface absorption of solar radiation due to surface albedo feedbacks related with sea-ice, ice, and snow-cover retreat as well as poleward energy transports, water-vapour-radiation and cloud-radiation feedbacks (Screen and Simmonds, 2010; Serreze and Barry, 2011; Pithan and Mauritsen, 2014; Bintanja and Krikken, 2016; Graversen and Burtu, 2016; Franzke et al., 2017; Stuecker et al., 2018). Precipitation in the Arctic is dominated by snowfall, with rainfall present mostly during the summer period. Arctic climate is influenced by the North Atlantic Oscillation, the leading mode of atmospheric variability in the North Atlantic basin with a northward extension into the Arctic affecting temperature, precipitation and sea ice over the region, with ENSO and Atlantic Multidecadal Variability also affecting parts of the region (Annex IV). Further, the Greenland Ice Sheet contribution to sea-level results from the imbalance between mass gain by net snow accumulation and mass loss by meltwater runoff and ice discharge into the ocean (IMBIE team, 2020), highlighting that the ice sheet is a major contributor to sea level changes.

Atlas.11.2.1.2 Findings from previous IPCC assessments

The following summary from previous IPCC reports is derived from the SROCC (IPCC, 2019a) unless otherwise stated. Arctic surface air temperatures have increased from the mid-1950s, with feedbacks from loss of sea ice and snow cover contributing to the amplified warming (*high confidence*) (IPCC, 2018c), and have *likely* increased by more than double the global average over the last two decades (*high confidence*). Arctic snow cover in June has declined from 1967 to 2018 (*high confidence*). Arctic glaciers are losing mass (*very high confidence*) and this along with changes in high-mountain snow melt have caused changes in hydrology, including river runoff, that are projected to continue in the near term (*high confidence*). The rate of ice loss from the Greenland Ice Sheet has increased; during 2006–2015 the loss was 278 ± 11 Gt yr^{-1} with the rate for 2012–2016 higher than for 2002–2011 and several times higher than during 1992–2001 (*high confidence*).

The Arctic sea-ice area is declining in all months of the year (*very high confidence*) with the September sea-ice minimum *very likely* having reduced by 12.8 ± 2.3% per decade during the satellite era (1979 to 2018) to levels unprecedented for at least 1000 years (*medium confidence*).

The high latitudes are *likely* to experience an increase in annual mean precipitation under RCP8.5 (IPCC, 2013c). Further, changes in precipitation will not be uniform. Autumn and spring snow cover duration are projected to decrease by a further 5–10% from current conditions in the near term (2031–2050). No further losses are projected under RCP2.6 whereas a further 15–25% reduction in snow cover duration is projected by the end of century under RCP8.5 (*high confidence*).

ACCEPTED VERSION SUBJECT TO FINAL EDITS

Atlas.11.2.2 Assessment and synthesis of observations, trends and attribution

The Arctic has warmed at more than twice the global rate over the past 50 years with the greatest warming during the cold season (Davy et al., 2018; Box et al., 2019; Przybylak and Wyszyński, 2020; Xiao et al., 2020) (*high confidence*). This is based on various Arctic amplification processes, in particular the combined effect of several related feedback processes including sea-ice and snow-cover albedo and water-vapour-cloud-radiation feedbacks as well as poleward energy transports. The annual average Arctic surface air temperature increased by 2.7°C from 1971 to 2017, with a 3.1°C increase in the cold season (October–May) and a 1.8°C increase in the warm season (June–September) (AMAP, 2019). Satellite-based data estimate the rate of annual warming for 1981–2012 over sea-ice covered regions to be 0.47°C per decade, whereas the trend was significantly higher at 0.77°C per decade over Greenland and amplified in the northern Barents and Kara seas (Comiso and Hall, 2014). The largest Arctic warming in 2003–2017 was reported over the Barents and Kara Seas with trends larger than 2.5°C per decade (Susskind et al., 2019) and Arctic temperatures from 2014 to 2018 have exceeded all previous records since 1900 (Blunden and Arndt, 2019).

Over the ARO, long-term temperature records are available from Spitsbergen (Svalbard Airport). For the period 1898–2018, the annual mean warming was 0.32°C per decade, about 3.5 times the global mean temperature for the same period and since 1991, 1.7°C per decade or about seven times the global average for the same period (Nordli et al., 2020). There is a positive trend in the annual temperature for all stations across Svalbard (Gjelten et al., 2016; Hanssen-Bauer et al., 2019; Dahlke et al., 2020) of 0.64°C–1.01°C per decade for 1971–2017 (Hanssen-Bauer et al., 2019) co-varying with regional changes in sea-ice conditions (Dahlke et al., 2020). The largest temperature trends *very likely* occur in winter, with Svalbard airport warming at 0.43°C per decade during 1898–2018 and 3.19°C per decade during 1991–2018 (Nordli et al., 2020) and Isaksen et al. (2016) reporting on substantial warming in western Spitsbergen, particularly in winter, while the summer warming is moderate.

A multi-dataset analysis for NEN shows a consistent warming (Rapaić et al., 2015), with the largest annual temperature trend greater than 0.3°C per decade during 1981 to 2010 over eastern NEN and also significant warming over northern Quebec and most of the Canadian Arctic north of the treeline. For the longer 1950–2010 period, a consistent warming is found over central and western NEN, but no trend or no consensus is found over the Labrador coast. The latter is related with cooling of the North Atlantic region during the 1970s. For western Greenland, however, summer temperatures increased (2.2°C in June, 1.1°C in July) from 1994 to 2015 (Saros et al., 2019). For neighbouring Arctic regions of NEU, WSE and ESB, datasets show a consistent warming of annual mean temperature since the mid-1970s and 1980 (see Sections Atlas.8 and Atlas.5.2).

Along with the amplified warming, the Arctic has become moister (Rinke et al., 2019; Nygård et al., 2020). AMAP reported Arctic precipitation increases of 1.5–2.0% per decade, with the strongest increase in the cold season (October–May) (AMAP, 2019) (*medium confidence*). Also, for neighbouring Arctic regions for example NEU, EEU and Northern Asia, mean annual precipitation has increased since the early 20th century (see Sections Atlas.8 and Atlas.5.2). Estimated trends for precipitation and snowfall fraction are mixed for Arctic, with increases and decreases for different regions and seasons (Vihma et al., 2016). However, annual precipitation trends derived from different reanalyses do not agree, differ in sign and have low significance (Lindsay et al., 2014; Boisvert et al., 2018). Direct precipitation measurements are difficult and include uncertainties (among others measuring frozen precipitation), therefore precipitation estimates in the Arctic rely on climate models and reanalyses.

An average of five reanalyses for 2000–2010 suggests around 40% of Arctic Ocean precipitation falls as snow, though there is large uncertainty in this estimate (Boisvert et al., 2018). Rainfall frequency is estimated to have increased over the Arctic by 2.7–5.4% over 2000–2016 (Boisvert et al., 2018) with more frequent rainfall events reported for NEU and ARO (Svalbard) (Maturilli et al., 2015; AMAP, 2019), and winter rain totals and frequency have increased in Svalbard since 2000 (Łupikasza et al., 2019) (*medium confidence*). Rain-free winters have rarely occurred since 1998 (Peeters et al., 2019).

Observational records (1966 to 2010) for the RAR region show changing precipitation characteristics (Ye et

ACCEPTED VERSION SUBJECT TO FINAL EDITS

al., 2016), with higher precipitation intensity but lower frequency and little change in annual precipitation total. Precipitation intensity is reported to have increased in all seasons, strongest in winter and spring, weakest in summer, and at a rate of about 1–3% per degree Celsius of air temperature increase.

Atlas.11.2.3 Assessment of model performance

Evaluating simulated temperature and precipitation is problematic in the Arctic due to sparse weather station observations. The lack of reliable observed precipitation datasets for the Arctic thus makes it *very unlikely* to be able to evaluate objectively the skill of models to reproduce precipitation patterns (Takhsha et al., 2018).

The CMIP5 models reproduce the observed Arctic warming over the past century (Chylek et al., 2016; Hao et al., 2018; Huang et al., 2019) (*medium confidence*). The simulated mean Arctic warming for 1900–2014 averaged over 40 CMIP5 models is 2.7°C compared to the observed values of 2.2°C (NASA GISS data smoothed using a 1200-km radius) or 1.7°C (using a 250-km smoothing radius) (Chylek et al., 2016). However, there are large inter-model differences in the simulated warming which ranges from 1.2°C to 5.0°C. Although the CMIP5 models reproduce the spatially averaged observed warming over the past 50 to 100 years, the pattern is different from that of observations and reanalysis (Xie et al., 2016; Franzke et al., 2017; Hao et al., 2018). Zonal mean temperature trends in the CMIP5 models overestimate the warming in the cold season over high latitudes in the northern hemisphere (Xie et al., 2016). Overall, the amplified Arctic warming in the recent decades is overestimated by CMIP5 models (Huang et al., 2019). Possible reasons are modelled sea surface temperature biases and an overestimated temperature response to the Arctic sea-ice decline. Furthermore, some models, which have a warm or weak bias in their Arctic temperature simulations, closely relate the Arctic warming to changes in the large-scale atmospheric circulation. In other models, which show large cold biases, the albedo feedback effect plays a more important role for the temperature trend magnitude. This implies that the dominant simulated Arctic warming mechanism and trend may be dependent on the bias of the model mean state (Franzke et al., 2017). Compared to CMIP5 models, Davy and Outten (2020) found lower biases in CMIP6 models' representation of sea-ice extent and volume with improved extents linked to a better seasonal cycle in the Barents Sea.

Rapid temperature changes, such as the pronounced increase of 2°C yr^{-1} during 2003–2012 over the Kara and Barents Seas in March is well captured in Arctic CORDEX simulations (Kohnemann et al., 2017). The models show adequate skill in capturing the general temperature patterns (Koenigk et al., 2015; Matthes et al., 2015; Hamman et al., 2016; Cassano et al., 2017; Brunke et al., 2018; Diaconescu et al., 2018; Takhsha et al., 2018), but tend to show a cold temperature bias which is largest in winter and depends on the reference dataset. Cassano et al. (2017) showed a large sensitivity of the simulated surface climate to changes in atmospheric model physics. In particular, large changes in radiative flux biases, driven by changes in simulated clouds, lead to large differences in temperature and precipitation biases.

The CMIP5 models perform well in simulating 20th-century snowfall for the northern hemisphere, although there is a positive bias in the multi-model ensemble relative to the observed data in many regions (Krasting et al., 2013b). Lack of sufficient spatial resolution in the model topography has a serious impact on the simulation of snowfall. The patterns of relative maxima and minima of snowfall, however, are captured reasonably well by the models.

Arctic CORDEX RCMs reproduce the dominant features of regional precipitation patterns and extremes (e.g., Glisan and Gutowski, 2014; Hamman et al., 2016). Due to their higher spatial resolution, RCMs simulates larger amounts of orographic precipitation compared to reanalyses. Overall, the simulated precipitation is within the reanalysis and global model ensemble spread, but the Arctic river basin precipitation is closer to observations (Brunke et al., 2018). However, Takhsha et al. (2018) show that the RCMs precipitation bias highly depends on the observational reference dataset used.

The annual mean precipitation pattern of ensemble global atmospheric simulations with a high horizontal resolution agrees well with the observations, with precipitation maxima over the Greenland and Norwegian Seas (Kusunoki et al., 2015). However, the simulated Arctic average annual precipitation shows a positive bias with excessive precipitation over Alaska and the western Arctic (Kattsov et al., 2017).

ACCEPTED VERSION SUBJECT TO FINAL EDITS

Regarding the Greenland Ice Sheet (region GIC), modelled surface mass balance (SMB) has decreased since the end of the 1990s (Fettweis et al., 2020). A multi-model inter-comparison study (Fettweis et al., 2020) emphasized a simulated positive mean annual SMB of 338 ± 68 Gt yr^{-1} between 1980 and 2012, with a decreasing average rate of 7.3 ± 2.0 Gt yr^{-2}, mainly driven by an increase in meltwater runoff. Mouginot et al. (2019) stated that SMB played a strong role in the ice sheet mass loss, where SMB dominated in the last two decades. Mottram et al. (2019) found that SMB processes dominate the ice sheet mass budget over most of the interior, highlighting that the ice sheet is a contributor to global mean sea level rise between 1991 and 2015. More specifically, SMB models have improved (Fettweis et al., 2020; Hanna et al., 2021) due to increased availability and quality of remotely sensed (Koenig et al., 2016; Overly et al., 2016) and in-situ observations (Machguth et al., 2016; Fausto et al., 2018; Vandecrux et al., 2019, 2020). Fettweis et al. (2020) showed that the models' ensemble mean provides the best estimate of the present-day SMB relative to observations. This is the case for the patterns in all seven regions (regional division after Mouginot et al., 2019) apart from the SE accumulation zone where large discrepancies in modelled snowfall accumulation occurred where the spread can reach 2 m water equivalent per year. Montgomery et al. (2020) confirmed this highlighting that RCMs (MAR and RACMO) are underestimating accumulation in southeast Greenland and that models misrepresent spatial heterogeneity due to an orographically forced bias in snowfall near the coast. Further, for northeast Greenland, Karlsson et al. (2020) found RCMs underestimate snow accumulation rates by up to 35%. The regional time series show that SMB has been gradually decreasing in all seven regions (1979–2017), although the trend is less strong in central-eastern and southeast regions. In the southwest, northeast and northwest, SMB turns negative or close to zero after 2000 and remains above zero in other regions (Figure Atlas.30) (*medium confidence*).

Atlas.11.2.4 Assessment and synthesis of projections

Mean temperature in the Arctic is projected to continue to rise through the 21st century significantly higher than the global average (Figure Atlas.29 and Interactive Atlas). For the regions NWN and NEN, see Section Atlas.9. The Arctic is projected to reach a 2°C annual mean warming above the 1981–2005 baseline about 25 to 50 years before the globe as a whole under RCP8.5 and RCP4.5 (Post et al., 2019). The Arctic warming may be as much as 4°C in the annual mean and 7°C in late autumn under 2°C global warming, regardless of which scenario is considered (Post et al., 2019) (*high confidence*).

Projections from 40 CMIP5 models of the 2014–2100 Arctic annual warming under RCP4.5 vary from 0.9°C to 6.7°C, with a multi-model mean of 3.7°C (Chylek et al., 2016). All models agree on a projected Arctic amplification (of at least 1.5 times), but they disagree on the magnitude and spatial patterns. Arctic warming trends projected by models that include a full direct and indirect aerosol effect ('fully aerosol-cloud interactive') are significantly higher than those projected by models without a full indirect aerosol effect (Chylek et al., 2016).

Projected Arctic warming exhibits a very pronounced seasonal cycle, with exceptionally strong warming in the winter. In projections from 30 CMIP5 models, winter warming over ARO varies regionally from 3°C to 5°C by mid-century and 5°C to 9°C by late-century under RCP4.5 (AMAP, 2017) (*high confidence*). Averaged over the Arctic and based on 36 CMIP5 models, winter warming is 5.8 ± 1.5°C by mid-century and 7.1 ± 2.3°C by 2100 under RCP4.5 (Overland et al., 2019), and an exceptionally strong warming of up to 14.1 ± 2.9°C is projected in December under RCP8.5 (Bintanja and Krikken, 2016). Bintanja and Van Der Linden (2013) estimated the Arctic winter warming over the 21st century to exceed the summer warming by at least a factor of four, irrespective of the magnitude of the climate forcing.

Overland et al. (2014) highlighted the difference between the near-term 'adaptation timescale' and the long-term 'mitigation timescale' for the Arctic. Only in the latter half of the century do the projections under RCP4.5 and RCP8.5 noticeably separate. End-of-the-century warming is approximately twice as large under RCP8.5 demonstrating the impact of the lower emissions under RCP4.5 (AMAP, 2017) (*high confidence*). More specifically under the strong forcing scenario, annual mean surface air temperature in the Arctic is projected to increase by 8.5 ± 2.1°C over the course of the 21st century (Bintanja and Andry, 2017), and emerges as a 'new Arctic' climate being significantly different from that of the mid-20th century (Landrum

ACCEPTED VERSION SUBJECT TO FINAL EDITS

and Holland, 2020). The end-of-the-century warming (2080–2099 relative to 1980–1999, RCP8.5) can exceed 15°C in autumn and winter over the Arctic Ocean (Koenigk et al., 2015). Projections averaged over the four best-performing CMIP5 models show an Arctic annual warming of 4.1°C (RCP2.6), 5.7°C (RCP4.5), and 10.6°C (RCP8.5) by 2100 compared to 1951–1980 (Hao et al., 2018). Also, for neighbouring Arctic regions, for example NEU, WSB and ESB, temperature is projected to increase towards the end of the century under both RCP4.5 and RCP8.5 (see Sections Atlas.8 and Atlas.5.2).

The ensemble of CMIP6 shows *likely* greater warming compared to CMIP5 (Figure Atlas.29). There is weak agreement among the models in projected temperature change over the Arctic North Atlantic under SSPs until the mid-century, but a robust warming signal clearly emerges even there by 2100 (Interactive Atlas). Generally, the largest annual warming is simulated over the Arctic Ocean, particularly over the Barents and Kara Seas. Future warming in CORDEX RCMs and the CMIP5 models are similar (Spinoni et al., 2020). The RCM warming over the AO is smaller, while the warming over land is larger in winter and spring but smaller in summer, compared with CMIP5 (Koenigk et al., 2015).

Mean precipitation in ARO, GIC and RAR is projected to rise in a warming climate (Figure Atlas.29), with different rates for the different seasons and scenarios. For NWN and NEN, see Section Atlas.9. The CMIP5 multi-model mean projected precipitation increase in the Arctic is *likely* of the order of 50% under RCP8.5 by the end of 21st century, which is among the highest globally (Bintanja and Selten, 2014). Over 70°N–90°N, the precipitation increase is *likely* 62 ± 20% and 56 ± 13% for RCP4.5 and RCP8.5 respectively. For ARO (Svalbard), the increase in annual precipitation by 2100 is estimated to be about 45% for RCP4.5 and 65% for RCP8.5 (CMIP5 ensemble median) (Van der Bilt et al., 2019). However, importantly the simulated Arctic precipitation increase varies by a factor of three to four between models (Bintanja and Selten, 2014). The projected increase is strongest in late autumn and winter (Vihma et al., 2016). The interannual variability of Arctic precipitation will likely increase markedly (up to 40% over the 21st century), especially in summer (Bintanja et al., 2020) (*medium confidence*)

The CMIP6 projections confirm precipitation will *likely* increase almost everywhere in the Arctic (see the Interactive Atlas). The largest increase is simulated over the Barents and Kara Seas and East Siberian Sea regions, and over northeast Greenland. A pronounced uncertainty in the projection exists over the Arctic North Atlantic and south Greenland. There, the precipitation signal is not significant even by the end of the 21st century and under high-emission scenarios (RCP8.5, SSP5-8.5). Consistent with the generally higher warming in CMIP6, compared to CMIP5, the projected precipitation increase is also higher (Figure Atlas.29) (*high confidence*).

The Arctic mean annual precipitation sensitivity has been estimated at 4.5% increase per degree Celsius of temperature rise, compared to a global average of 1.6–1.9% per degree Celsius of temperature rise (Bintanja and Selten, 2014) based on a set of 37 CMIP5 GCMs. Koenigk et al. (2015) stress the different precipitation sensitivity in winter (0.8 mm per month per degree Celsius of temperature rise) and summer (2 mm per month per degree Celsius of temperature rise). Dobler et al. (2016) support the high precipitation sensitivity for the projected temperature changes. The pattern and amplitude of precipitation changes agree in CORDEX simulations with their driving CMIP5 models (Koenigk et al., 2015; Spinoni et al., 2020) (*high confidence*). However, more small-scale variations over land and coastlines and significantly larger precipitation changes in summer are obvious in the downscaling.

Rain is projected to become the dominant form of precipitation in the Arctic region by the end of the 21st century (Bintanja, 2018). The CMIP5 models show a decrease in annual Arctic snowfall under both RCP4.5 and RCP8.5 (Krasting et al., 2013b; Bintanja and Andry, 2017) (*high confidence*). In the central Arctic, the snowfall fraction barely remains larger than 50%, with only Greenland still having snowfall fractions larger than 80% (Bintanja and Andry, 2017). The most dramatic reductions in snowfall fraction are projected to occur over the North Atlantic and especially the Barents Sea.

With ongoing warming and polar amplification in the Arctic, the Greenland Ice Sheet SMB will inevitably continue to change (Lenaerts et al., 2019) (*high confidence*). For the ice sheet, despite large differences between model scenarios, future projections and regions agree that increasing temperatures will increase

ACCEPTED VERSION SUBJECT TO FINAL EDITS

runoff which will in turn dominate the future decrease of SMB (Rae et al., 2012; van Angelen et al., 2014; Mottram et al., 2017; Hofer et al., 2020), confirming the high sensitivity of the SMB to atmospheric warming. Changes in SMB will continue to dominate future mass loss from the ice sheet, and likely even more when marine terminating glaciers retreat onto land, and solid ice discharge is reduced (Vizcaino, 2014; Lenaerts et al., 2019).

Atlas.11.2.5 Summary

It is *very likely* that the Arctic has warmed at more than twice the global rate over the past 50 years and *likely* that annual precipitation has increased with the highest increases during the cold season. This is based on various Arctic amplification processes, in particular combination of several feedback-related processes such as sea-ice and snow-cover albedo, poleward energy transports, and water-vapour-cloud-radiation feedbacks. The frequency of rainfall increased over the Arctic by 2.7 to 5.4% over the 2000–2016 period with more frequent rainfall events being reported for northern Europe and Svalbard (*medium confidence*).

The CMIP5 models reproduce the observed Arctic warming over the past century but overestimate the amplified Arctic warming in the recent decades (*medium confidence)*. Arctic CORDEX simulations show adequate skill in capturing regional temperature and precipitation patterns and precipitation extremes (*high confidence*). SMB models have improved due to increased availability and quality of remotely sensed and in-situ observations and an ensemble mean of SMB model simulations provides the best estimate of the present-day SMB (*medium confidence)*.

It is *very likely* that the Arctic annual mean temperature and precipitation will continue to increase, reaching around 11.5 ± 3.4°C and 49 ± 19% over the 2081–2100 period (with respect to a 1995–2014 baseline) under the SSP5-8.5 scenario or 4.0 ± 2.5°C and 17 ± 11% under the SSP1-2.6 scenario. These CMIP6 results show *likely* higher Arctic annual mean temperatures compared to CMIP5 for a given time-period and emissions scenario, though the projections are consistent for global warming levels.

Atlas.12 Final remarks

Developing from the WGI AR5 Atlas Annex (IPCC, 2013a), the Atlas is an innovation in the WGI contribution to the AR6, providing a region-by-region assessment of new knowledge on changes in mean climate and an online interactive tool, the Interactive Atlas. It demonstrates the diversity in the climate changes across these regions, in the evidence base for generating information on what changes have already occurred and why, and what further changes each region is likely to face in the future based on different emission scenarios. Finally, the Interactive Atlas allows for further exploration of the data underpinning assessment material generated by many of the other chapters.

The foundation of the regional information generated by the Atlas chapter is an assessment of the significant body of new literature on regional climate change though noting substantial heterogeneity in both its availability and the involvement of regional expertise. In many regions this allows for an in-depth assessment though in some the range of information that can be provided and/or the level of confidence in the information is limited. There is similar heterogeneity in the availability of observations to assess recent trends and evaluate model performance, with a lack of curated regional datasets in polar regions, northern South America and Africa.

Internal variability is a large contributor to the climate uncertainty at regional scales. Recent work has combined outputs of Single Model Initial-conditions Large Ensembles (SMILEs) with CMIP5 and CMIP6 to partition and gain insights on the modelled range and uncertainty arising from internal variability and from model response uncertainty for a given emission scenario (Deser et al., 2020; Lehner et al., 2020; Maher et al., 2021). The work highlights the notable role for internal variability at regional scales, particularly for precipitation in regions with weaker forced response, where internal variability can remain larger than model uncertainty or scenario uncertainty throughout the whole century. The Atlas (similar to the other regional

ACCEPTED VERSION SUBJECT TO FINAL EDITS

chapters) uses a single realization per model (CMIP6 models provide multiple realizations, but it is not the case for CORDEX and less so for CMIP5) which allows for the comparison of the different lines of evidence but at the expense of internal variability having a larger influence on the ability to detect or quantify changes.

The assessment produced in the Atlas is based on the individual results from the different lines of global and regional evidence and the consistency amongst them, as there is a lack of literature on methodologies that combine multiple lines of evidence to distil regional climate change information.

ACCEPTED VERSION
SUBJECT TO FINAL EDITS

References

Aalbers, E.E., G. Lenderink, E. van Meijgaard, and B.J.J.M. van den Hurk, 2018: Local-scale changes in mean and heavy precipitation in Western Europe, climate change or internal variability? *Climate Dynamics*, **50(11–12)**, doi:10.1007/s00382-017-3901-9.

Aalto, J., M. Kämäräinen, M. Shodmonov, N. Rajabov, and A. Venäläinen, 2017: Features of Tajikistan's past and future climate. *International Journal of Climatology*, **37(14)**, 4949–4961, doi:10.1002/joc.5135.

Abadi, A.M., R. Oglesby, C. Rowe, and R. Mawalagedara, 2018: Evaluation of GCMs historical simulations of monthly and seasonal climatology over Bolivia. *Climate Dynamics*, **51(1–2)**, 733–754, doi:10.1007/s00382-017-3952-y.

Abid, M.A., M. Almazroui, F. Kucharski, E. O'Brien, and A.E. Yousef, 2018: ENSO relationship to summer rainfall variability and its potential predictability over Arabian Peninsula region. *npj Climate and Atmospheric Science*, **1(1)**, 20171, doi:10.1038/s41612-017-0003-7.

Aceituno, P., 1988: On the functioning of the Southern Oscillation in the South American sector. Part I: surface climate. *Monthly Weather Review*, **116(3)**, 505–524, doi:10.1175/1520-0493(1988)116<0505:otfots>2.0.co;2.

Adler, R. et al., 2018: The Global Precipitation Climatology Project (GPCP) Monthly Analysis (New Version 2.3) and a Review of 2017 Global Precipitation. *Atmosphere*, **9(4)**, 138, doi:10.3390/atmos9040138.

Adusumilli, S., M. A. Fish, H.A. Fricker, and B. Medley, 2021: Atmospheric River Precipitation Contributed to Rapid Increases in Surface Height of the West Antarctic Ice Sheet in 2019. *Geophysical Research Letters*, **48(5)**, 1–11, doi:10.1029/2020gl091076.

Agel, L. and M. Barlow, 2020: How Well Do CMIP6 Historical Runs Match Observed Northeast U.S. Precipitation and Extreme Precipitation–Related Circulation? *Journal of Climate*, **33(22)**, 9835–9848, doi:10.1175/jcli-d-19-1025.1.

Agosta, C., X. Fettweis, and R. Datta, 2015: Evaluation of the CMIP5 models in the aim of regional modelling of the Antarctic surface mass balance. *The Cryosphere*, **9(6)**, 2311–2321, doi:10.5194/tc-9-2311-2015.

Agosta, C. et al., 2012: A 40-year accumulation dataset for Adelie Land, Antarctica and its application for model validation. *Climate Dynamics*, **38(1)**, 75–86, doi:10.1007/s00382-011-1103-4.

Agosta, C. et al., 2019: Estimation of the Antarctic surface mass balance using the regional climate model MAR (1979–2015) and identification of dominant processes. *The Cryosphere*, **13(1)**, 281–296, doi:10.5194/tc-13-281-2019.

Aguilar, E. et al., 2009: Changes in temperature and precipitation extremes in western central Africa, Guinea Conakry, and Zimbabwe, 1955-2006. *Journal of Geophysical Research Atmospheres*, doi:10.1029/2008jd011010.

Akinsanola, A.A., G.J. Kooperman, A.G. Pendergrass, W.M. Hannah, and K.A. Reed, 2020a: Seasonal representation of extreme precipitation indices over the United States in CMIP6 present-day simulations. *Environmental Research Letters*, **15(9)**, 094003, doi:10.1088/1748-9326/ab92c1.

Akinsanola, A.A., G.J. Kooperman, K.A. Reed, A.G. Pendergrass, and W.M. Hannah, 2020b: Projected changes in seasonal precipitation extremes over the United States in CMIP6 simulations. *Environmental Research Letters*, **15(10)**, 104078, doi:10.1088/1748-9326/abb397.

Akperov, M. et al., 2019: Future projections of cyclone activity in the Arctic for the 21st century from regional climate models (Arctic-CORDEX). *Global and Planetary Change*, **182**, 103005, doi:10.1016/j.gloplacha.2019.103005.

Albrecht, F., O. Pizarro, A. Montecinos, and X. Zhang, 2019: Understanding Sea Level Change in the South Pacific During the Late 20th Century and Early 21st Century. *Journal of Geophysical Research: Oceans*, **124(6)**, 3849–3858, doi:10.1029/2018jc014828.

Ali, S. et al., 2020: Spatio-Temporal Variability of Summer Monsoon Onset over Pakistan. *Asia-Pacific Journal of Atmospheric Sciences*, **56(1)**, 147–172, doi:10.1007/s13143-019-00130-z.

Allaberdiyev, G., 2010: *Climate change and Turkmenistan*. United Nations Development Programme (UNDP), 29 pp.

Almazroui, M., 2016: RegCM4 in climate simulation over CORDEX-MENA/Arab domain: selection of suitable domain, convection and land-surface schemes. *International Journal of Climatology*, **36(1)**, 236–251, doi:10.1002/joc.4340.

Almazroui, M., 2020a: Changes in Temperature Trends and Extremes over Saudi Arabia for the Period 1978–2019. *Advances in Meteorology*, **2020**, 1–21, doi:10.1155/2020/8828421.

Almazroui, M., 2020b: Rainfall Trends and Extremes in Saudi Arabia in Recent Decades. *Atmosphere*, **11(9)**, 964, doi:10.3390/atmos11090964.

Almazroui, M. and S. Saeed, 2020: Contribution of extreme daily precipitation to total rainfall over the Arabian Peninsula. *Atmospheric Research*, **231**, 104672, doi:10.1016/j.atmosres.2019.104672.

Almazroui, M., M.N. Islam, H. Athar, P.D. Jones, and M.A. Rahman, 2012: Recent climate change in the Arabian Peninsula: Annual rainfall and temperature analysis of Saudi Arabia for 1978-2009. *International Journal of Climatology*, **32(6)**, doi:10.1002/joc.3446.

Almazroui, M., M.N. Islam, S. Saeed, A.K. Alkhalaf, and R. Dambul, 2017: Assessment of uncertainties in projected temperature and precipitation over the Arabian Peninsula using three categories of CMIP5 multimodel

ACCEPTED VERSION SUBJECT TO FINAL EDITS

ensembles. *Earth Systems and Environment*, doi:10.1007/s41748-017-0027-5.
Almazroui, M., M.N. Islam, S. Saeed, F. Saeed, and M. Ismail, 2020a: Future changes in climate over the Arabian Peninsula based on CMIP6 multimodel simulations. *Earth Systems and Environment*, **4(4)**, 611–630, doi:10.1007/s41748-020-00183-5.
Almazroui, M., S. Saeed, F. Saeed, M.N. Islam, and M. Ismail, 2020b: Projections of Precipitation and Temperature over the South Asian Countries in CMIP6. *Earth Systems and Environment*, **4(2)**, 297–320, doi:10.1007/s41748-020-00157-7.
Almazroui, M. et al., 2020c: Projected Change in Temperature and Precipitation Over Africa from CMIP6. *Earth Systems and Environment*, **4(3)**, 455–475, doi:10.1007/s41748-020-00161-x.
Almazroui, M. et al., 2021: Projected Changes in Temperature and Precipitation Over the United States, Central America, and the Caribbean in CMIP6 GCMs. *Earth Systems and Environment*, **5(1)**, 1–24, doi:10.1007/s41748-021-00199-5.
Almeida, C.T., J.F. Oliveira-Júnior, R.C. Delgado, P. Cubo, and M.C. Ramos, 2017: Spatiotemporal rainfall and temperature trends throughout the Brazilian Legal Amazon, 1973–2013. *International Journal of Climatology*, doi:10.1002/joc.4831.
AlSarmi, S. and R. Washington, 2011: Recent observed climate change over the Arabian Peninsula. *Journal of Geophysical Research Atmospheres*, doi:10.1029/2010jd015459.
Altnau, S., E. Schlosser, E. Isaksson, and D. Divine, 2015: Climatic signals from 76 shallow firn cores in Dronning Maud Land, East Antarctica. *The Cryosphere*, **9(3)**, 925–944, doi:10.5194/tc-9-925-2015.
Alves, L., 2016: Análise estatística da sazonalidade e tendências das estações chuvosas e seca na Amazônia: Clima presente e projeções futuras., National Institute for Space Research (INPE), São José dos Campos, Brazil, 140 pp.
Alves, L.M., R. Chadwick, A. Moise, J. Brown, and J.A. Marengo, 2020: Assessment of rainfall variability and future change in Brazil across multiple timescales. *International Journal of Climatology*, joc.6818, doi:10.1002/joc.6818.
Amador, J., 1998: A climatic feature of the tropical Americas: The trade wind easterly jet. *Top. Meteor. Oceanogr.*, **5**, 91–102.
AMAP, 2017: *Snow, Water, Ice and Permafrost in the Arctic (SWIPA) 2017*. Arctic Monitoring and Assessment Programme (AMAP), Oslo, Norway, 269 pp.
AMAP, 2019: *AMAP Climate Change Update 2019: An Update to Key Findings of Snow, Water, Ice and Permafrost in the Arctic (SWIPA) 2017*. Arctic Monitoring and Assessment Programme (AMAP), Oslo, Norway, 12 pp.
Ambrizzi, T., M.S. Reboita, R.P. da Rocha, and M. Llopart, 2019: The state of the art and fundamental aspects of regional climate modeling in South America. *Annals of the New York Academy of Sciences*, **1436(1)**, 98–120, doi:10.1111/nyas.13932.
Anderson, T.G., K.J. Anchukaitis, D. Pons, and M. Taylor, 2019: Multiscale trends and precipitation extremes in the Central American Midsummer Drought. *Environmental Research Letters*, **14(12)**, 124016, doi:10.1088/1748-9326/ab5023.
Angeles-Malaspina, M., J.E. González-Cruz, and N. Ramírez-Beltran, 2018: Projections of Heat Waves Events in the Intra-Americas Region Using Multimodel Ensemble. *Advances in Meteorology*, **2018**, 1–16, doi:10.1155/2018/7827984.
Anyah, R.O. and W. Qiu, 2012: Characteristic 20th and 21st century precipitation and temperature patterns and changes over the Greater Horn of Africa. *International Journal of Climatology*, doi:10.1002/joc.2270.
Araya-Osses, D., A. Casanueva, C. Román-Figueroa, J.M. Uribe, and M. Paneque, 2020: Climate change projections of temperature and precipitation in Chile based on statistical downscaling. *Climate Dynamics*, **54(9–10)**, 4309–4330, doi:10.1007/s00382-020-05231-4.
Ashfaq, M. et al., 2016: High-resolution ensemble projections of near-term regional climate over the continental United States. *Journal of Geophysical Research: Atmospheres*, **121(17)**, 9943–9963, doi:10.1002/2016jd025285.
Ashfaq, M. et al., 2020: Robust late twenty-first century shift in the regional monsoons in RegCM-CORDEX simulations. *Climate Dynamics*, doi:10.1007/s00382-020-05306-2.
Atif, R.M. et al., 2020: Extreme precipitation events over Saudi Arabia during the wet season and their associated teleconnections. *Atmospheric Research*, **231**, 104655, doi:10.1016/j.atmosres.2019.104655.
Attada, R. et al., 2019: Surface air temperature variability over the Arabian Peninsula and its links to circulation patterns. *International Journal of Climatology*, **39(1)**, 445–464, doi:10.1002/joc.5821.
Bach, L., C. Schraff, J.D. Keller, and A. Hense, 2016: Towards a probabilistic regional reanalysis system for Europe: Evaluation of precipitation from experiments. *Tellus, Series A: Dynamic Meteorology and Oceanography*, **68(1)**, 1–21, doi:10.3402/tellusa.v68.32209.
Baidya Roy, S., M. Smith, L. Morris, N. Orlovsky, and A. Khalilov, 2014: Impact of the desiccation of the Aral Sea on summertime surface air temperatures. *Journal of Arid Environments*, **110**, 79–85, doi:10.1016/j.jaridenv.2014.06.008.
Bailey, R.T., A. Khalil, and V. Chatikavanij, 2015: Estimating Current and Future Groundwater Resources of the Maldives. *JAWRA Journal of the American Water Resources Association*, **51(1)**, 112–122,

ACCEPTED VERSION
SUBJECT TO FINAL EDITS

doi:10.1111/jawr.12236.
Bailey, R.T., K. Barnes, and C.D. Wallace, 2016: Predicting Future Groundwater Resources of Coral Atoll Islands. *Hydrological Processes*, **30(13)**, 2092–2105, doi:10.1002/hyp.10781.
Baker, M., 2016: 1,500 scientists lift the lid on reproducibility. *Nature*, doi:10.1038/533452a.
Balabukh, V. and L. Malitskaya, 2017: Assessment of the current changes in the thermal regime of Ukraine. *Geoinformatika*, **4(64)**, 34–49.
Ban, N. et al., 2021: The first multi-model ensemble of regional climate simulations at kilometer-scale resolution , Part I : Evaluation of precipitation. *Climate Dynamics*, doi:10.1007/s00382-021-05708-w.
Banwell, A.F., D.R. MacAyeal, and O. Sergienko, 2013: Breakup of the Larsen B Ice Shelf triggered by chain reaction drainage of supraglacial lakes. *Geophysical Research Letters*, **40(22)**, 5872–5876, doi:10.1002/2013gl057694.
Barkey, B. and R. Bailey, 2017: Estimating the Impact of Drought on Groundwater Resources of the Marshall Islands. *Water*, **9(1)**, 41, doi:10.3390/w9010041.
Barkhordarian, A., J. Bhend, and H. von Storch, 2012: Consistency of observed near surface temperature trends with climate change projections over the Mediterranean region. *Climate Dynamics*, doi:10.1007/s00382-011-1060-y.
Barlow, M., A. Hoell, and L. Agel, 2021: An evaluation of CMIP6 historical simulations of the cold season teleconnection between tropical Indo-Pacific sea surface temperatures and precipitation in Southwest Asia, the coastal Middle East, and Northern Pakistan and India. *Journal of Climate*, 1–43, doi:10.1175/jcli-d-19-1026.1.
Barreiro, M., 2010: Influence of ENSO and the South Atlantic Ocean on climate predictability over Southeastern South America. *Climate Dynamics*, **35(7–8)**, 1493–1508, doi:10.1007/s00382-009-0666-9.
Barros, V.R. and M.E. Doyle, 2018: Low-level circulation and precipitation simulated by CMIP5 GCMS over southeastern South America. *International Journal of Climatology*, **38(15)**, 5476–5490, doi:10.1002/joc.5740.
Barros, V.R. et al., 2015: Climate change in Argentina: trends, projections, impacts and adaptation. *Wiley Interdisciplinary Reviews: Climate Change*, **6(2)**, 151–169, doi:10.1002/wcc.316.
Bartók, B. et al., 2017: Projected changes in surface solar radiation in CMIP5 global climate models and in EURO-CORDEX regional climate models for Europe. *Climate Dynamics*, **49(7–8)**, 2665–2683, doi:10.1007/s00382-016-3471-2.
Bassiouni, M. and D.S. Oki, 2013: Trends and shifts in streamflow in Hawai'i, 1913-2008. *Hydrological Processes*, **27(10)**, 1484–1500, doi:10.1002/hyp.9298.
Beaumet, J., M. Déqué, G. Krinner, C. Agosta, and A. Alias, 2019: Effect of prescribed sea surface conditions on the modern and future Antarctic surface climate simulated by the ARPEGE atmosphere general circulation model. *Cryosphere*, **13(11)**, 3023–3043, doi:10.5194/tc-13-3023-2019.
Beck, H.E. et al., 2017: Global-scale evaluation of 22 precipitation datasets using gauge observations and hydrological modeling. *Hydrology and Earth System Sciences*, doi:10.5194/hess-21-6201-2017.
Bedia, J. et al., 2019: The METACLIP semantic provenance framework for climate products. *Environmental Modelling & Software*, **119**, 445–457, doi:10.1016/j.envsoft.2019.07.005.
Beharry, S.L., R.M. Clarke, and K. Kumarsingh, 2015: Variations in extreme temperature and precipitation for a Caribbean island: Trinidad. *Theoretical and Applied Climatology*, **122(3)**, 783–797, doi:10.1007/s00704-014-1330-9.
Belmar, Y.N., K.E. McNamara, and T.H. Morrison, 2016: Water security in small island developing states: the limited utility of evolving governance paradigms. *WIREs Water*, **3**, 181–193, doi:10.1002/wat2.1129.
Berg, P., L. Norin, and J. Olsson, 2016: Creation of a high resolution precipitation data set by merging gridded gauge data and radar observations for Sweden. *Journal of Hydrology*, **541**, 6–13, doi:10.1016/j.jhydrol.2015.11.031.
Berthou, S. et al., 2018: Pan-European climate at convection-permitting scale: a model intercomparison study. *Climate Dynamics*, doi:10.1007/s00382-018-4114-6.
Bettolli, M.L. and O.C. Penalba, 2018: Statistical downscaling of daily precipitation and temperatures in southern La Plata Basin. *International Journal of Climatology*, **38(9)**, 3705–3722, doi:10.1002/joc.5531.
Bettolli, M.L. et al., 2021: The CORDEX Flagship Pilot Study in southeastern South America: a comparative study of statistical and dynamical downscaling models in simulating daily extreme precipitation events. *Climate Dynamics*, doi:10.1007/s00382-020-05549-z.
Bian, Q. et al., 2020: Multiscale Changes in Snow Over the Tibetan Plateau During 1980–2018 Represented by Reanalysis Data Sets and Satellite Observations. *Journal of Geophysical Research: Atmospheres*, **125(19)**, e2019JD031914, doi:10.1029/2019jd031914.
Biasutti, M., 2013: Forced Sahel rainfall trends in the CMIP5 archive. *Journal of Geophysical Research Atmospheres*, doi:10.1002/jgrd.50206.
Biasutti, M., 2019: Rainfall trends in the African Sahel: Characteristics, processes, and causes. *Wiley Interdisciplinary Reviews: Climate Change*, doi:10.1002/wcc.591.
Bindoff, N.L. et al., 2013: Detection and attribution of climate change: from global to regional. In: *Climate Change 2013: The Physical Science Basis. Contribution of Working Group I to the Fifth Assessment Report of the Intergovernmental Panel on Climate Change* [Stocker, T.F., D. Qin, G.-K. Plattner, M. Tignor, S.K. Allen, J. Boschung, A. Nauels, Y. Xia, V. Bex, and P.M. Midgley (eds.)]. Cambridge University Press, Cambridge,

ACCEPTED VERSION SUBJECT TO FINAL EDITS

United Kingdom and New York, NY, USA, pp. 867–952, doi:10.1017/cbo9781107415324.022.
Bintanja, R., 2018: The impact of Arctic warming on increased rainfall. *Scientific Reports*, **8(1)**, 16001, doi:10.1038/s41598-018-34450-3.
Bintanja, R. and E.C. Van Der Linden, 2013: The changing seasonal climate in the Arctic. *Scientific Reports*, **3**, 1–8, doi:10.1038/srep01556.
Bintanja, R. and F.M. Selten, 2014: Future increases in Arctic precipitation linked to local evaporation and sea-ice retreat. *Nature*, **509(7501)**, 479–482, doi:10.1038/nature13259.
Bintanja, R. and F. Krikken, 2016: Magnitude and pattern of Arctic warming governed by the seasonality of radiative forcing. *Scientific Reports*, **6**, 1–7, doi:10.1038/srep38287.
Bintanja, R. and O. Andry, 2017: Towards a rain-dominated Arctic. *Nature Climate Change*, **7(4)**, 263–267, doi:10.1038/nclimate3240.
Bintanja, R., C. Severijns, R. Haarsma, and W. Hazeleger, 2014: The future of Antarctica's surface winds simulated by a high-resolution global climate model: 1. Model description and validation. *Journal of Geophysical Research: Atmospheres*, **119(12)**, 7136–7159, doi:10.1002/2013jd020847.
Bintanja, R. et al., 2020: Strong future increases in Arctic precipitation variability linked to poleward moisture transport. *Science Advances*, **6(7)**, eaax6869, doi:10.1126/sciadv.aax6869.
Blackport, R., J.A. Screen, K. van der Wiel, and R. Bintanja, 2019: Minimal influence of reduced Arctic sea ice on coincident cold winters in mid-latitudes. *Nature Climate Change*, **9(9)**, 697–704, doi:10.1038/s41558-019-0551-4.
Blázquez, J. and M.N. Nuñez, 2013a: Analysis of uncertainties in future climate projections for South America: comparison of WCRP-CMIP3 and WCRP-CMIP5 models. *Climate Dynamics*, **41(3–4)**, 1039–1056, doi:10.1007/s00382-012-1489-7.
Blázquez, J. and M.N. Nuñez, 2013b: Performance of a high resolution global model over southern South America. *International Journal of Climatology*, **33(4)**, 904–919, doi:10.1002/joc.3478.
Blunden, J. and D.S. Arndt, 2019: State of the Climate in 2018. *Bulletin of the American Meteorological Society*, **100(9)**, Si–S306, doi:10.1175/2019bamsstateoftheclimate.1.
Bodart, J.A. and R.J. Bingham, 2019: The Impact of the Extreme 2015–2016 El Niño on the Mass Balance of the Antarctic Ice Sheet. *Geophysical Research Letters*, **46(23)**, 13862–13871, doi:10.1029/2019gl084466.
Boé, J. and L. Terray, 2014: Land–sea contrast, soil-atmosphere and cloud-temperature interactions: interplays and roles in future summer European climate change. *Climate Dynamics*, **42(3–4)**, 683–699, doi:10.1007/s00382-013-1868-8.
Boé, J., S. Somot, L. Corre, and P. Nabat, 2020a: Large discrepancies in summer climate change over Europe as projected by global and regional climate models: causes and consequences. *Climate Dynamics*, **54(5–6)**, 2981–3002, doi:10.1007/s00382-020-05153-1.
Boé, J. et al., 2020b: Past long-term summer warming over western Europe in new generation climate models: Role of large-scale atmospheric circulation. *Environmental Research Letters*, **15(8)**, 84038, doi:10.1088/1748-9326/ab8a89.
Boening, C., M. Lebsock, F. Landerer, and G. Stephens, 2012: Snowfall-driven mass change on the East Antarctic ice sheet. *Geophysical Research Letters*, doi:10.1029/2012gl053316.
Boisier, J.P. et al., 2018: Anthropogenic drying in central-southern Chile evidenced by long-term observations and climate model simulations. *Elem Sci Anth*, **6(1)**, 74, doi:10.1525/elementa.328.
Boisvert, L.N. et al., 2018: Intercomparison of precipitation estimates over the Arctic ocean and its peripheral seas from reanalyses. *Journal of Climate*, **31(20)**, 8441–8462, doi:10.1175/jcli-d-18-0125.1.
Bollmeyer, C. et al., 2015: Towards a high-resolution regional reanalysis for the european CORDEX domain. *Quarterly Journal of the Royal Meteorological Society*, **141(686)**, 1–15, doi:10.1002/qj.2486.
BOM and CSIRO, 2014: *Climate Variability, Extremes and Change in the Western Tropical Pacific: New Science and Updated Country Reports 2014*. Australian Bureau of Meteorology (BOM) and Commonwealth Scientific and Industrial Research Organisation (CSIRO), 372 pp.
BOM and CSIRO, 2018: *State of the Climate 2018*. Australian Bureau of Meteorology (BOM) and Commonwealth Scientific and Industrial Research Organisation (CSIRO), 24 pp.
BOM and CSIRO, 2020: *State of the climate 2020*. Australian Bureau of Meteorology (BoM) and Commonwealth Scientific and Industrial Research Organisation (CSIRO), 23 pp.
Borges, P.A., K. Barfus, H. Weiss, and C. Bernhofer, 2017: Extended predictor screening, application and added value of statistical downscaling of a CMIP5 ensemble for single-site projections in Distrito Federal, Brazil. *International Journal of Climatology*, **37(1)**, 46–65, doi:10.1002/joc.4686.
Boulanger, J.P., A.F. Carril, and E. Sanchez, 2016: CLARIS-La Plata Basin: regional hydroclimate variability, uncertainties and climate change scenarios. *Climate Research*, **68(2–3)**, 93–94, doi:10.3354/cr01392.
Box, J.E. et al., 2019: Key indicators of Arctic climate change: 1971-2017. *Environmental Research Letters*, **14(4)**, doi:10.1088/1748-9326/aafc1b.
Boychenko, S. et al., 2016: Feaures of Climate Change on Ukraine: Scenarios, Consequences for Nature and Agroecosystems. *Proceedings of the National Aviation University*, **69(4)**, 96–113, doi:10.18372/2306-

ACCEPTED VERSION SUBJECT TO FINAL EDITS

1472.69.11061.
Bozkurt, D., M. Rojas, J.P. Boisier, and J. Valdivieso, 2018a: Projected hydroclimate changes over Andean basins in central Chile from downscaled CMIP5 models under the low and high emission scenarios. *Climatic Change*, **150(3)**, 131–147, doi:10.1007/s10584-018-2246-7.
Bozkurt, D., R. Rondanelli, J.C. Marín, and R. Garreaud, 2018b: Foehn Event Triggered by an Atmospheric River Underlies Record-Setting Temperature Along Continental Antarctica. *Journal of Geophysical Research: Atmospheres*, **123(8)**, 3871–3892, doi:10.1002/2017jd027796.
Bozkurt, D. et al., 2019: Dynamical downscaling over the complex terrain of southwest South America: present climate conditions and added value analysis. *Climate Dynamics*, **53(11)**, 6745–6767, doi:10.1007/s00382-019-04959-y.
Bozkurt, D. et al., 2020: Recent Near-surface Temperature Trends in the Antarctic Peninsula from Observed, Reanalysis and Regional Climate Model Data. *Advances in Atmospheric Sciences*, **37(5)**, 477–493, doi:10.1007/s00376-020-9183-x.
Bracegirdle, T.J., D.B. Stephenson, J. Turner, and T. Phillips, 2015: The importance of sea ice area biases in 21st century multimodel projections of Antarctic temperature and precipitation. *Geophysical Research Letters*, **42(24)**, 10,832–10,839, doi:10.1002/2015gl067055.
Bracegirdle, T.J. et al., 2019: Back to the Future: Using Long-Term Observational and Paleo-Proxy Reconstructions to Improve Model Projections of Antarctic Climate. *Geosciences*, **9(6)**, 255, doi:10.3390/geosciences9060255.
Bracegirdle, T.J. et al., 2020a: Improvements in Circumpolar Southern Hemisphere Extratropical Atmospheric Circulation in CMIP6 Compared to CMIP5. *Earth and Space Science*, **7(6)**, doi:10.1029/2019ea001065.
Bracegirdle, T.J. et al., 2020b: Twenty first century changes in Antarctic and Southern Ocean surface climate in CMIP6. *Atmospheric Science Letters*, **21(9)**, doi:10.1002/asl.984.
Brogli, R. et al., 2019: The Role of Hadley Circulation and Lapse-Rate Changes for the Future European Summer Climate. *Journal of Climate*, **32(2)**, 385–404, doi:10.1175/jcli-d-18-0431.1.
Bromwich, D.H. et al., 2013: Central West Antarctica among the most rapidly warming regions on Earth. *Nature Geoscience*, **6(2)**, 139–145, doi:10.1038/ngeo1671.
Bromwich, D.H. et al., 2014: Correction: Corrigendum: Central West Antarctica among the most rapidly warming regions on Earth. *Nature Geoscience*, **7(1)**, 76–76, doi:10.1038/ngeo2016.
Brown, J.R., A.F. Moise, and R.A. Colman, 2017: Projected increases in daily to decadal variability of Asian-Australian monsoon rainfall. *Geophysical Research Letters*, **44(11)**, 5683–5690, doi:10.1002/2017gl073217.
Brown, J.R., A.F. Moise, R. Colman, and H. Zhang, 2016: Will a Warmer World Mean a Wetter or Drier Australian Monsoon? *Journal of Climate*, **29(12)**, 4577–4596, doi:10.1175/jcli-d-15-0695.1.
Brown, R.D., B. Fang, and L. Mudryk, 2019: Update of Canadian Historical Snow Survey Data and Analysis of Snow Water Equivalent Trends, 1967–2016. *Atmosphere-Ocean*, **57(2)**, 149–156, doi:10.1080/07055900.2019.1598843.
Brunetti, M., M. Maugeri, F. Monti, and T. Nanni, 2006: Temperature and precipitation variability in Italy in the last two centuries from homogenised instrumental time series. *International Journal of Climatology*, **26(3)**, 345–381, doi:10.1002/joc.1251.
Brunke, M.A. et al., 2018: Evaluation of the atmosphere – land – ocean – sea ice interface processes in the Regional Arctic System Model version 1 (RASM1) using local and globally gridded observations. , 4817–4841, doi:10.5194/gmd-11-4817-2018.
Bucchignani, E., L. Cattaneo, H.J. Panitz, and P. Mercogliano, 2016: Sensitivity analysis with the regional climate model COSMO-CLM over the CORDEX-MENA domain. *Meteorology and Atmospheric Physics*, **128(1)**, 73–95, doi:10.1007/s00703-015-0403-3.
Bucchignani, E., P. Mercogliano, H.J. Panitz, and M. Montesarchio, 2018: Climate change projections for the Middle East–North Africa domain with COSMO-CLM at different spatial resolutions. *Advances in Climate Change Research*, **9(1)**, 66–80, doi:10.1016/j.accre.2018.01.004.
Bukovsky, M.S. and L.O. Mearns, 2020: Regional climate change projections from NA-CORDEX and their relation to climate sensitivity. *Climatic Change*, **162(2)**, 645–665, doi:10.1007/s10584-020-02835-x.
Bukovsky, M.S., D.J. Gochis, and L.O. Mearns, 2013: Towards Assessing NARCCAP Regional Climate Model Credibility for the North American Monsoon: Current Climate Simulations. *Journal of Climate*, **26(22)**, 8802–8826, doi:10.1175/jcli-d-12-00538.1.
Bukovsky, M.S. et al., 2015: Toward Assessing NARCCAP Regional Climate Model Credibility for the North American Monsoon: Future Climate Simulations. *Journal of Climate*, **28(17)**, 6707–6728, doi:10.1175/jcli-d-14-00695.1.
Bulygina, O.N., N.N. Korshunova, and V.N. Razuvaev, 2014: Specialized datasets for climate research. *Trudy of VNIIGMI-WDC*, **177**.
Bulygina, O.N., N.N. Korshunova, and V.N. Razuvaev, 2017: Monitoring snow cover on the territory of Russia. *Proceedings of Hydrometcentre of Russia*, **366**, 87–96.
Bulygina, O.N., P.Y. Groisman, V.N. Razuvaev, and N.N. Korshunova, 2011: Changes in snow cover characteristics over Northern Eurasia since 1966. *Environmental Research Letters*, **6(4)**, 45204–45214, doi:10.1088/1748-

ACCEPTED VERSION SUBJECT TO FINAL EDITS

9326/6/4/045204.
Burger, F., B. Brock, and A. Montecinos, 2018: Seasonal and elevational contrasts in temperature trends in Central Chile between 1979 and 2015. *Global and Planetary Change*, **162**, 136–147, doi:10.1016/j.gloplacha.2018.01.005.
Burns, W.C.G., 2002: Pacific Island Developing Country Water Resources and Climate Change. In: *World's Water 2002–2003: The Biennial Report on Freshwater Resources (Third Edit edition)* [Gleick, P.H., W.C.G. Burns, E.L. Chalecki, and M. Cohen (eds.)]. Island Press, Washington, DC, USA, pp. 113–131.
Bush, E. and D.S. Lemmen (eds.), 2019: *Canada's Changing Climate Report*. Government of Canada, Ottawa, ON, Canada, 444 pp.
Cabos, W. et al., 2018: Dynamical downscaling of historical climate over CORDEX Central America domain with a regionally coupled atmosphere--ocean model. *Climate Dynamics*, doi:10.1007/s00382-018-4381-2.
Cai, P. et al., 2019: Agriculture intensification increases summer precipitation in Tianshan Mountains, China. *Atmospheric Research*, **227**, 140–146, doi:10.1016/j.atmosres.2019.05.005.
Callaghan, T. et al., 2011: The Changing Face of Arctic Snow Cover: A Synthesis of Observed and Projected Changes. *AMBIO*, **40(S1)**, 17–31, doi:10.1007/s13280-011-0212-y.
Campbell, J.D., M.A. Taylor, T.S. Stephenson, R.A. Watson, and F.S. Whyte, 2011: Future climate of the Caribbean from a regional climate model. *International Journal of Climatology*, **31(12)**, 1866–1878, doi:10.1002/joc.2200.
Camuffo, D. et al., 2013: Western Mediterranean precipitation over the last 300 years from instrumental observations. *Climatic Change*, **117(1–2)**, 85–101, doi:10.1007/s10584-012-0539-9.
Candan, K.S., H. Liu, and R. Suvarna, 2001: Resource Description Framework : Metadata and Its Applications. *SIGKDD Explorations*, doi:10.1145/507533.507536.
Cantet, P., M. Déqué, P. Palany, and J.-L. Maridet, 2014: The importance of using a high-resolution model to study the climate change on small islands: the Lesser Antilles case. *Tellus A: Dynamic Meteorology and Oceanography*, **66(1)**, 24065, doi:10.3402/tellusa.v66.24065.
Cantet, P., M.A. Boucher, S. Lachance-Coutier, R. Turcotte, and V. Fortin, 2019: Using a particle filter to estimate the spatial distribution of the snowpack water equivalent. *Journal of Hydrometeorology*, **20(4)**, 577–594, doi:10.1175/jhm-d-18-0140.1.
Cardoso, R.M., P.M.M. Soares, D.C.A. Lima, and A. Semedo, 2016: The impact of climate change on the Iberian low-level wind jet: EURO-CORDEX regional climate simulation. *Tellus A: Dynamic Meteorology and Oceanography*, **68(1)**, 29005, doi:10.3402/tellusa.v68.29005.
Carvalho, A.A. et al., 2020: Trends of rainfall and temperature in Northeast Brazil. *Revista Brasileira de Engenharia Agrícola e Ambiental*, **24(1)**, 15–23, doi:10.1590/1807-1929/agriambi.v24n1p15-23.
Carvalho, L.M., 2020: Assessing precipitation trends in the Americas with historical data: A review. *WIREs Climate Change*, **11(2)**, doi:10.1002/wcc.627.
Casanueva, A. et al., 2016: Daily precipitation statistics in a EURO-CORDEX RCM ensemble: added value of raw and bias-corrected high-resolution simulations. *Climate Dynamics*, **47(3–4)**, 719–737, doi:10.1007/s00382-015-2865-x.
Casanueva, A. et al., 2020: Testing bias adjustment methods for regional climate change applications under observational uncertainty and resolution mismatch. *Atmospheric Science Letters*, **21(7)**, doi:10.1002/asl.978.
Cashman, A., 2014: Water Security and Services in the Caribbean. *Water*, **6(5)**, 1187–1203, doi:10.3390/w6051187.
Cassano, J.J. et al., 2017: Development of the Regional Arctic System Model (RASM): Near-surface atmospheric climate sensitivity. *Journal of Climate*, **30(15)**, 5729–5753, doi:10.1175/jcli-d-15-0775.1.
Castro, C.L. et al., 2012: Can a Regional Climate Model Improve the Ability to Forecast the North American Monsoon? *Journal of Climate*, **25(23)**, 8212–8237, doi:10.1175/jcli-d-11-00441.1.
Cavazos, T. and S. Arriaga-Ramírez, 2012: Downscaled Climate Change Scenarios for Baja California and the North American Monsoon during the Twenty-First Century. *Journal of Climate*, **25(17)**, 5904–5915, doi:10.1175/jcli-d-11-00425.1.
Cavazos, T. et al., 2020: Climatic trends and regional climate models intercomparison over the CORDEX-CAM (Central America, Caribbean, and Mexico) domain. *International Journal of Climatology*, **40(3)**, 1396–1420, doi:10.1002/joc.6276.
Cavicchia, L. et al., 2018: Mediterranean extreme precipitation: a multi-model assessment. *Climate Dynamics*, **51(3)**, 901–913, doi:10.1007/s00382-016-3245-x.
Centella-Artola, A. et al., 2015: Assessing the effect of domain size over the Caribbean region using the PRECIS regional climate model. *Climate Dynamics*, **44(7–8)**, 1901–1918, doi:10.1007/s00382-014-2272-8.
Centella-Artola, A. et al., 2020: Evaluation of Sixteen Gridded Precipitation Datasets over the Caribbean Region Using Gauge Observations. *Atmosphere* , **11(12)**, doi:10.3390/atmos11121334.
Cerezo-Mota, R. et al., 2015: CORDEX-NA: Factors inducing dry/wet years on the North American Monsoon region. *International Journal of Climatology*, **36**, doi:10.1002/joc.4385.
Charles, S.P., F.H. Chiew, and H. Zheng, 2016: *Climate change and water in south Asia - overview and literature review*. CSIRO Sustainable Development Investment Portfolio project. CSIRO Land and Water, Australia, 31

ACCEPTED VERSION SUBJECT TO FINAL EDITS

pp.
Chattopadhyay, M. and J. Katzfey, 2015: Simulating the climate of South Pacific islands using a high resolution model. *International Journal of Climatology*, **35(6)**, 1157–1171, doi:10.1002/joc.4046.
Chen, F.H., W. Huang, L.Y. Jin, J.H. Chen, and J.S. Wang, 2011: Spatiotemporal precipitation variations in the arid Central Asia in the context of global warming. *Science China Earth Sciences*, **54(12)**, 1812–1821, doi:10.1007/s11430-011-4333-8.
Chen, L., X. Qu, G. Huang, and Y. Gong, 2019: Projections of East Asian summer monsoon under 1.5°C and 2°C warming goals. *Theoretical and Applied Climatology*, **137(3)**, 2187–2201, doi:10.1007/s00704-018-2720-1.
Chen, S. et al., 2019: Added Value of a Dynamical Downscaling Approach for Simulating Precipitation and Temperature Over Tianshan Mountains Area, Central Asia. *Journal of Geophysical Research: Atmospheres*, **124(21)**, 11051–11069, doi:10.1029/2019jd031016.
Cheong, W.K. et al., 2018: Observed and modelled temperature and precipitation extremes over Southeast Asia from 1972 to 2010. *International Journal of Climatology*, **38(7)**, 3013–3027, doi:10.1002/joc.5479.
Cherif, S. et al., 2020: Drivers of change. In: *Climate and Environmental Change in the Mediterranean Basin – Current Situation and Risks for the Future. First Mediterranean Assessment Report* [Cramer, W., J. Guiot, and K. Marini (eds.)]. Union for the Mediterranean, Plan Bleu, UNEP/MAP, Marseille, France, pp. 128.
Chernokulsky, A. et al., 2019: Observed changes in convective and stratiform precipitation in Northern Eurasia over the last five decades. *Environmental Research Letters*, **14(4)**, doi:10.1088/1748-9326/aafb82.
Chinn, T., B.B. Fitzharris, A. Willsman, and M.J. Salinger, 2012: Annual ice volume changes 1976–2008 for the New Zealand Southern Alps. *Global and Planetary Change*, **92–93**, 105–118, doi:10.1016/j.gloplacha.2012.04.002.
Choi, J.-W. and Y. Cha, 2015: Interdecadal Variation in the Activity of Tropical Cyclones Affecting Korea. *Tropical Cyclone Research and Review*, **4(2)**, 88–93, doi:10.6057/2015tcrr02.05.
Chou, S.C. et al., 2014: Assessment of Climate Change over South America under RCP 4.5 and 8.5 Downscaling Scenarios. *American Journal of Climate Change*, **03(05)**, 512–527, doi:10.4236/ajcc.2014.35043.
Choudhary, A. and A.P. Dimri, 2018: Assessment of CORDEX-South Asia experiments for monsoonal precipitation over Himalayan region for future climate. *Climate Dynamics*, **50(7–8)**, 3009–3030, doi:10.1007/s00382-017-3789-4.
Christensen, J.H. et al., 2013: Climate Phenomena and their Relevance for Future Regional Climate Change. In: *Climate Change 2013: The Physical Science Basis. Contribution of Working Group I to the Fifth Assessment Report of the Intergovernmental Panel on Climate Change* [Stocker, T.F., D. Qin, G.-K. Plattner, M. Tignor, S.K. Allen, J. Boschung, A. Nauels, Y. Xia, V. Bex, and P.M. Midgley (eds.)]. Cambridge University Press, Cambridge, United Kingdom and New York, NY, USA, pp. 1217–1308, doi:10.1017/cbo9781107415324.028.
Chung, J.X., L. Juneng, F. Tangang, and A.F. Jamaluddin, 2018: Performances of BATS and CLM land-surface schemes in RegCM4 in simulating precipitation over CORDEX Southeast Asia domain. *International Journal of Climatology*, **38(2)**, 794–810, doi:10.1002/joc.5211.
Church, J.A. et al., 2013: Sea Level Change. *Climate Change 2013: The Physical Science Basis. Contribution of Working Group I to the Fifth Assessment Report of the Intergovernmental Panel on Climate Change*, 1137–1216.
Chylek, P. et al., 2016: Indirect aerosol effect increases CMIP5 models' projected arctic warming. *Journal of Climate*, **29(4)**, 1417–1428, doi:10.1175/jcli-d-15-0362.1.
Ciarlo, J.M. et al., 2020: A new spatially distributed added value index for regional climate models: the EURO-CORDEX and the CORDEX-CORE highest resolution ensembles. *Climate Dynamics*, doi:10.1007/s00382-020-05400-5.
Cinco, T.A., R.G. de Guzman, F.D. Hilario, and D.M. Wilson, 2014: Long-term trends and extremes in observed daily precipitation and near surface air temperature in the Philippines for the period 1951–2010. *Atmospheric Research*, **145–146**, 12–26, doi:10.1016/j.atmosres.2014.03.025.
Clark, J.P. and S. Lee, 2019: The Role of the Tropically Excited Arctic Warming Mechanism on the Warm Arctic Cold Continent Surface Air Temperature Trend Pattern. *Geophysical Research Letters*, doi:10.1029/2019gl082714.
Clem, K.R. et al., 2020: Record warming at the South Pole during the past three decades. *Nature Climate Change*, **10(8)**, 762–770, doi:10.1038/s41558-020-0815-z.
Cohen, J. et al., 2014: Recent Arctic amplification and extreme mid-latitude weather. *Nature Geoscience*, **7(9)**, 627–637, doi:10.1038/ngeo2234.
Collins, J.M., 2011: Temperature variability over Africa. *Journal of Climate*, **24**, 3649–3666, doi:10.1175/2011jcli3753.1.
Collins, M. et al., 2013: Long Term Climate Change: Projections, Commitments and Irreversibility. *Climate Change 2013: The Physical Science Basis. Contribution of Working Group I to the Fifth Assessment Report of the Intergovernmental Panel on Climate Change*, 1029–1136.
Colorado-Ruiz, G., T. Cavazos, J.A. Salinas, P. De Grau, and R. Ayala, 2018: Climate change projections from Coupled Model Intercomparison Project phase 5 multi-model weighted ensembles for Mexico, the North American monsoon, and the mid-summer drought region. *International Journal of Climatology*, **38(15)**, 5699–5716, doi:10.1002/joc.5773.

ACCEPTED VERSION SUBJECT TO FINAL EDITS

Comiso, J.C. and D.K. Hall, 2014: Climate trends in the Arctic as observed from space. *Wiley Interdisciplinary Reviews: Climate Change*, **5(3)**, 389–409, doi:10.1002/wcc.277.

Condom, T. et al., 2020: Climatological and Hydrological Observations for the South American Andes: In situ Stations, Satellite, and Reanalysis Data Sets. *Frontiers in Earth Science*, **8**, doi:10.3389/feart.2020.00092.

Coppola, E. et al., 2014: Present and future climatologies in the phase I CREMA experiment. *Climatic Change*, **125(1)**, 23–38, doi:10.1007/s10584-014-1137-9.

Coppola, E. et al., 2020: Assessment of the European climate projections as simulated by the large EURO-CORDEX regional and global climate model ensemble. *Journal of Geophysical Research: Atmospheres*, **125(e2019JD032356)**, doi:10.1029/2019jd032356.

Coppola, E. et al., 2021: Climate hazard indices projections based on CORDEX-CORE, CMIP5 and CMIP6 ensemble. *Climate Dynamics*, doi:10.1007/s00382-021-05640-z.

Cornes, R.C., G. van der Schrier, E.J.M. van den Besselaar, and P.D. Jones, 2018: An Ensemble Version of the E-OBS Temperature and Precipitation Data Sets. *Journal of Geophysical Research: Atmospheres*, **123(17)**, 9391–9409, doi:10.1029/2017jd028200.

Corrales-Suastegui, A., R. Fuentes-Franco, and E.G. Pavia, 2020: The mid-summer drought over Mexico and Central America in the 21st century. *International Journal of Climatology*, **40(3)**, 1703–1715, doi:10.1002/joc.6296.

Cruz, F.T. and H. Sasaki, 2017: Simulation of Present Climate over Southeast Asia Using the Non-Hydrostatic Regional Climate Model. *SOLA*, **13(0)**, 13–18, doi:10.2151/sola.2017-003.

Cruz, F.T. et al., 2017: Sensitivity of temperature to physical parameterization schemes of RegCM4 over the CORDEX-Southeast Asia region. *International Journal of Climatology*, **37(15)**, 5139–5153, doi:10.1002/joc.5151.

CSGM, 2012: *State of the Jamaican Climate 2012: Information for Resilience Building (Full Report)*. Climate Studies Group, Mona (CSGM). Produced for the Planning Institute of Jamaica (PIOJ), Kingston, Jamaica, 179 pp.

CSIRO and BOM, 2015: *Climate Change in Australia Information for Australia's Natural Resource Management Regions: Technical Report*. Commonwealth Scientific and Industrial Research Organisation (CSIRO) and Bureau of Meteorology (BOM), Australia, 222 pp.

Cucchi, M. et al., 2020: WFDE5: bias-adjusted ERA5 reanalysis data for impact studies. *Earth System Science Data*, **12(3)**, 2097–2120, doi:10.5194/essd-12-2097-2020.

Cueto, R.O.G., A.T. Martínez, and E.J. Ostos, 2010: Heat waves and heat days in an arid city in the northwest of México: current trends and in climate change scenarios. *International Journal of Biometeorology*, **54(4)**, 335–345, doi:10.1007/s00484-009-0283-7.

Dahlgren, P., T. Landelius, P. Kållberg, and S. Gollvik, 2016: A high-resolution regional reanalysis for Europe. Part 1: Three-dimensional reanalysis with the regional HIgh-Resolution Limited-Area Model (HIRLAM). *Quarterly Journal of the Royal Meteorological Society*, **142(698)**, 2119–2131, doi:10.1002/qj.2807.

Dahlke, S. et al., 2020: The observed recent surface air temperature development across Svalbard and concurring footprints in local sea ice cover. *International Journal of Climatology*, **40(12)**, 5246–5265, doi:10.1002/joc.6517.

Dai, A., 2011: Drought under global warming: A review. *Wiley Interdisciplinary Reviews: Climate Change*, doi:10.1002/wcc.81.

Darmaraki, S. et al., 2019: Future evolution of Marine Heatwaves in the Mediterranean Sea. *Climate Dynamics*, doi:10.1007/s00382-019-04661-z.

Daron, J. et al., 2018: Providing future climate projections using multiple models and methods: insights from the Philippines. *Climatic Change*, **148(1–2)**, 187–203, doi:10.1007/s10584-018-2183-5.

Daron, J.D., S. Lorenz, P. Wolski, R.C. Blamey, and C. Jack, 2015: Interpreting climate data visualisations to inform adaptation decisions. *Climate Risk Management*, **10**, 17–26, doi:10.1016/j.crm.2015.06.007.

Dash, S.K., M.A. Kulkarni, U.C. Mohanty, and K. Prasad, 2009: Changes in the characteristics of rain events in India. *Journal of Geophysical Research Atmospheres*, **114(10)**, doi:10.1029/2008jd010572.

Davin, E.L., E. Maisonnave, and S.I. Seneviratne, 2016: Is land surface processes representation a possible weak link in current Regional Climate Models? *Environmental Research Letters*, **11(7)**, 74027, doi:10.1088/1748-9326/11/7/074027.

Davy, R. and S. Outten, 2020: The Arctic Surface Climate in CMIP6: Status and Developments since CMIP5. *Journal of Climate*, **33(18)**, 8047–8068, doi:10.1175/jcli-d-19-0990.1.

Davy, R., L. Chen, and E. Hanna, 2018: Arctic amplification metrics. *International Journal of Climatology*, **38(12)**, 4384–4394, doi:10.1002/joc.5675.

de Abreu, R.C. et al., 2019: Contribution of Anthropogenic Climate Change to April–May 2017 Heavy Precipitation over the Uruguay River Basin. *Bulletin of the American Meteorological Society*, **100(1)**, S37–S41, doi:10.1175/bams-d-18-0102.1.

de Barros Soares, D., H. Lee, P.C. Loikith, A. Barkhordarian, and C.R. Mechoso, 2017: Can significant trends be detected in surface air temperature and precipitation over South America in recent decades? *International Journal of Climatology*, **37(3)**, 1483–1493, doi:10.1002/joc.4792.

de Coninck, H. et al., 2018: Strengthening and Implementing the Global Response. In: *Global Warming of 1.5°C. An IPCC Special Report on the impacts of global warming of 1.5°C above pre-industrial levels and related global*

ACCEPTED VERSION SUBJECT TO FINAL EDITS

greenhouse gas emission pathways, in the context of strengthening the global response to the threat of climate change, [Masson-Delmotte, V., P. Zhai, H.-O. Pörtner, D. Roberts, J. Skea, P.R. Shukla, A. Pirani, W. Moufouma-Okia, C. Péan, R. Pidcock, S. Connors, J.B.R. Matthews, Y. Chen, X. Zhou, M.I. Gomis, E. Lonnoy, T. Maycock, M. Tignor, and T. Waterfield (eds.)]. In Press, pp. 313–443.

de Jesus, E.M. et al., 2016: Contribution of cold fronts to seasonal rainfall in simulations over the southern La Plata Basin. *Climate Research*, **68(2–3)**, 243–255, doi:10.3354/cr01358.

Degirmendžić, J., K. Kożuchowski, and E. Żmudzka, 2004: Changes of air temperature and precipitation in Poland in the period 1951–2000 and their relationship to atmospheric circulation. *International Journal of Climatology*, **24(3)**, 291–310, doi:10.1002/joc.1010.

Dell'Aquila, A. et al., 2018: Evaluation of simulated decadal variations over the Euro-Mediterranean region from ENSEMBLES to Med-CORDEX. *Climate Dynamics*, **51(3)**, 857–876, doi:10.1007/s00382-016-3143-2.

Delworth, T.L. and F. Zeng, 2014: Regional rainfall decline in Australia attributed to anthropogenic greenhouse gases and ozone levels. *Nature Geoscience*, **7(8)**, 583–587, doi:10.1038/ngeo2201.

Deng, H. and Y. Chen, 2017: Influences of recent climate change and human activities on water storage variations in Central Asia. *Journal of Hydrology*, **544**, 46–57, doi:10.1016/j.jhydrol.2016.11.006.

Deng, H., Y. Chen, H. Wang, and S. Zhang, 2015: Climate change with elevation and its potential impact on water resources in the Tianshan Mountains, Central Asia. *Global and Planetary Change*, **135**, 28–37, doi:10.1016/j.gloplacha.2015.09.015.

Déqué, M. and S. Somot, 2008: Analysis of heavy precipitation for France using high resolution ALADIN RCM simulations. *Idöjaras Quaterly Journal of the Hungarian Meteorological Service*, **112(3–4)**, 179–190.

Deser, C. et al., 2020: Insights from Earth system model initial-condition large ensembles and future prospects. *Nature Climate Change*, **10(4)**, 277–286, doi:10.1038/s41558-020-0731-2.

Dey, R., S.C. Lewis, J.M. Arblaster, and N.J. Abram, 2019: A review of past and projected changes in Australia's rainfall. *Wiley Interdisciplinary Reviews: Climate Change*, **10(3)**, e577, doi:10.1002/wcc.577.

Dhurmea, K.R., R. Boojhawon, and S.D.D.V. Rughooputh, 2019: A drought climatology for Mauritius using the standardized precipitation index. *Hydrological Sciences Journal*, **64(2)**, 227–240, doi:10.1080/02626667.2019.1570209.

Di Luca, A., J.P. Evans, and F. Ji, 2018: Australian snowpack in the NARCliM ensemble: evaluation, bias correction and future projections. *Climate Dynamics*, **51(1)**, 639–666, doi:10.1007/s00382-017-3946-9.

Di Virgilio, G. et al., 2019: Evaluating reanalysis-driven CORDEX regional climate models over Australia: model performance and errors. *Climate Dynamics*, doi:10.1007/s00382-019-04672-w.

Di Virgilio, G. et al., 2020: Realised added value in dynamical downscaling of Australian climate change. *Climate Dynamics*, **54(11–12)**, 4675–4692, doi:10.1007/s00382-020-05250-1.

Diaconescu, E.P., A. Mailhot, R. Brown, and D. Chaumont, 2018: Evaluation of CORDEX-Arctic daily precipitation and temperature-based climate indices over Canadian Arctic land areas. *Climate Dynamics*, **50(5–6)**, 2061–2085, doi:10.1007/s00382-017-3736-4.

Díaz, L.B. and C.S. Vera, 2017: Austral summer precipitation interannual variability and trends over Southeastern South America in CMIP5 models. *International Journal of Climatology*, **37**, 681–695, doi:10.1002/joc.5031.

Díaz, L.B., R.I. Saurral, and C.S. Vera, 2021: Assessment of South America summer rainfall climatology and trends in a set of global climate models large ensembles. *International Journal of Climatology*, **41(S1)**, E59–E77, doi:10.1002/joc.6643.

Diedhiou, A. et al., 2018: Changes in climate extremes over West and Central Africa at 1.5 and 2 degree C global warming. *Environmental Research Letters*, **13(6)**, 65020, doi:10.1088/1748-9326/aac3e5.

Dieterich, C. et al., 2019: Surface Heat Budget over the North Sea in Climate Change Simulations. *Atmosphere*, **10(5)**, 272, doi:10.3390/atmos10050272.

Diffenbaugh, N.S., M. Scherer, and M. Ashfaq, 2013: Response of snow-dependent hydrologic extremes to continued global warming. *Nature Climate Change*, **3(4)**, 379–384, doi:10.1038/nclimate1732.

Diffenbaugh, N.S. et al., 2017: Quantifying the influence of global warming on unprecedented extreme climate events. *Proceedings of the National Academy of Sciences*, **114(19)**, 4881–4886, doi:10.1073/pnas.1618082114.

Dike, V.N. et al., 2015: Modelling present and future African climate using CMIP5 scenarios in HadGEM2-ES. *International Journal of Climatology*, doi:10.1002/joc.4084.

DiNezio, P.N. et al., 2009: Climate Response of the Equatorial Pacific to Global Warming. *Journal of Climate*, **22(18)**, 4873–4892, doi:10.1175/2009jcli2982.1.

Ding, Y. et al., 2014: Interdecadal variability of the East Asian winter monsoon and its possible links to global climate change. *Journal of Meteorological Research*, **28(5)**, 693–713, doi:10.1007/s13351-014-4046-y.

Dobler, A., J.E. Haugen, and R.E. Benestad, 2016: Regional climate change projections for the Barents region. *Earth System Dynamics Discussions*, **2016**, 1–22, doi:10.5194/esd-2016-27.

Donat, M.G. et al., 2014: Changes in extreme temperature and precipitation in the Arab region: Long-term trends and variability related to ENSO and NAO. *International Journal of Climatology*, doi:10.1002/joc.3707.

Donat-Magnin, M. et al., 2020: Interannual variability of summer surface mass balance and surface melting in the Amundsen sector, West Antarctica. *The Cryosphere*, **14(1)**, 229–249, doi:10.5194/tc-14-229-2020.

ACCEPTED VERSION SUBJECT TO FINAL EDITS

Dong, B., R.T. Sutton, and L. Shaffrey, 2017: Understanding the rapid summer warming and changes in temperature extremes since the mid-1990s over Western Europe. *Climate Dynamics*, **48(5–6)**, 1537–1554, doi:10.1007/s00382-016-3158-8.

Dong, X. et al., 2020: Robustness of the Recent Global Atmospheric Reanalyses for Antarctic Near-Surface Wind Speed Climatology. *Journal of Climate*, **33(10)**, 4027–4043, doi:10.1175/jcli-d-19-0648.1.

Dosio, A., 2016: Projections of climate change indices of temperature and precipitation from an ensemble of bias-adjusted high-resolution EURO-CORDEX regional climate models. *Journal of Geophysical Research*, **121(10)**, 5488–5511, doi:10.1002/2015jd024411.

Dosio, A. and H.J. Panitz, 2016: Climate change projections for CORDEX-Africa with COSMO-CLM regional climate model and differences with the driving global climate models. *Climate Dynamics*, **46(5–6)**, doi:10.1007/s00382-015-2664-4.

Dosio, A. and E.M. Fischer, 2018: Will Half a Degree Make a Difference? Robust Projections of Indices of Mean and Extreme Climate in Europe Under 1.5°C, 2°C, and 3°C Global Warming. *Geophysical Research Letters*, **45(2)**, 935–944, doi:10.1002/2017gl076222.

Dosio, A. et al., 2019: What can we know about future precipitation in Africa? Robustness, significance and added value of projections from a large ensemble of regional climate models. *Climate Dynamics*, **53(9–10)**, 5833–5858, doi:10.1007/s00382-019-04900-3.

Dozier, J., E.H. Bair, and R.E. Davis, 2016: Estimating the spatial distribution of snow water equivalent in the world's mountains. *Wiley Interdisciplinary Reviews: Water*, **3(3)**, 461–474, doi:10.1002/wat2.1140.

Drobinski, P. et al., 2018: North-western Mediterranean sea-breeze circulation in a regional climate system model.. *Climate Dynamics*, **51(3)**, 1077–1093, doi:10.1007/s00382-017-3595-z.

Drugé, T., P. Nabat, M. Mallet, and S. Somot, 2019: Model simulation of ammonium and nitrate aerosols distribution in the Euro-Mediterranean region and their radiative and climatic effects over 1979–2016. *Atmospheric Chemistry and Physics*, **19(6)**, 3707–3731, doi:10.5194/acp-19-3707-2019.

Duan, W. et al., 2015: Changes of precipitation amounts and extremes over Japan between 1901 and 2012 and their connection to climate indices. *Climate Dynamics*, **45(7)**, 2273–2292, doi:10.1007/s00382-015-2778-8.

Dunn, R.J.H. et al., 2020: Development of an Updated Global Land In Situ-Based Data Set of Temperature and Precipitation Extremes: HadEX3. *Journal of Geophysical Research: Atmospheres*, **125(16)**, doi:10.1029/2019jd032263.

Dunning, C.M., E. Black, and R.P. Allan, 2018: Later Wet Seasons with More Intense Rainfall over Africa under Future Climate Change. *Journal of Climate*, **31(23)**, 9719–9738, doi:10.1175/jcli-d-18-0102.1.

Dutheil, C. et al., 2019: Impact of surface temperature biases on climate change projections of the South Pacific Convergence Zone. *Climate Dynamics*, 1–23, doi:10.1007/s00382-019-04692-6.

Easterling, D.R. et al., 2017: Precipitation change in the United States. , doi:10.7930/j0h993cc.

EEA, 2018: National climate change vulnerability and risk assessments in Europe 2018. , 79, doi:10.2800/348489.

Elvidge, A.D. and I.A. Renfrew, 2016: The causes of foehn warming in the lee of mountains. *Bulletin of the American Meteorological Society*, **97(3)**, 455–466, doi:10.1175/bams-d-14-00194.1.

Elvidge, A.D., P. Kuipers Munneke, J.C. King, I.A. Renfrew, and E. Gilbert, 2020: Atmospheric Drivers of Melt on Larsen C Ice Shelf: Surface Energy Budget Regimes and the Impact of Foehn. *Journal of Geophysical Research: Atmospheres*, **125(17)**, doi:10.1029/2020jd032463.

Elvidge, A.D. et al., 2015: Foehn jets over the Larsen C Ice Shelf, Antarctica. *Quarterly Journal of the Royal Meteorological Society*, **141(688)**, 698–713, doi:10.1002/qj.2382.

Endo, H., A. Kitoh, R. Mizuta, and M. Ishii, 2017: Future Changes in Precipitation Extremes in East Asia and Their Uncertainty Based on Large Ensemble Simulations with a High-Resolution AGCM. *SOLA*, **13**, 7–12, doi:10.2151/sola.2017-002.

Endris, H.S. et al., 2013: Assessment of the performance of CORDEX regional climate models in simulating East African rainfall. *Journal of Climate*, doi:10.1175/jcli-d-12-00708.1.

Endris, H.S. et al., 2016: Teleconnection responses in multi-GCM driven CORDEX RCMs over Eastern Africa. *Climate Dynamics*, doi:10.1007/s00382-015-2734-7.

Enfield, D.B., A.M. Mestas-Nuñez, and P.J. Trimble, 2001: The Atlantic Multidecadal Oscillation and its relation to rainfall and river flows in the continental U.S.. *Geophysical Research Letters*, **28(10)**, 2077–2080, doi:10.1029/2000gl012745.

Engel, Z., K. Láska, D. Nývlt, and Z. Stachoň, 2018: Surface mass balance of small glaciers on James Ross Island, north-eastern Antarctic Peninsula, during 2009-2015. *Journal of Glaciology*, **64(245)**, 349–361, doi:10.1017/jog.2018.17.

Engelbrecht, F. et al., 2015: Projections of rapidly rising surface temperatures over Africa under low mitigation. *Environmental Research Letters*, doi:10.1088/1748-9326/10/8/085004.

Espinoza, J.C. et al., 2020: Hydroclimate of the Andes Part I: Main Climatic Features. *Frontiers in Earth Science*, **8**, doi:10.3389/feart.2020.00064.

Evans, A., D. Jones, R. Smalley, and S. Lellyett, 2020: An enhanced gridded rainfall analysis scheme for Australia. , 45.

ACCEPTED VERSION SUBJECT TO FINAL EDITS

Evans, J.P. et al., 2020: The CORDEX-Australasia ensemble: evaluation and future projections. *Climate Dynamics*, doi:10.1007/s00382-020-05459-0.
Eyring, V. et al., 2016: Overview of the Coupled Model Intercomparison Project Phase 6 (CMIP6) experimental design and organization. *Geoscientific Model Development*, **9(5)**, 1937–1958, doi:10.5194/gmd-9-1937-2016.
Falco, M., A.F. Carril, C.G. Menéndez, P.G. Zaninelli, and L.Z.X. Li, 2019: Assessment of CORDEX simulations over South America: added value on seasonal climatology and resolution considerations. *Climate Dynamics*, **52(7–8)**, 4771–4786, doi:10.1007/s00382-018-4412-z.
Fan, X., Q. Duan, C. Shen, Y. Wu, and C. Xing, 2020: Global surface air temperatures in CMIP6: Historical performance and future changes. *Environmental Research Letters*, **15(10)**, 104056, doi:10.1088/1748-9326/abb051.
Fantini, A. et al., 2018: Assessment of multiple daily precipitation statistics in ERA-Interim driven Med-CORDEX and EURO-CORDEX experiments against high resolution observations. *Climate Dynamics*, **51(3)**, 877–900, doi:10.1007/s00382-016-3453-4.
Fathian, F. et al., 2020: Assessment of changes in climate extremes of temperature and precipitation over Iran. *Theoretical and Applied Climatology*, **141(3–4)**, 1119–1133, doi:10.1007/s00704-020-03269-2.
Fausto, R.S. et al., 2018: A Snow Density Dataset for Improving Surface Boundary Conditions in Greenland Ice Sheet Firn Modeling. *Frontiers in Earth Science*, **6**, 51, doi:10.3389/feart.2018.00051.
Fay, A.R. and G.A. McKinley, 2014: Global open-ocean biomes: mean and temporal variability. *Earth System Science Data*, **6(2)**, 273–284, doi:10.5194/essd-6-273-2014.
Fei, L. and G. Yong-Qi, 2015: The Project Siberian High in CMIP5 Models. *Atmospheric and Oceanic Science Letters*, **8(4)**, 179–184, doi:10.3878/aosl20140101.
Fernandes, K., A. Giannini, L. Verchot, W. Baethgen, and M. Pinedo-Vasquez, 2015a: Decadal covariability of Atlantic SSTs and western Amazon dry-season hydroclimate in observations and CMIP5 simulations. *Geophysical Research Letters*, **42(16)**, 6793–6801, doi:10.1002/2015gl063911.
Fernandes, K., A. Giannini, L. Verchot, W. Baethgen, and M. Pinedo-Vasquez, 2015b: Decadal covariability of Atlantic SSTs and western Amazon dry-season hydroclimate in observations and CMIP5 simulations. *Geophysical Research Letters*, **42(16)**, 6793–6801, doi:10.1002/2015gl063911.
Fernández, J. et al., 2019: Consistency of climate change projections from multiple global and regional model intercomparison projects. *Climate Dynamics*, **52(1–2)**, 1139–1156, doi:10.1007/s00382-018-4181-8.
Fernandez-Granja, J.A., A. Casanueva, J. Bedia, and J. Fernandez, 2021: Improved atmospheric circulation over Europe by the new generation of CMIP6 earth system models. *Climate Dynamics*, 1–14, doi:10.1007/s00382-021-05652-9.
Fettweis, X. et al., 2020: GrSMBMIP: intercomparison of the modelled 1980–2012 surface mass balance over the Greenland Ice Sheet. *The Cryosphere*, **14(11)**, 3935–3958, doi:10.5194/tc-14-3935-2020.
Flaounas, E. et al., 2018: Assessment of an ensemble of ocean–atmosphere coupled and uncoupled regional climate models to reproduce the climatology of Mediterranean cyclones. *Climate Dynamics*, **51(3)**, 1023–1040, doi:10.1007/s00382-016-3398-7.
Flato, G. et al., 2013: Evaluation of Climate Models. In: *Climate Change 2013: The Physical Science Basis. Contribution of Working Group I to the Fifth Assessment Report of the Intergovernmental Panel on Climate Change* [Stocker, T.F., D. Qin, G.-K. Plattner, M. Tignor, S.K. Allen, J. Boschung, A. Nauels, Y. Xia, V. Bex, and P.M. Midgley (eds.)]. Cambridge University Press, Cambridge, United Kingdom and New York, NY, USA, pp. 741–866, doi:10.1017/cbo9781107415324.020.
Foley, A., 2018: Climate impact assessment and "islandness": Challenges and opportunities of knowledge production and decision-making for Small Island Developing States. *International Journal of Climate Change Strategies and Management*, **10(2)**, 289–302, doi:10.1108/ijccsm-06-2017-0142.
Ford, M., M.A. Merrifield, and J.M. Becker, 2018: Inundation of a low-lying urban atoll island: Majuro, Marshall Islands. *Natural Hazards*, **91(3)**, 1273–1297, doi:10.1007/s11069-018-3183-5.
Forster, P.M., A.C. Maycock, C.M. McKenna, and C.J. Smith, 2019: Latest climate models confirm need for urgent mitigation. *Nature Climate Change*, doi:10.1038/s41558-019-0660-0.
Franzke, C.L.E., S. Lee, and S.B. Feldstein, 2017: Evaluating Arctic warming mechanisms in CMIP5 models. *Climate Dynamics*, **48(9–10)**, 3247–3260, doi:10.1007/s00382-016-3262-9.
Frazier, A.G. and T.W. Giambelluca, 2017: Spatial trend analysis of Hawaiian rainfall from 1920 to 2012. *International Journal of Climatology*, **37(5)**, 2522–2531, doi:10.1002/joc.4862.
Frazier, A.G., O. Elison Timm, T.W. Giambelluca, and H.F. Diaz, 2018: The influence of ENSO, PDO and PNA on secular rainfall variations in Hawai'i. *Climate Dynamics*, **51(5–6)**, 2127–2140, doi:10.1007/s00382-017-4003-4.
Frei, P., S. Kotlarski, M.A. Liniger, and C. Schär, 2018: Future snowfall in the Alps: projections based on the EURO-CORDEX regional climate models. *The Cryosphere*, **12(1)**, 1–24, doi:10.5194/tc-12-1-2018.
Frezzotti, M., C. Scarchilli, S. Becagli, M. Proposito, and S. Urbini, 2013: A synthesis of the Antarctic surface mass balance during the last 800 yr. *Cryosphere*, **7(1)**, 303–319, doi:10.5194/tc-7-303-2013.
Frieler, K. et al., 2015: Consistent evidence of increasing Antarctic accumulation with warming. *Nature Climate*

ACCEPTED VERSION SUBJECT TO FINAL EDITS

Change, **5(4)**, 348–352, doi:10.1038/nclimate2574.
Frigg, R., L.A. Smith, and D.A. Stainforth, 2013: The myopia of imperfect climate models: The case of UKCP09. *Philosophy of Science*, **80(5)**, 886–897, doi:10.1086/673892.
Frolov, A. et al., 2014: *Second Roshydromet Assessment Report on Climate Change and its Consequences in the Russian Federation*. Federal Service for Hydrometeorology and Environmental Monitoring (Roshydromet), Moscow, Russia, 56 pp.
Fu, R. et al., 2013: Increased dry-season length over southern Amazonia in recent decades and its implication for future climate projection. *Proceedings of the National Academy of Sciences*, **110(45)**, 18110–18115, doi:10.1073/pnas.1302584110.
Fuentes-Franco, R., F. Giorgi, E. Coppola, and K. Zimmermann, 2017: Sensitivity of tropical cyclones to resolution, convection scheme and ocean flux parameterization over Eastern Tropical Pacific and Tropical North Atlantic Oceans in the RegCM4 model. *Climate Dynamics*, **49(1)**, 547–561, doi:10.1007/s00382-016-3357-3.
Fuentes-Franco, R., E. Coppola, F. Giorgi, F. Graef, and E.G. Pavia, 2014: Assessment of RegCM4 simulated inter-annual variability and daily-scale statistics of temperature and precipitation over Mexico. *Climate Dynamics*, **42(3)**, 629–647, doi:10.1007/s00382-013-1686-z.
Fuentes-Franco, R. et al., 2015: Inter-annual variability of precipitation over Southern Mexico and Central America and its relationship to sea surface temperature from a set of future projections from CMIP5 GCMs and RegCM4 CORDEX simulations. *Climate Dynamics*, **45(1)**, 425–440, doi:10.1007/s00382-014-2258-6.
Fumière, Q. et al., 2020: Extreme rainfall in Mediterranean France during the fall: added value of the CNRM-AROME Convection-Permitting Regional Climate Model. *Climate Dynamics*, **55(1–2)**, 77–91, doi:10.1007/s00382-019-04898-8.
Fyfe, J.C., N.P. Gillett, and G.J. Marshall, 2012: Human influence on extratropical Southern Hemisphere summer precipitation. *Geophysical Research Letters*, **39(L23711)**, doi:10.1029/2012gl054199.
Fyfe, J.C. et al., 2017: Large near-term projected snowpack loss over the western United States. *Nature Communications*, **8(1)**, 14996, doi:10.1038/ncomms14996.
Gaertner, M. et al., 2018: Simulation of medicanes over the Mediterranean Sea in a regional climate model ensemble: impact of ocean–atmosphere coupling and increased resolution. *Climate Dynamics*, **51(3)**, 1041–1057, doi:10.1007/s00382-016-3456-1.
Gaetani, M. et al., 2017: West African monsoon dynamics and precipitation: the competition between global SST warming and CO2 increase in CMIP5 idealized simulations. *Climate Dynamics*, doi:10.1007/s00382-016-3146-z.
García Cueto, O.R., N. Santillán Soto, M. Quintero Núñez, S. Ojeda Benítez, and N. Velázquez Limón, 2013: Extreme temperature scenarios in Mexicali, Mexico under climate change conditions. *Atmósfera*, **26(4)**, 509–520, doi:10.1016/s0187-6236(13)71092-0.
Gbobaniyi, E. et al., 2014: Climatology, annual cycle and interannual variability of precipitation and temperature in CORDEX simulations over West Africa. *International Journal of Climatology*, **34(7)**, doi:10.1002/joc.3834.
Ge, J., X. Jia, and H. Lin, 2016: The interdecadal change of the leading mode of the winter precipitation over China. *Climate Dynamics*, **47(7)**, 2397–2411, doi:10.1007/s00382-015-2970-x.
Gevorgyan, A., H. Melkonyan, T. Aleksanyan, A. Iritsyan, and Y. Khalatyan, 2016: An assessment of observed and projected temperature changes in Armenia. *Arabian Journal of Geosciences*, **9(1)**, 27, doi:10.1007/s12517-015-2167-y.
Ghebrezgabher, M.G., T. Yang, and X. Yang, 2016: Long-term trend of climate change and drought assessment in the Horn of Africa. *Advances in Meteorology*, **2016**, doi:10.1155/2016/8057641.
Gheuens, J., N. Nagabhatla, and E. Perera, 2019: Disaster-Risk, Water Security Challenges and Strategies in Small Island Developing States (SIDS). *Water*, **11(4)**, 637, doi:10.3390/w11040637.
Giannini, A., Y. Kushnir, and M.A. Cane, 2000: Interannual variability of Caribbean rainfall, ENSO, and the Atlantic Ocean. *Journal of Climate*, **13**, 297–311, doi:10.1175/1520-0442(2000)013<0297:ivocre>2.0.co;2.
Gibba, P. et al., 2019: State-of-the-art climate modeling of extreme precipitation over Africa: analysis of CORDEX added-value over CMIP5. *Theoretical and Applied Climatology*, doi:10.1007/s00704-018-2650-y.
Gibson, P.B., D.E. Waliser, H. Lee, B. Tian, and E. Massoud, 2019: Climate Model Evaluation in the Presence of Observational Uncertainty: Precipitation Indices over the Contiguous United States. *Journal of Hydrometeorology*, **20(7)**, 1339–1357, doi:10.1175/jhm-d-18-0230.1.
Gilbert, E. et al., 2020: Summertime cloud phase strongly influences surface melting on the Larsen C ice shelf, Antarctica. *Quarterly Journal of the Royal Meteorological Society*, **146(729)**, 1575–1589, doi:10.1002/qj.3753.
Giorgi, F., C. Jones, and G.R. Asrar, 2009: Addressing climate information needs at the regional level: the CORDEX framework. *WMO Bulletin*, **58(3)**, 175–183.
Giorgi, F., F. Raffaele, and E. Coppola, 2019: The response of precipitation characteristics to global warming from climate projections. *Earth System Dynamics*, **10(1)**, 73–89, doi:10.5194/esd-10-73-2019.
Giorgi, F. et al., 2016: Enhanced summer convective rainfall at Alpine high elevations in response to climate warming. *Nature Geoscience*, **9(8)**, 584–589, doi:10.1038/ngeo2761.

ACCEPTED VERSION SUBJECT TO FINAL EDITS

Giot, O. et al., 2016: Validation of the ALARO-0 model within the EURO-CORDEX framework. *Geoscientific Model Development*, **9(3)**, 1143–1152, doi:10.5194/gmd-9-1143-2016.
Gjelten, H.M. et al., 2016: Air temperature variations and gradients along the coast and fjords of western Spitsbergen. *Polar Research*, **35(0 SE – Research/review articles)**, doi:10.3402/polar.v35.29878.
Glisan, J.M. and W.J. Gutowski, 2014: WRF winter extreme daily precipitation over the North American CORDEX Arctic. *Journal of Geophysical Research*, **119(18)**, 10.738–10.748, doi:10.1002/2014jd021676.
Gloor, M. et al., 2015: Recent Amazon climate as background for possible ongoing and future changes of Amazon humid forests. *Global Biogeochemical Cycles*, **29(9)**, 1384–1399, doi:10.1002/2014gb005080.
Gnanaseelan, C., M. Mujumdar, A. Kulkarni, and S. Chakraborty, 2020: Assessment of Climate Change over the Indian Region: A Report of the Ministry of Earth Sciences (MoES), Government of India. , 226, doi:10.1007/978-981-15-4327-2.
Gong, H. et al., 2018: Revisiting the Northern Mode of East Asian Winter Monsoon Variation and Its Response to Global Warming. *Journal of Climate*, **31(21)**, 9001–9014, doi:10.1175/jcli-d-18-0136.1.
Gonzalez, S. and D. Fortuny, 2018: How robust are the temperature trends on the Antarctic Peninsula? *Antarctic Science*, **30(5)**, 322–328, doi:10.1017/s0954102018000251.
Gonzalez-Hidalgo, J.C., D. Peña-Angulo, M. Brunetti, and N. Cortesi, 2016: Recent trend in temperature evolution in Spanish mainland (1951-2010): from warming to hiatus. *International Journal of Climatology*, **36(6)**, 2405–2416, doi:10.1002/joc.4519.
Gorbatenko, V.P., V. Sevastyanov, D.A. Konstantinova, and O. Nosyreva, 2019: Characteristic of the snow cover for the Western Siberia territory. *IOP Conference Series: Earth and Environmental Science*, **232**, 012003, doi:10.1088/1755-1315/232/1/012003.
Gorodetskaya, I., T. Silva, H. Schmithüsen, and N. Hirasawa, 2020: Atmospheric River Signatures in Radiosonde Profiles and Reanalyses at the Dronning Maud Land Coast, East Antarctica. *Advances in Atmospheric Sciences*, **37(5)**, 455–476, doi:10.1007/s00376-020-9221-8.
Gorodetskaya, I. et al., 2014: The role of atmospheric rivers in anomalous snow accumulation in East Antarctica. *Geophysical Research Letters*, **41(17)**, 6199–6206, doi:10.1002/2014gl060881.
Gorodetskaya, I. et al., 2015: Cloud and precipitation properties from ground-based remote-sensing instruments in East Antarctica. *The Cryosphere*, **9(1)**, 285–304, doi:10.5194/tc-9-285-2015.
Gorte, T., J.T.M. Lenaerts, and B. Medley, 2020: Scoring Antarctic surface mass balance in climate models to refine future projections. *The Cryosphere*, **14(12)**, 4719–4733, doi:10.5194/tc-14-4719-2020.
Gossart, A. et al., 2019: An Evaluation of Surface Climatology in State-of-the-Art Reanalyses over the Antarctic Ice Sheet. *Journal of Climate*, **32(20)**, 6899–6915, doi:10.1175/jcli-d-19-0030.1.
Goswami, B.N., V. Venugopal, D. Sengupta, M.S. Madhusoodanan, and P.K. Xavier, 2006: Increasing trend of extreme rain events over India in a warming environment.. *Science (New York, N.Y.)*, **314(5804)**, 1442–5, doi:10.1126/science.1132027.
Gouirand, I., V. Moron, and B. Sing, 2020: Seasonal atmospheric transitions in the Caribbean basin and Central America. *Climate Dynamics*, **55(7)**, 1809–1828, doi:10.1007/s00382-020-05356-6.
Graversen, R.G. and M. Burtu, 2016: Arctic amplification enhanced by latent energy transport of atmospheric planetary waves. *Quarterly Journal of the Royal Meteorological Society*, **142(698)**, 2046–2054, doi:10.1002/qj.2802.
Grazioli, J. et al., 2017: Measurements of precipitation in Dumont d'Urville, Adélie Land, East Antarctica. *Cryosphere*, **11(4)**, 1797–1811, doi:10.5194/tc-11-1797-2017.
Gregor, L., A.D. Lebehot, S. Kok, and P.M. Scheel Monteiro, 2019: A comparative assessment of the uncertainties of global surface ocean CO2 estimates using a machine-learning ensemble (CSIR-ML6 version 2019a)-Have we hit the wall? *Geoscientific Model Development*, **12(12)**, 5113–5136, doi:10.5194/gmd-12-5113-2019.
Grise, K.M., S.-W. Son, and J.R. Gyakum, 2013: Intraseasonal and Interannual Variability in North American Storm Tracks and Its Relationship to Equatorial Pacific Variability. *Monthly Weather Review*, **141(10)**, 3610–3625, doi:10.1175/mwr-d-12-00322.1.
Gröger, M., C. Dieterich, M.H.E. Meier, and S. Schimanke, 2015: Thermal air–sea coupling in hindcast simulations for the North Sea and Baltic Sea on the NW European shelf. *Tellus A: Dynamic Meteorology and Oceanography*, **67(1)**, 26911, doi:10.3402/tellusa.v67.26911.
Groisman, P.Y. et al., 2016: Recent changes in the frequency of freezing precipitation in North America and Northern Eurasia. *Environmental Research Letters*, **11(4)**, 045007, doi:10.1088/1748-9326/11/4/045007.
Grose, M.R., S. Foster, J.S. Risbey, S. Osbrough, and L. Wilson, 2019a: Using indices of atmospheric circulation to refine southern Australian winter rainfall climate projections. *Climate Dynamics*, doi:10.1007/s00382-019-04880-4.
Grose, M.R. et al., 2017: Constraints on Southern Australian Rainfall Change Based on Atmospheric Circulation in CMIP5 Simulations. *Journal of Climate*, **30(1)**, 225–242, doi:10.1175/jcli-d-16-0142.1.
Grose, M.R. et al., 2019b: The role of topography on projected rainfall change in mid-latitude mountain regions. *Climate Dynamics*, doi:10.1007/s00382-019-04736-x.
Grose, M.R. et al., 2020: Insights From CMIP6 for Australia's Future Climate. *Earth's Future*, **8(5)**, e2019EF001469, doi:10.1029/2019ef001469.

ACCEPTED VERSION SUBJECT TO FINAL EDITS

Grosvenor, D.P., J.C. King, T.W. Choularton, and T. Lachlan-Cope, 2014: Downslope föhn winds over the antarctic peninsula and their effect on the larsen ice shelves. *Atmospheric Chemistry and Physics*, **14(18)**, 9481–9509, doi:10.5194/acp-14-9481-2014.

Gruza, G.V., E.Y. Rankova, E.V. Rocheva, and V.D. Smirnov, 2015: Current Global Warming: Geographical and Seasonal Features. *Фундаментальная и прикладная климатология*, **2**, 41–62.

Gudmundsson, L. and S.I. Seneviratne, 2016: Anthropogenic climate change affects meteorological drought risk in Europe. *Environmental Research Letters*, **11(4)**, 44005, doi:10.1088/1748-9326/11/4/044005.

Guhathakurta, P. and J. Revadekar, 2017: Observed Variability and Long-Term Trends of Rainfall Over India. In: *Observed Climate Variability and Change over the Indian Region* [Rajeevan, M. and S. Nayak (eds.)]. Springer, Singapore, doi:10.1007/978-981-10-2531-0_1.

Gulizia, C. and I. Camilloni, 2015: Comparative analysis of the ability of a set of CMIP3 and CMIP5 global climate models to represent precipitation in South America. *International Journal of Climatology*, **35(4)**, 583–595, doi:10.1002/joc.4005.

Gulizia, C., I. Camilloni, and M. Doyle, 2013: Identification of the principal patterns of summer moisture transport in South America and their representation by WCRP/CMIP3 global climate models. *Theoretical and Applied Climatology*, **112(1–2)**, 227–241, doi:10.1007/s00704-012-0729-4.

Guo, D.-L., J.-Q. Sun, and E.-T. Yu, 2018: Evaluation of CORDEX regional climate models in simulating temperature and precipitation over the Tibetan Plateau. *Atmospheric and Oceanic Science Letters*, **11(3)**, 219–227, doi:10.1080/16742834.2018.1451725.

Guo, H. et al., 2017a: Meteorological drought analysis in the Lower Mekong Basin using satellite-based long-term CHIRPS product. *Sustainability (Switzerland)*, **9(6)**, doi:10.3390/su9060901.

Guo, H. et al., 2017b: Systematical Evaluation of Satellite Precipitation Estimates Over Central Asia Using an Improved Error-Component Procedure. *Journal of Geophysical Research: Atmospheres*, **122(20)**, 10,906–910,927, doi:10.1002/2017jd026877.

Guo, H. et al., 2018: Spatial and temporal characteristics of droughts in Central Asia during 1966–2015. *Science of The Total Environment*, **624**, 1523–1538, doi:10.1016/j.scitotenv.2017.12.120.

Guo, H. et al., 2021: Assessment of CMIP6 in simulating precipitation over arid Central Asia. *Atmospheric Research*, **252**, 105451, doi:10.1016/j.atmosres.2021.105451.

Guo, L. and L. Li, 2015: Variation of the proportion of precipitation occurring as snow in the Tian Shan Mountains, China. *International Journal of Climatology*, **35(7)**, 1379–1393, doi:10.1002/joc.4063.

Gusain, A., S. Ghosh, and S. Karmakar, 2020: Added value of CMIP6 over CMIP5 models in simulating Indian summer monsoon rainfall. *Atmospheric Research*, **232**, 104680, doi:10.1016/j.atmosres.2019.104680.

Gutiérrez, C. et al., 2018: Impact of aerosols on the spatiotemporal variability of photovoltaic energy production in the Euro-Mediterranean area. *Solar Energy*, **174**, 1142–1152, doi:10.1016/j.solener.2018.09.085.

Gutiérrez, C. et al., 2020: Future evolution of surface solar radiation and photovoltaic potential in Europe: investigating the role of aerosols. *Environmental Research Letters*, **15(3)**, 034035, doi:10.1088/1748-9326/ab6666.

Gutowski Jr., W.J. et al., 2016: WCRP COordinated Regional Downscaling EXperiment (CORDEX): a diagnostic MIP for CMIP6. *Geoscientific Model Development*, **9(11)**, 4087–4095, doi:10.5194/gmd-9-4087-2016.

Haag, I., P.D. Jones, and C. Samimi, 2019: Central Asia's changing climate: How temperature and precipitation have changed across time, space, and altitude. *Climate*, **7(10)**, doi:10.3390/cli7100123.

Haarsma, R.J. et al., 2016: High Resolution Model Intercomparison Project (HighResMIP v1.0) for CMIP6. *Geoscientific Model Development*, **9(11)**, 4185–4208, doi:10.5194/gmd-9-4185-2016.

Haiden, T. et al., 2011: The integrated nowcasting through comprehensive analysis (INCA) system and its validation over the Eastern Alpine region. *Weather and Forecasting*, **26(2)**, 166–183, doi:10.1175/2010waf2222451.1.

Ham, S., J.-W. LEE, and K. YOSHIMURA, 2016: Assessing Future Climate Changes in the East Asian Summer and Winter Monsoon Using Regional Spectral Model. *Journal of the Meteorological Society of Japan. Ser. II*, **94A(0)**, 69–87, doi:10.2151/jmsj.2015-051.

Hamman, J. et al., 2016: Land surface climate in the regional Arctic system model. *Journal of Climate*, **29(18)**, 6543–6562, doi:10.1175/jcli-d-15-0415.1.

Han, S. and Z. Yang, 2013: Cooling effect of agricultural irrigation over Xinjiang, Northwest China from 1959 to 2006. *Environmental Research Letters*, **8(2)**, doi:10.1088/1748-9326/8/2/024039.

Hanna, E. et al., 2020: Mass balance of the ice sheets and glaciers – Progress since AR5 and challenges. *Earth-Science Reviews*, **201**, 102976, doi:10.1016/j.earscirev.2019.102976.

Hanna, E. et al., 2021: Greenland surface air temperature changes from 1981 to 2019 and implications for ice-sheet melt and mass-balance change. *International Journal of Climatology*, **41(S1)**, E1336–E1352, doi:10.1002/joc.6771.

Hannart, A., C. Vera, B. Cerne, and F.E.L. Otto, 2015: Causal Influence of Anthropogenic Forcings on the Argentinian Heat Wave of December 2013. *Bulletin of the American Meteorological Society*, **96(12)**, S41–S45, doi:10.1175/bams-d-15-00137.1.

Hanssen-Bauer, I., E.J. Førland, H. Hisdal, S. Mayer, S. AB, and A. Sorteberg (eds.), 2019: *Climate in Svalbard 2100 – a knowledge base for climate adaptation*. NCCS report no. 1/2019, Norwegian Centre for Climate Services (NCCS), 207 pp.

ACCEPTED VERSION SUBJECT TO FINAL EDITS

Hao, M. et al., 2018: Narrowing the surface temperature range in CMIP5 simulations over the Arctic. *Theoretical and Applied Climatology*, **132(3–4)**, 1073–1088, doi:10.1007/s00704-017-2161-2.
Harada, Y. et al., 2016: The JRA-55 Reanalysis: Representation of Atmospheric Circulation and Climate Variability. *Journal of the Meteorological Society of Japan. Ser. II*, **94(3)**, 269–302, doi:10.2151/jmsj.2016-015.
Harold, J., I. Lorenzoni, T.F. Shipley, and K.R. Coventry, 2016: Cognitive and psychological science insights to improve climate change data visualization. *Nature Climate Change*, **6(12)**, 1080–1089, doi:10.1038/nclimate3162.
Harris, I., P.D. Jones, T.J. Osborn, and D.H. Lister, 2014: Updated high-resolution grids of monthly climatic observations – the CRU TS3.10 Dataset. *International Journal of Climatology*, **34(3)**, 623–642, doi:10.1002/joc.3711.
Harris, I., T.J. Osborn, P. Jones, and D. Lister, 2020: Version 4 of the CRU TS monthly high-resolution gridded multivariate climate dataset. *Scientific Data*, **7(1)**, 109, doi:10.1038/s41597-020-0453-3.
Harter, D.E. et al., 2015: Impacts of global climate change on the floras of oceanic islands – Projections, implications and current knowledge. *Perspectives in Plant Ecology, Evolution and Systematics*, **17(2)**, 160–183, doi:10.1016/j.ppees.2015.01.003.
Hartmann, D.L. et al., 2013: Observations: Atmosphere and Surface. In: *Climate Change 2013: The Physical Science Basis. Contribution of Working Group I to the Fifth Assessment Report of the Intergovernmental Panel on Climate Change* [Stocker, T.F., D. Qin, G.-K. Plattner, M. Tignor, S.K. Allen, J. Boschung, A. Nauels, Y. Xia, V. Bex, and P.M. Midgley (eds.)]. Cambridge University Press, Cambridge, United Kingdom and New York, NY, USA, pp. 159–203, doi:10.1017/cbo9781107415324.008.
Harzallah, A. et al., 2018: Long term evolution of heat budget in the Mediterranean Sea from Med-CORDEX forced and coupled simulations. *Climate Dynamics*, **51(3)**, 1145–1165, doi:10.1007/s00382-016-3363-5.
Hasson, S., J. Böhner, and F. Chishtie, 2019: Low fidelity of CORDEX and their driving experiments indicates future climatic uncertainty over Himalayan watersheds of Indus basin. *Climate Dynamics*, **52(1–2)**, 777–798, doi:10.1007/s00382-018-4160-0.
Hawkins, E. and R. Sutton, 2016: Connecting Climate Model Projections of Global Temperature Change with the Real World. *Bulletin of the American Meteorological Society*, **97(6)**, 963–980, doi:10.1175/bams-d-14-00154.1.
Hawkins, E. et al., 2020: Observed Emergence of the Climate Change Signal: From the Familiar to the Unknown. *Geophysical Research Letters*, **47(6)**, doi:10.1029/2019gl086259.
Hazeleger, W. et al., 2015: Tales of future weather. *Nature Climate Change*, **5(2)**, doi:10.1038/nclimate2450.
He, C. and W. Zhou, 2020: Different Enhancement of the East Asian Summer Monsoon under Global Warming and Interglacial Epochs Simulated by CMIP6 Models: Role of the Subtropical High. *Journal of Climate*, **33(22)**, 9721–9733, doi:10.1175/jcli-d-20-0304.1.
He, C., Z. Wang, T. Zhou, and T. Li, 2019: Enhanced Latent Heating over the Tibetan Plateau as a Key to the Enhanced East Asian Summer Monsoon Circulation under a Warming Climate. *Journal of Climate*, **32(11)**, 3373–3388, doi:10.1175/jcli-d-18-0427.1.
He, S., Y. Gao, F. Li, H. Wang, and Y. He, 2017: Impact of Arctic Oscillation on the East Asian climate: A review. *Earth-Science Reviews*, **164**, 48–62, doi:10.1016/j.earscirev.2016.10.014.
Heidinger, H., L. Carvalho, C. Jones, A. Posadas, and R. Quiroz, 2018: A new assessment in total and extreme rainfall trends over central and southern Peruvian Andes during 1965-2010. *International Journal of Climatology*, **38**, e998–e1015, doi:10.1002/joc.5427.
Heikkilä, U. and A. Sorteberg, 2012: Characteristics of autumn-winter extreme precipitation on the Norwegian west coast identified by cluster analysis. *Climate Dynamics*, **39(3)**, 929–939, doi:10.1007/s00382-011-1277-9.
Hernández-Henríquez, M.A., S.J. Déry, and C. Derksen, 2015: Polar amplification and elevation-dependence in trends of Northern Hemisphere snow cover extent, 1971-2014. *Environmental Research Letters*, **10(4)**, 44010, doi:10.1088/1748-9326/10/4/044010.
Herrera, D. and T. Ault, 2017: Insights from a New High-Resolution Drought Atlas for the Caribbean Spanning 1950–2016. *Journal of Climate*, **30(19)**, 7801–7825, doi:10.1175/jcli-d-16-0838.1.
Herrera, D.A. et al., 2018: Exacerbation of the 2013–2016 Pan-Caribbean Drought by Anthropogenic Warming. *Geophysical Research Letters*, **45(19)**, 10,610–619,626, doi:10.1029/2018gl079408.
Herrera, S. et al., 2019: Iberia01: a new gridded dataset of daily precipitation and temperatures over Iberia. *Earth System Science Data*, **11(4)**, 1947–1956, doi:10.5194/essd-11-1947-2019.
Herrmann, M., T. Ngo-Duc, and L. Trinh-Tuan, 2020: Impact of climate change on sea surface wind in Southeast Asia, from climatological average to extreme events: results from a dynamical downscaling. *Climate Dynamics*, **54(3–4)**, 2101–2134, doi:10.1007/s00382-019-05103-6.
Hersbach, H. et al., 2020: The ERA5 global reanalysis. *Quarterly Journal of the Royal Meteorological Society*, **146(730)**, 1999–2049, doi:10.1002/qj.3803.
Hewitson, B. et al., 2014: Regional context. In: *Climate Change 2014: Impacts, Adaptation, and Vulnerability. Part B: Regional Aspects. Contribution of Working Group II to the Fifth Assessment Report of the Intergovernmental Panel on Climate Change* [Barros, V.R., C.B. Field, D.J. Dokken, M.D. Mastrandrea, K.J. Mach, T.E. Bilir, M. Chatterjee, K.L. Ebi, Y.O. Estrada, R.C. Genova, B. Girma, E.S. Kissel, A.N. Levy, S. MacCracken, P.R.

ACCEPTED VERSION SUBJECT TO FINAL EDITS

Mastrandrea, and L.L. White (eds.)]. Cambridge University Press, Cambridge, United Kingdom and New York, NY, USA, pp. 1133–1197, doi:10.1017/cbo9781107415386.001.

Hidalgo, H.G., E.J. Alfaro, and B. Quesada-Montano, 2017: Observed (1970–1999) climate variability in Central America using a high-resolution meteorological dataset with implication to climate change studies. *Climatic Change*, **141(1)**, 13–28, doi:10.1007/s10584-016-1786-y.

Hijioka, Y. et al., 2014: Asia. In: *Climate Change 2014: Impacts, Adaptation, and Vulnerability. Part B: Regional Aspects. Contribution of Working Group II to the Fifth Assessment Report of the Intergovernmental Panel on Climate Change (AR5 edition)* [Barros, V.R., C.B. Field, D.J. Dokken, M.D. Mastrandrea, K.J. Mach, T.E. Bilir, M. Chatterjee, K.L. Ebi, Y.O. Estrada, R.C. Genova, B. Girma, E.S. Kissel, A.N. Levy, S. MacCracken, P.R. Mastrandrea, and L.L. White (eds.)]. Cambridge University Press, Cambridge, United Kingdom and New York, NY, USA, pp. 1327–1370, doi:10.1017/cbo9781107415386.004.

Hines, K.M. et al., 2019: Microphysics of summer clouds in central West Antarctica simulated by the Polar Weather Research and Forecasting Model (WRF) and the Antarctic Mesoscale Prediction System (AMPS). *Atmospheric Chemistry and Physics*, **19(19)**, 12431–12454, doi:10.5194/acp-19-12431-2019.

Hock, R. et al., 2019a: GlacierMIP – A model intercomparison of global-scale glacier mass-balance models and projections. *Journal of Glaciology*, **65(251)**, 453–467, doi:10.1017/jog.2019.22.

Hock, R. et al., 2019b: High Mountain Areas. *IPCC Special Report on the Ocean and Cryosphere in a Changing Climate*.

Hoegh-Guldberg, O. et al., 2018: Impacts of 1.5°C Global Warming on Natural and Human Systems. In: *Global Warming of 1.5°C. An IPCC Special Report on the impacts of global warming of 1.5°C above pre-industrial levels and related global greenhouse gas emission pathways, in the context of strengthening the global response to the threat of climate change*, [Masson-Delmotte, V., P. Zhai, H.-O. Pörtner, D. Roberts, J. Skea, P.R. Shukla, A. Pirani, W. Moufouma-Okia, C. Péan, R. Pidcock, S. Connors, J.B.R. Matthews, Y. Chen, X. Zhou, M.I. Gomis, E. Lonnoy, T. Maycock, M. Tignor, and T. Waterfield (eds.)]. In Press, pp. 175–311.

Hoell, A., M. Hoerling, J. Eischeid, X.W. Quan, and B. Liebmann, 2017: Reconciling theories for human and natural attribution of recent East Africa drying. *Journal of Climate*, doi:10.1175/jcli-d-16-0558.1.

Hoerling, M., J. Hurrell, J. Eischeid, and A. Phillips, 2006: Detection and attribution of twentieth-century northern and southern African rainfall change. *Journal of Climate*, doi:10.1175/jcli3842.1.

Hofer, S. et al., 2020: Greater Greenland Ice Sheet contribution to global sea level rise in CMIP6. *Nature Communications*, **11(1)**, 1–11, doi:10.1038/s41467-020-20011-8.

Homar, V., C. Ramis, R. Romero, and S. Alonso, 2009: Recent trends in temperature and precipitation over the Balearic Islands (Spain). *Climatic Change*, **98(1–2)**, 199–211, doi:10.1007/s10584-009-9664-5.

Horinouchi, T., S. Matsumura, T. Ose, and Y.N. Takayabu, 2019: Jet–Precipitation Relation and Future Change of the Mei-Yu–Baiu Rainband and Subtropical Jet in CMIP5 Coupled GCM Simulations. *Journal of Climate*, **32(8)**, 2247–2259, doi:10.1175/jcli-d-18-0426.1.

Howard, E. and R. Washington, 2020: Tracing Future Spring and Summer Drying in Southern Africa to Tropical Lows and the Congo Air Boundary. *Journal of Climate*, **33(14)**, 6205–6228, doi:10.1175/jcli-d-19-0755.1.

Hu, Z., C. Zhang, Q. Hu, and H. Tian, 2014: Temperature Changes in Central Asia from 1979 to 2011 Based on Multiple Datasets. *Journal of Climate*, **27(3)**, 1143–1167, doi:10.1175/jcli-d-13-00064.1.

Hu, Z. et al., 2017: Variations and changes of annual precipitation in Central Asia over the last century. *International Journal of Climatology*, **37(S1)**, 157–170, doi:10.1002/joc.4988.

Huang, A. et al., 2014: Changes of the Annual Precipitation over Central Asia in the Twenty-First Century Projected by Multimodels of CMIP5. *Journal of Climate*, **27(17)**, 6627–6646, doi:10.1175/jcli-d-14-00070.1.

Huang, B. et al., 2017: Extended Reconstructed Sea Surface Temperature, Version 5 (ERSSTv5): Upgrades, Validations, and Intercomparisons. *Journal of Climate*, **30(20)**, 8179–8205, doi:10.1175/jcli-d-16-0836.1.

Huang, J., H. Yu, A. Dai, Y. Wei, and L. Kang, 2017: Drylands face potential threat under 2°C global warming target. *Nature Climate Change*, **7(6)**, 417–422, doi:10.1038/nclimate3275.

Huang, J., T. Ou, D. Chen, Y. Luo, and Z. Zhao, 2019: The Amplified Arctic Warming in the Recent Decades may Have Been Overestimated by CMIP5 Models. *Geophysical Research Letters*, **46(22)**, 13338–13345, doi:10.1029/2019gl084385.

Hurd, C.L., A. Lenton, B. Tilbrook, and P.W. Boyd, 2018: Current understanding and challenges for oceans in a higher-CO2 world. *Nature Climate Change*, **8(8)**, 686–694, doi:10.1038/s41558-018-0211-0.

IDOE, 2017: *Islamic Republic of Iran Third National Communication to United Nations Framework Convention on Climate Change (UNFCCC)*. Department of Environment of the Government of the Islamic Republic of Iran, Tehran, Iran, 255 pp.

Iles, C.E. et al., 2020: The benefits of increasing resolution in global and regional climate simulations for European climate extremes. *Geoscientific Model Development*, **13(11)**, 5583–5607, doi:10.5194/gmd-13-5583-2020.

Imbach, P. et al., 2018: Future climate change scenarios in Central America at high spatial resolution. *PLOS ONE*, **13(4)**, e0193570, doi:10.1371/journal.pone.0193570.

IMBIE team, 2020: Mass balance of the Greenland Ice Sheet from 1992 to 2018. *Nature*, **579(7798)**, 233–239, doi:10.1038/s41586-019-1855-2.

ACCEPTED VERSION SUBJECT TO MINOR EDITS

IMBIE team et al., 2018: Mass balance of the Antarctic Ice Sheet from 1992 to 2017. *Nature*, **558(7709)**, 219–222, doi:10.1038/s41586-018-0179-y.

IPCC, 2013a: Annex I: Atlas of Global and Regional Climate Projections [van Oldenborgh, G.J., M. Collins, J. Arblaster, J.H. Christensen, J. Marotzke, S.B. Power, M. Rummukainen and T. Zhou (eds.)]. In: *Climate Change 2013: The Physical Science Basis. Contribution of Working Group I to the Fifth Assessment Report of the Intergovernmental Panel on Climate Change* [Stocker, T.F., D. Qin, G.-K. Plattner, M. Tignor, S.K. Allen, J. Boschung, A. Nauels, Y. Xia, V. Bex, and P.M. Midgley (eds.)]. Cambridge University Press, Cambridge, United Kingdom and New York, NY, USA, pp. 1311–1394, doi:10.1017/cbo9781107415324.029.

IPCC, 2013b: Climate Change 2013: The Physical Science Basis. Contribution of Working Group I to the Fifth Assessment Report of the Intergovernmental Panel on Climate Change. [Stocker, T.F., D. Qin, G.-K. Plattner, M. Tignor, S.K. Allen, J. Boschung, A. Nauels, Y. Xia, V. Bex, and P.M. Midgley (eds.)]. Cambridge University Press, Cambridge, United Kingdom and New York, NY, USA, 1535 pp., doi:10.1017/cbo9781107415324.

IPCC, 2013c: Summary for Policymakers. In: *Climate Change 2013: The Physical Science Basis. Contribution of Working Group I to the Fifth Assessment Report of the Intergovernmental Panel on Climate Change* [Stocker, T.F., D. Qin, G.-K. Plattner, M. Tignor, S.K. Allen, J. Boschung, A. Nauels, Y. Xia, V. Bex, and P.M. Midgley (eds.)]. Cambridge University Press, Cambridge, United Kingdom and New York, NY, USA, pp. 3–29, doi:10.1017/cbo9781107415324.004.

IPCC, 2018a: Expert Meeting of the Intergovernmental Panel on Climate Change on Assessing Climate Information for Regions. , 50.

IPCC, 2018b: Global warming of 1.5°C. An IPCC Special Report on the impacts of global warming of 1.5°C above pre-industrial levels and related global greenhouse gas emission pathways, in the context of strengthening the global response to the threat of climate change. [Masson-Delmotte, V., P. Zhai, H.-O. Pörtner, D. Roberts, J. Skea, P.R. Shukla, A. Pirani, W. Moufouma-Okia, C. Péan, R. Pidcock, S. Connors, J.B.R. Matthews, Y. Chen, X. Zhou, M.I. Gomis, E. Lonnoy, T. Maycock, M. Tignor, and T. Waterfield (eds.)]. In Press, 616 pp.

IPCC, 2018c: Summary for Policymakers. In: *Global Warming of 1.5°C. An IPCC Special Report on the impacts of global warming of 1.5°C above pre-industrial levels and related global greenhouse gas emission pathways, in the context of strengthening the global response to the threat of climate change,* [Masson-Delmotte, V., P. Zhai, H.-O. Pörtner, D. Roberts, J. Skea, P.R. Shukla, A. Pirani, W. Moufouma-Okia, C. Péan, R. Pidcock, S. Connors, J.B.R. Matthews, Y. Chen, X. Zhou, M.I. Gomis, E. Lonnoy, T. Maycock, M. Tignor, and T. Waterfield (eds.)]. In Press, pp. 3–24.

IPCC, 2019a: Summary for Policymakers. In: *IPCC Special Report on the Ocean and Cryosphere in a Changing Climate* [Pörtner, H.-O., D.C. Roberts, V. Masson-Delmotte, P. Zhai, M. Tignor, E. Poloczanska, K. Mintenbeck, A. Alegría, M. Nicolai, A. Okem, J. Petzold, B. Rama, and N.M. Weyer (eds.)]. In Press, pp. 3–35.

IPCC, 2019b: Summary for Policymakers. In: *Climate Change and Land: an IPCC special report on climate change, desertification, land degradation, sustainable land management, food security, and greenhouse gas fluxes in terrestrial ecosystems* [Shukla, P.R., J. Skea, E.C. Buendia, V. Masson-Delmotte, H.-O. Pörtner, D.C. Roberts, P. Zhai, R. Slade, S. Connors, R. van Diemen, M. Ferrat, E. Haughey, S. Luz, S. Neogi, M. Pathak, J. Petzold, J.P. Pereira, P. Vyas, E. Huntley, K. Kissick, M. Belkacemi, and J. Malley (eds.)]. In Press, pp. 3–36.

IPCC, 2019c: Technical Summary. *IPCC Special Report on the Ocean and Cryosphere in a Changing Climate*.

Ippolitov, I.I., S. Loginov, E. Kharyutkina, and E.I. Moraru, 2014: Climate variability over the Asian territory of Russia during 1975–2012. *Geography and Natural Resources*, **35(4)**, 310–318, doi:10.1134/s1875372814040027.

Iqbal, W. et al., 2017: Mean climate and representation of jet streams in the CORDEX South Asia simulations by the regional climate model RCA4. *Theoretical and Applied Climatology*, **129(1–2)**, 1–19, doi:10.1007/s00704-016-1755-4.

Isaksen, K. et al., 2016: Recent warming on Spitsbergen – Influence of atmospheric circulation and sea ice cover. *Journal of Geophysical Research: Atmospheres*, **121(20)**, 11,911–913,931, doi:10.1002/2016jd025606.

Ito, R., T. Nakaegawa, and I. Takayabu, 2020a: Comparison of regional characteristics of land precipitation climatology projected by an MRI-AGCM multi-cumulus scheme and multi-SST ensemble with CMIP5 multi-model ensemble projections. *Progress in Earth and Planetary Science*, **7(1)**, 77, doi:10.1186/s40645-020-00394-4.

Ito, R., H. Shiogama, T. Nakaegawa, and I. Takayabu, 2020b: Uncertainties in climate change projections covered by the ISIMIP and CORDEX model subsets from CMIP5. *Geoscientific Model Development*, **13(3)**, 859–872, doi:10.5194/gmd-13-859-2020.

Iturbide, M. et al., 2019: The R-based climate4R open framework for reproducible climate data access and post-processing. *Environmental Modelling and Software*, **111**, 42–54, doi:10.1016/j.envsoft.2018.09.009.

Iturbide, M. et al., 2020: An update of IPCC climate reference regions for subcontinental analysis of climate model data: definition and aggregated datasets. *Earth System Science Data*, **12(4)**, 2959–2970, doi:10.5194/essd-12-2959-2020.

Iturbide, M. et al., 2021: Repository supporting the implementation of FAIR principles in the IPCC-WG1 Interactive Atlas. Zenodo, DOI: 10.5281/zenodo.3595626. Available from: https://github.com/IPCC-WG1/Atlas.

ACCEPTED VERSION SUBJECT TO FINAL EDITS

Ivanov, M., K. Warrach-Sagi, and V. Wulfmeyer, 2017: Field significance of performance measures in the context of regional climate model evaluation. Part 1: temperature. *Theoretical and Applied Climatology*, 1–19, doi:10.1007/s00704-017-2100-2.
Jacob, D. et al., 2012: Assessing the transferability of the regional climate model REMO to different coordinated regional climate downscaling experiment (CORDEX) regions. *Atmosphere*, doi:10.3390/atmos3010181.
Jacob, D. et al., 2018: Climate Impacts in Europe Under +1.5°C Global Warming. *Earth's Future*, doi:10.1002/2017ef000710.
James, R. et al., 2018: Evaluating climate models with an African lens. *Bulletin of the American Meteorological Society*, doi:10.1175/bams-d-16-0090.1.
Jeong, D. and L. Sushama, 2018: Rain-on-snow events over North America based on two Canadian regional climate models. *Climate Dynamics*, **50(1)**, 303–316, doi:10.1007/s00382-017-3609-x.
Jiang, D., D. Hu, Z. Tian, and X. Lang, 2020: Differences between CMIP6 and CMIP5 Models in Simulating Climate over China and the East Asian Monsoon. *Advances in Atmospheric Sciences*, **37(10)**, 1102–1118, doi:10.1007/s00376-020-2034-y.
Jiang, Y. et al., 2020: Assessment of Uncertainty Sources in Snow Cover Simulation in the Tibetan Plateau. *Journal of Geophysical Research: Atmospheres*, **125(18)**, 0–3, doi:10.1029/2020jd032674.
Jin, C.-S. et al., 2016: Evaluation of climatological tropical cyclone activity over the western North Pacific in the CORDEX-East Asia multi-RCM simulations. *Climate Dynamics*, **47(3)**, 765–778, doi:10.1007/s00382-015-2869-6.
Jin, Q. and C. Wang, 2017: A revival of Indian summer monsoon rainfall since 2002. *Nature Climate Change*, **7(8)**, 587–594, doi:10.1038/nclimate3348.
Jin, Q., J. Wei, Z.-L. Yang, and P. Lin, 2017: Irrigation-Induced Environmental Changes around the Aral Sea: An Integrated View from Multiple Satellite Observations. *Remote Sensing*, **9(9)**, doi:10.3390/rs9090900.
Joetzjer, E., H. Douville, C. Delire, and P. Ciais, 2013: Present-day and future Amazonian precipitation in global climate models: CMIP5 versus CMIP3. *Climate Dynamics*, **41(11–12)**, 2921–2936, doi:10.1007/s00382-012-1644-1.
Jones, C. and L.M. Carvalho, 2013: Climate Change in the South American Monsoon System: Present Climate and CMIP5 Projections. *Journal of Climate*, **26(17)**, 6660–6678, doi:10.1175/jcli-d-12-00412.1.
Jones, D. et al., 2013: An updated analysis of homogeneous temperature data at Pacific Island stations. *Australian Meteorological and Oceanographic Journal*, **63(2)**, 285–302, doi:10.22499/2.6302.002.
Jones, J.M. et al., 2016: Assessing recent trends in high-latitude Southern Hemisphere surface climate. *Nature Climate Change*, **6(10)**, 917–926, doi:10.1038/nclimate3103.
Jones, M.E. et al., 2019: Sixty Years of Widespread Warming in the Southern Middle and High Latitudes (1957–2016). *Journal of Climate*, **32(20)**, 6875–6898, doi:10.1175/jcli-d-18-0565.1.
Jones, P., C. Harpham, A. Burton, and C. Goodess, 2016: Downscaling regional climate model outputs for the Caribbean using a weather generator. *International Journal of Climatology*, **36**, n/a–n/a, doi:10.1002/joc.4624.
Jones, P.D. et al., 2016: Long-term trends in precipitation and temperature across the Caribbean. *International Journal of Climatology*, **36(9)**, 3314–3333, doi:10.1002/joc.4557.
Jovanovic, B., K. Braganza, D. Collins, and D. Jones, 2012: Climate variations and change evident in high-quality climate data for Australia's Antarctic and remote island weather stations. *Aust. Meteorol. Oceanogr. J.*, **62**, 247–261.
Juneng, L. et al., 2016: Sensitivity of Southeast Asia rainfall simulations to cumulus and air-sea flux parameterizations in RegCM4. *Climate Research*, **69(1)**, 59–77, doi:10.3354/cr01386.
Jury, M.R., 2013: Climate trends in southern Africa. *South African Journal of Science*, doi:10.1590/sajs.2013/980.
Jylhä, K., S. Fronzek, H. Tuomenvirta, T.R. Carter, and K. Ruosteenoja, 2008: Changes in frost, snow and Baltic sea ice by the end of the twenty-first century based on climate model projections for Europe. *Climatic Change*, **86(3–4)**, 441–462, doi:10.1007/s10584-007-9310-z.
Kagawa-Viviani, A.K. and T.W. Giambelluca, 2020: Spatial Patterns and Trends in Surface Air Temperatures and Implied Changes in Atmospheric Moisture Across the Hawaiian Islands, 1905–2017. *Journal of Geophysical Research: Atmospheres*, **125(2)**, e2019JD031571, doi:10.1029/2019jd031571.
Kaiser-Weiss, A.K. et al., 2019: Added value of regional reanalyses for climatological applications. *Environmental Research Communications*, **1(7)**, 071004, doi:10.1088/2515-7620/ab2ec3.
Kalognomou, E.-A. et al., 2013: A Diagnostic Evaluation of Precipitation in CORDEX Models over Southern Africa. *Journal of Climate*, **26(23)**, 9477–9506, doi:10.1175/jcli-d-12-00703.1.
Kamil, S. et al., 2019: Long-term ENSO relationship to precipitation and storm frequency over western Himalaya–Karakoram–Hindukush region during the winter season. *Climate Dynamics*, doi:10.1007/s00382-019-04859-1.
Kang, I.S., I.U. Rashid, F. Kucharski, M. Almazroui, and A.K. Alkhalaf, 2015: Multidecadal changes in the relationship between ENSO and wet-season precipitation in the Arabian Peninsula. *Journal of Climate*, doi:10.1175/jcli-d-14-00388.1.
Kang, S., E.-S. Im, and E.A.B. Eltahir, 2019: Future climate change enhances rainfall seasonality in a regional model of western Maritime Continent. *Climate Dynamics*, **52(1–2)**, 747–764, doi:10.1007/s00382-018-4164-9.

ACCEPTED VERSION SUBJECT TO FINAL EDITS

Kaplan, A. et al., 1998: Analyses of global sea surface temperature 1856-1991. *Journal of Geophysical Research: Oceans*, **103(C9)**, 18567–18589, doi:10.1029/97jc01736.
Karim, R., G. Tan, B. Ayugi, H. Babaousmail, and F. Liu, 2020: Evaluation of historical CMIP6 model simulations of seasonal mean temperature over Pakistan during 1970-2014. *Atmosphere*, **11(9)**, doi:10.3390/atmos11091005.
Karlsson, N.B. et al., 2020: Surface accumulation in Northern Central Greenland during the last 300 years. *Annals of Glaciology*, **61(81)**, 214–224, doi:10.1017/aog.2020.30.
Karmacharya, J., M. New, R. Jones, and R. Levine, 2016: Added value of a high-resolution regional climate model in simulation of intraseasonal variability of the South Asian summer monsoon. , doi:10.1002/joc.4767.
Karmacharya, J., R. Jones, W. Moufouma-Okia, and M. New, 2017: Evaluation of the added value of a high-resolution regional climate model simulation of the South Asian summer monsoon climatology. *International Journal of Climatology*, **37(9)**, 3630–3643, doi:10.1002/joc.4944.
Karmalkar, A., 2018: Interpreting Results from the NARCCAP and NA-CORDEX Ensembles in the Context of Uncertainty in Regional Climate Change Projections. *Bulletin of the American Meteorological Society*, **99(10)**, 2093–2106, doi:10.1175/bams-d-17-0127.1.
Karmalkar, A., R.S. Bradley, and H.F. Diaz, 2011: Climate change in Central America and Mexico: regional climate model validation and climate change projections. *Climate Dynamics*, **37(3–4)**, 605–629, doi:10.1007/s00382-011-1099-9.
Karmalkar, A.V. et al., 2013: A review of observed and projected changes in climate for the islands in the Caribbean. *Atmósfera*, **26(2)**, 283–309, doi:10.1016/s0187-6236(13)71076-2.
Katragkou, E. et al., 2015: Regional climate hindcast simulations within EURO-CORDEX: evaluation of a WRF multi-physics ensemble. *Geoscientific Model Development*, **8(3)**, 603–618, doi:10.5194/gmd-8-603-2015.
Kattsov, V.M., I.M. Shkolnik, and S. Efimov, 2017: Climate change projections in Russian regions: The detailing in physical and probability spaces. *Russian Meteorology and Hydrology*, **42(7)**, 452–460, doi:10.3103/s1068373917070044.
Katzfey, J. et al., 2016: High-resolution simulations for Vietnam – methodology and evaluation of current climate. *Asia-Pacific Journal of Atmospheric Sciences*, **52(2)**, 91–106, doi:10.1007/s13143-016-0011-2.
Kawase, H. et al., 2021: Regional characteristics of future changes in snowfall in Japan under RCP2.6 and RCP8.5 scenarios. *SOLA*, **advpub**, doi:10.2151/sola.2021-001.
Keener, V.W., J.J. Marra, M.L. Finucane, D. Spooner, and M.H. Smith (eds.), 2012: *Climate Change and Pacific islands: Indicators and Impacts. Report for the 2012 Pacific Islands Regional Climate Assessment (PIRCA)*. Island Press, Washington, DC, USA, 170 pp.
Keener, V.W. et al., 2018: Hawai'i and U.S.-Affiliated Pacific Islands. In: *Impacts, Risks, and Adaptation in the United States: Fourth National Climate Assessment, Volume II* [Reidmiller, D.R., C.W. Avery, D.R. Easterling, K.E. Kunkel, K.L.M. Lewis, T.K. Maycock, and B.C. Stewart (eds.)]. U.S. Global Change Research Program, Washington, DC, USA, pp. 1242–1308, doi:10.7930/nca4.2018.ch27.
Kelley, C., M. Ting, R. Seager, and Y. Kushnir, 2012: The relative contributions of radiative forcing and internal climate variability to the late 20th Century winter drying of the Mediterranean region. *Climate Dynamics*, **38(9–10)**, 2001–2015, doi:10.1007/s00382-011-1221-z.
Kendon, E.J. et al., 2019: Enhanced future changes in wet and dry extremes over Africa at convection-permitting scale. *Nature Communications*, **10(1)**, doi:10.1038/s41467-019-09776-9.
Kennedy, J.J., N.A. Rayner, C.P. Atkinson, and R.E. Killick, 2019: An Ensemble Data Set of Sea Surface Temperature Change From 1850: The Met Office Hadley Centre HadSST.4.0.0.0 Data Set. *Journal of Geophysical Research: Atmospheres*, **124(14)**, 7719–7763, doi:10.1029/2018jd029867.
Khan, N., S. Shahid, T. Ismail, and X.-J. Wang, 2019: Spatial distribution of unidirectional trends in temperature and temperature extremes in Pakistan. *Theoretical and Applied Climatology*, **136(3–4)**, 899–913, doi:10.1007/s00704-018-2520-7.
Khan, N., S. Shahid, E.S. Chung, F. Behlil, and M.S.J. Darwish, 2020: Spatiotemporal changes in precipitation extremes in the arid province of Pakistan with removal of the influence of natural climate variability. *Theoretical and Applied Climatology*, **142(3–4)**, 1447–1462, doi:10.1007/s00704-020-03389-9.
Kharyutkina, E., S. Loginov, and I.I. Ippolitov, 2016: Influence of radiation and circulation factors on climate change in Western Siberia at the end of the 20th century and beginning of the 21st century. *Izvestiya - Atmospheric and Ocean Physics*, **52(6)**, 579–586, doi:10.1134/s0001433816060098.
Khaydarov, M. and L. Gerlitz, 2019: Climate variability and change over Uzbekistan – an analysis based on high resolution CHELSA data. *Central Asian Journal of Water Research*, **5(2)**, 1–19, doi:10.29258/cajwr/2019-r1.v5-2/1-19.eng.
Khlebnikova, E.I., V.M. Kattsov, A.A. Pikaleva, and I.M. Shkolnik, 2018: Assessment of Climate Change Impacts on the Economic Development of the Russian Arctic in the 21st Century. *Russian Meteorology and Hydrology*, **43(6)**, 347–356, doi:10.3103/s1068373918060018.
Kieu-Thi, X. et al., 2016: Rainfall and Tropical Cyclone Activity over Vietnam Simulated and Projected by the Non-Hydrostatic Regional Climate Model - NHRCM. *Journal of the Meteorological Society of Japan. Ser. II*, **94A(0)**, 135–150, doi:10.2151/jmsj.2015-057.

ACCEPTED VERSION SUBJECT TO FINAL EDITS

Kim, G. et al., 2020: Evaluation and Projection of Regional Climate over East Asia in CORDEX-East Asia Phase I Experiment. *Asia-Pacific Journal of Atmospheric Sciences*, doi:10.1007/s13143-020-00180-8.
Kim, H.-S., Y.-S. Chung, P.P. Tans, and M.-B. Yoon, 2016: Climatological variability of air temperature and precipitation observed in South Korea for the last 50 years. *Air Quality, Atmosphere & Health*, **9(6)**, 645–651, doi:10.1007/s11869-015-0366-z.
Kim, I.W., J. Oh, S. Woo, and R.H. Kripalani, 2018: Evaluation of precipitation extremes over the Asian domain: observation and modelling studies. *Climate Dynamics*, **52(3–4)**, 1–26, doi:10.1007/s00382-018-4193-4.
Kim, Y., M. Jun, S.-K. Min, M.-S. Suh, and H.-S. Kang, 2016: Spatial analysis of future East Asian seasonal temperature using two regional climate model simulations. *Asia-Pacific Journal of Atmospheric Sciences*, **52(2)**, 237–249, doi:10.1007/s13143-016-0022-z.
King, J.C. et al., 2017: The Impact of Föhn Winds on Surface Energy Balance During the 2010–2011 Melt Season Over Larsen C Ice Shelf, Antarctica. *Journal of Geophysical Research: Atmospheres*, **122(22)**, 12,062–12,076, doi:10.1002/2017jd026809.
Kirchmeier-Young, M.C., H. Wan, X. Zhang, and S.I. Seneviratne, 2019: Importance of Framing for Extreme Event Attribution: The Role of Spatial and Temporal Scales. *Earth's Future*, **7(10)**, 1192–1204, doi:10.1029/2019ef001253.
Kirono, D.G. et al., 2015: Historical and future seasonal rainfall variability in Nusa Tenggara Barat Province, Indonesia: Implications for the agriculture and water sectors. *Climate Risk Management*, **12**, 45–58, doi:10.1016/j.crm.2015.12.002.
Kirtman, B., A. Adedoyin, and N. Bindoff, 2013: Near-term Climate Change: Projections and Predictability. In: *Climate Change 2013: The Physical Science Basis. Contribution of Working Group I to the Fifth Assessment Report of the Intergovernmental Panel on Climate Change* [Stocker, T.F., D. Qin, G.-K. Plattner, M. Tignor, S.K. Allen, J. Boschung, A. Nauels, Y. Xia, V. Bex, and P.M. Midgley (eds.)]. Cambridge University Press, Cambridge, United Kingdom and New York, NY, USA, pp. 953–1028, doi:10.1017/cbo9781107415324.023.
Kisembe, J. et al., 2018: Evaluation of rainfall simulations over Uganda in CORDEX regional climate models. *Theoretical and Applied Climatology*, doi:10.1007/s00704-018-2643-x.
Kitoh, A., 2017: The Asian Monsoon and its Future Change in Climate Models: A Review. *Journal of the Meteorological Society of Japan. Ser. II*, **95(1)**, 7–33, doi:10.2151/jmsj.2017-002.
Kittel, C. et al., 2021: Diverging future surface mass balance between the Antarctic ice shelves and grounded ice sheet. *The Cryosphere*, **15(3)**, 1215–1236, doi:10.5194/tc-15-1215-2021.
Kjellström, E. et al., 2018: European climate change at global mean temperature increases of 1.5 and 2 °C above pre-industrial conditions as simulated by the EURO-CORDEX regional climate models. *Earth System Dynamics*, **9(2)**, 459–478, doi:10.5194/esd-9-459-2018.
Klutse, N.A.B. et al., 2016: Daily characteristics of West African summer monsoon precipitation in CORDEX simulations. *Theoretical and Applied Climatology*, **123(1–2)**, doi:10.1007/s00704-014-1352-3.
Klutse, N.A.B. et al., 2018: Potential impact of 1.5°C and 2°C global warming on consecutive dry and wet days over West Africa. *Environmental Research Letters*, doi:10.1088/1748-9326/aab37b.
Knippertz, P., M. Christoph, and P. Speth, 2003: Long-term precipitation variability in Morocco and the link to the large-scale circulation in recent and future climates. *Meteorology and Atmospheric Physics*, doi:10.1007/s00703-002-0561-y.
Knowles, N., 2015: Trends in snow cover and related quantities at weather stations in the conterminous United States. *Journal of Climate*, **28(19)**, 7518–7528, doi:10.1175/jcli-d-15-0051.1.
Knutson, T. et al., 2019: Tropical Cyclones and Climate Change Assessment: Part I: Detection and Attribution. *Bulletin of the American Meteorological Society*, **100(10)**, 1987–2007, doi:10.1175/bams-d-18-0189.1.
Knutson, T.R. and F. Zeng, 2018: Model Assessment of Observed Precipitation Trends over Land Regions: Detectable Human Influences and Possible Low Bias in Model Trends. *Journal of Climate*, **31(12)**, 4617–4637, doi:10.1175/jcli-d-17-0672.1.
Knutti, R., D. Masson, and A. Gettelman, 2013: Climate model genealogy: Generation CMIP5 and how we got there. *Geophysical Research Letters*, **40**, 1194–1199, doi:10.1002/grl.50256.
Koenig, L.S. et al., 2016: Annual Greenland accumulation rates (2009–2012) from airborne snow radar. *The Cryosphere*, **10(4)**, 1739–1752, doi:10.5194/tc-10-1739-2016.
Koenigk, T., P. Berg, and R. Döscher, 2015: Arctic climate change in an ensemble of regional CORDEX simulations. *Polar Research*, **34(1)**, 24603, doi:10.3402/polar.v34.24603.
Kohler, J., O. Brandt, M. Johansson, and T. Callaghan, 2006: A long-term Arctic snow depth record from Abisko, northern Sweden, 1913–2004. *Polar Research*, **25(2)**, 91–113, doi:10.1111/j.1751-8369.2006.tb00026.x.
Kohnemann, S.H.E., G. Heinemann, D.H. Bromwich, and O. Gutjahr, 2017: Extreme Warming in the Kara Sea and Barents Sea during the Winter Period 2000–16. *Journal of Climate*, **30(22)**, 8913–8927, doi:10.1175/jcli-d-16-0693.1.
Kokorev, V.A. and A.B. Sherstiukov, 2015: Meteorological Data for Studying the Current and Projected for the Future Climate Change in Russia. *Arctica.Natural Sciences*, **2(3)**, 5–23.
Komurcu, M., K.A. Emanuel, M. Huber, and R.P. Acosta, 2018: High-Resolution Climate Projections for the

ACCEPTED VERSION SUBJECT TO FINAL EDITS

Northeastern United States Using Dynamical Downscaling at Convection-Permitting Scales. *Earth and Space Science*, **5(11)**, 801–826, doi:10.1029/2018ea000426.

Kotlarski, S. et al., 2014: Regional climate modeling on European scales: a joint standard evaluation of the EURO-CORDEX RCM ensemble. *Geoscientific Model Development*, **7(4)**, 1297–1333, doi:10.5194/gmd-7-1297-2014.

Kotlarski, S. et al., 2019: Observational uncertainty and regional climate model evaluation: A pan-European perspective. *International Journal of Climatology*, **39(9)**, 3730–3749, doi:10.1002/joc.5249.

Kovats, R.S. et al., 2014: Europe. In: *Climate Change 2014: Impacts, Adaptation, and Vulnerability. Part B: Regional Aspects. Contribution of Working Group II to the Fifth Assessment Report of the Intergovernmental Panel on Climate Change* [Barros, V.R., C.B. Field, D.J. Dokken, M.D. Mastrandrea, K.J. Mach, T.E. Bilir, M. Chatterjee, K.L. Ebi, Y.O. Estrada, R.C. Genova, B. Girma, E.S. Kissel, A.N. Levy, S. MacCracken, P.R. Mastrandrea, and L.L. White (eds.)]. Cambridge University Press, Cambridge, United Kingdom and New York, NY, USA, pp. 1267–1326, doi:10.1017/cbo9781107415386.003.

Krakovska, S.V., 2018: Optimal ensemble of regional climate models for the ssessment of temperature regime change in Ukraine. *Nature Management*, **12(1)**, 114–126.

Krakovska, S.V., L.V. Palamarchuk, N.V. Gnatiuk, T.M. Shpytal, and I.P. Shedemenko, 2017: Changes in precipitation distribution in Ukraine for the 21st century based on data of regional climate model ENSEMBLE. *Geoinformatika*, **4(64)**, 62–74.

Krasting, J.P., A.J. Broccoli, K.W. Dixon, and J.R. Lanzante, 2013a: Future changes in northern hemisphere snowfall. *Journal of Climate*, **26(20)**, 7813–7828, doi:10.1175/jcli-d-12-00832.1.

Krasting, J.P., A.J. Broccoli, K.W. Dixon, and J.R. Lanzante, 2013b: Future changes in northern hemisphere snowfall. *Journal of Climate*, **26(20)**, 7813–7828, doi:10.1175/jcli-d-12-00832.1.

Krinner, G., J. Beaumet, V. Favier, M. Déqué, and C. Brutel-Vuilmet, 2019: Empirical Run-Time Bias Correction for Antarctic Regional Climate Projections With a Stretched-Grid AGCM. *Journal of Advances in Modeling Earth Systems*, **11(1)**, 64–82, doi:10.1029/2018ms001438.

Krinner, G., V. Kharin, R. Roehrig, J. Scinocca, and F. Codron, 2020: Historically-based run-time bias corrections substantially improve model projections of 100 years of future climate change. *Communications Earth & Environment*, **1(1)**, 29, doi:10.1038/s43247-020-00035-0.

Krishnan, R. et al., 2016: Deciphering the desiccation trend of the South Asian monsoon hydroclimate in a warming world. *Climate Dynamics*, **47(3–4)**, 1007–1027, doi:10.1007/s00382-015-2886-5.

Kröner, N. et al., 2017: Separating climate change signals into thermodynamic, lapse-rate and circulation effects: theory and application to the European summer climate. *Climate Dynamics*, **48(9)**, 3425–3440, doi:10.1007/s00382-016-3276-3.

Kruger, A.C. and S. Shongwe, 2004: Temperature trends in South Africa: 1960-2003. *International Journal of Climatology*, doi:10.1002/joc.1096.

Kruger, A.C. and S.S. Sekele, 2013: Trends in extreme temperature indices in South Africa: 1962-2009. *International Journal of Climatology*, doi:10.1002/joc.3455.

Kruger, A.C. and M.P. Nxumalo, 2017: Historical rainfall trends in South Africa: 1921–2015. *Water SA*, doi:10.4314/wsa.v43i2.12.

Kruk, M.C. et al., 2015: On the state of the knowledge of rainfall extremes in the western and northern Pacific basin. *International Journal of Climatology*, **35(3)**, 321–336, doi:10.1002/joc.3990.

Kug, J.-S. et al., 2015: Two distinct influences of Arctic warming on cold winters over North America and East Asia. *Nature Geoscience*, **8(10)**, 759–762, doi:10.1038/ngeo2517.

Kuleshov, Y., P. Gregory, A.B. Watkins, and R.J.B. Fawcett, 2020: Tropical cyclone early warnings for the regions of the Southern Hemisphere: strengthening resilience to tropical cyclones in small island developing states and least developed countries. *Natural Hazards*, **104(2)**, 1295–1313, doi:10.1007/s11069-020-04214-2.

Kulkarni, A. et al., 2017: Observed climate variability and change over India. In: *Climate Change over India: An Interim Report* [Krishnan, R. and J. Sanjay (eds.)]. Centre for Climate Change Research (CCCR), Indian Institute of Tropical Meteorology (IITM), Pune, India, pp. 3–9.

Kumar, K.N., D. Entekhabi, and A. Molini, 2015: Hydrological extremes in hyperarid regions: A diagnostic characterization of intense precipitation over the Central Arabian Peninsula. *Journal of Geophysical Research: Atmospheres*, **120(5)**, 1637–1650, doi:10.1002/2014jd022341.

Kumar, R., M. Stephens, and T. Weir, 2013: Temperature trends in Fiji: a clear signal of climate change. *The South Pacific Journal of Natural and Applied Sciences*, **31(1)**, 27, doi:10.1071/sp13002.

Kumi, N. and B.J. Abiodun, 2018: Potential impacts of 1.5 °c and 2 °c global warming on rainfall onset, cessation and length of rainy season in West Africa. *Environmental Research Letters*, **13(5)**, 55009, doi:10.1088/1748-9326/aab89e.

Kunkel, K.E. et al., 2007: Trend identification in twentieth-century U.S. snowfall: The challenges. *Journal of Atmospheric and Oceanic Technology*, **24(1)**, 64–73, doi:10.1175/jtech2017.1.

Kunkel, K.E. et al., 2016: Trends and Extremes in Northern Hemisphere Snow Characteristics. *Current Climate Change Reports*, **2(2)**, 65–73, doi:10.1007/s40641-016-0036-8.

ACCEPTED VERSION SUBJECT TO FINAL EDITS

Kusunoki, S., 2017: Future changes in global precipitation projected by the atmospheric model MRI-AGCM3.2H with a 60-km size. *Atmosphere*, **8(5)**, 6–14, doi:10.3390/atmos8050093.
Kusunoki, S., 2018a: Future changes in precipitation over East Asia projected by the global atmospheric model MRI-AGCM3.2. *Climate Dynamics*, **51(11)**, 4601–4617, doi:10.1007/s00382-016-3499-3.
Kusunoki, S., 2018b: Is the global atmospheric model MRI-AGCM3.2 better than the CMIP5 atmospheric models in simulating precipitation over East Asia? *Climate Dynamics*, **51(11)**, 4489–4510, doi:10.1007/s00382-016-3335-9.
Kusunoki, S., R. Mizuta, and M. Hosaka, 2015: Future changes in precipitation intensity over the Arctic projected by a global atmospheric model with a 60-km grid size. *Polar Science*, **9(3)**, 277–292, doi:10.1016/j.polar.2015.08.001.
Kwan, M.S., F.T. Tangang, and L. Juneng, 2014: Present-day regional climate simulation over Malaysia and western Maritime Continent region using PRECIS forced with ERA40 reanalysis. *Theoretical and Applied Climatology*, **115(1–2)**, 1–14, doi:10.1007/s00704-013-0873-5.
Landelius, T., P. Dahlgren, S. Gollvik, A. Jansson, and E. Olsson, 2016: A high-resolution regional reanalysis for Europe. Part 2: 2D analysis of surface temperature, precipitation and wind. *Quarterly Journal of the Royal Meteorological Society*, **142(698)**, 2132–2142, doi:10.1002/qj.2813.
Landrum, L. and M.M. Holland, 2020: Extremes become routine in an emerging new Arctic. *Nature Climate Change*, **10(12)**, 1108–1115, doi:10.1038/s41558-020-0892-z.
Lange, S., 2019a: Trend-preserving bias adjustment and statistical downscaling with ISIMIP3BASD (v1.0). *Geoscientific Model Development*, **12(7)**, 3055–3070, doi:10.5194/gmd-12-3055-2019.
Lange, S., 2019b: WFDE5 over land merged with ERA5 over the ocean (W5E5). V. 1.0. GFZ Data Services.
Larue, F. et al., 2017: Validation of GlobSnow-2 snow water equivalent over Eastern Canada. *Remote Sensing of Environment*, **194**, 264–277, doi:10.1016/j.rse.2017.03.027.
Latif, M., 2017: Analysis of rainfall trends over Indo-Pakistan summer monsoon and related dynamics based on CMIP5 climate. , doi:10.1002/joc.5391.
Latif, M., F.S. Syed, and A. Hannachi, 2017: Rainfall trends in the South Asian summer monsoon and its related large-scale dynamics with focus over Pakistan. *Climate Dynamics*, **48(11)**, 3565–3581, doi:10.1007/s00382-016-3284-3.
Lavado Casimiro, W.S., D. Labat, J. Ronchail, J.C. Espinoza, and J.L. Guyot, 2012: Trends in rainfall and temperature in the Peruvian Amazon-Andes basin over the last 40 years (1965-2007). *Hydrological Processes*, n/a–n/a, doi:10.1002/hyp.9418.
Lee, J.-Y. et al., 2017: The long-term variability of Changma in the East Asian summer monsoon system: A review and revisit. *Asia-Pacific Journal of Atmospheric Sciences*, **53(2)**, 257–272, doi:10.1007/s13143-017-0032-5.
Lee, T.-C., T.R. Knutson, T. Nakaegawa, M. Ying, and E.J. Cha, 2020: Third assessment on impacts of climate change on tropical cyclones in the Typhoon Committee Region – Part I: Observed changes, detection and attribution. *Tropical Cyclone Research and Review*, **9(1)**, 1–22, doi:10.1016/j.tcrr.2020.03.001.
Legasa, M.N. et al., 2020: Assessing Multidomain Overlaps and Grand Ensemble Generation in CORDEX Regional Projections. *Geophysical Research Letters*, **47(4)**, e2019GL086799, doi:10.1029/2019gl086799.
Lehner, F. et al., 2020: Partitioning climate projection uncertainty with multiple large ensembles and CMIP5/6. *Earth System Dynamics*, **11(2)**, 491–508, doi:10.5194/esd-11-491-2020.
Lelieveld, J. et al., 2016: Strongly increasing heat extremes in the Middle East and North Africa (MENA) in the 21st century. *Climatic Change*, doi:10.1007/s10584-016-1665-6.
Lemos, M.C., C.J. Kirchhoff, and V. Ramprasad, 2012: Narrowing the climate information usability gap. *Nature Climate Change*, **2(11)**, 789–794, doi:10.1038/nclimate1614.
Lenaerts, J.T.M., J. Fyke, and B. Medley, 2018: The Signature of Ozone Depletion in Recent Antarctic Precipitation Change: A Study With the Community Earth System Model. *Geophysical Research Letters*, **45(23)**, 12,931–12,939, doi:10.1029/2018gl078608.
Lenaerts, J.T.M., B. Medley, M.R. Broeke, and B. Wouters, 2019: Observing and Modeling Ice Sheet Surface Mass Balance. *Reviews of Geophysics*, **57(2)**, 376–420, doi:10.1029/2018rg000622.
Lenaerts, J.T.M., M. Vizcaino, J. Fyke, L. van Kampenhout, and M.R. van den Broeke, 2016: Present-day and future Antarctic ice sheet climate and surface mass balance in the Community Earth System Model. *Climate Dynamics*, **47(5–6)**, 1367–1381, doi:10.1007/s00382-015-2907-4.
Lenaerts, J.T.M. et al., 2013: Recent snowfall anomalies in Dronning Maud Land, East Antarctica, in a historical and future climate perspective. *Geophysical Research Letters*, **40(11)**, 2684–2688, doi:10.1002/grl.50559.
Lenderink, G. et al., 2014: Preparing local climate change scenarios for the Netherlands using resampling of climate model output. *Environmental Research Letters*, **9(11)**, doi:10.1088/1748-9326/9/11/115008.
Lennard, C., G. Nikulin, A. Dosio, and W. Moufouma-Okia, 2018: On the need for regional climate information over Africa under varying levels of global warming. *Environmental Research Letters*, doi:10.1088/1748-9326/aab2b4.
Li, B., Y. Chen, and X. Shi, 2012: Why does the temperature rise faster in the arid region of northwest China? *Journal of Geophysical Research: Atmospheres*, **117(D16)**, doi:10.1029/2012jd017953.

ACCEPTED VERSION SUBJECT TO FINAL EDITS

Li, B., Y. Chen, X. Shi, Z. Chen, and W. Li, 2013: Temperature and precipitation changes in different environments in the arid region of northwest China. *Theoretical and Applied Climatology*, **112(3–4)**, 589–596, doi:10.1007/s00704-012-0753-4.

Li, D., T. Zhou, L. Zou, W. Zhang, and L. Zhang, 2018a: Extreme High-Temperature Events Over East Asia in 1.5°C and 2°C Warmer Futures: Analysis of NCAR CESM Low-Warming Experiments. *Geophysical Research Letters*, **45(3)**, 1541–1550, doi:10.1002/2017gl076753.

Li, D. et al., 2018b: Present climate evaluation and added value analysis of dynamically downscaled simulations of CORDEX-East Asia. *Journal of Applied Meteorology and Climatology*, **57(10)**, 2317–2341, doi:10.1175/jamc-d-18-0008.1.

Li, J., Z. Liu, Z. Yao, and R. Wang, 2019: Comprehensive assessment of Coupled Model Intercomparison Project Phase 5 global climate models using observed temperature and precipitation over mainland Southeast Asia. *International Journal of Climatology*, **39(10)**, 4139–4153, doi:10.1002/joc.6064.

Li, J. et al., 2015: Precipitation over East Asia simulated by NCAR CAM5 at different horizontal resolutions. *Journal of Advances in Modeling Earth Systems*, **7(2)**, 774–790, doi:10.1002/2014ms000414.

Li, Q. et al., 2017: Comparisons of Time Series of Annual Mean Surface Air Temperature for China since the 1900s: Observations, Model Simulations, and Extended Reanalysis. *Bulletin of the American Meteorological Society*, **98(4)**, 699–711, doi:10.1175/bams-d-16-0092.1.

Li, W., L. Li, M. Ting, and Y. Liu, 2012: Intensification of Northern Hemisphere subtropical highs in a warming climate. *Nature Geoscience*, **5(11)**, 830–834, doi:10.1038/ngeo1590.

Li, Z., Y. Sun, T. Li, Y. Ding, and T. Hu, 2019: Future Changes in East Asian Summer Monsoon Circulation and Precipitation Under 1.5 to 5°C of Warming. *Earth's Future*, **7(12)**, 1391–1406, doi:10.1029/2019ef001276.

Liebmann, B. et al., 2017: Climatology and interannual variability of boreal spring wet season precipitation in the eastern horn of Africa and implications for its recent decline. *Journal of Climate*, doi:10.1175/jcli-d-16-0452.1.

Limsakul, A. and P. Singhruck, 2016: Long-term trends and variability of total and extreme precipitation in Thailand. *Atmospheric Research*, **169**, 301–317, doi:10.1016/j.atmosres.2015.10.015.

Lin, L. et al., 2019: CAM6 simulation of mean and extreme precipitation over Asia: sensitivity to upgraded physical parameterizations and higher horizontal resolution. *Geoscientific Model Development*, **12(8)**, 3773–3793, doi:10.5194/gmd-12-3773-2019.

Lindsay, R., M. Wensnahan, A. Schweiger, and J. Zhang, 2014: Evaluation of seven different atmospheric reanalysis products in the arctic. *Journal of Climate*, **27(7)**, 2588–2606, doi:10.1175/jcli-d-13-00014.1.

Lindvall, J. and G. Svensson, 2015: The diurnal temperature range in the CMIP5 models. *Climate Dynamics*, **44(1)**, 405–421, doi:10.1007/s00382-014-2144-2.

Lionello, P. and L. Scarascia, 2018: The relation between climate change in the Mediterranean region and global warming. *Regional Environmental Change*, **18(5)**, 1481–1493, doi:10.1007/s10113-018-1290-1.

Lionello, P. et al., 2012: Introduction: Mediterranean Climate – Background Information. In: *The Climate of the Mediterranean Region: From the Past to the Future* [Lionello, P. (ed.)]. Elsevier, pp. xxxv–xc, doi:10.1016/b978-0-12-416042-2.00012-4.

Liu, C. et al., 2017: Continental-scale convection-permitting modeling of the current and future climate of North America. *Climate Dynamics*, **49(1)**, 71–95, doi:10.1007/s00382-016-3327-9.

Liu, H.W., T.J. Zhou, Y.X. Zhu, and Y.H. Lin, 2012: The strengthening East Asia summer monsoon since the early 1990s. *Chinese Science Bulletin*, **57(13)**, 1553–1558, doi:10.1007/s11434-012-4991-8.

Liu, W. et al., 2018: Global Freshwater Availability Below Normal Conditions and Population Impact Under 1.5 and 2 °C Stabilization Scenarios. *Geophysical Research Letters*, **45(18)**, 9803–9813, doi:10.1029/2018gl078789.

Llopart, M., E. Coppola, F. Giorgi, R.P. da Rocha, and S. Cuadra, 2014: Climate change impact on precipitation for the Amazon and La Plata basins. *Climatic Change*, **125(1)**, 111–125, doi:10.1007/s10584-014-1140-1.

Llopart, M. et al., 2020: Assessing changes in the atmospheric water budget as drivers for precipitation change over two CORDEX-CORE domains. *Climate Dynamics*, doi:10.1007/s00382-020-05539-1.

Lloyd, E.A. and N. Oreskes, 2018: Climate Change Attribution: When Is It Appropriate to Accept New Methods? *Earth's Future*, **6(3)**, 311–325, doi:10.1002/2017ef000665.

Loginov, S., I.I. Ippolitov, and E. Kharyutkina, 2014: The relationship of surface air temperature, heat balance at the surface, and radiative balance at the top of atmosphere over the Asian territory of Russia using reanalysis and remote-sensing data. *International Journal of Remote Sensing*, **35(15)**, 5878–5898, doi:10.1080/01431161.2014.945007.

Loginov, V.F. et al., 2018: Climate Research in the Institute for Nature Management of the National Academy of Sciences of Belarus. *Nature Management*, **1**, 67–86.

Loh, J., F. Tangang, L. Juneng, D. Hein, and D.-I. Lee, 2016: Projected rainfall and temperature changes over Malaysia at the end of the 21st century based on PRECIS modelling system. *Asia-Pacific Journal of Atmospheric Sciences*, **52(2)**, 191–208, doi:10.1007/s13143-016-0019-7.

López-Moreno, J.I., S. Goyette, and M. Beniston, 2009: Impact of climate change on snowpack in the Pyrenees: Horizontal spatial variability and vertical gradients. *Journal of Hydrology*, **374(3–4)**, 384–396, doi:10.1016/j.jhydrol.2009.06.049.

ACCEPTED VERSION SUBJECT TO FINAL EDITS

Lorenz, S., S. Dessai, P.M. Forster, and J. Paavola, 2015: Tailoring the visual communication of climate projections for local adaptation practitioners in Germany and the UK. *Philosophical Transactions of the Royal Society A: Mathematical, Physical and Engineering Sciences*, **373(2055)**, 20140457, doi:10.1098/rsta.2014.0457.

Losada, T. et al., 2010: Tropical response to the Atlantic Equatorial mode: AGCM multimodel approach. *Climate Dynamics*, **35(1)**, 45–52, doi:10.1007/s00382-009-0624-6.

Lowe, J. et al., 2018: *UKCP18 Science Overview Report*. UK Met Office, 73 pp.

Lucas-Picher, P., S. Somot, M. Déqué, B. Decharme, and A. Alias, 2013: Evaluation of the regional climate model ALADIN to simulate the climate over North America in the CORDEX framework. *Climate Dynamics*, **41(5)**, 1117–1137, doi:10.1007/s00382-012-1613-8.

Lucas-Picher, P. et al., 2012: Very high resolution regional climate model simulations over Greenland: Identifying added value. *Journal of Geophysical Research Atmospheres*, **117(2)**, doi:10.1029/2011jd016267.

Luo, J., H. Chen, and B. Zhou, 2020: Comparison of Snowfall Variations over China Identified from Different Snowfall/Rainfall Discrimination Methods. *Journal of Meteorological Research*, **34(qxxbywb–34–X–luojiangshan)**, 1114–1128, doi:10.1007/s13351-020-0004-z.

Luo, M. et al., 2018: Defining spatiotemporal characteristics of climate change trends from downscaled GCMs ensembles: how climate change reacts in Xinjiang, China. *International Journal of Climatology*, **38(5)**, 2538–2553, doi:10.1002/joc.5425.

Luo, M. et al., 2019: Spatiotemporal characteristics of future changes in precipitation and temperature in Central Asia. *International Journal of Climatology*, **39(3)**, 1571–1588, doi:10.1002/joc.5901.

Luo, X., B. Wang, A.G. Frazier, and T.W. Giambelluca, 2020: Distinguishing Variability Regimes of Hawaiian Summer Rainfall: Quasi-Biennial and Interdecadal Oscillations. *Geophysical Research Letters*, **47(23)**, doi:10.1029/2020gl091260.

Luomaranta, A., J. Aalto, and K. Jylhä, 2019: Snow cover trends in Finland over 1961–2014 based on gridded snow depth observations. *International Journal of Climatology*, **39(7)**, 3147–3159, doi:10.1002/joc.6007.

Łupikasza, E.B. et al., 2019: The Role of Winter Rain in the Glacial System on Svalbard. *Water*, **11(2)**, 334, doi:10.3390/w11020334.

Lussana, C. et al., 2018: seNorge2 daily precipitation, an observational gridded dataset over Norway from 1957 to the present day. *Earth System Science Data; Katlenburg-Lindau*, **10(1)**, 235–249, doi:10.5194/essd-10-235-2018.

Lyon, B., 2014: Seasonal drought in the Greater Horn of Africa and its recent increase during the March-May long rains. *Journal of Climate*, doi:10.1175/jcli-d-13-00459.1.

Lyon, B. and D.G. Dewitt, 2012: A recent and abrupt decline in the East African long rains. *Geophysical Research Letters*, doi:10.1029/2011gl050337.

Lyra, A. et al., 2018: Climate change projections over three metropolitan regions in Southeast Brazil using the non-hydrostatic Eta regional climate model at 5-km resolution. *Theoretical and Applied Climatology*, **132(1–2)**, 663–682, doi:10.1007/s00704-017-2067-z.

Lyu, Z., A.J. Orsi, and H. Goosse, 2020: Comparison of observed borehole temperatures in Antarctica with simulations using a forward model driven by climate model outputs covering the past millennium. *Climate of the Past*, **16(4)**, 1411–1428, doi:10.5194/cp-16-1411-2020.

MacAyeal, D.R. and O. Sergienko, 2013: The flexural dynamics of melting ice shelves. *Annals of Glaciology*, **54(63)**, 1–10, doi:10.3189/2013aog63a256.

Machguth, H. et al., 2016: Greenland surface mass-balance observations from the ice-sheet ablation area and local glaciers. *Journal of Glaciology*, **62(235)**, 861–887, doi:10.1017/jog.2016.75.

MacKellar, N., M. New, and C. Jack, 2014: Observed and modelled trends in rainfall and temperature for South Africa: 1960-2010. *South African Journal of Science*, doi:10.1590/sajs.2014/20130353.

Magaña, V., J.A. Amador, and S. Medina, 1999: The Midsummer Drought over Mexico and Central America. *Journal of Climate*, **12(6)**, 1577–1588, doi:10.1175/1520-0442(1999)012<1577:tmdoma>2.0.co;2.

Magnan, A.K. et al., 2019: Cross-Chapter Box 9: Integrative Cross-Chapter Box on Low-Lying Islands and Coasts.. *IPCC Special Report on the Ocean and Cryosphere in a Changing Climate*.

Magrin, G.O. et al., 2014: Central and South America. In: *Climate Change 2014: Impacts, Adaptation, and Vulnerability. Part B: Regional Aspects. Contribution of Working Group II to the Fifth Assessment Report of the Intergovernmental Panel on Climate Change* [Barros, V.R., C.B. Field, D.J. Dokken, M.D. Mastrandrea, K.J. Mach, T.E. Bilir, M. Chatterjee, K.L. Ebi, Y.O. Estrada, R.C. Genova, B. Girma, E.S. Kissel, A.N. Levy, S. MacCracken, P.R. Mastrandrea, and L.L. White (eds.)]. Cambridge University Press, Cambridge, United Kingdom and New York, NY, USA, pp. 1499–1566, doi:10.1017/cbo9781107415386.007.

Maher, N., S.B. Power, and J. Marotzke, 2021: More accurate quantification of model-to-model agreement in externally forced climatic responses over the coming century. *Nature Communications*, **12(1)**, 788, doi:10.1038/s41467-020-20635-w.

Mahmoudi, P., M. Mohammadi, and H. Daneshmand, 2019: Investigating the trend of average changes of annual temperatures in Iran. *International Journal of Environmental Science and Technology*, **16(2)**, 1079–1092, doi:10.1007/s13762-018-1664-4.

Mahoney, K. et al., 2021: Cool season precipitation projections for California and the Western United States in NA-

ACCEPTED VERSION SUBJECT TO FINAL EDITS

CORDEX models. *Climate Dynamics*, doi:10.1007/s00382-021-05632-z.
Maidment, R.I., R.P. Allan, and E. Black, 2015: Recent observed and simulated changes in precipitation over Africa. *Geophysical Research Letters*, **42(19)**, 8155–8164, doi:10.1002/2015gl065765.
Maldonado, T., A. Rutgersson, E. Alfaro, J. Amador, and B. Claremar, 2016: Interannual variability of the midsummer drought in Central America and the connection with sea surface temperatures. *Advances in Geosciences*, **42**, 35–50, doi:10.5194/adgeo-42-35-2016.
Maloney, E.D. et al., 2014: North American Climate in CMIP5 Experiments: Part III: Assessment of Twenty-First-Century Projections. *Journal of Climate*, **27(6)**, 2230–2270, doi:10.1175/jcli-d-13-00273.1.
Mankin, J.S. and N.S. Diffenbaugh, 2015: Influence of temperature and precipitation variability on near-term snow trends. *Climate Dynamics*, **45(3–4)**, 1099–1116, doi:10.1007/s00382-014-2357-4.
Mannig, B. et al., 2013: Dynamical downscaling of climate change in Central Asia. *Global and Planetary Change*, **110**, 26–39, doi:10.1016/j.gloplacha.2013.05.008.
Manomaiphiboon, K., M. Octaviani, K. Torsri, and S. Towprayoon, 2013: Projected changes in means and extremes of temperature and precipitation over Thailand under three future emissions scenarios. *Climate Research*, **58(2)**, 97–115, doi:10.3354/cr01188.
Manzanas, R., L.K. Amekudzi, K. Preko, S. Herrera, and J.M. Gutiérrez, 2014: Precipitation variability and trends in Ghana: An intercomparison of observational and reanalysis products. *Climatic Change*, doi:10.1007/s10584-014-1100-9.
Marengo, J.A. and J.C. Espinoza, 2016: Extreme seasonal droughts and floods in Amazonia: causes, trends and impacts. *International Journal of Climatology*, **36(3)**, 1033–1050, doi:10.1002/joc.4420.
Marengo, J.A. et al., 2012: Recent developments on the South American monsoon system. *International Journal of Climatology*, **32(1)**, 1–21, doi:10.1002/joc.2254.
Marengo, J.A. et al., 2018a: Climatic characteristics of the 2010-2016 drought in the semiarid Northeast Brazil region. *Anais da Academia Brasileira de Ciências*, **90(2 suppl 1)**, 1973–1985, doi:10.1590/0001-3765201720170206.
Marengo, J.A. et al., 2018b: Changes in Climate and Land Use Over the Amazon Region: Current and Future Variability and Trends. *Frontiers in Earth Science*, **6**, doi:10.3389/feart.2018.00228.
Mariotti, A., Y. Pan, N. Zeng, and A. Alessandri, 2015: Long-term climate change in the Mediterranean region in the midst of decadal variability. *Climate Dynamics*, **44(5–6)**, 1437–1456, doi:10.1007/s00382-015-2487-3.
Martinez, C., L. Goddard, Y. Kushnir, and M. Ting, 2019: Seasonal climatology and dynamical mechanisms of rainfall in the Caribbean. *Climate Dynamics*, **53(1)**, 825–846, doi:10.1007/s00382-019-04616-4.
Martínez-Asensio, A. et al., 2019: Relative sea-level rise and the influence of vertical land motion at Tropical Pacific Islands. *Global and Planetary Change*, **176**, 132–143, doi:10.1016/j.gloplacha.2019.03.008.
Martínez-Austria, P. and E. Bandala, 2017: Temperature and Heat-Related Mortality Trends in the Sonoran and Mojave Desert Region. *Atmosphere*, **8(12)**, 53, doi:10.3390/atmos8030053.
Martínez-Austria, P.F., E.R. Bandala, and C. Patiño-Gómez, 2016: Temperature and heat wave trends in northwest Mexico. *Physics and Chemistry of the Earth, Parts A/B/C*, **91(C)**, 20–26, doi:10.1016/j.pce.2015.07.005.
Martínez-Castro, D. et al., 2018a: The performance of RegCM4 over the Central America and Caribbean region using different cumulus parameterizations. *Climate Dynamics*, **50(11–12)**, 4103–4126, doi:10.1007/s00382-017-3863-y.
Martínez-Castro, D. et al., 2018b: The performance of RegCM4 over the Central America and Caribbean region using different cumulus parameterizations. *Climate Dynamics*, **50(11–12)**, 4103–4126, doi:10.1007/s00382-017-3863-y.
Marty, C., S. Schlögl, M. Bavay, and M. Lehning, 2017: How much can we save? Impact of different emission scenarios on future snow cover in the Alps. *The Cryosphere*, **11(1)**, 517–529, doi:10.5194/tc-11-517-2017.
Martynov, A. et al., 2013: Reanalysis-driven climate simulation over CORDEX North America domain using the Canadian Regional Climate Model, version 5: model performance evaluation. *Climate Dynamics*, **41(11–12)**, 2973–3005, doi:10.1007/s00382-013-1778-9.
Matsumoto, J., F. Fujibe, and H. Takahashi, 2017: Urban climate in the Tokyo metropolitan area in Japan. *Journal of Environmental Sciences*, **59**, 54–62, doi:10.1016/j.jes.2017.04.012.
Matthes, H., A. Rinke, and K. Dethloff, 2015: Recent changes in Arctic temperature extremes: Warm and cold spells during winter and summer. *Environmental Research Letters*, **10(11)**, 114020, doi:10.1088/1748-9326/10/11/114020.
Maturilli, M., A. Herber, and G. König-Langlo, 2015: Surface radiation climatology for Ny-Ålesund, Svalbard (78.9° N), basic observations for trend detection. *Theoretical and Applied Climatology*, **120(1–2)**, 331–339, doi:10.1007/s00704-014-1173-4.
Maúre, G. et al., 2018: The southern African climate under 1.5°C and 2°C of global warming as simulated by CORDEX regional climate models. *Environmental Research Letters*, **13(6)**, 065002, doi:10.1088/1748-9326/aab190.
Mayer, S. et al., 2015: Identifying added value in high-resolution climate simulations over Scandinavia. *Tellus A: Dynamic Meteorology and Oceanography*, **67(1)**, 24941, doi:10.3402/tellusa.v67.24941.
Mayowa, O.O. et al., 2015: Trends in rainfall and rainfall-related extremes in the east coast of peninsular Malaysia. *Journal of Earth System Science*, **124(8)**, 1609–1622, doi:10.1007/s12040-015-0639-9.

ACCEPTED VERSION SUBJECT TO FINAL EDITS

Mba, W.P. et al., 2018: Consequences of 1.5°C and 2°C global warming levels for temperature and precipitation changes over Central Africa. *Environmental Research Letters*, **13(5)**, 055011, doi:10.1088/1748-9326/aab048.
McCrary, R.R. and L.O. Mearns, 2019: Quantifying and Diagnosing Sources of Uncertainty in Midcentury Changes in North American Snowpack from NARCCAP. *Journal of Hydrometeorology*, **20(11)**, 2229–2252, doi:10.1175/jhm-d-18-0248.1.
Mccrary, R.R., S. Mcginnis, and L.O. Mearns, 2017: Evaluation of snow water equivalent in NARCCAP simulations, including measures of observational uncertainty. *Journal of Hydrometeorology*, **18(9)**, 2425–2452, doi:10.1175/jhm-d-16-0264.1.
McDermid, S.S. and J. Winter, 2017: Anthropogenic forcings on the climate of the Aral Sea: A regional modeling perspective. *Anthropocene*, **20**, 48–60, doi:10.1016/j.ancene.2017.03.003.
McGowan, H. et al., 2018: Global warming in the context of 2000 years of Australian alpine temperature and snow cover. *Scientific Reports*, **8(1)**, 4394, doi:10.1038/s41598-018-22766-z.
McGree, S., S. Schreider, and Y. Kuleshov, 2016: Trends and variability in droughts in the Pacific islands and Northeast Australia. *Journal of Climate*, **29(23)**, 8377–8397, doi:10.1175/jcli-d-16-0332.1.
McGree, S. et al., 2014: An updated assessment of trends and variability in total and extreme rainfall in the western Pacific. *International Journal of Climatology*, **34(8)**, 2775–2791, doi:10.1002/joc.3874.
McGree, S. et al., 2019: Recent Changes in Mean and Extreme Temperature and Precipitation in the Western Pacific Islands. *Journal of Climate*, **32(16)**, 4919–4941, doi:10.1175/jcli-d-18-0748.1.
McKenzie, M.M., T.W. Giambelluca, and H.F. Diaz, 2019: Temperature trends in Hawai'i: A century of change, 1917–2016. *International Journal of Climatology*, **39(10)**, 3987–4001, doi:10.1002/joc.6053.
McLean, N.M. et al., 2015: Characterization of Future Caribbean Rainfall and Temperature Extremes across Rainfall Zones. *Advances in Meteorology*, **2015**, 1–18, doi:10.1155/2015/425987.
McMahon, R., M. Stauffacher, and R. Knutti, 2015: The unseen uncertainties in climate change: reviewing comprehension of an IPCC scenario graph. *Climatic Change*, **133(2)**, 141–154, doi:10.1007/s10584-015-1473-4.
McSweeney, C.F. and R.G. Jones, 2016: How representative is the spread of climate projections from the 5 CMIP5 GCMs used in ISI-MIP? *Climate Services*, doi:10.1016/j.cliser.2016.02.001.
Mearns, L. et al., 2009: A Regional Climate Change Assessment Program for North America. *EOS Transactions*, **90**, 311, doi:10.1029/2009eo360002.
Mearns, L. et al., 2017: The NA-CORDEX dataset, version 1.0. NCAR Climate Data Gateway, Boulder, CO, USA.
Cramer, W., J. Guiot, and K. Marini (eds.), 2020: *Summary for Policymakers*. Union for the Mediterranean, Plan Bleu, UNEP/MAP, Marseille, France, 34 pp.
Medley, B. and E.R. Thomas, 2019: Increased snowfall over the Antarctic Ice Sheet mitigated twentieth-century sea-level rise. *Nature Climate Change*, **9(1)**, 34–39, doi:10.1038/s41558-018-0356-x.
Medley, B. et al., 2013: Airborne-radar and ice-core observations of annual snow accumulation over Thwaites Glacier, West Antarctica confirm the spatiotemporal variability of global and regional atmospheric models. *Geophysical Research Letters*, **40(14)**, 3649–3654, doi:10.1002/grl.50706.
Medley, B. et al., 2018: Temperature and Snowfall in Western Queen Maud Land Increasing Faster Than Climate Model Projections. *Geophysical Research Letters*, **45(3)**, 1472–1480, doi:10.1002/2017gl075992.
MEE, 2016: Second National Communication of Maldives to the United Nations Framework Convention on Climate Change. .
Meehl, G.A. and A. Hu, 2006: Megadroughts in the Indian Monsoon Region and Southwest North America and a Mechanism for Associated Multidecadal Pacific Sea Surface Temperature Anomalies. *Journal of Climate*, **19(9)**, 1605–1623, doi:10.1175/jcli3675.1.
Mei, R., M. Ashfaq, D. Rastogi, L.R. Leung, and F. Dominguez, 2015: Dominating controls for wetter South Asian summer monsoon in the twenty-first century. *Journal of Climate*, **28(8)**, 3400–3419, doi:10.1175/jcli-d-14-00355.1.
Meleshko, V.P. et al., 2019: The Arctic Climate Warming and Extremely Cold Winters in North Eurasia during 1979–2017. *Russian Meteorology and Hydrology*, **44(4)**, 223–230, doi:10.3103/s1068373919040010.
Mendes, D., J.A. Marengo, S. Rodrigues, and M. Oliveira, 2014: Downscaling Statistical Model Techniques for Climate Change Analysis Applied to the Amazon Region. *Advances in Artificial Neural Systems*, **2014**, 1–10, doi:10.1155/2014/595462.
Méndez, M. and V. Magaña, 2010: Regional Aspects of Prolonged Meteorological Droughts over Mexico and Central America. *Journal of Climate*, **23(5)**, 1175–1188, doi:10.1175/2009jcli3080.1.
Méndez-Lázaro, P.A., A. Nieves-Santiago, and J. Miranda, 2014: Trends in total rainfall , heavy rain events , and number of dry days in San Juan, Puerto Rico, 1955-2009. *Ecology and Society*, **19(2)**, doi:10.5751/es-06464-190250.
Menéndez, C.G., P.G. Zaninelli, A.F. Carril, and E. Sánchez, 2016: Hydrological cycle, temperature, and land surface-atmosphere interaction in the La Plata Basin during summer: response to climate change. *Climate Research*, **68(2–3)**, 231–241, doi:10.3354/cr01373.
Menon, S., 2002: Climate Effects of Black Carbon Aerosols in China and India. *Science*, **297(5590)**, 2250–2253,

ACCEPTED VERSION SUBJECT TO FINAL EDITS

doi:10.1126/science.1075159.
MENRPG, 2015: *Georgia's Third National Communication to the UNFCCC*. Ministry of Environment and Natural Resources Protection of Georgia (MENRPG), Tbilisi, Georgia, 262 pp.
Meque, A. and B.J. Abiodun, 2015: Simulating the link between ENSO and summer drought in Southern Africa using regional climate models. *Climate Dynamics*, doi:10.1007/s00382-014-2143-3.
Meredith, M. et al., 2019: Polar Regions. In: *IPCC Special Report on the Ocean and Cryosphere in a Changing Climate* [Pörtner, H.-O., D.C. Roberts, V. Masson-Delmotte, P. Zhai, M. Tignor, E. Poloczanska, K. Mintenbeck, A. Alegría, M. Nicolai, A. Okem, J. Petzold, B. Rama, and N.M. Weyer (eds.)]. In Press, pp. 203–320.
MESDDBM, 2016: *Republic of Mauritius Third National Communication: Report to the United Nations Framework Convention on Climate Change*. TNC Report 2016, Ministry of Environment, Sustainable Development, and Disaster and Beach Management (MESDDBM), Government of Mauritius, Port Louis, Republic of Mauritius, 210 pp.
Météo-France, 2020: *Bulletin climatologique 2019 de l'île de la Réunion*. Météo-France, Direction Interrégionale pour l'Océan Indien, Sainte Clotilde, Sainte Clotilde, La Réunion, 29 pp.
MfE, 2018: *Climate Change Projections for New Zealand: Atmosphere Projections Based on Simulations from the IPCC Fifth Assessment, 2nd Edition*. Ministry for the Environment (MfE), Wellington, NZ, 131 pp.
MfE and Stats NZ, 2017: *New Zealand's Environmental Reporting Series: Our atmosphere and climate 2017*. Ministry for the Environment (MfE) and Stats NZ, 58 pp.
MfE and Stats NZ, 2020: *New Zealand's Environmental Reporting Series: Our atmosphere and climate 2020*. Ministry for the Environment (MfE) & Stats NZ, New Zealand, 79 pp.
Miao, C. et al., 2014: Assessment of CMIP5 climate models and projected temperature changes over Northern Eurasia. *Environmental Research Letters*, **9**, 12, doi:10.1088/1748-9326/9/5/055007.
Miao, J. and T. Wang, 2020: Decadal variations of the East Asian winter monsoon in recent decades. *Atmospheric Science Letters*, **21(4)**, e960, doi:10.1002/asl.960.
Miao, J., T. Wang, and D. Chen, 2020: More robust changes in the East Asian winter monsoon from 1.5 to 2.0°C global warming targets. *International Journal of Climatology*, **40(11)**, 4731–4749, doi:10.1002/joc.6485.
Min, S.K. and A. Hense, 2007: A Bayesian assessment of climate change using multimodel ensembles. Part II: Regional and seasonal mean surface temperatures. *Journal of Climate*, doi:10.1175/jcli4178.1.
Mindlin, J. et al., 2020: Storyline description of Southern Hemisphere midlatitude circulation and precipitation response to greenhouse gas forcing. *Climate Dynamics*, **54(9)**, 4399–4421, doi:10.1007/s00382-020-05234-1.
Mioduszewski, J.R., A.K. Rennermalm, D.A. Robinson, and T.L. Mote, 2014: Attribution of snowmelt onset in Northern Canada. *Journal of Geophysical Research: Atmospheres*, **119(16)**, 9638–9653, doi:10.1002/2013jd021024.
Mioduszewski, J.R., A.K. Rennermalm, D.A. Robinson, and L. Wang, 2015: Controls on Spatial and Temporal Variability in Northern Hemisphere Terrestrial Snow Melt Timing, 1979–2012. *Journal of Climate*, **28(6)**, 2136–2153, doi:10.1175/jcli-d-14-00558.1.
Mirzabaev, A. et al., 2019: Desertification. In: *Climate Change and Land: an IPCC special report on climate change, desertification, land degradation, sustainable land management, food security, and greenhouse gas fluxes in terrestrial ecosystems* [Shukla, P.R., J. Skea, E.C. Buendia, V. Masson-Delmotte, H.-O. Pörtner, D.C. Roberts, P. Zhai, R. Slade, S. Connors, R. van Diemen, M. Ferrat, E. Haughey, S. Luz, S. Neogi, M. Pathak, J. Petzold, J.P. Pereira, P. Vyas, E. Huntley, K. Kissick, M. Belkacemi, and J. Malley (eds.)]. In Press, pp. 249–343.
Mishra, V., 2015: Climatic uncertainty in Himalayan water towers. *Journal of Geophysical Research: Atmospheres*, **120(7)**, 2689–2705, doi:10.1002/2014jd022650.
Mishra, V., U. Bhatia, and A.D. Tiwari, 2020: Bias-corrected climate projections for South Asia from Coupled Model Intercomparison Project-6. *Scientific Data*, **7(1)**, 1–13, doi:10.1038/s41597-020-00681-1.
Mokhov, I.I., 2015: Contemporary climate changes in the Arctic. *Herald of the Russian Academy of Sciences*, **85(3)**, 265–271, doi:10.1134/s1019331615030168.
Mokhov, I.I., A. Timazhev, and A.R. Lupo, 2014: Changes in atmospheric blocking characteristics within Euro-Atlantic region and Northern Hemisphere as a whole in the 21st century from model simulations using RCP anthropogenic scenarios. *Global and Planetary Change*, **122**, 265–270, doi:10.1016/j.gloplacha.2014.09.004.
Montgomery, L., L. Koenig, J.T.M. Lenaerts, and P. Kuipers Munneke, 2020: Accumulation rates (2009–2017) in Southeast Greenland derived from airborne snow radar and comparison with regional climate models. *Annals of Glaciology*, **61(81)**, 225–233, doi:10.1017/aog.2020.8.
Moon, S. and K.-J. Ha, 2017: Temperature and precipitation in the context of the annual cycle over Asia: Model evaluation and future change. *Asia-Pacific Journal of Atmospheric Sciences*, **53(2)**, 229–242, doi:10.1007/s13143-017-0024-5.
Mora, C. et al., 2013: The projected timing of climate departure from recent variability. *Nature*, doi:10.1038/nature12540.
Moreau, L., P. Groth, J. Cheney, T. Lebo, and S. Miles, 2015: The rationale of PROV. *Journal of Web Semantics*, doi:10.1016/j.websem.2015.04.001.
Morim, J. et al., 2019: Robustness and uncertainties in global multivariate wind-wave climate projections. *Nature*

ACCEPTED VERSION SUBJECT TO FINAL EDITS

Climate Change, **9(9)**, 711–718, doi:10.1038/s41558-019-0542-5.
Mortimer, C. et al., 2020: Evaluation of long-term Northern Hemisphere snow water equivalent products. *Cryosphere*, **14(5)**, 1579–1594, doi:10.5194/tc-14-1579-2020.
Mote, P.W., S. Li, D.P. Lettenmaier, M. Xiao, and R. Engel, 2018: Dramatic declines in snowpack in the western US. *npj Climate and Atmospheric Science*, **1(1)**, doi:10.1038/s41612-018-0012-1.
Mote, P.W. et al., 2016: Perspectives on the causes of exceptionally low 2015 snowpack in the western United States. *Geophysical Research Letters*, **43(20)**, 10,910–980,988, doi:10.1002/2016gl069965.
Mottram, R., K.P. Nielsen, E. Gleeson, and X. Yang, 2017: Modelling Glaciers in the HARMONIE-AROME NWP model. *Advances in Science and Research*, **14**, 323–334, doi:10.5194/asr-14-323-2017.
Mottram, R. et al., 2019: An Integrated View of Greenland Ice Sheet Mass Changes Based on Models and Satellite Observations. *Remote Sensing*, **11(12)**, 1407, doi:10.3390/rs11121407.
Mottram, R. et al., 2021: What is the Surface Mass Balance of Antarctica? An Intercomparison of Regional Climate Model Estimates. *The Cryosphere Discuss*, doi:10.5194/tc-2019-333.
Mouginot, J. et al., 2019: Forty-six years of Greenland Ice Sheet mass balance from 1972 to 2018. *Proceedings of the National Academy of Sciences*, **116(19)**, 9239–9244, doi:10.1073/pnas.1904242116.
Mouhamed, L., S.B. Traore, A. Alhassane, and B. Sarr, 2013: Evolution of some observed climate extremes in the West African Sahel. *Weather and Climate Extremes*, doi:10.1016/j.wace.2013.07.005.
Mudryk, L. et al., 2020: Historical Northern Hemisphere snow cover trends and projected changes in the CMIP6 multi-model ensemble. *The Cryosphere*, **14(7)**, 2495–2514, doi:10.5194/tc-14-2495-2020.
Mudryk, L.R., C. Derksen, P.J. Kushner, and R. Brown, 2015: Characterization of Northern Hemisphere snow water equivalent datasets, 1981-2010. *Journal of Climate*, **28(20)**, 8037–8051, doi:10.1175/jcli-d-15-0229.1.
Mudryk, L.R. et al., 2018: Canadian snow and sea ice: Historical trends and projections. *Cryosphere*, **12(4)**, 1157–1176, doi:10.5194/tc-12-1157-2018.
Murphy, C. et al., 2019: Multi-century trends to wetter winters and drier summers in the England and Wales precipitation series explained by observational and sampling bias in early records. *International Journal of Climatology*, joc.6208, doi:10.1002/joc.6208.
Musselman, K.N. et al., 2018: Projected increases and shifts in rain-on-snow flood risk over western North America. *Nature Climate Change*, **8(9)**, 808–812, doi:10.1038/s41558-018-0236-4.
Mycoo, M.A., 2018: Achieving SDG 6: water resources sustainability in Caribbean Small Island Developing States through improved water governance. *Nat Resour Forum*, **42**, 54–68, doi:10.1111/1477-8947.12141.
Nabat, P., F. Solmon, M. Mallet, J.F. Kok, and S. Somot, 2012: Dust emission size distribution impact on aerosol budget and radiative forcing over the Mediterranean region: a regional climate model approach. *Atmospheric Chemistry and Physics*, **12(21)**, 10545–10567, doi:10.5194/acp-12-10545-2012.
Nabat, P., S. Somot, M. Mallet, A. Sanchez-Lorenzo, and M. Wild, 2014: Contribution of anthropogenic sulfate aerosols to the changing Euro-Mediterranean climate since 1980. *Geophysical Research Letters*, **41(15)**, 5605–5611, doi:10.1002/2014gl060798.
Nabat, P. et al., 2013: A 4-D climatology (1979-2009) of the monthly tropospheric aerosol optical depth distribution over the Mediterranean region from a comparative evaluation and blending of remote sensing and model products. *Atmospheric Measurement Techniques*, **6(5)**, 1287–1314, doi:10.5194/amt-6-1287-2013.
Nabat, P. et al., 2015: Dust aerosol radiative effects during summer 2012 simulated with a coupled regional aerosol-atmosphere-ocean model over the Mediterranean. *Atmospheric Chemistry and Physics*, **15(6)**, doi:10.5194/acp-15-3303-2015.
Nabat, P. et al., 2020: Modulation of radiative aerosols effects by atmospheric circulation over the Euro-Mediterranean region. *Atmospheric Chemistry and Physics*, **20(14)**, 8315–8349, doi:10.5194/acp-20-8315-2020.
Nakaegawa, T., A. Kitoh, S. Kusunoki, H. Murakami, and O. Arakawa, 2014: Hydroclimate changes over Central America and the Caribbean in a global warming climate projected with 20-km and 60-km mesh MRI atmospheric general circulation models.. *Pap. Meteor. Geophys.*, **65**, 15–33, doi:10.2467/mripapers.65.15.
Naranjo-Diaz, L.R. and A. Centella, 1998: Recent trends in the climate of Cuba. *Weather*, **53(3)**, 78–85, doi:10.1002/j.1477-8696.1998.tb03964.x.
Narsey, S.Y. et al., 2020: Climate Change Projections for the Australian Monsoon From CMIP6 Models. *Geophysical Research Letters*, **47(13)**, e2019GL086816, doi:10.1029/2019gl086816.
Navarro-Estupiñan, J. et al., 2018: Observed trends and future projections of extreme heat events in Sonora, Mexico. *International Journal of Climatology*, **38(14)**, 5168–5181, doi:10.1002/joc.5719.
Nengker, T., A. Choudhary, and A.P. Dimri, 2018: Assessment of the performance of CORDEX-SA experiments in simulating seasonal mean temperature over the Himalayan region for the present climate: Part I. *Climate Dynamics*, **50(7–8)**, 2411–2441, doi:10.1007/s00382-017-3597-x.
Nesbitt, S.W., D.J. Gochis, and T.J. Lang, 2008: The Diurnal Cycle of Clouds and Precipitation along the Sierra Madre Occidental Observed during NAME-2004: Implications for Warm Season Precipitation Estimation in Complex Terrain. *Journal of Hydrometeorology*, **9(4)**, 728–743, doi:10.1175/2008jhm939.1.
Neukom, R. et al., 2010: Multi-centennial summer and winter precipitation variability in southern South America. *Geophysical Research Letters*, **37(14)**, doi:10.1029/2010gl043680.

ACCEPTED VERSION SUBJECT TO FINAL EDITS

New, M. et al., 2006: Evidence of trends in daily climate extremes over southern and west Africa. *Journal of Geophysical Research Atmospheres*, doi:10.1029/2005jd006289.

Ngo-Duc, T., C. Kieu, M. Thatcher, D. Nguyen-Le, and T. Phan-Van, 2014: Climate projections for Vietnam based on regional climate models. *Climate Research*, **60(3)**, 199–213, doi:10.3354/cr01234.

Ngo-Duc, T. et al., 2017: Performance evaluation of RegCM4 in simulating extreme rainfall and temperature indices over the CORDEX-Southeast Asia region. *International Journal of Climatology*, **37(3)**, 1634–1647, doi:10.1002/joc.4803.

Nguyen-Thi, T. et al., 2020: Climate analogue and future appearance of novel climate in Southeast Asia. *International Journal of Climatology*, joc.6693, doi:10.1002/joc.6693.

Nguyen-Thuy, H. et al., 2021: Time of emergence of climate signals over Vietnam detected from the CORDEX-SEA experiments. *International Journal of Climatology*, **41(3)**, 1599–1618, doi:10.1002/joc.6897.

Nguyen-Xuan, T. et al., 2016: The Vietnam Gridded Precipitation (VnGP) Dataset: Construction and Validation. *SOLA*, **12(0)**, 291–296, doi:10.2151/sola.2016-057.

Niang, I. et al., 2014: Africa. In: *Climate Change 2014: Impacts, Adaptation, and Vulnerability. Part B: Regional Aspects. Contribution of Working Group II to the Fifth Assessment Report of the Intergovernmental Panel on Climate Change* [Barros, V.R., C.B. Field, D.J. Dokken, M.D. Mastrandrea, K.J. Mach, T.E. Bilir, M. Chatterjee, K.L. Ebi, Y.O. Estrada, R.C. Genova, B. Girma, E.S. Kissel, A.N. Levy, S. MacCracken, P.R. Mastrandrea, and L.L. White (eds.)]. Cambridge University Press, Cambridge, United Kingdom and New York, NY, USA, pp. 1199–1265, doi:10.1017/cbo9781107415386.002.

Nicolas, J.P. et al., 2017: January 2016 extensive summer melt in West Antarctica favoured by strong El Niño. *Nature Communications*, **8**, doi:10.1038/ncomms15799.

Nikulin, G. et al., 2018: The effects of 1.5 and 2 degrees of global warming on Africa in the CORDEX ensemble. *Environmental Research Letters*, **13(6)**, 065003, doi:10.1088/1748-9326/aab1b1.

Ning, L. and R.S. Bradley, 2015: Snow occurrence changes over the central and eastern United States under future warming scenarios. *Scientific Reports*, **5**, 1–8, doi:10.1038/srep17073.

Nkrumah, F. et al., 2019: Recent Trends in the Daily Rainfall Regime in Southern West Africa. *Atmosphere*, **10(12)**, 741, doi:10.3390/atmos10120741.

Nobre, C.A. et al., 2016: Land-use and climate change risks in the Amazon and the need of a novel sustainable development paradigm. *Proceedings of the National Academy of Sciences*, **113(39)**, 10759 LP – 10768, doi:10.1073/pnas.1605516113.

Noël, B. et al., 2015: Evaluation of the updated regional climate model RACMO2.3: Summer snowfall impact on the Greenland Ice Sheet. *Cryosphere*, **9(5)**, 1831–1844, doi:10.5194/tc-9-1831-2015.

Nordli et al., 2020: Revisiting the extended Svalbard Airport monthly temperature series, and the compiled corresponding daily series 1898–2018. *Polar Research*, **39(SE – Research Articles)**, doi:10.33265/polar.v39.3614.

Notaro, M., V. Bennington, and S. Vavrus, 2015: Dynamically Downscaled Projections of Lake-Effect Snow in the Great Lakes Basin. *Journal of Climate*, **28(4)**, 1661–1684, doi:10.1175/jcli-d-14-00467.1.

Nowicki, S. et al., 2020: Experimental protocol for sea level projections from ISMIP6 stand-alone ice sheet models. *The Cryosphere*, **14(7)**, 2331–2368, doi:10.5194/tc-14-2331-2020.

Nurse, L.A. et al., 2014: Small Islands. In: *Climate Change 2014: Impacts, Adaptation, and Vulnerability. Part B: Regional Aspects. Contribution of working Group II to the Fifth Assessment Report of the Intergovernmental Panel on Climate Change* [Barros, V.R., C.B. Field, D.J. Dokken, M.D. Mastrandrea, K.J. Mach, T.E. Bilir, M. Chatterjee, K.L. Ebi, Y.O. Estrada, R.C. Genova, B. Girma, E.S. Kissel, A.N. Levy, S. MacCracken, P.R. Mastrandrea, and L.L. White (eds.)]. Cambridge University Press, Cambridge, United Kingdom and New York, NY, USA, pp. 1613–1654, doi:10.1017/cbo9781107415386.009.

Nygård, T., T. Naakka, and T. Vihma, 2020: Horizontal Moisture Transport Dominates the Regional Moistening Patterns in the Arctic. *Journal of Climate*, **33(16)**, 6793–6807, doi:10.1175/jcli-d-19-0891.1.

O'Neill, B.C. et al., 2016: The Scenario Model Intercomparison Project (ScenarioMIP) for CMIP6. *Geoscientific Model Development*, **9(9)**, 3461–3482, doi:10.5194/gmd-9-3461-2016.

Odry, J. et al., 2020: Using artificial neural networks to estimate snow water equivalent from snow depth. *Canadian Water Resources Journal*, **45(3)**, 252–268, doi:10.1080/07011784.2020.1796817.

Oh, S.G. and M.S. Suh, 2018: Changes in seasonal and diurnal precipitation types during summer over South Korea in the late twenty-first century (2081–2100) projected by the RegCM4.0 based on four RCP scenarios. *Climate Dynamics*, **51(7–8)**, 3041–3060, doi:10.1007/s00382-017-4063-5.

Olson, R., J.P. Evans, A. Di Luca, and D. Argüeso, 2016: The NARCliM project: model agreement and significance of climate projections. *Climate Research*, **69(3)**, 209–227.

Ongoma, V., H. Chena, and C. Gaoa, 2018: Projected changes in mean rainfall and temperature over east Africa based on CMIP5 models. *International Journal of Climatology*, doi:10.1002/joc.5252.

Onyutha, C., H. Tabari, A. Rutkowska, P. Nyeko-Ogiramoi, and P. Willems, 2016: Comparison of different statistical downscaling methods for climate change rainfall projections over the Lake Victoria basin considering CMIP3 and CMIP5. *Journal of Hydro-Environment Research*, doi:10.1016/j.jher.2016.03.001.

ACCEPTED VERSION SUBJECT TO FINAL EDITS

Orsolini, Y. et al., 2019: Evaluation of snow depth and snow cover over the Tibetan Plateau in global reanalyses using in situ and satellite remote sensing observations. *Cryosphere*, **13(8)**, 2221–2239, doi:10.5194/tc-13-2221-2019.
Osakada, Y. and E. Nakakita, 2018: Future Change of Occurrence Frequency of Baiu Heavy Rainfall and Its Linked Atmospheric Patterns by Multiscale Analysis. *SOLA*, **14**, 79–85, doi:10.2151/sola.2018-014.
Osborn, T.J., C.J. Wallace, I.C. Harris, and T.M. Melvin, 2016: Pattern scaling using ClimGen: monthly-resolution future climate scenarios including changes in the variability of precipitation. *Climatic Change*, **134(3)**, 353–369, doi:10.1007/s10584-015-1509-9.
Osborn, T.J. et al., 2021: Land Surface Air Temperature Variations Across the Globe Updated to 2019: The CRUTEM5 Data Set. *Journal of Geophysical Research: Atmospheres*, **126(2)**, doi:10.1029/2019jd032352.
Ose, T., 2017: Future precipitation changes during summer in East Asia and model dependence in high-resolution MRI-AGCM experiments. *Hydrological Research Letters*, **11(3)**, 168–174, doi:10.3178/hrl.11.168.
Osima, S. et al., 2018: Projected climate over the Greater Horn of Africa under 1.5°C and 2°C global warming. *Environmental Research Letters*, **13(6)**, 065004, doi:10.1088/1748-9326/aaba1b.
Otto, F.E.L. et al., 2015: Factors Other Than Climate Change, Main Drivers of 2014/15 Water Shortage in Southeast Brazil. *Bulletin of the American Meteorological Society*, **96(12)**, S35–S40, doi:10.1175/bams-d-15-00120.1.
Outten, S.D. and I. Esau, 2012: A link between Arctic sea ice and recent cooling trends over Eurasia. *Climatic Change*, **110(3–4)**, 1069–1075, doi:10.1007/s10584-011-0334-z.
Overland, J. et al., 2019: The urgency of Arctic change. *Polar Science*, doi:10.1016/j.polar.2018.11.008.
Overland, J.E., M. Wang, J.E. Walsh, and J.C. Stroeve, 2014: Future Arctic climate changes: Adaptation and mitigation time scales. *Earth's Future*, **2(2)**, 68–74, doi:10.1002/2013ef000162.
Overland, J.E. et al., 2016: Nonlinear response of mid-latitude weather to the changing Arctic. *Nature Climate Change*, **6(11)**, 992–999, doi:10.1038/nclimate3121.
Overly, T.B., R.L. Hawley, V. Helm, E.M. Morris, and R.N. Chaudhary, 2016: Greenland annual accumulation along the EGIG line, 1959–2004, from ASIRAS airborne radar and neutron-probe density measurements. *The Cryosphere*, **10(4)**, 1679–1694, doi:10.5194/tc-10-1679-2016.
Ozturk, T., M.T. Turp, M. Türkeş, and M.L. Kurnaz, 2017: Projected changes in temperature and precipitation climatology of Central Asia CORDEX Region 8 by using RegCM4.3.5. *Atmospheric Research*, **183**, 296–307, doi:10.1016/j.atmosres.2016.09.008.
Ozturk, T., M.T. Turp, M. Türkeş, and M.L. Kurnaz, 2018: Future projections of temperature and precipitation climatology for CORDEX-MENA domain using RegCM4.4. *Atmospheric Research*, **206**, 87–107, doi:10.1016/j.atmosres.2018.02.009.
Pabón-Caicedo, J.D. et al., 2020: Observed and Projected Hydroclimate Changes in the Andes. *Frontiers in Earth Science*, **8**, doi:10.3389/feart.2020.00061.
Pal, S., H.-I. Chang, C.L. Castro, and F. Dominguez, 2019: Credibility of Convection-Permitting Modeling to Improve Seasonal Precipitation Forecasting in the Southwestern United States. *Frontiers in Earth Science*, **7**, 11, doi:10.3389/feart.2019.00011.
Palerme, C. et al., 2014: How much snow falls on the Antarctic ice sheet? *The Cryosphere*, **8(4)**, 1577–1587, doi:10.5194/tc-8-1577-2014.
Palerme, C. et al., 2017: Evaluation of current and projected Antarctic precipitation in CMIP5 models. *Climate Dynamics*, **48(1–2)**, 225–239, doi:10.1007/s00382-016-3071-1.
Palomino-Lemus, R., S. Córdoba-Machado, S.R. Gámiz-Fortis, Y. Castro-Díez, and M.J. Esteban-Parra, 2015: Summer precipitation projections over northwestern South America from CMIP5 models. *Global and Planetary Change*, **131**, 11–23, doi:10.1016/j.gloplacha.2015.05.004.
Palomino-Lemus, R., S. Córdoba-Machado, S.R. Gámiz-Fortis, Y. Castro-Díez, and M.J. Esteban-Parra, 2017: Climate change projections of boreal summer precipitation over tropical America by using statistical downscaling from CMIP5 models. *Environmental Research Letters*, **12(12)**, 124011, doi:10.1088/1748-9326/aa9bf7.
Palomino-Lemus, R., S. Córdoba-Machado, S.R. Gámiz-Fortis, Y. Castro-Díez, and M.J. Esteban-Parra, 2018: High-resolution boreal winter precipitation projections over tropical America from CMIP5 models. *Climate Dynamics*, **51(5–6)**, 1773–1792, doi:10.1007/s00382-017-3982-5.
Panitz, H.J., A. Dosio, M. Büchner, D. Lüthi, and K. Keuler, 2014: COSMO-CLM (CCLM) climate simulations over CORDEX-Africa domain: Analysis of the ERA-Interim driven simulations at 0.44° and 0.22° resolution. *Climate Dynamics*, doi:10.1007/s00382-013-1834-5.
Panthou, G., A. Mailhot, E. Laurence, and G. Talbot, 2014: Relationship between surface temperature and extreme rainfalls: A multi-time-scale and event-based analysis. *Journal of Hydrometeorology*, doi:10.1175/jhm-d-14-0020.1.
Panthou, G., M. Vrac, P. Drobinski, S. Bastin, and L. Li, 2018a: Impact of model resolution and Mediterranean sea coupling on hydrometeorological extremes in RCMs in the frame of HyMeX and MED-CORDEX. *Climate Dynamics*, **51(3)**, 915–932, doi:10.1007/s00382-016-3374-2.
Panthou, G. et al., 2018b: Rainfall intensification in tropical semi-arid regions: The Sahelian case. *Environmental Research Letters*, doi:10.1088/1748-9326/aac334.
Park, B.-J. et al., 2017: Long-Term Warming Trends in Korea and Contribution of Urbanization: An Updated

ACCEPTED VERSION SUBJECT TO FINAL EDITS

Assessment. *Journal of Geophysical Research: Atmospheres*, **122(20)**, 10,610–637,654, doi:10.1002/2017jd027167.
Park, C. et al., 2016: Evaluation of multiple regional climate models for summer climate extremes over East Asia. *Climate Dynamics*, **46(7)**, 2469–2486, doi:10.1007/s00382-015-2713-z.
Park, C. et al., 2020: Evaluation of summer precipitation over Far East Asia and South Korea simulated by multiple regional climate models. *International Journal of Climatology*, **40(4)**, 2270–2284, doi:10.1002/joc.6331.
Partasenok, I.S., B. Geyer, and V.I. Melnik, 2015: Studies of possible scenarios of changes in the climate of Belarus based on ensemble concep. *Proceedings of Hydrometcentre of Russia*, **358**, 99–111.
Pavlidis, V. et al., 2020: Investigating the sensitivity to resolving aerosol interactions in downscaling regional model experiments with WRFv3.8.1 over Europe. *Geoscientific Model Development*, **13(6)**, 2511–2532, doi:10.5194/gmd-13-2511-2020.
Peel, M.C., B.L. Finlayson, and T.A. McMahon, 2007: Updated world map of the Köppen-Geiger climate classification. *Hydrology and Earth System Sciences*, **11(5)**, 1633–1644, doi:10.5194/hess-11-1633-2007.
Peeters, B. et al., 2019: Spatiotemporal patterns of rain-on-snow and basal ice in high Arctic Svalbard: detection of a climate-cryosphere regime shift. *Environmental Research Letters*, **14(1)**, 15002, doi:10.1088/1748-9326/aaefb3.
Peña-Angulo, D. et al., 2020: Long-term precipitation in Southwestern Europe reveals no clear trend attributable to anthropogenic forcing. *Environmental Research Letters*, **15(9)**, 094070, doi:10.1088/1748-9326/ab9c4f.
Peng, D. and T. Zhou, 2017: Why was the arid and semiarid northwest China getting wetter in the recent decades? *Journal of Geophysical Research: Atmospheres*, **122(17)**, 9060–9075, doi:10.1002/2016jd026424.
Peng, X. et al., 2019: Evaluation and quantification of surface air temperature over Eurasia based on CMIP5 models. *Climate Research*, **77(2)**, 167–180, doi:10.3354/cr01549.
Perdigón-Morales, J., R. Romero-Centeno, P.O. Pérez, and B.S. Barrett, 2018: The midsummer drought in Mexico: perspectives on duration and intensity from the CHIRPS precipitation database. *International Journal of Climatology*, **38(5)**, 2174–2186, doi:10.1002/joc.5322.
Perevedentsev, Y.P., A.A. Vasil'ev, K.M. Shantalinskii, and V. Gur'yanov, 2017: Long-term variations in surface air pressure and surface air temperature in the Northern Hemisphere mid-latitudes. *Russian Meteorology and Hydrology*, **42(7)**, 461–470, doi:10.3103/s1068373917070056.
Perry, S.J., S. McGregor, A. Sen Gupta, M.H. England, and N. Maher, 2020: Projected late 21st century changes to the regional impacts of the El Niño-Southern Oscillation. *Climate Dynamics*, **54(1–2)**, 395–412, doi:10.1007/s00382-019-05006-6.
Pham, T., J. Brauch, B. Früh, and B. Ahrens, 2017: Simulation of snowbands in the Baltic Sea area with the coupled atmosphere-ocean-ice model COSMO-CLM/NEMO. *Meteorologische Zeitschrift*, **26(1)**, 71–82, doi:10.1127/metz/2016/0775.
Philandras, C.M., P.T. Nastos, I.N. Kapsomenakis, and C.C. Repapis, 2015: Climatology of upper air temperature in the Eastern Mediterranean region. *Atmospheric Research*, **152**, 29–42, doi:10.1016/j.atmosres.2013.12.002.
Pichelli, E. et al., 2021: The first multi-model ensemble of regional climate simulations at kilometer-scale resolution part 2: historical and future simulations of precipitation. *Climate Dynamics*, doi:10.1007/s00382-021-05657-4.
Pinto, I., C. Jack, and B. Hewitson, 2018: Process-based model evaluation and projections over southern Africa from Coordinated Regional Climate Downscaling Experiment and Coupled Model Intercomparison Project Phase 5 models. *International Journal of Climatology*, doi:10.1002/joc.5666.
Pinto, I. et al., 2016: Evaluation and projections of extreme precipitation over southern Africa from two CORDEX models. *Climatic Change*, doi:10.1007/s10584-015-1573-1.
Pithan, F. and T. Mauritsen, 2014: Arctic amplification dominated by temperature feedbacks in contemporary climate models. *Nature Geoscience*, **7(3)**, 181–184, doi:10.1038/ngeo2071.
Planos Gutiérrez, E.O., R. Rivero Vega, and V. Guevara Velazco (eds.), 2012: *Impacto del Cambio Climático y Medidas de Adaptación en Cuba*. Agencia de Medio Ambiente, Ministerio de Ciencia Tecnología y Medio Ambiente, La Habana, Cuba, 520 pp.
Poan, E.D. et al., 2018: Investigating added value of regional climate modeling in North American winter storm track simulations. *Climate Dynamics*, **50(5)**, 1799–1818, doi:10.1007/s00382-017-3723-9.
Poli, P. et al., 2016: ERA-20C: An Atmospheric Reanalysis of the Twentieth Century. *Journal of Climate*, **29(11)**, 4083–4097, doi:10.1175/jcli-d-15-0556.1.
Post, E. et al., 2019: The polar regions in a 2°C warmer world. *Science Advances*, **5(12)**, eaaw9883, doi:10.1126/sciadv.aaw9883.
Post, V.E.A., A.L. Bosserelle, S.C. Galvis, P.J. Sinclair, and A.D. Werner, 2018: On the resilience of small-island freshwater lenses: Evidence of the long-term impacts of groundwater abstraction on Bonriki Island, Kiribati. *Journal of Hydrology*, **564**, 133–148.
Prakash, S., 2019: Performance assessment of CHIRPS, MSWEP, SM2RAIN-CCI, and TMPA precipitation products across India. *Journal of Hydrology*, doi:10.1016/j.jhydrol.2019.01.036.
Prakash, S. et al., 2014: Comparison of TMPA-3B42 Versions 6 and 7 Precipitation Products with Gauge-Based Data over India for the Southwest Monsoon Period. *Journal of Hydrometeorology*, **16(1)**, 346–362,

ACCEPTED VERSION SUBJECT TO FINAL EDITS

doi:10.1175/jhm-d-14-0024.1.
Prein, A., R. Rasmussen, and G. Stephens, 2017: Challenges and Advances in Convection Permitting Climate Modeling. *Bulletin of the American Meteorological Society*, **May**, 1027–1029, doi:10.1175/bams-d-16-0263.1.
Prein, A.F. and A. Gobiet, 2017: Impacts of uncertainties in European gridded precipitation observations on regional climate analysis. *International Journal of Climatology*, **37(1)**, 305–327, doi:10.1002/joc.4706.
Prein, A.F., M.S. Bukovsky, L.O. Mearns, C.L. Bruyère, and J.M. Done, 2019: Simulating North American Weather Types With Regional Climate Models. *Frontiers in Environmental Science*, **7**, 36, doi:10.3389/fenvs.2019.00036.
Prein, A.F. et al., 2015: A review on regional convection-permitting climate modeling: Demonstrations, prospects, and challenges. *Reviews of Geophysics*, **53(2)**, 323–361, doi:10.1002/2014rg000475.
Prein, A.F. et al., 2016: Precipitation in the EURO-CORDEX 0.11° and 0.44° simulations: high resolution, high benefits? *Climate Dynamics*, **46(1–2)**, 383–412, doi:10.1007/s00382-015-2589-y.
Prein, A.F. et al., 2017: Increased rainfall volume from future convective storms in the US. *Nature Climate Change*, **7(12)**, 880–884, doi:10.1038/s41558-017-0007-7.
Previdi, M. and L.M. Polvani, 2016: Anthropogenic impact on Antarctic surface mass balance, currently masked by natural variability, to emerge by mid-century. *Environmental Research Letters*, **11(9)**, doi:10.1088/1748-9326/11/9/094001.
Przybylak, R. and P. Wyszyński, 2020: Air temperature changes in the Arctic in the period 1951–2015 in the light of observational and reanalysis data. *Theoretical and Applied Climatology*, **139(1–2)**, 75–94, doi:10.1007/s00704-019-02952-3.
Pulliainen, J. et al., 2020: Patterns and trends of Northern Hemisphere snow mass from 1980 to 2018. *Nature*, **581(7808)**, 294–298, doi:10.1038/s41586-020-2258-0.
Rae, J.G.L. et al., 2012: Greenland ice sheet surface mass balance: evaluating simulations and making projections with regional climate models. *The Cryosphere*, **6(6)**, 1275–1294, doi:10.5194/tc-6-1275-2012.
Raghavan, S., M.T. Vu, and S.Y. Liong, 2016: Regional climate simulations over Vietnam using the WRF model. *Theoretical and Applied Climatology*, **126(1–2)**, 161–182, doi:10.1007/s00704-015-1557-0.
Raghavan, S., J. Liu, N.S. Nguyen, M.T. Vu, and S.-Y. Liong, 2018: Assessment of CMIP5 historical simulations of rainfall over Southeast Asia. *Theoretical and Applied Climatology*, **132(3–4)**, 989–1002, doi:10.1007/s00704-017-2111-z.
Rahimi, M. and S.S. Fatemi, 2019: Mean versus Extreme Precipitation Trends in Iran over the Period 1960–2017. *Pure and Applied Geophysics*, **176(8)**, 3717–3735, doi:10.1007/s00024-019-02165-9.
Rahmawati, N. and M.W. Lubczynski, 2018: Validation of satellite daily rainfall estimates in complex terrain of Bali Island, Indonesia. *Theoretical and Applied Climatology*, **134(1–2)**, 513–532, doi:10.1007/s00704-017-2290-7.
Ramanathan, V. and G. Carmichael, 2008: Global and regional climate changes due to black carbon. *Nature Geoscience*, **1(4)**, 221–227, doi:10.1038/ngeo156.
Ramanathan, V. et al., 2007: Atmospheric brown clouds: Hemispherical and regional variations in long-range transport, absorption, and radiative forcing. *Journal of Geophysical Research Atmospheres*, **112(22)**, 1–26, doi:10.1029/2006jd008124.
Ramarao, M.V.S. et al., 2018: On observed aridity changes over the semiarid regions of India in a warming climate. *Theoretical and Applied Climatology*, 1–10, doi:10.1007/s00704-018-2513-6.
Rana, A. et al., 2020: Contrasting regional and global climate simulations over South Asia. *Climate Dynamics*, **54(5–6)**, 2883–2901, doi:10.1007/s00382-020-05146-0.
Rao, V.B., S.H. Franchito, C.M.E. Santo, and M.A. Gan, 2016: An update on the rainfall characteristics of Brazil: seasonal variations and trends in 1979-2011. *International Journal of Climatology*, **36(1)**, 291–302, doi:10.1002/joc.4345.
Rapaić, M., R. Brown, M. Markovic, and D. Chaumont, 2015: An Evaluation of Temperature and Precipitation Surface-Based and Reanalysis Datasets for the Canadian Arctic, 1950-2010. *Atmosphere - Ocean*, **53(3)**, 283–303, doi:10.1080/07055900.2015.1045825.
Rasmussen, R. et al., 2014: Climate Change Impacts on the Water Balance of the Colorado Headwaters: High-Resolution Regional Climate Model Simulations. *Journal of Hydrometeorology*, **15(3)**, 1091–1116, doi:10.1175/jhm-d-13-0118.1.
Ratna, S.B., J.V. Ratnam, S.K. Behera, F.T. Tangang, and T. Yamagata, 2017: Validation of the WRF regional climate model over the subregions of Southeast Asia: climatology and interannual variability. *Climate Research*, **71(3)**, 263–280, doi:10.3354/cr01445.
Rauniyar, S.P. and S.B. Power, 2020: The Impact of Anthropogenic Forcing and Natural Processes on Past, Present, and Future Rainfall over Victoria, Australia. *Journal of Climate*, **33(18)**, 8087–8106, doi:10.1175/jcli-d-19-0759.1.
Rauscher, S.A., F. Giorgi, N.S. Diffenbaugh, and A. Seth, 2008: Extension and Intensification of the Meso-American mid-summer drought in the twenty-first century. *Climate Dynamics*, **31(5)**, 551–571, doi:10.1007/s00382-007-0359-1.
Rauthe, M., H. Steiner, U. Riediger, A. Mazurkiewicz, and A. Gratzki, 2013: A Central European precipitation

ACCEPTED VERSION SUBJECT TO FINAL EDITS

climatology – Part I: Generation and validation of a high-resolution gridded daily data set (HYRAS). *Meteorologische Zeitschrift*, **22(3)**, 235–256, doi:10.1127/0941-2948/2013/0436.
Reboita, M.S., R.P. da Rocha, C.G. Dias, and R.Y. Ynoue, 2014a: Climate Projections for South America: RegCM3 Driven by HadCM3 and ECHAM5. *Advances in Meteorology*, **2014**, 1–17, doi:10.1155/2014/376738.
Reboita, M.S., R.P. da Rocha, C.G. Dias, and R.Y. Ynoue, 2014b: Climate Projections for South America: RegCM3 Driven by HadCM3 and ECHAM5. *Advances in Meteorology*, **2014**, 1–17, doi:10.1155/2014/376738.
Reboita, M.S. et al., 2020: Future changes in the wintertime cyclonic activity over the CORDEX-CORE southern hemisphere domains in a multi-model approach. *Climate Dynamics*, doi:10.1007/s00382-020-05317-z.
Reisinger, A. et al., 2014: Australasia. In: *Climate Change 2014: Impacts, Adaptation, and Vulnerability. Part B: Regional Aspects. Contribution of Working Group II to the Fifth Assessment Report of the Intergovernmental Panel on Climate Change* [Barros, V.R., C.B. Field, D.J. Dokken, M.D. Mastrandrea, K.J. Mach, T.E. Bilir, M. Chatterjee, K.L. Ebi, Y.O. Estrada, R.C. Genova, B. Girma, E.S. Kissel, A.N. Levy, S. MacCracken, P.R. Mastrandrea, and L.L. White (eds.)]. Cambridge University Press, Cambridge, United Kingdom and NewYork, NY, USA, pp. 1371–1438, doi:10.1017/cbo9781107415386.005.
Ren, Y., B. Zhou, L. Song, and Y. Xiao, 2017: Interannual variability of western North Pacific subtropical high, East Asian jet and East Asian summer precipitation: CMIP5 simulation and projection. *Quaternary International*, **440**, 64–70, doi:10.1016/j.quaint.2016.08.033.
Retamales-Muñoz, G., C. Durán-Alarcón, and C. Mattar, 2019: Recent land surface temperature patterns in Antarctica using satellite and reanalysis data. *Journal of South American Earth Sciences*, **95**, 102304, doi:10.1016/j.jsames.2019.102304.
Retchless, D.P. and C.A. Brewer, 2016: Guidance for representing uncertainty on global temperature change maps. *International Journal of Climatology*, **36(3)**, 1143–1159, doi:10.1002/joc.4408.
Reyer, C.P.O. et al., 2017: Climate change impacts in Central Asia and their implications for development. *Regional Environmental Change*, **17(6)**, 1639–1650, doi:10.1007/s10113-015-0893-z.
Rhoades, A.M., A.D. Jones, and P.A. Ullrich, 2018: Assessing Mountains as Natural Reservoirs With a Multimetric Framework. *Earth's Future*, **6(9)**, 1221–1241, doi:10.1002/2017ef000789.
Rignot, E. et al., 2019: Four decades of Antarctic Ice Sheet mass balance from 1979–2017. *Proceedings of the National Academy of Sciences*, **116(4)**, 1095–1103, doi:10.1073/pnas.1812883116.
Ringard, J. et al., 2016: The intensification of thermal extremes in west Africa. *Global and Planetary Change*, doi:10.1016/j.gloplacha.2015.12.009.
Rinke, A. et al., 2019: Trends of vertically integrated water vapor over the Arctic during 1979-2016: Consistent moistening all over? *Journal of Climate*, **32(18)**, 6097–6116, doi:10.1175/jcli-d-19-0092.1.
Rivera, J.A. and G. Arnould, 2020: Evaluation of the ability of CMIP6 models to simulate precipitation over Southwestern South America: Climatic features and long-term trends (1901–2014). *Atmospheric Research*, **241**, 104953, doi:10.1016/j.atmosres.2020.104953.
Rizzi, J., I.B. Nilsen, J.H. Stagge, K. Gisnås, and L.M. Tallaksen, 2018: Five decades of warming: Impacts on snow cover in Norway. *Hydrology Research*, **49(3)**, 670–688, doi:10.2166/nh.2017.051.
RMetS, 2019: Warming Stripes show the changing climate across the globe. Royal Meteorological Soceity (RMetS), Reading, UK. Retrieved from: www.rmets.org/news/warming-stripes-show-changing-climate-across-globe.
Roach, L.A. et al., 2020: Antarctic Sea Ice Area in CMIP6. *Geophysical Research Letters*, **47(9)**, 1–10, doi:10.1029/2019gl086729.
Robel, A.A. and A.F. Banwell, 2019: A Speed Limit on Ice Shelf Collapse Through Hydrofracture. *Geophysical Research Letters*, **46(21)**, 12092–12100, doi:10.1029/2019gl084397.
Roberts, M.J. et al., 2018: The Benefits of Global High Resolution for Climate Simulation: Process Understanding and the Enabling of Stakeholder Decisions at the Regional Scale. *Bulletin of the American Meteorological Society*, **99(11)**, 2341–2359, doi:10.1175/bams-d-15-00320.1.
Roehrig, R., D. Bouniol, F. Guichard, F. Hourdin, and J.L. Redelsperger, 2013: The present and future of the west african monsoon: A process-oriented assessment of CMIP5 simulations along the AMMA transect. *Journal of Climate*, doi:10.1175/jcli-d-12-00505.1.
Rohde, R.A. and Z. Hausfather, 2020: The Berkeley Earth Land/Ocean Temperature Record. *Earth System Science Data*, **12(4)**, 3469–3479, doi:10.5194/essd-12-3469-2020.
Rosenzweig, C. et al., 2017: Assessing inter-sectoral climate change risks: the role of ISIMIP. *Environmental Research Letters*, **12(1)**, 010301, doi:10.1088/1748-9326/12/1/010301.
Roshydromet, 2019: *A Report on Climate Features on the Territory of the Russian Federation in 2018*. Russian Federal Service for Hydrometeorology and Environmental Monitoring (Roshydromet), Moscow, Russia, 79 pp.
Roussel, M.-L., F. Lemonnier, C. Genthon, and G. Krinner, 2020: Brief communication: Evaluating Antarctic precipitation in ERA5 and CMIP6 against CloudSat observations. *The Cryosphere*, **14(8)**, 2715–2727, doi:10.5194/tc-14-2715-2020.
Rowell, D.P., 2013: Simulating SST teleconnections to Africa: What is the state of the art? *Journal of Climate*, doi:10.1175/jcli-d-12-00761.1.
Rowell, D.P., B.B.B. Booth, S.E. Nicholson, and P. Good, 2015: Reconciling past and future rainfall trends over East

ACCEPTED VERSION SUBJECT TO FINAL EDITS

Africa. *Journal of Climate*, doi:10.1175/jcli-d-15-0140.1.
Rowell, D.P., C.A. Senior, M. Vellinga, and R.J. Graham, 2016: Can climate projection uncertainty be constrained over Africa using metrics of contemporary performance? *Climatic Change*, doi:10.1007/s10584-015-1554-4.
Roxy, M.K. et al., 2015: Drying of Indian subcontinent by rapid Indian Ocean warming and a weakening land-sea thermal gradient. *Nature Communications*, **6**, 7423, doi:10.1038/ncomms8423.
Roxy, M.K. et al., 2017: A threefold rise in widespread extreme rain events over central India. *Nature Communications*, **8(1)**, doi:10.1038/s41467-017-00744-9.
Rozante, J.R., E.R. Gutierrez, A.A. Fernandes, and D.A. Vila, 2020: Performance of precipitation products obtained from combinations of satellite and surface observations. *International Journal of Remote Sensing*, **41(19)**, 7585–7604, doi:10.1080/01431161.2020.1763504.
Rupp, D.E., P.W. Mote, N.L. Bindoff, P. Stott, and D. Robinson, 2013: Detection and Attribution of Observed Changes in Northern Hemisphere Spring Snow Cover. *Journal of Climate*, **26(18)**, 6904–6914, doi:10.1175/jcli-d-12-00563.1.
Ruscica, R.C., C.G. Menéndez, and A.A. Sörensson, 2016: Land surface-atmosphere interaction in future South American climate using a multi-model ensemble. *Atmospheric Science Letters*, **17(2)**, 141–147, doi:10.1002/asl.635.
Russo, E., I. Kirchner, S. Pfahl, M. Schaap, and U. Cubasch, 2019: Sensitivity studies with the Regional Climate Model COSMO-CLM 5.0 over the CORDEX Central Asia Domain. *Geoscientific Model Development Discussions*, **2019**, 1–33, doi:10.5194/gmd-2019-22.
Rutgersson, A. et al., 2015: Recent Change – Atmosphere. *Second Assessment of Climate Change for the Baltic Sea Basin*, 69–97, doi:10.1007/978-3-319-16006-1_4.
Ruti, P.M. et al., 2016: Med-CORDEX initiative for Mediterranean climate studies. *Bulletin of the American Meteorological Society*, **97(7)**, doi:10.1175/bams-d-14-00176.1.
Ryu, J.-H. and K. Hayhoe, 2014: Understanding the sources of Caribbean precipitation biases in CMIP3 and CMIP5 simulations. *Climate Dynamics*, **42(11)**, 3233–3252, doi:10.1007/s00382-013-1801-1.
Sa'adi, Z., S. Shahid, T. Ismail, E.-S. Chung, and X.-J. Wang, 2017: Trends analysis of rainfall and rainfall extremes in Sarawak, Malaysia using modified Mann–Kendall test. *Meteorology and Atmospheric Physics*, 1–15, doi:10.1007/s00703-017-0564-3.
Sabin, T.P. et al., 2013: High resolution simulation of the South Asian monsoon using a variable resolution global climate model. *Climate Dynamics*, **41(1)**, 173–194, doi:10.1007/s00382-012-1658-8.
Saeed, F. and H. Athar, 2018: Assessment of simulated and projected climate change in Pakistan using IPCC AR4-based AOGCMs. *Theoretical and Applied Climatology*, **134(3–4)**, 967–980, doi:10.1007/s00704-017-2320-5.
Safarianzengir, V. et al., 2020: Monitoring and Analysis of Changes in the Depth and Surface Area Snow of the Mountains in Iran Using Remote Sensing Data. *Journal of the Indian Society of Remote Sensing*, **48(11)**, 1479–1494, doi:10.1007/s12524-020-01145-0.
Saha, A., S. Ghosh, A.S. Sahana, and E.P. Rao, 2014: Failure of CMIP5 climate models in simulating post-1950 decreasing trend of Indian monsoon. *Geophysical Research Letters*, **41(20)**, 7323–7330, doi:10.1002/2014gl061573.
Salinger, M.J., B.B. Fitzharris, and T. Chinn, 2019: Atmospheric circulation and ice volume changes for the small and medium glaciers of New Zealand's Southern Alps mountain range 1977–2018. *International Journal of Climatology*, **39(11)**, 4274–4287, doi:10.1002/joc.6072.
Salinger, M.J., S. McGree, F. Beucher, S.B. Power, and F. Delage, 2014: A new index for variations in the position of the South Pacific convergence zone 1910/11-2011/2012. *Climate Dynamics*, **43(3–4)**, 881–892, doi:10.1007/s00382-013-2035-y.
Salio, P., M.P. Hobouchian, Y. García Skabar, and D. Vila, 2015: Evaluation of high-resolution satellite precipitation estimates over southern South America using a dense rain gauge network. *Atmospheric Research*, doi:10.1016/j.atmosres.2014.11.017.
Salman, S.A., S. Shahid, T. Ismail, E.-S. Chung, and A.M. Al-Abadi, 2017: Long-term trends in daily temperature extremes in Iraq. *Atmospheric Research*, **198**, 97–107, doi:10.1016/j.atmosres.2017.08.011.
Salman, S.A. et al., 2018: Unidirectional trends in daily rainfall extremes of Iraq. *Theoretical and Applied Climatology*, **134(3–4)**, 1165–1177, doi:10.1007/s00704-017-2336-x.
Sánchez, E. et al., 2015: Regional climate modelling in CLARIS-LPB: a concerted approach towards twentyfirst century projections of regional temperature and precipitation over South America. *Climate Dynamics*, **45(7–8)**, 2193–2212, doi:10.1007/s00382-014-2466-0.
Sanchez-Gomez, E. and S. Somot, 2018: Impact of the internal variability on the cyclone tracks simulated by a regional climate model over the Med-CORDEX domain. *Climate Dynamics*, **51(3)**, doi:10.1007/s00382-016-3394-y.
Sanchez-Lorenzo, A. et al., 2015: Reassessment and update of long-term trends in downward surface shortwave radiation over Europe (1939–2012). *Journal of Geophysical Research: Atmospheres*, **120(18)**, 9555–9569, doi:10.1002/2015jd023321.
Sanjay, J., M.V.S. Ramarao, M. Mujumdar, and R. Krishnan, 2017: Regional Climate Change Scenarios. In: *Observed Climate Variability and Change over the Indian Region* [Rajeevan, M. and S. Nayak (eds.)]. Springer,

ACCEPTED VERSION SUBJECT TO FINAL EDITS

Singapore, pp. 285–304, doi:10.1007/978-981-10-2531-0_16.
Sanogo, S. et al., 2015: Spatio-temporal characteristics of the recent rainfall recovery in West Africa. *International Journal of Climatology*, **35(15)**, 4589–4605, doi:10.1002/joc.4309.
Santer, B.D. et al., 2008: Consistency of modelled and observed temperature trends in the tropical troposphere. *International Journal of Climatology*, **28(13)**, 1703–1722, doi:10.1002/joc.1756.
Saros, J.E. et al., 2019: Arctic climate shifts drive rapid ecosystem responses across the West Greenland landscape. *Environmental Research Letters*, **14(7)**, 074027, doi:10.1088/1748-9326/ab2928.
Satgé, F., D. Ruelland, M.-P. Bonnet, J. Molina, and R. Pillco, 2019: Consistency of satellite-based precipitation products in space and over time compared with gauge observations and snow-hydrological modelling in the Lake Titicaca region. *Hydrol. Earth Syst. Sci.*, **23(1)**, 595–619, doi:10.5194/hess-23-595-2019.
Scarchilli, C. et al., 2020: Characterization of snowfall estimated by in situ and ground-based remote-sensing observations at Terra Nova Bay, Victoria Land, Antarctica. *Journal of Glaciology*, **66(260)**, 1006–1023, doi:10.1017/jog.2020.70.
Schaller, N. et al., 2016: Human influence on climate in the 2014 southern England winter floods and their impacts. *Nature Climate Change*, **6(6)**, 627–634, doi:10.1038/nclimate2927.
Schiermeier, Q., 2018: Droughts, heatwaves and floods: How to tell when climate change is to blame. *Nature*, **560**, 20–22, doi:10.1038/d41586-018-05849-9.
Schilling, J., K.P. Freier, E. Hertig, and J. Scheffran, 2012: Climate change, vulnerability and adaptation in North Africa with focus on Morocco. *Agriculture, Ecosystems and Environment*, doi:10.1016/j.agee.2012.04.021.
Schmucki, E., C. Marty, C. Fierz, and M. Lehning, 2015: Simulations of 21st century snow response to climate change in Switzerland from a set of RCMs. *International Journal of Climatology*, **35(11)**, 3262–3273, doi:10.1002/joc.4205.
Schneider, D.P., J.E. Kay, and J. Lenaerts, 2020: Improved clouds over Southern Ocean amplify Antarctic precipitation response to ozone depletion in an earth system model. *Climate Dynamics*, **55(5–6)**, 1665–1684, doi:10.1007/s00382-020-05346-8.
Schneider, U. et al., 2011: GPCC Full Data Reanalysis Version 6.0 at 1.0°: Monthly Land-Surface Precipitation from Rain-Gauges built on GTS-based and Historic Data. , doi:10.5676/dwd_gpcc/fd_m_v6_100.
Schwingshackl, C. et al., 2019: Regional climate model projections underestimate future warming due to missing plant physiological CO 2 response. *Environmental Research Letters*, **14(11)**, 114019, doi:10.1088/1748-9326/ab4949.
Scott, R.C., J.P. Nicolas, D.H. Bromwich, J.R. Norris, and D. Lubin, 2019: Meteorological Drivers and Large-Scale Climate Forcing of West Antarctic Surface Melt. *Journal of Climate*, **32(3)**, 665–684, doi:10.1175/jcli-d-18-0233.1.
Screen, J.A. and I. Simmonds, 2010: Increasing fall-winter energy loss from the Arctic Ocean and its role in Arctic temperature amplification. *Geophysical Research Letters*, doi:10.1029/2010gl044136.
Sellami, H., S. Benabdallah, I. La Jeunesse, and M. Vanclooster, 2016: Quantifying hydrological responses of small Mediterranean catchments under climate change projections. *Science of the Total Environment*, doi:10.1016/j.scitotenv.2015.07.006.
Sellar, A.A. et al., 2019: UKESM1: Description and evaluation of the UK Earth System Model. *Journal of Advances in Modeling Earth Systems*, **11(12)**, 4513–4558, doi:10.1029/2019ms001739.
Semenov, V.A., 2016: Link between anomalously cold winters in Russia and sea-ice decline in the Barents Sea. *Izvestiya, Atmospheric and Oceanic Physics*, **52(3)**, 225–233, doi:10.1134/s0001433816030105.
Semenov, V.A., I.I. Mokhov, and M. Latif, 2012: Influence of the ocean surface temperature and sea ice concentration on regional climate changes in Eurasia in recent decades. *Izvestiya, Atmospheric and Oceanic Physics*, **48(4)**, 355–372, doi:10.1134/s0001433812040135.
Seneviratne, S.I. and M. Hauser, 2020: Regional Climate Sensitivity of Climate Extremes in CMIP6 Versus CMIP5 Multimodel Ensembles. *Earth's Future*, **8(9)**, doi:10.1029/2019ef001474.
Seneviratne, S.I. et al., 2012: Changes in Climate Extremes and their Impacts on the Natural Physical Environment. In: *Managing the Risks of Extreme Events and Disasters to Advance Climate Change Adaptation. A Special Report of Working Groups I and II of the Intergovernmental Panel on Climate Change* [Field, C.B., V. Barros, T.F. Stocker, Q. Dahe, D.J. Dokken, K.L. Ebi, M.D. Mastrandrea, K.J. Mach, G.-K. Plattner, S.K. Allen, M. Tignor, and P.M. Midgley (eds.)]. Cambridge University Press, Cambridge, United Kingdom and New York, NY, USA, pp. 109–230, doi:10.1017/cbo9781139177245.006.
Šeparović, L. et al., 2013: Present climate and climate change over North America as simulated by the fifth-generation Canadian regional climate model. *Climate Dynamics*, **41(11–12)**, 3167–3201, doi:10.1007/s00382-013-1737-5.
Seroussi, H. et al., 2020: ISMIP6 Antarctica: a multi-model ensemble of the Antarctic ice sheet evolution over the 21st century. *The Cryosphere*, **14(9)**, 3033–3070, doi:10.5194/tc-14-3033-2020.
Serreze, M.C. and R.G. Barry, 2011: Processes and impacts of Arctic amplification: A research synthesis. *Global and Planetary Change*, **77(1–2)**, 85–96, doi:10.1016/j.gloplacha.2011.03.004.
Sharafi, S. and N. Mir Karim, 2020: Investigating trend changes of annual mean temperature and precipitation in Iran. *Arabian Journal of Geosciences*, **13(16)**, 759, doi:10.1007/s12517-020-05695-y.

ACCEPTED VERSION
SUBJECT TO FINAL EDITS

Sharma, A., H.-P. Huang, P. Zavialov, and V. Khan, 2018: Impact of Desiccation of Aral Sea on the Regional Climate of Central Asia Using WRF Model. *Pure and Applied Geophysics*, **175(1)**, 465–478, doi:10.1007/s00024-017-1675-y.

Shepherd, T.G. et al., 2018: Storylines: an alternative approach to representing uncertainty in physical aspects of climate change. *Climatic Change*, **151(3–4)**, 555–571, doi:10.1007/s10584-018-2317-9.

Sherstyukov, B.G., 2016: The climatic conditions of the Arctic and new approaches to the forecast of the climate change. *Арктика и Север*, 35–60, doi:10.17238/issn2221-2698.2016.24.39.

Shin, S.-H. and J.-Y. Moon, 2018: Prediction Skill for the East Asian Winter Monsoon Based on APCC Multi-Models. *Atmosphere* , **9(8)**, doi:10.3390/atmos9080300.

Shongwe, M.E. et al., 2015: An evaluation of CORDEX regional climate models in simulating precipitation over Southern Africa. *Atmospheric Science Letters*, doi:10.1002/asl2.538.

Shultz, J.M. et al., 2019: Risks, Health Consequences, and Response Challenges for Small-Island-Based Populations: Observations From the 2017 Atlantic Hurricane Season. *Disaster Medicine and Public Health Preparedness*, **13(01)**, 5–17, doi:10.1017/dmp.2018.28.

Sierra, J.P., P.A. Arias, and S.C. Vieira, 2015: Precipitation over Northern South America and Its Seasonal Variability as Simulated by the CMIP5 Models. *Advances in Meteorology*, **2015**, 1–22, doi:10.1155/2015/634720.

Sierra, J.P., P.A. Arias, S.C. Vieira, and J. Agudelo, 2018: How well do CMIP5 models simulate the low-level jet in western Colombia? *Climate Dynamics*, **51(5–6)**, 2247–2265, doi:10.1007/s00382-017-4010-5.

Siew, J.H., F.T. Tangang, and L. Juneng, 2013: Evaluation of CMIP5 coupled atmosphere-ocean general circulation models and projection of the Southeast Asian winter monsoon in the 21st century. *International Journal of Climatology*, **34(9)**, n/a–n/a, doi:10.1002/joc.3880.

Silber, I. et al., 2019: Persistent Supercooled Drizzle at Temperatures Below -25°C Observed at McMurdo Station, Antarctica. *Journal of Geophysical Research: Atmospheres*, **124(20)**, 10878–10895, doi:10.1029/2019jd030882.

Sillmann, J., V. Kharin, X. Zhang, F.W. Zwiers, and D. Bronaugh, 2013: Climate extremes indices in the CMIP5 multimodel ensemble: Part 1. Model evaluation in the present climate. *Journal of Geophysical Research: Atmospheres*, **118(4)**, 1716–1733, doi:10.1002/jgrd.50203.

Silvestri, G. and C. Vera, 2009: Nonstationary Impacts of the Southern Annular Mode on Southern Hemisphere Climate. *Journal of Climate*, **22(22)**, 6142–6148, doi:10.1175/2009jcli3036.1.

Singh, D., M. Tsiang, B. Rajaratnam, and N.S. Diffenbaugh, 2014: Observed changes in extreme wet and dry spells during the South Asian summer monsoon season. *Nature Climate Change*, **4**, 456.

Singh, M.S., Z. Kuang, E.D. Maloney, W.M. Hannah, and B.O. Wolding, 2017: Increasing potential for intense tropical and subtropical thunderstorms under global warming. *Proceedings of the National Academy of Sciences of the United States of America*, **114(44)**, 11657–11662, doi:10.1073/pnas.1707603114.

Singh, S., S. Ghosh, A.S. Sahana, H. Vittal, and S. Karmakar, 2017: Do dynamic regional models add value to the global model projections of Indian monsoon? *Climate Dynamics*, **48(3–4)**, 1375–1397, doi:10.1007/s00382-016-3147-y.

Skansi, M.M. et al., 2013: Warming and wetting signals emerging from analysis of changes in climate extreme indices over South America. *Global and Planetary Change*, **100**, 295–307, doi:10.1016/j.gloplacha.2012.11.004.

Skaugen, T., H.B. Stranden, and T. Saloranta, 2012: Trends in snow water equivalent in Norway (1931-2009). *Hydrology Research*, **43(4)**, 489–499, doi:10.2166/nh.2012.109.

Skrynyk, O. et al., 2020: Ukrainian early (pre-1850) historical weather observations. *Geoscience Data Journal*, gdj3.108, doi:10.1002/gdj3.108.

Slivinski, L.C. et al., 2019: Towards a more reliable historical reanalysis: Improvements for version 3 of the Twentieth Century Reanalysis system. *Quarterly Journal of the Royal Meteorological Society*, **145(724)**, 2876–2908, doi:10.1002/qj.3598.

Smith, C.D., A. Kontu, R. Laffin, and J.W. Pomeroy, 2017: An assessment of two automated snow water equivalent instruments during the WMO Solid Precipitation Intercomparison Experiment. *Cryosphere*, **11(1)**, 101–116, doi:10.5194/tc-11-101-2017.

Smith, D.M. et al., 2018: The Polar Amplification Model Intercomparison Project (PAMIP) contribution to CMIP6: investigating the causes and consequences of polar amplification. *Geoscientific Model Development Discussions*, **12**, 1–42, doi:10.5194/gmd-2018-82.

Soares, P.M.M. and R.M. Cardoso, 2018: A simple method to assess the added value using high-resolution climate distributions: application to the EURO-CORDEX daily precipitation. *International Journal of Climatology*, **38(3)**, 1484–1498, doi:10.1002/joc.5261.

Soares dos Santos, T., D. Mendes, and R. Rodrigues Torres, 2016: Artificial neural networks and multiple linear regression model using principal components to estimate rainfall over South America. *Nonlinear Processes in Geophysics*, **23(1)**, 13–20, doi:10.5194/npg-23-13-2016.

Solman, S.A., 2013: Regional Climate Modeling over South America: A Review. *Advances in Meteorology*, **2013**, 1–13, doi:10.1155/2013/504357.

Solman, S.A., 2016: Systematic temperature and precipitation biases in the CLARIS-LPB ensemble simulations over

ACCEPTED VERSION SUBJECT TO FINAL EDITS

South America and possible implications for climate projections. *Climate Research*, **68(2–3)**, 117–136, doi:10.3354/cr01362.

Solman, S.A. and J. Blázquez, 2019: Multiscale precipitation variability over South America: Analysis of the added value of CORDEX RCM simulations. *Climate Dynamics*, **53(3–4)**, 1547–1565, doi:10.1007/s00382-019-04689-1.

Solman, S.A., M.N. Nuñez, and M.F. Cabré, 2008: Regional climate change experiments over southern South America. I: present climate. *Climate Dynamics*, **30(5)**, 533–552, doi:10.1007/s00382-007-0304-3.

Solman, S.A. et al., 2013: Evaluation of an ensemble of regional climate model simulations over South America driven by the ERA-Interim reanalysis: Model performance and uncertainties. *Climate Dynamics*, **41(5–6)**, 1139–1157, doi:10.1007/s00382-013-1667-2.

Song, S. and J. Bai, 2016: Increasing Winter Precipitation over Arid Central Asia under Global Warming. *Atmosphere*, **7(10)**, doi:10.3390/atmos7100139.

Sørland, S.L., C. Schär, D. Lüthi, and E. Kjellström, 2018: Bias patterns and climate change signals in GCM-RCM model chains. *Environmental Research Letters*, **13(7)**, 074017, doi:10.1088/1748-9326/aacc77.

Souverijns, N. et al., 2019: A New Regional Climate Model for POLAR-CORDEX: Evaluation of a 30-Year Hindcast with COSMO-CLM2 Over Antarctica. *Journal of Geophysical Research: Atmospheres*, **124(3)**, 1405–1427, doi:10.1029/2018jd028862.

Souvignet, M., H. Gaese, L. Ribbe, N. Kretschmer, and R. Oyarzún, 2010: Statistical downscaling of precipitation and temperature in north-central Chile: an assessment of possible climate change impacts in an arid Andean watershed. *Hydrological Sciences Journal*, **55(1)**, 41–57, doi:10.1080/02626660903526045.

Sperber, K.R. et al., 2013: The Asian summer monsoon: An intercomparison of CMIP5 vs. CMIP3 simulations of the late 20th century. *Climate Dynamics*, **41(9–10)**, 2711–2744, doi:10.1007/s00382-012-1607-6.

Spinoni, J., G. Naumann, J. Vogt, and P. Barbosa, 2015a: The biggest drought events in Europe from 1950 to 2012. *Journal of Hydrology: Regional Studies*, **3**, 509–524, doi:10.1016/j.ejrh.2015.01.001.

Spinoni, J. et al., 2015b: Climate of the Carpathian Region in the period 1961-2010: Climatologies and trends of 10 variables. *International Journal of Climatology*, **35(7)**, 1322–1341, doi:10.1002/joc.4059.

Spinoni, J. et al., 2020: Future Global Meteorological Drought Hot Spots: A Study Based on CORDEX Data. *Journal of Climate*, **33(9)**, 3635–3661, doi:10.1175/jcli-d-19-0084.1.

Srivastava, A., R. Grotjahn, and P.A. Ullrich, 2020: Evaluation of historical CMIP6 model simulations of extreme precipitation over contiguous US regions. *Weather and Climate Extremes*, **29**, 100268, doi:10.1016/j.wace.2020.100268.

Srivastava, A.K. and T. Delsole, 2014: Robust forced response in South Asian summer monsoon in a future climate. *Journal of Climate*, **27(20)**, 7849–7860, doi:10.1175/jcli-d-13-00599.1.

Srivastava, A.K., D.R. Kothawale, and M.N. Rajeevan, 2017: Variability and Long-Term Changes in Surface Air Temperatures Over the Indian Subcontinent. In: *Observed Climate Variability and Change over the Indian Region* [Rajeevan, M. and S. Nayak (eds.)]. Springer, Singapore, pp. 17–35, doi:10.1007/978-981-10-2531-0_2.

Srivastava, A.K., J. Revadekar, and M. Rajeevan, 2019: South Asia [in "State of the climate in 2018"]. *Bulletin of the American Meteorological Society*, **100(9)**, S236–S240, doi:10.1175/2019bamsstateoftheclimate.1.

Steger, C., S. Kotlarski, T. Jonas, and C. Schär, 2013: Alpine snow cover in a changing climate: A regional climate model perspective. *Climate Dynamics*, **41(3–4)**, 735–754, doi:10.1007/s00382-012-1545-3.

Stennett-Brown, R., J.J. Jones, T. Stephenson, and M. Taylor, 2017: Future Caribbean temperature and rainfall extremes from statistical downscaling: statistical downscaling of Caribbean temperature and rainfall. *International Journal of Climatology*, **37**, doi:10.1002/joc.5126.

Stenni, B. et al., 2017: Antarctic climate variability on regional and continental scales over the last 2000 years. *Climate of the Past*, **13(11)**, 1609–1634, doi:10.5194/cp-13-1609-2017.

Stephenson, T.S. et al., 2014: Changes in extreme temperature and precipitation in the Caribbean region, 1961–2010. *International Journal of Climatology*, **34(9)**, 2957–2971, doi:10.1002/joc.3889.

Steptoe, H., S.E.O. Jones, and H. Fox, 2018: Correlations Between Extreme Atmospheric Hazards and Global Teleconnections: Implications for Multihazard Resilience. *Reviews of Geophysics*, **56(1)**, 50–78, doi:10.1002/2017rg000567.

Stocker, T.F. et al., 2013: Technical Summary. In: *Climate Change 2013: The Physical Science Basis. Contribution of Working Group I to the Fifth Assessment Report of the Intergovernmental Panel on Climate Change* [Stocker, T.F., D. Qin, G.-K. Plattner, M. Tignor, S.K. Allen, J. Boschung, A. Nauels, Y. Xia, V. Bex, and P.M. Midgley (eds.)]. Cambridge University Press, Cambridge, United Kingdom and New York, NY, USA, pp. 33–115, doi:10.1017/cbo9781107415324.005.

Stott, P.A., N. Christidis, and R.A. Betts, 2011: Changing return periods of weather-related impacts: The attribution challenge. *Climatic Change*, doi:10.1007/s10584-011-0265-8.

Stott, P.A. et al., 2010: Detection and attribution of climate change: A regional perspective. *Wiley Interdisciplinary Reviews: Climate Change*, doi:10.1002/wcc.34.

St-Pierre, M., J.M. Thériault, and D. Paquin, 2019: Influence of the Model Horizontal Resolution on Atmospheric

ACCEPTED VERSION SUBJECT TO FINAL EDITS

Conditions Leading to Freezing Rain in Regional Climate Simulations. *Atmosphere-Ocean*, **57(2)**, 101–119, doi:10.1080/07055900.2019.1583088.

Stratton, R.A. et al., 2018: A Pan-African Convection-Permitting Regional Climate Simulation with the Met Office Unified Model: CP4-Africa. *Journal of Climate*, **31(9)**, doi:10.1175/jcli-d-17-0503.1.

Strauch, A.M., R.A. MacKenzie, C.P. Giardina, and G.L. Bruland, 2015: Climate driven changes to rainfall and streamflow patterns in a model tropical island hydrological system. *Journal of Hydrology*, **523**, 160–169.

Stuecker, M.F. et al., 2018: Polar amplification dominated by local forcing and feedbacks. *Nature Climate Change*, **8(12)**, 1076–1081, doi:10.1038/s41558-018-0339-y.

Sturman, A. and H. Quénol, 2013: Changes in atmospheric circulation and temperature trends in major vineyard regions of New Zealand. *International Journal of Climatology*, **33(12)**, 2609–2621, doi:10.1002/joc.3608.

Sun, B., H. Wang, and B. Zhou, 2019: Climatic Condition and Synoptic Regimes of Two Intense Snowfall Events in Eastern China and Implications for Climate Variability. *Journal of Geophysical Research: Atmospheres*, **124(2)**, 926–941, doi:10.1029/2018jd029921.

Sun, H. et al., 2018: Impacts of global warming of 1.5°C and 2.0°C on precipitation patterns in China by regional climate model (COSMO-CLM). *Atmospheric Research*, **203**, 83–94, doi:10.1016/j.atmosres.2017.10.024.

Sun, Q. et al., 2018: A Review of Global Precipitation Data Sets: Data Sources, Estimation, and Intercomparisons. *Reviews of Geophysics*, doi:10.1002/2017rg000574.

Sun, Y. et al., 2014: Rapid increase in the risk of extreme summer heat in Eastern China. *Nature Climate Change*, **4(12)**, 1082–1085, doi:10.1038/nclimate2410.

Supari, F. Tangang, L. Juneng, and E. Aldrian, 2017: Observed changes in extreme temperature and precipitation over Indonesia. *International Journal of Climatology*, **37(4)**, 1979–1997, doi:10.1002/joc.4829.

Supari et al., 2018: ENSO modulation of seasonal rainfall and extremes in Indonesia. *Climate Dynamics*, **51(7–8)**, 2559–2580, doi:10.1007/s00382-017-4028-8.

Supari et al., 2020: Multi-model projections of precipitation extremes in Southeast Asia based on CORDEX-Southeast Asia simulations. *Environmental Research*, **184**, doi:10.1016/j.envres.2020.109350.

Suriano, Z.J. and D.J. Leathers, 2016: Twenty-first century snowfall projections within the eastern Great Lakes region: Detecting the presence of a lake-induced snowfall signal in GCMs. *International Journal of Climatology*, **36(5)**, 2200–2209, doi:10.1002/joc.4488.

Susskind, J., G.A. Schmidt, J.N. Lee, and L. Iredell, 2019: Recent global warming as confirmed by AIRS. *Environmental Research Letters*, **14(4)**, doi:10.1088/1748-9326/aafd4e.

Suzuki-Parker, A. et al., 2018: Contributions of GCM/RCM Uncertainty in Ensemble Dynamical Downscaling for Precipitation in East Asian Summer Monsoon Season. *SOLA*, **14**, 97–104, doi:10.2151/sola.2018-017.

Syed, F.S., W. Iqbal, A.A.B. Syed, and G. Rasul, 2014: Uncertainties in the regional climate models simulations of South-Asian summer monsoon and climate change. *Climate Dynamics*, **42(7)**, 2079–2097, doi:10.1007/s00382-013-1963-x.

Syed, F.S., M. Latif, A. Al-Maashi, and A. Ghulam, 2019: Regional climate model RCA4 simulations of temperature and precipitation over the Arabian Peninsula: sensitivity to CORDEX domain and lateral boundary conditions. *Climate Dynamics*, doi:10.1007/s00382-019-04974-z.

Sylla, M.B., F. Giorgi, E. Coppola, and L. Mariotti, 2013: Uncertainties in daily rainfall over Africa: Assessment of gridded observation products and evaluation of a regional climate model simulation. *International Journal of Climatology*, **33**, 1805–1817, doi:10.1002/joc.3551.

Sylla, M.B., A. Faye, N.A.B. Klutse, and K. Dimobe, 2018: Projected increased risk of water deficit over major West African river basins under future climates. *Climatic Change*, **151(2)**, 247–258, doi:10.1007/s10584-018-2308-x.

Sylla, M.B., P.M. Nikiema, P. Gibba, I. Kebe, and N.A.B. Klutse, 2016: Climate Change over West Africa: Recent Trends and Future Projections. In: *Adaptation to Climate Change and Variability in Rural West Africa* [Yaro, J. and J. Hesselberg (eds.)]. Springer, Cham, Switzerland, pp. 25–40, doi:10.1007/978-3-319-31499-0_3.

Tabary, P. et al., 2011: A 10-year (1997-2006) reanalysis of Quantitative Precipitation Estimation over France: methodology and first results. In: *Weather Radar and Hydrology (Proceedings of a symposium held in Exeter, UK, April 2011)*. pp. 255–260.

Takaya, Y., I. Ishikawa, C. Kobayashi, H. Endo, and T. Ose, 2020: Enhanced Meiyu-Baiu Rainfall in Early Summer 2020: Aftermath of the 2019 Super IOD Event. *Geophysical Research Letters*, **47(22)**, e2020GL090671, doi:10.1029/2020gl090671.

Takhsha, M. et al., 2018: Dynamical downscaling with the fifth-generation Canadian regional climate model (CRCM5) over the CORDEX Arctic domain: effect of large-scale spectral nudging and of empirical correction of sea-surface temperature. *Climate Dynamics*, **51(1)**, 161–186, doi:10.1007/s00382-017-3912-6.

Tan, J., C. Jakob, W.B. Rossow, and G. Tselioudis, 2015: Increases in tropical rainfall driven by changes in frequency of organized deep convection. *Nature*, **519(7544)**, 451–454, doi:10.1038/nature14339.

Tan, M.L., L. Juneng, F.T. Tangang, J.X. Chung, and R.B. Radin Firdaus, 2021: Changes in temperature extremes and their relationship with ENSO in Malaysia from 1985 to 2018. *International Journal of Climatology*, **41(S1)**, doi:10.1002/joc.6864.

ACCEPTED VERSION SUBJECT TO FINAL EDITS

Tang, J. et al., 2016: Building Asian climate change scenario by multi-regional climate models ensemble. Part I: surface air temperature. *International Journal of Climatology*, **36(13)**, 4241–4252, doi:10.1002/joc.4628.
Tangang, F. et al., 2017: Characteristics of precipitation extremes in Malaysia associated with El Niño and La Niña events. *International Journal of Climatology*, **37**, 696–716, doi:10.1002/joc.5032.
Tangang, F. et al., 2018: Future changes in annual precipitation extremes over Southeast Asia under global warming of 2°C. *APN Science Bulletin*, **8(1)**, 3–8, doi:10.30852/sb.2018.436.
Tangang, F. et al., 2020: Projected future changes in rainfall in Southeast Asia based on CORDEX–SEA multi-model simulations. *Climate Dynamics*, **55(5–6)**, 1247–1267, doi:10.1007/s00382-020-05322-2.
Tatebe, H. et al., 2019: Description and basic evaluation of simulated mean state, internal variability, and climate sensitivity in MIROC6. *Geoscientific Model Development*, **12(7)**, 2727–2765, doi:10.5194/gmd-12-2727-2019.
Taylor, A.L., S. Dessai, and W.B. de Bruin, 2015: Communicating uncertainty in seasonal and interannual climate forecasts in Europe. *Philosophical Transactions of the Royal Society A: Mathematical, Physical and Engineering Sciences*, **373(2055)**, 20140454, doi:10.1098/rsta.2014.0454.
Taylor, C.M. et al., 2017: Frequency of extreme Sahelian storms tripled since 1982 in satellite observations. *Nature*, doi:10.1038/nature22069.
Taylor, K.E., R.J. Stouffer, and G.A. Meehl, 2012: An Overview of CMIP5 and the Experiment Design. *Bulletin of the American Meteorological Society*, **93(4)**, 485–498, doi:10.1175/bams-d-11-00094.1.
Taylor, M., F. Whyte, T. Stephenson, and J. Campbell, 2013: Why dry? Investigating the future evolution of the Caribbean Low Level Jet to explain projected Caribbean drying. *International Journal of Climatology*, **33**, 784–792, doi:10.1002/joc.3461.
Taylor, M.A. and E.J. Alfaro, 2005: Central America and the Caribbean, Climate of. In: *Encyclopedia of World Climatology* [Oliver, J.E. (ed.)]. Springer, Dordrecht, The Netherlands, pp. 183–189, doi:10.1007/1-4020-3266-8_37.
Taylor, M.A., T.S. Stephenson, A.A. Chen, and K.A. Stephenson, 2012: Climate Change and the Caribbean: Review and Response. *Caribbean Studies*, **40(2)**, 169–200, doi:10.1353/crb.2012.0020.
Taylor, M.A. et al., 2013: The Precis Caribbean Story: Lessons and Legacies. *Bulletin of the American Meteorological Society*, **94(7)**, 1065–1073, doi:10.1175/bams-d-11-00235.1.
Taylor, M.A. et al., 2018: Future Caribbean Climates in a World of Rising Temperatures: The 1.5 vs 2.0 Dilemma. *Journal of Climate*, **31(7)**, 2907–2926, doi:10.1175/jcli-d-17-0074.1.
Tebaldi, C., J.M. Arblaster, and R. Knutti, 2011: Mapping model agreement on future climate projections. *Geophysical Research Letters*, **38(23)**, n/a–n/a, doi:10.1029/2011gl049863.
Tedeschi, R.G. and M. Collins, 2016: The influence of ENSO on South American precipitation during austral summer and autumn in observations and models. *International Journal of Climatology*, **36(2)**, 618–635, doi:10.1002/joc.4371.
Teichmann, C. et al., 2018: Avoiding Extremes: Benefits of Staying below +1.5°C Compared to +2.0°C and +3.0°C Global Warming. *Atmosphere*, **9(4)**, 115, doi:10.3390/atmos9040115.
Teichmann, C. et al., 2020: Assessing mean climate change signals in the global CORDEX-CORE ensemble. *Climate Dynamics*, doi:10.1007/s00382-020-05494-x.
Terzago, S., J. von Hardenberg, E. Palazzi, and A. Provenzale, 2017: Snow water equivalent in the Alps as seen by gridded data sets, CMIP5 and CORDEX climate models. *The Cryosphere*, **11(4)**, 1625–1645, doi:10.5194/tc-11-1625-2017.
Tetzner, D., E. Thomas, and C. Allen, 2019: A Validation of ERA5 Reanalysis Data in the Southern Antarctic Peninsula – Ellsworth Land Region, and Its Implications for Ice Core Studies. *Geosciences*, **9(7)**, 289, doi:10.3390/geosciences9070289.
Thirumalai, K., P.N. DiNezio, Y. Okumura, and C. Deser, 2017: Extreme temperatures in Southeast Asia caused by El Niño and worsened by global warming. *Nature Communications*, **8**, 15531, doi:10.1038/ncomms15531.
Thomas, E.R. et al., 2017: Regional Antarctic snow accumulation over the past 1000 years. *Climate of the Past*, **13(11)**, 1491–1513, doi:10.5194/cp-13-1491-2017.
Thompson, E., R. Frigg, and C. Helgeson, 2016: Expert Judgment for Climate Change Adaptation. *Philosophy of Science*, **83(5)**, 1110–1121, doi:10.1086/687942.
Thorarinsdottir, T.L., J. Sillmann, M. Haugen, N. Gissibl, and M. Sandstad, 2020: Evaluation of CMIP5 and CMIP6 simulations of historical surface air temperature extremes using proper evaluation methods. *Environmental Research Letters*, **15(12)**, 124041, doi:10.1088/1748-9326/abc778.
Thornton, P.E. et al., 2016: Daymet: Daily Surface Weather Data on a 1-km Grid for North America, Version 3. Oak Ridge National Laboratory Distributed Active Archive Center (ORNL DAAC), Oak Ridge, TN, USA.
Tian, T. et al., 2013: Resolved complex coastlines and land–sea contrasts in a high-resolution regional climate model: a comparative study using prescribed and modelled SSTs. *Tellus A: Dynamic Meteorology and Oceanography*, **65(1)**, 19951, doi:10.3402/tellusa.v65i0.19951.
Tierney, J.E., C.C. Ummenhofer, and P.B. DeMenocal, 2015: Past and future rainfall in the Horn of Africa. *Science Advances*, doi:10.1126/sciadv.1500682.
Timm, O.E., T.W. Giambelluca, and H.F. Diaz, 2015: Statistical downscaling of rainfall changes in Hawai‘i based on

ACCEPTED VERSION SUBJECT TO FINAL EDITS

the CMIP5 global model projections. *Journal of Geophysical Research: Atmospheres*, **120(1)**, 92–112, doi:10.1002/2014jd022059.
Top, S. et al., 2021: Evaluation of regional climate models ALARO-0 and REMO2015 at 0.22° resolution over the CORDEX Central Asia domain. *Geoscientific Model Development*, **14(3)**, 1267–1293, doi:10.5194/gmd-14-1267-2021.
Torma, C. and F. Giorgi, 2020: On the evidence of orographical modulation of regional fine scale precipitation change signals: The Carpathians. *Atmospheric Science Letters*, **21(6)**, doi:10.1002/asl.967.
Torres, R.R. and J.A. Marengo, 2013: Uncertainty assessments of climate change projections over South America. *Theoretical and Applied Climatology*, **112(1–2)**, 253–272, doi:10.1007/s00704-012-0718-7.
Torzhkov, I.O. et al., 2019: Assessment of Future Climate Change Impacts on Forestry in Russia. *Russian Meteorology and Hydrology*, **44(3)**, 180–186, doi:10.3103/s1068373919030038.
Trewin, B. et al., 2020: An updated long-term homogenized daily temperature data set for Australia. *Geoscience Data Journal*, **7(2)**, 149–169, doi:10.1002/gdj3.95.
Trinh-Tuan, L. et al., 2018: Application of Quantile Mapping Bias Correction for Mid-future Precipitation Projections over Vietnam. *Scientific Online Letters on the Atmosphere (SOLA)*, **15**, 1–6, doi:10.2151/sola.
Tripathi, O.P. and F. Dominguez, 2013: Effects of spatial resolution in the simulation of daily and subdaily precipitation in the southwestern US. *Journal of Geophysical Research: Atmospheres*, **118(14)**, 7591–7605, doi:10.1002/jgrd.50590.
Troin, M. et al., 2016: A complete hydro-climate model chain to investigate the influence of sea surface temperature on recent hydroclimatic variability in subtropical South America (Laguna Mar Chiquita, Argentina). *Climate Dynamics*, **46(5–6)**, 1783–1798, doi:10.1007/s00382-015-2676-0.
Trusel, L.D. et al., 2015: Divergent trajectories of Antarctic surface melt under two twenty-first-century climate scenarios. *Nature Geoscience*, **8(12)**, 927–932, doi:10.1038/ngeo2563.
Turner, J. et al., 2016: Absence of 21st century warming on Antarctic Peninsula consistent with natural variability. *Nature*, **535(7612)**, 411–415, doi:10.1038/nature18645.
Turner, J. et al., 2019: The Dominant Role of Extreme Precipitation Events in Antarctic Snowfall Variability. *Geophysical Research Letters*, **46(6)**, 3502–3511, doi:10.1029/2018gl081517.
Turner, J. et al., 2020: Antarctic temperature variability and change from station data. *International Journal of Climatology*, **40(6)**, 2986–3007, doi:10.1002/joc.6378.
Turton, J., A. Kirchgaessner, A.N. Ross, and J.C. King, 2017: Does high-resolution modelling improve the spatial analysis of föhn flow over the Larsen C Ice Shelf? *Weather*, **72(7)**, 192–196, doi:10.1002/wea.3028.
Turton, J., A. Kirchgaessner, A.N. Ross, J.C. King, and P. Kuipers Munneke, 2020: The influence of föhn winds on annual and seasonal surface melt on the Larsen C Ice Shelf, Antarctica. *The Cryosphere*, **14(11)**, 4165–4180, doi:10.5194/tc-14-4165-2020.
Ullah, S. et al., 2020: Evaluation of CMIP5 models and projected changes in temperatures over South Asia under global warming of 1.5°C, 2°C, and 3°C. *Atmospheric Research*, **246**, 105122, doi:10.1016/j.atmosres.2020.105122.
Vaittinada Ayar, P. et al., 2016: Intercomparison of statistical and dynamical downscaling models under the EURO- and MED-CORDEX initiative framework: present climate evaluations. *Climate Dynamics*, **46(3–4)**, 1301–1329, doi:10.1007/s00382-015-2647-5.
Valdés-Pineda, R., J.B. Valdés, H.F. Diaz, and R. Pizarro-Tapia, 2016: Analysis of spatio-temporal changes in annual and seasonal precipitation variability in South America-Chile and related ocean–atmosphere circulation patterns. *International Journal of Climatology*, doi:10.1002/joc.4532.
van Angelen, J.H., M.R. van den Broeke, B. Wouters, and J.T.M. Lenaerts, 2014: Contemporary (1960–2012) Evolution of the Climate and Surface Mass Balance of the Greenland Ice Sheet. *Surveys in Geophysics*, **35(5)**, 1155–1174, doi:10.1007/s10712-013-9261-z.
van den Besselaar, E.J.M. et al., 2017: SA-OBS: A Daily Gridded Surface Temperature and Precipitation Dataset for Southeast Asia. *Journal of Climate*, **30(14)**, 5151–5165, doi:10.1175/jcli-d-16-0575.1.
van den Hurk, B. et al., 2018: The match between climate services demands and Earth System Models supplies. *Climate Services*, **12**, 59–63, doi:10.1016/j.cliser.2018.11.002.
Van der Bilt, W. et al., 2019: *Climate in Svalbard 2100 – a knowledge base for climate adaptation*. NCCS report no. 1/2019, The Norwegian Centre for Climate Services (NCCS), 207 pp.
Van Khiem, M., G. Redmond, C. McSweeney, and T. Thuc, 2014: Evaluation of dynamically downscaled ensemble climate simulations for Vietnam. *International Journal of Climatology*, **34(7)**, 2450–2463, doi:10.1002/joc.3851.
Van Meerbeeck, C., 2020: OECS-Climate Trends and Projections 2020. .
Van Pham, T., J. Brauch, C. Dieterich, B. Frueh, and B. Ahrens, 2014: New coupled atmosphere-ocean-ice system COSMO-CLM/NEMO: assessing air temperature sensitivity over the North and Baltic Seas. *Oceanologia*, **56(2)**, 167–189, doi:10.5697/oc.56-2.167.
van Wessem, J.M. et al., 2016: The modelled surface mass balance of the Antarctic Peninsula at 5.5 km horizontal resolution. *The Cryosphere*, **10(1)**, 271–285, doi:10.5194/tc-10-271-2016.
van Wessem, J.M. et al., 2018: Modelling the climate and surface mass balance of polar ice sheets using RACMO2 –

ACCEPTED VERSION SUBJECT TO FINAL EDITS

Part 2: Antarctica (1979–2016). *The Cryosphere*, **12(4)**, 1479–1498, doi:10.5194/tc-12-1479-2018.
Vandecrux, B. et al., 2019: Firn data compilation reveals widespread decrease of firn air content in western Greenland. *The Cryosphere*, **13(3)**, 845–859, doi:10.5194/tc-13-845-2019.
Vandecrux, B. et al., 2020: The firn meltwater Retention Model Intercomparison Project (RetMIP): evaluation of nine firn models at four weather station sites on the Greenland ice sheet. *The Cryosphere*, **14(11)**, 3785–3810, doi:10.5194/tc-14-3785-2020.
Vaughan, D.G. et al., 2013: Observations: Cryosphere. *Climate Change 2013: The Physical Science Basis. Contribution of Working Group I to the Fifth Assessment Report of the Intergovernmental Panel on Climate Change*, 317–382, doi:10.1017/cbo9781107415324.012.
Vautard, R. et al., 2013: The simulation of European heat waves from an ensemble of regional climate models within the EURO-CORDEX project. *Climate Dynamics*, **41(9–10)**, 2555–2575, doi:10.1007/s00382-013-1714-z.
Vautard, R. et al., 2020: Evaluation of the large EURO-CORDEX regional climate model ensemble. *Journal of Geophysical Research: Atmospheres*, e2019JD032344, doi:10.1029/2019jd032344.
Vecchi, G.A. and B.J. Soden, 2007: Global Warming and the Weakening of the Tropical Circulation. *Journal of Climate*, **20(17)**, 4316–4340, doi:10.1175/jcli4258.1.
Vecchi, G.A. et al., 2006: Weakening of tropical Pacific atmospheric circulation due to anthropogenic forcing. *Nature*, **441(7089)**, 73–76, doi:10.1038/nature04744.
Vera, C.S. and L. Díaz, 2015: Anthropogenic influence on summer precipitation trends over South America in CMIP5 models. *International Journal of Climatology*, **35(10)**, 3172–3177, doi:10.1002/joc.4153.
Vermishev, M., 2015: *Armenia's Third National Communication on Climate Change*. Ministry of Nature Protection of the Republic of Armenia. "Lusabats" Publishing House, Yerevan, 165 pp.
Vicente-Serrano, S.M., E. Rodríguez-Camino, F. Domínguez-Castro, A. El Kenawy, and C. Azorín-Molina, 2017: An updated review on recent trends in observational surface atmospheric variables and their extremes over Spain. *Cuadernos de Investigacion Geografica*, **43(1)**, 209–232, doi:10.18172/cig.3134.
Vicente-Serrano, S.M. et al., 2018: Recent changes in monthly surface air temperature over Peru, 1964-2014. *International Journal of Climatology*, **38(1)**, 283–306, doi:10.1002/joc.5176.
Vichot-Llano, A. and D. Martínez-Castro, 2017: Estado actual de las representación de los principales factores del clima del Caribe por modelos climáticos regionales. Estudios de sensibilidad y validación. *Revista Cubana de Meteorología*, **23(2)**, 232–261.
Vichot-Llano, A., D. Martínez-Castro, A. Centella-Artola, and A. Bezanilla-Morlot, 2014: Sensibilidad al cambio de dominio y resolución de tres configuraciones del modelo climático regional RegCM 4.3 para la región de América Central y el Caribe. *Revista de Climatología*, **14**, 45–62.
Vichot-Llano, A., A. Bezanilla-Morlot, D. Martínez-Castro, and A. Centella-Artola, 2019: Present situation of the application of downscaling methods to the climate change pr ojections in Central America and the Caribbean. *Revista Cubana de Meteorología*, **25(2)**, 218–237.
Vichot-Llano, A., D. Martinez-Castro, F. Giorgi, A. Bezanilla-Morlot, and A. Centella-Artola, 2020: Comparison of GCM and RCM simulated precipitation and temperature over Central America and the Caribbean. *Theoretical and Applied Climatology*, doi:10.1007/s00704-020-03400-3.
Vichot-Llano, A., D. Martinez-Castro, A. Bezanilla-Morlot, A. Centella-Artola, and F. Giorgi, 2021: Projected changes in precipitation and temperature regimes and extremes over the Caribbean and Central America using a multiparameter ensemble of RegCM4. *International Journal of Climatology*, **41(2)**, 1328–1350, doi:10.1002/joc.6811.
Vidal, J.-P., E. Martin, L. Franchistéguy, M. Baillon, and J.-M. Soubeyroux, 2010: A 50-year high-resolution atmospheric reanalysis over France with the Safran system. *International Journal of Climatology*, **30(11)**, 1627–1644, doi:10.1002/joc.2003.
Vignon, O. Traullé, and A. Berne, 2019: On the fine vertical structure of the low troposphere over the coastal margins of East Antarctica. *Atmospheric Chemistry and Physics*, **19(7)**, 4659–4683, doi:10.5194/acp-19-4659-2019.
Vignon, E. et al., 2018: Modeling the Dynamics of the Atmospheric Boundary Layer Over the Antarctic Plateau With a General Circulation Model. *Journal of Advances in Modeling Earth Systems*, **10(1)**, 98–125, doi:10.1002/2017ms001184.
Vihma, T. et al., 2016: The atmospheric role in the Arctic water cycle: A review on processes, past and future changes, and their impacts. *Journal of Geophysical Research: Biogeosciences*, **121(3)**, 586–620.
Villafuerte, M.Q. and J. Matsumoto, 2015: Significant influences of global mean temperature and ENSO on extreme rainfall in Southeast Asia. *Journal of Climate*, **28(5)**, 1905–1919, doi:10.1175/jcli-d-14-00531.1.
Villafuerte, M.Q. et al., 2014: Long-term trends and variability of rainfall extremes in the Philippines. *Atmospheric Research*, **137**, 1–13, doi:10.1016/j.atmosres.2013.09.021.
Vincent, L.A. et al., 2015: Observed Trends in Canada's Climate and Influence of Low-Frequency Variability Modes. *Journal of Climate*, **28(11)**, 4545–4560, doi:10.1175/jcli-d-14-00697.1.
Viste, E., D. Korecha, and A. Sorteberg, 2013: Recent drought and precipitation tendencies in Ethiopia. *Theoretical and Applied Climatology*, doi:10.1007/s00704-012-0746-3.
Vizcaino, M., 2014: Ice sheets as interactive components of Earth System Models: progress and challenges. *Wiley*

ACCEPTED VERSION SUBJECT TO FINAL EDITS

Interdisciplinary Reviews: Climate Change, **5(4)**, 557–568, doi:10.1002/wcc.285.
Vizy, E.K. and K.H. Cook, 2012: Mid-twenty-first-century changes in extreme events over northern and tropical Africa. *Journal of Climate*, doi:10.1175/jcli-d-11-00693.1.
Voldoire, A. et al., 2019: Evaluation of CMIP6 DECK Experiments With CNRM-CM6-1. *Journal of Advances in Modeling Earth Systems*, **11(7)**, 2177–2213, doi:10.1029/2019ms001683.
Vose, R.S., D.R. Easterling, K.E. Kunkel, A.N. LeGrande, and M.F. Wehner, 2017: Temperature changes in the United States. In: *Climate Science Special Report: Fourth National Climate Assessment, Volume I* [Wuebbles, D.J., D.W. Fahey, K.A. Hibbard, D.J. Dokken, B.C. Stewart, and T.K. Maycock (eds.)]. U.S. Global Change Research Program, Washington, DC, USA, pp. 185–206, doi:10.7930/j0n29v45.
Vuille, M., E. Franquist, R. Garreaud, W.S. Lavado Casimiro, and B. Cáceres, 2015: Impact of the global warming hiatus on Andean temperature. *Journal of Geophysical Research: Atmospheres*, **120(9)**, 3745–3757, doi:10.1002/2015jd023126.
Wainwright, C.M. et al., 2019: 'Eastern African Paradox' rainfall decline due to shorter not less intense Long Rains. *npj Climate and Atmospheric Science*, doi:10.1038/s41612-019-0091-7.
Walsh, K. et al., 2010: The Tropical Cyclone Climate Model Intercomparison Project. *Hurricanes and Climate Change*, 1–24, doi:10.1007/978-90-481-9510-7_1.
Walters, D. et al., 2017: The Met Office Unified Model Global Atmosphere 6.0/6.1 and JULES Global Land 6.0/6.1 configurations. *Geoscientific Model Development*, **10(4)**, 1487–1520, doi:10.5194/gmd-10-1487-2017.
Wang, B., R. Wu, and X. Fu, 2000: Pacific–East Asian Teleconnection: How Does ENSO Affect East Asian Climate? *Journal of Climate*, **13(9)**, 1517–1536, doi:10.1175/1520-0442(2000)013<1517:peathd>2.0.co;2.
Wang, C., L. Zhang, S.K. Lee, L. Wu, and C.R. Mechoso, 2014: A global perspective on CMIP5 climate model biases. *Nature Climate Change*, doi:10.1038/nclimate2118.
Wang, G., S.B. Power, and S. McGree, 2016: Unambiguous warming in the western tropical Pacific primarily caused by anthropogenic forcing. *International Journal of Climatology*, **36(2)**, 933–944, doi:10.1002/joc.4395.
Wang, J. and V.R. Kotamarthi, 2015: High-resolution dynamically downscaled projections of precipitation in the mid and late 21st century over North America. *Earth's Future*, **3(7)**, 268–288, doi:10.1002/2015ef000304.
Wang, L. and W. Chen, 2014: The East Asian winter monsoon: re-amplification in the mid-2000s. *Chinese Science Bulletin*, **59(4)**, 430–436, doi:10.1007/s11434-013-0029-0.
Wang, L. and M.-M. Lu, 2016: The East Asian Winter Monsoon. In: *The Global Monsoon System: Research and Forecast (3rd Edition)* [Chang, C.-P., H.-C. Kuo, N.-C. Lau, R.H. Johnson, B. Wang, and M.C. Wheeler (eds.)]. World Scientific, pp. 51–61, doi:10.1142/9789813200913_0005.
Wang, Q., P.-M. Zhai, and D.-H. Qin, 2020: New perspectives on 'warming-wetting' trend in Xinjiang, China. *Advances in Climate Change Research*, **11(3)**, 252–260, doi:10.1016/j.accre.2020.09.004.
Wang, S. et al., 2015: Development and evaluation of a new regional coupled atmosphere–ocean model in the North Sea and Baltic Sea. *Tellus A: Dynamic Meteorology and Oceanography*, **67(1)**, 24284, doi:10.3402/tellusa.v67.24284.
Wang, T., J.-P. Miao, J.-Q. Sun, and Y.-H. Fu, 2018: Intensified East Asian summer monsoon and associated precipitation mode shift under the 1.5°C global warming target. *Advances in Climate Change Research*, **9(2)**, 102–111, doi:10.1016/j.accre.2017.12.002.
Wang, X.L., H. Xu, B. Qian, Y. Feng, and E. Mekis, 2017: Adjusted Daily Rainfall and Snowfall Data for Canada. *Atmosphere - Ocean*, **55(3)**, 155–168, doi:10.1080/07055900.2017.1342163.
Wang, Y. et al., 2015: Recent surface mass balance from Syowa Station to Dome F, East Antarctica: comparison of field observations, atmospheric reanalyses, and a regional atmospheric climate model. *Climate Dynamics*, **45(9–10)**, 2885–2899, doi:10.1007/s00382-015-2512-6.
Wang, Y. et al., 2019: A New 200-Year Spatial Reconstruction of West Antarctic Surface Mass Balance. *Journal of Geophysical Research: Atmospheres*, **124(10)**, 5282–5295, doi:10.1029/2018jd029601.
Wang, Z., Y. Jiang, H. Wan, J. Yan, and X. Zhang, 2017: Detection and Attribution of Changes in Extreme Temperatures at Regional Scale. *Journal of Climate*, **30(17)**, 7035–7047, doi:10.1175/jcli-d-15-0835.1.
Watterson, I.G., J. Bathols, and C. Heady, 2014: What Influences the Skill of Climate Models over the Continents? *Bulletin of the American Meteorological Society*, **95(5)**, 689–700, doi:10.1175/bams-d-12-00136.1.
Wegmann, M., Y. Orsolini, and O. Zolina, 2018: Warm Arctic-cold Siberia: comparing the recent and the early 20th-century Arctic warmings. *Environmental Research Letters*, **13(2)**, 025009, doi:10.1088/1748-9326/aaa0b7.
Wen, G. et al., 2014: Changes in the characteristics of precipitation over northern Eurasia. *Theoretical and Applied Climatology*, **119(3–4)**, 653–665, doi:10.1007/s00704-014-1137-8.
Wester, P., A. Mishra, A. Mukherji, and A.B. Shrestha (eds.), 2019: *The Hindu Kush Himalaya Assessment: Mountains, Climate Change, Sustainability and People*. Springer, Cham, Switzerland, 627 pp., doi:10.1007/978-3-319-92288-1.
Whan, K. and F. Zwiers, 2017: The impact of ENSO and the NAO on extreme winter precipitation in North America in observations and regional climate models. *Climate Dynamics*, **48(5–6)**, 1401–1411, doi:10.1007/s00382-016-3148-x.
Whan, K. et al., 2014: Trends and variability of temperature extremes in the tropical Western Pacific. *International*

ACCEPTED VERSION SUBJECT TO FINAL EDITS

Journal of Climatology, **34(8)**, 2585–2603, doi:10.1002/joc.3861.
Whetton, P., K. Hennessy, J. Clarke, K. McInnes, and D. Kent, 2012: Use of Representative Climate Futures in impact and adaptation assessment. *Climatic Change*, **115(3–4)**, 433–442, doi:10.1007/s10584-012-0471-z.
Whetton, P.H., M.R. Grose, and K.J. Hennessy, 2016: A short history of the future: Australian climate projections 1987–2015. *Climate Services*, **2–3**, 1–14, doi:10.1016/j.cliser.2016.06.001.
Whittleston, D., S.E. Nicholson, A. Schlosser, and D. Entekhabi, 2017: Climate models lack jet-rainfall coupling over West Africa. *Journal of Climate*, doi:10.1175/jcli-d-16-0579.1.
Whyte, F.S., M.A. Taylor, T.S. Stephenson, and J.D. Campbell, 2008: Features of the Caribbean low level jet. *International Journal of Climatology*, **28(1)**, 119–128, doi:10.1002/joc.1510.
Wilkinson, M.D. et al., 2016: The FAIR Guiding Principles for scientific data management and stewardship. *Scientific Data*, **3(1)**, 160018, doi:10.1038/sdata.2016.18.
Wille, J.D. et al., 2019: West Antarctic surface melt triggered by atmospheric rivers. *Nature Geoscience*, **12(11)**, 911–916, doi:10.1038/s41561-019-0460-1.
Williams, A.P. and C. Funk, 2011: A westward extension of the warm pool leads to a westward extension of the Walker circulation, drying eastern Africa. *Climate Dynamics*, doi:10.1007/s00382-010-0984-y.
WMO, 2017: *WMO Guidelines on the Calculation of Climate Normals*. WMO-No. 1203, World Meteorological Organization (WMO), Geneva, Switzerland, 18 pp.
Woo, S., G. Prakash, S. Jai, H. Oh, and K. Min, 2019: Projection of seasonal summer precipitation over Indian sub-continent with a high-resolution AGCM based on the RCP scenarios. *Meteorology and Atmospheric Physics*, **131(4)**, 897–916, doi:10.1007/s00703-018-0612-7.
Wöppelmann, G. and M. Marcos, 2016: Vertical land motion as a key to understanding sea level change and variability. *Reviews of Geophysics*, **54(1)**, 64–92, doi:10.1002/2015rg000502.
Wright, D.M., D.J. Posselt, and A.L. Steiner, 2013: Sensitivity of lake-effect snowfall to lake ice cover and temperature in the great lakes region. *Monthly Weather Review*, **141(2)**, 670–689, doi:10.1175/mwr-d-12-00038.1.
Wright, E.E., J.R.P. Sutton, N.T. Luchetti, M.C. Kruk, and J.J. Marra, 2016: Closing the Pacific Rainfall Data Void. *Eos*, **97**, doi:10.1029/2016eo055053.
Wu, C.-H., N. Freychet, C.-A. Chen, and H.-H. Hsu, 2017: East Asian presummer precipitation in the CMIP5 at high versus low horizontal resolution. *International Journal of Climatology*, **37(11)**, 4158–4170, doi:10.1002/joc.5055.
Wu, J. and X. Gao, 2020: Present day bias and future change signal of temperature over China in a series of multi-GCM driven RCM simulations. *Climate Dynamics*, **54(1)**, 1113–1130, doi:10.1007/s00382-019-05047-x.
Wu, P., Y. Ding, Y. Liu, and X. Li, 2019: The characteristics of moisture recycling and its impact on regional precipitation against the background of climate warming over Northwest China. *International Journal of Climatology*, **39(14)**, 5241–5255, doi:10.1002/joc.6136.
Wu, T. et al., 2019: The Beijing Climate Center Climate System Model (BCC-CSM): the main progress from CMIP5 to CMIP6. *Geoscientific Model Development*, **12(4)**, 1573–1600, doi:10.5194/gmd-12-1573-2019.
Xiao, H. et al., 2020: Long-term trends in Arctic surface temperature and potential causality over the last 100 years. *Climate Dynamics*, **55(5–6)**, 1443–1456, doi:10.1007/s00382-020-05330-2.
Xie, Y., Y. Liu, and J. Huang, 2016: Overestimated Arctic warming and underestimated Eurasia mid-latitude warming in CMIP5 simulations. *International Journal of Climatology*, **36(14)**, 4475–4487, doi:10.1002/joc.4644.
Xu, C., J. Li, J. Zhao, S. Gao, and Y. Chen, 2015: Climate variations in northern Xinjiang of China over the past 50 years under global warming. *Quaternary International*, **358**, 83–92, doi:10.1016/j.quaint.2014.10.025.
Xu, M., S. Kang, H. Wu, and X. Yuan, 2018: Detection of spatio-temporal variability of air temperature and precipitation based on long-term meteorological station observations over Tianshan Mountains, Central Asia. *Atmospheric Research*, **203**, 141–163, doi:10.1016/j.atmosres.2017.12.007.
Xu, Y., A. Jones, and A. Rhoades, 2019: A quantitative method to decompose SWE differences between regional climate models and reanalysis datasets. *Scientific Reports*, **9(1)**, 1–11, doi:10.1038/s41598-019-52880-5.
Yang, J., G. Fang, Y. Chen, and P. De-Maeyer, 2017: Climate change in the Tianshan and northern Kunlun Mountains based on GCM simulation ensemble with Bayesian model averaging. *Journal of Arid Land*, **9(4)**, 622–634, doi:10.1007/s40333-017-0100-9.
Yang, M., X. Wang, G. Pang, G. Wan, and Z. Liu, 2019: The Tibetan Plateau cryosphere: Observations and model simulations for current status and recent changes. *Earth-Science Reviews*, **190**, 353–369, doi:10.1016/j.earscirev.2018.12.018.
Yang, W., R. Seager, M.A. Cane, and B. Lyon, 2015: The rainfall annual cycle bias over East Africa in CMIP5 coupled climate models. *Journal of Climate*, doi:10.1175/jcli-d-15-0323.1.
Yang, Y., J. Tang, S. Wang, and G. Liu, 2018: Differential Impacts of 1.5 and 2°C Warming on Extreme Events Over China Using Statistically Downscaled and Bias-Corrected CESM Low-Warming Experiment. *Geophysical Research Letters*, **45(18)**, 9852–9860, doi:10.1029/2018gl079272.
Yao, J., Q. Yang, W. Mao, Y. Zhao, and X. Xu, 2016: Precipitation trend–Elevation relationship in arid regions of the China. *Global and Planetary Change*, **143**, 1–9, doi:10.1016/j.gloplacha.2016.05.007.
Yao, J. et al., 2017: Improved Performance of High-Resolution Atmospheric Models in Simulating the East Asian

ACCEPTED VERSION SUBJECT TO FINAL EDITS

Summer Monsoon Rain Belt. *Journal of Climate*, **30(21)**, 8825–8840, doi:10.1175/jcli-d-16-0372.1.
Yao, T., J. Pu, A. Lu, Y. Wang, and W. Yu, 2007: Recent glacial retreat and its impact on hydrological processes on the Tibetan Plateau, China, and surrounding regions. *Arctic, Antarctic, and Alpine Research*, **39(4)**, 642–650, doi:10.1657/1523-0430(07-510)[yao]2.0.co;2.
Yatagai, A., M. Maeda, S. Khadgarai, M. Masuda, and P. Xie, 2020: End of the Day (EOD) Judgment for Daily Rain-Gauge Data. *Atmosphere*, **11(8)**, 772, doi:10.3390/atmos11080772.
Yatagai, A. et al., 2012: APHRODITE: Constructing a Long-Term Daily Gridded Precipitation Dataset for Asia Based on a Dense Network of Rain Gauges. *Bulletin of the American Meteorological Society*, **93(9)**, 1401–1415, doi:10.1175/bams-d-11-00122.1.
Ye, H., E.J. Fetzer, S. Wong, and B.H. Lambrigtsen, 2017: Rapid decadal convective precipitation increase over Eurasia during the last three decades of the 20th century. *Science Advances*, **3(1)**, e1600944, doi:10.1126/sciadv.1600944.
Ye, H. et al., 2016: Increasing daily precipitation intensity associated with warmer air temperatures over northern Eurasia. *Journal of Climate*, **29(2)**, 623–636, doi:10.1175/jcli-d-14-00771.1.
Yeh, S.W. et al., 2018: ENSO Atmospheric Teleconnections and Their Response to Greenhouse Gas Forcing. *Reviews of Geophysics*, **56(1)**, 185–206, doi:10.1002/2017rg000568.
Yin, L., R. Fu, E. Shevliakova, and R.E. Dickinson, 2013: How well can CMIP5 simulate precipitation and its controlling processes over tropical South America? *Climate Dynamics*, **41(11–12)**, 3127–3143, doi:10.1007/s00382-012-1582-y.
Yoon, J.H. et al., 2015: Increasing water cycle extremes in California and in relation to ENSO cycle under global warming. *Nature Communications*, **6**, 1–6, doi:10.1038/ncomms9657.
Yoon, J.-H., L. Ruby Leung, and J. Correia, 2012: Comparison of dynamically and statistically downscaled seasonal climate forecasts for the cold season over the United States. *Journal of Geophysical Research Atmospheres*, **117(21)**, doi:10.1029/2012jd017650.
Yu, Y. et al., 2019: Climate change, water resources and sustainable development in the arid and semi-arid lands of Central Asia in the past 30 years. *Journal of Arid Land*, **11(1)**, 1–14, doi:10.1007/s40333-018-0073-3.
Yuan, X. et al., 2017: Vegetation changes and land surface feedbacks drive shifts in local temperatures over Central Asia. *Scientific Reports*, **7(1)**, 1–8, doi:10.1038/s41598-017-03432-2.
Zagorodnov, V. et al., 2012: Borehole temperatures reveal details of 20th century warming at Bruce Plateau, Antarctic Peninsula. *The Cryosphere*, **6(3)**, 675–686, doi:10.5194/tc-6-675-2012.
Zampieri, M. and P. Lionello, 2011: Anthropic land use causes summer cooling in -Central Europe. *Climate Research*, **46(3)**, 255–268, doi:10.3354/cr00981.
Zaninelli, P.G., C.G. Menéndez, M. Falco, N. López-Franca, and A.F. Carril, 2019: Future hydroclimatological changes in South America based on an ensemble of regional climate models. *Climate Dynamics*, **52(1–2)**, 819–830, doi:10.1007/s00382-018-4225-0.
Zappa, G., E. Bevacqua, and T.G. Shepherd, 2021: Communicating potentially large but non-robust changes in multi-model projections of future climate. *International Journal of Climatology*, joc.7041, doi:10.1002/joc.7041.
Zazulie, N., M. Rusticucci, and G.B. Raga, 2017a: Regional climate of the subtropical central Andes using high-resolution CMIP5 models-part I: past performance (1980–2005). *Climate Dynamics*, **49(11–12)**, 3937–3957, doi:10.1007/s00382-017-3560-x.
Zazulie, N., M. Rusticucci, and G.B. Raga, 2017b: Regional climate of the subtropical central Andes using high-resolution CMIP5 models-part I: past performance (1980–2005). *Climate Dynamics*, **49(11–12)**, 3937–3957, doi:10.1007/s00382-017-3560-x.
Zeng, X., P. Broxton, and N. Dawson, 2018: Snowpack Change From 1982 to 2016 Over Conterminous United States. *Geophysical Research Letters*, **45(23)**, doi:10.1029/2018gl079621.
Zhang, D. et al., 2018: High-resolution ensemble projections and uncertainty assessment of regional climate change over China in CORDEX East Asia. *Hydrology and Earth System Sciences*, **22(5)**, 3087–3103, doi:10.5194/hess-22-3087-2018.
Zhang, H., Z. Ouyang, H. Zheng, and X. Wang, 2009: Recent climate trends on the northern slopes of the Tianshan Mountains, Xinjiang, China. *Journal of Mountain Science*, **6(3)**, 255–265, doi:10.1007/s11629-009-0236-y.
Zhang, M., Y. Chen, Y. Shen, and Y. Li, 2017: Changes of precipitation extremes in arid Central Asia. *Quaternary International*, **436**, 16–27, doi:10.1016/j.quaint.2016.12.024.
Zhang, M., Y. Chen, Y. Shen, and B. Li, 2019a: Tracking climate change in Central Asia through temperature and precipitation extremes. *Journal of Geographical Sciences*, **29(1)**, 3–28, doi:10.1007/s11442-019-1581-6.
Zhang, M. et al., 2018: Coordination to Understand and Reduce Global Model Biases by U.S. and Chinese Institutions. *Bulletin of the American Meteorological Society*, **99(7)**, ES109–ES113, doi:10.1175/bams-d-17-0301.1.
Zhang, M. et al., 2019b: Numerical Simulation of the Irrigation Effects on Surface Fluxes and Local Climate in Typical Mountain-Oasis-Desert Systems in the Central Asia Arid Area. *Journal of Geophysical Research: Atmospheres*, **n/a(n/a)**, doi:10.1029/2019jd030507.
Zhao, S., J. Li, R. Yu, and H. Chen, 2015: Recent Reversal of the Upper-Tropospheric Temperature Trend and its Role in Intensifying the East Asian Summer Monsoon. *Scientific Reports*, **5**, doi:10.1038/srep11847.

ACCEPTED VERSION SUBJECT TO FINAL EDITS

Zhong, X. et al., 2018: Spatiotemporal variability of snow depth across the Eurasian continent from 1966 to 2012. *The Cryosphere*, **12(1)**, 227–245, doi:10.5194/tc-12-227-2018.

Zhou, B., Z. Wang, Y. Shi, Y. Xu, and Z. Han, 2018: Historical and Future Changes of Snowfall Events in China under a Warming Background. *Journal of Climate*, **31(15)**, 5873–5889, doi:10.1175/jcli-d-17-0428.1.

Zhou, C. and K. Wang, 2017: Quantifying the Sensitivity of Precipitation to the Long-Term Warming Trend and Interannual–Decadal Variation of Surface Air Temperature over China. *Journal of Climate*, **30(10)**, 3687–3703, doi:10.1175/jcli-d-16-0515.1.

Zhou, L., R.E. Dickinson, A. Dai, and P. Dirmeyer, 2010: Detection and attribution of anthropogenic forcing to diurnal temperature range changes from 1950 to 1999: Comparing multi-model simulations with observations. *Climate Dynamics*, doi:10.1007/s00382-009-0644-2.

Zhou, T., D. Gong, J. Li, and B. Li, 2009: Detecting and understanding the multi-decadal variability of the East Asian Summer Monsoon – Recent progress and state of affairs. *Meteorologische Zeitschrift*, **18(4)**, 455–467, doi:10.1127/0941-2948/2009/0396.

Zhou, T. et al., 2017: A Robustness Analysis of CMIP5 Models over the East Asia-Western North Pacific Domain. *Engineering*, **3(5)**, 773–778, doi:10.1016/j.eng.2017.05.018.

Zhou, W. et al., 2016: Evaluation of regional climate simulations over the CORDEX-EA-II domain using the COSMO-CLM model. *Asia-Pacific Journal of Atmospheric Sciences*, **52(2)**, 107–127, doi:10.1007/s13143-016-0013-0.

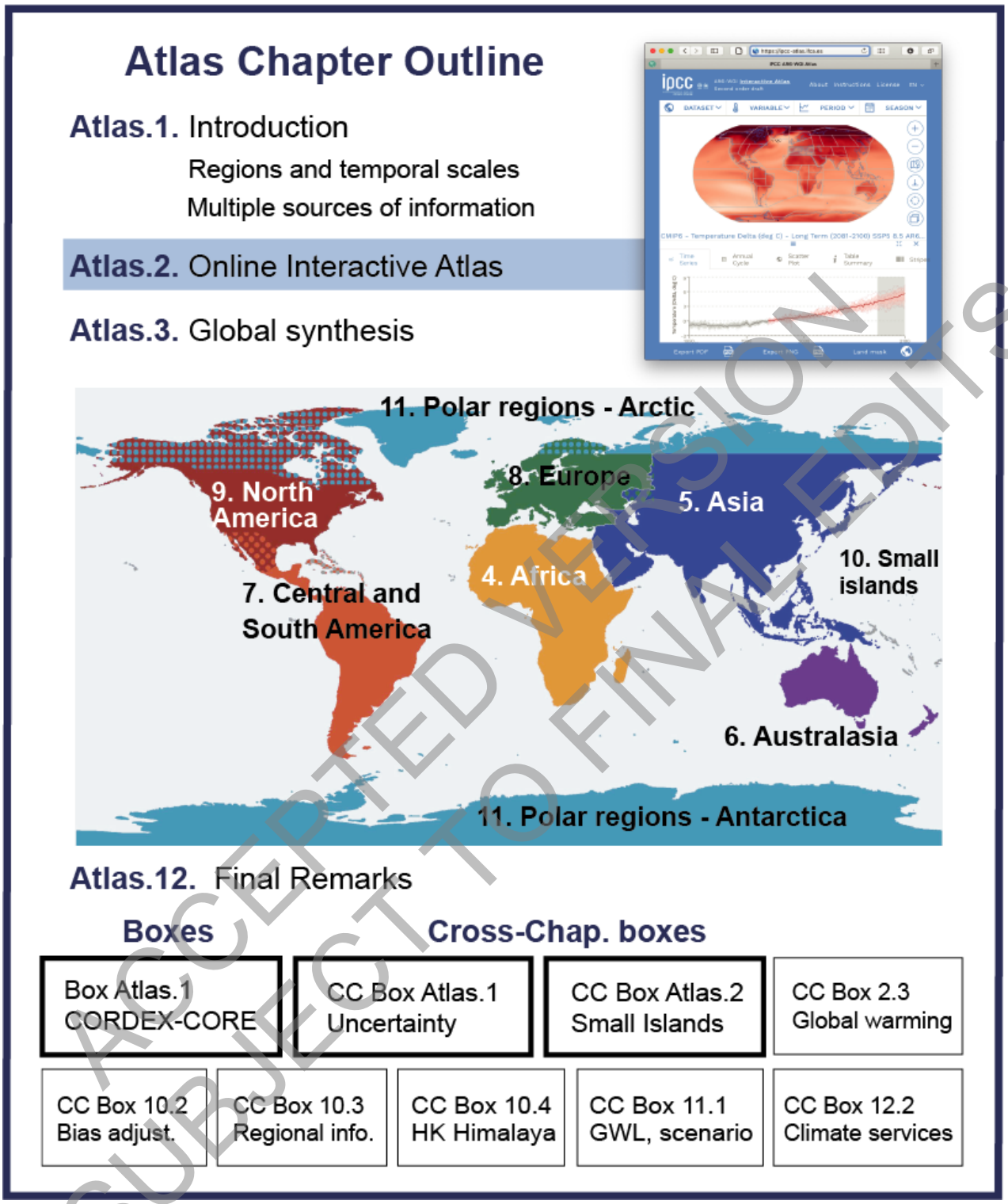
Zittis, G., 2018: Observed rainfall trends and precipitation uncertainty in the vicinity of the Mediterranean, Middle East and North Africa. *Theoretical and Applied Climatology*, **134(3–4)**, 1207–1230, doi:10.1007/s00704-017-2333-0.

Zittis, G. and P. Hadjinicolaou, 2017: The effect of radiation parameterization schemes on surface temperature in regional climate simulations over the MENA-CORDEX domain. *International Journal of Climatology*, **37(10)**, 3847–3862, doi:10.1002/joc.4959.

Zou, L. and T. Zhou, 2016: A regional ocean–atmosphere coupled model developed for CORDEX East Asia: assessment of Asian summer monsoon simulation. *Climate Dynamics*, **47(12)**, 3627–3640, doi:10.1007/s00382-016-3032-8.

ACCEPTED VERSION SUBJECT TO FINAL EDITS

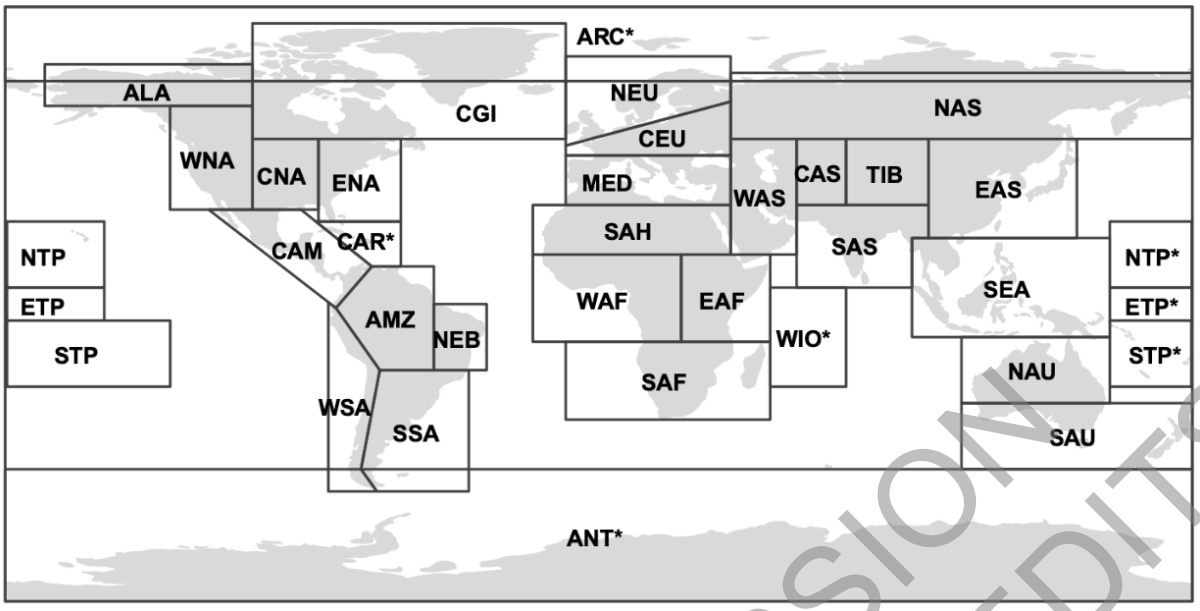
Figures



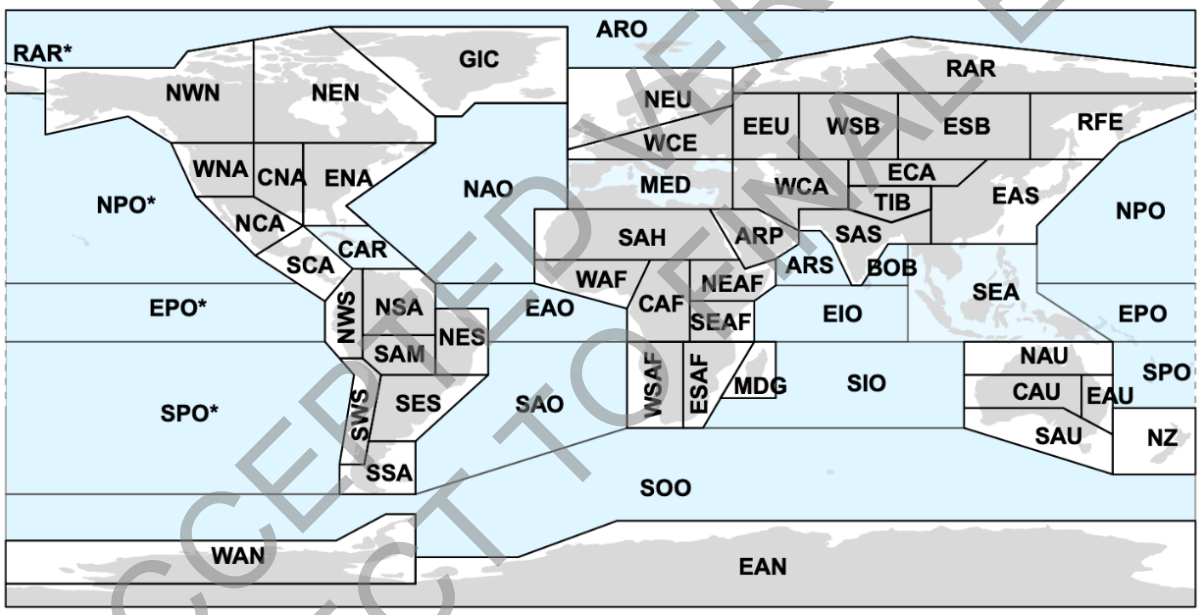
ACCEPTED VERSION SUBJECT TO FINAL EDITS

Figure Atlas.1: The main components of the Atlas chapter with, upper right, a screenshot from the online Interactive Atlas.

(a) IPCC-AR5 WGI Reference Regions



(b) IPCC-AR6 WGI Reference Regions



1	GIC	Greenland/Iceland
2	NWN	N.W.North-America
3	NEN	N.E.North-America
4	WNA	W.North-America
5	CNA	C.North-America
6	ENA	E.North-America
7	NCA	N.Central-America
8	SCA	S.Central-America
9-10	CAR	Caribbean
11	NWS	N.W.South-America
12	NSA	N.South-America
13	NES	N.E.South-America
14	SAM	South-American-Monsoon
15	SWS	S.W.South-America
16	SES	S.E.South-America
17	SSA	S.South-America
18	NEU	N.Europe
19	WCE	Western&Central-Europe
20	EEU	E.Europe
21-22	MED	Mediterranean

23	SAH	Sahara
24	WAF	Western-Africa
25	CAF	Central-Africa
26	NEAF	N.Eastern-Africa
27	SEAF	S.Eastern-Africa
28	WSAF	W.Southern-Africa
29	ESAF	E.Southern-Africa
30	MDG	Madagascar
31	RAR	Russian-Arctic
32	WSB	W.Siberia
33	ESB	E.Siberia
34	RFE	Russian-Far-East
35	WCA	W.C.Asia
36	ECA	E.C.Asia
37	TIB	Tibetan-Plateau
38	EAS	E.Asia
39	ARP	Arabian-Peninsula
40	SAS	S.Asia
41-42	SEA	S.E.Asia

43	NAU	N.Australia
44	CAU	C.Australia
45	EAU	E.Australia
46	SAU	S.Australia
47	NZ	New-Zealand
48	EAN	E.Antarctica
49	WAN	W.Antarctica
50	ARO	Arctic-Ocean
51	NPO	N.Pacific-Ocean
52	EPO	Equatorial.Pacific-Ocean
53	SPO	S.Pacific-Ocean
54	NAO	N.Atlantic-Ocean
55	EAO	Equatorial.Atlantic-Ocean
56	SAO	S.Atlantic-Ocean
57	ARS	Arabian-Sea
58	BOB	Bay-of-Bengal
59	EIO	Equatorial.Indic-Ocean
60	SIO	S.Indic-Ocean
61	SOO	Southern-Ocean

ACCEPTED VERSION
SUBJECT TO FINAL EDITS

1

Figure Atlas.2: WGI reference regions used in the (a) AR5 and (b) AR6 reports (Iturbide et al., 2020). The latter includes both land and ocean regions and it is used as the standard for the regional analysis of atmospheric variables in the Atlas chapter and the Interactive Atlas. The definition of the regions and companion notebooks and scripts are available at the Atlas repository (Iturbide et al., 2021).

ACCEPTED VERSION
SUBJECT TO FINAL EDITS

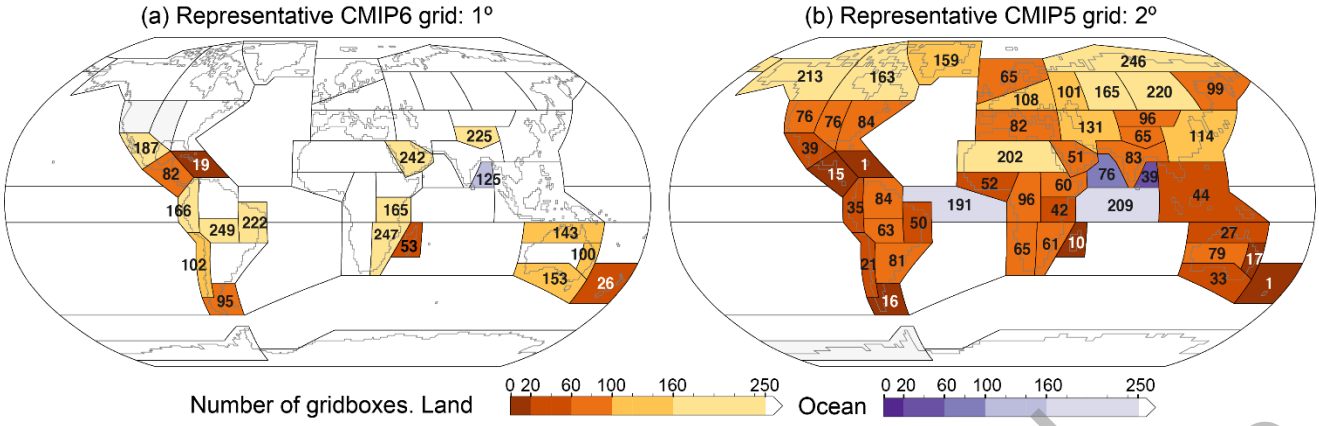


Figure Atlas.3: Number of land grid boxes (blue numbers) for the AR6 WGI reference regions for the reference grids representative of (a) CMIP6 and (b) CMIP5, at 1° and 2° resolution respectively. Colour shading indicate regions with fewer than 250 grid boxes indicating the number of grid boxes (darkest shading if fewer than 20 grid boxes). The polygons show the AR6 WGI reference regions of Figure Atlas.2.

ACCEPTED VERSION
SUBJECT TO FINAL EDITS

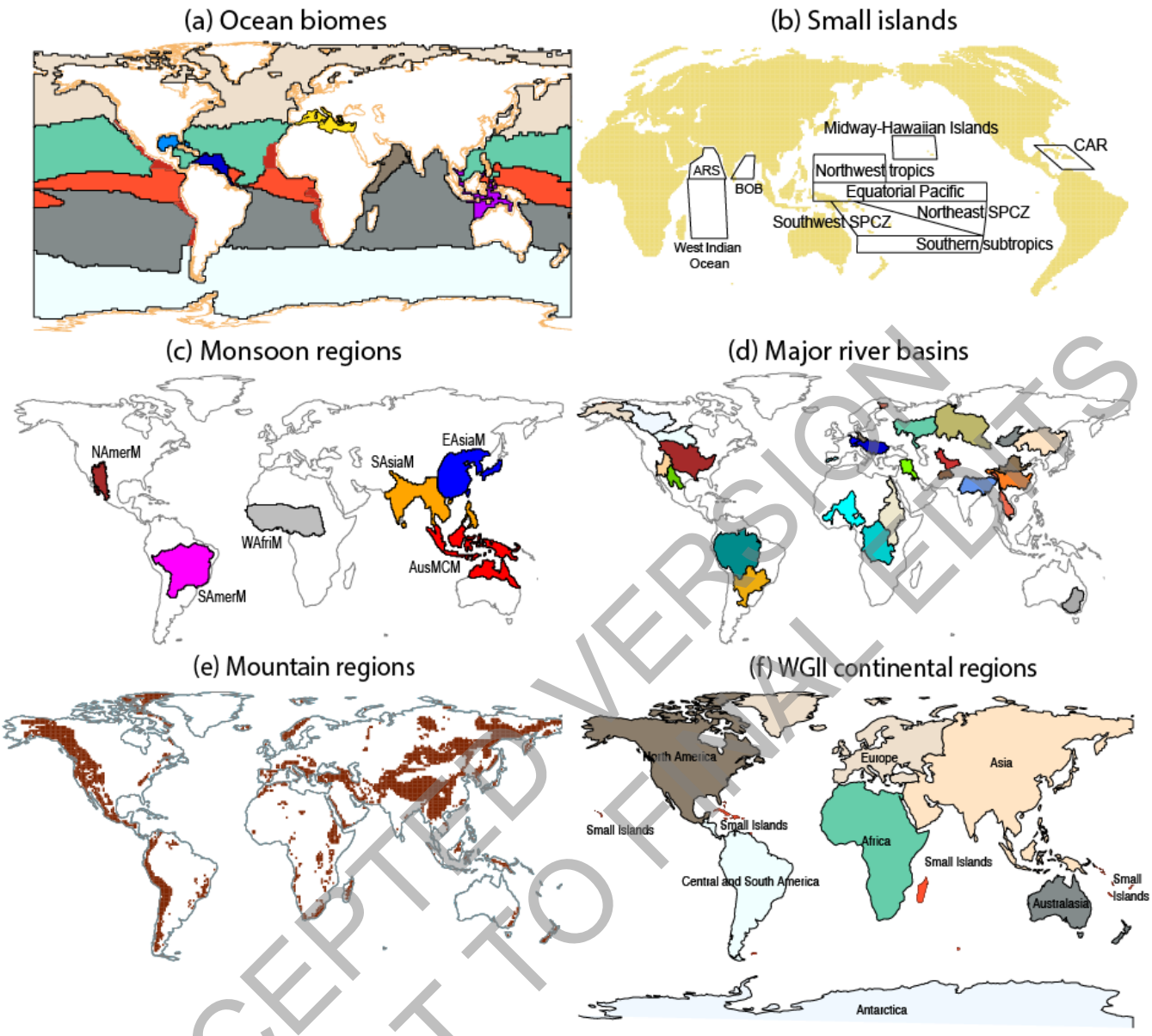
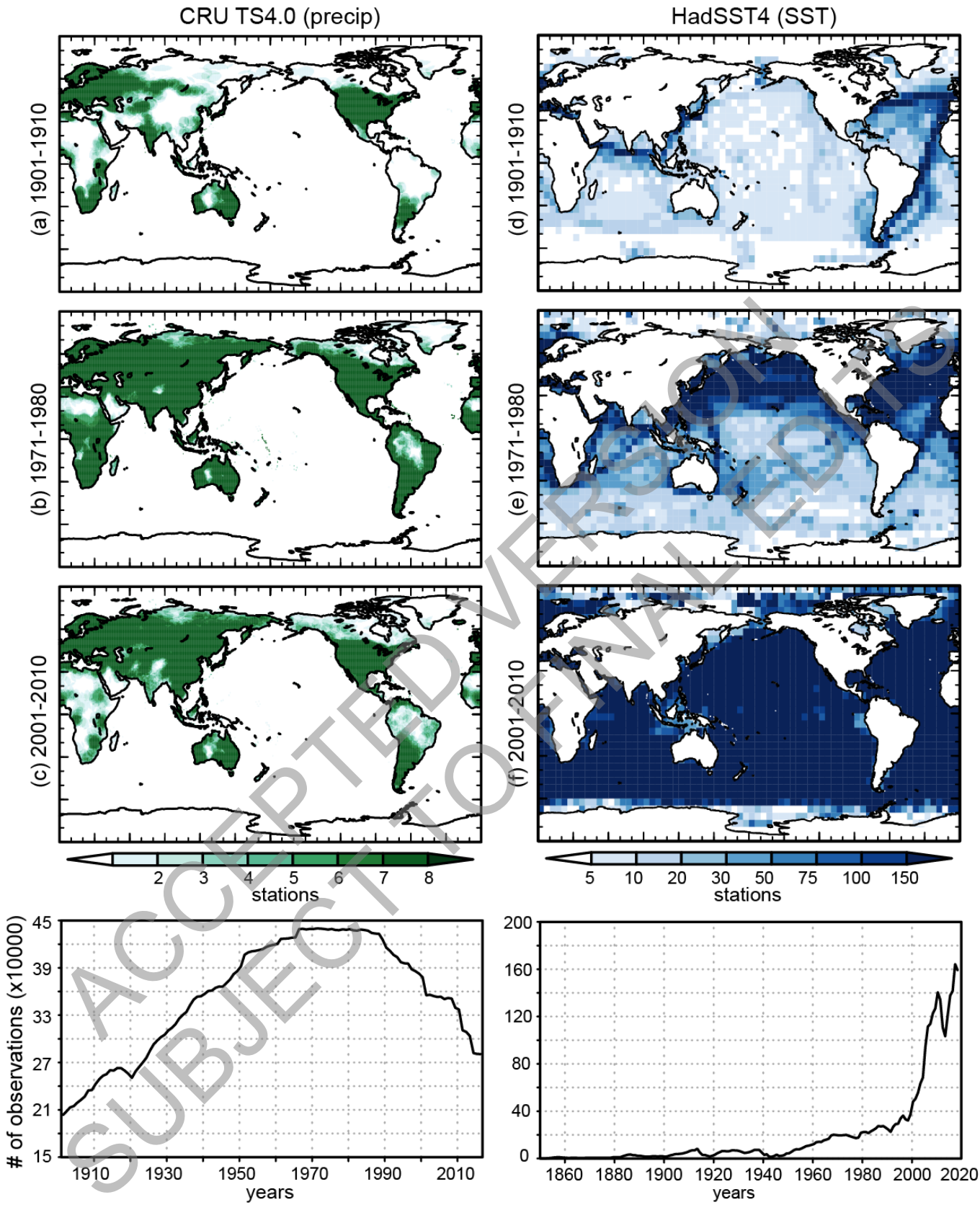


Figure Atlas.4: Typological and socio-economic regions used in the Interactive Atlas. (a) Eleven ocean regions defined by their biological activity used for the regional analysis of oceanic variables; (b) ocean regions for small islands, including the Caribbean (CAR) and the North Indian Ocean (ARS and BOB); (c) land monsoon regions of North America, South America, Africa, Asia and Australasia; (d) major river basins; (e) mountain regions; (f) WGII continental regions. These regions can be used alternatively to the reference regions for the regional analysis of climatic variables in the Interactive Atlas. The definition of the regions and companion notebooks and scripts are available at the Atlas repository (Iturbide et al., 2021).

ACCEPTED VERSION SUBJECT TO FINAL EDITS



ACCEPTED VERSION SUBJECT TO FINAL EDITS

Figure Atlas.5: Number of stations per 0.5° x 0.5° grid cell reported over the periods of 1901–1910, 1971–1980, and 2001–2010 (rows 1–3) and global total number of stations reported over the entire globe (bottom row) for precipitation in the CRU TS4.0 dataset (left) and the HadSST4 dataset (right). Further details on data sources and processing are available in the chapter data table (Table Atlas.SM.15).

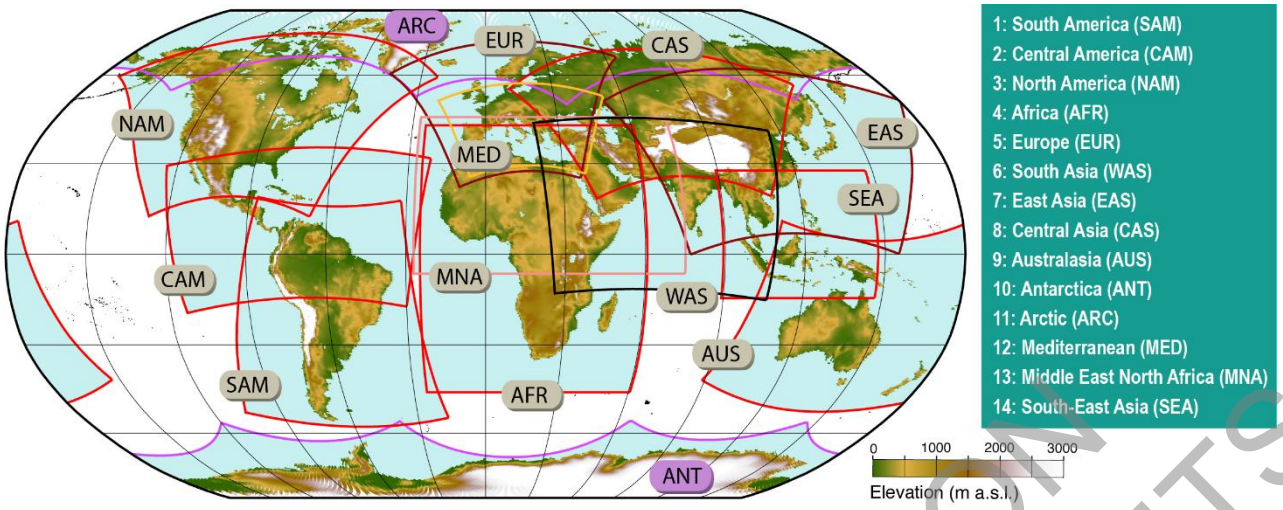


Figure Atlas.6: CORDEX domains showing the curvilinear projections resulting from the original rotated domains. The topography corresponding to the standard CORDEX 0.44° resolution is shown to illustrate the orographic gradients seen by the models over the different regions.

ACCEPTED VERSION
SUBJECT TO FINAL EDITS

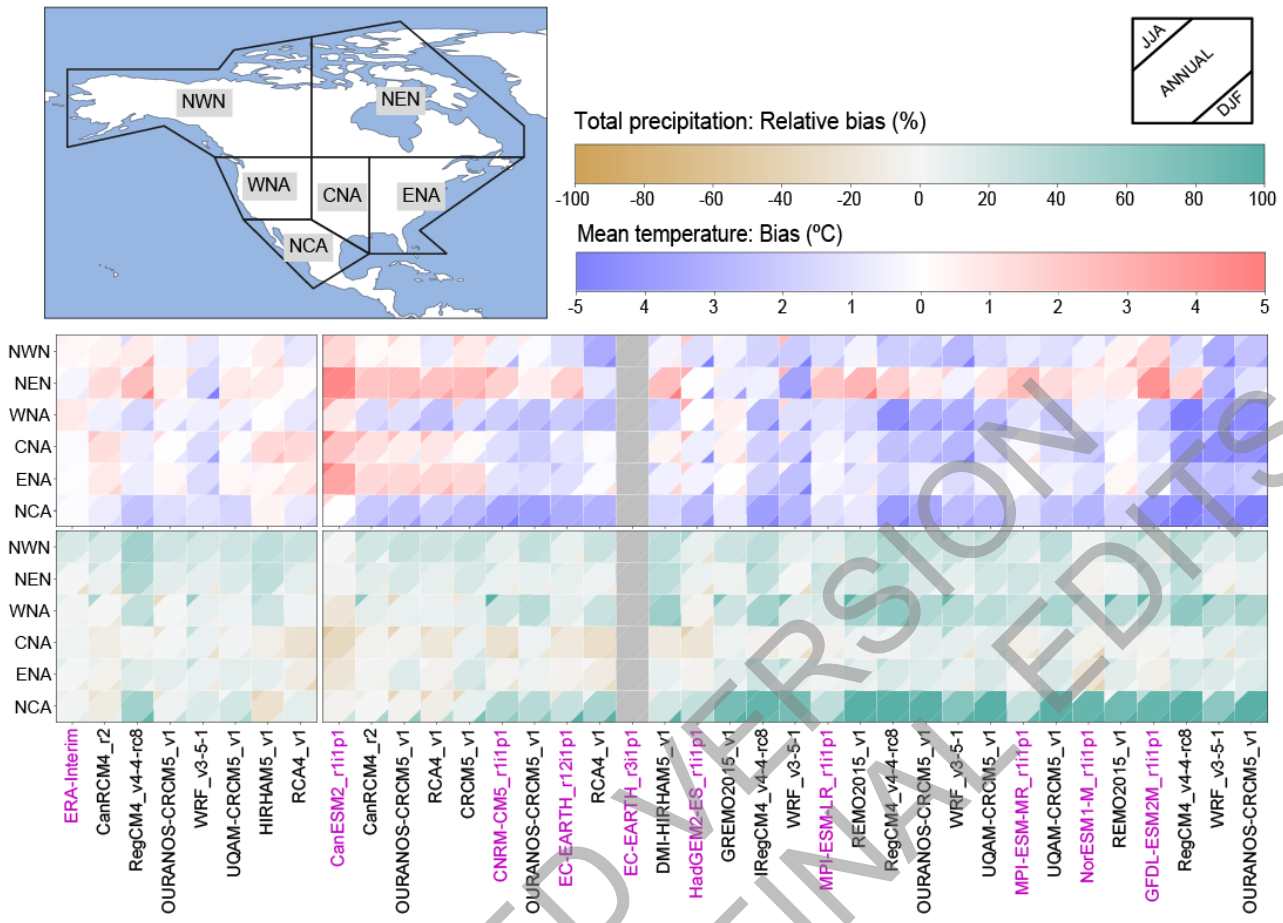
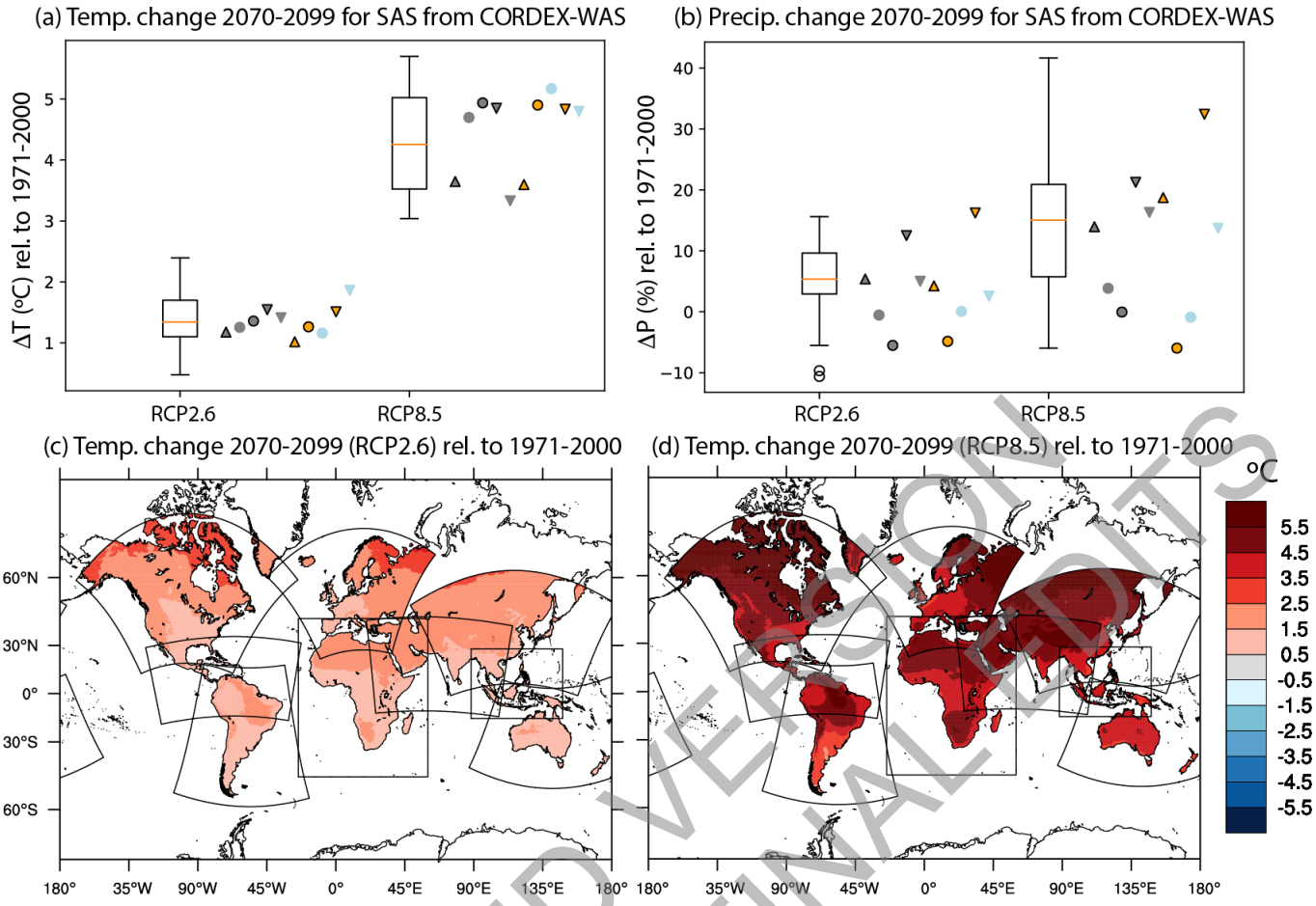


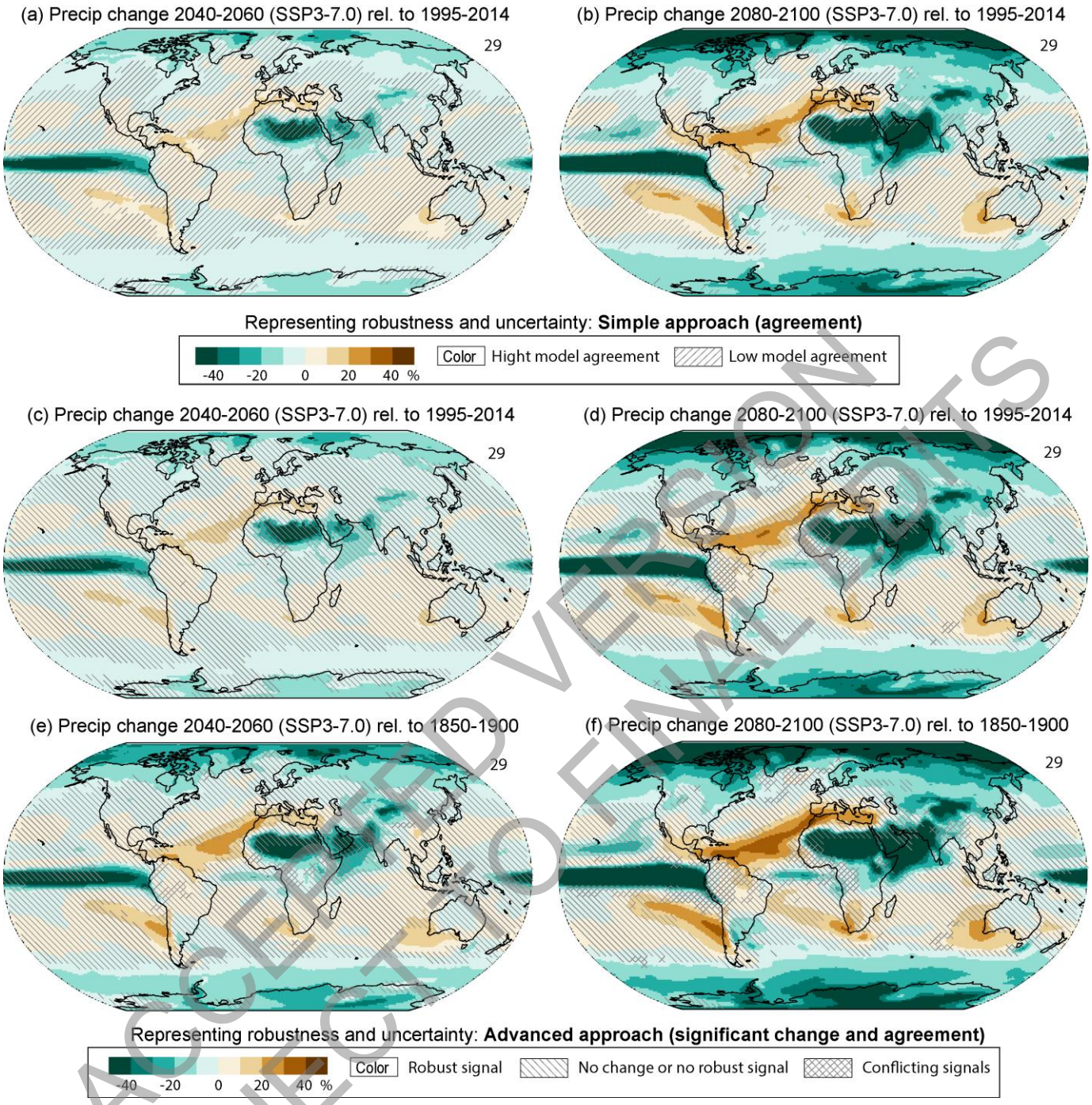
Figure Atlas.7: Evaluation of annual and seasonal air temperature and precipitation for the six North America subregions, NWN, NEN, WNA, CNA, ENA and NCA (land only) for CORDEX-NAM RCM simulations driven by reanalysis or historical GCMs. Seasons are June-July-August (JJA) and December-January-February (DJF). Rows represent subregions and columns correspond to the models. Magenta text indicates the driving historical CMIP5 GCMs (including ERA-Interim in first set of slightly separated columns) and the black text to the right of the magenta text represents the driven RCMs. The colour matrices show the mean spatial biases; all biases have been computed for the period 1985–2005 relative to the observational reference (E5W5, see Section Atlas.1.4.2). Further details on data sources and processing are available in the chapter data table (Table Atlas.SM.15).

ACCEPTED VERSION SUBJECT TO FINAL EDITS



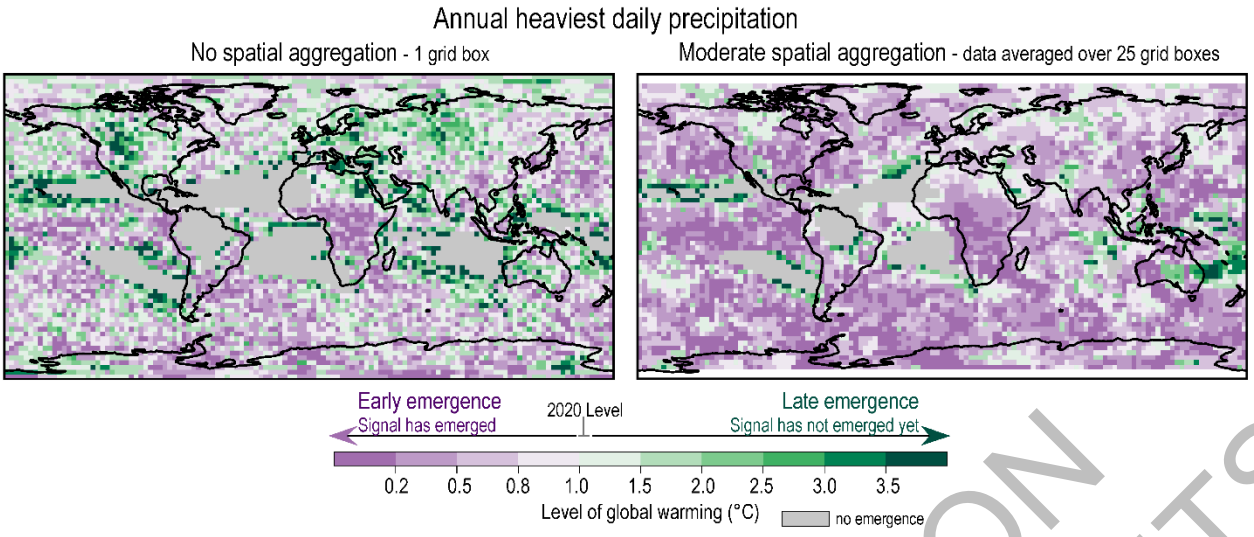
Box Atlas.1, Figure 1: Temperature (left) and precipitation (right) climate change signals at the end of the century (2070–2099) for the entire CMIP5 ensemble (box-whisker plots) and the CORDEX-CORE driving GCMs (grey symbols) of the respective CORDEX-CORE results (non-grey symbols) in the South Asia (SAS) reference region. The shape of the grey symbols represents the climate sensitivity of the driving GCMs: triangles pointing upwards (low equilibrium), circles (medium equilibrium), triangles pointing downwards (high equilibrium). The corresponding RCM results are drawn using the same symbols, but in orange for REMO and in blue for RegCM. The bottom panels show the warming signal by 2070–2099 over the CORDEX regions for RCP2.6 (left) and RCP8.5 (right) (Teichmann et al., 2020).

ACCEPTED VERSION SUBJECT TO FINAL EDITS



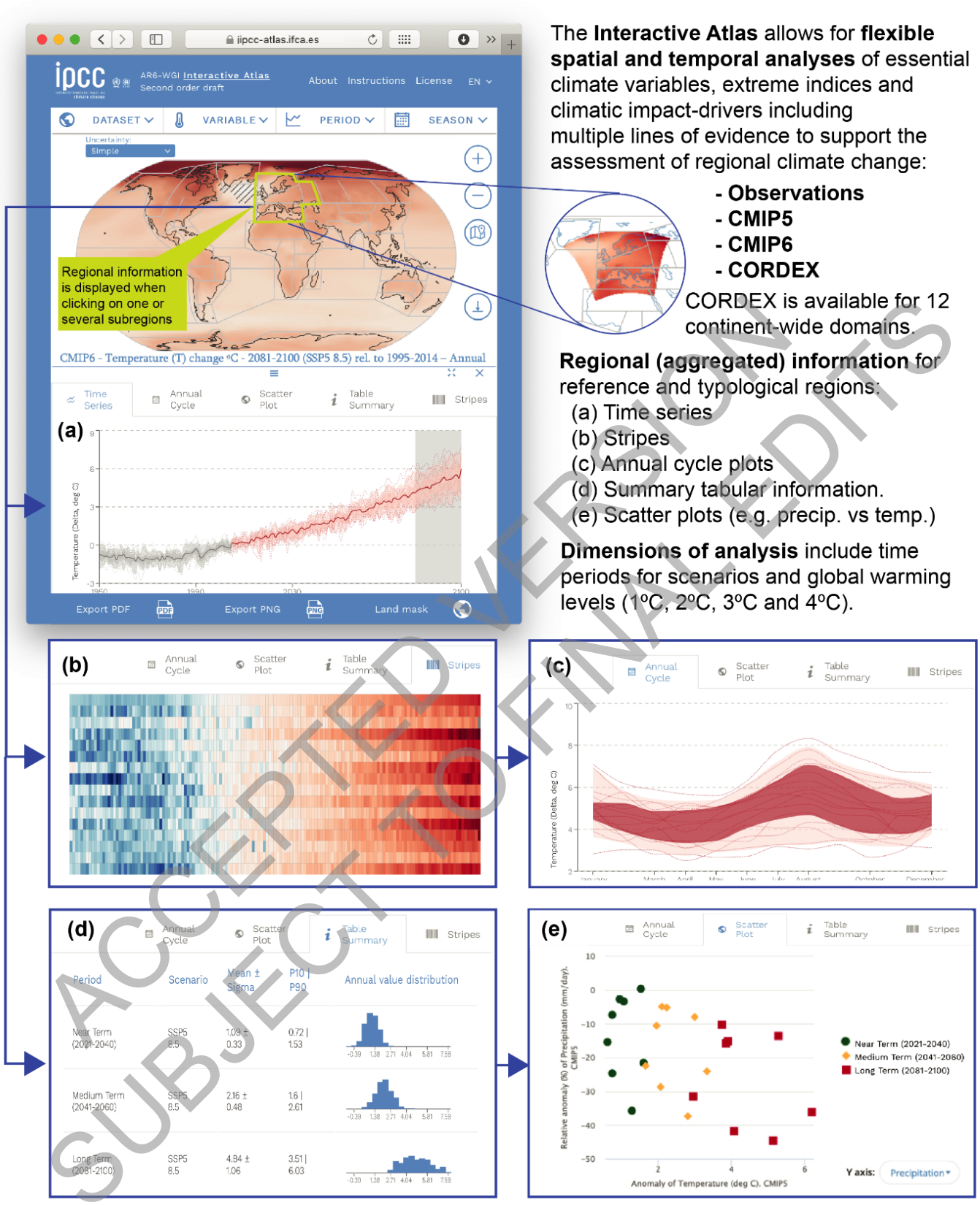
Cross-Chapter Box Atlas.1, Figure 1: Illustration of the simple (top) and advanced (bottom) approaches (B and C in Cross-Chapter Box Atlas.1, Table 1) for uncertainty representation in maps of future projections. Annual multi-model mean projected precipitation change (%) from CMIP6 for the period 2040–2060 (left) and 2080–2100 (right) relative to the baseline periods 1995–2014 (a–d) and 1850–1900 (e–g) under a high-emission (SSP3-7.0) future. Diagonal and crossed lines follow the indications in Cross-Chapter Box Atlas.1, Table 1. Further details on data sources and processing are available in the chapter data table (Table Atlas.SM.15).

ACCEPTED VERSION SUBJECT TO FINAL EDITS



Cross-Chapter Box Atlas.1, Figure 2: Climate change signals are more separable from noise at larger spatial scales. The figure is showing the global warming level associated with the emergence of a significant increase in the probability due to anthropogenic forcing in the 1-in-20-year daily precipitation event using a 500-year sample from the CanESM2 large ensemble simulations. The left panel uses data analysed over a single grid box, with no spatial aggregation, while the right box uses data averaged over 25 grid boxes to represent the regional scale, with moderate spatial aggregation. Aggregation over 25 grid boxes reduces natural variability, resulting in a smaller warming required for a clear separation between the signal and noise. Adapted from Kirchmeier-Young et al. (2019).

ACCEPTED VERSION SUBJECT TO FINAL EDITS



ACCEPTED VERSION SUBJECT TO FINAL EDITS

Figure Atlas.8: Screenshots from the Interactive Atlas. (a) The main interface includes a global map and controls to define a particular choice of dataset, variable, period (reference and baseline) and season (in this example, annual temperature change from CMIP6 for SSP3-7.0 for the long-term 2081–2100 period relative to 1995–2104). (b–e) Various visuals and summary tables for the regionally averaged information for the selected reference regions.

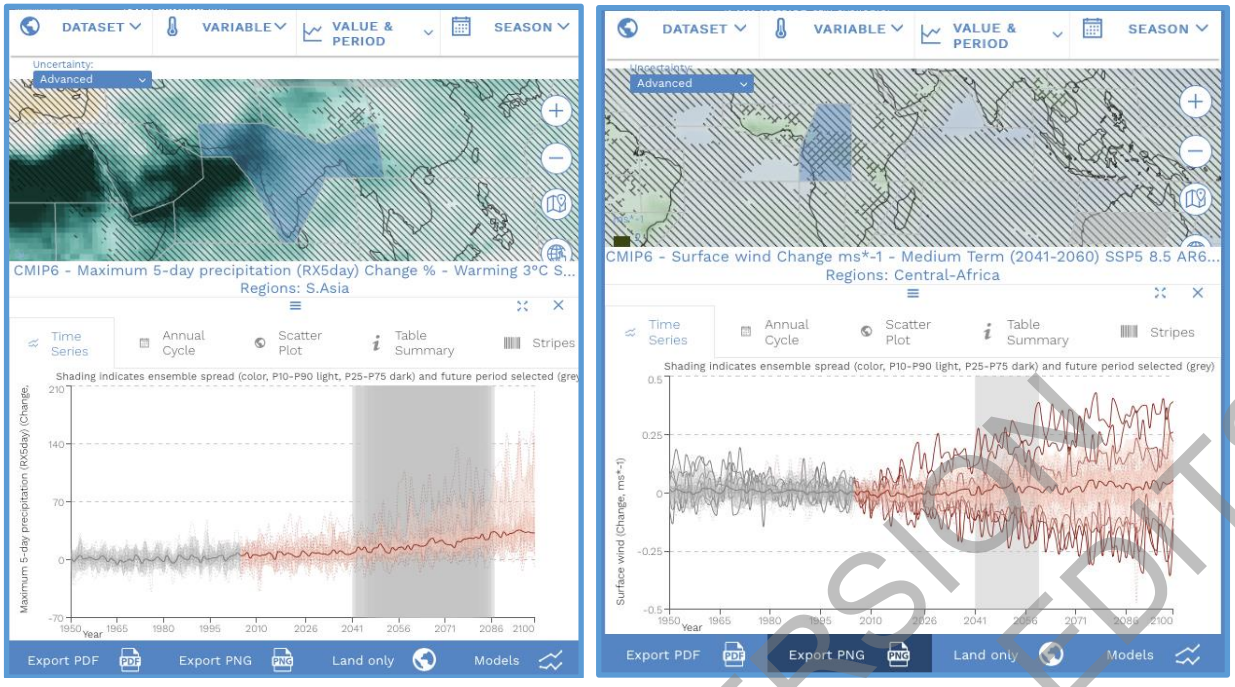
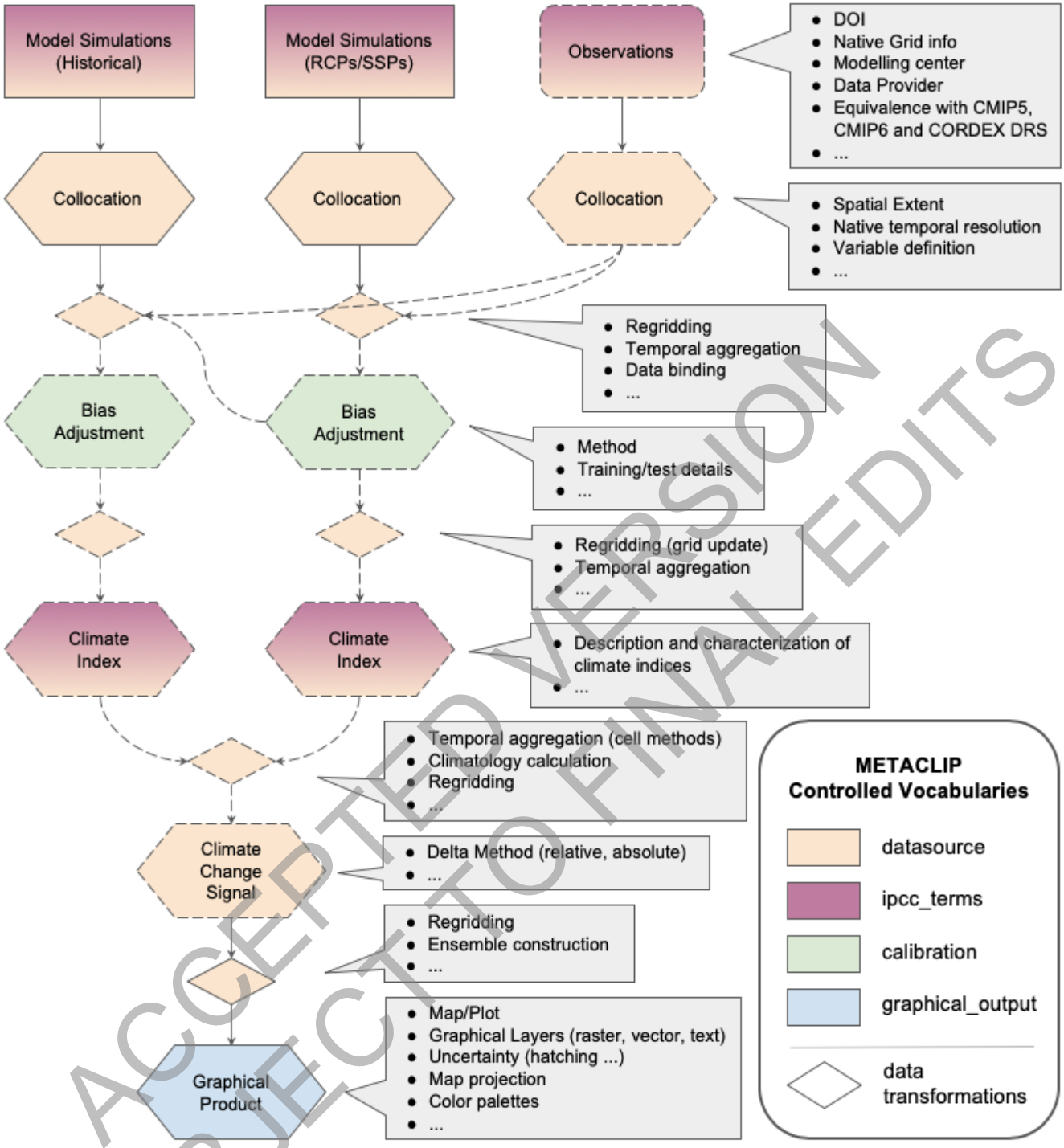


Figure Atlas.9: Analysing robustness and uncertainty in climate change signals across spatial scales using the Interactive Atlas. The left panel shows projected annual relative changes for maximum 5-day precipitation from CMIP6 at 3°C of global warming level relative to the 1850–1900 baseline, through a map of the ensemble mean changes (panel top) and information on the regional aggregated signal over the South Asia reference region as time series (panel bottom). This shows non-robust changes (diagonal lines) at the grid-box level (due to the large local variability), but a robust aggregated signal over the region. The right panel shows projected surface wind speed changes from CMIP6 models for 2041–2060 relative to a 1995–2014 baseline under the SSP5-8.5 scenario, again with the ensemble mean changes in the map (panel top) and regionally aggregated time series over Central Africa for each model (panel bottom). This shows conflicting changes (crossed lines) at the grid-box level due to signals of opposite sign in the individual models displayed in the time series.

ACCEPTED VERSION
SUBJECT TO FINAL EDITS



ACCEPTED VERSION SUBJECT TO FINAL EDITS

Figure Atlas.10: Schematic representation of the Interactive Atlas workflow, from database description, subsetting and data transformation to final graphical product generation (maps and plots). Product-dependent workflow steps are depicted with dashed borders. METACLIP specifically considers the different intermediate steps consisting of various data transformations, bias adjustment, climate index calculation and graphical product generation, providing a semantic description of each stage and the different elements involved. The different controlled vocabularies describing each stage are indicated by the colours, with gradients indicating several vocabularies involved, usually meaning that specific individual instances are defined in 'ipcc_terms' extending generic classes of 'datasource'. These two vocabularies, dealing with the primary data sources have specific annotation properties linking their own features with the CMIP5, CMIP6 and CORDEX Data Reference Syntax, taking as reference their respective controlled vocabularies. All products generated by the Interactive Atlas provide a METACLIP provenance description, including a persistent link to a reproducible source code under version control.

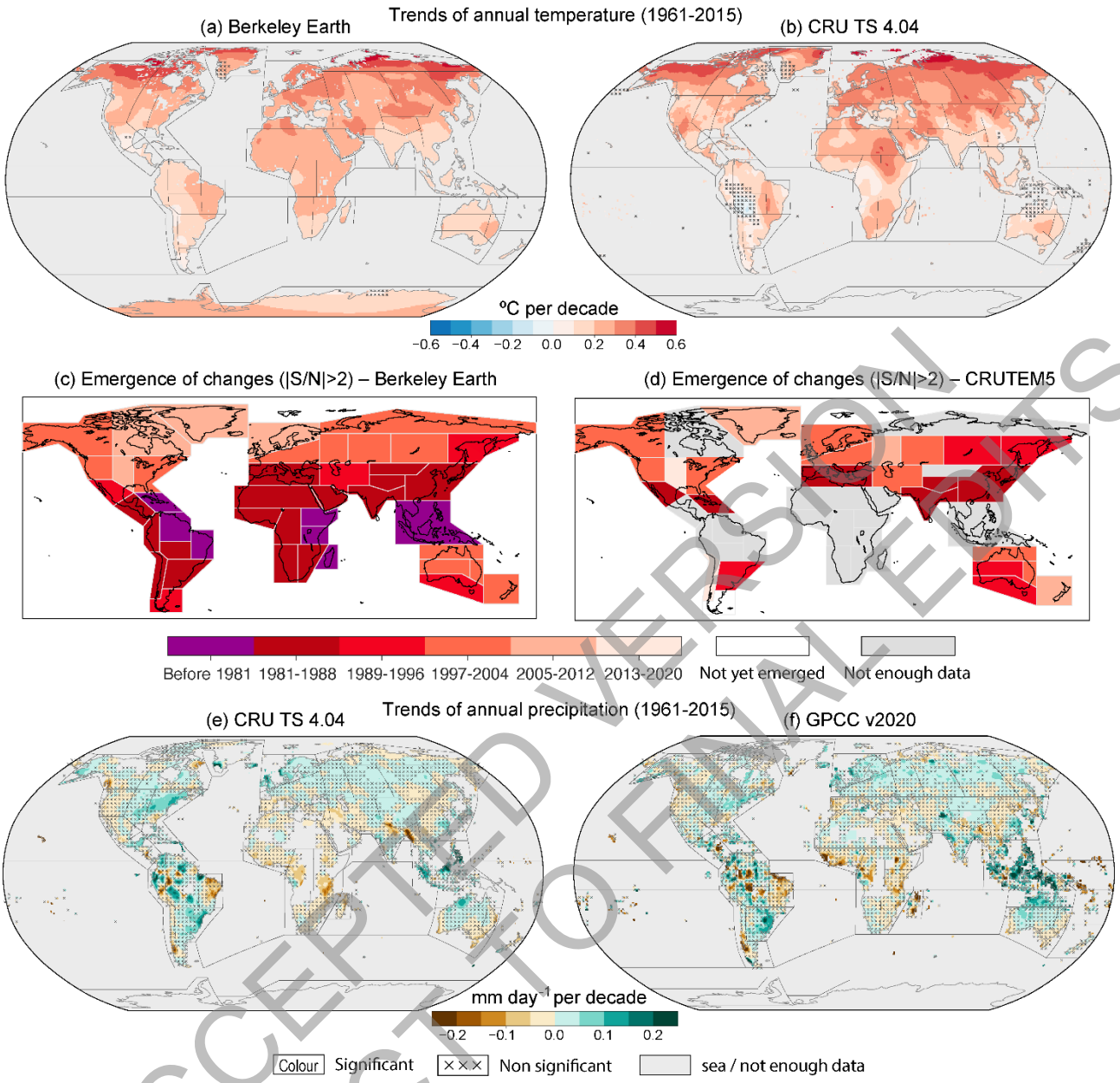


Figure Atlas.11: Observed linear trends of signals in annual mean surface air temperature (a, b) and precipitation (e, f) in the Berkeley Earth, CRU TS and GPCC datasets (see Section Atlas.1 for dataset details). Trends are calculated for the common 1960–2015 period and are expressed as ºC per decade for temperature and relative change (with respect to the climatological mean) per decade for precipitation. Crosses indicate regions where trends are not significant (at a 0.1 significance level) and the black lines mark out the reference regions defined in Section Atlas.1. Panels c and d display the period in which the signals of temperature change in data aggregated over the reference regions emerged from the noise of annual variability in the respective aggregated data. Emergence time is calculated for (c) Berkeley Earth (as used in (a)) and CRUTEM5. Regions in the CRUTEM5 map are shaded grey when data are available over less than 50% of the land area of the region. Further details on data sources and processing are available in the chapter data table (Table Atlas.SM.15).

ACCEPTED VERSION SUBJECT TO FINAL EDITS

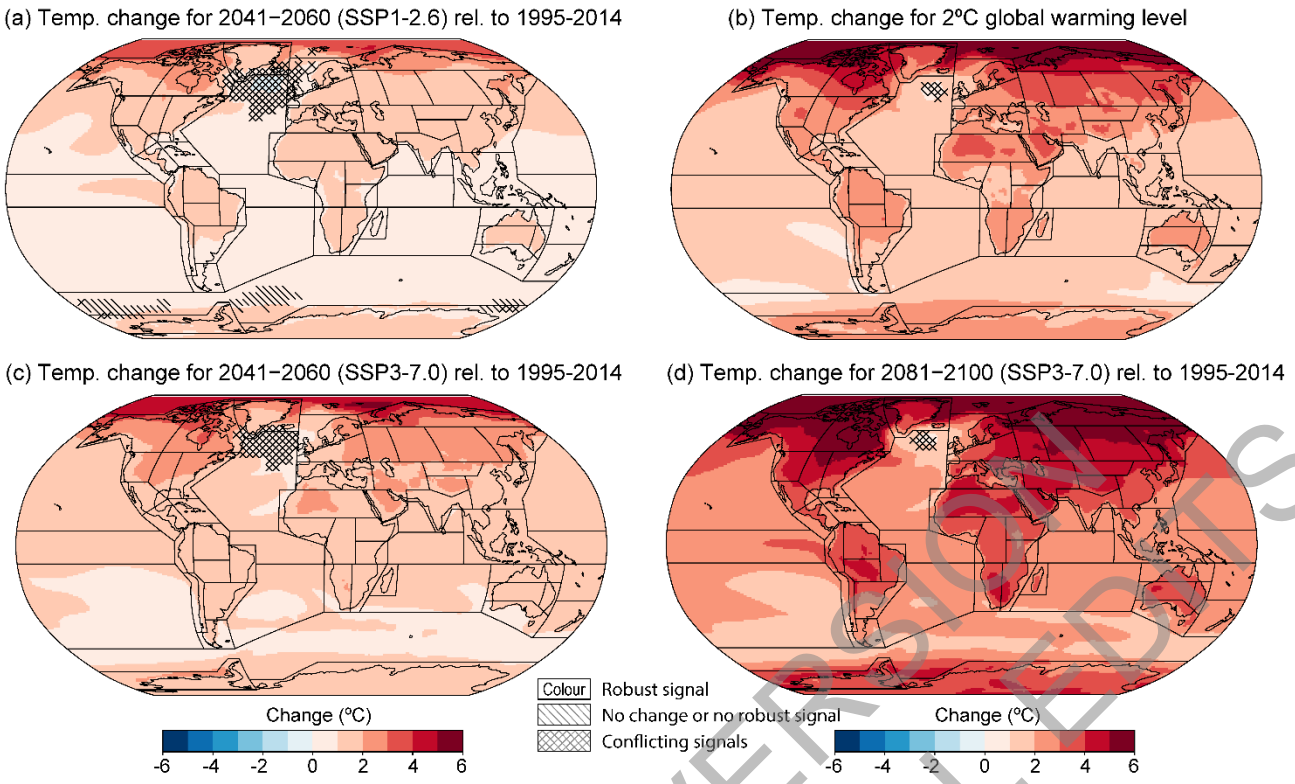


Figure Atlas.12: Global temperature changes projected for the mid-century under SSP1-2.6 (left, top) and SSP3-7.0 (left, bottom) compared with a 2°C global warming level (right, top) and the end of the century under SSP3-7.0 (right, bottom) from the CMIP6 ensemble. Note that the future period warmings are calculated against a baseline period of 1995–2014 whereas the global mean warming level is defined with respect to the baseline period of 1851–1900 used to define global warming levels. The other three SSP-based maps would show greater warmings with respect to this earlier baseline. Further details on data sources and processing are available in the chapter data table (Table Atlas.SM.15).

ACCEPTED VERSION
SUBJECT TO FINAL EDITS

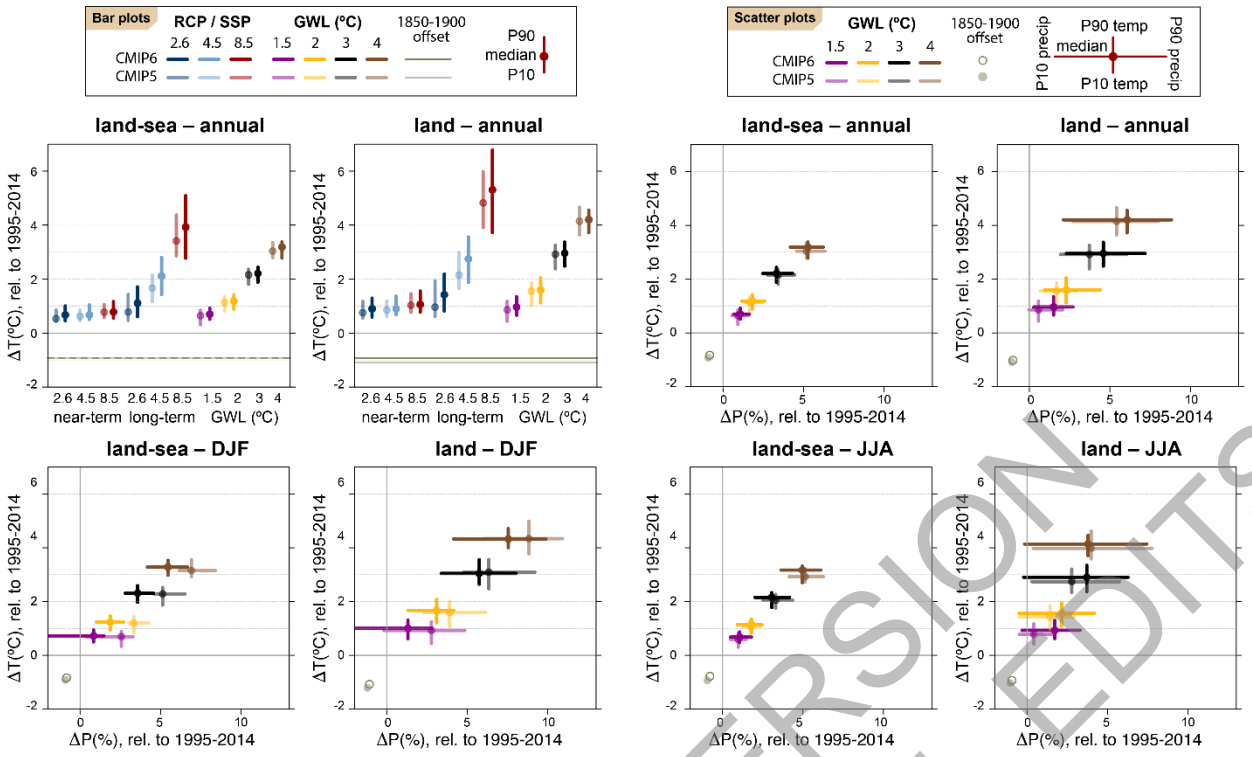


Figure Atlas.13: Changes in annual mean surface air temperature and precipitation averaged over the global (left) and global land areas (right) in each horizontal pair of panels. The top left two panels show the median (dots) and 10th–90th percentile range across each model ensemble for temperature change, for two datasets (CMIP5 and CMIP6) and two scenarios (SSP1-2.6/RCP2.6 and SSP5-8.5/RCP8.5). The first twelve bars represent the projected changes over three time periods (near-term 2021–2040, mid-term 2041–2060 and long-term 2081–2100) compared to the baseline period of 1995–2014 and the remaining four bars represent the additional warming projected relative to the same baseline to reach four global warming levels (GWL; 1.5°C, 2°C, 3°C and 4°C). The top right two panels show scatter diagrams of temperature against precipitation changes, displaying the median (dots) and 10th–90th percentile ranges for the same four GWLs, again representing the additional changes for the global temperature to reach the respective GWL from the baseline period of 1995–2014. In all panels the dark (light) grey lines or dots represent the CMIP6 (CMIP5) simulated changes in temperature and precipitation between the 1850–1900 baseline used for calculating GWLs and the recent past baseline of 1995–2014 used to calculate the changes in the bar diagrams and scatter-plots. Changes are absolute for temperature and relative for precipitation. The script used to generate this figure is available online (Iturbide et al., 2021) and similar results can be generated in the Interactive Atlas for flexibly defined seasonal periods. Further details on data sources and processing are available in the chapter data table (Table Atlas.SM.15).

ACCEPTED VERSION SUBJECT TO FINAL EDITS

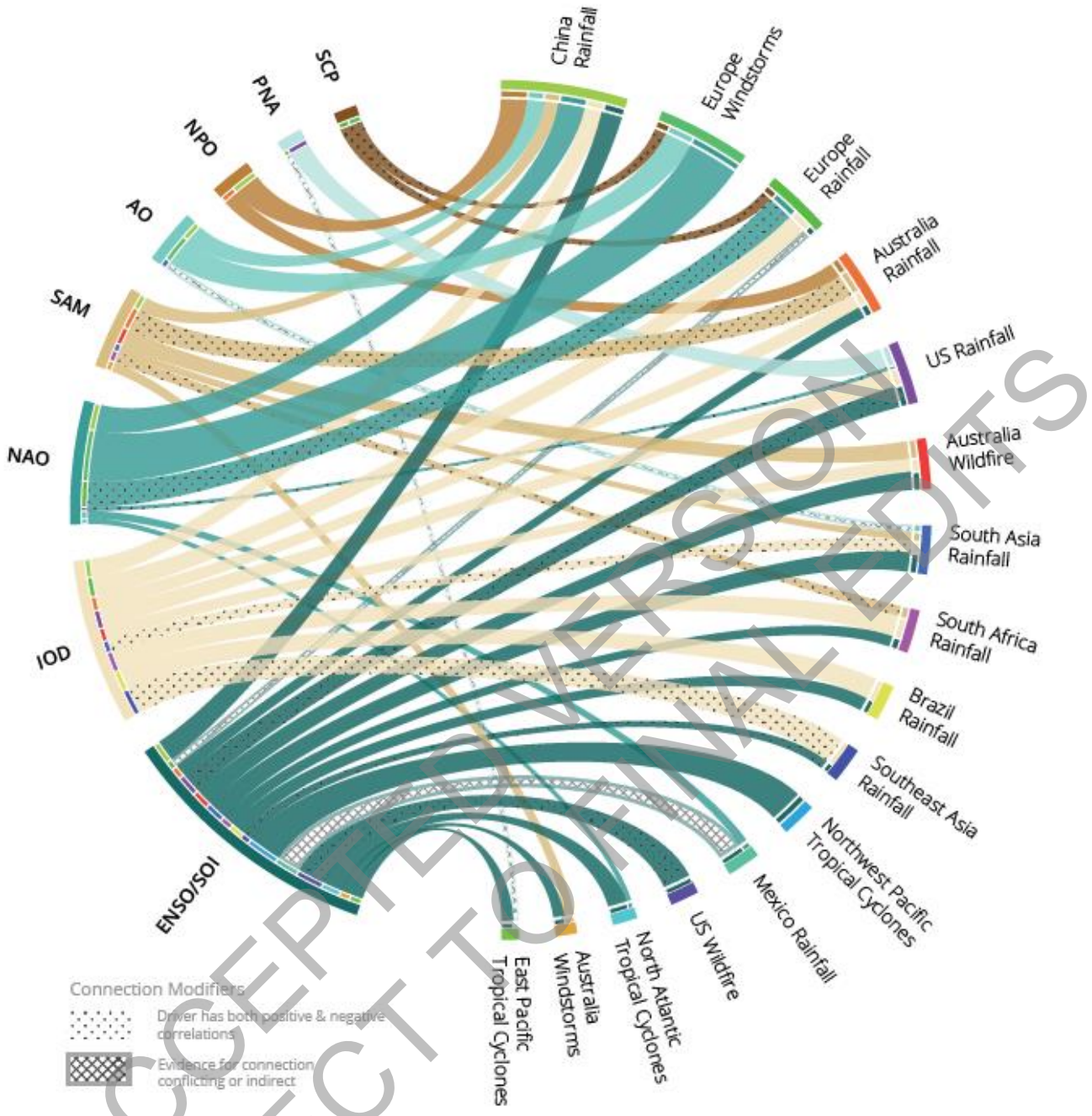


Figure Atlas.14: Influence of major modes of variability (see Annex IV) on regional extreme events relevant to assessing multi-hazard resilience. Ribbon colours define the driver from which they originate and their width is proportional to the correlation. Crossed lines represent where there is conflicting evidence for a correlation or where the driver is not directly related to the hazard and dots represent drivers that have both a positive and negative correlation with the hazard. Figure is copied from Steptoe et al. (2018) / CCBY4.0.

ACCEPTED VERSION SUBJECT TO FINAL EDITS

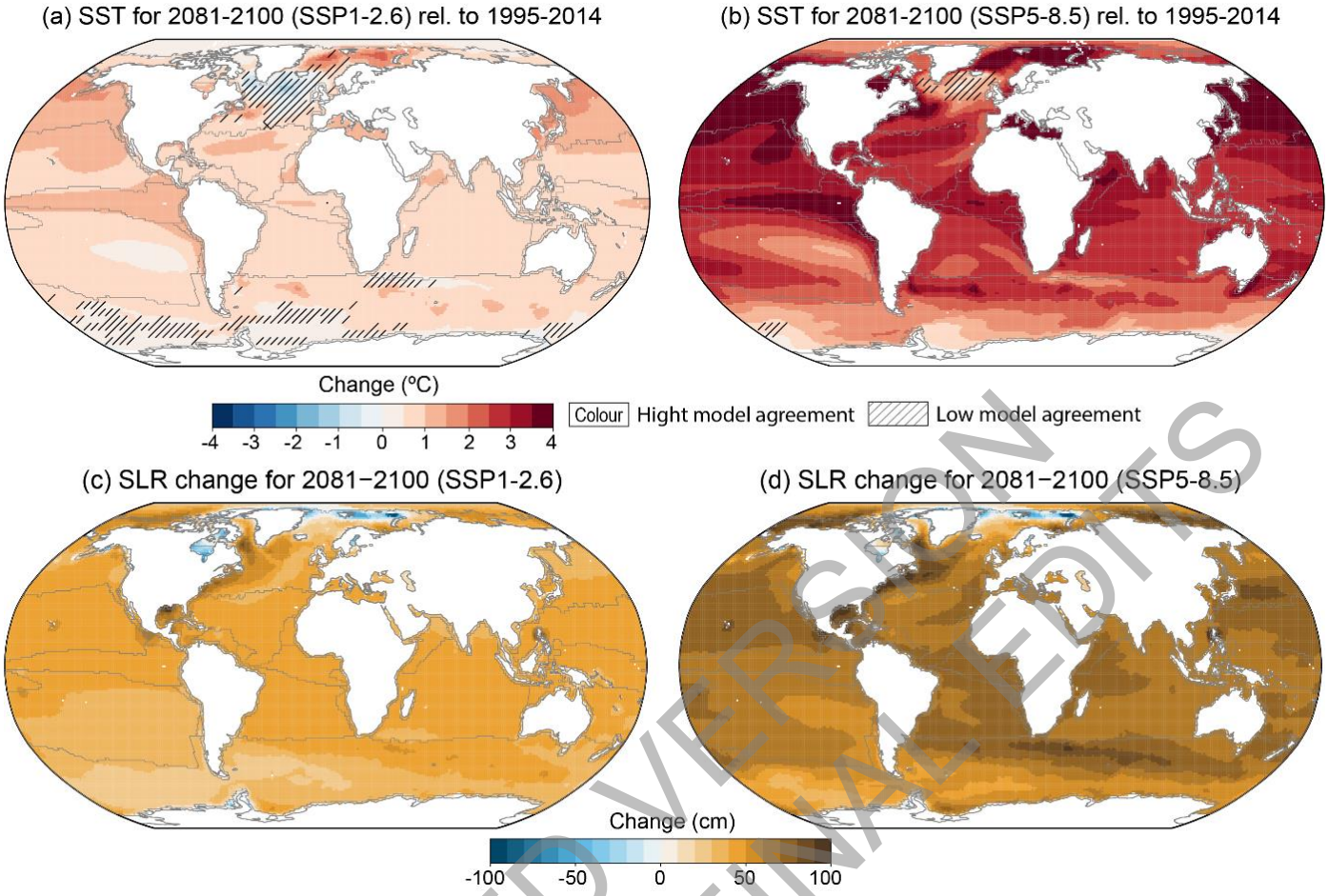


Figure Atlas.15: Projected changes in sea surface temperature (top), sea level rise (bottom) for 2081–2100 under the SSP1-2.6 (left) and SSP5-8.5 (right) emission scenarios compared to a 1995–2014 baseline period from the CMIP6 ensemble. For sea surface temperature, diagonal lines indicate regions where 80% of the models do not agree on the sign of the projected changes. Further details on data sources and processing are available in the chapter data table (Table Atlas.SM.15).

ACCEPTED VERSION SUBJECT TO FINAL EDITS

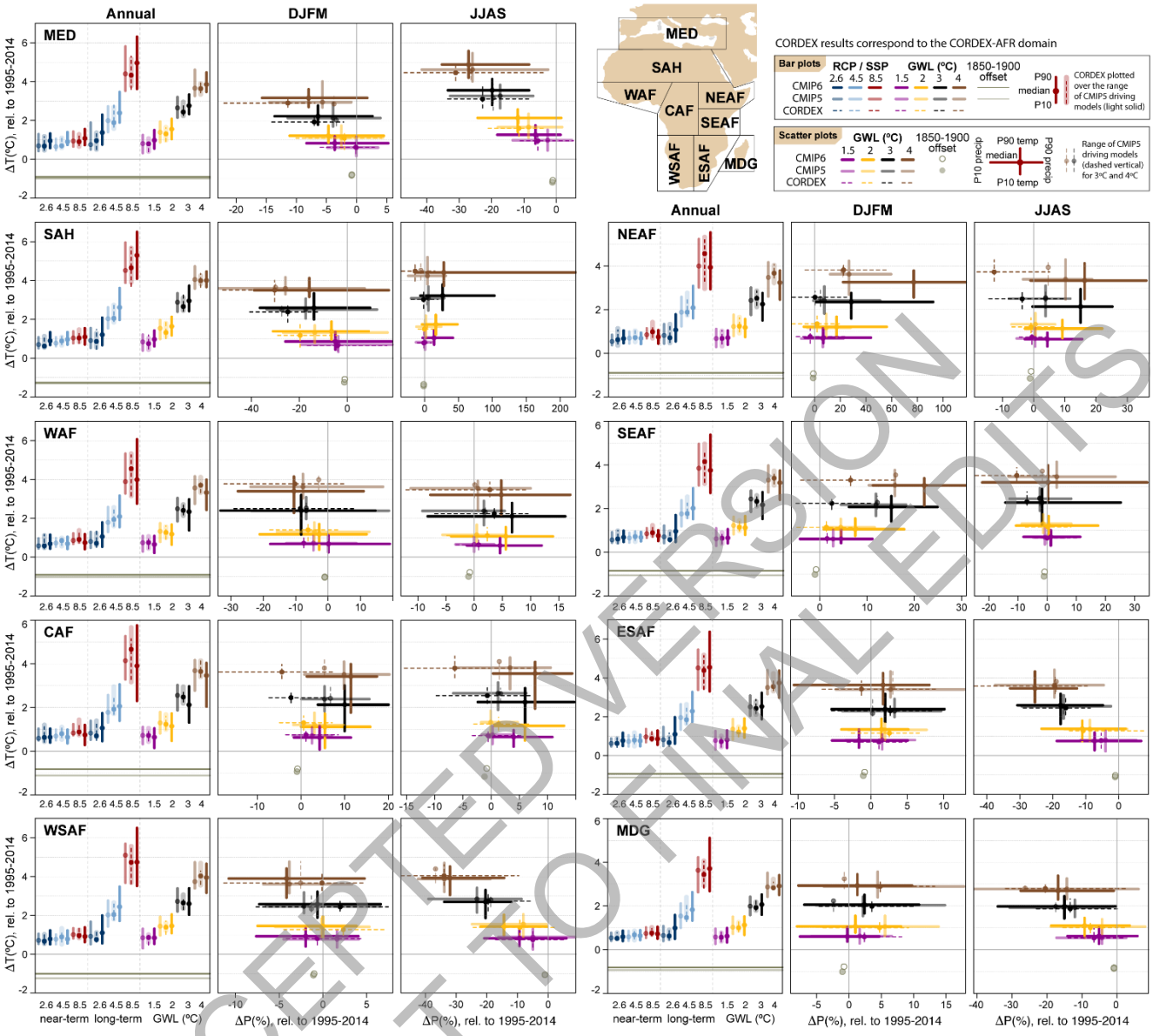
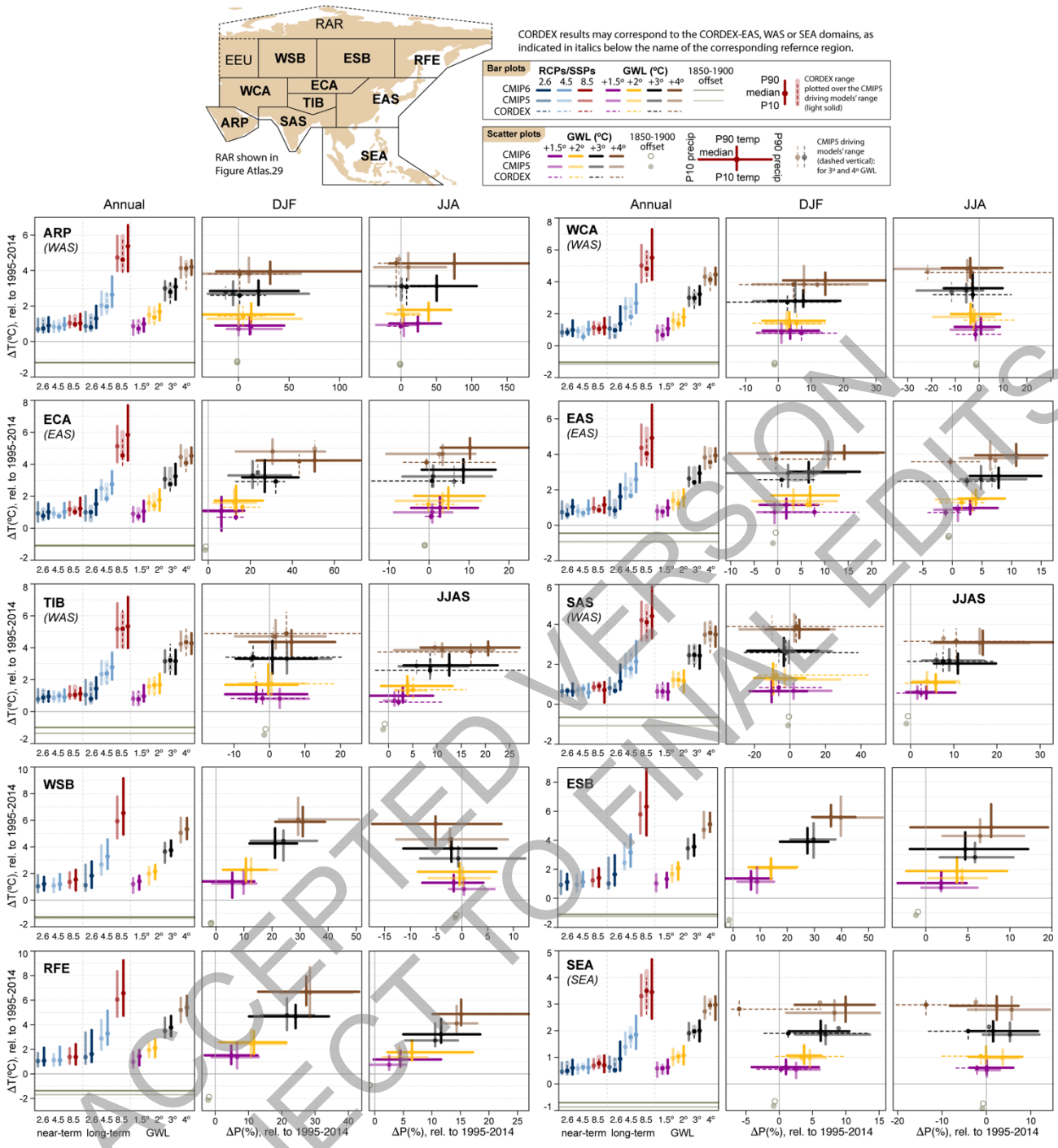


Figure Atlas.16: Regional mean changes in annual mean surface air temperature and precipitation relative to the 1995–2014 baseline for the reference regions in Africa (warming since the 1850–1900 pre-industrial baseline is also provided as an offset). Bar plots in the left panel of each region triplet show the median (dots) and 10th–90th percentile range (bars) across each model ensemble for annual mean temperature changes for four datasets (CMIP5 in intermediate colours; subset of CMIP5 used to drive CORDEX in light colours; CORDEX overlying the CMIP5 subset with dashed bars; and CMIP6 in solid colours); the first six groups of bars represent the regional warming over two time periods (near-term 2021–2040 and long-term 2081–2100) for three scenarios (SSP1-2.6/RCP2.6, SSP2-4.5/RCP4.5, and SSP5-8.5/RCP8.5), and the remaining bars correspond to four global warming levels (GWL: 1.5°C, 2°C, 3°C, and 4°C). The scatter diagrams of temperature against precipitation changes display the median (dots) and 10th–90th percentile ranges for the above four warming levels for December-January-February-March (DJFM; middle panel) and June-July-August-September (JJAS; right panel), respectively; for the CMIP5 subset only the percentile range of temperature is shown, and only for 3°C and 4°C GWLs. Changes are absolute for temperature (in °C) and relative (as %) for precipitation. See Section Atlas.1.3 for more details on reference regions (Iturbide et al., 2020) and Section Atlas.1.4 for details on model data selection and processing. The script used to generate this figure is available online (Iturbide et al., 2021) and similar results can be generated in the Interactive Atlas for flexibly defined seasonal periods. Further details on data sources and processing are available in the chapter data table (Table Atlas.SM.15).

ACCEPTED VERSION SUBJECT TO FINAL EDITS



ACCEPTED VERSION SUBJECT TO FINAL EDITS

Figure Atlas.17: Regional mean changes in annual mean surface air temperature and precipitation relative to the 1995–2014 baseline for the reference regions in Asia (warming since the 1850–1900 pre-industrial baseline is also provided as an offset). Bar plots in the left panel of each region triplet show the median (dots) and 10th–90th percentile range (bars) across each model ensemble for annual mean temperature changes for four datasets (CMIP5 in intermediate colours; subset of CMIP5 used to drive CORDEX in light colours; CORDEX overlying the CMIP5 subset with dashed bars; and CMIP6 in solid colours); the first six groups of bars represent the regional warming over two time periods (near-term 2021–2040 and long-term 2081–2100) for three scenarios (SSP1-2.6/RCP2.6, SSP2-4.5/RCP4.5, and SSP5-8.5/RCP8.5), and the remaining bars correspond to four global warming levels (GWL: 1.5°C, 2°C, 3°C, and 4°C). The scatter diagrams of temperature against precipitation changes display the median (dots) and 10th–90th percentile ranges for the above four warming levels for December-January-February (DJF; middle panel) and June-July-August (JJA; right panel), respectively; for the CMIP5 subset only the percentile range of temperature is shown, and only for 3°C and 4°C GWLs. Changes are absolute for temperature (in °C) and relative (as %) for precipitation. See Section Atlas.1.3 for more details on reference regions (Iturbide et al., 2020) and

Section Atlas.1.4 for details on model data selection and processing. The script used to generate this figure is available online (Iturbide et al., 2021) and similar results can be generated in the Interactive Atlas for flexibly defined seasonal periods. Further details on data sources and processing are available in the chapter data table (Table Atlas.SM.15).

ACCEPTED VERSION
SUBJECT TO FINAL EDITS

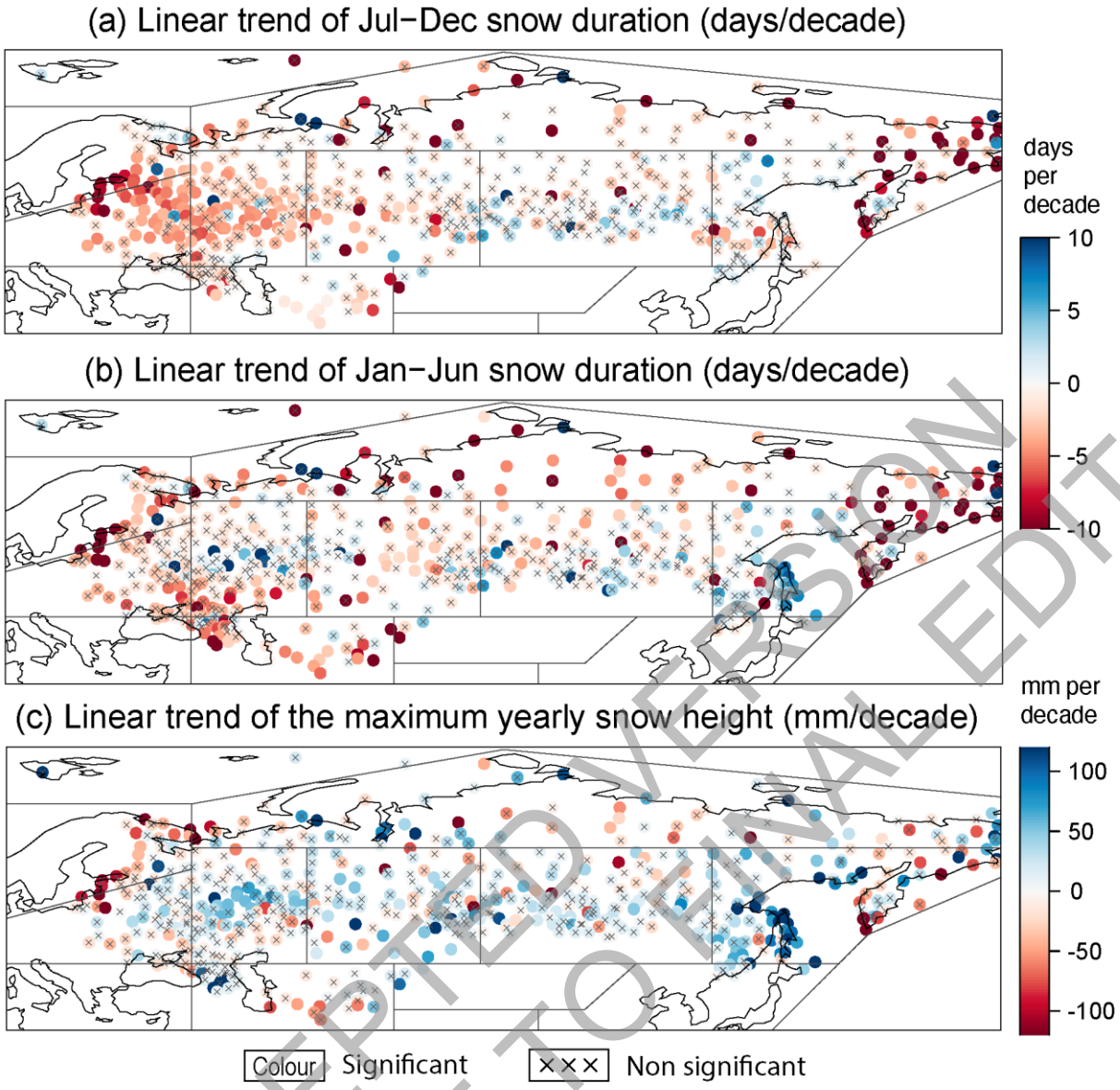
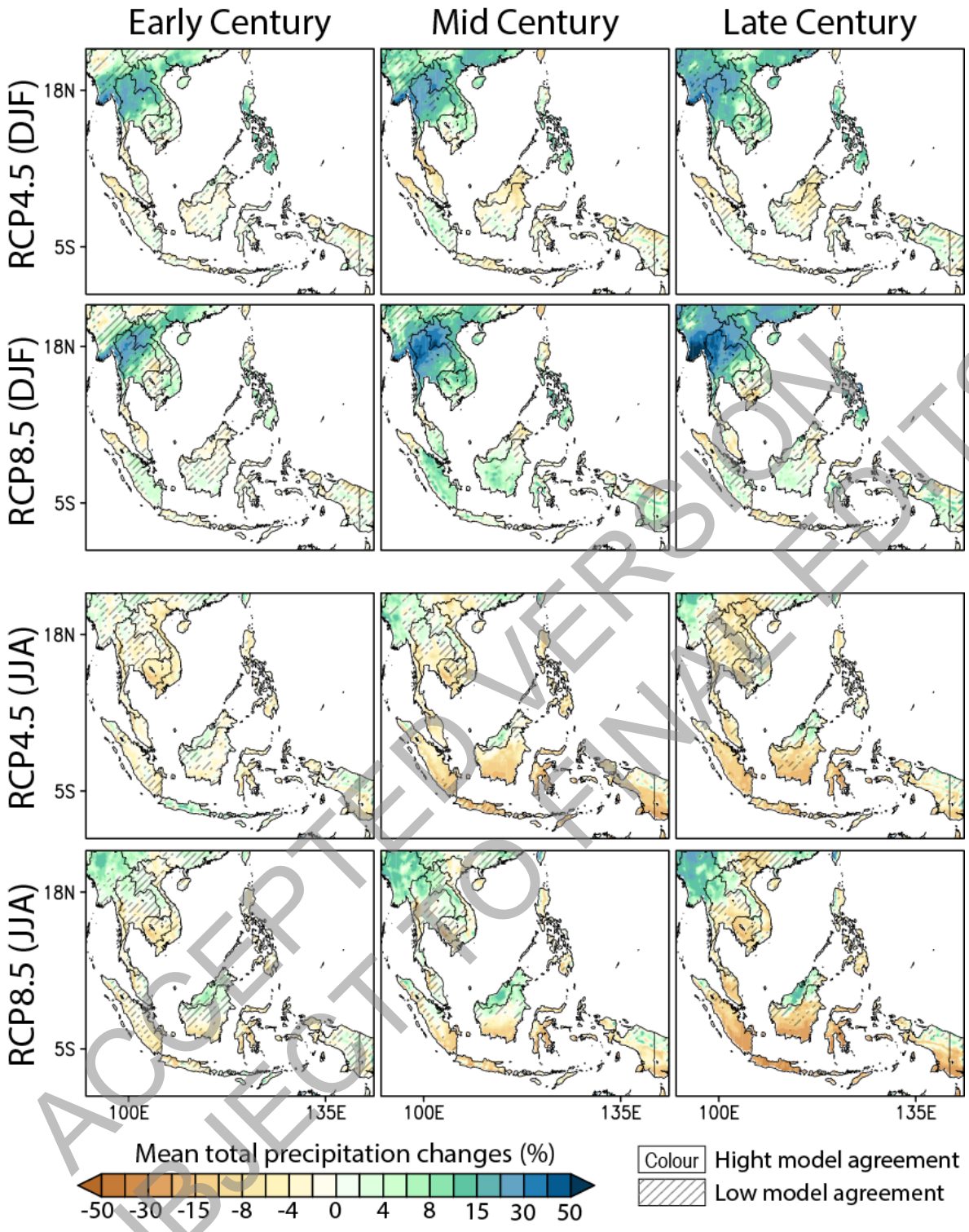


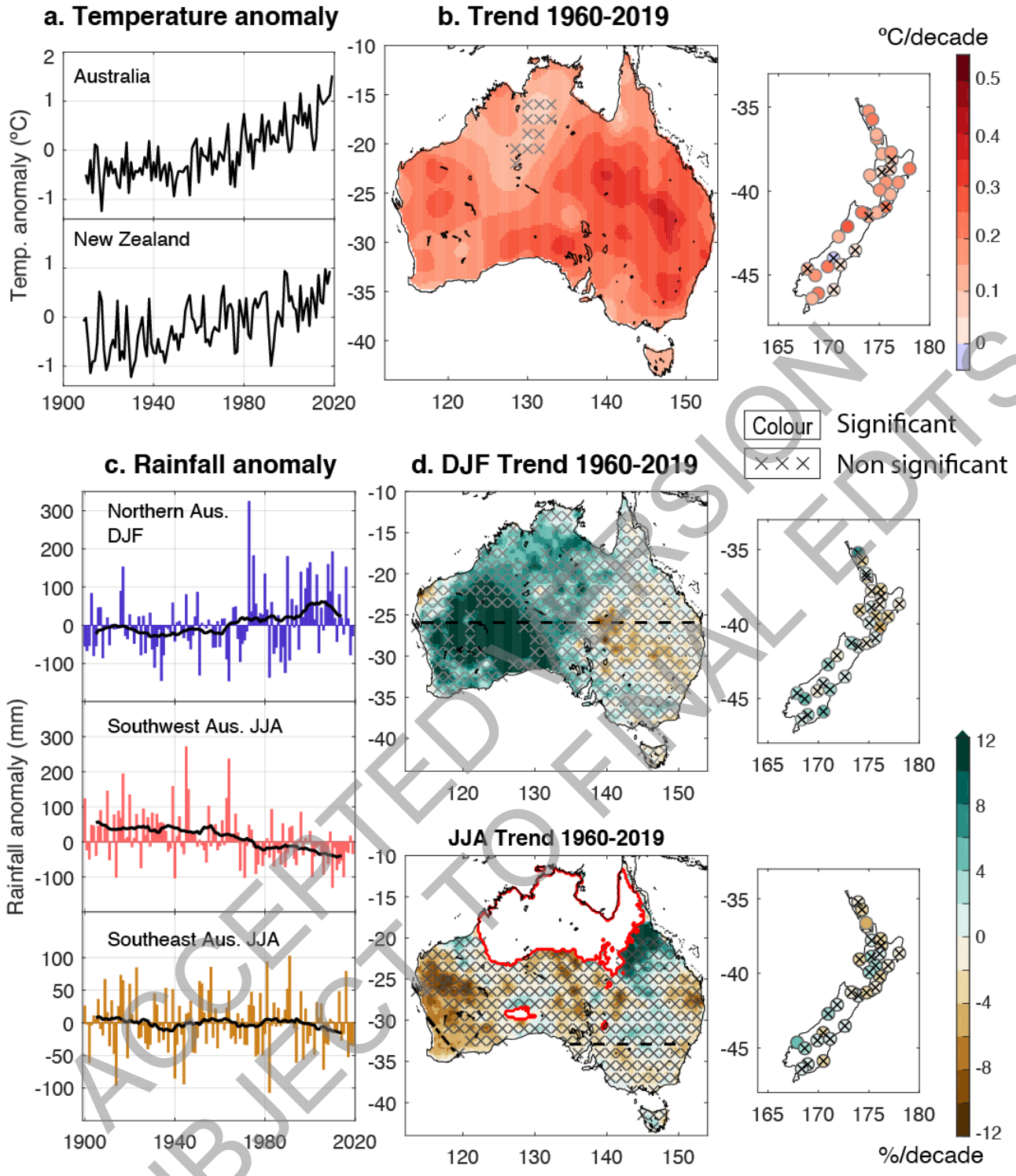
Figure Atlas.18: Linear trends for the 1980–2015 period based on station data from the World Data Centre of the Russian Institute for Hydrometeorological Information (RIHMI-WDC) (Bulygina et al., 2014). (a) Snow season duration from 1 July to 31 December (days per decade); (b) snow season duration from 1 January to 30 June (days per decade); (c) maximum annual height of snow cover (mm per decade). Trends have been calculated using ordinary least squares regression and the crosses indicate nonsignificant trend values (at the 0.1 level) following the method of Santer et al. (2008) to account for serial correlation. Further details on data sources and processing are available in the chapter data table (Table Atlas.SM.15).

ACCEPTED VERSION SUBJECT TO FINAL EDITS



ACCEPTED VERSION SUBJECT TO FINAL EDITS

Figure Atlas.19: The RCM projected changes in mean precipitation between the early (2011–2040), mid (2041–2070) and late (2071–2099) 21st century and the historical period 1976–2005. Data are obtained from the CORDEX-SEA downscaling simulations. Diagonal lines indicate areas with low model agreement (less than 80%). Adapted from Tangang et al. (2020).



ACCEPTED VERSION SUBJECT TO FINAL EDITS

Figure Atlas.20: Observed trends in mean annual temperature (a–b) and summer (DJF) and inter (JJA) precipitation (c–d) for Australia and New Zealand from high-quality regional datasets. Time series show anomalies from 1961–1990 average and 10-year running mean; maps show annual linear trends for 1960–2019; rainfall trends are shown in % per decade, crosses show areas and stations with a lack of significant trend and regions of seasonally dry conditions (<0.25 mm day–1) are masked and outlined in red. Datasets are Australian Climate Observation Reference Network – Surface Air Temperature version 2.1 (ACORN-SATv2.1) for Australian temperature, the Australian Gridded Climate Data (AGCD) for Australian rainfall (Evans et al., 2020), and the 30-station high-quality network for New Zealand temperature and rainfall. Further details on data sources and processing are available in the chapter data table (Table Atlas.SM.15).

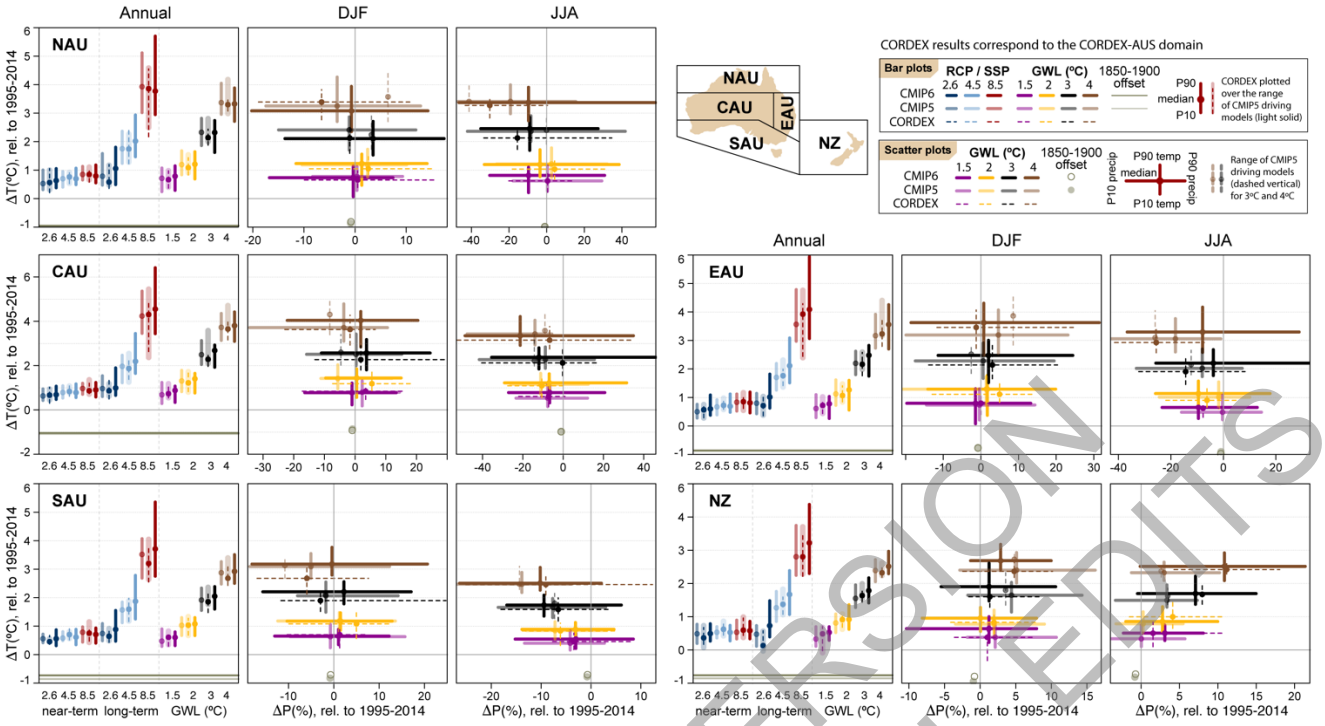
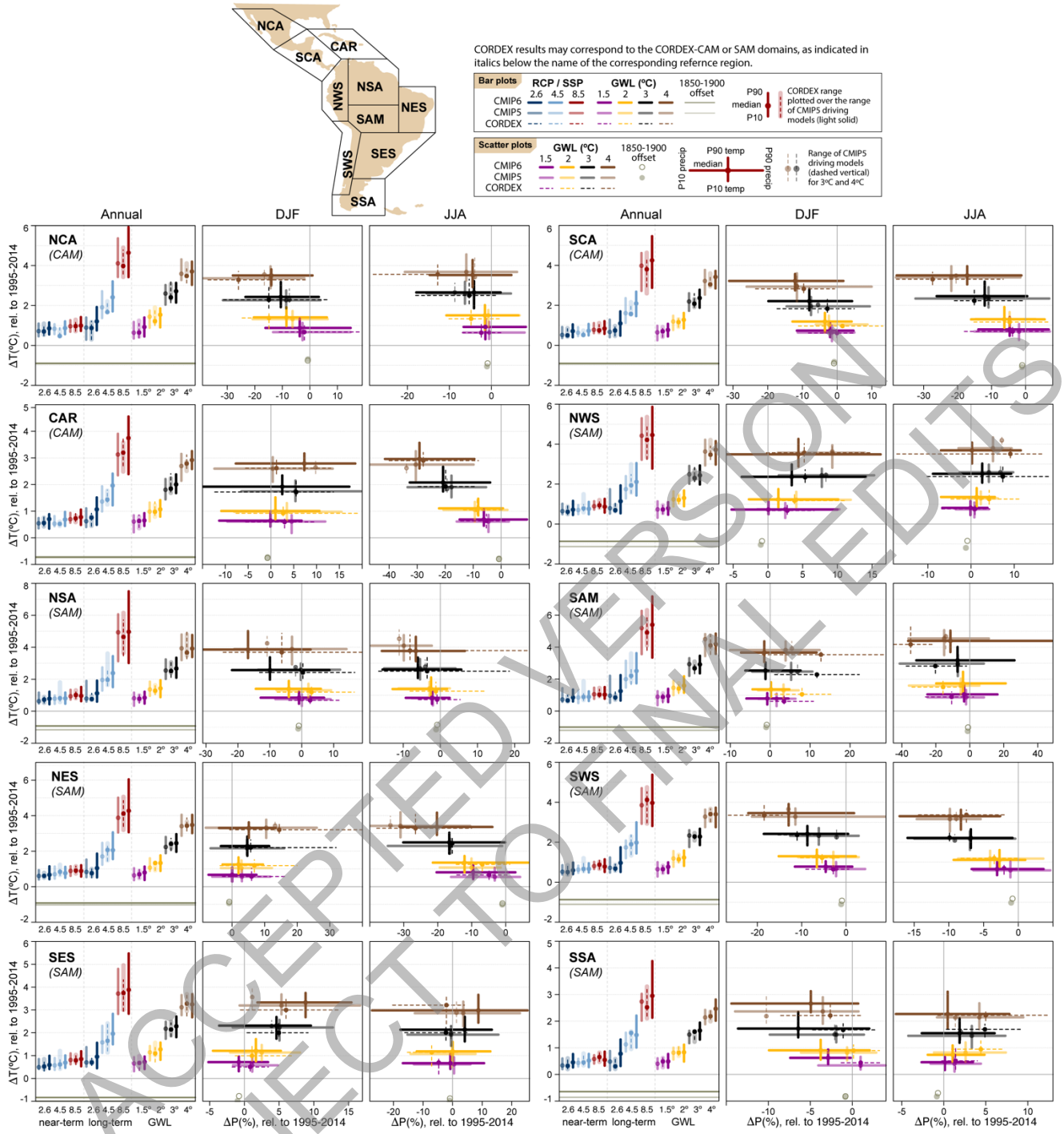


Figure Atlas.21: Regional mean changes in annual mean surface air temperature and precipitation relative to the 1995–2014 baseline for the reference regions in Australasia (warming since the 1850–1900 pre-industrial baseline is also provided as an offset). Bar plots in the left panel of each region triplet show the median (dots) and 10th–90th percentile range (bars) across each model ensemble for annual mean temperature changes for four datasets (CMIP5 in intermediate colours; subset of CMIP5 used to drive CORDEX in light colours; CORDEX overlying the CMIP5 subset with dashed bars; and CMIP6 in solid colours); the first six groups of bars represent the regional warming over two time periods (near-term 2021–2040 and long-term 2081–2100) for three scenarios (SSP1-2.6/RCP2.6, SSP2-4.5/RCP4.5, and SSP5-8.5/RCP8.5), and the remaining bars correspond to four global warming levels (GWL: 1.5°C, 2°C, 3°C, and 4°C). The scatter diagrams of temperature against precipitation changes display the median (dots) and 10th–90th percentile ranges for the above four warming levels for December-January-February (DJF; middle panel) and June-July-August (JJA; right panel), respectively; for the CMIP5 subset only the percentile range of temperature is shown, and only for 3°C and 4°C GWLs. Changes are absolute for temperature (in °C) and relative (as %) for precipitation. See Section Atlas.1.3 for more details on reference regions (Iturbide et al., 2020) and Section Atlas.1.4 for details on model data selection and processing. The script used to generate this figure is available online (Iturbide et al., 2021) and similar results can be generated in the Interactive Atlas for flexibly defined seasonal periods. Further details on data sources and processing are available in the chapter data table (Table Atlas.SM.15).

ACCEPTED VERSION SUBJECT TO FINAL EDITS

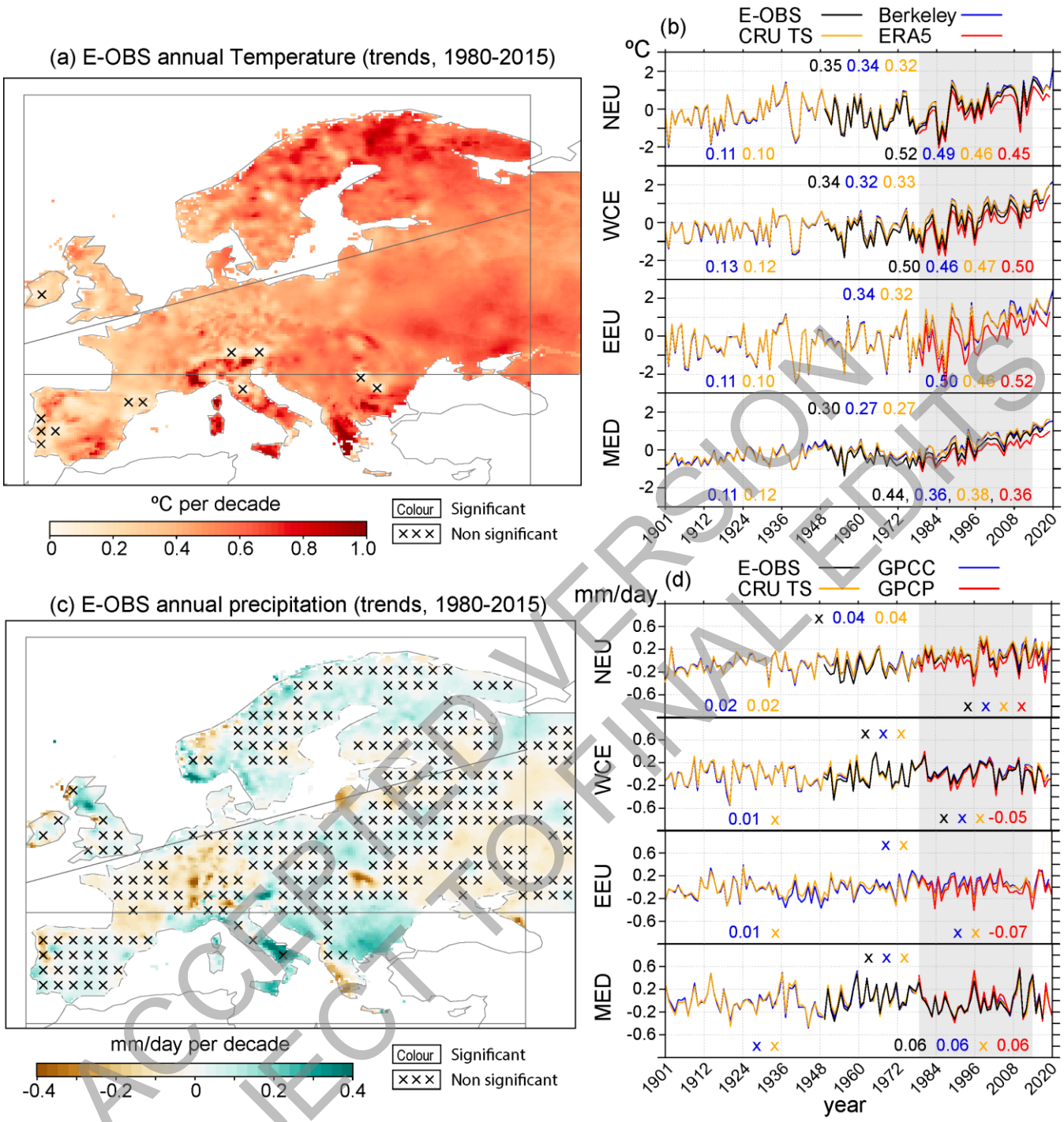


ACCEPTED VERSION SUBJECT TO FINAL EDITS

Figure Atlas.22: Regional mean changes in annual mean surface air temperature and precipitation relative to the 1995–2014 baseline for the reference regions in Central America, the Caribbean and South America (warming since the 1850–1900 pre-industrial baseline is also provided as an offset). Bar plots in the left panel of each region triplet show the median (dots) and 10th–90th percentile range (bars) across each model ensemble for annual mean temperature changes for four datasets (CMIP5 in intermediate colours; subset of CMIP5 used to drive CORDEX in light colours; CORDEX overlying the CMIP5 subset with dashed bars; and CMIP6 in solid colours); the first six groups of bars represent the regional warming over two time periods (near-term 2021–2040 and long-term 2081–2100) for three scenarios (SSP1-2.6/RCP2.6, SSP2-4.5/RCP4.5, and SSP5-8.5/RCP8.5), and the remaining bars correspond to four global warming levels (GWL: 1.5°C, 2°C, 3°C, and 4°C). The scatter diagrams of temperature against precipitation changes display the median (dots) and 10th–90th percentile ranges for the above four warming levels for December-January-February (DJF; middle panel) and June-July-August (JJA; right panel), respectively; for the CMIP5 subset only the percentile range of temperature is shown, and only for 3°C and 4°C GWLs. Changes are absolute for temperature (in °C)

and relative (as %) for precipitation. See Section Atlas.1.3 for more details on reference regions (Iturbide et al., 2020) and Section Atlas.1.4 for details on model data selection and processing. The script used to generate this figure is available online (Iturbide et al., 2021) and similar results can be generated in the Interactive Atlas for flexibly defined seasonal periods. Further details on data sources and processing are available in the chapter data table (Table Atlas.SM.15).

ACCEPTED VERSION
SUBJECT TO FINAL EDITS



ACCEPTED VERSION SUBJECT TO FINAL EDITS

Figure Atlas.23: (a) Mean 1980–2015 trend of annual mean surface air temperature (°C per decade) from E-OBS (Cornes et al., 2018). Data for non-European countries in the MED area are masked out. (b) Time series of mean annual temperature anomaly relative to the 1980–2015 period (shown with grey shading) aggregated for the land area in each of the four European subregions, from E-OBS, CRU, Berkeley and ERA5 (see Section Atlas.1.4.1 for description of global datasets). Mean trends for 1901–2015, 1961–2015 and 1980–2015 are shown for each data set in corresponding colours in the same units as panel (a) (see legend in upper panel). (c) As panel (a) for annual mean precipitation (mm day^{-1} per decade). (d) as panel (b) for annual mean precipitation, and data sets E-OBS, CRU, GPCC and GPCP. Note that E-OBS data are not shown in panels b and d for region EEU. For the MED region data are aggregated over the European countries alone. Trends have been calculated using ordinary least squares regression and the crosses indicate nonsignificant trend values (at the 0.1 level) following the method of Santer et al. (2008) to account for serial correlation. Further details on data sources and processing are available in the chapter data table (Table Atlas.SM.15).

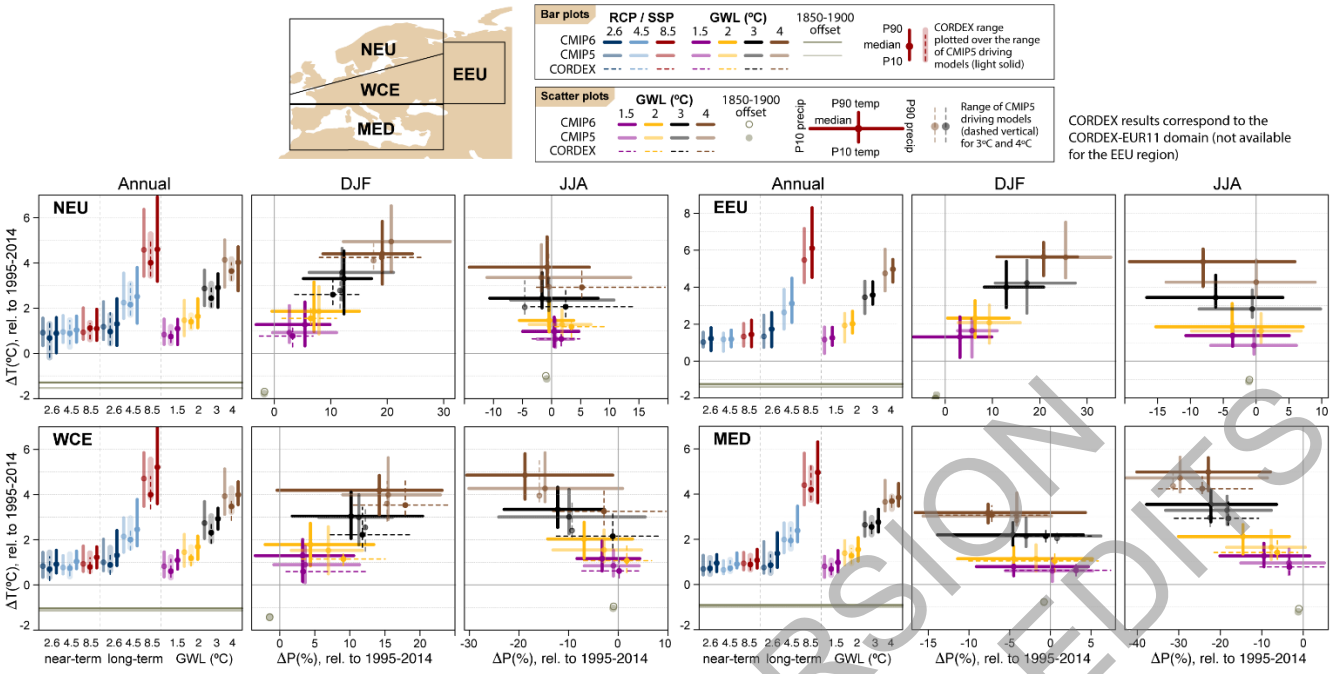


Figure Atlas.24: Regional mean changes in annual mean surface air temperature and precipitation relative to the 1995–2014 baseline for the reference regions in Europe (warming since the 1850–1900 pre-industrial baseline is also provided as an offset). Bar plots in the left panel of each region triplet show the median (dots) and 10th–90th percentile range (bars) across each model ensemble for annual mean temperature changes for four datasets (CMIP5 in intermediate colours; subset of CMIP5 used to drive CORDEX in light colours; CORDEX overlying the CMIP5 subset with dashed bars; and CMIP6 in solid colours); the first six groups of bars represent the regional warming over two time periods (near-term 2021–2040 and long-term 2081–2100) for three scenarios (SSP1-2.6/RCP2.6, SSP2-4.5/RCP4.5, and SSP5-8.5/RCP8.5), and the remaining bars correspond to four global warming levels (GWL: 1.5°C, 2°C, 3°C, and 4°C). The scatter diagrams of temperature against precipitation changes display the median (dots) and 10th–90th percentile ranges for the above four warming levels for December-January-February (DJF; middle panel) and June-July-August (JJA; right panel), respectively; for the CMIP5 subset only the percentile range of temperature is shown, and only for 3°C and 4°C GWLs. Changes are absolute for temperature (in °C) and relative (as %) for precipitation. See Section Atlas.1.3 for more details on reference regions (Iturbide et al., 2020) and Section Atlas.1.4 for details on model data selection and processing. The script used to generate this figure is available online (Iturbide et al., 2021) and similar results can be generated in the Interactive Atlas for flexibly defined seasonal periods. Further details on data sources and processing are available in the chapter data table (Table Atlas.SM.15).

ACCEPTED VERSION SUBJECT TO FINAL EDITS

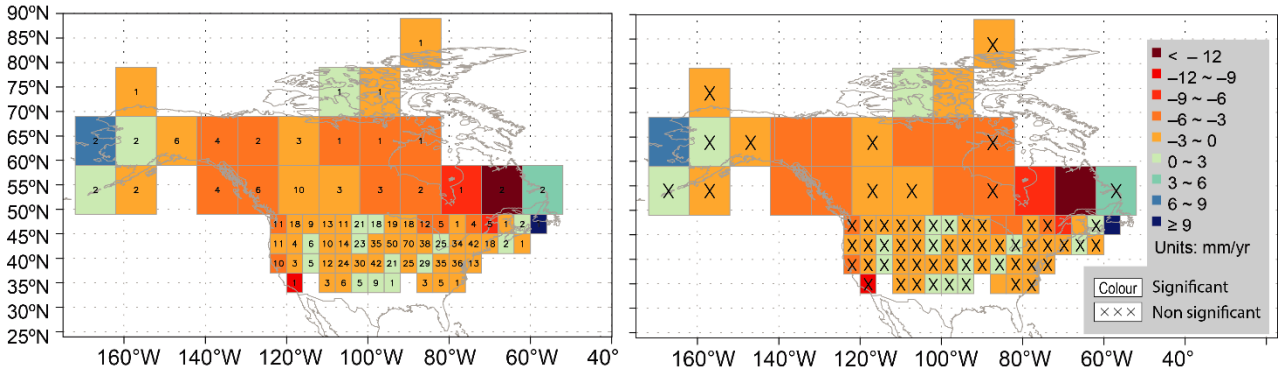


Figure Atlas.25: Grid-box trends (mm yr^{-1}) in annual maximum snow depth for cold season periods of 1960/1961 to 2014/2015. (Left) Numbers indicate number of stations available in that grid box. (Right) Boxes with 'x' indicate non-significant trends (at the $p < 0.05$ level of significance) (Kunkel et al., 2016).

ACCEPTED VERSION
SUBJECT TO FINAL EDITS

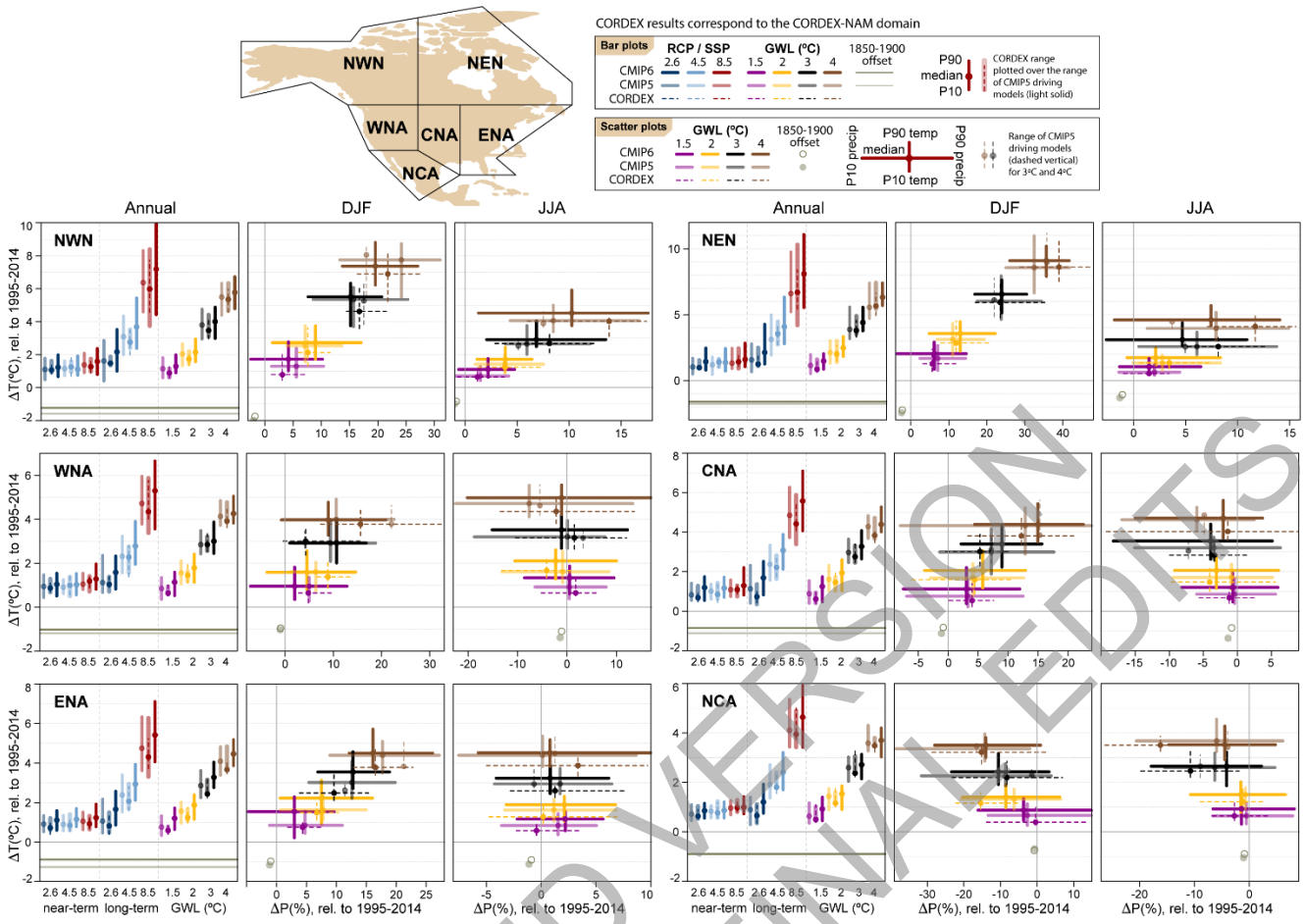


Figure Atlas.26: Regional mean changes in annual mean surface air temperature and precipitation relative to the 1995–2014 baseline for the reference regions in North America (warming since the 1850–1900 pre-industrial baseline is also provided as an offset). Bar plots in the left panel of each region triplet show the median (dots) and 10th–90th percentile range (bars) across each model ensemble for annual mean temperature changes for four datasets (CMIP5 in intermediate colours; subset of CMIP5 used to drive CORDEX in light colours; CORDEX overlying the CMIP5 subset with dashed bars; and CMIP6 in solid colours); the first six groups of bars represent the regional warming over two time periods (near-term 2021–2040 and long-term 2081–2100) for three scenarios (SSP1-2.6/RCP2.6, SSP2-4.5/RCP4.5, and SSP5-8.5/RCP8.5), and the remaining bars correspond to four global warming levels (GWL: 1.5°C, 2°C, 3°C, and 4°C). The scatter diagrams of temperature against precipitation changes display the median (dots) and 10th–90th percentile ranges for the above four warming levels for December-January-February (DJF; middle panel) and June-July-August (JJA; right panel), respectively; for the CMIP5 subset only the percentile range of temperature is shown, and only for 3°C and 4°C GWLs. Changes are absolute for temperature (in °C) and relative (as %) for precipitation. See Section Atlas.1.3 for more details on reference regions (Iturbide et al., 2020) and Section Atlas.1.4 for details on model data selection and processing. The script used to generate this figure is available online (Iturbide et al., 2021) and similar results can be generated in the Interactive Atlas for flexibly defined seasonal periods. Further details on data sources and processing are available in the chapter data table (Table Atlas.SM.15).

ACCEPTED VERSION SUBJECT TO FINAL EDITS

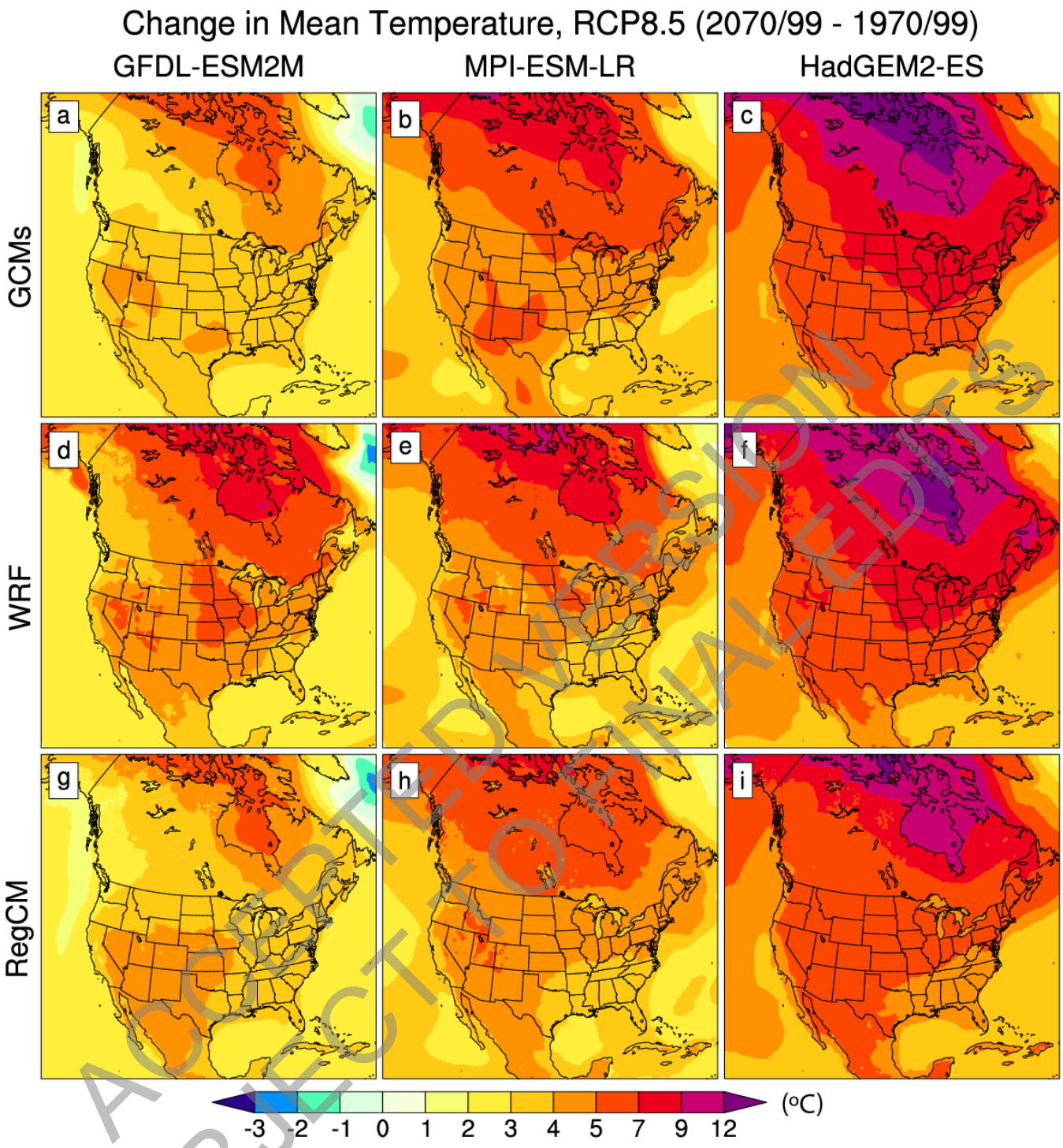
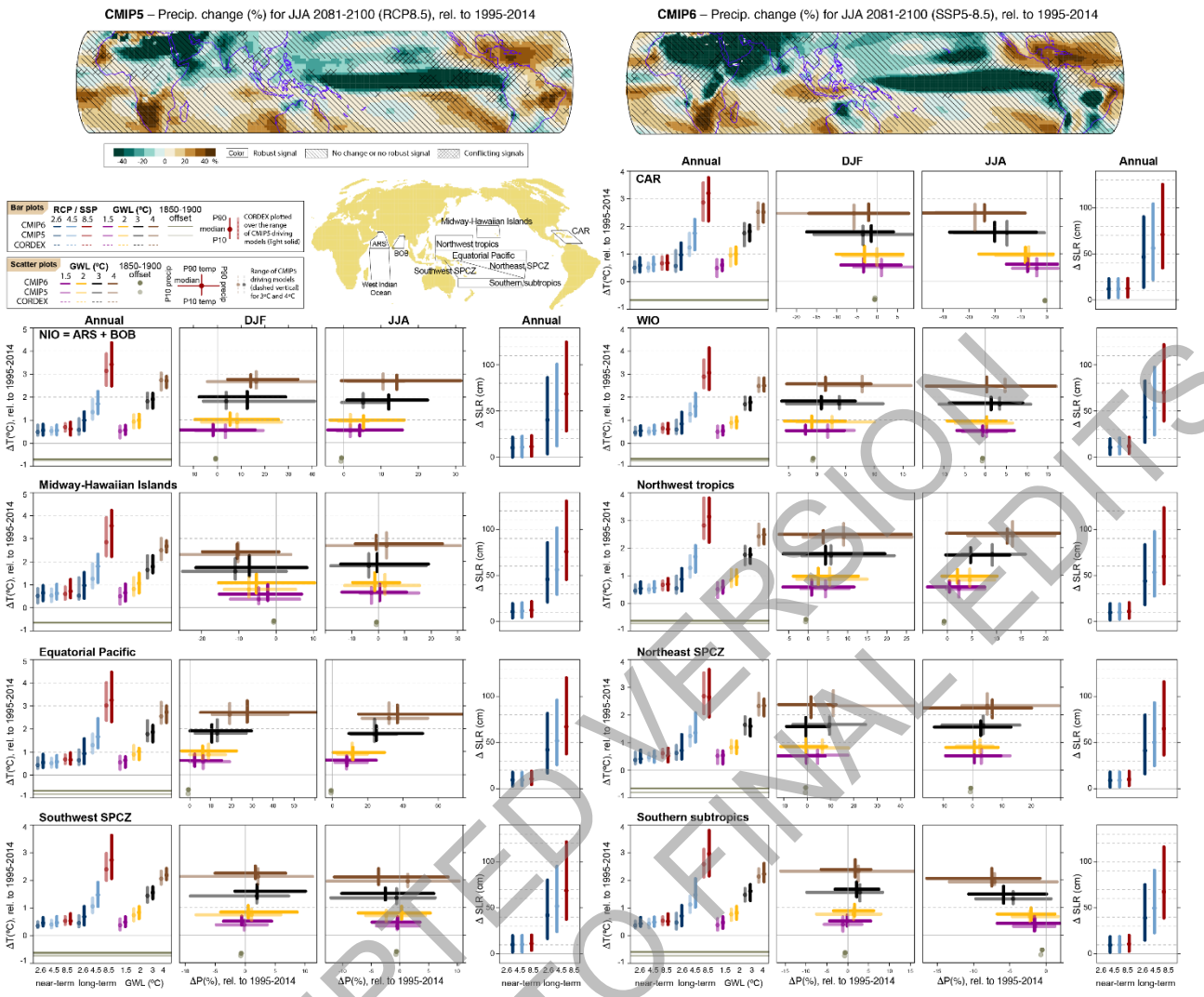


Figure Atlas.27: Changes (2070–2099 relative to 1970–1999) in the annual mean surface air temperature by three GCMs (GFDL ESM2M, MPI ESM-LR, HadGEM2-ES) and two RCMs (WRF and RegCM4) nested in the GCMs, for the RCP8.5 scenario (after Bukovsky and Mearns, 2020).

ACCEPTED VERSION SUBJECT TO FINAL EDITS



ACCEPTED VERSION SUBJECT TO FINAL EDITS

Figure Atlas.28: Regional mean changes in annual mean surface air temperature, precipitation and sea level rise relative to the 1995–2014 baseline for the reference regions in Small Islands (warming since the 1850–1900 pre-industrial baseline is also provided as an offset). Bar plots in the left panel of each region triplet show the median (dots) and 10th–90th percentile range (bars) across each model ensemble for annual mean temperature changes for four datasets (CMIP5 in intermediate colours; subset of CMIP5 used to drive CORDEX in light colours; CORDEX overlying the CMIP5 subset with dashed bars; and CMIP6 in solid colours); the first six groups of bars represent the regional warming over two time periods (near-term 2021–2040 and long-term 2081–2100) for three scenarios (SSP1-2.6/RCP2.6, SSP2-4.5/RCP4.5, and SSP5-8.5/RCP8.5), and the remaining bars correspond to four global warming levels (GWL: 1.5°C, 2°C, 3°C, and 4°C). Bar plots in the right panel show the median (dots) and 5th–95th percentile range (bars) sea level rise from the CMIP6 ensemble (see Chapter 9 for details) for the same time periods and scenarios. The scatter diagrams of temperature against precipitation changes display the median (dots) and 10th–90th percentile ranges for the above four warming levels for December-January-February (DJF; middle panel) and June-July-August (JJA; right panel), respectively; for the CMIP5 subset only the percentile range of temperature is shown, and only for 3°C and 4°C GWLs. Changes are absolute for temperature (in °C) and relative (as %) for precipitation. See Section Atlas.1.3 for more details on reference regions (Iturbide et al., 2020) and Section Atlas.1.4 for details on model data selection and processing. The script used to generate this figure is available online (Iturbide et al., 2021) and similar results can be generated in the Interactive Atlas for flexibly defined seasonal periods. Further details on data sources and processing are available in the chapter data table (Table Atlas.SM.15).

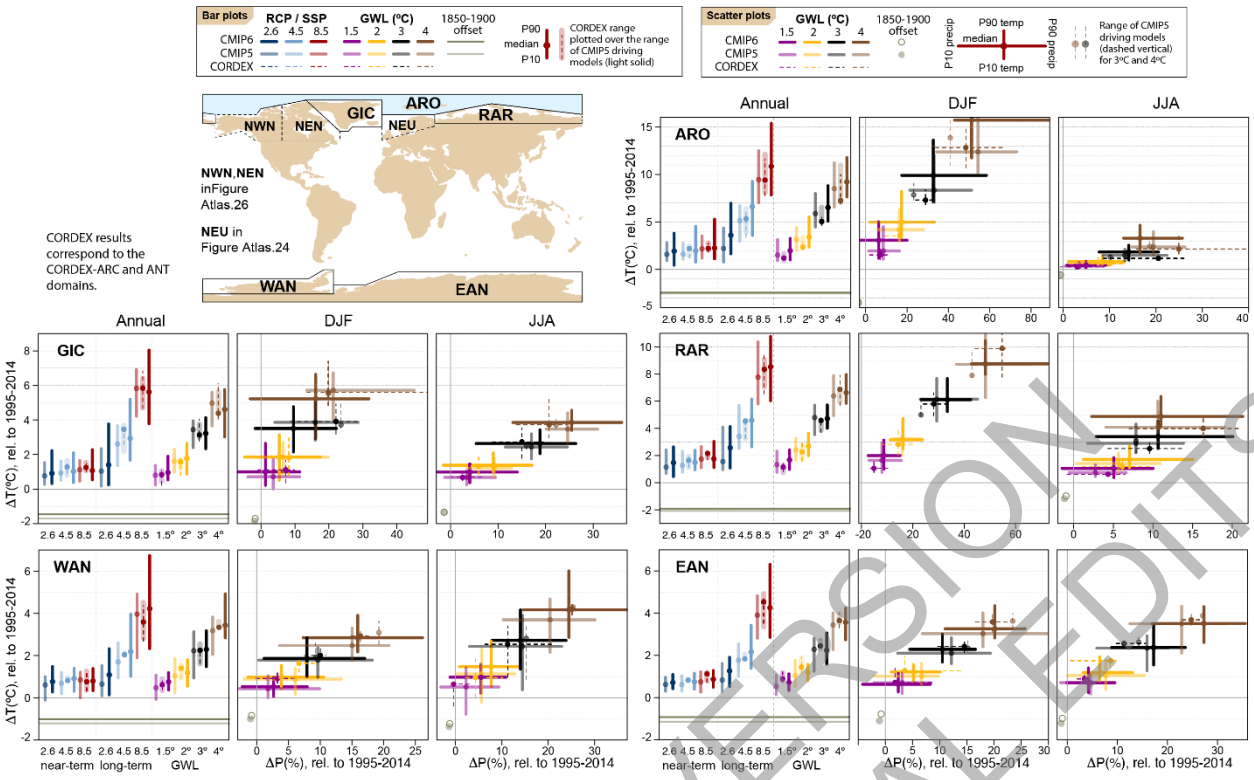


Figure Atlas.29: Regional mean changes in annual mean surface air temperature and precipitation relative to the 1995–2014 baseline for the reference regions in Arctic and Antarctica (warming since the 1850–1900 pre-industrial baseline is also provided as an offset). Bar plots in the left panel of each region triplet show the median (dots) and 10th–90th percentile range (bars) across each model ensemble for annual mean temperature changes for four datasets (CMIP5 in intermediate colours; subset of CMIP5 used to drive CORDEX in light colours; CORDEX overlying the CMIP5 subset with dashed bars; and CMIP6 in solid colours); the first six groups of bars represent the regional warming over two time periods (near-term 2021–2040 and long-term 2081–2100) for three scenarios (SSP1-2.6/RCP2.6, SSP2-4.5/RCP4.5, and SSP5-8.5/RCP8.5), and the remaining bars correspond to four global warming levels (GWL: 1.5°C, 2°C, 3°C, and 4°C). The scatter diagrams of temperature against precipitation changes display the median (dots) and 10th–90th percentile ranges for the above four warming levels for December-January-February (DJF; middle panel) and June-July-August (JJA; right panel), respectively; for the CMIP5 subset only the percentile range of temperature is shown, and only for 3°C and 4°C GWLs. Changes are absolute for temperature (in °C) and relative (as %) for precipitation. See Section Atlas.1.3 for more details on reference regions (Iturbide et al., 2020) and Section Atlas.1.4 for details on model data selection and processing. The script used to generate this figure is available online (Iturbide et al., 2021) and similar results can be generated in the Interactive Atlas for flexibly defined seasonal periods. Further details on data sources and processing are available in the chapter data table (Table Atlas.SM.15).

ACCEPTED VERSION SUBJECT TO FINAL EDITS

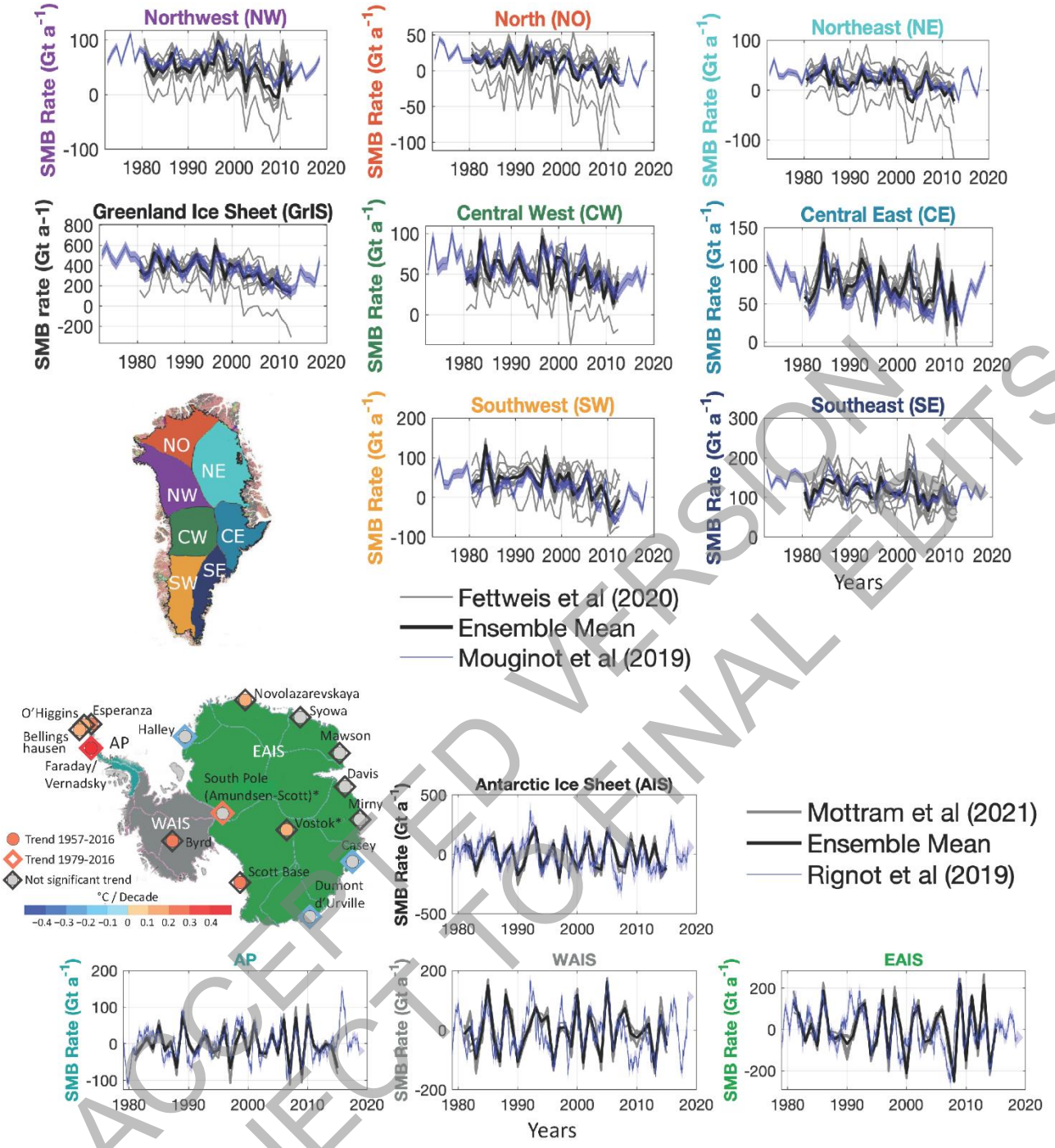


Figure Atlas.30: (Upper panels) Time series of annual surface mass balance (SMB) rates (in Gt a^{-1}) for Greenland ice sheet and its regions (shown in the inset map) for the periods 1972–2018 (Mouginot et al., 2019) and 1980–2012 (Fettweis et al., 2020) using 13 different models. (Lower panels) Time series of annual SMB rates (in Gt a^{-1}) for the grounded Antarctic ice sheet (excluding ice shelves) and its regions (shown in the inset map) for the periods 1979–2019 (Rignot et al., 2019) and 1980–2016 (Mottram et al., 2021) using five Polar-CORDEX regional climate models. The Antarctic inset map also shows the location of the stations discussed in section Atlas.11.1.2 where observations are available for at least 50 years. Colors indicate near surface air temperature trends for 1957-2016 (circles) and 1979-2016 (diamonds) statistically significant at 90% (Jones et al, 2019; Turner et al, 2020). Stations with an asterisk (*) are where significance estimates disagree between the two publications. Further details on data sources and processing are available in the chapter data table (Table Atlas.SM.15).

ACCEPTED VERSION SUBJECT TO FINAL EDITS

Atlas Supplementary Material

Coordinating Lead Authors:
José Manuel Gutiérrez (Spain), Richard G. Jones (United Kingdom), Gemma Teresa Narisma (Philippines)

Lead Authors:
Lincoln M. Alves (Brazil), Muhammad Amjad (Pakistan), Irina V. Gorodetskaya (Portugal/Belgium, Russian Federation), Michael Grose (Australia), Nana Ama Browne Klutse (Ghana), Svitlana Krakovska (Ukraine), Jian Li (China), Daniel Martínez-Castro (Cuba, Peru/Cuba), Linda O. Mearns (United States of America), Sebastian H. Mernild (Denmark, Norway/Denmark), Thanh Ngo-Duc (Vietnam), Bart van den Hurk (The Netherlands), Jin-Ho Yoon (Republic of Korea)

Contributing Authors (Atlas chapter):
Maialen Iturbide (Spain), Ma. Laurice Preciado Jamero (Philippines), Émilie Vanvyve United Kingdom/ Belgium), Guðfinna Aðalgeirsdóttir (Iceland), Cécile Agosta (France), Mansour Almazroui (Saudi Arabia), Jorge Baño-Medina (Spain), Joaquín Bedia (Spain), María Laura Bettolli (Argentina), Donovan Campbell (Jamaica), Ana Casanueva (Spain), Christophe Cassou (France), Tereza Cavazos (Mexico), Abel Centella-Artola (Cuba), Ruth Cerezo-Mota (Mexico), Haoming Chen (China), Annalisa Cherchi (Italy), Erika Coppola (Italy), Faye Abigail Cruz (Philippines), Joseph D. Daron (United Kingdom), Chirag Dhara (India), Alejandro di Luca (Australia, Canada/Argentina), Arona Diedhiou (Ivory Coast/Senegal), Javier Díez Sierra (Spain), Alessandro Dosio (Italy), Jason Evans (Australia), Vincent Favier (France), Erich Fischer (Switzerland), Sebastian Gerland (Norway/Germany), Subimal Ghosh (India), Natalia Gnatiuk (Russian Federation/Ukraine), Melissa I. Gomis (France/Switzerland), Patrick Grenier (Canada), David S. Gutzler (United States of America), Rein Haarsma (The Netherlands), Rafiq Hamdi (Belgium), Cédric Hananel (Belgium/France), Ed Hawkins (United Kingdom), Mark Hemer (Australia), Kevin Hennessy (Australia), Nazrul Islam (Bangladesh/Saudi Arabia), Sanjay Jayanarayanan (India), Liew Juneng (Malaysia), Eleni Katragkou (Greece), Elena Kharyutkina (Russian Federation), Megan Kirchmeier-Young (Canada/ United States of America), Akio Kitoh (Japan), Erik Kjellström (Sweden), Yu Kosaka (Japan), James Kossin (United States of America), Kenneth Kunkel (United States of America), June-Yi Lee (Republic of Korea), Christopher Lennard (South Africa), Piero Lionello (Italy), Marta Pereira Llopart (Brazil), Ian Macadam (Australia/ United Kingdom), Douglas Maraun (Austria/Germany), Seth McGinnis (United States of America), Simon McGree (Australia/Fiji, Australia), Wilfran Moufouma-Okia (France), Gregory Nikulin (Sweden/Russian Federation), Francis Nkrumah (Ghana), Dirk Notz (Germany), Andrew Orr (United Kingdom), Sarah Osima (Tanzania), Tugba Ozturk (Turkey), Mohammad Rahimi (Iran), Mehwish Ramzan (Pakistan), Rosh Ranasinghe (The Netherlands/Sri Lanka, Australia), Johan Reyns (The Netherlands/Belgium), Annette Rinke (Germany), Daniela Schmidt (United Kingdom), Stéphane Sénési (France), Sonia I. Seneviratne (Switzerland), Chris Shaw (United Kingdom), Stefan Sobolowski (Norway/ United States of America), Samuel Somot (France), Anna A. Sörensson (Argentina), Tannecia S. Stephenson (Jamaica), Mouhamadou Bamba Sylla (Rwanda/Senegal), Fredolin Tangang (Malaysia), Claas Teichmann (Germany), Peter W. Thorne (Ireland/United Kingdom), Blair Trewin (Australia), Geert-Jan van Oldenborgh (The Netherlands), Jan Melchior van Wessem (The Netherlands), Robert Vautard (France), Sergio M. Vicente-Serrano (Spain), Alejandro Vichot-Llano (Cuba), Etienne Vignon (France), Yu Xiaoyong (China, Germany), Xuebin Zhang (Canada)

Contributing Authors (Interactive Atlas):
Maialen Iturbide (Spain), Jorge Baño-Medina (Spain), Joaquín Bedia (Spain), Ana Casanueva (Spain), Ezequiel Cimadevilla (Spain), Antonio S. Cofiño (Spain), Javier Díez Sierra (Spain), Jesús Fernández (Spain), Markel García (Spain), Sixto Herrera (Spain), Rodrigo Manzanas (Spain), Josipa Milovac (Spain/Croatia), Juan José Sáenz de la Torre (Spain), Daniel San Martín (Spain), Iván Sánchez (Spain), Elena Suárez (Spain), Max Tuni (Spain)

Review Editors:
Inés Camilloni (Argentina), Jens Hesselbjerg Christensen (Denmark), Fatima Driouech (Morocco)

ACCEPTED VERSION SUBJECT TO FINAL EDITING

Chapter Scientists:
Maialen Iturbide (Spain), Ma. Laurice Preciado Jamero (Philippines), Émilie Vanvyve (United Kingdom/Belgium)

Gemma Teresa Narisma, *in memoriam*.

This Supplementary Material should be cited as:
Gutiérrez, J. M., R. G. Jones, G. T. Narisma, L. M. Alves, M. Amjad, I. V. Gorodetskaya, M. Grose, N. A. B. Klutse, S. Krakovska, J. Li, D. Martínez-Castro, L. O. Mearns, S. H. Mernild, T. Ngo-Duc, B. van den Hurk, J-H. Yoon, 2021, Atlas Supplementary Material. In: *Climate Change 2021: The Physical Science Basis. Contribution of Working Group I to the Sixth Assessment Report of the Intergovernmental Panel on Climate Change* [Masson-Delmotte, V., P. Zhai, A. Pirani, S. L. Connors, C. Péan, S. Berger, N. Caud, Y. Chen, L. Goldfarb, M. I. Gomis, M. Huang, K. Leitzell, E. Lonnoy, J. B. R. Matthews, T. K. Maycock, T. Waterfield, O. Yelekçi, R. Yu and B. Zhou (eds.)]. Available from https://ipcc.ch/static/ar6/wg1.

Date: August 2021

This document is subject to copy-editing, corrigenda and trickle backs.

ACCEPTED VERSION
SUBJECT TO FINAL EDITING

Table of Contents

Atlas.SM.1 Tables of global (CMIP) and regional (CORDEX) models used in the Atlas chapter 4
Atlas.SM.2 Figures of regional (CORDEX) model evaluation 16
Atlas.SM.3 Data Table 25
References 29

ACCEPTED VERSION
SUBJECT TO FINAL EDITING

Atlas.SM.1 Tables of global (CMIP) and regional (CORDEX) models used in the Atlas chapter

The following tables present the global and regional models and the specific variables used in the Atlas chapter (and in the Interactive Atlas) from the ensembles of CMIP5, CMIP6 and CORDEX historical and scenario simulations. Detailed information and salient features of these models are described in IPCC AR5 Appendix 9.A (for CMIP5), and Annexes AII.2 (Table AII.5) and AII.1 (Tables AII.1 to AII.4) for CMIP6 and CORDEX, respectively.

[START TABLE ATLAS.SM.1 HERE]

Table Atlas.SM.1: The CMIP5 models used in the Atlas for each of the historical and RCP scenario experiments. Salient features of these models are described in IPCC AR5 Appendix 9.A (model names are taken from Table 9.A.1). The first two columns indicate the model and the particular run used. Columns 4–7 indicate the availability of the different variables used in the Atlas. P: precipitation (pr); T: temperature (tas); X: tasmin and tasmax. A blank space indicates lack of data, usually because that scenario run was not available. P, T and X correspond to the *atmosphere* realm and daily frequency. Further details (including the specific ESGF versions used) are given in the Atlas GitHub repository (Iturbide et al., 2021).

#	Model	Run	Hist	RCP2.6	RCP4.5	RCP8.5
1	ACCESS1-0	r1i1p1	PTX		PTX	PTX
2	ACCESS1-3	r1i1p1	PTX		PTX	PTX
3	bcc-csm1-1	r1i1p1	PTX	PTX	PTX	PTX
4	bcc-csm1-1-m	r1i1p1	PTX	PTX	PTX	PTX
5	BNU-ESM	r1i1p1	PTX	PTX	PTX	PTX
6	CanESM2	r1i1p1	PTX	PTX	PTX	PTX
7	CCSM4	r1i1p1	PTX	PTX	PTX	PTX
8	CESM1-BGC	r1i1p1	PTX		PTX	PTX
9	CMCC-CM	r1i1p1	PTX		PTX	PTX
10	CMCC-CMS	r1i1p1	PTX		PTX	PTX
11	CNRM-CM5	r1i1p1	PTX	PTX	PTX	PTX
12	CSIRO-Mk3-6-0	r1i1p1	PTX	PTX	PTX	PTX
13	EC-EARTH	r12i1p1	PTX	PTX	PTX	PTX
14	GFDL-CM3	r1i1p1	PTX	PTX		PTX
15	GFDL-ESM2G	r1i1p1	PTX	PTX	PTX	PTX
16	GFDL-ESM2M	r1i1p1	PTX	PTX	PTX	PTX
17	HadGEM2-CC	r1i1p1	PTX		PTX	PTX
18	HadGEM2-ES	r1i1p1	PTX	PTX	PTX	PTX
19	inmcm4	r1i1p1	PTX		PTX	PTX
20	IPSL-CM5A-LR	r1i1p1	PTX	PTX	PTX	PTX
21	IPSL-CM5A-MR	r1i1p1	PTX	PTX	PTX	PTX
22	IPSL-CM5B-LR	r1i1p1	PTX		PTX	PTX
23	MIROC-ESM	r1i1p1	PTX	PTX	PTX	PTX
24	MIROC-ESM-CHEM	r1i1p1	PTX	PTX	PTX	PTX
25	MIROC5	r1i1p1	PTX	PTX	PTX	PTX
26	MPI-ESM-LR	r1i1p1	PTX	PTX	PTX	PTX
27	MPI-ESM-MR	r1i1p1	PTX	PTX	PTX	PTX
28	MRI-CGCM3	r1i1p1	PTX	PTX	PTX	PTX
29	NorESM1-M	r1i1p1	PTX	PTX	PTX	PTX

[END TABLE ATLAS.SM.1 HERE]

ACCEPTED VERSION SUBJECT TO FINAL EDITING

[START TABLE ATLAS.SM.2 HERE]

Table Atlas.SM.2: The CMIP6 models used in the Atlas for each of the historical and SSP scenario experiments, and for the PMIP experiment. Salient features of these models are described in Table AII.5. The first two columns indicate the model and the particular run used. Columns 3–7 indicate the availability of the different variables from historical and scenario experiments used in the Atlas. P: precipitation (pr); T: temperature (tas); X: tasmin and tasmax; W: wind (sfcWind), S: snow (prsn); I: sea-ice area fraction (siconc); O: sea-surface temperature (tos); H: pH (ph). A blank space indicates lack of data, usually because that scenario run was not available. P, T, X, W and S correspond to the *atmosphere* realm; I, O and H correspond to the *sea* realm. Daily frequency has been used for P, T and X (to compute the derived indices, see Atlas.2.3), whereas monthly frequency is used for the others. The last column indicates the availability of data (precipitation and temperature) from the particular periods of the PMIP experiment used in the Interactive Atlas: piControl (c), midPliocene-eoi400 (p), midHolocene (h), lig127k (i), lgm (g); see Cross-Chapter Box 2.1 for details. Further details (including the specific ESGF versions used) are given in the Atlas GitHub repository (Iturbide et al., 2021). Note: Run ri1p1f1 for CESM2 in PMIP.

#	Model	Run	Hist	SSP1.26	SSP2.45	SSP3.7	SSP5.85	PMIP
1	ACCESS-CM2	r1i1p1f1	PTXSWIO	PTXSWIO	PTXSWIO	PTXSWIO	PTXSWIO	
2	ACCESS-ESM1-5	r1i1p1f1	PTXSWIO	PTXSWIO	PTXSWIO	PTXSWIO	PTXSWIO	ci
3	AWI-CM-1-1-MR	r1i1p1f1	TXSWO	TXSWO	TXSWO	TXSWO	TXSWO	
4	BCC-CSM2-MR	r1i1p1f1	PTXSWIO	PTXSWIO	PTXSWIO	PTXSWIO	PTXSWIO	
5	CAMS-CSM1-0	r2i1p1f1	PTWIO	PTWIO	PTWIO	PTWIO	PTWIO	
6	CanESM5	r1i1p1f1	PTXSWIO	PTXSWIO	PTXSWIO	PTXSWIO	PTXSWIO	
7	CESM2	r4i1p1f1	PTSIH	PTSIH	PTSIH	PTSIH	PTSIH	cphi
8	CESM2-WACCM	r1i1p1f1	PTWIOH	PTWIOH	PTWIOH	PTWIOH	PTWIOH	
9	CMCC-CM2-SR5	r1i1p1f1	PTSWIO	PTSWIO	PTSWIO	PTSWIO	PTSWIO	
10	CNRM-CM6-1	r1i1p1f2	PTXSWIO	PTXSWIO	PTXSWIO	PTXSWIO	PTXSWIO	ci
11	CNRM-CM6-1-HR	r1i1p1f2	PTXSWIO	PTXSWIO	TSWIO	TSWIO	PTXSWIO	
12	CNRM-ESM2-1	r1i1p1f2	PTXSWIOH	PTXSWOH	PTXSWIOH	PTXSWOH	PTXSWOH	
13	EC-Earth3	r1i1p1f1	PTXSWIO	PTXSWIO	PTXSWIO	PTXSWIO	PTXSWIO	
14	EC-Earth3-Veg	r1i1p1f1	PTXSWIO	PTXSWIO	PTXSWIO	PTXSWIO	PTXSWIO	
15	EC-Earth3-Veg-LR	r1i1p1f1	PTXSWIO		PTXSWIO	PTXSWIO		chi
16	FGOALS-g3	r1i1p1f1	PTXSWIO	PTXSWIO	PTXSWIO	PTXSWIO	PTXSWIO	chi
17	GFDL-CM4	r1i1p1f1	PTXSWIO		PTXSWIO		PTXSWIO	
18	GFDL-ESM4	r1i1p1f1	PTXSWO	PTXSO	PTXSWO	PTXSO	PTXSWO	
19	HadGEM3-GC31-LL	r1i1p1f3	PTXSWIO	PTXSWIO	PTXSWIO		PTXSWIO	cphi
20	IITM-ESM	r1i1p1f1	PTO	PTO	PTO	PTO	PTO	
21	INM-CM4-8	r1i1p1f1	PTXSW	PTXSW	PTXSW	PTXSW	PTXSW	chig
22	INM-CM5-0	r1i1p1f1	PTXSWIO	PTXSWIO	PTXSWIO	PTXSWIO	PTXSWIO	
23	IPSL-CM6A-LR	r1i1p1f1	PTXSWIOH	PTXSWIOH	PTXSWIOH	PTXSWIOH	PTXSWIOH	cphi
24	KACE-1-0-G	r2i1p1f1	PTXSW	PTXSW	PTXSW	PTXSW	PTXSW	
25	KIOST-ESM	r1i1p1f1	PTXWIO	PTXWIO	PTXWIO		PTXWIO	
26	MIROC-ES2L	r1i1p1f2	PTXSWIH	PTXSWIH	PTXSWIH	PTXSWIH	PTXSWIH	chig
27	MIROC6	r1i1p1f1	PTXSWI	PTXSWI	PTXSWI	PTXSWI	PTXSWI	
28	MPI-ESM1-2-HR	r1i1p1f1	PTXSWIOH	PTXSWIOH	PTXSWIOH	PTXSWIOH	PTXSWIOH	
29	MPI-ESM1-2-LR	r1i1p1f1	PTXSWIOH	PTXSWIOH	PTXSWIOH	PTXSWIOH	PTXSWIOH	chg
30	MRI-ESM2-0	r1i1p1f1	PTXSWI	PTXSWI	PTXSWI	PTXSWI	PTXSWI	ch
31	NESM3	r1i1p1f1	PTXSO	PTXSO	PTXSO		PTXSO	chi
32	NorESM2-LM	r1i1p1f1	PTSWIOH	PTSWIOH	PTSWIOH	PTSWIOH	PTSWIOH	chi
33	NorESM2-MM	r1i1p1f1	PTXSWIOH	PTXSWIOH	PTXSWIOH	PTXSWIOH	PTXSWIOH	
34	TaiESM1	r1i1p1f1	PTSW				PTSW	

ACCEPTED VERSION SUBJECT TO FINAL EDITING

35	UKESM1-0-LL	r1i1p1f2	PTXSWIOH	PTXSWIOH	PTXSWIOH	PTXSWIOH	PTXSWIOH	
36	AWI-ESM-1-1-LR	r1i1p1f1						cig
37	FGOALS-f3-L	r1i1p1f1						chi
38	GISS-E2-1-G	r1i1p1f1						cphi
39	NorESM1-F	r1i1p1f1						cphi

[END TABLE ATLAS.SM.2 HERE]

[START TABLE ATLAS.SM.3 HERE]

Table Atlas.SM.3: Regional simulations from the CORDEX South America (SAM) domain (Figure Atlas.6) used in the Atlas for the historical and RCP scenario experiments. Column 2 indicates the domain and resolution. Columns 3–4 indicate the CMIP5 GCM (see Table Atlas.A.1) and RCM (see Table AII.2 for salient features of these models) pairs used in the simulations. Columns 5–8 indicate the availability of the different variables (with daily frequency) used in the Atlas. P: precipitation (pr); T: temperature (tas); X: tasmin and tasmax; W: wind (sfcWind); a blank space indicates lack of data. Further details (including the specific ESGF versions used) are given in the Atlas GitHub repository (Iturbide et al., 2021).

#	Domain	GCM_run	RCM	Hist	RCP2.6	RCP4.5	RCP8.5
1	SAM-22	HadGEM2-ES_r1i1p1	REMO2015_v1	PTXW	PTXW		PTXW
2	SAM-22	MPI-ESM-LR_r1i1p1	REMO2015_v1	PTXW	PTXW		PTXW
3	SAM-22	NorESM1-M_r1i1p1	REMO2015_v1	PTXW	PTXW		PTXW
4	SAM-22	HadGEM2-ES_r1i1p1	RegCM4-7_v0	PTXW	PTXW		PTXW
5	SAM-22	MPI-ESM-MR_r1i1p1	RegCM4-7_v0	PTXW	PTXW		PTXW
6	SAM-22	NorESM1-M_r1i1p1	RegCM4-7_v0	PTXW	PTXW		PTXW
7	SAM-44	HadGEM2-ES_r1i1p1	RegCM4-3_v4	PTXW		PTXW	PTXW
8	SAM-44	MPI-ESM-LR_r1i1p1	REMO2009_v1	PTXW	PTXW	PTXW	PTXW
9	SAM-44	CSIRO-Mk3-6-0_r1i1p1	RCA4_v3	PTXW		PTXW	PTXW
10	SAM-44	CanESM2_r1i1p1	RCA4_v3	PTXW		PTXW	PTXW
11	SAM-44	EC-EARTH_r12i1p1	RCA4_v3	PTXW	PTXW	PTXW	PTXW
12	SAM-44	IPSL-CM5A-MR_r1i1p1	RCA4_v3	PTXW		PTXW	PTXW
13	SAM-44	MIROC5_r1i1p1	RCA4_v3	PTXW	PTXW	PTXW	PTXW
14	SAM-44	HadGEM2-ES_r1i1p1	RCA4_v3	PTXW	PTXW	PTXW	PTXW
15	SAM-44	MPI-ESM-LR_r1i1p1	RCA4_v3	PTXW	PTXW	PTXW	PTXW
16	SAM-44	NorESM1-M_r1i1p1	RCA4_v3	PTXW	PTXW	PTXW	PTXW
17	SAM-44	GFDL-ESM2M_r1i1p1	RCA4_v3	PTXW		PTXW	PTXW
18	SAM-44	CanESM2_r1i1p1	WRF341I_v2	PTXW		PTXW	PTXW

[END TABLE ATLAS.SM.3 HERE]

ACCEPTED VERSION SUBJECT TO FINAL EDITING

[START TABLE ATLAS.SM.4 HERE]

Table Atlas.SM.4: Regional simulations from the CORDEX Central America (CAM) domain (Figure Atlas.6) used in the Atlas for the historical and RCP scenario experiments. Column 2 indicates the domain and resolution. Columns 3–4 indicate the CMIP5 GCM (see Table Atlas.A.1) and RCM (see Table AII.2 for salient features of these models) pairs used in the simulations. Columns 5–8 indicate the availability of the different variables (with daily frequency) used in the Atlas. P: precipitation (pr); T: temperature (tas); X: tasmin and tasmax; W: wind (sfcWind); a blank space indicates lack of data. Further details (including the specific ESGF versions used) are given in the Atlas GitHub repository (Iturbide et al., 2021).

#	Domain	GCM_run	RCM	Historical	RCP2.6	RCP4.5	RCP8.5
1	CAM-22	HadGEM2-ES_r1i1p1	REMO2015_v1	PTXW	PTXW		PTXW
2	CAM-22	MPI-ESM-LR_r1i1p1	REMO2015_v1	PTXW	PTXW		PTXW
3	CAM-22	NorESM1-M_r1i1p1	REMO2015_v1	PTXW	PTXW		PTXW
4	CAM-22	HadGEM2-ES_r1i1p1	RegCM4-7_v0	PTXW	PTXW		PTXW
5	CAM-22	MPI-ESM-MR_r1i1p1	RegCM4-7_v0	PTXW	PTXW		PTXW
6	CAM-22	GFDL-ESM2M_r1i1p1	RegCM4-7_v0	PTXW	PTXW		PTXW
7	CAM-22	GFDL-ESM2M_r1i1p1	CRCM5_v1	PTXW			PTXW
8	CAM-44	HadGEM2-ES_r1i1p1	RegCM4-3_v4	PTXW			PTXW
9	CAM-44	MPI-ESM-MR_r1i1p1	RegCM4-3_v4	PTXW			PTXW
10	CAM-44	CanESM2_r1i1p1	RCA4_v1	PTXW			PTXW
11	CAM-44	CNRM-CM5_r1i1p1	RCA4_v1	PTXW			PTXW
12	CAM-44	CSIRO-Mk3-6-0_r1i1p1	RCA4_v1	PTXW			PTXW
13	CAM-44	EC-EARTH_r12i1p1	RCA4_v1	PTXW	PTXW	PTXW	PTXW
14	CAM-44	IPSL-CM5A-MR_r1i1p1	RCA4_v1	PTXW			PTXW
15	CAM-44	MIROC5_r1i1p1	RCA4_v1	PTXW	PTXW		PTXW
16	CAM-44	HadGEM2-ES_r1i1p1	RCA4_v1	PTXW	PTXW	PTXW	PTXW
17	CAM-44	MPI-ESM-LR_r1i1p1	RCA4_v1	PTXW	PTXW	PTXW	PTXW
18	CAM-44	NorESM1-M_r1i1p1	RCA4_v1	PTXW	PTXW		PTXW
19	CAM-44	GFDL-ESM2M_r1i1p1	RCA4_v1	PTXW			PTXW
20	CAM-22	CNRM-CM5_r1i1p1	CRCM5_v1	PTXW			PTXW
21	CAM-22	CanESM2_r1i1p1	CRCM5_v1	PTXW			PTXW

[END TABLE ATLAS.SM.4 HERE]

ACCEPTED VERSION SUBJECT TO FINAL EDITING

[START TABLE ATLAS.SM.5 HERE]

Table Atlas.SM.5: Regional simulations from the CORDEX North America (NAM) domain (Figure Atlas.6) used in the Atlas for the historical and RCP scenario experiments. Column 2 indicates the domain and resolution. Columns 3–4 indicate the CMIP5 GCM (see Table Atlas.A.1) and RCM (see Table AII.2 for salient features of these models) pairs used in the simulations. Columns 5–8 indicate the availability of the different variables (with daily frequency) used in the Atlas. P: precipitation (pr); T: temperature (tas); X: tasmin and tasmax; W: wind (sfcWind); a blank space indicates lack of data. Further details (including the specific ESGF versions used) are given in the Atlas GitHub repository (Iturbide et al., 2021).

#	Domain	GCM_run	RCM	Hist	RCP2.6	RCP4.5	RCP8.5
1	NAM-22	HadGEM2-ES_r1i1p1	REMO2015_v1	PTXW	PTXW		PTXW
2	NAM-22	MPI-ESM-LR_r1i1p1	REMO2015_v1	PTXW	PTXW		PTXW
3	NAM-22	NorESM1-M_r1i1p1	REMO2015_v1	PTXW	PTXW		PTXW
4	NAM-22	CanESM2_r1i1p1	CRCM5_v1	PTXW		PTXW	PTXW
5	NAM-22	CNRM-CM5_r1i1p1	CRCM5_v1	PTXW		PTXW	PTXW
6	NAM-22	MPI-ESM-LR_r1i1p1	CRCM5_v1	PTXW		PTXW	PTXW
7	NAM-22	GFDL-ESM2M_r1i1p1	CRCM5_v1	PTXW		PTXW	PTXW
8	NAM-44	EC-EARTH_r3i1p1	HIRHAM5_v1	PTXW		PTXW	PTXW
9	NAM-44	CanESM2_r1i1p1	RCA4_v1	PTXW		PTXW	PTXW
10	NAM-44	EC-EARTH_r12i1p1	RCA4_v1	PTXW	PTXW	PTXW	PTXW
11	NAM-22	CanESM2_r1i1p1	CanRCM4_r2	PTXW		PTXW	PTXW
12	NAM-22	MPI-ESM-MR_r1i1p1	CRCM5_v1	PTXW			PTXW
13	NAM-22	ESM2M_r1i1p1	RegCM4_v4-4-rc8	PTXW			PTXW
14	NAM-22	HadGEM2-ES_r1i1p1	RegCM4_v4-4-rc8	PTXW			PTXW
15	NAM-22	MPI-ESM-LR_r1i1p1	RegCM4_v4-4-rc8	PTXW			PTXW
16	NAM-22	GFDL-ESM2M_r1i1p1	WRF_v3-5-1	PTXW			PTXW
17	NAM-22	HadGEM2-ES_r1i1p1	WRF_v3-5-1	PTXW			PTXW
18	NAM-22	MPI-ESM-LR_r1i1p1	WRF_v3-5-1	PTXW			PTXW
19	NAM-22	MPI-ESM-LR_r1i1p1	CRCM5_v1	PTXW		PTXW	PTXW
20	NAM-22	CanESM2_r1i1p1	CRCM5_v1	PTXW		PTXW	PTXW

[END TABLE ATLAS.SM.5 HERE]

ACCEPTED VERSION SUBJECT TO FINAL EDITING

[START TABLE ATLAS.SM.6 HERE]

Table Atlas.SM.6: Regional simulations from the CORDEX Africa (AFR) domain (Figure Atlas.6) used in the Atlas for the historical and RCP scenario experiments. Column 2 indicates the domain and resolution. Columns 3–4 indicate the CMIP5 GCM (see Table Atlas.A.1) and RCM (see Table AII.2 for salient features of these models) pairs used in the simulations. Columns 5–8 indicate the availability of the different variables (with daily frequency) used in the Atlas. P: precipitation (pr); T: temperature (tas); X: tasmin and tasmax; W: wind (sfcWind); a blank space indicates lack of data. Further details (including the specific ESGF versions used) are given in the Atlas GitHub repository (Iturbide et al., 2021).

#	Domain	GCM_run	RCM	Hist	RCP2.6	RCP4.5	RCP8.5
1	AFR-22	HadGEM2-ES_r1i1p1	CCLM5-0-15_v1	PTXW	PTXW		PTXW
2	AFR-22	MPI-ESM-LR_r1i1p1	CCLM5-0-15_v1	PTXW	PTXW		PTXW
3	AFR-22	NorESM1-M_r1i1p1	CCLM5-0-15_v1	PTXW	PTXW		PTXW
4	AFR-22	HadGEM2-ES_r1i1p1	REMO2015_v1	PTXW	PTXW		PTXW
5	AFR-22	MPI-ESM-LR_r1i1p1	REMO2015_v1	PTXW	PTXW		PTXW
6	AFR-22	NorESM1-M_r1i1p1	REMO2015_v1	PTXW	PTXW		PTXW
7	AFR-22	HadGEM2-ES_r1i1p1	RegCM4-7_v0	PTXW	PTXW		PTXW
8	AFR-22	MPI-ESM-MR_r1i1p1	RegCM4-7_v0	PTXW	PTXW		PTXW
9	AFR-22	NorESM1-M_r1i1p1	RegCM4-7_v0	PTXW	PTXW		PTXW
10	AFR-44	CNRM-CM5_r1i1p1	CCLM4-8-17_v1	PTXW		PTXW	PTXW
11	AFR-44	EC-EARTH_r12i1p1	CCLM4-8-17_v1	PTXW		PTXW	PTXW
12	AFR-44	HadGEM2-ES_r1i1p1	CCLM4-8-17_v1	PTXW		PTXW	PTXW
13	AFR-44	MPI-ESM-LR_r1i1p1	CCLM4-8-17_v1	PTXW		PTXW	PTXW
14	AFR-44	EC-EARTH_r3i1p1	HIRHAM5_v2	PTXW		PTXW	PTXW
15	AFR-44	IPSL-CM5A-LR_r1i1p1	REMO2009_v1	PTXW	PTXW		PTXW
16	AFR-44	MIROC5_r1i1p1	REMO2009_v1	PTXW	PTXW		PTXW
17	AFR-44	HadGEM2-ES_r1i1p1	REMO2009_v1	PTXW	PTXW		PTXW
18	AFR-44	HadGEM2-ES_r1i1p1	RACMO22T_v2	PTXW	PTXW	PTXW	PTXW
19	AFR-44	EC-EARTH_r12i1p1	REMO2009_v1	PTXW	PTXW	PTXW	PTXW
20	AFR-44	MPI-ESM-LR_r1i1p1	REMO2009_v1	PTXW	PTXW	PTXW	PTXW
21	AFR-44	CanESM2_r1i1p1	RCA4_v1	PTXW		PTXW	PTXW
22	AFR-44	CNRM-CM5_r1i1p1	RCA4_v1	PTXW		PTXW	PTXW
23	AFR-44	CSIRO-Mk3-6-0_r1i1p1	RCA4_v1	PTXW		PTXW	PTXW
24	AFR-44	EC-EARTH_r12i1p1	RCA4_v1	PTXW	PTXW	PTXW	PTXW
25	AFR-44	IPSL-CM5A-MR_r1i1p1	RCA4_v1	PTXW		PTXW	PTXW
26	AFR-44	MIROC5_r1i1p1	RCA4_v1	PTXW	PTXW	PTXW	PTXW
27	AFR-44	HadGEM2-ES_r1i1p1	RCA4_v1	PTXW	PTXW	PTXW	PTXW
28	AFR-44	MPI-ESM-LR_r1i1p1	RCA4_v1	PTXW	PTXW	PTXW	PTXW
29	AFR-44	NorESM1-M_r1i1p1	RCA4_v1	PTXW	PTXW	PTXW	PTXW
30	AFR-44	GFDL-ESM2M_r1i1p1	RCA4_v1	PTXW		PTXW	PTXW
31	AFR-22	CanESM2_r1i1p1	CanRCM4_r2	PTXW		PTXW	PTXW
32	AFR-44	GFDL-ESM2G_r1i1p1	REMO2009_v1	PTXW	PTXW		
33	AFR-44	EC-EARTH_r12i1p1	RACMO22T_v1	PTXW	PTXW		

ACCEPTED VERSION SUBJECT TO FINAL EDITING

34	AFR-44	CanESM2_r1i1p1	CRCM5_v1	PTXW		PTXW	
35	AFR-44	MPI-ESM-LR_r1i1p1	CRCM5_v1	PTXW		PTXW	

[END TABLE ATLAS.SM.6 HERE]

[START TABLE ATLAS.SM.7 HERE]

Table Atlas.SM.7: Regional simulations from the CORDEX Europe (EUR) domain (Figure Atlas.6) used in the Atlas for the historical and RCP scenario experiments. Column 2 indicates the domain and resolution. Columns 3–4 indicate the CMIP5 GCM (see Table Atlas.A.1) and RCM (see Table AII.2 for salient features of these models) pairs used in the simulations. Columns 5–8 indicate the availability of the different variables (with daily frequency) used in the Atlas. P: precipitation (pr); T: temperature (tas); X: tasmin and tasmax; W: wind (sfcWind); a blank space indicates lack of data. Further details (including the specific ESGF versions used) are given in the Atlas GitHub repository (Iturbide et al., 2021).

#	Domain	GCM_run	RCM	Hist	RCP2.6	RCP4.5	RCP8.5
1	EUR-11	EC-EARTH_r12i1p1	COSMO-crCLIM-v1-1_v1	PTXW			PTXW
2	EUR-11	HadGEM2-ES_r1i1p1	COSMO-crCLIM-v1-1_v1	PTXW			PTXW
3	EUR-11	MPI-ESM-LR_r1i1p1	COSMO-crCLIM-v1-1_v1	PTXW			PTXW
4	EUR-11	NorESM1-M_r1i1p1	COSMO-crCLIM-v1-1_v1	PTXW			PTXW
5	EUR-11	CNRM-CM5_r1i1p1	CCLM4-8-17_v1	PTXW		PTXW	PTXW
6	EUR-11	EC-EARTH_r12i1p1	CCLM4-8-17_v1	PTXW	PTXW	PTXW	PTXW
7	EUR-11	HadGEM2-ES_r1i1p1	CCLM4-8-17_v1	PTXW		PTXW	PTXW
8	EUR-11	MPI-ESM-LR_r1i1p1	CCLM4-8-17_v1	PTXW	PTXW	PTXW	PTXW
9	EUR-11	CNRM-CM5_r1i1p1	ALADIN63_v2	PTXW	PTXW	PTXW	PTXW
10	EUR-11	HadGEM2-ES_r1i1p1	ALADIN63_v1	PTXW			PTXW
11	EUR-11	MPI-ESM-LR_r1i1p1	ALADIN63_v1	PTXW			PTXW
12	EUR-11	NorESM1-M_r1i1p1	ALADIN63_v1	PTXW			PTXW
13	EUR-11	CNRM-CM5_r1i1p1	HIRHAM5_v2	PTXW			PTXW
14	EUR-11	EC-EARTH_r12i1p1	HIRHAM5_v1	PTXW			PTXW
15	EUR-11	EC-EARTH_r3i1p1	HIRHAM5_v2	PTXW	PTXW	PTXW	PTXW
16	EUR-11	HadGEM2-ES_r1i1p1	HIRHAM5_v2	PTXW		PTXW	PTXW
17	EUR-11	MPI-ESM-LR_r1i1p1	HIRHAM5_v1	PTXW			PTXW
18	EUR-11	IPSL-CM5A-MR_r1i1p1	HIRHAM5_v1	PTXW			PTXW
19	EUR-11	NorESM1-M_r1i1p1	HIRHAM5_v3	PTXW		PTXW	PTXW
20	EUR-11	IPSL-CM5A-MR_r1i1p1	REMO2015_v1	PTXW			PTXW
21	EUR-11	MPI-ESM-LR_r3i1p1	REMO2015_v1	PTXW			PTXW
22	EUR-11	NorESM1-M_r1i1p1	REMO2015_v1	PTXW	PTXW	PTXW	PTXW
23	EUR-11	CNRM-CM5_r1i1p1	REMO2015_v2	PTXW	PTXW		PTXW
24	EUR-11	HadGEM2-ES_r1i1p1	RegCM4-6_v1	PTXW	PTXW		PTXW
25	EUR-11	MPI-ESM-LR_r1i1p1	RegCM4-6_v1	PTXW	PTXW		PTXW
26	EUR-11	EC-EARTH_r12i1p1	RegCM4-6_v1	PTXW			PTXW
27	EUR-11	CNRM-CM5_r1i1p1	WRF381P_v2	PTXW			PTXW
28	EUR-11	IPSL-CM5A-MR_r1i1p1	WRF381P_v1	PTXW		PTXW	PTXW

ACCEPTED VERSION SUBJECT TO FINAL EDITING

29	EUR-11	HadGEM2-ES_r1i1p1	WRF381P_v1	PTXW			PTXW
30	EUR-11	NorESM1-M_r1i1p1	WRF381P_v1	PTXW			PTXW
31	EUR-11	EC-EARTH_r12i1p1	WRF381P_v1	PTXW			PTXW
32	EUR-11	CNRM-CM5_r1i1p1	RACMO22E_v2	PTXW	PTXW	PTXW	PTXW
33	EUR-11	EC-EARTH_r12i1p1	RACMO22E_v1	PTXW	PTXW	PTXW	PTXW
34	EUR-11	IPSL-CM5A-MR_r1i1p1	RACMO22E_v1	PTXW			PTXW
35	EUR-11	HadGEM2-ES_r1i1p1	RACMO22E_v2	PTXW	PTXW	PTXW	PTXW
36	EUR-11	MPI-ESM-LR_r1i1p1	RACMO22E_v1	PTXW	PTXW		PTXW
37	EUR-11	NorESM1-M_r1i1p1	RACMO22E_v1	PTXW	PTXW		PTXW
38	EUR-11	EC-EARTH_r12i1p1	HadREM3-GA7-05_v1	PTXW			PTXW
39	EUR-11	HadGEM2-ES_r1i1p1	HadREM3-GA7-05_v1	PTXW			PTXW
40	EUR-11	MPI-ESM-LR_r1i1p1	HadREM3-GA7-05_v1	PTXW			PTXW
41	EUR-11	NorESM1-M_r1i1p1	HadREM3-GA7-05_v1	PTXW			PTXW
42	EUR-11	CNRM-CM5_r1i1p1	HadREM3-GA7-05_v2	PTXW			PTXW
43	EUR-11	MPI-ESM-LR_r1i1p1	REMO2009_v1	PTXW	PTXW	PTXW	PTXW
44	EUR-11	CNRM-CM5_r1i1p1	ALARO-0_v1	PTXW	PTXW	PTXW	PTXW
45	EUR-11	CNRM-CM5_r1i1p1	RCA4_v1	PTXW		PTXW	PTXW
46	EUR-11	EC-EARTH_r12i1p1	RCA4_v1	PTXW	PTXW	PTXW	PTXW
47	EUR-11	IPSL-CM5A-MR_r1i1p1	RCA4_v1	PTXW		PTXW	PTXW
48	EUR-11	HadGEM2-ES_r1i1p1	RCA4_v1	PTXW	PTXW	PTXW	PTXW
49	EUR-11	MPI-ESM-LR_r1i1p1	RCA4_v1a	PTXW	PTXW	PTXW	PTXW
50	EUR-11	MPI-ESM-LR_r2i1p1	RCA4_v1	PTXW			PTXW
51	EUR-11	NorESM1-M_r1i1p1	RCA4_v1	PTXW	PTXW		PTXW

[END TABLE ATLAS.SM.7 HERE]

[START TABLE ATLAS.SM.8 HERE]

Table Atlas.SM.8: Regional simulations from the CORDEX South Asia (WAS) domain (Figure Atlas.6) used in the Atlas for the historical and RCP scenario experiments. Column 2 indicates the domain and resolution. Columns 3–4 indicate the CMIP5 GCM (see Table Atlas.A.1) and RCM (see Table AII.2 for salient features of these models) pairs used in the simulations. Columns 5–8 indicate the availability of the different variables (with daily frequency) used in the Atlas. P: precipitation (pr); T: temperature (tas); X: tasmin and tasmax; W: wind (sfcWind); a blank space indicates lack of data. Further details (including the specific ESGF versions used) are given in the Atlas GitHub repository (Iturbide et al., 2021).

#	Domain	GCM_run	RCM	Hist	RCP2.6	RCP4.5	RCP8.5
1	WAS-22	EC-EARTH_r12i1p1	COSMO-crCLIM-v1-1_v1	PTXW			PTXW
2	WAS-22	MPI-ESM-LR_r1i1p1	COSMO-crCLIM-v1-1_v1	PTXW	PTXW		PTXW
3	WAS-22	NorESM1-M_r1i1p1	COSMO-crCLIM-v1-1_v1	PTXW	PTXW		PTXW
4	WAS-22	HadGEM2-ES_r1i1p1	REMO2015_v1	PTXW	PTXW		PTXW
5	WAS-22	MPI-ESM-LR_r1i1p1	REMO2015_v1	PTXW	PTXW		PTXW
6	WAS-22	NorESM1-M_r1i1p1	REMO2015_v1	PTXW	PTXW		PTXW

ACCEPTED VERSION SUBJECT TO FINAL EDITING

7	WAS-22	MIROC5_r1i1p1	RegCM4-7_v0	PTXW	PTXW		PTXW
8	WAS-22	MPI-ESM-MR_r1i1p1	RegCM4-7_v0	PTXW	PTXW		PTXW
9	WAS-22	NorESM1-M_r1i1p1	RegCM4-7_v0	PTXW	PTXW		PTXW
10	WAS-44	CanESM2_r1i1p1	RegCM4-4_v5	PTXW		PTXW	PTXW
11	WAS-44	CNRM-CM5_r1i1p1	RegCM4-4_v5	PTXW		PTXW	PTXW
12	WAS-44	CSIRO-Mk3-6-0_r1i1p1	RegCM4-4_v5	PTXW		PTXW	PTXW
13	WAS-44	IPSL-CM5A-LR_r1i1p1	RegCM4-4_v5	PTXW		PTXW	PTXW
14	WAS-44	MPI-ESM-MR_r1i1p1	RegCM4-4_v5	PTXW		PTXW	PTXW
15	WAS-44	GFDL-ESM2M_r1i1p1	RegCM4-4_v5	PTXW		PTXW	PTXW
16	WAS-44	MPI-ESM-LR_r1i1p1	REMO2009_v1	PTXW	PTXW	PTXW	PTXW
17	WAS-44	CanESM2_r1i1p1	RCA4_v2	PTXW		PTXW	PTXW
18	WAS-44	CNRM-CM5_r1i1p1	RCA4_v2	PTXW		PTXW	PTXW
19	WAS-44	CSIRO-Mk3-6-0_r1i1p1	RCA4_v2	PTXW		PTXW	PTXW
20	WAS-44	EC-EARTH_r12i1p1	RCA4_v2	PTXW	PTXW	PTXW	PTXW
21	WAS-44	IPSL-CM5A-MR_r1i1p1	RCA4_v2	PTXW		PTXW	PTXW
22	WAS-44	MIROC5_r1i1p1	RCA4_v2	PTXW	PTXW	PTXW	PTXW
23	WAS-44	HadGEM2-ES_r1i1p1	RCA4_v2	PTXW	PTXW	PTXW	PTXW
24	WAS-44	MPI-ESM-LR_r1i1p1	RCA4_v2	PTXW	PTXW	PTXW	PTXW
25	WAS-44	NorESM1-M_r1i1p1	RCA4_v2	PTXW	PTXW	PTXW	PTXW
26	WAS-44	GFDL-ESM2M_r1i1p1	RCA4_v2	PTXW		PTXW	PTXW

[END TABLE ATLAS.SM.8 HERE]

[START TABLE ATLAS.SM.9 HERE]

Table Atlas.SM.9: Regional simulations from the CORDEX East Asia (EAS) domain (Figure Atlas.6) used in the Atlas for the historical and RCP scenario experiments. Column 2 indicates the domain and resolution. Columns 3–4 indicate the CMIP5 GCM (see Table Atlas.A.1) and RCM (see Table AII.2 for salient features of these models) pairs used in the simulations. Columns 5–8 indicate the availability of the different variables (with daily frequency) used in the Atlas. P: precipitation (pr); T: temperature (tas); X: tasmin and tasmax; W: wind (sfcWind); a blank space indicates lack of data. Further details (including the specific ESGF versions used) are given in the Atlas GitHub repository (Iturbide et al., 2021).

#	Domain	GCM_run	RCM	Hist	RCP2.6	RCP4.5	RCP8.5
1	EAS-22	HadGEM2-ES_r1i1p1	REMO2015_v1	PTXW	PTXW		PTXW
2	EAS-22	MPI-ESM-LR_r1i1p1	REMO2015_v1	PTXW	PTXW		PTXW
3	EAS-22	NorESM1-M_r1i1p1	REMO2015_v1	PTXW	PTXW		PTXW
4	EAS-44	CNRM-CM5_r1i1p1	CCLM5-0-2_v1	PTXW		PTXW	PTXW
5	EAS-44	EC-EARTH_r12i1p1	CCLM5-0-2_v1	PTXW		PTXW	PTXW
6	EAS-44	HadGEM2-ES_r1i1p1	CCLM5-0-2_v1	PTXW		PTXW	PTXW
7	EAS-44	MPI-ESM-LR_r1i1p1	CCLM5-0-2_v1	PTXW		PTXW	PTXW
8	EAS-44	EC-EARTH_r3i1p1	HIRHAM5_v1	PTXW		PTXW	PTXW
9	EAS-22	HadGEM2-ES_r1i1p1	RegCM4-4_v0	PTXW	PTXW		PTXW
10	EAS-22	MPI-ESM-MR_r1i1p1	RegCM4-4_v0	PTXW	PTXW		PTXW

ACCEPTED VERSION SUBJECT TO FINAL EDITING

11	EAS-22	NorESM1-M_r1i1p1	RegCM4-4_v0	PTXW	PTXW		PTXW

[END TABLE ATLAS.SM.9 HERE]

[START TABLE ATLAS.SM.10 HERE]

Table Atlas.SM.10: Regional simulations from the CORDEX Australasia (AUS) domain (Figure Atlas.6) used in the Atlas for the historical and RCP scenario experiments. Column 2 indicates the domain and resolution. Columns 3–4 indicate the CMIP5 GCM (see Table Atlas.A.1) and RCM (see Table AII.2 for salient features of these models) pairs used in the simulations. Columns 5–8 indicate the availability of the different variables (with daily frequency) used in the Atlas. P: precipitation (pr); T: temperature (tas); X: tasmin and tasmax; W: wind (sfcWind); a blank space indicates lack of data. Further details (including the specific ESGF versions used) are given in the Atlas GitHub repository (Iturbide et al., 2021).

#	Domain	GCM_run	RCM	Hist	RCP2.6	RCP4.5	RCP8.5
1	AUS-22	HadGEM2-ES_r1i1p1	REMO2015_v1	PTXW	PTXW		PTXW
2	AUS-22	MPI-ESM-LR_r1i1p1	REMO2015_v1	PTXW	PTXW		PTXW
3	AUS-22	NorESM1-M_r1i1p1	REMO2015_v1	PTXW	PTXW		PTXW
4	AUS-22	HadGEM2-ES_r1i1p1	RegCM4-7_v0	PTXW	PTXW		PTXW
5	AUS-22	MPI-ESM-MR_r1i1p1	RegCM4-7_v0	PTXW	PTXW		PTXW
6	AUS-22	NorESM1-M_r1i1p1	RegCM4-7_v0	PTXW	PTXW		PTXW
7	AUS-44	EC-EARTH_r12i1p1	CCLM4-8-17-CLM3-5_v1	PTXW		PTXW	PTXW
8	AUS-44	MPI-ESM-LR_r1i1p1	CCLM4-8-17-CLM3-5_v1	PTXW		PTXW	PTXW
9	AUS-22	HadGEM2-ES_r1i1p1	CCLM5-0-15_v1	PTXW	PTXW		PTXW
10	AUS-22	MPI-ESM-LR_r1i1p1	CCLM5-0-15_v1	PTXW	PTXW		PTXW
11	AUS-22	NorESM1-M_r1i1p1	CCLM5-0-15_v1	PTXW	PTXW		PTXW
12	AUS-44	CanESM2_r1i1p1	WRF360J_v1	PTXW		PTXW	PTXW
13	AUS-44	CanESM2_r1i1p1	WRF360K_v1	PTXW		PTXW	PTXW
14	AUS-44	ACCESS1-3_r1i1p1	WRF360J_v1	PTXW		PTXW	PTXW
15	AUS-44	ACCESS1-3_r1i1p1	WRF360K_v1	PTXW		PTXW	PTXW
16	AUS-44	ACCESS1-0_r1i1p1	WRF360J_v1	PTXW		PTXW	PTXW
17	AUS-44	ACCESS1-0_r1i1p1	WRF360K_v1	PTXW		PTXW	PTXW
18	AUS-44i	ACCESS1-0_r1i1p1	CCAM-2008_v1	PTXW		PTXW	PTXW
19	AUS-44i	CanESM2_r1i1p1	CCAM-2008_v1	PTXW		PTXW	PTXW
20	AUS-44i	MIROC5_r1i1p1	CCAM-2008_v1	PTXW		PTXW	PTXW
21	AUS-44i	NorESM1-M_r1i1p1	CCAM-2008_v1	PTXW		PTXW	PTXW
22	AUS-44i	GFDL-ESM2M_r1i1p1	CCAM-2008_v1	PTXW		PTXW	PTXW

[END TABLE ATLAS.SM.10 HERE]

ACCEPTED VERSION SUBJECT TO FINAL EDITING

[START TABLE ATLAS.SM.11 HERE]

Table Atlas.SM.11: Regional simulations from the CORDEX Antarctic (ANT) domain (Figure Atlas.6) used in the Atlas for the historical and RCP scenario experiments. Column 2 indicates the domain and resolution. Columns 3–4 indicate the CMIP5 GCM (see Table Atlas.A.1) and RCM (see Table AII.2 for salient features of these models) pairs used in the simulations. Columns 5–8 indicate the availability of the different variables (with daily frequency) used in the Atlas. P: precipitation (pr); T: temperature (tas); X: tasmin and tasmax; W: wind (sfcWind); a blank space indicates lack of data. Further details (including the specific ESGF versions used) are given in the Atlas GitHub repository(Iturbide et al., 2021).

#	Domain	GCM_run	RCM	Hist	RCP2.6	RCP4.5	RCP8.5
1	ANT-44	EC-EARTH_r3i1p1	HIRHAM5_v1	PTXW		PTXW	PTXW
2	ANT-44	EC-EARTH_r1i1p1	RACMO21P_v1	PTXW		PTXW	PTXW
3	ANT-44	HadGEM2-ES_r1i1p1	RACMO21P_v2	PTXW	PTXW	PTXW	PTXW
4	ANT-44	ACCESS1-3_r1i1p1	MAR311_v1	PTXW			PTXW
5	ANT-44	NorESM1-M_r1i1p1	MAR311_v1	PTXW			PTXW

[END TABLE ATLAS.SM.11 HERE]

[START TABLE ATLAS.SM.12 HERE]

Table Atlas.SM.12: Regional simulations from the CORDEX Arctic (ARC) domain (Figure Atlas.6) used in the Atlas for the historical and RCP scenario experiments. Column 2 indicates the domain and resolution. Columns 3–4 indicate the CMIP5 GCM (see Table Atlas.A.1) and RCM (see Table AII.2 for salient features of these models) pairs used in the simulations. Columns 5–8 indicate the availability of the different variables (with daily frequency) used in the Atlas. P: precipitation (pr); T: temperature (tas); X: tasmin and tasmax; W: wind (sfcWind); a blank space indicates lack of data. Further details (including the specific ESGF versions used) are given in the Atlas GitHub repository (Iturbide et al., 2021).

#	Domain	GCM_run	RCM	Hist	RCP2.6	RCP4.5	RCP8.5
1	ARC-44	EC-EARTH_r3i1p1	HIRHAM5_v1	PTXW		PTXW	PTXW
2	ARC-44	MPI-ESM-LR_r1i1p1	RRCM_v1	PTXW			PTXW
3	ARC-44	CanESM2_r1i1p1	RCA4_v1	PTXW		PTXW	PTXW
4	ARC-44	EC-EARTH_r12i1p1	RCA4-SN_v1	PTXW			PTXW
5	ARC-44	EC-EARTH_r12i1p1	RCA4_v1	PTXW	PTXW	PTXW	PTXW
6	ARC-44	MPI-ESM-LR_r1i1p1	RCA4-SN_v1	PTXW			PTXW
7	ARC-44	MPI-ESM-LR_r1i1p1	RCA4_v1	PTXW		PTXW	PTXW
8	ARC-44	NorESM1-M_r1i1p1	RCA4_v1	PTXW		PTXW	PTXW
9	ARC-22	CanESM2_r1i1p1	CanRCM4_r2	PTXW		PTXW	PTXW
10	ARC-44	CanESM2_r1i1p1	CRCM5_v1	PTXW			PTXW
11	ARC-44	MPI-ESM-MR_r1i1p1	CRCM5_v1	PTXW			PTXW

[END TABLE ATLAS.SM.12 HERE]

ACCEPTED VERSION SUBJECT TO FINAL EDITING

[START TABLE ATLAS.SM.13 HERE]

Table Atlas.SM.13: Regional simulations from the CORDEX Mediterranean (MED) domain (Figure Atlas.6) used in the Atlas for the historical and RCP scenario experiments. Columns 3–4 indicate the CMIP5 GCM (see Table Atlas.A.1) and RCM (see Table AII.2 for salient features of these models) pairs used in the simulations. The models selected in this domain are the coupled atmosphere-ocean regional models providing scenario simulations. Columns 5–8 indicate the availability of the sea surface temperature (with monthly frequency) used in the Atlas. Further details (including the specific ESGF versions used) are given in the Atlas GitHub repository (Iturbide et al., 2021).

#	Domain	GCM_run	RCM	Hist	RCP2.6	RCP4.5	RCP8.5
1	MED-44	IPSL-CM5A-MR_r1i1p1	LMD-LMDZ4NEMOMED8_v1	O		O	O
2	MED-44	IPSL-CM5A-MR_r1i1p1	LMD-LMDZ4NEMOMED8_v2	O			O
3	MED-44	CNRM-CM5_r1i1p1	LMD-LMDZ4NEMOMED8_v2	O			O
4	MED-44	MPI-ESM-MR_r1i1p1	LMD-LMDZ4NEMOMED8_v2	O			O
5	MED-22	MPI-ESM-LR_r1i1pi	GERICS-AWI-ROM	O		O	O
6	MED-44	MPI-ESM-LR_r1i1p1	GERICS-AWI-ROM	O			O
7	MED-11	EC-EARTH_r12i1p1	GUF-CCLM5-0-9-NEMOMED12-3-6_v1	O			O
8	MED-44	CNRM-CM5_r1i1p1	CNRM-RCSM4_v1	O	O	O	O
9	MED-44i	MPI-ESM-LR_r1i1p1	UBELGRADE-EBU	O			O
10	MED-11	CMCC-CM_r1i1p1	CMCC-CCLM4-21-NEMOMFS_v1	O		O	O

[END TABLE ATLAS.SM.13 HERE]

[START TABLE ATLAS.SM.14 HERE]

Table Atlas.SM.14: Regional simulations from the CORDEX South-East Asia (SEA) domain (Figure Atlas.6) used in the Atlas for the historical and RCP scenario experiments. Column 2 indicates the domain and resolution. Columns 3–4 indicate the CMIP5 GCM (see Table Atlas.A.1) and RCM (see Table AII.2 for salient features of these models) pairs used in the simulations. Columns 5–8 indicate the availability of the different variables (with daily frequency) used in the Atlas. P: precipitation (pr); T: temperature (tas); X: tasmin and tasmax; W: wind (sfcWind); a blank space indicates lack of data. Further details (including the specific ESGF versions used) are given in the Atlas GitHub repository (Iturbide et al., 2021).

#	Domain	GCM_run	RCM	Hist	RCP2.6	RCP4.5	RCP8.5
1	SEA-22	HadGEM2-ES_r1i1p1	REMO2015_v1	PTXW	PTXW		PTXW
2	SEA-22	MPI-ESM-LR_r1i1p1	REMO2015_v1	PTXW	PTXW		PTXW
3	SEA-22	NorESM1-M_r1i1p1	REMO2015_v1	PTXW	PTXW		PTXW
4	SEA-22	EC-EARTH_r1i1p1	RegCM4-3_v4	PTXW		PTXW	PTXW
5	SEA-22	IPSL-CM5A-LR_r1i1p1	RegCM4-3_v4	PTXW		PTXW	PTXW
6	SEA-22	MPI-ESM-MR_r1i1p1	RegCM4-3_v4	PTXW		PTXW	PTXW
7	SEA-22	HadGEM2-ES_r1i1p1	RCA4_v1	PTXW		PTXW	PTXW
8	SEA-22	HadGEM2-ES_r1i1p1	RegCM4-3_v4	PTXW		PTXW	PTXW
9	SEA-22	HadGEM2-ES_r1i1p1	RegCM4-7_v0	PTXW	PTXW		PTXW
10	SEA-22	MPI-ESM-MR_r1i1p1	RegCM4-7_v0	PTXW	PTXW		PTXW

ACCEPTED VERSION SUBJECT TO FINAL EDITING

11	SEA-22	NorESM1-M_r1i1p1	RegCM4-7_v0	PTXW	PTXW		PTXW

[END TABLE ATLAS.SM.14 HERE]

Atlas.SM.2 Figures of regional (CORDEX) model evaluation

The following figures expand the illustrative evaluation results shown in Atlas 1.4.4 (Figure Atlas.7) for the CORDEX North America domain (NAM) to the other domains considered in the Atlas and the Interactive Atlas (see Figure Atlas.6 and Tables Atlas.SM.3 to Atlas.SM.14). Detailed information and salient features of these models are described in Tables AII.2 to AII.4.

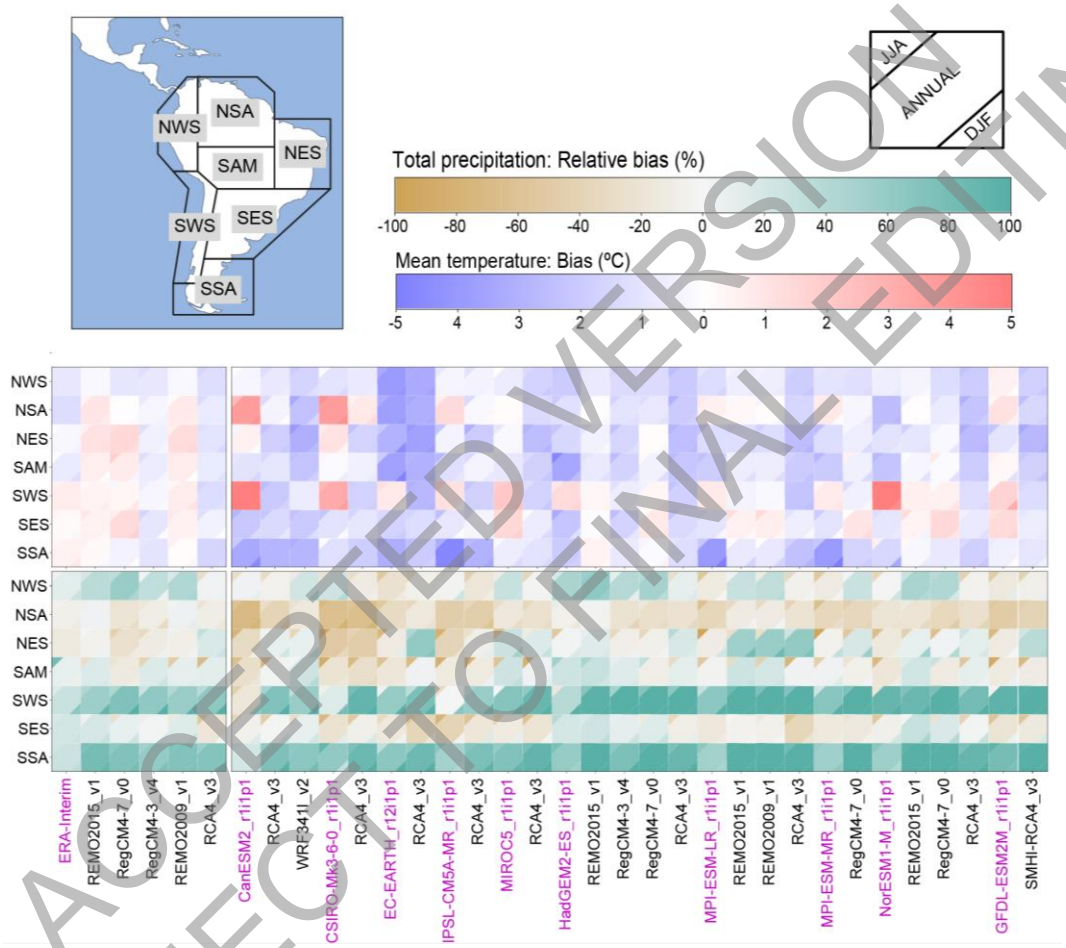


Figure Atlas.SM.1: Evaluation of annual and seasonal air temperature and precipitation for the seven South America subregions NWS, NSA, SAM, NES, SWS, SES, and SSA (land only) for CORDEX-SAM (see Figure Atlas.6) RCM simulations driven by reanalysis or historical GCMs. Seasons are June-July-August (JJA) and December-January-February (DJF). Rows represent subregions and columns correspond to the models. Magenta text indicates the driving historical CMIP5 GCMs (including ERA-Interim in first set of slightly separated columns) and the black text to the right of the magenta text represents the driven RCMs. The colour matrices show the mean spatial biases; all biases have been computed for the period 1985–2005 relative to the observational reference (E5W5, see Section Atlas 1.4.2).

ACCEPTED VERSION SUBJECT TO FINAL EDITING

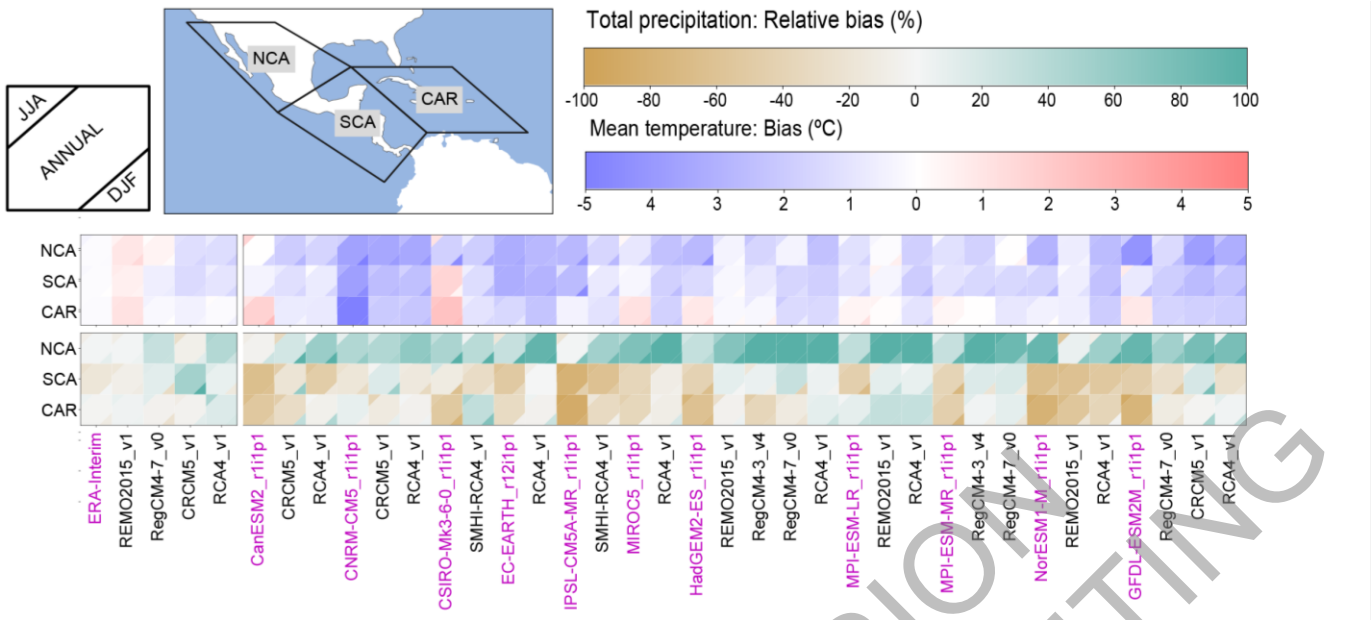


Figure Atlas.SM.2: Evaluation of annual and seasonal air temperature and precipitation for the three Central America subregions NCA, SCA and CAR (land only) for CORDEX-CAM (see Figure Atlas.6) RCM simulations driven by reanalysis or historical GCMs. Seasons are June-July-August (JJA) and December-January-February (DJF). Rows represent subregions and columns correspond to the models. Magenta text indicates the driving historical CMIP5 GCMs (including ERA-Interim in first set of slightly separated columns) and the black text to the right of the magenta text represents the driven RCMs. The colour matrices show the mean spatial biases; all biases have been computed for the period 1985–2005 relative to the observational reference (E5W5, see Section Atlas 1.4.2).

ACCEPTED VERSION
SUBJECT TO FINAL EDITING

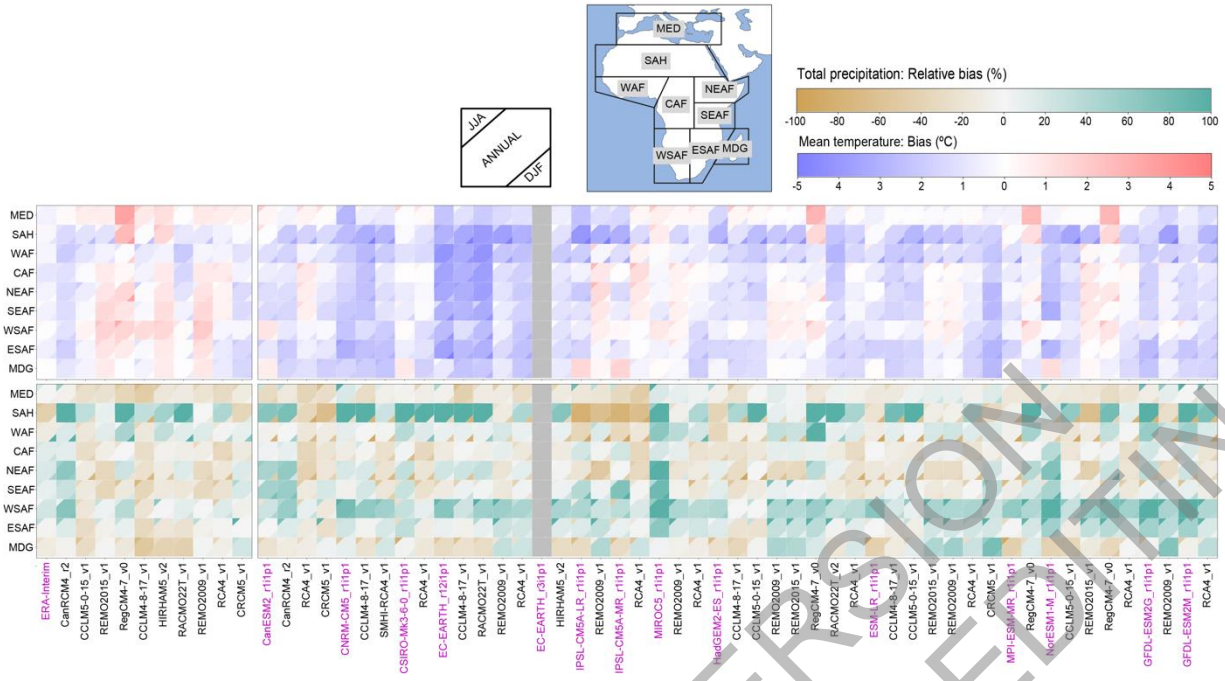


Figure Atlas.SM.3: Evaluation of annual and seasonal air temperature and precipitation for the nine African subregions MED, SAH, WAF, CAF, NEAF, SEAF, WSAF, ESAF, and MDG (land only) for the CORDEX-AFR (see Figure Atlas.6) RCM simulations driven by reanalysis or historical GCMs. Seasons are June-July-August (JJA) and December-January-February (DJF). Rows represent subregions and columns correspond to the models. Magenta text indicates the driving historical CMIP5 GCMs (including ERA-Interim in first set of slightly separated columns) and the black text to the right of the magenta text represents the driven RCMs. The colour matrices show the mean spatial biases; all biases have been computed for the period 1985–2005 relative to the observational reference (E5W5, see Section Atlas 1.4.2).

ACCEPTED VERSION SUBJECT TO FINAL EDITING

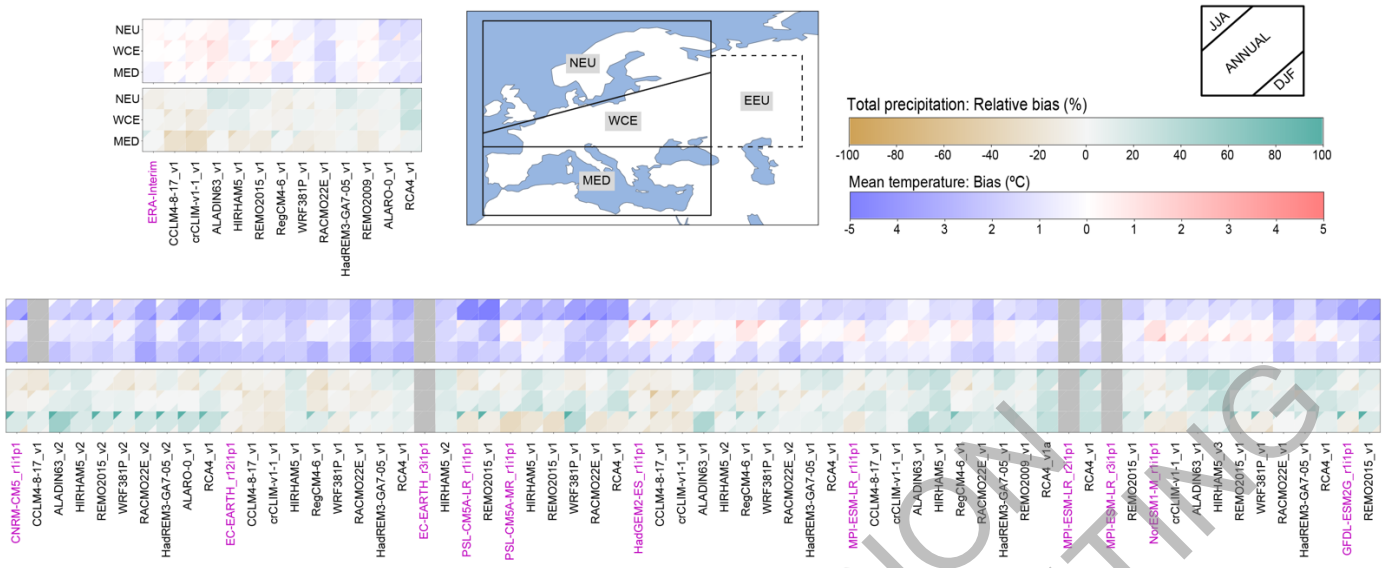


Figure Atlas.SM.4: Evaluation of annual and seasonal air temperature and precipitation for the three European subregions NEU, WCE and MED (land only) for CORDEX-EUR11 (see Figure Atlas.6) RCM simulations driven by reanalysis or historical GCMs. Seasons are June-July-August (JJA) and December-January-February (DJF). Rows represent subregions and columns correspond to the models. Magenta text indicates the driving historical CMIP5 GCMs (including ERA-Interim in first set of slightly separated columns) and the black text to the right of the magenta text represents the driven RCMs. The colour matrices show the mean spatial biases; all biases have been computed for the period 1985–2005 relative to the observational reference (E5W5, see Section Atlas 1.4.2).

ACCEPTED VERSION SUBJECT TO FINAL EDITING

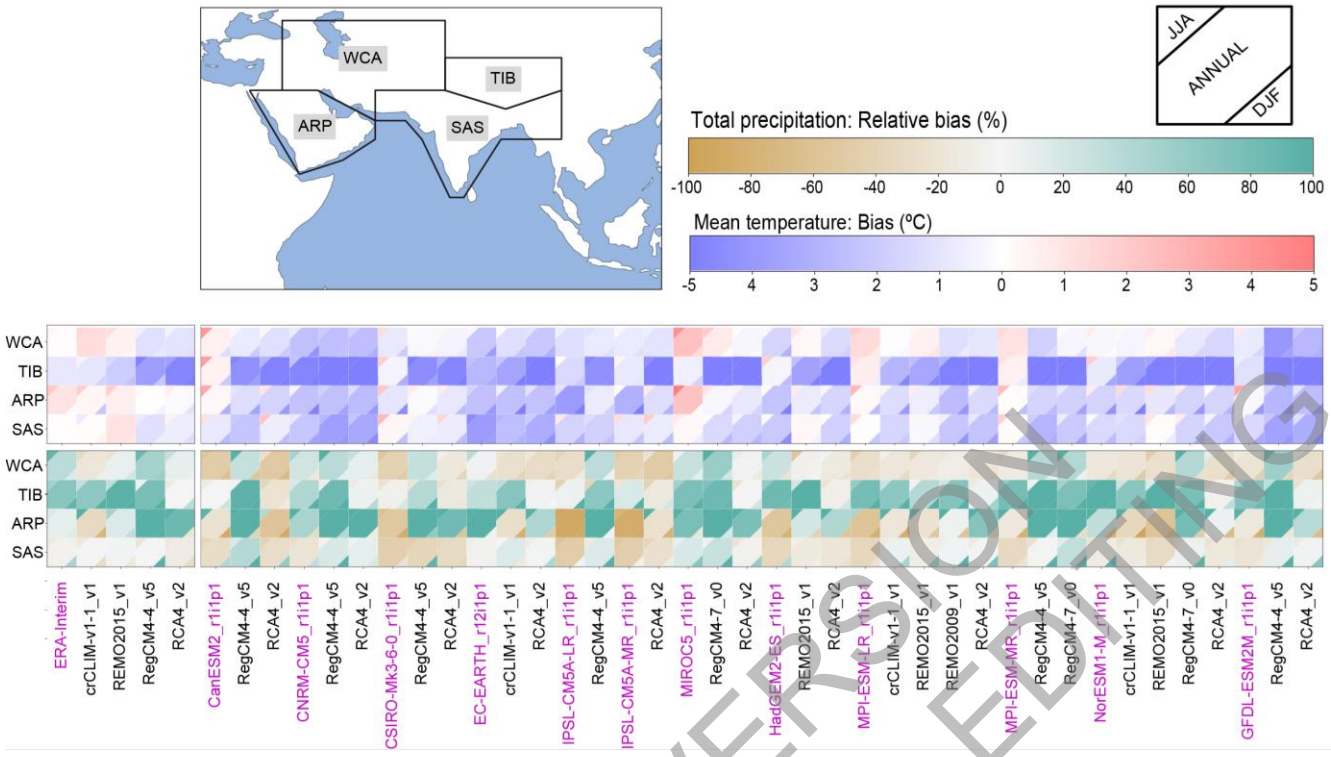


Figure Atlas.SM.5: Evaluation of annual and seasonal air temperature and precipitation for the four Asian subregions WCA, TIB, ARP and SAS (land only) for CORDEX-WAS (see Figure Atlas.6) RCM simulations driven by reanalysis or historical GCMs. Seasons are June-July-August (JJA) and December-January-February (DJF). Rows represent subregions and columns correspond to the models. Magenta text indicates the driving historical CMIP5 GCMs (including ERA-Interim in first set of slightly separated columns) and the black text to the right of the magenta text represents the driven RCMs. The colour matrices show the mean spatial biases; all biases have been computed for the period 1985–2005 relative to the observational reference (E5W5, see Section Atlas 1.4.2).

ACCEPTED VERSION SUBJECT TO FINAL EDITING

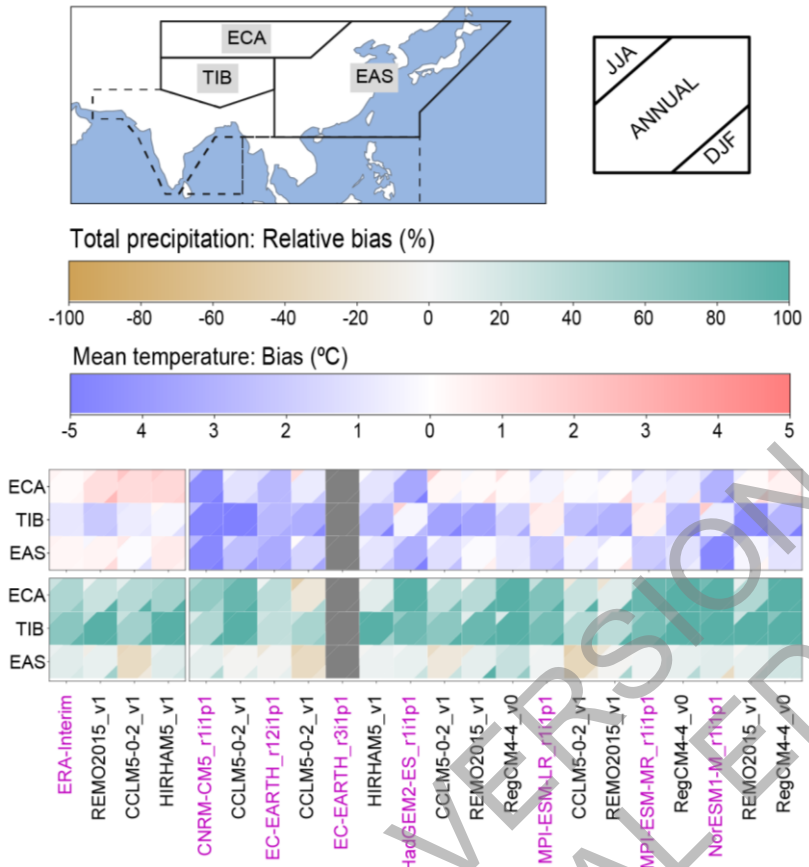


Figure Atlas.SM.6: Evaluation of annual and seasonal air temperature and precipitation for the three Asian subregions ECA, TIB and EAS (land only) for CORDEX-EAS (see Figure Atlas.6) RCM simulations driven by reanalysis or historical GCMs. Seasons are June-July-August (JJA) and December-January-February (DJF). Rows represent subregions and columns correspond to the models. Magenta text indicates the driving historical CMIP5 GCMs (including ERA-Interim in first set of slightly separated columns) and the black text to the right of the magenta text represents the driven RCMs. The colour matrices show the mean spatial biases; all biases have been computed for the period 1985–2005 relative to the observational reference (E5W5, see Section Atlas 1.4.2).

ACCEPTED VERSION SUBJECT TO FINAL EDITING

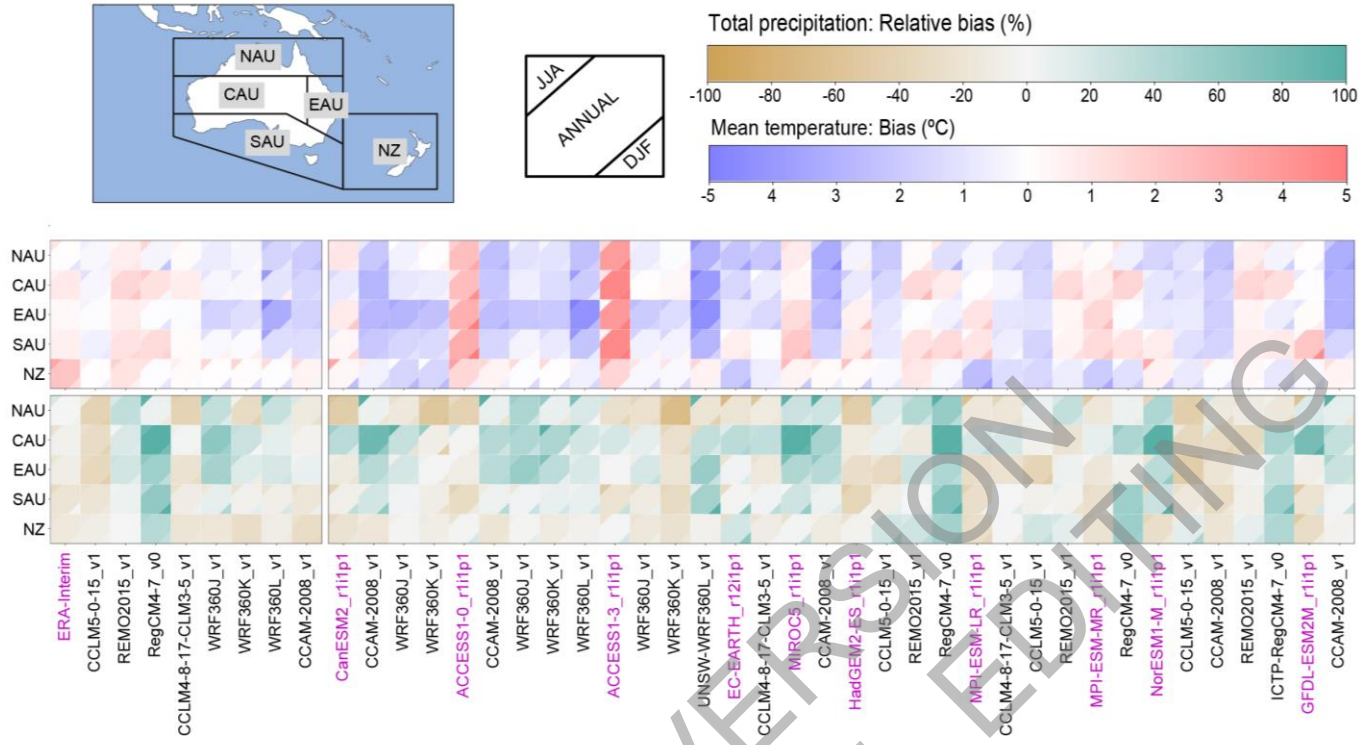


Figure Atlas.SM.7: Evaluation of annual and seasonal air temperature and precipitation for the five Australasia subregions NAU, CAU, EAU, SAU, and NZ (land only) for CORDEX-AUS (see Figure Atlas.6) RCM simulations driven by reanalysis or historical GCMs. Seasons are June-July-August (JJA) and December-January-February (DJF). Rows represent subregions and columns correspond to the models. Magenta text indicates the driving historical CMIP5 GCMs (including ERA-Interim in first set of slightly separated columns) and the black text to the right of the magenta text represents the driven RCMs. The colour matrices show the mean spatial biases; all biases have been computed for the period 1985–2005 relative to the observational reference (E5W5, see Section Atlas 1.4.2).

ACCEPTED VERSION SUBJECT TO FINAL EDITING

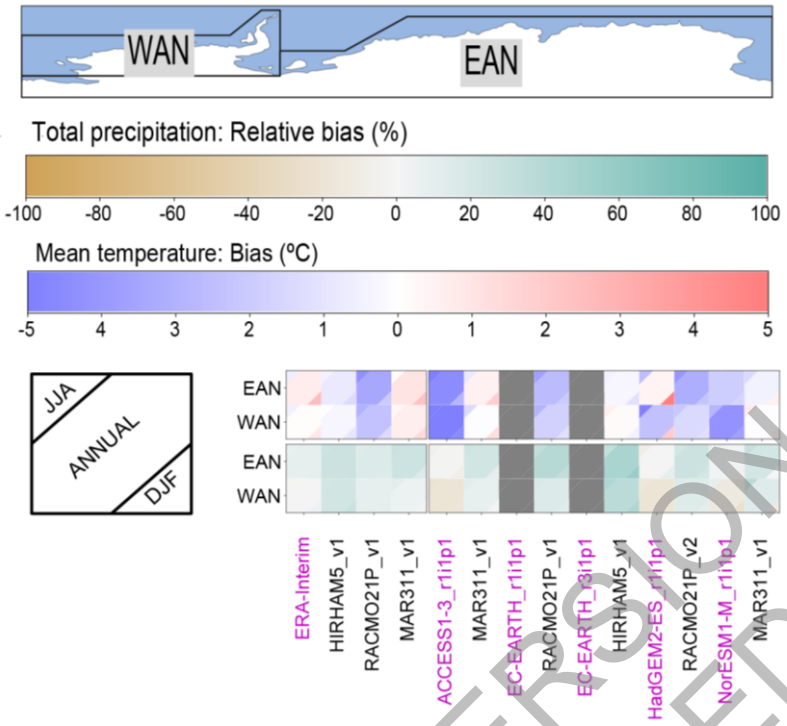


Figure Atlas.SM.8: Evaluation of annual and seasonal air temperature and precipitation for the Antarctic regions EAN and WAN (land only) for CORDEX-ANT (see Figure Atlas.6) RCM simulations driven by reanalysis or historical GCMs. Seasons are June-July-August (JJA) and December-January-February (DJF). Rows represent subregions and columns correspond to the models. Magenta text indicates the driving historical CMIP5 GCMs (including ERA-Interim in first set of slightly separated columns) and the black text to the right of the magenta text represents the driven RCMs. The colour matrices show the mean spatial biases; all biases have been computed for the period 1985–2005 relative to the observational reference (E5W5, see Section Atlas 1.4.2).

ACCEPTED VERSION SUBJECT TO FINAL EDITING

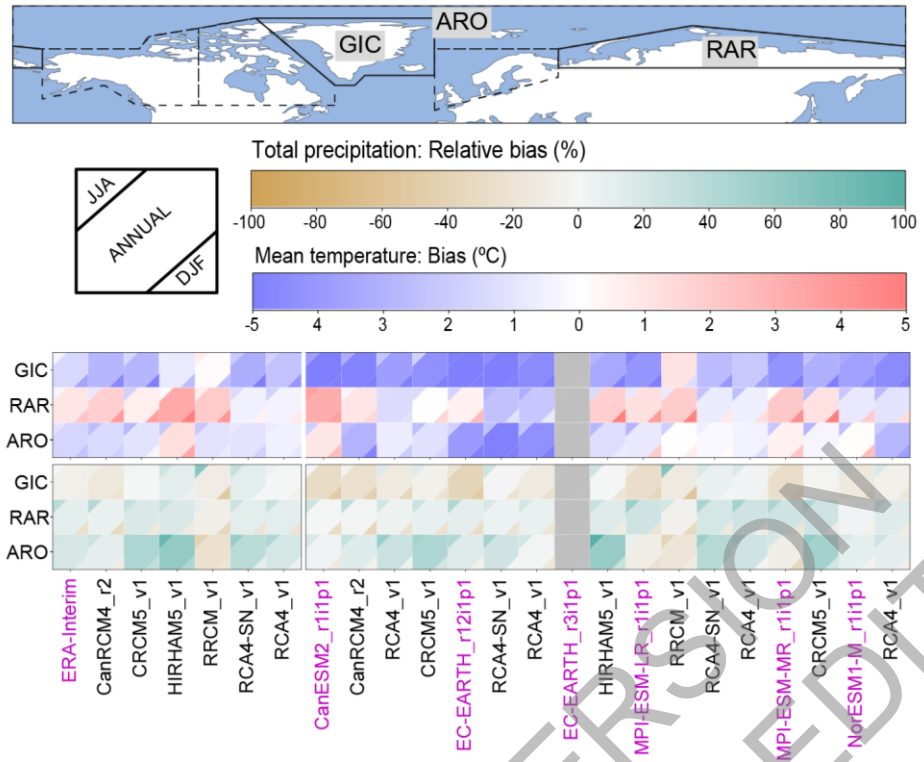


Figure Atlas.SM.9: Evaluation of annual and seasonal air temperature and precipitation for the Arctic regions GIC, RAR (land only), ARO for CORDEX-ARC (see Figure Atlas.6) RCM simulations driven by reanalysis or historical GCMs. Seasons are June-July-August (JJA) and December-January-February (DJF). Rows represent subregions and columns correspond to the models. Magenta text indicates the driving historical CMIP5 GCMs (including ERA-Interim in first set of slightly separated columns) and the black text to the right of the magenta text represents the driven RCMs. The colour matrices show the mean spatial biases; all biases have been computed for the period 1985–2005 relative to the observational reference (E5W5, see Section Atlas 1.4.2).

ACCEPTED VERSION SUBJECT TO FINAL EDITING

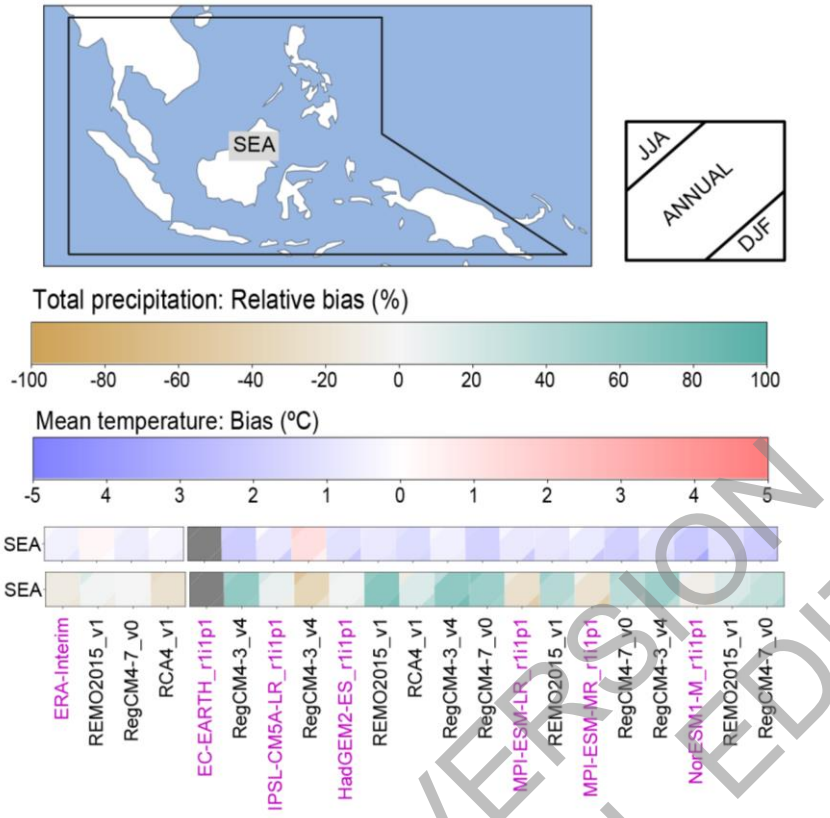


Figure Atlas.SM.10: Evaluation of annual and seasonal air temperature and precipitation for the Asian subregion SEA (land only) for CORDEX-SEA (see Figure Atlas.6) RCM simulations driven by reanalysis or historical GCMs. Seasons are June-July-August (JJA) and December-January-February (DJF). Rows represent subregions and columns correspond to the models. Magenta text indicates the driving historical CMIP5 GCMs (including ERA-Interim in first set of slightly separated columns) and the black text to the right of the magenta text represents the driven RCMs. The colour matrices show the mean spatial biases; all biases have been computed for the period 1985–2005 relative to the observational reference (E5W5, see Section Atlas 1.4.2).

Atlas.SM.3 Data Table

[START TABLE ATLAS.SM.15 HERE]

Table Atlas.SM.15: Input datasets and code used in the chapter.

Figure number	Dataset / Code name	Type	Filename / Specificities	License type	Dataset / Code citation	Dataset / Code URL	Related publications
Atlas.5	CRU-TS v4.04 HadSST.4	Input dataset		Open Government License: http://www.nationalarchives.gov.uk/doc/open-government-licence/version/3/		https://crudata.uea.ac.uk/cru/data/hrg/cru_ts_4.04/ https://www.metoffice.gov.uk/hadobs/hadsst4/	Harris et al., 2020 Kennedy et al., 2019

ACCEPTED VERSION SUBJECT TO FINAL EDITING

Atlas.11.a,c	Berkeley Earth	Input dataset		N/A		http://berkeleyearth.org/data/	Rohde and Hausfater 2020
	observations TrendsGlobal.R (for panel a)	Code				https://github.com/IPCC-WG1/Atlas/scripts	
Atlas.11.b,e	CRU-TS v4.04	Input dataset		Open Government License: http://www.nationalarchives.gov.uk/doc/open-government-licence/version/3/			Harris et al., 2020
	observations TrendsGlobal.R	Code				https://github.com/IPCC-WG1/Atlas/scripts	
Atlas.11.d	CRUTEM5	Input dataset		Open Government License: http://www.nationalarchives.gov.uk/doc/open-government-licence/version/3/		https://www.metoffice.gov.uk/hadobs/crutem5/	Osborn et al., 2021
Atlas.11.f	GPCC v2020	Input dataset		N/A			Schneider et al., 2020
	observations TrendsGlobal.R	Code				https://github.com/IPCC-WG1/Atlas/scripts	
Atlas.18	World Data Centre of the Russian Institute for Hydrometeorological Information (RIHMI-WDC)	Input dataset		N/A			Bulygina et al., 2014
	observations TrendsSnow.R	Code					

ACCEPTED VERSION SUBJECT TO FINAL EDITING

Atlas.20	ACORN-SAT V2.1 AGCD v2	Input dataset		N/A		https://doi.org/10.25941/5d28a5d352de7	
Atlas.23.a,c	E-OBS v21e	Input dataset		Data Policy for ECA&D and E-OBS: https://eca.knmi.nl/documents/ECAD_datapolicy.pdf		spatialMaps_onemodel.R	Cornes et al., 2018
	observationsTrendsEurope.R	Code				https://github.com/IPCC-WG1/Atlas/scripts	
Atlas.23.b	E-OBS v21e	Input dataset		Data Policy for ECA&D and E-OBS: https://eca.knmi.nl/documents/ECAD_datapolicy.pdf			Cornes et al., 2018
	CRU-TS v4.04	Input dataset		Open Government License: http://www.nationalarchives.gov.uk/doc/open-government-licence/version/3/			Harris et al., 2020
	Berkeley Earth	Input dataset		N/A			Rohde and Hausfater 2020
	ERA5	Input dataset		License to use Copernicus products: https://cds.climate.copernicus.eu/api/v2/terms/static/licence-to-use-copernicus-products.pdf			Hersbach et al., 2020
	observationsSeriesEurope.R	Code				https://github.com/IPCC-WG1/Atlas/scripts	

ACCEPTED VERSION SUBJECT TO FINAL EDITING

Atlas.23.d	E-OBS v21e	Input dataset	Temporal series	Data Policy for ECA&D and E-OBS: https://eca.knmi.nl/documents/ECAD_datapolicy.pdf			Cornes et al., 2018
	CRU-TS v4.04	Input dataset		Open Government License: http://www.nationalarchives.gov.uk/doc/open-government-licence/version/3/			Harris et al., 2020
	GPCC v2020	Input dataset		N/A			Schneider et al., 2020
	GPCP v2.3	Input dataset		N/A			Adler et al., 2003
	observationsSeriesEurope.R	Code				https://github.com/IPCC-WG1/Atlas/scripts	

[END TABLE ATLAS.SM.15 HERE]

ACCEPTED VERSION SUBJECT TO FINAL EDITING

References

Iturbide, M., Gutiérrez, J. M., Martín, D. S., Fernández, J., Bedia, J., Baño-Medina, J., et al. (2021). Repository supporting the implementation of FAIR principles in the IPCC-WG1 Interactive Atlas. doi:10.5281/zenodo.3595626.

ACCEPTED VERSION
SUBJECT TO FINAL EDITING

Annex I: Observational Products

Coordinating Lead Authors:
Blair Trewin (Australia)

Lead Authors:
Mansour Almazroui (Saudi Arabia), Lisa Bock (Germany), Josep G. Canadell (Australia), Rafiq Hamdi (Belgium), Masao Ishii (Japan), Pedro M. S. Monteiro (South Africa), Prabir K. Patra (Japan/India), Shilong Piao (China), Jin-Ho Yoon (Republic of Korea), Yongqiang Yu (China), Prodromos Zanis (Greece), Olga Zolina (Russian Federation/France)

This Annex should be cited as:
IPCC, 2021: Annex I: Observational Products [Trewin, B. (ed.)]. In: *Climate Change 2021: The Physical Science Basis. Contribution of Working Group I to the Sixth Assessment Report of the Intergovernmental Panel on Climate Change* [Masson-Delmotte, V., P. Zhai, A. Pirani, S. L. Connors, C. Péan, S. Berger, N. Caud, Y. Chen, L. Goldfarb, M. I. Gomis, M. Huang, K. Leitzell, E. Lonnoy, J.B.R. Matthews, T. K. Maycock, T. Waterfield, O. Yelekçi, R. Yu and B. Zhou (eds.)]. Cambridge University Press. In Press.

Date: August 2021

Note: Accepted version

This document is subject to copy-editing, corrigenda and trickle backs.

ACCEPTED VERSION
SUBJECT TO FINAL EDITING

Table of Content

AI.1 Introduction..... 3

References 22

ACCEPTED VERSION
SUBJECT TO FINAL EDITING

AI.1 Introduction

The purpose of this Annex is to document observational data sets used by Working Group I in the Sixth Assessment Report. This includes details of the types and versions of data sets, the time period they cover, the chapters in which they appear, and citations and (where available) web links to the data.

This list includes those observational data sets that contribute to values reported in the text or in figures, unless they are citing a specific result from a paper (as opposed to an ongoing data set for which that paper is a reference).

Reanalyses are within the scope of this Annex, but historical climate model simulations are not. Proxy data sets are also outside the scope of this Annex.

Data sets which are updated regularly on an operational basis are shown as ending in 2020, even if no 2020 data have yet been published at the time of writing.

Data sets are sorted alphabetically according to the data set name or, if there is no formal name, the name of the responsible institution or lead author.

[START Table AI.1]

Table AI.1: Observational products used by Working Group I in the Sixth Assessment Report.

ACCEPTED VERSION
SUBJECT TO FINAL EDITING

Name	Ver-sion	Type	Resolution (time and space)	Sect-ion(s)	Time period	Citation, link and DOI (where available)
NOAA-CIRES 20th Century Reanalysis (20CR)	2c	Reanalysis	3-hourly, 2 x 2°, 24 vertical levels	2.4.1	1851-2014	Compo et al., 2011 https://www.esrl.noaa.gov/psd/data/20thC_Rean/
NOAA-CIRES 20th Century Reanalysis (20CR)	3	Reanalysis	3-hourly, 0.5° x 0.5°	2.3.1 3.3.3 3.7.1	1851-2020	Slivinski et al., 2019 https://www.esrl.noaa.gov/psd/data/20thC_Rean/
Finland Climate (Aalto)		In situ	Daily 0.1° × 0.1°	10.2.1	1961-2010	Aalto et al., 2016 https://www.csc.fi/-/paituli
ACORN-SAT Australian temperature data	2.1	In situ	Daily, point-based	Atlas 6.2	1910-2020	Trewin et al., 2020 http://www.bom.gov.au/climate/data/acorn-sat/
AERONET AOD Level 2.0	3	Remote sensing	Monthly, point-based	2.2.6	1995-2020	Giles et al., 2019 https://aeronet.gsfc.nasa.gov/data_push/AOT_Level2_Monthly.tar.gz
Advanced Global Atmospheric Gases Experiment (AGAGE)		In situ	Up to 36 times per day, point-based	2.2.3 2.2.4 5.2.2 5.2.3	1978-2020	Prinn et al., 2018 http://agage.mit.edu/data
Australian Gridded Climate Data (AGCD)		In situ	Daily 0.05° × 0.05°	Atlas 6.2	1900-2020	Jones et al., 2009; Evans et al., 2020 http://www.bom.gov.au/climate/maps/rainfall
AIRS specific humidity	RetStd-v5	Remote sensing	Monthly,1° x1°	3.3.2	2003-2010	Susskind et al., 2006; Tian et al., 2013 https://esgf-node.llnl.gov/search/obs4mips/
AIRS-6 climate data products		Remote sensing	Various	2.3.1	2002-2020	Susskind et al., 2014 http://disc.sci.gsfc.nasa.gov/AIRS/data-holdings
Energy balance reconstruction (Allan)		Remote sensing	Monthly, 10 x 10°	7.2.2	1985-2012	Allan et al., 2014 http://met.reading.ac.uk/~sgs02rpa/research/DEEP-C/GRL/
AMOC data set		In situ and reanalysis	Monthly, regional time series	3.5.4	2004-2017	Smeed et al., 2018
Advanced Microwave Scanning Radiometer 2 (AMSR2)		Remote sensing	3-hourly	8.3.1	2012-2019	Kummerow, 2015 https://lance.nsstc.nasa.gov/amsr2-science/data/level2/rainocean/
Aqua's Advanced Microwave Scanning Radiometer for Earth Observing System (AMSR-E)		Remote sensing	5.4 to 56 km	8.3.1	2002-2011	Kawanishi et al., 2003
Arctic sea ice thickness from submarine transects		In situ	Intermittent, track-based	2.3.2	1975-2000	Rothrock et al., 2008
Asian Precipitation - Highly-Resolved Observ-ational Data Integration		In situ	Daily, 0.05° x 0.05°	8.3.2 10.2.1 10.6.3	1900-2020	Kamiguchi et al., 2010; Yatagai et al., 2012

ACCEPTED VERSION SUBJECT TO FINAL EDITING

Towards Evaluation (APHRO-DITE's) Precipitation						
Asian Precipitation -Highly-Resolved Observational Data Integration Towards Evaluation Monsoon Asia (APHRO-MA)	V1808	In situ	Daily, 0.5°	CCB 10.4	1961-2014	Yasutomi et al., 2011 http://aphrodite.st.hirosaki-u.ac.jp/products.html
Asian Precipitation -Highly-Resolved Observational Data Integration Towards Evaluation Monsoon Asia (APHRO-MA)	V1101	In situ	Daily, 0.5°	10.6.3	1956-2005	Yatagai et al., 2012 http://aphrodite.st.hirosaki-u.ac.jp/products.html
Advanced SCATtero-meter (ASCAT)		Remote sensing	Daily, 25 km	8.3.1	2006-2016	Wagner et al., 1999
Cross-calibrated multi-platform wind data set (Atlas)		Remote sensing and in situ	6-hourly, 25 km	2.3.1	1987-2020	Atlas et al., 2011 http://www.remss.com/measurements/ccmp/
Australian vineyard data		In situ	Annual, point-based	2.3.4	Varies by site	Webb et al., 2011
AVISO sea level observations		Remote sensing	Monthly, 0.25°	9.2.4	1995-2020	Legeais et al., 2018 https://www.aviso.altimetry.fr/en/data/products/ocean-indicators-products/mean-sea-level.html
Beaune grape harvest dates		In situ	Annual, point-based	2.3.4	1354-2018	Labbe et al., 2019 https://www.euroclimhist.unibe.ch/en/
Berkeley Earth surface air temperature		In situ	Monthly, 1 x 1° (or equivalent equal-area grid)	1.3.6 1.4.1 1.4.2 1.6.1 FAQ 1.2 2.3.1 CCB 2.3 3.3.1 3.7.3 10.3.3 10.6.4 Box 10.3 CCB10.4 Atlas	1750-2020	Rohde and Hausfather, 2020 http://www.berkeleyearth.org
Berlin City Measure-ment Network		In situ	1-minute	Box 10.3	On-going	www.geo.fu-berlin.de/en/met/service/stadtmessnetz/index.html
Bermuda Atlantic Time-series Study Data		In situ	Point-based	2.3.3	1988-2016	Bates et al., 2014; Bates and Johnson, 2020 http://bats.bios.edu/bats-data/

ACCEPTED VERSION SUBJECT TO FINAL EDITING

Czech Republic precipitation (Bližňák)		In situ	10 min 0.01° × 0.01°	10.2.1	2002-2011	Bližňák et al., 2018
Boulder stratospheric water vapour		In situ	Point-based, profiles approx.. monthly	2.2.5	1980-2010	Hurst et al., 2011
BUCL (Birming-ham)		In situ	Hourly	Box 10.3	2013-2020	Chapman et al., 2015
Global temperature data (Callendar)		In situ	Annual, global time series	1.3.3	1880-1935	Callendar, 1938; Hawkins and Jones, 2013
Cyprus precipitation (Camera)		In situ	Daily 0.01° × 0.01°	10.2.1	1980-2010	Camera et al., 2014
CAMS atmospheric composition reanalysis		Reanalysis	3-hourly, 1 x 1°	7.3.3	2003-2018	Inness et al., 2019 http://atmosphere.copernicus.eu
Data of CARIACO ocean time-series program in the Cariaco Basin		In situ	Point-based	5.3.2	1996-2017	Bates et al., 2014 http://imars.marine.usf.edu/cariaco
CCU 'IKI-Monitoring' satellite data archive		Remote sensing	Daily, resolution varies	Atlas	1984-2020	Loupian et al., 2015
Community Emissions Data System (CEDS)		In situ	Monthly, 50 km (nominal)	6.2.1	1750-2014	Hoesly et al., 2018 http://www.globalchange.umd.edu/ceds/
CERA-20C reanalysis		Reanalysis	3-hourly, 125 km, 91 levels	10.3.3	1901-2010	Laloyaux et al., 2018 https://www.ecmwf.int/en/forecasts/datasets/reanalysis-datasets/cera-20c
CERES EBAF	Ed2.8	Remote sensing	Monthly,1° x1°	3.8.2	2000-2018	Loeb et al., 2009, 2012 https://esgf-node.llnl.gov/search/obs4mips/
CERES EBAF	Ed4.0	Remote sensing	Monthly,1° x1°	7.2.2 9.2.1	2000-2016	Loeb et al., 2017, 2020 http://ceres-tool.larc.nasa.gov/ord-tool/jsp/EBAF4Selection.jsp
NCEP Climate Forecast System Reanalysis (CFSR)		Reanalysis	Hourly, T382 (approx. 38 km)	2.3.1 8.3.2	1979-2010	Saha et al., 2010 https://cfs.ncep.noaa.gov/cfsr/
High-Resolution Gridded Daily Meteorologi-cal Dataset over Sub-Saharan Africa (Chaney)		Reanalysis	Daily 0.1°×0.1°	10.2.1	1979-2005	Chaney et al., 2014
Cheng ocean heat content		In situ	Monthly, ocean basin	2.3.3	1960-2020	Cheng et al., 2017
Global mean sea level reconstructio n (Church and White)		In situ, remote sensing	Monthly, global time series	2.3.3	1880-2009	Church and White, 2011
Climate Hazards Group InfraRed	2.0	Remote sensing	Daily, Monthly 0.25°x 0.25°	10.2.1	1981-2018	Funk et al., 2015 https://www.chc.ucsb.edu/data/chirps

ACCEPTED VERSION SUBJECT TO FINAL EDITING

Precipitation with Station data (CHIRPS)						
CLIMATER		In situ	Daily, point-based	Atlas 5.2	1874-2020	Bulygina et al., 2014
China Land Surface Air Temperature (CLSAT)		In situ	Monthly, point-based	2.3.1	1900-2020	Xu et al., 2018
CPC Merged Analysis of Precipitation (CMAP)		Remote sensing	Monthly, 2.5°x2.5°	3.3.3 Atlas	1979-2020	Xie et al., 2007a https://www.esrl.noaa.gov/psd/data/gridded/data.cmap.html
Copernicus Marine Environment Monitoring Service (CMEMS) ocean pH		In situ	Annual, global mean	2.3.3	1985-2020	Gehlen et al., 2020 https://marine.copernicus.eu/access-data/ocean-monitoring-indicators
CMEMS global mean sea level		Remote sensing	10-day, global time series	2.3.3	1993-2020	Ablain et al., 2019
China Mean Surface Temperature (CMST)		In situ	Monthly, 5° x 5°	2.3.1	1854-2020	Sun et al., 2021
A gridded daily dataset over China CN05.1	5.1	In situ	Daily 0.25° × 0.25°	10.2.1	1961-2005	Wu and Gao, 2013
COBE Sea Surface Temperature	2	In situ	Daily, 1 x 1°	2.4.3 2.4.5 3.7.6 3.7.7	1845-2020	Hirahara et al., 2014 https://ds.data.jma.go.jp/tcc/tcc/products/elnino/cobesst/cobe-sst.html
Bootstrap Sea Ice Concent-rations from Nimbus-7 SMMR and DMSP SSM/I-SSMIS (Comiso)	3	Remote sensing	Monthly, 25 km	2.3.2 3.4.1	1979-2020	Comiso, 2017 https://nsidc.org/data/nsidc-0079
CORA Ocean Heat Content	5.2	In situ	Monthly, global time series	2.3.3	1950-2020	Cabanes et al., 2013 http://www.coriolis.eu.org/Science2/Global-Ocean/CORA
Co-WIN (Hong Kong)		In situ	15 minutes	Box 10.3	2007-2020	Hung and Wo, 2012
Cowtan and Way global temperature	2.0	In situ	Monthly, 5 x 5°	1.3.6 2.3.1 3.3.1	1850-2020	Cowtan and Way, 2014 http://www-users.york.ac.uk/~kdc3/papers/coverage2013/series.html
Climate Prediction Center (CPC) Niño indices		In situ	Monthly, regional time series	2.4.2 2.4.3	1950-2020	https://www.cpc.ncep.noaa.gov/data/indices/ Derived from ERSSTv5
Climate Prediction Centre (CPC) Precipitation		In situ	Hourly 2.0° x 2.5°, daily 0.25° x 0.25°	10.2.1	1948-2006	Higgins et al., 2000; Xie et al., 2007; Chen et al., 2008
CPC teleconnec-tion indices (AAO, AO, NAO, PNA)		In situ	Daily, regional means	2.4.1	1950-2020 (1979-2019 for AAO)	https://www.cpc.ncep.noaa.gov/products/precip/CWlink/daily_ao_index/teleconnections.shtml
CPC Unified Gauge-Based Analysis of Global Daily Precipitation		In situ and remote sensing	Daily, 0.5° x 0.5°	8.3.1	1979-2019	Xie et al., 2010 https://psl.noaa.gov/data/gridded/data.cpc.globalprecip.html

ACCEPTED VERSION SUBJECT TO FINAL EDITING

CloudSat Cloud Profiling Radar (CPR)		Remote sensing	1.5 km horizontal, 0.5 km vertical	8.3.1	2006-2019	Tanelli et al., 2008
CRU TS	4.02	In situ	Monthly, 0.5 x 0.5°	3.3.2 3.3.3 3.7.3 5.2.1	1901-2017	Harris et al., 2014 https://crudata.uea.ac.uk/cru/data/hrg/cru_ts_4.02/
CRU TS	4.03	In situ	Monthly, 0.5 x 0.5°	10.6.2	1901-2017	Harris et al., 2014 https://crudata.uea.ac.uk/cru/data/hrg/cru_ts_4.03/
CRU TS	4.04	In situ	Monthly, 0.5 x 0.5°	2.3.1 8.3.2 Box 8.1 10.3.3 10.3.4 10.4.2 10.6.3 10.6.4 Box 10.3 CCB10.4 Atlas	1901-2020	Harris et al., 2020 https://crudata.uea.ac.uk/cru/data/hrg/cru_ts_4.04/
CRUTEM	4	In situ	Monthly, 5 x 5°	10.6.4 Atlas	1850-2020	Jones et al., 2012 https://crudata.uea.ac.uk/cru/data/temperature/
CRUTEM	5	In situ	Monthly, 5 x 5°	Atlas	1850-2020	Osborn et al., 2021 https://crudata.uea.ac.uk/cru/data/temperature/
Cryosat Arctic sea ice thickness data		Remote sensing	Monthly, 25 x 25 km	2.3.2 9.4.1	2011-2020	Kwok and Cunningham, 2015; Bamber et al., 2018 http://nsidc.org/cryosphere/sotc/sea_ice.html https://science-pds.cryosat.esa.int/
CSIR-ML6 air-sea CO2 fluxes	2019	In situ	Monthly, 1° x 1°	5.2.1	1982-2015	Gregor, 2019 https://doi.org/10.6084/m9.figshare.7894976
CSIRO atmospheric gas measure-ments		In situ	Monthly, point-based	2.2.3 5.2.3	1976-2019	Langenfelds et al., 2002; Francey et al., 2003; Kirschke et al., 2013
CSIRO global mean sea level		Remote sensing	Monthly, 1° x 1°	2.3.3	1993-2020	Church and White, 2011
CSIRO ocean heat content		In situ	Annual, global	2.3.3	1950-2020	Domingues et al., 2008; Wijffels et al., 2016
Mexican climate (Cuervo-Robayo)		In situ	Monthly 30 arc sec	10.2.1	1910-2009	Cuervo-Robayo et al., 2014
3D-VAR regional reanalysis (Dahlgren)		Reanalysis	6-hourly, 0.2° x 0.2°	10.2.1	1989-2010	Dahlgren et al., 2016
Global sea level reconstructio n (Dangendorf)		In situ, remote sensing	Monthly, regional means	1.2.1 2.3.3	1900-2015	Dangendorf et al., 2017, 2019
DCNet (Washing-ton)		In situ	Hourly	Box 10.3	On-going	Hicks et al., 2012
Ethiopian precipitation (Dinku)		In situ	Sub-monthly 0.1° × 0.1°	10.2.1	1983-2013	Dinku et al., 2014
Data of DYFAMED station in the Ligurian Sea		In situ	Point-based	5.3.2	1991-2016	Merlivat et al., 2018 http://dyfbase.obs-vlfr.fr/
Eastern China spring phenology index		In situ	Annual, point-based	2.3.4	1834-2009	Ge et al., 2014
European Climate Assessment		In situ	Daily, point-based	10.6.4	1775-2020	Klein Tank et al., 2002 https://www.ecad.eu/

ACCEPTED VERSION SUBJECT TO FINAL EDITING

& Dataset (ECA&D)						
EDGARv4.3.2	2019	In situ	Monthly, 0.1° x 0.1°	6.7.1	1970-2012	Janssens-Maenhout et al., 2019 http://edgar.jrc.ec.europa.eu/overview.php?v=432_GHG&SECURE=123
EN4 ocean subsurface profiles		In situ	Monthly, point-based	2.3.3	1900-2020	Good et al., 2013 https://www.metoffice.gov.uk/hadobs/
E-OBS	V19.0	In situ	Daily, 0.1° and 0.25°	10.3.3 10.6.4 Atlas 8.2	1950-2020	Cornes et al., 2018 https://www.ecad.eu/
ERA 20th Century (ERA-20C) reanalysis		Reanalysis	3-hourly, ~125 km, 128 vertical levels	2.3.1 3.3.3 3.7.1	1900-2010	Hersbach et al., 2015; Poli et al., 2016 https://www.ecmwf.int/en/forecasts/datasets/reanalysis-datasets/era-20c
ERA-5		Reanalysis	Hourly, 30 km, 137 vertical levels	1.4.1 2.3.1 3.3.1 3.3.2 3.3.3 3.7.1 3.8.2 CCB 3.1 8.3.2 11.4.3 Box 11.4 Atlas	1979-2020	Hersbach et al., 2020 https://www.ecmwf.int/en/forecasts/datasets/reanalysis-datasets/era5
ECMWF ERA-Interim reanalysis		Reanalysis	6-hourly, T255 spectral (approx. 80 km), 60 vertical levels	2.3.1 3.3.3 3.7.1 8.3.2 10.3.3	1979-2019	Dee et al., 2011 https://www.ecmwf.int/en/forecasts/datasets/reanalysis-datasets/era-interim
ECMWF ERA-Interim reanalysis - Land		Reanalysis	6-hourly, T255 spectral (approx. 80 km), 60 vertical levels	10.2.1	1979-2010	Balsamo et al., 2015
NOAA ERSST sea surface temperature	5	In situ	Monthly, 2° x 2°	2.4.2 2.4.3 2.4.5 3.7.3 3.7.6 3.7.7 9.2.1 CCB 9.2 Atlas	1880-2020	Huang et al., 2017 https://www.ncdc.noaa.gov/data-access/marineocean-data/extended-reconstructed-sea-surface-temperature-ersst-v5
ESA CCI sea surface temperature	L4-GHRSST-SSTdepth-OSTIA-GLOB	Remote sensing	Monthly, 0.05°x0.05°	3.8.2	1992-2010	Merchant et al., 2014a, 2014b ftp://anon-ftp.ceda.ac.uk/neodc/esacci/sst/data/
ESA CCI Soil Moisture	L3S-SSMV-COMBINED-v4.2	Remote sensing	Monthly, 0.25°x0.25° ;daily, global images	3.8.2 8.3.1	1979-2016	Dorigo et al., 2017; Gruber et al., 2017; Liu et al., 2012 ftp://anon-ftp.ceda.ac.uk/neodc/esacci/soil_moisture/data/
European Station for Time series in the Ocean Canary Islands (ESTOC)		In situ	Point-based	5.3.2	1995-2018	González-Dávila et al., 2010 http://data.plocan.eu/thredds/catalog/aggregate/public/ESTOCInSitu/EMSOservices/Biogeochemistry/catalog.html
Alpine precipitation grid dataset (EURO4M-APGD)	1.0	In situ	Daily 0.04°× 0.04°	10.2.2	1971-2008	Isotta et al., 2014

ACCEPTED VERSION SUBJECT TO FINAL EDITING

FLO1K flow metrics data set		In situ	Annual, 1 km	2.3.1	1960-2015	Barbarossa et al., 2018
Fogt SAM recon-struction		In situ	Monthly, index	2.4.1	1865-2005	Fogt et al., 2009 http://polarmet.osu.edu/ACD/sam/sam_recon.html
Global mean sea level reconstruction (Frederikse)	2018	In situ	Annual, global time series	2.3.3	1958-2014	Frederikse et al., 2018
Global mean sea level reconstruction (Frederikse)	2020	In situ	Annual, global time series	2.3.3	1900-2018	Frederikse et al., 2020
GHCN precipitation	2	In situ	Monthly, 5°x5°	3.3.2 3.8.1 3.8.2	1900-2014	Jones and Moberg, 2003 https://www.esrl.noaa.gov/psd/data/gridded/data.ghcngridded.html
Global Historical Climatology Network (GHCN) - Monthly	4	In situ	Monthly, point-based	2.3.1 3.8.2 10.3.3	1880-2020	Menne et al., 2018 https://www.ncdc.noaa.gov/ghcnm/
GHCNDEX		In situ	Monthly, 2.5 x 2.5°	2.3.1	1951-2020	Donat et al., 2013b http://www.climdex.org
Global albedo change (Ghimire)		In situ	Monthly, 1 x 1°	2.2.7	1700-2005	Ghimire et al., 2014
GISTEMP	4	In situ	Monthly, 2°x2°	1.3.6 2.3.1 3.7.3 CCB 3.1 10.6.4 Box 10.3	1880-2020	Lenssen et al., 2019 https://data.giss.nasa.gov/gistemp/
Glacier Thickness Database (GlaThiDa)	3.0.1	In situ	Annual, point-based	9.5.1	1935-2018	GlaThiDa Consortium, 2019 https://www.gtn-g.ch/data_catalogue_glathida/ DOI: 10.5904/wgms-glathida-2019-03
GLDAS		Reanalysis	Monthly, 1°x1°	3.4.2 8.3.1	1951-2010	Rodell et al., 2004 https://hydro1.gesdisc.eosdis.nasa.gov/data/GLDAS/GLDAS_NOAH10_M.2.0/
Global Carbon Project		In situ	Global, spatial average	5.2.1 5.2.2	1959-2020	Friedlingstein et al., 2020; Saunois et al., 2020 https://www.globalcarbonproject.org/
Global Ocean Data Analysis Project (GLODAP)	2	In situ	Point-based	5.2.1	1972-2020	Olsen et al., 2019 https://www.glodap.info/
Global Space-based Strato-spheric Aerosol Climatology (GloSSAC)	1.0	Remote sensing	Monthly, 5° zonal means	2.2.2 7.3.2	1979-2016	Thomason et al., 2018 https://eosweb.larc.nasa.gov
Ghana Meteorologi-cal Agency (GMet) precipitation	1.0	In situ	Monthly 0.5°×0.5°	10.2.1	1990-2012	Aryee et al., 2018
GOME global total ozone (GTO) data set		Remote sensing	Monthly, 1 x 1°	2.2.5	1996-2020	Coldewey-Egbers et al., 2015 http://www.esa-ozone-cci.org/?q=node/163
GOME GSG ozone data set		Remote sensing	Monthly, 5° zonal means	2.2.5	1995-2020	Weber et al., 2018a http://www.iup.uni-bremen.de/gome/wfdoas/merged/
GOSAT	2019	Remote sensing	Hourly-monthly	5.2.1	2009-2017	Yoshida et al., 2013 www.gosat.nies.go.jp/en/recent-global-ch4.html

ACCEPTED VERSION SUBJECT TO FINAL EDITING

Global Precipitation Climatology Centre (GPCC)	8	In situ	Monthly, 0.25 x 0.25°	1.2.1 2.3.1 3.3.3 3.7.3 8.3.1 8.3.2 Box 8.1 10.3.3 10.4.2 10.6.3 10.6.4 11.6.2 Atlas	1981-2020	Becker et al., 2013; Schneider et al., 2017 ftp://ftp.dwd.de/pub/data/gpcc/html/fulldata-monthly_v2018_doi_download.html
Global Precipitation Climatology Project (GPCP)	2.3	Remote sensing and in situ	Monthly, 2.5 x 2.5°	2.3.1 3.3.2 3.3.3 3.7.3 3.8.2 8.2.3 8.3.1 9.2.1 10.4.2 Atlas	1979-2020	Adler et al., 2018 https://www.esrl.noaa.gov/psd/data/gridded/data.gpcp.html
Gravity Recovery and Climate Experiment (GRACE)		Remote sensing	3 days, 400 m	2.3.2 8.3.1	2002-2017	Tapley et al., 2004; Wouters et al., 2019 https://gracefo.jpl.nasa.gov/data/grace-fo-data/
Historical greenhouse gas concen-trations for climate modelling		In situ	Monthly, 15° zonal means	2.2.3	1850-2014	Meinshausen et al., 2017 http://www.climatecollege.unimelb.edu.au/cmip6
GRID-Sat		Remote sensing	15-minute, 4 km	8.3.1	1994-2016	Inamdar and Knapp, 2015
The oceanic sink for anthropogenic CO2 from 1994 to 2007 – the data (Gruber)		In situ	1°x1°	5.2.1		Gruber et al., 2019 https://www.nodc.noaa.gov/archive/arc0132/0186034/1.1/data/0-data/
Global Streamflow Indices and Metadata Archive (GSIM)		In situ	Daily, point-based	2.3.1	1806-2016	Do et al., 2018
GSMaP		Remote sensing	Hourly 0.1°	10.3.3	2007-2020	Kubota et al., 2020
GEWEX Water Vapour Assessment (G-VAP)		Reanalysis, remote sensing	Monthly, 2 x 2°	2.3.1	1988-2009	Schröder et al., 201) http://gewex-vap.org/
HadAT	2	In situ	Monthly, 5° latitude by 10° longitude	Atlas	1958-2012	Thorne et al., 2005 https://www.metoffice.gov.uk/hadobs/hadat/
HadCRUT	5	In situ	Monthly, 5 x 5°	1.2.1 1.3.6 1.4.1 1.6.1 2.3.1 CCB 2.3 3.3.1 3.6.1 3.8.1 CCB 3.1 Box 10.3	1850-2020	Morice et al., 2020 https://www.metoffice.gov.uk/hadobs/
HadCRUT	4	In situ	Monthly, 5 x 5°	3.3.1 FAQ 3.1 8.2.3 10.3.3	1850-2020	Morice et al., 2012 https://www.metoffice.gov.uk/hadobs/hadcrut4/

ACCEPTED VERSION SUBJECT TO FINAL EDITING

				10.6.4		
HadEX	2	In situ	Monthly, 3.75 x 2.5°	2.3.1	1901-2010	Donat et al., 2013a http://www.climdex.org
HadEX	3	In situ	Monthly, 1.875 x 1.25°	CCB 3.2 11.1.4 11.3.2 11.4.3 11.6.2	1901-2020	Dunn et al., 2020 https://www.metoffice.gov.uk/hadobs/hadex3/
HadGHCND		In situ	Daily, 3.75 x 2.5°	Atlas	1950-2014	Caesar et al., 2006 https://www.metoffice.gov.uk/hadobs/hadghcnd/
HadISD	2.0.2. 2017f	In situ	Sub-daily, point-based	2.3.1	1973-2020	Dunn et al., 2012, 2016 https://www.metoffice.gov.uk/hadobs/hadisd/
HadISDH	1.0.0. 2019f	In situ	Monthly, 5 x 5°	2.3.1	1973-2020	Willett et al., 2014, 2020 https://www.metoffice.gov.uk/hadobs/hadisdh/
Hadley Centre Sea Ice and Sea Surface Temperature data set (HadISST)	1	In situ and remote sensing	Monthly, 1 x 1°	2.4.3 2.4.5 3.5.1 3.7.3 3.7.6 3.7.7 3.8.1 7.4.4 9.2.1	1871-2020	Rayner et al., 2003 https://www.metoffice.gov.uk/hadobs/hadisst/
Hadley Centre HadNMAT2 night marine air temperature	2	In situ	Monthly, 5° x 5°	CCB 2.3	1880-2010	Kent et al., 2013 https://www.metoffice.gov.uk/hadobs/hadnmat2/
Hadley Centre Sea Level Pressure (HadSLP)	2r	In situ and reanalysis	Monthly, 5 x 5°	3.3.3	1850-2020	Allan and Ansell, 2006 https://www.metoffice.gov.uk/hadobs/hadslp2/
Hadley Centre HadSST sea surface temperature	4	In situ	Monthly, 5° x 5°	9.2.1 Atlas	1850-2020	Kennedy et al., 2019 https://www.metoffice.gov.uk/hadobs/
HadUK-Grid	1.0	In situ	Daily 0.009° × 0.009°	10.2.1	1862-2019	https://www.metoffice.gov.uk/climate/uk/data/haduk-grid/haduk-grid
Hawaii Ocean Time-series Data		In situ	Point-based	2.3.3	1988-2018	Dore et al., 2009 http://hahana.soest.hawaii.edu/hot/hot-dogs/interface.html
Global mean sea level reconstruction (Hay)		In situ	Annual, global mean	2.3.3	1901-2010	Hay et al., 2015
Hamburg Ocean Atmosphere Parameters and Fluxes from Satellite data record (HOAPS4)		Remote sensing	6-hourly, 0.5° x 0.5°	2.3.1	1987-2014	Andersson et al., 2010, 2017 https://wui.cmsaf.eu/safira/action/viewDoiDetails?acronym=HOAPS_V002 DOI: 10.5676/EUM_SAF_CM/HOAPS/V002
Boulder stratospheric water vapor (Hegglin)		In situ		2.2.5	1980-2010	Hegglin et al., 2014
Glacier and ice sheet data set (Hugonnet)		Remote sensing	Annual, point-based	2.3.2	2000-2019	Hugonnet et al., 2021
Central European high-resolution gridded daily data sets (HYRAS)	1.0	In situ	Daily 0.5°×0.5° 0.25°×0.25	10.2.1	1951-2006	Frick et.al., 2014

ACCEPTED VERSION SUBJECT TO FINAL EDITING

IAGOS airborne ozone data		In situ	Intermittent	2.2.5 6.3.2	1994-2020	Cohen et al., 2018; Cooper et al., 2020; Gaudel et al., 2020 http://www.iagos-data.fr/ DOI: 10.25326/20
ICESat sea ice thickness data		Remote sensing	Intermittent, 25 x 25 km	2.3.1	2003-2008	Kwok et al., 2009 http://nsidc.org/cryosphere/sotc/sea_ice.html
International Compre-hensive Ocean - Atmosphere Data Set (ICOADS)	3.0	In situ	Point-based, frequency varies; monthly, 1 x 1°	2.3.1	1662-2019	Freeman et al., 2017 https://icoads.noaa.gov/
IFREMER4	4	Remote sensing	Daily, 0.25° x 0.25°	9.2.1	1992-2017	de Boyer Montégut et al., 2004; Bentamy et al., 2017
Integrated Global Radiosonde Archive (IGRA)		In situ	Point-based	8.3.1	1900-2019	Durre et al., 2006 https://data.noaa.gov/dataset/dataset/integrated-global-radiosonde-archive-igra-version-2
IMBIE Greenland and Antarctic ice sheet mass		Remote sensing	Regional aggregate	2.3.2 9.4.1 9.4.2	1992-2017	IMBIE Consortium, 2018, 2019, 2020
Indian Monsoon Data Assimilation and Analysis (IMDAA)		Reanalysis	Sub-daily 0.11°× 0.11°	10.2.1	1979-2016	Mahmood et al., 2018
Indian Institute of Tropical Meteorology (IITM) all-India rainfall		In situ	Monthly, time series	10.6.3	1871-1993	Parthasarathy et al., 1994
IPRC subsurface temperature data		In situ	Monthly, 1° x 1°	2.3.3	2005-2020	http://apdrc.soest.hawaii.edu/projects/Argo/data/gridded/On_standard_levels/index-1.html
ISAS-15 temperature and salinity gridded fields		In situ	Monthly, 1° x 1°	2.3.3	2002-2015	Gaillard et al., 2016; Kolodziejczyk et al, 2017 https://www.seanoe.org/data/00412/52367/
Ishii et al ocean heat content		In situ	Annual, time series	2.3.3 9.2.2	1955-2020	Ishii et al., 2017
JAMSTEC Database for time-series stations K2 and S1		In situ	Point-based	5.3.2	1997-2018	Wakita et al., 2017 http://www.godac.jamstec.go.jp/catalog/data_catalog/metadataDisp/JAMSTEC_K2_S1?lang=en
Jena-MLS air-sea CO2 fluxes	2018	In situ	Daily, 4° x 5°	5.2.1	1982-2017	Rödenbeck et al., 2013, 2014 http://www.bgc-jena.mpg.de/CarboScope/?ID=oc
Global mean sea level reconstruction (Jevrejeva)		In situ	Annual, global time series	2.3.3	1807-2009	Jevrejeva et al., 2014
JMA-TRANS-COM		Reanalysis	Monthly, 1°x1°	3.6.1 3.8.2	1985-2008	Gurney et al., 2003
Japanese Ocean Flux Data Sets with Use of Remote Sensing Observations (J-OFURO3)	3	Remote sensing	Daily, 0.25° x 0.25°	8.3.1	1988-2013	Tomita, 2017

ACCEPTED VERSION SUBJECT TO FINAL EDITING

Belgium precipitation (Journée)		In situ	Daily 4km²	10.2.1	1981-2010	Journée et al., 2015
Japan Meteorological Agency JRA-55 reanalysis		Reanalysis	3-hourly, TL319 (~55 km), 60 vertical levels	2.3.1 3.3.3 3.7.1 3.8.2 8.3.2 10.3.3 CCB10.4	1958-2020	Kobayashi et al., 2015; Harada et al., 2016 https://jra.kishou.go.jp/JRA-55/index_en.html
JRA-25		Reanalysis	6-hourly T106 (~120km)	10.3.3	1979-2004	Onogi et al., 2007 https://jra.kishou.go.jp/JRA-25/index_en.html
Kadow global temperature data set		In situ	Monthly, 5 x 5°	1.4.1 1.6.1 2.3.1 CCB 2.3 3.3.1 CCB 3.1	1850-2020	Kadow et al., 2020
Kaplan Extended SST data set	2	In situ	Monthly, 5 x 5°	2.4.3 2.4.5 Atlas	1856-2019	Kaplan et al., 1998 https://www.esrl.noaa.gov/psd/data/gridded/data.kaplan_sst.html
Greenland ice sheet discharge (King)		Remote sensing	Annual, regional time series	9.4.1	1985-2018	King et al., 2020 https://datadryad.org/stash/dataset/doi:10.5061/dryad.qrfj6q5cb DOI: 10.5061/dryad.qrfj6q5cb
Kyoto cherry blossom data		In situ	Annual, point-based	2.3.4	801-2020	Aono and Saito, 2010 http://atmenv.envi.osakafu-u.ac.jp/aono/kyophenotemp4/
LAI3g		Remote sensing	Monthly, 0.5°x0.5°	3.6.1 3.8.2	1982-2011	Zhu et al., 2013
LandFlux-EVAL		In situ	Monthly	3.8.2 8.3.1	2000-2004	Mueller et al., 2013 http://www.iac.ethz.ch/groups/seneviratne/research/LandFlux-EVAL
Landsat Global Land Survey (GLS) database		Remote sensing	Daily, global images	8.3.1	1972-2019	Gutman et al., 2013
LAQN (London)		In situ	15 minutes	Box 10.3	1993-2019	www.londonair.org.uk
LDEO Global Ocean Surface Water Partial Pressure of CO2 Database		In situ	Point-based	5.3.2	1957-2018	Takahashi et al., 2014 https://www.nodc.noaa.gov/ocads/oceans/LDEO_Underway_Database/NDP-088_V2018.pdf
LEGOS sea level budget		Remote sensing	Monthly, global time series	2.3.3	1993-2020	Blazquez et al., 2018
Combined satellite and station data (Maidment)		Remote sensing and in situ	10-day 0.0375°× 0.0375°	10.2.1	1983-2012	Maidment et al., 2014
Marshall SAM index		In situ	Monthly, regional means	2.4.1	1957-2020	Marshall, 2003 http://www.nerc-bas.ac.uk/icd/gjma/sam.html
Princeton MEaSURES		Reanalysis, remote sensing and in situ	Monthly, 0.5° x 0.5°	8.3.1	1950-2019	Pan et al., 2012
Multivariate ENSO Index (MEI)		In situ	Monthly	5.2.3	1977-2017	Wolter and Timlin, 1998 https://www.esrl.noaa.gov/psd/enso/mei/
MERRA reanalysis	1	Reanalysis	3-hourly, 0.5° x 0.66°	8.3.2	1979-2016	Rienecker et al., 2011
MERRA-2 reanalysis	2	Reanalysis	Hourly, 0.5 x 0.66°, 72 vertical levels	2.3.1 3.3.3 8.3.2	1980-2020	Gelaro et al., 2017 https://gmao.gsfc.nasa.gov/reanalysis/MERRA-2/

ACCEPTED VERSION SUBJECT TO FINAL EDITING

MERRA-2 reanalysis - Land	2	Reanalysis	6-hourly, 0.5 x 0.66°, 72 vertical levels	8.3.1	1980-2020	Reichle, 2012 http://gmao.gsfc.nasa.gov/pubs/office_notes.
METROS (Tokyo)		In situ	15 minutes	Box 10.3	2000-2005	Takahashi et al., 2011
MIROC4-ACTM emission flux data	2018	Reanalysis	Monthly, 1 x 1°	5.2.2	1996-2016	Patra et al., 2016, 2018; Saeki and Patra, 2017 https://ebcrpa.jamstec.go.jp/~prabir/data/co2l2r84/s042_FaChOt_srcdf1/ https://ebcrpa.jamstec.go.jp/~prabir/data/ch4l2r53/gcp2019/ https://ebcrpa.jamstec.go.jp/~prabir/data/n2ol2r84/s037_edgman1/
MISR Component Global Aerosol Product	V4, Level 3	Remote sensing	Yearly, 0.5° x 0.5° grid	2.2.6	2000-2020	Garay et al., 2017 https://eosweb.larc.nasa.gov/project/misr/mil3yaen_table
MOCCA (Ghent)		In situ	15 minutes	Box 10.3	2016-2020	Vandemeulebroucke et al., 2019; Caluwaerts et al., 2020
NASA Merged Ozone Data (MOD)	8.6	Remote sensing	Monthly, 5° zonal means	2.2.6	1970-2020	Frith et al., 2017 https://acd-ext.gsfc.nasa.gov/Data_services/merged/index.html
MODIS Aerosol optical depth 550nm	MYD08_M3	Remote sensing	Monthly, 1°x1°	2.2.6	2003-2011	Platnick et al., 2003 https://ladsweb.modaps.eosdis.nasa.gov/search/order
MODIS NDVI/EVI vegetation greenness index	6	Remote sensing	16-day; 1km	5.2.1	2000-2018	Myneni et al., 2015 doi:10.5067/MODIS/MCD15A2H.006
Moderate resolution imaging spectro-radiometer (MODIS)	MCD12Q1	Remote sensing	Annual, 500 m	8.3.1	2001-2019	Loveland and Belward, 1997
MPI-SOMFFN air-sea CO2 fluxes	2016	In situ	Monthly, 1° x 1°	3.8.2 5.2.1	1982-2015	Landschützer et al., 2016 https://www.nodc.noaa.gov/ocads/oceans/SPCO2_1982_2015_ETH_SOM_FFN.html
Ozone multi-sensor reanalysis (MSR)	2	Reanalysis	6-hourly, 1 x 1°	2.2.5	1970-2019	Braesicke et al., 2018; Chipperfield et al., 2018; Weber et al., 2018b, 2020 https://www.temis.nl/protocols/O3global.php
Multi-Source Weighted-Ensemble Precipitation dataset (MSWEP)		Reanalysis, remote sensing and in situ	3-hourly, 0.25° x 0.25°	8.3.1	1979-2015	Beck et al., 2017 https://wald.anu.edu.au/data_services/data/mswep-multi-source-weighted-ensem%C2%ADble-pre%C2%ADcip%C2%ADi%C2%ADta%C2%ADtion/
MTE Gross Primary Productivity	May12	Reanalysis	Monthly, 0.5°x0.5°	3.8.2	1982-2011	Jung et al., 2011
Northern Hemisphere Blended Snow Cover Extent and Snow Mass Time Series (Mudryk)		Remote sensing, in situ	Monthly, time series	2.3.2 3.4.2 9.5.3	1980-2018	Mudryk et al., 2020 http://data.ec.gc.ca/data/climate/scientificknowledge/climate-research-publication-based-data/northern-hemisphere-blended-snow-extent-and-snow-mass-time-series/
NASA global mean sea level	4.2	Remote sensing	10-day, global time series	2.3.3	1993-2020	Beckley et al., 2016
NASA Team Sea Ice Concent-rations from Nimbus-7 SMMR and DMSP SSM/I-	1	Remote sensing	Monthly, 25 km	3.4.1	1979-2019	Cavalieri et al., 1996 https://nsidc.org/data/nsidc-0051

ACCEPTED VERSION SUBJECT TO FINAL EDITING

SSMIS Passive Microwave Data						
NCEI Ocean Heat Content		In situ	Annual, 1° x 1°	2.3.3 9.2.2 9.3.2	1955-2020	Levitus et al., 2012 https://www.ncei.noaa.gov/access/global-ocean-heat-content/
NCEP-NCAR Reanalysis		Reanalysis	Daily and monthly, 2.5°x2.5°	3.7.1 3.8.2 10.3.3	1980-2020	Kalnay et al., 1996 http://www.esrl.noaa.gov/psd/data/gridded/data.ncep.reanalysis.html
New Zealand temperature and rainfall datasets		In situ	Daily, point-based	Atlas 6.2	1870-2020	NIWA, 2020
NIWA $\delta^{13}C$-CO_2	2019	In situ	Monthly	5.2.1	1957-2015	Turnbull et al., 2017
NOAA atmospheric gas measure-ments		In situ	Point-based, time resolution depends on gas	2.2.3 2.2.4 3.6.1 5.1.2 5.2.1 5.2.2 5.2.3	Varies depending on gas	Masarie and Tans, 2004; Montzka et al., 2009, 2015; Hall et al., 2011; Dlugokencky and Tans, 2019 https://www.esrl.noaa.gov/gmd/ccgg/
NOAA ESRL MLO Carbon dioxide		In situ	Monthly, point-based	3.6.1	1980-2014	Zeng et al., 2014 https://www.esrl.noaa.gov/gmd/ccgg/trends/data.html
NOAA Global Temp	5	In situ	Monthly, 5 x 5°	1.3.6 10.6.4	1880-2020	Huang et al., 2020 https://www.ncdc.noaa.gov/data-access/marineocean-data/noaa-global-surface-temperature-noaaglobaltemp
NOAA Global Temp - Interim		In situ	Monthly, 5 x 5°	1.4.1 1.6.1 2.3.1 3.3.1 CCB 2.3 CCB 3.1	1850-2020	Vose et al., 2021
NOAA Merge ozone data (SBUV)	8.6	Remote sensing	Daily, 5° zonal means	2.2.5	1978-2020	Wild et al., 2016 ftp://ftp.cpc.ncep.noaa.gov/SBUV_CDR/
NOAA reconstruct-ed snow cover data set		Remote sensing and in situ	Monthly, hemi-spheric time series	3.4.2 9.5.3	1915-1997	Brown, 2002; Brown and Robinson, 2011 https://nsidc.org/data/g02131
NOAA CDR of sea-ice concent-ration	3.0	Remote sensing	Monthly, 25 km	2.3.2	1979-2020	Peng et al., 2013 https://nsidc.org/data/g02202
NOAA STAR satellite temperature	3.0	Remote sensing	Monthly, 2.5 x 2.5°, 3 vertical layers	2.3.1	1979-2020	Zou and Wang, 2011 https://www.star.nesdis.noaa.gov/smcd/emb/mscat/
National Oceanography Centre (NOC) surface flux and meteorological dataset	2.0	In situ	Monthly, 1 x 1°	2.3.1	1973-2014	Berry and Kent, 2011 http://badc.nerc.ac.uk/data/nocs_flux/
African Rainfall Climatology (Novella and Thiaw)	2.0	Remote sensing	Daily 0.1°×0.1°	10.2.1	1983-2010	Novella and Thiaw, 2013
National Sea and Ice Data Center (NSIDC) sea ice index	3	Remote sensing	Daily, 25 km	2.3.2	1978-2020	Fetterer et al., 2017 https://nsidc.org/data/G02135/versions/3
NASA Water Vapor Project		Remote sensing	Daily, 1°	2.3.1	1988-2008	Vonder Haar et al., 2012 https://public.satproj.klima.dwd.de/data/GVAP_data_archive/v1.0/TCWV/long/

ACCEPTED VERSION SUBJECT TO FINAL EDITING

MEaSUReS (NVAP-M)						
NYCMET-NET (New York)	2.0.0	In situ	15 minutes	Box 10.3	On-going	http://nycmetnet.ccny.cuny.edu
OAFlux		Remote sensing	Daily, 0.25 x 0.25°	2.3.1 9.2.1	1987-2019	Yu et al., 2008 http://oaflux.whoi.edu/
Ocean Colour Climate Change Initiative (OC-CCI)	4.2	Remote sensing	Daily, 4 km	2.3.4	1997-2019	Sathyendranath et al., 2019 https://climate.esa.int/en/projects/ocean-colour/
Ocean Satellite Oceanographic Datasets for Acidification (OCEAN SODA-ETHZ)		Remote sensing	Monthly, 1°	2.3.3	1985-2018	Gregor and Gruber, 2021 DOI: 10.25921/m5wx-ja34
NOAA Optimum Interpolation SST (OISST)	2	In situ and remote sensing	Daily, 0.25 x 0.25°	2.4.3	1981-2020	Reynolds et al., 2002; Banzon et al., 2016 https://www.ncdc.noaa.gov/oisst
OSISAF/ CCI sea-ice concent-ration	450	Remote sensing	Monthly, 25 km	2.3.2 3.4.1	1979-2015	Lavergne et al., 2019 http://osisaf.met.no/p/ice/
USA temperature (Oyler)		In situ	Daily 30-arcsec	10.2.1	1948-2012	Oyler et al., 2015
Swiss Alps (Panziera)		Remote sensing	Sub-daily 0.01° × 0.01°	10.2.1	2005-2017	Panziera et al., 2018
Gridded dataset of hourly precipitation in Germany (Paulat)		In situ	Hourly 0.06°× 0.06°	10.2.1	2001-2004	Paulat et al., 2008
Portland State University (PDX) CH_4, $\delta^{13}C$- CH_4	2017	In situ	Daily-monthly	5.2.2	1977-2010	Rice et al., 2016
PERSIANN-CDR		Remote sensing	Daily, 0.25 x 0.25°	10.2.1	1982-2020	Ashouri et al., 2015 https://www.ncdc.noaa.gov/cdr/atmospheric/precipitation-persiann-cdr
Philadelphia plant data		In situ	Annual, point-based	2.3.4	1840-2010	Panchen et al., 2012
PIOMAS Arctic sea ice reanalysis	2.1	Reanalysis	Monthly, 4-5°	7.2.2	1979-2020	Zhang and Rothrock, 2003; Schweiger et al., 2011 http://psc.apl.uw.edu/research/projects/arctic-sea-ice-volume-anomaly/
PMEL ocean heat content		In situ	Annual, global time series	2.3.3	1950-2011	Lyman and Johnson, 2014
PROMICE Greenland ice sheet discharge		Remote sensing	Annual, regional time series	9.4.1	1986-2018	Mankoff et al., 2019 http://promice.org/PromiceDataPortal
PROMICE ice sheet mass balance		Remote sensing	Annual, regional time series	9.4.1	1995-2019	Colgan et al., 2019 http://promice.org/PromiceDataPortal
Purkey and Johnson ocean heat content		In situ	Annual, global mean	2.3.3	1981-2010	Purkey and Johnson, 2010
High Resolution Gridded Data for	1.0	In situ	Daily 1° × 1°	10.6.3	1951-2003	Rajeevan et al., 2006

ACCEPTED VERSION SUBJECT TO FINAL EDITING

India (Rajeevan)						
Randolph Glacier Inventory	6	Remote sensing	Decametric shape files of glacier outlines, global. 0.5° global grid of glacierized area	2.3.2 9.5.1	1955-2014	Scherler et al., 2018 http://www.glims.org/RGI/rgi60_dl.html
RAOB-CORE radiosonde data set	1.7	In situ	Monthly, 10 x 5°, 12 vertical levels	2.3.1 3.3.1	1958-2020	Haimberger et al., 2012 https://www.univie.ac.at/theoret-met/research/raobcore/
Global mean sea level reconstruction (Ray and Douglas)		In situ	Annual, global time series	2.3.3	1900-2010	Ray and Douglas, 2011
REGEN global precipitation	1	In situ	Daily, 1 x 1°	10.3.2	1950-2016	Contractor et al., 2020 https://researchdata.ands.org.au/rainfall-estimates-gridded-v1-2019/1408744 DOI: 10.25914/5ca4c380b0d44
RICH radiosonde data set	1.7	In situ	Monthly, 10 x 5°, 12 vertical levels	2.3.1 3.3.1	1958-2020	Haimberger et al., 2012 https://www.univie.ac.at/theoret-met/research/raobcore/
Antarctic ice mass balance (Rignot)		Remote sensing	Annual, regional average	2.3.2	1979-2017	Rignot et al., 2019
Daily Dataset Romania ROCADA	1.0	In situ	Daily 0.1°×0.1°	10.2.1	1961-2013	Dumitrescu et al., 2016
MSG-based gridded datasets of clouds, precipitation and radiation (Roebeling and Holleman)		Remote sensing	Daily, 0.27° x 0.27°	10.2.1	2005-2019	Roebeling and Holleman, 2009
ROM SAF radio occultation climate data record		Remote sensing	Monthly, 5° latitude bins, 200 m vertical resolution	2.3.1	2001-2020	Gleisner et al., 2020 http://www.romsaf.org
Arctic permafrost layer temperature (Romanovsky)		In situ	Annual, site-based	2.3.2	1977-2020	Romanovsky et al., 2020
Israel precipitation (Rostkier-Edelstein)		Reanalysis	Seasonal 0.02°× 0.02°	10.2.1	1991-2009	Rostkier-Edelstein et al., 2014
Remote Sensing Systems (RSS) precipitation and water vapour	7	Remote sensing	2 per day, 0.25° x 0.25°	2.3.1 3.3.2	1987-2020	Wentz, 2013 http://www.remss.com/measurements/rain-rate/
Remote Sensing Systems RSS satellite temperature	4.0	Remote sensing	Monthly, 2.5° x 2.5°, 5 vertical layers	2.3.1	1979-2020	Mears and Wentz, 2017 http://www.remss.com/measurements/upper-air-temperature/
NOAA/ Rutgers University	V01r01	Remote sensing	Weekly, 100-200 km	2.3.2 9.5.3	1966-2020	Estilow et al., 2015 https://climate.rutgers.edu/snowcover/

ACCEPTED VERSION SUBJECT TO FINAL EDITING

snow cover extent data set						
SAFRAN temperature and precipitation for France		Reanalysis	Hourly 8km^2	10.2.1	1958-2008	Vidal et al., 2010
SAT1 NASA satellite ozone data		Remote sensing	Daily, 1° x 1°	2.2.5	2004-2020	Ziemke et al., 2019 https://acd-ext.gsfc.nasa.gov/Data_services/cloud_slice/new_data.html
SAT2 NASA satellite ozone data		Remote sensing	Daily, 1° x 1°	2.2.5	2004-2020	Heue et al., 2016
SAT3 NASA satellite ozone data		Remote sensing	Daily, 1° x 1°	2.2.5	2004-2020	Leventidou et al., 2018
Scripps atmospheric CO_2 data		In situ	Weekly, point-based	1.2.1 2.2.3 5.2.1	1958-2019	Keeling et al., 2001, 2005 http://scrippsco2.ucsd.edu/data/atmospheric_co2/
SeaWIFS FAPAR data	V2010.0	Remote sensing	Monthly, 1 km	2.3.4	1998-2017	Gobron, 2018 https://fapar.jrc.ec.europa.eu/Home.php
Norwegian seNorge2 precipitation	2.0	In situ	Daily 0.008°× 0.008°	10.2.1	1957-2019	Lussana et al., 2018
Merged precipitation in China (Shen)		In situ	Hourly 0.01° × 0.01°	10.2.1	2015	Shen et al., 2018
The Surface Ocean CO2 Atlas (SOCAT)	6	In situ	Point-based	5.2.1	1957-2020	Bakker et al., 2016 https://www.socat.info/
Southern Oscillation Index (SOI)		In situ	Monthly, regional time series	2.4.2	1876-2020	Troup, 1965 http://www.bom.gov.au/climate/current/soihtm1.shtml
Spain02	5.0	In situ	Daily 0.1°×0.1°	10.2.1	1948-2002	Herrera et al., 2016
Arosa stratospheric ozone data (Staehelin)		In situ	Time resolution varies, point-based	2.2.5	1926-2020	Staehelin et al., 2018
STAMMEX		In situ	Daily, 0.1°, 0.25° and 0.5°	8.3.1	1931-2000	Zolina et al., 2014
State University of New York (SUNY) radiosonde data set		In situ	Monthly, 10° x 10°	2.3.1	1958-2020	Zhou et al., 2021
Strato-spheric Water and Ozone Satellite Homogen-ized (SWOOSH)	2.5	Remote sensing	Monthly, 2.5° zonal mean, 12 vertical levels	2.2.5	1984-2020	Davis et al., 2016 https://data.nodc.noaa.gov/cgi-bin/iso?id=gov.noaa.ncdc:C00958
Tibetan plateau growing season		In situ	Annual, point-based	2.3.4	1960-2014	Yang et al., 2017a
Merged TM4NO2A tropospheric NO2 data set		Remote sensing	Monthly, 0.25°	6.3.3	1996-2016	Georgoulias et al., 2019 https://www.temis.nl/airpollution/no2.php
Tropo-spheric Ozone Assessment Report		In situ	Hourly, point-based	6.3.2	1970-2020	Schultz et al., 2017; Tarasick et al., 2019 http://www.igacproject.org/activities/TOAR

ACCEPTED VERSION SUBJECT TO FINAL EDITING

(TOAR) surface ozone database						
Tohoku Univ. N_2O, $\delta^{15}N$, $\delta^{15}N\alpha$	2018	In situ	Irregular	5.2.3	1950-2000	Ishijima et al., 2007
TOST composite ozonesonde product		In situ	Monthly, 5° × 5° × 1 km	2.2.5 6.3.2	1965-2012	Tarasick et al., 2010; Liu et al., 2013; Gaudel et al., 2018
TRMM Precipitation Radar 3A25	7	Remote sensing	Monthly, 0.5°	8.3.1	1997-2014	Iguchi et al., 2000
TRMM GPOF	GPOF	Remote sensing	Daily, 0.25° x 0.25°	8.3.1	1997-2015	Stocker et al., 2018
TRMM Microwave Imager (TRMM TMI)	TMI	Remote sensing	3-days, 0.25° x 0.25°	8.3.1	1997-2015	Wentz et al., 2001
TRMM Multi-Satellite Precipitation Analysis	7.0	Remote sensing	3-hourly, 0.25° x 0.25°	10.2.1	1997-2018	Huffman et al., 2007; TRMM, 2011; Liu et al., 2012b https://disc.gsfc.nasa.gov/datasets/TRMM_3B42_7/summary
Tropical Rainfall Measuring Mission Precipitation Radar (TRMM PR)	PR	Remote sensing	Monthly, 0.5° x 0.5°	8.3.1	1997-2015	Haddad et al., 1997
TWIN (Taipei)		In situ	Hourly	Box 10.3	2004-2020	Chang et al., 2010
University of Alabama at Huntsville (UAH) satellite temperature	6.0	Remote sensing	Monthly, 3 vertical layers	2.3.1	1979-2020	Spencer et al., 2017 https://www.nsstc.uah.edu/climate/
UC Berkeley, N_2O, $\delta^{15}N$, $\delta^{15}N\alpha$	2018	In situ	Event	5.2.3	1900-1995	Park et al., 2012
University of Colorado global mean sea level		Remote sensing	Monthly, global time series	2.3.3	1993-2017	Nerem et al., 2018
UCAR/ NOAA radio occultation data		Remote sensing	Monthly, 5° latitude bands	2.3.1	2002-2020	Steiner et al., 2020
University of California at Irvine (UCI) atmospheric gas measure-ments		In situ	Point-based, several sampling periods per year	2.2.3	1984-2020	Simpson et al., 2012 http://cdiac.ornl.gov/tracegases.html
UEA-SI air-sea CO2 fluxes	2015	In situ	Monthly, 2.5° x 2.5°	5.2.1	1985-2011	Jones et al., 2015 https://doi.pangaea.de/10.1594/PANGAEA.849262
UHH sea ice product		In situ, remote sensing	Monthly, area average	2.3.2	1850-2020	Doerr et al., 2021 https://www.fdr.uni-hamburg.de/record/8559#.YEtN09xxXIU DOI: 10.25592/uhhfdm.8525
UrBAN (Helsinki)		In situ	Sub-hourly	Box 10.3	2004-2020	Wood et al., 2013 http://urban.fmi.fi
Vaccaro et al global temperature data set		In situ	Monthly, 5° x 5°	2.3.1	1850-2020	Vaccaro et al., 2021

ACCEPTED VERSION SUBJECT TO FINAL EDITING

W5E5 bias-adjusted reanalysis	1.0	Reanalysis	Daily, 0.5° x 0.5°	Atlas	1979-2016	Lange, 2019 https://dataservices.gfz-potsdam.de/pik/showshort.php?id=escidoc:4855898 DOI: 10.5880/pik.2019.023
Walsh et al sea ice data		Remote sensing and in situ	Monthly	2.3.2	1850-2020	Walsh et al., 2017
WASWind marine wind data		In situ	Monthly, 4 x 4°	2.4.4	1950-2011	Tokinaga and Xie, 2011 https://climatedataguide.ucar.edu/climate-data/waswind-wave-and-anemometer-based-sea-surface-wind
WCRP/ Palmer global sea level		Remote sensing and in situ	Monthly, global time series	2.3.3	1901-2018	WCRP Global Sea Level Budget Group, 2018; Palmer et al., 2021
Wegener Centre radio occultation data set		Remote sensing	Monthly, 0.1 km vertical	2.3.1	2001-2020	Angerer et al., 2017
Global mean sea level reconstruction (Wenzel and Schröter)		In situ	Monthly, global time series	2.3.3	1900-2009	Wenzel and Schröter, 2014
WFDE5	1.0	Reanalysis	Hourly, 0.5 °	10.3.3	1979-2018	Cucchi et al., 2020
WMO Global Atmosphere Watch greenhouse gas measure-ments		In situ	Annual, point-based and global means.	2.2.3	1984-2020	Tsutsumi et al., 2009; WMO, 2019 https://gaw.kishou.go.jp/publications/global_mean_mole_fractions
World Ocean Atlas (WOA)	2018	In situ	Monthly, 1°x1°	3.5.1	2009	Levitus et al., 2012; Locarnini et al., 2019; Zweng et al., 2019 https://www.nodc.noaa.gov/OC5/woa18/woa18data.html
World Ozone and UV Data Center (WOUDC) ozone data set		In situ	Monthly, global and zonal means	2.2.5	1964-2020	Fioletov et al., 2002 https://woudc.org/
Global Earth Observation for Integrated Water Resource Assessment (Earth2Observe) Water Resources Reanalysis v2 (WRR2)	2	Reanalysis	Monthly, 0.5° x 0.5°	8.3.1	1979-2012	Schellekens et al., 2017
Brazil gridded met data 1980-2013 (Xavier)		In situ	Daily 0.25° × 0.25°	10.2.1	1980-2013	Xavier et al., 2016 http://careyking.com/data-downloads/
Chile precipitation (Yang)		In situ	Daily 0.04° × 0.04°	10.2.1	2009-2014	Yang et al., 2017 http://www.climatedatalibrary.cl/SOURCES/
Ocean heat content and thermosteric sea level reconstruction (Zanna)		In situ	Annual, global means	2.3.3	1871-2017	Zanna et al., 2019

ACCEPTED VERSION SUBJECT TO FINAL EDITING

[END TABLE AI.1 HERE]

References

Aalto, J., Pirinen, P., and Jylhä, K. (2016). New gridded daily climatology of Finland: Permutation-based uncertainty estimates and temporal trends in climate. *J. Geophys. Res. Atmos.* 121, 3807–3823. doi:10.1002/2015JD024651.

Ablain, M., Meyssignac, B., Zawadzki, L., Jugier, R., Ribes, A., Spada, G., et al. (2019). Uncertainty in satellite estimates of global mean sea-level changes, trend and acceleration. *Earth Syst. Sci. Data* 11, 1189–1202. doi:10.5194/essd-11-1189-2019.

Adler, R. F., Sapiano, M. R. P., Huffman, G. J., Wang, J. J., Gu, G., Bolvin, D., et al. (2018). The Global Precipitation Climatology Project (GPCP) monthly analysis (New Version 2.3) and a review of 2017 global precipitation. *Atmosphere (Basel).* 9. doi:10.3390/atmos9040138.

Allan, R., and Ansell, T. (2006). A new globally complete monthly historical gridded mean sea level pressure dataset (HadSLP2): 1850-2004. *J. Clim.* 19, 5816–5842. doi:10.1175/JCLI3937.1.

Allan, R. P., Liu, C., Loeb, N. G., Palmer, M. D., Roberts, M., Smith, D., et al. (2014). Changes in global net radiative imbalance 1985-2012. *Geophys. Res. Lett.* 41, 5588–5597. doi:10.1002/2014GL060962.

Andersson, A., Fennig, K., Klepp, C., Bakan, S., Graßl, H., and Schulz, J. (2010). The Hamburg Ocean Atmosphere Parameters and Fluxes from Satellite Data – HOAPS-3. *Earth Syst. Sci. Data* 2, 215–234. doi:10.5194/essd-2-215-2010.

Andersson, A., Graw, K., Schröder, M., Fennig, K., Liman, J., Bakan, S., et al. (2017). Hamburg Ocean Atmosphere Parameters and Fluxes from Satellite Data - HOAPS 4.0. *Satell. Appl. Facil. Clim. Monit.* doi:10.5676/EUM_SAF_CM/HOAPS/V002.

Angerer, B., Ladstädter, F., Scherllin-Pirscher, B., Schwärz, M., Steiner, A. K., Foelsche, U., et al. (2017). Quality aspects of the Wegener Center multi-satellite GPS radio occultation record OPSv5.6. *Atmos. Meas. Tech.* 10, 4845–4863. doi:10.5194/amt-10-4845-2017.

Aono, Y., and Saito, S. (2010). Clarifying springtime temperature reconstructions of the medieval period by gap-filling the cherry blossom phenological data series at Kyoto, Japan. *Int. J. Biometeorol.* 54, 211–219. doi:10.1007/s00484-009-0272-x.

Aryee, J. N. A., Amekudzi, L. K., Quansah, E., Klutse, N. A. B., Atiah, W. A., and Yorke, C. (2018). Development of high spatial resolution rainfall data for Ghana. *Int. J. Climatol.* 38, 1201–1215. doi:10.1002/joc.5238.

Ashouri, H., Hsu, K. L., Sorooshian, S., Braithwaite, D., Knapp, K. R., Cecil, L. C., et al. (2015). PERSIANN-CDR: Daily Precipitation Climate Data Record from Multisatellite Observations for Hydrological and Climate Studies. *Bull. Amer. Meteor. Soc*, 69–84. doi:10.1175/BAMS-D-13-00068.1.

Atlas, R., Hoffman, R., Ardizzone, J., Leidner, S., Jusem, J., Smith, D., et al. (2011). A cross-calibrated mutiplatform ocean wind velocity product for meteorlogical and oceanographic applications. *Bull. Am. Meteorol. Soc.* 92, 157–174.

Bakker, D. C. E., Pfeil, B., Landa, C. S., Metzl, N., O'Brien, K. M., Olsen, A., et al. (2016). A multi-decade record of high-quality CO2 data in version 3 of the Surface Ocean CO2 Atlas (SOCAT). *Earth Syst. Sci. Data* 8, 383–413. doi:10.5194/essd-8-383-2016.

Balsamo, G., Albergel, C., Beljaars, A., Boussetta, S., Brun, E., Cloke, H., et al. (2015). ERA-Interim/Land: A global land surface reanalysis data set. *Hydrol. Earth Syst. Sci.* 19, 389–407. doi:10.5194/hess-19-389-2015.

Bamber, J. L., Westaway, R. M., Marzeion, B., and Wouters, B. (2018). The land ice contribution to sea level during the satellite era. *Environ. Res. Lett.* 13, 63008. doi:10.1088/1748-9326/aac2f0.

Banzon, V., Smith, T. M., Chin, T. M., Liu, C., and Hankins, W. (2016). A long-term record of blended satellite and in situ sea-surface temperature for climate monitoring, modeling and environmental studies. *Earth Syst. Sci. Data* 8, 165–176. doi:10.5194/essd-8-165-2016.

Barbarossa, V., Huijbregts, M. A. J., Beusen, A. H. W., Beck, H. E., King, H., and Schipper, A. M. (2018). Data Descriptor: FLO1K, global maps of mean, maximum and minimum annual streamflow at 1 km resolution from 1960 through 2015. *Sci. Data* 5, 1–11. doi:10.1038/sdata.2018.52.

Bates, N. R., Astor, Y., Church, M., Currie, K., Dore, J., Gonzalez-Davila, M., et al. (2014). A Time-Series View of Changing Ocean Chemistry Due to Ocean Uptake of Anthropogenic CO2 and Ocean Acidification. *Oceanography* 27, 126–141. Available at: https://doi.org/10.5670/oceanog.2014.16.

Bates, N. R., and Johnson, R. J. (2020). Acceleration of ocean warming, salinification, deoxygenation and acidification in the surface subtropical North Atlantic Ocean. *Commun. Earth Environ.* 1, 33. doi:10.1038/s43247-020-00030-5.

Beck, H. E., van Dijk, A. I. J. M., Levizzani, V., Schellekens, J., Miralles, D. G., Martens, B., et al. (2017). MSWEP: 3-hourly 0.25{\degree} global gridded precipitation (1979--2015) by merging gauge, satellite, and reanalysis data. *Hydrol. Earth Syst. Sci.* 21, 589–615. doi:10.5194/hess-21-589-2017.

Becker, A., Finger, P., Meyer-Christoffer, A., Rudolf, B., Schamm, K., Schneider, U., et al. (2013). A description of the global land-surface precipitation data products of the Global Precipitation Climatology Centre with sample applications including centennial (trend) analysis from 1901-present. *Earth Syst. Sci. Data* 5, 71–99. doi:10.5194/essd-5-71-2013.

ACCEPTED VERSION SUBJECT TO FINAL EDITING

Beckley, B. ., Zelensky, N. P. ., Holmes, S. A. ., Lemoine, F. G. ., Ray, R. D. ., Mitchum, G. T. ., et al. (2016). Global Mean Sea Level Trend from Integrated Multi-Mission Ocean Altimeters TOPEX/Poseidon Jason-1 and OSTM/Jason-2 Version 4.2. doi:10.5067/GMSLM-TJ142.

Bentamy, A., Piollé, J. F., Grouazel, A., Danielson, R., Gulev, S., Paul, F., et al. (2017). Review and assessment of latent and sensible heat flux accuracy over the global oceans. *Remote Sens. Environ.* 201, 196–218. doi:https://doi.org/10.1016/j.rse.2017.08.016.

Berry, D. I., and Kent, E. C. (2011). Air – Sea fluxes from ICOADS : the construction of a new gridded dataset with uncertainty estimates. *Int. J. Climatol.* 31, 987–1001. doi:10.1002/joc.2059.

Blazquez, A., Meyssignac, B., Lemoine, J. M., Berthier, E., Ribes, A., and Cazenave, A. (2018). Exploring the uncertainty in GRACE estimates of the mass redistributions at the Earth surface: Implications for the global water and sea level budgets. *Geophys. J. Int.* 215, 415–430. doi:10.1093/gji/ggy293.

Bližňák, V., Kašpar, M., and Müller, M. (2018). Radar-based summer precipitation climatology of the Czech Republic. *Int. J. Climatol.* 38, 677–691. doi:10.1002/joc.5202.

Braesicke, A. P., Neu, J., Fioletov, V., Godin-Beekman, S., Hubert, D., Petropavlovskikh, I., et al. (2018). "Update on Global Ozone: Past, Present and Future," in *Scientific Assessment of Ozone Depletion: 2018* Global Ozone Research and Monitoring Project – Report No. 58. (Geneva, Switzerland: World Meteorological Organization (WMO)), 3.1-3.74. Available at: https://csl.noaa.gov/assessments/ozone/2018/downloads/.

Brown, R. D. (2002). Reconstructed North American, Eurasian, and Northern Hemisphere Snow Cover Extent, 1915-1997, Version 1. National Snow and Ice Center, Boulder, Colorado, USA. doi:10.7265/N5V985Z6.

Brown, R. D., and Robinson, D. A. (2011). Northern Hemisphere spring snow cover variability and change over 1922–2010 including an assessment of uncertainty. *Cryosph.* 5, 219–229. doi:10.5194/tc-5-219-2011.

Bulygina, O. N., Korshunova, N. N., and Razuvaev, V. N. (2014). Specialized datasets for climate research. *Tr. VNIIGMI-WDC* 177. Available at: http://meteo.ru/publications/125-trudy-vniigmi/trudy-vniigmi-mtsd-vypusk-177-2014-g/518-spetsializirovannye-massivy-dannykh-dlya-klimaticheskikh-issledovanij.

Cabanes, C., Grouazel, A., Von Schuckmann, K., Hamon, M., Turpin, V., Coatanoan, C., et al. (2013). The CORA dataset: Validation and diagnostics of in-situ ocean temperature and salinity measurements. *Ocean Sci.* 9, 1–18. doi:10.5194/os-9-1-2013.

Caesar, J., Alexander, L., and Vose, R. (2006). Large-scale changes in observed daily maximum and minimum temperatures: Creation and analysis of a new gridded data set. *J. Geophys. Res.* 111, D05101. doi:10.1029/2005JD006280.

Callendar, G. S. (1938). The artificial production of carbon dioxide and its influence on temperature. *Q. J. R. Meteorol. Soc.* 64, 223–240. doi:https://doi.org/10.1002/qj.49706427503.

Caluwaerts, S., Hamdi, R., Top, S., Lauwaet, D., Berckmans, J., Degrauwe, D., et al. (2020). The urban climate of Ghent, Belgium: A case study combining a high-accuracy monitoring network with numerical simulations. *Urban Clim.* 31, 100565. doi:https://doi.org/10.1016/j.uclim.2019.100565.

Camera, C., Bruggeman, A., Hadjinicolaou, P., Pashiardis, S., and Lange, M. A. (2014). Evaluation of interpolation techniques for the creation of gridded daily precipitation (1 × 1 km2); Cyprus, 1980–2010. *J. Geophys. Res. Atmos.* 119, 693–712. doi:10.1002/2013JD020611.

Cavalieri, D. J., Parkinson, C. L., Gloersen, P., and Zwally, H. J. (1996). Sea ice concentrations form Nimbus-7 SMMR and DMSP SSM/I passive microwave data, Version 1. *Boulder, Color. USA. NASA Natl. Snow Ice Data Cent. Distrib. Act. Arch. Center*. doi:10.5067/8GQ8LZQVL0VL.

Chaney, N. W., Sheffield, J., Villarini, G., and Wood, E. F. (2014). Development of a High-Resolution Gridded Daily Meteorological Dataset over Sub-Saharan Africa: Spatial Analysis of Trends in Climate Extremes. *J. Clim.* 27, 5815–5835. doi:10.1175/JCLI-D-13-00423.1.

Chang, B., Wang, H. Y., Peng, T. Y., and Hsu, Y. S. (2010). Development and evaluation of a city-wide wireless weather sensor network. *Educ. Technol. Soc.* doi:10.1172/JCI37539.as.

Chapman, L., Muller, C. L., Young, D. T., Warren, E. L., Grimmond, C. S. B., Cai, X.-M., et al. (2015). The Birmingham Urban Climate Laboratory: An Open Meteorological Test Bed and Challenges of the Smart City. *Bull. Am. Meteorol. Soc.* 96, 1545–1560. doi:10.1175/BAMS-D-13-00193.1.

Chen, M., Shi, W., Xie, P., Silva, V. B. S., Kousky, V. E., Wayne Higgins, R., et al. (2008). Assessing objective techniques for gauge-based analyses of global daily precipitation. *J. Geophys. Res.* 113, D04110. doi:10.1029/2007JD009132.

Cheng, L., Trenberth, K. E., Fasullo, J., Boyer, T., Abraham, J., and Zhu, J. (2017). Improved estimates of ocean heat content from 1960 to 2015. *Sci. Adv.* 3. doi:10.1126/sciadv.1601545.

Chipperfield, M. P., Dhomse, S., Hossaini, R., Feng, W., Santee, M. L., Weber, M., et al. (2018). On the Cause of Recent Variations in Lower Stratospheric Ozone. *Geophys. Res. Lett.* 45, 5718–5726. doi:10.1029/2018GL078071.

Church, J. A., and White, N. J. (2011). Sea-level rise from the late 19th to the early 21st Century. *Surv. Geophys.* 32, 585. doi:10.1007/s10712-011-9119-1.

Cohen, Y., Petetin, H., Thouret, V., Marécal, V., Josse, B., Clark, H., et al. (2018). Climatology and long-term evolution of ozone and carbon monoxide in the upper troposphere--lower stratosphere (UTLS) at northern

ACCEPTED VERSION SUBJECT TO FINAL EDITING

midlatitudes, as seen by IAGOS from 1995 to 2013. *Atmos. Chem. Phys.* 18, 5415–5453. doi:10.5194/acp-18-5415-2018.
Coldewey-Egbers, M., Loyola, D. G., Koukouli, M., Balis, D., Lambert, J.-C., Verhoelst, T., et al. (2015). The GOME-type Total Ozone Essential Climate Variable (GTO-ECV) data record from the ESA Climate Change Initiative. *Atmos. Meas. Tech.* 8, 3923–3940. doi:10.5194/amt-8-3923-2015.
Colgan, W., Mankoff, K. D., Kjeldsen, K. K., Bjørk, A. A., Box, J. E., Simonsen, S. B., et al. (2019). Greenland ice sheet mass balance assessed by PROMICE (1995–2015). *GEUS Bull.* 43. doi:10.34194/GEUSB-201943-02-01.
Comiso, J. C. (2017). Bootstrap Sea Ice Concentrations from Nimbus-7 SMMR and DMSP SSM/I-SSMIS, Version 3. *Boulder, Color. USA. NASA Natl. Snow Ice Data Cent. Distrib. Act. Arch. Cent.* doi:10.5067/7Q8HCCWS4I0R.
Compo, G. P., Whitaker, J. S., Sardeshmukh, P. D., Matsui, N., Allan, R. J., Yin, X., et al. (2011). The twentieth century reanalysis project. *Q. J. R. Meteorol. Soc.* 137, 1–28.
Contractor, S., Donat, M. G., Alexander, L. V, Ziese, M., Meyer-Christoffer, A., Schneider, U., et al. (2020). Rainfall Estimates on a Gridded Network (REGEN) -- a global land-based gridded dataset of daily precipitation from 1950 to 2016. *Hydrol. Earth Syst. Sci.* 24, 919–943. doi:10.5194/hess-24-919-2020.
Cooper, O. R., Schultz, M. G., Schröder, S., Chang, K.-L., Gaudel, A., Carbajal Benítez, G., et al. (2020). Multi-decadal surface ozone trends at globally distributed remote locations. *Elem. Sci. Anthr.* 8, 23. doi:10.1525/elementa.420.
Cornes, R. C., van der Schrier, G., van den Besselaar, E. J. M., and Jones, P. D. (2018). An Ensemble Version of the E-OBS Temperature and Precipitation Data Sets. *J. Geophys. Res. Atmos.* 123, 9391–9409. doi:10.1029/2017JD028200.
Cowtan, K., and Way, R. G. (2014). Coverage bias in the HadCRUT4 temperature series and its impact on recent temperature trends. *Q. J. R. Meteorol. Soc.* 140, 1935–1944. doi:10.1002/qj.2297.
Cucchi, M., Weedon, G. P., Amici, A., Bellouin, N., Lange, S., Müller Schmied, H., et al. (2020). WFDE5: bias-adjusted ERA5 reanalysis data for impact studies. *Earth Syst. Sci. Data* 12, 2097–2120. doi:10.5194/essd-12-2097-2020.
Cuervo-Robayo, A. P., Téllez-Valdés, O., Gómez-Albores, M. A., Venegas-Barrera, C. S., Manjarrez, J., and Martínez-Meyer, E. (2014). An update of high-resolution monthly climate surfaces for Mexico. *Int. J. Climatol.* 34, 2427–2437. doi:10.1002/joc.3848.
Dahlgren, P., Landelius, T., Kållberg, P., and Gollvik, S. (2016). A high-resolution regional reanalysis for Europe. Part 1: Three-dimensional reanalysis with the regional HIgh-Resolution Limited-Area Model (HIRLAM). *Q. J. R. Meteorol. Soc.* 142, 2119–2131. doi:10.1002/qj.2807.
Dangendorf, S., Hay, C., Calafat, F. M., Marcos, M., Piecuch, C. G., Berk, K., et al. (2019). Persistent acceleration in global sea-level rise since the 1960s. *Nat. Clim. Chang.* 9, 705–710. doi:10.1038/s41558-019-0531-8.
Dangendorf, S., Marcos, M., Wöppelmann, G., Conrad, C. P., Frederikse, T., and Riva, R. (2017). Reassessment of 20th century global mean sea level rise. *Proc. Natl. Acad. Sci.* 114, 5946–5951. doi:10.1073/pnas.1616007114.
Davis, S. M., Rosenlof, K. H., Hassler, B., Hurst, D. F., Read, W. G., Vömel, H., et al. (2016). The Stratospheric Water and Ozone Satellite Homogenized (SWOOSH) database: a long-term database for climate studies. *Earth Syst. Sci. Data* 8, 461–490. doi:10.5194/essd-8-461-2016.
de Boyer Montégut, C., Madec, G., Fischer, A. S., Lazar, A., and Iduicone, D. (2004). Mixed layer depth over the global ocean: An examination of profile data and a profile-based climatology. *J. Geophys. Res.* 109, C12003. doi:10.1029/2004JC002378.
Dee, D. P., Uppala, S. M., Simmons, A. J., Berrisford, P., Poli, P., Kobayashi, S., et al. (2011). The ERA-Interim reanalysis: configuration and performance of the data assimilation system. *Q. J. R. Meteorol. Soc.* 137, 553–597. doi:10.1002/qj.828.
Dinku, T., Hailemariam, K., Maidment, R., Tarnavsky, E., and Connor, S. (2014). Combined use of satellite estimates and rain gauge observations to generate high-quality historical rainfall time series over Ethiopia. *Int. J. Climatol.* 34, 2489–2504. doi:10.1002/joc.3855.
Dlugokencky, E., and Tans, P. (2019). Trends in atmospheric carbon dioxide, National Oceanic and Atmospheric Administration. *Earth Syst. Res. Lab.* Available at: http://www.esrl.noaa.gov/gmd/ccgg/trends/global.html [Accessed January 18, 2021].
Do, H. X., Gudmundsson, L., Leonard, M., and Westra, S. (2018). The Global Streamflow Indices and Metadata Archive (GSIM)-Part 1: The production of a daily streamflow archive and metadata. *Earth Syst. Sci. Data* 10, 765–785. doi:10.5194/essd-10-765-2018.
Doerr, J., Notz, D., and Kern, S. (2021). UHH Sea Ice Area Product (Version 2019_fv0.01). Available at: http://doi.org/10.25592/uhhfdm.8559.
Domingues, C. M., Church, J. A., White, N. J., Gleckler, P. J., Wijffels, S. E., Barker, P. M., et al. (2008). Improved estimates of upper-ocean warming and multi-decadal sea-level rise. *Nature* 453, 1090–1093. doi:10.1038/nature07080.
Donat, M. G., Alexander, L. V., Yang, H., Durre, I., Vose, R., and Caesar, J. (2013a). Global Land-Based Datasets for Monitoring Climatic Extremes. *Bull. Am. Meteorol. Soc.* 94, 997–1006. doi:10.1175/bams-d-12-00109.1.
Donat, M. G., Alexander, L. V., Yang, H., Durre, I., Vose, R., Dunn, R. J. H., et al. (2013b). Updated analyses of temperature and precipitation extreme indices since the beginning of the twentieth century: The HadEX2 dataset.

ACCEPTED VERSION SUBJECT TO FINAL EDITING

J. Geophys. Res. Atmos. doi:10.1002/jgrd.50150.
Dore, J. E., Lukas, R., Sadler, D. W., Church, M. J., and Karl, D. M. (2009). Physical and biogeochemical modulation of ocean acidification in the central North Pacific. *Proc. Natl. Acad. Sci.* 106, 12235–12240. doi:10.1073/pnas.0906044106.
Dorigo, W., Wagner, W., Albergel, C., Albrecht, F., Balsamo, G., Brocca, L., et al. (2017). ESA CCI Soil Moisture for improved Earth system understanding: State-of-the art and future directions. *Remote Sens. Environ.* 203, 185–215. doi:10.1016/j.rse.2017.07.001.
Dumitrescu, A., Birsan, M.-V., and Manea, A. (2016). Spatio-temporal interpolation of sub-daily (6 h) precipitation over Romania for the period 1975–2010. *Int. J. Climatol.* 36, 1331–1343. doi:10.1002/joc.4427.
Dunn, R. J. H., Alexander, L. V, Donat, M. G., Zhang, X., Bador, M., Herold, N., et al. (2020). Development of an Updated Global Land In Situ-Based Data Set of Temperature and Precipitation Extremes: HadEX3. *J. Geophys. Res. Atmos.* 125, e2019JD032263. doi:https://doi.org/10.1029/2019JD032263.
Dunn, R. J. H., Willett, K. M., Parker, D. E., and Mitchell, L. (2016). Expanding HadISD: quality-controlled, sub-daily station data from 1931. *Geosci. Instrumentation, Methods Data Syst.* 5, 473–491.
Dunn, R. J. H., Willett, K. M., Thorne, P. W., Woolley, E. V, Durre, I., Dai, A., et al. (2012). HadISD: A Quality Controlled global synoptic report database for selected variables at long-term stations from 1973-2011. *Clim. Past* 8, 1649–1679.
Durre, I., Vose, R. S., and Wuertz, D. B. (2006). Overview of the Integrated Global Radiosonde Archive. *J. Clim.* 19, 53–68. doi:10.1175/JCLI3594.1.
Estilow, T. W., Young, A. H., and Robinson, D. A. (2015). A long-term Northern Hemisphere snow cover extent data record for climate studies and monitoring. *Earth Syst. Sci. Data*. doi:10.5194/essd-7-137-2015.
Evans, A., Jones, D. A., Smalley, R., and Lellyett, S. (2020). *An enhanced gridded rainfall analysis scheme for Australia*. Australian Bureau of Meteorology Available at: http://www.bom.gov.au/research/publications/researchreports/BRR-041.pdf.
Fetterer, F., Knowles, K., Meier, W. N., Savoie, M. H., and Windnagel, A. K. (2017). Sea ice index: version 3. National Snow and Ice Data Center, Boulder, Colorado, USA. doi:10.7265/N5K072F8.
Fioletov, V. E., Bodeker, G. E., Miller, A. J., McPeters, R. D., and Stolarski, R. (2002). Global and zonal total ozone variations estimated from ground-based and satellite measurements: 1964–2000. *J. Geophys. Res. Atmos.* 107, ACH 21-1-ACH 21-14. doi:10.1029/2001JD001350.
Fogt, R. L., Perlwitz, J., Monaghan, A. J., Bromwich, D. H., Jones, J. M., and Marshall, G. J. (2009). Historical SAM variability. Part II: Twentieth-century variability and trends from reconstructions, Observations, and the IPCC AR4 models. *J. Clim.* 22, 5346–5365. doi:10.1175/2009JCLI2786.1.
Francey, R. J., Steele, L. P., Spencer, D. A., Langenfelds, R. L., Law, R. M., Krummel, P. B., et al. (2003). "The CSIRO (Australia) measurement of greenhouse gases in the global atmosphere," in *Baseline Atmospheric Program Australia 1999-2000*, 42–53. Available at: http://www.cmar.csiro.au/e-print/open/baseline_1999-2000.pdf.
Frederikse, T., Jevrejeva, S., Riva, R. E. M., and Dangendorf, S. (2018). A consistent sea-level reconstruction and its budget on basin and global scales over 1958-2014. *J. Clim.* 31, 1267–1280. doi:10.1175/JCLI-D-17-0502.1.
Frederikse, T., Landerer, F., Caron, L., Adhikari, S., Parkes, D., Humphrey, V. W., et al. (2020). The causes of sea-level rise since 1900. *Nature* 584, 393–397. doi:10.1038/s41586-020-2591-3.
Freeman, E., Woodruff, S. D., Worley, S. J., Lubker, S. J., Kent, E. C., Angel, W. E., et al. (2017). ICOADS Release 3.0: a major update to the historical marine climate record. *Int. J. Climatol.* 37, 2211–2232. doi:10.1002/joc.4775.
Friedlingstein, P., O'Sullivan, M., Jones, M. W., Andrew, R. M., Hauck, J., Olsen, A., et al. (2020). Global Carbon Budget 2020. *Earth Syst. Sci. Data* 12, 3269–3340. doi:10.5194/essd-12-3269-2020.
Frith, S. M., Stolarski, R. S., Kramarova, N. A., and McPeters, R. D. (2017). Estimating uncertainties in the SBUV Version 8.6 merged profile ozone data set. *Atmos. Chem. Phys.* 17, 14695–14707. doi:10.5194/acp-17-14695-2017.
Funk, C., Peterson, P., Landsfeld, M., Pedreros, D., Verdin, J., Shukla, S., et al. (2015). The climate hazards infrared precipitation with stations - A new environmental record for monitoring extremes. *Sci. Data.* doi:10.1038/sdata.2015.66.
Gaillard, F., Reynaud, T., Thierry, V., Kolodziejczyk, N., and von Schuckmann, K. (2016). In Situ–Based Reanalysis of the Global Ocean Temperature and Salinity with ISAS: Variability of the Heat Content and Steric Height. *J. Clim.* 29, 1305–1323. doi:10.1175/JCLI-D-15-0028.1.
Garay, M. J., Kalashnikova, O. V, and Bull, M. A. (2017). Development and assessment of a higher-spatial-resolution (4.4km) MISR aerosol optical depth product using AERONET-DRAGON data. *Atmos. Chem. Phys.* 17, 5095–5106. doi:10.5194/acp-17-5095-2017.
Gaudel, A., Cooper, O. R., Ancellet, G., Barret, B., Boynard, A., Burrows, J. P., et al. (2018). Tropospheric Ozone Assessment Report: Present-day distribution and trends of tropospheric ozone relevant to climate and global atmospheric chemistry model evaluation. *Elem Sci Anth* 6. doi:10.1525/elementa.291.
Gaudel, A., Cooper, O. R., Chang, K.-L., Bourgeois, I., Ziemke, J. R., Strode, S. A., et al. (2020). Aircraft observations since the 1990s reveal increases of tropospheric ozone at multiple locations across the Northern Hemisphere. *Sci.*

ACCEPTED VERSION SUBJECT TO FINAL EDITING

Adv. 6. doi:10.1126/sciadv.aba8272.
Ge, Q., Wang, H., Zheng, J., This, R., and Dai, J. (2014). A 170year spring phenology index of plants in eastern China. *J. Geophys. Res. Biogeosciences* 119. doi:10.1002/2013JG002565.
Gehlen, M., Chau, T., Conchon, A., Denvil-Sommer, A., Chevallier, F., Vrac, M., et al. (2020). Ocean acidification. In The Copernicus Marine Service Ocean State Report, issue 4. *J. Oper. Oceanogr.* 13, s64–s67. doi:DOI: 10.1080/1755876X.2020.1785097.
Gelaro, R., McCarty, W., Suárez, M. J., Todling, R., Molod, A., Takacs, L., et al. (2017). The Modern-Era Retrospective Analysis for Research and Applications, Version 2 (MERRA-2). *J. Clim.* 30, 5419–5454. doi:10.1175/JCLI-D-16-0758.1.
Georgoulias, A. K., van der A, R. J., Stammes, P., Boersma, K. F., and Eskes, H. J. (2019). Trends and trend reversal detection in 2 decades of tropospheric NO2 satellite observations. *Atmos. Chem. Phys.* 19, 6269–6294. doi:10.5194/acp-19-6269-2019.
Ghimire, B., Williams, C. A., Masek, J., Gao, F., Wang, Z., Schaaf, C., et al. (2014). Global albedo change and radiative cooling from anthropogenic land cover change, 1700 to 2005 based on MODIS, land use harmonization, radiative kernels, and reanalysis. *Geophys. Res. Lett.* 41, 9087–9096. doi:10.1002/2014GL061671.
Giles, D. M., Sinyuk, A., Sorokin, M. G., Schafer, J. S., Smirnov, A., Slutsker, I., et al. (2019). Advancements in the Aerosol Robotic Network (AERONET) Version 3 database – automated near-real-time quality control algorithm with improved cloud screening for Sun photometer aerosol optical depth (AOD) measurements. *Atmos. Meas. Tech.* 12, 169–209. doi:10.5194/amt-12-169-2019.
GlaThiDa Consortium (2019). *Glacier Thickness Database 3.0.1*. World Glacier Monitoring Service Available at: https://www.gtn-g.ch/data_catalogue_glathida/.
Gleisner, H., Lauritsen, K. B., Nielsen, J. K., and Syndergaard, S. (2020). Evaluation of the 15-year ROM SAF monthly mean GPS radio occultation climate data record. *Atmos. Meas. Tech.* 13, 3081–3098. doi:10.5194/amt-13-3081-2020.
Gobron, N. (2018). Terrestrial Vegetation Activity [in "State of the Climate in 2017"]. *Bull. Am. Meteorol. Soc.* 99, S62–S63. doi:10.1175/2018BAMSStateoftheClimate.1.
González-Dávila, M., Santana-Casiano, J. M., Rueda, M. J., and Llinás, O. (2010). The water column distribution of carbonate system variables at the ESTOC site from 1995 to 2004. *Biogeosciences* 7, 3067–3081. doi:10.5194/bg-7-3067-2010.
Good, S. A., Martin, M. J., and Rayner, N. A. (2013). EN4: Quality controlled ocean temperature and salinity profiles and monthly objective analyses with uncertainty estimates. *J. Geophys. Res. Ocean.* 118, 6704–6716. doi:10.1002/2013JC009067.
Gregor, L. (2019). Global surface ocean pCO2 from CSIR-ML6 (version 2019a). doi:10.6084/m9.figshare.7894976.v1.
Gregor, L., and Gruber, N. (2021). OceanSODA-ETHZ: a global gridded data set of the surface ocean carbonate system for seasonal to decadal studies of ocean acidification. *Earth Syst. Sci. Data* 13, 777–808. doi:10.5194/essd-13-777-2021.
Gruber, A., Dorigo, W. A., Crow, W., and Wagner, W. (2017). Triple Collocation-Based Merging of Satellite Soil Moisture Retrievals. *IEEE Trans. Geosci. Remote Sens.* 55, 6780–6792. doi:10.1109/TGRS.2017.2734070.
Gruber, N., Clement, D., Carter, B. R., Feely, R. A., van Heuven, S., Hoppema, M., et al. (2019). The oceanic sink for anthropogenic CO2 from 1994 to 2007. *Science (80-.).* 363, 1193–1199. doi:10.1126/science.aau5153.
Gurney, K. R., Law, R. M., Denning, A. S., Rayner, P. J., Baker, D., Bousquet, P., et al. (2003). TransCom 3 CO2inversion intercomparison: 1. Annual mean control results and sensitivity to transport and prior flux information. *Tellus, Ser. B Chem. Phys. Meteorol.* 55, 555–579. doi:10.1034/j.1600-0889.2003.00049.x.
Gutman, G., Huang, C., Chander, G., Noojipady, P., and Masek, J. G. (2013). Assessment of the NASA–USGS Global Land Survey (GLS) datasets. *Remote Sens. Environ.* 134, 249–265. doi:https://doi.org/10.1016/j.rse.2013.02.026.
Haddad, Z. S., Smith, E. A., Kummerow, C. D., Iguchi, T., Farrar, M. R., Durden, S. L., et al. (1997). The TRMM Day-1 Radar/Radiometer Combined Rain-Profiling Algorithm. *J. Meteorol. Soc. Japan. Ser. II* 75, 799–809. doi:10.2151/jmsj1965.75.4_799.
Haimberger, L., Tavolato, C., and Sperka, S. (2012). Homogenization of the Global Radiosonde Temperature Dataset through Combined Comparison with Reanalysis Background Series and Neighboring Stations. *J. Clim.* 25, 8108–8131. doi:10.1175/JCLI-D-11-00668.1.
Hall, B. D., Dutton, G. S., Mondeel, D. J., Nance, J. D., Rigby, M., Butler, J. H., et al. (2011). Improving measurements of SF6 for the study of atmospheric transport and emissions. *Atmos. Meas. Tech.* doi:10.5194/amt-4-2441-2011.
Harada, Y., Kamahori, H., Kobayashi, C., Endo, H., Kobayashi, S., Ota, Y., et al. (2016). The JRA-55 Reanalysis: Representation of atmospheric circulation and climate variability. *J. Meteorol. Soc. Japan* 94, 269–302. doi:10.2151/jmsj.2016-015.
Harris, I., Jones, P. D., Osborn, T. J., and Lister, D. H. (2014). Updated high-resolution grids of monthly climatic observations - the CRU TS3.10 Dataset. *Int. J. Climatol.* 34, 623–642. doi:10.1002/joc.3711.
Harris, I., Osborn, T. J., Jones, P., and Lister, D. (2020). Version 4 of the CRU TS monthly high-resolution gridded multivariate climate dataset. *Sci. Data* 7, 109. doi:10.1038/s41597-020-0453-3.
Hawkins, E., and Jones, P. D. (2013). On increasing global temperatures: 75 years after Callendar. *Q. J. R. Meteorol.*

ACCEPTED VERSION SUBJECT TO FINAL EDITING

Soc. 139, 1961–1963. doi:https://doi.org/10.1002/qj.2178.
Hay, C. C., Morrow, E., Kopp, R. E., and Mitrovica, J. X. (2015). Probabilistic reanalysis of twentieth-century sea-level rise. *Nature* 517, 481–484. doi:10.1038/nature14093.
Haylock, M. R., Hofstra, N., Klein Tank, A. M. G., Klok, E. J., Jones, P. D., and New, M. (2008). A European daily high-resolution gridded data set of surface temperature and precipitation for 1950–2006. *J. Geophys. Res.* 113, D20119. doi:10.1029/2008JD010201.
Hegglin, M. I., Plummer, D. A., Shepherd, T. G., Scinocca, J. F., Anderson, J., Froidevaux, L., et al. (2014). Vertical structure of stratospheric water vapour trends derived from merged satellite data. *Nat. Geosci.* 7, 768. doi:10.1038/ngeo2236.
Herrera, S., Fernández, J., and Gutiérrez, J. M. (2016). Update of the Spain02 gridded observational dataset for EURO-CORDEX evaluation: Assessing the effect of the interpolation methodology. *Int. J. Climatol.* doi:10.1002/joc.4391.
Hersbach, H., Bell, B., Berrisford, P., Hirahara, S., Horányi, A., Muñoz-Sabater, J., et al. (2020). The ERA5 global reanalysis. *Q. J. R. Meteorol. Soc.* 146, 1999–2049. doi:10.1002/qj.3803.
Hersbach, H., Peubey, C., Simmons, A., Berrisford, P., Poli, P., and Dee, D. (2015). ERA-20CM: a twentieth-century atmospheric model ensemble. *Q. J. R. Meteorol. Soc.* 141, 2350–2375. doi:10.1002/qj.2528.
Heue, K. P., Coldewey-Egbers, M., Delcloo, A., Lerot, C., Loyola, D., Valks, P., et al. (2016). Trends of tropical tropospheric ozone from 20 years of European satellite measurements and perspectives for the Sentinel-5 Precursor. *Atmos. Meas. Tech.* 9, 5037–5051. doi:10.5194/amt-9-5037-2016.
Hicks, B. B., Callahan, W. J., Pendergrass, W. R., Dobosy, R. J., and Novakovskaia, E. (2012). Urban turbulence in space and in time. *J. Appl. Meteorol. Climatol.* doi:10.1175/JAMC-D-11-015.1.
Higgins, R., Shi, W., Yarosh, E., and Joyce, R. (2000). Improved United States Precipitation Quality Control System and Analysis. *NOAA, Natl. Weather Serv. Natl. Centers Environ. Predict. Clim. Predict. Cent.*
Hirahara, S., Ishii, M., and Fukuda, Y. (2014). Centennial-Scale Sea Surface Temperature Analysis and Its Uncertainty. *J. Clim.* 27, 57–75. doi:10.1175/JCLI-D-12-00837.1.
Hoesly, R. M., Smith, S. J., Feng, L., Klimont, Z., Janssens-Maenhout, G., Pitkanen, T., et al. (2018). Historical (1750--2014) anthropogenic emissions of reactive gases and aerosols from the Community Emissions Data System (CEDS). *Geosci. Model Dev.* 11, 369–408. doi:10.5194/gmd-11-369-2018.
Huang, B., Menne, M. J., Boyer, T., Freeman, E., Gleason, B. E., Lawrimore, J. H., et al. (2020). Uncertainty estimates for sea surface temperature and land surface air temperature in NOAAGlobalTemp version 5. *J. Clim.* 33, 1351–1379. doi:10.1175/JCLI-D-19-0395.1.
Huang, B., Thorne, P. W., Banzon, V. F., Boyer, T., Chepurin, G., Lawrimore, J. H., et al. (2017). Extended Reconstructed Sea Surface Temperature, Version 5 (ERSSTv5): Upgrades, Validations, and Intercomparisons. *J. Clim.* 30, 8179–8205. doi:10.1175/JCLI-D-16-0836.1.
Huffman, G. J., Adler, R. F., Bolvin, D., Gu, G., Nelkin, E., Bowman, K. P., et al. (2007). The TRMM Multisatellite Precipitation Analysis (TMPA): Quasi-Global , Multiyear , Combined-Sensor Precipitation Estimates at Fine Scales. *J. Hydrometeorol.* 8, 38–55. doi:10.1175/JHM560.1.
Hugonnet, R., McNabb, R., Berthier, E., Menounos, B., Nuth, C., Girod, L., et al. (2021). Accelerated global glacier mass loss in the early twenty-first century. *Nat. (in Press.*
Hung, T. K., and Wo, O. C. (2012). Development of a Community Weather Information Network (Co-WIN) in Hong Kong. *Weather* 67, 48–50. doi:10.1002/wea.1883.
Hurst, D. F., Oltmans, S. J., Vömel, H., Rosenlof, K. H., Davis, S. M., Ray, E. A., et al. (2011). Stratospheric water vapor trends over Boulder, Colorado: Analysis of the 30 year Boulder record. *J. Geophys. Res. Atmos.* 116. doi:10.1029/2010JD015065.
Iguchi, T., Kozu, T., Meneghini, R., Awaka, J., and Okamoto, K. (2000). Rain-Profiling Algorithm for the TRMM Precipitation Radar. *J. Appl. Meteorol.* 39, 2038–2052. doi:10.1175/1520-0450(2001)040<2038:RPAFTT>2.0.CO;2.
IMBIE Consortium (2018). Mass balance of the Antarctic Ice Sheet from 1992 to 2017. *Nature*. doi:10.1038/s41586-018-0179-y.
IMBIE Consortium (2019). Mass balance of the Greenland Ice Sheet from 1992 to 2018. *Nature*. doi:10.1038/s41586-019-1855-2.
IMBIE Consortium (2020). Mass balance of the Greenland Ice Sheet from 1992 to 2018. *Nature* 579, 233–239. doi:10.1038/s41586-019-1855-2.
Inamdar, A. K., and Knapp, K. R. (2015). Intercomparison of Independent Calibration Techniques Applied to the Visible Channel of the ISCCP B1 Data. *J. Atmos. Ocean. Technol.* 32, 1225–1240. doi:10.1175/JTECH-D-14-00040.1.
Inness, A., Ades, M., Agustí-Panareda, A., Barré, J., Benedictow, A., Blechschmidt, A.-M., et al. (2019). The CAMS reanalysis of atmospheric composition. *Atmos. Chem. Phys.* 19, 3515–3556. doi:10.5194/acp-19-3515-2019.
Ishii, M., Fukuda, Y., Hirahara, S., Yasui, S., Suzuki, T., and Sato, K. (2017). Accuracy of Global Upper Ocean Heat Content Estimation Expected from Present Observational Data Sets. *SOLA* 13, 163–167. doi:10.2151/sola.2017-030.

ACCEPTED VERSION SUBJECT TO FINAL EDITING

Ishijima, K., Sugawara, S., Kawamura, K., Hashida, G., Morimoto, S., Murayama, S., et al. (2007). Temporal variations of the atmospheric nitrous oxide concentration and its δ15N and δ18O for the latter half of the 20th century reconstructed from firn air analyses. *J. Geophys. Res.* 112, D03305. doi:10.1029/2006JD007208.

Isotta, F. A., Frei, C., Weilguni, V., Perčec Tadić, M., Lassègues, P., Rudolf, B., et al. (2014). The climate of daily precipitation in the Alps: Development and analysis of a high-resolution grid dataset from pan-Alpine rain-gauge data. *Int. J. Climatol.* doi:10.1002/joc.3794.

Janssens-Maenhout, G., Crippa, M., Guizzardi, D., Muntean, M., Schaaf, E., Dentener, F., et al. (2019). EDGAR v4.3.2 Global Atlas of the three major Greenhouse Gas Emissions for the period 1970-2012. *Earth Syst. Sci. Data Discuss.* 2010, 1–52. doi:10.5194/essd-2018-164.

Jevrejeva, S., Moore, J. C., Grinsted, A., Matthews, A. P., and Spada, G. (2014). Trends and acceleration in global and regional sea levels since 1807. *Glob. Planet. Change* 113, 11–22. doi:https://doi.org/10.1016/j.gloplacha.2013.12.004.

Jones, D., Wang, W., and Fawcett, R. (2009). High-quality spatial climate data-sets for Australia. *Aust. Meteorol. Oceanogr. J.* 58, 233–248. doi:10.22499/2.5804.003.

Jones, P. D., Lister, D. H., Osborn, T. J., Harpham, C., Salmon, M., and Morice, C. P. (2012). Hemispheric and large-scale land-surface air temperature variations: An extensive revision and an update to 2010. *J. Geophys. Res. Atmos.* 117. doi:10.1029/2011JD017139.

Jones, P. D., and Moberg, A. (2003). Hemispheric and large-scale surface air temperature variations: An extensive revision and an update to 2001. *J. Clim.* 16, 206–223.

Jones, S. D., Le Quéré, C., Rödenbeck, C., Manning, A. C., and Olsen, A. (2015). Data and Code archive for the interpolation of surface ocean carbon dioxide. doi:10.1594/PANGAEA.849262.

Journée, M., Delvaux, C., and Bertrand, C. (2015). Precipitation climate maps of Belgium. *Adv. Sci. Res.* 12, 73–78. doi:10.5194/asr-12-73-2015.

Jung, M., Reichstein, M., Margolis, H. A., Cescatti, A., Richardson, A. D., Arain, M. A., et al. (2011). Global patterns of land-atmosphere fluxes of carbon dioxide, latent heat, and sensible heat derived from eddy covariance, satellite, and meteorological observations. *J. Geophys. Res. Biogeosciences* 116, 1–16. doi:10.1029/2010JG001566.

Kadow, C., Hall, D. M., and Ulbrich, U. (2020). Artificial intelligence reconstructs missing climate information. *Nat. Geosci.* 13, 408–413. doi:10.1038/s41561-020-0582-5.

Kalnay, E., Kanamitsu, M., Kistler, R., Collins, W., Deaven, D., Gandin, L., et al. (1996). The NCEP/NCAR 40-Year Reanalysis Project. *Bull. Am. Meteorol. Soc.* 77, 437–472. doi:10.1175/1520-0477(1996)077<0437:TNYRP>2.0.CO;2.

Kamiguchi, K., Arakawa, O., Kitoh, A., Yatagai, A., Hamada, A., and Yasutomi, N. (2010). Development of APHRO_JP, the first Japanese high-resolution daily precipitation product for more than 100 years. *Hydrol. Res. Lett.* 4, 60–64. doi:10.3178/hrl.4.60.

Kaplan, A., Cane, M. A., Kushnir, Y., Clement, A. C., Blumenthal, M. B., and Rajagopalan, B. (1998). Analyses of global sea surface temperature 1856–1991. *J. Geophys. Res. Ocean.* 103, 18567–18589. doi:10.1029/97JC01736.

Kawanishi, T., Sezai, T., Ito, Y., Imaoka, K., Takeshima, T., Ishido, Y., et al. (2003). The Advanced Microwave Scanning Radiometer for the Earth Observing System (AMSR-E), NASDA's contribution to the EOS for global energy and water cycle studies. *IEEE Trans. Geosci. Remote Sens.* 41, 184–194. doi:10.1109/TGRS.2002.808331.

Keeling, C. D., Piper, S. C., Bacastow, R. B., Wahlen, M., Whorf, T. P., Heimann, M., et al. (2001). Exchanges of atmospheric CO2 and 13CO2 with the terrestrial biosphere and oceans from 1978 to 2000. I. Global Aspects, SIO Reference Series, No.01-06, Scripps Institution of Oceanography. San Diego.

Keeling, C. D., Piper, S. C., Bacastow, R. B., Wahlen, M., Whorf, T. P., Heimann, M., et al. (2005). "Atmospheric CO2 and 13CO2 exchange with the terrestrial biosphere and oceans from 1978 to 2000: observations and carbon cycle implications, pages 83-113, in "A History of Atmospheric CO2 and its effects on Plants, Animals, and Ecosystems," in *A History of Atmospheric CO2 and its effects on Plants, Animals, and Ecosystems, editors Ehleringer, J.R., T. E. Cerling, M. D. Dearing,* eds. J. R. Ehleringer, T. E. Cerling, and M. D. Dearing (New York: Springer Verlag), 83–113.

Kennedy, J. J., Rayner, N. A., Atkinson, C. P., and Killick, R. E. (2019). An ensemble data set of sea-surface temperature change from 1850: the Met Office Hadley Centre HadSST.4.0.0.0 data set. *J. Geophys. Res. Atmos.* 124, 7719–7763. doi:10.1029/2018JD029867.

Kent, E. C., Rayner, N. A., Berry, D. I., Saunby, M., Moat, B. I., Kennedy, J. J., et al. (2013). Global analysis of night marine air temperature and its uncertainty since 1880: The HadNMAT2 data set. *J. Geophys. Res. Atmos.* 118, 1281–1298. doi:10.1002/jgrd.50152.

King, M. D., Howat, I. M., Candela, S. G., Noh, M. J., Jeong, S., Noël, B. P. Y., et al. (2020). Dynamic ice loss from the Greenland Ice Sheet driven by sustained glacier retreat. *Commun. Earth Environ.* 1, 1. doi:10.1038/s43247-020-0001-2.

Kirschke, S., Bousquet, P., Ciais, P., Saunois, M., Canadell, J. G., Dlugokencky, E. J., et al. (2013). Three decades of global methane sources and sinks. *Nat. Geosci.* doi:10.1038/ngeo1955.

ACCEPTED VERSION SUBJECT TO FINAL EDITING

Klein Tank, A. M. G., Wijngaard, J. B., Können, G. P., Böhm, R., Demarée, G., Gocheva, A., et al. (2002). Daily dataset of 20th-century surface air temperature and precipitation series for the European Climate Assessment. *Int. J. Climatol.* doi:10.1002/joc.773.

Kobayashi, S., Ota, Y., Harada, Y., Ebita, A., Moriya, M., Onoda, H., et al. (2015). The JRA-55 reanalysis: General specifications and basic characteristics. *J. Meteorol. Soc. Japan. Ser. II* 93, 5–48.

Kolodziejczyk, N., A. Prigent-Mazella, F. G. (2017). ISAS-15 temperature and salinity griddedfields. *SEANOE*. doi:10.17882/52367.

Kubota, T., Aonashi, K., Ushio, T., Shige, S., Takayabu, Y. N., Kachi, M., et al. (2020). "Global Satellite Mapping of Precipitation (GSMaP) Products in the GPM Era," in *Satellite Precipitation Measurement: Volume 1*, eds. V. Levizzani, C. Kidd, D. B. Kirschbaum, C. D. Kummerow, K. Nakamura, and F. J. Turk (Cham: Springer International Publishing), 355–373. doi:10.1007/978-3-030-24568-9_20.

Kummerow, C. (2015). NRT AMSR2 L2B Global Swath Goddard Profiling Algorithm 2010: Surface Precipitation, Wind Speed Over Ocean, Water Vapor over Ocean and Cloud Liquid Water over Ocean. doi:10.5067/AMSR2/A2_RainOcn_NRT.

Kwok, R., and Cunningham, G. F. (2015). Variability of arctic sea ice thickness and volume from CryoSat-2. *Philos. Trans. R. Soc. A Math. Phys. Eng. Sci.* 373, 2045. doi:10.1098/rsta.2014.0157.

Kwok, R., Cunningham, G. F., Wensnahan, M., Rigor, I., Zwally, H. J., and Yi, D. (2009). Thinning and volume loss of the Arctic Ocean sea ice cover: 2003-2008. *J. Geophys. Res. Ocean.* 114. doi:10.1029/2009JC005312.

Labbe, T., Pfister, C., Bronnimann, S., Rousseau, D., Franke, J., and Bois, B. (2019). The longest homogeneous series of grape harvest dates, Beaune 1354-2018, and its significance for the understanding of past and present climate. *Clim. Past Forum* 15, 1485–1501. doi:10.5194/cp-2018-179.

Laloyaux, P., de Boisseson, E., Balmaseda, M., Bidlot, J.-R., Broennimann, S., Buizza, R., et al. (2018). CERA-20C: A Coupled Reanalysis of the Twentieth Century. *J. Adv. Model. Earth Syst.* 10, 1172–1195. doi:https://doi.org/10.1029/2018MS001273.

Landschützer, P., Gruber, N., and Bakker, D. C. E. (2016). Decadal variations and trends of the global ocean carbon sink. *Global Biogeochem. Cycles* 30, 1396–1417. doi:10.1002/2015GB005359.

Lange, S. (2019). *WFDE5 over land merged with ERA5 over the ocean (W5E5)*. GFZ Data Services doi:10.5880/pik.2019.023.

Langenfelds, R. L., Francey, R. J., Pak, B. C., Steele, L. P., Lloyd, J., Trudinger, C. M., et al. (2002). Interannual growth rate variations of atmospheric CO2 and its δ13C, H2, CH4, and CO between 1992 and 1999 linked to biomass burning. *Global Biogeochem. Cycles*. doi:10.1029/2001GB001466.

Lavergne, T., Sørensen, A. M., Kern, S., Tonboe, R., Notz, D., Aaboe, S., et al. (2019). Version 2 of the EUMETSAT OSI SAF and ESA CCI sea-ice concentration climate data records. *Cryosph.* 13, 49–78. doi:10.5194/tc-13-49-2019.

Legeais, J.-F., Ablain, M., Zawadzki, L., Zuo, H., Johannessen, J. A., Scharffenberg, M. G., et al. (2018). An improved and homogeneous altimeter sea level record from the ESA Climate Change Initiative. *Earth Syst. Sci. Data* 10, 281–301. doi:10.5194/essd-10-281-2018.

Lenssen, N. J. L., Schmidt, G. A., Hansen, J. E., Menne, M. J., Persin, A., Ruedy, R., et al. (2019). Improvements in the GISTEMP Uncertainty Model. *J. Geophys. Res. Atmos.* 124, 6307–6326. doi:10.1029/2018JD029522.

Leventidou, E., Weber, M., Eichmann, K.-U. K. U., Burrows, J. P., Heue, K.-P. K. P., Thompson, A. M., et al. (2018). Harmonisation and trends of 20-year tropical tropospheric ozone data. *Atmos. Chem. Phys.* 18, 9189–9205. doi:10.5194/acp-18-9189-2018.

Levitus, S., Antonov, J. I., Boyer, T. P., Baranova, O. K., Garcia, H. E., Locarnini, R. A., et al. (2012a). World ocean heat content and thermosteric sea level change (0-2000m), 1955-2010. *Geophys. Res. Lett.* 39. doi:10.1029/2012GL051106.

Levitus, S., Antonov, J. I., Boyer, T. P., Baranova, O. K., Garcia, H. E., Locarnini, R. A., et al. (2012b). World ocean heat content and thermosteric sea level change (0–2000 m), 1955–2010. *Geophys. Res. Lett.* 39. doi:10.1029/2012GL051106.

Liu, G., Liu, J., Tarasick, D. W., Fioletov, V. E., Jin, J. J., Moeini, O., et al. (2013). A global tropospheric ozone climatology from trajectory-mapped ozone soundings. *Atmos. Chem. Phys.* 13, 10659–10675. doi:10.5194/acp-13-10659-2013.

Liu, Y. Y., Dorigo, W. A., Parinussa, R. M., De Jeu, R. A. M., Wagner, W., McCabe, M. F., et al. (2012a). Trend-preserving blending of passive and active microwave soil moisture retrievals. *Remote Sens. Environ.* 123, 280–297. doi:10.1016/j.rse.2012.03.014.

Liu, Z., Ostrenga, D., Teng, W., and Kempler, S. (2012b). Tropical Rainfall Measuring Mission (TRMM) Precipitation Data and Services for Research and Applications. *Bull. Am. Meteorol. Soc.* 93, 1317–1325. doi:10.1175/BAMS-D-11-00152.1.

Locarnini, R. A., Mishonov, A. V., Baranova, O. K., Boyer, T. P., Zweng, M. M., Garcia, H. E., et al. (2019). World Ocean Atlas 2018, Volume 1: Temperature. Available at: https://archimer.ifremer.fr/doc/00651/76338/.

Loeb, N. G., Doelling, D. R., Wang, H., Su, W., Nguyen, C., Corbett, J. G., et al. (2017). Clouds and the Earth's Radiant Energy System (CERES) Energy Balanced and Filled (EBAF) Top-of-Atmosphere (TOA) Edition-4.0

ACCEPTED VERSION SUBJECT TO FINAL EDITING

Data Product. *J. Clim.* 31, 895–918. doi:10.1175/JCLI-D-17-0208.1.
Loeb, N. G., Lyman, J. M., Johnson, G. C., Allan, R. P., Doelling, D. R., Wong, T., et al. (2012). Observed changes in top-of-the-atmosphere radiation and upper-ocean heating consistent within uncertainty. *Nat. Geosci.* 5, 110–113. doi:10.1038/ngeo1375.
Loeb, N. G., Wang, H., Allan, R. P., Andrews, T., Armour, K., Cole, J. N. S., et al. (2020). New Generation of Climate Models Track Recent Unprecedented Changes in Earth's Radiation Budget Observed by CERES. *Geophys. Res. Lett.* 47, e2019GL086705. doi:https://doi.org/10.1029/2019GL086705.
Loeb, N. G., Wielicki, B. A., Doelling, D. R., Smith, G. L., Keyes, D. F., Kato, S., et al. (2009). Toward optimal closure of the Earth's top-of-atmosphere radiation budget. *J. Clim.* 22, 748–766. doi:10.1175/2008JCLI2637.1.
Loupian, E., Burtsev, M. A., Bartalev, S. A., and Kashnitskii, A. (2015). IKI center for collective use of satellite data archiving , processing and analysis systems aimed at solving the problems of environmental study and monitoring. *Curr. Probl. Remote Sens. Earth From Sp.* 12, 263–284.
Loveland, T. R., and Belward, A. S. (1997). The IGBP-DIS global 1km land cover data set, DISCover: First results. *Int. J. Remote Sens.* 18, 3289–3295. doi:10.1080/014311697217099.
Lussana, C., Saloranta, T., Skaugen, T., Magnusson, J., Einar Tveito, O., and Andersen, J. (2018). SeNorge2 daily precipitation, an observational gridded dataset over Norway from 1957 to the present day. *Earth Syst. Sci. Data*. doi:10.5194/essd-10-235-2018.
Lyman, J., and Johnson, G. (2014). Estimating Global Ocean Heat Content Changes in the Upper 1800 m since 1950 and the Influence of Climatology Choice. *J. Clim.* 27, 1945–1957. doi:doi: 10.1175/jcli-d-12-00752.1.
Mahmood, S., Davie, J., Jermey, P., Renshaw, R., George, J. P., Rajagopal, E. N., et al. (2018). Indian monsoon data assimilation and analysis regional reanalysis: Configuration and performance. *Atmos. Sci. Lett.* 19, e808. doi:10.1002/asl.808.
Maidment, R. I., Grimes, D., Allan, R. P., Tarnavsky, E., Stringer, M., Hewison, T., et al. (2014). The 30 year TAMSAT African Rainfall Climatology And Time series (TARCAT) data set. *J. Geophys. Res. Atmos.* 119, 10, 610–619, 644. doi:10.1002/2014JD021927.
Mankoff, K. D., Colgan, W., Solgaard, A., Karlsson, N. B., Ahlstrøm, A. P., van As, D., et al. (2019). Greenland Ice Sheet solid ice discharge from 1986 through 2017. *Earth Syst. Sci. Data* 11, 769–786. doi:10.5194/essd-11-769-2019.
Marshall, G. J. (2003). Trends in the Southern Annular Mode from observations and reanalyses. *J. Clim.* 16, 4134–4143.
Masarie, K. A., and Tans, P. P. (2004). Extension and integration of atmospheric carbon dioxide data into a globally consistent measurement record. *J. Geophys. Res. Atmos.* 100, 11593–11610. doi:10.1029/95JD00859.
Mears, C. A., and Wentz, F. J. (2017). A Satellite-Derived Lower-Tropospheric Atmospheric Temperature Dataset Using an Optimized Adjustment for Diurnal Effects. *J. Clim.* 30, 7695–7718. doi:10.1175/JCLI-D-16-0768.1.
Meinshausen, M., Vogel, E., Nauels, A., Lorbacher, K., Meinshausen, N., Etheridge, D. M., et al. (2017). Historical greenhouse gas concentrations for climate modelling (CMIP6). *Geosci. Model Dev.* 10, 2057–2116. doi:10.5194/gmd-10-2057-2017.
Menne, M. J., Williams, C. N., Gleason, B. E., Rennie, J. J., and Lawrimore, J. H. (2018). The Global Historical Climatology Network Monthly Temperature Dataset, Version 4. *J. Clim.* 0, null. doi:10.1175/JCLI-D-18-0094.1.
Merchant, C. J., Embury, O., Roberts-Jones, J., Fiedler, E., Bulgin, C. E., Corlett, G. K., et al. (2014a). Sea surface temperature datasets for climate applications from Phase 1 of the European Space Agency Climate Change Initiative (SST CCI). *Geosci. Data J.* 1, 179–191. doi:10.1002/gdj3.20.
Merchant, C. J., Embury, O., Roberts-Jones, J., Fiedler, E. K., Bulgin, C. E., Corlett, G. K., et al. (2014b). "ESA Sea Surface Temperature Climate Change Initiative (ESA SST CCI): Analysis long term product version 1.0," in *NERC Earth Observation Data Centre, 24th February 2014* doi:10.5285/2262690A-B588-4704-B459-39E05527B59A.
Merlivat, L., Boutin, J., Antoine, D., Beaumont, L., Golbol, M., and Vellucci, V. (2018). Increase of dissolved inorganic carbon and decrease in pH in near-surface waters in the Mediterranean Sea during the past two decades. *Biogeosciences* 15, 5653–5662. doi:10.5194/bg-15-5653-2018.
Montzka, S. A., Hall, B. D., and Elkins, J. W. (2009). Accelerated increases observed for hydrochlorofluorocarbons since 2004 in the global atmosphere. *Geophys. Res. Lett.* doi:10.1029/2008GL036475.
Montzka, S. A., Mcfarland, M., Andersen, S. O., Miller, B. R., Fahey, D. W., Hall, B. D., et al. (2015). Recent trends in global emissions of hydrochlorofluorocarbons and hydrofluorocarbons: Reflecting on the 2007 Adjustments to the Montreal protocol. *J. Phys. Chem. A* 119, 4439–4449. doi:10.1021/jp5097376.
Morice, C. P., Kennedy, J. J., Rayner, N. A., and Jones, P. D. (2012). Quantifying uncertainties in global and regional temperature change using an ensemble of observational estimates: The HadCRUT4 data set. *J. Geophys. Res. Atmos.* 117. doi:10.1029/2011JD017187.
Morice, C. P., Kennedy, J. J., Rayner, N. A., Winn, J. P., Hogan, E., Killick, R. E., et al. (2020). An updated assessment of near-surface temperature change from 1850: the HadCRUT5 dataset. *J. Geophys. Res. Atmos.* 125, (in press). doi:https://doi.org/10.1029/2019JD032361.
Mudryk, L., Santolaria-Otín, M., Krinner, G., Ménégoz, M., Derksen, C., Brutel-Vuilmet, C., et al. (2020). Historical

ACCEPTED VERSION SUBJECT TO FINAL EDITING

Northern Hemisphere snow cover trends and projected changes in the CMIP6 multi-model ensemble. *Cryosph.* 14, 2495–2514. doi:10.5194/tc-14-2495-2020.

Mueller, B., Hirschi, M., Jimenez, C., Ciais, P., Dirmeyer, P. A., Dolman, A. J., et al. (2013). Benchmark products for land evapotranspiration: LandFlux-EVAL multi-data set synthesis. *Hydrol. Earth Syst. Sci.*

Myneni, R., Knyazikhin, Y., and Park, T. (2015). MCD15A2H MODIS/Terra+Aqua Leaf Area Index/FPAR 8-day L4 Global 500m SIN Grid V006 [Data set]. NASA EOSDIS Land Processes DAAC. doi:10.5067/MODIS/MCD15A2H.006.

Nerem, R. S., Beckley, B. D., Fasullo, J. T., Hamlington, B. D., Masters, D., and Mitchum, G. T. (2018). Climate-change–driven accelerated sea-level rise detected in the altimeter era. *Proc. Natl. Acad. Sci.* 115, 2022–2025. doi:10.1073/pnas.1717312115.

NIWA (2020). Ministry for the Environment Atmosphere and Climate Report 2020: Updated datasets supplied by NIWA. Available at: https://www.mfe.govt.nz/publications/environmental-reporting/ministry-environment-atmosphere-and-climate-report-2020-updated.

Novella, N. S., and Thiaw, W. M. (2013). African rainfall climatology version 2 for famine early warning systems. *J. Appl. Meteorol. Climatol.* doi:10.1175/JAMC-D-11-0238.1.

Olsen, A., Lange, N., Key, R. M., Tanhua, T., Álvarez, M., Becker, S., et al. (2019). GLODAPv2.2019 -- an update of GLODAPv2. *Earth Syst. Sci. Data* 11, 1437–1461. doi:10.5194/essd-11-1437-2019.

Onogi, K., Tsutsui, J., Koide, H., Sakamoto, M., Kobayashi, S., Hatsushika, H., et al. (2007). The JRA-25 Reanalysis. *J. Meteorol. Soc. Japan* 85, 369–432. doi:10.2151/jmsj.85.369.

Osborn, T. J., Jones, P. D., Lister, D. H., Morice, C. P., Simpson, I. R., Winn, J. P., et al. (2021). Land Surface Air Temperature Variations Across the Globe Updated to 2019: The CRUTEM5 Data Set. *J. Geophys. Res. Atmos.* 126. doi:10.1029/2019JD032352.

Oyler, J. W., Ballantyne, A., Jencso, K., Sweet, M., and Running, S. W. (2015). Creating a topoclimatic daily air temperature dataset for the conterminous United States using homogenized station data and remotely sensed land skin temperature. *Int. J. Climatol.* 35, 2258–2279. doi:10.1002/joc.4127.

Palmer, M. D., Domingues, C. M., Slangen, A. B. A., and Boeira Dias, F. (2021). An ensemble approach to quantify global mean sea-level rise over the 20th century from tide gauge reconstructions. *Environ. Res. Lett.* 16, 044043. doi:10.1088/1748-9326/abdaec.

Pan, M., Sahoo, A. K., Troy, T. J., Vinukollu, R. K., Sheffield, J., and Wood, E. F. (2012). Multisource Estimation of Long-Term Terrestrial Water Budget for Major Global River Basins. *J. Clim.* 25, 3191–3206. doi:10.1175/JCLI-D-11-00300.1.

Panchen, Z. A., Primack, R. B., Aniśko, T., and Lyons, R. E. (2012). Herbarium specimens, photographs, and field observations show philadelphia area plants are responding to climate change. *Am. J. Bot.* 99. doi:10.3732/ajb.1100198.

Panziera, L., Gabella, M., Germann, U., and Martius, O. (2018). A 12-year radar-based climatology of daily and sub-daily extreme precipitation over the Swiss Alps. *Int. J. Climatol.* 38, 3749–3769. doi:10.1002/joc.5528.

Park, S., Croteau, P., Boering, K. A., Etheridge, D. M., Ferretti, D., Fraser, P. J., et al. (2012). Trends and seasonal cycles in the isotopic composition of nitrous oxide since 1940. *Nat. Geosci.* 5, 261–265. doi:10.1038/ngeo1421.

Parthasarathy, B., Munot, A. A., and Kothawale, D. R. (1994). All-India monthly and seasonal rainfall series: 1871–1993. *Theor. Appl. Climatol.* 49, 217–224. doi:10.1007/BF00867461.

Patra, P. K., Saeki, T., Dlugokencky, E. J., Ishijima, K., Umezawa, T., Ito, A., et al. (2016). Regional methane emission estimation based on observed atmospheric concentrations (2002-2012). *J. Meteorol. Soc. Japan* 94. doi:10.2151/jmsj.2016-006.

Patra, P. K., Takigawa, M., Watanabe, S., Chandra, N., Ishijima, K., and Yamashita, Y. (2018). Improved Chemical Tracer Simulation by MIROC4.0-based Atmospheric Chemistry-Transport Model (MIROC4-ACTM). *SOLA* 14, 91–96. doi:10.2151/sola.2018-016.

Paulat, M., Frei, C., Hagen, M. ., and Wernli, H. (2008). A gridded dataset of hourly precipitation in Germany: Its construction, climatology and application. *Meteorol. Zeitschrift* 17, 719–732. doi:10.1127/0941-2948/2008/0332.

Peng, G., Meier, W. N., Scott, D. J., and Savoie, M. H. (2013). A long-term and reproducible passive microwave sea ice concentration data record for climate studies and monitoring. *Earth Syst. Sci. Data* 5, 311–318. doi:10.5194/essd-5-311-2013.

Platnick, S., King, M. D., Ackerman, S. A., Menzel, W. P., Baum, B. A., Riédi, J. C., et al. (2003). The MODIS cloud products: Algorithms and examples from terra. *IEEE Trans. Geosci. Remote Sens.* 41, 459–472. doi:10.1109/TGRS.2002.808301.

Poli, P., Hersbach, H., Dee, D. P., Berrisford, P., Simmons, A. J., Vitart, F., et al. (2016). ERA-20C: An Atmospheric Reanalysis of the Twentieth Century. *J. Clim.* 29, 4083–4097. doi:10.1175/JCLI-D-15-0556.1.

Prinn, R. G., Weiss, R. F., Arduini, J., Arnold, T., Langley Dewitt, H., Fraser, P. J., et al. (2018). History of chemically and radiatively important atmospheric gases from the Advanced Global Atmospheric Gases Experiment (AGAGE). *Earth Syst. Sci. Data*. doi:10.5194/essd-10-985-2018.

Purkey, S. G., and Johnson, G. C. (2010). Warming of Global Abyssal and Deep Southern Ocean Waters between the 1990s and 2000s: Contributions to Global Heat and Sea Level Rise Budgets. *J. Clim.* 23, 6336–6351.

SUBJECT TO FINAL EDITING ACCEPTED VERSION

doi:10.1175/2010JCLI3682.1.
Rajeevan, M., Bhate, J., Kale, J. D., and Lal, B. (2006). High resolution daily gridded rainfall data for the Indian region: Analysis of break and active monsoon spells. *Curr. Sci.* doi:10.1007/s12040-007-0019-1.
Ray, R. D., and Douglas, B. C. (2011). Experiments in reconstructing twentieth-century sea levels. *Prog. Oceanogr.* 91, 496–515. doi:https://doi.org/10.1016/j.pocean.2011.07.021.
Rayner, N. A., Parker, D. E., Horton, E. B., Folland, C. K., Alexander, L. V, Rowell, D. P., et al. (2003). Global analyses of sea surface temperature, sea ice, and night marine air temperature since the late nineteenth century. *J. Geophys. Res. Atmos.* 108. doi:10.1029/2002JD002670.
Reichle, R. H. (2012). The MERRA-Land Data Product. GMAO Office Note No. 3 (Version 1.2).
Reynolds, R. W., Rayner, N. A., Smith, T. M., Stokes, D. C., and Wang, W. (2002). An Improved In Situ and Satellite SST Analysis for Climate. *J. Clim.* 15, 1609–1625. doi:10.1175/1520-0442(2002)015<1609:AIISAS>2.0.CO;2.
Rice, A. L., Butenhoff, C. L., Teama, D. G., Röger, F. H., Khalil, M. A. K., and Rasmussen, R. A. (2016). Atmospheric methane isotopic record favors fossil sources flat in 1980s and 1990s with recent increase. *Proc. Natl. Acad. Sci.* 113, 10791–10796. doi:10.1073/pnas.1522923113.
Rienecker, M. M., Suarez, M. J., Gelaro, R., Todling, R., Bacmeister, J., Liu, E., et al. (2011). MERRA: NASA's Modern-Era Retrospective Analysis for Research and Applications. *J. Clim.* 24, 3624–3648. doi:10.1175/JCLI-D-11-00015.1.
Rignot, E., Mouginot, J., Scheuchl, B., van den Broeke, M., van Wessem, M. J., and Morlighem, M. (2019). Four decades of Antarctic Ice Sheet mass balance from 1979-2017. *Proc. Natl. Acad. Sci.* 116, 1095–1103. doi:10.1073/pnas.1812883116.
Rodell, M., Houser, P. R., Jambor, U. E. A., Gottschalck, J., Mitchell, K., Meng, C.-J., et al. (2004). The global land data assimilation system. *Bull. Am. Meteorol. Soc.* 85, 381–394.
Rödenbeck, C., Bakker, D. C. E., Metzl, N., Olsen, A., Sabine, C., Cassar, N., et al. (2014). Interannual sea–air CO2 flux variability from an observation-driven ocean mixed-layer scheme. *Biogeosciences* 11, 4599–4613. doi:10.5194/bg-11-4599-2014.
Rödenbeck, C., Keeling, R. F., Bakker, D. C. E., Metzl, N., Olsen, A., Sabine, C., et al. (2013). Global surface-ocean pCO2 and sea–air CO2 flux variability from an observation-driven ocean mixed-layer scheme. *Ocean Sci.* 9, 193–216. doi:10.5194/os-9-193-2013.
Roebeling, R. A., and Holleman, I. (2009). SEVIRI rainfall retrieval and validation using weather radar observations. *J. Geophys. Res. Atmos.* doi:10.1029/2009JD012102.
Rohde, R. A., and Hausfather, Z. (2020). The Berkeley Earth Land/Ocean Temperature Record. *Earth Syst. Sci. Data* 12, 3469–3479. doi:10.5194/essd-12-3469-2020.
Romanovsky, V., Smith, S., Isaksen, K., Nyland, K., Kholodov, A., Shiklomanov, N., et al. (2020). [Arctic] Terrestrial Permafrost [in "State of the Climate in 2019"]. *Bull. Am. Meteorol. Soc.* 101, 265–269. doi:10.1175/BAMS-D-20-0086.1.
Rostkier-Edelstein, D., Liu, Y., Wu, W., Kunin, P., Givati, A., and Ge, M. (2014). Towards a high-resolution climatography of seasonal precipitation over Israel. *Int. J. Climatol.* 34, 1964–1979. doi:10.1002/joc.3814.
Rothrock, D. A., Percival, D. B., and Wensnahan, M. (2008). The decline in arctic sea-ice thickness: Separating the spatial, annual, and interannual variability in a quarter century of submarine data. *J. Geophys. Res. Ocean.* 113. doi:10.1029/2007JC004252.
Saeki, T., and Patra, P. K. (2017). Implications of overestimated anthropogenic CO2 emissions on East Asian and global land CO2 flux inversion. *Geosci. Lett.* 4, 9. doi:10.1186/s40562-017-0074-7.
Saha, S., Moorthi, S., Pan, H.-L., Wu, X., Wang, J., Nadiga, S., et al. (2010). The NCEP Climate Forecast System Reanalysis. *Bull. Am. Meteorol. Soc.* 91, 1015–1058. doi:10.1175/2010BAMS3001.1.
Sathyendranath, S., Brewin, R. J. W., Brockmann, C., Brotas, V., Calton, B., Chuprin, A., et al. (2019). An Ocean-Colour Time Series for Use in Climate Studies: The Experience of the Ocean-Colour Climate Change Initiative (OC-CCI). *Sensors* 19. doi:10.3390/s19194285.
Saunois, M., Stavert, A. R., Poulter, B., Bousquet, P., Canadell, J. G., Jackson, R. B., et al. (2020). The Global Methane Budget 2000–2017. *Earth Syst. Sci. Data* 12, 1561–1623. doi:10.5194/essd-12-1561-2020.
Schellekens, J., Dutra, E., la Torre, A., Balsamo, G., van Dijk, A., Sperna Weiland, F., et al. (2017). A global water resources ensemble of hydrological models: the eartH2Observe Tier-1 dataset. *Earth Syst. Sci. Data* 9, 389–413. doi:10.5194/essd-9-389-2017.
Scherler, D., Wulf, H., and Gorelick, N. (2018). Global Assessment of Supraglacial Debris-Cover Extents. *Geophys. Res. Lett.* 45, 11,798-11,805. doi:10.1029/2018GL080158.
Schneider, U., Finger, P., Meyer-Christoffer, A., Rustemeier, E., Ziese, M., and Becker, A. (2017). Evaluating the hydrological cycle over land using the newly-corrected precipitation climatology from the Global Precipitation Climatology Centre (GPCC). *Atmosphere (Basel).* 8, 52. doi:10.3390/atmos8030052.
Schröder, M., Lockhoff, M., Fell, F., Forsythe, J., Trent, T., Bennartz, R., et al. (2018). The GEWEX Water Vapor Assessment archive of water vapour products from satellite observations and reanalyses. *Earth Syst. Sci. Data* 10, 1093–1117. doi:10.5194/essd-10-1093-2018.
Schultz, M. G., Schröder, S., Lyapina, O., Cooper, O., Galbally, I., Petropavlovskikh, I., et al. (2017). Tropospheric

ACCEPTED VERSION
SUBJECT TO FINAL EDITING

Ozone Assessment Report: Database and Metrics Data of Global Surface Ozone Observations. *Elem Sci Anth* 5, 58. doi:10.1525/elementa.244.

Schweiger, A., Lindsay, R., Zhang, J., Steele, M., Stern, H., and Kwok, R. (2011). Uncertainty in modeled Arctic sea ice volume. *J. Geophys. Res. Ocean.* 116. doi:https://doi.org/10.1029/2011JC007084.

Shen, Y., Hong, Z., Pan, Y., Yu, J., and Maguire, L. (2018). China's 1 km Merged Gauge, Radar and Satellite Experimental Precipitation Dataset. *Remote Sens.* 10. doi:10.3390/rs10020264.

Simpson, I. J., Andersen, M. P. S., Meinardi, S., Bruhwiler, L., Blake, N. J., Helmig, D., et al. (2012). Long-term decline of global atmospheric ethane concentrations and implications for methane. *Nature* 488, 490–494. doi:10.1038/nature11342.

Slivinski, L. C., Compo, G. P., Whitaker, J. S., Sardeshmukh, P. D., Giese, B. S., McColl, C., et al. (2019). Towards a more reliable historical reanalysis: Improvements for version 3 of the Twentieth Century Reanalysis system. *Q. J. R. Meteorol. Soc.* 145, 2876–2908. doi:10.1002/qj.3598.

Smeed, D. A., Josey, S. A., Beaulieu, C., Johns, W. E., Moat, B. I., Frajka-Williams, E., et al. (2018). The North Atlantic Ocean is in a state of reduced overturning. *Geophys. Res. Lett.* 45, 1527–1533.

Spencer, R. W., Christy, J. R., and Braswell, W. D. (2017). UAH Version 6 Global Satellite Temperature Products: Methodology and Results. *Asia-Pacific Jouurnal Atmos. Sci.* 53, 121–130. doi:10.1007/s13143-017-0010-y.

Staehelin, J., Viatte, P., Stübi, R., Tummon, F., and Peter, T. (2018). Stratospheric ozone measurements at Arosa (Switzerland): History and scientific relevance. *Atmos. Chem. Phys.* 18, 6567–6584. doi:10.5194/acp-18-6567-2018.

Steiner, A. K., Ladstädter, F., Ao, C. O., Gleisner, H., Ho, S.-P., Hunt, D., et al. (2020). Consistency and structural uncertainty of multi-mission GPS radio occultation records. *Atmos. Meas. Tech.* 13, 2547–2575. doi:10.5194/amt-13-2547-2020.

Stocker, E. F., Alquaied, F., Bilanow, S., Ji, Y., and Jones, L. (2018). TRMM Version 8 Reprocessing Improvements and Incorporation into the GPM Data Suite. *J. Atmos. Ocean. Technol.* 35, 1181–1199. doi:10.1175/JTECH-D-17-0166.1.

Sun, W., Li, Q., Huang, B., Cheng, J., Song, Z., Li, H., et al. (2021). The Assessment of Global Surface Temperature Change from 1850s: The C-LSAT2.0 Ensemble and the CMST-Interim Datasets. *Adv. Atmos. Sci.* doi:10.1007/s00376-021-1012-3.

Susskind, J., Barnet, C. D., Blaisdell, J., Iredell, L., Keita, F., Kouvaris, L., et al. (2006). Accuracy of geophysical parameters derived from Atmospheric Infrared Sounder/Advanced Microwave Sounding Unit as a function of fractional cloud cover. *J. Geophys. Res. Atmos.* 111. doi:10.1029/2005JD006272.

Susskind, J., Blaisdell, J. M., and Iredell, L. (2014). Improved methodology for surface and atmospheric soundings, error estimates, and quality control procedures: the atmospheric infrared sounder science team version-6 retrieval algorithm. *J. Appl. Remote Sens.* 8, 1–34. doi:10.1117/1.JRS.8.084994.

Takahashi, K., Mikami, T., and Takahashi, H. (2011). Influence of the Urban Heat Island Phenomenon in Tokyo on the Local Wind System at Nighttime in Summer. *J. Geogr. (Chigaku Zasshi)*. doi:10.5026/jgeography.120.341.

Takahashi, T., Sutherland, S. C., Chipman, D. W., Goddard, J. G., Ho, C., Newberger, T., et al. (2014). Climatological distributions of pH, pCO2, total CO2, alkalinity, and CaCO3 saturation in the global surface ocean, and temporal changes at selected locations. *Mar. Chem.* 164, 95–125. doi:https://doi.org/10.1016/j.marchem.2014.06.004.

Tanelli, S., Durden, S. L., Im, E., Pak, K. S., Reinke, D. G., Partain, P., et al. (2008). CloudSat's Cloud Profiling Radar After Two Years in Orbit: Performance, Calibration, and Processing. *IEEE Trans. Geosci. Remote Sens.* 46, 3560–3573. doi:10.1109/TGRS.2008.2002030.

Tapley, B. D., Bettadpur, S., Watkins, M., and Reigber, C. (2004). The gravity recovery and climate experiment: Mission overview and early results. *Geophys. Res. Lett.* 31. doi:10.1029/2004GL019920.

Tarasick, D., Galbally, I. E., Cooper, O. ., and Schultz, M. G. (2019). Tropospheric Ozone Assessment Report: Tropospheric ozone observations – How well do we know tropospheric ozone changes? Submitted. *Elementa.*

Tarasick, D. W., Jin, J. J., Fioletov, V. E., Liu, G., Thompson, A. M., Oltmans, S. J., et al. (2010). High-resolution tropospheric ozone fields for INTEX and ARCTAS from IONS ozonesondes. *J. Geophys. Res. Atmos.* 115. doi:https://doi.org/10.1029/2009JD012918.

Thomason, L. W., Ernest, N., Millán, L., Rieger, L., Bourassa, A., Vernier, J.-P., et al. (2018). A global space-based stratospheric aerosol climatology: 1979–2016. *Earth Syst. Sci. Data* 10, 469–492. doi:10.5194/essd-10-469-2018.

Thompson, R. L., Lassaletta, L., Patra, P. K., Wilson, C., Wells, K., Gressent, A., et al. Acceleration of global N2O emissions seen from two decades of atmospheric inversion. *J. Geophys. Res.*

Thorne, P. W., Parker, D. E., Tett, S. F. B., Jones, P. D., McCarthy, M., Coleman, H., et al. (2005). Revisiting radiosonde upper air temperatures from 1958 to 2002. *J. Geophys. Res. Atmos.* 110. doi:10.1029/2004JD005753.

Tian, B., Fetzer, E. J., Kahn, B. H., Teixeira, J., Manning, E., and Hearty, T. (2013). Dub Evaluating CMIP5 models using AIRS tropospheric air temperature and specific humidity climatology. *J. Geophys. Res. Atmos.* 118, 114–134. doi:10.1029/2012JD018607.

Tokinaga, H., and Xie, S.-P. (2011). Wave and anemometer-based sea surface wind (WASWind) for climate change analysis. *J. Clim.* 24, 267–285.

Tomita (2017). Correction of J-OFURO3 air specific humidity product from microwave radiometers. J-OFURO3

ACCEPTED VERSION SUBJECT TO FINAL EDITING

official document J-OFURO3-DOC-005 (in Japanese).
Trewin, B., Braganza, K., Fawcett, R., Grainger, S., Jovanovic, B., Jones, D., et al. (2020). An updated long-term homogenized daily temperature data set for Australia. *Geosci. Data J.* 7, 149–169. doi:10.1002/gdj3.95.
TRMM (2011). TRMM (TMPA) Rainfall Estimate L3 3-hour 0.25 degree x 0.25 degree V7, Greenbelt, MD, Goddard Earth Sciences Data and Information Services Center (GES DISC). doi:10.5067/TRMM/TMPA/3H/7.
Troup, A. J. (1965). The 'southern oscillation.' *Q. J. R. Meteorol. Soc.* 91, 490–506. doi:10.1002/qj.49709139009.
Tsutsumi, Y., Mori, K., Hirahara, T., Ikegami, M., and Conway, T. J. (2009). Technical Report of Global Analysis Method for Major Greenhouse Gases by the World Data Center for Greenhouse Gases, Global Atmosphere Watch Report No. 184. Geneva, Switzerland Available at: www.wmo.int/pages/prog/arep/gaw/documents/TD_1473_GAW184_web.pdf.
Turnbull, J. C., Mikaloff Fletcher, S. E., Ansell, I., Brailsford, G. W., Moss, R. C., Norris, M. W., et al. (2017). Sixty years of radiocarbon dioxide measurements at Wellington, New Zealand: 1954–2014. *Atmos. Chem. Phys.* 17, 14771–14784. doi:10.5194/acp-17-14771-2017.
Vaccaro, A., Emile-Geay, J., Guillot, D., Verna, R., Morice, C., Kennedy, J., et al. (2021). Climate field completion via Markov random fields – Application to the HadCRUT4.6 temperature dataset. *J. Clim.*, 1–66. doi:10.1175/JCLI-D-19-0814.1.
Vandemeulebroucke, I., Calle, K., Caluwaerts, S., De Kock, T., and Van Den Bossche, N. (2019). Does historic construction suffer or benefit from the urban heat island effect in Ghent and global warming across Europe? *Can. J. Civ. Eng.* doi:10.1139/cjce-2018-0594.
Vidal, J.-P., Martin, E., Franchistéguy, L., Baillon, M., and Soubeyroux, J.-M. (2010). A 50-year high-resolution atmospheric reanalysis over France with the Safran system. *Int. J. Climatol.* 30, 1627–1644. doi:10.1002/joc.2003.
Vonder Haar, T. H., Bytheway, J. L., and Forsythe, J. M. (2012). Weather and climate analyses using improved global water vapor observations. *Geophys. Res. Lett.* 39, 1–6. doi:10.1029/2012GL052094.
Vose, R. S., Huang, B., Yin, X., Arndt, D., Easterling, D. R., Lawrimore, J. H., et al. (2021). Implementing Full Spatial Coverage in NOAA's Global Temperature Analysis. *Geophys. Res. Lett.* 48, e2020GL090873. doi:10.1029/2020GL090873.
Wagner, W., Lemoine, G., and Rott, H. (1999). A Method for Estimating Soil Moisture from ERS Scatterometer and Soil Data. *Remote Sens. Environ.* 70, 191–207. doi:https://doi.org/10.1016/S0034-4257(99)00036-X.
Wakita, M., Nagano, A., Fujiki, T., and Watanabe, S. (2017). Slow acidification of the winter mixed layer in the subarctic western North Pacific. *J. Geophys. Res. Ocean.* 122, 6923–6935. doi:10.1002/2017JC013002.
Walsh, J. E., Fetterer, F., Scott Stewart, J., and Chapman, W. L. (2017). A database for depicting Arctic sea ice variations back to 1850. *Geogr. Rev.* doi:10.1111/j.1931-0846.2016.12195.x.
WCRP Global Sea Level Budget Group (2018). Global sea-level budget 1993–present. *Earth Syst. Sci. Data* 10, 1551–1590. doi:10.5194/essd-10-1551-2018.
Webb, L. B., Whetton, P. H., and Barlow, E. W. R. (2011). Observed trends in winegrape maturity in Australia. *Glob. Chang. Biol.* 17. doi:10.1111/j.1365-2486.2011.02434.x.
Weber, M., Coldewey-Egbers, M., Fioletov, V. E., Frith, S. M., Wild, J. D., Burrows, J. P., et al. (2018a). Total ozone trends from 1979 to 2016 derived from five merged observational datasets-the emergence into ozone recovery. *Atmos. Chem. Phys.* doi:10.5194/acp-18-2097-2018.
Weber, M., Steinbrecht, W., A, R. van der, Frith, S. M., Anderson, J., Coldewey-Egbers, M., et al. (2018b). Stratospheric ozone [in "State of the Climate in 2017"]. *Bull. Amer. Meteor. Soc* 99, S51-s54. doi:10.1175/2018BAMSStateoftheClimate.1.
Weber, M., Steinbrecht, W., Arosio, C., A, R. van der, Frith, S. M., Anderson, M., et al. (2020). Stratospheric ozone, in State of the Climate in 2019. *Bull. Amer. Meteor., 101 (8), S81–S83,* 101, S81–S83. doi:10.1175/ BAMS-D-20-0104.1.
Wentz, F. J. (2013). SSM/I Version-7 Calibration Report. Report number 011012, Remote Sensing Systems, Santa Rosa, CA. Available at: http://images.remss.com/papers/rsstech/2012_011012_Wentz_Version-7_SSMI_Calibration.pdf.
Wentz, F. J., Ashcroft, P. D., and Gentemann, C. L. (2001). Post-launch calibration of the TRMM microwave imager. *IEEE Trans. Geosci. Remote Sens.* 39, 415–422.
Wenzel, M., and Schröter, J. (2014). Global and regional sea level change during the 20th century. *J. Geophys. Res. Ocean.* 119, 7493–7508. doi:10.1002/2014JC009900.
Wijffels, S., Roemmich, D., Monselesan, D., Church, J., and Gilson, J. (2016). Ocean temperatures chronicle the ongoing warming of Earth. *Nat. Clim. Chang.* 6, 116–118. doi:10.1038/nclimate2924.
Wild, J. D., Yang, S.-K., and Long, C. S. (2016). Ozone Profile Trends: An SBUV/2 Perspective. in *Quadrennial Ozone Symposium 2016, Edinburgh, 2–9 September 2016* Available at: https://meetingorganizer.copernicus.org/QOS2016/QOS2016-133.pdf.
Willett, K. M., Dunn, R. J. H., Kennedy, J. J., and Berry, D. I. (2020). Development of the HadISDH.marine humidity climate monitoring dataset. *Earth Syst. Sci. Data* 12, 2853–2880. doi:10.5194/essd-12-2853-2020.
Willett, K. M., Dunn, R. J. H., Thorne, P. W., Bell, S., Podesta, M. De, Parker, D. E., et al. (2014). HadISDH land

ACCEPTED VERSION SUBJECT TO FINAL EDITING

surface multi-variable humidity and temperature record for climate monitoring. *Clim. Past* 10, 1983–2006. doi:10.5194/cp-10-1983-2014.

WMO (2019). WMO Greenhouse Gas Bulletin (GHG Bulletin) - No. 15: The State of Greenhouse Gases in the Atmosphere Based on Global Observations through 2018. *WMO Greenh. Gas Bull. (GHG Bull.* Available at: https://library.wmo.int/index.php?lvl=notice_display&id=21620#.YCEa8uj7SUk.

Wolter, K., and Timlin, M. S. (1998). Measuring the strength of ENSO events: How does 1997/98 rank? *Weather* 53, 315–324. doi:10.1002/j.1477-8696.1998.tb06408.x.

Wood, C. R., Järvi, L., Kouznetsov, R. D., Nordbo, A., Joffre, S., Drebs, A., et al. (2013). An Overview of the Urban Boundary Layer Atmosphere Network in Helsinki. *Bull. Am. Meteorol. Soc.* 94, 1675–1690. doi:10.1175/BAMS-D-12-00146.1.

Wouters, B., Gardner, A. S., and Moholdt, G. (2019). Global Glacier Mass Loss During the GRACE Satellite Mission (2002-2016). *Front. Earth Sci.* 7, 96. doi:10.3389/feart.2019.00096.

Wu, J., and Gao, X.-J. (2013). A gridded daily observation dataset over China region and comparison with the other datasets. *Chinese J. Geophys.* doi:10.6038/cjg20130406.

Xavier, A. C., King, C. W., and Scanlon, B. R. (2016). Daily gridded meteorological variables in Brazil (1980–2013). *Int. J. Climatol.* 36, 2644–2659. doi:10.1002/joc.4518.

Xie, P., Arkin, P. A., and Janowiak, J. E. (2007a). "CMAP: The CPC merged analysis of precipitation," in *Advances in Global Change Research* (Dordrecht: Springer Netherlands), 319–328. doi:10.1007/978-1-4020-5835-6_25.

Xie, P., Chen, M., and Shi, W. (2010). CPC unified gauge-based analysis of global daily precipitation. in *24th Conference of Hydrology, Atlanta, 16-21 January 2010*.

Xie, P., Chen, M., Yang, S., Yatagai, A., Hayasaka, T., Fukushima, Y., et al. (2007b). A Gauge-Based Analysis of Daily Precipitation over East Asia. *J. Hydrometeorol.* 8, 607–626. doi:10.1175/JHM583.1.

Xu, W., Li, Q., Jones, P., Wang, X. L., Trewin, B., Yang, S., et al. (2018). A new integrated and homogenized global monthly land surface air temperature dataset for the period since 1900. *Clim. Dyn.* 50, 2513–2536. doi:10.1007/s00382-017-3755-1.

Yang, B., He, M., Shishov, V., Tychkov, I., Vaganov, E., Rossi, S., et al. (2017a). New perspective on spring vegetation phenology and global climate change based on Tibetan Plateau tree-ring data. *Proc. Natl. Acad. Sci. U. S. A.* 114. doi:10.1073/pnas.1616608114.

Yang, Z., Hsu, K., Sorooshian, S., Xu, X., Braithwaite, D., Zhang, Y., et al. (2017b). Merging high-resolution satellite-based precipitation fields and point-scale rain gauge measurements-A case study in Chile. *J. Geophys. Res. Atmos.* 122, 5267–5284. doi:10.1002/2016JD026177.

Yasutomi, N., Hamada, A., and Yatagai, A. (2011). Development of a Long-term Daily Gridded Temperature Dataset and Its Application to Rain/Snow Discrimination of Daily Precipitation. *Glob. Environ. Res.* 15, 165–172.

Yatagai, A., Kamiguchi, K., Arakawa, O., Hamada, A., Yasutomi, N., and Kitoh, A. (2012). APHRODITE: Constructing a Long-Term Daily Gridded Precipitation Dataset for Asia Based on a Dense Network of Rain Gauges. *Bull. Am. Meteorol. Soc.* 93, 1401–1415. doi:10.1175/BAMS-D-11-00122.1.

Yoshida, Y., Kikuchi, N., Morino, I., Uchino, O., Oshchepkov, S., Bril, A., et al. (2013). Improvement of the retrieval algorithm for GOSAT SWIR XCO2 and XCH4 and their validation using TCCON data. *Atmos. Meas. Tech.* 6, 1533–1547. doi:10.5194/amt-6-1533-2013.

Yu, L., Jin, X., and Weller, R. A. (2008). Multidecade Global Flux Datasets from the Objectively Analyzed Air-sea Fluxes (OAFlux) Project: Latent and sensible heat fluxes, ocean evaporation, and related surface meteorological variables. Woods Hole Oceanographic Institution, OAFlux Project Technical Report. OA-2008-01, Woods Hole. Massachusetts.

Zanna, L., Khatiwala, S., Gregory, J. M., Ison, J., and Heimbach, P. (2019). Global reconstruction of historical ocean heat storage and transport. *Proc. Natl. Acad. Sci.* 116, 1126 LP – 1131. doi:10.1073/pnas.1808838115.

Zeng, N., Zhao, F., Collatz, G. J., Kalnay, E., Salawitch, R. J., West, T. O., et al. (2014). Agricultural Green Revolution as a driver of increasing atmospheric CO 2 seasonal amplitude. *Nature* 515, 394–397. doi:10.1038/nature13893.

Zhang, J., and Rothrock, D. A. (2003). Modeling Global Sea Ice with a Thickness and Enthalpy Distribution Model in Generalized Curvilinear Coordinates. *Mon. Weather Rev.* 131, 845–861. doi:10.1175/1520-0493(2003)131<0845:MGSIWA>2.0.CO;2.

Zhou, C., Wang, J., Dai, A., and Thorne, P. W. (2021). A New Approach to Homogenize Global Subdaily Radiosonde Temperature Data from 1958 to 2018. *J. Clim.* 34, 1163–1183. doi:10.1175/JCLI-D-20-0352.1.

Zhu, Z., Bi, J., Pan, Y., Ganguly, S., Anav, A., Xu, L., et al. (2013). Global data sets of vegetation leaf area index (LAI)3g and fraction of photosynthetically active radiation (FPAR)3g derived from global inventory modeling and mapping studies (GIMMS) normalized difference vegetation index (NDVI3G) for the period 1981 to 2. *Remote Sens.* 5, 927–948. doi:10.3390/rs5020927.

Ziemke, J. R., Oman, L. D., Strode, S. A., Douglass, A. R., Olsen, M. A., McPeters, R. D., et al. (2019). Trends in global tropospheric ozone inferred from a composite record of TOMS/OMI/MLS/OMPS satellite measurements and the MERRA-2 GMI simulation. *Atmos. Chem. Phys.* 19, 3257–3269. doi:10.5194/acp-19-3257-2019.

Zolina, O., Simmer, C., Kapala, A., Shabanov, P., Becker, P., Mächel, H., et al. (2014). Precipitation Variability and Extremes in Central Europe: New View from STAMMEX Results. *Bull. Am. Meteorol. Soc.* 95, 995–1002.

ACCEPTED VERSION SUBJECT TO FINAL EDITING

doi:10.1175/BAMS-D-12-00134.1.
Zou, C.-Z., and Wang, W. (2011). Intersatellite calibration of AMSU-A observations for weather and climate applications. *J. Geophys. Res. Atmos.* 116. doi:10.1029/2011JD016205.
Zweng, M. M., Reagan, J. R., Seidov, D., Boyer, T. P., Locarnini, R. A., Garcia, H. E., et al. (2019). World Ocean Atlas 2018, Volume 2: Salinity. Available at: https://archimer.ifremer.fr/doc/00651/76339/.

ACCEPTED VERSION
SUBJECT TO FINAL EDITING

Annex II: Models

Coordinating Lead Authors:
José Manuel Gutiérrez (Spain), Anne-Marie Treguier (France)

Lead Authors:
Paul J. Durack (United States of America/Australia), Seita Emori (Japan), Malte Meinhausen (Australia/Germany), Sophie Nowicki (United States of America /France), Lucas Ruiz (Argentina)

Contributing Authors:
Javier Díez Sierra (Spain), Eric Guilyardi (France), Yusuke Satoh (Japan), Martina Stockhause (Germany)

This Annex should be cited as:
IPCC, 2021: Annex II: Models [Gutiérrez, J. M., A-M. Treguier (eds.)]. In: *Climate Change 2021: The Physical Science Basis. Contribution of Working Group I to the Sixth Assessment Report of the Intergovernmental Panel on Climate Change* [Masson-Delmotte, V., P. Zhai, A. Pirani, S. L. Connors, C. Péan, S. Berger, N. Caud, Y. Chen, L. Goldfarb, M. I. Gomis, M. Huang, K. Leitzell, E. Lonnoy, J. B. R. Matthews, T. K. Maycock, T. Waterfield, O. Yelekçi, R. Yu and B. Zhou (eds.)]. Cambridge University Press. In Press.

Date: August 2021

This document is subject to copy-editing, corrigenda and trickle backs.

ACCEPTED VERSION
SUBJECT TO FINAL EDITING

AII.1 Regional Climate Models (RCMs) participating in CORDEX 3
AII.2 Earth System Models and General Circulation Models for climate projections 15
AII.3 Models used in Ice sheet and glacier model intercomparison studies 26
AII.4 CMIP model datasets used in the report 30

ACCEPTED VERSION
SUBJECT TO FINAL EDITING

This Annex provides information on the numerical models used in this assessment.

AII.1 Regional Climate Models (RCMs) participating in CORDEX

The Coordinated Regional Climate Downscaling Experiment (CORDEX, (Gutowski Jr. et al., 2016)) coordinates regional downscaling activities worldwide over a number of defined domains. Regional downscaling is performed using Regional Climate Models (RCMs) run over limited geographical regions, driven at the boundaries by the output from CMIP global model simulations. CORDEX relies on the same infrastructure as the Coupled Model Intercomparison Project (CMIP) to make the multi-model output publicly available in a standardized format: the data is disseminated via the Earth System Grid Federation (ESGF, Williams et al. 2016).

Table AII.1 lists the current CORDEX domains, displaying the different resolutions (from the lowest 0.44º, to the highest 0.11º, typically in rotated coordinates), with data available through the ESGF. Figure Atlas.7 provides a geographical map of the domains. Note that 0.44º and 0.22º are the prioritized resolution in the CORDEX and CORDEX-CORE experimental designs, respectively, and only some domains provide information for higher resolution (0.11º); see Atlas, Section Atlas.1.4.4 and https://cordex.org for further details. Table AII.1 also displays the number of simulations available for the following experiments: "evaluation" (ERA-Interim driven simulations), and the "historical", "RCP26", "RCP45" and "RCP85" CMIP5-driven simulations (Taylor et al., 2012). This table illustrates the heterogeneity of information available across the different domains which limits the assessment of some scenarios in some regions.

The RCMs contributing to CORDEX (as available from ESGF) are listed in Table AII.2, including the main references and details on model components relevant for the WGI AR6 assessment.

Finally, Tables AII.3 and AII.4 provide information on the CMIP5 and RCM models used in the different CORDEX domains, respectively (the numbers in each cell indicate the number of available simulations for each scenario). Note that CORDEX information is complex to describe since each particular simulation is produced by a single combination of a CMIP5 boundary forcing, or "driving model" (or reanalysis for the evaluation experiment) and an RCM model from Table AII.2. These two tables together provide comprehensive information on the GCM/RCM composition of the ensembles available in each domain, which is key to understanding the assessment done in WGI chapters (in particular the regional Chapters 10, 11, 12 and Atlas).

[START TABLE AII.1 HERE]

Table AII.1: CORDEX regional domains

List of CORDEX domains. Column 1: name of the domain. Column 2: domain code (as in ESGF specification). Column 2: horizontal grid resolutions (11, 22, 44 for 0.11º, 0.22º and 0.44º resolution in the original rotated coordinates, and the suffix "i" indicating regular interpolated domains). Columns 4 to 8 indicate the number of simulations available at each resolution, for the evaluation, historical, RCP26, RCP45, RCP85 experiments, respectively, as archived in the ESGF as of 31 January 2021. Note that MED-CORDEX data is stored on a dedicated server (details at http://www.medcordex.eu) and include experiments with only atmosphere (the standard for other domains) and atmosphere-ocean coupled regional climate models (denoted by MED and OMED, respectively). See Section Atlas 1.4.4 for more details on CORDEX and CORDEX-CORE experiments.

CORDEX Domains	Code	Resolutions	evaluation	historical	RCP26	RCP45	RCP85
1: South America	SAM	[20, 22, 44]	[1, 2, 5]	[3, 6, 14]	[0, 6, 6]	[3, 0, 12]	[3, 6, 13]
2: Central America	CAM	[22, 44]	[3, 2]	[9, 15]	[6, 5]	[0, 3]	[9, 14]
3: North America	NAM	[11, 22, 44]	[1, 5, 7]	[0, 17, 13]	[0, 3, 1]	[0, 5, 6]	[0, 17, 13]

ACCEPTED VERSION SUBJECT TO FINAL EDITING

4: Africa	AFR	[22, 44]	[4, 10]	[10, 33]	[9, 13]	[1, 22]	[10, 29]
5: Europe	EUR	[11, 22, 44]	[14, 2, 15]	[65, 3, 27]	[29, 3, 11]	[26, 0, 21]	[63, 3, 26]
6: South Asia	WAS	[22, 44, 44i]	[3, 3, 0]	[9, 18, 1]	[8, 7, 1]	[0, 18, 1]	[9, 18, 1]
7: East Asia	EAS	[22, 44]	[5, 3]	[6, 5]	[6, 0]	[0, 5]	[6, 5]
8: Central Asia	CAS	[22, 44]	[2, 2]	[4, 2]	[4, 0]	[1, 2]	[4, 2]
9: Australasia	AUS	[22, 44, 44i]	[2, 6, 1]	[6, 34, 24]	[6, 0, 0]	[0, 25, 17]	[6, 25, 17]
10: Antarctica	ANT	[22, 44]	[4, 0]	[12, 6]	[2, 0]	[8, 5]	[10, 5]
11: Arctic	ARC	[22, 44, 44i]	[2, 13, 2]	[1, 11, 0]	[0, 1, 0]	[1, 6, 0]	[1, 13, 1]
12: Mediterranean	MED	[11, 22, 44]	[6, 3, 20]	[2, 2,13]	[1, 0, 1]	[2, 0, 7]	[1, 2, 12
	OMED	[11, 22, 44]	[5, 4, 9]	[1, 1, 8]	[0, 0, 1]	[1, 0, 4]	[1, 1, 7]
13: Middle East North Africa	MNA	[22, 44]	[1, 2]	[2, 6]	[0, 1]	[0, 6]	[2, 6]
14: South-East Asia	SEA	[22]	[3]	[12]	[6]	[5]	[11]

[END TABLE AII.1 HERE]

[START TABLE AII.2 HERE]

Table AII.2: Regional Climate Models contributing to CORDEX experiments.

Salient features of the Regional Climate Models (RCMs) participating in CORDEX scenario experiments (CMIP5-driven). Column 1: sponsoring institution(s). Column 2: name of the model (and versions); subsequent columns for each of the model components with main references. Column 3: atmospheric component with number of vertical levels and main reference; Column 4: aerosols component (interactive or prescribed, with component details when interactive). Column 5: land component (number of levels and component name). Column 6: ocean component (prescribed or interactive, with model details when interactive). Column 7: additional components (lake, urban, river models) and comments on versions and/or different configurations of the same model. See Table AII.1 for the codes of CORDEX domains.

ACCEPTED VERSION
SUBJECT TO FINAL EDITING

Institution (Country)	Model	Atmosphere 1) number of levels 2) main references	Aerosols 1) interactive or prescribed 2) component name (when interactive)	Land 1) number of levels 2) component name	Ocean 1) interactive or prescribed 2) component name 3) details	Additional components / comments Lake (LK), urban (UR), or river (RI) models, etc. Comments on the different versions
CNRM (France)	ALADIN52_v1 ALADIN53_v1	1) 31 2) (Colin et al., 2010)	1) Prescribed; (Szopa et al., 2013) dataset for eval and GCM forcing for scen runs, 5 classes, 2D spatial pattern, vertical profile, seasonal cycle, temporal evolution	1) 3 2) ISBA (Noilhan and Mahfouf, 1996)	1) Prescribed SST (ice cover defined by a SST threshold)	LK: no UR: no ALADIN53_v1 is same as ALADIN52_v1 except for the radiation scheme (RRTM for the LW, Mlawer et al. (1997) and FMR-6bands for the SW, Fouquart and Bonnel, (1980); Morcrette et al. (2008), for the turbulent air-sea fluxes (ECUME) and for the mixing length based on Lenderink's work.
CNRM (France)	ALADIN63_v1 ALADIN63_v2	1) 91 2) (Nabat et al., 2020)	1) Prescribed; TACTIC dataset for eval and GCM forcing for scen, 5 classes, 2D spatial pattern, vertical profile, seasonal cycle, temporal evolution	1) 14 2) SURFEX8-ISBA (Decharme et al., 2019). No land use land cover change is taken into account	1) Prescribed SST (ice cover defined by a SST threshold)	LK: Flake (Le Moigne et al., 2016), pronostic lake ice. UR: Urban areas are considered as rock (Daniel et al., 2019) ALADIN63_v1 and ALADIN63_v2 are identical. v2 label is used to indicate that the runs driven by the CNRM-CM5 GCM use the corrected version of the CNRM-CM5 Atmospheric-LBCs contrary to ALADIN53_v1
RMIB-UGent (Belgium)	ALARO-0_v1	1) 46 2) (Giot et al., 2016; Top et al., 2021)	1) Prescribed	1) 2 2) ISBA (Douville et al., 2000)	1) Prescribed SST	N/A
CCCma (Canada)	CanRCM4_r2	1) 25 2) (Scinocca et al., 2016)	1) Interactive 2) described in main reference	1) 3 2) CLASS 2.7	1) Prescribed SST	Full atmospheric physics package identical to that used by parent global model, CanAM4, used by CanESM2 for CMIP5. Historical + RCP8.5 large ensemble (50 members) of 'NAM-44' available for large ensemble (50 members) of its parent model CanESM2.
CSIRO (Australia)	CCAM_v1 CCAM-1704_v1	1) 27 2) (Hoffmann et al., 2016)	1) Interactive 2) sulfate, black carbon, organic aerosol, mineral dust and sea salt (Rotstayn and Lohmann, 2002; Rotstayn et al., 2011)	1) 6 2) CABLE (Kowalczyk et al., 2013)	1) Prescribed SST after bias and variance correction (CCAM_V1) or just bias correction (CCAM-1704_v1)). No atmospheric nudging.	UR: UCLEM (Lipson et al., 2018)
CSIRO (Australia)	CCAM-2008_v1	1) 35 2) (Thatcher and McGregor, 2009)	1) Interactive 2) sulfate, black carbon, organic aerosol, mineral dust and sea salt (Rotstayn and Lohmann, 2002; Rotstayn et al., 2011)	1) 6 2) CABLE (Kowalczyk et al., 2013)	1) Prescribed SST	UR: UCLEM (Lipson et al., 2018)
CLM-	CCLM4-8-17-	1) 35	1) Prescribed	1) 9	1) Prescribed SST	N/A

ACCEPTED VERSION SUBJECT TO FINAL EDITING

Community: BTU, CMCC, DWD, ETH, GUF, HZG, JLU, KIT, WEGC ZAMG (Europe)	CLM3-5_v1	2) (Di Virgilio et al., 2019)		2) CLM (Dickinson et al., 2006)		
CLM-Community (Europe)	CCLM4-8-17_v1	1) 35 2) (Panitz et al., 2014)	1) Prescribed	1) 9 2) soil-vegetation-atmosphere-transfer TERRA-ML (Schrodin and Heise, 2002)	1) Prescribed SST	N/A
CLM-Community (Europe)	CCLM5-0-2_v1	1) 45 2) (Li et al., 2018)	1) Prescribed. Aerosol optical thickness: NASA/GISS (Global Aerosol Climatology Project)	1) 9 Multilayer soil model TERRA-ML (Schrodin and Heise, 2002)	1) Prescribed SST	Surface roughness: GLOBE (NOAA/NGDC); Global Land Cover 2000 Project (GLC2000)
CLM-Community: HZG and KIT (Germany)	CCLM5-0-15_v1	1) 57 2) N/A	1) Prescribed	1) 9 2) TERRA-ML (Schrodin and Heise, 2002)	1) Prescribed SST	LK: FLake (Mironov et al., 2010)
CLM-Community: GUF (Germany)	CCLM5-0-9-NEMOMED12-3-6	1) 40 2) (Akhtar et al., 2018)	1)Prescribed; AeroCom Global AOD data is used for Aerosol representation (Kinne et al., 2006)	1) 9 TERRA-ML (Schrodin and Heise, 2002)	1) Interactive 2) NEMOMED12 (1/12^{o} resolution) is the interactive ocean model component (Beuvier et al., 2012) 3) The CCLM and NEMOMED12 models are coupled via OASIS3-MCT (Valcke, 2013) with a 1-h coupling time.	RI: TRIP (Total Runoff Integrating Pathways) is used as the interactive river component for rivers over the Mediterranean Basin to feed runoff at the river mouths to the Mediterranean Sea (NEMOMED12)
CLM-Community: ETH (Switzerland)	COSMO-crCLIM-v1-1_v1	1) 40 (EUR-11), 57 (WAS-22) 2) (Leutwyler et al., 2017)	1) Prescribed; AeroCom1 aerosol monthly climatology dataset (Kinne et al., 2006).	1) 9 2) TERRA-ML with a soil hydrology scheme (Schlemmer et al., 2018)	1) Prescribed SST	COSMO-crCLIM is similar to CCLM. Its main characteristics are that it runs on GPUs and includes the soil hydrology scheme of Schlemmer et al. (2018). Other adjustments include changing the upper level damping to only relax the vertical velocity instead of all dynamical fields (Klemp et al., 2008)
OURANOS (Canada)	CRCM5_v1	1) 56 (TOA 10 hPa) 2) (Martynov et al., 2013; Šeparović et al., 2013)	1) Prescribed	1) 17 (to 15 m) 2) CLASS3.5c (Verseghy et al., 1993)	1) Prescribed SST and sea-ice fraction	LK: Flake

ACCEPTED VERSION SUBJECT TO FINAL EDITING

UQAM (Canada)	CRCM5_v1	1) 56 (TOA 10 hPa) 2) (Martynov et al., 2013)	1) Prescribed; not varying in time; higher values at the equator, lower at the poles; higher values over land than over the ocean	1) 26 (to 60 m) 2) CLASS3.5+	1) Prescribed SST and sea-ice fraction	LK: FLake
INPE (Brazil)	Eta_v1	1) 38 (TOA 25hPa) 2) (Chou et al., 2014a, 2014b)	1) Prescribed	1) 4 2) NOAH scheme (Ek et al., 2003) 12 Vegetation types and 9 soil types.	1) Prescribed SST	No orography smoothing; No internal or lateral boundary relaxation nudging.
DMI (Denmark)	HIRHAM5_v1 HIRHAM5_v2 HIRHAM5_v3	1) 31 2) (Christensen et al., 2007)	1) Prescribed	1) 5 2) ECHAM5	1) Prescribed SST and sea-ice	The different versions v1, v2, v3, are simulation versions due to necessary re-runs, not different model versions.
MOHC (U.K.)	HadREM3-GA7-05_v1 HadREM3-GA7-05_v2	1) 63 2) (Walters et al., 2019)	1) Prescribed. MACv2-SP dataset (Stevens et al., 2017), total aerosol properties, 9 bands. EasyAerosol (Voigt et al., 2014) RCP scenarios	1) 4 2) (Walters et al., 2019)	1) Prescribed SST and sea-ice from driving GCM/reanalysis	LK: no The "v2" runs are using CNRM boundary conditions from pressure level 3d data. No differences in the RCM, only a different source of lbcs.
LMD (France)	LMDZ4NEMOMED8_v1 LMDZ4NEMOMED8_v2	1) N/A 2) (L'Hévéder et al., 2013; Vadsaria et al., 2020)	1) Prescribed	1) 2 2) ORCHIDEE	1) interactive 2) NEMOMED8 (Beuvier et al., 2010) 3) Interactive Mediterranean Sea only; 43 vertical levels with a 6-m thick first level; daily coupling frequency by the OASIS coupler (Valcke, 2013)	RI: Interactive river coupling in v2. No river coupling in v1
ULg (Belgium)	MAR311_v1	1) 24 2) (Agosta et al., 2019; Kittel et al., 2021)	1) Prescribed, RCP scenarios	1) 7 2) SISVAT (De Ridder, 1997; De Ridder and Schayes, 1997), (Gallée and Duynkerke, 1997; Gallée et al., 2001; Lefebre, 2003)	1) Prescribed SST and SIC (evolution of the snow properties simulated by SISVAT)	SISVAT model: 30 snow/ice layers over the ice sheet and two sub-pixels (rocs and permanent ice-covered area)
UB Belgarde (Serbia)	EBU-POM2c_v1	1) 32 2) (Djurdjevic and Rajkovic, 2008, 2010; Kržič et al., 2011)	1) Prescribed	1) 4 2) NOAH-LSM (Ek et al., 2003)	1) Interactive 2) POM - Princeton ocean model (30km, L21, coupling frequency 6 min)	N/A
ENEA (Italy)	PROTHEUS_v2	1) 18 2) (Artale et al., 2010; Soto-Navarro et al., 2020)	1) no active aerosol chemical model	1) 2 2) BATS1e (Dickinson et al., 1993). Air–sea exchanges by Zeng et al.	1) Interactive 2) MITMED8 (1/8° resolution) is the interactive ocean model component (Sannino et al.,	RI: Fully interactive (daily coupling) using the TRIP river routine model

ACCEPTED VERSION SUBJECT TO FINAL EDITING

				(1998) to improve excessive evaporation from warm ocean surfaces (Pal et al., 2007) in the original BATS package.	2009)	
KNMI (Netherlands)	RACMO21P_v1 RACMO21P_v2	1) 40 2) (van Meijgaard et al., 2008)	1) Prescribed (Tegen et al., 1997) four classes (land, maritime, dust, urban) + stratospheric + (optionally) volcanic	1) 4 2) baseline LSM TESSEL (van den Hurk et al., 2000); Land-ice tile added for ice-sheet modelling. Multi-layer snow-ice-refreezing scheme (Ettema et al., 2010); snow albedo scheme (Kuipers Munneke et al., 2011); snow drift scheme (Lenaerts et al., 2012)	1) Prescribed SST and sea-ice concentration; inferred from re-analysis or GCM	Model versions: Simulations with RACMO21P_v2 are straight reruns of RACMO21P_v1 employing the same model system and parameter settings. In ANT-44 simulations, v2 is only used with MOHC-HadGEM2-ES forcing to fix the remapping of SST to the RACMO grid in the v1-simulation
KNMI (Netherlands)	RACMO22E_v1 RACMO22E_v2	1) 40 2) (van Meijgaard et al., 2012)	1) Prescribed; inferred from CAM inventory (except volcanic); historical and rcp pathways (Lamarque et al., 2010, 2011; van Vuuren et al., 2011); also used in evaluation. Sulfate, particulate organic matter black carbon, sea salt, desert dust stratospheric aerosols, volcanic aerosol. Spatial maps and vertical profiles per species. Monthly variations and decadal trends.	1) 4 2) HTESSEL (Balsamo et al., 2009)	1) Prescribed SST and sea-ice concentration; inferred from re-analysis or GCM	Model versions: Simulations with RACMO22E_v2 are straight reruns of RACMO22E_v1 employing the same model system and parameter settings. Meaning of v2 depends on forcing GCM: i) MOHC-HadGEM2-ES: remapping of GCM-SST to RACMO grid erroneous in v1, corrected in v2 ii) CNRM-CERFACS-CNRM-CM5: atmospheric forcings derived from pressure level fields, because of error in CNRM-CM5 model level fields
KNMI (Netherlands)	RACMO22T_v1 RACMO22T_v2	1) 40 2) (van Meijgaard et al., 2012)	1) Prescribed, as in RACMO22E	1) 4 2) HTESSEL (Balsamo et al., 2009)	1) Prescribed SST and sea-ice concentration; inferred from re-analysis of GCM	Model versions: Simulations with RACMO22T_v2 are straight reruns of RACMO22T_v1 employing the same model system and parameter settings. In AFR-44, v2 is only used with MOHC-HadGEM2-ES forcing to fix the remapping of SST to the RACMO grid in the v1-simulation
SMHI (Sweden)	RCA4_v1 RCA4_v1a RCA4_v2	1) 40 2) (Samuelsson et al., 2015; Strandberg et al., 2015)	1) Prescribed: single integrated class, parameterized aerosol effect on radiation fluxes,spatially uniform, static.	1) 3 2) a tile-based scheme with physiography based on ECOCLIMAP (Samuelsson et al., 2015)	1) Prescribed SST and sea-ice from daily driving GCMs/reanalysis	LK: Flake (pronostic lake ice). (Mironov et al., 2010) Model versions: i) RCA4-v1a is simply a re-run because a restart file to start the scenario experiment was taken from another

ACCEPTED VERSION SUBJECT TO FINAL EDITING

	RCA4_v3 RCA4-SN_v1					simulations, ii) RCA4-v2 and RCA4-v3 are slightly tuned versions of RCA4-v1 (some parameters) but parameterizations are the same. RCA-SN indicates spectral nudging.
CNRM (France)	RCSM4_v1	1) 31 2) (Sevault et al., 2014)	1) Prescribed (Szopa et al., 2013) dataset for evaluation and GCM forcing for scen runs, 5 classes, 2D spatial pattern, vertical profile, seasonal cycle, temporal evolution	1) 3 2) ISBA (Noilhan and Mahfouf, 1996)	1) Interactive 2) NEMOMED8 (Beuvier et al., 2010) 3) Mediterranean Sea only; 43 vertical levels with a 6-m thick first level; daily coupling frequency by the OASIS coupler (Valcke, 2013)	1) interactive rivers connecting the atmosphere to the ocean 2) TRIP (Oki and Sud, 1998; Decharme et al., 2010) 3) 50km spatial resolution
GERICS and MPI-CSC (Germany)	REMO2009_v1 REMO2015_v1 REMO2015_v2	1) 27 2) (Jacob and Podzun, 1997; Jacob, 2001)	1) Prescribed (Tanré et al., 1984)	1) 5 2) a tile-based scheme including annual cycle of albedo (Rechid et al., 2009)	1) Prescribed SST and SIC	REMO2009_v1 and REMO2015_v1 and V2 are essentially the same, just with some technical changes
GERICS-AWI (Germany)	ROM ROM_v1	1) 27 2) (Sein et al., 2015)	See above	See above	1) Interactive. 2) SST, SIC and SIT are calculated in ocean model MPIOM	1) interactive rivers connecting the atmosphere to the ocean 2) Hydrological Discharge (HD) model 3) 50km spatial
MGO (Russia)	RRCM_v1	1) 25 2) (Shkolnik and Efimov, 2013)	1) Prescribed	1) 4 2) MGO-2	1) Prescribed SST	N/A
ITU (Turkey)	RegCM4-BATS_v1	1) 18 2) (Ruti et al., 2016; Turuncoglu, 2019)	1) no active aerosol chemical model	1) 2 2) BATS1e	1) Prescribed; surface layer (Zeng et al., 1998)	In MED-11, Wave Model (WAM) Cycle-4 (4.5.3-MPI) coupled with Atmospheric model
ITU (Turkey)	RegESM	1) 18 2) (Ruti et al., 2016; Turuncoglu, 2019)	See above	See above	1) Interactive 2) ROMS-revision 809; (Haidvogel et al., 2008)	In MED-11, Wave Model (WAM) Cycle-4 (4.5.3-MPI) coupled with Atmospheric model
ICTP (Italy) RU-CORE (Thailand)	RegCM4-3_v4	1) 18 2) (Giorgi et al., 2012)	1) no active aerosol chemical model	1) 2 2) BATS1e [SAM-44: 1) 10 2) CLM3.5]	1) Prescribed; surface layer (Zeng et al., 1998)	N/A
ICTP (Italy) BOUN (Turkey)	RegCM4-3_v5	1) 18 2) (Ozturk et al., 2017, 2018)	1) no active aerosol chemical model	1) 1 2) BATS 1e	1) Prescribed; surface layer (Zeng et al., 1998)	N/A
ICTP (Italy)	RegCM4-4_v0	1) 18 2) (Giorgi et al., 2012)	1) no active aerosol chemical model	1) 2 2) BATS1e	1) Prescribed; surface layer (Zeng et al., 1998)	N/A
ICTP (Italy)	RegCM4-4_v5	1) 18 2) (Giorgi et al., 2012;	1) no active aerosol chemical model	1) 10 2) CLM4.5	1) Prescribed; surface layer (Zeng et al., 1998)	UR: CLM4.5

ACCEPTED VERSION SUBJECT TO FINAL EDITING

IITM (India)		Sanjay et al., 2017, 2020)				
ICTP (Italy)	RegCM4-6_v1	1) 23 2) (Giorgi et al., 2012)	1) no active aerosol chemical model	1) 10 2) CLM4.5	1) Prescribed; surface layer (Zeng et al., 1998)	UR: CLM4.5
ICTP (Italy) ORNL (USA)	RegCM4-7_v0	1) 23 2) (Giorgi et al., 2012)	1) no active aerosol chemical model	1) 10 2) CLM4.5	1) Prescribed; surface layer (Zeng et al., 1998)	UR: CLM4.5
ICTP (Italy) ISU (USA)	RegCM4_v4-4-rc8	1) 18 2) (Giorgi andAnyah, 2012; Mearns et al., 2017; Bukovsky and Mearns, 2020)	N/A	1) 3 soil layers 2) BATS	1) Prescribed SST; no sea-ice prescribed, atmospheric skin temperature instead	LK: (Hostetler et al., 1994)
UB (Serbia)	EBU	1) 32 2) N/A	Same as EBU-POM2c_v1	Same as EBU-POM2c_v1	1) Prescribed SST	N/A
UCAN (Spain)	WRF341I_v2	1) 30 2) (Skamarock et al., 2008)	1) Prescribed uniform background with vertical profile. Constant in time.	1) 4 2) Noah (Chen and Dudhia, 2001)	1) Prescribed SST and sea-ice	WRF v3.4.1. "I" stands for the coordinated physics configuration used within CORDEX. "v2" refers to the variable GHG input and noleap calendar in scenario (CanESM2) simulations. Otherwise, fully comparable to v1 in ERA-Interim (fixed GHG, standard cal.)
CYI (Cyprus)	WRF351_v1	1) 30 2) (Zittis et al., 2014; Zittis and Hadjinicolaou, 2017)	1) Prescribed	1) 4 2) Noah (Chen and Dudhia, 2001)	1) Prescribed SST	N/A
UNSW (Australia)	WRF360J_v1 WRF360K_v1	1) 30 2) (Powers et al., 2017; Evans et al., 2020)	1) Prescribed	1) 4 2) Noah (Chen and Dudhia, 2001)	1) Prescribed SST (ice with SST threshold)	N/A
UNSW (Australia)	WRF360L_v1	1) 30 2) (Powers et al., 2017; Di Virgilio et al., 2019)	1) Prescribed	1) 4 2) Noah (Chen and Dudhia, 2001)	1) Prescribed SST (ice with SST threshold)	N/A
UHOH (Germany)	WRF361H_v1	1) 50 2) (Skamarock et al., 2008)	1) Prescribed uniform background with vertical profile. Constant in time.	1) 4 2) NOAH (Chen and Dudhia, 2001)	1) Prescribed SST (ice with SST threshold)	N/A
CRC (France)	WRF381_v1	1) 50 2) https://doi.org/10.25666/dataosu-2021-03-05-02 https://doi.org/10.25666/dataosu-2021-03-05	1) Prescribed (Tegen et al., 1997)	1) 4 2) Noah_mp (Niu et al., 2011) Modis land categories	1) Prescribed SST (ice with SST threshold) from global model	Allow sub-grid cloud fraction interaction with radiation (Alapaty et al., 2012) The forcing variables have been bias-corrected using ERA-Interim fields for 1981-2005, as in Bruyère et al. (2014).
IPSL (France)	WRF381P_v1 WRF381P_v2	1) 31 2) (Skamarock et al., 2008)	1) Prescribed aerosols	1) 4	1) Prescribed SST and sea-ice (from global model)	N/A

ACCEPTED VERSION SUBJECT TO FINAL EDITING

NCAR and UA (USA)	WRF_v3-5-1	1) 28 2) (Skamarock et al., 2008; Mearns et al., 2017; Bukovsky and Mearns, 2020)	1) Prescribed	1) 4 soil levels 2) Noah	1) Prescribed SST, prescribed sea-ice for GFDL and MPI-driven simulations, sea-ice with an SST threshold for HadGEM-driven simulation	WRF v3.5.1 Spectral nudging used.

[END TABLE AII.2 HERE]

ACCEPTED VERSION
SUBJECT TO FINAL EDITING

[START TABLE AII.3 HERE]

Table AII.3: CMIP5 models used for downscaling in the different CORDEX domains

Climate models participating in CMIP5 (rows) used as boundary conditions for the CORDEX regional simulations in the different domains (columns). Each cell indicates the number of simulations available for the historical, RCP26, RCP45 and RCP85 experiments (see the color legend). Salient features of these models are described in IPCC-AR5 Appendix 9.A (model names are taken from table 9.A.1). Further details on these simulations (e.g. particular GCM-RCM combinations in each cell) are given in the November 2021 list of simulations available in the CORDEX website https://cordex.org. (*) For the Mediterranean domain, only the coupled atmosphere-ocean simulations are listed.

GCM/Domain	SAM	CAM	NAM	AFR	EUR-11	WAS	EAS	CAS	AUS	ANT	ARC	MED(*)	MNA	SEA
CanESM2_r1i1p1	3 3 3	3 3	6 5 6	4 4 3		2 2 2			3 3 3	1 1 1	4 3 4			
CNRM-CM5_r1i1p1		2 2	1 1 1	2 2 2	10 5 6 9	2 2 2	1 1 1	1 1 1 1	2 2 2			3 1 2 2	1 1 1	1
ACCESS1-0_r1i1p1									9 5 5	1 1 1				
ACCESS1-3_r1i1p1									6 2 2	1 1				
CSIRO-Mk3-6-0_r1i1p1	1 1 1	1 1		1 1 1		2 2 2								
EC-EARTH_r12i1p1	1 1 1 1	1 1 1 1	1 1 1 1	4 3 3 3	8 5 4 8	2 1 1 2	1 1 1		1 1 1	1 1	2 1 1 2	1 1	2 1 1 2	
EC-EARTH_r1i1p1				2 1 2	4 1 4					1 1 1				1 1 1
EC-EARTH_r3i1p1			1 1 1	2 1 2	4 1 1 4		1 1 1			1 1 1	1 1 1			
PSL-CM5A-LR_r1i1p1				1 1 1	1 1	1 1 1								1 1 1
IPSL-CM5A-MR_r1i1p1	1 1 1	1 1		1 1 1	5 2 5	1 1 1						2 1 2		
MIROC5_r1i1p1	2 1 2 2	1 1 1		2 2 1 2	2	2 2 1 2			2 2 2	1 1 1				
HadGEM2-CC_r1i1p1									1 1 1					
HadGEM2-ES_r1i1p1	5 3 3 5	4 3 1 4	5 1 5	8 6 3 8	9 6 5 9	2 2 1 2	3 2 1 3	2 1 1 2	2 2 2	1 1 1 1			1 1 1	4 2 2 4
HadGEM2-ES_r2i1p1		1 1												
MPI-ESM-LR_r1i1p1	3 3 2 3	2 2 1 2	8 1 2 8	6 4 4 5	9 4 3 #	5 5 3 5	2 1 1 2	1 1 1	4 2 2 4		3 1 5	3 1 3		1 1 1
MPI-ESM-LR_r2i1p1				1 1	3 1 1 3									
MPI-ESM-LR_r3i1p1				1 1	3 3									
MPI-ESM-MR_r1i1p1	2 1 2	2 1 2	2 2	2 1 2		2 1 1 2	1 1 1	1 1 1			1 1	1 1	1 1 1	2 1 1 2
MPI-ESM-MR_r2i1p1		1												
CCSM4_r1i1p1									1 1 1					
CCSM4_r6i1p1													1 1 1	
NorESM1-M_r1i1p1	3 3 1 3	2 2 2	1 1 1	4 4 1 4	8 3 3 8	4 4 1 4	2 2 2	1 1 1	5 2 3 5	2 1 2	1 1 1			2 2 2
GFDL-CM3_r1i1p1									1 1 1					

ACCEPTED VERSION SUBJECT TO FINAL EDITING

| | | |

| | | |

AII.2 Earth System Models and General Circulation Models for climate projections

Detailed and structured information about climate models, simulations and their conformance to common experimental protocols is not only important for scientific interpretation but, under increased scrutiny from society, it is also demanded of climate science that purports to be mature, credible, open, transparent and reproducible (Guilyardi et al., 2013). Scientific publications remain an essential way of documenting models but remain largely scattered and not easily accessible by the growing community of users of model output. To address these challenges, the Earth System Documentation (ES-DOC) project offers an eco-system of tools and services in support of Earth System modelling documentation creation, analysis and dissemination. ES-DOC is coordinated with other community efforts such as the Coupled Model Intercomparison Project (CMIP) via the World Climate Research Programme work group on Climate Modelling (WGCM) and its Infrastructure Panel WIP (Balaji et al., 2018).

The objective of CMIP is to better understand past, present and future global climate changes arising from natural, unforced variability or in response to changes in radiative forcing in a multi-model context (Chapter 1, Section 1.5.4). This understanding includes assessments of model performance during the historical period (Chapter 3) and quantifications of the causes of the spread in future projections (Chapters 4, 7). Idealised experiments are also used to increase understanding of the model responses. In addition to these long time scale responses, experiments are performed to investigate the predictability of the climate system on various time and space scales as well as making predictions from initialised climate states. The different activities (MIP) endorsed by CMIP6 are listed in Chapter 1, Table 1.3 (Eyring et al., 2016). A set of common experiments, the DECK (Diagnostic, Evaluation and Characterization of Klima) and CMIP historical simulations (1850–2014) were introduced that will maintain continuity with previous CMIP phases and help document basic and evolving characteristics of models. ScenarioMIP is the framework for future climate projections (O'Neill et al., 2016). The infrastructure panel of the World Climate Research Programme coordinates framework developments and defines data standards for CMIP. A key aspect is the dissemination of the data via the Earth System Grid Federation, ESGF (Williams et al., 2016; Petrie et al., 2021)

A new online service, ES-DOC, provides information about all aspects of CMIP6. Building on the Common Information Model concepts and standards (Lawrence et al., 2012), a number of documents are created for the CMIP6 Project, as illustrated on https://es-doc.org/cmip6/. These include documents to describe experiments, ensembles simulations, models, conformance to the numerical requirements of the CMIP6 protocol (see (Pascoe et al., 2019) for CMIP6 experiments) and other important aspects of the CMIP6 model archive. These different documents are either produced automatically or provided in a standard way by modelling groups. Hundreds of clearly structured properties are harvested and stored on a database to be used by clients and portals (e.g. https://search.es-doc.org/ and https://explore.es-doc.org/). Another entry point to the database is provided by the one-stop-shop "further_info_url" global attribute in each CMIP6 netcdf data file. ES-DOC also includes the CMIP6 errata system (https://errata.es-doc.org), which tracks issues with the model data and the potential corrections made. ES-DOC includes information at the model level and the experiment level.

Model datasets shared on ESGF are characterized by their institution, model, experiment, variable, and ensemble member (the different types of ensemble strategies are introduced in Chapter 1, Section 1.4). Each ensemble member is designated by a label of four letters, each associated with a number: "r" for realization, "i" for initialization, "p" for physics, and "f" for forcing. For example, Table Atlas.A.2 lists the ensemble member label of each CMIP6 dataset used in the Atlas. In the future, ES-DOC will document in more detail how each individual member differs from the other members of a given ensemble.

The key new model developments since AR5 are summarized in Chapter 1, Section 1.3.5, and model results are assessed in multiple chapters of this report. In this Annex, Table AII.5 presents the main features of the CMIP6 coupled models, in a format comparable with AR5 table 9.A.1 for CMIP5 (Flato et al., 2013). At the date of March 2021, 136 models had registered for CMIP6, including the 23 CMIP6-endorsed MIPs (Chapter 1, Table 1.3). For conciseness, Table AII.5 documents only the coupled models used in the CMIP6 "DECK" experiments and ScenarioMIP, excluding atmosphere-only and ocean-only components (AMIP and

ACCEPTED VERSION SUBJECT TO FINAL EDITING

OMIP), radiative transfer models (RFMIP), etc. Registered coupled model that have not submitted data in time to be used in this report are not included. The high-resolution models used for HighResMIP (Haarsma et al., 2016) are listed in Table AII.6, and ice sheet models are documented in section AII.3. The citation information for all CMIP6 model datasets is compiled in section AII.4, Table AII.10

ACCEPTED VERSION
SUBJECT TO FINAL EDITING

[START TABLE AII.5 HERE]

Table AII.5: Coupled Climate and Earth System Models participating in CMIP6 DECK, historical simulation, and ScenarioMIP

Salient features of the coupled General Circulation Models (GCMs) and Earth System Models (ESMs) participating in the CMIP6 DECK, historical simulation, and ScenarioMIP. Column 1: sponsoring institution(s), Column 2: names of model configurations; Column 3: main reference(s); subsequent columns for each of the model components, with names and main component reference(s). In addition, there are standard entries for the atmosphere component: horizontal grid resolution, number of vertical levels, grid top; and for the ocean component: horizontal grid resolution, number of vertical levels, vertical coordinate type. The horizontal resolution (rounded to 10km) is the square root of the number of grid points divided by the surface area of the Earth, or the number of surface ocean grid points divided by the area of the ocean surface, for the atmosphere and ocean respectively. When reported in hPa, the atmosphere top heights are converted into km assuming standard atmosphere (ISO 2533:1975, 1975). Aerosols are either prescribed or computed from emissions (emission-driven). For land carbon, a list of active processes is provided among: active land carbon cycle (Land carbon), active nitrogen cycle (N cycle), prognostic biogeography of vegetation (Prog. veg.), carbon included in a permafrost pool (Permafrost), and dynamic fires (Fires). A blank entry indicates that information was not available. The information contained in the table is consistent with version 6.2.55.10 of the CMIP6 Controlled Vocabularies (https://github.com/WCRP-CMIP/CMIP6_CVs).

ACCEPTED VERSION
SUBJECT TO FINAL EDITING

institution **full name** **country**	**Models**	**Main references**	**Atmosphere** **1) Component name** **2) resolution (km) and number of levels** **3) Top** **4) references**	**Aerosol** **1) Component name** **2) emission-driven or prescribed** **3) references**	**Atmospheric Chemistry** **1) Component name** **2) details** **3) references**	**Ocean** **1) Component name** **2) horizontal resolution and number of levels** **3) vertical grid** **4) references**	**Cryosphere** **1) Sea ice** **2) Land ice**	**Land** **1) component name** **2) reference**	**Land carbon** **Active processes**	**ocean interactive biogeochemistry** **1) component name** **2) reference**
AS-RCEC Research Center for Environmental Changes, Academia Sinica, **Taiwan**	**TaiESM1.0**	(Lee et al., 2020)	1) TaiAM1 2) 100 km, 30L 3) Top 43 km	1) SNAP 2) emission-driven 3) (Chen et al., 2013)	none	1) POP2 2) 60 km, 60 L 3) z	1) CICE4	1) CLM4.0 with modified surface solar radiation 2) (Lee et al., 2013)	Land carbon N cycle Fires	none
AWI Alfred Wegener Institute, **Germany**	**AWI-CM-1-1-LR** **AWI-CM-1-1-MR** **AWI-ESM-1-1-LR**	(Sidorenko et al., 2015) (Semmler et al., 2020)	1)ECHAM6.3.04p1 2) **LR**: 170 km, 47L ; **MR:** 80 km, 95L 3) Top 80 km	2) prescribed MACv2-SP 3) (Stevens et al., 2017)	none	1) FESOM1.4 2) **LR**: 50 km, 46L **MR** : 20km, 46L 3) z	1) FESOM1.4	JSBACH 3.20	**AWI-CM:** none **AWI-ESM**: Land carbon N cycle Prog. Veg. Fires	none
BCC Beijing Climate Centre, **China**	**BCC-CSM2-MR**	(Wu et al., 2019)	1) AGCM3 2) 100 km, 46L 3) Top 45 km	2) prescribed MACv2-SP 3) (Stevens et al., 2017)	1) none	1) MOM4 2) 80 km, 40L 3) z	1) SIS1	BCC_AVIM2 (Li et al., 2019)	none	none
BCC	**BCC-ESM1**	(Wu et al., 2020b)	1) AGCM3 2) 250 km, 26L 3) Top 42 km	2) emission-driven	1) BCC-AGCM3-Chem 2) interactive 3) (Wu et al., 2020b)	1) MOM4 2) 80 km, 40L 3) z	1) SIS1	BCC_AVIM2 (Li et al., 2019)	Land Carbon	none
CAMS Chinese Academy of Meteorological Sciences **China**	**CAMS-CSM1-0**	(Rong et al., 2018)	1) ECHAM5_CAMS 2) 100 km, 31L 3) Top 31.2 km	2) prescribed MACv2-SP 3) (Stevens et al., 2017)	none	1) MOM4 2) 90 km, 50L 3) z	1) SIS1	CoLM	none	none
CAS Chinese Academy of Sciences **China**	**FGOALS-f3-L**	(He et al., 2020)	1) FAMIL2.2 2) 90 km, 32 L 3) Top 42.1 km (He et al., 2019)	2) prescribed 3) (He et al., 2019)	none	1) LICOM3.0, 2) 80 km, 30L 3) z 4) (Lin et al., 2020a)	1) CICE4.0	CLM4.0 / CAS-LSM (Xie et al., 2018)	none	none

ACCEPTED VERSION SUBJECT TO FINAL EDITING

CAS	**FGOALS-g3**	(Li et al., 2020)	1) GAMIL3 2) 190 km, 26 L 3) Top 42 km	2) prescribed 3) (Li et al., 2020)	none	1) LICOM3.0, 2) 80 km, 30L 3) z 4) (Lin et al., 2020a)	1) CICE4.0	CLM4.0 / CAS-LSM (Xie et al., 2018)	none	none
CCCMa Canadian Centre for Climate Modelling and Analysis **Canada**	**CanESM5** **CanESM5-CanOE**	(Swart et al., 2019)	1) CanAM5 2) 250 km, 49L 3) Top 48. km	2) emission-driven 3) (von Salzen et al., 2013)	2) specified oxidants, interactive sulfur 3) (von Salzen et al., 2013)	2) NEMO3.4.1 2) 70 km, 45 L 3) z	1) LIM2	1)Physics, CLASS3.6 Biogeochemistry, CTEM1.2 2) (Verseghy, 2000; Arora and Boer, 2010)	Land carbon	**CanESM5:** CMOC **CanESM5-CanOE:** CanOE
CCCR-IITM Centre for Climate Change Research, Indian Institute of Tropical Meteorology, **India**	**IITM-ESM**	(Swapna et al., 2018)	1) IITM-GFS 2) 170 km, 64L 3) Top 61 km	2) prescribed MAC-v2 3) (Stevens et al., 2017; Fiedler et al., 2019)	none	1) MOM4p1 2) 90 km, 50L 3) z	1) SISv1.0	NOAH LSMv2.7.1	none	TOPAZv2.0
CMCC Centro Euro-Mediterraneo sui Cambiamenti Climatici **Italy**	**CMCC-CM2-SR5** **CMCC-ESM2**	(Cherchi et al., 2019)	1) CAM5.3 2) 100 km, 30L 3) Top 43 km	1) MAM3 2) emission-driven 3) (Liu et al., 2012a)	2) Specified oxidants based on MOZART simulations	1) NEMO3.6 2) 70 km, 50L 3) z	1) CICE4.0	1) CLM4.5 2) (Oleson et al., 2013)	Land cardon N cycle Permafrost Fires	**CM2-SR5**: none **ESM2:** BFM5.2
CNRM Centre National de Recherches Météorologiques, **and CERFACS** Centre Européen de Recherche et de Formation Avancée en Calcul Scientifique **France**	**CNRM-CM6-1** **CNRM-CM6-1-HR**	(Voldoire et al., 2019; Saint-Martin et al., 2020)	1) Arpege 6.3; 2) **CM6-1 :** 140 km, 91L; **CM6-1-HR:** 50km, 91L 3) Top 78 km 4) (Roehrig et al., 2020)	1) TACTIC_v2 2 prescribed 3) (Michou et al., 2020)	1) OZL_V2 2) linear ozone	1) NEMO3.6 2) **CM6-1:** 70 km, 75L **CM6-1-HR:** 20 km, 75L 3) z	1) Gelato 6.1	1) ISBA-CTRIP 2) (Voldoire et al., 2017; Decharme et al., 2019)	none	none
CNRM and CERFACS	**CNRM-ESM2-1**	(Séférian et al., 2019)	1) Arpege 6.3; 2) 140 km, 91L; 3) Top 78 km	1) TACTIC_v2 2) emission-driven 3) (Michou et al., 2020)	1) REPROBUS-C-V2 2) Stratosphere only (above 560hPa)	1) NEMO3.6 2) 70 km, 75L 3) z	1) Gelato 6.1	1) ISBA-CTRIP 2) (Delire et al., 2020)	Land carbon Fires	Pisces 2.s (Aumont et al., 2015; Séférian et al., 2020)
CSIRO Commonwealth Scientific and Industrial Research	**ACCESS-ESM1-5**	(Ziehn et al., 2020)	1) HadGAM2 r1.1 2) 140 km, 38L 3) Top 39 km	1) CLASSIC (v1.0) 2) emission-driven 3) (Bellouin et	2) Specified oxidants for aerosols	1) ACCESS-OM2 GFDL-MOM5 2) 70 km, 50L 3) z	1) CICE4.1	1) CABLE2.4 2) (Ziehn et al., 2020)	Land carbon N cycle	Wombat1.0

ACCEPTED VERSION SUBJECT TO FINAL EDITING

Organisation **Australia**				al., 2011)		4) (Kiss et al., 2020)				
CSIRO-ARCCSS CSIRO and Austr. Res. Council Centre of Excellence for Climate System Science **Australia**	**ACCESS-CM2**	(Bi et al., 2020)	1) HadGEM3-GA7.1 2) 140 km, 85L 3) Top 85 km	1) UKCA-GLOMAP-mode 2) emission-driven 3) (Mulcahy et al., 2020)	2) Specified oxidants for aerosols	ACCESS-OM2 GFDL-MOM5 2) 70 km, 50L 3) z 4) (Kiss et al., 2020)	1) CICE5.1.2 (Ridley et al., 2018a)	1) CABLE2.5 2) (Bi et al., 2020)	none	none
E3SM National laboratories consortium **U.S.A**	**E3SM 1.0** **E3SM-1-1** **E3SM-1-1-ECA**	(Golaz et al., 2019)	1) E3M v1.0 2) 100 km, 72L; 3) Top 66 km 4) (Rasch et al.)	1) MAM4 2) emission-driven 3) (Wang et al., 2020)	2) Specified oxidants for aerosols ; linear interactive stratospheric ozone (LINOZ v2)	1) MPAS-Ocean v6.0 2) 40 km, 60L 3) z* 4) (Petersen et al., 2019)	1) MPAS-Seaice v6.0	1) ELM v1.0, based on CLM4.5 2) **E3SM-1.0:** (Golaz et al., 2019) **E3SM-1.1**: (Burrows et al., 2020)	**ES3M 1.0**: none **ES3M1.1**: Land carbon, N cycle, Fires	none
EC-Earth consortium **Europe**	**EC-Earth3** **EC-Earth3-LR** **Options:** **AerChem,** **Veg**	(Döscher et al., 2021)	**1**) IFS cy36r4 **2) EC-Earth3:** 80 km, 91L; **EC-Earth3-LR:** 120 km, 62L 3) **EC-Earth3:** Top 80 km **EC-Earth3-LR:** Top 36 km	**EC-Earth3** 2) Prescribed, MACv2-SP **AerChem:** 1)TM5 2) emission-driven 3)(van Noije et al., 2014, 2020)	**EC-Earth3** none **AerChem :** 1) TM5 2) interactive 3) (van Noije et al., 2014, 2020)	**NEMO3.6** 2) 70 km, 75L 3) z	1) LIM3 (Rousset et al., 2015)	**EC-Earth3** 1) H-TESSEL 2) (Balsamo et al., 2009) **Veg**: 1) H-TESSEL and LPJ-GUESS 2) (Smith et al., 2014)	**EC-Earth3** none **Veg:** N cycle Prog. Veg Fires	none
EC-Earth	**EC-Earth3-CC**	(Döscher et al., 2021)	**1**) IFS cy36r4 **2)** 80 km, 91L; 3) Top 80 km	2) prescribed, MACv2-SP	none	**NEMO3.6** 2) 70 km, 75L 3) z	1) LIM3 (Rousset et al., 2015)	1) H-TESSEL and LPJ-GUESS 2)) (Smith et al., 2014)	Land carbon N cycle Prog. Veg Fires	PISCES v2
FIO-QNLM First Institute of Oceanography , and Pilot National Laboratory for Marine Science and Technology (Qingdao), **China**	**FIO-ESM-2-0**	(Bao et al., 2020)	1) CAM5 2) 100km, 26L 3) Top 43 km	2) prescribed MACv2-SP (Stevens et al., 2017)	none	POP-W with MASNUM surface wave model 2) 60 km, 60L 3) z 4) (Qiao et al., 2013)	1) CICE4.0 (Hunke and Lipscomp, 2008)	1) CLM4.0 2) (Lawrence et al., 2011)	Land carbon N cycle	BEC

ACCEPTED VERSION SUBJECT TO FINAL EDITING

HAMMOZ-Consortium Switzerland, Germany, UK, Finland	**MPI-ESM-1-2-HAM**	(Neubauer et al., 2019)	1) ECHAM6.3 2) 170 km, 47L 3) Top 80 km	1) HAM2.3 2) emission-driven 3) (Tegen et al., 2019)	2) Specified oxidants, sulfur chemistry 3)(Feichter et al., 1996; Inness et al., 2013)	1) MPIOM 1.63 2) 100 km, 40L 3) z	**1)** (Notz et al., 2013a)	1) JSBACH3.20 2) (Reick et al., 2021)	Land carbon N Cycle Prog. Veg. Fires	HAMOCC6
INM Institute for Numerical Mathematics **Russia**	**INM-CM4-8** **INM-CM5-0**	INM-CM4-8: (Volodin Evgenii M et al., 2018) INM-CM5-0: (Volodin et al., 2017)	**CM4:** 1) INM-AM4-8 : 2) 150 km, 21L 3) Top 31 km **CM5**: 1) INM-AM5.0 2) 150 km, 73L 3) Top 61 km	1) INM-AER1 2) emission-driven 3) (Volodin and Kostrykin, 2016)	none	INM-OM5 2) **CM4**: 70 km, 40L **CM5**: 30 km, 40L 3) sigma 4) (Zalesny et al., 2010)	1) INM-ICE1 (Yakovlev, 2009)	INM-LND1	Land carbon	none
IPSL Institut Pierre-Simon Laplace **France**	**IPSL-CM6A-LR**	(Boucher et al., 2020)	1) LMDZ NPv6 2) 160 km, 79L 3) Top 80 km (Hourdin et al., 2020)	2) prescribed 3) (Lurton et al., 2020)	2) specified oxidants for aerosols	1) NEMO 3.6 2) 70 km, 75L 3) z	1) NEMO-LIM3 (Rousset et al., 2015)	ORCHIDEE (v2.0, Water/Carbon/Energy mode)	none	PISCES
IPSL	**IPSL-CM5A2-INCA**		1) LMDZ APv5 2) 240 km, 79L, 3) Top 80 km (Hourdin et al., 2020)	1) INCA 2) emission-driven	1) INCA 2) interactive 3) (Hauglustaine et al., 2014)	1) NEMO 3.6 2) 150 km, 30L 3) z	1) NEMO-LIM3 (Rousset et al., 2015)	ORCHIDEE (IPSLCM5A2.1, Water/Carbon/Energy mode)	Land carbon	PISCES
KIOST Korea Institute of Ocean Science & Technology **Korea**	**KIOST-ESM**	(Pak et al., 2021)	1) GFDL-AM2.0 2) 190 km, 32L 3) Top 43 km 4) (Anderson et al., 2004)	1) GFDL-AM2.0 2) emission-driven 3) (Anderson et al., 2004)	none	1) GFDL-MOM5.0 2) 90km, 52L 3) z	1) GFDL-SIS	GFDL-LM3.0 (Milly et al., 2014)	Land Carbon N cycle Prog.Veg.	TOPAZ2
MIROC consortium JAMSTEC, AORI, NIES, R-CCS **Japan**	**MIROC-ES2L** **MIROC-ES2H** **MIROC6**	**ES2L:** (Hajima et al., 2020) **ES2H :** (Kawamiya et al., 2020) **MIROC6**: (Tatebe et al., 2019)	**ES2L**: 1) CCSR AGCM 2) 250 km, 40L; 3) Top 40 km **ES2H, MIROC6:** 1) CCSR AGCM 2) 120 km, 81L; 3) Top 80 km	1) SPRINTARS 2) emission-driven 3) (Takemura et al., 2000, 2005, 2009)	**ES2L, MIROC6:** 2) prescribed oxidants **ES2H**: 1) CHASER 2) interactive 3) (Sudo et al., 2002b, 2002a; Morgenstern et al., 2017)	1) COCO4.9 2) 80 km, 63L 3) z	1) COCO4.9	**MIROC6:** MATSIRO6.0 (Takata et al., 2003; Nitta et al., 2014, 2017) **ES2L & ES2H** MATSIRO6.0 And visit-e ver 1.0 (Hajima et al., 2020)	**MIROC6:** none **ES2L & ES2H** Land carbon N cycle	OECO v2.0
MOHC Met Office Hadley Centre **U.K.**	**HADGEM3-GC31-LL** **HADGEM3-GC31-MM**	(Williams et al., 2018) (Kuhlbrodt et al., 2018) (Sellar et al., 2019)	1) MetUM-HadGEM3-GA7.1 2) **LL**: 140 km, 85L **MM**: 60 km, 85L 3) Top 85 km	1) UK-GLOMAP 2) emission-driven 3) (Mulcahy et al., 2020)	none	1) NEMO-HadGEM3-GO6.0 2) **LL** : 70 km, 75L **MM**:20 km, 75L	1) CICE HadGEM3-GSI8 (Ridley et al., 2018b)	JULES-HadGEM3-GL7.1	none	none

ACCEPTED VERSION SUBJECT TO FINAL EDITING

						3) z				
MOHC	**UK-ESM1.0-LL**	(Sellar et al., 2019)	1) MetUM-HadGEM3-GA7.1 2) 140 km, 85L 3) Top 85 km	1) UK-GLOMAP 2) emission-driven 3) (Mulcahy et al., 2020)	1) UKCA-StratTrop 3) (Archibald et al., 2020)	1) NEMO-HadGEM3-GO6.0 2) 70 km, 75L 3) z	1) CICE HadGEM3-GSI8 (Ridley et al., 2018b)	JULES-HadGEM3-GL7.1 (Sellar et al., 2019; Wiltshire et al., 2020)	Land carbon N cycle Prog. Veg	MEDUSA2
MPI-M Max Planck Institute for Meteorology **Germany**	**MPI-ESM1-2-LR** **MPI-ESM1-2-HR**	**MPI-ESM** (Mauritsen et al., 2019) **MPI-ESM1-2-HR** (Müller et al., 2018)	1) ECHAM6.3 2) **LR:** 170 km, 47L **HR:** 80 km 95L 3) Top 80 km	2) prescribed MACv2-SP	none	**1)** MPIOM 1.63 **2)** **LR:**100 km, 40L **HR:** 40 km, 40L 3) z	1) (Notz et al., 2013b)	1) JSBACH3.20 2) (Reick et al., 2021)	**LR:** Land Carbon N cycle Prog. Veg. Fires **HR:** none	HAMOCC6
MRI Meteorological Research Institute **Japan**	**MRI-ESM-2.0**	**MRI-ESM-2.0** (Yukimoto et al., 2019) (Mizuta et al., 2012)	**1)** MRI-AGCM3.5 2) 100 km, 80L 3) Top 80 km	1) MASINGAR mk-2r4c 2) emission-driven 3) (Yukimoto et al., 2019; Oshima et al., 2020)	1) MRI-CCM2.1 2) interactive 3) (Deushi and Shibata, 2011)	**1)** MRI.COM4.4 2) 60 km, 61L 3) z 4) (Tsujino et al., 2017a)	**1)** MRI.COM4.4 (Tsujino et al., 2017b)	1) HAL 1.0 and MRI-LCCM2 2) (Obata and Shibata, 2012; Yukimoto et al., 2012; Obata and Adachi, 2019)	Land carbon Prog. veg. Fires	MRI.COM4.4 (Nakano et al., 2015)
NASA-GISS Goddard Institute for Space Studies **U.S.A.**	**GISS-E2-1-G** **GISS-E2-1-H** **GISS-E2.1-G-CC** **GISS-E2-2-G**	(Kelley et al., 2020) **GISS-E2-2-G:** (Rind et al., 2020)	**GISS-E2-1 :** 1) GISS-E2.1 2) 200 km, 40L 3) Top 66 km **GISS-E2-2-G :** 1) GISS-E2-2 2) 200km, 102L 3) Top 88 km	Varies with physics-version p1 p3 OMA, p5 MATRIX 3) (Bauer et al., 2020)	Varies with physics-version p1 None, p3, p5 GPUCCINI, interactive 3) (Shindell et al., 2006)	**GISS-E2-1-G, GISS-E2-2-G :** 1) GISS ocean 2) 100 km, 40L 3) z **GISS-E2-1-H :** 1) HYCOM 2) 70 km, 32L 3) hybrid	1) GISS-SI	1) GISS-LSM	none	**GISS-E2-1-G-CC:** NOBM Others: none
NCAR National Center for Atmospheric Research **U.S.A.**	**CESM2** **CESM2-FV2** **CESM2-WACCM** **CESM2-WACCM-FV2**	(Danabasoglu et al., 2020)	1) CAM6 **2) CESM2:** 100 km **FV2 variants**: 190 km 3) **CESM2:** 32L, Top 42 km **WACCM variants:** 70L, Top 80 km.	1) MAM4 2) emission-driven 3) (Liu et al., 2016)	**CESM2:** 2) prescribed oxidants **WACM variants**: 2) interactive 3) (Emmons et al., 2020)	1) POP2 2) 60 km, 60L 3) z	1) CICE5.1, (Hunke et al., 2015) 2) CISM2.1, (Lipscomb et al., 2019)	1) CLM5 **2)** (Lawrence et al., 2019)	Land carbon N cycle Permafrost Fires	MARBL, Moore et. al, 2013
NCC NorESM Climate Modelling Consortium **Norway**	**NorCPM1** **NorESM1-F**	**NorESM1-F:** (Guo et al., 2019)	1) CAM4 2) 190 km, 26L 3) Top 43 km	**NorCPM1:** 1) OsloAero4.1 2) emission-driven 3) **NorESM1-F:** 2) prescribed	**NorCPM1 :** 1) OsloAero4.1 2) prescribed oxidants for aerosols **NorESM1-F:** none	1) MICOM1.1 2) 60 km, 53L 3) isopycnal	1) CICE4	1) CLM4	Land carbon N cycle Fires	HAMOCC5.1 (Tjiputra et al., 2013; Schwinger et al., 2016)

ACCEPTED VERSION SUBJECT TO FINAL EDITING

NCC **NorESM2-LM** **NorESM2-MM**	**NorESM2:** (Seland et al., 2020)	1) CAM6-Nor 2) **NorESM2-LM:** 190 km, 32L **NorESM2-MM:** 100km, 32L 3) Top 40 km	1) OsloAero6 2) emission-driven 3) (Kirkevåg et al., 2018; Seland et al., 2020)	1) OsloAero6 2) prescribed oxidants, interactive sulfur chemistry, SOA precursor chemistry	1) BLOM1.0 2) 60 km, 70L 3) isopycnal;	**1)** CICE5.1	1) CLM5	Land carbon N cycle Permafrost Fires	iHAMOCC (Tjiputra et al., 2020)
NIMS-KMA National Institute of Meteorological Sciences, Korea Meteorological Administration**,** **Korea**	**KACE-1-0-G**	(Lee et al., 2019)	1) MetUM-HadGEM3-GA7.1 2) 140 km, 85L 3) Top 85 km	1) UKCA-GLOMAP-mode 2) emission-driven	2) specified oxidants for aerosols	**1)** MOM4p1 2) 90 km, 50L 3) z	1) CICE-HadGEM3-GSI8	JULES-HadGEM3-GL7.1	none	none
NOAA-GFDL National Oceanic and Atmospheric Administration, Geophysical Fluid Dynamics Laboratory **U.S.A.**	**GFDL-CM4**	(Held et al., 2019)	1) GFDL-AM4.0.1 2) 100 km, 33L 3) Top 48 km (Zhao et al., 2018a, 2018c)	1) GFDL-AM4.0.1; 2) emission-driven 3) (Zhao et al., 2018a, 2018c)	1) GFDL-AM4.0.1; 2) specified oxidants, fast chemistry, aerosol only	1) GFDL-OM4p25 (GFDL-MOM6); **2)** 20 km, 75L 3) hybrid; 4) (Adcroft et al., 2019a)	1) GFDL-SIM4p25 (GFDL-SIS2.0); (Adcroft et al., 2019b)	GFDL-LM4.0.1 (Zhao et al., 2018b, 2018d)	Land carbon Prog. Veg. Fires	GFDL-BLINGv2 (Dunne et al., 2020a)
NOAA-GFDL	**GFDL-ESM4**	(Dunne et al., 2020b)	1) GFDL-AM4.1; 2) 100 km, 49L 3) Top 80 km 4) (Horowitz et al., 2020)	1) GFDL-AM4.1 2) emission-driven 3) (Horowitz et al., 2020)	1) GFDL-ATMCHEM4.1; 2) interactive 3) (Horowitz et al., 2020)	GFDL-OM4p5 (GFDL-MOM6); 2) 40 km, 75L 3) hybrid 4) (Adcroft et al., 2019a)	1) GFDL-SIM4p5 (GFDL-SIS2.0); (Adcroft et al., 2019a)	GFDL-LM4.1	Land carbon Prog. Veg. Fires	GFDL-COBALTv2 (Stock et al., 2020)
NUIST Nanjing University of Information Science and Technology **China**	**NESM3**	(Cao et al., 2018)	1) ECHAM v6.3 2) 170 km, 47L 3) Top 48 km	2) prescribed	none	1) NEMO v3.4 2) 70 km, 46L 3) z	1) CICE 4.1	JSBACH v3.1	Land carbon Prog. Veg.	none
SNU Seoul National University **Korea**	**SAM0-UNICON**	(Park et al., 2019)	**1)** CAM5.3 with UNICON 2) 100 km 30L 3) Top 43 km	1) MAM3 2) emission-driven 3) (Liu et al., 2012b)	none	1) POP2 2) 60 km, 60L 3) z	1) CICE4.0	CLM 4.0	Land carbon N cycle Fires	none
THU Department of Earth System Science **China**	**CIESM**	(Lin et al., 2020b)	1) CIESM-AM 2) 100 km, 30L 3) Top 42 km	2) Prescribed MACv2-SP 3) (Stevens et al., 2017)	none	1) CIESM-OM 2) 60 km, 46L 3) z	1) CICE4	CIESM-LM (modified CLM4.0)	none	none

ACCEPTED VERSION SUBJECT TO FINAL EDITING

University of Arizona (U.S.A.)	**MCM-UA-1-0**	(Delworth et al., 2002)	1) Manabe R30L14 2) 260 km, 14L 3) Top 29 km	none	none	**1)** MOM1.0 2) 190 km, 18L 3) z	1) thermo-dynamic simplified sea ice	Manabe bucket scheme (Manabe, 1969)	none	none

[END TABLE AII.5 HERE]

ACCEPTED VERSION
SUBJECT TO FINAL EDITING

[START TABLE AII.6 HERE]

Table AII.6: High resolution coupled models participating in HighResMIP. Full names of the institutions are found in table AII.5. The horizontal resolution (rounded to 10 km, when larger than 10 km) is the square root of the number of grid points divided by the surface area of the Earth, or the number of surface ocean grid points divided by the area of the ocean surface, for the atmosphere and ocean respectively. When reported in hPa, the atmosphere top heights are converted into km assuming standard atmosphere (ISO 2533:1975, 1975).

Institution	**Model**	**Reference**	**Atmosphere top**	**Atmosphere resolution** *Horizontal (km), Number of vertical levels*	**Ocean resolution** *Horizontal (km), Number of vertical levels*
AWI	AWI-CM-1-1-HR	(Sein et al., 2017, 2018)	80 km	80 km, N=95	20 km, N=46
BCC	BCC-CSM2-HR	(Wu et al., 2020a)	66 km	40 km, N=56	20 km, N=40
CAS	FGOALS-f3-H		42 km	20 km, N=32	8 km, N=55
CMCC	CMCC-CM2-HR4	(Scoccimarro et al., 2020; Bellucci et al., 2021)	43 km	100 km, N=26	20 km, N=50
	CMCC-CM2-VHR4		43 km	20 km, N=26	20 km, N=50
CNRM	CNRM-CM6-1-HR	(Saint-Martin et al., 2020)	78 km	50 km, N=91	20 km, N=75
EC-Earth	EC-Earth3P-HR	(Haarsma et al., 2020)	80 km	40 km, N=91	20 km, N=75
ECMWF	ECMWF-IFS-MR	(Roberts et al., 2018)	80 km	60 km, N=91	20 km, N=75
	ECMWF-IFS-HR		80 km	30 km, N=91	20 km, N=75
INM	INM-CM5-H		61 km	50 km, N=73	10 km, N=40
MOHC	HadGEM3-GC31-MH	(Roberts et al., 2019)	85 km	60 km, N=85	7 km, N=75
	HadGEM3-GC31-HM		85 km	30 km, N=85	20 km, N=75
	HadGEM3-GC31-HH		85 km	30 km, N=85	7 km, N=75
MPI	MPI-ESM1-2-HR	(Gutjahr et al., 2019)	80 km	80 km, N=95	40 km, N=40
	MPI-ESM1-2-XR		80 km	40 km, N=95	40 km, N=40
NCAR	CESM1-CAM5-SE-HR	(Small et al., 2014; Meehl et al., 2019; Chang et al., 2020)	42 km	30 km, N=30	8 km, N=62
NOAA-GFDL	GFDL-CM4C192	(Zhao, 2020)	48 km	50 km, N=33	20 km, N=75

[END TABLE AII.6 HERE]

ACCEPTED VERSION SUBJECT TO FINAL EDITING

AII.3 Models used in Ice sheet and glacier model intercomparison studies

Ice sheet and glacier models are used to assess the contribution of ice sheets and glaciers to future sea level rise as described in Section 9.6.3. New to AR6, the projections of the future sea level contribution from ice sheets and glaciers comes from the ensemble of model intercomparison studies (Box 9.3; Section 9.4.1.2; Section 9.4.2.2; Section 9.5.1.3). The tables here describe the models used for Greenland ISMIP6 (Table AII.7), Antarctica ISMIP6 and LARMIP-2 (Table AII.8) and GlacierMIP (Table AII.9).

More specific information on the model capabilities and parameter choices used for each ice sheet and glacier MIPs are presented in the following papers: ISMIP6 initMIP-Greenland (Goelzer et al., 2018), ISMIP6 projection-Greenland (Goelzer et al., 2020), ISMIP6 initMIP-Antarctica (Seroussi et al., 2019), ISMIP6 Antarctica projection (Seroussi et al., 2020), LARMIP-2 Antarctica projections (Levermann et al., 2020), and GlacierMIP (Hock et al., 2019; Marzeion et al., 2020).

[START TABLE AII.7 HERE]

Table AII.7: Models used in Greenland model intercomparison studies (initMIP and/or ISMIP6 projections)

Institution **Full name** **Country**	**Model**	**Reference**	**Resolution** (min-max) (km)	**MIP activity**
AWI Alfred-Wegener-Institut Helmholtz-Zentrum für Polar- und Meeresforschung, and University of Bremen **Germany**	AWI-ISSM	(Larour et al., 2012) (Rückamp et al., 2020)	0.75-7.5	initMIP ISMIP6
BGC Bristol Glaciology Center **UK**	BGC-BISICLES	(Lee et al., 2015) (Cornford et al., 2013)	1.2-4.8	initMIP ISMIP6
DMI Danish Meteorological Institute **Denmark**	DMI-PISM	(Bueler and Brown, 2009) (Aschwanden et al., 2016)	5	initMIP
GSFC Goddard Space Flight Center NASA **U.S.A.**	GSFC-ISSM	(Larour et al., 2012)	0.5-25	ISMIP6
IGE Institut des Géosciences de L'Environnement **France**	IGE-ELMER	(Gillet-Chaulet et al., 2012)	1-4.5	initMIP
ILTSPIK Institute of Low Temperature Science **Japan** Potsdam Institute for Climate Impact Research **Germany**	ILTSPIK-SICOPOLIS	(Greve and Blatter, 2016) (Greve and SICOPOLIS Developer Team, 2019) (Greve et al., 2020)	5	initMIP ISMIP6
IMAU Institute for Marine and Atmospheric research **The Netherlands**	IMAUICE	(de Boer et al., 2014)	8-16	initMIP ISMIP6
JPL Jet Propulsion Laboratory **U.S.A**	JPL-ISSM	(Larour et al., 2012) (Seroussi et al., 2013)	0.25 – 15	initMIP ISMIP6
JPL Jet Propulsion Laboratory	JPL-ISSMPALEO	(Larour et al., 2012)	3 – 30	initMIP ISMIP6

ACCEPTED VERSION SUBJECT TO FINAL EDITING

U.S.A		(Cuzzone et al., 2018)		
LSCE Laboratoire des Sciences du Climat et de l'Environnement **France**	LSCE-GRISLI	(Quiquet et al., 2018)	5	initMIP ISMIP6
MIROC Japan Agency for Marine-Earth Science and Technology The University of Tokyo **Japan**	MIROC-IcIES	(Saito et al., 2016)	10	initMIP
MPIM Max Planck Institute for Meteorology **Germany**	MPIM-PISM	(Bueler and Brown, 2009) (Aschwanden et al., 2016)	5	initMIP
MUN Memorial University of Newfoundland **Canada**	MUN-GSM	(Tarasov and Peltier, 1999) (Tarasov and Peltier, 2003)	5-14	ISMIP6
NCAR National Center for Atmospheric Research **U.S.A**	NCAR-CISM	(Lipscomb et al., 2019)	4	initMIP ISMIP6
UAF University of Alaska Fairbanks **U.S.A**	UAF-PISM	(Bueler and Brown, 2009) (Aschwanden et al., 2016)	0.9	initMIP ISMIP6
UCIJPL University of California Irvine Jet Propulsion Laboratory **U.S.A**	UCIJPL-ISSM	(Larour et al., 2012) (Morlighem et al., 2010)	0.2-30	initMIP ISMIP6
ULB Université Libre de Bruxelles **Belgium**	ULB-FETISH	(Pattyn, 2017)	10	initMIP
VUB Vrije Universiteit Brussel **Belgium**	VUB-GISM	(Huybrechts, 2002) (Fürst et al., 2015)	5	initMIP ISMIP6
VUW Victoria University of Wellington **New Zealand**	VUW-PISM	(Bueler and Brown, 2009) (Golledge et al., 2019)	2	initMIP ISMIP6

[END TABLE AII.7 HERE]

[START TABLE AII.8 HERE]

Table AII.8: Models used in Antarctica model intercomparison studies (initMIP and/or ISMIP6 projections and/or LARMIP-2 projections)

Institution **Full name** **Country**	**Model**	**Reference**	**Resolution** (min-max) (km)	**MIP activity**
AWI Alfred-Wegener-Institut Helmholtz-Zentrum für Polar- und Meeresforschung, and	AWI-PISM	(Bueler and Brown, 2009) (Winkelmann et al., 2011)	8-16	initMIP ISMIP6 LARMIP-2

ACCEPTED VERSION SUBJECT TO FINAL EDITING

University of Bremen **Germany**				
LBL Lawrence Berkeley National Laboratory, **U.S.A** Swansea University, **UK**	LBL-BISICLES	(Cornford et al., 2013) (Cornford et al., 2015)	0.5-8	initMIP ISMIP6 LARMIP-2
DOE Los Alamos National Laboratory **U.S.A**	DOE-MALI	(Hoffman et al., 2018)	2-20	initMIP ISMIP6 LARMIP-2
DMI Danish Meteorological Institute **Danmark**	DMI-PISM	(Bueler and Brown, 2009)	5-16	initMIP LARMIP-2
IGE Institut des Géosciences de L'Environnement **France**	IGE-ELMER	(Gillet-Chaulet et al., 2012)	1-4.5	initMIP
ILTSPIK Institute of Low Temperature Science **Japan** Potsdam Institute for Climate Impact Research **Germany**	ILTSPIK-SICOPOLIS	(Greve and Blatter, 2016) (Greve and SICOPOLIS Developer Team, 2019) (Greve et al., 2020)	8	initMIP ISMIP6 LARMIP-2
IMAU Institute for Marine and Atmospheric research **The Netherlands**	IMAUICE	(de Boer et al., 2014)	32	initMIP ISMIP6 LARMIP-2
JPL Jet Propulsion Laboratory **U.S.A**	JPL-ISSM	(Larour et al., 2012) (Seroussi et al., 2013)	2-50	initMIP ISMIP6 LARMIP-2
LSCE Laboratoire des Sciences du Climat et de l'Environnement **France**	LSCE-GRISLI	(Quiquet et al., 2018)	16	initMIP ISMIP6 LARMIP-2
NCAR National Center for Atmospheric Research **U.S.A**	NCAR-CISM	(Lipscomb et al., 2019)	4	initMIP ISMIP6 LARMIP-2
PIK Potsdam Institute for Climate Impact Research **Germany**	PIK-PISM	(Winkelmann et al., 2011)	4-8	initMIP ISMIP6 LARMIP-2
PSU Pennsylvania State University **U.S.A**	PSUICE3D	(Pollard and DeConto 2012) (Pollard et al., 2015)	16	initMIP LARMIP-2
UCIJPL University of California Irvine Jet Propulsion Laboratory **U.S.A**	UCIJPL-ISSM	(Larour et al., 2012) (Morlighem et al., 2010)	3-50	initMIP ISMIP6 LARMIP-2
ULB Université Libre de Bruxelles **Belgium**	ULB-FETISH	(Pattyn, 2017)	16-32	initMIP ISMIP6 LARMIP-2
UNN University of Northumbria **UK**	UNN-UA	(Gudmundsson et al., 2012)	1-40	LARMIP-2

ACCEPTED VERSION SUBJECT TO FINAL EDITING

UTAS University of Tasmania, **Australia** University of Lapland, **Finland** CSC-IT Center for Science, **Finland**	UTAS-ELMER	(Gillet-Chaulet et al., 2016)	4-40	ISMIP6
VUB Vrije Universiteit Brussel **Belgium**	VUB-AISPALEO	(Huybrechts, 2002)	20	initMIP ISMIP6 LARMIP-2
VUW Victoria University of Wellington **New Zealand**	VUW-PISM	(Bueler and Brown, 2009) (Golledge et al., 2019)	16	initMIP ISMIP6 LARMIP-2

[END TABLE AII.8 HERE]

[START TABLE AII.9 HERE]

Table AII.9: Models used in the GlacierMIP2 model intercomparison.

Institution Full name, Country	**Model name**	**Reference**	**Resolution** (km)	**Domain** (global/regional)
Nagoya University, **Japan**	GLIMB	(Sakai and Fujita, 2017)	0.5° grid and 50 m elevation bands for mass balance, each glacier for geometry change	Global
ETH Zurich, **Switzerland** University of Fribourg, **Switzerland** University of Alaska Fairbanks, **USA** Uppsala University, **Sweden**	GloGEM	(Huss and Hock, 2015)	Each glacier, 10m elevation bands	Global
University of British Columbia, **Canada** University of Alaska Fairbanks, **USA** Scott Polar Research Institute, **UK** Trent University, **Canada**	RAD2014	(Radić et al., 2014)	Each glacier, 20-25 m elevation bands	Global
Utrecht University, **Netherlands** ETH Zurich, **Switzerland**	WAL2001	(Van de Wal and Wild, 2001)	Each glacier	Global
University of Exeter, **UK** University of Bristol, **UK** University of Reading, **UK** Met Office, **UK** University of Fribourg, **Switzerland** ETH Zurich, **Switzerland** University of Crete, **Greece** University of Exeter, **UK**	JULES	(Shannon et al., 2019)	0.5° grid, 250 m elevation bands	Global except Antarctica
University of Innsbruck,	MAR2012	(Marzeion et al.,	Each glacier, considering	Global except

ACCEPTED VERSION SUBJECT TO FINAL EDITING

Austria		2012)	elevation range	Antarctica
University of Innsbruck, **Austria** University of Bremen, **Germany** University of Grenoble Alpes, **France** ETH Zurich, **Switzerland** WSL, **Switzerland** University of Natural Resources and Life Sciences, **Austria** University of Canterbury, **New Zealand**	OGGM	(Maussion et al., 2019)	Each glacier, 20 - 400 m spacing of grid points on flow line	Global except Antarctica
Utrecht University, **Netherlands** FutureWater, **Netherlands** ICIMOD, **Nepal**	KRA2017	(Kraaijenbrink et al., 2017)	Each glacier, variable elevation bands	High Mountain Asia
University of Alaska Fairbanks, **USA** University of Washington, **USA**	PyGEM	(Rounce et al., 2020)	Each glacier, 20 m elevation bands	High Mountain Asia
Victoria University of Wellington, **New Zealand**	AND2012	(Anderson and Mackintosh, 2012)	100 m	New Zealand
ETH Zurich, **Switzerland** WSL, **Switzerland** University of Fribourg, **Switzerland**	GloGEMflow	(Zekollari et al., 2019)	Each glacier, 10 - 202 m spacing of grid points on flow line	Central Europe

[END TABLE AII.9 HERE]

AII.4 CMIP model datasets used in the report

[START TABLE AII.10 HERE]

Table AII.10: List of CMIP6 model datasets used in this report

Institute: Model	Activity ID	Data citation and DOI Link
AER:LBLRTM-12-8	RFMIP	Mlawer et al. (2019), https://doi.org/10.22033/ESGF/CMIP6.2003
AER:RRTMG-LW-4-91	RFMIP	Mlawer et al. (2020), https://doi.org/10.22033/ESGF/CMIP6.9961
AER:RRTMG-SW-4-02	RFMIP	Mlawer et al. (2020), https://doi.org/10.22033/ESGF/CMIP6.9963
AS-RCEC:HiRAM-SIT-HR	HighResMIP	Tu (2020), https://doi.org/10.22033/ESGF/CMIP6.13301
AS-RCEC:HiRAM-SIT-LR	HighResMIP	Tu (2020), https://doi.org/10.22033/ESGF/CMIP6.13303
AS-RCEC:TaiESM1	AerChemMIP	Tsai et al. (2020), https://doi.org/10.22033/ESGF/CMIP6.9682
AS-RCEC:TaiESM1	CFMIP	Shiu et al. (2020), https://doi.org/10.22033/ESGF/CMIP6.9683
AS-RCEC:TaiESM1	CMIP	Lee et al. (2019), https://doi.org/10.22033/ESGF/CMIP6.9684
AS-RCEC:TaiESM1	GMMIP	Wang et al. (2020), https://doi.org/10.22033/ESGF/CMIP6.9685
AS-RCEC:TaiESM1	PAMIP	Hong et al. (2020), https://doi.org/10.22033/ESGF/CMIP6.15214

ACCEPTED VERSION SUBJECT TO FINAL EDITING

AS-RCEC:TaiESM1	ScenarioMIP	Lee et al. (2020), https://doi.org/10.22033/ESGF/CMIP6.9688
AWI:AWI-CM-1-1-HR	HighResMIP	Semmler et al. (2017), https://doi.org/10.22033/ESGF/CMIP6.1202
AWI:AWI-CM-1-1-LR	HighResMIP	Semmler et al. (2017), https://doi.org/10.22033/ESGF/CMIP6.1209
AWI:AWI-CM-1-1-MR	CMIP	Semmler et al. (2018), https://doi.org/10.22033/ESGF/CMIP6.359
AWI:AWI-CM-1-1-MR	PAMIP	Semmler et al. (2019), https://doi.org/10.22033/ESGF/CMIP6.12021
AWI:AWI-CM-1-1-MR	ScenarioMIP	Semmler et al. (2019), https://doi.org/10.22033/ESGF/CMIP6.376
AWI:AWI-ESM-1-1-LR	CMIP	Danek et al. (2020), https://doi.org/10.22033/ESGF/CMIP6.9301
AWI:AWI-ESM-1-1-LR	PMIP	Shi et al. (2020), https://doi.org/10.22033/ESGF/CMIP6.9302
BCC:BCC-CSM2-HR	HighResMIP	Jie et al. (2020), https://doi.org/10.22033/ESGF/CMIP6.1722
BCC:BCC-CSM2-MR	C4MIP	Zhang et al. (2019), https://doi.org/10.22033/ESGF/CMIP6.1723
BCC:BCC-CSM2-MR	CFMIP	Zhang et al. (2019), https://doi.org/10.22033/ESGF/CMIP6.1724
BCC:BCC-CSM2-MR	CMIP	Xin et al. (2018), https://doi.org/10.22033/ESGF/CMIP6.1725
BCC:BCC-CSM2-MR	DAMIP	Xin et al. (2019), https://doi.org/10.22033/ESGF/CMIP6.1726
BCC:BCC-CSM2-MR	DCPP	Fang et al. (2019), https://doi.org/10.22033/ESGF/CMIP6.1727
BCC:BCC-CSM2-MR	GMMIP	Zhang et al. (2019), https://doi.org/10.22033/ESGF/CMIP6.1728
BCC:BCC-CSM2-MR	LS3MIP	Li et al. (2019), https://doi.org/10.22033/ESGF/CMIP6.1729
BCC:BCC-CSM2-MR	LUMIP	Zhang et al. (2019), https://doi.org/10.22033/ESGF/CMIP6.1730
BCC:BCC-CSM2-MR	ScenarioMIP	Xin et al. (2019), https://doi.org/10.22033/ESGF/CMIP6.1732
BCC:BCC-ESM1	AerChemMIP	Zhang et al. (2019), https://doi.org/10.22033/ESGF/CMIP6.1733
BCC:BCC-ESM1	CMIP	Zhang et al. (2018), https://doi.org/10.22033/ESGF/CMIP6.1734
CAMS:CAMS-CSM1-0	CMIP	Rong (2019), https://doi.org/10.22033/ESGF/CMIP6.1399
CAMS:CAMS-CSM1-0	GMMIP	Chinese Academy of Meteorological Sciences (CAMS) (2019), https://doi.org/10.22033/ESGF/CMIP6.11002
CAMS:CAMS-CSM1-0	HighResMIP	Rong (2020), https://doi.org/10.22033/ESGF/CMIP6.11003
CAMS:CAMS-CSM1-0	ScenarioMIP	Rong (2019), https://doi.org/10.22033/ESGF/CMIP6.11004
CAS:CAS-ESM2-0	CMIP	Chai (2020), https://doi.org/10.22033/ESGF/CMIP6.1944
CAS:CAS-ESM2-0	FAFMIP	Chai (2020), https://doi.org/10.22033/ESGF/CMIP6.1948
CAS:CAS-ESM2-0	OMIP	Chai (2020), https://doi.org/10.22033/ESGF/CMIP6.1954
CAS:FGOALS-f3-H	HighResMIP	Bao et al. (2019), https://doi.org/10.22033/ESGF/CMIP6.2041
CAS:FGOALS-f3-H	OMIP	Lin (2020), https://doi.org/10.22033/ESGF/CMIP6.13261
CAS:FGOALS-f3-L	CMIP	YU (2018), https://doi.org/10.22033/ESGF/CMIP6.1782
CAS:FGOALS-f3-L	GMMIP	He et al. (2019), https://doi.org/10.22033/ESGF/CMIP6.2043
CAS:FGOALS-f3-L	HighResMIP	Bao et al. (2019), https://doi.org/10.22033/ESGF/CMIP6.12001
CAS:FGOALS-f3-L	OMIP	Lin (2019), https://doi.org/10.22033/ESGF/CMIP6.2044
CAS:FGOALS-f3-L	PAMIP	He et al. (2019), https://doi.org/10.22033/ESGF/CMIP6.11497
CAS:FGOALS-f3-L	PMIP	Zheng et al. (2019), https://doi.org/10.22033/ESGF/CMIP6.12002
CAS:FGOALS-f3-L	ScenarioMIP	YU (2019), https://doi.org/10.22033/ESGF/CMIP6.2046
CAS:FGOALS-g3	CMIP	Li (2019), https://doi.org/10.22033/ESGF/CMIP6.1783
CAS:FGOALS-g3	DAMIP	Li (2020), https://doi.org/10.22033/ESGF/CMIP6.2048
CAS:FGOALS-g3	FAFMIP	Lin (2020), https://doi.org/10.22033/ESGF/CMIP6.2050

ACCEPTED VERSION
SUBJECT TO FINAL EDITING

CAS:FGOALS-g3	GMMIP	Li (2020), https://doi.org/10.22033/ESGF/CMIP6.2051
CAS:FGOALS-g3	LS3MIP	Jia et al. (2020), https://doi.org/10.22033/ESGF/CMIP6.2052
CAS:FGOALS-g3	PMIP	Zheng et al. (2019), https://doi.org/10.22033/ESGF/CMIP6.2054
CAS:FGOALS-g3	ScenarioMIP	Li (2019), https://doi.org/10.22033/ESGF/CMIP6.2056
CCCR-IITM:IITM-ESM	CMIP	AG et al. (2019), https://doi.org/10.22033/ESGF/CMIP6.44
CCCR-IITM:IITM-ESM	GMMIP	AG et al. (2019), https://doi.org/10.22033/ESGF/CMIP6.825
CCCR-IITM:IITM-ESM	ScenarioMIP	Panickal et al. (2020), https://doi.org/10.22033/ESGF/CMIP6.14741
CCCma:CanESM5	C4MIP	Swart et al. (2019), https://doi.org/10.22033/ESGF/CMIP6.1301
CCCma:CanESM5	CDRMIP	Swart et al. (2019), https://doi.org/10.22033/ESGF/CMIP6.10201
CCCma:CanESM5	CFMIP	Cole et al. (2019), https://doi.org/10.22033/ESGF/CMIP6.1302
CCCma:CanESM5	CMIP	Swart et al. (2019), https://doi.org/10.22033/ESGF/CMIP6.1303
CCCma:CanESM5	DAMIP	Swart et al. (2019), https://doi.org/10.22033/ESGF/CMIP6.1305
CCCma:CanESM5	DCPP	Sospedra-Alfonso et al. (2019), https://doi.org/10.22033/ESGF/CMIP6.1306
CCCma:CanESM5	FAFMIP	Swart et al. (2019), https://doi.org/10.22033/ESGF/CMIP6.1308
CCCma:CanESM5	GMMIP	Swart et al. (2019), https://doi.org/10.22033/ESGF/CMIP6.1309
CCCma:CanESM5	GeoMIP	Cole et al. (2019), https://doi.org/10.22033/ESGF/CMIP6.1310
CCCma:CanESM5	LUMIP	Swart et al. (2019), https://doi.org/10.22033/ESGF/CMIP6.1313
CCCma:CanESM5	OMIP	Swart et al. (2019), https://doi.org/10.22033/ESGF/CMIP6.1314
CCCma:CanESM5	PAMIP	Sigmond et al. (2019), https://doi.org/10.22033/ESGF/CMIP6.13942
CCCma:CanESM5	RFMIP	Cole et al. (2019), https://doi.org/10.22033/ESGF/CMIP6.1315
CCCma:CanESM5	ScenarioMIP	Swart et al. (2019), https://doi.org/10.22033/ESGF/CMIP6.1317
CCCma:CanESM5	VolMIP	Cole et al. (2019), https://doi.org/10.22033/ESGF/CMIP6.10202
CCCma:CanESM5-CanOE	C4MIP	Swart et al. (2019), https://doi.org/10.22033/ESGF/CMIP6.10203
CCCma:CanESM5-CanOE	CDRMIP	Swart et al. (2019), https://doi.org/10.22033/ESGF/CMIP6.10204
CCCma:CanESM5-CanOE	CMIP	Swart et al. (2019), https://doi.org/10.22033/ESGF/CMIP6.10205
CCCma:CanESM5-CanOE	OMIP	Swart et al. (2019), https://doi.org/10.22033/ESGF/CMIP6.10206
CCCma:CanESM5-CanOE	ScenarioMIP	Swart et al. (2019), https://doi.org/10.22033/ESGF/CMIP6.10207
CMCC:CMCC-CM2-HR4	CMIP	Scoccimarro et al. (2020), https://doi.org/10.22033/ESGF/CMIP6.1358
CMCC:CMCC-CM2-HR4	HighResMIP	Scoccimarro et al. (2017), https://doi.org/10.22033/ESGF/CMIP6.1359
CMCC:CMCC-CM2-HR4	OMIP	Fogli et al. (2020), https://doi.org/10.22033/ESGF/CMIP6.13161
CMCC:CMCC-CM2-SR5	CMIP	Lovato et al. (2020), https://doi.org/10.22033/ESGF/CMIP6.1362
CMCC:CMCC-CM2-SR5	DCPP	Nicolý et al. (2020), https://doi.org/10.22033/ESGF/CMIP6.1363
CMCC:CMCC-CM2-SR5	OMIP	Fogli et al. (2020), https://doi.org/10.22033/ESGF/CMIP6.13162
CMCC:CMCC-CM2-SR5	ScenarioMIP	Lovato et al. (2020), https://doi.org/10.22033/ESGF/CMIP6.1365
CMCC:CMCC-CM2-VHR4	HighResMIP	Scoccimarro et al. (2017), https://doi.org/10.22033/ESGF/CMIP6.1367

ACCEPTED VERSION SUBJECT TO FINAL EDITING

CMCC:CMCC-ESM2	C4MIP	Lovato et al. (2021), https://doi.org/10.22033/ESGF/CMIP6.13163
CMCC:CMCC-ESM2	CMIP	Lovato et al. (2021), https://doi.org/10.22033/ESGF/CMIP6.13164
CMCC:CMCC-ESM2	LS3MIP	Peano et al. (2020), https://doi.org/10.22033/ESGF/CMIP6.13165
CMCC:CMCC-ESM2	LUMIP	Peano et al. (2020), https://doi.org/10.22033/ESGF/CMIP6.13166
CMCC:CMCC-ESM2	OMIP	Lovato et al. (2021), https://doi.org/10.22033/ESGF/CMIP6.13167
CMCC:CMCC-ESM2	ScenarioMIP	Lovato et al. (2021), https://doi.org/10.22033/ESGF/CMIP6.13168
CMCC:CMCC-ESM2-SR5	LS3MIP	Peano et al. (2019), https://doi.org/10.22033/ESGF/CMIP6.1372
CMCC:CMCC-ESM2-SR5	LUMIP	Peano et al. (2019), https://doi.org/10.22033/ESGF/CMIP6.1373
CNRM-CERFACS:CNRM-CM6-1	CFMIP	Voldoire (2019), https://doi.org/10.22033/ESGF/CMIP6.1374
CNRM-CERFACS:CNRM-CM6-1	CMIP	Voldoire (2018), https://doi.org/10.22033/ESGF/CMIP6.1375
CNRM-CERFACS:CNRM-CM6-1	DAMIP	Voldoire (2019), https://doi.org/10.22033/ESGF/CMIP6.1376
CNRM-CERFACS:CNRM-CM6-1	DCPP	Voldoire (2019), https://doi.org/10.22033/ESGF/CMIP6.1377
CNRM-CERFACS:CNRM-CM6-1	GMMIP	Voldoire (2019), https://doi.org/10.22033/ESGF/CMIP6.1379
CNRM-CERFACS:CNRM-CM6-1	HighResMIP	Voldoire (2019), https://doi.org/10.22033/ESGF/CMIP6.1925
CNRM-CERFACS:CNRM-CM6-1	LS3MIP	Voldoire (2019), https://doi.org/10.22033/ESGF/CMIP6.1381
CNRM-CERFACS:CNRM-CM6-1	OMIP	Voldoire (2019), https://doi.org/10.22033/ESGF/CMIP6.10336
CNRM-CERFACS:CNRM-CM6-1	PAMIP	Voldoire (2021), https://doi.org/10.22033/ESGF/CMIP6.9561
CNRM-CERFACS:CNRM-CM6-1	PMIP	Voldoire (2020), https://doi.org/10.22033/ESGF/CMIP6.1382
CNRM-CERFACS:CNRM-CM6-1	RFMIP	Voldoire (2019), https://doi.org/10.22033/ESGF/CMIP6.1383
CNRM-CERFACS:CNRM-CM6-1	ScenarioMIP	Voldoire (2019), https://doi.org/10.22033/ESGF/CMIP6.1384
CNRM-CERFACS:CNRM-CM6-1-HR	CMIP	Voldoire (2019), https://doi.org/10.22033/ESGF/CMIP6.1385
CNRM-CERFACS:CNRM-CM6-1-HR	GMMIP	Voldoire (2019), https://doi.org/10.22033/ESGF/CMIP6.13921
CNRM-CERFACS:CNRM-CM6-1-HR	HighResMIP	Voldoire (2019), https://doi.org/10.22033/ESGF/CMIP6.1387

ACCEPTED VERSION SUBJECT TO FINAL EDITING

CNRM-CERFACS:CNRM-CM6-1-HR	OMIP	Voldoire (2021), https://doi.org/10.22033/ESGF/CMIP6.10337
CNRM-CERFACS:CNRM-CM6-1-HR	ScenarioMIP	Voldoire (2019), https://doi.org/10.22033/ESGF/CMIP6.1388
CNRM-CERFACS:CNRM-ESM2-1	AerChemMIP	Seferian (2019), https://doi.org/10.22033/ESGF/CMIP6.1389
CNRM-CERFACS:CNRM-ESM2-1	C4MIP	Seferian (2018), https://doi.org/10.22033/ESGF/CMIP6.1390
CNRM-CERFACS:CNRM-ESM2-1	CDRMIP	Seferian (2021), https://doi.org/10.22033/ESGF/CMIP6.9562
CNRM-CERFACS:CNRM-ESM2-1	CMIP	Seferian (2018), https://doi.org/10.22033/ESGF/CMIP6.1391
CNRM-CERFACS:CNRM-ESM2-1	GMMIP	Seferian (2019), https://doi.org/10.22033/ESGF/CMIP6.13922
CNRM-CERFACS:CNRM-ESM2-1	GeoMIP	Seferian (2019), https://doi.org/10.22033/ESGF/CMIP6.1392
CNRM-CERFACS:CNRM-ESM2-1	LS3MIP	Seferian (2019), https://doi.org/10.22033/ESGF/CMIP6.9564
CNRM-CERFACS:CNRM-ESM2-1	LUMIP	Seferian (2019), https://doi.org/10.22033/ESGF/CMIP6.1393
CNRM-CERFACS:CNRM-ESM2-1	OMIP	Seferian (2019), https://doi.org/10.22033/ESGF/CMIP6.1394
CNRM-CERFACS:CNRM-ESM2-1	RFMIP	Seferian (2019), https://doi.org/10.22033/ESGF/CMIP6.9565
CNRM-CERFACS:CNRM-ESM2-1	ScenarioMIP	Seferian (2019), https://doi.org/10.22033/ESGF/CMIP6.1395
CSIRO-ARCCSS:ACCESS-CM2	CMIP	Dix et al. (2019), https://doi.org/10.22033/ESGF/CMIP6.2281
CSIRO-ARCCSS:ACCESS-CM2	FAFMIP	Savita et al. (2019), https://doi.org/10.22033/ESGF/CMIP6.2282
CSIRO-ARCCSS:ACCESS-CM2	RFMIP	Dix et al. (2020), https://doi.org/10.22033/ESGF/CMIP6.2284
CSIRO-ARCCSS:ACCESS-CM2	ScenarioMIP	Dix et al. (2019), https://doi.org/10.22033/ESGF/CMIP6.2285
CSIRO:ACCESS-ESM1-5	C4MIP	Ziehn et al. (2019), https://doi.org/10.22033/ESGF/CMIP6.2286
CSIRO:ACCESS-ESM1-5	CDRMIP	Ziehn et al. (2019), https://doi.org/10.22033/ESGF/CMIP6.2287
CSIRO:ACCESS-ESM1-5	CMIP	Ziehn et al. (2019), https://doi.org/10.22033/ESGF/CMIP6.2288
CSIRO:ACCESS-ESM1-5	DAMIP	Ziehn et al. (2020), https://doi.org/10.22033/ESGF/CMIP6.14362

ACCEPTED VERSION SUBJECT TO FINAL EDITING

CSIRO:ACCESS-ESM1-5	PMIP	Yeung et al. (2019), https://doi.org/10.22033/ESGF/CMIP6.13701
CSIRO:ACCESS-ESM1-5	RFMIP	Ziehn et al. (2020), https://doi.org/10.22033/ESGF/CMIP6.2290
CSIRO:ACCESS-ESM1-5	ScenarioMIP	Ziehn et al. (2019), https://doi.org/10.22033/ESGF/CMIP6.2291
DKRZ:MPI-ESM1-2-HR	ScenarioMIP	Schupfner et al. (2019), https://doi.org/10.22033/ESGF/CMIP6.2450
DWD:MPI-ESM1-2-HR	ScenarioMIP	Steger et al. (2019), https://doi.org/10.22033/ESGF/CMIP6.1869
E3SM-Project:E3SM-1-0	CMIP	Bader et al. (2019), https://doi.org/10.22033/ESGF/CMIP6.2294
E3SM-Project:E3SM-1-1	C4MIP	Bader et al. (2019), https://doi.org/10.22033/ESGF/CMIP6.11441
E3SM-Project:E3SM-1-1	CMIP	Bader et al. (2019), https://doi.org/10.22033/ESGF/CMIP6.11442
E3SM-Project:E3SM-1-1	ScenarioMIP	Bader et al. (2020), https://doi.org/10.22033/ESGF/CMIP6.15103
E3SM-Project:E3SM-1-1-ECA	C4MIP	Bader et al. (2020), https://doi.org/10.22033/ESGF/CMIP6.11443
E3SM-Project:E3SM-1-1-ECA	CMIP	Bader et al. (2019), https://doi.org/10.22033/ESGF/CMIP6.11444
EC-Earth-Consortium:EC-Earth3	CMIP	EC-Earth Consortium (EC-Earth) (2019), https://doi.org/10.22033/ESGF/CMIP6.181
EC-Earth-Consortium:EC-Earth3	DAMIP	EC-Earth Consortium (EC-Earth) (2020), https://doi.org/10.22033/ESGF/CMIP6.14701
EC-Earth-Consortium:EC-Earth3	DCPP	EC-Earth Consortium (EC-Earth) (2019), https://doi.org/10.22033/ESGF/CMIP6.227
EC-Earth-Consortium:EC-Earth3	LS3MIP	EC-Earth Consortium (EC-Earth) (2020), https://doi.org/10.22033/ESGF/CMIP6.218
EC-Earth-Consortium:EC-Earth3	OMIP	EC-Earth Consortium (EC-Earth) (2020), https://doi.org/10.22033/ESGF/CMIP6.14702
EC-Earth-Consortium:EC-Earth3	RFMIP	EC-Earth Consortium (EC-Earth) (2020), https://doi.org/10.22033/ESGF/CMIP6.242
EC-Earth-Consortium:EC-Earth3	ScenarioMIP	EC-Earth Consortium (EC-Earth) (2019), https://doi.org/10.22033/ESGF/CMIP6.251
EC-Earth-Consortium:EC-Earth3-AerChem	AerChemMIP	EC-Earth Consortium (EC-Earth) (2020), https://doi.org/10.22033/ESGF/CMIP6.699
EC-Earth-Consortium:EC-Earth3-AerChem	CMIP	EC-Earth Consortium (EC-Earth) (2020), https://doi.org/10.22033/ESGF/CMIP6.639
EC-Earth-Consortium:EC-Earth3-AerChem	RFMIP	EC-Earth Consortium (EC-Earth) (2020), https://doi.org/10.22033/ESGF/CMIP6.15326
EC-Earth-Consortium:EC-Earth3-AerChem	ScenarioMIP	EC-Earth Consortium (EC-Earth) (2020), https://doi.org/10.22033/ESGF/CMIP6.724
EC-Earth-Consortium:EC-Earth3-CC	C4MIP	EC-Earth Consortium (EC-Earth) (2020), https://doi.org/10.22033/ESGF/CMIP6.650
EC-Earth-Consortium:EC-Earth3-CC	CMIP	EC-Earth Consortium (EC-Earth) (2020), https://doi.org/10.22033/ESGF/CMIP6.640
EC-Earth-Consortium:EC-Earth3-CC	ScenarioMIP	EC-Earth Consortium (EC-Earth) (2021), https://doi.org/10.22033/ESGF/CMIP6.15327
EC-Earth-Consortium:EC-	CMIP	EC-Earth Consortium (EC-Earth) (2019), https://doi.org/10.22033/ESGF/CMIP6.202

ACCEPTED VERSION SUBJECT TO FINAL EDITING

Earth3-LR		
EC-Earth-Consortium:EC-Earth3-LR	PMIP	EC-Earth Consortium (EC-Earth) (2020), https://doi.org/10.22033/ESGF/CMIP6.247
EC-Earth-Consortium:EC-Earth3-Veg	CMIP	EC-Earth Consortium (EC-Earth) (2019), https://doi.org/10.22033/ESGF/CMIP6.642
EC-Earth-Consortium:EC-Earth3-Veg	LS3MIP	EC-Earth Consortium (EC-Earth) (2020), https://doi.org/10.22033/ESGF/CMIP6.672
EC-Earth-Consortium:EC-Earth3-Veg	LUMIP	EC-Earth Consortium (EC-Earth) (2020), https://doi.org/10.22033/ESGF/CMIP6.692
EC-Earth-Consortium:EC-Earth3-Veg	ScenarioMIP	EC-Earth Consortium (EC-Earth) (2019), https://doi.org/10.22033/ESGF/CMIP6.727
EC-Earth-Consortium:EC-Earth3-Veg-LR	CMIP	EC-Earth Consortium (EC-Earth) (2020), https://doi.org/10.22033/ESGF/CMIP6.643
EC-Earth-Consortium:EC-Earth3-Veg-LR	PMIP	EC-Earth Consortium (EC-Earth) (2020), https://doi.org/10.22033/ESGF/CMIP6.718
EC-Earth-Consortium:EC-Earth3-Veg-LR	ScenarioMIP	EC-Earth Consortium (EC-Earth) (2020), https://doi.org/10.22033/ESGF/CMIP6.728
EC-Earth-Consortium:EC-Earth3P	HighResMIP	EC-Earth Consortium (EC-Earth) (2019), https://doi.org/10.22033/ESGF/CMIP6.2322
EC-Earth-Consortium:EC-Earth3P-HR	HighResMIP	EC-Earth Consortium (EC-Earth) (2018), https://doi.org/10.22033/ESGF/CMIP6.2323
EC-Earth-Consortium:EC-Earth3P-VHR	CMIP	EC-Earth Consortium (EC-Earth) (2020), https://doi.org/10.22033/ESGF/CMIP6.2326
ECMWF:ECMWF-IFS-HR	HighResMIP	Roberts et al. (2017), https://doi.org/10.22033/ESGF/CMIP6.2461
ECMWF:ECMWF-IFS-LR	HighResMIP	Roberts et al. (2017), https://doi.org/10.22033/ESGF/CMIP6.2463
ECMWF:ECMWF-IFS-MR	HighResMIP	Roberts et al. (2018), https://doi.org/10.22033/ESGF/CMIP6.2465
FIO-QLNM:FIO-ESM-2-0	CMIP	Song et al. (2019), https://doi.org/10.22033/ESGF/CMIP6.9047
FIO-QLNM:FIO-ESM-2-0	GMMIP	Song et al. (2019), https://doi.org/10.22033/ESGF/CMIP6.9049
FIO-QLNM:FIO-ESM-2-0	ScenarioMIP	Song et al. (2019), https://doi.org/10.22033/ESGF/CMIP6.9051
HAMMOZ-Consortium:MPI-ESM-1-2-HAM	AerChemMIP	Neubauer et al. (2019), https://doi.org/10.22033/ESGF/CMIP6.1621
HAMMOZ-Consortium:MPI-ESM-1-2-HAM	CMIP	Neubauer et al. (2019), https://doi.org/10.22033/ESGF/CMIP6.1622
HAMMOZ-Consortium:MPI-ESM-1-2-HAM	RFMIP	Neubauer et al. (2019), https://doi.org/10.22033/ESGF/CMIP6.14724
INM:INM-CM4-8	CMIP	Volodin et al. (2019), https://doi.org/10.22033/ESGF/CMIP6.1422
INM:INM-CM4-8	PMIP	Volodin et al. (2019), https://doi.org/10.22033/ESGF/CMIP6.2295

ACCEPTED VERSION SUBJECT TO FINAL EDITING

INM:INM-CM4-8	ScenarioMIP	Volodin et al. (2019), https://doi.org/10.22033/ESGF/CMIP6.12321
INM:INM-CM5-0	CMIP	Volodin et al. (2019), https://doi.org/10.22033/ESGF/CMIP6.1423
INM:INM-CM5-0	ScenarioMIP	Volodin et al. (2019), https://doi.org/10.22033/ESGF/CMIP6.12322
INM:INM-CM5-H	HighResMIP	Volodin et al. (2019), https://doi.org/10.22033/ESGF/CMIP6.14041
IPSL:4AOP-v1-5	RFMIP	Boucher et al. (2020), https://doi.org/10.22033/ESGF/CMIP6.12340
IPSL:IPSL-CM5A2-INCA	CMIP	Boucher et al. (2020), https://doi.org/10.22033/ESGF/CMIP6.13642
IPSL:IPSL-CM5A2-INCA	LUMIP	Boucher et al. (2020), https://doi.org/10.22033/ESGF/CMIP6.15666
IPSL:IPSL-CM5A2-INCA	ScenarioMIP	Boucher et al. (2020), https://doi.org/10.22033/ESGF/CMIP6.15667
IPSL:IPSL-CM6A-ATM-HR	HighResMIP	Boucher et al. (2019), https://doi.org/10.22033/ESGF/CMIP6.2361
IPSL:IPSL-CM6A-LR	C4MIP	Boucher et al. (2018), https://doi.org/10.22033/ESGF/CMIP6.1521
IPSL:IPSL-CM6A-LR	CFMIP	Boucher et al. (2018), https://doi.org/10.22033/ESGF/CMIP6.1522
IPSL:IPSL-CM6A-LR	CMIP	Boucher et al. (2018), https://doi.org/10.22033/ESGF/CMIP6.1534
IPSL:IPSL-CM6A-LR	DAMIP	Boucher et al. (2018), https://doi.org/10.22033/ESGF/CMIP6.13801
IPSL:IPSL-CM6A-LR	DCPP	Boucher et al. (2019), https://doi.org/10.22033/ESGF/CMIP6.1523
IPSL:IPSL-CM6A-LR	GMMIP	Boucher et al. (2018), https://doi.org/10.22033/ESGF/CMIP6.1525
IPSL:IPSL-CM6A-LR	GeoMIP	Boucher et al. (2018), https://doi.org/10.22033/ESGF/CMIP6.1526
IPSL:IPSL-CM6A-LR	HighResMIP	Boucher et al. (2019), https://doi.org/10.22033/ESGF/CMIP6.13803
IPSL:IPSL-CM6A-LR	LS3MIP	Boucher et al. (2019), https://doi.org/10.22033/ESGF/CMIP6.1527
IPSL:IPSL-CM6A-LR	LUMIP	Boucher et al. (2019), https://doi.org/10.22033/ESGF/CMIP6.1528
IPSL:IPSL-CM6A-LR	OMIP	Boucher et al. (2019), https://doi.org/10.22033/ESGF/CMIP6.1529
IPSL:IPSL-CM6A-LR	PAMIP	Boucher et al. (2019), https://doi.org/10.22033/ESGF/CMIP6.13802
IPSL:IPSL-CM6A-LR	PMIP	Boucher et al. (2018), https://doi.org/10.22033/ESGF/CMIP6.1530
IPSL:IPSL-CM6A-LR	RFMIP	Boucher et al. (2018), https://doi.org/10.22033/ESGF/CMIP6.1531
IPSL:IPSL-CM6A-LR	ScenarioMIP	Boucher et al. (2019), https://doi.org/10.22033/ESGF/CMIP6.1532
IPSL:IPSL-CM6A-LR-INCA	AerChemMIP	Boucher et al. (2020), https://doi.org/10.22033/ESGF/CMIP6.13581
IPSL:IPSL-CM6A-LR-INCA	CMIP	Boucher et al. (2021), https://doi.org/10.22033/ESGF/CMIP6.13582
IPSL:IPSL-CM6A-LR-INCA	RFMIP	Boucher et al. (2020), https://doi.org/10.22033/ESGF/CMIP6.14583
KIOST:KIOST-ESM	CMIP	Kim et al. (2019), https://doi.org/10.22033/ESGF/CMIP6.1922
KIOST:KIOST-ESM	ScenarioMIP	Kim et al. (2019), https://doi.org/10.22033/ESGF/CMIP6.11241
LLNL:E3SM-1-0	CFMIP	Qin et al. (2021), https://doi.org/10.22033/ESGF/CMIP6.15093
MIROC:MIROC-	CMIP	Watanabe et al. (2021),

ACCEPTED VERSION SUBJECT TO FINAL EDITING

ES2H		https://doi.org/10.22033/ESGF/CMIP6.901
MIROC:MIROC-ES2H	GeoMIP	Watanabe et al. (2021), https://doi.org/10.22033/ESGF/CMIP6.907
MIROC:MIROC-ES2H-NB	AerChemMIP	Sudo et al. (2020), https://doi.org/10.22033/ESGF/CMIP6.13305
MIROC:MIROC-ES2L	C4MIP	Hajima et al. (2019), https://doi.org/10.22033/ESGF/CMIP6.906
MIROC:MIROC-ES2L	CDRMIP	Hajima et al. (2020), https://doi.org/10.22033/ESGF/CMIP6.2161
MIROC:MIROC-ES2L	CMIP	Hajima et al. (2019), https://doi.org/10.22033/ESGF/CMIP6.902
MIROC:MIROC-ES2L	DAMIP	Ohgaito et al. (2020), https://doi.org/10.22033/ESGF/CMIP6.15241
MIROC:MIROC-ES2L	LUMIP	Hajima et al. (2019), https://doi.org/10.22033/ESGF/CMIP6.922
MIROC:MIROC-ES2L	OMIP	Watanabe et al. (2020), https://doi.org/10.22033/ESGF/CMIP6.934
MIROC:MIROC-ES2L	PMIP	Ohgaito et al. (2019), https://doi.org/10.22033/ESGF/CMIP6.932
MIROC:MIROC-ES2L	ScenarioMIP	Tachiiri et al. (2019), https://doi.org/10.22033/ESGF/CMIP6.936
MIROC:MIROC-ES2L	VolMIP	Abe et al. (2021), https://doi.org/10.22033/ESGF/CMIP6.918
MIROC:MIROC6	AerChemMIP	Takemura (2019), https://doi.org/10.22033/ESGF/CMIP6.9121
MIROC:MIROC6	CFMIP	Ogura et al. (2019), https://doi.org/10.22033/ESGF/CMIP6.885
MIROC:MIROC6	CMIP	Tatebe et al. (2018), https://doi.org/10.22033/ESGF/CMIP6.881
MIROC:MIROC6	DAMIP	Shiogama (2019), https://doi.org/10.22033/ESGF/CMIP6.894
MIROC:MIROC6	DCPP	Mochizuki et al. (2019), https://doi.org/10.22033/ESGF/CMIP6.890
MIROC:MIROC6	FAFMIP	Suzuki (2019), https://doi.org/10.22033/ESGF/CMIP6.892
MIROC:MIROC6	GMMIP	Watanabe et al. (2019), https://doi.org/10.22033/ESGF/CMIP6.886
MIROC:MIROC6	LS3MIP	Onuma et al. (2020), https://doi.org/10.22033/ESGF/CMIP6.887
MIROC:MIROC6	OMIP	Komuro (2019), https://doi.org/10.22033/ESGF/CMIP6.897
MIROC:MIROC6	PAMIP	Mori (2019), https://doi.org/10.22033/ESGF/CMIP6.2162
MIROC:MIROC6	RFMIP	Sekiguchi et al. (2019), https://doi.org/10.22033/ESGF/CMIP6.895
MIROC:MIROC6	ScenarioMIP	Shiogama et al. (2019), https://doi.org/10.22033/ESGF/CMIP6.898
MIROC:NICAM16-7S	HighResMIP	Kodama et al. (2019), https://doi.org/10.22033/ESGF/CMIP6.1033
MIROC:NICAM16-8S	HighResMIP	Kodama et al. (2019), https://doi.org/10.22033/ESGF/CMIP6.1034
MIROC:NICAM16-9S	HighResMIP	Kodama et al. (2019), https://doi.org/10.22033/ESGF/CMIP6.1036
MOHC:HadGEM3-GC31-HH	HighResMIP	Roberts (2018), https://doi.org/10.22033/ESGF/CMIP6.445
MOHC:HadGEM3-GC31-HM	HighResMIP	Roberts (2017), https://doi.org/10.22033/ESGF/CMIP6.446
MOHC:HadGEM3-GC31-LL	CFMIP	Webb (2019), https://doi.org/10.22033/ESGF/CMIP6.435
MOHC:HadGEM3-GC31-LL	CMIP	Ridley et al. (2018), https://doi.org/10.22033/ESGF/CMIP6.419
MOHC:HadGEM3-GC31-LL	DAMIP	Jones (2019), https://doi.org/10.22033/ESGF/CMIP6.471
MOHC:HadGEM3-GC31-LL	HighResMIP	Roberts (2017), https://doi.org/10.22033/ESGF/CMIP6.1901
MOHC:HadGEM3-GC31-LL	LS3MIP	Wiltshire et al. (2020), https://doi.org/10.22033/ESGF/CMIP6.14460
MOHC:HadGEM3-GC31-LL	LUMIP	Wiltshire et al. (2020), https://doi.org/10.22033/ESGF/CMIP6.14461

ACCEPTED VERSION SUBJECT TO FINAL EDITING

MOHC:HadGEM3-GC31-LL	RFMIP	Andrews (2019), https://doi.org/10.22033/ESGF/CMIP6.475
MOHC:HadGEM3-GC31-LL	ScenarioMIP	Good (2019), https://doi.org/10.22033/ESGF/CMIP6.10845
MOHC:HadGEM3-GC31-LM	HighResMIP	Roberts (2017), https://doi.org/10.22033/ESGF/CMIP6.1321
MOHC:HadGEM3-GC31-MH	HighResMIP	Roberts (2017), https://doi.org/10.22033/ESGF/CMIP6.1762
MOHC:HadGEM3-GC31-MM	CMIP	Ridley et al. (2019), https://doi.org/10.22033/ESGF/CMIP6.420
MOHC:HadGEM3-GC31-MM	DCPP	Hermanson (2020), https://doi.org/10.22033/ESGF/CMIP6.456
MOHC:HadGEM3-GC31-MM	HighResMIP	Roberts (2017), https://doi.org/10.22033/ESGF/CMIP6.1902
MOHC:HadGEM3-GC31-MM	PAMIP	Eade (2020), https://doi.org/10.22033/ESGF/CMIP6.14627
MOHC:HadGEM3-GC31-MM	ScenarioMIP	Jackson (2020), https://doi.org/10.22033/ESGF/CMIP6.10846
MOHC:UKESM1-0-LL	AerChemMIP	O'Connor (2019), https://doi.org/10.22033/ESGF/CMIP6.1561
MOHC:UKESM1-0-LL	C4MIP	Liddicoat et al. (2019), https://doi.org/10.22033/ESGF/CMIP6.1562
MOHC:UKESM1-0-LL	CDRMIP	Jones et al. (2019), https://doi.org/10.22033/ESGF/CMIP6.12181
MOHC:UKESM1-0-LL	CMIP	Tang et al. (2019), https://doi.org/10.22033/ESGF/CMIP6.1569
MOHC:UKESM1-0-LL	DAMIP	Rumbold et al. (2020), https://doi.org/10.22033/ESGF/CMIP6.14830
MOHC:UKESM1-0-LL	GeoMIP	Jones (2019), https://doi.org/10.22033/ESGF/CMIP6.1563
MOHC:UKESM1-0-LL	LS3MIP	Wiltshire et al. (2020), https://doi.org/10.22033/ESGF/CMIP6.14462
MOHC:UKESM1-0-LL	LUMIP	Wiltshire et al. (2019), https://doi.org/10.22033/ESGF/CMIP6.1564
MOHC:UKESM1-0-LL	RFMIP	O'Connor et al. (2019), https://doi.org/10.22033/ESGF/CMIP6.11061
MOHC:UKESM1-0-LL	ScenarioMIP	Good et al. (2019), https://doi.org/10.22033/ESGF/CMIP6.1567
MPI-M:MPI-ESM1-2-HR	CMIP	Jungclaus et al. (2019), https://doi.org/10.22033/ESGF/CMIP6.741
MPI-M:MPI-ESM1-2-HR	DCPP	Pohlmann et al. (2019), https://doi.org/10.22033/ESGF/CMIP6.768
MPI-M:MPI-ESM1-2-HR	FAFMIP	Haak et al. (2019), https://doi.org/10.22033/ESGF/CMIP6.774
MPI-M:MPI-ESM1-2-HR	GeoMIP	Niemeier et al. (2019), https://doi.org/10.22033/ESGF/CMIP6.15294
MPI-M:MPI-ESM1-2-HR	HighResMIP	von Storch et al. (2017), https://doi.org/10.22033/ESGF/CMIP6.762
MPI-M:MPI-ESM1-2-LR	C4MIP	Brovkin et al. (2019), https://doi.org/10.22033/ESGF/CMIP6.748
MPI-M:MPI-ESM1-2-LR	CMIP	Wieners et al. (2019), https://doi.org/10.22033/ESGF/CMIP6.742
MPI-M:MPI-ESM1-2-LR	DAMIP	M³ller et al. (2019), https://doi.org/10.22033/ESGF/CMIP6.15016
MPI-M:MPI-ESM1-2-LR	GeoMIP	Niemeier et al. (2019), https://doi.org/10.22033/ESGF/CMIP6.751
MPI-M:MPI-ESM1-2-LR	LS3MIP	Stracke et al. (2019), https://doi.org/10.22033/ESGF/CMIP6.760
MPI-M:MPI-ESM1-2-	LUMIP	Pongratz et al. (2019),

ACCEPTED VERSION SUBJECT TO FINAL EDITING

LR		https://doi.org/10.22033/ESGF/CMIP6.772
MPI-M:MPI-ESM1-2-LR	PMIP	Jungclaus et al. (2019), https://doi.org/10.22033/ESGF/CMIP6.787
MPI-M:MPI-ESM1-2-LR	RFMIP	Fiedler et al. (2019), https://doi.org/10.22033/ESGF/CMIP6.784
MPI-M:MPI-ESM1-2-LR	ScenarioMIP	Wieners et al. (2019), https://doi.org/10.22033/ESGF/CMIP6.793
MPI-M:MPI-ESM1-2-XR	HighResMIP	von Storch et al. (2017), https://doi.org/10.22033/ESGF/CMIP6.10290
MRI:MRI-AGCM3-2-H	HighResMIP	Mizuta et al. (2019), https://doi.org/10.22033/ESGF/CMIP6.10942
MRI:MRI-AGCM3-2-S	HighResMIP	Mizuta et al. (2019), https://doi.org/10.22033/ESGF/CMIP6.1625
MRI:MRI-ESM2-0	AerChemMIP	Yukimoto et al. (2019), https://doi.org/10.22033/ESGF/CMIP6.633
MRI:MRI-ESM2-0	C4MIP	Yukimoto et al. (2019), https://doi.org/10.22033/ESGF/CMIP6.623
MRI:MRI-ESM2-0	CFMIP	Yukimoto et al. (2019), https://doi.org/10.22033/ESGF/CMIP6.625
MRI:MRI-ESM2-0	CMIP	Yukimoto et al. (2019), https://doi.org/10.22033/ESGF/CMIP6.621
MRI:MRI-ESM2-0	DAMIP	Yukimoto et al. (2019), https://doi.org/10.22033/ESGF/CMIP6.634
MRI:MRI-ESM2-0	DCPP	Yukimoto et al. (2020), https://doi.org/10.22033/ESGF/CMIP6.630
MRI:MRI-ESM2-0	FAFMIP	Yukimoto et al. (2019), https://doi.org/10.22033/ESGF/CMIP6.632
MRI:MRI-ESM2-0	GMMIP	Yukimoto et al. (2019), https://doi.org/10.22033/ESGF/CMIP6.626
MRI:MRI-ESM2-0	OMIP	Yukimoto et al. (2020), https://doi.org/10.22033/ESGF/CMIP6.637
MRI:MRI-ESM2-0	PMIP	Yukimoto et al. (2019), https://doi.org/10.22033/ESGF/CMIP6.636
MRI:MRI-ESM2-0	RFMIP	Yukimoto et al. (2019), https://doi.org/10.22033/ESGF/CMIP6.635
MRI:MRI-ESM2-0	ScenarioMIP	Yukimoto et al. (2019), https://doi.org/10.22033/ESGF/CMIP6.638
NASA-GISS:GISS-E2-1-G	AerChemMIP	NASA Goddard Institute for Space Studies (NASA/GISS) (2019), https://doi.org/10.22033/ESGF/CMIP6.2059
NASA-GISS:GISS-E2-1-G	C4MIP	NASA Goddard Institute for Space Studies (NASA/GISS) (2019), https://doi.org/10.22033/ESGF/CMIP6.2060
NASA-GISS:GISS-E2-1-G	CFMIP	NASA Goddard Institute for Space Studies (NASA/GISS) (2018), https://doi.org/10.22033/ESGF/CMIP6.2061
NASA-GISS:GISS-E2-1-G	CMIP	NASA Goddard Institute for Space Studies (NASA/GISS) (2018), https://doi.org/10.22033/ESGF/CMIP6.1400
NASA-GISS:GISS-E2-1-G	DAMIP	NASA Goddard Institute for Space Studies (NASA/GISS) (2018), https://doi.org/10.22033/ESGF/CMIP6.2062
NASA-GISS:GISS-E2-1-G	ISMIP6	NASA Goddard Institute for Space Studies (NASA/GISS) (2018), https://doi.org/10.22033/ESGF/CMIP6.2066
NASA-GISS:GISS-E2-1-G	LS3MIP	NASA Goddard Institute for Space Studies (NASA/GISS) (2018), https://doi.org/10.22033/ESGF/CMIP6.2067
NASA-GISS:GISS-E2-1-G	LUMIP	NASA Goddard Institute for Space Studies (NASA/GISS) (2018), https://doi.org/10.22033/ESGF/CMIP6.2068
NASA-GISS:GISS-E2-1-G	PMIP	NASA Goddard Institute for Space Studies (NASA/GISS) (2019), https://doi.org/10.22033/ESGF/CMIP6.2071
NASA-GISS:GISS-E2-1-G	RFMIP	NASA Goddard Institute for Space Studies (NASA/GISS) (2019), https://doi.org/10.22033/ESGF/CMIP6.2072
NASA-GISS:GISS-E2-1-G	ScenarioMIP	NASA Goddard Institute for Space Studies (NASA/GISS) (2020), https://doi.org/10.22033/ESGF/CMIP6.2074

ACCEPTED VERSION SUBJECT TO FINAL EDITING

NASA-GISS:GISS-E2-1-G-CC	C4MIP	NASA Goddard Institute for Space Studies (NASA/GISS) (2019), https://doi.org/10.22033/ESGF/CMIP6.11656
NASA-GISS:GISS-E2-1-G-CC	CMIP	NASA Goddard Institute for Space Studies (NASA/GISS) (2019), https://doi.org/10.22033/ESGF/CMIP6.11657
NASA-GISS:GISS-E2-1-H	CFMIP	NASA Goddard Institute for Space Studies (NASA/GISS) (2019), https://doi.org/10.22033/ESGF/CMIP6.13941
NASA-GISS:GISS-E2-1-H	CMIP	NASA Goddard Institute for Space Studies (NASA/GISS) (2018), https://doi.org/10.22033/ESGF/CMIP6.1421
NASA-GISS:GISS-E2-2-G	CFMIP	NASA Goddard Institute for Space Studies (NASA/GISS) (2019), https://doi.org/10.22033/ESGF/CMIP6.11659
NASA-GISS:GISS-E2-2-G	CMIP	NASA Goddard Institute for Space Studies (NASA/GISS) (2019), https://doi.org/10.22033/ESGF/CMIP6.2081
NASA-GISS:GISS-E3-G	RFMIP	NASA Goddard Institute for Space Studies (NASA/GISS) (2019), https://doi.org/10.22033/ESGF/CMIP6.2098
NCAR:CESM1-1-CAM5-CMIP5	DCPP	Danabasoglu (2019), https://doi.org/10.22033/ESGF/CMIP6.11542
NCAR:CESM1-CAM5-SE-HR	HighResMIP	Gent (2020), https://doi.org/10.22033/ESGF/CMIP6.14220
NCAR:CESM1-CAM5-SE-LR	HighResMIP	Gent (2020), https://doi.org/10.22033/ESGF/CMIP6.14262
NCAR:CESM1-WACCM-SC	PAMIP	Peings (2020), https://doi.org/10.22033/ESGF/CMIP6.12281
NCAR:CESM2	AerChemMIP	Danabasoglu (2019), https://doi.org/10.22033/ESGF/CMIP6.2181
NCAR:CESM2	C4MIP	Danabasoglu (2019), https://doi.org/10.22033/ESGF/CMIP6.2182
NCAR:CESM2	CDRMIP	Danabasoglu (2019), https://doi.org/10.22033/ESGF/CMIP6.2183
NCAR:CESM2	CFMIP	Danabasoglu (2019), https://doi.org/10.22033/ESGF/CMIP6.2184
NCAR:CESM2	CMIP	Danabasoglu (2019), https://doi.org/10.22033/ESGF/CMIP6.2185
NCAR:CESM2	DAMIP	Danabasoglu (2019), https://doi.org/10.22033/ESGF/CMIP6.2187
NCAR:CESM2	FAFMIP	Danabasoglu (2020), https://doi.org/10.22033/ESGF/CMIP6.14052
NCAR:CESM2	GMMIP	Danabasoglu (2019), https://doi.org/10.22033/ESGF/CMIP6.2190
NCAR:CESM2	ISMIP6	Danabasoglu (2019), https://doi.org/10.22033/ESGF/CMIP6.2193
NCAR:CESM2	LS3MIP	Danabasoglu (2019), https://doi.org/10.22033/ESGF/CMIP6.2194
NCAR:CESM2	LUMIP	Danabasoglu (2019), https://doi.org/10.22033/ESGF/CMIP6.2195
NCAR:CESM2	OMIP	Danabasoglu (2019), https://doi.org/10.22033/ESGF/CMIP6.2196
NCAR:CESM2	PAMIP	Danabasoglu (2019), https://doi.org/10.22033/ESGF/CMIP6.2197
NCAR:CESM2	PMIP	Danabasoglu (2019), https://doi.org/10.22033/ESGF/CMIP6.2198
NCAR:CESM2	RFMIP	Danabasoglu (2019), https://doi.org/10.22033/ESGF/CMIP6.2199
NCAR:CESM2	ScenarioMIP	Danabasoglu (2019), https://doi.org/10.22033/ESGF/CMIP6.2201
NCAR:CESM2-FV2	CMIP	Danabasoglu (2019), https://doi.org/10.22033/ESGF/CMIP6.11281
NCAR:CESM2-WACCM	AerChemMIP	Danabasoglu (2019), https://doi.org/10.22033/ESGF/CMIP6.10023
NCAR:CESM2-WACCM	CMIP	Danabasoglu (2019), https://doi.org/10.22033/ESGF/CMIP6.10024
NCAR:CESM2-WACCM	GeoMIP	Danabasoglu (2019), https://doi.org/10.22033/ESGF/CMIP6.10025
NCAR:CESM2-WACCM	RFMIP	Danabasoglu (2019), https://doi.org/10.22033/ESGF/CMIP6.14053
NCAR:CESM2-WACCM	ScenarioMIP	Danabasoglu (2019), https://doi.org/10.22033/ESGF/CMIP6.10026
NCAR:CESM2-WACCM-FV2	CMIP	Danabasoglu (2019), https://doi.org/10.22033/ESGF/CMIP6.11282
NCC:NorCPM1	CMIP	Bethke et al. (2019),

ACCEPTED VERSION
SUBJECT TO FINAL EDITING

		https://doi.org/10.22033/ESGF/CMIP6.10843
NCC:NorCPM1	DCPP	Bethke et al. (2019), https://doi.org/10.22033/ESGF/CMIP6.10844
NCC:NorESM1-F	CMIP	Guo et al. (2019), https://doi.org/10.22033/ESGF/CMIP6.11543
NCC:NorESM1-F	PMIP	Guo et al. (2019), https://doi.org/10.22033/ESGF/CMIP6.11544
NCC:NorESM2-LM	AerChemMIP	OliviÞ et al. (2019), https://doi.org/10.22033/ESGF/CMIP6.574
NCC:NorESM2-LM	C4MIP	Schwinger et al. (2019), https://doi.org/10.22033/ESGF/CMIP6.13721
NCC:NorESM2-LM	CDRMIP	Tjiputra et al. (2019), https://doi.org/10.22033/ESGF/CMIP6.13722
NCC:NorESM2-LM	CMIP	Seland et al. (2019), https://doi.org/10.22033/ESGF/CMIP6.502
NCC:NorESM2-LM	DAMIP	Seland et al. (2019), https://doi.org/10.22033/ESGF/CMIP6.580
NCC:NorESM2-LM	LUMIP	Cai et al. (2020), https://doi.org/10.22033/ESGF/CMIP6.562
NCC:NorESM2-LM	OMIP	Bentsen et al. (2019), https://doi.org/10.22033/ESGF/CMIP6.598
NCC:NorESM2-LM	PAMIP	Graff et al. (2019), https://doi.org/10.22033/ESGF/CMIP6.13723
NCC:NorESM2-LM	PMIP	Zhang et al. (2019), https://doi.org/10.22033/ESGF/CMIP6.592
NCC:NorESM2-LM	RFMIP	OliviÞ et al. (2019), https://doi.org/10.22033/ESGF/CMIP6.586
NCC:NorESM2-LM	ScenarioMIP	Seland et al. (2019), https://doi.org/10.22033/ESGF/CMIP6.604
NCC:NorESM2-MM	CMIP	Bentsen et al. (2019), https://doi.org/10.22033/ESGF/CMIP6.506
NCC:NorESM2-MM	RFMIP	OliviÞ et al. (2020), https://doi.org/10.22033/ESGF/CMIP6.590
NCC:NorESM2-MM	ScenarioMIP	Bentsen et al. (2019), https://doi.org/10.22033/ESGF/CMIP6.608
NERC:HadGEM3-GC31-HH	HighResMIP	Coward et al. (2018), https://doi.org/10.22033/ESGF/CMIP6.1822
NERC:HadGEM3-GC31-HM	HighResMIP	Schiemann et al. (2019), https://doi.org/10.22033/ESGF/CMIP6.1824
NERC:HadGEM3-GC31-LL	FAFMIP	Gregory (2021), https://doi.org/10.22033/ESGF/CMIP6.12065
NERC:HadGEM3-GC31-LL	PMIP	Williams et al. (2020), https://doi.org/10.22033/ESGF/CMIP6.12067
NERC:UKESM1-0-LL	AerChemMIP	O'Connor (2020), https://doi.org/10.22033/ESGF/CMIP6.405
NIMS-KMA:KACE-1-0-G	CMIP	Byun et al. (2019), https://doi.org/10.22033/ESGF/CMIP6.2241
NIMS-KMA:KACE-1-0-G	ScenarioMIP	Byun et al. (2019), https://doi.org/10.22033/ESGF/CMIP6.2242
NIMS-KMA:UKESM1-0-LL	AerChemMIP	Shim et al. (2020), https://doi.org/10.22033/ESGF/CMIP6.2243
NIMS-KMA:UKESM1-0-LL	CMIP	Shim et al. (2020), https://doi.org/10.22033/ESGF/CMIP6.2245
NIMS-KMA:UKESM1-0-LL	ScenarioMIP	Shim et al. (2020), https://doi.org/10.22033/ESGF/CMIP6.2250
NIWA:UKESM1-0-LL	AerChemMIP	Dalvi et al. (2019), https://doi.org/10.22033/ESGF/CMIP6.1741
NOAA-GFDL:GFDL-AM4	CMIP	Zhao et al. (2018), https://doi.org/10.22033/ESGF/CMIP6.1401
NOAA-GFDL:GFDL-CM4	CFMIP	Silvers et al. (2018), https://doi.org/10.22033/ESGF/CMIP6.1641
NOAA-GFDL:GFDL-CM4	CMIP	Guo et al. (2018), https://doi.org/10.22033/ESGF/CMIP6.1402
NOAA-GFDL:GFDL-CM4	DAMIP	Ploshay et al. (2018), https://doi.org/10.22033/ESGF/CMIP6.11383
NOAA-GFDL:GFDL-CM4	GMMIP	Xiang et al. (2018), https://doi.org/10.22033/ESGF/CMIP6.1642
NOAA-GFDL:GFDL-CM4	OMIP	Adcroft et al. (2018), https://doi.org/10.22033/ESGF/CMIP6.1403

ACCEPTED VERSION SUBJECT TO FINAL EDITING

NOAA-GFDL:GFDL-CM4	RFMIP	Paynter et al. (2018), https://doi.org/10.22033/ESGF/CMIP6.1643
NOAA-GFDL:GFDL-CM4	ScenarioMIP	Guo et al. (2018), https://doi.org/10.22033/ESGF/CMIP6.9242
NOAA-GFDL:GFDL-CM4C192	HighResMIP	Zhao et al. (2018), https://doi.org/10.22033/ESGF/CMIP6.2262
NOAA-GFDL:GFDL-ESM2M	FAFMIP	Hurlin et al. (2018), https://doi.org/10.22033/ESGF/CMIP6.1645
NOAA-GFDL:GFDL-ESM4	AerChemMIP	Horowitz et al. (2018), https://doi.org/10.22033/ESGF/CMIP6.1404
NOAA-GFDL:GFDL-ESM4	C4MIP	Krasting et al. (2018), https://doi.org/10.22033/ESGF/CMIP6.1405
NOAA-GFDL:GFDL-ESM4	CDRMIP	John et al. (2018), https://doi.org/10.22033/ESGF/CMIP6.1981
NOAA-GFDL:GFDL-ESM4	CMIP	Krasting et al. (2018), https://doi.org/10.22033/ESGF/CMIP6.1407
NOAA-GFDL:GFDL-ESM4	DAMIP	Horowitz et al. (2018), https://doi.org/10.22033/ESGF/CMIP6.1408
NOAA-GFDL:GFDL-ESM4	LUMIP	Malyshev et al. (2018), https://doi.org/10.22033/ESGF/CMIP6.1411
NOAA-GFDL:GFDL-ESM4	RFMIP	Paynter et al. (2018), https://doi.org/10.22033/ESGF/CMIP6.11961
NOAA-GFDL:GFDL-ESM4	ScenarioMIP	John et al. (2018), https://doi.org/10.22033/ESGF/CMIP6.1414
NOAA-GFDL:GFDL-GRTCODE	RFMIP	Paynter et al. (2018), https://doi.org/10.22033/ESGF/CMIP6.10404
NOAA-GFDL:GFDL-OM4p5B	OMIP	Zadeh et al. (2018), https://doi.org/10.22033/ESGF/CMIP6.2264
NOAA-GFDL:GFDL-RFM-DISORT	RFMIP	Paynter et al. (2018), https://doi.org/10.22033/ESGF/CMIP6.10406
NTU:TaiESM1-TIMCOM	OMIP	Tseng et al. (2020), https://doi.org/10.22033/ESGF/CMIP6.14323
NUIST:NESM3	CMIP	Cao et al. (2019), https://doi.org/10.22033/ESGF/CMIP6.2021
NUIST:NESM3	PMIP	Cao (2019), https://doi.org/10.22033/ESGF/CMIP6.2026
NUIST:NESM3	ScenarioMIP	Cao (2019), https://doi.org/10.22033/ESGF/CMIP6.2027
RTE-RRTMGP-Consortium:RTE-RRTMGP-181204	RFMIP	Pincus (2019), https://doi.org/10.22033/ESGF/CMIP6.10124
SNU:SAM0-UNICON	CMIP	Park et al. (2019), https://doi.org/10.22033/ESGF/CMIP6.1489
THU:CIESM	CMIP	Huang (2019), https://doi.org/10.22033/ESGF/CMIP6.1352
THU:CIESM	GMMIP	Xue (2020), https://doi.org/10.22033/ESGF/CMIP6.1354
THU:CIESM	ScenarioMIP	Huang (2019), https://doi.org/10.22033/ESGF/CMIP6.1357
UA:MCM-UA-1-0	CMIP	Stouffer (2019), https://doi.org/10.22033/ESGF/CMIP6.2421
UA:MCM-UA-1-0	ScenarioMIP	Stouffer (2019), https://doi.org/10.22033/ESGF/CMIP6.13816
UHH:ARTS-2-3	RFMIP	Brath (2019), https://doi.org/10.22033/ESGF/CMIP6.2001

[END TABLE AII.10 HERE]

ACCEPTED VERSION SUBJECT TO FINAL EDITING

References

Adcroft, A., Anderson, W., Balaji, V., Blanton, C., Bushuk, M., Dufour, C. O., et al. (2019a). The GFDL Global Ocean and Sea Ice Model OM4.0: Model Description and Simulation Features. *J. Adv. Model. Earth Syst.* 11, 3167–3211. doi:10.1029/2019MS001726.

Adcroft, A., Anderson, W., Balaji, V., Blanton, C., Bushuk, M., Dufour, C. O., et al. (2019b). The GFDL Global Ocean and Sea Ice Model OM4.0: Model Description and Simulation Features. *J. Adv. Model. Earth Syst.* 11, 3167–3211. doi:10.1029/2019MS001726.

Agosta, C., Amory, C., Kittel, C., Orsi, A., Favier, V., Gallée, H., et al. (2019). Estimation of the Antarctic surface mass balance using the regional climate model MAR (1979–2015) and identification of dominant processes. *Cryosph.* 13, 281–296. doi:10.5194/tc-13-281-2019.

Akhtar, N., Brauch, J., and Ahrens, B. (2018). Climate modeling over the Mediterranean Sea: impact of resolution and ocean coupling. *Clim. Dyn.* 51, 933–948. doi:10.1007/s00382-017-3570-8.

Alapaty, K., Mathur, R., Pleim, J., Hogrefe, C., Rao, S. T., Ramaswamy, V., et al. (2012). New Directions: Understanding interactions of air quality and climate change at regional scales. *Atmos. Environ.* 49, 419–421. doi:10.1016/j.atmosenv.2011.12.016.

Anderson, B., and Mackintosh, A. (2012). Controls on mass balance sensitivity of maritime glaciers in the Southern Alps, New Zealand: The role of debris cover. *J. Geophys. Res. Earth Surf.* 117. doi:10.1029/2011JF002064.

Anderson, J. L., Balaji, V., Broccoli, A. J., Cooke, W. F., Delworth, T. L., Dixon, K. W., et al. (2004). The New GFDL Global Atmosphere and Land Model AM2–LM2: Evaluation with Prescribed SST Simulations. *J. Clim.* 17, 4641–4673. doi:10.1175/JCLI-3223.1.

Archibald, A. T., O'Connor, F. M., Abraham, N. L., Archer-Nicholls, S., Chipperfield, M. P., Dalvi, M., et al. (2020). Description and evaluation of the UKCA stratosphere--troposphere chemistry scheme (StratTrop vn 1.0) implemented in UKESM1. *Geosci. Model Dev.* 13, 1223–1266. doi:10.5194/gmd-13-1223-2020.

Arora, V. K., and Boer, G. J. (2010). Uncertainties in the 20th century carbon budget associated with land use change. *Glob. Chang. Biol.* 16, 3327–3348. doi:https://doi.org/10.1111/j.1365-2486.2010.02202.x.

Artale, V., Calmanti, S., Carillo, A., Dell'Aquila, A., Herrmann, M., Pisacane, G., et al. (2010). An atmosphere–ocean regional climate model for the Mediterranean area: assessment of a present climate simulation. *Clim. Dyn.* 35, 721–740. doi:10.1007/s00382-009-0691-8.

Aschwanden, A., Fahnestock, M. A., and Truffer, M. (2016). Complex Greenland outlet glacier flow captured. *Nat. Commun.* 7, 10524. doi:10.1038/ncomms10524.

Aumont, O., Ethé, C., Tagliabue, A., Bopp, L., and Gehlen, M. (2015). PISCES-v2: an ocean biogeochemical model for carbon and ecosystem studies. *Geosci. Model Dev.* 8, 2465–2513. doi:10.5194/gmd-8-2465-2015.

Balaji, V., Taylor, K. E., Juckes, M., Lawrence, B. N., Durack, P. J., Lautenschlager, M., et al. (2018). Requirements for a global data infrastructure in support of CMIP6. *Geosci. Model Dev.* 11, 3659–3680. doi:10.5194/gmd-11-3659-2018.

Balsamo, G., Beljaars, A., Scipal, K., Viterbo, P., van den Hurk, B., Hirschi, M., et al. (2009). A Revised Hydrology for the ECMWF Model: Verification from Field Site to Terrestrial Water Storage and Impact in the Integrated Forecast System. *J. Hydrometeorol.* 10, 623–643. doi:10.1175/2008JHM1068.1.

Bao, Y., Song, Z., and Qiao, F. (2020). FIO-ESM Version 2.0: Model Description and Evaluation. *J. Geophys. Res. Ocean.* 125, e2019JC016036. doi:https://doi.org/10.1029/2019JC016036.

Bauer, S. E., Tsigaridis, K., Faluvegi, G., Kelley, M., Lo, K. K., Miller, R. L., et al. (2020). Historical (1850–2014) Aerosol Evolution and Role on Climate Forcing Using the GISS ModelE2.1 Contribution to CMIP6. *J. Adv. Model. Earth Syst.* 12, e2019MS001978. doi:https://doi.org/10.1029/2019MS001978.

Bellouin, N., Rae, J., Jones, A., Johnson, C., Haywood, J., and Boucher, O. (2011). Aerosol forcing in the Climate Model Intercomparison Project (CMIP5) simulations by HadGEM2-ES and the role of ammonium nitrate. *J. Geophys. Res. Atmos.* 116. doi:https://doi.org/10.1029/2011JD016074.

Bellucci, A., Athanasiadis, P. J., Scoccimarro, E., Ruggieri, P., Gualdi, S., Fedele, G., et al. (2021). Air-Sea interaction over the Gulf Stream in an ensemble of HighResMIP present climate simulations. *Clim. Dyn.* doi:10.1007/s00382-020-05573-z.

Beuvier, J., Brossier, C. L., B´eranger, K., Arsouze, T., Bourdall´e-Badie, R., Deltel, C., et al. (2012). MED12, OCEANIC COMPONENT FOR THE MODELING OF THE REGIONAL MEDITERRANEAN EARTH SYSTEM. *Mercat. Ocean Q. Newsletter, #46 <hal-01138958>*.

Beuvier, J., Sevault, F., Herrmann, M., Kontoyiannis, H., Ludwig, W., Rixen, M., et al. (2010). Modeling the Mediterranean Sea interannual variability during 1961–2000: Focus on the Eastern Mediterranean Transient. *J. Geophys. Res.* 115, C08017. doi:10.1029/2009JC005950.

Bi, D., Dix, M., Marsland, S., O'Farrell, S., Sullivan, A., Bodman, R., et al. (2020). Configuration and spin-up of ACCESS-CM2, the new generation Australian Community Climate and Earth System Simulator Coupled Model. *J. South. Hemisph. Earth Syst. Sci.* doi:10.1071/es19040.

Boucher, O., Servonnat, J., Albright, A. L., Aumont, O., Balkanski, Y., Bastrikov, V., et al. (2020). Presentation and

ACCEPTED VERSION SUBJECT TO FINAL EDITING

Evaluation of the IPSL-CM6A-LR Climate Model. *J. Adv. Model. Earth Syst.* 12. doi:10.1029/2019MS002010.
Bruyère, C. L., Done, J. M., Holland, G. J., and Fredrick, S. (2014). Bias corrections of global models for regional climate simulations of high-impact weather. *Clim. Dyn.* 43, 1847–1856. doi:10.1007/s00382-013-2011-6.
Bueler, E., and Brown, J. (2009). Shallow shelf approximation as a "sliding law" in a thermomechanically coupled ice sheet model. *J. Geophys. Res.* 114, F03008. doi:10.1029/2008JF001179.
Bukovsky, M. S., and Mearns, L. O. (2020). Regional climate change projections from NA-CORDEX and their relation to climate sensitivity. *Clim. Change* 162, 645–665. doi:10.1007/s10584-020-02835-x.
Burrows, S. M., Maltrud, M., Yang, X., Zhu, Q., Jeffery, N., Shi, X., et al. (2020). The DOE E3SM v1.1 Biogeochemistry Configuration: Description and Simulated Ecosystem-Climate Responses to Historical Changes in Forcing. *J. Adv. Model. Earth Syst.* 12, e2019MS001766. doi:https://doi.org/10.1029/2019MS001766.
Cao, J., Wang, B., Yang, Y.-M., Ma, L., Li, J., Sun, B., et al. (2018). The NUIST Earth System Model~(NESM) version 3: description and preliminary evaluation. *Geosci. Model Dev.* 11, 2975–2993. doi:10.5194/gmd-11-2975-2018.
Chang, P., Zhang, S., Danabasoglu, G., Yeager, S. G., Fu, H., Wang, H., et al. (2020). An Unprecedented Set of High-Resolution Earth System Simulations for Understanding Multiscale Interactions in Climate Variability and Change. *J. Adv. Model. Earth Syst.* 12, e2020MS002298. doi:https://doi.org/10.1029/2020MS002298.
Chen, F., and Dudhia, J. (2001). Coupling an Advanced Land Surface–Hydrology Model with the Penn State–NCAR MM5 Modeling System. Part I: Model Implementation and Sensitivity. *Mon. Weather Rev.* 129, 569–585. doi:10.1175/1520-0493(2001)129<0569:CAALSH>2.0.CO;2.
Chen, J.-P., Tsai, I.-C., and Lin, Y.-C. (2013). A statistical–numerical aerosol parameterization scheme. *Atmos. Chem. Phys.* 13, 10483–10504. doi:10.5194/acp-13-10483-2013.
Cherchi, A., Fogli, P. G., Lovato, T., Peano, D., Iovino, D., Gualdi, S., et al. (2019). Global Mean Climate and Main Patterns of Variability in the CMCC-CM2 Coupled Model. *J. Adv. Model. Earth Syst.* 11, 185–209. doi:10.1029/2018MS001369.
Chou, S. C., Lyra, A., Mourão, C., Dereczynski, C., Pilotto, I., Gomes, J., et al. (2014a). Assessment of Climate Change over South America under RCP 4.5 and 8.5 Downscaling Scenarios. *Am. J. Clim. Chang.* 03, 512–527. doi:10.4236/ajcc.2014.35043.
Chou, S. C., Lyra, A., Mourão, C., Dereczynski, C., Pilotto, I., Gomes, J., et al. (2014b). Evaluation of the Eta Simulations Nested in Three Global Climate Models. *Am. J. Clim. Chang.* 03, 438–454. doi:10.4236/ajcc.2014.35039.
Christensen, O. B., Drews, M., Christensen, J. H., Danish Climate Centre, DMI, Dethloff, K., et al. (2007). The HIRHAM Regional Climate Model. Available at: www.dmi.dk/dmi/tr06-17.
Colin, J., Déqué, M., Radu, R., and Somot, S. (2010). Sensitivity study of heavy precipitation in Limited Area Model climate simulations: influence of the size of the domain and the use of the spectral nudging technique. *Tellus A Dyn. Meteorol. Oceanogr.* 62, 591–604. doi:10.1111/j.1600-0870.2010.00467.x.
Cornford, S. L., Martin, D. F., Graves, D. T., Ranken, D. F., Le Brocq, A. M., Gladstone, R. M., et al. (2013). Adaptive mesh, finite volume modeling of marine ice sheets. *J. Comput. Phys.* 232, 529–549. doi:10.1016/j.jcp.2012.08.037.
Cornford, S. L., Martin, D. F., Payne, A. J., Ng, E. G., Le Brocq, A. M., Gladstone, R. M., et al. (2015). Century-scale simulations of the response of the West Antarctic Ice Sheet to a warming climate. *Cryosph.* 9, 1579–1600. doi:10.5194/tc-9-1579-2015.
Cuzzone, J. K., Morlighem, M., Larour, E., Schlegel, N., and Seroussi, H. (2018). Implementation of higher-order vertical finite elements in ISSM v4.13 for improved ice sheet flow modeling over paleoclimate timescales. *Geosci. Model Dev.* 11, 1683–1694. doi:10.5194/gmd-11-1683-2018.
Danabasoglu, G., Lamarque, J.-F., Bacmeister, J., Bailey, D. A., DuVivier, A. K., Edwards, J., et al. (2020). The Community Earth System Model Version 2 (CESM2). *J. Adv. Model. Earth Syst.* 12, e2019MS001916. doi:10.1029/2019MS001916.
Daniel, M., Lemonsu, A., Déqué, M., Somot, S., Alias, A., and Masson, V. (2019). Benefits of explicit urban parameterization in regional climate modeling to study climate and city interactions. *Clim. Dyn.* 52, 2745–2764. doi:10.1007/s00382-018-4289-x.
de Boer, B., Stocchi, P., and van de Wal, R. S. W. (2014). A fully coupled 3-D ice-sheet–sea-level model: algorithm and applications. *Geosci. Model Dev.* 7, 2141–2156. doi:10.5194/gmd-7-2141-2014.
De Ridder, K. (1997). Radiative Transfer in the IAGL Land Surface Model. *J. Appl. Meteorol.* 36, 12–21. doi:10.1175/1520-0450(1997)036<0012:RTITIL>2.0.CO;2.
De Ridder, K., and Schayes, G. (1997). The IAGL Land Surface Model. *J. Appl. Meteorol.* 36, 167–182. doi:10.1175/1520-0450(1997)036<0167:TILSM>2.0.CO;2.
Decharme, B., Alkama, R., Douville, H., Becker, M., and Cazenave, A. (2010). Global Evaluation of the ISBA-TRIP Continental Hydrological System. Part II: Uncertainties in River Routing Simulation Related to Flow Velocity and Groundwater Storage. *J. Hydrometeorol.* 11, 601–617. doi:10.1175/2010JHM1212.1.
Decharme, B., Delire, C., Minvielle, M., Colin, J., Vergnes, J.-P., Alias, A., et al. (2019). Recent Changes in the ISBA-CTRIP Land Surface System for Use in the CNRM-CM6 Climate Model and in Global Off-Line Hydrological Applications. *J. Adv. Model. Earth Syst.* 11, 1207–1252. doi:https://doi.org/10.1029/2018MS001545.

ACCEPTED VERSION
SUBJECT TO FINAL EDITING

Delire, C., Séférian, R., Decharme, B., Alkama, R., Calvet, J.-C., Carrer, D., et al. (2020). The Global Land Carbon Cycle Simulated With ISBA-CTRIP: Improvements Over the Last Decade. *J. Adv. Model. Earth Syst.* 12, e2019MS001886. doi:https://doi.org/10.1029/2019MS001886.

Delworth, T., Ronald, S., Dixon, K., MJ, S., TR, K., Broccoli, A., et al. (2002). Simulation of climate variability and change by the GFDL R30 coupled climate model. *Clim. Dyn.* 19, 555–574. doi:10.1007/s00382-002-0249-5.

Deushi, M., and Shibata, K. (2011). Development of a Meteorological Research Institute Chemistry-Climate Model version 2 for the Study of Tropospheric and Stratospheric Chemistry. *Pap. Meteorol. Geophys.* 62, 1–46. doi:10.2467/mripapers.62.1.

Di Virgilio, G., Evans, J. P., Di Luca, A., Olson, R., Argüeso, D., Kala, J., et al. (2019). Evaluating reanalysis-driven CORDEX regional climate models over Australia: model performance and errors. *Clim. Dyn.* 53, 2985–3005. doi:10.1007/s00382-019-04672-w.

Dickinson, R. E., Henderson-Sellers, A., and Kennedy, P. J. (1993). Biosphere-Atmosphere Transfer Scheme (BATS) version le as coupled to the NCAR community climate model. Technical note. [NCAR (National Center for Atmospheric Research)]. United States Available at: https://www.osti.gov/biblio/5733868-biosphere-atmosphere-transfer-scheme-bats-version-le-coupled-ncar-community-climate-model-technical-note-ncar-national-center-atmospheric-research.

Dickinson, R. E., Oleson, K. W., Bonan, G., Hoffman, F., Thornton, P., Vertenstein, M., et al. (2006). The Community Land Model and Its Climate Statistics as a Component of the Community Climate System Model. *J. Clim.* 19, 2302–2324. doi:10.1175/JCLI3742.1.

Djurdjevic, V., and Rajkovic, B. (2008). Verification of a coupled atmosphere-ocean model using satellite observations over the Adriatic Sea. *Ann. Geophys.* 26, 1935–1954. doi:10.5194/angeo-26-1935-2008.

Djurdjevic, V., and Rajkovic, B. (2010). "Development of the EBU-POM coupled regional climate model and results from climate change experiments," in *Advances in Environmental Modeling and Measurements*, eds. T. D. Mihajlovic and B. Lalic (Nova Publishers), 23–32.

Döscher, R., Acosta, M., Alessandri, A., Anthoni, P., Arneth, A., Arsouze, T., et al. (2021). The EC-Earth3 Earth System Model for the Climate Model Intercomparison Project 6. *Geosci. Model Dev. Discuss.* 2021, 1–90. doi:10.5194/gmd-2020-446.

Douville, H., Planton, S., Royer, J.-F., Stephenson, D. B., Tyteca, S., Kergoat, L., et al. (2000). Importance of vegetation feedbacks in doubled-CO 2 climate experiments. *J. Geophys. Res. Atmos.* 105, 14841–14861. doi:10.1029/1999JD901086.

Dunne, J. P., Bociu, I., Bronselaer, B., Guo, H., John, J. G., Krasting, J. P., et al. (2020a). Simple Global Ocean Biogeochemistry With Light, Iron, Nutrients and Gas Version 2 (BLINGv2): Model Description and Simulation Characteristics in GFDL's CM4.0. *J. Adv. Model. Earth Syst.* 12, e2019MS002008. doi:https://doi.org/10.1029/2019MS002008.

Dunne, J. P., Horowitz, L. W., Adcroft, A. J., Ginoux, P., Held, I. M., John, J. G., et al. (2020b). The GFDL Earth System Model version 4.1 (GFDL-ESM 4.1): Overall coupled model description and simulation characteristics. *J. Adv. Model. Earth Syst.* n/a, e2019MS002015. doi:https://doi.org/10.1029/2019MS002015.

Ek, M. B., Mitchell, K. E., Lin, Y., Rogers, E., Grunmann, P., Koren, V., et al. (2003). Implementation of Noah land surface model advances in the National Centers for Environmental Prediction operational mesoscale Eta model. *J. Geophys. Res. Atmos.* 108, 2002JD003296. doi:10.1029/2002JD003296.

Emmons, L. K., Schwantes, R. H., Orlando, J. J., Tyndall, G., Kinnison, D., Lamarque, J.-F., et al. (2020). The Chemistry Mechanism in the Community Earth System Model Version 2 (CESM2). *J. Adv. Model. Earth Syst.* 12, e2019MS001882. doi:https://doi.org/10.1029/2019MS001882.

Ettema, J., van den Broeke, M. R., van Meijgaard, E., van de Berg, W. J., Box, J. E., and Steffen, K. (2010). Climate of the Greenland ice sheet using a high-resolution climate model – Part 1: Evaluation. *Cryosph.* 4, 511–527. doi:10.5194/tc-4-511-2010.

Evans, J. P., Di Virgilio, G., Hirsch, A. L., Hoffmann, P., Remedio, A. R., Ji, F., et al. (2020). The CORDEX-Australasia ensemble: evaluation and future projections. *Clim. Dyn.* doi:10.1007/s00382-020-05459-0.

Eyring, V., Bony, S., Meehl, G. A., Senior, C. A., Stevens, B., Stouffer, R. J., et al. (2016). Overview of the Coupled Model Intercomparison Project Phase 6 (CMIP6) experimental design and organization. *Geosci. Model Dev.* 9, 1937–1958. doi:10.5194/gmd-9-1937-2016.

Feichter, J., Kjellström, E., Rodhe, H., Dentener, F., Lelieveldi, J., and Roelofs, G.-J. (1996). Simulation of the tropospheric sulfur cycle in a global climate model. *Atmos. Environ.* 30, 1693–1707. doi:https://doi.org/10.1016/1352-2310(95)00394-0.

Fiedler, S., Stevens, B., Gidden, M., Smith, S. J., Riahi, K., and van Vuuren, D. (2019). First forcing estimates from the future CMIP6 scenarios of anthropogenic aerosol optical properties and an associated Twomey effect. *Geosci. Model Dev.* 12, 989–1007. doi:10.5194/gmd-12-989-2019.

Flato, G., Marotzke, J., Abiodun, B., Braconnot, P., Chou, S. C., Collins, W., et al. (2013). "Evaluation of Climate Models," in *Climate Change 2013: The Physical Science Basis. Contribution of Working Group I to the Fifth Assessment Report of the Intergovernmental Panel on Climate Change*, eds. T. F. Stocker, D. Qin, G.-K. Plattner, M. Tignor, S. K. Allen, J. Boschung, et al. (Cambridge, United Kingdom and New York, NY, USA: Cambridge

ACCEPTED VERSION SUBJECT TO FINAL EDITING

University Press), 741–866. doi:10.1017/CBO9781107415324.020.
Fouquart, Y., and Bonnel, B. (1980). Computations of solar heating of the Earth's atmosphere: A new parameterization. Available at: https://pascal-francis.inist.fr/vibad/index.php?action=getRecordDetail&idt=PASCAL8030435628.
Fürst, J. J., Goelzer, H., and Huybrechts, P. (2015). Ice-dynamic projections of the Greenland ice sheet in response to atmospheric and oceanic warming. *Cryosph.* 9, 1039–1062. doi:10.5194/tc-9-1039-2015.
Gallée, H., and Duynkerke, P. G. (1997). Air-snow interactions and the surface energy and mass balance over the melting zone of west Greenland during the Greenland Ice Margin Experiment. *J. Geophys. Res. Atmos.* 102, 13813–13824. doi:10.1029/96JD03358.
Gallée, H., Guyomarc'h, G., and Brun, E. (2001). Impact Of Snow Drift On The Antarctic Ice Sheet Surface Mass Balance: Possible Sensitivity To Snow-Surface Properties. *Boundary-Layer Meteorol.* 99, 1–19. doi:10.1023/A:1018776422809.
Gillet-Chaulet, F., Durand, G., Gagliardini, O., Mosbeux, C., Mouginot, J., Rémy, F., et al. (2016). Assimilation of surface velocities acquired between 1996 and 2010 to constrain the form of the basal friction law under Pine Island Glacier. *Geophys. Res. Lett.* 43, 10,311-10,321. doi:10.1002/2016GL069937.
Gillet-Chaulet, F., Gagliardini, O., Seddik, H., Nodet, M., Durand, G., Ritz, C., et al. (2012). Greenland ice sheet contribution to sea-level rise from a new-generation ice-sheet model. *Cryosph.* 6, 1561–1576. doi:10.5194/tc-6-1561-2012.
Giorgi, F., and Anyah, R. (2012). INTRODUCTION The road towards RegCM4 F. Giorgi1,*, R. O. Anyah2. *Clim. Res.* 52, 3–6. doi:10.3354/cr01089.
Giorgi, F., Coppola, E., Solmon, F., Mariotti, L., Sylla, M., Bi, X., et al. (2012). RegCM4: model description and preliminary tests over multiple CORDEX domains. *Clim. Res.* 52, 7–29. doi:10.3354/cr01018.
Giot, O., Termonia, P., Degrauwe, D., De Troch, R., Caluwaerts, S., Smet, G., et al. (2016). Validation of the ALARO-0 model within the EURO-CORDEX framework. *Geosci. Model Dev.* 9, 1143–1152. doi:10.5194/gmd-9-1143-2016.
Goelzer, H., Nowicki, S., Edwards, T., Beckley, M., Abe-Ouchi, A., Aschwanden, A., et al. (2018). Design and results of the ice sheet model initialisation experiments initMIP-Greenland: an ISMIP6 intercomparison. *Cryosph.* 12, 1433–1460. doi:10.5194/tc-12-1433-2018.
Goelzer, H., Nowicki, S., Payne, A., Larour, E., Seroussi, H., Lipscomb, W. H., et al. (2020). The future sea-level contribution of the Greenland ice sheet: a multi-model ensemble study of ISMIP6. *Cryosph.* 14, 3071–3096. doi:10.5194/tc-14-3071-2020.
Golaz, J.-C., Caldwell, P. M., Van Roekel, L. P., Petersen, M. R., Tang, Q., Wolfe, J. D., et al. (2019). The DOE E3SM Coupled Model Version 1: Overview and Evaluation at Standard Resolution. *J. Adv. Model. Earth Syst.* 11, 2089–2129. doi:10.1029/2018MS001603.
Golledge, N. R., Keller, E. D., Gomez, N., Naughten, K. A., Bernales, J., Trusel, L. D., et al. (2019). Global environmental consequences of twenty-first-century ice-sheet melt. *Nature* 566, 65–72. doi:10.1038/s41586-019-0889-9.
Greve, R., and Blatter, H. (2016). Comparison of thermodynamics solvers in the polythermal ice sheet model SICOPOLIS. *Polar Sci.* 10, 11–23. doi:10.1016/j.polar.2015.12.004.
Greve, R., Chambers, C., and Calov, R. (2020). ISMIP6 future projections for the Greenland ice sheet with the model SICOPOLIS. Zenodo. Available at: http://doi.org/10.5281/zenodo.4035941.
Greve, R., and SICOPOLIS Developer Team (2019). SICOPOLIS v5.1 (Version 5.1). Zenodo. doi:10.5281/zenodo.3727511.
Gudmundsson, G. H., Krug, J., Durand, G., Favier, L., and Gagliardini, O. (2012). The stability of grounding lines on retrograde slopes. *Cryosph.* 6, 1497–1505. doi:10.5194/tc-6-1497-2012.
Guilyardi, E., Balaji, V., Lawrence, B., Callaghan, S., Deluca, C., Denvil, S., et al. (2013). Documenting Climate Models and Their Simulations. *Bull. Am. Meteorol. Soc.* 94, 623–627. doi:10.1175/BAMS-D-11-00035.1.
Guo, C., Bentsen, M., Bethke, I., Ilicak, M., Tjiputra, J., Toniazzo, T., et al. (2019). Description and evaluation of NorESM1-F: a fast version of the Norwegian Earth System Model (NorESM). *Geosci. Model Dev.* 12, 343–362. doi:10.5194/gmd-12-343-2019.
Gutjahr, O., Putrasahan, D., Lohmann, K., Jungclaus, J. H., von Storch, J.-S., Brüggemann, N., et al. (2019). Max Planck Institute Earth System Model (MPI-ESM1.2) for the High-Resolution Model Intercomparison Project (HighResMIP). *Geosci. Model Dev.* 12, 3241–3281. doi:10.5194/gmd-12-3241-2019.
Gutowski Jr., W. J., Giorgi, F., Timbal, B., Frigon, A., Jacob, D., Kang, H.-S., et al. (2016). WCRP COordinated Regional Downscaling EXperiment (CORDEX): a diagnostic MIP for CMIP6. *Geosci. Model Dev.* 9, 4087–4095. doi:10.5194/gmd-9-4087-2016.
Haarsma, R., Acosta, M., Bakhshi, R., Bretonnière, P.-A., Caron, L.-P., Castrillo, M., et al. (2020). HighResMIP versions of EC-Earth: EC-Earth3P and EC-Earth3P-HR -- description, model computational performance and basic validation. *Geosci. Model Dev.* 13, 3507–3527. doi:10.5194/gmd-13-3507-2020.
Haarsma, R. J., Roberts, M. J., Vidale, P. L., Senior, C. A., Bellucci, A., Bao, Q., et al. (2016). High Resolution Model Intercomparison Project (HighResMIP v1.0) for CMIP6. *Geosci. Model Dev.* 9, 4185–4208. doi:10.5194/gmd-9-4185-2016.

ACCEPTED VERSION
SUBJECT TO FINAL EDITING

Haidvogel, D. B., Arango, H., Budgell, W. P., Cornuelle, B. D., Curchitser, E., Di Lorenzo, E., et al. (2008). Ocean forecasting in terrain-following coordinates: Formulation and skill assessment of the Regional Ocean Modeling System. *J. Comput. Phys.* 227, 3595–3624. doi:10.1016/j.jcp.2007.06.016.

Hajima, T., Watanabe, M., Yamamoto, A., Tatebe, H., Noguchi, M. A., Abe, M., et al. (2020). Development of the MIROC-ES2L Earth system model and the evaluation of biogeochemical processes and feedbacks. *Geosci. Model Dev.* 13, 2197–2244. doi:10.5194/gmd-13-2197-2020.

Hauglustaine, D. A., Balkanski, Y., and Schulz, M. (2014). A global model simulation of present and future nitrate aerosols and their direct radiative forcing of climate. *Atmos. Chem. Phys.* 14, 11031–11063. doi:10.5194/acp-14-11031-2014.

He, B., Bao, Q., Wang, X., Zhou, L., Wu, X., Liu, Y., et al. (2019). CAS FGOALS-f3-L Model Datasets for CMIP6 Historical Atmospheric Model Intercomparison Project Simulation. *Adv. Atmos. Sci.* 36, 771–778. doi:10.1007/s00376-019-9027-8.

He, B., Yu, Y., Bao, Q., LIN, P., LIU, H., LI, J., et al. (2020). CAS FGOALS-f3-L model dataset descriptions for CMIP6 DECK experiments. *Atmos. Ocean. Sci. Lett.* 13, 582–588. doi:10.1080/16742834.2020.1778419.

Held, I. M., Guo, H., Adcroft, A., Dunne, J. P., Horowitz, L. W., Krasting, J., et al. (2019). Structure and Performance of GFDL's CM4.0 Climate Model. *J. Adv. Model. Earth Syst.* 11, 3691–3727. doi:10.1029/2019MS001829.

Hock, R., Bliss, A., Marzeion, B. E. N., Giesen, R. H., Hirabayashi, Y., Huss, M., et al. (2019). GlacierMIP – A model intercomparison of global-scale glacier mass-balance models and projections. *J. Glaciol.* 65, 453–467. doi:10.1017/jog.2019.22.

Hoffman, M. J., Perego, M., Price, S. F., Lipscomb, W. H., Zhang, T., Jacobsen, D., et al. (2018). MPAS-Albany Land Ice (MALI): a variable-resolution ice sheet model for Earth system modeling using Voronoi grids. *Geosci. Model Dev.* 11, 3747–3780. doi:10.5194/gmd-11-3747-2018.

Hoffmann, P., Katzfey, J. J., McGregor, J. L., and Thatcher, M. (2016). Bias and variance correction of sea surface temperatures used for dynamical downscaling. *J. Geophys. Res. Atmos.* 121, 12,877-12,890. doi:10.1002/2016JD025383.

Horowitz, L. W., Naik, V., Paulot, F., Ginoux, P. A., Dunne, J. P., Mao, J., et al. (2020). The GFDL Global Atmospheric Chemistry-Climate Model AM4.1: Model Description and Simulation Characteristics. *J. Adv. Model. Earth Syst.* 12, e2019MS002032. doi:https://doi.org/10.1029/2019MS002032.

Hostetler, S. W., Giorgi, F., Bates, G. T., and Bartlein, P. J. (1994). Lake-Atmosphere Feedbacks Associated with Paleolakes Bonneville and Lahontan. *Science (80-.).* 263, 665–668. doi:10.1126/science.263.5147.665.

Hourdin, F., Rio, C., Grandpeix, J.-Y., Madeleine, J.-B., Cheruy, F., Rochetin, N., et al. (2020). LMDZ6A: The Atmospheric Component of the IPSL Climate Model With Improved and Better Tuned Physics. *J. Adv. Model. Earth Syst.* 12, e2019MS001892. doi:https://doi.org/10.1029/2019MS001892.

Hunke, E. C., Lipscomb, W. H., Turner, A. K., Jeffery, N., and Elliott, S. (2015). CICE: the Los Alamos Sea Ice Model Documentation and Software User's Manual Version 4.1 LA-CC-06-012.

Hunke, E., and Lipscomp, W. H. (2008). CICE: The Los Alamos Sea Ice Model Documentation and Software User's Manual Version 4.1. Los Alamos.

Huss, M., and Hock, R. (2015). A new model for global glacier change and sea-level rise. *Front. Earth Sci.* 3. doi:10.3389/feart.2015.00054.

Huybrechts, P. (2002). Sea-level changes at the LGM from ice-dynamic reconstructions of the Greenland and Antarctic ice sheets during the glacial cycles. *Quat. Sci. Rev.* 21, 203–231. doi:10.1016/S0277-3791(01)00082-8.

Inness, A., Baier, F., Benedetti, A., Bouarar, I., Chabrillat, S., Clark, H., et al. (2013). The MACC reanalysis: an 8 yr data set of atmospheric composition. *Atmos. Chem. Phys.* 13, 4073–4109. doi:10.5194/acp-13-4073-2013.

Jacob, D. (2001). A note to the simulation of the annual and inter-annual variability of the water budget over the Baltic Sea drainage basin. *Meteorol. Atmos. Phys.* 77, 61–73. doi:10.1007/s007030170017.

Jacob, D., and Podzun, R. (1997). Sensitivity studies with the regional climate model REMO. *Meteorol. Atmos. Phys.* 63, 119–129. doi:10.1007/BF01025368.

Kawamiya, M., Hajima, T., Tachiiri, K., Watanabe, S., and Yokohata, T. (2020). Two decades of Earth system modeling with an emphasis on Model for Interdisciplinary Research on Climate (MIROC). *Prog. Earth Planet. Sci.* 7, 64. doi:10.1186/s40645-020-00369-5.

Kelley, M., Schmidt, G. A., Nazarenko, L. S., Bauer, S. E., Ruedy, R., Russell, G. L., et al. (2020). GISS-E2.1: Configurations and Climatology. *J. Adv. Model. Earth Syst.* 12. doi:10.1029/2019MS002025.

Kinne, S., Schulz, M., Textor, C., Guibert, S., Balkanski, Y., Bauer, S. E., et al. (2006). An AeroCom initial assessment – optical properties in aerosol component modules of global models. *Atmos. Chem. Phys.* 6, 1815–1834. doi:10.5194/acp-6-1815-2006.

Kirkevåg, A., Grini, A., Olivié, D., Seland, Ø., Alterskjær, K., Hummel, M., et al. (2018). A production-tagged aerosol module for Earth system models, OsloAero5.3 -- extensions and updates for CAM5.3-Oslo. *Geosci. Model Dev.* 11, 3945–3982. doi:10.5194/gmd-11-3945-2018.

Kiss, A. E., McC Hogg, A., Hannah, N., Boeira Dias, F., B Brassington, G., Chamberlain, M. A., et al. (2020). ACCESS-OM2 v1.0: A global ocean-sea ice model at three resolutions. *Geosci. Model Dev.* 13, 401–442. doi:10.5194/gmd-13-401-2020.

ACCEPTED VERSION SUBJECT TO FINAL EDITING

Kittel, C., Amory, C., Agosta, C., Jourdain, N. C., Hofer, S., Delhasse, A., et al. (2021). Diverging future surface mass balance between the Antarctic ice shelves and grounded ice sheet. *Cryosph.* 15, 1215–1236. doi:10.5194/tc-15-1215-2021.

Klemp, J. B., Dudhia, J., and Hassiotis, A. D. (2008). An Upper Gravity-Wave Absorbing Layer for NWP Applications. *Mon. Weather Rev.* 136, 3987–4004. doi:10.1175/2008MWR2596.1.

Kowalczyk, E., Stevens, L., Law, R., Dix, M., Wang, Y., Harman, I., et al. (2013). The land surface model component of ACCESS: description and impact on the simulated surface climatology. *Aust. Meteorol. Oceanogr. J.* 63, 65–82. doi:10.22499/2.6301.005.

Kraaijenbrink, P. D. A., Bierkens, M. F. P., Lutz, A. F., and Immerzeel, W. W. (2017). Impact of a global temperature rise of 1.5 degrees Celsius on Asia's glaciers. *Nature* 549, 257–260. doi:10.1038/nature23878.

Kržič, A., Tošić, I., Djurdjević, V., Veljović, K., and Rajković, B. (2011). Changes in climate indices for Serbia according to the SRES-A1B and SRES-A2 scenarios. *Clim. Res.* 49, 73–86. doi:10.3354/cr01008.

Kuhlbrodt, T., Jones, C. G., Sellar, A., Storkey, D., Blockley, E., Stringer, M., et al. (2018). The Low-Resolution Version of HadGEM3 GC3.1: Development and Evaluation for Global Climate. *J. Adv. Model. Earth Syst.* 10, 2865–2888. doi:10.1029/2018MS001370.

Kuipers Munneke, P., van den Broeke, M. R., Lenaerts, J. T. M., Flanner, M. G., Gardner, A. S., and van de Berg, W. J. (2011). A new albedo parameterization for use in climate models over the Antarctic ice sheet. *J. Geophys. Res.* 116, D05114. doi:10.1029/2010JD015113.

L'Hévéder, B., Li, L., Sevault, F., and Somot, S. (2013). Interannual variability of deep convection in the Northwestern Mediterranean simulated with a coupled AORCM. *Clim. Dyn.* 41, 937–960. doi:10.1007/s00382-012-1527-5.

Lamarque, J.-F., Bond, T. C., Eyring, V., Granier, C., Heil, A., Klimont, Z., et al. (2010). Historical (1850–2000) gridded anthropogenic and biomass burning emissions of reactive gases and aerosols: methodology and application. *Atmos. Chem. Phys.* 10, 7017–7039. doi:10.5194/acp-10-7017-2010.

Lamarque, J.-F., McConnell, J. R., Shindell, D. T., Orlando, J. J., and Tyndall, G. S. (2011). Understanding the drivers for the 20th century change of hydrogen peroxide in Antarctic ice-cores. *Geophys. Res. Lett.* 38, n/a-n/a. doi:10.1029/2010GL045992.

Larour, E., Seroussi, H., Morlighem, M., and Rignot, E. (2012). Continental scale, high order, high spatial resolution, ice sheet modeling using the Ice Sheet System Model (ISSM). *J. Geophys. Res. Earth Surf.* 117, F01022. doi:10.1029/2011JF002140.

Lawrence, B. N., Balaji, V., Bentley, P., Callaghan, S., DeLuca, C., Denvil, S., et al. (2012). Describing Earth system simulations with the Metafor CIM. *Geosci. Model Dev.* 5, 1493–1500. doi:10.5194/gmd-5-1493-2012.

Lawrence, D. M., Fisher, R. A., Koven, C. D., Oleson, K. W., Swenson, S. C., Bonan, G., et al. (2019). The Community Land Model Version 5: Description of New Features, Benchmarking, and Impact of Forcing Uncertainty. *J. Adv. Model. Earth Syst.* 11, 4245–4287. doi:10.1029/2018MS001583.

Lawrence, D. M., Oleson, K. W., Flanner, M. G., Thornton, P. E., Swenson, S. C., Lawrence, P. J., et al. (2011). Parameterization improvements and functional and structural advances in Version 4 of the Community Land Model. *J. Adv. Model. Earth Syst.* 3. doi:10.1029/2011MS00045.

Le Moigne, P., Colin, J., and Decharme, B. (2016). Impact of lake surface temperatures simulated by the FLake scheme in the CNRM-CM5 climate model. *Tellus A Dyn. Meteorol. Oceanogr.* 68, 31274. doi:10.3402/tellusa.v68.31274.

Lee, J., Kim, J., Sun, M.-A., Kim, B.-H., Moon, H., Sung, H. M., et al. (2019). Evaluation of the Korea Meteorological Administration Advanced Community Earth-System model (K-ACE). *Asia-Pacific J. Atmos. Sci.* doi:10.1007/s13143-019-00144-7.

Lee, V., Cornford, S. L., and Payne, A. J. (2015). Initialization of an ice-sheet model for present-day Greenland. *Ann. Glaciol.* 56, 129–140. doi:10.3189/2015AoG70A121.

Lee, W.-L., Liou, K. N., and Wang, C. (2013). Impact of 3-D topography on surface radiation budget over the Tibetan Plateau. *Theor. Appl. Climatol.* 113, 95–103. doi:10.1007/s00704-012-0767-y.

Lee, W.-L., Wang, Y.-C., Shiu, C.-J., Tsai, I., Tu, C.-Y., Lan, Y.-Y., et al. (2020). Taiwan Earth System Model Version 1: description and evaluation of mean state. *Geosci. Model Dev.* 13, 3887–3904. doi:10.5194/gmd-13-3887-2020.

Lefebre, F. (2003). Modeling of snow and ice melt at ETH Camp (West Greenland): A study of surface albedo. *J. Geophys. Res.* 108, 4231. doi:10.1029/2001JD001160.

Lenaerts, J. T. M., van den Broeke, M. R., Déry, S. J., van Meijgaard, E., van de Berg, W. J., Palm, S. P., et al. (2012). Modeling drifting snow in Antarctica with a regional climate model: 1. Methods and model evaluation. *J. Geophys. Res. Atmos.* 117, n/a-n/a. doi:10.1029/2011JD016145.

Leutwyler, D., Lüthi, D., Ban, N., Fuhrer, O., and Schär, C. (2017). Evaluation of the convection-resolving climate modeling approach on continental scales. *J. Geophys. Res. Atmos.* 122, 5237–5258. doi:10.1002/2016JD026013.

Levermann, A., Winkelmann, R., Albrecht, T., Goelzer, H., Golledge, N. R., Greve, R., et al. (2020). Projecting Antarctica's contribution to future sea level rise from basal ice shelf melt using linear response functions of 16 ice sheet models (LARMIP-2). *Earth Syst. Dyn.* 11, 35–76. doi:10.5194/esd-11-35-2020.

Li, D., Yin, B., Feng, J., Dosio, A., Geyer, B., Qi, J., et al. (2018). Present Climate Evaluation and Added Value Analysis of Dynamically Downscaled Simulations of CORDEX—East Asia. *J. Appl. Meteorol. Climatol.* 57, 2317–2341. doi:10.1175/JAMC-D-18-0008.1.

ACCEPTED VERSION SUBJECT TO FINAL EDITING

Li, L., Yu, Y., Tang, Y., Lin, P., Xie, J., Song, M., et al. (2020). The Flexible Global Ocean-Atmosphere-Land System Model Grid-Point Version 3 (FGOALS-g3): Description and Evaluation. *J. Adv. Model. Earth Syst.* 12, e2019MS002012. doi:https://doi.org/10.1029/2019MS002012.

Li, W., Zhang, Y., Shi, X., Zhou, W., Huang, A., Mu, M., et al. (2019). Development of Land Surface Model BCC_AVIM2.0 and Its Preliminary Performance in LS3MIP/CMIP6. *J. Meteorol. Res.* 33, 851–869. doi:10.1007/s13351-019-9016-y.

Lin, P., Yu, Z., Liu, H., Yu, Y., Li, Y., Jiang, J., et al. (2020a). LICOM Model Datasets for the CMIP6 Ocean Model Intercomparison Project. *Adv. Atmos. Sci.* 37, 239–249. doi:10.1007/s00376-019-9208-5.

Lin, Y., Huang, X., Liang, Y., Qin, Y., Xu, S., Huang, W., et al. (2020b). Community Integrated Earth System Model (CIESM): Description and Evaluation. *J. Adv. Model. Earth Syst.* 12, e2019MS002036. doi:https://doi.org/10.1029/2019MS002036.

Lipscomb, W. H., Price, S. F., Hoffman, M. J., Leguy, G. R., Bennett, A. R., Bradley, S. L., et al. (2019). Description and evaluation of the Community Ice Sheet Model (CISM) v2.1. *Geosci. Model Dev.* 12, 387–424. doi:10.5194/gmd-12-387-2019.

Lipson, M. J., Thatcher, M., Hart, M. A., and Pitman, A. (2018). A building energy demand and urban land surface model. *Q. J. R. Meteorol. Soc.* 144, 1572–1590. doi:10.1002/qj.3317.

Liu, X., Easter, R. C., Ghan, S. J., Zaveri, R., Rasch, P., Shi, X., et al. (2012a). Toward a minimal representation of aerosols in climate models: description and evaluation in the Community Atmosphere Model CAM5. *Geosci. Model Dev.* 5, 709–739. doi:10.5194/gmd-5-709-2012.

Liu, X., Easter, R. C., Ghan, S. J., Zaveri, R., Rasch, P., Shi, X., et al. (2012b). Toward a minimal representation of aerosols in climate models: description and evaluation in the Community Atmosphere Model CAM5. *Geosci. Model Dev.* 5, 709–739. doi:10.5194/gmd-5-709-2012.

Liu, X., Ma, P.-L., Wang, H., Tilmes, S., Singh, B., Easter, R. C., et al. (2016). Description and evaluation of a new four-mode version of the Modal Aerosol Module (MAM4) within version 5.3 of the Community Atmosphere Model. *Geosci. Model Dev.* 9, 505–522. doi:10.5194/gmd-9-505-2016.

Lurton, T., Balkanski, Y., Bastrikov, V., Bekki, S., Bopp, L., Braconnot, P., et al. (2020). Implementation of the CMIP6 Forcing Data in the IPSL-CM6A-LR Model. *J. Adv. Model. Earth Syst.* 12, e2019MS001940. doi:https://doi.org/10.1029/2019MS001940.

Manabe, S. (1969). Climate and the Ocean Circulation : I. The Atmospheric Circulation and the Hydrology of the Earth's Surface. *Mon. Weather Rev.* 97, 739–774.

Martynov, A., Laprise, R., Sushama, L., Winger, K., Šeparović, L., and Dugas, B. (2013). Reanalysis-driven climate simulation over CORDEX North America domain using the Canadian Regional Climate Model, version 5: model performance evaluation. *Clim. Dyn.* 41, 2973–3005. doi:10.1007/s00382-013-1778-9.

Marzeion, B., Hock, R., Anderson, B., Bliss, A., Champollion, N., Fujita, K., et al. (2020). Partitioning the Uncertainty of Ensemble Projections of Global Glacier Mass Change. *Earth's Futur.* 8, e2019EF001470. doi:https://doi.org/10.1029/2019EF001470.

Marzeion, B., Jarosch, A. H., and Hofer, M. (2012). Past and future sea-level change from the surface mass balance of glaciers. *Cryosph.* 6, 1295–1322. doi:10.5194/tc-6-1295-2012.

Mauritsen, T., Bader, J., Becker, T., Behrens, J., Bittner, M., Brokopf, R., et al. (2019). Developments in the MPI-M Earth System Model version 1.2 (MPI-ESM 1.2) and its response to increasing CO2. *J. Adv. Model. Earth Syst.* 0. doi:10.1029/2018MS001400.

Maussion, F., Butenko, A., Eis, J., Fourteau, K., Jarosch, A. H., Landmann, J., et al. (2019). The Open Global Glacier Model (OGGM) v1.0. *Geosci. Model Dev.* 12, 909–931. doi:10.5194/gmd-2018-9.

Mearns, L., McGinnis, S., Korytina, D., Arritt, R., Biner, S., Bukovsky, M., et al. (2017). The NA-CORDEX dataset, version 1.0. NCAR Climate Data Gateway. Boulder CO doi:10.5065/D6SJ1JCH.

Meehl, G. A., Yang, D., Arblaster, J. M., Bates, S. C., Rosenbloom, N., Neale, R., et al. (2019). Effects of Model Resolution, Physics, and Coupling on Southern Hemisphere Storm Tracks in CESM1.3. *Geophys. Res. Lett.* 46, 12408–12416. doi:https://doi.org/10.1029/2019GL084057.

Michou, M., Nabat, P., Saint-Martin, D., Bock, J., Decharme, B., Mallet, M., et al. (2020). Present-Day and Historical Aerosol and Ozone Characteristics in CNRM CMIP6 Simulations. *J. Adv. Model. Earth Syst.* 12, e2019MS001816. doi:https://doi.org/10.1029/2019MS001816.

Milly, P. C. D., Malyshev, S. L., Shevliakova, E., Dunne, K. A., Findell, K. L., Gleeson, T., et al. (2014). An Enhanced Model of Land Water and Energy for Global Hydrologic and Earth-System Studies. *J. Hydrometeorol.* 15, 1739–1761. doi:10.1175/JHM-D-13-0162.1.

Mironov, D., Heise, E., Kourzeneva, E., Ritter, B., Schneider, N., and Terzhevik, A. (2010). Implementation of the lake parameterisation scheme FLake into the numerical weather prediction model COSMO. *Boreal Environ. Res. 15* 15, 218–230. Available at: https://helda.helsinki.fi/handle/10138/233087.

Mizuta, R., Yoshimura, H., Murakami, H., Matsueda, M., Endo, H., Ose, T., et al. (2012). Climate Simulations Using MRI-AGCM3.2 with 20-km Grid. *J. Meteorol. Soc. Japan. Ser. II* 90A, 233–258. doi:10.2151/jmsj.2012-A12.

Mlawer, E. J., Taubman, S. J., Brown, P. D., Iacono, M. J., and Clough, S. A. (1997). Radiative transfer for inhomogeneous atmospheres: RRTM, a validated correlated-k model for the longwave. *J. Geophys. Res. Atmos.*

ACCEPTED VERSION SUBJECT TO FINAL EDITING

102, 16663–16682. doi:10.1029/97JD00237.
Morcrette, J.-J., Barker, H. W., Cole, J. N. S., Iacono, M. J., and Pincus, R. (2008). Impact of a New Radiation Package, McRad, in the ECMWF Integrated Forecasting System. *Mon. Weather Rev.* 136, 4773–4798. doi:10.1175/2008MWR2363.1.
Morgenstern, O., Hegglin, M. I., Rozanov, E., O'Connor, F. M., Abraham, N. L., Akiyoshi, H., et al. (2017). Review of the global models used within phase 1 of the Chemistry–Climate Model Initiative (CCMI). *Geosci. Model Dev.* 10, 639–671. doi:10.5194/gmd-10-639-2017.
Morlighem, M., Rignot, E., Seroussi, H., Larour, E., Ben Dhia, H., and Aubry, D. (2010). Spatial patterns of basal drag inferred using control methods from a full-Stokes and simpler models for Pine Island Glacier, West Antarctica. *Geophys. Res. Lett.* 37, L14502. doi:10.1029/2010GL043853.
Mulcahy, J. P., Johnson, C., Jones, C. G., Povey, A. C., Scott, C. E., Sellar, A., et al. (2020). Description and evaluation of aerosol in UKESM1 and HadGEM3-GC3.1 CMIP6 historical simulations. *Geosci. Model Dev.* 13, 6383–6423. doi:10.5194/gmd-13-6383-2020.
Müller, W. A., Jungclaus, J. H., Mauritsen, T., Baehr, J., Bittner, M., Budich, R., et al. (2018). A Higher-resolution Version of the Max Planck Institute Earth System Model (MPI-ESM1.2-HR). *J. Adv. Model. Earth Syst.* 10, 1383–1413. doi:10.1029/2017MS001217.
Nabat, P., Somot, S., Cassou, C., Mallet, M., Michou, M., Bouniol, D., et al. (2020). Modulation of radiative aerosols effects by atmospheric circulation over the Euro-Mediterranean region. *Atmos. Chem. Phys.* 20, 8315–8349. doi:10.5194/acp-20-8315-2020.
Nakano, H., Ishii, M., Rodgers, K. B., Tsujino, H., and Yamanaka, G. (2015). Anthropogenic CO2 uptake, transport, storage, and dynamical controls in the ocean imposed by the meridional overturning circulation: A modeling study. *Global Biogeochem. Cycles* 29, 1706–1724. doi:10.1002/2015GB005128.
Neubauer, D., Ferrachat, S., Siegenthaler-Le Drian, C., Stier, P., Partridge, D. G., Tegen, I., et al. (2019). The global aerosol--climate model ECHAM6.3--HAM2.3 -- Part 2: Cloud evaluation, aerosol radiative forcing, and climate sensitivity. *Geosci. Model Dev.* 12, 3609–3639. doi:10.5194/gmd-12-3609-2019.
Nitta, T., Yoshimura, K., and Abe-Ouchi, A. (2017). Impact of Arctic Wetlands on the Climate System: Model Sensitivity Simulations with the MIROC5 AGCM and a Snow-Fed Wetland Scheme. *J. Hydrometeorol.* 18, 2923–2936. doi:10.1175/JHM-D-16-0105.1.
Nitta, T., Yoshimura, K., Takata, K., O'ishi, R., Sueyoshi, T., Kanae, S., et al. (2014). Representing Variability in Subgrid Snow Cover and Snow Depth in a Global Land Model: Offline Validation. *J. Clim.* 27, 3318–3330. doi:10.1175/JCLI-D-13-00310.1.
Niu, G.-Y., Yang, Z.-L., Mitchell, K. E., Chen, F., Ek, M. B., Barlage, M., et al. (2011). The community Noah land surface model with multiparameterization options (Noah-MP): 1. Model description and evaluation with local-scale measurements. *J. Geophys. Res.* 116, D12109. doi:10.1029/2010JD015139.
Noilhan, J., and Mahfouf, J.-F. (1996). The ISBA land surface parameterisation scheme. *Glob. Planet. Change* 13, 145–159. doi:10.1016/0921-8181(95)00043-7.
Notz, D., Haumann, F. A., Haak, H., Jungclaus, J. H., and Marotzke, J. (2013a). Arctic sea-ice evolution as modeled by Max Planck Institute for Meteorology's Earth system model. *J. Adv. Model. Earth Syst.* 5, 173–194. doi:10.1002/jame.20016.
Notz, D., Haumann, F. A., Haak, H., Jungclaus, J. H., and Marotzke, J. (2013b). Arctic sea-ice evolution as modeled by Max Planck Institute for Meteorology's Earth system model. *J. Adv. Model. Earth Syst.* 5, 173–194. doi:10.1002/jame.20016.
O'Neill, B. C., Tebaldi, C., van Vuuren, D. P., Eyring, V., Friedlingstein, P., Hurtt, G., et al. (2016). The Scenario Model Intercomparison Project (ScenarioMIP) for CMIP6. *Geosci. Model Dev.* 9, 3461–3482. doi:10.5194/gmd-9-3461-2016.
Obata, A., and Adachi, Y. (2019). Earth System Model Response to Large Midlatitude and High-latitude Volcanic Eruptions. *J. Geophys. Res. Biogeosciences* 124, 1865–1886. doi:10.1029/2018JG004696.
Obata, A., and Shibata, K. (2012). Damage of Land Biosphere due to Intense Warming by 1000-Fold Rapid Increase in Atmospheric Methane: Estimation with a Climate–Carbon Cycle Model. *J. Clim.* 25, 8524–8541. doi:10.1175/JCLI-D-11-00533.1.
Oki, T., and Sud, Y. C. (1998). Design of Total Runoff Integrating Pathways (TRIP)—A Global River Channel Network. *Earth Interact.* 2, 1–37. doi:10.1175/1087-3562(1998)002<0001:DOTRIP>2.3.CO;2.
Oleson, K., Lawrence, D. M., Bonan, G. B., Drewniak, B., Huang, M., Koven, C. D., et al. (2013). Technical description of version 4.5 of the Community Land Model (CLM). Boulder, CO, U.S.A. doi:http://dx.doi.org/10.5065/D6RR1W7M.
Oshima, N., Yukimoto, S., Deushi, M., Koshiro, T., Kawai, H., Tanaka, T. Y., et al. (2020). Global and Arctic effective radiative forcing of anthropogenic gases and aerosols in MRI-ESM2.0. *Prog. Earth Planet. Sci.* 7, 38. doi:10.1186/s40645-020-00348-w.
Ozturk, T., Turp, M. T., Türkeş, M., and Kurnaz, M. L. (2017). Projected changes in temperature and precipitation climatology of Central Asia CORDEX Region 8 by using RegCM4.3.5. *Atmos. Res.* 183, 296–307. doi:10.1016/j.atmosres.2016.09.008.

ACCEPTED VERSION SUBJECT TO FINAL EDITING

Ozturk, T., Turp, M. T., Türkeş, M., and Kurnaz, M. L. (2018). Future projections of temperature and precipitation climatology for CORDEX-MENA domain using RegCM4.4. *Atmos. Res.* 206, 87–107. doi:10.1016/j.atmosres.2018.02.009.

Pak, G., Noh, Y., Lee, M.-I., Yeh, S.-W., Kim, D., Kim, S.-Y., et al. (2021). Korea Institute of Ocean Science and Technology Earth System Model and its simulation characteristics. *Ocean Sci. J.* 56.

Pal, J. S., Giorgi, F., Bi, X., Elguindi, N., Solmon, F., Gao, X., et al. (2007). Regional Climate Modeling for the Developing World: The ICTP RegCM3 and RegCNET. *Bull. Am. Meteorol. Soc.* 88, 1395–1410. doi:10.1175/BAMS-88-9-1395.

Panitz, H.-J., Dosio, A., Büchner, M., Lüthi, D., and Keuler, K. (2014). COSMO-CLM (CCLM) climate simulations over CORDEX-Africa domain: analysis of the ERA-Interim driven simulations at 0.44° and 0.22° resolution. *Clim. Dyn.* 42, 3015–3038. doi:10.1007/s00382-013-1834-5.

Park, S., Shin, J., Kim, S., Oh, E., and Kim, Y. (2019). Global Climate Simulated by the Seoul National University Atmosphere Model Version 0 with a Unified Convection Scheme (SAM0-UNICON). *J. Clim.* 32, 2917–2949. doi:10.1175/JCLI-D-18-0796.1.

Pascoe, C., Lawrence, B. N., Guilyardi, E., Juckes, M., and Taylor, K. E. (2019). Designing and Documenting Experiments in CMIP6. *Geosci. Model Dev. Discuss.*, 1–27. doi:10.5194/gmd-2019-98.

Pattyn, F. (2017). Sea-level response to melting of Antarctic ice shelves on multi-centennial timescales with the fast Elementary Thermomechanical Ice Sheet model (f.ETISh v1.0). *Cryosph.* 11, 1851–1878. doi:10.5194/tc-11-1851-2017.

Petersen, M. R., Asay-Davis, X. S., Berres, A. S., Chen, Q., Feige, N., Hoffman, M. J., et al. (2019). An Evaluation of the Ocean and Sea Ice Climate of E3SM Using MPAS and Interannual CORE-II Forcing. *J. Adv. Model. Earth Syst.* 11, 1438–1458. doi:10.1029/2018MS001373.

Petrie, R., Denvil, S., Ames, S., Levavasseur, G., Fiore, S., Allen, C., et al. (2021). Coordinating an operational data distribution network for CMIP6 data. *Geosci. Model Dev.* 14, 629–644. doi:10.5194/gmd-14-629-2021.

Pollard, D., and DeConto, R. M. (2012). Description of a hybrid ice sheet-shelf model, and application to Antarctica. *Geosci. Model Dev.* 5, 1273–1295. doi:10.5194/gmd-5-1273-2012.

Pollard, D., DeConto, R. M., and Alley, R. B. (2015). Potential Antarctic Ice Sheet retreat driven by hydrofracturing and ice cliff failure. *Earth Planet. Sci. Lett.* 412, 112–121. doi:10.1016/j.epsl.2014.12.035.

Powers, J. G., Klemp, J. B., Skamarock, W. C., Davis, C. A., Dudhia, J., Gill, D. O., et al. (2017). The Weather Research and Forecasting Model: Overview, System Efforts, and Future Directions. *Bull. Am. Meteorol. Soc.* 98, 1717–1737. doi:10.1175/BAMS-D-15-00308.1.

Qiao, F., Song, Z., Bao, Y., Song, Y., Shu, Q., Huang, C., et al. (2013). Development and evaluation of an Earth System Model with surface gravity waves. *J. Geophys. Res. Ocean.* 118, 4514–4524. doi:10.1002/jgrc.20327.

Quiquet, A., Dumas, C., Ritz, C., Peyaud, V., and Roche, D. M. (2018). The GRISLI ice sheet model (version 2.0): calibration and validation for multi-millennial changes of the Antarctic ice sheet. *Geosci. Model Dev.* 11, 5003–5025. doi:10.5194/gmd-11-5003-2018.

Radić, V., Bliss, A., Beedlow, A. C., Hock, R., Miles, E., and Cogley, J. G. (2014). Regional and global projections of twenty-first century glacier mass changes in response to climate scenarios from global climate models. *Clim. Dyn.* 42, 37–58. doi:10.1007/s00382-013-1719-7.

Rasch, P. J., Xie, S., Ma, P.-L., Lin, W., Wang, H., Tang, Q., et al. An Overview of the Atmospheric Component of the Energy Exascale Earth System Model. *J. Adv. Model. Earth Syst.* 0. doi:10.1029/2019MS001629.

Rechid, D., Raddatz, T. J., and Jacob, D. (2009). Parameterization of snow-free land surface albedo as a function of vegetation phenology based on MODIS data and applied in climate modelling. *Theor. Appl. Climatol.* 95, 245–255. doi:10.1007/s00704-008-0003-y.

Reick, C. H., Gayler, V., Goll, D., Hagemann, S., Heidkamp, M., Nabel, J. E. M. S., et al. (2021). JSBACH 3 - The land component of the MPI Earth System Model: documentation of version 3.2. Hamburg, Germany doi:10.17617/2.3279802.

Ridley, J. K., Blockley, E. W., Keen, A. B., Rae, J. G. L., West, A. E., and Schroeder, D. (2018a). The sea ice model component of HadGEM3-GC3.1. *Geosci. Model Dev.* 11, 713–723. doi:10.5194/gmd-11-713-2018.

Ridley, J. K., Blockley, E. W., Keen, A. B., Rae, J. G. L., West, A. E., and Schroeder, D. (2018b). The sea ice model component of HadGEM3-GC3.1. *Geosci. Model Dev.* 11, 713–723. doi:10.5194/gmd-11-713-2018.

Rind, D., Orbe, C., Jonas, J., Nazarenko, L., Zhou, T., Kelley, M., et al. (2020). GISS Model E2.2: A Climate Model Optimized for the Middle Atmosphere—Model Structure, Climatology, Variability, and Climate Sensitivity. *J. Geophys. Res. Atmos.* 125. doi:10.1029/2019JD032204.

Roberts, C. D., Senan, R., Molteni, F., Boussetta, S., Mayer, M., and Keeley, S. P. E. (2018). Climate model configurations of the ECMWF Integrated Forecasting System (ECMWF-IFS cycle 43r1) for HighResMIP. *Geosci. Model Dev.* 11, 3681–3712. doi:10.5194/gmd-11-3681-2018.

Roberts, M. J., Baker, A., Blockley, E. W., Calvert, D., Coward, A., Hewitt, H. T., et al. (2019). Description of the resolution hierarchy of the global coupled HadGEM3-GC3.1 model as used in CMIP6 HighResMIP experiments. *Geosci. Model Dev.* 12, 4999–5028. doi:10.5194/gmd-12-4999-2019.

Roehrig, R., Beau, I., Saint-Martin, D., Alias, A., Decharme, B., Guérémy, J.-F., et al. (2020). The CNRM Global

ACCEPTED VERSION SUBJECT TO FINAL EDITING

Atmosphere Model ARPEGE-Climat 6.3: Description and Evaluation. *J. Adv. Model. Earth Syst.* 12, e2020MS002075. doi:https://doi.org/10.1029/2020MS002075.

Rong, X., Li, J., Chen, H., Xin, Y., Su, J., Hua, L., et al. (2018). The CAMS Climate System Model and a Basic Evaluation of Its Climatology and Climate Variability Simulation. *J. Meteorol. Res.* 32, 839–861. doi:10.1007/s13351-018-8058-x.

Rotstayn, L. D., Collier, M. A., Mitchell, R. M., Qin, Y., Campbell, S. K., and Dravitzki, S. M. (2011). Simulated enhancement of ENSO-related rainfall variability due to Australian dust. *Atmos. Chem. Phys.* 11, 6575–6592. doi:10.5194/acp-11-6575-2011.

Rotstayn, L. D., and Lohmann, U. (2002). Simulation of the tropospheric sulfur cycle in a global model with a physically based cloud scheme. *J. Geophys. Res. Atmos.* 107, AAC 20-1-AAC 20-21. doi:10.1029/2002JD002128.

Rounce, D. R., Hock, R., and Shean, D. E. (2020). Glacier Mass Change in High Mountain Asia Through 2100 Using the Open-Source Python Glacier Evolution Model (PyGEM). *Front. Earth Sci.* 7, 331. doi:10.3389/feart.2019.00331.

Rousset, C., Vancoppenolle, M., Madec, G., Fichefet, T., Flavoni, S., Barthélemy, A., et al. (2015). The Louvain-La-Neuve sea ice model LIM3.6: global and regional capabilities. *Geosci. Model Dev.* 8, 2991–3005. doi:10.5194/gmd-8-2991-2015.

Rückamp, M., Goelzer, H., and Humbert, A. (2020). Sensitivity of Greenland ice sheet projections to spatial resolution in higher-order simulations: the Alfred Wegener Institute (AWI) contribution to ISMIP6 Greenland using the Ice-sheet and Sea-level System Model (ISSM). *Cryosph.* 14, 3309–3327. doi:10.5194/tc-14-3309-2020.

Ruti, P. M., Somot, S., Giorgi, F., Dubois, C., Flaounas, E., Obermann, A., et al. (2016). Med-CORDEX Initiative for Mediterranean Climate Studies. *Bull. Am. Meteorol. Soc.* 97, 1187–1208. doi:10.1175/BAMS-D-14-00176.1.

Saint-Martin, D., Geoffroy, O., Voldoire, A., Cattiaux, J., Brient, F., Chauvin, F., et al. (2020). Tracking changes in climate sensitivity in CNRM climate models. *J. Adv. Model. Earth Syst.* n/a, e2020MS002190. doi:https://doi.org/10.1029/2020MS002190.

Saito, F., Abe-Ouchi, A., Takahashi, K., and Blatter, H. (2016). SeaRISE experiments revisited: potential sources of spread in multi-model projections of the Greenland ice sheet. *Cryosph.* 10, 43–63. doi:10.5194/tc-10-43-2016.

Sakai, A., and Fujita, K. (2017). Contrasting glacier responses to recent climate change in high-mountain Asia. *Sci. Rep.* 7, 13717. doi:10.1038/s41598-017-14256-5.

Samuelsson, P., Gollvik, S., Jansson, C., Kupiainen, M., Kourzeneva, E., and van de Berg, W. J. (2015). The surface processes of the Rossby Centre regional atmospheric climate model (RCA4). Available at: http://www.smhi.se/polopoly_fs/1.89799!/Menu/general/extGroup/attachmentColHold/mainCol1/file/meteorologi_157.pdf.

Sanjay, J., Krishnan, R., Shrestha, A. B., Rajbhandari, R., and Ren, G.-Y. (2017). Downscaled climate change projections for the Hindu Kush Himalayan region using CORDEX South Asia regional climate models. *Adv. Clim. Chang. Res.* 8, 185–198. doi:10.1016/j.accre.2017.08.003.

Sanjay, J., Revadekar, J. V., Ramarao, M. V. S., Borgaonkar, H., Sengupta, S., Kothawale, D. R., et al. (2020). "Temperature Changes in India," in *Assessment of Climate Change over the Indian Region* (Singapore: Springer Singapore), 21–45. doi:10.1007/978-981-15-4327-2_2.

Sannino, G., Herrmann, M., Carillo, A., Rupolo, V., Ruggiero, V., Artale, V., et al. (2009). An eddy-permitting model of the Mediterranean Sea with a two-way grid refinement at the Strait of Gibraltar. *Ocean Model.* 30, 56–72. doi:10.1016/j.ocemod.2009.06.002.

Schlemmer, L., Schär, C., Lüthi, D., and Strebel, L. (2018). A Groundwater and Runoff Formulation for Weather and Climate Models. *J. Adv. Model. Earth Syst.* 10, 1809–1832. doi:10.1029/2017MS001260.

Schrodin, E., and Heise, E. (2002). A New Multi-Layer Soil Model. COSMO Newsletter No. 2. 149–151. Available at: http://www.cosmo-model.org.

Schwinger, J., Goris, N., Tjiputra, J. F., Kriest, I., Bentsen, M., Bethke, I., et al. (2016). Evaluation of NorESM-OC (versions~1 and 1.2), the ocean carbon-cycle stand-alone configuration of the Norwegian Earth System Model (NorESM1). *Geosci. Model Dev.* 9, 2589–2622. doi:10.5194/gmd-9-2589-2016.

Scinocca, J. F., Kharin, V. V., Jiao, Y., Qian, M. W., Lazare, M., Solheim, L., et al. (2016). Coordinated Global and Regional Climate Modeling*. *J. Clim.* 29, 17–35. doi:10.1175/JCLI-D-15-0161.1.

Scoccimarro, E., Gualdi, S., Bellucci, A., Peano, D., Cherchi, A., Vecchi, G. A., et al. (2020). The typhoon-induced drying of the Maritime Continent. *Proc. Natl. Acad. Sci.* 117, 3983–3988. doi:10.1073/pnas.1915364117.

Séférian, R., Berthet, S., Yool, A., Palmiéri, J., Bopp, L., Tagliabue, A., et al. (2020). Tracking Improvement in Simulated Marine Biogeochemistry Between CMIP5 and CMIP6. *Curr. Clim. Chang. Reports* 6, 95–119. doi:10.1007/s40641-020-00160-0.

Séférian, R., Nabat, P., Michou, M., Saint-Martin, D., Voldoire, A., Colin, J., et al. (2019). Evaluation of CNRM Earth System Model, CNRM-ESM2-1: Role of Earth System Processes in Present-Day and Future Climate. *J. Adv. Model. Earth Syst.* 11, 4182–4227. doi:10.1029/2019MS001791.

Sein, D. V., Mikolajewicz, U., Gröger, M., Fast, I., Cabos, W., Pinto, J. G., et al. (2015). Regionally coupled atmosphere-ocean-sea ice-marine biogeochemistry model ROM: 1. Description and validation. *J. Adv. Model.*

ACCEPTED VERSION SUBJECT TO FINAL EDITING

Earth Syst. 7, 268–304. doi:10.1002/2014MS000357.
Sein, D. V, Koldunov, N. V, Danilov, S., Sidorenko, D., Wekerle, C., Cabos, W., et al. (2018). The Relative Influence of Atmospheric and Oceanic Model Resolution on the Circulation of the North Atlantic Ocean in a Coupled Climate Model. *J. Adv. Model. Earth Syst.* 10, 2026–2041. doi:10.1029/2018MS001327.
Sein, D. V, Koldunov, N. V, Danilov, S., Wang, Q., Sidorenko, D., Fast, I., et al. (2017). Ocean Modeling on a Mesh With Resolution Following the Local Rossby Radius. *J. Adv. Model. Earth Syst.* 9, 2601–2614. doi:https://doi.org/10.1002/2017MS001099.
Seland, Ø., Bentsen, M., Olivié, D., Toniazzo, T., Gjermundsen, A., Graff, L. S., et al. (2020). Overview of the Norwegian Earth System Model (NorESM2) and key climate response of CMIP6 DECK, historical, and scenario simulations. *Geosci. Model Dev.* 13, 6165–6200. doi:10.5194/gmd-13-6165-2020.
Sellar, A. A., Jones, C. G., Mulcahy, J. P., Tang, Y., Yool, A., Wiltshire, A., et al. (2019). UKESM1: Description and Evaluation of the U.K. Earth System Model. *J. Adv. Model. Earth Syst.* n/a. doi:10.1029/2019MS001739.
Semmler, T., Danilov, S., Gierz, P., Goessling, H. F., Hegewald, J., Hinrichs, C., et al. (2020). Simulations for CMIP6 With the AWI Climate Model AWI-CM-1-1. *J. Adv. Model. Earth Syst.* 12, e2019MS002009. doi:https://doi.org/10.1029/2019MS002009.
Šeparović, L., Alexandru, A., Laprise, R., Martynov, A., Sushama, L., Winger, K., et al. (2013). Present climate and climate change over North America as simulated by the fifth-generation Canadian regional climate model. *Clim. Dyn.* 41, 3167–3201. doi:10.1007/s00382-013-1737-5.
Seroussi, H., Morlighem, M., Rignot, E., Khazendar, A., Larour, E., and Mouginot, J. (2013). Dependence of century-scale projections of the Greenland ice sheet on its thermal regime. *J. Glaciol.* 59, 1024–1034. doi:10.3189/2013JoG13J054.
Seroussi, H., Nowicki, S., Payne, A. J., Goelzer, H., Lipscomb, W. H., Abe-Ouchi, A., et al. (2020). ISMIP6 Antarctica: a multi-model ensemble of the Antarctic ice sheet evolution over the 21st century. *Cryosph.* 14, 3033–3070. doi:10.5194/tc-14-3033-2020.
Seroussi, H., Nowicki, S., Simon, E., Abe-Ouchi, A., Albrecht, T., Brondex, J., et al. (2019). initMIP-Antarctica: an ice sheet model initialization experiment of ISMIP6. *Cryosph.* 13, 1441–1471. doi:10.5194/tc-13-1441-2019.
Sevault, F., Somot, S., Alias, A., Dubois, C., Lebeaupin-Brossier, C., Nabat, P., et al. (2014). A fully coupled Mediterranean regional climate system model: design and evaluation of the ocean component for the 1980–2012 period. *Tellus A Dyn. Meteorol. Oceanogr.* 66, 23967. doi:10.3402/tellusa.v66.23967.
Shannon, S., Smith, R., Wiltshire, A., Payne, T., Huss, M., Betts, R., et al. (2019). Global glacier volume projections under high-end climate change scenarios. *Cryosph.* 13, 325–350. doi:10.5194/tc-13-325-2019.
Shindell, D. T., Faluvegi, G., Unger, N., Aguilar, E., Schmidt, G. A., Koch, D. M., et al. (2006). Simulations of preindustrial, present-day, and 2100 conditions in the NASA GISS composition and climate model G-PUCCINI. *Atmos. Chem. Phys.* 6, 4427–4459. doi:10.5194/acp-6-4427-2006.
Shkolnik, I. M., and Efimov, S. V (2013). Cyclonic activity in high latitudes as simulated by a regional atmospheric climate model: added value and uncertainties. *Environ. Res. Lett.* 8, 045007. doi:10.1088/1748-9326/8/4/045007.
Sidorenko, D., Rackow, T., Jung, T., Semmler, T., Barbi, D., Danilov, S., et al. (2015). Towards multi-resolution global climate modeling with ECHAM6--FESOM. Part I: model formulation and mean climate. *Clim. Dyn.* 44, 757–780. doi:10.1007/s00382-014-2290-6.
Skamarock, W. C., Klemp, J. B., Dudhia, J., Gill, D. O., Barker, D., Duda, M. G., et al. (2008). A Description of the Advanced Research WRF Version 3 (No. NCAR/TN-475+STR). Available at: http://dx.doi.org/10.5065/D68S4MVH.
Small, R. J., Bacmeister, J., Bailey, D., Baker, A., Bishop, S., Bryan, F., et al. (2014). A new synoptic scale resolving global climate simulation using the Community Earth System Model. *J. Adv. Model. Earth Syst.* 6, 1065–1094. doi:10.1002/2014MS000363.
Smith, B., Wårlind, D., Arneth, A., Hickler, T., Leadley, P., Siltberg, J., et al. (2014). Implications of incorporating N cycling and N limitations on primary production in an individual-based dynamic vegetation model. *Biogeosciences* 11, 2027–2054. doi:10.5194/bg-11-2027-2014.
Soto-Navarro, J., Jordá, G., Amores, A., Cabos, W., Somot, S., Sevault, F., et al. (2020). Evolution of Mediterranean Sea water properties under climate change scenarios in the Med-CORDEX ensemble. *Clim. Dyn.* 54, 2135–2165. doi:10.1007/s00382-019-05105-4.
Stevens, B., Fiedler, S., Kinne, S., Peters, K., Rast, S., Müsse, J., et al. (2017). MACv2-SP: a parameterization of anthropogenic aerosol optical properties and an associated Twomey effect for use in CMIP6. *Geosci. Model Dev.* 10, 433–452. doi:10.5194/gmd-10-433-2017.
Stock, C. A., Dunne, J. P., Fan, S., Ginoux, P., John, J., Krasting, J. P., et al. (2020). Ocean Biogeochemistry in GFDL's Earth System Model 4.1 and Its Response to Increasing Atmospheric CO2. *J. Adv. Model. Earth Syst.* 12, e2019MS002043. doi:https://doi.org/10.1029/2019MS002043.
Strandberg, G., Bärring, L., Hansson, U., Jansson, C., Jones, C., Kjellström, E., et al. (2015). CORDEX scenarios for Europe from the Rossby Centre regional climate model RCA4. Available at: https://www.smhi.se/en/publications/cordex-scenarios-for-europe-from-the-rossby-centre-regional-climate-model-rca4-1.90274.

ACCEPTED VERSION SUBJECT TO FINAL EDITING

Sudo, K., Takahashi, M., and Akimoto, H. (2002a). CHASER: A global chemical model of the troposphere 2. Model results and evaluation. *J. Geophys. Res. Atmos.* 107, ACH 9-1-ACH 9-39. doi:https://doi.org/10.1029/2001JD001114.

Sudo, K., Takahashi, M., Kurokawa, J., and Akimoto, H. (2002b). CHASER: A global chemical model of the troposphere 1. Model description. *J. Geophys. Res. Atmos.* 107, ACH 7-1-ACH 7-20. doi:https://doi.org/10.1029/2001JD001113.

Swapna, P., Krishnan, R., Sandeep, N., Prajeesh, A. G., Ayantika, D. C., Manmeet, S., et al. (2018). Long-Term Climate Simulations Using the IITM Earth System Model (IITM-ESMv2) With Focus on the South Asian Monsoon. *J. Adv. Model. Earth Syst.* 10, 1127–1149. doi:https://doi.org/10.1029/2017MS001262.

Swart, N. C., Cole, J. N. S., Kharin, V. V, Lazare, M., Scinocca, J. F., Gillett, N. P., et al. (2019). The Canadian Earth System Model version 5 (CanESM5.0.3). *Geosci. Model Dev.* 12, 4823–4873. doi:10.5194/gmd-12-4823-2019.

Szopa, S., Balkanski, Y., Schulz, M., Bekki, S., Cugnet, D., Fortems-Cheiney, A., et al. (2013). Aerosol and ozone changes as forcing for climate evolution between 1850 and 2100. *Clim. Dyn.* 40, 2223–2250. doi:10.1007/s00382-012-1408-y.

Takata, K., Emori, S., and Watanabe, T. (2003). Development of the minimal advanced treatments of surface interaction and runoff. *Glob. Planet. Change* 38, 209–222. doi:https://doi.org/10.1016/S0921-8181(03)00030-4.

Takemura, T., Egashira, M., Matsuzawa, K., Ichijo, H., O'ishi, R., and Abe-Ouchi, A. (2009). A simulation of the global distribution and radiative forcing of soil dust aerosols at the Last Glacial Maximum. *Atmos. Chem. Phys.* 9, 3061–3073. doi:10.5194/acp-9-3061-2009.

Takemura, T., Nozawa, T., Emori, S., Nakajima, T. Y., and Nakajima, T. (2005). Simulation of climate response to aerosol direct and indirect effects with aerosol transport-radiation model. *J. Geophys. Res. Atmos.* 110. doi:https://doi.org/10.1029/2004JD005029.

Takemura, T., Okamoto, H., Maruyama, Y., Numaguti, A., Higurashi, A., and Nakajima, T. (2000). Global three-dimensional simulation of aerosol optical thickness distribution of various origins. *J. Geophys. Res. Atmos.* 105, 17853–17873. doi:https://doi.org/10.1029/2000JD900265.

Tanré, D., Geleyn, J.-F., and Slingo, J. M. (1984). "First results of the introduction of an advanced aerosol-radiation interaction in the ECMWF low resolution global model," in *Aerosols and their Climatic Effects*, eds. H. E. Gerber and A. Deepak (Hampton, Va, USA: Deepak Publishing), 133–177.

Tarasov, L., and Peltier, W. R. (1999). Impact of thermomechanical ice sheet coupling on a model of the 100 kyr ice age cycle. *J. Geophys. Res. Atmos.* 104, 9517–9545. doi:10.1029/1998JD200120.

Tarasov, L., and Peltier, W. R. (2003). Greenland glacial history, borehole constraints, and Eemian extent. *J. Geophys. Res. Solid Earth* 108. doi:10.1029/2001JB001731.

Tatebe, H., Ogura, T., Nitta, T., Komuro, Y., Ogochi, K., Takemura, T., et al. (2019). Description and basic evaluation of simulated mean state, internal variability, and climate sensitivity in MIROC6. *Geosci. Model Dev.* 12, 2727–2765. doi:10.5194/gmd-12-2727-2019.

Taylor, K. E., Stouffer, R. J., and Meehl, G. A. (2012). An Overview of CMIP5 and the Experiment Design. *Bull. Am. Meteorol. Soc.* 93, 485–498. doi:10.1175/BAMS-D-11-00094.1.

Tegen, I., Hollrig, P., Chin, M., Fung, I., Jacob, D., and Penner, J. (1997). Contribution of different aerosol species to the global aerosol extinction optical thickness: Estimates from model results. *J. Geophys. Res. Atmos.* 102, 23895–23915. doi:10.1029/97JD01864.

Tegen, I., Neubauer, D., Ferrachat, S., Siegenthaler-Le Drian, C., Bey, I., Schutgens, N., et al. (2019). The global aerosol--climate model ECHAM6.3--HAM2.3 -- Part 1: Aerosol evaluation. *Geosci. Model Dev.* 12, 1643–1677. doi:10.5194/gmd-12-1643-2019.

Thatcher, M., and McGregor, J. L. (2009). Using a Scale-Selective Filter for Dynamical Downscaling with the Conformal Cubic Atmospheric Model. *Mon. Weather Rev.* 137, 1742–1752. doi:10.1175/2008MWR2599.1.

Tjiputra, J. F., Roelandt, C., Bentsen, M., Lawrence, D. M., Lorentzen, T., Schwinger, J., et al. (2013). Evaluation of the carbon cycle components in the Norwegian Earth System Model (NorESM). *Geosci. Model Dev.* 6, 301–325. doi:10.5194/gmd-6-301-2013.

Tjiputra, J. F., Schwinger, J., Bentsen, M., Morée, A. L., Gao, S., Bethke, I., et al. (2020). Ocean biogeochemistry in the Norwegian Earth System Model version 2 (NorESM2). *Geosci. Model Dev.* 13, 2393–2431. doi:10.5194/gmd-13-2393-2020.

Top, S., Kotova, L., De Cruz, L., Aniskevich, S., Bobylev, L., De Troch, R., et al. (2021). Evaluation of regional climate models ALARO-0 and REMO2015 at 0.22° resolution over the CORDEX Central Asia domain. *Geosci. Model Dev.* 14, 1267–1293. doi:10.5194/gmd-14-1267-2021.

Tsujino, H., Nakano, H., Sakamoto, K., Urakawa, S., Hirabara, M., Ishizaki, H., et al. (2017a). Reference Manual for the Meteorological Research Institute Community Ocean Model version 4(MRI.COMv4). Available at: https://www.mri-jma.go.jp/Publish/Technical/DATA/VOL_80/index_en.html.

Tsujino, H., Nakano, H., Sakamoto, K., Urakawa, S., Hirabara, M., Ishizaki, H., et al. (2017b). Reference Manual for the Meteorological Research Institute Community Ocean Model version 4(MRI.COMv4).

Turuncoglu, U. U. (2019). Toward modular in situ visualization in Earth system models: the regional modeling system RegESM 1.1. *Geosci. Model Dev.* 12, 233–259. doi:10.5194/gmd-12-233-2019.

ACCEPTED VERSION
SUBJECT TO FINAL EDITING

Vadsaria, T., Li, L., Ramstein, G., and Dutay, J.-C. (2020). Development of a sequential tool, LMDZ-NEMO-med-V1, to conduct global-to-regional past climate simulation for the Mediterranean basin: an Early Holocene case study. *Geosci. Model Dev.* 13, 2337–2354. doi:10.5194/gmd-13-2337-2020.

Valcke, S. (2013). The OASIS3 coupler: a European climate modelling community software. *Geosci. Model Dev.* 6, 373–388. doi:10.5194/gmd-6-373-2013.

Van de Wal, R. S. W., and Wild, M. (2001). Modelling the response of glaciers to climate change by applying volume-area scaling in combination with a high resolution GCM. *Clim. Dyn.* 18, 359–366. doi:10.1007/s003820100184.

van den Hurk, B. J. J. M., Viterbo, P., Beljaars, A. C. M., and Betts, A. K. (2000). *Offline validation of the ERA40 surface scheme*. Reading: ECMWF doi:10.21957/9aoaspz8.

van Meijgaard, E., van Ulft, B., van de Berg, Willem Jan Bosveld, F. C., van den Hurk, B., Lenderink, G., and Siebesma, A. P. (2008). The KNMI regional atmospheric climate model RACMO, version 2.1, KNMI number: TR-302. Available at: https://www.knmi.nl/kennis-en-datacentrum/publicatie/the-knmi-regional-atmospheric-climate-model-racmo-version-2-1.

van Meijgaard, E., van Ulft, L. H., Lenderink, G., de Roode, S. R., Wipfler, E. L., Boers, R., et al. (2012). Refinement and application of a regional atmospheric model for climate scenario calculations of Western Europe. Available at: https://library.wur.nl/WebQuery/wurpubs/427097.

van Noije, T., Bergman, T., Le Sager, P., O'Donnell, D., Makkonen, R., Gonçalves-Ageitos, M., et al. (2020). EC-Earth3-AerChem, a global climate model with interactive aerosols and atmospheric chemistry participating in CMIP6. *Geosci. Model Dev. Discuss.* 2020, 1–46. doi:10.5194/gmd-2020-413.

van Noije, T. P. C., Le Sager, P., Segers, A. J., van Velthoven, P. F. J., Krol, M. C., Hazeleger, W., et al. (2014). Simulation of tropospheric chemistry and aerosols with the climate model EC-Earth. *Geosci. Model Dev.* 7, 2435–2475. doi:10.5194/gmd-7-2435-2014.

van Vuuren, D. P., Edmonds, J., Kainuma, M., Riahi, K., Thomson, A., Hibbard, K., et al. (2011). The representative concentration pathways: an overview. *Clim. Change* 109, 5–31. doi:10.1007/s10584-011-0148-z.

Verseghy, D. L. (2000). The Canadian land surface scheme (CLASS): Its history and future. *Atmosphere-Ocean* 38, 1–13. doi:10.1080/07055900.2000.9649637.

Verseghy, D. L., McFarlane, N. A., and Lazare, M. (1993). Class—A Canadian land surface scheme for GCMS, II. Vegetation model and coupled runs. *Int. J. Climatol.* 13, 347–370. doi:10.1002/joc.3370130402.

Voigt, A., Stevens, B., Bony, S., and Boucher, O. (2014). Easy Aerosol - a modeling framework to study robustness and sources of uncertainties in aerosol-induced changes of the large-scale atmospheric circulation. Available at: https://www.wcrp-climate.org/images/grand_challenges/clouds/documents/easyaerosol_projectdescription_expprotocol.pdf.

Voldoire, A., Decharme, B., Pianezze, J., Lebeaupin Brossier, C., Sevault, F., Seyfried, L., et al. (2017). SURFEX v8.0 interface with OASIS3-MCT to couple atmosphere with hydrology, ocean, waves and sea-ice models, from coastal \hack{\newline}to global scales. *Geosci. Model Dev.* 10, 4207–4227. doi:10.5194/gmd-10-4207-2017.

Voldoire, A., Saint-Martin, D., Sénési, S., Decharme, B., Alias, A., Chevallier, M., et al. (2019). Evaluation of CMIP6 DECK Experiments With CNRM-CM6-1. *J. Adv. Model. Earth Syst.* 11, 2177–2213. doi:10.1029/2019MS001683.

Volodin, E. M., and Kostrykin, S. V (2016). The aerosol module in the INM RAS climate model. *Russ. Meteorol. Hydrol.* 41, 519–528. doi:10.3103/S106837391608001X.

Volodin, E. M., Mortikov, E. V, Kostrykin, S. V, Galin, V. Y., Lykossov, V. N., Gritsun, A. S., et al. (2017). Simulation of the present-day climate with the climate model INMCM5. *Clim. Dyn.* 49, 3715–3734. doi:10.1007/s00382-017-3539-7.

Volodin Evgenii M, V, M. E., V, K. S., Ya., G. V., N, L. V., S, G. A., et al. (2018). Simulation of the modern climate using the INM-CM48 climate model. *Russ. J. Numer. Anal. Math. Model.* 33, 367. doi:10.1515/rnam-2018-0032.

von Salzen, K., Scinocca, J. F., McFarlane, N. A., Li, J., Cole, J. N. S., Plummer, D., et al. (2013). The Canadian Fourth Generation Atmospheric Global Climate Model (CanAM4). Part I: Representation of Physical Processes. *Atmosphere-Ocean* 51, 104–125. doi:10.1080/07055900.2012.755610.

Walters, D., Baran, A. J., Boutle, I., Brooks, M., Earnshaw, P., Edwards, J., et al. (2019). The Met Office Unified Model Global Atmosphere 7.0/7.1 and JULES Global Land 7.0 configurations. *Geosci. Model Dev.* 12, 1909–1963. doi:10.5194/gmd-12-1909-2019.

Wang, H., Easter, R. C., Zhang, R., Ma, P.-L., Singh, B., Zhang, K., et al. (2020). Aerosols in the E3SM Version 1: New Developments and Their Impacts on Radiative Forcing. *J. Adv. Model. Earth Syst.* 12, e2019MS001851. doi:10.1029/2019MS001851.

Williams, D. N., Balaji, V., Cinquini, L., Denvil, S., Duffy, D., Evans, B., et al. (2016). A global repository for planet-sized experiments and observations. *Bull. Am. Meteorol. Soc.* 97, 755–766. doi:10.1175/BAMS-D-15-00132.1.

Williams, K. D., Copsey, D., Blockley, E. W., Bodas-Salcedo, A., Calvert, D., Comer, R., et al. (2018). The Met Office Global Coupled Model 3.0 and 3.1 (GC3.0 and GC3.1) Configurations. *J. Adv. Model. Earth Syst.* 10, 357–380. doi:10.1002/2017MS001115.

Wiltshire, A. J., Burke, E. J., Chadburn, S. E., Jones, C. D., Cox, P. M., Davies-Barnard, T., et al. (2020). JULES-CN: a coupled terrestrial Carbon-Nitrogen Scheme (JULES vn5.1). *Geosci. Model Dev. Discuss.* 2020, 1–40.

ACCEPTED VERSION SUBJECT TO FINAL EDITING

doi:10.5194/gmd-2020-205.

Winkelmann, R., Martin, M. A., Haseloff, M., Albrecht, T., Bueler, E., Khroulev, C., et al. (2011). The Potsdam Parallel Ice Sheet Model (PISM-PIK) – Part 1: Model description. *Cryosph.* 5, 715–726. doi:10.5194/tc-5-715-2011.

Wu, T., Lu, Y., Fang, Y., Xin, X., Li, L., Li, W., et al. (2019). The Beijing Climate Center Climate System Model (BCC-CSM): the main progress from CMIP5 to CMIP6. *Geosci. Model Dev.* 12, 1573–1600. doi:10.5194/gmd-12-1573-2019.

Wu, T., Yu, R., Lu, Y., Jie, W., Fang, Y., Zhang, J., et al. (2020a). BCC-CSM2-HR: A High-Resolution Version of the Beijing Climate Center Climate System Model. *Geosci. Model Dev. Discuss.* 2020, 1–64. doi:10.5194/gmd-2020-284.

Wu, T., Zhang, F., Zhang, J., Jie, W., Zhang, Y., Wu, F., et al. (2020b). Beijing Climate Center Earth System Model version 1 (BCC-ESM1): model description and evaluation of aerosol simulations. *Geosci. Model Dev.* 13, 977–1005. doi:10.5194/gmd-13-977-2020.

Xie, Z., Liu, S., Zeng, Y., Gao, J., Qin, P., Jia, B., et al. (2018). A High-Resolution Land Model With Groundwater Lateral Flow, Water Use, and Soil Freeze-Thaw Front Dynamics and its Applications in an Endorheic Basin. *J. Geophys. Res. Atmos.* 123, 7204–7222. doi:10.1029/2018JD028369.

Yakovlev, N. G. (2009). Reproduction of the large-scale state of water and sea ice in the Arctic Ocean in 1948–2002: Part I. Numerical model. *Izv. Atmos. Ocean. Phys.* 45, 357–371. doi:10.1134/S0001433809030098.

Yukimoto, S., ADACHI, Y., HOSAKA, M., SAKAMI, T., YOSHIMURA, H., HIRABARA, M., et al. (2012). A New Global Climate Model of the Meteorological Research Institute: MRI-CGCM3 -Model Description and Basic Performance. *J. Meteorol. Soc. Japan. Ser. II* 90A, 23–64. doi:10.2151/jmsj.2012-A02.

Yukimoto, S., Kawai, H., Koshiro, T., Oshima, N., YOSHIDA, K., URAKAWA, S., et al. (2019). The Meteorological Research Institute Earth System Model Version 2.0, MRI-ESM2.0: Description and Basic Evaluation of the Physical Component. *J. Meteorol. Soc. Japan. Ser. II* 97, 931–965. doi:10.2151/jmsj.2019-051.

Zalesny, V. B., Marchuk, G. ., Agoshkov, V. I., Bagno, A. V., Gusev, A. V., Diansky, N. A., et al. (2010). Numerical simulation of large-scale ocean circulationbased on the multicomponent splitting method. *Russ. J. Numer. Anal. Math. Model.* 25, 581§609.

Zekollari, H., Huss, M., and Farinotti, D. (2019). Modelling the future evolution of glaciers in the European Alps under the EURO-CORDEX RCM ensemble. *Cryosph.* 13, 1125–1146. doi:10.5194/tc-13-1125-2019.

Zeng, X., Zhao, M., and Dickinson, R. E. (1998). Intercomparison of Bulk Aerodynamic Algorithms for the Computation of Sea Surface Fluxes Using TOGA COARE and TAO Data. *J. Clim.* 11, 2628–2644. doi:10.1175/1520-0442(1998)011<2628:IOBAAF>2.0.CO;2.

Zhao, M. (2020). Simulations of Atmospheric Rivers, Their Variability, and Response to Global Warming Using GFDL's New High-Resolution General Circulation Model. *J. Clim.* 33, 10287–10303. doi:10.1175/JCLI-D-20-0241.1.

Zhao, M., Golaz, J.-C., Held, I. M., Guo, H., Balaji, V., Benson, R., et al. (2018a). The GFDL Global Atmosphere and Land Model AM4.0/LM4.0: 1. Simulation Characteristics With Prescribed SSTs. *J. Adv. Model. Earth Syst.* 10, 691–734. doi:10.1002/2017MS001208.

Zhao, M., Golaz, J.-C., Held, I. M., Guo, H., Balaji, V., Benson, R., et al. (2018b). The GFDL Global Atmosphere and Land Model AM4.0/LM4.0: 1. Simulation Characteristics With Prescribed SSTs. *J. Adv. Model. Earth Syst.* 10, 691–734. doi:10.1002/2017MS001208.

Zhao, M., Golaz, J.-C., Held, I. M., Guo, H., Balaji, V., Benson, R., et al. (2018c). The GFDL Global Atmosphere and Land Model AM4.0/LM4.0: 2. Model Description, Sensitivity Studies, and Tuning Strategies. *J. Adv. Model. Earth Syst.* 10, 735–769. doi:10.1002/2017MS001209.

Zhao, M., Golaz, J.-C., Held, I. M., Guo, H., Balaji, V., Benson, R., et al. (2018d). The GFDL Global Atmosphere and Land Model AM4.0/LM4.0: 2. Model Description, Sensitivity Studies, and Tuning Strategies. *J. Adv. Model. Earth Syst.* 10, 735–769. doi:10.1002/2017MS001209.

Ziehn, T., Chamberlain, M. A., Law, R. M., Lenton, A., Bodman, R. W., Dix, M., et al. (2020). The Australian Earth System Model: ACCESS-ESM1.5. *J. South. Hemisph. Earth Syst. Sci.* 70, 193–214. Available at: https://doi.org/10.1071/ES19035.

Zittis, G., and Hadjinicolaou, P. (2017). The effect of radiation parameterization schemes on surface temperature in regional climate simulations over the MENA-CORDEX domain. *Int. J. Climatol.* 37, 3847–3862. doi:10.1002/joc.4959.

Zittis, G., Hadjinicolaou, P., and Lelieveld, J. (2014). Comparison of WRF Model Physics Parameterizations over the MENA-CORDEX Domain. *Am. J. Clim. Chang.* 03, 490–511. doi:10.4236/ajcc.2014.35042.

ACCEPTED VERSION SUBJECT TO FINAL EDITING

Annex III: Tables of historical and projected well-mixed greenhouse gas mixing ratios and effective radiative forcing of all climate forcers

Coordinating Lead Authors: Frank J. Dentener (EU, The Netherlands), Bradley Hall (United States of America), Chris Smith (United Kingdom)

Lead Authors: Jinho Ahn (Republic of Korea), William Collins (United Kingdom), Christopher G. Jones (United Kingdom), Malte Meinshausen (Australia/Germany),

Contributing Authors:
Ralph Keeling (United States of America), Paul B. Krummel (Australia), Jens Mühle (United States of America/Germany), Zebedee R. J. Nicholls (Australia), Isobel J. Simpson (Canada)

This Annex should be cites as:
IPCC, 2021: Annex III: Tables of historical and projected well-mixed greenhouse gas mixing ratios and effective radiative forcing of all climate forcers [Dentener F. J., B. Hall, C. Smith (eds.)]. In: *Climate Change 2021: The Physical Science Basis. Contribution of Working Group I to the Sixth Assessment Report of the Intergovernmental Panel on Climate Change* [Masson-Delmotte, V., P. Zhai, A. Pirani, S. L. Connors, C. Péan, S. Berger, N. Caud, Y. Chen, L. Goldfarb, M. I. Gomis, M. Huang, K. Leitzell, E. Lonnoy, J.B.R. Matthews, T. K. Maycock, T. Waterfield, O. Yelekçi, R. Yu and B. Zhou (eds.)]. Cambridge University Press. In Press.

Date: August 2021

This document is subject to copy-editing, corrigenda and trickle backs.

ACCEPTED VERSION
SUBJECT TO FINAL EDITS

AIII.1 Introduction

Annex III presents, in tabulated form, data related to historical and projected changes in greenhouse gas (GHG) mixing ratios and effective radiative forcing (ERF) of all climate forcers as assessed and used throughout Chapters 1-7. Where available 90 % confidence level uncertainties on observed GHG mixing ratios are given. For each species, the abundance is given as dry air mole fraction: ppm = micromoles per mole (10^{-6}); ppb = nanomoles per mole (10^{-9}); and ppt = picomoles per mole (10^{-12}). ERF is given in W m^{-2} for CO_2, N_2O, and CH_4 and mW m^{-2} for other components.

Pre-instrumental mixing ratios are estimated from ice core and firn air records that are described in Ahn et al., 2012; Bauska et al., 2015; Flückiger et al., 1999; Machida et al., 1995; Meinshausen et al., 2017; Mitchell et al., 2013; Rubino et al., 2020; Ryu et al., 2020; Siegenthaler et al., 2005; Sowers, 2001. Observed (instrumental) mixing ratios are described in Dlugokencky et al., 2011; Hall et al., 2011; Laube et al., 2016; Masarie and Tans, 2004; Montzka et al., 2009; Naus et al., 2019; Prinn et al., 2018; Rigby et al., 2014; Trudinger et al., 2004; Worton et al., 2006; Adcock et al., 2018; Droste et al., 2020; Leedham Elvidge et al., 2018; Mühle et al., 2019; Simmonds et al., 2017.

Projected concentrations for the 5 core scenarios discussed in the report (Section 1.6.1) are from (Gidden et al., 2019; Meinshausen et al., 2017, 2020; Velders et al., 2015). These scenarios span a wide range of plausible societal and climatic futures from potentially below 1.5°C best-estimate warming to over 4°C warming by 2100 (Section 4.3.4). Computational methods and assumptions to calculate historical and projected ERF are described in Chapter 7 and detailed information can be found in Chapter 7 Supplementary Material 7.SM.1.3 and 7.SM.1.4.

Extended datasets and further auxiliary data are made available via https://zenodo.org/xxxx

Chemical Abbreviations and Symbols of components regulated under the Kyoto[11] and Montreal Protocols.

CO_2	carbon dioxide	Kyoto
CH_4	methane	Kyoto
N_2O	nitrous oxide	Kyoto
HFC	hydrofluorocarbon (a class of compounds: HFC-32, HFC-134a, …)	Kyoto, Montreal
PFC	perfluorocarbon (a class of compounds: CF_4, C_2F_6,C_4F_{10}, …)	Kyoto
SF_6	sulphur hexafluoride	Kyoto
NF_3	nitrogen trifluoride	Kyoto
CFC	chlorofluorocarbon (a class of compounds: $CFCl_3$, CF_2Cl_2, …)	Montreal
HCFC	hydrochlorofluorocarbon (a class of compounds: HCFC-22, HCFC-141b, …)	Montreal
CCl_4	carbon tetrachloride	Montreal
CH_3CCl_3	methyl chloroform	Montreal
Halons	Bromo(chloro)fluorocarbon (a class of compounds: CF_2ClBr “Halon-1211”; $CBrF_3$ “Halon-1301”; $C2Br_2F_4$ “Halon-2402”)	Montreal

[1] The Kyoto protocol (1 December 1997-31 December 2020) regulated a basket of 6 GHGs. The term Kyoto gases is widely used in the scientific literature

ACCEPTED VERSION SUBJECT TO FINAL EDITS

1 **List of Tables:**

Table AIII.1	Historical Abundances of greenhouse gases
Table AIII.1a	Historical abundances and ERF(Wm^{-2}) for CO_2(ppm), CH_4(ppb), and N_2O(ppb)
Table AIII.1b	Historical abundances (ppt) and ERF (mWm^{-2}) of NF_3, SF_6, and PFCs
Table AIII.1c	Historical abundances (ppt) and ERF [mWm^{-2}] of HFCs
Table AIII.1d	Historical abundances (ppt) and ERF [mWm^{-2}] of HCFCs
Table AIII.1e	Historical abundances (ppt) and ERF [mWm^{-2}] of CFCs
Table AIII.1f	Historical abundances (ppt) and ERF [mWm^{-2}] of CH_3CCl_3, CCl_4, CH_3Br, $CHCl_3$ and Halons.
Table AIII.2	Future abundances of CO_2, CH_4, and N_2O for selected SSP scenarios [2020-2500]
Table AIII.3	Effective Radiative Forcing (Wm^{-2}) time series of all climate forcers from 1750-2019
Table AIII.4a	Effective Radiative Forcing (Wm^{-2}) time series of all climate forcers for SSP1-19
Table AIII.4b	Effective Radiative Forcing (Wm^{-2}) time series of all climate forcers for SSP1-26
Table AIII.4c	Effective Radiative Forcing (Wm^{-2}) time series of all climate forcers for SSP2-45
Table AIII.4d	Effective Radiative Forcing (Wm^{-2}) time series of all climate forcers for SSP3-70
Table AIII.4e	Effective Radiative Forcing (Wm^{-2}) time series of all climate forcers for SSP5-85
Table AIII.4f	Effective Radiative Forcing (mWm^{-2}) time series of halogen components for selected scenarios and Kyoto and Montreal gases
Table AIII.5	Total Anthropogenic and natural ERF relative to 1750 assessed in AR5 (RCP scenarios) and AR6 (SSP scenarios).

2
3

ACCEPTED VERSION
SUBJECT TO FINAL EDITS

Table AIII.1a: Historical abundances and ERF(Wm^{-2}) for CO_2(ppm), CH_4(ppb), and N_2O(ppb)

Year	CO_2	CH_4	N_2O	Year	CO_2	CH_4	N_2O	Year	CO_2	CH_4	N_2O
1750[1]	278.3	729	270.1	1968	322.5	1372	295.2	1995	360.0	1748	311.4
1850[1]	285.5	808	272.1	1969	323.4	1389	295.6	1996	361.8	1750	312.3
1860[2]	286.8	822	273.2	1970	324.9	1411	296.0	1997	362.9	1754	313.1
1870	288.4	852	274.9	1971	325.5	1431	296.5	1998	365.5	1764	313.9
1880	290.4	868	276.6	1972	327.4	1449	296.9	1999	367.6	1772	314.9
1890	293.3	896	277.6	1973	330.0	1463	297.3	2000	368.8	1773	315.9
1900	296.4	925	278.9	1974	330.8	1476	297.8	2001	370.4	1772	316.6
1905	298.0	947	280.2	1975	330.9	1492	298.3	2002	372.4	1773	317.3
1910	300.0	974	281.8	1976	331.6	1509	298.8	2003	375.0	1777	318.0
1915	302.5	991	283.6	1977	333.4	1528	299.3	2004	376.8	1776	318.6
1920	304.8	1025	284.5	1978	335.0	1547	299.8	2005	378.8	1774	319.3
1925	306.3	1052	285.3	1979	336.6	1566	300.4	2006	381.0	1774	320.2
1930	307.1	1072	285.6	1980	338.8[3]	1585	301.1[3]	2007	382.7	1781	320.9
1935	308.6	1097	286.3	1981	340.0	1603	301.9	2008	384.8	1788	321.8
1940	311.7	1120	287.3	1982	340.8	1619	303.1	2009	386.3	1793	322.6
1945	312.7	1139	289.0	1983	342.4	1633	303.7	2010	388.6	1798	323.4
1950	313.1	1164	289.5	1984	344.0	1645[3]	304.3	2011	390.5	1803	324.4
1955	314.6	1207	290.7	1985	345.5	1657	304.9	2012	392.5	1808	325.3
1960	316.8	1264	292.1	1986	346.9	1670	305.8	2013	395.2	1814	326.2
1961	317.5	1269	292.5	1987	348.6	1680	306.0	2014	397.1	1823	327.4
1962	318.2	1282	292.8	1988	351.2	1693	306.7	2015	399.4	1834	328.3
1963	318.8	1301	293.2	1989	352.8	1707	307.8	2016	402.9	1842	329.1
1964	319.5	1317	293.6	1991	354.0	1714	308.7	2017	405.0	1849	330.0
1965	320.0	1331	293.9	1992	355.3	1728	309.4	2018	407.4	1858	331.2
1966	321.0	1342	294.4	1993	356.0	1735	309.9	2019	409.9	1866	332.1
1967	321.6	1354	294.8	1994	356.7	1737	310.3	***ERF[4]***	**2.16**	**0.54**	**0.21**

Notes: [1] 1750/1850 CO_2, CH_4, N_2O from multiple ice cores assessed in Chapter 2. Uncertainties (90 % CI) for 1750 are 2.9 ppm, 9.4 ppb and 6.0 ppb for CO_2, CH_4 and N_2O, respectively. Uncertainties for 1850 are 2.1 ppm, 13.8 ppb and 5.7 ppb, based on variations of ice cores. [2] Mixing ratios from 1851- 1980/1984 are updated from the CMIP6 (Meinshausen et al., 2017) dataset, using a linear time-dependent offset correction function. [3] CO_2 from NOAA network; CH_4, N_2O from merged NOAA and AGAGE networks. Uncertainties (90 % CI) in 2019, derived from multiple global networks, are 0.36 ppm, 3.3 ppb and 0.4 ppb for CO_2, CH_4 and N_2O, respectively, and do not include estimates of analytical accuracy. Uncertainties for other years may differ. [4] ERF(2019-1750) from Chapter 7.

ACCEPTED VERSION SUBJECT TO FINAL EDITS

Table AIII.1b: Historical abundances (ppt) and ERF (mWm^{-2}) of NF_3, SF_6, and perfluorocarbons

Year	NF_3	SF_6	SO_2F_2	CF_4	C_2F_6	C_3F_8	c-C_4F_8	n-C_4F_{10}	n-C_5F_{12}	n-C_6F_{14}	i-C_6F_{14}	C_7F_{16}	C_8F_{18}
1750	0.00	0.00	0.00	34.05	0.00	0.00	0.00	0.00	0.00	0.00	0.00	0.00	0.00
1850	0.00	0.00	0.00	34.1	0.00	0.00	0.00	0.00	0.00	0.00	0.00	0.00	0.00
1900	0.00	0.00	0.00	34.1	0.00	0.00	0.00	0.00	0.00	0.00	0.00	0.00	0.00
1910	0.00	0.00	0.00	34.1	0.01	0.00	0.00	0.00	0.00	0.00	0.00	0.00	0.00
1920	0.00	0.00	0.00	34.4	0.04	0.00	0.00	0.00	0.00	0.00	0.00	0.00	0.00
1930	0.00	0.00	0.00	34.9	0.10	0.00	0.00	0.00	0.00	0.00	0.00	0.00	0.00
1940	0.00	0.00	0.00	35.8	0.19	0.01	0.00	0.00	0.00	0.00	0.00	0.00	0.00
1950	0.00	0.00	0.00	38.0	0.40	0.01	0.00	0.00	0.00	0.00	0.00	0.00	0.00
1960	0.00	0.09	0.00	40.1	0.51	0.02	0.00	0.00	0.00	0.00	0.00	0.00	0.00
1970	0.00	0.32	0.01	43.4	0.62	0.03	0.14	0.00	0.00	0.00	0.00	0.00	0.00
1980	0.00	0.86	0.35	53.5	1.22	0.05	0.38	0.02	0.02	0.01	0.00	0.01	0.01
1990	0.01	2.35	0.68	63.8	2.07	0.12	0.76	0.07	0.05	0.03	0.015	0.03	0.02
2000	0.17	4.56	1.07	71.5	3.11	0.28	0.98	0.13	0.10	0.14	0.038	0.07	0.06
2010	0.73	7.01	1.63	78.3	4.09	0.54	1.26	0.17	0.12	0.21	0.055	0.10	0.09
2015	1.30	8.57	2.11	81.9	4.49	0.62	1.50	0.19	0.14	0.22	0.062	0.11	n.a.
2019	2.05	9.95	2.50	85.5	4.85	0.68	1.75	n.a.	n.a.	n.a.	n.a.	n.a.	n.a.
Unc.	*0.03*	*0.03*	*0.05*	*0.2*	*0.05*	*0.01*	*0.06*	n.a.	n.a.	n.a.	n.a.	n.a.	n.a.
ERF	0.4	5.6	0.5	5.1	1.3	0.2	0.5	0.1	0.1	0.1	0.0[1]	0.1	0.1

Notes: Data merged from AR5 (1750;1850); CMIP6 compilation by Meinshausen et al. (2017) until ca. 1995, and data directly taken from merged AGAGE and NOAA networks, depending on date of availability. Perfluorocarbons from CMIP6 dataset (Meinshausen et al., 2017) or estimated from Droste et al. (2020), with CMIP6 n-C_6F_{14} and C_7F_{16} scaled to account for calibration changes in Droste et al. (2020). Uncertainties pertain to 2019, derived from observations made by global networks and literature, and do not include estimates of analytical accuracy. Uncertainties are not available for c-C_4F_8, n-C_4F_{10}, n-C_5F_{12}, n-C_6F_{14}, i-C_6F_{14}, C_7F_{16}, C_8F_{18}. ERF(2019-1750) from Chapter 7, except for c-C_4F_8, n-C_4F10, n-C_5F_{12}, n-C_6F_{14}, i-C_6F_{14}, C_7F_{16} use 2015 abundances and C_8F_{18} which uses 2014 abundance. [1]below <0.5 mWm^{-2}

ACCEPTED VERSION SUBJECT TO FINAL EDITS

Table AIII.1c: Historical abundances (ppt) and ERF [mWm^{-2}] of HFCs

Year	HFC-134a	HFC-23	HFC-32	HFC-125	HFC-143a	HFC-152a	HFC-227ea	HFC-236fa	HFC-245fa	HFC-365mfc	HFC-43-10mee
1750	0.0	0.0	0.0	0.0	0.0	0.0	0.00	0.00	0.00	0.00	0.00
1850	0.0	0.0	0.0	0.0	0.0	0.0	0.00	0.00	0.00	0.00	0.00
1900	0.0	0.0	0.0	0.0	0.0	0.0	0.00	0.00	0.00	0.00	0.00
1910	0.0	0.0	0.0	0.0	0.0	0.0	0.00	0.00	0.00	0.00	0.00
1920	0.0	0.0	0.0	0.0	0.0	0.0	0.00	0.00	0.00	0.00	0.00
1930	0.0	0.0	0.0	0.0	0.0	0.0	0.00	0.00	0.00	0.00	0.00
1940	0.0	0.0	0.0	0.0	0.0	0.0	0.00	0.00	0.00	0.00	0.00
1950	0.0	0.0	0.0	0.0	0.0	0.0	0.00	0.00	0.00	0.00	0.00
1960	0.0	0.5	0.0	0.0	0.0	0.0	0.00	0.00	0.00	0.00	0.00
1970	0.0	1.8	0.0	0.	0.0	0.0	0.00	0.00	0.00	0.00	0.00
1980	0.2	3.9	0.0	0.1	0.1	0.0	0.01	0.00	0.00	0.00	0.00
1990	0.5	8.3	0.1	0.1	0.5	0.2	0.01	0.00	0.00	0.01	0.00
2000	14.2	15.2	0.2	1.5	2.5	1.6	0.11	0.02	0.02	0.01	0.03
2010	57.5	23.3	3.8	8.8	10.8	6.2	0.66	0.09	1.34	0.55	0.20
2015	83.4	28.0	10.0	18.1	17.6	6.6	1.10	0.14	2.23	0.86	0.25
2019	107.6	32.4	20.0	29.4	24.0	7.1	1.59	0.19	3.06	1.09	0.29
Unc.	*0.5*	*0.1*	*1.4*	*0.6*	*0.4*	*0.4*	*0.06*	*n.a.*	*0.06*	*0.14*	*n.a.*
ERF	18.0	6.2	2.2	6.9	4.0	0.7	0.4	0.0	0.7	0.2	0.1

Notes: Data merged from AR5 (1750;1850); CMIP6 compilation by Meinshausen et al (2017)until ca. 1995, and data directly taken from merged AGAGE and NOAA networks, depending on date of availability for various components. Uncertainties pertain to 2019, derived from observations made by global networks, and do not include estimates of analytical accuracy. n.a.: not available. ERF(2019-1750) from Chapter 7.

ACCEPTED VERSION
SUBJECT TO FINAL EDITS

Table AIII.1d: Historical abundances (ppt) and ERF [mWm^{-2}] of HCFCs

Year	HCFC-22	HCFC-141b	HCFC-142b	HCFC-133a	HCFC-31	HCFC-124
1750	0.0	0.0	0.0	0.00	0.00	0.00
1850	0.0	0.0	0.0	0.00	0.00	0.00
1900	0.0	0.0	0.0	0.00	0.00	0.00
1910	0.0	0.0	0.0	0.00	0.00	0.00
1920	0.0	0.0	0.0	0.00	0.00	0.00
1930	0.0	0.0	0.0	0.00	0.00	0.00
1940	0.3	0.0	0.0	0.00	0.00	0.00
1950	0.9	0.0	0.0	0.00	0.00	0.00
1960	2.3	0.0	0.0	0.00	0.00	0.00
1970	13.1	0.0	0.0	0.00	0.00	0.00
1980	44.6	0.0	0.4	0.01	0.00	0.00
1990	89.6	0.3	1.5	0.05	0.00	0.00
2000	141.8	12.7	11.4	0.11	0.027	0.00
2010	206.3	20.5	20.4	0.31	0.084	1.10
2015	233.3	24.2	22.2	0.40	0.084	1.02
2019	246.8	24.4	22.3	n.a.	n.a.	n.a.
Unc.	*0.6*	*0.3*	*0.4*	n.a.	n.a.	n.a.
ERF	52.8	3.9	4.3	0.1	0.0	0.2

Notes: 1750/1850 from AR5.; 1900-1970 from CMIP6 dataset in Meinshausen et al. (2017). 1980-1995 AGAGE, or data directly taken from merged AGAGE and NOAA networks, depending on date of availability for various components; HCFC-31 from Schoenenberger et al (2015), HCFC-124 from Simmonds et al. (2017) Uncertainties pertain to 2019, derived from observations made by global networks, and do not include estimates of analytical accuracy. For HCFC-133a, HCFC-31, and HCFC-124 abundancies in 2019 and uncertainties are not available. ERF(2019-1750) from Chapter 7, except HCFC-133a, HCFC-31, and HCFC-124 which are for 2015.

ACCEPTED VERSION
SUBJECT TO FINAL EDITS

Table AIII.1e: Historical abundances (ppt) and ERF [mWm^{-2}] of CFCs

Year	CFC-12	CFC-11	CFC-113	CFC-114	CFC-115	CFC-13	CFC-112	CFC-112a	CFC-113a	CFC-114a
1750	0.0	0.0	0.0	0.0	0.00	0.00	0.00	0.00	0.00	0.00
1850	0.0	0.0	0.0	0.0	0.00	0.00	0.00	0.00	0.00	0.00
1900	0.0	0.0	0.0	0.0	0.00	0.00	0.00	0.00	0.00	0.00
1910	0.0	0.0	0.0	0.0	0.00	0.00	0.00	0.00	0.00	0.00
1920	0.0	0.0	0.0	0.0	0.00	0.00	0.00	0.00	0.00	0.00
1930	0.0	0.0	0.0	0.0	0.00	0.01	0.00	0.00	0.00	0.00
1940	0.0	0.0	0.5	0.0	0.00	0.03	0.00	0.00	0.00	0.00
1950	6.4	0.9	1.0	1.5	0.00	0.04	0.00	0.00	0.00	0.00
1960	31.6	10.2	2.0	3.9	0.00	0.05	0.00	0.00	0.00	0.00
1970	121.7	57.0	5.9	6.7	0.20	0.44	0.00	0.00	0.00	0.00
1980	304.0	166.8	20.8	10.1	1.75	1.20	0.11	0.00	0.06	0.44
1990	483.1	258.1	70.6	15.6	5.46	2.42	0.31	0.00	0.16	0.91
2000	542.3	259.2	82.1	16.4	8.16	2.83	0.49	0.07	0.28	1.03
2010	530.9	239.4	75.2	16.3	8.38	3.04	0.45	0.07	0.41	1.06
2015	516.6	231.0	72.0	16.0	8.46	3.16	0.42	0.07	0.62	1.05
2019	503.1	226.2	69.8	16.0	8.67	3.28	n.a	n.a	n.a	n.a
Unc.	*3.2*	*1.1*	*0.3*	*0.1*	*0.02*	*0.02*	n.a	n.a	n.a	n.a
ERF	180.3	66.3	21.0	5.0	2.1	0.9	0.1	0.0	0.2	0.3

Notes: 1750/1850 from AR5.; 1900-1970 from CMIP6 dataset in Meinshausen et al. (2017). 1980-1995 AGAGE, or data directly taken from merged AGAGE and NOAA networks, depending on date of availability for various components; CFC-13 from Vollmer et al. (2018) until 2015 then AGAGE; CFC-114 and CFC-114a from AGAGE and Laube et al. (2016) . CFC-112 from Laube et al.(2014); CFC-112a from Adcock et al. (2018). Uncertainties pertain to 2019, derived from observations made by global networks, and do not include estimates of analytical accuracy. For CFC-112, CFC-112a, CFC-113a, and CFC-114a abundances and uncertainties for 2019 are not available. ERF(2019-1750) from Chapter 7, except for CFC-112, CFC-112a, CFC-113a, and CFC-114a for 2015

ACCEPTED VERSION SUBJECT TO FINAL EDITS

Table AIII.1f: Historical abundances (ppt) and ERF [mWm^{-2}] of CH_3CCl_3, CCl_4, CH_3Br, $CHCl_3$ and Halons.

Year	CH_3CCl_3	CCl_4	CH_3Cl	CH_3Br	CH_2Cl_2	$CHCl_3$	Halon-1211	Halon-1301	Halon-2402
1750	0.00	0.03	457	5.30	7	4.8	0.00	0.00	0.00
1850	0.00	0.03	457	5.30	7	4.8	0.00	0.00	0.00
1900	0.00	0.03	457	5.30	7	4.8	0.00	0.00	0.00
1910	0.00	0.03	457	5.30	7	4.8	0.00	0.00	0.00
1920	0.00	1.2	457	5.30	7	4.8	0.00	0.00	0.00
1930	0.00	4.1	457	5.30	7	5.0	0.00	0.00	0.00
1940	0.00	14.1	457	5.66	7	5.3	0.00	0.00	0.00
1950	0.00	35.5	478	6.06	8	5.7	0.03	0.00	0.00
1960	1.70	53.2	512	6.50	11	6.4	0.02	0.00	0.00
1970	17.7	77.0	540	7.06	14	7.5	0.04	0.00	0.02
1980	85.9	93.8	549	7.77	18	8.8	0.71	0.38	0.15
1990	129.3	106.2	550	8.69	20	10.3	2.44	1.85	0.37
2000	45.4	98.1	547	9.09	20	7.5	4.12	2.82	0.48
2010	7.6	87.3	538	7.14	29	7.3	4.12	3.21	0.46
2015	3.1	81.6	547	6.68	35	8.6	3.66	3.31	0.42
2019	1.6	77.9	551	6.49	41	8.8	3.28	3.32	0.40
Unc.	*0.1*	*0.7*	*5*	*0.07*	*6*	*0.3*	*0.05*	*0.07*	*0.03*
ERF	0.1	12.9	0.4	0.0	1.0	0.3	1.0	1.0	0.1

Notes: 1750 from AR5.; 1850-1970 from CMIP6 dataset in Meinshausen (2017). 1980-2019 AGAGE or merged AGAGE and NOAA networks, depending on date of availability. ERF(2019-1750) from Chapter 7.

ACCEPTED VERSION
SUBJECT TO FINAL EDITS

Table AIII.2: Future abundances of CO_2, CH_4, and N_2O for selected SSP scenarios [2020-2500]

	CO_2 (ppm)					CH_4 (ppb)					N_2O (ppb)				
2019*	410					1866					332				
Year/ Scenario	SSP1-19	SSP-126	SSP2-45	SSP3-70	SSP5-58	SSP1-19	SSP-126	SSP2-45	SSP3-70	SSP5-58	SSP1-19	SSP-126	SSP2-45	SSP3-70	SSP5-58
2020	414	414	414	415	415	1894	1888	1911	1921	1907	332	332	332	332	332
2030	434	440	444	451	452	1796	1810	2002	2099	2018	337	337	340	341	341
2040	440	458	475	493	500	1593	1663	2045	2289	2209	341	341	348	351	350
2050	438	469	507	541	563	1428	1519	2020	2472	2446	344	344	356	362	358
2060	431	474	537	593	643	1305	1402	1942	2655	2613	346	346	363	373	366
2070	424	473	564	652	744	1220	1299	1854	2840	2670	348	348	369	385	374
2080	415	467	585	716	864	1150	1197	1779	3028	2652	350	349	373	397	380
2090	405	457	598	787	998	1088	1112	1719	3208	2549	352	352	376	409	387
2100	394	446	603	867	1135	1036	1056	1683	3372	2415	354	354	377	422	392
2200	343	403	643	1457	2108	929	928	1255	2572	1516	364	363	376	497	414
2300	342	396	621	1483	2162	872	864	1001	1988	1068	361	360	367	511	411
2400	339	389	598	1424	2080	871	864	999	1959	1038	358	358	362	514	408
2500	337	384	579	1371	2010	871	864	997	1938	1019	357	356	360	516	407

Note: *observed from Table AIII.1a. SSP GHG concentrations (Meinshausen et al., 2017, 2020) available at greenhousegases.science.unimelb.edu.au. Concentrations of halogens in electronic supplement. Major scenarios used in this report are selected.

ACCEPTED VERSION
SUBJECT TO FINAL EDITS

Table AIII.3: Effective Radiative Forcing (Wm^{-2}) time series of all climate forcers from 1750-2019.

year	CO_2	CH_4	N_2O	Halogens	O_3	H_2O STRAT	Contrail-cirrus	Aerosol radiation interactions	Aerosol cloud interactions	BC on snow	Land use	Volcanic	Solar	Total anthropogenic	Total natural	Total
1750	0.00	0.00	0.00	0.00	0.00	0.00	0.00	0.00	0.00	0.00	0.00	0.20	0.10	0.00	0.30	0.30
1850	0.14	0.05	0.01	0.00	0.03	0.00	0.00	-0.01	-0.07	0.01	-0.03	0.19	0.01	0.13	0.20	0.33
1900	0.35	0.12	0.03	0.00	0.08	0.01	0.00	-0.06	-0.29	0.02	-0.08	0.20	-0.04	0.18	0.16	0.34
1910	0.41	0.15	0.04	0.00	0.09	0.01	0.00	-0.10	-0.42	0.03	-0.10	0.20	-0.02	0.12	0.18	0.30
1920	0.50	0.17	0.05	0.00	0.10	0.02	0.00	-0.10	-0.43	0.03	-0.11	0.19	0.01	0.23	0.20	0.43
1930	0.54	0.20	0.06	0.00	0.12	0.02	0.00	-0.11	-0.46	0.03	-0.13	0.19	0.02	0.26	0.21	0.48
1940	0.62	0.22	0.06	0.00	0.14	0.02	0.00	-0.15	-0.52	0.03	-0.14	0.19	0.04	0.29	0.23	0.52
1950	0.65	0.24	0.07	0.01	0.17	0.02	0.00	-0.15	-0.55	0.03	-0.14	0.18	0.06	0.35	0.24	0.59
1960	0.71	0.29	0.08	0.03	0.22	0.03	0.01	-0.25	-0.73	0.04	-0.17	0.18	0.09	0.26	0.27	0.54
1970	0.85	0.36	0.09	0.08	0.28	0.03	0.02	-0.38	-0.92	0.05	-0.18	0.05	0.08	0.29	0.13	0.42
1980	1.09	0.43	0.11	0.20	0.33	0.04	0.02	-0.41	-1.04	0.06	-0.18	0.09	0.11	0.66	0.19	0.86
1990	1.33	0.49	0.13	0.33	0.36	0.04	0.03	-0.38	-1.05	0.07	-0.19	0.14	0.11	1.17	0.24	1.42
2000	1.56	0.51	0.16	0.37	0.40	0.05	0.04	-0.30	-0.92	0.07	-0.19	0.18	0.11	1.74	0.29	2.02
2010	1.85	0.52	0.18	0.39	0.44	0.05	0.04	-0.27	-0.99	0.08	-0.20	0.14	-0.01	2.10	0.13	2.23
2015	2.01	0.53	0.20	0.40	0.47	0.05	0.05	-0.23	-0.89	0.08	-0.20	0.11	0.03	2.47	0.14	2.61
2019	2.16	0.54	0.21	0.41	0.47	0.05	0.06	-0.22	-0.84	0.08	-0.20	0.14	-0.02	2.72	0.12	2.84

Note: O_3 includes tropospheric and stratospheric O_3, dominated by tropospheric O_3. Stratospheric water vapour from methane oxidation is a linear function of the methane ERF (Section 7.3.2.6). Contrail forcing is a linear scaling of aviation NOx emissions, scaled to ERF in 2018 (Lee et al., 2021). Present-day aerosol forcing is assessed in Section 7.3.3 as -0.3 (-0.6 to 0.0) W m^{-2} for aerosol-radiation interactions and -1.0 (-1.7 to -0.3) W m^{-2} for aerosol-cloud interactions for the 2005-2014 mean relative to 1750. Land use change considers albedo and irrigation effects (Section 7.3.4.1). BC on snow forcing is linear with emissions of BC (Section 7.3.4.3). Volcanic forcing is positive in years without large volcanic eruptions such that the long-term pre-industrial (500 BCE to 1749 CE) mean volcanic forcing is zero. Solar forcing is derived from the ^{14}C reconstruction of total solar irradiance in the combined PMIP4/CMIP6 dataset (Jungclaus et al., 2017; Matthes et al., 2017). Present-day solar forcing is assessed in Section 7.3.4.4 as +0.01 (-0.06 to +0.08) W m^{-2}, based on the mean total solar irradiance from solar cycle 24 (2009-2019) compared a long pre-industrial baseline period (6754 BCE - 1744 CE); the 2019 ERF value differs from this as it represents a single year near the solar minimum. Natural is the sum of volcanic and solar forcing, while anthropogenic includes all others. Further details on methods for computing ERF are in Chapter 7 Supplementary Material 7.SM.1.3.

ACCEPTED VERSION SUBJECT TO FINAL EDITS

Table AIII.4a: Effective Radiative Forcing (Wm-2) time series of all climate forcers for SSP1-19

year	CO_2	CH_4	N_2O	Halogens	O_3	H_2O STRAT	Contrail-cirrus	Aerosol radiation interactions	Aerosol cloud interactions	BC on snow	Land use	Volcanic	Solar	Total anthropogenic	Total natural	Total
2020	2.22	0.55	0.21	0.40	0.42	0.05	0.05	-0.20	-0.81	0.08	-0.20	0.06	-0.02	2.77	0.04	2.81
2030	2.49	0.52	0.23	0.38	0.25	0.05	0.03	-0.16	-0.39	0.03	-0.21	0.00	-0.02	3.22	-0.02	3.20
2040	2.56	0.44	0.24	0.32	0.19	0.04	0.02	-0.16	-0.28	0.02	-0.21	0.00	-0.01	3.18	-0.01	3.18
2050	2.53	0.37	0.25	0.27	0.14	0.03	0.02	-0.17	-0.20	0.01	-0.21	0.00	0.01	3.04	0.01	3.05
2060	2.45	0.31	0.26	0.23	0.12	0.03	0.01	-0.17	-0.16	0.01	-0.21	0.00	0.01	2.87	0.01	2.88
2070	2.35	0.27	0.26	0.21	0.11	0.02	0.01	-0.16	-0.13	0.00	-0.20	0.00	0.02	2.74	0.02	2.76
2080	2.23	0.24	0.27	0.19	0.09	0.02	0.01	-0.15	-0.09	0.00	-0.19	0.00	0.02	2.62	0.02	2.64
2090	2.09	0.21	0.28	0.17	0.09	0.02	0.01	-0.14	-0.05	0.00	-0.19	0.00	0.01	2.48	0.01	2.48
2100	1.92	0.18	0.28	0.15	0.08	0.02	0.01	-0.13	-0.01	0.00	-0.18	0.00	0.00	2.33	0.00	2.33
2200	1.16	0.12	0.32	0.07	0.06	0.01	0.00	-0.10	0.08	-0.01	-0.17	0.00	0.03	1.55	0.03	1.58
2300	1.14	0.09	0.31	0.04	0.03	0.01	0.00	-0.09	0.14	-0.01	-0.17	0.00	0.00	1.49	0.00	1.49
2400	1.09	0.09	0.30	0.03	0.03	0.01	0.00	-0.09	0.14	-0.01	-0.17	0.00	0.00	1.42	0.00	1.42
2500	1.05	0.09	0.30	0.02	0.03	0.01	0.00	-0.09	0.14	-0.01	-0.17	0.00	0.00	1.38	0.00	1.38

Note: ERF based on future abundancies of WMGHGs listed in AIII.2 . See notes of AIII.3. Future ozone forcing uses projected emissions of carbon monoxide, volatile organic carbon, nitrogen oxides, and concentrations of methane, nitrous oxide and halogenated compounds with relationships to forcing derived from Thornhill et al. (2021b, 2021a). Future contrail forcing is a linear scaling of future NOx emissions (Smith et al., 2018) and scaled to year-2018 ERF (Lee et al., 2021). Future aerosol forcing is based on emissions of black carbon, organic carbon, sulphur dioxide and ammonia using method described in Smith et al. (2018). Land use forcing scales with cumulative emissions of future land-use CO_2 (Smith et al., 2018). Future volcanic forcing set to zero from a 10-year linear transition from the end of the historical period following Eyring et al. (2016). Solar forcing is set to zero from 2300 CE. Further details on methods for computing SSP-projection ERF are in Chapter 7 Supplementary Material 7.SM.1.4

ACCEPTED VERSION SUBJECT TO FINAL EDITS

Table AIII.4b: Effective Radiative Forcing (Wm-2) time series of all climate forcers for SSP1-26

year	CO_2	CH_4	N_2O	Halogens	O_3	H_2O STRAT	Contrail-cirrus	Aerosol radiation interactions	Aerosol cloud interactions	BC on snow	Land use	Volcanic	Solar	Total anthropogenic	Total natural	Total
2020	2.22	0.55	0.21	0.40	0.42	0.05	0.05	-0.20	-0.81	0.08	-0.20	0.06	-0.02	2.76	0.04	2.80
2030	2.56	0.52	0.22	0.39	0.30	0.05	0.04	-0.19	-0.51	0.04	-0.21	0.00	-0.02	3.23	-0.02	3.21
2040	2.79	0.46	0.24	0.34	0.26	0.04	0.04	-0.16	-0.36	0.03	-0.20	0.00	-0.01	3.49	-0.01	3.48
2050	2.93	0.41	0.25	0.28	0.21	0.04	0.04	-0.15	-0.26	0.02	-0.20	0.00	0.01	3.56	0.01	3.58
2060	2.99	0.35	0.25	0.24	0.18	0.03	0.04	-0.13	-0.20	0.02	-0.20	0.00	0.01	3.58	0.01	3.58
2070	2.98	0.31	0.26	0.21	0.15	0.03	0.04	-0.13	-0.16	0.02	-0.19	0.00	0.02	3.52	0.02	3.54
2080	2.91	0.26	0.27	0.19	0.12	0.02	0.04	-0.13	-0.10	0.01	-0.18	0.00	0.02	3.40	0.02	3.42
2090	2.78	0.22	0.28	0.17	0.10	0.02	0.03	-0.13	-0.06	0.01	-0.17	0.00	0.01	3.24	0.01	3.25
2100	2.63	0.19	0.28	0.16	0.08	0.02	0.03	-0.12	-0.01	0.00	-0.17	0.00	0.00	3.10	0.00	3.10
2200	2.06	0.12	0.32	0.07	0.04	0.01	0.01	-0.10	0.08	-0.01	-0.15	0.00	0.03	2.47	0.03	2.50
2300	1.96	0.08	0.31	0.04	0.01	0.01	0.00	-0.09	0.14	-0.01	-0.15	0.00	0.00	2.30	0.00	2.30
2400	1.87	0.08	0.30	0.03	0.01	0.01	0.00	-0.09	0.14	-0.01	-0.15	0.00	0.00	2.19	0.00	2.19
2500	1.79	0.08	0.29	0.02	0.01	0.01	0.00	-0.09	0.14	-0.01	-0.15	0.00	0.00	2.11	0.00	2.11

Notes: see Table AIII.3 and Table AIII.4a.

ACCEPTED VERSION
SUBJECT TO FINAL EDITS

Table AIII.4c: Effective Radiative Forcing (Wm-2) time series of all climate forcers for SSP2-45

year	CO_2	CH_4	N_2O	Halogens	O_3	H_2O STRAT	Contrail-cirrus	Aerosol radiation interactions	Aerosol cloud interactions	BC on snow	Land use	Volcanic	Solar	Total anthropogenic	Total natural	Total
2020	2.22	0.56	0.21	0.40	0.45	0.05	0.05	-0.18	-0.88	0.10	-0.20	0.06	-0.02	2.79	0.04	2.83
2030	2.62	0.59	0.23	0.40	0.47	0.05	0.07	-0.21	-0.84	0.09	-0.21	0.00	-0.02	3.25	-0.02	3.24
2040	3.01	0.61	0.26	0.37	0.45	0.06	0.09	-0.20	-0.74	0.07	-0.22	0.00	-0.01	3.76	-0.01	3.75
2050	3.38	0.60	0.28	0.34	0.43	0.06	0.09	-0.18	-0.61	0.06	-0.22	0.00	0.01	4.23	0.01	4.24
2060	3.72	0.57	0.30	0.32	0.39	0.05	0.10	-0.18	-0.51	0.05	-0.22	0.00	0.01	4.59	0.01	4.60
2070	4.01	0.54	0.32	0.30	0.35	0.05	0.12	-0.19	-0.43	0.04	-0.21	0.00	0.02	4.89	0.02	4.91
2080	4.23	0.51	0.33	0.29	0.31	0.05	0.15	-0.19	-0.34	0.02	-0.20	0.00	0.02	5.15	0.02	5.16
2090	4.35	0.49	0.34	0.28	0.28	0.04	0.16	-0.19	-0.25	0.01	-0.19	0.00	0.01	5.32	0.01	5.33
2100	4.40	0.47	0.35	0.27	0.25	0.04	0.18	-0.19	-0.21	0.01	-0.18	0.00	0.00	5.40	0.00	5.40
2200	4.79	0.29	0.35	0.14	0.08	0.03	0.06	-0.13	-0.01	-0.01	-0.15	0.00	0.03	5.43	0.03	5.46
2300	4.59	0.16	0.32	0.05	-0.02	0.01	0.00	-0.11	0.09	-0.01	-0.15	0.00	0.00	4.94	0.00	4.94
2400	4.35	0.16	0.31	0.03	-0.02	0.01	0.00	-0.11	0.09	-0.01	-0.15	0.00	0.00	4.67	0.00	4.67
2500	4.17	0.16	0.30	0.03	-0.02	0.01	0.00	-0.11	0.09	-0.01	-0.15	0.00	0.00	4.47	0.00	4.47

Notes: see Table AIII.3 and Table AIII.4a.

ACCEPTED VERSION
SUBJECT TO FINAL EDITS

Table AIII.4d: Effective Radiative Forcing (Wm^{-2}) time series of all climate forcers for SSP3-70

year	CO_2	CH_4	N_2O	Halogens	O_3	H_2O STRAT	Contrail-cirrus	Aerosol radiation interactions	Aerosol cloud interactions	BC on snow	Land use	Volcanic	Solar	Total anthropogenic	Total natural	Total
2020	2.23	0.56	0.21	0.40	0.51	0.05	0.05	-0.19	-1.02	0.12	-0.20	0.06	-0.02	2.72	0.04	2.76
2030	2.71	0.63	0.23	0.39	0.57	0.06	0.07	-0.19	-1.04	0.12	-0.21	0.00	-0.02	3.33	-0.02	3.31
2040	3.22	0.69	0.26	0.37	0.62	0.06	0.08	-0.19	-1.06	0.13	-0.22	0.00	-0.01	3.97	-0.01	3.96
2050	3.76	0.75	0.29	0.36	0.66	0.07	0.09	-0.20	-1.06	0.13	-0.23	0.00	0.01	4.61	0.01	4.63
2060	4.31	0.80	0.33	0.35	0.69	0.07	0.09	-0.20	-1.03	0.12	-0.24	0.00	0.01	5.30	0.01	5.30
2070	4.87	0.86	0.36	0.35	0.71	0.08	0.10	-0.20	-0.99	0.12	-0.25	0.00	0.02	6.00	0.02	6.02
2080	5.45	0.91	0.39	0.35	0.73	0.08	0.10	-0.20	-0.95	0.11	-0.26	0.00	0.02	6.71	0.02	6.72
2090	6.04	0.96	0.42	0.35	0.75	0.09	0.10	-0.21	-0.92	0.11	-0.26	0.00	0.01	7.43	0.01	7.44
2100	6.64	1.00	0.45	0.36	0.77	0.09	0.11	-0.20	-0.87	0.10	-0.27	0.00	0.00	8.18	0.00	8.18
2200	10.00	0.77	0.64	0.22	0.38	0.07	0.04	-0.16	-0.32	0.03	-0.29	0.00	0.03	11.37	0.03	11.40
2300	10.11	0.58	0.68	0.08	0.15	0.05	0.00	-0.14	0.02	-0.01	-0.29	0.00	0.00	11.24	0.00	11.24
2400	9.84	0.57	0.69	0.06	0.14	0.05	0.00	-0.14	0.02	-0.01	-0.29	0.00	0.00	10.94	0.00	10.94
2500	9.60	0.56	0.70	0.06	0.13	0.05	0.00	-0.14	0.02	-0.01	-0.29	0.00	0.00	10.68	0.00	10.68

Notes: see Table AIII.3 and Table AIII.4a.

ACCEPTED VERSION
SUBJECT TO FINAL EDITS

Table AIII.4e: Effective Radiative Forcing (Wm^{-2}) time series of all climate forcers for SSP5-85

year	CO_2	CH_4	N_2O	Halogens	O_3	H_2O STRAT	Contrail-cirrus	Aerosol radiation interactions	Aerosol cloud interactions	BC on snow	Land use	Volcanic	Solar	Total anthropogenic	Total natural	Total
2020	2.23	0.56	0.21	0.40	0.48	0.05	0.06	-0.14	-0.86	0.11	-0.20	0.06	-0.02	2.90	0.04	2.94
2030	2.71	0.60	0.23	0.41	0.49	0.06	0.08	-0.13	-0.71	0.09	-0.21	0.00	-0.02	3.61	-0.02	3.59
2040	3.30	0.66	0.26	0.41	0.54	0.06	0.09	-0.14	-0.67	0.09	-0.23	0.00	-0.01	4.37	-0.01	4.37
2050	4.00	0.74	0.28	0.42	0.56	0.07	0.10	-0.15	-0.57	0.07	-0.23	0.00	0.01	5.29	0.01	5.30
2060	4.79	0.79	0.30	0.45	0.60	0.07	0.12	-0.18	-0.58	0.06	-0.24	0.00	0.01	6.21	0.01	6.22
2070	5.68	0.81	0.32	0.50	0.60	0.07	0.14	-0.20	-0.55	0.06	-0.24	0.00	0.02	7.19	0.02	7.21
2080	6.62	0.80	0.34	0.55	0.56	0.07	0.15	-0.20	-0.48	0.05	-0.23	0.00	0.02	8.24	0.02	8.25
2090	7.54	0.77	0.36	0.58	0.49	0.07	0.15	-0.21	-0.38	0.03	-0.23	0.00	0.01	9.18	0.01	9.19
2100	8.38	0.73	0.37	0.60	0.40	0.07	0.15	-0.21	-0.27	0.02	-0.23	0.00	0.00	10.01	0.00	10.00
2200	12.30	0.40	0.42	0.32	0.06	0.04	0.05	-0.16	-0.07	0.00	-0.22	0.00	0.03	13.14	0.03	13.17
2300	12.46	0.19	0.42	0.08	-0.11	0.02	0.00	-0.14	0.03	-0.01	-0.22	0.00	0.00	12.72	0.00	12.72
2400	12.22	0.18	0.42	0.06	-0.13	0.02	0.00	-0.14	0.03	-0.01	-0.22	0.00	0.00	12.43	0.00	12.43
2500	12.01	0.17	0.41	0.06	-0.14	0.02	0.00	-0.14	0.03	-0.01	-0.22	0.00	0.00	12.19	0.00	12.19

Notes: see Table AIII.3 and Table AIII.4a.

ACCEPTED VERSION SUBJECT TO FINAL EDITS

Table AIII.4f: Effective Radiative Forcing (mWm^{-2}) time series of halogen components for selected scenarios and Kyoto and Montreal gases.

	SSP1-19						**SSP3-70**						**SSP5-85**					
2019 (obs)	40	14	338	17	54	394	40	14	311	17	54	367	40	14	311	17	54	367
year	HFCs	NF3, SF_6, PFCs	CFCs, HCFCs	CH_3CCl_3,CCL_4, CH_3Cl,CH_3Br	Kyoto	Montreal	HFCs	NF3, SF_6, PFCs	CFCs, HCFCs	CH_3CCl_3,CCL_4, CH_3Cl,CH_3Br	Kyoto	Montreal	HFCs	NF3, SF_6, PFCs	CFCs, HCFCs	CH_3CCl_3,CCL_4, CH_3Cl,CH_3Br	Kyoto	Montreal
2020	43	14	330	16	57	390	42	14	330	16	56	389	43	14	330	17	57	390
2030	53	16	296	12	70	308	68	18	295	13	86	308	83	18	294	14	101	308
2040	41	17	249	9	59	258	92	21	248	10	113	258	130	21	246	11	151	257
2050	33	18	209	7	51	216	116	24	208	8	140	216	180	25	207	8	205	215
2060	28	19	180	5	47	185	138	27	178	6	164	184	238	28	177	7	266	184
2070	25	19	157	4	45	161	157	29	155	5	187	160	304	31	154	6	336	160
2080	24	20	139	3	44	141	176	32	136	4	208	140	370	35	135	5	405	140
2090	23	20	123	2	43	125	195	35	119	3	229	123	420	38	118	4	459	122
2100	22	20	110	1	43	111	212	38	105	3	250	108	447	41	104	4	489	107
2200	12	22	38	0	34	38	132	56	31	0	187	31	225	61	29	1	286	30

Notes: ERF for 2019 was calculated using concentrations list in Table AIII.1, 2020 and onward are scenario projections. ERF was calculated using concentrations of individual halogen components. Updated from (Meinshausen et al., 2017, 2020) available at greenhousegases.science.unimelb.edu.au.

ACCEPTED VERSION
SUBJECT TO FINAL EDITS

Table AIII.5: Total Anthropogenic and natural ERF relative to 1750 assessed in AR5 (RCP scenarios) and AR6 (SSP scenarios).

		2030			2050			2090		
		Anthro-pogenic	Natural	Total	Anthro-pogenic	Natural	Total	Anthro-pogenic	Natural	Total
AR5	RCP2.6[1]	2.52		2.50 ± 0.51	2.64		2.65 ± 0.47	2.35		2.44 ± 0.49
	RCP4.5[1]	2.67		2.61 ± 0.54	3.42		3.25 ± 0.56	3.91		3.78 ± 0.58
	RCP6.0[1]	2.52		2.41 ± 0.60	3.20		3.07 ± 0.61	4.93		4.64 ± 0.71
	RCP8.5[1]	2.91		2.92 ± 0.57	4.37		4.21 ± 0.63	7.32		7.13 ± 0.89
AR6	RCP2.6[2]	2.85	-0.02	2.83 (1.93-3.61)	3.11	0.01	3.12 (2.33-3.76)	2.70	0.01	2.71 (2.04-3.22)
	RCP4.5[2]	3.01	-0.02	2.99 (2.12-3.84)	3.90	0.01	3.91 (3.07-4.68)	4.48	0.01	4.49 (3.75-5.15)
	RCP6.0[2]	2.84	-0.02	2.82 (1.88-3.69)	3.56	0.01	3.58 (2.59-4.47)	5.51	0.01	5.52 (4.50-6.38)
	RCP8.5[2]	3.36	-0.02	3.34 (2.40-4.23)	5.01	0.01	5.03 (4.06-5.92)	8.46	0.01	8.46 (7.23-9.61)
	SSP1-1.9[3]	3.22	-0.02	3.20 (2.62-3.75)	3.04	0.01	3.05 (2.58-3.50)	2.48	0.01	2.48 (2.12-2.83)
	SSP1-2.6[3]	3.23	-0.02	3.21 (2.57-3.84)	3.56	0.01	3.58 (3.02-4.11)	3.24	0.01	3.25 (2.81-3.67)
	SSP2-4.5[3]	3.25	-0.02	3.24 (2.40-4.08)	4.23	0.01	4.24 (3.46-5.02)	5.32	0.01	5.33 (4.56-6.05)
	SSP3-7.0[3]	3.33	-0.02	3.31 (2.30-4.31)	4.61	0.01	4.63 (3.51-5.73)	7.43	0.01	7.44 (6.17-8.70)
	SSP3-7.0_lowNTCF[4]	3.40	-0.02	3.48 (2.53-4.24)	4.91	0.01	4.92 (4.13-5.70)	7.73	0.01	7.74 (6.70-8.76)
	SSP3-7.0_lowNTCFCH$_4$[5]	3.26	-0.02	3.24 (2.40-4.09)	4.28	0.01	4.29 (3.56-5.01)	6.67	0.01	6.67 (5.75-7.57)
	SSP4-3.4[3]	3.26	-0.02	3.24 (2.33-4.11)	3.90	0.01	3.91 (3.06-4.68)	4.18	0.01	4.19 (3.49-4.83)
	SSP4-6.0[3]	3.31	-0.02	3.30 (2.35-4.23)	4.44	0.01	4.46 (3.49-5.42)	6.12	0.01	6.13 (5.21-7.02)
	SSP5-3.4_over[3]	3.62	-0.02	3.60 (2.82-4.40)	5.04	0.01	5.05 (4.29-5.79)	3.93	0.01	3.93 (3.40-4.45)
	SSP5-8.5[3]	3.61	-0.02	3.59 (2.80-4.38)	5.29	0.01	5.30 (4.44-6.17)	9.18	0.01	9.19 (7.96-10.40)

Notes [1]Table AII.6.8 and 6.10 in Annex II of the IPCC AR5 WG1 report (Prather et al., 2013), for which total ERF is derived from CMIP5 models and anthropogenic ERF from a simple climate model emulator. [2]RCPs calculated for ERF as described in Chapter 7 Supplementary Material 7.SM.1.4. Similar to AR5, an emulator was used in AR6 to derive anthropogenic ERF (Cross Chapter Box 7.1 and Chapter 7 Supplementary Material 7.SM.1.4). Further discussion on the difference between AR5 and AR6 radiative forcing in section 4.6.2. [3] ScenarioMIP (O'Neill et al., 2016), [4]AerChemMIP (Collins et al., 2017) [5] Allen et al. (2021)

ACCEPTED VERSION SUBJECT TO FINAL EDIT

References

Adcock, K. E., Reeves, C. E., Gooch, L. J., Leedham Elvidge, E. C., Ashfold, M. J., Brenninkmeijer, C. A. M., et al. (2018). Continued increase of CFC-113a (CCl3CF3) mixing ratios in the global atmosphere: emissions, occurrence and potential sources. *Atmos. Chem. Phys.* 18, 4737–4751. doi:10.5194/acp-18-4737-2018.

Allen, R. J., Horowitz, L. W., Naik, V., Oshima, N., O'Connor, F. M., Turnock, S., et al. (2021). Significant climate benefits from near-term climate forcer mitigation in spite of aerosol reductions. *Environ. Res. Lett.* doi:10.1088/1748-9326/abe06b.

Collins, W. J., Lamarque, J.-F., Schulz, M., Boucher, O., Eyring, V., Hegglin, M. I., et al. (2017). AerChemMIP: quantifying the effects of chemistry and aerosols in CMIP6. *Geosci. Model Dev.* 10, 585–607. doi:10.5194/gmd-10-585-2017.

Dlugokencky, E. J., Nisbet, E. G., Fisher, R., and Lowry, D. (2011). Global atmospheric methane: Budget, changes and dangers. *Philos. Trans. R. Soc. A Math. Phys. Eng. Sci.* doi:10.1098/rsta.2010.0341.

Droste, E. S., Adcock, K. E., Ashfold, M. J., Chou, C., Fleming, Z., Fraser, P. J., et al. (2020). Trends and emissions of six perfluorocarbons in the Northern Hemisphere and Southern Hemisphere. *Atmos. Chem. Phys.* 20, 4787–4807. doi:10.5194/acp-20-4787-2020.

Eyring, V., Bony, S., Meehl, G. A., Senior, C. A., Stevens, B., Stouffer, R. J., et al. (2016). Overview of the Coupled Model Intercomparison Project Phase 6 (CMIP6) experimental design and organization. *Geosci. Model Dev.* 9, 1937–1958. doi:10.5194/gmd-9-1937-2016.

Gidden, M. J., Riahi, K., Smith, S. J., Fujimori, S., Luderer, G., Kriegler, E., et al. (2019). Global emissions pathways under different socioeconomic scenarios for use in CMIP6: a dataset of harmonized emissions trajectories through the end of the century. *Geosci. Model Dev.* 12, 1443–1475. doi:10.5194/gmd-12-1443-2019.

Hall, B. D., Dutton, G. S., Mondeel, D. J., Nance, J. D., Rigby, M., Butler, J. H., et al. (2011). Improving measurements of SF6 for the study of atmospheric transport and emissions. *Atmos. Meas. Tech.* doi:10.5194/amt-4-2441-2011.

Jungclaus, J. H., Bard, E., Baroni, M., Braconnot, P., Cao, J., Chini, L. P., et al. (2017). The PMIP4 contribution to CMIP6 - Part 3: The last millennium, scientific objective, and experimental design for the PMIP4 past1000 simulations. *Geosci. Model Dev.* 10, 4005–4033. doi:10.5194/gmd-10-4005-2017.

Laube, J. C., Mohd Hanif, N., Martinerie, P., Gallacher, E., Fraser, P. J., Langenfelds, R., et al. (2016). Tropospheric observations of CFC-114 and CFC-114a with a focus on long-term trends and emissions. *Atmos. Chem. Phys.* doi:10.5194/acp-16-15347-2016.

Laube, J. C., Newland, M. J., Hogan, C., Brenninkmeijer, C. A. M., Fraser, P. J., Martinerie, P., et al. (2014). Newly detected ozone-depleting substances in the atmosphere. *Nat. Geosci.* 7, 266–269. doi:10.1038/ngeo2109.

Lee, D. S., Fahey, D. W., Skowron, A., Allen, M. R., Burkhardt, U., Chen, Q., et al. (2021). The contribution of global aviation to anthropogenic climate forcing for 2000 to 2018. *Atmos. Environ.* 244, 117834. doi:https://doi.org/10.1016/j.atmosenv.2020.117834.

Leedham Elvidge, E., Bönisch, H., Brenninkmeijer, C. A. M., Engel, A., Fraser, P. J., Gallacher, E., et al. (2018). Evaluation of stratospheric age of air from CF4, C2F6, C3F8, CHF3, HFC-125, HFC-227ea and SF6; implications for the calculations of halocarbon lifetimes, fractional release factors and ozone depletion potentials. *Atmos. Chem. Phys.* 18, 3369–3385. doi:10.5194/acp-18-3369-2018.

Masarie, K. A., and Tans, P. P. (2004). Extension and integration of atmospheric carbon dioxide data into a globally consistent measurement record. *J. Geophys. Res.* doi:10.1029/95jd00859.

Matthes, K., Funke, B., Andersson, M. E., Barnard, L., Beer, J., Charbonneau, P., et al. (2017). Solar forcing for CMIP6 (v3.2). *Geosci. Model Dev.* 10, 2247–2302. doi:10.5194/gmd-10-2247-2017.

Meinshausen, M., Nicholls, Z. R. J., Lewis, J., Gidden, M. J., Vogel, E., Freund, M., et al. (2020). The shared socio-economic pathway (SSP) greenhouse gas concentrations and their extensions to 2500. *Geosci. Model Dev.* 13, 3571–3605. doi:10.5194/gmd-13-3571-2020.

Meinshausen, M., Vogel, E., Nauels, A., Lorbacher, K., Meinshausen, N., Etheridge, D. M., et al. (2017). Historical greenhouse gas concentrations for climate modelling (CMIP6). *Geosci. Model Dev.* 10, 2057–2116. doi:10.5194/gmd-10-2057-2017.

Montzka, S. A., Hall, B. D., and Elkins, J. W. (2009). Accelerated increases observed for hydrochlorofluorocarbons since 2004 in the global atmosphere. *Geophys. Res. Lett.* doi:10.1029/2008GL036475.

Mühle, J., Trudinger, C. M., Western, L. M., Rigby, M., Vollmer, M. K., Park, S., et al. (2019). Perfluorocyclobutane (PFC-318, C4F8) in the global atmosphere. *Atmos. Chem. Phys.* 19, 10335–10359. doi:10.5194/acp-19-10335-2019.

Naus, S., Montzka, S. A., Pandey, S., Basu, S., Dlugokencky, E. J., and Krol, M. (2019). Constraints and biases in a tropospheric two-box model of OH. *Atmos. Chem. Phys.* doi:10.5194/acp-19-407-2019.

O'Neill, B. C., Tebaldi, C., van Vuuren, D. P., Eyring, V., Friedlingstein, P., Hurtt, G., et al. (2016). The Scenario Model Intercomparison Project (ScenarioMIP) for CMIP6. *Geosci. Model Dev.* 9, 3461–3482. doi:10.5194/gmd-9-3461-2016.

Prather, M., Flato, G., Friedlingstein, P., Jones, C., Lamarque, J. F., Liao, H., et al. eds. (2013). "IPCC, 2013: Annex II:

ACCEPTED VERSION SUBJECT TO FINAL EDITS

Climate System Scenario Tables," in *Climate Change 2013: The Physical Science Basis. Contribution of Working Group I to the Fifth Assessment Report of the Intergovernmental Panel on Climate Change [Stocker, T.F., D. Qin, G.-K. Plattner, M. Tignor, S.K. Allen, J. Boschung, A. Nauels, Y. Xia* (Cambridge, United Kingdom and New York, NY, USA: Cambridge University Press), 52. Available at: https://www.ipcc.ch/pdf/assessment-report/ar5/wg1/WG1AR5_AnnexII_FINAL.pdf.

Prinn, R. G., Weiss, R. F., Arduini, J., Arnold, T., Langley Dewitt, H., Fraser, P. J., et al. (2018). History of chemically and radiatively important atmospheric gases from the Advanced Global Atmospheric Gases Experiment (AGAGE). *Earth Syst. Sci. Data*. doi:10.5194/essd-10-985-2018.

Rigby, M., Prinn, R. G., O'Doherty, S., Miller, B. R., Ivy, D., Mühle, J., et al. (2014). Recent and future trends in synthetic greenhouse gas radiative forcing. *Geophys. Res. Lett.* 41, 2623–2630. doi:10.1002/2013GL059099.

Schoenenberger, F., Vollmer, M. K., Rigby, M., Hill, M., Fraser, P. J., Krummel, P. B., Langenfelds, R. L., R., S., T., et al. (2015). First observations, trends, and emissions of HCFC-31 (CH2ClF) in the global atmosphere. *Geophys. Res. Lett.*, 42, 7817–. doi:10.1002/2015GL064709.

Simmonds, P. G., Rigby, M., McCulloch, A., O'Doherty, S., Young, D., Mühle, J., et al. (2017). Changing trends and emissions of hydrochlorofluorocarbons (HCFCs) and their hydrofluorocarbon (HFCs) replacements. *Atmos. Chem. Phys.* 17, 4641–4655. doi:10.5194/acp-17-4641-2017.

Smith, C. J., Forster, P. M., Allen, M., Leach, N., Millar, R. J., Passerello, G. A., et al. (2018). FAIR v1.3: a simple emissions-based impulse response and carbon cycle model. *Geosci. Model Dev.* 11, 2273–2297. doi:10.5194/gmd-11-2273-2018.

Thornhill, G., Collins, W., Olivié, D., Skeie, R. B., Archibald, A., Bauer, S., et al. (2021a). Climate-driven chemistry and aerosol feedbacks in CMIP6 Earth system models. *Atmos. Chem. Phys.* 21, 1105–1126. doi:10.5194/acp-21-1105-2021.

Thornhill, G. D., Collins, W. J., Kramer, R. J., Olivié, D., Skeie, R. B., O'Connor, F. M., et al. (2021b). Effective radiative forcing from emissions of reactive gases and aerosols -- a multi-model comparison. *Atmos. Chem. Phys.* 21, 853–874. doi:10.5194/acp-21-853-2021.

Trudinger, C. M., Etheridge, D. M., Sturrock, G. A., Fraser, P. J., Krummel, P. B., and McCulloch, A. (2004). Atmospheric histories of halocarbons from analysis of Antarctic firn air: Methyl bromide, methyl chloride, chloroform, and dichloromethane. *J. Geophys. Res. D Atmos.* doi:10.1029/2004JD004932.

Velders, G. J. M., Fahey, D. W., Daniel, J. S., Andersen, S. O., and McFarland, M. (2015). Future atmospheric abundances and climate forcings from scenarios of global and regional hydrofluorocarbon (HFC) emissions. *Atmos. Environ.* 123, 200–209. doi:https://doi.org/10.1016/j.atmosenv.2015.10.071.

Vollmer, M. K., Mühle, J., Trudinger, C. M., Rigby, M., Montzka, S. A., Harth, C. M., et al. (2016). Atmospheric histories and global emissions of halons H-1211 (CBrClF2), H-1301 (CBrF3), and H-2402 (CBrF2CBrF2). *J. Geophys. Res.* doi:10.1002/2015JD024488.

Worton, D. R., Sturges, W. T., Schwander, J., Mulvaney, R., Barnola, J. M., and Chappellaz, J. (2006). 20th century trends and budget implications of chloroform and related tri-and dihalomethanes inferred from firn air. *Atmos. Chem. Phys.* doi:10.5194/acp-6-2847-2006.

ACCEPTED VERSION
SUBJECT TO FINAL EDITS

Annex IV: Modes of Variability

Coordinating Lead Authors:
Christophe Cassou (France), Annalisa Cherchi (Italy), Yu Kosaka (Japan)

Lead Authors:
Susanna Corti (Italy), Francois Engelbrecht (South Africa), June-Yi Lee (Republic of Korea), Amanda Maycock (United Kingdom), Shayne McGregor (Australia), Olaf Morgenstern (New Zealand/Germany), Hyacinth C. Nnamchi (Nigeria, Germany/Nigeria), Juan A. Rivera (Argentina), Blair Trewin (Australia)

Contributing Author:
Adam S. Phillips (United States of America)

This Annex should be cited as:
IPCC, 2021: Annex IV: Modes of Variability [Cassou, C., A. Cherchi, Y. Kosaka (eds.)]. In: *Climate Change 2021: The Physical Science Basis. Contribution of Working Group I to the Sixth Assessment Report of the Intergovernmental Panel on Climate Change* [Masson-Delmotte, V., P. Zhai, A. Pirani, S. L. Connors, C. Péan, S. Berger, N. Caud, Y. Chen, L. Goldfarb, M. I. Gomis, M. Huang, K. Leitzell, E. Lonnoy, J.B.R. Matthews, T. K. Maycock, T. Waterfield, O. Yelekçi, R. Yu and B. Zhou (eds.)]. Cambridge University Press. In Press.

Date: August 2021

This document is subject to copy-editing, corrigenda and trickle backs.

ACCEPTED VERSION
SUBJECT TO FINAL EDITING

Table of Contents

AIV.1 Introduction 4
AIV.2 The main modes of climate variability assessed in AR6 5
AIV.2.1 North Atlantic Oscillation and Northern Annular Mode 5
AIV.2.1.1 Definition of the mode 5
AIV.2.1.2 Teleconnections and regional influence 7
AIV.2.1.3 Available proxy-based reconstruction 8
AIV.2.2 Southern Annular Mode 9
AIV.2.2.1 Definition of the mode 9
AIV.2.2.2 Teleconnections and regional influence 10
AIV.2.2.3 Available proxy-based reconstruction 11
AIV.2.3 El Niño-Southern Oscillation 11
AIV.2.3.1 Definition of the mode 11
AIV.2.3.2 Teleconnections and regional influence 13
AIV.2.3.3 Available proxy-based reconstruction 14
AIV.2.4 Indian Ocean Basin and Dipole Modes 14
AIV.2.4.1 Definition of the mode 14
AIV.2.4.2 Teleconnections and regional influence 16
AIV.2.4.3 Available proxy-based reconstruction 17
AIV.2.5 Atlantic Meridional and Zonal Modes 17
AIV.2.5.1 Definition of the mode 17
AIV.2.5.2 Teleconnections and regional influence 19
AIV.2.5.3 Available proxy-based reconstruction 20
AIV.2.6 Pacific Decadal Variability 20
AIV.2.6.1 Definition of the mode 20
AIV.2.6.2 Teleconnections and regional influence 22
AIV.2.6.3 Available proxy-based reconstruction 23
AIV.2.7 Atlantic Multidecadal Variability 23
AIV.2.7.1 Definition of the mode 23
AIV.2.7.2 Teleconnections and regional influence 25
AIV.2.7.3 Available proxy-based reconstruction 26

ACCEPTED VERSION
SUBJECT TO FINAL EDITING

AIV.2.8 Madden-Julian Oscillation 26
AIV.2.8.1 Definition of the mode 26
AIV.2.8.2 Teleconnections and regional influence 28
References 29
Figures 50

ACCEPTED VERSION
SUBJECT TO FINAL EDITING

AIV.1 Introduction

This Annex describes the fundamental features of the main modes of large-scale climate variability assessed across chapters in the AR6 WGI report. Modes are defined as recurrent space-time structures of variability of the climate system with intrinsic spatial patterns, seasonality and timescales. They can arise through the dynamical characteristics of the atmospheric circulation but also through coupling between the ocean and the atmosphere, with some interactions with land surfaces and sea ice. The variability of the climate system at ocean- or continental-basin scales, and in particular on seasonal-to-multidecadal timescales, can be described to a large extent by the occurrence and often combination of several modes of climate variability which lead to local impacts and remote responses through teleconnection processes on top of externally forced trends. More precisely, the concept of "teleconnection" refers to the ability of modes of variability to relate climate in remote regions through associated atmospheric or oceanic pathways. Regional climate variations are thus the complex outcome of local physical processes, such as thermodynamical and land-atmosphere feedback processes, and non-local large-scale phenomena.

Historically, modes have been identified based on evidence of correlations between regional climate variations at widely separated, mostly geographically fixed spatial locations. One of the oldest known space-time structured patterns of variability is the North Atlantic Oscillation (NAO, Section AIV.2.1), with some early description from seafaring activities available since several centuries ago (Stephenson et al., 2003). Similarly, empirical, albeit remarkably precise, documentation of trans-Pacific coherent variability in atmospheric and oceanic conditions can be traced back to the 19th century for the El Niño-Southern Oscillation (ENSO, Section AIV.2.3). The Southern Oscillation was named in 1924 and the first use of the name 'El Niño' to describe a climatic phenomenon appeared in South America in 1893 (see for instance Philander, 1983 for ENSO history). Since then, the increased spatial coverage of observations and the measurement of new climatic parameters have improved significantly. These advancements, along with the development of new theoretical background and statistical methods for combining different sources of information, have allowed substantial improvements in our understanding of the characteristic spatial scale of the coherent structures of variability as well as of the characteristic temporal expression of the modes.

There are several ways to document and describe the modes of climate variability based on more or less sophisticated statistical techniques and dynamical nature, interpretation and understanding of the variability (i.e., Feldstein and Franzke, 2017; Hannachi et al., 2017; Franzke et al., 2020; Ghil and Lucarini, 2020). The simplest method to evaluate the temporal evolution of a spatially coherent phenomenon is to take one or more spatial averages of a climate variable such as sea surface temperature (SST) or sea level pressure (SLP), as examples, within a latitude-longitude box. Another classical technique relies on principal component analysis (PCA), also known as empirical orthogonal function (EOF) analysis, to extract the patterns in the chosen climate variable with maximal spatial covariance. The method also extracts an associated climate index timeseries, i.e. principal component (PC), describing the temporal evolution tied to the spatial pattern. PCA/EOF is widely used with gridded datasets and model outputs. Correlation or regression maps between the climate index timeseries and other space-time variables, such as precipitation, temperature or wind, are then calculated to quantify the teleconnection patterns. Altogether, beyond their physical relevance, modes of climate variability and their teleconnection patterns provide a simplified representation of climate variation affecting weather, from regional (i.e. oceanic or continental scale) to worldwide scales (i.e. for some specific phenomena like ENSO), having important impacts on human activities and ecosystems. Modes are often associated with climatic impact-drivers (CIDs, as defined in Chapter 12, Section 12.1) including droughts, heavy rains, storms, heat waves and cold spells, affecting agriculture, water resources, availability and consumption of energy, fire risks, etc.

Many modes of variability are driven by internal climate processes and are a critical potential source of climate predictability on sub-seasonal to decadal timescales. It is essential to understand the physical processes behind the past evolution of the modes of climate variability in order to assess, with confidence, their future changes. External forcing may affect their temporal (occurrence, variance, seasonality, persistence etc.) or spatial properties and associated teleconnections.

Previous IPCC reports have described the observed and modelled behaviour of a large number of modes of

ACCEPTED VERSION SUBJECT TO FINAL EDITING

variability over the instrumental period and in a paleoclimate context. The projected evolution of those modes has been also documented based on future climate scenarios. In AR5, large-scale modes of variability and teleconnections were assessed in depth in Chapter 14, setting the physical basis of future regional climate changes contingent on global mean temperature increase. Modes were defined through so-called "indices of climate variability" in AR5 Chapter 2, dedicated to observed atmospheric and surface changes. Two boxes (AR5 Box 2.5 and AR5 Box 14.1) introduced the main concepts. AR4 had a similar structure, with a specific section on modes in the chapter dedicated to the observations (Chapter 3). In AR6, a different perspective has been adopted, as the modes are discussed in various chapters and assessed with respect to the specific objectives of each of them. Space-time past changes of the modes using proxy records and instrumental data are assessed in Chapter 2. Human influence on modes is assessed in Chapter 3 over the instrumental period, while their future changes are addressed in Chapter 4. Their influence at regional scale through large-scale teleconnection is assessed in Chapters10, 11, 12 and Atlas, while the contribution of the modes in past and future hydrological changes and related uncertainties are assessed in Chapter 8. Chapter 9 focuses on oceanic expression of the modes. The aim of this Annex is to set a common background for the assessment of the modes of climate variability and related regional climate anomalies for all the AR6 WG1 Chapters, and to provide this information for the readers of the report. In doing so, the Annex provides a more accessible summary of the main modes of variability allowing a more coherent assessment of this important aspect of the climate system.

The Annex summarizes the fundamental features of spatial structure, seasonality and teleconnections for a selection of modes of climate variability corresponding to those addressed in the report, namely: the NAO and Northern Annular Mode, the Southern Annular Mode, ENSO, the Indian Ocean Basin and Dipole Modes, the Atlantic Meridional and Zonal Modes, the Pacific Decadal Variability, the Atlantic Multidecadal Variability, and the Madden-Julian Oscillation. For each mode, the description follows a common structure, starting with a short definition of the mode (based on simple box-averaged indices and EOF) and related key physical mechanisms, then a description of the associated teleconnections (based on regression techniques), and when relevant, finishes with a short summary of paleoclimate reconstruction of the mode based on proxy-based records. An illustrative figure including patterns and timeseries is also provided for each mode.

AIV.2 The main modes of climate variability assessed in AR6

AIV.2.1 North Atlantic Oscillation and Northern Annular Mode

AIV.2.1.1 Definition of the mode

The North Atlantic Oscillation (NAO) is the leading mode of large-scale atmospheric variability in the North Atlantic basin. It is characterized by alternating (seesaw) variations in SLP between the Azores High in the subtropics and the Icelandic Low in the mid- to high latitudes, with some northward extension deep into the Arctic (Hurrell et al., 2003). The positive phase of the NAO corresponds to an anomalously strong Azores High and concomitant deepening of the Icelandic Low with some penetration in the subarctic basin (Greenland/Norwegian/Barents Sea), accompanied by a reinforced and northward shifted jet and storm track over a broad North Atlantic-European sector (Figure AIV.1a). The opposite, notwithstanding marginal spatial asymmetries, occurs for the negative phase.

The NAO is the main mode of climate variability over a broad North Atlantic-Europe region in all seasons (Hurrell and Deser, 2009) for intra-seasonal to multidecadal timescales, albeit with seasonally-dependent physical characteristics (fraction of explained variance, latitudinal shift and intensity of the related anomalous atmospheric circulation and SST fingerprint, etc.; Folland et al., 2009a; Woollings et al., 2015a). The phases of the NAO control a significant fraction of the variance of temperature and precipitation over the North Atlantic and surrounding continents and of the prevailing westerly winds and the related storm tracks (Woollings et al., 2014). It is also strongly related to the occurrence and intensity of blocking conditions especially over Greenland (Woollings et al., 2010; Davini et al., 2012) and controls a large part of the incidence of extremes (cold waves, very strong wind episodes related to explosive storminess, heavy precipitation events, etc.) over Europe (Matthews et al., 2014; Yiou et al., 2017) and eastern North America

ACCEPTED VERSION SUBJECT TO FINAL EDITING

(Durkee et al., 2008; Whan and Zwiers, 2017).

The NAO can be viewed as the regional expression of a hemispheric-scale mode of atmospheric variability that was identified in the late 1990s known as the Arctic Oscillation (AO; Thompson and Wallace, 1998) or Northern Annular Mode (NAM) (Thompson and Wallace, 2000a; Ambaum et al., 2001) to reflect the longitudinal scale that transcends the entire hemisphere. An additional centre of action is present for NAM over the North Pacific, albeit much weaker than its Atlantic counterpart, with a slackened Aleutian Low in the positive phase (Figure AIV.1b). The AO/NAM can be defined as the leading mode of variability across a range of atmospheric levels from the surface to the stratosphere (Baldwin and Dunkerton, 1999; Gerber et al., 2010). In the stratosphere, the AO/NAM corresponds to fluctuations in the strength of the boreal winter polar vortex over the Arctic. In the troposphere, the AO/NAM primarily corresponds to fluctuations in the position of the midlatitude westerly jet stream. Interactions between the stratospheric and tropospheric annular modes have been extensively studied and are important for the variability and predictability of the mode at intra-seasonal timescales (i.e. see Domeisen, 2019).

Despite the fact that NAM and NAO indices are strongly correlated (Figure AIV.1c), the debate on the relevance of the NAM as a mode of variability per se (Deser, 2000; Honda and Nakamura, 2001; Itoh, 2008) is not closed yet, despite progress in understanding the dynamical mechanisms linking the Pacific and Atlantic SLP cores on the basis of wave breaking theory that prevails at intra-seasonal timescales (e.g. Rivière and Drouard, 2015). Consequently, NAO and NAM are treated as indistinguishable in some studies (Feldstein and Franzke, 2006) while others still consider the NAO as a stand-alone mode even if associated circumpolar patterns exist (García-Serrano and Haarsma, 2017). In the latter case, the NAM is interpreted as a statistical artefact of two regional independent modes namely the NAO and the Pacific-North American pattern (Ambaum et al., 2001; Douville et al., 2017). Throughout the report, NAO and NAM are often considered as the same entity because the NAO explains most of the variance on the zonally-averaged hemispheric circulation and because the associated timeseries are highly correlated.

The NAO/NAM arise as large-scale signals primarily driven by internal atmospheric variability of midlatitude dynamics (e.g., Lorenz and Hartmann, 2003). By nature, these signals correspond to barotropic phenomena being partly controlled by eddy-mean flow interaction (Feldstein and Franzke, 2017). Their fingerprint can be found along the entire atmospheric column with maximum amplitude in the winter season when storminess is the most pronounced. In addition, the tropospheric NAO/NAM variability has been shown in boreal winter to be linked to the strength of the stratospheric polar vortex (Baldwin and Dunkerton, 1999) including sudden stratospheric warmings (Domeisen, 2019). On intra-seasonal timescales, downward propagation of associated geopotential height anomalies occurs from the lower stratosphere to the troposphere through wave-mean flow interaction resulting in some predictability at the surface for CIDs, through temperature, precipitation and wind anomalies at large spatial scales (e.g. Karpechko et al., 2017 over Europe).

The NAO/NAM includes a forced component arising from SST anomalies: key oceanic regions are identified but are dependent on the timescale of variability that is investigated (Baker et al., 2019). There is also growing evidence for the importance of cryosphere-atmosphere coupling to explain part of the observed variability of the NAO in response to recent Arctic sea-ice decline (Cohen et al., 2014), even if discrepancies remain in model estimates (Screen et al., 2018) and may not be stationary in time (Blackport and Screen, 2020). Finally, part of the NAO/NAM variability has also been documented to be influenced by external forcing such as volcanic eruptions (Swingedouw et al., 2017) and solar forcing (Ineson et al., 2011; Gray et al., 2016; Le Mouël et al., 2019) as well as anthropogenic factors (Gillett et al., 2003). However, internal variability is predominant and, because of signal-to-noise issues, very long observational records and large ensembles of climate simulations are needed to clearly evaluate the fraction of the forced component in the observed NAO/NAM, as assessed in detail in Sections 2.4.1.1 and 3.7.1. Sea ice-NAO/NAM coupling is comprehensively assessed in Cross-Chapter Box 10.1.

Given their equivalent barotropic structure, the NAO/NAM is usually defined from SLP fields or geopotential height anomalies at various levels (Fu et al., 2016). The NAO/NAM can be defined using pattern-based statistical techniques such as EOF or clustering techniques applied to seasonal gridded

ACCEPTED VERSION SUBJECT TO FINAL EDITING

atmospheric circulation fields (SLP or geopotential height anomalies) from observations or reanalysis data. The NAM pattern is traditionally defined as the leading EOF of pressure fields computed over the entire hemisphere, northward of 20ºN (Figure AIV.1b) and its related PC defines the NAM index (Figure AIV.1c). Similarly the NAO index can be defined as the PC of the leading EOF of the pressure field over the North Atlantic sector (Figure AIV.1a) or the temporal occurrence of the seasonal weather regimes extracted from clustering (Corti et al., 1999; Cassou et al., 2011; Hannachi et al., 2017).

An alternative and simpler estimate of the NAM/NAO uses differences in SLP between fixed locations. The NAM index can be calculated from the difference in normalized zonally averaged SLP between 35ºN and 65ºN (Li and Wang, 2003), which reflects the latitudinal fluctuation of the position and strength of the midlatitude westerlies at the hemispheric scale. Similarly, for the NAO, a weather station-based index is traditionally calculated as the difference of normalized SLP anomalies located in the Azores (Ponta Delgada) or continental Iberia (Lisbon/Gibraltar) minus those along the northern centre of action around Iceland (Stykkisholmur/Reykjavik) (Jones et al., 1997). Cornes et al. (2013) alternatively uses the Paris-London difference because of data availability back to the 17th century. The station-based NAO index is simple to compute, extends the longest over the instrumental period, and can be used year round, but caveats stand in its limitation to capture the seasonal latitudinal migration of the NAO variability pattern as well as potential shifts in the North Atlantic pressure centres of action at interannual to decadal timescales (Ulbrich and Christoph, 1999). Because it uses fixed locations, the index captures part of the variability that is not directly related to the latitudinal seesaw pressure balance and associated large-scale fluctuations of the zonal flow that characterize the NAO dynamics, and it also fails representing the spatial asymmetries between the positive and negative phases of the mode (Cassou et al., 2004).

The temporal correlation between the EOF and fixed latitude-based zonal NAM estimations is equal to 0.91 for December-January-February average and both are strongly correlated with the NAO indices (Figure AIV.1c). Correlations between all the NAO estimates are spatially and temporally very high in all the observational products over the modern reanalyses period (Gerber and Martineau, 2018); for instance, the correlation between the station-based and EOF-based NAO indices over 1959-2018 in boreal winter using JRA-55 is equal to 0.89 (Figure AIV.1c). EOF-based NAO and NAM indices are used in Section 3.7.1 for model evaluation. The fixed-latitude NAM index is used in Sections 2.4.1.1, 4.3.3.1, 4.4.3.1 and 4.5.3.1, and in Section 3.7.1 for attribution of past changes.

[START FIGURE AIV.1 HERE]

Figure AIV.1: The boreal wintertime NAO and NAM modes extracted as the leading EOF of December-January-February SLP anomalies over the North Atlantic-Europe Sector (20ºN-80ºN, 90ºW-30ºE, materialized by the red box, a) and the Northern Hemisphere (north of 20ºN, black domain, b), respectively, based on JRA-55 reanalysis over 1959-2019. (a,b) SLP anomalies regressed onto the leading principal component (PC) time series shown in (c). The NAO-PC is represented by red and blue bars, the NAM-PC by the black curve in (c); their variance explained is given in the legend. The NAO index based on weather stations (cyan dots in a) is given in cyan and the zonal-NAM index (latitude circles in b) is given in magenta. Correlation between each index and the NAO-PC timeseries is given in the legend. (d,e) Regression maps of blended SST and SAT over land from ERSST and BerkeleyEarth dataset, respectively, over for 1959-2019 (d) and of precipitation anomalies (e, shading based on GPCC for 1959-2016 and contours based on CMAP for 1979-2019 for every 0.1 mm/day). On maps, no-overlay indicates regions where the regressions are significant based on t-test accounting for false detection rate at 10% and crosses indicates no significance. Significance for CMAP precipitation is materialized by red contours in (e). All fields have been linearly detrended prior to computation.

[END FIGURE AIV.1 HERE]

AIV.2.1.2 Teleconnections and regional influence

Large-scale changes in the position and strength of the North Atlantic jet stream and storm tracks associated

ACCEPTED VERSION SUBJECT TO FINAL EDITING

with the NAO/NAM, as well as the related incidence in blocking episodes traditionally linked to extreme events, affect surface climate conditions over the entire North Atlantic and surrounding landmasses from daily to multidecadal timescales (Hurrell, 1995). Warmer and wetter weather over Northern Europe extending eastward in western Siberia with simultaneous cooler and drier conditions over a broad Mediterranean basin are distinct features of the positive boreal winter NAO/NAM (Figure AIV.1d,e). Over North America, regions around the Labrador Sea are significantly colder with excess sea-ice formation while milder conditions dominate the Great Plains forming altogether a typical quadripolar anomaly pattern for temperature linked to the winter NAO/NAM. The latter structure is tightly related to the latitudinal shift of the storm tracks that is particularly marked in precipitation over the ocean (Figure AIV.1e). More remotely, changes in North Atlantic storm track position and transient eddy activity associated with the positive (negative) phase of the NAO contribute downstream to negative (positive) SLP anomalies in north-eastern East Asia during boreal summer (Linderholm et al., 2011).

Related changes in both westerly winds at midlatitudes and trade winds in the tropics over the North Atlantic result in anomalous fluxes of sensible and latent heat at sea surface, which create ocean temperature anomalies that extend down to the base of the deep mixed layer during boreal winter (Deser and Timlin, 1997; Seager et al., 2000). The SST imprint of the NAO has a tripolar shape with positive anomalies at midlatitudes straddled by colder surface ocean in the subtropics and along the entire subpolar gyre (Figure AIV.1d). Weak feedbacks from SST on boreal winter NAO are found through forced Rossby wave mechanism (Baker et al., 2019) and local phenomena such as oceanic re-emergence in the North Atlantic Nordic seas (Cassou et al., 2007). Negative NAO phases are characterized by a wavier jet stream and a southward shift of storm tracks, which favours cold outbreaks over Northern Europe (Cattiaux et al., 2010) and reinforced storminess along the Mediterranean basin leading to heavy precipitation events (Sanchez-Gomez et al., 2008) and storm surge in southern Europe (Cid et al., 2016). Those are also often related to a collapse/split/displacement of the low-level stratospheric polar vortex and the occurrence of Stratospheric Sudden Warming (Sections 2.3.1.4.5 and 3.3.3.4). In boreal winter, NAM and NAO teleconnections are very similar over the Atlantic surrounding continents.

There is a strong seasonal asymmetry in observed NAO teleconnection patterns and NAO temporal evolution. Impacts over Europe are opposite between summer and winter months with dominant warmer and drier weather conditions over north-western Europe in summertime concurrently with wetter conditions over Southern Europe during positive NAO phases (Folland et al., 2009; Bladé et al., 2012). Extreme events (heat waves occurrence, droughts, etc.) are also linked to NAO phases (Cassou et al., 2005; Drouard et al., 2019) due to the related latitudinal shift of the North Atlantic storm tracks (Dong et al., 2013). Summer NAO trends also affect Arctic climate as assessed in Sections 3.4.1 and 9.4.1. The NAO is associated with storms or persistent mild wind period and dry/sunny spells affecting availability and power consumption (Jerez et al., 2013; Zubiate et al., 2017).

NAO fluctuations generate ocean responses due to altered buoyancy fluxes and wind stress anomalies (Barrier et al., 2014). Signatures of the NAO can be found in the gyre circulations (Marshall et al. 2001) and in the Atlantic Meridional Overturning Circulation (AMOC; Yeager and Danabasoglu, 2014), with a sea level imprint in observations (Han et al., 2017). The oceanic response is dependent on the timescale of the NAO variability (Delworth and Zeng, 2016) especially for AMOC in connection with the so-called Atlantic Multidecadal Variability (Section AIV.2.7). This is assessed in Section 9.2.3.1.

Implications of NAO/NAM variability in terms of observed and projected precipitation at a regional scale (Europe, Mediterranean basin, etc.) is comprehensively assessed in Sections 8.3.2.9, 8.4.2.9, and 8.5.2. NAO implications on extremes are assessed in Sections 11.3.1 and 11.4.1, and regional manifestations of NAM/NAO are further assessed in Sections Atlas.5, Atlas.7, Atlas.8 and Atlas.9 and Cross-Chapter Box Atlas.2.

AIV.2.1.3 Available proxy-based reconstruction

Sea level pressure records from Stykkisholmur, Akureyri, Reykjavik and from Gibraltar, Lisbon and Ponta

ACCEPTED VERSION SUBJECT TO FINAL EDITING

Delgada weather stations, all located close the NAO centres of action (i.e. Islandic Low and Azores high), allowed the reconstruction of the NAO index back to the mid-19th Century (Cropper et al., 2015; Hernández et al., 2020). The Paris-London sea level pressure difference used by Cornes et al. (2013) extends back to 1692, but it captures only part of the large-scale NAO phenomena because of the spatial proximity of the weather stations used. More reliable NAO reconstructions were recently developed based on the reconstruction of the sea level pressure field all over the North Atlantic and Europe (Delaygue et al., 2019; Mellado-Cano et al., 2019). Other long-term reconstructions involve proxy-based information from documents (Barriopedro et al., 2014), tree rings (Cook et al., 2019), ice cores (Sjolte et al., 2018), stalagmites (Baker et al., 2015), sediments (Faust et al., 2016) and a combination of multi-proxy information (Ortega et al., 2015), with large uncertainties due to diverse methodological approaches used for reconstruction (Michel et al., 2020) and disparate correlations between proxies and associated temporal resolution (Hernández et al., 2020). An additional difficulty for reconstruction lies on the fact that the spatial structure of North Atlantic variability might be time-scale dependent (Woollings et al., 2015). It is shown that on the shorter timescale (interannual), the NAO is dominated by variations in the latitude of the North Atlantic jet and storm track, whereas on the longer timescale (multidecadal and beyond) it represents changes in their strength instead. The two timescales also exhibit different regional impacts on temperature and precipitation and different relationships to sea surface temperatures, which makes proxy reconstructions of the NAO problematic.

Most of the reconstructed NAO/NAM indices describe the winter patterns of the last 500 years because the variability is the most pronounced and on larger-scale for that season (Luterbacher, 2001; Dezileau et al., 2011). Tree rings can however allow NAO boreal summer reconstruction back to the 16th century (Folland et al., 2009; Linderholm et al., 2009). Recent efforts to develop reconstructions of the NAO phases using pollen data (Mauri et al., 2014), speleothems (Ait Brahim et al., 2019) and lake sediments (Olsen et al., 2012) provide new evidence for multi-centennial NAO-type of variability along the Holocene (Hernández et al., 2020). A detailed description of the latest proxy-based reconstructions of the NAO and related conclusions placing the observations since the pre-industrial in a broader context of variability are given in Section 2.4.1.1.

AIV.2.2 Southern Annular Mode

AIV.2.2.1 Definition of the mode

The Southern Annular Mode (SAM), sometimes called the Antarctic Oscillation (AAO), is the leading mode of large-scale atmospheric circulation variability in the Southern Hemisphere extra tropics in all seasons and at intra-seasonal to multidecadal timescales, albeit with season-dependent physical characteristics such as fraction of explained variance, latitudinal shift and intensity of the related anomalous atmospheric circulation and SST fingerprint. It is characterized by synchronous SLP or geopotential height anomalies of opposite signs between the mid- and high latitudes, modulating the mean westerly winds near 50ºS. The SAM affects the frequency, strength, and position of cold fronts, and extratropical synoptic to mesoscale weather systems (Thompson and Wallace, 2000b; Manatsa et al., 2016; Mariani and Fletcher, 2016; Cerrone and Fusco, 2018). It controls a significant fraction of seasonal to multi-annual variance of the zonal mean precipitation in the Southern Hemisphere subtropics and extratropics (Kang et al., 2011). The SAM is also tightly linked to the fluctuations in the thermohaline properties of the Southern Ocean as well as its dynamics (Sen Gupta and England, 2006; Spence et al., 2014), and it modulates the Antarctic sea ice extent from interannual to multidecadal timescales (Ferreira et al., 2015).

Given its equivalent barotropic structure, the SAM is commonly quantified as the first EOF mode of extratropical geopotential height anomalies at various tropospheric levels or of SLP anomalies. However, it extends into the stratosphere, coupling lower and middle-atmosphere dynamics. As it essentially represents a meridional atmospheric mass transfer, an alternative definition is the difference in normalized zonal mean SLP at middle (40ºS) and high (65ºS) southern latitudes (Gong and Wang, 1999; Marshall, 2003). The polarity of the SAM is defined such that it is positive when pressure over Antarctica is anomalously low, and vice versa. While the SAM pattern is more zonally symmetric than its Northern Hemisphere counterpart (NAM, Section AIV.2.1), it does exhibit some asymmetries particularly in the midlatitude node over the

ACCEPTED VERSION SUBJECT TO FINAL EDITING

Pacific and Indian Ocean sectors (Fogt et al., 2012). Alternative interpretations of the SAM as a regional variability pattern in the South Pacific are also considered (Spensberger et al., 2020). The zonal asymmetries are present for all seasons, and illustrated in Figure AIV.2a for austral summer, to support the assessment in Section 3.7.2. A number of different SAM indices have been produced, and several are compared by Ho et al. (2012) and Barrucand et al. (2018), showing good agreement after the second half of the 20th century. Over the 1979-2019 period, the correlation between the EOF-based and zonal SLP-based indices for the summertime SAM reaches 0.94 (Figure AIV.2b).

During the positive phase of the SAM, the Antarctic air mass is isolated by an enhanced westerly jet that is located further south than during the negative phase. This leads to colder conditions over the entire continent and negative SST anomalies along the surrounding ocean (Figure AIV.2). During the opposite, negative phase, an equatorward displacement of the jet and related storm track brings low pressure systems toward the north with a strong effect on southern tip of South America (Mariani and Fletcher, 2016). The SAM is often used as a proxy for the location of the midlatitude westerly wind belt at seasonal to interannual timescales. However, Swart et al. (2015) noted that trends in the SAM and the Southern Hemisphere surface westerly jet are not directly interchangeable because multiple factors other than SAM can affect trends in the position, width and strength of the jet and surface wind.

The SAM is mainly driven by extratropical atmospheric dynamics, but its phase is affected by remote SST anomalies such as ENSO (Section AIV.2.3) and anthropogenic forcing as assessed in Section 3.7.2.

The EOF-based SAM index is used for model evaluation in Section 3.7.2. The fixed-latitude SAM index is used for the attribution assessment of the observed positive trend of the SAM that is maximum over the second half of the 20th century but reduced since about 2000 (Section 2.4.1.2) due to slackened ozone influence (Section 3.7.2). The fixed-latitude SAM index is also used in Sections 4.3.3.1, 4.4.3.1 and 4.5.3.1 to assess the future changes in Southern Hemispheric zonal circulation as a function of emissions scenarios and lead times.

[START FIGURE AIV.2 HERE]

Figure AIV.2: The austral summertime SAM extracted as the leading EOF of December-January-February SLP anomalies over the Southern Hemisphere (south of 20ºS, a) based on JRA-55 reanalysis over 1979-2019. (a) SLP anomalies regressed onto the leading principal component (PC) time series shown in (b); the variance explained is given in the legend in (b). The SAM-PC is represented by red and blue bars and the zonal-SAM index (latitude circles in a) is given in magenta. Correlation between the zonal SAM index and the SAM PC timeseries is given in the legend. (c, d) Regression maps of SST and SAT over land from ERSST and BerkeleyEarth dataset, respectively, over for 1979-2019 (d) and of precipitation anomalies (e, shading based on CMAP for 1979-2016 and contours based on GPCP for 1979-2019 for every 0.1 mm/day). On maps, no-overlay indicates regions where the regressions are significant based on *t*-test accounting for false detection rate at 10% and crosses indicates no significance. Significance for CMAP precipitation is materialized by red contours in (d). All fields have been linearly detrended prior computation.

[END FIGURE AIV.2 HERE]

AIV.2.2.2 Teleconnections and regional influence

Recent observational studies have enriched our understanding of the widespread influence of SAM variability on mean climate and related environmental parameters of the entire Southern Hemisphere extratropics (e.g. Holz et al., 2017; Jones et al., 2016; Kostov et al., 2017; Manatsa et al., 2013; Marshall et al., 2017; Raut et al., 2014; Waugh et al., 2013). The influence of the SAM extends over the midlatitude continental land masses with precipitation anomalies over Southern Australia (Cai and Watterson, 2002) and south-eastern South America (Silvestri and Vera, 2003) in link with the latitudinal migration and strength of the extratropical storm and mean westerly circulation. Consistently with NAM/NAO (Section AIV.2.1),

ACCEPTED VERSION SUBJECT TO FINAL EDITING

there is a strong seasonality in the teleconnection associated with SAM. In austral summer, during a positive phase of the SAM, drier conditions affect most of the southern Patagonia region and the southernmost tip of South America, while wetter conditions are found in South Africa and Madagascar, as well as in Southeast Australia where colder temperatures also prevail (Figure AIV.2c,d). Positive temperature anomalies are found in New Zealand, Tasmania and Southern tip of South America. These anomalies appear as the continental fingerprint of a warmer belt located around 40oS that is characterized by significant hemispheric-scale SST changes in consistence with the southern shift of the summertime storm track.

Moreover, several studies have described equatorward teleconnections linking the SAM to Asian precipitation across the equator (e.g., Liu et al., 2018; Prabhu et al., 2017). Coupling of seasonal stratospheric anomalies to the SAM can influence spring-time heat extremes in eastern Australia (Lim et al., 2019). Marshall et al. (2013) described a reversal in the relationship between the SAM and East Antarctic temperatures during austral summer/autumn in the first decade of the 21st century, due to regional variability of the pressure pattern associated with the zonal wavenumber 3. Other studies have analysed the temporal variability in the interactions between the SAM and ENSO at different timescales (e.g. Clem et al., 2016; Yu et al., 2015), being positive and significant during 1986-2014 (Vera and Osman, 2018).

Implications of SAM on observed and projected changes in water cycle and specific regional influences are assessed in Sections 8.3.2.9 and 8.4.2.9 and in Sections 12.4, Atlas.7 and Atlas.11, respectively.

AIV.2.2.3 Available proxy-based reconstruction

The regional influence of the SAM is recorded in tree rings (Holz et al., 2017; Dätwyler et al., 2018), lake sediments (Fletcher et al., 2018; Moreno et al., 2018), ice cores (Goodwin et al., 2004) and corals (Goodwin and Harvey, 2008) across the Southern Hemisphere extratropics. Multiproxy-based reconstructions of the SAM have been developed using temperature-sensitive proxy records that cover the last millennium (Villalba et al., 2012; Abram et al., 2014; Dätwyler et al., 2018). Villalba et al. (2012) used tree ring records to reconstruct the summertime SAM since 1409, while Abram et al. (2014) combined ice core records with tree ring data to derive a weighted composite-plus-scale reconstruction of the annual SAM index for the past millennium. Dätwyler et al. (2018) further included proxies from corals, speleothems and lake sediments using different stationarity criteria for the proxy record selection to build an austral summer SAM reconstruction. Hessl et al. (2017) compared three paleoclimatic reconstructions of the SAM, highlighting the need for additional proxy records over the Indian Ocean sector, to fully account for the annular structural properties of this mode of variability. Uncertainties also arise from the lack of proxy data related to cold season conditions, given that reconstructions relying on tree rings might be biased towards summertime thus accounting only for SAM austral summer variability (Hernández et al., 2020). Several studies attempted to reconstruct the SAM behaviour during the Holocene, inferred through changes in the Southern Hemisphere westerly wind belt, but uncertainties remain large without consensus in the SAM phases for most of the periods at multidecadal timescales (Hernández et al., 2020). These SAM reconstructions are assessed in Section 2.4.1.2 and compared with simulations in Section 3.7.2.

AIV.2.3 El Niño-Southern Oscillation

AIV.2.3.1 Definition of the mode

The El Niño-Southern Oscillation (ENSO) refers to the large-scale alternation between anomalous warming and cooling of central/eastern equatorial Pacific SSTs that coincide with changes in the overlaying winds and precipitation (Philander, 1990; Neelin et al., 1998; Wang, 2018). The main features of ENSO are displayed in Figure AIV.3. ENSO is the primary mode of tropical variability on interannual timescales and is considered as an internally occurring coupled ocean-atmosphere phenomenon. Whilst the ENSO phenomenon itself largely occurs in the tropical Pacific, it triggers climate teleconnections over the entire basin and in many other parts of the world (Figure AIV.3c,d). ENSO is consistently the main modulator of the global surface temperature at interannual timescales (Pan and Oort, 1983; Trenberth et al., 2002). ENSO

ACCEPTED VERSION SUBJECT TO FINAL EDITING

is the main source of climate predictability on seasonal to interannual timescales (Philander, 1990; Smith et al., 2012) and its status is consequently closely monitored by meteorological institutes around the globe. El Niño events are typically identified by warmer than normal central/eastern equatorial Pacific SSTs, negative SLP anomaly difference between the eastern and western portions of the tropical Pacific Ocean, anomalous westerly surface winds, and increases in cloudiness and precipitation over the central and eastern equatorial Pacific and adjacent land areas. By contrast, La Niña events are typically identified by cooler than normal central/eastern equatorial Pacific SSTs, positive surface pressure anomaly difference between the eastern and western portions of the tropical Pacific Ocean and anomalous easterly surface winds reflecting altogether an intensification of the climatological east-west thermal gradient across the equatorial Pacific Ocean.

ENSO has been monitored through a range of indices, which are based on SST or SLP anomalies during the instrumental period, and various proxies on longer timescales. Differences between indices and thresholds used to define the occurrence of an El Niño or La Niña event imply that no commonly accepted list of events and their magnitudes exists. The three most prominent (L'Heureux et al., 2017; Pepler, 2016) indices used to monitor ENSO are the averaged SST anomalies over the so-called NINO3 (5ºS-5ºN, 150ºW-90ºW) or NINO34 (5ºS-5ºN, 170ºW-120ºW) regions and the Southern Oscillation Index (SOI) based on the normalized SLP difference between Darwin and Tahiti (Troup, 1965). Decomposition into EOFs of the tropical SST is also used in the literature. Those indices are highly correlated, as shown in Figure AIV.3b. The correlation between NINO34 SST and EOF-SST index is about 0.97, and between NINO34 and SOI is about 0.89 over the 1959-2019 period.

SST anomalies from the NINO3 and NINO34 regions provide a direct measure of the events via its surface ocean fingerprint, while the SOI provides a measure in terms of atmospheric perturbation. Data are available back to 1876 for the SOI computation, whilst the uncertainty in SST-based indices, particularly those associated with the central equatorial Pacific, is large prior to the 1950s when the number of SST observations was much lower (Kennedy et al., 2019). The complexity of ENSO is at least partly demonstrated by the observed events, which are all different in the magnitude, spatial structure and/or seasonal timing. As a direct consequence, it is difficult to accurately represent ENSO with one single index. Over time, further indices have been introduced to monitor ENSO event evolution (i.e., Trans Niño Index – TNI, Trenberth and Stepaniak, 2001) and spatial structure (i.e., El Niño Modoki Index – EMI, Li et al., 2010). The limited length and quality of the observational records may further affect the choice of the index, whose relevance can depend on the specific application. The variety in ENSO indices also explains the non-universality in the qualification of ENSO status delivered by meteorological agencies responsible for operational monitoring, operational forecast and climate services for users.

A particular aspect of ENSO diversity is whether the event is centred in the eastern Pacific (EP events) or central Pacific (CP or "Modoki" events). This distinction is important as the type of event leads to different large-scale teleconnections and worldwide climatic impacts (e.g. Ashok et al., 2007; Ratnam et al., 2014; Capotondi et al., 2015; Timmermann et al., 2018; Taschetto et al., 2020). Differences can be significant at regional scale because of displaced source of diabatic heating associated with the position of the main SST anomalies. For instance, stronger precipitation teleconnections occur over Australia during CP than during EP events (Wang and Hendon 2007; Taschetto et al. 2009). It is noteworthy that central and eastern Pacific SST indices are more highly correlated with each other during La Niña than during El Niño events. This indicates that La Niña events have less geographic diversity than El Niño events (Kug and Ham, 2011) and that the CP/EP distinction is therefore more relevant for the latter. In the historical instrumental records, Banholzer and Donner (2014) found that CP events had a weaker influence on global surface temperature than EP events did.

However, the distinction between CP and EP events is not necessarily clearly defined, as different methods yield an inconsistent classification of the events, which implies that no robust consensus on the classification of CP or EP events is possible (Wiedermann et al. 2016). Furthermore, Giese and Ray (2011) found that the central longitude of peak SST anomalies associated with individual El Niño events had a distribution indistinguishable from a Gaussian distribution peaked at 140ºW, as opposed to a bimodal distribution implied by the EP/CP paradigm. There are also occasional "coastal Niño" events, such as those of 1925 (Takahashi and Martinez, 2019) or 2017 (Rodriguez-Marata et al., 2019), where abnormally warm waters are

ACCEPTED VERSION SUBJECT TO FINAL EDITING

confined to the South American coast. Even though these events are not conventionally classified as El Niños, they have some El Niño-like teleconnections in South America. Instrumental data have historically been of limited value in assessing the classification of events before 1955, because of the almost total lack of SST measurements in the western half of the NINO34 region (L'Heureux et al., 2013). It is not yet known whether newer SST data set versions, which benefit from improved data archives (Section 2.3.1.1), have reduced this uncertainty.

The description of ENSO in this Annex supports the assessments of Sections 2.4.2, 3.7.3, 4.3.3.2, 4.4.3.2 and 4.5.3.2. ENSO's influence on ocean circulation, heat transport and sea levels are assessed in Sections 9.2 and 9.6.

[START FIGURE AIV.3 HERE]

Figure AIV.3: The boreal wintertime ENSO mode defined by December-January-February SST anomalies averaged over the NINO34 region (5ºS-5ºN, 170ºW-120ºW, cyan box) or extracted as the leading EOF mode over the Tropical Pacific Ocean (the region denoted by the black box in a) for 1958-2019 using ERSSTv5. (a) SST anomalies regressed onto the NINO34 time series, which is shown in (b) as red and blue bars. Black curve in (b) represents the standardized leading principal component and the magenta curve stands for the SOI index. The percentage of explained variance of the leading EOF is given in the legend as well as the correlation between all indices and the NINO34 timeseries. (c) Same as (a) but for land SAT (shading; based on BerkeleyEarth) and 10-m level wind (arrows; based on JRA-55) anomalies over 1958-2018. (d) Same as (a) but for precipitation anomalies (shading based on GPCC for 1958-2016 and contours based on CMAP for 1979-2019 for every 0.5 mm/day). Magenta dots in (c,d) stands for the Darwin and Tahiti weather station used for the SOI computation. On maps, no-overlay indicates regions where the regressions are significant based on t-test accounting for false detection rate at 10% and crosses indicates no significance. Significance for CMAP precipitation is materialized by red contours in (d). All fields have been linearly detrended prior to computation.

[END FIGURE AIV.3 HERE]

AIV.2.3.2 Teleconnections and regional influence

ENSO has a broad range of teleconnections, both in and outside the Pacific region (Figure AIV.3c,d). Amongst the best-known teleconnections are the association of El Niño events with increased precipitation in the southwestern and southeastern United States, eastern Africa, coastal Ecuador and Peru, and northern Argentina, and with decreased precipitation in eastern Australia and the Maritime Continent, southern Africa, the Amazonian basin and much of the Indian subcontinent. A general reverse association is found during La Niña events although there are some asymmetries (Cai et al., 2010; Taschetto et al., 2020). ENSO also has a substantial impact on tropical cyclone occurrence (Wang and Chan, 2002; Chu, 2004; Kuleshov et al., 2008), with El Niño typically being associated with reduced tropical cyclone activity in the North Atlantic, and an eastward displacement of Northwest and South Pacific tropical cyclone genesis away from the Philippine Sea and the Australian continent and into the central Pacific. ENSO have been shown to control part of the interannual variability of fire, including wildfire and human-triggered fires, in many regions of the world including all the continents surrounding the Pacific (see for instance the devastating extreme fire emissions in Indonesia in 2015, Chisholm et al. 2016) but also remotely, e.g. over the Arctic (Monks et al., 2012).

Tropical climate impacts during ENSO events are largely driven by a reorganisation of the zonal Walker circulation that result from anomalous diabatic heating associated with deep atmospheric convection changes (e.g. Chiang and Sobel, 2002; Choi et al., 2015; Gill, 1980; Klein et al., 1999). The latter are also responsible for atmospheric teleconnections to higher latitudes (Yeh et al., 2018), acting as a source of forced large-scale Rossby waves (Hoskins and Karoly, 1981). Specific phases of the Pacific-North American (PNA) pattern (Horel and Wallace, 1981) and Pacific-South American (PSA) pattern (Karoly, 1989) are then favoured in the Northern and Southern Hemispheres, respectively, and are associated with shift and modulation of the

ACCEPTED VERSION SUBJECT TO FINAL EDITING

mean storm tracks. These teleconnections influence temperature and rainfall around the globe including extreme events (King et al., 2014). For instance, mild winter conditions dominate Alaska/Canada connected to the southeastward displacement and reinforcement of the Aleutian Low during El Niño, which generates anomalous southerlies and advects warmer air northward. By contrast, the anomalous cyclonic circulation favours cold outbreaks over the far-east Siberian region and Kamtchaka (Figure AIV.3c,d).

Being the dominant actor of variability at interannual timescale, ENSO is linked to many other modes of variability both in the tropics and midlatitudes, either in phase or with some seasonal lag. For instance, connection has been documented between EP ENSO events and SAM during austral summer (Ciasto et al., 2015). Relationship exists between ENSO and the NAO/NAM in boreal wintertime though various mechanisms such as stratosphere-troposphere coupling (Domeisen et al., 2015) and tropospheric pathways, including the eastward extension of the PNA during El Niño event and also through the alteration of the propagation of tropical Rossby wave trains from the Pacific to the Atlantic (Drouard et al., 2015). The tropical-extratropical teleconnection is not symmetrical with the phase of ENSO and nonstationary with considerable dependence on epochs being modulated by the inherent strong internal variability (Deser et al., 2017; Drouard and Cassou, 2019). In the Atlantic, relationship between ENSO and Atlantic Niño (Section AIV.2.5) is found in boreal spring (Tokinaga et al., 2019) while the South Atlantic Subtropical Dipole mode is mostly connected to ENSO in austral summer (Rodrigues et al., 2015).

Implications of ENSO in water cycle changes are further assessed in Sections 8.3.2.9 and 8.4.2.9. Association of ENSO with extremes and specific regional climate anomalies are assessed in Sections 11.4, 11.6, 11.7, 12.4, Atlas.4, Atlas.5, Atlas.6, Atlas.7, and Atlas.9 and Box 11.4.

AIV.2.3.3 Available proxy-based reconstruction

Model evidence suggests that ENSO characteristics vary on decadal to centennial timescales (e.g. Lewis and LeGrande, 2015; Deser et al., 2017), implying that a minimum of several hundred years of observations, which is much longer than the instrumental record, are required to determine the full natural range of ENSO complexity (Wittenberg, 2009). Thus, one way to understand if anthropogenic forcing has modulated ENSO is to understand ENSO behaviour prior to the observational record. Paleoclimate archives can be used to fill this gap as they provide quantitative estimates of ENSO behaviour during the pre-industrial era, while also providing information of ENSO characteristics under a variety of past natural climate background states controlled by external forcings. Extensive proxy-based studies, using a range of ENSO-sensitive records, have been carried out to assess the ENSO changes on various paleoclimate timescales, specifically the last few hundred years and back to the mid-Holocene (see Section 2.4.2).

Reconstructions of past ENSO behaviour traditionally merges information from multiple proxies that are considered sensitive to ENSO (Lu et al., 2018). This merging process may have multiple purposes, but is generally used to extend the reconstruction length and also to increase its signal to noise ratio. The resulting reconstructions can be broadly placed into two main categories: (i) those that utilise proxies in the central and eastern equatorial Pacific itself; and (ii) those that utilise proxies from other regions impacted through teleconnections, along with those that mix both categories. ENSO reconstructions from category (i) are considered to be a more accurate measure of ENSO behaviour. However, proxies from the central and eastern equatorial Pacific are generally rarer than those outside the region, due to the small number of land/reefs, and they also tend to be of shorter duration. Thus, the ideal case is a combination of both categories to get a robust quantitative estimates of ENSO behaviour in the past.

AIV.2.4 Indian Ocean Basin and Dipole Modes

AIV.2.4.1 Definition of the mode

The Indian Ocean basin (IOB) and Indian Ocean dipole (IOD) modes are the two dominant modes of interannual climate variability in the Indian Ocean. The IOB mode features the temporal alternation of basin-

ACCEPTED VERSION SUBJECT TO FINAL EDITING

wide warming and cooling of sea surface in the positive and negative phases, respectively (Figure AIV.4), while the IOD mode is characterized by a zonal dipole of SST anomalies in the tropics, with one lobe centred off Sumatra and Java and the other covering a large portion of the western basin (Figure AIV.5). The two modes mostly vary on interannual timescales and are both correlated positively with ENSO. In particular, the IOD tends to emerge during ENSO development from boreal summer to autumn (Stuecker et al., 2017), followed by the IOB which grows in ENSO peak season and persists for a few subsequent seasons (Tokinaga and Tanimoto, 2004).

The IOB mode is considered primarily as a response to ENSO associated with large-scale alteration of the Walker circulation, and thus matures in boreal spring, a season after the typical ENSO peak (Klein et al., 1999; Lau and Nath, 2000, 2003). By contrast, the Bjerknes feedback is key to the formation of the IOD. This feedback requires background surface easterlies and thermocline shallowing in the eastern part of the basin along the equator, and this condition sets in boreal spring and persists until autumn, then dissipating by early winter in association with climatological monsoon wind swing. The IOD mode therefore develops in boreal summer and reaches its maximum amplitude in autumn, then rapidly terminates before winter (Schott et al., 2009). Differently from the IOB, strong internal feedbacks enable the IOD mode to develop also without influence from ENSO, as noted for some specific events (Saji and Yamagata, 2003a; Meyers et al., 2007).

The IOB and IOD are identified as the first and second EOF modes, respectively, of monthly SST variability in the tropical Indian Ocean (Weare, 1979; Saji et al., 1999). The IOD can be extracted also as the first EOF of SST variability in boreal autumn, although the pattern depends on the analysis period (Pillai et al., 2019). The IOD mode has a subsurface signature and can be also calculated as the leading EOF mode of the 20ºC isotherm depth of the Indian Ocean seawater temperature (Saji et al., 2006). Apart from the EOF definitions, the Tropical Indian Ocean averaged SST (20ºS-20ºN, 40ºE-100ºE or 40ºE-120ºE) is often used as the IOB mode index (Figure AIV.4a). For March-April-May, its correlation with the leading PC of Indian Ocean SST (Figure AIV.4b) reaches 0.98. For the IOD, SST anomaly difference between the western (10ºS-10ºN, 50ºE-70ºE) and eastern (10ºS-0º, 90ºE-110ºE) equatorial Indian Ocean is a widely used index (Saji et al. 1999; Figure AIV.5). It is highly correlated (at 0.76) with the leading principal component of the Indian Ocean September-November SST when assessed over 1958-2019 (Figure AIV.5b).

The IOB (Han et al., 2014) and IOD (Ashok et al., 2004a; Tozuka et al., 2007) -like variability can also be identified at decadal timescales. The decadal IOB mode is defined as the leading EOF mode of linearly detrended monthly SST after decadal time filtering (Han et al., 2014; Dong and McPhaden, 2017). 10-year low pass filtered Indian Ocean basin-mean SST is an alternative index for the decadal IOB mode (Dong et al., 2016), with the global-mean SST subtracted in some cases as an estimation of the response component to radiative forcing (Huang et al., 2019). The decadal IOD mode can be extracted as the second EOF mode of 10-year low-pass filtered Indian Ocean SST in boreal autumn (Yang et al., 2017), while other studies use the 10-year low-pass filtered SST anomaly difference between the western and eastern equatorial Indian Ocean (Ashok et al., 2004a; Tozuka et al., 2007).

Paleo fluctuations of IOB and IOD as well as the changes over the instrumental record period are assessed in Section 2.4.3, while their model representations are assessed in Section 3.7.4. Future variations under global warming are assessed in Sections 4.4.3.3 (near-term) and 4.5.3.3 (mid- to long terms).

[START FIGURE AIV.4 HERE]

Figure AIV.4: The boreal springtime IOB mode defined by March-April-May SST anomalies averaged over the Indian Ocean (the region denoted by the cyan box in a) or extracted as the leading EOF mode over the same domain (black contour) for 1958-2019 using ERSSTv5. (a) SST anomalies regressed onto the IOB index timeseries shown in (b) in red and blue bars, while the black curve in (b) represents the leading principal component timeseries. Explained variance and correlation between indices are given in the legend in (b). (c) Same as (a) but for land SAT (shading; based on BerkeleyEarth) and 10-m level wind (arrows; based on JRA-55) anomalies for 1958-2018. (d) Same as (a) but for precipitation anomalies (shading based on GPCC for 1958-2016 and contours based on CMAP for 1979-2019 for

ACCEPTED VERSION SUBJECT TO FINAL EDITING

every 0.3 mm/day). On maps, no-overlay indicates regions where the regressions are significant based on t-test accounting for false detection rate at 10% and crosses indicates no significance. Significance for CMAP precipitation is materialized by red contours in (d). All fields have been linearly detrended prior to computation.

[END FIGURE AIV.4 HERE]

[START FIGURE AIV.5 HERE]

Figure AIV.5: The boreal autumn IOD mode defined by September-October-November standardized SST difference between the western (10ºS-10ºN, 50ºE-70ºE) and eastern (10ºS-0º, 90ºE-110ºE) equatorial Indian Ocean denoted by cyan boxes in (a) or extracted as the leading EOF mode over the Indian Ocean (the region denoted by black contour in a) over 1958-2019 using ERSSTv5. (a) SST anomalies regressed onto the IOD index timeseries shown in (b) in red and blue bars while the black curve represents the leading principal component timeseries. Explained variance and correlation between indices are given in the legend in (b). (c) Same as (a) but for land SAT (shading; based on BerkeleyEarth) and 10-m level wind (arrows; based on JRA-55) anomalies for 1958-2018. (d) Same as (a) but for precipitation anomalies (shading based on GPCC for 1958-2016 and contours based on CMAP for 1979-2019 for every 0.3 mm/day. On maps, no-overlay indicates regions where the regressions are significant based on t-test accounting for false detection rate at 10% and crosses indicates no significance. Significance for CMAP precipitation is materialized by red contours in (d). All fields have been linearly detrended prior to computation.

[END FIGURE AIV.5 HERE]

AIV.2.4.2 Teleconnections and regional influence

Since the IOB mode is tightly associated with ENSO, related climate anomalies can be viewed as part of ENSO's influence from boreal winter to subsequent spring. Still, the IOB mode plays an important role in modulating the ENSO influence on several regions. The positive phase of the IOB plays a major role in suppressing precipitation in the Maritime Continent from boreal winter to spring (Watanabe and Jin, 2002; Annamalai et al., 2005) and Northern Australia in austral summer (Taschetto et al., 2011) in concomitance with El Niño event (Figure AIV.3d). An anomalous surface anticyclone then forms over the Philippine Sea linked to the precipitation reduction in the tropical western Pacific and brings more precipitation to East Asia during El Niño winter and spring (Figure AIV.3d; Wang et al., 2000).

ENSO's equatorial Pacific SST anomalies typically dissipate by boreal summer, when the lingering IOB then plays the leading role in exerting climate anomalies in Asia and the Northwest Pacific (the Indian Ocean capacitor effect; Xie et al. 2009). The boreal summer IOB induces meridionally dipolar anomalies of precipitation and surface air temperature in Southeast and East Asia, with wetter and cooler summer in midlatitude East Asia and drier and warmer summer in Southeast Asia during positive IOB events (Kosaka et al., 2013; Wang et al., 2013). These conditions affect the occurrence of extremes such as heavy rainfall (often caused through atmospheric rivers; Kamae et al. 2017) and heat waves (Hu et al., 2012; Deng et al., 2019). The positive IOB suppresses summertime tropical cyclone formation in the Northwest Pacific (Du et al., 2011; Ueda et al., 2018), leading to a delayed onset of the typhoon season (Zhao et al., 2019). These regional influences are already present in the spring season (Figure AIV.4c,d) but tend to persist and even get reinforced due to the persistence of the IOB, while following the seasonal climatological displacement of tropical dynamics (monsoon etc.). In South Asia, tripolar precipitation anomalies form in boreal summer, with precipitation increase along the Western Ghats and in Bangladesh and decrease around the Ganges Delta during the positive IOB (Chowdary et al., 2013, 2019).

The IOD is associated with climate anomalies in broad regions (Figure AIV.5c,d). However, the related anomalies are interfered with influences from concomitant ENSO. The IOD affects rainfall in eastern Africa, South Asia, Indonesia and Australia (Figure AIV.5c,d). The IOD in the positive phase increases rainfall in eastern tropical Africa in boreal autumn to early winter (Figure AIV.5d), while the negative phase induces

ACCEPTED VERSION SUBJECT TO FINAL EDITING

the opposite anomalies. These anomalies are also found in association with ENSO (Figure AIV.3d), but the explained variance by IOD is larger (Saji and Yamagata, 2003b). Both positive IOD and El Niño events reduce precipitation and temperature over the entire Maritime Continent (Figure AIV.5c,d and Figure AIV.3c,d) because of strong low-level divergence coupled with upper-level convergence related to diminished convection, while the opposite anomalies are induced by negative IOD and La Niña episodes (Saji and Yamagata, 2003b). The positive phase of the IOD also decreases rainfall in western to south-eastern Australia (Ashok et al., 2003; Risbey et al., 2009) acting as preconditioning for fires (Cai et al., 2009). The rainfall anomalies cover the entire Australia when combined with simultaneous ENSO with the same polarity (Risbey et al., 2009). The IOD influences South Asian summer monsoon rainfall either directly through moisture transport over the western Indian Ocean or modification of the local Hadley cell (e.g., Ashok et al., 2001; Gadgil et al., 2004; Ashok and Saji, 2007; Behera and Ratnam, 2018), or indirectly in the framework of the tropospheric biennial oscillation (e.g., Meehl et al., 2003; Li et al., 2006; Webster and Hoyos, 2010). IOD and ENSO often interfere in their influence on the south Asian summer monsoon (e.g., Ashok et al., 2001, 2004b; Pepler et al., 2014; Crétat et al., 2017). Opposing influence of IOD and ENSO has been found on surface temperature in summertime Northeast Asia (Saji and Yamagata, 2003b).

Implications of these modes on water cycle changes and specific regional influences are further assessed in Sections 8.3.2.9 and 8.4.2.9 and in Sections 12.4, Atlas.5, Atlas.6, Atlas.7 and Cross-Chapter Box Atlas.2, respectively.

AIV.2.4.3 Available proxy-based reconstruction

Corals record interannual and longer variability in the Indian Ocean (Zinke et al., 2005, 2009). Several studies have developed IOD reconstructions based on oxygen isotope ratios from corals. These reconstructions include those based on samples from Kenya since 1887 (Kayanne et al., 2006), from the Mentawai Islands in western Indonesia for the last 6,500 years (Abram et al., 2007) and in combination with samples from Bali in southern Indonesia and the Seychelles since 1846 (Abram et al., 2008). Abram et al. (2020) developed a coral-based reconstruction of the IOD for the last millennium, albeit with some discontinuity. Niedermeyer et al. (2014) use isotope compositions in terrestrial plant wax to reconstruct rainfall changes over Northwest Sumatra, which is highly correlated with the IOD. Compared to the IOD, proxy-based IOB reconstruction is limited. Yet, Du et al. (2014) find that coral oxygen isotope records from the Seychelles are well correlated with the IOB, suggesting that they can be used as an IOB proxy. Evidence from other proxies that are potentially associated with the Indian Ocean variability is assessed in Section 2.4.3.

AIV.2.5 Atlantic Meridional and Zonal Modes

AIV.2.5.1 Definition of the mode

The Atlantic Zonal Mode (AZM), also commonly referred to as the Atlantic Niño, and the Atlantic Meridional Mode (AMM) are the two dominant modes of tropical Atlantic climate variability on interannual to decadal time scales. The AZM peaks during the boreal summer upwelling season with maximum SST anomalies in the eastern equatorial Atlantic and is commonly regarded as the Atlantic counterpart of the Pacific El Niño (Zebiak, 1993; Keenlyside and Latif, 2007; Lübbecke et al., 2018; Foltz et al., 2019). The AMM, which is more active on longer time scales, peaks during boreal spring and exhibits a cross-equatorial gradient of SST with opposite signs in the northern and southern portion of the Atlantic. Both modes are associated with changes in the Intertropical Convergence Zone (ITCZ) and related winds and exert a strong influence on the climate in adjacent and remote regions.

The AMM is thought to be primarily driven by air-sea heat fluxes and therefore thermodynamic in nature (Chang et al., 2000; Foltz and McPhaden, 2010), while various mechanisms for generating AZM events have been discussed. They mainly concern fluctuations in the wind field over the equatorial Atlantic. These wind stress anomalies can be excited by local SST changes, as part of Bjerknes feedback (i.e. weakening of trade

ACCEPTED VERSION SUBJECT TO FINAL EDITING

winds and thermocline slope adjustments via oceanic equatorial Kelvin wave propagation; Keenlyside and Latif, 2007; Deppenmeier et al., 2016). They can also be excited by meridional advection of temperature anomalies (Richter et al., 2013), generated remotely as a response to ENSO (Latif and Grötzner, 2000; Tokinaga et al., 2019) or to variations in the South Atlantic subtropical high (Lübbecke et al., 2014), or occur as stochastic wind variability (Richter et al., 2014). In contrast to previous mechanisms involving coupled atmosphere-ocean dynamics, Bellomo et al. (2015) and Nnamchi et al. (2015) suggested that a large part of the SST variability in the eastern equatorial Atlantic can be explained by thermodynamic feedbacks excited by stochastic atmospheric perturbations. A recent study based on observational and reanalysis products by Nnamchi et al. (2021) indicates that the seasonality of AZM is indeed largely controlled by the variability of the atmospheric diabatic heating. However, the balance between thermodynamic and dynamic processes determining SST variability in the equatorial Atlantic is subtle, and other studies (e.g. Jouanno et al., 2017; Dippe et al., 2018) conclude that, even if the thermodynamic component is not negligible, the dynamics is the dominant driver of the AZM.

The AZM and AMM represent the first and second EOF patterns of the tropical Atlantic variability identified using SST anomalies in this region (Figure AIV.6a and Figure AIV.7a). These modes may also be defined using box averages, with the AZM defined as SST anomalies averaged over the equatorial Atlantic region called ATL3 (3ºS-3ºS, 0º-20ºW), and the AMM defined as the difference between the SST anomalies averaged over the tropical North Atlantic and tropical South Atlantic (i.e. 5ºN-30ºN, 20ºW-60ºW minus 5ºN-20ºS, 5ºE-25ºW). In boreal summer, the ATL3 and the EOF-AZM PC are correlated at 0.87 during 1958-2019 (Figure AIV.6b). The correlation between the AMM-box index and the EOF-AMM PC is lower, i.e. 0.39 (Figure AIV.7b), but increases to 0.67 over 1900-2019.

For the AMM, the latitudinal polarity in SST anomalies is associated with wind gradient and flow from the cooler to the warmer hemisphere (Ruiz-Barradas et al., 2000; Chiang and Vimont, 2004; Lübbecke et al., 2018; Foltz et al., 2019; Figure AIV.7c). For the AZM, similarly to ENSO in the Pacific Ocean, anomalous westerlies lead to low-level convergence over warmer SST along the climatological cold tongue (Figure AIV.6c).

The temporal evolution of the Atlantic modes of variability and their model representation are assessed in Sections 2.4.4 and Section 3.7.5, respectively. Their near-term and long-term evolution is assessed in Sections 4.4.3.4 and 4.5.3.4, respectively.

[START FIGURE AIV.6 HERE]

Figure AIV.6: The boreal summertime AZM defined by June-July-August box-averaged SST anomalies over the ATL3 region (3ºS-3ºN, 0º-20ºW, cyan box in a) or estimated as the leading EOF over the tropical Atlantic Ocean (the region denoted by the black box in a) for 1958-2019 using ERSSTv5. (a) SST anomalies regressed onto the ATL3 time series, which is shown in (b) as red and blue bars, while the black curve represents the leading principal component timeseries. Explained variance and correlation between indices are given in the legend in (b). (c) Same as (a) but for land SAT and 10-m level wind (arrows; based on JRA-55 for 1958-2019) anomalies. (d) Same as (a) but for precipitation anomalies (shading based on GPCC for 1958-2016 and contours based on CMAP for 1979-2019 for every 0.2 mm/day). On maps, no-overlay indicates regions where the regressions are significant based on t-test accounting for false detection rate at 10% and crosses indicates no significance. Significance for CMAP precipitation is materialized by red contours in (d). All fields have been linearly detrended prior to computation.

[END FIGURE AIV.6 HERE]

[START FIGURE AIV.7 HERE]

Figure AIV.7: The boreal summertime AMM defined by June-July-August standardized SST difference between the north (5ºN-30ºN, 20ºW-60ºW) and south (5ºN-20ºS, 5ºE-25ºW) tropical Atlantic Ocean shown by the

ACCEPTED VERSION SUBJECT TO FINAL EDITING

cyan boxes in (a) or estimated as the leading EOF over the tropical Atlantic Ocean (the region denoted by the black box in a) for 1958-2019 using ERSSTv5. (a) SST anomalies regressed onto the AMM time series, which is shown in (b) as red and blue bars, while the black curve represents the leading principal component timeseries. Explained variance and correlation between indices are given in the legend in (b). (c) Same as (a) but for land SAT and 10-m level wind (arrows; based on JRA-55 for 1958-2019) anomalies. (d) Same as (a) but for precipitation anomalies (shading based on GPCC for 1958-2016 and contours based on CMAP for 1979-2019 for every 0.2 mm/day). On maps, no-overlay indicates regions where the regressions are significant based on t-test accounting for false detection rate at 10% and crosses indicates no significance. Significance for CMAP precipitation is materialized by red contours in (d). All fields have been linearly detrended prior to computation.

[END FIGURE AIV.7 HERE]

AIV.2.5.2 Teleconnections and regional influence

The tropical Atlantic variability has robust teleconnections with climate variability across the global tropics and beyond. There is evidence for two-way teleconnections between the tropical Atlantic and Pacific on interannual to decadal timescales such that the tropical Atlantic variability responds and feeds back to the Pacific ENSO (Section AIV.2.3) and Pacific Decadal Variability (Section AIV.2.6). A number of studies suggest the existence of a possible connection between the tropical North Atlantic and tropical Pacific variability (Wu et al., 2007; Ham et al., 2013a, 2013b; Wang et al., 2017b) at interannual timescales. This teleconnection appears to be modulated at decadal timescale by the AMV phases (Wang et al., 2017b) and it is also affected by global warming (Dong and Zhou, 2014).

The AZM-related boreal summer variability is linked with ENSO in the following boreal winter (Polo et al., 2008; Rodríguez-Fonseca et al., 2009; Ding et al., 2012; Keenlyside et al., 2013; Martín‐Rey et al., 2015; Cai et al., 2019). This relationship is strongest during negative AMV phases due to enhanced equatorial Atlantic variability (Martín-Rey et al., 2014, 2018; Polo et al., 2015). On the other hand, the persistence of SST anomalies during multi-year ENSO events affects the equatorial Atlantic variability through modifications of the Walker circulation (Tokinaga et al., 2019). An exhaustive analysis of the AZM characteristics and related teleconnections is given by Lübbecke et al. (2018b) and by Cabos et al. (2019).

The AZM affects the Indian summer monsoon (ISM), altering the ENSO-ISM connection (Kucharski et al., 2007, 2008; Wang et al., 2009; Barimalala et al., 2012, 2013; Kucharski and Joshi, 2017). Specifically, warm SST in the equatorial Atlantic leads to decreased monsoon rainfall over central India, and the opposite occurs for negative Atlantic SST anomalies via strengthening of the Somali Jet and low-level convergence (Kucharski et al., 2007, 2008; Pottapinjara et al., 2016). This relationship opens to predictive perspective of the ISM rainfall based on AZM phases (Sabeerali et al., 2019). In this framework, the AZM modulates SST variability in the Indian Ocean (Kajtar et al., 2017). The number of monsoon depressions over the Bay of Bengal increases during the cold phase of the AZM, which is remotely responsible for changes in low-level cyclonic vorticity and mid-tropospheric humidity (Pottapinjara et al., 2014). A relationship between AZM and the West African monsoon is documented as well, with reduction of rainfall over the Sahel and increase over Guinea (Losada et al., 2010). But the relationship with the Sahel shows significant changes across the 20th century (Joly and Voldoire, 2010; Losada et al., 2012), which is strongly indicative for non-stationarity of the teleconnection.

On the western side of the basin, a warm equatorial Atlantic delays the northward migration of the ITCZ and can thus influence rainfall over northeastern South America (Nobre and Srukla, 1996), even before the peak of the AZM (Losada et al., 2010; Mohino et al., 2011; Martín-Rey et al., 2018). When the Atlantic and Pacific basins act together, the response over northeastern South America is found to be strongly enhanced (Torralba et al., 2015). In the extratropics, the decaying phase of the AZM in boreal fall can modify the atmospheric circulation over Europe via a circum-global teleconnection pattern (Haarsma and Hazeleger, 2007; García-Serrano et al., 2011), and can remotely affect the NAO (Drévillon et al., 2003; Peng et al., 2005). AZM can also increase precipitation over southern Europe and the Mediterranean Sea during boreal summer through extra-tropical Rossby waves (Losada et al., 2012).

ACCEPTED VERSION SUBJECT TO FINAL EDITING

The fluctuation of the meridional SST gradient in the tropical Atlantic modulates the seasonal march of the ITCZ, thus influencing regional rainfall over northeast Brazil and Sahel (Hastenrath and Heller, 1977; Folland et al., 1986; Foltz et al., 2012). During a negative phase of the AMM, northerly wind anomalies are associated with a southward shift of the ITCZ (Cabos et al., 2019). During boreal spring, warmer SST over the tropical North Atlantic modulate winds over the western Indian Ocean and may strengthen the monsoon circulation over India, affecting the continental rainfall (Vittal et al., 2020). The AMM is also well known to affect the Atlantic hurricane activity (Vimont and Kossin, 2007; Patricola et al., 2014) and tropical cyclones over the western North Pacific (Zhang et al., 2017).

AIV.2.5.3 Available proxy-based reconstruction

Only a few paleo-reconstructions of AMM and AZM are available. Interhemispheric cross-equatorial SST gradients linked to changes in ITCZ locations characteristic of the AMM has been found during LGM, Heinrich Stadial 1 and the mid-Holocene (McGee et al., 2014). Similarly, the dipole-like SST pattern in the South Atlantic subtropics, which is related to the AZM (Lübbecke et al., 2018; Foltz et al., 2019), has been reconstructed with SST proxies from marine sediment cores during the past 12 kyr (Wainer et al., 2014).

Evidence from proxies associated with the AZM and AMM is assessed in Section 2.4.4.

AIV.2.6 Pacific Decadal Variability

AIV.2.6.1 Definition of the mode

The Pacific Decadal Variability (PDV) describes the large-scale fluctuations typically observed beyond ENSO timescales in a variety of instrumental records and proxy reconstructions over the entire Pacific Ocean and surrounding continents.

Historically, climate variability of the Pacific Ocean on timescales longer than 8-10 years has been described in terms of statistical modes, usually assessed through the decomposition into EOFs of the SST over oceanic sub-basins. The leading EOF mode of SST decadal variability in the extratropical North Pacific is called the Pacific Decadal Oscillation (PDO, Mantua et al., 1997; Mantua and Hare, 2002). The PDO is recognized to correspond to a collection of multiple processes (Newman et al., 2016). On interannual-to-decadal timescales, the PDO is thought to be driven by atmospheric forcing linked to stochastic changes in the Aleutian Low integrated by ocean mixed layer dynamics and related re-emergence processes, as well as to ENSO-forced teleconnections (Schneider and Cornuelle, 2005; Nidheesh et al., 2017). On decadal-to-interdecadal timescales, subpolar-subtropical gyre dynamics and related zonal advection of temperature anomalies in the Kuroshio-Oyashio extension and westward-propagating oceanic Rossby waves are thought to be key mechanisms (Qiu et al., 2007; Taguchi et al., 2007; Wills et al., 2019).

The PDO's South Pacific counterpart, called the South Pacific Decadal Oscillation (SPDO; Chen and Wallace 2015) is defined as the leading EOF mode of SST in the extratropical South Pacific. As for the PDO, the SPDO is thought to be driven by internal climate variability associated with extratropical atmospheric modes (e.g. SAM, Section AIV.2.2), ENSO teleconnections (Section AIV.2.3) and ocean dynamics through gyre circulation (Shakun and Shaman, 2009; Zhang et al., 2018).

In the tropical Pacific, while ENSO has a clear interannual spectral peak, decadal variability is also present with a similar spatial structure (Zhang et al., 1997), called tropical Pacific Decadal Variability (TPDV) or decadal ENSO. Relative occurrence of El Niño and La Niña events in a given decade correlates with the phase of the TPDV (Power and Colman, 2006).

Despite the PDO, SPDO and TPDV being considered to be physically distinct modes (Newman et al., 2016), they are highly correlated in observations (Chen and Wallace 2015) and they collectively constitute an equatorially symmetric pattern of basin-wide variability, often called the Interdecadal Pacific Oscillation

ACCEPTED VERSION SUBJECT TO FINAL EDITING

(IPO) (Power et al., 1999; Folland et al., 2002; Henley et al., 2015). There is evidence that ENSO and the TPDV drive the PDO and SPDO in the North and South Pacific through tropical-extratropical teleconnections and the "reddening" (i.e. selective retainment of decadal and longer variability) in the ocean, ensuring the synchronization of decadal variability in both hemispheres (Newman et al., 2016). Besides, positive feedbacks are suggested between the TPDV and the extratropical North Pacific through the Pacific Meridional Mode (Stuecker, 2018), which is the Pacific analogue of the AMM (Section AIV.2.5; Chiang and Vimont, 2004), and modulations of the shallow subtropical cell of the Pacific ocean circulation (Farneti et al., 2014).

Whether the IPO is a distinct mode of climate variability (Henley et al., 2017) or not (Tung et al., 2019) remains to be further assessed and clarified. However, since the PDO, SPDO, TPDV and IPO modes are highly correlated both spatially and temporally, they can be referred collectively as the Pacific Decadal Variability mode (PDV; Henley 2017b; Liu and Di Lorenzo 2018), similarly to the Atlantic (Section AIV.2.7). Besides, it is noteworthy that none of these modes are actually oscillations with clear spectral peaks in the instrumental period (Mann et al., 2020), which advocates for the use of the PDV acronym across the report.

De facto, there is no unique way to assess the PDV. It can be extracted from the IPO, defined as the leading EOF mode of decadal low-pass filtered SST variability over the entire Pacific to remove the overwhelming influence of ENSO at interannual timescales. Henley et al. (2015) introduced the tripole index (TPI) as the difference of SST anomalies between an equatorial Pacific domain (10ºS-10ºN, 170ºE-90ºW) and an average of midlatitude North (25ºN-45ºN, 140ºE-145ºW) and South (50º-15ºS, 150ºE-160ºW) Pacific domains (Figure AIV.8a). Section 2.4.5 describes the changes in the PDV phases over the instrumental record using a variety of SST products.

A positive phase of the PDV is characterized by warm conditions in the central-eastern tropical Pacific from the dateline to the coasts of the Americas, encircled to the west in the midlatitudes by negative SST anomalies forming a so-called horseshoe pattern. The pattern has a certain similarity with ENSO and related anomalous SST fingerprints through atmospheric teleconnections. However, the PDV features meridionally broader SST anomalies in the tropical Pacific extending to the subtropics compared to ENSO, and relatively stronger extratropical SST anomalies. Alternatively, the low-pass filtered SST regression on the PDO index defined as the leading principal component of SST (Mantua et al., 1997) or sea surface height (Di Lorenzo et al., 2008) over the extratropical North Pacific north of 20ºN are used in literature for PDV. Their corresponding spatial patterns are, by definition, weighted to the respective hemisphere of the Pacific. Figure AIV.8b provides evidence that they are all highly correlated to each other. The correlation value between TPI and the PDO index is equal to 0.76, and when low-pass filtered, it is greater than 0.9 for all the combination of indices.

In the following, and in Section 3.7.6 evaluating the model performance in reproducing PDV and assessing the human influence on the mode evolution, the TPI index is preferred. The latter definition is found to be less sensitive than classical EOF analysis to the possible interplay between internal processes that intrinsically drive the PDV (Wills et al., 2018) and the externally-forced SST response simulated in historical simulations. There is no unique way to remove the impact of the external forcing in the observations at decadal to multidecadal timescales, and the chosen method may have significant implications for the interpretation of the PDV expression during the instrumental era.

Since AR5, there has been considerable progress in the understanding of PDV itself but also in its critical role in modulating the evolution of observed global surface temperature (Cross-Chapter Box 3.1) as well as regional climate through teleconnections. On interannual time scales, ENSO is the leading internal driver of global surface tempeature variability (Section AIV.2.3). Since PDV encompasses decadal modulations of El Niño versus La Niña occurrences, PDV affects global surface tempeature on decadal timescales, with its positive and negative phases tied to higher and lower global surface tempeature, respectively. Indeed, studies identify PDV as the leading mode of variability associated with unforced decadal global surface tempeature fluctuations in observations and a majority of CMIP5 models (Brown et al., 2015; Dai et al., 2015), with additional influence from Atlantic Multidecadal Variability (AMV, Section AIV.2.7) (Tung and Zhou,

ACCEPTED VERSION SUBJECT TO FINAL EDITING

2013). PDV thus plays an important role in decadal acceleration and slowdown of global surface tempeature trends (Cross-Chapter Box 3.1). So far, little predictability has been found for decadal PDV, despite its global relevance and decadal prediction in the Pacific remains challenging with the current decadal forecast system (Section 4.4.3.5). Finally, there is an increasing body of evidence about the existence of a network of teleconnections related to decadal climate variability phenomena (Cassou et al., 2018; Cai et al., 2019). For instance, AMV has been hypothesized to influence in part the phase of the PDV (McGregor et al., 2014; Ruprich-Robert et al., 2017) and consistently, there is a significant negative correlation between PDV and AMV. Other studies suggest that the PDV may be the main driver of the decadal IOB and IOD modes (Section AIV.2.4), while influence from the Indian Ocean SST on PDV has been also suggested (Luo et al., 2012; Mochizuki et al., 2016).

The temporal evolution of PDV in the instrumental records and its model representation are assessed in Sections 2.4.5 and 3.7.6, respectively. Skill in predicting near-term temporal evolution of the PDV and mid- to long term PDV changes are assessed in Sections 4.4.3.5 and 4.5.3.5, respectively.

[START FIGURE AIV.8 HERE]

Figure AIV.8: The PDV based on TPI for 1900-2014 after 10-year low-pass filtering. (a) SST anomalies regressed onto TPI based on ERSSTv5. The cyan boxes indicate regions for the TPI definition. (b) Temporal evolution of the raw TPI (bars), the 10-year low-pass filtered TPI (cyan curve), the EOF-based PDO index (dashed black) and two estimations of the IPO EOF-based indices. In solid black, linear detrending is applied to annual data prior to the computation of the EOF of the low-pass filtered SST to remove the forced component in the SST field. In orange, the forced signal is estimated from CMIP5 historical simulations following Ting et al. (2009). The latter metric is used in CMIP6 DCPP-C sensitivity experiments (Boer et al. 2016). The correlation between the low-pass filtered TPI and all PDV indices is given in the legend. (c) Same as (a) but for land SAT (shading; based on BerkeleyEarth for 1900-2014) and 10-m level wind (arrows; based on JRA-55 for 1958-2014) anomalies. (d) Same as (a) but for precipitation anomalies (shading based on GPCC for 1900-2014). All are based on annual mean. On maps, no-overlay indicates regions where the regressions are significant based on t-test accounting for false detection rate at 10% and crosses indicates no significance.

[END FIGURE AIV.8 HERE]

AIV.2.6.2 Teleconnections and regional influence

Due to the similarity of the SST anomaly pattern with ENSO in the tropical Pacific, atmospheric teleconnections associated with the PDV are rather similar to those of ENSO but with a longer temporal expression. This includes the long-term alteration of the Walker circulation, the modification of the extratropical background driven by tropically-forced Rossby waves then favouring particular phases of the Pacific-North American (PNA) and Pacific-South American (PSA) patterns of atmospheric internal variability that are responsible for persistent influences over the continents (e.g. persistent drought over California and Australia, etc.). Those atmospheric patterns imprint a PDO-like and SPDO-like SST patterns with a reddening by the extratropical oceans, forming the pan-Pacific SST anomaly pattern of the PDV as described above (Newman et al., 2016; Henley, 2017; Liu and Di Lorenzo, 2018).

A positive phase of the PDV brings anomalously warm conditions in the northwestern corner of North America, with maximum loading over Alaska linked to reinforced and eastward displaced Aleutian Low and related anomalous southerlies (Figure AIV.8c). In contrast, concurrent cold conditions dominate far-eastern Siberia due to strengthened advection of Arctic air. The tail end of the storm track is strengthened leading to more precipitation along the Pacific coast of North America, especially in boreal winter. A positive PDV also induces a cooler and wetter climate in the southern part of the North American continent, with the wet anomalies being the most pronounced in boreal summer (Figure AIV.8d). The negative phase of the PDV is an important cause of droughts in the western and central United States (Dai, 2013). Besides the direct

ACCEPTED VERSION SUBJECT TO FINAL EDITING

influence of atmospheric teleconnections from the tropical branch of the mode, extratropical SST anomalies have been shown to modulate the amplitude of the precipitation anomalies in North America (Burgman and Jang, 2015).

In the tropics, a positive PDV is associated with warm and dry anomalies in the Maritime Continent and Amazon (Meehl and Teng, 2014; Figure AIV.8c,d). The Indian and African monsoons also tend to weaken (Meehl and Hu, 2006; Figure AIV.8d). Warm and dry anomalies also cover most of Australia while wet anomalies dominate in South America south of 15ºS. In particular, a positive PDV increases drought risk in Australia (Power et al., 1999; Vance et al., 2015). In the oceans, a positive PDV increases the occurrence of marine heat waves in the Bering Sea and subtropical Eastern Pacific, while a negative PDV increases ocean heat waves in the Kuroshio-Oyashio extension, Melanesia and over the tropical Indian Ocean (Holbrook et al., 2019). PDV also modulates tropical cyclone activity: a positive PDV increases tropical cyclone genesis over the Philippine Sea and the tropical eastern North Pacific and decreases it over the tropical North Atlantic and western South Pacific (Grant and Walsh, 2001; Liu and Chan, 2008; Li et al., 2015; Zhao et al., 2018, 2020). PDV, together with ENSO, have been shown to control part of the interannual to multidecadal wildfire variability, PDV-related persisting droughts and severe heatwave acting as preconditioning in many regions (see for instance Kitzberger et al., 2007; Ward et al., 2016).

Implications of PDV on water cycle changes are further assessed in Sections 8.3.2.4 and 8.4.2.4. Section 10.4 highlights the importance of PDV in regional climate change attribution, with an example in Section 10.6. Influence of PDV climate anomalies in specific regions, including extremes, are assessed in Sections 11.3, 11.4, 11.6, 11.7, Atlas.4, Atlas.5, Atlas.7 and Cross-Chapter Box Atlas.2. Its implications for ocean circulation and sea levels are assessed in Sections 9.2 and 9.6.

AIV.2.6.3 Available proxy-based reconstruction

PDV reconstructions have been developed with tree rings in North America and Asia (Biondi et al., 2001; D'Arrigo et al., 2001; Gedalof and Smith, 2001; MacDonald and Case, 2005; D'Arrigo and Wilson, 2006; D'Arrigo and Ummenhofer, 2015; Buckley et al., 2019), corals in the Pacific (Linsley et al., 2015; Williams et al., 2017) and Indian Ocean (Crueger et al., 2009), historical documents in China (Shen et al., 2006), ice cores (Vance et al., 2015), and multiproxy approaches (Verdon and Franks, 2006; Mann et al., 2009; McGregor et al., 2010) covering the past several centuries up to a millennium. Comparing 12 of these reconstructions, it has been found that respective correlations are generally low (Henley, 2017b), indicating large uncertainty in the PDV temporal history before instrumental records. On longer timescales, a variety of proxies consistently capture the variations of the Aleutian Low intensity throughout the Holocene, which can be used to reconstruct the PDV (see Section 2.4.5).

AIV.2.7 Atlantic Multidecadal Variability

AIV.2.7.1 Definition of the mode

The Atlantic Multidecadal Variability (AMV) describes the large-scale slow fluctuations observed from one decade to the next in a variety of instrumental records and proxy reconstructions over the entire North Atlantic Ocean and surrounding continents. Fingerprints of the AMV can be found at the surface ocean, which is characterized by swings in basin-scale SST anomalies reflecting the interaction with the atmosphere, with a nominal period in the order of 70 years (Deser et al., 2010). AMV markers can be also tracked at the subsurface ocean in terms of heat content and density anomalies. The latter have been traditionally linked to the low-frequency fluctuations in the Atlantic Meridional Overturning Circulation (AMOC) and related oceanic meridional heat/salinity transport and water masses formation through deep convection in the Subarctic Seas (Zhang, 2017).

The positive phase of the AMV is characterized by anomalous warming over the entire North Atlantic, with the strongest amplitude in the subpolar gyre and along sea-ice margin zones in the Labrador Sea and

ACCEPTED VERSION SUBJECT TO FINAL EDITING

Greenland/Barents Sea (approximately +0.5ºC) and in the subtropical North Atlantic basin to a lower extent (Figure AIV.9a). Concurrent, albeit weaker, anomalous cooling is found over the South Atlantic but also along the Pacific cold tongue sandwiched by warmer SST, a pattern reminiscent of the PDV (Section AIV.2.6). What stands out is the apparent inter-basin connectivity in AMV related SST anomalies, which is strongly indicative of the existence of a network of teleconnections linking neighbouring ocean basins, the tropics and the extra tropics, including Northern Hemisphere polar regions, and the oceans and land regions (Cassou et al., 2018). The AMV, together with the PDV, has been shown to modulate the observed time-evolving global surface temperature on multidecadal timescales since pre-industrial time (Cross-Chapter Box 3.1), whilst the level of their respective influence remains difficult to quantify because of their inter-connectivity (Tung and Zhou, 2013; Wu et al., 2019; Li et al., 2020).

The term "Atlantic Multidecadal Oscillation" (AMO) has been introduced in the literature (Kerr, 2000) and used in previous IPCC reports to describe this phenomenon and in particular to make the distinction with the so-called North Atlantic tripole pattern connected to the NAO (Section AIV.2.1) at interannual timescales (Enfield et al., 2001). However, since the observed slow variations of the North Atlantic SSTs consist of a broad band of low-frequency signals (Zhang, 2017; Sutton et al., 2018) rather than a single preferred timescale, as also confirmed from last-millennium reconstructions (e.g., Singh et al., 2018), the denomination "Atlantic Multidecadal Variability" wherein a distinct oscillatory timescale is less clearly implied, appears more appropriate to describe decadal climate variability phenomena as also suggested for the Pacific (Section AIV.2.6). The term AMV will be accordingly used subsequently and throughout the entire report.

The observed AMV is interpreted as the regional residual imprint in SST anomalies after removal of the externally-forced signal. There is no unique and preferred way to remove the impact of external forcing in observations. Linear detrending is used in the traditional definition of the AMV index, which corresponds to the average over the entire North Atlantic basin of the linearly detrended SST yearly anomalies on which a 10-year running mean is applied, as proposed by Enfield et al. (2001). To remove the residual nonlinear global-scale signal from the North Atlantic mean SST, different approaches have been proposed either based on observations applying specific statistics (e.g., Trenberth and Shea, 2006; Frajka-Williams et al., 2017; Frankignoul et al., 2017; Sutton et al., 2018; Yan et al., 2019) or based on model estimates of the externally-forced signal including both natural (solar and volcanoes) and anthropogenic (greenhouse gases and aerosols) influence assessed from historical simulations (Ting et al., 2009; Terray, 2012; Steinman et al., 2015; Tandon and Kushner, 2015). More specifically, in Trenberth and Shea (2006), the annual observed global-mean SST anomaly timeseries is subtracted from the observed annual North Atlantic spatially averaged timeseries to obtain the raw unfiltered AMV index. In Ting et al. (2009), a signal-to-noise maximizing EOF analysis is applied to global annual mean SSTs derived from the CMIP5 multi-model ensemble to extract an estimation of the forced component, which is a priori removed before computation of the AMV index, then defined as a low-frequency residual. The latter technique has been retained in the so-called CMIP6 DCPP-C sensitivity experiments (Boer et al., 2016) aimed at furthering a better understanding of the teleconnections associated with the AMV. The two latter indices are shown in Figure AIV.9b and compared to the traditional AMV index.

All AMV timeseries consistently show a few distinct phases over the approximately 120-year instrumental record, namely warm periods over 1930-1965 and since 1995, and cool periods between 1900 and 1925 and over 1965-1995 (Figure AIV.9b). The uncertainty introduced by the different definitions of the index is mainly related to the strength of the phase of the AMV and in particular the most recent ones, which are the most sensitive to the estimation of the externally-forced signal.

The temporal evolution of AMV in the instrumental records is assessed in Section 2.4.6. The transition between phases has been shown to involve various atmospheric and oceanic processes, leading to some predictability, but also influences from external forcing (both anthropogenic and natural), whose respective weight and interplay remain outstanding issues, as assessed in detail in Section 3.7.7 and Section 9.2.3.

ACCEPTED VERSION SUBJECT TO FINAL EDITING

[START FIGURE AIV.9 HERE]

Figure AIV.9: The AMV based on the AMV index defined from Trenberth and Shea (2006) for 1900-2014 after 10-year low-pass filtering. The index corresponds to the annual SST averaged over the North Atlantic domain (cyan box) minus near-global average [60ºN-60ºS]. (a) SST anomalies regressed onto the AMV index based on ERSSTv5. (b) The cyan curve indicates the 10-year low-pass filtered AMV index shown in bars. The orange curve stands for the AMV index used for the CMIP6 DCPP-C sensitivity experiments (Boer et al. 2016). (c) Same as (a) but for land SAT (shading; based on BerkeleyEarth for 1900-2014) and 10-m level wind (arrows; based on JRA-55 for 1958-2014) anomalies. (d) Same as (a) but for precipitation anomalies (shading based on GPCC for 1900-2014). All is based on annual mean. On maps, no-overlay indicates regions where the regressions are significant based on t-test accounting for false detection rate at 10% and crosses indicates no significance.

[END FIGURE AIV.9 HERE]

AIV.2.7.2 Teleconnections and regional influence

The important role of the AMV in observed low-frequency climate signals at a regional scale has been recognized for decades. The AMV is a key driver of temperature and precipitation anomalies along the North Atlantic surrounding continents but also remotely through global atmospheric teleconnections (e.g. monsoons). Considering AMV-induced regional influence is crucial because the AMV acts as a pronounced modulator of the impacts driven by external natural and anthropogenic forcings. For instance, the AMV can have a pronounced fingerprint in time-integrating processes, such as river flows, and could explain the largest fraction of observed variance in some specific local areas since the 1900s (e.g. Bonnet et al., 2020). It is thus a key phenomenon for regional-scale or process-based attribution of past observed climate variations as introduced in Cross-Chapter Box 1.4 and extensively developed in Section 10.4.1.

Positive AMV is associated with much warmer conditions over the north-western corner of the Atlantic, with marked positive anomalies on land around the Labrador Sea (Figure AIV.9c). There is a strong seasonality in the AMV teleconnection and this pattern is mostly explained by boreal winter atmospheric dynamics and a local reduction of sea-ice formation. There is a large-scale decrease of the wintertime midlatitude westerlies and, concurrently, a weakening of the trade winds in the North Atlantic tropical basin, which is reminiscent of a negative phase of the NAO (Peings and Magnusdottir, 2014; Gastineau and Frankignoul, 2015). Over Europe, AMV-related signals are weak on yearly average (Figure AIV.9c) but mask a pronounced seasonality of the teleconnection as well as some interplay between dynamical (i.e. atmospheric circulation) versus thermodynamical changes controlled by the AMV (O'Reilly et al., 2017; Ruprich-Robert et al., 2017, Qasmi et al. 2020). Summer tends to be warmer during positive AMV in Europe (Sutton and Dong, 2012; Nicolì et al., 2020) with constructive contribution of both dynamical and thermodynamical responses while destructive interference prevails in boreal winter leading to colder conditions with a reinforced occurrence of blocking (Rimbu et al., 2014; Davini et al., 2015) and a southward shift of the jet (Simpson et al., 2018). Anomalies are positive all year round over a broad Mediterranean region, including North Africa and the Middle East. Reduction of Arctic Sea Ice is also found during positive AMV with local warming extension over the adjacent polar land (Day et al., 2012; Yu et al., 2017; Castruccio et al., 2018).

In terms of precipitation (Figure AIV.9d), positive AMV is associated with a northward shift of the Atlantic ITCZ in response to changes in the meridional SST gradient with respect to the equator (Martin and Thorncroft, 2014; Friedman et al., 2017; Green et al., 2017). The AMV influence is the strongest in the boreal summer affecting the West African Monsoon, leading to reinforced Sahel rainfall, and wetter conditions in the Caribbean basin through the modulation of the occurrence of hurricanes (Dunstone et al., 2011; Hermanson et al., 2014). By contrast, dry conditions prevail in the Northeast Brazil and in the south-eastern corner of South America as well as in the Great Plains in North America. The signal of the positive AMV lead to an intensified precipitation and river runoff over Northern Eurasia (Nicolì et al., 2020) and controls the multidecadal variations in river flows over much of Europe (Boé and Habets, 2014; Hodgkins et al., 2017). Because of global teleconnections, especially in the tropics, the AMV also affects the other

ACCEPTED VERSION SUBJECT TO FINAL EDITING

monsoon systems with signals found over India, South East Asia, and the Maritime Continent and, more broadly, over the entire tropical Pacific (Chylek et al., 2014; Kucharski et al., 2016; Ruprich-Robert et al., 2017).

The weight of the AMV in observed low-frequency variations is assessed in detail in Section 10.4.2 for specific regional case studies, including the sectors listed above. Because of its long timescale due to persistent heat content anomalies, the AMV can be considered as a potential source of near-term climate predictability. Skill of the current decadal forecast systems in predicting the AMV temporal evolution and associated teleconnection at various lead time is assessed in Section 4.4.3.6, while long-term changes are assessed in Section 4.5.3.6.

AIV.2.7.3 Available proxy-based reconstruction

Paleoclimate reconstructions of AMV-related signals have been developed using terrestrial, marine and ice-core proxies. The AMV reconstruction in the last 1200 years by Wang et al. (2017a), using terrestrial proxy records, shows a clear broad band of enhanced spectral power at multidecadal timescales but no evidence of a distinct multidecadal or centennial spectral peak (Singh et al., 2018). This is largely consistent with the record of the instrumental period and with previous proxy-based studies (Gray et al., 2004; Mann et al., 2009) in the overlapping periods. Studies focusing on marine proxies also show persistent multidecadal variability over the last three centuries (Kilbourne et al., 2014; Svendsen et al., 2014; Moore et al., 2017). Multidecadal Arctic temperature variability related to the AMV is also evident in ice cores records over the last millennium (Chylek et al., 2011; Zhou et al., 2016) and beyond (Knudsen et al., 2011). High resolution sedimentary records from the Arctic were recently analyzed to reconstruct the AMV over the last 2900 years (Lapointe et al., 2020). However, this new reconstruction refers to the raw North Atlantic SST variability rather than to the residual of the Atlantic signal obtained after removal of the estimation of the external forcing influence. A multi-perspective assessment of the North Atlantic variability is thus necessary for understanding the origin of the AMV, its physics and its climatic implications over the paleoclimatic period.

The temporal evolution of the AMV is described and assessed in detail in Section 2.4.6.

AIV.2.8 Madden-Julian Oscillation

AIV.2.8.1 Definition of the mode

The Madden-Julian Oscillation (MJO) is the leading mode of tropical intra-seasonal variability with 20–90 days' timescale (Madden and Julian, 1994) and an important source of regional climate variability and predictability across the globe at subseasonal timescales from a week to months (Madden and Julian, 1994; Zhang, 2005; Vitart, 2017; Wheeler et al., 2017; Kim et al., 2018). It is characterized by planetary-scale disturbances (zonal wavenumber 1–3) of pressure, wind, clouds and rainfall moving predominantly eastward along the equator at average speed of 5 m s^{-1} (Roxy et al., 2019). More precisely, the MJO is characterized by alternating regions of suppressed and enhanced convection coupled to an anomalous zonal overturning circulation of the atmosphere (Zhang, 2005). The MJO is driven by internal ocean-atmosphere processes that occur all year round but exhibits prominent seasonality with more pronounced signals in boreal winter. During boreal summer, centres of convective activity associated with the MJO are shifted away from the equator to 10ºN–20ºN and propagate northward in the Asian monsoon region (Yasunari, 1980; Madden, 1986) in addition to eastward propagation, often called as the boreal summer intra-seasonal oscillation (BSISO; Madden, 1986; Kikuchi et al., 2012). Whereas the MJO is considered present in all seasons, albeit with weaker amplitude in boreal summer, the BSISO tends to prevail during boreal summer, with influences on monsoons, tropical cyclones and other water cycle aspects (Kikuchi et al., 2012; Lee et al., 2013).

The real-time multivariate MJO (RMM) index has been widely used to detect the MJO, based on the first two combined EOF modes of daily outgoing longwave radiation (OLR) and zonal winds at 850 and 200 hPa averaged over 15°N-15°S (Wheeler and Hendon, 2004). The OLR represents convective activity and zonal

ACCEPTED VERSION SUBJECT TO FINAL EDITING

winds at the lower and upper troposphere depict the overturning zonal circulation along the equator. The composite maps of convective activity and atmospheric circulation (Figure AIV.10a) and the phase diagram (Figure AIV.10b) based on eight phases constructed by the two PCs timeseries provide effective ways to understand and monitor spatial and temporal evolution of the MJO event. In general, the MJO disturbance are initiated in the equatorial western Indian Ocean and travel eastward mainly over the Indo-Pacific warm pool region. However dynamical fields in composite maps indicate that the MJO also propagates over climatological non-convective regions (e.g., the eastern Pacific, part of the tropical Atlantic) (Figure AIV.10a), then manifesting the planetary nature of the tropical intra-seasonal oscillation (Cassou, 2008). Each phase has a nominal persistence of about 7-8 days and the anti-clockwise rotation in this 2-dimensional diagram materializes the propagation of the MJO packets from west to east. Figure AIV.10b provides an example of that RMM index computed for the year 1997, with months highlighted in colours. When the value of the index lies in the centre of the diagram, the MJO is considered to be inactive; outside the circle, its distance from the centre quantifies the amplitude and spatial coherence of the MJO episode.

The evaluation of the MJO in climate models is done through phenomenological (Waliser et al., 2009) and process-oriented (Xavier, 2012) diagnostics. MJO simulation remains a challenge in both CMIP3 and CMIP5 models, even though overall improvements have been reported in the most recent model versions (Waliser et al., 2003; Lin et al., 2006; Sperber and Annamalai, 2008; Kim et al., 2009; Xavier et al., 2010; Jiang et al., 2016). Poor MJO simulation in coupled climate models has been attributed to many factors, including an insufficient build-up of atmospheric moisture for large-scale organized convection to occur (Kim et al., 2012; Mizuta et al., 2012), biases in models mean state (Inness et al., 2003; Hannah et al., 2015; Kim, 2017), coupling frequency with the ocean and representation of air-sea interactions (Bernie et al., 2008; DeMott et al., 2015). In CMIP5 simulations, the eastward propagation of boreal winter MJO convection from the Indian Ocean into the western Pacific (Hung et al., 2013) and the northward propagation during boreal summer (Sperber et al., 2013) are slightly better represented, even if major biases persist and still affect the monsoon systems. These improvements have been attributed to advances in parametrizing moist turbulence and convection (Hohenegger and Bretherton, 2011; Mapes and Neale, 2011; Del Genio et al., 2012; Kim et al., 2012; Hourdin et al., 2013), leading to greater MJO predictive skill of up to four weeks in operational subseasonal prediction centres (Vitart, 2014). Super-parametrized models (Benedict and Randall, 2009), global cloud system-resolving models (Miyakawa et al., 2014) and high-resolution global climate models with an improved seasonal cycle (Mizuta et al., 2012) have been shown to produce a more realistic simulation of the MJO. Progresses in the representation of the MJO across model generations are assessed in Section 1.5.4.6 and Section 8.3.2.9.1.

The assessment of changes in the MJO and related processes, mostly in terms of its implication for water cycle changes in the recent past and in future projections is provided in Sections 8.3.2.9 and 8.4.2.9, respectively. The MJO influence over south East Asia and Central and South America is further assessed in Sections Atlas.4, Atlas.5, Atlas.7, and Cross-Chapter Box Atlas.2.

[START FIGURE AIV.10 HERE]

Figure AIV.10: (a) The spatio-temporal properties of the MJO. Daily composites of Outgoing Longwave Radiation (OLR, W m^{-2}, shaded) anomalies and streamfunction anomalies at 300 hPa (STF, contours every 0.5 10^6 m^2 s^{-1}) for the 8 MJO phases in boreal winter (1st Dec. -31st March) based on NOAA interpolated satellite products and NCEP-NCAR reanalyzes over 1979-2019, respectively. Greenish (brownish) colours indicate enhanced (reduced) convective activity associated with wet (dry) conditions. Solid (dashed) contours show for positive (negative) STF anomalies which stand for anomalous anticyclonic circulation in the Northern (Southern) Hemisphere. (b) Phase diagram of the MJO constructed from the two leading principal components drawn from empirical orthogonal decomposition of combined wind@300hPa+OLR fields following Wheeler and Hendon (2004) for the winter 2007-2008 chosen as an example of active MJO years. (c) Schematic representation of MJO-related tropical—Northern Hemisphere interactions and teleconnections inferred from observational and numerical studies (adapted from Stan et al.(2017)). Because the interactions and teleconnections of the Southern Hemisphere are not as well understood but SAM, they are not included in the current schematic.

ACCEPTED VERSION SUBJECT TO FINAL EDITING

[END FIGURE AIV.10 HERE]

AIV.2.8.2 Teleconnections and regional influence

In AR5, the MJO has been described as a tropical phenomenon, yet with prominent impacts across the globe through teleconnections. The MJO exerts a strong influence on occurrences of extreme weather events in the tropics, including tropical cyclones, droughts, flooding, heat waves, fires, among others (Zhang, 2013), as well as those in the extratropics via teleconnections (Stan et al., 2017). This has opened new opportunities and scientific endeavours in the emerging field of sub-seasonal to seasonal forecasts of extremes (Vitart and Robertson, 2018) and for the development of new observational networks needed to initialize the forecast systems (Subramanian et al., 2019). The MJO can also impact the atmospheric composition, such as ozone, CO, CO_2, and aerosols (Tian et al., 2007, 2011; Li et al., 2010b; Lau et al., 2012).

The schematic in Figure AIV.10c shows the main regions of influence of the MJO. During boreal winter, the MJO fingerprint is mostly confined to the deep tropics with a zonal alternation of wet and dry zones depending on the MJO phase. For instance, in phase 4, enhanced rainfall is found over the Maritime Continent while suppression of convection is present over the central Pacific, northeast Brazil and equatorial Africa (Figure AIV.10a). The opposite is found during phase 8. Anomalous upper-level divergence in the deep tropics associated with altered convection and diabatic heating leads to anomalous vorticity in the subtropics (shown by streamfunction dipoles straddling the equator in Figure AIV.10a) acting as an efficient and primary source of teleconnections outside the tropics (L'Heureux and Higgins, 2008; Lin et al., 2009; Lukens et al., 2017). The extratropical influence of the MJO may occur via the excitation of forced tropospheric Rossby waves (Ferranti et al., 1990; Matthews et al., 2004; Cassou, 2008; Stan et al., 2017) that affect the climate variability over the North Pacific (Ferranti et al., 1990; Higgins and Mo, 1997), the North Atlantic (Ferranti et al., 1990; Cassou, 2008) and the Arctic (Zhou and Miller, 2005). For example, tropical convective heating associated with MJO phase 5 contributes to Arctic warming, while the opposite occurs for the MJO phase 1 (Yoo et al., 2011, 2012). Phase 2-3 of the MJO is clearly associated with the prevalence of the positive phase of the NAO with a 10 to 15-days lag after the MJO forcing. Stratospheric pathways are also reported to support tropical-extratropical teleconnections though the modified occurrence of sudden stratospheric warming (Liu et al., 2014; Garfinkel and Schwartz, 2017) with a 15 to 20-days delay leading to sub-seasonal predictability.

During boreal summer, the MJO/BSISO convective activities and related impacts propagate northward/northeastward over the Indian Ocean-South Asia region (Yasunari, 1980; Annamalai and Sperber, 2005) and northward/northwestward over the western North Pacific-East Asia region (Kemball-Cook and Wang, 2001; Lee et al., 2013). The MJO/BSISO significantly modulate occurrences of extreme rainfall and heat waves over Asia (Hsu et al., 2016, 2017; Chen and Zhai, 2017; Diao et al., 2018) and North America (Moon et al., 2013; Lee and Grotjahn, 2019). They also regulate tropical cyclone activities in Indian (Frank and Roundy, 2006), Pacific (Maloney and Hartmann, 2000; Diamond and Renwick, 2015; Zhao et al., 2015) and Atlantic (Klotzbach and Oliver, 2015) tropical oceans. They contribute to the intra-seasonal fluctuations of monsoons, including timing of its onset and termination during summer (Maloney and Shaman, 2008; Wheeler et al., 2009; Lee et al., 2013; Grimm, 2019) and its active/break phases (Pohl and Camberlin, 2006; Maloney and Shaman, 2008; Joseph et al., 2009; Lee et al., 2017).

ACCEPTED VERSION SUBJECT TO FINAL EDITING

References

Abram, N. J., Gagan, M. K., Cole, J. E., Hantoro, W. S., and Mudelsee, M. (2008). Recent intensification of tropical climate variability in the Indian Ocean. *Nat. Geosci.* 1, 849–853. doi:10.1038/ngeo357.

Abram, N. J., Gagan, M. K., Liu, Z., Hantoro, W. S., McCulloch, M. T., and Suwargadi, B. W. (2007). Seasonal characteristics of the Indian Ocean Dipole during the Holocene epoch. *Nature* 445, 299–302. doi:10.1038/nature05477.

Abram, N. J., Mulvaney, R., Vimeux, F., Phipps, S. J., Turner, J., and England, M. H. (2014). Evolution of the Southern Annular Mode during the past millennium. *Nat. Clim. Chang.* 4, 564–569. doi:10.1038/nclimate2235.

Abram, N. J., Wright, N. M., Ellis, B., Dixon, B. C., Wurtzel, J. B., England, M. H., et al. (2020). Coupling of Indo-Pacific climate variability over the last millennium. *Nature* 579, 385–392. doi:10.1038/s41586-020-2084-4.

Ait Brahim, Y., Wassenburg, J. A., Sha, L., Cruz, F. W., Deininger, M., Sifeddine, A., et al. (2019). North Atlantic Ice-Rafting, Ocean and Atmospheric Circulation During the Holocene: Insights From Western Mediterranean Speleothems. *Geophys. Res. Lett.* 46, 7614–7623. doi:10.1029/2019GL082405.

Ambaum, M. H. P., Hoskins, B. J., and Stephenson, D. B. (2001). Arctic Oscillation or North Atlantic Oscillation? *J. Clim.* 14, 3495–3507. doi:10.1175/1520-0442(2001)014<3495:AOONAO>2.0.CO;2.

Annamalai, H., Liu, P., and Xie, S.-P. (2005). Southwest Indian Ocean SST Variability: Its Local Effect and Remote Influence on Asian Monsoons*. *J. Clim.* 18, 4150–4167. doi:10.1175/JCLI3533.1.

Annamalai, H., and Sperber, K. R. (2005). Regional Heat Sources and the Active and Break Phases of Boreal Summer Intraseasonal (30–50 Day) Variability. *J. Atmos. Sci.* 62, 2726–2748. doi:10.1175/JAS3504.1.

Ashok, K., Behera, S. K., Rao, S. A., Weng, H., and Yamagata, T. (2007). El Niño Modoki and its possible teleconnection. *J. Geophys. Res. Ocean.* 112, C11007. doi:10.1029/2006JC003798.

Ashok, K., Chan, W.-L., Motoi, T., and Yamagata, T. (2004a). Decadal variability of the Indian Ocean dipole. *Geophys. Res. Lett.* 31, L24207. doi:10.1029/2004GL021345.

Ashok, K., Guan, Z., Saji, N. H., and Yamagata, T. (2004b). Individual and Combined Influences of ENSO and the Indian Ocean Dipole on the Indian Summer Monsoon. *J. Clim.* 17, 3141–3155. doi:10.1175/1520-0442(2004)017<3141:IACIOE>2.0.CO;2.

Ashok, K., Guan, Z., and Yamagata, T. (2001). Impact of the Indian Ocean dipole on the relationship between the Indian monsoon rainfall and ENSO. *Geophys. Res. Lett.* 28, 4499–4502. doi:10.1029/2001GL013294.

Ashok, K., Guan, Z., and Yamagata, T. (2003). Influence of the Indian Ocean Dipole on the Australian winter rainfall. *Geophys. Res. Lett.* 30, 1821. doi:10.1029/2003GL017926.

Ashok, K., and Saji, N. H. (2007). On the impacts of ENSO and Indian Ocean dipole events on sub-regional Indian summer monsoon rainfall. *Nat. Hazards* 42, 273–285. doi:10.1007/s11069-006-9091-0.

Baker, A., C. Hellstrom, J., Kelly, B. F. J., Mariethoz, G., and Trouet, V. (2015). A composite annual-resolution stalagmite record of North Atlantic climate over the last three millennia. *Sci. Rep.* 5, 10307. doi:10.1038/srep10307.

Baker, H. S., Woollings, T., Forest, C. E., and Allen, M. R. (2019). The Linear Sensitivity of the North Atlantic Oscillation and Eddy-Driven Jet to SSTs. *J. Clim.* 32, 6491–6511. doi:10.1175/JCLI-D-19-0038.1.

Baldwin, M. P., and Dunkerton, T. J. (1999). Propagation of the Arctic Oscillation from the stratosphere to the troposphere. *J. Geophys. Res. Atmos.* 104, 30937–30946. doi:10.1029/1999JD900445.

Banholzer, S., and Donner, S. The influence of different El Niño types on global average temperature. *Geophys. Res. Lett.* 41, 2093–2099. doi:10.1002/2014GL059520.

Barimalala, R., Bracco, A., and Kucharski, F. (2012). The representation of the South Tropical Atlantic teleconnection to the Indian Ocean in the AR4 coupled models. *Clim. Dyn.* 38, 1147–1166. doi:10.1007/s00382-011-1082-5.

Barimalala, R., Bracco, A., Kucharski, F., McCreary, J. P., and Crise, A. (2013). Arabian Sea ecosystem responses to the South Tropical Atlantic teleconnection. *J. Mar. Syst.* 117–118, 14–30. doi:10.1016/j.jmarsys.2013.03.002.

Barrier, N., Cassou, C., Deshayes, J., and Treguier, A.-M. (2014). Response of North Atlantic Ocean Circulation to Atmospheric Weather Regimes. *J. Phys. Oceanogr.* 44, 179–201. doi:10.1175/JPO-D-12-0217.1.

Barriopedro, D., Gallego, D., Alvarez-Castro, M. C., García-Herrera, R., Wheeler, D., Peña-Ortiz, C., et al. (2014). Witnessing North Atlantic westerlies variability from ships' logbooks (1685–2008). *Clim. Dyn.* 43, 939–955. doi:10.1007/s00382-013-1957-8.

Barrucand, M. G., Zitto, M. E., Piotrkowski, R., Canziani, P., and O'Neill, A. (2018). Historical SAM index time series: linear and nonlinear analysis. *Int. J. Climatol.* 38, e1091–e1106. doi:10.1002/joc.5435.

Behera, S. K., and Ratnam, J. V. (2018). Quasi-asymmetric response of the Indian summer monsoon rainfall to opposite phases of the IOD. *Sci. Rep.* 8, 123. doi:10.1038/s41598-017-18396-6.

ACCEPTED VERSION SUBJECT TO FINAL EDITING

Bellomo, K., Clement, A. C., Mauritsen, T., Rädel, G., and Stevens, B. (2015). The Influence of Cloud Feedbacks on Equatorial Atlantic Variability. *J. Clim.* 28, 2725–2744. doi:10.1175/JCLI-D-14-00495.1.

Benedict, J. J., and Randall, D. A. (2009). Structure of the Madden–Julian Oscillation in the Superparameterized CAM. *J. Atmos. Sci.* 66, 3277–3296. doi:10.1175/2009JAS3030.1.

Bernie, D. J., Guilyardi, E., Madec, G., Slingo, J. M., Woolnough, S. J., and Cole, J. (2008). Impact of resolving the diurnal cycle in an ocean–atmosphere GCM. Part 2: A diurnally coupled CGCM. *Clim. Dyn.* 31, 909–925. doi:10.1007/s00382-008-0429-z.

Biondi, F., Gershunov, A., and Cayan, D. R. (2001). North Pacific Decadal Climate Variability since 1661. *J. Clim.* 14, 5–10. doi:10.1175/1520-0442(2001)014<0005:NPDCVS>2.0.CO;2.

Blackport, R., and Screen, J. A. (2020). Weakened evidence for mid-latitude impacts of Arctic warming. *Nat. Clim. Chang.* 10, 1065–1066. doi:10.1038/s41558-020-00954-y.

Bladé, I., Liebmann, B., Fortuny, D., and van Oldenborgh, G. J. (2012). Observed and simulated impacts of the summer NAO in Europe: implications for projected drying in the Mediterranean region. *Clim. Dyn.* 39, 709–727. doi:10.1007/s00382-011-1195-x.

Boé, J., and Habets, F. (2014). Multi-decadal river flow variations in France. *Hydrol. Earth Syst. Sci.* 18, 691–708. doi:10.5194/hess-18-691-2014.

Boer, G. J., Smith, D. M., Cassou, C., Doblas-Reyes, F., Danabasoglu, G., Kirtman, B., et al. (2016). The Decadal Climate Prediction Project (DCPP) contribution to CMIP6. *Geosci. Model Dev.* 9, 3751–3777. doi:10.5194/gmd-9-3751-2016.

Bonnet, R., Boé, J., and Habets, F. (2020). Influence of multidecadal variability on high and low flows: the case of the Seine basin. *Hydrol. Earth Syst. Sci.* 24, 1611–1631. doi:10.5194/hess-24-1611-2020.

Brown, P. T., Li, W., and Xie, S.-P. (2015). Regions of significant influence on unforced global mean surface air temperature variability in climate models. *J. Geophys. Res. Atmos.* 120, 480–494. doi:10.1002/2014JD022576.

Buckley, B. M., Ummenhofer, C. C., D'Arrigo, R. D., Hansen, K. G., Truong, L. H., Le, C. L., et al. (2019). Interdecadal Pacific Oscillation reconstructed from trans-Pacific tree rings : 1350 – 2004 CE. *Clim. Dyn.* 53, 3181–3196. doi:10.1007/s00382-019-04694-4.

Burgman, R. J., and Jang, Y. (2015). Simulated U.S. drought response to interannual and decadal pacific SST variability. *J. Clim.* 28, 4688–4705. doi:10.1175/JCLI-D-14-00247.1.

Cabos, W., de la Vara, A., and Koseki, S. (2019). Tropical Atlantic Variability: Observations and Modeling. *Atmosphere (Basel).* 10, 502. doi:10.3390/atmos10090502.

Cai, W., Cowan, T., and Raupach, M. (2009). Positive Indian Ocean Dipole events precondition southeast Australia bushfires. *Geophys. Res. Lett.* 36, L19710. doi:10.1029/2009GL039902.

Cai, W., van Rensch, P., Cowan, T., and Sullivan, A. (2010). Asymmetry in ENSO Teleconnection with Regional Rainfall, Its Multidecadal Variability, and Impact. *J. Clim.* 23, 4944–4955. doi:10.1175/2010JCLI3501.1.

Cai, W., and Watterson, I. G. (2002). Modes of Interannual Variability of the Southern Hemisphere Circulation Simulated by the CSIRO Climate Model. *J. Clim.* 15, 1159–1174. doi:10.1175/1520-0442(2002)015<1159:MOIVOT>2.0.CO;2.

Cai, W., Wu, L., Lengaigne, M., Li, T., McGregor, S., Kug, J.-S., et al. (2019). Pantropical climate interactions. *Science (80-.).* 363, eaav4236. doi:10.1126/science.aav4236.

Capotondi, A., Wittenberg, A. T., Newman, M., Di Lorenzo, E., Yu, J.-Y., Braconnot, P., et al. (2015). Understanding ENSO Diversity. *Bull. Am. Meteorol. Soc.* 96, 921–938. doi:10.1175/BAMS-D-13-00117.1.

Cassou, C. (2008). Intraseasonal interaction between the Madden–Julian Oscillation and the North Atlantic Oscillation. *Nature* 455, 523–527. doi:10.1038/nature07286.

Cassou, C., Deser, C., and Alexander, M. A. (2007). Investigating the Impact of Reemerging Sea Surface Temperature Anomalies on the Winter Atmospheric Circulation over the North Atlantic. *J. Clim.* 20, 3510–3526. doi:10.1175/JCLI4202.1.

Cassou, C., Kushnir, Y., Hawkins, E., Pirani, A., Kucharski, F., Kang, I.-S., et al. (2018). Decadal Climate Variability and Predictability: Challenges and Opportunities. *Bull. Am. Meteorol. Soc.* 99, 479–490. doi:10.1175/BAMS-D-16-0286.1.

Cassou, C., Minvielle, M., Terray, L., and Périgaud, C. (2011). A statistical–dynamical scheme for reconstructing ocean forcing in the Atlantic. Part I: weather regimes as predictors for ocean surface variables. *Clim. Dyn.* 36, 19–39. doi:10.1007/s00382-010-0781-7.

Cassou, C., Terray, L., Hurrell, J. W., and Deser, C. (2004). North Atlantic Winter Climate Regimes: Spatial Asymmetry, Stationarity with Time, and Oceanic Forcing. *J. Clim.* 17, 1055–1068. doi:10.1175/1520-0442(2004)017<1055:NAWCRS>2.0.CO;2.

ACCEPTED VERSION SUBJECT TO FINAL EDITING

Cassou, C., Terray, L., and Phillips, A. S. (2005). Tropical Atlantic Influence on European Heat Waves. *J. Clim.* 18, 2805–2811. doi:10.1175/JCLI3506.1.

Castruccio, F. S., Ruprich-Robert, Y., Yeager, S. G., Danabasoglu, G., Msadek, R., and Delworth, T. L. (2018). Modulation of Arctic Sea Ice Loss by Atmospheric Teleconnections from Atlantic Multidecadal Variability. *J. Clim.* 32, 1419–1441. doi:10.1175/JCLI-D-18-0307.1.

Cattiaux, J., Vautard, R., Cassou, C., Yiou, P., Masson-Delmotte, V., and Codron, F. (2010). Winter 2010 in Europe: A cold extreme in a warming climate. *Geophys. Res. Lett.* 37, L20704. doi:10.1029/2010GL044613.

Cerrone, D., and Fusco, G. (2018). Low-frequency climate modes and Antarctic sea ice variations, 1982-2013. *J. Clim.* 31, 147–175. doi:10.1175/JCLI-D-17-0184.1.

Chang, P., Saravanan, R., Ji, L., and Hegerl, G. C. (2000). The Effect of Local Sea Surface Temperatures on Atmospheric Circulation over the Tropical Atlantic Sector. *J. Clim.* 13, 2195–2216. doi:10.1175/1520-0442(2000)013<2195:TEOLSS>2.0.CO;2.

Chen, X., and Wallace, J. M. (2015). ENSO-Like Variability: 1900–2013. *J. Clim.* 28, 9623–9641. doi:10.1175/JCLI-D-15-0322.1.

Chen, Y., and Zhai, P. (2017). Simultaneous modulations of precipitation and temperature extremes in Southern parts of China by the boreal summer intraseasonal oscillation. *Clim. Dyn.* 49, 3363–3381. doi:10.1007/s00382-016-3518-4.

Chiang, J. C. H., and Sobel, A. H. (2002). Tropical Tropospheric Temperature Variations Caused by ENSO and Their Influence on the Remote Tropical Climate. *J. Clim.* 15, 2616–2631. doi:10.1175/1520-0442(2002)015<2616:TTTVCB>2.0.CO;2.

Chiang, J. C. H., and Vimont, D. J. (2004). Analogous Pacific and Atlantic Meridional Modes of Tropical Atmosphere–Ocean Variability. *J. Clim.* 17, 4143–4158. doi:10.1175/JCLI4953.1.

Chisholm, R. A., Wijedasa, L. S., and Swinfield, T. (2016). The need for long-term remedies for Indonesia's forest fires. *Conserv. Biol.* 30, 5–6. doi:10.1111/cobi.12662.

Choi, K.-Y., Vecchi, G. A., and Wittenberg, A. T. (2015). Nonlinear Zonal Wind Response to ENSO in the CMIP5 Models: Roles of the Zonal and Meridional Shift of the ITCZ/SPCZ and the Simulated Climatological Precipitation. *J. Clim.* 28, 8556–8573. doi:10.1175/JCLI-D-15-0211.1.

Chowdary, J. S., Gnanaseelan, C., and Chakravorty, S. (2013). Impact of Northwest Pacific anticyclone on the Indian summer monsoon region. *Theor. Appl. Climatol.* 113, 329–336. doi:10.1007/s00704-012-0785-9.

Chowdary, J. S., Patekar, D., Srinivas, G., Gnanaseelan, C., and Parekh, A. (2019). Impact of the Indo-Western Pacific Ocean Capacitor mode on South Asian summer monsoon rainfall. *Clim. Dyn.* 53, 2327–2338. doi:10.1007/s00382-019-04850-w.

Chu, P. (2004). "ENSO and tropical cyclone activity," in *Hurricanes and typhoons: past, present and potential*, ed. K. B. Liu (New York, NY, USA: Columbia Press), 297–332.

Chylek, P., Dubey, M. K., Lesins, G., Li, J., and Hengartner, N. (2014). Imprint of the Atlantic multi-decadal oscillation and Pacific decadal oscillation on southwestern US climate: past, present, and future. *Clim. Dyn.* 43, 119–129. doi:10.1007/s00382-013-1933-3.

Chylek, P., Folland, C., Dijkstra, H., Lesins, G., and Dubey, M. (2011). Ice-core data evidence for a prominent near 20 year time-scale of the Atlantic Multidecadal Oscillation. *Geophys. Res. Lett.* 38, L13704. doi:10.1029/2011GL047501.

Ciasto, L. M., Simpkins, G. R., and England, M. H. (2015). Teleconnections between Tropical Pacific SST Anomalies and Extratropical Southern Hemisphere Climate. *J. Clim.* 28, 56–65. doi:10.1175/JCLI-D-14-00438.1.

Cid, A., Menéndez, M., Castanedo, S., Abascal, A. J., Méndez, F. J., and Medina, R. (2016). Long-term changes in the frequency, intensity and duration of extreme storm surge events in southern Europe. *Clim. Dyn.* 46, 1503–1516. doi:10.1007/s00382-015-2659-1.

Clem, K. R., Renwick, J. A., McGregor, J., and Fogt, R. L. (2016). The relative influence of ENSO and SAM on Antarctic Peninsula climate. *J. Geophys. Res. Atmos.* 121, 9324–9341. doi:10.1002/2016JD025305.Received.

Cohen, J., Screen, J. A., Furtado, J. C., Barlow, M., Whittleston, D., Coumou, D., et al. (2014). Recent Arctic amplification and extreme mid-latitude weather. *Nat. Geosci.* 7, 627–637. doi:10.1038/ngeo2234.

Cook, E. R., Kushnir, Y., Smerdon, J. E., Williams, A. P., Anchukaitis, K. J., and Wahl, E. R. (2019). A Euro-Mediterranean tree-ring reconstruction of the winter NAO index since 910 C.E. *Clim. Dyn.* 53, 1567–1580. doi:10.1007/s00382-019-04696-2.

Cornes, R. C., Jones, P. D., Briffa, K. R., and Osborn, T. J. (2013). Estimates of the North Atlantic Oscillation back to 1692 using a Paris-London westerly index. *Int. J. Climatol.* 33, 228–248. doi:10.1002/joc.3416.

Corti, S., Molteni, F., and Palmer, T. N. (1999). Signature of recent climate change in frequencies of natural atmospheric circulation regimes. *Nature* 398, 799–802. doi:10.1038/19745.

ACCEPTED VERSION SUBJECT TO FINAL EDITING

Crétat, J., Terray, P., Masson, S., Sooraj, K. P., and Roxy, M. K. (2017). Indian Ocean and Indian summer monsoon: relationships without ENSO in ocean–atmosphere coupled simulations. *Clim. Dyn.* 49, 1429–1448. doi:10.1007/s00382-016-3387-x.

Cropper, T., Hanna, E., Valente, M. A., and Jónsson, T. (2015). A daily Azores-Iceland North Atlantic Oscillation index back to 1850. *Geosci. Data J.* 2, 12–24. doi:10.1002/gdj3.23.

Crueger, T., Zinke, J., and Pfeiffer, M. (2009). Patterns of Pacific decadal variability recorded by Indian Ocean corals. *Int. J. Earth Sci.* 98, 41–52. doi:10.1007/s00531-008-0324-1.

D'Arrigo, R., and Ummenhofer, C. C. (2015). The climate of Myanmar: evidence for effects of the Pacific Decadal Oscillation. *Int. J. Climatol.* 35, 634–640. doi:10.1002/joc.3995.

D'Arrigo, R., Villalba, R., and Wiles, G. (2001). Tree-ring estimates of Pacific decadal climate variability. *Clim. Dyn.* 18, 219–224. doi:10.1007/s003820100177.

D'Arrigo, R., and Wilson, R. (2006). On the Asian expression of the PDO. *Int. J. Climatol.* 26, 1607–1617. doi:10.1002/joc.1326.

Dai, A. (2013). The influence of the inter-decadal Pacific oscillation on US precipitation during 1923–2010. *Clim. Dyn.* 41, 633–646. doi:10.1007/s00382-012-1446-5.

Dai, A., Fyfe, J. C., Xie, S. P., and Dai, X. (2015). Decadal modulation of global surface temperature by internal climate variability. *Nat. Clim. Chang.* 5, 555–559. doi:10.1038/nclimate2605.

Dätwyler, C., Neukom, R., Abram, N. J., Gallant, A. J. E., Grosjean, M., Jacques-Coper, M., et al. (2018). Teleconnection stationarity, variability and trends of the Southern Annular Mode (SAM) during the last millennium. *Clim. Dyn.* 51, 2321–2339. doi:10.1007/s00382-017-4015-0.

Davini, P., Cagnazzo, C., Neale, R., and Tribbia, J. (2012). Coupling between Greenland blocking and the North Atlantic Oscillation pattern. *Geophys. Res. Lett.* 39, L14701. doi:10.1029/2012GL052315.

Davini, P., Hardenberg, J. von, and Corti, S. (2015). Tropical origin for the impacts of the Atlantic Multidecadal Variability on the Euro-Atlantic climate. *Environ. Res. Lett.* 10, 094010. doi:10.1088/1748-9326/10/9/094010.

Day, J. J., Hargreaves, J. C., Annan, J. D., and Abe-Ouchi, A. (2012). Sources of multi-decadal variability in Arctic sea ice extent. *Environ. Res. Lett.* 7, 34011. doi:10.1088/1748-9326/7/3/034011.

Del Genio, A. D., Chen, Y., Kim, D., and Yao, M.-S. (2012). The MJO Transition from Shallow to Deep Convection in CloudSat /CALIPSO Data and GISS GCM Simulations. *J. Clim.* 25, 3755–3770. doi:10.1175/JCLI-D-11-00384.1.

Delaygue, G., Brönnimann, S., Jones, P. D., Blanchet, J., and Schwander, M. (2019). Reconstruction of Lamb weather type series back to the eighteenth century. *Clim. Dyn.* 52, 6131–6148. doi:10.1007/s00382-018-4506-7.

Delworth, T. L., and Zeng, F. (2016). The Impact of the North Atlantic Oscillation on Climate through Its Influence on the Atlantic Meridional Overturning Circulation. *J. Clim.* 29, 941–962. doi:10.1175/JCLI-D-15-0396.1.

DeMott, C. A., Klingaman, N. P., and Woolnough, S. J. (2015). Atmosphere-ocean coupled processes in the Madden-Julian oscillation. *Rev. Geophys.* 53, 1099–1154. doi:10.1002/2014RG000478.

Deng, K., Yang, S., Ting, M., Zhao, P., and Wang, Z. (2019). Dominant Modes of China Summer Heat Waves Driven by Global Sea Surface Temperature and Atmospheric Internal Variability. *J. Clim.* 32, 3761–3775. doi:10.1175/JCLI-D-18-0256.1.

Deppenmeier, A.-L., Haarsma, R. J., and Hazeleger, W. (2016). The Bjerknes feedback in the tropical Atlantic in CMIP5 models. *Clim. Dyn.* 47, 2691–2707. doi:10.1007/s00382-016-2992-z.

Deser, C. (2000). On the teleconnectivity of the "Arctic Oscillation." *Geophys. Res. Lett.* 27, 779–782. doi:10.1029/1999GL010945.

Deser, C., Alexander, M. A., Xie, S.-P., and Phillips, A. S. (2010). Sea Surface Temperature Variability: Patterns and Mechanisms. *Ann. Rev. Mar. Sci.* 2, 115–143. doi:10.1146/annurev-marine-120408-151453.

Deser, C., Simpson, I. R., McKinnon, K. A., and Phillips, A. S. (2017). The Northern Hemisphere Extratropical Atmospheric Circulation Response to ENSO: How Well Do We Know It and How Do We Evaluate Models Accordingly? *J. Clim.* 30, 5059–5082. doi:10.1175/JCLI-D-16-0844.1.

Deser, C., and Timlin, M. S. (1997). Atmosphere–Ocean Interaction on Weekly Timescales in the North Atlantic and Pacific. *J. Clim.* 10, 393–408. doi:10.1175/1520-0442(1997)010<0393:AOIOWT>2.0.CO;2.

Dezileau, L., Sabatier, P., Blanchemanche, P., Joly, B., Swingedouw, D., Cassou, C., et al. (2011). Intense storm activity during the Little Ice Age on the French Mediterranean coast. *Palaeogeogr. Palaeoclimatol. Palaeoecol.* 299, 289–297. doi:10.1016/j.palaeo.2010.11.009.

Di Lorenzo, E., Schneider, N., Cobb, K. M., Franks, P. J. S., Chhak, K., Miller, A. J., et al. (2008). North Pacific Gyre Oscillation links ocean climate and ecosystem change. *Geophys. Res. Lett.* 35, L08607. doi:10.1029/2007GL032838.

ACCEPTED VERSION SUBJECT TO FINAL EDITING

Diamond, H. J., and Renwick, J. A. (2015). The climatological relationship between tropical cyclones in the southwest pacific and the Madden-Julian Oscillation. *Int. J. Climatol.* 35, 676–686. doi:10.1002/joc.4012.

Diao, Y., Li, T., and Hsu, P. C. (2018). Influence of the Boreal Summer Intraseasonal Oscillation on Extreme Temperature Events in the Northern Hemisphere. *J. Meteorol. Res.* 32, 534–547. doi:10.1007/s13351-018-8031-8.

Ding, H., Keenlyside, N. S., and Latif, M. (2012). Impact of the Equatorial Atlantic on the El Niño Southern Oscillation. *Clim. Dyn.* 38, 1965–1972. doi:10.1007/s00382-011-1097-y.

Dippe, T., Greatbatch, R. J., and Ding, H. (2018). On the relationship between Atlantic Niño variability and ocean dynamics. *Clim. Dyn.* 51, 597–612. doi:10.1007/s00382-017-3943-z.

Domeisen, D. I. V. (2019). Estimating the Frequency of Sudden Stratospheric Warming Events From Surface Observations of the North Atlantic Oscillation. *J. Geophys. Res. Atmos.* 124, 3180–3194. doi:10.1029/2018JD030077.

Domeisen, D. I. V., Butler, A. H., Fröhlich, K., Bittner, M., Müller, W. A., and Baehr, J. (2015). Seasonal Predictability over Europe Arising from El Niño and Stratospheric Variability in the MPI-ESM Seasonal Prediction System. *J. Clim.* 28, 256–271. doi:10.1175/JCLI-D-14-00207.1.

Dong, B., Sutton, R. T., Woollings, T., and Hodges, K. (2013). Variability of the North Atlantic summer storm track: mechanisms and impacts on European climate. *Environ. Res. Lett.* 8, 034037. doi:10.1088/1748-9326/8/3/034037.

Dong, L., and McPhaden, M. J. (2017). Why has the relationship between Indian and Pacific Ocean decadal variability changed in recent decades? *J. Clim.* 30, 1971–1983. doi:10.1175/JCLI-D-16-0313.1.

Dong, L., and Zhou, T. (2014). The formation of the recent cooling in the eastern tropical Pacific Ocean and the associated climate impacts: A competition of global warming, IPO, and AMO. *J. Geophys. Res. Atmos.* 119, 11,272-11,287. doi:10.1002/2013JD021395.

Dong, L., Zhou, T., Dai, A., Song, F., Wu, B., and Chen, X. (2016). The Footprint of the Inter-decadal Pacific Oscillation in Indian Ocean Sea Surface Temperatures. *Sci. Rep.* 6, 21251. doi:10.1038/srep21251.

Douville, H., Peings, Y., and Saint-Martin, D. (2017). Snow-(N)AO relationship revisited over the whole twentieth century. *Geophys. Res. Lett.* 44, 569–577. doi:10.1002/2016GL071584.

Dréevillon, M., Cassou, C., and Terray, L. (2003). Model study of the North Atlantic region atmospheric response to autumn tropical Atlantic sea-surface-temperature anomalies. *Q. J. R. Meteorol. Soc.* 129, 2591–2611. doi:10.1256/qj.02.17.

Drouard, M., and Cassou, C. (2019). A Modeling- and Process-Oriented Study to Investigate the Projected Change of ENSO-Forced Wintertime Teleconnectivity in a Warmer World. *J. Clim.* 32, 8047–8068. doi:10.1175/JCLI-D-18-0803.1.

Drouard, M., Kornhuber, K., and Woollings, T. (2019). Disentangling Dynamic Contributions to Summer 2018 Anomalous Weather Over Europe. *Geophys. Res. Lett.* 46, 12537–12546. doi:10.1029/2019GL084601.

Drouard, M., Rivière, G., and Arbogast, P. (2015). The Link between the North Pacific Climate Variability and the North Atlantic Oscillation via Downstream Propagation of Synoptic Waves. *J. Clim.* 28, 3957–3976. doi:10.1175/JCLI-D-14-00552.1.

Du, Y., Xiao, J., and Yu, K. (2014). Tropical Indian Ocean Basin Mode recorded in coral oxygen isotope data from the Seychelles over the past 148 years. *Sci. China Earth Sci.* 57, 2597–2605. doi:10.1007/s11430-014-4956-7.

Du, Y., Yang, L., and Xie, S.-P. (2011). Tropical Indian Ocean Influence on Northwest Pacific Tropical Cyclones in Summer following Strong El Niño*. *J. Clim.* 24, 315–322. doi:10.1175/2010JCLI3890.1.

Dunstone, N. J., Smith, D. M., and Eade, R. (2011). Multi-year predictability of the tropical Atlantic atmosphere driven by the high latitude North Atlantic Ocean. *Geophys. Res. Lett.* 38, L14701. doi:10.1029/2011GL047949.

Durkee, J. D., Frye, J. D., Fuhrmann, C. M., Lacke, M. C., Jeong, H. G., and Mote, T. L. (2008). Effects of the North Atlantic Oscillation on precipitation-type frequency and distribution in the eastern United States. *Theor. Appl. Climatol.* 94, 51–65. doi:10.1007/s00704-007-0345-x.

Enfield, D. B., Mestas-Nuñez, A. M., and Trimble, P. J. (2001). The Atlantic Multidecadal Oscillation and its relation to rainfall and river flows in the continental U.S. *Geophys. Res. Lett.* 28, 2077–2080. doi:10.1029/2000GL012745.

Farneti, R., Molteni, F., and Kucharski, F. (2014). Pacific interdecadal variability driven by tropical–extratropical interactions. *Clim. Dyn.* 42, 3337–3355. doi:10.1007/s00382-013-1906-6.

Faust, J. C., Fabian, K., Milzer, G., Giraudeau, J., and Knies, J. (2016). Norwegian fjord sediments reveal NAO related winter temperature and precipitation changes of the past 2800 years. *Earth Planet. Sci. Lett.* 435, 84–93. doi:10.1016/j.epsl.2015.12.003.

Feldstein, S. B., and Franzke, C. (2006). Are the North Atlantic Oscillation and the Northern Annular Mode Distinguishable? *J. Atmos. Sci.* 63, 2915–2930. doi:10.1175/JAS3798.1.

ACCEPTED VERSION SUBJECT TO FINAL EDITING

Feldstein, S. B., and Franzke, C. L. E. (2017). "Atmospheric Teleconnection Patterns," in *Nonlinear and Stochastic Climate Dynamics*, eds. C. L. E. Franzke and T. J. OKane (Cambridge: Cambridge University Press), 54–104. doi:10.1017/9781316339251.004.

Ferranti, L., Palmer, T. N., Molteni, F., and Klinker, E. (1990). Tropical-Extratropical Interaction Associated with the 30–60 Day Oscillation and Its Impact on Medium and Extended Range Prediction. *J. Atmos. Sci.* 47, 2177–2199. doi:10.1175/1520-0469(1990)047<2177:TEIAWT>2.0.CO;2.

Ferreira, D., Marshall, J., Bitz, C. M., Solomon, S., and Plumb, A. (2015). Antarctic Ocean and Sea Ice Response to Ozone Depletion: A Two-Time-Scale Problem. *J. Clim.* 28, 1206–1226. doi:10.1175/JCLI-D-14-00313.1.

Fletcher, M.-S., Benson, A., Bowman, D. M. J. S., Gadd, P. S., Heijnis, H., Mariani, M., et al. (2018). Centennial-scale trends in the Southern Annular Mode revealed by hemisphere-wide fire and hydroclimatic trends over the past 2400 years. *Geology* 46, 363–366. doi:10.1130/G39661.1.

Fogt, R. L., Jones, J. M., and Renwick, J. (2012). Seasonal Zonal Asymmetries in the Southern Annular Mode and Their Impact on Regional Temperature Anomalies. *J. Clim.* 25, 6253–6270. doi:10.1175/JCLI-D-11-00474.1.

Folland, C. K., Knight, J., Linderholm, H. W., Fereday, D., Ineson, S., and Hurrell, J. W. (2009). The Summer North Atlantic Oscillation: Past, Present, and Future. *J. Clim.* 22, 1082–1103. doi:10.1175/2008JCLI2459.1.

Folland, C. K., Palmer, T. N., and Parker, D. E. (1986). Sahel rainfall and worldwide sea temperatures, 1901–85. *Nature* 320, 602–607. doi:10.1038/320602a0.

Folland, C. K., Renwick, J. A., Salinger, M. J., and Mullan, A. B. (2002). Relative influences of the Interdecadal Pacific Oscillation and ENSO on the South Pacific Convergence Zone. *Geophys. Res. Lett.* 29, 2–5. doi:10.1029/2001GL014201.

Foltz, G. R., Brandt, P., Richter, I., Rodríguez-Fonseca, B., Hernandez, F., Dengler, M., et al. (2019). The Tropical Atlantic Observing System. *Front. Mar. Sci.* 6, 206. doi:10.3389/fmars.2019.00206.

Foltz, G. R., and McPhaden, M. J. (2010). Interaction between the Atlantic meridional and Niño modes. *Geophys. Res. Lett.* 37, L18604. doi:https://doi.org/10.1029/2010GL044001.

Foltz, G. R., McPhaden, M. J., and Lumpkin, R. (2012). A Strong Atlantic Meridional Mode Event in 2009: The Role of Mixed Layer Dynamics*. *J. Clim.* 25, 363–380. doi:10.1175/JCLI-D-11-00150.1.

Frajka-Williams, E., Beaulieu, C., and Duchez, A. (2017). Emerging negative Atlantic Multidecadal Oscillation index in spite of warm subtropics. *Sci. Rep.* 7, 11224. doi:10.1038/s41598-017-11046-x.

Frank, W. M., and Roundy, P. E. (2006). The Role of Tropical Waves in Tropical Cyclogenesis. *Mon. Weather Rev.* 134, 2397–2417. doi:10.1175/MWR3204.1.

Frankignoul, C., Gastineau, G., and Kwon, Y.-O. (2017). Estimation of the SST Response to Anthropogenic and External Forcing and Its Impact on the Atlantic Multidecadal Oscillation and the Pacific Decadal Oscillation. *J. Clim.* 30, 9871–9895. doi:10.1175/JCLI-D-17-0009.1.

Franzke, C. L. E., Barbosa, S., Blender, R., Fredriksen, H., Laepple, T., Lambert, F., et al. (2020). The Structure of Climate Variability Across Scales. *Rev. Geophys.* 58, e2019RG000657. doi:10.1029/2019RG000657.

Friedman, A. R., Reverdin, G., Khodri, M., and Gastineau, G. (2017). A new record of Atlantic sea surface salinity from 1896 to 2013 reveals the signatures of climate variability and long-term trends. *Geophys. Res. Lett.* 44, 1866–1876. doi:10.1002/2017GL072582.

Fu, Z., Shi, L., Xie, F., and Piao, L. (2016). Nonlinear features of Northern Annular Mode variability. *Phys. A Stat. Mech. its Appl.* 449, 390–394. doi:10.1016/j.physa.2016.01.014.

Gadgil, S., Vinayachandran, P. N., Francis, P. A., and Gadgil, S. (2004). Extremes of the Indian summer monsoon rainfall, ENSO and equatorial Indian Ocean oscillation. *Geophys. Res. Lett.* 31, L12213. doi:10.1029/2004GL019733.

García-Serrano, J., and Haarsma, R. J. (2017). Non-annular, hemispheric signature of the winter North Atlantic Oscillation. *Clim. Dyn.* 48, 3659–3670. doi:10.1007/s00382-016-3292-3.

García-Serrano, J., Losada, T., and Rodríguez-Fonseca, B. (2011). Extratropical Atmospheric Response to the Atlantic Niño Decaying Phase. *J. Clim.* 24, 1613–1625. doi:10.1175/2010JCLI3640.1.

Garfinkel, C. I., and Schwartz, C. (2017). MJO-Related Tropical Convection Anomalies Lead to More Accurate Stratospheric Vortex Variability in Subseasonal Forecast Models. *Geophys. Res. Lett.* 44, 10054–10062. doi:10.1002/2017GL074470.

Gastineau, G., and Frankignoul, C. (2015). Influence of the North Atlantic SST Variability on the Atmospheric Circulation during the Twentieth Century. *J. Clim.* 28, 1396–1416. doi:10.1175/JCLI-D-14-00424.1.

Gedalof, Z., and Smith, D. J. (2001). Interdecadal climate variability and regime-scale shifts in Pacific North America. *Geophys. Res. Lett.* 28, 1515–1518. doi:10.1029/2000GL011779.

ACCEPTED VERSION SUBJECT TO FINAL EDITING

Gerber, E. P., Baldwin, M. P., Akiyoshi, H., Austin, J., Bekki, S., Braesicke, P., et al. (2010). Stratosphere-troposphere coupling and annular mode variability in chemistry-climate models. *J. Geophys. Res.* 115, D00M06. doi:10.1029/2009JD013770.

Gerber, E. P., and Martineau, P. (2018). Quantifying the variability of the annular modes: reanalysis uncertainty vs. sampling uncertainty. *Atmos. Chem. Phys.* 18, 17099–17117. doi:10.5194/acp-18-17099-2018.

Ghil, M., and Lucarini, V. (2020). The physics of climate variability and climate change. *Rev. Mod. Phys.* 92, 035002. doi:10.1103/RevModPhys.92.035002.

Giese, B. S., and Ray, S. (2011). El Niño variability in simple ocean data assimilation (SODA), 1871–2008. *J. Geophys. Res. Ocean.* 116, C02024. doi:10.1029/2010JC006695.

Gill, A. E. (1980). Some simple solutions for heat-induced tropical circulation. *Q. J. R. Meteorol. Soc.* 106, 447–462. doi:10.1002/qj.49710644905.

Gillett, N. P., Graf, H. F., and Osborn, T. J. (2003). "Climate change and the North Atlantic Oscillation," in *The North Atlantic Oscillation: Climatic Significance and Environmental Impact*, eds. J. W. Hurrell, Y. Kushnir, G. Ottersen, and M. Visbeck, 193–209. doi:10.1029/134GM09.

Gong, D., and Wang, S. (1999). Definition of Antarctic Oscillation index. *Geophys. Res. Lett.* 26, 459–462. doi:10.1029/1999GL900003.

Goodwin, I. D., and Harvey, N. (2008). Subtropical sea-level history from coral microatolls in the Southern Cook Islands, since 300 AD. *Mar. Geol.* 253, 14–25. doi:10.1016/j.margeo.2008.04.012.

Goodwin, I. D., van Ommen, T. D., Curran, M. A. J., and Mayewski, P. A. (2004). Mid latitude winter climate variability in the South Indian and southwest Pacific regions since 1300 AD. *Clim. Dyn.* 22, 783–794. doi:10.1007/s00382-004-0403-3.

Grant, A., and Walsh, K. J. E. (2001). Interdecadal variability in north-east Australian tropical cyclone formation. *Atmos. Sci. Lett.* 2, 9–17. doi:10.1006/asle.2001.0029.

Gray, L. J., Woollings, T. J., Andrews, M., and Knight, J. (2016). Eleven-year solar cycle signal in the NAO and Atlantic/European blocking. *Q. J. R. Meteorol. Soc.* 142, 1890–1903. doi:10.1002/qj.2782.

Gray, S. T., Graumlich, L. J., Betancourt, J. L., and Pederson, G. T. (2004). A tree-ring based reconstruction of the Atlantic Multidecadal Oscillation since 1567 A.D. *Geophys. Res. Lett.* 31, L12205. doi:10.1029/2004GL019932.

Green, B., Marshall, J., and Donohoe, A. (2017). Twentieth century correlations between extratropical SST variability and ITCZ shifts. *Geophys. Res. Lett.* 44, 9039–9047. doi:10.1002/2017GL075044.

Grimm, A. M. (2019). Madden–Julian Oscillation impacts on South American summer monsoon season: precipitation anomalies, extreme events, teleconnections, and role in the MJO cycle. *Clim. Dyn.* 53, 907–932. doi:10.1007/s00382-019-04622-6.

Haarsma, R. J., and Hazeleger, W. (2007). Extratropical Atmospheric Response to Equatorial Atlantic Cold Tongue Anomalies. *J. Clim.* 20, 2076–2091. doi:10.1175/JCLI4130.1.

Ham, Y.-G., Kug, J.-S., and Park, J.-Y. (2013a). Two distinct roles of Atlantic SSTs in ENSO variability: North Tropical Atlantic SST and Atlantic Niño. *Geophys. Res. Lett.* 40, 4012–4017. doi:10.1002/grl.50729.

Ham, Y.-G., Kug, J.-S., Park, J.-Y., and Jin, F.-F. (2013b). Sea surface temperature in the north tropical Atlantic as a trigger for El Niño/Southern Oscillation events. *Nat. Geosci.* 6, 112–116. doi:10.1038/ngeo1686.

Han, W., Meehl, G. A., Hu, A., Alexander, M. A., Yamagata, T., Yuan, D., et al. (2014). Intensification of decadal and multi-decadal sea level variability in the western tropical Pacific during recent decades. *Clim. Dyn.* 43, 1357–1379. doi:10.1007/s00382-013-1951-1.

Han, W., Meehl, G. A., Stammer, D., Hu, A., Hamlington, B., Kenigson, J., et al. (2017). Spatial Patterns of Sea Level Variability Associated with Natural Internal Climate Modes. *Surv. Geophys.* 38, 217–250. doi:10.1007/s10712-016-9386-y.

Hannachi, A., Straus, D. M., Franzke, C. L. E., Corti, S., and Woollings, T. (2017). Low-frequency nonlinearity and regime behavior in the Northern Hemisphere extratropical atmosphere. *Rev. Geophys.* 55, 199–234. doi:10.1002/2015RG000509.

Hannah, W. M., Maloney, E. D., and Pritchard, M. S. (2015). Consequences of systematic model drift in DYNAMO MJO hindcasts with SP-CAM and CAM5. *J. Adv. Model. Earth Syst.* 7, 1051–1074. doi:10.1002/2014MS000423.

Hastenrath, S., and Heller, L. (1977). Dynamics of climatic hazards in northeast Brazil. *Q. J. R. Meteorol. Soc.* 103, 77–92. doi:10.1002/qj.49710343505.

Henley, B. J. (2017). Pacific decadal climate variability: Indices, patterns and tropical-extratropical interactions. *Glob. Planet. Change* 155, 42–55. doi:10.1016/j.gloplacha.2017.06.004.

Henley, B. J., Gergis, J., Karoly, D. J., Power, S., Kennedy, J., and Folland, C. K. (2015). A Tripole Index for the Interdecadal Pacific Oscillation. *Clim. Dyn.* 45, 3077–3090. doi:10.1007/s00382-015-2525-1.

ACCEPTED VERSION SUBJECT TO FINAL EDITING

Henley, B. J., Meehl, G., Power, S. B., Folland, C. K., King, A. D., Brown, J. N., et al. (2017). Spatial and temporal agreement in climate model simulations of the Interdecadal Pacific Oscillation. *Environ. Res. Lett.* 12, 044011. doi:10.1088/1748-9326/aa5cc8.

Hermanson, L., Eade, R., Robinson, N. H., Dunstone, N. J., Andrews, M. B., Knight, J. R., et al. (2014). Forecast cooling of the Atlantic subpolar gyre and associated impacts. *Geophys. Res. Lett.* 41, 5167–5174. doi:10.1002/2014GL060420.

Hernández, A., Martin-Puertas, C., Moffa-Sánchez, P., Moreno-Chamarro, E., Ortega, P., Blockley, S., et al. (2020). Modes of climate variability: Synthesis and review of proxy-based reconstructions through the Holocene. *Earth-Science Rev.* 209, 103286. doi:10.1016/j.earscirev.2020.103286.

Hessl, A., Allen, K. J., Vance, T., Abram, N. J., and Saunders, K. M. (2017). Reconstructions of the southern annular mode (SAM) during the last millennium. *Prog. Phys. Geogr. Earth Environ.* 41, 834–849. doi:10.1177/0309133317743165.

Higgins, R. W., and Mo, K. C. (1997). Persistent North Pacific Circulation Anomalies and the Tropical Intraseasonal Oscillation. *J. Clim.* 10, 223–244. doi:10.1175/1520-0442(1997)010<0223:PNPCAA>2.0.CO;2.

Ho, M., Kiem, A. S., and Verdon-Kidd, D. C. (2012). The Southern Annular Mode: a comparison of indices. *Hydrol. Earth Syst. Sci.* 16, 967–982. doi:10.5194/hess-16-967-2012.

Hodgkins, G. A., Whitfield, P. H., Burn, D. H., Hannaford, J., Renard, B., Stahl, K., et al. (2017). Climate-driven variability in the occurrence of major floods across North America and Europe. *J. Hydrol.* 552, 704–717. doi:10.1016/j.jhydrol.2017.07.027.

Hohenegger, C., and Bretherton, C. S. (2011). Simulating deep convection with a shallow convection scheme. *Atmos. Chem. Phys.* 11, 10389–10406. doi:10.5194/acp-11-10389-2011.

Holbrook, N. J., Scannell, H. A., Sen Gupta, A., Benthuysen, J. A., Feng, M., Oliver, E. C. J., et al. (2019). A global assessment of marine heatwaves and their drivers. *Nat. Commun.* 10, 2624. doi:10.1038/s41467-019-10206-z.

Holz, A., Paritsis, J., Mundo, I. A., Veblen, T. T., Kitzberger, T., Williamson, G. J., et al. (2017). Southern Annular Mode drives multicentury wildfire activity in southern South America. *Proc. Natl. Acad. Sci.* 114, 9552–9557. doi:10.1073/pnas.1705168114.

Honda, M., and Nakamura, H. (2001). Interannual Seesaw between the Aleutian and Icelandic Lows. Part II: Its Significance in the Interannual Variability over the Wintertime Northern Hemisphere. *J. Clim.* 14, 4512–4529. doi:10.1175/1520-0442(2001)014<4512:ISBTAA>2.0.CO;2.

Horel, J. D., and Wallace, J. M. (1981). Planetary-Scale Atmospheric Phenomena Associated with the Southern Oscillation. *Mon. Weather Rev.* 109, 813–829. doi:10.1175/1520-0493(1981)109<0813:PSAPAW>2.0.CO;2.

Hoskins, B. J., and Karoly, D. J. (1981). The Steady Linear Response of a Spherical Atmosphere to Thermal and Orographic Forcing. *J. Atmos. Sci.* 38, 1179–1196. doi:10.1175/1520-0469(1981)038<1179:TSLROA>2.0.CO;2.

Hourdin, F., Grandpeix, J.-Y., Rio, C., Bony, S., Jam, A., Cheruy, F., et al. (2013). LMDZ5B: the atmospheric component of the IPSL climate model with revisited parameterizations for clouds and convection. *Clim. Dyn.* 40, 2193–2222. doi:10.1007/s00382-012-1343-y.

Hsu, P.-C., Lee, J.-Y., and Ha, K.-J. (2016). Influence of boreal summer intraseasonal oscillation on rainfall extremes in southern China. *Int. J. Climatol.* 36, 1403–1412. doi:10.1002/joc.4433.

Hsu, P.-C., Lee, J.-Y., Ha, K.-J., and Tsou, C.-H. (2017). Influences of boreal summer intraseasonal oscillation on heat waves in monsoon asia. *J. Clim.* 30, 7191–7211. doi:10.1175/JCLI-D-16-0505.1.

Hu, K., Huang, G., Qu, X., and Huang, R. (2012). The impact of Indian Ocean variability on high temperature extremes across the southern Yangtze River valley in late summer. *Adv. Atmos. Sci.* 29, 91–100. doi:10.1007/s00376-011-0209-2.

Huang, Y., Wu, B., Li, T., Zhou, T., and Liu, B. (2019). Interdecadal Indian Ocean Basin Mode Driven by Interdecadal Pacific Oscillation: A Season-Dependent Growth Mechanism. *J. Clim.* 32, 2057–2073. doi:10.1175/JCLI-D-18-0452.1.

Hung, M.-P., Lin, J.-L., Wang, W., Kim, D., Shinoda, T., and Weaver, S. J. (2013). MJO and Convectively Coupled Equatorial Waves Simulated by CMIP5 Climate Models. *J. Clim.* 26, 6185–6214. doi:10.1175/JCLI-D-12-00541.1.

Hurrell, J. W. (1995). Decadal Trends in the North Atlantic Oscillation: Regional Temperatures and Precipitation. *Science (80-.).* 269, 676–679. doi:10.1126/science.269.5224.676.

Hurrell, J. W., and Deser, C. (2009). North Atlantic climate variability: The role of the North Atlantic Oscillation. *J. Mar. Syst.* 78, 28–41. doi:10.1016/j.jmarsys.2008.11.026.

Hurrell, J. W., Kushnir, Y., Ottersen, G., and Visbeck, M. (2003). "An overview of the North Atlantic Oscillation," in *The North Atlantic Oscillation: Climatic Significance and Environmental Impact*, eds. J. W. Hurrell, Y. Kushnir, G. Ottersen, and M. Visbeck, 1–35. doi:10.1029/134GM01.

ACCEPTED VERSION SUBJECT TO FINAL EDITING

Ineson, S., Scaife, A. A., Knight, J. R., Manners, J. C., Dunstone, N. J., Gray, L. J., et al. (2011). Solar forcing of winter climate variability in the Northern Hemisphere. *Nat. Geosci.* 4, 753–757. doi:10.1038/ngeo1282.

Inness, P. M., Slingo, J. M., Guilyardi, E., and Cole, J. (2003). Simulation of the Madden–Julian Oscillation in a Coupled General Circulation Model. Part II: The Role of the Basic State. *J. Clim.* 16, 365–382. doi:10.1175/1520-0442(2003)016<0365:SOTMJO>2.0.CO;2.

Itoh, H. (2008). Reconsideration of the True versus Apparent Arctic Oscillation. *J. Clim.* 21, 2047–2062. doi:10.1175/2007JCLI2167.1.

Jerez, S., Trigo, R. M., Vicente-Serrano, S. M., Pozo-Vázquez, D., Lorente-Plazas, R., Lorenzo-Lacruz, J., et al. (2013). The Impact of the North Atlantic Oscillation on Renewable Energy Resources in Southwestern Europe. *J. Appl. Meteorol. Climatol.* 52, 2204–2225. doi:10.1175/JAMC-D-12-0257.1.

Jiang, X., Zhao, M., Maloney, E. D., and Waliser, D. E. (2016). Convective moisture adjustment time scale as a key factor in regulating model amplitude of the Madden-Julian Oscillation. *Geophys. Res. Lett.* 43, 10,412-10,419. doi:10.1002/2016GL070898.

Joly, M., and Voldoire, A. (2010). Role of the Gulf of Guinea in the inter-annual variability of the West African monsoon: what do we learn from CMIP3 coupled simulations? *Int. J. Climatol.* 30, 1843–1856. doi:10.1002/joc.2026.

Jones, J. M., Gille, S. T., Goosse, H., Abram, N. J., Canziani, P. O., Charman, D. J., et al. (2016). Assessing recent trends in high-latitude Southern Hemisphere surface climate. *Nat. Clim. Chang.* 6, 917–926. doi:10.1038/nclimate3103.

Jones, P. D., Jonsson, T., and Wheeler, D. (1997). Extension to the North Atlantic oscillation using early instrumental pressure observations from Gibraltar and south-west Iceland. *Int. J. Climatol.* 17, 1433–1450. doi:10.1002/(SICI)1097-0088(19971115)17:13<1433::AID-JOC203>3.0.CO;2-P.

Joseph, S., Sahai, A. K., and Goswami, B. N. (2009). Eastward propagating MJO during boreal summer and Indian monsoon droughts. *Clim. Dyn.* 32, 1139–1153. doi:10.1007/s00382-008-0412-8.

Jouanno, J., Hernandez, O., and Sanchez-Gomez, E. (2017). Equatorial Atlantic interannual variability and its relation to dynamic and thermodynamic processes. *Earth Syst. Dyn.* 8, 1061–1069. doi:10.5194/esd-8-1061-2017.

Kajtar, J. B., Santoso, A., England, M. H., and Cai, W. (2017). Tropical climate variability: interactions across the Pacific, Indian, and Atlantic Oceans. *Clim. Dyn.* 48, 2173–2190. doi:10.1007/s00382-016-3199-z.

Kamae, Y., Mei, W., Xie, S.-P., Naoi, M., and Ueda, H. (2017). Atmospheric Rivers over the Northwestern Pacific: Climatology and Interannual Variability. *J. Clim.* 30, 5605–5619. doi:10.1175/JCLI-D-16-0875.1.

Kang, S. M., Polvani, L. M., Fyfe, J. C., and Sigmond, M. (2011). Impact of Polar Ozone Depletion on Subtropical Precipitation. *Science (80-.).* 332, 951–954. doi:10.1126/science.1202131.

Karoly, D. J. (1989). Southern Hemisphere Circulation Features Associated with El Niño–Southern Oscillation Events. *J. Clim.* 2, 1239–1252. Available at: http://www.jstor.org/stable/26196374.

Karpechko, A. Y., Hitchcock, P., Peters, D. H. W., and Schneidereit, A. (2017). Predictability of downward propagation of major sudden stratospheric warmings. *Q. J. R. Meteorol. Soc.* 143, 1459–1470. doi:10.1002/qj.3017.

Kayanne, H., Iijima, H., Nakamura, N., McClanahan, T. R., Behera, S., and Yamagata, T. (2006). Indian Ocean Dipole index recorded in Kenyan coral annual density bands. *Geophys. Res. Lett.* 33, L19709. doi:10.1029/2006GL027168.

Keenlyside, N. S., Ding, H., and Latif, M. (2013). Potential of equatorial Atlantic variability to enhance El Niño prediction. *Geophys. Res. Lett.* 40, 2278–2283. doi:10.1002/grl.50362.

Keenlyside, N. S., and Latif, M. (2007). Understanding Equatorial Atlantic Interannual Variability. *J. Clim.* 20, 131–142. doi:10.1175/JCLI3992.1.

Kemball-Cook, S., and Wang, B. (2001). Equatorial Waves and Air–Sea Interaction in the Boreal Summer Intraseasonal Oscillation. *J. Clim.* 14, 2923–2942. doi:10.1175/1520-0442(2001)014<2923:EWAASI>2.0.CO;2.

Kennedy, J. J., Rayner, N. A., Atkinson, C. P., and Killick, R. E. (2019). An Ensemble Data Set of Sea Surface Temperature Change From 1850: The Met Office Hadley Centre HadSST.4.0.0.0 Data Set. *J. Geophys. Res. Atmos.* 124, 7719–7763. doi:10.1029/2018JD029867.

Kerr, R. A. (2000). A North Atlantic Climate Pacemaker for the Centuries. *Science (80-.).* 288, 1984–1985. doi:10.1126/science.288.5473.1984.

Kikuchi, K., Wang, B., and Kajikawa, Y. (2012). Bimodal representation of the tropical intraseasonal oscillation. *Clim. Dyn.* 38, 1989–2000. doi:10.1007/s00382-011-1159-1.

Kilbourne, K. H., Alexander, M. A., and Nye, J. A. (2014). A low latitude paleoclimate perspective on Atlantic multidecadal variability. *J. Mar. Syst.* 133, 4–13. doi:https://doi.org/10.1016/j.jmarsys.2013.09.004.

ACCEPTED VERSION SUBJECT TO FINAL EDITING

Kim, D., Sobel, A. H., Del Genio, A. D., Chen, Y., Camargo, S. J., Yao, M.-S., et al. (2012). The Tropical Subseasonal Variability Simulated in the NASA GISS General Circulation Model. *J. Clim.* 25, 4641–4659. doi:10.1175/JCLI-D-11-00447.1.

Kim, D., Sperber, K., Stern, W., Waliser, D., Kang, I.-S., Maloney, E., et al. (2009). Application of MJO Simulation Diagnostics to Climate Models. *J. Clim.* 22, 6413–6436. doi:10.1175/2009JCLI3063.1.

Kim, H.-M. (2017). The impact of the mean moisture bias on the key physics of MJO propagation in the ECMWF reforecast. *J. Geophys. Res. Atmos.* 122, 7772–7784. doi:10.1002/2017JD027005.

Kim, H., Vitart, F., and Waliser, D. E. (2018). Prediction of the Madden–Julian Oscillation: A Review. *J. Clim.* 31, 9425–9443. doi:10.1175/JCLI-D-18-0210.1.

King, A. D., Klingaman, N. P., Alexander, L. V, Donat, M. G., Jourdain, N. C., and Maher, P. (2014). Extreme Rainfall Variability in Australia: Patterns, Drivers, and Predictability. *J. Clim.* 27, 6035–6050. doi:10.1175/JCLI-D-13-00715.1.

Kitzberger, T., Brown, P. M., Heyerdahl, E. K., Swetnam, T. W., and Veblen, T. T. (2007). Contingent Pacific-Atlantic Ocean influence on multicentury wildfire synchrony over western North America. *Proc. Natl. Acad. Sci.* 104, 543–548. doi:10.1073/pnas.0606078104.

Klein, S. A., Soden, B. J., and Lau, N.-C. (1999). Remote Sea Surface Temperature Variations during ENSO: Evidence for a Tropical Atmospheric Bridge. *J. Clim.* 12, 917–932. doi:10.1175/1520-0442(1999)012<0917:RSSTVD>2.0.CO;2.

Klotzbach, P. J., and Oliver, E. C. J. (2015). Modulation of Atlantic Basin Tropical Cyclone Activity by the Madden–Julian Oscillation (MJO) from 1905 to 2011. *J. Clim.* 28, 204–217. doi:10.1175/JCLI-D-14-00509.1.

Knudsen, M. F., Seidenkrantz, M.-S., Jacobsen, B. H., and Kuijpers, A. (2011). Tracking the Atlantic Multidecadal Oscillation through the last 8,000 years. *Nat. Commun.* 2, 178. doi:10.1038/ncomms1186.

Kosaka, Y., Xie, S.-P., Lau, N.-C., and Vecchi, G. A. (2013). Origin of seasonal predictability for summer climate over the Northwestern Pacific. *Proc. Natl. Acad. Sci. U. S. A.* 110, 7574–7579. doi:10.1073/pnas.1215582110.

Kostov, Y., Marshall, J., Hausmann, U., Armour, K. C., Ferreira, D., and Holland, M. M. (2017). Fast and slow responses of Southern Ocean sea surface temperature to SAM in coupled climate models. *Clim. Dyn.* 48, 1595–1609. doi:10.1007/s00382-016-3162-z.

Kucharski, F., Bracco, A., Yoo, J. H., and Molteni, F. (2007). Low-Frequency Variability of the Indian Monsoon–ENSO Relationship and the Tropical Atlantic: The "Weakening" of the 1980s and 1990s. *J. Clim.* 20, 4255–4266. doi:10.1175/JCLI4254.1.

Kucharski, F., Bracco, A., Yoo, J. H., and Molteni, F. (2008). Atlantic forced component of the Indian monsoon interannual variability. *Geophys. Res. Lett.* 35, L04706. doi:10.1029/2007GL033037.

Kucharski, F., Ikram, F., Molteni, F., Farneti, R., Kang, I.-S., No, H.-H., et al. (2016). Atlantic forcing of Pacific decadal variability. *Clim. Dyn.* 46, 2337–2351. doi:10.1007/s00382-015-2705-z.

Kucharski, F., and Joshi, M. K. (2017). Influence of tropical South Atlantic sea-surface temperatures on the Indian summer monsoon in CMIP5 models. *Q. J. R. Meteorol. Soc.* 143, 1351–1363. doi:10.1002/qj.3009.

Kug, J.-S., and Ham, Y.-G. (2011). Are there two types of La Nina? *Geophys. Res. Lett.* 38, L16704. doi:10.1029/2011GL048237.

Kuleshov, Y., Qi, L., Fawcett, R., and Jones, D. (2008). On tropical cyclone activity in the Southern Hemisphere: Trends and the ENSO connection. *Geophys. Res. Lett.* 35. doi:10.1029/2007GL032983.

L'Heureux, M. L., and Higgins, R. W. (2008). Boreal Winter Links between the Madden–Julian Oscillation and the Arctic Oscillation. *J. Clim.* 21, 3040–3050. doi:10.1175/2007JCLI1955.1.

L'Heureux, M. L., Lee, S., and Lyon, B. (2013). Recent multidecadal strengthening of the Walker circulation across the tropical Pacific. *Nat. Clim. Chang.* 3, 571–576. doi:10.1038/nclimate1840.

L'Heureux, M. L., Takahashi, K., Watkins, A. B., Barnston, A. G., Becker, E. J., Di Liberto, T. E., et al. (2017). Observing and Predicting the 2015/16 El Niño. *Bull. Am. Meteorol. Soc.* 98, 1363–1382. doi:10.1175/BAMS-D-16-0009.1.

Lapointe, F., Bradley, R. S., Francus, P., Balascio, N. L., Abbott, M. B., Stoner, J. S., et al. (2020). Annually resolved Atlantic sea surface temperature variability over the past 2,900 y. *Proc. Natl. Acad. Sci.*, 202014166. doi:10.1073/pnas.2014166117.

Latif, M., and Grötzner, A. (2000). The equatorial Atlantic oscillation and its response to ENSO. *Clim. Dyn.* 16, 213–218. doi:10.1007/s003820050014.

Lau, N.-C., and Nath, M. J. (2000). Impact of ENSO on the Variability of the Asian–Australian Monsoons as Simulated in GCM Experiments. *J. Clim.* 13, 4287–4309. doi:10.1175/1520-0442(2000)013<4287:IOEOTV>2.0.CO;2.

Lau, N.-C., and Nath, M. J. (2003). Atmosphere–Ocean Variations in the Indo-Pacific Sector during ENSO Episodes. *J. Clim.* 16, 3–20. doi:10.1175/1520-0442(2003)016<0003:AOVITI>2.0.CO;2.

ACCEPTED VERSION SUBJECT TO FINAL EDITING

Lau, W. K. M., Waliser, D. E., and Tian, B. (2012). "Chemical and biological impacts," in *Intraseasonal Variability in the Atmosphere-Ocean Climate System* (Berlin, Heidelberg: Springer Berlin Heidelberg), 569–585. doi:10.1007/978-3-642-13914-7_18.

Le Mouël, J., Lopes, F., and Courtillot, V. (2019). A Solar Signature in Many Climate Indices. *J. Geophys. Res. Atmos.* 124, 2600–2619. doi:10.1029/2018JD028939.

Lee, J.-Y., Kwon, M. H., Yun, K.-S., Min, S.-K., Park, I.-H., Ham, Y.-G., et al. (2017). The long-term variability of Changma in the East Asian summer monsoon system: A review and revisit. *Asia-Pacific J. Atmos. Sci.* 53, 257–272. doi:10.1007/s13143-017-0032-5.

Lee, J.-Y., Wang, B., Wheeler, M. C., Fu, X., Waliser, D. E., and Kang, I.-S. (2013). Real-time multivariate indices for the boreal summer intraseasonal oscillation over the Asian summer monsoon region. *Clim. Dyn.* 40, 493–509. doi:10.1007/s00382-012-1544-4.

Lee, Y.-Y., and Grotjahn, R. (2019). Evidence of Specific MJO Phase Occurrence with Summertime California Central Valley Extreme Hot Weather. *Adv. Atmos. Sci.* 36, 589–602. doi:10.1007/s00376-019-8167-1.

Lewis, S. C., and LeGrande, A. N. (2015). Stability of ENSO and its tropical Pacific teleconnections over the Last Millennium. *Clim. Past* 11, 1347–1360. doi:10.5194/cp-11-1347-2015.

Li, G., Ren, B., Yang, C., and Zheng, J. (2010a). Indices of El Niño and El Niño Modoki: An improved El Niño Modoki index. *Adv. Atmos. Sci.* 27, 1210–1220. doi:10.1007/s00376-010-9173-5.

Li, J., and Wang, J. X. L. (2003). A new North Atlantic Oscillation index and its variability. *Adv. Atmos. Sci.* 20, 661–676. doi:10.1007/BF02915394.

Li, K.-F., Tian, B., Waliser, D. E., and Yung, Y. L. (2010b). Tropical mid-tropospheric CO2 variability driven by the Madden-Julian oscillation. *Proc. Natl. Acad. Sci.* 107, 19171–19175. doi:10.1073/pnas.1008222107.

Li, T., Liu, P., Fu, X., Wang, B., and Meehl, G. A. (2006). Spatiotemporal Structures and Mechanisms of the Tropospheric Biennial Oscillation in the Indo-Pacific Warm Ocean Regions*. *J. Clim.* 19, 3070–3087. doi:10.1175/JCLI3736.1.

Li, W., Li, L., and Deng, Y. (2015). Impact of the Interdecadal Pacific Oscillation on Tropical Cyclone Activity in the North Atlantic and Eastern North Pacific. *Sci. Rep.* 5, 12358. doi:10.1038/srep12358.

Li, Z., Zhang, W., Jin, F.-F., Stuecker, M. F., Sun, C., Levine, A. F. Z., et al. (2020). A robust relationship between multidecadal global warming rate variations and the Atlantic Multidecadal Variability. *Clim. Dyn.* 55, 1945–1959. doi:10.1007/s00382-020-05362-8.

Lim, E.-P., Hendon, H. H., Boschat, G., Hudson, D., Thompson, D. W. J., Dowdy, A. J., et al. (2019). Australian hot and dry extremes induced by weakenings of the stratospheric polar vortex. *Nat. Geosci.* 12, 896–901. doi:10.1038/s41561-019-0456-x.

Lin, H., Brunet, G., and Derome, J. (2009). An Observed Connection between the North Atlantic Oscillation and the Madden–Julian Oscillation. *J. Clim.* 22, 364–380. doi:10.1175/2008JCLI2515.1.

Lin, J.-L., Kiladis, G. N., Mapes, B. E., Weickmann, K. M., Sperber, K. R., Lin, W., et al. (2006). Tropical Intraseasonal Variability in 14 IPCC AR4 Climate Models. Part I: Convective Signals. *J. Clim.* 19, 2665–2690. doi:10.1175/JCLI3735.1.

Linderholm, H. W., Folland, C. K., and Walther, A. (2009). A multicentury perspective on the summer North Atlantic Oscillation (SNAO) and drought in the eastern Atlantic Region. *J. Quat. Sci.* 24, 415–425. doi:10.1002/jqs.1261.

Linderholm, H. W., Ou, T., Jeong, J.-H., Folland, C. K., Gong, D., Liu, H., et al. (2011). Interannual teleconnections between the summer North Atlantic Oscillation and the East Asian summer monsoon. *J. Geophys. Res.* 116, D13107. doi:10.1029/2010JD015235.

Linsley, B. K., Wu, H. C., Dassié, E. P., and Schrag, D. P. (2015). Decadal changes in South Pacific sea surface temperatures and the relationship to the Pacific decadal oscillation and upper ocean heat content. *Geophys. Res. Lett.* 42, 2358–2366. doi:10.1002/2015GL063045.

Liu, C., Tian, B., Li, K.-F., Manney, G. L., Livesey, N. J., Yung, Y. L., et al. (2014). Northern Hemisphere mid-winter vortex-displacement and vortex-split stratospheric sudden warmings: Influence of the Madden-Julian Oscillation and Quasi-Biennial Oscillation. *J. Geophys. Res. Atmos.* 119, 12,599-12,620. doi:10.1002/2014JD021876.

Liu, K. S., and Chan, J. C. L. (2008). Interdecadal Variability of Western North Pacific Tropical Cyclone Tracks. *J. Clim.* 21, 4464–4476. doi:10.1175/2008JCLI2207.1.

Liu, T., Li, J., Li, Y., Zhao, S., Zheng, F., Zheng, J., et al. (2018). Influence of the May Southern annular mode on the South China Sea summer monsoon. *Clim. Dyn.* 51, 4095–4107. doi:10.1007/s00382-017-3753-3.

Liu, Z., and Di Lorenzo, E. (2018). Mechanisms and Predictability of Pacific Decadal Variability. *Curr. Clim. Chang. Reports* 4, 128–144. doi:10.1007/s40641-018-0090-5.

Lorenz, D. J., and Hartmann, D. L. (2003). Eddy–Zonal Flow Feedback in the Northern Hemisphere Winter. *J. Clim.* 16, 1212–1227. doi:10.1175/1520-0442(2003)16<1212:EFFITN>2.0.CO;2.

ACCEPTED VERSION SUBJECT TO FINAL EDITING

Losada, T., Rodríguez-Fonseca, B., Janicot, S., Gervois, S., Chauvin, F., and Ruti, P. (2010). A multi-model approach to the Atlantic Equatorial mode: impact on the West African monsoon. *Clim. Dyn.* 35, 29–43. doi:10.1007/s00382-009-0625-5.

Losada, T., Rodríguez-Fonseca, B., and Kucharski, F. (2012). Tropical influence on the summer Mediterranean climate. *Atmos. Sci. Lett.* 13, 36–42. doi:10.1002/asl.359.

Lu, Z., Liu, Z., Zhu, J., and Cobb, K. M. (2018). A Review of Paleo El Niño-Southern Oscillation. *Atmosphere (Basel).* 9, 130. doi:10.3390/atmos9040130.

Lübbecke, J. F., Burls, N. J., Reason, C. J. C., and McPhaden, M. J. (2014). Variability in the South Atlantic Anticyclone and the Atlantic Niño Mode. *J. Clim.* 27, 8135–8150. doi:10.1175/JCLI-D-14-00202.1.

Lübbecke, J. F., Rodríguez-Fonseca, B., Richter, I., Martín-Rey, M., Losada, T., Polo, I., et al. (2018). Equatorial Atlantic variability-Modes, mechanisms, and global teleconnections. *Wiley Interdiscip. Rev. Clim. Chang.* 9, e527. doi:10.1002/wcc.527.

Lukens, K. E., Feldstein, S. B., Yoo, C., and Lee, S. (2017). The dynamics of the extratropical response to Madden-Julian Oscillation convection. *Q. J. R. Meteorol. Soc.* 143, 1095–1106. doi:10.1002/qj.2993.

Luo, J.-J., Sasaki, W., and Masumoto, Y. (2012). Indian Ocean warming modulates Pacific climate change. *Proc. Natl. Acad. Sci.* 109, 18701–18706. doi:10.1073/pnas.1210239109.

Luterbacher, J. (2001). Extending North Atlantic Oscillation reconstructions back to 1500. *Atmos. Sci. Lett.* 2, 114–124. doi:10.1006/asle.2001.0044.

MacDonald, G. M., and Case, R. A. (2005). Variations in the Pacific Decadal Oscillation over the past millennium. *Geophys. Res. Lett.* 32, L08703. doi:10.1029/2005GL022478.

Madden, R. A. (1986). Seasonal Variations of the 40-50 Day Oscillation in the Tropics. *J. Atmos. Sci.* 43, 3138–3158. doi:10.1175/1520-0469(1986)043<3138:SVOTDO>2.0.CO;2.

Madden, R. A., and Julian, P. R. (1994). Observations of the 40–50-Day Tropical Oscillation—A Review. *Mon. Weather Rev.* 122, 814–837. doi:10.1175/1520-0493(1994)122<0814:OOTDTO>2.0.CO;2.

Maloney, E. D., and Hartmann, D. L. (2000). Modulation of Eastern North Pacific Hurricanes by the Madden–Julian Oscillation. *J. Clim.* 13, 1451–1460. doi:10.1175/1520-0442(2000)013<1451:MOENPH>2.0.CO;2.

Maloney, E. D., and Shaman, J. (2008). Intraseasonal Variability of the West African Monsoon and Atlantic ITCZ. *J. Clim.* 21, 2898–2918. doi:10.1175/2007JCLI1999.1.

Manatsa, D., Morioka, Y., Behera, S. K., Yamagata, T., and Matarira, C. H. (2013). Link between Antarctic ozone depletion and summer warming over southern Africa. *Nat. Geosci.* 6, 934–939. doi:10.1038/ngeo1968.

Manatsa, D., Mudavanhu, C., Mushore, T. D., and Mavhura, E. (2016). Linking major shifts in East Africa "short rains" to the Southern Annular Mode. *Int. J. Climatol.* 36, 1590–1599. doi:10.1002/joc.4443.

Mann, M. E., Steinman, B. A., and Miller, S. K. (2020). Absence of internal multidecadal and interdecadal oscillations in climate model simulations. *Nat. Commun.* 11, 49. doi:10.1038/s41467-019-13823-w.

Mann, M. E., Zhang, Z., Rutherford, S., Bradley, R. S., Hughes, M. K., Shindell, D., et al. (2009). Global Signatures and Dynamical Origins of the Little Ice Age and Medieval Climate Anomaly. *Science (80-.).* 326, 1256–1260. doi:10.1126/science.1177303.

Mantua, N. J., and Hare, S. R. (2002). The Pacific Decadal Oscillation. *J. Oceanogr.* 58, 35–44. doi:10.1023/A:1015820616384.

Mantua, N. J., Hare, S. R., Zhang, Y., Wallace, J. M., and Francis, R. C. (1997). A Pacific Interdecadal Climate Oscillation with Impacts on Salmon Production*. *Bull. Am. Meteorol. Soc.* 78, 1069–1080. doi:10.1175/1520-0477(1997)078<1069:APICOW>2.0.CO;2.

Mapes, B., and Neale, R. (2011). Parameterizing Convective Organization to Escape the Entrainment Dilemma. *J. Adv. Model. Earth Syst.* 3, M06004. doi:10.1029/2011MS000042.

Mariani, M., and Fletcher, M. S. (2016). The Southern Annular Mode determines interannual and centennial-scale fire activity in temperate southwest Tasmania, Australia. *Geophys. Res. Lett.* 43, 1702–1709. doi:10.1002/2016GL068082.

Marshall, G. J. (2003). Trends in the Southern Annular Mode from Observations and Reanalyses. *J. Clim.* 16, 4134–4143.

Marshall, G. J., Orr, A., and Turner, J. (2013). A Predominant Reversal in the Relationship between the SAM and East Antarctic Temperatures during the Twenty-First Century. *J. Clim.* 26, 5196–5204. doi:10.1175/JCLI-D-12-00671.1.

Marshall, G. J., Thompson, D. W. J., and Broeke, M. R. (2017). The Signature of Southern Hemisphere Atmospheric Circulation Patterns in Antarctic Precipitation. *Geophys. Res. Lett.* 44, 11,580-11,589. doi:10.1002/2017GL075998.

ACCEPTED VERSION SUBJECT TO FINAL EDITING

Martín-Rey, M., Polo, I., Rodríguez-Fonseca, B., Losada, T., and Lazar, A. (2018). Is There Evidence of Changes in Tropical Atlantic Variability Modes under AMO Phases in the Observational Record? *J. Clim.* 31, 515–536. doi:10.1175/JCLI-D-16-0459.1.

Martín-Rey, M., Rodríguez-Fonseca, B., Polo, I., and Kucharski, F. (2014). On the Atlantic–Pacific Niños connection: a multidecadal modulated mode. *Clim. Dyn.* 43, 3163–3178. doi:10.1007/s00382-014-2305-3.

Martín-Rey, M., Rodríguez-Fonseca, B., and Polo, I. (2015). Atlantic opportunities for ENSO prediction. *Geophys. Res. Lett.* 42, 6802–6810. doi:10.1002/2015GL065062.

Martin, E. R., and Thorncroft, C. D. (2014). The impact of the AMO on the West African monsoon annual cycle. *Q. J. R. Meteorol. Soc.* 140, 31–46. doi:10.1002/qj.2107.

Matthews, A. J., Hoskins, B. J., and Masutani, M. (2004). The global response to tropical heating in the Madden–Julian oscillation during the northern winter. *Q. J. R. Meteorol. Soc.* 130, 1991–2011. doi:10.1256/qj.02.123.

Matthews, T., Murphy, C., Wilby, R. L., and Harrigan, S. (2014). Stormiest winter on record for Ireland and UK. *Nat. Clim. Chang.* 4, 738–740. doi:10.1038/nclimate2336.

Mauri, A., Davis, B. A. S., Collins, P. M., and Kaplan, J. O. (2014). The influence of atmospheric circulation on the mid-Holocene climate of Europe: A data-model comparison. *Clim. Past* 10, 1925–1938. doi:10.5194/cp-10-1925-2014.

McGee, D., Donohoe, A., Marshall, J., and Ferreira, D. (2014). Changes in ITCZ location and cross-equatorial heat transport at the Last Glacial Maximum, Heinrich Stadial 1, and the mid-Holocene. *Earth Planet. Sci. Lett.* 390, 69–79. doi:https://doi.org/10.1016/j.epsl.2013.12.043.

McGregor, S., Timmermann, A., Stuecker, M. F., England, M. H., Merrifield, M., Jin, F.-F., et al. (2014). Recent Walker circulation strengthening and Pacific cooling amplified by Atlantic warming. *Nat. Clim. Chang.* 4, 888–892. doi:10.1038/nclimate2330.

McGregor, S., Timmermann, A., and Timm, O. (2010). A unified proxy for ENSO and PDO variability since 1650. *Clim. Past* 6, 1–17. doi:10.5194/cp-6-1-2010.

Meehl, G. A., Arblaster, J. M., and Loschnigg, J. (2003). Coupled Ocean–Atmosphere Dynamical Processes in the Tropical Indian and Pacific Oceans and the TBO. *J. Clim.* 16, 2138–2158. doi:10.1175/2767.1.

Meehl, G. A., and Hu, A. (2006). Megadroughts in the Indian Monsoon Region and Southwest North America and a Mechanism for Associated Multidecadal Pacific Sea Surface Temperature Anomalies. *J. Clim.* 19, 1605–1623. doi:10.1175/JCLI3675.1.

Meehl, G. A., and Teng, H. (2014). Regional precipitation simulations for the mid-1970s shift and early-2000s hiatus. *Geophys. Res. Lett.* 41, 7658–7665. doi:10.1002/2014GL061778.

Mellado-Cano, J., Barriopedro, D., García-Herrera, R., Trigo, R. M., and Hernández, A. (2019). Examining the North Atlantic Oscillation, East Atlantic pattern and jet variability since 1685. *J. Clim.* 32, 6285–6298. doi:10.1175/JCLI-D-18-0135.1.

Meyers, G., McIntosh, P., Pigot, L., and Pook, M. (2007). The Years of El Niño, La Niña, and Interactions with the Tropical Indian Ocean. *J. Clim.* 20, 2872–2880. doi:10.1175/JCLI4152.1.

Michel, S., Swingedouw, D., Chavent, M., Ortega, P., Mignot, J., and Khodri, M. (2020). Reconstructing climatic modes of variability from proxy records using ClimIndRec version 1.0. *Geosci. Model Dev.* 13, 841–858. doi:10.5194/gmd-13-841-2020.

Miyakawa, T., Satoh, M., Miura, H., Tomita, H., Yashiro, H., Noda, A. T., et al. (2014). Madden–Julian Oscillation prediction skill of a new-generation global model demonstrated using a supercomputer. *Nat. Commun.* 5, 3769. doi:10.1038/ncomms4769.

Mizuta, R., Yoshimura, H., Murakami, H., Matsueda, M., Endo, H., Ose, T., et al. (2012). Climate Simulations Using MRI-AGCM3.2 with 20-km Grid. *J. Meteorol. Soc. Japan* 90A, 233–258. doi:10.2151/jmsj.2012-A12.

Mochizuki, T., Kimoto, M., Watanabe, M., Chikamoto, Y., and Ishii, M. (2016). Interbasin effects of the Indian Ocean on Pacific decadal climate change. *Geophys. Res. Lett.* 43, 7168–7175. doi:10.1002/2016GL069940.

Mohino, E., Rodríguez-Fonseca, B., Losada, T., Gervois, S., Janicot, S., Bader, J., et al. (2011). Changes in the interannual SST-forced signals on West African rainfall. AGCM intercomparison. *Clim. Dyn.* 37, 1707–1725. doi:10.1007/s00382-011-1093-2.

Monks, S. A., Arnold, S. R., and Chipperfield, M. P. (2012). Evidence for El Niño-Southern Oscillation (ENSO) influence on Arctic CO interannual variability through biomass burning emissions. *Geophys. Res. Lett.* 39, L14804. doi:10.1029/2012GL052512.

Moon, J.-Y., Wang, B., Ha, K.-J., and Lee, J.-Y. (2013). Teleconnections associated with Northern Hemisphere summer monsoon intraseasonal oscillation. *Clim. Dyn.* 40, 2761–2774. doi:10.1007/s00382-012-1394-0.

Moore, G. W. K., Halfar, J., Majeed, H., Adey, W., and Kronz, A. (2017). Amplification of the Atlantic Multidecadal Oscillation associated with the onset of the industrial-era warming. *Sci. Rep.* 7, 40861. doi:10.1038/srep40861.

ACCEPTED VERSION SUBJECT TO FINAL EDITING

Moreno, P. I., Vilanova, I., Villa-Martínez, R., Dunbar, R. B., Mucciarone, D. A., Kaplan, M. R., et al. (2018). Onset and Evolution of Southern Annular Mode-Like Changes at Centennial Timescale. *Sci. Rep.* 8, 3458. doi:10.1038/s41598-018-21836-6.

Neelin, J. D., Battisti, D. S., Hirst, A. C., Jin, F.-F., Wakata, Y., Yamagata, T., et al. (1998). ENSO theory. *J. Geophys. Res. Ocean.* 103, 14261–14290. doi:10.1029/97JC03424.

Newman, M., Alexander, M. A., Ault, T. R., Cobb, K. M., Deser, C., Di Lorenzo, E., et al. (2016). The Pacific Decadal Oscillation, Revisited. *J. Clim.* 29, 4399–4427. doi:10.1175/JCLI-D-15-0508.1.

Nicolì, D., Bellucci, A., Iovino, D., Ruggieri, P., and Gualdi, S. (2020). The impact of the AMV on Eurasian summer hydrological cycle. *Sci. Rep.* 10, 14444. doi:10.1038/s41598-020-71464-2.

Nidheesh, A. G., Lengaigne, M., Vialard, J., Izumo, T., Unnikrishnan, A. S., and Cassou, C. (2017). Influence of ENSO on the Pacific decadal oscillation in CMIP models. *Clim. Dyn.* 49, 3309–3326. doi:10.1007/s00382-016-3514-8.

Niedermeyer, E. M., Sessions, A. L., Feakins, S. J., and Mohtadi, M. (2014). Hydroclimate of the western Indo-Pacific Warm Pool during the past 24,000 years. *Proc. Natl. Acad. Sci.* 111, 9402–9406. doi:10.1073/pnas.1323585111.

Nnamchi, H. C., Latif, M., Keenlyside, N. S., Kjellsson, J., and Richter, I. (2021). Diabatic heating governs the seasonality of the Atlantic Niño. *Nat. Commun.* 12, 376. doi:10.1038/s41467-020-20452-1.

Nnamchi, H. C., Li, J., Kucharski, F., Kang, I.-S., Keenlyside, N. S., Chang, P., et al. (2015). Thermodynamic controls of the Atlantic Niño. *Nat. Commun.* 6, 8895. doi:10.1038/ncomms9895.

Nobre, P., and Srukla, J. (1996). Variations of Sea Surface Temperature, Wind Stress, and Rainfall over the Tropical Atlantic and South America. *J. Clim.* 9, 2464–2479. doi:10.1175/1520-0442(1996)009<2464:VOSSTW>2.0.CO;2.

O'Reilly, C. H., Minobe, S., Kuwano-Yoshida, A., and Woollings, T. (2017). The Gulf Stream influence on wintertime North Atlantic jet variability. *Q. J. R. Meteorol. Soc.* 143, 173–183. doi:10.1002/qj.2907.

Olsen, J., Anderson, N. J., and Knudsen, M. F. (2012). Variability of the North Atlantic Oscillation over the past 5,200 years. *Nat. Geosci.* 5, 808–812. doi:10.1038/ngeo1589.

Ortega, P., Lehner, F., Swingedouw, D., Masson-Delmotte, V., Raible, C. C., Casado, M., et al. (2015). A model-tested North Atlantic Oscillation reconstruction for the past millennium. *Nature* 523, 71–74. doi:10.1038/nature14518.

Pan, Y. H., and Oort, A. H. (1983). Global Climate Variations Connected with Sea Surface Temperature Anomalies in the Eastern Equatorial Pacific Ocean for the 1958–73 Period. *Mon. Weather Rev.* 111, 1244–1258. doi:10.1175/1520-0493(1983)111<1244:GCVCWS>2.0.CO;2.

Patricola, C. M., Saravanan, R., and Chang, P. (2014). The Impact of the El Niño–Southern Oscillation and Atlantic Meridional Mode on Seasonal Atlantic Tropical Cyclone Activity. *J. Clim.* 27, 5311–5328. doi:10.1175/JCLI-D-13-00687.1.

Peings, Y., and Magnusdottir, G. (2014). Forcing of the wintertime atmospheric circulation by the multidecadal fluctuations of the North Atlantic ocean. *Environ. Res. Lett.* 9, 034018. doi:10.1088/1748-9326/9/3/034018.

Peng, S., Robinson, W. A., Li, S., and Hoerling, M. P. (2005). Tropical Atlantic SST Forcing of Coupled North Atlantic Seasonal Responses. *J. Clim.* 18, 480–496. doi:10.1175/JCLI-3270.1.

Pepler, A. S. (2016). Seasonal climate summary southern hemisphere (summer 2015-16): strong El Niño begins to weaken. *J. South. Hemisph. Earth Syst. Sci.* 66, 361–379. doi:10.22499/3.6604.001.

Pepler, A., Timbal, B., Rakich, C., and Coutts-Smith, A. (2014). Indian Ocean Dipole Overrides ENSO's Influence on Cool Season Rainfall across the Eastern Seaboard of Australia. *J. Clim.* 27, 3816–3826. doi:10.1175/JCLI-D-13-00554.1.

Philander, S. G. (1990). El Niño, La Niña, and the southern oscillation, 293 pp. *San Diego, CA Acad.*

Philander, S. G. H. (1983). El Niño Southern Oscillation phenomena. *Nature* 302, 295–301. doi:10.1038/302295a0.

Pillai, P. A., Nair, R. C., and Vidhya, C. V (2019). Recent changes in the prominent modes of Indian Ocean dipole in response to the tropical Pacific Ocean SST patterns. *Theor. Appl. Climatol.* 138, 941–951. doi:10.1007/s00704-019-02875-z.

Pohl, B., and Camberlin, P. (2006). Influence of the Madden–Julian Oscillation on East African rainfall. I: Intraseasonal variability and regional dependency. *Q. J. R. Meteorol. Soc.* 132, 2521–2539. doi:10.1256/qj.05.104.

Polo, I., Lazar, A., Rodriguez-Fonseca, B., and Mignot, J. (2015). Growth and decay of the equatorial Atlantic SST mode by means of closed heat budget in a coupled general circulation model. *Front. Earth Sci.* 3, 37. doi:10.3389/feart.2015.00037.

Polo, I., Rodríguez-Fonseca, B., Losada, T., and García-Serrano, J. (2008). Tropical Atlantic Variability Modes (1979–2002). Part I: Time-Evolving SST Modes Related to West African Rainfall. *J. Clim.* 21, 6457–6475. doi:10.1175/2008JCLI2607.1.

ACCEPTED VERSION SUBJECT TO FINAL EDITING

Pottapinjara, V., Girishkumar, M. S., Ravichandran, M., and Murtugudde, R. (2014). Influence of the Atlantic zonal mode on monsoon depressions in the Bay of Bengal during boreal summer. *J. Geophys. Res. Atmos.* 119, 6456–6469. doi:10.1002/2014JD021494.

Pottapinjara, V., Girishkumar, M. S., Sivareddy, S., Ravichandran, M., and Murtugudde, R. (2016). Relation between the upper ocean heat content in the equatorial Atlantic during boreal spring and the Indian monsoon rainfall during June-September. *Int. J. Climatol.* 36, 2469–2480. doi:10.1002/joc.4506.

Power, S., Casey, T., Folland, C., Colman, A., and Mehta, V. (1999). Inter-decadal modulation of the impact of ENSO on Australia. *Clim. Dyn.* 15, 319–324. doi:10.1007/s003820050284.

Power, S., and Colman, R. (2006). Multi-year predictability in a coupled general circulation model. *Clim. Dyn.* 26, 247–272. doi:10.1007/s00382-005-0055-y.

Prabhu, A., Kripalani, R., Oh, J., and Preethi, B. (2017). Can the Southern annular mode influence the Korean summer monsoon rainfall? *Asia-Pacific J. Atmos. Sci.* 53, 217–228. doi:10.1007/s13143-017-0029-0.

Qiu, B., Schneider, N., and Chen, S. (2007). Coupled Decadal Variability in the North Pacific: An Observationally Constrained Idealized Model*. *J. Clim.* 20, 3602–3620. doi:10.1175/JCLI4190.1.

Ratnam, J. V, Behera, S. K., Masumoto, Y., and Yamagata, T. (2014). Remote Effects of El Niño and Modoki Events on the Austral Summer Precipitation of Southern Africa. *J. Clim.* 27, 3802–3815. doi:10.1175/JCLI-D-13-00431.1.

Raut, B. A., Jakob, C., and Reeder, M. J. (2014). Rainfall Changes over Southwestern Australia and Their Relationship to the Southern Annular Mode and ENSO. *J. Clim.* 27, 5801–5814. doi:10.1175/JCLI-D-13-00773.1.

Richter, I., Behera, S. K., Doi, T., Taguchi, B., Masumoto, Y., and Xie, S.-P. (2014). What controls equatorial Atlantic winds in boreal spring? *Clim. Dyn.* 43, 3091–3104. doi:10.1007/s00382-014-2170-0.

Richter, I., Behera, S. K., Masumoto, Y., Taguchi, B., Sasaki, H., and Yamagata, T. (2013). Multiple causes of interannual sea surface temperature variability in the equatorial Atlantic Ocean. *Nat. Geosci.* 6, 43–47. doi:10.1038/ngeo1660.

Rimbu, N., Lohmann, G., and Ionita, M. (2014). Interannual to multidecadal Euro-Atlantic blocking variability during winter and its relationship with extreme low temperatures in Europe. *J. Geophys. Res. Atmos.* 119, 13,621-13,636. doi:10.1002/2014JD021983.

Risbey, J. S., Pook, M. J., McIntosh, P. C., Wheeler, M. C., and Hendon, H. H. (2009). On the Remote Drivers of Rainfall Variability in Australia. *Mon. Weather Rev.* 137, 3233–3253. doi:10.1175/2009MWR2861.1.

Rivière, G., and Drouard, M. (2015). Understanding the contrasting North Atlantic Oscillation anomalies of the winters of 2010 and 2014. *Geophys. Res. Lett.* 42, 6868–6875. doi:10.1002/2015GL065493.

Rodrigues, R. R., Campos, E. J. D., and Haarsma, R. (2015). The Impact of ENSO on the South Atlantic Subtropical Dipole Mode. *J. Clim.* 28, 2691–2705. doi:10.1175/JCLI-D-14-00483.1.

Rodríguez-Fonseca, B., Polo, I., García-Serrano, J., Losada, T., Mohino, E., Mechoso, C. R., et al. (2009). Are Atlantic Niños enhancing Pacific ENSO events in recent decades? *Geophys. Res. Lett.* 36, L20705. doi:10.1029/2009GL040048.

Roxy, M. K., Dasgupta, P., McPhaden, M. J., Suematsu, T., Zhang, C., and Kim, D. (2019). Twofold expansion of the Indo-Pacific warm pool warps the MJO life cycle. *Nature* 575, 647–651. doi:10.1038/s41586-019-1764-4.

Ruiz-Barradas, A., Carton, J. A., and Nigam, S. (2000). Structure of Interannual-to-Decadal Climate Variability in the Tropical Atlantic Sector. *J. Clim.* 13, 3285–3297. doi:10.1175/1520-0442(2000)013<3285:SOITDC>2.0.CO;2.

Ruprich-Robert, Y., Msadek, R., Castruccio, F., Yeager, S., Delworth, T., and Danabasoglu, G. (2017). Assessing the Climate Impacts of the Observed Atlantic Multidecadal Variability Using the GFDL CM2.1 and NCAR CESM1 Global Coupled Models. *J. Clim.* 30, 2785–2810. doi:10.1175/JCLI-D-16-0127.1.

Sabeerali, C. T., Ajayamohan, R. S., and Rao, S. A. (2019). Loss of predictive skill of indian summer monsoon rainfall in NCEP CFSv2 due to misrepresentation of Atlantic zonal mode. *Clim. Dyn.* 52, 4599–4619. doi:10.1007/s00382-018-4390-1.

Saji, N. H., Goswami, B. N., Vinayachandran, P. N., and Yamagata, T. (1999). A dipole mode in the tropical Indian Ocean. *Nature* 401, 360–363. doi:10.1038/43854.

Saji, N. H., Xie, S.-P., and Yamagata, T. (2006). Tropical Indian Ocean Variability in the IPCC Twentieth-Century Climate Simulations*. *J. Clim.* 19, 4397–4417. doi:10.1175/JCLI3847.1.

Saji, N. H., and Yamagata, T. (2003a). Structure of SST and Surface Wind Variability during Indian Ocean Dipole Mode Events: COADS Observations*. *J. Clim.* 16, 2735–2751. doi:10.1175/1520-0442(2003)016<2735:SOSASW>2.0.CO;2.

Saji, N., and Yamagata, T. (2003b). Possible impacts of Indian Ocean Dipole mode events on global climate. *Clim. Res.* 25, 151–169. doi:10.3354/cr025151.

ACCEPTED VERSION SUBJECT TO FINAL EDITING

Sanchez-Gomez, E., Terray, L., and Joly, B. (2008). Intra-seasonal atmospheric variability and extreme precipitation events in the European-Mediterranean region. *Geophys. Res. Lett.* 35, L15708. doi:10.1029/2008GL034515.

Schneider, N., and Cornuelle, B. D. (2005). The Forcing of the Pacific Decadal Oscillation. *J. Clim.* 18, 4355–4373. doi:10.1175/JCLI3527.1.

Schott, F. A., Xie, S.-P., and McCreary, J. P. (2009). Indian Ocean circulation and climate variability. *Rev. Geophys.* 47, RG1002. doi:10.1029/2007RG000245.

Screen, J. A., Deser, C., Smith, D. M., Zhang, X., Blackport, R., Kushner, P. J., et al. (2018). Consistency and discrepancy in the atmospheric response to Arctic sea-ice loss across climate models. *Nat. Geosci.* 11, 155–163. doi:10.1038/s41561-018-0059-y.

Seager, R., Kushnir, Y., Visbeck, M., Naik, N., Miller, J., Krahmann, G., et al. (2000). Causes of Atlantic Ocean Climate Variability between 1958 and 1998*. *J. Clim.* 13, 2845–2862. doi:10.1175/1520-0442(2000)013<2845:COAOCV>2.0.CO;2.

Sen Gupta, A., and England, M. H. (2006). Coupled Ocean–Atmosphere–Ice Response to Variations in the Southern Annular Mode. *J. Clim.* 19, 4457–4486. doi:10.1175/JCLI3843.1.

Shakun, J. D., and Shaman, J. (2009). Tropical origins of North and South Pacific decadal variability. *Geophys. Res. Lett.* 36, L19711. doi:10.1029/2009GL040313.

Shen, C., Wang, W.-C., Gong, W., and Hao, Z. (2006). A Pacific Decadal Oscillation record since 1470 AD reconstructed from proxy data of summer rainfall over eastern China. *Geophys. Res. Lett.* 33, L03702. doi:10.1029/2005GL024804.

Silvestri, G. E., and Vera, C. S. (2003). Antarctic Oscillation signal on precipitation anomalies over southeastern South America. *Geophys. Res. Lett.* 30, 2115. doi:10.1029/2003GL018277.

Simpson, I. R., Deser, C., McKinnon, K. A., and Barnes, E. A. (2018). Modeled and Observed Multidecadal Variability in the North Atlantic Jet Stream and Its Connection to Sea Surface Temperatures. *J. Clim.* 31, 8313–8338. doi:10.1175/JCLI-D-18-0168.1.

Singh, H. K. A., Hakim, G. J., Tardif, R., Emile-Geay, J., and Noone, D. C. (2018). Insights into Atlantic multidecadal variability using the Last Millennium Reanalysis framework. *Clim. Past* 14, 157–174. doi:10.5194/cp-14-157-2018.

Sjolte, J., Sturm, C., Adolphi, F., Vinther, B. M., Werner, M., Lohmann, G., et al. (2018). Solar and volcanic forcing of North Atlantic climate inferred from a process-based reconstruction. *Clim. Past* 14, 1179–1194. doi:10.5194/cp-14-1179-2018.

Smith, D. M., Scaife, A. A., and Kirtman, B. P. (2012). What is the current state of scientific knowledge with regard to seasonal and decadal forecasting? *Environ. Res. Lett.* 7, 015602. doi:10.1088/1748-9326/7/1/015602.

Spence, P., Griffies, S. M., England, M. H., Hogg, A. M., Saenko, O. A., and Jourdain, N. C. (2014). Rapid subsurface warming and circulation changes of Antarctic coastal waters by poleward shifting winds. *Geophys. Res. Lett.* 41, 4601–4610. doi:10.1002/2014GL060613.

Spensberger, C., Reeder, M. J., Spengler, T., and Patterson, M. (2020). The Connection between the Southern Annular Mode and a Feature-Based Perspective on Southern Hemisphere Midlatitude Winter Variability. *J. Clim.* 33, 115–129. doi:10.1175/JCLI-D-19-0224.1.

Sperber, K. R., and Annamalai, H. (2008). Coupled model simulations of boreal summer intraseasonal (30–50 day) variability, Part 1: Systematic errors and caution on use of metrics. *Clim. Dyn.* 31, 345–372. doi:10.1007/s00382-008-0367-9.

Sperber, K. R., Annamalai, H., Kang, I.-S., Kitoh, A., Moise, A., Turner, A., et al. (2013). The Asian summer monsoon: an intercomparison of CMIP5 vs. CMIP3 simulations of the late 20th century. *Clim. Dyn.* 41, 2711–2744. doi:10.1007/s00382-012-1607-6.

Stan, C., Straus, D. M., Frederiksen, J. S., Lin, H., Maloney, E. D., and Schumacher, C. (2017). Review of Tropical-Extratropical Teleconnections on Intraseasonal Time Scales. *Rev. Geophys.* 55, 902–937. doi:10.1002/2016RG000538.

Steinman, B. A., Mann, M. E., and Miller, S. K. (2015). Atlantic and Pacific multidecadal oscillations and Northern Hemisphere temperatures. *Science (80-.).* 347, 988–991. doi:10.1126/science.1257856.

Stephenson, D. B., Wanner, H., Brönnimann, S., and Luterbacher, J. (2003). "The history of scientific research on the North Atlantic Oscillation," in *The North Atlantic Oscillation: Climatic Significance and Environmental Impact*, eds. J. W. Hurrell, Y. Kushnir, G. Ottersen, and M. Visbeck, 37–50. doi:10.1029/134GM02.

Stuecker, M. F. (2018). Revisiting the Pacific Meridional Mode. *Sci. Rep.* 8, 3216. doi:10.1038/s41598-018-21537-0.

Stuecker, M. F., Timmermann, A., Jin, F., Chikamoto, Y., Zhang, W., Wittenberg, A. T., et al. (2017). Revisiting ENSO/Indian Ocean Dipole phase relationships. *Geophys. Res. Lett.* 44, 2481–2492. doi:10.1002/2016GL072308.

ACCEPTED VERSION SUBJECT TO FINAL EDITING

Subramanian, A. C., Balmaseda, M. A., Centurioni, L., Chattopadhyay, R., Cornuelle, B. D., DeMott, C., et al. (2019). Ocean Observations to Improve Our Understanding, Modeling, and Forecasting of Subseasonal-to-Seasonal Variability. *Front. Mar. Sci.* 6, 427. doi:10.3389/fmars.2019.00427.

Sutton, R. T., and Dong, B. (2012). Atlantic Ocean influence on a shift in European climate in the 1990s. *Nat. Geosci.* 5, 788–792. doi:10.1038/ngeo1595.

Sutton, R. T., McCarthy, G. D., Robson, J., Sinha, B., Archibald, A. T., and Gray, L. J. (2018). Atlantic Multidecadal Variability and the U.K. ACSIS Program. *Bull. Am. Meteorol. Soc.* 99, 415–425. doi:10.1175/BAMS-D-16-0266.1.

Svendsen, L., Hetzinger, S., Keenlyside, N., and Gao, Y. (2014). Marine-based multiproxy reconstruction of Atlantic multidecadal variability. *Geophys. Res. Lett.* 41, 1295–1300. doi:10.1002/2013GL059076.

Swart, N. C., Fyfe, J. C., Gillett, N., and Marshall, G. J. (2015). Comparing Trends in the Southern Annular Mode and Surface Westerly Jet. *J. Clim.* 28, 8840–8859. doi:10.1175/JCLI-D-15-0334.1.

Swingedouw, D., Mignot, J., Ortega, P., Khodri, M., Menegoz, M., Cassou, C., et al. (2017). Impact of explosive volcanic eruptions on the main climate variability modes. *Glob. Planet. Change* 150, 24–45. doi:10.1016/j.gloplacha.2017.01.006.

Taguchi, B., Xie, S.-P., Schneider, N., Nonaka, M., Sasaki, H., and Sasai, Y. (2007). Decadal Variability of the Kuroshio Extension: Observations and an Eddy-Resolving Model Hindcast*. *J. Clim.* 20, 2357–2377. doi:10.1175/JCLI4142.1.

Tandon, N. F., and Kushner, P. J. (2015). Does External Forcing Interfere with the AMOC's Influence on North Atlantic Sea Surface Temperature? *J. Clim.* 28, 6309–6323. doi:10.1175/JCLI-D-14-00664.1.

Taschetto, A. S., Sen Gupta, A., Hendon, H. H., Ummenhofer, C. C., and England, M. H. (2011). The Contribution of Indian Ocean Sea Surface Temperature Anomalies on Australian Summer Rainfall during El Niño Events. *J. Clim.* 24, 3734–3747. doi:10.1175/2011JCLI3885.1.

Taschetto, A. S., Ummenhofer, C. C., Stuecker, M. F., Dommenget, D., Ashok, K., Rodrigues, R. R., et al. (2020). "ENSO Atmospheric Teleconnections," in *El Niño Southern Oscillation in a Changing Climate*, eds. M. J. McPhaden, A. Santoso, and W. Cai, 309–335. doi:10.1002/9781119548164.ch14.

Terray, L. (2012). Evidence for multiple drivers of North Atlantic multi-decadal climate variability. *Geophys. Res. Lett.* 39, L19712. doi:10.1029/2012GL053046.

Thompson, D. W. J., and Wallace, J. M. (1998). The Arctic oscillation signature in the wintertime geopotential height and temperature fields. *Geophys. Res. Lett.* 25, 1297–1300. doi:10.1029/98GL00950.

Thompson, D. W. J., and Wallace, J. M. (2000a). Annular Modes in the Extratropical Circulation. Part I: Month-to-Month Variability*. *J. Clim.* 13, 1000–1016. doi:10.1175/1520-0442(2000)013<1000:AMITEC>2.0.CO;2.

Thompson, D. W. J., and Wallace, J. M. (2000b). Annular modes in the extratropical circulation. Part II: Trends. *J. Clim.* 13, 1018–1036. doi:10.1175/1520-0442(2000)013<1018:AMITEC>2.0.CO;2.

Tian, B., Waliser, D. E., Kahn, R. A., and Wong, S. (2011). Modulation of Atlantic aerosols by the Madden-Julian Oscillation. *J. Geophys. Res.* 116, D15108. doi:10.1029/2010JD015201.

Tian, B., Yung, Y. L., Waliser, D. E., Tyranowski, T., Kuai, L., Fetzer, E. J., et al. (2007). Intraseasonal variations of the tropical total ozone and their connection to the Madden-Julian Oscillation. *Geophys. Res. Lett.* 34, L08704. doi:10.1029/2007GL029451.

Timmermann, A., An, S.-I., Kug, J.-S., Jin, F.-F., Cai, W., Capotondi, A., et al. (2018). El Niño–Southern Oscillation complexity. *Nature* 559, 535–545. doi:10.1038/s41586-018-0252-6.

Ting, M., Kushnir, Y., Seager, R., and Li, C. (2009). Forced and Internal Twentieth-Century SST Trends in the North Atlantic. *J. Clim.* 22, 1469–1481. doi:10.1175/2008JCLI2561.1.

Tokinaga, H., Richter, I., and Kosaka, Y. (2019). ENSO Influence on the Atlantic Niño, Revisited: Multi-Year versus Single-Year ENSO Events. *J. Clim.* 32, 4585–4600. doi:10.1175/JCLI-D-18-0683.1.

Tokinaga, H., and Tanimoto, Y. (2004). Seasonal transition of SST anomalies in the tropical Indian Ocean during El Niño and Indian Ocean dipole years. *J. Meteorol. Soc. Japan* 82, 1007–1018. doi:10.2151/jmsj.2004.1007.

Torralba, V., Rodríguez-Fonseca, B., Mohino, E., and Losada, T. (2015). The non-stationary influence of the Atlantic and Pacific Niños on North Eastern South American rainfall. *Front. Earth Sci.* 3, 55. doi:10.3389/feart.2015.00055.

Tozuka, T., Luo, J.-J., Masson, S., and Yamagata, T. (2007). Decadal Modulations of the Indian Ocean Dipole in the SINTEX-F1 Coupled GCM. *J. Clim.* 20, 2881–2894. doi:10.1175/JCLI4168.1.

Trenberth, K. E., Caron, J. M., Stepaniak, D. P., and Worley, S. (2002). Evolution of El Niño–Southern Oscillation and global atmospheric surface temperatures. *J. Geophys. Res.* 107, 4065. doi:10.1029/2000JD000298.

Trenberth, K. E., and Shea, D. J. (2006). Atlantic hurricanes and natural variability in 2005. *Geophys. Res. Lett.* 33, L12704. doi:10.1029/2006GL026894.

ACCEPTED VERSION SUBJECT TO FINAL EDITING

Trenberth, K. E., and Stepaniak, D. P. (2001). Indices of El Niño Evolution. *J. Clim.* 14, 1697–1701. doi:10.1175/1520-0442(2001)014<1697:LIOENO>2.0.CO;2.
Troup, A. J. (1965). The 'southern oscillation.' *Q. J. R. Meteorol. Soc.* 91, 490–506. doi:10.1002/qj.49709139009.
Tung, K.-K., Chen, X., Zhou, J., and Li, K.-F. (2019). Interdecadal variability in pan-Pacific and global SST, revisited. *Clim. Dyn.* 52, 2145–2157. doi:10.1007/s00382-018-4240-1.
Tung, K.-K., and Zhou, J. (2013). Using data to attribute episodes of warming and cooling in instrumental records. *Proc. Natl. Acad. Sci.* 110, 2058–2063. doi:10.1073/pnas.1212471110.
Ueda, H., Miwa, K., and Kamae, Y. (2018). Seasonal Modulation of Tropical Cyclone Occurrence Associated with Coherent Indo-Pacific Variability during Decaying Phase of El Niño. *J. Meteorol. Soc. Japan. Ser. II* 96, 381–390. doi:10.2151/jmsj.2018-044.
Ulbrich, U., and Christoph, M. (1999). A shift of the NAO and increasing storm track activity over Europe due to anthropogenic greenhouse gas forcing. *Clim. Dyn.* 15, 551–559. doi:10.1007/s003820050299.
Vance, T. R., Roberts, J. L., Plummer, C. T., Kiem, A. S., and van Ommen, T. D. (2015). Interdecadal Pacific variability and eastern Australian megadroughts over the last millennium. *Geophys. Res. Lett.* 42, 129–137. doi:10.1002/2014GL062447.
Vera, C. S., and Osman, M. (2018). Activity of the Southern Annular Mode during 2015 – 2016 El Niño event and its impact on Southern Hemisphere climate. 38, 1288–1295. doi:10.1002/joc.5419.
Verdon, D. C., and Franks, S. W. (2006). Long-term behaviour of ENSO: Interactions with the PDO over the past 400 years inferred from paleoclimate records. *Geophys. Res. Lett.* 33, L06712. doi:10.1029/2005GL025052.
Villalba, R., Lara, A., Masiokas, M. H., Urrutia, R., Luckman, B. H., Marshall, G. J., et al. (2012). Unusual Southern Hemisphere tree growth patterns induced by changes in the Southern Annular Mode. *Nat. Geosci.* 5, 793–798. doi:10.1038/ngeo1613.
Vimont, D. J., and Kossin, J. P. (2007). The Atlantic Meridional Mode and hurricane activity. *Geophys. Res. Lett.* 34, L07709. doi:10.1029/2007GL029683.
Vitart, F. (2014). Evolution of ECMWF sub-seasonal forecast skill scores. *Q. J. R. Meteorol. Soc.* 140, 1889–1899. doi:10.1002/qj.2256.
Vitart, F. (2017). Madden-Julian Oscillation prediction and teleconnections in the S2S database. *Q. J. R. Meteorol. Soc.* 143, 2210–2220. doi:10.1002/qj.3079.
Vitart, F., and Robertson, A. W. (2018). The sub-seasonal to seasonal prediction project (S2S) and the prediction of extreme events. *npj Clim. Atmos. Sci.* 1, 3. doi:10.1038/s41612-018-0013-0.
Vittal, H., Villarini, G., and Zhang, W. (2020). Early prediction of the Indian summer monsoon rainfall by the Atlantic Meridional Mode. *Clim. Dyn.* 54, 2337–2346. doi:10.1007/s00382-019-05117-0.
Wainer, I., Prado, L. F., Khodri, M., and Otto-Bliesner, B. (2014). Reconstruction of the South Atlantic Subtropical Dipole index for the past 12,000 years from surface temperature proxy. *Sci. Rep.* 4, 5291. doi:10.1038/srep05291.
Waliser, D. E., Jin, K., Kang, I.-S., Stern, W. F., Schubert, S. D., Wu, M. L. C., et al. (2003). AGCM simulations of intraseasonal variability associated with the Asian summer monsoon. *Clim. Dyn.* 21, 423–446. doi:10.1007/s00382-003-0337-1.
Waliser, D., Sperber, K., Hendon, H., Kim, D., Maloney, E., Wheeler, M., et al. (2009). MJO Simulation Diagnostics. *J. Clim.* 22, 3006–3030. doi:10.1175/2008JCLI2731.1.
Wang, B., and Chan, J. C. L. (2002). How Strong ENSO Events Affect Tropical Storm Activity over the Western North Pacific*. *J. Clim.* 15, 1643–1658. doi:10.1175/1520-0442(2002)015<1643:HSEEAT>2.0.CO;2.
Wang, B., Wu, R., and Fu, X. (2000). Pacific–East Asian Teleconnection: How Does ENSO Affect East Asian Climate? *J. Clim.* 13, 1517–1536. doi:10.1175/1520-0442(2000)013<1517:PEATHD>2.0.CO;2.
Wang, B., Xiang, B., and Lee, J.-Y. (2013). Subtropical High predictability establishes a promising way for monsoon and tropical storm predictions. *Proc. Natl. Acad. Sci.* 110, 2718–2722. doi:10.1073/pnas.1214626110.
Wang, C. (2018). A review of ENSO theories. *Natl. Sci. Rev.* 5, 813–825. doi:10.1093/nsr/nwy104.
Wang, C., Kucharski, F., Barimalala, R., and Bracco, A. (2009). Teleconnections of the tropical Atlantic to the tropical Indian and Pacific Oceans: A review of recent findings. *Meteorol. Zeitschrift* 18, 445–454. doi:10.1127/0941-2948/2009/0394.
Wang, J., Yang, B., Ljungqvist, F. C., Luterbacher, J., Osborn, T. J., Briffa, K. R., et al. (2017a). Internal and external forcing of multidecadal Atlantic climate variability over the past 1,200 years. *Nat. Geosci.* 10, 512–517. doi:10.1038/ngeo2962.
Wang, L., Yu, J.-Y., and Paek, H. (2017b). Enhanced biennial variability in the Pacific due to Atlantic capacitor effect. *Nat. Commun.* 8, 14887. doi:10.1038/ncomms14887.

ACCEPTED VERSION
SUBJECT TO FINAL EDITING

Ward, D. S., Shevliakova, E., Malyshev, S., Lamarque, J.-F., and Wittenberg, A. T. (2016). Variability of fire emissions on interannual to multi-decadal timescales in two Earth System models. *Environ. Res. Lett.* 11, 125008. doi:10.1088/1748-9326/11/12/125008.

Watanabe, M., and Jin, F. (2002). Role of Indian Ocean warming in the development of Philippine Sea anticyclone during ENSO. *Geophys. Res. Lett.* 29, 1478. doi:10.1029/2001GL014318.

Waugh, D. W., Primeau, F., DeVries, T., and Holzer, M. (2013). Recent Changes in the Ventilation of the Southern Oceans. *Science (80-.).* 339, 568–570. doi:10.1126/science.1225411.

Weare, B. C. (1979). A Statistical Study of the Relationships between Ocean Surface Temperatures and the Indian Monsoon. *J. Atmos. Sci.* 36, 2279–2291. doi:10.1175/1520-0469(1979)036<2279:ASSOTR>2.0.CO;2.

Webster, P. J., and Hoyos, C. D. (2010). Beyond the spring barrier? *Nat. Geosci.* 3, 152–153. doi:10.1038/ngeo800.

Whan, K., and Zwiers, F. (2017). The impact of ENSO and the NAO on extreme winter precipitation in North America in observations and regional climate models. *Clim. Dyn.* 48, 1401–1411. doi:10.1007/s00382-016-3148-x.

Wheeler, M. C., and Hendon, H. H. (2004). An All-Season Real-Time Multivariate MJO Index: Development of an Index for Monitoring and Prediction. *Mon. Weather Rev.* 132, 1917–1932. doi:10.1175/1520-0493(2004)132<1917:AARMMI>2.0.CO;2.

Wheeler, M. C., Hendon, H. H., Cleland, S., Meinke, H., and Donald, A. (2009). Impacts of the Madden–Julian Oscillation on Australian Rainfall and Circulation. *J. Clim.* 22, 1482–1498. doi:10.1175/2008JCLI2595.1.

Wheeler, M. C., Kim, H.-J., Lee, J.-Y., and Gottschalck, J. C. (2017). "Real-Time Forecasting of Modes of Tropical Intraseasonal Variability: The Madden-Julian and Boreal Summer Intraseasonal Oscillations," in *World Scientific Series on Asia-Pacific Weather and Climate*, 131–138. doi:10.1142/9789813200913_0010.

Wiedermann, M., Radebach, A., Donges, J. F., Kurths, J., and Donner, R. V (2016). A climate network-based index to discriminate different types of El Niño and La Niña. *Geophys. Res. Lett.* 43, 7176–7185. doi:10.1002/2016GL069119.

Williams, B., Halfar, J., Delong, K. L., Smith, E., Steneck, R., Lebednik, P. A., et al. (2017). North Pacific twentieth century decadal-scale variability is unique for the past 342 years. *Geophys. Res. Lett.* 44, 3761–3769. doi:10.1002/2017GL073138.

Wills, R. C. J., Battisti, D. S., Proistosescu, C., Thompson, L., Hartmann, D. L., and Armour, K. C. (2019). Ocean Circulation Signatures of North Pacific Decadal Variability. *Geophys. Res. Lett.* 46, 1690–1701. doi:10.1029/2018GL080716.

Wills, R. C., Schneider, T., Wallace, J. M., Battisti, D. S., and Hartmann, D. L. (2018). Disentangling Global Warming, Multidecadal Variability, and El Niño in Pacific Temperatures. *Geophys. Res. Lett.* 45, 2487–2496. doi:10.1002/2017GL076327.

Wittenberg, A. T. (2009). Are historical records sufficient to constrain ENSO simulations? *Geophys. Res. Lett.* 36, L12702. doi:10.1029/2009GL038710.

Woollings, T., Czuchnicki, C., and Franzke, C. (2014). Twentieth century North Atlantic jet variability. *Q. J. R. Meteorol. Soc.* 140, 783–791. doi:10.1002/qj.2197.

Woollings, T., Franzke, C., Hodson, D. L. R., Dong, B., Barnes, E. A., Raible, C. C., et al. (2015). Contrasting interannual and multidecadal NAO variability. *Clim. Dyn.* 45, 539–556. doi:10.1007/s00382-014-2237-y.

Woollings, T., Hannachi, A., Hoskins, B., and Turner, A. (2010). A Regime View of the North Atlantic Oscillation and Its Response to Anthropogenic Forcing. *J. Clim.* 23, 1291–1307. doi:10.1175/2009JCLI3087.1.

Wu, L., He, F., Liu, Z., and Li, C. (2007). Atmospheric Teleconnections of Tropical Atlantic Variability: Interhemispheric, Tropical–Extratropical, and Cross-Basin Interactions. *J. Clim.* 20, 856–870. doi:10.1175/JCLI4019.1.

Wu, T., Hu, A., Gao, F., Zhang, J., and Meehl, G. A. (2019). New insights into natural variability and anthropogenic forcing of global/regional climate evolution. *npj Clim. Atmos. Sci.* 2, 18. doi:10.1038/s41612-019-0075-7.

Xavier, P. K. (2012). Intraseasonal Convective Moistening in CMIP3 Models. *J. Clim.* 25, 2569–2577. doi:10.1175/JCLI-D-11-00427.1.

Xavier, P. K., Duvel, J.-P., Braconnot, P., and Doblas-Reyes, F. J. (2010). An Evaluation Metric for Intraseasonal Variability and its Application to CMIP3 Twentieth-Century Simulations. *J. Clim.* 23, 3497–3508. doi:10.1175/2010JCLI3260.1.

Xie, S.-P., Hu, K., Hafner, J., Tokinaga, H., Du, Y., Huang, G., et al. (2009). Indian Ocean Capacitor Effect on Indo–Western Pacific Climate during the Summer following El Niño. *J. Clim.* 22, 730–747. doi:10.1175/2008JCLI2544.1.

Yan, X., Zhang, R., and Knutson, T. R. (2019). A Multivariate AMV Index and Associated Discrepancies Between Observed and CMIP5 Externally Forced AMV. *Geophys. Res. Lett.* 46, 4421–4431. doi:10.1029/2019GL082787.

ACCEPTED VERSION
SUBJECT TO FINAL EDITING

Yang, Y., Li, J., Wu, L., Kosaka, Y., Du, Y., Sun, C., et al. (2017). Decadal Indian Ocean dipolar variability and its relationship with the tropical Pacific. *Adv. Atmos. Sci.* 34, 1282–1289. doi:10.1007/s00376-017-7009-2.

Yasunari, T. (1980). A Quasi-Stationary Appearance of 30 to 40 Day Period in the Cloudiness Fluctuations during the Summer Monsoon over India. *J. Meteorol. Soc. Japan. Ser. II* 58, 225–229. doi:10.2151/jmsj1965.58.3_225.

Yeager, S., and Danabasoglu, G. (2014). The Origins of Late-Twentieth-Century Variations in the Large-Scale North Atlantic Circulation. *J. Clim.* 27, 3222–3247. doi:10.1175/JCLI-D-13-00125.1.

Yeh, S.-W., Cai, W., Min, S.-K., McPhaden, M. J., Dommenget, D., Dewitte, B., et al. (2018). ENSO Atmospheric Teleconnections and Their Response to Greenhouse Gas Forcing. *Rev. Geophys.*, 77–117. doi:110.1002/2017RG000568.

Yiou, P., Jézéquel, A., Naveau, P., Otto, F. E. L., Vautard, R., and Vrac, M. (2017). A statistical framework for conditional extreme event attribution. *Adv. Stat. Climatol. Meteorol. Oceanogr.* 3, 17–31. doi:10.5194/ascmo-3-17-2017.

Yoo, C., Feldstein, S., and Lee, S. (2011). The impact of the Madden-Julian Oscillation trend on the Arctic amplification of surface air temperature during the 1979-2008 boreal winter. *Geophys. Res. Lett.* 38, L24804. doi:10.1029/2011GL049881.

Yoo, C., Lee, S., and Feldstein, S. B. (2012). Mechanisms of Arctic Surface Air Temperature Change in Response to the Madden–Julian Oscillation. *J. Clim.* 25, 5777–5790. doi:10.1175/JCLI-D-11-00566.1.

Yu, J.-Y., Paek, H., Saltzman, E. S., and Lee, T. (2015). The Early 1990s Change in ENSO – PSA – SAM Relationships and Its Impact on Southern Hemisphere Climate. *J. Clim.* 28, 9393–9408. doi:10.1175/JCLI-D-15-0335.1.

Yu, L., Zhong, S., Winkler, J. A., Zhou, M., Lenschow, D. H., Li, B., et al. (2017). Possible connections of the opposite trends in Arctic and Antarctic sea-ice cover. *Sci. Rep.* 7, 45804. doi:10.1038/srep45804.

Zebiak, S. E. (1993). Air–Sea Interaction in the Equatorial Atlantic Region. *J. Clim.* 6, 1567–1586. doi:10.1175/1520-0442(1993)006<1567:AIITEA>2.0.CO;2.

Zhang, C. (2005). Madden-Julian Oscillation. *Rev. Geophys.* 43, RG2003. doi:10.1029/2004RG000158.

Zhang, C. (2013). Madden–Julian Oscillation: Bridging Weather and Climate. *Bull. Am. Meteorol. Soc.* 94, 1849–1870. doi:10.1175/BAMS-D-12-00026.1.

Zhang, R. (2017). On the persistence and coherence of subpolar sea surface temperature and salinity anomalies associated with the Atlantic multidecadal variability. *Geophys. Res. Lett.* 44, 7865–7875. doi:10.1002/2017GL074342.

Zhang, W., Vecchi, G. A., Villarini, G., Murakami, H., Rosati, A., Yang, X., et al. (2017). Modulation of western North Pacific tropical cyclone activity by the Atlantic Meridional Mode. *Clim. Dyn.* 48, 631–647. doi:10.1007/s00382-016-3099-2.

Zhang, Y., Wallace, J. M., and Battisti, D. S. (1997). ENSO-like Interdecadal Variability: 1900–93. *J. Clim.* 10, 1004–1020. doi:10.1175/1520-0442(1997)010<1004:ELIV>2.0.CO;2.

Zhang, Y., Xie, S.-P., Kosaka, Y., and Yang, J.-C. (2018). Pacific Decadal Oscillation: Tropical Pacific Forcing versus Internal Variability. *J. Clim.* 31, 8265–8279. doi:10.1175/JCLI-D-18-0164.1.

Zhao, H., Wu, L., Wang, C., and Klotzbach, P. J. (2019). Consistent Late Onset of the Western North Pacific Tropical Cyclone Season Following major El Niño Events. *J. Meteorol. Soc. Japan. Ser. II* 97, 673–688. doi:10.2151/jmsj.2019-039.

Zhao, H., Yoshida, R., and Raga, G. B. (2015). Impact of the Madden–Julian Oscillation on Western North Pacific Tropical Cyclogenesis Associated with Large-Scale Patterns. *J. Appl. Meteorol. Climatol.* 54, 1413–1429. doi:10.1175/JAMC-D-14-0254.1.

Zhao, J., Zhan, R., Wang, Y., Xie, S.-P., and Wu, Q. (2020). Untangling impacts of global warming and Interdecadal Pacific Oscillation on long-term variability of North Pacific tropical cyclone track density. *Sci. Adv.* 6, eaba6813. doi:10.1126/sciadv.aba6813.

Zhao, J., Zhan, R., Wang, Y., and Xu, H. (2018). Contribution of the Interdecadal Pacific Oscillation to the Recent Abrupt Decrease in Tropical Cyclone Genesis Frequency over the Western North Pacific since 1998. *J. Clim.* 31, 8211–8224. doi:10.1175/JCLI-D-18-0202.1.

Zhou, J., Tung, K.-K., and Li, K.-F. (2016). Multi-decadal variability in the Greenland ice core records obtained using intrinsic timescale decomposition. *Clim. Dyn.* 47, 739–752. doi:10.1007/s00382-015-2866-9.

Zhou, S., and Miller, A. J. (2005). The Interaction of the Madden–Julian Oscillation and the Arctic Oscillation. *J. Clim.* 18, 143–159. doi:10.1175/JCLI3251.1.

Zinke, J., Pfeiffer, M., Timm, O., Dullo, W.-C., and Brummer, G. J. A. (2009). Western Indian Ocean marine and terrestrial records of climate variability: a review and new concepts on land–ocean interactions since AD 1660. *Int. J. Earth Sci.* 98, 115–133. doi:10.1007/s00531-008-0365-5.

ACCEPTED VERSION SUBJECT TO FINAL EDITING

Zinke, J., Pfeiffer, M., Timm, O., Dullo, W. –C., and Davies, G. R. (2005). Atmosphere–ocean dynamics in the Western Indian Ocean recorded in corals. *Philos. Trans. R. Soc. A Math. Phys. Eng. Sci.* 363, 121–142. doi:10.1098/rsta.2004.1482.

Zubiate, L., McDermott, F., Sweeney, C., and O'Malley, M. (2017). Spatial variability in winter NAO-wind speed relationships in western Europe linked to concomitant states of the East Atlantic and Scandinavian patterns. *Q. J. R. Meteorol. Soc.* 143, 552–562. doi:10.1002/qj.2943.

ACCEPTED VERSION
SUBJECT TO FINAL EDITING

Figures

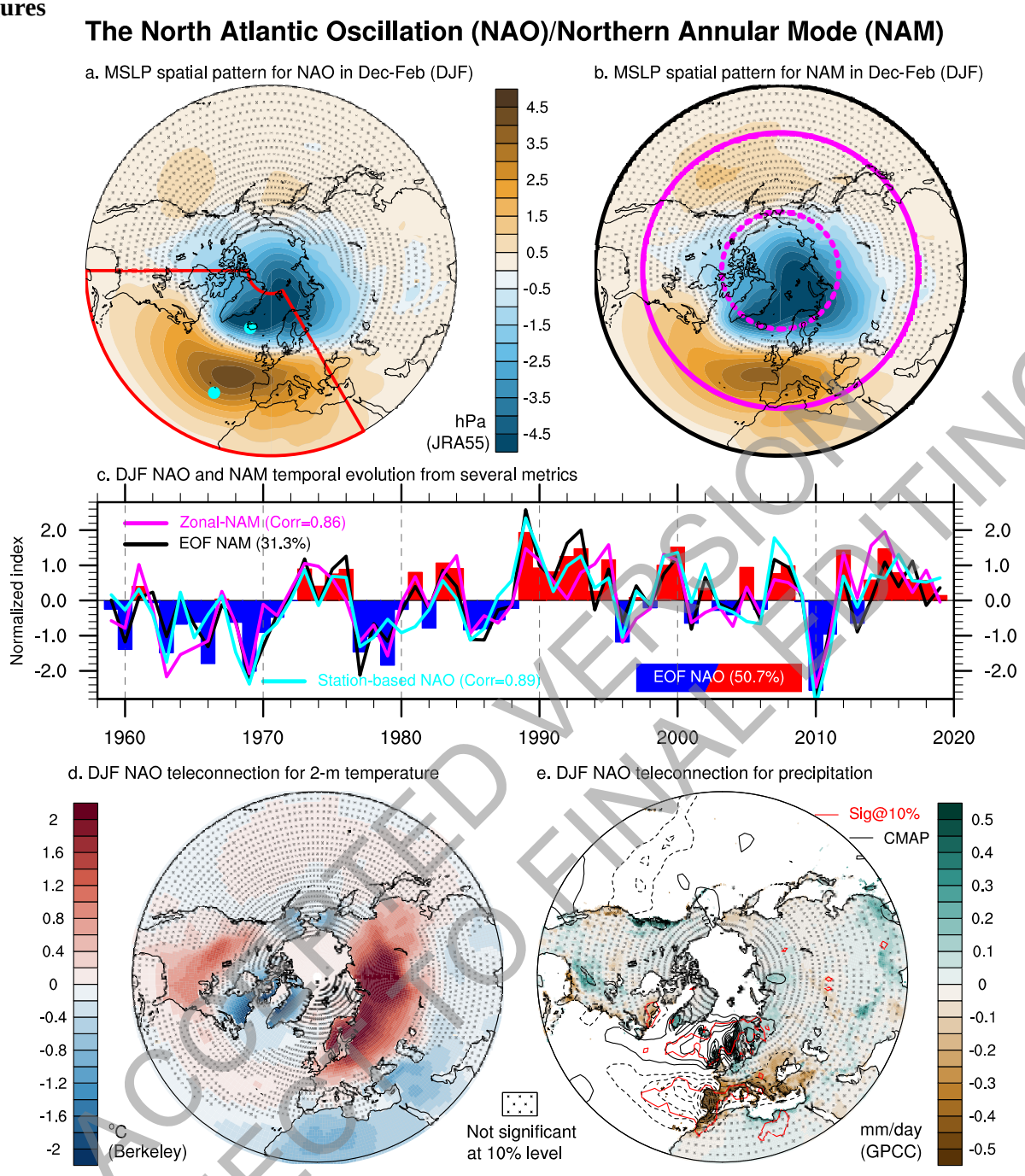
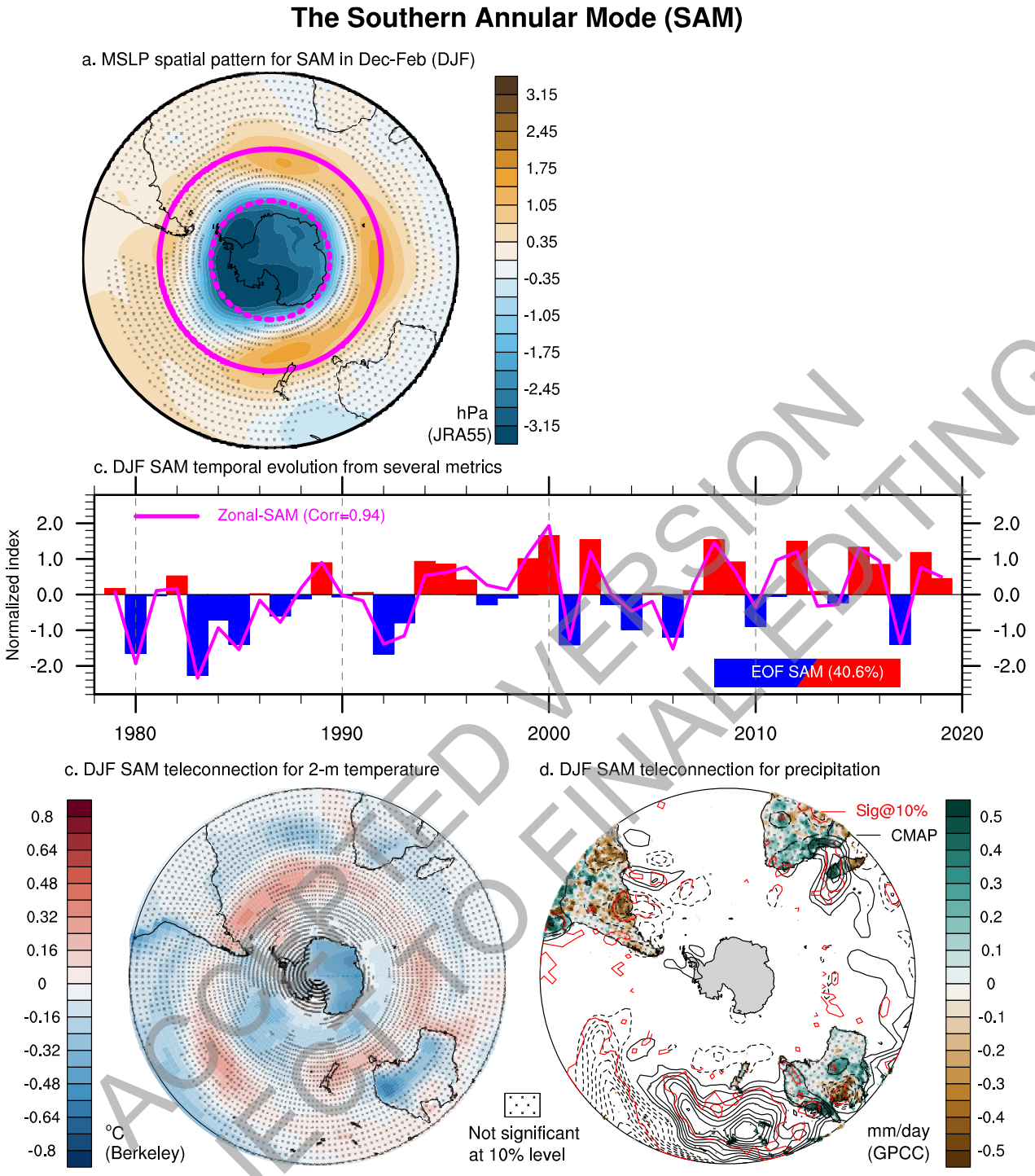


Figure AIV.1: The boreal wintertime NAO and NAM modes extracted as the leading EOF of December-January-February SLP anomalies over the North Atlantic-Europe Sector (20ºN-80ºN, 90ºW-30ºE, materialized by the red box, a) and the Northern Hemisphere (north of 20ºN, black domain, b), respectively, based on JRA-55 reanalysis over 1959-2019. (a,b) SLP anomalies regressed onto the leading principal component (PC) time series shown in (c). The NAO-PC is represented by red and blue bars, the NAM-PC by the black curve in (c); their variance explained is given in the legend. The NAO index based on weather stations (cyan dots in a) is given in cyan and the zonal-NAM index (latitude circles in b) is given in magenta. Correlation between each index and the NAO-PC timeseries is given in the legend. (d,e) Regression maps of blended SST and SAT over land from ERSST and BerkeleyEarth dataset, respectively, over for 1959-2019 (d) and of precipitation anomalies (e, shading based on GPCC for 1959-2016 and contours based on CMAP for 1979-2019 for every 0.1 mm/day). On maps, no-overlay indicates regions where the regressions are significant based on t-test accounting for false detection rate at 10% and crosses indicates no significance. Significance for CMAP precipitation is materialized by red contours in (e). All fields have been linearly detrended prior to computation.

ACCEPTED VERSION SUBJECT TO FINAL EDITING



ACCEPTED VERSION SUBJECT TO FINAL EDITING

Figure AIV.2: The austral summertime SAM extracted as the leading EOF of December-January-February SLP anomalies over the Southern Hemisphere (south of 20°S, a) based on JRA-55 reanalysis over 1979-2019. (a) SLP anomalies regressed onto the leading principal component (PC) time series shown in (b); the variance explained is given in the legend in (b). The SAM-PC is represented by red and blue bars and the zonal-SAM index (latitude circles in a) is given in magenta. Correlation between the zonal SAM index and the SAM PC timeseries is given in the legend. (c, d) Regression maps of SST and SAT over land from ERSST and BerkeleyEarth dataset, respectively, over for 1979-2019 (d) and of precipitation anomalies (e, shading based on CMAP for 1979-2016 and contours based on GPCP for 1979-2019 for every 0.1 mm/day). On maps, no-overlay indicates regions where the regressions are significant based on t-test accounting for false detection rate at 10% and crosses indicates no significance. Significance for CMAP precipitation is materialized by red contours in (d). All fields have been linearly detrended prior computation.

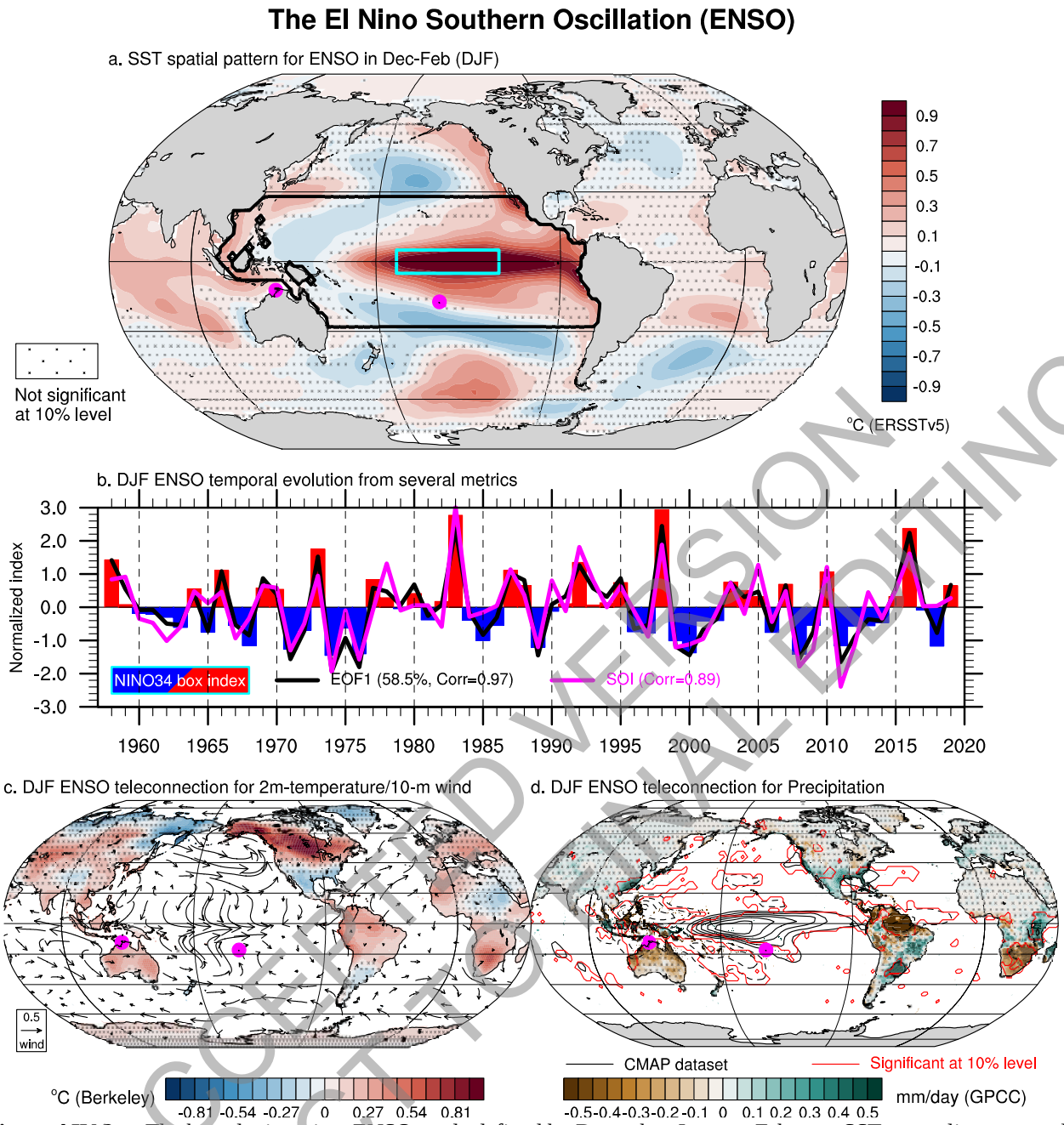


Figure AIV.3: The boreal wintertime ENSO mode defined by December-January-February SST anomalies averaged over the NINO34 region (5ºS-5ºN, 170ºW-120ºW, cyan box) or extracted as the leading EOF mode over the Tropical Pacific Ocean (the region denoted by the black box in a) for 1958-2019 using ERSSTv5. (a) SST anomalies regressed onto the NINO34 time series, which is shown in (b) as red and blue bars. Black curve in (b) represents the standardized leading principal component and the magenta curve stands for the SOI index. The percentage of explained variance of the leading EOF is given in the legend as well as the correlation between all indices and the NINO34 timeseries. (c) Same as (a) but for land SAT (shading; based on BerkeleyEarth) and 10-m level wind (arrows; based on JRA-55) anomalies over 1958-2018. (d) Same as (a) but for precipitation anomalies (shading based on GPCC for 1958-2016 and contours based on CMAP for 1979-2019 for every 0.5 mm/day). Magenta dots in (c,d) stands for the Darwin and Tahiti weather station used for the SOI computation. On maps, no-overlay indicates regions where the regressions are significant based on t-test accounting for false detection rate at 10% and crosses indicates no significance. Significance for CMAP precipitation is materialized by red contours in (d). All fields have been linearly detrended prior to computation.

ACCEPTED VERSION SUBJECT TO FINAL EDITING

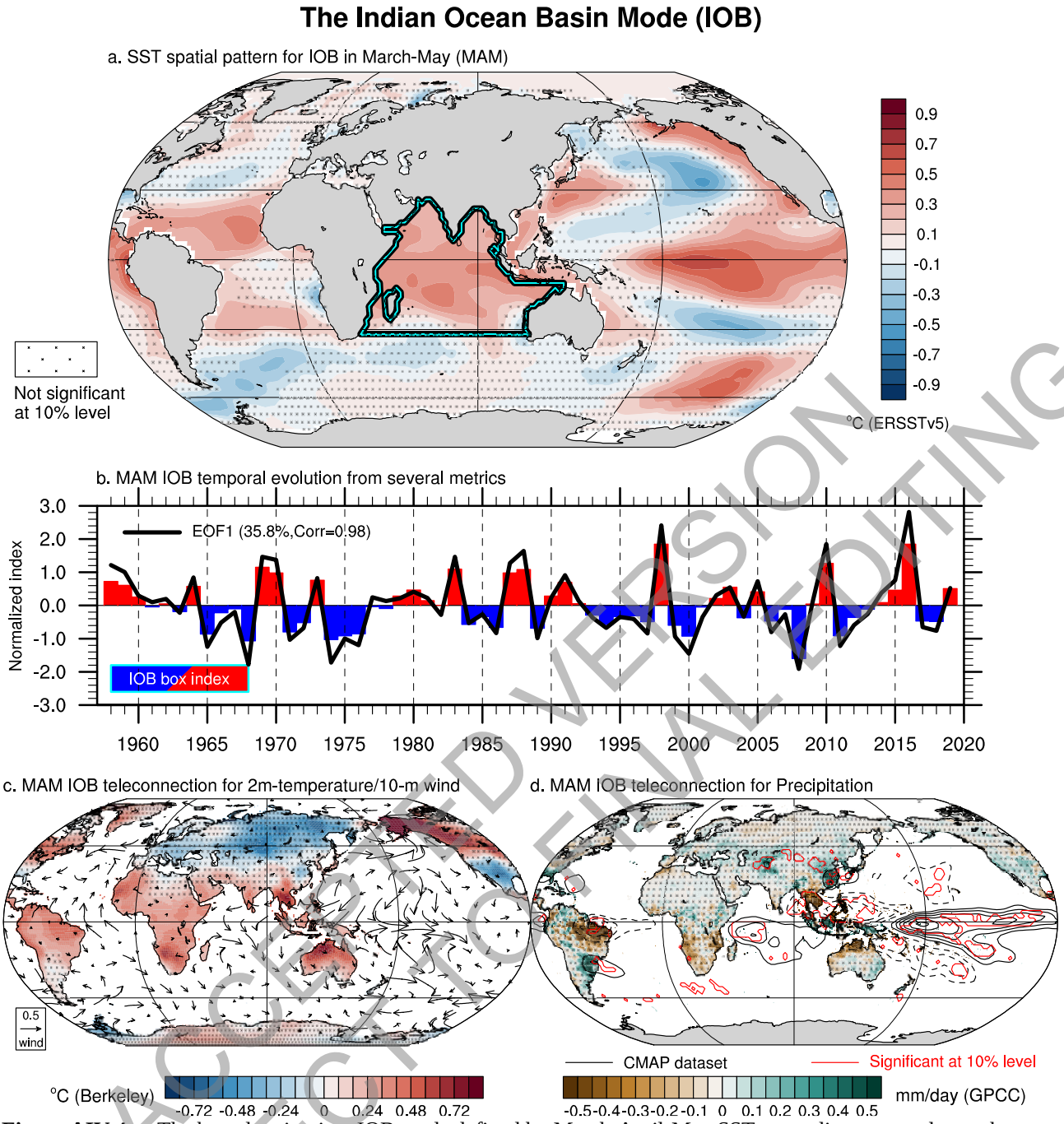


Figure AIV.4: The boreal springtime IOB mode defined by March-April-May SST anomalies averaged over the Indian Ocean (the region denoted by the cyan box in a) or extracted as the leading EOF mode over the same domain (black contour) for 1958-2019 using ERSSTv5. (a) SST anomalies regressed onto the IOB index timeseries shown in (b) in red and blue bars, while the black curve in (b) represents the leading principal component timeseries. Explained variance and correlation between indices are given in the legend in (b). (c) Same as (a) but for land SAT (shading; based on BerkeleyEarth) and 10-m level wind (arrows; based on JRA-55) anomalies for 1958-2018. (d) Same as (a) but for precipitation anomalies (shading based on GPCC for 1958-2016 and contours based on CMAP for 1979-2019 for every 0.3 mm/day). On maps, no-overlay indicates regions where the regressions are significant based on t-test accounting for false detection rate at 10% and crosses indicates no significance. Significance for CMAP precipitation is materialized by red contours in (d). All fields have been linearly detrended prior to computation.

ACCEPTED VERSION SUBJECT TO FINAL EDITING

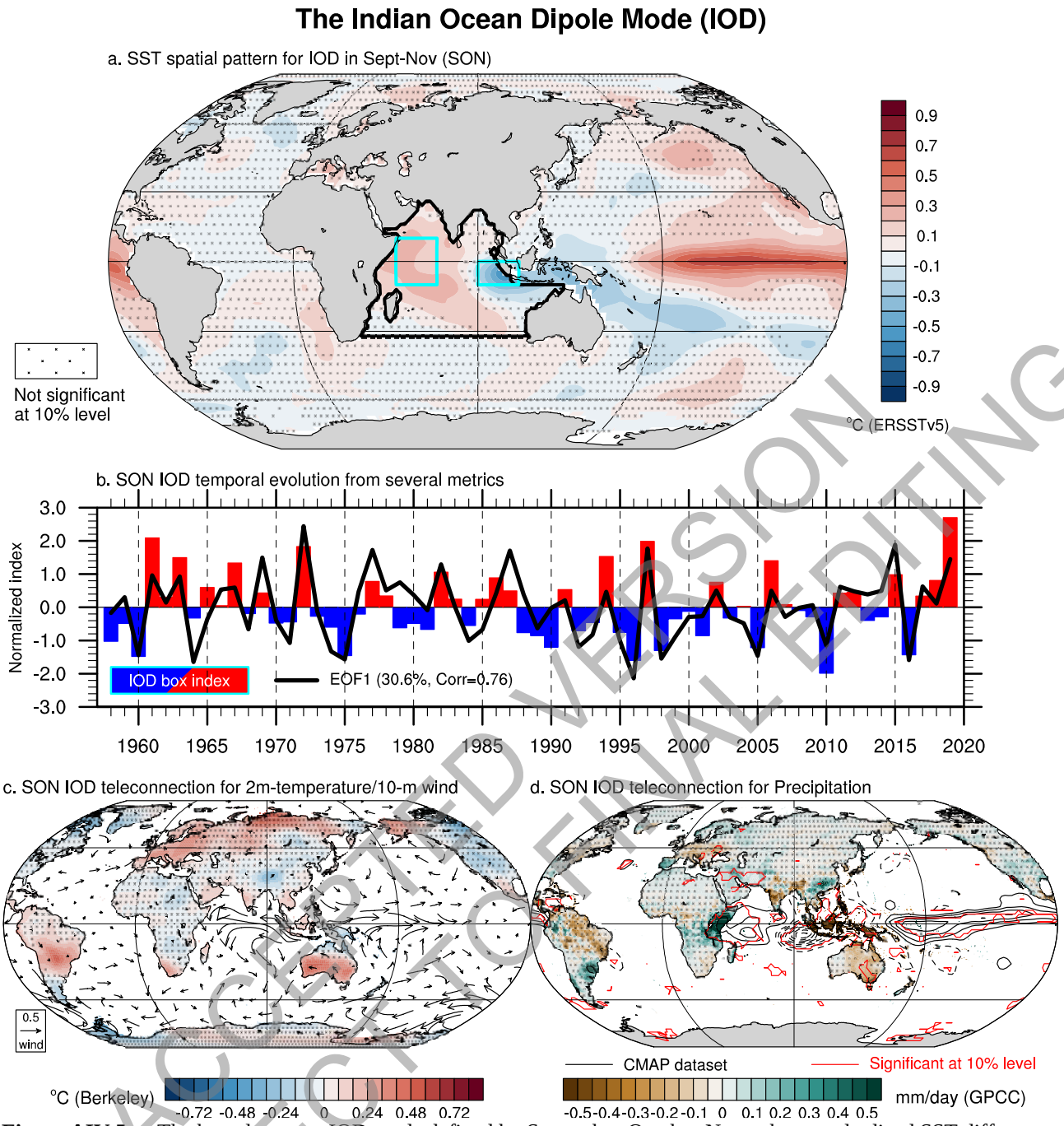


Figure AIV.5: The boreal autumn IOD mode defined by September-October-November standardized SST difference between the western (10ºS-10ºN, 50ºE-70ºE) and eastern (10ºS-0º, 90ºE-110ºE) equatorial Indian Ocean denoted by cyan boxes in (a) or extracted as the leading EOF mode over the Indian Ocean (the region denoted by black contour in a) over 1958-2019 using ERSSTv5. (a) SST anomalies regressed onto the IOD index timeseries shown in (b) in red and blue bars while the black curve represents the leading principal component timeseries. Explained variance and correlation between indices are given in the legend in (b). (c) Same as (a) but for land SAT (shading; based on BerkeleyEarth) and 10-m level wind (arrows; based on JRA-55) anomalies for 1958-2018. (d) Same as (a) but for precipitation anomalies (shading based on GPCC for 1958-2016 and contours based on CMAP for 1979-2019 for every 0.3 mm/day. On maps, no-overlay indicates regions where the regressions are significant based on t-test accounting for false detection rate at 10% and crosses indicates no significance. Significance for CMAP precipitation is materialized by red contours in (d). All fields have been linearly detrended prior to computation.

ACCEPTED VERSION SUBJECT TO FINAL EDITING

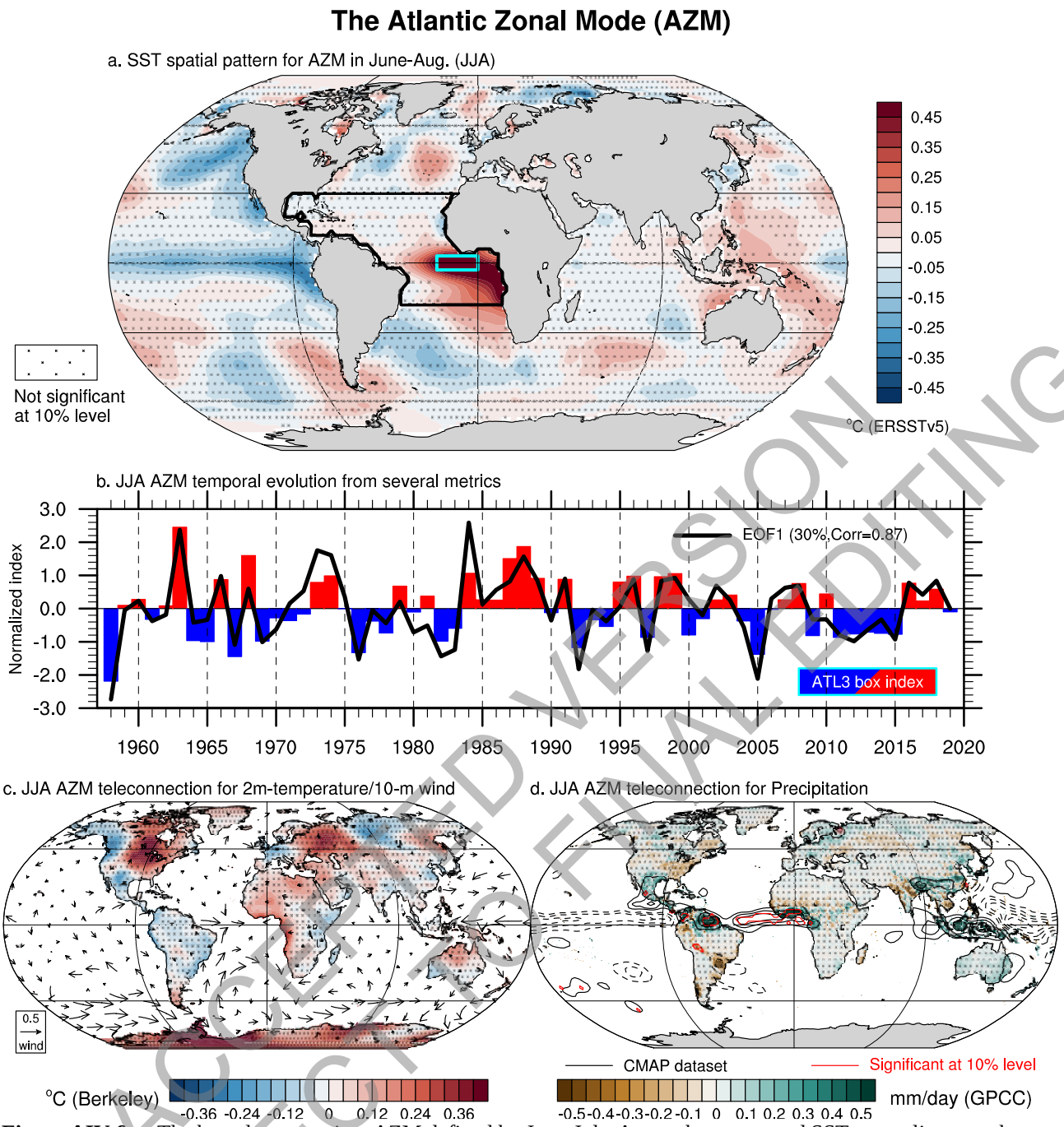


Figure AIV.6: The boreal summertime AZM defined by June-July-August box-averaged SST anomalies over the ATL3 region (3ºS-3ºN, 0º-20ºW, cyan box in a) or estimated as the leading EOF over the tropical Atlantic Ocean (the region denoted by the black box in a) for 1958-2019 using ERSSTv5. (a) SST anomalies regressed onto the ATL3 time series, which is shown in (b) as red and blue bars, while the black curve represents the leading principal component timeseries. Explained variance and correlation between indices are given in the legend in (b). (c) Same as (a) but for land SAT and 10-m level wind (arrows; based on JRA-55 for 1958-2019) anomalies. (d) Same as (a) but for precipitation anomalies (shading based on GPCC for 1958-2016 and contours based on CMAP for 1979-2019 for every 0.2 mm/day). On maps, no-overlay indicates regions where the regressions are significant based on t-test accounting for false detection rate at 10% and crosses indicates no significance. Significance for CMAP precipitation is materialized by red contours in (d). All fields have been linearly detrended prior to computation.

ACCEPTED VERSION SUBJECT TO FINAL EDITING

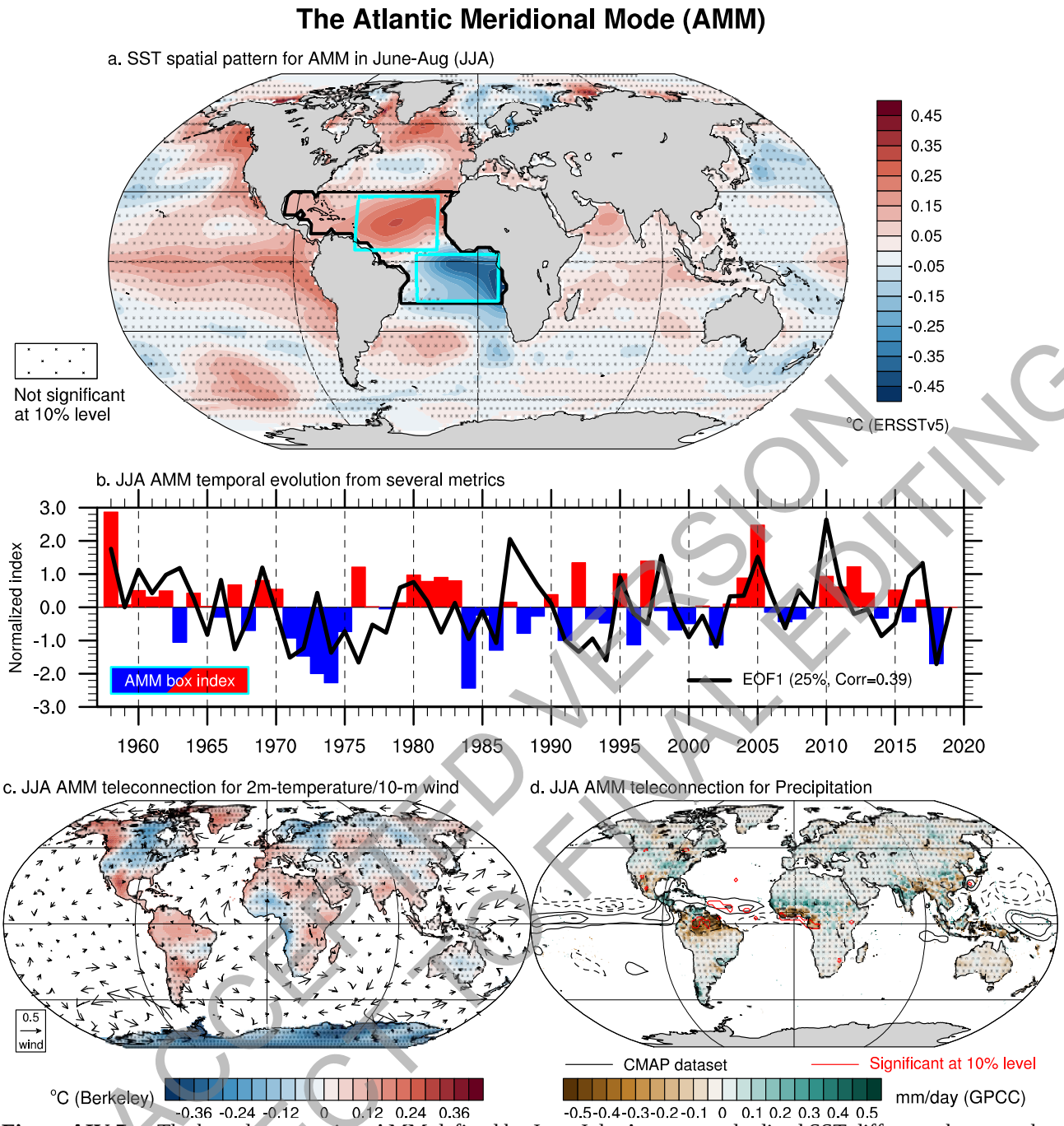
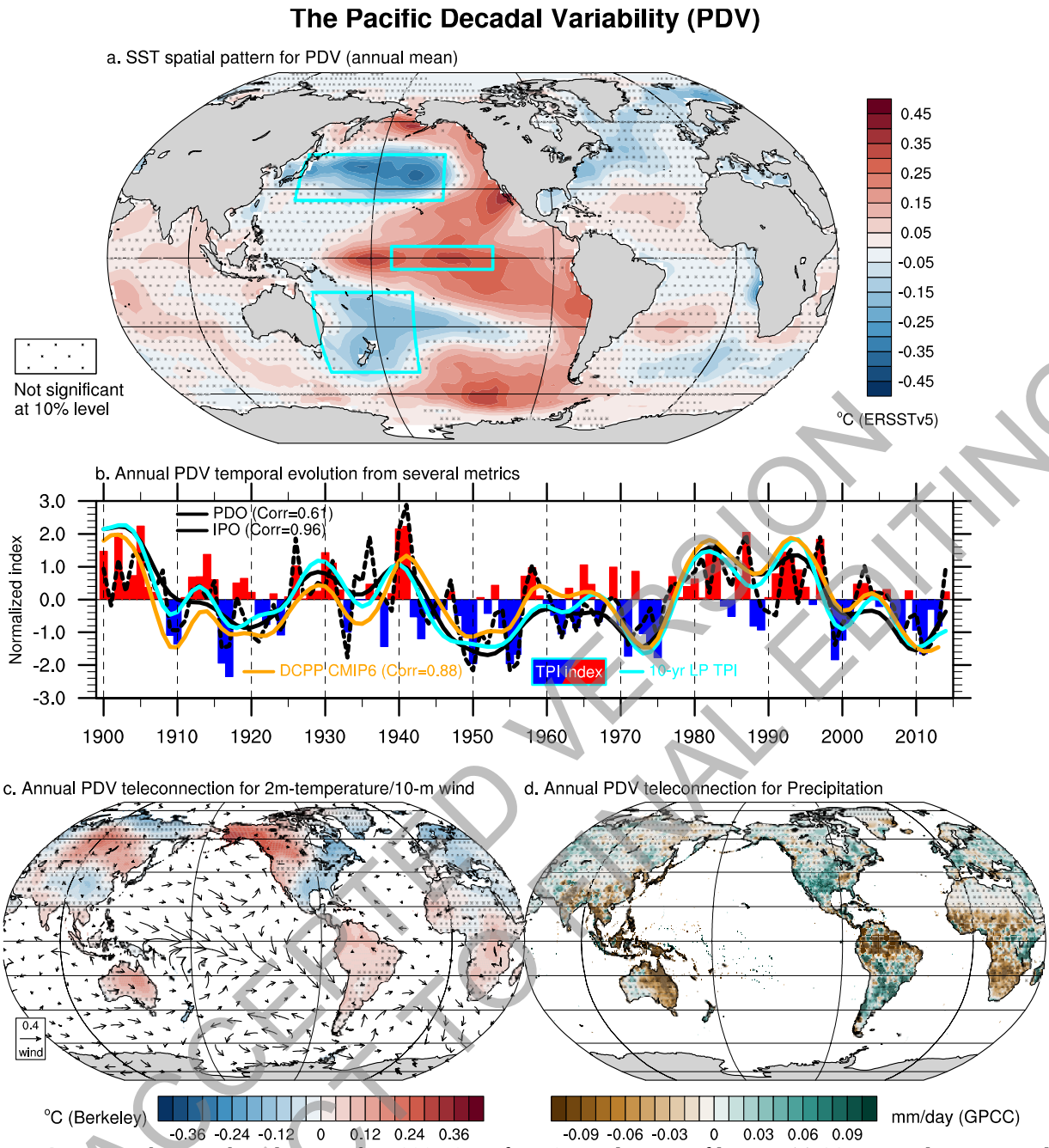


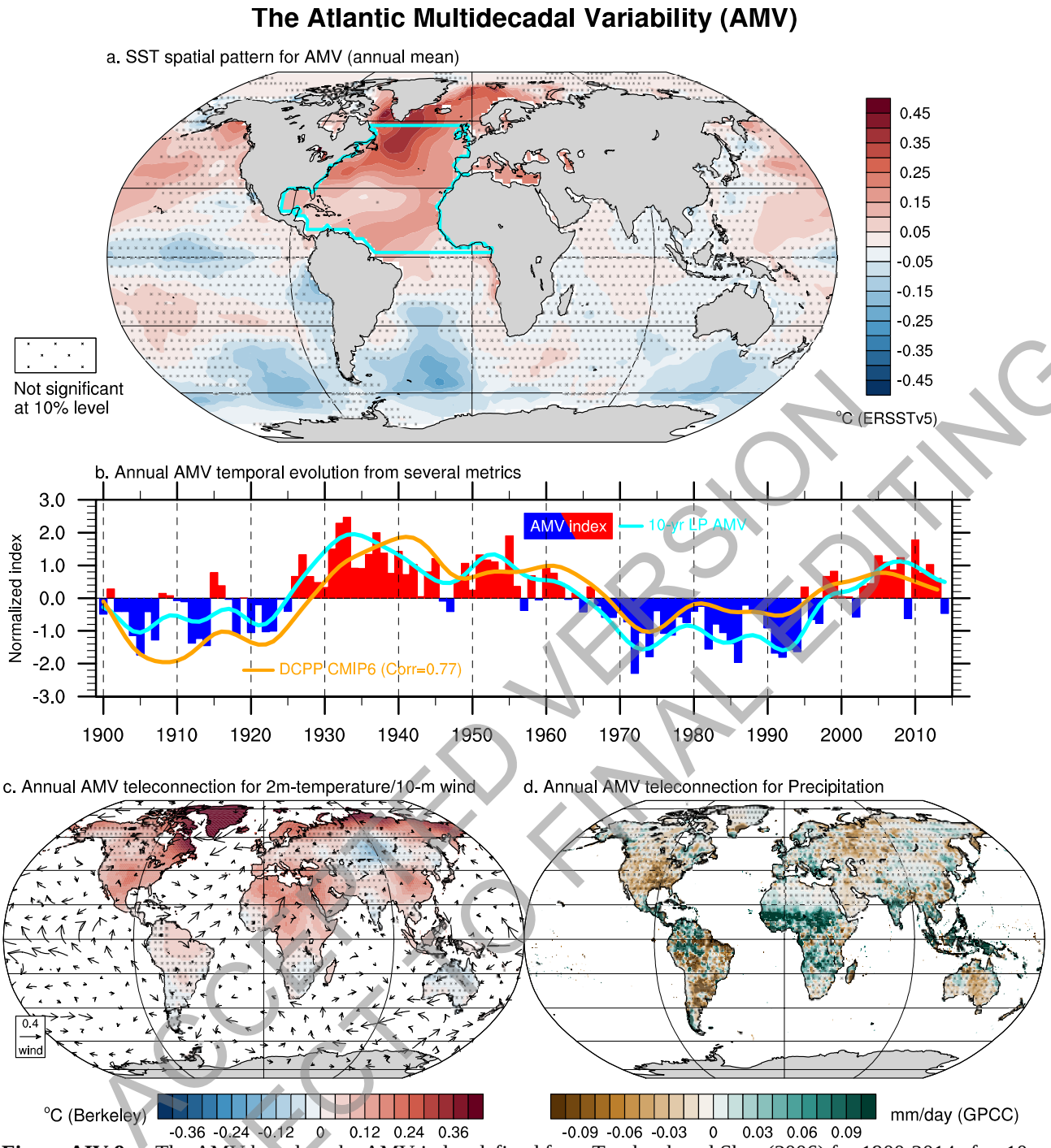
Figure AIV.7: The boreal summertime AMM defined by June-July-August standardized SST difference between the north (5ºN-30ºN, 20ºW-60ºW) and south (5ºN-20ºS, 5ºE-25ºW) tropical Atlantic Ocean shown by the cyan boxes in (a) or estimated as the leading EOF over the tropical Atlantic Ocean (the region denoted by the black box in a) for 1958-2019 using ERSSTv5. (a) SST anomalies regressed onto the AMM time series, which is shown in (b) as red and blue bars, while the black curve represents the leading principal component timeseries. Explained variance and correlation between indices are given in the legend in (b). (c) Same as (a) but for land SAT and 10-m level wind (arrows; based on JRA-55 for 1958-2019) anomalies. (d) Same as (a) but for precipitation anomalies (shading based on GPCC for 1958-2016 and contours based on CMAP for 1979-2019 for every 0.2 mm/day). On maps, no-overlay indicates regions where the regressions are significant based on t-test accounting for false detection rate at 10% and crosses indicates no significance. Significance for CMAP precipitation is materialized by red contours in (d). All fields have been linearly detrended prior to computation.

ACCEPTED VERSION SUBJECT TO FINAL EDITING



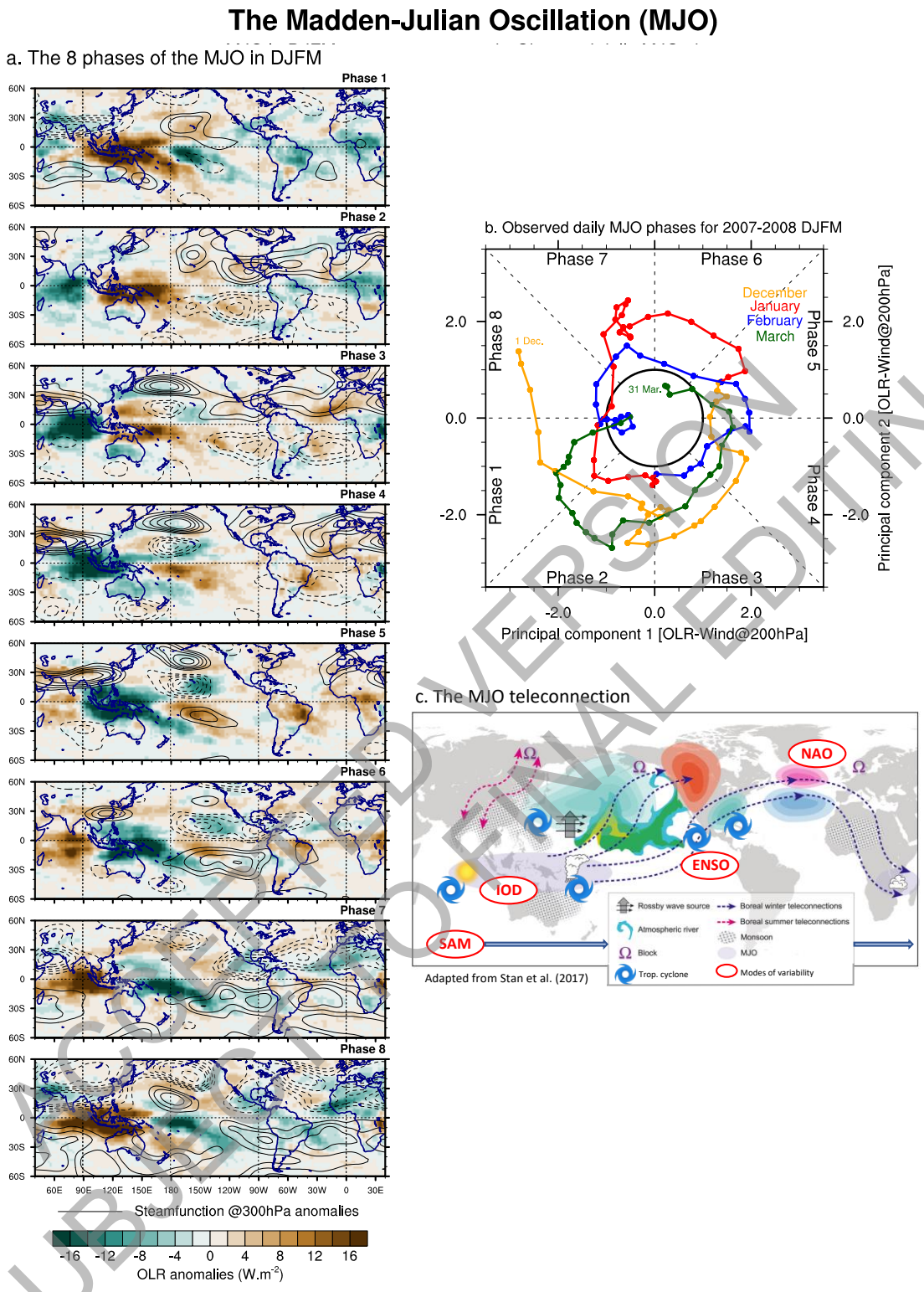
ACCEPTED VERSION SUBJECT TO FINAL EDITING

Figure AIV.8: The PDV based on TPI for 1900-2014 after 10-year low-pass filtering. (a) SST anomalies regressed onto TPI based on ERSSTv5. The cyan boxes indicate regions for the TPI definition. (b) Temporal evolution of the raw TPI (bars), the 10-year low-pass filtered TPI (cyan curve), the EOF-based PDO index (dashed black) and two estimations of the IPO EOF-based indices. In solid black, linear detrending is applied to annual data prior to the computation of the EOF of the low-pass filtered SST to remove the forced component in the SST field. In orange, the forced signal is estimated from CMIP5 historical simulations following Ting et al. (2009). The latter metric is used in CMIP6 DCPP-C sensitivity experiments (Boer et al. 2016). The correlation between the low-pass filtered TPI and all PDV indices is given in the legend. (c) Same as (a) but for land SAT (shading; based on BerkeleyEarth for 1900-2014) and 10-m level wind (arrows; based on JRA-55 for 1958-2014) anomalies. (d) Same as (a) but for precipitation anomalies (shading based on GPCC for 1900-2014). All are based on annual mean. On maps, no-overlay indicates regions where the regressions are significant based on t-test accounting for false detection rate at 10% and crosses indicates no significance.



ACCEPTED VERSION SUBJECT TO FINAL EDITING

Figure AIV.9: The AMV based on the AMV index defined from Trenberth and Shea (2006) for 1900-2014 after 10-year low-pass filtering. The index corresponds to the annual SST averaged over the North Atlantic domain (cyan box) minus near-global average [60ºN-60ºS]. (a) SST anomalies regressed onto the AMV index based on ERSSTv5. (b) The cyan curve indicates the 10-year low-pass filtered AMV index shown in bars. The orange curve stands for the AMV index used for the CMIP6 DCPP-C sensitivity experiments (Boer et al. 2016). (c) Same as (a) but for land SAT (shading; based on BerkeleyEarth for 1900-2014) and 10-m level wind (arrows; based on JRA-55 for 1958-2014) anomalies. (d) Same as (a) but for precipitation anomalies (shading based on GPCC for 1900-2014). All is based on annual mean. On maps, no-overlay indicates regions where the regressions are significant based on t-test accounting for false detection rate at 10% and crosses indicates no significance.



ACCEPTED VERSION SUBJECT TO FINAL EDITING

Figure AIV.10: (a) The spatio-temporal properties of the MJO. Daily composites of Outgoing Longwave Radiation (OLR, W m^{-2}, shaded) anomalies and streamfunction anomalies at 300 hPa (STF, contours every 0.5 10^6 m^2 s^{-1}) for the 8 MJO phases in boreal winter (1st Dec. -31st March) based on NOAA interpolated satellite products and NCEP-NCAR reanalyzes over 1979-2019, respectively. Greenish (brownish) colours indicate enhanced (reduced) convective activity associated with wet (dry) conditions. Solid

(dashed) contours show for positive (negative) STF anomalies which stand for anomalous anticyclonic circulation in the Northern (Southern) Hemisphere. (b) Phase diagram of the MJO constructed from the two leading principal components drawn from empirical orthogonal decomposition of combined wind@300hPa+OLR fields following Wheeler and Hendon (2004) for the winter 2007-2008 chosen as an example of active MJO years. (c) Schematic representation of MJO-related tropical—Northern Hemisphere interactions and teleconnections inferred from observational and numerical studies (adapted from Stan et al.(2017)). Because the interactions and teleconnections of the Southern Hemisphere are not as well understood but SAM, they are not included in the current schematic.

ACCEPTED VERSION
SUBJECT TO FINAL EDITING

Annex V: Monsoons

Coordinating Lead Authors:
Annalisa Cherchi (Italy), Andrew Turner (United Kingdom)

Lead Authors:
Lincoln M. Alves (Brazil), Paola A. Arias (Colombia), Mathew Barlow (United States of America), Ruth Cerezo-Mota (Mexico), Aïda Diongue-Niang (Senegal), Joelle Gergis (Australia), Sergey K. Gulev (Russian Federation), Dabang Jiang (China), Richard G. Jones (United Kingdom), Won-Tae Kwon (Republic of Korea), June-Yi Lee (Republic of Korea), Jian Li (China), Linda O. Mearns (United States of America), Wilfried Pokam Mba (Cameroon), Sabin Thazhe Purayil (India), Krishnan Raghavan (India), Juan A. Rivera (Argentina), Jessica Tierney (United States of America), Tianjun Zhou (China)

Contributing Author:
Josephine Brown (Australia)

This Annex should be cited as:
IPCC, 2021: Annex V: Monsoons [Cherchi, A., A. Turner (eds.)]. In: *Climate Change 2021: The Physical Science Basis. Contribution of Working Group I to the Sixth Assessment Report of the Intergovernmental Panel on Climate Change* [Masson-Delmotte, V., P. Zhai, A. Pirani, S. L. Connors, C. Péan, S. Berger, N. Caud, Y. Chen, L. Goldfarb, M. I. Gomis, M. Huang, K. Leitzell, E. Lonnoy, J.B.R. Matthews, T. K. Maycock, T. Waterfield, O. Yelekçi, R. Yu and B. Zhou (eds.)]. Cambridge University Press. In Press.

Date: August 2021

This document is subject to copy-editing, corrigenda and trickle backs.

ACCEPTED VERSION
SUBJECT TO FINAL EDITS

AV.1 Introduction 3
AV.2 Definition of the global monsoon 3
AV.3 Rationale for regional monsoons definitions in AR6 3
AV.4 Definition of regional monsoons 4
AV.4.1 The South and Southeast Asian monsoon 4
AV.4.2 The East Asian monsoon 5
AV.4.3 The West African Monsoon 6
AV.4.4 The North American Monsoon 7
AV.4.5 The South American Monsoon 8
AV.4.6 The Australian-Maritime Continent monsoon 9
References 11
Figures 19

ACCEPTED VERSION
SUBJECT TO FINAL EDITS

AV.1 Introduction

A monsoon refers to a seasonal transition of regimes in atmospheric circulation and precipitation in response to the annual cycle of solar insolation and the distribution of moist static energy (Wang and Ding, 2008; Wang et al., 2014; Biasutti et al., 2018). A global monsoon can be objectively identified based on precipitation contrasts in the solstice seasons to encompass all monsoon regions (Wang and Ding, 2008). In AR5, regional monsoon domains were identified starting from the definition of the global monsoon tailored over the continents and adjacent oceans, as in Kitoh et al. (2013). This Annex contains the definition of the global monsoon as used in AR6 (Section AV.2), it explains the rationale for the different definition of AR6 regional monsoons compared to AR5 (Section AV.3) and provides the definition and basic characteristics of each regional monsoon assessed (Section AV.4).

AV.2 Definition of the global monsoon

The concept of global monsoon (GM) emerged during the second half of the 20th century, representing the leading empirical orthogonal function (EOF) mode of the annual variations of precipitation and circulation in the global tropics and subtropics as a forced response of the coupled climate system to the annual cycle of solar insolation (Wang and Ding, 2008; An et al., 2015; Wang et al., 2017). GM variability represents, to a large extent, changes in the ITCZ and associated Hadley circulation (Wang et al., 2014). Changes in GM have been attributed to both internal variability and external forcings, ranging from interannual to millennial and orbital time scales (Wang et al., 2014, 2017; An et al., 2015; Geen et al., 2020). In AR6, the global monsoon is defined as the area in which the annual range (local summer minus local winter) of precipitation is greater than 2.5 mm/day (Kitoh et al. et al., 2013), and the domain is represented by the black contour in Figure AV.1. Simulation of the global monsoon and its variability is the subject of coordinated modelling experiments in the Global Monsoon Model Intercomparison Project (GMMIP; Zhou et al., 2016). Past changes, simulation and attribution, and projections of the GM are assessed in Sections 2.3.1.4.2, 3.3.3.2 and 4.4.1.4, respectively.

[START Figure AV.1 HERE]

Figure AV.1: Global and regional monsoons domains. AR6 global monsoon area is represented by the black contour. AR6 regional monsoons are: North American monsoon (shaded magenta), South American monsoon (shaded dark-orange), West African monsoon (shaded grey), South and Southeast Asian monsoon (shaded pink), East Asian monsoon (shaded purple) and Australian-Maritime Continent monsoon (shaded yellow). Areas over Equatorial America and South Africa (dotted red and magenta, respectively) are highlighted but not identified as specific regional monsoons (see explanation in the main text). For each regional monsoon, the seasonal characteristics associated with each domain are specified in the main text.

[END Figure AV.1 HERE]

AV.3 Rationale for regional monsoons definitions in AR6

The definition of the regional monsoons has been slightly modified in AR6 with respect to AR5, starting from the consideration that some of the continental areas identified using the global metric have a seasonality in precipitation that is not necessarily of monsoon origin. In particular, the dotted regions in Figure AV.1 located over South Africa, Central America and equatorial South America have a strong seasonality in precipitation but their qualification as monsoons is a subject of discussion. In the assessment of the regional monsoons in Sections 8.3.2.4 and 8.4.2.4, these regions are not considered as distinct regional monsoons, but they are discussed in Box 8.2 that is dedicated to changes in water cycle seasonality. The domains of the regional monsoons in AR6 are defined based on published literature and expert judgement, and accounting

ACCEPTED VERSION SUBJECT TO FINAL EDITS

for the fact that the climatological summer monsoon rainy season varies across the individual monsoon regions. As shown in Figure AV.1, AR6 regional monsoons are: South and Southeast Asian (Section AV.4.1), East Asian (Section AV.4.2), West African (Section AV.4.3), North American (Section AV.4.4), South American (Section AV.4.5) and Australian-Maritime Continent (Section AV.4.6). For each region the definition, regional justification and key features are provided, along with cross references to the main areas of assessment in AR6.

AV.4 Definition of regional monsoons

AV.4.1 The South and Southeast Asian monsoon

The South and Southeast Asian monsoon (SAsiaM) is characterized by pronounced seasonal reversal of wind and precipitation. It covers vast geographical areas and several countries including India, Bangladesh, Nepal, Myanmar, Sri Lanka, Pakistan, Thailand, Laos, Cambodia, Vietnam and the Philippines (Pant and Rupa Kumar, 1997; Goswami, 2006; Gadgil et al., 2010; Shige et al., 2017), with a domain roughly extending across 60°-110°E and 10°S-25°N as shown in Figure AV.1 (shaded pink). The SAsiaM is unique in its geographical features because of the orography surrounding the area (i.e., the Himalayas, Western Ghats and Arakan Yoma mountains, and Tibetan Plateau to the north) and the adjacent Indian Ocean.

The SAsiaM rainy season from June to September contributes to more than 75% of the annual rainfall over much of the region, including the southern slopes of the central and eastern Himalayas (Krishnan et al., 2019b). Considering the spatial domain of the SAsiaM, monsoon precipitation maxima are located over the west coast, northeast and central north India, Myanmar and Bangladesh, whereas minima are located over northwest and south-eastern India, western Pakistan, and south-eastern and northern Sri Lanka (Pant and Rupa Kumar, 1997; Gadgil et al., 2010). Prior to the SAsiaM rainy season, areas in the north-western Himalaya receive precipitation during winter and early spring from so-called “western disturbances”, which are extratropical synoptic systems originating over the Mediterranean region and propagating eastward along the sub-tropical westerly jet (Madhura et al., 2014; Cannon et al., 2015; Dimri et al., 2015; Hunt et al., 2018; Krishnan et al., 2019a, 2019b).

The climatological onset of the SAsiaM occurs around 20 May over the Andaman and Nicobar Islands and covers the central Bay of Bengal around 25 May, while it simultaneously advances into mainland India from the south through Kerala (Pai et al., 2020). The normal date of monsoon onset over Kerala is 1 June and the monsoon rains progress into India both from south to north and east to west, so as to cover the entire country by 15 July (Pai et al., 2020), although with large interannual and interdecadal variations (Ghanekar et al., 2019). Retreat of the SAsiaM typically begins from far northwest India around 1 September and withdraws completely from the country by 15 October; this is followed by establishment of the northeast monsoon rainy season over south peninsular India from October through December (Pai et al., 2020).

The SAsiaM exhibits prominent rainfall variability on subseasonal, interannual and interdecadal time scales with teleconnections to modes of climate variability (see Webster et al., 1998; Turner and Annamalai, 2012). While the gross features of the SAsiaM are simulated in GCMs, there are several large biases that have persisted over generations of climate models, in CMIP3 and CMIP5, including a large dry bias over India coupled to a lower-tropospheric circulation that is too weak (Sperber et al., 2013) and a related wet bias over the western equatorial Indian Ocean (Bollasina and Ming, 2013). In CMIP5, cold Arabian Sea SST biases in coupled GCMs were shown to worsen the monsoon dry bias by limiting the available moisture (Levine et al., 2013; Sandeep and Ajayamohan, 2015). Some improvements to the spatial pattern have been noted in CMIP6, particularly near orography (Gusain et al., 2020). The teleconnection to the El Niño-Southern Oscillation (ENSO) provides the main prospect for seasonal prediction and was too weak in CMIP5 (Sperber et al., 2013). The boreal summer intraseasonal oscillation (BSISO) controls the majority of subseasonal variations in SAsiaM rainfall, as well as affecting the East Asian monsoon region. While CMIP5 models better represented the BSISO than CMIP3 (especially its characteristic northward propagation), the spatial

ACCEPTED VERSION SUBJECT TO FINAL EDITS

pattern is still poorly simulated in most models (Sabeerali et al., 2013).

The SAsiaM is assessed in Sections 8.3.2.4.1, 8.4.2.4.1, Atlas.5.3.2 and Atlas.5.3.4. One of its main components, the Indian summer monsoon, is assessed in Section 10.6.3 as a case study on the construction of regional climate information from the distillation of multiple lines of evidence. Climate change over the Hindu Kush-Himalaya is assessed in CCB10.4.

AV.4.2 The East Asian monsoon

The East Asian monsoon (EAsiaM) is the seasonal reversal in wind and precipitation occurring over East Asia, including eastern China, Japan and the Korean Peninsula. The continental area influenced by this monsoon is roughly bounded by 102.5°-140°E and 20°-40°N (e.g., Wen et al., 2000; Wang and LinHo, 2002; Wang et al., 2010), and is shaded purple in Figure AV.1. Unlike other monsoons, it extends quite far north, out of the tropical belt, and it is largely influenced by subtropical systems, such as the Western North Pacific subtropical high, East Asian subtropical westerly jet, and by disturbances from the mid-latitudes (Chang et al., 2000; Lee et al., 2006, 2013b; Yim et al., 2008; Zhou et al., 2009).

The EAsiaM manifests during boreal summer with warm and wet southerly winds, but also during boreal winter with cold and dry northerly winds (Ha et al., 2012). The winter component has been linked to the subsequent summer (i.e., Wen et al., 2000, 2016; Ge et al., 2017; Yan et al., 2020).

AV.4.2.1 The summer EAsiaM

The summer EAsiaM is a subtropical monsoon system (e.g., Wang and LinHo, 2002; Ding et al., 2007). It is characterized by low-level southerly winds prevailing over eastern China, Korea and Japan in boreal summer. The monsoon flow brings abundant water vapour into East Asia that converges and forms the Meiyu/Baiu/Changma rain belt over the region (Zhou et al., 2009; Jin et al., 2013; Lee et al., 2017). In late April/early May, rainfall onsets in central Indochina Peninsula, and in mid-June the rainy season arrives over East Asia with the formation of the Meiyu front along the Yangtze River valley, Changma in Korea and Baiu in Japan. Later in July, the monsoon advances up to North China, the Korean peninsula and central Japan (Zhang et al., 2004; Yihui and Chan, 2005; Zhou et al., 2009).

Intraseasonal variability of the EAsiaM has been mostly related to the Madden Julian Oscillation (MJO) (Yasunari, 1979; Zhang et al., 2009; Chen et al., 2015), to the phase of the Pacific-Japan mode (Nitta, 1987) or the Indian summer monsoon (Li et al., 2018) and to the BSISO (Kikuchi et al., 2012; Chen et al., 2015), particularly for its onset (Lee et al., 2013a). At interannual time scales, changes in summer EAsiaM intensity lead to a position shift of the monsoon rain belt under the influence of ENSO (Wang et al., 2000) and the western Pacific subtropical high (Kosaka et al., 2013; Wang et al., 2013), Arctic sea ice (Guo et al., 2014) and solar and volcanic forcing (Peng et al., 2010; Man et al., 2012; Cui et al., 2014). Variability at interdecadal timescale is more prominent in the second half of the 20th century (Jiang, 2005; Ding et al., 2008; Wang et al., 2018), and a specific assessment about this aspect is provided in Section 8.3.2.4.2.

The basic features and interannual variations of the summer EAsiaM are well reproduced in climate models. For example, the climatological circulation structure is well reproduced in both atmospheric and coupled GCMs (Song and Zhou, 2013; Song et al., 2013; Jiang et al., 2016, 2020), and the relationship between the monsoon and ENSO is well represented (Sperber et al., 2013; Fu and Lu, 2017). In CMIP5 models, the main shortcomings relate to missing rainfall bands around 30°N and the northward shift of the western North Pacific subtropical high (Huang et al., 2013). Most coupled models show an inadequate strength of monsoon circulation over southern East Asia, and with little change in model performance from the TAR to AR6 (Jiang et al., 2016, 2020). In coupled model simulations, air-sea coupling helps improve the climatology and interannual variability of rainfall over the East Asia monsoon region (Wang, 2005; Song and Zhou, 2014).

ACCEPTED VERSION SUBJECT TO FINAL EDITS

The summer (June-July-August) component of the EAsiaM is assessed in Sections 8.3.2.4.2, 8.4.2.4.2, Atlas.5.1.2 and Atlas.5.1.4.

AV.4.2.2 The winter EAsiaM

The winter EAsiaM is characterized by strong north-westerlies over northeast China, Korea and Japan, and by strong north-easterlies along the coast of East Asia (Huang et al., 2003). The northerly wind extends from midlatitude East Asia to the equatorial South China Sea (Wen et al., 2000; Wang et al., 2010). The winter EAsiaM has one component mostly linked to mid-to-high latitude circulation systems and another mostly linked to the tropical circulation and largely controlled by ENSO (Ge et al., 2012; Chen et al., 2014a). The mid-latitude component has a close relationship with autumn Arctic sea-ice concentration changes (Chen et al., 2014b).

The winter EAsiaM exhibits significant variability ranging from intra-seasonal to interdecadal timescales. Its intra-seasonal variability is suggested to be influenced by both high-latitude and subtropical Eurasian wave trains (Jiao et al., 2019). At the interannual timescale, ENSO is an important factor modulating the winter EAsiaM (Wang et al., 2000), while the relationship between them is not stable (Wang and He, 2012; Fan et al., 2020). In addition, Arctic Oscillation (Gong et al., 2001), Arctic sea ice (Ge et al., 2012), Eurasian snow (Luo and Wang, 2019), and strong volcanic eruptions (Miao et al., 2016) also play vital roles in changing the winter EAsiaM intensity. At the interdecadal timescale, the winter EAsiaM weakened significantly in the mid-1980s, which resulted from atmospheric intrinsic quasi-stationary planetary waves (Wang et al., 2009) and external forcings (Miao et al., 2018). In the mid-2000s, the winter EAsiaM was observed to recover from its weak epoch (Wang and Chen, 2014).

The large-scale features of the winter EAsiaM are well reproduced by climate models, although the strength of monsoon circulation is underestimated. The ability of coupled models to simulate the winter EAsiaM shows little difference through the TAR to AR5, but has improved from AR5 to AR6 (Jiang et al., 2016, 2020). In CMIP5 models, reasonable simulations of the Siberian high and Aleutian low intensities and the ENSO-winter EAsiaM relationship help improve the climatology and interannual variability of the winter EAsiaM (Gong et al., 2014).

Model simulations of the winter component of the EAsiaM are assessed in chapter Atlas.5.1.3.

AV.4.3 The West African Monsoon

The West African monsoon (WAfriM) is a seasonal reversal in wind and precipitation extending over a vast and contrasted geographical region, from the Equator to the margins of the Sahara, and from the Atlantic coast inland. The WAfriM domain includes Togo, Guinea Bissau, Gambia, Senegal, Mauritania, Guinea, Sierra Leone, Liberia, Mali, Ivory Coast, Burkina Faso, Ghana, Benin, Chad, Cape Verde, northern Cameroon, Niger, Nigeria and northern Central African Republic. It can thus be roughly bounded by 18°W-30°E, 5°-18°N and is grey shaded in Figure AV.1 (e.g., Adedokun, 1978). The West African monsoon and Sahel are sometimes considered interchangeably. However, the Sahel lies in the northern part of the WAfriM region, often limited to the west and central north Africa (e.g., Nicholson et al. (2018) considered the domain to be 20°W-30°E, 10°-20°N) or sometimes extended to the east (e.g., Giannini and Kaplan (2019) considered the domain to be 20°W-40°E, 10°-20°N). The East African region with the Greater Horn of Africa, which includes Ethiopia, Sudan, and South Sudan, lies on the fringes of both the West African and Indian monsoons (Nicholson, 2017).

The WAfriM is characterized by the northward progression from May to September of moist low-level south-westerlies from the Gulf of Guinea, meeting the dry north-easterlies (Harmattan) from the Saharan heat low at the intertropical discontinuity (e.g., Hamilton et al., 1945; Omotosho, 1988). In May and June,

ACCEPTED VERSION SUBJECT TO FINAL EDITS

rainfall remains essentially along the Guinean coast with a maximum occurring near 5°N, then the rainfall maximum jumps suddenly over the Sudan-Sahel zone near 12°N, followed by a "little dry season" over the Guinea coast (Adejuwon and Odekunle, 2006). This apparent shift is known as the West African monsoon jump and it is concomitant with the monsoon onset over the Sahel (Sultan and Janicot, 2003; Cook, 2015). Rainfall continues to progress towards the north up to about 18-20°N. The rainfall maximum occurs in the Sahel in August/September, followed by a rapid retreat of rainfall to the Guinean Coast and a second maximum occurs over this region in October/November.

The WAfriM features variability at different timescales. Unprecedent droughts occurred in West Africa and particularly over the Sahel from the late 1960s to the mid-1990s, and a specific assessment of the understanding of mechanisms related to these changes is provided in Sections 8.3.2.4.3 and 10.4.2.1.

At interannual time scales, tropical oceans (Atlantic, Pacific and Indian) appear to be the major drivers with their SSTs anomalies leading to variations in the accumulated seasonal rainfall (e.g., Lamb, 1978; Diakhate et al, 2019). At intraseasonal time scales, equatorial waves (e.g., Mekonnen et al., 2008; Janicot et al., 2010) and interactions with mid-latitudes and the Mediterranean (e.g., Vizy and Cook, 2009; Roehrig et al., 2011) have an effect on WAfriM activity. African Easterly Waves (AEWs) and mesoscale convective systems (MCSs), including squall lines, are the prominent weather synoptic scale aspects of the WAfriM, supplying almost all rainfall in the Sahel. The strong coupling between AEWs and MCSs has been investigated in depth, as well as their interactions with the Saharan Heat Low, the moisture supply from East Africa and the Mediterranean region or from near the equator (e.g., Diongue et al., 2002; Brammer and Thorncroft, 2017; Lafore et al., 2017). Land surface processes are known to influence WAfriM precipitation (Boone et al., 2016).

Simulation of West Africa climate, including the monsoon, has received specific attention under coordinated programmes in the recent past: the African Multidisciplinary Monsoon Analysis Model Intercomparison Project (AMMA-MIP), the AMMA Land-surface Model Intercomparison Project (ALMIP), the West African Monsoon Modelling and Evaluation (WAMME) project and the Coordinated Regional Downscaling Experiment (CORDEX) (Raj et al., 2019). CMIP5 and CMIP6 struggle to reproduce the amplitude of observed decadal variability in the twenty century and to represent the mean climatology including the northward propagation of the monsoon (Roehrig et al., 2013; Monerie et al., 2020; Sow et al., 2020). A higher horizontal resolution improves the representation of the intensity and spatial distribution of WAfriM rainfall and related circulation, because of the effects of vegetation, orography and coastlines (Hourdin et al., 2010; Sylla et al., 2010; Xue et al., 2010; Raj et al., 2019).

The WAfriM is assessed in Sections 8.3.2.4.3 and 8.4.2.4.3. The observed Sahel and West African monsoon drought and recovery is assessed as a regional climate change attribution example in Section 10.4.2.1.

AV.4.4 The North American Monsoon

The North American monsoon (NAmerM) is a regional-scale atmospheric circulation system dominated by boreal summer precipitation over northwestern Mexico and southwest United States, where it contributes to almost 70% and 40% of the total annual precipitation, respectively (Douglas et al., 1993; Higgins et al., 1997). The NAmerM domain is shaded magenta in Figure AV.1, roughly bounded by 15°-35°N, 100°-115°W and defined where the July-August-September minus June mean precipitation exceeds 25mm/mon (Douglas et al., 1993; Adams and Comrie, 1997; Barlow et al., 1998; Cook and Seager, 2013).

The identification of a regional monsoon regime in North America dates back to the 1990s (Douglas et al., 1993; Adams and Comrie, 1997; Higgins et al., 1997; Barlow et al., 1998), although consideration of the monsoonal character of the southwestern United States precipitation goes back considerably further (e.g.,

ACCEPTED VERSION SUBJECT TO FINAL EDITS

Bryson and Lowry, 1955). The monsoonal characteristics of the region include a pronounced annual maximum of precipitation in boreal summer (June-July-August) accompanied by a surface low pressure system and an upper-level anticyclone, although the seasonal reversal of the surface winds is primarily limited to the northern Gulf of California. In particular, the summertime precipitation in the NAmerM region is dictated by the location of the upper-level anticyclone (Reed, 1933; Castro et al., 2001). The decay phase of the NAmerM is typically observed during late September-October, when convection migrates from Central to South America (Vera et al., 2006).

Mesoscale variability of the NAmerM comes from the pulsing of the Gulf of California low-level jet, the intensification/reduction of the land-sea contrast (Torres-Alavez et al., 2014) and moisture surges over the Gulf of California (Vera et al., 2006). Synoptic variability of the NAmerM is mainly associated with the activity of tropical cyclones and of easterly waves (Stensrud et al., 1997; Fuller and Stensrud, 2000). In addition, the NAmerM is strongly influenced by the ENSO variability at both the interannual (Higgins et al., 1999; Higgins and Shi, 2001) and decadal (e.g., Castro et al., 2001) time scales.

The region is challenging for climate modeling for several reasons, including complex topography, importance of Mesoscale Convective Systems (MCSs), and sensitivity to SST bias (e.g., Pascale et al., 2019). Many CMIP3 and CMIP5 models with resolutions coarser than 100 km are unable to realistically resolve the topography of the NAmerM region, thus inducing biases in simulating the monsoon (Geil et al., 2013). Among other factors, these biases are due to biases in the simulation of the Gulf of California summertime low-level flow (Kim et al., 2008; Pascale et al., 2017) and to failures in representing properly the diurnal cycle (Risanto et al., 2019) and the decay (Bukovsky et al., 2015) of the NAmerM precipitation. Simulations at higher horizontal resolution (i.e. with at least 0.25º grid) exhibit an improved representation of the regional topography, which provides a better representation of the regional circulation and therefore of the NAmerM (Varuolo-Clarke et al., 2019).

The NAmerM is assessed in Sections 8.3.2.4.4 and 8.4.2.4.4.

AV.4.5 The South American Monsoon

The South American monsoon (SAmerM) is a regional circulation system characterized by inflow of low-level winds from the Atlantic Ocean toward South America, involving Brazil, Perù, Bolivia and northern Argentina, associated with the development of surface pressure gradients (and intense precipitation) during austral summer (December-January-February). Based on climatological precipitation intensity, the SAmerM region is roughly bounded by 5°-25°S and 70°-50°W (Zhou and Lau, 1998; Vera et al., 2006; Raia and Cavalcanti, 2008) and is dark-orange shaded in Figure AV.1.

During austral spring (September-October-November), areas of intense convection migrate from northwestern South America to the south (Raia and Cavalcanti, 2008), forming the South Atlantic Convergence Zone (SACZ) during austral summer (Kodama, 1992; Jones and Carvalho, 2002; Vera et al., 2006). Associated with this regime, an upper-tropospheric anticyclone (the Bolivian High) forms over the Altiplano region during the monsoon onset (Lenters and Cook, 1997). The establishment of this upper-level anticyclone has been related to the transition from southerly to northerly winds and the occurrence of strong convective heating over the Amazon (Lenters and Cook, 1997; Wang and Fu, 2002). The SAmerM then retreats during austral autumn/fall (March-April-May) with a northeastward migration of the convection (e.g., Vera et al., 2006).

The SAmerM displays considerable variability on time scales raging from intraseasonal to decadal (Vera et al., 2006; Marengo et al., 2012; Vuille et al., 2012; Novello et al., 2017). The Madden-Julian Oscillation (MJO, Section AVI.2.8) influences the SACZ via changes in midlatitude synoptic disturbances (Jones and

ACCEPTED VERSION SUBJECT TO FINAL EDITS

Carvalho, 2002; Liebmann et al., 2004). At interannual time scales, ENSO explains most of the SAmerM variability (e.g., Paegle and Mo, 2002; Marengo et al., 2012).Tropical Atlantic temperatures also affect the SAmerM, with reduced atmospheric moisture transport to feed the monsoon under a warmer tropical north Atlantic conditions (e.g., Marengo et al., 2008; Zeng et al., 2008). In addition to SSTs, interannual variability of the SAmerM is linked to changes in land surface processes, cold-air incursions, the latitudinal location of the subtropical jet, and the Southern Annular Mode (Section AVI.2.2) (e.g., Silvestri, 2003; Li and Fu, 2004; Collini et al., 2008; Yin et al., 2014). At interdecadal timescales, the SAmerM is influenced by important modes of climate variability (e.g., Robertson and Mechoso, 2000; Paegle and Mo, 2002; Chiessi et al., 2009; Silvestri and Vera, 2009).

The general large-scale features of the SAmerM are reasonably well simulated by coupled climate models although they do not adequately reproduce maximum precipitation over the core of the monsoon, even when considering simulations under past natural forcings, such as those during the last millennium (Rojas et al., 2016; Díaz and Vera, 2018). However, CMIP5 models featured an improved representation of the SAmerM with respect to CMIP3 (Joetzjer et al., 2013; Jones and Carvalho, 2013; Gulizia and Camilloni, 2015; Díaz and Vera, 2017).

The SAmerM is assessed in Sections 8.3.2.4.5 and 8.4.2.4.5.

AV.4.6 The Australian-Maritime Continent monsoon

The Australian-Maritime Continent monsoon (AusMCM) occurs during austral summer (December-January-February), with the large-scale shift of the Inter-Tropical Convergence Zone into the Southern Hemisphere. It covers northern Australia and the Maritime Continent up to 10°N (e.g., McBride, 1987; Suppiah, 1992; Robertson et al., 2011), and it corresponds to the yellow shaded region in Figure AV.1. The identification of the Australian monsoon by meteorologists dates back to the early 20th century (see review of Suppiah, 1992), with later studies providing classifications of monsoon circulation regimes (e.g., McBride, 1987) and definitions of monsoon onset (Troup, 1961; Holland, 1986; Hendon and Liebmann, 1990; Drosdowsky, 1996).

The AusMCM is characterized by the seasonal reversal of prevailing easterly winds to westerly winds and the onset of periods of active convection and heavy rainfall (Zhang and Moise, 2016). Over northern Australia, the monsoon season generally lasts from December to March and is associated with west to northwesterly inflow of moist winds, producing convection and heavy precipitation. Over the Maritime Continent, the main rainy season south of the equator is centered on December to February with northwesterly monsoon flow at low levels.

Over Australia, the monsoon is strongly influenced by ENSO on interannual timescales: during El Niño years the monsoon onset tends to be delayed (Nicholls et al., 1982; McBride and Nicholls, 1983; Drosdowsky, 1996). This relationship breaks down after the onset of the wet season, leading to little correlation between ENSO phase and total monsoon rainfall or duration (e.g., Hendon et al., 2012). The Maritime Continent also experiences a delay in monsoon onset during El Niño years and monsoon rainfall is correlated with ENSO during the dry and transition seasons (Robertson et al., 2011). The AusMCM is also influenced by the Indian Ocean Dipole (peaking in September -November) that tends to weaken the following monsoon when in its positive phase (Cai et al., 2005).

The ability of climate models to simulate the Australian monsoon has improved in successive generations of coupled models (i.e., from CMIP3 to CMIP6, Moise et al., 2012; Brown et al., 2016; Narsey et al., 2020), with sensitivity of monsoon rainfall to the magnitude of SST biases in the equatorial Pacific (Brown et al., 2016).

ACCEPTED VERSION SUBJECT TO FINAL EDITS

The AusMCM is assessed in Sections 8.3.2.4.6 and 8.4.2.4.6.

ACCEPTED VERSION
SUBJECT TO FINAL EDITS

References

Adams, D. K., and Comrie, A. C. (1997). The North American Monsoon. *Bull. Am. Meteorol. Soc.* 78, 2197–2213. doi:10.1175/1520-0477(1997)078<2197:TNAM>2.0.CO;2.

Adedokun, J. A. (1978). West African precipitation and dominant atmospheric mechanisms. *Arch. für Meteorol. Geophys. und Bioklimatologie Ser. A* 27, 289–310. doi:10.1007/BF02247952.

Adejuwon, J. O., and Odekunle, T. O. (2006). Variability and the Severity of the "Little Dry Season" in Southwestern Nigeria. *J. Clim.* 19, 483–493. doi:10.1175/JCLI3642.1.

An, Z., Wu, G., Li, J., Sun, Y., Liu, Y., Zhou, W., et al. (2015). Global Monsoon Dynamics and Climate Change. *Annu. Rev. Earth Planet. Sci.* 43, 29–77. doi:10.1146/annurev-earth-060313-054623.

Barlow, M., Nigam, S., and Berbery, E. H. (1998). Evolution of the North American monsoon system. *J. Clim.* 11, 2238–2257. doi:10.1175/1520-0442(1998)011<2238:EOTNAM>2.0.CO;2.

Biasutti, M., Voigt, A., Boos, W. R., Braconnot, P., Hargreaves, J. C., Harrison, S. P., et al. (2018). Global energetics and local physics as drivers of past, present and future monsoons. *Nat. Geosci.* 11, 392–400. doi:10.1038/s41561-018-0137-1.

Bollasina, M. A., and Ming, Y. (2013). The general circulation model precipitation bias over the southwestern equatorial Indian Ocean and its implications for simulating the South Asian monsoon. *Clim. Dyn.* 40, 823–838. doi:10.1007/s00382-012-1347-7.

Boone, A. A., Xue, Y., De Sales, F., Comer, R. E., Hagos, S., Mahanama, S., et al. (2016). The regional impact of Land-Use Land-cover Change (LULCC) over West Africa from an ensemble of global climate models under the auspices of the WAMME2 project. *Clim. Dyn.* 47, 3547–3573. doi:10.1007/s00382-016-3252-y.

Brammer, A., and Thorncroft, C. D. (2017). Spatial and Temporal Variability of the Three-Dimensional Flow around African Easterly Waves. *Mon. Weather Rev.* 145, 2879–2895. doi:10.1175/MWR-D-16-0454.1.

Brown, J. R., Moise, A. F., Colman, R., and Zhang, H. (2016). Will a Warmer World Mean a Wetter or Drier Australian Monsoon? *J. Clim.* 29, 4577–4596. doi:10.1175/JCLI-D-15-0695.1.

Bryson, R., and Lowry, W. (1955). Synoptic climatology of the Arizona summer monsoon.

Bukovsky, M. S., Carrillo, C. M., Gochis, D. J., Hammerling, D. M., McCrary, R. R., and Mearns, L. O. (2015). Toward assessing NARCCAP regional climate model credibility for the North American monsoon: Future climate simulations. *J. Clim.* 28, 6707–6728. doi:10.1175/JCLI-D-14-00695.1.

Cai, W., Hendon, H. H., and Meyers, G. (2005). Indian Ocean Dipolelike Variability in the CSIRO Mark 3 Coupled Climate Model. *J. Clim.* 18, 1449–1468. doi:10.1175/JCLI3332.1.

Cannon, F., Carvalho, L. M. V., Jones, C., and Bookhagen, B. (2015). Multi-annual variations in winter westerly disturbance activity affecting the Himalaya. *Clim. Dyn.* 44, 441–455. doi:10.1007/s00382-014-2248-8.

Castro, C. L., McKee, T. B., and Pielke, R. A. (2001). The relationship of the North American Monsoon to tropical and North Pacific Sea surface temperatures as revealed by observational analyses. *J. Clim.* 14, 4449–4473. doi:10.1175/1520-0442(2001)014<4449:TROTNA>2.0.CO;2.

Chang, C.-P., Zhang, Y., and Li, T. (2000). Interannual and Interdecadal Variations of the East Asian Summer Monsoon and Tropical Pacific SSTs. Part I: Roles of the Subtropical Ridge. *J. Clim.* 13, 4310–4325. doi:10.1175/1520-0442(2000)013<4310:IAIVOT>2.0.CO;2.

Chen, J., Wen, Z., Wu, R., Chen, Z., and Zhao, P. (2015). Influences of northward propagating 25–90-day and quasi-biweekly oscillations on eastern China summer rainfall. *Clim. Dyn.* 45, 105–124. doi:10.1007/s00382-014-2334-y.

Chen, Z., Wu, R., and Chen, W. (2014a). Distinguishing Interannual Variations of the Northern and Southern Modes of the East Asian Winter Monsoon. *J. Clim.* 27, 835–851. doi:10.1175/JCLI-D-13-00314.1.

Chen, Z., Wu, R., and Chen, W. (2014b). Impacts of Autumn Arctic Sea Ice Concentration Changes on the East Asian Winter Monsoon Variability. *J. Clim.* 27, 5433–5450. doi:10.1175/JCLI-D-13-00731.1.

Chiessi, C. M., Mulitza, S., Pätzold, J., Wefer, G., and Marengo, J. A. (2009). Possible impact of the Atlantic Multidecadal Oscillation on the South American summer monsoon. *Geophys. Res. Lett.* 36, L21707. doi:10.1029/2009GL039914.

Collini, E. A., Berbery, E. H., Barros, V. R., and Pyle, M. E. (2008). How Does Soil Moisture Influence the Early Stages of the South American Monsoon? *J. Clim.* 21, 195–213. doi:10.1175/2007JCLI1846.1.

Cook, B. I., and Seager, R. (2013). The response of the North American Monsoon to increased greenhouse gas forcing. *J. Geophys. Res. Atmos.* 118, 1690–1699. doi:10.1002/jgrd.50111.

Cook, K. H. (2015). Role of inertial instability in the West African monsoon jump. *J. Geophys. Res. Atmos.* 120, 3085–3102. doi:10.1002/2014JD022579.

ACCEPTED VERSION SUBJECT TO FINAL EDITS

Cui, X., Gao, Y., and Sun, J. (2014). The response of the East Asian summer monsoon to strong tropical volcanic eruptions. *Adv. Atmos. Sci.* 31, 1245–1255. doi:10.1007/s00376-014-3239-8.

Diakhaté, M., Rodríguez-Fonseca, B., Gómara, I., Mohino, E., Dieng, A. L., and Gaye, A. T. (2019). Oceanic Forcing on Interannual Variability of Sahel Heavy and Moderate Daily Rainfall. *J. Hydrometeorol.* 20, 397–410. doi:10.1175/JHM-D-18-0035.1.

Díaz, L. B., and Vera, C. S. (2017). Austral summer precipitation interannual variability and trends over Southeastern South America in CMIP5 models. *Internatio*, 1–15. doi:10.1002/joc.5031.

Díaz, L. B., and Vera, C. S. (2018). South American precipitation changes simulated by PMIP3/CMIP5 models during the Little Ice Age and the recent global warming period. *Int. J. Climatol.* 38, 2638–2650. doi:10.1002/joc.5449.

Dimri, A. P., Niyogi, D., Barros, A. P., Ridley, J., Mohanty, U. C., Yasunari, T., et al. (2015). Western Disturbances: A review. *Rev. Geophys.* 53, 225–246. doi:10.1002/2014RG000460.

Ding, Y., Ren, G., Zhao, Z., Xu, Y., Luo, Y., Li, Q., et al. (2007). Detection, causes and projection of climate change over China: An overview of recent progress. *Adv. Atmos. Sci.* 24, 954–971. doi:10.1007/s00376-007-0954-4.

Ding, Y., Wang, Z., and Sun, Y. (2008). Inter-decadal variation of the summer precipitation in East China and its association with decreasing Asian summer monsoon. Part I: Observed evidences. *Int. J. Climatol.* 28, 1139–1161. doi:10.1002/joc.1615.

Diongue, A., Lafore, J.-P., Redelsperger, J.-L., and Roca, R. (2002). Numerical study of a Sahelian synoptic weather system: Initiation and mature stages of convection and its interactions with the large-scale dynamics. *Q. J. R. Meteorol. Soc.* 128, 1899–1927. doi:10.1256/003590002320603467.

Douglas, M. W., Maddox, R. A., Howard, K., and Reyes, S. (1993). The Mexican monsoon. *J. Clim.* 6, 1665–1677. doi:10.1175/1520-0442(1993)006<1665:TMM>2.0.CO;2.

Drosdowsky, W. (1996). Variability of the Australian Summer Monsoon at Darwin: 1957–1992. *J. Clim.* 9, 85–96. doi:10.1175/1520-0442(1996)009<0085:VOTASM>2.0.CO;2.

Fan, G., Lv, F., Zhang, J., and Fu, J. (2020). A possible way to extract a stationary relationship between ENSO and the East Asian winter monsoon. *Atmos. Ocean. Sci. Lett.* 13, 294–300. doi:10.1080/16742834.2020.1733918.

Fu, Y., and Lu, R. (2017). Improvements in Simulating the Relationship between ENSO and East Asian Summer Rainfall in the CMIP5 Models. *J. Clim.* 30, 4513–4525. doi:10.1175/JCLI-D-16-0606.1.

Fuller, R. D., and Stensrud, D. J. (2000). The Relationship between Tropical Easterly Waves and Surges over the Gulf of California during the North American Monsoon. *Mon. Weather Rev.* 128, 2983–2989. doi:10.1175/1520-0493(2000)128<2983:TRBTEW>2.0.CO;2.

Gadgil, S., Rajeevan, M., Zubair, L., and Yadav, P. (2010). "Interannual variations of the South Asian monsoon: Links with ENSO and EQUINOO," in *The Global Monsoon System - Research and Forecast*, eds. C.-P. Chang, Y. Ding, N.-C. Lau, H. R. Johnson, B. Wang, and T. Yasunari (World Scientific).

Ge, L., Li-Ren, J., Shu-Qing, S., and Yu-Fei, X. (2012). Low- and Mid-High Latitude Components of the East Asian Winter Monsoon and Their Reflecting Variations in Winter Climate over Eastern China. *Atmos. Ocean. Sci. Lett.* 5, 195–200. doi:10.1080/16742834.2012.11446985.

Ge, Q., Xue, Z., Yao, Z., Zang, Z., and Chu, F. (2017). Anti-phase relationship between the East Asian winter monsoon and summer monsoon during the Holocene? *J. Ocean Univ. China* 16, 175–183. doi:10.1007/s11802-017-3098-x.

Geen, R., Bordoni, S., Battisti, D. S., and Hui, K. (2020). Monsoons, ITCZs and the Concept of the Global Monsoon. *Rev. Geophys.* n/a, e2020RG000700. doi:https://doi.org/10.1029/2020RG000700.

Geil, K. L., Serra, Y. L., and Zeng, X. (2013). Assessment of CMIP5 model simulations of the North American monsoon system. *J. Clim.* doi:10.1175/JCLI-D-13-00044.1.

Ghanekar, S. P., Bansod, S. D., Narkhedkar, S. G., and Kulkarni, A. (2019). Variability of Indian summer monsoon onset over Kerala during 1971–2018. *Theor. Appl. Climatol.* 138, 729–742. doi:10.1007/s00704-019-02853-5.

Giannini, A., and Kaplan, A. (2019). The role of aerosols and greenhouse gases in Sahel drought and recovery. *Clim. Change* 152, 449–466. doi:10.1007/s10584-018-2341-9.

Gong, D.-Y., Wang, S.-W., and Zhu, J.-H. (2001). East Asian Winter Monsoon and Arctic Oscillation. *Geophys. Res. Lett.* 28, 2073–2076. doi:10.1029/2000GL012311.

Gong, H., Wang, L., Chen, W., Wu, R., Wei, K., and Cui, X. (2014). The Climatology and Interannual Variability of the East Asian Winter Monsoon in CMIP5 Models. *J. Clim.* 27, 1659–1678. doi:10.1175/JCLI-D-13-00039.1.

Goswami, B. N. (2006). "Intraseasonal variability in the atmosphere-ocean climate system," in *South Asian Monsoon*, eds. W. K. M. Lau and D. E. Waliser (Springer Praxis), 19–55.

Gulizia, C., and Camilloni, I. (2015). Comparative analysis of the ability of a set of CMIP3 and CMIP5 global climate models to represent precipitation in South America. *Int. J. Climatol.* 35, 583–595. doi:https://doi.org/10.1002/joc.4005.

ACCEPTED VERSION SUBJECT TO FINAL EDITS

Guo, D., Gao, Y., Bethke, I., Gong, D., Johannessen, O. M., and Wang, H. (2014). Mechanism on how the spring Arctic sea ice impacts the East Asian summer monsoon. *Theor. Appl. Climatol.* 115, 107–119. doi:10.1007/s00704-013-0872-6.

Gusain, A., Ghosh, S., and Karmakar, S. (2020). Added value of CMIP6 over CMIP5 models in simulating Indian summer monsoon rainfall. *Atmos. Res.* 232, 104680. doi:10.1016/j.atmosres.2019.104680.

Ha, K.-J., Heo, K.-Y., Lee, S.-S., Yun, K.-S., and Jhun, J.-G. (2012). Variability in the East Asian Monsoon: a review. *Meteorol. Appl.* 19, 200–215. doi:10.1002/met.1320.

Hamilton, R. A., Archbold, J. W., and Douglas, C. K. M. (1945). Meteorology of Nigeria and adjacent territory. *Q. J. R. Meteorol. Soc.* 71, 231–264. doi:10.1002/qj.49707130905.

Hendon, H. H., and Liebmann, B. (1990). A Composite Study of Onset of the Australian Summer Monsoon. *J. Atmos. Sci.* 47, 2227–2240. doi:10.1175/1520-0469(1990)047<2227:ACSOOO>2.0.CO;2.

Hendon, H. H., Lim, E.-P., and Liu, G. (2012). The Role of Air–Sea Interaction for Prediction of Australian Summer Monsoon Rainfall. *J. Clim.* 25, 1278–1290. doi:10.1175/JCLI-D-11-00125.1.

Higgins, R. W., Chen, Y., and Douglas, A. V. (1999). Interannual variability of the North American warm season precipitation regime. *J. Clim.* 12, 653–680. doi:10.1175/1520-0442(1999)012<0653:ivotna>2.0.co;2.

Higgins, R. W., and Shi, W. (2001). Intercomparison of the Principal Modes of Interannual and Intraseasonal Variability of the North American Monsoon System. *J. Clim.* 14, 403–417. Available at: http://www.jstor.org/stable/26247310.

Higgins, R. W., Yao, Y., and Wang, X. L. (1997). Influence of the North American monsoon system on the U.S. summer precipitation regime. *J. Clim.* 10, 2600–2622. doi:10.1175/1520-0442(1997)010<2600:IOTNAM>2.0.CO;2.

Holland, G. J. (1986). Interannual Variability of the Australian Summer Monsoon at Darwin: 1952–82. *Mon. Weather Rev.* 114, 594–604. doi:10.1175/1520-0493(1986)114<0594:IVOTAS>2.0.CO;2.

Hourdin, F., Musat, I., Guichard, F. se, Ruti, P. M., Favot, F., Filiberti, M.-A., et al. (2010). AMMA-Model Intercomparison Project. *Bull. Am. Meteorol. Soc.* 91, 95–104. doi:10.1175/2009BAMS2791.1.

Huang, D.-Q., Zhu, J., Zhang, Y.-C., and Huang, A.-N. (2013). Uncertainties on the simulated summer precipitation over Eastern China from the CMIP5 models. *J. Geophys. Res. Atmos.* 118, 9035–9047. doi:10.1002/jgrd.50695.

Huang, R., Zhou, L., and Chen, W. (2003). The Progresses of Recent Studies on the Variabilities of the East Asian Monsoon and Their Causes. *Adv. Atmos. Sci.* 20, 55–69. doi:10.1007/BF03342050.

Hunt, K. M. R., Turner, A. G., and Shaffrey, L. C. (2018). The evolution, seasonality and impacts of western disturbances. *Q. J. R. Meteorol. Soc.* 144, 278–290. doi:10.1002/qj.3200.

Janicot, S., Mounier, F., Gervois, S., Sultan, B., and Kiladis, G. N. (2010). The Dynamics of the West African Monsoon. Part V: The Detection and Role of the Dominant Modes of Convectively Coupled Equatorial Rossby Waves. *J. Clim.* 23, 4005–4024. doi:10.1175/2010JCLI3221.1.

Jiang, D. (2005). Natural interdecadal weakening of East Asian summer monsoon in the late 20th century. *Chinese Sci. Bull.* 50, 1923. doi:10.1360/982005-36.

Jiang, D., Hu, D., Tian, Z., and Lang, X. (2020). Differences between CMIP6 and CMIP5 Models in Simulating Climate over China and the East Asian Monsoon. *Adv. Atmos. Sci.* 37, 1102–1118. doi:10.1007/s00376-020-2034-y.

Jiang, D., Tian, Z., and Lang, X. (2016). Reliability of climate models for China through the IPCC Third to Fifth Assessment Reports. *Int. J. Climatol.* 36, 1114–1133. doi:10.1002/joc.4406.

Jiao, Y., Wu, R., and Song, L. (2019). Individual and Combined Impacts of Two Eurasian Wave Trains on Intraseasonal East Asian Winter Monsoon Variability. *J. Geophys. Res. Atmos.* 124, 4530–4548. doi:10.1029/2018JD029953.

Jin, Q., Yang, X.-Q., Sun, X.-G., and Fang, J.-B. (2013). East Asian summer monsoon circulation structure controlled by feedback of condensational heating. *Clim. Dyn.* 41, 1885–1897. doi:10.1007/s00382-012-1620-9.

Joetzjer, E., Douville, H., Delire, C., and Ciais, P. (2013). Present-day and future Amazonian precipitation in global climate models: CMIP5 versus CMIP3. *Clim. Dyn.* 41, 2921–2936. doi:10.1007/s00382-012-1644-1.

Jones, C., and Carvalho, L. M. V. (2002). Active and Break Phases in the South American Monsoon System. *J. Clim.* 15, 905–914. doi:10.1175/1520-0442(2002)015<0905:AABPIT>2.0.CO;2.

Jones, C., and Carvalho, L. M. V (2013). Climate Change in the South American Monsoon System: Present Climate and CMIP5 Projections. *J. Clim.* 26, 6660–6678. doi:10.1175/JCLI-D-12-00412.1.

Kikuchi, K., Wang, B., and Kajikawa, Y. (2012). Bimodal representation of the tropical intraseasonal oscillation. *Clim. Dyn.* 38, 1989–2000. doi:10.1007/s00382-011-1159-1.

Kim, H.-J., Wang, B., and Ding, Q. (2008). The Global Monsoon Variability Simulated by CMIP3 Coupled Climate Models. *J. Clim.* 21, 5271–5294. doi:10.1175/2008JCLI2041.1.

ACCEPTED VERSION SUBJECT TO FINAL EDITS

Kitoh et al., Kitoh, A., Endo, H., Krishna Kumar, K., Cavalcanti, I. F. A., Goswami, P., et al. (2013). Monsoons in a changing world: A regional perspective in a global context. *J. Geophys. Res. Atmos.* 118, 3053–3065. doi:10.1002/jgrd.50258.

Kodama, Y. (1992). Large-Scale Common Features of Subtropical Precipitation Zones (the Baiu Frontal Zone, the SPCZ, and the SACZ) Part I: Characteristics of Subtropical Frontal Zones. *J. Meteorol. Soc. Japan. Ser. II* 70, 813–836. doi:10.2151/jmsj1965.70.4_813.

Kosaka, Y., Xie, S.-P., Lau, N.-C., and Vecchi, G. A. (2013). Origin of seasonal predictability for summer climate over the Northwestern Pacific. *Proc. Natl. Acad. Sci.* 110, 7574–7579. doi:10.1073/pnas.1215582110.

Krishnan, R., Sabin, T. P., Madhura, R. K., Vellore, R. K., Mujumdar, M., Sanjay, J., et al. (2019a). Non-monsoonal precipitation response over the Western Himalayas to climate change. *Clim. Dyn.* 52, 4091–4109. doi:10.1007/s00382-018-4357-2.

Krishnan, R., Shrestha, A. B., Ren, G., Rajbhandari, R., Saeed, S., Sanjay, J., et al. (2019b). "Unravelling Climate Change in the Hindu Kush Himalaya: Rapid Warming in the Mountains and Increasing Extremes," in *The Hindu Kush Himalaya Assessment*, eds. P. Wester, A. Mishra, A. Mukherji, and A. B. Shrestha (Cham: Springer International Publishing), 57–97. doi:10.1007/978-3-319-92288-1_3.

Lafore, J.-P., Beucher, F., Peyrillé, P., Diongue-Niang, A., Chapelon, N., Bouniol, D., et al. (2017). A multi-scale analysis of the extreme rain event of Ouagadougou in 2009. *Q. J. R. Meteorol. Soc.* 143, 3094–3109. doi:10.1002/qj.3165.

Lamb, P. J. (1978). Large-scale Tropical Atlantic surface circulation patterns associated with Subsaharan weather anomalies. *Tellus* 30, 240–251. doi:10.3402/tellusa.v30i3.10338.

Lee, E.-J., Yeh, S.-W., Jhun, J.-G., and Moon, B.-K. (2006). Seasonal change in anomalous WNPSH associated with the strong East Asian summer monsoon. *Geophys. Res. Lett.* 33, L21702. doi:10.1029/2006GL027474.

Lee, J.-Y., Kwon, M., Yun, K.-S., Min, S.-K., Park, I.-H., Ham, Y.-G., et al. (2017). The long-term variability of Changma in the East Asian summer monsoon system: A review and revisit. *Asia-Pacific J. Atmos. Sci.* 53, 257–272. doi:10.1007/s13143-017-0032-5.

Lee, J.-Y., Wang, B., Wheeler, M. C., Fu, X., Waliser, D. E., and Kang, I.-S. (2013a). Real-time multivariate indices for the boreal summer intraseasonal oscillation over the Asian summer monsoon region. *Clim. Dyn.* 40, 493–509. doi:10.1007/s00382-012-1544-4.

Lee, S.-S., Seo, Y.-W., Ha, K.-J., and Jhun, J.-G. (2013b). Impact of the western North Pacific subtropical high on the East Asian monsoon precipitation and the Indian Ocean precipitation in the boreal summertime. *Asia-Pacific J. Atmos. Sci.* 49, 171–182. doi:10.1007/s13143-013-0018-x.

Lenters, J. D., and Cook, K. H. (1997). On the Origin of the Bolivian High and Related Circulation Features of the South American Climate. *J. Atmos. Sci.* 54, 656–678. doi:10.1175/1520-0469(1997)054<0656:OTOOTB>2.0.CO;2.

Levine, R. C., Turner, A. G., Marathayil, D., and Martin, G. M. (2013). The role of northern Arabian Sea surface temperature biases in CMIP5 model simulations and future projections of Indian summer monsoon rainfall. *Clim. Dyn.* 41, 155–172. doi:10.1007/s00382-012-1656-x.

Li, W., and Fu, R. (2004). Transition of the Large-Scale Atmospheric and Land Surface Conditions from the Dry to the Wet Season over Amazonia as Diagnosed by the ECMWF Re-Analysis. *J. Clim.* 17, 2637–2651. doi:10.1175/1520-0442(2004)017<2637:TOTLAA>2.0.CO;2.

Li, X., Gollan, G., Greatbatch, R. J., and Lu, R. (2018). Intraseasonal variation of the East Asian summer monsoon associated with the Madden-Julian Oscillation. *Atmos. Sci. Lett.* 19, e794. doi:10.1002/asl.794.

Liebmann, B., Kiladis, G. N., Vera, C. S., Saulo, A. C., and Carvalho, L. M. V. (2004). Subseasonal Variations of Rainfall in South America in the Vicinity of the Low-Level Jet East of the Andes and Comparison to Those in the South Atlantic Convergence Zone. *J. Clim.* 17, 3829–3842. doi:10.1175/1520-0442(2004)017<3829:SVORIS>2.0.CO;2.

Luo, X., and Wang, B. (2019). How autumn Eurasian snow anomalies affect east asian winter monsoon: a numerical study. *Clim. Dyn.* 52, 69–82. doi:10.1007/s00382-018-4138-y.

Madhura, R. K., Krishnan, R., Revadekar, J. V., Mujumdar, M., and Goswami, B. N. (2014). Changes in western disturbances over the Western Himalayas in a warming environment. *Clim. Dyn.* 44, 1157–1168. doi:10.1007/s00382-014-2166-9.

Man, W., Zhou, T., and Jungclaus, J. H. (2012). Simulation of the East Asian Summer Monsoon during the Last Millennium with the MPI Earth System Model. *J. Clim.* 25, 7852–7866. doi:10.1175/JCLI-D-11-00462.1.

Marengo, J. ., Nobre, C. ., Tomasella, J., Cardoso, M. ., and Oyama, M. . (2008). Hydro-climatic and ecological behaviour of the drought of Amazonia in 2005. *Philos. Trans. R. Soc. B Biol. Sci.* 363, 1773–1778. doi:10.1098/rstb.2007.0015.

ACCEPTED VERSION SUBJECT TO FINAL EDITS

Marengo, J. A., Liebmann, B., Grimm, A. M., Misra, V., Silva Dias, P. L., Cavalcanti, I. F. A., et al. (2012). Recent developments on the South American monsoon system. *Int. J. Climatol.* 32, 1–21. doi:10.1002/joc.2254.

McBride, J. L. (1987). "The Australian summer monsoon," in *Monsoon Meteorology*, eds. C. Chang and T. Kristinamurti (Oxford University Press), 203–231.

McBride, J. L., and Nicholls, N. (1983). Seasonal Relationships between Australian Rainfall and the Southern Oscillation. *Mon. Weather Rev.* 111, 1998–2004. doi:10.1175/1520-0493(1983)111<1998:SRBARA>2.0.CO;2.

Mekonnen, A., Thorncroft, C. D., Aiyyer, A. R., and Kiladis, G. N. (2008). Convectively Coupled Kelvin Waves over Tropical Africa during the Boreal Summer: Structure and Variability. *J. Clim.* 21, 6649–6667. doi:10.1175/2008JCLI2008.1.

Miao, J., Wang, T., Wang, H., Zhu, Y., and Sun, J. (2018). Interdecadal Weakening of the East Asian Winter Monsoon in the Mid-1980s: The Roles of External Forcings. *J. Clim.* 31, 8985–9000. doi:10.1175/JCLI-D-17-0868.1.

Miao, J., Wang, T., Zhu, Y., Min, J., Wang, H., and Guo, D. (2016). Response of the East Asian Winter Monsoon to Strong Tropical Volcanic Eruptions. *J. Clim.* 29, 5041–5057. doi:10.1175/JCLI-D-15-0600.1.

Moise, A. F., Colman, R. A., and Brown, J. R. (2012). Behind uncertainties in projections of Australian tropical climate: Analysis of 19 CMIP3 models. *J. Geophys. Res. Atmos.* 117, n/a-n/a. doi:10.1029/2011JD017365.

Monerie, P.-A., Wainwright, C. M., Sidibe, M., and Akinsanola, A. A. (2020). Model uncertainties in climate change impacts on Sahel precipitation in ensembles of CMIP5 and CMIP6 simulations. *Clim. Dyn.* doi:10.1007/s00382-020-05332-0.

Narsey, S. Y., Brown, J. R., Colman, R. A., Delage, F., Power, S. B., Moise, A. F., et al. (2020). Climate Change Projections for the Australian Monsoon From CMIP6 Models. *Geophys. Res. Lett.* 47, e2019GL086816. doi:https://doi.org/10.1029/2019GL086816.

Nicholls, N., McBride, J. L., and Ormerod, R. J. (1982). On Predicting the Onset of the Australian Wet Season at Darwin. *Mon. Weather Rev.* 110, 14–17. doi:10.1175/1520-0493(1982)110<0014:OPTOOT>2.0.CO;2.

Nicholson, S. E. (2017). Climate and climatic variability of rainfall over eastern Africa. *Rev. Geophys.* 55, 590–635. doi:10.1002/2016RG000544.

Nicholson, S. E., Fink, A. H., and Funk, C. (2018). Assessing recovery and change in West Africa's rainfall regime from a 161-year record. *Int. J. Climatol.* 38, 3770–3786. doi:10.1002/joc.5530.

Nitta, T. (1987). Convective Activities in the Tropical Western Pacific and Their Impact on the Northern Hemisphere Summer Circulation. *J. Meteorol. Soc. Japan. Ser. II* 65, 373–390. doi:10.2151/jmsj1965.65.3_373.

Novello, V. F., Cruz, F. W., Vuille, M., Stríkis, N. M., Edwards, R. L., Cheng, H., et al. (2017). A high-resolution history of the South American Monsoon from Last Glacial Maximum to the Holocene. *Sci. Rep.* 7, 1–8. doi:10.1038/srep44267.

Omotosho, J. 'Bay. (1988). Spatial variation of rainfall in Nigeria during the 'little dry season.' *Atmos. Res.* 22, 137–147. doi:10.1016/0169-8095(88)90004-X.

Paegle, J. N., and Mo, K. C. (2002). Linkages between Summer Rainfall Variability over South America and Sea Surface Temperature Anomalies. *J. Clim.* 15, 1389–1407. doi:10.1175/1520-0442(2002)015<1389:LBSRVO>2.0.CO;2.

Pai, D. S., Bangdar, A., Devi, S., Musale, M., Badwik, M., Kundale, A. P., et al. (2020). Normal dates of onset/progress and wthdrawal of southwest monsoon over India. *Mausam* 71, 553–570.

Pant, G., and Rupa Kumar, K. (1997). *Climates of South Asia*. John Wiley and Sons Ltd.

Pascale, S., Boos, W. R., Bordoni, S., Delworth, T. L., Kapnick, S. B., Murakami, H., et al. (2017). Weakening of the North American monsoon with global warming. *Nat. Clim. Chang.* 7, 806–812. doi:10.1038/nclimate3412.

Pascale, S., Carvalho, L. M. V. V, Adams, D. K., Castro, C. L., and Cavalcanti, I. F. A. A. (2019). Current and Future Variations of the Monsoons of the Americas in a Warming Climate. *Curr. Clim. Chang. Reports* 5, 125–144. doi:10.1007/s40641-019-00135-w.

Peng, Y., Shen, C., Wang, W.-C., and Xu, Y. (2010). Response of Summer Precipitation over Eastern China to Large Volcanic Eruptions. *J. Clim.* 23, 818–824. doi:10.1175/2009JCLI2950.1.

Raia, A., and Cavalcanti, I. F. A. (2008). The Life Cycle of the South American Monsoon System. *J. Clim.* 21, 6227–6246. doi:10.1175/2008JCLI2249.1.

Raj, J., Bangalath, H. K., and Stenchikov, G. (2019). West African Monsoon: current state and future projections in a high-resolution AGCM. *Clim. Dyn.* 52, 6441–6461. doi:10.1007/s00382-018-4522-7.

Reed, T. R. (1933). The North American high-level anticyclone. *Mon. Wea. Rev.* 61, 321–325. doi:10.1175/1520-0493(1933)61<321:TNAHA>2.0.CO;2.

Risanto, C. B., Castro, C. L., Moker, J. M., Arellano, A. F., Adams, D. K., Fierro, L. M., et al. (2019). Evaluating forecast skills of moisture from convective-permitting WRF-ARW Model during 2017 North American Monsoon season. *Atmosphere (Basel).* doi:10.3390/atmos10110694.

ACCEPTED VERSION SUBJECT TO FINAL EDITS

Robertson, A. W., and Mechoso, C. R. (2000). Interannual and Interdecadal Variability of the South Atlantic Convergence Zone. *Mon. Weather Rev.* 128, 2947–2957. doi:10.1175/1520-0493(2000)128<2947:IAIVOT>2.0.CO;2.

Robertson, A. W., Moron, V., Qian, J.-H., Chang, C.-P., Tangang, F., Aldrian, E., et al. (2011). "The Maritime Continent Monsoon," in, 85–98. doi:10.1142/9789814343411_0006.

Roehrig, R., Bouniol, D., Guichard, F., Hourdin, F., and Redelsperger, J.-L. L. (2013). The present and future of the west african monsoon: A process-oriented assessment of cmip5 simulations along the amma transect. *J. Clim.* 26, 6471–6505. doi:10.1175/JCLI-D-12-00505.1.

Roehrig, R., Chauvin, F., and Lafore, J.-P. (2011). 10–25-Day Intraseasonal Variability of Convection over the Sahel: A Role of the Saharan Heat Low and Midlatitudes. *J. Clim.* 24, 5863–5878. doi:10.1175/2011JCLI3960.1.

Rojas, M., Arias, P. A., Flores-Aqueveque, V., Seth, A., and Vuille, M. (2016). The South American monsoon variability over the last millennium in climate models. *Clim. Past* 12, 1681–1691. doi:10.5194/cp-12-1681-2016.

Sabeerali, C. T., Ramu Dandi, A., Dhakate, A., Salunke, K., Mahapatra, S., and Rao, S. A. (2013). Simulation of boreal summer intraseasonal oscillations in the latest CMIP5 coupled GCMs. *J. Geophys. Res. Atmos.* 118, 4401–4420. doi:10.1002/jgrd.50403.

Sandeep, S., and Ajayamohan, R. S. (2015). Origin of cold bias over the Arabian Sea in Climate Models. *Sci. Rep.* 4, 6403. doi:10.1038/srep06403.

Shige, S., Nakano, Y., and Yamamoto, M. K. (2017). Role of Orography, Diurnal Cycle, and Intraseasonal Oscillation in Summer Monsoon Rainfall over the Western Ghats and Myanmar Coast. *J. Clim.* 30, 9365–9381. doi:10.1175/JCLI-D-16-0858.1.

Silvestri, G. E. (2003). Antarctic Oscillation signal on precipitation anomalies over southeastern South America. *Geophys. Res. Lett.* 30, 2115. doi:10.1029/2003GL018277.

Silvestri, G., and Vera, C. (2009). Nonstationary Impacts of the Southern Annular Mode on Southern Hemisphere Climate. *J. Clim.* 22, 6142–6148. doi:10.1175/2009JCLI3036.1.

Song, F., and Zhou, T. (2013). FGOALS-s2 simulation of upper-level jet streams over East Asia: Mean state bias and synoptic-scale transient eddy activity. *Adv. Atmos. Sci.* 30, 739–753. doi:10.1007/s00376-012-2212-7.

Song, F., and Zhou, T. (2014). The Climatology and Interannual Variability of East Asian Summer Monsoon in CMIP5 Coupled Models: Does Air–Sea Coupling Improve the Simulations? *J. Clim.* 27, 8761–8777. doi:10.1175/JCLI-D-14-00396.1.

Song, F., Zhou, T., and Wang, L. (2013). Two modes of the silk road pattern and their interannual variability simulated by LASG/IAP AGCM SAMIL2.0. *Adv. Atmos. Sci.* 30, 908–921. doi:10.1007/s00376-012-2145-1.

Sow, M., Diakhaté, M., Dixon, R. D., Guichard, F., Dieng, D., and Gaye, A. T. (2020). Uncertainties in the Annual Cycle of Rainfall Characteristics over West Africa in CMIP5 Models. *Atmosphere (Basel).* 11, 216. doi:10.3390/atmos11020216.

Sperber, K. R., Annamalai, H., Kang, I.-S., Kitoh, A., Moise, A., Turner, A., et al. (2013). The Asian summer monsoon: an intercomparison of CMIP5 vs. CMIP3 simulations of the late 20th century. *Clim. Dyn.* 41, 2711–2744. doi:10.1007/s00382-012-1607-6.

Stensrud, D. J., Gall, R. L., and Nordquist, M. K. (1997). Surges over the Gulf of California during the Mexican Monsoon. *Mon. Weather Rev.* 125, 417–437. doi:10.1175/1520-0493(1997)125<0417:SOTGOC>2.0.CO;2.

Sultan, B., and Janicot, S. (2003). The West African Monsoon Dynamics. Part II: The "Preonset" and "Onset" of the Summer Monsoon. *J. Clim.* 16, 3407–3427. doi:10.1175/1520-0442(2003)016<3407:TWAMDP>2.0.CO;2.

Suppiah, R. (1992). The Australian summer monsoon: a review. *Prog. Phys. Geogr. Earth Environ.* 16, 283–318. doi:10.1177/030913339201600302.

Sylla, M. B., Gaye, A. T., Jenkins, G. S., Pal, J. S., and Giorgi, F. (2010). Consistency of projected drought over the Sahel with changes in the monsoon circulation and extremes in a regional climate model projections. *J. Geophys. Res.* 115, D16108. doi:10.1029/2009JD012983.

Torres-Alavez, A., Cavazos, T., and Turrent, C. (2014). Land-sea thermal contrast and intensity of the North American monsoon under climate change conditions. *J. Clim.* 27, 4566–4580. doi:10.1175/JCLI-D-13-00557.1.

Troup, A. (1961). Variations in upper troposheric flow associated with the onset of the Australian summer monsoon. *Indian J. Meteorol. Geophys.* 12, 217–230.

Turner, A. G., and Annamalai, H. (2012). Climate change and the South Asian summer monsoon. *Nat. Clim. Chang.* 2, 587–595. doi:10.1038/nclimate1495.

Varuolo-Clarke, A. M., Reed, K. A., and Medeiros, B. (2019). Characterizing the North American Monsoon in the Community Atmosphere Model: Sensitivity to Resolution and Topography. *J. Clim.* 32, 8355–8372. doi:10.1175/JCLI-D-18-0567.1.

ACCEPTED VERSION SUBJECT TO FINAL EDITS

Vera, C., Higgins, W., Amador, J., Ambrizzi, T., Garreaud, R., Gochis, D., et al. (2006). Toward a Unified View of the American Monsoon Systems. *J. Clim.* 19, 4977–5000. doi:10.1175/JCLI3896.1.

Vizy, E. K., and Cook, K. H. (2009). A mechanism for African monsoon breaks: Mediterranean cold air surges. *J. Geophys. Res. Atmos.* 114. doi:10.1029/2008JD010654.

Vuille, M., Burns, S. J., Taylor, B. L., Cruz, F. W., Bird, B. W., Abbott, M. B., et al. (2012). A review of the South American monsoon history as recorded in stable isotopic proxies over the past two millennia. *Clim. Past* 8, 1309–1321. doi:10.5194/cp-8-1309-2012.

Wang, B. (2005). Fundamental challenge in simulation and prediction of summer monsoon rainfall. *Geophys. Res. Lett.* 32, L15711. doi:10.1029/2005GL022734.

Wang, B., and Ding, Q. (2008). Global monsoon: Dominant mode of annual variation in the tropics. *Dyn. Atmos. Ocean.* 44, 165–183. doi:10.1016/j.dynatmoce.2007.05.002.

Wang, B., and LinHo (2002). Rainy Season of the Asian–Pacific Summer Monsoon*. *J. Clim.* 15, 386–398. doi:10.1175/1520-0442(2002)015<0386:RSOTAP>2.0.CO;2.

Wang, B., Wu, R., and Fu, X. (2000). Pacific–East Asian Teleconnection: How Does ENSO Affect East Asian Climate? *J. Clim.* 13, 1517–1536. doi:10.1175/1520-0442(2000)013<1517:PEATHD>2.0.CO;2.

Wang, B., Wu, Z., Chang, C.-P., Liu, J., Li, J., and Zhou, T. (2010). Another Look at Interannual-to-Interdecadal Variations of the East Asian Winter Monsoon: The Northern and Southern Temperature Modes. *J. Clim.* 23, 1495–1512. doi:10.1175/2009JCLI3243.1.

Wang, B., Xiang, B., and Lee, J.-Y. (2013). Subtropical High predictability establishes a promising way for monsoon and tropical storm predictions. *Proc. Natl. Acad. Sci.* 110, 2718–2722. doi:10.1073/pnas.1214626110.

Wang, H., and Fu, R. (2002). Cross-Equatorial Flow and Seasonal Cycle of Precipitation over South America. *J. Clim.* 15, 1591–1608. doi:10.1175/1520-0442(2002)015<1591:CEFASC>2.0.CO;2.

Wang, H., and He, S. (2012). Weakening relationship between East Asian winter monsoon and ENSO after mid-1970s. *Chinese Sci. Bull.* 57, 3535–3540. doi:10.1007/s11434-012-5285-x.

Wang, L., and Chen, W. (2014). The East Asian winter monsoon: re-amplification in the mid-2000s. *Chinese Sci. Bull.* 59, 430–436. doi:10.1007/s11434-013-0029-0.

Wang, L., Huang, R., Gu, L., Chen, W., and Kang, L. (2009). Interdecadal Variations of the East Asian Winter Monsoon and Their Association with Quasi-Stationary Planetary Wave Activity. *J. Clim.* 22, 4860–4872. doi:10.1175/2009JCLI2973.1.

Wang, P. X., Wang, B., Cheng, H., Fasullo, J., Guo, Z. T., Kiefer, T., et al. (2014). The global monsoon across timescales: coherent variability of regional monsoons. *Clim. Past* 10, 2007–2052. doi:10.5194/cp-10-2007-2014.

Wang, P. X., Wang, B., Cheng, H., Fasullo, J., Guo, Z. T., Kiefer, T., et al. (2017). The global monsoon across time scales: Mechanisms and outstanding issues. *Earth-Science Rev.* doi:10.1016/j.earscirev.2017.07.006.

Wang, T., Miao, J.-P., Sun, J.-Q., and Fu, Y.-H. (2018). Intensified East Asian summer monsoon and associated precipitation mode shift under the 1.5 °C global warming target. *Adv. Clim. Chang. Res.* 9, 102–111. doi:10.1016/j.accre.2017.12.002.

Webster, P. J., Magaña, V. O., Palmer, T. N., Shukla, J., Tomas, R. A., Yanai, M., et al. (1998). Monsoons: Processes, predictability, and the prospects for prediction. *J. Geophys. Res. Ocean.* 103, 14451–14510. doi:10.1029/97JC02719.

Wen, C., Graf, H.-F., and Ronghui, H. (2000). The interannual variability of East Asian Winter Monsoon and its relation to the summer monsoon. *Adv. Atmos. Sci.* 17, 48–60. doi:10.1007/s00376-000-0042-5.

Wen, X., Liu, Z., Wang, S., Cheng, J., and Zhu, J. (2016). Correlation and anti-correlation of the East Asian summer and winter monsoons during the last 21,000 years. *Nat. Commun.* 7, 11999. doi:10.1038/ncomms11999.

Xue, Y., De Sales, F., Lau, W. K.-M., Boone, A., Feng, J., Dirmeyer, P., et al. (2010). Intercomparison and analyses of the climatology of the West African Monsoon in the West African Monsoon Modeling and Evaluation project (WAMME) first model intercomparison experiment. *Clim. Dyn.* 35, 3–27. doi:10.1007/s00382-010-0778-2.

Yan, M., Liu, Z. Y., Ning, L., and Liu, J. (2020). Holocene EASM-EAWM Relationship Across Different Timescales in CCSM3. *Geophys. Res. Lett.* 47. doi:10.1029/2020GL088451.

Yasunari, T. (1979). Cloudiness Fluctuations Associated with the Northern Hemisphere Summer Monsoon. *J. Meteorol. Soc. Japan. Ser. II* 57, 227–242. doi:10.2151/jmsj1965.57.3_227.

Yihui, D., and Chan, J. C. L. (2005). The East Asian summer monsoon: an overview. *Meteorol. Atmos. Phys.* 89, 117–142. doi:10.1007/s00703-005-0125-z.

Yim, S.-Y., Yeh, S.-W., Wu, R., and Jhun, J.-G. (2008). The Influence of ENSO on Decadal Variations in the Relationship between the East Asian and Western North Pacific Summer Monsoons. *J. Clim.* 21, 3165–3179. doi:10.1175/2007JCLI1948.1.

ACCEPTED VERSION SUBJECT TO FINAL EDITS

Yin, L., Fu, R., Zhang, Y.-F., Arias, P. A., Fernando, D. N., Li, W., et al. (2014). What controls the interannual variation of the wet season onsets over the Amazon? *J. Geophys. Res. Atmos.* 119, 2314–2328. doi:10.1002/2013JD021349.

Zeng, N., Yoon, J.-H., Marengo, J. A., Subramaniam, A., Nobre, C. A., Mariotti, A., et al. (2008). Causes and impacts of the 2005 Amazon drought. *Environ. Res. Lett.* 3, 014002. doi:10.1088/1748-9326/3/1/014002.

Zhang, H., and Moise, A. (2016). "The Australian summer monsoon in current and future climate," in *The Monsoons and Climate Change*, eds. C. Jones and L. Carvalho (Berlin: Springer, , doi.org/10.1007/978-3-319-21650-8_5), 67–120.

Zhang, L., Wang, B., and Zeng, Q. (2009). Impact of the Madden–Julian Oscillation on Summer Rainfall in Southeast China. *J. Clim.* 22, 201–216. doi:10.1175/2008JCLI1959.1.

Zhang, Z., Chan, J. C. L., and Ding, Y. (2004). Characteristics, evolution and mechanisms of the summer monsoon onset over Southeast Asia. *Int. J. Climatol.* 24, 1461–1482. doi:10.1002/joc.1082.

Zhou, J., and Lau, K.-M. (1998). Does a Monsoon Climate Exist over South America? *J. Clim.* 11, 1020–1040. doi:10.1175/1520-0442(1998)011<1020:DAMCEO>2.0.CO;2.

Zhou, T., Gong, D., Li, J., and Li, B. (2009). Detecting and understanding the multi-decadal variability of the East Asian Summer Monsoon Recent progress and state of affairs. *Meteorol. Zeitschrift* 18, 455–467. doi:10.1127/0941-2948/2009/0396.

Zhou, T., Turner, A. G., Kinter, J. L., Wang, B., Qian, Y., Chen, X., et al. (2016). GMMIP (v1.0) contribution to CMIP6: Global Monsoons Model Inter-comparison Project. *Geosci. Model Dev.* 9, 3589–3604. doi:10.5194/gmd-9-3589-2016.

ACCEPTED VERSION
SUBJECT TO FINAL EDITS

Figures

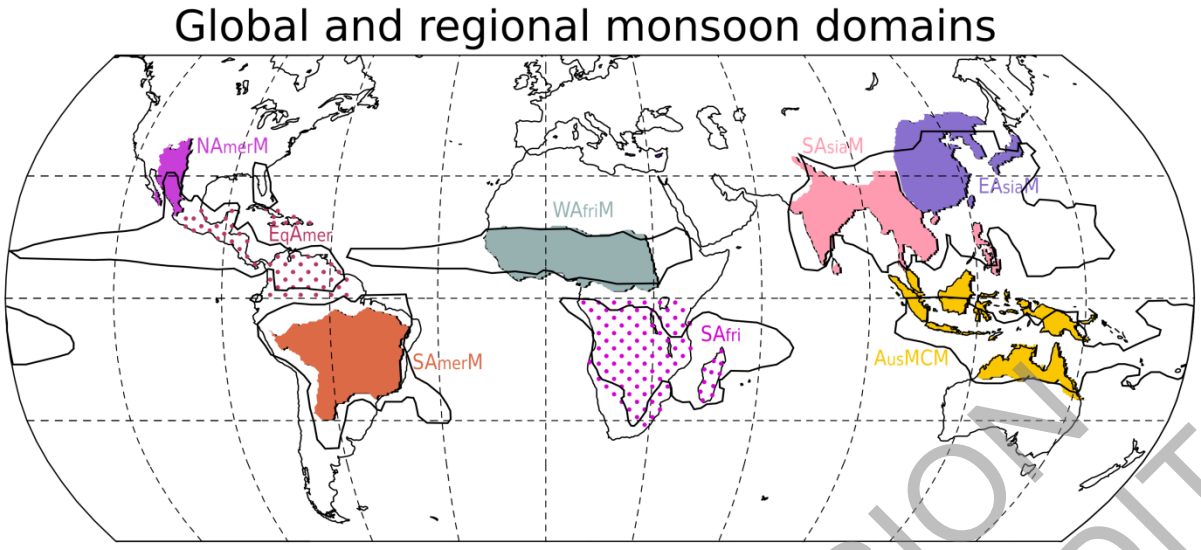


Figure AV.1: **Global and regional monsoons domains**. AR6 global monsoon area is represented by the black contour. AR6 regional monsoons are: North American monsoon (shaded magenta), South American monsoon (shaded dark-orange), West African monsoon (shaded grey), South and Southeast Asian monsoon (shaded pink), East Asian monsoon (shaded purple) and Australian-Maritime Continent monsoon (shaded yellow). Areas over Equatorial America and South Africa (dotted red and magenta, respectively) are highlighted but not identified as specific regional monsoons (see explanation in the main text). For each regional monsoon, the seasonal characteristics associated with each domain are specified in the main text.

ACCEPTED VERSION
SUBJECT TO FINAL EDITS

Annex VI: Climatic Impact-Driver and Extreme Indices

Coordinating Lead Authors:
José M. Gutiérrez (Spain), Roshanka Ranasinghe (The Netherlands/Sri Lanka, Australia), Alex C. Ruane (United States of America), Robert Vautard (France)

Lead Authors:
Nigel Arnell (United Kingdom), Erika Coppola (Italy), Izidine Pinto (South Africa/Mozambique), Daniel Ruiz Carrascal (United States of America/Colombia), Jana Sillmann (Norway/Germany), Claudia Tebaldi (United States of America)

Contributing Authors:
Clemens Schwingshakl (Norway/Italy)

Chapter Scientists:
Mathias Hauser (Switzerland), Carley E. Iles (Norway, France/United Kingdom), Maialen Iturbide (Spain),

This Annex should be cited as:
IPCC, 2021: Annex VI: Climatic Impact-Driver and Extreme Indices [Gutiérrez J. M., R. Ranasinghe, A. C. Ruane, R. Vautard (eds.)]. In: *Climate Change 2021: The Physical Science Basis. Contribution of Working Group I to the Sixth Assessment Report of the Intergovernmental Panel on Climate Change* [Masson-Delmotte, V., P. Zhai, A. Pirani, S. L. Connors, C. Péan, S. Berger, N. Caud, Y. Chen, L. Goldfarb, M. I. Gomis, M. Huang, K. Leitzell, E. Lonnoy, J.B.R. Matthews, T. K. Maycock, T. Waterfield, O. Yelekçi, R. Yu and B. Zhou (eds.)]. Cambridge University Press. In Press.

Date: August 2021

This document is subject to copy-editing, corrigenda and trickle backs.

ACCEPTED VERSION
SUBJECT TO FINAL EDITS

AVI.1 Introduction 3
AVI.2 Extreme indices selection 4
AVI.3 Climatic Impact-Drivers indices selection 6
AVI.3.1 Regional CID indices used in Chapter 12 and the Atlas 6
References 12

ACCEPTED VERSION
SUBJECT TO FINAL EDITS

AVI.1 Introduction

This Annex provides background information on indices used within Chapter 11, Chapter 12, and the Atlas, including technical details of calculation and related references.

In the climate science literature, a number of indices are used to characterize and quantify one or several aspects of climate phenomena occurring due to natural variability or due to long-term changes in the system. There is an extremely large number of examples. One can cite mean global climate indices, such as global mean sea level rise or global surface temperature, which characterize the state of the climate system and act as a shifting baseline for regional changes. One can also examine mean regional trends, for example in mean springtime precipitation, which reflect large-scale patterns and alter the background conditions within which episodic hazards may occur. One can also calculate indices of extremes characterizing episodic events within the tail of the distributions of specific variables within their variability range, for instance the annual maximal temperature at a given location or the 100-year return value of river discharge characterizing extreme floods. Such extreme indices have been the subject of a number of studies and have been used to characterize how climate change modifies extreme values of climate variables and subsequent impacts in the IPCC Special Report on "Managing the risks of Extreme Events and Disasters to Advance Climate Change Adaptation" (IPCC, 2012), as well other recent IPCC reports.

Indices can also characterize aspects of climatic impact-drivers (CIDs) (see Chapter 1 for the definition) that are key to impacts and risks to society and ecosystems. Chapter 12 proposes a definition of "climatic impact-driver indices" as "numerically computable indices using one or a combination of climate variables designed to measure the intensity of the climatic impact-driver, or the probability of exceedance of a threshold. For instance, an index of heat inducing human health stress is the Heat Index (HI) that combines temperature and relative humidity (e.g., (Burkart et al., 2011; Lin et al., 2012; Kent et al., 2014)) and is used among others by the US National Oceanic and Atmospheric Administration (NOAA) for issuing heat warnings".

Climatic impact-drivers may not be related only to extremes, and therefore require a much broader set of indices. For instance, the rate of coastline recession, due to sea level rise, assessed in Chapter 12, is involved in the risk of damage and losses in coastal settlements and infrastructures. Mean trends and changes themselves are considered throughout the report as CIDs. For instance, beyond the warming trend which has a large number of consequences, changes in other indices such 'snow season length' is often used to study economic impacts on winter tourism (Damm et al., 2017). Furthermore, (Mora et al., 2018) used a set of 11 very different key CID indices among which about half are related to extremes to characterize broader threats to society. Section 12.3 in Chapter 12 reviews the CIDs described in the literature to characterize impacts and risks, and reveal the wide variety of indices used to characterize them.

Indices are, in principle, computable from observations, reanalyses or model simulations, although it is important to consider scale in comparing across datasets. For example, an extreme precipitation event has a lower magnitude across a large grid cell than it would at a single station within that grid cell. In many cases, CIDs are simply characterized by the exceedance of a threshold for an Essential Climate Variable (ECV). For instance, the probability of crop failure dramatically increases as temperature rises above certain thresholds, which may differ from one species to another (Hatfield and Prueger, 2015; Grotjahn, 2021). To assess the effect of climate change on threshold-based indices (e.g., the change in the number of days with maximum temperature above 35°C), a bias adjustment of model outputs should be considered where sensible as model simulations can have biases compared to observations and reanalyses (Section 10.3.1.3, Cross Chapter Box 10.2, 12.2).

Indices are used in many chapters of this Report: in Chapter 4 for assessing changes in the global climate, in Chapter 8 for water cycle changes assessment, in Chapter 9 for oceans and the cryosphere, in Chapter 11 for assessing changes in extreme conditions, and in Chapter 12 for assessing CIDs and their changing characteristics due to climate change. The Atlas assesses changes in mean variables/indices (temperature, precipitation and snow). The Interactive Atlas includes indices of mean changes (for temperatures, precipitation, snowfall and wind) and a number of extreme indices and CIDs, allowing for flexible spatial and temporal analysis of the results.

ACCEPTED VERSION SUBJECT TO FINAL EDITS

AVI.2 Extreme indices selection

In Chapter 11, extreme weather and climate events (collectively referred to as extremes) are assessed and the main focus is on extreme events over land. Since the analysis of extremes often involves the examination of the tails of the statistical distributions, a parametric or non-parametric approach can be used to define extremes. The non-parametric approach is largely adopted in most of the literature to characterize moderate temperature and precipitation extremes with shorter return periods. The Expert Team on Climate Change Detection and Indices (ETCCDI -https://www.wcrp-climate.org/etccdi) defined 27 indices to characterize different aspects of moderate temperature and precipitation extremes, which are described by (Frich et al., 2002; Alexander et al., 2006; Zhang et al., 2011; Donat et al., 2013; Sillmann et al., 2013), and were also extensively used in previous IPCC reports. In Chapter 11, a subset of these indices is assessed in detail (Section 11.3 and Section 11.4). For events with longer return periods (e.g., events that occur once in 20 years or even rarer), the parametric approach based on Extreme Value Theory (EVT) (Coles, 2001) is used and adopted in the literature (e.g., (Kharin and Zwiers 2000; Brown et al. 2008; Kharin et al. 2013)). These events are also assessed throughout the chapter. Aside from temperature and precipitation, the chapter also assesses indices used to characterize droughts. Table AVI.1 list the indices used.

[START TABLE AVI.1 HERE]

Table AVI.1: Table listing extreme indices used in Chapter 11

Extreme	Label	Index name	Units	Variable
Temperature	TXx	Monthly maximum value of daily maximum temperature	°C	Maximum temperature
	TXn	Monthly minimum value of daily maximum temperature	°C	Maximum temperature
	TNn	Monthly minimum value of daily minimum temperature	°C	Minimum temperature
	TNx	Monthly maximum value of daily minimum temperature	°C	Minimum temperature
	TX90p	Percentage of days when daily maximum temperature is greater than the 90th percentile	%	Maximum temperature
	TX10p	Percentage of days when daily maximum temperature is less than the 10th percentile	%	Maximum temperature
	TN90p	Percentage of days when daily minimum temperature is greater than the 90th percentile	%	Minimum temperature
	TN10p	Percentage of days when daily minimum temperature is less than the 10th percentile	%	Minimum temperature
	ID	Number of icing days: Annual count of days when TX (daily maximum temperature) < 0°C	days	Maximum temperature
	FD	Number of frost days: Annual count of days when TN (daily minimum temperature) < 0°C	days	Minimum temperature
	WSDI	Warm spell duration index: Annual count of days with at least 6 consecutive days when TX >90th percentile	days	Maximum temperature
	CSDI	Cold spell duration index: Annual count of days with at least 6 consecutive days when TN <10th percentile	days	Minimum temperature
	SU	Number of summer days: Annual count of days when TX (daily maximum temperature) > 25°C	days	Maximum temperature
	TR	Number of tropical nights: Annual count of days when TN (daily minimum temperature) > 20°C	days	Minimum temperature

ACCEPTED VERSION SUBJECT TO FINAL EDITS

	DTR	Daily temperature range: Monthly mean difference between TX and TN	°C	Maximum and minimum temperature
	GSL	Growing season length: Annual (1st Jan to 31st Dec in Northern Hemisphere (NH), 1st July to 30th June in Southern Hemisphere (SH)) count between first span of at least 6 days with daily mean temperature TG>5°C and first span after July 1st (Jan 1st in SH) of 6 days with TG<5°C	days	Mean temperature
	20TXx	One-in-20 year return value of monthly maximum value of daily maximum temperature	°C	Maximum temperature
	20TXn	One-in-20 year return value of monthly minimum value of daily maximum temperature	°C	Maximum temperature
	20TNn	One-in-20 year return value of monthly minimum value of daily minimum temperature	°C	Minimum temperature
	20TNx	One-in-20 year return value of monthly maximum value of daily minimum temperature	°C	Minimum temperature
Precipitation	Rx1day	Maximum 1-day precipitation	mm	Precipitation
	Rx5day	Maximum 5-day precipitation	mm	Precipitation
	R5mm	Annual count of days when precipitation is greater than or equal to 5mm	days	Precipitation
	R10mm	Annual count of days when precipitation is greater than or equal to 10mm	days	Precipitation
	R20mm	Annual count of days when precipitation is greater than or equal to 20mm	days	Precipitation
	R50mm	Annual count of days when precipitation is greater than or equal to 50mm	days	Precipitation
	CDD	Maximum number of consecutive days with less than 1 mm of precipitation per day	days	Precipitation
	CWD	Maximum number of consecutive days with more than or equal to 1 mm of precipitation per day	days	Precipitation
	R95p	Annual total precipitation when the daily precipitation exceeds the 95th percentile of the wet-day (>1mm) precipitation	mm	Precipitation
	R99p	annual precipitation amount when the daily precipitation exceeds the 99th percentile of the wet-day precipitation	mm	Precipitation
	SDII	Simple precipitation intensity index	mm day^{-1}	Precipitation
	20Rx1day	One-in-20 year return value of maximum 1-day precipitation	mm day^{-1}	Precipitation
	20Rx5day	One-in-20 year return value of maximum 5-day precipitation	mm day^{-1}	Precipitation
Drought	SPI	Standardized Precipitation Index	months	Precipitation
	EDDI	Potential evaporation, Evaporative Demand Drought Index	months	Evaporation
	SMA	Soil moisture anomalies	months	Soil moisture
	SSMI	Standardized Soil Moisture Index	months	Soil moisture
	SRI	Standardized Runoff Index	months	Stream flow
	SSI	Standardized Streamflow Index	months	Stream flow
	PDSI	Palmer drought severity index	months	Precipitation, Evaporation
	SPEI	Standardized precipitation evapotranspiration index	months	Precipitation, Evaporation,

ACCEPTED VERSION SUBJECT TO FINAL EDITS

				Temperature

[END TABLE AVI.1 HERE]

Some of these indices are included in the Interactive Atlas allowing further analysis (seasons, regions, baselines and future periods – using both time-slices/scenarios and global warming levels): TXx, TNn, Rx1day, Rx5day, FD, CDD, and SPI.

AVI.3 Climatic Impact-Drivers indices selection

In Chapter 12, 33 CID types are identified on the basis of relevance for risks and impacts and available literature. They are classified into 7 categories: heat and cold, wet and dry, wind, snow and ice, coastal, oceanic, and other (see Tables 12.1 and 12.2). It would be impossible to cover all indices that have been developed in the literature. However, in order to illustrate how indices can inform on future regional climate, Chapter 12 and the Atlas use a limited number of indices to illustrate the main CIDs and their evolution with climate change.

The selection of indices, as displayed in Chapter 12 and the Atlas, is based on expert judgement using the following guiding principles. The set of indices should:

(i) describe the evolution of a manageable and illustrative number of indices,
(ii) cover these categories, while giving more weight to those with a higher number of potential impacts as described in the literature,
(iii) be used broadly in the literature,
(iv) allow easy computation from publicly available model outputs and observations, or be accessible from published material through contact with the authors,
(v) be well-evaluated in model simulations, or based on ECVs that are well-evaluated in model simulations, and
(vi) represent CIDs of interest to regional impacts and risk assessments.

The selection results in 16 regional indices that are reported in Table AVI.2. The description of the formulae used for processing is described below.

AVI.3.1 Regional CID indices used in Chapter 12 and the Atlas

Climatic impact-drivers indices

Length of frost-free period (LFFP): Many ecosystems and crops are sensitive to frost conditions, and can only develop over a frost-free period (e.g., Wolfe et al., 2018); the length of frost-free period is calculated in the Atlas as in McCabe et al., (2015) by counting the number of days between the last spring frost and first fall frost using 0°C as a threshold for the daily minimum temperature and adjusting for season between hemispheres (from January to December in the Northern Hemisphere and from July to June in the Southern Hemisphere).

Growing degree-days (GDD): Ecosystems and crop growth is often linked to a widely used index of thermal conditions, the cumulative number of degrees above a threshold (often between 0 and 10 °C, depending on species and farming system) during a given growing period. In Chapter 12 and the Atlas we use 5°C as an indicative threshold, which was also used in Ruosteenoja et al., (2016), and the calculation is taken from this reference. GDD calculations sometimes include a high temperature threshold above which plant development does not occur (e.g., Mu et al., 2017), but no cap was employed for our calculations. The GDD index used here is therefore the accumulated sum of the difference between daily mean temperature and the threshold (when higher than the threshold) over the April-September months that forms the primary growing season for mid-latitude agricultural areas in the northern Hemisphere; and October-March for the

ACCEPTED VERSION SUBJECT TO FINAL EDITS

Southern hemisphere.

Cooling Degree-days (CD): Energy consumption in hot environments typically depends on the excess of temperature above a given threshold, where cooling is required. In Chapter 12 and the Atlas we used the formulation of Spinoni et al., (2015), which uses the mean (T_M), max (T_X) and min daily (T_N) temperature with the formula taken from this reference:

$$CDD_i = \begin{cases} 0 \\ \frac{T_X - T_b}{4} \\ \frac{T_X - T_b}{2} - \frac{T_b - T_N}{4} \\ T_M - T_b \end{cases} \quad if \quad \begin{cases} T_X \le T_b \\ T_M \le T_b < T_X \\ T_N \le T_b < T_M \\ T_N \ge T_b \end{cases}$$

With T_b=22°C, then

$$CDD = \sum_{i=1}^{365} CDD_i$$

The difference between Chapter 12, Atlas, and the previous reference is that in this report the sum is cumulated over the entire year instead of 6 months, so it applies to all hemispheres.

Number of days with maximum daily temperature above threshold (TXnn): The number of days with maximum temperature above a threshold can be critical for human health, infrastructure, ecosystems, and agriculture. Different thresholds are used for different crops, generally varying between 30 degrees and 40 degrees (Hatfield and Prueger, 2015; Grotjahn, 2021).. Chapter 12 uses the 35°C threshold globally (Figure 12.4), which was identified as a critical temperature for maize pollination and production (Wolfe et al., 2008; Schlenker and Roberts, 2009; Hatfield et al., 2011, 2014; Lobell and Gourdji, 2012; Gourdji et al., 2013; Lobell et al., 2013; Deryng et al., 2014; Hatfield and Prueger, 2015; Tripathi et al., 2016; Schauberger et al., 2017; Tesfaye et al., 2017) as well as a notable threshold for human health hazards (Kingsley, Eliot, Gold, Vanderslice, & Wellenius, 2016; Petitti et al., 2016). The Interactive Atlas includes both TX35 and TX40 (both raw and bias adjusted; see Atlas 1.4.5).

NOAA Heat Index (HI): HI is used by the US National Oceanic and Atmospheric Administration (NOAA) for issuing heat warnings and was applied in several studies that investigated adverse health impacts due to heat stress (e.g., Burkart et al., 2011; Lin et al., 2012; Kent et al., 2014). HI is calculated as multiple linear regression with temperature (T_F in °F) and relative humidity (RH) as input variables (Steadman, 1979; Rothfusz, 1990):

$$\mathrm{HI} = \begin{cases} \mathrm{HI}_1 + \mathrm{HI}_{A1}, & \text{if RH} < 13\,\% \text{ and } 80\,^\circ\mathrm{F} < T_F < 112\,^\circ\mathrm{F} \\ \mathrm{HI}_1 + \mathrm{HI}_{A2}, & \text{if RH} > 85\,\% \text{ and } 80\,^\circ\mathrm{F} < T_F < 87\,^\circ\mathrm{F} \\ \mathrm{HI}_1, & \text{otherwise} \end{cases}$$

with:

$$\mathrm{HI}_1 = c_0 + c_1 \cdot T_F + c_2 \cdot \mathrm{RH} + c_3 \cdot T_F \cdot \mathrm{RH} + c_4 \cdot T_F^2 + c_5 \cdot \mathrm{RH}^2 + c_6 \cdot T_F^2 \cdot \mathrm{RH} + c_7 \cdot T_F \cdot \mathrm{RH}^2 + c_8 \cdot T_F^2 \cdot \mathrm{RH}^2$$

$$\mathrm{HI}_{A1} = (13 - \mathrm{RH})/4 \cdot \sqrt{(17 - |T_F - 95\,^\circ\mathrm{F}|)/17}$$

$$\mathrm{HI}_{A2} = (\mathrm{RH} - 85)/10 \cdot (87\,^\circ\mathrm{F} - T_F)/5$$

c_0 = -42.379 °F, c_1 = 2.04901523, c_2 = 10.14333127 °F, c_3 = -0.22475541,

c_4 = -0.00683783 $^\circ\mathrm{F}^{-1}$, c_5 = -0.05481717 °F, c_6 = 0.00122874 $^\circ\mathrm{F}^{-1}$, c_7 = 0.00085282

ACCEPTED VERSION SUBJECT TO FINAL EDITS

$c_8 = -0.00000199\ ^\circ\mathrm{F}^{-1}$

If $\mathrm{HI} < 80\ ^\circ\mathrm{F}$, the following equation is used:

$$\mathrm{HI} = 0.5 \cdot (T_F + 61\ ^\circ\mathrm{F} + 1.2 \cdot (T_F - 68\ ^\circ\mathrm{F}) + 0.094\ ^\circ\mathrm{F} \cdot \mathrm{RH})$$

The calculated HI is converted into °C.

HI is calculated for CMIP5, CMIP6 and CORDEX using daily mean near-surface specific humidity, daily mean surface pressure, and daily maximum near-surface air temperature. For CMIP5 and CMIP6, daily mean surface pressure is calculated from daily mean sea level pressure by applying a height adjustment (see Schwingshackl et al., (2021) for details) Additionally, HI is calculated for WFDE5, which is a bias adjusted version of the ERA5 reanalysis (Cucchi et al., 2020). Daily maximum temperature is calculated as maximum, daily mean pressure and humidity as average of the hourly WFDE5 variables near-surface air temperature, near-surface specific humidity, and surface air pressure.

To quantify heat stress, yearly sums of daily HI threshold exceedances are calculated using a threshold of 41°C, which corresponds to conditions that the US National Weather Service classifies into the category of "Danger" (Blazejczyk et al., 2012). Bias adjusted model simulations are used for calculating threshold exceedances of HI, employing the quantile delta mapping (QDM) approach as described by (Cannon et al., 2015). The QDM approach adjusts the model data in the application period to fit the reference data in the reference period (using quantile mapping). Subsequently, the climate change signal is added for each quantile by considering the change between the model's reference and application periods. QDM is directly applied to the HI data using WFDE5 as reference dataset and 1981-2010 as reference period. WFDE5 HI data are conservatively remapped to each model's grid before bias adjustment is performed. QDM is applied on each grid point individually and for each month separately. The application periods are the IPCC periods 1995-2014, 2041-2060, and 2081-2100 and 20-year periods for specific warming levels (1.5°C, 2°C, 3°C, and 4°C).

Heating Degree-days (HD): symmetrical to the Cooling Degree Day index, the HD index is used for illustrating energy demand for heating. It has been used in several studies of impacts of climate change on the energy sector. The Atlas follow the formulation proposed by (Spinoni et al., 2015). The calculation follows:

$$HDD_i = \begin{cases} T_b - T_M \\ \dfrac{T_b - T_N}{2} \dfrac{T_X - T_b}{4} \\ \dfrac{T_b - T_N}{4} \\ 0 \end{cases} \quad if \quad \begin{cases} T_X \le T_b \\ T_M \le T_b < T_X \\ T_N \le T_b < T_M \\ T_N \ge T_b \end{cases}$$

With T_b=15.5°C, then

$$HDD = \sum_{i=1}^{365} HDD_i$$

Where T_M, T_X and T_N correspond to daily mean, maximum and minimum temperature respectively.

To account for various geographic zones, however, the HD index is cumulated over the entire year, instead of 6 months, as in the previous reference. This index is included in the Interactive Atlas.

Number of frost days (FD): Frost affects crops (Barlow et al., 2015; Crimp et al., 2016; Cradock-Henry, 2017; Mäkinen et al., 2018), and there has been a number of studies investigating changes in the number of

ACCEPTED VERSION SUBJECT TO FINAL EDITS

frost days, with various thresholds, mostly between -10°C and 2°C. In Chapter 12 and the Atlas, we use the simple threshold of 0°C for the daily minimum temperature to define frost days as in Table AVI.1. This index is included in the Interactive Atlas.

River flood index using runoff (FI): As a flood indicator, the 100-year return value of discharge value (Q) has been used. The computation of the index follows Alfieri et al., (2015):

1. Annual maximum river discharges are selected and an Extreme Value Type I (Gumbel) distribution is fitted on time slices of 30 years and an analytical function is obtained.
2. The analytical function is used to estimate extreme discharge peaks with chosen return period Q(RP), by inverting the formulation of the Gumbel distribution:

$$Q(\mathrm{RP}) = \xi - \alpha \ln\left(-\ln\left(1 - \frac{1}{\mathrm{RP}}\right)\right)$$

   where α and ξ are the scale and location parameters of the analytical Gumbel distribution.

3. The peak discharge corresponding to the 100-year return period, Q(RP=100), is then calculated.

For CORDEX regional models the total runoff of each of the models has been used as an input of the hydrological model CHyM (Coppola et al., 2007, 2018) to produce the river discharge for all the European network. The Q(RP=100) value has been computed for each of the river segment and for each of the 29 CHyM simulations. The results are shown in the regional Figures of 12.4.

Standardized Precipitation Index (SPI): The SPI is a statistical index that compares cumulated precipitation for *n* months (*n*=6 or *n*=12) with the long-term precipitation distribution for the same location and cumulation period. The SPI months have been selected so SPI represent medium-term cumulated value and can be used to measure the medium term impact on river flow and reservoir storage (Mckee et al., 1993).

The index is computed in this way:

1. A monthly precipitation time series is selected (at least 30 years).
2. The running average for the *n*-months window is computed.
3. The Gamma distribution is used to fit the data. The fitting can be achieved through the maximum likelihood estimation of the Gamma distribution parameters.
4. The values from this probability distribution are then transformed into a normal distribution, so that the mean SPI for the location and desired period is zero and the standard deviation is 1 (Edwards and McKee, 1997).

Once SPI has been computed, the calculation of the Drought Frequency (DF) follows the method in (Spinoni et al., 2014): a drought event starts in the month when SPI falls below −1 and it ends when SPI returns to positive values, for at least two consecutive months.

It has to be noted that the SPI index has been recognized to be difficult to interpret in high latitudes and in arid areas due to statistical issues linked to inaccuracies in the estimation of the Gamma function (Spinoni et al., 2014). The duration of 6 months is considered in Figure 12.4.

This index is included in the Interactive Atlas, both SPI-6 and SPI-12 versions.

Soil moisture (SM):

The soil moisture index is used in Chapter 12 figures. It is simply using the total soil moisture content integrated over the soil depth, normalized by the recent past climatological values at each grid point.

Snow season length (SWE100): Several studies use the Snow Water Equivalent (SWE) variable (variable *snw* in model outputs) in order to define a "snow season length" as the number of days with enough snow on the ground. This index is particularly important for the winter tourism sector (Damm et al., 2017; Jacob et al., 2018). Several thresholds are used to define a day with "enough snow on the ground", with (Wobus et

ACCEPTED VERSION SUBJECT TO FINAL EDITS

al., 2017) marking 100mm as a key threshold for skiing. However, this index is important not only for winter tourism but also in other sectors such as water management. In several figures of Chapter 12 and the Atlas, the snow season length is calculated then as the number of days with SWE > 100mm, following the definition of (Damm et al., 2017; Wobus et al., 2017). Seasonal limits are given (November through March) for studies in the Northern hemisphere, and the index for the Southern Hemisphere is taken over the opposite season (May through September). SWE was assessed in several studies and its simulation depends on the representation of surface processes dealing with snow. Despite limitations, SWE was found to be useful in giving insight on the sign of changes (McCrary et al., 2017). When interpreting the figures shown in Chapter 12 and the Atlas, one should also keep in mind that 'altitudes' are model altitudes and may not correspond to real ones due to the coarse resolution, and the changes can be quite sensitive to such effects.

Extreme Total Water Level (ETWL): Factors contributing to extreme sea levels (ETWL) are sea level rise, storm surge (e.g. associated with tropical cyclones and extra-tropical cyclones), tide, and extreme waves (resulting in high wave setup at the shoreline). The ETWL used here is the summation of the aforementioned factors (Vitousek et al., 2017; Vousdoukas et al., 2018) and the commonly used 1 :100yr ETWL (the 100-year ETWL return value) is adopted here as the index relevant to episodic coastal flooding. Here, the median ETWL, together with the associated 5% -95 % confidence interval, resulting from a fully probabilistic model that incorporates storm surge and waves derived from models forced by an ensemble of 6 GCMs, is used as the index relevant for long-term coastal erosion.

Coastal Erosion (CE): Coastal erosion is generally accompanied by shoreline retreat, which can occur as a gradual process (e.g., due to sea level rise) or as an episodic event due to storm surge and/or extreme waves, especially when combined with high tide (Ranasinghe, 2016). The most commonly used shoreline retreat index is the magnitude of shoreline retreat by a pre-determined planning horizon such as 50 or 100 years into the future. Here, the median shoreline retreat, together with the associated 5% -95 % confidence interval, resulting from a fully probabilistic model that incorporates storm surge and waves derived from models forced by an ensemble of 6 GCMs, is used as the index relevant for long-term coastal erosion.

Some of these indices are included in the Interactive Atlas allowing flexible analysis (seasons, regions, baselines and future periods – using both time-slices/scenarios and global warming levels): TX35 and TX40 (both raw and bias adjusted; see Atlas 1.4.5), FD, CD, HD, SPI-6 and SPI-12.

[START TABLE AVI.2 HERE]

Table AVI.2: Regional CID indices table and relevant references.

CID category	Climatic impact-driver (from Table 12.1) and potential affected sectors	Index	Required ECVs	Way to calculate	Bias adjustment	References
Heat	Warming indicator for crops, ecosystems and hydrosystems	Length of Frost-Free period (LFFP)	Tasmin	from projections	yes	(Kunkel, 2004; McCabe et al., 2015; Wolfe et al., 2018)
Heat	Warming indicator for agriculture and ecosystems	yearly cumulated GDD over 5°C	Tas	from projections	yes	(Bonhomme, 2000; Cayton et al., 2015; Ruosteenoja et al., 2016)
Heat	Change in cooling demand for energy demand and building consumption	CD above 22°C	tas, tasmin, tasmax	from projections	yes	(Spinoni et al., 2015, 2018)
Heat	Heat, with thresholds important for agriculture	#days Tmax>35°C or 40°C (TX35, TX40)	Tasmax	from projections	yes	(Hatfield and Prueger, 2015; Hatfield et al., 2015; Grotjahn, 2021)
Heat	Heat stress index combining	NOAH Heat Index (HI) : Number of	tasmax huss ps	from projections	yes	(Burkart et al., 2011; Lin et al., 2012; Kent et al., 2014)

ACCEPTED VERSION SUBJECT TO FINAL EDITS

	humidity used in occupational and industrial health	days above 41°C threshold				
Cold	Heating Degree Day for Energy consumption	HD below 15.5°C	tas, tasmin, tasmax	from projections	yes	(Spinoni et al., 2015, 2018)
Cold	Frost	#Frost days below 0°C (FD)	Tasmin	from projections	yes	(Barlow et al., 2015; Rawlins et al., 2016)
Wet	River flooding	Flood index (FI)	srroff/ mrro	from projections and simplified routing model	no	(Forzieri et al., 2016; Alfieri et al., 2017)
Drought	Aridity	Soil Moisture (SM)	mrso	from projections	no	(Cook et al., 2020)
Drought	droughts	SPI accumulated over 6 months and 12 months (SPI-6 and SPI-12)	Pr	from projections	no	(Naumann et al., 2018)
Wind & storm	Mean wind speed	Annual mean wind speed	sfcWind	from projections	no	(Karnauskas et al., 2018; Li et al., 2018)
Snow/ice	Snow season length	Number of days with Snow Water Equivalent > 100 mm. (SWE100) over the snow season (NOV-MAR for NH)	Snw	from projections	no	(Damm et al., 2017; Wobus et al., 2017)
Coastal	Extreme Sea level (ETWL) inducing storm surges	100-year return period level (ETWL)		data from authors	no	(Vousdoukas et al., 2018)
Coastal	Coastal Erosion	Shoreline retreat by mid, end century		data from authors	no	(Vousdoukas et al., 2020)

[END TABLE AVI.2 HERE]

ACCEPTED VERSION
SUBJECT TO FINAL EDITS

References

Alexander, L. V., Zhang, X., Peterson, T. C., Caesar, J., Gleason, B., Klein Tank, A. M. G., et al. (2006). Global observed changes in daily climate extremes of temperature and precipitation. *J. Geophys. Res.* 111, D05109. doi:10.1029/2005JD006290.

Alfieri, L., Bisselink, B., Dottori, F., Naumann, G., de Roo, A., Salamon, P., et al. (2017). Global projections of river flood risk in a warmer world. *Earth's Futur.* 5, 171–182. doi:10.1002/2016EF000485.

Alfieri, L., Feyen, L., Dottori, F., and Bianchi, A. (2015). Ensemble flood risk assessment in Europe under high end climate scenarios. *Glob. Environ. Chang.* 35, 199–212. doi:10.1016/j.gloenvcha.2015.09.004.

Barlow, K. M., Christy, B. P., O'Leary, G. J., Riffkin, P. A., and Nuttall, J. G. (2015). Simulating the impact of extreme heat and frost events on wheat crop production: A review. *F. Crop. Res.* 171, 109–119. doi:https://doi.org/10.1016/j.fcr.2014.11.010.

Blazejczyk, K., Epstein, Y., Jendritzky, G., Staiger, H., and Tinz, B. (2012). Comparison of UTCI to selected thermal indices. *Int. J. Biometeorol.* 56, 515–535. doi:10.1007/s00484-011-0453-2.

Bonhomme, R. (2000). Bases and limits to using 'degree.day' units. *Eur. J. Agron.* 13, 1–10. doi:10.1016/S1161-0301(00)00058-7.

Brown, S. J., Caesar, J., and Ferro, C. A. T. (2008). Global changes in extreme daily temperature since 1950. *J. Geophys. Res. Atmos.* 113, D05115. doi:10.1029/2006JD008091.

Burkart, K., Schneider, A., Breitner, S., Khan, M. H., Krämer, A., and Endlicher, W. (2011). The effect of atmospheric thermal conditions and urban thermal pollution on all-cause and cardiovascular mortality in Bangladesh. *Environ. Pollut.* 159, 2035–2043. doi:https://doi.org/10.1016/j.envpol.2011.02.005.

Cannon, A. J., Sobie, S. R., and Murdock, T. Q. (2015). Bias Correction of GCM Precipitation by Quantile Mapping: How Well Do Methods Preserve Changes in Quantiles and Extremes? *J. Clim.* 28, 6938–6959. doi:10.1175/JCLI-D-14-00754.1.

Cayton, H. L., Haddad, N. M., Gross, K., Diamond, S. E., and Ries, L. (2015). Do growing degree days predict phenology across butterfly species? *Ecology* 96, 1473–1479. doi:10.1890/15-0131.1.

Coles, S. (2001). *An Introduction to Statistical Modeling of Extreme Values*. London, UK, UK: Springer Series in Statistics.

Cook, B. I., Mankin, J. S., Marvel, K., Williams, A. P., Smerdon, J. E., and Anchukaitis, K. J. (2020). Twenty-First Century Drought Projections in the CMIP6 Forcing Scenarios. *Earth's Futur.* 8, e2019EF001461. doi:10.1029/2019EF001461.

Coppola, E., Raffaele, F., and Giorgi, F. (2018). Impact of climate change on snow melt driven runoff timing over the Alpine region. *Clim. Dyn.* 51, 1259–1273. doi:10.1007/s00382-016-3331-0.

Coppola, E., Tomassetti, B., Mariotti, L., Verdecchia, M., and Visconti, G. (2007). Cellular automata algorithms for drainage network extraction and rainfall data assimilation. *Hydrol. Sci. J.* 52, 579–592. doi:10.1623/hysj.52.3.579.

Cradock-Henry, N. A. (2017). New Zealand kiwifruit growers' vulnerability to climate and other stressors. *Reg. Environ. Chang.* 17, 245–259. doi:10.1007/s10113-016-1000-9.

Crimp, S. J., Gobbett, D., Kokic, P., Nidumolu, U., Howden, M., and Nicholls, N. (2016). Recent seasonal and long-term changes in southern Australian frost occurrence. *Clim. Change* 139, 115–128. doi:10.1007/s10584-016-1763-5.

Cucchi, M., Weedon, G. P., Amici, A., Bellouin, N., Lange, S., Müller Schmied, H., et al. (2020). WFDE5: bias-adjusted ERA5 reanalysis data for impact studies. *Earth Syst. Sci. Data* 12, 2097–2120. doi:10.5194/essd-12-2097-2020.

Damm, A., Greuell, W., Landgren, O., and Prettenthaler, F. (2017). Impacts of +2 °C global warming on winter tourism demand in Europe. *Clim. Serv.* 7, 31–46. doi:10.1016/j.cliser.2016.07.003.

Deryng, D., Conway, D., Ramankutty, N., Price, J., and Warren, R. (2014). Global crop yield response to extreme heat stress under multiple climate change futures. *Environ. Res. Lett.* 9, 034011. doi:10.1088/1748-9326/9/3/034011.

Donat, M. G., Alexander, L. V., Yang, H., Durre, I., Vose, R., Dunn, R. J. H., et al. (2013). Updated analyses of temperature and precipitation extreme indices since the beginning of the twentieth century: The HadEX2 dataset. *J. Geophys. Res. Atmos.* 118, 2098–2118. doi:10.1002/jgrd.50150.

Edwards, D. C., and McKee, T. B. (1997). Characteristics of 20th century drought in the United States at multiple time scales. Available at: https://mountainscholar.org/handle/10217/170176 [Accessed March 24, 2019].

Forzieri, G., Feyen, L., Russo, S., Vousdoukas, M., Alfieri, L., Outten, S., et al. (2016). Multi-hazard assessment in Europe under climate change. *Clim. Change* 137, 105–119. doi:10.1007/s10584-016-1661-x.

Frich, P., Alexander, L., Della-Marta, P., Gleason, B., Haylock, M., Klein Tank, A., et al. (2002). Observed coherent changes in climatic extremes during the second half of the twentieth century. *Clim. Res.* 19, 193–212. doi:10.3354/cr019193.

Gourdji, S. M., Sibley, A. M., and Lobell, D. B. (2013). Global crop exposure to critical high temperatures in the reproductive period: historical trends and future projections. *Environ. Res. Lett.* 8, 024041. doi:10.1088/1748-

ACCEPTED VERSION SUBJECT TO FINAL EDITS

9326/8/2/024041.
Grotjahn, R. (2021). "Weather extremes that impact various agricultural commodities," in *Extreme Events and Climate Change: A Multidisciplinary Approach*, eds. F. Castillo, M. Wehner, and D. Stone (John Wiley & Sons, Inc.), 23–48. Available at: https://www.wiley.com/en-us/Extreme+Events+and+Climate+Change%3A+A+Multidisciplinary+Approach-p-9781119413622.
Hatfield, J. L., Boote, K. J., Kimball, B. A., Ziska, L. H., Izaurralde, R. C., Ort, D., et al. (2011). Climate Impacts on Agriculture: Implications for Crop Production. *Agron. J.* 103, 351. doi:10.2134/agronj2010.0303.
Hatfield, J. L., and Prueger, J. H. (2015). Temperature extremes: Effect on plant growth and development. *Weather Clim. Extrem.* 10, 4–10. doi:10.1016/J.WACE.2015.08.001.
Hatfield, J., Swanston, C., Janowiak, M., and Steele, R. (2015). USDA Midwest and Northern Forests Regional Climate Hub: Assessment of Climate Change Vulnerability and Adaptation and Mitigation Strategies. , ed. T. Anderson USA: U.S. Department of Agriculture Available at: https://www.climatehubs.oce.usda.gov/content/usda-midwest-and-northern-forests-regional-climate-hub-assessment-climate-change [Accessed February 22, 2019].
Hatfield, J., Takle, G., Grotjahn, R., Holden, P., Izaurralde, R. C., Mader, T., et al. (2014). "Ch. 6: Agriculture," in *Climate Change Impacts in the United States: The Third National Climate Assessment*, eds. J. M. Melillo, T. C. Richmond, and G. W. Yohe (USA: U.S Global Change Research Program), 150–174. doi:10.7930/J02Z13FR.
IPCC (2012). "IPCC 2012, Summary for policymakers," in *Managing the Risks of Extreme Events and Disasters to Advance Climate Change Adaptation*, eds. C. B. Field, V. Barros, T. F. Stocker, D. Qin, D. J. Dokken, K. L. Ebi, et al. (Cambridge, United Kingdom and New York, NY, USA: Cambridge University Press), 1–19. doi:10.1017/CBO9781139177245.
Jacob, D., Kotova, L., Teichmann, C., Sobolowski, S. P., Vautard, R., Donnelly, C., et al. (2018). Climate Impacts in Europe Under +1.5°C Global Warming. *Earth's Futur.* 6, 264–285. doi:10.1002/2017EF000710.
Karnauskas, K. B., Lundquist, J. K., and Zhang, L. (2018). Southward shift of the global wind energy resource under high carbon dioxide emissions. *Nat. Geosci.* 11, 38–43. doi:10.1038/s41561-017-0029-9.
Kent, S. T., McClure, L. A., Zaitchik, B. F., Smith, T. T., and Gohlke, J. M. (2014). Heat Waves and Health Outcomes in Alabama (USA): The Importance of Heat Wave Definition. *Environ. Health Perspect.* 122, 151–158. doi:10.1289/ehp.1307262.
Kharin, V. V., Zwiers, F. W., Zhang, X., and Wehner, M. (2013). Changes in temperature and precipitation extremes in the CMIP5 ensemble. *Clim. Change* 119, 345–357. doi:10.1007/s10584-013-0705-8.
Kharin, V. V, and Zwiers, F. W. (2000). Changes in the Extremes in an Ensemble of Transient Climate Simulations with a Coupled Atmosphere–Ocean GCM. *J. Clim.* 13, 3760–3788. doi:10.1175/1520-0442(2000)013<3760:CITEIA>2.0.CO;2.
Kingsley, S. L., Eliot, M. N., Gold, J., Vanderslice, R. R., and Wellenius, G. A. (2016). Current and Projected Heat-Related Morbidity and Mortality in Rhode Island. *Environ. Health Perspect.* 124, 460–467. doi:10.1289/ehp.1408826.
Kunkel, K. E. (2004). Temporal variations in frost-free season in the United States: 1895–2000. *Geophys. Res. Lett.* 31, L03201. doi:10.1029/2003GL018624.
Li, C., Michel, C., Seland Graff, L., Bethke, I., Zappa, G., Bracegirdle, T. J., et al. (2018). Midlatitude atmospheric circulation responses under 1.5 and 2.0 °C warming and implications for regional impacts. *Earth Syst. Dyn.* 9, 359–382. doi:10.5194/esd-9-359-2018.
Lin, Y.-K., Chang, C.-K., Li, M.-H., Wu, Y.-C., and Wang, Y.-C. (2012). High-temperature indices associated with mortality and outpatient visits: Characterizing the association with elevated temperature. *Sci. Total Environ.* 427–428, 41–49. doi:https://doi.org/10.1016/j.scitotenv.2012.04.039.
Lobell, D. B., and Gourdji, S. M. (2012). The Influence of Climate Change on Global Crop Productivity. *PLANT Physiol.* 160, 1686–1697. doi:10.1104/pp.112.208298.
Lobell, D. B., Hammer, G. L., McLean, G., Messina, C., Roberts, M. J., and Schlenker, W. (2013). The critical role of extreme heat for maize production in the United States. *Nat. Clim. Chang.* 3, 497–501. doi:10.1038/nclimate1832.
Mäkinen, H., Kaseva, J., Trnka, M., Balek, J., Kersebaum, K. C., Nendel, C., et al. (2018). Sensitivity of European wheat to extreme weather. *F. Crop. Res.* 222, 209–217. doi:10.1016/j.fcr.2017.11.008.
McCabe, G. J., Betancourt, J. L., and Feng, S. (2015). Variability in the start, end, and length of frost-free periods across the conterminous United States during the past century. *Int. J. Climatol.* 35, 4673–4680. doi:10.1002/joc.4315.
McCrary, R. R., McGinnis, S., and Mearns, L. O. (2017). Evaluation of Snow Water Equivalent in NARCCAP Simulations, Including Measures of Observational Uncertainty. *J. Hydrometeorol.* 18, 2425–2452. doi:10.1175/JHM-D-16-0264.1.
Mckee, T. B., Doesken, N. J., and Kleist, J. (1993). The relationship of drought frequency and duration to time scales. in *Eighth Conference on Applied Climatology, Anaheim California*, 17–22. Available at: http://www.droughtmanagement.info/literature/AMS_Relationship_Drought_Frequency_Duration_Time_Scales_1993.pdf [Accessed April 1, 2019].
Mora, C., Spirandelli, D., Franklin, E. C., Lynham, J., Kantar, M. B., Miles, W., et al. (2018). Broad threat to humanity from cumulative climate hazards intensified by greenhouse gas emissions. *Nat. Clim. Chang.* 8, 1062–1071.

ACCEPTED VERSION SUBJECT TO FINAL EDITS

doi:10.1038/s41558-018-0315-6.
Mu, J. E., Sleeter, B. M., Abatzoglou, J. T., and Antle, J. M. (2017). Climate impacts on agricultural land use in the USA: the role of socio-economic scenarios. *Clim. Change* 144, 329–345. doi:10.1007/s10584-017-2033-x.
Naumann, G., Alfieri, L., Wyser, K., Mentaschi, L., Betts, R. A., Carrao, H., et al. (2018). Global Changes in Drought Conditions Under Different Levels of Warming. *Geophys. Res. Lett.* 45, 3285–3296. doi:10.1002/2017GL076521.
Petitti, D. B., Hondula, D. M., Yang, S., Harlan, S. L., and Chowell, G. (2016). Multiple Trigger Points for Quantifying Heat-Health Impacts: New Evidence from a Hot Climate. *Environ. Health Perspect.* 124, 176–183. doi:10.1289/ehp.1409119.
Petkova, E. P., Vink, J. K., Horton, R. M., Gasparrini, A., Bader, D. A., Francis, J. D., et al. (2017). Towards More Comprehensive Projections of Urban Heat-Related Mortality: Estimates for New York City under Multiple Population, Adaptation, and Climate Scenarios. *Environ. Health Perspect.* 125, 47–55. doi:10.1289/EHP166.
Ranasinghe, R. (2016). Assessing climate change impacts on open sandy coasts: A review. *Earth-Science Rev.* 160, 320–332. doi:10.1016/j.earscirev.2016.07.011.
Rawlins, M. A., Bradley, R. S., Diaz, H. F., Kimball, J. S., and Robinson, D. A. (2016). Future Decreases in Freezing Days across North America. *J. Clim.* 29, 6923–6935. doi:10.1175/JCLI-D-15-0802.1.
Rothfusz, L. P. (1990). The heat index equation (or, more than you ever wanted to know about heat index). Fort Worth, TX, USA: National Oceanic and Atmospheric Administration, National Weather Service, Office of Meteorology Available at: https://wonder.cdc.gov/wonder/help/Climate/ta_htindx.PDF.
Ruosteenoja, K., Räisänen, J., Venäläinen, A., and Kämäräinen, M. (2016). Projections for the duration and degree days of the thermal growing season in Europe derived from CMIP5 model output. *Int. J. Climatol.* 36, 3039–3055. doi:10.1002/joc.4535.
Schauberger, B., Archontoulis, S., Arneth, A., Balkovic, J., Ciais, P., Deryng, D., et al. (2017). Consistent negative response of US crops to high temperatures in observations and crop models. *Nat. Commun.* 8, 13931. doi:10.1038/ncomms13931.
Schlenker, W., and Roberts, M. J. (2009). Nonlinear temperature effects indicate severe damages to U.S. crop yields under climate change. *Proc. Natl. Acad. Sci.* 106, 15594–15598. doi:10.1073/pnas.0906865106.
Sillmann, J., Kharin, V. V., Zwiers, F. W., Zhang, X., and Bronaugh, D. (2013). Climate extremes indices in the CMIP5 multimodel ensemble: Part 2. Future climate projections. *J. Geophys. Res. Atmos.* 118, 2473–2493. doi:10.1002/jgrd.50188.
Spinoni, J., Naumann, G., Carrao, H., Barbosa, P., and Vogt, J. (2014). World drought frequency, duration, and severity for 1951-2010. *Int. J. Climatol.* 34, 2792–2804. doi:10.1002/joc.3875.
Spinoni, J., Vogt, J., and Barbosa, P. (2015). European degree-day climatologies and trends for the period 1951-2011. *Int. J. Climatol.* 35, 25–36. doi:10.1002/joc.3959.
Spinoni, J., Vogt, J. V, Barbosa, P., Dosio, A., McCormick, N., Bigano, A., et al. (2018). Changes of heating and cooling degree-days in Europe from 1981 to 2100. *Int. J. Climatol.* 38, e191–e208. doi:10.1002/joc.5362.
Steadman, R. G. (1979). The assessment of sultriness. Part I: A temperature-humidity index based on human physiology and clothing science. *J. Appl. Meteorol.* 18, 861– 873. doi:10.1175/1520-0450(1979)018<0861:TAOSPI>2.0.CO;2.
Tesfaye, K., Zaidi, P. H., Gbegbelegbe, S., Boeber, C., Rahut, D. B., Getaneh, F., et al. (2017). Climate change impacts and potential benefits of heat-tolerant maize in South Asia. *Theor. Appl. Climatol.* 130, 959–970. doi:10.1007/s00704-016-1931-6.
Tripathi, A., Tripathi, D. K., Chauhan, D. K., Kumar, N., and Singh, G. S. (2016). Paradigms of climate change impacts on some major food sources of the world: A review on current knowledge and future prospects. *Agric. Ecosyst. Environ.* 216, 356–373. doi:10.1016/j.agee.2015.09.034.
Vitousek, S., Barnard, P. L., Fletcher, C. H., Frazer, N., Erikson, L., Storlazzi, C. D., et al. (2017). Doubling of coastal flooding frequency within decades due to sea-level rise. *Sci. Rep.* 7, 1399. doi:10.1038/s41598-017-01362-7.
Vousdoukas, M. I., Mentaschi, L., Voukouvalas, E., Verlaan, M., Jevrejeva, S., Jackson, L. P., et al. (2018). Global probabilistic projections of extreme sea levels show intensification of coastal flood hazard. *Nat. Commun.* 9, 2360. doi:10.1038/s41467-018-04692-w.
Vousdoukas, M. I., Ranasinghe, R., Mentaschi, L., Plomaritis, T. A., Athanasiou, P., Luijendijk, A., et al. (2020). Sandy coastlines under threat of erosion. *Nat. Clim. Chang.* 10, 260–263. doi:10.1038/s41558-020-0697-0.
Wobus, C., Small, E. E., Hosterman, H., Mills, D., Stein, J., Rissing, M., et al. (2017). Projected climate change impacts on skiing and snowmobiling: A case study of the United States. *Glob. Environ. Chang.* 45, 1–14. doi:10.1016/j.gloenvcha.2017.04.006.
Wolfe, D. W., DeGaetano, A. T., Peck, G. M., Carey, M., Ziska, L. H., Lea-Cox, J., et al. (2018). Unique challenges and opportunities for northeastern US crop production in a changing climate. *Clim. Change* 146, 231–245. doi:10.1007/s10584-017-2109-7.
Wolfe, D. W., Ziska, L., Petzoldt, C., Seaman, A., Chase, L., and Hayhoe, K. (2008). Projected change in climate thresholds in the Northeastern U.S.: implications for crops, pests, livestock, and farmers. *Mitig. Adapt. Strateg. Glob. Chang.* 13, 555–575. doi:10.1007/s11027-007-9125-2.
Zhang, X., Alexander, L., Hegerl, G. C., Jones, P., Tank, A. K., Peterson, T. C., et al. (2011). Indices for monitoring

ACCEPTED VERSION
SUBJECT TO FINAL EDITS

changes in extremes based on daily temperature and precipitation data. *Wiley Interdiscip. Rev. Clim. Chang.* 2, 851–870. doi:10.1002/wcc.147.

ACCEPTED VERSION
SUBJECT TO FINAL EDITS

Annex VII - Glossary

Coordinating Editors:
J. B. Robin Matthews (France/United Kingdom), Jan S. Fuglestvedt (Norway), Valérie Masson-Delmotte (France), Vincent Möller (Germany), Carlos Méndez (Venezuela), Renée van Diemen (The Netherlands/United Kingdom), Andy Reisinger (New Zealand), Sergey Semenov (Russian Federation)

Editorial Team:
Rondrotiana Barimalala (South Africa/Madagascar), Roxana Bojariu (Romania), Annalisa Cherchi (Italy), Peter M. Cox (United Kingdom), Sergio Henrique Faria (Spain/Brazil), Piers Forster (United Kingdom), Christopher Jones (United Kingdom), Nana Ama Browne Klutse (Ghana), Charles Koven (United States of America), Svitlana Krakovska (Ukraine), Sawsan K. Mustafa (Sudan), Friederike Otto (United Kingdom/Germany), Matthew D. Palmer (United Kingdom), Tamzin Palmer (United Kingdom), Wilfried Pokam Mba (Cameroon), Roshanka Ranasinghe (The Netherlands/Sri Lanka, Australia), Pedro Scheel Monteiro (South Africa), Joeri Rogelj (United Kingdom/ Belgium), Sharon L. Smith (Canada), Ying Sun (China), Andrew Turner (United Kingdom), Bart van den Hurk (The Netherlands), Émilie Vanvyve (United Kingdom/Belgium), Martin Wild (Switzerland), Cunde Xiao (China), Prodromos Zanis (Greece)

This glossary defines some specific terms as the Lead Authors intend them to be interpreted in the context of this report. Italicized words in definitions indicate that the italicized term is defined in the Glossary. Subterms appear in italics beneath main terms.

Date: August 2021

This document is subject to copy-editing, corrigenda and trickle backs.

ACCEPTED VERSION
SUBJECT TO FINAL EDITS

This Annex should be cited as:
IPCC, 2021: Annex VII: Glossary [Matthews, J. B. R., J. S. Fuglestvedt, V. Masson-Delmotte, V. Möller, C. Méndez, R. van Diemen, A. Reisinger, S. Semenov (ed.)]. In: *Climate Change 2021: The Physical Science Basis. Contribution of Working Group I to the Sixth Assessment Report of the Intergovernmental Panel on Climate Change* [Masson-Delmotte, V., P. Zhai, A. Pirani, S. L. Connors, C. Péan, S. Berger, N. Caud, Y. Chen, L. Goldfarb, M. I. Gomis, M. Huang, K. Leitzell, E. Lonnoy, J.B.R. Matthews, T. K. Maycock, T. Waterfield, O. Yelekçi, R. Yu and B. Zhou (eds.)]. Cambridge University Press. In Press.

1.5°C pathway See *Pathways*.

Ablation (of glaciers, ice sheets, or snow cover) See *Mass balance / budget (of glaciers or ice sheets)*.

Abrupt change A change in the system that is substantially faster than the typical rate of the changes in its history.

Abrupt climate change A large-scale *abrupt change* in the *climate system* that takes place over a few decades or less, persists (or is anticipated to persist) for at least a few decades and causes substantial *impacts* in *human and/or natural systems*. See also *Tipping point* and *Abrupt change*.

Accumulation (of glaciers, ice sheets, or snow cover) See *Mass balance / budget (of glaciers or ice sheets)*.

Active layer Layer of ground above *permafrost* subject to annual thawing and freezing.

Adaptation In *human systems*, the process of adjustment to actual or expected *climate* and its effects, in order to moderate harm or exploit beneficial opportunities. In natural systems, the process of adjustment to actual climate and its effects; human intervention may facilitate adjustment to expected climate and its effects. See also *Adaptation options*, *Adaptive capacity* and *Maladaptive actions (Maladaptation)*.

Adaptation options The array of strategies and measures that are available and appropriate for addressing *adaptation*. They include a wide range of actions that can be categorised as structural, *institutional*, ecological or behavioural.

Adaptive capacity The ability of systems, *institutions*, humans and other organisms to adjust to potential damage, to take advantage of opportunities, or to respond to consequences (IPCC, 2014; MA, 2005).

Added value Improvement of the representation of some climatic aspects by one methodology compared to another methodology. For instance, downscaling a coarse resolution *global climate model (GCM)* may improve the representation of regional climate in complex terrain.

Adjustment time See *Response time or adjustment time*.

Advection Transport of water or air along with its properties (e.g., temperature, chemical tracers) by winds or currents. Regarding the general distinction between advection and *convection*, the former describes transport by large-scale motions of the *atmosphere* or ocean, while convection describes the predominantly vertical, locally induced motions.

Aerosol A suspension of airborne solid or liquid particles, with typical diameters between a few nanometres and a few micrometres and atmospheric lifetimes of up to several days in the *troposphere* and up to years in the *stratosphere*. The term aerosol, which includes both the particles and the suspending gas, is often used in this report in its plural form to mean 'aerosol particles'. Aerosols may be of either natural or *anthropogenic* origin in the troposphere; stratospheric aerosol mostly stems from volcanic eruptions. Aerosols can cause an *effective radiative forcing* directly through scattering and absorbing radiation (*aerosol-radiation interactions*), and indirectly by acting as *cloud condensation nuclei* or ice nucleating particles which affect the properties of clouds (*aerosol-cloud interactions*), and upon deposition on snow- or ice-covered surfaces. Atmospheric aerosols may be emitted as primary particulate matter (PM), and form within the atmosphere from gaseous *precursors* (secondary production). Main classes of aerosol chemical composition are sea salt, organic carbon, *black carbon (BC)*, mineral species (mainly desert dust), sulphate, nitrate, and ammonium. See also *Short-lived climate forcers (SLCFs)*.

Aerosol effective radiative forcing (ERFari+aci) See *Aerosol-radiation interaction*.

Aerosol optical depth (AOD) Wavelength-dependent aerosol optical depth is a measure of the *aerosol*

ACCEPTED VERSION SUBJECT TO FINAL EDITS

contribution to extinction of top-of-the-atmosphere solar intensity measured at the ground. AOD is unitless.

Fine-mode aerosol optical depth Aerosol optical depth due to aerosol particles smaller than 1 μm in radius.

Aerosol-cloud interaction A process by which a perturbation to *aerosol* affects the microphysical properties and evolution of clouds through the aerosol role as *cloud condensation nuclei* or ice nuclei, particularly in ways that affect radiation or precipitation; such processes can also include the effect of clouds and precipitation on aerosol. The aerosol perturbation can be *anthropogenic* or come from some natural *source*. The *radiative forcing* from such interactions has traditionally been attributed to numerous indirect aerosol effects, but in this report, only two levels of radiative forcing (or effect) are distinguished: See also *Aerosol-radiation interaction*.

Effective radiative forcing (or effect) due to aerosol-cloud interactions (ERFaci) The final *radiative forcing* (or effect) from the *aerosol* perturbation including the adjustments to the initial change in droplet or crystal formation rate. These adjustments include changes in the strength of *convection*, precipitation efficiency, cloud fraction, *lifetime* or water content of clouds, and the formation or suppression of clouds in remote areas due to altered circulations. See also *Aerosol-radiation interaction*.

Instantaneous radiative forcing (or effect) due to aerosol-cloud interactions (IRFaci) The radiative forcing (or radiative effect, if the perturbation is internally generated) due to the change in number or size distribution of cloud droplets or ice crystals that is the proximate result of an aerosol perturbation, with other variables (in particular total cloud water content) remaining equal. In liquid clouds, an increase in cloud droplet concentration and surface area would increase the cloud albedo. This effect is also known as the cloud albedo effect, first indirect effect, or Twomey effect. It is a largely theoretical concept that cannot readily be isolated in observations or comprehensive process models due to the ubiquity of adjustments.

Aerosol-radiation interaction An interaction of *aerosol* directly with radiation produce *radiative effects*. In this report two levels of *radiative forcing* (or effect) are distinguished:

Aerosol effective radiative forcing (ERFari+aci) The total effective radiative forcing due to both aerosol-cloud and aerosol-radiation interactions is denoted aerosol effective radiative forcing (ERFari+aci).

Effective radiative forcing (or effect) due to aerosol-radiation interactions (ERFari) The final radiative forcing (or effect) from the aerosol perturbation including adjustments to the initial change in radiation. These adjustments include changes in cloud caused by the impact of the radiative heating on convective or larger-scale atmospheric circulations, traditionally known as semi-direct aerosol forcing (or effect). See also *Aerosol-cloud interaction*.

Instantaneous radiative forcing (or effect) due to aerosol-radiation interactions (IRFari) The radiative forcing (or radiative effect, if the perturbation is internally generated) of an aerosol perturbation due directly to aerosol-radiation interactions, with all environmental variables remaining unaffected. Traditionally known in the literature as the direct aerosol forcing (or effect).

Afforestation Conversion to *forest* of land that historically has not contained forests. [Note: For a discussion of the term forest and related terms such as afforestation, reforestation and deforestation, see the 2006 IPCC Guidelines for National Greenhouse Gas Inventories and their 2019 Refinement, and information provided by the United Nations Framework Convention on Climate Change (IPCC, 2006, 2019, UNFCCC, 2021a, 2021b).] See also *Deforestation, Reducing Emissions from Deforestation and Forest Degradation (REDD+), Reforestation, Anthropogenic removals* and *Carbon dioxide removal (CDR)*.

Agreement In this report, the degree of agreement within the scientific body of knowledge on a particular finding is assessed based on multiple lines of *evidence* (e.g., mechanistic understanding, theory, data, models, expert judgement) and expressed qualitatively (Mastrandrea et al., 2010). See also *Confidence, Likelihood, Uncertainty* and *Evidence*.

ACCEPTED VERSION SUBJECT TO FINAL EDITS

Agricultural or ecological drought See *Drought*.

Air mass A widespread body of air, the approximately homogeneous properties of which (1) have been established while that air was situated over a particular *region* of the Earth's surface, and (2) undergo specific modifications while in transit away from the source region (AMS, 2021).

Air pollution Degradation of air quality with negative effects on human health or the natural or built environment due to the introduction, by natural processes or human activity, into the *atmosphere* of substances (gases, *aerosols*) which have a direct (primary pollutants) or indirect (secondary pollutants) harmful effect. See also *Short-lived climate forcers (SLCFs)*.

Airborne fraction The fraction of total CO_2 emissions (from fossil fuel and land use change) remaining in the *atmosphere*.

Albedo The proportion of sunlight (*solar radiation*) reflected by a surface or object, often expressed as a percentage. Clouds, snow and ice usually have high albedo; soil surfaces cover the albedo range from high to low; vegetation in the dry season and/or in *arid zones* can have high albedo, whereas photosynthetically active vegetation and the *ocean* have low albedo. The Earth's planetary albedo changes mainly through changes in cloudiness and of snow, ice, leaf area and *land cover*.

Alkalinity See *Total alkalinity*.

Altimetry A technique for measuring the height of the Earth's surface with respect to the geocentre of the Earth within a defined terrestrial reference frame (geocentric sea level).

Annular modes Hemispheric scale patterns of atmospheric variability characterized by opposing and synchronous fluctuations in sea-level pressure between the polar caps and midlatitudes, with a structure exhibiting a high degree of zonal symmetry, and with no real preferred timescales ranging from days to decades. In each hemisphere, these fluctuations reflect changes in the latitudinal position and strength of the mid-latitude jets and associated storm tracks. Annular modes are defined as the leading mode of variability of extratropical sea-level pressure or geopotential heights and are known as the *Northern Annular Mode (NAM)* and *Southern Annular Mode (SAM)* in the two hemispheres, respectively.

Northern Annular Mode (NAM) A see-saw latitudinal fluctuation in Northern Hemisphere sea-level pressure or geopotential height between the Arctic and the mid-latitudes. The NAM has some links with the *stratospheric polar vortex* and is related to the fluctuation in strength and latitude of the mean westerlies. Its variance is maximum in winter and its pattern has a strong regional expression in the North Atlantic being strongly correlated with the *North Atlantic Oscillation* index. The NAM is also known as the Arctic Oscillation (AO). In its positive phase, the NAM is characterized by anomalously low pressure over the Arctic and high pressure over the mid-latitudes/subtropics, with a strengthening of the zonally averaged westerly winds on their polar flank that confines colder air across the Arctic. The negative NAM phase is characterized by a more distorted wind pattern and jet meanders which increases storminess in the midlatitude regions. See Section AIV.2.1 in Annex IV of the AR6 WGI report.

Southern Annular Mode (SAM) The leading mode of *climate variability* of Southern Hemisphere sea-level pressure and geopotential height, which is associated with the strength and latitudinal shifts in the mid- to high-latitudes westerly wind belt. The SAM is also known as the Antarctic Oscillation (AAO). A positive SAM phase is defined as lower-than-normal pressures over the polar regions and higher-than-normal pressures in the southern mid-latitudes, with a contraction towards Antarctica and strengthening of the westerly wind belt. The negative SAM phase exhibits positive high latitude pressure anomalies, negative mid-latitude pressure anomalies and a weaker westerly flow expanded towards the equator. See Section AIV.2.2 in Annex IV of the AR6 WGI report. See also *Annular modes*.

Anomaly The deviation of a variable from its value averaged over a *reference period.*

ACCEPTED VERSION SUBJECT TO FINAL EDITS

Antarctic amplification See *Polar amplification*.

Antarctic ice sheet (AIS) See *Ice sheet*.

Antarctic oscillation (AAO) See *Southern Annular Mode (SAM)* (under *Annular modes*).

Anthropocene A proposed new geological epoch resulting from significant human-driven changes to the structure and functioning of the Earth System, including the *climate system*. Originally proposed in the Earth System science community in 2000, the proposed new epoch is undergoing a formalization process within the geological community based on the stratigraphic *evidence* that human activities have changed the Earth System to the extent of forming geological deposits with a signature that is distinct from those of the *Holocene*, and which will remain in the geological record. Both the stratigraphic and Earth System approaches to defining the Anthropocene consider the mid-20th Century to be the most appropriate starting date (Steffen et al., 2016), although others have been proposed and continue to be discussed. The Anthropocene concept has already been informally adopted by diverse disciplines and the public to denote the substantive influence of humans on the Earth System.

Anthropogenic Resulting from or produced by human activities.

Anthropogenic emissions Emissions of *greenhouse gases (GHGs)*, precursors of GHGs and *aerosols* caused by human activities. These activities include the burning of *fossil fuels*, *deforestation, land use and land use changes (LULUC)*, livestock production, fertilisation, waste management, and industrial processes. See also *Anthropogenic* and *Anthropogenic removals*.

Anthropogenic removals The withdrawal of greenhouse gases (GHGs) from the atmosphere as a result of deliberate human activities. These include enhancing biological sinks of CO_2 and using chemical engineering to achieve long term removal and storage. Carbon capture and storage (CCS), which alone does not remove CO_2 from the atmosphere, can help reduce atmospheric CO_2 from industrial and energy-related sources if it is combined with bioenergy production (BECCS), or if CO_2 is captured from the air directly and stored (DACCS). [Note: In the 2006 IPCC Guidelines for national GHG Inventories (IPCC, 2006), which are used in reporting of emissions to the UNFCCC, 'anthropogenic' land-related GHG fluxes are defined as all those occurring on 'managed land', i.e. 'where human interventions and practices have been applied to perform production, ecological or social functions'. However, some removals (e.g. removals associated with CO_2 fertilisation and N deposition) are not considered as 'anthropogenic', or are referred to as 'indirect' anthropogenic effects, in some of the scientific literature assessed in this report. As a consequence, the land-related net GHG emission estimates from global models included in this report are not necessarily directly comparable with LULUCF estimates in national GHG Inventories.] See also *Carbon dioxide removal (CDR)*, *Afforestation*, *Biochar*, *Enhanced weathering*, *Ocean alkalinisation / Ocean alkalinity enhancement*, *Reforestation* and *Soil carbon sequestration (SCS)*.

Anthropogenic subsidence Downward motion of the land surface induced by anthropogenic drivers (e.g., loading, extraction of hydrocarbons and/or groundwater, drainage, mining activities) causing sediment compaction or subsidence/deformation of the sedimentary sequence, or oxidation of organic material, thereby leading to relative sea level rise.

Apparent hydrological sensitivity (η_a) The change in global mean precipitation per degree Celsius of global mean temperature change with units of % per °C although can also be calculated as W m^{-2} per °C. See also *Hydrological sensitivity (η)*.

Arctic amplification See *Polar amplification*.

Arid zone Areas where vegetation growth is severely constrained due to limited water availability. For the most part, the native vegetation of arid zones is sparse. There is high rainfall variability, with annual averages below 300 mm. Crop farming in arid zones requires irrigation.

ACCEPTED VERSION SUBJECT TO FINAL EDITS

Aridity The state of a long-term climatic feature characterised by low average precipitation or available water in a region. Aridity generally arises from widespread persistent *atmospheric* subsidence or anticyclonic conditions, and from more localised subsidence in the lee side of mountains (adapted from Gbeckor-Kove, 1989; Türkeş, 1999). See also *Drought*.

Artificial ocean upwelling (AOUpw) Artificial ocean upwelling (AOUpw) is a potential carbon dioxide removal method that aims to artificially pump up cooler, nutrient-rich waters from deep in the ocean to the surface. The aim is to stimulate phytoplankton activity and thereby increase ocean CO_2 uptake.

Assets Natural or human-made resources that provide current or future utility, benefit, economic or intrinsic value to natural or human systems.

Atlantic Equatorial Mode See *Atlantic Zonal Mode (AZM)* (under *Tropical Atlantic Variability (TAV)*).

Atlantic Meridional Mode (AMM) See *Tropical Atlantic Variability (TAV)*.

Atlantic Meridional Overturning Circulation (AMOC) See *Meridional overturning circulation (MOC)*.

Atlantic Multidecadal Oscillation (AMO) See *Atlantic Multidecadal Variability (AMV)*.

Atlantic Multidecadal Variability (AMV) Large-scale fluctuations observed from one decade to the next in a variety of instrumental records and *proxy* reconstructions over the entire North Atlantic ocean and surrounding continents. Fingerprints of Atlantic Multidecadal Variability (AMV) can be found at the surface ocean, which is characterized by swings in basin-scale *sea surface temperature* anomalies reflecting the interaction with the *atmosphere*. The positive phase of the AMV is characterized by anomalous warming over the entire North Atlantic, with the strongest amplitude in the subpolar gyre and along sea-ice margin zones in the Labrador Sea and Greenland/Barents Sea and in the subtropical North Atlantic basin to a lower extent. In the AR6 WGI report, the term AMV is preferred to Atlantic Multidecadal Oscillation (AMO) used in previous IPCC reports because there is no preferred timescale of decadal variability as the term oscillation would indirectly implied. See Section AIV.2.7 in Annex IV of the AR6 WGI report.

Atlantic Niño See *Atlantic Zonal Mode (AZM)* (under *Tropical Atlantic Variability (TAV)*).

Atlantic Zonal Mode (AZM) See *Tropical Atlantic Variability (TAV)*.

Atmosphere The gaseous envelope surrounding the Earth, divided into five layers – the *troposphere* which contains half of the Earth's atmosphere, the *stratosphere*, the mesosphere, the thermosphere, and the exosphere, which is the outer limit of the atmosphere. The dry atmosphere consists almost entirely of nitrogen (78.1% volume mixing ratio) and oxygen (20.9% volume mixing ratio), together with a number of trace gases, such as argon (0.93 % volume mixing ratio), helium and radiatively active *greenhouse gases (GHGs)* such as *carbon dioxide (CO_2)* (0.04% volume mixing ratio), *methane (CH_4)*, *nitrous oxide (N_2O)* and *ozone (O_3)*. In addition, the atmosphere contains the GHG water vapour (H_2O), whose concentrations are highly variable (0-5% volume mixing ratio) as the sources (*evapotranspiration*) and sinks (precipitation) of water vapour show large spato-temporal variations, and atmospheric temperature exerts a strong constraint on the amount of water vapour an air parcel can hold. The atmosphere also contains clouds and *aerosols*. See also *Hydrological cycle*, *Stratosphere* and *Troposphere*.

Atmosphere-ocean general circulation model (AOGCM) See *General circulation model (GCM)*.

Atmospheric boundary layer The atmospheric layer adjacent to the Earth's surface that is affected by friction against that boundary surface, and possibly by transport of heat and other variables across that surface (AMS, 2021). The lowest 100 m of the boundary layer (about 10% of the boundary layer thickness), where mechanical generation of turbulence is dominant, is called the surface boundary layer or surface layer.

Atmospheric lifetime See *Lifetime*.

ACCEPTED VERSION SUBJECT TO FINAL EDITS

Atmospheric rivers (ARs) Long, narrow (up to a few hundred km wide), shallow (up to a few km deep) and transient corridors of strong horizontal water vapour transport that are typically associated with a low-level jet stream ahead of the cold front of an *extratropical cyclone* (Ralph et al., 2018).

Attribution Attribution is defined as the process of evaluating the relative contributions of multiple causal factors to a change or event with an assessment of confidence.

Australian and Maritime Continent monsoon (AusMCM) See *Global monsoon*.

Autotrophic respiration Respiration by photosynthetic (see *photosynthesis*) organisms (e.g., plants and algae).

Avalanche A mass of snow, ice, earth or rocks, or a mixture of these, falling down a mountainside.

Barystatic See *Sea level change (sea level rise/sea level fall)*.

Basal lubrication Reduction of friction at the base of an *ice sheet* or *glacier* due to lubrication by meltwater. This can allow the glacier or ice sheet to slide over its base. Meltwater may be produced by pressure-induced melting, friction or geothermal heat, or surface melt may drain to the base through holes in the ice.

Baseline/reference The baseline (or reference) is the state against which change is measured.See *Baseline scenario* (under *Scenario*) and *Baseline/reference (period)*. See also *Baseline period* (under *Reference period*) and *Reference period*.

Baseline period See *Reference period*.

Baseline scenario See *Scenario*.

Bifurcation point See *Tipping point*.

Biodiversity Biodiversity or biological diversity means the variability among living organisms from all sources including, among other things, terrestrial, marine and other aquatic *ecosystems*, and the ecological complexes of which they are part; this includes diversity within species, between species, and of ecosystems (UN, 1992). See also *Ecosystem* and *Ecosystem services*.

Bioenergy with carbon dioxide capture and storage (BECCS) Carbon dioxide capture and storage (CCS) technology applied to a *bioenergy* facility. Note that depending on the total emissions of the BECCS supply chain, *carbon dioxide (CO_2)* can be removed from the *atmosphere*. See also *Bioenergy*, *Carbon dioxide capture and storage (CCS)*, *Anthropogenic removals* and *Carbon dioxide removal (CDR)*.

Biogenic volatile organic compounds (BVOCs) See *Volatile organic compounds (VOCs)*.

Biogeophysical potential See *Mitigation potential*.

Biological (carbon) pump A series of *ocean* processes through which inorganic carbon (as *carbon dioxide, CO_2*) is fixed as organic matter by photosynthesis in sunlit surface water and then transported to the ocean interior, and possibly the sediment, resulting in the storage of carbon.

Biomass Organic material excluding the material that is fossilised or embedded in geological formations. Biomass may refer to the mass of organic matter in a specific area (ISO, 2014). See also *Bioenergy* and *Biofuel*.

Biosphere (terrestrial and marine) The part of the Earth System comprising all *ecosystems* and living organisms, in the *atmosphere*, on land (terrestrial biosphere) or in the oceans (marine biosphere), including

ACCEPTED VERSION SUBJECT TO FINAL EDITS

derived dead organic matter, such as litter, soil organic matter and oceanic detritus.

Bipolar seesaw (also interhemispheric seesaw, interhemispheric asymmetry, hemispheric asymmetry) A phenomenon in which temperature changes in the northern and southern hemispheres are related but out of phase, generally inferred to represent a change in the magnitude or sign of net heat transport across the equator. Originally called hemispheric asymmetry and linked to changes in thermohaline overturning circulation on multi-millennial scales (Mix et al., 1986), later named bipolar seesaw and applied to millennial scales (Broecker, 1998) with a similar thermohaline mechanism (Stocker and Johnsen, 2003). See also *Meridional overturning circulation (MOC)* and *Deglacial or deglaciation or glacial termination*.

Black carbon (BC) A relatively pure form of carbon, also known as soot, arising from the incomplete combustion of fossil fuels, biofuel, and biomass. It only stays in the atmosphere for days or weeks. BC is a climate forcing agent with strong warming effect, both in the atmosphere and when deposited on snow or ice. See also *Aerosol* and *Atmosphere*.

Blocking Associated with persistent, slow-moving high-pressure systems that obstruct the prevailing westerly winds in the middle and high latitudes and the normal eastward progress of extratropical transient storm systems. It is an important component of the intraseasonal *climate variability* in the extratropics and can cause long-lived weather conditions such as cold spells in winter and summer *heat waves*.

Blue carbon Biologically-driven carbon fluxes and storage in marine systems that are amenable to management. Coastal blue carbon focuses on rooted vegetation in the coastal zone, such as tidal marshes, mangroves and seagrasses. These *ecosystems* have high carbon burial rates on a per unit area basis and accumulate carbon in their soils and sediments. They provide many non-climatic benefits and can contribute to ecosystem-based adaptation. If degraded or lost, coastal blue carbon ecosystems are likely to release most of their carbon back to the *atmosphere*. There is current debate regarding the application of the blue carbon concept to other coastal and non-coastal processes and ecosystems, including the open *ocean*. See also *Ecosystem services* and *Sequestration*.

Brewer-Dobson circulation The meridional overturning circulation of the *stratosphere* transporting air upward in the tropics, poleward to the winter hemisphere, and downward at polar and subpolar latitudes. The Brewer-Dobson circulation is driven by the interaction between upward propagating planetary waves and the mean flow.

Burden The total mass of a substance of concern in the *atmosphere*.

Business as usual (BAU) The term business as usual scenario has been used to describe a scenario that assumes no additional policies beyond those currently in place and that patterns of socio-economic development are consistent with recent trends. The term is now used less frequently than in the past. See also *Reference scenario* (under *Scenario*).

^{13}C Stable *isotope* of carbon having an atomic weight of approximately 13. Measurements of the ratio of $^{13}C/^{12}C$ in *carbon dioxide* molecules are used to infer the importance of different *carbon cycle* and *climate* processes and the size of the terrestrial carbon *reservoir*.

^{14}C Unstable *isotope* of carbon having an atomic weight of approximately 14, and a half-life of about 5700 years. It is often used for dating purposes going back some 40 kyr. Its variation in time is affected by the magnetic fields of the Sun and Earth, which influence its production from cosmic rays (see *Cosmogenic radioisotopes*).

Calcification The process of biologically precipitating calcium carbonate minerals to create organism shells, skeletons, otoliths, or other body structures. The chemical equation describing calcification is $Ca^{2+}(aq) + 2HCO_3^-(aq) \rightarrow CaCO_3(s) + CO_2 + H_2O$. Aragonite and calcite are two common crystalline forms of biologically precipitated calcium carbonate minerals that have different solubilities.

ACCEPTED VERSION SUBJECT TO FINAL EDITS

Calving (of glaciers or ice sheets) The breaking off of discrete pieces of ice from a *glacier*, *ice sheet* or an *ice shelf* into lake or seawater, producing *icebergs*. This is a form of mass loss from an ice body.

Canopy temperature The temperature within the canopy of a vegetation structure.

Carbon budget Refers to two concepts in the literature: (1) an assessment of carbon cycle *sources* and *sinks* on a global level, through the synthesis of evidence for *fossil-fuel* and cement emissions, emissions and removals associated with *land use* and *land use change*, ocean and natural land sources and sinks of *carbon dioxide (CO_2)*, and the resulting change in atmospheric CO_2 concentration. This is referred to as the Global Carbon Budget; (2) the maximum amount of cumulative net global *anthropogenic* CO_2 emissions that would result in limiting *global warming* to a given level with a given probability, taking into account the effect of other anthropogenic climate *forcers*. This is referred to as the Total Carbon Budget when expressed starting from the *pre-industrial* period, and as the Remaining Carbon Budget when expressed from a recent specified date.

Note 1: Net anthropogenic CO_2 emissions are anthropogenic CO_2 emissions minus anthropogenic CO_2 removals. See also *Carbon Dioxide Removal (CDR)*.

Note 2: The maximum amount of cumulative net global anthropogenic CO_2 emissions is reached at the time that annual net anthropogenic CO_2 emissions reach zero.

Note 3: The degree to which anthropogenic climate forcers other than CO_2 affect the Total Carbon Budget and Remaining Carbon Budget depends on human choices about the extent to which these forcers are mitigated and their resulting *climate* effects.

Note 4: The notions of a Total Carbon Budget and Remaining Carbon Budget are also being applied in parts of the scientific literature and by some entities at regional, national, or sub-national level. The distribution of global budgets across individual different entities and emitters depends strongly on considerations of equity and other value judgements.

Carbon cycle The flow of carbon (in various forms, e.g., as *carbon dioxide (CO_2)*, carbon in biomass, and carbon dissolved in the ocean as carbonate and bicarbonate) through the atmosphere, hydrosphere, terrestrial and marine biosphere and lithosphere. In this report, the reference unit for the global carbon cycle is $GtCO_2$ or GtC (one Gigatonne = 1 Gt = 10^{15} grams; 1GtC corresponds to 3.667 $GtCO_2$).

Carbon dioxide (CO_2) A naturally occurring gas, CO_2 is also a by-product of burning fossil fuels (such as oil, gas and coal), of burning *biomass*, of *land use* changes (LUC) and of industrial processes (e.g., cement production). It is the principal *anthropogenic* greenhouse gas (GHG) that affects the Earth's radiative balance. It is the reference gas against which other GHGs are measured and therefore has a Global Warming Potential (GWP) of 1. See also *Land use* and *Land-use change (LUC)*.

Carbon dioxide (CO_2) fertilisation The increase of plant photosynthesis and water-use efficiency in response to increased atmospheric *carbon dioxide (CO_2)* concentration. Whether this increased photosynthesis translates into increased plant growth and carbon storage on land depends on the interacting effects of temperature, moisture and nutrient availability.

Carbon dioxide capture and storage (CCS) A process in which a relatively pure stream of *carbon dioxide (CO_2)* from industrial and energy-related sources is separated (captured), conditioned, compressed and transported to a storage location for long-term isolation from the *atmosphere*. Sometimes referred to as Carbon Capture and Storage. See also *Bioenergy with carbon dioxide capture and storage (BECCS)*, *Carbon dioxide capture and utilisation (CCU)*, *Sequestration*, *Anthropogenic removals* and *Carbon dioxide removal (CDR)*.

Carbon dioxide removal (CDR) *Anthropogenic* activities removing *carbon dioxide (CO_2)* from the *atmosphere* and durably storing it in geological, terrestrial, or *ocean* reservoirs, or in products. It includes

ACCEPTED VERSION SUBJECT TO FINAL EDITS

existing and potential anthropogenic enhancement of biological or geochemical CO_2 *sinks* and direct air capture and storage, but excludes natural CO_2 *uptake* not directly caused by human activities. See also *Anthropogenic removals*, *Afforestation*, *Biochar*, *Enhanced weathering*, *Ocean alkalinisation / Ocean alkalinity enhancement*, *Reforestation*, *Soil carbon sequestration (SCS)*, *Bioenergy with carbon dioxide capture and storage (BECCS)* and *Carbon dioxide capture and storage (CCS)*.

Carbon neutrality Condition in which anthropogenic CO_2 emissions associated with a subject are balanced by anthropogenic CO_2 removals. The subject can be an entity such as a country, an organisation, a district or a commodity, or an activity such as a service and an event. Carbon neutrality is often assessed over the life cycle including indirect ("scope 3") emissions, but can also be limited to the emissions and removals, over a specified period, for which the subject has direct control, as determined by the relevant scheme.

Note 1: Carbon neutrality and *net zero CO_2 emissions* are overlapping concepts. The concepts can be applied at global or sub-global scales (e.g., regional, national and sub-national). At a global scale, the terms carbon neutrality and net zero CO_2 emissions are equivalent. At sub-global scales, net zero CO_2 emissions is generally applied to emissions and removals under direct control or territorial responsibility of the reporting entity, while carbon neutrality generally includes emissions and removals within and beyond the direct control or territorial responsibility of the reporting entity. Accounting rules specified by GHG programmes or schemes can have a significant influence on the quantification of relevant CO_2 emissions and removals.

Note 2: In some cases achieving carbon neutrality may rely on the supplementary use of *offsets* to balance emissions that remain after actions by the reporting entity are taken into account.

See also *Greenhouse gas neutrality*, *Land use, land-use change and forestry (LULUCF)* and *Net zero CO_2 emissions*.

Carbon sequestration See *Sequestration*.

Carbon sink See *Sink*.

Carbon source See *Source*.

Carbon-climate feedback See *Climate-carbon cycle feedback*.

Carbonaceous aerosol Aerosol consisting predominantly of organic substances and *black carbon*.

Carbonate counter pump See *Carbonate pump*.

Carbonate pump Ocean carbon fixation through the biological formation of carbonates, primarily by plankton that generate bio-mineral particles that sink to the *ocean* interior, and possibly the sediment. It is also called carbonate counter-pump, since the formation of calcium carbonate ($CaCO_3$) is accompanied by the release of *carbon dioxide (CO_2)* to surrounding water and subsequently to the *atmosphere*.

Catchment An area that collects and drains precipitation.

Cenozoic Era The third and current geological Era, which began 66.0 Ma. It comprises the Paleogene, Neogene and Quaternary Periods.

Central Pacific El Niño See *El Niño-Southern Oscillation (ENSO)*.

Chaotic A *dynamical system* such as the *climate system*, governed by nonlinear deterministic equations (see *Nonlinearity*), may exhibit erratic or chaotic behaviour in the sense that very small changes in the initial state of the system in time lead to large and apparently unpredictable changes in its temporal evolution. Such chaotic behaviour limits the *predictability* of the state of a nonlinear dynamical system at specific future

ACCEPTED VERSION SUBJECT TO FINAL EDITS

times, although changes in its statistics may still be predictable given changes in the system parameters or boundary conditions.

Charcoal Material resulting from charring of *biomass*, usually retaining some of the microscopic texture typical of plant tissues; chemically it consists mainly of carbon with a disturbed graphitic structure, with lesser amounts of oxygen and hydrogen.

Chlorofluorocarbons (CFCs) A chlorofluorocarbon is an organic compound that contains chlorine, carbon, hydrogen, and fluorine and is used for refrigeration, air conditioning, packaging, plastic foam, insulation, solvents, or aerosol propellants. Because they are not destroyed in the lower atmosphere, CFCs drift into the upper atmosphere where, given suitable conditions, they break down ozone (O_3). It is one of the greenhouse gases (GHGs) covered under the 1987 Montreal Protocol as a result of which manufacturing of these gases has been phased out and they are being replaced by other compounds, including hydrofluorocarbons (HFCs) which are GHGs covered under the Kyoto Protocol.

Chronology Arrangement of events according to dates or times of occurrence.

Cirrus cloud thinning (CCT) See *Solar radiation modification (SRM)*.

Clathrate (methane) A partly frozen slushy mix of *methane* gas and ice, usually found in sediments.

Clausius-Clapeyron equation/relationship The thermodynamic relationship between temperature and the vapour pressure of a substance in which two phases of the substance are in equilibrium (e.g., liquid water and *water vapour*). For gases such as water vapour, this relation gives the increase in equilibrium (or saturation) vapour pressure per unit change in air temperature.

Climate Climate in a narrow sense is usually defined as the average weather, or more rigorously, as the statistical description in terms of the mean and variability of relevant quantities over a period of time ranging from months to thousands or millions of years. The classical period for averaging these variables is 30 years, as defined by the World Meteorological Organization (WMO). The relevant quantities are most often surface variables such as temperature, precipitation and wind. Climate in a wider sense is the state, including a statistical description, of the *climate system*.

Climate change A change in the state of the *climate* that can be identified (e.g., by using statistical tests) by changes in the mean and/or the variability of its properties and that persists for an extended period, typically decades or longer. Climate change may be due to natural internal processes or external *forcings* such as modulations of the solar cycles, volcanic eruptions and persistent *anthropogenic* changes in the composition of the *atmosphere* or in *land use*. Note that the *United Nations Framework Convention on Climate Change (UNFCCC)*, in its Article 1, defines climate change as: 'a change of climate which is attributed directly or indirectly to human activity that alters the composition of the global atmosphere and which is in addition to natural climate variability observed over comparable time periods'. The UNFCCC thus makes a distinction between climate change attributable to human activities altering the atmospheric composition and *climate variability* attributable to natural causes. See also *Climate variability*, *Detection and attribution*, *Global warming* and *Ocean acidification (OA)*.

Climate change commitment Climate change commitment is defined as the unavoidable future *climate change* resulting from inertia in the geophysical and socio-economic systems. Different types of climate change commitment are discussed in the literature (see subterms). Climate change commitment is usually quantified in terms of the further change in temperature, but it includes other future changes, for example in the *hydrological cycle*, in *extreme weather events*, in extreme climate events, and in sea level.

Constant composition commitment The constant composition commitment is the remaining *climate change* that would result if atmospheric composition, and hence *radiative forcing*, were held fixed at a given value. It results from the thermal inertia of the ocean and slow processes in the cryosphere and land surface.

ACCEPTED VERSION SUBJECT TO FINAL EDITS

Constant emissions commitment The constant emissions commitment is the committed *climate change* that would result from keeping *anthropogenic emissions* constant.

Zero emissions commitment The zero emissions commitment is an estimate of the subsequent *global warming* that would result after *anthropogenic emissions* are set to zero. It is determined by both inertia in physical *climate system* components (*ocean*, *cryosphere*, land surface) and *carbon cycle* inertia. In its widest sense it refers to emissions of each climate *forcer* including *greenhouses gases*, *aerosols* and their pre-cursors. The climate response to this can be complex due to the different timescale of response of each climate forcer. A specific sub-category of zero emissions commitment is the Zero CO_2 Emissions Commitment which refers to the climate system response to CO_2 emissions after setting these to net zero. The CO_2-only definition is of specific use in estimating *remaining carbon budgets*.

Climate extreme (extreme weather or climate event) The occurrence of a value of a weather or *climate* variable above (or below) a threshold value near the upper (or lower) ends of the range of observed values of the variable. By definition, the characteristics of what is called *extreme weather* may vary from place to place in an absolute sense. When a pattern of extreme weather persists for some time, such as a season, it may be classified as an extreme climate event, especially if it yields an average or total that is itself extreme (e.g., high temperature, *drought*, or heavy rainfall over a season). For simplicity, both extreme weather events and extreme climate events are referred to collectively as 'climate extremes'.

Climate feedback An interaction in which a perturbation in one *climate* quantity causes a change in a second and the change in the second quantity ultimately leads to an additional change in the first. A negative feedback is one in which the initial perturbation is weakened by the changes it causes; a positive feedback is one in which the initial perturbation is enhanced. The initial perturbation can either be externally forced or arise as part of internal variability. See also *Climate-carbon cycle feedback*, *Cloud feedback* and *Ice-albedo feedback*.

Climate feedback parameter A way to quantify the radiative response of the *climate system* to a global surface temperature change induced by a *radiative forcing*. It is quantified as the change in net energy flux at the top of atmosphere for a given change in annual global surface temperature. It has units of W m^{-2} $°C^{-1}$.

Climate forecast See *Climate prediction*.

Climate index A time series constructed from climate variables that provides an aggregate summary of the state of the *climate system*. For example, the difference between sea level pressure in Iceland and the Azores provides a simple yet useful historical *NAO* index. Because of their optimal properties, climate indices are often defined using *principal components* – linear combinations of climate variables at different locations that have maximum variance subject to certain normalisation constraints (e.g., the *NAM* and *SAM* indices which are principal components of Northern Hemisphere and Southern Hemisphere gridded pressure anomalies, respectively). Definitions of observational indices for Modes of variability can be found in the Annex VI.

Climate indicator Measures of the *climate system* including large-scale variables and climate *proxies*. See also *Global surface temperature indicators* and *Climate metrics*.

Key climate indicators Key indicators constitute a finite set of distinct variables that may collectively point to important overall changes in the *climate system* of broad societal relevance across the atmospheric, oceanic, cryospheric and biospheric domains, with land as an implicit cross-cutting theme. Taken together, these indicators would be expected to both have changed and continue to change in the future in a coherent and consistent manner. See Cross-Chapter Box 2.2, Table 1 in the AR6 WGI report.

Climate information Information about the past, current state, or future of the *climate system* that is relevant for *mitigation*, *adaptation* and *risk management*. It may be tailored or “co-produced” for specific contexts, taking into account users' needs and values.

ACCEPTED VERSION SUBJECT TO FINAL EDITS

Climate metrics Measures of aspects of the overall *climate system* response to *radiative forcing*, such as *equilibrium climate sensitivity (ECS)*, *transient climate response (TCR)*, *transient climate response to cumulative CO_2 emissions (TCRE)* and the airborne fraction of *anthropogenic* carbon dioxide. See also *Greenhouse gas emission metric*, *Climate indicator* and *Key climate indicators* (under *Climate indicator*).

Climate model A qualitative or quantitative representation of the climate system based on the physical, chemical and biological properties of its components, their interactions and feedback processes and accounting for some of its known properties. The climate system can be represented by models of varying complexity; that is, for any one component or combination of components a spectrum or hierarchy of models can be identified, differing in such aspects as the number of spatial dimensions, the extent to which physical, chemical or biological processes are explicitly represented, or the level at which empirical parametrisations are involved. There is an evolution towards more complex models with interactive chemistry and biology. Climate models are applied as a research tool to study and simulate the climate and for operational purposes, including monthly, seasonal and interannual climate predictions. See also *Chemistry-climate model*, *Earth system model (ESM)*, *Earth system model of intermediate complexity (EMIC)*, *Energy balance model (EBM)*, *Simple climate model (SCM)*, *Regional climate model (RCM)*, *Dynamic global vegetation model (DGVM)*, *General circulation model (GCM)* and *Emulators*.

Climate pattern A set of spatially varying coefficients obtained by "projection" (regression) of *climate* variables onto a *climate index* time series. When the climate index is a principal component, the climate pattern is an eigenvector of the covariance matrix, referred to as an Empirical Orthogonal Function (EOF) in climate science.

Climate prediction A climate prediction or climate forecast is the result of an attempt to produce (starting from a particular state of the *climate system*) an estimate of the actual evolution of the climate in the future, for example, at seasonal, interannual or decadal time scales. Because the future evolution of the climate system may be highly sensitive to initial conditions, has chaotic elements and is subject to *natural variability*, such predictions are usually probabilistic in nature.

Climate projection Simulated response of the *climate system* to a *scenario* of future emissions or concentrations of *greenhouse gases (GHGs)* and *aerosols* and changes in *land use*, generally derived using *climate models*. Climate projections are distinguished from *climate predictions* by their dependence on the emission/concentration/radiative forcing *scenario* used, which is in turn based on assumptions concerning, for example, future socio-economic and technological developments that may or may not be realised.

Climate response A general term for how the *climate system* responds to a *radiative forcing*.

Climate scenario A plausible and often simplified representation of the future *climate*, based on an internally consistent set of climatological relationships that has been constructed for explicit use in investigating the potential consequences of *anthropogenic* climate change, often serving as input to impact models. *Climate projections* often serve as the raw material for constructing climate scenarios, but climate scenarios usually require additional information such as the observed current climate. See also *Regional climate scenario*.

Climate sensitivity The change in the surface temperature in response to a change in the atmospheric carbon dioxide (CO_2) concentration or other radiative forcing. See also *Climate feedback parameter*.

Earth system sensitivity The equilibrium surface temperature response of the coupled *atmosphere*-ocean-*cryosphere*-vegetation-*carbon cycle* system to a doubling of the atmospheric carbon dioxide (CO_2) concentration is referred to as Earth System sensitivity. Because it allows ice sheets to adjust to the external perturbation, it may differ substantially from the *equilibrium climate sensitivity* derived from coupled atmosphere-ocean models.

Equilibrium climate sensitivity (ECS) The equilibrium (steady state) change in the surface temperature following a doubling of the atmospheric *carbon dioxide (CO_2)* concentration from *pre-industrial* conditions.

ACCEPTED VERSION SUBJECT TO FINAL EDITS

Transient climate response (TCR) The surface temperature response for the hypothetical scenario in which atmospheric *carbon dioxide (CO_2)* increases at 1% yr^{-1} from *pre-industrial* to the time of a doubling of atmospheric CO_2 concentration (year 70).

Transient climate response to cumulative CO_2 emissions (TCRE) The transient surface temperature change per unit cumulative *carbon dioxide (CO_2)* emissions, usually 1000 GtC. TCRE combines both information on the airborne fraction of cumulative CO_2 emissions (the fraction of the total CO_2 emitted that remains in the *atmosphere*, which is determined by *carbon cycle* processes) and on the *transient climate response (TCR)*.

Climate services Climate services involve the provision of climate information in such a way as to assist decision-making. The service includes appropriate engagement from users and providers, is based on scientifically credible information and expertise, has an effective access mechanism, and responds to user needs (Hewitt et al., 2012).

Climate simulation ensemble A group of parallel model simulations characterising historical *climate* conditions, *climate predictions*, or *climate projections*. Variation of the results across the ensemble members may give an estimate of modelling-based uncertainty. Ensembles made with the same model but different initial conditions characterise the uncertainty associated with internal *climate variability*, whereas multi-model ensembles including simulations by several models also include the effect of model differences. Perturbed parameter ensembles, in which model parameters are varied in a systematic manner, aim to assess the uncertainty resulting from internal model specifications within a single model. Remaining sources of uncertainty unaddressed with model ensembles are related to systematic model errors or biases, which may be assessed from systematic comparisons of model simulations with observations wherever available.

Climate system The global system consisting of five major components: the *atmosphere*, the *hydrosphere*, the *cryosphere*, the *lithosphere* and the *biosphere* and the interactions between them. The climate system changes in time under the influence of its own internal dynamics and because of *external forcings* such as volcanic eruptions, solar variations, orbital forcing, and *anthropogenic* forcings such as the changing composition of the atmosphere and *land-use change*.

Climate threshold A limit within the *climate system* (or its *forcing*) beyond which the behaviour of the system is qualitatively changed. See also *Abrupt climate change* and *Tipping point*.

Climate variability Deviations of climate variables from a given mean state (including the occurrence of extremes, etc.) at all spatial and temporal scales beyond that of individual weather events. Variability may be intrinsic, due to fluctuations of processes internal to the *climate system* (*internal variability*), or extrinsic, due to variations in natural or anthropogenic *external forcing* (forced variability). See also *Climate change* and *Modes of climate variability*.

Decadal variability Decadal variability refers to *climate variability* on decadal time scales. See also *Pacific Decadal Variability (PDV)*, *Atlantic Multi-decadal Oscillation/Variability (AMO/AMV)* and *Pacific Decadal Oscillation (PDO)* (under *Pacific Decadal Variability (PDV)*).

Internal variability Fluctuations of the climate dynamical system when subject to a constant or periodic external forcing (such as the annual cycle). See also *Climate variability*.

Natural variability Natural variability refers to climatic fluctuations that occur without any human influence, i.e. *internal variability* combined with the response to external natural factors such as volcanic eruptions, changes in *solar activity* and, on longer time-scales, orbital effects and plate tectonics. See also *Orbital forcing*.

Climate velocity The speed at which isolines of a specified climate variable travel across landscapes or seascapes due to changing climate. For example, climate velocity for temperature is the speed at which

ACCEPTED VERSION SUBJECT TO FINAL EDITS

isotherms move due to changing climate (km yr^{-1}) and is calculated as the temporal change in temperature (°C yr^{-1}) divided by the current spatial gradient in temperature (°C km^{-1}). It can be calculated using additional climate variables such as precipitation or can be based on the climatic niche of organisms.

Climate-carbon cycle feedback A *climate feedback* involving changes in the properties of land and ocean *carbon cycle* in response to *climate change*. In the ocean, changes in oceanic temperature and circulation could affect the *atmosphere*-ocean CO_2 flux; on the continents, *climate change* could affect plant *photosynthesis* and soil microbial *respiration* and hence the flux of CO_2 between the *atmosphere* and the land *biosphere*.

Climatic impact-driver (CID) Climatic impact-drivers (CIDs) are physical *climate system* conditions (e.g., means, events, extremes) that affect an element of society or *ecosystems*. Depending on system tolerance, CIDs and their changes can be detrimental, beneficial, neutral, or a mixture of each across interacting system elements and regions. See also *Risk*, *Hazard* and *Impacts (consequences, outcomes)*.

Cloud condensation nuclei (CCN) The subset of *aerosol* particles that serve as an initial site for the condensation of liquid water, which can lead to the formation of cloud droplets, under typical cloud formation conditions. The main factor that determines which *aerosol* particles are CCN at a given supersaturation is their size.

Cloud feedback A climate feedback involving changes in any of the properties of clouds as a response to a change in the local or *global mean surface temperature*. Understanding cloud feedbacks and determining their magnitude and sign require an understanding of how a change in *climate* may affect the spectrum of cloud types, the cloud fraction and height, the radiative properties of clouds, and finally the Earth's radiation budget. At present, cloud feedbacks remain the largest source of *uncertainty* in *climate sensitivity* estimates.

Cloud radiative effect The *radiative effect* of clouds relative to the identical situation without clouds. In previous IPCC reports this was called cloud *radiative forcing*, but that terminology is inconsistent with other uses of the forcing term and is not maintained in this report.

Cloud-resolving models (CRMs) Numerical models that are that are of high enough resolution and have the necessary physics to represent the dynamical and physical processes of cloud formation.

CMIP6 See *Coupled Model Intercomparison Project (CMIP)*.

CO_2 equivalent (CO_2-eq) emission The amount of *carbon dioxide (CO_2)* emission that would have an equivalent effect on a specified key measure of *climate change*, over a specified time horizon, as an emitted amount of another *greenhouse gas (GHG)* or a mixture of other GHGs. For a mix of GHGs it is obtained by summing the CO_2-equivalent emissions of each gas. There are various ways and time horizons to compute such equivalent emissions (see *greenhouse gas emission metric*). CO_2-equivalent emissions are commonly used to compare emissions of different GHGs, but should not be taken to imply that these emissions have an equivalent effect across all key measures of climate change. [Note: Under the Paris Rulebook [Decision 18/CMA.1, annex, paragraph 37], parties have agreed to use GWP100 values from the IPCC AR5 or GWP100 values from a subsequent IPCC Assessment Report to report aggregate emissions and removals of GHGs. In addition, parties may use other metrics to report supplemental information on aggregate emissions and removals of GHGs.]

Coast The *land* near to the sea. The term ‘coastal’ can refer to that land (e.g., as in ‘coastal communities’), or to that part of the marine environment that is strongly influenced by land-based processes. Thus, coastal seas are generally shallow and near-shore. The landward and seaward limits of the coastal zone are not consistently defined, neither scientifically nor legally. Thus, coastal waters can either be considered as equivalent to territorial waters (extending 12 nautical miles / 22.2 km from mean low water), or to the full Exclusive Economic Zone, or to *shelf seas*, with less than 200 m water depth.

Cold days/cold nights Days where maximum temperature, or nights where minimum temperature, falls

ACCEPTED VERSION SUBJECT TO FINAL EDITS

below the 10th *percentile*, where the respective temperature distributions are generally defined with respect to the 1961-1990 reference period. For the corresponding indices, see Box 2.4.

Common era (CE) CE (Common Era) and BCE (Before the Common Era) are alternative names for AD (Anno Domini) and BC (Before Christ) in the Gregorian international standard calendar-year system. CE/BCE are preferred in an international context because they are neutral with respect to religion. The numbering of calendar years is the same under both terminologies. The CE began in year AD 1 and extends to the present day.

Compatible emissions Earth System Models that simulate the land and ocean *carbon cycle* can calculate CO_2 emissions that are compatible with a given atmospheric CO_2 concentration trajectory. The compatible emissions over a given period of time are equal to the increase of carbon over that same period of time in the sum of the three active *reservoirs*: the *atmosphere*, the land and the ocean.

Compound events See *Compound weather/climate events*.

Compound weather/climate events The combination of multiple *drivers* and/or *hazards* that contributes to societal and/or environmental *risk* (Zscheischler et al., 2018).

Concentrations scenario See *Scenario*.

Confidence The robustness of a finding based on the type, amount, quality and consistency of *evidence* (e.g., mechanistic understanding, theory, data, models, expert judgment) and on the degree of *agreement* across multiple lines of evidence. In this report, confidence is expressed qualitatively (Mastrandrea et al., 2010).

Constant composition commitment See *Climate change commitment*.

Constant emissions commitment See *Climate change commitment*.

Convection Vertical motion driven by buoyancy forces arising from static instability, usually caused by near-surface cooling or increases in salinity in the case of the ocean and near-surface warming or cloud-top radiative cooling in the case of the *atmosphere*. In the atmosphere, convection gives rise to cumulus clouds and precipitation and is effective at both scavenging and vertically transporting chemical species. In the ocean, convection can carry surface waters to deep within the ocean.

Convection-permitting models See *Cloud-resolving models (CRMs)*.

Coral bleaching Loss of coral pigmentation through the loss of intracellular symbiotic algae (known as zooxanthellae) and/or loss of their pigments.

Coral reef An underwater *ecosystem* characterised by structure-building stony corals. Warm-water coral reefs occur in shallow seas, mostly in the tropics, with the corals (animals) containing algae (plants) that depend on light and relatively stable temperature conditions. Cold-water coral reefs occur throughout the world, mostly at water depths of 50-500 m. In both kinds of reef, living corals frequently grow on older, dead material, predominantly made of calcium carbonate ($CaCO_3$). Both warm and cold-water coral reefs support high biodiversity of fish and other groups, and are considered to be especially vulnerable to *climate change*.

Cosmogenic radioisotopes Rare radioactive *isotopes* that are created by the interaction of a high-energy cosmic ray particles with atoms nuclei. They are often used as indicator of *solar activity* which modulates the cosmic rays intensity or as tracers of atmospheric transport processes, and are also called cosmogenic radionuclides.

Coupled Model Intercomparison Project (CMIP) A *climate* modelling activity from the World Climate

ACCEPTED VERSION SUBJECT TO FINAL EDITS

Research Programme (WCRP) which coordinates and archives *climate model* simulations based on shared model inputs by modelling groups from around the world. The CMIP3 multi-model data set includes projections using Special Report on Emissions Scenarios (SRES) scenarios. The CMIP5 data set includes projections using the *Representative Concentration Pathways (RCP)*. The CMIP6 phase involves a suite of common model experiments as well as an ensemble of CMIP-endorsed Model Intercomparison Projects (MIPs).

Cryosphere The components of the Earth System at and below the *land* and *ocean* surface that are frozen, including snow cover, *glaciers*, *ice sheets*, *ice shelves*, *icebergs*, *sea ice*, lake ice, river ice, *permafrost* and seasonally *frozen ground*.

Cumulative emissions The total amount of emissions released over a specified period of time. See also *Carbon budget* and *Transient climate response to cumulative CO_2 emissions (TCRE)* (under *Climate sensitivity*).

Dansgaard-Oeschger events (D-O events) Millennial-scale events first characterized in Greenland *ice cores* as abrupt warming from a cold *stadial* state to a warmer interstadial state, followed by a return to a cold stadial state (Dansgaard et al., 1993), and traced in the ocean via deposits of ice-rafted sand grains (Bond and Lotti, 1995). Named after Willi Dansgaard and Hans Oeschger by Bond and Lotti (1995). An example of a D-O event during the most recent *deglacial* transition is the Bølling-Allerød interstadial. Warm D-O events in Greenland are associated with cooling events in Antarctica (Blunier and Brook, 2001) through ocean *thermohaline circulation* (Stocker and Johnsen, 2003). See also *Bipolar seesaw (also interhemispheric seesaw, interhemispheric asymmetry, hemispheric asymmetry)*.

Data assimilation Mathematical method used to combine different sources of information in order to produce the best possible estimate of the state of a system. This information usually consists of observations of the system and a numerical model of the system evolution. Data assimilation techniques are used to create initial conditions for weather forecast models, and to construct *reanalyses* describing the trajectory of the *climate system* over the time period covered by the observations.

Dead zones Extremely *hypoxic* (i.e., low-oxygen) areas in oceans and lakes, caused by excessive nutrient input from human activities coupled with other factors that deplete the oxygen required to support many marine organisms in bottom and near-bottom water.

Decadal predictability Decadal predictability refers to the notion of predictability of the climate system on a decadal time scale. See also *Climate prediction*, *Predictability* and *Decadal prediction*.

Decadal prediction A decadal prediction is a climate prediction on decadal time scales.

Decadal variability See *Climate variability*.

Deep uncertainty See *Uncertainty*.

Deforestation Conversion of forest to non-forest. [Note: For a discussion of the term forest and related terms such as afforestation, reforestation and deforestation, see the 2006 IPCC Guidelines for National Greenhouse Gas Inventories and their 2019 Refinement, and information provided by the United Nations Framework Convention on Climate Change (IPCC, 2006, 2019, UNFCCC, 2021a, 2021b).]

See also *Reducing Emissions from Deforestation and Forest Degradation (REDD+)*, *Afforestation* and *Reforestation*.

Deglacial or deglaciation or glacial termination The period of transition from *glacial* conditions at the end of a glacial period to interglacial conditions characterized by a reduction in land ice volume. Gradual changes can be punctuated by *abrupt changes* linked to *stadial* / interstadial events and *bipolar seesaw* aspect. The last deglacial transition occurred between about 18,000 and 11,000 years ago. It encompasses

ACCEPTED VERSION SUBJECT TO FINAL EDITS

rapid events such as *Meltwater Pulse 1A (MWP-1A)* and millennial-scale fluctuations such as the *Younger Dryas*. See also *Glacial-interglacial cycles* and *Ice age*.

Detection Detection of change is defined as the process of demonstrating that climate or a system affected by climate has changed in some defined statistical sense, without providing a reason for that change. An identified change is detected in observations if its likelihood of occurrence by chance due to internal variability alone is determined to be small, for example, <10%.

Detection and attribution See *Detection* and *Attribution*.

Diatoms Silt-sized algae that live in surface waters of lakes, rivers and oceans and form shells of opal. Their species distribution in ocean cores is often related to past *sea surface temperatures*.

Dimensions of integration In IPCC AR6, concepts used to synthesize the knowledge of *climate change* across not just the physical sciences, but also across *impact* and *adaptation*, and *mitigation* research. The concept of 'dimensions of integration' includes (i) emission and c*oncentration scenarios* underlying the climate change *projections* assessed in this report, (ii) levels of projected global mean temperature change and (iii) total amounts of cumulative carbon emissions for projections.

Direct (aerosol) effect See *Aerosol-radiation interaction*.

Direct air capture (DAC) Chemical process by which a pure carbon dioxide (CO_2) stream is produced by capturing CO_2 from the ambient air. See also *Direct air carbon dioxide capture and storage (DACCS)*, *Anthropogenic removals* and *Carbon dioxide removal (CDR)*.

Direct emissions Emissions that physically arise from activities within well-defined boundaries of, for instance, a region, an economic sector, a company, or a process. See also *Indirect emissions*.

Disaster A 'serious disruption of the functioning of a community or a society at any scale due to hazardous events interacting with conditions of exposure, vulnerability and capacity, leading to one or more of the following: human, material, economic and environmental losses and impacts' (UNGA, 2016). See also *Exposure*, *Hazard*, *Risk* and *Vulnerability*.

Discharge (of ice) See *Mass balance / budget (of glaciers or ice sheets)*.

Dissolved inorganic carbon The combined total of different types of non-organic carbon in (seawater) solution, comprising carbonate (CO_3^{2-}), bicarbonate (HCO_3^-), carbonic acid (H_2CO_3) and *carbon dioxide (CO_2)*.

Diurnal temperature range (DTR) The difference between the maximum and minimum temperature during a 24-hour period.

Dobson unit (DU) A unit to measure the total amount of *ozone* in a vertical column above the Earth's surface (total column ozone). The number of Dobson Units is the thickness in units of 10^{-5} m that the *ozone* column would occupy if compressed into a layer of uniform density at a pressure of 1013 hPa and a temperature of 0°C. One DU corresponds to a column of ozone containing 2.69×10^{20} molecules per square metre. A typical value for the amount of ozone in a column of the Earth's *atmosphere*, although very variable, is 300 DU.

Downscaling A method that derives local- to regional-scale information from larger-scale models or data analyses. Two main methods exist: dynamical downscaling and empirical/statistical downscaling. The dynamical method uses the output of regional climate models, global models with variable spatial resolution, or high-resolution global models. The empirical/statistical methods are based on observations and develop statistical relationships that link the large-scale atmospheric variables with local/regional climate variables. In all cases, the quality of the driving model remains an important limitation on quality of the downscaled

ACCEPTED VERSION SUBJECT TO FINAL EDITS

information. The two methods can be combined, e.g., applying empirical/statistical downscaling to the output of a regional climate model, consisting of a dynamical downscaling of a global climate model.

Drought An exceptional period of water shortage for existing *ecosystems* and the human population (due to low rainfall, high temperature, and/or wind). See also *Plant evaporative stress*.

Agricultural or ecological drought Agricultural or ecological drought (depending on the affected *biome*): a period with abnormal *soil moisture* deficit, which results from combined shortage of precipitation and excess *evapotranspiration*, and during the growing season impinges on crop production or *ecosystem* function in general.

Hydrological drought A period with large *runoff* and water deficits in rivers, lakes and reservoirs.

Meteorological drought A period with an abnormal precipitation deficit.

Dynamic global vegetation model (DGVM) A model that simulates vegetation development and dynamics through space and time, as driven by climate and other environmental changes.

Dynamical downscaling See *Downscaling*.

Dynamical system A process or set of processes whose evolution in time is governed by a set of deterministic physical laws. The *climate system* is a dynamical system.

Early Eocene Climatic Optimum (EECO) The EECO is a period of geological time that occurred about 53 to 49 million years ago, during the Eocene Epoch. Continental positions at this time were somewhat different to present due to tectonic plate movements. Geological data indicate that the EECO was a period of relatively high atmospheric CO_2 concentrations (about 1150-2500 ppmv) and relative warmth (*global mean surface temperature* was about 10-18 °C above the 1850-1900 reference), and polar *ice sheets* were absent.

Earth system model (ESM) A coupled *atmosphere*–ocean general circulation model (AOGCM) in which a representation of the *carbon cycle* is included, allowing for interactive calculation of atmospheric *carbon dioxide (CO_2)* or compatible emissions. Additional components (e.g., atmospheric chemistry, *ice sheets*, dynamic vegetation, nitrogen cycle, but also urban or crop models) may be included. See also *Earth system model of intermediate complexity (EMIC)*.

Earth system model of intermediate complexity (EMIC) Earth system models of intermediate complexity (EMIC) represent *climate* processes at a lower *resolution* or in a simpler, more idealised fashion than an *Earth system model (ESM)*.

Earth's energy budget For a given time period, Earth's energy budget expresses the balance between *total earth system heating*, the time-integrated *effective radiative forcing* and time-integrated *Earth's radiative response*. Units: Joules. See also *Earth's top of atmosphere energy budget*, *Earth's energy imbalance*, *Earth's surface energy budget*, *Earth's radiative response*, *Earth's energy flows* and *Earth system heating*.

Earth's energy flows The time-mean (or representative) energy exchanges within the *climate system* (including energy energy exchanges at the surface and top-of-atmosphere). This also includes horizontal ocean and atmospheric heat transports. See also *Earth's energy budget*, *Earth's top of atmosphere energy budget*, *Earth's energy imbalance*, *Earth's surface energy budget*, *Earth system heating* and *Earth's radiative response*.

Earth's energy imbalance The persistent and positive (downward) net top of atmosphere energy flux associated with greenhouse gas *forcing* of the *climate system*. See also *Earth's energy budget*, *Earth's top of atmosphere energy budget*, *Earth's surface energy budget*, *Earth system heating*, *Earth's radiative response* and *Earth's energy flows*.

ACCEPTED VERSION SUBJECT TO FINAL EDITS

Earth's radiative response The product of *global mean surface air temperature (GSAT)* change and the net feedback parameter (i.e. sum of all feedbacks), which determines the net top-of-atmosphere radiative flux that opposes a change in *radiative forcing*. Units: W m^{-2}. See also *Earth's energy budget, Earth's top of atmosphere energy budget, Earth's energy imbalance, Earth's surface energy budget, Earth system heating* and *Earth's energy flows*.

Earth's surface energy budget Earth's surface energy budget comprises the exchanges of heat at the surface of the Earth associated with both radiative and non-radiative processes. See also *Earth's energy budget, Earth's top of atmosphere energy budget, Earth's energy imbalance, Earth system heating, Earth's radiative response* and *Earth's energy flows*.

Earth system sensitivity See *Climate sensitivity*.

Earth's top of atmosphere energy budget Earth's top of atmosphere energy budget comprises the energy fluxes associated with incoming solar radiation, reflected solar radiation and emitted thermal radiation. See also *Earth's energy budget, Earth's energy imbalance, Earth's surface energy budget, Earth system heating, Earth's radiative response* and *Earth's energy flows*.

East Antarctic ice sheet (EAIS) See *Ice sheet*.

East Asian monsoon (EAsiaM) See *Global monsoon*.

Eastern boundary upwelling systems (EBUS) Eastern boundary upwelling system (EBUS) are located at the eastern (landward) edges of major ocean basins in both hemispheres, where equatorward winds drive upwelling currents that bring cool, nutrient-rich (and often oxygen-poor) waters from the deep ocean to the surface near the coast.

Eastern Pacific El Niño See *El Niño-Southern Oscillation (ENSO)*.

Economic potential See *Mitigation potential*.

Ecosystem A functional unit consisting of living organisms, their non-living environment and the interactions within and between them. The components included in a given ecosystem and its spatial boundaries depend on the purpose for which the ecosystem is defined: in some cases they are relatively sharp, while in others they are diffuse. Ecosystem boundaries can change over time. Ecosystems are nested within other ecosystems and their scale can range from very small to the entire biosphere. In the current era, most ecosystems either contain people as key organisms, or are influenced by the effects of human activities in their environment. See also *Ecosystem services*.

Effective radiative forcing (ERF) See *Radiative forcing, Aerosol effective radiative forcing (ERFari+aci)* (under *Aerosol-radiation interaction*), *Effective radiative forcing (or effect) due to aerosol-cloud interactions (ERFaci)* (under *Aerosol-cloud interaction*) and *Effective radiative forcing (or effect) due to aerosol-radiation interactions (ERFari)* (under *Aerosol-radiation interaction*).

Ekman transport The total transport resulting from a balance between the Coriolis force and the frictional stress due to the action of the wind on the ocean surface.

El Niño See *El Niño-Southern Oscillation (ENSO)*.

El Niño-Southern Oscillation (ENSO) The term El Niño was initially used to describe a warm-water current that periodically flows along the coast of Ecuador and Peru, disrupting the local fishery. It has since become identified with warming of the tropical Pacific Ocean east of the dateline. This oceanic event is associated with a fluctuation of a global-scale tropical and subtropical surface pressure pattern called the Southern Oscillation. This coupled atmosphere–ocean phenomenon, with preferred time scales of two to about seven years, is known as the El Niño-Southern Oscillation (ENSO). The warm and cold phases of

ACCEPTED VERSION SUBJECT TO FINAL EDITS

ENSO are called El Niño and La Niña, respectively. ENSO is often measured by the surface pressure anomaly difference between Tahiti and Darwin and/or the sea surface temperatures in the central and eastern equatorial Pacific. This phenomenon has a great impact on the wind, sea surface temperature and precipitation patterns in the tropical Pacific. It has climatic effects throughout the Pacific region and in many other parts of the world through global *teleconnections*. See Section AIV.2.3 in Annex IV of the AR6 WGI report.

Central Pacific El Niño An El Niño event in which *sea surface temperature* anomalies are stronger in the central equatorial Pacific than in the east. Also known as a Modoki El Niño event.

Eastern Pacific El Niño An El Niño event in which *sea surface temperature* anomalies are largest in the eastern tropical Pacific.

Electromagnetic spectrum Wavelength, frequency or energy range of all electromagnetic radiation. In terms of *solar radiation*, the spectral irradiance is the power arriving at the Earth per unit area, per unit wavelength.

Elevation-dependent warming (EDW) Characteristic of many regions where mountains are located, in which past and/or future surface air temperature changes vary neither uniformly nor linearly with elevation. In many cases, warming is enhanced within or above a certain elevation range.

Emergence (of the climate signal) Emergence of a *climate change* signal or trend refers to when a change in *climate* (the 'signal') becomes larger than the amplitude of natural or internal variations (defining the 'noise'), This concept is often expressed as a 'signal-to-noise' ratio and emergence occurs at a defined threshold of this ratio (e.g., S/N > 1 or 2). Emergence can refer to changes relative to a historical or modern baseline (usually at least 20 years long) and can also be expressed in terms of time (*time of emergence*) or in terms of a global warming level. Emergence is also used to refer to a time when we can expect to see a response of reducing *greenhouse gas (GHG)* emissions (emergence with respect to *mitigation*). Emergence can be estimated using observations and/or model simulations. See also *Time of emergence (ToE)*.

Emergent constraint An attempt to reduce the uncertainty in climate projections, using an ensemble of ESMs to relate a specific feedback or future change to an observation of the past or current climate (typically some trend, variability or change in variability).

Emission factor/Emissions intensity A coefficient that quantifies the emissions or removals of a gas per unit activity. Emission factors are often based on a sample of measurement data, averaged to develop a representative rate of emission for a given activity level under a given set of operating conditions.

Emissions See *Indirect emissions, Negative CO_2 emissions, Production-based emissions, Scope 1, Scope 2, and Scope 3 emissions, Territorial emissions, Agricultural emissions, Cumulative emissions, Direct emissions, Embodied (embedded) [emissions, water, land], Anthropogenic emissions, Fossil fuel emissions, Non-CO_2 emissions and radiative forcing* and *Negative greenhouse gas emissions*. See also *Emissions scenario* (under *Scenario*), *Emission pathways* and *Emission trajectories*.

Emulation Reproducing the behaviour of complex, process-based models (namely, *Earth System Models, ESMs*) via simpler approaches, using either *emulators* or *simple climate models (SCMs)*. The computational efficiency of emulating approaches opens new analytical possibilities given that ESMs take a lot of computational resources for each simulation. See also *Emulators* and *Simple climate model (SCM)*.

Emulators A broad class of heavily parametrized models ('one-or-few-line climate models'), statistical methods like neural networks, genetic algorithms or other artificial intelligence approaches, designed to reproduce the responses of more complex, process-based Earth System Models (ESMs). The main application of emulators is to extrapolate insights from ESMs and observational constraints to a larger set of emission scenarios. See also *Emulation* and *Simple climate model (SCM)*.

ACCEPTED VERSION SUBJECT TO FINAL EDITS

Energy balance The difference between the total incoming and total outgoing energy. If this balance is positive, warming occurs; if it is negative, cooling occurs. Averaged over the globe and over long time periods, this balance must be zero. Because the *climate system* derives virtually all its energy from the Sun, zero balance implies that, globally, the absorbed *solar radiation*, that is, *incoming solar radiation* minus reflected *solar radiation* at the top of the *atmosphere* and *outgoing longwave radiation* emitted by the *climate system* are equal.

Energy balance model (EBM) An energy balance model is a simplified model that analyses the energy budget of the Earth to compute changes in the *climate*. In its simplest form, there is no explicit spatial dimension and the model then provides an estimate of the changes in globally averaged temperature computed from the changes in radiation. This zero-dimensional energy balance model can be extended to a one-dimensional or two-dimensional model if changes to the energy budget with respect to latitude, or both latitude and longitude, are explicitly considered.

Energy budget (of the Earth) The Earth is a physical system with an energy budget that includes all gains of incoming energy and all losses of outgoing energy. The Earth's energy budget is determined by measuring how much energy comes into the Earth System from the Sun, how much energy is lost to space, and accounting for the remainder on Earth and its *atmosphere*. *Solar radiation* is the dominant source of energy into the Earth System. Incoming solar energy may be scattered and reflected by clouds and *aerosols* or absorbed in the atmosphere. The transmitted radiation is then either absorbed or reflected at the Earth's surface. The average *albedo* of the Earth is about 0.3, which means that 30% of the incident solar energy is reflected into space, while 70% is absorbed by the Earth. Radiant solar or shortwave energy is transformed into sensible heat, latent energy (involving different water states), potential energy, and kinetic energy before being emitted as *infrared radiation*. With the average *surface temperature* of the Earth of about 15°C (288 K), the main outgoing energy flux is in the infrared part of the spectrum.

Enhanced weathering A proposed method to increase the natural rate of removal of *carbon dioxide (CO_2)* from the *atmosphere* using silicate and carbonate rocks. The active surface area of these minerals is increased by grinding, before they are actively added to soil, beaches or the open ocean. See also *Carbon dioxide removal (CDR)* and *Anthropogenic removals*.

Ensemble A collection of comparable datasets that reflect variations within the bounds of one or more sources of *uncertainty*, and that when averaged can provide a more robust estimate of underlying behaviour. Ensemble techniques are used by the observational, *reanalysis* and modelling communities. See also *Climate simulation ensemble*.

Equilibrium and transient climate experiment An equilibrium climate experiment is a *climate model* experiment in which the model is allowed to fully adjust to a change in *radiative forcing*. Such experiments provide information on the difference between the initial and final states of the model, but not on the time-dependent response. If the forcing is allowed to evolve gradually according to a prescribed *emission scenario*, the time-dependent response of a climate model may be analysed. Such an experiment is called a transient climate experiment.

Equilibrium climate sensitivity (ECS) See *Climate sensitivity*.

Equilibrium line The spatially averaged boundary at a given moment, usually chosen as the seasonal *mass budget* minimum at the end of summer, between the region on a *glacier* where there is a net annual loss of ice mass (ablation area) and that where there is a net annual gain (*accumulation* area). The altitude of this boundary is referred to as *equilibrium line* altitude (ELA).

Equivalent carbon dioxide (CO_2) emission See *CO_2 equivalent (CO_2-eq) emission*.

Eutrophication Over-enrichment of water by nutrients such as nitrogen and phosphorus. It is one of the leading causes of water quality impairment. The two most acute symptoms of eutrophication are *hypoxia* (or oxygen depletion) and harmful algal blooms.

ACCEPTED VERSION SUBJECT TO FINAL EDITS

Evaporation The physical process by which a liquid (e.g., water) becomes a gas (e.g., water vapour).

Evapotranspiration The combined processes through which water is transferred to the *atmosphere* from open water and ice surfaces, bare soil, and vegetation that make up the Earth's surface.

Potential evapotranspiration The potential rate of water loss from wet soils and from plant surfaces, without any limits imposed by the water supply.

Evidence Data and information used in the scientific process to establish findings. In this report, the degree of evidence reflects the amount, quality and consistency of scientific/technical information on which the Lead Authors are basing their findings. See also *Agreement*, *Confidence*, *Likelihood* and *Uncertainty*.

Exposure The presence of people; *livelihoods*; species or *ecosystems*; environmental functions, services, and resources; infrastructure; or economic, social, or cultural assets in places and settings that could be adversely affected.

Extended concentration pathways (ECPs) See *Representative concentration pathways (RCPs)* (under *Pathways*).

External forcing External forcing refers to a *forcing* agent outside the *climate system* causing a change in the climate system. Volcanic eruptions, solar variations and changes in Earth's orbit, as well as *anthropogenic* changes in the composition of the *atmosphere* or in *land use* are external forcings. See also *Orbital forcing*.

Extratropical cyclone (ETC) Any cyclonic-scale storm that is not a *tropical cyclone*. Usually refers to a middle- or high-latitude migratory storm system formed in regions of large horizontal temperature variations. Sometimes called extratropical storm or extratropical low.

Extratropical jets Extratropical jets are wind maxima in the upper *troposphere* marking zones of baroclinic instability. Anomalies in the position of these jets are often associated with storms, *blocking*, and weather extremes.

Extreme climate event See *Climate extreme (extreme weather or climate event)*.

Extreme coastal water level (ECWL) See *Extreme sea level (ESL)*.

Extreme sea level (ESL) The occurrence of an exceptionally low or high local sea-surface height, arising from (a combination of) short term phenomena (e.g. *storm surges*, tides and waves). *Relative sea-level changes* affect extreme sea levels directly by shifting the mean water levels and indirectly by modulating the propagation of tides, waves and/or surges due to increased water depth. In addition, extreme sea levels can be influenced by changes in the frequency, tracks, or strength of weather systems and storms, or due to anthropogenically induced changes such as the modification of coastlines or dredging. In turn, changes in any or all of the contributions to extreme sea levels may lead to long term relative sea-level changes. Alternate expressions for ESL may be used depending on the processes resolved.

Extreme Still Water Level (ESWL) refers to the combined contribution of relative sea-level change, tides and storm-surges. Wind-waves also contribute to coastal sea level via three processes: infragravity waves (lower frequency gravity waves generated by the wind waves); wave setup (time-mean sea-level elevation due to wave energy dissipation); and swash (vertical displacement up the shore-face induced by individual waves). Extreme Total Water Level (ETWL) is the ESWL plus wave setup. When considering coastal impacts, swash is also important, and Extreme Coastal Water Level (ECWL) is used. See also *Storm surge* and *Sea level change (sea level rise/sea level fall)*.

Extreme still water level (ESWL) See *Extreme sea level (ESL)*.

ACCEPTED VERSION SUBJECT TO FINAL EDITS

Extreme total water level (ETWL) See *Extreme sea level (ESL)*.

Extreme weather event An event that is rare at a particular place and time of year. Definitions of 'rare' vary, but an extreme weather event would normally be as rare as or rarer than the 10th or 90th percentile of a probability density function estimated from observations. By definition, the characteristics of what is called extreme weather may vary from place to place in an absolute sense. See also *Heatwave* and *Climate extreme (extreme weather or climate event)*.

Extreme/heavy precipitation event An extreme/heavy precipitation event is an event that is of very high magnitude with a very rare occurrence at a particular place. Types of extreme precipitation may vary depending on its duration, hourly, daily or multi-days (e.g., 5 days), though all of them qualitatively represent high magnitude. The intensity of such events may be defined with block maxima approach such as annual maxima or with peak over threshold approach, such as rainfall above 95th or 99th percentile at a particular space.

Faculae Bright patches on the Sun. The area covered by faculae is greater during periods of high *solar activity*.

Feedback See *Climate feedback*.

Fine-mode aerosol optical depth See *Aerosol optical depth (AOD)*.

Fingerprint The *climate* response pattern in space and/or time to a specific *forcing* is commonly referred to as a fingerprint. The spatial patterns of sea level response to melting of *glaciers* or *ice sheet*s (or other changes in surface loading) are also referred to as fingerprints. Fingerprints are used to detect the presence of this response in observations and are typically estimated using forced *climate model* simulations. See also *Detection and attribution*.

Fire weather Weather conditions conducive to triggering and sustaining wildfires, usually based on a set of indicators and combinations of indicators including temperature, soil moisture, humidity, and wind. Fire weather does not include the presence or absence of fuel load.

Firn Snow that has survived at least one *ablation* season but has not been transformed to *glacier* ice. Its pore space is at least partially interconnected, allowing air and water to circulate. Firn densities typically are 400–830 kg m^{-3}.

Fitness-for-purpose The suitability of a model (or other resource, such as a dataset or method) for a particular task, such as quantifying the contribution of increased *greenhouse gas* concentrations to recent changes in *global mean surface temperature* or projecting changes in *drought* frequency in a region under a given *scenario*. Assessment of a model's fitness-for-purpose can be informed both by how the model represents relevant physical processes and by how it scores on relevant performance metrics.

Flaring Open air burning of waste gases and volatile liquids, through a chimney, at oil wells or rigs, in refineries or chemical plants, and at landfills.

Flood The overflowing of the normal confines of a stream or other water body, or the accumulation of water over areas that are not normally submerged. Floods can be caused by unusually heavy rain, for example during storms and cyclones. Floods include river (fluvial) floods, flash floods, urban floods, rain (pluvial) floods, sewer floods, *coastal* floods, and *glacial lake outburst floods (GLOFs)*.

Flux A movement (a flow) of matter (e.g., water vapor, particles), heat or energy from one place to another, or from one medium (e.g., land surface) to another (e.g., atmosphere).

Foraminifera Single-celled, sand-sized marine organisms (protists) that possess a hard test mainly

ACCEPTED VERSION SUBJECT TO FINAL EDITS

composed of agglutinated walls (detrital grains glued together with organic cement) or calcium carbonate (predominantly calcite). They are used to reconstruct a range of (paleo)environmental variables such as salinity, temperature, oxygenation, oxygen isotope composition, and organic and nutrient flux.

Forcing See *Radiative forcing*.

Forest A vegetation type dominated by trees. Many definitions of the term forest are in use throughout the world, reflecting wide differences in biogeophysical conditions, social structure and economics. [Note: For a discussion of the term forest in the context of National GHG inventories, see the 2006 IPCC Guidelines for National GHG Inventories and their 2019 Refinement, and information provided by the United Nations Framework Convention on Climate Change (IPCC, 2006, 2019, UNFCCC, 2021a, 2021b).] See also *Afforestation*, *Deforestation* and *Reforestation*.

Fossil fuel emissions Emissions of *greenhouse gases* (in particular *carbon dioxide*), other trace gases and *aerosols* resulting from the combustion of fuels from fossil carbon deposits such as oil, gas and coal.

Fossil fuels Carbon-based fuels from fossil hydrocarbon deposits, including coal, oil, and natural gas.

Free atmosphere The atmospheric layer that is negligibly affected by friction against the Earth's surface, and which is above the *atmospheric boundary layer*.

Frozen ground Soil or rock in which part or all of the pore water consists of ice. See also *Active layer* and *Permafrost.*

General circulation The large-scale motions of the *atmosphere* and the ocean as a consequence of differential heating on a rotating Earth. General circulation contributes to the *energy balance* of the system through transport of heat and momentum.

General circulation model (GCM) A numerical representation of the atmosphere-ocean-sea ice system based on the physical, chemical and biological properties of its components, their interactions and feedback processes. General circulation models are used for weather forecasts, seasonal to decadal prediction, and *climate projections*. They are the basis of the more complex *Earth system models (ESMs)*. See also *Climate model*.

Geocentric sea-level change See *Sea level change (sea level rise/sea level fall)*.

Geoid The equipotential surface having the same geopotential at each latitude and longitude around the world (geodesists denoting this potential W0) that best approximates the *mean sea level*. It is the surface of reference for measurement of altitude. In practice, several variations of definitions of the *geoid* exist depending on the way the permanent tide (the zero-frequency gravitational tide due to the Sun and Moon) is considered in geodetic studies.

Geostrophic winds or currents A wind or current that is in balance with the horizontal pressure gradient and the Coriolis force, and thus is outside of the influence of friction. Thus, the wind or current is directly parallel to isobars and its speed is proportional to the horizontal pressure gradient.

Glacial isostatic adjustment (GIA) The ongoing changes in *gravity, rotation and viscoelastic solid Earth deformation (GRD)* in response to past changes in the distribution of ice and water on Earth's surface. On a timescale of decades to tens of millennia following mass redistribution, Earth's mantle flows viscously as it evolves toward isostatic equilibrium, causing solid Earth movement and *geoid* changes, which can result in regional to local sea-level variations. See also *Sea level change (sea level rise/sea level fall)*.

Glacial lake outburst flood (GLOF) / Glacier lake outburst A sudden release of water from a glacier lake, including any of the following types – a glacier-dammed lake, a pro-glacial moraine-dammed lake or water that was stored within, under or on the glacier.

ACCEPTED VERSION SUBJECT TO FINAL EDITS

Glacial or glaciation A period characterized by the establishment of expanded ice sheets and glaciers, and associated with global mean sea level (GMSL) substantially lower than present. Generally coincides with even-numbered *marine isotope stages*. Glacial intervals were interrupted by interglacial intervals. The Last Glacial Maximum (LGM) is a specific interval within the most recent glaciation, when ice sheets were near their global maximum volume (Clark et al., 2009; Gowan et al., 2021) and GMSL was near its most recent lowest stand (Lambeck et al., 2014; Yokoyama et al., 2018). Local or regional glacial maxima may be diachronous, for example ranging from about 29,000 years ago and 16,000 years ago. For purposes of global synthesis, IPCC AR6 adopts a practical chronostratigraphic definition of LGM of 23,000-19,000 years BP (before 1950; chronozone level 1 of Mix et al., 2001). For modeling purposes, LGM is defined by the model time step nearest to the center of this interval, 21,000 years ago (Kageyama et al., 2017). See also *Deglacial or deglaciation or glacial termination*, *Glacial-interglacial cycles*, *Ice age* and *Interglacial or interglaciation*.

Glacial termination See *Deglacial or deglaciation or glacial termination*.

Glacial-interglacial cycles Phase of the Earth's history marked by large changes in continental ice volume and global sea level. See also *Glacial or glaciation, Deglacial or deglaciation or glacial termination, Interglacial or interglaciation* and *Ice age*.

Glaciated State of a surface that was covered by *glacier* ice in the past, but not at present. See also *Glacierised*.

Glacier A perennial mass of ice, and possibly firn and snow, originating on the land surface by accumulation and compaction of snow and showing evidence of past or present flow. A glacier typically gains mass by accumulation of snow, and loses mass by ablation. Land ice masses of continental size (>50,000 km^2) are referred to as ice sheets (Cogley et al., 2011).

Outlet glacier A *glacier*, usually between rock walls, that is part of, and drains an *ice sheet*. See also *Ice stream*.

Glacierised A surface that is currently covered by *glacier* ice. See also *Glaciated*.

Global carbon budget See *Carbon budget*.

Global dimming Global dimming refers to the observed widespread reduction in the amount of *solar radiation* received at the Earth's surface from the 1950s to the 1980s, with an increase in anthropogenic aerosol emissions appearing to have contributed. This was followed by a partial recovery since the 1990s ("brightening"), particularly in industrialized areas, coincident with a reduction in anthropogenic aerosol emissions.

Global mean sea-level (GMSL) change See *Sea level change (sea level rise/sea level fall)*.

Global mean surface air temperature (GSAT) Global average of near-surface air temperatures over land, oceans and sea ice. Changes in GSAT are often used as a measure of global temperature change in *climate models*. See also *Global mean surface temperature (GMST)*.

Global mean surface temperature (GMST) Estimated global average of near-surface air temperatures over land and sea ice, and *sea surface temperature (SST)* over ice-free ocean regions, with changes normally expressed as departures from a value over a specified *reference period*. See also *Global mean surface air temperature (GSAT)*.

Global monsoon The global monsoon (GM) is a global-scale solstitial mode that dominates the annual variation of tropical and sub-tropical precipitation and circulation. The GM domain is defined as the area where the annual range of precipitation (local summer minus winter mean precipitation rate) is greater than

ACCEPTED VERSION SUBJECT TO FINAL EDITS

2.5 mm/day, following on from the definition as in Kitoh et al. (2013). Further details on how the GM is defined, used and related to regional monsoons throughout the report is provided by AnnexV.

Australian and Maritime Continent monsoon (AusMCM) The Australian-Maritime Continent monsoon (AusMCM) occurs during December-January-February, with the large-scale shift of the Inter-Tropical Convergence Zone into the Southern Hemisphere and covering northern Australia and the Maritime Continent up to 10N. The AusMCM is characterized by the seasonal reversal of prevailing easterly winds to westerly winds and the onset of periods of active convection and heavy rainfall. Over northern Australia, the monsoon season generally lasts from December to March and is associated with west to northwesterly inflow of moist winds, producing convection and heavy precipitation. Over the Maritime Continent, the main rainy season south of the equator is centered on December to February with northwesterly monsoon flow at low levels. Further details on how AusMCM is defined and used throughout the report is provided in the Annex V.

East Asian monsoon (EAsiaM) The East Asian monsoon (EAsiaM) is the seasonal reversal in wind and precipitation occurring over East Asia, including eastern China, Japan and the Korean peninsula. Differently from the other monsoons it extends quite far north, out of the tropical belt, and it is largely influenced by subtropical systems and by disturbances from the mid-latitudes. The EAsiaM manifests during boreal summer with warm and wet southerly winds, but also during boreal winter with cold and dry northerly winds. In late April/early May rainfall onsets in central Indochina Peninsula, and in mid-June the rainy season arrives over East Asia with the formation of the Meiyu front along the Yangtze River valley, Changma in Korea and Baiu in Japan. Lately in July, the monsoon advances up to North China, the Korean peninsula and central Japan. During boreal winter, strong north-westerlies manifest over north, northeast China, Korea and Japan, while strong north easterlies arrive along the coast of East Asia. Further details on how EAsiaM is defined and used throughout the report is provided in the Annex V.

North American monsoon (NAmerM) The North American monsoon (NAmerM) is a regional-scale atmospheric circulation system with increase in summer precipitation over northwestern Mexico and southwest United States. The monsoonal characteristics of the region include a pronounced annual maximum of precipitation in boreal summer (June-July-August) accompanied by a surface low pressure system and an upper-level anticyclone, although seasonal reversal of the surface winds is primarily limited to the northern Gulf of California. Further details on how NAmerM is defined and used throughout the report is provided in the Annex V.

South American monsoon (SAmerM) The South American monsoon (SAmerM) is a regional circulation characterized by inflow of low-level winds from the Atlantic to South America, including Brazil, Peru', Bolivia and northern Argentina, associated with the development of surface pressure gradients (and intense precipitation) during austral summer (December-January-February). During September-October-November areas of intense convection migrate from northwestern South America to the south. Associated to this regime, an upper-tropospheric anticyclone (a.k.a the Bolivian High) forms over the Altiplano region during the monsoon onset. The SAmerM then retreats during March-April-May with a northeastward migration of the convection. Further details on how SAmerM is defined and used throughout the report is provided in the Annex V.

South and Southeast Asian monsoon (SAsiaM) The South and Southeast Asian monsoon (SAsiaM) is characterized by pronounced seasonal reversals of wind and precipitation. The SAsiaM region extends across vast geographical areas and several countries including India, Bangladesh, Nepal, Myanmar, Sri Lanka, Pakistan, Thailand, Laos, Cambodia, Vietnam and Philippine. The SAsiaM starts in late May/early June and progresses toward northeast, ending in late September/early October. During the core monsoon season, maxima of SAsiaM precipitation are located over the west coast, northeast and central north India, Myanmar and Bangladesh, whereas minima are located over northwest and southeastern India, western Pakistan, southeastern and northern Sri Lanka. Further details on how SAsiaM is defined and used throughout the report is provided in the Annex V.

West African monsoon (WAfriM) The West African monsoon (WAfriM) is a seasonal reversal in wind and

ACCEPTED VERSION SUBJECT TO FINAL EDITS

precipitation whose domain includes Benin, Burkina-Faso, northern Cameroon, Cape Verde, northern Central African Republic, Chad, Gambia, Ghana, Guinea, Guinea Bissau, Ivory, Coast, Liberia, Mali, Mauritania, Niger, Nigeria, Senegal, Sierra Leone and Togo. The WAfriM is characterized by the northward progression from May to September of moist low-level south-westerlies from the Gulf of Guinea. In May and June, rainfall essentially remains along the Guinean coast with a maximum occurring near 5°N, followed by a sudden decrease of rainfall, marking the "short dry season" in the Guinean coast and the monsoon onset in the Sahel. Then rainfall continues to progress northward up to about 18-20°N, with a maximum near 12°N in late August/September, until it retreats starting from October towards the Guinean coast for a second maximum. Further details on how WAfriM is defined and used throughout the report is provided in the Annex V.

Global surface temperature See *Global mean surface temperature (GMST)* and *Global mean surface air temperature (GSAT)*. See also *Global warming*.

Global warming Global warming refers to the increase in *global surface temperature* relative to a baseline *reference period*, averaging over a period sufficient to remove interannual variations (e.g., 20 or 30 years). A common choice for the baseline is 1850-1900 (the earliest period of reliable observations with sufficient geographic coverage), with more modern baselines used depending upon the application. See also *Climate change* and *Climate variability*.

Global warming potential (GWP) An index measuring the *radiative forcing* following an emission of a unit mass of a given substance, accumulated over a chosen time horizon, relative to that of the reference substance, *carbon dioxide (CO_2)*. The GWP thus represents the combined effect of the differing times these substances remain in the atmosphere and their effectiveness in causing radiative forcing. See also *Lifetime* and *Greenhouse gas emission metric*.

Gravitational, rotational and deformational (GRD) effects See *Sea level change (sea level rise/sea level fall)*.

Gravity Recovery And Climate Experiment (GRACE) A pair of satellites to measure the Earth's gravity field anomalies from 2002 to 2017. These fields have been used, among other things, to study mass changes of the polar *ice sheets* and *glaciers*.

Greenhouse effect The infrared radiative effect of all infrared-absorbing constituents in the *atmosphere*. *Greenhouse gases (GHGs)*, clouds, and some *aerosols* absorb *terrestrial radiation* emitted by the Earth's surface and elsewhere in the atmosphere. These substances emit infrared radiation in all directions, but, everything else being equal, the net amount emitted to space is normally less than would have been emitted in the absence of these absorbers because of the decline of temperature with altitude in the *troposphere* and the consequent weakening of emission. An increase in the concentration of GHGs increases the magnitude of this effect; the difference is sometimes called the enhanced greenhouse effect. The change in a GHG concentration because of *anthropogenic* emissions contributes to an *instantaneous radiative forcing*. *Surface temperature* and *troposphere* warm in response to this forcing, gradually restoring the radiative balance at the top of the atmosphere.

Greenhouse gas emission metric A simplified relationship used to quantify the effect of emitting a unit mass of a given *greenhouse gas* on a specified key measure of *climate change*. A relative GHG emission metric expresses the effect from one gas relative to the effect of emitting a unit mass of a reference GHG on the same measure of climate change. There are multiple emission metrics and the most appropriate metric depends on the application. GHG emission metrics may differ with respect to (i) the key measure of climate change they consider, (ii) whether they consider climate outcomes for a specified point in time or integrated over a specified time horizon, (iii) the time horizon over which the metric is applied, (iv) whether they apply to a single emission pulse, emissions sustained over a period of time, or a combination of both, and (v) whether they consider the climate effect from an emission compared to the absence of that emission, or compared to a reference emissions level or climate state.

ACCEPTED VERSION SUBJECT TO FINAL EDITS

Notes: Most relative GHG emission metrics (such as the *Global Warming Potential (GWP)*, Global Temperature change Potential (GTP), Global Damage Potential, and GWP*), use carbon dioxide as the reference gas. Emissions of non-CO_2 gases, when expressed using such metrics, are often referred to as "carbon dioxide equivalent" emissions. A metric that establishes equivalence regarding one key measure of the *climate system* response to emissions does not imply equivalence regarding other key measures. The choice of a metric, including its time horizon, should reflect the policy objectives for which the metric is applied.

Greenhouse gas neutrality Condition in which metric-weighted anthropogenic greenhouse gas (GHG) emissions associated with a subject are balanced by metric-weighted anthropogenic GHG removals. The subject can be an entity such as a country, an organisation, a district or a commodity, or an activity such as a service and an event. GHG neutrality is often assessed over the life cycle including indirect ("scope 3") emissions, but can also be limited to the emissions and removals, over a specified period, for which the subject has direct control, as determined by the relevant scheme. The quantification of GHG emissions and removals depends on the GHG emission metric chosen to compare emissions and removals of different gases, as well as the time horizon chosen for that metric.

Note 1: GHG neutrality and net zero GHG emissions are overlapping concepts. The concepts can be applied at global or sub-global scales (e.g., regional, national and sub-national). At a global scale, the terms greenhouse gas neutrality and net zero greenhouse gas emissions are equivalent. At sub-global scales, net zero greenhouse gas emissions is generally applied to emissions and removals under direct control or territorial responsibility of the reporting entity, while greenhouse gas neutrality generally includes emissions and removals within and beyond the direct control or territorial responsibility of the reporting entity. Accounting rules specified by GHG programmes or schemes can have a significant influence on the quantification of relevant emissions and removals.

Note 2. Under the Paris Rulebook [Decision 18/CMA.1, annex, paragraph 37], parties have agreed to use GWP100 values from the IPCC AR5 or GWP100 values from a subsequent IPCC Assessment Report to report aggregate emissions and removals of GHGs. In addition, parties may use other metrics to report supplemental information on aggregate emissions and removals of GHGs.

Note 3: In some cases, achieving greenhouse gas neutrality may rely on the supplementary use of *offsets* to balance emissions that remain after actions by the reporting entity are taken into account.] See also *Carbon neutrality*, *Greenhouse gas emission metric*, *Land use, land-use change and forestry (LULUCF)* and *Net zero greenhouse gas emissions*.

Greenhouse gases (GHGs) Gaseous constituents of the *atmosphere*, both natural and *anthropogenic*, that absorb and emit radiation at specific wavelengths within the spectrum of radiation emitted by the Earth's surface, by the atmosphere itself, and by clouds. This property causes the *greenhouse effect*. Water vapour (H_2O), *carbon dioxide (CO_2)*, *nitrous oxide (N_2O)*, *methane (CH_4)* and *ozone (O_3)* are the primary GHGs in the Earth's atmosphere. Human-made GHGs include *sulphur hexafluoride (SF_6)*, *hydrofluorocarbons (HFCs)*, *chlorofluorocarbons (CFCs)* and *perfluorocarbons (PFCs)*; several of these are also O_3-depleting (and are regulated under the *Montreal Protocol*). See also *Well-mixed greenhouse gas*.

Greenland ice sheet (GrIS) See *Ice sheet*.

Gross Primary Production (GPP) See *Primary production*.

Ground-level ozone Atmospheric *ozone (O_3)* formed naturally or from human-emitted precursors near Earth's surface, thus affecting human health, agriculture, and ecosystems. Ozone is a *greenhouse gas (GHG)*, but ground-level ozone, unlike stratospheric ozone, also directly affects organisms at the surface. Ground-level ozone is sometimes referred to as tropospheric ozone, although much of the troposphere is well above the surface and thus does not directly expose organisms at the surface.

Grounding line The junction between a *glacier* or *ice sheet* and an *ice shelf*; the place where ice starts to float. This junction normally occurs over a zone, rather than at a line.

ACCEPTED VERSION SUBJECT TO FINAL EDITS

Gyre Basin-scale ocean horizontal circulation pattern with slow flow circulating around the ocean basin, closed by a strong and narrow (100 to 200 km wide) boundary current on the western side. The subtropical gyres in each ocean are associated with high pressure in the centre of the gyres; the subpolar gyres are associated with low pressure.

Hadley cell See *Hadley circulation*.

Hadley circulation A direct, thermally driven overturning cell in the *atmosphere* consisting of poleward flow in the upper *troposphere*, subsiding air into the subtropical anticyclones, return flow as part of the trade winds near the surface, and with rising air near the equator in the so-called *Inter-Tropical Convergence Zone*.

Halocarbons A collective term for the group of partially halogenated organic species, which includes the *chlorofluorocarbons (CFCs)*, hydrochlorofluorocarbons (HCFCs), *hydrofluorocarbons (HFCs)*, halons, methyl chloride and methyl bromide. Many of the halocarbons have large *global warming potentials*. The chlorine and bromine-containing halocarbons are also involved in the depletion of the ozone layer.

Halocline A layer in the oceanic water column in which salinity changes rapidly with depth. Generally saltier water is denser and lies below less salty water. In some high latitude oceans the surface waters may be colder than the deep waters and the halocline is responsible for maintaining water column stability and isolating the surface waters from the deep waters.

Halosteric See *Sea level change (sea level rise/sea level fall)*.

Halosteric sea-level change See *Sea level change (sea level rise/sea level fall)*.

Hazard The potential occurrence of a natural or human-induced physical event or trend that may cause loss of life, injury, or other health impacts, as well as damage and loss to property, infrastructure, livelihoods, service provision, ecosystems and environmental resources. See also *Impacts (consequences, outcomes)* and *Risk*.

Heat index A measure of how hot the air feels to the human body. The index is mainly based on surface air temperature and relative humidity, thus it reflects the combined effect of high temperature and humidity on human physiology and provides a relative indication of potential health risks.

Heat stress A range of conditions in, e.g., terrestrial or aquatic organisms when the body absorbs excess heat during overexposure to high air or water temperatures or thermal radiation. In aquatic water breathing animals, hypoxia and acidification can exacerbate vulnerability to heat. Heat stress in mammals (including humans) and birds, both in air, is exacerbated by a detrimental combination of ambient heat, high humidity and low wind-speeds, causing regulation of body temperature to fail.

Heatwave A period of abnormally hot weather often defined with reference to a relative temperature threshold, lasting from two days to months. Heatwaves and warm spells have various and, in some cases, overlapping definitions. See also *Marine heatwave*, *Warm spell*, *Blocking*, *Heat index* and *Heat stress*.

Heavy precipitation event See *Extreme/heavy precipitation event*.

Heinrich event Distinct layers of coarse-grained sediments comprised of ice-rafted debris identified across marine sediment cores in the North Atlantic. These sedimentary layers are closely associated with millennial-scale cooling events in the North Atlantic and a distinct pattern of global temperature and hydrological changes that are largely consistent with evidence for a slowdown, or even near-collapse, of the *Atlantic meridional ocean circulation (AMOC)* during these times.

Heterotrophic respiration The conversion of organic matter to *carbon dioxide* by organisms other than

ACCEPTED VERSION SUBJECT TO FINAL EDITS

autotrophs.

Hindcast or retrospective forecast A forecast made for a period in the past using only information available before the beginning of the forecast. A sequence of hindcasts can be used to calibrate the forecast system and/or provide a measure of the average skill that the forecast system has exhibited in the past as a guide to the skill that might be expected in the future.

Holocene The current *interglacial* geological epoch, the second of two epochs within the Quaternary Period, the preceding being the *Pleistocene*. The International Commission on Stratigraphy (ICS) defines the start of the Holocene Epoch at 11,700 years before 2000 (ICS, 2018). It encompasses the mid-Holocene (MH), the 1000-year-long interval centered at 6000 years before 1950; a period of long-standing focus for climate modelling, with enhanced seasonality in the Northern Hemisphere and decreased seasonality in the Southern Hemisphere. The early part of the Holocene is marked by the late stages of *deglaciation* of Pleistocene land ice, and sea level rise, and the occurrence of warm phases that affected different regions at different times, often referred to as the "Holocene thermal maximum". In addition, the epoch includes the post-glacial interval, which began approximately 7000 years ago when the fundamental features of the modern *climate system* were essentially in place, as the influence of remnant Pleistocene *ice sheets* waned. See also *Anthropocene*.

Holocene Thermal Maximum (HTM) See *Holocene*.

Human influence on the climate system Human-driven activities that lead to changes in the climate system due to perturbations of the Earth's energy budget (also called anthropogenic *forcing*). Human influence results from emissions of *greenhouse gases, aerosols, ozone-depleting substances (ODSs),* and *land-use change*. See also *Anthropogenic*, *Anthropogenic emissions* and *Anthropogenic removals*.

Human system Any system in which human organisations and institutions play a major role. Often, but not always, the term is synonymous with society or social system. Systems such as agricultural systems, urban systems, political systems, technological systems, and economic systems are all human systems in the sense applied in this report.

Hurricane See *Tropical cyclone*.

Hydroclimate Part of the *climate* pertaining to the hydrology of a *region*.

Hydrofluorocarbons (HFCs) One of the seven types of greenhouse gases (GHGs) or groups of GHGs to be mitigated under the Kyoto Protocol. They are produced commercially as a substitute for chlorofluorocarbons (CFCs). HFCs largely are used in refrigeration and semiconductor manufacturing.

Hydrological cycle The cycle in which water evaporates from the ocean and the land surface, is carried over the Earth in atmospheric circulation as water vapour, condenses to form clouds, precipitates over the ocean and land as rain or snow, which on land can be intercepted by trees and vegetation, potentially accumulating as snow or ice, provides runoff on the land surface, infiltrates into soils, recharges groundwater, discharges into streams, and ultimately, flows into the oceans as rivers, polar glaciers and ice sheets, from which it will eventually evaporate again. The various systems involved in the hydrological cycle are usually referred to as hydrological systems.

Hydrological drought See *Drought*.

Hydrological sensitivity (η) The change in global-mean precipitation per degree Celsius of global mean temperature change when precipitation changes related to fast atmospheric and land surface adjustments to radiative forcings are removed. Units are % per °C although can also be calculated as W m^{-2} per °C. See also *Apparent hydrological sensitivity (η_a)*.

Hydrosphere The component of the *climate system* comprising liquid surface and subterranean water,

ACCEPTED VERSION SUBJECT TO FINAL EDITS

such as in oceans, seas, rivers, freshwater lakes, underground water, *wetlands*, etc.

Hypoxic Conditions of low dissolved oxygen in shallow water ocean and freshwater environments. There is no universal threshold for hypoxia. A value around 60 μmol kg^{-1} has commonly been used for some estuarine systems, although this does not necessarily directly translate into biological impacts. Anoxic conditions occur where there is no oxygen present at all. See also *Eutrophication*.

Hypsometry The distribution of land or ice surface as a function of altitude.

Ice age An informal term for a geological period characterised by a long-term reduction in the temperature of the Earth's *climate*, resulting in the presence or expansion of *ice sheets* and *glaciers*. Among the Earth's ice ages is the current Quaternary Period, characterized by alternating *glacial* and *interglacial* intervals. See also *Deglacial or deglaciation or glacial termination* and *Glacial-interglacial cycles*.

Ice core A cylinder of ice drilled out of a *glacier* or *ice sheet* to determine the physical properties of the ice body, and to gain information on past changes in *climate* and composition of the *atmosphere* that are preserved in the ice or in air trapped in the ice.

Ice sheet An ice body originating on land that covers an area of continental size, generally defined as covering >50,000 km^2, and that has formed over thousands of years through *accumulation* and compaction of snow. An ice sheet flows outward from a high central ice plateau with a small average surface slope. The margins usually slope more steeply, and most ice is *discharged* through fast-flowing ice streams or outlet *glaciers*, often into the sea or into *ice shelves* floating on the sea. There are only two ice sheets in the modern world, one on Greenland and one on Antarctica. The latter is divided into the East Antarctic Ice Sheet (EAIS), the West Antarctic Ice Sheet (WAIS) and the Antarctic Peninsula ice sheet. During glacial periods, there were other ice sheets.

Ice shelf A floating slab of ice originating from *land* of considerable thickness extending from the *coast* (usually of great horizontal extent with a very gently sloping surface), resulting from the flow of *ice sheets*, initially formed by the accumulation of snow, and often filling embayments in the coastline of an ice sheet. Nearly all ice shelves are in Antarctica, where most of the ice *discharged* into the *ocean* flows via ice shelves.

Ice stream A stream of ice with strongly enhanced flow that is part of an *ice sheet*. It is often separated from surrounding ice by strongly sheared, crevassed margins.

Ice-albedo feedback A *climate feedback* involving changes in the Earth's surface *albedo*. Snow and ice have an albedo much higher (up to ~0.8) than the average planetary albedo (~0.3). With increasing temperatures, it is anticipated that snow and ice extent will decrease, the Earth's overall albedo will decrease and more *solar radiation* will be absorbed, warming the Earth further.

Iceberg Large piece of freshwater ice broken off from a *glacier* or an *ice shelf* during *calving* and floating in open water (at least five metres height above sea level). Smaller pieces of floating ice known as 'bergy bits' (less than 5 metres above sea level) or 'growlers' (less than 2 metres above sea level) can originate from glaciers or ice shelves, or from the breaking up of a large iceberg. Icebergs can also be classified by shape, most commonly being either tabular (steep sides and a flat top) or non-tabular (varying shapes, with domes and spires) (NOAA, 2021). In lakes, icebergs can originate by breaking off shelf ice, which forms through freezing of a lake surface.

Impacts (consequences, outcomes) The consequences of realised risks on natural and human systems, where risks result from the interactions of climate-related hazards (including extreme weather / climate events), exposure, and vulnerability. Impacts generally refer to effects on lives, livelihoods, health and wellbeing, ecosystems and species, economic, social and cultural assets, services (including ecosystem services), and infrastructure. Impacts may be referred to as consequences or outcomes, and can be adverse or beneficial. See also *Adaptation*, *Exposure*, *Hazard*, *Loss and Damage, and losses and damages*,

ACCEPTED VERSION SUBJECT TO FINAL EDITS

Vulnerability and *Risk*.

Incoming solar radiation See *Insolation*.

Indian Ocean Basin (IOB) mode A mode of interannual variability characterized by a temporal alternation of basin-wide warming and cooling of the Indian Ocean sea surface. It mostly develops in response to *El Niño-Southern Oscillation (ENSO)*, but often persists after ENSO's equatorial eastern Pacific signal has dissipated. The IOB affects atmospheric circulation, temperature, and precipitation in South, Southeast, and East Asia as well as Africa, and modulates *tropical cyclone* activity in the Northwestern Pacific. See Section AIV.2.4 in Annex IV of the AR6 WGI report. See also *Modes of climate variability* and *Indian Ocean Dipole (IOD)*.

Indian Ocean Dipole (IOD) A mode of interannual variability that features an east-west dipole of *sea surface temperature* anomalies in the tropical Indian Ocean. Its positive phase shows concurrent sea surface cooling off Sumatra and Java and warming off Somalia in the west, combined with anomalous surface easterlies along the equator, while the opposite anomalies are seen in the negative phase. The IOD typically develops in boreal summer and matures in boreal autumn and controls part of the rainfall interannual variability in Australia, South Eastern Asia and Eastern Africa. See Section AIV.2.4 in Annex IV of the AR6 WGI report. See also *Indian Ocean Basin (IOB) mode*.

Indirect aerosol effect See *Aerosol-cloud interaction*.

Indirect land-use change (iLUC) See *Land-use change (LUC)*.

Industrial revolution A period of rapid industrial growth with far-reaching social and economic consequences, beginning in Britain during the second half of the 18th century and spreading to Europe and later to other countries including the United States. The invention of the steam engine was an important trigger of this development. The industrial revolution marks the beginning of a strong increase in the use of *fossil fuels*, initially coal, and hence emission of *carbon dioxide (CO_2)*.

Infrared radiation See *Terrestrial radiation*.

Initial condition ensemble (ICE) See *Model ensemble*.

Insolation The amount of *solar radiation* reaching the Earth by latitude and by season measured in W m^{-2}. Usually insolation refers to the radiation arriving at the top of the *atmosphere*. Sometimes it is specified as referring to the radiation arriving at the Earth's surface. See also *Orbital forcing* and *Total solar irradiance (TSI)*.

Instantaneous radiative forcing (or effect) due to aerosol-cloud interactions (IRFaci) See *Aerosol-cloud interaction*.

Instantaneous radiative forcing (or effect) due to aerosol-radiation interactions (IRFari) See *Aerosol-radiation interaction*.

Integrated assessment model (IAM) Models that integrate knowledge from two or more domains into a single framework. They are one of the main tools for undertaking integrated assessments. One class of IAM used in respect of climate change mitigation may include representations of: multiple sectors of the economy, such as energy, land use and land use change; interactions between sectors; the economy as a whole; associated greenhouse gas (GHG) emissions and sinks; and reduced representations of the climate system. This class of model is used to assess linkages between economic, social and technological development and the evolution of the climate system. Another class of IAM additionally includes representations of the costs associated with climate change impacts, but includes less detailed representations of economic systems. These can be used to assess impacts and mitigation in a cost-benefit framework and have been used to estimate the social cost of carbon.

ACCEPTED VERSION SUBJECT TO FINAL EDITS

Interdecadal Pacific Oscillation (IPO) See *Pacific Decadal Variability (PDV)*.

Inter-Tropical Convergence Zone (ITCZ) The Inter-Tropical Convergence Zone is an equatorial zonal belt of low pressure, strong *convection* and heavy precipitation near the equator where the northeast trade winds meet the southeast trade winds. This band moves seasonally. See also *South Pacific Convergence Zone (SPCZ)*.

Interglacial or interglaciation A globally warm period lasting thousands of years between *glacial* periods within an *ice age*. Generally coincides with odd-numbered *marine isotope stages (MIS)* when mean sea level was close to present. The Last Interglacial (LIG) occurred between about 129 and 116 ka (thousand years) before present (defined as 1950) although the warm period started in some areas a few thousand years earlier. In terms of marine isotope stages (MIS), *interglaciations* are defined as the interval between the midpoint of the preceding termination and the onset of the next glaciation. The LIG coincides with MIS 5e. The present interglaciation, the *Holocene*, started at 11,700 years before 2000 CE, although global mean sea level did not approach its present position until roughly 7000 years ago. See also *Deglacial or deglaciation or glacial termination, Glacial-interglacial cycles, Glacial or glaciation* and *Ice age*.

Internal climate variability See *Internal variability* (under *Climate variability*).

Irreversibility A perturbed state of a *dynamical system* is defined as irreversible on a given timescale, if the recovery from this state due to natural processes takes substantially longer than the timescale of interest. See also *Tipping point*.

Isostatic or Isostasy Isostasy refers to the response of the earth to changes in surface load. It includes the deformational and gravitational response. This response is elastic on short time scales, as in the earth-ocean response to recent changes in mountain glaciation, or viscoelastic on longer time scales, as in the response to the last *deglaciation* following the *Last Glacial Maximum*.

Isotopes Atoms of the same chemical element that have the same the number of protons but differ in the number of neutrons. Some proton-neutron configurations are stable (stable isotopes), others are unstable undergoing spontaneous radioactive decay (radioisotopes). Most elements have more than one stable isotope. Isotopes can be used to trace transport processes or to study processes that change the isotopic ratio. Radioisotopes provide in addition time information that can be used for radiometric dating. See also ^{13}C and ^{14}C.

Key climate indicators See *Climate indicator*.

Kriging Kriging is a method of interpolation (normally spatial interpolation when used with atmospheric or oceanographic data), in which the interpolated values are estimated using a Gaussian process governed by prior covariances.

La Niña See *El Niño-Southern Oscillation (ENSO)*.

Land The terrestrial portion of the biosphere that comprises the natural resources (soil, near-surface air, vegetation and other biota, and water), the ecological processes, topography, and human settlements and infrastructure that operate within that system (UNCCD, 1994; FAO, 2007).

Land cover The biophysical coverage of *land* (e.g., bare soil, rocks, forests, buildings and roads or lakes). Land cover is often categorised in broad land-cover classes (e.g., deciduous forest, coniferous forest, mixed forest, grassland, bare ground). [Note: In some literature, land cover and land use are used interchangeably, but the two represent distinct classification systems. For example, the land cover class woodland can be under various land uses such as livestock grazing, recreation, conservation, or wood harvest.]

Land cover change Change from one *land cover* class to another, due to change in *land use* or change in

ACCEPTED VERSION SUBJECT TO FINAL EDITS

natural conditions (Pongratz et al., 2018). See also *Land management change* and *Land-use change (LUC)*.

Land surface air temperature (LSAT) The near-surface air temperature over land, typically measured at 1.25–2 m above the ground using standard meteorological equipment.

Land use The total of arrangements, activities and inputs applied to a parcel of land. The term land use is also used in the sense of the social and economic purposes for which land is managed (e.g., grazing, timber extraction, conservation and city dwelling). In national GHG inventories, land use is classified according to the IPCC land use categories of forest land, cropland, grassland, wetlands, settlements, other lands (see the 2006 IPCC Guidelines for National GHG Inventories and their 2019 Refinement for details (IPCC, 2006, 2019)).

Land water storage Land water storage (LWS) includes all surface water, soil moisture, groundwater storage and snow, but excludes water stored in *glaciers* and *ice sheets*. Changes in land water storage can be caused either by direct human intervention in the water cycle (e.g., storage of water in reservoirs by building dams in rivers, groundwater extraction from groundwater reservoirs for consumption and irrigation, or deforestation) or by *climate* variations (e.g., changes in the amount of water in endorheic lakes and wetlands, the canopy, the soil, the permafrost and the snowpack). Land water storage changes caused by climate variations may also be indirectly affected by *anthropogenic* influences. See also *Sea level change (sea level rise/sea level fall)*.

Land-use change (LUC) The change from one *land use* category to another. Note that in some scientific literature, land-use change encompasses changes in land-use categories as well as changes in land management. See also *Afforestation*, *Agriculture, Forestry and Other Land Use (AFOLU)*, *Deforestation*, *Land use, land-use change and forestry (LULUCF)* and *Reforestation*.

Indirect land-use change (iLUC) Land use change outside the area of focus, that occurs as a consequence of change in use or management of land within the area of focus, such as through market or policy drivers. For example, if agricultural land is diverted to biofuel production, forest clearance may occur elsewhere to replace the former agricultural production.See *Land-use change (LUC)*.

Lapse rate The rate of change of an atmospheric variable, usually temperature, with height. The lapse rate is considered positive when the variable decreases with height.

Large-scale The climate system involves process interactions from the micro- to the global-scale. Any threshold for defining “large-scale” is arbitrary. Understanding of large-scale climate variability and change requires knowledge of both the response to external forcings and the role of internal variability. Many external forcings have substantial hemispheric or continental scale variations. Modes of climate variability are driven by ocean basin scale processes. Thus we define large-scale to include ocean basin and continental scales as well as hemispheric and global scales.

Last deglacial transition See *Deglacial or deglaciation or glacial termination* and *Younger Dryas*.

Last Glacial Maximum (LGM) See *Glacial or glaciation*.

Last Interglacial (LIG) See *Interglacial or interglaciation*.

Last millennium The interval of the *Common Era (CE)* between 1001 and 2000 CE. Encompasses the Little Ice Age, a roughly defined period characterized by multiple expansions of mountain *glaciers* worldwide, the timing of which differs among regions, but generally occurred between 1400 CE and 1900 CE. The last millennium also mostly encompasses the Medieval Warm Period (also called the Medieval Climate Anomaly), a roughly defined period of relatively warm conditions or other *climate* excursions such as extensive *drought*, the timing and magnitude of which differ among regions, but generally occurred between 900 and 1400 CE. Transient *climate model* experiments by the Paleoclimate Modelling Intercomparison Project (PMIP) for the last millennium extend from 850-1849 CE.

ACCEPTED VERSION SUBJECT TO FINAL EDITS

Latent heat flux The turbulent flux of heat from the Earth's surface to the atmosphere that is associated with *evaporation* or condensation of water vapour at the surface; a component of the surface energy budget. See also *Atmosphere* and *Flux*.

Lifetime Lifetime is a general term used for various time scales characterizing the rate of processes affecting the concentration of trace gases. The following lifetimes may be distinguished:

Response time or adjustment time (Ta) Response time or adjustment time (T_a) is the time scale characterizing the decay of an instantaneous pulse input into the *reservoir*. The term adjustment time is also used to characterize the adjustment of the mass of a reservoir following a step change in the *source* strength. Half-life or decay constant is used to quantify a first-order exponential decay process. See *Response time or adjustment time* for a different definition pertinent to *climate* variations.

The term lifetime is sometimes used, for simplicity, as a surrogate for adjustment time.

In simple cases, where the global removal of the compound is directly proportional to the total mass of the reservoir, the adjustment time equals the *turnover time*: $T = T_a$. An example is CFC-11, which is removed from the *atmosphere* only by photochemical processes in the *stratosphere*. In more complicated cases, where several reservoirs are involved or where the removal is not proportional to the total mass, the equality $T = T_a$ no longer holds.

Carbon dioxide (CO_2) is an extreme example. Its turnover time is only about 4 years because of the rapid exchange between the atmosphere and the ocean and terrestrial biota. However, a large part of that CO_2 is returned to the atmosphere within a few years. The adjustment time of CO_2 in the atmosphere is determined from the rates of removal of carbon by a range of processes with timescales from months to hundreds of thousands of years. As a result, 15 to 40% of an emitted CO_2 pulse will remain in the atmosphere longer than 1,000 years, 10 to 25% will remain about ten thousand years, and the rest will be removed over several hundred thousand years.

In the case of *methane (CH_4)*, the adjustment time is different from the turnover time because the removal is mainly through a chemical reaction with the hydroxyl radical (OH), the concentration of which itself depends on the CH_4 concentration. Therefore, the CH_4 removal rate S is not proportional to its total mass M.

Turnover time (T) (also called global atmospheric lifetime) is the ratio of the mass M of a *reservoir* (e.g., a gaseous compound in the *atmosphere*) and the total rate of removal S from the *reservoir*: $T = M/S$. For each removal process, separate turnover times can be defined. In soil carbon biology, this is referred to as Mean Residence Time.

Light-absorbing particles Light-absorbing particles (LAP), e.g., black carbon, brown carbon, dust, are particles that absorb solar radiation and convert it into internal energy, thus raising the particle's temperature and emitting thermal-infrared radiation that is selectively absorbed by the surrounding medium. LAP affect the energy balance of the atmosphere, clouds, and when deposited on snow and ice, they reduce snow/ice albedo, increasing heating and accelerating smelting. These particles have a warming effect on climate.

Likelihood The chance of a specific outcome occurring, where this might be estimated probabilistically. Likelihood is expressed in this report using a standard terminology (Mastrandrea et al., 2010). See also *Agreement*, *Confidence*, *Evidence* and *Uncertainty*.

Lithosphere The upper layer of the solid Earth, both continental and oceanic, which comprises all crustal rocks and the cold, mainly elastic part of the uppermost mantle. Volcanic activity, although part of the *lithosphere*, is not considered as part of the *climate system*, but acts as an *external forcing* factor.

Livelihood The resources used and the activities undertaken in order for people to live. Livelihoods are usually determined by the entitlements and assets to which people have access. Such assets can be

ACCEPTED VERSION SUBJECT TO FINAL EDITS

categorised as human, social, natural, physical, or financial.

Local sea level change See *Sea level change (sea level rise/sea level fall)*.

Long-lived climate forcers (LLCFs) A set of well-mixed *greenhouse gases* with long atmospheric lifetimes. This set of compounds includes *carbon dioxide (CO_2)* and *nitrous oxide (N_2O)*, together with some fluorinated gases. They have a warming effect on *climate*. These compounds accumulate in the atmosphere at decadal to centennial timescales, and their effect on climate hence persists for decades to centuries after their emission. On timescales of decades to a century already emitted emissions of long-lived climate forcers can only be abated by *greenhouse gas removal (GGR)*.

Longwave radiation See *Terrestrial radiation*.

Low-likelihood, high impact events Events whose probability of occurrence is low or not well known (as in the context of deep uncertainty) but whose potential impacts on society and ecosystems could be high. To better inform risk assessment and decision-making, such low-likelihood outcomes are considered if they are associated with very large consequences and may therefore constitute material risks, even though those consequences do not necessarily represent the most likely outcome.

Madden-Julian Oscillation (MJO) The largest mode of tropical atmospheric intraseasonal variability with typical periods ranging from 20 to 90 days. The MJO corresponds to planetary-scale disturbances of pressure, wind and deep convection moving predominantly eastward along the equator. As it progresses, the MJO is associated with the temporal alternation of large-scale enhanced and suppressed rainfall, with maximum loading over the Indian and western Pacific oceans, although influences of the MJO can be tracked over the Atlantic/Africa in dynamical fields. See Section AIV.2.8 in Annex IV of the AR6 WGI report.

Maladaptive actions (Maladaptation) Actions that may lead to increased risk of adverse climate-related outcomes, including via increased greenhouse gas (GHG) emissions, increased vulnerability to climate change, or diminished welfare, now or in the future. Maladaptation is usually an unintended consequence.

Marine cloud brightening (MCB) See *Solar radiation modification (SRM)*.

Marine heatwave A period during which water temperature is abnormally warm for the time of the year relative to historical temperatures with that extreme warmth persisting for days to months. The phenomenon can manifest in any place in the ocean and at scales of up to thousands of kilometres. See also *Heatwave*.

Marine ice cliff instability (MICI) A hypothetic mechanism of an ice cliff failure. In case a marine-terminated *ice sheet* loses its buttressing *ice shelf*, an ice cliff can be exposed. If the exposed ice cliff is tall enough (about 800 m of the total height, or about 100 m of the above-water part), the stresses at the cliff face exceed the strength of the ice, and the cliff fails structurally in repeated *calving* events. See also *Marine ice sheet instability (MISI)*.

Marine ice sheet instability (MISI) A mechanism of irreversible (on the decadal to centennial time scale) retreat of a *grounding line* for the marine-terminating *glaciers*, in case the glacier bed slopes towards the *ice sheet* interior. See also *Marine ice cliff instability (MICI)*.

Marine isotope stage (MIS) Geological periods of alternating glacial and interglacial conditions, each typically lasting tens of thousands of years as inferred from the oxygen isotope composition of microfossils from deep sea sediment cores. MIS numbers increase back in time from the present, which is MIS 1. Even-number MISs coincide with glacial periods, and odd-numbered MISs are interglacials.

Marine-based ice sheet An *ice sheet* containing a substantial *region* that rests on a bed lying below sea level and whose perimeter is in contact with the ocean. The best known example is the West Antarctic ice sheet.

ACCEPTED VERSION SUBJECT TO FINAL EDITS

Mass balance / budget (of glaciers or ice sheets) Difference between the mass input (*accumulation*) and the mass loss (*ablation*) of an ice body (e.g., a glacier or ice sheet) over a stated time period, which is often a year or a season. Surface mass balance refers to the difference between surface accumulation and surface ablation.

Ablation (of glaciers, ice sheets, or snow cover) All processes that reduce the mass of a *glacier*, *ice sheet*, or snow cover. The main processes are melting, and for glaciers also *calving* (or, when the glacier nourishes an *ice shelf*, *discharge of ice* across the *grounding line*), but other processes such as sublimation and loss of wind-blown snow can also contribute to ablation. Ablation also refers to the mass lost by any of these processes.

Accumulation (of glaciers, ice sheets, or snow cover) All processes that add to the mass of a *glacier*, an *ice sheet*, or snow cover. The main process of accumulation is snowfall. Accumulation also includes deposition of hoar, freezing rain, other types of solid precipitation, gain of wind-blown snow, avalanching, and basal accumulation (often beneath floating ice).

Discharge (of ice) Rate of the flow of ice through a vertical section of a *glacier* perpendicular to the direction of the flow of ice. Often used to refer to the loss of mass at marine-terminating glacier fronts (mostly *calving* of *icebergs* and submarine melt), or to mass flowing across the *grounding line* of a floating ice shelf.

Mean sea level The surface level of the ocean at a particular point averaged over an extended period of time such as a month or year. Mean sea level is often used as a national datum to which heights on land are referred.

Medieval Climate Anomaly (MCA) See *Medieval Warm Period (MWP)*.

Megacity Urban agglomerations with 10 million inhabitants or more.

Meltwater Pulse 1A (MWP-1A) A particular interval of rapid global *sea level rise* between about 14,700 and 14,300 years ago, associated with the end of the last *ice age* and attributed to freshwater flux to the ocean from accelerated melting of *ice sheets* and *glaciers*. First defined based on oxygen *isotope* data (Duplessy et al., 1981), and later shown to be reflected by high rates of sea-level rise (Fairbanks, 1989). See also *Deglacial or deglaciation or glacial termination*.

Meridional overturning circulation (MOC) Meridional (north-south) overturning circulation in the *ocean* quantified by zonal (east-west) sums of mass transports in depth or density layers. In the North Atlantic, away from the subpolar regions, the MOC (which is in principle an observable quantity) is often identified with the thermohaline circulation (THC), which is a conceptual and incomplete interpretation. The MOC is also driven by wind, and can also include shallower overturning cells such as occur in the upper ocean in the tropics and subtropics, in which warm (light) waters moving poleward are transformed to slightly denser waters and subducted equatorward at deeper levels.

Atlantic Meridional Overturning Circulation (AMOC) The main current system in the South and North Atlantic Oceans. AMOC transports warm upper-ocean water northwards, and cold, deep water southwards, as part of the global ocean circulation system. Changes in the strength of AMOC can affect other components of the *climate system*.

Meteorological drought See *Drought*.

Methane (CH_4) One of the seven greenhouse gases (GHGs) to be mitigated under the Kyoto Protocol. Methane is the major component of natural gas and associated with all hydrocarbon fuels. Significant anthropogenic emissions also occur as a result of animal husbandry and paddy rice production. Methane is also produced naturally where organic matter decays under anaerobic conditions, such as in wetlands. Under

ACCEPTED VERSION SUBJECT TO FINAL EDITS

future global warming, there is risk of increased methane emissions from thawing permafrost, coastal wetlands and sub-sea gas hydrates. See also *Short-lived climate forcers (SLCFs)*.

Microclimate Local climate at or near the Earth's surface.

Microwave sounding unit (MSU) A microwave sounder on National Oceanic and Atmospheric Administration (NOAA) polar orbiter satellites, that estimates the temperature of thick layers of the *atmosphere* by measuring the thermal emission of oxygen molecules from a complex of emission lines near 60 GHz. A series of nine MSUs began making this kind of measurement in late 1978. Beginning in mid-1998, a follow-on series of instruments, the Advanced Microwave Sounding Units (AMSUs), began operation.

Mid-Holocene (MH) See *Holocene*.

Mid-Pliocene Warm Period (MPWP) See *Pliocene*.

Mineralisation/Remineralisation The conversion of an element from its organic form to an inorganic form as a result of microbial decomposition. In nitrogen mineralisation, organic nitrogen from decaying plant and animal residues (proteins, nucleic acids, amino sugars and urea) is converted to ammonia (NH_3) and ammonium (NH_4^+) by biological activity.

Mitigation (of climate change) A human intervention to reduce emissions or enhance the sinks of greenhouse gases.

Mitigation potential The quantity of net greenhouse gas emission reductions that can be achieved by a given mitigation option relative to specified emission baselines. [Note: Net greenhouse gas emission reductions is the sum of reduced emissions and/or enhanced sinks.] See also *Sequestration potential*.

Biogeophysical potential The mitigation potential constrained by biological, geophysical and geochemical limits and thermodynamics, without taking into account technical, social, economic, and/or environmental considerations.

Economic potential The portion of the technical potential for which the social benefits exceed the social costs, taking into account a social discount rate and the value of externalities

Technical potential The mitigation potential constrained by biogeophysical limits as well as availability of technologies and practices. Quantification of technical potentials takes into account primarily technical considerations, but social, economic and/or environmental considerations are occasionally also included, if these represent strong barriers for the deployment of an option.

Mitigation scenario See *Scenario*.

Mixing ratio See *Mole fraction or mixing ratio*.

Model bias See *Biases*.

Model drift Since model *climate* differs to some extent from observed climate, *climate forecasts* will typically 'drift' from the initial observation-based state towards the model's climate. This drift occurs at different time scales for different variables, can obscure the initial-condition forecast information and is usually removed a posteriori by an empirical, usually linear, adjustment.

Model initialization A *climate prediction* typically proceeds by integrating a *climate model* forward in time from an initial state that is intended to reflect the actual state of the *climate system*. Available observations of the climate system are 'assimilated' into the model. Initialization is a complex process that is limited by available observations, observational errors and, depending on the procedure used, may be

ACCEPTED VERSION SUBJECT TO FINAL EDITS

affected by *uncertainty* in the history of *climate* forcing. The initial conditions will contain errors that grow as the forecast progresses, thereby limiting the time for which the forecast will be useful.

Model spread The range or spread in results from *climate models*, such as those assembled for Coupled Model Intercomparison Project Phase 6 (CMIP6). Does not necessarily provide an exhaustive and formal estimate of the *uncertainty* in *feedbacks*, forcing or *projections* even when expressed numerically, for example, by computing a standard deviation of the models' responses. In order to quantify uncertainty, information from observations, physical constraints and expert judgement must be combined, using a statistical framework.

Modes of climate variability Recurrent space-time structures of *natural variability* of the *climate system* with intrinsic spatial patterns, seasonality and time scales. Modes can arise through the dynamical characteristics of the atmospheric circulation but also through coupling between the ocean and the *atmosphere*, with some interactions with land surfaces and *sea ice*. Many modes of variability are driven by internal climate processes and are a critical potential source of climate predictability on sub-seasonal to decadal time scales. See Annex IV of the AR6 WGI report. See also *Annular modes*, *Tropical Atlantic Variability (TAV)*, *Indian Ocean Dipole (IOD)*, *Indian Ocean Basin (IOB) mode*, *Pacific Decadal Variability (PDV)*, *Pacific Decadal Oscillation (PDO)* (under *Pacific Decadal Variability (PDV)*), *El Niño-Southern Oscillation (ENSO)*, *North Atlantic Oscillation (NAO)*, *Northern Annular Mode (NAM)* (under *Annular modes*), *Southern Annular Mode (SAM)* (under *Annular modes*), *Atlantic Meridional Mode (AMM)* (under *Tropical Atlantic Variability (TAV)*), *Atlantic Zonal Mode (AZM)* (under *Tropical Atlantic Variability (TAV)*), *Madden-Julian Oscillation (MJO)*, *Atlantic Multidecadal Variability (AMV)* and *Interdecadal Pacific Oscillation (IPO)* (under *Pacific Decadal Variability (PDV)*).

Mole fraction or mixing ratio Mole fraction, or mixing ratio, is the ratio of the number of moles of a constituent in a given volume to the total number of moles of all constituents in that volume. It is usually reported for dry air. Typical values for well-mixed greenhouse gases are in the order of μmol mol^{-1} (parts per million: ppm), nmol mol^{-1} (parts per billion: ppb), and fmol mol^{-1} (parts per trillion: ppt). Mole fraction differs from volume mixing ratio, often expressed in ppmv etc., by the corrections for non-ideality of gases. This correction is significant relative to measurement precision for many greenhouse gases (Schwartz and Warneck, 1995).

Monsoon See *Global monsoon*.

Montreal Protocol The Montreal Protocol on Substances that Deplete the Ozone Layer was adopted in Montreal in 1987, and subsequently adjusted and amended in London (1990), Copenhagen (1992), Vienna (1995), Montreal (1997) and Beijing (1999). It controls the consumption and production of chlorine- and bromine-containing chemicals that destroy stratospheric ozone (O_3), such as chlorofluorocarbons (CFCs), methyl chloroform, carbon tetrachloride and many others.

Multi-model ensemble (MME) See *Climate simulation ensemble*. See also *Ensemble*.

Narrative See *Storyline*. See also *Pathways*.

Natural systems The dynamic physical and biological components of the environment that would operate in the absence of human impacts. Most, if not all, natural systems are also now affected by human activities to some degree.

Natural variability See *Climate variability*.

Near-surface permafrost See *Permafrost*.

Negative greenhouse gas emissions Removal of *greenhouse gases (GHGs)* from the *atmosphere* by deliberate human activities, i.e., in addition to the removal that would occur via natural carbon cycle or atmospheric chemistry processes. See also *Carbon dioxide removal (CDR)*, *Greenhouse gas removal (GGR)*,

ACCEPTED VERSION SUBJECT TO FINAL EDITS

Negative CO_2 emissions, *Net negative greenhouse gas emissions*, *Net zero CO_2 emissions* and *Net zero greenhouse gas emissions*.

Net negative greenhouse gas emissions A situation of net negative greenhouse gas emissions is achieved when metric-weighted anthropogenic greenhouse gas (GHG) removals exceed metric-weighted anthropogenic GHG emissions. Where multiple GHG are involved, the quantification of net emissions depends on the metric chosen to compare emissions of different gases (such as *global warming potential*, global temperature change potential, and others, as well as the chosen time horizon). See also *Net zero CO_2 emissions*, *Net zero greenhouse gas emissions*, *Negative greenhouse gas emissions*, *Carbon dioxide removal (CDR)*, *Greenhouse gas removal (GGR)* and *Greenhouse gas emission metric*.

Net primary production (NPP) See *Primary production*.

Net zero CO_2 emissions Condition in which anthropogenic carbon dioxide (CO_2) emissions are balanced by anthropogenic CO_2 removals over a specified period. [Note: Carbon neutrality and net zero CO_2 emissions are overlapping concepts. The concepts can be applied at global or sub-global scales (e.g., regional, national and sub-national). At a global scale, the terms carbon neutrality and net zero CO_2 emissions are equivalent. At sub-global scales, net zero CO_2 emissions is generally applied to emissions and removals under direct control or territorial responsibility of the reporting entity, while carbon neutrality generally includes emissions and removals within and beyond the direct control or territorial responsibility of the reporting entity. Accounting rules specified by GHG programmes or schemes can have a significant influence on the quantification of relevant CO_2 emissions and removals.] See also *Net zero greenhouse gas emissions*, *Carbon neutrality* and *Land use, land-use change and forestry (LULUCF)*.

Net zero greenhouse gas emissions Condition in which metric-weighted anthropogenic greenhouse gas (GHG) emissions are balanced by metric-weighted anthropogenic GHG removals over a specified period. The quantification of net zero GHG emissions depends on the GHG emission metric chosen to compare emissions and removals of different gases, as well as the time horizon chosen for that metric.

[Note 1: GHG neutrality and net zero GHG emissions are overlapping concepts. The concept of net zero GHG emissions can be applied at global or sub-global scales (e.g., regional, national and sub-national). At a global scale, the terms GHG neutrality and net zero GHG emissions are equivalent. At sub-global scales, net zero GHG emissions is generally applied to emissions and removals under direct control or territorial responsibility of the reporting entity, while GHG neutrality generally includes anthropogenic emissions and anthropogenic removals within and beyond the direct control or territorial responsibility of the reporting entity. Accounting rules specified by GHG programmes or schemes can have a significant influence on the quantification of relevant emissions and removals.

Note 2. Under the Paris Rulebook [Decision 18/CMA.1, annex, paragraph 37], parties have agreed to use GWP100 values from the IPCC AR5 or GWP100 values from a subsequent IPCC Assessment Report to report aggregate emissions and removals of GHGs. In addition, parties may use other metrics to report supplemental information on aggregate emissions and removals of GHGs.]

See also *Net zero CO_2 emissions*, *Greenhouse gas emission metric*, *Greenhouse gas neutrality* and *Land use, land-use change and forestry (LULUCF)*.

Nitrogen deposition Nitrogen deposition is defined as the nitrogen transferred from the *atmosphere* to the Earth's surface by the processes of wet deposition and dry deposition.

Nitrous oxide (N_2O) One of the seven *greenhouse gases (GHGs)* to be mitigated under the Kyoto Protocol. The main anthropogenic source of N_2O is agriculture (soil and animal manure management), but important contributions also come from sewage treatment, *fossil fuel* combustion, and chemical industrial processes. N_2O is also produced naturally from a wide variety of biological sources in soil and water, particularly microbial action in wet tropical forests.

ACCEPTED VERSION SUBJECT TO FINAL EDITS

Non-CO_2 emissions and radiative forcing Non-CO_2 emissions included in this report are all *anthropogenic emissions* other than CO_2 that result in *radiative forcing*. These include *short-lived climate forcers*, such as *methane (CH_4)*, some fluorinated gases, *ozone (O_3)* precursors, *aerosols* or aerosol *precursors*, such as *black carbon* and sulphur dioxide, respectively, as well as long-lived *greenhouse gases*, such as *nitrous oxide (N_2O)* or other fluorinated gases. The radiative forcing associated with non-CO_2 emissions and changes in surface *albedo* (e.g., resulting from land-use change) is referred to as non-CO_2 radiative forcing.

Non-methane volatile organic compounds (NMVOCs) See *Volatile organic compounds (VOCs)*.

Nonlinearity A process is called nonlinear when there is no simple proportional relation between cause and effect. The *climate system* contains many such nonlinear processes, resulting in a system with potentially very complex behaviour. Such complexity may lead to *abrupt climate change*.

North American monsoon (NAmerM) See *Global monsoon*.

Northern Annular Mode (NAM) See *Annular modes*.

North Atlantic Oscillation (NAO) The leading mode of large-scale atmospheric variability in the North Atlantic basin characterized by alternating (see-saw) variations in sea-level pressure or geopotential height between the Azores High in the subtropics and the Icelandic Low in the mid- to high latitudes, with some northward extension deep into the Arctic. It is associated with fluctuations in strength and latitudinal position of the main westerly winds across a vast North Atlantic-Europe domain, and thus with fluctuations in the embedded extratropical cyclones and associated frontal systems leading to strong *teleconnection* over the entire North Atlantic adjacent continents. The positive and negative phases of the NAO show similar characteristics described for the *Northern Annular Mode (NAM)*. See Section AIV.2.1 in Annex IV of the AR6 WGI report.

Northern polar vortex See *Stratospheric polar vortex*.

Ocean The interconnected body of saline water that covers 71% of the Earth's surface, contains 97% of the Earth's water and provides 99% of the Earth's biologically-habitable space. It includes the Arctic, Atlantic, Indian, Pacific and Southern Oceans, as well as their marginal seas and coastal waters.

Ocean acidification (OA) A reduction in the *pH* of the *ocean*, accompanied by other chemical changes (primarily in the levels of carbonate and bicarbonate ions), over an extended period, typically decades or longer, which is caused primarily by *uptake* of *carbon dioxide (CO_2)* from the *atmosphere*, but can also be caused by other chemical additions or subtractions from the ocean. *Anthropogenic* OA refers to the component of pH reduction that is caused by human activity (IPCC, 2011, p. 37).

Ocean alkalinisation / Ocean alkalinity enhancement A proposed carbon dioxide removal method that involves deposition of alkaline minerals or their dissociation products at the ocean surface. This increases surface total alkalinity, and may thus increase ocean CO_2 uptake and ameliorate surface ocean acidification. See also *Anthropogenic removals* and *Carbon dioxide removal (CDR)*.

Ocean carbon cycle The ocean *carbon cycle* is the set of processes that exchange carbon between various pools within the ocean, as well as between the *atmosphere*, Earth's interior, *cryosphere*, and the seafloor. See also *Carbon cycle*.

Ocean deoxygenation The loss of oxygen in the *ocean*. It results from ocean warming, which reduces oxygen solubility and increases oxygen consumption and *stratification*, thereby reducing the mixing of oxygen into the ocean interior. Deoxygenation can also be exacerbated by the addition of excess nutrients in the *coastal* zone.

Ocean dynamic sea level change See *Sea level change (sea level rise/sea level fall)*.

ACCEPTED VERSION SUBJECT TO FINAL EDITS

Ocean fertilisation A proposed carbon dioxide removal method that relies on the deliberate increase of nutrient supply to the near-surface ocean with the aim of sequestering additional CO_2 from the atmosphere through biological production. Methods include direct addition of micro-nutrients or macro-nutrients. To be successful, the additional carbon needs to reach the deep ocean where it has the potential to be sequestered on climatically-relevant timescales. See also *Anthropogenic removals* and *Carbon dioxide removal (CDR)*.

Ocean heat uptake efficiency This is a measure ($W\ m^{-2}\ °C^{-1}$) of the rate at which heat storage by the global ocean increases as global surface temperature rises. It is a useful parameter for *climate change* simulations in which the *radiative forcing* is changing monotonically, when it can be compared with the c*limate feedback parameter* to gauge the relative importance of radiative response and ocean heat *uptake* in determining the rate of *climate change*. It can be estimated from such an experiment as the ratio of the rate of increase of ocean heat content to the surface temperature change.

Ocean stratification See *Stratification*.

Orbital forcing Orbital *forcing* is the influence of slow, systematic and predictable changes in orbital parameters (eccentricity, obliquity and precession of the equinox) on incoming solar radiation (*insolation*), especially its latitudinal and seasonal distribution. It is an *external forcing* and a key driver of *glacial-interglacial cycles*.

Organic aerosol Component of the *aerosol* that consists of organic compounds, mainly carbon, hydrogen, oxygen and lesser amounts of other elements.

Outgoing longwave radiation Net outgoing radiation in the infrared part of the spectrum at the top of the *atmosphere*.

Outlet glacier See *Glacier*.

Oxygen minimum zone (OMZ) The midwater layer (200–1000 m) in the open ocean in which oxygen saturation is the lowest in the ocean. The degree of oxygen depletion depends on the largely bacterial consumption of organic matter and the distribution of the OMZs is influenced by large-scale ocean circulation. In coastal oceans, OMZs extend to the shelves and may also affect benthic ecosystems.

Ozone (O_3) The triatomic form of oxygen, and a gaseous *atmospheric* constituent. In the troposphere, O_3 is created both naturally and by photochemical reactions involving gases resulting from human activities (e.g., smog). Tropospheric O_3 acts as a *greenhouse gas (GHG)*. In the stratosphere, O_3 is created by the interaction between solar ultraviolet radiation and molecular oxygen (O_2). Stratospheric O_3 plays a dominant role in the stratospheric radiative balance. Its concentration is highest in the ozone layer. See also *Ground-level ozone*, *Ozone hole*, *Ozone layer*, *Ozone-depleting substances (ODSs)*, *Ozonesonde* and *Short-lived climate forcers (SLCFs)*.

Ozone layer The ozone layer is a layer of Earth's *stratosphere* that absorbs most of the Sun's ultraviolet radiation. It contains high concentrations of *ozone (O_3)* in relation to other parts of the *atmosphere*, although still small in relation to other gases in the stratosphere. The ozone layer contains less than 10 parts per million of ozone, while the average ozone concentration in Earth's atmosphere as a whole is about 0.3 parts per million. The ozone layer is mainly found in the lower portion of the stratosphere, from approximately 15 to 35 kilometres (9.3 to 21.7 miles) above Earth, although its thickness varies seasonally and geographically. See also *Ozone hole* and *Ozone-depleting substances (ODSs)*.

Ozone-depleting substances (ODSs) Ozone-depleting substances (ODSs) are man-made gases that destroy *ozone (O_3)* once they reach the *ozone layer* in the *stratosphere*. Ozone depleting substances include: *chlorofluorocarbons (CFCs)*, hydrochlorofluorocarbons (HCFCs), hydrobromofluorocarbons (HBFCs), halons, methyl bromide, carbon tetrachloride and methyl chloroform. They are used as refrigerants in commercial, home and vehicle air conditioners and refrigerators, foam blowing agents, components in

ACCEPTED VERSION SUBJECT TO FINAL EDITS

electrical equipment, industrial solvents, solvents for cleaning (including dry cleaning), aerosol spray propellants and fumigants. See also *Ozone layer*, *Ozone (O_3)* and *Stratospheric ozone*.

Ozonesonde An ozonesonde is a radiosonde measuring *ozone (O_3)* concentrations. The radiosonde is usually carried on a weather balloon and transmits measured quantities by radio to a ground-based receiver.

Pacific Decadal Oscillation (PDO) See *Pacific Decadal Variability (PDV)*.

Pacific Decadal Variability (PDV) Coupled decadal-to-interdecadal variability of the atmospheric circulation and underlying ocean that is typically observed over the entire Pacific Basin beyond the *El Niño-Southern Oscillation (ENSO)* timescale. In the AR6 WGI report, PDV encapsulates the *Pacific Decadal Oscillation (PDO)*, the South Pacific Decadal Oscillation (SPDO), tropical Pacific decadal variability (also called decadal ENSO), and the Interdecadal Pacific Oscillation (IPO). Typically, the positive phase of the PDV is characterized by anomalously high *sea surface temperatures* in the central-eastern tropical Pacific that extend to the extratropical North and South Pacific along the American coasts, encircled to the west by cold sea surface anomalies in the mid-latitude North and South Pacific. The negative phase is accompanied by sea surface temperature anomalies in the opposite sign. Those sea surface temperature anomalies are linked to anomalies in atmospheric and oceanic circulation throughout the whole Pacific Basin. The PDV is associated with decadal modulations in the relative occurrence of El Niño and La Niña. See Section AIV.2.6 in Annex IV of the AR6 WGI report.

Interdecadal Pacific Oscillation (IPO) An equatorially symmetric pattern of *sea surface temperature* variability at decadal-to-interdecadal timescales. While the *Pacific Decadal Oscillation (PDO)* and its South Pacific counterpart, the South Pacific Decadal Oscillation (SPDO), are considered as physically distinct modes, the tropical Pacific decadal-interdecadal variability can drive both the PDO and SPDO, forming the IPO as a synchronized pan-Pacific variability. Its spatial pattern of sea surface temperature anomalies is similar to that of the *El Niño-Southern Oscillation (ENSO)*, but with a broader meridional extent in the tropical signal and more weights in the extratropics compared to the tropics. In the AR6 WGI report, it is encapsulated within the definition and description of the *Pacific Decadal Variability (PDV)*. See also Section AIV.2.6 in Annex IV of the AR6 WGI report.

Pacific Decadal Oscillation (PDO) The leading mode of variability obtained from decomposition in empirical orthogonal function of *sea surface temperature* over the North Pacific north of 20°N, and characterized by a strong decadal component. The positive phase of the PDO features a dipole of sea surface temperature anomalies in the North Pacific, with a cold lobe near the center of the basin and extending westward along the Kuroshio, encircled by warmer conditions along the coast of North America and in the subtropics. A positive PDO is accompanied by an intensified Aleutian Low and an associated cyclonic circulation enhancement leading to *teleconnections* over the continents adjacent to the North Pacific. In AR6 WGI report, the PDO is encapsulated within the definition and description of *Pacific Decadal Variability (PDV)*. See also Section AIV.2.6 in Annex IV of the AR6 WGI report.

Pacific-North American (PNA) pattern An atmospheric large-scale wave pattern featuring a sequence of tropospheric high and low pressure anomalies stretching from the subtropical west Pacific to the east coast of North America. See also *Pacific-South American (PSA) pattern*.

Palaeocene-Eocene Thermal Maximum (PETM) The PETM is a transient event that occurred between 55.9 and 55.7 million years ago. Continental positions at this time were somewhat different to present due to tectonic plate movements. Geological data indicate that the PETM was characterised by a warming (*global mean surface temperature* rose to about 4-7 °C warmer than the preceding mean state), and an increase in atmospheric CO_2 (from about 900 to about 2000 ppmv). In addition, ocean *pH* and oxygen content decreased; many deep-sea species went extinct and tropical *coral reefs* diminished.

Paleoclimate Climate during periods prior to the development of measuring instruments, including historic and geologic time, for which only *proxy* climate records are available.

ACCEPTED VERSION SUBJECT TO FINAL EDITS

Parameterisation In *climate models*, this term refers to the technique of representing processes that cannot be explicitly resolved at the spatial or temporal *resolution* of the model (sub-grid scale processes) by relationships between model-resolved larger-scale variables and the area- or time-averaged effect of such subgrid scale processes.

Pathways The temporal evolution of natural and/or human systems towards a future state. Pathway concepts range from sets of quantitative and qualitative *scenarios* or *narratives* of potential futures to solution-oriented decision-making processes to achieve desirable societal goals. Pathway approaches typically focus on biophysical, techno-economic, and/or socio-behavioural trajectories and involve various dynamics, goals, and actors across different scales. See also *Scenario storyline* (under *Storyline*), *Mitigation scenario* (under *Scenario*), *Baseline scenario* (under *Scenario*) and *Stabilisation (of GHG or CO_2-equivalent concentration)*.

1.5°C pathway A pathway of emissions of greenhouse gases and other climate forcers that provides an approximately one-in-two to two-in-three chance, given current knowledge of the climate response, of global warming either remaining below 1.5°C or returning to 1.5°C by around 2100 following an overshoot.

Representative concentration pathways (RCPs) *Scenarios* that include time series of *emissions* and concentrations of the full suite of *greenhouse gases (GHGs)* and *aerosols* and chemically active gases, as well as *land use*/*land cover* (Moss et al., 2010). The word representative signifies that each RCP provides only one of many possible scenarios that would lead to the specific *radiative forcing* characteristics. The term pathway emphasises that not only the long-term concentration levels are of interest, but also the trajectory taken over time to reach that outcome (Moss et al., 2010).

RCPs usually refer to the portion of the concentration pathway extending up to 2100, for which *Integrated assessment models* produced corresponding emission scenarios. Extended concentration pathways describe extensions of the RCPs from 2100 to 2300 that were calculated using simple rules generated by stakeholder consultations, and do not represent fully consistent scenarios. Four RCPs produced from Integrated assessment models were selected from the published literature and are used in the Fifth IPCC Assessment and also used in this Assessment for comparison, spanning the range from approximately below 2°C warming to high (>4°C) warming best-estimates by the end of the 21st century: RCP2.6, RCP4.5 and RCP6.0 and RCP8.5.

- RCP2.6: One pathway where radiative forcing peaks at approximately 3 W m^{-2} and then declines to be limited at 2.6 W m^{-2} in 2100 (the corresponding Extended Concentration Pathway, or ECP, has constant emissions after 2100).
- RCP4.5 and RCP6.0: Two intermediate stabilisation pathways in which radiative forcing is limited at approximately 4.5 W m^{-2} and 6.0 W m^{-2} in 2100 (the corresponding ECPs have constant concentrations after 2150).
- RCP8.5: One high pathway which leads to >8.5 W m^{-2} in 2100 (the corresponding ECP has constant emissions after 2100 until 2150 and constant concentrations after 2250).

See also *Coupled Model Intercomparison Project (CMIP)* and *Shared socio-economic pathways (SSPs)* (under *Pathways*).

Shared socio-economic pathways (SSPs) Shared socio-economic pathways (SSPs) have been developed to complement the *Representative concentration pathways (RCPs)*. By design, the RCP emission and concentration pathways were stripped of their association with a certain socio-economic development. Different levels of *emissions* and *climate change* along the dimension of the RCPs can hence be explored against the backdrop if different socio-economic development pathways (SSPs) on the other dimension in a matrix. This integrative SSP-RCP framework is now widely used in the climate *impact* and policy analysis literature, where *climate projections* obtained under the RCP scenarios are analysed against the backdrop of various SSPs. As several emission updates were due, a new set of emission scenarios was developed in conjunction with the SSPs. Hence, the abbreviation SSP is now used for two things: On the one hand SSP1, SSP2, …, SSP5 is used to denote the five socio-economic scenario families. On the other hand, the

ACCEPTED VERSION SUBJECT TO FINAL EDITS

abbreviations SSP1-1.9, SSP1-2.6, …, SSP5-8.5 are used to denote the newly developed emission scenarios that are the result of an SSP implementation within an integrated assessment model. Those SSP scenarios are bare of climate policy assumption, but in combination with so-called shared policy assumptions (SPAs), various approximate *radiative forcing* levels of 1.9, 2.6, …, or 8.5 W m^{-2} are reached by the end of the century, respectively.

Pattern scaling Techniques used to represent the spatial variations in *climate* at a given increase in *global mean surface air temperature (GSAT)* are referred to as 'pattern scaling'.

Peat Soft, porous or compressed, sedimentary deposit of which a substantial portion is partly decomposed plant material with high water content in the natural state (up to about 90%).

Peatlands Peatland is a land where soils are dominated by *peat*.

Percentile A partition value in a population distribution that a given percentage of the data values are below or equal to. The 50th percentile corresponds to the median of the population. Percentiles are often used to estimate the extremes of a distribution. For example, the 90th (10th) percentile may be used to refer to the threshold for the upper (lower) extremes.

Permafrost Ground (soil or rock, and included ice and organic material) that remains at or below 0°C for at least two consecutive years (Harris et al., 1988). Note that permafrost is defined via temperature rather than ice content and, in some instances, may be ice-free.

Near-surface permafrost Permafrost within ~3-4 m of the ground surface. The depth is not precise, but describes what commonly is highly relevant for people and *ecosystems*. Deeper permafrost is often progressively less ice-rich and responds more slowly to warming than near-surface permafrost. Presence or absence of near-surface permafrost is not the only significant metric of permafrost change, and deeper permafrost may persist when near-surface permafrost is absent.

Permafrost degradation Decrease in the thickness and/or areal extent of permafrost.

Permafrost thaw Progressive loss of ground ice in permafrost, usually due to input of heat. Thaw can occur over decades to centuries over the entire depth of permafrost ground, with impacts occurring while thaw progresses. During thaw, temperature fluctuations are subdued because energy is transferred by phase change between ice and water. After the transition from permafrost to non-permafrost, ground can be described as thawed.

Perturbed parameter ensemble See *Model ensemble*.

pH A dimensionless measure of the acidity of a solution given by its concentration of hydrogen ions (H^+). pH is measured on a logarithmic scale where $pH = -\log_{10}(H^+)$. Thus, a pH decrease of 1 unit corresponds to a 10-fold increase in the concentration of H^+, or acidity.

Phenology The relationship between biological phenomena that recur periodically (e.g., development stages, migration) and *climate* and seasonal changes.

Photosynthesis The production of carbohydrates in plants, algae and some bacteria using the energy of light. Carbon dioxide (CO_2) is used as the carbon source.

Physical climate storyline See *Storyline*.

Piacenzian warm period See *Pliocene*.

Plankton Microorganisms living in the upper layers of aquatic systems. A distinction is made between phytoplankton, which depend on *photosynthesis* for their energy supply, and zooplankton, which feed on

ACCEPTED VERSION SUBJECT TO FINAL EDITS

phytoplankton.

Plant evaporative stress Plant evaporative stress in both crops and natural vegetation can result from the combination of a high atmospheric evaporative demand and limited available water to supply this demand by means of evapotranspiration, further enhancing *agricultural or ecological drought*.

Pleistocene The Pleistocene Epoch is the earlier of two epochs in the *Quaternary* System, extending from 2.59 Ma to the beginning of the *Holocene* at 11.65 ka.

Pliocene The Pliocene Epoch is the more recent of two epochs of the Neogene Period within the *Cenozoic Era*. It extends from 5.33 Ma to the beginning of the *Pleistocene* Epoch at 2.59 Ma. The Neogene Period precedes the current geological period, the *Quaternary* Period, which is one of several ice ages that have occurred during Earth's geological history. It encompasses the mid-Pliocene warm period (MPWP), also known as the Piacenzian warm period, which occurred approximately 3.3 to 3.0 Ma. The MPWP, in turn, encompasses the interglacial episode, marine isotope stage (MIS) KM5c, which peaked at 3.205 Ma, when orbital forcing was similar to modern (Haywood et al., 2016).

Polar amplification Polar amplification describes the phenomenon where surface temperature change at high latitudes exceeds the global average surface temperature change. The terms Arctic Amplification or Antarctic Amplification are used when describing the phenomenon occurring at one of the poles.

Pollen analysis A technique of both relative dating and environmental *reconstruction*, consisting of the identification and counting of pollen types preserved in peat, lake sediments and other deposits.

Post-glacial period See *Holocene*.

Potential evapotranspiration See *Evapotranspiration*.

Pre-industrial (period) The multi-century period prior to the onset of large-scale industrial activity around 1750. The *reference period* 1850–1900 is used to approximate pre-industrial *global mean surface temperature (GMST)*. See also *Industrial revolution*.

Precipitable water The total amount of atmospheric water vapour in a vertical column of unit cross-sectional area. It is commonly expressed in terms of the height of the water if completely condensed and collected in a vessel of the same unit cross section.

Precursors Atmospheric compounds that are not *greenhouse gases (GHGs)* or *aerosols*, but that have an effect on GHG or aerosol concentrations by taking part in physical or chemical processes regulating their production or destruction rates.

Predictability The extent to which future states of a system may be predicted based on knowledge of current and past states of the system. Because knowledge of the climate system's past and current states is generally imperfect, as are the models that utilize this knowledge to produce a *climate prediction*, and because the *climate system* is inherently nonlinear and chaotic, predictability of the climate system is inherently limited. Even with arbitrarily accurate models and observations, there may still be limits to the predictability of such a nonlinear system (AMS, 2021).

Prediction quality/skill Measures of the success of a prediction against observationally based information. No single measure can summarize all aspects of forecast quality and a suite of *metrics* is considered. Metrics will differ for forecasts given in deterministic and probabilistic form.

Primary production The synthesis of organic compounds by plants and microbes, on land or in the ocean, primarily by photosynthesis using light and carbon dioxide (CO_2) as sources of energy and carbon respectively. It can also occur through chemosynthesis, using chemical energy, e.g., in deep sea vents.

ACCEPTED VERSION SUBJECT TO FINAL EDITS

Gross Primary Production (GPP) The total amount of carbon fixed by photosynthesis over a specified time period.

Net primary production (NPP) The amount of carbon fixed by photosynthesis minus the amount lost by respiration over a specified time period.

Probability density function (PDF) A probability density function is a function that indicates the relative chances of occurrence of different outcomes of a variable. The function integrates to unity over the domain for which it is defined and has the property that the integral over a sub-domain equals the probability that the outcome of the variable lies within that sub-domain. For example, the probability that a temperature anomaly defined in a particular way is greater than zero is obtained from its PDF by integrating the PDF over all possible temperature anomalies greater than zero. Probability density functions that describe two or more variables simultaneously are similarly defined.

Process-based model Theoretical concepts and computational methods that represent and simulate the behaviour of real-world systems derived from a set of functional components and their interactions with each other and the system environment, through physical and mechanistic processes occurring over time.

Projection A potential future evolution of a quantity or set of quantities, often computed with the aid of a model. Unlike predictions, projections are conditional on assumptions concerning, for example, future socio-economic and technological developments that may or may not be realised. See also *Climate projection*, *Pathways* and *Scenario*.

Proxy A proxy *climate indicator* is any biophysical property of materials formed during the past that is interpreted to represent some combination of climate-related variations back in time. Climate-related data derived in this way are referred to as proxy data and time series of proxy data are proxy records. Examples of proxy types include pollen assemblages, *tree ring* widths, speleothem and coral geochemistry, and various data derived from marine sediments and glacier ice. Proxy data can be calibrated to provide quantitative climate information.

Proxy records See *Proxy*.

Quasi-Biennial Oscillation (QBO) A near-periodic oscillation of the equatorial zonal wind between easterlies and westerlies in the tropical *stratosphere* with a mean period of around 28 months. The alternating wind maxima descend from the base of the mesosphere down to the *tropopause*, and are driven by wave energy that propagates up from the *troposphere*.

Quaternary The Quaternary Period is the last of three periods that make up the Cenozoic Era (66 Ma to present), extending from 2.58 Ma to the present, and includes the *Pleistocene* and *Holocene* Epochs.

Radiative effect The impact on a radiation flux or heating rate (most commonly, on the downward flux at the top of *atmosphere*) caused by the interaction of a particular constituent with either the *infrared* or *solar radiation* fields through absorption, scattering and emission, relative to an otherwise identical *atmosphere* free of that constituent. This quantifies the impact of the constituent on the *climate system*. Examples include the *aerosol-radiation interactions*, *cloud radiative effect*, and *greenhouse effect*. In this report, the portion of any top-of-atmosphere radiative effect that is due to *anthropogenic* or other external influences (e.g., volcanic eruptions or changes in the sun) is termed the instantaneous *radiative forcing*.

Radiative forcing The change in the net, downward minus upward, radiative flux (expressed in W m^{-2}) due to a change in an external *driver* of *climate change*, such as a change in the concentration of *carbon dioxide (CO_2)*, the concentration of volcanic *aerosols* or in the output of the Sun. The stratospherically adjusted radiative forcing is computed with all tropospheric properties held fixed at their unperturbed values, and after allowing for stratospheric temperatures, if perturbed, to readjust to radiative-dynamical equilibrium. Radiative forcing is called instantaneous if no change in stratospheric temperature is accounted for. The radiative forcing once both stratospheric and tropospheric adjustments are accounted for is termed

ACCEPTED VERSION SUBJECT TO FINAL EDITS

the effective radiative forcing.

Rapid adjustment The response to an agent perturbing the *climate system* that is driven directly by the agent, independently of any change in the *global mean surface temperature*. For example, *carbon dioxide* and *aerosols*, by altering internal heating and cooling rates within the *atmosphere*, can each cause changes to cloud cover and other variables thereby producing a *radiative effect* even in the absence of any surface warming or cooling. Adjustments are rapid in the sense that they begin to occur right away, before *climate feedbacks* which are driven by warming (although some adjustments may still take significant time to proceed to completion, for example those involving vegetation or *ice sheets*). It is also called the rapid response or fast adjustment.

Rapid climate change See *Abrupt change / abrupt climate change*.

Rapid dynamical change (of glaciers or ice sheets) Changes in *glacier* or *ice sheet* mass controlled by changes in flow speed and discharge rather than by *accumulation* or ablation. This can result in a rate of mass change larger than that due to any imbalance between accumulation and ablation. Rapid dynamical change may be initiated by a climatic trigger, such as incursion of warm ocean water beneath an *ice shelf*, or thinning of a grounded tidewater terminus, which may lead to reactions within the glacier system, that may result in rapid ice loss.

Reanalysis Reanalyses are created by processing past meteorological or oceanographic data using fixed state-of-the-art weather forecasting or ocean circulation models with *data assimilation* techniques. They are used to provide estimates of variables such as historical atmospheric temperature and wind or oceanographic temperature and currents, and other quantities. Using fixed data assimilation avoids effects from the changing analysis system that occur in operational analyses. Although continuity is improved, global reanalyses still suffer from changing coverage and biases in the observing systems.

Reasons for concern (RFCs) Elements of a classification framework, first developed in the IPCC Third Assessment Report, which aims to facilitate judgments about what level of climate change may be dangerous (in the language of Article 2 of the UNFCCC) by aggregating risks from various sectors, considering hazards, exposures, vulnerabilities, capacities to adapt, and the resulting impacts.

Reconstruction (of climate variable) Approach to reconstructing the past temporal and spatial characteristics of a *climate* variable from predictors. The predictors can be instrumental data if the reconstruction is used to infill missing data or *proxy* data if it is used to develop *paleoclimate* reconstructions. Various techniques have been developed for this purpose: linear multivariate regression based methods and nonlinear *Bayesian* and analogue methods.

Reference period The period relative to which *anomalies* are computed. See also *Baseline/reference (period)*.

Baseline period The period relative to which *anomalies* are computed. See also *Baseline/reference (period)*.

Reference scenario See *Scenario*.

Reforestation Conversion to forest of land that has previously contained forests but that has been converted to some other use. [Note: For a discussion of the term forest and related terms such as afforestation, reforestation and deforestation, see the 2006 IPCC Guidelines for National Greenhouse Gas Inventories and their 2019 Refinement, and information provided by the United Nations Framework Convention on Climate Change (IPCC, 2006, 2019, UNFCCC, 2021a, 2021b).] See also *Afforestation*, *Deforestation*, *Reducing Emissions from Deforestation and Forest Degradation (REDD+)*, *Anthropogenic removals* and *Carbon dioxide removal (CDR)*.

Region *Land* and/or *ocean* area characterised by specific geographical and/or climatological features. The

ACCEPTED VERSION SUBJECT TO FINAL EDITS

climate of a region emerges from a multiscale combination of its own features, remote influences from other regions, and global climate conditions.

Regional climate messages Regional climate messages translate *climate information* synthesized from different lines of *evidence* into the context of a user *vulnerable* to climate at regional scales taking into account the values of both the producer and user (WGI Section 10.5).

Regional climate model (RCM) A *climate model* at higher *resolution* over a limited area. Such models are used in *downscaling* global *climate* results over specific regional domains.

Regional climate scenario A narrative used to describe how the future might unfold for a region (IPCC-TGICA, 2007). These are often used to guide impact understanding and adaptation efforts. They can include quantitative information based on scaled historical data or derived from GCM-based internally consistent future climates. See also *Climate scenario*.

Regional sea level change See *Sea level change (sea level rise/sea level fall)*.

Relative humidity The relative humidity specifies the ratio of actual water vapour pressure to that at saturation with respect to liquid water or ice at the same temperature. See also *Specific humidity*.

Relative sea-level (RSL) change See *Sea level change (sea level rise/sea level fall)*.

Remaining carbon budget See *Carbon budget*.

Representative concentration pathways (RCPs) See *Pathways*.

Reservoir A component or components of the climate system where a *greenhouse gas (GHG)* or a *precursor* of a greenhouse gas is stored (UNFCCC Article 1.7 (UNFCCC, 1992)).

Resilience The capacity of interconnected social, economic and ecological systems to cope with a hazardous event, trend or disturbance, responding or reorganising in ways that maintain their essential function, identity and structure. Resilience is a positive attribute when it maintains capacity for adaptation, learning and/or transformation (Arctic Council, 2016). See also *Hazard*, *Risk* and *Vulnerability*.

Resolution In *climate models*, this term refers to the physical distance (metres or degrees) between each point on the grid used to compute the equations. Temporal resolution refers to the time step or time elapsed between each model computation of the equations.

Respiration The process whereby living organisms convert organic matter to *carbon dioxide (CO_2)*, releasing energy and consuming molecular oxygen.

Response time or adjustment time In the context of climate variations, the response time or adjustment time is the time needed for the *climate system* or its components to re-equilibrate to a new state, following a forcing resulting from external processes. It is very different for various components of the climate system. The response time of the *troposphere* is relatively short, from days to weeks, whereas the *stratosphere* reaches equilibrium on a time scale of typically a few months. Due to their large heat capacity, the oceans have a much longer response time: typically decades, but up to centuries or millennia. The response time of the strongly coupled surface-troposphere system is, therefore, slow compared to that of the stratosphere, and mainly determined by the oceans. The *biosphere* may respond quickly (e.g., to *droughts*), but also very slowly to imposed changes.

In the context of *lifetimes*, response time or adjustment time (T_a) is the time scale characterizing the decay of an instantaneous pulse input into the *reservoir*. See *Response time or adjustment time (Ta)* under *Lifetime*.

Return period An estimate of the average time interval between occurrences of an event (e.g., flood or

ACCEPTED VERSION SUBJECT TO FINAL EDITS

extreme rainfall) of (or below/above) a defined size or intensity.

Return value The highest (or, alternatively, lowest) value of a given variable, on average occurring once in a given period of time (e.g., in 10 years).

Risk The potential for adverse consequences for human or ecological systems, recognising the diversity of values and objectives associated with such systems. In the context of *climate change*, risks can arise from potential *impacts* of climate change as well as human responses to climate change. Relevant adverse consequences include those on lives, *livelihoods*, health and *well-being*, economic, social and cultural assets and investments, infrastructure, services (including *ecosystem services*), *ecosystems* and species.

In the context of climate change impacts, risks result from dynamic interactions between climate-related *hazards* with the *exposure* and *vulnerability* of the affected human or ecological system to the hazards. Hazards, exposure and vulnerability may each be subject to uncertainty in terms of magnitude and *likelihood* of occurrence, and each may change over time and space due to socio-economic changes and human decision-making (see also *risk management*, *adaptation* and *mitigation*).

In the context of climate change responses, risks result from the potential for such responses not achieving the intended objective(s), or from potential trade-offs with, or negative side-effects on, other societal objectives, such as the *Sustainable Development Goals (SDGs)* (see also *risk trade-off*). Risks can arise for example from uncertainty in implementation, effectiveness or outcomes of *climate policy*, climate-related investments, technology development or adoption, and system transitions. See also *Hazard* and *Impacts (consequences, outcomes)*.

Risk assessment The qualitative and/or quantitative scientific estimation of *risks*. See also *Risk management* and *Risk perception*.

Risk framework A common framework for describing and assessing risk across all three working groups is adopted to promote clear and consistent communication of risks and to better inform risk assessment and decision making related to climate change.

Risk management Plans, actions, strategies or policies to reduce the *likelihood* and/or magnitude of adverse potential consequences, based on assessed or perceived *risks*. See also *Risk assessment*, *Risk perception* and *Risk transfer*.

Risk perception The subjective judgment that people make about the characteristics and severity of a *risk*. See also *Risk assessment*, *Risk management* and *Risk transfer*.

Risk trade-off The change in the portfolio of *risks* that occurs when a countervailing risk is generated (knowingly or inadvertently) by an intervention to reduce the target risk (Wiener and Graham, 2009).

River discharge See *Streamflow*.

Rock glacier A debris landform (mass of rock fragments and finer material that contains either an ice core or an ice-cemented matrix) generated by a former or current gravity-driven creep of *permafrost* in mountain slopes (Harris et al., 1988; Giardino et al., 2011; IPA-RG, 2020). It is detectable in the landscape due to the occurrence of (i) a steep slope delimiting the terminal part; (2) generally well-defined lateral margins in a continuation of the front; (3) transversal or longitudinal ridges and furrows (ridge and furrow topography). These are geomorphological indicators of the occurrence of permafrost conditions. Although it is an ice storage feature, it is not a type of glacier since it is not originated over the surface by the recrystallization of snow.

Runoff The flow of water over the surface or through the subsurface, which typically originates from the part of liquid precipitation and/or snow/ice melt that does not evaporate, transpire or refreeze, and returns to water bodies.

ACCEPTED VERSION SUBJECT TO FINAL EDITS

Sampling uncertainty See *Uncertainty*.

Scenario A plausible description of how the future may develop based on a coherent and internally consistent set of assumptions about key driving forces (e.g., rate of technological change (TC), prices) and relationships. Note that scenarios are neither predictions nor forecasts, but are used to provide a view of the implications of developments and actions. See also *Climate scenario* and *Regional climate scenario*.

Baseline scenario See Reference ScenarioSee *Reference scenario* (under *Scenario*).

Concentrations scenario A plausible representation of the future development of atmospheric concentrations of substances that are radiatively active (e.g., *greenhouse gases (GHGs)*, *aerosols*, tropospheric *ozone*), plus human-induced *land cover changes* that can be radiatively active via *albedo* changes, and often used as input to a *climate model* to compute *climate projections.*

Emissions scenario A plausible representation of the future development of emissions of substances that are radiatively active (e.g., *greenhouse gases (GHGs)* or *aerosols*), plus human-induced land cover changes that can be radiatively active via albedo changes, based on a coherent and internally consistent set of assumptions about driving forces (such as demographic and socio-economic development, technological change, energy and *land use*) and their key relationships. *Concentration scenarios*, derived from emission scenarios, are often used as input to a *climate model* to compute *climate projections*. See also *Representative concentration pathways (RCPs)* (under *Pathways*) and *Shared socio-economic pathways (SSPs)* (under *Pathways*).

Mitigation scenario A plausible description of the future that describes how the (studied) system responds to the implementation of *mitigation* policies and measures. See also *Pathways, Socio-economic scenario* (under *Scenario*) and *Stabilisation (of GHG or CO_2-equivalent concentration)*.

Reference scenario Scenario used as starting or reference point for a comparison between two or more scenarios.

[Note 1: In many types of climate change research, reference scenarios reflect specific assumptions about patterns of socio-economic development and may represent futures that assume no climate policies or specified climate policies, for example those in place or planned at the time a study is carried out. Reference scenarios may also represent futures with limited or no climate impacts or adaptation, to serve as a point of comparison for futures with impacts and adaptation. These are also referred to as baseline scenarios in the literature.

Note 2: Reference scenarios can also be climate policy or impact scenarios, which in that case are taken as a point of comparison to explore the implications of other features, e.g., of delay, technological options, policy design and strategy or to explore the effects of additional impacts and adaptation beyond those represented in the reference scenario.

Note 3: The term business as usual scenario has been used to describe a scenario that assumes no additional policies beyond those currently in place and that patterns of socio-economic development are consistent with recent trends. The term is now used less frequently than in the past.

Note 4: In climate change attribution or impact attribution research reference scenarios may refer to counterfactual historical scenarios assuming no anthropogenic greenhouse gas emissions (climate change attribution) or no climate change (impact attribution).]

Socio-economic scenario A scenario that describes a plausible future in terms of population, *gross domestic product (GDP)*, and other socio-economic factors relevant to understanding the implications of *climate change*. See also *Baseline scenario* (under *Scenario*), *Mitigation scenario* (under *Scenario*) and *Pathways*.

ACCEPTED VERSION SUBJECT TO FINAL EDITS

Scenario storyline See *Storyline*.

Sea ice Ice found at the sea surface that has originated from the freezing of seawater. Sea ice may be discontinuous pieces (ice floes) moved on the *ocean* surface by wind and currents (pack ice), or a motionless sheet attached to the *coast* (land-fast ice). Sea ice concentration is the fraction of the ocean covered by ice. Sea ice less than one year old is called first-year ice. Perennial ice is sea ice that survives at least one summer. It may be subdivided into second-year ice and multi-year ice, where multiyear ice has survived at least two summers.

Sea ice area (SIA) Sea ice area is the area covered by sea ice. In contrast to *sea ice extent*, it is a linear measure of sea ice coverage that does not depend on grid resolution.

Sea ice concentration Sea ice concentration is the fraction of the ocean covered by ice.

Sea ice extent (SIE) Sea ice extent is calculated for gridded data products as the total area of all grid cells with *sea ice concentration* above a given threshold, usually 15 %. It hence is a grid-dependent, non-linear measure of sea ice coverage.

Sea level change (sea level rise/sea level fall) Change to the height of sea level, both globally and locally (*relative sea level* change) at seasonal, annual, or longer time scales due to (1) a change in *ocean* volume as a result of a change in the mass of water in the ocean (e.g., due to melt of *glaciers* and *ice sheets*), (2) changes in ocean volume as a result of changes in ocean water density (e.g., expansion under warmer conditions), (3) changes in the shape of the ocean basins and changes in the Earth's gravitational and rotational fields, and (4) local subsidence or uplift of the *land*. *Global mean sea level change* resulting from change in the mass of the ocean is called barystatic. The amount of barystatic sea level change due to the addition or removal of a mass of water is called its *sea level equivalent (SLE)*. Sea level changes, both globally and locally, resulting from changes in water density are called steric. Density changes induced by temperature changes only are called thermosteric, while density changes induced by salinity changes are called halosteric. Barystatic and steric sea level changes do not include the effect of changes in the shape of ocean basins induced by the change in the ocean mass and its distribution. See also *Vertical land motion (VLM)*, *Land water storage*, *Sea level commitment*, *Glacial isostatic adjustment (GIA)*, *Extreme sea level (ESL)* and *Storm surge*.

Geocentric sea-level change The change in local mean sea surface height with respect to the terrestrial reference frame, it is the sea-level change observed with instruments from space. See also *Altimetry*.

Global mean sea-level (GMSL) change The increase or decrease in the volume of the ocean divided by the ocean surface area. It is the sum of changes in ocean density through temperature changes (global mean *thermosteric sea-level change*) and changes in the ocean mass as a result of changes in the cryosphere or land water storage (barystatic sea-level change). See also *Terrestrial water storage (TWS)*.

Gravitational, rotational and deformational (GRD) effects Changes in Earth Gravity, Earth Rotation and viscoelastic solid Earth Deformation (GRD) result from the redistribution of mass between terrestrial ice and water reservoirs and the ocean. Contemporary terrestrial mass loss leads to elastic solid Earth uplift and a nearby relative sea-level fall (for a single source of terrestrial mass loss this is within ~2000 km, for multiple sources the distance depends on the interaction of the different relative sea-level patterns). Farther away (more than ~7000 km for a single source of terrestrial mass loss), relative sea level rises more than the global average, due, to first order, to gravitational effects. Earth deformation associated with adding water to the oceans and a shift of the Earth's rotation axis towards the source of terrestrial mass loss leads to second-order effects that increase spatial variability of the pattern globally. GRD effects due to the redistribution of ocean water within the ocean itself are referred to as self-attraction and loading effects.

Halosteric sea-level change Halosteric sea-level change occurs as a result of salinity variations: higher salinity leads to higher density and decreases the volume per unit of mass. Although both processes can be relevant on regional to local scales, only thermosteric changes impact the *global mean sea-level change*, whereas the global mean halosteric change is negligible (Gregory et al., 2019).

ACCEPTED VERSION SUBJECT TO FINAL EDITS

Local sea level change Change in sea level relative to a datum (such as present-day mean sea level) at spatial scales smaller than 10 km.

Ocean dynamic sea level change Change in mean sea level relative to the geoid associated with circulation and density-driven changes in the ocean. Ocean dynamic sea-level change is regionally varying but by definition has a zero global mean and conventionally is inverse-barometer corrected (i.e., the effect of the hydrostatic depression of the sea surface by atmospheric pressure changes is removed). Changes in ocean currents occur due to variations in heating and cooling, variability in winds and changes in seasonally- to annually-averaged air temperature and humidity.

Regional sea level change Change in sea level relative to a datum (such as present-day *mean sea level*) at spatial scales of about 100 km.

Relative sea-level (RSL) change The change in local mean *sea surface height (SSH)* relative to the local solid surface, i.e. the sea floor, as measured by instruments that are fixed to the Earth's surface, such as *tide gauges*. This reference frame is used when considering coastal *impacts*, *hazards* and *adaptation* needs.

Steric sea level change Steric sea-level change is caused by changes in the ocean density and is composed of *thermosteric sea-level change* and *halosteric sea-level change*.

Thermosteric sea-level change Thermosteric sea-level change (where thermosteric sea-level rise may also be referred to as thermal expansion) occurs as a result of changes in ocean temperature: increasing temperature reduces ocean density and increases the volume per unit of mass.

Sea level equivalent (SLE) The SLE of a mass of water, ice, or water vapour is that mass, converted to a volume using a density of 1000 kg m^{-3}, and divided by the present-day *ocean* surface area of 3.625 × 1000 m^2. Thus, 362.5 Gt of water mass added to the ocean correspond to 1 mm of global mean sea level rise. However, more accurate estimates of SLE must account for additional processes affecting mean sea level rise, such as shoreline migration, changes in ocean area, and for vertical land movements.

Sea level rise (SLR) See *Sea level change (sea level rise/sea level fall)*.

Sea surface temperature (SST) The subsurface bulk temperature in the top few metres of the ocean, measured by ships, buoys, and drifters. From ships, measurements of water samples in buckets were mostly switched in the 1940s to samples from engine intake water. Satellite measurements of skin temperature (uppermost layer; a fraction of a millimetre thick) in the infrared or the top centimetre or so in the microwave are also used, but must be adjusted to be compatible with the bulk temperature.

Semi-direct (aerosol) effect See *Aerosol-radiation interaction*.

Semi-empirical model Model in which calculations are based on a combination of observed associations between variables and theoretical considerations relating variables through fundamental principles (e.g., conservation of energy). For example, in sea level studies, semi-empirical models refer specifically to transfer functions formulated to project future *global mean sea level change*, or contributions to it, from future *global mean surface temperature* change or *radiative forcing*.

Sensible heat flux The turbulent or conductive flux of heat from the Earth's surface to the *atmosphere* that is not associated with phase changes of water; a component of the surface *energy budget*.

Sequestration The process of storing carbon in a carbon pool. See also *Uptake* and *Soil carbon sequestration (SCS)*.

Sequestration potential The quantity of greenhouse gases that can be removed from the atmosphere by anthropogenic enhancement of sinks and stored in a pool. See Mitigation potential for different subcategories

ACCEPTED VERSION SUBJECT TO FINAL EDITS

of sequestration potential. See also *Pool, carbon and nitrogen*, *Sequestration* and *Sink.*

Shared policy assumptions (SPAs) See *Shared socio-economic pathways (SSPs)* (under *Pathways*).

Shared socio-economic pathways (SSPs) See *Pathways*.

Short-lived climate forcers (SLCFs) A set of chemically reactive compounds with short (relative to CO_2) atmospheric lifetimes (from hours to decades) but characterised by different physiochemical properties and environmental effects. Their emission or formation has a significant effect on radiative forcing over a period determined by their respective atmospheric *lifetimes*. Changes in their *emissions* can also induce long-term *climate* effects via, in particular, their interactions with some biogeochemical cycles. SLCFs are classified as direct or indirect, with direct SLCFs exerting climate effects through their *radiative forcing* and indirect SLCFs being the *precursors* of other direct climate forcers. Direct SLCFs include *methane (CH_4)*, *ozone (O_3)*, primary *aerosols* and some halogenated species. Indirect SLCFs are precursors of ozone or secondary aerosols. SLCFs can be cooling or warming through interactions with radiation and clouds. They are also referred to as near-term climate forcers (NTCFs). Many SLCFs are also air pollutants. A subset of exclusively warming SLCFs is also referred to as short-lived climate pollutants (SLCPs), including methane, ozone, and black carbon.

Short-lived climate pollutants (SLCP) See *Short-lived climate forcers (SLCFs)*.

Shortwave radiation See *Solar radiation*.

Significant wave height The average trough-to-crest height of the highest one-third of the wave heights (sea and swell) occurring in a particular time period.

Simple climate model (SCM) A broad class of lower-dimensional models of the *energy balance*, radiative transfer, *carbon cycle*, or a combination of such physical components. SCMs are also suitable for performing *emulations* of climate-mean variables of *Earth system models (ESMs)*, given that their structural flexibility can capture both the parametric and structural uncertainties across process-oriented ESM responses. They can also be used to test consistency across multiple lines of evidence with regard to *climate sensitivity* ranges, *transient climate responses (TCRs)*, *transient climate response to cumulative emissions (TCREs)* and carbon cycle *feedbacks*. See also *Emulators* and *Earth system model of intermediate complexity (EMIC)*.

Sink Any process, activity or mechanism which removes a greenhouse gas, an aerosol or a precursor of a greenhouse gas from the atmosphere (UNFCCC Article 1.8 (UNFCCC, 1992)). See also *Source* and *Uptake*.

Small Island Developing States (SIDS) Small Island Developing States (SIDS), as recognised by the United Nations OHRLLS (Office of the High Representative for the Least Developed Countries, Landlocked Developing Countries and Small Island Developing States), are a distinct group of developing countries facing specific social, economic and environmental vulnerabilities (UN-OHRLLS, 2011). They were recognized as a special case both for their environment and development at the Rio Earth Summit in Brazil in 1992. Fifty-eight countries and territories are presently classified as SIDS by the UN OHRLLS, with 38 being UN member states and 20 being Non-UN Members or Associate Members of the Regional Commissions (UN-OHRLLS, 2018).

Snow cover Snow cover refers to all the snow that has accumulated on the ground at a given time (UNESCO/IASH/WMO, 1970).

Snow cover duration (SCD) How long snow continuously remains on the land surface, or the period between snow-on and snow-off dates.

Snow cover extent (SCE) The areal extent of snow covered ground.

Snow water equivalent (SWE) The depth of liquid water that would result if a mass of snow melted

ACCEPTED VERSION SUBJECT TO FINAL EDITS

completely.

Socio-economic scenario See *Scenario*.

Soil moisture Water stored in the soil in liquid or frozen form. Root-zone soil moisture is of most relevance for plant activity.

Soil temperature The temperature of the soil. This can be measured or modelled at multiple levels within the depth of the soil.

Solar activity General term collectively describing a variety of magnetic phenomena on the Sun such as *sunspots*, *faculae* (bright areas), and flares (emission of high-energy particles). It varies on time scales from minutes to millions of years. The *solar cycle*, with an average duration of 11 years, is an example of a quasi-regular change in solar activity.

Solar cycle (11-year) A quasi-regular modulation of *solar activity* with varying amplitude and a period of between 8 and 14 years.

Solar radiation Electromagnetic radiation emitted by the Sun with a spectrum close to the one of a black body with a temperature of 5770 K. The radiation peaks in visible wavelengths. When compared to the *terrestrial radiation* it is often referred to as shortwave radiation. See also *Insolation* and *Total solar irradiance (TSI)*.

Solar radiation modification (SRM) Solar radiation modification (SRM) refers to a range of radiation modification measures not related to greenhouse gas (GHG) mitigation that seek to limit global warming. Most methods involve reducing the amount of incoming solar radiation reaching the surface, but others also act on the longwave radiation budget by reducing optical thickness and cloud lifetime.

Cirrus cloud thinning (CCT) Cirrus cloud thinning is one of several radiation modification approaches to counter the warming caused by greenhouse gases. In the approach, it is proposed to reduce the amount of cirrus clouds by injecting ice nucleating substances in the upper troposphere. The reduction in cirrus clouds is expected to increase the amount of longwave cooling to space resulting in a planetary cooling. Although cirrus cloud thinning primarily affects the longwave radiation budget of our planet, it is often identified as one of the *solar radiation modification (SRM)* approaches in the literature.

Marine cloud brightening (MCB) Marine cloud brightening is one of several solar radiation modification (SRM) approaches to increase the planetary albedo. In the approach, it is proposed to inject sea salt aerosols into the persistent marine lows clouds. This is expected to increase the cloud droplet concentration of these clouds and their reflectivity.

Stratospheric aerosol injection (SAI) Stratospheric aerosol injection is one of several solar radiation modification (SRM) approaches to increase the planetary albedo. In the approach, it is proposed to inject highly reflective aerosols such as sulphates into the lower stratosphere. This is expected to increase the fraction of solar radiation deflected to space resulting in a planetary cooling.

Solubility pump A physicochemical process that transports dissolved inorganic carbon from the *ocean*'s surface to its interior. The solubility pump is primarily driven by the solubility of *carbon dioxide (CO_2)* (with more CO_2 dissolving in colder water) and the large-scale, thermohaline patterns of ocean circulation.

Source Any process or activity which releases a greenhouse gas, an aerosol or a precursor of a greenhouse gas into the atmosphere (UNFCCC Article 1.9 (UNFCCC, 1992)). See also *Sink*.

South American monsoon (SAmerM) See *Global monsoon*.

South and Southeast Asian monsoon (SAsiaM) See *Global monsoon*.

ACCEPTED VERSION SUBJECT TO FINAL EDITS

Southern Annular Mode (SAM) See *Annular modes*.

South Pacific Convergence Zone (SPCZ) A band of low-level convergence, cloudiness and precipitation ranging from the west Pacific warm pool south-eastwards towards French Polynesia, which is one of the most significant features of subtropical Southern Hemisphere *climate*. It shares some characteristics with the *Inter-Tropical Convergence Zone (ITCZ)*, but is more extratropical in nature, especially east of the Dateline.

Southern Oscillation See *El Niño-Southern Oscillation (ENSO)*.

Specific humidity The specific humidity specifies the ratio of the mass of water vapour to the total mass of moist air. See also *Relative humidity*.

Stadial A period of North Atlantic cooling during the last glacial period, lasting anywhere from several centuries to millennia, as inferred from oxygen *isotopes* in Greenland *ice cores*. These episodes are often referred to as examples of "abrupt climate change events", as they are often terminated by abrupt warming. They occur repeatedly during the last glacial period, and are associated with a distinct pattern of global temperature and hydrological variations recorded in *paleoclimate* records from this interval. See also *Younger Dryas*.

Statistical downscaling See *Downscaling*.

Steric sea level change See *Sea level change (sea level rise/sea level fall)*.

Storm surge The temporary increase, at a particular locality, in the height of the sea due to extreme meteorological conditions (low atmospheric pressure and/or strong winds). The storm surge is defined as being the excess above the level expected from the tidal variation alone at that time and place. See also *Sea level change (sea level rise/sea level fall)* and *Extreme sea level (ESL)*.

Storm tracks Originally, a term referring to the tracks of individual cyclonic weather systems, but now often generalized to refer to the main *regions* where the tracks of extratropical disturbances occur as sequences of low (cyclonic) and high (anticyclonic) pressure systems.

Storyline A way of making sense of a situation or a series of events through the construction of a set of explanatory elements. Usually it is built on logical or causal reasoning. In *climate* research, the term storyline is used both in connection to *scenarios* as related to a future trajectory of the climate and human systems or to a weather or climate event. In this context, storylines can be used to describe plural, conditional possible futures or explanations of a current situation, in contrast to single, definitive futures or explanations.

Physical climate storyline A self-consistent and plausible unfolding of a physical trajectory of the *climate system*, or a weather or climate event, on timescales from hours to multiple decades (Shepherd et al., 2018). Through this, storylines explore, illustrate and communicate uncertainties in the *climate system* response to *forcing* and in *internal variability*.

Scenario storyline A narrative description of a *scenario* (or family of scenarios), highlighting the main scenario characteristics, relationships between key driving forces and the dynamics of their evolution.

Stratification Process of forming of layers of (*ocean*) water with different properties such as salinity, density and temperature that act as barrier for water mixing. The strengthening of near-surface stratification generally results in warmer surface waters, decreased oxygen levels in deeper water, and intensification of *ocean acidification (OA)* in the upper ocean.

Stratosphere The highly stratified region of the atmosphere above the *tropopause*, extending to about 50 km altitude. See also *Troposphere*.

ACCEPTED VERSION SUBJECT TO FINAL EDITS

Stratospheric aerosol injection (SAI) See *Solar radiation modification (SRM)*.

Stratosphere-troposphere exchange (STE) Stratosphere-troposphere exchange (STE) is understood as the flux of air or trace constituents across the tropopause, including both directions: the stratosphere to troposphere transport (STT) and troposphere to stratosphere transport (TST). STE is one of the key factors controlling the budgets of ozone, water vapour and other substances in both the *troposphere* and the lower *stratosphere*.

Stratospheric ozone Stratospheric ozone describes the *ozone (O_3)* that resides in the *stratosphere*, the region of the *atmosphere* which exists between 10 and 50 kilometres above the surface of the earth. Ninety percent of total-column ozone resides in the stratosphere.See *Ozone layer* and *Ozone (O_3)*. See also *Ozone-depleting substances (ODSs)*.

Stratospheric polar vortex A large-scale region of cold air poleward of approximately 60 degrees that is contained by a strong westerly jet from the tropopause (8-10km) to the stratopause (50-60km) and that forms in each hemisphere during the winter half-year. Planetary waves can temporarily disrupt the vortex, producing easterly winds and rapid warming over polar regions in the stratosphere, and leading to substantial weakening or breakdown of the vortex.

Stratospheric sounding unit (SSU) A three-channel infrared sounder on operational NOAA polar-orbiting satellites. The three channels are used to determine profiles of temperature in the *stratosphere* (AMS, 2020).

Streamflow Water flow within a river channel, for example, expressed in $m^3 s^{-1}$. A synonym for river discharge.

Subduction Ocean process in which surface waters enter the ocean interior from the surface mixed layer through *Ekman pumping* and lateral *advection*. The latter occurs when surface waters are advected to a *region* where the local *surface layer* is less dense and therefore must slide below the surface layer, usually with no change in density.

Sudden stratospheric warming (SSW) A phenomena of rapid warming in the *stratosphere* at high latitudes (sometimes more than 50°C in 1-2 days) that can cause breakdown of *stratospheric polar vortices*.

Sulphur hexafluoride (SF_6) One of the seven types of *greenhouse gases (GHGs)* to be mitigated under the Kyoto Protocol. SF_6 is largely used in heavy industry to insulate high-voltage equipment and to assist in the manufacturing of cable-cooling systems and semi-conductors.

Sunspots Dark areas on the Sun where strong magnetic fields reduce the convection causing a temperature reduction of about 1500 K compared to the surrounding regions. The number of sunspots is higher during periods of higher *solar activity*, and varies in particular with the *solar cycle*.

Surface air temperature See *Land surface air temperature (LSAT)* and *Global mean surface air temperature (GSAT)*.

Surface mass balance (SMB) See *Mass balance / budget (of glaciers or ice sheets)*.

Surface temperature See *Global mean surface air temperature (GSAT)*, *Global mean surface temperature (GMST)*, *Land surface air temperature (LSAT)* and *Sea surface temperature (SST)*.

Surprises A class of risk that can be defined as low-likelihood but well-understood events, and events that cannot be predicted with current understanding (see 1.4.4.3 in AR6 WGI Chapter 1). See also *Unknown unknowns*.

ACCEPTED VERSION SUBJECT TO FINAL EDITS

Swash See *Extreme sea level (ESL)*.

Talik A layer or body of unfrozen ground in a *permafrost* area due to a local anomaly in thermal, hydrological, hydrogeological or hydrochemical conditions (IPA, 2005).

Technical potential See *Mitigation potential*.

Teleconnection Association between *climate* variables at widely separated, geographically fixed locations related to each other through physical processes and oceanic and/or atmospheric dynamical pathways. Teleconnections can be caused by several climate phenomena, such as Rossby wave-trains, mid-latitude jet and storm track displacements, fluctuations of the *Atlantic Meridional Overturning Circulation*, fluctuations of the Walker circulation, etc. They can be initiated by *modes of climate variability* thus providing the development of remote climate *anomalies* at various temporal lags.

Teleconnection pattern A correlation map obtained by calculating the correlation between variables at different spatial locations and a *climate index*. It is the special case of a *climate pattern* obtained for standardized variables and a standardized climate index, that is, the variables and index are each centred and scaled to have zero mean and unit variance. One-point *teleconnection* maps are made by choosing a variable at one of the locations to be the climate index.

Temperature overshoot Exceedance of a specified global warming level, followed by a decline to or below that level during a specified period of time (e.g., before 2100). Sometimes the magnitude and likelihood of the overshoot is also characterized. The overshoot duration can vary from one *pathway* to the next but in most *overshoot pathways* in the literature and referred to as overshoot pathways in the AR6, the overshoot occurs over a period of at least one and up to several decades. See also *Pathways*.

Terrestrial radiation Radiation emitted by the Earth's surface, the *atmosphere* and the clouds. It is also known as thermal infrared or long-wave radiation, and is to be distinguished from the near-infrared radiation that is part of the solar spectrum. Infrared radiation, in general, has a distinctive range of wavelengths (spectrum) longer than the wavelength of the red light in the visible part of the spectrum. The spectrum of terrestrial radiation is almost entirely distinct from that of shortwave or *solar radiation* because of the difference in temperature between the Sun and the Earth-atmosphere system.

Thermal expansion See *Steric sea level change* (under *Sea level change (sea level rise/sea level fall)*).

Thermocline The layer of maximum vertical temperature gradient in the ocean, lying between the surface ocean and the abyssal ocean. In subtropical regions, its source waters are typically surface waters at higher latitudes that have subducted (see *Subduction*) and moved equatorward. At high latitudes, it is sometimes absent, replaced by a *halocline*, which is a layer of maximum vertical salinity gradient.

Thermohaline circulation (THC) See *Meridional overturning circulation (MOC)*.

Thermokarst Process by which characteristic landforms result from thawing of ice-rich *permafrost* or melting of massive ice (IPA, 2005).

Thermosteric See *Sea level change (sea level rise/sea level fall)*.

Tide gauge A device at a coastal or deep-sea location that continuously measures the level of the sea with respect to the adjacent land. Time averaging of the sea level so recorded gives the observed secular changes of the *relative sea level*.

Time of emergence (ToE) Time when a specific *anthropogenic* signal related to *climate change* is statistically detected to emerge from the background noise of natural *climate variability* in a *reference period*, for a specific *region* (Hawkins and Sutton, 2012). See also *Emergence (of the climate signal)*.

ACCEPTED VERSION SUBJECT TO FINAL EDITS

Tipping element A component of the Earth System that is susceptible to a *tipping point*.

Tipping point A critical threshold beyond which a system reorganizes, often abruptly and/or irreversibly. See also *Tipping element*, *Irreversibility* and *Abrupt change*.

Total alkalinity Total Alkalinity (A_T) is a measurable parameter of the seawater acid-base system which, when expressed in micromoles per kilogram of seawater, is a conservative variable both on mixing, and for changes in temperature and/or pressure. Changes in total alkalinity in the oceans can result from a variety of biogeochemical processes that affect the acid-base composition of the seawater itself. However, its value is not affected by the exchange of carbon dioxide gas between seawater and the atmosphere. Measurements of total alkalinity can thus be used to help study these biogeochemical processes, and can also be used to help calculate the state of the seawater acid-base system. Total alkalinity is most commonly measured using an acidimetric titration technique, that determines how much acid is required to titrate a seawater sample to a specified equivalence point.

Total carbon budget See *Carbon budget*.

Total solar irradiance (TSI) The total amount of *solar radiation* in watts per square metre received outside the Earth's *atmosphere* on a surface normal to the incident radiation, and at the Earth's mean distance from the Sun. Reliable measurements of solar radiation can only be made from space and the precise record extends back only to 1978. It has recently been estimated to 1360.8 ± 0.5 W m^{-2} for the solar minimum of 2008. Variations of a few tenths of a percent are common, usually associated with the passage of *sunspots* across the solar disk. The *solar cycle* variation of TSI is of the order of 0.1% (AMS, 2000). See also *Insolation*.

Total water level See *Extreme sea level (ESL)*.

Trace gas A minor constituent of the *atmosphere*, next to nitrogen and oxygen that together make up 99 % of all volume. The most important trace gases contributing to the *greenhouse effect* are *carbon dioxide (CO_2)*, *ozone (O_3)*, *methane (CH_4)*, *nitrous oxide (N_2O)*, perfluorocarbons (PFCs), *chlorofluorocarbons (CFCs)*, hydrofluorocarbons (HFCs), *sulphur hexafluoride (SF_6)* and water vapour (H_2O).

Transient climate response (TCR) See *Climate sensitivity*.

Transient climate response to cumulative CO2 emissions (TCRE) See *Climate sensitivity*.

Tree rings Concentric rings of secondary wood evident in a cross section of the stem of a woody plant. The difference between the dense, small-celled late wood of one season and the wide-celled early wood of the following spring enables the age of a tree to be estimated, and the ring widths or density can be related to *climate* parameters such as temperature and precipitation.

Tropical Atlantic modes See *Tropical Atlantic Variability (TAV)*.

Tropical Atlantic Variability (TAV) A generic term to describe the *climate variability* of the tropical Atlantic which is dominated at interannual to decadal timescale by two main climate modes: the *Atlantic Zonal Mode (AZM)* and the *Atlantic Meridional Mode (AMM)*. The Atlantic Zonal Mode, also commonly referred to as the Atlantic Niño or Atlantic equatorial mode, is associated with *sea surface temperature* anomalies near the equator, peaking in the eastern basin, while the Atlantic meridional mode is characterized by an inter-hemispheric gradient of sea surface temperature and wind anomalies. Both modes are associated with significant *teleconnections* over Africa and South America.

Atlantic Meridional Mode (AMM) The Atlantic Meridional Mode (AMM) refers to the interannual to *decadal variability* of the cross-equatorial *sea surface temperature* gradients and surface wind anomalies in the tropical Atlantic. It modulates the strength and latitudinal shifts of the *Inter-tropical Convergence Zone (ITCZ)*, which impacts regional rainfall over Northeast Brazil and Atlantic hurricane activity. See Section

ACCEPTED VERSION SUBJECT TO FINAL EDITS

AIV.2.5 in Annex IV of the AR6 WGI report.

Atlantic Zonal Mode (AZM) An equatorial coupled mode in the Atlantic similar to *El Niño-Southern Oscillation (ENSO)* in the Pacific, and therefore sometimes referred to as "Atlantic Niño". The AZM is associated with *sea surface temperature* anomalies near the equatorial Atlantic and rainfall disturbances over the African monsoon domain. Its variations are mostly observed in the interannual scale. It is called also Atlantic equatorial mode. See Section AIV.2.5 in Annex IV of the AR6 WGI report.

Tropical cyclone The general term for a strong, cyclonic-scale disturbance that originates over tropical oceans. Distinguished from weaker systems (often named tropical disturbances or depressions) by exceeding a threshold wind speed. A tropical storm is a tropical cyclone with one-minute average surface winds between 18 and 32 m s^{-1}. Beyond 32 m s^{-1}, a tropical cyclone is called a hurricane, typhoon, or cyclone, depending on geographic location.

Tropopause The boundary between the *troposphere* and the *stratosphere*. It ranges from 8-9 km at high latitudes to 15-16 km in the tropics.

Troposphere The lowest part of the atmosphere, below the *tropopause*, where clouds and weather phenomena occur. In the troposphere, temperatures generally decrease with height. See also *Stratosphere*.

Tropospheric ozone See *Ozone (O_3)* and *Ground-level ozone*.

Tundra A treeless biome characteristic of polar and alpine regions.

Turnover time (T) See *Lifetime*.

Typhoon See *Tropical cyclone*.

Typological domains See *Typological regions*.

Typological regions Regions of the Earth that share one or more specific features (known as 'typologies'), such as geographic location (e.g., coastal), physical processes (e.g., *monsoons*), and biological (e.g., coral reefs, tropical *forests*), geological (e.g., mountains) or *anthropogenic* (e.g., megacities) formation, and for which it is useful to consider the common *climate* features. Typological regions are smaller than climatic zones (e.g., a mountain region) and can be discontinuous (e.g., a group of megacities affected by the *urban heat island* effect, or monsoon regions).

Uncertainty A state of incomplete knowledge that can result from a lack of information or from disagreement about what is known or even knowable. It may have many types of sources, from imprecision in the data to ambiguously defined concepts or terminology, incomplete understanding of critical processes, or uncertain projections of *human behaviour*. Uncertainty can therefore be represented by quantitative measures (e.g., a probability density function) or by qualitative statements (e.g., reflecting the judgment of a team of experts) (see Moss and Schneider, 2000; IPCC, 2004; Mastrandrea et al., 2010). See also *Confidence* and *Likelihood*.

Deep uncertainty A situation of deep uncertainty exists when experts or stakeholders do not know or cannot agree on: (1) appropriate conceptual models that describe relationships among key driving forces in a system; (2) the probability distributions used to represent uncertainty about key variables and parameters; and/or (3) how to weigh and value desirable alternative outcomes (Lempert et al., 2003).

Sampling uncertainty Uncertainty arising from incomplete or uneven availability of measurements in either space or time or both.

United Nations Framework Convention on Climate Change (UNFCCC) The UNFCCC was adopted in May 1992 and opened for signature at the 1992 Earth Summit in Rio de Janeiro. It entered into force in

ACCEPTED VERSION SUBJECT TO FINAL EDITS

March 1994 and as of September 2020 had 197 Parties (196 States and the European Union). The Convention's ultimate objective is the 'stabilisation of greenhouse gas concentrations in the atmosphere at a level that would prevent dangerous anthropogenic interference with the climate system'. The provisions of the Convention are pursued and implemented by two further treaties: the Kyoto Protocol and the Paris Agreement.

Uptake The transfer of substances (such as carbon) or energy (e.g., heat) from one compartment of a system to another; for example, in the Earth System from the atmosphere to the ocean or to the land. See also *Sequestration*.

Upwelling region A region of an ocean where cold, typically nutrient-rich waters well up from the deep ocean.

Urban heat island (UHI) The relative warmth of a city compared with surrounding rural areas, associated with changes in *runoff*, effects on heat retention, and changes in surface albedo.

Ventilation The exchange of ocean properties with the atmospheric *surface layer* such that property concentrations are brought closer to equilibrium values with the *atmosphere* (AMS, 2021), and the processes that propagate these properties into the ocean interior.

Vertical land motion (VLM) Vertical land motion (VLM) is the change in height of the land surface or the sea floor and can have several causes in addition to elastic deformation associated with contemporary changes in *gravity, rotation and viscoelastic solid Earth deformation (GRD)* and viscoelastic deformation associated with *glacial isostatic adjustment (GIA)*. Subsidence (sinking of the land surface or sea floor) can, for instance, occur through compaction of alluvial sediments in deltaic regions, removal of fluids such as gas, oil, and water, or drainage of peatlands. Tectonic deformation of the Earth's crust can occur as a result of earthquakes and volcanic eruptions. See also *Sea level change (sea level rise/sea level fall)*.

Very short-lived halogenated substances (VSLSs) Very short-lived halogenated substances (VSLSs) are considered to include source gases (very short-lived halogenated substances present in the *atmosphere* in the form they were emitted from natural and *anthropogenic* sources), halogenated product gases arising from source gas degradation, and other sources of *tropospheric* inorganic halogens. VSLSs have tropospheric *lifetimes* of around 0.5 years or less.

Volatile organic compounds (VOCs) Important class of organic chemical air pollutants that are volatile at ambient air conditions. Other terms used to represent VOCs are hydrocarbons (HCs), reactive organic gases (ROGs) and non-methane volatile organic compounds (NMVOCs). NMVOCs are major contributors – together with nitrogen oxides (NOx), and carbon monoxide (CO) – to the formation of photochemical oxidants such as ozone (O_3).

Biogenic volatile organic compounds (BVOCs) Organic gas-phase compounds emitted from terrestrial and aquatic ecosystems that are critical in ecology and plant physiology, from abiotic and biotic stress functions to integrated components of metabolism. BVOCs are important in atmospheric chemistry as precursors for ozone and secondary organic aerosol formation. Other terms used to represent BVOCs are hydrocarbons (HCs), reactive organic gases (ROGs) and non-methane volatile organic compounds (NMVOCs).

Vulnerability The propensity or predisposition to be adversely affected. Vulnerability encompasses a variety of concepts and elements including sensitivity or susceptibility to harm and lack of capacity to cope and adapt. See also *Exposure*, *Hazard* and *Risk*.

Walker circulation Direct thermally driven zonal overturning circulation in the *atmosphere* over the tropical Pacific Ocean, with rising air in the western and sinking air in the eastern Pacific.

Warm days/warm nights Days where maximum temperature, or nights where minimum temperature, exceeds the 90th percentile, where the respective temperature distributions are generally defined with respect

ACCEPTED VERSION SUBJECT TO FINAL EDITS

to the 1961-1990 reference period.

Warm spell A period of abnormally warm weather. *Heatwaves* and warm spells have various and, in some cases, overlapping definitions.

Water cycle See *Hydrological cycle*.

Water mass A body of ocean water with identifiable properties (temperature, salinity, density, chemical tracers) resulting from its unique formation process. Water masses are often identified through a vertical or horizontal extremum of a property such as salinity. North Pacific Intermediate Water (NPIW) and Antarctic Intermediate Water (AAIW) are examples of water masses.

Water security 'The capacity of a population to safeguard sustainable access to adequate quantities of acceptable quality water for sustaining livelihoods, human well-being, and socio-economic development, for ensuring protection against water-borne pollution and water-related disasters, and for preserving ecosystems in a climate of peace and political stability' (UN-Water, 2013).

Wave run-up See *Extreme sea level (ESL)*.

Wave setup See *Extreme sea level (ESL)*.

Weathering The gradual removal of atmospheric CO_2 through dissolution of silicate and carbonate rocks. Weathering may involve physical processes (mechanical weathering) or chemical activity (chemical weathering).

Well-mixed greenhouse gas A *greenhouse gas* that has an atmospheric *lifetime* long enough (> several years) to be homogeneously mixed in the *troposphere*, and as such the global average mixing ratio can be determined from a network of surface observations. For many well-mixed greenhouse gases, measurements made in remote regions differ from the global mean by < 15%.

West African monsoon (WAfriM) See *Global monsoon*.

West Antarctic ice sheet (WAIS) See *Ice sheet*.

Wetland Land that is covered or saturated by water for all or part of the year (e.g., *peatland*).

Younger Dryas A period 12.85 to 11.65 ka (thousand years before 1950), during the *last deglacial transition*, characterized by a temporary return to colder conditions in many locations, especially around the North Atlantic. See also *Stadial* and *Last deglacial transition*.

Zero emissions commitment See *Climate change commitment*.

ACCEPTED VERSION SUBJECT TO FINAL EDITS

References

AMS, 2021: Glossary of Meteorology. American Meteorological Society (AMS), Boston, MA, USA. Retrieved from: http://glossary.ametsoc.org.

Carson, M. and G. Peterson (eds.), 2016: *Arctic Resilience Report 2016*. Stockholm Environment Institute and Stockholm Resilience Centre, Stockholm, Sweden, 218 pp.

Blunier, T. and E.J. Brook, 2001: Timing of Millennial-Scale Climate Change in Antarctica and Greenland During the Last Glacial Period. *Science*, **291(5501)**, 109 LP – 112, doi:10.1126/science.291.5501.109.

Bond, G.C. and R. Lotti, 1995: Iceberg Discharges into the North Atlantic on Millennial Time Scales During the Last Glaciation. *Science*, **267(5200)**, 1005 LP – 1010, doi:10.1126/science.267.5200.1005.

Broecker, W.S., 1998: Paleocean circulation during the Last Deglaciation: A bipolar seesaw? *Paleoceanography*, **13(2)**, 119–121, doi:10.1029/97pa03707.

Cogley, J.G. et al., 2011: *Glossary of Glacier Mass Balance and Related Terms*. IHP-VII Technical Documents in Hydrology No. 86, IACS Contribution No. 2, UNESCO-IHP, Paris, France, 114 pp.

Dansgaard, W. et al., 1993: Evidence for general instability of past climate from a 250-kyr ice-core record. *Nature*, **364(6434)**, 218–220, doi:10.1038/364218a0.

Duplessy, J.C., G. Delibrias, J.L. Turon, C. Pujol, and J. Duprat, 1981: Deglacial warming of the northeastern Atlantic ocean: correlation with the paleoclimatic evolution of the european continent. *Palaeogeography, Palaeoclimatology, Palaeoecology*, **35(C)**, 121–144, doi:10.1016/0031-0182(81)90096-1.

Fairbanks, R.G., 1989: A 17,000-year glacio-eustatic sea level record: influence of glacial melting rates on the Younger Dryas event and deep-ocean circulation. *Nature*, **342(6250)**, 637–642, doi:10.1038/342637a0.

FAO, 2007: Land evaluation: Towards a revised framework. Land and water discussion paper. .

Gbeckor-Kove, 1989: Lectures on drought, desertification. *Drought and Desertification*, 41–73.

Giardino, J.R., N.R. Regmi, and J.D. Vitek, 2011: Rock Glaciers. In: *Encyclopedia of Snow, Ice and Glaciers*. Springer Netherlands, Dordrecht, The Netherlands, pp. 943–948, doi:10.1007/978-90-481-2642-2_453.

Gowan, E.J. et al., 2021: A new global ice sheet reconstruction for the past 80 000 years. *Nature Communications*, **12(1)**, 1199, doi:10.1038/s41467-021-21469-w.

Harris, S.A. et al., 1988: *Glossary of Permafrost and Related Ground-Ice Terms*. Technical Memorandum No. 142, Permafrost Subcommittee, Associate Committee on Geotechnical Research, National Research Council of Canada, Ottawa, ON, Canada, 159 pp., doi:10.4224/20386561.

Hawkins, E. and R. Sutton, 2012: Time of emergence of climate signals. *Geophysical Research Letters*, **39(1)**, doi:10.1029/2011gl050087.

Haywood, A.M. et al., 2016: The Pliocene Model Intercomparison Project (PlioMIP) Phase 2: scientific objectives and experimental design. *Climate of the Past*, **12(3)**, 663–675, doi:10.5194/cp-12-663-2016.

Hewitt, C., S. Mason, and D. Walland, 2012: The Global Framework for Climate Services. *Nature Climate Change*, **2(12)**, 831–832, doi:10.1038/nclimate1745.

IPA, 2005: *Multi-language Glossary of Permafrost and Related Ground-Ice Terms*. International Permafrost Association (IPA), 159 pp.

Delaloye, R. and T. Echelard (eds.), 2020: *Towards standard guidelines for inventorying rock glaciers: Baseline concepts (Version 4.0)*. International Permafrost Association (IPA) Action Group Rock glacier inventories and kinematics, Longyearbyen, Svalbard, 13 pp.

IPCC, 2004: *IPCC Workshop on Describing Scientific Uncertainties in Climate Change to Support Analysis of Risk and of Options*. Intergovernmental Panel on Climate Change (IPCC), Geneva, Switzerland, 138 pp.

IPCC, 2006: 2006 IPCC Guidelines for National Greenhouse Gas Inventories, Prepared by the National Greenhouse Gas Inventories Programme. [Eggleston, H.S., L. Buendia, K. Miwa, T. Ngara, and K. Tanabe (eds.)]. Institute for Global Environmental Strategies (IGES), Hayama, Japan.

IPCC, 2011: Workshop Report of the Intergovernmental Panel on Climate Change Workshop on Impacts of Ocean Acidification on Marine Biology and Ecosystems. [Field, C.B., V. Barros, T.F. Stocker, D. Qin, K.J. Mach, G.-K. Plattner, M.D. Mastrandrea, M. Tignor, and K.L. Ebi (eds.)]. IPCC Working Group II Technical Support Unit, Carnegie Institution, Stanford, California, United States of America, 164 pp.

IPCC, 2019: 2019 Refinement to the 2006 IPCC Guidelines for National Greenhouse Gas Inventories. [Calvo Buendia, E., K. Tanabe, A. Kranjc, J. Baasansuren, M. Fukuda, S. Ngarize, A. Osako, Y. Pyrozhenko, P. Shermanau, and S. Federici (eds.)]. Intergovernmental Panel on Climate Change (IPCC), Geneva, Switzerland.

IPCC-TGICA, 2007: *General guidelines on the use of scenario data for climate impact and adaptation assessment*. Task Group on Data and Scenario Support for Impact and Climate Assessment (TGICA), Intergovernmental Panel on Climate Change (IPCC), Geneva, Switzerland, 66 pp.

ISO, 2014: ISO 16559:2014(en). Solid biofuels – Terminology, definitions and descriptions. International Standards Organisation (ISO). Retrieved from: www.iso.org/obp/ui/#iso:std:iso:16559:ed-1:v1:en.

Kageyama, M. et al., 2017: The PMIP4 contribution to CMIP6 – Part 4: Scientific objectives and experimental design of the PMIP4-CMIP6 Last Glacial Maximum experiments and PMIP4 sensitivity experiments. *Geoscientific*

ACCEPTED VERSION SUBJECT TO FINAL EDITS

Model Development, **10(11)**, 4035–4055, doi:10.5194/gmd-10-4035-2017.
Lempert, R.J., S.W. Popper, and S.C. Bankes, 2003: *Shaping the Next One Hundred Years: New Methods for Quantitative, Long-Term Policy Analysis*. RAND Corporation, Santa Monica, CA, USA, 186 pp.
MA, 2005: Appendix D: Glossary. In: *Ecosystems and Human Well-being: Current States and Trends. Findings of the Condition and Trends Working Group* [Hassan, R., R. Scholes, and N. Ash (eds.)]. Millennium Ecosystem Assessment (MEA). Island Press, Washington, DC, USA, pp. 893–900.
Mastrandrea, M.D. et al., 2010: *Guidance Note for Lead Authors of the IPCC Fifth Assessment Report on Consistent Treatment of Uncertainties*. Intergovernmental Panel on Climate Change (IPCC), Geneva, Switzerland, 6 pp.
Mix, A.C., W.F. Ruddiman, and A. McIntyre, 1986: Late Quaternary paleoceanography of the Tropical Atlantic, 1: Spatial variability of annual mean sea-surface temperatures, 0-20,000 years B.P.. *Paleoceanography*, **1(1)**, 43–66, doi:10.1029/pa001i001p00043.
Mix, A.C., E. Bard, and R. Schneider, 2001: Environmental processes of the ice age: land, oceans, glaciers (EPILOG). *Quaternary Science Reviews*, **20(4)**, 627–657, doi:10.1016/s0277-3791(00)00145-1.
Moss, R.H. and S.H. Schneider, 2000: Uncertainties in the IPCC TAR: Recommendations to Lead Authors for More Consistent Assessment and Reporting. In: *Guidance Papers on the Cross Cutting Issues of the Third Assessment Report of the IPCC* [Pachauri, R., T. Taniguchi, and K. Tanaka (eds.)]. Intergovernmental Panel on Climate Change (IPCC), Geneva, Switzerland, pp. 33–51.
Moss, R.H. et al., 2010: The next generation of scenarios for climate change research and assessment. *Nature*, **463(7282)**, 747–756, doi:10.1038/nature08823.
NOAA, 2021: What is an iceberg? National Oceanic and Atmospheric Administration (NOAA). National Ocean Service website. Retrieved from: https://oceanservice.noaa.gov/facts/iceberg.html.
Pongratz, J. et al., 2018: Models meet data: Challenges and opportunities in implementing land management in Earth system models. *Global Change Biology*, **24(4)**, 1470–1487, doi:10.1111/gcb.13988.
Ralph, F.M., M.D. Dettinger, M.M. Cairns, T.J. Galarneau, and J. Eylander, 2018: Defining "Atmospheric River": How the Glossary of Meteorology Helped Resolve a Debate. *Bulletin of the American Meteorological Society*, **99(4)**, 837–839, doi:10.1175/bams-d-17-0157.1.
Schwartz, S.E. and P. Warneck, 1995: Units for use in atmospheric chemistry (IUPAC Recommendations 1995). *Pure and Applied Chemistry*, **67(8/9)**, 1377–1406.
Shepherd, T.G. et al., 2018: Storylines: an alternative approach to representing uncertainty in physical aspects of climate change. *Climatic Change*, **151(3–4)**, 555–571, doi:10.1007/s10584-018-2317-9.
Stocker, T.F. and S.J. Johnsen, 2003: A minimum thermodynamic model for the bipolar seesaw. *Paleoceanography*, **18(4)**, doi:10.1029/2003pa000920.
Türkeş, M., 1999: Vulnerability of Turkey to Desertification With Respect to Precipitation and Aridity Conditions. *Turkish Journal of Engineering and Environmental Sciences*, **23**, 363–380.
UNCCD, 1994: *United Nations Convention to Combat Desertification in countries experiencing serious drought and/or desertification, particularly in Africa*. 58 pp.
UNESCO/IASH/WMO, 1970: *Seasonal snow cover: A guide for measurement, compilation and assemblage of data*. United Nations Educational, Scientific and Cultural Organization (UNESCO), Paris, France, 38 pp.
UNFCCC, 1992: *United Nations Framework Convention on Climate Change*. FCCC/INFORMAL/84, United Nations Framework Convention on Climate Change (UNFCCC), 24 pp.
UNFCCC, 2021a: Reporting and accounting of LULUCF activities under the Kyoto Protocol. United Nations Framework Convention on Climate Change (UNFCCC). Retrieved from: https://unfccc.int/topics/land-use/workstreams/land-use-land-use-change-and-forestry-lulucf/reporting-and-accounting-of-lulucf-activities-under-the-kyoto-protocol.
UNFCCC, 2021b: Reporting and Review under the Paris Agreement. United Nations Framework Convention on Climate Change (UNFCCC). Retrieved from: https://unfccc.int/process-and-meetings/transparency-and-reporting/reporting-and-review-under-the-paris-agreement.
UNGA, 2016: *Report of the open-ended intergovernmental expert working group on indicators and terminology relating to disaster risk reduction*. A/71/644, United Nations General Assembly (UNGA), 41 pp.
UN-OHRLLS, 2011: *Small Island Developing States: Small Islands Big(ger) Stakes*. Office for the High Representative for the Least Developed Countries, Landlocked Developing Countries and Small Island Developing States (UN-OHRLLS), New York, NY, USA, 32 pp.
UN-OHRLLS, 2018: Small Island Developing States: Country profiles. Office for the High Representative for the Least Developed Countries, Landlocked Developing Countries and Small Island Developing States (UN-OHRLLS). Retrieved from: http://unohrlls.org/about-sids/country-profiles.
UN-Water, 2013: What is Water Security? Infographic. UN-Water, Geneva, Switzerland. Retrieved from: www.unwater.org/publications/water-security-infographic.
Zscheischler, J. et al., 2018: Future climate risk from compound events. *Nature Climate Change*, **8(6)**, 469–477, doi:10.1038/s41558-018-0156-3.

ACCEPTED VERSION SUBJECT TO FINAL EDITS